

Handbook of Optical Constants of Solids

edited by

Edward D. Palik

This book is printed on acid-free paper.

Copyright © 1998, 1985 by Academic Press

All rights reserved.
No part of this publication may be reproduced or transmitted in any form or by any means, electronic or mechanical, including photocopy, recording, or any information storage and retrieval system, without permission in writing from the publisher.

ACADEMIC PRESS
525 B Street, Suite 1900, San Diego, CA 92101-4495, USA
1300 Boylston Street, Chestnut Hill, MA 02167, USA
http://www.apnet.com

Academic Press Limited
24–28 Oval Road, London NW1 7DX, UK
http://www.hbuk.co.uk/ap/

Library of Congress Cataloging-in-Publication Data

Handbook of optical constants of solids / edited by Edward D. Palik.
p. cm.
Includes bibliographical references.
ISBN 0-12-544420-6
1. Solids. 2. Optical properties. 3. Handbooks, manuals, etc.
I. Palik, Edward D.
QC176.8.06H36 1985 530.4'1 84—15870 CIP

Printed in the United States of America
97 98 99 00 01 IC 9 8 7 6 5 4

Contents

List of Contributors xv

Part I DETERMINATION OF OPTICAL CONSTANTS

Chapter 1 Introductory Remarks 3
EDWARD D. PALIK

I. Introduction 3
II. The Chapters 4
III. The Critiques 5
IV. The Tables 6
V. The Figures of the Tables 7
VI. General Remarks 8
References 9

Chapter 2 Basic Parameters for Measuring Optical Properties 11
ROY F. POTTER

I. Introduction 11
II. Intrinsic Material Parameters in Terms of Optical Constants 16
III. Reflectance, Transmittance, and Absorptance of Layered Structures 18
IV. The General Lamelliform — Phase Coherency Throughout 19
V. The General Lamelliform — Phase Incoherency in Substrate 21
VI. Summary 24
Appendix A. Basic Formulas for Fresnel Coefficients 24
Appendix B. General Formulas for the Case of a Parallel-Sided Slab 25
Appendix C. Reflectance, R_{jk} at $j-k$ Interface 26
Appendix D. Reflectance of Single Layer on Each Side of a Slab and Single Layer on Either Side of a Slab 26
Appendix E. Critical Angle of Incidence 30
Definition of Terms 33
References 34

Chapter 3 Dispersion Theory, Sum Rules, and Their Application to the Analysis of Optical Data 35
D. Y. SMITH

I. Introduction 36
II. Optical Sum Rules and Their Physical Interpretation 36

III. Finite-Energy Sum Rules 45
IV. Sum Rules for Reflection Spectroscopy 51
V. Analysis of Optical Data and Sum-Rule Applications 55
VI. Summary 64
References 64

Chapter 4 **Measurement of Optical Constants in the Vacuum Ultraviolet Spectral Region** 69
W. R. HUNTER

I. Introduction 69
II. General Discussion of Reflectance Methods 70
III. Reflectance Method for Two Media 85
References 87

Chapter 5 **The Accurate Determination of Optical Properties by Ellipsometry** 89
D. E. ASPNES

I. Reflection Techniques; Background and Overview 89
II. Measurement Configurations 92
III. Accurate Determination of Optical Properties: Overlayer Effects 96
IV. Living with Overlayers 99
V. Eliminating Overlayers 102
VI. Bulk and Thin-Film Effects; Effective-Medium Theory 104
VII. Conclusion 108
References 110

Chapter 6 **Interferometric Methods for the Determination of Thin-Film Parameters** 113
JOSEPH SHAMIR

I. Introduction 113
II. Basic Principles 114
III. Nonlaser Interferometers 117
IV. Kösters-Prism Interferometers 123
V. A Self-Calibrating Method 126
VI. Surface Effects 131
VII. Conclusions 132
References 133

Chapter 7 **Thin-Film Absorptance Measurements Using Laser Calorimetry** 135
P. A. TEMPLE

I. Introduction 135
II. Single-Layer Films 138
III. Wedged-Film Laser Calorimetry 139
IV. Electric-Field Considerations in Laser Calorimetry 143
V. Entrance versus Exit Surface Films 147

VI. Experimental Determination of α_f, a_{af}, and a_{fs} 149
References 153

Chapter 8 **Complex Index of Refraction Measurements at Near-Millimeter Wavelengths** 155
GEORGE J. SIMONIS

I. Introduction 155
II. Fourier Transform Spectroscopy 156
III. Free-Space Resonant Cavity 161
IV. Mach–Zehnder Interferometer 163
V. Direct Birefringence Measurement 164
VI. Overmoded Nonresonant Cavity 165
VII. Crystal Quartz as Index Reference 165
VIII. Conclusion 167
References 167

Chapter 9 **The Quantum Extension of the Drude–Zener Theory in Polar Semiconductors** 169
B. JENSEN

I. Introduction 169
II. Quantum Theory of Free-Carrier Absorption 172
III. Theoretical Results 174
IV. Comparison with Experimental Data 176
Appendix 187
References 188

Chapter 10 **Interband Absorption — Mechanisms and Interpretation** 189
DAVID W. LYNCH

I. Introduction 189
II. One-Electron Model 190
III. Electron–Hole Interaction, Excitons 198
IV. Local Field Effects 203
V. Examples 204
References 210
General References 211

Chapter 11 **Optical Properties of Nonmetallic Solids for Photon Energies below the Fundamental Band Gap** 213
SHASHANKA S. MITRA

I. Introduction 213
II. Infrared Dispersion by Polar Crystals 215
III. Kramers–Kronig Dispersion Relations 227
IV. Determination of Absorption Coefficient in the Intermediate Region 229
V. Absorption Coefficient in the Transparent Regime 230
VI. Multiphonon Absorption 232

VII. Infrared Absorption by Defects and Disorders 254
VIII. Infrared Dispersion by Plasmons 263
References 267

Part II CRITIQUES

Subpart 1 Metals

Comments on the Optical Constants of Metals and an Introduction to the Data for Several Metals 275
DAVID W. LYNCH AND W. R. HUNTER

I. Introduction 275
II. Anomalous Skin Effect 277
References 279
III. Copper (Cu) 280
References 280
IV. Gold (Au) 286
References 287
V. Iridium (Ir) 296
References 296
VI. Molybdenum (Mo) 303
References 304
VII. Nickel (Ni) 313
References 314
VIII. Osmium (Os) 324
References 324
IX. Platinum (Pt) 333
References 334
X. Rhodium (Rh) 342
References 342
XI. Silver (Ag) 350
References 351
XII. Tungsten (W) 357
References 358

The Optical Properties of Metallic Aluminum 369
D. Y. SMITH, E. SHILES, AND MITIO INOKUTI

I. General Features 369
II. Optical Measurements and Sample Conditions 372
III. Tabulated Data 377
References 383

Subpart 2 Semiconductors

Cadmium Telluride (CdTe) 409
EDWARD D. PALIK

References 413

Gallium Arsenide (GaAs) 429
EDWARD D. PALIK

References 432

Gallium Phosphide (GaP) 445
A. BORGHESI AND G. GUIZZETTI

References 449

Germanium (Ge) 465
ROY F. POTTER

References 469

Indium Arsenide (InAs) 479
EDWARD D. PALIK AND R. T. HOLM

References 481

Indium Antimonide (InSb) 491
R. T. HOLM

References 494

Indium Phosphide (InP) 503
O. J. GLEMBOCKI AND H. PILLER

References 506

Lead Selenide (PbSe) 517
G. BAUER AND H. KRENN

References 518

Lead Sulfide (PbS) 525
G. GUIZZETTI AND A. BORGHESI

References 528

Lead Telluride (PbTe) 535
G. BAUER AND H. KRENN

References 538

Silicon (Si) 547
DAVID F. EDWARDS

References 552

Silicon (Amorphous) (a-Si) 571
H. PILLER
References 573

Silicon Carbide (SiC) 587
W. J. CHOYKE AND EDWARD D. PALIK
References 589

Zinc Sulfide (ZnS) 597
EDWARD D. PALIK AND A. ADDAMIANO
References 602

Subpart 3 Insulators

Arsenic Selenide (As_2Se_3) 623
D. J. TREACY
References 625

Arsenic Sulfide (As_2S_3) 641
D. J. TREACY
References 644

Cubic Carbon (Diamond) 665
DAVID F. EDWARDS AND H. R. PHILIPP
References 668

Lithium Fluoride (LiF) 675
EDWARD D. PALIK AND W. R. HUNTER
References 678

Lithium Niobate ($LiNbO_3$) 695
EDWARD D. PALIK
References 697

Potassium Chloride (KCl) 703
EDWARD D. PALIK
References 706

Silicon Dioxide (SiO_2), Type α (Crystalline) 719
H. R. PHILIPP

References 721

Silicon Dioxide (SiO_2) (Glass) 749
H. R. PHILIPP

References 752

Silicon Monoxide (SiO) (Noncrystalline) 765
H. R. PHILIPP

References 766

Silicon Nitride (Si_3N_4) (Noncrystalline) 771
H. R. PHILIPP

References 772

Sodium Chloride (NaCl) 775
J. E. ELDRIDGE AND EDWARD D. PALIK

References 779

Titanium Dioxide (TiO_2) (Rutile) 795
M. W. RIBARSKY

References 798

List of Contributors

Numbers in parentheses indicate the pages on which the authors' contributions begin.

A. ADDAMIANO (597), Naval Research Laboratory, Washington, D.C. 20375

D. E. ASPNES (89), Bell Communications Research, Inc., Murray Hill, New Jersey 07974

G. BAUER (517, 535), Institut für Physik, Montanuniversität Leoben, A-8700 Leoben, Austria

A. BORGHESI (445, 525), Dipartimento di Fisica "A. Volta" and Gruppo Nazionale di Struttura della Materia del CNR, Università di Pavia, Pavia, Italy

W. J. CHOYKE (587), Westinghouse Research and Development Center, Pittsburgh, Pennsylvania 15235, and University of Pittsburgh, Pittsburgh, Pennsylvania 15260

DAVID F. EDWARDS* (547, 665), University of California, Los Alamos National Laboratory, Los Alamos, New Mexico 87545

J. E. ELDRIDGE (775), Department of Physics, University of British Columbia, Vancouver V6T 1W5, British Columbia, Canada

O. J. GLEMBOCKI (503), Naval Research Laboratory, Washington, D.C. 20375

G. GUIZZETTI (445, 525), Dipartimento di Fisica "A. Volta" and Gruppo Nazionale di Struttura della Materia del CNR, Università di Pavia, Pavia, Italy

R. T. HOLM (479, 491), Naval Research Laboratory, Washington, D.C. 20375

W. R. HUNTER† (69, 275, 675), Naval Research Laboratory, Washington, D.C. 20375

MITIO INOKUTI (369), Argonne National Laboratory, Argonne, Illinois 60439

B. JENSEN (169), Department of Physics, Boston University, Boston, Massachusetts 02215

H. KRENN (517, 535), Institut für Physik, Montanuniversität Leoben, A-8700 Leoben, Austria

* Present address: Lawrence Livermore National Laboratory, Livermore, California 94550.

† Present address: Sachs/Freeman Associates, Inc., Bowie, Maryland 20715.

DAVID W. LYNCH (189, 275), Department of Physics and Ames Laboratory, U.S. Department of Energy, Iowa State University, Ames, Iowa 50011
SHASHANKA S. MITRA (213), Department of Electrical Engineering, University of Rhode Island, Kingston, Rhode Island 02881
EDWARD D. PALIK (3, 409, 429, 479, 587, 597, 675, 695, 703, 775), Naval Research Laboratory, Washington, D.C. 20375
H. R. PHILIPP (665, 719, 749, 765, 771), General Electric Research and Development Center, Schenectady, New York 12301
H. PILLER (503, 571), Department of Physics and Astronomy, Louisiana State University, Baton Rouge, Louisiana 70803
ROY F. POTTER (11, 465), Department of Physics and Astronomy, Western Washington University, Bellingham, Washington 98225
M. W. RIBARSKY (795), School of Physics, Georgia Institute of Technology, Atlanta, Georgia 30332
JOSEPH SHAMIR (113), Faculty of Electrical Engineering, Technion — Israel Institute of Technology, Haifa 32000, Israel
E. SHILES* (369), Argonne National Laboratory, Argonne, Illinois 60439
GEORGE J. SIMONIS (155), Electronics Research and Development Command, Harry Diamond Laboratories, Adelphi, Maryland 20783
D. Y. SMITH (35, 369), Argonne National Laboratory, Argonne, Illinois 60439, and Max-Planck-Institut für Festkörperforschung, 7 Stuttgart 80, Federal Republic of Germany
P. A. TEMPLE (135), Michelson Laboratory, Physics Division, Naval Weapons Center, China Lake, California 93555
D. J. TREACY (623, 641), Physics Department, U.S. Naval Academy, Annapolis, Maryland 21402

* Present address: Gulf Research and Development Company, Houston, Texas 37048.

Chapter 1

Introductory Remarks

EDWARD D. PALIK
Naval Research Laboratory
Washington, D.C.

I. Introduction 3
II. The Chapters 4
III. The Critiques 5
IV. The Tables 6
V. The Figures of the Tables 7
VI. General Remarks 8
References 9

INTRODUCTION I

During a professional career covering molecular spectroscopy, magneto-optical properties of semiconductors, internal-reflection spectroscopy, and general optical properties of electronic materials, I rarely measured refractive index n or extinction coefficient k to better than two significant figures and then only when the experiment really demanded it. However, there was always a need for n and k values for estimating an optical effect, internal reflection in a prism with multilayers, band-edge transmission of a thin semiconductor film on a substrate, or free-carrier reflection effects, for example. Such numbers were not very handy, especially for a variety of metals into the infrared to the far infrared and for semiconductors with various free-carrier concentrations.

The present handbook is an attempt to collect references and tabulate n and k for a reasonably large number of materials of technological and physics interest, so that a person having the need could easily find the numbers over the widest spectral range, ideally x-ray to microwave, in a grid fine enough to yield the number by inspection or by a simple interpolation, and provide the pertinent references if more details were needed. For each material a critique is provided to indicate how the numbers were obtained from experiment and how good they are.

HANDBOOK OF OPTICAL CONSTANTS OF SOLIDS ISBN 0-12-544420-6

II THE CHAPTERS

To preface and supplement the critiques for each material, there are 11 chapters (including this one) that discuss various aspects of optical constants with some emphasis on experimental techniques and sample preparation. While n and k are oblivious to the units used in Maxwell's equations, deriving these numbers both theoretically and experimentally can be done in various units that the individual contributors have indicated when necessary (primarily cgs and mks).

In Chapter 2 Roy F. Potter develops R, T, and A for a general sample of multiple films on both sides of a thick substrate. This simplifies to the single slab and the single film on a slab substrate, the two most prevalent kinds of samples. In Chapter 3 D. Y. Smith reviews the world of sum rules over infinite and finite frequency ranges and stresses how such analysis can spot experimental errors.

In Chapter 4 W. R. Hunter discusses polarized nonnormal incidence reflection techniques especially as they are practiced in the ultraviolet–visible (UV–vis) spectral region, with emphasis on how errors in R are propagated to errors in n and k and the effects of oxide layers. In Chapter 5 D. E. Aspnes outlines wavelength ellipsometry with emphasis on the effects of surface preparation and the properties of a deposited or grown film on a substrate. In Chapter 6 Joseph Shamir reviews standard interferometric techniques for transparent samples and then discusses his more recent laser interferometric technique for measuring both n and k for a film on a substrate. In Chapter 7 P. A. Temple deals with calorimetry for bulk material and for a film on a substrate to determine small absorption constants. In Chapter 8 George J. Simonis discusses the more-specialized techniques used in the far-IR and submillimeter-wave region to determine optical constants. These are of considerable interest now with the advent of gyratron sources. In Chapter 9 B. Jensen summarizes the quantum free-carrier-absorption theory for semiconductors and gives numerical results for the contributions to n and k for GaAs, InP, and InAs for various free-carrier densities. Thus, the reader can calculate from scratch (or use an abbreviated table) to determine the free-carrier contribution to ε_1 and ε_2 and thus n and k. The regular critiques for GaAs, InP, and InAs were done for "pure" material, and these values of n and k can be combined with the free-carrier contributions to estimate the optical constants for any sample of arbitrary free-carrier concentration.

Finally in Chapter 10 David W. Lynch discusses the absorption mechanisms above the fundamental band gap with emphasis on the variety of interband, plasma, core-level, exciton, and Urbach-tail absorption processes. In Chapter 11 Shashanka S. Mitra describes the absorption mechanisms below the fundamental band gap, such as single- and multiphonon processes, free-carrier absorption, and impurity absorption.

Special attention has been given to aluminum by D. Y. Smith in a long critique since it is the most-studied metal and its optical constants have been determined over a wide spectral range with the aid of dispersion relations. It would be hoped that the data given for some of the other materials might spur further such analysis.

We have stressed the film-on-a-substrate sample because this is becoming more and more the sample confronting us in materials studies since the upsurge in (1) epitaxial film growth, (2) use of insulator films on semiconductors, (3) surface studies of adsorbed layers under ultrahigh-vacuum (UHV) conditions, and (4) reflection and antireflection coatings.

THE CRITIQUES III

Thirty-seven materials have been examined with some crystalline and amorphous forms included for a few materials. The critiques have been done by 21 people. Thus, the styles vary somewhat. We wanted a common thread of discussion of experimental techniques, reasons for choices of numbers used in the table, the most important literature references, and some idea of accuracy and precision. This last requirement has been met head-on by some of the contributors (and original workers) who quote plus/minus variations in experimental scatter for a Sellmeier-type fit to express the data, who discuss limits of systematic and random errors, or who (more vaguely) discuss which decimal place is becoming unreliable or uncertain. Because of the wide spectral range along with the number of different experimental techniques used for a given material, this becomes a task impossible to do in detail, and we can only refer the reader back to the original references. In most tables we have overlapped n and k values from different experiments to give the reader an idea of the mismatch. Sometimes, we can figure out the reasons for this mismatch and suggest which is the better set of data. For example, Kramers–Kronig (KK) analysis deteriorates when k becomes smaller than n and at the edges of a particular spectral region; also, the purity and structure of the material can vary among laboratories. Unfortunately, the variations in n and k are such that for nontransmission experiments generally, only one or two figures should be used in quoting absolute values (accuracy), while more are often carried along to show spectral structure as a function of wavelength (precision). Only in the case of measurement of refractive index by minimum deviation or fringes are we able to set down values to four decimal places with some confidence. While we can give examples of ellipsometric measurements and KK analysis of reflectivity in an overlap region (1.5–6.0 eV) that agree to two figures, we also have examples

in which two laboratories measuring R and doing KK analysis hardly agree to two figures among themselves.

Much of the work cited was done by physicists interested in absorption peaks so as to be able to identify phonon absorption and interband absorption transitions in detail. Their precision is generally high in order to distinguish peaks and shoulders, but their accuracy is not necessarily high, as a comparison of two experiments measuring multiphonon absorption in silicon or gallium arsenide will show, for example.

We do think that a single set of values of n and k is desirable in contrast to a collection of all the work ever done since the dawn of time with no selectivity or hints as to what is what. To some extent, we feel this handbook accomplishes this goal.

There have been a number of previous collections of optical data that have been helpful. The most useful is "The Refractive Index of Alkali Halides," by Li [1], in which Sellmeier-type fits have been given to many materials. The work of Haelbich *et al.* [2], "Optical Properties of Some Insulators in the Vacuum Ultraviolet Region," was especially useful because it catalogued all the x-ray to UV work of a number of insulators and proved to be a good starting point. Another older collection was published by Moses [3], "Refractive Index of Optical Materials in the Infrared Region." My copy of Ballard *et al.* [4], "Optical Materials for Infrared Instrumentation," is dog-eared from use. Another more recent starting point was Wolfe's [5] "Properties of Optical Materials." The table of Hass and Hadley [6], "Optical Properties of Metals," was useful, as was the more recent compilation of Weaver *et al.* [7] based on synchrotron data for metals.

IV THE TABLES

A few general comments about the format of the tables are in order. We have used photon energy in electron volts, wave number in reciprocal centimeters, and wavelength in micrometers for each material to aid the reader. It is natural to think in electron volts and angstroms in the x-ray–UV region, while in the infrared reciprocal centimeters and micrometers are more comfortable. We will never get used to a number like 110,000 cm^{-1}, although this usage appears in older atomic spectroscopy books [8]. Therefore, we introduce reciprocal centimeters usually near 50,000 cm^{-1} ($\sim$6 eV), keeping them to all lower energies.

It is usually obvious what the units were for the original data because of the systematic trends of the simple numbers given to one, two, or three figures. The other two units are usually given to four figures just for consistency and to help identify the original units. To convert electron volts to reciprocal

centimeters we use 8065.48 cm^{-1}/eV rounded off from the most recently determined [9] fundamental constants e/hc.

The real and imaginary parts of the dielectric function ε are given by $\varepsilon = \varepsilon_1 \pm i\varepsilon_2 = (n \pm ik)^2$. One obtains $n \pm ik$ by choosing the form of the plane-wave solution to Maxwell's equations as $\exp[i(\mp\omega t \pm \mathbf{q}\cdot\mathbf{r})]$. This choice also determines signs in the Lorentz-oscillator formula for lattice vibrations. We have elected to tabulate n and k because it is then an easy matter to obtain $\varepsilon_1 = n^2 - k^2$ and $\varepsilon_2 = 2nk$ as well as reflectivity $R = [(n-1)^2 + k^2]/[(n+1)^2 + k^2]$.

The extinction coefficient is often given in powers of 10. This power is understood to be the same down the column until this power repeats itself just before a new power of 10 appears or the number becomes a pure decimal at 10^{-1}.

In most instances, the values for n and k have been obtained from tables and graphs in the original references. In some cases, the original workers have kindly supplied detailed tables to the critiquers. The tables are acknowledged as private communications. To obtain n and k from a graph produces all sorts of eyestrain problems. Many authors do not provide fiduciary marks on all four sides of the graph or omit the marks for 2–9 on log plots. Tables that are too small to read must be expanded. For some reason, artists and/or experimenters cannot draw a linear scale with evenly spaced fiduciary marks. Therefore, some of these numbers probably have an uncertainty larger than the experimental uncertainty quoted in the original paper.

When absorption is due to extrinsic mechanisms such as impurities and surface quality, the critiquer has mentioned this and either omitted the data or noted its extrinsic character.

The references are given in brackets next to the beginning n and k and are understood to apply down the column until a new reference appears. This may get a little confusing when a significant overlap of two sets of data occurs.

THE FIGURES OF THE TABLES V

The tables are plotted for each critique, usually as Fig. 1, on a log–log scale, so that the reader can see at a glance what is going on. Admittedly, the details are lost. The solid line is for n; the dashed line is for k. After plotting over 30 such tables, I find the optical constants of solids to be a boring subject with the same old reststrahlen bands, the same old multiphonon bands, the same old free-carrier absorption, the same fundamental band gap and higher-lying band gaps and the same K, L, M atomic absorption edges.

VI GENERAL REMARKS

A few interesting observations have been made while I was doing several of the critiques and reading all of them. Room temperature was anything from 292 to 300 K, and it was surprising how many authors neglected to report this number at all. This is no problem except for the refractive-index variation typically in the fourth decimal place for a 1-K change in temperature. Some critiques do quote temperature dependences.

Description of the sample surface preparation was often neglected, as was the free-carrier concentration in semiconductors. Mechanical (nonchemical) polishing of the surface should have been outlawed 20 years ago, although whether it affects an optical measurement often depends on the wavelength-to-damage size and the kind of material—metal, semiconductor, or insulator. We sometimes run into trouble with surface roughness at reststrahlen minima at which reflection is low ($R \approx 0.02$) and at maxima at which surface-optical-phonon features weakly occur because roughness can couple light to the surface-phonon modes. Deposited films were often undercharacterized as to state of crystallinity.

The great majority of far-IR determinations of n and k are indirect via the Lorentz-oscillator-model and Drude-model fits to R. The former is notoriously poor in the wings, but it is all we have in many cases, and many of the materials in the handbook are analyzed in the IR by this technique. In a few cases, KK analysis for R was also done, with some agreement with the results of an oscillator-model fit. Fortunately, asymmetric Fourier transform spectroscopy can now give both the real and imaginary parts of R, ε_1, and ε_2, and n and k directly, thus avoiding the oscillator model and KK analysis. The other, more direct, technique of polarized nonnormal incidence reflection is not so widespread in the IR yet.

The nomenclature for optics gets a little mixed up on occasion in the original references and in the present chapters and critiques. While reflection and transmission are general processes, the measurement one makes on a laboratory sample yields numbers, the reflectance and transmittance. This, of course, includes multiple-reflection effects. As the sample becomes opaque or as the sample is wedged, the reflectance approaches the single-surface reflectivity, and this is the quantity that is used in KK analysis.

Since $\alpha = 4\pi k/\lambda$ defines the absorption constant, most people measure α directly and do not convert to k. In converting some α data to k data over a considerable range of λ, I noticed that detailed structure was often washed out somewhat in the final plot of k in contrast to the plot of α. Also, a peak in α did not necessarily fall at the same wavelength as a peak in k. Since power absorption is proportional to α, measurement of α is a better approach to locating resonances.

Very few of the measurements were done to determine n and k for their own sake, except when the material was new, such as in the case of InSb in 1953. The interest in laser-window materials spurred such measurements in selected transparent materials such as NaCl and KCl. The availability of synchrotron-radiation sources is now producing physics interests in material structure and will yield better values.

Some general reviews of how to calculate and measure optical constants are also listed in the references [10–14].

REFERENCES

1. H. H. Li, *J. Phys. Chem. Ref. Data* **5**, 329 (1976).
2. R.-P. Haelbich, M. Iwan, and E. E. Koch, "Physik Daten, Physics Data," Fach-information zentrum, Karlsruhe, 1977.
3. A. J. Moses, Refractive Index of Optical Materials in the Infrared Region, Report on Contract F33615-68-C-1225, Air Force Systems Command, Hughes Aircraft Company, Culver City, California, 1970.
4. S. S. Ballard, K. A. McCarthy, and W. L. Wolfe, Optical Materials for Infrared Instrumentation, Report from Infrared Information and Analysis Center, University of Michigan, Willow Run Laboratories, Ann Arbor, Michigan, 1959.
5. W. L. Wolfe, *in* "Handbook of Optics OSA," Section 7, McGraw-Hill, New York, 1978.
6. G. Hass and L. Hadley, *in* "AIP Handbook," Section 6, pp. 118–169, McGraw-Hill, New York, 1972.
7. J. H. Weaver, C. Krafka, D. W. Lynch, and E. E. Koch, "Physik Daten, Physics Data," "Optical Properties of Metals," Vol. 18-1, Fach-information zentrum, Karlsruhe, 1981.
8. H. E. White, "Introduction to Atomic Spectra," McGraw-Hill, New York, 1934.
9. M. Aguilar-Benitez, R. L. Crawford, F. Frosch, G. P. Gopal, R. E. Hendrick, R. L. Kelly, M. J. Losty, L. Montanet, F. C. Porter, A. Rittenberg, M. Roos, L. D. Roper, T. Shimada, R. E. Shrock, T. G. Trippe, C. Walek, C. G. Wohl, and G. P. Yost, *Phys. Lett.* **111B**, 1 (1982).
10. E. E. Bell, *in* "Handbuch der Physik," Vol. 25, Part 2a, p. 1 (S. Flugge, ed.), Springer-Verlag, Berlin, 1967.
11. F. Abeles, *in* "Progress in Optics," Vol. 11, p. 251 (E. Wolf, ed.), North-Holland Publ., Amsterdam, 1963.
12. H. E. Bennett and J. M. Bennett, *in* "Physics of Thin Films," Vol. 4, p. 1 (G. Hass and R. E. Thun, eds.), Academic Press, New York, 1967.
13. O. S. Heavens, "Optical Properties of Thin Solid Films," Dover, New York, 1965.
14. P. H. Berning, *in* "Physics of Thin Films," Vol. 1, p. 69 (G. Hass, ed.), Academic Press, New York, 1963.

Chapter 2

Basic Parameters for Measuring Optical Properties

ROY F. POTTER
Department of Physics and Astronomy
Western Washington University
Bellingham, Washington

I. Introduction 11
II. Intrinsic Material Parameters in Terms of Optical Constants 16
III. Reflectance, Transmittance, and Absorptance of Layered Structures 18
IV. The General Lamelliform—Phase Coherency Throughout 19
V. The General Lamelliform—Phase Incoherency in Substrate 21
A. Absorptance of a General Lamelliform 22
B. Reflectance of Single Film on Nontransmitting Substrate 23
VI. Summary 24
Appendix A. Basic Formulas for Fresnel Coefficients 24
Appendix B. General Formulas for the Case of a Parallel-Sided Slab 25
Appendic C. Reflectance R_{jk} at j–k Interface 26
Appendix D. Reflectance of Single Layer on Each Side of a Slab and Single Layer on Either Side of a Slab 26
Appendix E. Critical Angle of Incidence 30
Definitions of Terms 33
References 34

INTRODUCTION I

The interaction of electromagnetic (em) radiation with matter has provided over the years an effective and powerful tool for understanding and probing the electronic and vibrational states of condensed materials. Maxwell's equations describing the propagation of em waves are so well established and accepted that they serve as the underlying bases for optical studies. Based on Faraday's law of induction and Maxwell's extension of Ampere's

HANDBOOK OF OPTICAL CONSTANTS OF SOLIDS

Copyright © 1985 by Academic Press, Inc.
All rights of reproduction in any form reserved.
ISBN 0-12-544420-6

law, they are given, in partial differential form, as

$$\nabla \times \mathbf{E} = -\partial \mathbf{B}/\partial t, \qquad \nabla \times \mathbf{H} = \mathbf{J} + \partial \mathbf{D}/\partial t, \tag{1}$$

along with the divergence relations for induction and displacement

$$\nabla \cdot \mathbf{B} = 0, \qquad \nabla \cdot \mathbf{D} = 0$$

(assuming that no free charge exists), where **E** is the electric field, **H** the magnetic field, **B** the magnetic induction, **D** the electric displacement, and **J** the electric current flux [1]. (Expressions are in mks units.)

However, these expressions are not sufficient in themselves to completely describe em propagation through a medium; i.e., no "optical constants" are contained in Maxwell's equations. A full description must include the trio of "material equations"

$$\mathbf{D} = \varepsilon\varepsilon_0\mathbf{E}, \qquad \mathbf{B} = \mu\mu_0\mathbf{H}, \qquad \mathbf{J} = \sigma\mathbf{E} \quad \text{(Ohm's law)}, \tag{2}$$

where the coefficients $\varepsilon\varepsilon_0$, $\mu\mu_0$, and σ are restricted for present purposes to be time- and field- independent scalar quantities. (See Born and Wolf [2] for more general tensor treatments.) These restrictions follow the assumption of isotropic media and linear responses. An additional important assumption is that these quantities are continuous in the *immediate* vicinity of the points where the fields are considered or measured. The coefficients $\varepsilon\varepsilon_0$, $\mu\mu_0$, and σ are known as the electric permittivity, the magnetic permeability, and the electrical conductivity, respectively; while ε_0 and μ_0 are the free-space permittivity and permeability, respectively. The so-called optical constants are contained in the coefficients ε, μ, and σ. Used for describing the macroscopic optical properties of matter, these coefficients can be related to polarizabilities on the atomic scale and provide details on the physics of the condensed state.

The expressions used in this section are based on the rationalized mks system of units. A consequence is that the propagation velocity in a given medium is given by $(\mu\varepsilon\mu_0\varepsilon_0)^{-1/2} = c(\mu\varepsilon)^{-1/2}$, where $c = (\mu_0\varepsilon_0)^{-1/2}$ is the free-space velocity of light. However, when Gaussian units are used, the propagation velocity is stated explicitly in Maxwell's equations, and the free-space velocity defined by $(\mu_0\varepsilon_0)^{-1/2}$. At the risk of belaboring the point, the refractive index for a given medium c/v is defined by the dimensionless quantity $(\mu\hat{\varepsilon})^{1/2}$. The Fresnel coefficients, reflectivity and transmittivity, are also defined by dimensionless ratios, namely, of the field strengths. Thus the complex refractive indices (as well as the corresponding complex dielectric functions $\hat{\varepsilon}$) carry no reference to any system of units. When they are used to determine field strength values relative to given input values, the fields must be stated in a consistent set of units (see Table I).

An additional point to keep in mind is that the dielectric susceptibility term in the polarization vector **P** in the rationalized system of units is 4π times the susceptibility term in an unrationalized system.

TABLE I

Conversion of Units

Quantity	mks	Practical cgs	Gaussian
Permittivity of free space ε_0	$\frac{10^{-9}}{4\pi a^2}\frac{\text{F}}{\text{m}}$	$\frac{10^{-11}}{4\pi a^2}\frac{\text{F}}{\text{cm}}$	$\frac{1}{4\pi}$
Permeability of free space μ_0	$4\pi \times 10^{-7}\frac{\text{H}}{\text{m}}$	$4\pi \times 10^{-9}\frac{\text{H}}{\text{cm}}$	$\frac{4\pi}{c^2}$
Speed of light $c = (\mu_0\varepsilon_0)^{-1/2}$	$a \times 10^8\frac{\text{m}}{\text{sec}}$ $(a = 2.9979)$	$a \times 10^{10}\frac{\text{cm}}{\text{sec}}$	$a \times 10^{10}\frac{\text{cm}}{\text{sec}}$
Impedance of free space $Z_0 = (\mu_0/\varepsilon_0)^{1/2}$	$40\pi a\ \Omega$	$40\pi a\ \Omega$	$4\pi/c$
Electric intensity E	$\frac{\text{V}}{\text{m}}$	$\frac{\text{V}}{\text{cm}}$	$\frac{1}{300}\frac{\text{V}}{\text{cm}}$
Electric displacement D	$\frac{\text{C}}{\text{m}^2}$	$4\pi\frac{\text{C}}{\text{cm}^2}$	$12\pi \times 10^9\frac{\text{C}}{\text{cm}^2}$
Magnetic intensity H	$\frac{\text{ampere-turn}}{\text{m}}$	Oe	Oe
Magnetic induction B	$\frac{\text{Wb}}{\text{m}^2}$ $(10^4\ \text{G})$	G	G

Table I lists several parameters in terms of three systems of units in common use.

Introducing the material equations permits Maxwell's equations to be expressed as a modified set of partial differential equations involving only two of the four field parameters, namely, **E** and **H**. Assuming that the fields have time dependence proportional to $e^{i\omega t}$, the modified Maxwell's equations become

$$\begin{aligned}\nabla \times \mathbf{E} &= -\mu\mu_0\dot{\mathbf{H}} = -i\mu\mu_0\omega\mathbf{H} = -i\frac{2\pi\mu}{\lambda}Z_0H,\\ \nabla \times \mathbf{H} &= \mathbf{J} + \dot{\mathbf{D}} = \mathbf{J} + \varepsilon\varepsilon_0\mathbf{E}\omega = i\left(\varepsilon - \frac{i\sigma}{\varepsilon_0\omega}\right)\varepsilon_0\omega\mathbf{E} = \frac{2\pi}{\lambda}\frac{\hat{\varepsilon}}{Z_0}\mathbf{E},\end{aligned} \tag{3}$$

where

$$\hat{\varepsilon} = \varepsilon - (i\sigma/\varepsilon_0\omega) = \varepsilon - i\sigma\lambda Z_0/2\pi = \varepsilon' - i\varepsilon''$$

and

$$c = (\mu_0\varepsilon_0)^{-1/2}, \qquad Z_0 = (\mu_0/\varepsilon_0)^{1/2}, \qquad \lambda = 2\pi c/\omega.$$

The complex function $\hat{\varepsilon}$ has a real term equal to the ratio of the medium permittivity to that of free space, i.e., ε, and an imaginary term proportional to the frequency-dependent conductivity σ. The wave velocity, impedance, and wavelength for free space are given by c, Z_0, and λ, respectively.

For the infrared, visible, and ultraviolet spectral regions, the em radiation is considered to be propagating as plane waves. When such waves are incident upon a specimen composed of one or more homogeneous phases separated by specular surfaces, the amount and degree of transmission, reflection, and refraction are direct measures of the material parameters. Many of the usual and useful experimental arrangements have the em waves incident upon a set of parallel-sided slabs, with zero separation between the slabs (lamelliforms). The two field components E and H are orthogonal to each other and are contained in a plane orthogonal to the propagation direction. One needs to consider two cases only: (1) the electric field E normal to the plane of incidence (POI) (TE mode) and (2) the magnetic field component H normal to the POI (TM mode). (The POI is defined as the plane containing the propagation vector and the normal to the surface upon which the wave is incident.) Consider that the normal to the incident surfaces lies parallel to the z axis and that the x axis is normal to the POI. The y axis lies in the POI and is parallel to the surface.

Both the TE (also known as s or perpendicular polarization) and TM (p or parallel polarization) modes are treated in similar manners by using separation of variables techniques. The following are taken as solutions for each polarization:

TE polarization	TM polarization
$E_x = U(z)X(t, y)$	$H_x = U(z)X(t, y)$
$H_y = V(z)X(t, y)$	$E_y = V(z)X(t, y)$
$H_z = W(z)X(t, y)$	$E_z = W(z)X(t, y)$

(4)

where

$$X = \exp i(\omega t - \kappa S y),$$

in which

$$\kappa = \omega/c = 2\pi/\lambda = (\mu_0\varepsilon_0)^{1/2}\omega, \qquad S = (\mu\hat{\varepsilon})^{1/2} \sin \phi,$$

and ϕ is the angle of incidence in the medium. Operating on these with the modified Maxwell's equations,

$$\nabla \times \mathbf{E} = -\mu\mu_0 \, \partial\mathbf{H}/\partial t, \qquad \nabla \times \mathbf{H} = \hat{\varepsilon}\varepsilon_0 \, \partial\mathbf{E}/\partial t,$$

yields for either polarization the expressions

$$U' = -i\hat{m}V, \qquad V' = -i\hat{\gamma}^2/\hat{m}U, \qquad SU = -\hat{m}W, \tag{5}$$

where $\hat{\gamma} = \alpha - i\beta$, $\hat{\gamma}^2 = \mu\hat{\varepsilon} - S^2$, and $\mu\hat{\varepsilon} = \hat{n}^2 = (n - ik)^2$. The $\hat{m}$ is defined for each mode as

$$\hat{m} = \begin{cases} \mu Z_0 = \hat{n}\hat{Z} & \text{(TE)}, \\ -\varepsilon/Z_0 = -\hat{n}/\hat{Z} & \text{(TM)}. \end{cases} \tag{6}$$

It should be noted that in this section the prime denotes the use of the operator $(1/\kappa)\,\partial/\partial z$. Eliminating W yields two second-order ordinary differential equations in U and V:

$$\begin{aligned} U'' + \hat{\gamma}^2(z)U - f'(z)U' &= 0, \\ V'' + \hat{\gamma}^2(z)V + g'(z)V' &= 0, \end{aligned} \tag{7}$$

where

$$\begin{aligned} f &= \ln(\hat{m}) = \ln(\hat{\zeta}/\hat{\gamma}), \\ g &= \ln(\hat{m}/\hat{\gamma}^2) = \ln(\hat{\zeta}/\hat{\gamma}), \end{aligned}$$

and where the material parameters m and ζ are still to be considered to vary along z; also:

$$\hat{\zeta} = \frac{\hat{m}}{\hat{\gamma}} = \begin{cases} \hat{Z}\hat{n}/\hat{\gamma} = Z_0\mu/\hat{\gamma} & \text{(TE)}, \\ -\hat{n}/Z\hat{\gamma} = -\hat{\varepsilon}/\hat{\gamma}Z_0 & \text{(TM)}. \end{cases} \tag{8}$$

The pair of differential equations (7) can be solved analytically for only a few special cases. (See Jacobsson [3] for a comprehensive discussion of this problem.) Two cases are considered here, the first of which is that for an abrupt interface; i.e., $\hat{n}'$ is infinite. This is expressed in matrix form as

$$\begin{bmatrix} U_0 \\ V_0 \end{bmatrix} = \begin{bmatrix} 1 & 0 \\ 0 & 1 \end{bmatrix} \begin{bmatrix} U_f \\ V_f \end{bmatrix}, \tag{9}$$

where the subscripts refer to the initial side (0) and the opposite side (f) of the slab or interface. This matrix expression is the statement that tangential fields are equal across the interface.

The second case is that for a medium characterized as having a uniform refractive index n, i.e., f' and g' vanish. This results in the usual homogeneous wave equation whose solutions are expressed in the "characteristic matrix"

$$\begin{bmatrix} U_0 \\ V_0 \end{bmatrix} = \begin{bmatrix} \cos(\hat{\gamma}z) & i\hat{\zeta}\sin(\hat{\gamma}z) \\ [i\sin(\hat{\gamma}z)]/\hat{\zeta} & \cos(\hat{\gamma}z) \end{bmatrix} \begin{bmatrix} U_f \\ V_f \end{bmatrix} = \hat{M} \begin{bmatrix} U_f \\ V_f \end{bmatrix}, \tag{10}$$

where U, V, and ζ are appropriately defined for either polarization mode. Note that z is the dimensionless product of the distance between points 0 and f with $\kappa = \omega/c$. The determinants for both of these 2×2 matrices are constants and the particular solutions have been chosen to make both equal to unity.

The characteristic matrix for a uniform layer is the basis for calculating the resultant matrix M_R for a series of parallel layers. Applying matrix multiplication to the matrices for the individual layers gives

$$\hat{M}_0 \times \hat{M}_1 \times \cdots \times \hat{M}_f = \hat{M}_R = \begin{bmatrix} \hat{A}_R & \hat{B}_R \\ \hat{C}_R & \hat{D}_R \end{bmatrix} \tag{11}$$

(see Macleod [4]).

An alternative approach is to apply Eqs. (5) and express the matrix for each interface and layer in terms of the forward and reverse field components:

$$U = U^+ + U^- = (V^+ - V^-)\zeta, \qquad V = V^+ + V^- = (U^+ - U^-)\zeta^{-1} \quad (12)$$

(note that $\hat{\zeta}V^{\pm} = \pm U^{\pm}$). The superscripts + and − refer to forward and reverse components, respectively.

For the ith abrupt interface, the matrix equations are

$$\begin{bmatrix} U_0^+ \\ U_0^- \end{bmatrix} = \frac{1}{\hat{t}_{0f}} \begin{bmatrix} 1 & \hat{r}_{0f} \\ \hat{r}_{0f} & 1 \end{bmatrix} \begin{bmatrix} U_f^+ \\ U_f^- \end{bmatrix} = \hat{C}_s(U) \begin{bmatrix} U_f^+ \\ U_f^- \end{bmatrix},$$

$$\hat{r}_{0f} = \frac{\hat{\zeta}_f - \hat{\zeta}_0}{\hat{\zeta}_f + \hat{\zeta}_0}, \qquad \hat{t}_{0f} = 1 + \hat{r}_{0f} = \frac{2\hat{\zeta}_f}{\hat{\zeta}_f + \hat{\zeta}_0}, \quad (13)$$

$$\hat{C}_s(V) = \frac{1}{\hat{t}'_{0f}} \begin{bmatrix} 1 & -\hat{r}_{0f} \\ -\hat{r}_{0f} & 1 \end{bmatrix}, \qquad \hat{C}_s(W) = \frac{\hat{m}_f}{\hat{m}_0} \hat{C}_s(U),$$

$$\hat{t}'_{0f} = 1 - \hat{r}_{0f} = (\hat{\zeta}_0/\hat{\zeta}_f)t_{0f},$$

while that for the medium with a uniform index is

$$\begin{bmatrix} U_0^+ \\ U_0^- \end{bmatrix} = \begin{bmatrix} e^{i\hat{\gamma}d} & 0 \\ 0 & e^{-i\hat{\gamma}d} \end{bmatrix} \begin{bmatrix} U_f^+ \\ U_f^- \end{bmatrix} = \hat{C}_l \begin{bmatrix} U_f^+ \\ U_f^- \end{bmatrix} \quad (14)$$

with $d = z_f - z_0$.

Each interface and intervening homogeneous layer can be described by its appropriate matrix. Matrix multiplication must be applied in the proper sequence, beginning with the initial interface matrix (s0) and ending with that for the final interface (sf) and alternating uniform layer–interface–uniform layer, etc., matrices. The result, C_R, corresponding to Eq. (11) is

$$\hat{C}_R = \hat{C}_{s0} \times \hat{C}_{l1} \times \hat{C}_{s1} \times \hat{C}_{l2} \times \hat{C}_{s2} \times \cdots \times \hat{C}_{lf} \times \hat{C}_{sf}. \quad (15)$$

The matrices expressed in Eqs. (13) and (14) are given in terms of the Fresnel terms $\hat{r}$ and $\hat{t}$ as well as the phase factor $\hat{\gamma}$ and are the bases for ellipsometry. The reader is referred to Heavens for a discussion of this approach [5].

II INTRINSIC MATERIAL PARAMETERS IN TERMS OF THE OPTICAL CONSTANTS

This section outlines the connections between the macroscopic optical constants and the electric-dipole excitations on the atomic scale. Thus, the accurate determination of the optical parameters of a given medium provide intrinsic information about that medium. At optical frequencies these parameters exhibit rich and varied features unique to the particular composition

under study. Even the presence of a small amount of an impurity can significantly alter portions of the spectral behavior. In addition, these parameters can be modified by temperature variations and by additional spectral features introduced by the application of external fields such as electric, magnetic, and stress fields, which can bring about symmetry changes, injection of charges, and so on.

It should be understood that the expanded Ampere's law is a generalized statement, that the motion of charges in an oscillating electric field has two components: (1) 90° out of phase with the field with no absorption of power and (2) in phase with energy from the field being dissipated in the material, corresponding to the usual Ohm's law. The optical conductivity is not to be confused with the dc conductivity σ_0, however.

From Ohm's law [Eq. (2)] the mean power P dissipated per unit volume is given by

$$P = \sigma \langle E^2 \rangle. \tag{16}$$

Let $p(t)$ be the probability that a photon of energy $\hbar\omega$ is absorbed in time t per unit volume; then

$$P = \hbar\omega p(t)/t. \tag{17}$$

This is a consequence of the observation that on the atomic scale, radiation must be treated as if it is absorbed or emitted in quanta or photons with magnitude $\hbar\omega$.

Equating the macroscopic term with that of the atomic gives

$$P = \varepsilon''\omega\varepsilon_0\langle E^2\rangle = \hbar\omega p(t)/t \qquad \text{or} \qquad \varepsilon'' = \hbar p(t)/\varepsilon_0\langle E^2\rangle t. \tag{18}$$

These expressions relate the macroscopic parameter ε'' to that of $p(t)$ at the atomic level for the interaction of electromagnetic radiation while propagating through matter. If the physics of condensed matter gives a value or estimate for $p(t)$, it can be checked and validated by measurements of the optical constants [6].

For example, the semiclassical quantum-mechanical treatment of a bound electron shows that ε'' is proportional to the product of the matrix element for this transition and the joint density of states for the initial and final states. The matrix element provides the base for determining selection rules based on lattice symmetry as well as indicating the strength of the transition. The joint density of states, on the other hand, gives a measure of the availability of sites available for transitions between states. These topics are handled in further detail elsewhere in this handbook.

The classical-oscillator case for an electron is an example of absorption and dispersion due to free carriers. Since there are no restoring forces, the real and imaginary parts of the dielectric function are written as

$$\varepsilon' - \varepsilon'_\infty = \frac{(e^2/\varepsilon_0)(N/m^*)}{\omega^2 + g^2}, \qquad \varepsilon'' = \frac{ge^2}{\varepsilon_0\omega}\frac{N/m^*}{(\omega^2 + g^2)}, \tag{19}$$

where ε_∞ is the dielectric function at frequencies sufficiently high that free-carrier effects are negligible, N is the free-carrier concentration, g is a damping term, and m^* is the isotropic free-carrier effective mass. These expressions describe the optical properties of many semiconductors in the spectral region between the reststrahlen frequencies and those for the interband electronic transitions (see Moss [6]).

Other absorption mechanisms can exist which contribute to the optical properties of the condensed phase. The classical treatment already sketched illustrates the type of microscopic information on the atomic scale to be inferred and derived from the macroscopic measurements of the so-called optical constants.

III REFLECTANCE, TRANSMITTANCE, AND ABSORPTANCE OF LAYERED STRUCTURES

A common type of specimen structure for use in the experimental determination of the optical parameters is that of the lamelliform, which is a structure consisting of parallel-sided lamellae in intimate contact and with each interface a specular surface. Such structures include the plain slab as well as a slab with a single film.

Ellipsometry is a general class of experimental techniques for studying such specimens. Matrices (13) and (14) are the bases for describing the Fresnel coefficients and determining the ratio of the amplitudes of the reflected TM and TE modes as well as the phase difference between them (see Chapter 5).

The other principal class of experiments consists of those that measure the intensity ratios: reflectance R, transmittance T, and absorptance A. For a given experimental setup, these quantities are related by

$$A + R + T = 1. \tag{20}$$

Most measurements of one or more of these quantities have been made at zero, or near zero, angles of incidence. This section will develop expressions for them that are generalized for either polarization as well as for *all* angles of incidence. (See Chapter 4 for more details of nonnormal-incidence reflectance measurements.)

The source of em radiation is considered to be on one side of the lamelliform only, i.e., the incident side (subscript 0), and no backward wave exists in the medium opposite the source (subscript f), i.e., $U_f^- = 0$. Taking the z axis along the normal to the lamelliform, the Poynting vector components along that axis for the three field amplitudes are proportional to $U_0^+ V_0^{+*}$, $U_0^- V_0^{-*}$, and $U_f^+ V_f^{+*}$ for the incident, the reflected, and the transmitted

waves, respectively. In terms of the matrix C_R [Eq. (15)], the field amplitudes are related as

$$\begin{bmatrix} U_0^+ \\ U_0^- \end{bmatrix} = \frac{1}{t_{0f}} \begin{bmatrix} a & b \\ c & d \end{bmatrix} \begin{bmatrix} U_f^+ \\ 0 \end{bmatrix} = C_R \begin{bmatrix} U_f^+ \\ 0 \end{bmatrix}, \tag{21}$$

with $t_{0f} = t_0 \cdot t_1 \cdot t_2 \cdots t_f$.

The reflectance R and the transmittance T are defined by

$$\begin{aligned} R_{0f} &= \frac{U_0^- U_0^{-*}}{U_0^+ U_0^{+*}} = \frac{\hat{c}\hat{c}^*}{\hat{a}\hat{a}^*} = \hat{r}_{0f}\hat{r}_{0f}^*, \\ T_{0f} &= \frac{\mathrm{Re}[U_f^{+*}\sqrt{(V_f^+)^2 + (W_f^+)^2}\cos\phi_f]}{\mathrm{Re}[U_0^{+*}\sqrt{(V_0^+)^2 + (W_0^+)^2}\cos\phi_f]} \\ &= \frac{U_f^+ U_f^{+*}\,\mathrm{Re}(1/\hat{\zeta}_f)}{U_0^+ U_0^{+*}\,\mathrm{Re}(1/\hat{\zeta}_0)} = \frac{\hat{t}_{0f}\hat{t}_{0f}^*\,\mathrm{Re}(1/\hat{\zeta}_f)}{\hat{a}\hat{a}^*\,\mathrm{Re}(1/\hat{\zeta}_0)}, \\ \frac{\mathrm{Re}(1/\hat{\zeta}_f)}{\mathrm{Re}(1/\hat{\zeta}_0)} &= \zeta_0\,\mathrm{Re}\left(\frac{1}{\hat{\zeta}_f}\right) = \frac{1 - \hat{r}_{0f}\hat{r}_{0f}^*}{1 + \hat{r}_{0f}\hat{r}_{0f}^* + 2\,\mathrm{Re}(\hat{r}_{0f})} \\ &= \frac{1 - R_{0f}}{1 + \hat{R}_{0f} + 2\,\mathrm{Re}(\hat{r}_{0f})}. \end{aligned} \tag{22}$$

The resultant matrix C_R can also be expressed in terms of the characteristic matrix M_R of Eq. (11). Although the characteristic matrix Eq. (11) is often preferred for calculations because each submatrix is defined for its own particular lammella, the elements of M_R must be directly related to those of Eq. (21), thus the components a and c of Eq. (21), in terms of Eq. (11), become

$$\begin{aligned} \hat{a} &= \tfrac{1}{2}[\hat{A}_R + \zeta_0\hat{C}_R + (\hat{B}_R/\hat{\zeta}_f) + (\zeta_0/\hat{\zeta}_f)\hat{D}_R], \\ \hat{c} &= \tfrac{1}{2}[\hat{A}_R - \zeta_0\hat{C}_R + (\hat{B}_R/\hat{\zeta}_f) - (\zeta_0/\hat{\zeta}_f)\hat{D}_R]. \end{aligned} \tag{23}$$

In most instances, the reflectance and the transmittance are measured in the same medium, i.e., $\hat{\zeta}_0 = \hat{\zeta}_f$, but experimental conditions exist for which the ratio $\mathrm{Re}(1/\hat{\zeta}_f)/\mathrm{Re}(1/\hat{\zeta}_0)$ must be included for T in Eq. (22).

IV THE GENERAL LAMELLIFORM— PHASE COHERENCY THROUGHOUT

A lamelliform of general interest is that of a parallel-sided dielectric or semiconductor slab, coated in either side with one or more lamellae, each sufficiently thin so as to transmit radiation of a given frequency (or wavelength). The approach here is to use Eqs. (13) and (14) to form $\hat{C}_R$ as the

product of three matrices:

(1) $\hat{C}_f$ for the n lamellae on the front or source side,
(2) $\hat{C}_s$ for the substrate slab itself, and
(3) $\hat{C}_b$ for the m lamellae on the back side, opposite the source.

The resulting matrices are represented as

$$C_f = \frac{1}{t_f}\begin{bmatrix} a_f & b_f \\ c_f & d_f \end{bmatrix} = \frac{a_f}{t_f}\begin{bmatrix} 1 & r'_f \\ r_f & D_f \end{bmatrix}, \tag{24a}$$

where $t_f = t_{f1} \cdot t_{f2} \cdots t_{fn}$ (n lamellae), $r_f = c_f/a_f$, $r'_f = b_f/a_f$, and $D_f = d_f/a_f$;

$$C_s = a_s\begin{bmatrix} 1 & 0 \\ 0 & D_s \end{bmatrix}, \tag{24b}$$

where $a_s = \exp i\hat{\gamma}_s d_s$, $D_s = a^{-2} = E\hat{e}$, $E = \exp(-2\beta_s d_s)$, and $\hat{e} = \exp(-2i\alpha_s d_s)$;

$$C_b = \frac{a_b}{t_b}\begin{bmatrix} 1 & r'_b \\ r_b & D_b \end{bmatrix}, \tag{24c}$$

where $t_b = t_{b1} \cdot t_{b2} \cdots t_{bm}$ (m lamellae), $r_b = c_b/a_b$, $r'_b = b_b/a_b$, and $D_b = d_b/a_b$. Multiplying these matrices in proper sequence gives

$$C_R = \frac{a_f a_s a_b(1 + r'_f r_b D_s)}{t_f t_b}\begin{bmatrix} 1 & r' \\ r & \dfrac{r_f r'_b + D_f D_s D_b}{1 + r'_f r_b D_s} \end{bmatrix},$$
$$r = \frac{r_f + r_b D_s D_f}{1 + r'_f r_b D_s}, \qquad r' = \frac{r'_b + r'_f D_s D_b}{1 + r'_f r_b D_s}. \tag{25}$$

From Eq. (22) the reflectance for either polarization is

$$R = rr^* = \frac{R_f + R_b D_f D_f^* E^2 + 2E\,\mathrm{Re}(r_f^* r_b D_f \hat{e})}{1 + R'_f R_b E^2 + 2E\,Re(r'_f r_b \hat{e})}, \tag{26}$$

where $R_f = r_f r_f^*$, $R'_f = r'_f r_f^*$, $R_b = r_b r_b^*$, and R_f is the reflectance of the front lamellae when the reflection from the substrate back surface R_b is zero. Here R'_f is the back reflectance from the front lamellae as though the source were located beyond the slab; i.e., the product $R'_f R_b$ is invariant when the slab is reversed 180° with respect to the source. (See Fig. 1 in Appendix D.)

The transmittance for the system is given by

$$T = \frac{T_f T_b T_s}{1 + R'_f R_b E^2 + 2E\,\mathrm{Re}(r'_f r_b \hat{e})},$$
$$T_f = \frac{t_f t_f^*}{a_f a_f^*}\frac{\mathrm{Re}(1/\hat{\zeta}_s)}{\mathrm{Re}(1/\hat{\zeta}_{f0})}; \qquad T_b = \frac{t_b t_b^*}{a_b a_b^*}\frac{\mathrm{Re}(1/\hat{\zeta}_{b0})}{\mathrm{Re}(1/\hat{\zeta}_s)}, \tag{27}$$
$$T_s = \sqrt{D_s D_s^*} = (a_s a_s^*)^{-1} = \exp(-2\beta_s d_s) = E.$$

Here T_f is the transmittance into the slab (medium s) through the lamellae on the source side, and the incident medium is characterized by $\hat{\zeta}_{f0}$. T_b is the transmittance from the slab through the lamellae on the back side into the b medium characterized by $\hat{\zeta}_{b0}$. $T_s = E$, analogous to the Lambert–Beer law, i.e., the transmittance through the substrate interior characterized by $\hat{\zeta}_s$.

V THE GENERAL LAMELLIFORM—PHASE INCOHERENCY IN SUBSTRATE

A case of particular interest is that for the substrate whose thickness-to-wavelength ratio d_s becomes so large that most experimental setups have insufficient resolution to sense the phase coherence of the transmitted and reflected beams through the substrate. In this case it becomes necessary to average the real part of the phase change across the substrate (assuming $k_s/n_s \ll 1$) [7].

Rearranging the terms of Eq. (26) gives

$$R = \frac{R_f + R_b D_f D_f^* E^2 + 2\sqrt{R_f R_b D_f^* D_f}\, E(\cos\theta \cos Y + \sin\theta \sin Y)}{(1 + R_f' R_b E^2)\,[1 + 2\sqrt{R_f' R_b}\, E \cos Y/(1 + R_f' R_b E^2)]} \tag{28}$$

where

$$\cos\theta = \frac{\mathrm{Re}(r_f' r_f D_f^*)}{(R_f' R_f D_f D_f^*)^{1/2}} \qquad \text{and} \qquad Y = 2\alpha_s d_s + \text{const.}$$

Averaging the quantity Y over $(2m + 1)\,\pi \geq Y \geq 0$, where the integer m is very large, gives the average reflectance $\bar{R}$ and transmittance $\bar{T}$ as

$$\bar{R} = \frac{1}{(2m+1)\pi}\int_0^{(2m+1)\pi} R\, dY = \frac{R_f + R_b G_f E^2}{1 - R_f' R_b E^2}, \qquad \bar{T} = \frac{T_f T_b E}{1 - R_f' R_b E^2}, \tag{29}$$

where

$$G_f = D_f D_f^* - 2\,\mathrm{Re}(r_f' r_f D_f^*) = (D_f - r_f' r_f)(D_f - r_f' r_f)^* - R_f R_f'.$$

Inductive arguments show that [using Eqs. (13), (14), and (21)]

$$D_f - r_f r_f' = \prod_{j=0}^{f} \det(m_j) = \left[\prod_{j=0}^{f} e^{-2\gamma_j d_j}(1 - \hat{r}_j^2)\right] \Big/ a_T^2. \tag{30}$$

Therefore,

$$G = T_f T_f' - R_f R_f',$$

where

$$T_f' = \frac{\hat{t}_f' \hat{t}_f'^*\,\mathrm{Re}(1/\zeta_{f_0})}{\hat{a}_f \hat{a}_f^*\,\mathrm{Re}(1/\zeta_s)}, \qquad \hat{t}_f' = 1 - \hat{r}_f,$$

giving the result that

$$\bar{R} = \frac{R_f + (T_f T'_f - R_f R'_f) R_b E^2}{1 - R'_f R_b E^2} = R_f + \frac{T_f T'_f R_b E^2}{1 - R'_f R_b E^2}, \tag{31}$$

where T'_f is the transmittance in the front lamellae, as though the radiation were to propagate from the substrate to the front surface. Gabriel and Nedoluha [8] give similar expressions using a different approach.

A Absorptance of a General Lamelliform

Most experiments measure either or both of the pair, transmittance and reflectance. The third quantity, absorptance, A (also known as emittance, through Kirchhoff's law), is the fraction of the incident radiation that has been absorbed by the lamelliform. From Eqs. (20), (29), and (30) it follows that

$$\bar{A} = 1 - R_f - E\frac{T_f(T'_f R_b E + T_b)}{1 - R'_f R_b E^2} = A_f + T_f\left[1 - E\frac{(T_b + R_b T'_f E)}{1 - R'_f R_b E^2}\right]. \tag{32}$$

These expressions for $\bar{A}$, $\bar{R}$, and $\bar{T}$ bring out an interesting point. When the lamelliform is not symmetric about its center plane, the reflectance and absorptance would differ if the lamelliform were to be inverted 180° with respect to the source. Since both of the products $T_f T_b$ and $R'_f R_b$ are invariant for the 180° reversal, the transmittance is the same. Palik *et al.* [9] measured the reflectance for a series of asymmetric Si slabs and explicitly showed these results.

When the various lamellae are weakly absorbing, formulas such as these provide insight into the optical properties of an otherwise complex system. For example, if the lamellae on either side of the slab have negligible absorption, then

$$\bar{A} = \frac{(1 - R_f)(1 + R_b E)(1 - E)}{1 - R'_f R_b E^2} \simeq \frac{2\beta_s d_d (1 - R_f)(1 + R_b)}{1 - R'_f R_b}. \tag{33}$$

Whenever the optical properties of the lamellae are symmetrical with respect to the slab, i.e., $R_b = R'_f$, the total absorptance is approximated by

$$\bar{A} = \frac{(1 - E)(1 - R_f)}{1 - R'_f E} \simeq 2\beta_s d_s \tag{34}$$

(which is also true for the bare-substrate case). The approximations in Eqs. (33) and (34) hold for the weakly absorbing substrate case. Measurements of these types can be very useful in determining the optical properties in the infrared spectral region. Stierwalt and Potter [10] studied the infrared properties of semiconductors by using this approach.

Reflectance of Single Film on Nontransmitting Substrate B

When the substrate is opaque ($E = 0$) or infinite in depth (or sufficiently nonparallel, i.e., $R_b = 0$), a reflectance experiment measures the front-surface reflectance R_f only. The use of the matrix multiplication for a single layer will demonstrate the approach for determining R_f for Eqs. (29)–(34). The resulting formulas have been found to be useful in optical measurements of metals, dielectrics, and semiconductors.

Using matrices in the form given in Eqs. (13) and (14) [Eqs. (10) and (23) can be used but Eqs. (13) and (14) have the Fresnel relations already given], the front surface resultant matrix m_f is

$$\begin{aligned}\hat{m}_f &= \frac{1}{\hat{t}_{01}}\begin{bmatrix}1 & \hat{r}_{01}\\ \hat{r}_{01} & 1\end{bmatrix}\begin{bmatrix}\exp i\hat{\gamma}d & 0\\ 0 & \exp -i\hat{\gamma}d\end{bmatrix}\frac{1}{\hat{t}_{12}}\begin{bmatrix}1 & \hat{r}_{12}\\ \hat{r}_{12} & 1\end{bmatrix}\\ &= \frac{1}{(Ww)^{1/2}}\begin{bmatrix}1 + \hat{r}_{01}\hat{r}_{12}W\hat{w} & \hat{r}_{12} + \hat{r}_{01}W\hat{w}\\ \hat{r}_{01} + \hat{r}_{12}W\hat{w} & Ww + \hat{r}_{01}\hat{r}_{12}\end{bmatrix}\frac{1}{\hat{t}_{01}\hat{t}_{12}},\end{aligned} \tag{35}$$

where $W\hat{w} = \exp(-2i\hat{\gamma}d)$, $W = \exp(-2\beta d)$, $\hat{w} = \exp(-2i\delta)$, $\delta = \alpha d$, and $\hat{\gamma} = \alpha - i\beta$ for the layer.

The reflectivity is written

$$\begin{aligned}\hat{r}_f &= \frac{\hat{r}_{01} + \hat{r}_{12} - \hat{r}_{12}(1 - W\hat{w})}{1 + \hat{r}_{01}\hat{r}_{12} - \hat{r}_{01}\hat{r}_{12}(1 - W\hat{w})}\\ &= \frac{\hat{r}_{02} - \hat{r}_{12}(1 - W\hat{w})/(1 + \hat{r}_{01}\hat{r}_{12})}{1 - \hat{r}_{01}\hat{r}_{12}(1 - W\hat{w})/(1 + \hat{r}_{01}\hat{r}_{12})},\end{aligned}$$

giving, in turn, the reflectance

$$\begin{aligned}R_f &= \hat{r}_f\hat{r}_f^*\\ &= \frac{\begin{aligned}&R_{02} - \{R_{12}(1 - W^2) + 2(1 - W)\,\mathrm{Re}(\hat{r}_{01}\hat{r}_{12}^*)\\ &\quad + 4W\sin\delta\,[\sin\delta\,\mathrm{Re}(\hat{r}_{01}\hat{r}_{12}^*) + \cos\delta\,\mathrm{Im}(\hat{r}_{01}\hat{r}_{12}^*)]\}/D\end{aligned}}{\begin{aligned}&1 - \{R_{01}R_{12}(1 - W^2) + 2(1 - W)\,\mathrm{Re}(\hat{r}_{01}\hat{r}_{12})\\ &\quad + 4W\sin\delta\,[\sin\delta\,\mathrm{Re}(\hat{r}_{01}\hat{r}_{12}) - \cos\delta\,\mathrm{Im}(\hat{r}_{01}\hat{r}_{12})]\}/D\end{aligned}}\end{aligned} \tag{36}$$

with

$$D = 1 + R_{01}R_{12} + 2\,\mathrm{Re}(\hat{r}_{01}\hat{r}_{12}), \qquad R_{02} = [R_{01} + R_{12} + 2\,\mathrm{Re}(\hat{r}_{01}\hat{r}_{12}^*)]/D$$

(the front surface reflectance of bare substrate).

As W approaches zero, i.e., the film becomes opaque, R_f approaches the value for R_{01}. For the weakly absorbing layer, i.e., $W \cong 1 - 2\beta d$, $\mathrm{Im}(r_{01}) \cong 0$,

$$R_f = \frac{R_{02} - 4[\beta d(R_{12} + r_{01}g) + r_{01}\sin\delta\,(g\sin\delta - h\cos\delta)]/D}{1 - 4[\beta d(R_{01}R_{12} + r_{01}g) + r_{01}\sin\delta\,(g\sin\delta - h\cos\delta)]/D}, \tag{37}$$

where

$$D = (1 + r_{01}g)^2 + (r_{01}h)^2, \qquad g = \mathrm{Re}(\hat{r}_{12}), \qquad h = \mathrm{Im}(\hat{r}_{12}).$$

The expression for the completely nonabsorbing case ($\beta = 0$) has been given elsewhere [11]. When the layer is so thin that d_s^2 can be ignored compared to unity, Eq. (36) becomes

$$R_f = \frac{R_{02} - 4\{\beta d[R_{12} + \mathrm{Re}(\hat{r}_{01}\hat{r}_{12}^*)] + \delta\,\mathrm{Im}(\hat{r}_{01}\hat{r}_{12}^*)\}/D}{1 - 4\{\beta d[R_{01}R_{12} + \mathrm{Re}(\hat{r}_{01}\hat{r}_{12})] - \delta\,\mathrm{Im}(\hat{r}_{01}\hat{r}_{12})\}/D}. \tag{38}$$

This expression is equivalent to that given by McIntyre and Aspnes [12].

VI SUMMARY

This brief chapter is a summary of the relations between the optical constants and the macroscopic equations (Maxwell's equations for propagation through the material), as well as the constitutive (material) equations and the intrinsic microscopic parameters of the physics of the condensed state. A series of formulas has been developed on the basis of those relationships that are useful to the experimenter in interpreting his optical measurements. The application of either the characteristic or Fresnel matrices permits descriptions of systems of varying complexity. A small sample of the possible lamellar systems has been given here.

APPENDIX A BASIC FORMULAS FOR FRESNEL COEFFICIENTS

The Fresnel coefficients $\hat{r}_{ij}$ and $\hat{t}_{ij}$ are functions of the real and imaginary parts of the complex dielectric functions $\hat{\varepsilon}_i$, and $\hat{\varepsilon}_j$, the incident dielectric function n_0^2 and the angle of incidence ϕ. Following is a compact set of formulas defining the coefficients in terms of these parameters.

The incident medium is considered to be completely transparent and to have a dielectric function n_0^2. Snell's law defines the quantity $S = n_0 \sin\phi$, which is a real quantity throughout the system; i.e., $\hat{n}_j \sin\phi_j = S$ is real in the jth medium. The phase term $\gamma_0 = n_0 \cos\phi$ is also real but $\hat{\gamma}_j = \hat{n}_j \cos\phi_j$ is, in general, a complex quantity.

In the jth layer one has

$$\hat{\varepsilon}_j\mu_j = \hat{n}_j^2 = \varepsilon_j' - i\varepsilon_j'', \qquad \hat{n}_j = \hat{n}_j - ik_j, \qquad \hat{\gamma}_j = \alpha_j - i\beta_j,$$

where

$$\hat{\gamma}_j\hat{\gamma}_j^* = P_j^2 = \alpha_j^2 + \beta_j^2 = \sqrt{(\varepsilon_j' - S^2)^2 + \varepsilon_j''^2},$$
$$2\alpha_j^2 = P_j^2 + \varepsilon_j' - S^2, \qquad 2\beta_j^2 = P_j^2 - \varepsilon_j' + S^2.$$

The function $\hat{\zeta}_j$ is defined for either polarization as

$$\hat{\zeta}_j = \begin{cases} \mu Z_0/\hat{\gamma}_j & \text{(TE, s)}, \\ -\hat{\varepsilon}_j/(\hat{\gamma}_j Z_0) & \text{(TM, p)}. \end{cases} \tag{8'}$$

The Fresnel coefficients can be expressed for either polarization in terms of the functions $\hat{\zeta}_j$ and $\hat{\zeta}_k$. The positive direction is taken as going from the jth medium to the kth medium:

$$\hat{r}_{jk} = (\hat{\zeta}_k - \hat{\zeta}_j)/(\hat{\zeta}_j + \hat{\zeta}_k) = q_{jk} + ih_{jk},$$
$$\hat{t}_{jk} = 1 + \hat{r}_{jk} = 2\hat{\zeta}_k/(\hat{\zeta}_j + \hat{\zeta}_k).$$

Note. An alternative convention for defining $\hat{n}_j$ and $\hat{n}_j^2$ is in common use. The solutions for Eq. (7) can be expressed as the inverse of the matrix in Eq. (10) as well as Eq. (14). This requires that $\hat{n}_j$ and $\hat{n}_j^2$ be expressed as $\hat{n}_j = n_j + ik_j$ and $\hat{n}_j^2 = \varepsilon_j' + i\varepsilon_j''$. The formulas, as developed in this chapter, are compatible with this convention because the product $h_{jk} \sin \alpha_j d_j$ is invariant.

APPENDIX B GENERAL FORMULAS FOR THE CASE OF A PARALLEL-SIDED SLAB

a. Asymmetrically Layered Slab (Absorbing Layers)

$$\bar{R} = R_f + \frac{T_f T_f' R_b E^2}{1 - R_f' R_b E^2}, \tag{31}$$

$$\bar{T} = \frac{T_f T_b E}{1 - R_f' R_b E^2}, \tag{29}$$

$$\bar{A} = A_f + T_f\left[1 - \frac{E(T_b + R_b T_f' E)}{1 - R_f' R_b E^2}\right]. \tag{32}$$

Here $E = \exp(-2\beta_s d_s)$ and f, b refer to the front and back sides of the slab, respectively. It is assumed that d_s is sufficiently large that the phase coherency in $\exp(i\alpha_s d_s)$ is averaged out and that $k_s/n_s \ll 1$, where s refers to the substrate.

b. Symmetrically Layered Slab (Absorbing Layers). For $R_f' = R_b$ and $T_f' = T_b$

$$\bar{R} = R_f + \frac{T_f T_f' R_f' E^2}{1 - R_f'^2 E^2},$$

$$\bar{T} = \frac{T_f T_f' E}{1 - R_f'^2 E^2},$$

$$\bar{A} = (1 - R_f) - \frac{E T_f T_f'}{1 - R_f' E}$$

$$= \frac{(1 - R_f)(1 - E)}{1 - R_f' E} + E\left[\frac{A_f(1 - R_f') + A_f'(1 - R_f) - A_f A_f'}{1 - R_f' E}\right].$$

c. Nonabsorbing Layers with Symmetry. For $R_f = R'_f$ and $T_f \cdot T'_f = (1 - R_f)^2$

$$\bar{R} = R_f\left[\frac{1 + E^2(1 - 2R_f)}{1 - R_f^2E^2}\right] \simeq \frac{2R_f}{1 + R_f}\left(1 - \frac{2\beta_s d_s}{1 + R_f}\right),$$

$$\bar{T} = \frac{(1 - R_f)^2E}{1 - R_f^2E^2} \simeq \frac{1 - R_f}{1 + R_f}\left(1 - 2\beta_s d_s \frac{1 + R_f^2}{1 - R_f^2}\right),$$

$$\bar{A} = \frac{1 - R_f}{1 - R_fE}(1 - E_\infty) \simeq 2\beta_s d_s(1 - 2\beta_s d_s R_f).$$

Approximations hold for $E \simeq 1 - 2\beta_s d_s$. (See Appendix D for single layer and bare substrate.)

APPENDIX C REFLECTANCE, R_{jk} AT j–k INTERFACE

$$R_{jk} = \hat{r}_{jk}\hat{r}^*_{jk} = \begin{cases} \dfrac{P_j^2 + P_k^2 - 2(\alpha_j\alpha_k + \beta_j\beta_k)}{P_j^2 + P_k^2 + 2(\alpha_j\alpha_k + \beta_j\beta_k)} = R_{jks} & \text{(TE, s)} \\ R_{jks}\dfrac{S^4 + P_j^2P_k^2 - 2S^2(\alpha_j\alpha_k - \beta_j\beta_k)}{S^4 + P_j^2P_k^2 + 2S^2(\alpha_j\alpha_k - \beta_j\beta_k)} = R_{jkp} & \text{(TM, p).} \end{cases}$$

Whenever $j = 0$ or $k = 0$, i.e., whenever the interface is between a nonabsorbing ambient and another medium, terms in S^2 and γ_0 can be consolidated to give

$$R_{0ks} = \frac{\gamma_0^2 + P_k^2 - 2\gamma_0\alpha_k}{\gamma_0^2 + P_k^2 + 2\gamma_0\alpha_k}$$

and the ratio

$$\mathscr{R}_{0k} = \frac{R_{0kp}}{R_{0ks}} = \frac{X_0^2 + P_k^2 - 2X_0\alpha_k}{X_0^2 + P_k^2 + 2X_0\alpha_k}, \qquad \text{where} \quad X_0 = \frac{S^2}{\gamma_0}.$$

APPENDIX D REFLECTANCE OF SINGLE LAYER ON EACH SIDE OF A SLAB AND SINGLE LAYER ON EITHER SIDE OF A SLAB

In Eqs. (29), (31), and (32), the transmittance $\bar{T}$, reflectance $\bar{R}$, and absorptance $\bar{A}$ are given for a transparent, paralled-sided slab, with the phase coherency averaged out in terms of the front and back-surface reflectances and transmittances. These terms will be evaluated for the case of a single layer on each side of the slab. If each layer has identical properties and thickness, the system is said to be symmetrical. For that case $T_b = T'_f$ and $R'_f = R_b$; otherwise, they must be evaluated separately in the same manner as that illustrated below for the front surface.

The following expressions for the front-surface reflectance R_f for a single layer on a substrate are given in terms of parameters that are explicit functions

of the real and imaginary parts of the dielectric functions $\hat{\varepsilon}_j$, the angle of incidence ϕ, and the front-layer-thickness-to-wavelength ratio d. [For example, 0 labels the incident ambient, 1 the film, 2 the substrate, and 0 the back ambient (film on front surface); for film on back surface, 0 labels the incident ambient, 2 the substrate, 1 the film, and 0 the back ambient.]

Expressions for single layer on transparent substrate with interfaces 01 and 12 (Eq. 36) for use in Eqs. (31), (29), and (32):

$$\begin{aligned}
R_f &= \{R_{02} - \{R_{12}(1 - W^2) + 2(1 - W)(g_{01}g_{12} + h_{01}h_{12}) \\
&\quad + 4W[(g_{01}g_{12} + h_{01}h_{12}) \sin^2 \delta \\
&\quad - (g_{01}h_{12} - g_{12}h_{01}) \sin \delta \cos \delta]\}/D\}/D_f, \\
D_f &= 1 - \{R_{01}R_{12}(1 - W^2) + 2(1 - W)(g_{01}g_{12} - h_{01}h_{12}) \\
&\quad + 4W[(g_{01}g_{12} - h_{01}h_{12}) \sin^2 \delta \\
&\quad - (g_{01}h_{12} + g_{12}h_{01}) \sin \delta \cos \delta]\}/D; \qquad (36') \\
R_{02} &= [R_{01} + R_{12} + 2(g_{01}g_{12} + h_{01}h_{12})]/D \\
&= g_{02}^2 + h_{02}^2 \qquad \text{(see Appendix C)}, \\
D &= 1 + R_{01}R_{12} + 2(g_{01}g_{12} - h_{01}h_{12}), \\
R_{01} &= g_{01}^2 + h_{01}^2 \qquad \text{(see Appendix C)}, \\
R_{12} &= g_{12}^2 + h_{12}^2 \qquad \text{(see Appendix C)}, \\
W &= \exp(-2\beta_1 d_1), \qquad \delta = \alpha_1 d_1.
\end{aligned}$$

TE, s polarization $\hat{\zeta}_j = \mu Z_0/\hat{\gamma}_j$:

$$\begin{aligned}
g_{jk} &= (P_j^2 - P_k^2)/D_{jk}, \qquad h_{jk} = 2(\alpha_j\beta_k - \alpha_k\beta_j)/D_{jk}, \\
D_{jk} &= P_j^2 + P_k^2 + 2(\alpha_j\alpha_k + \beta_j\beta_k).
\end{aligned}$$

TM, p polarization $\hat{\zeta}_j = -\hat{\varepsilon}_j\mu/\hat{\gamma}_j$:

$$\begin{aligned}
g_{jk} &= [(P_j^2P_k^2 - S^2)(P_k^2 - P_j^2) - 4S^2(\alpha_j^2\beta_k^2 - \alpha_k^2\beta_j^2)]/D_{jk}, \\
h_{jk} &= 2[(\varepsilon_j'\varepsilon_k' + \varepsilon_j''\varepsilon_k'')(\alpha_j\beta_k - \alpha_k\beta_j) \\
&\quad + (\varepsilon_j''\varepsilon_k' - \varepsilon_k''\varepsilon_j')(\alpha_j\alpha_k + \beta_j\beta_k)]/D_{jk}, \\
D_{jk} &= [P_j^2 + P_k^2 + 2(\alpha_j\alpha_k + \beta_j\beta_k)][(P_j^2P_k^2 + S^4 + 2S^2(\alpha_j\alpha_k - \beta_j\beta_k)].
\end{aligned}$$

R_f' is evaluated from the expression for R_f by interchanging the subscripts 01 and 12. Figure 1 shows the configurations for a film on the front surface of a slab substrate and a second configuration for a film on the back surface. The film is labeled 1, the substrate 2, and the front and back ambients 0 in each case.

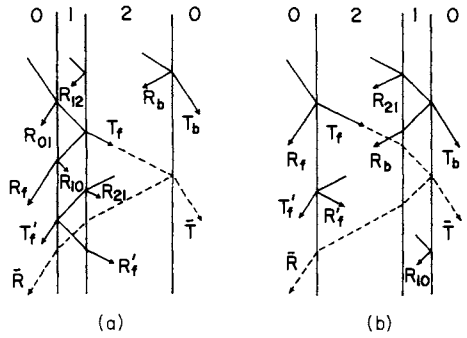

Fig. 1. Single layer on either side of parallel-sided slab. The number zero denotes ambient; one, single layer; and two, slab. (a) Layer on front side, (b) layer on back side.

For the first configuration Ia, R_f and R_f' are as given above;

$$R_b = R_{02}, \qquad T_f = (1 + R_{02} + 2g_{02})\frac{W}{D_f}\,\mathrm{Re}\,\frac{\zeta_0}{\zeta_2},$$

$$T_f' = (1 + R_{02} - 2g_{02})\frac{W}{D_f}\,\mathrm{Re}^{-1}\,\frac{\zeta_0}{\zeta_2},$$

$$\frac{T_b(1 - R_{02})}{1 + R_{02} - 2g_{02}}\,\mathrm{Re}\left(\frac{\zeta_0}{\zeta_2}\right) = T_{02}, \qquad g_{jk} = -g_{kj}, \qquad h_{jk} = -h_{kj}, \qquad R_{jk} = R_{kj}.$$

For the second configuration Ib,

$$R_f = R_{02} = R_f', \qquad R_b = R_f' \qquad \text{(configuration Ia)},$$

$$T_f = (1 - R_{02}), \quad T_f' = (1 - R_{02})\left(1 + \left(\frac{2h_{02}}{1 - R_{02}}\right)^2\right)$$

$$T_b = T_f' \qquad \text{(configuration Ia)}.$$

For a symmetrically layered slab, $R_b = R_f'$ and $T_b = T_f'$. Also,

$$T_f = (1 + R_{02} + 2g_{02})\frac{W}{D_f}\,\mathrm{Re}\left(\frac{\zeta_0}{\zeta_2}\right), \qquad T_f' = (1 + R_{02} + 2g_{02})\frac{W}{D_f}\,\mathrm{Re}^{-1}\left(\frac{\zeta_0}{\zeta_2}\right)$$

$$T_f T_f' = \frac{[(1 - R_{02})^2 + 4h_{02}^2]W^2}{D_f^2}, \qquad T_f T_f' = T_f T_b.$$

(N.B.: h_{02} vanishes for the nonopaque slab because $k_2/n_2 = k_s/n_s \ll 1$, so that $\beta_0 = \beta_2 = 0$.)

Here R_f is expressed in a manner that emphasizes the presence of the substrate reflectance R_{02}. Whenever the absorption of the film is small, this substrate reflectance will be apparent. However, when the layer is opaque, the expression for R_f becomes that for R_{01}, the front-surface reflectance of the layer itself.

For the symmetrical case of an identical film on each side, Eqs. (31), (29), and (32) can be expressed as

$$\bar{R} = R_f + \frac{[(1 - R_{02})^2 + 4h_{02}^2]E^2W^2R_f'}{(1 - R_f'^2E^2)D_f^2}, \tag{31'}$$

$$\bar{T} = \frac{[(1 - R_{02})^2 + 4h_{02}^2]E^2W^2}{(1 - R_f'^2E^2)D_f^2}, \tag{29'}$$

$$\bar{A} = 1 - R_f - \frac{E[(1 - R_{02})^2 + 4h_{02}^2]W2}{D_f^2(1 - R_f'E)}. \tag{32'}$$

These are general expressions for the three measurable parameters $\bar{A}$, $\bar{R}$ and $\bar{T}$, but two special cases are often encountered.

(1) For a transparent film for which β_1, h_{02}, h_{12} vanish, $W = 1$, $D_f = 1 - C$, $R_f = R_f' = (R_{02} - C)/(1 - C)$, and $C = 4g_{01}g_{12}\sin^2\delta$, these expressions become

$$\bar{R} = \frac{R_f[1 + E^2(1 - 2R_f)]}{1 - R_f^2E^2} = \frac{(R_{02} - C)[1 + E^2(1 - 2R_{02}) - C(1 - E)]}{1 - R_{02}^2E^2 - 2C[1 - 2R_{02}E^2 + C^2(1 - E^2)]}, \tag{31''}$$

$$\bar{T} = \frac{(1 - R_f)^2E}{1 - R_f^2E^2} = \frac{(1 - R_{02})^2E}{1 - R_{02}^2E^2 - 2C[1 - 2R_{02}E^2 + C^2(1 - E^2)]}, \tag{29''}$$

$$\bar{A} = \frac{(1 - R_f)(1 - E)}{1 - R_fE} = \frac{(1 - R_{02})(1 - E)}{1 - R_{02}E - C(1 - E)}. \tag{32''}$$

It is evident why the reflectance $\bar{R}$ exhibits the strongest interference effects due to the presence of a film while the absorbtance $\bar{A}$ shows the least. These same expressions hold for the bare-substrate case since $C = 0$ and $R_f = R_{02}$.

(2) The other special case is that for nonabsorbing films on a weakly absorbing substrate, i.e., $E \simeq 1 - 2\beta_s d_s$:

$$\bar{R} \simeq \frac{2R_f}{1 + R_f}\left[\frac{1 - \dfrac{2\beta_s d_s(1 - 2R_f)}{1 - R_f}}{1 + \dfrac{4\beta_s d_s R_f^2}{1 - R_f^2}}\right] \simeq \frac{2R_f}{1 + R_f}\left[1 - \frac{2\beta_s d_s}{1 + R_f}\right], \tag{31'''}$$

$$\bar{T} \simeq \left[\frac{1 - R_f}{1 + R_f}\right]\frac{[1 - 2\beta_s d_s]}{\left[1 + \dfrac{4R_f^2\beta_s d_s}{1 - R_f^2}\right]} \simeq \frac{1 - R_f}{1 + R_f}\left[1 - \frac{2\beta_s d_s(1 + R_f^2)}{1 - R_f^2}\right], \tag{29'''}$$

$$\bar{A} \simeq 2\beta_s d_s\left[1 - \frac{2R_f\beta_s d_s}{1 - R_f}\right]. \tag{32'''}$$

Again, as above, these hold for the bare-substrate case in which $R_f = R_{02}$.

At normal incidence ($\phi = 0$),

$$R_{02} = \left(\frac{n_2 - n_0}{n_2 + n_0}\right)^2, \qquad g_{01}g_{12} = \frac{n_1 - n_0}{n_1 + n_0}\frac{n_2 - n_1}{n_1 + n_2},$$

$$\beta_s = k_2 \qquad \text{and} \qquad \delta = n_2 d_s.$$

APPENDIX E CRITICAL ANGLE OF INCIDENCE

Whenever a layer in a lamelliform is characterized with the real part of its dielectric function ε_j' less than that of the incident medium n_0^2, a special condition exists for the reflectivity from that jth layer at those angles at which $S^2 > \varepsilon_j'$. The transition angle is commonly referred to as the "critical angle of incidence."

In the convention used here $\gamma_j = \alpha_j - i\beta_j$ is complex with α_j and β_j both real and positive quantities, where

$$\alpha_j^2 + \beta_j^2 = P_j^2 = [(\varepsilon_j' - S^2)^2 + \varepsilon_j''^2]^{1/2},$$

$$2\alpha_j^2 = P_j^2 + \varepsilon_j' - S^2, \qquad 2\beta_j^2 = P_j^2 + S^2 - \varepsilon_j'.$$

If $n_0^2 > \varepsilon_j'$, there exists a critical angle of incidence ϕ_c at which

$$\alpha_j(\phi_c) = \beta_j(\phi_c) = \varepsilon_j''/2^{1/2},$$

where

$$\phi_c = \arcsin\,(\varepsilon_j'/n_0^2)^{1/2}.$$

(N.B.: Many texts define ϕ_c as $\arcsin(n_j/n_0)$, but this is the special case for a nonabsorbing medium with $\alpha_j(\phi_c) = \beta_j(\phi_c) = 0$.) Although the Fresnel relations for $\phi > \phi_c$ can differ markedly from those for $\phi < \phi_c$, the formalism developed in this chapter is directly applicable.

Two examples for the three-medium expression of Eq. (36) will illustrate the point.

Example 1. Frustrated Total Reflectance. Consider that the third medium is optically identical to the incident medium and that the intervening medium is completely nonabsorbing, i.e., $n_2 = n_0$, $\varepsilon_1'' < 0$, and $n_1 < n_0$. The term R_{02} in Eq. (36) is zero for all angles of incidence. Also note that $R_{01} = R_{12} = g_{01}^2 + h_{01}^2$, $g_{01} = -g_{12}$, and $h_{01} = -h_{12}$. Also $\delta_1 = \alpha_1 d_1$ and $W = \exp(-2\beta_1 d_1)$.

Rearranging Eq. (36) with $R_{02} = 0$ gives

$$R_f = \frac{R_{01}[4W \sin^2 \delta_1 + (1 - W)^2]}{(1 - R_{01}W)^2 + 4W[h_{01}^2 + (g_{01}^2 - h_{01}^2)\sin^2 \delta_1 - 2g_{01}h_{01} \sin \delta_1 \cos \delta_1]}. \tag{36''}$$

It is evident that below the critical angle the reflectance varies between zero

and $4R_{01}/(1 + R_{01})^2$ as a function of $\alpha_1 d_1$, while above the critical angle, $R_{01} = 1$, $\alpha_1 = 0$ and R_f has values between zero (zero thickness) and unity (i.e. thickness d_1 is sufficiently large that $\beta_1 d_1$ is such a large number that $W \to 0$).

What is termed *frustrated total reflection* occurs for intermediate thicknesses. For small values of $2(S^2 - n_1^2)^{1/2} d_1 = 2\beta_1 d_1$,

$$R_f \simeq \frac{(S^2 - n_1^2) d_1^2}{h_{01}^2 + (S^2 - n_1^2) d_1^2}$$

vanishes as d_1^2 and becomes zero, as expected. On the other hand, as the thickness-to-wavelength ratio d_1 is increased, W decreases exponentially; and as it becomes small in value, R_f can be approximated as

$$R_f \simeq 1 - [4Wh_{01}^2/(1 - W)^2].$$

Although the front-surface reflectance R_{01} is unity, it is modified by the factor W. This is the result of penetration of the fields into the rarer medium. The W term is a measure of the damping of these fields, and if the two surfaces are not separated by a suitable amount, the evanescent waves couple into the third medium—frustrating the totality of the reflectance. Equations (13), (14), and (22) contain the information necessary for studying the amplitudes and intensities of the fields present in the rarer medium.

The following list of equations gives the parameters needed for the frustrated total-reflectance case:

$$R_f = \frac{R_{01}[4W \sin^2 \delta + (1 - W)^2]}{(1 - R_{01})^2 + 4W[h_{01}^2 + (g_{01}^2 - h_{01}^2) \sin^2 \delta - 2g_{01} h_{01} \sin \delta \cos \delta]},$$

$$\gamma_1 = \alpha_1 - i\beta_1, \qquad P_1^2 = \alpha_1^2 + \beta_1^2, \qquad \gamma_1^2 = \alpha_1^2 - \beta_1^2 - 2i\alpha_1\beta_1 = n_1^2 - S^2,$$

$$\gamma_0 = n_0 \cos \phi, \qquad X_0 = S^2/\gamma_0, \qquad S^2 = n_0^2 \sin^2 \phi.$$

	$\phi < \phi_c$		$\phi > \phi_c$
α_1:	$(n_1^2 - S^2)^{1/2}$		0
β_1:	0		$(S^2 - n_1^2)^{1/2}$
γ_1:	α_1		$-i\beta_1$
P_1:	$\alpha_1^2 = \gamma_1^2$		$\beta_1^2 = -\gamma_1^2$
W:	1		$\exp(-2\beta_1 d_1)$
δ:	$\gamma_1 d_1$		0
g_{01}:	$\dfrac{\gamma_0 - \gamma_1}{\gamma_0 + \gamma_1}$	(TE, s)	$\dfrac{\gamma_0^2 + \gamma_1^2}{\gamma_0^2 - \gamma_1^2} = \dfrac{n_0^2 + n_1^2 - 2S^2}{n_0^2 - n_1^2}$
	$\dfrac{(\gamma_1 - X_0)(\gamma_1 - \gamma_0)}{(\gamma_1 + X_0)(\gamma_1 + \gamma_0)}$	(TM, p)	$\dfrac{\gamma_1^2(X_0 + \gamma_0)^2 + (\gamma_1^2 + X_0\gamma_0)^2}{(X_0^2 - \gamma_1^2)(\gamma_0^2 - \gamma_1^2)} = \dfrac{(\gamma_1^2/\gamma_0^2) n_0^4 + n_1^4}{(n_0^2 - n_1^2)[(n_0^2/\gamma_0) X_0 - n_1^2]}$

(*continued on next page*)

(*continued from preceding page*)

$$h_{01}: \begin{cases} 0 & \text{(TE, s)} \quad \dfrac{2i\gamma_1\gamma_0}{\gamma_0^2-\gamma_1^2} = \dfrac{2\{(S^2-n_1^2)(n_0^2-S^2)\}^{1/2}}{n_0^2-n_1^2} \\ 0 & \text{(TM, p)} \quad \dfrac{2i\gamma_1(\gamma_0+X_0)(\gamma_1^2+S^2)}{(X_0^2-\gamma_1^2)(\gamma_0^2-\gamma_1^2)} = \dfrac{2(S^2-n_1^2)^{1/2}(n_0^2/\gamma_0)n_1^2}{[(X_0/\gamma_0)n_0^2-n_1^2](n_0^2-n_1^2)} \end{cases}$$

$$R_{01}: \begin{cases} \left(\dfrac{\gamma_0-\gamma_1}{\gamma_0+\gamma_1}\right)^2 & \text{(TE, s)} \quad 1 \\ \left[\dfrac{(\gamma_1-X_0)(\gamma_1-\gamma_0)}{(\gamma_1+X_0)(\gamma_1+\gamma_0)}\right]^2 & \text{(TM, p)} \quad 1 \end{cases}$$

Example 2. Attenuated Total Reflectance. A more interesting experimental situation exists when either medium 1 or 2 absorbs a fraction of the radiation; i.e., $\varepsilon_j'' \neq 0$. In this case, the radiation is also attenuated by the factors $\exp(-\beta_j d_j)$, hence the name *attenuated total reflectance* (ATR). Two cases are considered: (1) the layer is the rarer medium but slightly absorbing and (2) the third medium is the rarer one, slightly absorbing and sufficiently thick that $\exp(-\beta_2 d_2)$ is zero. The weak absorption is determined by $\varepsilon_j''^2/(\varepsilon_j'' - S^2)^2 \ll 1$. Above the critical angle the following approximations can be made:

$$P_j^2 = [(S^2-\varepsilon_j')^2 + \varepsilon_j''^2]^{1/2} \simeq (S^2-\varepsilon_j')\left[1 + \frac{\varepsilon_j''^2}{2(S^2-\varepsilon_j')^2}\right] \simeq (S^2-\varepsilon_j'),$$

$$2\alpha_j^2 \simeq \frac{\varepsilon_j''^2}{2(S^2-\varepsilon_j')}, \qquad 2\beta_j^2 \simeq 2(S^2-\varepsilon_j')\left[1 + \frac{\varepsilon_j''^2}{2(S^2-\varepsilon_j')}\right] \simeq 2(S^2-\varepsilon_j'),$$

$$\alpha_j \simeq \frac{\varepsilon_j''}{2(S^2-\varepsilon_j')^{1/2}}, \qquad \beta_j \simeq (S^2-\varepsilon_j')^{1/2}.$$

Case 1. Medium 1 is rarer than the incident medium; $\varepsilon_1' < n_0^2$. An example is a low-index thick film deposited on a high-index internal-reflection prism. For angles above the critical angle where $(S^2-\varepsilon_1')^{1/2}d$ is sufficiently large that $W = \exp(-2\beta_1 d_1) \ll 1$ and $W \sin\delta$ also becomes vanishingly small, Eq. (36) reduces to $R_f = R_{01}$, and the reflectance measurement probes the properties of the layer.

For TE, s polarization

$$R_f = \frac{\gamma_0^2 + P_1^2 - 2\alpha_1\gamma_0}{\gamma_0^2 + P_1^2 + 2\alpha_1\gamma_0} \simeq 1 - \frac{4\alpha_1\gamma_0}{\gamma_0^2 + P_1^2},$$

$$R_f \simeq 1 - \frac{2\varepsilon_1''\gamma_0}{(S^2-\varepsilon_1')^{1/2}(n_0^2-\varepsilon_1')}.$$

Similarly for TM, p polarization

$$R_f \simeq 1 - \frac{4\alpha(P_1^2 + X_0\gamma_0)(X_0 + \gamma_0)}{(P^2 + X_0^2)(P^2 + \gamma_0^2) + 4\alpha^2 X_0\gamma_0}$$

$$\simeq 1 - \frac{2\varepsilon_1''(2S^2 - \varepsilon_1')\gamma_0 n_0^2}{(S^2 - \varepsilon_1')^{1/2}(n_0^2 - \varepsilon_1')(n_0^2 S^2 - \varepsilon_1'\gamma_0^2)}.$$

It should be noted that the ratio $\mathscr{R} = R_s/R_p$ can also be used as a probe in ATR:

$$\mathscr{R} = 1 - \frac{2\varepsilon_1'' S^2 \gamma_0}{(S^2 - \varepsilon_1')^{1/2}(S^2 n_0^2 - \varepsilon_1'\gamma_0^2)}.$$

Whenever W does not vanish, terms involving it must be included in Eq. (36).

Case 2. Medium 2 is considered to be rarer, i.e., $n_0^2 > \varepsilon_2'$, as well as weakly absorbing. An example is a coupling prism spaced by air from a sample surface. The intervening layer, medium 1, is nonabsorbing with a refractive index such that $\varepsilon_1' > S^2$ for all angles of interest so that $\beta_1 \simeq 0$ and $W = 1$, so that

$$R_f = \frac{R_{02} - C_{s,p}}{1 - C_{s,p}}, \qquad C_{s,p} = 4g_{01} \sin\delta\,(g_{12} \sin\delta - h_{12} \cos\delta).$$

Evaluating R_{02} in the same manner as that for R_{01} for case 1 gives

$$R_{02} \simeq 1 - \frac{2\varepsilon_2''\gamma_0}{(S^2 - \varepsilon_2')^{1/2}(n_0^2 - \varepsilon_2')}$$

$$R_f \simeq 1 - \frac{2\varepsilon_2''\gamma_0}{(S^2 - \varepsilon_2')^{1/2}(n_0^2 - \varepsilon_2')(1 - C_s)} \qquad \text{(TE, s)},$$

$$R_{02} \simeq 1 - \frac{2\varepsilon_2''\gamma_0 n_0^2(2S^2 - \varepsilon_2')}{(S^2 - \varepsilon_2')^{1/2}(n_0^2 - \varepsilon_2')(n_0^2 S^2 - \varepsilon_2'\gamma_0^2)}$$

$$R_f \simeq 1 - \frac{2\varepsilon_2''(\gamma_0 n_0^2)(2S^2 - \varepsilon_2')}{(S^2 - \varepsilon_2')^{1/2}(n_0^2 - \varepsilon_2')(n_0^2 S^2 - \varepsilon_2'\gamma_0^2)(1 - C_p)} \qquad \text{(TM, p)}.$$

Depending on the thickness of the intervening layer, the ATR for case 2 is modulated by the factor $(1 - C)^{-1}$. In both cases, the reflectance becomes total as the absorption vanishes. Although the ratio $\mathscr{R} = R_p/R_s$ can be useful as a probe, care must be taken in case 2 with terms $C_{s,p}$.

DEFINITIONS OF TERMS

$\mu\mu_0$ Magnetic permeability of a medium
μ_0 Magnetic permeability of free space
$\varepsilon\varepsilon_0$ Permittivity of a medium

ε_0 Permittivity of free space
c Speed of light in free space: $c = 1/\sqrt{\mu_0 \varepsilon_0}$
$\hat{n}$ Complex refractive index of medium: $\hat{n} = \sqrt{\mu\hat{\varepsilon}} = n - ik$
$\hat{n}^2$ Complex dielectric function: $\hat{n}^2 = (\varepsilon' - i\varepsilon'') = n^2 - k^2 - 2ink$
S Snell's law, S is constant: $S = \hat{n} \sin \phi = n_0 \sin \phi_0 = n_2 \sin \phi_2$
$\hat{\gamma}$ Complex phase term: $\hat{\gamma} = \hat{n} \cos \phi = \sqrt{\hat{n}^2 - S^2} = \alpha - i\beta$
Z_0 Impedance of free space: $Z_0 = \sqrt{\mu_0/\varepsilon_0}$
Z Complex impedance of medium: $\hat{Z} = \sqrt{\mu/\hat{\varepsilon}}\, Z_0$
λ Wavelength of light in free space: $\lambda = c/\nu$
$\hat{r}_{if}$ Fresnel coefficient for reflectivity: $\hat{r}_{if} = (\hat{\zeta}_f - \hat{\zeta}_i)/(\hat{\zeta}_f + \hat{\zeta}_i)$
$\hat{t}_{if}$ Fresnel coefficient for transmittivity across interface in forward direction: $\hat{t}_{if} = 1 + \hat{r}_{if} = 2\hat{\zeta}_f/(\hat{\zeta}_f + \hat{\zeta}_i)$
$\hat{t}'_{if}$ Fresnel coefficient for transmittivity across interface in backward direction: $\hat{t}'_{if} = 1 - \hat{r}_{if} = 2\hat{\zeta}_i/(\hat{\zeta}_f + \hat{\zeta}_i)$
κ Propagation vector in free space: $\kappa = 2\pi/\lambda$
z Dimensionless parameter for propagation vector × distance along z axis: $z = \kappa \times$ physical distance
d Dimensionless parameter for fixed distance: $d = (z_f - z_i)$

REFERENCES

1. J. C. Slater and N. I. T. Frank, "Electromagnetism," McGraw-Hill, New York, 1947, or Dover, New York, 1969.
2. M. Born and E. Wolf, "Principles of Optics," Pergamon, New York, 1975.
3. R. Jacobsson, "Progress in Optics," Vol. 5 (E. Wolf, ed.), North-Holland Publ., New York, 1966.
4. I. A. Macleod, "Thin Film Optical Filter," American Elsevier, New York, 1969.
5. O. S. Heavens, "Optical Properties of Thin Films," Butterworth, London, 1955, or Dover, New York, 1965.
6. T. Moss, "Optical Properties of Semi-Conductors," Butterworth, London, 1959.
7. R. F. Potter, *SPIE Proceedings* **276**, 204 (1981).
8. C. Gabriel and A. Nedoluha, *Opt. Acta* **18**, 415 (1971).
9. Edward D. Palik, N. Ginsburg, H. B. Rosenstock, and R. T. Holm, *Appl. Opt.* **17**, 3345 (1978).
10. D. L. Stierwalt and R. F. Potter, "Semiconductor and Semimetals," Vol. 3 (R. K. Willardson and A. C. Beer, eds.), p. 71, Academic Press, New York, 1967.
11. Roy F. Potter, "Optical Properties" (S. Nudelman and S. S. Mitra, eds.), Plenum, New York, 1969.
12. J. D. McIntyre and D. E. Aspnes, *Surf. Sci.* **24**, 417 (1971).

Chapter 3

Dispersion Theory, Sum Rules, and Their Application to the Analysis of Optical Data*

D. Y. Smith
Argonne National Laboratory
Argonne, Illinois
and
Max-Planck-Institut für Festkörperforschung
Stuttgart, Federal Republic of Germany

I. Introduction 36
II. Optical Sum Rules and Their Physical Interpretation 36
A. Superconvergence Sum Rules for $\varepsilon(\omega)$ 38
B. Superconvergence Sum Rules for $N(\omega)$ 41
C. Superconvergence Sum Rules for Functions of N and ε 42
D. Superconvergence Relations Employing Weighting Functions 44
E. Static-Limit Sum Rules 44
III. Finite-Energy Sum Rules 45
A. Defect Absorptions and Smakula's Equation 47
B. Finite Oscillator Strength Sums and $n_{\text{eff}}(\omega)$ 49
IV. Sum Rules for Reflection Spectroscopy 51
A. Normal-Incidence Spectroscopy 51
B. Reflectance between Media at Nonnormal Incidence, Ellipsometry, and Transmission 55
V. Analysis of Optical Data and Sum-Rule Applications 55
A. Construction of Composite Data Sets 56
B. Sum-Rule Tests 60
VI. Summary 64
References 64

* Work supported by the U.S. Department of Energy and the Max-Planck Gesellschaft.

HANDBOOK OF OPTICAL CONSTANTS OF SOLIDS

Copyright © 1985 by Academic Press, Inc.
All rights of reproduction in any form reserved.
ISBN 0-12-544420-6

I INTRODUCTION

The basic optical properties of solids [1, 2], despite their great diversity, are rigorously limited by nature. These limitations take the form of sum rules and dispersion relations that reflect the physical laws governing the dynamics of matter and its interaction with light. Many of these limitations were enumerated in the first half of this century, but in the early 1970s, the discovery of a large number of new sum rules [3–15] deepened our understanding of these constraints and their application. Thus, it is now known that in addition to the celebrated f sum rule for absorption processes, there are companion sum rules for dispersive processes. For example, the real part of the complex refractive index $N(\omega) = n(\omega) + ik(\omega)$ satisfies [3, 4]

$$\int_0^\infty [n(\omega) - 1]\, d\omega = 0. \tag{1}$$

That is, the refractive index averaged over all frequencies must be unity. Moreover, it may be shown that this restriction arises in part from the inertial property of matter. Related rules—with a similar physical interpretation—have been shown to apply to the complex dielectric function and its inverse.

Formally rules such as these are a consequence [4] of the asymptotic behavior of the optical functions and the Kramers–Kronig dispersion relations [16–18]. They are the optical analog of the superconvergence relations [19–21] of high-energy physics. However, physically they arise simply from causality and the dynamical laws of motion [7] and may be viewed as a restatement of these laws in frequency space.

Besides giving insight into the mathematical structure of the optical functions, the various sum rules provide a means of relating different physical properties without model fits to spectra and are valuable as self-consistency tests. This chapter is intended as a brief introduction to this topic† with emphasis on the underlying physics and applications. Throughout, the cgs system of units will be used since this is most common in practice. In addition, isotropic media and scalar dielectric functions are assumed. In the case of anisotropic media or symmetry-breaking external fields, the individual dielectric tensor elements must be treated separately. This is reviewed for magneto-optics [11–13] by Smith [23a] and for natural optical activity by Thomaz and Nussenzveig [23b].

II OPTICAL SUM RULES AND THEIR PHYSICAL INTERPRETATION

The best-known optical sum rule is the f sum rule [1, 24], which may be written in a variety of forms useful in optical analysis [1, 14]:

$$\int_0^\infty \omega\varepsilon_2(\omega)\, d\omega = 2\int_0^\infty \omega n(\omega)k(\omega)\, d\omega = \frac{\pi}{2}\omega_p^2, \tag{2}$$

† For some representative references for a broader treatment of linear response theory and sum rules, see Gross, Macdonald *et al.*, Pines *et al.*, Marten *et al.*, and Kubo *et al.* [22].

$$\int_0^\infty \omega k(\omega)\, d\omega = \frac{\pi}{4}\omega_p^2, \tag{3}$$

and

$$\int_0^\infty \omega\, \mathrm{Im}[\varepsilon^{-1}(\omega)]\, d\omega = -\frac{\pi}{2}\omega_p^2, \tag{4}$$

where $\varepsilon(\omega) = \varepsilon_1(\omega) + i\varepsilon_2(\omega)$ is the complex dielectric function. In the case† of nonrelativistic electrons in a solid under consideration here, ω_p denotes the plasma frequency $[4\pi\mathcal{N}e^2/m]^{1/2}$; with $\mathcal{N}$ the total electron density and e and m the electronic charge $[e < 0]$ and mass, respectively. As will become apparent, the factor of $\frac{1}{2}$ difference between the right-hand sides of Eqs. (2) and (3) arises because the complex refractive index is the square root of the dielectric function [cf. Eqs. (8) and (22)].

These rules are occasionally rewritten in terms of the optical oscillator strength density [18]

$$f(\omega)|_\varepsilon = (m/2\pi^2e^2)\,\omega\varepsilon_2(\omega), \tag{5}$$

or the absorption coefficient,

$$\alpha(\omega) = 2\omega k(\omega)/c, \tag{6}$$

where c is the speed of light *in vacuo*. Note that Eq. (5) is the traditional optical definition of oscillator strength density and arises from the classical notion of the density of Lorentz oscillators. In other applications—such as charged particle energy loss—ε^{-1} plays the fundamental role, and the oscillator strength density for energy-loss processes is taken as [30]

$$f(\omega)|_{\varepsilon^{-1}} = -(m/2\pi^2e^2)\omega\ \mathrm{Im}[\varepsilon^{-1}(\omega)]. \tag{7}$$

The f sum rule was first proved by Thomas and Reiche [31] and by Kuhn [32] for nonrealistic systems in 1925. It has played a crucial part in the development of quantum mechanics [33], atomic [24, 34] and nuclear [35]‡ spectroscopy, and it is fundamental to determining the concentrations of defects and dopants in condensed phases via Smakula's equation [36–38].§ In

† The f sum rules given here are exact for a system of nonrelativistic electrons and infinitely heavy nuclei interacting via a local, velocity-independent potential. Finite nuclear mass may be taken into account via an effective mass. The formalism required for arbitrary nonrelativistic particles of arbitrary mass and a generalization to all electric multipole orders has been given by Sachs and Austern [25]. However, for practical purposes this effective mass correction is generally negligible in treating the optical properties of solids. Relativistic corrections are important for the inner shells of heavy elements. In first order these corrections arise from the mass–velocity term in the approximate relativistic wave equation describing the electrons. These appear to have been first described by Levinger *et al.* [26] and later found independently by Dogliani and Bailey [27]. Relativistic oscillator strengths for individual transitions have been given by Jacobsohn [28] and by Payne and Levinger [29].

‡ Chapter 1 of Levinger [35] contains an insightful introduction to these rules.

§ For a modern treatment see Dexter [37].

addition to the f sum rule, several less familiar sum rules for moments of the absorption spectrum have been given by Vinti [39] and others [40, 41]. These have been widely applied to atomic spectra [34], nuclear photodisintegration [35] and quantum chemistry [40], but only limited applications have been made to the spectroscopy of solids [41–43]. Values of the various moments of the absorption spectrum involved in several sum rules have been shown to be interrelated by the uncertainty principle [35, 44].

The existence of numerous sum rules for the absorptive process suggests analogous rules hold for the dispersive process. However, no hint of them is given by the commonly employed [24] proofs of the absorption rules that involve combining the time-dependent Schrödinger equation and the fermion commutator. Here, an alternative approach [4], employing the high-frequency (or short-time) behavior of matter, will be used. This has the advantage of allowing the systematic construction of a large class of sum rules and of emphasizing the underlying physics.

A Superconvergence Sum Rules for $\varepsilon(\omega)$

1 Formal Development

At frequencies higher than any characteristic absorption of the system, the excitation frequency dominates the expression for the polarizability, and the complex dielectric function has the asymptotic form [1, 45]

$$\lim_{\omega \to \infty} \varepsilon(\omega) = 1 - (\omega_p^2/\omega^2) + \cdots . \tag{8}$$

This series expansion is universal: The term in ω^{-1} is missing; the term in ω^{-2} involves only the electron density through the plasma frequency. These first terms are independent of interactions within the system. Physically, the reason is that at frequencies well above the highest characteristic absorption, inertial effects, not restoring or dissipative forces, dominate the dynamics. The latter forces enter into succeeding terms. [For example, the next term in the expansion of $\varepsilon(\omega)$ for a Lorentz oscillator with damping constant γ is $i\omega_p^2\gamma/\omega^3$.]

Formally, the physics and mathematics may be combined to get the sum rules by comparing the limiting behavior of $\varepsilon(\omega)$, Eq. (8), with the Kramers–Kronig relations [1, 16–18]:

$$\varepsilon_1(\omega) - 1 = \frac{2}{\pi} P \int_0^\infty \frac{\omega' \varepsilon_2(\omega')}{\omega'^2 - \omega^2} \, d\omega', \tag{9}$$

$$\varepsilon_2(\omega) - 4\pi \frac{\sigma(0)}{\omega} = -\frac{2}{\pi} \omega P \int_0^\infty \frac{\varepsilon_1(\omega') - 1}{\omega'^2 - \omega^2} \, d\omega'. \tag{10}$$

Here P denotes the principal value integral, and $\sigma(0)$ is the dc value of the

conductivity. The conductivity term is, of course, not present for insulators. These relations hold for linear, causal systems, and their use guarantees the functions involved are analytic, square-integrable, causal response functions [46, 47].

To proceed, note that Eq. (8) actually makes two statements, one for the real part of $\varepsilon(\omega)$,

$$\lim_{\omega\to\infty} \varepsilon_1(\omega) = 1 - (\omega_p^2/\omega^2), \tag{11}$$

and a second for the imaginary part,

$$\lim_{\omega\to\infty} \varepsilon_2(\omega) \text{ falls off faster than } \omega^{-2}. \tag{12}$$

The first of these may be compared with the high-frequency limit of the first Kramers–Kronig relation

$$\lim_{\omega\to\infty} \varepsilon_1(\omega) - 1 = -\frac{2}{\pi}\frac{1}{\omega^2}\int_0^\infty \omega'\varepsilon_2(\omega')\,d\omega' + \cdots. \tag{13}$$

Equating powers of ω^{-2} in Eqs. (11) and (13) yields the f sum rule[†]

$$\int_0^\infty \omega\varepsilon_2(\omega)\,d\omega = \frac{\pi}{2}\omega_p^2. \tag{14}$$

Similarly, the high-frequency limit of the second Kramers–Kronig relation is

$$\lim_{\omega\to\infty} \varepsilon_2(\omega) = \frac{4\pi\sigma(0)}{\omega} + \frac{2}{\pi}\frac{1}{\omega}\int_0^\infty [\varepsilon_1(\omega') - 1]\,d\omega' + \cdots. \tag{15}$$

Since by Eq. (12) there is no term in ω^{-1} in ε_2, equating powers of ω^{-1} in Eqs. (12) and (15) yields [4].[‡,§]

$$\int_0^\infty [\varepsilon_1(\omega) - 1]\,d\omega + 2\pi^2\sigma(0) = 0. \tag{16}$$

[†] The first proof of the f sum rule employing this method appears to have been given by R. de Laer Kronig [17] in his original work on the Kramers–Kronig relations.

[‡] An alternative proof [8] of Eq. (16) can be made by simply integrating $\varepsilon(\omega)$ over the contour consisting of the real axis and the semicircle at infinity in the upper half-plane. In the case of metals $\varepsilon(\omega)$ has a pole at the origin $i4\pi\sigma(0)/\omega$; this contributes the term in $\sigma(0)$ to Eq. (16), and the remainder of the real axis gives the integral over $\varepsilon(\omega)$, while the semicircle at infinity gives a vanishing contribution. At first this proof seems simpler, but the vanishing of the contribution of the semicircle at infinity does not follow directly from the asymptotic behavior along the real axis [Eq. (8)]. Rather, an argument based on the Phragmén–Lindelöf theorem is required. For details on this point see Titchmarsh [48]; Sec. 5.61. See also Nussenzveig [19], Theorems 2.5.4 and 7.5.1.

[§] $\sigma(\omega)$ has units sec^{-1} in cgs electrostatic units. To convert σ in $\text{ohm}^{-1}\,\text{cm}^{-1}$ to σ in sec^{-1} multiply by 8.9876×10^{11} ohm cm sec^{-1}. Generally, sum-rule integrals are done over an energy scale resulting in values of $\hbar\sigma$. The corresponding multipliers for electron volt and cm^{-1} energy scales are 5.9158×10^{-4} ohm cm eV and 4.7713 ohm cm cm^{-1}, respectively.

This is the analog for $\varepsilon_1(\omega)$ of Eq. (1). Note that this sum rule provides independent information on the parameters describing free-carrier absorption. Traditionally, these are found by making Drude-model fits to $\varepsilon(\omega)$. However, the integral of $[\varepsilon_1(\omega) - 1]$ provides an additional constraint since $\sigma(0) = ne^2\tau/m_0$, where n is the carrier concentration, τ their lifetime, and m_0 their optical mass (see Stern [1] for details).

In taking the high-frequency limit of the dispersion relations, we have relied on the intuitive notion that at large ω the denominator of the integrals is dominated by ω^2 [or, more precisely, that $(\omega^2 - \omega'^2)^{-1}$ may be expanded in a power series in inverse powers of ω^2]. This will be true provided that the numerator decreases fast enough as $\omega' \to \infty$. The necessary restrictions on the numerator are embodied in the superconvergence theorem [49–50].† For the present, it is sufficient to note that these limits hold provided that $\varepsilon_2(\omega)$ falls off at least as fast as $\omega^{-2} \ln^{-\alpha} \omega$, for $\alpha > 1$, as $\omega \to \infty$. This is a mild restriction on $\varepsilon_2(\omega)$ since it decreases faster than this in actual systems. For example, the contribution to $\varepsilon_2(\omega)$ from K-shell electrons that dominate the high-frequency absorption falls off as $\omega^{-4.5}$ (neglecting retardation and relativistic effects) [51]. (For more information see Bethe *et al.* [24] and Rau *et al.* [51].)

In discussing the optical properties of metals and superconductors, it is common to rewrite the rules in terms of the complex frequency-dependent conductivity as

$$\sigma(\omega) = -(i\omega/4\pi)\varepsilon(\omega). \tag{17}$$

The f sum rule then takes the form

$$\int_0^\infty \mathrm{Re}\, \sigma(\omega)\, d\omega = \frac{\pi}{2}\frac{\mathcal{N}e^2}{m}. \tag{18}$$

This rule and its generalizations [9, 52] as well as related rules for the surface impedance [53, 54] have been used extensively to relate the difference in conductivity between the superconducting and the normal states in the region of the superconducting gap to the δ-function conductivity at zero frequency in superconductors [53, 55–57].

2 Physical Picture

The physical basis of the f sum rule [Eq. (14)] and the dc conductivity rule [Eq. (16)] lies in the dynamical laws of motion. This is most easily seen using the linear-response-theory [7] result that the polarization $P_\delta(\tau)$ induced by a δ-function pulse electric field as a function of the time τ following the

† The term *superconvergent* was introduced into particle physics to describe the convergence properties of dispersion relation integrals; the corresponding sum rules are often referred to as superconvergence relations. (For an introduction to this theorem see the appendix of Altarelli *et al.* [4]. Details are given in de Alfaro *et al.* [49] and Frey *et al.* [50].)

pulse is just the Fourier transform of the electric susceptibility $[\varepsilon(\omega) - 1]/4\pi$. That is,

$$P_\delta(\tau) = \frac{1}{2\pi} \int_{-\infty}^{\infty} \left(\frac{\varepsilon(\omega) - 1}{4\pi} \right) e^{-i\omega\tau} \, d\omega. \tag{19a}$$

Taking account of the pole in $\varepsilon(\omega)$ at the origin for conductors and by using the fact that $\varepsilon_1(\omega)$ is an even function of ω while $\varepsilon_2(\omega)$ is odd leads to

$$P_\delta(\tau) = \frac{1}{4\pi^2} \left\{ \int_0^\infty \mathrm{Re}[\varepsilon(\omega) - 1] \cos(\omega\tau) \, d\omega, \right.$$
$$\left. + \int_0^\infty \mathrm{Im}\, \varepsilon(\omega) \sin(\omega\tau) \, d\omega + 2\pi^2\sigma(0) \right\}. \tag{19b}$$

The sum rules then follow [7] by using elementary arguments to determine $P_\delta(\tau)$ at small τ.

For example, inertia requires that the response cannot be instantaneous; $P_\delta(\tau)$ for $\tau \geq 0$ must join onto $P_\delta(\tau)$ for $\tau < 0$ without a discontinuity. By causality the latter values are all zero (no response before excitation) so that $P_\delta(\tau = 0) = 0$. Setting $\tau = 0$ in Eq. (19) then leads to the dc conductivity rule [Eq. (16)]. This rule and, by analogy, the corresponding relation for $n(\omega)$ [Eq. (1)] are therefore direct consequences of causality and the law of inertia; they are thus often referred to as inertial sum rules.

The f sum rule may be similarly derived by calculating the initial rate of change of polarization $P_\delta(\tau)$ in the impulse approximation and equating this to the time derivative of Eq. (19) at $\tau = 0$. In this case the determining factor is the dynamical law of motion—Newton's law in a classical picture. The details are given by Altarelli and Smith [7]. In the commonly quoted quantum-mechanical derivation employing commutation relations [24], the dynamics enters through the time-dependent Schrödinger equation.

Superconvergence Sum Rules for $N(\omega)$ B

A parallel development [7] may be given for the refractive index. The only difference lies in that for metals there is no pole in the index at the origin arising from the conductivity term. Rather, there is a square-root singularity

$$[i4\pi\sigma(0)/\omega]^{1/2} = (1 + i)\sqrt{2\pi\sigma(0)}\, \omega^{-1/2},$$

at the origin, and the Kramers–Kronig dispersion relations take the form†

$$n(\omega) - 1 = \frac{2}{\pi} P \int_0^\infty \frac{\omega' k(\omega')}{\omega'^2 - \omega^2} \, d\omega', \tag{20}$$

† For a derivation of these relations for insulator see Section 1.9 in Nussenzveig [19] and for conductors see Smith [58].

$$k(\omega) = -\frac{2\omega}{\pi} P \int_0^\infty \frac{n(\omega') - 1}{\omega'^2 - \omega^2} d\omega'. \tag{21}$$

Comparing the high-frequency limits of these with the limit for $N(\omega)$ obtained from the square root of Eq. (8),

$$\lim_{\omega \to \infty} N(\omega) = 1 - \tfrac{1}{2}(\omega_p^2/\omega^2) + \cdots, \tag{22}$$

yields the f sum rule for $k(\omega)$ and the companion inertial sum rule for $n(\omega)$

$$\int_0^\infty \omega k(\omega)\, d\omega = \frac{\pi}{4}\omega_p^2, \tag{23}$$

and

$$\int_0^\infty [n(\omega) - 1]\, d\omega = 0. \tag{24}$$

A physical interpretation [7] of these rules in terms of a response function is similar to that for $\varepsilon(\omega)$.

In addition to sum rules involving integral equations, a variety of integral inequalities hold for the dielectric function, the refractive index, and the reflectance. These have received some formal treatment recently [6, 59] but have not yet been applied to experimental problems.

C Superconvergence Sum Rules for Functions of N and ε

Since an analytic function of an analytic function is also analytic, it is possible to construct analytic functions of $N(\omega)$ and $\varepsilon(\omega)$ and develop sum rules and dispersion relations for them. For example, starting with $N(\omega)$, $N^2(\omega)$ would yield the sum rules for $\varepsilon(\omega)$. The number of such rules is limited only by one's imagination and a large number of generalized rules involving powers of ω and the real and imaginary parts of $[N(\omega) - 1]^m$, and so on, have been given in the literature [6–8]. In general the higher the power m, the faster the convergence of the sum rule, so that a given rule is more sensitive to a particular spectral range than to others. A few preliminary applications [7] of these rules have been made to test optical data. Since they are based on the same asymptotic behavior as the rules for $N(\omega)$ and $\varepsilon(\omega)$, they must contain the same physics, but with emphasis on different spectral regions.

A number of examples [7] of these rules for an insulating system are

$$\int_0^\infty \mathrm{Re}\{[N(\omega') - 1]^m\}\, d\omega' = 0, \tag{25}$$

and

$$\int_0^\infty \omega' \,\mathrm{Im}\{[N(\omega') - 1]^m\}\, d\omega' = \begin{cases} \frac{1}{4}\pi\omega_p^2 & (m = 1), \\ 0 & (m > 1). \end{cases} \tag{26}$$

For $m = 1$ these yield the familiar inertial and f sum rules, respectively. For higher powers Eq. (25) yields

$$m = 2: \quad \int_0^\infty \{[n(\omega') - 1]^2 - k^2(\omega')\}\, d\omega' = 0, \tag{27}$$

$$m = 3: \quad \int_0^\infty [n(\omega') - 1]\{[n(\omega') - 1]^2 - 3k^2(\omega')\}\, d\omega' = 0. \tag{28}$$

Similarly, Eq. (26) yields the rules

$$m = 2: \quad \int_0^\infty \omega' k(\omega')[n(\omega') - 1]\, d\omega' = 0, \tag{29}$$

$$m = 3: \quad \int_0^\infty \omega' k(\omega')\{3[n(\omega') - 1]^2 - k^2(\omega')\}\, d\omega' = 0. \tag{30}$$

Equation (29) has been previously noted by Stern [1]. Observe that this rule, together with the inertial sum rule for $n(\omega)$ [Eq. (24)] states that $[n(\omega) - 1]$ averages to zero *either alone or when weighted by* $\omega k(\omega)$. Analogous rules may be derived [7] for conductors by taking $\omega[N(\omega) - 1]$ as the starting point. The reader is referred to the literature [6–8] for details and related rules involving $(N - 1)^m$ multipled by powers of ω.

Equation (27) deserves further comment. It can be rewritten in the more suggestive form

$$\int_0^\infty [n(\omega') - 1]^2\, d\omega' = \int_0^\infty k^2(\omega')\, d\omega'. \tag{31}$$

As such it provides a potentially useful check on Kramers–Kronig inversions. It is a particular case of the general theorem [60, Theorems 90 and 91] that the norm of a function is preserved in a Hilbert transformation. Using the identity $\varepsilon_1(\omega) = n^2(\omega) - k^2(\omega)$ and the inertial sum rule for $n(\omega)$, it follows from Eq. (16) that the generalization of Eq. (31) for conductors is

$$\int_0^\infty \{[n(\omega) - 1]^2 - k^2(\omega)\}\, d\omega + 2\pi^2\sigma(0) = 0. \tag{32}$$

The extra term in $\sigma(0)$ arises from the pole at the origin. (Note: Separately $[n(\omega) - 1]^2$ and $k^2(\omega)$ have poles at the origin but their difference does not; hence, they have been written together under the same integral to avoid undefined expressions.)

Since $N(\omega)$ has at most a $\omega^{-1/2}$ singularity for conductors, $\omega N(\omega)$ is square integrable for both insulators and conductors. It then follows that its real and imaginary parts are related by Hilbert transforms. Thus, in analogy with Eq. (31), the norm of the transform is preserved [6],

$$\int_0^\infty \omega^2[n(\omega) - 1]^2\, d\omega = \int_0^\infty \omega^2 k^2(\omega)\, d\omega. \tag{33}$$

The fact that both Eqs. (33) and (31) or, in the case of a conductor Eq. (32), must hold is another remarkable example of the constraints imposed on the optical functions.

Before leaving this section, it might be noted that a generalization of the f sum rule for higher powers of ω_p has been found by Villani and Zimerman [5], who considered powers of $\omega^2[N(\omega) - 1]$ and $\omega^2[\varepsilon(\omega) - 1]$. In the case of the refractive index their result is

$$\int_{-\infty}^{\infty} \omega^{2m-1}[N(\omega) - 1]^m \, d\omega = (-1)^{m+1} 2^{-m} i\pi\omega_p^{2m}. \tag{34}$$

D Superconvergence Relations Employing Weighting Functions

Superconvergence techniques can be applied to quantities consisting of the optical functions multiplied by an appropriate analytic weighting function. Weighting with powers of ω mentioned in the preceding section is perhaps the simplest example of this. The technique has been applied by using algebraic, exponential, and Gaussian weighting functions by Villani and Zimerman [6], King [8], and Kimel [61]; a general discussion has been given by Fischer *et al.* [62]. A major result of Villani and Zimmerman based on the Lin–Okubo [63] weighting function is

$$\int_0^a \frac{[n(\omega) - 1] \, d\omega}{(a^2 - \omega^2)^{1/2}} = \int_a^{\infty} \frac{k(\omega) \, d\omega}{(\omega^2 - a^2)^{1/2}}. \tag{35}$$

This is particularly interesting since it relates the index in the interval $[0, a]$ to the extinction coefficient in the remainder of the spectrum. While this relation does not seem to have been used in practical data analysis to date, it should be a helpful guide to constructing composite sets of data. For example, in semiconductors and insulators $n(\omega)$ is often available with high accuracy for ω less than the band gap, ω_g, while above ω_g, $k(\omega)$ may be imprecisely or only partially known. By using Eq. (35) with $a \leq \omega_g$ and requiring that the f sum rule be also satisfied, it should be possible to sharpen the limits on the values of $k(\omega)$ for $\omega > \omega_g$.

E Static-Limit Sum Rules

The sum rules discussed thus far all derive from the high-frequency behavior. The static limit also yields several well-known rules [18] that follow directly from the dispersion relations. For insulators both $\varepsilon(\omega)$ and $N(\omega)$ are well behaved at the origin, and the Kramers–Kronig relations yield the dc dielectric constant and index as

$$\varepsilon_1(0) = 1 + (2/\pi) \int_0^{\infty} \omega^{-1} \varepsilon_2(\omega) \, d\omega, \tag{36}$$

and

$$n(0) = 1 + (2/\pi) \int_0^\infty \omega^{-1} k(\omega)\, d\omega. \tag{37}$$

The other dispersion relations give the trivial results $\varepsilon_2(0) = 0$ and $k(0) = 0$.

In the case of conductors $\varepsilon(\omega)$ has a pole at the origin arising from the term $i4\pi\sigma(0)/\omega$ in the dielectric function. Along the real axis this yields an ω^{-1} divergence in $\varepsilon_2(\omega)$, but $\varepsilon_1(\omega)$ remains finite. The latter finite value of $\varepsilon_1(0)$ can be recovered by considering dispersion relations for the function $\varepsilon(\omega) - [i4\pi\sigma(0)/\omega] - 1$. The result is

$$\varepsilon_1(0) = 1 + \frac{2}{\pi} \int_0^\infty \frac{\omega' \varepsilon_2(\omega') - 4\pi\sigma(0)}{\omega'^2}\, d\omega'. \tag{38}$$

Note that this limit holds only as ω approaches zero along the real axis. Because of the singularity, the limit of Re $\varepsilon(\omega)$ depends on the direction in the complex ω plane along which the limit is taken.

In the case of the refractive index of a conductor, both $n(\omega)$ and $k(\omega)$ have $\omega^{-1/2}$ singularities and diverge in the static limit.

FINITE-ENERGY SUM RULES III

The sum rules discussed to this point involve the infinite frequency interval $[0, \infty]$ and include all absorptive processes. However, a typical spectrum consists of different regions corresponding primarily to a single class of absorptions such as excitation of phonons, conduction, valence, or core electron. It is tempting to seek a means of treating these individual processes. In those favorable cases in which a particular absorptive process is not overlapped by other absorptions, finite-energy sum rules and dispersion relations may be developed [14, 64].

The key requirement [14] is that the absorption in question be sufficiently isolated that it can be viewed to a good approximation as taking place in a transparent medium with real background dielectric function $\varepsilon_b(\omega)$ arising from the dispersion of absorptive processes in all other spectral ranges.

The situation is illustrated in Fig. 1. Examples include phonon absorptions in polar insulators and free-carrier absorption in wide-gap semiconductors. In both instances, the absorptions in question are well separated from interband transitions that provide the polarizable background. On a wider spectral range, the valence electrons of a solid may be regarded as moving in a dielectric "medium" consisting of the polarizable ion cores in those materials for which valence and core absorptions do not overlap.

To proceed, consider an energy $\hat{\omega}$ large compared with that of the isolated absorption—or group of absorptions—but well below the energy of the

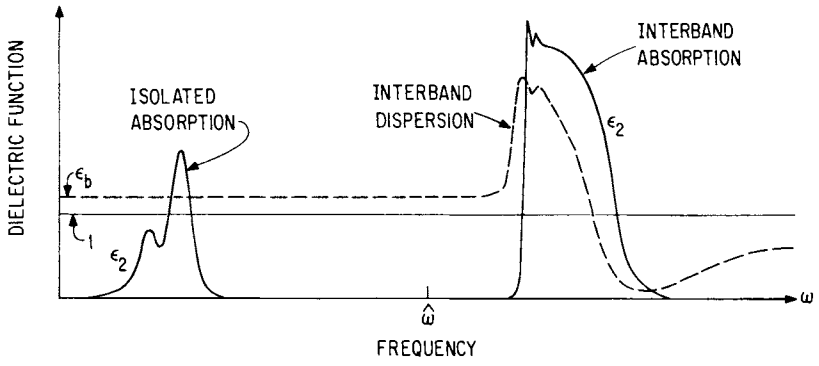

Fig. 1. Absorption spectra for nonoverlapping bands. (Solid curve, absorption; dashed curve, interband dispersion.)

transitions responsible for the dispersive dielectric background. Such an energy is indicated in Fig. 1. The dielectric function may then be expanded in the neighborhood of $\hat{\omega}$ as [14]

$$\lim_{\omega \to \hat{\omega}} \varepsilon(\omega) = \varepsilon_b(\omega) - \omega_{pi}^2/\omega^2 + \cdots, \tag{39}$$

where ω_{pi} is the plasma frequency associated with the isolated absorption. In the limit of large separation between the isolated absorption and the other absorptions of the system, $\varepsilon_b(\omega)$ may be taken as a constant so that

$$\lim_{\omega \to \hat{\omega}} \varepsilon(\omega) = \varepsilon_b - \omega_{pi}^2/\omega^2 + \cdots, \tag{40}$$

$$\lim_{\omega \to \hat{\omega}} N(\omega) = \varepsilon_b^{1/2} - \omega_{pi}^2/2\,\varepsilon_b^{1/2}\omega^2 + \cdots, \tag{41}$$

$$\lim_{\omega \to \hat{\omega}} \varepsilon^{-1}(\omega) = \varepsilon_b^{-1} + \omega_{pi}^2/\varepsilon_b^2\omega^2 + \cdots. \tag{42}$$

In taking the square root and the inverse of Eq. (40) to obtain Eqs. (41) and (42), it has been assumed that $\omega \gg \omega_{pi}$. Notice particularly that the dielectric constant ε_b appears in the coefficient of the ω^{-2} term in the limiting values of $N(\omega)$ and $\varepsilon^{-1}(\omega)$.

Finite-energy sum rules for the frequency interval containing the isolated absorption then follow either by applying superconvergence methods to the idealized problem of an isolated absorption in a medium with a constant ε_b at all frequencies or by employing [21] a Cauchy-theorem integration over a semicircular path of radius $\hat{\omega}$ in the upper half-plane.

The resulting finite-energy f sum rules are

$$\int_0^{\hat{\omega}} \omega' \varepsilon_2(\omega')\, d\omega' \approx \frac{\pi}{2}\,\omega_{pi}^2, \tag{43}$$

$$\int_0^{\hat{\omega}} \omega' k(\omega')\, d\omega' \approx \frac{\pi}{4}\,\frac{\omega_{pi}^2}{\varepsilon_b^{1/2}}, \tag{44}$$

$$\int_0^{\hat{\omega}} \omega' \operatorname{Im}[\varepsilon^{-1}(\omega')]\, d\omega' \approx -\frac{\pi}{2}\frac{\omega_{pi}^2}{\varepsilon_b^2}. \tag{45}$$

Similarly, the inertial sum rules are

$$\int_0^{\hat{\omega}} [\varepsilon_1(\omega') - \varepsilon_b]\, d\omega' + 2\pi^2\sigma(0) \approx 0, \tag{46}$$

$$\int_0^{\hat{\omega}} [n(\omega') - \varepsilon_b^{1/2}]\, d\omega' \approx 0, \tag{47}$$

$$\int_0^{\hat{\omega}} \{\operatorname{Re}[\varepsilon(\omega')^{-1}] - \varepsilon_b^{-1}\}\, d\omega' \approx 0. \tag{48}$$

These rules are exact in the limit of $\hat{\omega} \to \infty$. For finite $\hat{\omega}$ the f sums are accurate to within terms of the order of $\omega_{pi}^2(\gamma/\hat{\omega})$, and the inertial rules hold to terms of order $\omega_{pi}^2/\hat{\omega}$, where γ is the effective damping constant for the low-energy absorption.

The inertial sum rules are what one would expect intuitively: The dispersion associated with the isolated absorption is superimposed—though not linearly in the case of $N(\omega)$ or $\varepsilon^{-1}(\omega)$—on the background ε_b, $\varepsilon_b^{1/2}$, or ε_b^{-1} and averages to zero (or $-2\pi^2$ times the dc conductivity) with respect to that background.

The finite-energy f sum rules are more noteworthy in that the background dielectric constant appears in the right-hand side of the rules for $k(\omega)$ and $\operatorname{Im}[\varepsilon^{-1}(\omega)]$. That is, the integral of $\omega\varepsilon_2(\omega)$ gives ω_{pi} for an isolated absorption directly. However, the areas under $\omega k(\omega)$ or $\omega \operatorname{Im}[\varepsilon^{-1}(\omega)]$ do not; in these f sums *it is necessary to include the effect of virtual processes from all other transitions* via ε_b. This is manifest in the factors $\varepsilon_b^{1/2}$ and ε_b^2 in Eqs. (44) and (45), respectively, which may be thought of as correcting for the dielectric shielding of the isolated transition by the remainder of the system. The greater the background dielectric function, the weaker the apparent strength of an absorption as measured by $k(\omega)$ or $\operatorname{Im}[\varepsilon^{-1}(\omega)]$ for a fixed ω_{pi} (i.e., for a fixed oscillator strength of the isolated absorption).

Defect Absorptions and Smakula's Equation A

A particularly striking example [64] of the dependence of the amplitude of an isolated absorption on the remainder of the system occurs for defects or impurities that introduce absorption bands in the region of transparency of insulators. This is illustrated in Fig. 2, which shows the modeled absorption spectra for a series of four different defects. Each exhibits a single absorption band; they all have the same strength as measured by ω_{pi}^2 and the same half-width but have different absorption frequencies ω_d. In the figure the bands are labeled by $\nu = \omega_d/\omega_{host}$, where ω_{host} is the frequency of the host's fundamental absorption edge. As the defect absorption frequency approaches

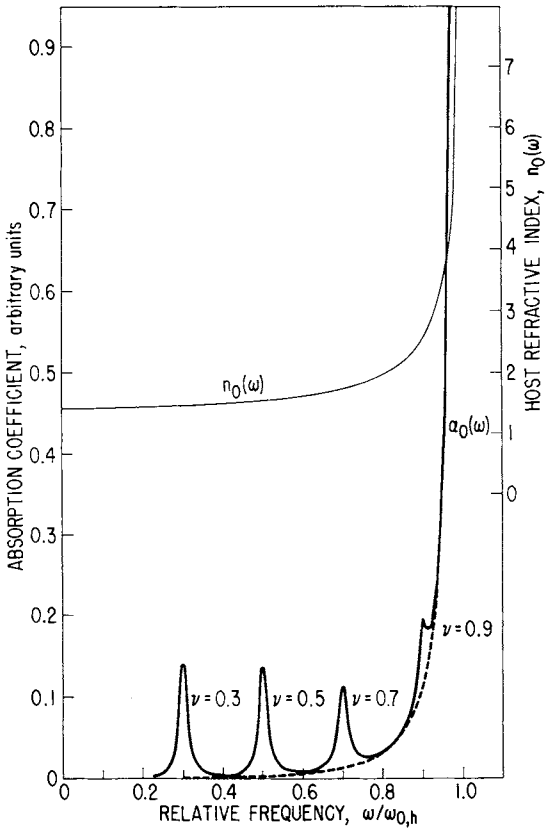

Fig. 2. Modeled spectra of a weak defect absorption on the low-energy side of the fundamental crystal absorption. Four possible defect absorptions are shown for energies $\omega_d = \nu\omega_{0,h}$, where $\omega_{0,h}$ is host absorption energy. Although all four absorptions have the same oscillator strengths, the absorption coefficient for bands at higher energies are reduced as a result of the larger values of the host refractive index, $n_0(\omega)$. (After Smith and Graham [64].)

that of the host's fundamental absorption edge, $\varepsilon_b(\omega)$ increases sharply with frequency and the apparent strength of the defect absorption as measured by the absorption coefficient $\alpha(\omega) = 2\omega k(\omega)/c$ decreases markedly.

In this case, it is necessary to treat the case in which the background dielectric function varies over the band. The result is a generalization of Smakula's equation [36–38] for the integrated oscillator strength $f = (m/4\pi e^2)\omega_{pi}^2$ of a defect or impurity in a transparent medium [64]

$$\rho f = \frac{m}{\pi^2 e^2} \int \omega n_0(\omega)\, \Delta k(\omega)\, d\omega. \tag{49}$$

Here ρ is the density of defects that is taken to be much less than the density of host atoms and effective-field effects have been omitted for simplicity. The

refractive index of the host is denoted by $n_0(\omega) = \varepsilon_b^{1/2}(\omega)$ (the change in index induced by the defect is negligible), and $\Delta k(\omega)$ is the absorption induced by the defect.

B Finite Oscillator Strength Sums and $n_{eff}(\omega)$

In analogy with the f sum rule it has become common practice to define the effective number density of electrons contributing to the optical properties up to an energy ω by the partial f sums [14, 45]

$$n_{eff}(\omega)|_{\varepsilon} = \frac{m}{2\pi^2 e^2} \int_0^{\omega} \omega' \varepsilon_2(\omega')\, d\omega', \tag{50}$$

$$n_{eff}(\omega)|_{k} = \frac{m}{\pi^2 e^2} \int_0^{\omega} \omega' k(\omega')\, d\omega, \tag{51}$$

$$n_{eff}(\omega)|_{\varepsilon^{-1}} = -\frac{m}{2\pi^2 e^2} \int_0^{\omega} \omega' \operatorname{Im}[\varepsilon^{-1}(\omega')]\, d\omega'. \tag{52}$$

Here the subscripts ε, k, and ε^{-1} are used to distinguish the partial f sums involving $\varepsilon_2(\omega)$, $k(\omega)$, and $\operatorname{Im}[\varepsilon^{-1}(\omega)]$, respectively. The f sum rule guarantees that in the limit $\omega \to \infty$ all three values of $n_{eff}(\omega)$ approach the number of electrons $\mathcal{N}$ in the system.

For intermediate values of ω the three values generally do not coincide. This is illustrated in Fig. 3a for the simple classical Drude-model of a metal in which core-electron x-ray transitions are neglected. Starting at zero for $\omega = 0$, the three values increase monotonically, but on different paths until in the vicinity of the plasma frequency they draw together and asymptotically approach $\mathcal{N}$ at infinity.

In discussing the spectra of materials with valence or conduction electron absorptions that are well separated from those of core transitions, it is common to calculate $n_{eff}(\hat{\omega})$ for the valence or conduction electrons. Then $\hat{\omega}$ is chosen to exhaust the valence- or conduction-electron oscillator strength but to lie below the lowest-energy core transitions. A comparison of this situation with the finite-energy f sum rules [Eqs. (43)–(45)] shows that the various $n_{eff}(\hat{\omega})$ values for conduction or valence electrons should not be equal when the polarizability of the core electrons is accounted for. Rather [14],

$$n_{eff}(\hat{\omega})|_{\varepsilon} = \varepsilon_b^{1/2} n_{eff}(\hat{\omega})|_{k} = \varepsilon_b^{2} n_{eff}(\hat{\omega})|_{\varepsilon^{-1}}, \tag{53}$$

where ε_b is the background dielectric constant of the fictitious medium consisting of the polarizable atomic cores alone.

This is illustrated in Fig. 3b. Again a Drude model has been employed, but a background dielectric constant $\varepsilon_b = 1.05$ has been included to take

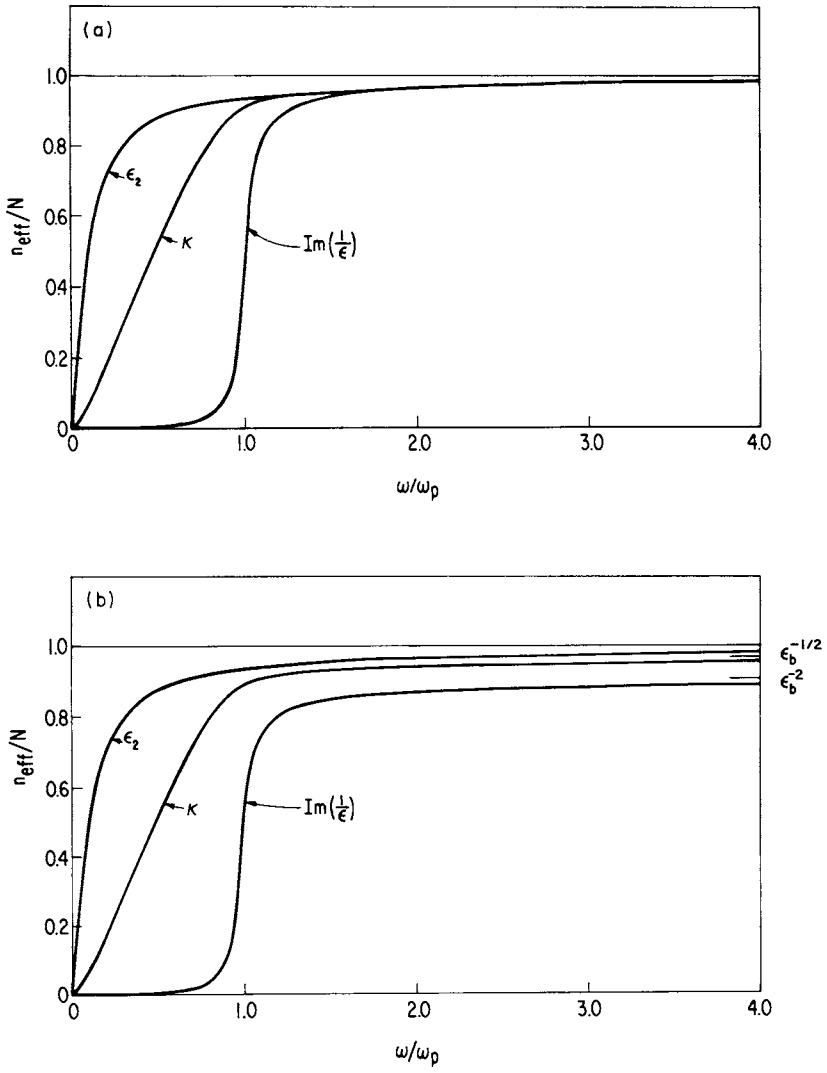

Fig. 3. The functions $n_{\mathrm{eff}}(\omega)$ for a Drude metal (a) with unpolarizable cores, i.e., $\varepsilon_b = 1$, and (b) embedded in a dielectric medium with $\varepsilon_b = 1.05$ corresponding to the core polarizability for a light element such as aluminum. (From Smith and Shiles [14].)

account of the core transitions which lie at higher energies. This value is typical for a light element such as aluminum. A plot of the actual $n_{\mathrm{eff}}(\omega)$ for both conduction and core transitions of aluminum is discussed in Section V.

It should be further noted that the asymptotic limit of $n_{\mathrm{eff}}(\hat{\omega})|_\varepsilon$ is generally *not* the actual number of valence or conduction electrons. It is their oscillator strength. To start with the distinction between valence and conduction electrons is only approximate. The separation is never complete because of Cou-

lomb and exchange interactions, and in the one-electron approximation this leads to an "exchange" of oscillator strength between core and valence electrons [2, 38, 65]: The major contribution to this effect can be understood by observing that the Pauli principle prohibits transitions of core electrons to the occupied valence or conduction states, so that the core-electron oscillator strength is less than their number. Similarly, electrons in higher-lying states cannot make transitions to the occupied core states, and they consequently exhibit an oscillator strength greater than their number (Note: Emissive processes have negative oscillator strength.)

Typically this Pauli principle effect increases the valence-electron oscillator strength by a few percentages for light elements and from 10 to 20% for heavy elements.† In addition a small correction arises from the exchange part of the potential that occurs when electrons are treated in the one-electron approximation. Briefly, the f sum rule for dipole matrix elements applies strictly only for systems in which the interaction operator and spatial coordinates commute [24]. This does not hold for the (nonlocal) exchange part of one-electron Hamiltonian that leads to a small correction in the one-electron model oscillator strength. This has been treated by Fock [66], who found the effect to be less than 20% of the Pauli principle correction. However, note that what is a prohibited absorption for one particular electron is a prohibited emission for another, so that the f sum taken over transitions to all levels still totals to the electronic number of the whole system in accord with the f sum rule.

SUM RULES FOR REFLECTION SPECTROSCOPY IV

Reflection spectroscopy has become a widely used method for determining optical constants of highly absorbing materials, since it was shown that reflectance spectra could be analyzed for the unknown phase by dispersion methods [67, 68].

Normal-Incidence Spectroscopy A

The simplest situation occurs for normal incidence from vacuum or, to a good approximation, air. In this case the complex reflectivity (for the magnetic field vector) is given by [1]

$$\tilde{r}(\omega) = r(\omega)e^{i\theta(\omega)} = [N(\omega) - 1]/[N(\omega) + 1]. \tag{54}$$

† See, for example, Table 1 of Smith and Dexter [38].

Since N is analytic, $\tilde{r}(\omega)$ is also analytic, and its real and imaginary parts satisfy sum rules and dispersion relations similar to those for $N(\omega)$ [69–71]. For example,

$$\int_0^\infty r^m(\omega) \cos[m\theta(\omega)]\, d\omega = 0 \qquad (m = 1, 2, 3, \ldots) \tag{55}$$

and

$$\int_0^\infty \omega r^m(\omega) \sin[m\theta(\omega)]\, d\omega = \begin{cases} \frac{\pi}{8}\omega_p^2 & (m = 1), \\ 0 & (m \geq 2). \end{cases} \tag{56}$$

These and similar superconvergence relations for powers of $\tilde{r}(\omega)$, and so on, all involve a mixture of reflectivity amplitude and phase. They are, therefore, currently of little practical value since the phase is generally not measured.

The phase and amplitude may be separated by considering the analytic function

$$\ln \tilde{r}(\omega) = \ln r(\omega) + i\theta(\omega). \tag{57}$$

There is, however, a major difference between this and the dielectric function, refractive index, and so on. The latter approach unity as $\omega \to \infty$, whereas $\ln \tilde{r}(\omega)$ diverges logarithmically since $\lim_{\omega\to\infty} r(\omega) = 0$. Thus, the dispersion relations and sum rules for $\ln \tilde{r}(\omega)$ are not of the same form as those for $\varepsilon(\omega)$ or $N(\omega)$.

The dispersion relations for $\ln \tilde{r}(\omega)$ may be obtained by a number of methods† that yield [68, 72, 73].‡

$$\theta(\omega) = -\frac{2\omega}{\pi} P \int_0^\infty \frac{\ln r(\omega')}{\omega'^2 - \omega^2}\, d\omega' \tag{58}$$

and its inverse [76, 77]

$$\ln r(\omega) - \ln r(\omega_0) = \frac{2}{\pi} P \int_0^\infty \omega'\theta(\omega')\left(\frac{1}{\omega'^2 - \omega^2} - \frac{1}{\omega'^2 - \omega_0^2}\right) d\omega', \tag{59}$$

where it is necessary to assume that the reflectance is known at some frequency ω_0. The equation for $\theta(\omega)$ [Eq. (58)] has the usual Kramers–Kronig form, while the second is a subtracted dispersion relation. Note that, while the second appears to simply involve the difference between two Kramers-Kronig integrals—one for $r(\omega)$ and one for $r(\omega_0)$—such an interpretation is invalid. The reason is that $\theta(\omega) \to \pi$ as $\omega \to \infty$, leading to integrals that are divergent when taken separately.

Equation (59) displays a further point. The phase does not determine the

† For a detailed discussion of the phase retrieval problem see Toll [46], Roman and Marathay [74], and Burge *el al.* [75]; a brief, but physical, discussion is given by Stern [1].

‡ The sign convention used here assumes a time dependence $\exp[-i\omega t]$. If $\exp[i\omega t]$ is used, the index must be written as $N = n - ik$ and Eq. (58) for $\theta(\omega)$ changes sign.

reflectance uniquely [77]. One must know the reflectivity amplitude at one point $\omega = \omega_0$, to fix the ratio $r(\omega)/r(\omega_0)$. In other words, two systems with reflectances differing by a constant multiplier have the same phase. [This is clear from Eq. (58) since multiplying the reflectance by a constant c contributes $\ln c \int_0^\infty (\omega'^2 - \omega^2)^{-1}\, d\omega'$ to the phase which is identically zero.†]

Sum rules are similarly limited [71]. Several methods have been proposed for circumventing this. They are (1) use of convergence factors [13, 70], (2) consideration of the normalized function [71] $r(\omega)/r(0)$ or of the ratio of the reflectances of two materials [13], and (3) finite-energy sum rules [71]. In general, the reflectance sum rules are too new to have been widely studied or utilized, but a number of them appear promising and will be mentioned briefly.

For insulators a sum rule for the derivative of the phase in the static limit that involves the ratio $\ln|r(\omega)/r(0)|$ has been developed [71].

$$\int_0^\infty \omega^{-1}\left[\frac{r'(\omega)}{r(\omega)}\right] d\omega = \int_0^\infty \omega^{-2} \ln\left|\frac{r(\omega)}{r(0)}\right| d\omega$$

$$= -\frac{\pi}{2}\frac{d\theta}{d\omega}\bigg|_{\omega=0} = -\frac{\pi}{n^2(0)-1}\frac{dk}{d\omega}\bigg|_{\omega=0}, \qquad (60)$$

where in the first integral $r'(\omega)$ denotes the derivative. The two integrals are related by integration by parts, and $d\theta/d\omega|_{\omega=0}$ has been written in terms of $dk/d\omega|_{\omega=0}$ by employing Eq. (54).

In most instances, $dk/d\omega|_{\omega=0}$ is small so that there is a large degree of cancellation within the integrals of Eq. (60). This has been demonstrated in an application [71] to the reststrahl absorption of NaCl. The negative contribution to $\omega^{-1}[r'(\omega)/\omega(r)]$ exceeds the positive contribution by roughly 10%, the remainder giving $dk/d\omega|_{\omega=0}$ to within experimental accuracy.

The derivative form of the normalized reflectance sum rule is of potential interest in connection with modulation spectroscopy [78–80], where the measured quantity is the relative change $\Delta R/R$ induced in the intensity reflection coefficient $R = |\tilde{r}|^2$ by an oscillatory external perturbation or wavelength modulation.

Finite-energy sum rules are particularly useful in reflection spectroscopy of systems with well-isolated absorptions such as polar insulators or wide-band-gap semiconductors in which the infrared vibrational modes or free-carrier absorption is separated from band-to-band electronic transitions by a wide region of transparency. In this region of transparency the reflectance arising from the band-to-band transition r_b is, to a good approximation, constant except as the fundamental edge is approached, and the infrared reflectance spectra appears superimposed on this constant "optical" reflectance as a background. This superposition is complicated and nonlinear, but one can

† Note that $P\int_0^\infty [dx/(x^2 - a^2)] = \frac{1}{2}aP\int_{-\infty}^{\infty}[dx/(x-a)] = \frac{1}{2}aP\int_{-\infty}^{\infty}(dy/y) \equiv 0$.

proceed in analogy with the development of finite-energy rules for $N(\omega)$, etc., in Section III.

Finite-energy dispersion relations and sum rules are then found for the quantity $\tilde{r}(\omega)/r_b$ over the finite energy internal $[0, \hat{\omega}]$, where, as in Section III , $\hat{\omega}$ is a frequency in the region of transparency below the point at which dispersion in r_b becomes significant but well above the highest of the isolated absorption bands in the infrared. The two sum rules that appear to have the greatest utility are [71]

(1) A reflectance conservation rule for isolated reflection bands

$$\int_0^{\hat{\omega}} \omega[r'(\omega)/r(\omega)]\, d\omega = \int_0^{\hat{\omega}} \ln|r(\omega)/r_b|\, d\omega \approx 0. \tag{61}$$

Here $r_b = (\varepsilon_b^{1/2} - 1)/(\varepsilon_b^{1/2} + 1)$ is the background reflectance with ε_b the "optical" dielectric constant. The integrals are related by integration by parts as in Eq. (60).

(2) A phase f sum rule

$$\int_0^{\hat{\omega}} \omega\theta(\omega)\, d\omega \approx \frac{\pi\omega_{pi}^2}{2\varepsilon_b^{1/2}(\varepsilon_b - 1)}, \tag{62}$$

where ω_{pi}^2 is the plasma frequency of the infrared absorption.

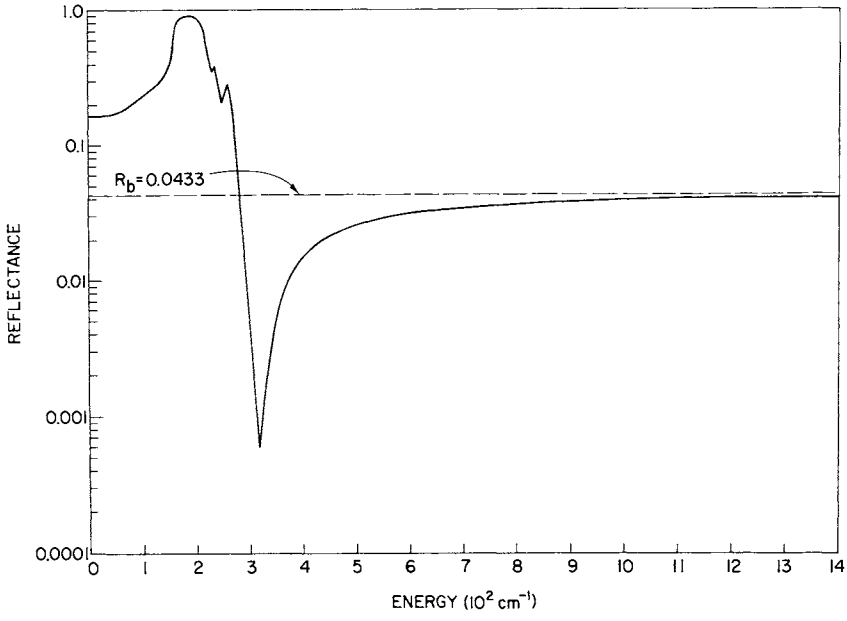

Fig. 4. The reflectance of crystalline NaCl in the infrared plotted on a logarithmic scale versus energy. Note the equality of areas between the curve above and below the background reflectance line at $R_b = 0.0433$, the reflectance in the visible. (From Smith and Manogue [71].)

The content of the reflectance conservation rule [Eq. (61)] is that, regardless of the processes involved, the logarithm of the reflectance of the low-energy process averages to the logarithm of the background reflectance. This is illustrated [71] for the NaCl reststrahl band in Fig. 4. Notice the equality of the areas above and below the dashed line, which denotes the reflectance in the visible or background reflectance $R_b = r_b^2$.

The second rule [Eq. (62)] allows the direct calculation of the oscillator strength of the low-energy absorption without the usual intermediate calculation of $\varepsilon_2(\omega)$ from the phase and reflectance. It must be stressed that this only applies for a finite frequency interval.

Reflectance between Media at Nonnormal Incidence, Ellipsometry, and Transmission B

The case of normal incidence already discussed leads to particularly simple dispersion relations and sum rules. In the case of reflection in a medium other than vacuum [81–84] or at nonnormal incidence [81, 84–86], the dispersion relations must be modified to account for more complex terms in the phase shift [46]. The interested reader is referred to the literature [8–86] for details. While this more complex situation has led to discussions of the validity of dispersion analysis [87, 88], sum rules have not been investigated for these more general cases except in the case of ellipsometry. In this procedure the ratio of the reflectivities for light polarized parallel and perpendicular to the plane of incidence is considered. Dispersion relations [89] and sum rules [90] for the real and imaginary parts of the ellipsometric function have been developed. Their use has been limited by the small wavelength range over which ellipsometry is now feasible. However, applications to highly localized absorptions in a finite energy interval is an attractive possibility.

Dispersion relations have also been developed for the analysis of transmission measurements [91–93].

ANALYSIS OF OPTICAL DATA AND SUM-RULE APPLICATIONS V

Wide-spectral-range composites of optical data have been constructed with increasing frequency as sufficient measurements become available. Some examples of this work are given in Ehrenreich *et al.* [94], Hagemann *et al.* [95], Inagaki *et al.* [96], Shiles *et al.* [97], and Cardona [98]. The various sum rules provide a means of testing such composites against both theoretical

constraints and independently measured quantities. We briefly consider several aspects of dispersion analysis and the use of sum rules to eliminate systematic errors.

A Construction of Composite Data Sets

In principle, exact knowledge of both the real and imaginary parts of a single-valued analytic function over a finite interval is sufficient to determine the function for all values of the argument by analytic continuation. However, in practice optical data are subject to experimental errors, so any such continuation outside the measured interval has virtually no meaning. It is thus necessary to have optical measurements at all significant frequencies to determine optical properties over the complete spectral range. While this strict requirement is generally not satisfied, good results over a limited range can be had in favorable cases. We consider this situation first.

1 *Dispersion Analysis over a Limited Range*

For argument, suppose a single optical function is known (or can be estimated) over all frequencies. Then the others are given by a Kramers–Kronig analysis. As a specific example, if the reflectance for normal incidence from vacuum is known, the phase can be found by using the Šimon–Robinson–Price method [67, 68] by the phase dispersion relation Eq. (58):

$$\theta(\omega) = -\frac{\omega}{\pi} P \int_0^\infty \frac{\ln R(\omega')}{\omega'^2 - \omega^2} d\omega', \tag{63}$$

where the expression has been rewritten in terms of the intensity reflection coefficient $R(\omega) = |\tilde{r}(\omega)|^2$, the quantity usually measured. Jahoda's proof [72] of this dispersion relation for the optical case was completed by Velický [73] using Toll's general theory [46]. The other optical functions then follow from Fresnel's equations [1]. In practice dispersion integrals are usually integrated numerically after eliminating [1] the principle value by subtracting an integral that is identically zero† to get

$$\theta(\omega) = -\frac{\omega}{\pi} \int_0^\infty \frac{\ln R(\omega') - \ln R(\omega)}{\omega'^2 - \omega^2} d\omega'. \tag{63'}$$

Graphical [68, 99] and, more recently, Fourier-integral [100] and Fourier-series [101–103]‡ methods have also been developed to evaluate Eq. (63).

Usually only reflection measurements over a limited frequency interval $\omega_1 \leq \omega' \leq \omega_2$ are available and without further information $\theta(\omega)$ cannot be

† See footnote to the discussion of Eq. (59) in Section IV.

‡ Similar methods have been applied to phase determination in electron microscopy [104, 105].

determined since the contributions to Eq. (63) from $0 \leq \omega' < \omega_1$ and $\omega_2 < \omega' < \infty$ are unknown. However, "physically reasonable" estimates and extrapolations of $R(\omega')$ can often be made and, for ω in the measured interval, considerable information about the structure of $\theta(\omega)$—though not its absolute value—can be found.

The important point is that the denominator of Eq. (63) tends to emphasize values of $R(\omega')$ near ω more than those far away. This is particularly evident if Eq. (63) is integrated by parts [72, 106, 107]

$$\theta(\omega) = -\frac{1}{2\pi}\int_0^\infty \frac{d\ln|R(\omega')|}{d\omega'} \ln\left|\frac{\omega' + \omega}{\omega' - \omega}\right| d\omega'. \tag{64}$$

The factor $\ln|(\omega' + \omega)/(\omega' - \omega)|$ is sharply peaked at ω and weights $R(\omega')$ near ω strongly. Thus, for ω within the measured range, the portion of the dispersion integral from ω_1 to ω_2 contributes the structure to $\theta(\omega)$. The values of $R(\omega')$ outside this measured interval typically supply a slowly varying "background" contribution $\Delta\theta(\omega)$[†]. Only under special conditions is this background negligible [111, 112], and tests indicate that errors may be significant particularly in regions of small k [113].

The presence of a slowly varying background component in $\theta(\omega)$ is crucial to estimating $\theta(\omega)$ since if $\theta(\omega)$ is known even at a single point, the transform Eq. (63) or (64) can be "anchored" there. The more such points, the better the estimate of $\Delta\theta(\omega)$. The additional information required can be obtained by ellipsometry in reflecting regions and by absorption or index measurements in transparent regions.

Traditionally, such additional data have been used either (1) to establish an extrapolation for $R(\omega)$ or (2) to determine the slowly varying component $\Delta\theta(\omega)$ of the phase directly. The two methods are equivalent but have been compared in only a few cases [114].

In the first approach methods used include trial-and-error searches [115] for an extrapolation of $R(\omega)$ that reproduces the additional data, and the determination of free parameters in a simple reflectance extrapolation function. Some common examples of high-energy parametric extrapolations are the power law [116, 117][‡] $R(\omega) = R(\omega_2)(\omega_2/\omega)^p$, the exponential [119] $R(\omega) = R(\omega_2)\exp[B(\omega_2 - \omega)]$, and a closely related power-law development [120] of $\ln R(\omega)$. These are useful when reflectance measurements extend to energies high enough so that the strength of conduction or valence electrons is largely exhausted. The parameters p and B are generally chosen to make $\theta(\omega)$ zero below the fundamental edge in nonmetals.

In infrared studies of molecular and lattice modes, constant reflectance extrapolations $R(\omega') = R_L$, $0 \leq \omega' < \omega_1$, and $R(\omega') = R_H$, $\omega_2 < \omega' < \infty$, for the reflectance above and below the measured interval are common [76, 121]. The two constants R_L and R_H are chosen to reproduce the auxiliary data.

[†] Explicit examples of this are given in Roessler [108], Velický [109], and MacRae *et al.* [110].

[‡] For correction to Cardona and Greenaway [117] see Scouler [118].

A closely related method employs a mean-value approximation to the dispersion integrals in the unmeasured regions [107, 108]. More detailed schemes [122] using parameters to define harmonic-oscillator extrapolations have been developed for cases in which sufficient data is at hand. Arkatova *et al.* [123] have critically reviewed several of these extrapolation methods.

The second approach to the finite measurement interval problem involves finding the slowly varying component of the phase. Methods include calculating $\Delta\theta(\omega)$ at specific points at which additional data are available and then fitting the result with a simple function [109, 124] or determining a power-series expansion of $\Delta\theta(\omega)$ [125–127]. The latter approach is based on Velický's observation [109] that since $\ln \tilde{r}(\omega)$ is analytic, the difference between the actual phase $\theta(\omega)$ and the phase calculated from Eq. (63) by using measured data plus a "smooth" extrapolation can be expressed in a power series. The coefficients of the series are determined from the auxiliary measurements of $\theta(\omega)$. [Since $\theta(\omega)$ is an odd function, only odd powers of ω are present.]

The remarkable success of these methods in treating reflectance measurements over a finite interval plus one or more auxiliary data points to anchor the phase can be best understood in terms of subtracted dispersion relations, a technique widely used in high-energy physics [19, 20]. If $\theta(\omega)$ is known at a frequency $\omega = a$, then by Eq. (63)

$$\theta(a) = -\frac{a}{\pi} P \int_0^\infty \frac{\ln R(\omega')}{\omega'^2 - a^2} d\omega'. \tag{65}$$

Subtracting this from Eq. (63) yields [128]

$$\theta(\omega) = \left(\frac{\omega}{a}\right)\theta(a) - \frac{\omega}{\pi}(\omega^2 - a^2)P \int_0^\infty \frac{\ln R(\omega')}{(\omega'^2 - \omega^2)(\omega'^2 - a^2)} d\omega'. \tag{66}$$

This new expression manifestly gives the correct value of $\theta(\omega)$ at $\omega = a$ and is odd in ω as required. By way of qualitative comparison with the Velický [109] series expansion of $\theta(\omega)$, Eq. (66) has the form of a modified dispersion relation plus a term linear in ω. Most important, the modified dispersion integral converges more rapidly than Eq. (63); at large ω' the denominator of the integrand behaves as ω'^4 compared with ω'^2 for Eq. (63). Thus, the knowledge of additional data in the form of the phase at $\omega = a$ has anchored $\theta(\omega)$ at the point $\theta(a)$ and has significantly reduced the dependence of the dispersion integral on the unknown details of $R(\omega)$ far from the measured interval.

The procedure may be carried as far as one has extra data points. For example, with two points the doubly subtracted dispersion relation becomes

$$\theta(\omega) = \frac{\omega}{a}\frac{\omega^2 - b^2}{a^2 - b^2}\theta(a) + \frac{\omega}{b}\frac{\omega^2 - a^2}{b^2 - a^2}\theta(b)$$
$$-\frac{\omega}{\pi}(\omega^2 - a^2)(\omega^2 - b^2)P \int_0^\infty \frac{\ln R(\omega')\, d\omega'}{(\omega'^2 - \omega^2)(\omega'^2 - a^2)(\omega'^2 - b^2)}. \tag{67}$$

Now $\theta(\omega)$ is anchored at two points a and b; moreover, the dispersion integral is even less dependent on the high-energy extrapolation.

The method of subtracted dispersion relations has had only limited applications [128, 129] in optics, but it should provide a systematic scheme utilizing all available data and offering significant savings in effort particularly over trial-and-error extrapolation.

2 Dispersion Analysis over a Wide Spectral Range

For an increasing number of substances some optical data are available in all significant spectral ranges. However, the same type of data are not available at all frequencies. Reflectance or ellipsometric measurements are practical in opaque spectral regions, while the absorption coefficient or refractive index can be measured in regions of near transparency. As a consequence of this mix of data, the Kramers–Kronig method cannot be applied directly since it requires knowledge of a single optical function over all frequencies. However, the combination of Kramers–Kronig and Fresnel equations can be solved as coupled equations.

In practice, one employs a method of successive approximations in which a trial value of one of the optical functions is estimated as best as can be from the available data. A Kramers–Kronig analysis is performed on this trial function. A new trial function is then constructed (generally by substitution of measured values in place of the calculated ones) and the procedure repeated until measurements and calculations agree [97, 132].

In principle, any optical function could be chosen as the starting point for an iteration. For materials with large regions of transparency—such as insulators—the extinction coefficient has been found to be convenient in practice [96]. However, transmission data can also be treated directly by using a dispersion relation for the phase shift in terms of the transmittance [91–93] that is analogous to Eq. (63). In the case of metals [97], the reflectance is a particularly favorable starting point since in opaque regions reflectance data are the most common, while the reflectance can often be approximated from Fresnel's equations in transparent regions. In the latter, both absorption coefficient and refractive index data can be measured and, even if only absorption data is at hand in the region of transparency, simple extrapolations or model fits give reasonable starting values for the index.

This procedure, or at least one cycle of the procedure, has been carried out in a large number of studies by using the reflectance (for example, Ehrenreich *et al.* [94]) or a combination of reflectance and transmittance data (for example, Hagemann *et al.* [95]). In principle, there should be no difference in the final result whatever starting function is chosen, provided that the calculation is iterated to self-consistency, although this is not often done.

A full self-consistent iterative analysis has been applied to polystyrene by Inagaki *et al.* [96] and to aluminum by Shiles *et al.* [97] and preliminary results have been reported for silicon [130] and gallium arsenide [131]. Aluminum is particularly favorable for this procedure since one form or another of optical data are now available from approximately 0.04 to 10,000 eV. In addition, in the region near the plasma frequency where optical experiments are difficult, there are accurate electron energy-loss measurements that give the shape of $\mathrm{Im}[\varepsilon^{-1}(\omega)]$ (though not its absolute magnitude). Specific results are discussed in the section of this handbook devoted to the optical properties of aluminum.

B Sum-Rule Tests

Sum rules provide significant guidance in the construction of composite sets of data, particularly in selecting the most probable values from the available optical measurements and in pinpointing systematic errors. In the case of metallic aluminum mentioned earlier [97], it has proven possible to generate a comprehensive set of optical functions that satisfies all principal sum rules and is compatible with electron-energy-loss and stopping-power data.

1 *The Inertial Sum Rule for $n(\omega)$*

The rule

$$\int_0^\infty [n(\omega) - 1]\, d\omega = 0 \tag{68}$$

must be satisfied for any $n(\omega)$ corresponding to a physically acceptable absorption spectrum. Provided that $k(\omega)$ has an acceptable high-frequency behavior (no ω^{-1} component), the rule tests the acceptability of $n(\omega)$ as part of an analytic function. Hence, it tests the accuracy of the Kramer–Kronig transform procedure and any high- or low-frequency extrapolation of $n(\omega)$ that may have been used.

In practice, it is convenient to define a verification parameter [7]

$$\xi = \int_0^\infty [n(\omega) - 1]\, d\omega \Big/ \int_0^\infty |n(\omega) - 1|\, d\omega \tag{69}$$

to assess the extent to which a spectrum satisfies the rule. Shiles *et al.* [97] found that values of the order of 2×10^{-3} were obtained for self-consistent solutions with ordinary numerical procedures.

Application of the rule to several composite data sets in the literature disclosed large values of ξ (some as large as 0.2) [7, 97]. These unacceptable values appear to arise primarily from nonanalytic modifications of the results

of a Kramers–Kronig transformation. Such modifications include fitting inappropriate extrapolations or otherwise forcing $n(\omega)$ to pass through data points inconsistent with the absorption spectrum.

The DC-Conductivity Sum Rule 2

A second consequence of causality and inertia is the expression for the dc conductivity

$$\int_0^\infty [\varepsilon_1(\omega) - 1]\, d\omega = -2\pi^2\sigma(0). \tag{70}$$

In the case of insulators, there are only interband transitions, and the right-hand side is zero. In metals both inter- and intraband transitions occur. To a good approximation the two processes contribute to $\varepsilon(\omega)$ by linear superposition, and the nonzero term on the right-hand side of Eq. (70) arises primarily from the intraband part. Thus, the dc-conductivity rule measures the conduction-electron contribution to $\varepsilon_1(\omega)$. Generally, this dispersive contribution extends over a wider and experimentally more accessible range than the corresponding absorptive contribution to $\varepsilon_2(\omega)$. Hence, Eq. (70) can be expected to give a more reliable optically derived value of $\sigma(0)$ for comparison with the measured dc conductivity than a Drude-model fit to $\varepsilon_2(\omega)$ in the far infrared.

In comparing values of $\sigma(0)$ derived from optical measurements with the bulk dc conductivity, it must be borne in mind that optical measurements are sensitive to the state of the sample at the surface. Moreover, many measurements are made on evaporated films that may have properties differing significantly from those of the bulk. In applying this rule to aluminum Shiles *et al.* [97] found that the optical and electrical values were equal within experimental error for unoxidized evaporated samples prepared in ultrahigh vacuum. This would generally not have been the case for contaminated films.

The f Sum Rule 3

The various f sum rules test the conformity of optical data with the known electron density. Further, to the extent that absorptions can be attributed to a particular group of levels, the finite-energy rules test the distribution of oscillator strength within broad spectral regions.

The concept of the effective number of electrons contributing to processes up to energy ω [14, 45]

$$n_{\text{eff}}(\omega)|_\Phi = \frac{m}{2\pi^2 e^2} \int_0^\omega \omega' \Phi(\omega')\, d\omega', \tag{71}$$

where $\Phi(\omega')$ may be $\varepsilon_2(\omega')$, $2k(\omega')$, or $-\text{Im}[\varepsilon^{-1}(\omega')]$, is particularly useful in applying the f sum rule. A plot of these three quantities for aluminum is

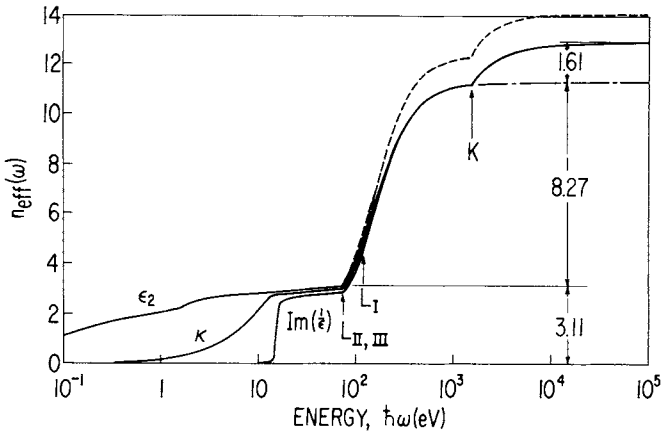

Fig. 5. The functions $n_{eff}(\omega)$ for metallic aluminum. The dashed curve shows the results for experimental data exhibiting a total oscillator strength over 14 rather than 13 e/at. The solid curve shows $n_{eff}(\omega)$ after correction of the magnitude of the L-shell data. (From Shiles *et al.* [97].)

shown in Fig. 5. Notice that the three quantities differ significantly as a function of energy. They describe different processes: The $\varepsilon_2(\omega)$ function concerns the dissipation of energy from an electromagnetic wave, the $k(\omega)$ function the attenuation of the wave's amplitude, and Im $\varepsilon^{-1}(\omega)$ the energy loss of a charged particle.

The requirement that the three forms of $n_{eff}(\omega)$ be equal at $\omega = \infty$, while trivial, is a test of the arithmetic consistency of ε, N, and ε^{-1}. The further requirement that $n_{eff}(\infty)$ is the observed electron density has more substance and serves as a test for net systematic error. In applying it, one must remember that reflection data measures the state of matter near the surface and that transmission measurements on thin films may not be representative of the bulk. In both instances, surface contamination and impurities introduced in preparation, or differences in density between thin-film and bulk samples may lead to spurious effects.

An example of an apparent systematic error can be seen in the aluminum data of Fig. 5. The dashed curve shows $n_{eff}(\omega)$ for what initially appeared to be the best available experimental data. However, the total f sum approaches a limit of approximately 14.1 electrons/atom (e/at.) rather than the actual density of 13 e/at. This indicates a significant systematic error in an important spectral region.

The partial f sum rules serve as a guide to the location of such errors. Aluminum is an especially favorable case for this since the conduction, L-shell, and K-shell absorptions are well separated and the oscillator strength of one absorption is virtually exhausted before the onset of the next. The partial f sums for the conduction electrons show a plateau region from the plasmon frequency ($\sim$15.0 eV) to the $L_{II,III}$ edge at $\sim$72.7 eV. As explained in Section

TABLE I

The "Effective" Number of Electrons per Atom for the Various Energy Levels in Aluminum[a]

Electronic shell	Atomic parentage	Occupation	Raw data	$n_{\text{eff}}(\omega)\|_{\varepsilon}$ modified data	HFS theory
Conduction	$(3s^2, 3p)$	3	3.1_1	3.1_1	3.12
L shell	$(2s^2, 2p^6)$	8	9.3_5	8.2_7	8.33
K shell	$(1s^2)$	2	1.6_1	1.6_1	1.55
Total		13	14.0_8	12.9_9	13.00

[a] After Shiles *et al.* [97].

III, the three forms of $n_{\text{eff}}(\omega)$ differ in this asymptotic region because of virtual processes in the polarizable cores. A fit of Eq. (53) to the plateau yields the core background dielectric constant $\varepsilon_b \approx 1.03_5$. The total conduction electron oscillator strength is given by the limiting value of $n_{\text{eff}}(\omega)|_{\varepsilon}$; extrapolating the plateau gives a total oscillator strength for the three conduction electrons of 3.1_1 e/at. Above the $L_{II,III}$ edge the effects of shielding decrease sharply, and the three forms of $n_{\text{eff}}(\omega)$ draw together.

The oscillator strengths for the various energy levels in metallic aluminum as derived from a self-consistent composite of the reported data are listed in Table I under raw data. Also given is the oscillator strength calculated for the corresponding *atomic* energy levels in a one-electron Hartree–Fock–Slater (HFS) model that takes into account the Pauli principle redistribution of oscillator strength. In going from the atom to the solid, the valence-electron energies and wave functions are vastly altered, leading to a completely different absorption spectrum of the outermost electrons. However, the core levels are not changed significantly, and the net oscillator strength of each group of levels in the metal and the atom should be qualitatively comparable. Making this comparison in Table I, one sees that the L-shell strength of the reported data is too strong by approximately 1 e/at. corresponding to a systematic overestimate of 12–13% averaged over the whole L absorption.

In the high-absorption region between the L edge and 500 eV, virtually all measurements have been made on thin evaporated films prepared in conventional vacuum and subsequently exposed to the atmosphere. It is known that such films are highly reactive and form surface layers. Moreover, their absorption shows a surface as well as a bulk component [133, 134].

It was found by trial and error that an *ad hoc* reduction of the reported thin-film absorption data by 14% from the L edge to 300 eV followed by a smooth interpolation to the rolled-foil data above 500 eV gave satisfactory agreement with the partial f sum rules. Independent experiments by Balzarotti *et al.* [134] provide additional evidence for this correction. Using films of

various thickness, these authors separated surface and bulk effects and found absorption coefficients some 15% below those generally reported in this region. Unfortunately, their measurements extend only 10 eV above the L edge, but as far as they go, they are in agreement with the values inferred by demanding the f sum rule be satisfied.

VI SUMMARY

The optical constants obey a large number of integral constraints in the form of sum rules. We have shown that some of the simpler of these rules arise directly from the requirements of causality, inertia, and the dynamical laws. These optical rules may therefore be viewed as the ω-space equivalent of the dynamical laws of motion in time space. The sum rules provide a useful means of testing optical measurements, particularly wide-range composite data, both against theoretical constraints and independently measured quantities.

ACKNOWLEDGMENTS

The author wishes to express his thanks to Professor Dr. H. Bilz for his hospitality and encouragement and to the Max-Planck-Institut für Festkörperforschung for support during the early stages of preparation of this review. Thanks are also due to Dr. M. Inokuti for stimulating discussions and Mrs. Janice Grant for her aid in preparing the manuscript.

REFERENCES

1. F. Stern, *in* "Solid State Physics" (F. Seitz and D. Turnbull eds.), Vol. 15, p. 299, Academic Press, New York, 1963.
2. F. Wooten, "Optical Properties of Solids," Academic Press, New York, 1972.
3. W. M. Saslow, *Phys. Lett.* **33A**, 157 (1970).
4. M. Altarelli, D. L. Dexter, H. M. Nussenzveig, and D. Y. Smith, *Phys. Rev. B* **6**, 4502 (1972).
5. A. Villani and A. H. Zimerman, *Phys. Lett.* **44A**, 295 (1973).
6. A. Villani and A. H. Zimerman, *Phys. Rev. B* **8**, 3914 (1973).
7. M. Altarelli and D. Y. Smith, *Phys. Rev. B* **9**, 1290 (1974); M. Altarelli and D. Y. Smith, *Phys. Rev. B* **12**, 3511 (1975).
8. F. W. King, *J. Math. Phys.* **17**, 1509 (1976).
9. K. Furuya, A. H. Zimerman, and A. Villani, *Phys. Rev. B* **13**, 1357 (1976).
10. D. Y. Smith, *J. Opt. Soc. Am.* **66**, 547 (1976).
11. D. Y. Smith, *Phys. Rev. B* **13**, 5303 (1976).
12. K. Furuya, A. H. Zimerman, and A. Villani, *J. Phys. C* **9**, 4329 (1976).
13. K. Furuya, A. Villani, and A. H. Zimerman, *J. Phys. C* **10**, 3189 (1977).
14. D. Y. Smith and E. Shiles, *Phys. Rev. B* **17**, 4689 (1978).
15. C. K. Mukhtarov, *Dok. Akad. Nauk SSSR* **249**, 851 (1979); C. K. Mukhtarov, *Sov. Phys. Dokl.* **24**, 991 (1979).
16. H. A. Kramers, *Nature* **117**, 775 (1926) [abstract]; H. A. Kramers, *Atti Congr. Intern. Fisici, Como-Pavia-Roma* (N. Zanichelli, Bologna, 1928) **2**, 545–557 [reprinted in H. A.

Kramers, "Collected Scientific Papers," North-Holland Publ., Amsterdam, 1956]; H. A. Kramers, *Phys. Z.* **30**, 522 (1929).
17. R. de L. Kronig, *J. Opt. Soc. Am.* **12**, 547 (1926).
18. L. D. Landau and E. M. Lifshitz, "Electrodynamics of Continuous Media," Pergamon, Oxford, 1960.
19. H. M. Nussenzveig, "Causality and Dispersion Relations," Academic Press, New York, 1972.
20. H. Burkhardt, "Dispersion Relation Dynamics," North Holland Publ., Amsterdam, 1969.
21. C. Ferro Fontán, N. M. Queen, and G. Violini, *Riv. Nuovo Cimento* **2**, 357 (1972).
22. B. Gross, *Nuovo Cimento Suppl.* **3**, 235 (1956); J. R. Macdonald and M. K. Brachman, *Rev. Mod. Phys.* **28**, 393 (1956); D. Pines and P. Nozières, "The Theory of Quantum Liquids," W. A. Benjamin, New York, 1966; P. C. Martin, *Phys. Rev.* **161**, 143 (1967); J. des Cloizeaux, *in* "Theory of Condensed Matter," p. 325 Int. At. Energy Ag., Vienna, 1968; R. Kubo and M. Ichimura, *J. Math. Phys.* **13**, 1454 (1972).
23a. D. Y. Smith, *in* "Theoretical Aspects and New Developments in Magnetooptics" (J. T. Devreese ed.), p. 133, Plenum, New York, 1980.
23b. M. T. Thomaz and H. M. Nussenzveig, *Ann. Phys. (N.Y.)* **139**, 14 (1982).
24. H. A. Bethe and E. E. Salpeter, "Quantum Mechanics of One- and Two-Electron Atoms," Sec. 61 and 62, pp. 357 and 358, Springer-Verlag, Berlin, 1957.
25. R. G. Sachs and N. Austern, *Phys. Rev.* **81**, 705 (1951).
26. J. S. Levinger, M. L. Rustgi, and K. Okamoto, *Phys. Rev.* **106**, 1191 (1957).
27. H. O. Dogliani and W. F. Bailey, *J. Quant. Spectrosc. Radiat. Transfer* **9**, 1643 (1969).
28. B. Jacobsohn, Ph.D. dissertation, University of Chicago, Chicago, 1947 (unpublished). [Available in part through DOE Technical Information Center, Oak Ridge, Tennessee, as ANL-HDY-423 (Del).]
29. W. B. Payne and J. S. Levinger, *Phys. Rev.* **101**, 1020 (1956).
30. U. Fano, *in* "Annual Review of Nuclear Science" (E. Segrè, G. Friedlander, and H. P. Noyes eds.) Vol. 13, p. 1, Annual Reviews, Palo Alto, California, 1963.
31. W. Thomas, *Naturwiss.* **28**, 627 (1925); and F. Reiche and W. Thomas, *Z. Phys.* **34**, 510 (1925).
32. W. Kuhn, *Z. Phys.* **33**, 408 (1925).
33. B. L. van der Waerden, "Sources of Quantum Mechanics," North-Holland Publ., Amsterdam, 1967.
34. U. Fano and J. W. Cooper, *Rev. Mod. Phys.* **40**, 441 (1968); U. Fano and J. W. Cooper, *Rev. Mod. Phys.* **41**, 724 (1969).
35. J. S. Levinger, "Nuclear Photo-Disintegration," Oxford Univ. Press, London, 1960.
36. A. Smakula, *Z. Phys.* **59**, 603 (1930).
37. D. L. Dexter, *in* "Solid State Physics" (F. Seitz and D. Turnbull eds.), Vol. 6, p. 353, Academic, New York, 1958.
38. D. Y. Smith and D. L. Dexter, *in* "Progress in Optics" (E. Wolf, ed.), Vol. 10, Sec. 3.1, North-Holland Publ., Amsterdam, 1972.
39. J. P. Vinti, *Phys. Rev.* **41**, 432 (1932).
40. J. O. Hirschfelder, W. B. Brown, and S. T. Epstein, *in* "Advances in Quantum Chemistry" (P.-O. Löwdin, ed.), Vol. 1, Sec. 10. Academic Press, New York, 1964.
41. J. J. Hopfield, *Phys. Rev. B* **2**, 973 (1970).
42. M. Brauwers, R. Evrard, and E. Kartheuser, *Phys. Rev. B* **12**, 5864 (1975).
43. C.-H. Wu, G. Mahler, and J. L. Birman, *Phys. Rev. B* **18**, 4221 (1978).
44. J. Gardavský, *Coll. Phen.* **1**, 193 (1974).
45. H. Ehrenreich, *in* "The Optical Properties of Solids" (J. Tauc, ed.), p. 106, Academic Press, New York, 1966.
46. J. S. Toll, Ph.D. thesis Princeton University, Princeton, New Jersey, 1952; J. S. Toll, *Phys. Rev.* **104**, 1760 (1956).
47. N. G. van Kampen, *J. Phys, Rad.* **22**, 179 (1961).

48. E. C. Titchmarsh, "The Theory of Functions," Oxford Univ. Press, London, 1968.
49. V. de Alfaro, S. Fubini, G. Rossetti, and G. Furlan, *Phys. Lett.* **21**, 576 (1966).
50. G. Frey and R. L. Warnock, *Phys. Rev.* **130**, 478 (1963).
51. A. R. P. Rau and U. Fano, *Phys. Rev.* **162**, 68 (1967).
52. R. A. Ferrell and R. E. Glover, *Phys. Rev.* **109**, 1398 (1958).
53. G. Brändli, *Phys. Rev. Lett.* **28**, 159 (1972); G. Brändli and A. J. Sievers, *Helv. Phys. Acta* **45**, 847 (1972); G. Brandli and A. J. Sievers, *Phys. Rev. B* **5**, 3550 (1972).
54. G. Brändli, *Phys. Rev. B* **9**, 342 (1974).
55. M. Tinkham and R. A. Ferrell, *Phys. Rev. Lett.* **2**, 331 (1959).
56. D. M. Ginsberg and M. Tinkham, *Phys. Rev.* **118**, 990 (1960).
57. L. H. Palmer and M. Tinkham, *Phys. Rev.* **165**, 588 (1968).
58. D. Y. Smith, *J. Opt. Soc. Am.* **66**, 454 (1976).
59. F. W. King, *J. Math. Phys.* **22**, 1321 (1981); F. W. King, *Phys. Rev. B* **25**, 1381 (1982).
60. E. C. Titchmarsh, "Introduction to the Theory of Fourier Integrals," Oxford Univ. Press, London, 1962.
61. I. Kimel, *Phys. Rev. B* **25**, 6561 (1982).
62. J. Fischer, J. Pišút, P. Prešnajder, and J. Šebesta, *Czech. J. Phys. B* **19**, 1486 (1969).
63. Y. C. Liu and S. Okubo, *Phys. Rev. Lett.* **19**, 190 (1967).
64. D. Y. Smith and G. Graham, *J. Phys. (Paris)* **41**, Colloque C6, C6-80 (1980).
65. R. de L. Kronig and H. A. Kramers, *Z. Phys.* **48**, 174 (1928).
66. V. Fock, *Z. Phys.* **89**, 744 (1934).
67. I. Šimon, *J. Opt. Soc. Am.* **41**, 336 (1951).
68. T. S. Robinson, *Proc. Phys. Soc. (London) B* **65**, 910 (1952); T. S. Robinson and W. C. Price, *Proc. Phys. Soc. (London) B* **66**, 969 (1953); T. S. Robinson and W. C. Price, *in* "Molecular Spectroscopy" (G. Sell ed.), p. 211, Inst. Petroleum, London, 1955; J. K. Wilmshurst and S. Senderoff, *J. Chem. Phys.* **35**, 1078 (1961).
69. T. Inagaki, A. Ueta, and H. Kuwata, *Phys. Lett.* **66A**, 329 (1978).
70. F. W. King, *J. Chem. Phys.* **71**, 4726 (1979); I. Kimel, *Phys. Lett.* **88A**, 62 (1982).
71. D. Y. Smith and C. A. Manogue, *J. Opt. Soc. Am.* **71**, 935 (1981).
72. F. C. Jahoda, Ph.D. thesis, Cornell University, Ithaca, New York, 1957; F. C. Jahoda, *Phys. Rev.* **107**, 1261 (1957).
73. B. Velický, Czech. *J. Phys. B* **11**, 541 (1961).
74. P. Roman and A. S. Marathay, *Nuovo Cimento* **30**, 1452 (1963).
75. R. E. Burge, M. A. Fiddy, A. H. Greenaway, and G. Ross, *J. Phys. D* **7**, L65 (1974).
76. M. Gottlieb, Ph.D. thesis, University of Pennsylvania, Phildelphia, Pennsylvania 1959; M. Gottlieb, *J. Opt. Soc. Am.* **50**, 343 (1960); M. Gottlieb, *J. Opt. Soc. Am.* **50**, 350 (1960).
77. D. Y. Smith, *J. Opt. Soc. Am.* **67**, 570 (1977).
78. G. Bonfiglioli and P. Brovetto, *Phys. Lett.* **5**, 248 (1963); G. Bonfiglioli and P. Brovetto, *Appl. Opt.* **3**, 1417 (1964).
79. B. O. Seraphin, *in* "Optical Properties of Solids" (F. Abelès, ed.), p. 163, North-Holland Publ. Amsterdam, 1972.
80. A Balzarotti, E. Colavita, S. Gentile, and R. Rosei, *Appl. Opt.* **14**, 2412 (1975).
81. J. S. Plaskett and P. N. Schatz, *J. Chem. Phys.* **38**, 612 (1963).
82. E. A. Lupashko, V. K. Miloslavskii, and I. N. Shklyarevskii, *Opt. Spectrosk.* **29**, 789 (1970); E. A. Lupashko, V. K. Miloslavskii, and I. N. Shklyarevskii, *Opt. Spectrosc.* **29**, 419 (1970).
83. E. A. Lupashko, V. K. Miloslavskii, and I. N. Shklyarevskii, *Opt. Spectrosk.* **24**, 257 (1968); Lupashko, Miloslavskii, and Shklyarevskii, *Opt. Spectrosc.* **24**, 132 (1968).
84. A. A. Clifford, M. I. Duckels, and B. Walker, *J. Chem. Soc. (London), Faraday Transactions II*, **68**, 407 (1972).
85. D. M. Roessler, *Brit. J. Appl. Phys.* **16**, 1359 (1965).
86. D. W. Berreman, *Appl. Opt.* **6**, 1519 (1967).
87. W. G. Chambers, *Infrared Phys.* **15**, 139 (1975).
88. R. H. Young, *J. Opt. Soc. Am.* **67**, 520 (1977).

89. G. M. Hale, W. E. Holland, and M. R. Querry, *Appl. Opt.* **12**, 48 (1973); M. R. Querry and W. E. Holland *Appl. Opt.*, **13**, 595 (1974).
90. T. Inagaki, H. Kuwata, and A. Ueda, *Phys. Rev. B* **19**, 2400 (1979); T. Inagaki, H. Kuwata, and A. Ueda, *Surf. Sci.* **96**, 54 (1980).
91. S. Maeda, G. Thyagarajan, and P. N. Schatz, *J. Chem. Phys.* **39**, 3474 (1963); K. Kozima, W. Suëtaka, and P. N. Schatz, *J. Opt. Soc. Am.* **56**, 181 (1966).
92. P.-O. Nilsson, *Appl. Opt.* **7**, 435 (1968).
93. J. D. Neufeld and G. Andermann, *J. Opt. Soc. Am.* **62**, 1156 (1972).
94. H. Ehrenreich, H. R. Philipp, and B. Segall, *Phys. Rev.* **132**, 1918 (1963); H. R. Philipp and H. Ehrenreich, *J. Appl. Phys.* **35**, 1416 (1964).
95. H.-J. Hagemann, W. Gudat, and C. Kunz, *J. Opt. Soc. Am.* **65**, 742 (1975); H.-J. Hagemann, W. Gudat, and C. Kunz, DESY Report SR 74/7, "Optical Constants from the Far Infrared to the X-Ray Region," Deutsches Elektronen-Synchrotron, Hamburg, 1974.
96. T. Inagaki, E. T. Arakawa, R. N. Hamm, and M. W. Williams, *Phys. Rev. B* **15**, 3243 (1977).
97. E. Shiles, T. Sasaki, M. Inokuti, and D. Y. Smith, *Phys. Rev. B* **22**, 1612 (1980).
98. M. Cardona, *in* "Optical Properties of Solids," (S. Nudelman and S. S. Mitra eds.), p. 137 Plenum, New York, 1969.
99. L. D. Kislovskii, *Opt. Spektrosk.* **1**, 672 (1956); L. D. Kislovskii, *Opt. Spektrosk.* **2**, 186 (1957); L. D. Kislovskii, *Opt. Spektrosk.* **5**, 66 (1958); L. D. Kislovskii, *Opt. Spektrosk.* **6**, 810 (1959); L. D. Kislovskii, *Opt. Spectrosc.* **6**, 529 (1959); L. D. Kislovskii, *Opt. Spektrosk.* **7**, 311 (1959); L. D. Kislovskii, *Opt. Spectrosc.* 7, 201 (1959).
100. C. W. Peterson and B. W. Knight, *J. Opt. Soc. Am.* **63**, 1238 (1973).
101. D.W. Johnson, *J. Phys. A* **8**, 490 (1975).
102. F. W. King, *J. Phys. C* **10**, 3199 (1977).
103. F. W. King, *J. Opt. Soc. Am.* **68**, 994 (1978).
104. W. O. Saxton, *J. Phys. D* **7**, L63 (1974).
105. D. L. Misell, *J. Phys. D* 7, L69 (1974).
106. H. W. Bode, "Network Analysis and Feedback Amplifier Design," D. Van Nostrand, New York, 1945.
107. D. M. Roessler, *Brit. J. Appl. Phys.* **16**, 1119 (1965); D. M. Roessler, *Brit. J. Appl. Phys.* **16**, 1777 (1965).
108. D. M. Roessler, *Brit. J. Appl. Phys.* **17**, 1313 (1966).
109. B. Velický, Czech. *J. Phys. B* **11**, 787 (1961).
110. R. A. MacRae, E. T. Arakawa, and M. W. Williams, *Phys. Rev.* **162**, 615 (1967).
111. G. R. Anderson and W. B. Person, *J. Chem. Phys.* **36**, 62 (1962).
112. H. J. Bowlden and J. K. Wilmshurst, *J. Opt. Soc. Am.* **53**, 1073 (1963).
113. W. G. Spitzer and D. A. Kleinman, *Phys. Rev.* **121**, 1324 (1961).
114. O. Castaño, M. de Dios, and R. Pérez, *comunicaciones (Havana)* **17**, 65 (1975); O. D. Castaño, M. de Dios Leyva, and R. Pérez Alvarez, *Phys. Stat. Solidi B* **71**, 111 (1975).
115. B. W. Veal *in* "The Actinides: Electronic Structure and Related Properties, Vol. 2, pp. 87–88, Academic Press, New York, 1974.
116. H. R. Philipp and E. A. Taft, *Phys. Rev.* **113**, 1002 (1959); H. R. Philipp and E. A. Taft, *Phys. Rev.* **136**, A1445 (1964).
117. M. Cardona and D. L. Greenaway, *Phys. Rev.* **133**, A1685 (1964).
118. W. J. Scouler, *Phys. Rev.* **178**, 1353 (1969).
119. M. P. Rimmer and D. L. Dexter, *J. Appl. Phys.* **31**, 775 (1960); M. G. Doane, M.S. thesis, University of Rochester, Rochester, New York, 1961.
120. V. B. Tulvinskii and N. I. Terentev, *Opt. Spektrosk.* **28**, 894 (1970); V. B. Tulvinskii and N. I. Terentev, *Opt. Spectrosc.* **28**, 484 (1970).
121. P. N. Schatz, S. Maeda, and K. Kozima, *J. Chem. Phys.* **38**, 2658 (1963); D. W. Barnes and P. N. Schatz, *J. Chem. Phys.* **38**, 2662 (1963).
122. G. Andermann, A. Caron, and D. A. Dows, *J. Opt. Soc. Am.* **55**, 1210 (1965); G. Andermann

and D. A. Dows, *J. Phys. Chem. Sol.* **28**, 1307 (1967); C.–K. Wu and G. Andermann, *J. Opt. Soc. Am.* **58**, 519 (1968).
123. T. G. Arkatova, N. M. Gopshtein, E. G. Makarova, and B. A. Mikhailov, *Opt. Mekh. Promst.* **48**, 44 (1981); T. G. Arkatova, N. M. Gopshtein, E. G. Makatova, and B. A. Mikhailov, *Sov. J. Opt. Technol.* **48**, 552 (1981).
124. D. G. Thomas and J. J. Hopfield, *Phys. Rev.* **116**, 573 (1959).
125. V. K. Miloslavskii, *Opt. Spektrosk.* **21**, 343 (1966); V. K. Miloslavskii, *Opt. Spectrosc.* **21**, 193 (1966).
126. P.-O. Nilsson and L. Munkby, *Phys. Kondens. Materie* **10**, 290 (1969).
127. V. K. Zaitsev and M. I. Fedorov, *Opt. Spektrosk.* **44**, 1186 (1978); V. K. Zaitsev and M. I. Fedorov, *Opt. Spectrosc.* **44**, 691 (1978).
128. R. K. Ahrenkiel, *J. Opt. Soc. Am.* **61**, 1651 (1971); R. K. Ahrenkiel, *J. Opt. Soc. Am.* **62**, 1009 (1972).
129. R. Z. Bachrach and F. C. Brown, *Phys. Rev. B* **1**, 818 (1970); N. J. Carrera and F. C. Brown, *Phys. Rev. B* **4**, 3651 (1971).
130. E. Shiles and D. Y. Smith, *Bull. Am. Phys. Soc.* **23**, 226 (1978).
131. E. Shiles and D. Y. Smith, *Bull. Am. Phys. Soc.* **24**, 335 (1979).
132. G. Leveque, *J. Phys. C* **10**, 4877 (1977).
133. D. H. Tomboulian and E. M. Pell, *Phys. Rev.* **83**, 1196 (1951).
134. A. Balzarotti, A. Bianconi, and E. Burattini, *Phys. Rev. B* **9**, 5003 (1974).

Chapter 4

Measurement of Optical Constants in the Vacuum Ultraviolet Spectral Region*

W. R. HUNTER†
Naval Research Laboratory
Washington, D.C.

I. Introduction 69
II. General Discussion of Reflectance Methods 70
A. Reflection at Normal Incidence—Measurement of Index of Refraction 70
B. Reflection at Oblique Incidence 71
C. Effect of Layer Thickness 78
D. Critical-Angle Method 79
E. Measurement of Extinction Coefficients 81
III. Reflectance Method for Two Media 85
References 87

INTRODUCTION I

The optical constants of an isotropic material are the index of refraction n and the extinction coefficient k. They are the real and imaginary components of the complex index of refraction $N = n - ik$. They can be measured at a given wavelength by direct methods or inferred from photometric or polarimetric measurements. For wavelengths less than 2000 Å, the vacuum ultraviolet (VUV) spectral region, polarimetric methods are seldom useful because the phase-discriminating components of the system are strongly absorbing, consequently, reflectance methods are almost exclusively used for obtaining

* This chapter is a condensed version of a paper, "Measurement of Optical Properties of Materials in the Vacuum Ultraviolet Spectral Region," published in *Applied Optics* **21**, 2103 (1982).

† Present address: Sachs/Freeman Associates, Inc., Bowie, Maryland.

Copyright © 1985 by Academic Press, Inc.
All rights of reproduction in any form reserved.
ISBN 0-12-544420-6

n and k. A number of methods exist for extracting n and k from specular-reflectance measurements at both normal and oblique incidence and for semi-infinite media as well as layers on substrates.

This chapter will discuss the most useful methods for obtaining n and k in the VUV and the problems encountered in applying these methods. The Kramers–Kronig method will not be discussed here (see Chapter 3) because it cannot be used to deduce n and k from measurements at a single wavelength.

II GENERAL DISCUSSION OF REFLECTANCE METHODS

The specular reflectance of a substance at an angle of incidence ϕ, measured from the surface normal, is related to the complex index of refraction by the generalized Fresnel reflection coefficients,

$$R_s = [(a - \cos\phi)^2 + b^2]/[(a + \cos\phi)^2 + b^2]$$

$$R_p = R_s[(a - \sin\phi \tan\phi)^2 + b^2]/[(a + \sin\phi \tan\phi)^2 + b^2]$$

$$R_a = \tfrac{1}{2}[R_p(1 + p) + R_s(1 - p)],$$

where R_s is the component of specular reflection perpendicular to the plane of incidence, R_p the parallel component, and R_a the reflectance for non-polarized radiation. The polarization of the incident radiation is given by

$$p = (I_p - I_s)/(I_p + I_s),$$

and

$$a^2 = \tfrac{1}{2}\{[(n^2 - k^2 - \sin^2\phi) + 4n^2k^2]^2 + (n^2 - k^2 - \sin^2\phi)\},$$

$$b^2 = \tfrac{1}{2}\{[(n^2 - k^2 - \sin^2\phi) + 4n^2k^2]^2 - (n^2 - k^2 - \sin^2\phi)\}.$$

These equations cannot be solved explicitly for n and k; hence one must resort to graphical or numerical means to solve them [1–11]. Since the equations have two unknowns, two independent measurements are necessary if a solution is to be obtained.

A Reflection at Normal Incidence—Measurement of Index of Refraction

At normal incidence the two components of reflection are indistinguishable and, for nonabsorbing media, the equations may be reduced to

$$R = (n - 1)^2/(n + 1)^2.$$

Unlike the generalized coefficients, this equation can be solved for n as

$$n = (1 + R^{0.5})/(1 - R^{0.5}).$$

The values of n of transparent media in the VUV usually range from 1.3 to 2.0. Over this range the absolute error in determining n from reflectance measurements is approximately 10 times the absolute error in measuring R. Thus, n is sensitive to small errors in R and the accuracy of the method makes it suitable only for determining provisional values to two significant figures at best.

This simple method may be used for any material that is transparent in the VUV and can be polished or cleaved to give a specularly reflecting surface. Precautions must be taken to measure reflectance from the first surface only. Reflections from the second surface can be eliminated by making the sample wedge shaped or can be suppressed by grinding the second surface and blackening it.

Reflection at Oblique Incidence B

Humphreys–Owen [6] lists nine methods by which n and k can be deduced from reflectance measurements at oblique incidence. These methods are divided into two classes: (1) two reflectance measurements at one angle of incidence or one reflectance measurement at each of two angles of incidence and (2) one reflectance measurement at any angle of incidence and measurement of a special angle of incidence capable of supplying the necessary second measurement. There are only two special angles: (1) the principal angle of incidence, which must be determined by polarimetric methods and so it will not be discussed, and (2) the Brewster, or pseudo-Brewster (pB), angle. The Brewster angle is defined only in terms of dielectric media and is given by $n = \tan \phi_B$. At this angle $R_p = 0$. As k increases, R_p always has a minimum value, but it is not zero. The angle at which this minimum occurs in the pB angle and, if $k > 0$, $\phi_{pB} > \phi_B$. Humphreys–Owen's list has been rearranged as follows:

Class 1

Method 1 Reflectance at two angles of incidence using natural or polarized radiation; sometimes referred to as *the* reflectance-versus-angle of incidence method

Method 2 The ratio R_p/R_s at two angles of incidence

Method 3 R_s and R_p at one angle of incidence

Class 2

Method 4 Pseudo-Brewster angle and R_s or R_p at that angle

Method 5 Pseudo-Brewster angle and R_p/R_s at that angle

Method 6 Pseudo-Brewster angle and R_s, R_p, or R_p/R_s at any other angle of incidence

In principle, only two measurements are required, but, because of possible errors in the measurements, a redundancy of measurements is more useful and will give an indication of the errors involved in determining n and k.

Although these methods can be used at any wavelength, their sensitivities to errors in measurements of reflectance, of the angles involved, or of the state of polarization are functions of both n and k, as well as the angle of incidence and the state of polarization. Thus, there may be parts of the n, k plane, angles of incidence, and states of polarization, for which the lack of sensitivity reduces their accuracy to unacceptable values.

Since the sensitivities of the methods are dependent on n and k, hence on the shape of the R-versus-ϕ curves, a collection of these curves is shown in Fig. 1 [11] for reference during the ensuing discussion. The large numbers give the values of n and k used in calculating a particular set of curves. These values cover the range of n and k most likely to be encountered in the VUV. The small numbers along the abscissa and ordinate show the angle of incidence and percent reflectance, respectively. The upper curve is always R_s, the lower curve R_p, and the curve between R_a. Generally, for a given n, as k increases

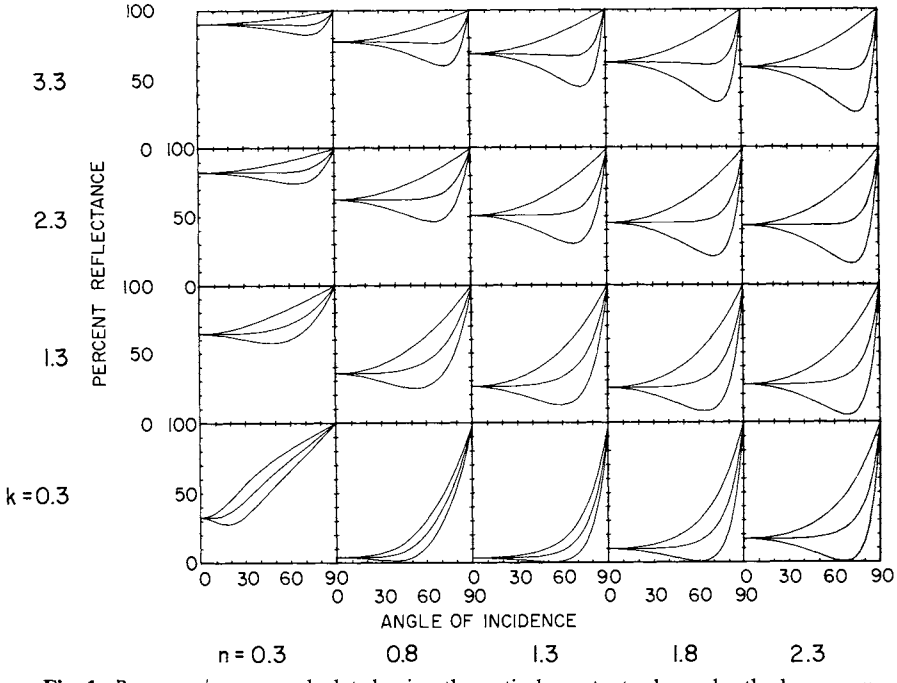

Fig. 1. R-versus-ϕ curves calculated using the optical constants shown by the large numbers. The small numbers shown on the abscissa and ordinate are the values of ϕ and R, respectively.

the reflectance at normal incidence increases, the change in R with ϕ becomes small, especially for R_a, except at the pB angle, and the pB angle becomes larger. For a given k, as n increases the reflectance at normal incidence decreases. the change in R with ϕ becomes more pronounced, especially for R_p, and again the pB angle becomes larger. The value of R_p at the pB angle appears to be zero for $n \geq 1.3$ and $k = 0.3$. This is not so, but the values are extremely small.

Method 1 1

The sensitivity of this method is most easily investigated by means of isoreflectance curves. An isoreflectance curve is the locus of points in the n, k plane corresponding to a given value of R for a specific value of ϕ. If isoreflectance curves are plotted for perfect data, i.e., reflectance values calculated using the Fresnel formula, an insight into the sensitivity of the method can be obtained. Figure 2 [11] shows such a set of curves for the parallel component covering that part of the n, k plane $0.3 \leq n \leq 2.3$ and $0.3 \leq k \leq 3.3$.

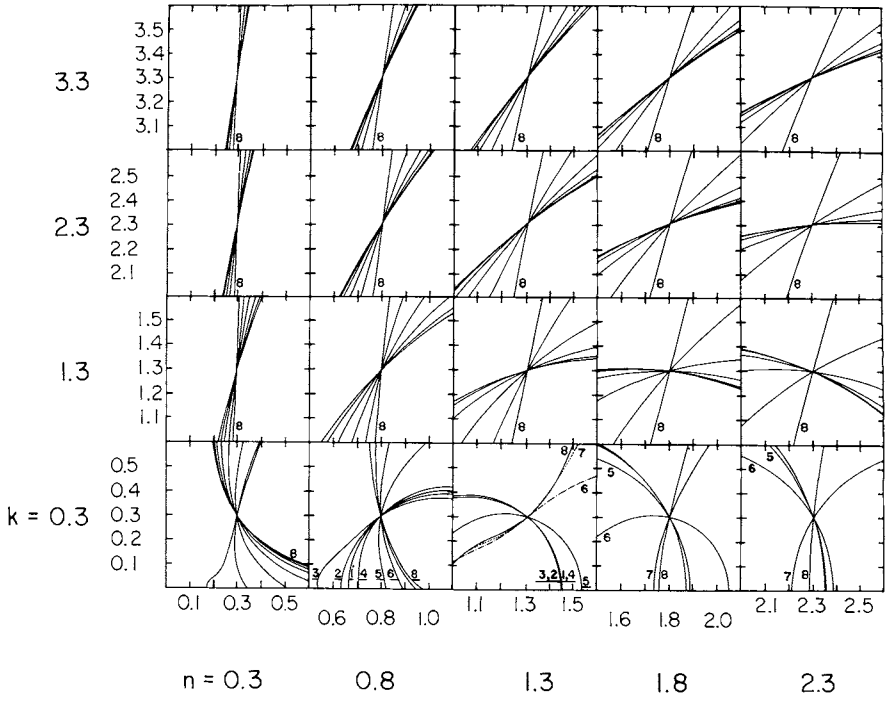

Fig. 2. Isoreflectance curves for R_p calculated using the optical constants shown by the larger numbers. The small numbers used for the abscissa and ordinate show the scale in the n, k plane. The numeral 8 designates the isoreflectance curve corresponding to 80°. The other curves are for angles of incidence 70, 60, through 10°. The curves usually occur in descending order; when they do not, each curve is labeled with a single digit to avoid confusion (method 1).

An indication of the sensitivity is the angle of intersection of the isoreflectance curves. If there is an error in the reflectance, the isoreflectance curve will be shifted parallel to itself by an amount depending on the magnitude of the error and in a direction depending on its sign. Thus, if two curves intersect at a small angle, a slight displacement of one with respect to the other may shift the intersection point by a large amount. Such a displacement could be due either to an error in measuring R or an error in measuring ϕ. The figure indicates that for $n = 0.3$, the sensitivity with respect to k decreases as k increases. Thus, for small n and $k > n$, the R-versus-ϕ method can provide reasonable values for n but may result in large errors for k. Metals with large reflectance values, e.g., Al, Mg, etc., usually have small n and $k > n$. For example, at 1216 Å, Al has $n \approx 0.06$ and $k \approx 1.0$.

For $n > 0.3$, the isoreflectance curves for small angles of incidence are more nearly parallel than those for the larger angles. Thus, the sensitivity is greatest if measurements are made at the larger angles of incidence. For $n = 0.3$, however, the maximum sensitivity for small k is obtained using small angles and as n increases, maximum sensitivity is shifted only slowly to larger angles. Generally, the angles with which maximum sensitivity is obtained are those angles at which the curvature in R is maximum, which is not necessarily the angles at which R changes most rapidly with ϕ. Similar sets of isoreflectance curves have been calculated for R_s and R_a [11].

Although the curves in Fig. 2 furnish an idea of the sensitivity of the method, the accuracy of the method can only be found by using false data. By adding positive and negative errors to perfect reflectance data, the magnitude of the displacement of the isoreflectance curves can be obtained and the accuracy of the method determined. Hunter [11] has investigated the accuracy of method 1 using angles of incidence of 20 and 70°. His results are shown in Fig. 3 for both R_p and R_a. The blackened parallelopipeds represent the error in determining n and k for $\pm 1\%$ errors in measuring the reflectance. The parallelopipeds correspond to the values of n and k shown in large numbers. Lines connect the extremities of these parallelopipeds to indicate the magnitude of the errors at intermediate points. The magnitude of the errors is in keeping with the sensitivity as discussed in connection with Fig. 2. For example, for small n (0.3), the error in n as k increases grows comparatively slowly, but the corresponding error in k becomes large quite rapidly because the parallelopipeds are almost parallel to the k axis. As n increases and for large k, the long axis of the parallelopipeds rotates in a clockwise direction so that the error in determining n increases while that for k decreases. It is evident that R_p is more tolerant of errors than R_a.

In using the R-versus-ϕ method it is not necessary to know the actual R values [11]. The fact that reflectance is defined as the ratio of the reflected intensity at angle ϕ to the incident intensity is equivalent to normalizing the reflected intensity at angle ϕ to the reflected intensity at 90° angle of incidence, which is defined as unity. For use in the R-versus-ϕ method, normalization

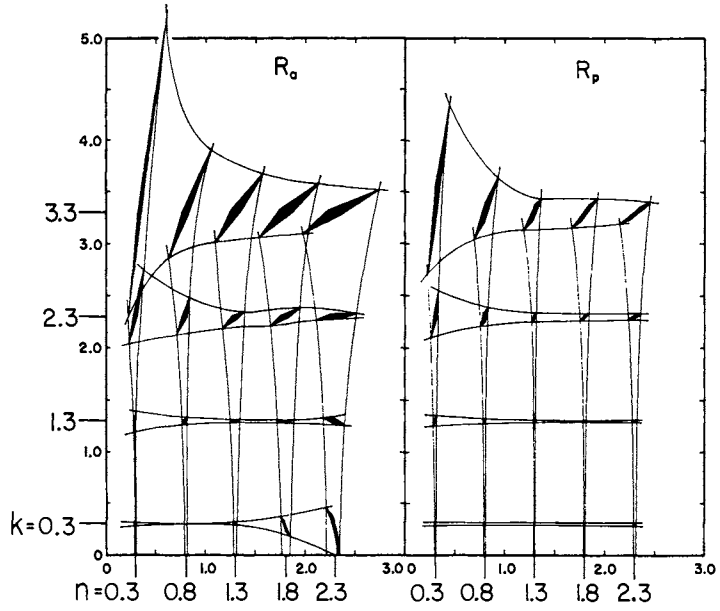

Fig. 3. The effect of $\pm 1\%$ error in the measurement of reflectance on the determination of n and k using method 1. The angles of incidence are 20 and 70°.

can be done at any angle of incidence and is referred to as oblique normalization. Field and Murphy [12] have published an analysis of the R-versus-ϕ method for oblique normalization. For oblique normalization the angle between the isoreflectance curves may not be a good indicator of sensitivity, and one should plot known errors in the obliquely normalized reflectance values to get a correct indication of sensitivity. Oblique normalization has no advantages over the usual mode of normalization and is only used when the physical arrangement of the reflectometer makes measurement of the incident intensity impractical.

Method 2 2

Figure 4 shows two sets of curves for the ratio R_p/R_s. To the left is a set for small angles of incidence and to the right a set for large angles. According to Humphreys–Owen, an indication of the sensitivity is the spacing between contours—if the spacing is large, the sensitivity is good and vice versa. Assuming that his assertion is correct, the large-angle contours are obviously not useful if n and k are large but might be used to obtain good values if n and k are small. The small-angle contours are only useful if n and k are small. Humphreys–Owen showed a limited set of contours of R_p/R_s for 80 and 60°, and a more extended, calculated set indicates that these two angles may be more useful than those shown here for larger values of n and k.

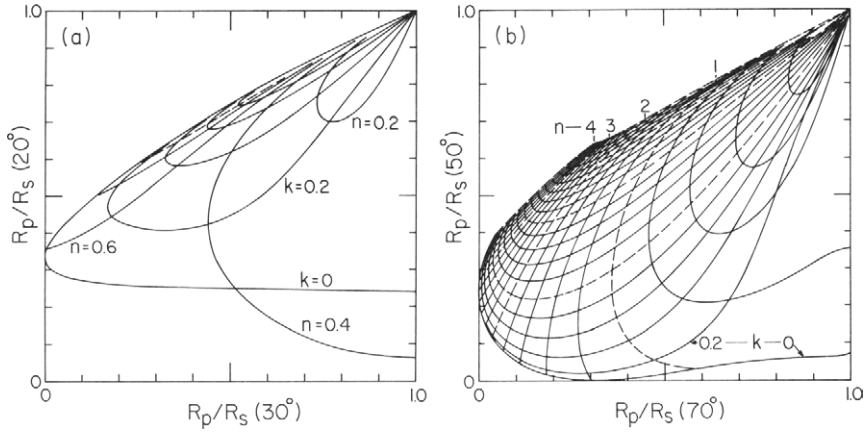

Fig. 4. Curves of constant n and k as a function of R_p/R_s for (a) small (30–20°) and (b) large (70–50°) angles of incidence. Δn and Δk are each 0.2. Curves for integer n and k values are dashed (method 2).

3 *Method 3*

Figure 5 shows two sets of curves for R_s and R_p at both 20 and 70° angles of incidence. Judging from sets of curves obtained for other angles of incidence, these two angles are the most useful. For the 20° angle of incidence, the curves of constant k are spaced 0.01 apart from $k = 0$ to $k = 0.1$. The next k contour is for $k = 0.2$ and thereafter $\Delta k = 0.2$. The n contours have $\Delta n = 0.1$.

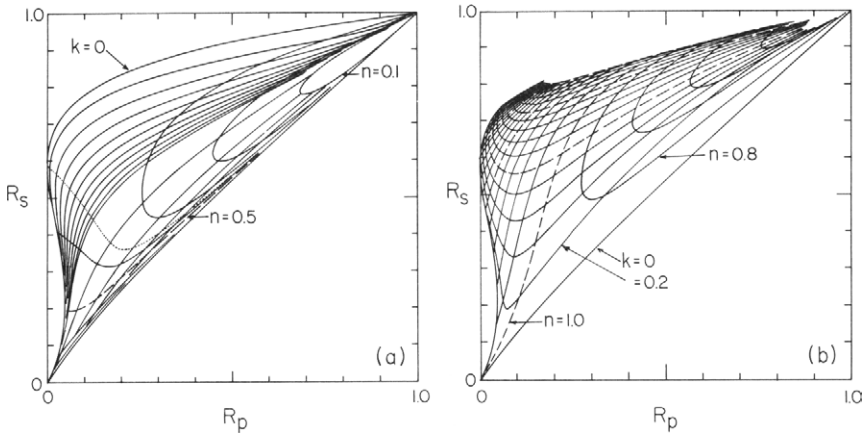

Fig. 5. Curves of constant n and k as a function of R_p and R_s for (a) small (20°) and (b) large (70°) angles of incidence. For (a) Δk is 0.01 for $0 \leq k \leq 0.1$; otherwise Δk is 0.2. Δn is 0.1 and the curve for $n = 0.5$ is dashed. The dotted line corresponds to the value of n for the Brewster angle, $n = 0.364$. For (b) $\Delta k = \Delta n = 0.2$. Curves for integer n and k values are dashed (method 3).

The dotted line is the contour of $n = 0.364 = \tan 20°$. This set of curves might be useful for $n < 0.5$ and $k < 0.4$.

The set of curves of 70° is less useful for small n and k but more useful for larger values. For this set $R_p = 0$ when $n = 2.747 = \tan 70°$. Both Δn and Δk are 0.2 for this set.

The envelope of the 20° contours consists of the curves $k = 0$ and, ultimately, the curve for large n values. The 70° contours are enveloped by the two curves for $k = 0$, which coincide at $R_s = R_p = 0$. At 45°, where $R_p = R_s^2$ for any n and k, the envelope is compressed to a line that has the form of a parabola.

Methods 4 and 5 4

Figure 6 shows sets of curves for R_p/R_s (method 4) and R_s (method 5) versus the pB angle. The R_p/R_s set favors small values of n and k and the R_s set favors somewhat larger n and k. Note that the R_s curves can give double values. For example, if the pB angle is 15° and $R_s = 0.56$, k would be 0.3 but n could be 0.2 or 0.3. Thus, the region with double values is not useful. Contours for R_p-versus-pB angle are similar to those for R_p/R_s.

According to Humphreys–Owen, method 6 gives no advantages over the other methods.

In order to obtain quantitative data on the accuracy of methods 2–5, it is necessary to plot the contours for $R \pm \Delta R$, or pB $\pm$ ΔpB, which has not been done. The existence of large spacings between the contours suggests but does not guarantee small displacements of the contours when errors are introduced Humphreys–Owen points out that R_p, at the pB angle, can be quite

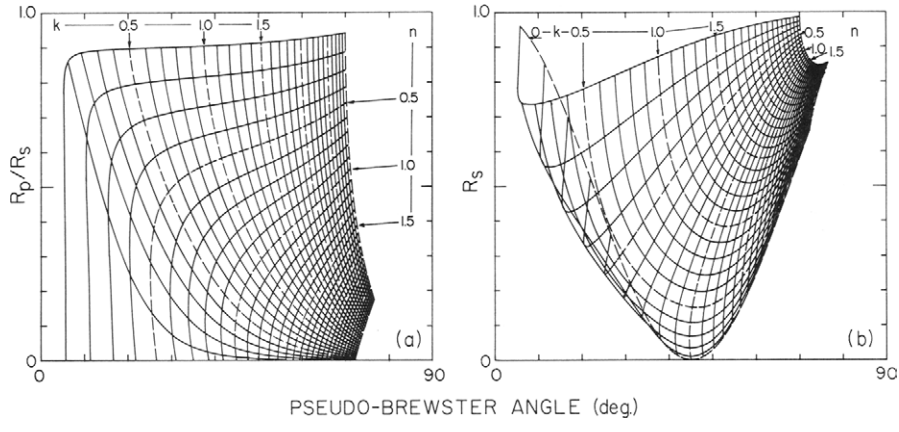

Fig. 6. Curves of constant n and k as a function (a) of R_p/R_s and the pseudo-Brewster (pB) angle and (b) of R_s and the pB angle (methods 4 and 5, respectively). $\Delta n = \Delta k = 0.1$ and curves for integer and half-integer; n and k values are dashed.

small; thus, there may be a large error in measuring it. Furthermore, the minimum in R_p at the pB angle is usually broad, so accurate location of the angle may be difficult.

If method 2 or 5 is to be used, normalization to get actual reflectance values is unnecessary.

The equation for R_p can be manipulated to obtain the pB angle in terms of n and k [6]. It is given below,

$$2(p^2 + q)v^3 + p^2(p^2 - 3)v^2 - 2p^4v + p^4 = 0,$$

where

$$p = n^2 + k^2, \qquad q = n^2 - k^2, \qquad \text{and} \qquad v = \sin(\text{pB}).$$

The experimental values for n and k obtained from the curves can be substituted in the formula to help verify the correctness of the results.

C Effect of Layer Thickness

Preparing a material for reflectance measurements from which n and k are to be obtained is often done by vacuum evaporation of the material onto a highly polished substrate. Since methods 1–5 are intended for use with semi-infinite media, the layer must be thick enough to qualify in this respect. Generally, as the thickness of a vacuum-deposited layer increases, so does its surface roughness. If the layer is not too thick, the error introduced by scattering due to the surface roughness will be small compared to errors from other causes. If, however, the thickness is too small, radiation will penetrate to the substrate/layer boundary, be reflected back to the layer/vacuum boundary, and interfere with the radiation reflected at the layer/vacuum boundary. If this interference is significant, the measured reflectances will not be representative of the reflectances of a semi-infinite medium and the reflectance methods 1–5 will not be useful. Hunter and Hass [13] have investigated the effects of interference on method 1 and found that the thickness required to reduced errors in n and k to approximately 1% depends on the n, k values of the layer. Their Table I shows that for $n = k = 0.3$, the geometrical thickness of the layer must be approximately one wavelength, and as n and k increase, the required thickness decreases. At $n = 2.3$ and $k = 3.3$, for example, a geometrical thickness of approximately 0.1 wavelength is required.

The effect of layer thickness on methods 2–5 has not been investigated but is expected to be generally the same as for method 1.

The general behavior of R-versus-ϕ and isoreflectance curves indicates that for large k/n, the method is not very accurate. Since metals with large reflectance values in the visible and infrared usually have large k/n, reflectance methods appear not to be suitable for obtaining n and k of metals in these spectral regions.

There are wavelength ranges in the VUV in which the n of some substances is less than unity and $k < 0.1$. This occurs for Al, Mg, Si, for example [14], and the alkali metals [15] at wavelengths less than their critical wavelength. For such values of n and k, the R-versus-ϕ curves exhibit the behavior shown in Fig. 7 [16]. This figure shows curves for a substance with $n = 0.707$, corresponding to a critical angle ϕ_c of 45°, and for different values of k. For $k = 0$, ϕ_c is well defined and $\sin \phi_c = n$. As k increases, however, ϕ_c is no longer well defined because the R-versus-ϕ curves become rounded at angles larger than ϕ_c. The point of maximum slope of the curve, however, occurs quite close to ϕ_c and can be used as a good approximation to ϕ_c. Since only the angle of incidence at which the maximum slope occurs is required, the reflectance values need not be known. To get correct values of n, k must be known and

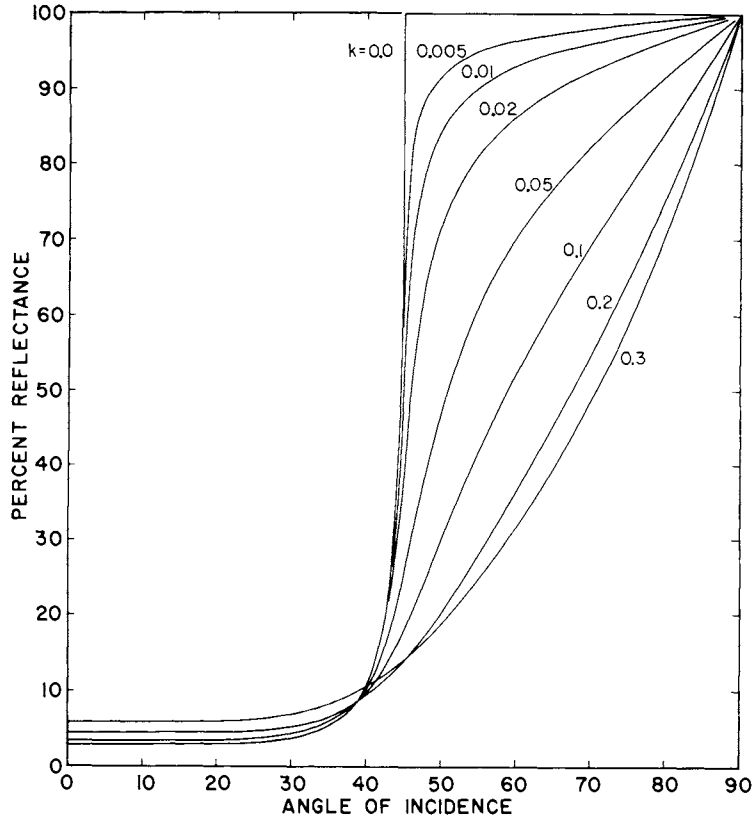

Fig. 7. Calculated R-versus-ϕ curves for $n = 0.707$, $\phi_c = 45°$, and different values of k showing the behavior of the reflectance for nonpolarized light in the vicinity of the critical angle.

a correction made. The figure shows that as k increases, the correction required to obtain the true n also increases.

Corrections must also be made for the state of polarization of the incident radiation. These corrections decrease with increasing n, becoming small for $n = 0.7$.

Hunter [16] has used this technique to measure n of evaporated layers of quasi-free electron metals such as Al, Mg, Si, and others at wavelengths less than their critical wavelengths. In order to correct the measured angle of maximum slope for the effect of k, he used extinction coefficients obtained from transmittance measurements through thin, unbacked films of the metal under investigation. The presence of the oxide layer that forms readily on the chemically active metals can shift the position of maximum slope. Hunter found that the natural oxide thickness for Al (30–40 Å) tends to shift the

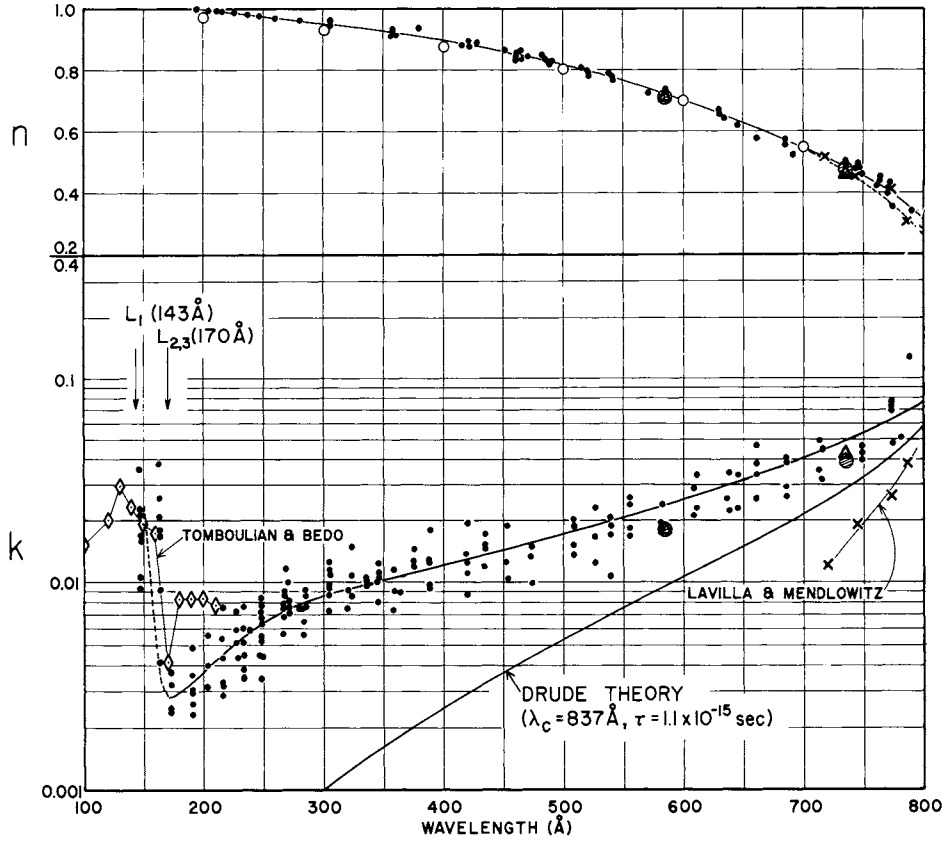

Fig. 8. The curve at the top shows n values for Al obtained using the critical angle method. The curve at the bottom shows the extinction coefficient of Al deduced from transmittance measurements. The scatter of points indicates that the critical angle method gives fairly accurate values for n, but that the transmittance method for finding k can give quite variable results.

maximum slope to larger angles, especially for small values of n, but that the magnitude of the shift is small.

For this method the layer thickness is also important because interference effects can shift the position of maximum slope. Usually, if the thickness exceeds 2000 Å, interference effects are negligible. This method is also advantageous because of its relative insensitiveness to surface roughness frequently encountered for layer thicknesses in excess of 2000–3000 Å.

Whang *et al.* [17] have extended the method to obtain k from the maximum slope of the R-versus-ϕ curve. Because the value of the slope is required when using their method, actual reflectance values must be measured. In addition, the polarization of the incident radiation must be known. They estimate that the critical-angle method, in spectral regions in which it can be used, gives more accurate results than using method 1. Hunter [18] found that the scatter of data points is quite small when using this method, as illustrated by the top part of Fig. 8.

Measurement of Extinction Coefficients E

The extinction coefficient can be determined by measuring the transmittance of a known thickness of material and calculating k using Lambert's law after correcting the transmittance measurements for reflection losses at the surfaces. If the light is not coherent, these corrections involve only reflected intensities, and if two different thicknesses of the material are used, the corrections usually can be eliminated.

Lambert's law relates transmittance T, thickness t, and k through the equation

$$T = I/I_0 = e^{-4\pi kt/\lambda}.$$

For two thicknesses, k is obtained from

$$k = \lambda \ln(T_1/T_2)/[4\pi(t_2 - t_1)],$$

where λ is the wavelength in the same units as t.

If the film has surface layers, such as oxide layers, they are frequently much more absorbing than the material to be measured. If the oxide layers are always the same thickness, however, their absorptance does not affect the ratio T_1/T_2 and their reflectance values are independent of the test-material film thickness for all practical film thicknesses. Therefore, transmittance values obtained using two different test-material thicknesses should give reasonable values for k.

This method for determining k can be applied to thin, unbacked films or thin films on a transparent substrate if the value of k is small enough so that the transmitted signal has a reasonable signal/noise ratio. Hass *et al.* [19]

obtained k values for unbacked films of Al at 736 and 584 Å, and Hunter [18, 20] has made extensive measurements on unbacked films of Al and other materials.

Despite the apparent simplicity of the method, there are two possible sources of error: (1) anomalous dependence of transmittance on thickness and wavelength caused by interference effects and (2) methods of preparation of the sample.

For most materials in the VUV, the absorptance is so large that transmittances can only be obtained through thin films a few thousand angstroms thick. The coherence length of the light is usually larger than the film thickness, so interference effects will be present, and the simple intensity correction for reflection losses may not be valid.

Figure 9 shows the calculated transmittance of an Al film as a function of the Al thickness with a 40-Å-thick oxide coating on either surface. The k value used for Al is 0.0233. As the Al film thickness increases, the interference effects decrease in magnitude. At a thickness of 2000 Å the amplitude of the interference effect is about 10% of the transmittance, and at 3000 Å about 4%. By choosing thicknesses corresponding to interference maxima and minima, k values as large as 0.0698 can be obtained, and even negative k values

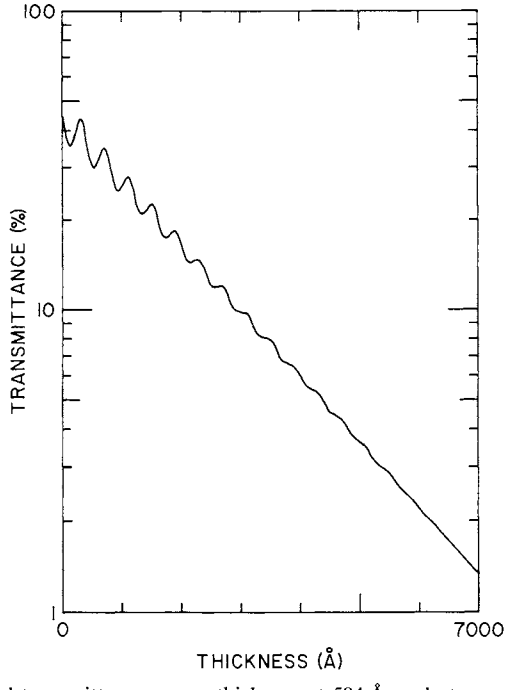

Fig. 9. Calculated transmittance versus thickness at 584 Å, and at normal incidence, for an unbacked Al film with 40 Å of oxide on both surfaces. The curve shows how interference effects alter the transmittance as the Al thickness changes.

can be calculated. Calculated from transmittance values at thicknesses of 6000 and 7000 Å, k is 0.0216, about a 7% error, and for thicknesses of 9000 and 10,000 Å, not shown in Fig. 9, a value of 0.0299 was obtained, an error of 1.7%. Thus, in principle, more accurate values of k are obtained as the thickness is increased. In practice, the transmittance values become too small for accurate measurement, so thinner films must be used.

Although interference effects are always present in the transmittance values, the experimental error in measuring the transmittance can mask the error caused by interference. For example, if the experimental error is $\pm 1\%$ of full scale, a transmittance of 16.5% ($t = 2000$ Å) can be in error by $\pm 6\%$, but the error introduced by interference would be 1.6% (10% of the transmittance value). Thus, for this example, the error in transmittance caused by interference would contribute little to the error in determining k for film thicknesses in excess of 2000 Å.

The transmittance of a thin film can also show interference effects as a function of wavelength. An example is given in Fig. 10 [21] which shows the measured transmittance of an unbacked film of Al 800 Å thick as a function of wavelength. Also shown for comparison are the calculated transmittances of an Al film of the same thickness with and without oxide layers 40 Å thick on either surface. The oxide is much more strongly absorbing than the Al, which decreases the transmittance of the oxidized film over that of the non-oxidized film, and its presence accentuates the interference effects. If interference-modulated transmittance spectra are used to provide transmittance values for the equation for k, k will also have a wavelength-dependent modulation. Reduction of this modulation is achieved by using thick films.

The transmittance method for finding k using thin films is perhaps more susceptible to errors arising from the method of preparation of the sample than from oscillatory terms in the transmittance equation or interference-modulated transmittance spectra. Unbacked metal films are made most simply by evaporating the metal onto a water-soluble layer [22]. Both the act of removal of the evaporated film from the substrate and the evaporation conditions under which it is made can strongly affect its optical properties. After the layer is dissolved, the films are allowed to float free on the water surface until picked up on a suitable frame for transmittance measurements. No two exposures to water will be alike; therefore, there may be considerable variability in the thicknesses of the oxide layers on either side of the metal film and also in k deduced from transmittance measurements made on such films. Figure 8 [18] shows measurements of k for Al. The scatter of points is quite large, primarily because of differences in the thicknesses of the oxide layers on either side of a metal film and because of differences in thicknesses of the oxide films on the different samples. Some of the scatter, however, is caused by interference effects of the type shown in Figs. 9 and 10.

Evaporation conditions are most apt to affect chemically active metals, such as Al, which adsorb oxygen readily. The amount of residual oxygen

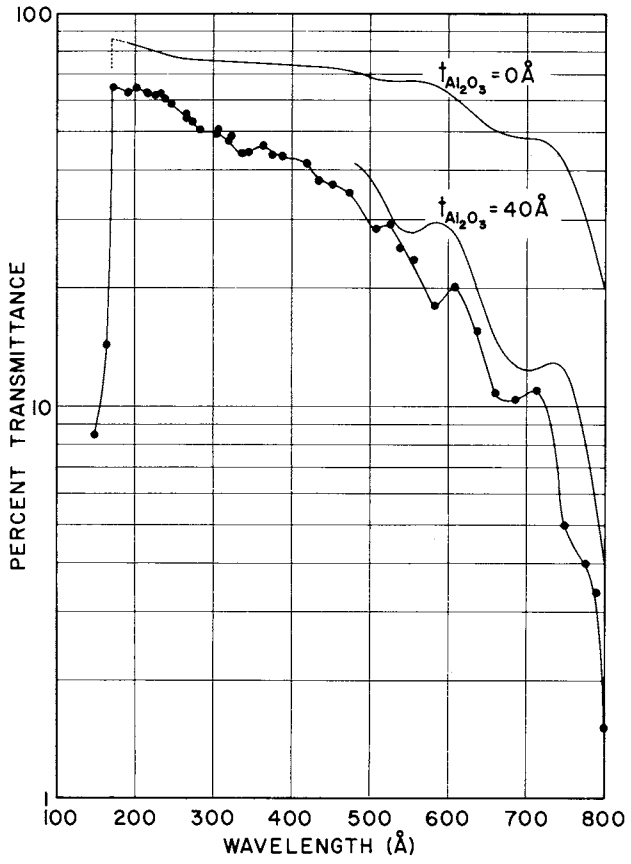

Fig. 10. The measured transmittance of an unbacked Al film 800 Å thick as a function of wavelength. Included for comparison are calculated curves for Al with and without 40-Å oxide layers on both surfaces. Interference effects cause the fluctuations in transmittance that are accentuated by the presence of the oxide layers.

captured in the film during evaporation must be reduced as much as possible. This can be done by evaporating in an ultrahigh-vacuum evaporator, or by doing a very fast evaporation in a conventional evaporator. If the residual oxygen is not removed or reduced sufficiently, Al films tend to have transmittances almost independent of thickness.[†]

A more specialized technique exists for measuring k of a material, if it is small ($k < 0.1$) and if n is known. At a given wavelength the reflectance at near-normal incidence of a substrate/layer combination, wherein the material to be measured forms the layer, is determined as a function of layer thickness.

[†] D. N. Steele, Luxel Corporation, 515 Tucker Avenue, Friday Harbor, Washington 98250, and C. Kunz, DESY HASYLAB, Notkestieg 1, Hamburg 52, Federal Republic of Germany; private communications.

The reflectance of the combination is then calculated as a function of layer thickness, with different k values, until a best fit to the experimental points is found. For this technique n and k of the substrate must be known. Canfield *et al.* [23] have used this method to determine k of MgF_2 layers on Al at 1216 Å, and Cox *et al.* [24] have used it to determine k of LiF layers on Al at 1026 Å.

REFLECTANCE METHOD FOR TWO MEDIA III

In principle, reflectance methods can be used to measure n and k of either component of a layer–substrate combination. One must know n and k of either layer or substrate, the layer thickness, and the layer–substrate transition region must be small compared to the wavelength used to make the measurement. Using such measurements, one could determine the optical constants of the natural oxide that forms on aluminum or of iron or cobalt films that cannot be made opaque because of their large internal strains.

Juencker [10] has discussed using method 1 for substrate–layers but did not discuss the conditions under which the method is valid. It is difficult to generalize for two media because of the large number of parameters involved, but there are some avenues of approach as well as some problems that will be discussed in the following paragraphs.

In contrast with single-medium reflectance methods, the two-medium reflectance method requires interference between the light reflected from the vacuum–layer and layer–substrate interfaces. Therefore, the layer must be thin enough for this interference to take place. The amount of light available for interference depends on the optical constants of both the layer and substrate, on the layer thickness, and on the angle of incidence. An example will be given to illustrate the method.

Assume a substrate with $N = 0.4 + i0.1$ and a layer with $N = 2.0 + i0.1$. The upper left panel of Fig. 11 shows how the reflectance of the substrate–layer varies with layer thickness. Choosing the first half-wave thickness, $0.13t/\lambda$, which may not be the optimum thickness, one calculates the R-versus-ϕ curves shown in 11b. Then, isoreflectance curves are plotted. Studies showed that for this particular layer–substrate combination, the parallel component gave the best isoreflectance curves for both layer and substrate. They are shown in 11c and d, respectively. Note that if only the large angles of incidence are used, there appear to be two solutions. This ambiguity can be resolved by using some reflectance measurements at smaller angles of incidence or by using a second, different thickness. In the latter case the correct intersection remains unmoved, but the spurious intersection shifts to a new location in the n, k plane.

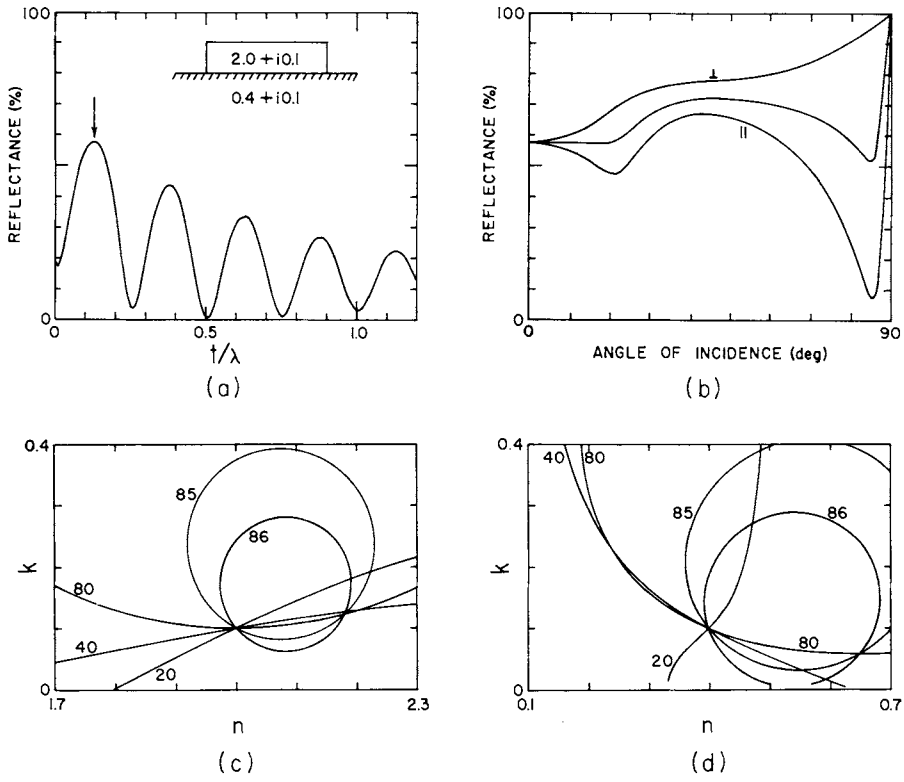

Fig. 11. Illustration of the procedure tor obtaining isoreflectance curves for determining n and k using two media. (a) Reflectance versus thickness is shown at normal incidence; choosing $t/\lambda = 0.13$ (arrow), (b) R-versus-ϕ curves are calculated; isoreflectance curves are obtained (c) for the layer assuming that the substrate is known and (d) for the substrate assuming the layer is known.

There are a number of problems associated with the two-medium reflectance method. First, there is the possibility of interdiffusion between substrate and layer, giving rise to a transition-region dimension comparable to, or greater than, the wavelength. If glass or fused silica is used for the substrate, the probability of interdiffusion is remote. There may be situations, however, when a substrate with a large reflectance adds to the contrast of the interference effects; for example, the effective substrate could be an opaque layer of Al on glass. Unoxidized Al interdiffuses readily with some other metals, notably Au [25]. Thus, some advance research must be done to ascertain the compatibility of the substrate and layer vis-à-vis interdiffusion.

Another problem is nonuniformity of the layer. The two-medium reflectance method tacitly assumes that the layer has a constant n and k as a function of distance into the layer. Such an assumption is not necessarily true. Reflectance measurements made on aged Al + MgF_2 mirrors at 1216 Å

with polarized radiation indicate that n or k or both may not be constant throughout the layer. Magnesium fluoride is known to adsorb water vapor which can modify the optical constants of the MgF_2 layer.

Fabre *et al.* [26] have devised a method for measuring n and k of slightly absorbing films in the VUV and have applied it to a study of MgF_2 films [27]. The film is vacuum deposited onto a suitable substrate (glass) such that its thickness varies along the long dimension of the coated area. After the actual thickness and its variation have been determined, the reflectance is measured as a function of thickness by moving the substrate/film uniformly past the radiation beam. The resultant reflectance curve resembles the curve shown in Fig. 11a. Using the enveloping curves for the reflectance maxima and minima, and the position of these extremes, Fabre *et al.* were able to calculate values for n and k.

Daude *et al.* [28] have used a technique similar to that employed by Canfield *et al.* and Cox *et al.* to determine both n and k of MgF_2 films on Al but that they consider applicable to any thin film with small absorptance. They measure the reflectance of the substrate/film combination as a function of film thickness and fit a curve to the measurements by calculating the reflectance as a function of layer thickness while varying n and k to achieve best fit.

REFERENCES

1. C. Boeckner, *J. Opt. Soc. Am.* **19**, 7 (1919).
2. R. Tousey, *J. Opt. Soc. Am.* **29**, 235 (1939).
3. J. R. Collins and R. O. Bock, *Rev. Sci. Inst.* **14**, 135 (1943).
4. I. Simon, *J. Opt. Soc. Am.* **41**, 336 (1951).
5. D. G. Avery, *Proc. Phys. Soc. (London)* **65**, 425 (1952).
6. S. P. F. Humphreys–Owen, *Proc. Phys. Soc. (London)* **77**, 949 (1961).
7. T. Sasaki and K. Ishiguro, *Japan J. Appl. Phys.* **2**, 289 (1963).
8. A. P. Prishivalko, "Otrazhenie Sveta ot Poglishchaoiuchikh Sred" ["Reflection of Light from Absorbing Media"], Izdate'lstvo, Akademii Nauk, Beloruskoi SSR Minsk, 1963.
9. A Vasicek, "Tables of Determination of Optical Constants from the Intensities of Reflected Light," Nakladatelstvi Ceskoslovenske Akademie Vec, Prague, 1964.
10. D. W. Juenker, *J. Opt. Soc. Am.* **55**, 295 (1965).
11. W. R. Hunter, *J. Opt. Soc. Am.* **55**, 1197 (1965).
12. G. R. Field and E. Murphy, *Appl. Opt.* **10**, 1402 (1971).
13. W. R. Hunter and G. Hass, *J. Opt. Soc. Am.* **64**, 429 (1974).
14. D. Pines, *Rev. Mod. Phys.* **28**, 184 (1956).
15. C. Zener, *Nature*, **132**, 968 (1933).
16. W. R. Hunter, *J. Opt. Soc. Am.* **54**, 15 (1964).
17. U. S. Whang, R. N. Hamm, E. T. Arakawa, and M. W. Williams, *J. Opt. Soc. Am.* **63**, 305 (1973).
18. W. R. Hunter, *J. de Physique* **25**, 154 (1964).
19. G. Hass, W. R. Hunter, and R. Tousey, *J. Opt. Soc. Am.* **47**, 120A (1957).
20. W. R. Hunter, "Proceedings of the International Colloquium on Optical Properties and Electronic Structure of Metals and Alloys" (F. Abélès, ed.), p. 136, North-Holland Publ., Amsterdam, 1966.

21. W. R. Hunter and R. Tousey, *J. de Physique* **25**, 148 (1964).
22. W. R. Hunter, *in* "Physics of Thin Films" (G. Hass, M. Francombe, and R. W. Hoffman, eds.), p. 43, Academic Press, New York, 1973.
23. L. R. Canfield, G. Hass, and J. E. Waylonis, *Appl. Opt.* **5**, 45 (1966).
24. J. T. Cox, G. Hass, and J. E. Waylonis, *Appl Opt.* **7**, 1535 (1968).
25. W. R. Hunter, T. L. Mikes, and G. Hass, *Appl. Opt.* **11**, 1594 (1972).
26. D. Fabre, J. Romand, and B. Vodar, *J. Phys. Radium* **21**, 263 (1960).
27. D. Fabre and J. Romand, *J. Phys. Radium* **22**, 324 (1961).
28. A. Daude, A. Savary, A. Seignac, and S. Robin, *Opt. Acta* **20**, 353 (1973).

Chapter 5

The Accurate Determination of Optical Properties by Ellipsometry

D. E. ASPNES
Bell Communications Research, Inc.
Murray Hill, New Jersey

I. Reflection Techniques; Background and Overview 89
II. Measurement Configurations 92
III. Accurate Determination of Optical Properties: Overlayer Effects 96
IV. Living with Overlayers 99
V. Eliminating Overlayers 102
VI. Bulk and Thin-Film Effects; Effective-Medium Theory 104
VII. Conclusion 108
References 110

I REFLECTION TECHNIQUES; BACKGROUND AND OVERVIEW

In this section, we give some background in electromagnetic theory to aid in understanding the different techniques used to determine optical properties of materials. An incident plane wave propagating in the z-direction of a local orthogonal coordinate system can be represented as [1, 2]

$$\mathbf{E}_i(\mathbf{r}, t) = \mathrm{Re}[(\hat{x}E_x + \hat{y}E_y)e^{ikz - i\omega t}], \tag{1}$$

where E_x and E_y are the *complex field coefficients* describing the amplitude and phase dependences of the projections of $\mathbf{E}_i(\mathbf{r}, t)$ along the x and y axes. If the electromagnetic wave is reflected by a smooth surface, the outgoing wave can be represented in the absence of anisotropic effects in another local coordinate system as

$$\mathbf{E}_r(\mathbf{r}, t) = \mathrm{Re}[(\hat{x}r_p E_x + \hat{y}r_s E_y)e^{ikz' - i\omega t}], \tag{2}$$

HANDBOOK OF OPTICAL CONSTANTS OF SOLIDS

Copyright © 1985 by Academic Press, Inc.
All rights of reproduction in any form reserved.
ISBN 0-12-544420-6

where in both local coordinate systems the x axes are in the plane of incidence, the y axis is perpendicular to the plane of incidence, and the z axes define the plane of incidence.

In this approximation the effect of the surface is described by two coefficients r_p and r_s. These *complex reflectances* describe the action of the sample on the field components parallel (p) and perpendicular (s = German senkrecht) to the plane of incidence. Thus, four parameters—two amplitudes and two phases—are necessary to describe completely the incoming wave and four more to describe the sample. The properties of the sample therefore are obtainable if the properties of both incident and reflected waves are known. *Reflectometry* and *ellipsometry* are two techniques for obtaining this information. Neither extracts all the available data, but each is an incomplete form of a still more general technique, *polarimetry* [3].

To appreciate the different types of information obtained in reflectometry, ellipsometry, and polarimetry, it is useful to recast the four parameters describing the plane waves of Eqs. (1) and (2) into four new parameters by means of the concept of the *polarization ellipse.* The polarization ellipse is the locus traced out in time by the real (observable) electric field vector $\mathbf{E}(\mathbf{r}, t)$ at any fixed plane $z = z_i$. The polarization ellipse has two attributes that can be termed *size* and *shape.* The size $E = (|E_x|^2 + |E_y|^2)^{1/2}$ is a scalar whose square is proportional to the power flow or *intensity* I. The intensity is the only quantity of interest in a reflectance or transmittance measurement and one of the quantities of interest in a polarimetric measurement.

The shape is an intensity-independent quantity that clearly requires two parameters to specify, such as the minor/major axis ratio and the azimuth angle of the major axis of the polarization ellipse. One convenient representation of the shape is the *polarization state* $\chi = E_x/E_y$ [2]. Since E_x and E_y are complex, χ is also complex and therefore contains the required two parameters. For example, if E_x and E_y are in phase, then χ is real, both field components are strictly proportional at all times, and the light is linearly polarized with an azimuth angle $\psi = \tan^{-1} \chi$. If E_x and E_y are 90° out of phase, then χ is purely imaginary and one field component is at a maximum while the other is at zero and vice versa; if, in addition, $|E_x| = |E_y|$, then $\chi = \pm i$, and the light is circularly polarized. The polarization state is the only quantity of interest in ellipsometry and another of the quantities of interest in polarimetry. In addition, polarimetry is also concerned with depolarized or unpolarized light, the superposition of electromagnetic waves in uncorrelated states of polarization.

Given either intensities or polarization states for the incident and reflected beams, the sample properties can be calculated by taking appropriate ratios. In reflectometry, we distinguish between p- and s-polarized light. By Eqs. (1) and (2), the intensity ratios are

$$(I_r/I_i)_p = |r_p E_x|^2/|E_x|^2 = |r_p|^2 = R_p, \tag{3a}$$

$$(I_r/I_i)_s = |r_s E_y|^2/|E_y|^2 = |r_s|^2 = R_s. \tag{3b}$$

The *reflectances* R_p and R_s are the absolute squares of the respective complex reflectance coefficients. At normal incidence both polarizations are equivalent and $R_p = R_s$. In ellipsometry, the ratio of polarization states yields a somewhat different perspective of the sample. By Eqs. (1) and (2)

$$\chi_r/\chi_i = (r_p E_x/r_s E_y)/(E_x/E_y) = r_p/r_s \tag{4a}$$

$$= \rho = (\tan \psi)e^{i\Delta}. \tag{4b}$$

The *complex reflectance ratio* ρ is often expressed as an amplitude $(\tan \psi)$ and a phase Δ. Depolarization or cross-polarization effects determined by polarimetry are important in more complex sample configurations and in the presence of scattering [3], topics that we shall not discuss here.

We can now make some general remarks about the relative advantages and disadvantages of reflectometry, ellipsometry, and polarimetry. For isotropic samples ellipsometry is strictly a nonnormal-incidence technique, while reflectometry and polarimetry can be performed at either normal or nonnormal incidence. Reflectometry deals with intensities and is therefore a power measurement, while ellipsometry deals with intensity-independent complex quantities and is therefore more nearly analogous to an impedance measurement. Because more complicated quantities are involved, an ellipsometer is necessarily more complicated than a reflectometer and a polarimeter is more complicated than an ellipsometer. The most serious drawback of ellipsometers and polarimeters is that transmission through optical elements (e.g., polarizers) is generally required. Therefore, such measurments are limited to those wavelength ranges in which good-quality transmitting elements are available.

Leaving polarimetry as a topic not yet sufficiently developed for detailed discussion, we now consider the relative advantages and disadvantages of reflectometry and ellipsometry. Ellipsometry is unquestionably the more powerful for a number of reasons. First, two parameters instead of one are independently determined in any single-measurement operation. Consequently, both real and imaginary parts of the complex dielectric function ε of a homogeneous material can be obtained directly on a wavelength-by-wavelength basis without having to resort to multiple measurements or to Kramers–Kronig analysis. Two independent parameters also place tighter constraints on models representing more complicated, e.g., laminar microstructures. While two independent parameters R_s and R_p are also available in nonnormal-incidence reflectance measurements, these parameters can be obtained separately only after additional adjustments of system components. Second, ellipsometric measurements are relatively insensitive to intensity fluctuations of the source, temperature drifts of electronic components, and macroscopic roughness. Macroscopic roughness causes light loss by scattering the incident radiation out of the field of the instrument, which can be

a serious problem in reflectometry but not in ellipsometry, for which absolute intensity measurements are not required.

Third, accurate reflectometric measurements are difficult, in general requiring double-beam methods. In contrast, ellipsometry is intrinsically a double-beam method in which one polarization component serves as amplitude and phase reference for the other. Finally, ρ explicitly contains phase information that makes ellipsometry generally more sensitive to surface conditions. Insensitivity to surface conditions is often considered to be an advantage of reflectometry, but this is not correct if the objective is to obtain accurate values of the intrinsic dielectric responses of bulk materials. Because small differences in R can result in large differences in ε, reflectances in general must be measured more accurately. Surface artifacts affect ellipsometric results at the measurement level at which they can be identified and often corrected on the spot, whereas they affect reflectometric results at the data-reduction level at which it may be too late to do anything about them.

II MEASUREMENT CONFIGURATIONS

Despite the intrinsic advantages of ellipsometry, reflectometry historically has been a far more significant factor in advancing our general knowledge of the optical properties of materials. Reflectometers are well suited for spectral measurements, while the classical null ellipsometer is by nature a single-wavelength instrument. The development of photometric ellipsometers has now changed the picture, although spectroscopic instruments must still be built by the user. For this reason, we review in this section some configurations of interest (as of July 1982). More detailed discussions have been given by Azzam and Bashara [2], Hauge [3], Muller [4], and Rzhanov and Svitashev [5].

A schematic diagram of the general optical configuration for reflectometry, ellipsometry, or polarimetry is shown in Fig. 1. The source provides collimated

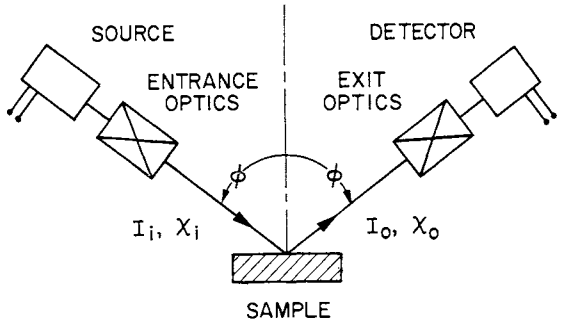

Fig. 1. General configuration for determining optical properties by reflectance techniques.

monochromatic light. The entrance and exit optics establish and analyze, respectively, the intensities, and/or polarization states. The detector may determine absolute or relative intensities or their time dependences.

The simplest configuration is that of a normal-incidence reflectometer. Here, there are no entrance or exit optics. The detector may be moved to intercept either entrance or exit beam or a rotating light pipe may be used. The movable-detector approach is particularly well suited for synchrotron radiation sources because they provide light in spectral ranges in which transmission elements are not available.

Because reflectometry is discussed in detail elsewhere in this volume [6], we now restrict the discussion to ellipsometry. As already implied, the most important instrument until recently was the classical null ellipsometer. Here, the entrance optics consist of a polarizer and compensator, or quarter-wave plate, and the exit optics consist of a second polarizer, or analyzer. The polarizer–compensator combination functions as a general *elliptical* polarizer. In normal operation the ellipticity is adjusted so that it is exactly cancelled by reflection. The reflected beam can then be blocked by properly adjusting the azimuth of the analyzer. The null ellipsometer is the optical analog of the ac impedance bridge.

The twin advantages of the null ellipsometer are mechanical simplicity and high accuracy. If the light source is sufficiently intense, the accuracy limit is determined solely by the mechanical components and their alignment and is not affected by detector nonlinearity. However, these advantages are relatively minor compared to its disadvantages. The null condition cannot be achieved by independent adjustments because the polarizer and analyzer azimuth settings interact. The intensity near null depends quadratically on both azimuths, so the null is not well defined. While Faraday-cell modulation of the plane of polarization can be used to improve null sensitively [7, 8], the detector still operates at minimum light levels so the rate of information flow is small and dark-current and shot noise may be significant. The traditional approach toward dealing with these problems has been to increase the source intensity, which means that in practice most null ellipsometric measurements have been performed at the Hg green line $\lambda = 5461$ Å or more recently at the HeNe laser line $\lambda = 6328$ Å. Consequently, the use of a compensator, a component with a relatively narrow useful wavelength range, has not proved to be the significant handicap.

The modern era in ellipsometry can essentially be traced back to the automatic photometric ellipsometer described by Cahan and Spanier in 1969 [9]. Photometric instruments operate on entirely different principles than do null ellipsometers. One of the components is a modulator that is used to produce a time dependence on the transmitted intensity that is later decoded for the properties of interest. Because most of the light is transmitted, photometric systems are compatible with the relatively weak continuum sources suitable for infrared–visible–near-UV spectroscopy. In the Cahan–Spanier design

[9], the modulator consisted simply of the final analyzer prism, which was rotated mechanically to produce a sinusoidal variation of the transmitted intensity (see the next paragraph). In addition, the data were obtained automatically, with operator feedback not required. A number of configurations [2–5] have also been developed involving photoelastic modulators [10–13] and Pockels cells [14] as well as mechanically rotating elements [15–20] and featuring also digital encoding and analysis of the transmitted intensity. The more elaborate designs [3, 17, 18] also can distinguish between polarized and unpolarized light. Photometric ellipsometers now totally dominate the field as far as research and spectroscopic applications are concerned, with null ellipsometers now mainly relegated to routine measurements on simple systems, such as determining oxide thicknesses on semiconductor wafers.

Only a few of the many photometric designs have been considered sufficiently practical to warrant the time and effort of actual development. The simplest of these are the rotating-analyzer ellipsometer (RAE) [15, 16] and its complement, the rotating-polarizer ellipsometer (RPE) [20]. In these configurations, the entrance and exit optics consist of single polarizing elements, the polarizer and analyzer, respectively. As the names imply, one of these is rotated mechanically while the other is held fixed. The advantages are simplicity and the absence of a compensator; the only wavelength-dependent element is the sample itself. A second advantage is that the transmitted intensity has a very simple Fourier spectrum consisting of a single ac component on a dc background. Disadvantages include the requirement of either a rigorously unpolarized source for an RPE or a rigorously polarization-insensitive detector for an RAE. In addition, as with all photometric systems, the detector must be rigorously linear. Finally, these configurations cannot distinguish between circularly polarized or unpolarized light or the handedness of circularly polarized light, and a significant loss of accuracy occurs for ε_2 if $\varepsilon_2 \cong 0$.

Because photodiodes and end-on photomultipliers are relatively polarization insensitive while equivalently unpolarized sources do not exist, the RAE is preferred over the RPE unless the samples or their environments are themselves sources of significant amounts of radiation. Stray light suppression is much better in an RPE because the monochromator can be placed between sample and detector. With respect to the other limitations, depolarization is not usually a factor unless sample quality is poor. Handedness can be determined from spectral dependences. The inability to measure ε_2 accurately for $\varepsilon_2 \cong 0$ can be circumvented by using a compensator, but this introduces another wavelength-dependent element into the system. A combination of a rotating analyzer followed by a fixed analyzer has been found useful in the infrared [19], where the principal objective is to determine threshold energies of line structures rather than to determine accurate values of dielectric functions.

If a compensator must be used, then the rotating-compensator ellipsometer (RCE) [18] is a more practical alternative. In this configuration, the entrance optics consist of a fixed polarizer and the exit optics of a rotating compensator followed by a fixed analyzer. The fixed polarizers at either end completely eliminate polarization sensitivity artifacts due to source or detector. Moreover, the RCE is capable of measuring handedness and can also distinguish between circularly polarized and unpolarized light [18]. The only reason that RCEs have not completely replaced RAEs and RPEs is that suitable achromatic compensators do not yet exist. With currently available elements, the usable wavelength range of an RCE is about a factor of 2. For fixed-wavelength operation the RCE is superior to an RAE, an RPE, or a null ellipsometer.

Photometric systems that rely on mechanically rotating components are relatively slow, with complete optical cycles requiring about 10 msec. Much higher speeds can be obtained with photoelastic modulators or with Pockels cells. Ellipsometers using these elements are identical to the null ellipsometer except that the compensator is replaced with the modulating element. Modulation frequencies are of the order of 100 kHz for photoelastic units [10–13] and upwards of 1 MHz for Pockels cells [14]. Disadvantages of birefringent-modulation systems include the introduction of another degree of freedom, the modulation amplitude, which in principle should also be measured on a wavelength-by-wavelength basis and should also be correlated with the wavelength for optimum sensitivity. In principle, the modulation amplitude can be obtained from an analysis of the higher-frequency harmonics. Because the operational frequency is much higher, digital analysis may be impractical and several lock-in amplifiers may be required. This introduces the usual calibration and gain uncertainties associated with several independent demodulators. Higher speeds also require higher source intensities.

Other configurations have also been developed, but those already discussed have accounted for most published work and appear entirely adequate when used within their limitations. Future developments will take advantage of the capabilities of photometric configurations to measure absolute intensities as well as polarization states and therefore to determine reflectances as well as complex reflectance ratios. At present, this capability has only been exploited differentially in thin-film measurements in which changes in the reflectance, rather than the reflectance itself, are measured [21]. The development of a truly achromatic compensator would be significant because an RCE using this element could perform spectroscopic measurements over a wide energy range without the limitations of an RAE or RPE.

But for most purposes, at least in the near IR–visible–near UV, instrumentation is a solved problem. The most significant factor responsible for differences among ε spectra is now sample preparation and maintenance, not measurement method or instrumentation. We discuss sample effects in the next section.

III ACCURATE DETERMINATION OF OPTICAL PROPERTIES: OVERLAYER EFFECTS

The accurate determination of the intrinsic optical properties of a material in its pure bulk form is a double challenge, requiring not only accurate instrumentation but also well-characterized samples. Indeed, all reflection techniques for determining ε are model dependent, and the key to success is to prepare and maintain the sample in such a way that it can be described by fewer variables than independent experimental quantities. This is not a trivial matter: visible–near-UV optical properties are so strongly affected by microstructure and surface conditions that optical measurements are a convenient means of characterizing both microstructure [22] and surface quality [23]. As a particular case, the optical properties of evaporated metal films may not be accurately described by intrinsic bulk properties of the constituent material because the samples generally contain a significant volume fraction of voids [24]. We shall return to bulk problems after first discussing difficulties associated with imperfect surfaces.

It is useful to begin with the ideal case, in which the substrate is homogeneous and isotropic and the surface is mathematically sharp. Then ε and the normal incidence reflectance R are given by the two-phase (substrate–ambient) model [2]:

$$\varepsilon/\varepsilon_a = \sin^2\phi + \sin^2\phi \tan^2\phi \left[(1-\rho)/(1+\rho)\right]^2, \tag{5a}$$

$$R = \left|(n-n_a)/(n+n_a)\right|^2, \tag{5b}$$

where ϕ is the angle of incidence and $n = \varepsilon^{1/2}$ and $n_a = \varepsilon_a^{1/2}$ are the complex and ordinary indices of refraction of substrate and ambient, respectively. (We assume that the ambient is transparent.) Although ε and ρ may be transformed interchangeably by Eq. (5a), there are no corresponding expressions for ε and R, R_s, and R_p. The analogous equations for these quantities must be solved numerically for ε [25].

For real samples, the assumption of a mathematically sharp interface leads to immediate practical difficulties. Transition-region widths are finite even if the lattice termination is atomically perfect. Under typical laboratory conditions, surfaces are covered with oxides or adsorbed contaminants. Surfaces are usually microscopically rough, often as a result of cleaning processes used to remove the other overlayers. If such effects are not taken into account, the optical parameters calculated from Eqs. (5) may be considerably in error [26]. However, in the analysis of ellipsometric data it is often useful to assume perfection anyway and to convert the measured quantity ρ into a derived quantity, the *pseudodielectric function* $\langle\varepsilon\rangle$, by Eq. (5a). The pseudodielectric function necessarily is an average of the dielectric responses of substrate and overlayer, and the accuracy by which it actually represents ε depends on the accuracy by which the sample configuration approximates

that of the ideal two-phase model. The pseudodielectric function is useful simply because it expresses ρ in a form related to the fundamental quantity of interest. The complex reflectance ratio can always be recovered from $\langle\varepsilon\rangle$ by inverting Eq. (5a).

The importance of surface conditions can be appreciated by noting that penetration depths of light in opaque materials are typically 100–500 Å in the near UV, whence a 1-Å surface film can affect ρ, $\langle\varepsilon\rangle$, or R as much as several percentage points. This can be shown quantitatively by expanding ρ, $\langle\varepsilon\rangle$, and R to first order in d/λ, where d is the film thickness. We have [26, 27]

$$\rho \cong \rho_0\left[1 + \frac{4\pi i d n_a \cos\phi}{\lambda}\frac{\varepsilon(\varepsilon-\varepsilon_o)(\varepsilon_o-\varepsilon_a)}{\varepsilon_o(\varepsilon-\varepsilon_a)(\varepsilon\cot^2\phi-\varepsilon_a)}\right]; \tag{6a}$$

$$\langle\varepsilon\rangle \cong \varepsilon + \frac{4\pi i d}{\lambda}\frac{\varepsilon(\varepsilon-\varepsilon_o)(\varepsilon_o-\varepsilon_a)}{\varepsilon_o(\varepsilon-\varepsilon_a)}(\varepsilon-\varepsilon_a\sin^2\phi)^{1/2}; \tag{6b}$$

$$\cong \varepsilon + (4\pi i d/\lambda)\varepsilon^{3/2}; \tag{6c}$$

$$R \cong R_0\left[1 + \frac{8\pi n_a d}{\lambda}\,\mathrm{Im}\left(\frac{\varepsilon_o-\varepsilon_a}{\varepsilon-\varepsilon_a}\right)\right]. \tag{6d}$$

In Eqs. (6), ε_o is the effective dielectric function of the overlayer and ρ_0 and R_0 are the corresponding values for the ideal system. The quantity ε_o may be anisotropic because ε_o can be defined in terms of spatial averages that are different for s- and p-polarized light [28]. However, effects due to anisotropy are usually small, and we ignore them here. Equation (6c) follows from (6b) in the limit that $|\varepsilon| \gg |\varepsilon_o| \gg |\varepsilon_a|$. Note that ε_o has dropped out of Eq. (6c) completely, so that relative changes in d can be investigated through $\langle\varepsilon\rangle$ without having to identify the nature of the overlayer materials [29].

Effects of oxide overlayers and microscopic roughness on $\langle\varepsilon\rangle$ and R are shown in Figs. 2 and 3 for a typical semiconductor, GaAs. These calculations were done by using the exact three-phase (substrate–overlayer–ambient) model [2] instead of Eqs. (6). The dielectric function of the oxide was assumed to be that of an electrochemically grown anodic film [30]. Microscopic roughness was modeled in the Bruggeman effective medium approximation [31] as a layer consisting of 60% substrate material and 40% voids, values typical of microscopically rough surface on semiconductors [29, 32]. The effect on $\langle\varepsilon\rangle$ of a microscopically rough layer 14 Å thick is identical to that of a 10-Å oxide on the scale of Fig. 2. Figures 2 and 3 show that at higher energies $\langle\varepsilon\rangle$ is about three times more sensitive than R to the presence of overlayers; the quantitative ratio of the relative sensitivities of R and $\langle\varepsilon\rangle$ is seen by Eqs. (6c) and (6b) to be

$$\left|\frac{\delta R/R}{\delta\langle\varepsilon\rangle/\langle\varepsilon\rangle}\right| \cong \frac{2n_a}{|\varepsilon|^{3/2}}\,\mathrm{Im}\left(\frac{\varepsilon_o-\varepsilon_a}{\varepsilon-\varepsilon_a}\right), \tag{7}$$

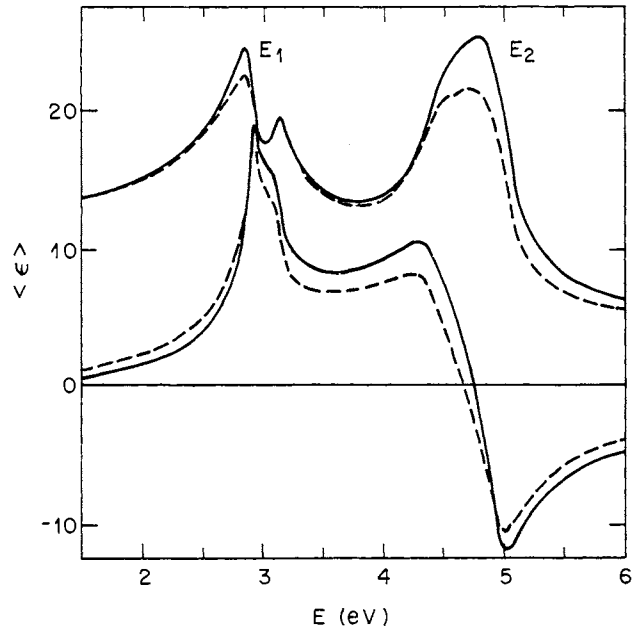

Fig. 2. Effect of a 10-Å oxide on $\langle \varepsilon \rangle$ for GaAs. The results for a 14-Å-thick microscopically rough surface are identical to this scale. [——, abrupt; – – – –, oxidized (d = 10 Å).]

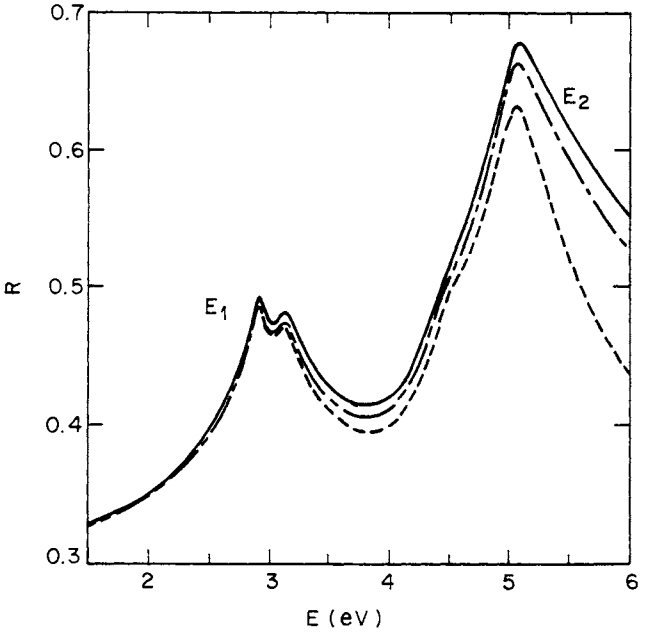

Fig. 3. As in Fig. 2 but for R. Note that the film thicknesses are larger than those in Fig. 2. [——, abrupt; — — —, rough (d = 30 Å); – – – –, oxidized (d = 30 Å).]

about $\frac{1}{3}$ at the 4.78-eV E_2 peak in ε_2 for an oxide on GaAs. At low energies where ε and ε_o are real, the first-order dependence of R on d vanishes. Figure 3 shows that the effect of microscopic roughness on R, as with $\langle\varepsilon\rangle$, is also qualitatively similar to that of an oxide overlayer.

The spectroscopic dependence of the effect of an overlayer on $\langle\varepsilon\rangle$ can be understood from Eq. (6c). At low energies $\varepsilon^{3/2}$ is real, so overlayers affect only $\langle\varepsilon_2\rangle$. Or, equivalently, Eq. (6a) shows that $\Delta = \arg(\rho)$ is affected, but not $\psi = \tan^{-1}|\rho|$. The importance of Δ in providing information about surface films has long been known [26, 33–42]. As the energy increases, $\varepsilon^{3/2}$ becomes purely imaginary and the effect of the overlayer shifts entirely over to $\langle\varepsilon_1\rangle$. At still higher energies, $\varepsilon^{3/2}$ becomes completely real and the effect again shifts back to $\langle\varepsilon_2\rangle$.

LIVING WITH OVERLAYERS IV

Basically, there are two courses of action to follow in dealing with overlayers. First, overlayers can be accepted as a necessary evil and their effects identified by proper data acquisition and reduction. In this approach the sample is represented by a more complicated three-phase (substrate–overlayer–ambient) model and additional measurements are made to determine the extra parameters. For example, auxiliary measurements can be used to independently determine the overlayer thickness. Alternatively, the data can be effectively overdetermined and the inadequacy of the two-phase model made apparent by varying the angle of incidence or the refractive index of the ambient medium. To use this approach successfully, all parameters of the three-phase model (itself an approximation) must be obtained independently. Second, overlayers may be removed as far as possible and the sample maintained in a state that most nearly approximates the ideal two-phase model. Both approaches have their advantages and limitations.

We consider the laissez-faire approach first. Most work of this type has been done with null ellipsometers at single wavelengths on samples for which overlayers are nominally transparent oxides. Overlayer transparency already represents a considerable simplification because if $\mathrm{Im}(\varepsilon_o) = 0$, then only the thickness and ordinary refractive index of the overlayer need be determined. If the substrate is also transparent or nearly transparent, as is the situation for Si at the 5461- and 6328-Å wavelengths commonly used with null ellipsometers, then ψ and Δ become essentially independent, with ψ being only a function of ε_1 and Δ of ε_2 and the overlayer thickness in the form of the product $(n_o d)$. Thus, ε_1 can be obtained directly with essentially no interference from the overlayer.

Even with these simplications, considerably more effort is required to obtain ε_2, and a number of approaches have been tried. The most direct is

simply to measure d by an alternative method and then to assume that the thickness so determined is also appropriate for the optical measurement. As an example, Claussen and Flower [35] used reflection electron scattering to determine the thickness of the residual SiO_2 layer on hydrogen-annealed Si wafers and obtained a complex refractive index of $n = 4.05 + i0.03$ at 5461 Å for Si, in rather good agreement with the current best value [43] $n = (4.086 \pm 0.003) + i(0.031 \pm 0.0015)$. However, the validity of the assumption of equivalent optical and SiO_2 thicknesses is questionable in view of the recent work by Chang and Boulin [44], who showed that ellipsometrically determined "SiO_2" thicknesses for overlayers with $d \lesssim 120$ Å were consistently larger than those determined by Auger spectroscopy. The discrepancy was attributed to a Si-rich interface region.

A second approach is to use transmission measurements to determine a small substrate extinction coefficient and to use this value in the data-reduction process. Where applicable, transmission measurements are invariably much more accurate than reflection measurements simply because more material interacts with the electromagnetic radiation. The combined transmission–ellipsometric method works well for Si at 5461 and 6328 Å and was used by Taft [43] to obtain the accurate refractive index value quoted in the preceding paragraph. This approach has been used numerous times in the analysis of optical properties and oxide thicknesses on Si [39, 40, 43].

"Self-contained" approaches involving only ellipsometry must rely on multiple measurements at the same wavelength to determine all parameters of the system. Most methods that have been developed are useful only when the overlayer is transparent. In fact, most of these have only been tested on Si, a material whose technological importance and ready availability in high-quality, single-crystal form has made it a favorite for this purpose. Thus, measurements of a sample in air can be compared with measurements of the same sample immersed in liquids of various indices of refraction [37, 45, 46]. The assumption is that immersion does not affect the properties of the sample. Another approach is to make measurements at different angles of incidence [47–50] or to modulate directly the angle of incidence [51–53]. The latter approach was used by Bermudez in a spectroscopic ellipsometric study of F-center generation by UV irradiation of KCl [53]. Hunderi [50] has shown that to terms linear in d/λ the quantity $\bar{N} = (\langle\varepsilon\rangle - \varepsilon_a \sin^2\phi)^{1/2}$ [as represented by using parameters defined in Eq. (5a) and the ensuing discussion] differs from $N = (\varepsilon - \varepsilon_a \sin^2\phi)^{1/2}$ by a quantity independent of ϕ. Therefore, by examining the rate of change of $\bar{N}$ with ϕ, one can determine ε regardless of the values of ε_0 or d. Several workers have also proposed to use the approximate invariance of R to provide a third condition and thereby to place another constraint on the system [54, 55].

The capabilities and limitations of these techniques with respect to very thin films can be understood from Eq. (6b). In this expression, the leading terms $\langle\varepsilon\rangle$ and ε are already independent of d, ε_a, and ϕ, so the possibility

of determining the correction term from its functional dependence on these variables can be examined directly. The dependences on d and λ are not very useful because d is not generally under direct experimental control (or we would simply make it zero), and the functional dependence of ε on λ is the quantity being sought. In principle, the choice $\varepsilon_a = \varepsilon_o$ eliminates the correction term entirely; a good example [46] is the use of CCl_4 with Si because CCl_4 index-matches fused silica almost exactly. However, the method does not work if ε_o is complex, and in fact the approach can never provide unique information unless ε_a is also allowed to take on complex values. The same limitation is encountered by varying ϕ. Moreover, the variation of the correction term with ϕ is already very weak, especially for large values of ε, as seen directly in Eq. (6b). The same comments apply to Hunderi's approach [50], since his expression is also equivalent to Eq. (6b). The condition provided by the invariance of R likewise cannot provide unique information because only a single-phase projection is involved. In short, nothing works well if $d/\lambda \ll 1$ and if ε_o takes on arbitrary values.

However, variations in d can be useful if the film is transparent and $d \sim \lambda$. The method of Lukes *et al.* [45] involves measurements at various thicknesses as well as immersion in various ambients, although later refinements [49] incorporated measurements at multiple angles of incidence in addition to circumventing the immersion requirement. Taft and Cordes [56] used controlled etching to systematically reduce the thickness of a 7000-Å thermally grown oxide on a Si wafer; ellipsometric measurements at 5461 Å at various stages of etching yielded not only the ordinary refractive index of the oxide but also the small strain birefringence of the film and showed in addition the existence of a 6-Å interfacial layer of refractive index 2.8. Similar single-wavelength ellipsometric measurements were performed on anodized GaAs samples by Dinges [57]. It is noteworthy that oxide-removal techniques were the first to determine by optical means the existence of fairly wide ($\sim$5–10-Å) interface regions between oxides and substrates, a consequence of the sensitivity of optical measurements to interface conditions at wavelengths and angles of incidence corresponding to antireflection [58]. In this regard, we mention the reflectance technique developed by Jungk [59] in which half the sample is stripped of its oxide and the angle of incidence adjusted so there is no difference in R_p between the two halves. Then ϕ is just equal to the Brewster's angle of the oxide, and its index can be readily calculated.

Spectral measurements offer other alternatives for overlayer correction, and they also illustrate shortcomings not evident from single-wavelength measurements. In principle, a thickness determined at a wavelength where the overlayer is known to be transparent should be valid at all wavelengths. However, attempts [60] to determine substrate optical properties for GaSb by solving simultaneously the exact three-phase equations for both ε and ε_o from data for two samples with 30- and 2000-Å oxides showed about a 10%

overcorrection in ε_2 in the near UV when compared with more recent data [61]. Daunois and Aspnes [62] assumed an SiO_2 layer on a Si wafer and established the thickness by requiring that $\varepsilon_2 \to 0$ as $E \to 1.5$ eV; the resultant height of the E_2 peak in $\langle \varepsilon_2 \rangle$ went from 40.46 at 4.22 eV to 52.35 at 4.25 eV compared to the current "best" value 46.8 at 4.25 eV [61]. Consequently, the assumption of uniform overlayers with the optical properties of ideal oxides cannot always be justified, although it continues to be used [12, 63].

In fact, there is mounting evidence [30, 56, 57, 64, 65] that interfaces do not have the optical properties of either oxide or substrate. Philipp [65] noted that the characteristic SiO_2 structure did not appear as expected at 10.2 eV in normal-incidence reflectance data for Si [66] and so corrected these data for 15 Å of SiO instead of SiO_2. In single-wavelength null-ellipsometric work on the Si–thermally oxidized SiO_2 system, Taft and Cordes [56] found a 6-Å interface of refractive index 2.8 as already mentioned, while in spectroscopic ellipsometric measurements on similar oxides Aspnes and Theeten [64] found 7 ± 2 Å of $SiO_{0.4 \pm 0.2}$. Some $\langle \varepsilon \rangle$ data have been corrected by assuming that the residual interface layer after chemical stripping is that of the oxide interface itself [30, 64]. While the variations in the "best" values of ε obtained by *post hoc* correction procedures are getting smaller, this approach obviously still leaves something to be desired. The subject has been discussed recently by Jellison and Modine [67].

V ELIMINATING OVERLAYERS

The preparation of high-quality samples with minimal overlayer thickness is an approach that actually has seen surprisingly little use. The importance of sample preparation and of maintaining surfaces in inert ambients such as dry N_2 was stressed as early as 1958 by Archer [68] and re-emphasized by Donovan *et al.* in 1963 [69]. It is no accident that the discrete-wavelength ellipsometric data of Archer [68] and the reflectance spectra of Donovan *et al.* [69], both on Ge, agree within several percentage points with recent work [61] in a field where discrepancies of 10–20% are not uncommon.

To successfully eliminate overlayers requires an unambiguous means of assessing overlayer thickness in real time. Null ellipsometers are simply too slow, and moreover the long-wavelength sensitivity of Δ to the presence of overlayers is not useful because it is not unique. For example, the refractive index of amorphous silicon at long wavelengths is about 10% greater than that of crystalline material, so changes in Δ can have either sign according to whether the overlayer is an oxide or is simply disordered material. Some techniques, such as vacuum ultraviolet reflectometry, are incompatible with real-time assessment, and also involve environments in which samples undergo some oxidation during preparation (loading and pumpdown). The early

reflectance data of Philipp and co-workers [66, 70, 71] show evidence of such artifacts [61].

Photometric instrumentation has solved the speed problem because measurements can be made within seconds of processing if the sample is optically prealigned [72]. The uniqueness problem can also be solved by measuring at the energy corresponding to the E_2 peak in $\langle\varepsilon\rangle$ [29]. The argument is as follows. The magnitude of the peak and the energy at which it occurs are the combined result of the type of atoms constituting the crystal and the long-range order. If either is modified, e.g., by oxidation, disorder, or microscopic roughness, then the dielectric response of the surface region will drop below its bulk value. This tends to impedance-match ambient to substrate, thereby lowering R and $\langle\varepsilon\rangle$. The effect can be summarized qualitatively as "biggest is best" and is illustrated in Fig. 4, which shows $\langle\varepsilon_2\rangle$ spectra of a single InSb sample after various surface treatments [29, 72]. The similarity to Fig. 2 is apparent. The spectrum that most nearly approximates the true bulk dielectric response is that with the highest value of $\langle\varepsilon_2\rangle$. Other advantages of measurements at the E_2 peak are that the penetration depth of light is near its minimum value so that surface effects are most pronounced. Also, the wavelength is shorter so the expansion term d/λ is larger for a given d. A similar connection between sample quality and the height of the E_2 peak also occurs in reflectance [73, 74].

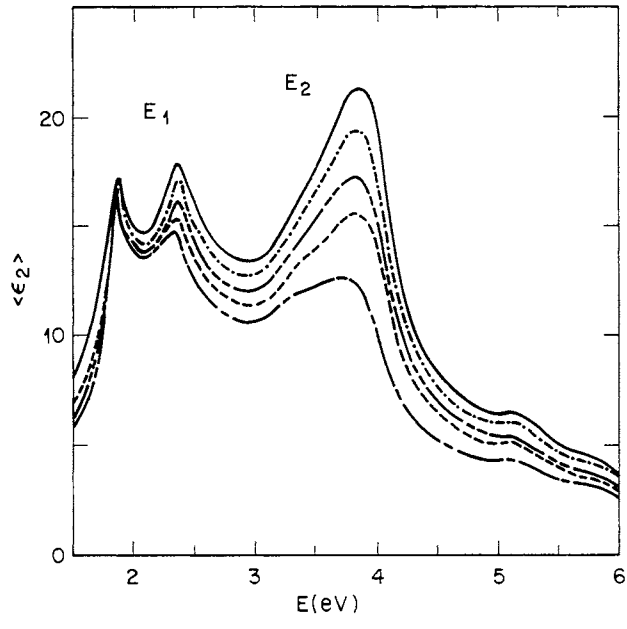

Fig. 4. $\langle\varepsilon_2\rangle$ spectra for InSb for various surface conditions: (a–c) ⟨100⟩ surface after chemomechanical polishing and after 6- and 27-h exposures to 1:1 HCl:methanol; (d and e) ⟨110⟩ surface after 1:1 HCl:methanol and after the procedure described by Aspnes and Studna [61]. (——, e; —·—·, d; – – – –, c; – – –, b; ———, a.)

Aspnes and Studna [72, 75] investigated various procedures for obtaining surfaces with narrow transition regions on semiconductors. The best surfaces on Si and Ge were obtained by chemical etching. Atomically clean surfaces prepared in ultrahigh vacuum by ion bombardment and annealing were poorer [76], probably as the result of subsurface damage and reconstruction that occurs in the direction normal to the surface plane. Cleavage was also observed to give poor results: Transition regions were broader, and the surfaces oxidized at a much faster rate than chemically etched surfaces, consistent with previous work [37, 39] and indicative of a large number of active sites from cracks or damage. The best chemical procedures involved a chemomechanical polish with Syton or a weak ($\sim$0.05-vol. %) solution of bromine in methanol, followed by crystal- and orientation-specific procedures for removing residual overlayers [72, 75]. Standard chemical polishing solutions such as CP-4 (HNO_3:HF:CH_3COOH 5:3:3) left the surfaces microscopically rough. However, microscopically smooth $\langle 111 \rangle$ surfaces could be obtained on Si with an etch consisting of HNO_3:HF 10:1. Other surfaces were not investigated in detail.

In retrospect, the superior performance of chemical processing probably follows because the correct combination of reagents should produce an etch that only attacks edge and corner atoms and leaves the surface atomically flat. The process is the inverse of habit plane formation in crystal growth. While such surfaces are not atomically clean, the chemisorbed monolayer(s) provides a more natural termination of the electronic wave functions and appears to preserve bulk dielectric function behavior closer to the surface.

Even greater control should be obtainable with the sample immersed in an electrolyte. Here, various oxidation potentials could be established with proper reactants, and interface potentials could also be controlled externally. Ellipsometric measurements on such surfaces have been reported for InSb [77] and appear to be promising for preparing high-quality surfaces on other materials.

While attractive for low-index faces of single crystals, the chemical preparation approach may not be useful for composite materials or for highly reactive materials such as Al or Ti. In the former case, sharp interfaces probably cannot be obtained owing to the microstructure of the material, while in the latter case, the only appropriate environment is ultrahigh vacuum.

VI BULK AND THIN-FILM EFFECTS; EFFECTIVE-MEDIUM THEORY

The preceding discussion on overlayers presumes homogeneous bulk material. It is often necessary to determine the optical properties of heterogeneous or composite systems that are more accurately described as mixtures of separate regions of two or more materials, each of which retains its

own dielectric identity. This is the objective of effective-medium theory. Examples of composite materials include metal films, which can be described as heterogeneous mixtures of material and voids owing to the inability of forming grain boundaries in close-packed systems without some loss of material [24]. Other examples include polycrystalline films, amorphous materials, and glasses; in the latter two cases, the inhomogeneity is essentially on the atomic scale and concerns the number of polarizable elements (bonds) per unit volume. A microscopically rough surface can also be considered a heterogeneous medium, being a mixture of bulk and ambient on a microscopic scale. In this discussion, we assume that the characteristic dimensions of the microstructure are large enough ($\gtrsim$10–20 Å) so that the individual regions retain essentially their bulk dielectric responses, but small ($\lesssim$0.1–0.2λ) compared to the wavelength of light. Then, the macroscopic **E** and **H** fields of Maxwell's equations will not vary appreciably over any single region, and quasistatic theory can be used. This avoids complications due to scattering and retardation effects that are dominant in macroscopically inhomogeneous systems [78].

The optical properties of heterogeneous systems are calculated in the same way that macroscopic quantities or observables are calculated in thermodynamics or quantum mechanics. First, the microscopic problem is solved exactly; then the microscopic quantities are averaged to obtain their macroscopic counterparts. The dielectric function is obtained from the macroscopic average electric field **E** and polarization **P** according to

$$\mathbf{D} = \varepsilon\mathbf{E} = \mathbf{E} + 4\pi\mathbf{P}, \tag{7a}$$

$$\mathbf{P} = \frac{1}{V}\sum q_i \, \Delta\mathbf{x}_i, \tag{7b}$$

where $\Delta\mathbf{x}_i$ is the displacement of the charge q_i under the action of the local field at q_i. It is the appearance of the volume normalizing factor in Eq. (7b) that is responsible for the sensitivity of ε to density.

A qualitative understanding of effective-medium effects can be obtained by considering the configuration of a metal sphere in an insulating dielectric, as shown in Fig. 5 [79]. Owing to its large polarizability, screening charge collects on the surface of the sphere and prevents the electric field from penetrating. The distortions in the microscopic field and polarization that result are what give rise to "local-field effects" and dielectric functions that differ from simple averages of those of the constituents. As indicated in Fig. 5, the more-polarizable species in any composite provides the screening charge and tends to contribute less than expected from simple volume arguments. Consequently, the less-polarizable species (e.g., voids) tends to dominate the dielectric response of composite materials.

If the electrostatic solution for the dielectric sphere in a dielectric host is volume averaged, then the Maxwell–Garnett effective-medium expression is

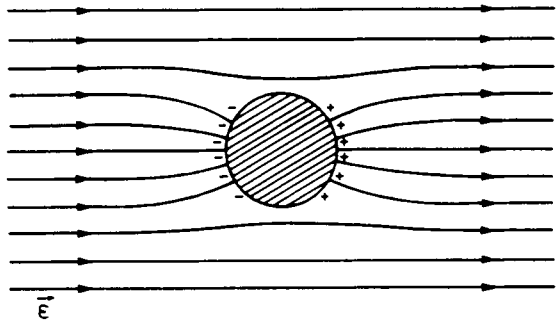

Fig. 5. Effect of screening on the local field near a metal sphere in an insulating matrix.

obtained. A general representation of two-phase effective-medium theories appropriate to three-dimensionally isotropic systems is [32]

$$\frac{\varepsilon - \varepsilon_h}{\varepsilon + 2\varepsilon_h} = f_a \frac{\varepsilon_a - \varepsilon_h}{\varepsilon_a + 2\varepsilon_h} + f_b \frac{\varepsilon_b - \varepsilon_h}{\varepsilon_b + 2\varepsilon_h}, \tag{8}$$

where ε_a, ε_b and f_a, f_b are the dielectric functions and volume fractions of the phases a and b. The quantity ε_h is a host dielectric function that is assigned different values according to the model. To obtain the Maxwell–Garnett expressions [80], a or b is considered the host medium, so $\varepsilon_h = \varepsilon_a$ or ε_b, and one of the two terms on the right-hand side of Eq. (8) vanishes. The Bruggeman effective-medium approximation (EMA) [31] is obtained by making the self-consistent choice $\varepsilon_h = \varepsilon$, in which case the left-hand side vanishes. The Lorentz–Lorenz expression [81, 82] is obtained by choosing $\varepsilon_h = 1$, i.e., empty space.

The various effective-medium theories actually differ only in the choice of host material, but this choice does imply different microstructures. Thus, the Maxwell–Garnett theories, with one medium completely surrounded by another, are appropriate to the cermet or coated sphere microstructures, while the Bruggeman theory is appropriate to random or aggregate configurations [83]. The aggregate microstructure can also be considered as an average over grain shapes, and probably more accurately describes most thin films.

Effective-medium theory can be used to understand differences in optical properties of metal films, as shown in Fig. 6. Here, representative ε spectra from among the 30 or so available in the literature are presented for Au. The data of Thèye [84] were obtained by combined transmittance–reflectance measurements of thin ($\sim$200-Å) films deposited and annealed in ultrahigh vacuum. The spectroscopic ellipsometric data of Aspnes *et al.* [85] fall into three categories: films deposited by electron-beam evaporation under conditions similar to those of Thèye but not annealed and films prepared at moderate ($\sim 10^{-6}$-torr) pressures by filament evaporation onto room-temperature

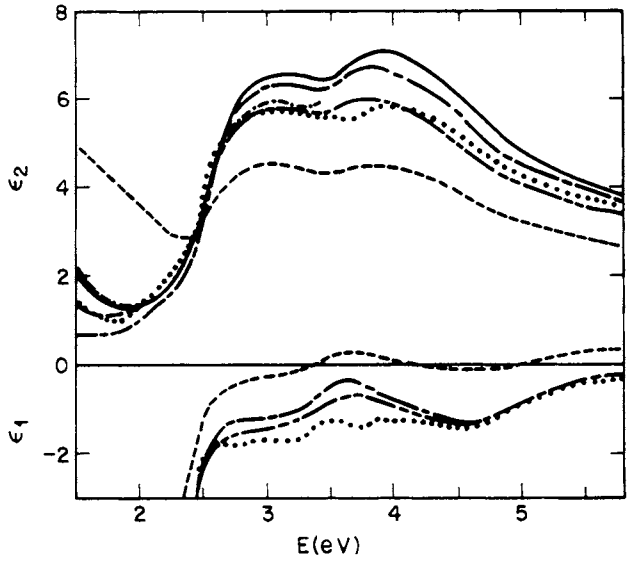

Fig. 6. Representative ε spectra for Au as described in the text. Thèye [84] (——); Johnson and Christy [86] (·····); Winsemius [87] (–·–·–·–); Aspnes *et al.* [85]: electron-beam deposition (— — —), evaporation onto room-temperature substrate (— · — · —), and evaporation onto liquid-nitrogen-cooled substrate (– – – –).

and liquid-nitrogen-cooled substrates. The data of Johnson and Christy [86] were obtained by combined transmittance–reflectance measurements on films deposited by filament evaporation on room-temperature substrates. The agreement between ε_2 spectra for the two films deposited under basically identical conditions indicates again that sample preparation is more important than measurement method. The data of Winsemius [87] were obtained ellipsometrically on bulk samples cleaned and annealed at 700 K for several hours in ultrahigh vacuum.

All data clearly show the plasma edge at 2.5 eV and higher-energy structures, but there are significant differences in amplitude. These can be understood by supposing that the densities of the various films are different. If $\varepsilon_b = 1$ represents the void phase and ε_a the metal, with $f_b \ll 1$, then to first order in f_b either the Bruggeman or Maxwell–Garnett forms of Eq. (8) yields

$$\varepsilon = \varepsilon_a\{1 - 3f_b[(\varepsilon_a - 1)/(2\varepsilon_a + 1)]\}, \tag{9a}$$

$$\varepsilon \cong \varepsilon_a(1 - \tfrac{3}{2}f_b), \tag{9b}$$

where Eq. (9b) follows if $|\varepsilon_a| \gg 1$. For increasing concentrations of voids, the dielectric response simply scales to lower values approaching $\varepsilon_b = 1 + i0$. The decrease in ε is $\frac{3}{2}$ times the actual density deficit, a result of the metal screening itself more effectively as discussed in connection with Fig. 5. The void fraction of 0.21 calculated by comparing the electron-beam-evaporated

and liquid-nitrogen-cooled film data of Fig. 6 is consistent with TEM micrographs, which show 12% clear aperture in the 500-Å film deposited on the cooled substrate. The remaining 9% missing material can be accounted as voids in the film network. Below 2.5 eV a pronounced Drude tail appears in ε_2 for the porous film, indicating increased broadening from surface collisions and therefore a smaller grain size. Surface scattering becomes important when the grain size drops significantly below the intrinsic mean free path, which for Au is 400 Å at room temperature.

A careful examination of Fig. 6 shows that both ε_1 and ε_2 spectra of the films evaporated on room-temperature substrates have been displaced downward with respect to the corresponding spectra for the electron-beam-evaporated film, while Eqs. (9) would predict that the ε_1 spectra should be displaced upward. This effect is due to surface roughness, which is an increasingly important factor for thicker films. The separation of surface roughness and density effects can only be done if both ε_1 and ε_2 spectra are available.

From the preceding analysis, we can conclude that the ε_2 spectrum most representative of the intrinsic dielectric response of Au is that of Thèye, while the spectrum most representative of the dielectric response of films deposited e.g., under the pressure and substrate temperature conditions used by Johnson and Christy, are those of Johnson and Christy.

The effective-medium arguments apply in general to optical data on metal films and allow differences among conflicting handbook data for a particular metal to be understood. For example, the "American Institute of Physics Handbook" [88] gives three sets of data for the complex refractive index of Ag at $\lambda = 10$ μm, from which we calculate $\varepsilon = -2700 + i1400$ [89], $-3570 + i1310$ [90], and $-4650 + i1480$ [91]. From this discussion, it follows that both real and imaginary parts of ε are related to film density but that ε_2 depends in addition on grain size. It follows that the first datum [89] corresponds to the least dense material with the smallest grain size and that the last datum [91] most accurately represents the true bulk dielectric function of Ag.

VII CONCLUSION

We have discussed a number of methods developed to determine accurate values for bulk dielectric properties of materials. Which is best? The following comments, applicable primarily but not exclusively to spectral work in the visible–near UV, can be made.

Kramers–Kronig and related analyses of reflectance data are probably least accurate because they require reflectance data over the entire energy range or complete ε_1, ε_2 data at certain wavelenghts or ranges of wave-

lengths [92, 93] or accurate extrapolations into experimentally inaccessible spectral regions. Unfortunately, these procedures are also sensitive both to small errors in reflectances and to extrapolations, and reflectances are generally difficult to measure accurately. For example, reflectance measurements on Si have been performed and analyzed from 0 to 25 eV by Philipp and coworkers [65, 66] and from 0.5 to 10 eV by Verleur [94]. The values obtained for the E_2 peak in R near 4.6 eV were 0.73 and 0.82, respectively. While one would expect Verleur's data to yield the higher value for the corresponding E_2 peak in ε_2 at 4.25 eV, the actual values determined in the analysis of the reflectance data were 41.2 and 27.8, respectively. The difference was due essentially to extrapolation procedures, even though data were available in both analyses to 10 eV, seemingly sufficiently far from the evaluated point.

In a more extreme case, Morrison [73] calculated a "peak" value of 5 at the 4 eV E_2 peak of ε_2 for InAs from reflectance results determined experimentally from 0 to 6 eV and extrapolated via a power-law relationship to higher energy. Here, the error is due almost entirely to the extrapolation procedure; in a Kramers–Kronig analysis of their 0–27-eV reflectance data, Philipp and Ehrenreich [70] obtained 21 at 4.45 eV, in quite reasonable agreement with the value of 22.81 at the same energy obtained via an optimized-surface approach [61].

Extrapolation errors can be reduced in principle by making use of fixed-phase points established by independently measured values of ε_1 and ε_2 [92, 93]. However this procedure can also lead to considerable error. For example, Grasso *et al.* [95] obtained an E_2 peak of 31 for ε_2 at 4.8 eV for GaAs from an R peak of 0.59, compared to ellipsometric values [61] of 25.22 and 0.677, respectively. The low value of R observed by Grasso *et al.* indicates that the actual sample was covered with a significant overlayer. Nevertheless, the calculated ε_2 value was larger, which indicates a probable error in the Kramers–Kronig analysis of the order of 50%. The error arises because even though the integrand in the Ahrenkel algorithm [92] used in the calculation converges as E^{-4}, the prefactor is proportional to E^3. Thus, extrapolation is still important. The message is clear: A Kramers–Kronig analysis should be attempted only if accurate reflectance data are available over a very, very wide energy range.

The second approach is to overdetermine the data enough to be able to determine the substrate parameters and those describing the overlayer independently. This approach requires some assumptions about the nature of the surface and substrate, but it may be the only alternative for reactive materials for which clean surfaces are difficult to obtain or for composite materials for which smooth surfaces may be difficult to obtain. This approach has been used widely for Si at 5461 Å and has given fairly consistent results, although in some respects the transparent oxide and nearly transparent substrate characteristic of this system make it particularly favorable for this type of analysis. The results at higher energies are less convincing: at 3655 Å,

Ibrahim and Bashara [48] and So and Vedam [49] obtained $36.93 + i36.69$ and $(39.43 \pm 0.44) + i(29.57 \pm 0.6)$, respectively, a substantial difference in view of the expected accuracy of the technique. Nevertheless, over-determination seems preferable to the Kramers–Kronig approach if for no other reason than that it offers some self-consistency checks.

The third approach is to concentrate on preparing high-quality samples and eliminating surface overlayers as far as possible. The most consistent results for a given material, regardless of measurement technique, have been obtained in this way. The observed consistency instills some confidence that the values obtained are representative of the intrinsic dielectric response. Although arbitrarily accurate values can never be obtained in this manner, it appears that errors introduced by the neglect of finite transition region widths are less than those resulting from overdetermination, correction, or Kramers–Kronig analysis procedures.

We have not discussed explicitly the determination of intrinsic optical properties of glasses, polycrystalline semiconductors, polymers, anisotropic materials, or other important classes of solids and thin films. The same general remarks apply, but each material seems to give rise to its own special problems. The problem of the accurate determination of intrinsic dielectric properties has not yet been solved in general.

REFERENCES

1. J. D. Jackson, "Classical Electrodynamics," 5th ed., Wiley, New York, 1975.
2. R. M. A. Azzam and N. M. Bashara, "Ellipsometry and Polarized Light," North-Holland Publ., Amsterdam, 1977.
3. P. S. Hauge, *Surf. Sci.* **96**, 108 (1979).
4. R. H. Muller, *Surf. Sci.* **56**, 19 (1976).
5. A. V. Rzhanov and K. K. Svitashev, *Adv. Electron. Electron Phys.* **49**, 1 (1979).
6. See Chapter 4, this volume.
7. A. B. Winterbottom, *in* "Ellipsometry in the Measurement of Surfaces and Thin Films" (E. Passaglia, R. R. Stromberg, and J. Kruger eds.), p. 97, National Bureau of Standards Special Publication 256, 1963.
8. H. J. Mathieu, D. E. McClure, and R. H. Muller, *Rev. Sci. Instrum.* **45**, 798 (1974).
9. B. D. Cahan and R. F. Spanier, *Surf. Sci.* **16**, 166 (1969).
10. S. N. Jasperson and S. E. Schnatterly, *Rev. Sci. Instrum.* **40**, 761 (1969).
11. V. M. Bermudez and V. H. Ritz, *Appl. Opt.* **17**, 542 (1978).
12. G. E. Jellison, Jr., and F. A. Modine, *J. Appl. Phys.* **53**, 3745 (1982).
13. B. Drevillon, J. Perrin, R. Marbot, A. Violet, and J. L. Dalby, *Rev. Sci. Instrum.* **53**, 104 (1982).
14. B. H. Billings, *J. Opt. Soc. Am.* **42**, 12 (1952).
15. P. S. Hauge and F. H. Dill, *IBM J. Res. Dev.* **17**, 472 (1973).
16. D. E. Aspnes and A. A. Studna, *Appl. Opt.* **14**, 220 (1975).
17. D. E. Aspnes, *J. Opt. Soc. Am.* **65**, 1274 (1975).
18. P. S. Hauge and F. H. Dill, *Opt. Commun.* **14**, 431 (1975).
19. R. W. Stobie, B. Rao, and M. J. Dignam, *Appl. Opt.* **14**, 999 (1975).
20. J. B. Theeten, R. P. H. Chang, D. E. Aspnes, and T. E. Adams, *J. Electrochem. Soc.* **127**, 379 (1980).
21. B. D. Cahan, *Surf. Sci.* **56**, 354 (1976).

22. D. E. Aspnes, *SPIE Proc.* **276**, 188 (1981).
23. D. E. Aspnes and A. A. Studna, *SPIE Proc.* **276**, 227 (1981).
24. P. Rouard and A. Meessen, *in* "Progress in Optics" (E. Wolf ed.), Vol. 15, p. 77, North-Holland, Publ., Amsterdam, 1977.
25. S. P. F. Humphreys–Owen, *Proc. Roy. Soc. (London)* **77**, 949 (1961).
26. D. K. Burge and H. E. Bennett, *J. Opt. Soc. Am.* **54**, 1428 (1964).
27. D. E. Aspnes, in "Optical Properties of Solids: New Developments" (B. O. Seraphin, ed.), p. 799, North-Holland Publ., Amsterdam, 1976.
28. W. J. Plieth and K. Naegele, *Surf. Sci.* **64**, 84 (1977).
29. D. E. Aspnes, *J. Vac. Sci. Technol.* **17**, 1057 (1980).
30. D. E. Aspnes, G. P. Schwartz, A. A. Studna, G. J. Gualtieri, and B. Schwartz, *J. Electrochem. Soc.* **128**, 590 (1981).
31. D. A. G. Bruggeman, *Ann. Phys. (Leipzig)* **24**, 636 (1935).
32. D. E. Aspnes, J. B. Theeten, and F. Hottier, *Phys. Rev. B* **20**, 3292 (1979).
33. A. B. Winterbottom, *K. Nor. Vidensk. Selsk. Sk.* **1**, 61 (1955).
34. R. J. Archer, *J. Electrochem. Soc.* **104**, 619 (1957).
35. B. H. Claussen and M. Flower, *J. Electrochem. Soc.* **110**, 983 (1963).
36. A. N. Saxena, *Appl. Phys. Lett.* **7**, 113 (1965).
37. F. Lukes, *Optik* **31**, 83 (1970).
38. K. Vedam and S. S. So, *Surf. Sci.* **29**, 379 (1972).
39. S. S. So and K. Vedam, *J. Opt. Soc. Am.* **62**, 596 (1972).
40. Y. J. van der Meulen, *J. Electrochem. Soc.* **119**, 530 (1972).
41. K. Vedam, *Surf. Sci.* **56**, 221 (1976).
42. B.-L. Twu, *J. Electrochem. Soc.* **126**, 1589 (1979).
43. E. A. Taft, *J. Electrochem. Soc.* **125**, 968 (1978).
44. C. C. Chang and D. M. Boulin, *Surf. Sci.* **69**, 385 (1977).
45. F. Lukes, W. H. Knausenberger, and K. Vedam. *Surf. Sci.* **16**, 112 (1969).
46. G. A. Egorova, N. S. Ivanova, E. V. Potapov, and A. V. Rakov, *Opt. Spektrosk.* **36**, 773 (1974); G. A. Egorova, N. S. Ivanova, E. V. Potapov, and A. V. Rakov, *Opt. Spectrosc.* **36**, 449 (1974).
47. J. Shewchun and E. C. Rowe, *J. Appl. Phys.* **41**, 4125 (1970).
48. M. M. Ibrahim and N. M. Bashara, *J. Opt. Soc.* **61**, 1622 (1971).
49. S. S. So and K. Vedam, *J. Opt. Soc. Am.* **62**, 16 (1972).
50. O. Hunderi, *Surf. Sci.* **61**, 515 (1976).
51. O. Hunderi, *Appl. Opt.* **11**, 1572 (1972).
52. P. Picozzi, S. Santucci, and A. Balzarotti, *Surf. Sci.* **45**, 227 (1974).
53. V. M. Bermudez, *Surf. Sci.* **94**, 29 (1980).
54. K. Vedam, W. Knausenberger, and F. Lukes, *J. Opt. Soc. Am.* **59**, 64 (1969).
55. R. C. O'Handley, *Surf. Sci.* **46**, 24 (1974).
56. E. A. Taft and L. Cordes, *J. Electrochem. Soc.* **126**, 131 (1979).
57. H. W. Dinges, *Thin Solid Films* **50**, L17 (1978).
58. J. B. Theeten and D. E. Aspnes, *Thin Solid Films* **60**, 183 (1979).
59. G. Jungk, *Phys. Status Solidi A* **34**, 69 (1976).
60. D. E. Aspnes, *Surf. Sci.* **56**, 322 (1976).
61. D. E. Aspnes and A. A. Studna, *Phys. Rev. B* **27**, 985 (1983).
62. A. Daunois and D. E. Aspnes, *Phys. Rev. B* **18**, 1824 (1978).
63. H. Burkhard, H. W. Dinges, and E. Kuphal, *J. Appl. Phys.* **53**, 655 (1982).
64. D. E. Aspnes and J. B. Theeten, *J. Electrochem. Soc.* **127**, 1359 (1980).
65. H. R. Philipp, *J. Appl. Phys.* **43**, 2835 (1972).
66. H. R. Philipp and H. Ehrenreich, *Phys. Rev.* **129**, 1550 (1963).
67. G. E. Jellison and F. A. Modine, *J. Opt. Soc. Am.* **72**, 1253 (1982).
68. R. J. Archer, *Phys. Rev.* **110**, 354 (1958).
69. T. M. Donovan, E. J. Ashley, and H. E. Bennett, *J. Opt. Soc. Am.* **53**, 1403 (1963).

70. H. R. Philipp and E. A. Taft, *Phys. Rev.* **120**, 37 (1960).
71. H. R. Philipp and H. Ehrenreich, in "Optical Properties of Solids: New Developments" (R. K. Willardson and A. C. Beer eds.), p. 93, Academic Press, New York, 1967.
72. D. E. Aspnes and A. A. Studna, *SPIE Proc.* **276**, 227 (1981).
73. R. E. Morrison, *Phys. Rev.* **124**, 1314 (1961).
74. M. Cardona, *J. Appl. Phys.* **32**, 958 (1961).
75. D. E. Aspnes and A. A. Studna, *Appl. Phys. Lett.* **39**, 316 (1981).
76. D. E. Aspnes and A. A. Studna, *Surf. Sci.* **96**, 294 (1980).
77. N. P. Syoseva and B. M. Ayupov, *Opt. Spectrosk.* **47**, 300 (1979).
78. P. Beckmann, *The Depolarization of Electromagnetic Waves*, Golem, Boulder, Colorado, 1968.
79. D. E. Aspnes, *Am. J. Phys.* **50**, 704 (1982).
80. J. C. M. Garnett, *Philos. Trans. Roy. Soc. (London)* **203**, 385 (1904); J. C. M. Garnett, *Philos. Trans. Roy. Soc.* (London). *A* **205**, 237 (1906).
81. L. Lorenz, *Ann. Phys. Chem. (Leipzig)* **11**, 70 (1880).
82. H. A. Lorentz, "Theory of Electrons," 2nd ed., Teubner, Leipzig, 1916.
83. G. A. Niklasson, C. G. Granquist, and O. Hunderi, *Appl. Opt.* **20**, 26 (1981).
84. M.-L. Thèye, *Phys. Rev. B* **2**, 3060 (1970).
85. D. E. Aspnes, E. Kinsbron, and D. D. Bacon, *Phys. Rev. B* **21**, 3290 (1980).
86. P. B. Johnson and R. W. Christy, *Phys. Rev. B* **6**, 4370 (1972).
87. M. Guerrisi, R. Rosei, and P. Winsemius, *Phys. Rev. B* **12**, 557 (1975).
88. D. E. Gray (ed.), pp. 6–150, "American Institute of Physics Handbook," McGraw-Hill, New York, 1972.
89. B. Dold and R. Mecke, *Optik* **22**, 435 (1965).
90. V. G. Padalka and I. N. Shklyarevskii, *Opt, Spectrosk.* **11**, 527 (1961); V. G. Padalka and I. N. Shklyarevskii, *Opt. Spectrosc.* **11**, 285 (1961).
91. J. R. Beattie, *Physica* **23**, 898 (1957).
92. R. K. Ahrenkiel, *J. Opt. Soc. Am.* **61**, 1651 (1971).
93. R. Hulthén, *J. Opt. Soc. Am.* **72**, 794 (1982).
94. H. W. Verleur, *J. Opt. Soc. Am.* **58**, 1356 (1968).
95. V. Grasso, G. Mondio, G. Saitta, S. U. Campisano, G. Foti, and E. Rimini, *Appl. Phys. Lett.* **33**, 632 (1978).

Chapter 6

Interferometric Methods for the Determination of Thin-Film Parameters

JOSEPH SHAMIR
Faculty of Electrical Engineering
Technion—Israel Institute of Technology
Haifa, Israel

I. Introduction 113
II. Basic Principles 114
III. Nonlaser Interferometers 117
A. The Fizeau Method 117
B. The FECO Method 118
C. Shearing Interferometers 119
D. Discussion 121
IV. Kösters-Prism Interferometers 123
A. Transmission Phase Measurement 123
B. Reflection Phase Measurement 124
C. Ellipsometric Interferometry 124
D. Measuring Thermal Expansion and Index Variation 125
E. Response Linearization 126
V. A Self-Calibrating Method 126
VI. Surface Effects 131
VII. Conclusions 132
References 133

I INTRODUCTION

The optical parameters of thin films frequently deviate from those determined for bulk material. Therefore, special methods are required for the measurement of optical parameters of thin films in their final form and, as far as possible, with no special preparation for the measurement. While some of the methods discussed can also be applied for measuring the optical properties of bulk material, emphasis will be on thin films deposited on known bulk slabs.

HANDBOOK OF OPTICAL CONSTANTS OF SOLIDS

Copyright©1985 by Academic Press, Inc.
All rights of reproduction in any form reserved.
ISBN 0-12-544420-6

Among the optical measuring techniques, interferometry is capable of the highest accuracy. However, before the invention of the laser, its usefulness was quite limited, and other methods had been developed to a high level of sophistication. The highly advanced methods for thin-film analysis, such as the ellipsometric methods discussed in Chapter 5, made interferometric techniques a second choice at best. Nevertheless, recent advances in laser interferometry should lead to a renewal of interest in this field and result in the synthesis of novel methods with extremely high accuracies and simplified operating procedures.

The first part of this chapter will deal with the description of traditional interferometric methods for the measurement of thin-film parameter [1–5], while the rest will be devoted to the description of novel laser interferometric techniques.

II BASIC PRINCIPLES

For typical experimental situations the investigated sample will be assumed to consist of a uniform slab of thickness h and complex refractive index

$$n_2 = n - ik, \tag{1}$$

situated between two media of respective refractive indices n_1 and n_3. In most cases $n_1 \simeq 1$ (air) and n_3 is a known, transparent substrate (Fig. 1); however, opaque substrates may be used in reflection measurements. For high-sensitivity measurements the simplest practical situation is a bare substrate (n_3) with a thin, equivalent layer representing the combined effect of surface roughness and adsorbed matter, to be discussed in Section VI.

The sample is probed by light beams incident on either or both sides. Each polarization component of a light beam will be represented by its analytic signal

$$V = E \exp(i\omega t). \tag{2}$$

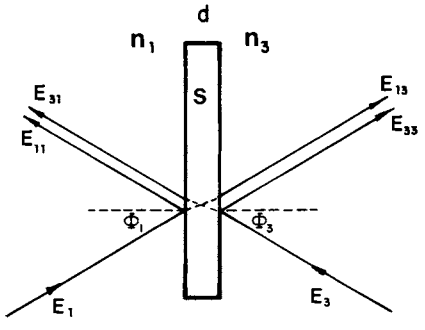

Fig. 1. Illumination configurations. S is the sample film imbedded between two media of respective refractive indices n_1 and n_3. Two possible illuminating beams are E_1 and E_3 that produce the respective two pairs of outgoing beams E_{11}, E_{13} and E_{33}, E_{31}.

In the figure, E_1 represents one polarization component of the complex amplitude of the light incident from medium I. A fraction

$$E_{11} = r_1 E_1 \tag{3}$$

of the beam is reflected into medium I, while the fraction

$$E_{13} = t_1 E_1 \tag{4}$$

is transmitted into medium III. In a similar way, the sample may be interrogated by a beam E_3 from the other side to produce the two outgoing beams

$$E_{33} = r_3 E_3 \tag{3a}$$

and

$$E_{31} = t_3 E_3. \tag{4a}$$

The complex amplitude reflectances and transmittances are defined by

$$r_j = |r_j| \exp(i\rho_j), \qquad (j = 1, 3) \tag{5a}$$

$$t_j = |t_j| \exp(i\theta_j), \tag{5b}$$

where ρ_j and θ_j are the phase shifts upon reflection and transmission, respectively.

It should be noted here that usually the light beams inside the substrate medium n_3 are inaccessible for detection, and measurements made outside the substrate should take into account the effects of the back surface and possibly internal losses as well. In particular, back-surface reflections may interfere with all detected beams and require special arrangements for their elimination. Such arrangements may be based on spatial filtering configurations and index matching.

Most noninterferometric methods involve the measurement of intensity reflectances

$$R_j = |r_j|^2 \tag{6}$$

and transmittances

$$T_1 = (p_3/p_1)|t_1|^2; \qquad T_3 = (p_1/p_3)|t_3|^2, \tag{7}$$

where

$$p_j = n_j \cos \phi_j, \tag{8}$$

with ϕ the incidence angle.

At first sight, there appear to be eight real measurable parameters defined in Eqs. (5). However, these parameters are not independent and some basic relations interconnect them. Apart from the two simple general relations [1, 6]

$$T_1 = T_2 \equiv T, \tag{9}$$

and

$$\theta_1 = \theta_2 \equiv \theta, \tag{10}$$

there are a number of other, more complicated ones. If a single, homogeneous film on a known substrate is considered, these relations may be used to reduce the number of independent measurables to three, adequate in principle for the determination of the three film parameters n, k, and h. Unfortunately, the transcendental and multivalued nature of these relations [2, 3, 7] prohibits, in general, the unique determination of film parameters from only three measurements. Therefore, in most cases, some *a priori* information about the film is required, or additional measurements should be performed.

The phase shift under transmission θ and the two phase shifts due to reflection ρ_1 and ρ_3 are the main subjects for interferometric measurements. The major problem in interferometry is that these phases cannot usually be determined absolutely in an independent way. In fact, most methods are only able to measure the variations of these phases in space and time. The parameters of Eqs. (5) are functions of wavelength, angle of incidence, and polarization. Thus, by varying these factors, the required phase shift changes may be obtained. Sometimes, external parameters such as pressure or temperature may be utilized as well; however, the common procedure in interferometry is the utilization of an actual reference surface.

The attainable accuracies in interferometric setups are limited by the quality of the optical components, stability of the system, and stability and coherence of the light source. The restricted coherence of nonlaser sources was the main cause for the neglect of interferometry as a major technological tool in the field of thin-film analysis. Nevertheless, a number of interferometric principles were developed for application with conventional thermal sources. Some of the interferometers representative of these principles will be discussed in Section III.

While nonlaser interferometers should involve very small optical path differences, this restriction can be greatly relaxed when lasers are used. However, even laser interferometers are strongly affected by environmental noise and special designs are required for high-accuracy measurements. A compact and relatively immune laser interferometer will be introduced in Section IV, and its various applications for optical parameter determination will be described.

Most interferometric methods require a reference for a comparative measurement. Such a reference may be an optical flat with a very high-quality surface like in the Fizeau and fringes of equal chromatic order (FECO) interferometers, [1, 4] to be described in Section III, a mirror in a Michelson interferometer, or a portion of uncoated substrate as used in some of the Kösters-prism configurations described in Section IV. A self-calibrating method that dispenses with a reference surface will be described in Section V.

At this point one should mention also a new concept in interferometry that is based on phase conjugation [8]. This new method is very promising

because information can be evaluated from the comparison of a wave front with its complex conjugate providing a measure of absolute phase value. However, since they are still in a research stage, phase conjugating methods will not be considered here. This chapter will be concluded by a discussion of the effects of surface quality and some comparisons among the various interferometric methods.

NONLASER INTERFEROMETERS III

The term *nonlaser interferometer* refers to systems designed primarily for application with conventional light sources. Naturally, this does not imply that these interferometers cannot be used also with laser light, and in most cases the converse is true—laser illumination will improve the performance of the system.

A number of common characteristics for the nonlaser interferometers can be pointed out. First of all, the fact that they have to utilize very small optical path differences between the interfering beams results also in a relatively high stability. Usually, these interferometers are easy to operate for low-sensitivity measurement and can be applied in quite hostile environments; however, when accuracy requirements become more stringent, laser interferometers may become preferable. In this section, we shall discuss three methods: (1) the Fizeau method that uses multiple reflection of monochromatic light, (2) the FECO method that uses multiple reflection of white light, and (3) shearing methods.

The Fizeau Method A

Probably the most popular method for the optical measurement of the thickness of thin films is the Fizeau method [1, 4]. The advantages here are simple construction and ease of use, while the main drawback is the special sample preparation that is required for high-sensitivity measurements. The sample film is deposited onto a high-quality optical surface, usually with a channel left uncoated (Fig. 2a), and then the whole surface is overcoated by a high-reflectance metal coating. Fizeau fringes are obtained by multiple reflection of diffused monochromatic light between the sample and a second optical flat (overplate) placed above it at a slight inclination.

The Fizeau method has been extensively studied in the cited literature; thus, here we shall only mention its main characteristics and applicability. Fizeau fringes originate from the interference among the multiple reflected beams and are described by the Airy formula that gives the intensity distribution

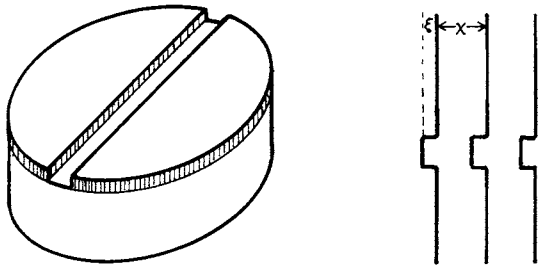

Fig. 2. (a) Thin-film sample on optical flat for Fizeau interferometry and (b) fringe pattern.

over the surface [1]:

$$I = \frac{I_{\max}}{1 + F \sin^2 \pi[(2nt \cos \phi)/\lambda]}, \tag{11}$$

where $I_{\max}$ is the maximum intensity at fringe center, nt the equivalent optical distance (including phase shift on reflection) between the two reflecting surfaces, ϕ the illumination angle, λ the observation wavelength, and F the finesse of the system defined by

$$F = 4R/(1 - R)^2, \tag{12}$$

with $R = |r_1||r_2|$ being the average intensity reflectance of the two surfaces. With monochromatic illumination, fringes are observed over the whole sample surface with lateral spacing x determined by the overplate inclination. With normal-incidence illumination, the vertical optical path difference between adjacent fringes is $\lambda/2$. Film thickness is determined by the ratio between fringe shift ε (Fig. 2b) and x.

The Fizeau method is very useful for high-accuracy (up to 0.001λ) thickness measurement of properly prepared samples and also for quick, low-sensitivity estimation of step height in any reflective sample. In principle, this method is also applicable for the determination of ρ_j; however, the interpretation of the result may be ambiguous, since it is difficult to separate the phase shift due to reflection from that induced by optical path length.

Improvements in the sensitivity of the Fizeau method are possible by multiple-pass arrangements [9, 10].

B The FECO Method

The FECO method [1, 4, 11] differs from the Fizeau method by two main features. First, here, too, reference is made to Eq. (11); however, instead of varying nt, in the FECO method the wavelength is varied. Second, instead of

making observation over a large portion of the sample, only a narrow line is observed at a time. The second difference may be considered a drawback, but at the same time it is an advantage in that it greatly reduces the quality requirements of the sample and absolute determination of nt is, in principle, possible at each point on its surface. The basic constituent of the FECO method is a multiple-beam interferometer similar to the one used for the Fizeau method; however, here the illumination is by white light, and the interferometer surface is imaged onto the entrance slit of a spectrometer. On the output plane of the spectrometer, one obtains a strong spectral line for each wavelength that, according to Eq. (11), produces a maximum for the portion of the interferometer imaged on the slit.

For the purpose of the determination of general optical parameters, the FECO method appears to be superior to the Fizeau method because it is capable of the absolute determination of the optical thickness of transparent films (reflectively coated on two sides) through the whole visible region. As a matter of fact, there is no reason not to use the method on both sides of the visible spectrum as well.

In summary, one can state that the Fizeau and FECO methods are based on a quite stable interferometric setup; thus, they are applicable, in relatively hostile environment, for the determination of optical thickness and surface topography with moderate accuracy. High accuracies are also attainable, but with highly sophisticated sample preparation and very careful experimental procedures.

A third way of using Eq. (11) was also proposed by Pliskin and Conrad [12]: In this method the illumination angle ϕ was varied during measurement also facilitating the determination of the thickness and refractive index of transparent films [12].

Shearing Interferometers C

The requirement of a reflective overcoat on the sample limits the possible applications of the Fizeau and FECO methods to the determination of film thickness only, with some exceptions when refractive index can be determined as well. Furthermore, the apparently simple method may become quite expensive and inconvenient due to the requirement of a well-aligned, high-quality optical reference flat. All these difficulties are resolved by using the shearing interferometric method. Instead of using a physical reference, in the shearing techniques the wave front, transmitted or reflected from the object, is compared with itself after a transversal shift has been imparted to it. Any nonuniformity in the wave front will result in the production of interference fringes determined by the local phase difference δ (Fig. 3), provided that the shear Δ does not exceed the spatial coherence of the source. In most systems,

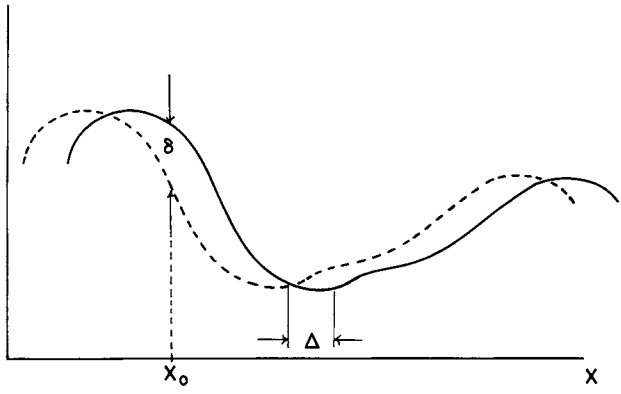

Fig. 3. One-dimensional representation of a sheared wave front. Δ is the shear and δ is the measured phase shift at point x_0.

the shear is very small, which leads to the determination of phase gradients rather than phase magnitudes.

For the purpose of analyzing thin films, usually the gradient measurement is adequate for the determination of the optical thickness, i.e., nh for transmission measurement and h for reflection measurement of an overcoated sample. For shearing interferometric measurement, the sample should be prepared in the same way as for the Fizeau method or just with a film edge on a useful part of the substrate. For the measurement of such a sample a mere shear is inadequate as demonstrated by the single "infinite" broad fringe in Fig. 4a. To produce a useful, "finite" fringe pattern, a slight inclination is imparted to the sheared wave front as in Fig. 4b. Similar to the Fizeau fringes, here too the phase shift δ can be determined from the ratio of the fringe shift ε to the fringe spacing.

Shearing interferometers differ from each other mainly by the optical arrangement used for imparting the required shear. For the analysis of small objects, as is the case in thin-film measurements, the best choice will be a single-component shearing configuration, which makes the interferometer into a "common path" interferometer in which both interfering waves traverse effectively the same path. Common-path interferometers are very stable and can be easily used in noisy and unfavorable environments.

Probably the most popular component to produce the required shear, together with the inclination mentioned earlier, is the Wollaston prism. The Wollaston prism is made of a doubly refracting crystal that splits a light beam into its two polarization components separating them by a small angle. A number of useful configurations, with a Wollaston prism as their central component, have been described for various applications by Nomarski [13] and Francon and Mallick [5]. Another component worth mentioning here is the Kösters prism [14, 15], which will be discussed in Section IV from a different point of view.

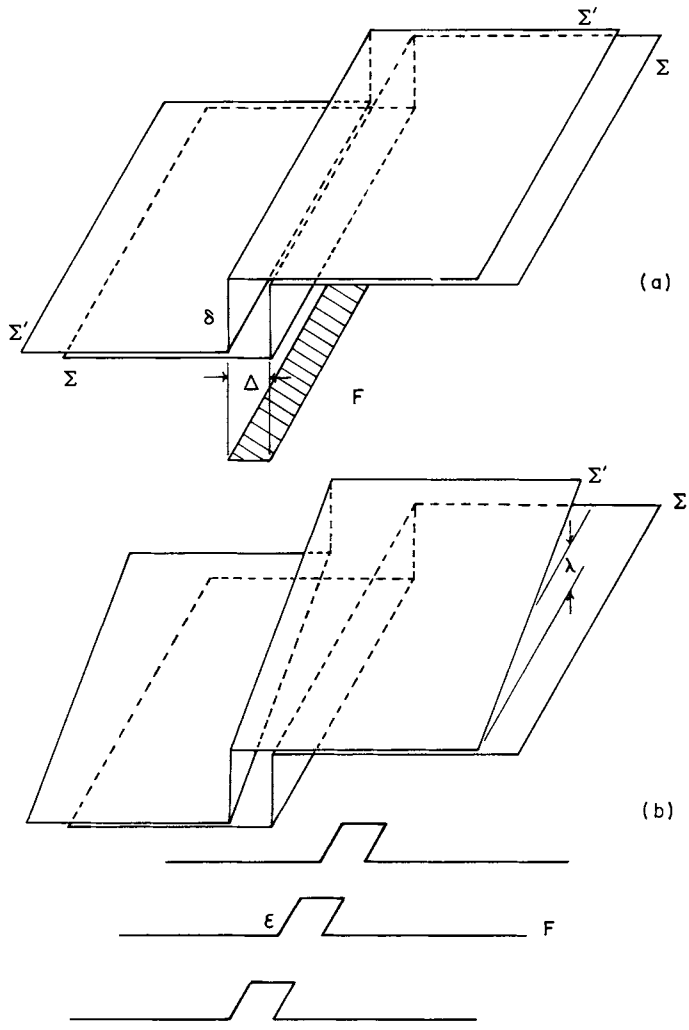

Fig. 4. Sheared wave fronts from a sample with a step of height δ with lateral shear Δ; Σ is the original wave front, Σ' is the sheared one, and F represents the shape of the fringe pattern. (a) Lateral shear only and (b) lateral shear with inclination.

D Discussion

Three approaches have been described for nonlaser interferometric analysis of thin films. The Fizeau and shearing methods are used to visualize a whole region of the sample, while the FECO method investigates only a line at a time. The FECO method is capable of measuring absolute optical thickness;

this usually is not possible with the two other methods unless measurements are performed at a number of wavelengths.

Owing to the high finesse of multiple-beam interference fringes, one would expect much higher accuracy for the Fizeau and FECO methods than for the shearing methods, which are essentially double-beam interferometers. Actually, however, the monochromatic shearing interferometers may be used with laser light that produces very high-luminosity fringes. These fringes may be analyzed by simple electronic means [16] to yield high-sensitivity measurements. At first sight, it appears that the Fizeau method may also be improved by laser illumination, but for high-accuracy measurements the benefits of coherent light may be upset by the coherent noise (i.e., due to speckle, dust particles, and irregularities in the optical components of the whole system) that will effectively reduce the finesse of the fringes.

The rest of this chapter is devoted to laser-illuminated interferometers all of them being essentially double-beam interferometers where high luminosity and electronic detection play a cardinal role.

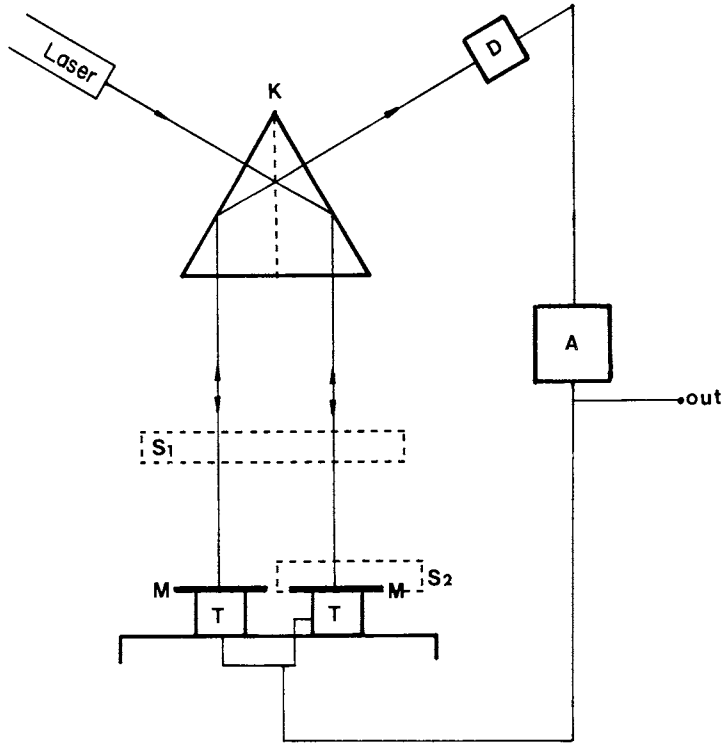

Fig. 5. Kösters-prism interferometer. K, Kösters prism; M, mirrors; T, piezoelectric transducers; D, fringe position detector; A, integrating amplifier; S, possible sample positions.

KÖSTERS-PRISM INTERFEROMETERS IV

The main advantage of the Kösters-prism interferometer as represented schematically in Fig. 5 is its high immunity to environmental noise due to the close vicinity of the two interfering beams. This immunity makes it an ideal tool for high-precision measurements [15–19]. Here, the basic principle will be discussed, while the description of actual measuring systems can be found in the literature cited.

The central constituent of the interferometer is the Kösters-prism beam splitter [14] K, which produces two parallel coherent beams (see Fig. 5). Transparent samples may be inserted in region S_1, while reflective samples will replace one or both reflecting mirrors M at position S_2. The two reflected beams recombine in K, and the interference is observed in detector D. The rest of the system constitutes a feedback arrangement to be discussed later.

The principle of measurement is demonstrated in Fig. 6; the thin film F is deposited on part of the substrate S. The two parallel beams from the Kösters prism E_1 and E_2 impinge on the sample as shown, part of them is reflected and part transmitted.

Transmission Phase Measurement A

For the measurement of the transmission phase θ [Eq. (10)], the sample is inserted at S_1. The phase shift is determined by detecting the interference fringe motion while translating the sample in such a way that the beams cross

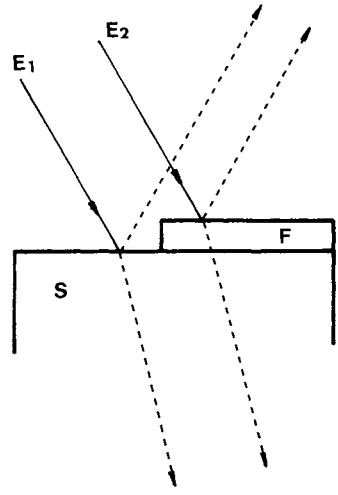

Fig. 6. Thin film (F) on substrate (S) configuration for measurement with two parallel beams E_1 and E_2 in Kösters-prism interferometer.

the film border in succession. This system is capable of measuring θ with a sensitivity of 10^{-4} rad [18]. For films with small absorption, this phase shift is independent of k; therefore, the method is suitable for the accurate determination of either n or d, provided that the other is known *a priori*. When neither is known, additional measurements may be performed at different angles or different wavelengths.

B Reflection Phase Measurement

The second mode of operation of the interferometer is in reflection for measuring ρ_1 or ρ_2. With the sample inserted at S_2, the phase shifts can be measured by sample translation as before. In contrast to transmission phase shift θ, the reflection phase shift is strongly dependent on all three optical parameters. Thus, in principle, more information is attainable by reflection measurements than by transmission measurements; however, the transmission mode of operation is more convenient for transparent samples since it is much less sensitive to sample vibration and misalignment. Furthermore, reflection measurements on transparent samples may be greatly disturbed by spurious reflection, especially from the substrate's second surface.

To summarize these two operating modes, we note that for transparent samples one should use transmission measurements if possible. Usually, these will be adequate for the determination of n and h. Reflection measurements may be used as well, but they are more difficult. Nevertheless, for reflecting samples, especially overcoated ones, reflection measurements are ideal for thickness measurements. Accuracies better than 0.5 Å are attainable without too much effort.

C Ellipsometric Interferometry

The main drawback of the procedures described in the preceding subsections is the requirement of a physical, relative translation between the scanning beams and the sample. This translation induces some stringent quality requirements on the sample and mechanical (or electro-optic) translation systems. To overcome this difficulty, in the third mode of operation the sample is stationary and the *polarization* of the incident illumination is varied. In principle, this converts the system into a kind of ellipsometer [19] in which the ellipsometric phase shift is directly measured. The ellipsometric phase shifts are the changes of θ and ρ upon 90° rotation of the polarization. Alternative interferometric ellipsometers have also been suggested [20].

Measuring Thermal Expansion and Index Variation D

This subsection describes a system that is proposed for the accurate determination of the thermal expansion together with thermal index variation of optical materials. For the measuring process, a sample with two flat surfaces (not necessarily parallel) should be prepared and inserted in the system of Fig. 5. However, this time the sample transmits only one of the beams, and it serves also as a second interferometer (Fig. 7). Part of the beam is reflected by the two surfaces of the sample, and the two reflected beams interfere to form fringes in the detector D_2. The position of the interference fringes is a function of the optical path $2nt$ in the sample, where n is its refractive index and t the geometrical path length in the sample. A temperature change dT of the sample introduces a change in its optical thickness $l = nt$:

$$\frac{dl}{dT} = n\frac{dt}{dT} + t\frac{dn}{dT}. \tag{13}$$

The change in the optical path difference of the interfering beams in D_2 is

$$dl_2 = 2dl. \tag{14}$$

However, for the second pair of interfering beams we obtain a change

$$dl_1 = 2dl - 2\frac{dt}{dT}dT, \tag{15}$$

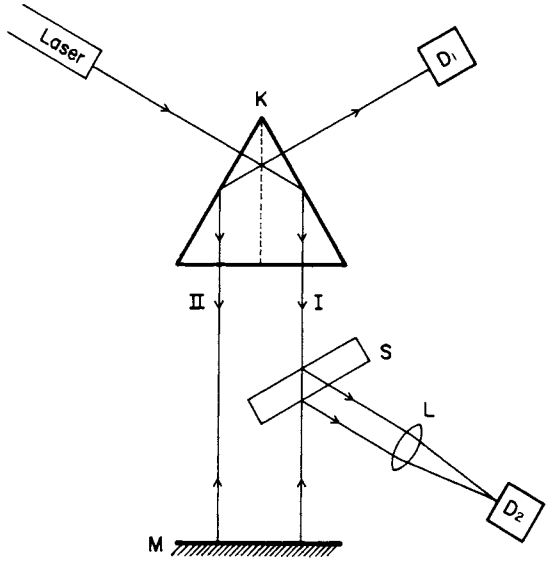

Fig. 7. Modified interferometer for measuring thermal effects.

since the expanding sample occupies a portion of the original path in air. From Eqs. (13–15) one may determine dt/dT and dn/dT separately.

The expected sensitivity of this method can easily be estimated. Assuming a conservative fringe shift measuring sensitivity of 10^{-3} fringe and a measuring wavelength of 600 nm, an expansion of 0.3 nm is measurable. Thus, for a sample 3 mm thick, a thermal expansion coefficient of 10^{-7} is measurable with a temperature change of 1°C. The thermal variation of n may be determined to the same order of magnitude. With a stable system, thicker sample and larger temperature change, the measuring sensitivity could be increased about two orders of magnitude, but then the effects of air refraction and possible system deformation should be taken into account.

E Response Linearization

One drawback of double-beam interferometers is their sinusoidal response. In classical interferometry this fact limited measuring capability to about $1/10\lambda$. Although this limitation does not exist with laser interferometers [16], still the nonlinearities may be troublesome. The solution of this problem involves the electronic part of the system in Fig. 5; the signal from the detector is amplified, integrated, and fed into piezoelectric (PZT) transducers T that impart a relative translation to the two reflecting mirrors. The result is a cancellation of the phase shift induced by the sample. Thus, the fringe pattern is locked into position, and the measure of the phase shift is the voltage on the transducer, the quality of which determines the linearity.

An additional benefit of the feedback arrangement is its directional dependence that facilitates phase measurements accompanied by their algebraic sign.

V A SELF-CALIBRATING METHOD

As mentioned in the introduction, most interferometric methods require a reference for comparison: The Fizeau method uses a reference flat and so does the FECO method unless the investigated film itself can be reflectively coated on its two sides. All interferometers based on the Michelson interferometer, including the Kösters prism, configurations utilize a reference surface or a comparison between two parts of the sample itself. Even shearing interferometers are based on a comparison between pairs of points on the surface of the sample.

The need for a reference constitutes a drawback of the interferometric methods as compared with other techniques such as ellipsometry or photo-

metry. In this section we describe an interferometric method that performs the measurement at a single point and, being self-calibrating, does not require any reference. The penalties paid for these advantages are some inconvenient alignment problems and the fact that the method is applicable only for transparent samples.

The basic principle, theory, and experimental verification have already been discussed in the literature [21, 22, 6]. Nevertheless, considering the new concepts involved, the method will be treated here in some length, though in a simplified manner.

In Fig. 1, the sample S may be any stratified layer situated between two media of respective indices of refraction n_1 and n_3. In the measuring system, the sample serves as a beam splitter in an interferometric arrangement in which two coherent beams of complex amplitudes E_1 and E_3 are incident on its two sides. The alignment is such that the reflected fraction of each beam is superposed on the transmitted fraction of the other beam. Assuming a linear medium, one will observe two emerging beams with respective intensities given by

$$I_1 = a_1|E_{11} + E_{31}|^2, \tag{16}$$

and

$$I_3 = a_3|E_{33} + E_{13}|^2, \tag{17}$$

where a_1 and a_3 are constants depending on the environment and angle of incidence. The components of each beam are given by Eqs. (3) and (4). Naturally, if n_3 is a substrate, measurements are performed outside, and a corresponding modification has to be made in the relevant expressions. Furthermore, reflections from the back surface of the substrate should be removed by spatial filtering or index matching.

The definition of a complex ratio between the two incident complex amplitudes

$$E_3 = \eta E_1 \exp(j\phi), \tag{18}$$

leads to

$$I_1 = a_1|E_1|^2[|r_1|^2 + \eta^2|t_3|^2 + 2|r_1||t_3|\eta \cos(\theta - \rho_1 + \phi)], \tag{19a}$$

$$I_3 = a_3|E_1|^2[\eta^2|r_3|^2 + |t_1|^2 + 2|r_2||t_1|\eta \cos(\rho_3 - \theta + \phi)]. \tag{19b}$$

If one records the two emerging intensities and plots them one against the other on an xy recorder in such a way that

$$x \propto I_1; \qquad y \propto I_3, \tag{20}$$

one may write,

$$x = x_0 + A_x \cos(\phi - \rho_1 + \theta), \tag{21a}$$

$$y = y_0 + A_y \cos(\phi + \rho_2 - \theta), \tag{21b}$$

where

$$x_0 = F_x(|r_1|^2 + \eta^2|t_3|^2), \tag{22a}$$

$$y_0 = F_y(\eta^2|r_3|^2 + |t_1|^2), \tag{22b}$$

$$A_x = 2F_x|r_1||t_3|\eta, \tag{22c}$$

and

$$A_y = 2F_y|r_3||t_1|\eta, \tag{22d}$$

where F_x and F_y are some scaling factors. Equations (21) may be considered as a parametric representation of an ellipse, with ϕ as parameter. Thus, if y is plotted against x as ϕ is continuously varied, an ellipse is produced (Fig. 8). An ellipse is determined by three independent parameters; therefore, in principle, measurements made on the ellipse should be adequate for the determination of three independent sample parameters. The scaling factors F_x and F_y depend on the calibration of the electronic measuring instruments, the quality of the optical components, and the back surface of the sample

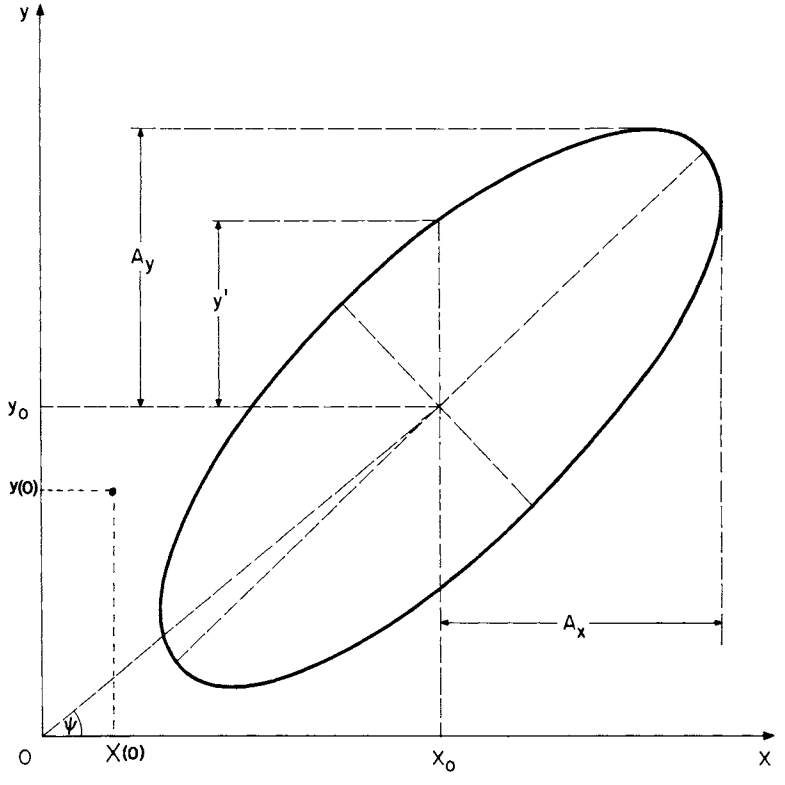

Fig. 8. Definition of parameters on interferometer xy output recording.

substrate. One of the advantages of this method is that it is possible to define measurable parameters that are independent of these uncertain factors. One such quantity is the phase difference between x and y that can be determined by putting $x = x_0$, which implies

$$\phi - \rho_1 + \theta = \pi/2.$$

Therefore, at this point,

$$y - y_0 \equiv y' = A_y \sin \Delta, \tag{23}$$

where y' is defined in the figure and

$$\Delta = \rho_1 + \rho_3 - 2\theta \tag{24}$$

is a dimensionless quantity that may be determined from the measured ratio between y' and A_y. Thus, Δ is our first observable that has already been noted as an indicator of absorption [2]. The angle ψ, which is a function of the intensity ratio of the incident beams η, defines the direction toward the center of the ellipse. One may define a function

$$f(\eta) \equiv \tan \psi = y_0/x_0$$

or, according to Eqs. (22),

$$f(\eta) = \frac{F_y}{F_x} \frac{\eta^2 |r_3|^2 + |t_1|^2}{|r_1|^2 + \eta^2 |t_3|^2}, \tag{25}$$

which is also a dimensionless observable, but dependent on F_y/F_x. Another dimensionless quantity also depending on F_y/F_x is the ratio between the respective variation amplitudes (or modulation depth) of the two intensities

$$A_y/A_x = \frac{F_y}{F_x} \frac{|r_3||t_1|}{|r_1||t_3|}. \tag{26}$$

The uncertain scaling factor F_y/F_x may be cancelled between Eqs. (25) and (26), but this would reduce the number of independent measurables. Instead, an additional measurement is possible by recording one point with one of the incident beams blocked. Blocking the beam E_3 is equivalent to a substitution $\eta = 0$. The point recorded has the coordinates

$$x(0) = F_x |r_1|^2; \qquad y(0) = F_y |t_1|^2, \tag{27}$$

from which one has

$$f(0) = \frac{F_y}{F_x} \frac{|t_1|^2}{|r_1|^2}. \tag{28}$$

A new measurable is obtained by dividing Eq. (26) by (28)

$$A \equiv \frac{A_y/A_x}{f(0)} = \frac{|r_1||r_3|}{|t_1||t_3|}, \tag{29}$$

which can be evaluated from measurements performed solely on the recorded intensities.

Two additional measurables can be defined by dividing Eqs. (22a) and (22b) by the respective Eqs. (27). A rearrangement of terms yields the two new measurables

$$B \equiv [x_0/x(0) - 1]\eta^2 = |t_3|^2/|r_1|^2,$$
$$C \equiv [y_0/y(0) - 1]\eta^2 = |r_3|^2/|t_1|^2, \tag{30}$$

which are also independent of the factors F_x and F_y but depend on the intensity ratio of the two incident beams that have to be measured separately. The two quantities B and C are not independent since they are related through Eq. (29). Other observables that are derivable by blocking the other beam are also simply related to the previous ones, and they may be used for cross-checking.

The schematic diagram of Fig. 9 shows a possible setup for the application of this method; beam splitter BS splits a laser beam to produce the two coherent measuring beams. The transmitted fraction is directed into the sample via mirrors M_1 and M_2 as beam E_1. The reflected fraction is incident on mirror M_3 mounted on a piezoelectric transducer T and returned through the beam splitter as E_3. The transducer is used to vary ϕ during measurement

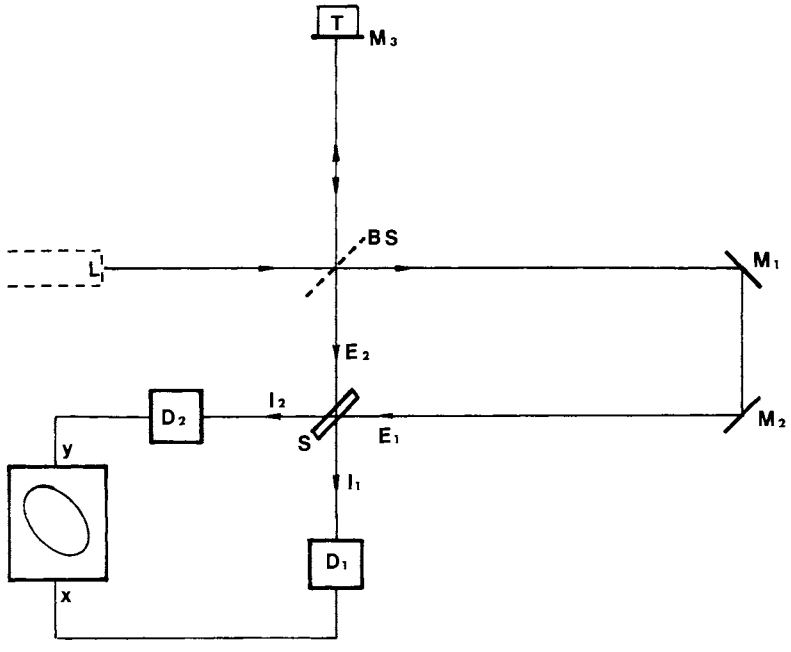

Fig. 9. Possible configuration for self-calibrating interferometer. L, laser; BS, beam splitter; S, sample; D, detectors; M, mirrors; T, piezoelectric transducer; xy recorder.

while the two emerging intensities are recorded on the xy recorder. An ellipse is recorded when ϕ is varied through 2π and the point $[x(0); y(0)]$ is obtained by blocking E_3. Equations (24), (29), and (30) are now utilized in a computer program to find the film parameters h, n, and k that correspond to the measured quantities Δ, A, B, and C. The four measured quantities are required to determine three parameters since the scaling factor F_y/F_x is also unknown.

This scheme of measuring procedure is one in a number of possibilities, leading to accuracies indicated by the results cited in Section VI. More sophisticated electronics and high-quality optics provide at least one order of magnitude improvement. Such an improvement is very helpful for extremely thin layers where ambiguities may arise [23, 24].

The phase shift Δ [Eq. (24)] is very sensitive to the extinction coefficient k, and its measurement is the most accurate. Therefore, this method is most useful for the direct determination of k in very weakly absorbing films. An important advantage is also the fact that the method, unlike many other techniques, can be applied for measurements in a wide spectral range [25] and also for anisotropic samples [23].

VI SURFACE EFFECTS

For high-accuracy measurements surface roughness and material adsorption may be quite troublesome. The effects of surface roughness have been extensively discussed in Bennett [26] and Elson *et al.* [27], but not much has been done with regard to optical effects of adsorption.

A comprehensive treatment of these problems is outside the scope of this chapter, and here we shall briefly discuss only their influence on the measuring methods described.

Surface effects are important for very thin films that are, in most cases, coherent with the substrate (i.e., the film surface is nearly identical in form with the substrate surface). For these cases, the effects of roughness may be cancelled by measurements of the type described in Subsections IV.A and IV.B if the size of the measuring spot is large enough to perform an averaging process. The form of fringes in the Fizeau and FECO methods may be used as a direct measure for the roughness; however, irregular fringes greatly reduce measuring accuracy.

Most sensitive to surface effects are single-point measurements demonstrated by some results obtained by using the method of Section V; measurements at 6328 Å performed on bare fused quartz flats [6, 22] yielded equivalent surface layers with $h = 10$–20 nm, $n \simeq 1.3$, and $k \simeq 10^{-4}$. This result corresponds to expectations and is due to a combined effect of surface roughness and adsorbed water and hydrocarbons. A more striking effect has been observed in measurements performed with a CO_2 laser at 10.6 μm by

using the same method [25]: (1) The surface layer on an NaCl window (that was completely transparent for visible light) was found to have the parameters $h = 1.7\ \mu m$, $n = 1.8$, and $k = 0.03$. Integral absorption calculated by using these values was in full agreement with transmission measurements at the same wavelength. The measured effect should be attributed to water absorbed in the outer salt layer. (2) An amorphous layer of As_2Se_3 deposited on an NaCl substrate was also investigated, and the derived parameters were $h = 3.67 \pm 0.04\ \mu m$, $n = 2.80 \pm 0.03$, and $k = 0.02$. Here, too, the results were in correspondence with transmission measurements.

The large influence of surface effects was conclusively demonstrated by independent measurements performed on the As_2Se_3 film by using a method that is very insensitive to surface effects when they are restricted to a layer that is much less than the wavelength and the total film thickness. This method is based on the wave-guiding properties of thin dielectric films [28]: The electromagnetic wave is coupled into the thin film by using a prism or grating. The coupling angle and guiding properties are strong functions of film thickness, absorption, and refractive index; thus, they can be used for accurate determination of these parameters. Measurements performed on this layer yielded results that are identical with the interferometric measurements for film thickness and refractive index. However, the guiding properties revealed an absorption that should be at least one order of magnitude less than the mentioned result. The definite conclusion is that the waveguiding was not affected by a thin absorbing layer that is responsible for absorption of light transversally incident on the sample.

VII CONCLUSIONS

The interferometric methods described in this chapter are, almost exclusively, adapted to the optical analysis of thin films. General properties of bulk material have not been considered since conventional, noninterferometric techniques are usually better suited for these purposes. The advantages of interferometry manifest themselves when the quantities to be measured are small. The best method for each application should be selected by considering a number of factors. First of all, one should specify the parameters to be measured and the parameters already known. Among the other factors, one should mention sample preparation, required accuracy, environment, available equipment, and personnel. For example, if only thickness is the required parameter, the sample may be prepared in any form and there are no interferometric experts around, one should choose the Fizeau method. On the other hand, if for the same purpose the sample is given with a film edge, the Kösters-prism interferometer may be the best choice. Actually, this would probably be the best choice also for thickness and index determination,

especially if the substrate and film are of relatively low optical quality. If all three optical parameters are required for a weakly absorbing film or just the absorption of that film, one should choose the method of Section V, provided that the film surface can be properly cleaned and at least one good technician is available.

As a final remark, one should remember that interferometric parameters are usually multivalued and, in many cases, measured parameters will be in correspondence with a number of possible parameter sets. This is especially so if all three film parameters are not known in advance. Therefore, it is very useful to obtain additional information on the sample, even if it is of relatively low accuracy.

REFERENCES

1. S. Tolansky, "Multibeam Interferometry of Surfaces and Films" Clarendon Press, Oxford, 1948.
2. F. Abélès, *in* "Progress in Optics" (E. Wolf, ed.), Vol. 2, p. 251, North-Holland Publ. Amsterdam, 1963.
3. O. S. Heavens, *in* "Physics of Thin Films" (G. Hass and R. E. Thun, eds.), Vol. 2, p. 193, Academic Press, New York, 1964.
4. H. E. Bennett and J. M. Bennett, *in* "Physics of Thin Films" (G. Hass and R. E. Thun, eds.), p. 1, Academic Press, New York, 1967.
5. M. Francon and S. Mallick, "Polarization Interferometers," Wiley, New York, 1971.
6. Y. Demner and J. Shamir, *Appl. Opt.* **17**, 3738 (1978).
7. M. Born and E. Wolf, "Principles of Optics," Pergamon, New York, 1959.
8. Y. Fainman, E. Lenz, and J. Shamir, *Appl. Opt.* **20**, 158 (1981).
9. H. D. Polster, *Appl. Opt.* **8**, 522 (1969).
10. P. Langenbeck, *in* "Optical Instrument and Techniques" (J. H. Dickson, ed.), p. 276, Oriel Press, England, 1970.
11. J. N. Israelachvili, *J. Colloid Interface Sci.* **44**, 259 (1973).
12. W. A. Pliskin and E. E. Conrad, *IBM J. Res. Devel.* **8**, 43 (1964).
13. M. G. Nomarski, *J. Phys. Rad.* **16**, 9 (S) (1955).
14. W. Kösters, "Interferenzdopplprisma für Messwecke," German patent 595211, 1934.
15. J. B. Saunders, *J. Res. Nat. Bur. Stand. Sec. C*, **73**, 1 (1969); J. B. Saunders, *J. Opt. Soc. Am.* **62**, 6 (1972)
16. J. Shamir, R. Fox, and S. G. Lipson, *Appl. Opt.* **8**, 103 (1969).
17. Th. Kwaaitaal, "A New Interferometric Method for Measuring Small Magnetostrictive Effects," private communication, 1976.
18. J. Shamir, *J. Phys. E* **9**, 499 (1976).
19. H. Rosen and J. Shamir, *J. Phys. E* **11**, 905 (1978).
20. H. F. Hazebroek and A. A. Holscher, *J. Phys. E* **6**, 822 (1973).
21. J. Shamir and P. Graff, *Appl. Opt.* **14**, 3053 (1975).
22. J. Shamir, *Appl. Opt.* **15**, 120 (1976).
23. R. A. Soli and H. H. Soonpaa, *Appl. Opt.* **18**, 3367 (1979).
24. J. Shamir and Y. Demner, *Appl. Opt.* **19**, 2658 (1980).
25. D. Apter and J. Shamir, *Appl. Opt.* **21**, 1512 (1982).
26. J. M. Bennett, *Appl. Opt.* **15**, 2705 (1976).
27. J. M. Elson, H. E. Bennett, and J. M. Bennett, *in* "Applied Optics and Optical Engineering" (R. R. Shannon and J. C. Wyant, eds.), Vol. 7, p. 191, Academic Press, New York, 1979.
28. R. Th. Kersten, *Opt. Acta* **22**, 503 (1975); R. Th. Kersten *Opt. Comm.* **13**, 327 (1975).

Chapter 7

Thin-Film Absorptance Measurements Using Laser Calorimetry

P. A. TEMPLE
Michelson Laboratory, Physics Division
Naval Weapons Center
China Lake, California

I. Introduction 135
II. Single-Layer Films 138
III. Wedged-Film Laser Calorimetry 139
IV. Electric-Field Considerations in Laser Calorimetry 143
V. Entrance versus Exit Surface Films 147
VI. Experimental Determination of α_f, a_{af}, and a_{fs} 149
References 153

INTRODUCTION I

Laser calorimetry has been used for several years as a method for measuring the absorptive loss in materials in both bulk and thin-film form. Two review articles on bulk absorption coefficient measurements in low-absorption, transparent materials were written by Skolnik [1] and Hordvik [2]. Skolnik includes a table showing bulk absorption coefficients as low as 10^{-6} cm^{-1}. The technique is not limited to low-absorption materials or to those wavelengths at which intense laser lines are available. In the work by Bos and Lynch [3], calorimetry was used to measure the absorption of chromium and two chromium alloys over the spectral range from 0.24 to 14.0 μm at liquid-helium temperatures.

Calorimetry has the advantage of simplicity and high sensitivity. The fundamental quantity measured is the absorptance A, where

$$A = \text{absorbed energy/incident energy.} \quad (1)$$

HANDBOOK OF OPTICAL CONSTANTS OF SOLIDS

Copyright © 1985 by Academic Press, Inc.
All rights of reproduction in any form reserved.
ISBN 0-12-544420-6

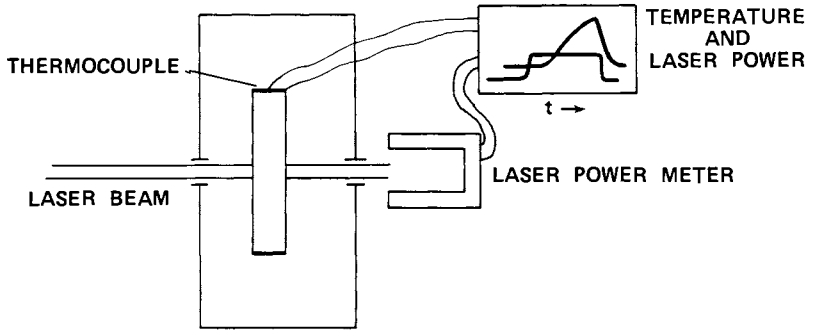

Fig. 1. Typical laser rate calorimeter.

With optical materials, laser calorimetry is generally used to measure samples with absorptances of 1×10^{-2} and less. Figure 1 is a schematic of a typical laser calorimeter. In this apparatus, the sample is heated by a laser beam of constant intensity for a period of time sufficient to raise the temperature of the sample above ambient. The laser is then turned off, and the sample slowly returns to thermal equilibrium with its surroundings. Both the laser power and sample temperature are recorded on a strip-chart recorder. Several analysis techniques have been described in the literature. Figure 2 shows schematically five sample temperature-versus-time curves. In technique (a) Pinnow and Rich [4] placed the sample in a laser cavity to take advantage of high intercavity power, allowed it to come to thermal equilibrium, and abruptly turned the laser off and observed the cooling curve. In technique (b) Allen *et al.* [5] irradiated the sample for 4 min and, using computer modeling, determined the absorptance by measuring the temperature

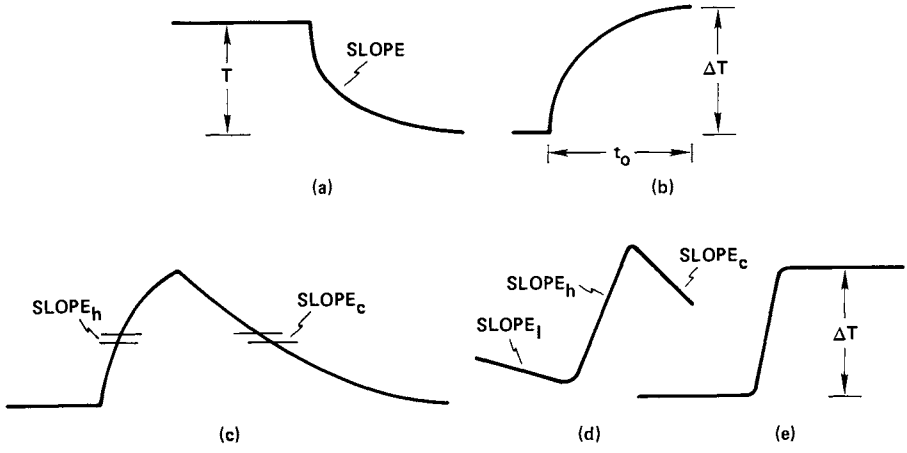

Fig. 2. Sample temperature as a function of time for five temperature-versus-time analysis schemes.

rise at the 4-min point. Technique (c), called the rate method, has been used by various workers and is probably the most common analysis technique [1, 2]. The three-slope method, shown in (d), is not unlike the rate technique shown in (c), but it has the advantage of not requiring the sample to be initially in thermal equilibrium with its surroundings [6]. Finally, technique (e), described by Decker and Temple [7], is a truly adiabatic technique in which the sample enclosure is temperature controlled and is caused to follow the temperature of the sample as it is heated by the laser. This technique overcomes some of the temperature-gradient problems of the other methods and is easily calibrated electrically.

There are a number of instrumental considerations involved in accurately determining the absorptance [8]. Probably the most serious of these is that of temperature nonuniformity in the sample during irradiation. In the usual analysis, it is assumed that the rate of temperature increase is uniform throughout the sample. As discussed by Bernal G. [9], this is correct only if the sample's thermal diffusivity is large and the heat losses are small. Only techniques (b), in which a theoretical correction is made, and (e), in which the sample is allowed to come to thermal equilibrium with itself, are free of this problem.

A second experimental consideration that is often neglected for both bare and coated samples is that of substrate interference effects. In any calorimetric technique using transparent substrates, the sample will have a rear surface from which the beam must emerge and from which the beam will be partially reflected. Because of the long coherence length of laser radiation, the substrate may act as an added thin film of some unknown thickness. This will cause a substantial uncertainty in the transmittance of the substrate–film system and in the electric-field distribution within both the substrate and any films present. In order to avoid this undesirable situation, we are forced to defeat laser coherence effects in the substrate. Figure 3 shows three ways of

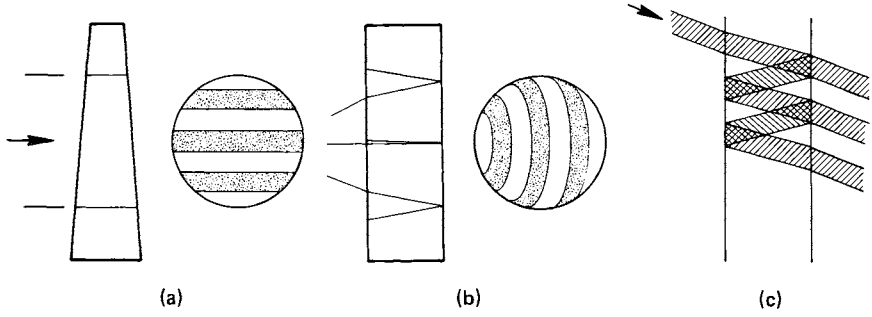

Fig. 3. Three techniques for defeating laser coherence effects in a substrate. (a) Wedged substrate and a large parallel beam, (b) plane-parallel substrate and divergent beam, tilted sample shown, and (c) plane-parallel sample using small beam at nonnormal angle of incidence to avoid overlap.

accomplishing this. All three methods result in the same average electric-field intensity distribution in the various regions of the sample. In the first case, the substrate is slightly wedged and the beam is quite large. The wedge causes the substrate to go through several cycles in optical thickness. The second case uses a plane-parallel substrate but a large diverging beam. The optical path length is different for various angles of incidence within the beam, causing a mixing similar to the preceding case. In this case, tilting the sample slightly enhances the mixing. In the third case, a small-diameter beam is incident on a plane-parallel sample at slightly off-normal incidence. Nonoverlap of beams on the entrance (or exit) surface assures us that no interference will exist within the substrate. This is essentially the classical incoherent-beam, multiple-bounce picture, and this model is used to calculate the effect of a real substrate in data given later in this chapter.

When these experimental considerations are taken into account, any of the calorimetric analysis techniques described can be used to measure the absorptance of either uncoated or coated substrates. In this chapter, we are concerned with measuring the absorptive properties of a single-layer, thin film deposited on a highly transparent substrate.

II SINGLE-LAYER FILMS

The most common way of determining the absorption properties of a material in thin-film form is to first measure the absorptance A_1 of a suitable substrate. A film of known thickness l, usually a half-wave in optical thickness (OT), is then deposited on the substrate, and the absorptance A_2 is again measured. The film absorption coefficient β, where

$$\beta = (A_2 - A_1)/l, \tag{2}$$

is then calculated. The variation in the electric field both throughout the film and from material to material is not accounted for in Eq. (2). Because of this, one typically finds that β measured when the sample is illuminated from the filmed side will be different from that measured when illuminated from the uncoated side. It is generally recognized that the increased absorption of the filmed substrate is due not only to the bulk of the film, but also to the newly introduced film–substrate interface and the film–air interface, where there is a change in material type with possible stoichiometry problems, as well as residual cleaning compound, etc., that may lead to higher absorption. In addition, the work of MacLeod [10] suggests that water migrates into the film system through pinholes and spreads out laterally into the interface regions. Donovan [11] has shown, by a nuclear resonance technique, that water is present in the film–substrate interface for discontinuous silicon films but is absent when the film is continuous. His work suggests

that the interface layer in this system is at most a few hundred angstroms thick. In spite of the presence of interface absorption, nearly all thin-film, absorption-coefficient data reported in the literature have been calculated by using Eq. (2) since it is a simple and convenient scheme for quickly characterizing coating materials.

A more complete analysis is possible by using a larger set of samples or, more elegantly, a single sample with a wedge-shaped film deposited on the incident face [12]. In this technique a simple model of a film is assumed, where the bulk absorption coefficient of the film is constant throughout the thickness of the film and all the interface absorption occurs in infinitesimally thin sheets at the two film boundaries. Then, a minimum of two measurements, using $\lambda/4$ and $3\lambda/4$ OT (or $\lambda/2$ and 1λ OT) films, will give the bulk absorption coefficient of the film without interface absorption present. Two more measurements, one on the bare substrate and one on a $\lambda/2$ (or $3\lambda/4$ OT) coating, can be used to determine the contribution from the film–substrate interface and the air–film interface. This technique will now be described in detail.

WEDGED-FILM LASER CALORIMETRY III

Figure 4 shows a sample with a beam normally incident from the left. The time average of the square of the electric field of the beam far from the sample is $\langle E_0^2 \rangle$. Reflection of the beam from the various film and substrate interfaces causes a redistribution of electric field within the sample. The time average of the square of this field is $\langle E^2(z) \rangle$, a quantity that varies sinusoidally in the vicinity of sample interfaces. For a sample of total thickness L including any films, Lambert's law can be written to give the absorptance as

$$A = \int_0^L \frac{n(z)\langle E^2(z)\rangle}{n_0 \langle E_0^2 \rangle} \alpha(z)\, dz, \tag{3a}$$

$$A = \int_0^L p(z)\alpha(z)\, dz, \tag{3b}$$

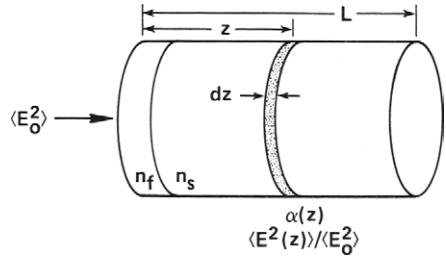

Fig. 4. Configuration for calculating the absorptance of a sample as per Eq. (3).

where $\alpha(z)$ and $n(z)$ are the absorption coefficient and the real part of the index of refraction, respectively, of the sample at the position z and n_0 is the index of the material outside the sample, which is normally air. Here $\alpha(z)$ is related to the extinction coefficient by $\alpha(z) = 4\pi k(z)/\lambda$.

The relative energy density, which contains the incident beam normalization factor, is $p(z)$. The purpose of wedged-film laser calorimetry is to determine $\alpha(z)$ for the film and the film interfaces by using Eq. (3b). This equation relates the measured absorptance A and the calculable quantity $p(z)$ to the material property $\alpha(z)$. Equation (3a) makes it clear that the contribution that any region in the sample makes to sample heating is proportional to $\alpha(z)$ in that region times the electric-field strength in that same region.

In order to make use of Eq. (3b), one assumes that the bulk absorption coefficient of the film α_f is constant throughout the film and is independent of film thickness. We also assume that all of the air–film interface absorption takes place in a thin sheet of material of absorption coefficient α_{af} and thickness Δ_{af}, and the film–substrate interface absorption takes place in a thin sheet of thickness Δ_{fs}, with absorption coefficient α_{fs}. Then the air–film and film–substrate interface absorption are characterized by the specific absorptances $a_{af} = \alpha_{af}\Delta_{af}$ and $a_{fs} = \alpha_{fs}\Delta_{fs}$. Finally, in calculating $p(z)$, which will be described in Section IV, we assume no absorptive attenuation of the illuminating beam in passing through the sample. In samples where $A < 10^{-2}$, this approximation is certainly acceptable. Without this simplification, knowledge of $\alpha(z)$ is necessary to calculate $p(z)$, and the entire problem becomes more difficult.

Under these approximations, the absorptance of a single-layer film on a transparent substrate can be written as†

$$A = p_{af}a_{af} + \bar{p}_f\alpha_f l_f + p_{fs}a_{fs} + \bar{p}_s A_0, \tag{4}$$

where $\bar{p}_f$ and $\bar{p}_s$ are the spatially averaged relative energy densities within the film and substrate and A_0 is the absorptance measured on the uncoated substrate. Here p_{af} and p_{fs} are the relative energy density at the air–film and film–substrate interfaces, respectively. As the film thickness is varied, a_{af}, $\alpha_f a_{fs}$, and A_0 remain constant and A, l_f, p_{af}, $\bar{p}_f$, p_{fs}, and $\bar{p}_s$ change. Of these A, A_0, and l_f are the experimentally measured absorptances and physical film thickness. And p_{af}, $\bar{p}_f$, p_{fs}, and $\bar{p}_s$ are calculated quantities. Values of p_{af}, $\bar{p}_f$, p_{fs}, and $\bar{p}_s$ for $\lambda/4$ and $\lambda/2$ thickness films are given in graphical form at the end of this chapter. By measuring the absorptances of an appropriate set of film thicknesses, we obtain a set of linearly independent equations that can be solved for α_f, a_{af}, and a_{fs}, the three coefficients that characterize a single film on a transparent substrate.

In order to use Eq. (4) to determine the bulk absorption of the film α_f, one measures the absorptance of a pair of film thicknesses that have the same

† The last term in this expression has a further approximation, which is discussed in Section V.

relative power densities at the interfaces, in the bulk of the film, and in the substrate. Such a pair consists of any two films that differ by $\lambda/2$ in optical thickness. Differentiating Eq. (4) and using absorptances from this pair of film thicknesses, we obtain

$$\alpha_f = (A_{t+\lambda/2} - A_t)/\bar{p}_f l_{\lambda/2}, \tag{5}$$

where $\bar{p}_f$ is calculated for film thickness t and $l_{\lambda/2}$, the physical thickness of a film of $\lambda/2$ OT. Like Eq. (2), two measurements are required; but in contrast to Eq. (2), this expression accounts for interface absorption and electric-field strength in the film and gives the bulk absorption coefficient of the thin-film coating.

A convenient sample configuration for this measurement is a sample one-half of which has been masked for part of the deposition. In this way, one side of a diameter has a coating of OT t while the other side has a coating of OT $t + \lambda/2$. While any thickness t will suffice, values of $\bar{p}_f$ for the $\lambda/2$, λ pair (or the $\lambda/4$, $3\lambda/4$ pair) are given here. When measuring the absorptances of these two coatings, the beam is aligned slightly off-center so that it passes through one or the other of the coating halves. The use of one sample eliminates substrate-to-substrate and deposition-to-deposition variations that are present when two substrates and two depositions are needed to obtain the t and $t + \lambda/2$ samples.

With additional measurements on the bare substrate and on a $\lambda/4$ OT film, we can determine a_{af} and a_{fs}. The relative power densities at both interfaces, within the film, and within the substrate all change in going from a $\lambda/4$ OT film to a $\lambda/2$ OT film. This fact is utilized in the determination of a_{af} and a_{fs}. By rewriting Eq. (4) for these two cases (unprimed for $\lambda/2$ OT and primed for $\lambda/4$ OT) with all measured and/or calculated quantities on the right, including α_f, which is determined by using Eq. (5), we have

$$a_{af}p_{af} + a_{fs}p_{fs} = [A - \bar{p}_f\alpha_f l_f - \bar{p}_s A_0] = [F], \tag{6a}$$

$$a_{af}p'_{af} + a_{fs}p'_{fs} = [A' - \bar{p}'_f\alpha_f l'_f - \bar{p}'_s A_0] = [F'], \tag{6b}$$

which have the solutions

$$a_{af} = \frac{[F]p'_{fs} - [F']p_{fs}}{p_{af}p'_{fs} - p'_{af}p_{fs}}, \tag{7a}$$

$$a_{fs} = \frac{[F']p_{af} - [F]p'_{af}}{p_{af}p'_{fs} - p'_{af}p_{fs}}. \tag{7b}$$

Figure 5 shows a convenient sample configuration for making this type of measurement. The maximum film thickness is $\sim 1\lambda$ OT, allowing measurement at the four regions required for obtaining A_0, $A_{1/4}$, $A_{1/2}$, and A_1. A small-diameter laser beam is used with the sample tilted slightly. The required thickness is found by moving the sample until the transmittance minimum

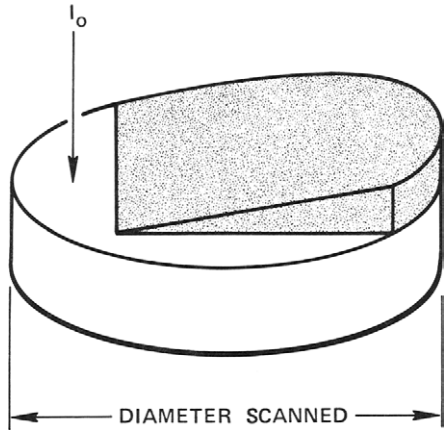

Fig. 5. Wedged-film sample used to obtain film bulk and interface absorption for single-layer films. The film varies from zero to $\sim 1\lambda$ OT. (From Temple [12].)

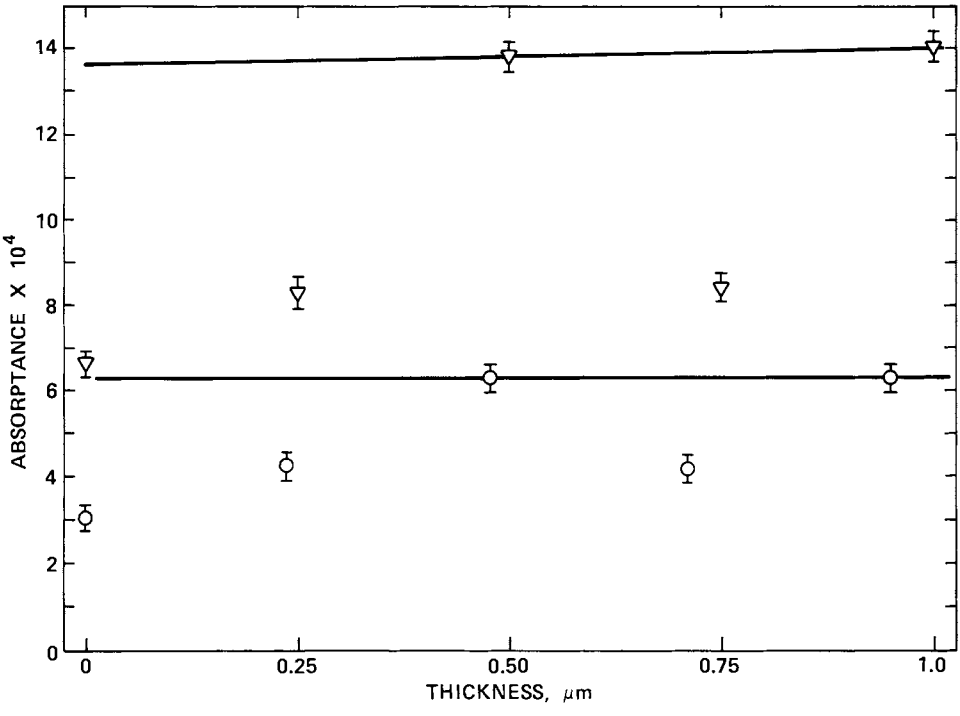

Fig. 6. The absorptance of an entrance surface film on As_2Se_3 on a CaF_2 substrate measured at two wavelengths and at $\lambda/4$, $\lambda/2$, $3\lambda/4$, and 1λ OT. The two data points at 0.0-μm thickness are bare substrate absorptances A_0. The two lines have been drawn through $\lambda/2$ and 1λ OT data points. The $\lambda/4$ and $3\lambda/4$ data points have lower absorptances because of reduced p_{fs} for these thicknesses. (∇, 2.87 μm; $\circ$, 2.72 μm; for the upper curve $\alpha = 0.4\ cm^{-1}$, $a_{af} \cong 0.0$, and $a_{fs} = 4.2 \times 10^{-4}$; for the lower curve, $\alpha = 0.0\ cm^{-1}$, $a_{af} \cong 0.0$, and $a_{fs} = 2.3 \times 10^{-4}$.) (From Temple [12].)

or maximum is found. This type of sample is particularly useful when absorptances are to be measured at a variety of wavelengths, since precise $\lambda/4$, $\lambda/2$, and 1λ OTs can be found for any wavelength. As in the case in which two film thicknesses are present on the same substrate, this type of sample eliminates substrate-to-substrate and deposition-to-deposition variation present when three separate depositions are made to obtain the $\lambda/4$, $\lambda/2$, and λ OT films.

Figure 6, which is an example of this type of measurement [12, 13], shows the absorptance measured on the bare CaF_2 substrate (shown at 0.0 film thickness) and at $\lambda/4$, $\lambda/2$, $3\lambda/4$, and λ OT positions of an As_2Se_3 wedged film. Measurements were made at 2.72- and 2.87-μm wavelength by using a line-tuned HF cw gas laser. The substrate index is 1.42 and the film index is 2.6, which causes a $\lambda/2$ OT film to be ~ 0.5 μm thick. The values of α_f were calculated from the $\lambda/2$ and λ OT data (solid lines through data). The presence of water in the filmed substrate is evidenced by the higher absorptance as measured at 2.87 rather than at 2.72 μm. However, the bulk absorption coefficient of the film is quite low. The analysis of interface absorption indicates that nearly all the absorption is taking place at the film–substrate interface. Analysis of the bare substrate and $\lambda/2$ OT data and Eq. (2) gives a β of 14.60 cm^{-1}, which is ~ 35 times greater than α_f calculated by the wedged-film technique.

IV ELECTRIC-FIELD CONSIDERATIONS IN LASER CALORIMETRY

The technique and considerations in calculating $p(z)$ for use in Eqs. (7a) and (7b) will now be described. The accurate determination of $p(z)$ must take into consideration (1) the coherent interaction of a single beam with a dielectric interface and (2) the effect of the multiple (but incoherent) bounces the beam undergoes between the two faces of the sample.

A convenient method of making the first calculation was first given by Leurgans [14] and was more recently detailed by DeBell [15]. As originally described, the technique uses the Smith chart, but it is easily adapted to a computer or even a hand calculator. Leurgans's method, which we will briefly describe, is restricted to normal-incidence plane waves and lossless films. While only single films are of concern here, the general multilayer description will be given.

Figure 7 shows the layer-labeling system. The substrate is of index n_0, and the incident medium is of index n_k. The layers are labeled 1 through $k-1$ and are of physical thickness l_1 to l_{k-1}.

A right-traveling, normally incident plane wave of wavelength λ is represented by $\hat{E}^+ = E^+ e^{i(\omega t - \delta)}$, where $\delta = 2\pi nz/\lambda$. At a dielectric boundary, the

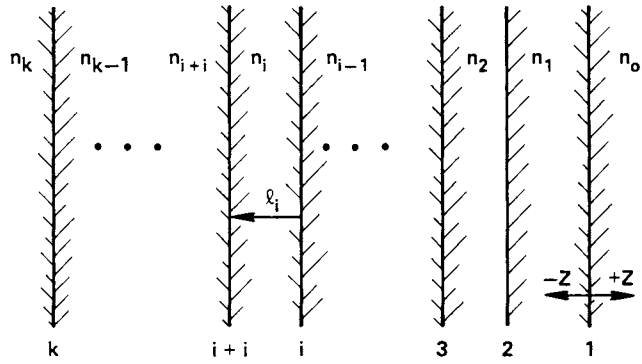

Fig. 7. The layer-labeling system for a thin-film stack.

partially reflected left-going field is given by

$$\hat{E}^- = E^+ \hat{\rho} e^{i(\omega t + \delta)},$$

where the reflection coefficient $\hat{\rho}$ is complex. Now, in general,

$$\hat{\rho}(z) = |\hat{\rho}(z)| e^{i(2\delta + \phi)}$$

within any given layer. In the lossless case, $|\hat{\rho}(z)|$ is constant within a layer and $\hat{\rho}$ only changes in phase through the layer. To calculate $\hat{\rho}$ across a boundary, we use the boundary condition requiring continuity of $E_{\tan}$ and $H_{\tan}$. This is done by using the reduced admittance $\hat{y}(z)$:

$$\hat{y}(z) = \hat{H}(z)/n\hat{E}(z).$$

The boundary condition then requires that

$$\hat{y}_{i+1}(z_b) n_{i+1} = \hat{y}_i(z_b) n_i,$$

where z_b is the position of the boundary between the ith and $(i + 1)$th layers. Finally, $\hat{y}(z)$ and $\hat{\rho}(z)$ are related by

$$\hat{\rho}_i(z) = \frac{1 - \hat{y}_i(z)}{1 + \hat{y}_i(z)}; \qquad \hat{y}_i(z) = \frac{1 - \hat{\rho}_i(z)}{1 + \hat{\rho}_i(z)}.$$

These expressions, along with the condition that there is no beam incident on the exit surface from the right, are sufficient to uniquely determine $\hat{\rho}(z)$.

The calculation begins within the substrate and proceeds from right to left. The procedure is the following:

(1) Realize that $\hat{\rho}_0 = 0$ and $\hat{y}_0 = 1$;
(2) use $\hat{y}_1(0) = \hat{y}_0 n_0/n_1$ to cross the substrate–film (1) interface;
(3) use $\hat{\rho}_1(0) = [1 - \hat{y}_1(0)]/[1 + \hat{y}_1(0)]$ to find $\hat{\rho}_1(0)$;
(4) use $\hat{\rho}_1(z) = |\hat{\rho}_1(0)| e^{i2\delta}$ to find $\hat{\rho}_1(z)$ in the first film;
(5) use $\hat{y}_1(z_1) = [1 - \hat{\rho}_1(z_1)]/[1 + \hat{\rho}_1(z_1)]$ and
(6) $\hat{y}_2(z_1) = \hat{y}_1(z_1) n_1/n_2$ to find $\hat{y}_2(z_1)$;
(7) now proceed as at step (3) above to find $\hat{\rho}_2(z)$, and so on.

In the work by Leurgans [14] and DeBell [15], the calculation was used to determine the reflectance R of the stack, which is given by $R = \hat{\rho}_k \hat{\rho}_k^*$.

Having found $\hat{\rho}(z)$ throughout the system by the method of Leurgans [14], we will now calculate the electric-field strengths throughout the layered system. At any point z in the ith layer, the net field is

$$\hat{E}_i(z) = \hat{E}_i^+(z) + \hat{E}_i^-(z) = [1 + \hat{\rho}_i(z)]\hat{E}^+(z).$$

The time average of the square of the field is given by

$$\langle E^2(z)\rangle = \frac{1}{T}\int_0^T \frac{[\hat{E}_i(z) + \hat{E}_i^*(z)]^2}{2}\, dt = \frac{E_{i\max}^{+2}}{2}[1 + \hat{\rho}_i(z)][1 + \hat{\rho}_i^*(z)],$$

or, finally

$$\langle E_i^2(z)\rangle = \langle E_i^{+2}\rangle[1 + \hat{\rho}_i(z)][1 + \hat{\rho}_i^*(z)]. \tag{8}$$

While $\langle E^2(z)\rangle$ in general varies throughout a layer, $\langle E_i^{+2}\rangle$ is constant in any given layer. Using the continuity of $E_{\tan}$ across a boundary, we derive the recursion relation

$$\langle E_i^{+2}\rangle = \langle E_{i+1}^{+2}\rangle \frac{[1 + \hat{\rho}_{i+1}(z_{i+1})][1 + \hat{\rho}_{i+1}^*(z_{i+1})]}{[1 + \hat{\rho}_i(z_{i+1})][1 + \hat{\rho}_i^*(z_{i+1})]}, \tag{9}$$

where the numerator is evaluated just to the left of the $(i + 1)$th boundary and the denominator just to the right of it. Knowing ρ and using the recursion relation, we can now determine the electric-field distribution throughout the system.

The starting point in calculating the set of $\langle E_i^{+2}\rangle$ is within the incident medium where the right-traveling field is $\langle E_k^{+2}\rangle$, a known quantity. Equation (9) is used to find $\langle E_i^{+2}\rangle$ for successive layers to the right of the incident medium. Equation (8) is used to determine $\langle E_i^2(z)\rangle$. Finally, the relative energy density is

$$p_i(z) = n_i\langle E_i^2(z)\rangle / n_k\langle E_k^{+2}\rangle.$$

This value does not take into account the multiple bounces that the beam undergoes between the two faces of the sample; this will be done next.

Figure 8 shows the right- and left-going beams within and to the right of the substrate. These are expressed in terms of the incident field $\langle E_{\text{inc}}^2\rangle$ and the first and second surface reflectance and transmittance of the coated sample R_1, R_2 and T_1, T_2 (calculable from Leurgans's method); n_s is the substrate index.

When using Eq. (3), we must include the contribution of the field of each of the individual beams in Fig. 8. Since there is no beam overlap and therefore no interference, this can be done by adding all of the right-going beams to form an effective right-going beam and all the left-going beams to form

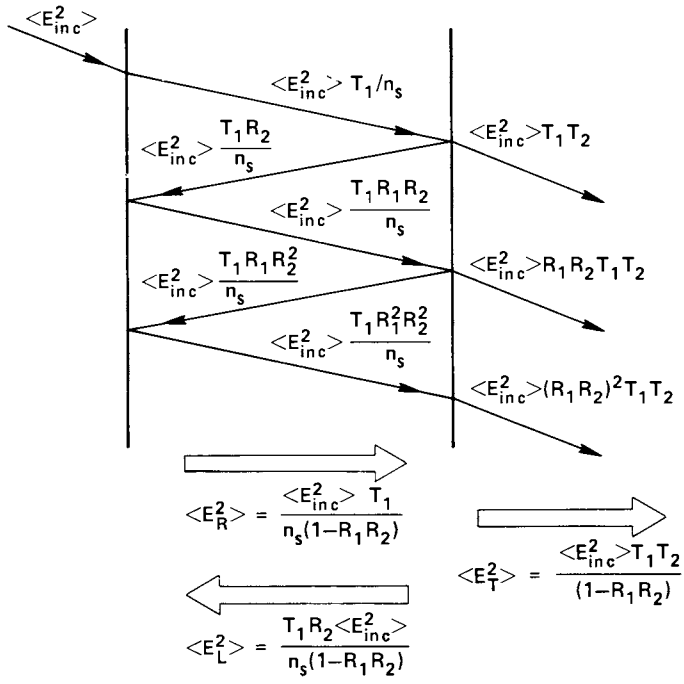

Fig. 8. The electric-field intensities within a substrate for multiple bounces of nonoverlapping beams. The entrance surface has reflectance R_1 and the exit surface R_2. Assumed are $T_1 = 1 - R_1$ and $T_2 = 1 - R_2$.

an effective left-going beam. These values are

$$\langle E_R^2 \rangle = \frac{\langle E_{inc}^2 \rangle T_1}{n_s(1 - R_1 R_2)}, \tag{10a}$$

$$\langle E_L^2 \rangle = \frac{\langle E_{inc}^2 \rangle T_1 R_2}{n_s(1 - R_1 R_2)}. \tag{10b}$$

To calculate $p(z)$ in the region near the exit surface of the sample, the right-going field $\langle E_R^2 \rangle$ is used as the starting value in the recursion relation Eq. (9). This and Eq. (8) are used to calculate $\langle E^2(z) \rangle$. The average value of $\langle E^2 \rangle$ within the substrate is the sum of Eqs. (10a) and (10b)

$$\langle E_{subst}^2 \rangle = \frac{\langle E_{inc}^2 \rangle T_1(1 + R_1)}{n_s(1 - R_1 R_2)}. \tag{11}$$

To calculate $p(z)$ in the region near the entrance surface, we add the field resulting from the incident beam $\langle E_{inc}^2 \rangle$ to the field resulting from the left-going beam $\langle E_L^2 \rangle$. This is done since, while the transmittance of a lossless filmed surface is the same when illuminated from either side, the electric-field distribution is not. This is illustrated in Fig. 9, in which the values of $\langle E(z)^2 \rangle / \langle E_{inc}^2 \rangle$ (solid lines) and $p(z)$ (dashed lines) are shown for a single

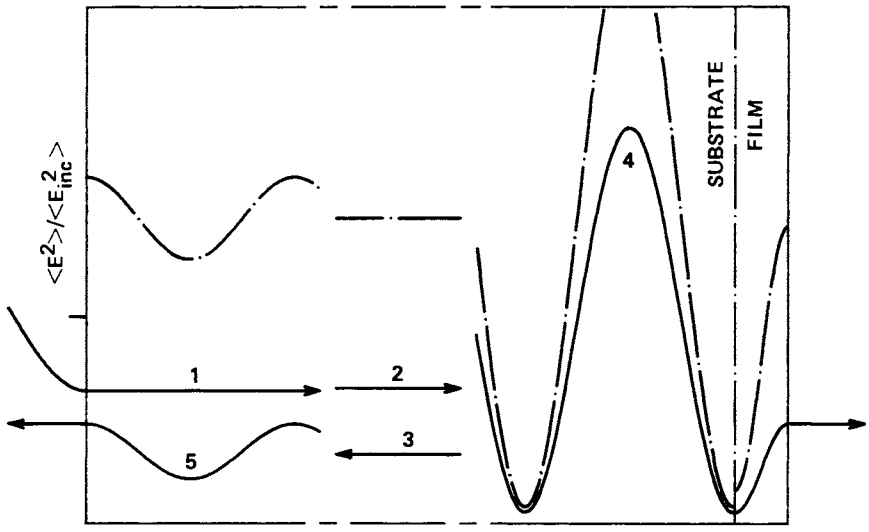

Fig. 9. The relative electric-field intensity (solid curve) and the relative energy density (dashed curve) for a $\lambda/4$ exit surface film. Line 1 is the incident beam, $\langle E_{inc}^2 \rangle T_1/n_s$, while lines 2 and 3 are $\langle E_R^2 \rangle$ and $\langle E_L^2 \rangle$. Line 4 is the coherent combination of 2 and 3 near the exit surface where the beams overlap; line 5 is the coherent combination of 2 and 3 *less* 1 near the entrance surface. The dashed lines are n_s/n_0 times 1 plus 5, 2 plus 3, and 4 at the entrance surface, in the central region, and near the exit surface, respectively. (Substrate index = 1.50; film index = 3.00; film thickness = 0.250; transmittance = 0.480.)

layer of material of index 3.0 and $\lambda/4$ OT deposited on the exit surface of a substrate of index 1.5. A film of this thickness and index has a high reflectance and accentuates the various effects just described. The line labeled 1 is the value of $\langle E^2(z) \rangle / \langle E_{inc}^2 \rangle$ resulting from the incident beam encountering the entrance surface of the substrate. Lines 2 and 3 are the net right- and left-traveling beams $\langle E_R^2 \rangle / \langle E_{inc}^2 \rangle$ and $\langle E_L^2 \rangle / \langle E_{inc}^2 \rangle$, respectively. Line 4 is the value of $\langle E^2(z) \rangle / \langle E_{inc}^2 \rangle$ in the vicinity of the exit surface of the substrate. Line 5 is the value of $\langle E^2(z) \rangle / \langle E_{inc}^2 \rangle$ near the entrance surface due to the left-traveling beam. The total relative field intensity near the entrance surface is the sum of lines 1 and 5, and the total within the bulk is the sum of lines 2 and 3. The values of $p(z)$ are then these sums multiplied by n_s/n_0. It is this value of $p(z)$, which includes all substrate multibounce effects, that is to be used in Eq. (3).

ENTRANCE VERSUS EXIT SURFACE FILMS V

Figure 10 shows the value of $\langle E^2 \rangle / \langle E_{inc}^2 \rangle$ at the entrance surface of the substrate, within the bulk of the substrate, at the film–substrate interface, the average value within the film, and at the air–film interface for an exit

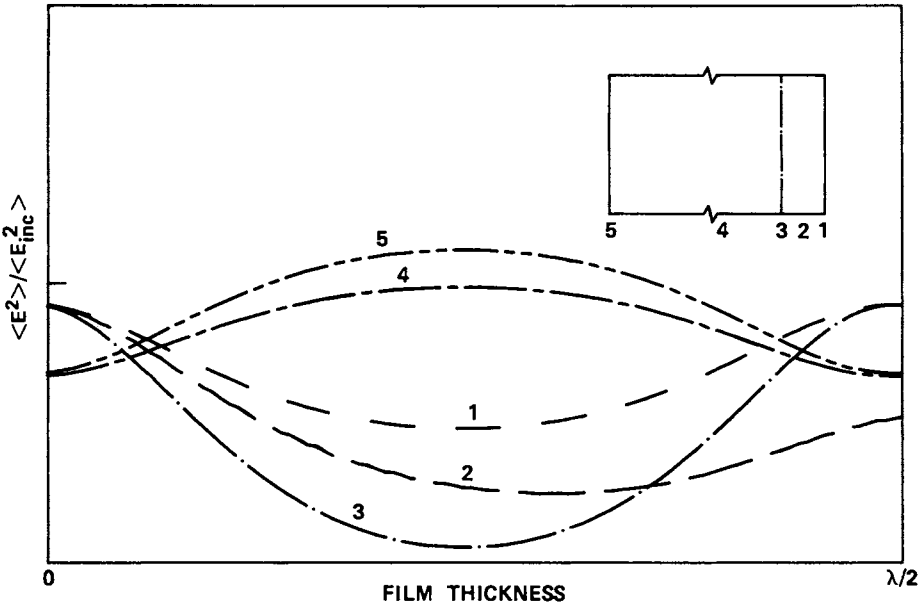

Fig. 10. The value of $\langle E^2 \rangle \langle E_{inc}^2 \rangle$ for five regions in a single-layer exit surface film. The film thickness varies from zero to $\lambda/2$ OT. (Substrate index = 1.50; film index = 3.00.)

surface film, all as functions of film thickness. This graph shows how the fields gradually change with changing film thickness, causing each region in the system to contribute a different proportion to the measured absorptance.

The three significant regions of the substrate are the central or bulk region and the two interfaces, shown as regions 4, 5, and 3, respectively, in Fig. 10. Also in Fig. 10 we see that these three quantities change relative to each other as film thickness changes. For example, a $\lambda/2$ OT film causes nearly equal weighting, while a $\lambda/4$ OT film accentuates the incident surface and the bulk over the exit surface. Without knowing the values of $\alpha(z)$ throughout the substrate and in particular at the interfaces, it is not possible to properly account for the substrate contribution for an exit surface film.

Figure 11 is similar to Fig. 10, except here the film is on the entrance surface. In this case, $\langle E^2 \rangle / \langle E_{inc}^2 \rangle$ for the two interfaces and in the bulk of the substrate (i.e., at 3, 5, and 4) maintain a nearly constant ratio to each other for all film thicknesses. A careful inspection shows that the ratio between the bulk and the exit surface values of p is identically constant and that the ratio between the bulk and the film–substrate interface value of p is constant to within $\sim 2\%$ over the thickness range shown. This is an important advantage in analysis, since now the substrate can be treated as a single entity whose contribution is directly proportional to the transmittance of the entrance surface of the sample. We do not need prior knowledge of $\alpha(z)$ for the

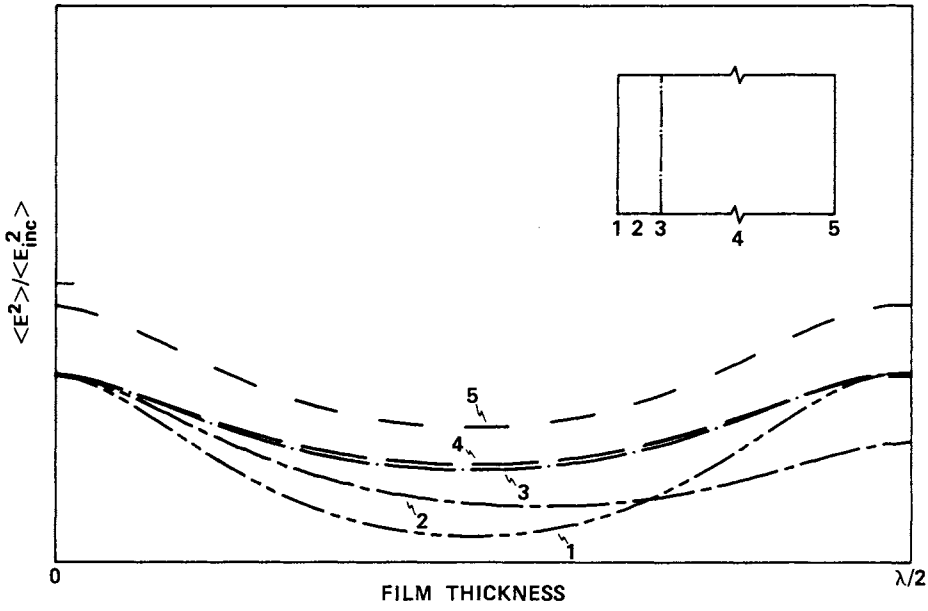

Fig. 11. The value of $\langle E^2 \rangle / \langle E_{inc}^2 \rangle$ for five regions in a single-layer entrance surface film. The film thickness varies from zero to $\lambda/2$ OT. (Substrate index = 1.50; film index = 3.00.)

substrate as we would in the exit surface analysis. It is this property of entrance surface films that permits us to account for the substrate contribution with the single term $\bar{p}_s A_0$ in Eq. (4).

VI EXPERIMENTAL DETERMINATION OF α_f, a_{af}, AND a_{fs}

Several values of relative energy density p are needed in the analysis of two-thickness films using Eq. (5) or of wedge-shaped films using Eqs. (7a) and (7b). Figures 12–17 show plots of relative energy densities for substrates illuminated at normal incidence from the film side for $\lambda/4$ and $\lambda/2$ OT films. These calculations include substrate multibounce effects. All the figures are families of curves for substrates ranging in index from 1.0 to 4.0 by steps of 0.2. The film index also ranges from 1.0 to 4.0 and is given as the abscissa. The corresponding relative energy density is shown as the ordinate.

Figure 12 uses Eq. (11) and shows $\bar{p}_s$, the average substrate relative power density for a $\lambda/4$ OT film. The value of $\bar{p}_s$ for $3\lambda/4$, $5\lambda/4$, ... OT films are identical to that for the $\lambda/4$ OT film. The value of $\bar{p}_s$ for a bare substrate and for $\lambda/2$, λ, ... OT films are identically 1.0 for all film and substrate indices and are not shown graphically.

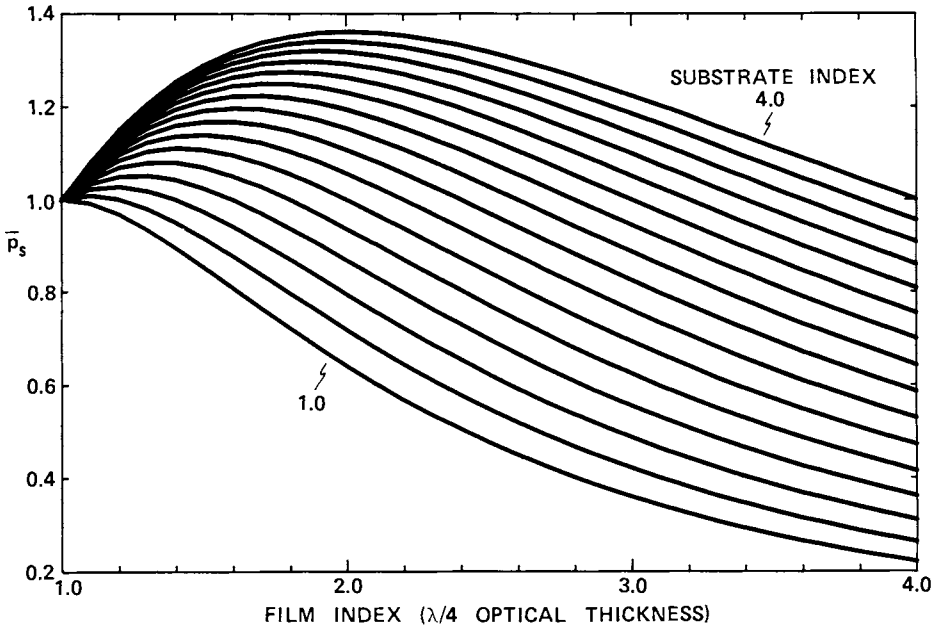

Fig. 12. The average relative energy density $\bar{p}_s$ within the bulk of a substrate with a $\lambda/4$, $3\lambda/4, \ldots$ film on the entrance surface.

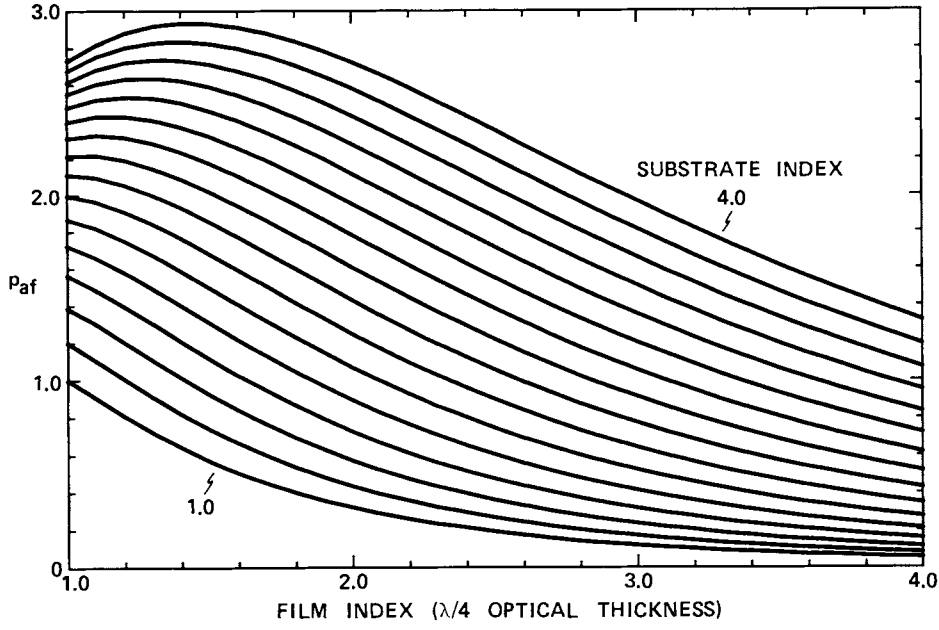

Fig. 13. The relative energy density p_{af} at the air–film interface for an entrance surface film of $\lambda/4$, $3\lambda/4, \ldots$ OT.

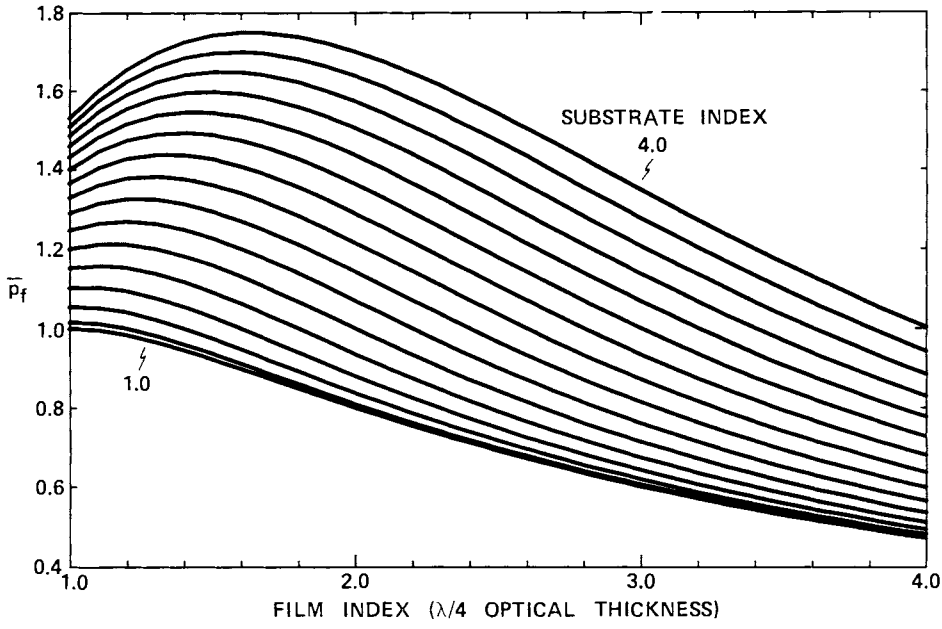

Fig. 14. The average relative energy density $\bar{p}_f$ within the bulk of an entrance surface film of $\lambda/4, 3\lambda/4, \ldots$ OT.

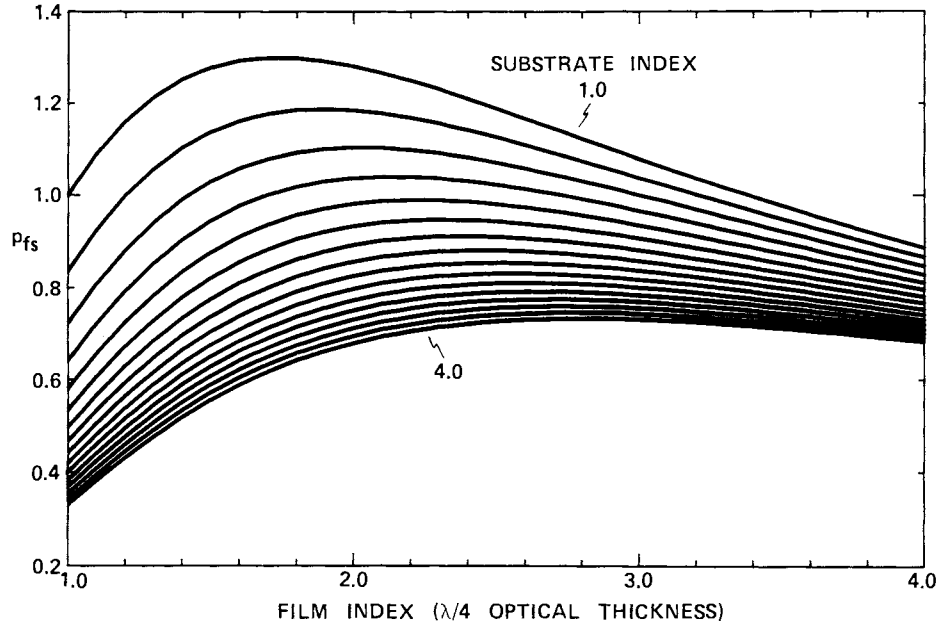

Fig. 15. The relative energy density p_{fs} at the film–substrate interface for an entrance surface film of $\lambda/4, 3\lambda/4, \ldots$ OT.

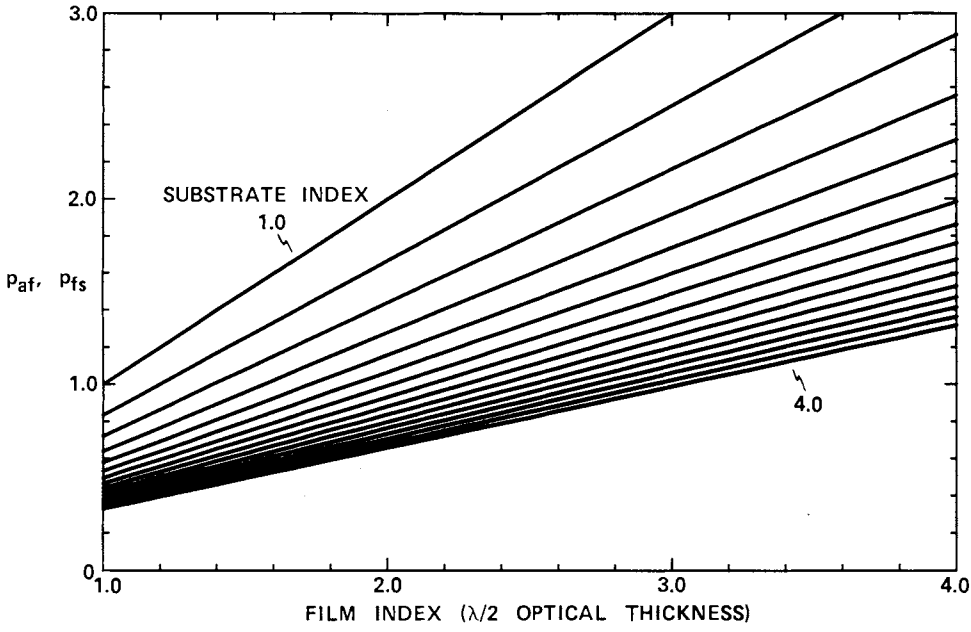

Fig. 16. The relative energy density at the air–film p_{af} and the film–substrate p_{fs} interface for an entrance surface film of $\lambda/2, \lambda, \ldots$ OT.

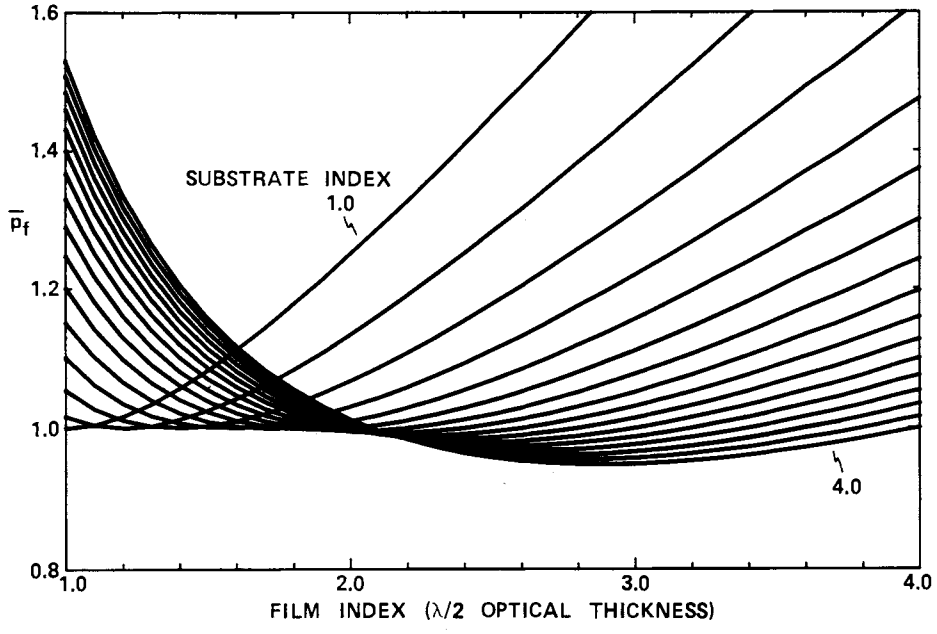

Fig. 17. The average relative energy density $\bar{p}_f$ within the bulk of an entrance surface film of $\lambda/2, \lambda, \ldots$ OT.

Figures 13–15 show p_{af}, $\bar{p}_f$, and p_{fs}, the air-film, average in the film, and film–substrate relative power density for a $\lambda/4$ OT film. As in the preceding section, these same values apply to a $3\lambda/4$, $5\lambda/4$, . . . OT film. Figure 16 shows p_{af} and p_{fs} for films of $\lambda/2$, λ, . . . thickness. Figure 17 shows $\bar{p}_f$ for $\lambda/2$, λ, . . . OT films.

In evaluating a sample, the values of p_{af}, $\bar{p}_f$, $\bar{p}_{fs}$, and $\bar{p}_s$ for the applicable substrate and film index are extracted from Figs. 12–17. If only the bulk absorption coefficient of the film is to be determined, then the absorptance for $\lambda/2$ and 1λ films are measured calorimetrically, and Eq. (5) is used, along with the value of $\bar{p}_f$ from Fig. 17, to find α_f.

If the interface absorptances are to be determined, then the absorptance of the bare substrate and a $\lambda/4$ OT film must be measured, in addition to the $\lambda/2$ and 1λ OT films. The values of p_{af}, $\bar{p}_f$, p_{fs}, and $\bar{p}_s$ for $\lambda/4$, $\lambda/2$, and 1λ OT films are taken from Figs. 12–17. Then, Eqs. (7a) and (7b) are used to determine a_{af} and a_{fs}.

REFERENCES

1. L. Skolnik, *in* "Optical Properties of Highly Transparent Solids" (S. S. Mitra and B. Bendow, eds.) pp. 405–533, Plenum, New York, 1975.
2. A. Hordvik, *Appl. Opt.* **16**, 2827 (1977).
3. L. W. Bos and D. W. Lynch, *Phys. Rev. B* **2**, 4567 (1970).
4. D. A. Pinnow and T. C. Rich, *Appl. Opt.* **12**, 984 (1973).
5. T. H. Allen, J. H. Apfel, and C. K. Carniglia, *in* "Laser Induced Damage in Optical Materials: 1978" (A. J. Glass and A. H. Guenther, eds.), pp. 33–36, National Bureau of Standards Spec. Publ. 541, Washington, D.C., 1978.
6. M. J. Hass, J. W. Davisson, P. H. Klein, and L. L. Boyer, *J. Appl. Phys.* **45**, 3959 (1974).
7. D. L. Decker and P. A. Temple, *in* "Laser Induced Damage in Optical Materials: 1977" (A. J. Glass and A. H. Guenther, eds.), pp. 281–285, National Bureau of Standards, Spec. Publ. 509, Washington, D.C., 1977.
8. P. A. Temple, *SPIE Proc.* **325**, 156 (1982).
9. E. Bernal G., *Appl. Opt.* **14**, 314 (1975).
10. H. A. MacLeod and D. Richmond, *Thin Solid Films* **37**, 163 (1976).
11. T. M. Donovan, P. A. Temple, Shiu-Chin Wu, and T. A. Tombrello, *in* "Laser Induced Damage in Optical Materials: 1979" (H. E. Bennett, A. J. Glass, A. H. Guenther, and B. E. Newnam eds.) pp. 237–246, National Bureau of Standards, Spec. Publ. 568, Washington, D.C., 1980.
12. P. A. Temple, *Appl. Phys. Lett.* **34**, 677 (1979).
13. P. A. Temple, D. L. Decker, T. M. Donovan, and J. W. Bethke, *in* "Laser Induced Damage in Optical Materials: 1978" (A. J. Glass and A. H. Guenther, eds.), pp. 37–42. National Bureau of Standards, Washington, D.C., 1978.
14. P. J. Leurgans, *J. Opt. Soc. Am.* **41**, 714 (1951).
15. G. W. DeBell, *SPIE Proc.* **140**, 2 (1978).

Chapter 8

Complex Index of Refraction Measurements at Near-Millimeter Wavelengths

GEORGE J. SIMONIS
Electronics Research and Development Command
Harry Diamond Laboratories
Adelphi, Maryland

I. Introduction 155
II. Fourier Transform Spectroscopy 156
III. Free-Space Resonant Cavity 161
IV. Mach–Zehnder Interferometer 163
V. Direct Birefringence Measurement 164
VI. Overmoded Nonresonant Cavity 165
VII. Crystal Quartz as Index Reference 165
VIII. Conclusion 167
References 167

I INTRODUCTION

The measurement of the complex index of refraction $\hat{n}$ at wavelengths in the range from hundreds of micrometers to several millimeters, or "near-millimeter" wavelengths (roughly 100 to 1000 GHz), can draw on a diversity of techniques. These wavelengths fall between the far-infrared wavelengths, at which the *optical* techniques are predominant, and the conventional millimeter wavelengths, at which *microwave* techniques are predominant. The wavelengths are short enough that quasi-optical apparatus can have clear apertures of many wavelengths for acceptable apparatus dimensions in the laboratory and long enough that single-mode microwave apparatus can have dimensions and tolerances accessible with established fabrication techniques. However, if the measurement accuracy requirements are high,

HANDBOOK OF OPTICAL CONSTANTS OF SOLIDS ISBN 0-12-544420-6

then many optical techniques can be a serious challenge because of diffraction effects, as can microwave techniques due to dimension tolerances. Many different approaches have been used in dealing with these challenges, but adaptations of optical techniques seem to predominate for this frequency range.

An extensive review of available data on the near-millimeter wave (NMMW) properties of materials is available [1]. Some of the different approaches used to measure these properties will be introduced and discussed briefly in the following sections. Space limitations will not allow a comprehensive discussion of this topic. The precise measurement of n and α at *fixed* NMMW frequencies, at which $\hat{n} = n - \hat{i}(\alpha\lambda/4\pi)$ and α is the exponential power absorption coefficient, is very useful because there are few strong narrow material resonances compared to those in the infrared range. The NMMW index dispersion is generally lower, and measurement at a fixed frequency can generally be extrapolated to neighboring frequencies to more significant figure accuracy than would be possible in the infrared. Debye relaxation effects are most often more pronounced at lower frequencies. The losses for "low-loss" materials typically get progressively higher as the NMMW frequency increases and acquire a nonlinear frequency dependence more typical of the far-infrared with broad features as the wings of infrared absorption bands are approached.

II FOURIER TRANSFORM SPECTROSCOPY

The vast majority of the interferometers in use for far-infrared Fourier transform spectroscopy (FTS) are of a Michelson interferometer configuration with Mylar beam splitters as portrayed in Fig. 1. Many good discussions of FTS techniques are available [2–5]. Fourier transform spectroscopy techniques have the advantage over grating spectrometer techniques of being able to collect data simultaneously at many frequencies and over a large solid angle. This becomes progressively more important, when blackbody sources are used, as measurements are sought at lower frequencies at which the signal level decreases as the frequency squared. Fourier transform spectroscopy techniques have the attractive feature of being able to provide measurements of n and α continuously as a function of frequency over large frequency ranges. This is in contrast to some of the fixed-frequency techniques.

Fourier transform spectroscopy techniques also have several unattractive features for NMMW studies. Even with their signal-to-noise advantage, it is most often very difficult to obtain useful data below 8 cm^{-1} (240 GHz) unless the instrumentation is specially adapted for low-frequency operation. The instrumentation and data processing are conceptually simple, but the implementation can become quite complicated. Also, at low frequencies the beam splitters must be very thick in order to get constructive interference from the

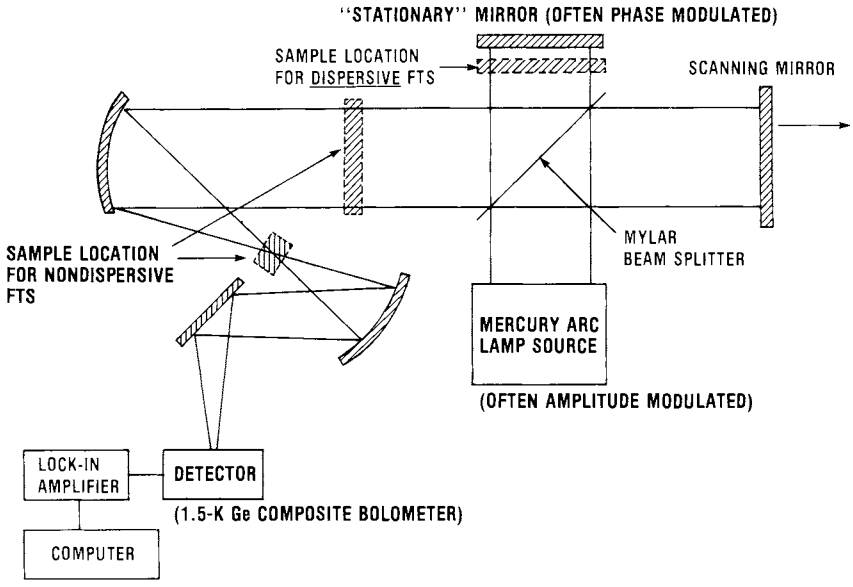

Fig. 1. Fourier transform spectroscopy configuration with a Mylar beam splitter. Dispersive or nondispersive data can be obtained depending on sample position.

two splitter surface reflections, and even then there is a low-frequency roll-off to a null reflected signal level. This thickness introduces significant beam splitter absorption losses at Mylar absorption frequencies and periodic null signal levels due to coherent interference effects from the two surfaces of the splitter. The low NMMW signal levels lead to the use of detectors cooled to 1.5 K, extensive filtering that limits the frequency coverage, and averaging of many scans. Enhanced diffraction effects at NMMW frequencies lead to a need for larger beam and sample diameters. Even under optimized conditions, it is difficult to get accurate data on lossy samples or accurate loss information on low-loss samples. In spite of these difficulties, remarkable results have been achieved at frequencies as low as 100 GHz with specially adapted FTS systems [6]. Polarizing interferometer configurations using wire grating beam splitters alleviate some of the beam splitter problems [6–8]. Such beam splitters do not have material resonance absorptions or periodic reflection nulls. They also have a flat, uniform, high efficiency for all wavelengths considerably greater than the grating wire spacing. The use of phase modulation [5] along with careful detector choice, filtering, source regulation, and cooling can make dramatic improvements in the NMMW signal-to-noise ratio.

Fourier transform spectroscopy measurements of $\hat{n}$ can be divided up into two basic approaches—dispersive and nondispersive FTS. The two are distinguished by the different placement of the sample in the interferometer (Fig. 1). In dispersive FTS, the sample is placed in one arm of the interferometer, while in nondispersive FTS, the sample is placed in the output

where the two beams are already recombined. In the nondispersive FTS configuration, the output beam is often focused onto the sample, allowing measurements to be made on relatively small samples. This is also an attractive feature for use with temperature- and pressure-controlled cells, in which small apertures are needed. However, if thick samples are needed for measurement accuracy, then errors can be introduced in focused-beam configurations due to beam defocusing by the sample. The real-index component is determined from multiple-reflection interference effects and the known spacing of the two surfaces of the sample. The imaginary component is obtained from throughout signal attenuation. The nondispersive approach must deal with a progressively smaller signal for real n determination as the sample index gets smaller or as α gets bigger. The multiple-surface reflection signal gets smaller for decreasing n until, finally, with materials such as styrofoam ($n = 1.017$) there are no observable multiple reflections, and the real index cannot be measured.

The dispersive FTS approach can be contrasted with the nondispersive approach inasmuch as the transmitted signal unreflected in the sample carries

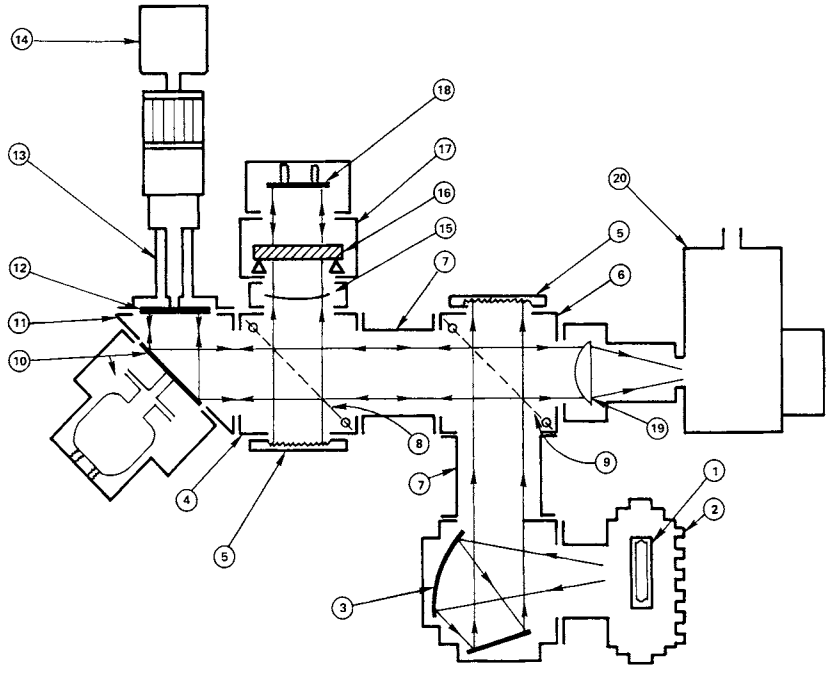

Fig. 2. Polarizing interferometer using wire-grating beam splitters and phase modulation to conduct dispersive Fourier transform spectroscopy. (1) Mercury lamp, (2) water-cooled lamp housing, (3) two-mirror collimator, (4) central cube, (5) radiation dump, (6) cube 2, (7) connectors (spacers), (8) wire-grid beam splitter, (9) wire-grid polarizer/analyzer, (10) 45° mirror and phase modulation assembly, (11) half-cube, (12) scanning mirror, (13) micrometer, (14) stepping motor, (15) Mylor window, (16) solid specimen, (17) specimen holder, (18) adjustable fixed mirror, (19) focusing lens, and (20) InSb Rollin detector. (From Afsar and Button [6].)

the real-index information for dispersive FTS. Thus, a relatively good signal-to-noise ratio exists for low index or lossy materials. The dispersive FTS index information is obtained from the shifting of the primary feature of the interferogram rather than in the appearance of secondary features, an important distinction when signal-to-noise ratio is such a serious problem. An extensive review of the dispersive FTS approach is available [9]. The sample is placed in the collimated beam of one arm that, combined with a requirement for small diffraction effects, leads to a need for NMMW samples with clear apertures of several inches. A dispersive FTS interferometer [6] employing wire-grating beam splitters, phase modulation, and a cooled-InSb Rollin detector is presented in Fig. 2 [6]. One polarization is reflected into

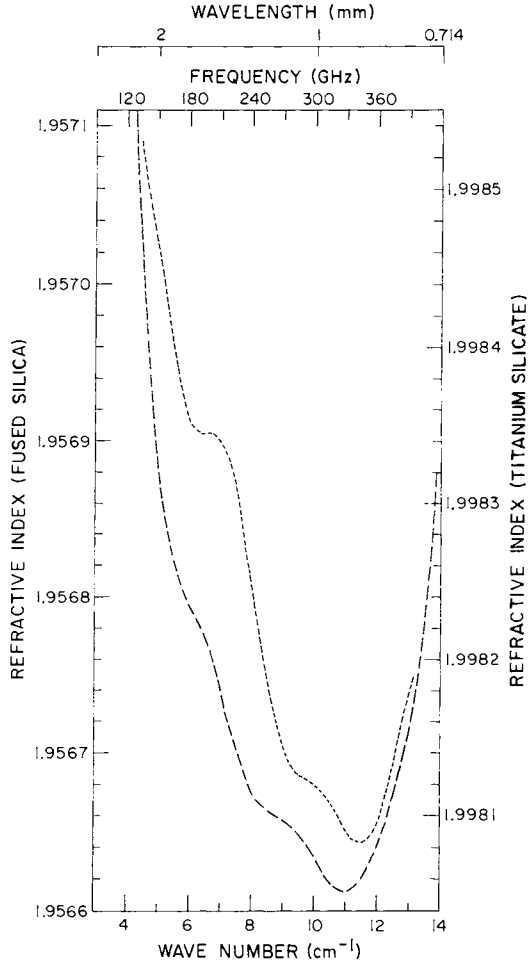

Fig. 3. Refractive index data obtained at 25°C using the instrumentation of Fig. 2. [·····, Corning 7940 (fused silica); – – –, Corning 7971 (titanium silicate).] (From Afsar and Button [6].)

the interferometer from the source with the other being disposed of. The reflected linear polarization is split into two orthogonal linear components that are separately phase shifted in different amounts, recombined, and sent on to the detector through the first grating, which also functions as a polarization filter for the detector. When sufficiently large flat plane-parallel samples are available and the technique is carried to extreme, remarkable results can be achieved with this approach. Figure 3 shows recent NMMW index of refraction data reported to six significant figures [6]. It is expected that NMMW features observed in such data for the first time will be relatable to physical sample characteristics. Figure 4 shows associated material-loss data reported here in terms of the imaginary component of the dielectric constant [6].

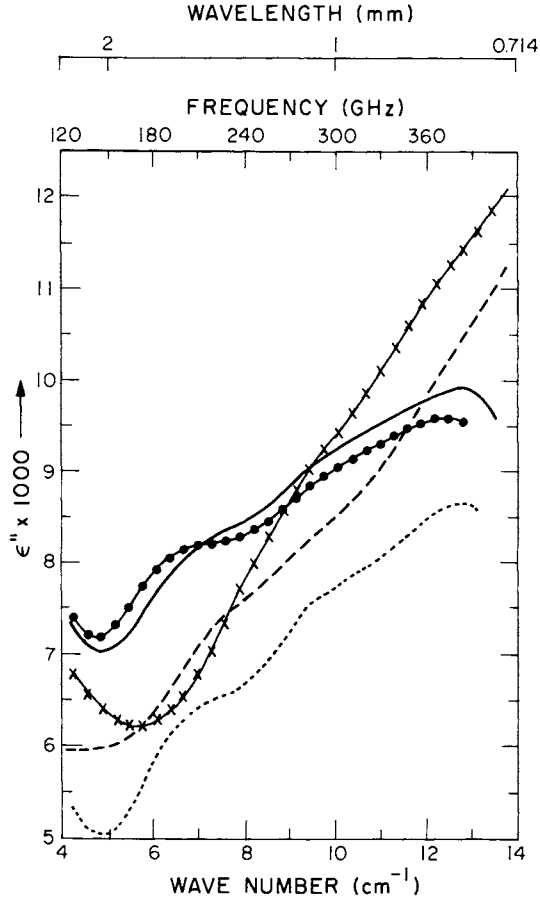

Fig. 4. Measurements of the imaginary component of the relative dielectric constant at 25°C using the instrumentation of Fig. 2. [×, alumma 995; ●, BeO; ——, Corning 9606 (glass ceramic); ·····, Corning 7940 (fused silica); and – – – –, Corning 7971 (titanium silicate).] (From Afsar and Button [6].)

Thus, it can be seen that, despite the difficulties of the FTS approach, very useful results can be achieved across the NMMW range with appropriate samples and experimental procedure.

FREE-SPACE RESONANT CAVITY III

The NMMW free-space resonant cavity techniques (usually Fabry–Perot cavities; see Figs. 5 and 6) are somewhat analogous to the popular microwave closed-resonant-cavity techniques in that they also rely on the perturbation of the cavity Q and resonant frequencies (or, alternatively, resonant-cavity length at fixed frequency) for the determination of the complex index. These cavities are driven by narrow-band sources providing a very good signal-to-noise ratio. The closed-microwave-resonant-cavity technique is difficult

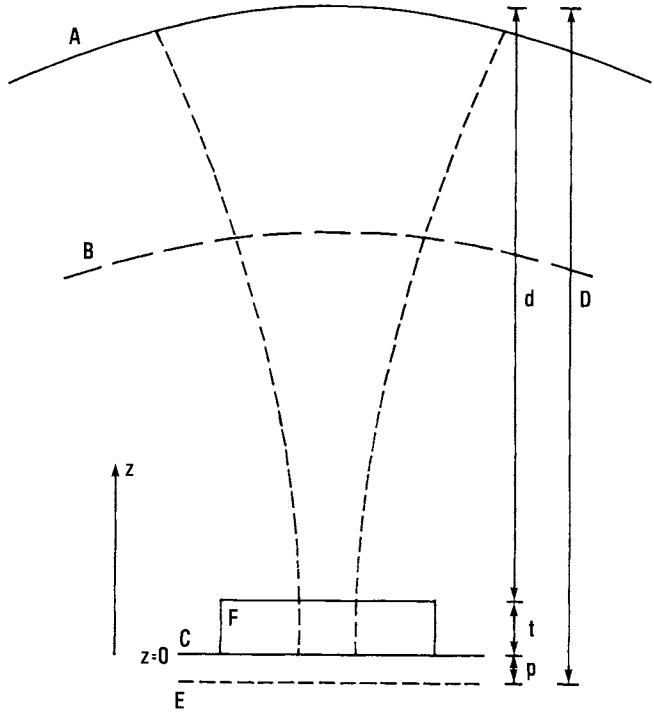

Fig. 5. Semiconfocal cavity configuration used for the measurement of the complex index of refraction. A, concave mirror; B, phase front; C, plane mirror at resonant position with sample; D, resonance-cavity length without sample; E, plane mirror at resonant position without sample; F, sample; t, sample thickness; $t + d$, resonance-cavity length with sample; and p, shift in resonance-cavity length due to sample. (From Jones [10]. Copyright 1976, The Institute of Physics.)

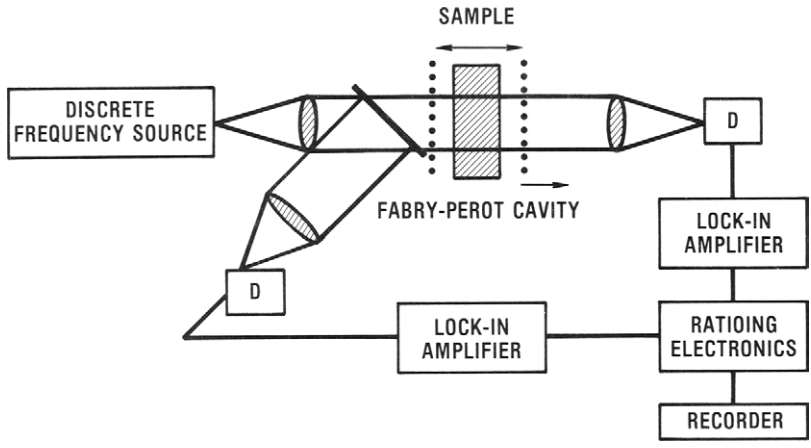

Fig. 6. Plane-parallel mesh-cavity configuration used for the measurement of the index of refraction. Detectors are labeled D.

to apply in the NMMW range because the dimensions and tolerances on fundamental-mode cavities are difficult to work with and larger overmoded closed cavities have too many competing modes to deal with. Also, it is difficult to insert and remove the sample without perturbing the tiny cavity. The free-space resonant cavities have dimensions large relative to the wavelength, require close tolerances only on two quasi-optical end reflectors (easily achievable by using optical fabrication techniques), allow the simple insertion and removal of samples, and have only a few low-loss modes if properly apertured. Also, they can achieve very high Q values because no sidewall losses are involved. The high Q values can be thought of as providing the equivalent of many passes through the sample, making the technique a sensitive method of measuring the material losses of very-low-loss samples. The sharp cavity resonance also allows accurate index determinations to be made.

Figure 5 presents schematically a semiconfocal configuration (used by Jones [10] at 35 GHz) that several groups including ourselves are extending to the NMMW range. Insertion of the sample, labeled F, causes the resonance-cavity length to be shortened by an amount p. Errors in the determination of the real dielectric constant on the order of 0.1% were reported. References to several similar efforts in resonant cavities can be found in Cullon and Yu [11], and Simonis and Felock [12]. Various plane-parallel, confocal, and semiconfocal Fabry–Perot cavities have been used. Simonis and Felock [12] used a plane-parallel cavity having metal-mesh reflectors selected for use with the 245-GHz output of an optically pumped $C^{13}H_3F$ laser (Fig. 6). Such crossed-wire meshes can be produced to high accuracy by using photolithographic techniques and are commercially available. Single or multiple

meshes can serve the purpose in the NMMW range that single or multiple dielectric layers often serve in the infrared for achieving desired reflectivities.

A number of publications cited in the preceding references also discuss the use of changing open-cavity Q with sample insertion for the determination of the sample loss tangent, power absorption coefficient, or imaginary component of the dielectric constant. Some careful examinations of the sources of error of this approach are provided. The resonant-cavity approach provides a high sensitivity to small sample losses. However, samples with large losses degrade the cavity Q so badly that this technique becomes very difficult to employ with lossy samples.

The resonant-cavity technique requires a highly stabilized and narrow-band-source frequency so that small shifts in resonance frequency or, equivalently, resonance-cavity length can be accurately measured. The use of optically pumped NMMW lasers alleviates some of these problems. Another difficulty with resonant-cavity techniques is that there are multiple roots to the index equations, providing multiple possible answers. The correct index must be distinguished by working with multiple sample thicknesses or by knowing what the approximate value should be.

MACH–ZEHNDER INTERFEROMETER IV

The Mach–Zehnder interferometer is the optical analog of the balanced-bridge techniques used at microwave and lower frequencies. The sample is placed in one arm and balanced against a calibrated variable phase shift and attenuation in the other arm. This configuration has the advantage of requiring only one pass through the sample. Thus, higher-loss samples can be dealt with.

The results are more straightforward to interpret and source-frequency drift is less of a problem than with resonant-cavity techniques. The signal-to-noise ratio is generally very good. However, one does need calibrated variable phase shifters and attenuators. The phase shift is readily obtainable as a variable optical path length [13] or as a variable sample thickness in the case of liquids [14]. The attenuator can be based on total internal reflection in a closely spaced pair of prisms [15, 16] or on crossed wire gratings [17].

The beam splitters generally are sheet material that has pronounced frequency-dependent properties. This frequency dependence can be removed by using wire-grating beam splitters as discussed in Section II. Such a polarizing Mach–Zehnder interferometer is shown in Fig. 7. Instead of having an attenuator in one arm, the relative signal level in the two arms is changed by rotating the initial polarizer [18]. The Mach–Zehnder approach also yields several possible index values that must be distinguished as with the resonant-cavity method.

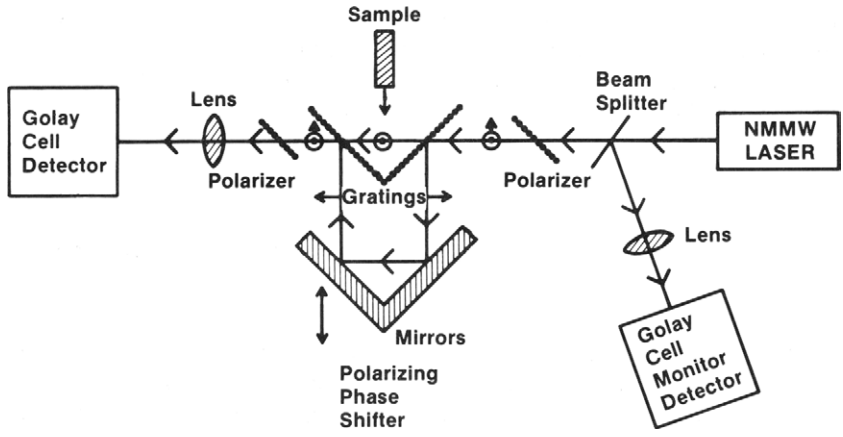

Fig. 7. Polarizing Mach–Zehnder configuration for the measurement of the index of refraction. Dotted beam splitters are wire gratings.

V DIRECT BIREFRINGENCE MEASUREMENT

The birefringence of a material can be measured *directly* without first measuring the individual indices by canceling its birefringent with a tunably birefringent wire-grating configuration as shown in Fig. 8. The sample and tunably birefringent grating assembly are placed in series between crossed polarizers and adjusted until a null signal level is achieved [19]. Effects due

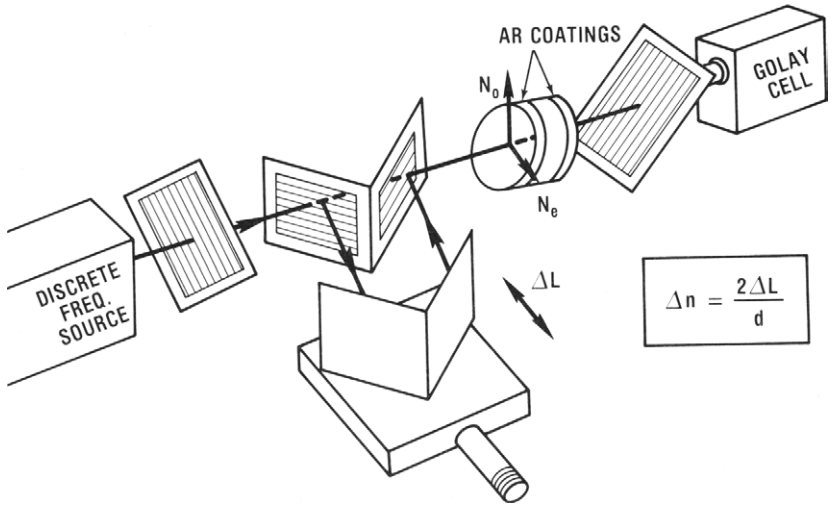

Fig. 8. A configuration similar to that of Fig. 7 but used to measure material birefringence directly. (From Simonis [19].)

to multiple reflections from the sample surfaces can be minimized by antireflection coating the sample or can be allowed for in the analytical treatment of the data. Measurements on crystal quartz yielded a value of $\Delta n = 0.047$ at 245 GHz [19], in good agreement with other reported measurements at nearby frequencies.

OVERMODED NONRESONANT CAVITY VI

Overmoded nonresonant cavities have been in use for many years for microwave dielectric studies. Their most common utilization has been for gas spectroscopy. Energy from a blackbody or narrow-band source is coupled into a greatly overmoded closed metal cavity through a small hole and sensed by detectors in the cavity or through a small output coupling hole. Mode stirring devices are often rotated inside the cavity (much as in microwave ovens) or the source frequency is slightly dithered in order to average out standing-wave patterns. There are no critical cavity dimensions. The use of such cavities for the study of the NMMW properties of solid materials has been explored [20–23]. The technique allows the study of irregularly shaped samples and powders since the reflected radiation is just returned to the cavity and eventually returns to the sample again. The technique can facilitate the NMMW study of the dielectric properties of biological material (including those in *in vivo*), a topic of current interest. This technique could also provide good NMMW metal reflectivity data. However, the analysis can get complicated for lossy materials. The technique shows promise for some special applications but is not likely to displace the techniques previously described for routine measurements.

CRYSTAL QUARTZ AS INDEX REFERENCE VII

As mentioned in Section I, many techniques are being employed for the determination of the NMMW properties of materials. It would be useful to have materials with well-known indices of refraction that reproduced well from one sample to another. Such materials could be used to prove out and compare apparatuses and techniques. Many materials have not been carefully measured or vary significantly in their NMMW properties from sample to sample [1]. These NMMW variations may be due, for example, to variations in crystallinity, density, chemical impurities, or available free carriers.

Single-crystal quartz appears to be a useful NMMW reference material for index of refraction measurements. Its NMMW index has been measured

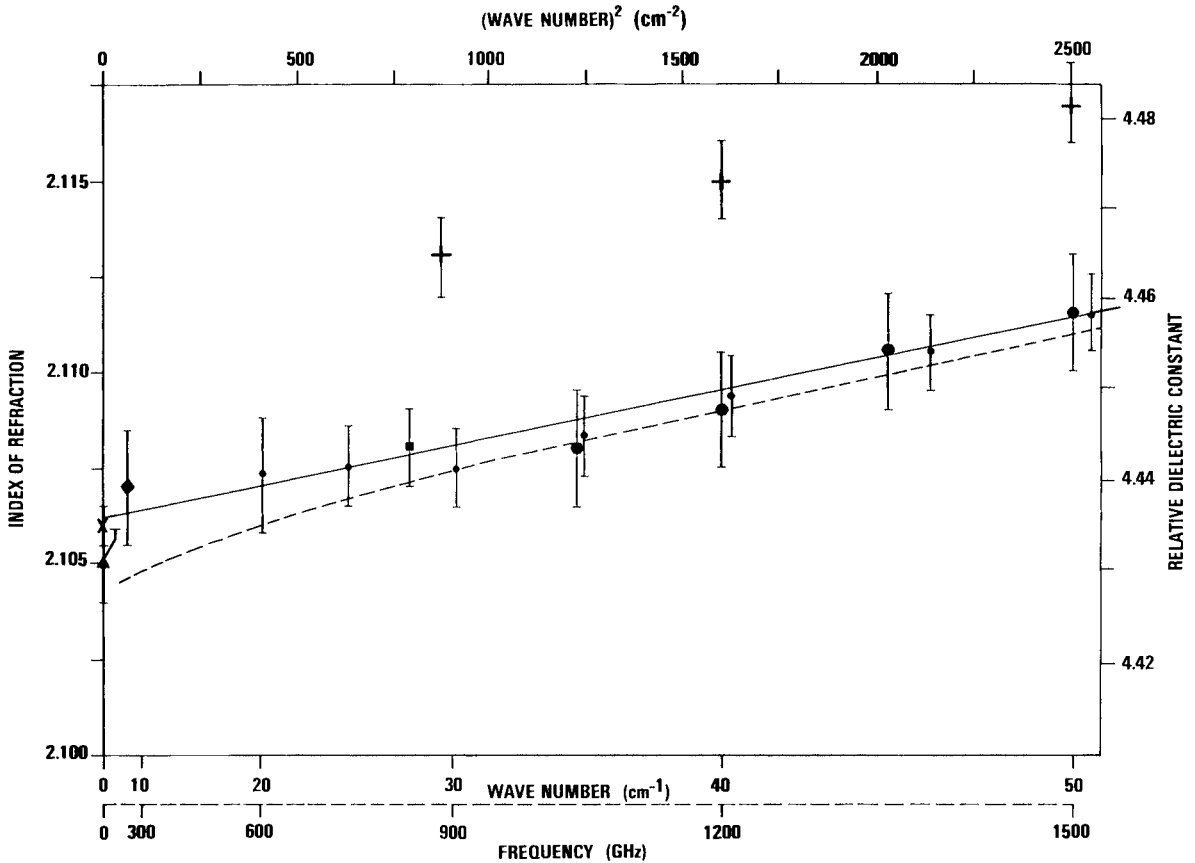

Fig. 9. The ordinary index of refraction of crystalline quartz as measured by many researchers using many techniques. The solid line is a frequency-square dependence fit to the zero-frequency and 50-cm^{-1} values of Russell and Bell [25]. ●, Russell and Bell [25]; ▲, Jones [10]; ◆, Simonis and Ferlock [12]; ×, Fontanella [24]; ●, Passchier *et al.* [26]; +, Loewenstien *et al.* [27]; ■, Charlemagne and Hadni [28]; – – –, Afsar [29]; and ——Russell and Bell [25].

accurately by a number of researchers using various techniques. The absorption losses of crystal quartz are extremely small and therefore present no problems. Its ordinary index is well behaved in the NMMW range, and there is good agreement between different measurements. Figure 9 [12] presents the semiconfocal resonant-cavity measurements of Jones [10] at 35 GHz, the bridge-substitution measurements of Fontanella [24] at 1 kHz, the mesh Fabry–Perot measurements of Simonis and Felock [12] at 245 GHz, the dispersive FTS measurements of Russell and Bell [25], the dispersive FTS measurements of Passchier *et al.* [26], the nondispersive FTS measurements of Loewenstein *et al.* [27], the laser measurement of Charlemagne and Hadni [28] at 890 GHz, and the dispersive FTS measurements of Afsar [29]. The solid line is a fit of a frequency-squared dependence to the "zero frequency" and 50-cm^{-1} values of Russell and Bell [25] when dispersion from an infrared resonance is assumed. The discrepancies between the data of Loewenstein *et al.* [27] and those of others remain unexplained (Loewenstein *et al.* [27] were aware of the discrepancy).

One concern about the use of crystalline quartz as a reference is that it is birefringent. A misoriented Z-cut sample would show a mix of the two indices, yielding erroneously large ordinary-index results.

VIII CONCLUSION

Adaptations of several quasi-optical techniques of complex index measurement can provide NMMW values of sufficient accuracy for most purposes. Several examples have been given. Many materials do not have sufficiently reproducible NMMW properties to be reliable confirmations of techniques being tested by different laboratories, but some materials, such as Z-cut crystalline quartz, can be very helpful in this regard. Equipment designed and employed for NMMW characterization of materials is readily available if such data are needed.

REFERENCES

1. G. J. Simonis, *Int. J. Infrared Millimeter Waves* **3**, 439 (1982).
2. R. J. Bell, "Introductory Fourier Transform Spectroscopy," Academic Press, New York, 1972.
3. G. W. Chantry, "Submillimetre Spectroscopy," Academic Press, New York, 1971.
4. P. R. Griffiths, "Transform Techniques in Chemistry," Plenum, New York, 1978.
5. J. E. Chamberlain, "The Principles of Interferometric Spectroscopy," Wiley, New York, 1979.
6. M. N. Afsar and K. J. Button, *Int. J. Infrared Millimeter Waves* **2**, 1029 (1981).
7. D. H. Martin and E. Puplett, *Infrared Phys.* **10**, 105 (1969).
8. T. J. Parker, D. A. Ledsham, and W. G. Chambers, *Infrared Phys.* **18**, 179 (1978).

9. J. R. Birch and T. J. Parker, *in* "Infrared and Millimeter Waves" (K. J. Button, ed.), Vol. 2, p. 138, Academic Press, New York, 1979.
10. R. G. Jones, *J. Phys. D* **9**, 819 (1976).
11. A. L. Cullen and P. K. Yu, *Proc. R. Soc. London Ser. A.* **325**, 493 (1971).
12. G. J. Simonis and R. D. Felock, *Appl. Opt.* **22**, 194 (1983).
13. J. E. Allnutt and J. A. Staniforth, *J. Phys. E* **4**, 730 (1971).
14. J. Chamberlain, J. Haigh, and M. J. Hine, *Infrared Phys.* **11**, 75 (1971).
15. E. R. Schineller, *Proc. Symp. Quasi-Optics* **14**, 517 (1964).
16. J. J. Taub, H. J. Hindin, O. F. Hinchselmann, and M. L. Wright, *IEEE Trans. Microwave Theory Tech.* **MTT-11**, 338 (1963).
17. J. A. Staniforth and J. E. Allnutt, *Proc. IEE* **118**, 343 (1971).
18. G. J. Simonis and B. C. Redman (to be published).
19. G. J. Simonis, *IEEE Trans. Microwave Theory Tech.* **MTT-31**, 356 (1983).
20. D. T. Llewellyn-Jones, R. J. Knight, P. H. Moffat, and H. A. Gebbie, *Proc. IEE A*, **127**, 535 (1980)
21. H. A. Gebbie and D. T. Llewellyn-Jones, *Int. J. Infrared Millimeter Waves* **2**, 197 (1981).
22. J. R. Izatt and F. Kremer, *Appl. Opt.* **20**, 2555 (1981).
23. F. Kremer and J. R. Izatt, *Int. J. Infrared Millimeter Waves* **2**, 675 (1981).
24. J. Fontanella, *J. Appl. Phys.* **45**, 2852 (1974).
25. E. E. Russell and E. E. Bell, *J. Opt. Soc. Am.* **57**, 341 (1967).
26. W. F. Passchier, D. D. Konijk, M. Mandel, and M. N. Afsar, *J. Phys. D* **10**, 509 (1977).
27. E. V. Loewenstien, D. R. Smith, and R. L. Morgan, *Appl. Opt.* **12**, 398 (1973).
28. D. Charlemagne and A. Hadni, *Opt. Acta* **16**, 53 (1969).
29. M. N. Afsar, Ph.D. thesis, University of London, London, England, 1978.

Chapter 9

The Quantum Extension of the Drude–Zener Theory in Polar Semiconductors*

B. JENSEN
Department of Physics
Boston University
Boston, Massachusetts

I. Introduction 169
II. Quantum Theory of Free-Carrier Absorption 172
III. Theoretical Results 174
IV. Comparison with Experimental Data 176
Appendix 187
References 188

INTRODUCTION I

The classical Drude model for the complex dielectric constant of a semiconductor can be used to extract the mobility and the free-carrier density n_e from an analysis of the reflectivity and transmittance data in the far infrared [1–4]. The dielectric constant ε is the square of the complex refractive index, which determines the optical properties of a given material. One has

$$\varepsilon = \varepsilon_1 - i\varepsilon_2 = N^2, \tag{1}$$

where the real and imaginary parts of the complex dielectric constant ε_1 and ε_2 are functions of the complex refractive index N as

$$N = n - ik, \tag{2}$$

* This research was supported by the Department of Energy under contract No. DE-AC02-79ER10444.A000

HANDBOOK OF OPTICAL CONSTANTS OF SOLIDS

Copyright © 1985 by Academic Press, Inc.
All rights of reproduction in any form reserved.
ISBN 0-12-544420-6

$$\varepsilon_1 = n^2 - k^2, \tag{3}$$

$$\varepsilon_2 = 2nk = 4\pi\sigma/\omega. \tag{4}$$

The choice of $n - ik$ rather than $n + ik$ is determined by the original use of $\exp i(\omega t - \mathbf{q} \cdot \mathbf{r})$ in the assumed plane-wave solution of Maxwell's equations.

In Eqs. (1)–(4), n is the real part of the complex refractive index, k the imaginary part or extinction coefficient, and σ the optical conductivity. The absorption coefficient α is proportional to σ, to ε_2, and to k:

$$n\alpha = 4\pi\sigma/c = (\omega/c)\varepsilon_2, \tag{5}$$

$$\alpha/2 = (\omega/c)k = 1/\delta. \tag{6}$$

The extinction coefficient k is essentially the ratio of the free-space wavelength of light of frequency ω to the skin depth δ.

The Drude theory gives the free-carrier contribution to ε_1 and ε_2 in terms of the plasma frequency $\bar{\omega}_p$ and the electron scattering time τ as

$$\varepsilon_1 = \varepsilon_\infty(1 - \bar{\omega}_p^2/\omega^2\eta), \tag{7}$$

$$\varepsilon_2 = (\omega_p^2/\omega^2\eta)1/\omega\tau, \tag{8}$$

where

$$\omega_p^2 = 4\pi n_e e^2/m_n, \qquad \bar{\omega}_p^2 = \omega_p^2/\varepsilon_\infty, \tag{9}$$

$$\eta = 1 + (1/\omega^2\tau^2) \to 1, \qquad \omega\tau \gg 1, \tag{10}$$

and ε_∞ is the high-frequency lattice dielectric constant. The real and imaginary parts of the complex refractive index are obtained from ε_1 and ε_2. One has

$$\varepsilon = (\varepsilon_1^2 + \varepsilon_2^2)^{1/2} = n^2 + k^2, \tag{11}$$

$$n = [(\varepsilon + \varepsilon_1)/2]^{1/2}, \tag{12}$$

$$k = \varepsilon_2/2n = [(\varepsilon - \varepsilon_1)/2]^{1/2}. \tag{13}$$

Experimentally, n and k are found from measurements of the reflectivity R of a bulk, opaque sample and the transmittance T of a slab, which are given in terms of n and k as

$$R = \frac{(n-1)^2 + k^2}{(n+1)^2 + k^2} \tag{14}$$

and

$$T = \frac{(1-R)^2 e^{-2\omega kd/c}}{1 - R^2 e^{-4\omega kd/c}}, \tag{15}$$

where d is the sample thickness. For the slab multiple-reflection effects are averaged, so that interface fringes are not resolved.

For the III–V and II–VI semiconducting compounds GaAs, InP, InAs, CdTe, and ZnSe, it is known that free-carrier absorption at frequencies just below the fundamental absorption edge, which lie in the near-infrared region of the spectrum, requires a quantum-mechanical description. The experimentally observed λ^3 wavelength dependence [5–9] of the optical conductivity in this region can be accounted for by a quantum-mechanical treatment based on time-dependent perturbation theory [10–12] that utilizes the band structure of the Kane theory [13]. In the far infrared, for photon energies small compared with k_0T (k_0 is the Boltzmann constant) and with the energy $\hbar\omega_Q$ of the phonon involved in the scattering, the quantum result reduces to the λ^2 dependence given by the Drude theory, and the quasi-classical Boltzmann transport equation [1–3]. The departures from the Drude theory at high frequencies are associated mainly with k rather than n, and hence, the transmission is affected more than the reflectivity. The latter depends on k in the region of the reflectivity minimum, where $n \simeq 1$, but is determined essentially by n over the region of the absorption spectrum for which $n > k$, which is the region where departures from the Drude theory would occur.

The quantum theory of free-carrier absorption has been treated by various investigators [10–12]. The problem is of theoretical as well as practical interest, since it is related to the question of the limits of validity of the quasi-classical Boltzmann transport equation, which describes many transport phenomena in solids. It is expected that deviations from the quasi-classical Boltzmann equation, or Drude theory, which gives the same result, should occur when photon energies become large compared with electron energies. The latter are of the order of k_0T or E_f for nondegenerate or degenerate materials, respectively, where E_f is the Fermi energy measured relative to the conduction band edge. The quantum result, which predicts a λ^3 wavelength dependence of the absorption coefficient for polar-optical-mode scattering and a $\lambda^{3.5}$ to λ^4 dependence for ionized-impurity scattering, can be derived from the equation of motion of the quantum density matrix [14]. The response of electrons to a driving field may be followed from the quasi-classical limit of small ω to the quantum limit that occurs when $\hbar\omega$ is no longer small compared with characteristic energies of the system. In this case, a generalized Boltzmann equation is obtained that reduces to the quasi-classical Boltzmann transport equation when the electron wave vector q tends to zero and ω is small [14–17]. When ω is appreciable, one obtains, under certain conditions, a solution of the Boltzmann equation in terms of a frequency-dependent relaxation time. This relaxation rate, which has been tabulated as a function of frequency and carrier concentration for various materials [18–20], can be used in the usual expressions of the classical Drude theory to obtain the quantum result. In particular, the low-frequency $\hbar\omega \simeq k_0T$ limit gives a good estimate for the dc mobility as a function of carrier concentration. At high frequencies, in lightly doped materials in which polar scattering dominates, $n\alpha$ is proportional to λ^3 and ε_2 and k are proportional

to λ^4 rather than λ^3. The real part of the dielectric constant is given approximately by the Drude-theory expression and $n \simeq (\varepsilon_\infty)^{1/2}$ for $\bar{\omega}_p \ll \omega \ll G/\hbar$, where $G/\hbar$ is the frequency of the fundamental absorption edge and G is the direct-band-gap energy of the semiconductor. As ω approaches $G/\hbar$ there is a small quantum-mechanical correction to ε_1 and hence to n. A summary of the results of the quantum theory is given in Section II.

II QUANTUM THEORY OF FREE-CARRIER ABSORPTION

Free-carrier absorption in semiconductors refers to the process of optical absorption in which the electron makes a transition from an initial state to a final state in the same band. The absorption or emission of a photon is then accompanied by scattering by optical- or acoustical-mode phonons or by charged impurities. The scattering mechanism is necessary for the conservation of crystal momentum, since the interaction with the photon provides energy but negligible momentum transfer.

To formulate the problem in terms of the quantum density-matrix equation of motion, we consider a system of dynamically independent electrons in interaction with a scattering system and an equilibrium radiation field. A perturbing electromagnetic field is then applied. The total system is now described by a quantum density matrix R with the equation of motion

$$R = R^0 + p, \qquad i\hbar\dot{p} = [H, R], \tag{16}$$

where R^0 is the equilibrium density matrix and p the deviation from equilibrium. Here H is the total Hamiltonian of the system and is given by

$$H = H^0 + H' + H^{er}, \tag{17}$$

where H^0 is the sum of the Hamiltonians of the noninteracting subsystems consisting of electrons, phonons, and photons, respectively. The scattering interaction of the electrons with the phonon field is denoted by H' and the interaction of the electrons with the quantum radiation field by H^{er}

$$H^{er} = -(e/mc)\mathbf{A} \cdot \mathbf{P}, \tag{18}$$

where $\mathbf{A}$ is the vector potential of the radiation field, $\mathbf{P}$ the momentum of the electron system, and the Coulomb gauge is used. This implies that $\mathbf{A}$ and $\mathbf{E}$ are transverse, where

$$\mathbf{E} = -(1/c)\dot{\mathbf{A}}. \tag{19}$$

The form of H' depends on the scattering mechanism. Various cases are considered [12, 14]. The complete derivation is given in Jensen [14].

We work in the number representation and take matrix elements of p between the eigenstates of $|N)$ and $|N')$ of H^0. We define*

$$|N) = |n)|v)|\gamma), \tag{20}$$

where $|n)$, $|v)$, and $|\gamma)$ are the wave functions of the subsystems consisting of electrons, phonons, and photons.

A generalized Boltzmann equation can be derived for the matrix element of p. The deviation from equilibrium of the Fourier component of the electron distribution function g_k^q is obtained by taking the trace over $|n)|v)$ of

$$p_{nv}^{(2)} = (nv|p^{(2)}|nv) \tag{21}$$

and the electron number operator $(n|\hat{N}_k|n) = n_k$ as follows

$$\sum_{nv} n_k p_{nv}^{(2)} = R(\gamma) g_k^q. \tag{22}$$

The superscript on p_{nv} in Eqs. (21) and (22) denotes the result of an expansion to second order of the density-matrix equation of motion in powers of $(1/\omega)$, which is permissible when $\omega\tau \gg 1$, and $R(\gamma)$ is the photon density matrix. The electron current $\mathbf{j}^q$ is given by the expression

$$\mathbf{j}^q = \sum_k e\mathbf{v}_k g_k^q, \tag{23}$$

where $\mathbf{v}_k$ is the matrix element of the electron momentum operator between the Bloch functions of the Kane theory divided by the electron mass.

The optical conductivity is obtained by taking the trace over the remaining photon subspace of

$$\langle \mathbf{j} \cdot \mathbf{E} \rangle_q = \sigma \langle E^2 \rangle_q. \tag{24}$$

The coefficient of $\langle E^2 \rangle_q$ in Eq. (24) is identified as the optical conductivity and is related to the absorption coefficient α obtained by using second-order perturbation theory by Eq. (5). That is, one obtains the same result when using either method. The advantage of the more cumbersome density-matrix approach is that it allows insight into the extension of the Boltzmann equation at high frequencies and permits an identification of the frequency-dependent relaxation rate that reduces to a constant in the far infrared and predicts the dc mobility. In the derivation of $n\alpha$ or ε_2 using second-order, time-dependent perturbation theory, one finds

$$\alpha = n_e \Sigma, \tag{25}$$

where Σ is the scattering cross section per electron, which at high frequencies may be written as an analytical function of $\hbar\omega/G$ [12–21], where G is the

* No confusion should arise from the double definition of N and n.

band-gap energy in electron volts. One does not address the question of an electron relaxation time in this formulation of the problem. While the cross section is, in fact, proportional to the generalized relaxation rate, this relaxation rate does not reduce to that obtained from transport theory unless scattering is elastic and the photon energy is small compared with the average electron energy. In the case of an inelastic scattering mechanism, such as interaction with optical mode phonons (polar scattering), a modified scattering rate is found that, however, does reduce to a constant in the far infrared so that the λ^2 dependence of the Drude theory is obtained for $\omega\tau \gg 1$.

III THEORETICAL RESULTS

The results obtained for the conductivity σ by using the above method can be written in terms of a generalized relaxation rate $1/\tau$, where τ reduces to the usual relaxation time under conditions previously discussed. When H' is the interaction between electrons and polar-optical-mode phonons, the conductivities $\sigma_\pm$ are found as follows, where the subscripts + and − correspond to photon absorption accompanied by phonon absorption and phonon emission, respectively, and the total optical conductivity for polar scattering is the sum of the two terms:

$$\sigma_\pm = (\omega_p^2/4\pi\omega^2)\langle 1/\tau\rangle_\pm, \qquad \omega\tau \gg 1. \tag{26}$$

The generalized relaxation rate is defined as follows:

$$\langle 1/\tau\rangle_\pm = (1/\tau_p^0)[F_\pm(\omega, \omega_Q)/X](I_\pm/12n_eV_c). \tag{27}$$

The conductivity and generalized relaxation times in Eqs. (26) and (27) are given in terms of the following parameters, which are obtained experimentally:

$$1/\tau_p^0 = g_p/\pi\hbar^2\alpha_0 c, \qquad \alpha_0 = (G/2m_nc^2)^{1/2}, \tag{28}$$

$$g_p = 2\pi e^2\hbar\omega_Q[(1/e_\infty) - (1/e_0)], \qquad X = \hbar\omega/G, \tag{29}$$

$$1/V_c = 2/\pi^2\lambda\!\!\!^{-3}_c, \qquad \lambda\!\!\!^{-}_c = \hbar/m_n\alpha_0 c. \tag{30}$$

In Eq. (27), $F_\pm(\omega, \omega_Q)$ is a function of temperature and frequency that involves the optical-phonon occupation probability, G is the band-gap energy at $k = 0$, m_n is the effective mass at the band edge, $\hbar\omega_Q$ is the optical-phonon energy, and ε_0 and ε_∞ are the static and high-frequency lattice dielectric constants, respectively. The term V_c is a characteristic volume element associated with the electron density of states, and it has been written in terms

of the wavelength $\lambda\!\!\!^{-}_c \to \hbar/mc$, $m_n \to m$, $\alpha_0 \to 1$ to utilize the analogy between the Kane theory and the Dirac theory [12, 13]. The quantity $I_\pm/12n_eV_cX$, where $I_\pm$ is an integral over initial electron energies, is essentially frequency independent at low frequencies and becomes independent of carrier concentration and a function only of frequency at high frequencies. In this limit, the absorption coefficient becomes proportional to the carrier concentration times a frequency-dependent cross section $\Sigma_\pm$, which is related to the scattering rate as follows for $\omega\tau \gg 1$:

$$n\Sigma_\pm = (1/n_e)(\omega_p^2/\omega^2 c)\langle 1/\tau\rangle_\pm = n\Sigma_0 \frac{F_\pm(\omega, \omega_Q)}{X^3} \frac{I_\pm}{n_eV_c}, \tag{31}$$

$$n\Sigma_0 = (1/12n_e)(\omega_p^2/\omega_g^2 c)1/\tau_p^0, \tag{32}$$

$$w_g = G/\hbar. \tag{33}$$

For the case of impurity scattering, the optical conductivity σ^I assumes the form

$$\sigma^I = (\omega_p^2/4\pi\omega^2)\langle 1/\tau^I\rangle, \tag{34}$$

$$\langle 1/\tau^I\rangle = (1/\tau_I^0)I_+^I/6n_eV_cX, \tag{35}$$

$$1/\tau_I^0 = g^I/\pi\hbar^2\alpha_0 c, \tag{36}$$

$$g^I = 8N_iV_c(e^2/e_0)^2/\lambda\!\!\!^{-}_c, \tag{37}$$

where N_i is the impurity concentration and I_+^I is again an integral over initial electron energies of a function appropriate to impurity scattering. The optical conductivity can be expressed in terms of a cross section per electron Σ^I calculated from perturbation theory as

$$4\pi\sigma^I/c = n\alpha^I = nn_e\Sigma^I, \tag{38}$$

$$n\Sigma^I = (n\Sigma_0^I/X^3)I_+^I/2n_eV_c, \tag{39}$$

$$n\Sigma_0^I = (1/12n_e)(\omega_p^2/\omega_g^2 c)1/\tau_I^0. \tag{40}$$

The optical conductivity due to impurity scattering thus assumes the form of the usual Drude expression if written in terms of an effective relaxation rate $\langle 1/\tau^I\rangle$ that is related to the cross section per electron as

$$n\Sigma^I = (1/n_e)(\omega_p^2/\omega^2 c)\langle 1/\tau^I\rangle. \tag{41}$$

The total conductivity σ, which is the sum of the conductivities due to polar optical mode and impurity scattering, is proportional to the total relaxation rate and the total absorption coefficient α, where

$$4\pi\sigma = 4\pi(\sigma_+ + \sigma_- + \sigma^I) = (\omega_p^2/\omega^2)1/\tau = cn\alpha, \tag{42}$$

$$1/\tau = \langle 1/\tau\rangle_+ + \langle 1/\tau\rangle_- + \langle 1/\tau^I\rangle. \tag{43}$$

Equation (42) gives the high-frequency limit in which $\omega\tau \gg 1$. The transition to the low-frequency regime $\omega\tau \leq 1$ is given by

$$\sigma = \sigma_0/\omega^2\tau^2\eta = \sigma_0/(1 + \omega^2\tau^2) \rightarrow \begin{cases} \sigma_0, & \omega\tau \ll 1 \\ \sigma_0/\omega^2\tau^2, & \omega\tau \gg 1, \end{cases} \tag{44}$$

where

$$\sigma_0 = n_e e^2\tau/m_n = en_e\mu, \qquad \mu = e\tau/m_n. \tag{45}$$

For degenerate materials, m_n in Eq. (45) should be replaced by

$$m^* = m_n(1 + 2E_f/G), \tag{46}$$

which is the effective mass at the Fermi surface from the Kane theory. Detailed calculations of the scattering rates are given by Jensen [12, 14, 21]. Numerical results for various compounds are also given by Jensen [18–20] for $1/\tau$ as a function of n_e and ω, from which the complex dielectric constant in Eq. (8) can be immediately calculated. The remaining quantities, including the complex refractive index, absorption coefficient, optical conductivity, and skin depth, then follow as discussed in Section I.

Values of n, k, and R versus wavelength, calculated by using the method discussed for GaAs, InP, and InAs, are tabulated in Section IV.

IV COMPARISON WITH EXPERIMENTAL DATA

The theoretical results are calculated by using experimental values for the various quantities given in Table I. For polar-optical mode scattering, no adjustable parameters are involved. Theoretical results are obtained for the scattering rate $1/\tau$ in Eq. (43). This enables one to calculate ε_1 and ε_2 in Eqs. (7) and (8), from which n and k are obtained by using Eqs. (11–13). The reflectivity R is found as a function of n and k from Eq. (14). This is the quantity measured experimentally.

A calculation of ε_1 appropriate to electrons in polar semiconductors with the band structure of the Kane theory and based on the quantum density-matrix equation of motion yields a high-frequency modification to Eq. (7). For $\omega\tau \gg 1$ and $X < 0.1$, one obtains [18, 22]

$$\begin{aligned} \varepsilon_1 &= [\varepsilon_\infty/(1 - X)][1 - (X/\varepsilon_\infty) - \bar{\omega}_p^2/\omega^2] \\ &\cong [\varepsilon_\infty/(1 - X)](1 - \bar{\omega}_p^2/\omega^2) \\ &\rightarrow \varepsilon_\infty(1 - \bar{\omega}_p^2/\omega^2), \qquad X \ll 1. \end{aligned} \tag{47}$$

TABLE I

Parameters Used to Calculate Optical Constants

	InP	GaAs	InAs
G (eV)	1.35	1.43	0.36
m_n/m	0.073	0.071	0.024
$\hbar\omega_Q$ (eV)	0.0428	0.0349	0.0299
ε_∞	9.61	11.1	11.6
$1/\varepsilon_\infty - 1/\varepsilon_0$	0.02767	0.0135	0.01619
α_0	$\frac{1}{234}$	$\frac{1}{224}$	$\frac{1}{266}$
g (eV^2 cm)	1.13×10^{-9}	4.25×10^{-10}	4.39×10^{-10}
$1/\tau_p$ sec^{-1}	6.46×10^{12}	2.33×10^{12}	2.86×10^{12}
$e\tau_p/m_n$ (cm^2)/V sec[a]	3.37×10^3	1.06×10^4	2.59×10^4
μ (cm^2)/V sec[b]	4.53×10^3	8.3×10^3	
μ (cm^2)/V sec[c]	4.5×10^3	8.5×10^3	3×10^4

[a] $T = 300$ K.
[b] Theoretical value.
[c] Experimental value.

We note that $1/\varepsilon_\infty \lesssim 0.1$ and hence $X/\varepsilon_\infty \ll 1$ for compounds we consider, and this term can be neglected. In the limit $X \ll 1$, the quasi-classical high-frequency Drude result is recovered, as required. For $X \sim 0.1$, there is a high-frequency correction given by Eq. (47), which is used to calculate the numerical values of $\varepsilon_1 = n^2 - k^2$. The major modification of the classical result is dispersion in n as one approaches the fundamental absorption edge [22].

Figure 1 shows the impurity scattering rate calculated for various samples of InP described in Table II. As the free-carrier density increases from sample 1 to sample 8, the scattering rate increases. In Fig. 2 the relaxation rate for polar scattering $1/\tau_p = \langle 1/\tau_+ \rangle + \langle 1/\tau_- \rangle$ is shown for the same samples. In the quantum limit, this quantity varies as λ and is roughly independent of carrier concentration. At low frequencies, such that $\hbar\omega \sim k_0 T$, the Drude limit is recovered and the polar scattering rate converges to a concentration-dependent constant. If the scattering rate for impurity scattering is now included, the total relaxation time τ in the Drude limit can be used to predict the dc mobility. The total scattering rate is $1/\tau$ plotted for the samples of InP in Fig. 3. The calculated optical constants n and k for some of the samples of Table II are listed in Table III.

Figure 4 shows the total scattering rate for various samples of GaAs (Table IV) versus $X = \hbar\omega/G$ at $T = 300$ K. The intersection of the curve $1/\tau$ with ω gives the point at which $\omega\tau = 1$ for a given sample. Sample a shows the contribution of polar scattering only while all other samples include the contributions of polar plus impurity scattering for various values of the

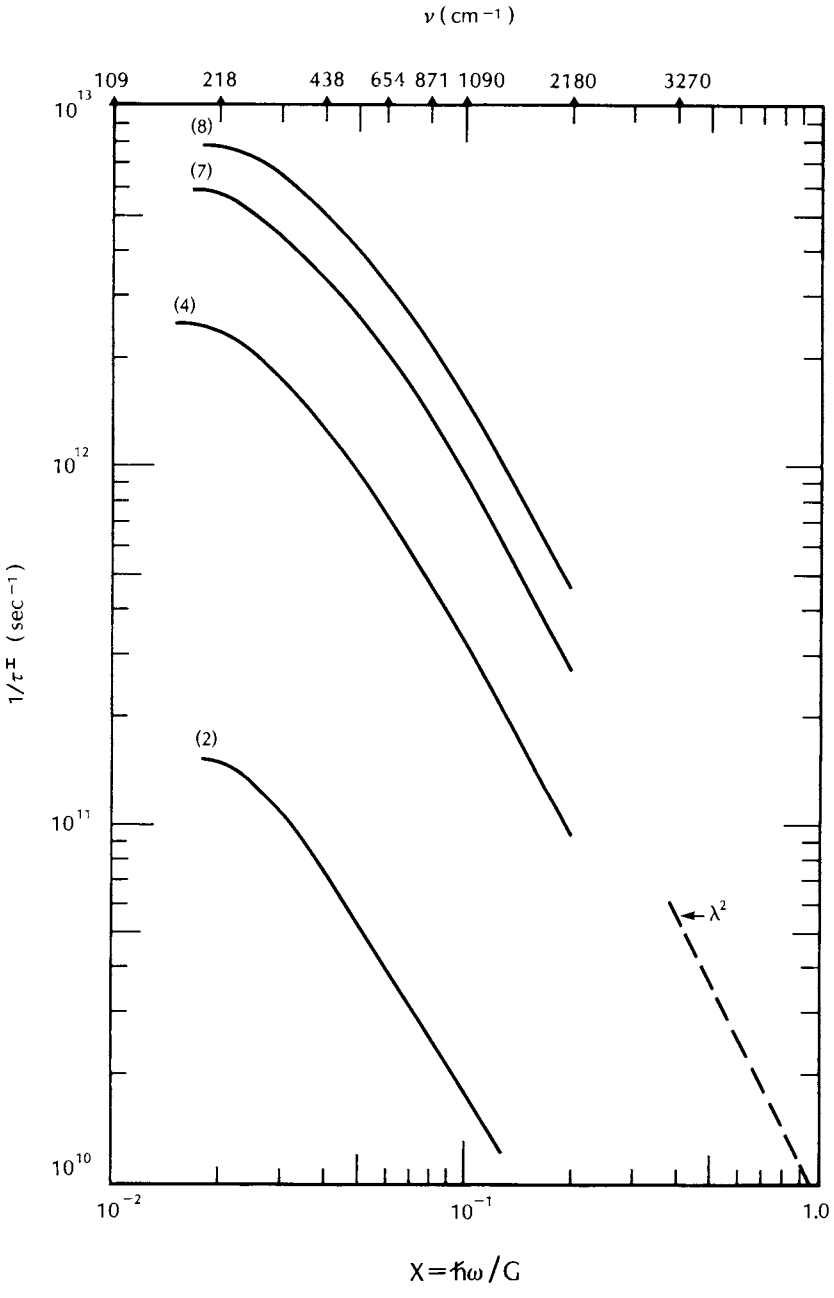

Fig. 1. The relaxation rate for impurity scattering calculated for the samples of InP at 300 K as described in Table II. (Sample numbers in parentheses.)

TABLE II

InP Samples of Varying Free-Carrier Concentration[a]

Sample	Carrier concentration n_e (cm^{-3})
1	4.69×10^{15}
2	2.25×10^{16}
3	6.27×10^{16}
4	4.13×10^{17}
6	6.17×10^{17}
7	1.23×10^{18}
8	2.13×10^{18}

[a] Data tabulated in Table III and/or plotted in Figs. 1–3.

carrier concentration. Uncompensated samples such that $N_i = n_e$ are considered. Polar scattering dominates at high frequencies for all but the most heavily doped samples shown, while in the Drude limit one obtains a frequency-independent scattering rate that is a function of carrier concentration. In Fig. 5, the Drude limit is used to calculate the dc mobility at $T = 300$ K as a function of free-carrier density for GaAs and comparison is made with various experimental results. In Figs. 6 and 7, the scattering rate at $T = 300$ K has been used to calculate the real and imaginary parts of the complex index of refraction of GaAs samples that are listed in Table IV.

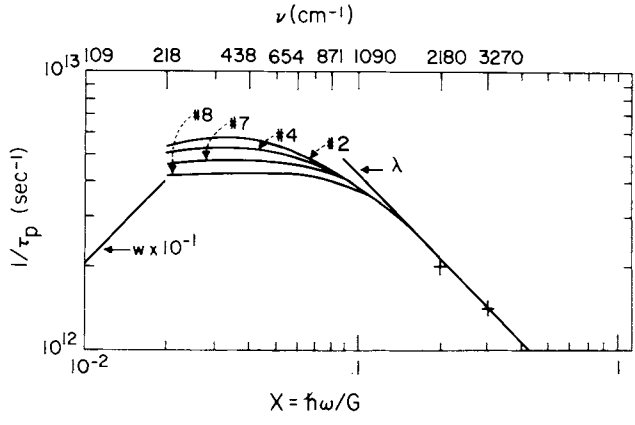

Fig. 2. The relaxation rate for polar scattering calculated for the samples of InP described in Table II. The high-frequency quantum limit is indicated by crossmarks.

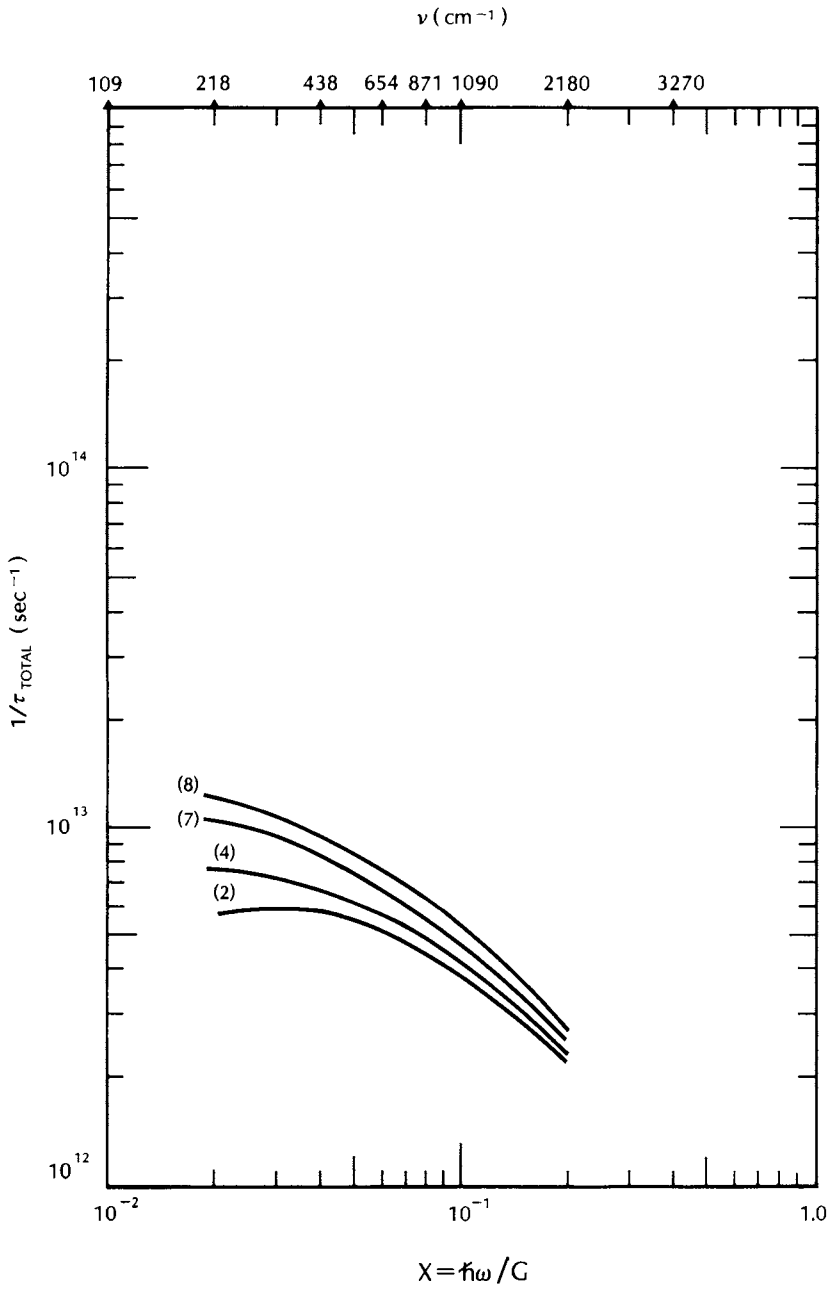

Fig. 3. The total relaxation rate for samples of InP at 300 K, given by the sum of the relaxation rates for polar and for impurity scattering. (Sample numbers in parentheses.)

TABLE III

Optical Constants of InP at 300 K as a Function of Free-Carrier Density

Sample			1		3		6		8	
eV	cm^{-1}	μm	n	k	n	k	n	k	n	k
0.1351	1089	9.18	3.25	1.12×10^{-5}	3.24	1.53×10^{-4}	3.14	1.88×10^{-3}	2.85	1.01×10^{-2}
0.1078	869.6	11.5	3.22	2.53×10^{-5}	3.20	3.47×10^{-4}	3.05	4.51×10^{-3}	2.57	2.66×10^{-2}
0.08103	653.6	15.3	3.19	7.02×10^{-5}	3.16	9.82×10^{-4}	2.88	1.37×10^{-2}	1.92	0.106
0.06199	500.0	20	3.16	1.74×10^{-4}	3.115	2.46×10^{-3}	2.62	3.92×10^{-2}	0.516	1.04
0.05391	434.8	23	3.15	2.72×10^{-4}	3.09	3.90×10^{-3}	2.42	6.83×10^{-2}	0.421	2.08
0.04959	400.0	25	3.15	3.52×10^{-4}	3.07	5.08×10^{-3}	2.25	9.98×10^{-2}	0.458	2.62
0.04133	333.3	30	3.14	6.02×10^{-4}	3.03	8.87×10^{-3}	1.73	0.241	0.597	3.72
0.03542	285.7	35	3.13	9.40×10^{-4}	2.98	1.43×10^{-2}	0.999	0.702	0.795	4.68
0.03100	250	40	3.12	1.36×10^{-3}	2.93	2.15×10^{-2}	0.662	1.61	1.02	5.52
0.02701	217.9	45.9	3.11	2.03×10^{-3}	2.86	3.35×10^{-2}	0.674	2.49	1.33	6.49
0.01351	108.9	91.8	3.04	1.61×10^{-2}	1.91	0.384	1.72	6.88	4.14	12.5

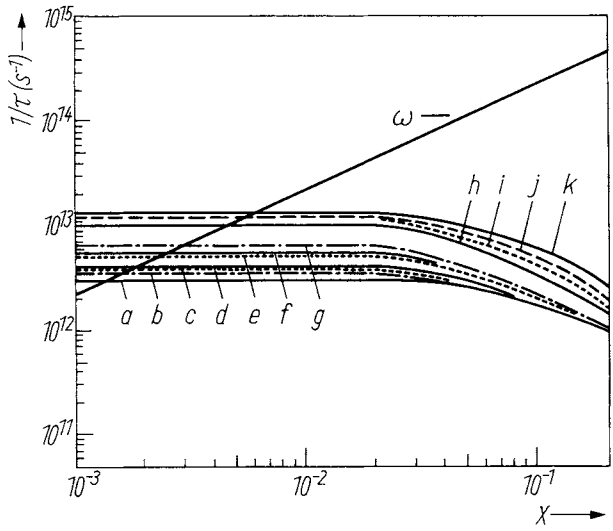

Fig. 4. The total frequency-dependent relaxation rate versus $x = \hbar\omega/G$ for samples of GaAs of varying carrier concentration listed in Table IV. The intersection of the curve ω with the curve $1/\tau$ for a given sample specifies the point at which $\omega\tau = 1$.

TABLE IV

GaAs Samples of Varying Free-Carrier (Electron) Concentration[a]

Sample	Carrier concentration n_e (cm^{-3})
a	3.38×10^{15}
b	2.75×10^{16}
c	6.33×10^{16}
d	1.41×10^{17}
e	3.37×10^{17}
f	4.27×10^{17}
g	5.84×10^{17}
h	2.16×10^{18}
i	3.38×10^{18}
j	4.85×10^{18}
k	8.73×10^{18}

[a] Data tabulated in Table V and/or Figs. 4–8.

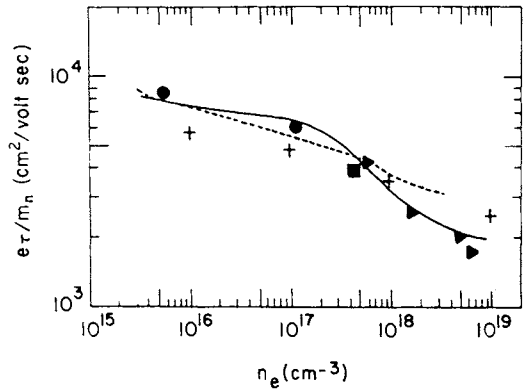

Fig. 5. Theoretical results (for GaAs) for mobility $e\tau/m_n$, $m_n = 0.071$ m, are given by the solid curve. The effective mass at the Fermi surface should be used to calculate the mobility at high carrier concentrations $\gtrsim 10^{18}$ cm^{-3}. The ratio of the effective mass at the Fermi surface to m_n is 1.10, 1.14, 1.18, and 1.26 for samples h, i, j, and k, described in Table IV, respectively. Prior results are: theoretical: ----, Madelung [31]; +, Perkowitz [3]; ■, Vakulenko [23]; experimental: ▲, ●, Madelung [31].

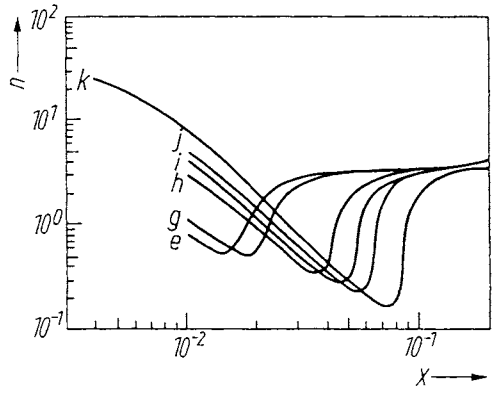

Fig. 6. The real part of the refractive index versus the photon energy in units of G for samples of GaAs described in Table IV.

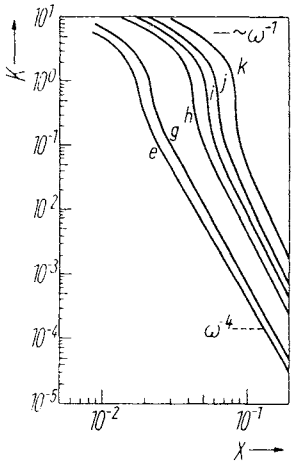

Fig. 7. The imaginary part of the refractive index versus the photon energy in units of G for samples of GaAs described in Table IV.

TABLE V

Optical Constants of GaAs at 300 K as a Function of Free-Carrier Density

Sample			a		b		g		h		j		k	
eV	cm^{-1}	μm	n	k	n	k	n	k	n	k	n	k	n	k
0.1430	1153	8.67	3.51	3.57×10^{-6}	3.51	2.89×10^{-5}	3.42	8.14×10^{-4}	3.17	4.90×10^{-3}	2.69	1.89×10^{-2}	1.78	6.37×10^{-2}
0.1287	1038	9.63	3.49	8.19×10^{-6}	3.49	4.34×10^{-5}	3.38	1.24×10^{-3}	3.07	7.89×10^{-3}	2.44	3.15×10^{-2}	0.972	0.171
0.1148	925.9	10.8	3.47	8.29×10^{-6}	3.47	6.72×10^{-5}	3.33	1.99×10^{-3}	2.93	1.32×10^{-2}	2.07	5.89×10^{-2}	0.186	1.40
0.09999	806.5	12.4	3.45	1.37×10^{-5}	3.45	1.11×10^{-4}	3.27	3.41×10^{-3}	2.73	2.41×10^{-2}	1.37	0.144	0.169	2.48
0.09537	769.2	13									0.920	0.259		
0.08856	714.3	14									0.306	1.03		
0.08551	689.7	14.5	3.44	2.38×10^{-5}	3.43	1.93×10^{-4}	3.19	6.20×10^{-2}	2.40	4.90×10^{-2}	0.262	1.34	0.205	3.53
0.07167	578.0	17.3	3.42	4.49×10^{-5}	3.40	3.65×10^{-4}	3.06	1.27×10^{-2}	1.76	0.132	0.244	2.76	0.293	4.78
0.06888	555.6	18							1.55	0.173				
0.06526	526.3	19							1.19	0.280				
0.06199	500.0	20							0.732	0.542				
0.05714	460.8	21.7	3.40	9.48×10^{-5}	3.38	8.00×10^{-4}	2.82	3.12×10^{-2}	0.394	1.35	0.345	4.26	0.453	6.45
0.04290	346.0	28.9	3.38	2.38×10^{-4}	3.34	2.05×10^{-3}	2.27	0.108	0.425	3.44	0.632	6.35	0.835	9.00
0.03875	312.5	32	3.37	3.30×10^{-4}	3.32	2.90×10^{-3}	1.94	0.187	0.540	4.10	0.778	7.17	1.12	10.0
0.03647	294.1	34	3.36	4.00×10^{-4}	3.31	3.49×10^{-3}	1.67	0.263	0.599	4.51	0.892	7.69	1.28	10.7
0.03444	277.8	36	3.36	4.75×10^{-4}	3.30	4.17×10^{-3}	1.36	0.390	0.664	4.90	1.01	8.20	1.45	11.3
0.03263	263.2	38	3.36	5.59×10^{-4}	3.29	4.93×10^{-3}	1.01	0.627	0.742	5.27	1.12	8.69	1.61	12.0
0.02857	230.4	43.4	3.35	8.47×10^{-4}	3.27	7.49×10^{-3}	0.575	1.70	0.895	6.25	1.48	9.99	2.07	13.6
0.02254	181.8	55	3.34	1.70×10^{-3}	3.20	1.57×10^{-2}	0.598	3.31	1.38	8.21	2.27	12.7	3.26	17.1
0.01879	151.5	66					0.765	4.53	1.86	9.97	3.15	15.1	4.45	20.3
0.01746	140.8	71	3.32	3.66×10^{-3}	3.08	3.47×10^{-2}	0.833	5.00	2.17	10.7	3.58	16.1	5.12	21.6
0.01430	115.3	86.7	3.30	6.57×10^{-3}	2.94	6.54×10^{-2}	1.16	6.46	3.00	13.0	5.06	19.2	8.08	24.4
0.01240	100.0	100	3.28	1.02×10^{-2}	2.79	0.105	1.46	7.59	3.90	14.7	6.40	21.6	9.05	28.5
0.007948	64.10	156					3.11	11.8	7.72	21.1	12.4	29.9	17.1	39.1
0.004959	40.00	250	2.98	0.155	1.34	2.98	6.50	17.4	14.4	28.1	21.9	39.4	29.3	50.4
0.003723	30.03	333					9.62	21.1	19.4	33.2	28.8	45.3	38.2	58.3

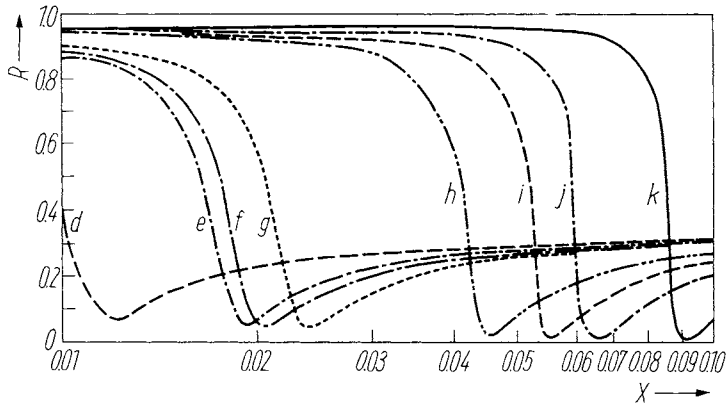

Fig. 8. Reflectivity curves for samples of GaAs of varying carrier concentration calculated from values of n and k shown in Figs. 6 and 7.

The ω^{-4} dependence of k at high frequencies, which corresponds to a λ^3 rather than a λ^2 dependence of the absorption coefficient, has been reported by many authors [23–30]. The absorption coefficient is calculated and compared with experimental results by Jensen [12]. The reflectivity calculated from the n and k values is shown in Fig. 8 for GaAs. Note that the rest-strahlen features near $X = 0.024$ are not present. The addition of these features is discussed in the appendix.

For InAs samples listed in Table VI, the optical constants are given in Table VII. Enough points are tabulated to allow the reader to plot the data and interpolate for other wavelengths.

In summary, the Drude theory of the optical constants of III–V and II–VI polar semiconductors can be extended into the near infrared in terms of a frequency-dependent electron scattering rate formulated to give the quantum result when used in the classical Drude theory. In the far infrared, this scattering rate reduces to a concentration-dependent but frequency-independent constant that predicts the dc mobility as a function of carrier concentration for the various samples.

TABLE VI

InAs Samples of Varying Free-Carrier (Electron) Concentration[a]

Sample	Carrier concentration n_e (cm^{-3})
E	5.07×10^{16}
H	1.12×10^{17}
J	2.16×10^{17}

[a] Data tabulated in Table VII.

TABLE VII

Optical Constants of InAs at 300 K as a Function of Free-Carrier Density

Sample		E			H		J	
eV	cm^{-1}	μm	n	k	n	k	n	k
0.07208	581.4	17.2	3.68	7.91×10^{-4}	3.60	1.75×10^{-3}	3.42	3.90×10^{-3}
0.03604	290.7	34.4	3.21	1.04×10^{-2}	2.84	2.59×10^{-2}	1.93	8.25×10^{-2}
0.03444	277.8	36	3.17	1.22×10^{-2}	2.60	3.72×10^{-2}	1.12	0.194
0.03263	263.2	38	3.11	1.50×10^{-2}	2.46	4.77×10^{-2}	0.473	0.561
0.03100	250.0	40	3.05	1.80×10^{-2}	2.31	6.06×10^{-2}	0.256	1.23
0.02877	232.0	43.1	2.95	2.30×10^{-2}	2.04	8.85×10^{-2}	0.210	1.91
0.02480	200.0	50	2.71	4.14×10^{-2}	1.14	0.259	0.221	3.03
0.02160	174.2	57.4	2.38	7.10×10^{-2}	0.572	0.712	0.265	3.43
0.01440	116.1	86.1	0.357	1.61	0.349	3.92	0.478	6.37
0.01078	86.95	115	0.367	3.68	0.536	6.00	0.798	8.94
0.007208	58.14	172	0.676	6.66	1.10	9.64	1.70	13.7
0.003604	29.07	344	2.37	14.1	3.93	19.2	6.08	26.4
0.002877	23.20	431	3.55	17.4	5.81	23.4	8.89	31.8
0.002160	17.42	574	5.86	22.4	9.33	29.6	14.0	39.6
0.001440	11.61	861	11.2	30.8	16.8	39.3	24.3	51.6
0.0007200	5.807	1772	26.5	46.9	36.1	57.2	49.1	73.4
0.0003600	2.904	3444	48.1	64.7	61.6	78.0	81.3	99.7
0.0002880	2.323	4305	56.2	71.4	71.1	86.0	93.4	110
0.0002160	1.742	5740	67.7	81.0	84.8	97.7	111	125
0.00007200	0.5807	17220	126	134	155	163	201	210
0.00003600	0.2904	34440	181	187	223	228	288	294

APPENDIX

The optical constants n and k have been calculated in this chapter for the free carriers in the limit that the lattice dielectric constant can be approximated by a constant $\varepsilon_l = \varepsilon_\infty$. This approximation is not valid in the frequency range in which the reststrahlen contribution of the lattice is important, i.e., for $\omega_T \lesssim \omega \lesssim \omega_L$, where ω_L and ω_T are the angular frequencies of the longitudinal and transverse optical phonons, respectively. This covers a range from approximately 268 to 292 cm^{-1} for GaAs, from 307 to 351 cm^{-1} for InP, and from 219 to 243 cm^{-1} for InAs [31]. The purpose of this appendix is to consider how the results given here can be combined with the results in the critiques of InP, GaAs, and InAs to obtain the total n_t and k_t in the reststrahlen region and elsewhere.

The results in Tables III, V, and VII of this chapter are n_f and k_f for free carriers such that

$$(n_f - ik_f)^2 = \varepsilon_f = \varepsilon_{f1} - i\varepsilon_{f2}, \tag{A.1}$$

where ε_{f1} and ε_{f2} are as given by Eqs. (7) and (8).

The results in the critiques for InP, GaAs, and InAs, n_l and k_l may be considered as having been obtained from the Lorentz oscillator model with

$$(n_l - ik_l)^2 = \varepsilon_l = \varepsilon_{l1} - i\varepsilon_{l2} = \varepsilon_\infty\left(1 + \frac{\omega_L^2 - \omega_T^2}{\omega_T^2 - \omega^2 + i\Gamma\omega}\right). \tag{A.2}$$

Generally, we can assume that dielectric functions are additive (while n and k are not), so that the total dielectric function is

$$\varepsilon_t = \varepsilon_f + \varepsilon_l - \varepsilon_\infty. \tag{A.3}$$

It is necessary to subtract off one ε_∞ either from ε_f or ε_l since each separate consideration of ε_f and ε_l contains an ε_∞. Then it is straightforward, for example, to construct $\varepsilon_{l1} = n_l^2 - k_l^2$ and $\varepsilon_{l2} = 2n_l k_l$ from Table I in the GaAs critique as well as $\varepsilon_{f1} = n_f^2 - k_f^2$ and $\varepsilon_{f2} = 2n_f k_f$ from Table V of this Chapter. We have

$$\begin{aligned}(n_t - ik_t)^2 &= \varepsilon_{t1} - i\varepsilon_{t2} = \varepsilon_{f1} - i\varepsilon_{f2} + \varepsilon_{l1} - i\varepsilon_{l2} - \varepsilon_\infty \\ &= (\varepsilon_{f1} + \varepsilon_{l1} - \varepsilon_\infty) - i(\varepsilon_{f2} + \varepsilon_{l2}).\end{aligned} \tag{A.4}$$

Then we find that

$$\varepsilon_{t1} = n_t^2 - k_t^2 = \varepsilon_{f1} + \varepsilon_{l1} - \varepsilon_\infty, \qquad \varepsilon_{t2} = 2n_t K_t = \varepsilon_{f2} + \varepsilon_{l2}. \tag{A.5}$$

We then extract n_t and k_t from

$$2n_t^2 = \varepsilon_{t1} \pm \sqrt{\varepsilon_{t1}^2 + \varepsilon_{t2}^2}, \qquad 2k_t^2 = -\varepsilon_{t1} \pm \sqrt{\varepsilon_{t1}^2 + \varepsilon_{t2}^2}. \tag{A.6}$$

Since the ε_∞ used to construct Table V is slightly different from the ε_∞ used to obtain Table I in the GaAs critique and approximations are made in the calculation of ε_f, this procedure is not accurate for short wavelengths when $\lambda < 10\ \mu m$.

Well below the reststrahlen region (say $\omega < \omega_T/2$), the lattice contribution to ε_t approaches ε_0, the static dielectric constant. Then the determination of ε_t becomes especially simple, only requiring the subtraction of ε_∞ from $\varepsilon_{f1} = n_f^2 - k_f^2$ and the addition of ε_0. Nothing need be done to $\varepsilon_{f2} = 2n_f k_f$.

REFERENCES

1. E. D. Palik and R. T. Holm., *in* "Nondestructive Evaluation of Semiconductor Materials and Devices" (J. N. Zemel, ed.), Chap. 7, Plenum, New York, 1979.
2. R. T. Holm, J. W. Gibson, and E. D. Palik, *J. Appl. Phys.* **48**, 212 (1977).
3. S. Perkowitz and R. H. Thorland, *Phys. Rev. B* **9**, 545 (1974); S. Perkowitz, *J. Phys. Chem. Solids* **32**, 2267 (1971).
4. H. Y. Fan, *in* "Semiconductors and Semimetals" (R. K. Willardson and A. C. Beer eds.), Vol. 3, Academic Press, New York, 1967.
5. J. K. Kung and W. G. Spitzer, *J. Electrochem. Soc.* **121**, 1482 (1974).
6. W. G. Spitzer and J. W. Whelan, *Phys. Rev.* **114**, 59 (1959).
7. W. P. Dumke, M. R. Lorenz, and G. D. Pettit, *Phys. Rev. B* **1**, 4668 (1970).
8. B. V. Dutt, O. Kim, and W. G. Spitzer, *J. Appl. Phys.* **48**, 2110 (1977).
9. B. V. Dutt, M. Al-Delaimi, and W. G. Spitzer, *J. Appl. Phys.* **47**, 565 (1976).
10. W. P. Dumke, *Phys. Rev.* **124**, 1813 (1961).
11. E. Haga and H. J. Kimura, *J. Phys. Soc. Jpn.* **18**, 777 (1963); E. Haga and H. J. Kimura *J. Phys. Soc. Jpn.* **19**, 471, 658, 1596 (1964).
12. B. Jensen, *Ann. Phys.* **80**, 284 (1973).
13. E. O. Kane, *J. Phys. Chem. Solids* **1**, 249 (1957).
14. B. Jensen, *Ann. Phys.* **95**, 229 (1975).
15. P. J. Price, *IBM J. Res. Dev.* **10**, 395 (1966).
16. P. N. Argyres, *J. Phys. Chem. Solids* **19**, 66 (1961).
17. W. Kohn and J. M. Luttinger, *Phys. Rev.* **108**, 590 (1957); W. Kohn and J. M. Luttinger, *Phys. Rev.* **109**, 1892 (1958).
18. B. Jensen, *Phys. Status Solidi* **86**, 291 (1978); B. Jensen, *Solid State Commun.* **24**, 853 (1977).
19. B. Jensen, *J. Appl. Phys.* **50**, 5800 (1979).
20. B. Jensen, *in* "Laser Induced Damage in Optical Materials; 1980" (H. E. Bennett, A. J. Glass, A. H. Guenther, and B. D. Newman, eds.), p. 416, National Bureau of Standards Special Publication 620, Boulder, Colorado, 1981.
21. B. Jensen, *in* "Infrared and Submillimeter Waves" (K. J. Button, ed.), Vol. 8, Academic Press, New York, 1983.
22. B. Jensen, *IEEE J. Quantum Electron.* **QE-18**, 1361 (1982); B. Jensen and A. Torabi, *IEEE J. Quantum Electron.* **QE-19**, 448–457, 877–882, 1362–1365 (1983); B. Jensen and A. Torabi, *J. Appl. Phys.* **54**, 2030–2035, 3623–3625, 5945–5949 (1983).
23. O. V. Vakulenko and M. P. Lisitsa, *Sov. Phys, Solid State* **9**, 769 (1967).
24. M. G. Mil'vidskii, V. B. Osvenskii, E. P. Rashevskaya, and T. G. Yugova, *Sov. Phys. Solid State* **7**, 2784 (1966).
25. E. P. Rashevskaya and V. I. Fistul', *Sov. Phys. Solid State* **9**, 2849 (1968).
26. J. Dixon, *Proc. Int. Conf. Phys. Semicond., Prague, 1960*, p. 366, Publishing House Czech. Acad. Sci., Prague, 1961.
27. R. M. Culpepper and J. R. Dixon, *J. Opt. Soc. Am.* **58**, 96 (1968).
28. A. J. Strauss and G. W. Isler, *Bull. Am. Phys. Soc.* **17**, 326 (1972).
29. R. Newman, *Phys. Rev.* **111**, 1518 (1958).
30. A. Kahan, AFCRL, Physical Sciences Research Paper. 537, AFCRL-TR-73-0122 (1973).
31. O. Madelung, "Physics of the III–V Compounds," Wiley, New York, 1964.

Chapter 10

Interband Absorption —Mechanisms and Interpretation

DAVID W. LYNCH
Department of Physics and Ames Laboratory, U.S. Department of Energy
Iowa State University
Ames, Iowa

I. Introduction 189
II. One-Electron Model 190
III. Electron–Hole Interaction, Excitons 198
IV. Local Field Effects 203
V. Examples 204
References 210
General References 211

INTRODUCTION I

In this chapter we discuss the origin or interpretation of the optical properties of solids at and above the band gap. We thus discuss interband transitions but not intraband transitions (Drude or free-carrier absorption) or optical absorption arising from the excitation of phonons or electrons on impurities. Plasmons, collective excitations of an electron gas, can be excited optically in special geometries, but we omit discussing them. At rather high energies, e.g., above 10 or 20 eV, electrons can be excited from core levels that are localized in space and in energy. These have some characteristics of interband transitions, but space does not permit a description of the phenomena contributing to the edge shapes and structures above the edges that are observed in some spectra above about 10 eV. These, too, are optical properties, but they are studied mainly by transmission through thin films or by photoemission. This chapter will be without great depth, and we refer the reader to many references that cover more extensively the material to be presented in this chapter.

HANDBOOK OF OPTICAL CONSTANTS OF SOLIDS

Copyright © 1985 by Academic Press, Inc.
All rights of reproduction in any form reserved.
ISBN 0-12-544420-6

We shall begin with the one-electron picture and go as far as we can with it. Specific many-body effects will be introduced in this chapter. The one-electron picture can be applied quantitatively to many solids, although if the number of atoms per unit cell becomes large, it is impractical to do so. Many-body effects are much more difficult to incorporate in an arbitrary material. As expected, most progress has been made on a model solid, the free-electron gas, with extensions to a free-electron gas with a band gap, which may resemble adequately a semiconductor or insulator. However, to calculate realistically many-body effects in an arbitrary material is not yet feasible, and we can make only qualitative interpretations based on calculations on model systems. We conclude this chapter with a few examples of spectra of typical solids and attempt to point out what we do and do not know at this time.

II ONE-ELECTRON MODEL

The calculation of the one-electron optical properties of solids arising from interband transitions can be carried out in a number of ways, all leading to essentially the same result. These calculations often are analogous to the calculation of the optical absorption spectrum of an atom. In the outline that follows, the electric field of the incident electromagnetic wave is treated as a time-dependent perturbation that induces transitions from filled eigenstates to empty eigenstates of the crystal Hamiltonian or an approximation to it. The same method is applicable to amorphous and crystalline solids, and to alloys as well, although only in the case of crystalline solids are the other quantum numbers known, simplifying the problem considerably.

The solution to the Schrödinger equation for a single electron in the crystal is assumed to be known. The eigenfunctions are Bloch functions characterized by an energy $E_n(\mathbf{k})$, a wave vector $\mathbf{k}$ in the first Brillouin zone, a band index n, and a spin index. The relationship $E_n(\mathbf{k})$ is the band structure of the crystal. We suppress the spin index and write the wave function as $\psi_{n,\mathbf{k}}(\mathbf{r})$.

In the sample there is an electromagnetic wave with electric field

$$\mathbf{E}(\mathbf{r}, t) = \mathrm{Re}[\mathbf{E}_0 \exp(i\mathbf{q} \cdot \mathbf{r} - i\omega t)]$$

and a corresponding magnetic field. The latter plays a negligible role, as can be seen by examining the classical expression for the force on an electron,

$$\mathbf{F} = (-e)(\mathbf{E} + (\mathbf{v}/c) \times \mathbf{B}).$$

In free space $|\mathbf{B}| = |\mathbf{E}|$ in Gaussian units, and since $v/c \ll 1$, the magnetic force is negligible when dealing with transitions as strong as those to be considered

in Section IV. The effect of the magnetic field on the electron spin is also negligible. The electric and magnetic fields can be derived from a vector potential **A** as

$$\mathbf{B} = \nabla \times \mathbf{A}, \qquad \mathbf{E} = (1/c)(\partial \mathbf{A}/\partial t),$$

with

$$\mathbf{A}(\mathbf{r}, t) = \mathrm{Re}[-(ic/\omega)\mathbf{E}_0 \exp(i\mathbf{q} \cdot \mathbf{r} - i\omega t)].$$

In the presence of the electromagnetic field the Hamiltonian for an electron in the crystal is modified by replacing the momentum operator **p** by $(\mathbf{p} + e\mathbf{A}/c)$, which introduces several new terms into the Hamiltonian

$$(1/2m)[(e/c)(\mathbf{p} \cdot \mathbf{A} + \mathbf{A} \cdot \mathbf{p}) + (e^2/c^2)A^2].$$

The last term is negligible when considering only linear optical absorption, so we drop it. The other two terms are treated as a perturbation. The vector potential is assumed to be known, but, in fact, it may not be known. We assume for now that it is the average **A** in the material, averaged over a volume large compared with the wavelength of the radiation, that is itself larger than unit-cell dimensions. We return to this problem in Section IV.

We assume the eigenfunctions and eigenvalues of the unperturbed Hamiltonian are known and apply time-dependent perturbation theory to obtain the transition rate between an initial state i and a final state f as

$$W_{if} = (2\pi/\hbar)|\langle f|M|i\rangle|^2 f_{\mathrm{FD}}(E_i)[1 - f_{\mathrm{FD}}(E_f)]\,\delta(E_f - E_i - \omega),$$

where

$$M = (e/2mc)(\mathbf{p} \cdot \mathbf{A} + \mathbf{A} \cdot \mathbf{p})$$

and f_{FD} is the Fermi–Dirac distribution function and the factors containing it ensure that the initial state is occupied and the final state empty before the transition. The radiation also stimulates transitions from f to i, but, except for the infrared, the distribution functions make this process ignorable for weak exciting fields. By expanding the exponential in the vector potential as

$$\mathbf{A}_0 e^{i(\mathbf{q} \cdot \mathbf{r} - \omega t)} = \mathbf{A}_0 e^{-i\omega t}[1 - i\mathbf{q} \cdot \mathbf{r} + \cdots]$$

and keeping only the first term, we obtain the electric-dipole approximation, which is adequate for all observable interband transitions at and above the band gap, except at energies high enough that q^{-1} approaches the interatomic distance. Then $\mathbf{p} \cdot \mathbf{A} + \mathbf{A} \cdot \mathbf{p} = 2\mathbf{A} \cdot \mathbf{p}$, so that

$$|\langle f|\mathbf{M}|i\rangle|^2 = (e/mc)^2|\mathbf{A}_0 \cdot \mathbf{p}_{if}|^2,$$

with $\langle f|\mathbf{p}|i\rangle = \mathbf{p}_{if}$ the momentum matrix element.

Next, one sums over initial and final states. For a crystalline solid this can be done by integration over the Brillouin zone, after letting the wave vector

be the summation index. Setting $\mathbf{A}_0 = \hat{e}\mathbf{A}_0$, we get

$$W(\hbar\omega) = \frac{\pi e^2}{2m^2}\frac{A_0^2}{c^2}\int \frac{d^3k}{4\pi^3}\,|\hat{e}\cdot\mathbf{p}_{if}|^2 f_{\mathrm{FD}}(E_i)[1 - f_{\mathrm{FD}}(E_f)]\,\delta(E_f - E_i - \omega).$$

This is the probability per unit time and volume that the electromagnetic wave loses energy $\hbar\omega$ to the electronic system by exciting an electron.

The power absorbed per unit volume is $\hbar\omega W(\hbar\omega)$. The incident flux is

$$\langle \mathbf{S} \rangle = (\omega^2 A^2/2\pi c) n\hbar k,$$

with n the refractive index (real part). The absorption coefficient μ is defined as

$$\mu = (1/\langle S \rangle)(d/dr)\langle \mathbf{S} \rangle = (1/\langle S \rangle)\hbar\omega W.$$

Since $\mu = (\omega\varepsilon_2/cn)$, we end with

$$\varepsilon_2(\omega) = \frac{e^2}{\pi m^2\omega^2}\int d^3k|\hat{e}\cdot\mathbf{p}_{if}|^2 f_{\mathrm{FD}}(E_i)[1 - f_{\mathrm{FD}}(E_f)]\,\delta(E_f - E_i - \omega).$$

The real part of the dielectric function can be obtained from the imaginary part by an integral transform, the Kramers–Kronig integral. Both parts of $\tilde{\varepsilon}$ arise from similar transitions, except that they are real in the case of ε_2 but may be virtual in the case of ε_1.

Other functions frequently are used to describe the optical properties of absorbing media. The complex refractive index is $N = n + i\kappa$, where n is the refractive index so useful for transparent ($\kappa = 0$) media. Since $\tilde{\varepsilon} = \varepsilon_1 + \varepsilon_2 = \tilde{N}^2$, we have

$$\varepsilon_1 = n^2 - \kappa^2, \qquad \varepsilon_2 = 2n\kappa,$$

or

$$n = [+\varepsilon_1 + \sqrt{\varepsilon_1^2 + \varepsilon_2^2}]^{1/2}/\sqrt{2}, \qquad \kappa = [-\varepsilon_1 + \sqrt{\varepsilon_1^2 + \varepsilon_2^2}]^{1/2}/\sqrt{2}.$$

The absorption coefficient is

$$\mu = (\varepsilon_2\omega/nc) = (4\pi\kappa/\lambda).$$

Finally, for metals the optical conductivity σ is useful. In Gaussian units it is

$$\sigma = \sigma_1 + i\sigma_2 = -i(\omega/4\pi)(\tilde{\varepsilon} - 1).$$

The foregoing expressions are valid for cubic crystals or randomly oriented polycrystalline samples. For noncubic crystals, $\tilde{\varepsilon}$ and $\tilde{\sigma}$ become tensors and $\tilde{N}$ and μ become anisotropic as well. In the following, we shall drop the distribution-function factors and deal with fully occupied initial states and unoccupied final states.

Shortly we shall neglect the dipole matrix element, but this can be justified only if one is not interested in a complete interpretation of the optical prop-

erties. Upon neglecting the matrix element, the optical properties become independent of the orientation of the electric vector with respect to the crystallographic axes of a single crystal; all optical anisotropy is lost. Even for unpolarized radiation some effects of anisotropy are expected. Unpolarized radiation incident normally on a surface parallel to the basal plane of a hexagonal crystal will give a different reflectance spectrum than the same radiation normally incident on a plane face containing the c axis, but an explanation of the anisotropy requires consideration of the matrix elements.

One can show that $\mathbf{p}_{if} = im\omega_{if}\mathbf{r}_{if}$, where $\mathbf{er}_{if}$ is the transition dipole moment and $\hbar\omega_{if} = E_f - E_i$. This is often used, but is it correct only when one is dealing with exact eigenfunctions. For approximate eigenfunctions the use of each side of the preceding expression may not give the same results, and it is not clear, *a priori*, which will be better. The right-hand side emphasizes the regions of large r in the integrand, while the left-hand side emphasizes the regions of large gradient, closer to the ion cores than the regions of large r. The evaluation of $\mathbf{p}_{if}$ and $\mathbf{r}_{if}$ is very sensitive to small changes in the wave functions used.

When Bloch states are used, the evaluation of the dipole matrix element leads to the selection rule that the wave vectors of the initial and final states are the same. Physically, this corresponds to conservation of momentum $\mathbf{k}$ because the absorbed photon has a wave vector that is very small on the scale of electron wave vectors in the crystal. Thus, in an energy-band diagram allowed optical transitions are vertical.

Group theory is useful for deciding when the dipole matrix elements vanish, i.e., for determining the other selection rules. The symmetry of the Bloch states limits the number of transitions for states with wave vectors lying in symmetry planes, along symmetry lines, and at symmetry points in the Brillouin zone. However, for those transitions for which the matrix element does not vanish, the magnitude of the matrix element cannot be obtained from group theory; the integral must be evaluated. The same application of group theory also gives polarization selection rules, describing some of the anisotropy in noncubic crystals. Often such calculations are carried out on nonrelativistic energy bands that lack spin-orbit effects. Upon including these effects, a similar calculation leads to new selection rules that usually are less "selective." This is the crystal analog of the spin-orbit term in an atomic Hamiltonian that makes spin-forbidden or orbitally forbidden transitions allowed by mixing spin and orbital angular momentum. Again, however, it is difficult to assess whether a transition that is allowed only in the presence of the spin-orbit interaction is strong enough to be detected in an actual spectrum. Tabulations of selection rules for simple crystal structures can be found in Eberhardt and Himpsel [1], Borstel *et al.* [2], and Benbow [3].

The evaluation of the dipole matrix elements can be carried out during a band calculation by "keeping" the wave functions used in the calculation, but

the accuracy of the results may not be very high. Such calculations have not been done very often in the past, and, except for semiconductors and a few simple metals, the agreement with experiment has not been very gratifying. Smith [4] and Lässer *et al.* [5] have used an interpolation scheme, often used for energy bands alone, to obtain dipole matrix elements rather easily and accurately for several noble metals and for a series of alloys. It requires a basis set larger than that normally used for interpolation of the bands, but one that is manageable.

To proceed with the simplification of the expression for ε_2, we make a common approximation that the dipole matrix element may be replaced by an average value. Often this is not evaluated, and only the shape of the ε_2 spectrum, slightly distorted by the energy dependence of the actual matrix element, is considered. This gives

$$\varepsilon_2(\omega) = \frac{e^2}{\pi m^2 \omega^2} \overline{|\hat{e} \cdot \mathbf{p}_{if}|^2} \int d^3k \, \delta(E_f - E_i - \omega),$$

which can be placed in the form

$$\varepsilon_2(\omega) = \frac{e^2}{\pi m^2 \omega^2} \overline{|\hat{e} \cdot \mathbf{p}_{if}|^2} \int \frac{dS}{\nabla_k |E_{if}(\mathbf{k})|}.$$

Often the integrand denominator causes the structure in the spectrum. The points in k space $\mathbf{k}_0$ at which the denominator vanishes are called critical points. At symmetry critical points $\nabla_k E_i(\mathbf{k}) = \nabla_k E_f(\mathbf{k}) = 0$, while general critical points have $\nabla_k E_i(\mathbf{k}) = \nabla_k E_f(\mathbf{k}) \neq 0$. If we expand the interband energy in a series about $\mathbf{k}_0$ we obtain

$$E_f(\mathbf{k}) - E_i(\mathbf{k}) = E_0 + 0 + \sum_{i=1}^{3} \frac{\hbar^2}{2m_i^*} [(\mathbf{k} - \mathbf{k}_0)_i]^2 + \ldots,$$

in which local principal axes have been assumed. The critical points are classified by the number of negative values of the principal interband effective masses m_i^* and by the dimensionality. (If the bands are very flat, one or two effective masses become very large and the system is effectively two- or one-dimensional when a particular critical point is being discussed.) In all cases the integral for ε_2 can be evaluated for one critical point at a time, and characteristic shapes in the ε_2 spectrum result. These can be written in compact form as

$$\varepsilon(E) = \frac{C_n}{\omega^2} i^{r-n} \int_0^{E - E_0 + i\Gamma} t \left(\frac{n-4}{2} \right) dt = \varepsilon_1 + i\varepsilon_2,$$

Fig. 1. Characterictic shapes of spectra of $E^2\varepsilon_1$ and $E^2\varepsilon_2$ from interband critical points in one, two, and three dimensions, with schematic energy bands for each type of transition. (a) One-dimensional critical points, (b) two-dimensional critical points, and (c) three-dimensional critical points. The terms m^* are interband effective-mass components in a local system of principal axes.

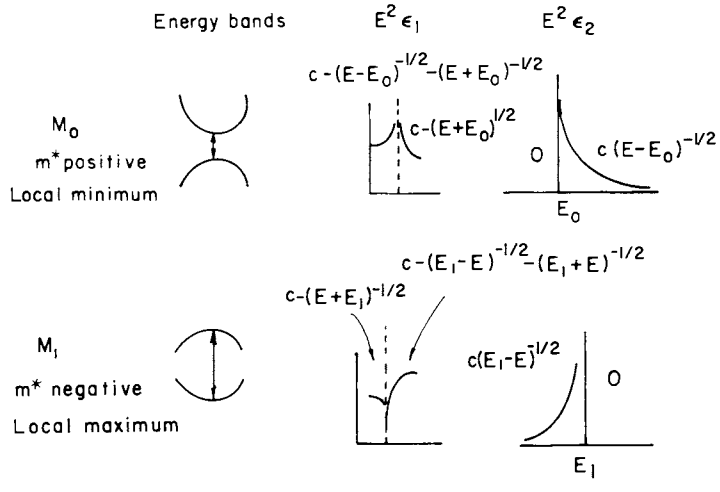
Energy bands
$E^2\epsilon_1$
$E^2\epsilon_2$
M_0
m^* positive
Local minimum
$c-(E-E_0)^{-1/2}-(E+E_0)^{-1/2}$
$c-(E+E_0)^{-1/2}$
$c\,(E-E_0)^{-1/2}$
0
E_0
M_1
m^* negative
Local maximum
$c-(E_1-E)^{-1/2}-(E_1+E)^{-1/2}$
$c-(E+E_1)^{-1/2}$
$c(E_1-E)^{-1/2}$
0
E_1

(a)

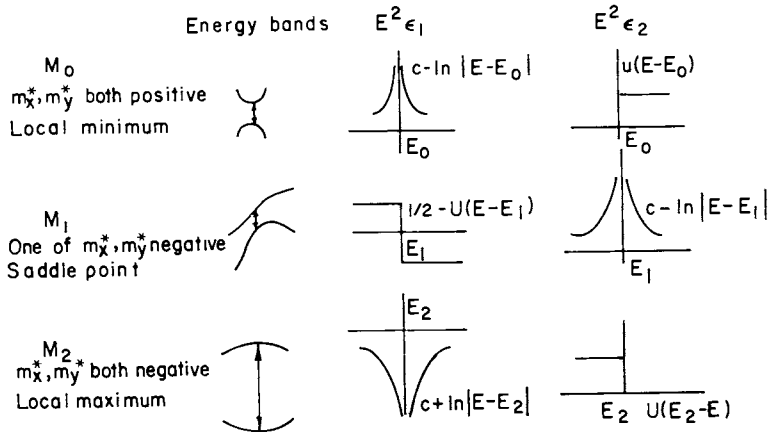
Energy bands
$E^2\epsilon_1$
$E^2\epsilon_2$
M_0
m_x^*, m_y^* both positive
Local minimum
$c-\ln|E-E_0|$
$u(E-E_0)$
E_0
E_0
M_1
One of m_x^*, m_y^* negative
Saddle point
$1/2-U(E-E_1)$
$c-\ln|E-E_1|$
E_1
E_1
M_2
m_x^*, m_y^* both negative
Local maximum
E_2
$c+\ln|E-E_2|$
E_2
$U(E_2-E)$

(b)

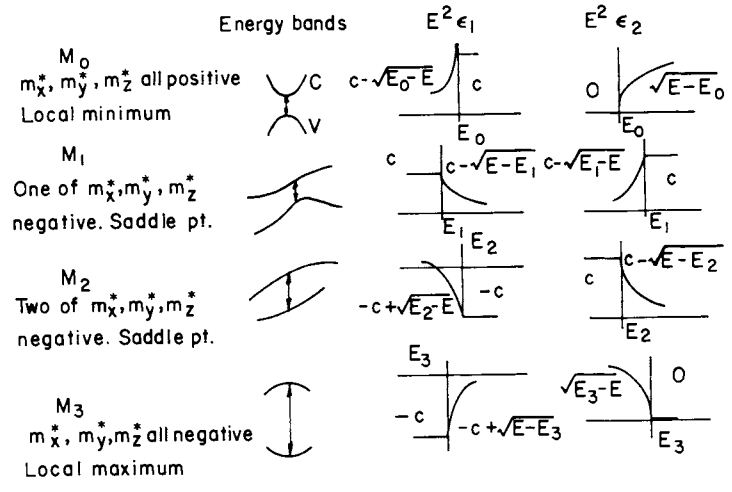
Energy bands
$E^2\epsilon_1$
$E^2\epsilon_2$
M_0
m_x^*, m_y^*, m_z^* all positive
Local minimum
C
V
$c-\sqrt{E_0-E}$
c
0
$\sqrt{E-E_0}$
E_0
E_0
M_1
One of m_x^*, m_y^*, m_z^*
negative. Saddle pt.
c
$c-\sqrt{E-E_1}$
$c-\sqrt{E_1-E}$
c
E_1
E_1
M_2
Two of m_x^*, m_y^*, m_z^*
negative. Saddle pt.
E_2
$-c+\sqrt{E_2-E}$
$-c$
c
$c-\sqrt{E-E_2}$
E_2
M_3
m_x^*, m_y^*, m_z^* all negative
Local maximum
E_3
$-c$
$-c+\sqrt{E-E_3}$
$\sqrt{E_3-E}$
0
E_3

(c)

in which n is the dimensionality of the system and r the type of critical point ($r \leq n$), t is a dummy variable, and Γ takes account of broadening processes. The corresponding shapes of ε_1 and ε_2 for all possible n and r are displayed in Fig. 1 with $\Gamma = 0$. In three dimensions the singularity in the integrand for ε_2 leads only to a singularity in the first energy derivative of ε_2. The three-dimensional critical points are better studied in derivative measurements (modulation spectroscopy) unless the energy bands involved are nearly two-dimensional, or one is at the fundamental absorption edge, always an M_0. Interesting illustrations of how critical points evolve as the dimensionality changes are included in Nakao [6], Sasaki *et al.* [7], and Okuyana *et al.* [8]. Diamond- and zincblende-structured semiconductors have a peaked structure in their ε_2 spectra due to a nearly two-dimensional critical point in these cubic materials.

A feature resembling a critical point structure in $\tilde{\varepsilon}$ can occur in metals if there is a very flat band, e.g., a d band, if it is flat enough. Transitions between this band and the others at the Fermi energy "turn on" very suddenly as the photon energy is increased. This provides a sudden increase in ε_2 roughly like that provided by an M_0 critical point, but one whose width is determined by the width of the Fermi–Dirac distribution function edge and by the flatness of the "flat" band.

Critical points are expected to provide features in the ε spectra of all crystals, but they may be difficult to observe. All materials with a band gap will have an M_0 interband critical point at the fundamental absorption edge if the gap is a direct one. However, it may not be found with the expected shape for reasons soon to be given. Parallel bands often occur in simple polyatomic metals. Such a band structure and the resultant optical properties can be treated in closed form by using a simple but realistic model with the result that in the absence of broadening ε_2 displays a singularity of the form

$$\varepsilon_2 \sim (E - E_0)^{-1/2} E \geq E_0, \qquad \varepsilon \sim \text{const}\, E < E_0.$$

This is like an M_0 critical point in one dimension. By and large, however, it is difficult to see critical point effects in metals because they are not large and they lie on a large background. They are best seen in semiconductors when exciton effects are disturbing but not of obliterating strength. Insulators tend to have such strong exciton effects that they dominate the above critical point line shapes.

The foregoing discussion assumed that the electronic excitations were perfectly sharp. The radiative lifetimes of the excited states usually are long enough so that radiative lifetime broadening is negligible. The transitions are broadened by electron–electron scattering of the excited electron and hole and by phonon absorption and emission. Both of these are usually incorporated phenomenologically in the expression for ε_2 by introducing an interband lifetime or energy width, as Γ above, to account for the electron–electron scattering, and convolving the resultant spectrum with a phonon density of states, weighted with a suitable coupling coefficient. If such a con-

volution is omitted, the interband lifetimes become temperature dependent, representing all broadening processes.

The fundamental band gap is an exception, for here the electron–phonon interaction plays a more obvious role. If the band gap is direct, i.e., if the valence-band maximum and the lowest conduction-band minimum (there may be several of each, all degenerate) lie at the same point in reciprocal space, then one has only an M_0 critical point whose phonon broadening is easy to detect on the low-energy side of the critical point transition. If the two band edges are at different points in k space, the selection rule on k prohibits transitions across the indirect gap. Such transitions can occur only if a second interaction occurs to allow conservation of wave vector, and the most common is the simultaneous absorption or emission of a phonon when the photon is absorbed. This process requires two interactions, so it occurs in second-order perturbation theory only, with consequently weak absorption. Thus, indirect transitions are observed only at the fundamental absorption edge (Fig. 2). The electron at the valence-band maximum may be photoexcited, producing a virtual intermediate state "after" which the electron may be scattered either by absorption or emission of a phonon of the appropriate wave vector. An electron with the wave vector of the conduction-band maximum instead may be photoexcited with the hole and "then" scattered by phonon absorption or emission. Both processes may occur and their matrix elements must be added before squaring, leading to the possibility of interference effects. However, usually one or the other of the routes shown in Fig. 2 dominates, and the resultant expression for the absorption edge

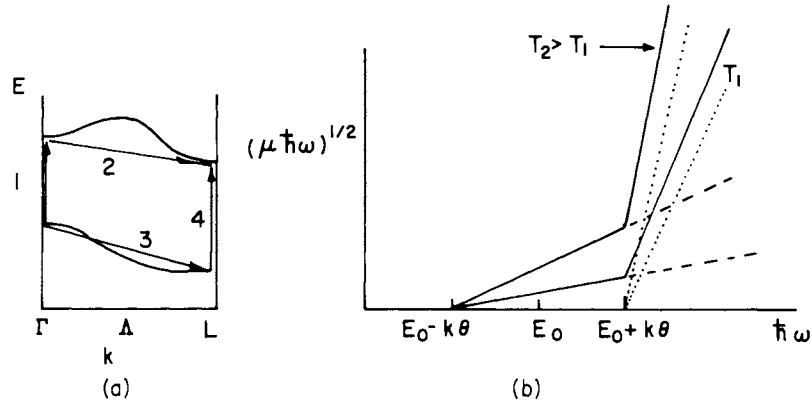

Fig. 2. (a) Indirect interband transitions between a valence band maximum at Γ(k = 0, 0, 0) and a conduction-band minimum at $L(k = (\pi/a_0)(1, 1, 1))$, separated by wave vector $k = (\pi a_0)$ (1, 1, 1). Transitions 1 + 2 and 3 + 4 are both possible and may interfere. Transitions 1 and 3 are photon absorption processes, while 2 and 4 are electron and hole scattering processes, respectively, caused by phonon absorption or emission. (b) Indirect absorption edge from processes 1 + 2 or 3 + 4 at two temperatures. The dashed line represents phonon absorption; the dotted line, phonon emission; and the solid line, the sum. It is assumed (incorrectly) that E_0 does not depend on temperature.

contains two terms, one for phonon absorption and one for phonon emission:

$$\mu = \frac{\text{const}}{(\hbar\omega)^2}\left[\frac{(\hbar\omega - E_0 + k\theta)^2}{e^{\theta/T} - 1} + \frac{(\hbar\omega - E_0 - k\theta)^2}{1 - e^{-\theta/T}}\right],$$

$$\hbar\omega > E_0 - k\theta, \qquad \hbar\omega > E_0 + k\theta.$$

The phonon has energy $k\theta$ and wave vector q, the separation of the band edges in reciprocal space. In general, there are several phonons, one from each branch, which may scatter, so the absorption edge is then a sum of terms like the equations above with different values of θ and different scattering matrix elements (hidden in the constant prefactor). Symmetry considerations sometimes lead to a vanishing scattering probability for some phonons. The resultant absorption coefficients have characteristic shapes, as shown in Fig. 2. (The foregoing assumed the electron excitation by the photon was allowed by the electric-dipole selection rules. If not, then the wave functions are expanded in a series in k. The term in k^1 gives the first nonvanishing absorption. The exponent 2 in the preceding equation then becomes 3, for these indirect forbidden transitions.)

In small-band-gap semiconductors and in heavily doped semiconductors, the foregoing absorption-edge description is incorrect because the Fermi level may lie inside the conduction or valence band. Then one gets a sharp turn-on of absorption with a shape dominated by the Fermi–Dirac distribution function. In this case, the position of the Fermi level rises with increasing doping for n-type material, giving a shift in the edge energy with doping level, the Burstein–Moss shift.

This is as far as we shall go with the one-electron picture. It provides a qualitatively good picture for metals; indeed, often a quantitatively good one. (One must first subtract the intraband contribution to ε_2 from the measured ε_2 spectrum.) For semiconductors the electron–hole interaction, discussed in Section III, alters the expected spectrum appreciably near threshold but apparently not strongly in regions far above threshold. As the band gap increases, such effects become stronger and, in some cases, the band picture may not be the best starting point.

III ELECTRON–HOLE INTERACTION, EXCITONS

The excited electron and the hole are created at the same lattice site, so their interaction cannot be neglected. This leads to excitons, and to other effects as well. We first consider only the lowest energy M_0 critical point transition with gap energy E_0. There are two extreme models for the electron–hole interaction. The Wannier–Mott model assumes that the electron–hole

interaction is weak. The effective-mass model is employed and the hydrogen atom Hamiltonian results, but with the factors e^2 and m replaced by e^2/ε and $\mu^* = m_e^* m_h^*/(m_e^* + m_h^*)$, respectively. The static dielectric constant is ε, and the m^* are the electron and hole effective masses, here assumed to be isotropic. This Hamiltonian leads to discrete levels and a continuum. The former, nonconducting excited states, have energies of $E_0 - R_{ex}/n^2$ with $R_{ex} = 13.6\ \text{eV}\ (\mu^*/m)\varepsilon^{-2}$ and n an integer. The radii of the exciton "orbits" are $r_n = 0.53\ \text{Å}\ \{\varepsilon m n^2/\mu^*\}$, and if the model is to be self-consistent, the smallest radius must be at least several interatomic spacings in order to make the picture of dielectric screening meaningful. This is usually the case for small-band-gap materials that usually have small effective masses and high dielectric constants, but it may be less valid for the lowest energy exciton than for the others. In such cases a central-cell correction is needed to account for the departure of the potential from the simple $-e^2/\varepsilon r$ assumed when the electron and hole are nearby. This may be done with a nonlocal dielectric function $\varepsilon(r)$.

The other extreme model is the Frenkel exciton, basically an excited atom or ion in the crystal. The electron and hole are localized on one site or a small number of sites. The solid is polarized about this site, so free-atom or free-ion energy levels are not expected. Such a model was formerly believed to be the appropriate one for all large-band-gap insulators, e.g., the solid rare gases and the alkali halides, but now it seems that the Wannier model is quite suitable for all of them, except for the $n = 1$ exciton, and perhaps for a few higher levels in solid Ne. The Frenkel model is very useful for describing excitons in organic crystals.

An electron–hole interaction of intermediate strength requires the use of the Frenkel model with the excitation "localized" on a large number of sites or the Wannier model with Bloch functions employed with many wave vectors, not just those near the critical point wave vector. Thus, as the electron–hole interaction increases in strength, more and more of the band wave functions are used in the Wannier model, and the exciton is no longer associated with a particular critical point; possibly more than one conduction band may have to be used. In such a case, the band picture may not be the best starting point for an understanding of all the optical properties of insulators.

In both of these models the excitation is not permanently localized. It propagates through the crystal with a wave vector $\mathbf{K}$ and, in the case of the Wannier exciton, with a kinetic energy $\hbar^2 K^2/2(m_e^* + m_h^*)$, giving rise to a band. The selection rule on wave vector, however, limits the excitons that can be directly photoexcited to those with $\mathbf{K} = 0$. For indirect transitions, one can excite part of the exciton band because the phonon participating in the transition supplies the proper wave vector to allow this to happen.

The hydrogen-atom problem also has unbound continuum states that differ from free-electron states, especially near threshold. In the crystal, the

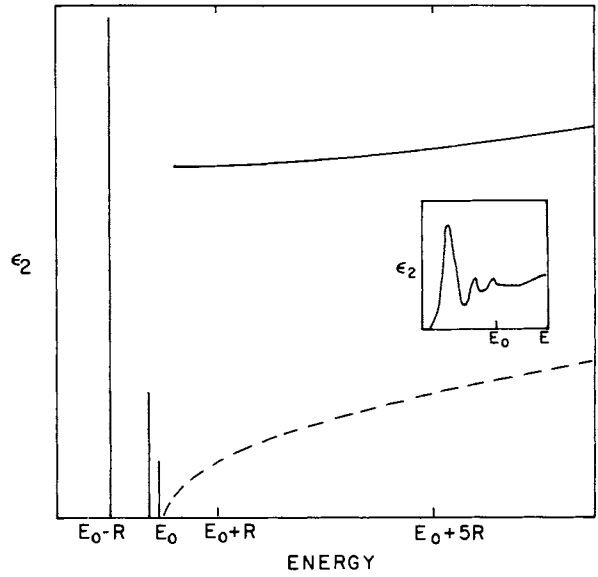

Fig. 3. An M_0 absorption-edge spectrum (dashed line) and how it is modified by the electron–hole interaction (solid line). Only the $n = 1$, 2, and 3 excitons are shown, and these are shown unbroadened as delta functions, with heights proportional to their oscillator strengths. An observed spectrum resembles the spectrum in inset.

electron–hole interaction modifies the absorption above the critical point as well. Elliott [9] has given a description of the effects of the electron–hole interaction for an M_0 critical point for a direct-band-gap material and for an indirect-band-gap absorption threshold. As shown schematically in Fig. 3, the series of excitons merges into a continuum. The enhanced absorption of the Coulomb states above E_0 meets them, the result being a series of lines merging into a continuum with no apparent structure at E_0. If there is any broadening present, as there must be, the continuum begins further below E_0, possibly leaving only the $n = 1$ exciton resolved. For M_0 critical points in two-dimensional crystals, the exciton spectrum is different, with $E = E_0 - R_{ex}/(2n - 1)^2$, and the dependence of absorption strength on n is different from the three-dimensional case [10, 11]. For an indirect gap, the edge is also distorted, and its analysis into two terms according to Fig. 2 is then invalid over an energy range from about R_{ex} below to several times R_{ex} above E_0. For direct-band-gap materials with large values of R_{ex}, the entire valence-to-conduction-band transitions can be distorted by the electron–hole interaction [12].

The electron–hole interaction is present for electron–hole pairs produced by exciting any electron to any excited state, not just at M_0 thresholds. At an M_1 critical point any discrete bound electron–hole pair we try to make will be degenerate with other excited states into which it may decay, for the

M_1 critical point transitions overlap other transitions. Such an excited state is called a hyperbolic exciton, after the nature of the $E_{if}(\mathbf{k})$ surface, and if the decay rate is not too great, it may be observable. Such excitons are believed to have been observed in several semiconductors, although the subject is controversial [13–15]. The electron–hole interaction decreases the absorption strength below that expected for the one-electron picture for M_2 and M_3 critical points, making them *less* prominent in spectra than expected by the one-electron model [16].

At energies above the band-gap energy, it is possible to think of other types of discrete excited states overlapping the continuum of excitations above the fundamental edge. Such discrete excitations could arise from the excitation of excitons below another M_0 critical point involving a second, higher, conduction band or a deeper valence band, e.g., the spin-orbit "partner" of the highest one. Core-electron excitation may also give rise to such a situation. In such cases, the two excitations may not be independent, and the absorption spectrum is not the sum of the two individual spectra. The final excited state of the system is a superposition of both the discrete and continuum excited states. When this superposition is used to evaluate the electric-dipole matrix element, interference effects occur upon squaring, and the strength of the coupling of two types of excitations has a strong effect on the appearance of the resultant absorption spectrum. There can be shifts of the absorption peak, which now is broadened, and a dip may appear on either the high- or low-energy side. Fano [17–19] first described such effects, and the resultant line shapes are called Fano line shapes. (Hyperbolic excitons give rise to Fano line shapes.)

The electron–hole interaction is not just the Coulomb attraction. This is also an exchange term that is important, and the net interaction may be attractive or repulsive. Toyozawa *et al.* [20] have considered the electron–hole interaction at each type of critical point and have summarized the results in a figure, reproduced here as Fig. 4. It shows how the interaction mixes the line shape expected for a given critical point with the line shape for an "adjacent" critical point, the mixing increasing with increasing strength of the electron–hole interaction. The result is that one cannot identify properly a critical point in the observed spectrum of an insulator without consideration of the effect of the electron–hole interaction. The inclusion of exchange also can alter considerably the apparent spin-orbit features in the spectrum [21].

Electrons and holes each interact with the vibrating lattice, and despite the apparent electrical neutrality of an exciton, the exciton–phonon interaction may be rather strong. The strength is described by the ratio of the average coupling energy to the bandwidth of the excitons. The coupling is usually to the longitudinal optical phonons or to zone-boundary acoustic phonons [22], and the bandwidth is a measure of exciton mobility. The exciton line shape is an asymmetric Lorentzian for weak coupling and

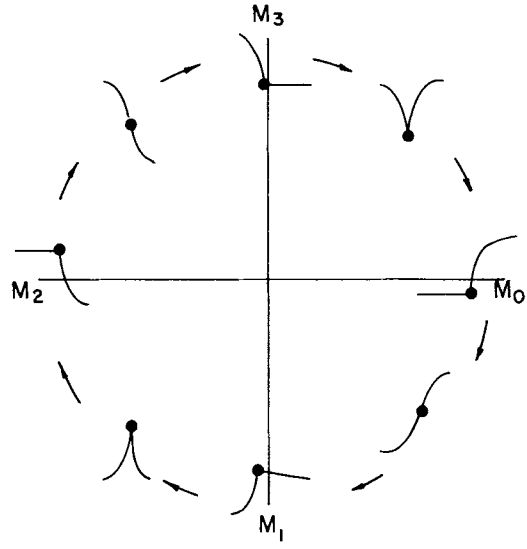

Fig. 4. Metamorphosis of critical points by an attractive electron–hole interaction. A three-dimensional critical point of type $M_j (j = 0, 1, 2, 3)$ is as shown with no electron–hole interaction. As this interaction grows, the shape distorts according to the arrow until at very large interaction the M_j has become M_{j+1} ($j = 4 \rightarrow j = 0$). A repulsive interaction acts similarly but with the arrows pointing counterclockwise. (From Toyozawa *et al.* [20].)

Gaussian for strong coupling [23, 24]; both shapes are temperature dependent. As a result of the phonon coupling, there is a shift in the energy of the peak in the exciton from that calculated for the electronic system alone [23, 24].

On the low-energy side of the first exciton absorption peak, the absorption coefficient is found to be exponential with energy over a range of up to four decades for a variety of insulating and semiconducting materials. This is the "Urbach rule" [25], according to which

$$\mu(E) = \mu_0 \exp[-b(E_0 - E)].$$

In some materials, e.g., highly doped semiconductors, b is a constant, while for many other materials, e.g., alkali halides,

$$b = b_0(2kT/\hbar\omega_0) \tanh(\hbar\omega_0/2kT)$$

with $\hbar\omega_0$ an effective phonon energy. An Urbach tail is found in amorphous semiconductors, as well. At low temperatures in some crystals, e.g., CdTe [26], the exponential edge shape changes, and phonon sidebands become resolved. There are two models that give the observed exponential absorption edge. One is based on the electric fields arising from impurities, defects, and

phonons [27]. There is convincing evidence that this model applies to heavily doped semiconductors [28] and disordered materials [29]. The other model is the standard exciton–phonon coupling model [23, 24], which can yield an exponential edge [30–34] or phonon sidebands [32], depending on the coupling strength to the phonons. There is convincing evidence that this mechanism is operative in GeS, for the phonons involved have been identified as phonons with no accompanying electric field [37]. In many other materials with exponential absorption edges, the two models cannot be so clearly distinguished. A phenomenological model [35, 36] also has been used for a number of materials.

LOCAL FIELD EFFECTS IV

We have just described what appears to be a two-body effect, but, in fact, all the valence electrons participate in screening the electron–hole interaction. Their roles are subsumed in $\varepsilon(r)$. There are other many-body effects that play a real role. We consider only the local field effect, an old classical problem. The electric field acting on an electron, in our case causing it to become excited, is the local field caused by the incident electromagnetic wave and by the polarization of the medium around the electron in response to that wave and to the polarization in the medium. A self-consistent local field must be found [38–45]. The resultant local field depends on the degree of localization of the electron under consideration. For a spatially delocalized electron, we can use just the average field in the medium. For a highly localized electron, one confined to a unit cell, the local field "correction" becomes the largest. Classically it is given by

$$\mathbf{E}_{\text{loc}}(r) = (\varepsilon + 2/3)\mathbf{E}(r)$$

for a cubic or isotropic crystal, and $\varepsilon \to \tilde{\varepsilon}$ in regions of absorption. As the electron becomes more delocalized, the size the correction decreases to unity. Also, at high energies $\tilde{\varepsilon} \to 1$, and the correction is negligible, no matter how localized the electron may be. The use of a local field correction depending on ε alters the shape of the ε_2 spectrum obtained from experiment [46, 47]. In Fig. 5 we show some data for an alkali halide. The dielectric function has been derived from a reflectance measurement by Kramers–Kronig analysis, with two different assumptions about the local field, the most extreme assumptions. The differences in the spectra are very large, and it is not at all clear which may be the more correct in a given spectral region, for we do not really know how much local field correction should be applied to a given transition. This is clearly an area in which more understanding is needed.

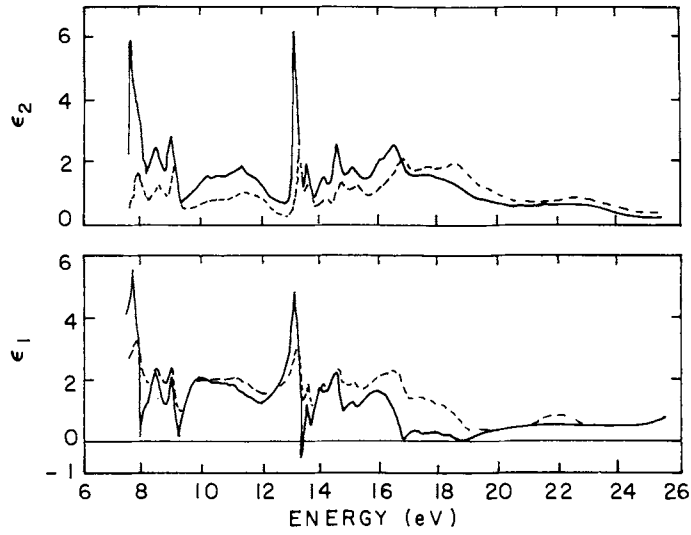

Fig. 5. Dielectric function spectra for CsCl obtained by Kramers–Kronig analysis of reflectance spectra; solid line represents no local field correction used and dashed line full Lorentz–Lorenz local field correction used. (From Bergstresser and Rubloff [46].)

V EXAMPLES

We now give some examples of interband spectra for some simple materials. Figure 6 shows the interband optical conductivity of an Al single crystal at 4.2 K, obtained by a Kramers–Kronig analysis of absorptance and reflectance [48]. The theoretical result presented is a fit to the parallel-band model for a polyvalent, nearly free-electron metal [49]. The model is based on the pseudopotential formalism, and in the case of Fig. 6, four parameters have been used to fit both the shape and the magnitude, with two of the parameters consonant with Fermi-surface data on Al. Moreover, a more elaborate pseudopotential band calculation has been carried out, and the optical properties calculated from it [50]. The results are in good agreement with the measured 1.5-eV peak and in reasonably good agreement for the 0.5-eV peak, but the calculated results are uncertain at low energy because they result from small differences in nearly equal energy eigenvalues. Reasonably good fits have been achieved for other similar metals—In, Ga, Pb, and Tl—although in Pb and Tl, spin-orbit splitting of certain bands contributes features in the experimental spectra not considered in the model. Other polyvalent metals—Be, Zn, Cd—and the alkaline earths do not conform to this simple (local) pseudopotential model.

Figure 7 shows the measured [51] ε_2 for Cu and the results of an empirical, nonlocal pseudopotential calculation of the band structure and the dielectric

TABLE I

Important Interband Transitions in Cu

Energy (eV)	Bands involved	Location in Brillouin zone	Type of transition
2.1	$4, 5 \rightarrow 6$	$\Delta_5 \rightarrow \Delta_1(E_F)$	Fermi edge
3.2	$4, 5 \rightarrow 6$	Near X	Volume
3.7	$3 \rightarrow 6$	$\Sigma_1 \rightarrow \Sigma_1(E_F)$	Fermi edge
3.7	$3, 4, 5 \rightarrow 6$	Near X	Volume
3.96	$4, 5 \rightarrow 6$	$X_5 \rightarrow X_4'$	M_1
4.25	$6 \rightarrow 7'$	$L_2' \rightarrow L_1^u$	M_0
4.33	$1 \rightarrow 6$	$\Sigma_1 \rightarrow \Sigma_1(E_F)$	Fermi edge
4.5	$3, 4, 5 \rightarrow 6$		Volume
5.0	$1, 2 \rightarrow 6$		Volume

function [52]. This calculation also used optical and photoemission data to fix a total of eight parameters in the band calculation. Although onsets of structure may be attributed to transitions to the Fermi level from the relatively flat 3d bands and to a few critical points, much of the large background giving the magnitude of ε_2 comes from transitions occurring in large volumes of the Brillouin zone. The contributing transitions are shown in Table I.

The optical properties of Cu have also been calculated quite accurately from first principles. Janak *et al.* [53] have calculated the (self-consistent) energy bands, dielectric function, and photoemission spectra from a potential for copper adjusted only to give the correct Fermi surface. The only other adjustable parameter characterized the electron–electron interaction, and it was adjusted to improve agreement with ε_2. The agreement is about the same as shown in Fig. 7, but only one parameter was adjusted to produce the fit. Finally, Lässer *et al.* [5] have calculated the dielectric function for the noble metals by using an interpolation scheme, evaluating the dipole matrix elements from $E(k)$ by simple differentiation [5]. The fit, although not quite as good as that shown in Fig. 7, extends to an energy of 24 eV, and the departures from the experimental spectra seem understandable on the basis of the model.

Figure 8 shows the measured interband ε_2 for Mo obtained by Kramers–Kronig analysis of reflectance spectra [54, 55], and one calculated ε_2 [56]. The calculation began with energy bands but ignored electric-dipole matrix elements. Thus, the calculated ε_2 is in arbitrary units. By using only specific regions of the Brillouin zone, the origin of structures or large featureless contributions to ε_2 could be identified. However, another group [57] used a different set of energy bands as a starting point and a different technique for locating the origin of structures by using energy, rather than momentum, windows, and obtained comparably good agreement with experiment (again without dipole matrix elements) but different assignments for a number of the

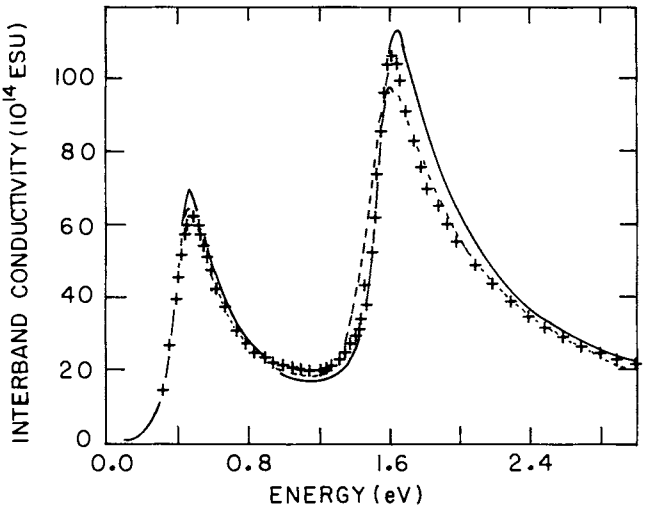

Fig. 6. Interband contribution to the optical conductivity of Al (solid). The crosses and dashed curve represent model calculations of the interband conductivity. (From Benbow and Lynch [48].)

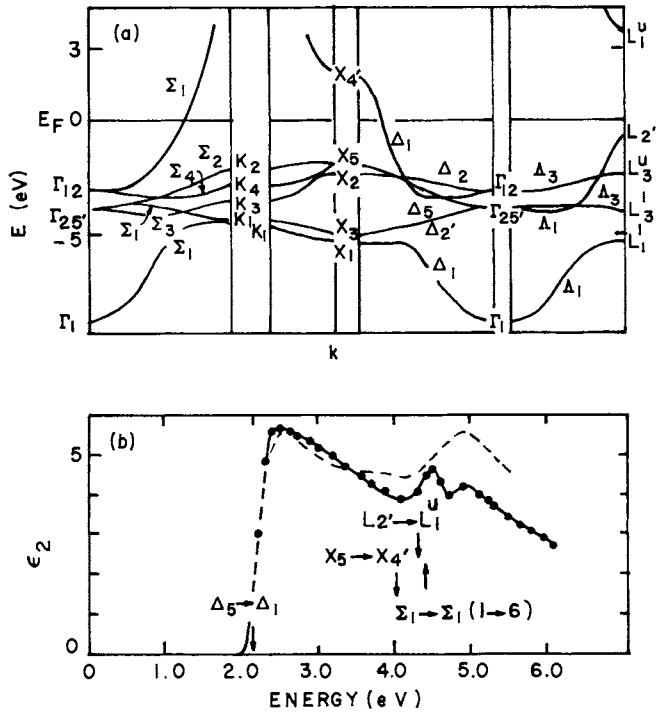

Fig. 7. (a) Band structure of Cu calculated by an empirical pseudopotential method, (b) interband contribution to ε_2 for Cu (dashed) ([51]) and an empirical pseudopotential calculation of ε_2 (solid). Some important transitions are labeled. (See also Table I and Fig. 7a.) (From Fong *et al.* [52].)

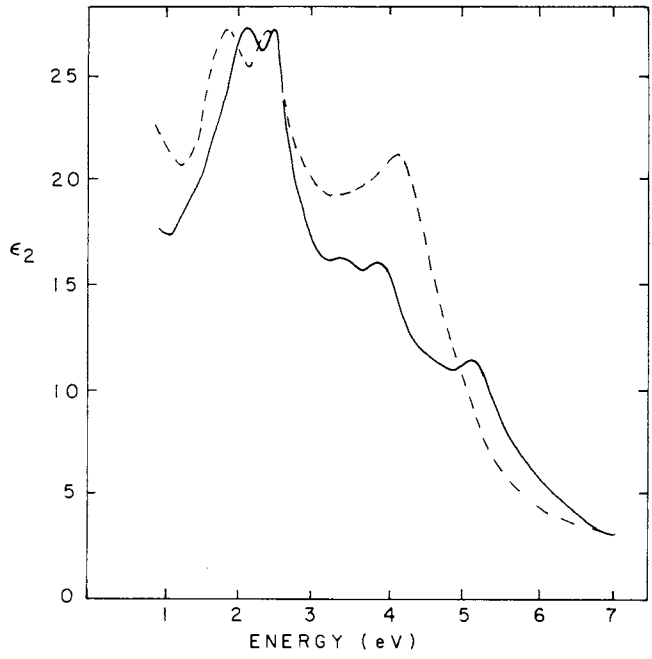

Fig. 8. ε_2 of Mo. Solid line represents values measured by Weaver *et al.* [54]; dashed line values calculated by Pickett and Allen [56].

transitions. It would be most useful to evaluate ε_2 for a transition metal by using dipole matrix elements to see if ε_2 can be calculated well for a material with unfilled d bands.

In both the transition metals and the noble metals, it now is clear that some of the structure and much of the magnitude in the ε_2 spectra arise from transitions throughout large volumes of the Brillouin zone, and such transitions are not easily accounted for in any way other than a numerical integration over the Brillouin zone. Simpler models, such as are appropriate for simple metals, do not suffice. Calcium is an example of a simple metal in which the Fermi surface and critical points play no role in the optical properties [58].

Figure 9 shows the ε_2 spectrum for Si, a covalently bonded semiconductor [59]. Although the one-electron calculation of ε_2 was quite successful for Ge, a similar material it is clear that the peak at 3.5 eV in Si appears as only a shoulder at 3.4 eV in the one-electron calculation, whose integrated area is too small by about 30% [42].

A number of critical points have been identified in derivative spectra, so the problem seems not to be grossly inadequate energy bands in the calculation. The bonding electrons, those being excited in this spectrum, are highly localized in Si, and several calculations of local field effects have shown that they have a large effect, although some of the early calculations did not lead

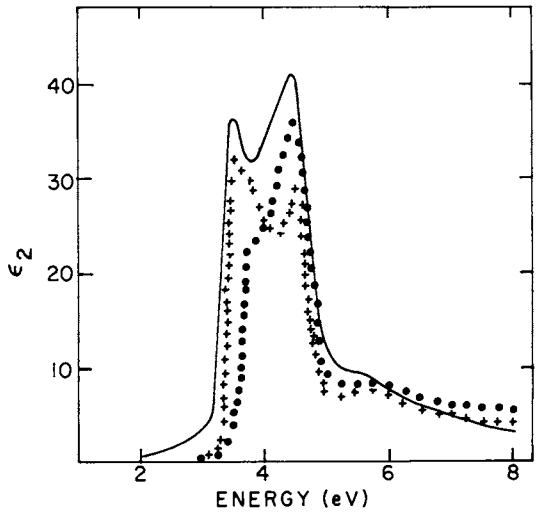

Fig. 9. ε_2 of Si. Solid line represents experiment by Philipp and Ehrenreich [59]; filled circles, values calculated by a one-electron empirical pseudopotential method (Louie *et al.* [41]; crosses) calculated by using a local field correction. (From Hanke and Sham [45].)

to an effect that produced better agreement with experiment. The recent calculations [45] show that proper treatment of the local field and other many-electron effects is a *sine qua non* to the quantitative understanding of the optical spectrum of silicon and of diamond. Such calculations have not been carried out on other solids for which local field effects are believed to be important.

The absorption-edge region is shown in Fig. 10 [60, 61]. These data were taken with high resolution at a number of temperatures. There is considerable resemblance to the spectrum shown schematically in Fig. 2, indicating the occurrence of indirect transitions with the participation of a phonon. Detailed analysis of all the spectra shows that the band-gap energy is temperature dependent, that the slopes near threshold are not as expected because of the electron-hole interaction, and that there are several overlapping structures at higher temperatures because phonons with four different energies (i.e., from four different branches) participate. A second indirect edge, at which the electrons are excited into a higher-lying set of conduction-band minima, has been observed [62] with great difficulty, for it is weak and lies at 1.65 eV, where the absorption shown in Fig. 10 is very large.

As an example of an insulator we can use CsCl, shown in Fig. 5. The sharp structures near 8 and 13 eV are clearly excitons, those near 8 eV arising from the valence-to-conduction-band transitions, and those at 13.5 eV from the excitation of Cs 5p core levels. Considerable analysis has been carried out on the valence and core excitons in alkali halides and solid rare gases, but far less is known about the other structures. (Many weaker exciton features,

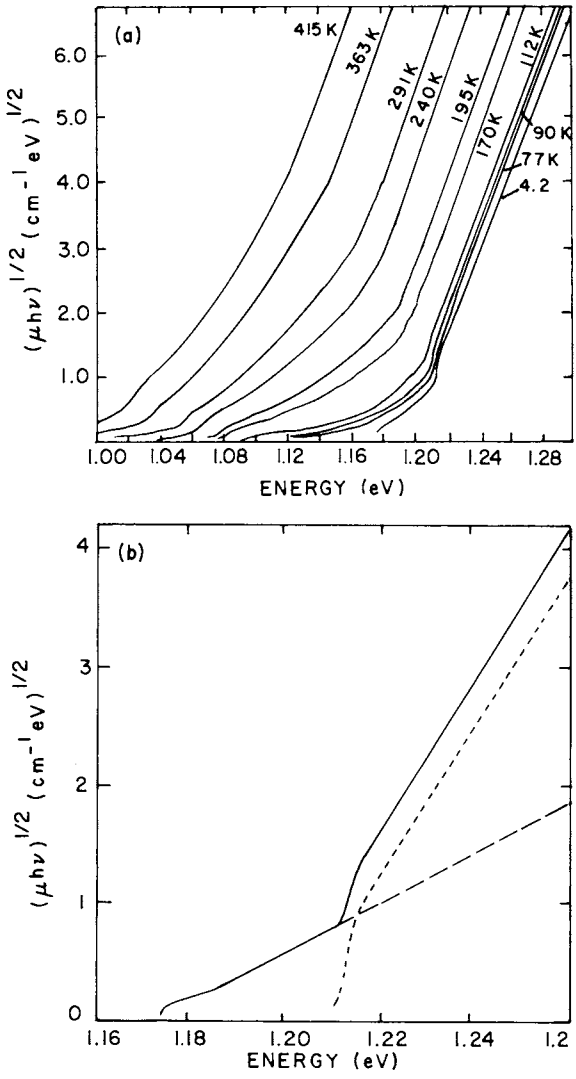

Fig. 10. (a) Absorption-coefficient spectra for Si at the fundamental (indirect) edge at several temperatures (from Macfarlane *et al.* [60]) and (b) decomposition of the 4.2 K spectrum into two components, phonon emission (dotted line beginning at higher energy) and phonon absorption (dashed line lying under the solid line, then leaving it). The solid line is the spectrum from both components together.

not apparent in Fig. 2, are known in many alkali halides.) These have been associated with structures expected in the joint density of states for interband transitions, but the large electron–hole interaction leads one not to expect a one-to-one correspondence between the one-electron spectrum and the experimental spectrum.

ACKNOWLEDGMENT

The Ames Laboratory is operated for the U.S. Department of Energy by Iowa State University under contract No. W-7405-Eng-82. This research was supported by the Director for Energy Research, Office of Basic Energy Sciences.

REFERENCES

1. W. Eberhardt and F. D. Himpsel, *Phys. Rev. B* **21**, 5572 (1980).
2. G. Borstel, M. Neumann and M. Wohlecke, *Phys. Rev. B* **23**, 3121 (1981).
3. R. L. Benbow, *Phys. Rev. B* **22**, 3225 (1980).
4. N. V. Smith, *Phys. Rev. B* **19**, 5019 (1979).
5. R. Lässer, N. V. Smith, and R. L. Benbow, *Phys. Rev. B* **24**, 1895 (1981).
6. K. Nakao, *J. Phys. Soc. Jpn.* **25**, 1343 (1968).
7. Y. Sasaki, C. Hamaguchi, A. Moritani, and J. Nakai, *J. Phys. Soc. Jpn.* **36**, 177 (1974).
8. M. T. Okuyana, T. Nishino, and Y. Hamakawa, *J. Phys. Soc. Jpn.* **37**, 431 (1974).
9. R. J. Elliott, *Phys. Rev.* **108**, 1384 (1957).
10. H. I. Ralph, *Solid State Commun.* **3**, 303 (1965).
11. M. Shinada and S. Sugano, *J. Phys. Soc. Jpn.* **20**, 1274 (1965).
12. U. Rössler and O. Schütz, *Phys. Stat. Solidi B* **56**, 483 (1973).
13. C. B. Duke and B. Segall, *Phys. Rev. Lett.* **17**, 19 (1966).
14. J. Hermanson, *Phys. Rev. Lett.* **18**, 170 (1967).
15. J. E. Rowe, F. H. Pollak, and M. Cardona, *Phys. Rev. Lett.* **22**, 933 (1969).
16. B. Velický and J. Sak, *Phys. Stat. Solidi* **16**, 147 (1966).
17. U. Fano, *Phys. Rev.* **124**, 1866 (1961).
18. K. P. Jain, *Phys. Rev.* **139**, A544 (1965).
19. Y. Onodera, *Phys. Rev. B* **4**, 2751 (1971).
20. Y. Toyozawa, M. Inoue, T. Inui, and E. Hanamura, *J. Phys. Soc. Jpn.* **22**, 1337, 1349 (1967).
21. Y. Onodera and Y. Toyozawa, *J. Phys. Soc. Jpn.* **22**, 833 (1967); Y. Onodera and Y. Toyozawa, *J. Phys. Soc. Jpn.* **22**, 1337, 1349 (1967).
22. Y. Toyozawa and M. Inoue, *J. Phys. Soc. Jpn.* **21**, 1663 (1966).
23. Y. Toyozawa, *Prog. Theor. Phys.* **20**, 53 (1958).
24. H. Sumi, *J. Phys. Soc. Jpn.* **32**, 616 (1972).
25. F. Urbach, *Phys. Rev.* **92**, 1325 (1953).
26. D. T. F. Marple, *Phys. Rev.* **150**, 728 (1966).
27. J. D. Dow and D. Redfield, *Phys. Rev. B* **5**, 594 (1972).
28. D. Redfield and M. A. Aframovitz, *Appl. Phys. Lett.* **11**, 138 (1967).
29. J. Szczyrbowski, *Phys. Stat. Solidi B* **105**, 515 (1981).
30. K. Cho and Y. Toyozawa, *J. Phys. Soc. Jpn.* **30**, 1555 (1971).
31. H. Sumi and Y. Toyozawa, *J. Phys. Soc. Jpn.* **31**, 342 (1971).
32. H. Miyazaki and E. Hanamura, *J. Phys. Soc. Jpn.* **50**, 1310 (1981).
33. S. Schmitt-Rink, H. Haug, and E. Mohler, *Phys. Rev. B* **24**, 6043 (1981).
34. M. Schreiber and Y. Toyozawa, *J. Phys. Soc. Jpn.* **51**, 1544 (1982).
35. T. Skettrup, *Phys. Rev. B* **18**, 2622 (1978).
36. D. J. Dunstan, *J. Phys. C* **30**, L419 (1982).
37. J. D. Wiley, E. Schonherr, and A. Breitschwerdt, *Solid State Commun.* **34**, 891 (1980).
38. S. L. Adler, *Phys. Rev.* **126**, 413 (1962).
39. N. Wiser, *Phys. Rev.* **129**, 62 (1963).
40. Y. Onodera, *Prog. Theor. Phys.* **49**, 37 (1973).
41. S. G. Louie, J. R. Chelikowski, and M. L. Cohen, *Phys. Rev. Lett.* **34**, 155 (1975).
42. W. Hanke and L. J. Sham, *Phys. Rev. B* **12**, 4501 (1975).
43. R. D. Turner and J. C. Inkson, *J. Phys. C* **9**, 3585 (1976).

44. R. Bonneville, *Phys. Rev. B* **21**, 368 (1980).
45. W. Hanke and L. J. Sham, *Phys. Rev. B* **21**, 4656 (1980).
46. T. K. Bergstresser and G. W. Rubloff, *Phys. Rev. Lett.* **30**, 794 (1973).
47. S. R. Nagel and T. A. Witten, *Phys. Rev. B* **11**, 1623 (1975).
48. R. L. Benbow and D. W. Lynch, *Phys. Rev. B* **12**, 5615 (1975).
49. N. W. Ashcroft and K. Sturm, *Phys. Rev. B* **3**, 1898 (1971).
50. D. Brust, *Phys. Rev. B* **2**, 818 (1970).
51. U. Gerhardt, *Phys. Rev.* **172**, 651 (1968).
52. C. Y. Fong, M. L. Cohen, R. R. L. Zucca, J. Stokes, and Y. R. Shen, *Phys. Rev. Lett.* **25**, 1486 (1970).
53. J. F. Janak, A. R. Williams, and V. L. Moruzzi, *Phys. Rev. B* **11**, 1522 (1971).
54. J. H. Weaver, D. W. Lynch, and C. G. Olson, *Phys. Rev. B* **10**, 501 (1974).
55. B. W. Veal and A. P. Paulikas, *Phys. Rev. B* **10**, 1280 (1974).
56. W. E. Pickett and P. B. Allen, *Phys. Rev. B* **11**, 3599 (1975).
57. D. D. Koelling, F. M. Mueller, and B. W. Veal, *Phys. Rev. B* **10**, 1290 (1974).
58. P. O. Nilsson and G. Forssell, *J. Phys. F* **5**, L159 (1975).
59. H. R. Philipp and H. Ehrenreich, *Phys. Rev.* **129**, 1550 (1963).
60. G. G. Macfarlane, T. P. McLean, J. E. Quarrington, and V. Roberts, *Phys. Rev.* **111**, 1245 (1958).
61. G. G. Macfarlane, T. P. McLean, J. E. Quarrington, and V. Roberts, *J. Phys. Chem. Solids* **8**, 388 (1959).
62. R. A. Forman, W. R. Thurber, and D. E. Aspnes, *Sol. State Commun.* **14**, 1007 (1974).

GENERAL REFERENCES

Abélès, F., *in* "Optical Properties of Solids" (F. Abélès, ed.), p. 93, North-Holland Publ., Amsterdam, 1972.
Altarelli, M., *J. de Phys.* **39**, C4–95 (1978).
Aspnes, D. E., *in* "Handbook of Semiconductors" (M. Balkanski, ed.), Vol. 2, p. 109, North-Holland Publ., Amsterdam, 1980.
Bassani, F., *Appl. Opt.* **19**, 4093 (1980).
Bassani, F., and Pastori Parravicini, G., "Electronic States and Optical Transitions in Solids," Pergamon, Oxford, 1975.
Brown, F. C., *in* "Synchrotron Radiation Research" (H. Winick and S. Doniach, eds.), p. 61, Plenum, New York, 1980.
Brown, F. C., *Solid State Phys.* **29**, 1 (1974).
Brown, G. S., and Doniach, S., *in* "Synchrotron Radiation Research" (H. Winick and S. Doniach, eds.), p. 353, Plenum, New York, 1980.
Cardona, M., *in* "Semiconductors and Semimetals" (R. K. Willardson and A. C. Beer, eds.), Vol. 3, p. 125, Academic Press, New York, 1967.
Cardona, M., "Modulation Spectroscopy," *Solid State Phys.* **Supp. 11** (1969).
Cohen, M. H., *in* "Optical Properties of Solids" (J. Tauc, ed.), p. 1, Academic Press, New York, 1966.
Dexter, D. L., and Knox, R. S., "Excitons," Wiley, New York, 1963.
Dow, J. D., *in* "Optical Properties of Solids—New Developments" (B. O. Seraphin, ed.), p. 3, North-Holland Publ., Amsterdam, 1976.
Ehrenreich, H., *in* "Optical Properties of Solids" (J. Tauc, ed.), p. 106, Academic Press, New York, 1966.
Evans, B. L., *in* "Optical and Electrical Properties" (P. A. Lee, ed), p. 1, Reidel, Dordrecht, 1976.
Greenaway, D. L., and Harbeke, G., "Optical Properties and Band Structure of Semiconductors," Pergamon, New York, 1968.

Hamakawa, Y., and Nishino, T., *in* "Optical Properties of Solids—New Developments" (B. O. Seraphin, ed.), p. 255, North-Holland Publ., Amsterdam, 1976.
Hanke, W., *in* "Festkorper Probleme XIX—Advances in Solid State Physics" (J. Treusch, ed.), p. 43, Vieweg, Braunschweig, 1979.
Harbeke, G., *in* "Optical Properties of Solids" (F. Abélès, ed), p. 21, North-Holland Publ., Amsterdam, 1972.
Johnson, E. J., *in* "Semiconductors and Semimetals" (R. K. Willardson and A. C. Beer, eds.), Vol. 3, p. 154, Academic Press, New York, 1967.
Koch, E. E., Kunz, C., and Sonntag, B., *Phys. Rep.* **28C**, 154 (1977).
Kotani, A., and Toyozowa, Y., *in* "Synchrotron Radiation Techniques and Applications" (C. Kunz, ed.), p. 169, Springer-Verlag, Heidelberg, 1979.
Knox, R. S., "Theory of Excitons," *Solid State Phys.* **Supp. 5** (A63).
Kunz, C., *J. de Phys.* **39**, C4–112 (1978).
Kunz, C., *in* "Optical Properties of Solids—New Developments" (B. O. Seraphin, ed.), p. 423, North-Holland Publ., Amsterdam, 1976.
Lynch, D. W., *in* "Synchrotron Radiation, Techniques and Applications" (C. Kunz, ed.), p. 357, Springer-Verlag, Heidelberg, 1979.
Moss, T. S., "Optical Properties of Semiconductors," Butterworth, London, 1959.
Nilsson, P. O., *Solid State Phys.* **29**, 139 (1974).
Pankove, J. I., "Optical Processes in Semiconductors," Prentice-Hall, Englewood Cliffs, New Jersey, 1971.
Petroff, Y., *in* "Handbook of Semiconductors" (M. Balkanski, ed.), Vol. 2, p. 1, North-Holland Publ., Amsterdam, 1980.
Philipp, H. R., and Ehrenreich, H., *in* "Semiconductors and Semimetals" (R. K. Willardson and A. C. Beer, eds.), Vol. 3, p. 93, Academic Press, New York, 1967.
Phillips, J. C., *in* "Optical Properties of Solids" (J. Tauc, ed.), p. 155, Academic Press, New York, 1966.
Phillips, J. C. *Solid State Phys.* **18**, 55 (1966).
Reynolds, D. C., and Collins, T. C., "Excitons, Their Properties and Uses," Academic Press, New York, 1981.
Schwentner, N., *Appl. Opt.* **19**, 4104 (1980).
Skibowski, M., Sprussel, G., and Saile, V., *Appl. Opt.* **19**, 3978 (1980).
Tauc, J., *in* "Optical Properties of Solids" (J. Tauc, ed.), p. 277, Academic Press, New York, 1966.
Toyozawa, Y., *Appl. Opt.* **19**, 4101 (1980).
Wooten, F., "Optical Properties of Solids," Academic Press, New York, 1972.
Zavetova, M., and Velicky, B., *in* "Optical Properties of Solids—New Developments" (B. O. Seraphin, ed.), p. 379, North-Holland, Publ., Amsterdam, 1976.

Chapter 11

Optical Properties of Nonmetallic Solids for Photon Energies below the Fundamental Band Gap

SHASHANKA S. MITRA
Department of Electrical Engineering
University of Rhode Island
Kingston, Rhode Island

I. Introduction 213
II. Infrared Dispersion by Polar Crystals 215
III. Kramers–Kronig Dispersion Relations 227
IV. Determination of Absorption Coefficient in the Intermediate Region 229
V. Absorption Coefficient in the Transparent Regime 230
VI. Multiphonon Absorption 232
A. General Remarks 232
B. Absorption in the Region $\omega > \omega_{LO}$ 236
C. Absorption in the Region $\omega < \omega_{TO}$ 249
VII. Infrared Absorption by Defects and Disorders 254
A. General Remarks 254
B. Crystals with Substitutional Impurities 255
C. Amorphous and Glassy Systems 259
VIII. Infrared Dispersion by Plasmons 263
References 267

I INTRODUCTION

There are two chief sources of absorption in a pure solid, viz., lattice vibrations and electronic transitions. For most materials, a sufficiently wide spectral window exists between these two limits where the material is transparent (see Fig. 1). However, this transparent regime displays residual absorption

HANDBOOK OF OPTICAL CONSTANTS OF SOLIDS

Copyright © 1985 by Academic Press, Inc.
All rights of reproduction in any form reserved.
ISBN 0-12-544420-6

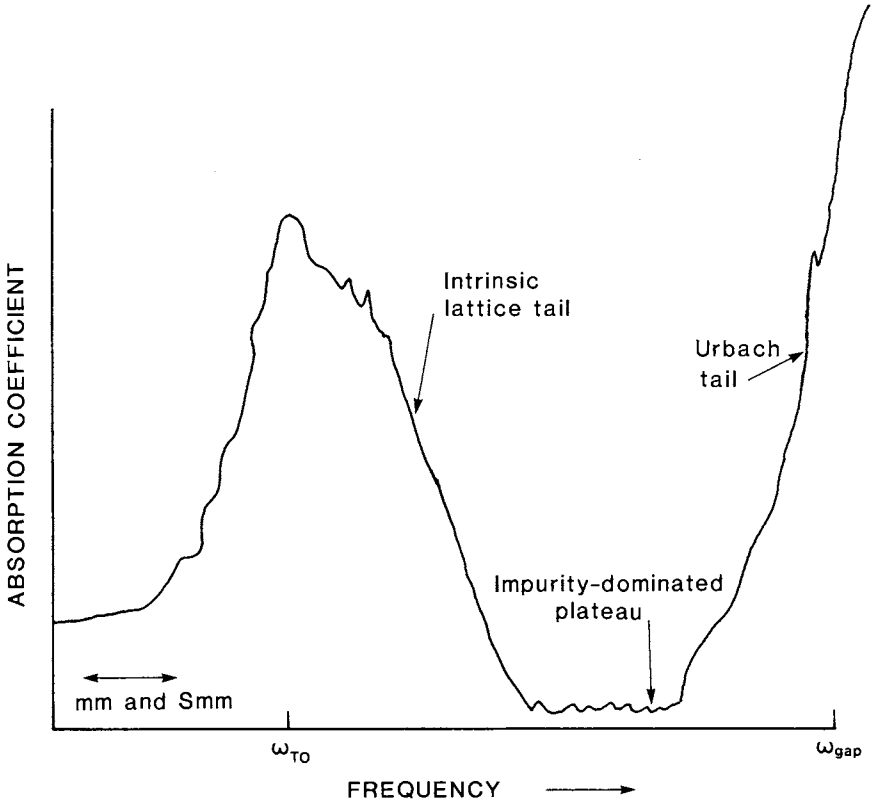

Fig. 1. The absorption gap between the fundamental electronic absorption edge and the one-phonon adsorption process in a polar crystal (schematic).

due to (a) multiphonon processes, (b) defects and impurities, (c) phonon-assisted electronic transitions in the long-wavelength tail of the fundamental absorption edge, and/or (d) multiphoton electronic transitions in the case of high-photon flux. As is evident from Fig. 1, for most solids, the mid- and near-infrared regions fall at energies substantially higher than the reststrahlen region and yet far below the electronic absorption edge. Thus, the primary source of absorption in this region is multiphonon summation processes. The millimeter and submillimeter spectral regions, on the other hand, occur on the low-energy side of the one-phonon reststrahlen region. The primary source of absorption in the region is thus two-phonon difference processes, although there will be some contribution from the sum processes involving low-energy acoustical phonons, and one-phonon absorption processes in the case of structurally disordered solids, and solids containing imperfections and impurities.

In this chapter we discuss optical properties of solids in the infrared spectral region that are caused by interaction of electromagnetic radiation with

lattice vibrations. This chapter is organized in the following manner: We start with optical interactions in crystals resulting from one-phonon processes; next we treat multiphonon interactions both at energies higher and lower than the fundamental one-phonon processes; this is followed by a description of phonon processes induced by defects and impurities and their interaction with infrared radiation. Finally, photon–phonon interaction in crystals that have substantial amount of charge carriers (plasma effects) is considered.

We regard a crystal as a mechanical system of nN particles, where n is the number of particles per unit cell and N the number of unit cells. Such a crystal shall have $3nN$ degrees of freedom, of which $3nN - 3$ are the linearly independent normal modes and three are pure translations. The very large number ($\sim 10^{24}$) of modes of a macroscopic crystalline sample necessitates the description of the frequency spectrum in terms of a frequency distribution function. The frequency spectrum of the ionic motions in a solid can be obtained by constructing the classical equations of motion for the lattice points and solving for the normal modes as plane waves of the form $\exp i(\omega_i t - \mathbf{k}_i \cdot \mathbf{r})$, where ω_i and $\mathbf{k}_i$ are, respectively, the frequency and the wave vector of the ith mode. The vibration frequencies occur as the $3n$ roots of the secular equation, involving the wave vector, which may take N values. The $3nN$ modes are thus distributed on $3n$ branches, $3n - 3$ of which are termed optical that have nonvanishing mode frequencies for all values of k and three are acoustic branches that have vanishing frequencies at $k = 0$.

The energy of each of the $3nN$ modes is quantized, and the term *phonon* is used to describe a quantized lattice vibration. Throughout the rest of this chapter we have considered lattice vibrations as phonons or quantized excitations, rather than as waves of vibrating ions; and thus in their interactions with photons, other phonons, electrons, or neutrons, the requirement of the conservation of energy and momentum are tacitly implied. The formulas developed use cgs units.

INFRARED DISPERSION BY POLAR CRYSTALS II

In the long-wave limit ($k \cong 0$), the optical branch vibrations of a diatomic lattice corresponds to the motion of one type of atoms, all in phase, relative to the other kind. In polar crystals, such a motion is associated with strong electric moments and hence can directly interact with the electric field of proper polarization of the incident electromagnetic radiation, provided that energy and wave vectors are conserved. The wave vectors associated with an infrared photon are essentially zero (10^4–10^5 cm^{-1}) compared with those of most optical phonons (10^9 cm^{-1}) of the same energy. For example, in rock salt, a diatomic crystal, there are three optic branches. At $k = 0$ one

corresponds to the long-wavelength longitudinal optical mode and the other two to the doubly degenerate transverse optical mode. The electromagnetic radiation being transverse cannot directly interact with longitudinal phonons in an infinite crystal. The $k \cong 0$ transverse optical mode, on the other hand, will interact and can be observed as a resonant frequency by measuring the transmittance of infrared radiation by thin films. In the vicinity of the resonance frequency, one thus expects drastic changes in the optical properties of such a crystal. In the case of strong photon–phonon coupling encountered in ionic solids, it is thus impossible to distinguish between purely photon or phononlike modes. On the other hand, in a homopolar crystal such as diamond, germanium, or silicon, one does not expect any such resonant interaction.

We will briefly discuss the dispersion of infrared radiation by cubic diatomic ionic crystals with optical isotropy. Huang [1] (also see Born and Huang [2]) was the first to give a phenomenological theory of infrared dispersion by long-wavelength optical phonons of ionic crystals. In terms of a reduced displacement vector $\mathbf{w} = \mathbf{u}(\mu/v)^{1/2}$, where $\mathbf{u}$ represents the displacement of the positive ions relative to the negative ions and μ/v is the reduced ionic mass per Bravais cell. The polar motions and the dielectric polarization may then be described by

$$\ddot{\mathbf{w}} = b_1\mathbf{w} + b_2\mathbf{E} \tag{1}$$

and

$$\mathbf{P} = b_2\mathbf{w} + b_3\mathbf{E} = [(\varepsilon - 1)/4\pi]\mathbf{E}, \tag{2}$$

where $\mathbf{E}$ is the electric field and $\varepsilon(\omega)$ the dielectric response function. The b's are constants characteristic of the solid; b_1 is related to the near-neighbor force constant, b_2 to a transverse effective ionic charge, and b_3 to polarizability. Considering the periodic solutions

$$(\mathbf{w}, \mathbf{E}, \mathbf{P}) = (\mathbf{w}_0, \mathbf{E}_0, \mathbf{P}_0)e^{-i\omega t}, \tag{3}$$

one obtains by manipulation of Eqs. (1)–(3) the expression for ε

$$\varepsilon(\omega) = \varepsilon_\infty + \frac{(\varepsilon_0 - \varepsilon_\infty)\omega_0^2}{\omega_0^2 - \omega^2}, \tag{4}$$

where ω_0 is the dispersion frequency and ε_0 and ε_∞ are static and high-frequency dielectric constants, respectively. The coefficients of Eqs. (1) and (2) may be identified as

$$b_1 = -\omega_0^2, \tag{5}$$

$$b_2 = \omega_0[(\varepsilon_0 - \varepsilon_\infty)/4\pi]^{1/2}, \tag{6}$$

and

$$b_3 = (\varepsilon_\infty - 1)/4\pi. \tag{7}$$

Equations (1) and (2) describe the electrostatic interaction between the ions. To include propagation of the excitations with finite velocity, one must solve these equations along with Maxwell's equations. Now considering $\mathbf{w}$, $\mathbf{P}$, $\mathbf{E}$ and the magnetic field $\mathbf{H}$ all varying as $\exp[i(\mathbf{q}\cdot\mathbf{r} - \omega t)]$, one obtains

$$\mathbf{q}\cdot(\mathbf{E} + 4\pi\mathbf{P}) = 0, \tag{8}$$

$$\mathbf{q}\cdot\mathbf{H} = 0, \tag{9}$$

$$\mathbf{q}\times\mathbf{E} = (\omega/c)\mathbf{H}, \tag{10}$$

$$\mathbf{q}\times\mathbf{H} = -(\omega/c)(\mathbf{E} + 4\pi\mathbf{P}). \tag{11}$$

Equations (2) and (8) yield

$$\varepsilon(\omega)(\mathbf{q}\cdot\mathbf{E}) = 0. \tag{12}$$

Equation (12) is satisfied by either

$$\mathbf{q}\cdot\mathbf{E} = 0 \tag{13}$$

or

$$\varepsilon(\omega) = 0. \tag{14}$$

Let us consider Eq. (13) first, which signifies that $\mathbf{E}$ is perpendicular to $\mathbf{q}$. Considering Eq. (10) also, we find that $\mathbf{E}$, $\mathbf{H}$, and $\mathbf{q}$ are all perpendicular to each other. From Eqs. (1) and (2) it follows that $\mathbf{w}$ and $\mathbf{P}$ are both parallel to $\mathbf{E}$. Thus Eq. (13) describes transverse waves. Elimination of $\mathbf{H}$ between Eqs. (10) and (11) yields

$$\varepsilon(\omega) = (qc/\omega)^2, \tag{15}$$

signifying propagating transverse waves that are simultaneously electromagnetic and lattice waves known as *polaritons.*

To understand the nature of the dielectric response function (4) we shall consider the electrostatic approximation in which the transverse modes are purely mechanical. Considering $\mathbf{E} = 0$, Eq. (1) becomes

$$\ddot{\mathbf{w}}_t = b_1\mathbf{w}. \tag{16}$$

If ω_{TO} is considered the natural frequency of the transverse oscillator, one has

$$\omega_{TO}^2 = -b_1 = \omega_0^2. \tag{17}$$

Thus, the dispersion frequency in Eq. (4) is identical with the long-wavelength transverse optical-mode frequency.

Returning to the second case [Eq. (~~14~~)], one can rewrite Eq. (2) as

$$\mathbf{E} = -4\pi\mathbf{P}. \tag{18}$$

Equation (18) along with Eqs. (9) and (11) gives $\mathbf{H} = 0$. Because of Eq. (10) it follows that $\mathbf{q}$ and $\mathbf{E}$ are parallel to each other and also parallel to $\mathbf{w}$ and

P [see Eqs. (1) and (2)]. Thus, Eq. (14) signifies longitudinal waves. Denoting the natural frequency of the longitudinal oscillator as ω_{LO} and solving Eq. (14) with the aid of Eq. (4) one obtains

$$\varepsilon_\infty + \frac{(\varepsilon_0 - \varepsilon_\infty)\omega_0^2}{\omega_0^2 - \omega_{LO}^2} = 0.$$

Solving for ω_{LO} one has

$$\omega_{LO} = (\varepsilon_0/\varepsilon_\infty)^{1/2}\omega_0 = (\varepsilon_0/\varepsilon_\infty)^{1/2}\omega_{TO}. \tag{19}$$

This relation between the long-wavelength longitudinal and transverse optical-mode frequencies is known as the Lyddane–Sachs–Teller (LST) relation [3].

In a homopolar crystal such as Si or Ge, in the absence of polar interactions the atomic motions are determined only by the local elastic restoring forces, i.e., $b_2 = 0$ in Eq. (1). From Eqs. (6) and (19) it follows that for such crystals $\varepsilon_0 = \varepsilon_\infty$ and $\omega_{LO} = \omega_{TO}$.

Electromagnetic radiation with frequencies in the vicinity of the dispersion frequency ω_0, will strongly interact with an ionic solid. Unfortunately, relation (4) is inadequate to describe this interaction realistically. The dielectric function given by Eq. (4) is a real quantity and thus is incapable of describing selective absorption of radiation. However, reflection of radiation could be

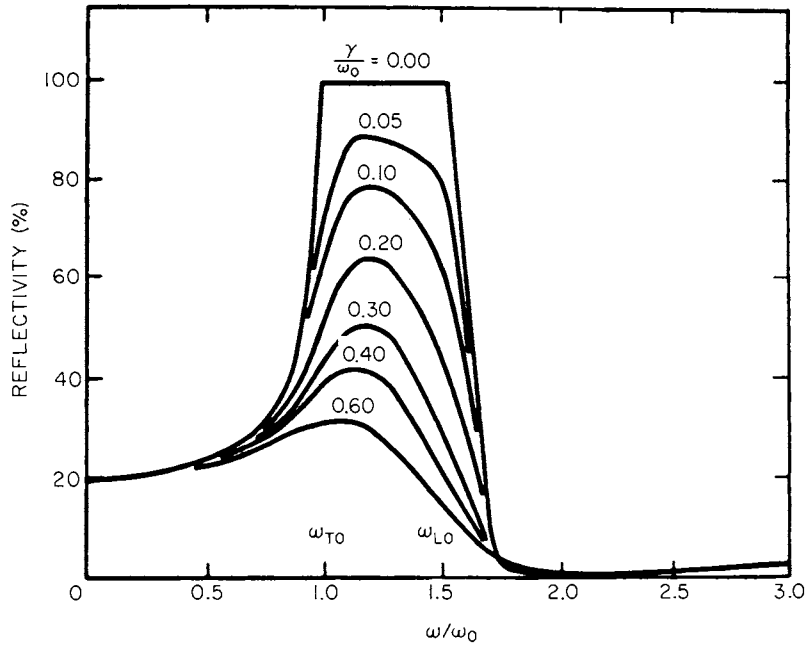

Fig. 2. Reflection spectra of a damped oscillator for various values of the damping factor.

understood by Eq. (4) along with the Fresnel formula

$$R = [(n - 1)/(n + 1)]^2, \tag{20}$$

where $n = \sqrt{\varepsilon(\omega)}$ is the refractive index. The selective reflection of infrared radiation in the vicinity of optical lattice-mode frequencies is known as the *reststrahlen phenomenon.* The reststrahlen band for an ionic crystal in the harmonic approximation [Eq. (1)] is shown in Fig. 2 (top curve). We notice that such a crystal becomes totally reflecting between the frequencies ω_{TO} and ω_{LO}.

In any real ionic or partially ionic diatomic crystal, the observed reflectivity shows a characteristic reststrahlen band with high reflectivity between the frequencies ω_{TO} and ω_{LO}. However, in shape or intensity the observed reflectivity does not agree quantitatively with the ideal case represented by Eqs. (4) and (20). This is evident from Fig. 3, in which the reflection spectrum of AlSb is shown [4]. In real crystals, the strong reflection in the reststrahlen region is also associated with strong absorption, whereas Eq. (4), being a real quantity for all values of ω, predicts no such selective absorption. Equation

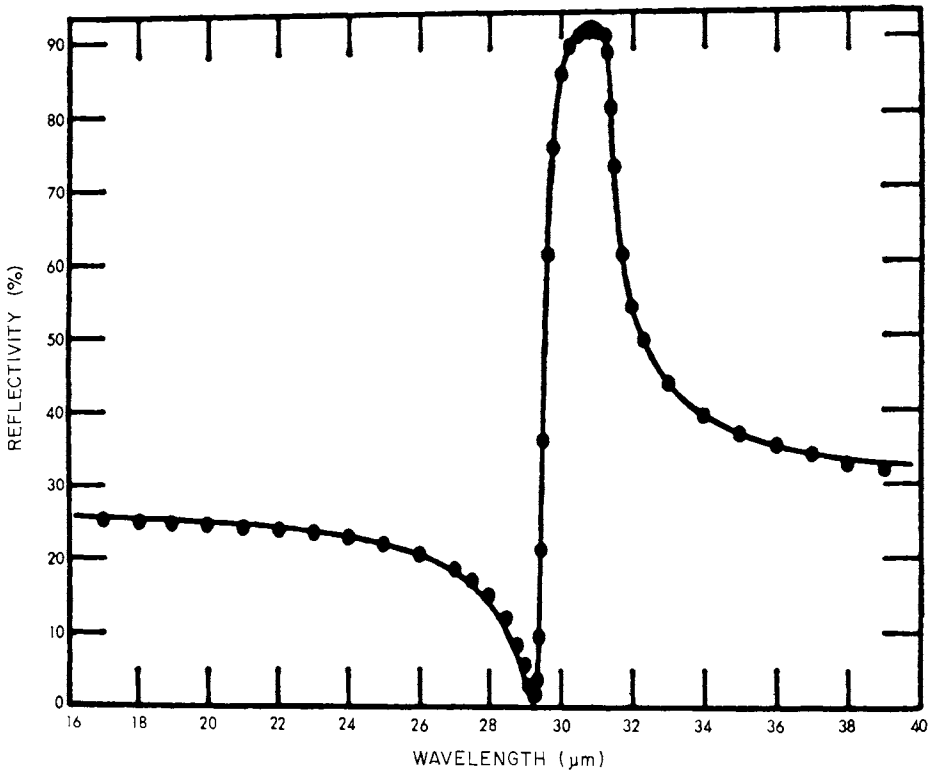

Fig. 3. Reststrahlen spectrum of AlSb. (From Turner and Reese [4].)

(4) was obtained from the phenomenological equations of motion [Eqs. (1) and (2)], which neglected all but linear terms giving rise to mutually independent lattice waves of infinite lifetimes. In real crystals, the lattice waves are coupled by anharmonic and higher-order electric-moment terms, which play an important role in the dissipation of energy, through lattice waves of finite lifetimes.

A more realistic expression for the dielectric response function may be obtained by the phenomenological introduction of a damping term that represents a force always opposed to the ionic motions and proportional to the velocity. The damping factor then represents the phonon half-width or its reciprocal, the phonon lifetime for ω_{TO}. This procedure thus provides a crude method for including the effect of energy dissipation in the neighborhood of ω_0. Equation (1) now takes the form

$$\ddot{\mathbf{w}} = b_1\mathbf{w} - \gamma\dot{\mathbf{w}} + b_2\mathbf{E}. \tag{21}$$

Because of the periodic nature of $\mathbf{w}$, the introduction of the additional term amounts to replacing the coefficient b_1 with $(b_1 + i\omega\gamma)$. Therefore, the dielectric response function [Eq. (4)] including damping now becomes

$$\varepsilon(\omega) = \varepsilon_\infty + \frac{\varepsilon_0 - \varepsilon_\infty}{1 - (\omega/\omega_0)^2 - i\gamma(\omega/\omega_0^2)}, \tag{22}$$

which is a complex quantity, as expected of a lossy medium.

A plane electromagnetic wave of phase velocity $c/\sqrt{\varepsilon} = \omega/k$ and frequency ω may be represented by

$$\mathbf{E} = \mathbf{E}_0 \exp i\omega(\mathbf{e}\cdot\mathbf{r}(\sqrt{\varepsilon}/c) - t), \tag{23}$$

where $\mathbf{e}$ is a unit vector in the direction of propagation. In an absorbing medium, the dielectric constant $\varepsilon(\omega)$ and hence the refractive index represent complex quantities

$$n^* = \sqrt{\varepsilon(\omega)} = n + ik$$

and

$$\varepsilon(\omega) = \varepsilon_1 + i\varepsilon_2 = (n^2 - k^2) + 2ink, \tag{24}$$

where n and k are refractive index and extinction coefficient, respectively, and ε_1 and ε_2 real and imaginary parts of the dielectric constant. Equation (23) accordingly becomes

$$\mathbf{E} = \mathbf{E}_0 \exp\left(-\frac{\omega k}{c}\mathbf{e}\cdot\mathbf{r}\right)\exp\left[i\omega\left(\frac{n}{c}\mathbf{e}\cdot\mathbf{r} - t\right)\right] \tag{25}$$

and describes the simultaneous effects of refraction and attenuation. In terms of the absorption coefficient α, the attenuation is given by the Beer–Lambert law

$$|E^2| = |E_0^2| \exp(-\alpha r). \tag{26}$$

Comparison of Eqs. (25) and (26) give the relation between α and k

$$\alpha = 2\omega k/c = 4\pi k/\lambda.$$

In terms of the real and the imaginary parts of $\varepsilon(\omega)$ [Eq. (22)], one has

$$\varepsilon_1 = n^2 - k^2 = \varepsilon_\infty + \frac{(\varepsilon_0 - \varepsilon_\infty)[1 - (\omega/\omega_0)^2]}{[1 - (\omega/\omega_0)^2]^2 + (\gamma/\omega_0)^2(\omega/\omega_0)^2} \tag{27}$$

and

$$\varepsilon_2 = 2nk = \frac{(\varepsilon_0 - \varepsilon_\infty)(\gamma/\omega_0)(\omega/\omega_0)}{[1 - (\omega/\omega_0)^2]^2 + (\gamma/\omega_0)^2(\omega/\omega_0)^2}. \tag{28}$$

The reflectance R of an absorbing medium is now given by

$$R = \frac{(n-1)^2 + k^2}{(n+1)^2 + k^2} \tag{29}$$

instead of Eq. (20). The reststrahlen spectrum of a damped oscillator for several values of the damping factor γ/ω_0 is shown in Fig. 2.

The optical constants n and k, or ε_1 and ε_2, are obtained by fitting the reststrahlen band by Eqs. (27)–(29). Usually, a best set of oscillator parameters ω_0, γ/ω_0, ε_0, and ε_∞ are chosen so as to minimize the difference between calculated and observed reflectivity as a function of frequency. The fit to the experimental data is obtained by minimizing the quantity

$$S = \sum_{i=1}^{M} [R_{i,\,\mathrm{exp}} - R_{i,\,\mathrm{calc}}]^2, \tag{30}$$

where S is the square of the difference between the calculated and experimental reflectivity and the summation extends over the number of experimental points M. The computations may be performed utilizing a computer program based on the method of steepest descent outlined by Verleur [5].

Figure 4 gives the calculated optical constants for AlSb from its reststrahlen spectrum shown in Fig. 3 [4]. Although the maximum of k occurs very near ω_0, it is ε_2 and the conductivity ($nk\omega$) that undergo maxima precisely at $\omega = \omega_0$. Obviously, one identifies ω_0 with the long-wavelength ω_{TO} and the corresponding ω_{LO} may be obtained from the LST relation [Eq. (19)]. In the case of diatomic cubic crystals, ω_{LO} may also be identified with the minimum in ε_2 versus ω curves.

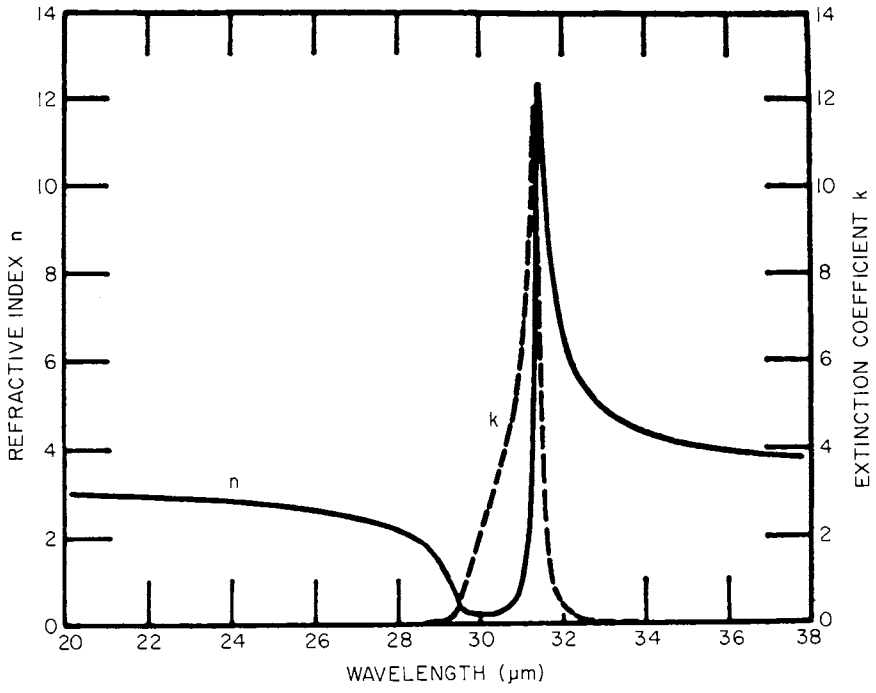

Fig. 4. Optical constants of AlSb in the one-phonon region. (From Turner and Reese [4].)

Crystals with more than two particles per unit cell may possess more than one reflection maximum, and analysis of such data requires a multioscillator fit of the observed data. Additional resonances may also occur as a result of a strong two-phonon or a strong impurity process. For the multiresonance case, Eq. (22) is replaced by the phenomenological relation

$$\varepsilon(\omega) = \varepsilon_\infty + \sum_{j=1}^{n} \frac{4\pi\rho_j}{1 - (\omega/\omega_j)^2 - i(\gamma_j/\omega_j)(\omega/\omega_j)}, \tag{31}$$

where $\varepsilon_0 = \varepsilon_\infty + \sum_{j=1}^{n} 4\pi\rho_j$. The sum is intended to include all resonances necessary to represent the reststrahlen spectrum and the dielectric response function. An example of such a reflection spectrum is shown in Fig. 5 for single-crystal GeO_2 with light polarized perpendicular to the unique axis of the crystal [6]. This spectrum was fitted with three oscillators.

For crystals with more than two atoms per unit cell a modified LST relation holds [7] involving the transverse and longitudinal phonons of the same symmetry types

$$\prod_i (\omega_{\mathrm{LO}_j}/\omega_{\mathrm{TO}_j}) = (\varepsilon_0/\varepsilon_\infty)^{1/2}. \tag{32}$$

In the presence of damped phonons, Eqs. (19) and (32) undergo slight modifications as pointed out by Barker [8] and Chang *et al.* [9]. It is also realized

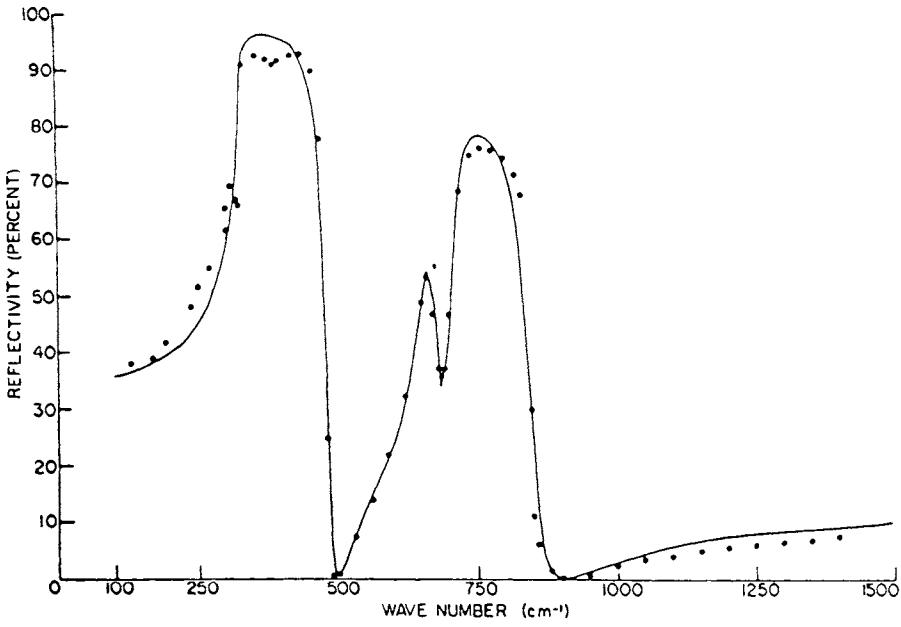

Fig. 5. Reststrahlen spectrum of tetragonal GeO_2 with $E \perp c$. Solid line is classical oscillator fit to experimental data (open circle). (From Kahan *et al.* [6].)

that in the case of multimode crystals, LO frequencies are not readily available from the TO frequencies through Eq. (32). Chang *et al.* [9] have given analytical relations for ω_{LO}'s in terms of the ω_{TO}'s and other oscillator parameters including damping. They also suggest that in the case of crystals with multimode damped oscillators, the ω_{TO}'s may be identified with the maxima of the modulus of dielectric response function $|\varepsilon(\omega)| = (\varepsilon_1^2 + \varepsilon_2^2)^{1/2}$, while ω_{LO}'s with the minima in $|\varepsilon(\omega)|$ to a very good approximation. Barker [10] suggests identification of ω_{TO}'s with maxima in ε_2 and ω_{LO}'s with maxima in $\mathrm{Im}(-1/\varepsilon)$. Either method gives good agreement with the analytical solution or other measurements of ω_{LO}'s if the damping terms are not too large.

The long-wavelength transverse optical-mode frequency of a polar crystal may also be determined directly by transmission measurements. However, for an ionic crystal, the strong absorption in the neighborhood of the dispersion frequencies calls for the use of thin samples. For very thin (< 1-μm) samples, it may be shown that the minima in transmission occur exactly at the infrared-active ($k = 0$), TO-mode frequencies. If transmission measurements on thin films are done with p-polarized light incident obliquely to the surface, transmission minima occur also at the corresponding LO mode frequencies as shown by Berreman [11]. The three different infrared measurement configurations described and the information they reveal are illustrated in Fig. 6 for a crystal with a single damped oscillator.

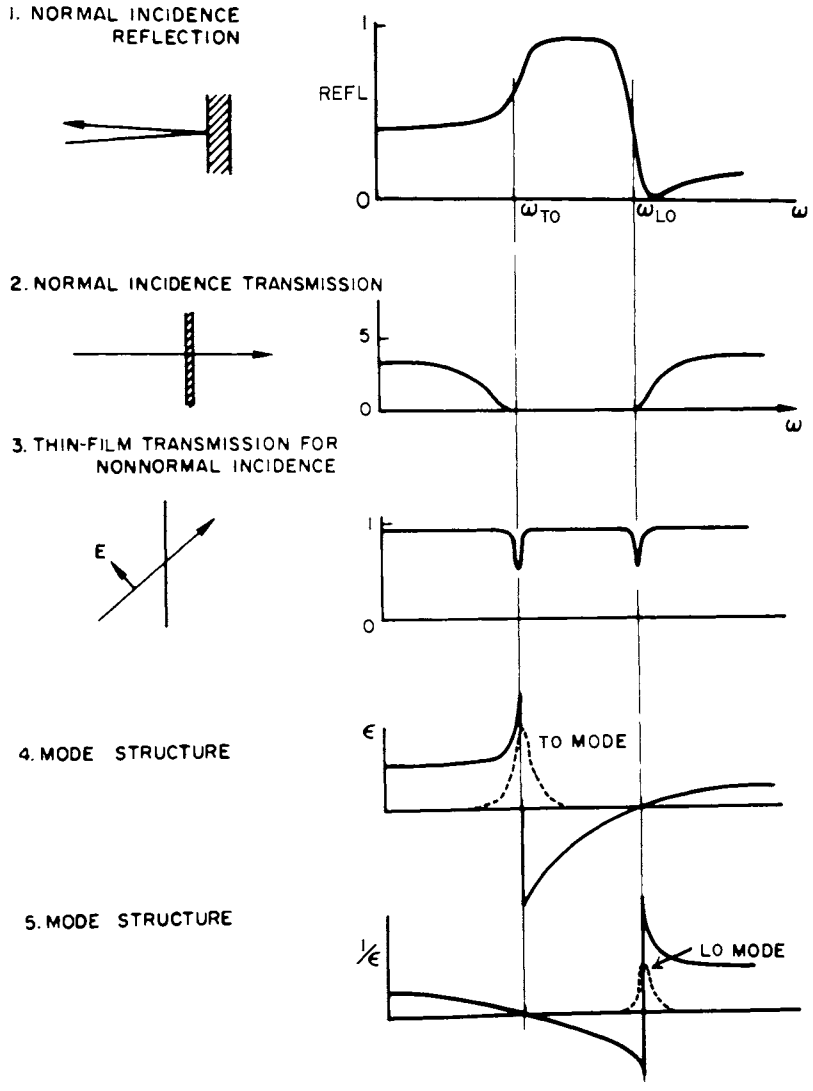

Fig. 6. Infrared spectra of three types of sample configuration. The sample is taken to have the idealized one-oscillator-mode structure given at the bottom of the figure with one TO frequency, one LO frequency and a constant (frequency-independent) damping factor. In part 4, the solid line represents real (ε) and the broken line imaginary (ε); in part 5, real ($1/\varepsilon$) and imaginary ($-1/\varepsilon$). (From Barker [10].)

As as example of the usefulness of Eq. (31) in obtaining optical constants, we present the case of MgO studied by Jasperse *et al.* [12]. The reflection spectra at several temperatures ranging from 8 to 1950 K and their fit by Eq. (31) requiring two oscillators are presented in Fig. 7, with the

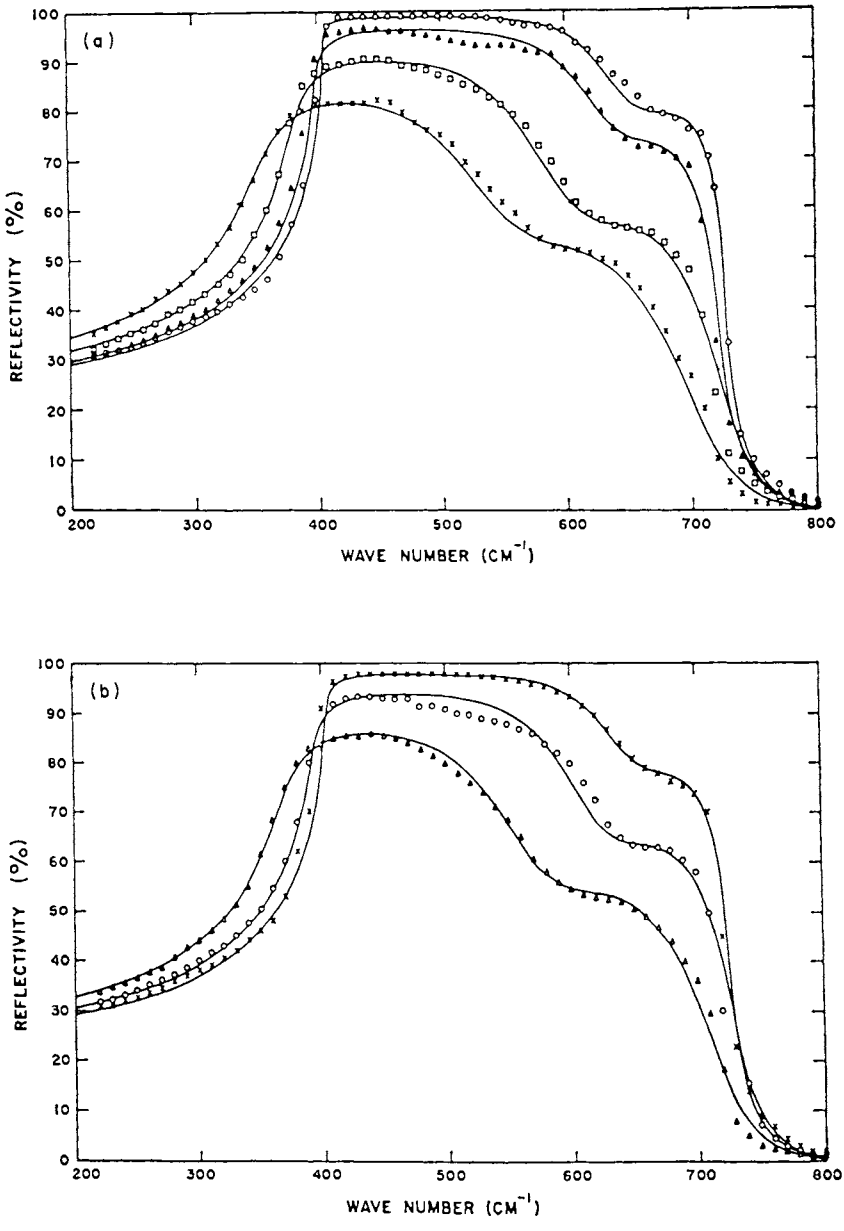

Fig. 7. Infrared reflectivity of MgO as a function of wave number and temperature. The various symbols are experimental points, and the solid lines are the theoretical curves calculated from the dispersion parameters of Table I. (a) ○, 8 K; ▲, 295 K; □, 950 K; ×, 1950 K; (b) ×, 85 K; ○, 545 K; ▲, 1410 K. (From Jasperse *et al.* [12].)

TABLE I

Infrared-Dispersion Parameters and Related Quantities for MgO, Temperature Independent[a,b]

Temperature (K)	ν_1 cm^{-1}	ν_2 cm^{-1}	γ_1/ν_1	γ_2/ν_2	$4\pi\rho_1$	$4\pi\rho_2$	ε_0	ν_{LO} (cm^{-1})	LST
8	408	653	0.0045	0.140	6.30	0.025	9.34	724	719
85	406	650	0.0100	0.145	6.40	0.030	9.44	725	719
295	401	640	0.0190	0.160	6.60	0.045	9.64	725	718
545	394	630	0.0325	0.170	6.75	0.075	9.84	724	712
950	382	610	0.0570	0.195	7.10	0.120	10.23	720	705
1410	368	590	0.0850	0.225	7.45	0.175	10.64	711	692
1950	355	566	0.1200	0.260	7.95	0.225	11.19	703	685

[a] From Jasperse *et al.* [12].

[b] ν_{LO} is determined from the zero in the dielectric response function ε' and from the LST relation, and $\varepsilon_\infty = 3.01$.

corresponding fitting parameters given in Table I. The index of refraction and extinction coefficient as functions of frequency and temperature can be easily obtained from these parameters as shown in Fig. 8 and 9.

It should be emphasized that the classical dispersion theory, even with the inclusion of damping factors and several poles, is only an approximation of the true frequency dependence of the dielectric response function. It is useful because it has a simple form, can represent the frequency dependence of reflectivity reasonably well, and enables one to obtain the various optical constants as functions of frequency in a fairly straightforward manner.

In the pseudoharmonic approximation a damping constant was introduced in Eq. (21) in an arbitrary manner. In an equally arbitrary manner a number of discrete poles were introduced to obtain Eq. (31). In reality, the phonon spectrum of a crystal is quasi-continuous extending from $\omega = 0$ to $\omega = \omega_{LO}$. Potentially any and all combinations of these phonons obeying certain conservation rules may contribute to the dielectric and optical response. Thus, γ is no longer frequency or temperature independent and the summation of Eq. (31) should be replaced by integrations involving joint densities of phonon states. A complete analytical expression for $\varepsilon(\omega)$ that includes all possible combinations of phonons and all possible decay channels is well nigh impossible. However, several approximations to include the factors previously described have been attempted [13–17] with varying success. It is interesting to note that in the vicinity of a resonance frequency (ω_j) all of these treatments reduce to the expression one obtains for the classical case. Thus, it is safe to conclude that Eq. (31) is useful in determining optical constants in the vicinities of resonances only where α has high values.

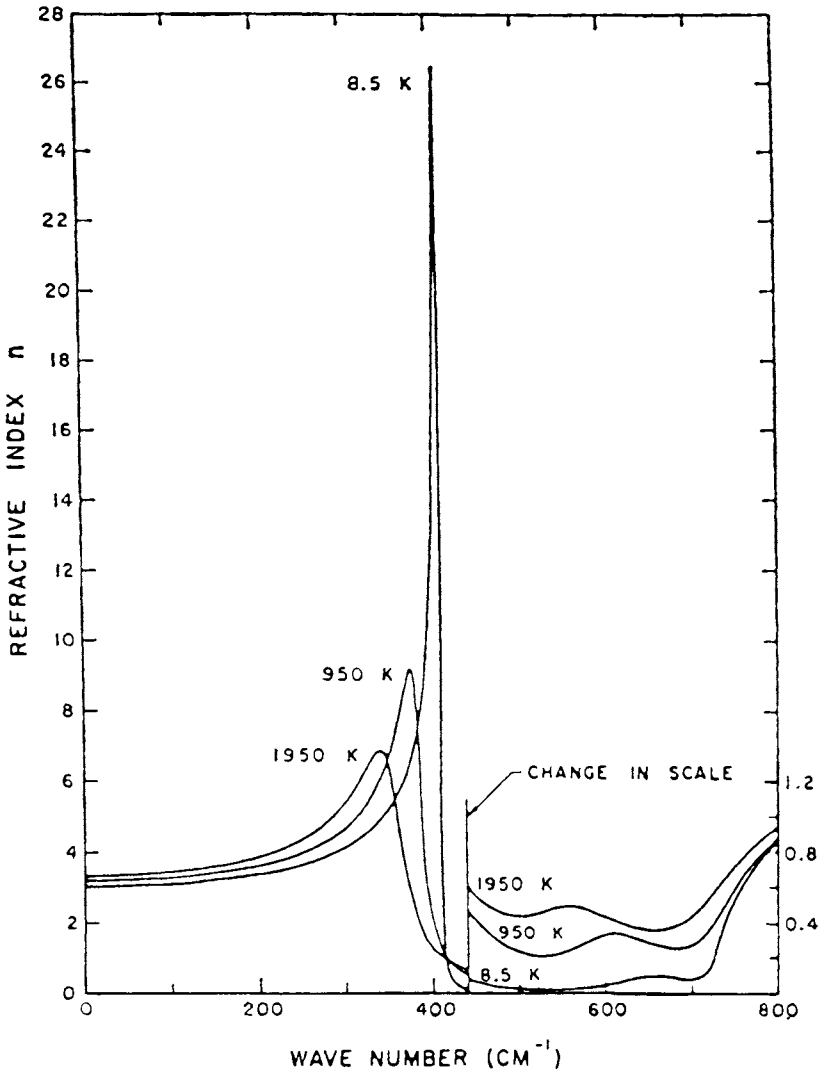

Fig. 8. Calculated refractive indices of MgO as functions of wave number and temperature (note change in vertical scale). (From Jasperse *et al.* [12].)

KRAMERS–KRONIG DISPERSION RELATIONS III

The optical constants and hence the long-wavelength optical phonon frequencies may also be obtained from the observed reflection spectrum by performing a Kramers–Kronig (KK) dispersion analysis [18]. The KK relations

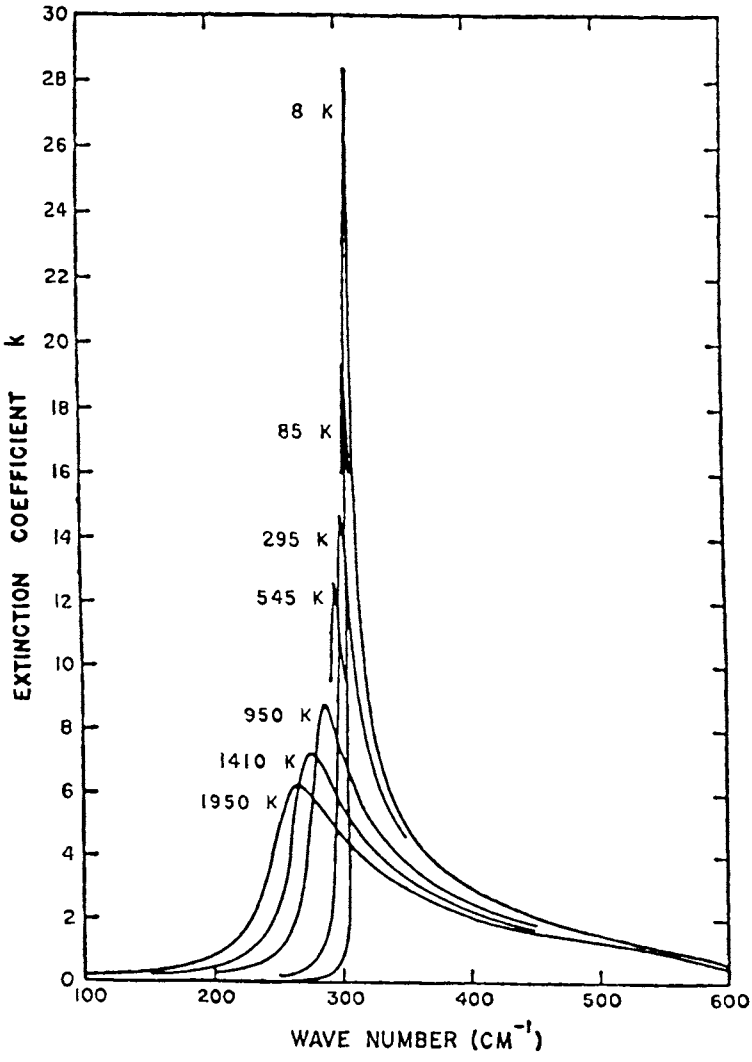

Fig. 9. Computed extinction coefficients of MgO as functions of wave number and temperature. (From Jasperse *et al.* [12].)

express an exact relationship between the real and imaginary parts of the dielectric constant and do not assume a model for calculating ε. This can be derived as a direct consequence of the principles of causality and the fact that the dielectric constant must be an analytically continuous function of the complex frequency [19]. The optical constants are given by

$$n = \frac{1 - r^2}{1 + r^2 - 2r\cos\theta}, \qquad k = \frac{-2r\sin\theta}{1 + r^2 - 2r\cos\theta}, \tag{33}$$

where the quantity $R = r^2$ is the experimentally observed reflectivity (single-surface reflection). The phase difference θ between the incident and the reflected waves is obtained from the relation

$$\theta_c = \frac{1}{\pi}\int_0^\infty \frac{d \ln r}{d\omega} \ln\left|\frac{\omega + \omega_c}{\omega - \omega_c}\right| d\omega$$

$$= 2\frac{\omega_c}{\pi}\int_0^\infty \frac{\ln r(\omega) - \ln r(\omega_c)}{\omega^2 - \omega_c^2} d\omega. \tag{34}$$

Here, θ_c is the value of the phase difference at frequency ω_c. The integral is evaluated numerically. The limits of integration are, in practice, the two extremities of the spectrum where the reflection approaches constant values. Compared to the oscillator-fit technique described in Section II, the KK relations impose much less restrictive conditions on ε. In practice, however, the damped-oscillator representation of ε actually fits the experimental reflectivity data to a reasonable degree of accuracy, although one may often have to use a large number of oscillators [20]. The basic problem with the KK method is the limits of integration in Eq. (34) that necessitates extrapolation of data, often with large inaccuracies in the optical constants at frequencies away from the region of high reflectivity. Some of these difficulties have been discussed in detail in the literature [21–24] and will not be further discussed here. Procedures that combine the oscillator fit with KK analysis have also been tried with some success [25].

Thus, in principle, the absorption coefficient as a function of frequency can be determined from only one type of measurement, e.g., reflection or transmission, over a large spectral region. This could be accomplished by the use of KK analysis. However, since an error at any wavelength may influence the results over the entire spectral region of consideration, this method (in conjunction with pole fit or not) is only useful in the strong absorption ($\alpha \geq 10^3$ cm^{-1}) regime also.

In fact, the KK integrals exist [18] for pairs of complementary optical constants, e.g., ε_1 and ε_2, n and k, and so on. In principle, if one has experimental values of one of these optical constants as a function of frequency, all others could be obtained.

IV DETERMINATION OF ABSORPTION COEFFICIENT IN THE INTERMEDIATE REGION

Usually the absorption coefficient in the intermediate region (10^0 cm^{-1} < $\alpha < 10^3$ cm^{-1}) as a function of frequency is determined by two independent measurements, e.g., reflection and transmission at each frequency.

Considering the multiple reflection and interference, transmittance of a monochromatic beam incident normally on a slab of thickness d and with parallel faces is given by [26]

$$T = \frac{I}{I_0} = \frac{(1-R)^2 + 4R\sin^2\phi}{\exp(\alpha d) + R^2\exp(-\alpha d) - 2R\cos 2(\psi+\phi)}, \tag{35}$$

where R is given by Eq. (29),

$$\tan\phi = 2k/(n^2 + k^2 - 1), \tag{36}$$

and

$$\psi = 2\pi nd. \tag{37}$$

Equation (35) is simplified in the case of low resolution [27], when interference fringes cannot be resolved, to

$$T = \frac{(1-R)^2 + 4R\sin^2\phi}{\exp(\alpha d) + R^2\exp(-\alpha d)}. \tag{38}$$

At infrared wavelengths, the second term of the numerator can be neglected compared to the first one; thus

$$T = \frac{(1-R)^2}{\exp(\alpha d) - R^2\exp(-\alpha d)}, \tag{39}$$

or solving for αd,

$$\alpha d = \log\left\{\frac{(1-R)^2}{2T} + \left[R^2 + \frac{(1-R)^2}{4T^2}\right]^{1/2}\right\}. \tag{40}$$

Tables are available [28, 29] for the determination of α by using Eq. (39) or (40) from measured values of R and T. Provided that samples of different thicknesses varying from a few tens of micrometers to a few millimeters are available, measured α for ionic and partially ionic solids could vary from a few reciprocal centimeters to a few hundred reciprocal centimeters.

V ABSORPTION COEFFICIENT IN THE TRANSPARENT REGIME

The transparent regime could be broadly defined as the spectral region for which $\alpha < 10^0\ \text{cm}^{-1}$, although Barker *et al.* [30] have defined the onset of transparency as the frequency (ω_{onset}) at which α becomes $10^{-2}\ \text{cm}^{-1}$ and thus for $\omega > \omega_{\text{onset}}$, $\alpha < 10^{-2}\ \text{cm}^{-1}$. They have also shown that this transparent regime starts around $\omega_{\text{onset}} \simeq 3\,\omega_{\text{LO}}$ as shown in Table II. The

TABLE II

Frequency of Onset of Transparency Compared with the Three-Phonon Cutoff Frequency[a]

Material	$\omega_{max} = \omega_{LO}$ (cm^{-1})	$3\omega_{LO}$	ω_{onset}[b]
LiF	665	1995	2000
NaF	422	1226	1350
NaCl	265	795	700
KCl	205	615	580
KBr	163	489	430
CsBr	114	342	330
CsI	90	270	240
MgO	728	2184	1750
AgCl	189	567	500
CuCl	216	648	620
CuBr	169	507	500
ZnS	347	1041	1000
AlSb	340	1020	1110
InSb	197	591	550
GaP	403	1209	1200
GaAs	286	858	810
CaF_2	479	1437	1470
SrF_2	389	1167	1250
BaF_2	338	1014	1070
Si	508	1524	1520
Ge	300	900	880
C (diamond)	1332	3996	3950

[a] From Barker *et al.* [30].
[b] For $\alpha = 0.01\ cm^{-1}$ (see text).

measurement of absorption coefficient in this regime by straightforward transmission measurement utilizing thick slabs is not always possible. The chief uncertainties in the measured values come from surface effects and scattering, because these contributions are often comparable to the absorption coefficient itself. The surface effects could be minimized by difference measurements involving slabs of two different thicknesses as is usually done with attenuation measurements in optical fibers.

A number of different techniques have evolved in the past several years for the measurement of very low absorption coefficients ($10^{-2}\ cm^{-1} > \alpha > 10^{-5}\ cm^{-1}$). They include laser calorimetry, band-edge-shift calorimetry, surface-acoustic-wave calorimetry, differential spectrophotometry, and so on. The various experimental methods for the measurement of low absorption coefficients have been thoroughly reviewed by Skolnik [32] and Hordvik [33]; we refer the reader to these articles for further information. The various methods and their range of suitability are summarized in Table III (reproduced from Skolnik [32]).

TABLE III

"Readily" Measurable Optical-Loss Levels[a]

Method	Absorption loss (cm^{-1})	Reference(s)
Thermal methods		
Thermocouple laser calorimetry	1×10^{-3}–1×10^{-4}	Many [1–7]
Laser Doppler calorimetry	5×10^{-5}	Skolnik [24]
Band-edge-shift calorimetry	1×10^{-4}–5×10^{-5}	Nurmikko [27]
Photoacoustic calorimetry	1×10^{-6}	Kerr [33] Rosencwaig [31, 32]
Thermoacoustic calorimetry	5×10^{-6}	Hordvik [34]
Surface acoustic wave calorimetry	1×10^{-5}–5×10^{-6}	Parks [35]
Thermal lens (IR-solids)	1×10^{-2}–5×10^{-3}	Hordvik [41]
Direct loss methods		
Laser differential loss	1×10^{-4}–1×10^{-5}	Rehn [46]
Optical bridge Q-meter	1×10^{-5}	Birnbaum [47]
Differential spectrophotometry	5×10^{-3}–2×10^{-3}	Deutsch [48, 49]
Emittance spectroscopy	1×10^{-5}	Stierwalt [51, 52] Skolnik [54]

[a] From Skolnik [32]. For references in the last column, see the original reference [32].

VI MULTIPHONON ABSORPTION

A General Remarks

In the harmonic approximation, electric-dipole selection rules permitting only the long-wavelength ($k = 0$) optical phonons display resonances in the infrared spectrum. Combinations and overtones do not arise. Furthermore, the phonon resonances should appear as sharp lines. The appearance of multiphonon spectra, the line broadening, and the phenomenon of thermal expansion of solids, however, indicate the presence of cubic and higher-order terms in the vibrational potential energy of a solid. Inclusion of anharmonicity in the general theory of the vibrational spectra of crystals not only allows combinations and overtones but, in fact, puts very little restriction on the selection rules applicable to such transitions.

For polar crystals, the mechanism of the interaction of electromagnetic radiation with phonons is due to the anharmonic (mechanical) part of the potential energy associated with the lattice vibrations. The interaction takes place through the dipole moment associated with the lattice mode. In homopolar crystals the long-wavelength optical phonons are infrared inactive because the associated electric-dipole moment is zero, and thus the above mechanism does not apply. For such crystals Lax and Burstein [34] have shown that two or more phonons can interact directly with the radiation

through terms in the electric moment of second or higher order in the atomic displacements. For a semiconductor such as GaAs, which is partially covalent and partially ionic, both mechanisms contribute. Multiphonon spectra of either origin will be allowed, space-group selection rules permitting, if the energy and wave vectors are conserved:

$$\hbar\omega = \sum_i (\pm \hbar\omega_i) \tag{41}$$

and

$$\mathbf{k} + n\mathbf{K} = \sum_i (\pm \mathbf{q}_i), \tag{42}$$

where $\hbar\omega$ and $\mathbf{k}$ are the energy and wave vector of the absorbed photon; $\hbar\omega_i$ and $\mathbf{q}_i$ are the energy and the wave vector of the ith phonon; $\mathbf{K}$ is a reciprocal lattice vector; and n is an integer. The positive and negative signs indicate emission and absorption of phonons, respectively. Since the wave vector of the photon in the infrared region is small compared to the phonon wave vectors, the second condition becomes

$$n\mathbf{K} = \sum_i (\pm \mathbf{q}_i). \tag{43}$$

Strictly speaking, the multiphonon process should give rise to a continuous spectrum. Features in multiphonon spectra, however, occur because of singularities in the phonon frequency distribution. Any structure in the spectrum thus reflects structure in the frequency dependence of the combined phonon density of states. The regions of high phonon concentration in a phonon dispersion occur at critical points (CP). The singularities corresponding to the CPs occur where the dispersion curves for the individual branches are flat. A CP in a phonon branch occurs where $\nabla_q \omega(q)$ (gradient of ω with respect to q) either is zero or changes sign discontinuously. In the case of the cubic diamond and zincblende structures, the relevant CPs, e.g., are

- Γ, the center of the Brillouin zone (0, 0, 0),
- L, the center of a face with coordinates $(\frac{1}{2}, \frac{1}{2}, \frac{1}{2})$,
- X, the center of a face with coordinates (1, 0, 0),
- W, the density peak at coordinates $(1, \frac{1}{2}, 0)$, and
- K, the edge of the zone with coordinates $(\frac{3}{4}, \frac{3}{4}, 0)$

Each of the CP phonons is related to one of the irreducible representations of the cystal space group. With the use of group theory, one may, in principle, enumerate the selection rules governing the infrared spectra of a crystal allowing for the possibility of creation and/or annihilation of one or more of these CP phonons. One derives the reduction coefficients of the so-called Clebsch–Gordon coefficients for the Kronecker products of space-group irreducible representations. This corresponds to the problem of finding whether a combination of two, three, or many phonons from different or same critical points can interact with a photon through an electric-dipole, an induced electric-dipole, an electric-quadrupole, or a magnetic-dipole change. Birman [35] has worked out the space-group selection rules for the diamond

and zincblende structures. Mitra [36] has applied these selection rules to the understanding of the infrared spectrum of GaAs . Johnson and Loudon [37] have applied them to the interpretation of the spectra of diamond, Si, and Ge. Burstein *et al.* [38] have obtained the selection rules for the NaCl structure, and Ganesan and Burstein [39] have done so for the fluorite structure.

The temperature dependence of the infrared absorption at any frequency depends on the number of phonons available to participate in a proposed multiphonon process at a given temperature. The occupation number of a phonon of frequency ω_i is given by

$$n_i = [\exp(\hbar\omega_i/kT) - 1]^{-1}. \tag{44}$$

The probability of emission or absorption of one of these phonons is proportional to the square of the matrix elements of the phonon creation a^+ or annihilation a^- operator, respectively. These matrix elements are given by

$$\langle\psi(n_i)|a^+|\psi(n_i + 1)\rangle = (n_i + 1)^{1/2} \tag{45}$$

for emission and

$$\langle\psi(n_i)|a^-|\psi(n_i - 1)\rangle = n_i^{1/2}. \tag{46}$$

for absorption. The probability of absorption of a phonon is thus proportional to n_i, and that of emission of a phonon is proportional to $(1 + n_i)$. Let us suppose that a feature in the infrared absorption spectrum is assigned to a two-phonon process such that the absorption of a photon is accompanied by the emission of two phonons ($i = 1, 2$) in accordance with the conservation principles Eqs. (41) and (42). The probability of the process is proportional to $(1 + n_1)(1 + n_2)$. The net absorption is obtained by correcting for spontaneous emission of the photon by the reverse process in which two phonons are absorbed. Then the temperature dependence of the net absorption is proportional to $(1 + n_1)(1 + n_2) - n_1n_2 = 1 + n_1 + n_2$. The temperature-dependence factors for some two- and three-phonon processes are given in Table IV. The two conservation laws and the temperature dependence of the absorption intensity subject the phenomenological analysis of infrared spectral data to rather stringent self-consistency requirements.

TABLE IV

Temperature-Dependence Factors for Two- and Three-Phonon Absorption Processes

Combination	Description	Infrared absorption intensity
2ν	First overtone	$1 + 2n$
$\nu_1 + \nu_2$	Sum	$1 + n_1 + n_2$
$\nu_1 - \nu_2$	Difference	$n_2 - n_1$
3ν	Second overtone	$1 + 3n + 3n^2$
$\nu_1 + \nu_2 + \nu_3$	Sum	$1 + n_1n_2 + n_2n_3 + n_3n_1 + n_1 + n_2 + n_3$
$\nu_1 + \nu_2 - \nu_3$	Sum and difference	$(1 + n_1)(1 + n_2)n_3 - n_1n_2(1 + n_3)$

It is implicit from the foregoing discussion that the absorption coefficient for a multiphonon event will depend on three factors, viz., the strength of the multiphonon interaction (the dipole-moment matrix element contributing to the oscillator strength), the joint density of states at the frequency of consideration, and the phonon-occupation-number function at the temperature of interest. There are many different ways of expressing these dependences; we shall outline here a well-understood treatment due to Szigeti [40]. When the anharmonic contributions are included, the vibrational potential energy of a solid has the form

$$V = \sum_{j}^{q} f_j^{\mathbf{q}}(Q_j^{\mathbf{q}})^2 + \sum_{i,j,k}^{\mathbf{q}_1\mathbf{q}_2\mathbf{q}_3} b_{ijk}^{\mathbf{q}_1,\mathbf{q}_2,\mathbf{q}_3} Q_i^{\mathbf{q}_1} Q_j^{\mathbf{q}_2} Q_k^{\mathbf{q}_3} + \sum_{ijkl}^{\mathbf{q}_1\mathbf{q}_2\mathbf{q}_3\mathbf{q}_4} c_{ijkl}^{\mathbf{q}_1\mathbf{q}_2\mathbf{q}_3\mathbf{q}_4} Q_1^{\mathbf{q}_1} Q_j^{\mathbf{q}_2} Q_k^{\mathbf{q}_3} Q_l^{\mathbf{q}_4} + \cdots . \tag{47}$$

Here, f, b, c, and so on, are harmonic, cubic, quartic, and so on, force constants in suitable units [see Eq. (1), for example], and Q_i is a normal coordinate. The superscripts refer to wave vectors, and the subscripts refer to branches. Similarly, the dipole moment M [see Eq. (2)] can be written as

$$\mathbf{M} = \alpha_0 \mathbf{Q}_0 + \sum_{ij}^{\mathbf{q}_1\mathbf{q}_2} \beta_{ij}^{\mathbf{q}_1\mathbf{q}_2} Q_i^{\mathbf{q}_1} Q_j^{\mathbf{q}_2} + \cdots . \tag{48}$$

The subscript 0 refers to the resonance absorption or ω_0 denotes the frequency of resonance ω_{TO} and $\alpha_0 Q_0$ the associated first-order dipole moment [b_2 of Eq. (2)].

For a region of spectrum sufficiently away from the resonance frequency, Szigeti [40] has derived the combined contributions from anharmonicity and higher-order electric moment to the imaginary part of the dielectric constant $\varepsilon_2(\omega)$ as

$$\varepsilon_2(\omega) = \frac{h\pi^2}{V\omega\,\delta\omega} \sum_{ij} \frac{\omega}{\omega_i \omega_j} D_{ij}^2 \begin{Bmatrix} 1 + n_i + n_j \\ |n_i - n_j| \end{Bmatrix} + \cdots , \tag{49}$$

where

$$D_{ij}^2 = \left[\beta_{ij}^{\mathbf{q}_1\mathbf{q}_2} - \frac{\alpha_0 b_{0ij}^{\mathbf{q}_0\mathbf{q}_i\mathbf{q}_j}}{\omega_0^2 - \omega^2} \right]^2 .$$

The summation goes over pairs of modes for which $\omega_i \pm \omega_j$ is between ω and $\omega + \delta\omega$ so that $\omega = \omega_{ij}$ in D_{ij}. The population factors $(1 + n_i + n_j)$ and $(n_i - n_j)$ refer to sum and difference processes as given in Table IV. An expression for $\varepsilon_1(\omega)$, the real part of the dielectric function, could also be written in an analogous manner. However, at $\omega \gg \omega_0$, ε_1 is not much different from ε_∞. The absorption coefficient $\alpha(\omega)$ is easily obtained through manipulation of Eqs. (24) and (28). The terms described in Eq. (49) are almost impossible to obtain from a realistic solid, except under certain very special approximations, as we shall see in Section B.

B Absorption in the Region $\omega > \omega_{LO}$

1 *Two- and Three-Phonon Processes*

In ionic crystals like NaCl the absorption in the frequency region $\omega_{LO} < \omega < 3\omega_{LO}$ is still dominated by the tail of the strong one-phonon absorption often accompanied by some broad features due to two-phonon processes [41] as illustrated in Fig. 10. Such a one-phonon absorption process is absent in a homopolar crystal such as silicon and germanium. In the latter case, for pure crystals (without free carriers), the entire absorption process originates from multiphonon interactions. Figure 11 shows the experimental data [42] for Si at three temperatures along with a CP analysis of the multiphonon singularities due to Bilz and Genzel [43].

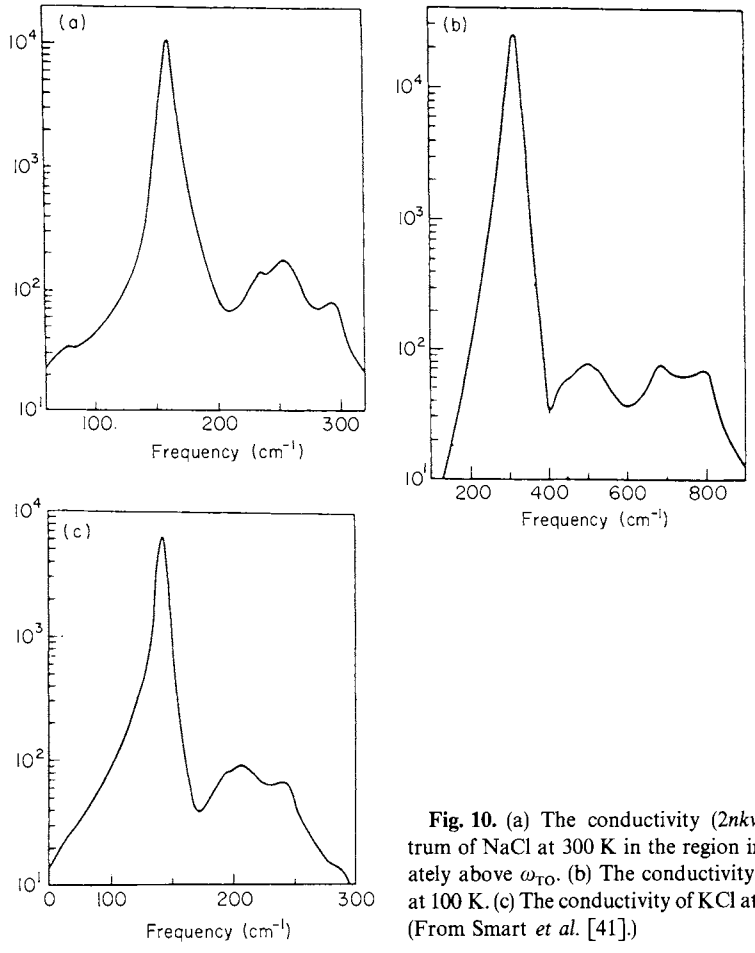

Fig. 10. (a) The conductivity ($2nkv$) spectrum of NaCl at 300 K in the region immediately above ω_{TO}. (b) The conductivity of LiF at 100 K. (c) The conductivity of KCl at 300 K. (From Smart *et al.* [41].)

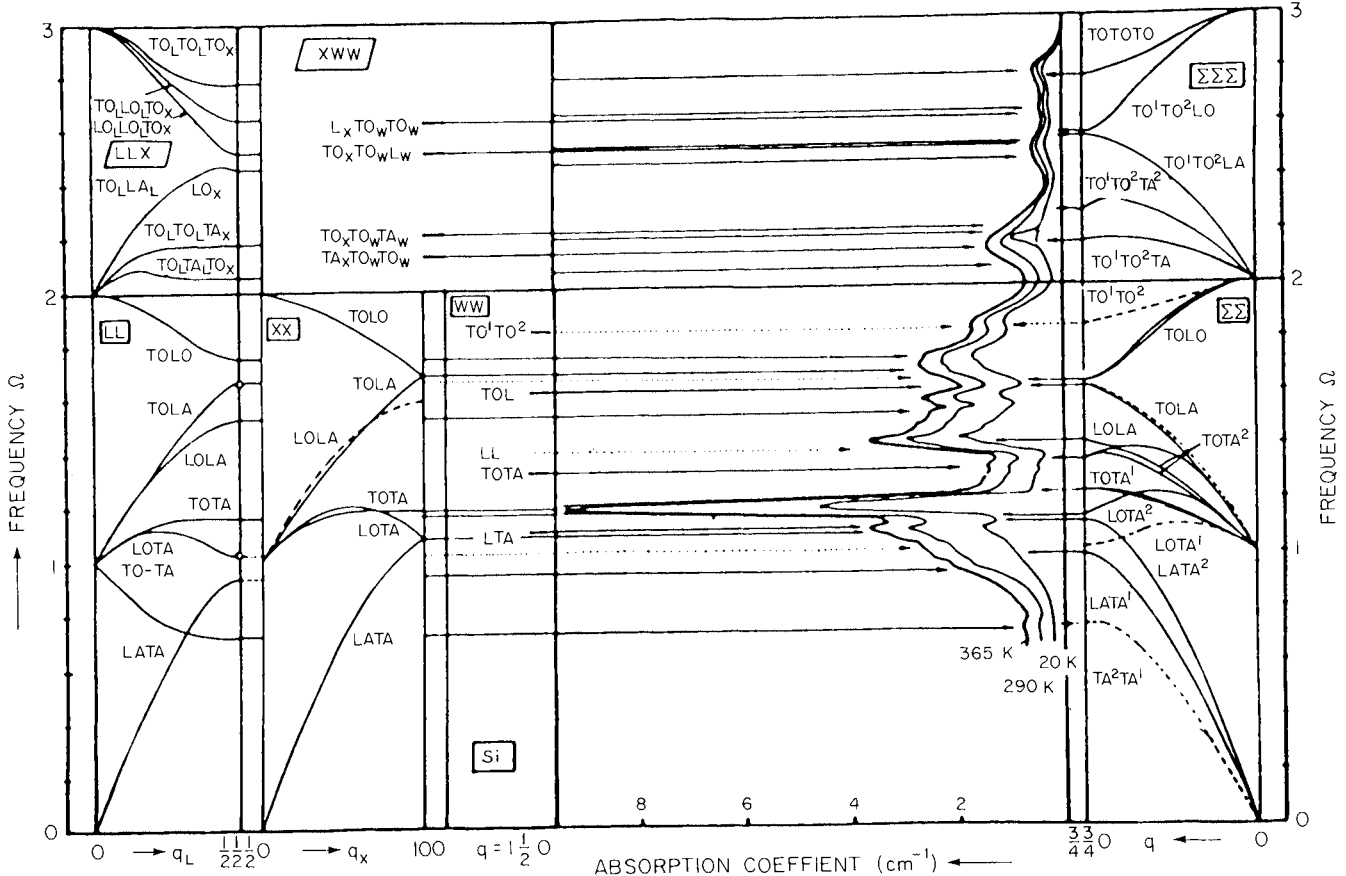

Fig. 11. Critical point analysis of infrared spectra of Si (experimental data from Johnson [42] and analysis from Bilz and Genzel [43]).

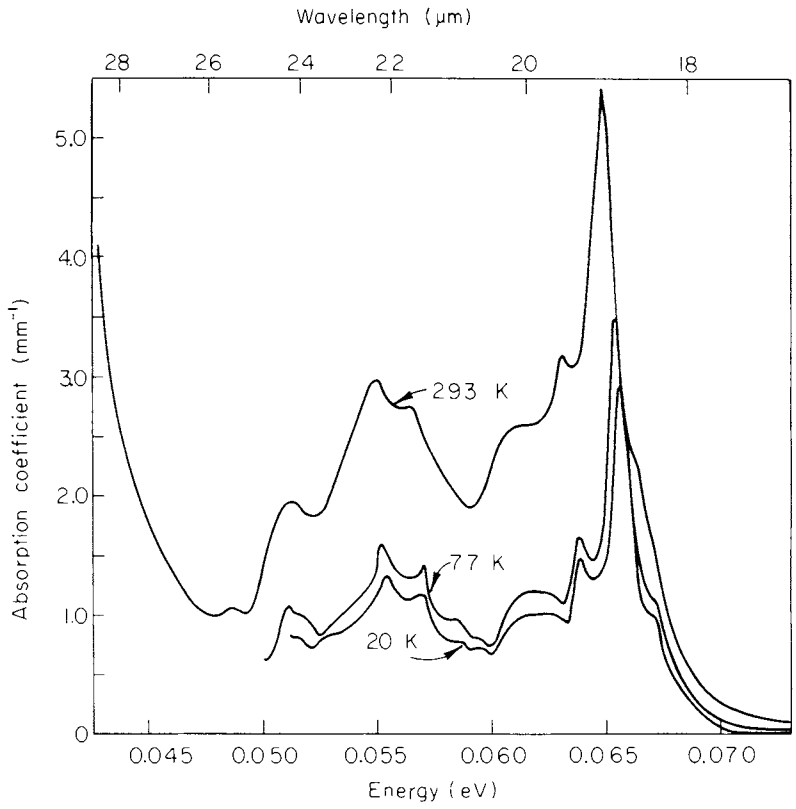

Fig. 12. Infrared absorption spectrum of high-resistivity *n*-type GaAs in the two-phonon region. (From Cochran *et al.* [44].)

Partially ionic crystals such as the II–VI and III–V semiconductors combine both of the preceding features, viz., tail from the one-phonon absorption process superimposed with rich features from two- and three-phonon processes. Examples of this are GaAs (Cochran *et al.* [44]), AlSb (Turner and Reese [4]), and ZnSe (Mitra [45]). We shall discuss the case of GaAs and AlSb (shown in Figs. 12 and 13) in somewhat greater detail. The reststrahlen spectrum of AlSb was described in Section II. The analysis of this spectrum yields $\omega_{TO} = 319\ \text{cm}^{-1}$ and $\omega_{LO} = 340\ \text{cm}^{-1}$. The spectrum in the region $\omega > 340\ \text{cm}^{-1}$ was assigned by Turner and Reese [4] in terms of combinations of four Brillouin zone-boundary characteristic phonons. The positions of these zone-boundary characteristic phonons are estimated from the seven two-phonon band assignments as indicated in Fig. 13. The triplet 2LO, LO + TO, and 2TO is better resolved at 77 K. The peaks shift toward higher frequencies by $5\ \text{cm}^{-1}$ at 77 K. The assignment is confirmed by a comparison of the net power absorbed in a two-phonon summation at two temperatures. A temperature factor f is defined as the ratio of the magnitudes of absorption

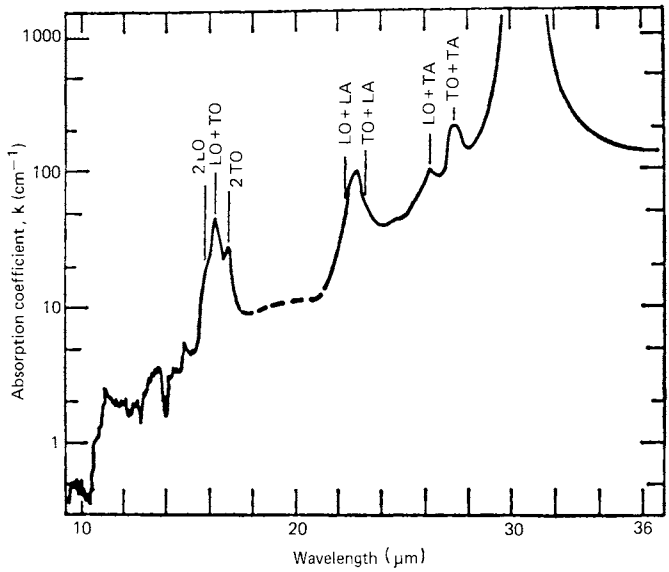

Fig. 13. High-frequency tail of the infrared absorption in AlSb. (From Turner and Reese [4].)

coefficient of a feature at two temperatures. Thus

$$f_{\text{calc}} = \frac{(1 + n_1 + n_2)_{300\,\text{K}}}{(1 + n_1 + n_2)_{77\,\text{K}}} \tag{50}$$

in the present case for a two-phonon sum process. The observed temperature factor f_{obs} was obtained after correction for the background due to free-carrier absorption, impurity absorption, and the tail of the fundamental absorptions. The assignment for the two-phonon features along with their temperature dependence is given in Table V. Thirty-eight additional features at the $\omega > 2\omega_{\text{LO}}$ cutoff ($680\,\text{cm}^{-1}$) were assigned to three- and four-phonon processes.

A more thorough analysis [36] is possible for GaAs (Fig. 12) for which neutron-scattering data on critical-point phonons are available. The assignment of the CP phonons at X and L is straightforward from the dispersion relations given by Waugh and Dolling [46]. The CP at W presents some problems. The W is located at $(1, \frac{1}{2}, 0)$ and is not in a (110) plane, for which the experimental values are available. For reasons given by Phillips [47] it is a good approximation to assume $\omega(\text{W}) = \omega(\Sigma)$, where Σ denotes a CP along the (110) direction near $k = (0.75, 0.75, 0)$. There is, however, a lack of clear separation at W of branches into transverse and longitudinal. The CP phonon assignment of GaAs is given in Table VI [36]. There is a total of 16 different phonon frequencies that may take part in infrared-active combinations.

TABLE V

Two-Phonon Combination Bands in AlSb [a,b]

λ (μm)	ν_{obs} (cm^{-1})	f_{obs}	Assignment	ν_{calc} (cm^{-1})	f_{calc}
27.50	363	2.83	TO + TA	362	2.84
26.30	380	2.86	LO + TA	381	2.82
23.29	429	2.27	TO + LA	429	2.23
22.33	448	1.91	LO + LA	448	2.20
16.81	595	1.70	2TO	594	1.62
16.31	613	1.57	LO + TO	613	1.59
15.80	633	1.56	2LO	632	1.55

[a] From Turner and Reese [4].

[b] Data calculated from the four characteristic zone-boundary phonon frequencies: LO = 316 cm^{-1}, TO = 297 cm^{-1}, LA = 132 cm^{-1}, and TA = 65 cm^{-1}.

TABLE VI

Critical Points, Coordinates, and Phonon Modes for GaAs (Space Group T_d^2) [a]

Critical point	Coordinate	Phonon mode	Frequency[b] (cm^{-1})
Γ	(0, 0, 0)(1/a)	TO(Γ)	267 (273)[c]
		LO(Γ)	285 (297)[c]
X	(2π, 0, 0)(1/a)	TO(X)	252
		LO(X)	241
		LA(X)	227
		TA(X)	79
L	(π, π, π)(1/a)	TO(L)	261
		LO(L)	238
		LA(L)	209
		TA(L)	62
W(Σ)[d]	(2π, π, 0)(1/a)	O_1(W)	263
		O_2(W)	215
		O_3(W)	250
		A_1(W)	116
		A_2(W)	188
		A_3(W)	79

[a] Based on Mitra [36].

[b] Data from Waugh and Dolling [46] if not stated otherwise.

[c] The values obtained by Hass and Henvis [48] from infrared reflection measurements. A value of 290 cm^{-1} has been obtained by Iwasa *et al.* [49] for the LO(Γ) mode from infrared transmission measurements on thin films.

[d] See text for explanation.

TABLE VII

Infrared-Active Two-Phonon Processes in GaAs[a]

Assignment	Calculated (cm^{-1})	Observed[b]
$2TO(\Gamma)$[c]	534 (546)[c]	
$2LO(\Gamma)$	570 (594)	578; 593
$TO(\Gamma) + LO(\Gamma)$	552 (570)	578
2TO(X)	504	509
2TA(X)	158	
2TO(L)	522	533
2TA(L)	124	
2LO(L)	476	468
2LA(L)	418	411
TO(X) + LO(X)	493	494
TO(X) + LA(X)	479	
TA(X) + LO(X)	320	321
TA(X) + LA(X)	306	307
TO(X) + TA(X)	331	333
LO(X) + LA(X)	468	468
TO(L) + LO(L)	499	494
TO(L) + LA(L)	470	468
TA(L) + LO(L)	300	307
TA(L) + LA(L)	271	
TO(L) + TA(L)	323	321
LO(L) + LA(L)	447	442
$O_1(W) + O_2(W)$	478	
$O_1 + O_3$[d]	513	509
$O_1 + A_1$	379	387
$O_1 + A_2$	451	456
$O_1 + A_3$	342	
$O_2 + O_3$	465	468
$O_2 + A_1$	331	333
$O_2 + A_2$	403	411
$O_2 + A_3$	294	
$O_3 + A_1$	366	(360)
$O_3 + A_2$	438	442
$O_3 + A_3$	329	333
$A_1 + A_2$	304	307
$A_1 + A_3$	195	
$A_2 + A_3$	267	

[a] Based on Mitra [36].

[b] Data from Cocharan *et al.* [44]. The values in the parentheses are not listed by Cochran *et al.* but are estimated from their diagrams.

[c] Based on Hass and Henvis [48] assignment.

[d] In the rest of this column, O_i and A_i (where $i = 1, 2, 3$) mean $O_i(W)$ and $A_i(W)$.

All infrared-active two-phonon combinations are listed in Table VII. It is evident that the total number of possible combinations far exceeds the absorption maxima recorded by Cochran *et al.* [44]. However, all observed features below 600 cm^{-1} can be assigned to one or the other of the multitude of binary combinations. The infrared-active three-phonon processes are even more numerous. In Table VIII, some possible assignments of the high-frequency bands are shown.

Although the observed infrared spectra of zincblende and diamond types of crystals can be completely understood in terms of the CP phonons known from the neutron scattering, the reverse, i.e., an unambiguous assignment of the CP phonons from the observed infrared absorption spectrum may not always be possible. In the absence of detailed phonon dispersion curves, however, it is still possible to obtain approximate Brillouin zone-boundary values of longitudinal and transverse optical and acoustic phonons in the so-called spherical Brillouin-zone-approximation, often consistent with the requirements of the space-group selection rules, as was demonstrated in the case of AlSb.

TABLE VIII

Some Infrared-Active Three-Phonon Processes in GaAs[a]

Observed[b] (cm^{-1})	Assignment	Calculated (cm^{-1})
578	TA(X) + TO(Γ) + LA(X)	573 (579)[c]
	TA(X) + TO(X) + LO(X)	572
	TO(L) + LO(L) + TA(X)	578
593	TA(X) + LO(Γ) + LA(X)	591 (603)
	TA(X) + TO(Γ) + LO(X)	587 (593)
	2TO(L) + TA(X)	601
694	TO(L) + LA(L) + LA(X)	697
	LO(L) + LA(L) + TO(X)	699
714	TO(L) + LA(L) + LO(X)	711
	TO(X) + LA(X) + LO(X)	720
(752)	TO(L) + LO(L) + TO(X)	751
	LO(X) + LA(X) + LO(X)	753 (765)
	TO(X) + TO(Γ) + LA(X)	746 (752)
	3TO(X)	756
770	2TO(L) + TO(X)	774
	TO(X) + LO(Γ) + LA(X)	764 (776)

[a] Based on Mitra [36].

[b] Data from Cocharan *et al.* [44]. The values in the parentheses are not listed by Cochran *et al.* but are estimated from their diagrams.

[c] Based on Hass and Henvis [48] assignment.

The Transparent Regime 2

As described in the preceding subsection, the two- and three-phonon processes usually produce a structure in the absorption, particularly in the high-frequency side of the one-phonon absorption band (reststrahlen region) of ionic solids [41], and the absorption coefficient is still so substantial that the crystal can hardly be considered transparent. An operational definition of the range of transparency may be the frequency region in which approximately four- to eight-phonon processes are operative. In this subsection we consider the problem of absorption due to higher-order multiphonon processes. In ionic solids such as alkali halides (Fig. 14 and Sparks [50]), the absorption spectrum in this region is already nearly structureless, although a considerable number of features persist in a covalent solid such as Si [Fig. 15], and some structure is evident in a partially ionic solid such as ZnSe [51].

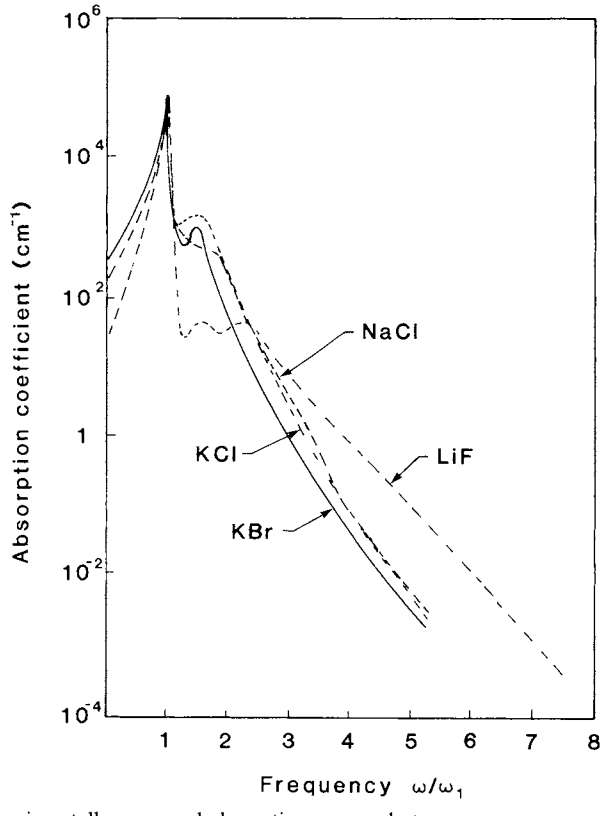

Fig. 14. Experimentally measured absorption versus photon energy at room temperature for several alkali halides. (From Sparks [50].)

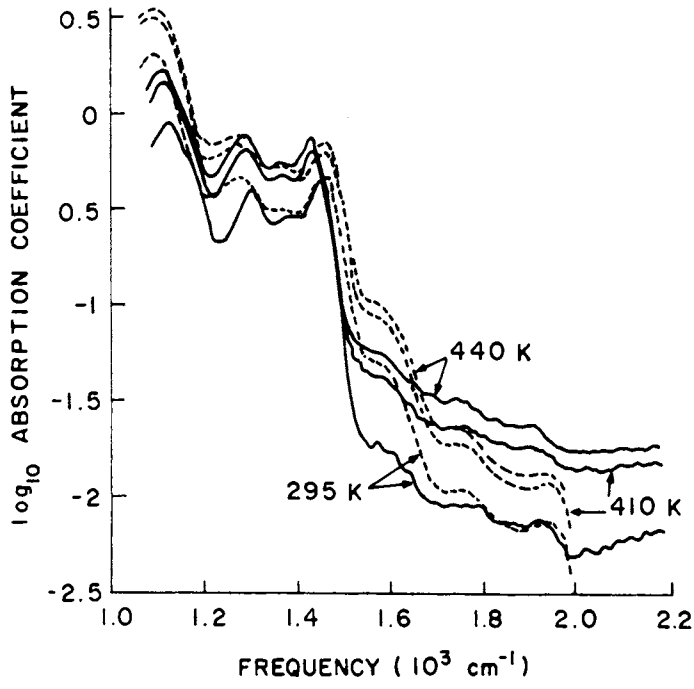

Fig. 15. Multiphonon absorption spectrum of Si in the highly transparent regime. (——, experiment; – – –, theory.) (From Bendow *et al.* [51].)

Recent compilation [52] of experimental data on the absorption coefficient of a large number of dielectric solids in the transparent regime has revealed a striking, almost universal, dependence on frequency. In a wide variety of solids, including alkali halides, alkaline earth fluorides, oxides, and semiconductors, the absorption coefficient is observed [53] to vary exponentially with frequency as

$$\alpha = A \exp(-\gamma\omega), \tag{51}$$

where A and γ are characteristic material parameters. The temperature dependence of α has also been measured for a number of solids [52], and α increases with increasing temperature.

A number of theoretical attempts [54–61] have been made to show that the absorption coefficient indeed varies as Eq. (51), starting from the basic equation for multiphonon interaction [see Eq. (49)]. The most successful of these treatments are the so-called oscillator models in which the solid is approximated by a series of diatomic molecules. The interatomic interaction is approximated by empirical potential functions such as Born–Mayer or Morse potentials, and the molecular dipole moment is assumed to be either linear or nonlinear. Here we shall briefly describe a theoretical model due

to Namjoshi and Mitra [55]. In terms of ε_1 and ε_2, α is given by

$$\alpha = \varepsilon_2 \omega / c\varepsilon_1^{1/2} \tag{52}$$

where

$$\begin{aligned}\varepsilon &= \varepsilon_1 + i\varepsilon_2 \\ &= \varepsilon_\infty + \frac{A_0}{[1-(\omega/\omega_0)^2] + i(\gamma_0\omega/\omega_0^2)} + \sum_j \frac{A_j}{[1-(\omega/\omega_j)^2] + i(\gamma_j\omega/\omega_j^2)}\end{aligned} \tag{53}$$

and γ_j's are the damping factors, ω_j's the oscillator frequencies, and A_j's the oscillator-strength parameters. The subscript zero stands for the fundamental process and the subscript j stands for a multiphonon process. In the limit when γ_j's go to zero [55], the imaginary part of the dielectric constant reduces to

$$\varepsilon_2 = \frac{A_0\gamma_0\omega}{[1-(\omega/\omega_0)^2]^2 + (\gamma_0\omega/\omega_0^2)^2} - \sum_j A_j(\omega)\rho_j(\omega)\frac{\omega\pi}{2}. \tag{54}$$

Here $\rho_j(\omega)$ corresponds to the j-phonon density of states. Contributions to α from the multiphonon processes of the order higher than two are shown [55] to be equal to

$$\alpha = \sum_{j\geq 2} A_j\rho_j(\omega)\pi\omega^2/2c\varepsilon_1^{1/2}. \tag{55}$$

For the calculation of higher-order-phonon densities of states, Namjoshi and Mitra [55] have shown that the wave vector conservation rule is not important and that as the order increases, the combined density-of-states function resembles more and more a normal distribution function. Therefore, higher-order density-of-states functions do not show any structure. From three phonons onward, the density-of-states function is calculated from the relation

$$\begin{aligned}\rho_n(\omega) = \int_{\omega_1=0}^{\omega}\int_{\omega_2=0}^{\omega-\omega_1}\cdots\int_{\omega_{n-1}=0}^{\omega-\omega_1-\omega_2\cdots\omega_{n-2}} &\rho(\omega_1)\rho(\omega_2)\cdots\rho(\omega_{n-1}) \\ &\cdot\rho(\omega-\omega_1-\omega_2\cdots\omega_{n-1})\,d\omega_1\,d\omega_2\cdots d\omega_{n-1},\end{aligned} \tag{56}$$

where $\rho(\omega)$ is the one-phonon density of state and $\rho_n(\omega)$ is the n-phonon density of state. Figure 16 shows the result of these iterations for the one- to six-phonon processes for KBr. It may be noted that higher-order-phonon densities of states gradually approach a normal distribution.

The oscillator strengths were assumed [55] to depend on the corresponding derivatives of the crystal potential energy. Namjoshi and Mitra [55] had originally used a Born–Mayer-type potential for this purpose, although other authors [30, 62] have used a Morse-type potential. The calculated and experimental absorption coefficient as a function of frequency is shown in Fig. 17 for three alkaline earth fluorides [63].

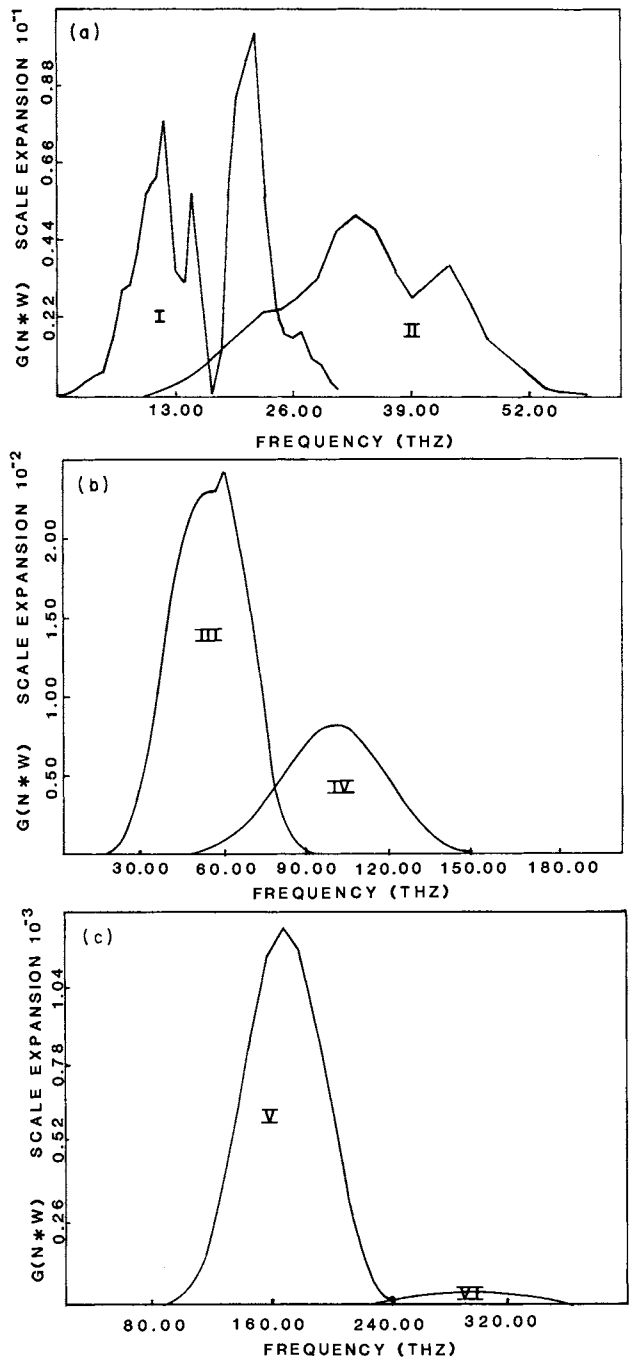

Fig. 16. One- to six-phonon densities of states for KBr: (a) one (I) and two (II), (b) three (III) and four (IV), and (c) five (V) and six (VI). Note that the vertical scale has been expanded to show the normal distribution behavior of higher-order processes. One-phonon density of states has been normalized to one. (From Barker *et al.* [30].)

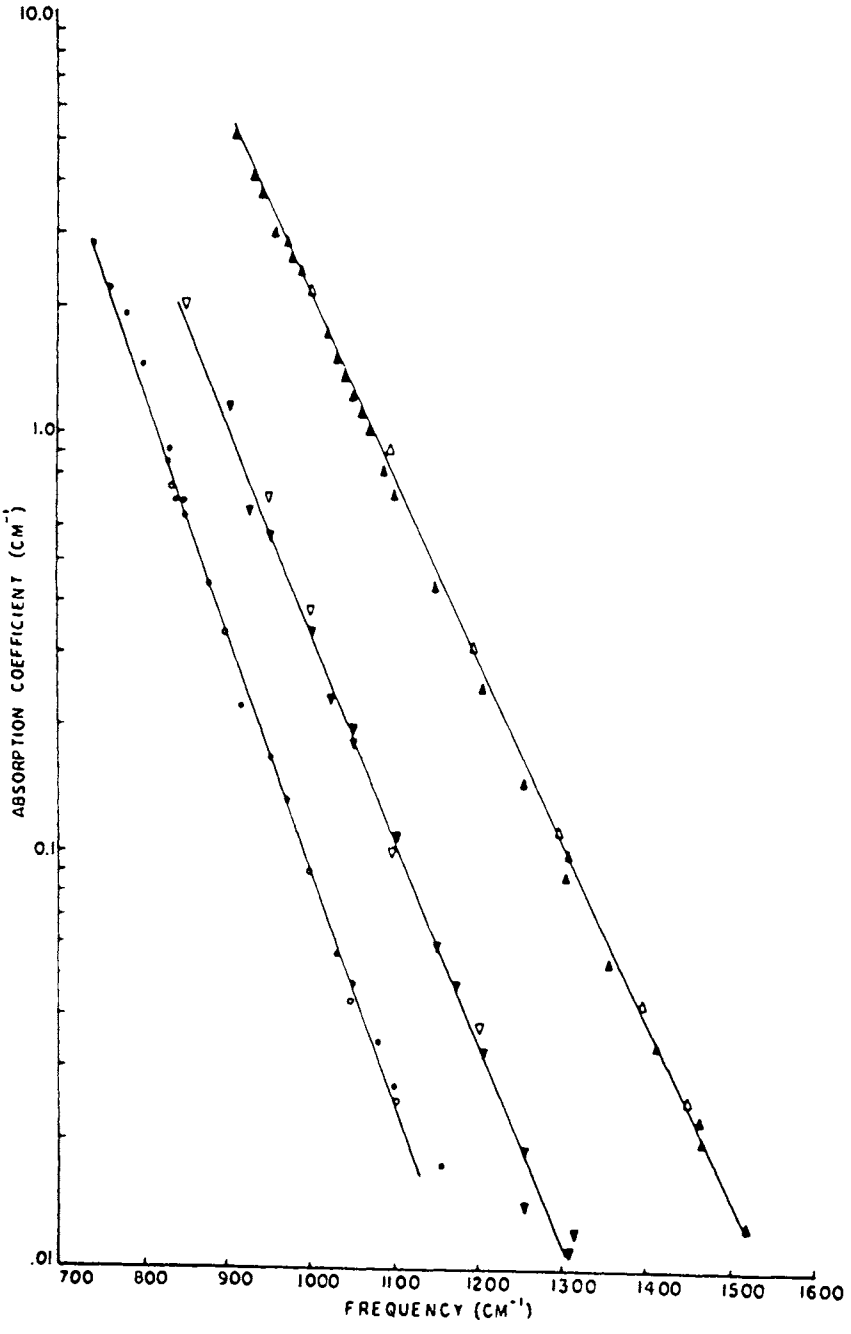

Fig 17. The room-temperature (293-K) absorption coefficient as a function of frequency for the three alkaline earth fluorides. Symbols represent experimental data and lines calculation using the Namjoshi–Mitra model. ▲, △: CaF_2; ▼, ▽: SrF_2; ●, ○: BeF_2. (From Lipson *et al.* [63].)

Namjoshi and Mitra [55] have also done first-principle calculation of the temperature dependence of α in the transparent regime by separately considering the temperature dependence of the oscillator strength A_j and the joint density of state function $\rho_j(\omega)$. They have shown that A_j varies as T^{j-1} for $j > 2$, indeed a strong temperature dependence. The temperature dependence of $\rho_j(\omega)$, in principle, is easy to estimate. In general crystal-mode frequencies decrease with temperature with a different temperature dependence for each mode. Hence, a one-phonon density-of-states function will shift to lower frequencies with increasing temperature, in addition to undergoing any deformation in its shape. Accordingly, the higher-order-phonon density-of-states functions also shift toward lower frequencies. Therefore, the order of the processes making significant contribution to α increases. Since the higher-order processes are weaker than the corresponding lower-order processes, these two effects [i.e., the temperature dependence of A_j and the temperature dependence of $\rho_j(\omega)$] have opposite contributions to the temperature dependence of α. One-phonon density-of-states function at different temperatures can be obtained by solving the lattice dynamics for different temperatures, provided that the temperature dependence of input parameters is known. Namjoshi and Mitra [55] made the simplifying approximation that all the normal-mode frequencies have the same temperature dependence and that it is equal to the corresponding temperature dependence of the bulk modulus of the solid. Under this assumption, one-phonon density of states will shift to lower frequencies as the temperature increases and thus can be obtained from its room-temperature values through multiplication of a suitable scaling factor. Neglecting any deformation in shape, higher phonon density-of-states functions can be obtained from their room-temperature values in an analogous manner. Table IX gives results for the absorption coefficient of NaCl at 10.6 μm for several temperatures that show surprisingly good agreement with the experimental results [64].

The preceding approach to the understanding to the temperature dependence is absolute, albeit approximate, and requires tedious calculations. The same considerations could be incorporated into the framework of a model due to Mitra [30, 63] that aims at calculating relative values and has proved

TABLE IX

Temperature Dependence of α for NaCl at 10.6 μm[a]

Temperature (K)	α_{calc} (10^{-3} cm^{-1})	α_{exp} (10^{-3} cm^{-1})
300	1.5	2.7
600	8.2	6.5
900	17.0	20
1000	18.2	22

[a] From Namjoshi and Mitra [55].

extremely useful. Including temperature dependence, the observed behavior of $\alpha(\omega)$ in the transparent regime as given in Eq. (51) can be rewritten [65] as

$$\alpha(\omega, T) = \alpha_0 \frac{\{n[\omega_0(T)] + 1\}^{\omega/\omega_0(T)}}{n(\omega) + 1} \exp[-\beta\omega/\omega_0(T)] \tag{57}$$

in terms of an effective phonon frequency ω_0. Here n is the phonon occupation number defined in Eq. (44) and α_0 and β depend weakly on ω_0 and/or T. It is clear that α is enhanced at high T according to the T^{j-1} dependence mentioned earlier for a j $(= \omega/\omega_0)$ phonon process, provided that ω_0 is independent of temperature. In general, $\omega_0(T)$ decreases with increasing T, which tends to suppress the T dependence of α as remarked before.

To apply Eq. (57) we must specify the effective oscillator frequency $\omega_0(T)$. Because the contributions of acoustic phonons are suppressed due to energy conservation, the average frequency ω defined as the first moment of the density of states should not be an appropriate choice. On the other hand, an average optical phonon frequency, such as Brout frequency [66] ω_B, should be more appropriate [30, 63].

It turns out that ω_B is close to the Debye frequency ω_D for most polyatomic crystals [67] and that both are related to the bulk modulus [68]. Regarding the T dependence of ω_0, one notes that for ionic solids the principal T dependence arises from thermal-expansion effects [69]. A small contribution arises from anharmonicity of the crystal potential and may be neglected [69] in many cases because of cancellation between the contributions of cubic and quartic terms.

C Absorption in the Region $\omega < \omega_{TO}$

So far our discussion of optical absorption processes in a solid has been confined to allowed one-phonon, and multiphonon sum processes in the high-frequency side of ω_{LO}. As is evident from Fig. 1, there is a considerable amount of optical absorption present in the low-frequency side of the reststrahlen region. This spectral region for a typical solid ranges from the far-infrared to submillimeter- and millimeter-wave regions. Experimental work on far-infrared absorption in solids dates back to the beginning of the century. For example, as early as 1912, Rubens and Hertz [70] measured the absorption coefficient of several ionic solids at 33 cm^{-1} as a function of temperature and found it to vary linearly. More recently, careful measurements of the frequency and temperature dependence of absorption coefficient have been conducted and the materials range from ionic solids [71], to partially ionic solids such as GaAs [72] and CdTe [73] to a host of refractory, amorphous, and polymeric materials. The primary source of absorption in this region is expected to be two-phonon difference processes, although

in general one also expects contribution from three-phonon difference processes and sum processes involving low-energy acoustical phonons, and one-phonon absorption processes in the case of structurally disordered solids and solids containing imperfections and impurities.

That the far-infrared spectrum in the region immediately below the reststrahlen region could consist of two-phonon difference and/or sum processes is illustrated by the example of CdTe. The real and imaginary parts of the dielectric response of CdTe were determined by Birch and Murray [73] as a function of frequency (40–240 cm^{-1}) at room temperature from measurements of the amplitude and phase reflection spectra by Fourier transform spectroscopy. This experimental result was used by Parker *et al.* [74] to obtain the frequency dependence of the imaginary part of the self-energy. Twenty or more features were revealed in the spectrum and were assigned to two- and three-phonon decay processes involving CP phonons. Table X shows a typical example of such an analysis.

At frequencies farther removed from the reststrahlen region ($\omega \ll \omega_{TO}$) one will expect a featureless absorption spectrum, and its temperature dependence will be useful in delineating the absorption processes. Advances in far-infrared techniques and the development of high-power microwave

TABLE X

Assignment of Peaks of the Imaginary Part of Self-Energy of CdTe versus Frequency in Terms of Two- and Three-Phonon Combinations[a]

Feature	Assignment	Expected frequency	Observed frequency
1	TO(L) − LA(L)	39	40
3	2TA(L)	62	62.5
4	2TA(X)	69	69
5	LA(L) − TA(L)	73	73
8	LA(X) − TA(X)	91	91
9	LO(X) − TA(X)	102	102
10	TO(L) − TA(L)	112	112
11	TO(X) − TA(X)	115	116
12	LA(L) + TA(L)	135	134
16	LA(X) + TA(X)	160	160
17	LO(X) + TA(X)	171	171
18	TO(L) + TA(L)	174	173
19	TO(X) + TA(X)	184	184
21	2LA(L)	208	208
2	TO(L) + TA(L) − LA(X)	48.5	49.5
13	TA(L) + LO(L) − TA(X)	140.5	140.5
15	TO(X) + TO(Γ) − LO(X)	153.5	152.5
22	TO(L) + LA(L) − TA(X)	212.5	212.5
23	2TA(X) + TO(X)	218.5	219

[a] From Billard [75].

sources and millimeter-wave lasers have helped produce a plethora of such data. For example, the temperature dependence (up to 450 K) of the far-infrared absorption in GaAs measured by Stolen [72] indicated that both two- and three-phonon difference processes contribute to the absorption. He further speculated that the two-phonon part of the absorption is dominated by processes that involve optical and longitudinal acoustic phonons rather than longitudinal and transverse acoustic phonons. The far-infrared absorption in Al_2O_3 and MgO has been measured by Billard *et al.* [75] in the region covering 1 to 300 cm^{-1} and the temperature range of 200 to 2000 K. Their result is shown in Fig. 18 for Al_2O_3. At high temperatures, the absorption coefficient essentially vary as T^{n-1}, where n is the order of the difference process. The data of Fig. 18 show a temperature dependence of the type

$$\alpha = AT + BT^2, \tag{58}$$

thus indicating the presence of both two- and three-phonon difference mechanisms.

Considerable experimental data also exist on amorphous solids, glasses, and polymers [76–79]. The absorption coefficient of partially crystalline solids in the far-infrared region has more complicated frequency and temperature dependence. The long-wavelength (4–8-mm) region is still dominated by temperature-dependent multiphonon difference processes, whereas the shorter-wavelength (< 1-mm) region is primarily dominated by disorder-induced, one-phonon absorption (see Section VII) involving the entire phonon density of states and is essentially temperature independent. In general, the magnitude of the absorption in amorphous solids in this region is an order of magnitude higher than that in their crystalline counterparts. Some amorphous materials exhibit an additional anomalous behavior. For example, silica-based glasses display [79] a distinct minimum in the temperature dependence of the very-far-infrared (1–10-cm^{-1}) absorption coefficient near 10 K. This anomalous behavior is interpreted [79] by a two-level tunneling model.

The frequency and temperature dependence of the absorption coefficient in the millimeter and submillimeter regions can, in general, be understood in terms of the multiphonon theory outlined in Subsection VI B. In particular, this absorption will consist of (a) multiphonon difference processes, (b) less significantly, multiphonon sum processes, (c) disorder-induced, one-phonon processes, and (d) a host of anomalous behavior at very long wavelengths and very low temperatures. For example, Hardy and Karo [80] explained the long-wavelength absorption in a number of alkali halides in terms of difference processes caused by third-order anharmonic terms. They found that a nearest-neighbor approximation to the anharmonic potential and deformation-dipole-model-generated eigenvectors and eigenfrequencies can account for most of the absorption. The discrepancies between theory and experiment were understood in terms of three-phonon processes. At

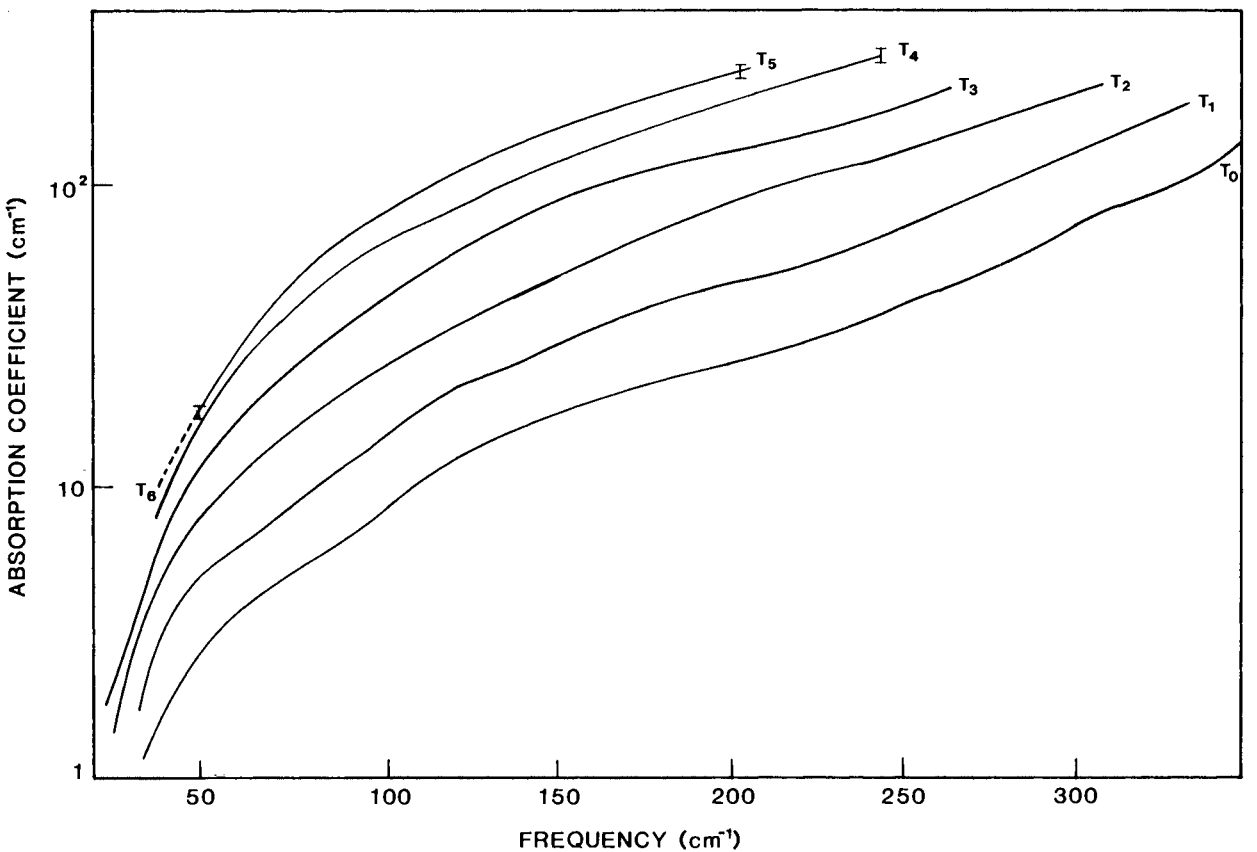

Fig. 18a. Far-infrared absorption spectrum of crystalline Al_2O_3 with $E \perp c$ at several temperatures. ($T_0 = 295$ K; $T_1 = 400$ K; $T_2 = 555$ K; $T_3 = 795$ K; $T_4 = 1050$ K; $T_5 = 1090$ K; and $T_6 = 1310$ K.) (From Billard [75].)

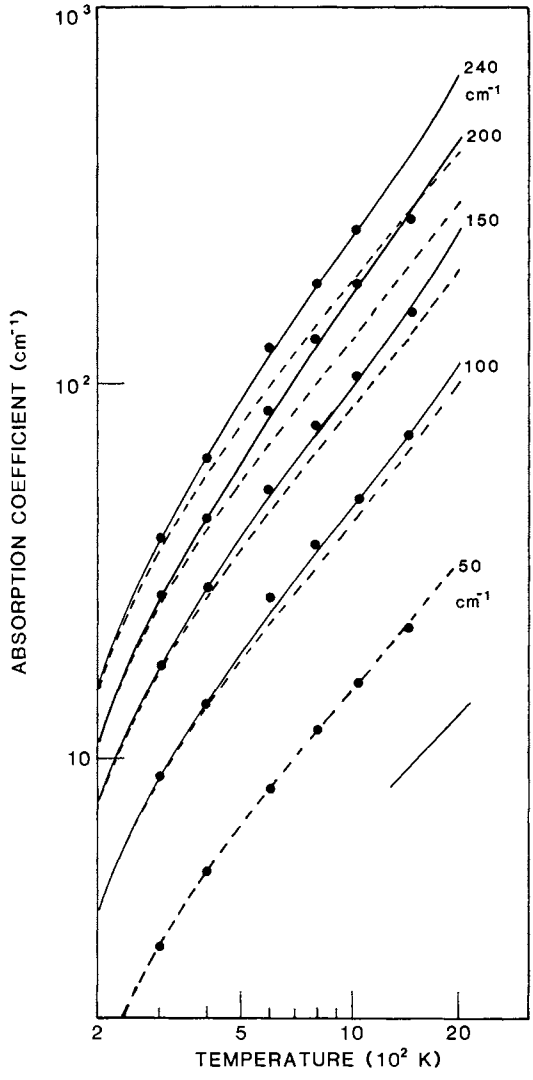

Fig. 18b. Temperature dependence of absorption coefficient of Al_2O_3 with $E \perp c$. (From Billard [75].)

longer wavelengths ($\sim$3 mm) further discrepancies occurred and were explained by invoking the effects of lifetime broadening of the final-state phonons. The latter mechanism is further emphasized by Sparks *et al.* [81]. They show that at long wavelengths lifetime-broadened, two-phonon processes dominate in contrast to energy-conserving, two- and three-phonon processes. Defining a critical frequency ω_c as originally proposed by Stolen and Dransfeld [71] as the difference between an optical phonon frequency and an acoustical phonon frequency at a critical point in the Brillouin zone

boundary. Sparks *et al.* [81] claim that their lifetime-broadened results agree with previous energy-conserving results and experimental results in the region $\omega > \omega_c + \gamma$, where γ is the combined-phonon inverse lifetime at room temperature. The purely energy-conserving results were shown to disagree with experimental results for both the magnitude and the temperature and frequency dependence of absorption coefficients in the region $\omega < \omega_c$.

VII INFRARED ABSORPTION BY DEFECTS AND DISORDERS

A General Remarks

Impurities and defects in an otherwise perfect crystal are widely known to give rise to localized, gap, and/or resonance modes of oscillation. Furthermore, because of their presence, the translational symmetry of the lattice breaks down and the $q \simeq 0$ selection rule is relaxed, making it potentially possible to obtain optical excitation of the entire phonon density of states. Of particular interest is the case of silicon or germanium. Because of their homopolar nature, the perfect crystal does not absorb infrared radiation by a one-phonon process. However, the presence of defects modifies the situation and leads to the excitation of one-phonon infrared absorption as was observed by Fan and Ramdas [82] in neutron-irradiated Si. Simple theoretical considerations indicate that the absorption in the allowed frequency range, in addition to being dependent on the defect concentration, will, in general, follow the density of states modified by a frequency-dependent, dipole-moment matrix element that depends on the detailed nature of the defect. The defects may be chemical in nature (e.g., an impurity atom) or mechanical in nature (e.g., vacancies at particular lattice sites), or they may be extended defects (e.g., dislocation). If the impurity content of a solid is increased to such an extent that interactions between impurity atoms become significant, the system is then termed a disordered solid rather than an impure crystal. Disordered lattices are of two main types: the disordered alloy (mixed crystals) and the glasslike substance in which the disorder is spatial rather than configurational.

Absorption of infrared radiation by a crystal containing defects as compared to a perfect crystal will have the following characteristics: (a) appearance of new absorption peaks, electric-dipole selection rule permitting, due to localized modes of vibration occurring in regions outside of the normal frequency spectrum of the perfect crystal; (b) appearance of features from the entire phonon frequency spectrum due to relaxation of selection rules; and (c) weakening and broadening of allowed one-phonon characteristics. Thus, one often encounters lower absorption near the one-phonon peaks and increased absorption in the wings.

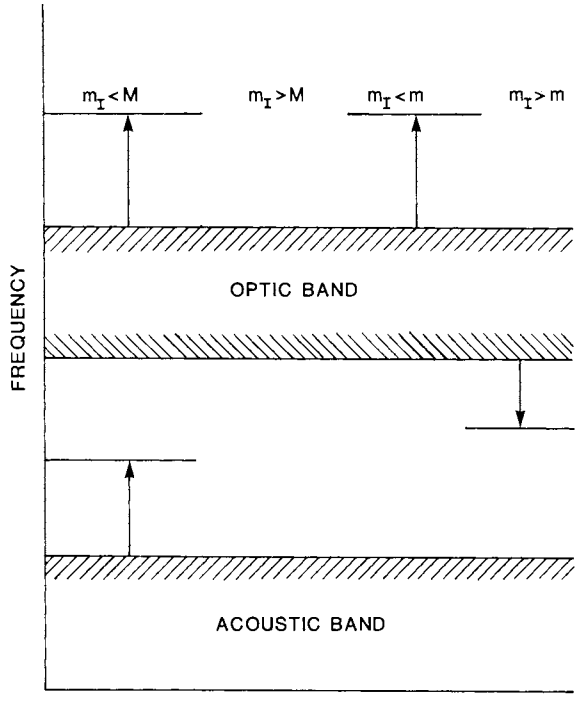

Fig. 19. Impurity modes in a linear diatomic chain ($m < M$). Four cases shown are a light impurity atom replaces the heavy atom of the host lattice ($m_I < M$); a heavy impurity atom replaces the heavy atom ($m_I > M$); a light impurity atom replaces the light atom ($m_I < m$); a heavy impurity atom replaces the light atom ($m_I > m$).

Crystals with Substitutional Impurities B

The introduction of impurity atoms modifies the potential-energy function in a lattice. Hence, the phonon spectrum of the crystal is modified as is any physical property of the crystal in which the lattice vibrations play a central role. In the case of a substitutional impurity whose mass is different from that of the atom it replaces, the modification of the phonon spectrum is usually manifested in the appearance of localized frequencies. These frequencies may appear within the allowable frequency range of the perfect crystal, in which case they are known as resonant modes, or outside the frequency spectrum, in which case they are known as gap or local modes, as shown in Fig. 19.

The first theoretical discovery of impurity-induced localized vibrational modes in crystals was made by Lifshitz [83] in 1943. This work was followed by the work of Montroll and Potts [84] and Mazur *et al.* [85]. However, the early work was restricted on one- and two-dimensional lattices and, therefore, was only of qualitative value. The direct experimental observation, in 1960, of the existence of localized modes due to U centers (H^- ions) in alkali

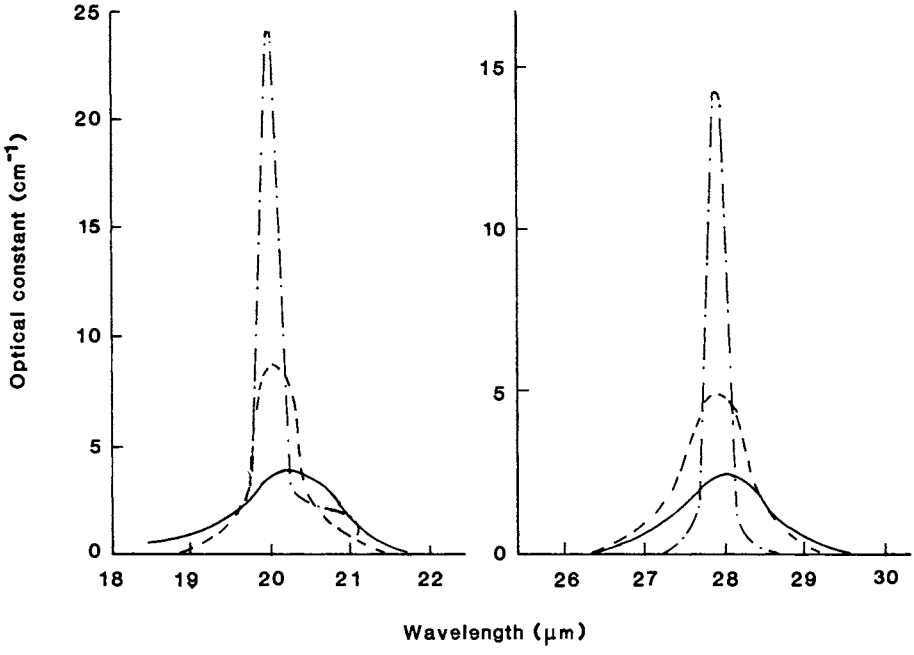

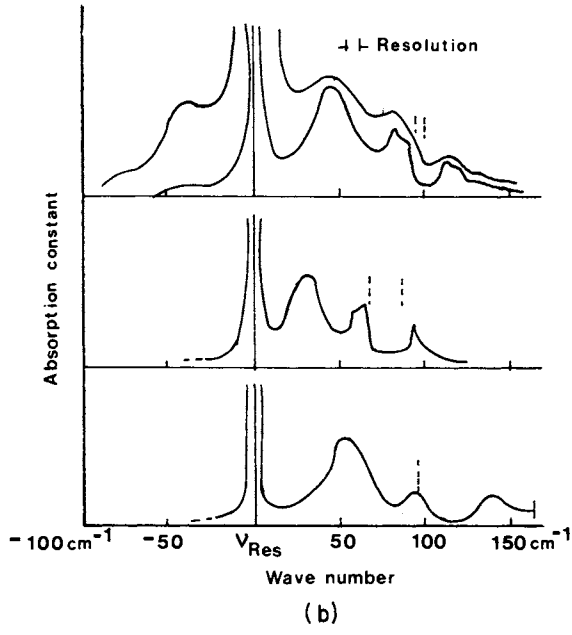

Fig. 20. (a) U-center local-mode absorption due to H^- and D^- impurities in KCl and its temperature dependence. For KCl·KH, $N = 8.7 \times 10^{17}$ cm^{-3} and for KCl·KD, $N = 5.1 \times 10^{17}$ cm^{-3}. The lines represent various temperatures:——, 300 K; – – –, 200 K; —·—, 100 K. (b) One-phonon side bands of U-center absorption in KBr, KI, and NaBr. For KBr:H^-, $T =$ 90 K and 20 K, $\nu_{Res} = 446$ cm^{-1}, for KI:H^-, $T = 9$ K, $\nu_{Res} = 380$ cm^{-1}; for NaBr:H^-, $T = 9$ K, $\nu_{Res} = 498$ cm^{-1}. (From Klein [96].)

halides by Schaefer [86] paved the way for a serious study of three-dimensional lattices. The U-center absorption spectra in KCl due to H^- and D^- ions are shown in Fig. 20.

The dynamical behavior of the impurities has been described theoretically by either a Green's function technique and by a molecular model. The Green's function technique introduced by Lifshitz [87] has been applied extensively to describe the dynamical behavior of an impurity atom in a lattice (for example, see Dawber and Elliot [88], Lifshitz [89], Izyumov [90], and Gaur *et al.* [91]). In this model, it is usually assumed that the defect-induced excitations are localized. This enables one to express the defect problem in terms of the elementary excitations of the unperturbed host crystal. Thus, for a simple mass defect perturbing the phonon spectrum of the host lattice, knowledge of the complete phonon dispersion relation and the eigenvectors of the host-lattice phonons are essential. Under such conditions, this method has an advantage over the conventional perturbation techniques in that it provides, in principle, an exact solution to the defect problem. It is expected that in addition to the change in mass, a softening (or hardening, depending on the impurity) of short-range forces around the impurity ion will also occur. The Green's function technique does not allow one to incorporate such effects easily. A molecular model, introduced by Jaswal [92] to study the U-center local mode in alkali halides, on the other hand, is capable of determining the changes in short-range forces around the impurity. The molecular model was adapted for the impurities in zincblende-type semiconductors by Singh and Mitra [93]. A large body of data on point-defect-induced local, gap, and, band-mode absorption and theoretical interpretation exist in the literature (see Genzel [94], Maradudin [95], Klein [96], Newman [97], and Vetelino and Mitra [98]) and will not be elaborated here.

Before leaving the subject of defect-induced absorption, it is worthwhile to comment on at least two interesting aspects of it. Absorption of infrared radiation resulting in the simultaneous creation (or annihilation) of a local-mode phonon and a lattice phonon giving rise to sidebands around a local-mode resonance are not an uncommon occurrence. An example of this is shown in Fig. 20 for the case of U centers. Resonant absorption of infrared radiation by molecular impurities and defect clusters have also been observed extensively (see, for example, Newman [97]), and although the latter are qualitatively understood, an exact theory is not straightforward. As an example, the absorption spectrum from boron–lithium pairs in silicon is shown in Fig. 21.

If the impurity content of a solid is increased to such an extent that interaction between impurity atoms begins to play an effective role, the system should then be termed a mixed crystal rather than an impure crystal. The study of mixed crystals dates back to as early as 1928 (see Krueger *et al.* [99]). Dyson [100] was the first to obtain a formal solution for the frequency spectrum of the disordered linear chain. Several phenomenological models

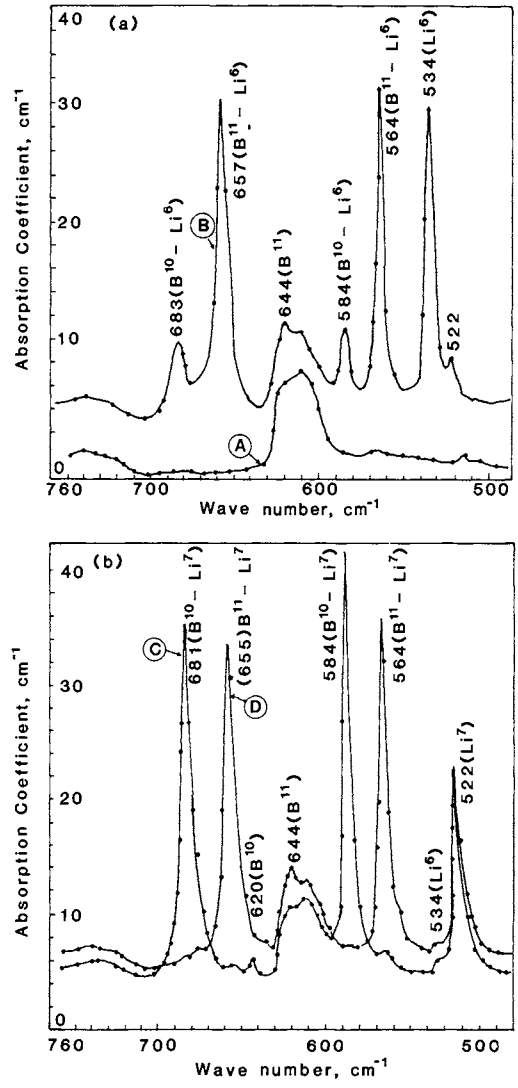

Fig. 21. The absorption spectrum from B–Li pairs in Si. (a) High-purity Si (A) and ^{6}Li doping (B); (b) ^{10}B and Li (C) and ^{11}B and Li (D). (From Newman [97].)

[101–107] have been proposed to explain the vibrations of mixed-crystal systems and their interaction with infrared radiation. As far as the behavior of the long-wavelength optical phonons is concerned, there seem to exist two types of mixed crystals. In one class of mixed systems, termed here the one-mode-behavior type, each of the $q = 0$ optical-mode frequencies varies continuously and approximately linearly with concentration from the frequency characteristic of one end member to that of the other end member. Further-

more, the strength of the resonant absorption remains approximately constant. The examples of this behavior are most of the mixed alkali halides, $GaAs_xSb_{1-x}$, $Zn_xCd_{1-x}S$, $ZnSe_xTe_{1-x}$, and so on. In the other class of mixed-crystal systems, termed here the two-mode behavior type, two phonon frequencies for each of the allowed optical modes of the pure crystal are observed to occur at frequencies close to those of the pure end members. In addition, the strength of absorption by each phonon mode of the mixed crystal is approximately proportional to the mole fraction of the component it represents. Examples of the two-mode type of behavior are in $InAs_xP_{1-x}$, $GaAs_xP_{1-x}$, CdS_xSe_{1-x}, ZnS_xSe_{1-x}, and so on. As examples, the reststrahlen spectra of $Zn_xCd_{1-x}S$ and ZnS_xSe_{1-x} are shown in Fig. 22.

It has been observed that the model using the concept of a unit cell does provide some basic understanding of mixed-crystal behavior. Verleur and Barker [103] considered a cluster model to account for the two-mode behavior. This model assumed that like negative ions cluster around positive ions or vice versa, depending on whether the ad-atom is an anion or a cation. In the random element isodisplacement (REI) model, Chen *et al.* [104] assumed that in a mixed crystal $AB_{1-x}C_x$ the B and C atoms are distributed on the anion sublattice and the anions of like species vibrate in phase with identical amplitudes against the cations, which also vibrate as a rigid unit. Chang and Mitra [105] modified the REI model to include the polarization field. Subsequently, Chang and Mitra [108] proposed the pseudo-unit-cell model and predicted the zone-boundary phonons of systems exhibiting the two-mode behavior at the zone center. Kutty [109] applied the Green's function technique to derive the phonon dispersion relations in mixed crystals as a function of wave vector. Sen and Hartman [110] explained the switching from one- to two-mode-type behavior observed in some III–V mixed semiconductors by using the coherent-potential-approximation technique in one dimension. Varshney *et al.* [111] have given a complete lattice dynamics of a mixed linear diatomic chain by using the pseudo-unit-cell model of Chang and Mitra [108]. Massa *et al.* [112] have extended this model to three dimensions and successfully explained the optical absorption and lattice dynamics of mixed alkali halides.

C Amorphous and Glassy Systems

In contrast to the crystalline state, in which the positions of atoms are fixed into a definite structure except for small thermal vibrations, the amorphous state of the same material displays varying degrees of departure from this fixed structure. The amorphous state almost always shows no long-range order. Short-range order, up to several neighbors, may often be retained, although averaged considerably around their crystalline values. In the discussion of

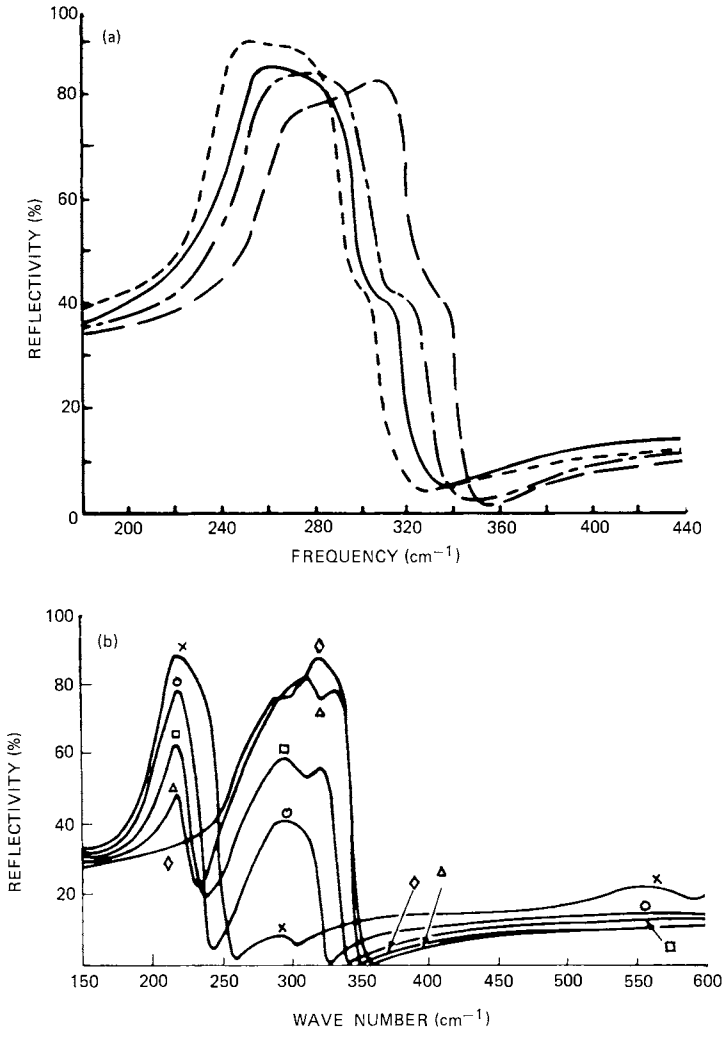

Fig. 22. Reststrahlen spectra of (a) $Zn_xCd_{1-x}S$ for $E \perp c$ (one-mode type) at 300 K [106]. (----, $Zn_{0.19}Cd_{0.81}S$; ——, $Zn_{0.36}Cd_{0.64}S$; ———, $Zn_{0.55}Cd_{0.45}S$; and ——, $Zn_{0.88}Cd_{0.12}S$.) (b) ZnS_xSe_{1-x} (two-mode type). (◇, $x = 1.00$; △, $x = 0.82$; □, $x = 0.60$; ○, $x = 0.33$; and ×, $x = 0.015$.) (From Brafman *et al.* [107].)

absorption of light by the vibrational modes of a glassy or an amorphous material, it is useful to distinguish between modes that are allowed or forbidden in a one-phonon absorption process. For a crystal of the diamond structure, e.g., Si or Ge, there is no one-phonon infrared absorption as could be seen from the lower curve of Fig. 21a. On the other hand, the absorption spectrum of a neutron-irradiated sample shows [113] (Fig. 23) a rich absorption spectrum almost mimicking the phonon density of states of the crystalline

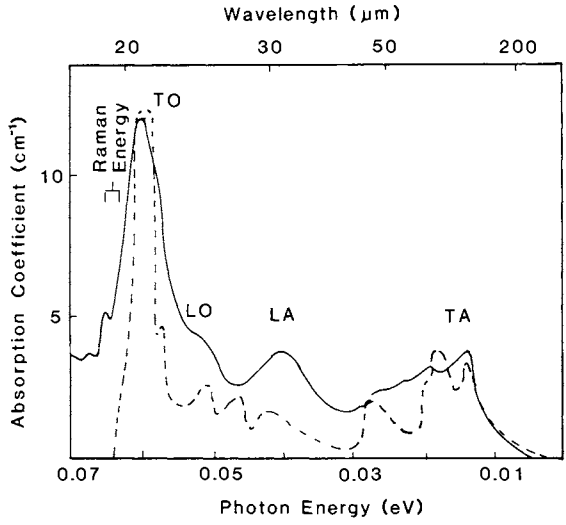

Fig. 23. One-phonon absorption in Si irradiated with 9.3×10^{18} fast neutrons/cm^2. The dashed line represents a calculated density of states curve. (From Angress *et al.* [113].)

counterpart but somewhat broadened. On the other hand, a crystal like SiC displays a strong one-phonon infrared absorption. Spectrum of its amorphous form [114] is still dominated by the one-phonon process, albeit considerably broadened, as shown in Fig. 24. It is worth noting that the areas under the absorption spectra for the crystalline and amorphous materials are almost equal and that while the peak absorption of the crystalline material is more than an order of magnitude higher than its amorphous counterpart, the opposite is true in the wings.

These two contrasting examples (viz., Si and SiC) emphasize the necessity for distinguishing between crystalline-forbidden and crystalline-allowed analog processes. While in the former case the entire density of states plays an important role and a nonvanishing dipole-moment matrix element appears in the entire spectral range [88], a statistical approach to the prediction of infrared absorption in amorphous solids is used by Mitra *et al.* [115] in the latter crystalline-allowed analog processes. In the statistical model of Mitra, a small degree of microscopic density disorder is introduced in which the properties of the disordered solid are related to those of its crystalline counterpart. The infrared response is treated by determining the changes in the phonon spectrum as functions of local density. As an example of application of this model, the crystal-allowed case of SiC is shown in Fig. 24, in which the calculated amorphous one-phonon absorption spectrum consists of nothing but a broadened version of the allowed crystalline case broadened by the radial distribution function of the amorphous phase. This kind of analysis provides a quantitative gauge of the departure from crystallinity in the optical

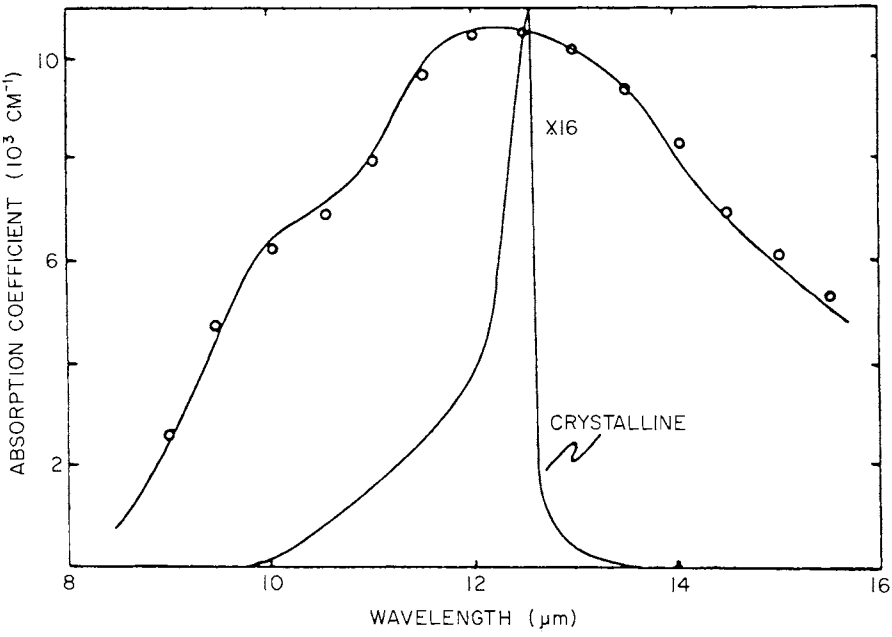

Fig. 24. Infrared absorption in amorphous SiC. Circles represent experimental data [114]. Solid line is a calculation on the basis of local-density-disorder model due to Mitra [115]. The spectrum of the crystalline phase is also indicated (note the multiplicative factor in the vertical scale). (From Vetelino and Mitra [98].)

spectrum, i.e., the relative contribution of processes that do not conserve crystal momentum.

In the preceding examples, both Si and SiC are tetrahedrally bonded semiconductors, and in structure their amorphous counterparts are not that drastically different from their crystalline phases. We should conclude this section with a more dramatic example of disorder, viz., silica glass and quartz. In both their crystalline and vitreous forms, SiO_2 is composed of tetrahedra with SiO_4 units, although in the vitreous phase significant variations in bond angles and distances have been reported and also an almost complete absence of order beyond a few near neighbors. Yet the basic SiO_4 tetrahedron offers a plethora of infrared-active absorption bonds in the range of 300 to 1400 cm^{-1}. In Fig. 25 we compare the infrared reflection spectra of crystalline quartz with that of vitreous silica and neutron-irradiated quartz and silica glass [116]. The following points are worth noting: (a) the dielectric response in quartz and glass [116] shows resonances approximately in the same regions of the spectrum, indicating the integrity of SiO_4 units; (b) the glass spectra, as expected, are smeared out; (c) with increasing neutron dosage, the spectrum of crystalline quartz approaches that of silica glass; and (d) irradiation has very little or no effect on the spectrum of vitreous silica, indicating an equilibrium disordered state.

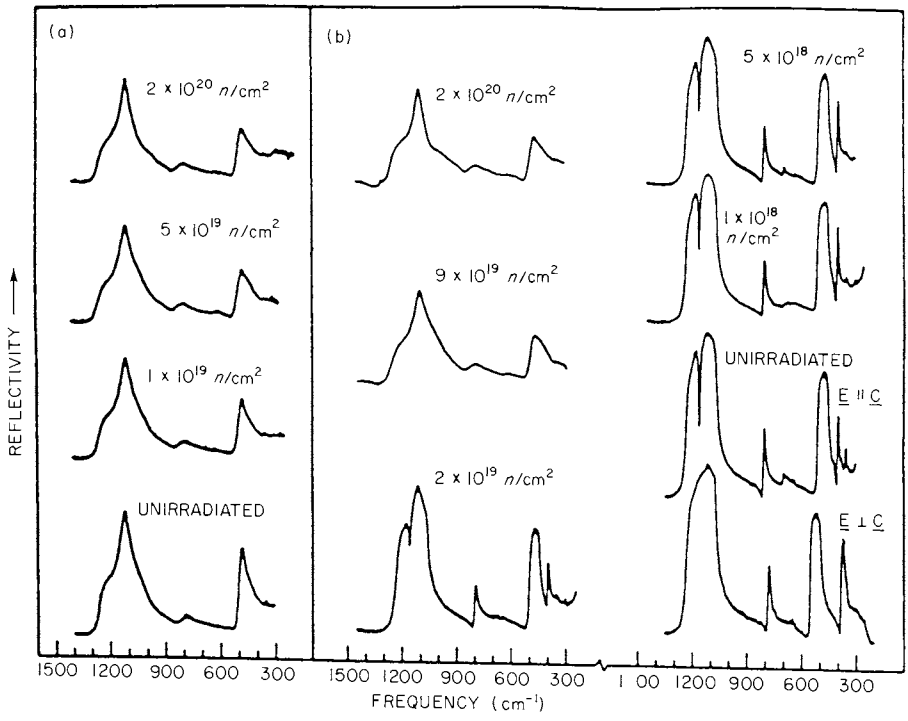

Fig. 25. Infrared reflection spectra of neutron-irradiated (a) vitreous silica and (b) quartz. (From Bates *et al.* [116].)

INFRARED DISPERSION BY PLASMONS VIII

In the preceding discussion of absorption of infrared radiation by phonons in a solid, it was tacitly assumed that the solid was an insulator. This assumption does not hold well for a narrow-gap semiconductor at ordinary temperatures or for a doped semiconductor with a partially filled conduction or valence band. The collective excitation of this free-carrier electron gas (plasma) in such a crystal will modify the infrared absorption by phonons, as discussed earlier. The dispersion mechanisms through which electromagnetic radiation interacts with a solid should include the contribution of free-charge carriers in solids for which their numbers are significant, in addition to contributions from bound electrons and phonons. The dielectric response function of such a solid can now be written as

$$\varepsilon = 1 + 4\pi(\chi_{BE} + \chi_L + \chi_{FC}), \tag{59}$$

where χ_{BE}, χ_L, and χ_{FC}, respectively, represent the bound electron, lattice, and free-carrier contributions to the electrical susceptibility. For the spectral

region of interest, we are not concerned with the bound-electron dispersion; thus this term, as usual, will be represented by a dispersion-free, high-frequency dielectric-constant term

$$\varepsilon_\infty = 1 + 4\pi\chi_{\mathrm{BE}}. \tag{60}$$

An approximate expression for the dielectric response function for a free-electron gas in a solid can be obtained from the classical Drude model in which a free electron of effective mass m^* and charge e is displaced by an amount $\mathbf{x}$ as a result of interaction with the electric field $\mathbf{E}$, with the equation of motion

$$m^*\ddot{\mathbf{x}} + m^*\gamma\dot{\mathbf{x}} = e\mathbf{E}_0 e^{-i\omega t}. \tag{61}$$

The damping term proportional to the velocity obviously represents the electron–phonon scattering in a phenomenological manner. Solving for $\mathbf{x}$, one obtains

$$\mathbf{x} = -e\mathbf{E}/m^*\omega(\omega + i\gamma). \tag{62}$$

The polarization, defined as the electric-dipole moment per unit volume, is given by

$$\mathbf{P} = N\mathbf{e}\mathbf{x}, \tag{63}$$

where N is the carrier concentration. Recalling that

$$\mathbf{P} = [(\varepsilon - 1)/4\pi]\mathbf{E}, \tag{64}$$

one readily obtains

$$\varepsilon_{\mathrm{FC}} = \varepsilon_\infty - \{4\pi Ne^2/[m^*\omega(\omega + i\gamma)]\} \tag{65}$$

for the dielectric response function due to a single-component plasma. In terms of the plasma frequency defined as

$$\omega_{\mathrm{p}} = (4\pi Ne^2/\varepsilon_\infty m^*)^{1/2} \tag{66}$$

$\varepsilon_{\mathrm{FC}}$ becomes

$$\varepsilon_{\mathrm{FC}} = \varepsilon_\infty\{1 - [\omega_{\mathrm{p}}^2/\omega(\omega + i\gamma)]\}. \tag{67}$$

For a number of semiconductors there exists a region of the infrared spectrum in which the free-carrier contribution dominates, and both the bound-electron and lattice contributions to the dielectric response function are negligible. For a semiconductor, such a situation prevails in a region of the infrared spectrum in which $\omega_{\mathrm{g}} \gg \omega_{\mathrm{p}} \gg \omega_{\mathrm{TO}}$, where $\hbar\omega_{\mathrm{g}}$ is the electronic band gap. The analysis of optical response is also simpler in a region in which the reflection coefficient is independent of carrier scattering. For such a situation to prevail, one usually finds $\gamma \ll \omega$ and $\varepsilon_1 \gg \varepsilon_2$. In a few semiconductors for which all these conditions are met, the reflectivity spectrum in the appropriate ($\sim\omega_{\mathrm{p}}$) infrared region becomes a function of carrier concentration. Here

PbTe satisfies the preceding specified conditions, and its infrared reflection spectrum [117] as a function of hole carrier concentration is shown in Fig. 26. Since this case satisfies the preceding outlined conditions, the reflectivity minimum is a measure of the effective mass

$$m^* \cong [1/(\varepsilon_\infty - 1)](Ne^2/\pi c^2)\lambda_{\min}^2, \tag{68}$$

and the real and imaginary part of ε are given by

$$\varepsilon_1 = \varepsilon_\infty - \frac{e^2}{\pi c^2}\left(\frac{N}{m^*}\right)\lambda^2 \qquad \text{and} \qquad \varepsilon_2 = \frac{e^2}{2\pi c^3}\left(\frac{N}{m^*}\right)\gamma\lambda^3. \tag{69}$$

The λ^2 dependence of ε_1 is confirmed experimentally [117].

For most polar semiconductors, however, lattice dispersion contributes significantly. For such cases,

$$\varepsilon(\omega) = \varepsilon_\infty\left[1 - \frac{\omega_p^2}{\omega(\omega + i\gamma)}\right] + \frac{(\varepsilon_o - \varepsilon_\infty)\omega_o^2}{\omega_o^2 - \omega^2}, \tag{70}$$

where the last term represents a single undamped oscillator representing the long-wavelength optical phonons. It may be recalled from Subsection B that

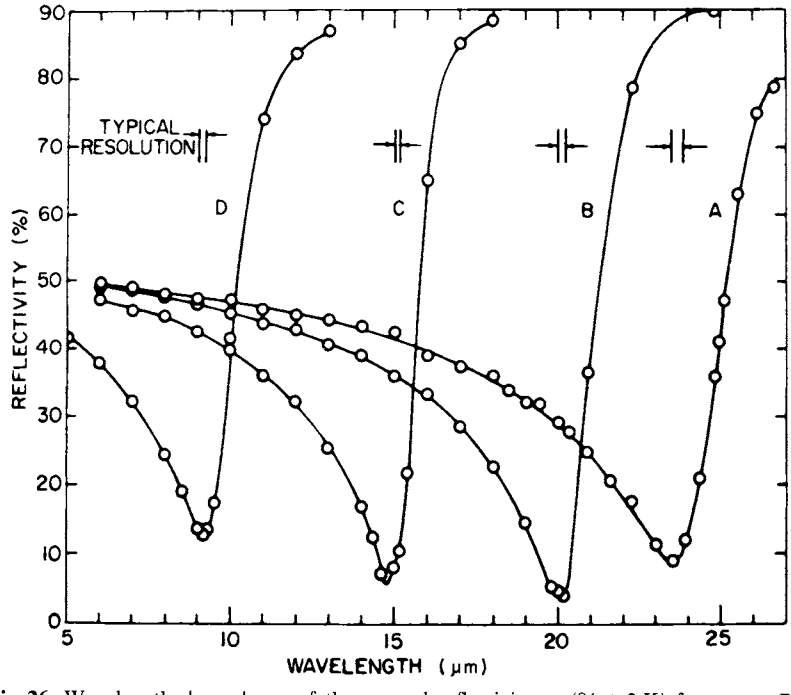

Fig. 26. Wavelength dependence of the normal reflectivity at (81 ± 2 K) for *p*-type PbTe samples having carrier concentration ranging from 3.5×10^{18} cm^{-3} (A) to 4.8×10^{19} cm^{-3} (D). (From Dixon and Riedl [117].)

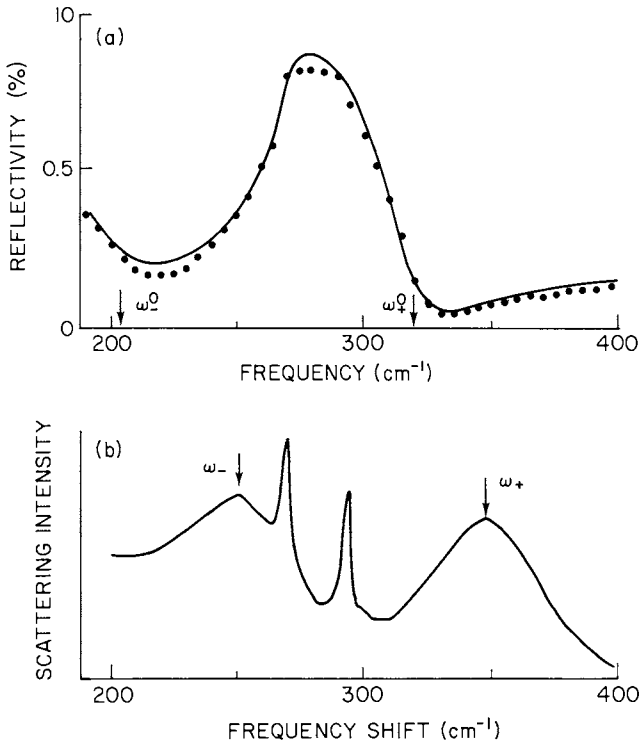

Fig. 27. (a) Infrared reflection spectrum of *n*-GaAs ($n = 5 \times 10^{17}$ cm^{-3}). The solid curve is the calculated spectrum and the dots are experimental data. The calculated ω_+^0 and ω_-^0 are marked by arrows. (b) Raman scattering spectrum of the same sample. Notice the difference in the position of the arrows, indicating a wave vector dependence of ω_+ and ω_-. (From Zemski *et al.* [121].)

$\omega_{TO} = \omega_0$ was identified with the maximum in ε, whereas ω_{LO} with its zero. Because of the first term, the second condition is now altered: i.e., ω_{TO} can still be identified with the maximum in ε but not ω_{LO} with its minimum. Thus for a polar semiconductor with an appreciable carrier concentration, the resonance corresponding to the long-wavelength LO frequency will no longer correspond to the real LO phonon frequency. In the limit of negligible damping for both electrons and phonons, the solution of Eq. (70) is given by

$$\omega_\pm^2 = \tfrac{1}{2}(\omega_{LO}^2 + \omega_p^2) \pm \tfrac{1}{2}[(\omega_{LO}^2 + \omega_p^2) - 4\omega_p^2\omega_{TO}^2]^{1/2} \tag{71}$$

where ω_+ and ω_- represent new resonances above and below ω_{LO}.

The plasmon–phonon interaction obviously will be modified by the inclusion of both plasmon and phonon damping terms. The influence of damping and the wave vector dependence on the phonon–plasmon interaction in semiconductors have been theoretically treated by Gurevich *et al.* [118],

Varga [119], and Singwi and Tosi [120]. Such effects have indeed been observed experimentally. The wave vector dependence of the plasmon-phonon interaction has been investigated by Zemski *et al.* [121], who studied *n*-InP and *n*-GaAs by both infrared reflection spectroscopy and Raman light scattering. Whereas the former measurement gives coupled LO plasmon–phonon modes with $q \simeq 10^3\ \text{cm}^{-1}$, the latter measurement gives modes with $q \simeq 10^6\ \text{cm}^{-1}$. This is illustrated in Fig. 27 for GaAs. Note the difference in the positions of ω_+ and ω_- in the two spectra.

REFERENCES

1. K. Huang, *Proc. R. Soc. London Ser. A* **208**, 352 (1951).
2. M. Born and K. Huang, "Dynamical Theory of Crystal Lattices," p. 82, Oxford Univ. Press, New York, 1954.
3. R. H. Lyddane, R. G. Sachs, and E. Teller, *Phys. Rev.* **59**, 673 (1941).
4. W. J. Turner and W. E. Reese, *Phys. Rev.* **127**, 126 (1962).
5. H. W. Verleur, *J. Opt. Soc. Am.* **58**, 1356 (1968).
6. A. Kahan, J. W. Goodman, R. S. Singh, and S. S. Mitra, *J. Appl. Phys.* **42**, 4444 (1971).
7. W. Cochran, *Z. Krist.* **112**, 465 (1959).
8. A. S. Barker, *Phys. Rev.* **136A**, 1290 (1964).
9. I. F. Chang, S. S. Mitra, J. N. Plendl, and L. C. Mansur, *Phys. Status Solidi* **28**, 663 (1968).
10. A. S. Barker, *in* "Far Infrared Properties of Solids" (S. S. Mitra and S. Nudelman eds.), p. 247, Plenum, New York, 1970.
11. D. W. Berreman, *Phys. Rev.* **130**, 2193 (1963).
12. J. R. Jasperse, A. Kahan, J. N. Plendl, and S. S. Mitra, *Phys. Rev.* **146**, 526 (1966).
13. M. Born and K. Huang, "Dynamical Theory of Crystal Lattices," p. 341, Oxford Univ. Press, New York, 1954.
14. A. A. Maradudin and R. F. Wallis, *Phys. Rev.* **125**, 4 (1962).
15. V. V. Mitskevich, *Fiz. Tverd. Tela* **4**, 3035 (1962); V. V. Mitskevich, [English transl.: *Soviet Phys.—Solid State* **4**, 2224 (1963)].
16. J. Neuberger and R. D. Hatcher, *J. Chem. Phys.* **34**, 5 (1961).
17. R. A. Cowley, *Adv. Phys.* **12**, 421 (1963).
18. R. de L. Kronig *J. Opt. Soc. Am.* **12**, 547 (1926); H. A. Kramers, *Atti Congr. Intern. Fis. Como.* **2**, 545 (1927); M. Cardona, *in* "Optical Properties of Solids" (S. Nudelman and S. S. Mitra. eds.), p.137, Plenum, New York, 1969.
19. M. Sharnoff, *Am. J. Phys.* **32**, 1 (1964).
20. W. G. Spitzer and D. A. Kleinman, *Phys. Rev.* **121**, 1324 (1961).
21. P. N. Schatz, S. Maeda, and K. Kozima, *J. Chem. Phys.* **38**, 2658 (1963).
22. H. J. Bowlden and J. K. Wilmshurst, *J. Opt. Soc. Am.* **53**, 1073 (1963).
23. M. Gottlieb, *J. Opt. Soc. Am.* **50**, 343 (1960).
24. R. B. Sanderson, *J. Phys. Chem. Solids* **26**, 803 (1965).
25. G. Andermann, A. Caron, and D. A. Dows, *J. Opt. Soc. Am.* **55**, 1210 (1965).
26. L. Kellner, *Z. Phys.* **56**, 212 (1929).
27. H. Y. Fan and M. Becker, *in* "Proceedings of Conference on Semiconducting Materials: Reading, U.K.," p. 132, Academic Press, New York, 1951.
28. A. Kahan and H. G. Lipson, Air Force Cambridge Research Laboratory Report AFCRL-63-325, Bedford, Massachusetts [limited circulation].
29. W. Nazarewicz, P. Rolland, E. da Silva, and M. Balkanski, *Appl. Opt.* **1**, 369 (1962).
30. A. J. Barker, G. R. Wilkinson, N. E. Massa, and S. S. Mitra, *in* "Optical Properties of Highly Transparent Solids" (S. S. Mitra and B. Bendow, eds.), p. 45, Plenum, New York, 1975.

31. A. J. Barker, G. R. Wilkinson, N. E. Massa, and S. S. Mitra, *in* "Optical Properties of Highly Transparent Solids" (S. S. Mitra and B. Bendow, eds.), p. 405–525, Plenum, New York, 1975.
32. L. H. Skolnik, *in* "Optical Properties of Highly Transparent Solids" (S. S. Mitra and B. Bendow, eds.), pp. 405–433, Plenum, New York, 1975.
33. A. Hordvik, *Appl. Opt.* **16**, 2827 (1977).
34. M. Lax and E. Burstein, *Phys. Rev.* **97**, 39 (1955).
35. J. L. Birman, *Phys. Rev.* **127**, 1093 (1962); J. L. Birman, Phys. Rev. **131**, 1489 (1963).
36. S. S. Mitra, *Phys. Lett.* **11**, 119 (1964).
37. F. A. Johnson and R. Loudon, *Proc. R. Soc. London Ser.* **A 231**, 274 (1964).
38. E. Burstein, F. A. Johnson, and R. Loudon, *Phys. Rev.* **139A**, 1239 (1965).
39. S. Ganesan and E. Burstein, *J. Phys. Paris* **26**, 645 (1965).
40. B. Szigeti, *in* "Lattice Dynamics" (R. F. Wallis ed.), p. 405, Pergamon, Oxford, 1965.
41. C. Smart, G. R. Wilkinson, A. M. Karo, and J. R. Hardy, *in* "Lattice Dynamics" (R. F. Wallis, ed.), p. 387, Pergamon, Oxford, 1965.
42. F. A. Johnson, *Proc. Phys. Soc. London* **73**, 265 (1959).
43. H. Bilz and L Genzel, *Z. Phys.* **169**, 53 (1962).
44. W. Cochran, S. J. Fray, F. A. Johnson, J. E. Quarrington, and N. Williams, *J. Appl. Phys.* **32**, 2102 (1961).
45. S. S. Mitra, *J. Phys. Soc. Jpn.* **21** (suppl.), 61 (1966).
46. J. L. T. Waugh and G. Dolling, *Phys. Rev.* **132**, 2410 (1963).
47. J. C. Phillips, *Phys. Rev.* **113**, 147 (1959).
48. M. Hass and B. W. Henvis, *J. Phys. Chem. Solids* **23**, 1099 (1962).
49. S. Iwasa, I. Balslev, and E. Burstein, *Bull. Am. Phys. Soc.* **9**, 237 (1964).
50. M. Sparks, *Phys. Rev. B* **9**, 827 (1974).
51. B. Bendow, H. G. Lipson, and S. P. Yukon, *Phys. Rev. B* **16**, 2684 (1977).
52. B. Bendow, *Solid State Phys.* **33**, 249 (1978).
53. G. Ruprecht, *Phys. Rev. Lett.* **12**, 580 (1964).
54. T. C. McGill, R. W. Hellwarth, M. Mangir, and H. V. Winston, *J. Phys. Chem. Solids.* **34**, 2105 (1973).
55. K. V. Namjoshi and S. S. Mitra, *Phys. Rev. B* **9**, 815 (1974); K. V. Namjoshi and S. S. Mitra, *Solid State Commun.* **15**, 317 (1974).
56. D. L. Mills and A. A. Maradudin, *Phys. Rev. B* **8**, 1617 (1973).
57. B. Bendow, S. C. Ying, and S. P. Yukon, *Phys. Rev. B* **8**, 1679 (1973).
58. L. J. Sham and M. Sparks, *Phys. Rev. B* **9**, 827 (1974).
59. H. B. Rosenstock, *Phys. Rev. B* **9**, 1963 (1974).
60. D. L. Mills and A. A. Maradudin, *Phys. Rev. B* **10**, 1713 (1974).
61. B. Bendow, S. P. Yukon, and S. C. Ying, *Phys. Rev. B* **10**, 2286 (1974).
62. L. L. Boyer, J. A., Harrington, M. Hass, and H. B. Rosenstock, *in* "Optical Properties of Highly Transparent Solids" (S. S. Mitra and B. Bendow, eds.), p. 59, Plenum, New York, 1975.
63. H. G. Lipson, B. Bendow, N. E. Massa, and S. S. Mitra, *Phys. Rev. B* **13**, 2614 (1976).
64. J. A. Harrington and M. Hass, *Phys. Rev. Lett.* **11**, 710 (1973); K. V. Namjoshi and S. S. Mitra, *Solid State Commun.* **15**, 317 (1974).
65. B. Bendow, *Appl. Phys. Lett.* **23**, 133 (1973).
66. R. Brout, *Phys. Rev.* **113**, 43 (1959); S. S. Mitra and R. Marshall, *J. Chem. Phys.* **41**, 3158 (1964).
67. S. S. Mitra, unpublished.
68. S. S. Mitra and S. K. Joshi, *Physica* **26**, 825 (1960); S. S. Mitra and S. K. Joshi, *Physica* **27**, 345 (1961).
69. S. S. Mitra, *in* "Optical Properties of Solids" (S. Nudelman and S. S. Mitra, eds.), p. 333, Plenum, New York, 1969.

70. H. Rubens and G. Hertz, *Preuss. Akad. Wiss. Berlin* **14**, 256 (1912).
71. H. Dotsch and H. Happ. *Z. Phys*, **177**, 360 (1964); J. E. Eldridge and P. R. Staal, *Phys. Rev. B* **16**, 4608 (1977); R. H. Stolen and K. Dransfeld, *Phys. Rev.* **139A**, 1295 (1965).
72. R. H. Stolen, *Phys. Rev. B* **11**, 767 (1975).
73. J. R. Birch and D. K. Murray, *Infrared Phys.* **18**, 283 (1978).
74. T. J. Parker, W. G. Chambers, and J. F. Angress, *Infrared Phys.* **14**, 207 (1974).
75. D. Billard, private communication, 1980; D. Billard, seminar given at the University of Rhode Island, Kingston, Rhode Island, December 19, 1979.
76. R. H. Stolen, *Phys. Chem. Glasses*, **11**, 83 (1970).
77. E. M. Armhein and H. Heil, *J. Phys. Chem. Solids*, **32**, 1925 (1971).
78. U. Strom and P. C. Taylor, *Phys. Rev. B* **16**, 5512 (1977).
79. M. A. Bosch, *Phys. Rev. Lett.* **40**, 879 (1978).
80. J. R. Hardy and A. M. Karo, *Phys. Rev. B* **26**, 3327 (1982).
81. M. Sparks, D. F. King, and D. L. Mills, *Phys. Rev.* **26**, 6987 (1982).
82. H. Y. Fan and A. K. Ramdas, *J. Appl. Phys.* **30.** 1127 (1959).
83. I. M. Lifshitz, *J. Phys. (USSR)* 7, 215 (1943); I. M. Lifshitz, *J. Phys (USSR)* **7**, 249 (1943); I. M. Lifshitz, *J. Phys. (USSR)* **8**, 89 (1944).
84. E. W. Montroll and R. B. Potts, *Phys. Rev.* **100**, 525 (1955).
85. P. Mazur, E. W. Montroll, and R. E. Potts, *J. Wash, Acad. Sci.* **46**, 2 (1956).
86. G. Schaefer, *J. Phys. Chem. Solids* **12**, 233 (1960).
87. I. M. Lifshitz, *Nuovo Cimento Suppl.* **3**, 716 (1956).
88. P. G. Dawber and R. J. Elliot, *Proc. R. Soc. London* **272**, 222 (1963); P. G. Dawber and R. J. Elliot, *Proc. Phys. Soc. London* **81**, 453 (1963).
89. I. M. Lifshitz, *Adv. Phys.* **13**, 485 (1964).
90. Yu. A. Izyumov. *Adv. Phys.* **14**, 569 (1965).
91. S. P. Gaur, J. F. Vetelino, and S. S. Mitra, *J. Phys. Chem. Solids* **32**, 2737 (1971).
92. S. S. Jaswal. *Phys. Rev.* **137A**, 302 (1965).
93. R. S. Singh and S. S. Mitra, *Phys. Rev. B* **5**, 733 (1972).
94. L. Genzel, *in* "Optical Properties of Solids" (S. Nudelman and S. S. Mitra, eds.), pp. 453–487, Plenum, New York, 1969.
95. A. A. Maradudin, *Solid State Phys.* **18**, 273 (1966); A. A. Maradudin, *Solid State Phys.* **19**, 2 (1966).
96. M. V. Klein, *in* "Physics of Color Centers" (W. B. Fowler, ed.), pp. 430–531, Academic Press, New York, 1968.
97. R. C. Newman, "Infrared Studies of Crystal Defects," Taylor and Francis, London, 1974.
98. J. F. Vetelino and S. S. Mitra, *in* "Physics of Structurally Disordered Solids" (S. S. Mitra, ed.), pp. 541–622, New York, 1974.
99. F. Krueger, O. Reinkober, and E. Koch-Holm, *Ann. Phys.* **85**, 110 (1928).
100. F. J. Dyson, *Phys. Rev.* **92**, 133 (1953).
101. R. H. Braunstein, R. Moore, and F. Herman, *Phys. Rev.* **109**, 695 (1958).
102. J. S. Langer, *J. Math. Phys.* **2**, 584 (1961).
103. H. W. Verleur and A. S. Barker, *Phys. Rev.* **149**, 715 (1966).
104. Y. S. Chen, W. Shockley, and G. L. Pearson, *Phys. Rev.* **151**, 648 (1966).
105. I. F. Chang and S. S. Mitra, *Phys. Rev.* **172**, 924 (1968).
106. G. Lucovsky, E. Lind, and E. A. Davis, *in* "II–VI Semiconducting Compounds" (D. G. Thomas, ed.), p. 1150, Benjamin, New York, 1967.
107. O. Brafman, I. F. Chang, G. Lengyel, S. S. Mitra, and E. Carnall, *Phys. Rev. Lett.* **19**, 1120 (1967).
108. I. F. Chang and S. S. Mitra, *Adv. Phys.* **20**, 359 (1971).
109. A. P. G. Kutty, *Solid State Commun.* **14**, 213 (1974).
110. P. N. Sen and W. M. Hartman, *Phys. Rev. B* **9**, 367 (1974).
111. S. C. Varshney, J. F. Vetelino, S. S. Mitra, and I. F. Chang, *Phys. Rev. B* **12**, 5912 (1975).

112. N. E. Massa, S. S. Mitra, and J. F. Vetelino, *Phys. Rev. B* **26**, 4579, 4606 (1982).
113. J. F. Angress, S. D. Smith, and K. F. Renk, *in* "Lattice Dynamics" (R. F. Wallis, ed.), p. 467, Pergamon, Oxford, 1965.
114. E. A. Fagan, *Proc. Int. Conf. Amorphous Liq. Semicond. 5th, Garmisch-Partenkirchen*, 6701 (1973).
115. S. S. Mitra, Y. F. Tsay, D. K. Paul, and B. Bendow, *Phys. Stat. Solidi*, **72**, 475 (1975).
116. J. D. Bates, R. W. Hendricks, and L. B. Shaffer, *J. Chem. Phys.* **61**, 4163 (1974).
117. J. E. Dixon and H. R. Riedl, *Phys. Rev.* **138**, A873 (1965).
118. V. I. Gurevich. A. I. Larkin, and Yu. A. Firsov, *Fiz. Tverd. Tela*, **4**, 185 (1962).
119. B. H. Varga, *Phys. Rev.* **137A**, 1896 (1965).
120. K. B. Singwi and M. P. Tosi, *Phys. Rev.* **147**, 658 (1966).
121. V. I. Zemski, E. L. Ivchenko, D. N. Mirlin, and I. I. Reshina, *Solid State Commun.* **16**, 221 (1975).

Comments on the Optical Constants of Metals and an Introduction to the Data for Several Metals

DAVID W. LYNCH
Department of Physics and Ames Laboratory, U.S. Department of Energy
Iowa State University
Ames, Iowa

W. R. HUNTER*
Naval Research Laboratory
Washington, D.C.

INTRODUCTION I

Tables and plots of the optical constants $N = n - ik$ for the metals Ag, Au, Cu, Ir, Mo, Ni, Os, Pt, Rh, W, and Al, are presented in the following sections as a function of wavelength from the soft x-ray region to the near infrared. Preceding each data set is a short critique outlining the procedures used to obtain the constants and the conditions under which they were measured. Most measurements were made at room temperature (297–300 K).

Each critique has its own independent set of references. We tried to choose metals that are of practical value to the designer of optical filters as well as of interest for their electronic properties. Of these metals, aluminum appears to have the most widespread spectral application, being used in optical components from the infrared to the soft x-ray region. It also has the distinction of having been measured and studied more thoroughly than the other metals; therefore more space has been allotted for its critique than for the other

* Present address: Sachs/Freeman Associates, Inc., Bowie, Maryland.

Copyright © 1985 by Academic Press, Inc.
All rights of reproduction in any form reserved.
ISBN 0-12-544420-6

metals. Aluminum is discussed further by Smith *et al.* in the section on metallic aluminum in this handbook.

The following paragraphs serve to remind the reader of the methods (discussed in more detail elsewhere in this volume) used to obtain the optical constants. There are also some general comments on the data. Comments germane to a particular metal are included in the individual critique for that metal. We finish with some warnings about attempting to use infrared optical data for free-electron-like metals (here, Cu, Au, Ag, and, to some extent, Al) to calculate accurately some expected optical characteristic, e.g., a reflectance value for a given sample. There is an inherent difficulty in defining optical constants in such cases because of the anomalous skin effect.

The optical constants for the metals listed have been measured by a number of investigators, and there is a large scatter in the reported values for any one metal. Instrumental sources beyond the investigator's control, e.g., second-order radiation or scattered light from the monochromator, are responsible for some of the scatter. Other contributing factors arise from errors in the quantities measured and from genuine differences in the samples caused by the methods of preparation. Methods of sample preparation are given, when known, in the individual critiques.

To plot n and k over such a large wavelength range, data from a number of investigators have been used. Agreement at the junctions of the data sets is rare. Rather than interpolate values to form a smooth junction between disjointed data sets, which sometimes requires an exercise of judgment bordering on the omniscient, we usually give only the data. Readers may create their own smooth junction if one is required.

There are four general methods for obtaining experimental data from which the optical constants can be deduced. The first three are based on the Fresnel relations for the reflection and transmission of radiation at a flat, smooth interface between two media. The first method that is widely used is known as the Kramers–Kronig method and is discussed by Smith in Chapter 3. The second method, sometimes referred to as the reflectance method, requires measuring reflectances at two or more angles of incidence. A description of this method is given by Hunter in Chapter 4. Ellipsometry is the third method for obtaining n and k and is described by Aspnes in Chapter 5.

The fourth method is the use of the electron-loss spectrum [1, 2]. The passage of fast (10-keV) electrons through a thin-film sample yields a spectrum of energy loss proportional to $\mathrm{Im}(-1/\tilde{\varepsilon})$. This spectrum can be measured over a wide energy range and analyzed by using the Kramers–Kronig relations to give $\mathrm{Re}(-1/\tilde{\varepsilon})$, hence $\tilde{\varepsilon}$ from which $\tilde{N} = \sqrt{\tilde{\varepsilon}}$ can be obtained. Such an analysis is subject to the usual restrictions inherent in the Kramers–Kronig method. Furthermore, the absolute magnitude of $\tilde{\varepsilon}$ is dependent on either a determination of the film thickness or an adjustment to fit some independently determined optical datum. The spectra obtained this way can be in good accord with those determined by genuine optical methods, but usually data

at energies less than 1 eV (wavelengths longer than about 1 μm) cannot be obtained in this way.

Optical constants in the soft x-ray spectral region (10–100 Å) have attracted much interest in recent years because they are required to design grazing incidence optical systems for both x-ray astronomy and synchrotron radiation instrumentation. Because of this interest, the plots and tables have been extended to 2 keV (6.2 Å) and for three metals (Au, Ag, and Ni) to approximately 9.9 keV (1.25 Å). Many of these values are not measured but are calculated from atomic scattering factors, based on absorption measurements, that have been presented by Henke *et al.* [3]. This method contains no adjustable parameters, depending only on the density of atoms used to construct the solid. The values for Au and Ni were taken from tables presented by Zombeck *et al.* [4] that contain some measured values originally obtained by Ershov *et al.* [5] and to which Van Speybroeck [6] has fitted calculated values obtained by using the Kallman–Mark dispersion formalism described by Compton and Allison [7]. The data for Ag were obtained by Hagemann *et al.* [8] and are described in the section on Ag. Where overlap or near overlap occurs with values measured at longer wavelengths, the agreement with the calculated soft x-ray data is often very good.

The accuracy with which optical constants can be obtained from reflectance or ellipsometric measurements is not great. In the tables we have usually retained three significant figures, but this is probably too generous. When compiling the indices of refraction for the soft x-ray region, we have retained the first three digits after the repeating nines, rounding the third digit. This is essentially quoting δ, where $n = 1 - \delta$, to three significant figures.

ANOMALOUS SKIN EFFECT II

A problem with free-electron metals in the infrared is that the optical constants may not be well defined. All of the optical constants of such metals arise from the response of the electrons to the electromagnetic field of the wave. As an example, consider the conductivity, which, for a cubic crystal or random polycrystal, relates the current density $\mathbf{J}$ to the electric field $\mathbf{E}$ as $\mathbf{J} = \sigma\mathbf{E}$. This really means that $\mathbf{J}$ at each point in space and moment in time is directly proportional to the electric field at that point and moment, i.e., $\mathbf{J}(\mathbf{r}, t) = \sigma\mathbf{E}(\mathbf{r}, t)$. We know that because of the inertia of the electrons, this response must decrease if $\mathbf{E}$ varies rapidly in time. We then Fourier analyze the fields with respect to time and treat one component at a time: $\mathbf{J}_\omega(\mathbf{r}) = \sigma(\omega)\mathbf{E}_\omega(\mathbf{r})$, and $\sigma(\omega)$ becomes smaller as ω increases. Now $\mathbf{J}$ arises from the driven motion of the electrons and is proportional to the velocity of the electrons at the point $\mathbf{r}$. The constitutive relations used so far imply that the velocity of an electron at $\mathbf{r}$ is proportional to the electric field at $\mathbf{r}$. This is often

a good approximation, but it is not always valid. When it is not valid, we cannot relate fields and currents algebraically unless we are willing to Fourier analyze the fields with respect to space as well. This leads to the replacement of $\sigma(\omega)$ by $\sigma(\omega, \mathbf{k})$, so that a spectrum of σ versus ω would be needed for each component $\mathbf{k}$.

Classically, the electric field decreases exponentially with depth in a metal, with a decay length equal to the skin depth $\delta_0 = c/(2\pi\sigma_0\omega)^{1/2}$, where σ_0 is the dc conductivity. (Note that the skin depth is derived by assuming that $\mathbf{J} = \sigma_0\mathbf{E}$.) For a free-electron gas at high frequency, the conductivity becomes $\sigma_0/(1 + \omega^2\tau^2)$, and so we use $\delta = \delta_0(1 + \omega^2\tau^2)^{1/2}$ as the length over which electric fields in a metal are approximately constant. If the electron mean free path $l = v_F\tau$, where v_F is the average speed of an electron on the Fermi surface, becomes of the order of δ or larger, the electron then samples a nonconstant electric field between its last scattering event and its arrival at $\mathbf{r}$. The velocity at $\mathbf{r}$ no longer is proportional to the field at $\mathbf{r}$ but is proportional to an integral of the varying electric field over the electron's path before it reached $\mathbf{r}$. We then cannot write $J_\omega(\mathbf{r}) = \sigma(\omega)\mathbf{E}_\omega(\mathbf{r})$. We are left with an integral constitutive relation or, if we Fourier analyze with respect to $\mathbf{r}$, the quantity $\sigma(\omega, \mathbf{k})$ already mentioned. In using the Fresnel relations to obtain the reflected electric field at some frequency, we must integrate over all spatial frequencies or wave numbers $\mathbf{k}$. Even though only one component $\mathbf{k}$ may be present in the wave in the vacuum, many components will appear in the fields induced in the metal when the response is nonlocal. The term $\sigma(\omega, \mathbf{k})$ can be obtained from a solution of the Boltzmann equation, and under some ranges of the parameters, closed-form solutions exist. Often, instead of relating bulk quantities, the surface impedance $\tilde{Z} = (4\pi/c)(E/H)_0$ is calculated, where the field magnitudes are evaluated on the surface. From this, reflectances can be found.

The nonlocal nature of the response of the electrons is crucial whenever the mean free path becomes long compared with the classical skin depth, e.g., for pure metal single crystals at low temperatures. In such cases the classical picture can lead to calculated results in error by orders of magnitude. At room temperature, if the film grain size is large enough so that the scattering is nearly all by phonons, i.e., if the film and single-crystal samples have the same electrical and optical properties, the nonlocality is marginal and causes small but nonnegligible corrections. For Cu at 300 K and for a frequency corresponding to 10-μm wavelength, we have $\omega\tau = 5.1$, $\delta_0 = 1.2 \times 10^{-6}$ cm, $\delta = 5.9 \times 10^{-6}$ cm, and $l = 4.2 \times 10^{-6}$ cm. If we assume that $\omega\tau \gg 1$, the classical expression for the reflectance at normal incidence is $R = 1 - A$ with absorptance $A = 2/(\omega_p\tau)$. For Cu at 300 K, $A = 0.0045$. The anomalous-skin-effect theory gives two possible corrections to this, one for the fraction p of electrons that scatter specularly from the metal surface and one for the fraction $(1 - p)$ that scatter diffusely. These corrections are simply additive to A; they are not calculated via optical constants. If we assume only diffuse scattering, the correction to A is the addition of a term $\frac{3}{4}(v_F/c)$, which thus reduces R. For copper this term is 0.0039, about as large as the classical de-

parture of R from unity. Thus, the anomalous skin effect makes a small correction to R but a correction of the order of 100% to A. This large departure from the classical value will have a large effect on any values of the optical constants determined from the reflectance. The corrections are much larger at low temperatures, for upon cooling τ gets very large and the classical result for A may become very small, 10^{-5} or less. The term $\frac{3}{4}(v_F/c)$ remains and dominates R. (In fact, at low temperatures there are other mechanisms that also contribute to A, which we neglect here.)

In addition to the mathematical complexity of the anomalous skin effect [9–12], one also must contend with the problem of specular versus diffuse scattering of the conduction electrons from the sample surface, i.e., deciding a value for p. Perhaps the best experimental study of this problem to date is that on Ag at 300 K by Bennett *et al.* [13], to which the reader is referred. Gold, too, requires consideration of the anomalous skin effect in the infrared region [14]. Other general references to the anomalous skin effect are also listed [15–20].

REFERENCES

1. H. Raether, *Springer Tracts Mod. Phys.* **38**, 84 (1965).
2. J. Daniels, C. V. Festenburg, H. Raether, and K. Zeppenfeld, *Springer Tracts Mod. Phys.* **54**, 77 (1970).
3. B. L. Henke, P. Lee, T. J. Tanaka, R. L. Shimabukuro, and B. K. Fujikawa, "Low Energy X-Ray Diagnostics—1981" (D. T. Attwood and B. L. Henke, eds.), p. 340, *AIP Conf. Proc.* No. 75, American Institute of Physics, New York, 1981.
4. M. V. Zombeck, G. K. Austin, and D. T. Torgerson, Smithsonian Astrophysical Observatory Report SAO-AXAF-80-003, Appendix B, Tables B1 (Au) and B2 (Ni), Cambridge, Massachusetts, 1980.
5. O. A. Ershov, I. A. Brytov, and A. P. Lukirskii, *Opt. Spectros.* **22**, 66 (1967).
6. L. Van Speybroeck, Smithsonian Astrophysical Observatory, Cambridge, Massachusetts, private communication (1982).
7. A. H. Compton and S. K. Allison, "X-Rays in Theory and Experiment," p. 263, Van Nostrand-Reinhold, Princeton, New Jersey, 1935.
8. H. J. Hagemann, W. Gudat, and C. Kunz, DESY Report SR-74/7, Hamburg, 1974; H. J. Hagemann, W. Gudat and C. Kunz, *J. Opt. Soc. Am.* **65**, 742 (1975).
9. G. E. H. Reuter and E. H. Sondheimer, *Proc. R. Soc. Ser. A* **195**, 336 (1948).
10. R. B. Dingle, *Physica* **19**, 311 (1953).
11. K. L. Kliewer and R. Fuchs, *Phys. Rev.* **172**, 607 (1968).
12. K. L. Kliewer and R. Fuchs, *Phys. Rev. B* **2**, 2923 (1970).
13. H. E. Bennett, J. M. Bennett, E. J. Ashley, and R. J. Motyka, *Phys. Rev.* **165**, 755 (1968).
14. M. L. Thèye, *Phys. Lett.* **25A**, 764 (1967); M. L. Thèye, *Phys. Rev. B* **2**, 3061 (1970).
15. A. B. Pippard, "*Dynamics of Conduction Electrons*," p. 58, Gordon and Breach, New York, 1965.
16. A. V. Sokolov, "*Optional Properties of Metals*," Chapter 8, Blackie, Glasgow and London, 1967.
17. F. Stern, *Solid State Physics* **15**, 299 (1963).
18. H. Jones, *in* "Handbuch der Physik," Vol. 19 (S. Flugge, ed.), p. 308, Springer-Verlag, Berlin, 1956.
19. F. Wooten, "Optical Properties of Solids," Chapter 4, Academic Press, New York, 1972.
20. H. B. G. Casimir and J. Ubbink, *Philips Tech. Rev.* **28**, 300 (1967).

III COPPER (Cu)

Although there have been many measurements of the optical properties of Cu [1–34], there are limited data in the infrared and vacuum ultraviolet spectral regions.

Table I lists the values of n and k chosen and the pertinent references. These data are plotted in Fig. 1 as smooth curves. The data used from 1.38 Å to 1.237 μm are those of Hagemann *et al.* [22], and those of Dold and Mecke [14] are used in the infrared.

Hagemann *et al.* [22] prepared their samples by evaporating thin films of copper onto substrates of collodion that were supported on copper screen of the type used for electron microscopy. The evaporation was done from resistance-heated boats at a pressure of about 5×10^{-7} torr at rates of 10–50 Å/sec. The plastic substrates were dissolved away, leaving copper films on copper screens. These processes required exposing the copper films to air before measurements. Transmittance measurements were made from 954 to 83 Å (13–150 eV) to obtain an absorption spectrum that was extended by using the data of others [11, 15, 17, 20] to provide an absorption spectrum large enough for a Kramers–Kronig analysis.

Dold and Mecke [14] evaporated copper onto polished glass substrates from molybdenum boats. The films were measured in air by using an ellipsometric technique described by Beattie and Conn [35]. If these data are used to calculate the normal-incidence reflectance R, a spectrum with a broad peak at 8 μm results. The reflectance should increase monotonically with increasing wavelength. Neglect of the anomalous skin effect causes a calculated R to be too high at longer wavelengths, not lower. The cause of the peak probably is erroneously low k values at the longer wavelengths.

REFERENCES

1. G. Joos and A. Klopfer, *Z. Physik* **138**, 251 (1954).
2. L. G. Schulz, *J. Opt. Soc. Am.* **44**, 357, 540 (1954).
3. L. G. Schulz and D. R. Tangherlini, *J. Opt. Soc. Am.* **44**, 362 (1954).
4. J. R. Beattie and G. K. T. Conn, *Philos. Mag.* **46**, 989 (1955).
5. J. N. Hodgson, *Proc. Phys. Soc. London Ser. B* **68**, 593 (1955).
6. M. A. Biondi, *Phys. Rev.* **102**, 964 (1956).
7. L. G. Schulz, *Adv. Phys.* **6**, 102 (1957).
8. M. A. Biondi and J. R. Rayne, *Phys. Rev.* **115**, 1522 (1959).
9. S. Roberts, *Phys. Rev.* **118**, 1509 (1960).
10. M. Otter, *Z. Phyzik* **161**, 163 (1961).
11. H. Ehrenreich and H. R. Philipp, *Phys. Rev.* **128**, 1622 (1962).
12. W. T. Spencer and M. P. Givens, *J. Opt. Soc. Am.* **54**, 1337 (1964).
13. D. Beaglehole, *Proc. Phys. Soc. London* **85**, 1007 (1965).
14. B. Dold and R. Mecke, *Optik* **22**, 435 (1965).
15. L. R. Canfield and G. Hass, *J. Opt. Soc. Am.* **55**, 61 (1965).
16. M. A. Biondi and A. I. Guobadia, *Phys. Rev.* **166**, 667 (1968).

17. R. Haensel, C. Kunz, T. Sasaki, and B. Sonntag, *Appl. Opt.* **7**, 301 (1968).
18. G. P. Pells and M. Shiga, *J. Phys. C* **2**, 1835 (1969).
19. D. H. Seib and W. E. Spicer, *Phys. Rev. B* **2**, 1676 (1970).
20. P. B. Johnson and R. W. Christy, *Phys. Rev. B* **6**, 4370 (1972).
21. I. I. Sasovskaya and M. M. Noskov, *Fiz. Tverd. Tela* **14**, 999 (1972); I. I. Sasovskaya and M. M. Noskov, *Sov. Phys. Solid State* **14**, 857 (1972).
22. H. J. Hagemann, W. Gudat, and C. Kunz, DESY Report SR-74/7, Hamburg, 1974; H. J. Hagemann, W. Gudat, and C. Kunz, *J. Opt. Soc. Am.* **65**, 742 (1975).
23. P. B. Johnson and R. W. Christy, *Phys. Rev. B* **11**, 1315 (1975).
24. J. Rivory and M. L. Thèye, *J. Physique* **36**, L129 (1975).
25. H. J. Hagemann, W. Gudat, and C. Kunz, *Phys. Stat. Solidi B* **74**, 507 (1976).
26. J. A. MacKay and J. R. Rayne, *Phys. Rev. B* **13**, 673 (1976).
27. P. Winsemius, F. F. van Kampen, H. P. Lengkeek, and C. G. van Went, *J. Phys. F* **6**, 1583 (1976).
28. D. Beaglehole and B. Thiéblemont, *Il Nuovo Cimento B* **39**, 477 (1977).
29. L. A. Feldkamp, L. C. Davis, and M. B. Stearns, *Phys. Rev. B* **15**, 5535 (1977).
30. K. G. Ramanathan, S. H. Yen, and E. A. Estalote, *Appl. Opt.* **16**, 2810 (1977).
31. T. Smith, *J. Opt. Soc. Am.* **67**, 48 (1977).
32. R. Smalley and A. J. Sievers, *J. Opt. Soc. Am.* **68**, 1516 (1978).
33. D. Beaglehole, M. DeCrescenzi, M. L. Thèye, and G. Vuye, *Phys. Rev. B* **19**, 6303 (1979).
34. B. Window and G. Harding, *J. Opt. Soc. Am.* **71**, 354 (1981).
35. J. R. Beattie and G. K. T. Conn, *Philos. Mag.* **46**, 222 (1955).

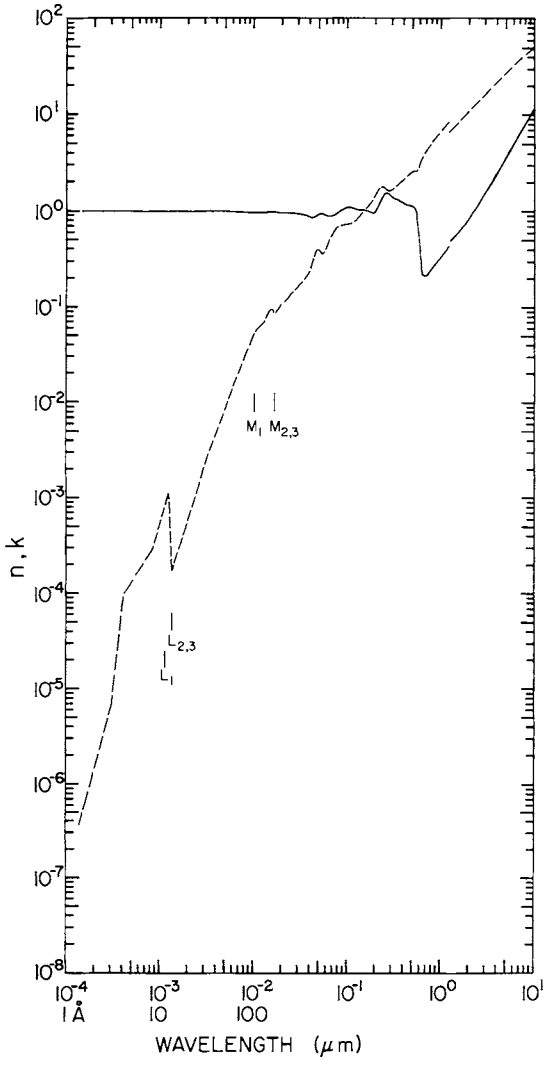

Fig. 1. Log–log plot of n (——) and k (– – – –) versus wavelength in micrometers for copper.

TABLE I

Values of n and k Obtained from Various References for Copper[a]

eV	cm^{-1}	Å	n	k
9000		1.378	1.0010 [22]	3.65×10^{-7} [22]
8900		1.393	1.0010	3.56
8000		1.550	1.0010	5.38×10^{-7}
4000		3.099	1.0000	6.62×10^{-6}
3000		4.133	1.0000	9.49×10^{-5}
1500		8.265	1.0000	2.73×10^{-4}
1200		10.33	0.999	6.24
1100		11.27	0.999	8.23
1000		12.40	0.999	8.51
900		13.78	1.000	1.74
800		15.50	0.999	2.63
700		17.71	0.998	3.95
600		20.66	0.997	6.51×10^{-4}
500		24.80	0.997	1.11×10^{-3}
400		30.99	0.993	2.45
300		41.33	0.988	5.13×10^{-3}
200		61.99	0.978	1.59×10^{-2}
150		82.65	0.969	3.10
120		103.3	0.965	5.40
110		112.7	0.968	5.99
105		118.1	0.968	6.25
100		124.0	0.967	6.53
95		130.5	0.965	6.93
92		134.8	0.963	7.44
90		137.8	0.963	7.88
88		140.9	0.963	8.34
86		144.2	0.966	8.77
84		147.6	0.969	9.11
83		149.4	0.971	9.23
82		151.2	0.973	9.34
81		153.1	0.974	9.43
80		155.0	0.977	9.46
79		156.9	0.979	9.41
78		158.9	0.980	9.36
77		161.0	0.982	9.21
76		163.1	0.984	9.10
75		165.3	0.983	8.72
74		167.5	0.979	8.50
73		169.8	0.977	8.57
72		172.2	0.975	8.68
71		174.6	0.974	8.81
70		177.1	0.972	8.93
68		182.3	0.968	9.27
66		187.8	0.967	9.63×10^{-2}
64		193.7	0.965	0.102
62		200.0	0.965	0.107
60		206.6	0.966	0.109
58		213.8	0.964	0.110
56		221.4	0.960	0.114
54		229.6	0.957	0.120
52		238.4	0.954	0.126
50		248.0	0.953	0.134
48		258.3	0.952	0.140
46		269.5	0.951	0.146

(*continued*)

[a] The references from which the values were extracted are given in brackets.

TABLE I (*Continued*)

Copper

eV	cm^{-1}	Å	n	k
44		281.8	0.948	0.151
42		295.2	0.942	0.157
40		309.9	0.934	0.167
38		326.3	0.927	0.180
36		344.4	0.922	0.193
34		364.6	0.910	0.205
32		387.4	0.891	0.223
30		413.3	0.856	0.262
29		427.5	0.849	0.302
28		442.8	0.862	0.346
27		459.2	0.884	0.382
26		476.8	0.921	0.403
25		495.9	0.960	0.396
24		516.6	0.961	0.373
23		539.0	0.943	0.366
22		563.5	0.917	0.381
21		590.4	0.897	0.411
20		619.9	0.882	0.455
19		652.5	0.883	0.507
18		688.8	0.890	0.561
17		729.3	0.913	0.620
16		774.9	0.954	0.673
15.5		799.9	0.981	0.695
15		826.5	1.01	0.707
14.5		855.0	1.03	0.717
14		885.6	1.06	0.724
13		953.7	1.08	0.724
eV	cm^{-1}	μm	n	k
12		0.1033	1.09	0.731
11		0.1127	1.07	0.754
10		0.1240	1.04	0.818
9.5		0.1305	1.03	0.867
9.0		0.1378	1.03	0.921
8.5		0.1459	1.03	0.979
8.0		0.1550	1.03	1.03
7.5		0.1653	1.01	1.09
7.0		0.1771	0.972	1.20
6.5		0.1907	0.958	1.37
6.0	48,390	0.2066	1.04	1.59
5.8	46,780	0.2138	1.10	1.67
5.6	45,170	0.2114	1.18	1.74
5.4	43,550	0.2296	1.28	1.78
5.2	41,940	0.2384	1.38	1.80
5.0	40,330	0.2480	1.47	1.78
4.8	38,710	0.2583	1.53	1.71
4.6	37,100	0.2695	1.52	1.67
4.4	35,490	0.2818	1.49	1.64
4.2	33,880	0.2952	1.42	1.64
4.0	32,260	0.3099	1.34	1.72
3.8	30,650	0.3263	1.34	1.81
3.6	29,040	0.3444	1.31	1.87
3.4	27,420	0.3646	1.27	1.95

TABLE I (*Continued*)

Copper

eV	cm^{-1}	μm	*n*	*k*
3.2	25,810	0.3874	1.18	2.21
3.0	24,200	0.4133	1.18	2.21
2.8	22,580	0.4428	1.17	2.36
2.6	20,970	0.4768	1.15	2.50
2.4	19,360	0.5166	1.12	2.60
2.3	18,550	0.5390	1.04	2.59
2.2	17,740	0.5635	0.826	2.60
2.1	16,940	0.5904	0.468	2.81
2.0	16,130	0.6199	0.272	3.24
1.9	15,320	0.6525	0.214	3.67
1.85	14,920	0.6702	0.215	3.86
1.80	14,520	0.688	0.213	4.05
1.75	14,110	0.7084	0.214	4.24
1.70	13,710	0.7293	0.223	4.43
1.50	12,100	0.8265	0.260	5.26
1.00	8,065	1.240	0.433	8.46
0.98	7,904	1.265	0.496 [14]	6.78 [14]
0.96	7,743	1.291	0.505	6.92
0.94	7,582	1.319	0.515	7.06
0.92	7,420	1.348	0.525	7.21
0.90	7,259	1.378	0.536	7.36
0.88	7,098	1.409	0.547	7.53
0.86	6,937	1.442	0.559	7.70
0.84	6,775	1.476	0.572	7.88
0.82	6,614	1.512	0.586	8.06
0.80	6,453	1.550	0.606	8.26
0.78	6,291	1.589	0.627	8.47
0.76	6,130	1.631	0.649	8.69
0.74	5,969	1.675	0.672	8.92
0.72	5,807	1.722	0.697	9.16
0.70	5,646	1.771	0.723	9.41
0.68	5,485	1.823	0.752	9.68
0.66	5,323	1.878	0.782	9.97
0.64	5,162	1.937	0.815	10.3
0.62	5,001	2.000	0.850	10.6
0.60	4,839	2.066	0.890	11.0
0.58	4,678	2.138	0.933	11.3
0.56	4,517	2.214	0.980	11.8
0.54	4,355	2.296	1.03	12.2
0.52	4,194	2.384	1.09	12.7
0.50	4,033	2.480	1.15	13.2
0.48	3,872	2.583	1.22	13.7
0.46	3,710	2.695	1.29	14.4
0.44	3,549	2.818	1.37	15.0
0.42	3,388	2.952	1.47	15.7
0.40	3,226	3.100	1.59	16.5
0.38	3,065	3.263	1.73	17.4
0.36	2,904	3.444	1.90	18.4
0.34	2,742	3.646	2.09	19.6
0.32	2,581	3.874	2.32	20.8
0.30	2,420	4.133	2.59	22.2
0.28	2,258	4.428	2.92	23.7
0.26	2,097	4.768	3.32	25.4
0.24	1,936	5.166	3.81	27.5

(*continued*)

TABLE I (*Continued*)

Copper

eV	cm^{-1}	μm	n	k
0.22	1,774	5.635	4.44	30.0
0.20	1,613	6.199	5.23	33.0
0.18	1,452	6.888	6.23	36.3
0.16	1,291	7.749	7.66	40.3
0.15	1,210	8.265	8.57	42.6
0.14	1,129	8.856	9.64	45.1
0.13	1,049	9.537	10.8	47.5

IV GOLD (Au)

There have been more measurements of the optical properties of Au [1–53] than of any other metal, but most of them have been made in the visible region. As with other metals that show free-electron gas behavior in the infrared, the infrared data are very limited and agreement in the n spectra is not good. Moreover, the scatter in the vacuum ultraviolet spectra is far larger than one would expect from a relatively inert metal.

Table II lists the values of n and k chosen and the pertinent references. These data are plotted in Fig. 2 as smooth curves. The data from 1.25 to 124 Å are those reported by Zombeck *et al.* [53], from 140 to 470 Å those reported by Hagemann *et al.* [39], from 470 to 2000 Å those of Canfield *et al.* [10], from 1000 Å to 2 μm those reported by Thèye [27], and in the infrared those of Dold and Mecke [14].

All investigators except Hagemann *et al.* [39] stated that the gold used in their investigations was better than 99.99% pure. Hagemann *et al.* [39] prepared their samples by evaporating thin films of gold onto substrates of collodion that were supported on copper screen of the type used for electron microscopy. The evaporation was done from resistance-heated boats at a pressure of about 5×10^{-7} torr at rates of 10–50 Å/sec. The plastic substrates were dissolved away, leaving gold films on copper screens. These processes required exposing the gold films to air before measurements were performed. Transmittance measurements were made from 13 to 150 eV to obtain an absorption spectrum that was extended by using the data of others [19, 26, 31, 33] to provide an absorption spectrum large enough for a Kramers–Kronig analysis.

Canfield *et al.* [10] used the reflectance method to obtain n and k from gold films vacuum evaporated onto polished glass substrates at room temperature (30–40°C) in a conventional vacuum system. The pressures during

evaporation were approximately 10^{-6} torr and deposition rates were on the order of hundreds of angstroms per second. Some reflectance measurements were made without exposing the films to air, and others were made after exposure. Exposure had no effect on reflectance.

Thèye [27] prepared her films by evaporation in ultrahigh vacuum (10^{-10}–10^{-11} torr) onto superpolished fused silica substrates. The substrate temperature ranged from room temperature to 100°C. Annealing at 100 to 150°C was done. She measured reflectance and transmittance at normal incidence in air for known film thicknesses (100–250 Å) from which she obtained n and k.

Dold and Mecke [14] evaporated gold onto polished glass substrates from tantalum boats. The films were measured in air by using an ellipsometric technique described by Beattie and Conn [54]. If these data are used to calculate the normal-incidence reflectance R, a spectrum with a broad peak at 5–6 μm results. The reflectance should increase monotonically with increasing wavelength. Neglect of the anomalous skin effect causes a calculated R to be too high at longer wavelengths, not lower. The cause of the peak probably is erroneously low k values at the longer wavelengths.

Aspnes *et al.* [52] made an extensive study of the optical properties of gold films. In the region of interband absorption they that found the most important cause of disagreement among different sets of data results not from experimental errors, but from genuine sample differences caused by different sample preparation methods. Of these differences, voids are the most important. The best films are those that have the highest value of ε_2 in this spectral region. The data we have chosen, those of Thèye [27], meet this criterion, which is discussed further by Aspnes in Chapter 5 of this handbook. In the intraband region, just below the interband threshold, Aspnes *et al.* [52] show that the most important differences in data sets arise from crystallite size in the films, with large-grained films giving the more bulklike results. In this case the criterion for quality is the smallest value of ε_2. Further in the infrared, measurement errors increase, and this criterion becomes less valid. In comparing the limited amount of data for Cu, Ag, and Au for wavelengths longer than 2 μm, there is no one investigator or group of investigators whose data yield consistently lower values of ε_2 for all three metals. We therefore did not use this criterion.

REFERENCES

1. G. Joos and A. Klopfer, *Z. Physik* **138**, 251 (1954).
2. L. G. Schulz, *J. Opt. Soc. Am.* **44**, 357, 540 (1954).
3. L. G. Schulz and F. R. Tangherlini, *J. Opt. Soc. Am.* **44**, 362 (1954).
4. J. R. Beattie and G. K. T. Conn, *Philos. Mag.* **46**, 989 (1955).
5. J. N. Hodgson, *Proc. Phys. Soc.* London Ser. B **68**, 593 (1955).
6. L. G. Schulz, *Adv. Phys.* **6**, 102 (1957).

7. M. Otter, *Z. Physik* **161**, 163 (1961).
8. P. R. Wessel, *Phys. Rev.* **132**, 2062 (1963).
9. H. Mayer and H. Bohme, *J. Physique* **25**, 81 (1964).
10. L. R. Canfield, G. Hass, and W. R. Hunter, *J. Physique* **25**, 124 (1964).
11. A. P. Lukirskii, E. P. Savinov, O. A. Ershov, and Y. F. Shepelev, *Opt. Spektrosk.* **16**, 310 (1964); A. P. Lukirskii, E. P. Savinov, O. A. Ershov, and Y. F. Shepelev, *Opt. Spectrosc.* **16**, 168 (1964).
12. D. Beaglehole, *Proc. Phys. Soc. London* **85**, 1007 (1965).
13. B. R. Cooper, H. Ehrenreich, and H. R. Philipp, *Phys. Rev.* **138**, A494 (1965).
14. B. Dold and R. Mecke, *Optik* **22**, 435 (1965).
15. H. E. Bennett and J. M. Bennett, *in* "Optical Properties and Electronic Structure of Metals and Alloys" (F. Abélès, ed.), p. 175, North-Holland Publ., Amsterdam, 1966.
16. H. Fukutani and O. Sueoka, *in* "Optical Properties and Electronic Structure of Metals and Alloys" (F. Abélès, ed.), p. 565, North-Holland Publ., Amsterdam, 1966.
17. D. Beaglehole, *in* "Optical Properties and Electronic Structure of Metals and Alloys" (F. Abélès, ed.), p. 154, North-Holland Publ., Amsterdam, 1966.
18. D. Jaegle and G. Missoni, *C. R. Acad. Sci. Paris* **262B**, 71 (1966).
19. E. Meyer, H. Frede, and H. Knof, *J. Appl. Phys.* **38**, 3682 (1967).
20. W. J. Scouler, *Phys. Rev. Lett.* **18**, 445 (1967).
21. W. Koster and R. Stahl, *Z. Metallkd.* **58**, 768 (1967).
22. R. Haensel, C. Kunz, T. Sasaki, and B. Sonntag, *Appl. Opt.* **7**, 301 (1968).
23. J. N. Hodgson, *J. Phys. Chem. Solids* **29**, 2175 (1968).
24. K. Platzöder and W. Steinmann, *J. Opt. Soc. Am.* **58**, 588 (1968).
25. G. P. Pells and M. Shiga, *J. Phys. C* **2**, 1835 (1969).
26. R. Haensel, K. Radler, B. Sonntag, and C. Kunz, *Solid State Commun.* **7**, 1495 (1969).
27. M. L. Thèye, *Phys. Rev. B* **2**, 3060 (1970).
28. P. O. Nilsson, *Phys. Kondens. Mater.* **11**, 1 (1970).
29. G. Jungk, *Phys. Stat. Solidi A* **3**, 965 (1970).
30. W. R. Hunter, *Proc. 3rd Int. Conf. Vac. Ultraviolet Radiation Physics, Tokyo*, p. 2aC2-1 (1971).
31. G. B. Irani, T. Huen, and F. Wooten, *J. Opt. Soc. Am.* **61**, 128 (1971).
32. G. B. Irani, T. Huen, and F. Wooten, *Phys. Rev. B* **6**, 2904 (1972).
33. P. B. Johnson and R. W. Christy, *Phys. Rev. B* **11**, 1315 (1975).
34. R. C. Linton, NASA Tech. Note D-7061 (1972).
35. M. Schlüter, *Z. Physik* **250**, 87 (1972).
36. D. E. Aspnes, *Opt. Commun.* **8**, 222 (1973).
37. O. Hunderi, *Phys. Rev. B* **7**, 3419 (1973).
38. L. N. Aksyutov, *Inzh-Fiz. Zh.* **27**, 197 (1974); L. N. Aksyutov, *J. Eng. Phys.* **27**, 913 (1974).
39. H. J. Hagemann, W. Gudat, and C. Kunz, DESY Report SR-74/7, Hamburg, 1974; H. J. Hagemann, W. Gudat, and C. Kunz, *J. Opt. Soc. Am.* **65**, 742 (1975).
40. C. Wehenkel and B. Gauthé, *Opt. Commun.* **11**, 62 (1974).
41. N. Fuschillo, B. Lalevic, W. Slusark, and A. Delahoy. *J. Vac. Sci. Technol.* **12**, 84 (1975).
42. C. G. Granquist and O. Hunderi, *Solid State Commun.* **19**, 939 (1976).
43. J. A. MacKay and J. A. Rayne, *Phys. Rev. B* **13**, 673 (1976).
44. P. Winsemius, F. F. van Kampen, H. P. Lengkeek, and C. G. van Went, *J. Phys. F* **6**, 1583 (1976).
45. G. Jungk and R. Grundler, *Phys. Stat. Solidi B* **76**, 541 (1976).
46. D. Beaglehole and B. Thiéblemont, *Il Nuovo Cimento B* **39**, 477 (1977).
47. T. Hollstein, V. Kreibig, and F. Leis, *Phys. Stat. Solidi B* **83**, K49 (1977).
48. T. A. McMath, R. A. D. Hewko, O. Singh, A. E. Curzon, and J. C. Irwin, *J. Opt. Soc. Am.* **67**, 630 (1977).
49. R. Kirsch, *Phys. Stat. Solidi A* **46**, 459 (1978).
50. D. Beaglehole, M. DeCrescenzi, M. L. Thèye, and G. Vuye, *Phys. Rev. B* **19**, 6303 (1979).

51. M. L. Scott and G. T. Johnston, *Appl. Opt.* **18**, 2905 (1979).
52. D. E. Aspnes, E. Kinsbron, and D. D. Bacon, *Phys. Rev. B* **21**, 3290 (1980).
53. M. V. Zombeck, G. K. Austin, and D. T. Torgerson, Smithsonian Astrophysical Observatory Report SAO-AXAF-80-003, Appendix B, Table B1, Cambridge, Massachusetts, 1980.
54. J. R. Beattie and G. K. T. Conn, *Philos. Mag.* **46**, 222 (1955).

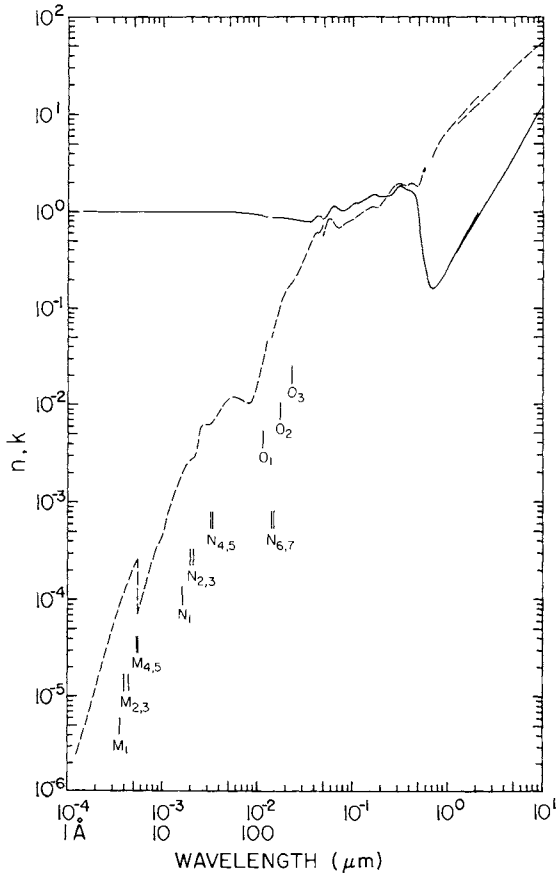

Fig. 2. Log–log plot of n (——) and k (– – – –) versus wavelength in micrometers for gold.

TABLE II

Values of n and k Obtained from Various References for Gold[a]

eV	cm^{-1}	Å	n	k
9919		1.25	0.9999719 [28]	2.39×10^{-6} [53]
9184		1.35	0.9999665	3.13
8551		1.45	0.9999608	4.02
8266		1.50	0.9999578	4.52
7085		1.75	0.9999415	7.78×10^{-6}
6199		2.00	0.9999227	1.25×10^{-5}
4959		2.50	0.999879	2.75
4133		3.00	0.999831	5.25
3542		3.50	0.999794	9.07×10^{-5}
3100		4.00	0.999769	1.20×10^{-4}
2480		5.00	0.999706	2.36×10^{-4}
2066		6.00	0.999637	9.88×10^{-5}
1771		7.00	0.999395	1.68×10^{-4}
1550		8.00	0.999156	2.67
1487		8.34	0.999085	3.10
1254		9.89	0.99885	4.40
1188		10.44	0.99871	5.33
1012		12.25	0.99820	9.40×10^{-4}
929.4		13.34	0.99788	1.23×10^{-3}
851.5		14.56	0.99759	1.57
776.4		15.97	0.99734	1.86
704.9		17.59	0.99708	2.34
637.5		19.45	0.99665	2.68
572.9		21.64	0.99652	2.85
524.9		23.62	0.99624	3.76
500.3		24.78	0.99600	5.60
452.2		27.42	0.99592	6.10
395.4		31.36	0.99525	6.15
300.0		41.33	0.99100	8.95×10^{-3}
260.0		47.69	0.988	1.06×10^{-2}
220.0		56.36	0.986	1.18
200		61.99	0.983	1.15
180		68.88	0.979	1.07
150		82.65	0.963	1.01
120		103.3	0.929	1.78
110		112.7	0.911	2.83
105		118.1	0.900	3.53
100		124.0	0.889	4.54
88		140.9	0.889 [39]	5.54×10^{-2} [39]
87.5		141.7	0.888	5.58
87		142.5	0.887	5.76
86		144.2	0.886	6.13
85		145.9	0.887	6.48
84.5		146.7	0.888	6.54
84		147.6	0.888	6.33
83.5		148.5	0.885	6.37
83		149.4	0.884	6.53
82		151.2	0.881	6.82
80		155.0	0.878	7.52
78		158.9	0.875	8.18
76		163.1	0.873	8.71
74		167.5	0.869	9.27
72		172.2	0.862	9.97×10^{-2}
70		177.1	0.857	0.112

[a] The references from which the values were extracted are given in brackets.

TABLE II (*Continued*)

Gold

eV	cm^{-1}	Å	n	k
68		182.3	0.855	0.124
66		187.8	0.856	0.136
64		193.7	0.857	0.147
62		200.0	0.859	0.156
60		206.6	0.863	0.162
58		213.8	0.861	0.166
56		221.4	0.856	0.171
54		229.6	0.848	0.180
52		238.4	0.839	0.190
50		248.0	0.828	0.204
49		253.0	0.821	0.213
48		258.3	0.814	0.225
47		263.8	0.809	0.238
46		269.5	0.805	0.254
45		275.5	0.805	0.270
44		281.8	0.807	0.282
43		288.3	0.807	0.292
42		295.2	0.804	0.303
41		302.4	0.799	0.317
40		309.9	0.795	0.334
39		317.9	0.793	0.353
38		326.3	0.791	0.371
37		335.1	0.788	0.391
36		344.4	0.786	0.414
35		354.2	0.783	0.439
34		364.6	0.779	0.473
33		375.7	0.781	0.515
32		387.4	0.805	0.570
31		399.9	0.851	0.596
30.5		406.5	0.870	0.601
30		413.3	0.887	0.603
29.5		420.3	0.900	0.601
29		427.5	0.905	0.599
28		442.8	0.901	0.607
27		459.2	0.895	0.635

eV	cm^{-1}	μm	n	k
26.38		0.0470	0.855 [10]	0.548 [10]
26		0.04768	0.896 [39]	0.679 [39]
25.83		0.0480	0.846 [10]	0.565 [10]
25.30		0.0490	0.846	0.600
24.80		0.0500	0.850	0.645
24.31		0.0510	0.860	0.695
23.84		0.0520	0.872	0.740
23.39		0.0530	0.890	0.795
22.96		0.0540	0.915	0.825
22.54		0.0550	0.950	0.840
22.14		0.0560	0.985	0.848
21.75		0.0570	1.022	0.850
21.38		0.0580	1.055	0.842
21.01		0.0590	1.085	0.830
20.66		0.0600	1.113	0.813
20.33		0.0610	1.134	0.795

(*continued*)

TABLE II (*Continued*)

Gold

eV	cm^{-1}	μm	n	k
20.00		0.0620	1.146	0.770
19.68		0.0630	1.153	0.750
19.37		0.0640	1.157	0.730
19.07		0.0650	1.155	0.710
18.79		0.0660	1.140	0.700
18.51		0.0670	1.125	0.694
18.23		0.0680	1.107	0.687
17.97		0.0690	1.088	0.680
17.71		0.0700	1.075	0.678
17.46		0.0710	1.060	0.680
17.22		0.0720	1.050	0.685
16.98		0.0730	1.042	0.690
16.75		0.0740	1,038	0.697
16.53		0.0750	1.033	0.704
16.31		0.0760	1.030	0.713
16.10		0.0770	1.029	0.720
15.90		0.0780	1.028	0.730
15.69		0.0790	1.028	0.739
15.50		0.0800	1.029	0.745
15.31		0.0810	1.030	0.752
15.12		0.0820	1.033	0.759
14.94		0.0830	1.037	0.765
14.76		0.0840	1.041	0.770
14.59		0.0850	1.048	0.775
14.42		0.0860	1.053	0.780
14.25		0.0870	1.061	0.784
14.09		0.0880	1.070	0.789
13.93		0.0890	1.080	0.793
13.78		0.0900	1.090	0.798
13.62		0.0910	1.100	0.801
13.48		0.0920	1.110	0.806
13.33		0.0930	1.121	0.809
13.19		0.0940	1.133	0.812
13.05		0.0950	1.146	0.815
12.92		0.0960	1.159	0.819
12.78		0.0970	1.170	0.823
12.65		0.0980	1.180	0.826
12.52		0.0990	1.190	0.831
12.40		0.100	1.200	0.836
12.28		0.101	1.207	0.842
12.16		0.102	1.210	0.848
12.04		0.103	1.213	0.853
11.92		0.104	1.215	0.860
11.81		0.105	1.217	0.865
11.70		0.106	1.217	0.870
11.59		0.107	1.218	0.878
11.48		0.108	1.218	0.885
11.37		0.109	1.220	0.893
11.27		0.110	1.222	0.900
11.17		0.111	1.223	0.907
11.07		0.112	1.225	0.914
10.97		0.113	1.228	0.922
10.88		0.114	1.232	0.927
10.78		0.115	1.237	0.932

TABLE II (*Continued*)

Gold

eV	cm^{-1}	μm	n	k
10.69		0.116	1.242	0.935
10.60		0.117	1.247	0.942
10.51		0.118	1.250	0.950
10.42		0.119	1.255	0.955
10.33		0.120	1.260	0.962
10.25		0.121	1.265	0.967
10.16		0.122	1.270	0.975
10.08		0.123	1.275	0.982
10.00		0.124	1.280	0.987
9.919		0.125	1.285	0.994
9.840		0.126	1.290	1.000
9.763		0.127	1.295	1.005
9.686		0.128	1.300	1.012
9.611		0.129	1.304	1.017
9.537		0.130	1.308	1.020
9.465		0.131	1.313	1.027
9.393		0.132	1.318	1.032
9.322		0.133	1.323	1.038
9.253		0.134	1.328	1.045
9.184		0.135	1.333	1.050
9.117		0.136	1.338	1.053
9.050		0.137	1.345	1.058
8.984		0.138	1.350	1.063
8.920		0.139	1.355	1.067
8.856		0.140	1.360	1.072
8.551		0.145	1.386	1.089
8.266		0.150	1.419	1.102
7.999		0.155	1.450	1.108
7.749		0.160	1.483	1.106
7.514		0.165	1.512	1.093
7.293		0.170	1.519	1.070
7.085		0.175	1.500	1.070
6.888		0.180	1.470	1.085
6.702		0.185	1.442	1.107
6.526		0.190	1.427	1.135
6.358		0.195	1.424	1.170
6.199		0.200	1.427	1.215
6.0	48,390	0.2066	1.422 [27]	1.306 [27]
5.9	47,590	0.2101	1.430	1.334
5.8	46,780	0.2138	1.432	1.364
5.7	45,970	0.2175	1.438	1.388
5.6	45,170	0.2214	1.442	1.418
5.5	44,360	0.2254	1.452	1.442
5.4	43,550	0.2296	1.454	1.478
5.3	42,750	0.2339	1.462	1.510
5.2	41,940	0.2384	1.470	1.550
5.1	41,130	0.2431	1.478	1.590
5.0	40,330	0.2480	1.484	1.636
4.9	39,520	0.2530	1.490	1.698
4.8	38,710	0.2583	1.504	1.748
4.7	37,910	0.2638	1.546	1.784
4.6	37,100	0.2695	1.598	1.822
4.5	36,290	0.2755	1.648	1.852
4.4	34,590	0.2818	1.690	1.882

(*continued*)

TABLE II (*Continued*)

Gold

eV	cm^{-1}	μm	n	k
4.3	34,680	0.2883	1.742	1.900
4.2	33,880	0.2952	1.776	1.918
4.1	33,070	0.3024	1.812	1.920
4.0	32,260	0.3100	1.830	1.916
3.9	31,460	0.3179	1.840	1.904
3.8	30,650	0.3263	1.824	1.878
3.7	29,840	0.3351	1.798	1.860
3.6	29,040	0.3444	1.766	1.846
3.5	28,230	0.3542	1.740	1.848
3.4	27,420	0.3647	1.716	1.862
3.3	26,620	0.3757	1.696	1.906
3.2	25,810	0.3875	1.674	1.936
3.1	25,000	0.4000	1.658	1.956
3.0	24,200	0.4133	1.636	1.958
2.9	23,390	0.4275	1.616	1.940
2.8	22,580	0.4428	1.562	1.904
2.7	21,780	0.4592	1.426	1.846
2.6	20,970	0.4769	1.242	1.796
2.5	20,160	0.4959	0.916	1.840
2.4	19,360	0.5166	0.608	2.120
2.3	18,550	0.5391	0.402	2.540
2.2	17,740	0.5636	0.306	2.88
2.1	16,940	0.5904	0.236	
2.0	16,130	0.6199	0.194	
1.9	15,320	0.6526	0.166	3.15
1.8	14,520	0.6888	0.160	3.80
1.7	13,710	0.7293	0.164	4.35
1.6	12,900	0.7749	0.174	4.86
1.5	12,100	0.8266	0.188	5.39
1.4	11,290	0.8856	0.210	5.88
1.3	10,490	0.9537	0.236	6.47
1.2	9,679	1.033	0.272	7.07
1.1	8,872	1.127	0.312	7.93
1.0	8,065	1.240	0.372	8.77
0.98	7,904	1.265	0.389 [14]	8.09 [14]
0.96	7,743	1.291	0.403	8.25
0.94	7,582	1.319	0.419	8.42
0.92	7,420	1.384	0.436	8.59
0.90	7,259	1.378	0.454	8.77
			0.458 [27]	9.72 [27]
0.88	7,098	1.409	0.473 [14]	8.96 [14]
0.86	6,936	1.442	0.493	9.15
0.84	6,775	1.476	0.515	9.36
0.82	6,614	1.512	0.537	9.58
0.80	6,452	1.550	0.559	9.81
			0.550 [27]	11.5 [27]
0.78	6,291	1.590	0.583 [14]	10.1 [14]
0.76	6,130	1.631	0.609	10.3
0.74	5,968	1.675	0.636	10.6
0.72	5,807	1.722	0.665	10.9
0.70	5,646	1.771	0.696	11.2
			0.726	12.9
0.68	5,485	1.823	0.730	11.5
0.66	5,323	1.879	0.767	11.9

TABLE II (*Continued*)

Gold

eV	cm^{-1}	μm	n	k
0.64	5,162	1.937	0.807	12.2
0.62	5,001	2.000	0.850	12.6
0.60	4,839	2.066	0.896	13.0
			0.976 [27]	15.1 [27]
0.58	4,678	2.138	0.947 [14]	13.4 [14]
0.56	4,517	2.214	1.002	13.9
0.54	4,355	2.296	1.063	14.4
0.52	4,194	2.384	1.130	14.9
0.50	4,033	2.480	1.205	15.5
0.48	3,871	2.583	1.287	16.1
0.46	3,710	2.695	1.379	16.8
0.44	3,549	2.818	1.482	17.5
0.42	3,388	2.952	1.598	18.3
0.40	3,226	3.100	1.728	19.2
0.39	3,146	3.179	1.800	19.7
0.38	3,065	3.263	1.876	20.2
0.37	2,984	3.351	1.958	20.7
0.36	2,904	3.444	2.046	21.3
0.35	2,823	3.542	2.141	21.9
0.34	2,742	2.647	2.242	22.5
0.33	2,662	3.757	2.352	23.1
0.32	2,581	3.875	2.471	23.9
0.31	2,500	4.000	2.600	24.6
0.30	2,420	4.133	2.749	25.4
0.29	2,339	4.275	2.912	26.3
0.28	2,258	4.428	3.091	27.2
0.27	2,178	4.592	3.289	28.2
0.26	2,097	4.769	3.507	29.3
0.25	2,016	4.959	3.748	30.5
0.24	1,936	5.166	4.007	31.7
0.23	1,855	5.391	4.292	32.9
0.22	1,774	5.636	4.611	34.3
0.21	1,694	5.904	4.971	35.9
0.20	1,613	6.199	5.423	37.5
0.195	1,573	6.358	5.684	38.3
0.19	1,532	6.526	5.966	39.1
0.185	1,492	6.702	6.270	40.1
0.18	1,452	6.888	6.598	41.0
0.175	1,411	7.085	6.937	42.0
0.17	1,371	7.293	7.282	43.0
0.165	1,331	7.514	7.655	44.1
0.16	1,290	7.749	8.060	45.2
0.155	1,250	7.999	8.500	46.4
0.15	1,210	8.266	9.016	47.6
0.145	1,169	8.551	9.582	48.8
0.14	1,129	8.856	10.21	50.2
0.135	1,089	9.184	10.84	51.6
0.13	1,049	9.537	11.51	53.1
0.125	1,008	9.919	12.24	54.7

V IRIDIUM (Ir)

There are not many optical studies of Ir[1–7]. Table III lists the n and k values of Weaver *et al.* [7] from 310 Å to approximately 12.4 μm and of Henke [8] from 6.2–124 Å. These data are presented as smooth curves in Fig. 3. It is tempting to interpolate between the data set with smooth curves; however, there is an hiatus of 186 Å, where both O and N absorption edges are located so such an interpolation would be highly speculative. Further measurements are necessary to fill the gap.

Weaver *et al.* [7] used large polycrystalline samples cut from a crystal rod of iridium of unstated purity. The samples were mechanically polished, boiled in aqua regia, and heated *in vacuo* (10^{-7} torr) at temperatures of 1200–1500°C for several hours. The samples were then transferred in air to ion-pumped experimental chambers. From 6.2 μm to 2818 Å, a calorimetric technique [9] was used and at the shorter wavelengths (4312–310 Å) the reflectance at 10° angle of incidence was measured. These data were combined with other data [4], Drude infrared extrapolations, and a power-law decay in R extending to 10^5 eV to obtain n and k by using the Kramers–Kronig technique.

REFERENCES

1. B. T. Barnes, *J. Opt. Soc. Am.* **56**, 1546 (1966).
2. G. Hass, G. F. Jacobus, and W. R. Hunter, *J. Opt. Soc. Am.* **57**, 758 (1967).
3. J. A. R. Samson, J. P. Padur, and A. Sharma, *J. Opt. Soc. Am.* **57**, 966 (1967).
4. R. Haensel, K. Radler, B. Sonntag, and C. Kunz, *Solid State Commun.* **7**, 1495 (1972).
5. M. M. Kirillova, L. V. Nomerovannaya, and M. M. Noskov, *Fiz. Met. Metalloved.* **34**, 291 (1972); M. M. Kirillova, L. V. Nomerovannaya, and M. M. Noskov, *Phys. Met. Metall.* **34** (2), 61 (1972).
6. J. H. Weaver, *Phys. Rev. B* **11**, 1416 (1975).
7. J. H. Weaver, C. G. Olson, and D. W. Lynch, *Phys. Rev. B* **15**, 4115 (1977).
8. B. L. Henke, P. Lee, T. J. Tanaka, R. L. Shimabukuro, and B. K. Fujikawa, "Low Energy X-Ray Diagnostics—1981" (D. T. Attwood and B. L. Henke, eds.), p. 340, *AIP Conf. Proc.* No. 75, American Institute of Physics, New York, 1981.
9. L. W. Bos and D. W. Lynch, *Phys. Rev. B* **2**, 4567 (1970).

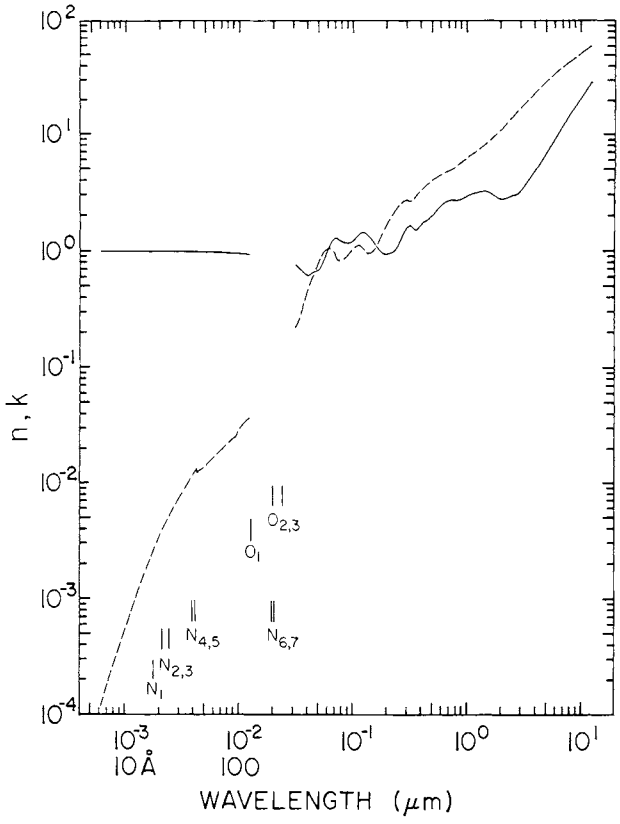

Fig. 3. Log–log plot of n (——) and k (– – – –) versus wavelength in micrometers for iridium.

TABLE III

Values of n and k Obtained from Various References for Iridium[a]

eV	cm^{-1}	Å	n	k
2000		6.199	0.999710 [8]	1.22×10^{-4} [8]
1952		6.351	0.999585	1.31
1905		6.508	0.999451	1.42
1860		6.665	0.999388	1.53
1815		6.831	0.999335	1.65
1772		6.997	0.999284	1.78
1730		7.166	0.999235	1.92
1688		7.345	0.999185	2.07
1648		7.523	0.999134	2.23
1609		7.705	0.999082	2.40
1570		7.897	0.999028	2.59
1533		8.087	0.99897	2.79
1496		8.287	0.99892	3.00
1460		8.492	0.99886	3.23
1426		8.694	0.99880	3.48
1392		8.906	0.99873	3.74
1358		9.129	0.99867	4.03
1326		9.350	0.99860	4.34
1294		9.581	0.99853	4.67
1263		9.816	0.99846	5.03
1233		10.05	0.99838	5.41
1204		10.30	0.99830	5.80
1175		10.55	0.99822	6.24
1147		10.81	0.99814	6.71
1119		11.08	0.99805	7.22
1093		11.34	0.99796	7.75
1067		11.62	0.99787	8.33
1041		11.91	0.99777	8.97
1016		12.20	0.99768	9.64×10^{-4}
992		12.50	0.99758	1.03×10^{-3}
968		12.81	0.99747	1.11
945		13.12	0.99737	1.19
923		13.43	0.99726	1.27
901		13.76	0.99715	1.36
879		14.10	0.99703	1.45
858		14.45	0.99692	1.55
838		14.79	0.99680	1.66
818		15.16	0.99668	1.77
798		15.54	0.99655	1.89
779		15.92	0.99643	2.02
760		16.31	0.99630	2.16
742		16.71	0.99618	2.30
725		17.10	0.99607	2.45
707		17.54	0.99598	2.62
690		17.97	0.99587	2.70
674		18.39	0.99571	2.79
658		18.84	0.99553	2.96
642		19.31	0.99536	3.19
627		19.77	0.99522	3.34
612		20.26	0.99507	3.53
597		20.77	0.99491	3.74
583		21.27	0.99477	3.95

[a] The references from which the values were extracted are given in brackets.

TABLE III (*Continued*)

Iridium

eV	cm^{-1}	Å	n	k
569		21.79	0.99463	4.17
555		22.34	0.99449	4.40
542		22.87	0.99436	4.62
529		23.44	0.99423	4.85
516		24.03	0.99411	5.07
504		24.60	0.99397	5.26
492		25.20	0.99380	5.46
480		25.83	0.99362	5.68
469		26.43	0.99343	5.89
458		27.07	0.99322	6.11
447		27.74	0.99297	6.38
436		28.44	0.99273	6.71
426		29.10	0.99252	7.03
415		29.87	0.99229	7.41
406		30.54	0.99212	7.74
396		31.31	0.99193	8.14
386		32.12	0.99176	8.51
377		32.89	0.99159	8.86
368		33.69	0.99140	9.24
359		34.53	0.99121	9.64×10^{-3}
351		35.32	0.99104	1.00×10^{-2}
342		36.25	0.99086	1.05
334		37.12	0.99070	1.09
326		38.03	0.99056	1.14
318		38.99	0.99045	1.19
311		39.86	0.99040	1.23
303		40.92	0.99045	1.29
296		41.88	0.99072	1.34
289		42.90	0.99109	1.26
282		43.96	0.99044	1.29
275		45.08	0.99006	1.32
269		46.09	0.9898	1.33
262		47.32	0.9894	1.35
256		48.43	0.9889	1.38
250		49.59	0.9885	1.41
244		50.81	0.9880	1.45
238		52.09	0.9876	1.49
232		53.44	0.9870	1.52
227		54.62	0.9866	1.56
221		56.10	0.9860	1.60
216		57.40	0.9855	1.64
211		58.76	0.9850	1.68
206		60.18	0.9843	1.72
201		61.68	0.9836	1.76
196		63.25	0.9828	1.82
191		64.91	0.9823	1.90
187		66.30	0.9819	1.93
182		68.12	0.9812	1.95
178		69.65	0.9804	1.98
174		71.25	0.9795	2.02
170		72.93	0.9786	2.05
166		74.69	0.9776	2.10

(*continued*)

TABLE III (*Continued*)

Iridium

eV	cm^{-1}	Å	n	k
162		76.53	0.9764	2.15
158		78.47	0.9752	2.22
154		80.51	0.9739	2.30
150		82.65	0.9729	2.39
147		84.34	0.9720	2.42
143		86.70	0.9708	2.46
140		88.56	0.9696	2.49
136		91.16	0.9676	2.52
133		93.22	0.9658	2.54
130		95.37	0.9634	2.57
127		97.62	0.9609	2.72
124		99.98	0.9588	2.88
121		102.5	0.9570	3.05
118		105.1	0.9555	3.18
115		107.8	0.9536	3.27
112		110.7	0.9513	3.37
110		112.7	0.9498	3.45
107		115.9	0.9473	3.53
104		119.2	0.9443	3.62
102		121.5	0.9419	3.68
100		124.0	0.9394	3.74
eV	cm^{-1}	μm	n	k
40		0.03100	0.76 [7]	0.22 [7]
38		0.03263	0.73	0.24
36		0.03444	0.69	0.27
34		0.03647	0.64	0.35
32		0.03875	0.62	0.44
30		0.04133	0.64	0.53
29.5		0.04203	0.64	0.55
29		0.04275	0.65	0.57
28.5		0.04350	0.66	0.59
28		0.04428	0.66	0.61
27.5		0.04509	0.66	0.63
27		0.04592	0.66	0.66
26.5		0.04678	0.67	0.69
26		0.04769	0.67	0.72
25.5		0.04862	0.68	0.76
25		0.04959	0.69	0.79
24.5		0.05060	0.70	0.83
24		0.05166	0.73	0.87
23.5		0.05276	0.76	0.92
23		0.05391	0.79	0.96
22.5		0.05510	0.84	0.99
22		0.05636	0.89	1.00
21.5		0.05766	0.94	1.02
21		0.05904	0.99	1.04
20.5		0.06048	1.04	1.05
20		0.06199	1.10	1.06
19.6		0.06326	1.15	1.05
19.2		0.06458	1.20	1.03

TABLE III (*Continued*)

Iridium

eV	cm^{-1}	μm	n	k
18.8		0.06595	1.24	1.00
18.4		0.06738	1.27	0.97
18		0.06888	1.30	0.93
17.6		0.07045	1.30	0.87
17.2		0.07208	1.28	0.83
16.8		0.07380	1.25	0.82
16.4		0.07560	1.23	0.82
16		0.07749	1.21	0.83
15.6		0.07948	1.20	0.83
15.2		0.08157	1.19	0.84
14.8		0.08377	1.18	0.87
14.4		0.08610	1.17	0.88
14		0.08856	1.16	0.91
13.6		0.09117	1.17	0.95
13.2		0.09393	1.18	0.96
12.8		0.09686	1.19	1.01
12.4		0.09999	1.21	1.05
12		0.1033	1.24	1.08
11.8		0.1051	1.25	1.10
11.6		0.1069	1.28	1.12
11.4		0.1088	1.31	1.13
11.2		0.1107	1.34	1.14
11.0		0.1127	1.38	1.13
10.8		0.1148	1.41	1.12
10.6		0.1170	1.43	1.09
10.4		0.1192	1.44	1.07
10.2		0.1216	1.45	1.04
10.0		0.1240	1.45	1.01
9.9		0.1252	1.44	1.00
9.8		0.1265	1.44	0.99
9.7		0.1278	1.43	0.98
9.6		0.1291	1.42	0.97
9.5		0.1305	1.40	0.96
9.4		0.1319	1.39	0.95
9.3		0.1333	1.38	0.95
9.2		0.1348	1.36	0.95
9.1		0.1362	1.35	0.94
9.0		0.1378	1.33	0.94
8.9		0.1393	1.31	0.94
8.8		0.1409	1.29	0.95
8.7		0.1425	1.27	0.95
8.6		0.1442	1.26	0.96
8.5		0.1459	1.24	0.97
8.4		0.1476	1.22	0.98
8.3		0.1494	1.20	0.99
8.2		0.1512	1.18	1.00
8.1		0.1531	1.15	1.01
8.0		0.1550	1.13	1.03
7.9		0.1569	1.11	1.05
7.8		0.1590	1.08	1.06
7.7		0.1610	1.05	1.10
7.6		0.1631	1.03	1.14

(*continued*)

TABLE III (*Continued*)

Iridium

eV	cm^{-1}	μm	n	k
7.5		0.1653	1.03	1.18
7.4		0.1675	1.02	1.20
7.3		0.1698	1.00	1.23
7.2		0.1722	0.99	1.27
7.1		0.1746	0.98	1.30
7.0		0.1771	0.97	1.34
6.9		0.1797	0.96	1.38
6.8		0.1823	0.95	1.42
6.7		0.1851	0.95	1.46
6.6		0.1879	0.94	1.50
6.5		0.1907	0.95	1.54
6.4		0.1937	0.94	1.59
6.3		0.1968	0.94	1.63
6.2		0.2000	0.94	1.68
6.1		0.2033	0.94	1.73
6.0	48,390	0.2066	0.95	1.78
5.9	47,590	0.2101	0.97	1.82
5.8	46,780	0.2138	0.96	1.86
5.7	45,970	0.2175	0.97	1.92
5.6	45,170	0.2214	0.98	1.98
5.5	44,360	0.2254	0.99	2.03
5.4	43,550	0.2296	1.00	2.09
5.3	42,750	0.2339	1.02	2.15
5.2	41,940	0.2384	1.04	2.22
5.1	41,130	0.2431	1.07	2.29
5.0	40,330	0.2480	1.10	2.35
4.9	39,520	0.2530	1.13	2.42
4.8	38,710	0.2583	1.18	2.49
4.7	37,910	0.2638	1.24	2.56
4.6	37,100	0.2695	1.31	2.60
4.5	36,290	0.2755	1.37	2.65
4.4	35,490	0.2818	1.45	2.68
4.3	34,680	0.2883	1.51	2.70
4.2	33,880	0.2952	1.58	2.71
4.1	33,070	0.3024	1.62	2.70
4.0	32,260	0.3100	1.64	2.68
3.9	31,460	0.3179	1.64	2.67
3.8	30,650	0.3263	1.61	2.69
3.7	29,840	0.3351	1.57	2.72
3.6	29,040	0.3444	1.52	2.81
3.5	28,230	0.3542	1.50	2.93
3.4	27,420	0.3647	1.53	3.05
3.3	26,620	0.3757	1.57	3.15
3.2	25,810	0.3875	1.62	3.26
3.1	25,000	0.4000	1.68	3.35
3.0	24,200	0.4133	1.73	3.43
2.9	23,390	0.4275	1.77	3.51
2.8	22,580	0.4428	1.81	3.61
2.7	21,780	0.4592	1.85	3.73
2.6	20,970	0.4769	1.91	3.86
2.5	20,160	0.4959	1.98	4.00
2.4	19,360	0.5166	2.07	4.14
2.3	18,550	0.5391	2.18	4.26
2.2	17,740	0.5636	2.29	4.38

TABLE III (*Continued*)

Iridium

eV	cm^{-1}	μm	n	k
2.1	16,940	0.5904	2.40	4.48
2.0	16,130	0.6199	2.50	4.57
1.9	15,320	0.6526	2.57	4.68
1.8	14,520	0.6888	2.64	4.81
1.7	13,710	0.7293	2.69	4.92
1.6	12,900	0.7749	2.68	5.08
1.5	12,100	0.8266	2.65	5.39
1.4	11,290	0.8856	2.72	5.74
1.3	10,490	0.9537	2.85	6.07
1.2	9,679	1.033	2.96	6.41
1.1	8,872	1.127	3.04	6.84
1.0	8,065	1.240	3.15	7.31
0.9	7,259	1.378	3.19	7.88
0.8	6,452	1.550	3.14	8.61
0.7	5,646	1.771	2.93	9.78
0.6	4,839	2.066	2.79	11.6
0.5	4,033	2.480	2.98	14.1
0.45	3,629	2.755	3.05	15.8
0.4	3,226	3.100	3.42	18.1
0.35	2,823	3.542	4.11	20.8
0.3	2,420	4.133	5.16	24.3
0.25	2,016	4.959	6.85	28.8
0.2	1,613	6.199	9.69	35.3
0.15	1,210	8.266	15.3	45.2
0.1	806.5	12.40	28.5	60.6

MOLYBDENUM (Mo) VI

The optical properties of Mo [1–30] have been measured many times and the results generally agree rather well. Table IV lists the n and k values of Weaver *et al.* [19] and Henke *et al.* [31]. These data are plotted in Fig. 4 as smooth curves.

Weaver *et al.* [19] used samples spark-cut from Mo buttons of high purity that had been melted with an electron-beam gun. The samples were macro-etched, mechanically polished, electropolished, and annealed. After annealing, they were recleaned, electropolished, washed in acetone and then in ethyl alcohol, and transferred in air to the measuring apparatus. In the infrared region measurements were made by using a calorimetric technique [32], and at shorter wavelengths reflectance measurements at near-normal incidence

were made. These data were then analyzed by using the Kramers–Kronig method to obtain n and k.

There may be some influence of surface oxides on the vacuum ultraviolet data, but truly clean surfaces have not been measured, nor have oxidation studies been carried out. For wavelengths longer than about 3 μm, molybdenum resembles a free-electron metal, but, in principle, there are interband transitions at longer wavelengths that would affect the fit to a free-electron model for wavelengths shorter than about 10 μm.

REFERENCES

1. L. J. LeBlanc, J. S. Farrell, and D. W. Juenker, *J. Opt. Soc. Am.* **54**, 956 (1964).
2. J. P. Waldron and D. W. Juenker, *J. Opt. Soc. Am.* **54**, 204 (1964).
3. M. M. Kirillova and B. A. Charikov, *Fiz. Met. Metalloved.* **19**, 495 (1965); M. M. Kirillova and B. A. Charikov, *Phys. Met. Metallogr.* **19**(4), 13 (1965).
4. H. R. Apholte and K. Ulmer, *Phys. Lett.* **22**, 552 (1966).
5. B. T. Barnes, *J. Opt. Soc. Am.* **56**, 1546 (1966).
6. A. P. Lenham and D. M. Treherne, *J. Opt. Soc. Am.* **56**, 1137 (1966).
7. A. P. Lenham and D. M. Treherne, *in* "Optical Properties and Electronic Structure of Metals and Alloys" (F. Abélès, ed.), p. 196, North-Holland, Publ., Amsterdam, 1966.
8. M. M. Kirillova, G. A. Bolotin, and M. V. Mayevskiy, *Fiz. Met. Metalloved.* **24**, 95 (1967); M. M. Kirillova, G. A. Bolotin, and M. V. Mayevskiy, *Phys. Met. Metallogr.* **24**(1), 91 (1967).
9. A. P. Lenham, *J. Opt. Soc. Am.* **57**, 473 (1967).
10. D. W. Juenker, L. J. LeBlanc, and C. R. Martin, *J. Opt. Soc. Am.* **58**, 164 (1968).
11. M. L. Kapitsa, Y. P. Udoev, and E. I. Shirokikh, *Fiz. Tverd. Tela.* **11**, 814 (1969); M. L. Kapitsa, Y. P. Udoev, and E. I. Shirokikh, *Sov. Solid State Phys.* **11**, 665 (1969).
12. A. Cezairliyan, M. S. Morse, H. A. Berman, and C. W. Beckett, *J. Res. National Bureau of Standards* **74A**, 65 (1970).
13. K. A. Kress and G. J. Lapeyre, *J. Opt. Soc. Am.* **60**, 1681 (1970).
14. M. M. Kirillova, L. V. Nomerovannaya, and M. M. Noskov, *Zh. Eksp. Teor. Fiz.* **60**, 2252 (1971); M. M. Kirillova, L. V. Nomerovannaya, and M. M. Noskov, *Sov. Phys. JETP* **33**, 1210 (1971).
15. Y. P. Udoyev, N. S. Koz'yakova and M. L. Kapitsa, *Fit. Met. Metalloved.* **31**, 439 (1971); Y. P. Udoyev, N. S. Koz'yakova and M. L. Kapitsa, *Phys. Met. Metallogr.* **31**(2), 229 (1971).
16. P. Gravier, *Thin Solid Films* **11**, 135 (1972).
17. V. Vujnovic and V. Grzeta, *Fizika (Yugoslavia)* **4**, 173 (1972).
18. D. N. Baria, T. S. Kin, and R. G. Bautista, *High Temp.-High Press.* **5**, 545 (1973).
19. J. H. Weaver, D. W. Lynch, and C. G. Olson, *Phys. Rev. B* **10**, 501 (1974).
20. B. W. Veal and A. P. Paulikas, *Phys. Rev. B* **10**, 1280 (1974).
21. Y. Ballu, J. Lecante, and H. Rousseau, *Phys. Rev. B* **14**, 3201 (1976).
22. G. Chassaing, P. Granier, and M. Sigrist, *Thin Solid Films* **35**, L25 (1976).
23. J. H. Weaver and C. G. Olson, *Phys. Rev. B* **14**, 3251 (1976).
24. E. S. Black, D. W. Lynch, and C. G. Olson, *Phys. Rev. B* **16**, 2337 (1977).
25. H. S. Gurev and C. Selvage, *Proc. Soc. Photo-Opt. Instrum. Eng.* **85**, 32 (1977).
26. A. S. Siddiqui and D. M. Treherne, *Infrared Phys.* **17**, 33 (1977).
27. P. Gravier, G. Chassaing, and M. Sigrist, *Thin Solid Films* **57**, 93 (1979).
28. G. E. Carver and B. O. Seraphin, *Appl. Phys. Lett.* **34**, 279 (1979).
29. R. Manzke, *Phys. Stat. Solidi B* **97**, 157 (1980).
30. J. E. Nestell, Jr. and R. W. Christy, *Phys. Rev. B*, **21**, 3173 (1980).

31. B. L. Henke, P. Lee, T. J. Tanaka, R. L. Shimabukuro, and B. K. Fujikawa, "Low Energy X-Ray Diagnostics—1981" (D. T. Attwood and B. L. Henke, eds.), p. 340, *AIP Conf. Proc.* No. 75, American Institute of Physics, New York 1981.
32. L. W. Bos and D. W. Lynch, *Phys. Rev. B* **2**, 4567 (1970).

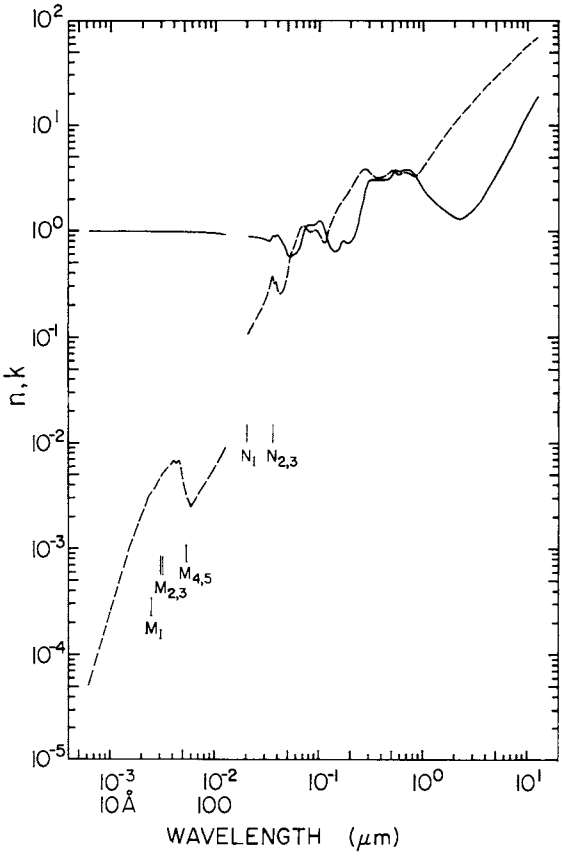

Fig. 4. Log–log plot of n (——) and k (– – – –) versus wavelength in micrometers for molybdenum.

TABLE IV

Values of n and k Obtained from Various References for Molybdenum[a]

eV	cm^{-1}	Å	n	k
2000		6.199	0.999622 [31]	4.84×10^{-5} [31]
1952		6.351	0.999600	5.26
1905		6.508	0.999577	5.73
1860		6.665	0.999555	6.22
1851		6.831	0.999530	6.77
1772		6.997	0.999505	7.36
1730		7.166	0.999479	7.99
1688		7.345	0.999451	8.69
1648		7.523	0.999423	9.44×10^{-5}
1609		7.705	0.999393	1.02×10^{-4}
1570		7.897	0.999361	1.11
1533		8.087	0.999329	1.21
1496		8.287	0.999294	1.31
1460		8.492	0.999258	1.43
1426		8.694	0.999222	1.54
1392		8.906	0.999183	1.68
1358		9.129	0.999142	1.82
1326		9.350	0.999100	1.97
1294		9.581	0.999055	2.14
1263		9.816	0.999008	2.32
1233		10.05	0.99896	2.52
1204		10.30	0.99891	2.72
1175		10.55	0.99886	2.95
1147		10.81	0.99880	3.19
1119		11.08	0.99875	3.47
1093		11.34	0.99869	3.75
1067		11.62	0.99863	4.06
1041		11.91	0.99856	4.40
1016		12.20	0.99850	4.77
992		12.50	0.99843	5.15
968		12.81	0.99836	5.57
945		13.12	0.99829	6.02
923		13.43	0.99821	6.49
901		13.76	0.99813	7.01
879		14.10	0.99805	7.59
858		14.45	0.99797	8.19
838		14.79	0.99789	8.83
818		15.16	0.99781	9.53×10^{-4}
798		15.54	0.99772	1.03×10^{-3}
779		15.92	0.99764	1.11
760		16.31	0.99755	1.19
742		16.71	0.99747	1.27
725		17.10	0.99738	1.35
707		17.54	0.99728	1.44
690		17.97	0.99718	1.54
674		18.39	0.99708	1.64
658		18.84	0.99699	1.75
642		19.31	0.99688	1.87
627		19.77	0.99678	1.99
612		20.26	0.99668	2.13
597		20.77	0.99658	2.28
583		21.27	0.99649	2.43

[a] The references from which the values were extracted are given in brackets.

TABLE IV (*Continued*)

Molybdenum

eV	cm^{-1}	Å	n	k
569		21.79	0.99639	2.59
555		22.34	0.99631	2.77
542		22.87	0.99625	2.95
529		23.44	0.99621	3.15
516		24.03	0.99622	3.28
504		24.60	0.99618	3.38
492		25.20	0.99612	3.48
480		25.83	0.99604	3.59
469		26.43	0.99595	3.69
458		27.07	0.99583	3.80
447		27.74	0.99568	3.95
436		28.44	0.99554	4.16
426		29.10	0.99544	4.37
415		29.87	0.99535	4.61
406		30.54	0.99528	4.83
396		31.31	0.99526	5.09
386		32.12	0.99528	5.28
377		32.89	0.99529	5.41
368		33.69	0.99526	5.55
359		34.53	0.99522	5.70
351		35.32	0.99518	5.84
342		36.25	0.99514	6.00
334		37.12	0.99512	6.15
326		38.03	0.99510	6.31
318		38.99	0.99511	6.48
311		39.86	0.99517	6.63
303		40.92	0.99541	6.82
296		41.88	0.99558	6.63
289		42.90	0.99569	6.39
282		43.96	0.99568	6.15
275		45.08	0.99565	5.85
269		46.09	0.99552	5.43
262		47.32	0.99520	4.98
256		48.43	0.99480	4.61
250		49.59	0.99433	4.26
244		50.81	0.99379	3.93
238		52.09	0.99315	3.62
232		53.44	0.99243	3.33
227		54.62	0.99176	3.10
221		56.10	0.99085	2.83
216		57.40	0.9900	2.60
211		58.76	0.9890	2.40
206		60.18	0.9879	2.58
201		61.68	0.9869	2.69
196		63.25	0.9859	2.80
191		64.91	0.9848	2.91
187		66.30	0.9839	3.00
182		68.12	0.9828	3.12
178		69.65	0.9818	3.22
174		71.25	0.9807	3.33
170		72.93	0.9795	3.45
166		74.69	0.9783	3.60

(*continued*)

TABLE IV (*Continued*)

Molybdenum

eV	cm^{-1}	Å	n	k
162		76.53	0.9770	3.75
158		78.47	0.9757	3.92
154		80.51	0.9742	4.10
150		82.65	0.9726	4.28
147		84.34	0.9713	4.42
143		86.70	0.9695	4.62
140		88.56	0.9680	4.78
136		91.16	0.9659	5.01
133		93.22	0.9641	5.19
130		95.37	0.9623	5.38
127		97.62	0.9603	5.59
124		99.98	0.9581	5.80
121		102.5	0.9557	6.03
118		105.1	0.9532	6.28
115		107.8	0.9504	6.54
112		110.7	0.9473	6.90
110		112.7	0.9451	7.19
107		115.9	0.9415	7.64
104		119.2	0.9377	8.14
102		121.5	0.9349	8.50
100		124.0	0.9318	8.89×10^{-3}
eV	cm^{-1}	μm	n	k
60.0		0.02066	0.897 [19]	0.106 [10]
50.0		0.02480	0.868	0.151
45.0		0.02755	0.850	0.187
40.0		0.03100	0.828	0.235
39.5		0.03139	0.823	0.241
39.0		0.03179	0.818	0.250
38.5		0.03220	0.813	0.261
38.0		0.03263	0.810	0.273
37.75		0.03284	0.809	0.281
37.5		0.03306	0.808	0.289
37.25		0.03328	0.809	0.297
37.0		0.03351	0.810	0.303
36.75		0.03374	0.811	0.312
36.5		0.03397	0.812	0.321
36.25		0.03420	0.815	0.331
36.0		0.03444	0.819	0.341
35.8		0.03463	0.825	0.350
35.6		0.03483	0.831	0.358
35.4		0.03502	0.841	0.367
35.2		0.03522	0.853	0.373
35.0		0.03542	0.867	0.375
34.8		0.03563	0.880	0.373
34.6		0.03583	0.893	0.368
34.4		0.03604	0.901	0.360
34.2		0.03625	0.907	0.352
34.0		0.03647	0.911	0.344
33.8		0.03668	0.912	0.334
33.6		0.03690	0.910	0.326
33.5		0.03701	0.907	0.322

TABLE IV (*Continued*)

Molybdenum

eV	cm^{-1}	μm	*n*	*k*
33.4		0.03712	0.903	0.321
33.2		0.03734	0.897	0.323
33.0		0.03757	0.896	0.327
32.8		0.03780	0.898	0.330
32.6		0.03803	0.901	0.331
32.4		0.03827	0.907	0.331
32.2		0.03850	0.912	0.327
32.0		0.03875	0.915	0.323
31.75		0.03905	0.918	0.315
31.5		0.03936	0.919	0.307
31.25		0.03968	0.918	0.298
31.0		0.04000	0.915	0.288
30.75		0.04032	0.909	0.279
30.5		0.04065	0.902	0.271
30.25		0.04099	0.892	0.263
30.0		0.04133	0.879	0.259
29.75		0.04168	0.868	0.256
29.5		0.04203	0.855	0.257
29.25		0.04239	0.844	0.256
29.0		0.04275	0.832	0.259
28.75		0.04313	0.822	0.261
28.5		0.04350	0.811	0.263
28.25		0.04389	0.799	0.265
28.0		0.04428	0.788	0.269
27.75		0.04468	0.776	0.272
27.5		0.04509	0.764	0.276
27.25		0.04550	0.750	0.281
27.0		0.04592	0.734	0.289
26.75		0.04635	0.721	0.298
26.5		0.04679	0.706	0.308
26.25		0.04723	0.694	0.319
26.0		0.04769	0.680	0.329
25.8		0.04806	0.666	0.341
25.6		0.04843	0.656	0.353
25.4		0.04881	0.645	0.367
25.2		0.04920	0.636	0.380
25.0		0.04959	0.624	0.393
24.8		0.04999	0.612	0.410
24.6		0.05040	0.603	0.429
24.4		0.05081	0.596	0.447
24.2		0.05123	0.588	0.468
24.0		0.05166	0.583	0.491
23.8		0.05209	0.581	0.511
23.6		0.05254	0.579	0.532
23.4		0.05299	0.579	0.553
23.2		0.05344	0.579	0.575
23.0		0.05391	0.582	0.595
22.8		0.05438	0.586	0.614
22.6		0.05486	0.589	0.633
22.4		0.05535	0.594	0.650
22.2		0.05585	0.596	0.668
22.0		0.05636	0.602	0.685

(*continued*)

TABLE IV (*Continued*)

Molybdenum

eV	cm^{-1}	μm	n	k
21.8		0.05687	0.607	0.700
21.6		0.05740	0.608	0.715
21.4		0.05794	0.609	0.733
21.2		0.05848	0.610	0.752
21.0		0.05904	0.612	0.773
20.8		0.05961	0.616	0.794
20.6		0.06019	0.621	0.815
20.4		0.06078	0.626	0.838
20.2		0.06138	0.632	0.862
20.0		0.06199	0.639	0.887
19.8		0.06262	0.648	0.913
19.6		0.06326	0.660	0.940
19.4		0.07391	0.674	0.968
19.2		0.06458	0.691	0.996
19.0		0.06526	0.712	1.02
18.8		0.06595	0.737	1.05
18.6		0.06666	0.766	1.08
18.4		0.06738	0.799	1.10
18.2		0.06812	0.833	1.11
18.0		0.06888	0.866	1.12
17.8		0.06965	0.903	1.13
17.6		0.07045	0.940	1.14
17.4		0.07126	0.978	1.14
17.2		0.07208	1.01	1.13
17.0		0.07293	1.04	1.12
16.8		0.07380	1.07	1.11
16.6		0.07469	1.10	1.10
16.4		0.07560	1.12	1.08
16.2		0.07653	1.13	1.06
16.0		0.07749	1.14	1.04
15.8		0.07847	1.15	1.02
15.6		0.07948	1.15	1.01
15.4		0.08051	1.15	0.994
15.2		0.08157	1.14	0.989
15.0		0.08266	1.14	0.987
14.8		0.08377	1.14	0.987
14.6		0.08492	1.13	0.990
14.4		0.08610	1.13	0.997
14.2		0.08731	1.14	1.01
14.0		0.08856	1.15	1.01
13.8		0.08984	1.15	1.02
13.6		0.09117	1.17	1.02
13.4		0.09253	1.18	1.02
13.2		0.09393	1.20	1.03
13.0		0.09537	1.21	1.02
12.8		0.09686	1.23	1.01
12.6		0.09840	1.24	0.993
12.4		0.09999	1.25	0.975
12.2		0.1016	1.26	0.953
12.0		0.1033	1.26	0.921
11.8		0.1051	1.25	0.886
11.6		0.1069	1.23	0.845

TABLE IV (*Continued*)

Molybdenum

eV	cm^{-1}	μm	n	k
11.4		0.1088	1.18	0.802
11.2		0.1107	1.12	0.782
11.0		0.1127	1.05	0.774
10.8		0.1148	0.977	0.791
10.6		0.1170	0.909	0.835
10.4		0.1192	0.859	0.881
10.2		0.1216	0.812	0.930
10.0		0.1240	0.770	0.987
9.8		0.1265	0.735	1.05
9.6		0.1291	0.707	1.12
9.4		0.1319	0.685	1.19
9.2		0.1348	0.670	1.25
9.0		0.1378	0.652	1.33
8.8		0.1409	0.647	1.41
8.6		0.1442	0.649	1.49
8.4		0.1476	0.659	1.57
8.2		0.1512	0.672	1.65
8.0		0.1550	0.685	1.73
7.9		0.1569	0.697	1.77
7.8		0.1590	0.711	1.81
7.7		0.1610	0.726	1.85
7.6		0.1631	0.745	1.90
7.5		0.1653	0.781	1.93
7.4		0.1675	0.808	1.95
7.3		0.1698	0.816	1.96
7.2		0.1722	0.813	1.98
7.1		0.1746	0.808	2.00
7.0		0.1771	0.798	2.04
6.9		0.1797	0.791	2.08
6.8		0.1823	0.784	2.12
6.7		0.1851	0.777	2.18
6.6		0.1879	0.779	2.24
6.5		0.1907	0.783	2.30
6.4		0.1937	0.789	2.36
6.3		0.1968	0.798	2.43
6.2		0.2000	0.813	2.50
6.1	49,200	0.2033	0.836	2.57
6.0	48,390	0.2066	0.850	2.64
5.9	47,590	0.2101	0.873	2.72
5.8	46,780	0.2138	0.895	2.80
5.7	45,970	0.2175	0.924	2.89
5.6	45,170	0.2214	0.959	2.99
5.5	44,360	0.2254	1.00	3.09
5.4	43,550	0.2296	1.06	3.20
5.3	42,750	0.2339	1.13	3.31
5.2	41,940	0.2384	1.22	3.42
5.1	41,130	0.2431	1.33	3.53
5.0	40,330	0.2480	1.46	3.62
4.9	39,520	0.2530	1.61	3.70
4.8	38,710	0.2583	1.75	3.76
4.7	37,910	0.2638	1.90	3.81
4.6	37,100	0.2695	2.06	3.84

(*continued*)

TABLE IV (*Continued*)

Molybdenum

eV	cm^{-1}	μm	n	k
4.5	36,290	0.2755	2.21	3.87
4.4	35,490	0.2818	2.39	3.88
4.3	34,680	0.2883	2.59	3.86
4.2	33,880	0.2952	2.77	3.77
4.1	33,070	0.3024	2.91	3.67
4.0	32,260	0.3100	3.01	3.51
3.9	31,460	0.3179	3.04	3.40
3.8	30,650	0.3263	3.04	3.31
3.7	29,840	0.3351	3.04	3.27
3.6	29,040	0.3444	3.05	3.24
3.5	28,230	0.3542	3.06	3.21
3.4	27,420	0.3647	3.06	3.19
3.3	26,620	0.3757	3.06	3.18
3.2	25,810	0.3875	3.05	3.18
3.1	25,000	0.4000	3.03	3.22
3.0	24,200	0.4133	3.04	3.27
2.9	23,390	0.4275	3.05	3.33
2.8	22,580	0.4428	3.08	3.42
2.7	21,780	0.4592	3.13	3.51
2.6	20,970	0.4769	3.22	3.61
2.5	20,160	0.4959	3.36	3.73
2.4	19,360	0.5166	3.59	3.78
2.3	18,550	0.5391	3.79	3.61
2.2	17,740	0.5636	3.76	3.41
2.1	16,940	0.5904	3.68	3.45
2.0	16,130	0.6199	3.68	3.52
1.9	15,320	0.6526	3.74	3.58
1.8	14,520	0.6888	3.81	3.58
1.7	13,710	0.7293	3.84	3.51
1.6	12,900	0.7749	3.77	3.41
1.5	12,100	0.8266	3.53	3.30
1.4	11,290	0.8856	3.15	3.40
1.3	10,490	0.9537	2.77	3.74
1.2	9,679	1.033	2.44	4.22
1.1	8,872	1.127	2.16	4.85
1.0	8,065	1.240	1.94	5.58
0.9	7,259	1.378	1.74	6.48
0.86	6,936	1.442	1.70	6.90
0.82	6,614	1.512	1.64	7.35
0.78	6,291	1.590	1.60	7.83
0.74	5,968	1.675	1.52	8.38
0.70	5,646	1.771	1.48	8.99
0.66	5,323	1.879	1.43	9.67
0.62	5,001	2.000	1.38	10.4
0.58	4,678	2.138	1.34	11.3
0.54	4,355	2.296	1.35	12.4
0.50	4,033	2.480	1.37	13.5
0.46	3,710	2.695	1.46	14.9
0.42	3,388	2.952	1.57	16.5
0.38	3,065	3.263	1.70	18.4
0.34	2,742	3.647	1.99	20.8
0.30	2,420	4.133	2.44	23.8
0.29	2,339	4.275	2.58	24.7
0.28	2,258	4.428	2.74	25.6

TABLE IV (*Continued*)

Molybdenum

eV	cm^{-1}	μm	n	k
0.27	2,178	4.592	2.92	26.6
0.26	2,097	4.769	3.14	27.6
0.25	2,016	4.959	3.36	28.8
0.24	1,936	5.166	3.61	30.0
0.23	1,855	5.391	3.92	31.3
0.22	1,774	5.636	4.26	32.7
0.21	1,694	5.904	4.65	34.3
0.20	1,613	6.109	5.10	36.0
0.19	1,532	6.526	5.61	37.8
0.18	1,452	6.888	6.21	39.9
0.17	1,371	7.293	6.90	42.2
0.16	1,291	7.749	7.74	44.7
0.15	1,210	8.266	8.78	47.5
0.14	1,129	8.856	9.96	50.7
0.13	1,049	9.537	11.4	54.4
0.12	967.9	10.33	13.4	58.4
0.11	887.2	11.27	15.6	63.1
0.10	806.5	12.40	18.5	68.5

NICKEL (Ni) VII

Overall agreement among the published n and k spectra of Ni [1–42] is good. Table V lists n and k values chosen and the pertinent references. These data are plotted in Fig. 5 as smooth curves.

The data extending from 1.3 to 124 Å are those of Zombeck *et al.* [40] determined as described in the introduction. Data calculated from a model of Henke *et al.* [43] overlap in the 6.1- to 124- Å region. The data from 88 to 248 Å are those of Bartlett *et al.* [42] (extinction coefficient) and Feldkamp *et al.* [39] (index of refraction). The data from 248 to 495 Å (Weaver *et al.* [41]), from 495 to 3540 Å (Vehse and Arakawa [13]), and from 4132 Å to 15.5 μm (Lynch *et al.* [17]) were combined for a Kramers–Kronig (KK) analysis, and the results are listed in the table and shown in Fig. 5 for 248 Å to 12.4 μm. The data of Henke [41] agree well with those of Feldkamp *et al.* [39] and Bartlett and Olson [42] in the overlap region.

Bartlett and Olson [42] used evaporated Ni films to obtain an absorption spectrum of Ni. They evaporated Ni onto thin-film substrates of carbon (1600 Å thick) or aluminum (900 Å thick). The pressure during deposition was less than 10^{-8} torr. The Ni was of high purity (resistivity ratio of 100 to 200).

Feldkamp *et al.* [39] obtained the electron energy loss spectrum of unbacked Ni films and used a KK analysis to obtain n and k. They evaporated Ni of unspecified purity from an alumina crucible at a deposition rate of 100 Å/min at a pressure of 10^{-7} torr. The substrate was a cleaned and polished {001} surface of NaCl and was maintained at 150°C during deposition. The film was floated off the substrate in water and collected on a 75-mesh electron-microscope grid. Film thicknesses were 500–1000 Å; the films were polycrystalline and continuous (hole free).

Vehse and Arakawa [13] used evaporated Ni films for their reflectance measurements. The Ni had a purity of 99.9995%. The evaporation and measurements took place in the same vacuum system with no exposure to air. Nickel was evaporated from resistance-heated filaments at a pressure of about 10^{-8} torr onto microscope slides. The films were 1800–2200 Å thick and were probably deposited onto the slides at room temperature. Near-normal-incidence reflectance data were obtained from 495 to 3540 Å, and some reflectance versus angle of incidence measurements were also made at selected wavelengths within this range. A KK analysis was then done by using the n, k values obtained at the selected wavelengths as guiding values.

Lynch *et al.* [17] used a single crystal at 4 K ({111} face). The crystal was spark-cut, polished, and etched. A calorimetric technique [44] was used.

A number of sharp structures have been reported in the visible and in the near infrared that are suspected of being spurious and are not reported here. The remaining infrared structures have been determined to be present by all investigators. Nickel is not a free-electron-like metal, except at wavelengths longer than about 20 μm. This accounts for the good agreement among investigators of Ni in the infrared. A number of VUV measurements are all in general agreement. The structure in the spectra at about 187 Å arises from the excitation of 3p electrons, and there is considerable scatter in the magnitudes of adsorption coefficient values reported in this region.

REFERENCES

1. S. Roberts, *Phys. Rev.* **114**, 104 (1959).
2. H. Ehrenreich, H. R. Philipp, and D. J. Olechna, *Phys. Rev.* **131**, 2469 (1963).
3. B. Dold and R. Mecke, *Optik* **22**, 435 (1965).
4. A. P. Lenham and D. M. Treherne, *J. Opt. Soc. Am.* **56**, 1137 (1966).
5. A. P. Lenham, *J. Opt. Soc. Am.* **57**, 473 (1967).
6. A. P. Lenham and D. M. Treherne, *in* "Optical Properties and Electronic Structure of Metals and Alloys" (F. Abélès, ed.), p. 196, North-Holland Publ., Amsterdam, 1966.
7. M. M. Noskov and I. I. Sasovskaya, *Opt. Spektrosk.* **22**, 358 (1966); M. M. Noskov and I. I. Sasovskaya, *Opt. Spectrosc.* **22**, 657 (1966).
8. R. H. W. Graves and A. P. Lenham, *J. Opt. Soc. Am.* **58**, 884 (1968).
9. M. A. Biondi and A. I. Guobadia, *Phys. Rev.* **166**, 667 (1968).
10. J. Feinleib, W. J. Scouler, and J. Hanus, *J. Appl. Phys.* **40**, 1400 (1969).
11. B. Sonntag, R. Haensel, and C. Kunz, *Solid State Commun.* **7**, 597 (1969).
12. M. Shiga and G. P. Pells, *J. Phys. C* **2**, 1847 (1969).
13. R. C. Vehse and E. T. Arakawa, *Phys. Rev.* **180**, 695 (1969).

14. D. H. Seib and W. E. Spicer, *Phys. Rev. B* **2**, 1694 (1970).
15. M. Ph. Stoll, *Solid State Commun.* **8**, 1207 (1970).
16. F. C. Brown, C. Gahwiller, and A. B. Kunz, *Solid State Commun.* **9**, 487 (1971).
17. D. W. Lynch, R. Rosei, and J. H. Weaver, *Solid State Commun.* **9**, 2195 (1971).
18. I. I. Sasovskaya and M. M. Noskov, *Fiz. Met. Metalloved.* **32**, 723 (1971); I. I. Sasovskaya and M. M. Noskov, *Phys. Met. Metallogr.* **32**(4), 48 (1971).
19. M. P. Stoll, *J. Appl. Phys.* **42**, 1717 (1971).
20. G. L. Zuppardo and K. G. Ramanatham, *J. Opt. Soc. Am.* **61**, 1607 (1971).
21. J. C. Jones, D. C. Palmer, and C. L. Tien, *J. Opt. Soc. Am.* **62**, 353 (1972).
22. M. M. Kirillova, *Zh. Eksp. Teor. Fiz.* **61**, 336 (1971); M. M. Kirillova, *Sov. Phys. JEPT* **34**, 178 (1972).
23. N. Ya. Gorban, V. S. Stashchuk, A. V. Shirin, and A. A. Shishlovskii, *Opt. Spektrosk.* **35**, 508 (1973); N. Ya. Gorban, V. S. Stashchuk, A. V. Shirin, and A. A. Shishlovskii, *Opt. Spectrosc.* **35**, 295 (1973).
24. B. W. Veal and A. P. Paulikas, *Int. J. Magn.* **4**, 57 (1973).
25. P. B. Johnson and R. W. Christy, *Phys. Rev. B* **9**, 5056 (1974).
26. C. Wehenkel and B. Gauthe, *Phys. Lett.* **47A**, 253 (1974).
27. C. Wehenkel and B. Gauthe, *Phys. Stat. Solidi B* **64**, 515 (1974).
28. B. K. Reddy and T. C. Goel, *Indian J. Appl. Phys.* **13**, 138 (1975).
29. I. I. Sasovskaya and M. M. Noskov, *Opt. Spektrosk.* **39**, 111 (1975); I. I. Sasovskaya and M. M. Noskov, *Opt. Spectrosc.* **39**, 64 (1975).
30. A. A. Studna, *Solid State Commun.* **16**, 1063 (1975).
31. S. Moritani, K. Kondo, and J. Nakai, *Jpn. J. Appl. Phys.* **15**, 1549 (1976).
32. T. J. Moravec, J. C. Rife, and R. N. Dexter, *Phys. Rev. B* **13**, 3297 (1976).
33. T. Smith, *J. Opt. Soc. Am.* **67**, 48 (1977).
34. A. S. Siddiqui and D. M. Treherne, *Infrared Phys.* **17**, 33 (1977).
35. M. Tokumoto, H. D. Drew, and A. Bagchi, *Phys. Rev. B* **16**, 3497 (1977).
36. V. S. Gushchin, K. M. Shvarev, B. A. Baum, and P. V. Gel'd, *Fiz. Tverd. Tela* **20**, 1637 (1978); V. S. Gushchin, K. M. Shvarev, B. A. Baum, and P. V. Gel'd, *Sov. Phys. Solid State* **20**, 948 (1978).
37. M. P. Stoll and C. Jung, *J. Physique* **39**, 389 (1978).
38. M. P. Stoll and C. Jung, *J. Phys. F* **9**, 2491 (1979).
39. L. A. Feldkamp, M. B. Stearns, and S. S. Shinozaki, *Phys. Rev. B* **20**, 1310 (1979).
40. M. V. Zombeck, G. K. Austin, and D. T. Torgerson, Smithsonian Astrophysica Observatory Report SAO-AXAF-80-003, Appendix B, Table B1, Cambridge, Massachusetts, 1980.
41. J. H. Weaver, C. Krafka, D. W. Lynch, and E. E. Kohn, "Physik Daten, Physics Data, Optical Properties of Metals," Part 1, Fach-information-zentrum, Karlsruhe, 1981.
42. R. J. Bartlett and C. G. Olson, *Phys. Stat. Solidi B* **111**, K33 (1982).
43. B. L. Henke, P. Lee, T. J. Tanaka, R. L. Shimabukuro, and B. K. Fujikawa, "Low Energy X-Ray Diagnostics—1981" (D. T. Attwood and B. L. Henke, eds.), p. 340, *AIP Conf. Proc.* no. 75, American Institute of Physics, New York, 1981.
44. L. W. Bos and D. W. Lynch, *Phys. Rev. B* **2**, 4567 (1970).

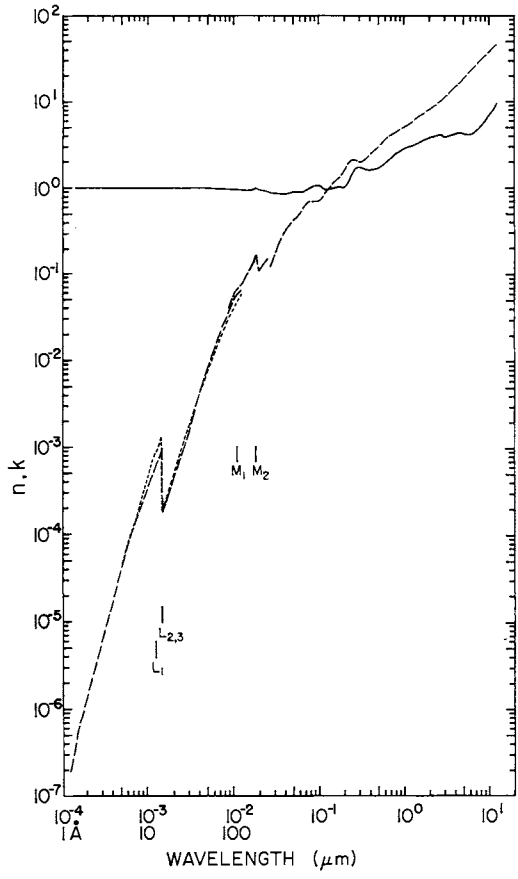

Fig. 5. Log–log plot of n (——) and k (– – – –) versus wavelength in micrometers for nickel.

TABLE V

Values of n and k Obtained from Various References for Nickel[a]

eV	cm^{-1}	Å	n		k	
9919		1.25	0.9999827	[40]	1.92×10^{-6}	[40]
9184		1.35	0.9999808		2.54	
8551		1.45	0.9999804		3.29×10^{-6}	
8266		1.50	0.9999816		4.98×10^{-7}	
7085		1.75	0.9999687		8.74×10^{-7}	
6199		2.00	0.9999579		1.43×10^{-6}	
4959		2.50	0.9999325		3.23	
4133		3.00	0.9999012		6.35×10^{-6}	
3542		3.50	0.999864		1.12×10^{-5}	
3100		4.00	0.999820		1.84	
2480		5.00	0.999715		4.19	
2066		6.00	0.999585		8.23	
2000		6.199	0.999559	[43]	8.81	[43]
1952		6.351	0.999538		9.61×10^{-5}	
1905		6.508	0.999516		1.05×10^{-4}	
1860		6.665	0.999493		1.14	
1815		6.831	0.999468		1.25	
1772		6.997	0.999444		1.36	
1771		7.00	0.999436	[40]	1.46	[40]
1730		7.166	0.999418	[43]	1.48	[43]
1688		7.345	0.999391		1.62	
1648		7.523	0.999363		1.76	
1609		7.705	0.999335		1.91	
1570		7.897	0.999304		2.09	
1550		8.00	0.999415	[40]	1.78	[40]
1533		8.087	0.999274	[43]	2.27	[43]
1496		8.287	0.999242		2.48	
1487		8.340	0.999409	[40]	1.90	[40]
1460		8.492	0.999210	[43]	2.70	[43]
1426		8.694	0.999178		2.92	
1392		8.906	0.999145		3.18	
1358		9.129	0.999109		3.46	
1326		9.350	0.999075		3.76	
1294		9.581	0.999040		4.09	
1263		9.816	0.999005		4.45	
1254		9.890	0.999200	[40]	3.20	[40]
1233		10.05	0.99897	[43]	4.83	[43]
1204		10.30	0.99894		5.24	
1188		10.44	0.999130	[40]	4.40	[40]
1175		10.55	0.99891	[43]	5.69	[43]
1147		10.81	0.99888		6.18	
1119		11.08	0.99885		6.72	
1093		11.34	0.99883		7.28	
1067		11.62	0.99881		7.91	
1041		11.91	0.99881		8.60	
1016		12.20	0.99883		9.33	
1012		12.25	0.999115	[40]	5.30	[40]
992		12.50	0.99886		9.09	[43]
968		12.81	0.99885		9.69×10^{-4}	
945		13.12	0.99886		1.05×10^{-3}	
929.4		13.34	0.99898	[40]	7.20×10^{-4}	[40]
923		13.43	0.99892	[43]	1.14×10^{-3}	[43]

(*continued*)

[a] The references from which the values were extracted are given in brackets.

TABLE V (*Continued*)

Nickel

eV	cm^{-1}	Å	n		k	
901		13.76	0.999081		1.23	
879		14.10	0.999565		1.34	
858		14.45	0.999820		6.30×10^{-4}	
851.5		14.56	0.99886	[40]	9.60	[40]
838		14.79	0.99299	[43]	1.95	[43]
818		15.16	0.99890		2.09	
798		15.54	0.99870		2.25	
779		15.92	0.99853		2.42	
776.4		15.97	0.99877	[40]	2.10	[40]
760		16.31	0.99837	[43]	2.63	[43]
742		16.71	0.99822		2.84	
725		17.10	0.99809		3.06	
707		17.54	0.99793		3.32	
704.9		17.59	0.99825	[40]	2.80	[40]
690		17.97	0.99779	[43]	3.59	[43]
674		18.39	0.99764		3.87	
658		18.84	0.99749		4.19	
642		19.31	0.99733		4.53	
637.5		19.45	0.99783	[40]	3.70	[40]
627		19.77	0.99717	[43]	4.89	[43]
612		20.26	0.99701		5.28	
597		20.77	0.99683		5.71	
583		21.27	0.99665		6.16	
572.9		21.64	0.99695	[40]	6.10	[40]
569		21.79	0.99646	[43]	6.65	[43]
555		22.34	0.99626		7.19	
542		22.87	0.99607		7.75	
529		23.44	0.99585		8.36	
524.9		23.62	0.99667	[40]	7.30	[40]
516		24.03	0.99563	[43]	9.03	[43]
504		24.60	0.99540		9.72	
500.3		24.78	0.99606	[40]	9.10×10^{-4}	[40]
492		25.20	0.99517	[43]	1.05×10^{-3}	[43]
480		25.83	0.99491		1.13	
469		26.43	0.99466		1.21	
458		27.07	0.99440		1.31	
452.2		27.42	0.99527	[40]	1.00	[40]
447		27.74	0.99411	[43]	1.41	[43]
436		28.44	0.99381		1.52	
426		29.10	0.99352		1.63	
415		29.87	0.99317		1.77	
406		30.54	0.99287		1.89	
396		31.31	0.99251		2.03	
395.4		31.36	0.99400	[40]	1.50	[40]
386		32.12	0.99213	[43]	2.20	[43]
377		32.89	0.99177		2.36	
368		33.69	0.99138		2.53	
359		34.53	0.99096		2.72	
351		35.32	0.99056		2.91	
342		36.25	0.99009		3.14	
334		37.12	0.9896		3.37	
326		38.03	0.9892		3.61	

TABLE V (*Continued*)

Nickel

eV	cm^{-1}	Å	n		k		
308		38.99	0.9887		3.88		
311		39.86	0.9882		4.14		
303		40.92	0.9876		4.47		
300.0		41.33	0.9880	[40]	5.13		[40]
296		41.88	0.9871	[43]	4.77		[43]
289		42.90	0.9865		5.11		
282		43.96	0.9859		5.47		
275		45.08	0.9853		5.88		
269		46.09	0.9847		6.25		
262		47.32	0.9840		6.72		
260.0		47.69	0.9851	[40]	7.65		[40]
256		48.43	0.9834	[43]	7.16		[43]
250		49.59	0.9827		7.64		
244		50.81	0.9820		8.17		
238		52.09	0.9812		8.74		
232		53.44	0.9804		9.35		
227		54.62	0.9797		9.91×10^{-3}		
221		56.10	0.9788		1.06×10^{-2}		
220		56.35	0.9809	[40]	1.22		[40]
216		57.40	0.9781	[43]	1.13		[43]
211		58.76	0.9772		1.20		
206		60.18	0.9764		1.28		
201		61.68	0.9755		1.36		
200		61.99	0.9780	[40]	1.59		[40]
196		63.25	0.9746	[43]	1.45		[43]
191		64.91	0.9736		1.55		
187		66.30	0.9728		1.63		
182		68.12	0.9717		1.74		
180		68.88	0.9751	[40]	2.03		[40]
178		69.65	0.9708	[43]	1.84		[43]
174		71.25	0.9699		1.94		
170		72.93	0.9689		2.05		
166		74.69	0.9679		2.17		
162		76.53	0.9668		2.30		
158		78.47	0.9658		2.44		
154		80.51	0.9647		2.58		
150		82.65	0.9635		2.73		
			0.9690	[40]	3.10		[40]
147		84.34	0.9625	[43]	2.86		[43]
143		86.70	0.9612		3.04		
140		88.56	0.9603		3.18		
			0.951	[39]	4.16		[42]
136		91.16	0.9589	[43]	3.39		[43]
133		93.22	0.9578		3.57		
130		95.37	0.9570		3.75		
			0.948	[39]	5.13		[42]
127		97.62	0.9560	[43]	3.91		[43]
124		99.98	0.9549		4.09		
121		102.5	0.9538		4.27		
120		103.3	0.9650	[40]	5.40		[40]
			0.948	[39]	6.21		[42]
118		105.1	0.9525	[43]	4.47		[43]

(*continued*)

TABLE V (*Continued*)

Nickel

eV	cm^{-1}	Å	n		k	
115		107.8	0.9511		4.69	
112		110.7	0.9497		4.92	
110		112.7	0.9487		5.08	
			0.9680	[40]	5.99	[40]
			0.950	[39]	7.03	[42]
107		115.9	0.9471	[43]	5.34	[43]
105		118.1	0.9680	[40]	6.25	[40]
104		119.2	0.9454	[43]	5.63	[43]
102		121.5	0.9443		5.83	
100		124.0	0.9430		6.04	
			0.9670	[40]	6.53	[40]
			0.943	[39]	7.75	[42]
98		126.5	0.939		8.01	
96		129.1	0.938		8.36	
94		131.9	0.936		8.73	
92		134.8	0.935		9.11	
90		137.8	0.936		9.44	
88		140.9	0.936		9.81×10^{-2}	
86		144.2	0.934		0.102	
84		147.6	0.932		0.107	
82		151.2	0.933		0.114	
80		155.0	0.936		0.121	
78		159.0	0.942		0.128	
76		163.1	0.944		0.135	
74		167.5	0.947		0.137	
72		172.2	0.952		0.144	
70		177.1	0.952		0.156	
69		179.7	0.960		0.161	
68		182.3	0.975		0.168	
67		185.1	0.986		0.166	
66		187.9	1.009		0.163	
65		190.7	1.002		0.124	
64		193.7	0.980		0.106	
63		196.8	0.971		0.108	
62		200.0	0.964		0.112	
61		203.3	0.960		0.115	
60		206.6	0.955		0.118	
58		213.8	0.948		0.123	
56		221.4	0.942		0.129	
54		229.6	0.937		0.135	
52		238.4	0.931		0.143	
50		248.0	0.926	[41]	0.151	[41]
45		275.5	0.884		0.129	
40		310.0	0.865		0.179	
35		354.2	0.858		0.241	
30		413.3	0.860		0.318	
29		427.5	0.863		0.336	
28		442.8	0.868		0.354	
27		459.2	0.873		0.372	
26		476.9	0.877		0.394	
25		495.9	0.888	[13]	0.418	[13]
24.5		506.1	0.897		0.427	

TABLE V (*Continued*)

Nickel

eV	cm^{-1}	Å	n	k
24		516.6	0.905	0.431
23.5		527.6	0.911	0.438
23		539.1	0.915	0.436
22.5		551.0	0.911	0.443
22		563.6	0.909	0.451
21.5		576.7	0.906	0.458
21		590.4	0.898	0.471
20.5		604.8	0.893	0.493
20		619.9	0.894	0.513
19.5		635.8	0.896	0.537
19		652.6	0.904	0.560
18.5		670.2	0.912	0.582
18		688.8	0.924	0.606
17.5		708.5	0.941	0.628
17		729.3	0.959	0.643
16.5		751.4	0.975	0.660
16		774.9	0.993	0.674
15.75		787.2	1.00	0.680
15.5		799.9	1.01	0.687
15.25		813.0	1.02	0.694
15		826.6	1.03	0.700
14.75		840.5	1.04	0.704
14.5		855.1	1.05	0.703
14.25		870.0	1.05	0.705
14		885.6	1.07	0.707
13.75		901.7	1.07	0.704
13.5		918.4	1.07	0.705
13.25		935.7	1.08	0.706
13		953.7	1.08	0.706
12.75		972.4	1.08	0.709
12.5		991.9	1.08	0.709
eV	cm^{-1}	μm	n	k
12.25		0.1012	1.07	0.712
12		0.1033	1.07	0.715
11.75		0.1055	1.07	0.714
11.5		0.1078	1.05	0.715
11.25		0.1102	1.04	0.717
11		0.1127	1.01	0.727
10.8		0.1148	0.993	0.747
10.6		0.1170	0.974	0.759
10.4		0.1192	0.951	0.800
10.2		0.1216	0.948	0.833
10		0.1240	0.946	0.867
9.8		0.1265	0.948	0.895
9.6		0.1291	0.949	0.927
9.4		0.1319	0.954	0.957
9.2		0.1348	0.959	0.987
9		0.1378	0.966	1.01
8.8		0.1409	0.972	1.05
8.6		0.1442	0.981	1.08

(*continued*)

TABLE V (*Continued*)

Nickel

eV	cm^{-1}	μm	n		k	
8.4		0.1476	0.992		1.11	
8.2		0.1512	1.00		1.13	
8.0		0.1550	1.01		1.15	
7.8		0.1590	1.02		1.18	
7.6		0.1631	1.02		1.21	
7.4		0.1675	1.03		1.24	
7.2		0.1722	1.03		1.27	
7.0		0.1771	1.03		1.30	
6.8		0.1823	1.02		1.35	
6.6		0.1879	1.01		1.40	
6.4		0.1937	1.01		1.46	
6.2		0.2000	1.00		1.54	
5.9	47,590	0.2101	1.02		1.67	
5.8	46,780	0.2138	1.04		1.73	
5.7	45,970	0.2175	1.06		1.78	
5.6	45,170	0.2214	1.09		1.83	
5.5	44,360	0.2254	1.12		1.88	
5.4	43,550	0.2296	1.16		1.94	
5.3	42,750	0.2339	1.21		1.99	
5.2	41,940	0.2384	1.27		2.04	
5.1	41,130	0.2431	1.33		2.07	
5.0	40,330	0.2480	1.40		2.10	
4.9	39,520	0.2530	1.47		2.11	
4.8	38,710	0.2583	1.53		2.11	
4.7	37,910	0.2638	1.59		2.10	
4.6	37,100	0.2695	1.63		2.09	
4.5	36,290	0.2755	1.67		2.07	
4.4	35,490	0.2818	1.71		2.06	
4.3	34,680	0.2883	1.73		2.03	
4.2	33,880	0.2952	1.74		2.01	
4.1	33,070	0.3024	1.74		1.99	
4.0	32,260	0.3100	1.73		1.98	
3.9	31,460	0.3179	1.72		1.98	
3.8	30,650	0.3263	1.69		1.99	
3.7	29,840	0.3351	1.66		2.02	
3.6	29,040	0.3444	1.64		2.07	
3.5	28,230	0.3542	1.63		2.11	
3.4	27,420	0.3647	1.62		2.17	
3.3	26,620	0.3757	1.61		2.23	
3.2	25,810	0.3875	1.61		2.30	
3.1	25,000	0.4000	1.61		2.36	
3.0	24,200	0.4133	1.61	[17]	2.44	[17]
2.9	23,390	0.4275	1.62		2.52	
2.8	22,580	0.4428	1.62		2.61	
2.7	21,780	0.4592	1.64		2.71	
2.6	20,970	0.4769	1.66		2.81	
2.5	20,160	0.4959	1.67		2.93	
2.4	19,360	0.5166	1.71		3.06	
2.3	18,550	0.5391	1.75		3.19	
2.2	17,740	0.5636	1.80		3.33	
2.1	16,940	0.5904	1.85		3.48	
2.0	16,130	0.6199	1.93		3.65	

TABLE V (*Continued*)

Nickel

eV	cm^{-1}	μm	n	k
1.95	15,730	0.6358	1.98	3.74
1.90	15,320	0.6526	2.02	3.82
1.85	14,920	0.6702	2.08	3.91
1.80	14,520	0.6888	2.14	4.00
1.75	14,110	0.7085	2.21	4.09
1.70	13,710	0.7293	2.28	4.18
1.65	13,310	0.7514	2.36	4.25
1.60	12,900	0.7749	2.43	4.31
1.55	12,500	0.7999	2.48	4.38
1.50	12,100	0.8266	2.53	4.47
1.45	11,690	0.8551	2.59	4.55
1.40	11,290	0.8856	2.65	4.63
1.35	10,890	0.9184	2.69	4.73
1.30	10,490	0.9537	2.74	4.85
1.25	10,080	0.9919	2.80	4.97
1.20	9,679	1.033	2.85	5.10
1.15	9,275	1.078	2.91	5.24
1.10	8,872	1.127	2.97	5.38
1.05	8,469	1.181	3.01	5.55
1.00	8,065	1.240	3.06	5.74
0.95	7,662	1.305	3.11	5.98
0.90	7,259	1.378	3.18	6.23
0.85	6,856	1.459	3.27	6.51
0.80	6,452	1.550	3.38	6.82
0.75	6,049	1.653	3.49	7.13
0.70	5,646	1.771	3.59	7.48
0.65	5,243	1.907	3.69	7.92
0.60	4,839	2.066	3.84	8.35
0.55	4,436	2.254	3.90	8.92
0.50	4,033	2.480	4.03	9.64
0.45	3,629	2.755	4.20	10.2
0.40	3,226	3.100	3.84	11.4
0.38	3,065	3.263	3.92	12.1
0.36	2,904	3.444	4.00	12.7
0.34	2,742	3.647	4.07	13.4
0.32	2,581	3.875	4.12	14.2
0.30	2,420	4.133	4.19	15.0
0.28	2,258	4.428	4.30	16.0
0.26	2,097	4.769	4.29	17.1
0.24	1,936	5.166	4.16	18.4
0.22	1,774	5.636	4.11	20.2
0.20	1,613	6.199	4.12	22.5
0.19	1,533	6.526	4.30	23.8
0.18	1,452	6.888	4.45	25.2
0.17	1,371	7.293	4.68	26.8
0.16	1,290	7.749	5.00	28.6
0.15	1,210	8.266	5.45	30.6
0.14	1,129	8.856	5.83	32.8
0.13	1,049	9.537	6.44	35.3
0.12	967.9	10.33	7.11	38.3
0.11	887.2	11.27	8.12	41.8
0.10	806.5	12.40	9.54	45.8

VIII OSMIUM (Os)

There have been only two measurements of the optical constants of Os that have been reported, and they do not agree very well in magnitude although their spectral dependences are approximately the same. Because one set of measurements used evaporated films and the other bulk samples, the differences in the results may be caused by differences in sample density.

Cox *et al.* [1] measured the reflectance of osmium films prepared in a conventional vacuum system. An electron beam was used to evaporate the osmium of 99.8% purity, and the films were condensed on both hot (300°C) and room-temperature (40°C), superpolished, fused-silica substrates. The deposition rates were approximately 50 Å/sec. The coated substrates were transferred in air to a reflectometer for measurements. There was very little difference in the reflectance values of films deposited on hot and cold substrates. The optical constants were obtained by using the reflectance method.

Lynch *et al.* [2] used a polycrystalline bulk sample of unknown crystallite orientation that was optically polished, boiled in aqua regia, and then heated *in vacuo* to 1200–1500°C for several hours. After cooling, the samples were transferred in air to a reflectometer. The optical constants were obtained from reflectance measurements at near-normal incidence by using the Kramers–Kronig method.

The data of Lynch *et al.* [2] are presented on Table VI and in Fig. 6, along with the soft *x*-ray data of Henke *et al.* [37]. Some of the data of Cox *et al.* [1] are also given in the table, so that the results obtained from films can be compared with those obtained from the bulk samples.

Osmium is a noncubic metal; therefore its optical properties are anisotropic. Presumably, the data of Lynch *et al.* [2] are characteristic of a random crystallite orientation. An evaporated film may not be similarly random in that the film often consists of crystallites with their basal planes in the plane of the film. Thus, differences between n and k for bulk and film samples are to be expected but predominantly for wavelengths longer than 0.1 to 0.2 μm.

REFERENCES

1. J. T. Cox, G. Hass, J. B. Ramsey, and W. R. Hunter, *J. Opt. Soc. Am.* **63**, 435 (1973).
2. D. W. Lynch, C. G. Olson, and J. H. Weaver, *in* "Physics Data" (J. H. Weaver, C. Krafka, D. W. Lynch, and E. E. Koch, eds.), Part 1, p. 253, Fach-informations-zentrum, Karlsruhe, 1981.
3. B. L. Henke, P. Lee, T. J. Tanaka, R. L. Shimabukuro, and B. K. Fujikawa, "Low Energy X-Ray Diagnostics—1981" (D. T. Attwood and B. L. Henke, eds.), p. 340, *AIP Conf. Proc.* No. 75, American Institute of Physics, New York, 1981.

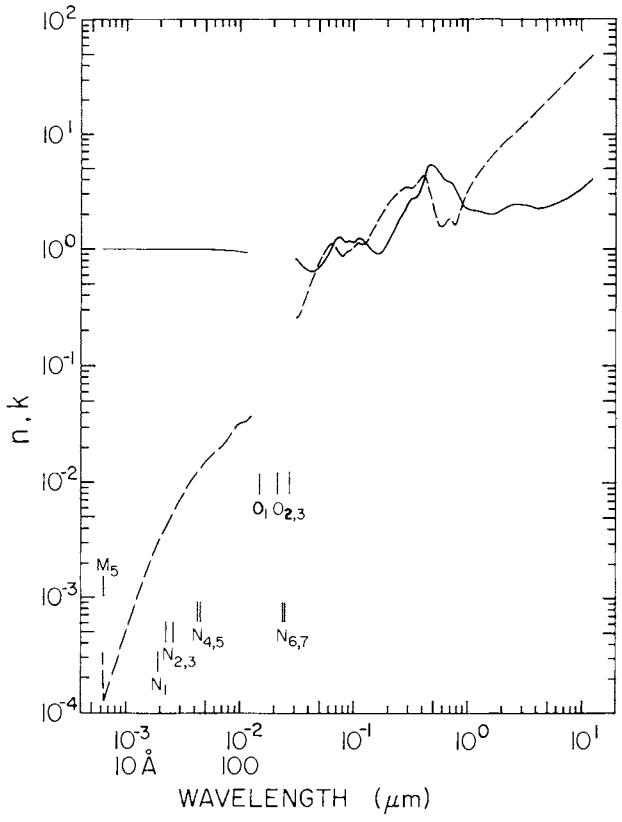

Fig. 6. Log–log plot of n (——) and k (– – – –) versus wavelength in micrometers for osmium.

TABLE VI

Values of n and k Obtained from Various References for Osmium[a]

eV	cm^{-1}	Å	n	k
2000		6.199	0.999626 [3]	3.36×10^{-4} [3]
1952		6.351	0.999529	1.25
1905		6.508	0.999467	1.35
1860		6.665	0.999405	1.45
1815		6.831	0.999350	1.57
1772		6.997	0.999297	1.69
1730		7.166	0.999245	1.82
1688		7.345	0.999192	1.96
1648		7.523	0.999140	2.11
1609		7.705	0.999087	2.28
1570		7.897	0.999031	2.45
1533		8.087	0.99898	2.64
1496		8.287	0.99892	2.85
1460		8.492	0.99886	3.06
1426		8.694	0.99880	3.29
1392		8.906	0.99873	3.54
1358		9.129	0.99866	3.82
1326		9.350	0.99860	4.11
1294		9.581	0.99852	4.42
1263		9.816	0.99845	4.76
1233		10.05	0.99837	5.12
1204		10.30	0.99830	5.49
1175		10.55	0.99821	5.91
1147		10.81	0.99813	6.35
1119		11.08	0.99804	6.84
1093		11.34	0.99795	7.34
1067		11.62	0.99785	7.88
1041		11.91	0.99775	8.49
1016		12.20	0.99765	9.12
992		12.50	0.99755	9.77×10^{-4}
968		12.81	0.99744	1.05×10^{-3}
945		13.12	0.99733	1.12
923		13.43	0.99722	1.20
901		13.76	0.99710	1.29
879		14.10	0.99698	1.38
858		14.45	0.99686	1.47
838		14.79	0.99674	1.57
818		15.16	0.99661	1.68
798		15.54	0.99647	1.80
779		15.92	0.99634	1.92
760		16.31	0.99620	2.05
741		16.71	0.99607	2.18
725		17.10	0.99594	2.32
707		17.54	0.99579	2.48
690		17.97	0.99567	2.64
674		18.39	0.99556	2.80
658		18.84	0.99543	2.91
642		19.31	0.99527	3.03
627		19.77	0.99509	3.19
612		20.26	0.99491	3.38
597		20.77	0.99473	3.58
583		21.27	0.99456	3.79

[a] The references from which the values were extracted are given in brackets.

TABLE VI (*Continued*)

Osmium

eV	cm^{-1}	Å	n	k
569		21.79	0.99440	4.01
555		22.34	0.99422	4.25
542		22.87	0.99408	4.48
529		23.44	0.99395	4.72
516		24.03	0.99383	4.93
504		24.60	0.99369	5.11
492		25.20	0.99351	5.29
480		25.83	0.99331	5.49
469		26.43	0.99310	5.68
458		27.07	0.99286	5.88
447		27.74	0.99257	6.14
436		28.44	0.99230	6.46
426		29.10	0.99205	6.78
415		29.87	0.99179	7.16
406		30.54	0.99159	7.49
396		31.31	0.99139	7.89
386		32.12	0.99122	8.23
377		32.89	0.99101	8.53
368		33.69	0.99078	8.85
359		34.53	0.99054	9.20
351		35.32	0.99030	9.52
342		36.25	0.99002	9.91×10^{-3}
334		37.12	0.9897	1.03×10^{-2}
326		38.03	0.9895	1.07
318		38.99	0.9892	1.11
311		39.86	0.9889	1.15
303		40.92	0.9886	1.19
296		41.88	0.9883	1.24
289		42.90	0.9880	1.28
282		43.96	0.9878	1.33
275		45.08	0.9876	1.38
269		46.09	0.9873	1.41
262		47.32	0.9870	1.45
256		48.43	0.9867	1.49
250		49.59	0.9863	1.53
244		50.81	0.9860	1.57
238		52.09	0.9855	1.61
232		53.44	0.9851	1.65
227		54.62	0.9846	1.69
221		56.10	0.9841	1.74
216		57.40	0.9836	1.78
211		58.76	0.9832	1.82
206		60.18	0.9827	1.85
201		61.68	0.9820	1.89
196		63.25	0.9812	1.92
190		64.91	0.9804	1.97
187		66.30	0.9796	2.00
182		68.12	0.9785	2.05
178		69.65	0.9775	2.09
174		71.25	0.9764	2.13
170		72.93	0.9752	2.20
166		74.69	0.9741	2.28

(*continued*)

TABLE VI (*Continued*)

Osmium

eV	cm^{-1}	Å	*n*	*k*
162		76.53	0.9729	2.36
158		78.47	0.9717	2.45
154		80.51	0.9704	2.54
150		82.65	0.9690	2.63
147		84.34	0.9680	2.71
143		86.70	0.9665	2.82
140		88.56	0.9654	2.91
136		91.16	0.9639	3.03
133		93.22	0.9626	3.13
130		95.37	0.9619	3.22
127		97.62	0.9608	3.24
124		99.98	0.9593	3.26
121		102.5	0.9574	3.29
118		105.1	0.9552	3.31
115		107.8	0.9526	3.34
112		110.7	0.9495	3.36
110		112.7	0.9471	3.38
107		115.9	0.9431	3.48
104		119.2	0.9389	3.59
102		121.5	0.9356	3.66
100		124.0	0.9323	3.74

eV	cm^{-1}	μm	*n*	*k*	*n*	*k*
41.33		0.030	0.833 [1]	0.127 [1]		
40.00		0.031	0.800	0.138		
39		0.03179			0.81 [2]	0.26 [2]
38.75		0.032	0.768	0.155		
38		0.03263			0.79	0.26
37.57		0.033	0.740	0.173		
37		0.03351			0.77	0.27
36.47		0.034	0.710	0.193		
36		0.03444			0.74	0.29
35.42		0.035	0.685	0.222		
35		0.0354			0.72	0.31
34.44		0.036	0.660	0.247		
34		0.03646			0.70	0.34
33.51		0.037	0.638	0.279		
33		0.03757			0.68	0.37
32.63		0.038	0.620	0.315		
32		0.03874			0.66	0.41
31.79		0.039	0.613	0.350		
31		0.04000	0.590	0.390	0.65	0.45
30.24		0.041	0.580	0.432		
30		0.04133			0.65	0.49
29.6		0.04189			0.65	0.51
29.52		0.042	0.572	0.473		
29.2		0.04246			0.65	0.53
28.83		0.043	0.566	0.513		
28.4		0.04365			0.64	0.57
28.18		0.044	0.562	0.552		
28		0.04428			0.64	0.59

TABLE VI (*Continued*)

Osmium

eV	cm^{-1}	Å	n	k	n	k
27.55		0.045	0.557	0.590		
27.2		0.04558			0.65	0.62
26.95		0.046	0.557	0.627		
26.8		0.04626			0.63	0.66
26.4		0.04696			0.65	0.69
26.38		0.047	0.560	0.662		
26		0.04768			0.66	0.72
25.83		0.048	0.563	0.695		
25.6		0.04843			0.67	0.75
25.30		0.049	0.568	0.739		
24.8		0.04999			0.70	0.80
24.80		0.050	0.578	0.760		
24.4		0.05081			0.72	0.82
24.31		0.051	0.588	0.790		
24		0.05166			0.73	0.84
23.84		0.052	0.597	0.817		
23.6		0.05253			0.75	0.86
23.39		0.053	0.603	0.842		
23.2		0.05344			0.75	0.88
22.96		0.054	0.610	0.868		
22.8		0.05438			0.77	0.90
22.54		0.055	0.617	0.890		
22.4		0.05535			0.78	0.93
22.14		0.056	0.627	0.910		
22		0.05635			0.80	0.96
21.75		0.057	0.630	0.932		
21.6		0.05740			0.83	0.99
21.38		0.058	0.642	0.952		
21.2		0.05848			0.86	1.02
21.01		0.059	0.653	0.973	0.87	1.04
20.8		0.05961			0.89	1.05
20.66		0.060	0.667	0.992		
20.6		0.06018			0.91	1.07
20.4		0.06077			0.93	1.09
20.33		0.061	0.687	1.01		
20.2		0.06138			0.96	1.10
20.00		0.062	0.708	1.03		
19.8		0.06262			1.02	1.11
19.68		0.063	0.730	1.05		
19.6		0.06326			1.05	1.11
19.4		0.06391			1.07	1.11
19.37		0.064	0.760	1.06		
19.2		0.06457			1.10	1.10
19.07		0.065	0.788	1.08		
19.0		0.06525			1.12	1.10
18.8		0.06595			1.14	1.10
18.79		0.066	0.824	1.08		
18.6		0.06666			1.17	1.09
18.51		0.067	0.857	1.09		
18.4		0.06738			1.19	1.08
18.23		0.068	0.887	1.08		
18.2		0.06812			1.21	1.06

(*continued*)

TABLE VI (*Continued*)

Osmium

eV	cm^{-1}	μm	n	k	n	k
18.0		0.0688			1.23	1.04
17.97		0.069	0.920	1.08		
17.8		0.06965			1.24	1.03
17.71		0.070	0.857	1.09		
17.6		0.07044			1.26	1.01
17.46		0.071	0.975	1.05		
17.4		0.07125			1.27	0.99
17.22		0.072	0.995	1.03		
17.2		0.07208			1.27	0.97
17.0		0.07293			1.28	0.96
16.98		0.073	1.01	1.01		
16.8		0.07380			1.28	0.94
16.75		0.074	1.03	0.993		
16.6		0.07469			1.28	0.92
16.53		0.075	1.03	0.963		
16.4		0.07560			1.28	0.90
16.31		0.076	1.03	0.942		
16.2		0.7653			1.26	0.88
16.10		0.077	1.03	0.922		
16.0		0.07749			1.25	0.87
15.90		0.078	1.03	0.908		
15.8		0.07847			1.22	0.86
15.69		0.079	1.03	0.902		
15.6		0.07947			1.20	0.86
15.50		0.080	1.02	0.902		
15.4		0.08051			1.18	0.87
15.31		0.081	1.01	0.908		
15.2		0.08157			1.17	0.89
15.12		0.082	1.01	0.918		
15.0		0.08265			1.16	0.90
14.94		0.083	1.01	0.927		
14.8		0.08377			1.16	0.91
14.76		0.084	1.00	0.935		
14.6		0.08492			1.15	0.93
14.59		0.085	0.999	0.945		
14.42		0.086	0.997	0.953		
14.4		0.08610			1.16	0.94
14.25		0.087	1.00	0.963		
14.2		0.08731			1.17	0.96
14.09		0.088	1.00	0.972		
14.0		0.08856			1.17	0.96
13.93		0.089	1.01	0.983		
13.8		0.08984			1.18	0.96
13.78		0.090	1.02	0.993		
13.62		0.091	1.04	1.01		
13.6		0.09116			1.17	0.97
13.48		0.092	1.06	1.01		
13.4		0.09252			1.17	0.97
13.33		0.093	1.07	1.03		
13.2		0.09392			1.16	0.98
13.19		0.094	1.09	1.04		
13.05		0.095	1.10	1.05		

TABLE VI (*Continued*)

Osmium

eV	cm^{-1}	μm	n	k	n	k
13.0		0.09537			1.16	0.99
12.92		0.096	1.12	1.06		
12.8		0.09686			1.15	1.01
12.78		0.097	1.13	1.07		
12.65		0.098	1.14	1.08		
12.6		0.09840			1.17	1.12
12.52		0.099	1.15	1.09		
12.4		0.09998			1.14	1.03
12.40		0.100	1.16	1.10		
12.2		0.1016			1.14	1.06
12.0		0.1033			1.15	1.08
11.81		0.105	1.21	1.14		
11.8		0.1051			1.16	1.10
11.6		0.1069			1.17	1.12
11.4		0.1088			1.19	1.15
11.27		0.110	1.24	1.17		
11.2		0.1107			1.23	1.14
11.0		0.1127			1.24	1.13
10.8		0.1148			1.25	1.11
10.78		0.115	1.25	1.18		
10.6		0.1170			1.24	1.10
10.4		0.1192			1.22	1.08
10.33		0.120	1.26	1.18		
10.3		0.1204			1.20	1.08
10.2		0.1216			1.19	1.08
10.0		0.1240			1.16	1.10
9.919		0.125	1.25	1.19		
9.8		0.1265			1.13	1.11
9.6		0.1292			1.10	1.14
9.537		0.130	1.23	1.23		
9.4		0.1319			1.08	1.16
9.2		0.1348			1.04	1.19
9.184		0.135	1.20	1.27		
9.0		0.1378			1.01	1.24
8.856		0.140	1.17	1.33		
8.8		0.1409			0.98	1.29
8.6		0.1442			0.96	1.34
8.551		0.145	1.12	1.41		
8.4		0.1476			0.94	1.40
8.266		0.150	1.08	1.49		
8.2		0.1512			0.91	1.48
8.0		0.1550			0.91	1.55
7.999		0.155	1.05	1.59		
7.8		0.1590			0.90	1.63
7.749		0.160	1.03	1.69		
7.6		0.1631			0.90	1.72
7.514		0.165	1.02	1.78		
7.4		0.1675			0.91	1.81
7.293		0.170	1.02	1.88		
7.2		0.1722			0.92	1.91
7.085		0.175	1.03	1.97		
7.0		0.1771			0.95	2.00

(*continued*)

TABLE VI (*Continued*)

Osmium

eV	cm^{-1}	μm	n	k	n	k
6.888		0.180	1.05	1.05		
6.8		0.1823			0.97	2.11
6.702		0.185	1.08	2.13		
6.6		0.1879			1.01	2.21
6.526		0.190	1.12	2.20		
6.4		0.1937			1.06	2.33
6.358		0.195	1.16	2.27		
6.2		0.2000			1.13	2.44
6.199		0.200	1.18	2.33		
6.0	48,390	0.2066			1.20	2.54
5.9	47,590	0.2101			1.24	2.60
5.8	46,780	0.2138			1.27	2.65
5.7	45,970	0.2175			1.32	2.71
5.6	45,170	0.2214			1.36	2.77
5.5	44,360	0.2254			1.41	2.83
5.4	43,550	0.2296			1.46	2.88
5.3	42,750	0.2339			1.52	2.94
5.2	41,940	0.2384			1.58	3.00
5.1	41,140	0.2431			1.65	3.07
5.0	40,330	0.2480			1.74	3.12
4.9	39,520	0.2530			1.82	3.15
4.8	38,720	0.2583			1.88	3.19
4.7	37,910	0.2638			1.94	3.24
4.6	37,100	0.2695			2.01	3.31
4.5	36,300	0.2755			2.11	3.38
4.4	35,490	0.2818			2.24	3.44
4.3	34,680	0.2883			2.39	3.47
4.2	33,880	0.2952			2.53	3.44
4.1	33,070	0.3024			2.64	3.40
4.0	32,260	0.3100			2.71	3.34
3.9	31,460	0.3179			2.73	3.31
3.8	30,650	0.3263			2.73	3.32
3.7	29,840	0.3351			2.73	3.37
3.6	29,040	0.3444			2.75	3.45
3.5	28,230	0.3542			2.79	3.59
3.4	27,420	0.3647			2.93	3.79
3.3	26,620	0.3757			3.15	3.88
3.2	25,810	0.3874			3.29	3.96
3.1	25,000	0.3999			3.51	4.21
3.0	24,200	0.4133			4.05	4.40
2.9	23,390	0.4275			4.65	4.18
2.8	22,580	0.4428			5.05	3.78
2.7	21,780	0.4592			5.30	3.38
2.6	20,970	0.4769			5.36	2.82
2.5	20,160	0.4959			5.28	2.38
2.4	19,360	0.5166			5.10	2.01
2.3	18,550	0.5390			4.84	1.76
2.2	17,740	0.5636			4.58	1.62
2.1	16,940	0.5904			4.26	1.54
2.0	16,130	0.6199			3.98	1.60
1.95	15,730	0.6358			3.88	1.67
1.90	15,320	0.6525			3.81	1.75

TABLE VI (*Continued*)

Osmium

eV	cm^{-1}	μm	n	k	n	k
1.85	14,920	0.6702			3.79	1.81
1.80	14,520	0.6888			3.78	1.83
1.75	14,110	0.7085			3.76	1.80
1.70	13,710	0.7293			3.70	1.75
1.65	13,310	0.7514			3.57	1.66
1.60	12,910	0.7749			3.36	1.62
1.57	12,660	0.7897			3.21	1.63
1.53	12,340	0.8103			2.99	1.70
1.50	12,100	0.8265			2.84	1.80
1.45	11,700	0.8550			2.65	2.01
1.40	11,290	0.8856			2.49	2.23
1.35	10,890	0.9184			2.35	2.48
1.30	10,490	0.9537			2.25	2.77
1.25	10,080	0.9918			2.19	3.04
1.20	9,679	1.033			2.16	3.35
1.15	9,276	1.078			2.17	3.59
1.10	8,872	1.127			2.15	3.84
1.05	8,469	1.181			2.12	4.11
1.00	8,065	1.240			2.09	4.41
0.95	7,662	1.305			2.05	4.74
0.90	7,259	1.378			2.03	5.10
0.85	6,856	1.459			2.01	5.51
0.80	6,452	1.550			2.00	5.95
0.75	6,049	1.653			2.00	6.46
0.70	5,646	1.771			2.02	7.04
0.65	5,243	1.907			2.11	7.68
0.60	4,839	2.066			2.21	8.37
0.55	4,436	2.254			2.33	9.12
0.50	4,033	2.480			2.41	9.97
0.45	3,630	2.755			2.43	11.0
0.40	3,226	3.100			2.45	12.3
0.35	2,823	3.542			2.33	14.1
0.30	2,420	4.133			2.23	16.6
0.25	2,016	4.959			2.35	20.0
0.20	1,613	6.199			2.44	25.1
0.15	1,210	8.265			2.90	33.6
0.10	806.5	12.40			4.08	50.2

PLATINUM (Pt) IX

Measurements of the optical properties of Pt [1–24] range over the vacuum ultraviolet to the infrared. Table VII lists the n and k values chosen and the pertinent references. These data are plotted in Fig. 7 as smooth curves. From 150–2200 Å the data are those of Hunter *et al.* [23] and from 2000 Å to about

12.4 μm the data are those of Weaver [21], and Henke *et al.'s* [25] calculated data cover the wavelength region from 6.2–124 Å.

Weaver [21] used reflectance [9, 16, 18] and transmittance [11] data from a number of sources to obtain n and k by the Kramers–Kronig technique.

Hunter *et al.* [23] made reflectance-versus-angle-of-incidence measurements on evaporated films of platinum. They used a conventional evaporation system with an electron-beam gun to evaporate the platinum, substrates heated to 300°C, and deposition rates of about 5–10 Å/sec. During deposition the pressure was about 10^{-6} torr. The purity of the Pt was 99.9%.

Except for the n spectra, Weaver's data [2] and those of Hunter *et al.* [23] show good agreement at 2200 Å. Although Henke *et al.'s* [25] data and those of Hunter *et al.* [23] do not meet or overlap, interpolations connecting the n and k spectra appear to be quite reasonable. It should be borne in mind that platinum films condensed on room-temperature substrates will have different values of n and k than those shown here and different reflectance values.

As with other transition metals, platinum is not expected to exhibit the optical properties of a free-electron metal in the infrared region.

REFERENCES

1. G. Hass and R. Tousey, *J. Opt. Soc. Am.* **49**, 593 (1959).
2. R. P. Madden and L. R. Canfield, *J. Opt. Soc. Am.* **51**, 838 (1961).
3. G. F. Jacobus, R. P. Madden, and L. R. Canfield, *J. Opt. Soc. Am.* **53**, 1084 (1963).
4. B. T. Barnes, *J. Opt. Soc. Am.* **56**, 1546 (1966).
5. A. P. Lenham and D. M. Treherne, *J. Opt. Soc. Am.* **56**, 1137 (1966).
6. A. P. Lenham and D. M. Treherne, *in* "Optical Properties and Electronic Structure of Metal Alloys" (F. Abélès, ed.), p. 196, North-Holland Publ., Amsterdam, 1966.
7. A. P. Lenham, *J. Opt. Soc. Am.* **57**, 473 (1967).
8. P. Jaegle, F. Combet Farnoux, P. Dhez, M. Cremonese, and G. Oroni, *Phys. Lett.* **26A**, 364 (1968).
9. A. Y.-C. Yu, W. E. Spicer, and G. Hass, *Phys. Rev.* **171**, 834 (1968).
10. G. Hass, J. B. Ramsey, and W. R. Hunter, *Appl. Opt.* **8**, 2255 (1969).
11. R. Haensel, K. Radler, B. Sonntag, and C. Kunz, *Sol. State Commun.* **7**, 1495 (1969).
12. W. R. Hunter, *Proc. Int. Conf. Vac. Ultraviolet Rad. Physics, 3rd. Tokyo* p. 2aC2-1 (1971).
13. J. C. Jones, D. C. Palmer, and C. L. Tien, *J. Opt. Soc. Am.* **62**, 353 (1972).
14. M. M. Kirillova, L. V. Nomerovannaya, and M. M. Noskov, *Phys. Met. Metallogr.* **34**, 291 (1972); M. M. Kirillova, L. V. Nomerovannaya, and M. M. Noskov, *Phys. Met. Metallogr.* **34**(2), 61 (1972).
15. R. C. Linton, NASA Technical Note D-7061 (1972).
16. A. Seignac and S. Robin, *Solid State Commun.* **11**, 217 (1972).
17. L. N. Aksyutov, *Inzh.-Fiz. Zh.* **27**, 197 (1974); L. N. Aksyutov, *J. Eng. Phys.* **27**, 913 (1974).
18. G. Hass and W. R. Hunter, *in* "Space Optics" (B. J. Thompson and R. R. Shannon, eds.), p. 525, National Academy of Sciences, Washington, D.C., 1974.
19. A. H. Madjid, R. L. Stover, and J. M. Martinez, *Phys. Kond. Matter.* **17**, 125 (1974).
20. C. Wehenkel and B. Gauthé, *Opt. Commun.* **11**, 62 (1974).
21. J. H. Weaver, *Phys. Rev. B* **11**, 1416 (1975).
22. A. S. Siddiqui and D. M. Treherne, *Infrared Phys.* **17**, 33 (1977).

23. W. R. Hunter, D. W. Angel, and G. Hass, *J. Opt. Soc. Am.* **69**, 1695 (1979).
24. R. E. Dietz, E. G. McRae, and J. H. Weaver, *Phys. Rev. B* **21**, 2229 (1980).
25. B. L. Henke, P. Lee, T. J. Tanaka, R. L. Shimabukuro, and B. K. Fujikawa, "Low Energy X-Ray Diagnostics—1981" (D. T. Attwood and B. L. Henke, eds.), p. 340, *AIP Conf. Proc.* No. 75, American Institute of Physics, New York, 1981.

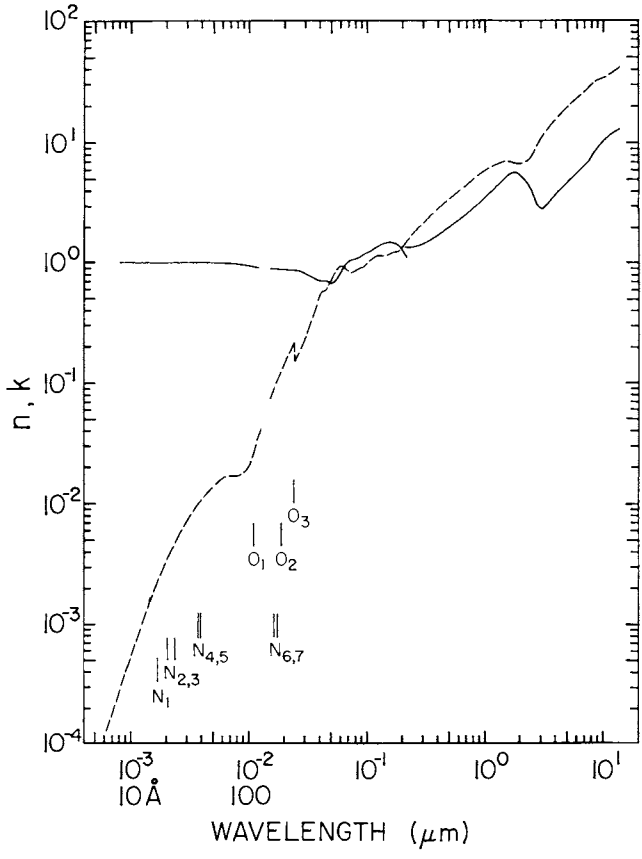

Fig. 7. Log–log plot of n (——) and k (– – –) versus wavelength in micrometers for platinum.

TABLE VII

Values of n and k Obtained from Various References for Platinum[a]

eV	cm^{-1}	Å	n	k
2000		6.199	0.999528 [25]	1.23×10^{-4} [25]
1952		6.351	0.999476	1.33
1905		6.508	0.999421	1.43
1860		6.665	0.999377	1.54
1815		6.831	0.999332	1.67
1772		6.997	0.999288	1.80
1730		7.166	0.999243	1.94
1688		7.344	0.999197	2.09
1648		7.523	0.999150	2.25
1609		7.705	0.999102	2.43
1570		7.897	0.999051	2.62
1533		8.087	0.999000	2.82
1496		8.287	0.99895	3.04
1460		8.492	0.99889	3.27
1426		8.694	0.99883	3.51
1392		8.906	0.99877	3.78
1358		9.129	0.99871	4.06
1326		9.350	0.99865	4.38
1294		9.581	0.99858	4.72
1263		9.816	0.99851	5.08
1233		10.05	0.99844	5.46
1204		10.30	0.99837	5.86
1175		10.55	0.99829	6.30
1147		10.81	0.99821	6.77
1119		11.08	0.99813	7.29
1093		11.34	0.99805	7.82
1067		11.62	0.99796	8.40
1041		11.91	0.99787	9.05
1016		12.20	0.99778	9.72×10^{-4}
992		12.50	0.99769	1.04×10^{-3}
968		12.81	0.99759	1.12
945		13.12	0.99749	1.20
923		13.43	0.99739	1.28
901		13.76	0.99729	1.37
879		14.10	0.99718	1.47
858		14.45	0.99707	1.57
838		14.79	0.99697	1.68
818		15.16	0.99686	1.79
798		15.54	0.99675	1.92
779		15.92	0.99666	2.05
760		16.31	0.99656	2.16
742		16.71	0.99646	2.27
725		17.10	0.99634	2.38
707		17.54	0.99620	2.51
690		17.97	0.99606	2.66
674		18.39	0.99592	2.82
658		18.84	0.99579	2.99
642		19.31	0.99566	3.19
627		19.77	0.99555	3.37
612		20.26	0.99544	3.55
597		20.77	0.99532	3.76
583		21.27	0.99521	3.96

[a] The references from which the values were extracted are given in brackets.

TABLE VII (*Continued*)

Platinum

eV	cm^{-1}	Å	n	k
569		21.79	0.99513	4.17
555		22.34	0.99508	4.37
542		22.87	0.99498	4.46
529		23.44	0.99482	4.54
516		24.03	0.99458	4.74
504		24.60	0.99437	4.98
492		25.20	0.99419	5.23
480		25.84	0.99400	5.51
469		26.43	0.99384	5.78
458		27.07	0.99368	6.07
447		27.74	0.99353	6.38
436		28.44	0.99338	6.70
426		29.10	0.99324	7.00
415		29.87	0.99310	7.37
406		30.54	0.99300	7.70
396		31.31	0.99293	8.08
386		32.12	0.99290	8.36
377		32.89	0.99284	8.59
368		33.69	0.99273	8.84
359		34.53	0.99260	9.09
351		35.32	0.99246	9.33
342		36.25	0.99228	9.62
334		37.12	0.99212	9.88×10^{-3}
326		38.03	0.99193	1.02×10^{-2}
318		38.99	0.99174	1.05
311		39.86	0.99155	1.07
303		40.92	0.99130	1.11
296		41.88	0.99108	1.14
289		42.90	0.99085	1.17
282		43.96	0.99060	1.20
275		45.08	0.99034	1.24
269		46.09	0.99010	1.27
262		47.32	0.9898	1.31
256		48.43	0.9896	1.35
250		49.59	0.9893	1.38
244		50.81	0.9891	1.41
238		52.09	0.9888	1.45
232		53.44	0.9885	1.48
227		54.62	0.9881	1.51
221		56.10	0.9877	1.54
216		57.40	0.9874	1.58
211		58.76	0.9870	1.61
206		60.18	0.9866	1.64
201		61.68	0.9863	1.68
196		63.25	0.9859	1.69
191		64.91	0.9855	1.69
187		66.30	0.9850	1.69
182		68.12	0.9841	1.70
178		69.65	0.9834	1.70
174		71.25	0.9826	1.70
170		72.93	0.9816	1.70
166		74.69	0.9805	1.70

(*continued*)

TABLE VII (*Continued*)

Platinum

eV	cm^{-1}	Å	n	k
162		76.53	0.9793	1.70
158		78.47	0.9778	1.71
154		80.51	0.9762	1.72
150		82.65	0.9745	1.74
147		84.34	0.9730	1.75
143		86.70	0.9708	1.77
140		88.56	0.9690	1.79
136		91.16	0.9661	1.81
133		93.22	0.9637	1.86
130		95.37	0.9612	1.92
127		97.62	0.9584	1.99
124		99.98	0.9553	2.06
121		102.5	0.9518	2.18
118		105.1	0.9481	2.34
115		107.8	0.9442	2.50
112		110.7	0.9399	2.71
110		112.7	0.9369	2.87
107		115.9	0.9322	3.14
104		119.2	0.9269	3.50
102		121.5	0.9232	3.77
100		124.0	0.9190	4.08
eV	cm^{-1}	μm	n	k
82.66		0.015	0.885 [23]	7.5 [23]
77.49		0.016	0.892	8.6
72.93		0.017	0.893	9.9×10^{-2}
68.88		0.018	0.892	0.114
65.26		0.019	0.887	0.129
61.99		0.020	0.882	0.145
59.04		0.021	0.877	0.162
56.36		0.022	0.869	0.180
53.91		0.023	0.860	0.198
51.66		0.024	0.881	0.217
45.59		0.025	0.872	0.157
47.69		0.026	0.862	0.166
45.92		0.027	0.850	0.180
44.28		0.028	0.838	0.194
42.75		0.029	0.826	0.210
41.33		0.030	0.810	0.227
40.00		0.031	0.794	0.249
38.75		0.032	0.779	0.272
37.57		0.033	0.762	0.297
36.47		0.034	0.742	0.322
35.42		0.035	0.722	0.350
34.44		0.036	0.696	0.379
33.51		0.037	0.674	0.412
32.63		0.038	0.663	0.447
31.79		0.039	0.675	0.502
31.00		0.040	0.687	0.551
30.24		0.041	0.699	0.581
29.52		0.042	0.709	0.573
28.83		0.043	0.718	0.654

TABLE VII (*Continued*)

Platinum

eV	cm^{-1}	μm	n	k
28.18		0.044	0.722	0.579
27.55		0.045	0.722	0.605
26.95		0.046	0.719	0.622
26.38		0.047	0.717	0.637
25.83		0.048	0.714	0.656
25.30		0.049	0.712	0.679
24.80		0.050	0.709	0.718
24.31		0.051	0.709	0.766
23.84		0.052	0.711	0.797
23.39		0.053	0.713	0.826
22.96		0.054	0.720	0.845
22.54		0.055	0.729	0.867
22.14		0.056	0.744	0.887
21.75		0.057	0.763	0.905
21.38		0.058	0.792	0.924
21.01		0.059	0.812	0.935
20.66		0.060	0.835	0.938
20.33		0.061	0.862	0.937
20.00		0.062	0.887	0.930
19.68		0.063	0.914	0.924
19.37		0.064	0.937	0.915
19.07		0.065	0.957	0.900
18.79		0.066	0.975	0.884
18.51		0.067	0.993	0.869
18.23		0.068	1.01	0.856
17.97		0.069	1.02	0.837
17.71		0.070	1.03	0.826
17.22		0.072	1.04	0.809
16.75		0.074	1.05	0.817
16.31		0.076	1.06	0.835
15.90		0.078	1.07	0.850
15.50		0.080	1.08	0.866
15.12		0.082	1.09	0.878
14.76		0.084	1.10	0.891
14.42		0.086	1.12	0.899
14.09		0.088	1.14	0.903
13.78		0.090	1.16	0.912
13.48		0.092	1.18	0.919
13.19		0.094	1.20	0.930
12.92		0.096	1.19	0.942
12.65		0.098	1.17	0.957
12.40		0.100	1.19	0.981
12.16		0.102	1.22	1.01
11.92		0.104	1.22	1.02
11.70		0.106	1.23	1.04
11.48		0.108	1.24	1.05
11.27		0.110	1.24	1.07
11.07		0.112	1.25	1.09
10.88		0.114	1.27	1.11
10.69		0.116	1.28	1.13
10.51		0.118	1.30	1.15
10.33		0.120	1.32	1.17

(*continued*)

TABLE VII (*Continued*)

Platinum

eV	cm^{-1}	μm	*n*	*k*
10.16		0.122	1.35	1.18
9.999		0.124	1.37	1.18
9.840		0.126	1.40	1.17
9.686		0.128	1.42	1.17
9.537		0.130	1.43	1.16
9.393		0.132	1.43	1.15
9.253		0.134	1.43	1.15
9.117		0.136	1.43	1.14
8.984		0.138	1.43	1.14
8.856		0.140	1.45	1.15
8.731		0.142	1.46	1.15
8.610		0.144	1.46	1.15
8.492		0.146	1.47	1.15
8.377		0.148	1.47	1.15
8.266		0.150	1.47	1.15
7.999		0.155	1.46	1.16
7.749		0.160	1.46	1.22
7.514		0.165	1.48	1.21
7.293		0.170	1.49	1.22
7.085		0.175	1.46	1.23
6.888		0.180	1.42	1.23
6.702		0.185	1.38	1.24
6.526		0.190	1.34	1.26
6.358		0.195	1.30	1.29
6.199	50,000	0.200	1.24	1.34
			1.39 [21]	1.35 [21]
6.1	49,200	0.2033	1.38	1.37
6.048	48,780	0.205	1.19 [23]	1.40 [23]
6.0	48,390	0.2066	1.38 [21]	1.40 [21]
5.9	47,590	0.2101	1.37	1.43
5.8	46,780	0.2138	1.36	1.47
5.6	45,170	0.2214	1.36	1.54
5.4	43,550	0.2296	1.36	1.61
5.2	41,940	0.2384	1.36	1.67
5.0	40,330	0.2480	1.36	1.76
4.8	38,720	0.2583	1.38	1.85
4.6	37,100	0.2695	1.39	1.95
4.4	35,490	0.2818	1.43	2.04
4.2	33,880	0.2952	1.45	2.14
4.0	32,260	0.3100	1.49	2.25
3.9	31,460	0.3179	1.51	2.32
3.8	30,650	0.3263	1.53	2.37
3.7	29,840	0.3351	1.56	2.42
3.6	29,040	0.3444	1.58	2.48
3.5	28,230	0.3542	1.60	2.55
3.4	27,420	0.3647	1.62	2.62
3.3	26,620	0.3757	1.65	2.69
3.2	25,810	0.3874	1.68	2.76
3.1	25,000	0.3999	1.72	2.84
3.0	24,200	0.4133	1.75	2.92
2.9	23,390	0.4275	1.79	3.01
2.8	22,580	0.4428	1.83	3.10

TABLE VII (*Continued*)

Platinum

eV	cm^{-1}	μm	n	k
2.7	21,780	0.4592	1.87	3.20
2.6	20,970	0.4769	1.91	3.30
2.5	20,160	0.4959	1.96	3.42
2.4	19,360	0.5166	2.03	3.54
2.3	18,550	0.5390	2.10	3.67
2.2	17,740	0.5636	2.17	3.77
2.1	16,940	0.5904	2.23	3.92
2.0	16,130	0.6199	2.30	4.07
1.9	15,320	0.6525	2.38	4.26
1.8	14,520	0.6888	2.51	4.43
1.7	13,710	0.7293	2.63	4.63
1.6	12,910	0.7749	2.76	4.84
1.5	12,100	0.8265	2.92	5.07
1.4	11,290	0.8856	3.10	5.32
1.3	10,490	0.9537	3.29	5.61
1.2	9,679	1.033	3.55	5.92
1.15	9,276	1.078	3.70	6.08
1.1	8,872	1.127	3.86	6.24
1.05	8,469	1.181	4.03	6.44
1.0	8,065	1.240	4.25	6.62
0.95	7,662	1.305	4.50	6.77
0.90	7,259	1.378	4.77	6.91
0.88	7,098	1.409	4.91	6.95
0.85	6,856	1.459	5.05	6.98
0.82	6,614	1.512	5.17	7.01
0.80	6,452	1.550	5.31	7.04
0.77	6,210	1.610	5.44	7.04
0.75	6,049	1.653	5.57	7.02
0.73	5,888	1.698	5.67	6.95
0.70	5,646	1.771	5.71	6.83
0.68	5,485	1.823	5.66	6.73
0.65	5,243	1.907	5.52	6.66
0.63	5,081	1.968	5.34	6.70
0.60	4,839	2.066	5.13	6.75
0.57	4,597	2.175	4.86	6.89
0.55	4,436	2.254	4.58	7.14
0.52	4,194	2.384	4.30	7.40
0.50	4,073	2.455	3.91	7.71
0.47	3,791	2.638	3.36	8.40
0.45	3,629	2.755	3.03	9.31
0.43	3,468	2.883	2.92	10.3
0.40	3,226	3.100	2.81	11.4
0.38	3,065	3.263	3.03	12.5
0.35	2,823	3.542	3.28	13.7
0.32	2,581	3.875	3.57	14.9
0.30	2,420	4.133	3.92	16.2
0.28	2,258	4.428	4.24	17.7
0.25	2,016	4.959	4.70	19.4
0.22	1,774	5.636	5.24	21.5
0.20	1,613	6.199	5.90	24.0
0.17	1,371	7.293	6.78	27.2
0.15	1,210	8.266	8.18	31.2
0.13	1,049	9.537	9.91	36.7
0.10	806.5	12.40	13.2	44.7

X RHODIUM (Rh)

Studies of the optical properties of Rh are listed in the references [1–15]. Table VIII lists the n and k values chosen and the pertinent references. These data are plotted in Fig. 8 as smooth curves. The data from 150 to 2000 Å are those of Cox *et al.* [9], from 2000 Å to about 12.4 μm the data are those of Weaver *et al.* [15], and Henke *et al.'s* [16] calculated data extend from 6.2 to 124 Å.

Cox *et al.* [9] obtained n and k values from evaporated films of rhodium by using the reflectance-versus-angle-of-incidence method. The films were evaporated with an electron gun at pressures of 10^{-5} torr in a conventional vacuum system. Deposition rates ranged from 10 to 100 Å/sec and substrate temperatures were 300°C. The purity of the Rh was 99.9%. The films were transferred in air to the reflectometer.

Weaver *et al.* [15] used large polycrystalline samples cut from an electron-beam-melted button of rhodium of unstated purity. The samples were mechanically polished, boiled in aqua regia, and heated *in vacuo* (10^{-7} torr) at temperatures of 1200 to 1500°C for several hours. The samples were then transferred in air to ion-pumped experimental chambers. From 6.2 μm to 2818 Å a calorimetric technique [17] was used, and at the shorter wavelengths the reflectance at 10° angle of incidence was measured. These data were combined with other data [7], Drude infrared extrapolations, and a power-law decay in the reflectance extending to 10^5 eV to obtain n and k by using the Kramers–Kronig method.

REFERENCES

1. G. Hass and R. Tousey, *J. Opt. Soc. Am.* **49**, 593 (1959)
2. R. P. Madden and L. R. Canfield, *J. Opt. Soc. Am.* **51**, 838 (1961).
3. I. Y. Leksina and N. V. Penkina, *Fiz. Met. Metalloved.* **22**, 264 (1966); I. Y. Leksina and N. V. Penkina, *Phys. Met. Metallogr.* **22**(2), 104 (1966).
4. G. A. Bolotin and T. P. Chukina, *Opt. Spektrosk.* **23**, 620 (1967); G. A. Bolotin and T. P. Chukina, *Opt. Spectrosc.* **23**, 333 (1967).
5. F. I. Vilesov, A. A. Azgrubskii, and M. M. Kirillova, *Opt. Spektrosk.* **23**, 153 (1967); F. I. Vileson, A. A. Azgrubskii, and M. M. Kirillova, *Opt. Spectrosc.* **23**, 79 (1967).
6. M. M. Kirillova, L. V. Nomerovannaya, G. A. Bolotin, V. M. Mayevskiy, M. M. Noskov, and M. L. Bolotina, *Fiz. Met. Metalloved.* **25**, 459 (1968); M. M. Kirillova, L. V. Nomerovannaya, G. A. Bolotin, V. M. Mayevkiy, M. M. Noskov, and M. L. Bolotina, *Phys. Met. Metallogr.* **25**(3), 81 (1968).
7. R. Haensel, K. Radler, B. Sonntag, and C. Kunz, *Solid State Commun.* **7**, 1495 (1969).
8. A. Seignac and S. Robin, *C. R. Acad. Sci Ser. B* **271**, 919 (1970).
9. J. T. Cox, G. Hass, and W. R. Hunter, *J. Opt. Soc. Am.* **61**, 360 (1971).
10. W. R. Hunter, *Proc. Int. Conf. Vac. Ultraviolet Rad. Physics*, 3rd, *Tokyo*, p. 2aC2-1 (1971).
11. A. Seignac and S. Robin, *Solid State Commun.* **11**, 217 (1972).
12. D. T. Pierce and W. E. Spicer, *Phys. Stat. Solidi B* **60**, 689 (1973).
13. J. H. Weaver, *Phys. Rev. B* **11**, 1416 (1975).
14. J. H. Weaver and C. G. Olson, *Phys. Rev. B* **14**, 3251 (1976).

15. J. H. Weaver, C. G. Olson, and D. W. Lynch, *Phys. Rev. B* **15**, 4115 (1977).
16. B. L. Henke, P. Lee, T. J. Tanaka, R. L. Shimabukuro, and B. K. Fujikawa, "Low Energy X-Ray Diagnostics—1981" (D. T. Attwood and B. L. Henke, eds.), p. 340, *AIP Conf. Proc.* No. 75, American Institute of Physics, New York, 1981.
17. L. W. Bos and D. W. Lynch, *Phys. Rev. B* **2**, 4567 (1970).

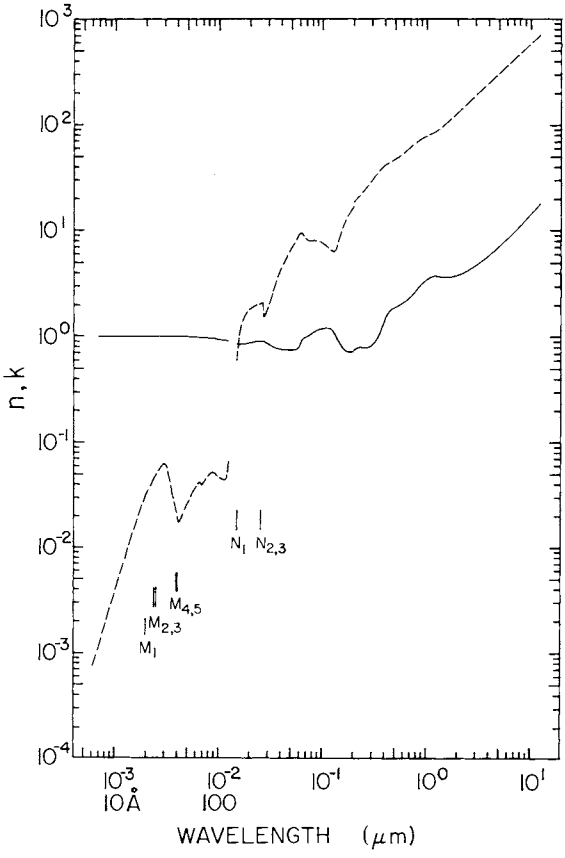

Fig. 8. Log–log plot of n (——) and k (– – –) versus wavelength in micrometers for rhodium.

TABLE VIII

Values of n and k Obtained from Various References for Rhodium[a]

eV	cm^{-1}	Å	n	k
2000		6.199	0.999512 [16]	7.50×10^{-5} [16]
1952		6.351	0.999486	8.16
1905		6.508	0.999459	8.87
1860		6.665	0.999432	9.63×10^{-5}
1815		6.831	0.999402	1.05×10^{-4}
1772		6.997	0.999372	1.14
1730		7.166	0.999341	1.24
1688		7.345	0.999307	1.34
1648		7.523	0.999272	1.46
1609		7.705	0.999236	1.58
1570		7.897	0.999198	1.71
1533		8.087	0.999158	1.86
1496		8.287	0.999117	2.02
1460		8.492	0.999073	2.19
1426		8.694	0.999029	2.36
1392		8.906	0.99898	2.56
1358		9.129	0.99893	2.78
1326		9.350	0.99888	3.00
1294		9.581	0.99883	3.25
1263		9.816	0.99877	3.52
1233		10.05	0.99871	3.81
1204		10.30	0.99865	4.13
1175		10.55	0.99859	4.47
1147		10.81	0.99852	4.84
1119		11.08	0.99845	5.25
1093		11.34	0.99839	5.67
1067		11.62	0.99831	6.14
1041		11.91	0.99824	6.66
1016		12.20	0.99816	7.21
992		12.50	0.99808	7.79
968		12.81	0.99800	8.42
945		13.12	0.99792	9.10
923		13.43	0.99783	9.81×10^{-4}
901		13.76	0.99774	1.06×10^{-3}
879		14.10	0.99765	1.14
858		14.45	0.99756	1.23
838		14.79	0.99747	1.33
818		15.16	0.99738	1.43
798		15.54	0.99728	1.54
779		15.92	0.99718	1.66
760		16.31	0.99709	1.79
741		16.73	0.99700	1.93
725		17.10	0.99691	2.07
707		17.54	0.99682	2.23
690		17.97	0.99674	2.39
674		18.39	0.99666	2.55
658		18.84	0.99658	2.74
642		19.31	0.99654	2.96
627		19.77	0.99652	3.13
612		20.26	0.99650	3.29
597		20.77	0.99645	3.46
583		21.27	0.99641	3.63
569		21.79	0.99636	3.82

[a] The references from which the values were extracted are given in brackets.

TABLE VIII (*Continued*)

Rhodium

eV	cm^{-1}	Å	*n*	*k*
555		22.34	0.99632	4.05
542		22.87	0.99631	4.27
529		23.44	0.99634	4.51
516		24.03	0.99639	4.72
504		24.60	0.99643	4.90
492		25.20	0.99648	5.09
480		25.83	0.99654	5.30
469		26.43	0.99661	5.50
458		27.07	0.99672	5.72
447		27.74	0.99692	6.01
436		28.44	0.99721	6.07
426		29.10	0.99744	6.12
415		29.87	0.99773	6.18
406		30.54	0.99808	6.23
396		31.31	0.99863	5.97
386		32.12	0.99887	5.30
377		32.89	0.99882	4.75
368		33.69	0.99867	4.25
359		34.53	0.99840	3.79
351		35.32	0.99808	3.41
342		36.25	0.99765	3.02
334		37.12	0.99720	2.71
326		38.03	0.99669	2.42
318		38.99	0.99611	2.16
311		39.86	0.99554	1.94
303		40.92	0.99473	1.72
296		41.88	0.99400	1.77
289		42.90	0.99329	1.87
282		43.96	0.99261	1.98
275		45.08	0.99195	2.09
269		46.09	0.99137	2.20
262		47.32	0.99066	2.33
256		48.43	0.99002	2.45
250		49.59	0.9894	2.59
244		50.81	0.9887	2.73
238		52.09	0.9879	2.89
232		53.44	0.9872	3.06
227		54.62	0.9865	3.21
221		56.10	0.9857	3.41
216		57.40	0.9849	3.59
211		58.76	0.9842	3.75
206		60.18	0.9834	3.90
201		61.68	0.9825	4.06
196		63.25	0.9817	4.23
190		64.91	0.9808	4.17
187		66.30	0.9799	4.09
182		68.12	0.9785	3.98
178		69.65	0.9773	4.08
174		71.25	0.9761	4.20
170		72.93	0.9748	4.32
166		74.69	0.9734	4.44
162		76.53	0.9719	4.57

(*continued*)

TABLE VIII (*Continued*)

Rhodium

eV	cm^{-1}	Å	*n*	*k*
158		78.47	0.9703	4.71
154		80.51	0.9686	4.86
150		82.65	0.9667	5.01
147		84.34	0.9653	5.14
143		86.70	0.9632	5.20
140		88.56	0.9615	5.12
136		91.16	0.9589	5.02
133		93.22	0.9567	4.93
130		95.37	0.9543	4.85
127		97.62	0.9517	4.77
124		99.98	0.9487	4.69
121		102.5	0.9455	4.61
118		105.1	0.9419	4.52
115		107.8	0.9379	4.44
112		110.7	0.9333	4.36
110		112.7	0.9300	4.39
107		115.9	0.9243	4.43
104		119.2	0.9174	4.73
102		121.5	0.9124	5.59
100		124.0	0.9072	6.62×10^{-3}
eV	cm^{-1}	μm	*n*	*k*
82.66		0.015	0.852 [9]	6.0×10^{-2} [9]
77.49		0.016	0.852	0.112
72.93		0.017	0.853	0.140
68.88		0.018	0.854	0.158
65.26		0.019	0.857	0.172
61.99		0.020	0.865	0.183
59.04		0.021	0.875	0.190
56.36		0.022	0.888	0.195
53.91		0.023	0.900	0.199
51.66		0.024	0.910	0.203
49.59		0.025	0.915	0.205
47.69		0.026	0.915	0.208
45.92		0.027	0.907	0.153
44.28		0.028	0.890	0.162
42.75		0.029	0.863	0.177
41.33		0.030	0.838	0.194
40.00		0.031	0.808	0.212
38.75		0.032	0.779	0.237
37.57		0.033	0.753	0.260
36.47		0.034	0.739	0.285
35.42		0.035	0.731	0.312
34.44		0.036	0.727	0.337
33.51		0.037	0.725	0.360
32.63		0.038	0.727	0.390
31.79		0.039	0.729	0.416
31.00		0.040	0.732	0.445
30.24		0.041	0.735	0.468
29.52		0.042	0.737	0.488
28.83		0.043	0.739	0.511

TABLE VIII (*Continued*)

Rhodium

eV	cm^{-1}	μm	*n*	*k*
28.18		0.044	0.739	0.536
27.55		0.045	0.739	0.560
26.95		0.046	0.738	0.580
26.38		0.047	0.733	0.603
25.83		0.048	0.728	0.627
25.30		0.049	0.727	0.645
24.80		0.050	0.732	0.673
24.31		0.051	0.742	0.696
23.84		0.052	0.757	0.720
23.39		0.053	0.780	0.743
22.96		0.054	0.795	0.771
22.54		0.055	0.807	0.798
22.14		0.056	0.815	0.832
21.75		0.057	0.821	0.821
21.38		0.058	0.823	0.893
21.01		0.059	0.832	0.925
20.66		0.060	0.875	0.942
20.33		0.061	0.926	0.949
20.00		0.062	0.987	0.950
19.68		0.063	1.02	0.948
19.37		0.064	1.03	0.938
19.07		0.065	1.04	0.913
18.79		0.066	1.05	0.877
18.51		0.067	1.06	0.851
18.23		0.068	1.06	0.834
17.97		0.069	1.07	0.820
17.71		0.070	1.08	0.812
17.46		0.071	1.09	0.805
17.22		0.072	1.10	0.803
16.98		0.073	1.10	0.802
16.75		0.074	1.11	0.802
16.53		0.075	1.12	0.802
16.31		0.076	1.13	0.802
16.10		0.077	1.14	0.802
15.90		0.078	1.15	0.802
15.69		0.079	1.15	0.802
15.50		0.080	1.17	0.802
15.31		0.081	1.17	0.802
15.12		0.082	1.18	0.802
14.94		0.083	1.19	0.802
14.76		0.084	1.20	0.801
14.59		0.085	1.21	0.800
14.42		0.086	1.21	0.799
14.25		0.087	1.22	0.798
14.09		0.088	1.23	0.796
13.93		0.089	1.24	0.793
13.78		0.090	1.24	0.791
13.62		0.091	1.25	0.788
13.48		0.092	1.26	0.787
13.33		0.093	1.26	0.784
13.19		0.094	1.26	0.782
13.05		0.095	1.27	0.778

(*continued*)

TABLE VIII (*Continued*)

Rhodium

eV	cm^{-1}	μm	*n*	*k*
12.92		0.096	1.27	0.773
12.78		0.097	1.27	0.769
12.65		0.098	1.27	0.764
12.52		0.099	1.27	0.758
12.40		0.100	1.27	0.755
11.81		0.105	1.26	0.730
11.27		0.110	1.24	0.707
10.78		0.115	1.22	0.682
10.33		0.120	1.18	0.655
9.919		0.125	1.11	0.638
9.537		0.130	1.03	0.638
9.184		0.135	0.953	0.675
8.856		0.140	0.880	0.750
8.551		0.145	0.820	0.843
8.266		0.150	0.766	0.940
7.999		0.155	0.720	1.03
7.749		0.160	0.691	1.12
7.514		0.165	0.681	1.22
7.293		0.170	0.677	1.30
7.085		0.175	0.675	1.38
6.888		0.180	0.672	1.45
6.702		0.185	0.672	1.51
6.526		0.190	0.671	1.57
6.358		0.195	0.672	1.63
6.199		0.200	0.675	1.69
6.2	50,010	0.2000	0.78 [15]	1.85 [15]
6.0	48,390	0.2066	0.76	1.93
5.8	46,780	0.2138	0.79	2.00
5.6	45,170	0.2214	0.80	2.06
5.4	43,550	0.2296	0.80	2.14
5.2	41,490	0.2384	0.79	2.23
5.0	40,330	0.2480	0.79	2.34
4.9	39,520	0.2530	0.79	2.39
4.8	38,710	0.2583	0.79	2.46
4.7	37,910	0.2638	0.79	2.52
4.6	37,100	0.2695	0.78	2.60
4.5	36,290	0.2755	0.79	2.68
4.4	35,490	0.2818	0.80	2.76
4.3	34,680	0.2883	0.83	2.85
4.2	33,880	0.2952	0.84	2.94
4.1	33,070	0.3024	0.84	3.03
4.0	32,260	0.3100	0.86	3.12
3.9	31,460	0.3179	0.88	3.23
3.8	30,650	0.3263	0.91	3.34
3.7	29,840	0.3351	0.95	3.45
3.6	29,040	0.3444	0.99	3.58
3.5	28,230	0.3542	1.04	3.71
3.4	27,420	0.3647	1.11	3.84
3.3	26,620	0.3757	1.20	3.97
3.2	25,810	0.3875	1.30	4.09
3.1	25,000	0.4000	1.41	4.20
3.0	24,200	0.4133	1.53	4.29

TABLE VIII (*Continued*)

Rhodium

eV	cm^{-1}	μm	*n*	*k*
2.9	23,390	0.4275	1.63	4.36
2.7	21,780	0.4592	1.80	4.49
2.6	20,970	0.4769	1.85	4.55
2.5	20,160	0.4959	1.88	4.65
2.4	19,360	0.5166	1.90	4.78
2.3	18,550	0.5391	1.94	4.94
2.2	17,740	0.5636	2.00	5.11
2.1	16,940	0.5904	2.05	5.30
2.0	16,130	0.6199	2.12	5.51
1.9	15,320	0.6526	2.20	5.76
1.8	14,520	0.6888	2.30	6.02
1.7	13,710	0.7293	2.42	6.33
1.6	12,900	0.7749	2.60	6.64
1.5	12,100	0.8266	2.78	6.97
1.4	11,290	0.8856	3.01	7.31
1.3	10,490	0.9537	3.26	7.63
1.25	10,080	0.9919	3.38	7.80
1.2	9,679	1.033	3.51	7.94
1.15	9,275	1.078	3.60	8.09
1.1	8,872	1.127	3.67	8.26
1.05	8,469	1.181	3.72	8.44
1.0	8,065	1.240	3.71	8.67
0.95	7,662	1.305	3.69	8.94
0.90	7,259	1.378	3.62	9.36
0.85	6,856	1.459	3.64	9.81
0.80	6,452	1.550	3.63	10.3
0.75	6,049	1.653	3.63	11.0
0.70	5,646	1.771	3.67	11.7
0.65	5,243	1.907	3.77	12.6
0.60	4,839	2.066	3.87	13.5
0.55	4,436	2.254	3.97	14.7
0.50	4,033	2.480	4.20	16.1
0.45	3,629	2.755	4.45	17.7
0.40	3,226	3.100	4.74	19.8
0.35	2,823	3.542	5.22	22.4
0.30	2,420	4.133	5.85	25.9
0.25	2,016	4.959	7.01	30.7
0.20	1,613	6.199	8.66	37.5
0.15	1,210	8.266	11.5	48.6
0.10	806.5	12.40	18.5	69.4

XI SILVER (Ag)

From among the many studies of the optical properties of Ag [1–36], four have been chosen as representative. They are (1) the data of Hagemann *et al.* [28] from approximately 1.5 to 460 Å, (2) the data of Leveque *et al.* [35] from 460 to 3600 Å, (3) the data of Winsemius *et al.* [33] from 3600 Å to 2.07 μm, and (4) the data of Dold and Mecke [14] from 1.265 to 10 μm. Table IX lists the values of n and k and the pertinent references. These data are plotted in Fig. 9 as smooth curves.

Hagemann *et al.* [28] prepared their samples by evaporating thin films of silver onto substrates of collodion that were supported on copper screens of the type used for electron microscopy. The evaporation was done from resistance heated boats at a pressure of about 5×10^{-7} torr at rates of 10–50 Å/sec. The plastic substrates were dissolved away, leaving Ag films on copper screens. These processes required exposing the Ag films to air before measurements. Transmission measurements were made from 13 to 150 eV to obtain an absorption spectrum that was extended by using the data of others [10, 15, 22, 24, 26] to provide an absorption spectrum large enough for a Kramers–Kronig analysis.

Leveque *et al.* [35] prepared their samples by the evaporation of silver in a vacuum of about 10^{-7} torr. Reflectance measurements were made in the same chamber, and so there was no exposure to air. A variety of substrates was used, but for the data reported, the substrates were Pyrex plates at room temperature. Reflectance measurements were made in the 3.5–30-eV region by using synchrotron radiation. These data were augmented prior to Kramers–Kronig analysis by using absorptance data, $A = 1 - R$, in the 0.1–2.8-eV region (Weaver [36]), a smooth interpolation to the reflectance at 3.5 eV, a reflectance derived from the absorption coefficient data of Haensel *et al.* [22] between 30 and 150 eV and the data from Hagemann *et al.* [28] for higher energies.

Winsemius *et al.* [33] used polycrystalline silver of $99.999^{+}\%$ purity. Samples were spark-cut from larger pieces and electrolytically and chemically polished [37]. The samples were then transferred in air to a reflectometer, where they were vacuum annealed at 700 K for four or more hours. Values of n and k were obtained by using a polarimetric method described by Beattie [38].

Dold and Mecke [14] evaporated $99.99^{+}\%$ pure silver onto polished glass plates from a Mo boat. The substrate temperature was not stated but was probably room temperature. Polarimetric measurements were made in air to obtain n and k.

Henke *et al.*'s [39] data showed good agreement with that of Hagemann *et al.* [28], especially from 80 to 124 Å. At 460 Å the n spectra of Hagemann *et al.* [28] and Leveque *et al.* [35] are in very close agreement, but they diverge to longer wavelengths. The k spectra of these two sets of investigators

show rather poor agreement at 460 Å but converge and become equal at about 1000 Å. The agreement for both n and k is good at 3600 Å, where the data of Leveque *et al.* [35] and Winsemius *et al.* [33] meet. The data of the latter group show only fair agreement with the data of Dold and Mecke [14] where their data overlap. If the data of Dold and Mecke [14] are used to calculate the normal-incidence reflectance R, a spectrum with a broad peak at 5 μm results. The reflectance should increase monotonically with increasing wavelength. Neglect of the anomalous skin effect causes a calculated R to be too high at longer wavelengths, not lower. The cause of the peak probably is erroneously low k values at longer wavelengths. The measured reflectance of silver is higher than that given by the data presented here, and it increases smoothly to longer wavelengths.

It should be noted that in the longer-wavelength region, the spectra are expected to be somewhat sample dependent, for the electron relaxation time depends on impurity content and crystallite size to an extent sufficient to appear in the spectra. See the discussion of the data for gold.

REFERENCES

1. G. Joos and A. Klopfer, *Z. Physik* **138**, 251 (1954).
2. L. G. Schulz, *J. Opt. Soc. Am.* **44**, 357, 540 (1954).
3. L. G. Schulz and F. R. Tangherlini, *J. Opt. Soc. Am.* **44**, 362 (1954).
4. J. R. Beattie and G. K. T. Conn, *Philos. Mag.* **46**, 989 (1955).
5. J. N. Hodgson, *Proc. Phys. Soc. London Ser. B* **68**, 593 (1955).
6. M. A. Biondi, *Phys. Rev.* **102**, 964 (1956).
7. J. R. Beattie, *Physica* **23**, 898 (1957).
8. L. G. Schulz, *Adv. Phys.* **6**, 102 (1957).
9. M. Otter, *Z. Physik* **161**, 163 (1961).
10. H. Ehrenreich and H. R. Philipp, *Phys. Rev.* **128**, 1622 (1962).
11. P. R. Wessel, *Phys. Rev.* **132**, 2062 (1963).
12. R. H. Huebner, E. T. Arakawa, R. A. MacRae, and R. N. Hamm, *J. Opt. Soc. Am.* **54**, 1434 (1964).
13. A. P. Lukirskii, E. P. Savinov, O. A. Ershov, and Y. F. Shepelev, *Opt. Spektrosk.* **16**, 310 (1964); A. P. Lukirskii, E. P. Savinov, O. A. Ershov, and Y. F. Shepelev, *Opt. Spectrosc.* **16**, 168 (1964).
14. B. Dold and R. Mecke, *Optik* **22**, 435 (1965).
15. L. R. Canfield and G. Hass, *J. Opt. Soc. Am.* **55**, 61 (1965).
16. R. G. Yarovaya and I. N. Shklyarevskii, *Opt. Spektrosk.* **18**, 832 (1964); R. G. Yarovaya and I. N. Shklyarevskii, *Opt. Spectrosc.* **18**, 465 (1965).
17. H. E. Bennett and J. M. Bennett, *in* "Optical Properties and Electronic Structure of Metals and Alloys" (F. Abélès, ed.), p. 175, North-Holland Publ., Amsterdam, 1966.
18. S. Robin, *in* "Optical Properties and Electronic Structure of Metals and Alloys" (F. Abélès, ed.), p. 202, North-Holland Publ., Amsterdam, 1966.
19. J. Daniels, *Z. Physik* **203**, 235 (1967).
20. E. Meyer, H. Frede, and H. Knof, *J. Appl. Phys.* **38**, 3682 (1967).
21. H. E. Bennett, J. M. Bennett, E. J. Ashley, and R. J. Motyka, *Phys. Rev.* **165**, 755 (1968).
22. R. Haensel, C. Kunz, T. Sasaki, and B. Sonntag, *Appl. Opt.* **7**, 301 (1968).
23. J. Daniels, *Z. Physik* **277**, 234 (1969).
24. G. B. Irani, T. Huen, and F. Wooten, *J. Opt. Soc. Am.* **61**, 128 (1971).
25. G. B. Irani, T. Huen, and F. Wooten, *Phys. Rev. B* **3**, 2385 (1971).
26. P. B. Johnson and R. W. Christy, *Phys. Rev. B* **6**, 4370 (1972).

27. M. Schlüter, *Z. Physik* **250**, 87 (1972).
28. H. J. Hagemann, W. Gudat, and C. Kunz, DESY Report SR-74/7, Hamburg (1974); H. J. Hagemann, W. Gudat, and C. Kunz, *J. Opt. Soc. Am.* **65**, 742 (1975).
29. C. Wehenkel and B. Gauthé, *Opt. Commun.* **11**, 62 (1974).
30. C. J. Flaten and E. A. Stern, *Phys. Rev. B* **11**, 638 (1975).
31. J. Rivory and M. L. Thèye, *J. Physique* **36**, L129 (1975).
32. J. A. Mackay and J. A. Rayne, *Phys. Rev. B* **13**, 673 (1976).
33. P. Winsemius, F. F. van Kampen, H. P. Lengkeek, and C. G. van Went, *J. Phys. F* **6**, 1583 (1976).
34. K. G. Ramanathan, S. H. Yen, and E. A. Estalote, *Appl. Opt.* **16**, 2810 (1977).
35. G. Leveque, C. G. Olson, and D. W. Lynch, *Phys. Rev. B* **24**, 4654 (1983).
36. J. H. Weaver, private communication (1978).
37. P. Winsemius, H. P. Lengkeek, and F. F. van Kampen, *Physica* **79 B**, 529 (1975).
38. J. R. Beattie, *Philos. Mag.* **46**, 235 (1955).
39. B. L. Henke, P. Lee, T. J. Tanaka, R. L. Shimabukuro and B. K. Fujikawa, "Low Energy X-Ray Diagnostics—1981" (D. T. Attwood and B. L. Henke, eds.), p. 340, *AIP Conf. Proc.* No. 75, American Institute of Physics, New York, 1981.

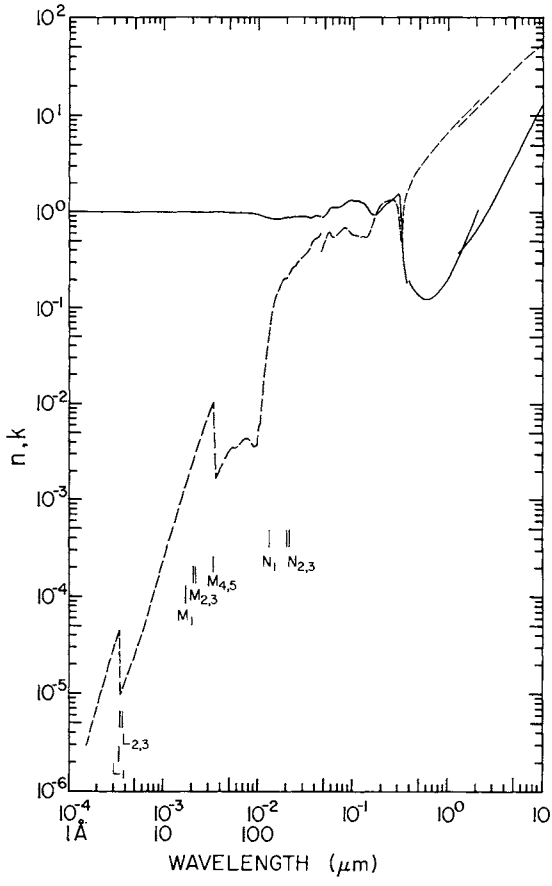

Fig. 9. Log–log plot of n (——) and k (– – – –) versus wavelength in micrometers for silver.

TABLE IX

Values of n and k Obtained from Various References for Silver[a]

eV	cm^{-1}	Å	n	k
10000		1.240	0.9990 [28]	1.29×10^{-6} [28]
8000		1.550	1.000	2.92
6000		2.066	1.002	8.36×10^{-6}
5000		2.480	1.001	1.52×10^{-5}
4500		2.755	1.001	2.21
4000		3.099	1.003	3.57
3600		3.444	1.003	3.24
3500		3.542	1.003	1.72
3000		4.133	1.001	1.43
2500		4.959	1.001	2.40
2000		6.199	1.001	4.72×10^{-5}
1500		8.265	0.999	1.21×10^{-4}
1000		12.40	0.998	5.23×10^{-4}
800		15.50	0.997	1.08×10^{-3}
740		16.75	0.998	1.42
600		20.66	0.997	2.69
500		24.80	0.997	4.57
400		30.99	0.998	8.82
370		33.51	1.007	8.23
350		35.42	1.001	1.68
300		41.33	0.996	2.32
280		44.28	0.994	2.70
260		47.68	0.992	3.11
240		51.66	0.989	3.50
220		56.35	0.987	3.45
200		61.99	0.982	3.77
180		68.88	0.978	4.31
170		72.93	0.973	4.42
160		77.49	0.968	4.38
150		82.65	0.963	4.07
140		88.56	0.955	3.54
130		95.37	0.943	3.66
120		103.3	0.926	6.22×10^{-3}
110		112.7	0.902	1.72×10^{-2}
105		118.1	0.890	2.61
100		124.0	0.876	3.82
95		130.5	0.861	5.65
90		137.8	0.849	8.24×10^{-2}
85		145.9	0.846	0.111
80		155.0	0.848	0.139
78		158.9	0.851	0.149
76		163.1	0.853	0.158
74		167.5	0.853	0.166
72		172.2	0.851	0.181
70		177.1	0.859	0.197
68		182.3	0.871	0.208
66		187.8	0.883	0.211
64		193.7	0.885	0.210
62		200.0	0.881	0.211
60		206.6	0.873	0.221
58		213.8	0.868	0.237
56		221.4	0.871	0.259
54		229.6	0.885	0.274
53		233.9	0.890	0.275

(*continued*)

[a] The references from which the values were extracted are given in brackets.

TABLE IX (*Continued*)

Silver

eV	cm^{-1}	Å	n	k
52		238.4	0.889	0.276
51		243.1	0.886	0.281
50		248.0	0.884	0.290
49		253.0	0.885	0.300
48		258.3	0.888	0.309
47		263.8	0.893	0.317
46		269.5	0.896	0.323
44		281.8	0.899	0.334
42		295.2	0.897	0.349
40		309.9	0.896	0.368
39		317.9	0.895	0.378
38		326.3	0.892	0.388
37		335.1	0.885	0.400
36		344.4	0.876	0.418
35		354.2	0.865	0.454
34		364.6	0.879	0.489
33		375.7	0.899	0.514
32		387.4	0.921	0.528
31		399.9	0.932	0.534
30		413.2	0.931	0.541
29		427.5	0.919	0.557
28.5		435.0	0.911	0.572
28		442.8	0.902	0.590
27.5		450.8	0.851	0.616
27		459.2	0.886	0.650
			0.882 [35]	0.399 [35]
26.5		467.9	0.886	0.421
26		476.9	0.887	0.444
25.5		486.2	0.891	0.468
24.5		506.1	0.906	0.522
23.5		527.6	0.943	0.584
23		539.1	0.980	0.614
22.5		551.0	1.029	0.624
22		563.6	1.075	0.615
21.5		576.7	1.104	0.584
21		590.4	1.109	0.561
20.5		604.8	1.105	0.549
20		619.9	1.098	0.548
19		652.6	1.096	0.565
18		688.8	1.101	0.593
17		729.3	1.121	0.635
16		774.9	1.167	0.676
15.5		799.9	1.202	0.691
15		826.6	1.243	0.693
14.5		855.1	1.281	0.679
14		885.6	1.308	0.656
13.5		918.4	1.322	0.628
13		953.7	1.322	0.603
12.5		991.9	1.315	0.588
eV	cm^{-1}	μm	n	k
12.1		0.1025	1.308	0.581
11.8		0.1051	1.304	0.578

TABLE IX (*Continued*)

Silver

eV	cm^{-1}	μm	n	k
11.5		0.1078	1.300	0.573
11.2		0.1107	1.293	0.566
10.9		0.1137	1.280	0.560
10.6		0.1170	1.265	0.560
10.3		0.1204	1.252	0.564
10.0		0.1240	1.241	0.568
9.7		0.1278	1.229	0.566
9.2		0.1348	1.182	0.550
9.0		0.1378	1.149	0.552
8.8		0.1409	1.112	0.563
8.6		0.1442	1.073	0.581
8.4		0.1476	1.032	0.610
8.2		0.1512	0.993	0.653
8.0		0.1550	0.962	0.706
7.8		0.1590	0.940	0.770
7.6		0.1631	0.935	0.832
7.4		0.1675	0.936	0.892
7.2		0.1722	0.942	0.951
7.0		0.1771	0.953	1.01
6.8		0.1823	0.969	1.07
6.6		0.1879	0.995	1.13
6.4		0.1937	1.028	1.18
6.3		0.1968	1.048	1.21
6.2		0.2000	1.072	1.24
6.1	49,200	0.2033	1.098	1.26
6.0	48,390	0.2066	1.125	1.27
5.8	46,780	0.2138	1.173	1.29
5.6	45,170	0.2214	1.208	1.30
5.4	43,550	0.2296	1.238	1.31
5.2	41,940	0.2384	1.265	1.33
5.0	40,330	0.2480	1.298	1.35
4.9	39,520	0.2530	1.320	1.35
4.8	38,710	0.2583	1.343	1.35
4.7	37,910	0.2638	1.372	1.35
4.6	37,100	0.2695	1.404	1.33
4.5	36,290	0.2755	1.441	1.31
4.4	35,490	0.2818	1.476	1.26
4.3	34,680	0.2883	1.502	1.19
4.2	33,880	0.2952	1.519	1.08
4.15	33,470	0.2988	1.522	0.992
4.1	33,070	0.3024	1.496	0.882
4.05	32,670	0.3061	1.432	0.766
4.0	32,260	0.3100	1.323	0.647
3.98	32,100	0.3115	1.246	0.586
3.95	31,860	0.3139	1.149	0.540
3.93	31,700	0.3155	1.044	0.514
3.9	31,460	0.3179	0.932	0.504
3.88	31,290	0.3195	0.815	0.526
3.85	31,050	0.3220	0.708	0.565
3.83	30,890	0.3237	0.616	0.609
3.8	30,650	0.3263	0.526	0.663
3.75	30,250	0.3306	0.371	0.813
3.73	30,090	0.3324	0.321	0.902
3.7	29,840	0.3351	0.294	0.986

(*continued*)

TABLE IX (*Continued*)

Silver

eV	cm^{-1}	μm	n	k
3.65	29,440	0.3397	0.259	1.12
3.6	29,040	0.3444	0.238	1.24
3.5	28,230	0.3542	0.209	1.44
3.4	27,420	0.3647	0.186	1.61
3.3	26,620	0.3757	0.200 [33]	1.67 [33]
3.2	25,810	0.3875	0.192	1.81
3.1	25,000	0.4000	0.173	1.95
3.0	24,200	0.4133	0.173	2.11
2.9	23,390	0.4275	0.160	2.26
2.8	22,580	0.4428	0.157	2.40
2.7	21,780	0.4592	0.144	2.56
2.6	20,970	0.4769	0.132	2.72
2.5	20,160	0.4959	0.130	2.88
2.4	19,360	0.5166	0.130	3.07
2.3	18,550	0.5391	0.129	3.25
2.2	17,740	0.5636	0.120	3.45
2.1	16,940	0.5904	0.121	3.66
2.0	16,130	0.6199	0.131	3.88
1.9	15,320	0.6526	0.140	4.15
1.8	14,520	0.6888	0.140	4.44
1.7	13,710	0.7293	0.148	4.74
1.6	12,900	0.7749	0.143	5.09
1.5	12,100	0.8266	0.145	5.50
1.4	11,290	0.8856	0.163	5.95
1.3	10,490	0.9537	0.198	6.43
1.2	9,679	1.033	0.226	6.99
1.1	8,872	1.127	0.251	7.67
1.0	8,065	1.240	0.329	8.49
0.98	7,904	1.265	0.375 [14]	7.78 [14]
0.96	7,743	1.291	0.383	7.92
0.95	7,662	1.305	0.358	8.95
0.94	7,582	1.319	0.392	8.06
0.92	7,420	1.348	0.401	8.21
0.90	7,259	1.378	0.411	8.37
			0.396 [33]	9.48 [33]
0.88	7,098	1.409	0.421 [14]	8.37 [14]
0.86	6,936	1.442	0.431	8.70
0.85	6,856	1.459	0.446 [33]	10.1 [33]
0.84	6,775	1.476	0.442 [14]	8.88 [14]
0.82	6,614	1.512	0.455	9.08
0.80	6,452	1.550	0.469	9.32
			0.514 [33]	10.8 [33]
0.78	6,291	1.590	0.485	9.57
0.76	6,130	1.631	0.501	9.84
0.75	6,049	1.653	0.624 [33]	11.5 [33]
0.74	5,968	1.675	0.519 [14]	10.1 [14]
0.72	5,807	1.722	0.537	10.4
0.70	5,646	1.771	0.557	10.7
			0.844 [33]	12.2 [33]
0.68	5,485	1.823	0.578 [14]	11.1 [14]
0.66	5,323	1.879	0.600	11.4
0.65	5,243	1.907	0.873 [33]	13.3 [33]
0.64	5,162	1.937	0.624 [14]	11.8 [14]
0.62	5,001	2.000	0.650	12.2

TABLE IX (*Continued*)

Silver

eV	cm^{-1}	μm	n	k
0.60	4,839	2.066	0.668	12.6
			1.064 [33]	14.4 [33]
0.58	4,678	2.138	0.729 [14]	13.0 [14]
0.56	4,517	2.214	0.774	13.5
0.54	4,355	2.296	0.823	14.0
0.52	4,194	2.384	0.878	14.5
0.50	4,033	2.480	0.939	15.1
0.48	3,871	2.583	1.007	15.7
0.46	3,710	2.695	1.083	16.4
0.44	3,549	2.818	1.168	17.1
0.42	3,388	2.952	1.265	17.9
0.40	3,226	3.100	1.387	18.8
0.38	3,065	3.263	1.536	19.8
0.36	2,904	3.444	1.710	20.9
0.34	2,742	3.647	1.915	22.1
0.32	2,581	3.875	2.160	23.5
0.30	2,420	4.133	2.446	25.1
0.28	2,258	4.428	2.786	26.9
0.26	2,097	4.769	3.202	29.0
0.24	1,936	5.166	3.732	31.3
0.22	1,774	5.636	4.425	34.0
0.20	1,631	6.199	5.355	37.0
0.19	1,532	6.526	5.960	38.6
0.18	1,452	6.888	6.670	40.4
0.17	1,371	7.293	7.461	42.5
0.16	1,290	7.749	8.376	44.8
0.15	1,210	8.266	9.441	47.1
0.14	1,129	8.856	10.69	49.4
0.13	1,049	9.537	12.21	52.2
0.125	1,008	9.919	13.11	53.7

TUNGSTEN (W) XII

Most measurements of the optical properties of W are in good agreement [1–35]. Table X lists the n and k values of Weaver *et al.* [26] and Henke *et al.* [36]. These data are plotted in Fig. 10 as smooth curves.

Weaver *et al.* [26] used W of unstated purity that had been melted into buttons by an electron beam. Samples were spark-cut from the buttons and after macroetching showed large (3-mm), unoriented, crystal grains. The samples were polished first by using an alumina abrasive and again, immediately prior to loading into the reflectometer, by electropolishing. During loading there was about a 3-min exposure to air. From 2818 Å to 8.3 μm a calorimetric technique [37] was used, and for wavelengths less than 2818 Å,

the reflectance at room temperature was measured at 10° angle of incidence. These data were used with the absorption spectrum obtained by Haensel *et al.* [12] to do a Kramers–Kronig analysis.

There may be some influence on the reflectance in the VUV because of oxidation, but oxidation effects have never been studied. Above about 5 μm tungsten resembles a free-electron metal, but interband transitions persist to longer wavelengths. Infrared data do not cover a wide enough range to give a definitive limit for the shortest wavelength at which Drude parameters are expected to be free of the influence of interband transitions, but probably it is roughly 10 μm.

REFERENCES

1. S. Roberts, *Phys. Rev.* **114**, 104 (1959).
2. L. J. LeBlanc, J. S. Farrell, and D. W. Juenker, *J. Opt. Soc. Am.* **54**, 956 (1964).
3. C. Tingwaldt, U. Schley, J. Verch, and S. Takata, *Optik* **22**, 48 (1965).
4. H. R. Apholte and K. Ulmer, *Phys, Lett.* **22**, 552 (1966).
5. B. T. Barnes, *J. Opt. Soc. Am.* **56**, 1546 (1966).
6. I. Ye. Leksina and N. V. Penkina, *Fiz. Met. Metalloved.* **22**, 264 (1966); I. Ye. Leksina and N. V. Penkina, *Phys. Met. Metallogr.* **22**(2), 104 (1966).
7. A. P. Lenham and D. M. Treherne, *J. Opt. Soc. Am.* **56**, 1137 (1966).
8. A. P. Lenham and D. M. Treherne, *in* "Optical Properties and Electronic Structure of Metals and Alloys" (F. Abélès, ed.), p. 196, North-Holland, Publ., Amsterdam, 1966.
9. A. P. Lenham, *J. Opt. Soc. Am.* **57**, 473 (1967).
10. D. W. Juenker, L. J. LeBlanc, and C. R. Martin, *J. Opt. Soc. Am.* **58**, 164 (1968).
11. J. J. Carroll and A. J. Melmed, *Surf. Sci.* **16**, 251 (1969).
12. R. Haensel, K. Radler, B. Sonntag, and C. Kunz, *Solid State Commun.* **7**, 1495 (1969).
13. B. A. Konyaev, *Teplo. Vys. Temp.* **7**, 1029 (1969).
14. L. N. Latyev, V. Y. Cheknovskoi, and E. N. Shestakov, *High Temp.-High Press.* **2**, 175 (1970).
15. V. Vujnovic, *J. Opt. Soc. Am.* **60**, 177 (1970).
16. J. J. Carroll and A. J. Melmed, *J. Opt. Soc. Am.* **61**, 470 (1971).
17. W. R. Hunter, *Proc. Int. Conf. Vac. Ultraviolet Rad. Physics, 3rd, Tokyo*, p. 2aC2-1 (1971).
18. Y. P. Udoyev, N. S. Kozyakova, and M. L. Kapitsa, *Fiz. Met Metalloved.* **31**, 439 (1971); Y. P. Udoyev, N. S. Kozyakova, and M. L. Kapitsa, *Phys. Met. Metallogr.* **31**(2), 229 (1971).
19. J. T. Cox, G. Hass, J. B. Ramsey and W. R. Hunter, *J. Opt. Soc. Am.* **62**, 781 (1972).
20. L. N. Latyev, V. Ya. Checkovskoi and E. N. Shestakov, *High Temp.-High Press.* **4**, 679 (1972).
21. L. V. Nomerovannaya, M. M. Kirillova, and M. M. Noskov, *Fiz. Tverd. Tela.* **14**, 633 (1972); L. V. Nomerovannaya, M. M. Kirillova, and M. M. Noskov, *Sov. Phys. Solid State* **14**, 541 (1972).
22. J. J. Rogers, *High Temp.-High Press.* **4**, 271 (1972).
23. T. Smith, *J. Opt. Soc. Am.* **62**, 774 (1972).
24. L. N. Aksyutov. *Inzh.-Fiz. Zh.* **27**, 197 (1974); L. N. Aksyutov, *J. Eng. Phys.* **27**, 913 (1974).
25. G. A. Zhorov, *Teplo. Vys. Temp.* **10**, 1332 (1974).
26. J. H. Weaver, C. G. Olson, and D. W. Lynch, *Phys. Rev. B* **12**, 1293 (1975).
27. J. O. Hylton and R. L. Reid, *AIAA J.* **14**, 1303 (1976).
28. L. K. Thomas and S. Thurm, *J. Phys. F* **6**, 279 (1976).
29. J. H. Weaver and C. G. Olson, *Phys. Rev B* **14**, 3251 (1976).
30. B. V. Habedank, L. K. Thomas, and S. Thurm, *J. Phys. F* **7**, 2217 (1977).
31. H. S. Gurev and C. Selvage, *Proc. Soc. Photo-Opt. Instrum. Eng.* **85**, 32 (1977).

32. P. Gravier, G. Chassaing, and M. Sigrist, *Thin Solid Films* **57**, 93 (1979).
33. J. E. Nestell, Jr., and R. W. Christy, *Phys. Rev. B* **21**, 3173 (1980).
34. J. E. Nestell, Jr., R. W. Christy, M. H. Cohen, and G. C. Ruben, *J. Appl. Phys.* **51**, 655 (1980).
35. L. A. Wojeik, A. J. Sievers, G. W. Graham, and T. N. Rhodin, *J. Opt. Soc. Am.* **70**, 443 (1980).
36. B. L. Henke, P. Lee, T. J. Tanaka, R. L. Shimabukuro, and B. K. Fujikawa, *At. Data Nucl. Data Tables* **27**, 1 (1982).
37. L. W. Bos and D. W. Lynch, *Phys. Rev. B* **2**, 4567 (1970).

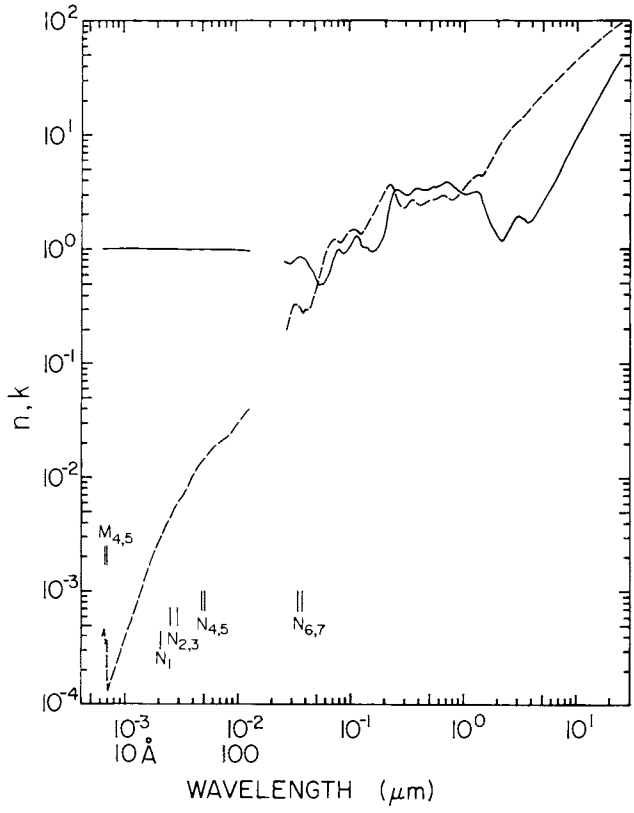

Fig. 10. Log–log plot of n (——) and k (– – – –) versus wavelength in micrometers for tungsten.

TABLE X

Values of n and k Obtained from Various References for Tungsten[a]

eV	cm^{-1}	Å	n	k
2000		6.199	0.999560 [37]	4.00×10^{-4} [36]
1952		6.351	0.999637	4.34
1905		6.508	0.999721	4.71
1860		6.665	0.999810	3.44
1815		6.831	0.999908	3.69
1772		6.997	0.999656	1.31
1730		7.166	0.999536	1.42
1688		7.345	0.999458	1.53
1648		7 523	0.999390	1.65
1609		7.705	0.999330	1.78
1570		7.897	0.999273	1.92
1533		8.088	0.999218	2.07
1496		8.287	0.999161	2.23
1460		8.492	0.999106	2.41
1426		8.694	0.999051	2.59
1392		8.906	0.99899	2.79
1358		9.129	0.99893	3.01
1326		9.350	0.99887	3.24
1294		9.581	0.99881	3.50
1263		9.816	0.99874	3.77
1233		10.05	0.99868	4.05
1204		10.30	0.99861	4.35
1175		10.55	0.99854	4.68
1147		10.81	0.99846	5.03
1119		11.08	0.99838	5.41
1093		11.34	0.99831	5.81
1067		11.62	0.99822	6.24
1041		11.91	0.99814	6.72
1016		12.20	0.99805	7.22
992		12.50	0.99796	7.74
968		12.81	0.99786	8.31
945		13.12	0.99777	8.90
923		13.43	0.99767	9.53×10^{-4}
901		13.76	0.99757	1.02×10^{-3}
879		14.10	0.99746	1.09
858		14.45	0.99735	1.17
838		14.79	0.99724	1.25
818		15.16	0.99712	1.34
798		15.54	0.99700	1.44
779		15.92	0.99688	1.54
760		16.31	0.99678	1.65
742		16.71	0.99663	1.76
725		17.10	0.99651	1.87
707		17.54	0.99637	2.00
690		17.97	0.99625	2.13
674		18.39	0.99611	2.26
658		18.84	0.99598	2.41
642		19.31	0.99586	2.57
627		19.77	0.99574	2.71
612		20.26	0.99561	2.84
597		20.77	0.99547	2.98
583		21.27	0.99531	3.13
569		21.79	0.99513	3.29
555		22.34	0.99494	3.49

[a] The references from which the values were extracted are given in brackets.

TABLE X (*Continued*)

Tungsten

eV	cm^{-1}	Å	*n*	*k*
542		22.87	0.99478	3.70
529		23.44	0.99462	3.91
516		24.03	0.99446	4.14
504		24.60	0.99430	4.35
492		25.20	0.99414	4.58
480		25.83	0.99397	4.83
469		26.43	0.99382	5.07
458		27.07	0.99369	5.34
447		27.74	0.99357	5.57
436		28.44	0.99343	5.78
426		29.10	0.99326	5.97
415		29.87	0.99305	6.20
406		30.54	0.99284	6.40
396		31.31	0.99258	6.63
386		32.12	0.99229	6.95
377		32.89	0.99203	7.26
368		33.69	0.99177	7.59
359		34.53	0.99150	7.95
351		35.32	0.99126	8.29
342		36.25	0.99098	8.70
334		37.12	0.99072	9.10
326		38.03	0.99046	9.52
318		38.99	0.99020	9.97×10^{-3}
311		39.86	0.9900	1.04×10^{-2}
303		40.92	0.9897	1.09
296		41.88	0.9895	1.14
289		42.90	0.9893	1.19
282		43.96	0.9891	1.25
275		45.08	0.9890	1.30
269		46.09	0.9888	1.34
262		47.32	0.9887	1.38
256		48.43	0.9884	1.42
250		49.59	0.9882	1.46
244		50.81	0.9879	1.50
238		52.09	0.9876	1.55
232		53.44	0.9874	1.60
227		54.62	0.9871	1.64
221		56.10	0.9867	1.70
216		57.40	0.9864	1.75
211		58.76	0.9861	1.80
206		60.18	0.9858	1.84
201		61.68	0.9855	1.89
196		63.25	0.9852	1.94
191		64.91	0.9848	1.99
187		66.30	0.9845	2.02
182		68.12	0.9840	2.05
178		69.65	0.9835	2.09
174		71.25	0.9829	2.12
170		72.93	0.9823	2.15
166		74.69	0.9816	2.19
162		76.53	0.9808	2.23
158		78.47	0.9800	2.26
154		80.51	0.9791	2.30
150		82.65	0.9782	2.34

(*continued*)

TABLE X (*Continued*)

Tungsten

eV	cm^{-1}	Å	*n*	*k*
147		84.34	0.9774	2.39
143		86.70	0.9760	2.48
140		88.56	0.9745	2.56
136		91.16	0.9717	2.67
133		93.22	0.9690	2.75
130		95.37	0.9661	2.85
127		97.62	0.9647	2.94
124		99.98	0.9637	3.03
121		102.5	0.9627	3.13
118		105.1	0.9612	3.22
115		107.8	0.9594	3.33
112		110.7	0.9573	3.44
110		112.7	0.9558	3.51
107		115.9	0.9532	3.63
104		119.2	0.9502	3.76
102		121.5	0.9479	3.85
100		124.0	0.9452	3.95
eV	cm^{-1}	μm	*n*	*k*
47.0		0.02638	0.774 [26]	0.195 [26]
46.0		0.02695	0.762	0.205
45.0		0.02755	0.750	0.225
44.0		0.02818	0.746	0.245
43.0		0.02883	0.744	0.274
42.0		0.02952	0.756	0.304
41.0		0.03024	0.778	0.319
40.0		0.03100	0.797	0.328
39.0		0.03179	0.814	0.330
38.0		0.03263	0.826	0.330
37.0		0.03351	0.837	0.328
36.0		0.03444	0.846	0.320
35.0		0.03542	0.848	0.306
34.5		0.03594	0.844	0.298
34.0		0.03647	0.838	0.291
33.5		0.03701	0.829	0.285
33.0		0.03757	0.816	0.278
32.5		0.03815	0.797	0.286
32.0		0.03875	0.791	0.295
31.5		0.03936	0.788	0.294
31.0		0.04000	0.778	0.293
30.5		0.04065	0.765	0.292
30.0		0.04133	0.750	0.295
29.75		0.04168	0.742	0.296
29.5		0.04203	0.733	0.297
29.25		0.04239	0.724	0.298
29.0		0.04275	0.712	0.301
28.75		0.04313	0.700	0.306
28.5		0.04350	0.690	0.310
28.25		0.04389	0.679	0.318
28.0		0.04428	0.671	0.322
27.75		0.04468	0.656	0.328
27.5		0.04509	0.643	0.336
27.25		0.04550	0.631	0.346

TABLE X (*Continued*)

Tungsten

eV	cm^{-1}	μm	n	k
27.0		0.04592	0.619	0.357
26.8		0.04626	0.610	0.365
26.6		0.04661	0.600	0.375
26.4		0.04696	0.591	0.383
26.2		0.04732	0.580	0.394
26.0		0.04769	0.571	0.404
25.8		0.04806	0.560	0.415
25.6		0.04843	0.548	0.429
25.4		0.04881	0.537	0.444
25.2		0.04920	0.528	0.461
25.0		0.04959	0.521	0.476
24.8		0.04999	0.511	0.494
24.6		0.05040	0.503	0.513
24.4		0.05081	0.497	0.534
24.2		0.05123	0.491	0.554
24.0		0.05166	0.487	0.575
23.8		0.05209	0.483	0.598
23.6		0.05254	0.484	0.621
23.4		0.05299	0.486	0.643
23.2		0.05344	0.490	0.663
23.0		0.05391	0.494	0.679
22.8		0.05438	0.494	0.695
22.6		0.05486	0.493	0.712
22.4		0.05535	0.492	0.730
22.2		0.05585	0.491	0.751
22.0		0.05636	0.491	0.773
21.8		0.05687	0.492	0.796
21.6		0.05740	0.496	0.819
21.4		0.05794	0.499	0.842
21.2		0.05848	0.503	0.866
21.0		0.05904	0.508	0.892
20.8		0.05961	0.517	0.918
20.6		0.06019	0.525	0.943
20.4		0.06078	0.537	0.969
20.2		0.06138	0.549	0.994
20.0		0.06199	0.563	1.02
19.8		0.06262	0.579	1.05
19.6		0.06326	0.599	1.07
19.4		0.06391	0.621	1.09
19.2		0.06458	0.642	1.11
19.0		0.06526	0.665	1.13
18.8		0.06595	0.688	1.15
18.6		0.06666	0.712	1.16
18.4		0.06738	0.738	1.18
18.2		0.06812	0.766	1.19
18.0		0.06888	0.796	1.20
17.8		0.06965	0.822	1.20
17.6		0.07045	0.847	1.21
17.4		0.07126	0.874	1.21
17.2		0.07208	0.900	1.20
17.0		0.07293	0.922	1.20
16.8		0.07380	0.944	1.19
16.6		0.07469	0.959	1.18
16.4		0.07560	0.973	1.17

(*continued*)

TABLE X (*Continued*)

Tungsten

eV	cm^{-1}	μm	n	k
16.2		0.07653	0.980	1.15
16.0		0.07749	0.981	1.14
15.8		0.07847	0.976	1.13
15.6		0.07948	0.966	1.12
15.4		0.08051	0.951	1.12
15.2		0.08157	0.933	1.13
15.0		0.08266	0.917	1.14
14.8		0.08377	0.904	1.17
14.6		0.08492	0.900	1.20
14.4		0.08610	0.901	1.23
14.2		0.08731	0.906	1.25
14.0		0.08856	0.913	1.28
13.8		0.08984	0.923	1.32
13.6		0.09117	0.941	1.35
13.4		0.09253	0.962	1.37
13.2		0.09393	0.984	1.40
13.0		0.09537	1.01	1.42
12.8		0.09686	1.04	1.44
12.6		0.09840	1.07	1.46
12.4		0.09999	1.10	1.47
12.2		0.1016	1.13	1.48
12.0		0.1033	1.16	1.48
11.9		0.1042	1.18	1.48
11.8		0.1051	1.20	1.48
11.7		0.1060	1.21	1.48
11.6		0.1069	1.22	1.48
11.5		0.1078	1.24	1.47
11.4		0.1088	1.25	1.46
11.3		0.1097	1.26	1.45
11.2		0.1107	1.27	1.44
11.1		0.1117	1.28	1.43
11.0		0.1127	1.28	1.42
10.9		0.1137	1.29	1.41
10.8		0.1148	1.29	1.39
10.7		0.1159	1.28	1.38
10.6		0.1170	1.28	1.36
10.5		0.1181	1.26	1.34
10.4		0.1192	1.24	1.33
10.3		0.1204	1.22	1.33
10.2		0.1216	1.19	1.33
10.1		0.1228	1.16	1.33
10.0		0.1240	1.13	1.34
9.9		0.1252	1.11	1.36
9.8		0.1265	1.09	1.38
9.7		0.1278	1.07	1.41
9.6		0.1291	1.05	1.44
9.5		0.1305	1.04	1.47
9.4		0.1319	1.03	1.50
9.3		0.1333	1.03	1.52
9.2		0.1348	1.02	1.55
9.1		0.1362	1.02	1.57
9.0		0.1378	1.01	1.60
8.9		0.1393	1.02	1.63
8.8		0.1409	1.01	1.65

TABLE X (*Continued*)

Tungsten

eV	cm^{-1}	μm	*n*	*k*
8.7		0.1425	0.999	1.67
8.6		0.1442	0.986	1.70
8.5		0.1459	0.973	1.73
8.4		0.1476	0.956	1.76
8.3		0.1494	0.943	1.81
8.2		0.1512	0.935	1.86
8.1		0.1531	0.935	1.91
8.0		0.1550	0.937	1.95
7.9		0.1569	0.932	2.00
7.8		0.1590	0.930	2.06
7.7		0.1610	0.937	2.12
7.6		0.1631	0.950	2.18
7.5		0.1653	0.964	2.24
7.4		0.1675	0.979	2.29
7.3		0.1698	0.993	2.36
7.2		0.1722	1.01	2.43
7.1		0.1746	1.04	2.49
7.0		0.1771	1.06	2.56
6.9		0.1797	1.09	2.63
6.8		0.1823	1.12	2.70
6.7		0.1851	1.16	2.78
6.6		0.1879	1.21	2.87
6.5		0.1907	1.26	2.95
6.4		0.1937	1.31	3.04
6.3		0.1968	1.38	3.14
6.2		0.2000	1.47	3.24
6.1	49,200	0.2033	1.58	3.33
6.0	48,390	0.2066	1.70	3.42
5.9	47,590	0.2101	1.83	3.52
5.8	46,780	0.2138	2.00	3.61
5.7	45,970	0.2175	2.20	3.67
5.6	45,170	0.2214	2.43	3.70
5.5	44,360	0.2254	2.68	3.68
5.4	43,550	0.2296	2.92	3.58
5.3	42,750	0.2339	3.11	3.43
5.2	41,940	0.2384	3.27	3.27
5.1	41,130	0.2431	3.38	3.05
5.0	40,330	0.2480	3.40	2.85
4.9	39,520	0.2530	3.37	2.68
4.8	38,710	0.2583	3.33	2.57
4.7	37,910	0.2638	3.29	2.48
4.6	37,100	0.2695	3.24	2.41
4.5	36,290	0.2755	3.19	2.35
4.4	35,490	0.2818	3.13	2.32
4.3	34,680	0.2883	3.07	2.31
4.2	33,880	0.2952	3.01	2.33
4.1	33,070	0.3024	2.97	2.37
4.0	32,260	0.3100	2.95	2.43
3.95	31,860	0.3139	2.95	2.46
3.9	31,460	0.3179	2.96	2.50
3.85	31,050	0.3220	2.98	2.53
3.8	30,650	0.3263	2.99	2.56
3.75	30,250	0.3306	3.02	2.60
3.7	29,840	0.3351	3.05	2.62

(*continued*)

TABLE X (*Continued*)

Tungsten

eV	cm^{-1}	μm	n	k
3.65	29,440	0.3397	3.09	2.65
3.6	29,040	0.3444	3.13	2.67
3.55	28,630	0.3493	3.18	2.69
3.5	28,230	0.3542	3.24	2.70
3.45	27,830	0.3594	3.32	2.70
3.4	27,420	0.3647	3.39	2.66
3.35	27,020	0.3701	3.43	2.60
3.3	26,620	0.3757	3.45	2.55
3.25	26,210	0.3815	3.45	2.49
3.2	25,810	0.3875	3.43	2.45
3.15	25,410	0.3936	3.41	2.43
3.1	25,000	0.4000	3.39	2.41
3.05	24,600	0.4065	3.37	2.42
3.0	24,200	0.4133	3.35	2.42
2.95	23,790	0.4203	3.33	2.43
2.9	23,390	0.4275	3.32	2.45
2.85	22,990	0.4350	3.31	2.47
2.8	22,580	0.4428	3.30	2.49
2.75	22,180	0.4509	3.31	2.53
2.7	21,780	0.4592	3.31	2.55
2.65	21,370	0.4679	3.32	2.59
2.6	20,970	0.4769	3.34	2.62
2.55	20,570	0.4862	3.35	2.64
2.5	20,160	0.4959	3.38	2.68
2.45	19,760	0.5061	3.42	2.71
2.4	19,360	0.5166	3.45	2.72
2.35	18,950	0.5276	3.48	2.72
2.3	18,550	0.5391	3.50	2.72
2.25	18,150	0.5510	3.50	2.73
2.2	17,740	0.5636	3.49	2.75
2.15	17,340	0.5767	3.51	2.81
2.1	16,940	0.5904	3.54	2.84
2.05	16,530	0.6048	3.57	2.86
2.0	16,130	0.6199	3.60	2.89
1.95	15,730	0.6358	3.65	2.92
1.9	15,320	0.6526	3.70	2.94
1.85	14,920	0.6702	3.76	2.95
1.8	14,520	0.6888	3.82	2.91
1.75	14,110	0.7085	3.85	2.86
1.7	13,710	0.7293	3.84	2.78
1.65	13,310	0.7514	3.78	2.72
1.6	12,900	0.7749	3.67	2.68
1.55	12,500	0.7999	3.56	2.73
1.5	12,100	0.8266	3.48	2.79
1.45	11,690	0.8551	3.38	2.85
1.4	11,290	0.8856	3.29	2.96
1.35	10,900	0.9184	3.20	3.07
1.3	10,490	0.9537	3.12	3.24
1.25	10,080	0.9919	3.05	3.39
1.2	9,679	1.033	3.00	3.64
1.15	9,275	1.078	3.02	3.83
1.1	8,872	1.127	3.05	4.04
1.05	8,469	1.181	3.11	4.19
1.0	8,065	1.240	3.14	4.32

TABLE X (*Continued*)

Tungsten

eV	cm^{-1}	μm	n	k
0.98	7,904	1.265	3.15	4.36
0.96	7,743	1.291	3.15	4.41
0.94	7,582	1.319	3.15	4.43
0.92	7,420	1.348	3.14	4.45
0.90	7,259	1.378	3.11	4.44
0.88	7,098	1.409	3.05	4.42
0.87	7,017	1.425	3.00	4.39
0.86	6,936	1.442	2.92	4.37
0.85	6,856	1.459	2.80	4.33
0.84	6,775	1.476	2.62	4.37
0.83	6,694	1.494	2.47	4.47
0.82	6,614	1.512	2.36	4.61
0.80	6,452	1.550	2.22	4.85
0.78	6,291	1.590	2.12	5.05
0.76	6,131	1.630	1.97	5.27
0.74	5,969	1.675	1.83	5.52
0.72	5,807	1.722	1.70	5.81
0.70	5,646	1.771	1.59	6.13
0.68	5,485	1.823	1.52	6.45
0.66	5,323	1.879	1.45	6.78
0.64	5,162	1.937	1.36	7.14
0.62	5,001	2.000	1.28	7.52
0.60	4,839	2.066	1.21	7.96
0.58	4,678	2.138	1.18	8.44
0.56	4,517	2.214	1.20	8.94
0.54	4,355	2.296	1.23	9.45
0.52	4,194	2.384	1.30	9.98
0.50	4,033	2.480	1.40	10.5
0.48	3,817	2.583	1.54	11.1
0.46	3,710	2.695	1.69	11.6
0.44	3,549	2.818	1.82	12.1
0.42	3,388	2.952	1.92	12.6
0.40	3,226	3.100	1.94	13.2
0.38	3,065	3.263	1.86	13.9
0.36	2,904	3.444	1.82	14.7
0.34	2,742	3.647	1.71	15.7
0.32	2,581	3.875	1.72	16.9
0.30	2,420	4.133	1.83	18.3
0.25	2,016	4.959	2.56	22.4
0.20	1,613	6.199	3.87	28.3
0.18	1,452	6.888	4.72	31.5
0.16	1,290	7.749	5.92	35.3
0.14	1,129	8.856	7.58	40.2
0.12	967.9	10.33	10.1	46.4
0.10	806.5	12.40	14.1	54.7
0.09	725.9	13.78	17.0	60.0
0.08	645.2	15.50	20.9	66.3
0.07	564.6	17.71	26.5	73.8
0.06	483.9	20.66	34.5	82.9
0.05	403.3	24.80	46.5	93.7

The Optical Properties of Metallic Aluminum*

D. Y. SMITH
Argonne National Laboratory
Argonne, Illinois
and
Max-Planck-Institut für Festkörperforschung
Stuttgart, Federal Republic of Germany

E. SHILES† and MITIO INOKUTI
Argonne National Laboratory
Argonne, Illinois

GENERAL FEATURES I

The optical properties of metallic aluminum are among the most widely measured and analyzed of any material [1–7]. They are dominated by three practically nonoverlapping groups of electronic transitions corresponding to absorptions by conduction band, L-shell, and K-shell electrons. The absorption spectrum for the crystalline solid is shown in Fig. 11.

The 3 e/at. (electrons/atom) donated to the conduction band by the atomic $3s^2 3p$ valence levels give rise to a typical metallic absorption from zero to ~ 15 eV, the bulk plasmon frequency ω_p. In crystalline samples this portion of the spectrum is dominated by intraband transitions in the far infrared and by two strong interband absorptions at ~ 0.5 eV ($\lambda \approx 2.5$ μm) and ~ 1.5 eV ($\lambda \approx 0.8$ μm). In the noncrystalline or partially crystalline solid state and in the liquid state, the interband spectrum is strongly modified or absent; this effect will be discussed further in Subsection II.C.

Intraband Spectrum A

The intraband contribution to the optical properties can be described phenomenologically to within experimental error with a Drude-model dielectric

* Work supported by the U.S. Department of Energy.

† Present address: Gulf Research and Development Company, Houston, Texas.

Copyright © 1985 by Academic Press, Inc.
All rights of reproduction in any form reserved.
ISBN 0-12-544420-6

function [8, 9] for the electron gas:

$$\varepsilon_{\text{Drude}} = \varepsilon_0 - [\Omega_p^2/\omega(\omega + i/\tau)], \tag{1}$$

where the contribution to the dielectric function from core interband transitions has been included in ε_0. Here Ω_p is the (phenomenological) plasma frequency for intraband transitions and τ the intraband relaxation time. The quantity ε_0 is effectively constant throughout the region of conduction–electron absorption (that is, to well above the plasma frequency) with a value [7] of 1.03_5.

In addition to using the quantity Ω_p, the strength of the intraband transitions is commonly expressed in terms of the effective number density of electrons participating in intraband transitions

$$n_{\text{eff,intraband}} = m_e\Omega_p^2/4\pi e^2. \tag{2}$$

Here m_e and e are the free-electron mass and charge, respectively. A second alternative is the optical mass defined by [8, 9]

$$m_{\text{opt}} = m_e(n_c/n_{\text{eff,intraband}}), \tag{3}$$

where n_c is the density of conduction electrons.

Similarly, the intraband relaxation time is often given in terms of the damping coefficient

$$\gamma = \tau^{-1}. \tag{4}$$

A quantity often cited for comparison with electrical experiments is the dc conductivity in the Drude model

$$\sigma(0) = \Omega_p^2/4\pi\gamma. \tag{5}$$

A variety of fits of Eq. (1) have been made to infrared data for polycrystalline samples of metallic aluminum [1, 3, 5, 10–15], but early work was incomplete because the interband transitions at ~ 0.5 and ~ 1.5 eV were not always reckoned with. Some of the more recent determinations of the Drude parameters and the experimental bulk dc conductivity are given in Table XI. The "0.5-eV" interband transition was not accounted for by Ehrenreich *et al.* [1] or by Powell [3], so that some interband absorption strength, as well as damping, is included in their Drude terms. This leads to a conductivity significantly smaller than the measured bulk value. Bennett and Bennett [12] assumed the measured value of $\sigma(0)$ but also neglected the 0.5 eV transition leading to an overestimate of Ω_p. Dresselhaus *et al.* [13], Mathewson and Myers [5], and Benbow and Lynch [14] accounted for both interband transitions, the last two studies with the Ashcroft–Sturm [18] model of the interband spectrum. The values reported by Smith and Segall [15] were derived by fitting the dielectric function of Shiles *et al.* [7] over the range of 0.04 to 3.0 eV, assuming that it is a linear superposition of a Drude term and the two principal interband transitions. No detailed assumptions as to the form of the interband spectrum were made. The resulting parameters thus yield

the least model-dependent description of the room-temperature interband absorption presently available.

Interband Spectrum B

The two strong interband transitions of the conduction-electron spectrum in the crystalline material are a consequence of the "parallel-band" effect [1, 18–20] that occurs in almost free-electron polyvalent metals. In these materials the occupied and unoccupied conduction bands are effectively parallel over substantial regions of k space in the vicinity of high-symmetry planes parallel to the zone faces. Allowed transitions between these parallel bands lead to prominent interband absorptions at energies approximately twice the Fourier component of the effective crystal potential V_K for the reciprocal lattice vector K corresponding to the face in question. In aluminum, absorption between almost parallel bands occurs in the neighborhood of surfaces parallel to the hexagonal (111) and the square (200) zone faces. The corresponding energy gaps predicted by a two-band model [18] using parameters derived by Ashcroft [21] from de Haas–van Alphen measurements below 4 K are $2V_{111} = 0.487$ eV and $2V_{200} = 1.53$ eV. The parallel-band absorption shows sharp rises near these energies followed by long tails toward higher energies that joins smoothly onto the band-to-band absorption arising from the remainder of the Brillouin zone [18, 20]. In addition, theory predicts [22, 23] an accidental degeneracy of the energy bands leading to a weak but finite interband absorption down to zero energy. However, this has not been verified experimentally because the interband component is overwhelmed by the intraband absorption below a few tenths of an electron volt.

The 1.5-eV (0.8-μm) interband absorption is readily apparent as a pronounced drop in the reflectance for crystalline samples (Fig. 12) and as a small peak in the extinction coefficient (Fig. 11). The former appears to have been first reported by Strong [24] and the latter by Schulz [25]. The absorption responsible for these features was identified as a transition between pairs of parallel bands by Ehrenreich *et al.* [1]. Shklyarevskii and Yarovaya [26] independently identified the absorption as an interband transition but did not recognize the crucial importance of energy-band parallelism near the Fermi energy.

The second major interband absorption at $\sim$0.5 eV is almost completely hidden by the Drude absorption. There is a suggestion of it in the early infrared measurements of Beattie [27] and in the ultrahigh vacuum (uhv) reflectance data of Bennett *et al.* that show a small drop in reflectance near 25 μm. (see Bennett *et al.* [28] Fig. 3). This transition was first definitively observed in low-temperature absorbtivity experiments by Bos and Lynch [29]. Figure 13 shows subsequent results of Benbow and Lynch [14] for single-crystal aluminum at 4.2 K together with Smith and Segall's [15] separation of room-temperature data for uhv evaporated films. The results are

presented in terms of the real part of the interband conductivity

$$\sigma_{\text{interband}}(\omega) = (-i\omega/4\pi)[\varepsilon(\omega) - \varepsilon_{\text{Drude}}(\omega)]. \tag{6}$$

Below approximately 0.3 eV the uncertainty in the experimental data and in the Drude parameters is so large that the interband contribution cannot be determined reliably from the available measurements.

Note the shift of the interband absorption toward higher energies as the temperature is lowered. Mathewson and Myers [5] studied this temperature dependence in detail for the "1.5-eV" transition (see also Fig. 17).

At low temperatures ($\sim$20 K) a weak fine structure is superimposed on the tail of the 1.5-eV absorption in the range 2–2.5 eV [30]. Some of these structures appear to arise [31] from transitions near the corners of the Brillouin zone in the vicinity of the intersections of the two groups of planes responsible for the two strong parallel-band absorptions. Along these lines of intersection three bands are almost parallel with band gaps determined by both V_{200} and V_{111}. However, the transitions arising from this "trio" of parallel bands along the intersections are not as prominent as those associated with the "duos" of parallel bands in the planes because of the smaller momentum space involved in the neighborhood of the lines of intersection. The result is two weak absorptions, one near the strong 0.5-eV interband transition and the second just above the strong 1.5-eV transition. These have been predicted in detail by band-structure calculations [23, 31]. (See also Hunderi and Nilsson [30].)

Further interband fine structure has been resolved in recent piezo-modulation experiments by Jiles and Staines [31a]. This includes strain-induced changes around 2–2.5 eV and 4.6 eV, in addition to structure near the 1.5 eV parallel-band transition.

The possibility that excitons may be associated with the interband absorption edges has been investigated theoretically [32]. While excitonic states are predicted, their binding energies are found to be only 5 (singlet) and 20 (triplet) meV as a result of the highly effective screening of the coulomb interaction by the conduction electrons. Such structure is unobservable in conventional optical experiments but may contribute to the broadening of the interband peaks.

II OPTICAL MEASUREMENTS AND SAMPLE CONDITIONS

A Polished Polycrystalline Samples

Serious studies of the optical properties of aluminum were begun in 1874 by Quincke [33]. Early studies employed polished bulk or rolled samples [33–40]. Even though bulk aluminum takes a "high polish," it always retains

a "hazy white surface" [36] and has a reflectance well below that of an uncontaminated evaporated film. As will become apparent, this is presumably the result of both scattering and absorption by the microscopically rough, oxide-coated surface. A composite of reflectance data for polished surfaces is given in Fig. 12. The curve generally follows the data of Coblentz [36] (IR), Luckiesh [38] (visible + UV), Quincke [33] (visible), and Wulff [40] (visible + UV). The polished bulk-metal data are strongly affected by surface contamination and light scattering, particularly at shorter wavelengths. In the visible, Nutting [35] reports reflectance values $\sim 10\%$ higher than those shown, while values measured by Coblentz and Stair [39] are 10% lower. An even more dramatic range is given by Taylor [41], who quotes reflectances from 33 (mill finish) to 84% (electropolished) at 296.7 nm.

Thin-Film Polycrystalline Samples B

The key factor in obtaining accurate values of the optical properties was the discovery that aluminum could be sputtered [42] or evaporated [43] to form highly reflecting metal films. Early sputtered films were described as "brilliant" [44, 45]. However, evaporation by the tungsten-coil method [46, 47] has become the preferred method of sample preparation because of its high speed and potential for low contamination. The major impetus for these developments was the production of interferometer and telescope mirrors [24]. (The superior reflectance of evaporated aluminum films over silver at short wavelengths extended stellar spectroscopy some 250 Å into the violet.)

Evaporated films show reflectances much higher than polished surfaces particularly in the ultraviolet. Generally, the higher the vacuum and the faster the evaporation, the higher is the reflectance [48–51]. Two curves for evaporated surfaces are shown in Fig. 12. The upper is for unoxidized, smooth films produced in ultrahigh vacuum (10^{-9}–10^{-10} torr), and the other is for films evaporated in conventional high vacuum ($\sim 10^{-5}$ torr). The first is believed to correspond to a smooth, uncontaminated aluminum surface. The second is for more-or-less contaminated surfaces having oxide coating with no special attempts made to eliminate surface roughness. The uhv curve generally follows the data of Bennett *et al.* [28], Hass and Waylonis [51] (though not uhv films, a high evaporation rate was employed that has been shown to yield the same results as an uhv preparation [52]), and Endriz and Spicer [53]. Beyond 11.8 eV the curve follows the analysis of Shiles *et al.* [7], which relies heavily on electron-energy-loss measurements [54] near ω_p and on transmission and reflectance data of Ditchburn and Freeman [55] and x-ray absorption measurements† beyond ω_p.

The high-vacuum curve generally follows the data of Beattie [11], Strong [24], Hass [48, 56], Sabine [57], Banning [58], and Walker *et al.* [59]. The

† For a list of sources used for x-ray cross sections, see Shiles *et al.* [7].

curve shown is in close agreement from 250 to 2500 nm with the U.S. National Bureau of Standards' reference standard first-surface aluminum mirror #2003a [60], which has an aged oxide coating. The curve also generally has the same reflectance from 200 to 2000 nm as commercially available evaporated mirrors.† Films evaporated under higher vacuum or at high deposition rates generally have reflectances between the high-vacuum and uhv curves shown. (For references to additional measurements see Shiles *et al.* [7] and the sources cited in Schopper [61].)

The differences between the various evaporated film data arises from surface oxide layers [48, 62–66], residual gas incorporated in the film [49, 50], surface roughness [53, 67, 68], and film morphology [52, 69–71].

1 *Surface Oxide Layers*

A layer of Al_2O_3 forms rapidly on an aluminum surface even in high vacuum [72, 73]. The layer is both adherent and relatively impervious so that once formed it protects the underlying metal from further oxidation [74]. The thickness of the surface layer and its composition depend strongly on sample structure and history, particularly on chemical treatment [24, 52, 69, 71, 74, 75]. Polarimetric studies of evaporated films simply exposed to the atmosphere indicate that the surface oxide layer is from 20 to 55 Å thick [50, 62–66] but that thicker layers readily form in moist environments [74]. The surface layers are probably hydrated to varying degrees depending on formation conditions. Preparation conditions [48, 52, 76], purity [76], structure [69, 71], partial oxidation in vacuum before exposure to the atmosphere [65], etc.; all influence the reported thickness. In addition, exposure of aluminum surfaces in air to ultraviolet light has been found to decrease their reflectance at short wavelengths; this is attributable to an increase in the oxidation rate of the surface [48, 69, 76, 77].

The oxide of aluminum is highly transparent from approximately 6 μm (0.2 eV) [78] to 180 nm (6.8 eV) [6, 79], so that a surface oxide film does not decrease the reflectance significantly over this range. Moreover, in the infrared a light wave does not "see" the film [48]. (The incident and reflected electric waves must be out of phase by approximately π to create the required node in the electric field at the metal surface. Thus, provided that the oxide thickness is much less than the wavelength of light, the electric fields of the incident and reflected waves almost cancel in the oxide layer and coupling to the layer is negligible.) However, at the shorter wavelengths of the vacuum ultraviolet, the oxide layer has a strong effect. For example, at 121.6 nm

† The authors are indebted to Professor Wayne Major of the University of Richmond for providing measurements for a commercially supplied, aluminum-film ($\sim$1000-Å) reflector on optical glass prepared by D. and E. Technology, Santa Clara, California. Evaporation was performed at $\sim 10^{-6}$ torr.

(~ 10 eV) an oxide layer 17 Å thick decreases the reflectance by a factor of two [63, 76].

Considerable research has been devoted to developing thin-film dielectric coatings to preserve or enhance the optical qualities of aluminum front-surface mirrors. For many applications, the natural oxide film is either too thin to offer the required protection from chemical change and mechanical damage—particularly when frequent cleaning is needed—or too absorbing for use in the ultraviolet. Coatings of the silicon oxides and Al_2O_3 that offer a high degree of mechanical and chemical protection have been developed [48, 80, 81] for use in the IR, visible, and near UV. At high angles of incidence, silicon oxide coatings show a reduced reflectance in the infrared. For such applications, protective coatings of Y_2O_3 and HfO_2 have been found to be highly successful [82]. At shorter wavelengths, overcoatings of MgF_2 and LiF preserve the high reflectance of aluminum down to ~ 1000 Å by preventing surface oxidation [48, 83]. Multiple dielectric layer coatings to enhance reflectance over a limited wavelength range have also been developed; enhancement of a 90% reflector to 99% reflectance have been reported [84].

Bulk Inclusion of Residual Gas 2

Studies of films evaporated at different rates and pressures indicate that the optical constants are very sensitive to residual gas incorporated into the bulk of the films [49, 50], specifically to the film composition within the penetration depth [50]. This is generally attributed [48–50, 85] to oxide formation arising from the gettering of molecular oxygen or to the reduction of water vapor to form Al_2O_3 and hydrogen. The relevant parameter appears to be the ratio of the residual gas pressure to the deposition rate, which is a measure of the arrival rate of residual gas molecules to that of aluminum atoms [49, 50]. Films deposited from high-purity starting material at terminal pressure-to-rate ratios of the order 10^{-8}–10^{-9} torr min $Å^{-1}$ or less [50] have similar reflectances and appear to be uncontaminated for the purpose of optical property measurements, provided that subsequent oxide formation is avoided.

The presence of surface effects has also been demonstrated in x-ray absorption measurements in the neighborhood of the L edge [86, 87]. This has not been investigated in detail, but it has been associated with an apparent systematic overestimate of the L-shell absorption [7].

Surface Roughness and Morphology 3

An extremely important factor in determining effective optical properties, particularly in the ultraviolet, is the roughness of the sample surfaces [53, 67, 68]. Surface roughness causes both scattering [88] and coupling to surface

plasmons [89] (the latter lie at an energy of $\hbar\omega_p/\sqrt{2} \approx 10.6$ eV for an aluminum-vacuum interface). Reflectance curves for two low-contamination films [53, 90, 91] with slight surface roughness are shown in Fig. 12 for comparison with the smooth, uhv surface reflectance. The main reflectance drop lies near the surface-plasmon frequency, but the drop extends well into the visible, largely as a result of scattering. Even a slight surface roughness produces dramatic effects. For example, a film with an rms surface roughness of only 27 Å is reported [53] to exhibit a reflectance drop of 20% at 3 eV (400 nm). These effects account for the wide variation of reflectance found in the UV and often previously attributed to contamination.

Film morphology, particularly grain size and orientation, has a substantial effect on optical properties. This is particularly apparent in aluminum films deposited by evaporation at oblique angles of incidence [92–94]. The optical properties of these films are anisotropic and the films develop diffusely reflecting surfaces with increasing thickness as a result of an increasingly coarse microstructure [80]. During the initial stages of deposition, films prepared in good vacuum systems appear to be compact and to have relatively small grain size, regardless of deposition angle; but beyond a critical film thickness diffuse scattering becomes substantial. For example, aluminum films 300 to 400 Å thick show surface roughness (as measured by scattering in the visible) for deposition angles of 60° or more. Holland [92] showed that the critical film thickness for diffuse reflection decreases sharply as the angle of incidence increases. These properties result from the preferential growth of crystallites in the form of columns parallel to the vapor beam [95] that are "self-shadowing." The amount and nature of the residual gas in the evaporating system have a major effect on the microstructure and, hence, the optical properties both because of gettering [96] and scattering of the metal vapor that alters the angle of incidence on the substrate [94].

C Noncrystalline and Liquid Samples

Vapor-quenched solid and liquid aluminum exhibit typical metallic properties but with a wide range of modifications in the interband spectrum. In the liquid state, aluminum exhibits no interband structure [97]. Rather, the conduction-electron absorption appears to follow a free-electron Drude model to within experimental error. This is in agreement with the expectation that in the liquid state there is no long-range order and, hence, no well-defined band structure nor Brillouin-zone boundaries [98].

Similar properties might be anticipated for samples with a low degree of crystallinity. However, the optical spectrum of vapor-quenched aluminum films deposited at low temperature exhibits a complex behavior [5, 99]. Films deposited at 25, 140, and 198 K show a progressive reduction in the intensity

of the 1.5-eV interband absorption with decreasing substrate temperature. Essentially no 1.5-eV absorption remains in films deposited at 25 K [99]. The reduced 1.5-eV absorption does not show a shift in position or broadening, only a decrease in magnitude. Further, annealing of the films at room temperature restores the 1.5-eV absorption. These observations are taken [5] to indicate that deposition from the vapor on a cooled substrate yields a two-phase system that is partly crystalline and partly amorphous but that crystallizes on annealing.

This interpretation cannot be complete since it is not consistent with analysis [99] of the 25-K films. These films show no 1.5-eV interband component, and consequently they would be considered to be noncrystalline in this interpretation. However, their optical properties are not described by the Drude model as those of the liquid can be. Rather, the conduction–electron absorption appears to consist of a Drude term plus a residual absorption near 0.5 eV that is attributed to interband transitions characteristic of a $2V_{111}$ energy gap. A possible explanation [99] is that the film consists of small-diameter, close-packed planar clusters with characteristic (111) translational symmetry but lacking the (200) translational symmetry of bulk aluminum.

TABULATED DATA III

Room-Temperature Optical Constants A

The most reliable optical data presently available are for uncontaminated polycrystalline aluminum films prepared in uhv. Measurements generally are made in reflectance at room temperature (18–25°C) and are presently available over the range 0.04 eV (32 μm) to 11.8 eV (105 nm) [28, 53]. In addition, a number of ellipsometric studies [5, 65, 71, 100, 101] of thin films in the near IR and visible have recently become available, particularly through the studies of Mathewson and Myers [5, 100] and of Liljenvall *et al.* [101]. (The former also includes high- and low-temperature measurements.) Studies [14, 29] of electropolished polycrystalline and single-crystal samples have also been reported, but absolute optical properties were not measured. The results are, however, consistent with absolute measurements on thin films.

Ellipsometric measurements yield the optical constants directly, but reflectance measurements at normal incidence must be analyzed by using dispersion theory. This has recently been done over a wide spectral range for the room-temperature uhv reflectance measurements by Shiles *et al.* [7],

who used a self-consistent Kramers–Kronig analysis. This involved combining the reflectance measurements below 11.8 eV with (1) electron-energy-loss measurements in the vicinity of the plasma frequency and (2) transmission and angular-variation-of-reflectance measurements in the extreme UV and x-ray regions. The energy-loss measurements were mainly those of Gibbons *et al.* [54]. The higher-energy optical data were taken primarily from Ditchburn and Freeman [55], Haensel *et al.* [102], Gähwiller and Brown [103], Fomichev *et al.* [104–106], Singer [107], Ershov *et al.* [108, 109], Cooke and Stewardson [110], Bearden [111], Henke *et al.* [112, 113], Singman [114], Lublin *et al.* [115], Hubbel *et al.* [116], and Davisson [117]. These additional data were for room temperature but were not for uhv samples and may suffer from surface effects to some degree, particularly in the transmission measurements on thin films near the $L_{II,III}$ edge [86, 87] and to a lesser degree between the plasmon energy and the $L_{II,III}$ edge [104] (see later in this section).

Since the Kramers–Kronig relations require knowledge of one optical function over the entire spectrum, the analysis proceeded by successive approximations. A trial reflectance function was constructed by employing estimates from transmission, electron-energy-loss, and similar data above 11.8 eV. This was then analyzed and the resulting optical functions compared with the input. The trial function was successively modified—primarily by the substitution of experimental data where available—until the calculated and measured optical functions agreed.

Throughout, the results were checked against a number of optical sum rules to ensure agreement with independent theoretical and experimental constraints (see Chapter 3 of this volume). This disclosed that the reported oscillator strength in the L-absorption region was consistently too high by $\sim 14\%$. The absorption coefficient in this region has generally been measured in transmission by using thin films that exhibit a surface component to their absorption [86, 87]. To compensate for this, an *ad hoc* reduction was made in the data based on the thin-film measurements of Lukirskii *et al.* [118], Fomichev and Lukirskii [104, 105], Haensel *et al.* [102], and Gähwiller and Brown [103]. This brought the calculated absorption coefficient into agreement with both the f sum rule and later measurements by Balzarotti *et al.* [87], who separated surface and bulk absorption. While the data of Balzarotti *et al.* [87] extend only 10 eV above the L edge, the $k(\omega)$ values are consistently some 15% below those used by Shiles *et al.* [7] in preparing their original input in this range. This is in agreement with the conclusion that previous measurements of the absorption cross section in the neighborhood of the $L_{II,III}$ edge were systematically too large.

While this correction is very important in the soft x-ray region of the spectrum, it was found to have negligible effect on the optical constants below the plasma frequency as determined by the Kramers–Kronig analysis.

The results of the analysis for the refractive index and the reflectance between the infrared and the $L_{II,III}$ edge are listed in Table XII. Given for

comparison are the *in situ* uhv ellipsometric measurements of Mathewson and Myers [100], the uhv reflectance data of Bennett *et al.* [28], and the vacuum ultraviolet transmission and reflectance-angular-variation measurements of Ditchburn and Freeman [55]. The index results are graphed in Fig. 14. It will be seen that the Kramers–Kronig analysis is in good agreement with the ellipsometric measurements of Mathewson and Myers [100] in the visible and the IR. The differences—less than 11% in $n(\omega)$ and 8% or less in $k(\omega)$—give an indication of the uncertainty of the data.

A large number of optical constant measurements [10, 11, 25–27, 51, 55, 56, 65, 66, 73, 75, 91, 119–129] have been reported for films prepared on normal substrates in high vacuum and subsequently exposed to the air. The resulting "effective" optical constants describe good but contaminated aluminum surfaces made with no special attempt to produce ultrasmooth films. A number of these measurements are compared with values derived from uhv films in Fig. 14. Over most of the spectrum the effective optical constants for the oxidized surface lie below those for the uhv films. This is most pronounced in the IR, where effective optical constants 25% or more smaller than the uhv values are common. In the visible the effective constants are generally 10 to 15% lower than the uhv values, while in the UV the effective constants are surprisingly close to the uhv values. The exception is for the effective $n(\omega)$ near the surface plasmon frequency ω_s. Here there is a "bump" in the effective index, presumably arising from dispersion associated with the apparent "absorption" of the surface plasma and light scattering by films with rough surfaces.

Reflectance at Normal Incidence B

The reflectance for smooth unoxidized films at normal incidence as calculated from the results of Shiles *et al.* [7] by using the Fresnel relation

$$R(\omega) = \frac{[n(\omega) - 1]^2 + k^2(\omega)}{[n(\omega) + 1]^2 + k^2(\omega)}, \tag{7}$$

is given in Table XII and Fig. 15. Also given in Table XII are the direct reflectance measurements of Bennett *et al.* [28] and the reflectance calculated from the ellipsometric measurements of Mathewson and Myers [100]. These data cover the infrared and visible and apply to films prepared in uhv. Values of the reflectance in the vacuum ultraviolet are also given; these were taken from the work of Ditchburn and Freeman [55] on films evaporated in high vacuum and are likely to suffer from surface-roughness and surface-oxide effects. (See Fomichev and Lukirskii [104].)

The last column of Table XII gives a composite set of reflectance data for the more common high-quality evaporated aluminum mirrors that are prepared in conventional high vacuum (10^{-5}–10^{-6} torr) and subsequently

exposed to the atmosphere. These same data are plotted as the curve marked high-vacuum films in air in Fig. 12. The properties of such films vary widely depending on formation conditions, atmospheric exposure history, and substrate surface roughness. The composite given is for films formed by rapid evaporation in high vacuum on optically polished (but not supersmooth) substrate and subsequently exposed to clean dry air. Such films generally show reflections $\sim 1\%$ lower than smooth oxide-free films in the infrared and visible. In the ultraviolet, their reflectance drops rapidly from the smooth oxide-free film value as a result of scattering and surface-plasmon excitation. A wide range of reflectance is reported at these wavelengths because surface roughness is generally not controlled.

C Room-Temperature Dielectric Function

The dielectric function covering the complete energy range involved in the Kramers–Kronig analysis is given in Table XIII and Fig. 16. This set of data includes the 14% reduction in the high-energy side of the $L_{II,III}$ edge needed to obtain agreement with the f sum rule and recent transmission measurements [87] taking surface effects into account. The energy intervals used in the table have been chosen to give closely spaced points in regions of pronounced structure such as interband absorption and x-ray edges. Intermediate points can be found by interpolation noting that the dielectric function generally has a power-law dependence on energy in regions far removed from interband edges. Near the edges the energy spacing is too course to show all the x-ray fine structure. For details of this the reader is referred to Balzarotti *et al.* [87] and Haensel *et al.* [130] for L-edge structure and to Kiyono *et al.* [131] for K-edge spectra.

The $\varepsilon_2(\omega)$ curve in Fig. 16 discloses unexpected discontinuities in slope: a small discontinuity at approximately 7 eV and a larger discontinuity near 15 eV. These are not readily apparent in the other optical functions, specifically in $n(\omega)$ and $k(\omega)$. These features may be extraneous, arising from the joining of data from different sources. This is most probably the case for the discontinuity near 7 eV when additional uncertainty was introduced from reading published graphic data.

However, the situation is not as clear for the larger discontinuity near 15 eV (the plasmon energy). Here the ε_2 data fall off significantly faster below 15 eV than in the interval between 15 eV and the $L_{II,III}$ edge. This is contrary to the simple expectation, based on single-particle excitations, that at photon energies high compared to the principal interband transition energies, the valence electrons should behave almost as free electrons so that their contribution to ε_2 should be approximately Drude-like; i.e., $\varepsilon_2(\omega) \sim \omega^{-3}$. A possible explanation is that the change in slope is an experimental artifact: below 15 eV, the $\varepsilon_2(\omega)$ data are based primarily on samples prepared in

uhv, whereas from 15 eV to the $L_{II,III}$ edge, the samples were prepared in conventional vacua and the measurements were made in air. Over the latter range, surface contamination could lead to significant errors in the optical constants reported by Ditchburn and Freeman [55]. Such an error cannot be detected as a violation of the f sum rule to within the accuracy of present data, since the contribution to the f sum rule over the region in question is of the order of a few tenths of an electron per atom.

A second and more intriguing possibility is that there is a deviation of the optical properties from the random-phase-approximation values above the plasmon energy. Just such an effect has been proposed by Hopfield [132] as a result of the dynamic screening of the phonon—or disorder—contribution to the optical absorption. A third possibility [133] is the excitation of bulk plasmons by oscillating charges induced at the metal surface by the exciting light; however, studies [134] of the surface photoelectric effect suggest the latter process is negligible. New measurements on well-characterized uhv samples in this energy range are needed to clarify this situation. Such experiments should be possible with the increasing availability of synchrotron radiation sources. Recent inelastic electron-scattering studies by Livins *et al.* [134a] confirm a deviation from Drude behavior near the plasmon energy that is consistent with Hopfield's suggestion.

D Temperature Dependence

The effect of temperature on the optical properties of aluminum has been studied directly with ellipsometry by Liljenvall *et al.* [101] and by Mathewson and Myers [5], who found $\sigma(\omega)$ as a function of energy and temperature as shown in Fig. 17. As the temperature rises, the 1.5-eV interband transition shows a pronounced broadening, shifts toward lower energies, and becomes weaker. The free-electron contribution also shows a broadening but becomes stronger with rising temperature. This is in line with the fact that in the liquid metal interband transitions are not observed [97], all the conduction electron oscillator strength having been transferred to the Drude-like intraband term. The ellipsometric results have been analyzed [5] within the framework of the Ashcroft–Sturm [18] two-band model to obtain the temperature dependence of the Drude parameters, the Fourier components of the crystal field, and the interband relaxation time (see Table XI and Mathewson and Myers [5]).

As a result of the high values of $n(\omega)$ and $k(\omega)$ in the visible and infrared, even a large variation of the optical constants with temperature produces only a small change in the reflectance R. This effect has been investigated qualitatively in thermomodulation studies by Rosei and Lynch [135]. The results are rather featureless except near the "1.5-eV" interband absorption. They show that dR/dT is negative below approximately 1.3 eV (0.95 μm) and positive at higher energies. This is consistent with the ellipsometric results [5]

and may be understood as arising primarily from (1) a broadening and shift toward lower energy of the "1.5-eV" interband transition with rising temperature, combined with (2) a decrease in reflectance in the Drude region (below ~ 1 eV) as a result of a shortening of the intraband lifetime at higher temperatures. Although the temperature modulation involved was not determined, the scale of the effect is given by Pudkov's measurements [136] at 1.96 eV (0.633 μm) that yield a value for dR/dT of approximately 3×10^{-5} $(°C)^{-1}$.

The temperature dependence of the reflectance and absorptance is of particular interest for high-power laser applications (see, for example, Pudkov [136] and Konov and Tokarev [137]). A detailed study of the wavelength and temperature dependence of the absolute reflectance of metallic Al (as well as Ag and Cu) from 4000 Å to 10 μm has been made by Decker and Hodgkin [138]. Measurements were made to a precision of a few parts in 10^5 and are in agreement with the qualitative discussion given above. The reader is referred to Decker and Hodgkin [138] for numerical results.

E Pressure Dependence

The effect of pressure on the reflectance of aluminum has been investigated at room temperature by Tups and Syassen [139] in both the infrared and the visible (0.5–3.0 eV). Polycrystalline samples were studied by using the gasketed diamond-anvil technique [140] with the reflectance measured relative to the diamond windows of the pressure cell. Representative results are shown in Fig. 18. Note that the reflectance of the diamond–aluminum interface shown in Fig. 18 for a pressure of 1 kbar is significantly less than that shown in Fig. 12 for the air–aluminum interface at 1 atm because of the higher refractive index of diamond ($n \approx 2.4$). Tups and Syassen [139] found that as pressure is increased, the reflectance drop arising from the strong interband transitions associated with the square (200) faces of the Brillouin zone shifts toward higher energies. From a value of ~ 1.47 eV at 1 atm, the transition energy rises monotonically to ~ 2.34 eV at 310 kbar. This shift is indicated by the upper set of arrows in the figure. The initial rate of charge of the transition energy is 4.35 ± 0.3 meV/kbar.

Near pressures of 100 kbar, a shoulder developed on the reflectance curve at about 1 eV. With increasing pressure this shoulder moved toward higher energies, and a well-defined reflectance minimum develops at low energies. This feature corresponds to the second strong interband transition associated with the hexagonal (111) faces of the Brillouin zone. At normal pressure and temperature, this transition lies at ~ 0.4 eV and is obscured by the intraband absorption, but it shifts toward higher energies with increasing pressure reaching ~ 1.32 eV at 310 kbar, where it is well resolved from lower-energy intraband processes. The peak positions of this low-energy interband transition are indicated by the lower set of arrows.

In a detailed analysis, Tups and Syassen [139] show that both the interband transitions become stronger at the expense of the oscillator strength of the intraband absorption. This exchange of strength reflects the partial f sum rule for conduction-electron absorption [147], which enters the theory of Ashcroft and Sturm [18]. The weakening of intraband processes is evident in the reflectance spectra as the retreat of the high-reflectance almost-free-electron region that lies below ~ 1 eV under normal conditions, toward lower energies with increasing pressure. A fitting of the data to the theory of Ashcroft and Sturm [18] indicates that the optical mass, which is inversely proportional to the intraband strength, increases by approximately a factor of 1.4 in going from atmospheric pressure to 310 kbar. This corresponds to a transfer of $\sim 28\%$ of the intraband strength of approximately 0.5 e/at. to the interband transitions.

ACKNOWLEDGMENTS

The authors would like to express appreciation to innumerable colleagues for discussions and aid during the course of their studies of aluminum. Particular thanks are due Dr. J. M. Bennett, Professor F. C. Brown, Professor H. P. Myers, Dr. E. M. Pell, Professor S. E. Schnatterly, Professor B. Segall, Dr. K. Syassen, and Dr. B. W. Veal, Jr., for counsel and for supplying unpublished or prepublication copies of their results.

REFERENCES

1. H. Ehrenreich, H. R. Philipp, and B. Segall, *Phys. Rev.* **132**, 1918 (1963).
2. H. R. Philipp and H. Ehrenreich, *J. Appl. Phys.* **35**, 1416 (1964).
3. C. J. Powell, *J. Opt. Soc. Am.* **60**, 78 (1970).
4. T. Sasaki and M. Inokuti, "Conference Digest of the Third International Conference on Vacuum Ultraviolet Radiation Physics" (Y. Nakai, ed.), paper 2aC2–2. Phys. Soc. of Japan, Tokyo, 1971.
5. A. G. Mathewson and H. P. Myers, *J. Phys. F* **2**, 403 (1972).
6. H.-J. Hagemann, W. Gudat, and C. Kunz, *J. Opt. Soc. Am.* **65**, 742 (1975); H.-J. Hagemann, W. Gudat, and C. Kunz, DESY Report SR 74/7, Hamburg, 1974 (unpublished).
7. E. Shiles, T. Sasaki, M. Inokuti, and D. Y. Smith, *Phys. Rev. B* **22**, 1612 (1980).
8. F. Wooten, "Optical Properties of Solids," Section 3.2. Academic Press, New York, 1972.
9. M. H. Cohen, *Philos. Mag.* **3**, 762 (1958).
10. J. N. Hodgson, *Proc. Phys. Soc. London Sec. B* **68**, 593 (1955).
11. J. R. Beattie, *Physica (Utrecht)* **23**, 898 (1957).
12. H. E. Bennett and J. M. Bennett, *in* "Optical Properties and Electronic Structure of Metals and Alloys" (F. Abelès ed.), p. 175. North-Holland Publ., Amsterdam, 1966.
13. G. Dresselhaus, M. S. Dresselhaus, and D. Beaglehole, *in* "Electronic Density of States" (L. H. Bennett ed.). National Bureau of Standards Special Publication 323, Washington, D.C., 1971.
14. R. L. Benbow and D. W. Lynch, *Phys. Rev. B* **12**, 5615 (1975).
15. D. Y. Smith and B. Segall, *Bull. Am. Phys. Soc.* **26**, 209 (1981); D. Y. Smith and B. Segall, (to be published).
16. "Handbook of Chemistry and Physics," 58th ed. (R. C. Weast, ed.). CRC Press, Cleveland, 1977.
17. G. T. Meaden, "Electrical Resistance of Metals." Plenum, New York, 1965.
18. N. W. Ashcroft and K. Sturm, *Phys. Rev. B* **3**, 1898 (1971).

19. W. A. Harrison, *Phys. Rev.* **147**, 467 (1966).
20. A. I. Golovashkin, A. I. Kopeliovich, and G. P. Motulevich, *Zh. Eksp. Teor. Fiz.* **53**, 2053 (1967); A. I. Golovashkin, A. I. Kopeliovich, and G. P. Motulevich, *Soviet Phys. JETP* **26**, 1161 (1968).
21. N. W. Ashcroft, *Philos. Mag.* **8**, 2055 (1963).
22. D. Brust, *Phys. Rev. B* **2**, 818 (1970).
23. F. Szmulowicz and B. Segall, *Phys. Rev. B* **24**, 892 (1981).
24. J. Strong, *Astrophys. J.* **83**, 401 (1936).
25. L. G. Schulz, *J. Opt. Soc. Am.* **44**, 357 (1954); L. G. Schulz and F. R. Tañgherlini, *J. Opt. Soc. Am.* **44**, 362 (1954).
26. I. N. Shklyarevskii and R. G. Yarovaya, *Opt. Spektrosk.* **16**, 85 (1964); I. N. Shklyarevskii and R. G. Yarovaya, *Opt. Spectrosc. (USSR)* **16**, 45 (1964).
27. J. R. Beattie, *Philos. Mag.* **46**, 235 (1955).
28. H. E. Bennett, M. Silver, and E. J. Ashley, *J. Opt. Soc. Am.* **53**, 1089 (1963).
29. L. W. Bos and D. W. Lynch, *Phys. Rev. Lett.* **25**, 156 (1970).
30. O. Hunderi and P. O. Nilsson, *Solid State Commun.* **19**, 921 (1976); O Hunderi and P. O. Nilsson, *Nuovo Cimento* **39 B**, 459 (1977).
31. D. Y. Smith, D. D. Koelling, and B. Segall, *Bull. Am. Phys. Soc.* **28**, 387 (1983); D. Y. Smith, D. D. Koelling, and B. Segall, to be published.

31a. D. C. Jiles and M. P. Staines, *Solid State Commun.* **47**, 37 (1983).

32. M. S. Miller and N. D. Drew, *J. Phys. F*, **13**, 1885 (1983).
33. G. Quincke, *Ann. Physik, Series 2, Jubelband*, p. 336 (1874); W. Voigt, *Ann. Physik, Series 3*, **23**, 142 (1884); F. F. Martens, "Landolt-Börnstein," 5th ed., Vol. 2, Section 165, p. 906. Springer, Berlin, 1923.
34. P. Drude, *Ann. Physik, Series 3*, **39**, 481 (1890).
35. P. G. Nutting, *Phys. Rev.* **13**, 193 (1901).
36. W. W. Coblentz, *Bull. U.S. Bureau Standards* **2**, 457 (1906).
37. W. v. Uljain, *Phys. Z.* **11**, 784 (1910).
38. M. Luckiesh, *J. Opt. Soc. Am.* **19**, 1 (1929).
39. W. W. Coblentz and R. Stair, *U. S. Bureau Standards J. Res.* **4**, 189 (1930).
40. J. Wulff, *J. Opt. Soc. Am.* **24**, 223 (1934).
41. A. H. Taylor, *J. Opt. Soc. Am.* **24**, 192 (1934).
42. W. R. Grove, *Philos. Trans. R. Soc. London* **142**, 87 (1852); W. Crookes, *Proc. R. Soc. London* **50**, 88 (1891).
43. P. Pringsheim and R. Pohl, *Verh. Dtsh. Phys. Ges.* **14**, 506 (1912).
44. E. O. Hulburt, *Astrophys. J.* **42**, 203 (1915).
45. P. R. Gleason, *Proc. Nat. Acad. Sci. (USA)* **15**, 551 (1929).
46. R. Ritschl, *Z. Instrumentenkunde* **41**, 158 (1929); R. Ritschl, *Z. Instrumentenkunde* **50**, 230 (1930); R. Ritschl, *Z. Phys.* **69**, 578 (1931); H. S. Jones, *Nature* **134**, 522 (1934).
47. J. Strong, *Phys. Rev.* **43**, 498 (1933).
48. G. Hass, *J. Opt. Soc. Am.* **45**, 945 (1955).
49. J. C. Burridge, H. Kuhn, and A. Pery, *Proc. Phys. Soc. London Ser. B* **66**, 963 (1953).
50. J. Halford, F. K. Chin, and J. E. Norman, *J. Opt. Soc. Am.* **63**, 786 (1973).
51. G. Hass and J. E. Waylonis, *J. Opt. Soc. Am.* **51**, 719 (1961).
52. E. T. Hutcheson, G. Hass, and J. K. Coulter, *Opt. Commun.* **3**, 213 (1971).
53. J. G. Endriz and W. E. Spicer, *Phys. Rev. B* **4**, 4144 (1971).
54. P. C. Gibbons, S. E. Schnatterly, J. J. Ritsko, and J. R. Fields, *Phys. Rev. B* **13**, 2451 (1976).
55. R. W. Ditchburn and G. H. Freeman, *Proc. R. Soc. London Sec. A* **294**, 20 (1966).
56. G. Hass, *Optik* **1**, 8 (1946).
57. G. B. Sabine, *Phys. Rev.* **55**, 1064 (1939).
58. M. Banning, *Phys. Rev.* **59**, 914 (1941); M. Banning, *J. Opt. Soc. Am.* **32**, 98 (1942).
59. W. C. Walker, J. A. R. Samson, and O. P. Rustig, *J. Opt. Soc. Am.* **48**, 71 (1958); W. C. Walker, O. P. Rustig, and G. L. Weissler, *J. Opt. Soc. Am.* **49**, 471 (1959).

60. V. R. Weidner and J. J. Hsia, National Bureau of Standards Certificate for Standard Reference Material 2003a, Washington, D.C., 1981; V. R. Weidner and J. J. Hsia, National Bureau of Standards Report NBS-SP-260-75, Washington, D.C., 1982.
61. H. Schopper, *in* "Landolt-Börnstein Zahlenwerte and Funktionen," 6th ed., (K.-H. Hellwege and A. M. Hellwege, eds.), Vol. 2, Part 8, Section 281, pp. 1-1–1-41. Springer Verlag, Berlin, 1962; R. C. Willams and G. B. Sabine, *Astrophys. J.* **77**, 316 (1933); H. S. Jones, *Nature* **133**, 552 (1934); B. K. Johnson, *Nature* **134**, 216 (1934); M. Auwärter, *Z. Tech. Phys.* **18**, 457 (1937); B. K. Johnson, *Proc. Phys. Soc. London* **53**, 258 (1941); A. Boettcher, *Z. Angew. Phys.* **2**, 340 (1950).
62. G. Hass, *Z. Anorg. Allg. Chem.* **254**, 96 (1947).
63. P. H. Berning, G. Hass, and R. P. Madden, *J. Opt. Soc. Am.* **50**, 586 (1960).
64. I. N. Shklyarevskii and R. G. Yarovaya, *Opt. Spektrosk.* **14**, 252 (1963); I. N. Shklyarevskii and R. G. Yarovaya, *Opt. Spectrosc. (USSR)* **14**, 130 (1963).
65. R. W. Fane and W. E. J. Neal, *J. Opt. Soc. Am.* **60**, 790 (1970).
66. J. Shewchun and E. C. Rowe, *J. Appl. Phys.* **41**, 4128 (1970).
67. B. P. Feuerbacher and W. Steinmann, *Opt. Commun.* **1**, 81 (1969).
68. A. Daude, A. Savary, and S. Robin, *Thin Solid Films* **13**, 255 (1972); A. Daude, A. Savary, and S. Robin, *J. Opt. Soc. Am.* **62**, 1 (1972).
69. W. Walkenhorst, *Z. Tech. Phys.* **22**, 14 (1941).
70. R. S. Sennett and G. D. Scott, *J. Opt. Soc. Am.* **40**, 203 (1950); M. F. Crawford, W. M. Gray, A. L. Schawlow, and F. M. Kelly, *J. Opt. Soc. Am.* **39**, 888 (1949).
71. W. E. J. Neal, R. W. Fane, and N. W. Grimes, *Philos. Mag.* **21**, 167 (1970).
72. R. P. Madden and L. R. Canfield, *J. Opt. Soc. Am.* **51**, 838 (1961).
73. R. P. Madden, L. R. Canfield, and G. Hass, *J. Opt. Soc. Am.* **53**, 620 (1963).
74. R. K. Hart, *Proc. R. Soc. London Sec. A* **236**, 68 (1956).
75. G. Hass, *Ann. Phys. (Leipzig)* **31**, 245 (1938).
76. G. Hass, W. R. Hunter, and R. Tousey, *J. Opt. Soc. Am.* **46**, 1009 (1956); G. Hass, W. R. Hunter, and R. Tousey, *J. Opt. Soc. Am.* **47**, 1070 (1957).
77. N. Cabrera, J. Terrien, and J. Hamon, *Compt. Rend.* **224**, 1558 (1947); N. Cabrera, *Philos. Mag.* **40**, 175 (1949).
78. R. P. Chasmar, J. L. Craston, G. Isaacs, and A. S. Young, *J. Sci. Instrum.* **28**, 206 (1951).
79. G. H. C. Freeman, *Br. J. Appl. Phys.* **16**, 927 (1965); E. T. Arakawa and M. W. Williams, *J. Phys. Chem. Sol.* **29**, 735 (1968).
80. G. Hass and N. W. Scott, *J. Opt. Soc. Am.* **39**, 179 (1949).
81. A. P. Bradford and G. Hass, *J. Opt. Soc. Am.* **53**, 1096 (1963); J. T. Cox, G. Hass, and J. B. Ramsey, *J. de Phys. (Paris)* **25**, 250 (1964); H. Herzig, R. S. Spencer, and J. J. Zaniewski, *Appl. Opt.* **17**, 3031 (1978); J. T. Cox and G. Hass, *Appl. Opt.* **17**, 333 (1978); R. J. Francis, *UV Spectrom. Group Bull.*, No. 6, 35 (December, 1978); and G. Hass, *J. Opt. Soc. Am.* **72**, 27 (1982).
82. J. T. Cox and G. Hass, *Appl. Opt.* **17**, 2125 (1978).
83. G. Hass and R. Tousey, *J. Opt. Soc. Am.* **49**, 593 (1959); P. H. Berning, G. Hass, and R. P. Madden, *J. Opt. Soc. Am.* **50**, 586 (1960); D. W. Angel, W. R. Hunter, R. Tousey, and G. Hass, *J. Opt. Soc. Am.* **51**, 913 (1961); W. R. Hunter, *Opt. Acta* **9**, 255 (1962); L. R. Canfield, G. Hass, and J. E. Waylonis, *Appl. Opt.* **5**, 45 (1966); J. T. Cox, G. Hass, and J. E. Waylonis, *Appl. Opt.* **7**, 1535 (1968); E. T. Hutcheson, G. Hass, and J. T. Cox, *Appl. Opt.* **11**, 2245 (1972); G. Hass and W. R. Hunter, *in* "Space Optics" (B. J. Thompson and R. R. Shannon, eds.), p. 525, National Academy of Sciences, Washington, D.C., 1974.
84. J. D. Armitage and M. A. Grimm, *IBM Tech. Disclosure Bull.* **23**, 3580 (1981).
85. L. Holland, "Vacuum Deposition of Thin Films." Wiley, New York, 1958.
86. D. H. Tomboulian and E. M. Pell, *Phys. Rev.* **83**, 1196 (1951).
87. A. Balzarotti, A Bianconi, and E. Burattini, *Phys. Rev. B* **9**, 5003 (1974).
88. J. M. Elson and R. H. Ritchie, *Phys. Rev. B* **4**, 4129 (1971).
89. R. H. Ritchie and R. E. Wilems, *Phys. Rev.* **178**, 372 (1969); J. Crowell and R. H. Ritchie, *J. Opt. Soc. Am.* **60**, 794 (1970); J. M. Elson and R. H. Ritchie, *Phys. Lett.* **33A**, 255 (1970).

90. R. C. Vehse, E. T. Arakawa, and J. L. Stanford, *J. Opt. Soc. Am.* **57**, 551 (1967).
91. M. W. Williams, E. T. Arakawa, and L. C. Emerson, *Surf. Sci.* **6**, 127 (1967).
92. L. Holland, *J. Opt. Soc. Am.* **43**, 376 (1953).
93. N. G. Nakhodkin and A. I. Shaldervan, *Thin Solid Films* **10**, 109 (1972).
94. R. T. Kivaisi, *Thin Solid Films* **97**, 153 (1982).
95. J. M. Nieuwenhuizen and H. B. Haanstra, *Philips Tech. Rev.* **27**, 87 (1966).
96. L. Holland, *B. J. Appl. Phys.* **9**, 336 (1958).
97. J. C. Miller, *Philos. Mag.* **20**, 1115 (1969).
98. T. E. Faber, *in* "Optical Properties and Electronic Structure of Metals and Alloys" (F. Abelès ed.), p. 259. North-Holland Publ., Amsterdam, 1966.
99. L. G. Bernland, O. Hunderi, and H. P. Myers, *Phys. Rev. Lett.* **31**, 363 (1973).
100. A.G. Mathewson and H. P. Myers, *Phys. Scr.* **4**, 291 (1971).
101. H. G. Liljenvall, A. G. Mathewson, and H. P. Myers, *Solid State Commun.* **9**, 169 (1971).
102. R. Haensel, B. Sonntag, C. Kunz, and T. Sasaki, *J. Appl. Phys.* **40**, 3046 (1969).
103. C. Gähwiller and F. C. Brown, *Phys. Rev. B* **2**, 1918 (1970).
104. V. A. Fomichev and A. P. Lukirskii, *Opt. Spektrosk.* **22**, 796 (1967); V. A. Fomichev and A. P. Lukirskii, *Opt. Spectrosc. (USSR)* **22**, 432 (1967).
105. V. A. Fomichev and A. P. Lukirskii, *Fiz. Tverd. Tela* **8**, 2104 (1966); V. A. Fomichev and A. P. Lukirskii, *Sov. Phys.-Solid State* **8**, 1674 (1967).
106. V. A. Fomichev, *Fiz. Tverd. Tela* **8**, 2892 (1966); V. A. Fomichev, *Sov. Phys.-Solid State* **8**, 2312 (1967).
107. S. Singer, *J. Appl. Phys.* **38**, 2897 (1967).
108. O. A. Ershov, I. A. Brytov, and A. P. Lukirskii, *Opt. Spektrosk.* **22**, 127 (1967); O. A. Ershov, I. A. Brytov, and A. P. Lukirskii, *Opt. Spectrosc. (USSR)* **22**, 66 (1967).
109. O. A. Ershov and I. A. Brytov, *Opt. Spektrosk.* **22**, 305 (1967); O. A. Ershov and I. A. Brytov, *Opt. Spectrosc. (USSR)* **22**, 165 (1967).
110. B. A. Cooke and E. A. Stewardson, *Br. J. Appl. Phys.* **15**, 1315 (1964).
111. A. J. Bearden, *J. Appl. Phys.* **37**, 1681 (1966).
112. B. L. Henke and R. L. Elgin, *in* "Advances in X-Ray Analysis" (B. L. Henke, J. B. Newkirk, and G. R. Mallett, eds.), Vol. 13, p. 639. Plenum, New York, 1970.
113. B. L. Henke and E. S. Ebisu, *in* "Advances in X-Ray Analysis" (C. L. Grant, C. S. Barrett, J. B. Newkirk, and C. O. Ruud, eds.), Vol. 17, p. 150. Plenum, New York, 1974.
114. L. Singman, *J. Appl. Phys.* **45**, 1885 (1974).
115. P. Lublin, P. Cukor, and R. J. Jaworowski, *in* "Advances in X-Ray Analysis" (B. L. Henke, J. B. Newkirk, and G. R. Mallett, eds.), Vol. 13, p. 632. Plenum, New York, 1970.
116. J. H. Hubbell, W. H. McMaster, N. K. Del Grande, and J. H. Mallett, *in* "International Tables for X-Ray Crystallography" (J. A. Ibers and W. C. Hamilton, eds.), Vol. IV, p. 47. Kynoch, Birmingham, England, 1974.
117. C. M. Davisson, *in* "Alpha-, Beta-, and Gamma-Ray Spectroscopy" (K. Siegbahn, ed.), Vol. I, p. 37. North-Holland Publ., Amsterdam, 1965.
118. A. P. Lukirskii, E. P. Savinov, O. A. Ershov, and Yu. F. Shepelev, *Opt. Spektrosk.* **16**, 310 (1964); A. P. Lukirskii, E. P. Savinov, O. A. Ershov, and Yu. F. Shepelev, *Opt. Spectrosc. (USSR)* **16**, 168 (1964).
119. A. Smakula, *Z. Phys.* **88**, 114 (1934).
120. W. Woltersdorff, *Z. Phys.* **91**, 230 (1934).
121. H. M. O'Bryan, *J. Opt. Soc. Am.* **26**, 122 (1936).
122. K. B. Hunt, Investigations of the Reflectivity and Transmissivity of Selected Materials in the Infrared Region. M.S. thesis, Purdue University, West Lafayette, Indiana, 1945 (unpublished).
123. A. I. Golovashkin, G. P. Motulevich, and A. A. Shubin, *Zh. Eksp. Teor. Fiz.* **38**, 51 (1960); A. I. Golovashkin, G. P. Motulevich, and A. A. Shubin, *Sov. Phys.-JETP* **11**, 38 (1960).
124. T. T. Cole and F. Oppenheimer, *Appl. Opt.* **1**, 709 (1962).
125. W. R. Hunter, *J. Appl. Phys.* **34**, 1565 (1963); W. R. Hunter, *J. Opt. Soc. Am.* **54**, 208 (1964); W. R. Hunter, *J. Phys. (Paris)* **25**, 154 (1964).

126. G. P. Motulevich, A. A. Shubin, and O. F. Shustova, *Zh. Eksp. Teor. Fiz.* **49**, 1431 (1965); G. P. Motulevich, A. A. Shubin, and O. F. Shustova, *Sov. Phys.-JETP* **22**, 984 (1966).
127. A. P. Lenham and D. M. Terherne, *J. Opt. Soc. Am.* **56**, 752 (1966).
128. A. Daude, M. Priol, and S. Robin, *C. R. Acad. Sci. (Paris) B* **263**, 1178 (1966).
129. A. Daude, A. Savary, G. Jezequel, and S. Robin, *C. R. Acad. Sci. (Paris) B* **269**, 901 (1969).
130. R. Haensel, G. Keitel, B. Sonntag, C. Kunz, and P. Schreiber, *Phys. Status Solidi A* **2**, 85 (1970); J. J. Ritsko, S. E. Schnatterly, and P. C. Gibbons, *Phys. Rev. Lett.* **32**, 671 (1974); H. Peterson and C. Kunz, *Phys. Rev. Lett.* **35**, 863 (1975); C. G. Olson and D. W. Lynch, *Solid State Commun.* **31**, 601 (1979); and C. G. Olson and D. W. Lynch, *Solid State Commun.* **36**, 513 (1980).
131. S. Kiyono, S. Chiba, Y. Hayasi, S. Kato, and S. Mochimaru, *Jpn. J. Appl. Phys.* **17** (Suppl. 17-2), 212 (1978); and M. H. Heinonen and J. A. Leiro, *Philos. Mag. B* **46**, 669 (1982).
132. J. J. Hopfield, *Phys. Rev.* **139**, A419 (1965).
133. K. L. Kliewer and R. Fuchs, *Phys. Rev.* **172**, 607 (1968).
134. H. J. Levinson and E. W. Plummer, *Phys. Rev. B* **24**, 628 (1981).
134a. P. Livins, S. E. Schnatterly, T. Aton, and A. Cafolla, *Bull. Am. Phys. Soc.* **29**, 517 (1984).
135. R. Rosei and D. W. Lynch, *Phys. Rev. B* **5**, 3883 (1972).
136. S. D. Pudkov, *Zh. Tekh. Fiz.* **47**, 649 (1977); S. D. Pudkov, *Sov. Phys.-Tech. Phys.* **22**, 389 (1977).
137. V. I. Konov and V. N. Tokarev, *Kvantovaya Elektron.* **10**, 327 (1983); V. I. Konov and V. N. Tokarev, *Sov. J. Quantum Electron.* **13**, 177 (1983).
138. D. L. Decker and V. A. Hodgkin, National Bureau of Standards Special Publication NBS-SP-620, Washington, D.C. 1981, p. 190.
139. H. Tups and K. Syassen, *J. Phys. F* **14**, 2753 (1984).
140. A. Jayaraman, *Rev. Mod. Phys.* **55**, 65 (1983).
141. D. Y. Smith and E. Shiles, *Phys. Rev. B* **17**, 4689 (1978).
142. D. Y. Smith, E. Shiles, and M. Inokuti, "The Optical Properties and Complex Dielectric Function of Metallic Aluminum from 0.04 to 10^4 eV." Argonne National Laboratory Report ANL-83-24, Argonne, Illinois, March 1983.
143. A. R. P. Rau and V. Fano, *Phys. Rev.* **162**, 68 (1967).

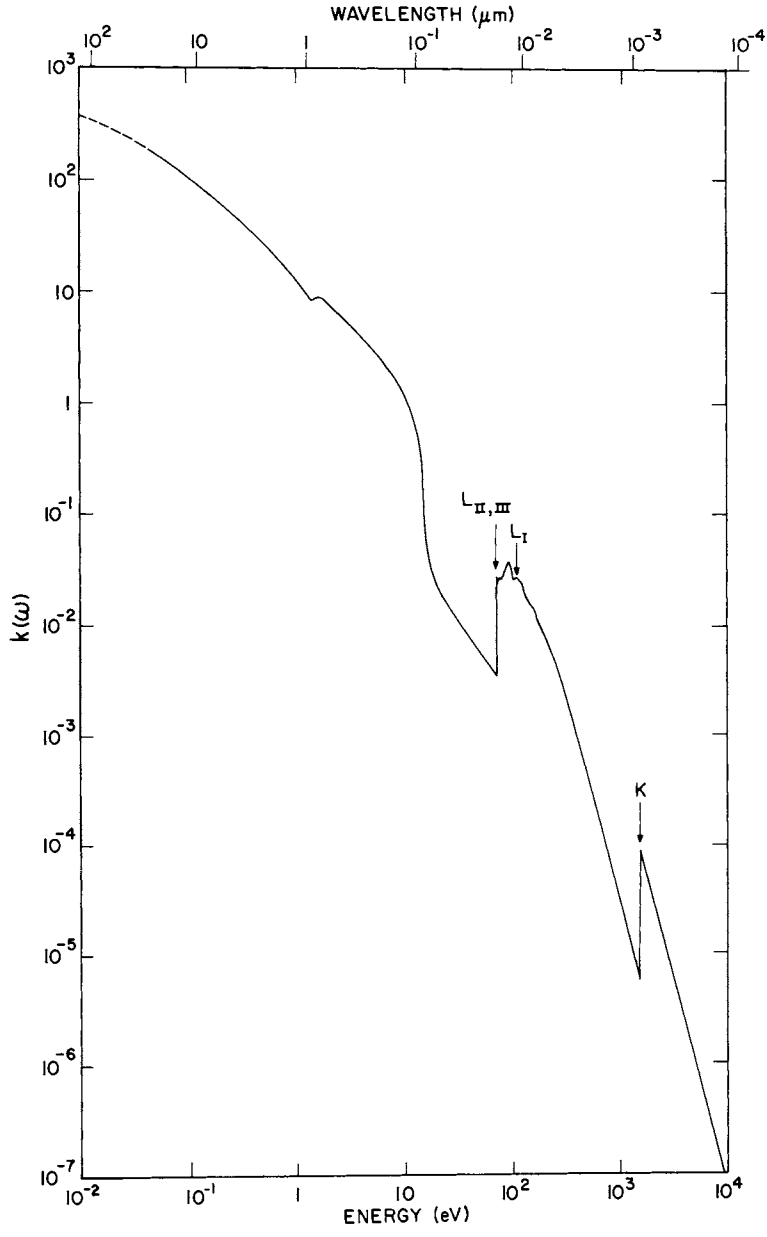

Fig. 11. The extinction coefficient $k(\omega)$; i.e., the imaginary part of the refractive index, for metallic aluminum at room temperature. (After Shiles *et al.* [7].)

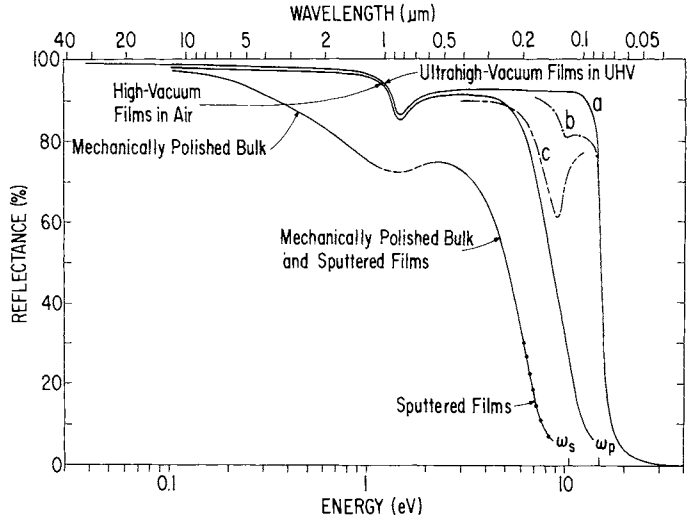

Fig. 12. The reflectance of metallic aluminum at room temperature. The uppermost curve gives the reflectance of opaque evaporated aluminum films prepared in ultrahigh vacuum. These films are presumed to be free of bulk and surface oxide contamination. The effect of light scattering and coupling to surface plasmons (at $\omega_s \approx 10.6$ eV) is illustrated by curves b and c. Curve b was obtained by Vehse *et al.* [90] for a film on a microscope slide cleaned by vapor decreasing and evaporated in a vacuum of $\sim 3 \times 10^{-8}$ torr; the "oxide-free" reflectance was obtained by extrapolation of the reflectance back to the time that the evaporation was completed. Curve c is for a uhv film with rms surface roughness σ of 18 Å, as reported by Endriz and Spicer [53]. The curve labeled high vacuum is an average for films evaporated in vacuum of the order of 10^{-5} torr. At this pressure surface and bulk oxidation occurs. The values reported for such films vary widely, especially in the ultraviolet, presumably because of surface roughness. The third curve is representative of mechanically polished samples, but the reported range of measurements is extremely large. Data for sputtered films are available from 380 nm well into the UV [44, 45]; curiously enough, they track the data for polished samples very closely.

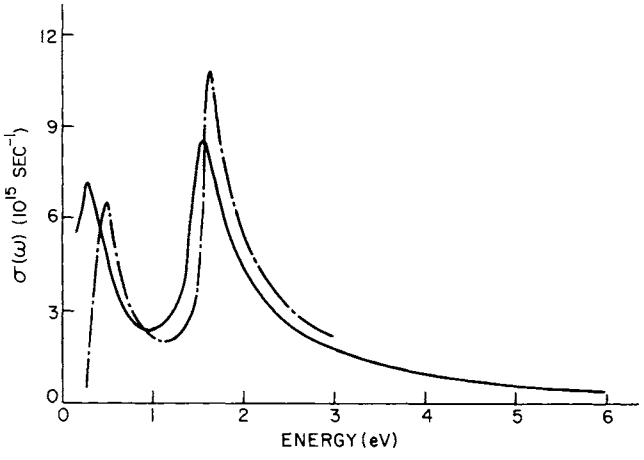

Fig. 13. The real part of the interband conductivity for aluminum obtained by subtracting the intraband contribution in the Drude model from the measured optical conductivity. The solid curve is for room temperature and was calculated by Smith and Segall [15], who employed Shiles *et al.*'s [7] analysis of uhv reflectance data. The dashed curve is taken from Benbow and Lynch [14] and applies to electropolished samples at 4.2 K.

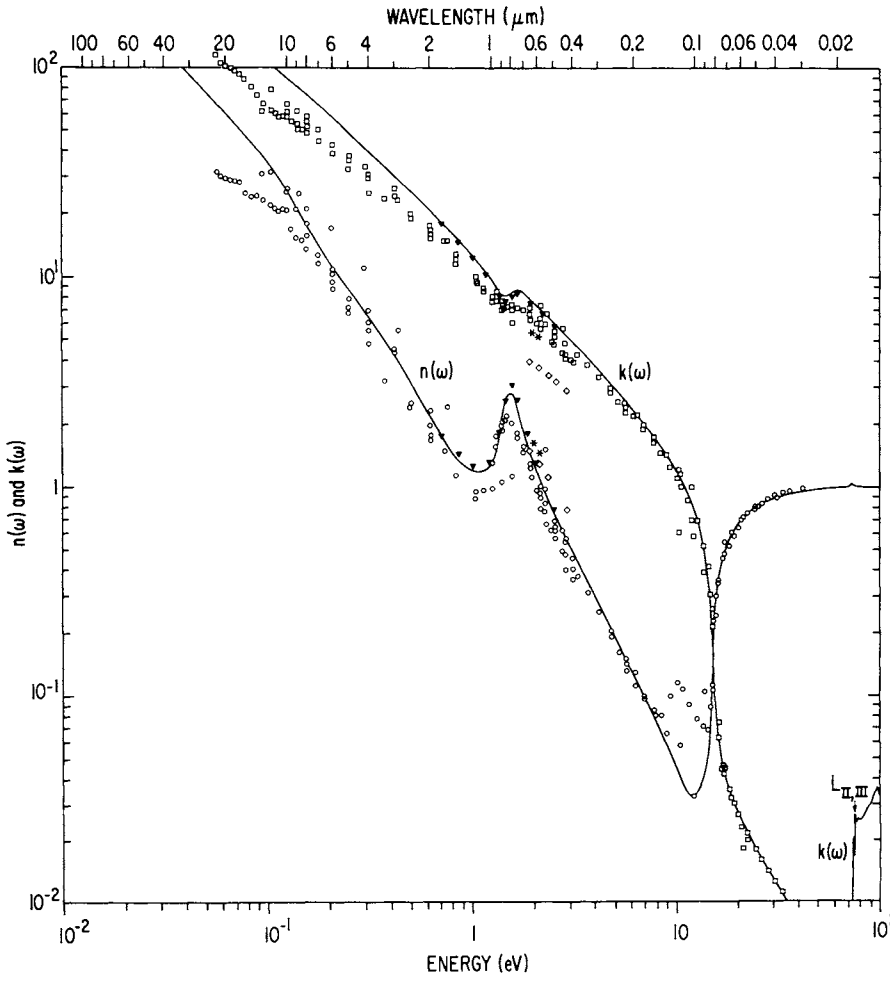

Fig. 14. The complex refractive index $n(\omega) + ik(\omega)$ for aluminum. The curves are taken from Shiles *et al.*'s [7] analysis of uhv reflectance data. A portion of the uhv ellipsometric data of Mathewson and Myers [100] is given for comparison. Quincke's [33] and Drude's [34] results for polished bulk samples are shown for historical interest; considering the materials and techniques available, these early measurements are remarkably good, especially for $n(\omega)$. The remainder of the data points are given to show the range of values of $n(\omega)$ (○) and $k(\omega)$ (□) reported in the literature. Most refer to evaporated films prepared in conventional or high vacuum and measured by using polarimetric, interferometric, and like methods. The sources of these data are given in the references [10, 11, 25, 26, 27, 51, 55 56, 65, 66, 73, 75, 91, and 121–129]. Note that the curves for $n(\omega)$ and $k(\omega)$ curve cross each other at roughly 15 eV, the plasmon energy. This corresponds to the plasmon condition $\varepsilon_1(\omega_p) = n^2(\omega_p) - k^2(\omega_p) \approx 0$. The onset of the L-shell absorption appears in the lower-right-hand corner. The corresponding dispersion is visible as a little "pimple" on the index curve near 72 eV. (Mathewson and Myers [100], ▼; Quincke [33], ◇; Drude [34], *.)

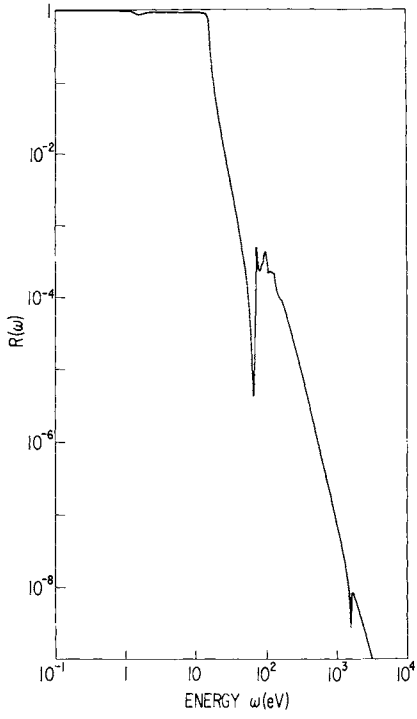

Fig. 15. The reflectance $R(\omega)$ at normal incidence of a smooth oxide-free metallic aluminum surface in vacuum. (After Shiles *et al.* [7].)

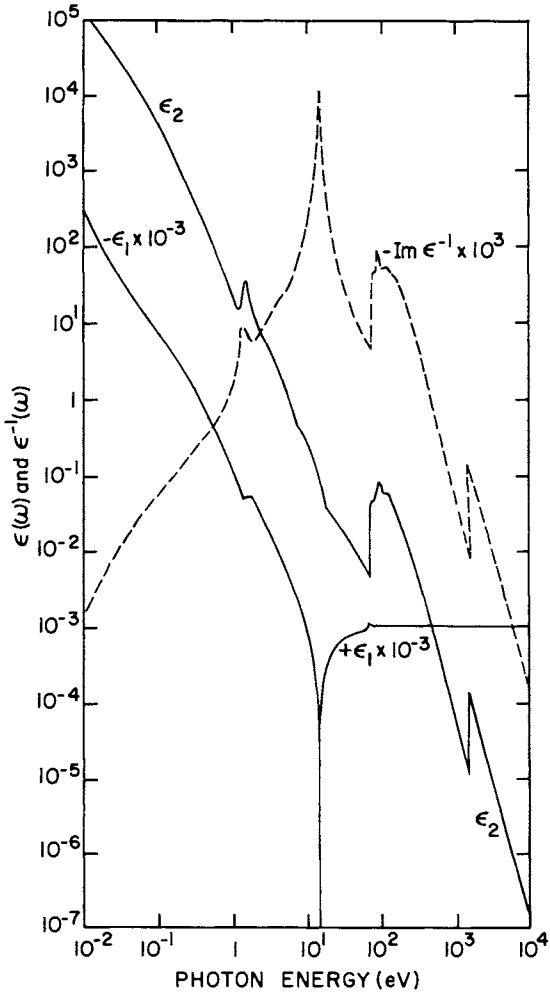

Fig. 16. The dielectric-response function of metallic aluminum. The real part $\varepsilon_1(\omega)$ is negative with large absolute values at low energies, vanishes at $\hbar\omega_p \approx 15.0$ eV (the plasmon energy for conduction electrons), and is positive and approaches unity at higher energies. The imaginary part $\varepsilon_2(\omega)$ is also largest at low energies and decreases with energy except at thresholds for newer modes of excitation (first at the beginning of interband excitation of valence electrons, next at the L-shell threshold, and finally at the K-shell threshold). The quantity $\mathrm{Im}[-1/\varepsilon(\omega)]$, which governs the energy transfer from fast charged particles, shows a prominent maximum near $\hbar\omega_p$ and is small at both lower and higher energies. (After Shiles *et al.* [7].)

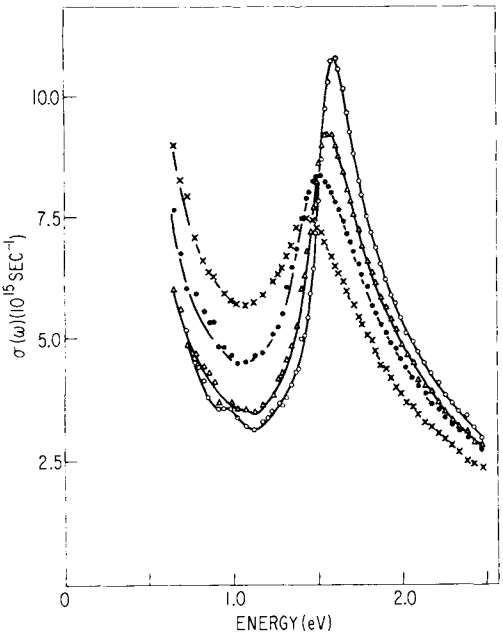

Fig. 17. The real part of the optical conductivity as a function of temperature for clean polycrystalline aluminum films deposited at room temperature. (198 K, ○; 298 K, △; 404 K, ●; and 552 K, ×.) (After Mathewson and Myers [5].) (Copyright © 1972 by the Institute of Physics).

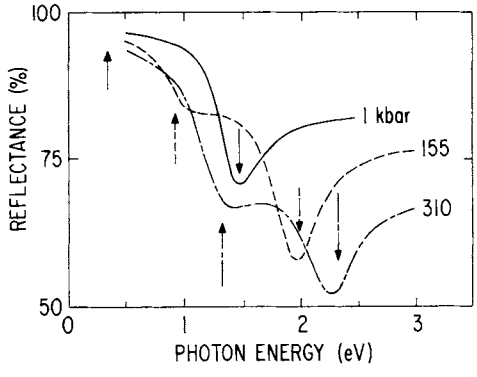

Fig. 18. The reflectance of aluminum at an interface with diamond as a function of pressure and photon energy. Pressures are given in kilobars to the right of each curve. The positions of the principal interband transitions, as determined by a fitting to the theory of Ashcroft and Sturm [18], are indicated by arrows coded to the corresponding reflectance curve. The position of the high-energy transition $2V_{200}$ is indicated by the upper set of arrows. That of the low-energy transition $2V_{111}$ is indicated by the lower set of arrows. (After Tups and Syassen [139].)

TABLE XI

Drude Parameters for the Intraband Absorption of Metallic Aluminum[a]

Source	Strength[b]				Damping		DC conductivity $\sigma(0)$ $(10^{17}\ \text{sec}^{-1})$	
	Temperature (K)	$\hbar\Omega_p$ (eV)	n_{eff} (e/at.)	m_{opt} (m_e)	τ $(10^{-14}$ sec)	$\hbar\gamma = \hbar\tau^{-1}$ (meV)	Optical	Electrical
Ehrenreich *et al.* [1]	RT	12.7	1.94	1.55	0.512	129	1.52	3.18 [16]–3.28 [17]
Bennett *et al.* [12]	RT	14.7	2.60	1.15	0.801	82.2	3.18 (input)[c]	
Powell [3]	RT	12.2	1.80	1.67	0.66	100	1.81	
Dresselhaus *et al.* [13]	RT	12.9 ± 0.7	2.0 ± 0.2	1.5 ∓ 0.15	0.5 ± 0.2	160 ∓ 60	1.60 ± 0.8	
Mathewson and Myers [5]	198	12.8	1.99	1.51[d]	1.18	55.8	3.58	5.49 [5]
Mathewson and Myers [5]	298	13.0	2.03	1.48[d]	1.02	64.5	3.14	3.21 [5]
Mathewson and Myers [5]	404	13.2	2.10	1.43[d]	0.62	105	1.96	2.30 [5]
Mathewson and Myers [5]	552	13.3	2.13	1.41[d]	0.52	128	1.65	1.63 [5]
Benbow and Lynch [14]	4.2	12.7	1.94	1.55 (input)[e]	1.10	60	3.25	
Smith and Segall [15]	RT	12.5 ± 0.3	1.88 ± 0.09	1.60 ∓ 0.08	1.06 ± 0.12	63 ∓ 7	3.00 ± 0.3	3.18 [16]–3.28 [17]

[a] See Eqs. (1)–(4) in the text.

[b] The effective density of electrons n_{eff} is given in electrons per atom (e/at.). In aluminum the actual density of conduction electrons is 3 e/at. The optical conductivity at $\omega = 0$ has been calculated from Eq. (5); the electrical values of $\sigma(0)$ are for dc measurements on bulk samples.

[c] The measured bulk value of $\sigma(0)$ was used to fix the ratio Ω_p^2/γ via Eq. (5).

[d] Evaluated by fitting the interband absorption and use of Eq. (42) of Ashcroft and Sturm [18].

[e] Assumed on the basis of a fit by Ashcroft and Sturm [18].

TABLE XII

The Optical Constants n and k and Reflectivity of Evaporated Metallic Aluminum Films at Room Temperature from 32 μm to the $L_{II,III}$ Edge[a,b]

eV	cm^{-1}	μm	n	n	k	k	R	R	R	R_{hv}
75		0.01653	1.01 [7]		2.40×10^{-2} [7]		1.74×10^{-4} [7]			
74		0.01676	1.01		2.42×10^{-2}		1.97			
73		0.01698	1.02		1.91×10^{-2}		2.33×10^{-4}			
72		0.01722	1.02		3.46×10^{-3}		6.85×10^{-5}			
71		0.01746	1.01		3.46		2.75			
70		0.01771	1.01		3.52		1.27×10^{-5}			
65		0.01908	0.995		4.17		9.85×10^{-6}			
60		0.02066	0.987		4.41		4.64×10^{-5}			
55		0.02254	0.979		5.08		1.21×10^{-4}			
50		0.02480	0.969		5.87		2.57			
45		0.02755	0.957		6.82		5.01			
40		0.03100	0.940		8.16		9.89×10^{-4}			
38		0.03263	0.931		8.71		1.30×10^{-3}			
36		0.03444	0.921	0.96 [55]	9.32×10^{-3} [7]	9.5×10^{-3} [55]	1.73	4.40×10^{-4} [55]		
34		0.03647	0.909		1.02×10^{-2}		2.33			
33		0.03757	0.902	0.943	1.07	1.10×10^{-2}	2.71	8.93×10^{-4}		
32		0.03875	0.894		1.11		3.17			
31		0.04000	0.885		1.16		3.75			

(*continued*)

[a] Columns labeled [7] are the composite data of Shiles *et al.* [7]; the values tabulated are based primarily on the Kramers-Kronig analysis of reflectance measurements of uhv films from 32 to 0.1 μm. The uhv reflectance data of Bennett *et al.* [28], are given in columns labeled [28]. The *in situ* uhv ellipsometric data of Mathewson and Myers [100] are given in columns labeled [100], and the vacuum-UV transmission and angular-dependence-of-reflection measurements of Ditchburn and Freeman [55] are given in columns labeled [55]. Composite reflectance values for films evaporated in high vacuum and measured in air, R_{hv}, are given in columns labeled [142]. These data are taken from Smith *et al.* [142] and are also shown as the "high vacuum" curve in Fig. 12. The reflectance of these oxidized films is not unique. However, films prepared by rapid evaporation in high vacuum and exposed to a normal laboratory environment are generally reported to have reflectances throughout the IR and visible which are roughly 1% below the values for smooth, unoxidized films prepared in uhv. At higher energies, the high-vacuum films show a sharp fall-off in reflectance because of surface-oxide absorption and because of the scattering and surface-plasmon absorption caused by surface roughness. A wide range of optical properties is generally observed in the ultraviolet unless special precautions are taken to control the film's surface roughness.

[b] A tabulation of optical constants at energies higher than those given here is available in Reference 142.

TABLE XII (*Continued*)

Metallic Aluminum

eV	cm^{-1}	μm	n	n	k	k	R	R	R	R_{hv}
30		0.04133	0.876	0.912	1.25	1.25×10^{-2}	4.44	2.16×10^{-3}		
29		0.04275	0.865		1.35		5.28			
28		0.04428	0.854	0.880	1.45	1.41	6.30	4.13		
27		0.04592	0.841		1.55		7.58			
26		0.04769	0.826	0.838	1.65	1.59	9.20×10^{-3}	7.84×10^{-3}		
25		0.04959	0.809		1.77		1.13×10^{-2}			
24		0.05166	0.789	0.785	1.90	1.82	1.40	1.46×10^{-2}		
23		0.05391	0.766		2.05		1.77			
22		0.05636	0.740	0.718	2.22	2.13	2.26	2.71		
21		0.05904	0.707		2.42		2.96			
20		0.06199	0.668	0.635	2.68	2.67	3.98	5.01		
19.5		0.06358	0.646		2.84		4.67			
19		0.06526	0.620	0.580	3.02	3.07	5.54	7.10×10^{-2}		
18.5		0.06702	0.591		3.24		6.64			
18		0.06888	0.558	0.520	3.48	3.55	8.09×10^{-2}	0.10		
17.5		0.07085	0.520		3.81		0.100			
17		0.07293	0.474	0.445	4.23	4.24	0.128	0.148		
16.5		0.07514	0.419		4.87		0.168			
16		0.07749	0.351	0.345	5.95	6.32×10^{-2}	0.233	0.239		
15.5		0.07999	0.258		7.77×10^{-2}		0.350			
15		0.08266	0.125	0.225	0.153	0.220	0.612	0.419		0.050 [142]
14.5		0.08551	0.0616		0.301		0.798			0.057
14		0.08856	0.0481		0.416		0.849			0.064
13.5		0.09184	0.0409	0.104	0.517	0.390	0.879	0.697		0.074
13		0.09537	0.0376		0.609		0.896			0.086
12.5		0.09919	0.0344		0.700		0.912			0.102
12	96,790	0.1033	0.0328	0.033	0.791	0.580	0.922	0.906		0.127
11.5	92,750	0.1078	0.0331		0.883		0.928			0.165

11	88,720	0.1127	0.0356	0.978	0.930		0.215
10.5	84,690	0.1181	0.0396	1.08	0.929		0.270
10	80,660	0.1240	0.0442	1.18	0.929		0.328
9.5	76,620	0.1305	0.0495	1.29	0.928		0.388
9	72,590	0.1378	0.0557	1.40	0.928		0.448
8.75	70,570	0.1417	0.0592	1.46	0.927		0.478
8.5	68,560	0.1459	0.0630	1.53	0.927		0.510
8.25	66,540	0.1503	0.0671	1.59	0.927		0.543
8	64,520	0.1550	0.0716	1.66	0.927		0.579
7.75	62,510	0.1600	0.0765	1.74	0.927		0.616
7.5	60,490	0.1653	0.0820	1.81	0.927		0.656
7.25	58,480	0.1710	0.0880	1.90	0.926		0.698
7	56,460	0.1771	0.0946	1.98	0.926		0.735
6.75	54,440	0.1837	0.102	2.07	0.926		0.766
6.5	52,430	0.1907	0.110	2.17	0.926		0.793
6.25	50,410	0.1984	0.119	2.28	0.926		0.820
6	48,390	0.2066	0.130	2.39	0.926		0.841
5.75	46,380	0.2156	0.141	2.51	0.926		0.858
5.5	44,360	0.2254	0.155	2.64	0.926		0.873
5.25	42,340	0.2362	0.172	2.79	0.925		0.884
5	40,330	0.2480	0.190	2.94	0.924		0.894
4.75	38,310	0.2610	0.209	3.11	0.925		0.901
4.5	36,300	0.2755	0.233	3.30	0.925		0.905
4.25	34,280	0.2917	0.261	3.51	0.925		0.908
4.133	33,330	0.300	0.276	3.61	0.925	0.9208 [28]	0.909
4	32,260	0.3100	0.294	3.74	0.925		0.910
3.9	31,460	0.3179	0.310	3.84	0.925		0.911
3.8	30,650	0.3263	0.326	3.95	0.925		0.912
3.7	29,840	0.3351	0.344	4.06	0.925		0.913
3.6	29,040	0.3444	0.364	4.17	0.925		0.913
3.542	28,570	0.350	0.375	4.24	0.925	0.9205	0.914
3.5	28,230	0.3542	0.385	4.30	0.925		0.914

(*continued*)

TABLE XII (*Continued*)

Metallic Aluminum

eV	cm^{-1}	μm	n	n	k	k	R	R	R	R_{hv}
3.4	27,420	0.3647	0.407		4.43		0.924			0.914
3.3	26,620	0.3757	0.432		4.56		0.924			0.915
3.2	25,810	0.3875	0.460		4.71		0.924			0.915
3.1	25,000	0.400	0.490		4.86		0.924	0.9194		0.915
3.0	24,200	0.4133	0.523		5.02		0.924			0.914
2.9	23,390	0.4275	0.558		5.20		0.924			0.914
2.8	22,580	0.4428	0.598		5.38		0.924			0.913
2.755	22,220	0.450	0.618		5.47		0.924	0.9175		0.913
2.7	21,780	0.4592	0.644		5.58		0.924			0.913
2.6	20,970	0.4769	0.695		5.80		0.924			0.912
2.5	20,160	0.4959	0.755	0.779 [100]	6.03	5.84 [100]	0.923		0.916 [100]	0.911
2.480	20,000	0.500	0.769		6.08		0.923	0.9162		0.911
2.45	19,760	0.5061	0.789	0.818	6.15	5.93	0.923		0.915	0.911
2.4	19,360	0.5166	0.826	0.852	6.28	6.10	0.923		0.916	0.910
2.35	18,950	0.5276	0.867	0.891	6.42	6.23	0.922		0.916	0.909
2.3	18,550	0.5391	0.912	0.944	6.55	6.36	0.922		0.915	0.909
2.254	18,180	0.550	0.958		6.69		0.921	0.9157		0.908
2.25	18,150	0.5510	0.963	1.00	6.70	6.52	0.921		0.914	0.908
2.2	17,740	0.5636	1.02	1.07	6.85	6.64	0.920		0.912	0.907
2.15	17,340	0.5767	1.08	1.15	7.00	6.77	0.919		0.909	0.906
2.1	16,940	0.5904	1.15	1.22	7.15	6.93	0.918		0.908	0.905
2.066	16,670	0.600	1.20		7.26		0.917	0.9117		0.904
2.05	16,530	0.6048	1.22	1.31	7.31	7.09	0.916		0.906	0.904
2.0	16,130	0.6199	1.30	1.40	7.48	7.21	0.915		0.903	0.903
1.95	15,730	0.6358	1.39	1.51	7.65	7.37	0.913		0.900	0.901
1.908	15,390	0.650	1.47		7.79		0.912	0.9057		0.899
1.9	15,320	0.6526	1.49	1.63	7.82	7.49	0.912		0.897	0.899

1.85	14,920	0.6702	1.60	1.78	8.01	7.66	0.910		0.893	0.896
1.8	14,520	0.6888	1.74	1.94	8.21	7.83	0.907		0.889	0.893
1.771	14,290	0.700	1.83		8.31		0.905	0.8977		0.890
1.75	14,120	0.7085	1.91	2.13	8.39	8.00	0.903		0.885	0.888
1.7	13,710	0.7293	2.14	2.34	8.57	8.15	0.897		0.880	0.882
1.653	13,330	0.750	2.40		8.62		0.888	0.8862		0.876
1.65	13,310	0.7514	2.41	2.57	8.62	8.25	0.888		0.873	0.876
1.6	12,905	0.7749	2.63	2.87	8.60	8.23	0.879	0.8773	0.861	0.868
1.55	12,500	0.7999	2.80	3.04	8.45	8.08	0.869	0.8676	0.851	0.860
1.503	12,120	0.825	2.75		8.31		0.868	0.8657		0.858
1.5	12,100	0.8266	2.74	2.94	8.31	7.76	0.868		0.845	0.858
1.459	11,770	0.850	2.61		8.22		0.870	0.8677		0.859
1.45	11,700	0.8551	2.58	2.53	8.21	7.61	0.872		0.856	0.860
1.417	11,430	0.875	2.38		8.18			0.878	0.8744	0.868
1.4	11,290	0.8856	2.24	2.14	8.21	7.75	0.885		0.878	0.874
1.378	11,110	0.900	2.06		8.30		0.895	0.8908		0.884
1.35	10,890	0.9184	1.86	1.82	8.44	8.14	0.906		0.902	0.897
1.340	10,810	0.925	1.77		8.49		0.911	0.9075		0.902
1.305	10,530	0.950	1.49		8.88		0.930	0.9243		0.916
1.3	10,490	0.9537	1.47	1.58	8.95	8.69	0.932		0.923	0.918
1.25	10,080	0.9919	1.37	1.41	9.49	9.19	0.943		0.937	0.932
1.240	10,000	1.000	1.35		9.58		0.944	0.9402		0.934
1.2	9,679	1.033	1.26	1.32	10.0	9.73	0.952		0.947	0.942
1.15	9,275	1.078	1.21	1.25	10.6	10.3	0.958		0.955	0.948
1.1	8,872	1.127	1.20	1.23	11.2	10.9	0.963		0.960	0.953
1.05	8,469	1.181	1.21	1.22	11.8	11.6	0.967		0.965	0.957
1.033	8,333	1.200	1.21		12.0		0.968	0.9637		0.958
1	8,066	1.240	1.21	1.25	12.5	12.2	0.970		0.967	0.960
0.95	7,662	1.305	1.23	1.30	13.2	12.9	0.973		0.970	0.963
0.9	7,259	1.378	1.26	1.35	14.0	13.7	0.975		0.972	0.964
0.85	6,856	1.459	1.33	1.43	14.9	14.5	0.977		0.974	0.966
0.8266	6,667	1.500	1.38		15.4		0.977	0.9742		0.967

(*continued*)

TABLE XII (*Continued*)

Metallic Aluminum

eV	cm^{-1}	μm	n	n	k	k	R	R	R	R_{hv}
0.8	6,452	1.550	1.44	1.50	16.0	15.5	0.978		0.976	0.967
0.75	6,049	1.653	1.59	1.59	17.1	16.5	0.979		0.977	0.968
0.7	5,646	1.771	1.77	1.75	18.3	17.8	0.979		0.978	0.969
0.65	5,243	1.907	1.99		19.8		0.980			0.970
0.6199	5,000	2.0	2.15		20.7		0.980	0.9779		0.970
0.6	4,839	2.065	2.27		21.4		0.981			0.970
0.55	4,436	2.254	2.62		23.3		0.981			0.971
0.5	4,033	2.480	3.07		25.6		0.982			0.972
0.45	3,629	2.755	3.68		28.3		0.982			0.973
0.4133	3,333	3.0	4.24		30.6		0.982	0.9805		0.973
0.4	3,226	3.100	4.45		31.5		0.983			0.974
0.375	3,025	3.306	4.88		33.4		0.983			0.974
0.35	2,823	3.542	5.44		35.6		0.983			0.975
0.325	2,621	3.815	6.00		38.1		0.984			0.975
0.3100	2,500	4.0	6.43		39.8		0.984	0.9826		0.975
0.3	2,420	4.133	6.76		41.0		0.984			0.976
0.275	2,218	4.509	7.61		44.3		0.985			0.976
0.25	2,016	4.959	8.59		48.2		0.986			0.977
0.2480	2,000	5.0	8.67		48.6		0.986	0.9843		0.977
0.225	1,815	5.510	9.85		53.2		0.987			0.977
0.2066	1,667	6.0	11.1		57.6		0.987	0.9856		0.978
0.2	1,613	6.199	11.7		59.4		0.987			0.978
0.19	1,532	6.526	12.7		62.2		0.987			0.978
0.18	1,452	6.888	13.7		65.2		0.988			0.979
0.1771	1,429	7.0	14.0		66.2		0.988	0.9866		0.979
0.17	1,371	7.293	14.9		68.8		0.988			0.979
0.16	1,290	7.749	16.5		72.7		0.988			0.980
0.1550	1,250	8.0	17.5		74.9		0.988	0.9872		0.980

0.15	1,210	8.266	18.6	77.0	0.988		0.980
0.14	1,129	8.856	20.9	81.5	0.988		0.980
0.1378	1,111	9.0	21.5	82.6	0.988	0.9874	0.980
0.13	1,049	9.537	23.5	86.5	0.988		0.981
0.1240	1,000	10.0	25.3	89.8	0.988	0.9876	0.981
0.12	967.9	10.33	26.6	92.2	0.989		0.981
0.1127	909.1	11.0	29.2	96.6	0.989	0.9879	0.982
0.11	887.2	11.27	30.2	98.4	0.989		0.982
0.1033	833.3	12.0	33.0	103	0.989	0.9882	0.982
0.1	806.5	12.40	34.5	106	0.989		0.982
0.09537	769.2	13.0	36.6	109	0.989	0.9884	0.982
0.095	766.2	13.05	36.8	110	0.989		0.982
0.09	725.9	13.78	39.7	114	0.989		0.983
0.08856	714.3	14.0	40.5	116	0.989	0.9886	0.983
0.085	685.6	14.59	42.8	119	0.989		0.983
0.08	645.2	15.50	46.0	124	0.990		0.983
0.07749	625.0	16.0	47.7	127	0.990	0.9892	0.983
0.075	604.9	16.53	49.7	129	0.990		0.983
0.07	564.6	17.71	53.8	136	0.990		0.983
0.06888	555.6	18.0	54.7	137	0.990	0.9896	0.983
0.065	524.3	19.07	57.6	143	0.990		0.984
0.06199	500.0	20.0	60.7	147	0.990	0.9902	0.984
0.06	483.9	20.66	62.9	151	0.991		0.984
0.05636	454.6	22.0	66.9	157	0.991	0.9907	0.984
0.055	443.6	22.54	68.3	160	0.991		0.984
0.05166	416.7	24.0	72.2	168	0.991	0.9912	0.984
0.05	403.3	24.80	75.0	172	0.992		0.984
0.04769	384.6	26.0	79.1	178	0.992	0.9918	0.985
0.045	362.9	27.55	84.7	186	0.992		0.985
0.04428	357.1	28.0	86.3	189	0.992	0.9923	0.985
0.04133	333.3	30.0	94.2	199	0.992	0.9928	0.985
0.04	322.6	31.00	98.6	204		0.992	0.985
0.03875	312.5	32.0	103	208	0.992	0.9933	0.985

TABLE XIII

The Dielectric Function for Evaporated Metallic Aluminum Films at Room Temperature from 0.04 to 10,000 eV[a-d]

eV	Å	ε_1	ε_2	eV	Å	ε_1	ε_2
10,000	1.240	0.99999	1.42×10^{-7}	1,556	7.968	0.99982	6.209
9,000	1.378	0.99999	2.16	1,555	7.973	0.99983	5.909
8,000	1.550	0.99998	3.40	1,550	7.999	0.99978	1.200
7,000	1.771	0.99998	5.80×10^{-7}	1,540	8.051	0.99974	1.230
6,000	2.066	0.99997	1.046×10^{-6}	1,530	8.104	0.99971	1.260
5,000	2.480	0.99996	2.08	1,520	8.157	0.99969	1.290
4,000	3.100	0.99993	4.900	1,510	8.211	0.99968	1.324
3,500	3.542	0.99991	8.006×10^{-6}	1,500	8.266	0.99966	1.356
3,000	4.133	0.99988	1.420×10^{-5}	1,450	8.551	0.99961	1.560
2,500	4.959	0.99983	2.718	1,400	8.856	0.99957	1.780
2,000	6.199	0.99974	6.406	1,300	9.537	0.99947	2.319
1,900	6.526	0.99972	7.691	1,200	10.33	0.99936	3.119
1,800	6.888	0.99970	9.426×10^{-5}	1,100	11.27	0.99922	4.312
1,700	7.293	0.99968	1.159×10^{-4}	1,000	12.40	0.99904	6.222
1,650	7.514	0.99968	1.309	900	13.78	0.99879	9.355×10^{-5}
1,600	7.749	0.99970	1.476	800	15.50	0.99845	1.462×10^{-4}
1,590	7.798	0.99971	1.520	700	17.71	0.99796	2.363
1,580	7.847	0.99973	1.570	600	20.66	0.99717	4.408
1,570	7.897	0.99976	1.622	500	24.80	0.99590	8.695×10^{-4}
1,565	7.922	0.99979	1.686	400	31.00	0.99378	1.939×10^{-3}
1,564	7.927	0.99981	1.709	300	41.33	0.9898	4.684
1,563	7.933	0.99983	1.636	250	49.59	0.9862	8.325×10^{-3}
1,562	7.938	0.99985	1.437	200	61.99	0.9820	1.490×10^{-2}
1,561	7.943	0.99985	1.220	190	65.26	0.9810	1.680
1,560	7.948	0.99985	1.000×10^{-4}	180	68.88	0.9797	1.913
1,559	7.953	0.99985	8.229×10^{-5}	170	72.93	0.9776	2.174
1,558	7.958	0.99984	6.583	160	77.49	0.9785	2.718
1,557	7.963	0.99983	5.860	150	82.68	0.9791	2.925

145	85.51	0.9782	3.055×10^{-2}	88	140.9	1.010	5.823×10^{-2}
140	88.56	0.9772	3.225	86	144.2	1.011	5.680
135	91.84	0.9756	3.511	84	147.6	1.013	5.402
130	95.37	0.9746	4.070	82	151.2	1.014	5.129
125	99.19	0.9780	4.634	80	155.0	1.013	4.928
120	103.3	0.9814	4.769	79	156.9	1.013	4.933
115	107.8	0.9840	4.947	78	159.0	1.014	4.987
110	112.7	0.9871	5.059	77	161.0	1.018	5.082
105	118.1	0.9860	4.850	76	163.1	1.020	4.818
100	124.0	0.9804	5.927	75.5	164.2	1.021	4.841
98	126.5	0.9832	6.559	75	165.3	1.022	4.856
96	129.2	0.9915	7.150	74.5	166.4	1.025	4.928
94	131.9	0.9998	7.066	74	167.5	1.029	4.904
92	134.8	1.007	6.706	73.9	167.8	1.030	4.915
90	137.8	1.010	6.218	73.8	168.0	1.031	4.928

(*continued*)

[a] Based on Shiles *et al.* [7].

[b] These data are based primarily on the analysis of reflectance measurements below the $L_{II,III}$ edge and on transmission measurements above the edge. They are in close agreement with direct ellipsometric measurements on oxide-free films by Mathewson and Myers [100] in the range 0.7 to 2.5 eV (see Table XII). Suggested extrapolations are given in the footnotes *c* and *d*.

[c] Low-energy extrapolations. The room-temperature dielectric function presented here may be extrapolated to lower energies by using the Drude model [Eq. (1)] with $\hbar\Omega_p = 11.5$ eV and $\hbar\gamma = 50.6$ meV [$\sigma(0) = 3.16 \times 10^{17}$ sec^{-1}]. This extrapolation fits on continuously at 0.04 eV, but with a small discontinuity in slope. However, it should be recognized that, while the dc conductivity is in excellent agreement with the measured value ($3.18 - 3.28 \times 10^{17}$ sec^{-1}) [16, 17], Ω_p and γ are somewhat outside the range recommended by Smith and Segall [5] (see Table XI). This represents a negligible conflict since, for the high reflectances (>99%) beyond 20 μm, the experimental error ($\pm 0.1\%$) in the reflectance measurements used to obtain the dielectric function translates into an uncertainty of the order of $\pm 25\%$ in $\varepsilon(\omega)$ even in favorable cases. The values of Smith and Segall [15] arise from fits over the range 0.04–3 eV, not just the lowest energy point, which is subject to considerable uncertainty.

[d] High-energy extrapolations. For $\varepsilon_1(\omega)$: at frequencies well above the K edge the real part of the dielectric function approaches $\varepsilon_1 \approx 1 - \omega_{p,t}^2/\omega^2$, where $\omega_{p,t}$ is the plasma frequency for the *total* electron density (13 e/at.). For aluminum at room temperature $\omega_{p,t} \approx 32.86$ eV and the asymptotic region is achieved by $\omega \simeq 3000$ eV. For $\varepsilon_2(\omega)$: beyond the K edge $\varepsilon_2(\omega)$ falls off very nearly as a power of energy $\varepsilon_2(\omega) \sim \omega^{-\delta}$. The exponent varies slowly with energy. At 5000 eV, $\delta \sim 3.8$; at 10^4 eV, $\delta \sim 4.0$; and from 10^4 to 10^5 eV, it increases to $\delta = 4.2$. An extrapolation from 10^4 eV using $\delta = 4.1$ reproduces photoelectric data up to 10^5 eV reasonably well. Theory predicts an asymptotic value of $\delta = 4.5$ [143].

TABLE XIII (*Continued*)

Metallic Aluminum

eV	Å	ε_1	ε_2	eV	Å	ε_1	ε_2
73.7	168.2	1.032	4.949×10^{-2}	55	225.4	0.9581	9.942×10^{-3}
73.6	168.5	1.033	4.976	50	248.0	0.9389	1.138×10^{-2}
73.5	168.7	1.035	5.048	45	275.5	0.9153	1.304
73.4	168.9	1.038	5.177	40	310.0	0.8827	1.533
73.3	169.1	1.043	5.308	35	354.2	0.8368	1.797
73.2	169.4	1.050	4.955	30	413.3	0.7665	2.197
73.1	169.6	1.052	3.998	25	495.9	0.6536	2.863
73	169.8	1.049	3.910	20	619.9	0.4460	3.582
72.9	170.1	1.051	4.089	19	652.6	0.3835	3.745
72.8	170.3	1.061	4.118	18	688.8	0.3103	3.885
72.7	170.5	1.069	2.549×10^{-2}	17	729.3	0.2232	4.013
72.6	170.8	1.061	8.139×10^{-3}	16	774.9	0.1195	4.174
72.5	171.0	1.050	7.264	15.8	784.7	0.09693	4.161
72.4	171.3	1.044	6.789	15.6	794.8	0.07327	4.081
72.3	171.5	1.040	6.871	15.4	805.1	0.04769	3.941
72.2	171.7	1.037	6.940	15.2	815.7	0.02019	3.855
72.1	172.0	1.035	6.949	15.0	826.6	−0.007825	3.834
72	172.2	1.033	7.042	14.8	837.7	−0.03727	3.613
71	174.6	1.020	6.982	14.6	849.2	−0.07038	3.644
70	177.1	1.012	7.086	14.4	861.0	−0.1033	3.802
68	182.3	1.002	7.339	14.2	873.1	−0.1365	3.928
66	187.9	0.9940	7.776	14.0	885.6	−0.1712	4.011
64	193.7	0.9876	8.204	13.5	918.4	−0.2656	4.229
62	200.0	0.9810	8.457	13.0	953.7	−0.3701	4.588
60	206.6	0.9746	8.709	12.5	991.9	−0.4887	4.814
eV	μm	ε_1	ε_2	eV	μm	ε_1	ε_2
12.0	0.1033	−0.6241	5.190×10^{-2}	1.90	0.6526	−58.96	23.28
11.5	0.1078	−0.7794	5.854	1.85	0.6702	−61.65	25.72

11.0	0.1127	−0.9562	6.971×10^{-2}	1.80	0.6888	−64.29	28.57
10.5	0.1181	−1.157	8.517×10^{-2}	1.75	0.7085	−66.68	32.00
10.0	0.1240	−1.386	0.1042	1.70	0.7293	−68.91	36.74
9.5	0.1305	−1.651	0.1273	1.65	0.7514	−68.52	41.61
9.0	0.1378	−1.962	0.1560	1.60	0.7749	−67.03	45.13
8.5	0.1459	−2.327	0.1922	1.58	0.7847	−66.27	46.67
8.0	0.1550	−2.762	0.2381	1.56	0.7948	−64.31	47.38
7.5	0.1653	−3.285	0.2974	1.54	0.8051	−62.95	47.06
7.0	0.1771	−3.923	0.3753	1.52	0.8157	−62.05	46.39
6.5	0.1907	−4.711	0.4791	1.50	0.8266	−61.50	45.61
6.0	0.2066	−5.700	0.6208	1.48	0.8377	−60.96	44.56
5.5	0.2254	−6.965	0.8192	1.46	0.8492	−60.71	43.08
5.0	0.2480	−8.617	1.120	1.44	0.8610	−60.94	41.51
4.5	0.2755	−10.83	1.538	1.42	0.8731	−61.07	39.28
4.0	0.3100	−13.90	2.203	1.40	0.8856	−62.42	36.74
3.8	0.3263	−15.47	2.575	1.38	0.8984	−64.45	34.50
3.6	0.3444	−17.29	3.035	1.36	0.9117	−66.70	32.54
3.4	0.3647	−19.42	3.606	1.34	0.9253	−69.01	30.03
3.2	0.3875	−21.95	4.327	1.32	0.9393	−72.93	27.48
3.0	0.4133	−24.97	5.258	1.30	0.9537	−77.92	26.28
2.9	0.4275	−26.71	5.800	1.28	0.9686	−82.27	26.11
2.8	0.4428	−28.64	6.440	1.26	0.9840	−86.20	26.10
2.7	0.4592	−30.78	7.188	1.24	0.9999	−89.97	25.92
2.6	0.4769	−33.15	8.066	1.22	1.016	−93.97	25.47
2.5	0.4959	−35.81	9.111	1.20	1.033	−98.61	25.23
2.4	0.5166	−38.79	10.38	1.15	1.078	−110.5	25.66
2.3	0.5391	−42.13	11.96	1.10	1.127	−123.6	26.86
2.2	0.5636	−45.83	13.94	1.05	1.181	−137.7	28.45
2.1	0.5904	−49.86	16.43	1.00	1.240	−153.9	30.21
2.0	0.6199	−54.24	19.50	0.95	1.305	−172.8	32.45
1.95	0.6358	−56.52	21.25	0.90	1.378	−195.0	35.45

(*continued*)

TABLE XIII (*Continued*)

Metallic Aluminum

eV	μm	ε_1	ε_2	eV	μm	ε_1	ε_2
0.85	1.459	−221.5	39.82	0.23	5.391	−2,622	994.9
0.80	1.550	−252.5	46.07	0.22	5.636	−2,845	1,104
0.75	1.653	−289.0	54.33	0.21	5.904	−3,096	1,231
0.70	1.771	−332.8	64.88	0.20	6.199	−3,387	1,393
0.65	1.907	−386.4	78.53	0.19	6.526	−3,703	1,578
0.60	2.066	−452.9	97.30	0.18	6.888	−4,065	1,791
0.55	2.254	−536.6	122.2	0.17	7.293	−4,512	2,054
0.50	2.480	−645.0	157.2	0.16	7.749	−5,016	2,407
0.45	2.755	−785.7	208.3	0.15	8.266	−5,578	2,859
0.40	3.100	−971.5	280.4	0.14	8.856	−6,205	3,410
0.39	3.179	−1,018	296.8	0.13	9.537	−6,930	4,065
0.38	3.263	−1,068	315.8	0.12	10.33	−7,787	4,899
0.37	3.351	−1,122	337.7	0.11	11.27	−8,769	5,940
0.36	3.444	−1,178	361.8	0.10	12.40	−9,964	7,279
0.35	3.542	−1,238	387.1	0.095	13.05	−10,720	8,080
0.34	3.647	−1,302	413.6	0.090	13.78	−11,450	9,049
0.33	3.757	−1,374	441.6	0.085	14.59	−12,260	10,160
0.32	3.875	−1,454	473.8	0.080	15.50	−13,210	11,380
0.31	4.000	−1,540	511.5	0.075	16.53	−14,290	12,860
0.30	4.133	−1,632	553.7	0.070	17.71	−15,470	14,580
0.29	4.275	−1,731	598.7	0.065	19.07	−16,990	16,420
0.28	4.428	−1,841	647.0	0.060	20.66	−18,790	18,960
0.27	4.592	−1,964	701.3	0.055	22.54	−20,840	21,810
0.26	4.769	−2,098	760.6	0.050	24.80	−24,030	25,830
0.25	4.959	−2,253	828.3	0.045	27.55	−27,580	31,590
0.24	5.166	−2,424	905.2	0.040	31.00	−31,770	40,170

Cadmium Telluride (CdTe)

EDWARD D. PALIK
Naval Research Laboratory
Washington, D.C. 20375

The UV–visible spectrum has been measured by wavelength ellipsometry by Marple and Ehrenreich [1] in the 5–1.5-eV region. Samples were high-resistivity, single crystals with cleaved surfaces. The measurements were completed in less than an hour after cleavage in air. The temperature was 300 K. The reflectivity has been measured to higher photon energies, but no Kramers–Kronig analysis was done [2]. The positions of peaks in ε_1 and ε_2 were in agreement with reflectivity peaks. Table I lists n and k as determined from reading the graph in Marple and Ehrenreich [1]. Figure 1 shows n and k.

Myers *et al.* [3] have measured n and k for both single crystals and polycrystalline film samples in the region 0.45–1.9 μm. The films were made by sublimation of the compound with deposition on heated fused-quartz substrates. Their resistivities were $>10^8\ \Omega$ cm. Films of cubic structure as well as films with mixed cubic-hexagonal structure were produced. However, the percentage mixture was not clearly determined. The thin-film constants were determined directly from measurements of R (at 6° by using an absolute reflectance attachment) and T. As expected, the constants varied with substrate preparation temperature and probably with cubic-hexagonal mixing. Roughly, the higher the temperature, the larger was n, while the reverse was true for k. The single-crystal material was mechanically polished with 0.25-μm grit. Only the reflectance was measured directly. In this case average values of k for the films were assumed, and then n was calculated. This was a reasonable assumption, since $n > k$ (~ 3 compared to ~ 0.4 at 0.5 μm). For the deposited films k ranged from 0.35 to 0.45 at 0.5 μm, for example, while its value from Marple and Ehrenreich [1] is 0.5. We have chosen to list the single-crystal data of Myers *et al.* [3] for n for comparison with the data of Marple and Ehrenreich [1]. In the transparent region to 1.9 μm, the n values [3] agree with Marple's values [4] to ~ 0.01. In the opaque region, they are lower than the values of Marple and Ehrenreich [1] by ~ 0.1. We also list an average k determined for films because of the peculiar behavior of k of

HANDBOOK OF OPTICAL CONSTANTS OF SOLIDS ISBN 0-12-544420-6

Marple and Ehrenreich [1] near the fundamental band gap; also the film data tend to extrapolate to agree with data of Marple [5].

The absorption at the fundamental band edge was measured by Marple [5] and Konak *et al.* [6]. In Marple's [5] research a series of slab samples were mechanically polished with Linde A to thicknesses of 3 mm to 100 μm and then chemically polished to remove 10 μm of additional material. Temperature was 297 K. The results of Marple's [5] findings, which are tabulated, and those of Konak *et al.* [6] were reasonably close at 1.47 eV within 20%, but below 1.43 eV they deviated to a factor of 4. Konak *et al.*'s [6] k value remains excessively high, suggesting impurity- and defect-absorption problems.

Marple [4] measured the refractive index by minimum deviation with a prism made of melt-grown material with mechanically polished surfaces. The data in the 1.45–0.5-eV region were fitted with the formula

$$n^2 = A + [B\lambda^2]/[\lambda^2 - C^2], \tag{1}$$

with $A = 5.68$, $B = 1.53$, and $C^2 = 0.366\ \mu\text{m}^2$. Notice that at large λ, $n^2 \to A + B = 7.21 = \varepsilon_\infty$, the high-frequency dielectric constant often used in the Lorentz- oscillator-model equation given later. Random error in n was quoted as ± 0.001, while systematic error was ± 0.002.

Pikhtin and Yas'kov [7] have refitted these data with a more detailed oscillator-model formula of the form

$$n^2 = 1 + \frac{A}{\pi} \ln \frac{E_1^2 - (\hbar\omega)^2}{E_0^2 - (\hbar\omega)^2} + \frac{G_1}{E_1^2 - (\hbar\omega)^2} + \frac{G_2}{E_2^2 - (\hbar\omega)^2} + \frac{G_3}{E_3^2 - (\hbar\omega)^2}, \tag{2}$$

with $E_0 = 1.5$ eV, $E_1 = 3.5$ eV, $E_2 = 5.5$ eV, $E_3 = 17.4 \times 10^{-3}$ eV, $G_1 = 64.375\ \text{eV}^2$, $G_2 = 17.664\ \text{eV}^2$, $G_3 = 1.08 \times 10^{-3}\ \text{eV}^2$, $A = 0.7\sqrt{E_0} = 0.857$. A lattice-vibration term G_3 presumably improves the fit at lower energy. We have listed these values of n for the spectral region 1.45–0.05 eV. Where they overlap Marple's data [4], they are in agreement to ± 0.003.

Danielewicz and Coleman [8] quote n data of Ladd [9] for hot-pressed CdTe in the near infrared at 300 K and have fitted it with an oscillator model together with their single-crystal n data in the 15–45-cm^{-1} region. We list n for some near-infrared wavelengths for comparison with the results of Pikhtin and Yas'kov [7]. Agreement is usually to one digit or better in the third significant figure. However, the agreement among three types of CdTe samples in Ladd [9], Harvey and Wolfe [10], and De Bell *et al.* [11] at 8 μm, for example, suggests that the n values of Pihktin and Yas'kov [7] are about 0.01 too small at the longer wavelengths.

The far IR has been studied by Danielewicz and Coleman [8], Mitsuishi *et al.* [12, 13], Manabe *et al.* [14, 15], Vodop'yanov *et al.* [16], and Johnson *et al.* [17]. The reststrahlen reflectivity spectrum has been measured at 300 K at an angle of incidence of 12° [12, 14]. The surface was mechanically polished. The reflectivity was fitted by using both KK analysis and an oscillator-model fit [12, 14]. The resultant values of n and k agree to $\pm 30\%$ in the spectral

region 50–75 μm. The oscillator-model fit is listed in Table I. It is obtained with the formula

$$(n - ik)^2 = \varepsilon_\infty \left[1 + \frac{(\omega_L^2 - \omega_T^2)}{\omega_T^2 - \omega^2 + i\Gamma\omega} \right], \tag{3}$$

with the parameters $\varepsilon_\infty = 7.1$, $\omega_T = 141\ \text{cm}^{-1}$, $\omega_L = 169\ \text{cm}^{-1}$, and $\Gamma = 6.6\ \text{cm}^{-1}$; T = transverse and L = longitudinal. We have allowed some overlap with the n of Pikhtin and Yas'kov [7] for comparison.

While we have concentrated on the oscillator fit to reflectivity, which is in reasonable agreement with the KK analysis, Birch and Murray [18] have carried out asymmetric Fourier-transform spectroscopy at 290 K to obtain directly the complex dielectric function (or complex refractive index). Their n and k data show ripples that have been analyzed in detail as multiphonon structure below and above the resonant frequency [19]. The complex frequency-dependent dielectric function is given as

$$\varepsilon(\nu) = \varepsilon_\infty + \frac{(\varepsilon_0 - \varepsilon_\infty)\nu(oj)^2}{\nu(oj)^2 - \nu^2 + 2\nu(oj)[\Delta(oj, \nu) - i\Gamma(oj, \nu)]}, \tag{4}$$

where $\nu(oj)$ is the harmonic frequency of the TO phonon and Δ and Γ are the real and imaginary parts, respectively, of the irreducible self-energy of the TO phonon. After determining ε experimentally, analysis gives Γ, which suppresses the TO resonance but shows much weak structure that can be assigned to a large number of multiphonon modes through which the TO phonon decays. We have determined the values of n and k in the reststrahlen region by reading a graph but smoothing out the ripples and therefore losing the details. These are listed in Table I and are probably the best numbers in this spectral region. While we have plotted the oscillator fit in the region 180–120 cm^{-1} (55.56–83.33 μm), there is no difference on the coarse scale of the graph. However, at longer wavelengths to 125 μm, the values are larger than the oscillator fit and begin to approach the data of Manabe *et al.* [15] somewhat better than the oscillator fit.

Danielewicz and Coleman [8] and Johnson *et al.* [17] fitted n data on both sides of ω_T with similar Lorentz oscillators as Manabe *et al.* [14] and obtained similar parameters. In view of the fact that the data of Manabe *et al.* [14] fit the experimental reflectivity over a wider range and that we do not know how well the other two fits of n actually fit the reflectivity, we chose to tabulate the data of Manabe *et al.* [14].

Vodop'yanov *et al.* [16] did a more detailed study of the reststrahlen spectrum that demonstrated changes in R with surface preparation and analyzed R by KK analysis. Unfortunately, they did not present numerical data. They also applied an oscillator model and discussed the frequency dependence of the lattice damping constant, which is neglected in the usual fitting procedure.

Multiphonon absorption straddles the resonant frequency ω_T for many tens of reciprocal centimeters. The two-phonon summation band region from 33 to 52 μm has been measured by transmission at 300 K [15], and the k data as read from a graph are tabulated. The data of Johnson *et al.* [17] and Stafsudd *et al.* [20] are in reasonable agreement with this result. Note that the oscillator-model fit for k is larger than the experimental values at 49 μm, indicating a poor fit. The 20–26-μm region (three-phonon absorption) has been measured by Deutsch [21], who also quotes the absorption coefficient at 10.6 μm. Data of Sherman [22] are quoted in Danielewicz and Coleman [8] for the 22–30-μm region.

The low-frequency region below ω_T has been measured in some detail [8, 15, 17] with transmission samples at 300 K. Some of the k values determined are listed and are to be compared with the oscillator-model values. The samples of Johnson *et al.* [17] had resistivities of $8.5 \times 10^5\ \Omega$ cm. Danielewicz and Coleman [8] made measurements by using the channel-spectrum technique with both Fourier-transform and grating spectrometers. Samples were single crystals with resistivities of $10^8\ \Omega$ cm polished with alumina. They also quote k values that were presumably obtained from thicker samples. The data from different laboratories differ by factors of 2, and it is not clear what structural differences would cause such differences in the optical-phonon features. At longer wavelengths of > 100 μm, some free-carrier absorption might be present.

We have included n data for two other types of CdTe, hot-pressed [9, 10] and chemical vapor deposition (CVD) [11] in the transparent IR region. These measurements, done by a modified minimum-deviation technique [23], give six significant figures. Accuracies are about one part in the fourth decimal place, so that the change in index as a function of temperature could be closely followed.

For the hot-pressed material of Harvey and Wolfe [10] the temperature was 297.5 K. The mean value of dn/dT at 10 μm was 0.951×10^{-4}/K. For the hot-pressed material of Ladd [9] room temperature was not specified. For CVD material the temperature was 300 K. A Sellmeier equation of the following form was fitted to the data:

$$n^2 - 1 = A_1\lambda^2/(\lambda^2 - \lambda_1^2) + A_2\lambda^2/(\lambda^2 - \lambda_2^2), \tag{5}$$

with $A_1 = 6.1977889$, $A_2 = 3.2243821$, $\lambda_1^2 = 0.1005326\ \mu\text{m}^2$, and $\lambda_2^2 = 5279.518\ \mu\text{m}^2$. A Herzberger equation gave a similar fit with the residual no more than one part in the fourth decimal place. The temperature coefficient in the range 80–300 K is 1.0×10^{-4}/K.

Table I shows a little systematic variation in n from single crystal to hot pressed to CVD material. Since the temperature varies about three degrees kelvin among these materials the fourth decimal place is touchy.

The far-IR (50–10-cm^{-1}) properties of hot-pressed Irtran VI have been measured by Randall and Rawcliffe [24]. Room temperature was not speci-

fied. The n values are slightly larger in the third significant figure than those of Danielewicz and Coleman [8], but the k values are consistently about a factor of 2 larger than for crystalline material.

REFERENCES

1. D. T. F. Marple and H. Ehrenreich, *Phys. Rev. Lett.* **8**, 87 (1962).
2. M. Cardona and D. C. Greenaway, *Phys. Rev.* **131**, 98 (1963).
3. T. H. Myers, S. W. Edwards, and J. F. Schetzina, *J. Appl. Phys.* **52**, 4231 (1981); T. H. Myers, S. W. Edwards, and J. F. Schetzina, private communication (1983).
4. D. T. F. Marple, *J. Appl. Phys.* **35**, 539 (Part 1) (1964).
5. D. T. F. Marple, *Phys. Rev.* **150**, 728 (1966).
6. C. Konak, J. Dillinger, and V. Prosser, *Proc. II–VI Semiconducting Compounds, 1967 Int. Conf.* (D. G. Thomas, ed.), p. 850, Benjamin, New York, 1967.
7. A. N. Pikhtin and A. D. Yas'kov, *Sov. Phys. Semicond.* **12**, 622 (1978); A. N. Pikhtin and A. D. Yas'kov, *Fiz. Tekh. Poluprovodn.* **12**, 1047 (1978).
8. E. J. Danielewicz and P. D. Coleman, *Appl. Opt.* **13**, 1164 (1974).
9. L. S. Ladd, *Infrared Phys.* **6**, 145 (1966).
10. J. E. Harvey and W. L. Wolfe, *J. Opt. Soc. Am.* **65**, 1267 (1975).
11. A. G. DeBell, E. L. Dereniak, J. Harvey, J. Nissley, J. Palmer, A. Selvarajin, and W. L. Wolfe, *Appl. Opt.* **18**, 3114 (1979).
12. A. Mitsuishi, *J. Phys. Soc. Jpn.* **16**, 533 (1961).
13. A. Mitsuishi, H. Yoshinaga, K. Yata, and A. Manabe, *Jpn. J. Appl. Phys.* **4**, 581 (1965).
14. A. Manabe, A. Mitsuishi, and H. Yoshinga, *Jpn. J. Appl. Phys.* **6**, 593 (1967).
15. A. Manabe, A. Mitsuishi, H. Yoshinaga, Y. Ueda, and H. Sei, *Technol. Rep. Osaka Univ. Jpn.* **17**, 263 (1967).
16. L. K. Vodop'yanov, E. A. Vinogradov, V. V. Kolotkov, and Y. A. Mityagin, *Sov. Phys.-Solid State* **16**, 912 (1974); L. K. Vodop'yanov, E. A. Vinogradov, V. V. Kolotkov, and Y. A. Mityagin, *Fiz. Tverd. Tela.* **16**, 1419 (1974).
17. C. J. Johnson, G. H. Sherman, and R. Weil, *Appl. Opt.* **8**, 1667 (1969).
18. J. R. Birch and D. K. Murray, *Infrared Phys.* **18**, 283 (1978).
19. T. J. Parker, J. R. Birch, and C. L. Mok, *Solid State Commun.* **36**, 581 (1980).
20. O. M. Stafsudd, F. A. Haak, and K. Radisavljevic, *J. Opt. Soc. Am.* **57**, 1475 (1967).
21. T. F. Deutsch, *J. Phys. Chem. Solids* **34**, 2091 (1973).
22. G. H. Sherman, Ph.D. dissertation, University of Illinois, Urbana, Illinois (1972).
23. B. C. Platt, H. W. Jeenogle, J. E. Harvey, R. Korinski, and W. Wolfe, *J. Opt. Soc. Am.* **654**, 1264 (1975).
24. C. M. Randall and R. D. Rawcliffe, *Appl. Opt.* **7**, 213 (1968).

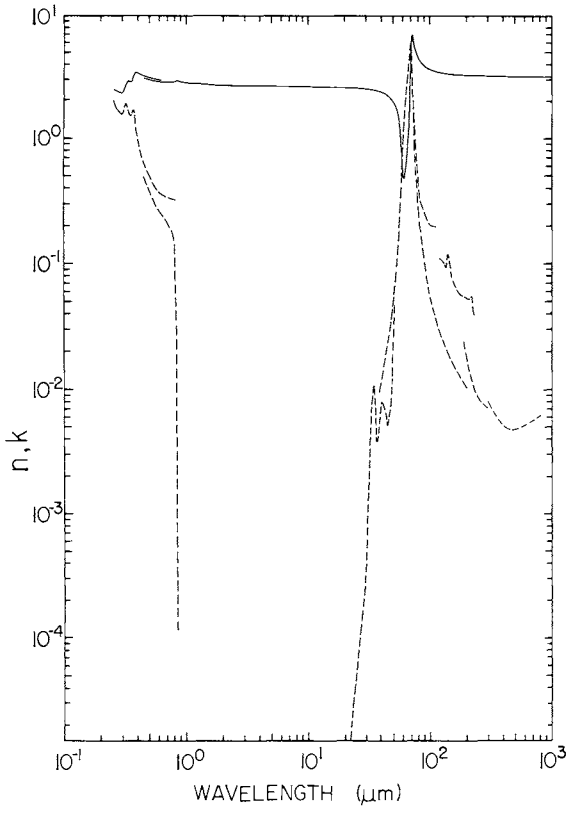

Fig. 1. Log–log plot of n (——) and k (– – – –) versus wavelength in micrometers for cadmium telluride. Data from various references sometimes do not join together in overlap regions.

TABLE I

Values of n and k for Cadmium Telluride Obtained from Various References[a]

eV	cm^{-1}	μm	n	n	n	k	k
4.9	39,520	0.2530	2.48 [1]			2.04 [1]	
4.8	38,710	0.2583	2.49			1.89	
4.7	37,910	0.2638	2.48			1.80	
4.6	37,100	0.2695	2.45			1.73	
4.5	36,290	0.2755	2.43			1.67	
4.4	35,490	0.2818	2.41			1.64	
4.3	34,680	0.2883	2.38			1.60	
4.2	33,880	0.2952	2.36			1.57	
4.1	33,070	0.3024	2.33			1.59	
4.0	32,260	0.3100	2.39			1.71	
3.9	31,460	0.3179	2.57			1.90	
3.8	30,650	0.3263	2.80			1.77	
3.7	29,840	0.3351	2.92			1.61	
3.6	29,040	0.3444	2.93			1.54	
3.5	28,230	0.3542	2.89			1.52	
3.4	27,420	0.3647	2.91			1.67	
3.3	26,620	0.3757	3.30			1.67	
3.2	25,810	0.3875	3.44			1.16	
3.1	25,000	0.4000	3.43			1.02	
3.0	24,200	0.4133	3.37			0.861	
2.755	22,220	0.45	3.080 [3]			0.485 [3]	
2.75	22,180	0.4509	3.23 [1]			0.636 [1]	
2.610	21,050	0.475	3.045 [3]				
2.5	20,160	0.4959	3.14 [1]			0.525	

(*continued*)

[a] The reference from which the values were extracted is given in brackets next to the first n and first k value. Reading down, the reference is the same until another set of brackets appears for a new reference.

TABLE I (*Continued*)

Cadmium Telluride

eV	cm^{-1}	μm	n	n	n	k	k
2.480	20,000	0.50	3.010 [3]			0.380 [3]	
2.362	19,050	0.525	2.970				
2.254	18,180	0.55	2.945			0.300	
2.25	18,150	0.5510	3.05 [1]			0.411 [1]	
2.156	17,390	0.575	2.917 [3]				
2.066	16,670	0.60	2.894			0.261 [3]	
2.0	16,130	0.6199	2.99 [1]			0.351 [1]	
1.984	16,000	0.625	2.873 [3]				
1.907	15,380	0.65	2.860			0.238 [3]	
1.837	14,810	0.675	2.860				
1.771	14,290	0.70	2.861			0.210	
1.75	14,110	0.7085	2.95 [1]			0.338 [1]	
1.710	13,790	0.725	2.868 [3]				
1.653	13,330	0.75	2.870			0.185 [3]	
1.631	13,160	0.76				0.179	
1.610	12,990	0.77				0.174	
1.600	12,900	0.775	2.872				
1.590	12,820	0.78				0.165	
1.569	12,740	0.79				0.155	
1.550	12,500	0.80	2.876			0.125	
1.531	12,350	0.81				8.0×10^{-2}	
1.512	12,200	0.82	2.880			4.0×10^{-2}	
1.50	12,100	0.8266	2.98 [1]			0.319 [1]	
1.494	12,050	0.83				2.0×10^{-2} [3]	
1.475	11,900	0.840	2.905 [3]			1.34×10^{-3} [5]	
1.47	11,860	0.8434				6.71×10^{-4}	
1.465	11,820	0.8463				3.37	

1.46	11,780	0.8492		1.89
1.459	11,760	0.850	2.948	
1.455	11,740	0.8521		1.08×10^{-4}
1.45	11,690	0.8551	2.9565 [7]	5.10×10^{-5}
1.445	11.650	0.8580		2.73
1.442	11,630	0.860	2.952 [3]	
1.44	11,610	0.8610	2.9479 [7]	1.37
1.43	11,530	0.8670	2.9402	
1.42	11,450	0.8731	2.9331	
1.41	11,370	0.8793	2.9266	
1.409	11,360	0.880	2.920 [3]	
1.40	11,290	0.8856	2.9205 [7]	
1.39	11,210	0.8920	2.9147	
1.38	11,130	0.8984	2.9092	
1.378	11,110	0.900	2.899 [3]	
1.36	10,970	0.9116	2.8989 [7]	
1.35	10,890	0.9184	2.8940	
1.34	10,810	0.9252	2.8894	
1.340	10,810	0.925	2.878 [3]	
1.33	10,730	0.9322	2.8848 [7]	
1.32	10,650	0.9393	2.8804	
1.31	10,570	0.9464	2.8761	
1.305	10,530	0.950	2.860 [3]	
1.30	10,490	0.9537	2.8720 [7]	
1.29	10,400	0.9611	2.8679	
1.28	10,320	0.9686	2.8640	
1.272	10,260	0.975	2.850 [3]	
1.27	10,240	0.9762	2.8601 [7]	
1.26	10,160	0.9840	2.8563	
1.25	10,080	0.9919	2.8527	
1.24	10,000	0.9999	2.8490	

(*continued*)

TABLE I (*Continued*)

Cadmium Telluride

eV	cm^{-1}	μm	n	n	n	k	k
1.240	10,000	1.0	2.840 [3]				
1.23	9,921	1.008	2.8455 [7]				
1.22	9,840	1.016	2.8420				
1.21	9,759	1.025	2.8386				
1.20	9,679	1.033	2.8353				
1.19	9,598	1.042	2.8320				
1.18	9,518	1.051	2.8288				
1.17	9,437	1.060	2.8257				
1.16	9,356	1.069	2.8226				
1.15	9,275	1.078	2.8195				
1.14	9,195	1.088	2.8165				
1.13	9,114	1.097	2.8136				
1.12	9,034	1.107	2.8107				
1.11	8,953	1.117	2.8078				
1.10	8,872	1.127	2.8050				
1.09	8,792	1.137	2.8023				
1.08	8,711	1.148	2.7996				
1.07	8,630	1.159	2.7969				
1.06	8,550	1.170	2.7943				
1.05	8,469	1.181	2.7917				
1.04	8,388	1.192	2.7891				
1.03	8,308	1.204	2.7866				
1.02	8,227	1.216	2.7842				
1.01	8,146	1.228	2.7817				
1.00	8,065	1.240	2.7793				
0.99	7,985	1.252	2.7770				
0.98	7,904	1.265	2.7747				

0.97	7,824	1.278	2.7724
0.96	7,743	1.291	2.7701
0.95	7,662	1.305	2.7679
0.94	7,582	1.319	2.7657
0.93	7,501	1.333	2.7636
0.92	7,420	1.348	2.7615
0.91	7,340	1.362	2.7594
0.90	7,259	1.378	2.7573
0.89	7,170	1.393	2.7553
0.88	7,098	1.409	2.7533
0.87	7,017	1.425	2.7514
0.86	6,936	1.442	2.7494
0.85	6,856	1.459	2.7475
0.84	6,775	1.476	2.7457
0.83	6,694	1.494	2.7438
0.82	6,614	1.512	2.7420
0.81	6,533	1.531	2.7402
0.80	6,452	1.550	2.7384
0.79	6,372	1.569	2.7367
0.78	6,291	1.589	2.7350
0.77	6,210	1.610	2.7333
0.76	6,130	1.631	2.7317
0.75	6,049	1.653	2.7301
0.74	5,968	1.675	2.7285
0.73	5,888	1.698	2.7269
0.72	5,807	1.722	2.7253
0.71	5,726	1.746	2.7238
0.70	5,646	1.771	2.7223
0.69	5,565	1.797	2.7208
0.68	5,485	1.823	2.7194
0.67	5,404	1.851	2.7180

(*continued*)

TABLE I (*Continued*)

Cadmium Telluride

eV	cm^{-1}	μm	n	n	n	k	k
0.66	5,323	1.879	2.7166				
0.65	5,243	1.907	2.7152				
0.64	5,162	1.937	2.7138				
0.63	5,081	1.968	2.7125				
0.62	5,001	2.000	2.7112				
0.6199	5,000	2.0	2.713 [9]	2.71772 [10]			
0.61	4,920	2.033	2.7099 [7]				
0.60	4,839	2.066	2.7086				
0.59	4,759	2.101	2.7074				
0.58	4.678	2.138	2.7062				
0.57	4,597	2.175	2.7050				
0.56	4,517	2.214	2.7038				
0.55	4,436	2.254	2.7027				
0.54	4,355	2.296	2.7015				
0.53	4,275	2.339	2.7004				
0.52	4,194	2.384	2.6993				
0.51	4,113	2.431	2.6983				
0.50	4,033	2.480	2.6972				
0.4959	4,000	2.5	2.702 [9]				
0.49	3,952	2.530	2.6962 [7]				
0.48	3,871	2.583	2.6952				
0.47	3,791	2.638	2.6942				
0.46	3,710	2.695	2.6932				
0.45	3,629	2.755	2.6923				
0.44	3,549	2.818	2.6914				
0.43	3,468	2.883	2.6904				
0.42	3,388	2.952	2.6895				

0.4133	3,333	3.0	2.695 [9]	2.69933	
0.41	3,307	3.024	2.6887 [7]		
0.40	3,226	3.100	2.6878		
0.39	3,146	3.179	2.6870		
0.38	3,065	3.263	2.6861		
0.37	2,984	3.351	2.6853		
0.36	2,904	3.444	2.6845		
0.3542	2,857.1	3.5	2.691 [9]		
0.35	2,823	3.542	2.6837 [7]		
0.34	2,742	3.647	2.6829		
0.33	2,662	3.757	2.6822		
0.32	2,581	3.875	2.6814		
0.31	2,500	4.000	2.6807	2.69258 [10]	
			2.688 [9]		
0.30	2,420	4.133	2.6800 [7]		
0.29	2,339	4.275	2.6792		
0.28	2,258	4.428	2.6785		
0.27	2,178	4.592	2.6778		
0.26	2,097	4.769	2.6770		
0.25	2,016	4.959	2.6763		
0.2480	2,000	5.0	2.684 [9]		
0.24	1,936	5.166	2.6755 [7]		
0.23	1,855	5.391	2.6747		
0.22	1,774	5.636	2.6739		
0.21	1,694	5.904	2.6731		
0.2066	1,667	6.0	2.681 [9]	2.68570	2.68198 [11]
0.20	1,613	6.199	2.6722 [7]		
0.19	1,532	6.526	2.6713		
0.18	1,452	6.888	2.6703		
0.1771	1,428.6	7.0	2.679 [9]		
0.17	1,371	7.293	2.6692 [7]		

(*continued*)

TABLE I (*Continued*)

Cadmium Telluride

eV	cm^{-1}	μm	n	n	n	k	k
0.16	1,290	7.749	2.6679				
0.1550	1,250	8.0	2.677 [9]	2.68044	2.67730		
0.15	1,210	8.266	2.6665 [7]				
0.14	1,129	8.856	2.6649				
0.13	1,049	9.537	2.6628				
0.1240	1,000	10.0	2.653 [14] 2.672 [9]	2.67513 [10]	2.67242 [11]		
0.12	967.9	10.33	2.6605 [7]				
0.1178	950.0	10.53	2.651 [14]				
0.1170	943	10.6				5.1×10^{-8} [21]	
0.1116	900	11.11	2.650				
0.11	887.2	11.27	2.6574 [7]				
0.1054	850	11.76	2.648 [14]				
0.1033	833.3	12.0		2.66932	2.66677		
0.10	806.5	12.40	2.6535 [7]				
0.09919	800	12.50	2.646 [14]				
0.09299	750	13.33	2.643				
0.09	725.9	13.78	2.6482 [7]				
0.08856	714.3	14.0		2.66280	2.66020		
0.08679	700	14.29	2.640 [14]				
0.08059	650	15.38	2.636				
0.08	645.2	15.50	2.6407 [7]				
0.07749	625.0	16.0		2.65451	2.65253		
0.07439	600	16.67	2.630 [14]				
0.07	564.6	17.71	2.6296 [7]				
0.06888	555.6	18.0		2.64492	2.64366		

0.06819	550	18.18	2.623 [14]			
0.0625	504	19.8				3.9×10^{-7}
0.06199	500.0	20.0	2.614	2.63428	2.63343	
0.06	483.9	20.66	2.6118 [7]			
0.0573	462	21.6				3.8×10^{-6}
0.05636	454.5	22.0		2.62265	2.62177	
0.05579	450	22.22	2.601 [14]			
0.0521	420	23.8				3.4×10^{-5}
0.05166	416.7	24.0		2.60928		
0.05061	408.2	24.5				3.51×10^{-5} [22]
0.05	403.3	24.80	2.5801 [7]			
0.04959	400	25	2.581 [14]			
0.04835	390	25.64	2.576			
0.04769	384.6	26		2.59466		
0.04711	380	26.32	2.570			
0.0469	378	26.5				8.0×10^{-5} [21]
0.04592	370.3	27				9.88×10^{-5} [22]
0.04587	370	27.03	2.564			
0.04463	360	27.78	2.557			
0.04428	357.1	28		2.57724		
0.04215	340	29.41	2.541			2.97×10^{-3} [14]
0.04133	333.3	30		2.55916		2.86×10^{-4} [22]
0.04092	330	30.30	2.531			3.34 [14]
0.03968	320	31.25	2.521			3.79
0.03844	310	32.26	2.508			4.32
0.03757	303.0	33.00				6.57 [15]
0.03720	300	33.33	2.494			4.97 [14]
0.03701	298.5	33.50				8.13 [15]
0.03647	294.1	34.00				8.93
0.03596	290	34.48	2.478			5.77×10^{-3} [14]

(*continued*)

TABLE I (*Continued*)

Cadmium Telluride

eV	cm^{-1}	μm	n	n	n	k	k
0.03594	289.9	34.50				1.08×10^{-2} [15]	
0.03542	285.7	35.00				9.19×10^{-3}	
0.03493	281.7	35.5				7.91	
0.03472	280	35.71	2.459			6.76 [14]	
0.03444	277.8	36.0				4.58 [15]	
0.03397	274.0	36.5				3.92	
0.03351	270.3	37.0				3.83	
0.03348	270	37.04	2.437			8.01 [14]	
0.03306	266.7	37.5				4.03 [15]	
0.03263	263.2	38.0				4.54	
0.03224	260	38.46	2.410			9.62 [14]	
0.03220	259.7	38.5				5.06 [15]	
0.03179	256.4	39.0				6.21	
0.03139	253.2	39.5				7.23	
0.03100	250	40	2.378			1.18×10^{-2} [14]	
						7.96×10^{-3} [15]	
0.03061	246.9	40.5				7.57	
0.03024	243.9	41.0				7.83	
0.02988	241.0	41.5				7.43	
0.02976	240	41.67	2.339			1.46×10^{-2} [14]	
0.02952	238.1	42.0				7.35×10^{-3} [15]	
0.02917	235.3	42.5				6.93	
0.02883	232.6	43.0				6.50	
0.02852	230	43.48	2.289	2.28 [18]		1.87 [14]	
0.02850	229.9	43.5				6.23 [15]	
0.02818	227.3	44.0				5.95	
0.02786	224.7	44.5				5.31	

0.02755	222.2	45.0			5.19	
0.02728	220	45.45	2.224	2.23	2.47×10^{-2} [14]	
0.02725	219.8	45.5			5.43×10^{-3} [15]	
0.02695	217.4	46.0			5.86	
0.02666	215.1	46.5			5.92	
0.02638	212.8	47.0			6.54	
0.02610	210.5	47.5			6.80	
0.02604	210	47.62	2.137	2.18	3.40×10^{-2} [14]	
0.02583	208.3	48.0			8.02×10^{-3} [15]	
0.02556	206.2	48.5			1.12×10^{-2}	
0.02530	204.1	49.0			1.44	
0.02505	202.0	49.5			1.60	
0.02480	200	50.00	2.013	2.05	4.97×10^{-2} [14]	
					2.07 [15]	
0.02455	198.0	50.5			2.65	
0.02431	196.1	51.0			3.69	
0.02407	194.2	51.5			5.33	
0.02384	192.3	52.0			6.21	
0.02356	190	52.63	1.824	1.9	8.00×10^{-2} [14]	
0.02232	180	55.56	1.498	1.5	0.154	0.1 [18]
0.02108	170	58.82	0.8021	0.80	0.522	0.5
0.02046	165	60.61	0.5183	0.40	1.17	0.9
0.01984	160	62.50	0.5085	0.20	1.89	1.8
0.01922	155	64.52	0.6392	0.40	2.71	2.75
0.01860	150	66.67	1.021	0.80	3.81	3.7
0.01835	148	67.57	1.353		4.41	
0.01810	146	68.49	1.939		5.12	
0.01798	145	68.97		1.8		5.2
0.01785	144	69.44	3.053		5.87	
0.01767	142.5	70.18		3.8		6.2
0.01760	142	70.42	5.009		6.02	

(*continued*)

TABLE I (*Continued*)

Cadmium Telluride

eV	cm^{-1}	μm	n	n	n	k	k
0.01736	140	71.43	6.778	5.5		4.50	5.5
0.01711	138	72.46	6.917			2.65	
0.01686	136	73.53	6.399			1.59	
0.01674	135	74.07		6.75			2.2
0.01661	134	74.63	5.882			1.03	
0.01636	132	75.76	5.468			0.722	
0.01612	130	76.92	5.146	5.1		0.534	0.8
0.01550	125	80.00	4.598	4.7		0.294	0.55
0.01488	120	83.33	4.260	4.4		0.187	0.3
0.01426	115	86.96	4.032			0.129	
0.01364	110	90.91	3.868	3.9		9.47×10^{-2}	0.25
0.01302	105	95.24	3.745			7.23	
0.01240	100	100	3.649	3.62		5.68	0.2 [18]
0.01118	90	111.1	3.510	3.45		3.75×10^{-2}	0.2
0.01033	83.33	120				0.111 [15]	
0.009919	80	125	3.415	3.32		2.62×10^{-2} [14]	0.2
0.009537	76.92	130				0.103 [15]	
0.009184	74.07	135				9.34×10^{-2}	
0.008856	71.43	140				0.116	
0.008679	70	142.9	3.348	3.3		1.89×10^{-2} [14]	0.2
0.008551	68.97	145				0.108 [15]	
0.008266	66.67	150				8.27×10^{-2}	
0.007749	62.50	160				6.86	
0.007439	60	166.7	3.299	3.3		1.39 [14]	
0.007293	58.82	170				6.05 [15]	
0.006888	55.56	180				5.67	
0.006526	52.63	190				5.56	
						2.42 [17]	

0.006199	50	200	3.263	3.3	1.03 [14] 1.83 [17] 5.32 [15]
0.005904	47.62	210			5.18
0.005767	46.51	215			5.37
0.0056956	45.938	217.68	3.2733 [8]		
0.005636	45.45	220			5.46
0.0055904	45.089	221.78	3.2720		
0.005510	44.44	225			4.24
0.005391	43.48	230			3.96×10^{-2}
0.0052828	42.608	234.70	3.2628		
0.0051798	41.778	239.36	3.2597		
0.0050756	40.937	244.28	3.2574		
0.0049712	40.095	249.41	3.2550		
0.004959	40	250.0	3.236 [14]		7.52×10^{-3} [14]
0.0042395	34.194	292.45	3.2360 [8]		8.55 [17]
0.004133	33.33	300			7.17 8.12 [8]
0.0041293	33.305	300.25	3.2371		
0.0038128	30.752	325.18	3.2294		
0.003720	30	333.3	3.217 [14]		
0.0031678	25.550	391.39	3.2203 [8]		
0.003100	25.00	400			5.09
0.0028443	22.941	435.90	3.2155		
0.0025176	20.306	492.46	3.2136		
0.002480	20	500.0			4.77
0.0023015	18.563	538.71	3.2096		
0.002066	16.67	600			5.16
0.0019749	15.929	627.78	3.2062		
0.001771	14.29	700			5.57
0.001550	12.50	800			6.18

Gallium Arsenide (GaAs)

EDWARD D. PALIK
Naval Research Laboratory
Washington, D.C.

The optical constants of pure (semi-insulating) GaAs are derived from a number of papers including the far-infrared reststrahlen work of Johnson *et al.* [1], Kachare *et al.* [2], and Holm *et al.* [3]; the mid-IR work of Cochran *et al.* [4]; the near-IR work of Pikhtin and Yas'kov [5]; the calorimetry work of Christensen *et al.* [6]; the fundamental band gap work of Casey *et al.* [7]; the visible–UV ellipsometry work of Theeten *et al.* [8]; the UV reflection work of Philipp and Ehrenreich [9]; and the synchrotron transmission work of Cardona *et al.* [10]. A smooth plot of the n and k data, given in Fig. 2, is obtained from the data of Table II.

The measurements of Johnson *et al.* [1] to determine n and k were 300-K transmission measurements of thin samples of resistivity $3.5 \times 10^8\ \Omega$ cm. Slab thickness was known to $\pm 1\%$. The transmittance was measured to $\pm 5\%$ with a Beckmann IR-11 spectrometer system. Surface preparation was described as optical polish. If this were a mechanical grit polish, then the surfaces were damaged, as discussed by Holm and Palik [11]. The effect of a damage layer thousands of angstroms thick can probably be neglected except at the reststrahlen peak itself. The n data listed were obtained from a graph of a calculated oscillator fit to the experimental points, the scatter of the points being ± 0.02 from the fit. The k data listed were read directly off a smooth-curve graph (no fit in this case). Similar less-detailed measurements for k have been made by Stolen [12], and his 294-K data (as read from a graph) are also listed for comparison.

In the reststrahlen region reflectivity data have been fitted by an oscillator model of the form

$$(n - ik)^2 = \varepsilon_\infty \left[1 + \frac{\omega_L^2 - \omega_T^2}{\omega_T^2 - \omega^2 + i\Gamma\omega} \right] \tag{1}$$

used by Kachare *et al.* [2] and Holm *et al.* [3]. We averaged these parameters to obtain $\omega_L = 292.1\ \text{cm}^{-1}$, $\omega_T = 268.7\ \text{cm}^{-1}$, $\Gamma = 2.4\ \text{cm}^{-1}$, and $\varepsilon_\infty = 11.0$. Surfaces were chemically polished to remove saw-cut and grinding damage. The reference was an aluminum mirror whose reflectivity is given by Bennett

HANDBOOK OF OPTICAL CONSTANTS OF SOLIDS
ISBN 0-12-544420-6

et al. [13]. A comparison can be made in the longer-wavelength overlap region with the data of Johnson *et al.* [1] showing agreement to ~ 0.03 and better in n. The calculated values of k are almost a factor of 2 smaller than those measured by Johnson *et al.* [1] probably because on the low-frequency side of ω_T difference bands occur in the 80–200-μm region that would make the experimental values of k larger than the single-oscillator model, as is observed. However, k measurements of Iwasa *et al.* [14] on thin mechanically polished and epitaxial films are only $\sim 10\%$ smaller than those calculated in the 240–320-cm^{-1} region (after a decimal point correction in Fig. 2. of Iwasa *et al.* [14], so we chose the oscillator-model fit through this region. The oscillator model can be modified to include a frequency-dependent damping constant to account for some of the structure away from ω_T [15]. The static dielectric constant is found to be 13.00.

The oscillator fit for n is extended up to 480 cm^{-1}. However, several multiphonon bands occur above ω_L that have been measured directly by Cochran *et al.* [4] in the 347–807-cm^{-1} region. They measured transmission and reflection of thin slabs. Surface preparation was not described. Room temperature varies among the samples and is usually 297 or 300 K, except for these samples for which it was 292 K (a cold English laboratory or ice water in the dewar?). Dopant impurities such as Si, Li, and B give rise to local vibration modes that often fall in this spectral region [16].

Calorimetry measurements at CO_2 laser wavelengths [6] produced the small k values listed in the 1000-cm^{-1} region for Czochrolski-grown, undoped, high-resistivity GaAs. No surface preparation was given, although surely a chemical polish was used. These numbers varied from sample to sample by a factor of 2 and with other measurements also [17]. Temperature-dependence studies suggest that this absorption is primarily intrinsic due to multiphonon absorption, although the variation from sample to sample suggests that residual impurities and surface effects may still be present.

Pikhtin and Yas'kov [5] have measured the index of refraction in the near IR by using prism (minimum deviation) and interference-fringe techniques. The authors fitted theirs and Marple's data [18] to an oscillator formula of the form

$$n^2 = 1 + \frac{A}{\pi} \ln \frac{E_1^2 - (\hbar\omega)^2}{E_0^2 - (\hbar\omega)^2} + \frac{G_1}{E_1^2 - (\hbar\omega)^2} + \frac{G_2}{E_2^2 - (\hbar\omega)^2} + \frac{G_3}{E_3^2 - (\hbar\omega)^2}, \qquad (2)$$

with the parameters $E_0 = 1.428$ eV, $E_1 = 3.0$ eV, $E_2 = 5.1$ eV, $E_3 = 0.0333$ eV, $G_1 = 39.194$ eV^2, $G_2 = 136.08$ eV^2, $G_3 = 0.00218$ eV^2, and $A = 0.7/\sqrt{E_0} = 0.5858$. No damping was assumed. These results for n are listed from 0.1 to 1.4 eV and fit the experimental values to a few units in the third decimal place. This fit of Eq. (2) agrees with the reststrahlen oscillator fit of Eq. (1) to within 0.02 at 0.06 eV, but n is smaller primarily due to the fact that in Eq. (1) $\varepsilon_\infty = 11.0$, while in Eq. (2) the first four terms give 10.9 to three figures from 5000 to 0 cm^{-1} when $G_3 = 0$. Usually, ε_∞ is the high-frequency back-

ground dielectric constant conveniently defined, where n^2 in Eq. (2) is equal to its low-frequency value when $G_3 = 0$. The second term in Eq. (1) could replace (without ε_∞) the last term in Eq. (2) for better description of n over the entire IR region along with k in the reststrahlen region.

At the fundamental band gap, Casey *et al.* [7] have measured k for "pure" and doped thin films by transmission and Kramers–Kronig (KK) analysis of reflectivity. A 1-m Jarrell Ash monochromator was used. The Burstein–Moss effect, the change in interband absorption due to free carriers blocking interband transitions, does change k significantly, but this effect is not discussed here. Transmission samples were bulk samples thinned down to appropriate thicknesses. Surface preparation was not described. For near-normal-incidence reflection, epitaxial films of GaAs on $Al_xGa_{1-x}As$ were used. The surfaces in this case would be undamaged. Uncertainty in absorption coefficient $\alpha = 4\pi k/\lambda$ was quoted to $\pm 5\%$ for the transmission data for $\alpha \leq 10^3$ cm^{-1}, primarily due to uncertainty in thickness measurements.

Theeten *et al.* [8] have performed continuous wavelength ellipsometry measurements on chemically polished samples and their results are presented in the 1.5–6.0-eV region. We have overlapped the Casey *et al.* [7] and the Theeten *et al.* [8] data to demonstrate how these data can differ; at 1.5 eV the respective k's are 0.079 and 0.041, while are 1.6 eV they are 0.095 and 0.066. The transmission measurements are preferred if the film thickness is well determined and the surface quality is good. However, in the Casey [7]/Theeten [8] overlap region the KK analysis was done by Casey *et al.* [7], so we prefer the more direct ellipsometric data.

The ellipsometric data [8] are considered better than the KK analyzed reflection data of Philipp and Ehrenreich [9], since it is a more direct determination with few approximations and assumptions. At 6 eV n is 1.264 compared to 1.395, a difference of 0.1, while k is 2.472 compared to 2.048, a difference of 0.4. Above 6 eV we list the results of Philipp and Ehrenreich [9] as tabulated by Seraphin and Bennett [19]. These were near-normal-incidence reflection measurements taken over the range 1–25 eV in a vacuum spectrometer system. Surfaces were chemically prepared.

Transmission of synchrotron radiation was measured by Cardona *et al.* [10] in the 15–155-eV region to determine k only. Normal incidence and grazing incidence vacuum spectrometers were used. Films were flash evaporated on carbon foils or on microscope slides coated with KCl. The films could be floated on water and picked up on a copper screen. To obtain polycrystalline rather than amorphous samples, the substrate temperature was ≥ 250°C. The k data listed were obtained from a graph readable to three figures. At 15 eV the KK-analyzed reflection data [9] give $k = 0.41$ while the transmission data give $k = 0.28$.

Throughout the visible–UV region we are plagued with values of k from various laboratories that differ by as much as a factor of 2, although the usual differences are $< 50\%$. Differences in n are usually less than 10%. Often,

absolute reflectivity is quoted to $\pm 3\%$, which could account for much of the differences between KK analysis, between two laboratories, or between KK analysis and ellipsometric measurements.

Except for the spectral regions in which the minimum deviation and interference-fringe techniques are used, we are hard-pressed to quote n to better than two significant figures. Things are even worse for k that is generally not determined better than $\pm 30\%$. Physicists, who did most of the measurements cited, were more interested in positions of peaks to identify vibrational frequencies and interband transitions, so relative values of k were typically good but absolute values varied as has been discussed.

The temperature dependence of n in the near IR between 5 and 20 μm has been found by Cardona [20] to be

$$(1/n)(dn/dT) = (4.5 \pm 0.2) \times 10^{-5}\,(\mathrm{C}^{-1}). \tag{3}$$

Near strong absorption features like band edges and lattice vibrations, the effects are no doubt even stronger. Data are usually quoted at 297 or 300 K, which would mean a variation of a few units in the fourth decimal place. Therefore, we cannot use this decimal place with confidence, although it is sometimes quoted in Table II.

It is clear that all samples probably have a native oxide in the form of Ga_2O_3 and As_2O_3 of $\sim$20-Å thickness. This layer presents little or no problems in the IR region but must be considered in the region above the band gap of this mixed oxide ($\sim$5 eV). Theeten *et al.* [8] and Philipp and Ehrenreich [9] prepared surfaces by chemical etching and polishing, but the samples may have been exposed to air before being put into the inert gas system or the vacuum system. Native oxides typically grow to their final thickness in a few hours in air but grow rapidly at first exposure. Therefore, we must assume that an oxide was growing on the samples. This may cause uncertainties in the determination of k in the UV. Only work with cleaved or evaporated surfaces in UHV would be free of oxides for a few hours.

REFERENCES

1. C. J. Johnson, G. H. Sherman, and R. Weil, *Appl. Opt.* **8**, 1667 (1969).
2. A. H. Kachare, W. G. Spitzer, F. K. Euler, and A. Kahan, *J Appl. Phys.* **45**, 2938 (1974).
3. R. T. Holm, J. W. Gibson, and E. D. Palik, *J. Appl. Phys.* **48**, 212 (1977).
4. W. Cochran, S. J. Fray, F. A. Johnson, J. E. Quarrington, and N. Williams, *J. Appl. Phys. Suppl.* **32**, 2102 (1961).
5. A. N. Pikhtin and A. D. Yas'kov, *Sov. Phys. Semicond.* **12**, 622 (1978); A. N. Pikhtin and A. D. Yas'kov, *Fiz. Tekh. Poluprovodn.* **12**, 1047 (1978).
6. C. P. Christensen, R. Joiner, S. K. T. Nieh, and W. H. Steier, *J. Appl. Phys.* **45**, 4957 (1974).
7. H. C. Casey, D. D. Sell, and K. W. Wecht, *J. Appl.* Phys. **46**, 250 (1975).
8. J. B. Theeten, D. E. Aspnes, and R. P. H. Chang, *J. Appl. Phys.* **49**, 6097 (1978); J. B. Theeten, D. E Aspnes, and R. P. H. Chang, private communication (1982).
9. H. R. Philipp and H. Ehrenreich, *Phys. Rev.* **129**, 1550 (1963).
10. M. Cardona, W. Gudat, B. Sonntag, and P. Y. Yu, *in Proc. Int. Conf. Phys. Semicond., 10th Cambridge*, 1970, p. 208. U.S. Atomic Energy Commission, Oak Ridge, Tennessee, 1970.

11. R. T. Holm and E. D. Palik, *J. Vac. Sci. Technol.* **13**, 889 (1976).
12. R. H. Stolen, *Phys. Rev. B* **11**, 767 (1975); R. H. Stolen, *Appl. Phys. Lett.* **15**, 74 (1969).
13. H. E. Bennett, M. Silver, and E. J. Ashley, *J. Opt. Soc. Am.* **53**, 1089 (1963).
14. S. Iwasa, I. Balslev, and E. Burstein, *in Int. Conf. Phys. Semicond., Paris*, 1964, p. 1077. Dunod, Paris, and Academic Press, New York, 1964.
15. A. S. Barker, Jr., *Phys. Rev.* **165**, 917 (1968).
16. W. G. Spitzer, *in* "Semiconductors and Semimetals" (R. K. Willardson and A. C. Beer, eds.), Vol. 3, p. 17. Academic Press, New York, 1967.
17. L. H. Skolnik, H. G. Lipson, and B. Bendow, *Appl. Phys. Lett.* **25**, 442 (1974).
18. D. T. F. Marple, *J. Appl. Phys.* **35**, 1241 (1964).
19. B. O. Seraphin and H. E. Bennett, *in* "Semiconductors and Semimetals" (R. K. Willardson and A. C. Beer, eds.), Vol. 3, p. 499. Academic Press, New York, 1967.
20. M. Cardona, *Proc. Int. Conf. Semicond. Phys., Prague*, 1960, p. 388. Czech. Acad. Sci., Prague, and Academic Press, New York, 1961.

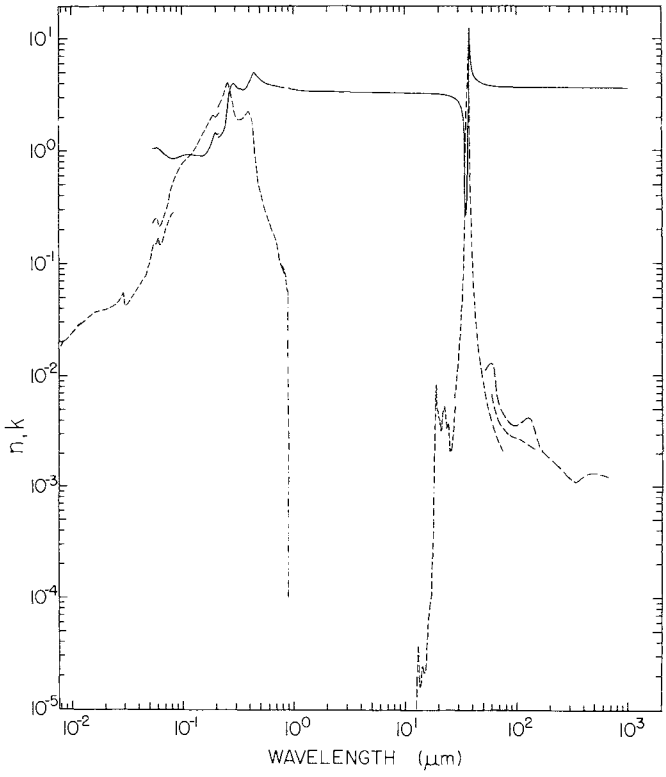

Fig. 2. Log–log plot of n (——) and k (– – – –) versus wavelength in micrometers for gallium arsenide. Data from various references sometimes do not join together in overlap regions.

TABLE II

Values of n and k for Gallium Arsenide Obtained from Various References[a]

eV	cm^{-1}	μm	n	k
155		0.007999		0.0181 [10]
150		0.008266		0.0193
145		0.008551		0.0203
144		0.008610		0.0204
143		0.008670		0.0206
142		0.008731		0.0204
141		0.008793		0.0205
140		0.008856		0.0206
135		0.009184		0.0213
130		0.009537		0.0224
125		0.009919		0.0234
120		0.01033		0.0245
115		0.01078		0.0256
113		0.01097		0.0263
111		0.01117		0.0274
110		0.01127		0.0278
109		0.01137		0.0281
108		0.01148		0.0283
107		0.01159		0.0276
106		0.01170		0.0288
105		0.01181		0.0293
104		0.01192		0.0284
103		0.01204		0.0294
102		0.01215		0.0289
100		0.01240		0.0294
95		0.01305		0.0308
90		0.01378		0.0323
85		0.01459		0.0338
80		0.01550		0.0353
75		0.01653		0.0368
70		0.01771		0.0376
65		0.01907		0.0387
60		0.02066		0.0389
55		0.02254		0.0407
50		0.02480		0.0430
48		0.02583		0.0448

[a] The data of Philipp and Ehrenreich [9] given in Seraphin and Bennett [19] are specified by the wavelength (in micrometers). However, the original data were given in electron volts, and it is obvious that most of the n, k values were determined for energies in whole numbers or tenths of a whole number. They were rounded off to three significant figures and then given the wavelength listed in Seraphin and Bennett [19]. Sometimes we list these wavelengths and then recalculate energy (in electron volts), thus producing roundoff error in election volts. The reference is given at the beginning of a tabulation of n and k, for example, and is understood to refer to all n's and k's below it until a new reference appears in brackets. The value of k is frequently given as an exponent of 10. This value of exponent is understood to refer to all k's below it in the table until a new exponent appears or the number changes from 10^{-2} to 10^{-1} when a decimal only is used.

TABLE II (*Continued*)

Gallium Arsenide

eV	cm^{-1}	μm	n	k
46		0.02695		0.0476
44		0.02818		0.0518
43		0.02883		0.0546
42		0.02952		0.0470
41		0.03024		0.0426
40		0.03100		0.0426
38		0.03263		0.0452
35		0.03542		0.0513
30		0.04133		0.0648
29		0.04275		0.0683
28		0.04428		0.0740
27		0.04592		0.0785
26		0.04769		0.0872
25		0.04959		0.0986
24		0.05166		0.115
23.5		0.05276		0.126
23		0.05391	1.037 [9, 19]	0.141
				0.228 [9, 19]
22.5		0.05510		0.146 [10]
22		0.05636	1.043	0.148
				0.243 [9, 19]
21.5		0.05767		0.147 [10]
21		0.05904	1.058	0.162
				0.245 [9, 19]
20.5		0.06048		0.164 [10]
20		0.06199	1.025	0.144
				0.212 [9, 19]
19.5		0.06358		0.147 [10]
19		0.06526	0.981	0.152
				0.234 [9, 19]
18		0.06888	0.936	0.178 [10]
				0.267 [9, 19]
17		0.07293	0.889	0.223 [10]
				0.324 [9, 19]
16		0.07749	0.850	0.261 [10]
				0.411 [9, 19]
15		0.08266	0.836	0.282 [10]
				0.503 [9, 19]
14		0.08856	0.840	0.602
13		0.09537	0.864	0.709
12.0		0.1033	0.895	0.791
10.8		0.1148	0.923	0.881
10.0		0.1240	0.913	0.974
9.0		0.1378	0.901	1.136
8.0		0.1550	0.899	1.435
7.0		0.1771	1.063	1.838

(*continued*)

TABLE II (*Continued*)

Gallium Arsenide

eV	cm^{-1}	μm	n	k
6.6		0.1879	1.247	2.047
6.3		0.1968	1.441	1.988
6.2		0.2000	1.424	1.976
6.0	48,390	0.2066	1.264 [8]	2.472 [8]
			1.395 [9, 19]	2.048 [9, 19]
5.94	47,910	0.2087	1.287 [8]	2.523 [8]
5.90	47,590	0.2101	1.288	2.556
5.84	47,100	0.2123	1.304	2.592
5.80	46,780	0.2138	1.311	2.625
5.74	46,300	0.2160	1.321	2.673
5.70	45,970	0.2175	1.325	2.710
5.64	45,490	0.2198	1.339	2.772
5.60	45,170	0.2214	1.349	2.815
5.54	44,680	0.2238	1.367	2.885
5.50	44,360	0.2254	1.383	2.936
5.44	43,880	0.2279	1.410	3.019
5.40	43,550	0.2296	1.430	3.079
5.34	43,070	0.2322	1.468	3.181
5.30	42,750	0.2339	1.499	3.255
5.24	42,260	0.2366	1.552	3.384
5.20	41,940	0.2384	1.599	3.484
5.14	41,460	0.2412	1.699	3.660
5.10	41,130	0.2431	1.802	3.795
5.04	40,650	0.2460	2.044	3.992
5.00	40,330	0.2480	2.273	4.084
4.94	39,840	0.2510	2.654	4.106
4.90	39,520	0.2530	2.890	4.047
4.84	39,040	0.2562	3.187	3.898
4.80	38,710	0.2583	3.342	3.770
4.74	38,230	0.2616	3.511	3.574
4.70	37,910	0.2638	3.598	3.452
4.64	37,420	0.2672	3.708	3.280
4.60	37,100	0.2695	3.769	3.169
4.54	36,620	0.2731	3.850	3.018
4.50	36,290	0.2755	3.913	2.919
4.44	35,810	0.2792	4.004	2.715
4.40	35,490	0.2818	4.015	2.563
4.34	35,000	0.2857	3.981	2.368
4.30	34,680	0.2883	3.939	2.260
4.24	34,200	0.2924	3.864	2.132
4.20	33,880	0.2952	3.810	2.069
4.14	33,390	0.2995	3.736	2.001
4.10	33,070	0.3024	3.692	1.969
4.04	32,580	0.3069	3.634	1.935
4.00	32,260	0.3100	3.601	1.920
3.94	31,780	0.3147	3,559	1.907
3.90	31,460	0.3179	3.538	1.904

TABLE II (*Continued*)

Gallium Arsenide

eV	cm^{-1}	μm	n	k
3.84	30,970	0.3229	3.512	1.905
3.80	30,650	0.3263	3.501	1.909
3.74	30,160	0.3315	3.488	1.920
3.70	29,840	0.3351	3.485	1.931
3.64	29,360	0.3406	3.489	1.950
3.60	29,040	0.3444	3.495	1.965
3.54	28,550	0.3502	3.513	1.992
3.50	28,230	0.3542	3.531	2.013
3.48	28,070	0.3563	3.541	2.024
3.46	27,910	0.3583	3.553	2.036
3.44	27,750	0.3604	3.566	2.049
3.42	27,580	0.3625	3.580	2.062
3.40	27,420	0.3647	3.596	2.076
3.38	27,260	0.3668	3.614	2.091
3.36	27,100	0.3690	3.635	2.107
3.34	26,940	0.3712	3.657	2.123
3.32	26,780	0.3734	3.681	2.142
3.30	26,620	0.3757	3.709	2.162
3.28	26,450	0.3780	3.740	2.183
3.26	26,290	0.3803	3.776	2.207
3.24	26,130	0.3827	3.818	2.232
3.22	25,970	0.3850	3.871	2.260
3.20	25,810	0.3875	3.938	2.288
3.18	25,650	0.3899	4.023	2.307
3.16	25,490	0.3924	4.126	2.304
3.14	25,330	0.3949	4.229	2.270
3.12	25,160	0.3974	4.313	2.212
3.10	25,000	0.4000	4.373	2.146
3.08	24,840	0.4025	4.413	2.082
3.06	24,680	0.4052	4.439	2.029
3.04	24,520	0.4078	4.462	1.988
3.02	24,360	0.4105	4.483	1.961
3.00	24,200	0.4133	4.509	1.948
2.98	24,040	0.4161	4.550	1.952
2.96	23,870	0.4189	4.626	1.967
2.94	23,710	0.4217	4.755	1.960
2.92	23,550	0.4246	4.917	1.885
2.90	23,390	0.4275	5.052	1.721
2.88	23,230	0.4305	5.107	1.529
2.86	23,070	0.4335	5.102	1.353
2.84	22,910	0.4366	5.065	1.206
2.82	22,740	0.4397	5.015	1.088
2.80	22,580	0.4428	4.959	0.991
2.78	22,420	0.4460	4.902	0.912
2.76	22,260	0.4492	4.845	0.846
2.74	22,100	0.4525	4.793	0.789

(*continued*)

TABLE II (*Continued*)

Gallium Arsenide

eV	cm^{-1}	μm	n	k
2.72	21,940	0.4558	4.741	0.739
2.70	21,780	0.4592	4.694	0.696
2.68	21,660	0.4626	4.649	0.659
2.66	21,450	0.4661	4.605	0.626
2.64	21,290	0.4696	4.567	0.595
2.62	21,130	0.4732	4.525	0.569
2.60	20,970	0.4769	4.492	0.539
2.58	20,810	0.4806	4.456	0.517
2.56	20,650	0.4843	4.423	0.497
2.54	20,490	0.4881	4.392	0.476
2.52	20,330	0.4920	4.362	0.458
2.50	20,160	0.4959	4.333	0.441
2.48	20,000	0.4999	4.305	0.426
2.46	19,840	0.5040	4.279	0.411
2.44	19,680	0.5081	4.254	0.398
2.42	19,520	0.5123	4.229	0.385
2.40	19,360	0.5166	4.205	0.371
2.38	19,200	0.5209	4.183	0.359
2.36	19,030	0.5254	4.162	0.347
2.34	18,870	0.5299	4.141	0.337
2.32	18,710	0.5344	4.120	0.327
2.30	18,550	0.5391	4.100	0.320
2.28	18,390	0.5438	4.082	0.308
2.26	18,230	0.5486	4.063	0.301
2.24	18,070	0.5535	4.045	0.294
2.22	17,910	0.5585	4.029	0.285
2.20	17,740	0.5636	4.013	0.276
2.18	17,580	0.5687	3.998	0.266
2.16	17,420	0.5740	3.983	0.257
2.14	17,260	0.5794	3.968	0.251
2.12	17,100	0.5848	3.954	0.245
2.10	16,940	0.5904	3.940	0.240
2.08	16,780	0.5961	3.927	0.232
2.06	16,610	0.6019	3.914	0.228
2.04	16,450	0.6078	3.902	0.223
2.02	16,290	0.6138	3.890	0.213
2.00	16,130	0.6199	3.878	0.211
1.98	15,970	0.6262	3.867	0.203
1.96	15,810	0.6326	3.856	0.196
1.94	15,650	0.6391	3.846	0.187
1.92	15,490	0.6458	3.836	0.183
1.90	15,320	0.6526	3.826	0.179
1.88	15,160	0.6595	3.817	0.173
1.86	15,000	0.6666	3.809	0.173
1.84	14,840	0.6738	3.799	0.168
1.82	14,680	0.6812	3.792	0.158
1.80	14,520	6.8888	3.785	0.151

TABLE II (*Continued*)

Gallium Arsenide

eV	cm^{-1}	μm	n	k
1.78	14,360	0.6965	3.779	0.152
1.76	14,200	0.7045	3.772	0.134
1.74	14,030	0.7126	3.762	0.127
1.72	13,870	0.7208	3.752	0.118
1.70	13,710	0.7293	3.742	0.112
1.68	13,550	0.7380	3.734	0.105
1.66	13,390	0.7469	3.725	0.101
1.64	13,230	0.7560	3.716	0.097
1.62	13,070	0.7653	3.707	0.093
1.60	12,900	0.7749	3.700	0.091
1.58	12,740	0.7847	3.693	0.089
1.56	12,580	0.7948	3.685	0.087
1.54	12,420	0.8051	3.679	0.085
1.52	12,260	0.8157	3.672	0.083
1.50	12,100	0.8266	3.666	0.080
				7.89×10^{-2} [7]
1.49	12,020	0.8321		7.28
1.48	11,940	0.8377		6.86
1.47	11,860	0.8434		6.64
1.46	11,780	0.8492		6.28
1.45	11,690	0.8551		6.12
1.44	11,610	0.8610		5.68
1.435	11,570	0.8640		5.57
1.43	11,530	0.8670		5.72
1.425	11,490	0.8700		5.54
1.42	11,450	0.8731		2.71×10^{-2}
1.41	11,370	0.8793		5.95×10^{-3}
1.40	11,290	0.8856	3.6140 [5]	1.69×10^{-3}
1.39	11,210	0.8920		5.68×10^{-4}
1.38	11,130	0.8984		2.50
1.37	11,050	0.9050		1.33×10^{-4}
1.35	10,890	0.9184	3.5690	
1.30	10,490	0.9537	3.5388	
1.25	10,080	0.9919	3.5138	
1.20	9,679	1.033	3.4920	
1.15	9,275	1.078	3.4724	
1.10	8,872	1.127	3.4546	
1.05	8,469	1.181	3.4383	
1.00	8,065	1.240	3.4232	
0.95	7,662	1.305	3.4094	
0.90	7,259	1.378	3.3965	
0.85	6,856	1.459	3.3847	
0.80	6,452	1.550	3.3737	
0.75	6,049	1.653	3.3636	
0.70	5,646	1.771	3.3543	
0.65	5,243	1.907	3.3457	

(*continued*)

TABLE II (*Continued*)

Gallium Arsenide

eV	cm^{-1}	μm	n	k
0.60	4,839	2.066	3.3378	
0.55	4,436	2.254	3.3306	
0.50	4,033	2.480	3.3240	
0.45	3,629	2.755	3.3180	
0.40	3,226	3.100	3.3125	
0.35	2,823	3.542	3.3075	
0.30	2,420	4.133	3.3027	
0.29	2,339	4.275	3.3017	
0.28	2,258	4.428	3.3008	
0.27	2,178	4.592	3.2998	
0.26	2,097	4.768	3.2988	
0.25	2,016	4.959	3.2978	
0.24	1,936	5.166	3.2968	
0.23	1,855	5.391	3.2954	
0.22	1,774	5.636	3.2946	
0.21	1,694	5.904	3.2934	
0.20	1,613	6.199	3.2921	
0.19	1,532	6.526	3.2907	
0.18	1,452	6.888	3.2891	
0.17	1,371	7.293	3.2874	
0.16	1,290	7.749	3.2854	
0.15	1,210	8.266	3.2831	
0.14	1,129	8.856	3.2803	
0.1347	1,087	9.2		4.4×10^{-7} [6]
0.13	1,048	9.537	3.2769	
0.1239	1,042	9.6		6.1
0.12	967.9	10.33	3.2727	
0.1169	943.4	10.6		7.6×10^{-7}
0.11	887.2	11.27	3.2671	
0.100	806.5	12.40	3.2597	4.93×10^{-6} [4]
0.098	790.4	12.65		1.61×10^{-5}
0.096	774.3	12.91		3.49
0.095	766.2	13.05		3.63
0.094	758.2	13.19		2.72
0.092	742.0	13.48		1.61
0.090	725.9	13.78	3.2493	1.64
0.088	709.8	14.09		2.24
0.086	693.6	14.42		2.40
0.084	677.5	14.76		2.11
0.082	661.4	15.12		2.16
0.080	645.2	15.50	3.2336	2.83
0.078	629.1	15.90		4.55
0.076	613.0	16.31		7.66
0.074	596.8	16.75		9.46×10^{-5}
0.073	588.8	16.98		1.00×10^{-4}
0.072	580.7	17.22		1.50
0.071	572.6	17.46		2.05

TABLE II (*Continued*)

Gallium Arsenide

eV	cm^{-1}	μm	n	k
0.070	564.6	17.71	3.2081	2.32
0.069	556.5	17.97		6.00×10^{-4}
0.068	548.5	18.23		1.17×10^{-3}
0.067	540.4	18.51		2.59
0.066	532.3	18.79		4.18
0.0655	528.3	18.93		6.10
0.065	524.3	19.07	3.1886	8.27
0.0645	520.2	19.22	3.205 [2, 3]	6.27
0.064	516.2	19.37		4.85
0.0635	512.2	19.53		4.83
0.063	508.1	19.68		4.85
0.0625	504.1	19.84		4.23
0.062	500.1	20.00		4.17
0.0615	496.0	20.16		4.18
0.061	492.0	20.33		4.09
0.060	483.9	20.66	3.1609 [5]	3.45
0.0595	480.0	20.84	3.176 [2, 3]	3.18
0.059	475.9	21.01		3.19
0.058	467.8	21.38		3.57
0.057	459.7	21.75	3.157	4.50
0.0565	455.7	21.94		4.78
0.056	451.7	22.14		4.84
0.0555	447.6	22.34		4.97
0.055	443.6	22.54		5.32
0.054	435.5	22.96	3.126	4.56
0.053	427.5	23.39		3.68
0.0525	423.4	23.62		3.38
0.052	419.4	23.84	3.100	3.43
0.051	411.3	24.31		3.71
0.050	403.3	24.80		2.74
0.0495	399.2	25.05	3.058	2.07
0.049	395.2	25.30		2.07
0.0485	391.2	25.56		2.17
0.048	387.1	25.83		2.10
0.047	379.1	26.38	2.997	2.33
0.046	371.0	26.95		2.91
0.045	362.9	27.55		3.94
0.04463	360	27.78	2.913	6.50 [2, 3]
0.044	354.9	28.18		5.15 [4]
0.04339	350	28.57	2.851	8.40 [2, 3]
0.043	346.8	28.83		8.95×10^{-3} [4]
0.04215	340	29.41	2.770	1.13×10^{-2} [2, 3]
0.04092	330	30.30	2.659	1.59
0.03968	320	31.25	2.495	2.43
0.03906	315	31.75	2.380	3.14

(*continued*)

TABLE II (*Continued*)

Gallium Arsenide

eV	cm^{-1}	μm	n	k
0.03844	310	32.26	2.229	4.21
0.03782	305	32.79	2.020	6.02
0.03720	300	33.33	1.707	9.59×10^{-2}
0.03707	299	33.44	1.623	0.107
0.03695	298	33.56	1.529	0.122
0.03682	297	33.67	1.422	0.141
0.03670	296	33.78	1.298	0.166
0.03658	295	33.90	1.151	0.201
0.03645	294	34.01	0.975	0.257
0.03633	293	34.13	0.761	0.357
0.03620	292	34.25	0.536	0.552
0.03608	291	34.36	0.391	0.826
0.03596	290	34.48	0.323	1.09
0.03583	289	34.60	0.291	1.34
0.03571	288	34.72	0.275	1.57
0.03558	287	34.84	0.267	1.79
0.03546	286	34.96	0.266	2.01
0.03534	285	35.09	0.270	2.23
0.03521	284	35.21	0.278	2.46
0.03509	283	35.33	0.290	2.69
0.03496	282	35.46	0.307	2.94
0.03484	281	35.59	0.329	3.20
0.03472	280	35.71	0.358	3.48
0.03459	279	35.84	0.395	3.79
0.03447	278	35.97	0.443	4.14
0.03434	277	36.10	0.506	4.52
0.03422	276	36.23	0.592	4.97
0.03409	275	36.36	0.713	5.49
0.03397	274	36.50	0.890	6.12
0.03385	273	36.63	1.17	6.91
0.03372	272	36.76	1.64	7.94
0.03360	271	36.90	2.56	9.32
0.03348	270	37.04	4.66	11.0
0.03341	269.5	37.10	6.63	11.6
0.03335	269	37.17	9.30	11.3
0.03329	268.5	37.24	11.6	9.37
0.03323	268	37.31	12.4	6.74
0.03317	267.5	37.38	12.0	4.66
0.03310	267	37.45	11.3	3.30
0.03304	266.5	37.52	10.6	2.43
0.03298	266	37.59	9.90	1.87
0.03286	265	37.74	8.87	1.20
0.03273	264	37.88	8.12	0.844
0.03261	263	38.02	7.55	0.629
0.03248	262	38.17	7.11	0.489
0.03236	261	38.31	6.76	0.393
0.03224	260	38.46	6.47	0.323

TABLE II (*Continued*)

Gallium Arsenide

eV	cm^{-1}	μm	n	k
0.03162	255	39.22	5.57	0.153
0.03100	250	40.00	5.08	9.02×10^{-2}
0.02976	240	41.67	4.57	4.26
0.02852	230	43.48	4.30	2.49
0.02728	220	45.45	4.13	1.63
0.02604	210	47.62	4.02	1.15×10^{-2}
0.02480	200	50.00	3.93	8.49×10^{-3}
			3.87 [1]	
0.02356	190	52.63		1.09×10^{-2} [12]
0.02232	180	55.56		1.22
0.02108	170	58.82		1.25×10^{-2}
0.02066	166.7	60	3.77 [2, 3]	3.89×10^{-3} [2, 3]
			3.74 [1]	6.92×10^{-3} [1]
0.01984	160	62.50		1.15×10^{-2} [12]
0.01860	150	66.67		6.4×10^{-3}
0.01771	142.9	70	3.71 [2, 3]	3.79 [1]
			3.68 [1]	
0.01736	140	71.43		5.0 [12]
0.01612	130	76.92		4.4
0.01550	125	80	3.681 [2, 3]	1.84 [2, 3]
			3.65 [1]	3.18 [1]
0.01488	120	83.33		3.9 [12]
0.01378	111.1	90	3.662 [2, 3]	
			3.635 [1]	2.86 [1]
0.01364	110	90.91		3.6 [12]
0.01240	100	100	3.650 [2, 3]	3.6
			3.625 [1]	2.78 [1]
0.01116	90	111.1		3.8 [12]
0.009919	80	125.0		4.2
0.008679	70	142.9		3.5
0.008266	66.67	150	3.623 [2, 3]	2.14 [1]
			3.62 [1]	
0.007439	60	166.7		2.1 [12]
0.006199	50.00	200	3.615 [2, 3]	1.8 [12]
			3.61 [1]	
0.004959	40	250.0		1.4
0.004133	33.33	300	3.611 [2, 3]	
			3.60 [1]	
0.003720	30	333.3		1.1
0.003100	25	400		1.2
0.002480	20	500	3.607 [2, 3]	1.3
0.001860	15	667		1.2
0.001240	10	1000	3.606	

Gallium Phosphide (GaP)

A. BORGHESI and G. GUIZZETTI
Dipartimento di Fisica "A. Volta" and
Gruppo Nazionale di Struttura della Materia del CNR
Università di Pavia
Pavia, Italy

The room-temperature values of n and k tabulated here were obtained from the following works and references therein: Kleinman and Spitzer [1], Barker [2], Parsons and Coleman [3], Abagyan *et al.* [4, 5], Giehler and Jahne [6], and Pikhtin *et al.* [7] for the medium and far infrared; Spitzer *et al.* [8], Bond [9], Dean and Thomas [10], Dean *et al.* [11], Remenyuk *et al.* [12], Nelson and Turner [13], and Pikhtin and Yas'kov [7, 14, 15] for the near infrared and visible; and Philipp and Ehrenreich [16], Cardona *et al.* [17, 18], Stokowski and Sell [19], Gudat *et al.* [20], and Jungk [21] for the visible–ultraviolet and the vacuum ultraviolet.

A composite smooth-curve plot is given in Fig. 3. Numerical values are given in Table IV with appropriate references.

In the infrared near the transverse optic mode ($\nu_T \simeq 27.5$ μm), where the absorption coefficient α is too large to allow transmission T measurements using the thinnest samples available, bulk reflectance R measurements at near-normal incidence were performed [1, 6]. Values for n and k were obtained from a Kramers–Kronig (KK) analysis [2] or by fitting R (from 13 to 42 μm) within the experimental error by classical dispersion theory [1]. As a by-product of this procedure, the optical constants were calculated and checked against T measurements in the regions outside the fundamental band. At longer wavelengths, transmission samples of thicknesses from 30 μm to 1 mm were used; k was derived from T and R, including multiple-reflection effects; n was deduced from the interference transmission pattern.

All the samples, except those in Kleinman and Spitzer [1], were single crystals grown by different techniques [floating zone, Czochralski, vapor transport, and liquid encapsulation Czochralski (*LEC*)], both of n- and p-type with free-carrier density N ranging from $< 5 \times 10^{15}$ to 10^{18} cm^{-3}. Some transmission samples [1, 4] were copper compensated to reduce the background absorption, and their surfaces were mechanically polished and etched

HANDBOOK OF OPTICAL CONSTANTS OF SOLIDS

Copyright © 1985 by Academic Press, Inc.
All rights of reproduction in any form reserved.
ISBN 0-12-544420-6

in concentrated bromine. In the other cases no description of the surface treatment was given.

The R values in the infrared from various labs agree to within the experimental uncertainty. It was determined that differences in the free-carrier concentration had no effect on R. The n values for $\lambda \geq 50$ μm from Parsons and Coleman [3] and Abagyan *et al.* [4] present a difference of 0.28% at $\lambda = 50$ μm, which lowers to 0.2% at $\lambda = 1000$ μm. In Abagyan *et al.* [4] the error Δn in n, resulting from the measurement of the sample thickness and of wavelength λ, is quoted not exceeding 0.005, while in Parsons and Coleman [3] n is quoted with four decimal places and its values are those reported in Table IV for 50 μm $\leq \lambda \leq 400$ μm.

Parsons and Coleman [3] fit the infrared data and the accurate n data from Bond [9] and Nelson and Turner [13] in the 0.5–4.0-μm range by using for the complex dielectric function $\tilde{\varepsilon}$ the following form proposed by Barker [2]:

$$\tilde{\varepsilon}(\nu) = 1 + \sum_{i=1}^{3} \frac{S_{ei}\nu_{ei}^2}{\nu_{ei}^2 - \nu^2} + \frac{S_0\left(1 - \sum_{j=1}^{2} S_j\right)}{\nu_0^2 - \nu^2 + i\nu\gamma_0 - \nu_0^2 \sum_{j=1}^{2} [S_j\nu_j^2/(\nu_j^2 - \nu^2 + i\nu\gamma_j)]}, \tag{1}$$

i.e., a classical-oscillator equation, where S_i, ν_i^2, and γ_i are the oscillator strength, restoring force, and linewidth, respectively. The second term in Eq. (1) represents the electronic contribution and the third one the lattice contribution with frequency-dependent damping. The fit parameters, given in Table III, are the same used by Barker [2] to fit α, R, and Raman data near the transverse optic mode, except S_0, which had to be increased from 2.01 to 2.056 for best fit. The net result of this fit is that the refractive index of GaP can be calculated from Eq. (1) to an accuracy somewhat better than four figures from microwave to visible frequencies. In particular, in the range 30–200 μm the fit agrees with the experimental n to a few units in the fourth decimal place ($\pm 0.03\%$) and yields the precise value $\varepsilon_0 = 11.147$ for the static relative dielectric constant. In Table IV we have labeled this fit with n_f for the data of Barker [2].

Also, Pikhtin *et al.* [7] proposed an analytic dispersion relationship for n in the 0.5–1000-μm spectral range; it has only six parameters and is simpler than Eq. (1) but less accurate ($\pm 0.8\%$). However, it is useful to report it, since by means of a relation in Pikhtin *et al.* [7] it has been possible also to fit spectra at 105 K. The fit parameters are from Pikhtin *et al.* [7].

For frequencies above or below $\nu_T \equiv \nu_0$, the k spectrum has considerable structure and values much higher than those predicted from Eq. (1). Since the same bands are observed in compensated and uncompensated samples, they are attributed to absorption by the lattice (combination bands) [1, 2]. However, the α spectra from different labs are in qualitative but not in quantitative agreement. In the 12–20-μm region we have tabulated the

data from Pikhtin and Yas'kov [15] because the n-type sample was monocrystalline, not intentionally doped, with the lowest carrier concentration (1.15×10^{17} cm^{-3}). Besides, T spectra were obtained with a double-beam spectrophotometer, and R was checked against accurate measurements of n. Near ν_T the reported values (labeled k_f) were obtained from Eq. (1).

As for the 4–23-μm range, Table IV contains experimental values of n deduced from the positions of interference peaks in T [5, 7]. The thickness of the samples and the interference order were accurately determined by comparing, in the 0.5–4-μm range, the results obtained with this method and with the more precise results obtained by using the prism method. The data from Abagyan *et al.* [5] and Pikhtin *et al.* [7] agree to within the 0.1%, with an error [7] of $\pm 0.2\%$ at 4 μm and of $\pm 0.47\%$ at 23 μm. The samples were n type, undoped, and high resistivity ($N < 5 \times 10^{16}$ cm^{-3}). Measurements performed on low-resistivity samples, doped both n- and p-type up to 1.7×10^{18} cm^{-3} have shown that for $\lambda \geq 3$-μm doping reduces n [5, 7]. For this reason we have disregraded older data for n [22, 23] that are $\sim 2\%$ lower. The absorption coefficient between 1 and 12 μm is free-carrier-like; it typically increases with wavelength and with free-carrier concentration. Besides, all the n-type samples show a broad absorption band in the 1–4-μm region that does not occur in p-type material. In this region there are many measurements of α [8, 12, 15] on crystals doped with different impurities and with carrier densities ranging from 10^{17} to 10^{18} cm^{-3}. We have tabulated those from Pikhtin and Yas'kov [15] on the basis of the same reasons that determined the choice in the 12–20-μm region.

In the 0.53–4-μm range, where GaP is nearly transparent, n measurements were carried out by the method of prism minimum deviation [7, 9, 13] and by interference spacing [11] at 2.24 eV (0.5536 μm) and 2.62 eV (0.4733 μm). The scattering of n data from different authors is within ± 0.0025. In Pikhtin *et al.* [7] the absolute values of n were determined to within ± 0.0025; in Bond [9] n was measured to the fourth decimal. In Nelson and Turner [13] the uncertainty in the individual value was ± 0.0002; however, the value obtained for different prisms differed by substantially more than this. The differences are believed to be real and to reflect the variation that can be expected from different samples of GaP. To include the value for all of the prisms, an uncertainty of ± 0.0012 would have to be assigned to the n values from 0.545 to 0.70 μm in Table IV. These variations were not correlated with the level of doping, which varied from no intentional doping to 10^{18} cm^{-3} with the type of dopant (Te, Sn, Zn) or the method of crystal growth (high-pressure boat growth, floating zone, or solution growth).

The intrinsic electronic absorption edge of single crystals was presented and analyzed by Spitzer *et al.* [8] at 300 K, by Dean and Thomas [10] between 1.6 and 300 K, and by Pikhtin and Yas'kov [14] between 4.2 and 500 K. The results agree qualitatively, although there is some quantitative difference. In Table IV we have reported in the 0.54–0.57-μm range the values from Dean and Thomas [10] that are a little lower than those reported

by Spitzer *et al.* [8] and Pikhtin and Yas'kov [14] and were obtained with exceptionally perfect single crystals grown by a modified wet-hydrogen transport process. All crystals had very high resistivities and three different thicknesses (0.0212, 0.0724, and 0.362 cm).

The 0.8–0.2-μm region straddling the fundamental band gap has been measured more recently by ellipsometry on surfaces containing native oxides that are mathematically "removed" in the analysis, or samples are chemically polished to remove this oxide and then put into an inert atmosphere while the measurement of the ellipsometric parameters ψ and Δ are performed [24]. We have included these values and at the ends of this spectral region have overlapped other data for comparison.

The optical properties from the fundamental absorption edge (0.53 μm) to about 0.08 μm can be determined by KK analysis of normal-incidence reflectance data. The R data between 0.53 and 0.21 μm obtained with a sensitive double-beam spectrophotometer by Stokowski and Sell [19] provide a considerable improvement in sensitivity over the older measurements reported by Philipp and Ehrenreich [16] and Seraphin and Bennett [23]. The samples used in Stokowski and Sell [19] were grown by the Czochralski method, were sliced parallel to a {111} face, and a weak ($\sim$0.2%) bromine–methanol solution was used as a polishing etch. The absolute-reflectance values were accurate to within $\pm$3% of the reflectivity. The data were about 10% higher than those in Philipp and Ehrenreich [16], in agreement within 1% with those calculated from n at 0.4733 μm as measured by Dean *et al.* [11]. In the 0.21–0.08-μm range no other R data are available except those from Philipp and Ehrenreich [16].

Absorption and reflection measurements in the 0.08–0.03-μm range [18, 20] and only absorption measurements in the 0.08–0.008-μm range [17] were performed with synchrotron radiation and with a typical resolution of 2 Å over the whole spectral range. The crystalline samples for transmission were obtained by flash evaporation and samples of at least three different thicknesses between 500 and 1500 Å were used. The thicknesses were determined with a Tolansky interferometer with an accuracy of about 10% and also during evaporation with a calibrated quartz-crystal monitor. The absolute values determined for the absorption coefficient were affected by an error of less than 20%, which arose mainly from uncertainties in the thicknesses. The R measurements [20] were performed under nearly normal incidence [15] on polished bulk samples, etched in bromine–methanol solution. Since the incoming and reflected intensities were not determined simultaneously, no accurate absolute values of R were obtained ($\pm$50%); therefore the measured reflectivities were scaled so as to coincide around the first maximum at 0.059 μm with the ones calculated by the KK analysis transforms from α data. Some discrepancies between scaled R and R from KK analysis may be due to a structural difference between the thin films used to measure T and the bulk samples for R. Also, there may be some influence of the surface treatment and of light scattering. Larger discrepancies be-

tween the α experimental data from Cardona *et al.* [17, 18] and the α values obtained from KK processing of early R data [16] can be attributed to R-limited range of R spectra and to the inadequacy of the conventional gas-discharge spectroscopic sources; in fact, hot-cathode argon lamps have typical separation of about 1 eV between adjacent lines, equal to the expected spin-orbit splitting of core levels (0.53 eV for Ga) and to separation between peaks in the density of conduction states.

In Table IV n and k values in the 0.44–0.08-μm range have been obtained by KK transform on R spectra from Philipp and Ehrenreich [16] and Stokowski and Sell [19], extended to shorter wavelengths with the data of Gudat *et al.* [20] and longer wavelengths (visible and infrared) with those of Kleiman and Spitzer [1], Giehler and Jahne [6], and Bond [9]. The results are in fair agreement with the dielectric function ellipsometrically determined between 0.36 and 0.31 μm [21].

REFERENCES

1. D. A. Kleinman and W. G. Spitzer, *Phys. Rev.* **118**, 110 (1960).
2. A. S. Barker, Jr., *Phys. Rev.* **165**, 917 (1968).
3. D. F. Parsons and P. D. Coleman, *Appl. Opt.* **10**, 1683 (1971).
4. S. A. Abagyan, G. A. Ivanov, Y. E. Shanurin, and V. I. Amosov, *Sov. Phys. Semicond.* **5**, 889 (1971).
5. S. A. Abagyan, G. A. Ivanov, A. P. Izergin, and Y. E. Shanurin, *Sov. Phys. Semicond.* **6**, 985 (1972).
6. M. Giehler and E. Jahne, *Phys. Status Solidi B* **73**, 503 (1976).
7. A. N. Pikhtin, V. T. Prokopenko, and A. D. Yas'kov, *Sov. Phys. Semicond.* **10**, 1224 (1976).
8. W. G . Spitzer, M. Gershenzon, C. J. Forsch, and D. F. Gibbs, *J. Phys. Chem. Sol.* **11**, 339 (1959).
9. W. L. Bond, *J. Appl. Phys.* **36**, 1674 (1965).
10. P. J. Dean and D. G. Thomas, *Phys. Rev.* **150**, 690 (1966).
11. P. J. Dean, G. Kaminsky, and R. B. Zetterstrom, *J. Appl. Phys.* **38**, 3551 (1967).
12. A. D. Remenyuk, L. G. Zabelina, Yu. I. Ukhanov, and Y. V. Shmartzev, *Sov. Phys. Semicond.* **2**, 557 (1968).
13. D. F. Nelson and E. H. Turner, *J. Appl. Phys.* **39**, 3337 (1968).
14. A. N. Pikhtin and D. A. Yas'kov. *Sov. Phys. Solid State* **11**, 455 (1969).
15. A. N. Pikhtin and D. A. Yas'kov. *Phys. Status Solidi* **34**, 815 (1969).
16. H. R. Philipp and H. Ehrenreich, *in* "Semiconductors and Semimetals" (R. K. Willardson and A. C. Beer, eds.), Vol. 3, Chapter 4. Academic, New York, 1967.
17. M. Cardona, W. Gudat, B. Sonntag, and P. Y. Yu, *Proc. Int. Conf. Phys. Semicond. Cambridge, 1970*, p. 208. U.S. Atomic Energy Commission, Oak Ridge, Tennessee, 1970.
18. M. Cardona, W. Gudat, E. E. Koch, M. Skibowski, B. Sonntag, and P. Yu, *Phys. Rev. Lett.* **25**, 659 (1970).
19. S. E. Stokowski and D. D. Sell, *Phys. Rev. B* **5**, 1636 (1972).
20. W. Gudat, E. E. Koch, P. Y. Yu, M. Cardona, and C. M. Penchina, *Phys. Status Solidi B* **52**, 505 (1972).
21. G. Jungk, *Phys. Status Solidi B* **67**, 85 (1975).
22. H. Welker, *J. Electron.* **1**, 181 (1955).
23. B. O. Seraphin and H. E. Bennett, *in* "Semiconductors and Semimetals" (R. K. Willardson and A. C. Beer, eds.), Vol. 3, p. 219. Academic, New York, 1967.
24. D. E. Aspnes and A. A. Studna, *Phys. Rev. B* **27**, 985 (1983); D. E. Aspnes and A. A. Studna, private communication (1982).

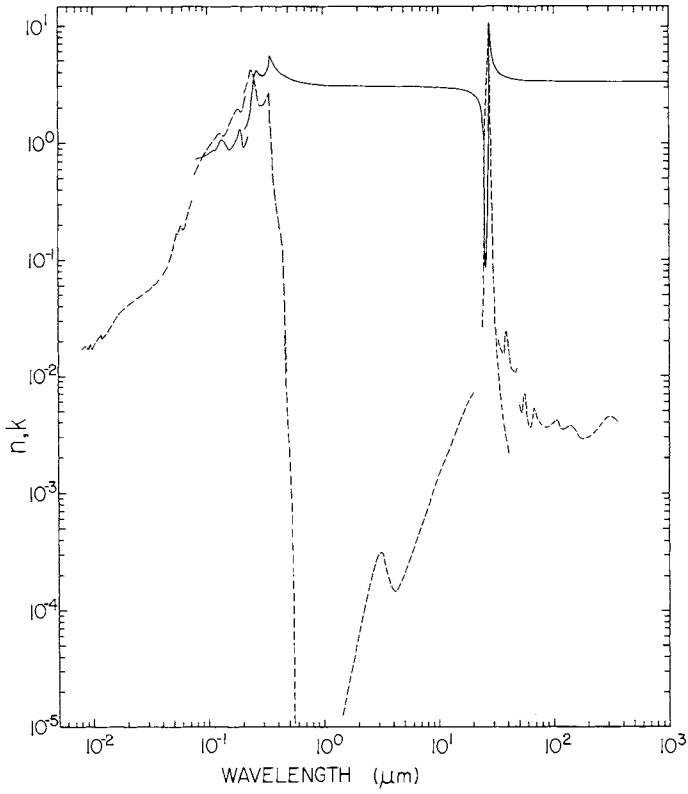

Fig 3. Log–log plot of n (——) and k(– – –) versus wavelength in micrometers for gallium phosphide.

TABLE III

Dielectric Parameters for Gallium Phosphide at 300 K[a]

Electronic		Ionic	
S_{e1}	2.570	ε_∞	9.091
ν_{e1}	29,000 cm^{-1}	S_0	2.056
S_{e2}	4.131	ν_0	363.4 cm^{-1}
ν_{e2}	42,700 cm^{-1}	γ_0	1.1 cm^{-1}
S_{e3}	1.390	S_1	7.0×10^{-4}
ν_{e3}	58,000 cm^{-1}	ν_1	349.4 cm^{-1}
		γ_1	21 cm^{-1}
		S_2	3.5×10^{-4}
		ν_2	358.4 cm^{-1}
		γ_2	12.6 cm^{-1}

[a] Data from Parsons and Coleman [3].

TABLE IV

Values of n and k for Gallium Phosphide Obtained from Various References[a]

eV	cm^{-1}	μm	n	n_f	k	k_f
154.0		0.00805			1.7×10^{-2} [17]	
144.0		0.00861			1.8	
134.0		0.00925			1.7	
131.2		0.00945			1.85	
126.0		0.00985			1.7	
122.0		0.0102			1.8	
119.0		0.0104			1.9	
115.0		0.0108			2.0	
110.0		0.0113			2.15	
109.2		0.0114			2.2	
107.0		0.0116			2.2	
106.1		0.0117			2.25	
105.0		0.0118			2.25	
104.0		0.0119			2.1	
100.0		0.0124			2.15	
96.0		0.0129			2.25	
90.0		0.0138			2.5	
80.0		0.0155			3.0	
70.0		0.0177			3.6	
66.0		0.0188			3.8	
60.0		0.0207			4.15	
50.0		0.0248			4.7	
45.0		0.0275			5.0	
40.0		0.0310			5.5	
37.0		0.0335			6.1	

(*continued*)

[a] References are indicated in brackets. Here n_f and k_f are fits to experimental data obtained with Eq. (1) and the parameters of Table III.

TABLE IV (*Continued*)

Gallium Phosphide

eV	cm^{-1}	μm	n	n_f	k	k_f
35.0		0.0354			6.1	
33.0		0.0376			6.7	
31.0		0.0400			7.3 [20]	
29.0		0.0427			8.0	
27.0		0.0459			9.3×10^{-2}	
25.0		0.0496			0.122	
24.2		0.0512			0.141	
23.5		0.0528			0.162	
23.1		0.0537			0.169	
22.6		0.0549			0.167	
22.2		0.0558			0.174	
21.8		0.0569			0.187	
21.4		0.0579			0.193	
21.2		0.0585			0.197	
21.0		0.0590			0.195	
20.6		0.0602			0.190	
20.5		0.0605			0.188	
20.0		0.0620			0.180	
19.5		0.0636			0.192	
19.0		0.0652			0.213	
18.0		0.0689			0.269	
17.0		0.0729			0.323	
16.0		0.0775	0.730 [16–20]		0.537 [16–20]	
15.0		0.0826	0.748		0.628	
14.0		0.0886	0.759		0.718	
13.0		0.0954	0.780		0.825	
12.0		0.1033	0.822		0.938	

11.0		0.1127	0.873	1.040
10.5		0.1181	0.875	1.104
9.95		0.1246	0.998	1.224
9.5		0.1305	1.076	1.183
9.05		0.1370	1.047	1.151
8.5		0.1459	0.943	1.224
8.05		0.1540	0.872	1.401
7.5		0.1653	0.944	1.652
7.0		0.1771	1.054	1.876
6.75		0.1837	1.200	1.968
6.55		0.1893	1.301	1.896
6.4		0.1937	1.207	1.836
6.0	48,390	0.2066	0.906	2.281
			1.309 [24]	2.690 [24]
5.94	47,910	0.2087	1.327	2.766
5.9	47,590	0.2101	1.327	2.803
5.84	47,100	0.2123	1.342	2.882
5.8	46,780	0.2138	1.348	2.934
			0.988 [16–20]	2.657 [16–20]
5.74	46,300	0.2160	1.368 [24]	3.028 [24]
5.7	45,970	0.2175	1.385	3.096
5.64	45,490	0.2198	1.418	3.211
5.6	45,170	0.2214	1.444	3.297
5.54	44,680	0.2238	1.494	3.441
5.5	44,360	0.2254	1.543	3.556
5.44	43,880	0.2279	1.660	3.752
5.4	43,550	0.2296	1.778	3.889
5.38	43,390	0.2305	1.851	3.955
5.36	43,230	0.2313	1.936	4.019
5.34	43,070	0.2322	2.028	4.077

(*continued*)

TABLE IV (*Continued*)

Gallium Phosphide

eV	cm^{-1}	μm	n	n_f	k	k_f
5.32	42,910	0.2331	2.134		4.128	
5.30	42,750	0.2339	2.248		4.168	
5.28	42,590	0.2348	2.368		4.192	
5.26	42,420	0.2357	2.490		4.201	
5.24	42,260	0.2366	2.607		4.197	
5.22	42,100	0.2375	2.718		4.185	
5.20	41,940	0.2384	2.825		4.170	
5.18	41,780	0.2394	2.930		4.150	
5.16	41,620	0.2403	3.036		4.123	
5.14	41,460	0.2412	3.144		4.086	
5.12	41,300	0.2422	3.248		4.036	
5.10	41,130	0.2431	3.342		3.975	
5.08	40,970	0.2441	3.424		3.909	
5.06	40,810	0.2450	3.498		3.839	
5.04	40,650	0.2460	3.561		3.768	
5.02	40,490	0.2470	3.615		3.698	
5.00	40,330	0.2480	3.661		3.631	
4.98	40,170	0.2490	3.701		3.567	
4.96	40,000	0.2500	3.739		3.509	
4.94	39,840	0.2510	3.774		3.454	
4.92	39,680	0.2552	3.806		3.404	
4.90	39,520	0.2530	3.844		3.358	
4.88	39,360	0.2541	3.880		3.316	
4.86	39,200	0.2551	3.923		3.269	
4.84	39,040	0.2562	3.970		3.218	
4.82	38,880	0.2572	4.018		3.162	

4.80	38,710	0.2583	4.062	3.096
4.78	38,550	0.2594	4.100	3.024
4.76	38,390	0.2605	4.132	2.949
4.74	38,230	0.2616	4.157	2.871
4.72	38,070	0.2627	4.173	2.791
4.70	37,910	0.2638	4.181	2.712
4.68	37,750	0.2649	4.181	2.634
4.66	37,590	0.2661	4.173	2.560
4.64	37,420	0.2672	4.158	2.491
4.62	37,260	0.2684	4.137	2.427
4.60	37,100	0.2695	4.113	2.371
4.54	36,620	0.2731	4.031	2.241
4.50	36,290	0.2755	3.978	2.180
4.44	35,810	0.2792	3.907	2.117
4.40	35,490	0.2818	3.867	2.090
4.34	35,000	0.2857	3.817	2.066
4.30	34,680	0.2883	3.792	2.058
4.24	34,200	0.2924	3.765	2.057
4.20	33,880	0.2952	3.754	2.063
4.14	33,390	0.2995	3.748	2.082
4.10	33,070	0.3024	3.752	2.100
4.04	32,580	0.3069	3.769	2.137
4.00	32,260	0.3100	3.790	2.171
3.94	31,780	0.3147	3.840	2.240
3.90	31,460	0.3179	3.890	2.303
3.88	31,290	0.3195	3.923	2.343
3.86	31,130	0.3212	3.966	2.389
3.84	30,970	0.3229	4.021	2.443
3.82	30,810	0.3246	4.095	2.502
3.80	30,650	0.3263	4.196	2.562

(*continued*)

TABLE IV (*Continued*)

Gallium Phosphide

eV	cm^{-1}	μm	n	n_f	k	k_f
3.78	30,490	0.3280	4.328		2.615	
3.76	30,330	0.3297	4.497		2.649	
3.74	30,160	0.3315	4.700		2.646	
3.72	30,000	0.3333	4.927		2.585	
3.70	29,840	0.3351	5.149		2.451	
3.68	29,680	0.3369	5.328		2.250	
3.66	29,520	0.3388	5.437		2.010	
3.64	29,360	0.3406	5.472		1.766	
3.62	29,200	0.3425	5.454		1.550	
3.60	29,040	0.3444	5.406		1.368	
3.58	28,870	0.3463	5.339		1.217	
3.56	28,710	0.3483	5.268		1.089	
3.54	28,550	0.3502	5.194		0.982	
3.52	28,390	0.3522	5.121		0.893	
3.50	28,230	0.3542	5.050		0.819	
3.48	28,070	0.3563	4.983		0.752	
3.46	27,910	0.3583	4.920		0.697	
3.44	27,750	0.3604	4.861		0.649	
3.42	27,580	0.3625	4.805		0.605	
3.40	27,420	0.3647	4.751		0.568	
3.38	27,260	0.3668	4.700		0.534	
3.36	27,100	0.3690	4.651		0.503	
3.34	26,940	0.3712	4.604		0.475	
3.32	26,780	0.3734	4.560		0.449	
3.30	26,620	0.3757	4.518		0.426	
3.28	26,450	0.3780	4.479		0.407	

3.26	26,290	0.3803	4.442	0.388
3.24	26,130	0.3827	4.406	0.369
3.22	25,970	0.3850	4.372	0.353
3.20	25,810	0.3875	4.339	0.337
3.18	25,650	0.3899	4.308	0.323
3.16	25,490	0.3924	4.278	0.310
3.14	25,330	0.3949	4.249	0.298
3.12	25,160	0.3974	4.222	0.285
3.10	25,000	0.4000	4.196	0.275
3.08	24,840	0.4025	4.171	0.264
3.06	24,680	0.4052	4.147	0.253
3.04	24,520	0.4078	4.124	0.244
3.02	24,360	0.4105	4.102	0.233
3.00	24,200	0.4133	4.081	0.224
2.98	24,040	0.4161	4.060	0.218
2.96	23,870	0.4189	4.041	0.208
2.94	23,710	0.4217	4.023	0.202
2.92	23,550	0.4246	4.006	0.194
2.90	23,390	0.4275	3.990	0.183
2.88	23,230	0.4305	3.976	0.176
2.86	23,070	0.4335	3.964	0.165
2.84	22,910	0.4366	3.952	0.152
2.82	22,740	0.4397	3.936	0.135
2.80	22,580	0.4428	3.919	0.118
2.78	22.420	0.4460	3.904	0.103
2.76	22,260	0.4492	3.896	8.5×10^{-2}
2.743	22,120	0.452		3.12 [8, 23]
2.74	22,100	0.4525	3.869	5.7 [24]
2.731	22,030	0.454		2.36 [8, 23]
2.72	21,940	0.4558	3.835	3.5 [24]

(*continued*)

TABLE IV (*Continued*)

Gallium Phosphide

eV	cm^{-1}	μm	n	n_f	k	k_f
2.719	21,930	0.456			1.87 [8, 23]	
2.713	21,880	0.457			1.59	
2.701	21,780	0.459			1.43	
2.70	21,780	0.4592	3.805		2.7 [24]	
2.678	21,600	0.463			1.16×10^{-2} [8, 23]	
2.672	21,550	0.464			9.49×10^{-3}	
2.64	21,290	0.4696	3.730		1.5×10^{-2} [24]	
2.638	21,280	0.470			7.68×10^{-3} [8, 23]	
2.621	21,140	0.473	3.73 [11]		6.37	
2.60	20,970	0.4769	3.691 [24]			
2.599	20,960	0.477			5.47	
2.583	20,830	0.480			4.66	
2.572	20,750	0.432			4.29	
2.541	20,490	0.488			3.41	
2.54	20,490	0.4881	3.638 [24]			
2.52	20,320	0.492			3.06	
2.500	20,160	0.496	3.605		2.54	
2.480	20,000	0.500	3.590		2.47	
			3.4595 [9]			
2.475	19,960	0.501			2.18	
2.460	19,840	0.504			1.85	
2.44	19,680	0.5081	3.561 [24]			
2.431	19,610	0.510			1.42	
2.412	19,450	0.514			1.19	
2.40	19,360	0.5166	3.535			
2.389	19,270	0.519			1.04×10^{-3}	
2.380	19,190	0.521			8.57×10^{-4}	

2.34	18,870	0.5299	3.497		
2.339	18,870	0.530			5.34
2.322	18,730	0.534			3.34
2.322	18,730	0.534			3.34
2.30	18,550	0.5391	3.474		2.48 [10]
2.29	18,470	0.5414			1.88 [10]
2.28	18,390	0.5438	3.463		1.3×10^{-4}
2.275	18,350	0.545	3.4522 [13]	3.4491	
2.27	18,310	0.5462			9.3×10^{-5}
2.26	18,230	0.5486	3.452 [24]		6.2
2.254	18,180	0.55	3.4411 [13]	3.4382	4.2
2.24	18,070	0.5535	3.441 [24]		2.7
2.23	17,990	0.5560			1.5×10^{-5}
2.22	17,910	0.5585	3.430		3.1×10^{-6}
2.214	17,860	0.56	3.4203 [13]		
2.21	17,820	0.5610			3.0
2.20	17,740	0.5636	3.421 [24]		1.4×10^{-6}
2.19	17,660	0.5661			6.5×10^{-7}
2.18	17,580	0.5687	3.411		2.8
2.175	17,540	0.57	3.4012 [13]		
2.14	17,260	0.5794	3.393 [24]		
2.138	17,240	0.58	3.3837 [13]		
2.101	16,950	0.59	3.3675		
2.10	16,940	0.5904	3.375 [24]		
2.066	16,670	0.60	3.3524 [13]		
2.04	16,450	0.6078	3.350 [24]		
2.033	16,390	0.61	3.3384 [13]		
2.000	16,130	0.62	3.3254		
			3.334 [24]		
1.968	15,870	0.63	3.3132 [13]		

(*continued*)

TABLE IV (*Continued*)

Gallium Phosphide

eV	cm^{-1}	μm	n	n_f	k	k_f
1.94	15,650	0.6391	3.311 [24]			
1.937	15,630	0.64	3.3018 [13]			
1.907	15,380	0.65	3.2912	3.2891		
1.90	15,320	0.6526	3.295 [24]			
1.879	15,150	0.66	3.2811 [13]			
1.851	14,930	0.67	3.2716			
1.84	14,840	0.6738	3.275 [24]			
1.823	14,710	0.68	3.2626 [13]			
1.80	14,520	0.6888	3.262 [24]			
1.797	14,490	0.69	3.2541 [13]			
1.771	14,290	0.70	3.2462			
1.74	14,030	0.7126	3.245 [24]			
1.70	13,710	0.7293	3.234			
1.64	13,230	0.7560	3.219			
1.60	12,900	0.7749	3.209			
1.550	12,500	0.80	3.1830 [9]			
1.54	12,420	0.8051	3.191 [24]			
1.50	12,100	0.8266	3.178			
1.378	11,110	0.90	3.1430 [9]			
1.240	10,000	1.0	3.1192	3.1173		
1.127	9,091	1.1	3.0981			
1.033	8,333	1.2	3.0844			
0.8856	7,143	1.4	3.0646	3.0646		
0.8551	6,897	1.45			1.27×10^{-5} [15]	
0.7749	6,250	1.6	3.0509	3.0522		
0.7085	5,714	1.75			3.27	

0.6888	5,556	1.8	3.0439		
0.6199	5,000	2.0	3.0379		
0.5767	4,651	2.15			7.70×10^{-5}
0.5636	4,545	2.2	3.0331		
0.5166	4,167	2.4	3.0296	3.0292	
0.4959	4,000	2.5			1.71×10^{-4}
0.4769	3,846	2.6	3.0271		
0.4428	3,571	2.8	3.0236		
0.4275	3,448	2.9			2.88
0.4133	3,333	3.0	3.0215	3.0217	
0.3875	3,125	3.2			3.18
0.3647	2,941	3.4	3.0181		
0.3444	2,778	3.6	3.0166	3.0166	
0.3263	2,632	3.8	3.0159		1.69
0.3100	2,500	4.0	3.0137	3.0137	1.53
0.2952	2,381	4.2			1.47
0.2583	2,083	4.8			1.91
0.2480	2,000	5.0	3.004 [5, 7]	3.007	
0.2254	1,818	5.5	3.001		
0.2175	1,754	5.7			2.95
0.2066	1,667	6.0	2.998	3.001	
0.1907	1,538	6.5	2.995		4.29
0.1771	1,429	7.0	2.992	2.993	
0.1653	1,333	7.5	2.98		
0.1590	1,282	7.8			7.14×10^{-4}
0.1550	1,250	8.0	2.984	2.985	
0.1459	1,176	8.5	2.980		
0.1378	1,111	9.0	2.975	2.975	
0.1305	1,053	9.5	2.970		
0.1292	1,042	9.6			1.3×10^{-3}
0.1240	1,000	10	2.964	2.964	

(*continued*)

TABLE IV (*Continued*)

Gallium Phosphide

eV	cm^{-1}	μm	n	n_f	k	k_f
0.1127	909.1	11	2.951			
0.1033	833.3	12	2.936		2.29	
0.09537	769.2	13	2.918			
0.08856	714.3	14	2.896			
0.08266	666.7	15	2.871	2.868		
0.07749	625.0	16	2.841		4.49	
0.07293	588.2	17	2.803			
0.06888	555.6	18	2.755			
0.06526	526.3	19	2.694 [7]			
0.06199	500.0	20	2.615	2.606	7.16×10^{-3}	
0.05904	476.2	21	2.511			
0.05636	454.5	22	2.354			
0.05391	434.8	23		2.076		
0.05166	416.7	24.0		1.585		2.6×10^{-2}
0.05123	413.2	24.2		1.421		3.3
0.05081	409.8	24.4		1.208		4.6
0.05040	406.5	24.6		0.908		7.2×10^{-2}
0.04999	403.2	24.8		0.360		0.22
0.04959	400.0	25.0		0.108		0.89
0.04881	393.7	25.4		0.086		1.74
0.04805	387.6	25.8		0.103		2.52
0.04769	384.6	26.0		0.123		2.96
0.04696	378.8	26.4		0.208		4.05
0.04626	373.1	26.8		0.515		5.86
0.04592	370.4	27.0		1.064		7.48
0.04575	369.0	27.1		1.740		8.69
0.04558	367.6	27.2		3.231		10.22

0.04541	366.3	27.3		6.580		11.19
0.04525	365.0	27.4		10.314		8.62
0.04509	363.6	27.5		10.483		5.15
0.04492	362.3	27.6		9.501		3.40
0.04460	359.7	27.8		8.060		2.10
0.04428	357.1	28.0		7.348		1.54
0.04366	352.1	28.4		6.431		0.78
0.04275	344.8	29.0		5.578		0.31
0.04217	340.1	29.4		5.182		0.16
0.04133	333.3	30	4.732 [4]	4.765		6.5×10^{-2}
0.04000	322.6	31	4.339			
0.03875	312.5	32	4.115			
0.03815	307.7	32.5			2.07×10^{-2} [2]	
0.03757	303.0	33	3.971			
0.03647	294.1	34	3.869			
0.03542	285.7	35	3.793	3.809	1.67	5.18×10^{-3}
0.03397	274.0	36.5			1.54	
0.03306	266.7	37.5			2.24	
0.03163	255.1	39.2			2.09	
0.03100	250.0	40	3.594	3.606	1.81	2.31
0.02917	235.3	42.5			1.15	
0.02755	222.2	45	3.508	3.518	1.11	1.46
0.02695	217.4	46			1.06	
0.02610	210.5	47.5			1.17×10^{-2}	
0.02480	200.0	50	3.461	3.470	5.77×10^{-3} [3]	1.06×10^{-3}
0.02356	190.0	52.63			4.90	
0.02280	183.93	54.37	3.4440 [3]	3.4435		
0.02244	181.0	55.25			7.03	
0.02173	175.29	57.05	3.4302		5.67	
0.02080	167.78	59.60	3.4238		4.03	

(*continued*)

TABLE IV (*Continued*)

Gallium Phosphide

eV	cm^{-1}	μm	n	n_f	k	k_f
0.02066	166.7	60		3.4200		6.9×10^{-4}
0.02009	162.00	61.73	3.4134		3.67	
0.01859	149.96	66.68	3.4010	3.4015	5.31	
0.01771	142.9	70		3.3947		5.2
0.01727	139.27	71.80	3.3922	3.3915	4.34	
0.01594	128.54	77.80	3.3830	3.3826	3.84	
0.01459	117.70	84.96	3.3754	3.3747	3.65	
0.01363	109.90	90.99	3.3706	3.3697	3.77	
0.01240	100.0	100		3.3639		3.0
0.01168	94.21	106.1	3.3621	3.3609	4.26	
0.01090	87.92	113.7	3.3584	3.3579	3.53	
0.008935	72.07	138.8	3.3522	3.3513	3.81	
0.008266	66.67	150		3.3494		
0.007360	59.36	168.5	3.3463	3.3472	2.95	
0.006567	52.97	188.8	3.3450	3.3454	3.00	
0.006199	50.00	200		3.3447		1.3×10^{-4}
0.005724	46.17	216.6	3.3438	3.3438	3.19	
0.004186	33.76	296.2	3.3399	3.3414	4.53	
0.004133	33.33	300		3.3413		
0.003387	27.32	366.0	3.3407	3.3405	3.93	7.2×10^{-5}
0.003100	25.00	400	3.3331 [4]	3.3402		
0.002480	20.00	500	3.3326	3.3397		
0.002066	16.67	600	3.3323	3.3394		
0.001771	14.29	700	3.3321	3.3392		
0.001550	12.50	800	3.3320	3.3391		
0.001378	11.11	900	3.33195	3.3390		
0.001240	10.00	1000	3.3319	3.3389		

Germanium (Ge)

ROY F. POTTER
Department of Physics and Astronomy
Western Washington University
Bellingham, Washington

Germanium transistor technology in the 1950s was the basis for extensive research activity. Good-quality single crystals became available for studies of the electrical, elastic, and optical properties. Because infrared systems were also developing, Ge was investigated for its photoelectric characteristics as well as its optical properties. Much of the work during this period concerned impurity or doping effects in terms of free-carrier absorption and forbidden-gap determinations. Early optical measurements made on evaporated Ge films had widely scattered results, depending strongly on the conditions of preparation. However, when quality bulk samples became available, measurement results were obtained that have withstood the passage of time remarkably well. Briggs's tabular data [1] for refractive indices between 1.8 and 2.6 μm are within 0.25% of the present-day accepted values. We include these values since they have stood the test of time. Salzberg and Villa [2] measured single-crystal and polycrystalline material almost a decade later for wavelengths between 2 and 16 μm. Their data served as the basis for IR optical design parameters until present day and are within 0.025% of present-day measurements. Cardona *et al.* [3] published results for Ge for several temperatures between 87 and 197 K. An examination of their figures indicates a similar degree of agreement with today's values.

In 1976, Icenogle *et al.* [4] reported refractive-index values for a series of temperatures and wavelengths between 2.5 and 13 μm. These authors claimed a conservative error of approximately 6×10^{-4} in index n for a percentage error of $\sim 0.0125\%$. A few years later, Edwin *et al.* [5] reported very precise results for wavelengths between 8 and 14 μm. The value of their results lies in the fact that two different experimental setups, each in a separate laboratory, were used on the same crystal sample of Ge. The differences between the two laboratories were between 1×10^{-4} and 3×10^{-4} (10^{-2} and $3 \times 10^{-2}\%$). This represents the apparent level of precision currently available for measuring refractive indices of high-index materials. All the experiments discussed so far are based on high-quality, single-crystal (in most instances) germanium

HANDBOOK OF OPTICAL CONSTANTS OF SOLIDS

Copyright © 1985 by Academic Press, Inc.
All rights of reproduction in any form reserved.
ISBN 0-12-544420-6

cut as polished prisms having included angles ranging between 5 and 18°. The angle of minimum deviation was measured to obtain the refractive index. Data of Icenogle *et al.* [4] at 297 K and some data of Edwin *et al.* [5] at 25°C, originally given in tabular form, are listed in Table V. The tabulated data are plotted in Fig. 4.

The precision of the data of Icenogle *et al.* [4] was such that Barnes and Piltch [6] used them as a basis for evaluating the coefficients of a temperature-dependent, Sellmeier-type equation

$$n^2 = A + B\lambda^2/(\lambda^2 - C) + D\lambda^2/(\lambda^2 - E).$$

Using the temperature-dependent values of n, they found the following values for the coefficients:

$$A = -6.040 \times 10^{-3}T + 11.05128,$$

$$B = 9.295 \times 10^{-3}T + 4.00536,$$

$$C = -5.392 \times 10^{-4}T + 0.5999034,$$

$$D = 4.151 \times 10^{-4}T + 0.09145,$$

$$E = 1.51408T + 3426.5.$$

We have evaluated this expression for "room temperture" of 18°C (291 K), over a large infrared wavelength range, and these values are included in Table V. Some comparison with the results from the several experiments outlined here can be made in the table. The Sellmeier equation represents the accurate values for high-grade optical-quality germanium within 0.025%, or better, over the infrared spectral range 2.5–14 μm and can be extrapolated to 2.0 and 40 μm.

Many more measurements have been reported for this spectral range, but in most cases the specimens were thin films, amorphous material, or heavily doped. Evaporated films do not, in general, have properties representative of bulk material, so such results are applicable only to material evaporated or sputtered by a given recipe. Li [7] tabulates most such measurements that have appeared in the literature in the past half-century. Li [7] also gives a table of recommended values for the infrared at various temperatures.

In the infrared spectral region there are two contributions to the intrinsic absorption properties of germanium. When the infrared radiation field interacts with the crystal lattice, it is described as a photon–phonon interaction. Since selection rules include the conservation of energy and wave vector or momentum, the spectrum will include features related to the photon excitation of multiple phonons. Such "phonon" bands have been observed for Ge. Collins and Fan [8] reported absorption coefficients for phonon bands for 300 K. These have been read from a graph and are listed in Table V. Values of Lax and Burstein [9] are comparable. More recently, Aronson *et al.* [10] have measured the absorption coefficient for high-resistivity Ge ($\sim 50\ \Omega$ cm) at 300 K. They used samples of different thickness measuring the transmit-

tance. We have read values from a graph and tabulate these. Their results overlap the data of Collins and Fan [8]. The band at 300 cm^{-1} in the data of Collins and Fan [8] occurs at 280 cm^{-1} in the data of Aronsen *et al.* [10]. Stierwalt and Potter [11] measured the spectral emittance of Ge at 50°C from 24 $\mu m > \lambda > 10$ μm. The reader should note that $k \sim 10^{-5}$ at 10 μm and becomes very much smaller at shorter wavelengths corresponding to three and more phonon interactions.

Randall and Rawcliffe [12] used channel spectra, while Afsar *et al.* [13] used asymmetric Fourier-transform spectroscopy to measure n and k for high-resistivity Ge (10–50 $\Omega\ cm^{-1}$). Their results are in good agreement and the data of Randall and Rawcliffe [12] are in Table V, although room temperature was not defined. At $\lambda > 200$-μm free-carrier absorption is beginning to appear.

As the photon energy is increased, the values of k due to phonon bands will decrease to insignificant values until the onset of electronic transitions in the near IR. Absorption increases for frequencies less than the first "edge" in Ge, again due to phonon or lattice interactions with electrons. Some of the data of MacFarlane and Roberts [14] obtained on ultrathin bulk samples by using transmittance at 291 K, as read from a graph, have been tabulated to show that k has measured values in the 10^{-7} range.

At wavelengths shorter than 2 μm, Ge becomes increasingly absorbing because of the dominance of electronic interband transitions; hence it is no longer possible to use the angle-of-deviation method for determining n. Transmittance measurements can be used to measure the absorption coefficient α (or k), but data are not valid for $\lambda < 0.6$ μm. Data of Dash and Newman [15] at 300 K, as read from a graph, are given for 2 $\mu m > \lambda > 0.7$ μm. The agreement in the wavelength overlap with MacFarlane and Roberts [14] is good, except for the shift of the indirect absorption edge due to the temperature difference.

The optical-measurement methods remaining for shorter wavelengths are related to aspects of the Fresnel reflectivity coefficients, i.e., ellipsometry and reflectance. Because the Fresnel reflectivity is a complex quantity obeying causality laws, it can be expressed as a modulus $R^{1/2}$ and a phase function. The Kramers–Kronig (KK) relation yields the spectral phase function, given R over the entire frequency spectrum [16]. Philipp and Taft [17] determined the reflectance R over a wide spectral region, applying the KK relations to give n and k. Some of their results as extracted from a graph are tabulated for $\lambda < 0.25$ μm for 300 K.

Another type of reflectance method is to measure reflectances at nonzero angles of incidence. Potter [18] measured the ratio R_p/R_s at several angles of incidence to get the minimum value R_p/R_s and the associated pseudo-Brewster angle. Some room-temperature values of n and k for Ge are given for the spectral range 1.77 $\mu m > \lambda > 0.6$ μm.

Ellipsometry has been used to measure optical properties from the visible spectral region to 6 eV (0.207 μm). The tabulated data of Aspnes and Studna

[19] are listed in Table V. Room temperature was not stated. Archer [20] also measured the optical properties over a reduced spectral range with less spectral detail. Cardona *et al.* [21] prepared crystalline and amorphous Ge films on heated and room-temperature KCl substrates, respectively. Samples were floated off and picked up with a copper mesh. Transmission measurements were done with synchrotron radiation. The data in Table V were read from a graph. Room temperature was not stated.

Lukirskii *et al.* [22] have measured the unpolarized reflectance for Ge as a function of angle of incidence at four x-ray wavelengths (since $\varepsilon < 1$, this gives a type of external attenuated total reflection). Samples were deposited on glass substrates. Room temperature was not specified. Note that the angles as given in Lukirskii *et al.* [22] are grazing angles, i.e., $\pi/2 - \phi$, where ϕ is angle of incidence. These data are obtained from a table and are listed as four points but plotted in Fig. 4 as a continuous line. Note in Fig. 4 that the k data tend to join the longer-wavelength data of Cardona *et al.* [21] and that these data, in turn, tend to join the data of Philipp and Taft [17].

Aspens and Studna's data [19] overlap Potter's [18] for $0.83\ \mu\text{m} > \lambda > 0.41\ \mu\text{m}$ (1.5–3eV). When the extinction coefficient is low, the agreement in n between the two sets is quite good (better than 0.25% for $0.83\ \mu\text{m} > \lambda > 0.74\ \mu\text{m}$). As k becomes larger, the discrepancy increases to about 1% at 2 eV and 4% at 3 eV. At the longer wavelengths Archer's data [20] are about 4% below those of Aspnes and Studna [19], coming into reasonable agreement (less than 1% difference) for $0.54\ \mu\text{m} > \lambda > 0.36\ \mu\text{m}$. Thus, the data of Aspnes and Studna [19] for $0.82\ \mu\text{m} > \lambda > 0.2\ \mu\text{m}$ appear to be the best choice for refractive-index values. Data of Philipp and Taft [17] appear to be too low.

In the spectral region of interband transitions the extinction coefficient becomes quite large ($k > 4$), corresponding to absorption coefficients of the order of $10^6\ \text{cm}^{-1}$. Reflectance-type measurements must be used. However, some overlap with transmittance measurements exists for comparison. Measurements of Dash and Newman [15] extend to $0.69\ \mu\text{m}$, which permits comparison with Potter [18] as well as with Aspnes and Studna [19]. The former appears to be low by about a factor of 2, whilte the agreement with the latter is within 10–20%, which, given sample treatment and technique differences, must be considered good. As k becomes larger, Potter's data [18] come closer to agreeing with those of Aspnes and Studna [19]. For $0.62\ \mu\text{m} > \lambda > 0.4\ \mu\text{m}$, Potter's data [18] are consistently larger than the data of Aspnes and Studna [19] by 10–20%. Again, it seems that the data of Aspnes and Studna [19] would be the choice for values of k.

For values of n overlap regions occur for the data of Briggs [1], Potter [18], and the Sellmeier fit. Given that the data of Briggs [1] and Potter [18] were taken at 20°C or more, the agreement is good. Below about $2\ \mu\text{m}$, the Sellmeier results would increasingly deviate from the measured values. That the reflectance method agrees with the angle-of-deviation method better than 0.25% in this spectral region establishes the compatibility of the two methods.

Reflectivity-type experiments can presents serious problems to the unwary for reducing the experimental data to intrinsic material parameters such as n and k. The condition of the reflecting surface must be well established. Any damage layer present due to grinding, polishing, etc., must be removed. Chemical polishes can avoid this problem. Another incipient problem is the likely presence of a native oxide. A stable oxide grows on germanium to thicknesses of 50 to 100 Å in ambient air. For high-index materials such as Ge, such a layer must be removed or accounted for. Aspnes *et al.* [19] stripped the oxide and took steps to inhibit the oxide growth during the experimental run. While ellipsometry is very sensitive to the presence of a low-index layer, reflectance measurements also become quite sensitive to such a layer as k becomes significant. Both Potter [18] and Archer [20] assumed the presence of an oxide on their specimens and corrected for it. Archer [20] assumed a thickness of 10 to 20 Å, while Potter [18] assumed a layer with thickness of 50 Å and an index of 2.0. (See Aspnes and Stunda [19] for further discussion.)

REFERENCES

1. H. B. Briggs, *Phys. Rev.* **77**, 286 (1950).
2. C. D. Salzberg and J. J. Villa, *J. Opt. Soc. Am.* **47**, 244 (1957).
3. M. Cardona, W. Paul, and H. Brooks, *J. Phys. Chem. Solids* **8**, 204 (1959).
4. H. W. Icenogle, B. C. Platt, and W. L. Wolfe, *Appl. Opt.* **15**, 2348 (1976).
5. R. P. Edwin, M. T. Dudermel, and M. Lamare, *Appl. Opt* **17**, 1066 (1978).
6. N. P. Barnes and M. S. Piltch, *J. Opt. Soc. Am.* **69**, 178 (1979).
7. H. H. Li, *J. Phys. Chem. Ref. Data*, **9**, 561 (1980).
8. R. J. Collins and H. Y. Fan, *Phys. Rev.* **93**, 674 (1954).
9. M. Lax and E. Burstein, *Phys. Rev.* **97**, 39 (1955).
10. J. R. Aronson, H. G. McLinden, and P. J. Gielisse, *Phys, Rev.* **135**, A785 (1964).
11. D. L. Stierwalt and Roy F. Potter, *Rep. Int. Conf. Phys. Semicond., Exter*, 1962, p. 513. Institute of Physics and Physical Society, London, 1962.
12. C. M. Randall and R. D. Rawcliffe, *Appl. Opt.* **6**, 1889 (1967).
13. M. N. Afsar, D. D. Honijk, W. F. Passchier, and J. Goulon, *IEEE Trans. Micro. Theor. Tech.* **MTT-25**, 505 (1977).
14. G. G. MacFarlane and V. Roberts, *Phys. Rev.* **98**, 1865 (1955).
15. W. C. Dash and R. Newman, *Phys. Rev.* **99**, 1151 (1955).
16. M. Cardona, *in* "Optical Properties of Solids" (S. Nudelman and S. S. Mitra, eds.), p. 137. Plenum, New York, 1969.
17. H. R. Philipp and E. A. Taft, *Phys. Rev.* **113**, 1002 (1959).
18. Roy F. Potter, *Phys. Rev.* **150**, 562 (1966).
19. D. E. Aspnes and A. A. Studna, *Phys. Rev. B* **27**, 985 (1983); D. E. Aspnes, private communication (1983).
20. R. J. Archer, *Phys. Rev*, **110**, 354 (1958).
21. M. Cardona, W. Gudat, B. Sonntag, and P. Y. Yu, *Proc. 10th Int. Conf. Phys. Semicond., Cambridge, 1970*, p. 208. U.S. Atomic Energy Commission, Oak Ridge, Tennessee, 1970.
22. A. P. Lukirskii, E. P. Savinov, O. A. Ershov, and Y. F. Shepelov, *Opt. Spectrosc.* **16**, 168 (1964); A. P. Lukirskii, E. P. Savinov, O. A. Ershov, and Y. F. Shepelov, *Opt. Spektrosk.* **16**, 310 (1964).

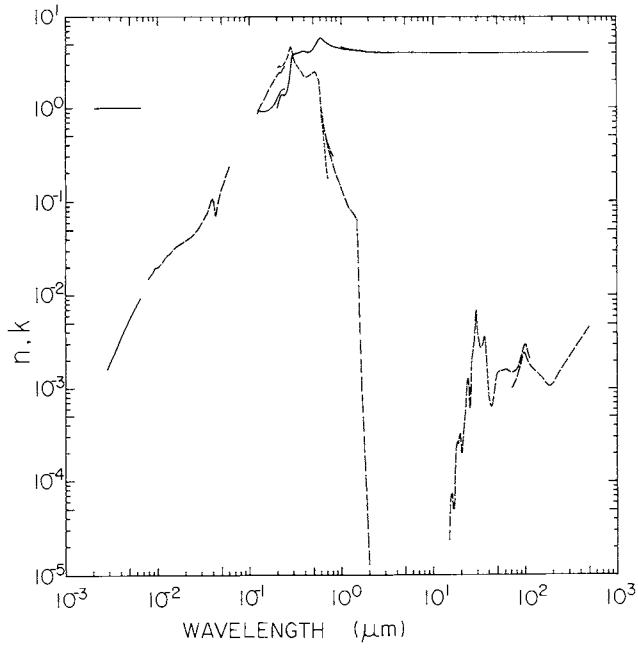

Fig. 4. Log–log plot of n (——) and k (– – – –) versus wavelength in micrometers for germanium. Data from various references sometimes do not join together in overlap regions.

TABLE V

Values of n and k for Germanium Obtained from Various References[a]

eV	cm^{-1}	μm	n	k	k
525.3		0.00236	0.99741 [22]	9.8×10^{-4} [22]	
394.8		0.00314	0.99590	2.05×10^{-3}	
281.8		0.0044	0.99385	4.30	
185.1		0.0067	0.99050	9.50×10^{-3}	
155		0.007999		1.47×10^{-2} [21]	
150		0.008266		1.55	
145		0.008550		1.63	
140		0.008856		1.71	
135		0.009184		1.77	
130		0.009537		1.98	
127.5		0.009725		1.94	
125		0.009919		1.98	
122.5		0.01012		2.02	
120		0.01033		1.99	
115		0.01078		2.06	
110		0.01127		2.21	
105		0.01181		2.37	
100		0.01240		2.57	
97.5		0.01272		2.65	
95		0.01305		2.71	
90		0.01378		2.79	
85		0.01459		3.03	
80		0.01550		3.26	
75		0.01653		3.39	
70		0.01771		3.52	
65		0.01907		3.67	
60		0.02066		3.94	
55		0.02254		4.23	
50		0.02480		4.52	
45		0.02755		5.04	
40		0.03100		6.04	
38		0.03263		6.51	
36		0.03444		7.40	
34		0.03647		8.56	
32		0.03875		9.99×10^{-2}	
31		0.04000		0.106	
30		0.04133		0.102	
29		0.04275		7.14×10^{-2}	
28		0.04428		7.47×10^{-2}	
26		0.04769		0.110	
24		0.05166		0.144	
22		0.05636		0.179	
20		0.06199		0.237	
10		0.1240	0.93 [17]	0.86 [17]	
9.5		0.1305		1.0	

(*continued*)

[a] References are indicated in brackets. Data from Stierwalt and Potter [11] obtained at 50°C are included because no room-temperature data were available in the 10–15-μm region.

TABLE V (*Continued*)

Germanium

eV	cm^{-1}	μm	n	k	k
9		0.1378	0.92	1.14	
8.5		0.1459	0.92	1.2	
8		0.1550	0.92	1.4	
7.5		0.1653		1.6	
7		0.1771	1.0	1.8	
6.5		0.1907	1.1	2.05	
6	48,390	0.2066	1.3	2.34	
			1.022 [19]	2.774 [19]	
5.94	47,910	0.2087	1.073	2.801	
5.9	47,590	0.2101	1.108	2.831	
5.84	47,100	0.2123	1.167	2.862	
5.8	46,780	0.2138	1.209	2.873	
5.75	46,380	0.2156	1.48 [17]	2.4 [17]	
5.74	46,300	0.2160	1.273 [19]	2.874 [19]	
5.7	45,970	0.2175	1.293	2.163	
5.64	45,490	0.2198	1.345	2.852	
5.6	45,170	0.2214	1.360	2.846	
5.54	44,680	0.2238	1.372	2.842	
5.5	44,360	0.2254	1.380	2.842	
			1.55 [17]	2.4 [17]	
5.44	43,880	0.2279	1.387 [19]	2.849 [19]	
5.4	43,550	0.2296	1.383	2.854	
5.34	43,070	0.2322	1.377	2.877	
5.3	42,750	0.2339	1.371	2.897	
5.25	42,340	0.2362	1.57 [17]	2.7 [17]	
5.24	42,260	0.2366	1.366 [19]	2.938 [19]	
5.2	41,940	0.2384	1.364	2.973	
5.14	41,460	0.2412	1.366	3.031	
5.1	41,130	0.2431	1.370	3.073	
5.04	40,650	0.2460	1.382	3.146	
5.0	40,330	0.2480	1.394	3.197	
			1.6 [17]	2.86 [17]	
4.94	39,840	0.2510	1.417 [19]	3.282 [19]	
4.9	39,520	0.2530	1.435	3.342	
4.84	39,040	0.2562	1.470	3.439	
4.8	38,710	0.2583	1.498	3.509	
4.74	38,230	0.2616	1.546	3.624	
4.7	37,910	0.2638	1.586	3.709	
4.64	37,420	0.2672	1.659	3.852	
4.6	37,100	0.2695	1.720	3.960	
4.54	36,620	0.2731	1.839	4.147	
4.5	36,290	0.2755	1.953	4.297	
4.44	35,910	0.2792	2.226	4.543	
4.4	35,080	0.2818	2.516	4.669	
4.34	35,000	0.2857	3.038	4.653	
4.3	34,680	0.2883	3.338	4.507	
4.24	34,200	0.2924	3.633	4.207	
4.2	33,880	0.2952	3.745	4.009	
4.14	33,390	0.2995	3.837	3.756	

TABLE V (*Continued*)

Germanium

eV	cm^{-1}	μm	n	k	k
4.1	33,070	0.3024	3.869	3.614	
4.04	32,580	0.3069	3.896	3.436	
4.0	32,260	0.3100	3.905	3.336	
3.94	31,780	0.3147	3.916	3.209	
3.9	31,460	0.3179	3.920	3.137	
3.84	30,970	0.3229	3.930	3.043	
3.8	30,650	0.3263	3.936	2.986	
3.74	30,160	0.3315	3.949	2.909	
3.7	29,840	0.3351	3.958	2.863	
3.64	29,360	0.3406	3.974	2.799	
3.6	29,040	0.3444	3.985	2.759	
3.54	28,550	0.3502	4.005	2.702	
3.5	28,230	0.3542	4.020	2.667	
3.44	27,750	0.3604	4.048	2.615	
3.4	27,420	0.3647	4.070	2.579	
3.34	26,940	0.3712	4.106	2.517	
3.3	26,620	0.3757	4.128	2.469	
3.24	26,130	0.3827	4.150	2.392	
3.2	25,810	0.3875	4.157	2.340	
3.14	25,330	0.3949	4.153	2.262	
3.1	25,000	0.4000	4.141	2.215	
3.04	24,520	0.4078	4.107	2.164	
3.0	24,200	0.4133	4.082	2.145	
2.94	23,710	0.4217	4.052	2.135	
2.9	23,390	0.4275	4.037	2.140	
2.84	22,910	0.4366	4.030	2.162	
2.8	22,580	0.4428	4.035	2.181	
2.74	22,100	0.4525	4.058	2.215	
2.7	21,780	0.4592	4.082	2.240	
2.64	21,290	0.4696	4.133	2.281	
2.6	20,970	0.4769	4.180	2.309	
2.54	20,490	0.4881	4.267	2.353	
2.5	20,160	0.4959	4.340	2.384	
2.44	19,680	0.5081	4.482	2.429	
2.4	19,360	0.5166	4.610	2.455	
2.34	18,870	0.5299	4.883	2.434	
2.3	18,550	0.5391	5.062	2.318	
2.24	18,070	0.5535	5,198	2.125	
2.2	17,740	0.5636	5.283	2.049	
2.14	17,260	0.5794	5.554	1.924	
2.1	16,940	0.5904	5.748	1.634	
2.05	16,530	0.6048	5.9 [18]		1.1 [18]
2.04	16,450	0.6078	5.708 [19]	1.150 [19]	
2.0	16,130	0.6199	5.588	0.933	
			5.64 [18]		0.8
1.95	15,730	0.6358	5.5		0.66
1.9	15,320	0.6526	5.38		0.54
			5.294 [19]	0.638	

(*continued*)

TABLE V (*Continued*)

Germanium

eV	cm^{-1}	μm	n	k	k
1.85	14,920	0.6702	5.21 [18]		0.4
1.84	14,840	0.6738	5.152 [19]	0.537	
1.8	14,520	0.6888	5.067	0.500	
			5.08 [18]		0.26
				0.466 [15]	
1.75	14,110	0.7085	4.99		0.2
1.74	14,030	0.7126	4.961 [19]	0.430 [19]	
1.7	13,710	0.7293	4.897	0.401	
			4.95 [18]		0.18
				0.389 [15]	
1.64	13,230	0.7560	4.816 [19]	0.364 [19]	
1.6	12,900	0.7749	4.763	0.345	
			4.75 [18]	0.308 [15]	
1.54	12,420	0.8051	4.684 [19]	0.316 [19]	
1.5	12,100	0.8266	4.653	0.298	
			4.64 [18]	0.237 [15]	
1.4	11,280	0.8856	4.56	0.190	
1.3	10,490	0.9537	4.495	0.167	
1.240	10,000	1.0	4.61733 [6]		
1.2	9,679	1.033	4.42 [18]	0.123	
1.1	8,872	1.127	4.385	0.103	
1.033	8,333	1.2	4.35673 [6]		
1.0	8,065	1.240	4.325 [18]	8.09×10^{-2}	
0.9	7,259	1.378	4.285	7.45	
0.8856	7,143	1.4	4.23840 [6]		
0.88	7,098	1.409		6.73	
0.86	6,936	1.442		6.88	
0.84	6,775	1.476		6.58	
0.82	6,614	1.512		5.66×10^{-2}	
0.8	6,452	1.550	4.275 [16]	5.67×10^{-3}	
0.78	6,291	1.590		3.42×10^{-3}	
0.775	6,251	1.600	4.17262 [6]		8.15×10^{-4} [19]
0.76	6,130	1.631		7.79×10^{-4}	
0.75	6,049	1.653			5.06
0.74	5,968	1.675		6.67	
0.725	5,847	1.710			3.01
0.72	5,807	1.722		4.66	
0.7	5,646	1.771	4.18 [18]	2.82	1.27×10^{-4}
0.6888	5,556	1.8	4.13164 [6]		
			4.143 [1]		
0.68	5,485	1.823		1.31×10^{-4}	
0.675	5,444	1.837			4.22×10^{-5}
0.6702	5,405	1.85	4.135		
0.66	5,323	1.879		6.73×10^{-5}	
0.6525	5,263	1.90	4.129		
0.65	5,243	1.907			9.71×10^{-6}
0.64	5,162	1.937		7.71×10^{-6}	
0.625	5,041	1.984			1.42×10^{-6}
0.6199	5,000	2.0	4.116		

TABLE V (*Continued*)

Germanium

eV	cm^{-1}	μm	n	k	k
			4.10415 [6]		
0.6	4,839	2.066			6.58×10^{-7}
0.5904	4,762	2.1	4.104 [1]		
0.5636	4,545	2.2	4.092		
			4.08469 [6]		
0.5391	4,348	2.3	4.085 [1]		
0.5166	4,167	2.4	4.078		
			4.07038 [6]		
0.4959	4,000	2.5	4.072 [1]		
0.4854	3,915	2.554	4.06230 [4]		
0.4769	3,846	2.6	4.068 [1]		
			4.05951 [6]		
0.4675	3,771	2.652	4.05754 [4]		
0.4538	3,660	2.732	4.05310		
0.4428	3,571	2.8	4.05105 [6]		
0.4341	3,501	2.856	4.04947 [4]		
0.4191	3,381	2.958	4.04595		
0.4133	3,333	3.0	4.04433 [6]		
0.4012	3,236	3.09	4.04292 [4]		
0.3874	3,125	3.2	4.03889 [6]		
0.3647	2,941	3.4	4.03443		
0.3444	2,778	3.6	4.03072		
0.3263	2,632	3.8	4.02760		
0.3100	2,500	4.0	4.02495		
0.3009	2,427	4.12	4.02457 [4]		
0.2952	2,381	4.2	402268 [6]		
0.2818	2,273	4.4	4.02072		
0.2695	2,174	4.6	4.01901		
0.2583	2,083	4.8	4.01751		
0.2480	2,000	5.0	4.01619		
0.2389	1,927	5.19	4.01617 [4]		
0.2384	1,923	5.2	4.01503 [6]		
0.2296	1,852	5.4	4.01399		
0.2214	1,786	5.6	4.01305		
0.2138	1,724	5.8	4.01222		
0.2066	1,667	6.0	4.01146		
0.2000	1,613	6.2	4.01078		
0.1937	1,563	6.4	4.01015		
0.1879	1,515	6.6	4.00958		
0.1823	1,471	6.8	4.00906		
0.1771	1,429	7.0	4.00858		
0.1722	1,389	7.2	4.00814		
0.1675	1,351	7.4	4.00773		
0.1631	1,316	7.6	4.00736		
0.1590	1,282	7.8	4.00701		
0.1550	1,250	8.0	4.00668		
			4.00748 [5]		
0.1512	1,220	8.2	4.00637 [6]		

(*continued*)

TABLE V (*Continued*)

Germanium

eV	cm^{-1}	μm	n	k	k
0.1506	1,215	8.23	4.00743 [4]		
0.1476	1,190	8.4	4.00609 [6]		
0.1442	1,163	8.6	4.00582		
0.1409	1,136	8.8	4.00556		
0.1378	1,111	9.0	4.00533		
			4.00620 [5]		
0.1348	1,087	9.2	4.00510 [6]		
0.1319	1,064	9.4	4.00489		
0.1292	1,042	9.6	4.00469		
0.1265	1,020	9.8	4.00449		
0.1240	1,000	10.0	4.00431		
			4.00525 [5]		1.43×10^{-5} [11]
0.1207	973.7	10.27	4.00571 [4]		
0.1181	952.4	10.5	4.00389 [6]		
0.1137	917.4	10.9			1.30
0.1127	909.1	11.0	4.00351		
			4.00436 [5]		
0.1078	869.6	11.5	4.00316 [6]		
0.1033	833.3	12.0	4.00285		3.82
			4.00398 [5]		
0.1003	809.1	12.36	4.00627 [4]		
0.09919	800.0	12.5	4.00255 [6]		
0.09840	793.7	12.6			3.51
0.09537	769.2	13.0	4.00228		
			4.00352 [5]		
0.09460	763.4	13.1			4.59
0.09184	740.7	13.5	4.00202 [6]		
0.08920	719.4	13.9			3.98
0.08856	714.3	14.0	4.00177		
			4.00315 [5]		
0.08551	689.7	14.5	4.00153 [6]		5.77
0.08431	680	14.71		2.34×10^{-5} [8]	
0.08307	670	14.93		3.56	
0.08266	666.7	15.0	4.00130		9.78×10^{-5}
0.08183	660	15.15		5.30	
0.08157	657.9	15.2			1.2×10^{-4}
0.08059	650	15.38		6.24	
0.07999	645.2	15.5	4.00107		1.71×10^{-4}
0.07935	640	15.63		7.34	
0.07811	630	15.87		7.33	
0.07749	625.0	16.0	4.00086		9.55×10^{-5}
0.07687	620	16.13		6.54	
0.07563	610	16.39		5.61	
0.07514	606.1	16.5			1.58×10^{-4}
0.07439	600	16.67		4.91	
0.07377	595	16.81		6.02	
0.07315	590	16.95		9.44×10^{-5}	
0.07293	588.2	17.0	4.00043		2.57
0.07191	580	17.24		1.64×10^{-4}	

TABLE V (*Continued*)

Germanium

eV	cm^{-1}	μm	n	k	k
0.07085	571.4	17.5			3.90
0.07067	570	17.54		2.09	
0.06943	560	17.86		2.56	
0.06888	555.6	18.0	4.00001		3.01
0.06819	550	18.18		2.68	
0.06757	545	18.35		2.63	
0.06702	540.5	18.5			4.27
0.06695	540	18.52		2.51	
0.06633	535	18.69		2.68	
0.06571	530	18.87		3.00	
0.06526	526.3	19.0	3.99958		4.53
0.06447	520	19.23		3.21	
0.06358	512.8	19.5			4.03
0.06323	510	19.61		3.12	
0.06199	500	20.00	3.99915	2.39	3.98
0.06075	490	20.41		1.94	
0.06048	487.8	20.5			3.92
0.05951	480	20.83		2.49	
0.05904	476.2	21			5.01
0.05827	470	21.28		3.39	
0.05767	465.1	21.5			7.70×10^{-4}
0.05703	460	21.74		4.67	
0.05636	454.5	22.0	3.99825		1.02×10^{-3}
0.05579	450	22.22		5.84	6.0×10^{-4} [10]
0.05455	440	22.73		7.24×10^{-4}	8.0×10^{-4}
0.05331	430	23.26		1.11×10^{-3}	1.1×10^{-3}
0.05269	425	23.53		1.27	
0.05207	420	23.81		1.10×10^{-3}	1.35
0.05166	416.7	24.0	3.99728		
0.05083	410	24.39		7.77×10^{-4}	1.4×10^{-3}
0.05021	405	24.69			9.0×10^{-4}
0.04959	400	25.00		6.17	8.0×10^{-4}
0.04897	395	25.32		8.06×10^{-4}	1.5×10^{-3}
0.04835	390	25.64		1.73×10^{-3}	2.0
0.04769	384.6	26.0	3.99621		
0.04711	380	26.32		2.30	2.1
0.04587	370	27.03		2.80	2.5
0.04463	360	27.78		3.76	3.4
0.04428	357.1	28.0	3.99500		
0.04401	355	28.17			5.5
0.04370	352.5	28.37			6.7
0.04339	350	28.57		5.23	6.3
0.04308	347.5	28.78			6.7
0.04277	345	28.99		6.92	6.5
0.04215	340	29.41		4.68	3.2
0.04133	333.3	30.0	3.99363		
0.04092	330	30.30		3.62	2.95
0.03968	320	31.25		2.98	2.9

(*continued*)

TABLE V (*Continued*)

Germanium

eV	cm^{-1}	μm	n	k	k
0.03844	310	32.26		2.82	2.7
0.03782	305	32.79		3.00	
0.03720	300	33.33		3.18	2.75
0.03658	295	33.90		2.83	
0.03596	290	34.48		2.74	3.05
0.03542	285.7	35	3.98925		
0.03534	285	35.09			3.45
0.03472	280	35.71			3.55
0.03410	275	36.36			3.3
0.03348	270	37.04			2.75
0.03224	260	38.46			1.55
0.03100	250	40.00	3.98272		0.85
0.02976	240	41.67			0.7
0.02852	230	43.48			0.65
0.02728	220	45.45			0.85
0.02604	210	47.62			1.25
0.02480	200	50.00			1.5
0.02356	190	52.63			1.53
0.02232	180	55.56			1.55
0.02108	170	58.82			1.6
0.01984	160	62.50			1.6
0.1860	150	66.67			1.5
0.01736	140	71.43	4.0060 [12]	1.02 [12]	1.5
0.01643	132.5	75.47	4.0060	1.14	
0.01612	130	76.92			1.55
0.01550	125	80.00	4.0060	1.27	
0.01488	120	83.33			1.7
0.01457	117.05	85.11	4.0060	1.62	
0.01364	110	90.91	4.0063	2.10	2.4
0.01302	105	95.24			2.8
0.01271	102.5	97.56	4.0064	2.41	
0.01240	100	100.0			3.0
0.01178	95	105.3	4.0067	2.01	2.5
0.01116	90	111.1			2.1×10^{-3}
0.01085	87.5	114.3	4.0068	1.73	
0.009919	80	125.0	4.0067	1.59	
0.008989	72.5	137.9	4.0067	1.43	
0.008059	65	153.8	4.0065	1.34	
0.007129	57.5	173.9	4.0061	1.10	
0.006199	50	200.0	4.0059	1.11	
0.005269	42.5	235.3	4.0056	1.50	
0.004339	35	285.7	4.0052	2.04	
0.003410	27.5	363.6	4.0047	2.89	
0.002480	20	500.0	4.0043	4.77×10^{-3}	

Indium Arsenide (InAs)

EDWARD D. PALIK and R. T. HOLM
Naval Research Laboratory
Washington, D.C.

The UV–visible reflectivity of InAs was measured by Philipp and Ehrenreich [1] in the spectral region from 1 to 25 eV. Chemically polished surfaces were used. Kramers–Kronig (KK) analysis yielded n and k, which were tabulated by Seraphin and Bennett [2]. Measurements by Morrison [3] in the 1–6-eV region are significantly different, probably because of poorer surface preparation and/or a wider range of extrapolation for the KK analysis. For 6 to 1.5 eV the ellipsometric results of Aspnes and Studna [4] are used. The absorption of deposited films was measured from 20 to 150 eV but these data were not given [5]; only peaks due to interband transitions were listed. The data of Seraphin and Bennett [2] and Aspnes and Stunda [4] are listed in Table VI. Figure 5 is a smooth-curve plot of all the data.

Dixon and Ellis [6] measured the band-edge absorption at 300 K for thin samples mechanically polished. Samples were polished on a beeswax lap with aluminum oxide powder. They were unsupported, or for samples less than 30 μm thick, they were glued on sapphire with glycol phthalate. Their lowest carrier density, 3.6×10^{16} cm^{-3}, did not show signs of the Burstein–Moss effect. The k values listed in Table VI were obtained from our reading of a graph in Dixon and Ellis [6] to three figures.

Lorimor and Spitzer [7] measured transmission interference fringes at room temperature in the near IR and fitted the data with the formula

$$n^2 = A + \frac{B}{1 - (\nu/3920)^2} + \frac{C}{1 - (\nu/219)^2} + \frac{D}{\nu^2}. \tag{1}$$

The B term is the contribution from the band-edge resonance, the C term is the contribution from the reststrahlen band, and the D term comes from the free-carrier susceptibility since the free-carrier effects were significant for $N = 2 \times 10^{16}$ cm^{-3}. The values were $A = 11.1 \pm 0.1$, $B = 0.71 \pm 0.1$, $C = 2.75 \pm 0.2$, and $D = 5.64 \times 10^4$ cm^{-2}. It is obvious that n is uncertain in the third significant figure by a digit or two.

ISBN 0-12-544420-6

Pikhtin and Yas'kov [8] have refitted these data with a more detailed formula

$$n^2 = 1 + \frac{A}{\pi} \ln \frac{E_1^2 - (\hbar\omega)^2}{E_0^2 - (\hbar\omega)^2} + \frac{G_1}{E_1^2 - (\hbar\omega)^2} + \frac{G_2}{E_2^2 - (\hbar\omega)^2} + \frac{G_3}{E_3^2 - (\hbar\omega)^2}, \quad (2)$$

with $A = 0.7/\sqrt{E_0}$, $E_0 = 0.356$ eV, $E_1 = 2.2$ eV, $E_2 = 4.9$ eV, $E_3 = 2.714 \times 10^{-2}$ eV, $G_1 = 28.748$ eV^2, $G_2 = 79.354$ eV^2, and $G_3 = 2.01 \times 10^{-3}$ eV^2. The second term is the contribution of the fundamental band gap. The third and fourth terms are contributions from two higher-lying band gaps treated as oscillators, while the fifth term is the contribution of the lattice oscillator in the far infrared. These values are tabulated in the near IR. While four figures are given, the third figure is probably uncertain to a digit or two.

Multiphonon absorption in the 450–250-cm^{-1} region has been measured by Lorimor and Spitzer [7]. Their sample showed free-carrier absorption ($N = 2 \times 10^{16}$ cm^{-3}) that was subtracted off, assuming a λ^2 dependence. The tabulated data were read off a graph. Absorption in the same spectral region was measured at 15 K for a sample with $N = 3 \times 10^{16}$ cm^{-3}, but no quantitative numbers were given [9].

The reststrahlen reflectivity data are scant [10], and we have elected to take values of $\omega_T = 218$ cm^{-1}, $\omega_L = 240$ cm^{-1}, and $\Gamma = 4$ cm^{-1} from Raman data [11, 12] with $\varepsilon_\infty = 11.7$ [7, 13] and calculate n and k from the formula

$$(n - ik)^2 = \varepsilon_\infty \left[1 + \frac{\omega_L^2 - \omega_T^2}{\omega_T^2 - \omega^2 + i\Gamma\omega} \right]. \quad (3)$$

These are indicted in Table VI as footnote *b*. No free carriers are assumed. The n's for Pikhtin and Yas'kov [8] and from the oscillator model [Eq. (3)] are compared, starting at 10 μm, and vary by one digit in the third significant figure. This agreement worsens to three digits by 25 μm. We prefer the oscillator model here because of the more precise parameters used from the Raman data.

Direct experimental measurement of n and k at 300 K has been made by Memon *et al.* [14], who used the asymmetric Fourier-transform spectroscopy technique. While the sample was described as undoped, it showed strong free-carrier effects below 200 cm^{-1}. They analyzed a dispersion equation by using experimental values of n and k to obtain the frequency-dependent damping parameter. We have read a graph to obtain n and k and list them in the 290–140-cm^{-1} region in Table VI. We have plotted in Fig. 5 the data of Memon *et al.* [14] in the vicinity of ω_T but have included some oscillator model data to lower frequency for n and k since no free-carrier effects are included. Note that the peak in k is ~ 9 and occurs at 219 cm^{-1} for values from Eq. (3) and is ~ 7 and occurs at 221 cm^{-1} for Memon *et al.* [14]. The data of Memon *et al.* [14] are preferred.

At low frequency, $n^2 = 14.18$ is smaller than, but in reasonable agreement with, the static dielectric constant 14.55 ± 0.3 [7, 13].

REFERENCES

1. H. R. Philipp and H. Ehrenreich, *Phys. Rev.* **129**, 1550 (1963).
2. B. O. Seraphin and H. E. Bennett, *in* "Semiconductors and Semimetals" (R. K. Willardson and A. C. Beer, eds.), Vol. 3, p. 499. Academic Press, New York, 1967.
3. R. E. Morrison, *Phys. Rev.* **124**, 1314 (1961).
4. D. E. Aspnes and A. A. Studna, *Phys. Rev. B* **27**, 985 (1983); D. E. Aspnes and A. A. Studna, private communication (1982).
5. M. Cardona, W. Gudat, B. Sonntag, and P. Y. Yu, *Proc. Int. Conf. Phys. Semicond., 10th Cambridge, 1970*, p. 208. U.S. Atomic Energy Commission, Oak Ridge, Tennessee, 1970.
6. J. R. Dixon and J. M. Ellis, *Phys. Rev.* **123**, 1560 (1961).
7. O. G. Lorimor and W. G. Spitzer, *J. Appl. Phys.* **36**, 1841 (1965).
8. A. N. Pikhtin and A. D. Yas'kov, *Sov. Phys. Semicond.* **12**, 622 (1978); A. N. Pikhtin and A. D. Yas'kov, *Fiz. Tekh. Poluprovodu.* **12**, 1047 (1978).
9. E. S. Koteles and W. R. Datars, *Can. J. Phys.* **54**, 1676 (1976).
10. M. Hass and B. W. Henvis, *J. Phys. Chem. Solids* **23**, 1099 (1962).
11. R. C. C. Leite and J. F. Scott, *Phys. Rev. Lett.* **22**, 130 (1969).
12. E. L. Ivchenko, D. N. Mirlin, and I. I. Reshina, *Sov. Phys. Solid State* **17**, 1510 (1975); E. L. Ivchenko, D. N. Mirlin, and I. I. Reshina, *Fiz. Tverd. Tela.* **17**, 2282 (1975).
13. M. Hass, *in* "Semiconductors and Semimetals" (R. K. Willardson and A. C. Beer, eds.), Vol. 3, p. 3. Academic Press, New York, 1967.
14. A. Memon, T. J. Parker, and J. R. Birch, *Proc. SPIE*, **289**, 20 (1981).

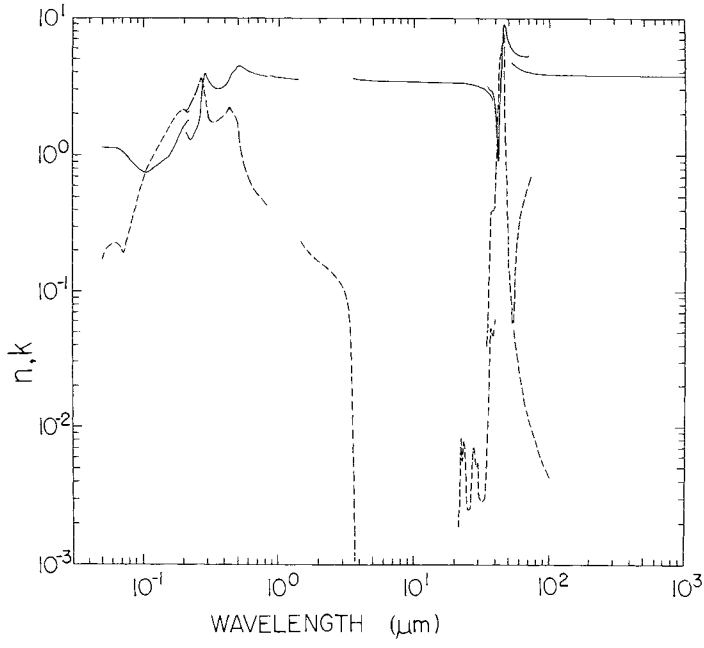

Fig. 5. Log–log plot of n (——) and k (– – –) versus wavelength in micrometers for indium arsenide. The transmission data for k at 1.5 μm are probably more reliable than the KK data and can be extrapolated to the first peak in k at 0.45 μm.

TABLE VI

Values of n and k for Indium Arsenide Obtained from Various References[a]

eV	cm^{-1}	μm	n	k
25		0.04959	1.139 [1, 2]	0.168 [1, 2]
24		0.05166	1.135	0.195
23		0.05391	1.135	0.207
22		0.05636	1.133	0.215
21		0.05904	1.131	0.222
20		0.06199	1.125	0.225
19.5		0.06358	1.120	0.224
18.5		0.06702	1.110	0.215
17.5		0.07085	1.047	0.189
16		0.07749	0.948	0.272
15		0.08266	0.894	0.336
14		0.08856	0.829	0.426
13		0.09537	0.766	0.563
12		0.1033	0.745	0.727
11.5		0.1078	0.751	0.830
11		0.1127	0.775	0.905
10		0.1240	0.835	1.071
9.1		0.1362	0.890	1.260
8.1		0.1531	0.967	1.552
7.2		0.1722	1.184	1.889
6.9		0.1797	1.332	1.998
6.6		0.1879	1.483	2.020
6.35		0.1953	1.583	2.120
6.0	48,390	0.2066	1.434 [4]	2.112 [4]
5.94	47,910	0.2087	1.401	2.085
5.9	47,590	0.2101	1.383	2.084
5.84	47,100	0.2123	1.350	2.089
5.8	46,780	0.2138	1.333	2.102
5.74	46,300	0.2160	1.306	2.135
5.7	45,970	0.2175	1.293	2.163
5.64	45,490	0.2198	1.281	2.212
5.6	45,170	0.2214	1.276	2.248
5.54	44,680	0.2238	1.277	2.304
5.5	44,360	0.2254	1.282	2.344

[a] The data of Philipp and Ehrenreich [1] given in Seraphin and Bennett [2] are specified by the wavelength (in micrometers). However, the original data were given in electron volts, and it is obvious that most of the n, k, values were determined for energies in whole numbers or tenths of a whole number. The values were rounded off to three significant figures and then given the wavelength listed in Seraphin and Bennett [2]. Sometimes we list these wavelengths and then recalculate energy (in electron volts), thus producing roundoff error in electron volts. The reference is given at the beginning of the tabulation for n and k and is understood to refer to all n's or all k's below it until a new reference appears. When an exponent of 10 is given, all numbers below it have the same exponent until the power of 10 changes. The power of 10 repeats at the end of a particular set of data or when the next number has 10^{-1}, which is then written as a decimal.

TABLE VI (*Continued*)

Indium Arsenide

eV	cm^{-1}	μm	n	k
			1.765 [1, 2]	2.202 [1, 2]
5.44	43,880	0.2279	1.297 [4]	2.407 [4]
5.4	43,550	0.2296	1.312	2.449
5.34	43,070	0.2322	1.341	2.514
5.3	42,750	0.2339	1.366	2.555
5.24	42,260	0.2366	1.408	2.612
5.2	41,940	0.2384	1.436	2.646
5.14	41,460	0.2412	1.469	2.694
5.1	41,130	0.2431	1.484	2.732
5.04	40,650	0.2460	1.505	2.807
5.0	40,330	0.2480	1.524	2.871
4.98	40,170	0.2490	1.535	2.907
4.96	40,000	0.2500	1.550	2.946
4.94	39,840	0.2510	1.566	2.988
4.92	39,680	0.2520	1.586	3.034
4.9	39,520	0.2530	1.608	3.081
4.88	39,360	0.2541	1.635	3.129
4.86	39,200	0.2551	1.668	3.182
4.84	39,040	0.2562	1.705	3.236
4.82	38,880	0.2572	1.751	3.291
4.8	38,710	0.2583	1.803	3.348
4.78	38,550	0.2594	1.866	3.404
4.76	38,390	0.2605	1.938	3.456
4.74	38,230	0.2616	2.019	3.504
4.72	38,070	0.2627	2.108	3.545
4.7	37,910	0.2638	2.204	3.575
4.68	37,750	0.2649	2.305	3.595
4.66	37,590	0.2661	2.407	3.604
4.64	37,420	0.2672	2.510	3.604
4.62	37,260	0.2684	2.609	3.596
4.6	37,100	0.2695	2.705	3.581
4.58	36,940	0.2707	2.799	3.564
4.56	36,780	0.2719	2.894	3.543
4.54	36,620	0.2731	2.990	3.519
4.52	36,460	0.2743	3.091	3.487
4.5	36,290	0.2755	3.194	3.445
4.48	36,130	0.2768	3.298	3.389
4.46	35,970	0.2780	3.399	3.320
4.44	35,810	0.2792	3.490	3.239
4.42	35,650	0.2805	3.573	3.146
4.4	35,080	0.2818	3.644	3.042
4.38	35,330	0.2831	3.701	2.931
4.36	35,170	0.2844	3.742	2.814
4.34	35,000	0.2857	3.765	2.697
4.32	34,840	0.2870	3.770	2.584
4.3	34,680	0.2883	3.761	2.478

(*continued*)

TABLE VI (*Continued*)

Indium Arsenide

eV	cm^{-1}	μm	n	k
4.28	34,520	0.2897	3.742	2.382
4.26	34,360	0.2910	3.715	2.297
4.24	34,200	0.2924	3.684	2.222
4.22	34,040	0.2938	3.650	2.156
4.2	33,880	0.2952	3.615	2.099
4.18	33,710	0.2966	3.580	2.049
4.16	33,550	0.2980	3.545	2.005
4.14	33,390	0.2995	3.512	1.967
4.12	33,230	0.3009	3.480	1.933
4.1	33,070	0.3024	3.449	1.903
4.08	32,910	0.3039	3.419	1.877
4.06	32,750	0.3054	3.391	1.854
4.04	32,580	0.3069	3.364	1.833
4.02	32,420	0.3084	3.338	1.815
4.0	32,260	0.3100	3.313	1.799
3.94	31,780	0.3147	3.246	1.761
3.9	31,460	0.3179	3.208	1.743
3.84	30,970	0.3229	3.158	1.726
3.8	30,650	0.3263	3.129	1.719
3.74	30,160	0.3315	3.091	1.714
3.7	29,840	0.3351	3.069	1.715
3.64	29,360	0.3406	3.044	1.721
3.6	29,040	0.3444	3.030	1.728
3.54	28,550	0.3502	3.015	1.742
3.5	28,230	0.3542	3.008	1.754
3.44	27,750	0.3604	3.003	1.774
3.4	27,420	0.3647	3.004	1.790
3.34	26,940	0.3712	3.010	1.817
3.3	26,620	0.3757	3.018	1.836
3.24	26,130	0.3827	3.035	1.868
3.2	25,810	0.3875	3.051	1.891
3.14	25,330	0.3949	3.083	1.929
3.1	25,000	0.4000	3.108	1.957
3.04	24,520	0.4078	3.157	2.001
3.0	24,200	0.4133	3.197	2.034
2.98	24,040	0.4161	3.220	2.051
2.96	23,870	0.4189	3.244	2.069
2.94	23,710	0.4217	3.272	2.088
2.92	23,550	0.4246	3.302	2.108
2.9	23,390	0.4275	3.337	2.129
2.88	23,230	0.4305	3.377	2.151
2.86	23,070	0.4335	3.425	2.174
2.84	22,910	0.4366	3.482	2.194
2.82	22,740	0.4397	3.550	2.207
2.8	22,580	0.4428	3.626	2.208
2.78	22,420	0.4460	3.705	2.189
2.76	22,260	0.4492	3.776	2.153
2.74	22,100	0.4525	3.834	2.108

TABLE VI (*Continued*)

Indium Arsenide

eV	cm^{-1}	μm	n	k
2.72	21,940	0.4558	3.878	2.060
2.7	21,780	0.4592	3.911	2.016
2.68	21,620	0.4626	3.935	1.977
2.66	21,450	0.4661	3.956	1.943
2.64	21,290	0.4696	3.976	1.917
2.62	21,130	0.4732	3.996	1.898
2.6	20,970	0.4769	4.021	1.885
2.58	20,810	0.4806	4.052	1.881
2.56	20,650	0.4843	4.098	1.882
2.54	20,490	0.4881	4.168	1.879
2.52	20,330	0.4920	4.265	1.855
2.5	20,160	0.4959	4.364	1.786
2.48	20,000	0.4999	4.437	1.686
2.46	19,840	0.5040	4.476	1.575
2.44	19,680	0.5081	4.489	1.466
2.42	19,520	0.5123	4.484	1.368
2.4	19,360	0.5166	4.466	1.283
2.38	19,200	0.5209	4.443	1.209
2.36	19,030	0.5254	4.417	1.144
2.34	18,870	0.5299	4.389	1.086
2.32	18,710	0.5344	4.360	1.035
2.3	18,550	0.5391	4.331	0.991
2.28	18,390	0.5438	4.303	0.951
2.26	18,230	0.5486	4.276	0.914
2.24	18,070	0.5535	4.249	0.880
2.22	17,910	0.5585	4.224	0.850
2.2	17,740	0.5636	4.199	0.822
2.18	17,580	0.5687	4.176	0.794
2.16	17,420	0.5740	4.153	0.771
2.14	17,260	0.5794	4.131	0.750
2.12	17,100	0.5848	4.109	0.730
2.1	16,940	0.5904	4.088	0.712
2.08	16,780	0.5961	4.068	0.694
2.06	16,610	0.6019	4.050	0.677
2.04	16,450	0.6078	4.031	0.661
2.02	16,290	0.6138	4.012	0.648
2.0	16,130	0.6199	3.995	0.634
1.98	15,970	0.6262	3.979	0.619
1.96	15,810	0.6326	3.962	0.606
1.94	15,650	0.6391	3.947	0.594
1.92	15,490	0.6458	3.932	0.582
1.9	15,320	0.6526	3.917	0.572
1.88	15,160	0.6595	3.902	0.564
1.86	15,000	0.6666	3.889	0.554
1.84	14,840	0.6738	3.875	0.547
1.82	14,680	0.6812	3.862	0.539
1.8	14,520	0.6888	3.851	0.530

(*continued*)

TABLE VI (*Continued*)

Indium Arsenide

eV	cm^{-1}	μm	n	k
1.78	14,360	0.6965	3.839	0.523
1.76	14,200	0.7045	3.828	0.515
1.74	14,030	0.7126	3.817	0.508
1.72	13,870	0.7208	3.807	0.500
1.7	13,710	0.7293	3.798	0.493
1.68	13,550	0.7380	3.788	0.486
1.66	13,390	0.7469	3.780	0.478
1.64	13,230	0.7560	3.770	0.475
1.62	13,070	0.7653	3.761	0.473
1.6	12,900	0.7749	3.755	0.463
1.58	12,740	0.7847	3.746	0.457
1.56	12,580	0.7948	3.735	0.458
1.54	12,420	0.8051	3.729	0.448
1.52	12,260	0.8157	3.720	0.444
1.5	12,100	0.8266	3.714	0.432
1.4	11,290	0.8856	3.696 [1, 2]	
1.2	9,679	1.033	3.613	
1.00	8,065	1.240	3.548	
0.90	7,259	1.378	3.516	
0.85	6,856	1.459		0.232 [6]
0.80	6,452	1.550		0.210
0.75	6,049	1.653		0.191
0.70	5,646	1.771		0.183
0.65	5,243	1.907		0.167
0.60	4,839	2.066		0.161
0.55	4,436	2.254		0.149
0.50	4,033	2.480		0.136
0.45	3,629	2.755		0.120
0.40	3,226	3.100		9.62×10^{-2}
0.37	2,984	3.351		6.4
0.365	2,944	3.397		5.13
0.36	2,904	3.444		3.70
0.355	2,863	3.493		2.17×10^{-2}
0.35	2,823	3.542	3.608 [8]	9.58×10^{-3}
0.345	2,783	3.594		5.14
0.34	2,742	3.647	3.556	2.29
0.335	2,702	3.701		1.12×10^{-3}
0.33	2,662	3.757	3.530	5.08×10^{-4}
0.325	2,621	3.815		2.52
0.32	2,581	3.875	3.512	1.23×10^{-4}
0.31	2,500	4.000	3.499	
0.30	2,420	4.133	3.488	
0.29	2,339	4.275	3.478	
0.28	2,258	4.428	3.470	
0.27	2,178	4.592	3.463	
0.26	2,097	4.769	3.457	
0.25	2,016	4.959	3.451	
0.24	1,936	5.166	3.445	

TABLE VI (*Continued*)

Indium Arsenide

eV	cm^{-1}	μm	n	k
0.23	1,855	5.391	3.441	
0.22	1,774	5.636	3.436	
0.21	1,694	5.904	3.432	
0.20	1,613	6.199	3.427	
0.19	1,532	6.526	3.423	
0.18	1,452	6.888	3.420	
0.17	1,371	7.293	3.416	
0.16	1,290	7.749	3.412	
0.15	1,210	8.266	3.408	
0.14	1,129	8.856	3.404	
0.13	1,049	9.537	3.400	
0.1240	1,000	10.00	3.402[b]	
0.12	967.9	10.33	3.394 [8]	
0.1116	900	11.11	3.398[b]	
0.11	887.2	11.27	3.388 [8]	
0.10	806.5	12.40	3.381	
0.09919	800	12.50	3.391[b]	
0.09	725.9	13.78	3.372 [8]	
0.08679	700	14.29	3.381[b]	
0.08	645.2	15.50	3.358 [8]	
0.07439	600	16.67	3.365[b]	
0.07	564.6	17.71	3.338 [8]	
0.06199	500	20.00	3.334[b]	
0.06	483.9	20.66	3.304 [8]	
0.05641	455	21.98		1.92×10^{-3} [7]
0.05579	450	22.22		3.36
0.05517	445	22.47		8.23
0.05455	440	22.73		5.61
0.05393	435	22.99		5.85
0.05331	430	23.26		7.96
0.05269	425	23.53		7.49
0.05207	420	23.81		7.20
0.05145	415	24.10		4.60
0.05083	410	24.39	3.275[b]	3.88
0.05021	405	24.69		2.55
0.05	403.3	24.80	3.237 [8]	
0.04959	400	25.00	3.264[b]	
0.04711	380	26.32		2.72
0.04649	375	26.67		3.40
0.04587	370	27.03		4.73
0.04525	365	27.38		6.54
0.04463	360	27.78		7.07
0.04401	355	28.17		6.73
0.04339	350	28.57	3.182	5.46
0.04277	345	28.99		5.07

(*continued*)

[b] Obtained from oscillator model [Eq. (3)].

TABLE VI (*Continued*)

Indium Arsenide

eV	cm^{-1}	μm	n	k
0.04215	340	29.41		5.15
0.04154	335	29.85		5.46
0.04092	330	30.30		3.38
0.03720	300	33.33	2.988	
0.03658	295	33.90		3.24
0.03596	290	34.48	2.912	4.94×10^{-3}
			3.18 [14]	4×10^{-2} [14]
0.03534	285	35.09	3.10	6×10^{-2}
				7.54×10^{-3} [7]
0.03472	280	35.71	2.808[b]	1.31×10^{-2}
			3.00 [14]	0.17 [14]
0.03410	275	36.36	2.93	0.27
				2.60×10^{-2} [7]
0.03348	270	37.04	2.658[b]	5.45
			2.92 [14]	0.39 [14]
				3.7×10^{-2} [b]
0.03286	265	37.74	2.92	0.40 [14]
				5.11×10^{-2} [7]
0.03224	260	38.46	2.418[b]	4.74
			2.73 [14]	0.40 [14]
				6.3×10^{-2} [b]
0.03199	258	38.76	2.352[b]	7.1
0.03174	256	39.06	2.277	8.1
0.03162	255	39.22	2.37 [14]	0.50 [14]
				5.62×10^{-2} [7]
0.03149	254	39.37	2.190[b]	9.4[b]
0.03124	252	39.68	2.089	0.11
0.03100	250	40.00	1.970[b]	6.37×10^{-2} [7]
			2.03 [14]	0.83 [14]
				0.13[b]
0.03075	248	40.32	1.827[b]	0.16
			1.88 [14]	0.97 [14]
0.03050	246	40.65	1.60	1.1
			1.649[b]	0.21[b]
0.03025	244	40.98	1.424	0.28
			1.24 [14]	1.44 [14]
0.03000	242	41.32	0.98	2.02
			1.128[b]	0.41[b]
0.02976	240	41.67	0.779	0.71
			0.92 [14]	2.77 [14]
0.02951	238	42.02	1.08	3.50
			0.563[b]	1.19[b]
0.02926	236	42.37	0.493	1.67
			1.27 [14]	4.20 [14]
0.02901	234	42.74	2.08	4.87
			0.485[b]	2.14[b]
0.02876	232	43.10	0.514	2.62
			2.79 [14]	5.17 [14]

TABLE VI (*Continued*)

Indium Arsenide

eV	cm^{-1}	μm	n	k
0.02852	230	43.48	3.30	5.36
			0.578[b]	3.15[b]
0.02827	228	43.86	0.690	3.76
			3.85 [14]	5.60 [14]
0.02802	226	44.25	4.35	5.83
			0.882[b]	4.50[b]
0.02777	224	44.64	1.24	5.45
			4.90 [14]	6.12 [14]
0.02765	222	44.84	5.90	6.53
			1.99[b]	6.76[b]
0.02728	220	45.45	3.99	8.44
			7.50 [14]	6.40 [14]
0.02703	218	45.87	8.89	5.05
			8.58[b]	7.87[b]
0.02678	216	46.30	9.16	3.53
			9.24 [14]	3.50 [14]
0.02653	214	46.73	9.13	2.40
			8.32[b]	1.63[b]
0.02628	212	47.17	7.33	0.92
			9.13 [14]	1.53 [14]
0.02604	210	47.62	8.32	1.04
			6.67[b]	0.60[b]
0.02542	205	48.78	5.72	0.27
			7.48 [14]	0.48 [14]
0.02480	200	50.00	6.91	0.30
			5.22[b]	0.16[b]
0.02418	195	51.28	6.42 [14]	8×10^{-2} [14]
0.02356	190	52.63	6.14	6
0.02294	185	54.05	5.97	6×10^{-2}
0.02232	180	55.56	5.64	0.17
			4.41[b]	4.2×10^{-2}[b]
0.02170	175	57.14	5.58 [14]	0.20 [14]
0.02108	170	58.82	5.41	0.32
0.02046	165	60.61	5.31	0.40
0.01984	160	62.50	5.27	0.41
			4.13[b]	1.9×10^{-2}[b]
0.01922	155	64.52	5.30 [14]	0.51 [14]
0.01860	150	66.67	5.27	0.51
0.01798	145	68.97	5.26	0.60
0.01736	140	71.43	5.30	0.71
			3.99[b]	1.1×10^{-2}[b]
0.01488	120	83.33	3.91	6.6×10^{-3}
0.01240	100	100.0	3.85	4.3
0.009919	80	125.0	3.817	
0.007439	60	166.7	3.793	
0.004959	40	250.0	3.778	
0.002480	20	500.0	3.769	
0.001240	10	1000	3.766	

Indium Antimonide (InSb)

R. T. HOLM
Naval Research Laboratory
Washington, D.C.

The collected data for n and k in Table VII are plotted in Fig. 6. The high-energy regime 155–14 eV has been investigated by Cardona *et al.* [1], who measured k by transmission through evaporated thin films either freely suspended on copper mesh or on transparent substrates of carbon. A synchrotron source provided the wide range of photon energies. The films were polycrystalline but no doubt had a native oxide, since some of the preparation was done outside of vacuum. Samples were presumably at room temperature. These data show several peaks, including three in the 20-eV region that were assigned to interband transitions.

However, Philipp and Ehrenreich [2] found no structure in this region after Kramers–Kronig (KK) analysis, probably because the corresponding reflectivity was $<2\%$; there could be problems in surface preparation even though a chemical polish was used; and a thin native oxide was present on the surface. Native oxides on most semiconductors have band gaps in the 4–10-eV region that means that above these energies even thin films (20–30 Å thick) begin to absorb when α becomes greater than 10^5 cm^{-1}. The factor of 2 disparity in k is illustrated in Table VII in the overlap region between the data of Cardona *et al.* [1] and Philipp and Ehrenreich [2]. The n and k data of Philipp and Ehrenreich [2], as tabulated by Seraphin and Bennett [3], are used down to 0.8 eV except for the region 6–1.5 eV. Here, ellipsometrically determined values of n and k by Aspnes and Studna [4] have been inserted.

At this point, it joins to the k results of Moss *et al.* [5], also tabulated in Seraphin and Bennett [3]. The near IR measurements were on slabs of intrinsic InSb of various thickness ranging from 5.5 to 40 μm, which were mechanically polished (surface damage present) and prepared so as to be unbacked but mounted on their edges. Although not specified, samples were at room temperature. Because of free-carrier effects at the fundamental band edge and at lower photon energies, we have elected to tabulate IR results for only intrinsic InSb with a free-carrier density of holes and electrons of

ISBN 0-12-544420-6

$N = P = 2 \times 10^{16}$ cm^{-3}. The Burstein–Moss effect at the band gap, originally discovered in heavily doped InSb [6, 7], is not appreciable in intrinsic material.

The near IR values for n were determined by Moss *et al.* [5] from interference fringe measurements. Values tabulated in Seraphin and Bennett [3] are listed in Table VII. Uncertainty in n is $\pm 0.5\%$. This work was the first to point out problems of fringe counting when there is significant dispersion in the refractive index.

Additional results for k are given by Kurnick and Powell [8] just below the band gap near 0.2 eV for a temperature of 298 K. Again, transmission measurements were used. Elaborate mechanical polishing to keep the slab faces parallel produced free samples of thicknesses in the range 0.08 to 3 mm. Reflectivity R was determined by measuring T as a function of sample thickness. Corrections for wide slit widths in a spectral range of rapidly changing absorption were made. The data for n- and p-type samples with carrier densities in the range 2×10^{15}–2×10^{17} cm^{-3} were presented. We chose the most suitable intrinsic sample that at low temperature had $N = 2 \times 10^{15}$ cm^{-3} and read the values of absorption coefficient α from the graph.

The far IR properties of nearly intrinsic material ($N = 6 \times 10^{15}$ cm^{-3} at low temperature) have been studied by Yoshinaga and Oetjen [9] and Sanderson [10]. Yoshinaga and Oetjen [9] measured reflectance at an angle of incidence of 45° (no light polarization was mentioned) and normal-incidence transmission in the spectral range 20–220 μm. They determined n and k directly in the transparent region 20–45 μm as tabulated Seraphin and Bennett [3]. The sample temperature was 298 K. The experiment involved a grating spectrometer with filters that did not give adequate spectral purity at long wavelengths beyond the reststrahlen as was subsequently shown by Sanderson [10], who used a lamellar grating interferometric modulator to measure reflectivity. He analyzed the results by a combined Drude and Lorentz oscillator model and also by the KK technique. The results of the two analyses were very close except in the region near the reststrahlen peak. We have used the oscillator model to calculate n and k. These are tabulated in the 10–1000-μm region. The formula used is

$$\varepsilon = (n - ik)^2 = \varepsilon_\infty \left[1 + \frac{\omega_L^2 - \omega_T^2}{\omega_T^2 - \omega^2 + i\Gamma\omega} - \frac{\omega_p^2}{\omega(\omega + i\gamma)} \right],$$

with $\varepsilon_\infty = 15.68$, $\omega_T = 179.1$ cm^{-1}, $\omega_L = 190.4$ cm^{-1}, $\Gamma = 2.86$ cm^{-1}, $\omega_p = 81.0$ cm^{-1}, and $\gamma = 10.7$ cm^{-1} and with ω_p the plasma frequency, γ the electron damping constant characterizing the free carriers, ω_T the TO frequency, ω_L the LO frequency, Γ the vibration damping constant, and ε_∞ the high-frequency lattice background dielectric constant. Above ω_L, these n and k values deviate significantly from those of Yoshinaga and Oetjen [9] in the overlap region as Table VII indicates. We have extended the calculated values of n to 1000 cm^{-1} to demonstrate the ultimate good agreement with the experimental values of Moss *et al.* [5].

We are hard-pressed to specify uncertainties in n and k. The values of Γ and γ are probably uncertain to $\pm 20\%$ and peaks in n and k near ω_T are very sensitive to these values. Here, n and k are probably reliable to one significant figure at best and a factor of 2 at worst. Of course, n and k as given do yield R over the range 20–200 cm^{-1} to within ± 0.02 reflectivity units everywhere except at the reststrahlen minimum. The calculated value of R is probably better here because the surface is mechanically damaged. A perusal of other data [11, 12] suggests that the reflection minimum should be nearer to 5% than to the experimentally measured value of 12% for intrinsic InSb.

It is obvious from the discussion of wavelength dependence of free-carrier absorption as discussed by Jensen for GaAs, InP, and InAs in Chapter 9 of this handbook that the Drude model with fixed damping constant is not expected to give good values of k above ω_L, although the wavelength dependence of α is λ^2 in agreement with a simple Drude model [13]. On the other hand, in the spectral region 30–45 μm the values of n from Yoshinaga and Oetjen [9] appear significantly smaller than those of Sanderson [10], the difference being larger than the usual discrepancy between measured n and calculated n as obtained with a Lorentz–Drude oscillator fit. The Lorentz oscillator parameters of Sanderson [10] (ε_∞, ω_T, ω_L) appear reasonable compared to another determination [11]; likewise for the free-carrier parameters (ω_p, γ). The data of Yoshinaga and Oetjen [9] do indicate some multiple-phonon absorption in the region 20–45 μm, but such absorption has very little effect on n as determined from an oscillator model.

Moss *et al.* [5] calculated the refractive index in the 5–21-μm region including various contributions to absorption due to higher-energy band gaps, the fundamental band gap, free carriers, and the reststrahlen band. Their resultant values are about 0.01 higher in the 11–21-μm region than the experimental values, indicating some problems with various oscillator models and the definition of ε_∞. Usually, the dielectric function due to all interband transitions (omitting free-carrier and lattice-vibration contributions) has a value at zero frequency that is the same as its value at about $E_g/3$ to one unit in the second decimal place. The practical value of ε_∞ is then easy to estimate. In a small-band-gap material such as InSb with the lattice vibration absorption being so close to the fundamental band edge, the practical definition of ε_∞ becomes harder. Pihktin and Yas'kov [14] have reanalyzed n in terms of dispersion equation for interband and lattice vibration contributions (no free carriers) and their values of n are significantly larger (~ 0.3) than those of Yoshinaga and Oetjen [9] and Sanderson [10] in the 25-μm region, indicating that the free-carrier contribution is important. It follows that the carrier density must be well determined for meaningful comparison.

The temperature dependence of n has both a lattice part and a free-carrier part. In the near IR transparent region, Cardona [15] determined both of these components, the latter being somewhat complicated due to the temperature dependence of the intrinsic free-carrier density. For the lattice part $(1/n)(dn/dT) = (11.9 \pm 0.2) \times 10^{-5}\,°C^{-1}$.

REFERENCES

1. M. Cardona, W. Gudat, B. Sonntag, and P. Y. Yu, *Proc. Int. Conf. Phys. Semicond., 10th, Cambridge, 1970*, p. 208. U.S. Atomic Energy Commission, Oak Ridge, Tennessee, 1970.
2. H. R. Philipp and H. Ehrenreich, *Phys. Rev.* **129**, 1550 (1963).
3. B. O. Seraphin and H. E. Bennett, *in* "Semiconductors and Semimetals" (R. K. Willardson and A. C. Beer eds.), Vol. 3, p. 499. Academic Press, New York, 1967.
4. D. E. Aspnes and A. A. Studna, *Phys. Rev. B* **27**, 985 (1983); D. E. Aspnes and A. A. Studna, private communication (1982).
5. T. S. Moss, S. D. Smith, and T. D. F. Hawkins, *Proc. Phys. Soc. London* **70B**, 776 (1957).
6. E. Burstein, *Phys. Rev.* **93**, 632 (1954).
7. T. S. Moss, *Proc. Phys. Soc. London* **67**, 775 (1954).
8. S. W. Kurnick and J. M. Powell, *Phys. Rev.* **116**, 597 (1959).
9. H. Yoshinaga and R. A. Oetjen, *Phys. Rev.* **101**, 526 (1956).
10. R. B. Sanderson, *J. Phys. Chem. Solids* **26**, 803 (1965).
11. R. T. Holm and E. D. Palik, *CRC Crit. Rev. Solid State Sci.* **5**, 397 (1975).
12. R. W. Gammon and E. D. Palik, *J. Opt. Soc. Am.* **64**, 350 (1974).
13. W. G. Spitzer and H. Y. Fan, *Phys. Rev.* **106**, 882 (1957).
14. A. N. Pikhtin and A. D. Yas'kov, *Soviet Phys. Semicond.* **12**, 622 (1978); A. N. Pikhtin and A. D. Yas'kov, *Fiz. Tekh. Poluprovodn.* **12**, 1047 (1978).
15. M. Cardona, *Proc. Int. Conf. Semicond. Phys., Prague, 1960*, p. 349. Czech. Acad. Sci., Prague, and Academic Press, New York, 1961.

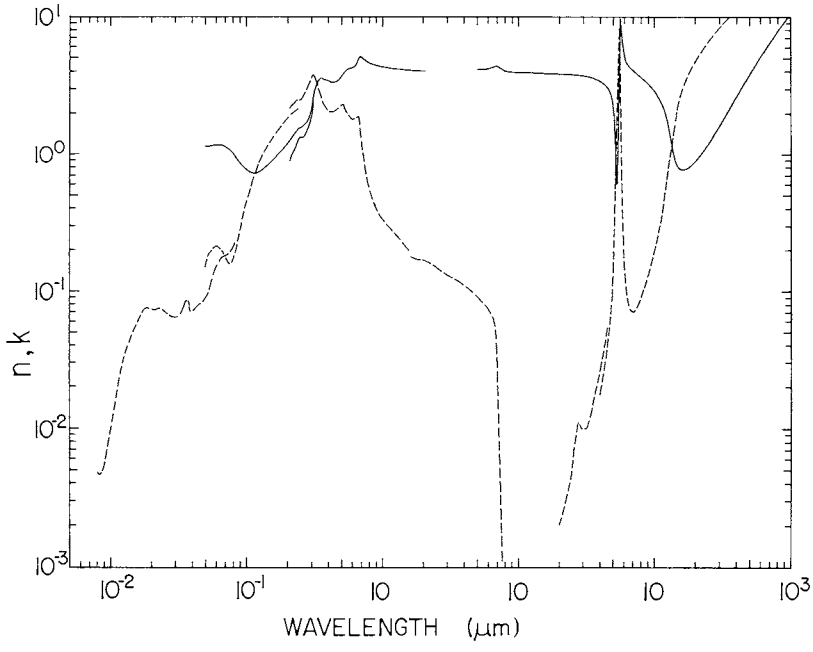

Fig. 6. Log–log plot of n (——) and k (– – –) versus wavelength in micrometers for indium antimonide. Note that this is intrinsic InSb with strong free-carrier absorption in the far infrared.

TABLE VII

Values of n and k for Indium Antimonide Obtained from Various References[a]

eV	cm^{-1}	μm	n	k
155		0.007999		4.77×10^{-3} [1]
150		0.008266		4.60
145		0.008551		4.83
140		0.008856		5.28
135		0.009184		6.13
130		0.009537		7.59
125		0.009919		9.70×10^{-3}
120		0.01033		1.25×10^{-2}
115		0.01078		1.59
110		0.01127		2.06
105		0.01181		2.63
100		0.01240		3.25
95		0.01305		3.79
90		0.01378		4.45
85		0.01459		5.02
80		0.01550		5.77
75		0.01653		6.60
70		0.01771		7.45
65		0.01907		7.46
60		0.02066		7.30
55		0.02254		7.50
50		0.02480		7.10
45		0.02755		6.51
40		0.03100		6.51
38		0.03263		6.75
37		0.03351		7.06
36		0.03444		7.67
35		0.03542		8.51
34		0.03647		8.56
33		0.03757		8.37
32		0.03875		7.09
31		0.04000		7.16
30		0.04133		7.23
29		0.04275		7.55
28		0.04428		7.89
27		0.04592		8.11
26		0.04769		8.34
25		0.04959	1.15 [2]	8.88×10^{-2} 0.15 [2]
24		0.05166	1.15	9.37×10^{-2} [1] 0.18 [2]

(continued)

[a] The value of k is often given in powers of 10 down to 10^{-2}, whereupon we revert to decimals only. The exponent of 10 is understood down the column until the next exponent is about to appear. We have sometimes overlapped data of different references to demonstrate discrepancies. It is not always obvious why the discrepancies exist. The references are given in brackets.

TABLE VII (*Continued*)

Indium Antimonide

eV	cm^{-1}	μm	n	k
23		0.05391	1.15	0.105 [1]
				0.19 [2]
22		0.05636	1.16	0.125 [1]
				0.20 [2]
21		0.05904	1.17	0.145 [1]
				0.21 [2]
20		0.06199	1.17	0.160 [1]
				0.21 [2]
19.5		0.06358		0.163 [1]
19		0.06526	1.18	0.173
				0.20 [2]
18.5		0.06702		0.178 [1]
18		0.06888	1.15	0.178
				0.18 [2]
17.5		0.07085		0.180 [1]
17		0.07293	1.11	0.181
				0.16 [2]
16.5		0.07514		0.191 [1]
16		0.07749		0.205
15.5		0.07999	1.02	0.17 [2]
15		0.08266	0.97	0.230 [1]
				0.19 [2]
14		0.08856	0.88	0.269 [1]
				0.26 [2]
13		0.09537	0.80	0.37
12		0.1033	0.75	0.51
11		0.1127	0.72	0.69
10		0.1240	0.74	0.88
9		0.1378	0.80	1.08
8		0.1550	0.88	1.32
7.6		0.1631	0.94	1.41
6.8		0.1823	1.06	1.61
6.0	48,390	0.2066	1.23	1.91
			0.861 [4]	2.139 [4]
5.94	47,910	0.2087	0.900	2.180
5.90	47,590	0.2101	0.922	2.185
5.84	47,100	0.2123	0.951	2.204
5.80	46,780	0.2138	0.969	2.210
5.74	46,300	0.2160	0.992	2.227
5.70	45,970	0.2175	1.000	2.235
			1.36 [2]	1.97 [2]
5.64	45,490	0.2198	1.016 [4]	2.257 [4]
5.60	45,170	0.2214	1.025	2.275
5.54	44,680	0.2238	1.042	2.307
5.50	44,360	0.2254	1.057	2.333
5.44	43,880	0.2279	1.088	2.369

TABLE VII (*Continued*)

Indium Antimonide

eV	cm^{-1}	μm	n	k
5.40	43,550	0.2296	1.116	2.394
5.34	43,070	0.2322	1.161	2.424
5.30	42,750	0.2339	1.194	2.435
5.24	42,260	0.2366	1.242	2.446
5.20	41,940	0.2384	1.270	2.444
5.14	41,460	0.2412	1.301	2.435
5.10	41,130	0.2431	1.309	2.430
5.04	40,650	0.2460	1.311	2.431
5.00	40,330	0.2480	1.307	2.441
4.94	39,840	0.2510	1.301	2.470
4.90	39,520	0.2530	1.301	2.495
4.84	39,040	0.2562	1.306	2.542
4.80	38,710	0.2583	1.312	2.576
4.74	38,230	0.2616	1.328	2.630
4.70	37,910	0.2638	1.341	2.669
4.64	37,420	0.2672	1.366	2.732
4.60	37,100	0.2695	1.385	2.776
4.54	36,620	0.2731	1.419	2.845
4.50	36,290	0.2755	1.443	2.894
4.44	35,810	0.2792	1.484	2.975
4.40	35,490	0.2818	1.515	3.034
4.34	35,000	0.2857	1.571	3.134
4.30	34,680	0.2883	1.618	3.209
4.24	34,200	0.2924	1.708	3.337
4.20	33,880	0.2952	1.791	3.433
4.14	33,390	0.2995	1.966	3.582
4.10	33,070	0.3024	2.127	3.666
4.04	32,580	0.3069	2.425	3.720
4.00	32,260	0.3100	2.632	3.694
3.94	31,780	0.3147	2.902	3.581
3.90	31,460	0.3179	3.044	3.479
3.84	30,970	0.3229	3.204	3.314
3.80	30,650	0.3263	3.287	3.204
3.74	30,160	0.3315	3.383	3.039
3.70	29,840	0.3351	3.427	2.933
3.64	29,360	0.3406	3.468	2.789
3.60	29,040	0.3444	3.485	2.705
3.54	28,550	0.3502	3.504	2.589
3.50	28,230	0.3542	3.511	2.517
3.44	27,750	0.3604	3.515	2.424
3.40	27,420	0.3647	3.520	2.369
3.34	26,940	0.3712	3.528	2.280
3.30	26,620	0.3757	3.525	2.217
3.24	26,130	0.3827	3.502	2.137
3.20	25,810	0.3875	3.482	2.093

(*continued*)

TABLE VII (*Continued*)

Indium Antimonide

eV	cm^{-1}	μm	n	k
3.14	25,330	0.3949	3.445	2.038
3.10	25,000	0.4000	3.419	2.015
3.04	24,520	0.4078	3.384	1.997
3.00	24,200	0.4133	3.366	1.994
2.94	23,710	0.4217	3.348	1.997
2.90	23,390	0.4275	3.342	2.004
2.84	22,910	0.4366	3.340	2.021
2.80	22,580	0.4428	3.345	2.036
2.74	22,100	0.4525	3.360	2.062
2.70	21,780	0.4592	3.377	2.083
2.64	21,290	0.4696	3.413	2.119
2.60	20,970	0.4769	3.447	2.145
2.54	20,490	0.4881	3.512	2.188
2.50	20,160	0.4959	3.570	2.221
2.48	20,000	0.4999	3.605	2.238
2.46	19,840	0.5040	3.646	2.254
2.44	19,680	0.5081	3.694	2.271
2.42	19,520	0.5123	3.752	2.283
2.40	19,360	0.5166	3.822	2.287
2.38	19,200	0.5209	3.900	2.274
2.36	19,030	0.5254	3.976	2.239
2.34	18,870	0.5299	4.040	2.183
2.32	18,710	0.5344	4.084	2.121
2.30	18,550	0.5391	4.111	2.060
2.28	18,390	0.5438	4.126	2.005
2.26	18,230	0.5486	4.133	1.957
2.24	18,070	0.5535	4.136	1.915
2.22	17,910	0.5585	4.136	1.880
2.20	17,740	0.5636	4.135	1.850
2.18	17,580	0.5687	4.134	1.826
2.16	17,420	0.5740	4.132	1.806
2.14	17,260	0.5794	4.132	1.790
2.12	17,100	0.5848	4.133	1.779
2.10	16,940	0.5904	4.136	1.770
2.08	16,780	0.5961	4.142	1.765
2.06	16,610	0.6019	4.149	1.763
2.04	16,450	0.6078	4.161	1.763
2.02	16,290	0.6138	4.175	1.767
2.00	16,130	0.6199	4.194	1.773
1.98	15,970	0.6262	4.218	1.784
1.96	15,810	0.6326	4.249	1.799
1.94	15,650	0.6391	4.290	1.818
1.92	15,490	0.6458	4.347	1.844
1.90	15,320	0.6526	4.433	1.873
1.88	15,160	0.6595	4.566	1.879
1.86	15,000	0.6666	4.723	1.816

TABLE VII (*Continued*)

Indium Antimonide

eV	cm^{-1}	μm	n	k
1.84	14,840	0.6738	4.841	1.685
1.82	14,680	0.6812	4.898	1.534
1.80	14,520	0.6888	4.909	1.396
			5.13 [2]	1.37 [2]
1.78	14,360	0.6965	4.894 [4]	1.275 [4]
1.76	14,200	0.7045	4.867	1.171
1.74	14,030	0.7126	4.830	1.085
1.72	13,870	0.7208	4.793	1.010
1.70	13,710	0.7293	4.754	0.949
1.68	13,550	0.7380	4.712	0.897
1.66	13,390	0.7469	4.675	0.848
1.64	13,230	0.7560	4.637	0.808
1.62	13,070	0.7653	4.602	0.776
1.60	12,900	0.7749	4.568	0.749
			4.72 [2]	0.60 [2]
1.58	12,740	0.7847	4.534 [4]	0.723 [4]
1.56	12,580	0.7948	4.501	0.701
1.54	12,420	0.8051	4.473	0.675
1.52	12,260	0.8157	4.442	0.659
1.50	12,100	0.8266	4.418	0.643
1.4	11,290	0.8856	4.40 [2]	0.40 [2]
1.2	9,679	1.033	4.24	0.32
1.0	8,065	1.240	4.15	0.26
0.8	6,452	1.550	4.08	0.20
0.7749.	6,250	1.6		0.18 [5]
0.6888	5,556	1.8		0.17
0.6199	5,000	2.0		0.17
0.6	4,839	2.066	4.03	
0.4959	4,000	2.5		0.15
0.4133	3,333	3.0		0.13
0.3542	2,857	3.5		0.12
0.3100	2,500	4.0		0.11
0.2755	2,222	4.5		0.10
0.2480	2,000	5.0	4.14 [5]	9.1×10^{-2}
0.2254	1,818	5.5	4.15	
0.2066	1,667	6.0	4.19	7.4
0.2033	1,639	6.1		7.2
0.2000	1,613	6.2		7.0
0.1968	1,587	6.3		6.8
0.1937	1,563	6.4		6.6
0.1907	1,538	6.5	4.30	6.3
0.1879	1,515	6.6		5.9
0.1851	1,493	6.7		5.5
0.1823	1,471	6.8		4.9
0.1797	1,449	6.9		3.7

(*continued*)

TABLE VII (*Continued*)

Indium Antimonide

eV	cm^{-1}	μm	n	k
0.1771	1,429	7.0	4.37	2.8
0.175	1,411	7.085		1.46×10^{-2} [8]
0.1722	1,389	7.2		9.2×10^{-3} [5]
0.170	1,371	7.293		5.68 [8]
0.1675	1,351	7.4		3.5 [5]
0.1653	1,333	7.5	4.18	2.7 [5]
0.165	1,331	7.5144		2.63 [8]
0.1631	1,316	7.6		1.3 [5]
0.160	1,290	7.749		1.57 [8]
0.1575	1,271	7.87	4.001	
0.155	1,251	7.999		1.18×10^{-3}
0.1550	1,250	8.0	3.995	
0.150	1,210	8.266		9.86×10^{-4}
0.145	1,169	8.551		9.52
0.140	1,129	8.856		9.15
0.1376	1,110	9.01	3.967	
0.135	1,089	9.184		9.13
0.130	1,049	9.537		9.10×10^{-4}
0.1240	1,000	10.00	3.938 [10]	
0.1232	994.0	10.06	3.953 [5]	
0.1126	908.3	11.01	3.937	
0.1116	900	11.11	3.933 [10]	
0.1028	829.2	12.06	3.920 [5]	
0.09919	800	12.50	3.926 [10]	
0.09552	770.4	12.98	3.912 [5]	
0.08920	719.4	13.90	3.902	
0.08679	700	14.29	3.915 [10]	
0.08194	660.9	15.13	3.881 [5]	
0.07852	633.3	15.79	3.873	
0.07439	600	16.67	3.898 [10]	
0.07310	589.6	16.96	3.866 [5]	
0.06946	560.2	17.85	3.850	
0.06577	530.5	18.85	3.843	
0.06205	500.5	19.98	3.826	
0.06199	500	20.00	3.869 [10]	2.0×10^{-3} [9]
0.05862	472.8	21.15	3.814 [5]	
0.05585	450.5	22.20	3.805	
0.04959	400.0	25.00	3.78 [9] 3.811 [10]	5.1
0.04769	384.6	26.00	3.74 [9]	7.5
0.04592	370.4	27.0	3.66	9.7×10^{-3}
0.04463	360	27.78	3.770 [10]	
0.04428	357.1	28.0	3.56 [9]	1.1×10^{-2}
0.04275	344.8	29.0	3.50	1.0
0.04215	340	29.41	3.743 [10]	
0.04133	333.3	30.0	3.47 [9]	1.0

TABLE VII (*Continued*)

Indium Antimonide

eV	cm^{-1}	μm	n	k
0.04000	322.6	31.0	3.44	1.0
0.03968	320	31.25	3.708 [10]	
0.03875	312.5	32.0	3.39 [9]	1.0
0.03757	303.0	33.0	3.34	1.1×10^{-2}
0.03720	300	33.33	3.662 [10]	7.84×10^{-3} [10]
0.03647	294.1	34.0	3.30 [9]	1.2×10^{-2} [9]
0.03596	290	34.48	3.63 [10]	8.96×10^{-3} [10]
0.03542	285.7	35.0	3.25 [9]	1.4×10^{-2} [9]
0.03472	280	35.71	3.60 [10]	1.03×10^{-2} [10]
0.03348	270	37.04	3.56	1.21
0.03224	260	38.46	3.51	1.44
0.03100	250	40.00	2.98 [9]	2.6 [9]
			3.45 [10]	1.75 [10]
0.02976	240	41.67	3.37	2.20
0.02914	235	42.55	3.32	2.51
0.02852	230	43.48	3.26	2.91
0.02790	225	44.44	3.18	3.44
0.02755	222.2	45.0	2.57 [9]	5.4 [9]
0.02728	220	45.45	3.09 [10]	4.16 [10]
0.02666	215	46.51	2.97	5.23
0.02604	210	47.62	2.82	6.92
0.02542	205	48.78	2.59	9.93×10^{-2}
0.02480	200	50.00	2.22	0.165
0.02455	198	50.51	2.00	0.217
0.02430	196	51.02	1.69	0.311
0.02405	194	51.55	1.25	0.525
0.02393	193	51.81	0.989	0.753
0.02380	192	52.08	0.776	1.10
0.02368	191	52.36	0.663	1.49
0.02356	190	52.63	0.618	1.88
0.02343	189	52.91	0.611	2.27
0.02331	188	53.19	0.632	2.67
0.02318	187	53.48	0.680	3.10
0.02306	186	53.76	0.760	3.57
0.02294	185	54.05	0.884	4.10
0.02281	184	54.35	1.08	4.73
0.02269	183	54.64	1.39	5.48
0.02256	182	54.95	1.95	6.43
0.02244	181	55.25	3.05	7.59
0.02232	180	55.56	5.34	8.56
0.02219	179	55.87	8.68	7.34
0.02207	178	56.18	9.61	4.20
0.02194	177	56.50	8.82	2.31
0.02182	176	56.82	7.97	1.42

(*continued*)

TABLE VII (*Continued*)

Indium Antimonide

eV	cm^{-1}	μm	n	k
0.02170	175	57.14	7.32	0.963
0.02157	174	57.47	6.82	0.699
0.02145	173	57.80	6.44	0.534
0.02132	172	58.14	6.14	0.424
0.02120	171	58.48	5.89	0.347
0.02108	170	58.82	5.69	0.291
0.02083	168	59.52	5.37	0.216
0.02058	166	60.24	5.13	0.170
0.02033	164	60.98	4.94	0.140
0.02009	162	61.73	4.79	0.119
0.01984	160	62.50	4.66	0.105
0.01922	155	64.52	4.42	8.38×10^{-2}
0.01860	150	66.67	4.24	7.43
0.01798	145	68.97	4.09	7.10
0.01736	140	71.43	3.96	7.15
0.01674	135	74.07	3.85	7.49
0.01612	130	76.92	3.74	8.08
0.01550	125	80.00	3.62	8.91×10^{-2}
0.01488	120	83.33	3.51	0.100
0.01426	115	86.96	3.38	0.115
0.01364	110	90.91	3.25	0.134
0.01302	105	95.24	3.10	0.159
0.01240	100	100.0	2.92	0.193
0.01178	95	105.3	2.71	0.240
0.01116	90	111.1	2.45	0.310
0.01054	85	117.6	2.12	0.423
0.009919	80	125.0	1.68	0.633
0.009299	75	133.3	1.19	1.09
0.008679	70	142.9	0.881	1.79
0.008059	65	153.8	0.781	2.51
0.007439	60	166.7	0.771	3.21
0.006819	55	181.8	0.811	3.94
0.006199	50	200.0	0.894	4.72
0.005579	45	222.2	1.02	5.59
0.004959	40	250.0	1.21	6.61
0.004339	35	285.7	1.50	7.83
0.003720	30	333.3	1.93	9.35
0.003100	25	400.0	2.63	11.3
0.002480	20	500.0	3.81	14.0
0.001860	15	666.7	6.03	17.9
0.001240	10	1000	10.7	24.0

Indium Phosphide (InP)

O. J. GLEMBOCKI
Naval Research Laboratory
Washington, D.C.

H. PILLER
Department of Physics and Astronomy
Louisiana State University
Baton Rouge, Louisiana

As with other semiconductors, the index of refraction of InP has been reported by various investigators over a wide range of photon energies, 1.2 meV to 20 eV. The number of papers for InP, however, is somewhat limited. Various techniques were employed in these measurements, and there is some overlap in data obtained from different sources. In many cases, values in the overlap regions do not coincide and a choice was made of one set over another based on the technique used and its limitations. We shall discuss the overlap problems when they arise. The values of n and k are listed in Table VIII and a plot is shown in Fig. 7.

Cardona [1] has measured the reflectivity of InP in the 1–20-eV range. The sample surfaces were prepared by mechanical polishing with Linde A-5175 compound. The reflection spectra were then measured and the samples were etched in a 1:1 solution of HNO_3 and HCl to remove any damage and to improve the reflectivity. The reflection spectra were then Kramers–Kronig (KK) analyzed to obtain ε_1 and ε_2 as well as n and k. We read values from a published graph. Above 20 eV Cardona [1] assumed the reflectivity to be proportional to E^{-4} (free-electron gas). In a subsequent work [2] measurements were made to 150 eV, but the data were not given. In Table VIII we list the data of Cardona [1] from 6–20 eV.

The 6-eV cutoff of Cardona's [1] values of n and k results from the availability of better measurements from 1.5 to 6 eV. Recently, Aspnes and Studna [3] have obtained the optical constants of InP, as well as of other semiconductors, through the use of spectroscopic ellipsometry. These measurements allowed them to determine ε_1 and ε_2 or, alternatively, n and k directly without a KK analysis. The values in Table I were obtained from a numerical table. Their samples were of $\langle 100 \rangle$ orientation and undoped. Extensive care

Copyright © 1985 by Academic Press, Inc.
All rights of reproduction in any form reserved.
ISBN 0-12-544420-6

was taken to avoid both surface damage and unintentional overlayers such as oxides. Their sample-preparation techniques involved an initial pretreatment with bromine–methanol (0.02-vol % bromine in methanol) chemomechanical polish. Afterward, the final polishing techniques involved a 20-sec polish on a lens paper saturated with the bromine–methanol solution, followed by a-10 sec quench in methanol, and, last, the sample was rinsed in a 1:1 NH_4O_4:OH solution. The final polishing and the measurements were performed in an N_2 atmosphere.

Aspnes and Studna [3] have corrected their values near 1.5 eV so that both ε_1 and ε_2 are KK consistent to within $\pm 0.4\%$. At 5.07 eV they obtain a value of $R = 0.621$, while Cardona [1] measured 0.553. This indicates that the sample surfaces of Cardona [1] were not as good as those of Aspnes and Studna [3].

Below 1.5 eV Pettit and Turner [4] measured n by the minimum-deviation method on an n-type sample of carrier density $N = 5 \times 10^{16}\ \text{cm}^{-3}$. The surface was mechanically polished to a flatness of 0.5 μm or better. A precision of ± 0.0003 in n is quoted. The data for n between 0.5 and 1.4 eV were found to fit to the expression

$$n^2 = A + B\lambda^2/(\lambda^2 - C^2), \tag{1}$$

where λ is in angstroms and the constants for room temperature are $A = 7.255$, $B = 2.316$, and $C^2 = 0.3922 \times 10^8$. Calculated values obtained from Eq. (1) are tabulated.

The transmission measurements of Newman [5] allow us to obtain k below 1.4 eV. These experiments were performed at 300 K by using an n-type sample with a carrier density of $N = 5 \times 10^{15}\ \text{cm}^{-3}$. Sample preparation is not discussed. Newman's data [5] for $\lambda > 14$ μm are presented in terms of the transmission spectrum. To obtain k, we used the relationship $T = (1 - R)^2 \exp(-4\pi kd/\lambda)$, which accounts for multiple reflections. The thickness was $d = 0.01$ cm, and R was computed from the oscillator model for n by using $R = [(n-1)^2 + k^2]/[(n+1)^2 + k^2]$; k was negligibly small in most cases. Seraphin and Bennett [6] present a tabular form of Newman's data [5] for shorter wavelengths between 0.92 and 0.98 μm.

Overlapping the data of Newman [5] is the work of Pikhtin and Yas'kov [7], in which they fit the n data [4] to a lattice-vibration oscillator model given by

$$n^2 = 1 + \frac{A}{\pi} \ln \frac{E_1^2 - (\hbar\omega)^2}{E_0^2 - (\hbar\omega)^2} + \frac{G_1}{E_1^2 - (\hbar\omega)^2} + \frac{G_2}{E_2^2 - (\hbar\omega)^2} + \frac{G_3}{E_3^2 - (\hbar\omega)^2}, \tag{2}$$

where $E_0 = 1.345$ eV, $E_1 = 3.2$ eV, $E_2 = 5.1$ eV, $E_3 = 37.65 \times 10^{-3}$ eV, $G_1 = 57.889\ \text{eV}^2$, $G_2 = 65.937\ \text{eV}^2$, $G_3 = 0.392 \times 10^{-2}\ \text{eV}^2$, and $A = 0.7\sqrt{E_0}$. A

comparison of these values with those of Pettit and Turner [4] reveals some differences, but only in the third decimal place. At longer wavelengths, we expect that the above data will be better than those of Pettit and Turner [4]. This is a consequence of the fact that for $\hbar\omega = 0$ and $G_3 = 0$, $n^2 = 9.52$, corresponding to the high-frequency dielectric constant ε_∞, which will be used in the analysis of Raman scattering data. The value of $n^2 = 9.52$ holds to within three figures, even up to 560 cm^{-1}.

Reynolds *et al.* [8] measured by transmission the multiphonon absorption in the 12–20-μm range. The temperature used was 293 K. The sample was n-type with a carrier density of $N \approx 10^{15}$ cm^{-3}, and the surfaces were cleaned and etched in hot or cold HCl. The data of Reynolds *et al.* [8] (read from a graph) and Newman [5] are in good agreement in the ranges of 0.060 to 0.062 eV and 0.083 to 0.085 eV. However, at the vibration peaks near 0.08 eV, they deviate by as much as a factor of 2 and by an order of magnitude in the transparent region near 0.07 eV. We tabulate portions of both data sets; from 12 to 20 μm we plot the values of Reynolds [8], whereas from 20 to 29 μm the Newman [5] data are used.

Koteles and Datars [9] performed absorption measurements at 20 K over the range of 0.025 to 0.10 eV. Their data were rich in structure. However, values of k are not provided, just absorption on a linear scale.

In the far infrared (<0.05 eV), we found little detailed analysis of the reflectance by a KK inversion or fit to an oscillator model. Newman's [5] data (at 300 K) indicate 100% reflectivity at the reststrahlen peak near 0.04 eV, which is unrealistic. The room-temperature data of Hass and Henvis [10] show too much variation from the simple reststrahlen curve. This may be attributable to free-carrier plasma and mechanical polishing effects. In order to obtain refractive-index data in this region, we used the oscillator model, which yields

$$(n - ik)^2 = \varepsilon_\infty \left[1 + \frac{\omega_L^2 - \omega_T^2}{\omega_T^2 - \omega^2 - i\Gamma\omega} \right], \tag{3}$$

with the parameters $\omega_L = 345.0 \pm 0.3$ cm^{-1}, $\omega_T = 303.7 \pm 0.3$ cm^{-1}, and $\Gamma = 3.5 \pm 0.5$ cm^{-1} from the Raman scattering data of Mooradian and Wright [11], while $\varepsilon_\infty = 9.61$ was obtained from Hass [12]. Other Raman work gave virtually the same values for ω_T and ω_L [13, 14]. In Table VIII we list our values for n and k below 410 cm^{-1} (as footnote *b*). Near $\omega = \omega_T \pm 30$ cm^{-1}, the n and k values are probably good to $\pm 50\%$. This is based on the systematic variation of the parameters within their probable values. Consequently, the model can only serve as an order-of-magnitude estimate for k far from ω_T. For example, at 0.044 eV the measured k is 2.39×10^{-2}, while the oscillator-model k is 9.9×10^{-2}, a factor of 4 larger. To force the oscillator model to fit better would require increasing Γ significantly, which is not warranted by the Raman linewidth data. We therefore conclude that

the oscillator model is a poor approximation away from the resonant frequency.

Jamshidi and Parker [15] have measured n and k by using asymmetric Fourier-transform spectroscopy, which is a more direct technique for obtaining optical constants. The values of n and k that we list have been taken from a graph. We find that their peak reststrahlen reflectivity of 0.897 occurs at 333 cm^{-1}. This is considerably different from the value of $R = 0.924$ at 314 cm^{-1}, which the oscillator model yields and much larger than the experimental value of 0.79 from Hass and Henvis [10]. This experimental value is too low, if anything, and may be due to surface quality and/or stray radiation. Their (Jamshidi and Parker [15]) value of n near 450 cm^{-1} is 2.29, significantly smaller than $n = 2.66$ from Pikhtin and Yas'kov [7]. We feel that the analysis of Pikhtin and Yas'kov [7] cannot be that much in error. In addition, the low-frequency dielectric constant of Jamshidi and Parker [15] is 12.18, much smaller than the value of 12.37 given in the analysis of reststrahlen reflectivity in Hass [12]. It is interesting to note that the values of n and k measured by asymmetric Fourier-transform spectroscopy in the case of CdTe were in good agreement with those obtained by other means, while those for InAs were in poorer agreement (perhaps due to different free-carrier densities).

Jamshidi and Parker [15] suggest that their data for n and k are better in the range 300–380 cm^{-1} than the results from previous reststrahlen analyses. However, outside of this regime, their measured phase is not satisfactorily determined because it is very close to the phase of the reference mirror. This may be the source of the discrepancies in n as noted. Jamshidi and Parker [15] state that the k values are only well determined in the range 300–380 cm^{-1} even though structure outside this region is reproducible. As reported by Newman [5], direct transmission measurements would be better outside the 300–380-cm^{-1} regime. Despite this, we still feel that asymmetric Fourier-transform spectroscopy is a powerful tool because, as in ellipsometry, one directly obtains n and k without a KK analysis.

REFERENCES

1. M. Cardona, *J. Appl. Phys.* **32**, 958 (1961); M. Cardona, *J. Appl. Phys.* **36**, 2181 (1965).
2. M. Cardona, W. Gudat, B. Sonntag, and P. Y. Yu, *Proc. Int. Conf. Phys. Semicond., 10th, Cambridge, 1970*, p. 209. U.S. Atomic Energy Commission, Oak Ridge, Tennessee, 1970.
3. D. E. Aspnes and A. A. Studna, *Phys. Rev. B* **27**, 985 (1983); D. E. Aspnes and A. A. Studna, private communication (1982).
4. G. D. Pettit and W. J. Turner, *J. Appl. Phys.* **36**, 2081 (1965).
5. R. Newman, *Phys. Rev.* **111**, 1518 (1958).
6. B. O. Seraphin and H. E. Bennett, *in* "Semiconductors and Semimetals" (R. K. Willardson and A. C. Beer eds.), Vol. 3, p. 499. Academic Press, New York, 1967.
7. A. N. Pikhtin and A. D. Yas'kov, *Sov. Phys. Semicond.* **12**, 622 (1978); A. N. Pikhtin and A. D. Yas'kov, *Fiz. Tekh. Poluprovodu.* **12**, 1047 (1978).
8. W. N. Reynolds, M. T. Lilburne, and R. M. Dell, *Proc. Phys. Soc. London* **71**, 416 (1958).

9. E. S. Koteles and W. R. Datars, *Solid State Commun.* **19**, 221 (1976).
10. M. Hass and B. W. Henvis, *J. Phys. Chem. Solids* **23**, 1099 (1962).
11. A. Mooradian and G. B. Wright, *Solid State Commun.* **4**, 431 (1966).
12. M. Hass, *in* "Semiconductors and Semimetals" (R. K. Willardson and A. C. Beer, eds.), Vol. 3, p. 3. Academic Press, New York, 1967.
13. V. I. Zemski, E. L. Ivchenko, D. N. Mirlin, and I. I. Reshina, *Solid State Commun.* **16**, 221 (1975).
14. C. Hilsum, S. Fray, and C. Smith, *Solid State Commun.* **7**, 1057 (1969).
15. H. Jamshidi and T. J. Parker, *Int. Meet. Infrared Mm Waves, 7th, Marseilles, 1983*; H. Jamshidi and T. J. Parker, private communication (1983).

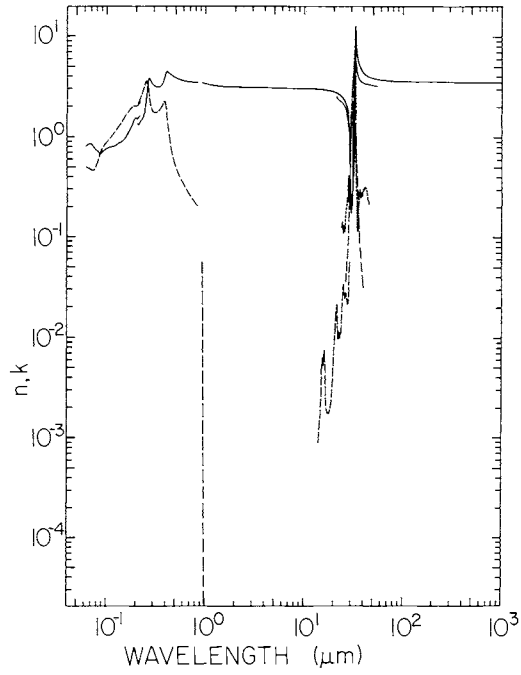

Fig. 7. Log–log plot of n (——) and k (– – –) versus wavelength in micrometers for indium phosphide.

TABLE VIII

Values of n and k for Indium Phosphide Obtained from Various References[a]

eV	μm	cm^{-1}	n	k	n	k
20	0.06199		0.793 [1]	0.494 [1]		
19.5	0.06358		0.815	0.499		
19	0.06526		0.834	0.493		
18.5	0.06702		0.843	0.487		
18	0.06888		0.846	0.477		
17.5	0.07085		0.840	0.469		
17	0.07293		0.824	0.454		
16.5	0.07514		0.785	0.457		
16	0.07749		0.742	0.491		
15.5	0.07999		0.719	0.529		
15	0.08266		0.695	0.574		
14.5	0.08851		0.675	0.645		
14	0.08856		0.688	0.706		
13.5	0.09184		0.701	0.765		
13	0.09537		0.726	0.820		
12.5	0.09919		0.754	0.861		
12	0.1033		0.771	0.899		
11.5	0.1078		0.781	0.946		
11	0.1127		0.793	0.996		
10.5	0.1181		0.797	1.056		
10	0.1240		0.806	1.154		
9.9	0.1252		0.820	1.172		
9.8	0.1265		0.832	1.185		
9.7	0.1278		0.840	1.198		
9.6	0.1291		0.847	1.210		
9.5	0.1305		0.852	1.225		
9.4	0.1319		0.859	1.237		
9.3	0.1333		0.861	1.253		
9.2	0.1348		0.865	1.269		
9.1	0.1362		0.868	1.287		
9.0	0.1378		0.872	1.304		
8.9	0.1393		0.874	1.324		
8.8	0.1409		0.875	1.346		
8.7	0.1425		0.877	1.375		
8.6	0.1442		0.885	1.403		
8.5	0.1459		0.894	1.433		
8.4	0.1476		0.909	1.458		
8.3	0.1494		0.919	1.486		
8.2	0.1512		0.934	1.512		
8.1	0.1513		0.947	1.539		
8.0	0.1550		0.960	1.566		
7.9	0.1569		0.973	1.594		
7.8	0.1590		0.984	1.627		
7.7	0.1610		1.000	1.664		
7.6	0.1631		1.022	1.700		
7.5	0.1653		1.046	1.736		
7.4	0.1675		1.072	1.771		

TABLE VIII (*Continued*)

Indium Phosphide

eV	μm	cm^{-1}	n	k	n	k
7.3	0.1698		1.100	1.812		
7.2	0.1722		1.136	1.847		
7.1	0.1746		1.174	1.882		
7.0	0.1771		1.215	1.915		
6.9	0.1797		1.261	1.941		
6.8	0.1823		1.307	1.966		
6.7	0.1851		1.354	1.986		
6.6	0.1879		1.402	2.994		
6.5	0.1907		1.453	2.010		
6.4	0.1937		1.496	2.008		
6.3	0.1968		1.526	1.991		
6.2	0.2000	50,010	1.525	1.982		
6.1	0.2033	49,200	1.508	2.005		
6.0	0.2066	48,390	1.500	2.063		
			1.336 [3]	2.113 [3]		
5.94	0.2087	47,910	1.318	2.151		
5.9	0.2101	47,590	1.301	2.183		
			1.516 [1]	2.130 [1]		
5.84	0.2123	47,100	1.301 [3]	2.239 [3]		
5.8	0.2138	46,780	1.299	2.280		
			1.544 [1]	2.191 [1]		
5.74	0.2160	46,290	1.311 [3]	2.341 [3]		
5.7	0.2175	45,970	1.325	2.383		
			1.573 [1]	2.267 [1]		
5.64	0.2198	45,490	1.352 [3]	2.446 [3]		
5.6	0.2214	45,170	1.375	2.484		
			1.616 [1]	2.349 [1]		
5.54	0.2238	44,680	1.407 [3]	2.532 [3]		
5.5	0.2254	44,360	1.426	2.562		
5.44	0.2279	43,880	1.447	2.611		
5.4	0.2296	43,550	1.455	2.652		
5.34	0.2322	43,070	1.467	2.734		
5.3	0.2339	42,750	1.482	2.802		
5.24	0.2366	42,260	1.519	2.922		
5.2	0.2384	41,940	1.558	3.016		
5.14	0.2412	41,460	1.649	3.176		
5.1	0.2431	41,130	1.745	3.291		
5.04	0.2460	40,650	1.958	3.438		
5.0	0.2480	40,330	2.131	3.495		
4.94	0.2510	39,840	2.391	3.519		
4.9	0.2530	39,520	2.546	3.514		
4.84	0.2562	39,040	2.782	3.523		
4.8	0.2583	38,710	2.984	3.517		
4.74	0.2616	38,230	3.344	3.401		
4.7	0.2638	37,910	3.560	3.223		
4.64	0.2672	37,420	3.757	2.877		

(*continued*)

TABLE VIII (*Continued*)

Indium Phosphide

eV	μm	cm^{-1}	n	k	n	k
4.6	0.2695	37,100	3.800	2.637		
4.54	0.2731	36,620	3.759	2.335		
4.5	0.2755	36,290	3.697	2.186		
4.44	0.2792	35,810	3.593	2.024		
4.4	0.2818	35,490	3.527	1.948		
4.34	0.2857	35,000	3.437	1.865		
4.3	0.2883	34,680	3.384	1.826		
4.24	0.2924	34,200	3.314	1.782		
4.2	0.2952	33,880	3.275	1.762		
4.14	0.2995	33,390	3.224	1.742		
4.1	0.3024	33,070	3.196	1.735		
4.04	0.3069	32,580	3.161	1.730		
4.0	0.3100	32,260	3.141	1.730		
3.94	0.3147	31,780	3.119	1.737		
3.9	0.3179	31,460	3.108	1.744		
3.84	0.3229	30,970	3.097	1.760		
3.8	0.3263	30,650	3.095	1.773		
3.74	0.3315	30,160	3.097	1.797		
3.7	0.3351	29,840	3.103	1.816		
3.64	0.3406	29,360	3.118	1.848		
3.6	0.3444	29,040	3.133	1.872		
3.54	0.3502	28,550	3.165	1.915		
3.5	0.3542	28,230	3.193	1.948		
3.44	0.3604	27,740	3.248	2.009		
3.4	0.3647	27,420	3.299	2.060		
3.34	0.3712	26,940	3.426	2.159		
3.3	0.3757	26,620	3.576	2.209		
3.24	0.3827	26,130	3.819	2.177		
3.2	0.3875	25,810	3.976	2.143		
3.14	0.3948	25,320	4.296	1.966		
3.1	0.4000	25,000	4.415	1.735		
3.04	0.4078	24,520	4.433	1.414		
3.0	0.4133	24,200	4.395	1.247		
2.94	0.4217	23,710	4.314	1.061		
2.9	0.4275	23,390	4.256	0.964		
2.84	0.4366	22,900	4.173	0.847		
2.8	0.4428	22,580	4.121	0.786		
2.74	0.4525	22,100	4.048	0.712		
2.7	0.4592	21,780	4.004	0.667		
2.64	0.4696	21,290	3.940	0.614		
2.6	0.4769	20,970	3.903	0.579		
2.54	0.4881	20,490	3.851	0.536		
2.5	0.4959	20,160	3.818	0.511		
2.44	0.5081	19,680	3.773	0.479		
2.4	0.5166	19,360	3.745	0.457		
2.34	0.5298	18,870	3.706	0.431		
2.3	0.5391	18,550	3.682	0.416		

TABLE VIII (*Continued*)

Indium Phosphide

eV	μm	cm^{-1}	n	k	n	k
2.24	0.5535	18,070	3.649	0.393		
2.2	0.5636	17,740	3.629	0.380		
2.14	0.5794	17,260	3.602	0.358		
2.1	0.5904	16,940	3.585	0.347		
2.04	0.6078	16,450	3.563	0.329		
2.0	0.6199	16,130	3.549	0.317		
1.94	0.6391	15,650	3.530	0.299		
1.9	0.6526	15,320	3.517	0.293		
1.84	0.6738	14,840	3.501	0.278		
1.8	0.6888	14,520	3.492	0.270		
1.74	0.7125	14,030	3.481	0.255		
1.7	0.7293	13,710	3.476	0.242		
1.64	0.7560	13,230	3.469	0.225		
1.6	0.7749	12,900	3.467	0.218		
1.54	0.8051	12,420	3.459	0.209		
1.5	0.8266	12,100	3.456	0.203		
1.345	0.921	10,850		5.71×10^{-2} [5, 6]		
1.340	0.925	10,810	3.3962 [4]	3.55		
1.335	0.928	10,770		2.04		
1.333	0.930	10,750	3.3905	1.09×10^{-2}		
1.326	0.935	10,700	3.3850	5.90×10^{-3}		
1.319	0.940	10,640	3.3797	3.18		
1.315	0.942	10,610		1.71×10^{-3}		
1.312	0.945	10,580	3.3746	9.67×10^{-4}		
1.305	0.950	10,530	3.3696	5.27		
1.30	0.9534	10,487	3.362 [7]	2.81×10^{-4}		
1.297	0.955	10,470	3.3647 [4]			
1.295	0.957	10,450		1.45×10^{-4}		
1.291	0.960	10,420	3.3600	7.39×10^{-5}		
1.29	0.9608	10,408	3.353 [7]			
1.284	0.965	10,360	3.3555 [4]	3.92		
1.28	0.9683	10,327	3.345 [7]	2.46		
1.277	0.970	10,310	3.3510 [4]			
1.275	0.972	10,290		1.66		
1.271	0.975	10,260	3.3467	1.13		
1.27	0.9759	10,247	3.337 [7]			
1.26	0.9837	10,166	3.330			
1.25	0.9915	10,085	3.324			
1.24	0.9995	10,005	3.318			
1.239	1.000	10,000	3.3269 [4]			
1.23	1.008	9,924	3.312 [7]			
1.22	1.016	9,843	3.307			
1.21	1.024	9,763	3.302			
1.20	1.033	9,682	3.297			
1.15	1.078	9,279	3.274			
1.127	1.10	9,091	3.2687 [4]			

(*continued*)

TABLE VIII (*Continued*)

Indium Phosphide

eV	μm	cm^{-1}	n	k	n	k
1.10	1.127	8,875	3.254 [7]			
1.05	1.180	8,472	3.236			
1.033	1.20	8,333	3.2312 [4]			
1.00	1.239	8,068	3.220 [7]			
0.9534	1.30	7,692	3.2053 [4]			
0.95	1.305	7,665	3.205 [7]			
0.90	1.377	7,261	3.191			
0.8853	1.40	7,143	3.1864 [4]			
0.85	1.458	6,858	3.178 [7]			
0.80	1.549	6,455	3.167			
0.75	1.653	6,051	3.156			
0.70	1.771	5,648	3.146			
0.65	1.907	5,244	3.137			
0.60	2.066	4,841	3.129			
0.55	2.254	4,438	3.121			
0.50	2.479	4,034	3.114			
0.45	2.754	3,631	3.107			
0.40	3.099	3,227	3.101			
0.35	3.541	2,824	3.095			
0.30	4.131	2,420	3.089			
0.25	4.958	2,017	3.083			
0.20	6.197	1,614	3.074			
0.18	6.886	1,452	3.069			
0.16	7.746	1,291	3.062			
0.14	8.853	1,130	3.053			
0.12	10.33	968.2	3.038			
0.1033	12.00	833.3		5.27×10^{-4} [6, 8]		
0.10	12.39	806.8	3.012			
0.09476	13.08	764.5		6.67		
0.09	13.77	726.1	2.990			
0.08853	14.00	714.3		8.86×10^{-4}		
0.08607	14.40	694.4		1.28×10^{-3}		
0.085	14.58	685.8	2.975	1.48×10^{-3} [5]		
0.084	14.75	677.7		1.81		
0.08346	14.85	673.4		3.00 [6, 8]		
0.083	14.93	669.7		6.34 [5]		
0.08263	15.00	666.7		3.71×10^{-3} [6, 8]		
0.082	15.11	661.6		1.15×10^{-2} [5]		
0.08133	15.24	656.2		5.25×10^{-3} [6, 8]		
0.081	15.30	653.5		1.76×10^{-2} [5]		
0.08090	15.32	652.7		6.17×10^{-3} [6, 8]		
0.08022	15.45	647.2		6.26		
0.08	15.49	645.5	2.956	3.90 [5]		
0.07986	15.52	644.3		5.63 [6, 8]		
0.079	15.69	637.4		9.72 [5]		
0.07874	15.74	635.3		5.22 [6, 8]		
0.07820	15.85	630.9		6.13		

TABLE VIII (*Continued*)

Indium Phosphide

eV	μm	cm^{-1}	n	k	n	k
0.078	15.89	629.3		8.83 [5]		
0.07746	16.00	625.0		7.12 [6, 8]		
0.077	16.10	621.2		3.00 [5]		
0.07679	16.14	619.6		7.46 [6, 8]		
0.07646	16.21	616.9		6.67		
0.07613	16.28	614.3		5.16		
0.07562	16.39	610.1		3.33		
0.075	16.53	605.1	2.932			
0.07489	16.55	604.2		2.31		
0.7291	17.00	588.2		1.77		
0.07	17.71	564.8	2.898			
0.06886	18.00	555.6		1.81		
0.06547	18.93	528.3		2.32		
0.065	19.07	524.4	2.851			
0.06353	19.51	512.6		3.84		
0.06317	19.62	509.7		4.73		
0.063	19.67	508.3		1.52 [5]		
0.06266	19.78	505.6		6.02 [6, 8]		
0.062	19.99	500.2		8.29 [5]		
0.06197	20.00	500.0		7.94 [6, 8]		
0.06139	20.19	495.3		9.49×10^{-3}		
0.061	20.32	492.2		1.04×10^{-2} [5]		
0.06094	20.34	491.6		1.08×10^{-2} [6, 8]		
0.06070	20.42	489.7		1.15		
0.06025	20.57	486.1		1.3		
0.06	20.66	484.1	2.780	1.46 [5]		
0.05951	20.83	480			2.51 [15]	
0.059	21.01	476.0		1.81		
0.058	21.37	468.0		2.17		
0.05765	21.51	465			2.34	
0.057	21.74	459.9		1.58×10^{-2}		
0.056	22.13	451.8		9.92×10^{-3}		
0.05579	22.22	450			2.24	
0.055	22.53	443.8	2.662	1.15×10^{-2}		
0.054	22.95	435.7		1.01		
0.05393	22.99	435			2.23	
0.053	23.38	427.6		1.15		
0.05207	23.81	420			2.19	0.126 [15]
0.052	23.83	419.6		1.36		
0.05170	23.98	417			2.16	0.135
0.05133	24.15	414			2.14	0.145
0.051	24.30	411.5		2.21		
0.05096	24.33	411			2.14	0.123
0.05083	24.39	410	2.494[b]			

(*continued*)

TABLE VIII (*Continued*)

Indium Phosphide

eV	μm	cm^{-1}	n	k	n	k
0.05059	24.51	408			2.12	0.112
0.05021	24.69	405			2.11	0.120
0.050	24.79	403.4	2.429 [7]	3.35		
0.04984	24.88	402			2.09	0.132
0.04959	25.00	400	2.411[b]			
0.04947	25.06	399			2.07	0.129
0.04910	25.25	396			2.04	0.126
0.04897	25.32	395	2.361	1.9[b]		
				2.89 [5]		
0.04873	25.45	393			2.02	0.126
0.04835	25.64	390	2.305	2.1[b]	2.00	0.115
0.048	25.83	387.1		2.49 [5]		
0.04798	25.84	387			1.93	0.129
0.04773	25.97	385	2.239	2.5[b]		
0.04761	26.04	384			1.86	0.182
0.04724	26.25	381			1.84	0.229
0.04711	26.32	380	2.163	2.9		
0.047	26.37	379.2		2.81 [5]		
0.04687	26.46	378			1.84	0.234
0.04649	26.67	375	2.072	3.5[b]	1.76	0.234
0.04612	26.88	372			1.70	0.240
0.046	26.94	371.1		2.51 [5]		
0.04587	27.03	370	1.963	4.3[b]		
0.04575	27.10	369			1.68	0.224
0.04538	27.32	366			1.51	0.234
0.04525	27.40	365	1.827	5.4		
0.045	27.54	363.1		2.15 [5]		
0.04501	27.55	363			1.45	0.316
0.04463	27.78	360	1.653	7.0[b]	1.41	0.398
0.04426	28.01	357			1.41	0.427
0.04401	28.17	355	1.418	9.9		
				2.39×10^{-2} [5]		
0.04389	28.25	354			1.32	0.324
0.04352	28.49	351			1.00	0.240
0.04339	28.57	350	1.069	0.16[b]		
0.04315	28.74	348	0.869	0.22	0.631	0.398
0.043	28.82	346.9		5.62×10^{-2} [5]		
0.04290	28.90	346	0.611	0.34[b]		
0.04277	28.99	345			0.355	0.794
0.04265	29.07	344	0.372	0.61		
0.04240	29.24	342	0.273	0.92	0.282	1.12
0.04215	29.41	340	0.234	1.20		
0.04203	29.50	339			0.224	1.48
0.04191	29.59	338	0.216	1.45		
0.04166	29.76	336	0.209	1.69	0.174	1.86
0.04141	29.94	334	0.209	1.93		
0.04129	30.03	333			0.170	2.29

TABLE VIII (*Continued*)

Indium Phosphide

eV	μm	cm^{-1}	h	k	n	k
0.04116	30.12	332	0.213	2.16		
0.04092	30.30	330	0.221	2.41	0.251	2.75
0.04067	30.49	328	0.234	2.67		
0.04054	30.58	327			0.447	3.31
0.04042	30.67	326	0.251	2.94		
0.04017	30.86	324	0.275	3.24	0.759	3.94
0.03992	31.06	322	0.307	3.57		
0.03980	31.15	321			1.20	4.52
0.03968	31.25	320	0.350	3.94		
0.03943	31.45	318	0.409	4.37	2.09	5.25
0.03918	31.65	316	0.493	4.87		
0.03906	31.75	315			3.24	5.50
0.03893	31.85	314	0.619	5.48		
0.03868	32.05	312	0.822	6.26	4.57	5.56
0.03844	32.26	310	1.81	7.32		
0.03831	32.36	309			5.89	5.25
0.03819	32.47	308	1.94	8.83		
0.03806	32.57	307	2.69	9.85		
0.03794	32.68	306	4.00	11.1	7.41	3.31
0.03782	32.79	305	6.42	12.1		
0.03369	32.89	304	10.2	11.6		
0.03757	33.00	303	12.7	8.24	7.24	1.26
0.03744	33.11	302	12.5	5.00		
0.03732	33.22	301	11.4	3.14		
0.03720	33.33	300	10.4	2.13	6.17	0.447
0.03695	33.56	298	8.93	1.17		
0.03682	33.67	297			5.01	0.162
0.03670	33.78	296	7.95	0.749		
0.03664	33.84	295.5				0.115
0.03645	34.01	294	7.28	0.525	4.68	0.120
0.03620	34.25	292	6.78	0.391		
0.03608	34.36	291			4.37	0.162
0.03596	34.48	290	6.39	0.304		
0.03571	34.72	288			4.12	0.219
0.03534	35.09	285	5.73	0.183	3.98	0.229
0.03496	35.46	282			3.89	0.282
0.03472	35.71	280	5.31	0.124		
0.03459	35.84	279			3.80	0.302
0.03422	36.23	276			3.76	0.282
0.03410	36.36	275	5.01	8.9×10^{-2}		
0.03385	36.63	273			3.72	0.257
0.03366	36.83	271.5				0.245
0.03348	37.04	270	4.79	6.8	3.67	0.263
0.03310	37.45	267			3.55	0.282
0.03273	37.88	264			3.55	0.282
0.03236	38.31	261			3.51	0.257

(*continued*)

TABLE VIII (*Continued*)

Indium Phosphide

eV	μm	cm^{-1}	n	k	n	k
0.03224	38.46	260	4.48	4.3		
0.03199	38.76	258			3.47	0.302
0.03162	39.22	255			3.47	0.295
0.03124	39.68	252			3.47	0.309
0.03100	40.00	250	4.27	3.0		
0.03087	40.16	249			3.47	0.320
0.03050	40.65	246			3.47	0.324
0.03013	41.15	243			3.44	0.320
0.02976	41.67	240	4.13	2.2	3.43	0.316
0.02938	42.19	237			3.43	0.302
0.02901	42.74	234			3.40	0.288
0.02864	43.29	231			3.39	0.234
0.02852	43.48	230	4.02	1.7		
0.02827	43.86	228			3.39	0.234
0.02790	44.48	225			3.35	0.214
0.02728	45.45	220	3.93	1.3		
0.02604	47.62	210	3.87	1.1×10^{-2}	3.31	
0.02480	50.00	200	3.81	8.7×10^{-3}		
0.02418	51.28	195			3.19	
0.02232	55.56	180			3.19	
0.01860	66.67	150	3.65			
0.01240	100.0	100	3.57			
0.009919	125.0	80	3.551			
0.007439	166.7	60	3.538			
0.004959	250.0	40	3.529			
0.002480	500.0	20	3.523			
0.001240	1000.0	10	3.522			

[a] References are indicated in brackets.

[b] Present work: fit by using oscillator model and Raman parameters.

Lead Selenide (PbSe)

G. BAUER and H. KRENN
Institut für Physik
Montanuniversität Leoben
Leoben, Austria

Lead selenide is in many respects similar to the other members of the lead-salt family PbS and PbTe; however, the literature on this compound is not as extensive.

In the far infrared Burstein *et al.* [1] have determined the transverse optic phonon mode ω_T by transmission experiments by using epitaxial thin PbSe films. Burkhard *et al.* [2] investigated the reflectivity of bulk *n*-type material ($N = 10^{17}$ cm^{-3}) in the 20–250-cm^{-1} range by using Fourier-transform spectroscopy. The data were analyzed by a classical oscillator fit (see PbTe), including a Drude term for the free carriers and by Kramers–Kronig (KK) analysis. For room temperature the following parameters were obtained: $\varepsilon_\infty = 23$, $\varepsilon_s = 203 \pm 15$, $\omega_T = 39 \pm 2$ cm^{-1}, and the phonon damping parameter $\Gamma = 24$ cm^{-1}; a plasma frequency $\omega_p = (Ne^2/\varepsilon_0 m_p)^{1/2}$ is 419 cm^{-1} and a free-carrier damping parameter is $\gamma = 20$ cm^{-1}. For frequencies above 40 cm^{-1} the results of the oscillator fit are essentially in agreement with the KK analysis, which was obtained by extrapolating the reflectivity in the low-frequency region according to the Hagen–Rubens law and in the high-frequency region to an asymptotic value given by ε_∞. Another far-infrared investigation on *p*-PbSe films deposited epitaxially on NaCl substrates ($d \simeq 2$ μm) was performed by Amirtharaj *et al.* [3] in the frequency range 20–350 cm^{-1}. An oscillator fit to the film/substrate reflectivity spectra yielded slightly different parameters than those found in Burkhard *et al.* [2]. Thus, both sets of data are shown in Fig. 8, and in Table IX $\varepsilon_\infty = 23.4$, $\varepsilon_s = 212$, $\omega_T = 45$ cm^{-1}, and $\Gamma = 19.6$ cm^{-1} for a sample with a hole concentration of 8.7×10^{17} cm^{-3} with $\omega_p = 880$ cm^{-1} and $\gamma = 170$ cm^{-1}.

In the region of the plasma minimum and at higher frequencies, several investigations have been performed [4–8], and a comparison of the longitudinal-optic-mode frequency from optical data with a value from tunneling experiments [9] is possible. Optical constants below and close to the fundamental absorption edge were obtained by Vyatkin *et al.* [7], who used

HANDBOOK OF OPTICAL CONSTANTS OF SOLIDS

Copyright © 1985 by Academic Press, Inc.
All rights of reproduction in any form reserved.
ISBN 0-12-544420-6

epitaxial p- and n-type films on BaF_2 substrates in the wavelength region 5–15 μm for the determination of n and 7.5–12 μm for the determination of k. For the absorption constant α an experimental dependence $\alpha \simeq 5 \times 10^{-10} N\lambda^2 \text{ cm}^{-1}$ was found for $\lambda > 8$ μm.

Refractive-index data in the region of the fundamental absorption edge and above (0.1–0.5 eV) were obtained by Zemel *et al.* [10], who used epitaxially grown films on NaCl and optical techniques described in the critique on PbS. At $T = 300$ K, around 0.3 eV the well-known peak in n (see Table IX) is present. The precision of the n measurements was estimated to be $\pm 3\%$. Further information on the temperature dependence of n in this region is found in Preier [11]. Absorption in this region has been measured by Scanlon [12], and Moss [13] has cited unpublished work by Avery [as cited by Moss [13], p. 187] in the 0.5–5-μm range. Avery measured the reflectance for incident light polarized in as well as perpendicular to the plane of incidence, choosing three angles of incidence per wavelength. Both data sets are given in Table IX.

In the region above the fundamental absorption edge, several authors have studied reflectivity in the 1–6-eV [14–17] and 1–22-eV [15, 17] ranges. Synchrotron radiation was used for a study in the 14–26-eV region [18]. Whereas up to 6 eV the results of a KK analysis of reflectivity data obtained with cleaved bulk samples can be compared with optical constants derived from reflectivity and transmission of thin films ($d \simeq 300$ Å), from 6 to 22 eV only reflectivity data could be analyzed. For the KK analysis and for the extrapolation to energies higher than 25 eV, it was assumed that the reflectivity is given by $R \propto C\omega^{-4}$, where C is calculated so as to have the reflectivity continuous at 25 eV. Actually n and k values were quoted up to 15 eV [17] and are tabulated in Table IX. The structure in the optical constants in the region is due to interband transitions and the effect of the d electrons of lead.

For review papers on the optical and electronic properties of PbSe, we refer the reader to Dalven [19, 20], Ravich *et al.* [21], and Nimtz [22].

REFERENCES

1. E. Burstein, R. Wheeler, and J. Zemel, *Proc. Int. Conf. Phys. Semicond.* (M. Hulin, ed.), p. 1065. Dunod, Paris, 1964.
2. H. Burkhard, R. Geick, P. Kästner, and K. H. Unkelbach, *Phys. Stat. Solidi B* **63**, 89 (1974).
3. P. M. Amirtharaj, B. L. Bean, and S. Perkowitz, *J. Opt. Soc. Am.* **67**, 939 (1977).
4. A. Aziza, E. Amzallag, and M. Balkanski, *Solid State Commun.* **8**, 873 (1970).
5. A. Mycielski, A. Aziza, M. Balkanski, M. Y. Moulin, and J. Mycielski, *Phys. Stat. Solidi B* **52**, 187 (1972).
6. I. V. Kucherenko, Y. A. Mityagin, L. K. Vodopyanov, and A. P. Shotov, *Sov. Phys. Semicond.* **11**, 282 (1977); I. V. Kucherenko, Y. A. Mityagin, L. K. Vodopyanov, and A. P. Shotov, *Fiz. Tekh. Poluprovodn* **11**, 488 (1977).
7. K. V. Vyatkin and A. P. Shotov, *Sov. Phys. Semicond.* **14**, 785 (1980); K. V. Vyatkin and A. P. Shotov, *Fiz. Tekh. Poluprovodn.* **14**, 1331 (1980).

8. A. Maitre, R. Le Toullec, and M. Balkanski, *Proc. Int. Conf. Phys. Semicond.* (M. Miasek, ed.), p. 826. PWN-Polish Scientific Publishers, Warsaw, 1972.
9. R. N. Hall and J. H. Racette, *J. Appl. Phys.* (Suppl.) **32**, 2078 (1961).
10. J. N. Zemel, J. D. Jensen, and R. B. Schoolar, *Phys. Rev. A* **140**, 330 (1965).
11. H. Preier, *Appl. Phys.* **20**, 189 (1979).
12. W. W. Scanlon, *J. Phys. Chem Solids*, **8**, 423 (1959).
13. T. S. Moss, "Optical Properties of Semiconductors," p. 189. Butterworth, London, 1959.
14. M. L. Belle, *Sov. Phys. Solid State*, **5**, 2401 (1964); M. L. Belle, *Fiz. Tverd. Tela* **5**, 3282 (1963).
15. S. E. Kohn, P. Y. Yu, Y. Petroff, Y. R. Shen, Y. Tsang, and M. L. Cohen, *Phys. Rev. B* **8**, 1477 (1973).
16. F. I. Bogacki, A. K. Sood, C. Y. Yang, S. Rabii, and J. E. Fischer, *Surf. Sci.* **37**, 494 (1973).
17. M. Cardona and D. L. Greenaway, *Phys. Rev. A* **133**, 1685 (1964).
18. M. Cardona, C. M. Penchina, E. E. Koch, and P. Y. Yu, *Phys. Stat. Solidi B* **53**, 327 (1972).
19. R. Dalven, *Infrared Phys.* **9**, 141 (1969).
20. R. Dalven, *Solid State Phys.* **28**, 179 (1973).
21. Y. I. Ravich, B. A. Efimova, and I. A. Smirnov, *in* "Semiconducting Lead Chalcogenides." Plenum, New York, 1979.
22. G. Nimtz, *in* "Landolt-Börnstein, Numerical Data and Functional Relationships in Science and Technology" (K.-H. Hellwege and O. Madelung, eds.), Group III, Vol. 17, Subvolume f, pp. 168, 110. Springer-Verlag, Berlin, 1983.

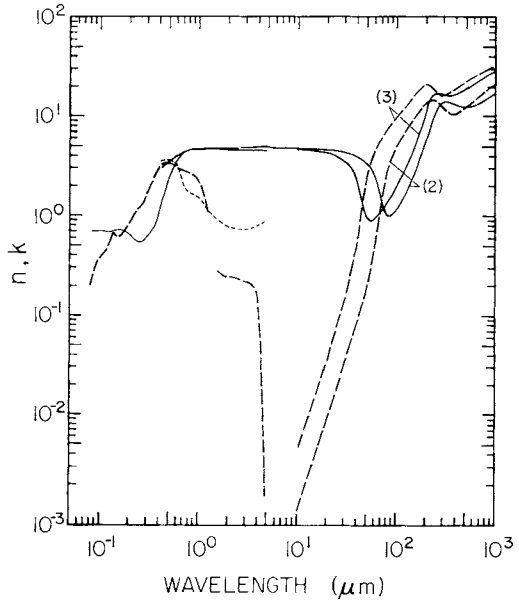

Fig. 8. Log–log plot of n (——) and k (– – –) versus wavelength in micrometers for lead selenide. Curves marked (2) and (3) are for samples of two different free-carrier concentrations from Burkbard *et al.* [2] and Amirtharaj *et al.* [3], respectively.

TABLE IX

Values of n and k for Lead Selenide Obtained from Various References[a]

eV	cm^{-1}	μm	n	k	n	k
14.5		0.08551	0.72 [17]	0.20 [17]		
14.0		0.08856	0.70	0.25		
13		0.09537	0.70	0.35		
12		0.1033	0.70	0.38		
11.5		0.1078	0.70	0.40		
11		0.1127	0.71	0.44		
10.5		0.1181	0.70	0.46		
10		0.1240	0.68	0.50		
9.5		0.1305	0.68	0.56		
9		0.1378	0.7	0.66		
8.5		0.1459	0.725	0.63		
8		0.1550	0.715	0.62		
7.5		0.1653	0.71	0.66		
7		0.1771	0.70	0.71		
6.5		0.1907	0.68	0.78		
6	48,390	0.2066	0.64	0.86		
5.5	44,360	0.2254	0.58	1.0		
5	40,330	0.2480	0.54	1.2		
4.5	36,290	0.2755	0.56	1.3		
4	32,260	0.3100	0.64	1.9		
3.5	28,230	0.3542	0.74	2.4		
3.0	24,200	0.4133	1.25 [17]	3.20 [17]	3.00 [13]	3.50 [13]
2.0	16,130	0.6199	3.65	2.9	3.90	3.20
1.65	13,310	0.7514			4.51	1.73
1.5	12,100	0.8266	4.64	2.64		
1.24	10,000	1.000			4.67	1.54
1.0	8,065	1.240	4.65	1.1		
0.99	7,985	1.252			4.69	1.14
0.83	6,694	1.494			4.64	0.950
0.80	6,452	1.550		0.284 [12]		
0.75	6,049	1.653		0.269		
0.71	5,726	1.746			4.61	0.830
0.70	5,646	1.771		0.251		
0.65	5,243	1.907		0.240		
0.62	5,001	2.000			4.59	0.770
0.60	4,839	2.066		0.254		
0.55	4,436	2.254		0.238	4.59	0.740
0.50	4,033	2.480		0.235		
			4.70	0.450 [17]		
0.495	3,992	2.505			4.58	0.740
0.48	3,871	2.583	4.90 [10]			
0.46	3,710	2.695	4.88			
0.45	3,629	2.755		0.220 [12]	4.57	0.740
0.44	3,549	2.818	4.885			
0.42	3,388	2.952	4.895			
0.41	3,307	3.024			4.57	0.740

TABLE IX (*Continued*)

Lead Selenide

eV	cm^{-1}	μm	n	k	n	k
0.40	3,226	3.100	4.91			
0.39	3,146	3.179	4.85	0.219		
0.38	3,065	3.263	4.93	0.225	4.57	0.740
0.36	2,904	3.444	4.95			
0.354	2,855	3.502			4.56	0.756
0.35	2,823	3.542		0.199		
0.34	2,742	3.647	4.96	0.194		
0.33	2,662	3.757		0.189	4.54	0.782
0.32	2,581	3.875	4.98	0.173		
0.31	2,500	4.000		0.127	4.52	0.796
0.30	2,420	4.133		0.104	5.05 [12]	
					5.29 [7]	
0.292	2,355	4.246			4.48 [13]	0.836
0.29	2,339	4.275		5.72×10^{-2}		
0.28	2,258	4.428	4.94	3.53×10^{-2} [10]		
					5.13 [7]	
0.275	2,218	4.509			4.48 [13]	0.836
0.27	2,178	4.592		9.17×10^{-3} [12]		
0.26	2,097	4.769	4.94	2.85	4.47	0.890
0.25	2,016	4.959		1.54	5.02 [7]	
0.248	2,000	5.000			4.45 [13]	
0.24	1,936	5.166	4.90	1.38		
0.23	1,855	5.391	4.83	1.28	4.91 [7]	
0.22	1,774	5.636	4.86			
0.20	1,613	6.199	4.82		4.90	
0.18	1,452	6.888			4.87	
0.17	1,371	7.293			4.86	
0.16	1,290	7.749	4.80		4.85	2.22×10^{-2} [7]
0.15	1,210	8.266	4.78			2.48
0.14	1,129	8.856	4.77			2.69
0.13	1,049	9.537	4.75		4.82	3.4
0.124	1,000	10.00	4.75 [2]	1.06×10^{-3} [2]	4.72 [3]	4.10×10^{-3} [3]
0.1215	980	10.20	4.75	1.13	4.71	4.36
0.1190	960	10.42	4.74	1.20	4.71	4.64
0.1165	940	10.64	4.74	1.28	4.70	4.95
0.1141	920	10.87	4.74	1.37	4.69	5.29
0.1116	900	11.11	4.74	1.46	4.69	5.66
0.1091	880	11.36	4.73	1.57	4.68	6.06
0.1066	860	11.63	4.73	1.68	4.67	6.51
0.1041	840	11.90	4.73	1.80	4.66	6.99
0.1017	820	12.20	4.73	1.94	4.66	7.53
0.09919	800	12.50	4.72	2.09	4.65	8.13
0.09671	780	12.82	4.72	2.26	4.64	8.79
0.09423	760	13.16	4.71	2.44	4.62	9.52×10^{-3}
0.09175	740	13.51	4.71	2.65	4.61	1.03×10^{-2}

(*continued*)

TABLE IX (*Continued*)

Lead Selenide

eV	cm^{-1}	μm	n	k	n	k
0.08927	720	13.89	4.70	2.88	4.60	1.13
0.08679	700	14.29	4.70	3.14	4.59	1.23
0.08431	680	14.71	4.69	3.43	4.57	1.34
0.08183	660	15.15	4.69	3.75	4.55	1.48
0.07935	640	15.63	4.68	4.12	4.53	1.63
0.07687	620	16.13	4.67	4.54	4.51	1.80
0.07439	600	16.67	4.66	5.02	4.49	1.99
0.07191	580	17.24	4.65	5.58	4.47	2.22
0.06943	560	17.86	4.64	6.21	4.44	2.48
0.06699	540	18.52	4.63	6.95	4.41	2.78
0.06447	520	19.23	4.62	7.80	4.37	3.14
0.06199	500	20.00	4.60	8.81×10^{-3}	4.33	3.56
0.05951	480	20.83	4.59	1.00×10^{-2}	4.29	4.07
0.05703	460	21.74	4.57	1.14	4.23	4.68
0.05455	440	22.73	4.55	1.31	4.17	5.43
0.05207	420	23.81	4.52	1.52	4.10	6.34
0.04959	400	25.00	4.49	1.77	4.02	7.49
0.04711	380	26.32	4.46	2.08	3.92	8.95×10^{-2}
0.04463	360	27.78	4.42	2.47	3.80	0.11
0.04215	340	29.41	4.37	2.97	3.66	0.13
0.03968	320	31.25	4.31	3.62	3.48	0.17
0.03720	300	33.33	4.24	4.48	3.26	0.22
0.03472	280	35.71	4.15	5.64	2.96	0.30
0.03224	260	38.46	4.04	7.26	2.55	0.43
0.02976	240	41.67	3.89	9.61×10^{-2}	1.97	0.70
0.02728	220	45.45	3.69	0.13	1.27	1.41
0.02480	200	50.00	3.42	0.19	0.96	2.49
0.02232	180	55.56	3.01	0.30	0.91	3.58
0.01984	160	62.50	2.34	0.56	0.99	4.71
0.01736	140	71.43	1.34	1.49	1.15	6.00
0.01488	120	83.33	1.02	3.19	1.45	7.57
0.01240	100	100.0	1.18	5.02	1.97	9.64
0.01215	98	102.0	1.21	5.22	2.04	9.89
0.01190	96	104.2	1.25	5.43	2.12	10.1
0.01165	94	106.4	1.29	5.64	2.21	10.4
0.01141	92	108.7	1.34	5.87	2.30	10.7
0.01116	90	111.1	1.39	6.09	2.39	11.0
0.01091	88	113.6	1.44	6.33	2.50	11.3
0.01066	86	116.3	1.51	6.58	2.61	11.6
0.01041	84	119.0	1.57	6.83	2.73	11.9
0.01017	82	122.0	1.65	7.10	2.87	12.3
0.009919	80	125.0	1.73	7.38	3.02	12.7
0.009671	78	128.2	1.83	7.67	3.18	13.1
0.009423	76	131.6	1.93	7.97	3.36	13.5
0.009175	74	135.1	2.05	8.29	3.56	13.9
0.008927	72	138.9	2.18	8.62	3.79	14.4

TABLE IX (*Continued*)

Lead Selenide

eV	cm^{-1}	μm	n	k	n	k
0.008679	70	142.9	2.33	8.97	4.04	14.9
0.008431	68	147.1	2.50	9.34	4.33	15.4
0.008183	66	151.5	2.69	9.73	4.67	16.0
0.007935	64	156.3	2.91	10.1	5.05	16.6
0.007687	62	161.3	3.16	10.6	5.51	17.2
0.007439	60	166.7	3.46	11.0	6.10	17.9
0.007191	58	172.4	3.80	11.5	6.71	18.6
0.006943	56	178.6	4.20	12.0	7.51	19.3
0.006695	54	185.2	4.68	12.5	8.49	20.0
0.006447	52	192.3	5.25	13.1	9.68	20.6
0.006199	50	200.0	5.93	13.6	11.1	21.1
0.005951	48	208.3	6.7	14.1	12.7	21.2
0.005703	46	217.4	7.7	14.5	14.4	20.9
0.005455	44	227.3	8.8	14.7	15.9	20.1
0.005207	42	238.1	10.0	14.8	16.9	19.0
0.004959	40	250.0	11.2	14.6	17.4	17.8
0.004711	38	263.2	12.3	14.1	17.4	16.9
0.004463	36	277.8	13.2	13.4	17.1	16.4
0.004215	34	294.1	13.8	12.5	16.8	16.3
0.003968	32	312.5	14.1	11.7	16.5	16.5
0.003720	30	333.3	14.0	11.0	16.3	17.0
0.003472	28	357.1	13.8	10.6	16.4	17.7
0.003224	26	384.6	13.4	10.5	16.6	18.1
0.002976	24	416.7	13.0	10.1	17.1	19.7
0.002728	22	454.5	12.7	11.3	17.8	20.9
0.002480	20	500.0	12.6	12.2	18.7	22.3
0.002232	18	555.6	12.8	13.4	19.9	23.1
0.001984	16	625.0	13.2	14.9	21.4	25.4
0.001736	14	714.3	14.1	16.6	23.3	27.3
0.001488	12	833.3	15.5	18.1	25.6	29.6
0.001240	10	1000	17.4	21.1	28.6	32.5

[a] References are indicated in brackets.

Lead Sulfide (PbS)

G. GUIZZETTI and A. BORGHESI
Dipartimento di Fisica "A. Volta" and
Gruppo Nazionale di Struttura della Materia del CNR
Università di Pavia
Pavia, Italy

The room-temperature values of n and k tabulated here were obtained from the following works and references therein: Riedl and Schoolar [1], Geick [2], Schoolar and Zemel [3], Schoolar and Dixon [4], Zemel *et al.* [5], Dixon and Riedl [6], and Vakulenko *et al.* [7] for the medium and far infrared; Schoolar and Dixon [4], Avery [8], Scanlon [9], Wessel [10], and Semenov and Shileika [11] for the near infrared and visible; Wessel [10], Cardona and Greenaway [12], Rossi and Paul [13], Cardona and Haensel [14], Cardona *et al.* [15], and Heckelmann *et al.* [16] for the visible–ultraviolet and vacuum–ultraviolet. For the review papers on the optical and electronic properties of PbS we refer to Moss [17], Zemel [18], Dalven [19, 21], and Ravich *et al.* [20].

A composite smooth-curve plot is given in Fig. 9. Numerical values are given in Table X with appropriate references listed in brackets.

The optical constants were obtained generally by reflectance R and/or transmittance T measurement on single-crystal bulk or film samples. After 1963 almost everyone producing PbS films adopted the technique described by Schoolar and Zemel [3]: single-crystal n-type films were grown in vacuum ($\sim 10^{-6}$ torr) from bulk PbS on heated rocksalt substrates (generally cleaved from synthetic single-crystal of NaCl or KCl). The good crystalline quality of such films, which have very uniform thickness, has been well established [3, 5]. The film's surfaces require on further treatment to make them suitable for either optical T or R measurement. Furthermore, experiments dealing with the electrical, optical, and mechanical properties indicate that the films behave like the best available bulk crystals. No significant thickness dependence of the optical constants has been detected [3–5, 7].

In the far-infrared ($\lambda > 30\ \mu$m) bulk reflectance measurements at near normal incidence (8–10°) [2, 6] and transmission on films [2, 18] were performed. We have disregarded earlier R spectra [22, 23] that were in qualitative agreement with the findings of Geick and Dixon and Riedl [2, 6] but had

HANDBOOK OF OPTICAL CONSTANTS OF SOLIDS

Copyright © 1985 by Academic Press, Inc.
All rights of reproduction in any form reserved.
ISBN 0-12-544420-6

values too low. The n and k values were obtained by fitting R in the 30–2000-μm range by a single classical dispersion oscillator (calculations including a Drude term suggested that the influence of free carriers on the optical constants is negligible for $N \lesssim 10^{16}$ cm^{-3}, at least out to 1000 μm). The R samples were natural or synthetic single crystals with different carrier concentrations N ranging from $\sim 10^{16}$ to $\sim 10^{19}$ cm^{-3}. The optical surfaces were ground mechanically and polished chemically, and it was checked that the damage caused by mechanical polishing does not significantly affect the R spectrum in this spectral region. Experimental and calculated spectra from Geick [2] and Dixon and Riedl [6] were in agreement to within the experimental uncertainties. In Table X n and k values obtained through the fit have been labeled according to Geick [2]. The parameters for the sample with the lowest carrier concentration were [2] $\varepsilon_0 = 150$ for the static relative dielectric constant; $\varepsilon_\infty = 16.8$ for the optical dielectric constant; $\nu_T = 71$ cm^{-1} and $\nu_L = 212$ cm^{-1} for the transverse and longitudinal optical phonon frequencies, respectively; and $\gamma = 15$ cm^{-1} for the damping. The fit values for ε_0 and ν_T agree within 7% with those derived directly (ε_0 from R value at $\lambda = 2$ mm and ν_T from the minimum in T spectra [2, 18]). Besides, the fit values are in good agreement with those deduced from phonon-assisted tunneling by Hall and Racette [24], microwave measurements by Sokoloski and Fang [25], inelastic neutron scattering by Cochran *et al.* [26], and n data in the medium infrared by plotting n^2 versus λ^2 and extrapolating the linear region to zero wavelength [1, 5, 6]. The sight dependence of ε_∞ on carrier density [6] is discussed in the PbTe critique.

As for the 0.95–26-μm range, Table X contains experimental n values deduced from the position of interference peaks in R and/or T for films [3–5]. The thicknesses, ranging from ~ 0.4 to ~ 5 μm, were determined by using the interferometric and weighing techniques described in Riedl and Schoolar [1], with an estimated error less than $\pm 3\%$. The typical carrier concentration was $N = 2 \times 10^{18}$ e/cm^3. At such high carrier density n is a slight function of N and is not expected to join smoothly to the calculated n [2] with no free-carrier contribution. The values of n [2] have been listed to 10 μm and can represent n for pure PbS. Although Geick [2] also lists k values, they are only a qualitative description of the lattice absorption of pure PbS. Phase shifts at the interfaces due to the nonzero values of the extinction coefficients and the optical properties of the substrate were estimated and found to be negligible. The basic precision of the n measurements was estimated to be $\pm 3\%$. The n values for the films are in excellent agreement with those obtained from bulk-reflectivity data [1]; their differences are within the experimental uncertainty. The same agreement exists among the data from [3–5] and the data obtained by other authors [1, 7, 11] with the same technique on films, in narrower spectral ranges. The refractive index in the 2–15-μm region was determined also at 77 and 373 K [5]. We observe that the sharp peak in the n spectrum at ~ 3 μm results from the rapid change in the absorption at the fundamental absorption edge.

The absorption coefficient α between 3 and 15 μm was measured by using a single crystal of n-type galena 0.22 mm thick, with $N = 2 \times 10^{17}$ cm^{-3} [7]. This absorption coefficient, typical of free carriers, was found to vary as $\lambda^{2.8 \pm 0.2}$ giving k to vary as $\lambda^{3.8}$. We would not expect this k to join smoothly on the k calculated for a purer sample in Dixon and Riedl [6]. Multiple-reflection effects were taken into account. Values for α were determined with an error not exceeding 20% and were in agreement, at short wavelengths, with those from Schoolar and Dixon [4] Scanlon [9], while the values from Semiletov *et al.* [27] were systematically too high (about one order of magnitude over the entire 3–15-μm range).

In the spectral region of the fundamental absorption edge, α has been measured at room temperature several times. The most recent and accurate measurements have been performed by Schoolar and Dixon [4], who, moreover, have discussed the previous results and the large discrepancies. Reflectance (at an angle of incidence less than 15°) and transmittance measurements were made in [4] on n-type films, with $N \simeq 3 \times 10^{18}$ cm^{-3} and thicknesses from 0.37 to 2.36 μm. The experimental error in R and T was estimated to be less than $\pm 4\%$, and the spectral energy resolution was less than 0.01 eV in the vicinity of the edge. Extinction coefficient k was derived from T and R, including multiple-reflection effects and the influence of the film backing. The results were estimated to be uncertain to $\pm 7\%$. In particular, the results approach those of Avery [8] in the higher energy region; in addition, they agree with those of Scanlon [9] in the steep portion of the edge but are greater by amounts up to 30% out to 1.2 μm. This fact and the long absorption plateau reported by Scanlon [9] were probably due to the presence of pinholes in the samples or scattered light in the monochromator, as suggested by Cardona and Greenaway [12]. The room-temperature Burstein–Moss effect is probably negligible at the fundamental band gap [28]. For all shorter wavelengths, the free-carrier effects are probably negligible.

The optical constants from 1.2 μm to about 0.2 μm were determined either by Kramers–Kronig (KK) analysis of near-normal-incidence reflectance data of bulk samples [12, 14] or from systematic and accurate measurement of R and T on thin films [10, 13]. The R values of more than 25 films and bulk agree in both magnitude and structure within about 4% [13]. The same agreement exists between R data from [10] and [13], which are higher than those reported in [12] and [16]. In Wessel [10] the error in R was taken to be $\pm 2\%$ and from 3 to 10% in T. In Rossi and Paul [13] R was repeatable to within $\pm 3\%$ absolute, and the total error was estimated $\pm 5\%$ absolute; the total error in T was estimated to be between 10 and 25%, including errors caused by scattered light from other wavelengths in the thicker samples and errors caused by imperfections in the films and film substrates (NaCl or KCl). No attempt was made to determine the impurity levels, but it was found [12] that the R spectra were not influenced by normally encountered variations in impurity concentrations. The films' thicknesses, ranging from

~ 200 to ~ 800 Å, were determined by assuming the carefully obtained optical constants of Schoolar and Dixon [4] near 1 μm and adding several methods of cross-checking. The thickness was considered to be accurate to approximately $\pm 15\%$. The optical constants obtained from R and T in Wessel [10] and Rossi and Paul [13] agree quite well (within 10%) with those obtained from KK analysis [13], and their error was about the same as the one involved in the R and T measurements, i.e., $\pm 5\%$ or less, if the thickness can be obtained accurately. This is true except in the energy range in which n and k values are such that a small uncertainty in R can lead to a large uncertainty in n [29]; this occurs in PbS near 0.4 μm. In Table X we have reported n and k values derived from thin-film optical data, which are in several respects more reliable than those derived from dispersion relations.

In the region between 0.2 and 0.05 μm only R measurements [12, 15, 16] were performed, either on expitaxial layers or on cleaved single crystals. The optical constants have been obtained from the KK analysis on R spectra from [12] and [15], extended to longer wavelengths with the data from [2] and [6] for the infrared and from [10] and [13] for the visible–ultraviolet. The R values of [12] and [15] were multiplied by a constant factor to make them agree with results from [13] at 0.2 μm and were extrapolated as $R = R_0(\lambda_0/\lambda)^{-P}$ for $\lambda < \lambda_0 = 0.05$ μm. Value P was adjusted to give values of k nearly equal to zero below the energy gap and agreeing with the values of [4, 10, 13] above the gap. The final value of $P = 2.77$ was used.

Transmission measurements on films in the 0.033–0.008-μm range were performed by Cardona and Haensel [14] with synchrotron radiation and with a typical resolution of 2 Å over the whole spectral range. The T technique was chosen over that of reflectance because of the small R or PbS ($< 1\%$) in this region, which increases the error due to scattered light of long wavelengths. The thin carbon substrates of the films made it impossible to extend the measurements to longer wavelengths. The thicknesses were determined with a Tolansky interferometer and also during evaporation with a calibrated quartz-crystal monitor. The absorption coefficient values were affected by a scaling error of about 20% because of uncertainties in the thicknesses.

REFERENCES

1. H. R. Riedl and R. B. Schoolar, *Phys. Rev.* **131**, 2082 (1963).
2. R. Geick, *Phys. Lett.* **10**, 51 (1964).
3. R. B. Schoolar and J. N. Zemel, *J. Appl. Phys.* **35**, 1848 (1964).
4. R. B. Schoolar and J. R. Dixon, *Phys. Rev. A* **137**, 667 (1965).
5. J. N. Zemel, J. D. Jensen, and R. B. Schoolar, *Phys. Rev. A* **140**, 330 (1965).
6. J. R. Dixon and H. R. Riedl, *Phys. Rev. A* **140**, 1283 (1965).
7. O. V. Vakulenko, M. P. Lisitsa, and Ya. F. Kononets, *Sov. Phys. Solid State* **8**, 1356 (1966).
8. D. G. Avery, *Proc. Phys. Soc. London Ser. B* **67**, 2 (1954).
9. W. W. Scanlon, *Solid State Phys.* **9**. 109 (1959).
10. P. R. Wessel, *Phys. Rev.* **153**, 836 (1967).

11. Ya. A. Semenov and A. Yu. Shileika, *Sov. Phys. Solid State* 1419 (1967).
12. M. Cardona and D. L. Greenaway, *Phys. Rev. A* **133**, 1685 (1964).
13. C. E. Rossi and W. Paul, *J. Appl. Phys.* **38**, 1803 (1967).
14. M. Cardona and R. Haensel, *Phys. Rev. B* **1**, 2605 (1970).
15. M. Cardona, C. M. Penchina, E. E. Koch, and P. Y. Yu, *Phys. Stat. Solidi B* **53**, 327 (1972).
16. G. H. Heckelmann, H. H. Landfermann, U. Nielsen, and T. S. Wagner, *Phys. Stat. Solidi B* **69**, K99 (1975).
17. T. S. Moss, *in* "Optical Properties of Semiconductors," p. 183. Butterworth, London, 1959.
18. J. N. Zemel, *Proc. Int. Conf. Phys. Semicond., Paris, 1964*, p. 1061. Dunod, Paris, 1964.
19. R. Dalven, *Infrared Phys.* **9**, 141 (1969).
20. Yu. I. Ravich, B. A. Efimova, and I. A. Smirnov, *in* "Semiconducting Lead Chalcogenides," p. 43. Plenum, New York, 1970.
21. R. Dalven, Solid State Phys. **28**, 179 (1973).
22. J. Strong, *Phys. Rev.* **38**, 1818 (1931).
23. H. Yoshinaga, *Phys. Rev.* **100**, 753 (1955).
24. R. N. Hall and J. H. Racette, *J. Appl. Phys., Suppl.* **32**, 2078 (1961).
25. M. M. Sokoloski and P. H. Fang, *Phys. Lett.* **16**, 222 (1965).
26. W. Cochran, R. Cowley, and G. Dolling, *Proc. R. Soc. London Ser. A* **293**, 433 (1966).
27. S. A. Semiletov, I. P. Voronina, and E. I. Kortukova, *Soviet Phys. Crystallogr. (Eng. Trans.)* **10**, 429 (1966).
28. Edward D. Palik, D. L. Mitchell, and J. N. Zemel, *Phys. Rev. A* **135**, 763 (1964).
29. P. M. Grant, *Bull. Am. Phys. Soc., Ser. II* **10**, 546 (1965).

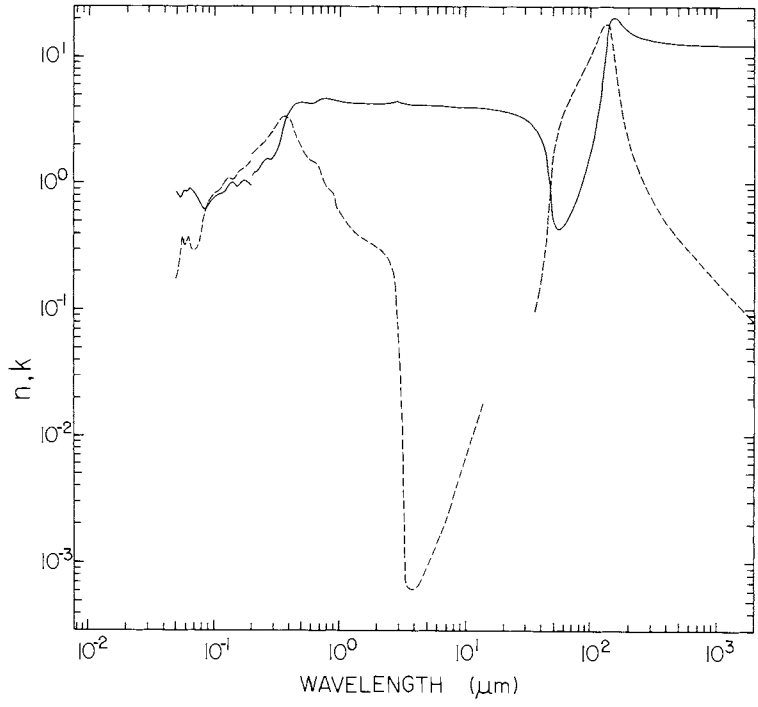

Fig. 9. Log–log plot of n (——) and k (– – – –) versus wavelength in micrometers for lead sulfide. Data from various references do not join together in overlap regions on occasion.

TABLE X

Values of n and k for Lead Sulfide from Various References[a]

eV	cm^{-1}	μm	n	k
150		0.008266		3.86×10^{-3} [14]
145		0.008551		4.09
140		0.008856		4.37
135		0.009184		4.66
130		0.009537		5.10
125		0.009919		5.59
120		0.01033		6.40
115		0.01078		8.96×10^{-3}
110		0.01127		1.05×10^{-2}
105		0.01181		1.26
100		0.01240		1.54
95		0.01305		1.78
90		0.01378		2.06
85		0.01459		2.38
80		0.01550		2.88
75		0.01653		3.72
70		0.01771		4.64
65		0.01907		5.48
60		0.02066		6.17
58		0.02138		6.44
55		0.02254		6.73
50		0.02480		7.05
45		0.02755		5.43
40		0.03100		4.28
38		0.03263		4.23×10^{-2}
25		0.04959	0.845 [12, 15]	0.171 [12, 15]
24		0.05166	0.800	0.196
23.3		0.05321	0.772	0.238
22.7		0.05462	0.760	0.291
21.9		0.05661	0.831	0.372
21.5		0.05767	0.870	0.339
21.3		0.05821	0.858	0.324
20.6		0.06019	0.847	0.339
19.8		0.06262	0.881	0.370
19.2		0.06457	0.911	0.332
18.6		0.06667	0.881	0.300
18.0		0.06888	0.846	0.294
17.5		0.07084	0.814	0.298
17.0		0.07293	0.778	0.307
16.5		0.07514	0.734	0.327
16.0		0.07749	0.687	0.364
15.6		0.07948	0.651	0.412
15.2		0.08157	0.628	0.472
14.8		0.08377	0.619	0.538
14.4		0.08610	0.627	0.606
14.0		0.08856	0.651	0.665
13.5		0.09183	0.687	0.725

TABLE X (*Continued*)

Lead Sulfide

eV	cm^{-1}	μm	n	k
13.0		0.09537	0.725	0.769
12.5		0.09918	0.758	0.807
12.0		0.1033	0.789	0.843
11.5		0.1078	0.811	0.872
11.0		0.1127	0.821	0.912
10.5		0.1181	0.836	0.974
10.0		0.1240	0.879	1.050
9.5		0.1305	0.968	1.096
9.0		0.1378	1.007	1.066
8.6		0.1442	0.997	1.060
8.2		0.1512	0.921	1.140
7.7		0.1610	0.999	1.273
7.2		0.1722	1.037	1.299
6.8		0.1823	1.024	1.361
6.4		0.1937	0.951	1.489
6.2	50,010	0.2000	1.13 [13]	1.70 [13]
5.9	47,590	0.2101	1.22	1.78
5.65	45,570	0.2194	1.22	1.85
5.4	43,550	0.2296	1.33	1.95
5.15	41,540	0.2407	1.43	2.05
4.95	39,920	0.2505	1.52	2.10
4.75	38,310	0.2610	1.53	2.20
4.6	37,100	0.2695	1.55	2.30
4.45	35,890	0.2786	1.53	2.45
4.30	34,680	0.2883	1.57	2.53
4.15	33,470	0.2988	1.67	2.70
4.0	32,260	0.3100	1.73	2.83
3.85	31,050	0.3220	1.90	3.00
3.75	30,250	0.3306	2.07	3.17
3.65	29,440	0.3397	2.33	3.32
3.55	28,630	0.3493	2.58	3.37
3.45	27,830	0.3594	2.98	3.37
3.35	27,020	0.3701	3.17	3.37
3.25	26,210	0.3815	3.32	3.30
3.15	25,410	0.3936	3.62	3.17
3.00	24,200	0.4133	3.88	3.00
2.90	23,390	0.4275	4.12	2.70
2.75	22,180	0.4509	4.25	2.33
2.55	20,570	0.4862	4.35	2.00
2.35	18,950	0.5276	4.33	1.67
2.20	17,740	0.5636	4.30	1.55
2.00	16,130	0.6199	4.29 [10, 13]	1.48 [10, 13]
1.80	14,520	0.6888	4.53 [10]	1.30 [10]
1.60	12,910	0.7749	4.62	0.94
1.40	11,290	0.8856	4.50	0.83
1.30	10,490	0.9537	4.48 [4, 10]	0.627 [4, 10]

(*continued*)

TABLE X (*Continued*)

Lead Sulfide

eV	cm^{-1}	μm	n	k
1.24	10,000	1.00	4.43	0.597 [4]
1.18	9,524	1.05	4.385	0.543
1.13	9,091	1.1	4.355	0.508
1.03	8,333	1.2	4.30	0.458
0.953	7,692	1.3	4.275 [4]	0.403
0.885	7,143	1.4	4.26	0.390
0.825	6,667	1.5	4.25	0.370
0.775	6,250	1.6	4.24	0.357
0.730	5,882	1.7	4.235	0.341
0.690	5,556	1.8	4.235	0.334
0.650	5,263	1.9	4.24	0.318
0.620	5,000	2.0	4.25 [4, 5]	0.310
0.590	4,762	2.1	4.245 [5]	0.304
0.563	4,545	2.2	4.255	0.285
0.539	4,348	2.3	4.26	0.271
0.516	4,167	2.4	4.28	0.255
0.496	4,000	2.5	4.30	0.235
0.477	3,846	2.6	4.335	0.212
0.459	3,704	2.7	4.38	0.182
0.443	3,571	2.8	4.42	0.144
0.432	3,484	2.87	4.435	9.03×10^{-2}
0.413	3,333	3.0	4.345	4.59 [9]
0.400	3,226	3.1	4.30	2.27
0.393	3,175	3.15		1.43
0.387	3,125	3.2		7.9×10^{-3}
0.381	3,077	3.25	4.26	3.46
0.3542	2,857	3.5	4.215	6.48×10^{-4}
0.3306	2,667	3.75	4.185	6.22
0.3100	2,500	4.0	4.16	6.38
0.2917	2,353	4.25	4.14	6.51
0.2755	2,222	4.5	4.125	7.47
0.2480	2,000	5	4.115	9.25×10^{-4}
0.2066	1,667	6	4.10	1.38×10^{-3}
0.1771	1,429	7	4.09	2.06
0.1550	1,250	8	4.07	3.06
0.1378	1,111	9	4.04	4.42
0.1240	1,000	10	4.01 4.02 [2]	6.32×10^{-3}
0.1178	950	10.53	4.01	
0.1116	900	11.11	4.00	
0.1054	850	11.76	3.98	
0.1033	833.3	12	3.90 [3]	1.14×10^{-2}
0.09919	800	12.50	3.97 [2]	
0.09299	750	13.33	3.95	
0.08856	714.3	14	3.795 [3]	1.83
0.08679	700	14.29	3.93 [2]	
0.08059	650	15.38	3.90	

TABLE X (*Continued*)

Lead Sulfide

eV	cm^{-1}	μm	n	k
0.07749	625.0	16	3.68 [3]	
0.07439	600	16.67	3.86 [2]	
0.06888	555.6	18	3.545 [3]	
0.06819	550	18.18	3.81 [2]	
0.06199	500.0	20	3.39 [3]	
			3.75 [2]	
0.05636	454.5	22	3.205 [3]	
0.05579	450	22.22	3.66 [2]	
0.05166	416.7	24	2.995 [3]	
0.04959	400	25.00	3.53 [2]	
0.04339	350	28.57	3.33	
0.03720	300	33.33	2.99	
0.03444	277.8	36	2.74	9.77×10^{-2} [2]
0.03263	263.2	38	2.53	0.127
0.03100	250.0	40	2.28	0.167
0.02952	238.1	42	1.98	0.226
0.02818	227.3	44	1.61	0.326
0.02695	217.4	46	1.13	0.540
0.02583	208.3	48	0.688	1.03
0.02480	200.0	50	0.514	1.59
0.02254	181.8	55	0.433	2.67
0.02066	166.7	60	0.452	3.55
0.01771	142.9	70	0.582	5.14
0.01550	125.0	80	0.809	6.74
0.01378	111.1	90	1.175	8.48
0.01240	100.0	100	1.79	10.51
0.01033	83.33	120	5.06	15.98
0.008856	71.43	140	17.41	17.94
0.007749	62.50	160	20.47	7.10
0.006888	55.56	180	17.87	3.47
0.006199	50.00	200	16.27	2.20
0.004959	40.00	250	14.40	1.15
0.004133	33.33	300	13.62	0.785
0.003542	28.57	350	13.21	0.604
0.003100	25.00	400	12.96	0.495
0.002480	20.00	500	12.69	0.367
0.001653	13.33	750	12.44	0.228
0.001240	10.00	1,000	12.35	0.167
0.0008266	6.667	1,500	12.29	0.109
0.0006199	5.000	2,000	12.27	0.0815

[a] Values obtained from the various references are indicated in brackets.

Lead Telluride (PbTe)

G. BAUER and H. KRENN
Institut für Physik
Montanuniversität Leoben
Leoben, Austria

Lead telluride is a member of the IV–VI compound semiconductor family, crystallizing in the cubic rocksalt structure with 10 electrons in the unit cell. The optical direct energy gap is very small, located at the L point of the Brillouin zone, which is the case for all three lead salts: PbS, PbSe, and PbTe [1–3]. The dielectric properties are characterized by unusually high dielectric constants ε_∞ and ε_s, where in PbTe strong temperature dependence of ε_s indicates the inherent tendency of the lattice to undergo a structural phase transition [4].

The room-temperature values of n and k tabulated in Table XI and plotted in Fig. 10 were obtained from the following works and references cited therein: the far-infrared results from 10 cm^{-1} (1000 μm) to 1000 cm^{-1} (10 μm) are from Buss and Kinch [5], Burkhard *et al.* [6], Perkowitz [7], and Lowney and Senturia [8] (2.5–40 μm). Values of n and k in the mid-infrared region are from Zemel *et al.* [9] (0.1–0.6 eV), Piccioli *et al.* [10] (1500–3500 cm^{-1}), Globus *et al.* [11] (0.15–0.6 eV), McCarthy *et al.* [21] (1000–2600 cm^{-1}), Walz [31] (0.25–0.35 eV); in the visible and UV region, from Cardona and Greenaway [12] (0.1–17 eV), Korn and Braunstein [13] (0.1–21 eV), and Cardona and Haensel [14] (36–150 eV).

In the low-energy part of the spectrum, the far-infrared results were usually obtained by reflectivity measurements [4–7, 15, 17]. Single-crystal bulk material as well as epitaxially grown films were used. The latter method yield high-quality material with relatively low free-carrier concentration and high carrier mobilities. For more than 10 years the hot wall technique [16] has been used to deposit films of uniform thickness on alkali halide (NaCl, KCl) or BaF_2 substrates. Due to the differences in the lattice constants and the thermal expansion coefficients, stresses appear that influence the electrical and optical properties [29], especially at low temperatures. The PbTe–BaF_2 system is the one in which stresses play the smallest role at room temperature.

Copyright © 1985 by Academic Press, Inc.
All rights of reproduction in any form reserved.
ISBN 0-12-544420-6

Epitaxially grown films usually do not require any surface treatment such as grinding, polishing, or etching after growth; bulk materials require electropolishing after surface treatment.

The n and k values in the far infrared were obtained by fitting the reflectivity data [4–8, 15, 17], taken at near normal incidence ($\sim 10°$) with a classical dispersion oscillator for the infrared active phonon and Drude term for the free carriers as given by

$$\varepsilon = (n - ik)^2 = \varepsilon_\infty + \frac{(\varepsilon_s - \varepsilon_\infty)\omega_T^2}{\omega_T^2 - \omega^2 + i\Gamma\omega} - \frac{\omega_p^2}{\omega(\omega + i\gamma)}$$

Here, units of inverse centimeters are used instead of radians per second.

The values given in Table I were obtained by using the following fitting parameters: $\varepsilon_\infty = 32.8$ for the high-frequency dielectric constant [8, 19, 20], $\varepsilon_s = 400 \pm 20$ for the static dielectric constant [4, 6], $\omega_T = 32\ \text{cm}^{-1}$ for the transverse optic phonon frequency (which is also in agreement with inelastic neutron scattering data [18]), and $\Gamma = 10\ \text{cm}^{-1}$ for the phonon damping parameter. The room-temperature electron damping parameter in the Drude term was taken to be $30\ \text{cm}^{-1}$. The plasma frequency given by $\omega_p^2 = Ne^2/\varepsilon_0 m_p$ in mks units is determined by the electron concentration N and effective mass m_p. ($\varepsilon_0 = 8.9 \times 10^{-12}\ C/Nm^2$ is the permittivity of free space.) We obtain $\omega_p = 1320\ \text{cm}^{-1}$ from the fit with $N = 10^{18}\ \text{cm}^{-3}$. The relaxation time τ is the reciprocal of γ if we stay in radians per second and $\gamma\ (\text{cm}^{-1}) = \gamma\ (\text{rad/sec})/2\pi c$. Experimental and calculated spectra are usually in agreement within experimental and calculated errors. A detailed discussion on improvements of classical oscillator fits has been given by Perkowitz [7].

At frequencies much greater than the longitudinal optic phonon frequency ω_L and the plasma frequency but less than that of the fundamental absorption edge, n can be expressed by

$$[n(\omega)]^2 = \varepsilon_\infty + \Delta\varepsilon(\omega) - \frac{\omega_p^2}{\omega^2} + \left(1 - \frac{\varepsilon_\infty}{\varepsilon_s}\right)\frac{\omega_L^2\varepsilon_\infty}{\omega^2}. \tag{1}$$

Here, $\Delta\varepsilon$ is a function that describes additional dispersion due to bound carriers at frequencies near the fundamental absorption edge, and Eq. (1) is valid for $(\omega\tau)^2 > 1$ [8, 19].

Lowney and Senturia [8] describe in detail the determination of the dispersion of n with the aid of thin-film transmission and reflectance data exhibiting interference fringes. A carrier-concentration dependence of ε_∞ is related to Im $\varepsilon(\omega)$ by Dionne and Woolley [19] and Moss [30].

$$\varepsilon_\infty = 1 + \frac{2}{\pi}\int_0^\infty \frac{\text{Im}\ \varepsilon(\omega)}{\omega}\, d\omega. \tag{2}$$

It turns out that for carrier densities below $10^{19}\ \text{cm}^{-3}$, the values of ε_∞ are also independent of electron concentration N.

In the region below and around the fundamental absorption edge, optical constants have been determined and discussed in a number of works [9–11, 21–28]. Early precise measurements on the refractive index in the 0.1–0.5-eV

range were performed by Zemel *et al.* [9] on epitaxial films by using an interferometric and weighing technique with an experimental error in n of about $\pm 3\%$. There exists a peak in the refractive index close to the fundamental band edge (see Table XI). Piccioli *et al.* [10] repeated the experiments of Zemel *et al.* [9] but freed the PbTe films ($p \sim 10^{18}$ cm^{-3}) from the substrate and gave data on absorption as well. The error in refractive index is estimated to be $\pm 1\%$ and in absorption index $\pm 5\%$. The maximum values of n fit Zemel *et al.*'s [9] results, apart from a small shift in wavelength. McCarthy *et al.* [21] investigated PbTe films on BaF_2 substrates in the 5-12-μm range and showed that a significant reduction in absorption occurs below the band gap as compared with PbTe–NaCl films, presumably due to chlorine surface contamination. Whereas the overall agreement of the refractive-index data with those of Piccioli *et al.* [10] and Zemel *et al.* [9] are satisfactory, the absorption coefficient data are smaller than those of Piccioli *et al.* [10] and of Riedl [22] for samples with carrier concentrations of the order of 10^{17} cm^{-3} by about a factor of 10 to 50.

The most recent data on PbTe–BaF_2 films are those by Globus *et al.* [11]. Reflectivity and transmission were measured by using PbTe films (thickness: 0.6 μm) grown on BaF_2 substrates in the wavelength region $\lambda = 2$–8 μm. Reflectivity has been determined with an 8° angle of incidence by using samples of comparatively low carrier concentrations (10^{16} cm^{-3}). With expressions for interference and multiple reflection of the complete film–substrate system, a careful analysis of their data and a comparison with previously published data [9, 10, 24, 27] were performed.

The refractive-index data compare favorably with those of Piccioli *et al.* [10], Zemel *et al.* [9], and McCarthy *et al.* [21]; only in the region near the absorption edge are there some differences (see Table XI). Scanlon's data [24] for k are substantially lower (about 40%) than those of Globus *et al.* [11]. The results by Globus *et al.* [11] are not influenced by a Burstein–Moss shift at room temperature. However, there is some fine structure in the absorption spectrum, probably due to phonon-assisted transitions. In addition, the authors suggest that apart from transitions at the L point ($\varepsilon_{gL} \sim 0.32$ eV), transitions originate from other close-lying, valence-band extrema presumably in the direction of Λ. The influence of free carriers on the absorption constant is discussed in the framework of several band models (Kane, two-band, six-band, Cohen models) in [11, 27, 28]. Optical constants of the important $Pb_{1-x}Sn_xTe$ system can be found [31, 32] in the range of the fundamental absorption edge.

The optical constants above the fundamental absorption gap and in the visible and UV region from 0.5 to 25 eV were determined by Kramers–Kronig (KK) analysis of near-normal-incidence reflectance data of bulk [12, 13, 24, 30] and thin-film samples [12] and from measurements of reflectivity and transmission (below 6 eV) of thin films [12] with thicknesses of the order of 300 Å. Wavelength modulation spectroscopy [13, 35] and thermoreflectance [33, 34] have also been used to detect fine structure in the

reflectance spectra, at low temperatures [35] that are related to critical points in the joint density of states. Cardona *et al.* [36] used synchrotron radiation to measure reflectivity in the 14–26-eV range.

Since there are systematic differences between the data of Cardona and Greenaway [12], who used cleaved bulk material and epitaxial films, and those obtained by Korn and Braunstein [13], who worked on polished and electrochemically etched samples, we decided to show both sets of data in Table XI and Fig. 10. Korn and Braunstein [13] cite a maximum absolute reflectance error of about 2% throughout the spectral range 0.1–21 eV. Despite some differences in the extrapolations in the KK analysis between the two papers [12, 13], the discrepancy probably results from the different sample preparation.

In the 36–150-eV region, transmission experiments have been performed with thin PbTe films by Cardona and Haensel [14], who used synchrotron radiation. Whereas below 20 eV the structures are due to valence-band to conduction-band transitions, above 20 eV structures appear to be due to transitions from the outermost d electrons [37].

The measurements were performed on films deposited on carbon substrates, and reflectivity measurements could not be performed because the small reflectivity in the 36–150-eV region ($R < 0.01$) would increase the error due to scattered light. Measurements of the thickness were made by using the Tolansky interferometric method with films deposited on glass substrates next to the carbon substrate used for the transmission experiments in the far-UV range. From uncertainties in the thickness evaluation, the absorption index Cardona and Haensel's [14] data are supposed to be affected by an error of about 20%.

Absorption constant and reflectivity data below and above the fundamental gap were recently compiled by Nimtz and Schlicht [38], and Nimtz [39].

REFERENCES

1. R. Dalven, *Infrared Phys.* **9**, 141 (1969).
2. R. Dalven, *Solid State Phys.* **28**, 179 (1973).
3. Yu. I. Ravich, B. A. Efimova, and I. A. Smirnov, *in* "Semiconducting Lead Chalcogenides." Plenum, New York, 1970.
4. G. Bauer, H. Burkhard, W. Jantsch, F. Unterleitner, A. Lopex-Otero, and G. Schleussner, *in* "Lattice Dynamics" (M. Balkanski ed.), p. 669. Flammarion, Paris, 1978.
5. D. D. Buss and M. A. Kinch, *J. Nonmet.* **1**, 111 (1973).
6. H. Burkhard, G. Bauer, and A. Lopez-Otero, *J. Opt. Soc. Am.* **67**, 943 (1979).
7. S. Perkowitz, *Phys. Rev. B* **12**, 3210 (1975).
8. J. R. Lowney and S. D. Senturia, *J. Appl. Phys.* **47**, 1771 (1976).
9. J. N. Zemel, J. D. Jensen, and R. B. Schoolar, *Phys. Rev.* **140**, A330 (1965).
10. N. Piccioli, J. M. Beson, and M. Balkanski, *J. Phys. Chem. Solids*, **35**, 971 (1974).
11. T. R. Globus, B. L. Gelmont, K. I. Geiman, V. A. Kondrashov, and A. V. Matveenko, *Sov. Phys. JETP* **53**, 1000 (1981); T. R. Globus, B. L. Gelmont, K. I. Geiman, V. A. Kondrashov, and A. V. Matveenko, *Zh. Eksp. Teor. Fiz.* **80**, 1926 (1981).

12. M. Cardona and D. L. Greenaway, *Phys. Rev.* **133**, A1685 (1964).
13. D. M. Korn and R. Braunstein, *Phys. Rev. B* **5**, 4837 (1972).
14. M. Cardona and R. Haensel, *Phys. Rev. B* **1**, 2605 (1970).
15. W. E. Tennant and J. A. Cape, *Phys. Rev. B* **13**, 2540 (1976).
16. A. Lopez-Otero, *Thin Solid Films*, **49**, 1 (1978).
17. E. G. Bylander and M. Hass, *Solid State Commun.* **4**, 51 (1966).
18. W. Cochran, R. A. Cowley, G. Dolling, and M. M. Elcombe, *Proc. R. Soc. London* **293**, 433 (1966).
19. G. Dionne and J. C. Woolley, *Phys. Rev. B* **6**, 3898 (1972).
20. E. Burstein, S. Perkowitz, M. H. Brodsky, *J. Phys. C*4 **29**, 78 (1968).
21. S. L. McCarthy, W. H. Weber, and M. Mikkor, *J. Appl. Phys.* **45**, 4907 (1974).
22. H. R. Riedl, *Phys. Rev.* **127**, 162 (1962).
23. J. R. Dixon and H. R. Riedl, *Phys. Rev.* **138**, A873 (1965).
24. W. W. Scanlon, *J. Phys. Chem. Solids* **8**, 423 (1959).
25. R. N. Tauber, A. A. Machonis, and I. B. Cadoff, *J. Appl. Phys.* **37**, 4855 (1966).
26. F. Stern, *Phys. Rev.* **133**, A1653 (1964).
27. D. Genzow, A. G. Mironov, and O. Ziep, *Phys. Status Solidi B* **90**, 535 (1978).
28. W. W. Anderson, *Infrared Phys.* **20**, 363 (1980).
29. E. D. Palik, D. L. Mitchell, and J. N. Zemel, *Phys. Rev.* **135**, A763 (1964).
30. T. S. Moss, "Optical Properties of Solids," p. 181. Butterworth, London, 1959.
31. V. M. Walz, thesis, Naval Postgraduate School, Monterey, California (1972); available from NTIS, Springfield, Virginia, order No. AD 767-677.
32. W. G. Opyd, thesis, Naval Postgrade School, Monterey, California (1973); available from NTIS, Springfield, Virginia, order No. AD 767-677.
33. M. Baleva, *Phys. Status Solidi B* **88**, 335 (1978).
34. R. I. Bogacki, A. K. Sood, C. Y. Yang, S. Rabii, and J. E. Fischer, *Surf. Sci.* **37**, 494 (1973).
35. S. E. Kohn, P. Y. Yu, Y. Petroff, Y. R. Shen, Y. Tsang, and M. L. Cohen, *Phys. Rev. B* **8**, 1477 (1973).
36. M. Cardona, C. M. Penchina, E. E. Koch, and P. Y. Yu, *Phys. Status Solidi B* **53**, 327 (1972).
37. D. E. Aspnes and M. Cardona, *Phys. Rev.* **173**, 714 (1968).
38. G. Nimtz and B. Schlicht, *in* "Springer Tracts in Modern Physics" (G. Höhler, ed.), Vol. 98, p. 1. Springer-Verlag, Berlin, 1983.
39. G. Nimtz, *in* "Landolt-Börnstein, Numerical Data and Functional Relationships in Science and Technology" (K.-H. Hellwege and O. Madelung, eds.), Group III, Vol. 17, Subvolume f, pp. 177 and 473. Springer-Verlag, Berlin, 1983.

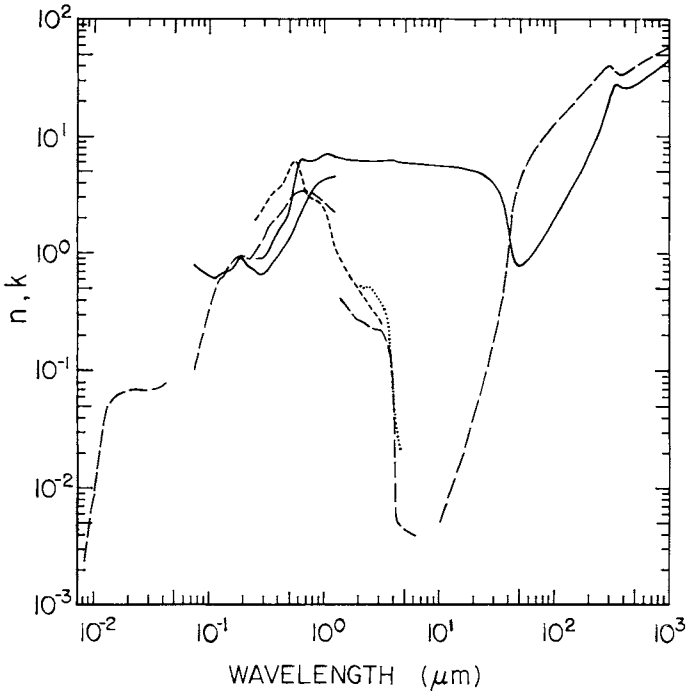

Fig. 10. Log–log plot of n (——) and k (– – – –) versus wavelength in micrometers for lead telluride. Data from various references do not join together in overlap regions on occasion.

TABLE XI

Values of n and k for Lead Telluride Obtained from Various References[a]

eV	cm^{-1}	μm	n	k	n	k
150		0.008266		2.37×10^{-3} [14]		
145		0.008551		3.06		
140		0.008856		4.37		
135		0.009184		5.85		
130		0.009537		7.59		
125		0.009919		9.71×10^{-3}		
120		0.01033		1.31×10^{-2}		
115		0.01078		1.79		
110		0.01127		2.43		
105		0.01181		3.43		
100		0.01240		4.39		
95		0.01305		4.94		
90		0.01378		5.36		
85		0.01459		5.73		
80		0.01550		6.09		
75		0.01653		6.43		
70		0.01771		6.62		
65		0.01907		6.76		
60		0.02066		6.84		
55		0.02254		6.80		
50		0.02480		6.87		
45		0.02755		6.78		
40		0.03100		6.81		
35		0.03542		7.10		
30		0.04133		7.77×10^{-2}		
17		0.07293	0.8 [12]	0.1 [12]		
16.5		0.07514	0.78	0.1		
16		0.07749	0.75	0.1		
15.5		0.07999	0.73	0.15		
15		0.08266	0.72	0.17		
14.5		0.08551	0.70	0.2		
14		0.08856	0.67	0.22		
13.5		0.09184	0.65	0.26		
13		0.09537	0.63	0.3		
12.5		0.09919	0.63	0.35		
12		0.1033	0.62	0.37		
11.5		0.1078	0.60	0.45		
11		0.1127	0.62	0.50		
10.5		0.1181	0.65	0.58		
10		0.1240	0.66	0.60		
9.5		0.1305	0.68	0.62		
9		0.1378	0.68	0.7		
8.5		0.1459	0.7	0.78		
8		0.1550	0.73	0.82		
7.5		0.1653	0.8	0.92		

(*continued*)

TABLE XI (*Continued*)

Lead Telluride

eV	cm^{-1}	μm	n	k	n	k
7		0.1771	0.9	0.92		
6.5		0.1907	0.9	0.94		
6	48,390	0.2066	0.8	0.92		
5.5	44,360	0.2254	0.75	0.87		
5.0	40,330	0.2480	0.72	1.0	0.90 [13]	1.88 [13]
4.8	38,710	0.2583			0.9	2.02
4.6	37,100	0.2695			0.9	2.16
4.5	36,290	0.2755	0.65	1.22		
4.4	35,490	0.2818			0.9	2.34
4.2	33,880	0.2952			0.91	2.54
4	32,260	0.3100	0.7	1.55	0.96	2.75
3.8	30,650	0.3263			1.05	2.96
3.6	29,040	0.3444			1.2	3.18
3.5	28,230	0.3542	0.86	1.85		
3.4	27,420	0.3647			1.4	3.35
3.2	25,810	0.3875			1.55	3.54
3.0	24,200	0.4133	1.0	2.2	1.65	3.8
2.8	22,580	0.4428			1.8	4.2
2.6	20,970	0.4769			2.14	5.0
2.5	20,160	0.4959	1.35	2.86		
2.4	19,360	0.5166			3.3	5.8
2.2	17,740	0.5636			5.4	5.9
2.0	16,130	0.6199			6.4	4.3
1.8	14,520	0.6888			6.16	3.1
1.6	12,900	0.7749			6.0	2.85
1.5	12,100	0.8266	3.8	3.1		
1.4	11,290	0.8856			6.4	2.74
1.2	9,679	1.033			7	1.8
1.0	8,065	1.240	4.55	2.2	6.5	1.04
0.90	7,259	1.378		0.413 [24]		
0.85	6,856	1.459		0.367		
0.80	6,452	1.550		0.348	6.25	0.71
0.75	6,049	1.653		0.311		
0.70	5,646	1.771		0.289		
0.65	5,243	1.907		0.271		
0.62	5,001	2.000				0.527 [11]
0.61	4,920	2.033				0.529
0.60	4,839	2.066		0.261	6.10 [11]	0.521
					6.10 [13]	0.46 [13]
0.59	4,759	2.101			6.11 [11]	0.516 [11]
0.58	4,678	2.138			6.10	0.508
0.57	4,597	2.175			6.10	0.492
0.56	4,517	2.214			6.10	0.496
0.55	4,436	2.254			6.11	0.505

TABLE XI (*Continued*)

Lead Telluride

eV	cm^{-1}	μm	n	k	n	k
0.54	4,355	2.296			6.10	0.522
0.53	4,275	2.339			6.07	0.523
0.52	4,194	2.384			6.10	0.504
0.51	4,113	2.431			6.10	0.509
0.50	4,033	2.480	5.76	1.4 [12]	6.07	0.507
				0.228 [24]		
0.49	3,952	2.530			6.06	0.505
0.48	3,871	2.583	6.04 [9]		6.05	0.493
0.47	3,791	2.638			6.06	0.465
0.46	3,710	2.695	6.04		6.09	0.447
0.45	3,629	2.755		0.220	6.10	0.438
0.44	3,549	2.818	6.05		6.11	0.427
0.43	3,468	2.883		0.370 [10]	6.14	0.407
0.42	3,388	2.952	6.08	0.374	6.07	0.399
0.41	3,307	3.024	6.06 [10]	0.345	6.07	0.381
0.40	3,226	3.100	6.075	0.331	6.09	0.382
			6.12 [9]	0.220 [24]	6.00 [13]	0.24 [13]
					6.10 [11]	0.349 [11]
0.39	3,146	3.179				
0.38	3,065	3.263	6.15	0.285 [10]	6.13	0.345
				0.195 [24]		
0.37	2,984	3.351	6.13 [10]	0.284 [10]	6.14	0.320
0.36	2,904	3.444	6.09	0.261	6.15	0.307
			6.16 [9]	0.178 [24]		
0.35	2,823	3.542	6.12 [10]	0.227 [10]	6.17	0.245
				0.188 [24]		0.175 [31]
0.34	2,742	3.647	6.23	0.145	6.17	0.183 [11]
			6.05 [9]			0.151 [31]
0.335	2,702	3.701	6.17 [10]	0.177 [10]		0.134 [11]
0.33	2,662	3.757		0.119 [24]	6.12 [11]	0.149 [31]
0.322	2,597	3.850	6.16	$7.81^{*}10^{-2}$ [10]	6.08	5.50×10^{-2} [11]
			5.96 [9]	7.32 [24]		2.75 [31]
0.31	2,500	4.000	6.02 [10]	5.61 [10]	6.02	1.13 [11]
				3.78 [24]		1.13 [31]
				9.55×10^{-3} [22]		
0.30	2,420	4.133	5.95	3.55×10^{-2} [10]	5.97	7.95×10^{-3}
			5.89 [9]	1.23 [24]		
0.29	2,339	4.275		5.2×10^{-3}	5.91	7.14
				5.11 [22]		
0.28	2,258	4.428	5.90 [10]	2.49×10^{-2} [10]	5.89	1.04 [21]
			5.82 [9]	4.20×10^{-3} [24]	5.92 [8]	7.05 [31]
0.27	2,178	4.592	5.88 [10]	2.17×10^{-2} [10]	5.86 [11]	6.94
				4.35×10^{-3} [24]		
0.26	2,097	4.769	5.85	4.44 [22]	5.85	7.02
			5.82 [9]			

(*continued*)

TABLE XI (*Continued*)

Lead Telluride

eV	cm^{-1}	μm	n	k	n	k
0.25	2,016	4.959	5.84 [10]		5.84	7.18
			5.79 [9]			
0.24	1,936	5.166	5.79		5.83	7.32
0.235	1,895	5.276	5.82 [10]			
0.23	1,855	5.391			5.82	
0.226	1,823	5.486			5.83 [8]	
0.22	1,774	5.636	5.80		5.82 [11]	
			5.76 [9]			6.72×10^{-4} [21]
0.21	1,694	5.904	5.78 [10]		5.8	
0.20	1,613	6.199	5.77		5.80	
			5.74 [9]		5.70 [8]	
0.19	1,532	6.526		3.9×10^{-3}	5.79 [11]	
0.185	1,492	6.702	5.74			
			5.76 [10]			
0.18	1,452	6.888	5.72 [9]		5.77	1.1×10^{-3} [21]
0.175	1,411	7.085			5.69 [8]	
0.17	1,371	7.293			5.77 [11]	
0.16	1,290	7.749	5.70		5.76	8.45×10^{-4}
0.155	1,250	7.999	5.72 [9, 10]	5.68 [8]		
0.15	1,210	8.266			5.76 [11]	
0.14	1,129	8.856	5 68 [9]			
0.124	1,000	10.00	5.66 [9, 10]		5.67 [8]	
			5.56 [4–7]	4.97 [15, 17]		
0.1215	980	10.20	5.55	5.29		
0.1190	960	10.42	5.54	5.63		
0.1165	940	10.64	5.54	6.01		
0.1141	920	10.87	5.53	6.42		
0.1116	900	11.11	5.52	6.87		
0.1103	890	11.24	5.66 [8]			
0.1091	880	11.36	5.51 [4–7]	7.37		
0.1066	860	11.63	5.49	7.91		
0.1041	840	11.90	5.48	8.5		
0.1017	820	12.20	5.47	9.16		
0.09199	800	12.50	5.45	9.9×10^{-3}		
0.09671	780	12.82	5.44	1.07×10^{-2}		
0.09423	760	13.16	5.64 [8]			
			5.51 [9, 10]			
0.09299	750	13.33	5.42 [4–7]	1.16		
0.09175	740	13.51	5.40	1.26		
0.08927	720	13.89	5.38	1.37		
0.08679	700	14.29	5.36	1.50		
0.08431	680	14.71	5.34	1.64		
0.08183	660	15.15	5.31	1.81		
			5.57 [8]			

TABLE XI (*Continued*)

Lead Telluride

eV	cm^{-1}	μm	n	k	n	k
0.07935	640	15.63	5.28 [4–7]	1.99		
0.07687	620	16.13	5.25	2.2		
0.07439	600	16.67	5.22	2.45		
0.07191	580	17.24	5.18	2.73		
0.06943	560	17.86	5.13	3.06		
0.06695	540	18.52	5.09	3.45		
			5.48 [8]			
0.06447	520	19.23	5.03 [4–7]	3.90		
0.06199	500	20.00	4.97	4.44		
0.05951	480	20.83	4.90	5.09		
0.05703	460	21.74	4.82	5.88		
0.05455	440	22.73	4.72	6.85		
0.05207	420	23.81	4.61	8.1		
0.04959	400	25.00	4.50	9.6×10^{-2}		
0.04711	380	26.23	4.32	0.12		
0.04463	360	27.78	4.13	0.14		
0.04215	340	29.41	3.89	0.18		
0.03968	320	31.25	3.58	0.23		
0.03720	300	33.33	3.18	0.32		
0.03472	280	35.71	2.62	0.48		
0.03224	260	38.46	1.79	0.87		
0.02976	240	41.67	1.01	1.9		
0.02728	220	45.45	0.80	3.2		
0.02480	200	50.00	0.78	4.4		
0.02232	180	55.56	0.84	5.6		
0.01984	160	62.50	0.95	6.9		
0.1736	140	71.43	1.15	8.5		
0.01488	120	83.33	1.47	10.4		
0.01240	100	100.0	2.00	13.0		
0.01215	98	102.0	2.07	13.3		
0.01190	96	104.2	2.14	13.6		
0.01165	94	106.4	2.22	13.9		
0.01141	92	108.7	2.31	14.3		
0.01116	90	111.1	2.40	14.6		
0.01091	88	113.6	2.50	15.0		
0.01066	86	116.3	2.60	15.4		
0.01041	84	119.0	2.71	15.8		
0.01017	82	122.0	2.83	16.2		
0.009919	80	125.0	2.95	16.6		
0.009671	78	128.2	3.1	17.1		
0.009423	76	131.6	3.2	17.6		
0.009175	74	135.1	3.4	18.1		
0.008927	72	138.9	3.6	18.6		
0.008679	70	142.9	3.7	19.2		

(*continued*)

TABLE XI (*Continued*)

Lead Telluride

eV	cm^{-1}	μm	n	k	n	k
0.008431	68	147.1	3.9	19.8		
0.008183	66	151.5	4.2	20.4		
0.007935	64	156.3	4.4	21.1		
0.007687	62	161.3	4.7	21.8		
0.007439	60	166.7	4.9	22.5		
0.007191	58	172.4	5.3	23.3		
0.006695	54	185.2	6.0	25.1		
0.006447	52	192.3	6.4	26.1		
0.006199	50	200.0	6.9	27.2		
0.005951	48	208.3	7.5	28.4		
0.005703	46	217.4	8.2	29.8		
0.005455	44	227.3	9.1	31.3		
0.005207	42	238.1	10.2	32.9		
0.004959	40	250.0	11.6	34.8		
0.004711	38	263.2	13.6	36.9		
0.004463	36	277.8	16.6	38.8		
0.004215	34	294.1	20.8	39.9		
0.003968	32	312.5	25.3	38.8		
0.003720	30	333.3	27.7	35.7		
0.003472	28	357.1	27.5	33.4		
0.003224	26	384.6	26.5	33.2		
0.002976	24	416.7	26.0	34.5		
0.002728	22	454.5	26.4	36.6		
0.002480	20	500.0	27.6	39.1		
0.002232	18	555.6	29.4	42.0		
0.001984	16	625.0	32.0	45.1		
0.001736	14	714.3	35.4	48.7		
0.001488	12	833.3	39.6	52.8		
0.001240	10	1000	45.1	57.8		

[a] References are indicated in brackets.

Silicon (Si)*

DAVID F. EDWARDS†
University of California
Los Alamos National Laboratory
Los Alamos, New Mexico

Index of refraction values have been reported for the transparent region ($\lambda \geqq 1.12$ μm) of silicon by a number of investigators. For these reports the samples have ranged from single cystals to evaporated thin films. The measuring techniques with their inherent differences in accuracy have varied from investigator to investigator as have the measured wavelength ranges. For a given group of investigators using equivalent measurement techniques on samples of about the same quality, the index values disagree by amounts greater than their stated precisions [1–3]. Rather than attempting to resolve this disagreement, we have selected those data by using the criteria given below and present them in Table XII as representative of average values. The data extend from 1.12 to 588 μm and are the results of six investigative groups. Essentially two different measuring techniques were used; angle of minimum deviation for the near infrared and channel spectra for the far infrared. The data-selection criteria are as follows: The samples were single crystal of good or optical quality. The reported refractive-index values were either tabulated or given in a figure which was readable to at least a few places in the third decimal place. We also required agreement in overlap areas to less than five in the third place between different data sets.

Meeting these criteria were the following investigators: Primak [1], who determined the index from 1.12 to 2.16 μm from the angle of minimum deviation measured by an autocollimation technique; Salzberg and Villa [2], who measured the index from 1.3570 to 11.04 μm by a similar autocollimation technique; Edwards and Ochoa [3], who used a channel-spectra technique to measure the index from 2.4373 to 25 μm; Icenogle *et al.* [4], who used the autocollimator technique to measure the index from 2.554 to 10.270 μm; Loewenstein *et al.* [5], who determined the far-IR index (28.57–333 μm) from

* Work performed under the auspices of the U.S. Department of Energy.

† Present address: Lawrence Livermore National Laboratory, Livermore, California.

Copyright © 1985 by Academic Press, Inc.
All rights of reproduction in any form reserved.
ISBN 0-12-544420-6

the channel spectra; and Randall and Rawcliffe [6], who also used the channel-spectra technique to determine the index from 67.8 to 588 μm. Each of these investigators report the index values for room-temperature samples. We have fit these data to both a Herzberger-type and a Sellmeier-type dispersion formula. A total of 184 data points was used.

The Herzberger-type dispersion formula [7] is

$$n = A + BL + CL^2 + D\lambda^2 + E\lambda^4,$$

where $L = 1/(\lambda^2 - 0.028)$ with the wavelength λ in micrometers and 0.028 is the square of the mean asymptote for the short-wavelength abrupt rise in index for 14 materials (silicon included) [7]. For the 184 data points, from 1.12 to 588 μm, the coefficients are $A = 3.41906$, $B = 1.23172 \times 10^{-1}$, $C = 2.65456 \times 10^{-2}$, $D = -2.66511 \times 10^{-8}$, and $E = 5.45852 \times 10^{-14}$. The quality of the fit of reported indices to the dispersion formula is good with differences in the third and fourth decimal places. The pertinent temperature is 26°C.

The Sellmeier-type dispersion formula [8] is

$$n^2 = \varepsilon + A/\lambda^2 + B\lambda_1^2/(\lambda^2 - \lambda_1^2),$$

where $\lambda_1 = 1.1071$ μm for silicon [8]. For the same 184 data points the coefficients are $\varepsilon = 1.16858 \times 10^1$, $A = 9.39816 \times 10^{-1}$, and $B = 8.10461 \times 10^{-3}$. The quality of the fit is similar to that for the Herzberger-type formula.

In addition to their room-temperature measurements, Icenogle *et al.* [4] have measured the index for a number of temperatures between about 100 and 296 K for the range from 2.554 to 10.270 μm. For a given wavelength their temperature-dependent indices were fit to a polynomial from which we have evaluated dn/dT. These dn/dT are given in Table XIII for four wavelengths. Loewenstein *et al.* [5] report the far-infrared index at 1.5 K in addition to 300 K.

Channel spectra used for far-infrared index determination has been described by Randall and Rawcliffe [6] and by Loewenstein *et al.* [5]. This technique is particularly well suited for the far infrared because of the low order of the interference, typically 20 or 30. For the near infrared, special care must be exercised in using the channel spectra because of the very large fringe order and the difficulty in its determination [9]. A method suggested by Baumeister [10], and Edwards and Ochoa [3] was used to avoid this problem. The Baumeister method has a broad application, and the details are given here.

For the channel-spectra technique, the samples must have faces that are flat to $\lambda/4$ (visible) or better and parallel to a second of arc or better. The flatness and wedge can be the determining factors in the accuracy of the measurement. Fringes of equal chromatic order [11] are produced when radiation undergoes multiple reflections between the parallel surfaces of the sample. The spacing between the fringes depends only on the sample thickness

and the real part of the refractive index. Knowing the sample thickness and the wavelength of the fringe, one can, in principle, determine the index. A limitation is knowing the order of the fringe [9]. To overcome this [10], an arbitrary order number is assigned to a fringe and the entire channel spectra is fit to the polynomial

$$m = a_0 + a_1\sigma + a_2\sigma^2 + a_3\sigma^3, \tag{1}$$

where the a_i coefficients are determined by a least-squares fit and m is the order number of the fringes at wave number σ. The slope for this curve at any wave number is

$$dm/d\sigma = a_1 + 2a_2\sigma + 3a_3\sigma^2. \tag{2}$$

In terms of the sample parameters, the order of the fringe is given by

$$m = 2n(\sigma)h\sigma, \tag{3}$$

where $n(\sigma)$ is the refractive index at wave number σ and h the metric thickness. For most materials, such as silicon, with broad transparent regions, the index is a slowly varying function of σ and can accurately be represented as a polynomial

$$n = n_0 + n_1\sigma + n_2\sigma^2, \tag{4}$$

where the n_i are coefficients that can be evaluated from the a_i coefficients and the metric thickness

$$n_0 = a_1/(2h), \qquad n_1 = a_2/(2h), \qquad n_2 = a_3/(2h). \tag{5}$$

The channel spectrum is usually taken in a beam of finite angle, and thus the n_i coefficients must be corrected [6]. In Eq. (5) this beam-angle correction is accomplished by replacing h by $h(1 + \cos \beta_m)/2$, where β_m is the maximum internal angle of a ray with the normal to the surface. The index values evaluated by this Baumeister method are insensitive to the choice of the initial order. The accuracy of the index values is set by the sample thickness, flatness, and parallelism. Good optical practices will ensure sufficient flatness and parallelism. In a metrology laboratory the metric thickness can be determined to a few parts in 10^5, and thus the uncertainty in the index will be determined to first order by the uncertainty in the sample thickness. For index 2 this means an index uncertainty of about $1 - 5 \times 10^{-4}$.

Optical-quality silicon is highly transparent from the band edge at 1.1071 μm to the far infrared with the exception of the 5- to 25-μm lattice absorption band. Outside this lattice band and for $\lambda > 1.1071$ μm, the absorption coefficient has been measured at a few select laser wavelengths. Using a photoacoustic technique, Hordvik and Skolnik [12] have measured the absorption coefficient for silicon at the HF and DF laser wavelengths, 2.7 and 3.8 μm, respectively. Their results are given in Table XII.

Multiphonon absorption limits the transparency in the lattice band of silicon and other wide-gap semiconductors. Because of crystal symmetry, the fundamental vibration in silicon has no dipole moment and is infrared inactive. Lax and Burstein [13] have shown that the phonons can interact directly with the radiation field through terms in the electric moment of second order (or higher) in the atomic displacement. Johnson [14] analyzed the absorption in the 6.7- to 25-μm region for oxygen-free silicon. He verified the absorption to be two phonon. Bendow *et al.* [15] extended these measurements to wider frequency and temperature ranges and found the multiphonon absorption structure to persist to low absorption levels and high temperatures. The work of Johnson [14] and Bendow *et al.* [15] confirms multiphonon interpretation of the 5- to 25-μm band. The absorption coefficient values of Johnson [14] and Bendow *et al.* [15] are given in Table XII for the major absorption peaks and shoulders. These correspond to combinations of four characteristic phonon energies. At wavelengths longer than 28 μm, the values for α of Loewenstein *et al.* [5] are approximately an order of magnitude larger than the extrapolation of the work of Lax and Burstein [13] and Johnson [14]. Therefore, we must omit this work as being anomalous due to surface damage or some other mechanism, as the authors suggest.

Several recent Fourier-transform measurements of n and k (not using Kramers–Kronig analysis) have given smaller values of k [16–19]. The Si used was 10 Ω cm [16–18] or 1000 Ω cm [19] resistivity with carrier type not specified. These showed free-carrier effects below 100 cm^{-1} with n decreasing and k increasing. The plasma frequency for 10 Ω cm n-type material is $\sim 4\ cm^{-1}$, and the carrier density is $\sim 5 \times 10^{14}\ cm^{-3}$. The data in the lattice-band region near 600 cm^{-1} in Honijk *et al.* [16] and Passchier *et al.* [17] appear to be in error both in peak value and in shape of bands compared to Lax and Burstein [13] and Johnson [14]. For example, the peak at 606 cm^{-1} is not 17 Np/cm but 9.5 cm^{-1}. Also, there is no band of Si at 650 cm^{-1}. The neper is usually a unit of amplitude attenuation and is $\alpha/2$ in optics language. Therefore, we do not use these data to lower frequency. Since the k values below 100 cm^{-1} varied among the reports of Loewenstein *et al.* [5], Randall and Rawcliffe [6], Honijk *et al.* [16], Passchier *et al.* [17], Birch [18], and Afsar and Hasted [19], we conclude that the free-carrier densities were different. We choose the data of Afsar and Hasted [19] for k below 160 cm^{-1} (measured at 303 K) because the resistivity was the largest, which should minimize the free-carrier effects on k.

Wavelength ellipsometry measurements have been carried out by Aspnes and Theeten [20] to determine n and k in the 1.5–6.0-eV region. Temperature was not stated but was probably 298 K. Samples of resistivity $\sim 26\ \Omega$ cm with {100}, {111}, and {110} surface orientations were prepared by Syton polishing; and dry thermal oxides were grown, stripped, and regrown so that a study of the transition layer between SiO_2 and Si could be made. The analysis involved mathematical removal of the oxide and its 6-Å transition

layer to obtain the final optical constants. The data were combined with ε_2 data of Hulthèn [21] below 2.5 eV to generate the final values we have tabulated.

The Hulthèn work was transmission measurements of epitaxial films of silicon on sapphire substrates, so that surface damage was not a problem as might be the case for Dash and Newman [22], who used mechanically polished thin samples. Temperature was not stated but was probably 298 K. This is fairly important, since the band gap is quite sensitive to temperature [23]. It would also be useful to know whether the entire optical image was focused on the sample (possibly raising the temperature) or if the radiation was predispersed. Strain in the film might also cause a shift in band gap. We obtained n and k from reading graphs [21] and list them so as to get some overlap with data of Aspnes and Theeten [20] near the band edge.

To slightly lower energy (1.0–1.3 eV), the absorption has been measured by McFarlane and Roberts [23] at 290 K for 100-Ω-cm material, mechanically polished. The absorption coefficient is dependent on optical–phonon emission and absorption processes for the indirect transitions, thus being temperature sensitive. Since the data of Hulthèn [21] and McFarlane and Roberts [23] were at 298 and 290 K, respectively, the discrepancy at 1.2 eV is not too surprising (bearing in mind the graph-reading process, also). However, a factor of 5 difference at 1.2 eV is puzzling and leads us to believe that sample surface preparation, the type and magnitude of impurity doping, and possibly strain must produce significant absorption effects near the band edge.

It has been pointed out by Russo [24] through reflection measurements of unpolarized incident radiation that n and k above the fundamental band gap do depend on resistivity (free-carrier density). However, sample resistivity was in the range $10^{-2}\ \Omega$ cm ($n \approx 1 \times 10^{19}\ \text{cm}^{-3}$) compared to 95 Ω cm ($\sim 5 \times 10^{13}\ \text{cm}^{-3}$) for the effect to be large. For example, at 0.5750 μm k increased by a factor of 3 while n increased by 10%. This is probably a combination of free-carrier absorption coming in from the infrared and the Burstein–Moss effect at the fundamental and other higher-lying band gaps.

Several investigators have measured reflectivity in the visible–ultraviolet region and then determined n and k from a Kramers–Kronig analysis [25–28]. The effect of native oxide on reflectivity measurements in this spectral region is discussed by Philipp [26]. It appears that the samples of Sasaki and Ishiguro [28] were mechanically polished, which would make them suspect at high energies. Philipp [25–27] used chemically prepared surfaces with minimum time spent in air before insertion into the vacuum spectrometer. We have therefore elected to tabulate the Philipp data from 5 to 25 eV overlapping the ellipsometric data for comparison. Interestingly, the data of Philipp [26] and Sasaki and Ishiguro [28] are in reasonable agreement at higher energies, typically $\lesssim 30\%$ for n but $\lesssim 10\%$ for k as well as at lower energy, despite the apparently different surface preparation. The

data of Aspnes and Theeten [20] and Philipp [26] are typically within $\lesssim 5\%$ for k and $\lesssim 10\%$ for n in the overlap region 5–6 eV.

For the range 20–95 eV we found data of Hunter [29]. Samples were evaporated Si on glass plates for measurement of n by a critical-angle method; they were freestanding for measurement of k by transmission. While the samples were probably amorphous, we find that the data fit reasonably well between the results of Henke [30] and Philipp [26].

An interpolation has been done between 95 and 99 eV to keep the continuity.

The absorption coefficient near the $L_{2,3}$ absorption edge of Si at ~ 100 eV has been measured [31, 32] with chemically etched and polished samples and with films flash evaporated onto NaCl substrates and floated off; the latter were polycrystalline. A synchroton source was used. Some of the extended fine structure is apparent.

From 99 to 2000 eV we have calculated n and k from a model of Henke *et al.* [30] as discussed by Lynch and Hunter in the metal section of this handbook. While the calculation cannot account for the fine structure, the magnitude of k is in reasonable agreement with experiment [31, 32].

Very recently, new measurements [33] of ε' and ε'' have been made on n-type Si wafers at 23°C in the millimeter-wave region at 107.3 GHz ($\lambda = 2.796$ mm). The resistivity varied from 5 to 50 Ω cm ($N = 1 \times 10^{15}$ to 1×10^{14} cm^{-3}). A transmission–reflection technique with the sample in free space was used. It was shown that a Drude model fit the data well with

$$\varepsilon' = \varepsilon_\infty \left[1 - \frac{\omega_p^2 \tau^2}{(1 + \omega^2 \tau^2)} \right], \qquad \varepsilon'' = \frac{\varepsilon_\infty \omega_p^2 \tau}{\omega(1 + \omega^2 \tau^2)},$$

where $\omega_p^2 = Ne^2/\varepsilon_0 \varepsilon_\infty m^*$ is the plasma frequency, N is the free-electron density, $\varepsilon_\infty = 11.7$ is the high-frequency dielectric constant, $m^* = 0.26$ is the effective mass, $\tau = 1 \times 10^{-13}$ sec is the constant scattering time, and mks units are used. Since the data fit well over the order-of-magnitude change in N, it is probably safe to extend the calculation of ε' and ε'' at least another order of magnitude in N in both directions to estimate how transparent a sample will be. Also, it is probably safe to calculate the reflectance and transmittance an order of magnitude to either side of 107.3 GHz.

REFERENCES

1. W. Primak, *App. Opt.* **10**, 759 (1971).
2. C. D. Salzberg and J. J. Villa, *J. Opt. Soc. Am.*, **47**, 244 (1957).
3. D. F. Edwards and E. Ochoa, *Appl. Opt.* **19**, 4130 (1980).
4. H. W. Icenogle, B. C. Platt, and W. L. Wolfe, *Appl. Opt.* **15**, 2348 (1976).
5. E. V. Loewenstein, D. R. Smith, and R. L. Morgan, *Appl. Opt.* **12**, 398 (1973).
6. C. M. Randall and R. D. Rawcliffe, *Appl. Opt.* **6**, 1889 (1967).
7. M. Herzberger and C. D. Salzberg, *J. Opt. Soc. Am.* **52**, 420 (1962); M. Herzberger, *Opt. Acta.* **6**, 197 (1959).

8. H. H. Li, *J. Phys. Chem. Ref. Data* **9**, 561 (1980).
9. T. S. Moss, "Optical Properties of Semi-Conductors." Butterworth, London, 1959.
10. P. Baumeister, Optical Coating Laboratory, Inc., private communication (1979).
11. S. Tolansky, *Philos. Mag.* **36**, 225 (1945).
12. A. Hordvik and L. Skolnik, *Appl. Opt.* **16**, 2919 (1977).
13. M. Lax and E. Burstein, *Phys. Rev.* **97**, 39 (1955).
14. F. A. Johnson, *Proc. Phys. Soc. London* **73**, 265 (1959).
15. B. Bendow, H. G. Lipson, and S. P. Yukon, *Appl. Opt.* **16**, 2909 (1977).
16. D. D. Honijk, W. F. Passchier, M. Mandel, and M. N. Afsar, *Infrared Phys.* **17**, 9 (1977).
17. W. F. Passchier, D. D. Honijk, M. Mandel, and M. N. Afsar, *J. Phys. D* **10**, 509 (1977).
18. J. R. Birch, *Infrared Phys.* **18**, 613 (1978).
19. M. N. Afsar and J. B. Hasted, *Infrared Phys.* **18**, 835 (1978).
20. D. E. Aspnes and J. B. Theeten, *J. Electrochem. Soc.* **127**, 1359 (1980); D. E. Aspnes and J. B. Theeten, private communication (1980).
21. R. Hulthèn, *Phys. Scr.* **12**, 342 (1975).
22. W. C. Dash and R. Newman, *Phys. Rev.* **99**, 1151 (1955).
23. G. G. McFarlane and V. Roberts, *Phys. Rev.* **98**, 1865 (1955).
24. O. I. Russo, *J. Electrochem. Soc.* **127**, 953 (1980).
25. H. R. Philipp and E. A. Taft, *Phys. Rev.* **120**, 37 (1960).
26. H. R. Philipp, *J. Appl. Phys.* **43**, 2836 (1972); H. R. Philipp, private communication (1982).
27. H. R. Philipp and H. Ehrenreich, *in* "Semiconductors and Semimetals" (R. K. Willardson and A. C. Beer, eds.), Vol. 2, p. 93. Academic Press, New York, 1967.
28. T. Sasaki and K. Ishiguro, *Phys. Rev.* **127**, 1091 (1962).
29. W. R. Hunter, private communication of unpublished data (1982).
30. B. L. Henke, P. Lee, T. J. Tanaka, R. L. Shimabukuro, and B. K. Fujikawa, "Low Energy X-Ray Diagnostics—1981" (D. T. Attwood and B. L. Henke, eds.), *AIP Conference Proc.*, No. 75, p. 340. American Institute of Physics, New York, 1981.
31. C. Gähwiller and F. C. Brown, *Proc. Int. Conf. Phys. Semicond., 10th, Cambridge, 1970*, p. 213. U.S. Atomic Energy Commission, Oak Ridge, Tennessee, 1970.
32. F. C. Brown, R. Z. Bachrach, and M. Skibowski, *Phys. Rev. B* **15**, 478 (1977).
33. H. T. Kinasewitz and D. Senitzky, *J. Appl. Phys.* **54**, 3394 (1983).

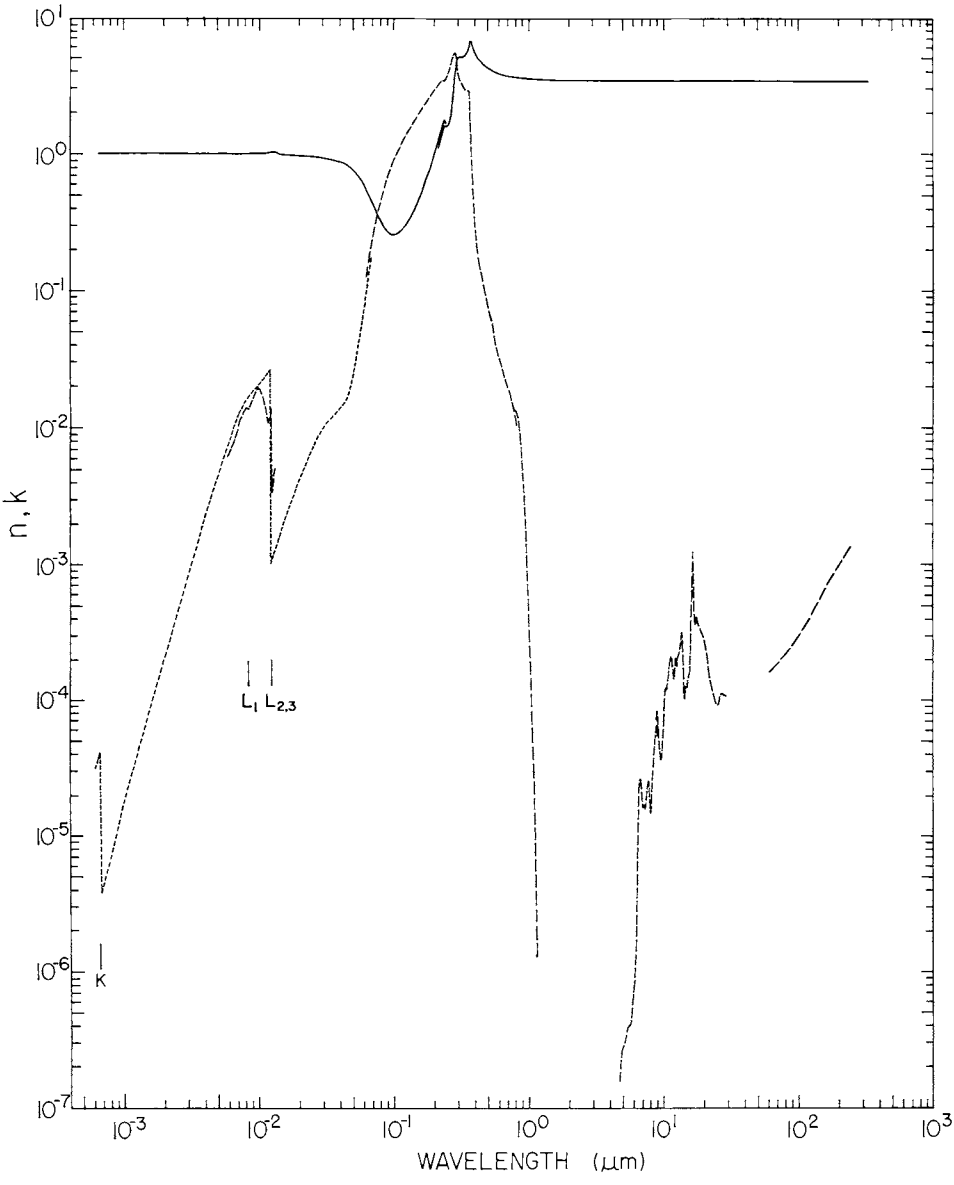

Fig. 11. Log–log plot of n (——) and k (– – – –) versus wavelength in micrometers for silicon. Data from various references sometimes do not join together in overlap regions.

TABLE XII

Values of n and k for Silicon Obtained from Various References[a]

eV	cm^{-1}	Å	n	k	n	k
2,000		6.199	0.9999048 [30]	3.19×10^{-5} [30]		
1,952		6.351	0.9999131	3.46		
1,905		6.508	0.9999222	3.76		
1,860		6.665	0.9999318	4.08×10^{-5}		
1,815		6.831	0.9999113	3.93×10^{-6}		
1,772		6.997	0.999885	4.32		
1,730		7.166	0.999874	4.74		
1,688		7.345	0.999863	5.20		
1,648		7.523	0.999854	5.70		
1,609		7.705	0.999844	6.24		
1,570		7.897	0.999834	6.85		
1,533		8.087	0.999824	7.49		
1,496		8.287	0.999814	8.22		
1,460		8.492	0.999803	8.99		
1,426		8.694	0.999792	9.81×10^{-6}		
1,392		8.906	0.999781	1.07×10^{-5}		
1,358		9.129	0.999769	1.17		
1,326		9.350	0.999756	1.28		
1,294		9.581	0.999743	1.40		
1,263		9.816	0.999729	1.53		
1,233		10.05	0.999715	1.67		
1,204		10.30	0.999700	1.83		
1,175		10.55	0.999684	2.00		
1,147		10.81	0.999667	2.18		
1,119		11.08	0.999649	2.39		
1,093		11.34	0.999631	2.60		
1,067		11.62	0.999612	2.84		
1,041		11.91	0.999591	3.10		
1,016		12.20	0.999570	3.39		
992		12.50	0.999548	3.70		
968		12.81	0.999524	4.04		
945		13.12	0.999500	4.41		
923		13.43	0.999474	4.80		
901		13.76	0.999447	5.24		
879		14.10	0.999418	5.73		
858		14.45	0.999388	6.25		
838		14.79	0.999358	6.80		
818		15.16	0.999325	7.42		
798		15.54	0.999289	8.11		
779		15.92	0.999253	8.84		
760		16.31	0.999214	9.66×10^{-5}		
742		16.71	0.999174	1.05×10^{-4}		
725		17.10	0.999134	1.14		
707		17.54	0.999088	1.25		
690		17.97	0.999041	1.36		
674		18.39	0.99899	1.48		

(*continued*)

TABLE XII (*Continued*)

Silicon

eV	cm^{-1}	Å	n	k	n	k
658		18.84	0.99894	1.61		
642		19.31	0.99889	1.76		
627		19.77	0.99883	1.91		
612		20.26	0.99878	2.08		
597		20.77	0.99871	2.27		
583		21.27	0.99865	2.47		
569		21.79	0.99858	2.69		
555		22.34	0.99851	2.94		
542		22.87	0.99843	3.19		
529		23.44	0.99836	3.47		
516		24.03	0.99827	3.79		
504		24.60	0.99819	4.11		
492		25.20	0.99810	4.47		
480		25.83	0.99800	4.87		
469		26.43	0.99791	5.27		
458		27.07	0.99781	5.72		
447		27.74	0.99770	6.22		
436		28.44	0.99759	6.77		
426		29.10	0.99748	7.34		
415		29.87	0.99735	8.01		
406		30.54	0.99723	8.63		
396		31.31	0.99710	9.39×10^{-4}		
386		32.12	0.99695	1.02×10^{-3}		
377		32.89	0.99682	1.11		
368		33.69	0.99667	1.20		
359		34.53	0.99651	1.31		
351		35.32	0.99636	1.41		
342		36.25	0.99619	1.53		
334		37.12	0.99602	1.66		
326		38.03	0.99585	1.80		
318		38.99	0.99566	1.95		
311		39.86	0.99549	2.10		
303		40.92	0.99528	2.29		
296		41.88	0.99509	2.47		
289		42.90	0.99489	2.67		
282		43.96	0.99468	2.88		
275		45.08	0.99446	3.13		
269		46.09	0.99427	3.36		
262		47.32	0.99403	3.65		
256		48.43	0.99382	3.93		
250		49.59	0.99361	4.23		
244		50.81	0.99339	4.57		
238		52.09	0.99318	4.94		
232		53.44	0.99296	5.34		
227		54.62	0.99277	5.70		
221		56.10	0.99254	6.19		
216		57.40	0.99236	6.63		

TABLE XII (*Continued*)

Silicon

eV	cm^{-1}	Å	n	k	n	k
211		58.76	0.99219	7.12		
210		59.04				6.30×10^{-3} [31]
206		60.18	0.99206	7.63		
205		60.48				6.59
201		61.68	0.99192	8.18		
200		61.99				6.96
196		63.25	0.99179	8.79		
195		63.58				7.34
191		64.91	0.99169	9.46×10^{-3}		
190		65.26				7.84
187		66.30	0.99167	1.00×10^{-2}		
185		67.02				8.48
182		68.12	0.99164	1.07		
180		68.88				9.21×10^{-3}
178		69.65	0.99164	1.14		
175		70.85				1.01×10^{-2}
174		71.25	0.99167	1.21		
170		72.93	0.99176	1.28		1.14
166		74.69	0.99235	1.45		
165		75.14				1.21
162		76.53	0.99235	1.45		
160		77.49				1.29
158		78.47	0.99287	1.52		
155		79.99				1.38
154		80.51	0.99340	1.57		
152.5		81.30				1.42
150		82.66	0.99384	1.62		1.40
147.5		84.05				1.37
147		84.34	0.99415	1.66		
145		85.51				1.43
143		86.70	0.99460	1.72		
140		88.56	0.99496	1.77		1.54
136		91.16	0.99549	1.83		
135		91.84				1.66
133		93.22	0.99594	1.88		
130		95.37	0.99645	1.94		1.81
127.5		97.24				1.88
127		97.62	0.99705	2.00		
125		99.19				1.91
124		99.98	0.99773	2.06		
121		102.5	0.99856	2.12		
120		103.3				1.85
118		105.1	0.99958	2.19		
115		107.8	1.0008	2.26		1.63
112		110.7	1.0024	2.33		
110		112.7	1.0039	2.39		1.38

(*continued*)

TABLE XII (*Continued*)

Silicon

eV	cm^{-1}	Å	n	k	n	k
107		115.9	1.0070	2.47		
105		118.1				1.08 [32]
104.8		118.3				1.09
104.6		118.5				1.08
104.4		118.8				1.08
104.2		119.0				1.09
104		119.2	1.0132	2.56		1.09
103.8		119.4				1.07
103.6		119.7				1.09
103.4		119.9				1.14
103.2		120.1				1.14
103		120.4				1.12
102.8		120.6				1.16
102.6		120.8				1.17
102.4		121.1				1.13
102.2		121.3				1.13
102		121.6	1.0241	2.62		1.16
101.8		121.8				1.22
101.6		122.0	1.025	2.4×10^{-2}		1.29
101.4		122.3				1.36
101.2		122.5				1.37
101		122.8				1.40
100.8		123.0	1.030	5.0×10^{-3}		1.40
100.6		123.2				1.34
100.4		123.5				1.12
100.2		123.7				1.00×10^{-2}
100		124.0	1.032	1.54		9.7×10^{-3}
99.8		124.2				4.9
99.6		124.5				3.6
99.4		124.7				3.4
99.2		125.0				3.4
99.19		125	1.034 [29]	1.0 [29]		
99.0		125.2				3.4
98.40		126	1.034	1.02		
96.86		128	1.034	1.09		
95.37		130	1.03	1.13		
95		130.5				4.9 [31]
93.93		132	1.022	1.2		
91.17		136	1.008	1.3		
88.56		140	1.000	1.43		
82.66		150	0.993	1.78		
77.49		160	0.991	2.15		
72.93		170	0.988	2.54		
68.88		180	0.985	2.97		
65.26		190	0.982	3.43		
61.99		200	0.978	3.93		
59.04		210	0.976	4.43		

TABLE XII (*Continued*)

Silicon

eV	cm $^{-1}$	Å	n	k	n	k
56.36		220	0.972	5.0		
53.91		230	0.968	5.53		
51.66		240	0.964	6.1		
49.59		250	0.960	6.7		
47.69		260	0.956	7.3		
45.92		270	0.952	7.85		
44.28		280	0.947	8.4		
42.75		290	0.942	9.0		
41.33		300	0.937	9.5×10^{-3}		
40.00		310	0.930	1.0×10^{-2}		
38.75		320	0.925	1.04		
37.57		330	0.918	1.0		
36.47		340	0.913	1.13		
35.42		350	0.906	1.17		
34.44		360	0.899	1.21		
33.51		370	0.893	1.24		
32.63		380	0.885	1.28		
31.79		390	0.877	1.32		
31.00		400	0.869	1.35		
30.24		410	0.860	1.38		
29.52		420	0.853	1.42		
28.83		430	0.843	1.47		
28.18		440	0.834	1.52		
27.55		450	0.824	1.58		
26.95		460	0.814	1.68		
26.38		470	0.803	1.78		
25.83		480	0.792	1.92		
25.30		490	0.778	2.05		
24.80		500	0.766	2.23		
24.31		510	0.752	2.43		
23.84		520	0.737	2.64		
23.39		530	0.722	2.92		
22.96		540	0.706	3.25		
22.54		550	0.691	3.65		
22.14		560	0.675	4.05		
21.75		570	0.659	4.55		
21.38		580	0.644	5.1		
21.01		590	0.627	5.8		
20.66		600	0.61	6.5		
20.33		610	0.59	7.4		
20.00		620	0.567	8.35×10^{-2}		
			0.569 [26]	0.122 [26]		
19.68		630	0.549 [29]	9.3×10^{-2}		
19.5		635.8	0.542 [26]	0.140 [26]		
10.37		640	0.53 [29]	0.10 [29]		
19.07		650	0.513	0.113		

(*continued*)

TABLE XII (*Continued*)

Silicon

eV	cm^{-1}	μm	*n*	*k*	*n*	*k*
19.0		0.06526	0.514 [26]	0.163 [26]		
18.5		0.06702	0.485	0.189		
18.0		0.06888	0.455	0.219		
17.75		0.06985	0.440	0.237		
17.5		0.07085	0.426	0.255		
17.25		0.07187	0.411	0.275		
17.0		0.07293	0.397	0.296		
16.80		0.07380	0.386	0.314		
16.7		0.07424	0.379	0.323		
16.6		0.07469	0.374	0.333		
16.5		0.07514	0.369	0.342		
16.25		0.07630	0.357	0.367		
16.0		0.07749	0.345	0.394		
15.75		0.07872	0.333	0.421		
15.5		0.07999	0.323	0.450		
15.25		0.08130	0.313	0.479		
15.0		0.08266	0.304	0.510		
14.75		0.08406	0.296	0.541		
14.5		0.08551	0.288	0.573		
14.25		0.08700	0.281	0.607		
14.0		0.08856	0.275	0.641		
13.75		0.09017	0.269	0.677		
13.5		0.09184	0.265	0.714		
13.25		0.09357	0.261	0.752		
13.0		0.09537	0.258	0.792		
12.75		0.09724	0.256	0.833		
12.5		0.09919	0.255	0.875		
12.25		0.10120	0.256	0.918		
12.0		0.1033	0.257	0.963		
11.75		0.1055	0.259	1.01		
11.5		0.1078	0.263	1.06		
11.25		0.1102	0.267	1.11		
11.0		0.1127	0.272	1.16		
10.75		0.1153	0.278	1.21		
10.5		0.1181	0.286	1.26		
10.25		0.1210	0.295	1.32		
10.0		0.1240	0.306	1.38		
9.75		0.1272	0.318	1.45		
9.5		0.1305	0.332	1.51		
9.25		0.1340	0.348	1.58		
9.0		0.1378	0.367	1.66		
8.75		0.1417	0.389	1.73		
8.5		0.1459	0.414	1.82		
8.25		0.1503	0.444	1.90		
8.0		0.1550	0.478	2.00		
7.75		0.1600	0.517	2.10		
7.5		0.1653	0.563	2.21		
7.25		0.1710	0.618	2.32		

TABLE XII (*Continued*)

Silicon

eV	cm^{-1}	μm	n	k	n	k
7.0		0.1771	0.682	2.45		
6.75		0.1837	0.756	2.58		
6.5		0.1907	0.847	2.73		
6.25		0.1984	0.968	2.89		
6.0	48,390	0.2066	1.11	3.05	1.010 [20]	2.909 [20]
5.98	48,230	0.2073			1.036	2.928
5.96	48,070	0.2080			1.046	2.944
5.94	47,910	0.2087			1.066	2.937
5.92	47,750	0.2094			1.070	2.963
5.9	47,590	0.2101			1.083	2.982
5.88	47,430	0.2109			1.088	2.987
5.86	47,260	0.2116			1.102	3.005
5.84	47,100	0.2123			1.109	3.015
5.82	46,940	0.2130			1.119	3.025
5.8	46,780	0.2138	1.24	3.18	1.133	3.045
5.78	46,620	0.2145			1.139	3.061
5.76	46,460	0.2153			1.155	3.073
5.74	46,300	0.2160			1.164	3.086
5.72	46,130	0.2168			1.175	3.102
5.7	45,970	0.2175			1.180	3.112
5.68	45,810	0.2183			1.195	3.135
5.66	45,640	0.2191			1.211	3.150
5.64	45,490	0.2198			1.222	3.169
5.62	45,330	0.2206			1.235	3.190
5.6	45,170	0.2214	1.40	3.33	1.247	3.206
5.58	45,010	0.2222			1.265	3.228
5.56	44,840	0.2230			1.280	3.245
5.54	44,680	0.2238			1.299	3.267
5.52	44,520	0.2246			1.319	3.285
5.5	44,360	0.2254	1.51	3.40	1.340	3.302
5.48	44,200	0.2263			1.362	3.319
5.46	44,040	0.2271			1.389	3.334
5.44	43,880	0.2279			1.416	3.350
5.42	43,710	0.2288			1.445	3.359
5.4	43,550	0.2296	1.64	3.44	1.471	3.366
5.38	43,390	0.2305			1.502	3.368
5.36	43,230	0.2313			1.526	3.368
5.34	43,070	0.2322			1.548	3.364
5.32	42,910	0.2331			1.566	3.358
5.3	42,750	0.2339	1.75	3.42	1.579	3.353
5.28	42,590	0.2348			1.585	3.346
5.26	42,420	0.2357			1.590	3.344
5.24	42,260	0.2366			1.591	3.344
5.22	42,100	0.2375			1.592	3.347
5.2	41,940	0.2384	1.78	3.36	1.589	3.354
5.18	41,780	0.2394			1.586	3.363
5.16	41,620	0.2403			1.582	3.376

(*continued*)

TABLE XII (*Continued*)

Silicon

eV	cm^{-1}	μm	n	k	n	k
5.14	41,460	0.2412			1.579	3.389
5.12	41,300	0.2422			1.573	3.408
5.1	41,130	0.2431	1.72	3.42	1.571	3.429
5.08	40,970	0.2441			1.570	3.451
5.06	40,810	0.2450			1.569	3.477
5.04	40,650	0.2460			1.568	3.504
5.02	40,490	0.2470			1.569	3.533
5.0	40,330	0.2480	1.68	3.58	1.570	3.565
4.98	40,170	0.2490			1.575	3.598
4.96	40,000	0.2500			1.580	3.632
4.94	39,840	0.2510			1.584	3.670
4.92	39,680	0.2520			1.591	3.709
4.9	39,520	0.2530			1.597	3.749
4.88	39,360	0.2541			1.608	3.789
4.86	39,200	0.2551			1.618	3.835
4.84	39,040	0.2562			1.629	3.880
4.82	38,880	0.2572			1.643	3.928
4.8	38,710	0.2583			1.658	3.979
4.78	38,550	0.2594			1.673	4.031
4.76	38,390	0.2605			1.692	4.088
4.74	38,230	0.2616			1.713	4.149
4.72	38,070	0.2627			1.737	4.211
4.7	37,910	0.2638			1.764	4.278
4.68	37,750	0.2649			1.794	4.350
4.66	37,590	0.2661			1.831	4.426
4.64	37,420	0.2672			1.874	4.506
4.62	37,260	0.2684			1.927	4.590
4.6	37,100	0.2695			1.988	4.678
4.58	36,940	0.2707			2.059	4.764
4.56	36,780	0.2719			2.140	4.849
4.54	36,620	0.2731			2.234	4.933
4.52	36,460	0.2743			2.339	5.011
4.5	36,290	0.2755			2.451	5.082
4.48	36,130	0.2768			2.572	5.148
4.46	35,970	0.2780			2.700	5.206
4.44	35,810	0.2792			2.833	5.257
4.42	35,650	0.2805			2.974	5.304
4.4	35,490	0.2818			3.120	5.344
4.38	35,330	0.2831			3.277	5.381
4.36	35,170	0.2844			3.444	5.414
4.34	35,000	0.2857			3.634	5.435
4.32	34,840	0.2870			3.849	5.439
4.3	34,680	0.2883			4.086	5.395
4.28	34,520	0.2897			4.318	5.301
4.26	34,360	0.2910			4.525	5.158
4.24	34,200	0.2924			4.686	4.989
4.22	34,040	0.2938			4.805	4.812
4.2	33,880	0.2952			4.888	4.639

TABLE XII (*Continued*)

Silicon

eV	cm^{-1}	μm	n	k	n	k
4.18	33,710	0.2966			4.941	4.480
4.16	33,550	0.2980			4.977	4.335
4.14	33,390	0.2995			4.999	4.204
4.12	33,230	0.3009			5.012	4.086
4.1	33,070	0.3024			5.020	3.979
4.08	32,910	0.3039			5.021	3.885
4.06	32,750	0.3054			5.020	3.798
4.04	32,580	0.3069			5.018	3.720
4.02	32,420	0.3084			5.015	3.650
4.0	32,260	0.3100			5.010	3.587
3.98	32,100	0.3115			5.009	3.529
3.96	31,940	0.3131			5.010	3.477
3.94	31,780	0.3147			5.009	3.429
3.92	31,620	0.3163			5.012	3.386
3.9	31,460	0.3179			5.016	3.346
3.88	31,290	0.3195			5.021	3.310
3.86	31,130	0.3212			5.029	3.275
3.84	30,970	0.3229			5.040	3.242
3.82	30,810	0.3246			5.052	3.211
3.8	30,650	0.3263			5.065	3.182
3.78	30,490	0.3280			5.079	3.154
3.76	30,330	0.3297			5.095	3.128
3.74	30;160	0.3315			5.115	3.103
3.72	30,000	0.3333			5.134	3.079
3.7	29,840	0.3351			5.156	3.058
3.68	29,680	0.3369			5.179	3.039
3.66	29,520	0.3388			5.204	3.021
3.64	29,360	0.3406			5.231	3.007
3.62	29,200	0.3425			5.261	2.995
3.6	29,040	0.3444			5.296	2.987
3.58	28,870	0.3463			5.336	2.983
3.56	28,710	0.3483			5.383	2.984
3.54	28,550	0.3502			5.442	2.989
3.52	28,390	0.3522			5.515	2.999
3.5	28,230	0.3542			5.610	3.014
3.48	28,070	0.3563			5.733	3.026
3.46	27,910	0.3583			5.894	3.023
3.44	27,750	0.3604			6.089	2.982
3.42	27,580	0.3625			6.308	2.881
3.4	27,420	0.3647			6.522	2.705
3.38	27,260	0.3668			6.695	2.456
3.36	27,100	0.3690			6.796	2.169
3.34	26,940	0.3712			6.829	1.870
3.32	26,780	0.3734			6.799	1.577
3.3	26,620	0.3757			6.709	1.321
3.28	26,450	0.3780			6.585	1.110
3.26	26,290	0.3803			6.452	0.945

(*continued*)

TABLE XII (*Continued*)

Silicon

eV	cm^{-1}	μm	n	k	n	k
3.24	26,130	0.3827			6.316	0.815
3.22	25,970	0.3850			6.185	0.714
3.2	25,810	0.3875			6.062	0.630
3.18	25,650	0.3899			5.948	0.561
3.16	25,490	0.3924			5.842	0.505
3.14	25,330	0.3949			5.744	0.456
3.12	25,160	0.3974			5.654	0.416
3.1	25,000	0.4000			5.570	0.387
3.08	24,840	0.4025			5.493	0.355
3.06	24,680	0.4052			5.420	0.329
3.04	24,520	0.4078			5.349	0.313
3.02	24,360	0.4105			5.284	0.291
3.0	24,200	0.4133			5.222	0.269
2.98	24,040	0.4161			5.164	0.255
2.96	23,870	0.4189			5.109	0.244
2.94	23,710	0.4217			5.058	0.228
2.92	23,550	0.4246			5.009	0.211
2.9	23,390	0.4275			4.961	0.203
2.88	23,230	0.4305			4.916	0.194
2.86	23,070	0.4335			4.872	0.185
2.84	22,910	0.4366			4.831	0.185
2.82	22,740	0.4397			4.791	0.170
2.8	22,580	0.4428			4.753	0.163
2.78	22,420	0.4460			4.718	0.149
2.76	22,260	0.4492			4.682	0.149
2.74	22,100	0.4525			4.648	0.133
2.72	21,940	0.4558			4.615	0.131
2.7	21,780	0.4592			4.583	0.130
2.68	21,660	0.4626			4.553	0.131
2.66	21,450	0.4661			4.522	0.134
2.64	21,290	0.4696			4.495	0.120
2.62	21,130	0.4732			4.466	0.120
2.6	20,970	0.4769			4.442	0.090
2.58	20,810	0.4806			4.416	0.094
2.56	20,650	0.4843			4.391	0.083
2.54	20,490	0.4881			4.367	0.079
2.52	20,330	0.4920			4.343	0.077
2.5	20,160	0.4959			4.320	0.073
2.48	20,000	0.4999			4.298	0.073
2.46	19,840	0.5040			4.277	0.066
2.44	19,680	0.5081			4.255	0.072
2.42	19,520	0.5123			4.235	0.060
2.4	19,360	0.5166			4.215	0.060
2.38	19,200	0.5209			4.196	0.056
2.36	19,030	0.5254			4.177	0.053
2.34	18,870	0.5299			4.159	0.043
2.32	18,710	0.5344			4.140	0.045

TABLE XII (*Continued*)

Silicon

eV	cm^{-1}	μm	n	k	n	k
2.3	18,550	0.5391			4.123	0.048
2.28	18,390	0.5438			4.106	0.044
2.26	18,230	0.5486			4.089	0.044
2.24	18,070	0.5535			4.073	0.032
2.22	17,910	0.5585			4.057	0.038
2.2	17,740	0.5636			4.042	0.032
2.18	17,580	0.5687			4.026	0.034
2.16	17,420	0.5740			4.012	0.030
2.14	17,260	0.5794			3.997	0.027
2.12	17,100	0.5848			3.983	0.030
2.1	16,940	0.5904			3.969	0.030
2.08	16,780	0.5961			3.956	0.027
2.06	16,610	0.6019			3.943	0.025
2.04	16,450	0.6078			3.931	0.025
2.02	16,290	0.6138			3.918	0.024
2.0	16,130	0.6199		2.96×10^{-2} [21]	3.906	0.022
1.98	15,970	0.6262			3.893	0.022
1.96	15,810	0.6326			3.882	0.019
1.94	15,650	0.6391			3.870	0.018
1.92	15,490	0.6458			3.858	0.017
1.9	15,320	0.6526		2.4	3.847	0.016
1.88	15,160	0.6595			3.837	0.016
1.86	15,000	0.6666			3.826	0.015
1.84	14,840	0.6738			3.815	0.014
1.82	14,680	0.6812			3.805	0.013
1.8	14,520	0.6888		2.25	3.796	0.013
1.78	14,360	0.6965			3.787	0.013
1.76	14,200	0.7045			3.778	0.012
1.74	14,030	0.7126			3.768	0.011
1.72	13,870	0.7208			3.761	0.011
1.7	13,710	0.7293		1.97	3.752	0.010
1.68	13,550	0.7380			3.745	0.010
1.66	13,390	0.7469			3.736	0.009
1.64	13,230	0.7560			3.728	0.009
1.62	13,070	0.7653			3.721	0.008
1.6	12,900	0.7749		1.42	3.714	0.008
1.58	12,740	0.7847			3.705	0.007
1.56	12,580	0.7948			3.697	0.007
1.54	12,420	0.8051			3.688	0.006
1.52	12,260	0.8157			3.681	0.006
1.5	12,100	0.8266		1.25×10^{-2}	3.673	0.005
1.4	11,290	0.8856		7.75×10^{-3}		
1.3	10,490	0.9537		2.26		
1.28	10,320	0.9686				6.4×10^{-4} [23]
1.26	10,160	0.9840				5.1
1.24	10,000	0.9999				4.0

(*continued*)

TABLE XII (*Continued*)

Silicon

eV	cm^{-1}	μm	n	k	n	k
1.22	9,840	1.016				2.8
1.2	9,679	1.033		1.07		1.8
1.18	9,518	1.051				1.2×10^{-4}
1.16	9,356	1.069				6.7×10^{-5}
1.14	9,195	1.088				4.2
1.12	9,034	1.107				2.5
1.107	8,929	1.12	3.5361 [1, 2, 3, 8]			
1.10	8,872	1.127				1.3×10^{-5}
1.084	8,741	1.144	3.5295			
1.08	8,711	1.148				5.8×10^{-6}
1.06	8,550	1.170				1.5
1.033	8,333	1.20	3.5193			
0.9037	7,289	1.372	3.5007			
0.8856	7,143	1.4	3.4876			
0.8093	6,527	1.532	3.4784			
0.7749	6,250	1.6	3.4710			
0.7310	5,896	1.696	3.4644			
0.6888	5,556	1.8	3.4578			
0.6199	5,000	2.0	3.4490			
0.5087	4,103	2.4373	3.4434			
0.4959	4,000	2.50	3.4424			
0.4568	3,684	2.7144	3.4393	2.5×10^{-9} [12]		
0.4133	3,333	3.00	3.4361			
0.3753	3,027	3.3033	3.4335			
0.3626	2,925	3.4188	3.4327			
0.3542	2,857	3.50	3.4321			
0.3263	2,632	3.80		1.3×10^{-8}		
0.3100	2,500	4.00	3.4294			
0.2480	2,000	5.00	3.4261	1.99×10^{-7} [15]		
0.2418	1,950	5.128		2.82×10^{-7}		
0.2356	1,900	5.263		2.97		
0.2294	1,850	5.405		3.26		
0.2232	1,800	5.556		3.94		
0.2170	1,750	5.714		4.05		
0.2108	1,700	5.882		4.17		
0.2066	1,667	6.00	3.4242			
0.2046	1,650	6.061		5.64		
0.1984	1,600	6.250		8.46×10^{-7}		
0.1922	1,550	6.452		1.74×10^{-6}		
0.1860	1,500	6.667		2.66×10^{-6}		
0.1798	1,450	6.897		2.45×10^{-5}		
0.1771	1,428	7.00	3.4231			
0.1736	1,400	7.143		1.68		
				1.87 [14]		
0.1674	1,350	7.407		1.62 [15]		
0.1612	1,300	7.692		2.49		
				2.82 [14]		

TABLE XII (*Continued*)

Silicon

eV	cm^{-1}	μm	n	k	n	k
0.1550	1,250	8.000	3.4224	1.53 [15]		
0.1488	1,200	8.333		2.41		
				2.52 [14]		
0.1426	1,150	8.696		5.13 [15]		
0.1401	1,130	8.850		7.11 [14]		
0.1395	1,125	8.889		6.44 [15]		
0.1389	1,120	8.929		8.38 [14]		
0.1378	1,111	9.00	3.4219			
0.1376	1,110	9.009		8.46		
0.1364	1,100	9.091		5.49 [15]		
				7.38 [14]		
0.1339	1,080	9.259		4.72		
0.1314	1,060	9.434		3.75		
0.1289	1,040	9.615		3.67		
0.1265	1,020	9.804		4.84		
0.1240	1,000	10.00	3.4215	6.76×10^{-5}		
0.1215	980	10.20		1.09×10^{-4}		
0.1203	970	10.31		1.22		
0.1190	960	10.42		1.24		
0.1178	950	10.53		1.22		
0.1165	940	10.64		1.27		
0.1141	920	10.87		1.66		
0.1116	900	11.11		2.02		
0.1103	890	11.24		2.08		
0.1091	880	11.36		2.02		
0.1079	870	11.49		2.01		
0.1066	860	11.63		1.73		
0.1054	850	11.76		1.53		
0.1041	840	11.90		1.44		
0.1029	830	12.05		1.77		
0.1017	820	12.20		2.06		
0.1004	810	12.35		1.97		
0.09919	800	12.50		1.77		
0.09795	790	12.66		2.07		
0.09671	780	12.82		2.14		
0.09547	770	12.99		2.27		
0.09423	760	13.16		2.39		
0.09299	750	13.33		2.59		
0.09184	740.7	13.50	3.4209			
0.09175	740	13.51		3.12		
0.09051	730	13.70		3.03		
0.08927	720	13.89		2.21		
0.08803	710	14.08		1.57		
0.08679	700	14.29		1.02		
0.08555	690	14.49		1.12		
0.08550	689.7	14.50	3.4208			

(*continued*)

TABLE XII (*Continued*)

Silicon

eV	cm^{-1}	μm	n	k	n	k
0.08431	680	14.71		1.25		
0.08307	670	14.93		1.24		
0.08265	666.7	15.00	3.4207			
0.08183	660	15.15		1.41		
0.08059	650	15.38		1.52		
0.07935	640	15.63		1.64		
0.07811	630	15.87		5.05		
0.07687	620	16.13		9.63×10^{-4}		
0.07563	610	16.39		1.11×10^{-3}		
0.07513	608	16.50		1.25×10^{-3}		
0.07439	600	16.67		7.16×10^{-4}		
0.07315	590	16.95		4.18		
0.07191	580	17.24		3.65		
0.07067	570	17.54		4.15		
0.06943	560	17.86		3.84		
0.06695	540	18.52		3.40		
0.06447	520	19.23		3.18		
0.06199	500	20.00	3.4204	2.86		
0.05951	480	20.83		2.22		
0.05703	460	21.74		1.56		
0.05455	440	22.73		1.27		
0.05207	420	23.81		1.06×10^{-4}		
0.04959	400	25.00	3.4201	9.15×10^{-5}		
0.04835	390	25.64		9.39×10^{-5}		
0.04711	380	26.32		1.05×10^{-4}		
0.04587	370	27.03		1.12		
0.04463	360	27.78		1.08		
0.04339	350	28.57				
0.04215	340	29.41		1.08		
0.04092	330	30.30	3.4200 [5, 6]			
0.03720	300	33.33				
0.03100	250	40.00	3.4199			
0.02480	200	50.00	3.4197			
0.01984	160	62.50	3.4195	1.7 [19]		
0.01736	140	71.43	3.4192	1.9		
0.01488	120	83.33	3.4190	2.3		
0.01364	110	90.91	3.4188			
0.01240	100	100.0	3.4185	2.9		
0.01116	90	111.1		3.5		
0.009919	80	125.0	3.4180	4.3		
0.008679	70	142.9		5.5		
0.007430	60	166.7	3.4170	7.2×10^{-4}		
0.006199	50	200.0	3.4165	1.0×10^{-3}		
0.004959	40	250.0	3.4160	1.4		
0.003720	30	333.3	3.4155			

[a] References are indicated in brackets.

TABLE XIII

Temperature Dependence of Index of Refraction[a]

λ (μm)	B_1	B_2	B_3
2.554	-1.1127×10^{-4}	2.0722×10^{-6}	-4.0×10^{-9}
2.732	-1.0255×10^{-5}	9.6748×10^{-7}	-1.2145×10^{-9}
5.190	-4.0089×10^{-5}	1.3368×10^{-6}	-2.3458×10^{-9}
10.270	-6.5198×10^{-5}	1.6358×10^{-6}	-3.2457×10^{-9}

[a] dn/dT for $T = 100$ to 296 K; $dn/dT = B_1 + B_2T + B_3T^2$.

Silicon (Amorphous) (a-Si)

H. PILLER
Department of Physics and Astronomy
Louisiana State University
Baton Rouge, Louisiana

The optical properties of amorphous silicon (a-Si) are sensitive to preparation conditions and to doping with hydrogen. Surface conditions and oxide films on the surface affect the optical measurements strongly, especially in the ultraviolet (UV). The optical properties of a-Si are also affected by the amount of disorder in the samples. Disorder is determined by substrate temperature, deposition rate, deposition method, impurities, vacuum conditions, annealing conditions, and environmental conditions. The mismatch of the expansion coefficients of the sample and the substrate introduces stress that can cause grain boundaries and voids in the sample. Annealing of the samples will reduce the strain but will generally increase the surface roughness. The a-Si samples should never be exposed to air before making the optical measurements. A measurement of the surface roughness should be performed, since specular reflectance measurements need to be corrected for imperfect (rough) surfaces. X-ray and low-energy electron-diffraction (LEED) measurements should be made to investigate the amorphous and surface properties of the samples.

Pierce and Spicer [1] measured reflectance R from 0.4 to 11.8 eV. Kramers–Kronig (KK) analysis was used to calculate the optical constants. The samples were evaporated in a vacuum of less than 5×10^{-6} torr by using low evaporation rates of 2 to 5 Å/sec and large evaporator-to-substrate distance (~ 40 cm). Silicon single crystals (1000 Ω cm) were used as substrates. The R measurements were made *in situ* on a 600-Å-thick film. The scattering in the R data indicated a relative measurement accuracy of $\pm 1\%$. The optical constants above 12 eV were derived from an extrapolation of the measured R and transmittance T and are less accurate. A zero-frequency refractive index n of 3.4, identical to that in crystalline Si (c-Si), was obtained. The maximum of the extinction coefficient k occurs at 4 eV compared to a maximum in k at 4.3 eV in c-Si. The data are listed in Table XIV and shown in Fig. 12 for both

Copyright © 1985 by Academic Press, Inc.
All rights of reproduction in any form reserved.
ISBN 0-12-544420-6

n and k. Weiser *et al.* [2] measured R of amorphous glow-discharge Si (g-Si) in the energy range of up to 10 eV. The g-Si films were deposited on quartz substrates in a rf discharge in pure silane at 0.2 mbar. The deposition rate was 2 Å/sec. The H:Si ratio in the samples varied as a function of deposition temperature (room temperature to 400°C) between 50 and 4%. The optical constants quoted in Table XIV and shown in Fig. 12 were determined from the measurements on a sample with a substrate temperature of 400°C. Here, R of g-Si shows a strong dependence on deposition temperature but a small dependence on annealing.

Brodsky *et al.* [3] measured the optical constants in a-Si films deposited on single-crystal sapphire substrates. The films were deposited by rf sputtering of c-Si onto a room-temperature substrate in an Ar atmosphere at a pressure of 0.01 torr. The deposition rates varied between 200 and 600 Å/min. Thicknesses of the films varied from 0.3 to 10 μm and were measured to within $\pm 10\%$. The films were stored in air. The data quoted in the table and shown in the figure were determined on a room-temperature sample. The k values agree very well with the data of Pierce *et al.* [1].

Zanzucchi *et al.* [4] measured the absorption in g-Si. Films prepared from silane contain up to an estimated 15–20 at. % of H. The films were deposited by either dc or rf glow discharge in silane at a pressure of 0.5 to 2.0 torr of silane and at deposition rates in the range 0.1–0.5 μm/min. It was found that n of g-Si is within 10 to 20% of the c-Si values. Vibration-band absorption due to bonded hydrogen was observed in g-Si associated with two modes, one at 2050 cm^{-1} and the other one at 635 cm^{-1}. These modes are associated with the Si-H stretching mode and the low-energy wagging mode, respectively. The data given in Table XIV and shown in Fig. 12 are for rf g-Si deposited at 215 and 300°C, respectively. The k values of rf g-Si, with substrate temperature of 420°C, agree very well with the values of Weiser *et al.* [2] in the band-edge region. Here, the absorption coefficient was determined from the amplitude of interference fringes in 1- to 3-μm-thick films. The measurement accuracy was $\pm(100\text{–}200)\ cm^{-1}$, which at 0.6 μm translates into $\pm(4.7\text{–}9.4) \times 10^{-4}$ for k. The experimental data show that the type of discharge is an important factor in determining the optical properties of g-Si. The Si-H bond was shown to be stable to thermal treatments.

Moddel *et al.* [5] determined the low-energy absorption in a-Si:H. The measurements were made on a 10-μm-thick sputtered film. The range of photon energy $h\nu$ was extended to lower energy by making use of photoconductivity (PC) data. The samples were made by rf sputtering of c-Si onto glass substrates in an Ar-H atmosphere. Interference fringes in the PC resulting from front and back surface reflections were not observed because of the low resolution of the spectrometer. Optical constants are shown in Fig. 12 and are listed in Table XIV.

Evangelisti *et al.* [6] determined the absorption coefficient α of a-Si:H from the spectral dependence of the PC over four decades. The samples were

grown by rf glow discharge in a capacitive reactor in pure silane or in a silane–argon mixture. Film thicknesses ranged between 0.5 and 1 μm; the hydrogen content varied between 9 and 17%. The exponential dependence of the PC on photon flux and $h\nu$ was studied, and it was found that the exponent β varies with $h\nu$. Value α was then evaluated by means of a recurrent expression. The optical constants presented in Table XIV and shown in Fig. 12 were determined by this procedure. Transmission data were used to normalize α deduced from PC.

Freeman and Paul [7] studied the transmission spectra of a-Si:H as a function of H content and substrate temperature. The samples were prepared by rf sputtering of a c-Si target in an Ar and H plasma. Corning 7059 glass was used as a substrate. The deposition rate was 1 Å/sec and the Ar pressure was 5×10^{-3} torr. The hydrogenated sample (22 at. %) shows a lower n for $h\nu$ between 0.04 and 0.50 eV; n decreases with increasing H pressure; n of a-Si and a-Si:H show very little $h\nu$ dependence for $h\nu < 0.5$ eV. Resonance effects due to Si–H vibrational modes are observed in n of a-Si:H. Here, n of a-Si:H is about 25% less than n of a-Si. The error in n is $\pm 4\%$. An increase in the H content in the film shifts the absorption edge to larger $h\nu$ and also causes a decrease of the density. Refractive indices are shown in Fig. 12 and are listed in Table XIV.

Brodsky and Lurio [8] measured the IR vibrational spectra of a-Si between 35 and 700 cm^{-1}. The absorption spectrum is interpreted in terms of a disorder-induced breakdown of the selection rules for vibronic transitions. Wedged c-Si substrates were used to suppress internal multiple-reflection effects in the substrate. Interference effects within the thin a-Si films are negligibly small because of the low reflection coefficient at the a-Si to c-Si interface (approximately 0.03). Extinction coefficients are shown in Fig. 12 and are listed in Table XIV.

Brown and Rustgi [9] studied the soft x-ray absorption spectra of a-Si. The spectrum for a-Si shows none of the detailed structure observed in c-Si. Extinction coefficients are shown in Fig. 12 and are listed in Table XIV.

Jackson and Amer [10] measured α at the absorption edge in a-Si:H down to $h\nu = 0.6$ eV by using the photothermal deflection spectroscopy (PDS), which measures directly the optical absorption and is insensitive to scattering. No optical constants are listed here, however.

Additional work is discussed by Chaleravertz and Kaplan [11].

REFERENCES

1. D. T. Pierce and W. E. Spicer, *Phys. Rev. B* **5**, 3017 (1972).
2. G. Weiser, D. Ewald, and M. Milleville, *J. Non-Cryst. Solids* **35/36**, 447 (1980).
3. M. H. Brodsky, R. S. Title, K. Weiser, and G. D. Pettit, *Phys. Rev. B* **1**, 2632 (1970).
4. P. J. Zanzucchi, C. R. Wronski, and D. E. Carlson, *J. Appl. Phys.* **48**, 5227 (1977).
5. G. Moddel, D. A. Anderson, and W. Paul, *Phys. Rev. B* **22**, 1918 (1980).
6. F. Evangelisti, P. Fiorini, G. Fortunato, A. Frova, C. Giovannella, and R. Peruzzi, *J. Non-Cryst. Solids* **55**, 191 (1983).

7. E. C. Freeman and W. Paul, *Phys. Rev. B* **20**, 716 (1979).
8. M. H. Brodsky and A. Lurio, *Phys. Rev. B* **9**, 1646 (1974).
9. F. C. Brown and O. P. Rustgi, *Phys. Rev. Lett.* **28**, 497 (1972).
10. B. Jackson and N. M. Amer, *Phys. Rev. B* **25**, 5559 (1982).
11. B. K. Chakravertz and D. Kaplan, *J. de Phys.* **42**, Colloque C-4 (1981).

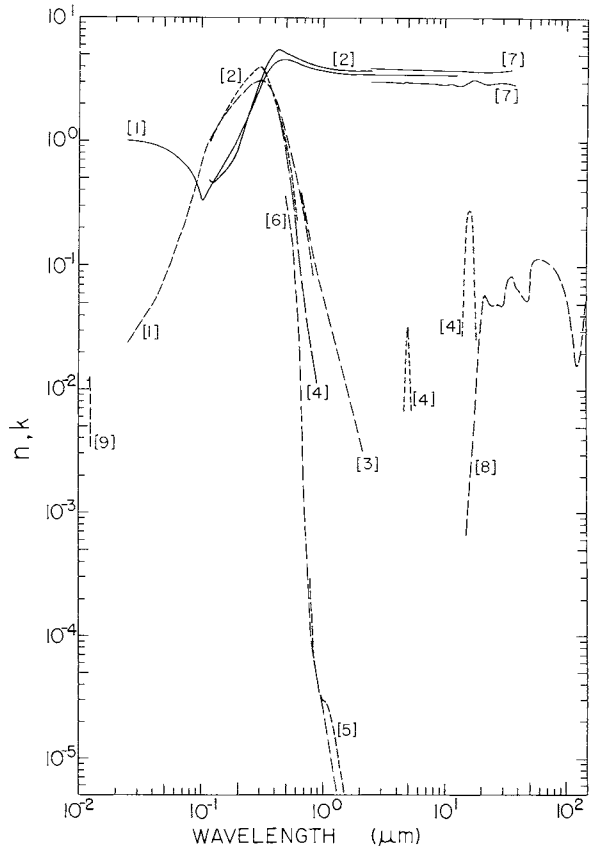

Fig. 12. Log–log plot of n (——) and k (– – – –) versus wavelength in micrometers for amorphous silicon. Various references are indicated in brackets.

TABLE XIV

Values of n and k for Amorphous Silicon Obtained from Various References[a]

eV	Å	cm^{-1}	n	k
105.0	118.1			1.16×10^{-2} [9]
104.5	118.6			1.13
103.9	119.3			1.12
103.1	120.2			1.11
102.6	120.8			1.11
102.0	121.5			1.13
101.7	122.0			1.14
101.3	122.4			1.16
101.0	122.8			1.19
100.8	123.0			1.22
100.6	123.2			1.23
100.5	123.4			1.19
100.45	123.43			1.12
100.4	123.5			1.05×10^{-2}
100.3	123.6			9.99×10^{-3}
100.2	123.7			9.99
100.1	123.9			9.94
99.93	124.1			9.03
99.83	124.2			7.40
99.72	124.3			5.78
99.68	124.4			4.57
99.45	124.7			3.68
99.13	125.1			3.42
98.86	125.4			3.37
50	248.0		0.995 [1]	2.35×10^{-2} [1]
49	253.0		0.992	2.42
48	258.3		0.990	2.50
47	263.8		0.988	2.58
46	269.5		0.986	2.67
45	275.5		0.984	2.75

(*continued*)

TABLE XIV (*Continued*)

Amorphous Silicon

eV	Å	cm^{-1}	n	k
44	281.8		0.981	2.85
43	288.3		0.979	2.94
42	295.2		0.976	3.04
41	302.4		0.973	3.14
40	310.0		0.970	3.26
39	317.9		0.967	3.37
38	326.3		0.963	3.50
37	335.1		0.959	3.64
36	344.4		0.955	3.79
35	354.2		0.950	3.95
34	364.7		0.945	4.13
33	375.7		0.939	4.33
32	387.5		0.933	4.55
31	400.0		0.926	4.80
30	413.3		0.918	5.08
29	427.5		0.909	5.41
28	442.8		0.899	5.79
27	459.2		0.888	6.23
26	476.9		0.876	6.75
25	495.9		0.862	7.37
24	516.6		0.846	8.12
23	539.1		0.828	9.03×10^{-2}
22	563.6		0.808	0.101
21	590.4		0.785	0.115
20	619.9		0.758	0.132
19	652.6		0.727	0.154
18	688.8		0.691	0.181
17	729.3		0.651	0.216
16	774.9		0.603	0.261
15	826.6		0.549	0.321
14	885.6		0.485	0.403
13	953.7		0.410	0.519

eV	μm	cm^{-1}	n	k	$n(H)$	$k(H)$	$k(H)$
12	0.1033		0.327	0.726			
11.5	0.1078		0.363	0.847			
11	0.1127		0.392	0.946			
10.5	0.1181		0.423	1.04	0.488 [2]	1.00 [2]	
10	0.1240		0.459	1.14	0.466	1.09	
9.5	0.1305		0.497	1.24	0.467	1.20	
9	0.1378		0.543	1.35	0.499	1.33	
8.5	0.1459		0.597	1.47	0.515	1.49	
8	0.1550		0.660	1.60	0.554	1.66	
7.5	0.1653		0.735	1.74	0.614	1.83	
7	0.1771		0.832	1.89	0.670	2.08	
6.5	0.1907		0.951	2.07	0.774	2.35	
6	0.2066	48,390	1.11	2.28	0.961	2.65	
5.5	0.2254	44,360	1.35	2.51	1.23	2.99	
5	0.2480	40,330	1.69	2.76	1.66	3.38	
4.8	0.2583	38,710	1.86	2.85			
4.6	0.2695	37,100	2.07	2.93			
4.5	0.2755	36,290			2.31	3.71	
4.4	0.2818	35,490	2.30	2.99			
4.2	0.2952	33,880	2.56	3.04			
4	0.3100	32,260	2.87	3.06	3.36	3.92	
3.8	0.3263	30,650	3.21	3.00			
3.6	0.3444	29,040	3.55	2.88			
3.5	0.3543	28,230	3.73	2.79	4.59	3.38	
3.4	0.3647	27,420	3.90	2.66			
3.2	0.3875	25,810	4.17	2.38			

(*continued*)

TABLE XIV (*Continued*)

Amorphous Silicon

eV	μm	cm^{-1}	n	k	$n(H)$	$k(H)$	$k(H)$
3.0	0.4133	24,200	4.38	2.02	5.43	2.19	
2.897	0.4279	23,370				1.80 [4]	
2.8	0.4428	22,580	4.47	1.64			
2.705	0.4584	21,820				1.40	
2.6	0.4769	20,970	4.49	1.28		0.850	
2.514	0.4932	20,280					0.367 [6]
2.500	0.4960	20,160	4.47	1.12	5.25	0.992 [2]	0.361
2.425	0.5112	19,560					0.288
2.4	0.5166	19,360	4.46	0.969			
2.382	0.5205	19,210				0.620 [4]	
2.318	0.5350	18,690					0.216
2.216	0.5596	17,870					0.175
2.205	0.5623	17,780				0.401	
2.20	0.5636	17,740	4.36	0.690			
2.100	0.5904	16,940				0.253	
2.090	0.5933	16,860					8.92×10^{-2}
2.009	0.6171	16,210				0.154	
2.0	0.6199	16,130	4.23	0.461	4.71	0.217 [2]	
1.970	0.6295	15,890					3.48×10^{-2}
1.907	0.6503	15,380				9.14×10^{-2} [4]	
1.9	0.6526	15,320	4.17	0.363			
1.857	0.6675	14,980					8.57×10^{-3}
1.856	0.6679	14,970		0.384 [3]			
1.804	0.6872	14,550				6.46	
1.8	0.6888	14,520	4.09	0.271 [1]			
1.770	0.7006	14,270					2.13
1.767	0.7016	14,250		0.310 [3]			

1.704	0.7275	13,750		0.251			
1.7	0.7293	13,710	4.01	0.199 [1]			
1.693	0.7323	13,660					6.57×10^{-4}
1.643	0.7546	13,250		0.221 [3]			
1.612	0.7694	13,000					2.32×10^{-4}
1.6	0.7749	12,900	3.93	0.136 [1]		2.37×10^{-2}	
1.581	0.7841	12,750		0.174 [3]			
1.533	0.8089	12,360				2.90×10^{-4} [5]	
1.526	0.8123	12,310					9.60×10^{-5}
1.514	0.8190	12,210				2.23	
1.513	0.8194	12,200		0.137			
1.5	0.8266	12,100	3.86	8.12×10^{-2} [1]	4.13		
1.498	0.8276	12,080				1.66×10^{-4}	
1.457	0.8509	11,750				7.99×10^{-5}	
1.440	0.8613	11,610					5.89
1.437	0.8631	11,590		0.110 [3]			
1.409	0.8799	11,360				5.45×10^{-5}	
1.4	0.8856	11,290	3.77	4.01×10^{-2} [1]			
1.397	0.8876	11,270				1.15×10^{-2} [4]	
1.363	0.9094	11,000		8.31 [3]			
1.357	0.9140	10,940				4.09×10^{-5} [5]	
1.333	0.9301	10,750					3.70
1.304	0.9505	10,520				3.41×10^{-5}	
1.3	0.9538	10,480	3.68				
1.291	0.9608	10,410		6.80			
1.290	0.9613	10,400				1.10×10^{-2} [4]	
1.262	0.9824	10,180				3.17×10^{-5} [5]	
1.243	0.9978	10,020					2.82
1.234	1.005	9,950		5.50			
1.211	1.024	9,764				2.94	
1.2	1.033	9,678	3.61				

(*continued*)

TABLE XIV (*Continued*)

Amorphous Silicon

eV	μm	cm^{-1}	n	k	$n(H)$	$k(H)$	$k(H)$
1.158	1.070	9,342				2.87	
1.137	1.090	9,172					1.69×10^{-5}
1.130	1.098	9,110		4.20			
1.114	1.113	8,988				2.57×10^{-5}	
1.1	1.127	8,872	3.57				
1.086	1.141	8,762				1.06×10^{-2} [4]	
1.062	1.167	8,567				2.06×10^{-5} [5]	
1.032	1.201	8,324					9.01×10^{-6}
1.023	1.211	8,254		2.86			
1.014	1.223	8,176				1.88	
1.0	1.240	8,065	3.54		3.83		
0.9649	1.285	7,782					6.08
0.9634	1.287	7,770				1.30×10^{-5}	
0.9286	1.335	7,489		1.99			
0.9160	1.354	7,388				9.88×10^{-6}	
0.90	1.378	7,259	3.50				
0.8870	1.398	7,154					3.70
0.8637	1.435	6,966				7.19	
0.8561	1.448	6,905		1.40×10^{-2}			
0.8637	1.435						
0.8159	1.520	6,581				4.87	
0.80	1.550	6,452	3.48				
0.7522	1.648	6,067		9.33×10^{-3}			
0.7035	1.762	5,674		6.88			
0.70	1.771	5,646	3.45				
0.6509	1.905	5,250		5.03			
0.6120	2.026	4,936		3.64			

0.60	2.066	4,839	3.44		
0.5647	2.196	4,555		2.85	
0.5014	2.473	4,044	3.88 [7]		
0.50	2.480	4,033			3.74
0.4920	2.520	3,968	3.87		
0.4918	2.521	3,966			2.99 [7]
0.4738	2.617	3,822			3.00
0.4718	2.628	3,805	3.86		
0.4538	2.732	3,660			2.99
0.4406	2.814	3,553	3.86		
0.4344	2.854	3,504			2.99
0.4202	2.951	3,389	3.85		
0.4146	2.990	3,344			3.00
0.3976	3.119	3,207	3.85		
0.3942	3.145	3,180			3.00
0.3777	3.282	3,047	3.84		
0.3751	3.305	3,026			2.99
0.3628	3.417	2,926	3.85		
0.3537	3.506	2,853			2.99
0.3458	3.586	2,789	3.84		
0.3337	3.716	2,691			2.99
0.3334	3.718	2,689	3.84		
0.3227	3.842	2,603	3.82		
0.3142	3.946	2,534			2.98
0.3093	4.008	2,495	3.84		
0.2948	4.206	2,377			2.98
0.2856	4.341	2,304	3.84		
0.2799	4.430	2,257	3.81		
0.2773	4.471	2,237			2.96
0.2702	4.589	2,179	3.81		
0.2664	4.654	2,149			2.93

(*continued*)

TABLE XIV (*Continued*)

Amorphous Silicon

eV	μm	cm^{-1}	n	k	$n(H)$	$k(H)$	$k(H)$
0.2654	4.672	2,140				6.63×10^{-3} [4]	
0.2629	4.716	2,120				1.02×10^{-2}	
0.2624	4.725	2,117			2.97		
0.2604	4.761	2,100				1.41	
0.2593	4.782	2,091				1.80	
0.2578	4.809	2,080				2.06	
0.2567	4.831	2,070				2.22	
0.2555	4.853	2,061				2.48	
0.2541	4.880	2,049				2.69	
0.2537	4.887	2,046	3.80				
0.2529	4.904	2,039				2.92	
0.2518	4.925	2,031				3.09	
0.2506	4.948	2,021			3.01		
0.2505	4.949	2,020				3.13	
0.2492	4.975	2,010				3.34	
0.2479	5.001	1,999				3.06	
0.2466	5.028	1,989				2.72	
0.2455	5.051	1,980				2.34	
0.2443	5.075	1,970				2.35	
0.2436	5.090	1,965			2.99		
0.2430	5.102	1,960				1.80	
0.2416	5.132	1,949				1.67	
0.2404	5.157	1,939				1.46×10^{-2}	
0.2379	5.211	1,919				9.66×10^{-3}	
0.2366	5.240	1,909				6.91	
0.2326	5.330	1,876	3.80				
0.2320	5.344	1,871			2.99		

0.2269	5.463	1,830	3.79		
0.2221	5.582	1,791		2.98	
0.2188	5.668	1,764	3.80		
0.2133	5.812	1,721		2.99	
0.2055	6.034	1,657	3.79		
0.2049	6.051	1,653		2.98	
0.1948	6.365	1,571		2.98	
0.1911	6.489	1,541	3.79		
0.1850	6.701	1,492		2.96	
0.1752	7.079	1,413	3.78		
0.1749	7.089	1,411		2.95	
0.1628	7.618	1,313		2.95	
0.1602	7.740	1,292	3.77		
0.1523	8.142	1,228		2.94	
0.1478	8.389	1,192	3.75		
0.1458	8.503	1,176		2.91	
0.1417	8.748	1,143	3.72		
0.1284	9.655	1,036	3.71		
0.1280	9.683	1,033		2.85	
0.1184	10.47	955.0	3.74		
0.1161	10.68	936.3		2.85	
0.1106	11.21	892.0	3.75		
0.1037	11.95	836.6		2.90	
0.1009	12.29	813.8	3.75		
0.09577	12.95	772.4	3.73		
0.09487	13.07	765.2		2.82	
0.08934	13.88	720.6			2.73×10^{-2}
0.08801	14.09	709.9			4.31
0.08795	14.10	709.3	3.73		
0.08792	14.10	709.1		2.80	
0.08666	14.31	698.9			6.85

(*continued*)

TABLE XIV (*Continued*)

Amorphous Silicon

eV	μm	cm^{-1}	n	k	$n(H)$	$k(H)$	$k(H)$
0.08567	14.47	690.9				9.82×10^{-2}	
0.08438	14.69	680.6				0.153	
0.08323	14.90	671.3				0.201	
0.08180	15.16	659.8				0.246	
0.08086	15.33	652.1				0.266	
0.08066	15.37	650.6		6.72×10^{-4} [8]			
0.07957	15.58	641.7				0.277	
0.07895	15.70	636.8	3.73				
0.07846	15.80	632.8				0.283	
0.07691	16.12	620.3				0.277	
0.07574	16.37	610.9				0.254	
0.07439	16.67	600.0				0.204	
0.07411	16.73	597.7	3.67	2.83×10^{-3}			
0.07318	16.94	590.2				0.193	
0.07203	17.21	580.9				0.151	
0.07171	17.29	578.4		4.43			
0.07066	17.55	569.9				7.08×10^{-2}	
0.06995	17.72	564.2		6.98×10^{-3}			
0.06935	17.88	559.3				3.19	
0.06908	17.95	557.1	3.62				
0.06811	18.21	549.3				2.52	
0.06808	18.21	549.1		1.06×10^{-2}			
0.06764	18.33	545.6			3.12		
0.06717	18.46	541.7		1.49			
0.06625	18.72	534.3		1.90			
0.06553	18.92	528.5		2.27			
0.06475	19.15	522.2		2.68			

0.06421	19.31	517.8		3.09	
0.06345	19.54	511.7		3.46	
0.06316	19.63	509.4		3.92	
0.06263	19.80	505.1		4.21	
0.06157	20.14	496.5		4.85	
0.06079	20.40	490.3		5.37	
0.05996	20.68	483.6			2.94
0.05953	20.83	480.2	3.62		
0.05917	20.95	477.2		5.94	
0.05745	21.58	463.4		5.76	
0.05657	21.92	456.3		5.47	
0.05531	22.42	446.1		5.20	
0.05385	23.03	434.3		5.02	
0.05318	23.32	428.9			2.87
0.05226	23.73	421.5	3.62		
0.05009	24.75	404.0		4.91	
0.04595	26.98	370.6		5.03	
0.04496	27.57	362.7	3.68		
0.04385	28.27	353.7		4.84	
0.04242	29.23	342.1		4.74	
0.04232	29.30	341.3		4.82	
0.04209	29.46	339.5			2.96
0.04083	30.36	329.3		5.56	
0.04028	30.78	324.9		6.16	
0.04005	30.96	323.0		6.77	
0.03762	32.96	303.4		7.86	
0.03642	34.05	293.7		8.24	
0.03491	35.52	281.5	3.74		
0.03404	36.42	274.6		7.99	
0.03311	37.44	267.1		7.45	
0.03261	38.03	263.0		6.83	

(*continued*)

TABLE XIV (*Continued*)

Amorphous Silicon

eV	μm	cm^{-1}	n	k	$n(H)$	$k(H)$	$k(H)$
0.03178	39.02	256.3			2.78		
0.03132	39.59	252.6		6.53			
0.03084	40.21	248.7		6.38			
0.02981	41.60	240.4		6.13			
0.02833	43.77	228.5		5.66			
0.02568	48.27	207.2		5.23			
0.02494	49.71	201.2		7.22			
0.02481	49.98	200.1		7.30			
0.02470	50.20	199.2		8.51			
0.02454	50.53	197.9		9.45×10^{-2}			
0.02333	53.14	188.2		0.110			
0.02078	59.66	167.6		0.114			
0.01884	65.82	151.9		0.112			
0.01725	71.86	139.2		0.104			
0.01565	79.25	126.2		9.63×10^{-2}			
0.01476	84.01	119.0		8.62			
0.01382	89.69	111.5		7.27			
0.01313	94.46	105.9		6.21			
0.01208	102.6	97.44		4.43			
0.01127	110.0	90.90		2.86			
0.01023	121.2	82.54		1.57			
0.009225	134.4	74.41		2.97			
0.008818	140.6	71.12		5.63			
0.008396	147.7	67.72		8.16			

[a] Values of n and k, obtained from various references indicated in brackets. Note the distinction between a-Si and a-Si:H data.

Silicon Carbide (SiC)

W. J. CHOYKE
Westinghouse Research and Development Center
and University of Pittsburgh
Pittsburgh, Pennsylvania

EDWARD. D. PALIK
Naval Research Laboratory
Washington, D.C.

The most widely studied polytype of this material is denoted as SiC II or 6H SiC. We list only room-temperature results for it in Table XV. The samples often used are in the form of hexagonal platelets as indicated in the inset of Fig. 13, with the c axis perpendicular to the surface. Thus, a normal-incidence transmission or reflection experiment measures the ordinary (o) ray properties. A prism cut in the manner shown is often used to determine both n_o and n_e (e for extraordinary ray). A slice parallel to the c axis is used to measure transmission and reflection of both polarizations.

The UV–visible data are a combination of the work of Rehn *et al.* [1] from 25 to 13 eV and Leveque and Lynch [2] from 30 to 3 eV. In Rehn *et al.* [1] samples were single crystals heated to 700°C for 30 min before etching in concentrated HF acid for 10 min. The sample was mounted in an absolute reflectometer and reflectance was measured at five angles of incidence (15°, 30°, 45°, 60°, 75°). The p-polarized reflectance was generally measured.

The absolute accuracy in R was quoted as ± 0.03. Analysis of the data finally yielded n and k, although it was not stated whether this was o or e or a mixture. These results are in good agreement with results of Leveque and Lynch [2], who utilized reflectivity of synchrotron radiation and Kramers–Kronig analysis. We quote the data of Leveque and Lynch [2] to three figures, although even two significant figures is probably generous.

At lower energy (4.75–3.2 eV) the band-edge absorption has been measured by Choyke and Patrick [3], who used hexagonal platelets. Thus, they measured k_o. Samples of thickness 3.6–200 μm were unsupported, while thinner ones were prepared by grinding and polishing samples glued to Suprasil II substrates. This work was undertaken to reveal direct and indirect

Copyright © 1985 by Academic Press, Inc.
All rights of reproduction in any form reserved.
ISBN 0-12-544420-6

transitions in the absorption edge that are not obvious from the data plotted in Fig. 13.

At lower energy the band-edge region has been studied by Groth and Kauer [4], who determined the temperature dependence of the ordinary absorption coefficient. We use their 20°C = 293 K for k_o as read from a graph in the region 3.12–2.5 eV. At still lower energy in the IR, they measured free-carrier absorption as a function of temperature. This absorption is evident at the low-energy side of the band edge.

Note that the Leveque and Lynch [2] values for k are too large near 3 μm by factors of 2, this points out that transmission measurements of k (where feasible) generally give better values than reflectivity analyses.

In the transparent region just below the band edge, measurements of n have typically been done with minimum-deviation prisms or plates exhibiting interference fringes. A typical prism (see insert of Fig. 13) is cut from a hexagonal plate so that the c axis is parallel to the prism apex edge. Then, both o ($E \perp c$) and e ($E \parallel c$) polarization can be used. Thibault [5] measured n_o and n_e at several wavelengths of H, Na, and Hg. Shaffer [6] fitted his data with the formulas

$$n_o = A' + (B'/\lambda_2), \qquad n_e = A + (B/\lambda_2),$$

with $A' = 2.5531$, $B' = 0.0334 \times 10^6$, $A = 2.5852$, and $B = 0.0368 \times 10^6$ and with wavelength λ in nanometers. The birefringence can, of course, be obtained from these results. Accuracy in n was limited by the estimated error of <1 min of angle to be <0.001.

Choyke and Patrick [7] measured n_o by utilizing interference fringes formed by their plates with the c axis perpendicular to the surface. They fitted their data with the formula

$$n_o^2 - 1 = 5.52/[1 - (h\nu/7.53)^2],$$

with $h\nu$ given in electron volts for the range 4–0.5 eV. These data are listed in Table XV for 20°C.

Spitzer *et al.* [8] have measured the absorption coefficient α_o from 2 to 10 μm by using plates. The samples were green in color with a resistivity greater than $\sim 1\ \Omega$ cm, although the individual resistivities were not specified.

Their results for several samples showed free-carrier absorption, and we chose the data for the weakest absorbing sample. While they measured both o and e absorption, there were no significant differences, so we give k_o.

Spitzer *et al.* [8, 9] also measured the reststrahlen reflection in the 2–22-μm region for o and e polarization. They fitted the reflection with an oscillator model of the form

$$(n - ik)^2 = \varepsilon = \varepsilon_\infty \left[1 + \frac{\omega_L^2 - \omega_T^2}{\omega_T^2 - \omega^2 + i\Gamma\omega} \right],$$

with $\omega_L = 969\ cm^{-1}$, $\omega_T = 793\ cm^{-1}$, $\Gamma = 4.76\ cm^{-1}$, and $\varepsilon_\infty = 6.7$ for the ordinary ray. We list the calculated n_o and k_o. While they also fitted the reflectance for the extraordinary ray, the numbers are very similar, and we are not sure whether the differences are very meaningful. Their experiment was not precise enough to give different values for $\varepsilon_{\infty o}$ and $\varepsilon_{\infty e}$ either. With all the shortcomings of the oscillator model, we still list n_o, k_o but caution that the numbers are probably uncertain in the first significant figure at least in the vicinity of ω_T.

The static dielectric constant has been measured at 20 K to be 10.2 ± 0.2 in the 1–100-kHz region, although conducting samples were a problem [10]. From an analysis of published data using the Lyddane–Sachs–Teller relation, $\varepsilon_o = \varepsilon_\infty(\omega_L/\omega_T)^2$, Patrick and Choyke [11] get $\varepsilon_\infty(\perp, o) = 6.52$, $\varepsilon_\infty(\parallel, e) = 6.70$ and $\varepsilon_s(\perp, o) = 9.66$, $\varepsilon_s(\parallel, e) = 10.03$ at room temperature.

REFERENCES

1. V. Rehn, J. L. Stanford, and V. O. Jones, *Proc. Int. Conf.* Phys. *Semicond., 13th*, Rome, *1976* (F. G. Fumi, ed.), p. 985. Typografia Marves, Rome, 1976.
2. G. Leveque and D. A. Lynch, private communication (1982).
3. W. J. Choyke and L. Patrick, *Phys. Rev.* **172**, 769 (1968).
4. R. Groth and E. Kauer, *Phys. Status Solidi* **1**, 445 (1961).
5. N. W. Thibault, *Am. Mineral.* **29**, 327 (1944).
6. P. T. B. Shaffer, *Appl. Opt.* **10**, 1034 (1971).
7. W. J. Choyke and L. Patrick *J. Opt. Soc. Am.* **58**, 377 (1968).
8. W. G. Spitzer, D. A. Kleinman, C. J. Frosch, and D. J. Walsh, *in* "Silicon Carbide, A High Temperature Semiconductor" (J. R. O'Connor and J. Smiltens, eds.), p. 347. Pergamon, New York, 1960.
9. W. G. Spitzer, D. Kleinman, and D. Walsh, *Phys. Rev.* **113**, 127 (1959).
10. D. Hofman, J. A. Lely, and J. Volger, *Physica* **23**, 236 (1957).
11. L. Patrick and W. J. Choyke, *Phys. Rev. B* **2**, 2255 (1970).

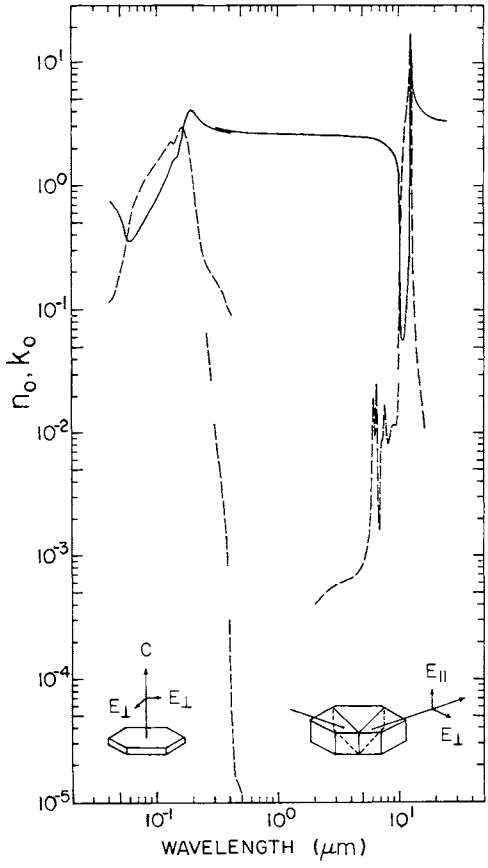

Fig. 13. Log–Log plot of n_o (——) and k_o (– – – –) versus wavelength in micrometers for silicon carbide. Typical sample orientations are shown in the insets.

TABLE XV

Values of n_o and k_o for Silicon Carbide Obtained from Various References[a]

eV	cm^{-1}	μm	n_o	k_o	n_e
30.0		0.04133	0.739 [1, 2]	0.114 [1, 2]	
29.1		0.04261	0.718	0.115	
28.2		0.04397	0.689	0.123	
27.6		0.04492	0.670	0.132	
27.0		0.04592	0.650	0.143	
26.4		0.04696	0.630	0.156	
26.1		0.04750	0.621	0.163	
25.5		0.04862	0.601	0.177	
25.1		0.04940	0.587	0.186	
24.5		0.05061	0.562	0.200	
24.1		0.05145	0.543	0.209	

TABLE XV (*Continued*)

Silicon Carbide

eV	cm^{-1}	μm	n_o	k_o	n_e
23.5		0.05276	0.505	0.225	
23.1		0.05367	0.474	0.243	
22.5		0.05510	0.424	0.285	
22.1		0.05610	0.392	0.326	
21.5		0.05767	0.360	0.402	
21.1		0.05876	0.348	0.481	
20.5		0.06048	0.347	0.532	
20.1		0.06168	0.349	0.581	
19.5		0.06358	0.359	0.653	
19.1		0.06491	0.369	0.699	
18.5		0.06702	0.387	0.766	
18.1		0.06850	0.401	0.810	
17.5		0.07085	0.424	0.873	
17.1		0.07251	0.438	0.915	
16.5		0.07514	0.461	0.983	
15.9		0.07798	0.490	1.05	
15.5		0.07999	0.512	1.10	
15.1		0.08211	0.536	1.15	
14.5		0.08551	0.574	1.23	
14.1		0.08793	0.602	1.28	
13.5		0.09184	0.649	1.36	
13.1		0.09465	0.681	1.41	
12.5		0.09919	0.729 [2]	1.51 [2]	
12.1		0.1025	0.769	1.58	
11.5		0.1078	0.844	1.71	
11.1		0.1117	0.909	1.80	
10.95		0.1132	0.937	1.84	
10.80		0.1148	0.969	1.88	
10.65		0.1164	1.00	1.92	
10.45		0.1186	1.05	1.97	
10.25		0.1210	1.11	2.03	
10.05		0.1234	1.18	2.08	
9.9		0.1252	1.23	2.13	
9.7		0.1278	1.33	2.19	
9.5		0.1305	1.46	2.21	
9.3		0.1333	1.56	2.18	
9.0		0.1378	1.60	2.15	
8.8		0.1409	1.61	2.19	
8.6		0.1442	1.63	2.26	
8.4		0.1476	1.66	2.39	
8.2		0.1512	1.77	2.57	
8.0		0.1550	1.99	2.73	
7.8		0.1590	2.27	2.82	
7.6		0.1631	2.59	2.87	
7.5		0.1653	2.78	2.85	
7.35		0.1687	3.04	2.74	

(*continued*)

TABLE XV (*Continued*)

Silicon Carbide

eV	cm^{-1}	μm	n_o	k_o	n_e
7.15		0.1734	3.33	2.55	
7.0		0.1771	3.51	2.38	
6.8		0.1823	3.69	2.17	
6.6		0.1879	3.97	1.88	
6.4		0.1937	4.05	1.42	
6.2		0.2000	3.96	1.06	
6.0	48,390	0.2066	3.83	0.803	
5.8	46,780	0.2138	3.68	0.609	
5.6	45,170	0.2214	3.54	0.464	
5.4	43,550	0.2296	3.39	0.367	
5.2	41,940	0.2384	3.27	0.304	
5.0	40,330	0.2480	3.16	0.259	
4.75	38,310	0.2610		6.58×10^{-2} [3]	
4.7	37,910	0.2638		5.85	
4.65	37,500	0.2666		5.16	
4.6	37,100	0.2695		4.57	
4.55	36,700	0.2725		4.13	
4.5	36,290	0.2755		3.73×10^{-2}	
			2.96	0.203 [2]	
4.45	35,890	0.2786		3.35×10^{-2} [3]	
4.4	35,490	0.2818		3.02	
4.35	35,080	0.2850		2.72	
4.1	33.070	0.3024		1.18×10^{-2}	
4.0	32,260	0.3100		9.48×10^{-3}	
			2.85	0.174 [2]	
			2.948 [7]		
3.9	31,460	0.3179	2.923	7.65×10^{-3} [3]	
3.8	30,650	0.3263	2.899	5.98	
3.7	29,840	0.3351	2.877	4.93	
3.6	29,040	0.3444	2.856	3.75	
3.5	28,230	0.3542	2.836	2.89	
3.4	27,420	0.3647	2.817	2.04×10^{-3}	
			2.76 [2]	0.119 [2]	
3.3	26,600	0.3757	2.799 [7]	1.38×10^{-3} [3]	
3.2	25,810	0.3875	2.781	8.39×10^{-4} [4]	
3.12	25,160	0.3974		3.00×10^{-4} [4]	
3.10	25,000	0.4000	2.765	1.91	
3.08	24,840	0.4025		1.19×10^{-4}	
3.06	24,680	0.4052		8.06×10^{-5}	
3.04	24,520	0.4078		6.49	
3.02	24,360	0.4105		5.39	
3.0	24,200	0.4133	2.750	4.44×10^{-5}	
			2.69 [2]	0.090 [2]	
2.98	24,040	0.4161		3.74×10^{-5} [4]	
2.96	23,870	0.4189		3.33	
2.94	23,710	0.4217		2.82	
2.92	23,550	0.4246		2.53	

TABLE XV (*Continued*)

Silicon Carbide

eV	cm^{-1}	μm	n_o	k_o	n_e
2.90	23,390	0.4275		2.31	
2.85	22,990	0.4350		1.87	
2.845	22,950	0.4358	2.7305 [5]		2.7824 [5]
2.8	22,580	0.4428		1.55	
2.7	21,780	0.4592		1.46	
2.655	21,410	0.467	2.7074 [6]		2.7553 [6]
2.6	20,970	0.4769		1.37	
2.5	20,160	0.4959	2.684 [7]	1.18×10^{-5}	
2.490	20,080	0.498	2.6870 [6]		2.7331 [6]
2.407	19,420	0.515	2.6789		2.7236
2.270	18,310	0.5461	2.6631 [5]		2.7064 [5]
2.183	17,610	0.568	2.6557 [6]		2.6979 [6]
2.145	17,300	0.5781	2.6511 [5]		2.6933 [5]
2.105	16,980	0.589	2.6488 [6]		2.6911 [6]
2.103	16,960	0.5895	2.6475 [5]		2.6889 [5]
2.013	16,230	0.616	2.6411 [6]		2.6820 [6]
2.0	16,130	0.6199	2.634 [7]		
1.889	15,240	0.6563	2.6296 [5]		2.6696 [5]
1.794	14,470	0.691	2.6243 [6]		2.6639 [6]
1.5	12,100	0.8266	2.598 [7]		
1.0	8,065	1.248	2.573		
0.6199	5,000	2	2.572 [8]	3.98×10^{-4} [8]	
0.5579	4,500	2.222	2.568		
0.5	4,033	2.480	2.558 [7]		
0.4959	4,000	2.5	2.562 [8]	5.17	
0.4339	3,500	2.857	2.554		
0.4133	3,333	3.0		5.73	
0.4	3,226	3.100	2.556 [7]		
0.3720	3,000	3.333	2.540 [8]		
0.3542	2,857	3.5		6.13	
0.3100	2,500	4.0	2.516	6.37	
0.3	2,420	4.133	2.555 [7]		
0.2755	2,222	4.5		7.16	
0.2480	2,000	5.0	2.467 [8]	8.75	
0.2384	1,923	5.2		9.93×10^{-4}	
0.2356	1,900	5.263	2.450		
0.2296	1,852	5.4		1.16×10^{-3}	
0.2232	1,800	5.556	2.430		
0.2214	1,786	5.6		1.56	
0.2138	1,724	5.8		2.68	
0.2108	1,700	5.882	2.404		
0.2066	1,667	6.0		6.21×10^{-3}	
0.2033	1,639	6.1		1.46×10^{-2}	
0.2000	1,613	6.2		1.92	
0.1984	1,600	6.250	2.372		
0.1968	1,587	6.3		9.53×10^{-3}	

(*continued*)

TABLE XV (*Continued*)

Silicon Carbide

eV	cm^{-1}	μm	n_o	k_o	n_e
0.1937	1,563	6.4		1.02×10^{-2}	
0.1907	1,538	6.5		2.59	
0.1879	1,515	6.6		2.10×10^{-2}	
0.1860	1,500	6.667	2.328		
0.1851	1,493	6.7		3.20×10^{-3}	
0.1823	1,471	6.8		1.62	
0.1797	1,449	6.9		3.07	
0.1771	1,429	7.0		5.57	
0.1746	1,408	7.1		7.91	
0.1736	1,400	7.143	2.267		
0.1722	1,389	7.2		8.59	
0.1698	1,370	7.3		8.71×10^{-3}	
0.1675	1,351	7.4		1.06×10^{-2}	
0.1653	1,333	7.5		1.43	
0.1631	1,316	7.6		1.69	
0.1612	1,300	7.692	2.178		
0.1610	1,299	7.7		1.59	
0.1590	1,282	7.8		1.24×10^{-2}	
0.1569	1,266	7.9		9.43×10^{-3}	
0.1550	1,250	8.0		8.28	
0.1512	1,220	8.2		7.96	
0.1488	1,200	8.333	2.034		
0.1476	1,190	8.4		8.96×10^{-3}	
0.1442	1,163	8.6		1.03×10^{-2}	
0.1409	1,136	8.8		1.11	
0.1378	1,111	9.0		1.15	
0.1364	1,100	9.091	1.768		
0.1348	1,087	9.2		1.16	
0.1339	1,080	9.259	1.684		
0.1319	1,064	9.4		1.14	
0.1314	1,060	9.434	1.581		
0.1292	1,042	9.6		1.15	
0.1289	1,040	9.615	1.453		
0.1265	1,020	9.8	1.286	1.40	
0.1240	1,000	10.0		2.55	
			1.051	3.4 [8]	
0.1227	990	10.10	0.888	4.5	
0.1215	980	10.20	0.663	6.7×10^{-2}	
0.1203	970	10.31	0.274	0.18	
0.1190	960	10.42	0.0872	0.63	
0.1178	950	10.53	0.0663	0.95	
0.1165	940	10.64	0.0593	1.21	
0.1153	930	10.75	0.0569	1.45	
0.1141	920	10.87	0.0569	1.69	
0.1128	910	10.99	0.0587	1.93	
0.1116	900	11.11	0.0621	2.18	
0.1103	890	11.24	0.0672	2.45	

TABLE XV (*Continued*)

Silicon Carbide

eV	cm^{-1}	μm	n_o	k_o	n_e
0.1091	880	11.36	0.0746	2.75	
0.1079	870	11.49	0.0850	3.08	
0.1066	860	11.63	0.0999	3.47	
0.1054	850	11.76	0.122	3.93	
0.1041	840	11.90	0.156	4.51	
0.1029	830	12.05	0.215	5.27	
0.1023	825	12.12	0.262	5.77	
0.1017	820	12.20	0.332	6.38	
0.1010	815	12.27	0.443	7.18	
0.1004	810	12.35	0.639	8.27	
0.09981	805	12.42	1.05	9.93	
0.09919	800	12.50	2.22	12.8	
0.09857	795	12.58	8.74	18.4	
0.09795	790	12.66	17.7	6.03	
0.09733	785	12.74	12.7	1.76	
0.09671	780	12.82	10.3	0.868	
0.09609	775	12.90	8.91	0.531	
0.09547	770	12.99	8.00	0.364	
0.09485	765	13.07	7.35	0.268	
0.09423	760	13.16	6.86	0.208	
0.09299	750	13.33	6.16	0.136	
0.09175	740	13.51	5.68	9.7×10^{-2}	
0.09051	730	13.70	5.32	7.4	
0.08927	720	13.89	5.05	5.8	
0.08803	710	14.08	4.83	4.7	
0.08679	700	14.29	4.65	3.9	
0.08059	650	15.38	4.09	1.8	
0.07439	600	16.67	3.80	1.1	
0.06819	550	18.18	3.61		
0.06199	500	20.00	3.49		
0.05579	450	22.22	3.40		
0.04959	400	25.00	3.34		

[a] References are indicated in brackets.

Zinc Sulfide (ZnS)

EDWARD D. PALIK and A. ADDAMIANO
Naval Research Laboratory
Washington, D.C.

Natural ZnS The complete phase diagram of the system Zn–S is not known [1–3]. Natural crystal forms include zinc blende (also called sphalerite), and wurtzite. Zinc blende (cubic, space group $F\bar{4}3m$) is the prototype of the B-3 structure [4] (see inset of Fig. 14). Wurtzite (hexagonal, space group C6mc) is the prototype of the B-4 structure [5] (see inset of Fig. 15). Other crystal modifications of natural zinc sulfide are known [6–8]. Substantial amounts of impurities are usually found in zinc sulfide minerals, the principal one being iron. Other common impurities include Cu, Ag, Pb, K, Na, Ga, Hg, Cd, In, Tl, As, Ni, Cr, Ca, Co, Mn, Sn, Ge, and rare earths[9]. These impurities affect the body color of the minerals [10]. The purest crystals are rarely colorless, usually having a light yellow body color [9, 10]. White zinc blende from Franklin, New Jersey, and from Nordmark, Sweden, was named cleiophane [9]. Natural ZnS crystals usually have hydrothermal or metamorphic origin [11].

Synthetic ZnS A variety of techniques have been developed to obtain large, well-formed, high-purity crystals. These include different "evaporation" or "sublimation" techniques, the high-pressure growth from molten ZnS, hydrothermal techniques, growth from solution, and so on. In addition, thin-layer ZnS coatings on a variety of substrates and sintered hot-pressed polycrystalline ZnS windows (IRTRAN 2 in the USA and KO-2 in the USSR) are being routinely produced for a variety of applications. Owing to differences in composition, their preparative methods, and/or history, all these materials differ somewhat in their physical properties. The differences derive from changes in the impurity background and from changes in the crystal structure. It must be stressed, in particular, that x-ray diffraction work on crystals grown by sublimation has shown that ZnS, like SiC, exists in a very large number of related crystal modifications, usually referred to as polytypes. Alexander *et al.* [12], for instance, observed about 150 new polytypes in their crystals. Approximately a total of some 200 polytypes have been characterized by x-ray diffraction [13–19]. Oftentimes, many polytypes

HANDBOOK OF OPTICAL CONSTANTS OF SOLIDS ISBN 0-12-544420-6

coexist side by side in minute needles or small plates. Since the preparative method, as well as the history (e.g., cooling rate) of a crystal may influence the fine structure of the material, it is not too surprising to read that the same growing procedure often resulted in different crystals [20]. The optical properties of all the ZnS polytypes have not been measured. The available data are limited to crystals with the zinc blende and the wurtzite structure to thin layers and to sintered ZnS (IRTRAN 2).

Cubic ZnS Data We shall discuss the data for cubic ZnS, starting in the x-ray region and working to longer wavelength. Because of the success of the model of Henke *et al.* [21] for calculating optical constants in the x-ray region (6–124 Å), we have included n and k results for ZnS (see the discussion by Lynch and Hunter on metals in this handbook). No attention is paid to the crystal structure, and the data should hold for any form of ZnS, except for scaling the density. The agreement with experimental data [22] in the small overlap region (85–124 Å) encourages us. These results, listed in Table XVI and plotted in Fig. 14, show the characteristic absorption edges due to the Zn and S atoms.

Cardona and Haensel [22] reported the absorption spectra of evaporated thin films in the 150–60-eV region. The experiments were performed by using the Deutsches Elektron Synchrotron (DESY) facility at Hamburg, Germany. The samples were prepared by vacuum deposition at pressures of about 10^{-6} torr *in situ* and *ex situ*. The substrates were carbon films supported by a copper grid and were kept at room temperature during evaporation. While the polycrystallinity of the samples was not discussed, there should be no essential differences between zinc blende and wurtzite spectra. We list k in Table XVI. A double peak in k at 135 Å is suggested to be due to transitions of electrons from 3p levels of Zn into conduction band states.

Hunter [23] has interpolated between 124 and 160 Å to provide the data listed there. Hunter *et al.* [24] and Cox *et al.* [25] measured the near-normal-incidence reflectance between 160 and 2200 Å of films vacuum-deposited onto glass. The ZnS was evaporated by using radiant heat. Kramers–Kronig (KK) analysis yielded the n and k values listed in Table XVI. The polycrystallinity of this material was not discussed in detail. However, the interband transitions in the 0.15-μm region are not nearly as sharp as those obtained by Cardona and Harbecke [26] with bulk crystals, suggesting some structure-related differences. In this experiment cubic crystals were freshly cleaved prior to measurement. Below 6 eV the measurements were done with a 50-cm Bausch and Lomb grating spectrometer. At higher photon energies a 1-m Jarrell–Ash vacuum UV spectrometer was used in windowless operation. The reflectivity was analyzed by the KK method. We list n and k from 20 to 2 eV. Reflectivity was measured between 25 and 4 eV and KK analyzed by Balkanski and Petroff [27], also.

While the KK analysis gives values of k at the absorption edge, we cannot trust these over direct transmission measurements such as given by Czyzak

et al. [20]. As mentioned previously, the color of different ZnS samples varies owing to impurity absorption near the band edge and to structure differences. We have chosen one of the synthetic crystals of low absorption measured by Czyzak *et al.* [20] and tabulated its k. These values are much smaller than those obtained from the KK analysis.

The optical constants of thin evaporated films were also obtained by Khawaja and Tomlin [28] from measurements of reflectance and transmittance at normal incidence as suggested by Denton *et al.* [29]. The films of thickness 50 to 300 nm were prepared on quartz substrates at room temperture and 180°C in the form of wedges of 3° angle, by evaporation from an aluminum crucible heated by an external tungsten wire coil in a vacuum of 10^{-5} torr. The films were predominantly cubic crystallites with a small proportion of the hexagonal phase. It was stressed by Khawaja and Tomlin [28] that surface roughness, clearly visible by electron microscopy of Pd-shadowed carbon replicas of the surface, must be taken into account in an interpretation of the data. Results were similar to Czyzak *et al.* [20, 30].

Refractive-index measurements of sphalerite crystals were made over a century ago. These early determinations have been reviewed by Mellor [31] and Gmelin [32]. Routinely, the crystals were described as having a light yellow body color. The refractive index was found to increase with iron content [32]. Mell [33] has measured the refractive indices of 0 and 20°C between 0.4 and 0.8 μm, fitting the data with a dispersion formula. He also fitted the temperature dependence with an empirical formula.

Bond [34] reported refractive index measurements of a zinc blende from Spain that were "not transparent beyond 2.4 μm." He used the minimum-deviation method. His data were fitted by Pikhtin and Yas'kov [35] with a detailed dispersion formula with agreement to one unit in the third decimal place. We list these calculated values in Table XVI along with extrapolation to longer wavelengths.

DeVore [36] reported room-temperature values of the refractive index of a sphalerite prism made from a "clear, water-like natural crystal." The deviation of the mercury light was measured by a photographic technique from 3650 to 15,296 Å. The data were fitted with the dispersion formula

$$n^2 = 5.164 + (1.208 \times 10^7)/(\lambda^2 - 0.732 \times 10^7). \quad (1)$$

Czyzak *et al.* [30] measured the room-temperature refractive index of sublimation-grown "cubic" ZnS by using the prism method. The data from 4000 to 14,000 Å were fitted with the formula

$$n^2 = 5.131 + (1.275 \times 10^7)/(\lambda^2 - 0.732 \times 10^7) \quad (2)$$

and are in good agreement with DeVore's data [36] for natural zinc blende.

The refractive index of sputtered and evaporated films was reported by Burgiel *et al.* [37] in the 4–1-eV region. The data are in close agreement with results of Hall [38] on vacuum-evaporated ZnS deposited on quartz.

In the infrared region, the three- and two-phonon absorption was measured by Klein and Donadio [39] at an unspecified room temperature. Their samples were grown by chemical vapor deposition but were not characterized except as cubic. It is not obvious whether their thin sample ($t = 0.018$ cm) for the two-phonon region (700–400 cm^{-1}) was on a substrate, so we do not calculate the absorption coefficient from their transmission data. For the three-phonon region (1000–750 cm^{-1}), the sample was 1.59 cm thick. Assuming that it was not on a substrate and using the reflectivity as calculated from the n's in Table XVI, we determined k and listed it in Table XVI.

Deutsch [40] measured the room-temperature transmission of crystals from Czyzak *et al.* [20] and a sample grown elsewhere [41] that had fewer stacking faults. The spectra in the two-phonon region were similar except that the sample of Nitsche [41] had a weak additional band at 19 μm. We list Deutsch's k values in Table XVI. Kwasniewski *et al.* [42] have measured absorption in the 800–200-cm^{-1} region to locate phonon peaks, but they give no values for absorption coefficient.

The reflectance was measured in the reststrahlen region (15–34 μm) and fitted with an oscillator model by Deutsch [40]. However, we have selected the more recent data of Manabe *et al.* [43]. They measured the reflectance at a 12° angle of incidence from 20 to 100 μm with a grating spectrometer at 300 K. The cubic sample was mechanically polished. Reflectivity was determined by using an aluminum mirror standard and was quoted to $\pm 1\%$. The reflectivity was fitted with an oscillator model to determine n and k with the formulas

$$R = [(n-1)^2 + k^2]/[(n+1)^2 + k^2] \tag{3}$$

and

$$(n - ik)^2 = \varepsilon_\infty \left[1 + \frac{\omega_L^2 - \omega_T^2}{\omega_T^2 - \omega^2 + i\Gamma\omega} \right], \tag{4}$$

with $\varepsilon_\infty = 5.7$, $\omega_T = 282\ cm^{-1}$, $\omega_L = 352\ cm^{-1}$, and $\Gamma = 6.77\ cm^{-1}$. The resulting n and k are listed in Table XVI.

At still-longer wavelengths (133–666 μm) Hattori *et al.* [44] studied the refractive index and absorption of ZnS crystals grown by the Bridgman method under high temperature and high pressure. These were described as of "mixed cubic and hexagonal type." The deviation of the surface flatness was smaller than 0.4%. The measurements were made at 300, 80, and 2 K with an evacuated Michelson interferometer coupled to a germanium bolometer through a light-pipe system. The refractive index was obtained from analysis of transmission interference maxima. We list values of n and k in Table XVI for 300 K.

Hexagonal ZnS Data The data for the wurtzite crystal are much sparser. Cardona and Harbecke [26] measured the reflectivity at 298 K of cleaved samples in the spectral region 11–2 eV and performed the KK analysis. They used polarized light (produced by reflection from LiF) to determine both

R_o ($E \perp c$) and R_e ($E \| c$). Significant differences were noted. In Table XVII we list their data for n_o, k_o and n_e, k_e as read from a graph and plot them in Fig. 15. Similar results were obtained by Freeouf [45] and Balkanski and Petroff [27]. Baars [46] also measured the reflectivity of several polytypes. Ebina *et al.* [47] have pointed out that considerable differences in the reflectivity spectra of structurally pure wurtzite and zinc blende crystals exist. They used melt-grown wurtzite crystals stabilized by the addition of 10^{-3}-mol Al per mole ZnS. Crystals grown without Al additions were found to have cubic structure with broadened x-ray diffraction spots on the n layers of the $\langle 111 \rangle$ diffraction patterns where $n \neq 3m$ (m an integer). For A1 additions of 10^{-4}-mol Al per mole ZnS, the crystals were found to be mixtures of 6H and 3C (hexagonal and cubic polytypes). The conclusion is made that melt-grown ZnS crystals are superior to other synthetic crystals because of higher crystal perfection, reproducibility, and short production time.

Bieniewski and Czyzak [48] reported refractive indices of synthetic crystals between 0.36 and 1.4 μm for 298 K. Only very small traces ($\leqq 0.0001\%$) of B, Mg, Si, Cu, and Fe were detected in these crystals. The crystals had to be heat treated to ensure the hexagonal structure. We list the data in Table XVII. Piper *et al.* [49] give similar data.

Pikhtin and Yas'kov [50] have fitted a detailed oscillator model to data of Voronkova *et al.* [51] and discussed the birefringence. Unfortunately, their table of parameters seems incomplete since they refer to work of Sobolev *et al.* [52] for parameters for three exciton peaks that we could not find. Therefore, we could not calculate the exciton contribution δn, although they did provide a plot of δn versus λ from 0.4 to 1.5 μm from which we might extrapolate $\delta n < 0.03$ for $\lambda > 1.5$ μm. Geidur and Yas'kov [53] had previously discussed the birefringence and given a curve for δn; this suggests that it is significantly smaller. Kulakovskii *et al.* [54] have also studied the birefringence. We list a few values of n_o for the near infrared as read off a graph in Pikhtin and Yas'kov [50].

Marshall and Mitra [55] give percentage transmission spectra of multiple-phonon absorption (presumably T_o) in the 775–350-cm^{-1} region but no optical constants. Samples were platelet crystals grown from the vapor phase.

Manabe *et al.* [43] measured R_o ($E \perp c$) in the 20–100-μm spectral region at 300 K and performed an oscillator fit to the data. Their parameters were used in Eq. (4) to obtain n_o and k_o, which are listed in Table XVII. The parameters are $\varepsilon_\infty = 5.7$, $\omega_T = 274\ \text{cm}^{-1}$, $\omega_L = 356\ \text{cm}^{-1}$, and $\Gamma = 4.66\ \text{cm}^{-1}$. We extrapolated the data to 10 μm to compare with the data of Pikhtin and Yas'kov [50]. A significant difference is probably due to the ε_∞ value of Manabe *et al.* [43] being too large.

Hot-Pressed ZnS Data IRTRAN 2 is the trade name of hot-pressed polycrystalline ZnS manufactured by the Eastman Kodak Company. The material is composed of 95% cubic and 5% hexagonal phases [56]. The room-temperature refractive index, listed in Table XVI, was measured in the region

1–10 μm and the values were extrapolated to 13 μm [57]. The method of measurement was presumably minimum deviation.

Transmittance and reflectance of a 1-mm-thick sample were measured by McCarthy [58]. Reflection at 30° incidence was compared to an aluminum mirror. No optical constants were given. Transmission data for various thicknesses were also reported by Eastman Kodak in the 0.4–15-μm range [57, 59]. Packard [60] compared the measured ("actual") transmittance of a 1-mm-thick sample with the "typical" (i.e., advertised) transmittance of the same sample and stressed the fact that there are considerable differences. For example, for one sample at 10 μm the actual transmittance was 62%, versus 66% reported as typical transmittance.

Considerable variations in the spectral transmission of KO-2 ceramics prepared "by the recrystallization vacuum-molding method from commercially manufactured zinc sulfide powder" were reported by Nosov and Dronova [61]. The KO-2 samples are known to contain some 0.1–1.5% of SO_4^{2-} ions by weight. Inclusions of sulfur and zinc oxide probably are responsible for the measured changes in transmission and for absorption bands appearing in the 9–11-μm region.

Stierwalt *et al.* [62] have reported the spectral absorptance between 3 and 15 μm of 2-mm-thick IRTRAN 2 at 60, 120, and 180°C. Stierwalt [63] measured the spectral emittance at 4.2, 77, and 373 K by using a modified Beckman IR-3 spectrophotometer.

Deposited Thin Films The optical constants of various types of deposited and grown ZnS films on a substrate have been discussed in some detail, since ZnS is a useful antireflection coating. We mentioned a few examples earlier. The subject is too complicated to organize in a few paragraphs, so we refer the reader to Pulker [64], who discusses the dependence of optical constants on structure, microstructure, packing density, chemical composition, and homogeneity, among other things, with some reference to ZnS [65]. Evaluations of sputtered and molecular-beam-deposited films [66] show wide variations in k and small systematic variations in n. Ever-present problems are the control of the initial constituents, the specification of the deposition process and the nonoptical characterization of the films as to structure and content.

In Jones *et al.* [66] the bulk index of refraction is given in the visible with no description of the measurement (presumably a prism technique). These numbers are consistently $\sim$0.004 less than the numbers given in Table XVI for cubic ZnS.

REFERENCES

1. M. Hansen, *in* "Constitution of Binary Alloys," p. 1171. McGraw-Hill, New York, 1958.
2. R. P. Elliott, *in* "Constitution of Binary Alloys," first suppl., p. 800. McGraw-Hill, New York, 1965.

3. F. A. Shunk, *in* "Constitution of Binary Alloys," second suppl., p. 644. McGraw-Hill, New York, 1969.
4. P. P. Ewald and C. Hermann, "Strukturbericht 1913–28," p. 76. Akademische Verlagsgesellschaft M. B. H., Leipzig, 1931.
5. P. P. Ewald and C. Hermann, "Strukturbericht 1913–28," p. 78. Akademische Verlagsgesellschaft M. B. H., Leipzig, 1931.
6. H. T. Evans and E. T. McKnight, *Am. Mineral* **44**, 210 (1959).
7. C. Frondel and C. Palache, *Am. Mineral* **35**, 29 (1950); C. Frondel and C. Palache, *Science* **107**, 602 (1948).
8. D. C. Buck and L. W. Strock, *Am. Mineral* **39**, 318 (1944); D. C. Buck and L. W. Strock, *Am. Mineral* **40**, 192 (1955).
9. J. W. Mellor, "Inorganic and Theoretical Chemistry," Vol. 4, p. 586. New Impression, New York, 1957.
10. L. Gmelin, "Handbuch der anorganischen Chemie," 8th ed. System-Nummer 32, pp. 123 and 521. Springer-Verlag, Berlin, 1956.
11. L. Gmelin, "Handbuch der anorganischen Chemie," 8th ed. System-Nummer 32, p. 25. Springer-Verlag, Berlin, 1956.
12. E. Alexander, Z. H. Kafman, S. Mardix, and I. T. Steinberger, *Philos. Mag.* **21**, 1237 (1970).
13. Y. Sonnenblick and I. Kiflawi, *Israel J. Chem.* **10**, 7 (1972).
14. I. T. Steinberger, E. Alexander, Y. Brada, Z. H. Kalman, I. Kiflawi, and S. Mardix, *J. Cryst. Growth* **13/14**, 285 (1972).
15. I. Kiflawi, Z. H. Kalman, S. Mardix, and I. T. Steinberger, *Acta Cryst.* **B 28**, 2110 (1972).
16. S. Kume, E. Kodera, T. Aikami, and J. Kakinoki, *J. Phys. Soc. Jpn.* **32**, 288 (1972).
17. I. Kiflawi, S. Mardix, and I. T. Steinberger, *Acta Cryst.* **B 27**, 378 (1971).
18. I. Kiflawi and S. Mardix, *Acta Cryst.* **B 26**, 1192 (1970); I. Kiflawi and S. Mardix, *Acta Cryst*, **B 25**, 1195 (1969).
19. R. W. G. Wyckoff, "Crystal Structures," 2nd ed., Vol. 1, p. 113. Interscience, New York, 1963.
20. S. L. Czyzak, D. C. Reynolds, R. C. Allen, and C. C. Reynolds, *J. Opt. Soc. Am.* **44**, 864 (1954).
21. B. L. Henke, P. L. Lee, T. J. Tanaka, R. L. Shimabukuro, and B. F. Fujikawa, "Low Energy X-Ray Diagnostics—1981" (D. T. Attwood and B. L. Henke, eds.). *AIP Conf. Proc.*, No. 75. American Institute of Physics, New York, 1981.
22. M. Cardona and R. Haensel, *Phys. Rev. B* **1**, 2605 (1970).
23. W. R. Hunter, private communication, (1983).
24. W. R. Hunter, D. W. Angel, and G. Hass, *J. Opt. Soc. Am.* **68**, 1319 (1978).
25. J. T. Cox, J. E. Waylonis, and W. R. Hunter, *J. Opt. Soc. Am.* **59**, 807 (1959).
26. M. Cardona and G. Harbeke, *Phys. Rev.* **137**, A1467 (1965).
27. M. Balkanski and Y. Petroff, *Proc. Conf. Phys. Semicond., 7th, Paris, 1964*, p. 245. Dunod, Paris, 1964.
28. E. Khawaja and S. G. Tomlin, *J. Phys. D.* **8**, 581 (1975).
29. R. E. Denton, R. D. Campbell, and S. G. Tomlin, *J. Phys. D* **5**, 852 (1972).
30. S. J. Czyzak, W. M. Baker, R. C. Crane, and J. B. Home, *J. Opt. Soc. Am.* **47**, 240 (1957).
31. J. W. Mellor, "Inorganic and Theoretical Chemical," Vol. 4, p. 597. New Impression, New York, 1957.
32. L. Gmelin, "Handbuch der anorganischen Chemie," 8th ed. System-Nummer 32, p. 200. Springer-Verlag, Berlin, 1956.
33. M. Mell, *Z. Phys.* **16**, 244 (1923).
34. W. L. Bond, *J. Appl. Phys.* **36**, 1674 (1965).
35. A. N. Pikhtin and A. D. Yas'kov, *Sov. Phys. Semicond.* **12**, 622 (1978).
36. J. R. DeVore, *J. Opt. Soc. Am.* **41**, 416 (1951).
37. J. C. Burgiel, Y. S. Chen, F. Vratny, and G. Smolinsky, *J. Electrochem. Soc.* **115**, 729 (1968).
38. J. F. Hall, Jr., *J. Opt. Soc. Am.* **46**, 1013 (1956).
39. C. A. Klein and R. N. Donadio, *J. Appl. Phys.* **51**, 797 (1980).

40. T. Deutsch, *Proc. Int. Conf. Phys. Semicond., 6th Exeter 1962*, p. 505. The Institute of Physics and the Physical Society, London, 1962.
41. R. Nitsche, *J. Phys. Chem. Solids* **17**, 163 (1960).
42. E. A. Kwasniewski, E. S. Koteles, and W. R. Datars, *Canada J. Phys.* **54**, 1053 (1976).
43. A. Manabe, A. Mitsuishi and H. Yoshinaga, *Jpn. J. Appl. Phys.* **6**, 593 (1967).
44. T. Hattori, Y. Homma, and A. Mitsuishi, *Opt. Commun.* **7**, 229 (1973).
45. J. L. Freeouf, *Phys. Rev. B* **7**, 3810 (1973).
46. J. W. Baars, *Proc. Int. Conf. II–VI Semicond. Comp., Providence, 1968* (D. G. Thomas, ed.), p. 631. Benjamin, New York, 1968.
47. A. Ebina, E. Fukunaga, and T. Takahashi, *Phys. Rev. B* **12**, 687 (1975).
48. T. M. Bieniewski and S. J. Czyzak, *J. Opt. Soc. Am.* **53**, 496 (1963).
49. W. W. Piper, D. T. F. Marple, and P. D. Johnson, *Phys. Rev.* **110**, 323 (1958).
50. A. N. Pikhtin and A. D. Yas'kov, *Sov. Phys. Semicond.* **15**, 8 (1981).
51. E. M. Voronkova, B. N. Grechushnikov, G. I. Distler, and I. P. Petrov, "*Optical Materials for Infrared Technology.*" Nauka, Moscow, 1965 [in Russian].
52. V. V. Sobolev, V. I. Donetskikh, and E. F. Zagaĭnov, *Sov. Phys. Semicond.* **12**, 646 (1978).
53. S. A. Geidur and A. D. Yas'kov, *Opt. Spectrosc.* **48**, 618 (1980); S. A. Geidur and A. D. Yas'kov, *Opt. Spektrok.* **48**, 1130 (1980).
54. V. D. Kulakovskii, V. I. Grinev, and M. P. Kulakov, *Sov. Phys. Solid State* **19**, 345 (1977).
55. R. Marshall and S. S. Mitra, *Phys. Rev.* **134**, A1019 (1964).
56. A. J. Moses, "Refractive Index of Optical Materials in the Infrared Region," D. S. 166 (January 1970), p. 5, Air Force Materials Laboratory, Culver City, California; A. J. Moses, A. D. 704555 (1970).
57. Eastman Kodak, publication No. U-72 Rochester, New York (1981).
58. D. E. McCarthy, *Appl. Opt.* **2**, 591 (1963).
59. W. L. Wolfe, *in* "Handbook of Optics," pp. 7–33. McGraw-Hill, New York, 1978.
60. R. D. Packard, *Appl. Opt.* **8**, 1901 (1969).
61. V. B. Nosov and G. N. Dronova, *Sov. J. Opt. Technol.* **47**, 470 (1980).
62. D. L. Stierwalt, J. D. Bernstein, and D. D. Kirth, *Appl. Opt.* **2**, 1169 (1963).
63. D. L. Stierwalt, *Appl. Opt.* **5**, 1911 (1966).
64. H. K. Pulker, *Appl. Opt.* **18**, 1969 (1979).
65. H. K. Pulker, *Thin Solid Films* **34**, 343 (1976).
66. P. L. Jones, D. R. Cotton, and D. Moore, *Thin Solid Films* **88**, 163 (1982).

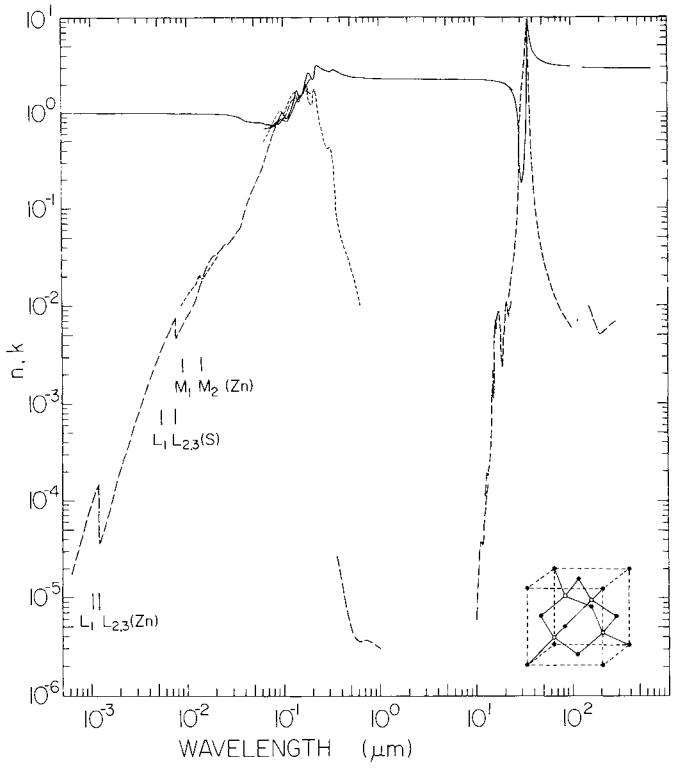

Fig. 14. Log–log plot of n (——) and k (– – – –) versus wavelength in micrometers for cubic ZnS. (Inset: ●, Zn; ○, S.)

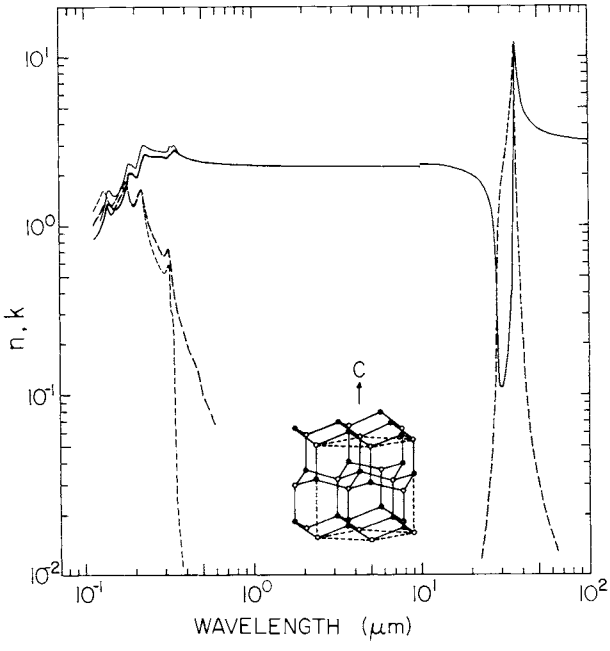

Fig. 15. Log–log plot of n_o (——), k_o (– – – –), n_e (——), and k_e (– – – –) versus wavelength in micrometers for hexagonal ZnS. (Inset: ●, Zn; ○, S.)

TABLE XVI

Values of n and k for Cubic Zinc Sulfide Obtained from Various References[a]

eV	Å	n	k	n	k
2000	6.199	0.999904 [21]	1.76×10^{-5} [21]		
1952	6.351	0.999900	1.92		
1905	6.508	0.999894	2.09		
1860	6.665	0.999889	2.27		
1815	6.831	0.999884	2.48		
1772	6.997	0.999878	2.70		
1730	7.166	0.999873	2.94		
1688	7.345	0.999867	3.20		
1648	7.523	0.999861	3.48		
1609	7.705	0.999855	3.78		
1570	7.897	0.999848	4.12		
1533	8.087	0.999841	4.47		
1496	8.287	0.999835	4.87		
1460	8.492	0.999828	5.30		
1426	8.694	0.999821	5.74		
1392	8.906	0.999814	6.24		
1358	9.129	0.999807	6.80		
1326	9.350	0.999800	7.38		
1294	9.581	0.999793	8.03		
1263	9.816	0.999787	8.74		
1233	10.05	0.999781	9.39×10^{-5}		
1204	10.30	0.999777	1.00×10^{-4}		
1175	10.55	0.999774	1.08		
1147	10.81	0.999770	1.15		
1119	11.08	0.999769	1.24		
1093	11.34	0.999769	1.32		
1067	11.62	0.999773	1.41		
1041	11.91	0.999791	1.52		
1038	11.95	0.99979	1.1×10^{-4}		
1033	12.00	0.999805	9.3×10^{-5}		
1029	12.05	0.999813	7.0		
1025	12.10	0.999822	4.4		
1020	12.15	0.999833	3.0		
1016	12.20	0.999838	3.61		
992	12.50	0.999774	3.91		
968	12.81	0.999734	4.24		
945	13.12	0.999694	4.60		
923	13.43	0.999671	4.98		
901	13.76	0.999647	5.42		
879	14.10	0.999622	5.91		
858	14.45	0.999597	6.43		
838	14.79	0.999573	6.99		
818	15.16	0.999547	7.60		
798	15.54	0.999520	8.29		
779	15.92	0.999493	9.01		
760	16.31	0.999464	9.80×10^{-5}		
742	16.71	0.999435	1.06×10^{-4}		

TABLE XVI (*Continued*)

Cubic Zinc Sulfide

eV	Å	n	k	n	k
725	17.10	0.999405	1.15		
707	17.54	0.999372	1.25		
690	17.97	0.999338	1.35		
674	18.39	0.999304	1.46		
658	18.84	0.999269	1.58		
642	19.31	0.999230	1.72		
627	19.77	0.999191	1.87		
612	20.26	0.999150	2.02		
597	20.77	0.999106	2.19		
583	21.27	0.999062	2.37		
569	21.79	0.999015	2.57		
555	22.34	0.99896	2.79		
542	22.87	0.99892	3.02		
529	23.44	0.99886	3.26		
516	24.03	0.99881	3.54		
504	24.60	0.99875	3.82		
492	25.20	0.99869	4.14		
480	25.83	0.99863	4.49		
469	26.43	0.99857	4.84		
458	27.07	0.99850	5.22		
447	27.74	0.99843	5.63		
436	28.44	0.99836	6.09		
426	29.10	0.99829	6.54		
415	29.87	0.99821	7.10		
406	30.54	0.99814	7.60		
396	31.31	0.99806	8.20		
386	32.12	0.99797	8.86		
377	32.89	0.99789	9.50×10^{-4}		
368	33.69	0.99781	1.02×10^{-3}		
359	34.53	0.99772	1.10		
351	35.32	0.99763	1.17		
342	36.25	0.99753	1.26		
334	37.12	0.99744	1.35		
326	38.03	0.99734	1.45		
318	38.99	0.99724	1.55		
311	39.86	0.99715	1.66		
303	40.92	0.99704	1.79		
296	41.88	0.99694	1.91		
289	42.90	0.99685	2.04		
282	43.96	0.99676	2.19		
275	45.08	0.99667	2.34		
269	46.09	0.99660	2.47		
262	47.32	0.99650	2.62		
256	48.43	0.99641	2.76		
250	49.59	0.99632	2.92		
244	50.81	0.99622	3.09		

(*continued*)

TABLE XVI (*Continued*)

Cubic Zinc Sulfide

eV	Å	n	k	n	k
238	52.09	0.99612	3.27		
232	53.44	0.99602	3.46		
227	54.62	0.99594	3.64		
221	56.10	0.99583	3.86		
216	57.40	0.99574	4.07		
211	58.76	0.99566	4.29		
206	60.18	0.99558	4.55		
201	61.68	0.99553	4.82		
196	63.25	0.99549	5.12		
191	64.91	0.99549	5.44		
187	66.30	0.99553	5.71		
182	68.12	0.99561	6.07		
178	69.65	0.99575	6.37		
174	71.25	0.99604	6.69		
170	72.93	0.99678	7.04		
166	74.69	0.99838	7.42		
165.3	75.00	0.9981	7.3		
164.2	75.50	0.99767	6.1		
163.1	76.00	0.99733	5.0		
162	76.53	0.99703	4.62		
158	78.47	0.99611	4.86		
154	80.51	0.99550	5.10		
150	82.65	0.99504	5.36		
147	84.34	0.99476	5.57		
145	85.51				1.00×10^{-2} [22]
143	86.70	0.99439	5.87		
140	88.56	0.99411	6.11		1.04
136	91.16	0.99375	6.45		
135	91.84				1.10
133	93.22	0.99347	6.73		
130	95.37	0.99321	7.02		1.16
127	97.62	0.99293	7.35		
125	99.18				1.23
124	99.98	0.99265	7.69		
121	102.5	0.99237	8.07		
120	103.3				1.32
118	105.1	0.99209	8.47		
115	107.8	0.99180	8.90		1.40
112	110.7	0.99151	9.36		
110	112.7	0.99132	9.69×10^{-3}		1.50
107	115.9	0.99105	1.02×10^{-2}		
105	118.1				1.59
104	119.2	0.99081	1.08		
102	121.5	0.99068	1.12		
100	124.0	0.99061	1.17		1.66
98	126.5				1.72
97	127.8				1.77

TABLE XVI (*Continued*)

Cubic Zinc Sulfide

eV	Å	n	k	n	k
96	129.2				1.85
95.37	130	0.989 [23]	1.37 [23]		
95	130.5				1.95
94	131.9				1.98
93	133.3				1.97
92	134.8				2.03
91.84	135	0.988	1.52		
91	136.2				2.04
90	137.8				1.96
88.56	140	0.987	1.68		
87.5	141.6				1.88
85	145.9				1.93
82.66	150	0.982	1.79		
80	155.0				2.08
77.49	160	0.974 [24]	2.55 [24]		
75	165.3				2.32
72.93	170	0.974	2.81		
70	177.1				2.55
68.88	180	0.973	3.06		
65.26	190	0.969	3.32		
65	190.7				2.87
61.99	200	0.964	3.32		
60	206.6				3.24
59.04	210	0.964	3.57		
56.36	220	0.962	3.83		
53.91	230	0.962	3.83		
51.66	240	0.962	4.34		
49.59	250	0.957	4.34		
47.69	260	0.957	4.34		
45.92	270	0.954	4.34		
44.28	280	0.949	4.59		
42.75	290	0.944	4.85		
41.33	300	0.941	5.10		
38.75	320	0.929	5.61		
36.47	340	0.911	6.12		
34.44	360	0.890	6.89		
32.63	380	0.867	7.91		
31.00	400	0.847	9.95×10^{-2}		
29.52	420	0.819	0.110		
28.18	440	0.809	0.125		
26.95	460	0.801	0.145		
25.83	480	0.798	0.158		
24.80	500	0.796	0.171		
23.84	520	0.793	0.189		
22.96	540	0.793	0.204		
22.14	560	0.788	0.222		

(*continued*)

TABLE XVI (*Continued*)

Cubic Zinc Sulfide

eV	Å	n	k	n	k
21.38	580	0.788	0.242		
20.66	600	0.783	0.260		
20.00	620	0.776	0.286		
				0.68 [26]	0.49 [26]
19.37	640	0.765	0.314		
19.0	652.6			0.68	0.53
18.79	660	0.758	0.347		
18.0	688.8			0.68	0.59
17.71	700	0.747	0.431		
17.22	720	0.747	0.464		
17.0	729.3			0.69	0.67
16.75	740	0.742	0.500		
16.31	760	0.737	0.543		
16.0	774.9			0.70	0.76
15.90	780	0.737	0.584		
15.50	800	0.742	0.620		
15.12	820	0.758	0.679		
15.0	826.6			0.72	0.86
14.76	840	0.791	0.735		
14.42	860	0.798	0.773		
14.09	880	0.783	0.801		
14.0	885.6			0.81	0.99
13.78	900	0.758	0.824		
13.5	918.4			0.89	1.04
13.48	920	0.765	0.842		
13.19	940	0.793	0.857		
13.0	953.7			0.97	1.04
12.92	960	0.827	0.862		
12.65	980	0.852	0.867		
12.5	991.9			1.00	0.99

eV	cm^{-1}	μm	n	k	n	k
12.40		0.1000	0.862	0.876		
12.0		0.1033			0.95	0.98
11.81		0.105	0.834	0.903		
11.5		0.1078			0.87	1.10
11.27		0.110	0.819	1.02		
11.0		0.1127			0.89	1.26
10.78		0.115	0.855	1.14		
10.5		0.1181			0.99	1.41
10.33		0.120	0.929	1.27		
10.0		0.1240			1.13	1.54
9.919		0.125	1.02	1.36		
9.537		0.130	1.13	1.42		
9.5		0.1305			1.40	1.66
9.184		0.135	1.23	1.44		

TABLE XVI (*Continued*)

Cubic Zinc Sulfide

eV	cm^{-1}	μm	n	k	n	k
9.0		0.1378			1.71	1.50
8.856		0.140	1.33	1.44		
8.551		0.145	1.38	1.45		
8.5		0.1459			1.53	1.28
8.266		0.150	1.41	1.47		
7.999		0.155	1.48	1.53	1.49	1.55
7.749		0.160	1.55	1.58	1.58	1.69
7.514		0.165	1.65	1.64		
7.5		0.1653			1.68	1.75
7.293		0.170	1.76	1.70		
7.25		0.1710			2.05	1.91
7.085		0.175	1.88	1.72		
7.0		0.1771			2.40	2.02
6.888		0.180	2.01	1.72		
6.75		0.1837			2.64	1.40
6.702		0.185	2.11	1.68		
6.526		0.190	2.19	1.64		
6.5		0.1907			2.50	1.25
6.358		0.195	2.26	1.62		
6.25		0.1984			2.35	1.21
6.199		0.200	2.32	1.62		
6.0	48,390	0.2066			2.24	1.65
5.75	46,380	0.2156			2.80	1.72
5.5	44,360	0.2254			3.18	1.30
5.25	42,340	0.2362			3.06	0.85
5.0	40,330	0.2480			2.97	0.68
4.75	38,310	0.2610			2.90	0.54
4.5	36,290	0.2755			2.81	0.46
4.25	34,280	0.2917			2.74	0.42
4.0	32,260	0.3100			2.70	0.44
3.75	30,250	0.3306			2.84	0.30
3.542	28,570	0.35		2.78×10^{-5} [20]		
3.5	28,230	0.3542			2.79	0.10
3.25	26,210	0.3815			2.64	6×10^{-2}
3.100	25,000	0.40		1.46×10^{-5}		
3.0	24,200	0.4133			2.54	4
2.755	22,220	0.45		7.52×10^{-6}		
2.75	22,180	0.4509	2.4687 [35]			
2.70	21,780	0.4592	2.4593			
2.65	21,370	0.4679	2.4502			
2.60	20,970	0.4769	2.4414			
2.55	20,570	0.4862	2.4330			
2.50	20,160	0.4959	2.4248		2.42	3
2.480	20,000	0.50		4.77×10^{-6}		
2.45	19,760	0.5061	2.4170			
2.40	19,360	0.5166	2.4094			

(*continued*)

TABLE XVI (*Continued*)

Cubic Zinc Sulfide

eV	cm^{-1}	μm	n	k	n	k
2.35	18,950	0.5276	2.4021			
2.30	18,550	0.5391	2.3950			
2.254	18,180	0.55		3.85		
2.25	18,150	0.5510	2.3882			
2.20	17,740	0.5636	2.3816			
2.15	17,340	0.5767	2.3753			
2.10	16,940	0.5904	2.3692			
2.066	16,670	0.60		3.58		
2.05	16,530	0.6048	2.3633			
2.00	16,130	0.6199	2.3576		2.37	1
1.95	15,730	0.6358	2.3520			
1.907	15,380	0.65		3.62×10^{-6}		
1.90	15,320	0.6526	2.3467			
1.85	14,920	0.6702	2.3416			
1.80	14,520	0.6888	2.3367			
1.771	14,290	0.70		3.68		
1.75	14,110	0.7085	2.3319			
1.70	13,710	0.7293	2.3274			
1.653	13,330	0.75		3.64		
1.65	13,310	0.7514	2.3229			

eV	cm^{-1}	μm	n	k	n_{IRTRAN}	k_{IRTRAN}
1.60	12,900	0.7749	2.3187			
1.55	12,500	0.7999	2.3146	3.50		
1.50	12,100	0.8266	2.3107			
1.459	11,760	0.85		3.38		
1.45	11,690	0.8551	2.3069			
1.40	11,290	0.8856	2.3033			
1.378	11,110	0.90		3.22		
1.35	10,890	0.9184	2.2998			
1.305	10,530	0.95		3.17		
1.30	10,490	0.9537	2.2965			
1.25	10,080	0.9919	2.2933			
1.240	10,000	1.00		3.02	2.2907 [57]	
1.20	9,679	1.033	2.2903			
1.15	9,275	1.078	2.2874			
1.10	8,872	1.127	2.2846			
1.05	8,469	1.181	2.2820			
1.00	8,065	1.240	2.2795			
0.9919	8,000	1.25			2.2777	
0.95	7,662	1.305	2.2771			
0.90	7,259	1.378	2.2748			
0.85	6,856	1.459	2.2727			
0.8266	6,667	1.50			2.2706	
0.80	6,452	1.550	2.2706			
0.75	6,049	1.653	2.2687			

TABLE XVI (*Continued*)

Cubic Zinc Sulfide

eV	cm^{-1}	μm	n	k	n_{IRTRAN}	k_{IRTRAN}
0.7085	5,714	1.75			2.2662	
0.70	5,646	1.771	2.2669			
0.65	5,243	1.907	2.2651			
0.6199	5,000	2.0			2.2631	6.2×10^{-6} [57]
0.60	4,839	2.066	2.2634			
0.5510	4,444	2.25			2.2608	
0.55	4,436	2.254	2.2618			
0.50	4,033	2.480	2.2603			
0.4959	4,000	2.5			2.2589	
0.4509	3,636	2.75			2.2573	
0.45	3,629	2.755	2.2587			
0.4133	3,333	3.0			2.2558	5.3
0.40	3,226	3.100	2.2570			
0.3815	3,077	3.25			2.2544	
0.3542	2,857	3.5			2.2531	
0.35	2,823	3.542	2.2552			
0.3306	2,667	3.75			2.2518	
0.3100	2,500	4.0			2.2504	3.8
0.30	2,420	4.133	2.2529			
0.2917	2,353	4.25			2.2491	
0.2755	2,222	4.5			2.2477	
0.2610	2,105	4.75			2.2462	
0.25	2,016	4.959	2.2497			
0.2480	2,000	5.0			2.2447	2.8
0.2362	1,905	5.25			2.2432	
0.2254	1,818	5.5			2.2416	
0.2156	1,739	5.75			2.2399	
0.2066	1,667	6.0			2.2381	2.9
0.20	1,613	6.199	2.2443			
0.1984	1,600	6.25			2.2363	
0.1907	1,538	6.5			2.2344	
0.1837	1,481	6.75			2.2324	
0.18	1,452	6.888	2.2409			
0.1771	1,429	7.0			2.2304	3.9
0.1710	1,379	7.25			2.2282	
0.1653	1,333	7.5			2.2260	
0.16	1,290	7.749	2.2362		2.2237	
0.1550	1,250	8.0			2.2213	4.5
0.1503	1,212	8.25			2.2188	
0.1459	1,176	8.5			2.2162	
0.1417	1,143	8.75			2.2135	
0.14	1,129	8.856	2.2290			
0.1378	1,111	9.0			2.2107	5.7
0.1340	1,081	9.25			2.2078	
0.1305	1,053	9.5			2.2048	
0.1272	1,026	9.75			2.2018	

(*continued*)

TABLE XVI (*Continued*)

Cubic Zinc Sulfide

eV	cm^{-1}	μm	n	k	n_{IRTRAN}	k_{IRTRAN}
0.1240	1,000	10.00		6.09×10^{-6} [39]	2.1986	8.8×10^{-6}
0.1209	975	10.26		1.14×10^{-5}		
0.12	967.9	10.33	2.2176			
0.1178	950	10.53		1.82		
0.1170	943.4	10.6				2.4×10^{-5}
0.1147	925	10.81		3.26		
0.1127	909.1	11			2.1846	3.9
0.1116	900	11.11		3.78		
0.1085	875	11.43		3.67		
0.1054	850	11.76		3.49		
0.1033	833.3	12			2.1688	4.5
0.1017	825	12.12		5.19		
0.10	806.5	12.40	2.1969			
0.09919	800	12.50		8.19×10^{-5}		
				1.09×10^{-4} [40]		
0.09724	784.3	12.75		1.88		
0.09537	769.2	13.0		1.86	2.1508	
0.09357	754.7	13.25		1.79		
0.09299	750	13.33		1.53 [39]		
0.09184	740.7	13.5		2.04 [40]		
0.09017	727.3	13.75		2.30		
0.09	725.9	13.78	2.1793			
0.08856	714.3	14.0		2.56		
0.08701	701.8	14.25		3.63		
0.08551	689.7	14.5		6.35		
0.08492	684.9	14.6		8.13×10^{-4}		
0.08377	675.7	14.80		1.53×10^{-3}		
0.08266	666.7	15.0		2.27		
0.08157	657.9	15.2		1.11		
0.08051	649.4	15.4		2.21		
0.07999	645.2	15.5	2.1518	3.82		
0.07948	641.0	15.6		5.21		
0.07847	632.9	15.8		7.04		
0.07749	625.0	16.0		5.79		
0.07653	617.3	16.2		5.87		
0.07560	609.8	16.4		7.05		
0.07514	606.1	16.5		7.48		
0.07469	602.4	16.6		7.86		
0.07380	595.2	16.8		8.56		
0.07293	588.2	17.0		8.79		
0.07188	579.7	17.25		8.51		
0.07085	571.4	17.5		7.24		
0.07	564.6	17.71	2.1040			
0.06985	563.4	17.75		5.93		
0.06888	555.6	18.0		4.66		
0.06794	547.9	18.25		3.27		
0.06702	540.5	18.5		2.44		
0.06613	533.3	18.75		2.40		

TABLE XVI (*Continued*)

Cubic Zinc Sulfide

eV	cm^{-1}	μm	n	k	n_{IRTRAN}	k_{IRTRAN}
0.06526	526.3	19.0		3.02		
0.06441	519.5	19.25		4.01		
0.06358	512.8	19.5		5.04		
0.06278	506.3	19.75		6.00		
0.06199	500.0	20.0		7.56		
			2.05 [43]	7.2 [43]		
0.06123	493.8	20.25		9.35 [40]		
0.06075	490	20.41	2.03	8.0 [43]		
0.06048	487.8	20.5		1.07×10^{-2} [40]		
0.06	483.9	20.66	2.0041 [35]			
0.05975	481.9	20.75		1.09		
0.05951	480	20.83	2.01 [43]	9.0×10^{-3} [43]		
0.05904	476.2	21.0		1.01×10^{-2} [40]		
0.05835	470.6	21.25		9.13×10^{-3}		
0.05827	470	21.28	1.98	1.0×10^{-2} [43]		
0.05767	465.1	21.5		8.16×10^{-3} [40]		
0.05703	460	21.74	1.95	1.2×10^{-2} [43]		
0.05700	459.8	21.75		7.65×10^{-3} [40]		
0.05636	454.5	22.0		8.05×10^{-3}		
0.05579	450	22.22	1.91	1.3×10^{-2} [43]		
0.05572	449.4	22.25		9.15×10^{-3} [40]		
0.05510	444.4	22.5		9.31		
0.05455	440	22.73	1.87	1.5×10^{-2} [43]		
0.05450	439.6	22.75		9.56×10^{-3} [40]		
0.05391	434.8	23.0		9.98×10^{-3}		
0.05333	430.1	23.25		1.11×10^{-2}		
0.05331	430	23.26	1.83	1.82 [43]		
0.05207	420	23.81	1.76	2.2		
0.05083	410	24.39	1.69	2.6		
0.05	403.3	24.80	1.6866 [35]			
0.04959	400	25.00	1.60 [43]	3.3		
0.04835	390	25.64	1.49	4.2		
0.04711	380	26.32	1.35	5.7		
0.04587	370	27.03	1.14	8.4×10^{-2}		
0.04463	360	27.78	0.83	0.15		
0.04339	350	28.57	0.31	0.52		
0.04215	340	29.41	0.19	1.1		
0.04092	330	30.30	0.19	1.7		
0.03968	320	31.25	0.23	2.3		
0.03844	310	32.26	0.31	3.1		
0.03720	300	33.33	0.53	4.2		
0.03695	298	33.56	0.62	4.6		
0.03670	296	33.78	0.74	4.9		
0.03645	294	34.01	0.90	5.4		
0.03620	292	34.25	1.15	5.9		
0.03596	290	34.48	1.52	6.6		
0.03571	288	34.72	2.15	7.4		

(*continued*)

TABLE XVI (*Continued*)

Cubic Zinc Sulfide

eV	cm^{-1}	μm	n	k	n_{IRTRAN}	k_{IRTRAN}
0.03546	286	34.97	3.29	8.3		
0.03521	284	35.21	5.42	9.0		
0.03496	282	35.46	8.32	8.0		
0.03472	280	35.71	9.54	5.2		
0.03447	278	35.97	9.02	3.1		
0.03422	276	36.23	8.20	2.0		
0.03397	274	36.50	7.48	1.3		
0.03372	272	36.76	6.91	0.99		
0.03348	270	37.04	6.46	0.76		
0.03323	268	37.31	6.10	0.60		
0.03298	266	37.59	5.80	0.49		
0.03273	264	37.88	5.55	0.41		
0.03248	262	38.17	5.34	0.35		
0.03224	260	38.46	5.15	0.30		
0.03100	250	40.00	4.52	0.16		
0.02976	240	41.67	4.15	0.10		
0.02852	230	43.48	3.90	7.1×10^{-2}		
0.02728	220	45.45	3.72	5.2		
0.02604	210	47.62	3.58	4.0		
0.02480	200	50.00	3.48	3.1		
0.02356	190	52.63	3.39	2.5		
0.02232	180	55.56	3.33	2.1		
0.02108	170	58.82	3.27	1.7		
0.01984	160	62.50	3.22	1.5		
0.01860	150	66.67	3.18	1.2		
0.01736	140	71.43	3.15	1.0×10^{-2}		
0.01612	130	76.92	3.12	9.1×10^{-3}		
0.01488	120	83.33	3.10	7.8		
0.01364	110	90.91	3.07	6.7		
0.01240	100	100.0	3.06	5.8		
0.009299	75	133.3	2.950 [44]			
0.008679	70	142.9	2.940	1.0×10^{-2} [44]		
0.008369	67.5	148.1		1.0×10^{-2}		
0.008059	65	153.0	2.932	8.6×10^{-3}		
0.007749	62.5	160.0		8.0		
0.007439	60	166.7	2.924	7.4		
0.007129	57.5	173.9		6.1		
0.006819	55	181.8	2.918	5.4		
0.006199	50	200.0	2.913	5.1		
0.005579	45	222.2	2.908	5.6		
0.004959	40	250.0	2.903	6.2		
0.004339	35	285.7	2.899	7.0		
0.003720	30	333.3	2.896			
0.003100	25	400.0	2.894			
0.002480	20	500.0	2.892			
0.001860	15	666.7	2.890			

[a] References are indicated in brackets. Some values for IRTRAN-2 are also listed. When a value of n or k appears by itself on a line, the pertinent wavelength is on the preceding line.

TABLE XVII

Values of n_o, k_o and n_e, k_e for Hexagonal Zinc Sulfide Obtained from Various References[a]

eV	cm^{-1}	μm	n_o	k_o	n_e	k_e
11		0.1127	0.84 [26]	1.02 [26]		1.23 [26]
10.75		0.1153		1.09		1.30
10.5		0.1181	0.89	1.13		1.36
10.25		0.1210		1.16		1.42
10.0		0.1240	0.99	1.21	1.08 [26]	1.50
9.75		0.1272		1.29		1.59
9.5		0.1305	1.15	1.34	1.30	1.61
9.25		0.1340	1.24	1.33	1.48	1.54
9.0		0.1378	1.37	1.26	1.62	1.44
8.75		0.1417	1.36	1.18	1.62	1.33
8.5		0.1459	1.29	1.18	1.53	1.33
8.25		0.1503	1.27	1.26	1.50	1.39
8.0		0.1550	1.27	1.34	1.52	1.46
7.75		0.1600	1.33	1.45	1.55	1.57
7.5		0.1653	1.42	1.54	1.69	1.72
7.25		0.1710	1.51	1.66	1.83	1.79
7.0		0.1771	1.73	1.75	2.10	1.81
6.75		0.1837	2.08	1.50	2.34	1.49
6.5		0.1907	2.07	1.34	2.30	1.35
6.25		0.1984	2.00	1.33	2.23	1.36
6.0	48,390	0.2066	1.97	1.50	2.28	1.54
5.75	46,380	0.2156	2.30	1.65	2.85	1.66
5.5	44,360	0.2254	2.65	1.37	3.01	1.20
5.25	42,340	0.2362	2.63	1.05	2.94	0.91
5.0	40,330	0.2480	2.60	0.91	2.88	0.76
4.75	38,310	0.2610	2.60	0.84	2.81	0.67
4.5	36,290	0.2755	2.60	0.74	2.80	0.59
4.25	34,280	0.2917	2.58	0.67	2.77	0.53
4.0	32,260	0.3100	2.57	0.72	2.76	0.58
3.75	30,250	0.3306	2.75	0.45	2.97	0.27
3.5	28,230	0.3542	2.69	0.30	2.80	2.5×10^{-2}
3.444	27,780	0.360	2.705 [48]		2.709 [48]	
3.306	26,670	0.375	2.637		2.640	
3.25	26,210	0.3815	2.62 [26]	0.24	2.64 [26]	1.0×10^{-2}
3.100	25,000	0.400	2.560 [48]		2.564 [48]	
3.024	24,390	0.410	2.539		2.544	
3.0	24,200	0.4133	2.54 [26]	0.18	2.54 [26]	
2.952	23,810	0.420	2.522 [48]		2.525 [48]	
2.917	23,530	0.425	2.511		2.514	
2.883	23,260	0.430	2.502		2.505	
2.818	22,730	0.440	2.486		2.488	
2.755	22,220	0.450	2.473		2.477	
2.75	22,180	0.4509	2.49 [26]	0.15	2.49 [26]	
2.695	21,740	0.460	2.459 [48]		2.463 [48]	
2.638	21,280	0.470	2.448		2.453	
2.610	21,050	0.475	2.445		2.449	
2.583	20,830	0.480	2.438		2.443	

(*continued*)

TABLE XVII (*Continued*)

Hexagonal Zinc Sulfide

eV	cm^{-1}	μm	n_o	k_o	n_e	k_e
2.530	20,410	0.490	2.428		2.433	
2.5	20,160	0.4959	2.42 [26]	0.10	2.42 [26]	
2.480	20,000	0.500	2.421 [48]		2.425 [48]	
2.362	19,050	0.525	2.402		2.407	
2.254	18,180	0.550	2.386		2.392	
2.25	18,150	0.5510		8×10^{-2}		
2.156	17,390	0.575	2.375		2.378	
2.066	16,670	0.600	2.363		2.368	
2.0	16,130	0.6199	2.38 [26]	6	2.36 [26]	
1.984	16,000	0.625	2.354 [48]		2.358 [48]	
1.907	15,380	0.650	2.346		2.350	
1.837	14,810	0.675	2.339		2.343	
1.771	14,290	0.700	2.332		2.337	
1.550	12,500	0.800	2.324		2.328	
1.378	11,110	0.900	2.310		2.315	
1.240	10,000	1.00	2.301		2.303	
1.033	8,333	1.20	2.290		2.294	
0.8856	7,143	1.40	2.285		2.288	
0.6199	5,000	2.0	2.27 [50]			
0.4133	3,333	3.0	2.26			
0.3100	2,500	4.0	2.255			
0.2480	2,000	5.0	2.25			
0.2066	1,667	6.0	2.245			
0.1771	1,492	7.0	2.24			
0.1550	1,250	8.0	2.235			
0.1378	1,111	9.0	2.23			
0.1240	1,000	10.0	2.225			
			2.32 [43]			
0.1033	833.3	12.0	2.29			
0.08856	714.3	14.0	2.24			
0.07749	625.0	16.0	2.18			
0.06888	555.6	18.0	2.11			
0.06199	500.0	20.0	2.00	5.6×10^{-3} [43]		
0.06075	490	20.41	1.98	6.2		
0.05951	480	20.83	1.95	7.0		
0.05827	470	21.28	1.92	7.9		
0.05703	460	21.74	1.88	9.0×10^{-3}		
0.05579	450	22.22	1.84	1.0×10^{-2}		
0.05455	440	22.73	1.79	1.2		
0.05331	430	23.26	1.74	1.4		
0.05207	420	23.81	1.67	1.7		
0.05083	410	24.39	1.59	2.0		
0.04959	400	25.00	1.49	2.5		
0.04835	390	25.64	1.37	3.3		
0.04711	380	26.32	1.21	4.5		

TABLE XVII (*Continued*)

Hexagonal Zinc Sulfide

eV	cm^{-1}	μm	n_o	k_o	n_e	k_e
0.04587	370	27.03	0.97	6.8×10^{-2}		
0.04463	360	27.78	0.57	0.15		
0.04339	350	28.57	0.15	0.72		
0.04215	340	29.41	0.11	1.3		
0.04092	330	30.30	0.11	1.7		
0.03968	320	31.25	0.13	2.2		
0.03844	310	32.26	0.17	2.9		
0.03720	300	33.33	0.25	3.7		
0.03695	298	33.56	0.27	4.0		
0.03670	296	33.78	0.30	4.2		
0.03645	294	34.01	0.34	4.5		
0.03620	292	34.25	0.40	4.8		
0.03596	290	34.48	0.46	5.1		
0.03571	288	34.72	0.56	5.6		
0.03546	286	34.97	0.69	6.1		
0.03521	284	35.21	0.88	6.7		
0.03496	282	35.46	1.19	7.5		
0.03472	280	35.71	1.75	8.6		
0.03447	278	35.97	2.88	10.1		
0.03422	276	36.23	5.61	11.8		
0.03397	274	36.50	10.9	10.6		
0.03372	272	36.76	12.3	5.4		
0.03348	270	37.04	10.7	2.7		
0.03323	268	37.31	9.34	1.6		
0.03298	266	37.59	8.36	1.1		
0.03273	264	37.88	7.64	0.78		
0.03248	262	38.17	7.09	0.59		
0.03224	260	38.46	6.56	0.47		
0.03100	250	40.00	5.38	0.20		
0.02976	240	41.67	4.74	0.11		
0.02852	230	43.48	4.35	7.4×10^{-2}		
0.02728	220	45.45	4.09	5.2		
0.02604	210	47.62	3.90	3.8		
0.02480	200	50.00	3.75	3.0		
0.02356	190	52.63	3.64	2.4		
0.02232	180	55.56	3.55	1.9		
0.02108	170	58.82	3.47	1.6		
0.01984	160	62.50	3.41	1.3		
0.01860	150	66.67	3.36	1.1×10^{-2}		
0.01736	140	71.43	3.32	9.4×10^{-3}		
0.01612	130	76.92	3.28	8.0		
0.01488	120	83.33	3.25	6.9		
0.01364	110	90.91	3.22	5.9		
0.01240	100	100.0	3.20	5.1		

[a] References are given in brackets.

Arsenic Selenide (As_2Se_3)

D. J. TREACY
Physics Department
U.S. Naval Academy
Annapolis, Maryland

The values of n_a, k_a and n_c, k_c listed in Table I and plotted in Fig. 1 are for crystalline material, while the values of n, k listed in Table II and plotted in Fig. 2 are for vitreous (amorphous) material. Values are for room temperature unless otherwise noted.

Crystalline As_2Se_3 In the crystalline phase the results are incomplete, with the major part of the experimental work having been done by reflectance in the one-phonon region, 200 μm (50 cm^{-1}) to 20 μm (500 cm^{-1}) by Zallen *et al.* [1], and in the electronic absorption region, 1.24 μm (1 eV) to 0.089 μm (14 eV) by Zallen *et al.* [2]. There are also transmission measurements in limited portions of both of these ranges.

In the infrared region of the spectrum reflectance measurements were made. Since the samples were opaque, this yielded one-surface reflectivity that was fitted with a Lorentz oscillator model. The fitting procedure was supplemented by including transmission measurements on weaker absorption bands to fix the position and strength of these bands. The root-mean-square uncertainty of the reflectance is quoted. Typically, reflectance measurements can be uncertain by about $\pm 3\%$, but this leads to about a 10% uncertainty in the index of refraction. There are limitations on the data obtained in this fashion. When n and k are substantially different, the value of the smaller is very uncertain.

Arsenic selenide crystallizes in a monoclinic structure [3] and possesses three principal indices of refraction. It exhibits micaceous cleavage perpendicular to the (010) axis, and so the plane of the cleaved sample contains the a and c axes. Therefore, it is difficult to obtain data for E $\|$ b. The data listed were obtained from the published [1] oscillator parameters for E $\|$ a (n_a, k_a) and E $\|$ c (n_c, k_c). The experiment was performed as an investigation of the structure of As_2Se_3 rather than as a definitive work on the optical constants of this material.

For the electronic absorption portion of the spectrum, while a Kramers–Kronig (KK) analysis of reflectivity is discussed for the 1–14-eV region [2],

HANDBOOK OF OPTICAL CONSTANTS OF SOLIDS

Copyright © 1985 by Academic Press, Inc.
All rights of reproduction in any form reserved.
ISBN 0-12-544420-6

no results for ε_1, ε_2 or n, k were given. Values of k listed were obtained in a limited range from 0.69 μm (1.8 eV) to 0.54 μm (2.3 eV), for which transmission measurements were made by using thin samples in a foreprism double-monochromator instrument.

Vitreous As_2Se_3 The vitreous form of As_2Se_3 has been widely investigated. The material is isotropic and thus possesses only one set of n and k. The low-frequency index of refraction is usually stated in the literature as the square root of the real part of the dielectric constant with values ranging from 3.29 ($\varepsilon_1 = 10.84$) at $\lambda \to \infty$ (dc) [4] to 3.03 ± 0.02 ($\varepsilon_1 = 9.2 \pm 0.15$) [5] at $\lambda = 400$ μm to 2.97 ($\varepsilon_1 = 8.87$) [6] at $\lambda = 10^8$ μm. The value of 3.03 ± 0.02 is a good value since it was obtained from a fringe-counting experiment, but it must still be viewed with some caution since k is down by slightly less than an order of magnitude from its value in the reststrahlen region at this wavelength. Since k is comparable to n at this wavelength, the dc and the 400-μm measurements are in substantial agreement.

The k data for the region $\lambda = 8.6 \times 10^4$ to 270 μm are taken from work of Strom and Taylor [7] and were listed in the original paper as $n\alpha$ versus $\bar{\nu}$. This implies that none of the values listed can be more accurate than the value of n used to obtain k. The value of n used in this region was taken from Austin and Garbett [5].

There have been numerous studies of the reflectivity of amorphous As_2Se_3 in the reststrahlen region [5, 8–14]. The values of $\Delta\varepsilon$ for this entire region range from 1.9 [5] to 2.25 [11]. If either the high or the low estimate of $\Delta\varepsilon$ due to the reststrahlen region is used in conjunction with the high-frequency index of refraction, this projects to a low-frequency index of refraction that ranges from 3.1 to 3.2, in reasonable agreement with [4] and [5].

In the reststrahlen region the main features of the reflectivity spectrum can be fit with a combination of damped oscillators [11]. There is a simplicity to this model in that it uses a minimum number of parameters to fit the observed spectrum. There are some drawbacks to this approach in that it does not fit the observed reflectivity spectrum perfectly on the high-energy side of the reststrahlen region and that it overestimates the value of k as one moves away from the resonant frequency. The values of n and k for the region $\lambda = 200$ μm to $\lambda = 25$ μm are taken from the osillator parameters of Lucovsky [11].

In the relatively transparent region there are two transmission studies [15, 16]. In this region the value of n is slowly varying and ranges from 2.77 at 8 μm [17] to 2.81 around 16.7 μm [18]. Both of these measurements are fringe measurements and agree to almost 1%. The differences between measurements are due to uncertainty in the thickness of the sample and composition (impurity content) of the glass. Both measurements were on nominally pure material, and a 3% variation could be expected, depending on the composition of any particular glass.

In the multiphonon region, sample in–sample out measurements of k on

the amorphous material [16] from 25 to 16.7 μm and double-beam measurements [15] from 25 to 11 μm have been made. These measurements are in agreement and both were made on pure materials. Substantial differences can arise, depending on impurity content. Many of these impurity absorptions are referenced in Moynihan *et al.* [15].

There is one study that uses laser calorimetry on As_2Se_3 covering the range from 11 to 4.57 μm [15].The values of k listed in this region were taken for samples that approximate intrinsic absorption.

At the electronic absorption edge there is a prism measurement of the index of refraction from 1.5 to 0.82 μm [19]. The data were fit with a one-oscillator Drude-type model (Sellmeier equation) and for reasonably pure material over this spectral region represents better than a 1% fit. Some caution should be exercised as to the purity of the material before applying these indices uncritically.

Absorption data are available from 0.84 to 0.60 μm [2, 20]. In the low k region this material is very sensitive to impurities. The values listed represent pure material.

Reflectivity data are available [2] to 0.1 μm, but the details of the KK analysis done on both crystalline and amorphous materials have not been given.

Vitreous has been used here to describe a material that when cooled down in the molten state solidifies into the amorphous state. There are, of course, other ways to make amorphous materials.

REFERENCES

1. R. Zallen, M. L. Slade, and A. T. Ward, *Phys. Rev. B* **3**, 4257 (1971).
2. R. Zallen, R. E. Drews, R. L. Emerald, and M. L. Slade, *Phys. Rev Lett.* **26**, 1564 (1971).
3. A. A. Vaipolin, *Sov. Phys. Cryst.* **10**, 509 (1966).
4. J. J. Fontenella, private communication, (1975).
5. I. G. Austin and E. S. Garbett, *Philos. Mag.* **23**, 17 (1971).
6. E. B. Ivkin and B. T. Kolomiets, *J. Non-Cryst. Solids* **3**, 41 (1970).
7. U. Strom and P. C. Taylor, *Phys. Rev. B* **16**, 5512 (1977).
8. M. Onomichi, T. Arai, and K. Kudo, *J. Non-Cryst. Solids* **6**, 362 (1971).
9. L. B. Zlatkin and Y. F. Markov. *Phys. Stat. Solidi A* **4**, 391 (1971).
10. G. Lucovsky, *Mater. Res. Bull.* **4**, 505 (1969).
11. G. Lucovsky, *Phys. Rev. B* **6**, 1480 (1972).
12. P. C. Taylor, S. G. Bishop, and D. L. Mitchell, *Solid State Commun.* **8**, 1783 (1970).
13. D. L. Mitchell, S. G. Bishop, and P. C. Taylor, *J. Non-Cryst. Solids* **8–10**, 231 (1972).
14. P. C. Taylor, S. G. Bishop, and D. L. Mitchell, *Proc. Int. Conf. Phonons, Rennes, 1971*, p. 199. Flammarion Science, Paris, 1971.
15. C. T. Moynihan, P. B. Macedo, M. S. Maklad, R. K. Mohr, and R. E. Howard, *J. Non-Cryst. Solids* **17**, 369 (1975).
16. D. J. Treacy and P. C. Taylor, *in* "Optical Properties of Highly Transparent Solids" (S. S. Mitra and B. Bendow, eds.), p. 261. Plenum, New York, 1975.
17. J. T. Edmond and H. W. Redfern, *Proc. Phys. Soc. London* **81**, 382 (1963).
18. D. J. Treacy, unpublished fringe measurements (1978).
19. Y. Ohmachi, *J. Opt. Soc. Am.* **63**, 630 (1973).
20. D. J. Treacy, P. C. Taylor, and P. B. Klein, *Solid State Commun.* **32**, 423 (1979).

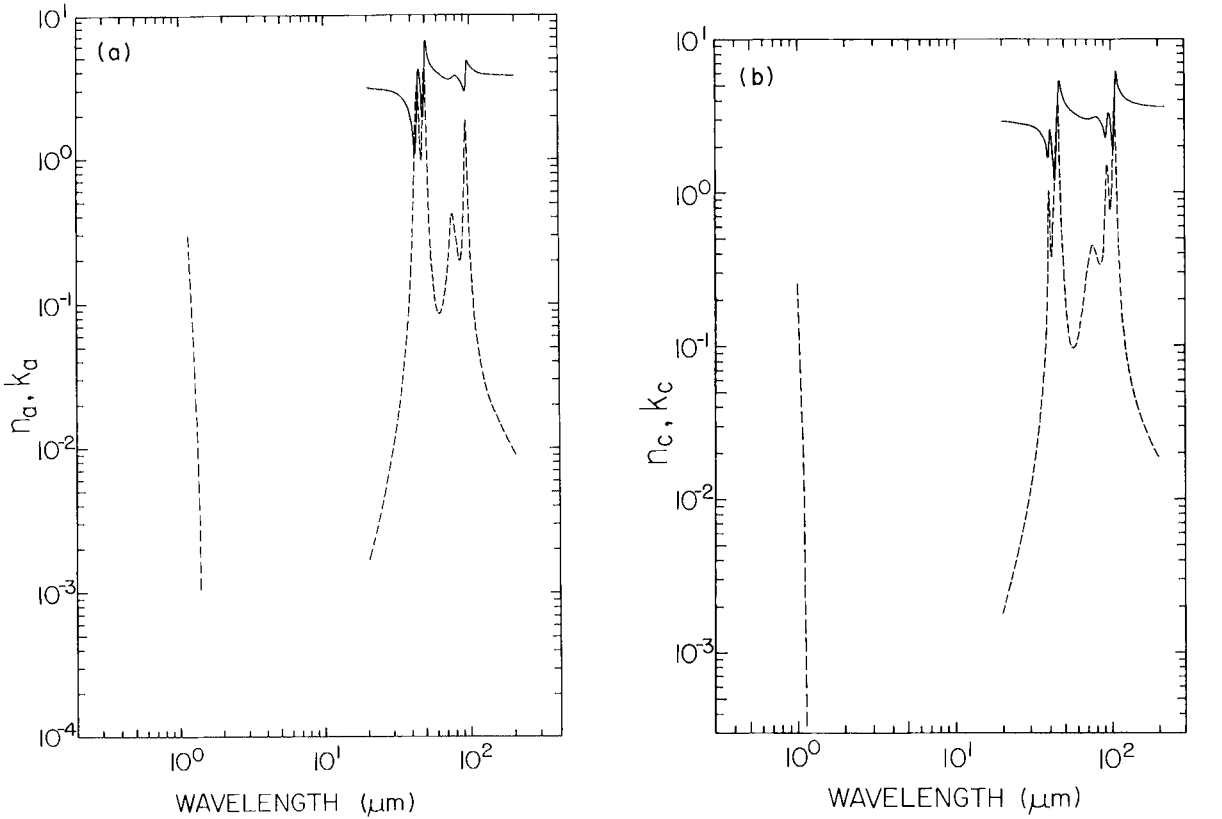

Fig. 1. (a) Log–log plot of n_a(——) and k_a(– – – –) versus wavelength in micrometers for crystalline As_2Se_3. (b) Log–log plot of n_c(——) and k_c(– – – –) versus wavelength in micrometers for crystalline As_2Se_3.

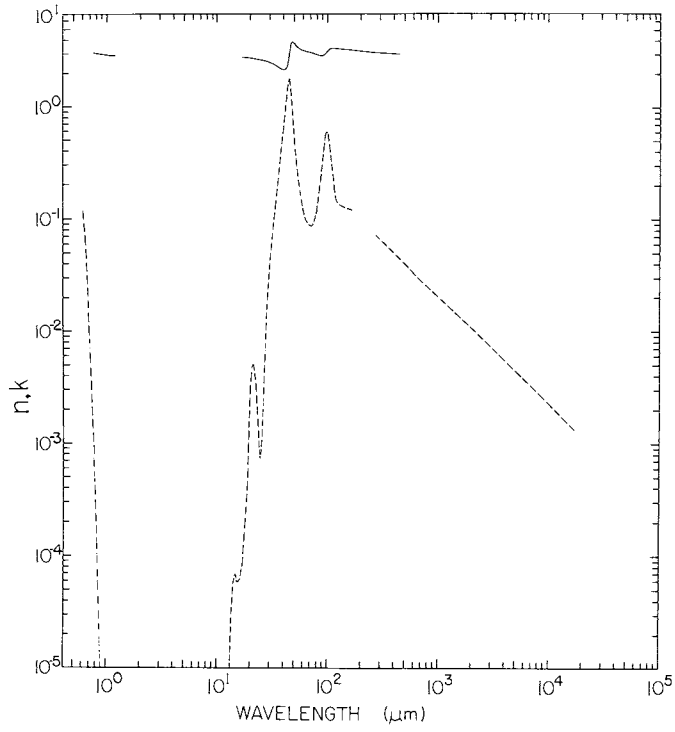

Fig. 2. Log–log plot of n (——) and k(– – – –) versus wavelength in micrometers for vitreous As_2Se_3. Two significant figures are sometimes not enough to show a smooth variation in n and k, and so the curves have been drawn through these points to smooth out steps.

TABLE I

Values of n and k for Crystalline As_2Se_3 from Various References[a]

eV	cm^{-1}	μm	n_a	n_c	k_a	k_c
2.194	17,700	0.565			0.30 [2]	
2.168	17,480	0.572			0.25	
2.141	17,270	0.579			0.20	
2.123	17,120	0.584			0.17	
2.098	16,920	0.591			0.13	
2.094	16,890	0.592				0.26 [2]
2.091	16,860	0.593				0.26
2.073	16,720	0.598			0.10	0.23
2.060	16,610	0.602				0.20
2.049	16,530	0.605			0.079	0.17
2.036	16,420	0.609				0.15
2.023	16,310	0.613				0.12
2.013	16,230	0.616			0.050	
2.009	16,210	0.617				0.097

(*continued*)

TABLE I (*Continued*)

Crystalline As_2Se_3

eV	cm^{-1}	μm	n_a	n_c	k_a	k_c
2.000	16,130	0.620				0.082
1.987	16,030	0.624				0.063
1.977	15,940	0.627			0.031	
1.974	15,920	0.628				0.051
1.962	15,820	0.632				0.038
1.953	15,750	0.635				0.030
1.949	15,720	0.636			0.020	
1.937	15,630	0.640				0.022
1.925	15,530	0.644				0.017
1.922	15,500	0.645			0.012	
1.905	15,360	0.651			8.6×10^{-3}	
1.893	15,270	0.655			6.4	
1.881	15,170	0.659			5.2	
1.859	14,990	0.667			3.1	
1.848	14,900	0.671				1.7×10^{-3}
1.845	14,880	0.672			2.0	
1.842	14,860	0.673				1.2×10^{-3}
1.831	14,770	0.677			1.3×10^{-3}	9.0×10^{-4}
1.826	14,730	0.679				6.4
1.821	14,680	0.681				4.7
1.818	14,660	0.682			8.6×10^{-4}	
1.815	14,640	0.683				3.4
1.807	14,580	0.686			5.5	
1.802	14,530	0.688			4.1	
0.06199	500.0	20.0	3.2 [1]	2.9 [1]	1.7×10^{-3} [1]	1.8×10^{-3} [1]
0.05904	476.2	21.0	3.1	2.9	2.1	2.2
0.05636	454.5	22.0	3.1	2.9	2.5	2.6
0.05391	434.8	23.0	3.1	2.9	3.0	3.1
0.05166	416.7	24.0	3.1	2.8	3.6	3.7
0.04959	400.0	25.0	3.1	2.8	4.3	4.5
0.04769	384.6	26.0	3.1	2.8	5.2	5.3
0.04592	370.4	27.0	3.0	2.8	6.3	6.4
0.04428	357.1	28.0	3.0	2.8	7.6	7.7
0.04275	344.8	29.0	3.0	2.8	9.2×10^{-3}	9.3×10^{-3}
0.04133	333.3	30.0	3.0	2.7	0.011	0.011
0.04065	327.9	30.5	2.9	2.7	0.012	0.012
0.04000	322.6	31.0	2.9	2.7	0.014	0.014
0.03936	317.5	31.5	2.9	2.7	0.015	0.015
0.03875	312.5	32.0	2.9	2.7	0.017	0.017
0.03815	307.7	32.5	2.9	2.6	0.019	0.019
0.03757	303.0	33.0	2.8	2.6	0.021	0.021
0.03701	298.6	33.5	2.8	2.6	0.024	0.023
0.03647	294.1	34.0	2.8	2.6	0.027	0.027
0.03594	289.9	34.5	2.7	2.6	0.031	0.030
0.03542	285.7	35.0	2.7	2.5	0.037	0.034
0.03493	281.7	35.5	2.7	2.5	0.040	0.040
0.03444	277.8	36.0	2.6	2.4	0.046	0.046

TABLE I (*Continued*)

Crystalline As_2Se_3

eV	cm^{-1}	μm	n_a	n_c	k_a	k_c
0.03397	274.0	36.5	2.6	2.4	0.053	0.054
0.03351	270.3	37.0	2.5	2.3	0.063	0.066
0.03306	266.7	37.5	2.4	2.3	0.083	0.081
0.03263	263.2	38.0	2.4	2.2	0.089	0.10
0.03220	259.7	38.5	2.3	2.1	0.11	0.14
0.03179	256.4	39.0	2.2	2.0	0.14	0.21
0.03139	253.2	39.5	2.1	1.7	0.19	0.41
0.03100	250.0	40.0	1.9	1.7	0.38	1.0
0.03061	247.0	40.5	2.0	2.6	0.33	0.95
0.03024	244.0	41.0	1.7	2.4	0.41	0.46
0.02988	241.0	41.5	1.4	2.1	0.62	0.38
0.02952	238.1	42.0	1.2	1.9	1.0	0.44
0.02917	235.3	42.5	1.1	1.6	1.6	0.61
0.01883	232.6	43.0	1.2	1.3	2.2	0.94
0.02850	229.9	43.5	1.6	1.2	2.8	1.4
0.02818	227.3	44.0	2.3	1.2	3.3	2.0
0.02786	224.7	44.5	3.4	1.5	3.3	2.7
0.02755	222.2	45.0	4.2	2.0	2.5	3.3
0.02725	219.8	45.5	4.1	3.0	1.6	3.9
0.02695	217.4	46.0	3.7	4.4	1.2	3.7
0.02666	215.1	46.5	3.3	5.2	1.0	2.6
0.02638	212.8	47.0	2.8	5.3	1.1	1.6
0.02610	210.5	47.5	2.3	5.0	1.5	1.0
0.02583	208.3	48.0	2.0	4.7	2.2	0.71
0.02556	206.2	48.5	2.2	4.5	3.2	0.52
0.02530	204.1	49.0	3.0	4.3	4.3	0.40
0.02505	202.0	49.5	4.8	4.2	4.8	0.32
0.02480	200.0	50.0	6.5	4.0	3.6	0.26
0.02455	198.0	50.5	6.6	3.9	2.0	0.22
0.02431	196.1	51.0	6.1	3.9	1.2	0.19
0.02407	194.2	51.5	5.7	3.8	0.76	0.17
0.02384	192.3	52.0	5.4	3.7	0.54	0.15
0.02362	190.5	52.5	5.2	3.7	0.41	0.14
0.02339	188.7	53.0	5.0	3.6	0.33	0.13
0.02317	186.9	53.5	4.8	3.6	0.27	0.12
0.02296	185.2	54.0	4.7	3.5	0.23	0.11
0.02275	183.5	54.5	4.6	3.5	0.20	0.11
0.02254	181.8	55.0	4.5	3.5	0.17	0.10
0.02234	180.2	55.5	4.5	3.4	0.15	0.10
0.02214	178.6	56.0	4.4	3.4	0.14	0.099
0.02194	177.0	56.5	4.3	3.4	0.13	0.098
0.02175	175.4	57.0	4.3	3.4	0.12	0.097
0.02156	173.9	57.5	4.2	3.3	0.11	0.097
0.02138	172.4	58.0	4.2	3.3	0.10	0.097
0.02119	170.9	58.5	4.1	3.3	0.098	0.098
0.02101	169.5	59.0	4.1	3.3	0.094	0.10

(*continued*)

TABLE I (*Continued*)

Crystalline As_2Se_3

eV	cm^{-1}	μm	n_a	n_c	k_a	k_c
0.02084	168.1	59.5	4.1	3.3	0.091	0.10
0.02066	166.7	60.0	4.0	3.2	0.089	0.10
0.02049	165.3	60.5	4.0	3.2	0.087	0.11
0.02033	163.9	61.0	4.0	3.2	0.086	0.11
0.02016	162.6	61.5	4.0	3.2	0.085	0.12
0.02000	161.3	62.0	3.9	3.2	0.085	0.12
0.01984	160.0	62.5	3.9	3.2	0.086	0.13
0.01968	158.7	63.0	3.9	3.1	0.087	0.13
0.01953	157.5	63.5	3.9	3.1	0.088	0.14
0.01937	156.3	64.0	3.8	3.1	0.091	0.15
0.01922	155.0	64.5	3.8	3.1	0.093	0.15
0.01907	153.8	65.0	3.8	3.1	0.097	0.16
0.01893	152.7	65.5	3.8	3.1	0.10	0.17
0.01879	151.5	66.0	3.8	3.1	0.11	0.18
0.01864	150.4	66.5	3.7	3.0	0.11	0.20
0.01851	149.3	67.0	3.7	3.0	0.12	0.21
0.01837	148.1	67.5	3.7	3.0	0.13	0.22
0.01823	147.1	68.0	3.7	3.0	0.14	0.24
0.01810	146.0	68.5	3.7	3.0	0.15	0.25
0.01797	144.9	69.0	3.6	3.0	0.16	0.27
0.01784	143.9	69.5	3.6	3.0	0.18	0.28
0.01771	142.9	70.0	3.6	3.0	0.19	0.30
0.01759	141.8	70.5	3.6	3.0	0.21	0.32
0.01746	140.8	71.0	3.6	3.0	0.23	0.33
0.01734	139.9	71.5	3.6	3.0	0.26	0.35
0.01722	138.9	72.0	3.6	3.0	0.28	0.37
0.01710	137.9	72.5	3.6	3.0	0.31	0.38
0.01698	137.0	73.0	3.6	3.0	0.33	0.40
0.01687	136.1	73.5	3.6	3.0	0.36	0.41
0.01675	135.1	74.0	3.6	3.0	0.38	0.42
0.01664	134.2	74.5	3.6	3.0	0.40	0.43
0.01653	133.3	75.0	3.7	3.0	0.41	0.44
0.01642	132.4	75.5	3.7	3.0	0.42	0.44
0.01631	131.6	76.0	3.7	3.1	0.42	0.45
0.01621	130.7	76.5	3.7	3.1	0.41	0.45
0.01610	129.9	77.0	3.7	3.1	0.40	0.44
0.01600	129.0	77.5	3.8	3.1	0.38	0.44
0.01590	128.2	78.0	3.8	3.1	0.37	0.43
0.01579	127.4	78.5	3.8	3.1	0.35	0.43
0.01569	126.6	79.0	3.8	3.1	0.33	0.42
0.01560	125.8	79.5	3.8	3.1	0.31	0.41
0.01550	125.0	80.0	3.8	3.1	0.29	0.40
0.01540	124.2	80.5	3.8	3.1 [1]	0.27	0.39
0.01531	123.4	81.0	3.8 [1]	3.1	0.26	0.38
0.01521	122.7	81.5	3.7	3.1	0.24	0.37
0.01512	122.0	82.0	3.7	3.1	0.23	0.37
0.01503	121.2	82.5	3.7	3.0	0.22	0.36

TABLE I (*Continued*)

Crystalline As_2Se_3

eV	cm^{-1}	μm	n_a	n_c	k_a	k_c
0.01494	120.5	83.0	3.7	3.0	0.21	0.35
0.01485	119.8	83.5	3.7	3.0	0.21	0.35
0.01476	119.0	84.0	3.7	3.0	0.20	0.34
0.01467	118.3	84.5	3.6	3.0	0.20	0.34
0.01459	117.6	85.0	3.6	2.9	0.20	0.34
0.01450	117.0	85.5	3.6	2.9	0.20	0.34
0.01442	116.3	86.0	3.5	2.9	0.21	0.34
0.01433	115.6	86.5	3.5	2.9	0.21	0.34
0.01425	114.9	87.0	3.5	2.8	0.22	0.35
0.01417	114.3	87.5	3.4	2.8	0.24	0.36
0.01409	113.6	88.0	3.4	2.8	0.26	0.37
0.01401	113.0	88.5	3.4	2.7	0.28	0.39
0.01393	112.3	89.0	3.3	2.7	0.32	0.42
0.01384	111.7	89.5	3.2	2.6	0.37	0.45
0.01378	111.1	90.0	3.2	2.6	0.43	0.49
0.01370	110.5	90.5	3.1	2.5	0.52	0.55
0.01362	109.9	91.0	3.0	2.4	0.64	0.62
0.01355	109.3	91.5	3.0	2.4	0.81	0.71
0.01348	108.7	92.0	3.0	2.3	1.0	0.83
0.01340	108.1	92.5	3.0	2.3	1.3	0.97
0.01333	107.5	93.0	3.2	2.4	1.6	1.1
0.01326	107.0	93.5	3.5	2.4	1.8	1.3
0.01319	106.4	94.0	4.0	2.6	1.9	1.5
0.01312	105.8	94.5	4.4	2.8	1.8	1.5
0.01305	105.3	95.0	4.7	3.0	1.5	1.5
0.01298	104.7	95.5	4.8	3.2	1.2	1.5
0.01292	104.2	96.0	4.8	3.3	0.94	1.3
0.01284	103.6	96.5	4.8	3.3	0.74	1.2
0.01278	103.1	97.0	4.7	3.3	0.59	1.0
0.01272	102.6	97.5	4.7	3.3	0.48	0.92
0.01265	102.0	98.0	4.6	3.2	0.40	0.84
0.01259	101.5	98.5	4.5	3.1	0.34	0.79
0.01252	101.0	99.0	4.5	3.0	0.29	0.77
0.01246	100.5	99.5	4.5	2.8	0.25	0.78
0.01240	100.0	100.0	4.4	2.7	0.22	0.81
0.01228	99.01	101.0	4.3	2.4	0.18	1.0
0.01216	98.04	102.0	4.3	2.1	0.15	1.4
0.01204	97.09	103.0	4.2	1.9	0.12	2.1
0.01192	96.15	104.0	4.2	2.2	0.11	3.0
0.01181	95.24	105.0	4.2	3.0	0.094	3.9
0.01170	94.34	106.0	4.1	4.7	0.084	4.1
0.01159	93.46	107.0	4.1	6.0	0.076	3.0
0.01148	92.59	108.0	4.1	6.1	0.069	1.7
0.01137	91.74	109.0	4.1	5.7	0.064	1.0
0.01127	90.91	110.0	4.1	5.3	0.059	0.70
0.01117	90.09	111.0	4.0	5.1	0.055	0.51

(*continued*)

TABLE I (*Continued*)

Crystalline As_2Se_3

eV	cm^{-1}	μm	n_a	n_c	k_a	k_c
0.01107	89.29	112.0	4.0	4.9	0.051	0.39
0.01097	88.50	113.0	4.0	4.8	0.048	0.31
0.01088	87.72	114.0	4.0	4.7	0.045	0.26
0.01078	86.96	115.0	4.0	4.6	0.043	0.22
0.01069	86.21	116.0	4.0	4.5	0.041	0.19
0.01060	85.47	117.0	4.0	4.4	0.039	0.17
0.01051	84.75	118.0	4.0	4.3	0.037	0.15
0.01042	84.03	119.0	4.0	4.3	0.036	0.14
0.01033	83.33	120.0	3.9	4.2	0.034	0.13
0.01025	82.64	121.0	3.9	4.2	0.033	0.12
0.01016	81.97	122.0	3.9	4.2	0.032	0.11
0.01008	81.30	123.0	3.9	4.1	0.030	0.10
0.009999	80.65	124.0	3.9	4.1	0.029	0.094
0.009919	80.00	125.0	3.9	4.1	0.028	0.088
0.009840	79.37	126.0	3.9	4.0	0.028	0.083
0.009763	78.74	127.0	3.9	4.0	0.027	0.079
0.009686	78.12	128.0	3.9	4.0	0.026	0.075
0.009611	77.52	129.0	3.9	4.0	0.025	0.072
0.009537	76.92	130.0	3.9	4.0	0.024	0.069
0.009465	76.34	131.0	3.9	4.0	0.024	0.066
0.009393	75.76	132.0	3.9	3.9	0.023	0.063
0.009322	75.19	133.0	3.9	3.9	0.023	0.061
0.009253	74.63	134.0	3.9	3.9	0.022	0.059
0.009184	74.07	135.0	3.9	3.9	0.022	0.057
0.009117	73.53	136.0	3.9	3.9	0.021	0.055
0.009050	72.99	137.0	3.9	3.9	0.021	0.053
0.008984	72.46	138.0	3.9	3.9	0.020	0.051
0.008920	71.94	139.0	3.9	3.9	0.020	0.050
0.008856	71.43	140.0	3.9	3.8	0.019	0.048
0.008551	68.97	145.0	3.9	3.8	0.018	0.043
0.008266	66.67	150.0	3.8	3.8	0.016	0.038
0.007999	64.52	155.0	3.8	3.7	0.015	0.034
0.007749	62.50	160.0	3.8	3.7	0.014	0.032
0.007514	60.61	165.0	3.8	3.7	0.013	0.029
0.007293	58.82	170.0	3.8	3.7	0.012	0.027
0.007085	57.14	175.0	3.8	3.7	0.012	0.025
0.006888	55.55	180.0	3.8	3.7	0.011	0.024
0.006702	54.05	185.0	3.8	3.7	0.010	0.022
0.006526	52.63	190.0	3.8	3.6	0.010	0.021
0.006358	51.28	195.0	3.8	3.6	9.5×10^{-3}	0.020
0.006199	50.00	200.0	3.8	3.6	9.1	0.019

[a] The radiation electric field is parallel to the *a* and *c* axes of the crystal. References are indicated in brackets and a reference applies down the column until a new bracket appears. Usually, two significant figures are given.

TABLE II

Values of n and k for Vitreous As_2Se_3[a]

eV	cm^{-1}	μm	n	k
2.056	16,580	0.603		0.12 [2]
2.039	16,450	0.608		0.11
2.026	16,340	0.612		0.11
2.006	16,180	0.618		9.9×10^{-2}
1.990	16,050	0.623		9.0
1.965	15,850	0.631		7.6
1.946	15,700	0.637		6.8
1.925	15,530	0.644		5.6
1.905	15,360	0.651		4.5
1.876	15,130	0.661		3.1
1,848	14,900	0.671		2.1
1.826	14,730	0.679		1.4
1.810	14,600	0.685		1.2×10^{-2}
1.794	14,470	0.691		8.9×10^{-3}
1.771	14,290	0.700		6.2
1.749	14,100	0.709		4.5
1.729	13,950	0.717		3.3
1.715	13,830	0.723		2.6
1.701	13,720	0.729		2.2×10^{-3}
1.647	13,280	0.753		4.6×10^{-4}
1.629	13,140	0.761	3.07 [19]	4.0
1.596	12,870	0.777	3.06	2.7
1.579	12,740	0.785	3.05	1.9
1.562	12,590	0.794	3.05	1.3×10^{-4}
1.544	12,450	0.803	3.04	9.4×10^{-5}
1.529	12,330	0.811	3.03	6.3
1.512	12,200	0.820	3.03	4.2
1.494	12,050	0.830	3.02	2.8
1.476	11,910	0.840	3.01	1.8
1.442	11,630	0.86	3.00	
1.409	11,360	0.88	2.99	
1.378	11,110	0.90	2.98	
1.348	10,870	0.92	2.97	
1.319	10,640	0.94	2.96	
1.292	10,420	0.96	2.95	
1.265	10,200	0.98	2.94	
1.240	10,000	1.00	2.93	
1.216	9,804	1.02	2.93	
1.192	9,615	1.04	2.92	
1.170	9,434	1.06	2.92	
1.148	9,259	1.08	2.92	
1.127	9,091	1.10	2.90	
1.107	8,929	1.12	2.90	
1.088	8,772	1.14	2.89	
1.069	8,621	1.16	2.89	
1.051	8,475	1.18	2.89	

(*continued*)

TABLE II (*Continued*)

Vitreous As_2Se_3

eV	cm^{-1}	μm	n	k
1.033	8,333	1.20	2.88	
0.2555	1,980	5.05		1.6×10^{-7} [15]
0.2380	1,919	5.21		9.9×10^{-8}
0.2344	1,890	5.29		1.1×10^{-7}
0.1345	1,085	9.22		4.4
0.1339	1,080	9.26		3.7
0.1333	1,075	9.30		4.4
0.1308	1,055	9.48		4.5
0.1302	1,050	9.52		4.9
0.1289	1,040	9.62		6.1
0.1277	1,030	9.71		6.6
0.1227	990	10.10		8.4 [15]
0.1215	980	10.20		8.9
0.1203	970	10.31		9.9×10^{-7}
0.1196	965	10.36		1.0×10^{-6}
0.1178	950	10.53		1.1
0.1170	943.4	10.60		1.3
0.1165	940	10.64		1.1
0.1159	935	10.70		1.1
0.1147	925	10.81		1.2
0.1141	920	10.87		1.1
0.1116	900	11.11		1.8
0.1103	890	11.24		1.8
0.1091	880	11.36		1.8
0.1079	870	11.49		1.8
0.1066	860	11.63		1.9
0.1054	850	11.76		1.9
0.1041	840	11.90		2.3
0.1029	830	12.05		2.9
0.1017	820	12.20		3.9
0.1004	810	12.35		4.9
0.09919	800	12.50		7.0×10^{-6}
0.09795	790	12.66		1.0×10^{-5}
0.09671	780	12.82		1.5
0.09547	770	12.99		2.2
0.09423	760	13.16		2.9
0.09299	750	13.33		3.7
0.09175	740	13.51		4.3
0.09051	730	13.70		5.5
0.08927	720	13.89		6.1
0.08803	710	14.08		6.7
0.08679	700	14.29		6.8
0.08555	690	14.49		6.9
0.08431	680	14.71		5.9
0.08307	670	14.93		5.9
0.08183	660	15.15		6.0
0.08059	650	15.38		6.1

TABLE II (*Continued*)

Vitreous As_2Se_3

eV	cm^{-1}	μm	n	k
0.07935	640	15.63		6.2
0.07811	630	15.87		6.3
0.07687	620	16.13		7.7
0.07563	610	16.39		7.8
0.07439	600	16.67		9.3×10^{-5} [16]
0.07315	590	16.95	2.8 [16]	1.2×10^{-4}
0.07191	580	17.24	2.8	1.4
0.07067	570	17.54	2.8	1.8
0.06943	560	17.86	2.8	2.8
0.06819	550	18.18	2.8	3.3
0.06695	540	18.52	2.8	4.3
0.06633	535	18.69	2.8	5.2
0.06571	530	18.87	2.8	7.2×10^{-4}
0.06509	525	19.05	2.8	1.2×10^{-3}
0.06447	520	19.23	2.8	1.7
0.06385	515	19.42	2.8	2.2
0.06323	510	19.61	2.8	2.8
0.06261	505	19.80	2.8	3.3
0.06199	500	20.00	2.8	4.0
0.06137	495	20.20	2.7	4.3
0.06075	490	20.41	2.7	4.9
0.06024	485.9	20.58	2.7	5.2
0.06013	485	20.62	2.7	5.1
0.05951	480	20.83	2.7	5.1
0.05889	475	21.05	2.7	5.2
0.05827	470	21.28	2.7	4.9
0.05765	465	21.51	2.7	4.6
0.05703	460	21.74	2.7	4.2
0.05641	455	21.98	2.7	3.7
0.05579	450	22.22	2.7	3.2
0.05517	445	22.47	2.7	2.5
0.05455	440	22.73	2.7	2.2
0.05393	435	22.99	2.7	1.7
0.05331	430	23.26	2.7	1.4
0.05269	425	23.53	2.7	1.1×10^{-3}
0.05207	420	23.81	2.7	8.5×10^{-4}
0.05145	415	24.10	2.7	7.3
0.05083	410	24.39	2.7	8.3
0.05021	405	24.69	2.7	9.4×10^{-4}
0.04959	400	25.0	2.7 [11]	1.2×10^{-3} [11]
0.04862	392.2	25.5	2.6	1.6
0.04769	384.6	26.0	2.6	3.9
0.04679	377.4	26.5	2.6	5.0
0.04592	370.4	27.0	2.6	8.0×10^{-3}
0.04509	363.6	27.5	2.6	1.2×10^{-2}

(*continued*)

TABLE II (*Continued*)

Vitreous As_2Se_3

eV	cm^{-1}	μm	n	k
0.04428	357.1	28.0	2.6	1.7
0.04350	350.9	28.5	2.6	2.2
0.04275	344.8	29.0	2.6	2.8
0.04203	339.0	29.5	2.6	3.6
0.04133	333.3	30.0	2.5	4.4
0.04065	327.9	30.5	2.5	5.3
0.04000	322.6	31.0	2.5	6.3
0.03936	317.5	31.5	2.5	7.3
0.03875	312.5	32.0	2.5	8.2
0.03815	307.7	32.5	2.5	9.3×10^{-2}
0.03757	303.0	33.0	2.4	0.11
0.03701	298.5	33.5	2.4	0.12
0.03647	294.1	34.0	2.4	0.14
0.03594	289.9	34.5	2.4	0.16
0.03542	285.7	35.0	2.3	0.18
0.03493	281.7	35.5	2.3	0.21
0.03444	277.8	36.0	2.3	0.24
0.03397	274.0	36.5	2.3	0.28
0.03351	270.3	37.0	2.2	0.32
0.03306	266.7	37.5	2.2	0.37
0.03263	263.2	38.0	2.2	0.42
0.03220	259.7	38.5	2.2	0.48
0.03179	256.4	39.0	2.2	0.54
0.03139	253.2	39.5	2.2	0.60
0.03100	250.0	40.0	2.2	0.67
0.03061	246.9	40.5	2.2	0.73
0.03024	243.9	41.0	2.2	0.81
0.02988	241.0	41.5	2.2	0.89
0.02952	238.1	42.0	2.2	1.0
0.02917	235.3	42.5	2.2	1.1
0.02883	232.6	43.0	2.2	1.3
0.02850	229.9	43.5	2.3	1.4
0.02818	227.3	44.0	2.5	1.6
0.02786	224.7	44.5	2.7	1.7
0.02755	222.2	45.0	2.9	1.8
0.02725	219.8	45.5	3.2	1.8
0.02695	217.4	46.0	3.5	1.7
0.02666	215.1	46.5	3.7	1.5
0.02638	212.8	47.0	3.8	1.3
0.02610	210.5	47.5	3.8	1.1
0.02583	208.3	48.0	3.9	0.94
0.02556	206.2	48.5	3.8	0.80
0.02530	204.1	49.0	3.8	0.68
0.02505	202.0	49.5	3.8	0.59
0.02480	200.0	50.0	3.7	0.52
0.02455	198.0	50.5	3.7	0.45
0.02431	196.1	51.0	3.7	0.40

TABLE II (*Continued*)

Vitreous As_2Se_3

eV	cm^{-1}	μm	n	k
0.02407	194.2	51.5	3.6	0.36
0.02384	192.3	52.0	3.6	0.33
0.02362	190.5	52.5	3.6	0.30
0.02339	188.7	53.0	3.5	0.27
0.02317	186.9	53.5	3.5	0.25
0.02296	185.2	54.0	3.4	0.23
0.02275	183.5	54.5	3.5	0.22
0.02254	181.8	55.0	3.4	0.20
0.02234	180.2	55.5	3.4	0.19
0.02214	178.6	56.0	3.4	0.18
0.02194	177.0	56.5	3.4	0.17
0.02175	175.4	57.0	3.4	0.16
0.02156	173.9	57.5	3.4	0.15
0.02138	172.4	58.0	3.3	0.14
0.02119	170.9	58.5	3.3	0.14
0.02101	169.5	59.0	3.3	0.13
0.02184	168.1	59.5	3.3	0.13
0.02066	166.7	60.0	3.3	0.12
0.02049	165.3	60.5	3.3	0.12
0.02033	163.9	61.0	3.3	0.11
0.02016	162.6	61.5	3.3	0.11
0.02000	161.3	62.0	3.2	0.10
0.01984	160.0	62.5	3.2	0.10
0.01968	158.7	63.0	3.2	0.10
0.01953	157.5	63.5	3.2	0.10
0.01937	156.2	64.0	3.2	0.10
0.01922	155.0	64.5	3.2	9.6×10^{-2}
0.01907	153.8	65.0	3.2	9.4
0.01893	152.7	65.5	3.2	9.3
0.01879	151.5	66.0	3.2	9.1
0.01864	150.4	66.5	3.2	9.0
0.01851	149.2	67.0	3.2	8.9
0.01837	148.1	67.5	3.2	8.8
0.01823	147.1	68.0	3.2	8.8
0.01810	146.0	68.5	3.1	8.7
0.01797	144.9	69.0	3.1	8.7
0.01784	143.9	69.5	3.1	8.7
0.01771	142.9	70.0	3.1	8.7
0.01759	141.8	70.5	3.1	8.7
0.01746	140.8	71.0	3.1	8.7
0.01734	139.9	71.5	3.1	8.7
0.01722	138.9	72.0	3.1	8.8
0.01710	137.9	72.5	3.1	8.8
0.01698	137.0	73.0	3.1	8.9
0.01687	136.1	73.5	3.1	9.0

(*continued*)

TABLE II (*Continued*)

Vitreous As_2Se_3

eV	cm^{-1}	μm	n	k
0.01675	135.1	74.0	3.1	9.1
0.01664	134.2	74.5	3.1	9.2
0.01653	133.3	75.0	3.1	9.4
0.01642	132.5	75.5	3.1	9.6×10^{-2}
0.01631	131.6	76.0	3.0	0.10
0.01621	130.7	76.5	3.0	0.10
0.01610	129.9	77.0	3.0	0.10
0.01600	129.0	77.5	3.0	0.10
0.01590	128.2	78.0	3.0	0.11
0.01579	127.4	78.5	3.0	0.11
0.01569	126.6	79.0	3.0	0.11
0.01560	125.8	79.5	3.0	0.12
0.01550	125.0	80.0	3.0	0.12
0.01540	124.2	80.5	3.0	0.13
0.01531	123.5	81.0	3.0	0.13
0.01521	122.7	81.5	3.0	0.14
0.01512	121.9	82.0	3.0	0.14
0.01503	121.2	82.5	3.0	0.15
0.01494	120.5	83.0	3.0	0.15
0.01485	119.8	83.5	2.9	0.16
0.01476	119.0	84.0	2.9	0.17
0.01467	118.3	84.5	2.9	0.18
0.01459	117.6	85.0	2.9	0.19
0.01450	117.0	85.5	2.9	0.19
0.01442	116.3	86.0	2.9	0.21
0.01433	115.6	86.5	2.9	0.22
0.01425	114.9	87.0	2.9	0.23
0.01417	114.3	87.5	2.9	0.24
0.01409	113.6	88.0	2.9	0.25
0.01401	113.0	88.5	2.9	0.27
0.01393	112.4	89.0	2.9	0.29
0.01384	111.7	89.5	2.9	0.30
0.01378	111.1	90.0	2.9	0.32
0.01370	110.5	90.5	2.9	0.34
0.01362	109.9	91.0	2.9	0.36
0.01355	109.3	91.5	2.9	0.38
0.01348	108.7	92.0	2.9	0.40
0.01340	108.1	92.5	2.9	0.42
0.01333	107.5	93.0	2.9	0.44
0.01326	106.9	93.5	2.9	0.47
0.01319	106.4	94.0	2.9	0.49
0.01312	105.8	94.5	2.9	0.51
0.01305	105.3	95.0	3.0	0.53
0.01298	104.7	95.5	3.0	0.55
0.01292	104.2	96.0	3.0	0.56
0.01285	103.6	96.5	3.0	0.58
0.01278	103.1	97.0	3.1	0.59

TABLE II (*Continued*)

Vitreous As_2Se_3

eV	cm^{-1}	μm	n	k
0.01272	102.6	97.5	3.1	0.60
0.01265	102.0	98.0	3.1	0.60
0.01259	101.5	98.5	3.2	0.60
0.01252	101.0	99.0	3.2	0.60
0.01246	100.5	99.5	3.2	0.60
0.01240	100.0	100.0	3.2	0.59
0.01228	99.01	101.0	3.3	0.57
0.01216	98.04	102.0	3.3	0.54
0.01204	97.09	103.0	3.4	0.51
0.01192	96.15	104.0	3.4	0.47
0.01181	95.24	105.0	3.4	0.43
0.01170	94.34	106.0	3.4	0.40
0.01159	93.46	107.0	3.4	0.37
0.01148	92.59	108.0	3.4	0.34
0.01137	91.74	109.0	3.4	0.31
0.01127	90.91	110.0	3.4	0.28
0.01117	90.09	111.0	3.4	0.26
0.01107	89.28	112.0	3.4	0.24
0.01097	88.49	113.0	3.4	0.23
0.01088	87.72	114.0	3.4	0.21
0.01078	86.96	115.0	3.4	0.20
0.01025	82.64	121.0	3.4	0.14
0.007606	61.35	163.0	3.3	0.12
0.006199	50.00	200.0	3.2	
0.004592	37.04	270.0	3.1	7.2×10^{-2} [7]
0.002799	22.57	443.0	3.0	4.5
0.001826	14.73	679.0	3.0	2.8
0.001273	10.27	974.0	3.0	2.1
0.0006491	5.236	1910.0	3.0	1.1×10^{-2}
0.0004376	3.530	2833.0	3.0	7.5×10^{-3}
0.0002903	2.341	4271.0	3.0	5.0
0.0001716	1.384	7224.0	3.0	3.1
0.00009047	0.7297	13704	3.0	1.6×10^{-3}
0.00005621	0.4534	22056	3.0	9.9×10^{-4}
0.00002774	0.2237	44699	3.0	5.2
0.00001439	0.1161	86153	3.0	2.6

[a] The material is now isotropic with one set of n and k. At 400 cm^{-1}, data of Lucovsky [11] and Treacy and Taylor [16] were matched by averaging. At 163 and 200 μm, data of Strom and Taylor [7] and Lucovsky [11] were matched by averaging. Two significant figures are given in most cases.

Arsenic Sulfide (As_2S_3)

D. J. TREACY
Physics Department
U.S. Naval Academy
Annapolis, Maryland

The values of n and k listed in Tables III and IV are room-temperature values. The discussion will cover both the crystalline and vitreous phases.

Crystalline As_2S_3 The crystalline phase has been investigated, primarily, as a comparison with the vitreous phase, and there are substantial gaps in the data. The crystalline form of As_2S_3, orpiment, is a naturally occurring mineral, but it is difficult to obtain large crystals of good optical quality. The crystal exhibits micaceous cleavage, and this makes it difficult to obtain optical data perpendicular to its layers. The crystalline form is monoclinic [1]; hence the results will be tabulated as n_a, k_a ($E \| a$); n_b, k_b ($E \| b$); and n_c, k_c ($E \| c$) in Table III. The data are plotted in Fig. 3.

In the spectral region from 100 to 25 μm, the spectra are reflection spectra [2, 3] with some transmission measurements at the position of weaker bands. The spectra were fit employing a superposition of several oscillators. In Zallen *et al.* [2] the criterion used to determine the oscillator fit was to minimize the root mean square of the deviation of the theoretical fit from the observed reflectivity spectra. The two studies agree essentialiy but differ systematically with n from Zallen *et al.* [2] in general being greater than Treacy and Taylor [3]. The systematic difference in n is due to the choice of the high-frequency dielectric constant. In Zallen *et al.* [2] higher reflectivities were observed at short wavelength, leading to a higher dielectric constant. Both choices of the dielectric constant, however, are probably in error because one overestimates and the other underestimates the index of refraction as determined from accurate fringe measurements by Evans and Young [4] in the near infrared and the visible.

This is a fairly common problem in attempting to determine optical constants from reflectivity data, for the reflectivity can vary over a substantial range, particularly in crystals showing micaceous cleavage. For the spectral region from 100 to 25 μm, the data presented for $E \| a$ and $E \| c$ are from Zallen

HANDBOOK OF OPTICAL CONSTANTS OF SOLIDS

Copyright © 1985 by Academic Press, Inc.
All rights of reproduction in any form reserved.
ISBN 0-12-544420-6

et al. [2] and are probably accurate to about 10% in n and k. The data for $E \| b$ are from Treacy and Taylor [3] and are probably good within the same limits. A point was added to the table at 35.8 μm to account for a weak mode that was observed in transmission studies.

In the spectral range from $\lambda = 21.7$ to 9.35 μm (the multiphonon region) the data for $E \| a$, $E \| c$, are taken from Klein *et al.* [5]. These are transmission measurements and are probably good to about 10% with a somewhat better accuracy in the stronger absorption bonds. The values of k in the relatively transparent region were limited by the quality of the natural crystals and probably are representative of impurity absorption and scattering. The values of k observed in this region decrease with wavelength near 25 μm faster than the oscillator fits used from 100 to 25 μm.

In the spectral range from 2 to 0.42 μm, the data for n are taken from Evans and Young [4]. The measurements for $E \| a$ and $E \| c$ were very accurate fringe measurements that involved an absolute determination of the order of interference. The results for n_a and n_c are probably accurate to better than 1% and are in substantial agreement with an earlier determination [6]. The measurements for $E \| b$ were again fringe measurements, but an intermediate step involving the birefringence was necessary.

The values of k for $E \| a$ and $E \| c$ are a mixture from Evans and Young [4] and Zallen *et al.* [7]. The data at small values of k were taken from Evans and Young [4]; for the moderate values of k Evans and Young [4] and Zallen *et al.* [7] agree, and for large values of k the data are from Zallen *et al.* [7]. Values of k for low temperatures may be obtained from Evans and Young [4] ($T = 77$ K) and from Zallen *et al.* [7] ($T = 10$ K). It is difficult to evaluate what limits of confidence can be placed on these data and what effect, if any, impurities have at low absorption levels. Both measurements agree for moderate values of k and are probably good to about 10%. At high values of k the data from Zallen *et al.* were used, but these values of k are probably good only within about 20%.

Since the reflectivity data for $\lambda < 0.4$ μm [7] have not been analyzed but rather presented for their qualitative features, no further constants will be listed.

Vitreous As_2S_3 The glassy (amorphous) form of As_2S_3 has been investigated in substantially greater depth than the crystalline form due to its possible technological applications. The values for n and k are listed in Table IV and plotted in Fig. 4.

There is one very accurate low-frequency measurement of the dielectric constant and the loss factor [8]. The loss is sufficiently low that it may be considered negligible, and the index of refraction is determined directly from the real part of the dielectric constant.

At this point it should be emphasized that there are substantial differences between commercially available forms of a-As_2S_3. It should also be noted

that the commercially available forms of a-As_2S_3 differ from a-As_2S_3 that was prepared specifically for its purity. It is worthwhile when using this set of tables to make allowance for the specific type of a-As_2S_3 in use.

The measurements reported by Fontanella [8] are accurate to substantially better than 1% within one batch of commercial material but are not better than 3% when different melts and suppliers are considered. This measurement [8] was taken at 300 K.

In the region from $\lambda = 1.2 \times 10^4$ to 116 μm, the data are taken from Strom and Taylor [9]. The first point in this study was taken from microwave perturbation techniques and is probably good within a factor of 2. The remainder of the points were taken in transmission by using a laser source. These points are probably good to within 20%.

From $\lambda = 100$ μm to $\lambda = 25$ μm, the data are taken from Lucovsky [10]. These data were taken as a reflectance spectrum and fit with oscillator parameters. The caveat given earlier concerning reflectance spectra applies here, but since the glass can be polished better than the crystal, the values of n and k are probably somewhat better than 15%.

The values of n from 24.69 to 12.5 μm were taken from Young [15]. When these values are compared with the extrapolation of the oscillator fit in Lucovsky [10], it is seen that the values given by the oscillator fit do not rise as quickly as the measured points as wavelength decreases. These measured values of n were determined from fringe measurements in transmission. The absolute value of the order of the fringes was obtained, and the measurements are probably good to about 1%.

The values of k for $\lambda = 25$ to 12.5 μm were taken from Klein *et al.* [11]. This was a sample in–sample out transmission spectrum, and the values of k listed are within 10%.

The values of n for 12.2 to 0.5600 μm were taken from Rodney *et al.* [12]. These are accurate prism measurements and the original values were listed to six significant figures. The data were fit with a five-term Sellmeier equation, and the fit was typically less than one part in 10^4. The authors note, however, that this is for a particular sample and that the difference between samples is of the order of 4% in the visible and of the order of 0.1% near 12 μm. (The values from Rodney *et al.* [12] and Young [15] agree to better than 1% at 12 μm.) This underscores the earlier comment concerning the difference between commercial suppliers and different melts of glass from any single commercial source.

The values of k for $\lambda = 12.2$ to 6.6 μm are taken from Maklad *et al.* [16]. At 12.5 μm Klein *et al.* [11] and Maklad *et al.* [16] agree. Most points were taken in transmission on a double-beam instrument and are good to within 20%. The points between 9.2 and 10.9 μm were taken by using laser calorimetry. For the points taken on the double-beam instrument, it is difficult to estimate the absolute magnitude of scattering losses, and the values of k listed can be interpreted as an upper bound.

The value of k at $\lambda = 1.0$ μm is taken from Wood and Tauc [13] and is probably good to 20%.

The values of k from $\lambda = 0.8$ to 0.56 μm were taken from Zallen *et al.* [7]. These were done in transmission with a foreprism monochrometer instrument and are probably good to within 20%. In the region of overlap between Zallen *et al.* and Wood and Tauc [13], the values quoted in Wood and Jauc [13] are slightly higher (about 25% higher at 0.5 μm).

The values of n and k from $\lambda = 0.5585$ to 0.22 μm were taken from Young [15]. For the values of n, 0.05 was added to the data presented by Young [15]. This was done because (a) this is well within the uncertainty between melts quoted in Rodney *et al.* [12], (b) there is greater uncertainty in the values of thickness for the thin samples quoted in Young [15], and (c) the curves run parallel to each other in the region of overlap. It must be emphasized that the differences in the index of refraction are representative differences between melts. The values of k listed here were taken on a prism-grating double monochrometer and should be accurate to better than 20%. In the region in which Zallen *et al.* [7] was used, the values from Young [15] agree quite well, but Zallen *et al.* [7] is consistently quite a bit lower for values of λ less than 0.56 μm.

REFERENCES

1. N. Morimoto, *Mineral J. Sapporo* **1**, 160 (1954).
2. R. Zallen, M. L. Slade, and A. T. Ward, *Phys. Rev. B* **3**, 4257 (1971).
3. D. J. Treacy and P. C. Taylor, *Phys. Rev. B* **11**, 2941 (1975).
4. B. L. Evans and P. A. Young, *Proc. R. Soc. Ser. A* **297**, 230 (1967).
5. P. G. Klein, P. C. Taylor, and D. J. Treacy, *Phys. Rev. B* **16**, 4501 (1977).
6. E. S. Larsen and H. Berman, *U. S. Geol. Surv. Bull.* **848**, 213 (1934).
7. R. Zallen, R. E. Drew, R. L. Emerald, and M. L. Slade, *Phys. Rev. Lett.* **26**, 1564 (1971).
8. J. J. Fontanella, private communication (1975).
9. U. Strom and P. C. Taylor, *in* "Amorphous and Liquid Semiconductors" (J. Stuke and W. Brenig, eds.), p. 375, Taylor and Francis, London, 1974; U. Strom and P. C. Taylor, *Phys. Rev. B.* **16**, 5512 (1977).
10. G. Lucovsky, *Phys. Rev. B* **6**, 1480 (1972).
11. P. B. Klein, P. C. Taylor, and D. J. Treacy, *Phys. Rev. B* **16**, 4511 (1977).
12. W. S. Rodney, I. H. Malitson, and T. A. King, *J. Opt. Soc. Am.* **48**, 633 (1958).
13. D. L. Wood and J. Tauc, *Phys. Rev. B* **5**, 3144 (1972).
14. E. L. Zorina, *Sov. Phys. Solid State* **7**, 269 (1965).
15. P. A. Young, *J. Phys. C* **4**, 93 (1971).
16. M. S. Maklad, R. K. Mohr, R. E. Howard, P. B. Macedo, and C. T. Moynihan, *Solid State Commun.* **15**, 855 (1974).

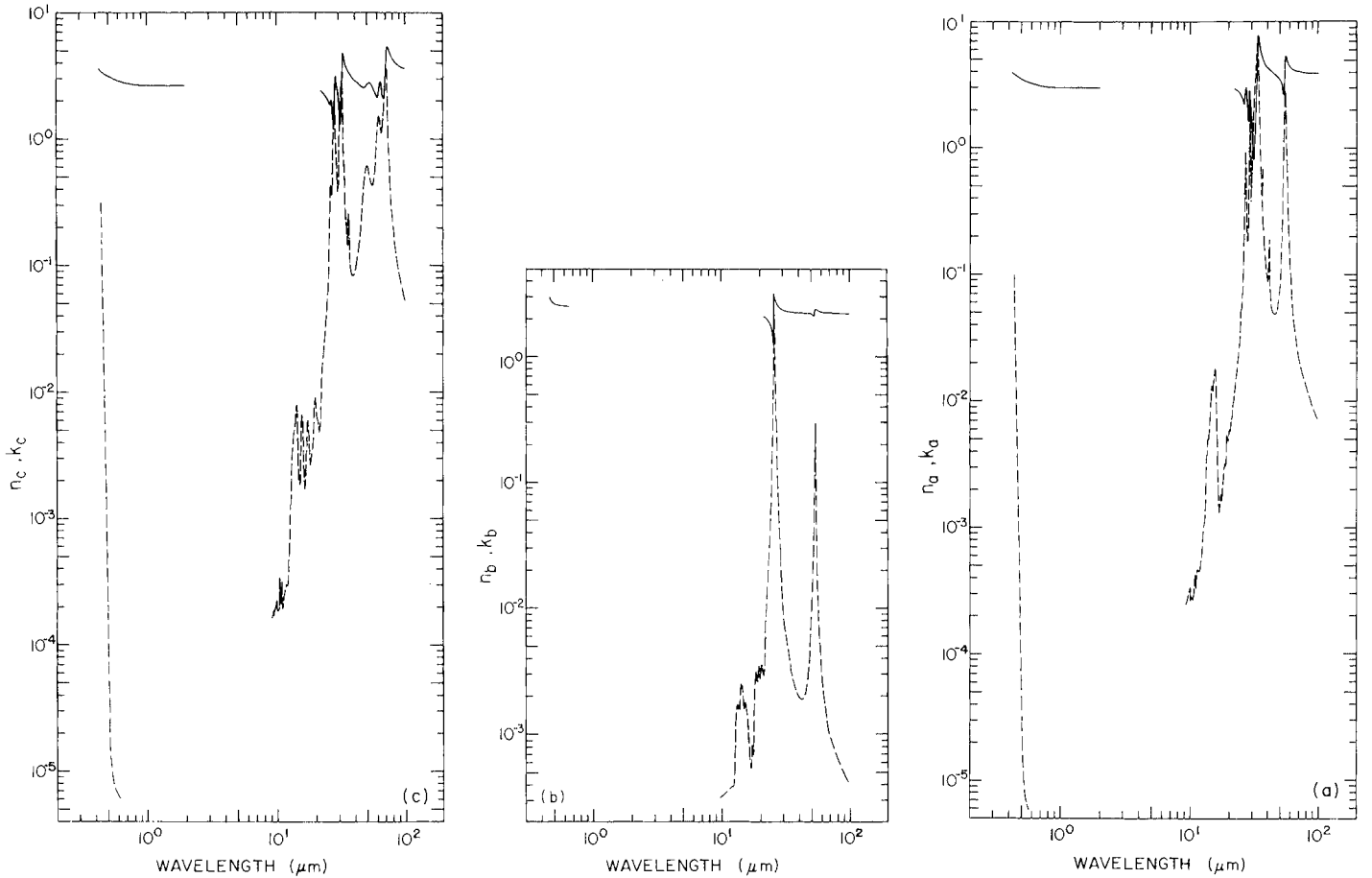

Fig. 3. (a) Log–log plot of n_a (——) and k_a (– – – –) versus wavelength in micrometers for crystalline As_2S_3. (b) Log–log plot of n_b (——) and k_b (– – – –) versus wavelength in micrometers for crystalline As_2S_3. (c) Log–log plot of n_c (——) and k_c (– – – –) versus wavelength in micrometers for crystalline As_2S_3.

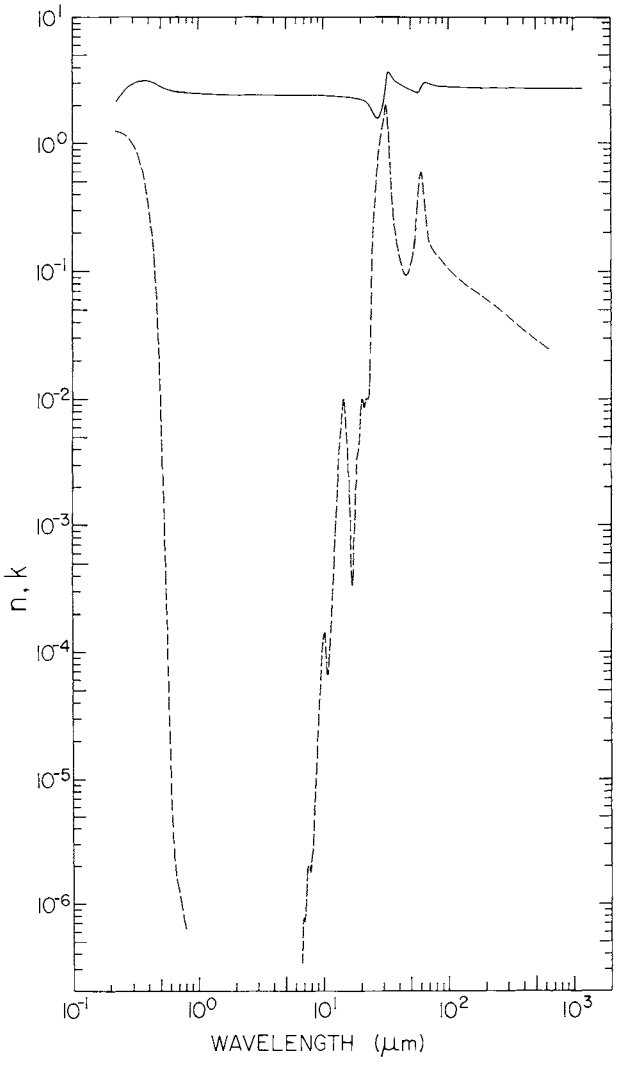

Fig. 4. Log–log plot of n (——) and (– – – –) k versus wavelength in micrometers for vitreous As_2S_3. Two significant figures are sometimes not enough to show a smooth variation in n and k, so the curves have been drawn through these points to smooth out steps.

TABLE III

Values of n and k for Crystalline As_2S_3 from Various References[a]

eV	cm^{-1}	μm	n_a	n_b	n_c	k_a	k_b	k_c
2.914	23,500	0.4255	3.92 [4]		3.60 [4]			
2.852	23,000	0.4348	3.84		3.51	9.8×10^{-2} [7]		
2.790	22,500	0.4444	3.77		3.43	3.5		0.32 [7]
2.728	22,000	0.4545	3.70		3.36	1.2×10^{-2}		9.4×10^{-2}
2.666	21,500	0.4651	3.64	3.02 [4]	3.29	3.7×10^{-3}		2.6×10^{-2}
2.604	21,000	0.4762	3.58	2.79	3.24	1.0×10^{-3} [4]		6.1×10^{-3} [4]
2.542	20,500	0.4878	3.53	2.69	3.18	2.5×10^{-4}		8.5×10^{-4}
2.480	20,000	0.5000	3.48	2.64	3.13	4.8×10^{-5}		1.4×10^{-4}
2.418	19,500	0.5128	3.44	2.62	3.08	2.4		1.9×10^{-5}
2.356	19,000	0.5263	3.39	2.60	3.04	1.2×10^{-5}		1.3×10^{-5}
2.294	18,500	0.5405	3.35	2.58	3.00	7.3×10^{-6}		9.4×10^{-6}
2.232	18,000	0.5556	3.32	2.57	2.96	6.8		8.2
2.170	17,500	0.5714	3.28	2.56	2.93	5.9		7.3
2.108	17,000	0.5882	3.25	2.55	2.90			6.7
2.046	16,500	0.6061	3.22	2.54	2.87			6.4
1.984	16,000	0.6250	3.19	2.53	2.84			6.2
1.922	15,500	0.6452	3.16	2.52	2.81			
1.860	15,000	0.6667	3.14	2.51	2.79			
1.798	14,500	0.6897	3.11		2.76			
1.736	14,000	0.7143	3.09		2.74			
1.674	13,500	0.7407	3.07		2.72			
1.612	13,000	0.7692	3.05		2.70			
1.550	12,500	0.8000	3.03		2.68			
1.488	12,000	0.8333	3.01		2.67			
1.426	11,500	0.8696	2.99		2.65			
1.364	11,000	0.9091	2.98		2.64			

(*continued*)

TABLE III (*Continued*)

Crystalline As_2S_3

eV	cm^{-1}	μm	n_a	n_b	n_c	k_a	k_b	k_c
1.302	10,500	0.9524	2.98		2.64			
1.240	10,000	1.000	2.98		2.64			
1.178	9,500	1.053	2.98		2.64			
1.116	9,000	1.111	2.98		2.64			
1.054	8,500	1.177	2.98		2.64			
0.9919	8,000	1.250	2.98		2.64			
0.9299	7,500	1.333	2.98		2.64			
0.8679	7,000	1.429	2.98		2.64			
0.8059	6,500	1.539	2.98		2.64			
0.7439	6,000	1.667	2.98		2.64			
0.6819	5,500	1.818	2.98		2.64			
0.6199	5,000	2.000	2.98		2.64			
0.1327	1,070	9.346				2.4×10^{-4} [5]		1.6×10^{-4} [5]
0.1314	1,060	9.434				2.6		1.9
0.1302	1,050	9.524				2.6		1.7
0.1289	1,040	9.615				2.9		1.9
0.1277	1,030	9.709				3.0		1.9
0.1265	1,020	9.804				3.2	3.1×10^{-4} [5]	2.0
0.1252	1,010	9.901				3.2	3.2	2.0
0.1240	1,000	10.00				3.4	3.2	2.3
0.1227	990	10.10				2.6	3.2	1.8
0.1215	980	10.20				2.8	3.2	1.8
0.1203	970	10.31				2.7	3.3	1.9
0.1190	960	10.42				2.6	3.3	3.4
0.1178	950	10.53				2.7	3.3	1.9
0.1165	940	10.64				2.8	3.4	1.9
0.1153	930	10.75				2.9	3.4	2.1
0.1141	920	10.87				3.5	3.5	2.6

0.1128	910	10.99	4.2	3.5	3.2
0.1116	900	11.11	3.3	3.5	1.9
0.1103	890	11.24	4.4	3.6	2.5
0.1091	880	11.36	4.7	3.6	2.5
0.1079	870	11.49	4.6	3.7	2.5
0.1066	860	11.63	4.5	3.7	2.6
0.1054	850	11.76	4.6	3.8	2.9
0.1041	840	11.90	4.6	3.8	3.0
0.1029	830	12.05	4.7	3.8	2.9
0.1017	820	12.20	5.1	3.8	3.1
0.1004	810	12.35	7.3	3.9	3.6
0.09919	800	12.50	8.0	4.0	6.8
0.09869	796	12.56	9.0×10^{-4}	5.0	6.0
0.09795	790	12.66	1.0×10^{-3}	6.1	8.1×10^{-4}
0.09720	784	12.76	1.1	7.1	1.0×10^{-3}
0.09646	778	12.85	1.4	9.2	1.3
0.09571	772	12.95	1.6	9.3×10^{-4}	2.1
0.09497	766	13.05	1.8	1.3×10^{-3}	2.6
0.09423	760	13.16	2.1	1.4	3.2
0.09348	754	13.26	3.5	1.7	3.6
0.09274	748	13.37	4.7	1.7	4.1
0.09199	742	13.48	4.8	1.6	4.6
0.09125	736	13.59	5.0	1.7	4.9
0.09051	730	13.70	4.9	1.7	5.2
0.08976	724	13.81	5.2	1.6	5.5
0.08902	718	13.93	5.8	1.8	6.2
0.08828	712	14.04	5.9	1.8	7.0
0.08753	706	14.16	7.1	2.3	7.5
0.08679	700	14.29	8.3	2.5	7.7
0.08617	695	14.39	8.7×10^{-3}	2.4	5.5
0.08555	690	14.49	0.013	2.3	4.5

(continued)

TABLE III (*Continued*)

Crystalline As_2S_3

eV	cm^{-1}	μm	n_a	n_b	n_c	k_a	k_b	k_c
0.08493	685	14.60				0.013	2.4	2.9
0.08431	680	14.71				0.013	2.3	2.9
0.08369	675	14.81				0.013	2.1	1.9
0.08307	670	14.93				0.012	1.9	2.5
0.08245	665	15.04				0.013	1.7	2.6
0.08183	660	15.15				0.015	1.6	3.6
0.08121	655	15.27				0.016	1.8	4.4
0.08059	650	15.38				0.017	1.8	5.6
0.07997	645	15.50				0.018	1.7	6.7
0.07935	640	15.63				0.017	1.6	5.8
0.07873	635	15.75				0.012	1.5	4.4
0.07811	630	15.87				8.2×10^{-3}	1.3	3.3
0.07749	625	16.00				6.7	1.0×10^{-3}	2.9
0.07687	620	16.13				4.5	9.0×10^{-4}	2.3
0.07625	615	16.26				1.9	9.0	1.7
0.07563	610	16.39				1.7	6.5	2.3
0.07501	605	16.53				1.5	5.3	2.9
0.07439	600	16.67				1.3	5.3	3.5
0.07377	595	16.81				1.5	6.7	3.9
0.07315	590	16.95				1.7	8.1	4.8
0.07253	585	17.09				1.8	8.1	5.7
0.07191	580	17.24				1.6	6.8	5.9
0.07129	575	17.39				1.7	8.3	5.4
0.07067	570	17.54				1.8	9.7×10^{-4}	4.5
0.07005	565	17.70				2.1	1.4×10^{-3}	3.7
0.06943	560	17.86				2.4	1.7	2.8
0.06881	555	18.02				2.7	2.1	2.6
0.06819	550	18.18				3.0	2.6	2.9

0.06757	545	18.35				3.2	2.9	3.1
0.06695	540	18.52				3.1	3.1	3.5
0.06633	535	18.69				3.3	2.7	4.0
0.06571	530	18.87				4.8	2.6	5.1
0.06509	525	19.05				5.3	2.7	6.5
0.06447	520	19.23				5.2	2.9	7.6
0.06385	515	19.42				4.8	3.4	8.0
0.06323	510	19.61				5.3	3.3	8.9
0.06261	505	19.80				5.7	2.8	8.5
0.06199	500	20.00				5.9	2.9	7.2
0.06150	496	20.16				5.8	3.2	6.3
0.06075	490	20.41				6.5	3.4	6.2
0.06001	484	20.66				7.1	3.5	5.9
0.05926	478	20.92				7.5	3.2	5.5
0.05852	472	21.19				8.1	3.0	4.7
0.05778	466	21.46		2.1 [3]		9.9×10^{-3}	3.1	5.5
0.05703	460	21.74		2.1		0.011	3.3	6.0×10^{-3}
0.05636	454.6	22.0	2.9 [2]	2.0	2.4 [2]	0.013 [2]	7.7×10^{-3} [3]	0.011 [2]
0.05510	444.4	22.5	2.9	2.0	2.4	0.016	0.011	0.017
0.05391	434.8	23.0	2.9	2.0	2.3	0.019	0.016	0.023
0.05276	425.5	23.5	2.8	1.9	2.3	0.023	0.024	0.031
0.05166	416.7	24.0	2.8	1.9	2.2	0.029	0.042	0.041
0.05060	408.2	24.5	2.7	1.7	2.1	0.050	0.080	0.057
0.04959	400.0	25.0	2.6	1.5	2.0	0.053	0.24	0.089
0.04862	392.2	25.5	2.5	1.3	1.9	0.087	1.1	0.18
0.04769	384.6	26.0	2.3	3.1	1.9	0.20	1.4	0.44
0.04679	377.4	26.5	2.3	2.9	2.0	0.84	0.30	0.37
0.04592	370.4	27.0	2.9	2.7	1.6	0.41	0.11	0.42
0.04508	363.6	27.5	2.5	2.5	1.4	0.19	0.057	1.0
0.04428	357.1	28.0	2.2	2.5	2.0	0.20	0.036	2.0
0.04350	350.9	28.5	1.6	2.4	3.1	0.50	0.024	1.3

(*continued*)

TABLE III (*Continued*)

Crystalline As_2S_3

eV	cm^{-1}	μm	n_a	n_b	n_c	k_a	k_b	k_c
0.04275	344.8	29.0	2.9	2.4	2.8	1.8	0.018	0.54
0.04203	339.0	29.5	2.4	2.4	2.4	0.39	0.014	0.39
0.04133	333.3	30.0	1.8	2.3	2.1	0.45	0.011	0.43
0.04065	327.9	30.5	1.2	2.3	1.6	1.4	9.4×10^{-3}	0.75
0.03999	322.6	31.0	0.83	2.3	1.3	1.7	8.0	1.6
0.03936	317.5	31.5	0.86	2.3	1.8	2.6	6.9	2.7
0.03874	312.5	32.0	1.1	2.3	3.5	3.6	6.0	3.4
0.03815	307.7	32.5	1.8	2.3	4.8	4.9	5.3	1.9
0.03757	303.0	33.0	3.5	2.3	4.5	6.3	4.7	0.79
0.03701	298.5	33.5	7.0	2.3	4.1	5.5	4.3	0.43
0.03647	294.1	34.0	7.6	2.3	3.8	2.4	3.9	0.28
0.03594	289.9	34.5	6.7	2.3	3.6	1.2	3.6	0.20
0.03542	285.7	35.0	6.0	2.3	3.5	0.69	3.3	0.16
0.03492	281.7	35.5	5.6	2.3	3.3	0.48	3.1	0.15
0.03459	279.0	35.9				0.55		
0.03444	277.8	36.0	5.3	2.3	3.3	0.38	2.9	0.26
0.03397	274.0	36.5	5.1	2.3	3.3	0.26	2.7	0.11
0.03351	270.2	37.0	4.9	2.3	3.2	0.20	2.5	0.094
0.03306	266.7	37.5	4.7	2.2	3.1	0.16	2.4	0.087
0.03263	263.2	38.0	4.6	2.2	3.1	0.14	2.3	0.084
0.03220	259.7	38.5	4.5	2.2	3.0	0.12	2.2	0.082
0.03179	256.4	39.0	4.4	2.2	3.0	0.10	2.1	0.083
0.03139	253.2	39.5	4.4	2.2	3.0	0.094	2.1	0.084
0.03100	250.0	40.0	4.3	2.2	2.9	0.087	2.0	0.087
0.03061	246.9	40.5	4.2	2.2	2.9	0.094	1.9	0.092
0.03024	243.9	41.0	4.2	2.2	2.9	0.19	1.9	0.097
0.02988	241.0	41.5	4.2	2.2	2.8	0.080	1.9×10^{-3}	0.10
0.02952	238.1	42.0	4.1	2.2	2.8	0.063	1.9	0.11

0.02917	235.3	42.5	4.1	2.2	2.8	0.058	1.9	0.12
0.02883	232.6	43.0	4.1	2.2	2.7	0.054	1.9	0.14
0.02850	229.9	43.5	4.0	2.2	2.7	0.052	1.9	0.15
0.02818	227.3	44.0	4.0	2.2	2.7	0.050	1.9	0.17
0.02786	224.7	44.5	4.0	2.2	2.6	0.048	2.0	0.19
0.02755	222.2	45.0	3.9	2.2	2.6	0.048	2.0	0.21
0.02725	219.8	45.5	3.9	2.2	2.6	0.048	2.1	0.24
0.02695	217.4	46.0	3.9	2.2	2.6	0.048	2.3	0.28
0.02666	215.1	46.5	3.8	2.2	2.5	0.049	2.5	0.31
0.02638	212.8	47.0	3.8	2.2	2.5	0.051	2.6	0.36
0.02610	210.5	47.5	3.8	2.2	2.5	0.053	2.9	0.40
0.02583	208.3	48.0	3.7	2.2	2.5	0.056	3.3	0.46
0.02556	206.2	48.5	3.7	2.2	2.5	0.061	3.8	0.50
0.02530	204.1	49.0	3.6	2.2	2.6	0.068	4.5	0.55
0.02505	202.0	49.5	3.5	2.2	2.6	0.076	5.4	0.58
0.02480	200.0	50.0	3.5	2.2	2.6	0.088	6.8	0.60
0.02455	198.0	50.5	3.5	2.2	2.7	0.11	8.9×10^{-3}	0.61
0.02431	196.1	51.0	3.4	2.2	2.7	0.13	0.012	0.60
0.02407	194.2	51.5	3.3	2.2	2.7	0.16	0.018	0.59
0.02384	192.3	52.0	3.2	2.1	2.8	0.21	0.029	0.56
0.02362	190.5	52.5	3.1	2.1	2.8	0.31	0.054	0.53
0.02339	188.7	53.0	2.9	2.1	2.8	0.47	0.12	0.51
0.02317	186.9	53.5	2.7	2.4	2.8	0.79	0.28	0.48
0.02296	185.2	54.0	2.6	2.4	2.7	1.4	0.27	0.46
0.02275	183.5	54.5	2.9	2.4	2.7	2.2	0.11	0.44
0.02254	181.8	55.0	4.0	2.3	2.7	2.7	0.054	0.43
0.02234	180.2	55.5	5.1	2.3	2.6	2.1	0.031	0.42
0.02214	178.6	56.0	5.3	2.3	2.6	1.2	0.020	0.42
0.02194	177.0	56.5	5.2	2.3	2.5	0.73	0.014	0.43
0.02175	175.4	57.0	5.0	2.3	2.5	0.47	0.011	0.45
0.02156	173.9	57.5	4.8	2.3	2.4	0.32	8.3×10^{-3}	0.48

(*continued*)

TABLE III (*Continued*)

Crystalline As_2S_3

eV	cm^{-1}	μm	n_a	n_b	n_c	k_a	k_b	k_c
0.02138	172.4	58.0	4.7	2.3	2.3	0.24	6.7	0.52
0.02119	170.9	58.5	4.6	2.3	2.3	0.18	5.6	0.57
0.02101	169.5	59.0	4.5	2.3	2.2	0.15	4.7	0.65
0.02084	168.1	59.5	4.4	2.3	2.2	0.12	4.1	0.75
0.02066	166.7	60.0	4.4	2.3	2.1	0.10	3.6	0.87
0.02049	165.3	60.5	4.3	2.3	2.1	0.088	3.2	1.0
0.02033	163.9	61.0	4.3	2.3	2.1	0.077	2.9	1.2
0.02016	162.6	61.5	4.3	2.3	2.3	0.068	2.6	1.3
0.02000	161.3	62.0	4.2	2.3	2.4	0.061	2.4	1.4
0.01984	160.0	62.5	4.2	2.2	2.6	0.055	2.2	1.5
0.01968	158.7	63.0	4.2	2.2	2.7	0.050	2.1	1.4
0.01953	157.5	63.5	4.2	2.2	2.8	0.046	1.9	1.4
0.01937	156.3	64.0	4.2	2.2	2.8	0.042	1.8	1.3
0.01922	155.0	64.5	4.1	2.2	2.8	0.039	1.7	1.2
0.01907	153.9	65.0	4.1	2.2	2.7	0.036	1.6	1.1
0.01893	152.7	65.5	4.1	2.2	2.6	0.034	1.5	1.1
0.01879	151.5	66.0	4.1	2.2	2.5	0.032	1.5	1.1
0.01864	150.4	66.5	4.1	2.2	2.4	0.030	1.4	1.2
0.01851	149.3	67.0	4.1	2.2	2.2	0.029	1.3	1.3
0.01837	148.2	67.5	4.1	2.2	2.1	0.027	1.3	1.5
0.01823	147.1	68.0	4.1	2.2	2.1	0.026	1.2	1.8
0.01810	146.0	68.5	4.1	2.2	2.1	0.025	1.2	2.1
0.01797	144.9	69.0	4.0	2.2	2.2	0.024	1.1	2.5
0.01784	143.9	69.5	4.0	2.2	2.5	0.023	1.1	2.9
0.01771	142.9	70.0	4.0	2.2	2.9	0.022	1.1	3.3
0.01759	141.8	70.5	4.0	2.2	3.5	0.021	1.0×10^{-3}	3.5
0.01746	140.9	71.0	4.0	2.2	4.2	0.020	9.9×10^{-4}	3.5
0.01734	139.9	71.5	4.0	2.2	4.8	0.019	9.6	3.2

0.01722	138.9	72.0	4.0	2.2	5.3	0.019	9.4	2.7
0.01710	137.9	72.5	4.0	2.2	5.4	0.018	9.1	2.1
0.01698	137.0	73.0	4.0	2.2	5.4	0.018	8.9	1.7
0.01687	136.1	73.5	4.0	2.2	5.3	0.017	8.6	1.3
0.01675	135.1	74.0	4.0	2.2	5.2	0.017	8.4	1.1
0.01664	134.2	74.5	4.0	2.2	5.1	0.016	8.2	0.86
0.01653	133.3	75.0	4.0	2.2	4.9	0.016	8.1	0.72
0.01642	132.5	75.5	4.0	2.2	4.8	0.015	7.9	0.61
0.01631	131.6	76.0	4.0	2.2	4.7	0.015	7.7	0.52
0.01621	130.7	76.5	4.0	2.2	4.6	0.015	7.6	0.46
0.01610	129.9	77.0	4.0	2.2	4.6	0.014	7.4	0.40
0.01600	129.0	77.5	4.0	2.2	4.5	0.014	7.3	0.36
0.01590	128.2	78.0	3.9	2.2	4.4	0.014	7.1	0.32
0.01579	127.4	78.5	3.9	2.2	4.4	0.013	7.0	0.29
0.01569	126.6	79.0	3.9	2.2	4.3	0.013	6.9	0.27
0.01560	125.8	79.5	3.9	2.2	4.3	0.013	6.7	0.25
0.01550	125.0	80.0	3.9	2.2	4.2	0.013	6.6	0.23
0.01540	124.2	80.5	3.9	2.2	4.2	0.012	6.5	0.21
0.01531	123.5	81.0	3.9	2.2	4.1	0.012	6.4	0.20
0.01521	122.7	81.5	3.9	2.2	4.1	0.012	6.3	0.18
0.01512	122.0	82.0	3.9	2.2	4.1	0.012	6.2	0.17
0.01503	121.2	82.5	3.9	2.2	4.1	0.011	6.1	0.16
0.01494	120.5	83.0	3.9	2.2	4.0	0.011	6.0	0.15
0.01485	119.8	83.5	3.9	2.2	4.0	0.011	5.9	0.15
0.01476	119.1	84.0	3.9	2.2	4.0	0.0108	5.8	0.14
0.01467	118.3	84.5	3.9	2.2	4.0	0.0106	5.8	0.13
0.01459	117.7	85.0	3.9	2.2	3.9	0.0105	5.7	0.13
0.01450	117.0	85.5	3.9	2.2	3.9	0.0103	5.6	0.12
0.01442	116.3	86.0	3.9	2.2	3.9	0.0101	5.5	0.12
0.01433	115.6	86.5	3.9	2.2	3.9	0.0100	5.5	0.11
0.01425	114.9	87.0	3.9	2.2	3.9	9.8×10^{-3}	5.4	0.11

(continued)

TABLE III (*Continued*)

Crystalline As_2S_3

eV	cm^{-1}	μm	n_a	n_b	n_c	k_a	k_b	k_c
0.01417	114.3	87.5	3.9	2.2	3.8	9.7	5.3	0.10
0.01409	113.6	88.0	3.9	2.2	3.8	9.6	5.3	0.099
0.01401	113.0	88.5	3.9	2.2	3.8	9.4	5.2	0.095
0.01393	112.4	89.0	3.9	2.2	3.8	9.3	5.1	0.092
0.01385	111.7	89.5	3.9	2.2	3.8	9.2	5.1	0.089
0.01378	111.1	90.0	3.9	2.2	3.8	9.0	5.0	0.086
0.01370	110.5	90.5	3.9	2.2	3.8	9.0	5.0	0.083
0.01362	109.9	91.0	3.9	2.2	3.8	8.8	4.9	0.081
0.01355	109.3	91.5	3.9	2.2	3.7	8.7	4.8	0.078
0.01348	108.7	92.0	3.9	2.2	3.7	8.6	4.8	0.076
0.01340	108.1	92.5	3.9	2.2	3.7	8.5	4.7	0.074
0.01333	107.5	93.0	3.9	2.2	3.7	8.4	4.7	0.072
0.01326	107.0	93.5	3.9	2.2	3.7	8.3	4.7	0.070
0.01319	106.4	94.0	3.9	2.2	3.7	8.2	4.6	0.068
0.01310	105.8	94.5	3.9	2.2	3.7	8.1	4.6	0.067
0.01305	105.3	95.0	3.9	2.2	3.7	8.0	4.5	0.065
0.01298	104.7	95.5	3.9	2.2	3.7	7.9	4.5	0.064
0.01292	104.2	96.0	3.9	2.2	3.7	7.8	4.4	0.062
0.01285	103.6	96.5	3.9	2.2	3.7	7.7	4.4	0.061
0.01278	103.1	97.0	3.9	2.2	3.7	7.7	4.3	0.059
0.01272	102.6	97.5	3.9	2.2	3.6	7.6	4.3	0.058
0.01265	102.0	98.0	3.9	2.2	3.6	7.5	4.3	0.057
0.01259	101.5	98.5	3.9	2.2	3.6	7.4	4.2	0.056
0.01252	101.0	99.0	3.9	2.2	3.6	7.3	4.2	0.055
0.01246	100.5	99.5	3.9	2.2	3.6	7.3	4.1	0.053
0.01240	100.0	100	3.9	2.2	3.6	7.2	4.1	0.052

[a] The radiation electric field is parallel to the *a*, *b*, and *c* axes of the crystal.

TABLE IV
Values of n and k for Vitreous As_2S_3 from Various References[a]

eV	cm^{-1}	μm	n	k
5.636	45,460	0.2200	2.10 [15]	1.24 [15]
5.390	43,480	0.2300	2.20	1.23
5.166	41,670	0.2400	2.34	1.22
4.959	40,000	0.2500	2.48	1.21
4.769	38,460	0.2600	2.60	1.19
4.592	37,040	0.27	2.73	1.15
4.428	35,710	0.28	2.79	1.11
4.275	34,480	0.29	2.85	1.05
4.133	33,330	0.30	2.90	1.01
3.999	32,260	0.31	2.98	0.95
3.874	31,250	0.32	3.02	0.89
3.757	30,300	0.33	3.05	0.82
3.647	29,410	0.34	3.07	0.73
3.542	28,570	0.35	3.09	0.66
3.444	27,780	0.36	3.10	0.61
3.351	27,030	0.37	3.11	0.55
3.263	26,320	0.38	3.11	0.49
3.179	25,610	0.39	3.10	0.42
3.100	25,000	0.40	3.09	0.34
3.024	24,390	0.41	3.06	0.28
2.952	23,810	0.42	3.04	0.24
2.883	23,260	0.43	3.02	0.20
2.818	22,730	0.44	3.00	0.16
2.80	22,520	0.4428	3.00	0.15
2.79	22,500	0.4444	2.99	0.15
2.78	22,420	0.4460	2.99	0.14
2.77	22,340	0.4476	2.99	0.14
2.76	22,220	0.4492	2.99	0.13
2.75	22,180	0.4508	2.98	0.126
2.74	22,100	0.4525	2.98	0.122
2.73	22,020	0.4542	2.98	0.117
2.72	21,940	0.4558	2.97	0.112
2.71	21,860	0.4575	2.97	0.105
2.70	21,780	0.4592	2.97	0.099
2.69	21,700	0.4609	2.96	0.096
2.68	21,620	0.4626	2.96	0.091
2.67	21,540	0.4644	2.95	0.084
2.66	21,460	0.4661	2.95	0.078
2.65	21,370	0.4679	2.94	0.076
2.64	21,290	0.4696	2.94	0.071
2.63	21,210	0.4714	2.93	0.067
2.62	21,130	0.4732	2.93	0.060
2.61	21,050	0.4750	2.92	0.055
2.60	20,970	0.4769	2.92	0.052
2.59	20,890	0.4787	2.91	0.047
2.58	20,810	0.4806	2.90	0.044

(*continued*)

TABLE IV (*Continued*)

Vitreous As_2S_3

eV	cm^{-1}	μm	n	k
2.57	20,730	0.4824	2.89	0.040
2.56	20,650	0.4843	2.89	0.035
2.55	20,570	0.4862	2.88	0.030
2.54	20,490	0.4881	2.88	0.026
2.53	20,410	0.4901	2.87	0.022
2.52	20,260	0.4920	2.87	0.019
2.51	20,250	0.4940	2.86	0.017
2.50	20,160	0.4959	2.85	0.016
2.49	20,080	0.4979	2.84	0.014
2.48	20,000	0.4999	2.83	0.013
2.47	19,920	0.5020	2.82	0.011
2.46	19,840	0.5040	2.82	9.8×10^{-3}
2.45	19,760	0.5061	2.81	8.7
2.44	19,680	0.5081	2.80	8.0
2.43	19,600	0.5102	2.80	7.0
2.42	19,520	0.5123	2.79	6.4
2.41	19,440	0.5145	2.78	5.5
2.40	19,360	0.5166	2.78	4.7
2.39	19,280	0.5188	2.77	4.1
2.38	19,200	0.5209	2.76	3.6
2.37	19,120	0.5231	2.76	3.2
2.36	19,040	0.5254	2.76	2.7
2.35	18,950	0.5276	2.75	2.4
2.34	18,870	0.5298	2.74	2.1
2.33	18,790	0.5321	2.73	1.8
2.32	18,710	0.5344	2.72	1.6
2.31	18,630	0.5367	2.72	1.3
2.30	18,550	0.5391	2.72	1.1×10^{-3}
2.29	18,470	0.5414	2.71	9.2×10^{-4}
2.28	18,390	0.5438	2.71	8.1
2.27	18,310	0.5462	2.70	7.0
2.26	18,230	0.5486	2.70	6.0
2.25	18,150	0.5510	2.70	5.1
2.24	18,070	0.5535	2.69	4.3
2.23	17,990	0.5560	2.69	3.8
2.22	17,910	0.5585	2.69	3.3
2.214	17,860	0.56	2.69 [12]	2.4×10^{-4} [7]
2.138	17,240	0.58	2.66	5.6×10^{-5}
2.066	16,670	0.60	2.64	1.5×10^{-5}
2.000	16,130	0.62	2.62	5.1×10^{-6}
1.937	15,630	0.64	2.60	2.6
1.879	15,150	0.66	2.59	1.7
1.823	14,710	0.68	2.57	1.5
1.771	14,290	0.70	2.56	1.2
1.722	13,890	0.72	2.55	1.03×10^{-6}
1.675	13,510	0.74	2.54	9.1×10^{-7}
1.631	13,160	0.76	2.53	7.4

TABLE IV (*Continued*)

Vitreous As_2S_3

eV	cm^{-1}	μm	n	k
1.590	12,820	0.78	2.53	6.5
1.550	12,500	0.80	2.52	6.2
1.512	12,200	0.82	2.51	
1.476	11,900	0.84	2.51	
1.442	11,630	0.86	2.50	
1.409	11,360	0.88	2.50	
1.378	11,110	0.90	2.50	
1.348	10,870	0.92	2.49	
1.319	10,640	0.94	2.49	
1.291	10,420	0.96	2.48	
1.265	10,200	0.98	2.48	
1.240	10,000	1.0	2.48	2.4×10^{-7} [13]
1.033	8,333	1.2	2.46	
0.8856	7,143	1.4	2.44	
0.7749	6,250	1.6	2.44	
0.6888	5,556	1.8	2.43	
0.6199	5,000	2.0	2.43	
0.5636	4,546	2.2	2.42	
0.5166	4,167	2.4	2.42	
0.4769	3,846	2.6	2.42	
0.4428	3,571	2.8	2.42	
0.4133	3,333	3.0	2.42	
0.3874	3,125	3.2	2.41	
0.3647	2,941	3.4	2.41	
0.3444	2,778	3.6	2.41	
0.3263	2,632	3.8	2.41	
0.3100	2,500	4.0	2.41	
0.2952	2,381	4.2	2.41	
0.2818	2,273	4.4	2.41	
0.2695	2,174	4.6	2.41	
0.2583	2,083	4.8	2.41	
0.2480	2,000	5.0	2.41	
0.2384	1,923	5.2	2.41	
0.2296	1,852	5.4	2.41	
0.2214	1,786	5.6	2.40	
0.2138	1,724	5.8	2.40	
0.2066	1,667	6.0	2.40	
0.2000	1,613	6.2	2.40	
0.1937	1,563	6.4	2.40	
0.1879	1,515	6.6	2.40	
0.1860	1,500	6.667	2.40	3.4 [16]
0.1829	1,475	6.780	2.40	5.4
0.1798	1,450	6.897	2.40	6.5
0.1767	1,425	7.018	2.40	6.4
0.1736	1,400	7.143	2.40	7.4
0.1705	1,375	7.273	2.40	8.7×10^{-7}

(*continued*)

TABLE IV (*Continued*)

Vitreous As_2S_3

eV	cm^{-1}	μm	n	k
0.1674	1,350	7.407	2.40	1.2×10^{-6}
0.1643	1,325	7.547	2.40	1.4
0.1612	1,300	7.692	2.40	1.4
0.1581	1,275	7.843	2.39	1.2
0.1550	1,250	8.000	2.39	1.3
0.1519	1,225	8.163	2.39	1.8
0.1488	1,200	8.333	2.39	3.1
0.1457	1,175	8.511	2.39	5.5×10^{-6}
0.1426	1,150	8.696	2.39	1.04×10^{-5}
0.1395	1,125	8.889	2.39	1.6
0.1364	1,100	9.091	2.38	2.9
0.1339	1,080	9.259	2.38	3.5
0.1314	1,060	9.434	2.38	4.5
0.1289	1,040	9.615	2.38	6.4
0.1265	1,020	9.804	2.38	9.9×10^{-5}
0.1240	1,000	10.00	2.38	1.3×10^{-4}
0.1215	980	10.20	2.38	1.4
0.1190	960	10.42	2.38	1.03×10^{-4}
0.1165	940	10.64	2.38	9.3×10^{-5}
0.1141	920	10.87	2.37	6.5
0.1116	900	11.11	2.37	9.3×10^{-5}
0.1011	880	11.36	2.37	1.3×10^{-4}
0.1066	860	11.63	2.37	1.9
0.1041	840	11.91	2.36	2.8
0.1017	820	12.20	2.36	3.6
0.09919	800	12.50	2.36 [15]	5.0 [11]
0.09795	790	12.66	2.36	6.5
0.09671	780	12.82	2.36	9.0×10^{-4}
0.09547	770	12.99	2.36	1.8×10^{-3}
0.09423	760	13.16	2.35	2.4
0.09299	750	13.33	2.35	3.0
0.09175	740	13.51	2.35	3.8
0.09051	730	13.70	2.35	4.6
0.08989	725	13.79	2.35	5.3
0.08927	720	13.89	2.34	6.1
0.08865	715	13.99	2.34	6.7
0.08803	710	14.09	2.34	7.7
0.08679	700	14.29	2.34	8.6
0.08555	690	14.49	2.34	9.7×10^{-3}
0.08493	685	14.60	2.34	1.0×10^{-2}
0.08431	680	14.71	2.34	9.6×10^{-3}
0.08307	670	14.93	2.33	8.3
0.08183	660	15.15	2.33	6.0
0.08059	650	15.39	2.33	5.3
0.07935	640	15.63	2.33	4.4
0.07811	630	15.87	2.32	3.0
0.07687	620	16.13	2.32	1.8×10^{-3}

TABLE IV (*Continued*)

Vitreous As_2S_3

eV	cm^{-1}	μm	n	k
0.07563	610	16.39	2.31	9.1×10^{-4}
0.07439	600	16.67	2.31	4.6
0.07315	590	16.95	2.31	3.4
0.07191	580	17.24	2.30	4.1
0.07067	570	17.54	2.30	8.4×10^{-4}
0.06943	560	17.86	2.29	1.1×10^{-3}
0.06819	550	18.18	2.28	1.9
0.06695	540	18.52	2.27	2.4
0.06571	530	18.87	2.26	3.5
0.06447	520	19.23	2.25	4.0
0.06323	510	19.61	2.24	5.5
0.06199	500	20.00	2.23	9.4×10^{-3}
0.06100	492	20.33	2.22	0.010
0.06050	488	20.49	2.22	0.011
0.05951	480	20.83	2.21	9.6×10^{-3}
0.05852	472	21.19	2.20	8.4
0.05802	468	21.37	2.19	8.6×10^{-3}
0.05703	460	21.74	2.17	0.010
0.05579	450	22.22	2.15	9.9×10^{-3}
0.05269	425	23.53	2.07	0.014
0.05083	410	24.39	2.01	0.050
0.05021	405	24.69	1.94	0.098
0.04959	400.0	25.0	1.79 [10]	0.20 [10]
0.04862	392.1	25.5	1.73	0.25
0.04769	384.6	26.0	1.67	0.33
0.04679	377.4	26.5	1.61	0.42
0.04592	370.4	27.0	1.57	0.55
0.04508	363.6	27.5	1.55	0.70
0.04428	357.1	28.0	1.56	0.86
0.04350	350.9	28.5	1.62	1.0
0.04275	344.8	29.0	1.70	1.1
0.04203	339.0	29.5	1.79	1.3
0.04133	333.3	30.0	1.86	1.4
0.04065	327.9	30.5	1.96	1.5
0.03999	322.6	31.0	2.12	1.8
0.03936	317.5	31.5	2.43	2.0
0.03874	312.5	32.0	2.88	2.0
0.03815	307.7	32.5	3.33	1.8
0.03757	303.0	33.0	3.59	1.4
0.03701	298.5	33.5	3.65	1.1
0.03647	294.1	34.0	3.61	0.83
0.03594	289.9	34.5	3.53	0.64
0.03542	285.7	35.0	3.45	0.51
0.03492	281.7	35.5	3.37	0.42
0.03444	277.8	36.0	3.30	0.35
0.03397	274.0	36.5	3.24	0.30

(*continued*)

TABLE IV (*Continued*)

Vitreous As_2S_3

eV	cm^{-1}	μm	n	k
0.03351	270.3	37.0	3.19	0.26
0.03306	266.7	37.5	3.14	0.23
0.03263	263.2	38.0	3.10	0.21
0.03220	259.7	38.5	3.07	0.19
0.03179	256.4	39.0	3.03	0.17
0.03139	253.2	39.5	3.00	0.16
0.03100	250.0	40.0	2.98	0.15
0.03024	243.9	41	2.93	0.13
0.02952	238.1	42	2.89	0.12
0.02883	232.6	43	2.85	0.11
0.02818	227.3	44	2.82	0.10
0.02755	222.2	45	2.79	0.096
0.02695	217.4	46	2.76	0.094
0.02638	212.8	47	2.74	0.094
0.02583	208.3	48	2.71	0.096
0.02530	204.1	49	2.68	0.10
0.02480	200.0	50	2.66	0.11
0.02431	196.1	51	2.63	0.12
0.02384	192.3	52	2.61	0.13
0.02339	188.7	53	2.58	0.15
0.02296	185.2	54	2.55	0.18
0.02254	181.8	55	2.53	0.22
0.02214	178.6	56	2.50	0.27
0.02175	175.4	57	2.50	0.34
0.02138	172.4	58	2.51	0.42
0.02101	169.5	59	2.56	0.51
0.02066	166.7	60	2.64	0.57
0.02032	163.9	61	2.76	0.60
0.02000	161.3	62	2.87	0.58
0.01968	158.7	63	2.96	0.52
0.01937	156.3	64	3.01	0.44
0.01908	153.9	65	3.03	0.37
0.01879	151.5	66	3.04	0.31
0.01850	149.3	67	3.03	0.26
0.01823	147.1	68	3.02	0.22
0.01797	144.9	69	3.00	0.19
0.01771	142.9	70	2.99	0.17
0.01722	138.9	72	2.96	0.15
0.01676	135.1	74	2.94	0.15
0.01631	131.6	76	2.92	0.15
0.01590	128.2	78	2.90	0.14
0.01550	125.0	80	2.89	0.14
0.01512	122.0	82	2.87	0.14
0.01476	119.1	84	2.86	0.14
0.01442	116.3	86	2.85	0.14
0.01409	113.6	88	2.84	0.13
0.01378	111.1	90	2.84	0.12

TABLE IV (*Continued*)

Vitreous As_2S_3

eV	cm^{-1}	μm	n	k
0.01348	108.7	92	2.83	0.12
0.01319	106.4	94	2.82	0.11
0.01292	104.2	96	2.82	0.11
0.01265	102.0	98	2.81	0.10
0.01240	100	100	2.81	0.10
0.01066	86	116	2.79 [9]	0.095 [9]
0.008183	66	152	2.76	0.072
0.006447	52	192	2.75	0.054
0.005393	43.5	230	2.75	0.055
0.004587	37	270	2.74	0.047
0.004029	32.5	308	2.74	0.044
0.003162	25.5	392	2.74	0.033
0.002418	19.5	513	2.74	0.031
0.002170	17.5	571	2.74	0.027
0.001984	16	625	2.74	0.025
0.001048	8.45	1,180	2.73	8.8×10^{-3}
0.0001033	0.833	12,000	2.73	1.3
4.129×10^{-12}	3.33×10^{-8}	3×10^{11}	2.73 [8]	

[a] Reference are indicated in brackets.

Cubic Carbon (Diamond)

DAVID F. EDWARDS*,†
University of California
Los Alamos National Laboratory
Los Alamos, New Mexico

H. R. PHILIPP
General Electric Research and Development Center
Schenectady, New York

Diamond is classified into four types depending on its optical and electrical properties. Common to each type is an absorption band in the 2- to 6-μm infrared region, which, as explained later, is due to a multiphonon absorption [1, 2]. Most natural diamonds are of type Ia and, in addition to the intrinsic 2- to 6-μm band, contain nitrogen [3] as an impurity that absorbs in the 6- to 12-μm region. The ultraviolet absorption edge of type Ia diamonds is at about 291 nm. Synthetic diamonds are type Ib and contain nitrogen as an impurity in a dispersed form. This, too, absorbs in the 6- to 12-μm region. Type IIa diamonds are effectively free of nitrogen and exhibit only the intrinsic 2- to 6-μm absorption. The ultraviolet absorption edge is at about 222 nm. Type IIb diamonds exhibit semiconducting properties [4] at ordinary temperatures, have a narrow absorption band from 7 to 10 μm, and are generally blue in color. Irradiation with neutrons or electrons will produce absorption in the 6- to 12-μm band (characteristic of type I diamonds) in previously transparent type IIa diamonds [1].

Type IIa diamonds have the optical properties best suited for infrared optical components. They absorb only in the intrinsic 2- to 6-μm band and their ultraviolet transmittance extends to 222 nm. Optical components with flat surfaces (e.g., windows, prisms, wedge plates, interferometer plates, infrared diffusers) can be produced to specification from diamond. It has not been cost-effective to produce polished curved surfaces (e.g., lenses) of optical quality on diamond. However, it should be possible to produce diamond Fresnel lenses, diffraction gratings, and other components with flat surface patterns [5].

* Work performed under the auspices of the U.S. Department of Energy.

† Present address: Lawrence Livermore National Laboratory, Livermore, California.

Copyright © 1985 by Academic Press, Inc.
All rights of reproduction in any form reserved.
ISBN 0-12-544420-6

Seal [6], Vishnerskiy *et al.* [7], and others have shown that the index of refraction of diamond sensitively depends on the properties of the crystal. The crystal internal structure, defects, impurities, and mechanical inclusions can alter the index. This is true of natural as well as synthetically grown diamonds. As stated earlier, the presence of nitrogen as an impurity can shift the ultraviolet absorption edge (222 nm for nitrogen free to 291 nm for a few parts in 10^4) and produce infrared absorption bands (6 to 12 μm). The effect of impurities on the index of refraction is greater in the infrared than the visible regions. For example, Vishnevskiy *et al.* [7] measured a 0.4% index variation for 26 diamonds (22 synthetic and 4 natural) at 580 nm, and Seal [6], working at 10 μm, saw a 4.7% variation for 11 samples (types Ia and IIa natural stones).

Tabulated in Table V and plotted in Fig. 5 are the room-temperature indices of refraction and extinction coefficients for natural types Ia and IIa diamonds; no values are included for synthetic diamond. For the visible region (226 to 722 nm) three results [7–9] were for diamonds either identified as or assumed to be type Ia. Two samples were IIa diamonds [10]. For common wavelengths the visible indices of types Ia and IIa diamonds as measured by different investigators [7–11] agree within three parts or less in the fourth decimal place. Because of this small difference, no distinction is made as to type for the visible indices in Table I. For the infrared, the sample-to-sample index variation is much greater for type Ia diamonds than for type IIa diamonds. Therefore, the listed infrared indices ($\lambda \geq 2.5$ μm) are for type IIa diamond exclusively.

The visible refractive indices were determined from the dispersion of a small diamond prism. Peter [10], using type IIa diamond samples, measured the index from 226 to 643 nm. His measurements are perhaps the most complete for the visible. Other investigations [7–9, 11] have also reported refractive indices for the visible region but for limited wavelengths. Each used some variation of a prism measuring technique with the exception of Bartoshinskii *et al.* [9], who developed a technique for determining the index using total internal reflections from {111} crystallographic planes in diamond.

The infrared index values from 2.5 to 25 μm are the measurements of Edwards and Ochoa [12] and are for a type IIa diamond. They used the channel spectrum technique [13], and it is the only known report for the infrared. The details of the channel technique can be found elsewhere in this publication and will not be repeated here. (See the critique on silicon in this handbook.)

The visible and infrared indices of refraction given in Table V as n_c are obtained by a fit of data with the Herzberger-type dispersion formula [14]

$$n = A + BL + CL^2 + D\lambda^2 + E\lambda^4,$$

where

$$L = 1/(\lambda^2 - 0.028)$$

with λ in micrometers. As explained by Herzberger *et al.* [14], the 0.028 is the square of the mean asymptote for the short-wavelength abrupt rise in the index for 14 materials (diamond not included). The coefficients, evaluated by least squares, are $A = 2.37837$, $B = 1.18897 \times 10^{-2}$ $C = -1.0083 \times 10^{-4}$, $D = -2.3676 \times 10^{-5}$, and $E = 3.24263 \times 10^{-8}$. The agreement between measured and calculated values is 0.001 in the IR from 20 to 2.5 μm but then deteriorates to 0.003 from 2.5 to 0.30 μm and to 0.01 at 0.23 μm. Peter [10], on the other hand, was able to fit his data from 0.60 to 0.22 μm with a Sellmeier-type formula to 0.0003. This suggests that further work is needed to fit the total spectrum from IR to UV because of apparent systematic variations over this long spectral range among various investigators.

The index data of Table V can also be fit to the Sellmeier-type formula

$$n^2 = \varepsilon + A\lambda_1^2 + B\lambda_1^2/(\lambda^2 - \lambda_1^2).$$

In view of the difficulties of fitting the Herzberger-type formula to the wide spectral range 20 to 0.22 μm, we have not done a similar fit for the Sellmeier-type formula.

For the infrared values in the region 2.5 to 25 μm, the relative uncertainty in the measured index is set by the relative uncertainty in the sample thickness. Edwards and Ochoa [12] report an index uncertainty of about 10^{-3}.

Results for the extinction coefficient in the UV–visible transparent region have been given by Peter [10] and Clark *et al.* [15].

Lax and Burstein [2] and Smith *et al.* [1] have verified that the 2- to 6-μm band in all diamond types is the result of two- and three-phonon absorption processes. Hardy and Smith [1] measured the absorption coefficient in this band for two diamonds with good optical surfaces. One type Ia and one type IIa were measured giving identical results within experimental error. Their absorption coefficient values are given in Table V for selected multiphonon frequencies in the 2 to 6 μm band.

The index of refraction n of cubic carbon (diamond) has been precisely documented in the region of optical transparency [10, 11]. However, in the region of intrinsic absorption $h\nu > 5.2$ eV, few attempts have been made to obtain a self-consistent set of optical constants n and k for this material. In the region of relatively low absorption, difficulties occur in preparing thin, intrinsic specimens for transmission measurements [16–19]. In the region of strong absorption, this information must be obtained by analysis of reflectance data. In some of these studies, problems in the evaluation of the reflectance and in its analysis were apparent [15, 20–23]. However, two studies were subsequently published [24, 25] that indicated reasonable but far from exact agreement in the reflectance values and their analysis by the Kramers–

Kronig technique. In these two studies the reflectance data differ by as much as $\pm 10\%$ in their relative values for $h\nu > 13$ eV, and the need for additional work is indicated. The results of Philipp and Taft [24], rather than those of Roberts and Walker [25], are given in Table V for two reasons. First, it is not clear whether the results of [25] are for room temperature (~ 300 K) or for 77 K. The data they analyze show two peaks in reflectance near 7 eV that only show up clearly at low temperature [26]. Second, their results give negative k value for $h\nu \geq 31.25$ eV [27], indicating a problem with their reflectance values or extrapolation procedures.

In most of the table entries for the ultraviolet, the values for n are given to four places and those for k to three places. The accuracy of these values does not in general warrant this precision. This is done to show the possible presence of weak structure in the optical properties that can often be discerned by comparison of precise but not necessarily accurate values over narrow energy ranges. In the region $4.5 \leq h\nu \leq 5.8$ eV, the k values are taken from the transmission data of Clark *et al.* [15] and Peter [10]. The table entries were obtained from a smooth curve drawn through these data and do not show up all of the fine details present in their measurements. The values of n for $h\nu \geq 6.0$ eV are taken from Philipp and Taft [24].

It is recommended that anyone who uses Table V carefully examine the material and references cited by the preceding authors.

REFERENCES

1. J. R. Hardy and S. D. Smith, *Philos. Mag.* **6**, 1163 (1961); S. D. Smith, J. R. Hardy, and E. W. J. Mitchell, *Rep. Int. Conf. Phys. Semicond., 6th, Exeter*, p. 529. Institute of Physics and the Physical Society, London, 1962.
2. M. Lax and E. Burstein, *Phys. Rev.* **97**, 39 (1955).
3. W. Kaiser and W. L. Bond, *Phys. Rev.* **115**, 857 (1959).
4. J. F. H. Custers, Physica **18**, 489 (1952).
5. D. Drukker and Zn. N. V., Amsterdam, The Netherlands (1979).
6. M. Seal, D. Drukker, and Zn. N. V., private communication (1979).
7. A. S. Vishnevskiy and V. G. Malogolovets, *Dopov. Akad. Nauk. Ukr. RSR Ser. A* **35**, 892 (1973).
8. S. von Rosch, *Opt. Acta* **12**, 253 (1965).
9. Z. V. Bartoshinskii, N. S. Pidzyraelo, I. V. Stefanski, and N. I. Tretyak, *Mineral. Sb. Lvov.* **29**, 24 (1975).
10. F. Peter, *Z. Phys.* **15**, 358 (1923).
11. Martens, *Ann. Physik* **8**, 463 (1902).
12. D. F. Edwards and E. Ochoa, *J. Opt. Soc. Am.* **71**, 607 (1981).
13. E. V. Loewenstein and D. R. Smith, *Appl. Opt.* **10**, 577 (1971).
14. M. Herzberger and C. D. Salzberg, *J. Opt. Soc. Am.* **52**, 420 (1962); M. Herzberger, *Opt. Acta* **6**, 197 (1959).
15. C. D. Clark, P. J. Dean, and P. V. Harris, *Proc. R. Soc. London* **A 277**, 312 (1964).
16. C. D. Clark, *J. Phys. Chem. Solids* **8**, 481 (1959).
17. J. F. H. Custers and F. A. Raal, *Nature* **179**, 268 (1957).
18. E. W. J. Mitchell, *J. Phys Chem. Solids* **8**, 444 (1959).
19. W. Kaiser and W. L. Bond, *Phys. Rev.* **115**, 857 (1959).

20. S. Robin, *Rev. Opt.* **33**, 377 (1954).
21. J. R. Nelson and W. C. Crocker, *Bull, Am. Phys. Soc.* **5**, 431 (1960).
22. H. R. Philipp and E. A. Taft, *Phys. Rev.* **127**, 159 (1962).
23. W. C. Walker and J. Osantowski, *Phys. Rev.* **134**, A153 (1964).
24. H. H. Philipp and E. A. Taft, *Phys. Rev.* **136**, A1445 (1964).
25. R. A. Roberts and W. C. Walker, *Phys. Rev.* **161**, 730 (1967).
26. R. A. Roberts, D. M. Roessler, and W. C. Walker, *Phys. Rev. Lett.* **17**, 302 (1966).
27. R. A. Roberts, Technical Report, NASA Research grant No. NSG91-60, Supplement 4, January 1967.

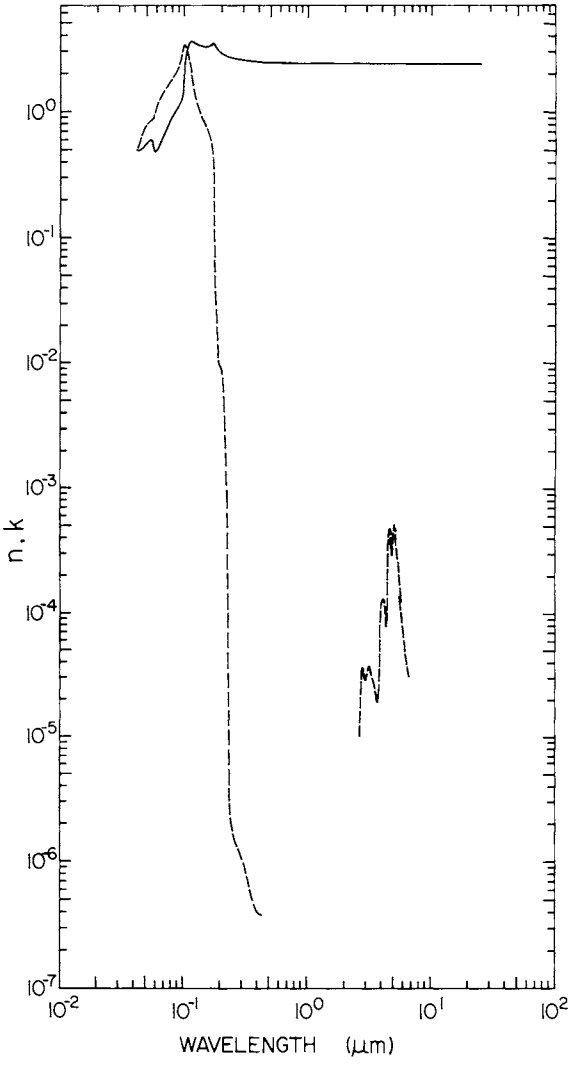

Fig. 5. Log–log plot of n(——) and k(– – –) versus wavelength in micrometers for cubic carbon.

TABLE V

Values of n and k for Cubic Carbon Obtained from Various References[a]

eV	μm	cm^{-1}	n	n_c	k
30.0	0.04133		0.493 [24]		0.490 [24]
29.5	0.04203		0.493		0.521
29.0	0.04275		0.494		0.552
28.5	0.04350		0.496		0.584
28.0	0.04428		0.501		0.616
27.5	0.04508		0.508		0.648
27.0	0.04592		0.516		0.679
26.5	0.04678		0.527		0.708
26.0	0.04769		0.538		0.736
25.5	0.04862		0.550		0.763
25.0	0.04959		0.562		0.787
24.5	0.05060		0.574		0.810
24.0	0.05166		0.586		0.829
23.5	0.05276		0.595		0.843
23.0	0.05391		0.597		0.850
22.5	0.05510		0.579		0.846
22.0	0.05635		0.518		0.888
21.5	0.05767		0.483		0.969
21.0	0.05904		0.487		1.052
20.5	0.06048		0.503		1.130
20.0	0.06199		0.527		1.203
19.5	0.06358		0.557		1.273
19.0	0.06525		0.589		1.341
18.5	0.06702		0.626		1.408
18.0	0.06888		0.665		1.476
17.5	0.07085		0.707		1.546
17.0	0.07293		0.753		1.619
16.5	0.07514		0.805		1.692
16.0	0.07749		0.861		1.767
15.5	0.07999		0.917		1.845
15.0	0.08266		0.972		1.929
14.75	0.08405		0.994		1.978
14.5	0.08551		1.018		2.034
14.25	0.08700		1.041		2.102
14.0	0.08856		1.070		2.178
13.75	0.09017		1.098		2.268
13.5	0.09184		1.129		2.379
13.25	0.09357		1.166		2.522
13.0	0.09537		1.223		2.722
12.8	0.09686		1.312		2.953
12.6	0.09839		1.532		3.265
12.4	0.09998		1.983		3.382
12.2	0.1016		2.383		3.354
12.0	0.1033		2.736		3.228
11.75	0.1055		3.090		2.986
11.5	0.1078		3.346		2.693
11.25	0.1102		3.507		2.380

TABLE V (*Continued*)

Cubic Carbon

eV	μm	cm^{-1}	n	n_c	k
11.0	0.1127		3.582		2.078
10.75	0.1153		3.600		1.813
10.5	0.1181		3.565		1.581
10.25	0.1210		3.514		1.403
10.0	0.1240		3.453		1.258
9.75	0.1272		3.398		1.147
9.5	0.1305		3.348		1.055
9.25	0.1340		3.308		0.978
9.0	0.1378		3.272		0.910
8.75	0.1417		3.247		0.855
8.5	0.1459		3.228		0.806
8.25	0.1503		3.232		0.765
8.0	0.1550		3.251		0.712
7.8	0.1590		3.276		0.659
7.6	0.1631		3.306		0.592
7.5	0.1653		3.321		0.553
7.4	0.1675		3.335		0.515
7.3	0.1698		3.376		0.473
7.2	0.1722		3.437		0.388
7.15	0.1734		3.464		0.307
7.1	0.1746		3.444		0.210
7.0	0.1771		3.322		9.35×10^{-2}
6.9	0.1797		3.220		5.24
6.8	0.1823		3.146		3.44
6.7	0.1851		3.085		2.20
6.6	0.1879		3.031		1.47
6.5	0.1907		2.985		1.10×10^{-2}
6.4	0.1937		2.944		9.87×10^{-3}
6.3	0.1968		2.910		9.74
6.2	0.2000		2.879		9.30
6.1	0.2033	49,200	2.852		8.62
6.0	0.2066	48,390	2.826		7.99
5.8	0.2138	46,780	2.780		5.02
5.6	0.2214	45,170	2.740		1.48×10^{-3} [15]
5.55	0.2234	44,760			5.48×10^{-4}
5.5	0.2254	44,360			3.41×10^{-5}
5.47386	0.226504	44,149.3	2.7151 [10]	2.7029	2.662 [10]
5.45	0.2275	43,960			1.48 [15]
5.4	0.2296	43,550			1.04×10^{-5}
5.36064	0.231288	43,236.1	2.6950		7.10×10^{-6} [10]
5.34131	0.232125	43,080.2	2.6917		
5.35	0.2317	43,150			6.45 [15]
5.32267	0.232938	42,929.9	2.6881	2.6849	
5.3	0.2339	42,750			2.98
5.0	0.25	40,000		2.6383	
4.8187	0.25730	38,865	2.6145	2.6205	1.47 [10]

(*continued*)

TABLE V (*Continued*)

Cubic Carbon

eV	μm	cm^{-1}	n	n_c	k
4.5112	0.27484	36,385	2.5786		1.29×10^{-6}
4.1596	0.29807	33,549	2.5429	2.5465	
4.133	0.30	33,330		2.5439	
3.961	0.313	31,950			8.97×10^{-7}
3.576	0.3467	28,840	2.4954	2.4955	
3.542	0.35	28,570		2.4929	
3.434	0.3611	27,690	2.4854	2.4849	
3.3924	0.36548	27,361			4.65
3.100	0.40	25,000		2.4627	
3.064	0.4047	24,710	2.4626	2.4605	3.86
2.8447	0.43584	22,944			3.82×10^{-7}
2.755	0.45	22,220		2.4432	
2.6503	0.46782	21,376	2.4408	2.4380	
2.5504	0.48614	20,570	2.4354 [8]	2.4332	
2.480	0.50	20,000		2.4299	
2.4379	0.50858	19,663	2.4306 [10]	2.4280	
2.2705	0.54608	18,312	2.4235 [8]	2.4210	
2.254	0.55	18,180		2.4203	
2.105	0.589	16,980	2.4175	2.4147	
2.066	0.60	16,670		2.4133	
1.9257	0.64385	15,531	2.4111 [10]	2.4084	
1.907	0.65	15,380		2.4079	
1.8892	0.65629	15,237	2.4104 [8]	2.4073	
1.771	0.70	14,290		2.4036	
1.653	0.75	13,330		2.4003	
1.550	0.80	12,500		2.3975	
1.459	0.85	11,760		2.3953	
1.378	0.90	11,110		2.3934	
1.305	0.95	11,760		2.3918	
1.240	1.0	10,000		2.3905	
0.8266	1.5	6,667		2.3837	
0.6199	2.0	5,000		2.3813	
0.4959	2.5	4,000		2.3801	
0.48	2.583	3,872			6.17×10^{-6} [1]
0.47	2.638	3,791			1.57×10^{-5}
0.46	2.695	3,710			3.22
0.45	2.755	3,630			3.62
0.44	2.818	3,549			3.14
0.43	2.883	3,468			2.87
0.42	2.952	3,388			2.94
0.4133	3.0	3,333		2.3795	
0.41	3.024	3,307			3.25
0.40	3.099	3,226			3.58
0.39	3.179	3,146			3.67
0.38	3.263	3,065			3.11
0.37	3.351	2,984			2.80
0.36	3.444	2,904			2.47

TABLE V (*Continued*)

Cubic Carbon

eV	μm	cm^{-1}	n	n_c	k
0.3542	3.5	2,857			
0.35	3.542	2,823			2.11
0.34	3.646	2,742			1.89
0.33	3.757	2,662			2.99×10^{-5}
0.32	3.874	2,581			1.11×10^{-4}
0.31	3.999	2,500		2.3787	1.30
0.30	4.133	2,420			1.32
0.2955	4.203	2,379			1.07×10^{-4}
0.29	4.275	2,339			7.82×10^{-5}
0.285	4.350	2,299			1.45×10^{-4}
0.28	4.428	2,258			2.75
0.275	4.508	2,218			3.52
0.27	4.592	2,178			4.39
0.2675	4.635	2,158			4.79
0.265	4.679	2,137			4.06
0.2625	4.723	2,117			3.38
0.26	4.768	2,097			2.96
0.255	4.862	2,057			3.87
0.2525	4.910	2,037			4.69
0.25	4.959	2,016			5.21
0.2480	5.0	2,000		2.3783	
0.2475	5.009	1,996			4.82
0.245	5.060	1,976			4.87
0.2425	5.113	1,956			4.68
0.24	5.166	1,936			3.82
0.235	5.276	1,895			2.90
0.23	5.391	1,855			2.36
0.2254	5.5	1,818			1.4 [2]
0.225	5.510	1,815			1.93 [1]
0.22	5.636	1,774			1.21
0.2066	6.0	1,667		2.3779	5.7×10^{-5} [2]
0.1907	6.5	1,538			3.1
0.1771	7.0	1,429			
0.1550	8.0	1,250		2.3772	
0.1378	9.0	1,111			
0.1240	10.0	1,000		2.3765	
0.1033	12.0	833.3		2.3757	
0.08856	14.0	714.3		2.3750	
0.07749	16.0	625.0		2.3745	
0.06888	18.0	555.6		2.3741	
0.06199	20.0	500.0		2.3741	

[a] The column headed n_c contains refractive index values calculated with the Herzberger-type formula. References are indicated in brackets.

Lithium Fluoride (LiF)

EDWARD D. PALIK and W. R. HUNTER*
Naval Research Laboratory
Washington, D.C.

The data are tabulated in Table VI and plotted in Fig. 6. These data are for room-temperature samples unless otherwise specified. When investigators make measurements at other than room temperature, they usually say so; consequently, we assume no statement of temperature implies room temperature, $\sim 20°C$.

The Henke *et al.* model [1] has been used to calculate n and k from approximately 6 to 123 Å. Lukirskii *et al.* [2] have measured n and k for vacuum-deposited films about 1000 Å thick (as determined by multiple-beam interferometry) on glass substrates at discrete wavelengths from 23.6 to 113 Å. They used a version of the reflectance method to find n and k. Brown *et al.* [3] measured the transmittance of thin vacuum-deposited films of different thicknesses on Formvar substrates from 53.9 Å (230 eV) to 206.6 Å (60 eV) and calculated the absorption coefficient from their measurements. The film thicknesses were determined by a quartz-crystal monitor that had been calibrated by the Tolansky technique (multiple-beam, interferometry). The spectral features did not sharpen much at 77 K. Milgram and Givens [4] also used thin vacuum-deposited films on celluloid substrates. They evaporated LiF from Pt boats at about 900°C at a pressure of $\sim 5 \times 10^{-5}$ torr, and by comparing the transmission of different thicknesses using a photographic method [5], they obtained values for the absorption coefficient. Film thicknesses were determined by using multiple-beam interferometry. Their data between 206 and 496 Å are included. Data of Rao *et al.* [6] are also included between 413 Å (30 eV) and 496 Å (25 eV). They used freshly cleaved crystals kept in vacuum continually while reflectance was measured with synchrotron radiation over the energy range 6–35 eV. Sample temperature was 100 K. Kramers–Kronig analysis was used. Roessler and Walker [7] measured the near-normal incidence reflectance of freshly cleaved crystal from 7 to 25 eV (1770–496 Å) at 300 K and used a Kramers–Kronig

* Present address: Sachs/Freeman Associates, Bowie, Maryland.

Copyright © 1985 by Academic Press, Inc.
All rights of reproduction in any form reserved.
ISBN 0-12-544420-6

analysis. Data of Rao *et al.* [6] and Roessler and Walker [7] are in reasonable agreement from 25 to 7 eV.

Tomiki and Miyata [8] have measured the absorption coefficient on thin cleaved slabs of UV-quality LiF at 298.5 K in the band-edge region to study the Urbach tail. The band-edge location is very temperature dependent. At room temperature there was some evidence for extrinsic absorption in the edge. At photon energies less than the edge, the absorption bottomed out to values near $k = 8 \times 10^{-7}$, which varied by a factor of 2 in different samples. We tabulate results for an intermediate sample. The steeply changing values of k in the band edge are much smaller than those of Roessler and Walker [7] and are to be preferred.

A number of investigators have measured the refractive index of LiF at wavelengths longer than the absorption edge. Early measurements were made by Gyulai [9] and Schneider [10], who used prisms of LiF. The most recent measurements that use prisms are those of Laporte and Subtil [11] at 25°C, which are reported here. They obtained index values from 1043.5 to 2000 Å. Li [12] has analyzed much of the existing n data and fitted it with a dispersion relation at 293 K:

$$n^2 = 1 + \frac{0.92549\lambda^2}{\lambda^2 - (0.07376)^2} + \frac{6.96747\lambda^2}{\lambda^2 - (32.79)^2}.$$

We list these values from 0.18 to 11 μm. Estimated uncertainty is given as ± 0.0002 in the 0.35–3-μm region. This increases to ± 0.005 for 0.25–0.35 and 3.0–5.0 μm, to ± 0.001 for 0.15–0.25 and 5.0–7.0 μm. The results of Laporte and Subtil [11] at 0.2 μm are 0.002 larger than Li's [12] value and are preferable to shorter wavelength.

Calorimetry measurements in the UV–visible region have been done by Harrington *et al.* [13] Values of k listed in Table VI are somewhat smaller than the results of Tomiki and Miyata [8] obtained nearer to the band edge. The origin of this extrinsic absorption is not known.

Deutsch [14] has measured the absorption coefficient from 1500 to 2300 cm^{-1} with slabs of different thicknesses. He noted that his α data and those of Hohls [15] from 900 to 1800 cm^{-1} plotted on a log scale fall on a straight line. We read the data from this graph. This is absorption due to two- and three-phonon processes and contains little structure at room temperature [16, 17]. This is consistent with theoretical calculations. Klier [18] has also measured the absorption at 300 K from 5.5 to 14 μm. His data nicely bridge the data of Deutsh [14] and the oscillator-model results of Kachare *et al.* [19].

Jasperse *et al.* [20] measured the reflectance of LiF in the 200–800-cm^{-1} region at many temperatures, including 295 K. The average angle of incidence was 11°. High-purity, single-crystal LiF was polished flat to $\frac{1}{2}$ wavelength at the sodium d line. The sample was then annealed in a vacuum furnance for two days at a temperature of about $\frac{3}{4}$ of the melting temperature (842°C). Presumably, the surface mechanical damage was annealed out. The

reflection standard was an aluminum mirror assumed to have 98.5% reflectivity over the entire spectral range. This will introduce some uncertainty in R since the reflectivity of Al† does vary steady through this spectral region from 0.994 to 0.988. A two-oscillator model was used to fit the data. The pertinent equations are

$$\varepsilon' = n^2 - k^2 = \varepsilon_\infty + \sum_i \frac{4\pi\rho_i \nu_i^2(\nu_i^2 - \nu^2)}{(\nu_i^2 - \nu^2)^2 + (\gamma_i \nu)^2},$$

$$\varepsilon'' = 2nk = \sum_i \frac{4\pi\rho_i \nu\gamma_i \nu_i^2}{(\nu_i^2 - \nu^2)^2 + (\gamma_i \nu)^2}.$$

Kachare *et al.* [19] reanalyzed the data forcing a fit to R by comparing the entire reflectance curve with a calculated one and minimizing a certain error function. While their values of the oscillator parameters were very near those of Japerse *et al.* for 295 K, they noted a large deviation in the damping constants at low temperature, suggesting that the classical oscillator model was not adequate for obtaining accurate values of the damping constant for strongly anharmonic lattice modes of ionic crystals. The values of Kachare *et al.* [19] were $\varepsilon_\infty = 1.96$, $\nu_1 = 307.5\,\text{cm}^{-1}$, $\nu_2 = 501.4\,\text{cm}^{-1}$, $4\pi\rho_1 = 6.67$, $4\pi\rho_2 = 0.116$, $\gamma_1/\nu_1 = 0.057$, and $\gamma_2/\nu_2 = 0.173$. We have used these to calculate n and k in the 200–1000-cm^{-1} region. The results for k are in reasonable agreement with the composite results of Seger and Genzel [21]. The refractive index of Li is comparable near 10 μm. The oscillator model gives $n = 2.96$ at 400 μm which is much smaller than the value of $n = 3.70 \pm 0.03$ measured by Genzel and Klier [22]: This suggests that the oscillator strength ($4\pi\rho_i$) is too small in the fit of Kachare *et al.* [19].

Genzel and Klier [22] and Seger and Genzel [21] have measured the absorption coefficient from 70 to 1000 μm at 20°C and in some cases the refractive index, also. Transmittances of slabs of various thicknesses were measured along with some reflectance. Results of Stolen and Dransfeld [23] for k at 320 μm at 300 K are similar. Eldridge [17] discusses the two-phonon difference-band region below ν_1.

The data of Seger and Genzel appear to extrapolate nicely to the lower-frequency results of Owens [24] at 116, 35.4, and 9.8 GHz (2.584, 8.469, 30.590 mm) at 25°C, Owens used a filled-resonant-cavity method and transmission through a dielectric plug in a section of waveguide to determine ε' and ε'', the real and imaginary parts of the dielectric function, from a measurement of the loss tangent $\tan\delta = \varepsilon'/\varepsilon''$ and ε'. His value of $n = 3.02$ at $\lambda = 2.584$ mm is the same as that of Dianov and Irisova [25] at $\lambda = 2$ mm at 300 K.

Breckenridge [26] used a capacitor technique to measure ε' and $\tan\delta$ over a wide range of frequencies from 4.5×10^7 to 10^2 Hz at 80°C. We list values of n and k obtained at 4.5×10^7 and 1×10^7 Hz (666.2 and 3335 cm).

† See the discussion of the optical properties of metallic aluminum by Smith *et al.* in this handbook.

It appears that k is leveling off in this region if extrapolation from higher frequency is made in Fig. 6, suggesting some extrinsic absorption mechanism.

Theoretical calculations support a decreasing exponential dependence of that absorption as a function of frequency in the multiphonon region (above ν_1) with essentially no structure. In the difference multiphonon, region, an increasing exponential dependence can be observed for NaCl, (below ν_1), but some structure appears to be present for other alkali halides. The exponential dependence with no structure for NaCl is probably fortuitous, and some structure for the other materials is consistent with theoretical expectations. While there is general agreement about the sum multiphonon region, the theoretical situation in the difference multiphonon region is still unsettled.

The magnitude and wavelength dependence of the millimeter-wave absorption coefficients of the alkali halides is consistent with recent theoretical calculations of Hardy and Karo [27] and of Sparks *et al.* [28] However, these two theoretical attempts to calculate the absorption as due to multiphonon difference processes are based on somewhat different models. The shape of the experimental data does suggest that the absorption, at least above 35 GHz, is essentially intrinsic in character.

ACKNOWLEDGMENT

We thank M. Hass of the Naval Research Laboratory for discussions of the far-infrared, submillimeter properties of LiF.

REFERENCES

1. B. L. Henke, P. Lee, T. J. Tanaka, R. L. Shimabukuro, and B. K. Fujikawa, "Low Energy X-ray Diagnostics—1981" (D. T. Attwood and B. L. Henke eds.). AIP Conf. Proc. No. 75, American Institute of Physics, New York, 1981.
2. A. P. Lukirskii, E. P. Savinov, O. A. Ershov, and Y. F. Shepelev, *Opt. Spektrosk.* **16**, 310 (1964); A. P. Lukirskii, E. P. Savinov, O. A. Ershov, and Y. F. Shepelev, *Opt. Spectrosc.* **16**, 168 (1964).
3. F. C. Brown, C. Gahwiller, A. B. Kunz, and N. O. Lipari, *Phys. Rev. Lett.* **25**, 927 (1970).
4. A. Milgram and M. P. Givens, *Phys. Rev.* **125**, 1506 (1962).
5. W. M. Cady and D. H. Tomboulian, *Phys. Rev.* **59**, 381 (1941).
6. K. K. Rao, T. J. Moravec, J. C. Rife, and R. N. Dexter, *Phys. Rev. B* **12**, 5937 (1975).
7. D. M. Roessler and W. C. Walker, *J. Opt. Soc. Am.* **57**, 835 (1967).
8. T. Tomiki and T. Miyata, *J. Phys. Soc. Jpn.* **27**, 658 (1969).
9. Z. Gyulai, *Z. Physik* **46**, 80 (1927).
10. E. G. Schneider, *Phys. Rev.* **49**, 341 (1936).
11. P. Laporte and J. L. Subtil, *J. Opt. Soc. Am.* **72**, 1558 (1982).
12. H. H. Li, *J. Phys. Chem. Ref. Data* **9**, 561 (1980).
13. J. A. Harrington, B. L. Bobbs, M. Braunstein, R. K. Kim, R. Stearns, and R. Braunstein, *Appl. Opt.* **17**, 1541 (1978).
14. T. F. Deutsch, *J. Phys. Chem. Solids* **34**, 2091 (1973).
15. H. W. Hohls, *Ann. Physik* **29**, 433 (1937).
16. V. V. Mitskevich, *Soc. Phys.-Solid State* **4**, 2224 (1963); V. V. Mitskerich, *Fiz. Tverd. Tela* **4**, 3035 (1962).
17. J. E. Eldridge, *Phys. Rev. B* **6**, 1510 (1972).

18. M. Klier, *Z. Physik* **150**, 49 (1958).
19. A. Kachare, G. Andermann, and L. R. Brantley, *J. Phys. Chem. Solids* **33**, 467 (1972).
20. J. R. Jasperse, A. Kahan, J. N. Plendl, and S. S. Mitra, *Phys. Rev.* **146**, 526 (1966).
21. G. Seger and L. Genzel, *Z. Physik* **169**, 66 (1962).
22. L. Genzel and M. Klier, *Z. Physik* **144**, 25 (1956).
23. R. Stolen and K. Dransfeld, *Phys. Rev.* **139**, A1295 (1965).
24. J. C. Owens, *Phys. Rev.* **181**, 1228 (1969).
25. E. M. Dianov and N. A. Irisova, *Sov. Phys.-Solid State* **8**, 1807 (1967); E. M. Dianov and N. A. Irisova, *Fiz. Tverd. Tela* **8**, 2265 (1966).
26. R. G. Breckenridge, *J. Chem. Phys.* **16**, 959 (1948).
27. J. R. Hardy and A. M. Karo, *Phys. Rev. B* **26**, 3327 (1982).
28. M. Sparks, D. F. King, and D. L. Mills *Phys. Rev. B* **26**, 6987 (1982).

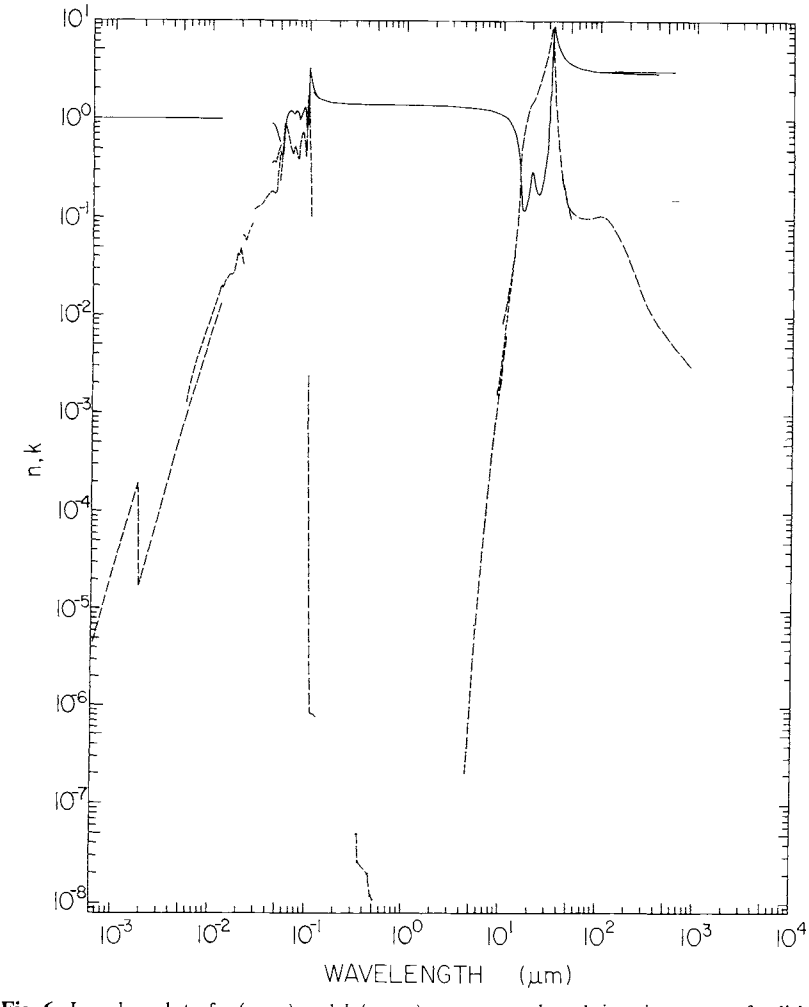

Fig. 6. Log–log plot of n (——) and k (– – – –) versus wavelength in micrometers for lithium fluoride. Note the incredibly small values of k in the transparent region centered near 1 μm.

TABLE VI

Values of n and k for Lithium Fluoride Obtained from Various References[a]

eV	Å	n	k
2000	6.199	0.9999347 [1]	4.33×10^{-6} [1]
1952	6.351	0.9999314	4.74
1905	6.508	0.9999279	5.19
1860	6.665	0.9999244	5.68
1815	6.831	0.9999206	6.23
1772	6.997	0.9999167	6.82
1730	7.166	0.9999126	7.46
1688	7.345	0.9999082	8.18
1648	7.523	0.9999037	8.94
1609	7.705	0.999899	9.78×10^{-6}
1570	7.897	0.999894	1.07×10^{-5}
1533	8.087	0.999889	1.17
1496	8.287	0.999883	1.28
1460	8.492	0.999878	1.40
1426	8.694	0.999872	1.53
1392	8.906	0.999866	1.67
1358	9.129	0.999859	1.83
1326	9.350	0.999852	2.00
1294	9.581	0.999845	2.18
1263	9.816	0.999838	2.38
1233	10.05	0.999830	2.60
1204	10.30	0.999822	2.83
1175	10.55	0.999814	3.09
1147	10.81	0.999805	3.36
1119	11.08	0.999796	3.67
1093	11.34	0.999787	3.99
1067	11.62	0.999778	4.35
1041	11.91	0.999768	4.75
1016	12.20	0.999757	5.18
992	12.50	0.999747	5.64
968	12.81	0.999736	6.14
945	13.12	0.999726	6.67
923	13.43	0.999715	7.23
901	13.76	0.999704	7.85
879	14.10	0.999692	8.53
858	14.45	0.999681	9.28×10^{-5}
838	14.79	0.999670	1.0×10^{-4}
818	15.16	0.999660	1.10
798	15.54	0.999650	1.20
779	15.92	0.999643	1.31
760	16.31	0.999638	1.42
742	16.71	0.999637	1.53
725	17.10	0.999643	1.62
707	17.54	0.999658	1.76
690	17.97	0.999758	1.90×10^{-4}
674	18.39	0.999663	1.70×10^{-5}
658	18.84	0.999606	1.86

TABLE VI (*Continued*)

Lithium Fluoride

eV	Å	n	k
642	19.31	0.999556	2.04
627	19.77	0.999517	2.23
612	20.26	0.999481	2.43
597	20.77	0.999443	2.67
583	21.27	0.999407	2.91
569	21.79	0.999369	3.18
555	22.34	0.999330	3.49
542	22.87	0.999291	3.80
529	23.44	0.999250	4.16×10^{-5}
525.4	23.6	0.99886 [2]	1.1×10^{-4} [2]
516	24.03	0.999206 [1]	4.55×10^{-5} [1]
504	24.60	0.999162	4.96
492	25.20	0.999116	5.42
480	25.83	0.999066	5.93
469	26.43	0.999017	6.46
458	27.07	0.99896	7.04
447	27.74	0.99891	7.69
436	28.44	0.99885	8.42
426	29.10	0.99879	9.16×10^{-5}
415	29.87	0.99872	1.01×10^{-4}
406	30.54	0.99866	1.09
396	31.31	0.99859	1.19
394.9	31.4	0.99814 [2]	2.0 [2]
386	32.12	0.99851 [1]	1.31 [1]
377	32.89	0.99843	1.43
368	33.69	0.99835	1.55
359	34.53	0.99826	1.70
351	35.32	0.99818	1.84
342	36.25	0.99807	2.02
334	37.12	0.99798	2.20
326	38.03	0.99787	2.40
318	38.99	0.99776	2.63
311	39.86	0.99765	2.84
303	40.92	0.99752	3.12
296	41.88	0.99740	3.39
289	42.90	0.99727	3.70
282	43.96	0.99713	4.03
281.8	44.0	0.99592 [2]	8.9 [2]
275	45.08	0.99697 [1]	4.41 [1]
269	46.09	0.99683	4.77
262	47.32	0.99666	5.23
256	48.43	0.99650	5.68
250	49.59	0.99632	6.17
244	50.81	0.99613	6.72
238	52.09	0.99593	7.34
232	53.44	0.99576	8.02

(*continued*)

TABLE VI (*Continued*)

Lithium Fluoride

eV	Å	n	k
227	54.62	0.99552	8.66
221	56.10	0.99528	9.51×10^{-4}
220	56.36		1.26×10^{-3} [3]
216	57.40	0.99505	1.03 [1]
211	58.76	0.99481	1.12
210	59.04		1.83 [3]
206	60.18	0.99456	1.21 [1]
201	61.68	0.99429	1.32
200	61.99		2.12 [3]
196	63.25	0.99399	1.44 [1]
191	64.91	0.99368	1.57
190	65.26		2.70 [3]
187	66.30	0.99341	1.69 [1]
185	67.0	0.99180 [2]	3.12 [2]
182	68.12	0.99305 [1]	1.85 [1]
180	68.88		3.29 [3]
178	69.65	0.99274	2.00 [1]
174	71.25	0.99241	2.16
170	72.93	0.99206	2.33
			4.06 [3]
166	74.69	0.99168	2.53 [1]
162	76.53	0.99128	2.74
160	77.49		4.75 [3]
158	78.47	0.99086	2.98 [1]
154	80.51	0.99040	3.25
150	82.65	0.9899	3.54
			5.79 [3]
147	84.34	0.9895	3.78 [1]
143	86.70	0.9890	4.14
140	88.56	0.9885	4.45
			7.05 [3]
136	91.16	0.9879	4.90 [1]
133	93.22	0.9874	5.28
130	95.37	0.9869	5.69
			8.56 [3]
127	97.62	0.9864	6.13 [1]
124	99.98	0.9858	6.61
121	102.5	0.9852	7.15×10^{-3}
120	103.3		1.16×10^{-2} [3]
118	105.1	0.9845	7.75×10^{-3} [1]
115	107.8	0.9839	8.42
112	110.7	0.9832	9.13
110	112.7	0.9827	9.65×10^{-3}
			1.44×10^{-2} [3]
109.7	113	0.98330 [2]	1.17 [2]
107	115.9	0.9819 [1]	1.05 [1]
104	119.2	0.9811	1.16
102	121.5	0.9806	1.24

TABLE VI (*Continued*)

Lithium Fluoride

eV	Å	n	k
100	124.0	0.9801	1.32
			1.94 [3]
97.5	127.2		2.00
95	130.5		1.96
92.5	134.0		2.06
90	137.8		2.28
87.5	141.7		2.40
85	145.9		2.48
82.5	150.3		2.62
80	155.0		2.64
77.5	160.0		2.61
75	165.3		2.63
72.5	171.0		2.86
70	177.1		3.81
67.5	183.7		4.22
65	190.7		4.16
62.5	198.4		7.74
60	206.6		3.78
			6.74 [4]
57.5	215.6		6.52
			3.26 [3]
55	225.4		5.92 [4]
52.5	236.2		6.77
50	248.0		7.89
47.5	261.0		8.72×10^{-2}
45	275.5		0.123
42.5	291.7		0.130
40	310.0		0.133
37.5	330.6		0.142
35	354.2		0.158
32.5	381.5		0.173
30	413.3	0.869 [7]	0.184
			0.367 [6]
29	427.5	0.861	0.376
			0.180 [4]
28	442.8	0.844	0.176
			0.363 [6]
27	459.2	0.749	0.401
			0.194 [4]
26	476.9	0.662	0.296
			0.467 [6]
25	495.9	0.558	0.521
			0.434 [4]
		0.47 [7]	0.23 [7]
24.5	506.1	0.44	0.31
24	516.6	0.43	0.42

(*continued*)

TABLE VI (*Continued*)

Lithium Fluoride

eV	Å	n	k
23.7	523.1	0.42	0.50
23.6	525.4	0.43	0.56
23.4	529.9	0.43	0.59
23.3	532.1	0.44	0.62
23.2	534.4	0.45	0.66
23.1	536.7	0.46	0.70
23.05	537.9	0.47	0.72
23	539.1	0.48	0.74
22.95	540.2	0.50	0.76
22.9	541.4	0.51	0.78
22.8	543.8	0.55	0.81
22.6	548.6	0.62	0.87
22.4	553.5	0.70	0.91
22.2	558.5	0.80	0.94
22	563.6	0.91	0.93
21.8	568.7	0.99	0.88
21.6	574.0	1.04	0.84
21.4	579.4	1.08	0.80
21	590.4	1.14	0.73
20.5	604.8	1.18	0.65
20	619.9	1.20	0.58
19.5	635.8	1.21	0.53
19	652.6	1.19	0.47
18.6	666.6	1.17	0.44
18.5	670.2	1.15	0.44
18.4	673.8	1.14	0.44
18.3	677.5	1.13	0.45
18	688.8	1.11	0.48
17.7	700.5	1.13	0.52
17.6	704.5	1.14	0.52
17.5	708.5	1.16	0.53
17.4	712.6	1.18	0.52
17.3	716.7	1.19	0.51
16.9	733.6	1.20	0.47
16.4	756.0	1.16	0.40
16.2	765.3	1.12	0.39
16.1	770.1	1.09	0.39
16	774.9	1.06	0.41
15.9	779.8	1.02	0.42
15.8	784.7	0.99	0.47
15.7	789.7	0.98	0.52
15.5	799.9	1.00	0.59
15.3	810.4	1.04	0.64
15.1	821.1	1.08	0.68
14.9	832.1	1.12	0.71
14.7	843.4	1.17	0.73
14.6	849.2	1.19	0.74

TABLE VI (*Continued*)

Lithium Fluoride

eV	Å	n	k
14.5	855.1	1.22	0.74
14.4	861.0	1.25	0.73
14.3	867.0	1.27	0.72
14.2	873.1	1.30	0.71
14.1	879.3	1.32	0.68
14	885.6	1.32	0.64
13.95	888.9	1.32	0.62
13.9	892.0	1.32	0.59
13.85	895.2	1.31	0.56
13.8	898.4	1.29	0.52
13.75	901.7	1.24	0.46
13.7	905.0	1.15	0.42
13.65	908.3	1.05	0.43
13.6	911.7	0.95	0.50
13.55	915.0	0.88	0.58
13.5	918.4	0.84	0.67
13.45	921.8	0.82	0.76
13.4	925.3	0.81	0.84
13.35	928.7	0.80	0.92
13.3	932.2	0.80	1.01
13.25	935.7	0.80	1.10
13.2	939.3	0.81	1.20
13.15	942.9	0.84	1.33
13.1	946.5	0.91	1.43
13.05	950.1	0.97	1.53
13	953.7	1.04	1.64
12.95	957.4	1.13	1.77
12.9	961.1	1.26	1.90
12.85	964.9	1.42	2.02
12.8	968.6	1.64	2.13
12.75	972.4	1.92	2.20
12.7	976.3	2.24	2.19
12.65	980.1	2.57	2.08
12.6	984.0	2.89	1.90
12.5	991.9	3.34	1.17
12.4	999.9	2.93	0.48

eV	cm^{-1}	μm	n	k
12.3		0.1008	2.68	0.33
12.2		0.1016	2.51	0.23
				2.42×10^{-3} [8]
12.1		0.1025		4.89×10^{-4}
12.0		0.1033	2.28	0.11 [7]
				9.86×10^{-5} [8]
11.9		0.1042		2.32×10^{-5}

(*continued*)

TABLE VI (*Continued*)

Lithium Fluoride

eV	cm^{-1}	μm	n	k
11.88		0.10435	2.003 [11]	
11.85		0.10465	1.985	
11.8		0.1051		4.18×10^{-6}
11.78		0.10525	1.951	
11.75		0.1055	2.08 [7]	4×10^{-2} [7]
11.75		0.10552	1.937 [11]	
11.70		0.10600	1.914	1.60×10^{-6} [8]
11.6		0.1069		1.10×10^{-6}
11.59		0.10695	1.875	
11.50		0.10781	1.844	
11.5		0.1078	1.94 [7]	9.44×10^{-7}
11.46		0.10815	1.833 [11]	
11.4		0.1088		8.40
11.33		0.10940	1.798	
11.3		0.1097		8.29
11.25		0.1102	1.84 [7]	
11.24		9.11025	1.777 [11]	
11.2		0.1107		8.37
11.13		0.11142	1.751	
11.1		0.1117		8.62
11.01		0.11265	1.729	
11.0		0.1127	1.77 [7]	8.07
11.00		0.11271	1.728 [11]	
10.82		0.11455	1.699	
10.8		0.1148		8.22
10.66		0.11625	1.677	
10.6		0.1170		8.19
10.52		0.11785	1.659	
10.50		0.11808	1.656	
10.5		0.1181	1.67 [7]	
10.4		0.1192		8.06
10.35		0.11980	1.639 [11]	
10.20		0.12153	1.624	7.74
10.09		0.12285	1.614	
10.00		0.12398	1.606	7.70×10^{-7}
			1.60 [7]	
9.927		0.12490	1.599 [11]	
9.717		0.12760	1.583	
9.526		0.13015	1.569	
9.357		0.13250	1.558	
9.184		0.13500	1.548	
9		0.1375	1.53 [7]	
9.004		0.13770	1.538 [11]	
8.856		0.14000	1.530	
8.551		0.14500	1.515	
8.266		0.15000	1.503	

TABLE VI (*Continued*)

Lithium Fluoride

eV	cm^{-1}	μm	n	k
8		0.15500	1.493	
			1.49 [7]	
7.749		0.16000	1.484 [11]	
7.293		0.17000	1.469	
7		0.1771	1.46 [7]	
7.000		0.17712	1.461 [11]	
6.888		0.18000	1.458	
			1.4533 [12]	
6.812		0.182	1.4516	
6.738		0.184	1.4500	
6.666		0.186	1.4484	
6.595		0.188	1.4469	
6.526		0.190	1.4455	
			1.449 [11]	
6.458		0.192	1.4441 [12]	
6.391		0.194	1.4428	
6.326		0.196	1.4415	
6.262		0.198	1.4403	
6.199	50,000	0.200	1.4391	
			1.441 [11]	
6.048	48,780	0.205	1.4363 [12]	
5.904	47,620	0.210	1.4337	
5.767	46,510	0.215	1.4313	
5.636	45,450	0.220	1.4291	
5.510	44,440	0.225	1.4271	
5.391	43,480	0.230	1.4252	
5.276	42,550	0.235	1.4235	
5.166	41,670	0.240	1.4219	
5.061	40,820	0.245	1.4203	
4.959	40,000	0.250	1.4189	
4.862	39,220	0.255	1.4176	
4.769	38,460	0.260	1.4164	
4.679	37,740	0.265	1.4152	
4.592	37,040	0.270	1.4141	
4.509	36,360	0.275	1.4131	
4.428	35,710	0.280	1.4121	
4.350	35,090	0.285	1.4112	
4.275	34,480	0.290	1.4103	
4.203	33,900	0.295	1.4095	
4.133	33,330	0.300	1.4087	
4.000	32,260	0.31	1.4073	
3.875	31,250	0.32	1.4060	
3.757	30,300	0.33	1.4048	
3.647	29,410	0.34	1.4037	
3.542	28,570	0.35	1.4028	

(*continued*)

TABLE VI (*Continued*)

Lithium Fluoride

eV	cm^{-1}	μm	n	k
3.531	28,480	0.3511		5.0×10^{-8} [13]
3.444	27,780	0.36	1.4019	
3.408	27,490	0.3638		2.6
3.351	27,030	0.37	1.4010	
3.263	26,320	0.38	1.4003	
3.179	25,640	0.39	1.3996	
3.100	25,000	0.40	1.3989	
2.952	23,810	0.42	1.3978	
2.818	22,730	0.44	1.3968	
2.708	21,840	0.4579		1.5
2.695	21,740	0.46	1.3959	
2.583	20,830	0.48	1.3951	
2.541	20,490	0.4880		1.2
2.480	20,000	0.50	1.3944	
2.410	19,440	0.5145		1.1×10^{-8}
2.384	19,230	0.52	1.3938	
2.296	18,520	0.54	1.3933	
2.214	17,860	0.56	1.3928	
2.138	17,240	0.58	1.3923	
2.066	16,670	0.60	1.3919	
2.000	16,130	0.62	1.3915	
1.937	15,630	0.64	1.3912	
1.879	15,150	0.66	1.3908	
1.823	14,710	0.68	1.3905	
1.771	14,290	0.70	1.3902	
1.722	13,890	0.72	1.3900	
1.675	13,510	0.74	1.3897	
1.631	13,160	0.76	1.3894	
1.590	12,820	0.78	1.3892	
1.550	12,500	0.80	1.3890	
1.512	12,200	0.82	1.3888	
1.476	11,900	0.84	1.3886	
1.442	11,630	0.86	1.3884	
1.409	11,360	0.88	1.3882	
1.378	11,110	0.90	1.3880	
1.348	10,870	0.92	1.3878	
1.319	10,640	0.94	1.3876	
1.292	10,420	0.96	1.3875	
1.265	10,200	0.98	1.3873	
1.240	10,000	1.00	1.3871	
1.181	9,524	1.05	1.3867	
1.127	9,091	1.10	1.3863	
1.087	8,696	1.15	1.3859	
1.033	8,333	1.20	1.3855	
0.9919	8,000	1.25	1.3851	
0.9537	7,692	1.30	1.3847	
0.9184	7,407	1.35	1.3844	

TABLE VI (*Continued*)

Lithium Fluoride

eV	cm^{-1}	μm	n	k
0.8856	7,143	1.40	1.3840	
0.8551	6,897	1.45	1.3836	
0.8266	6,667	1.50	1.3832	
0.7999	6,452	1.55	1.3828	
0.7749	6,250	1.60	1.3823	
0.7514	6,061	1.65	1.3819	
0.7293	5,882	1.70	1.3815	
0.7085	5,714	1.75	1.3810	
0.6888	5,556	1.80	1.3806	
0.6702	5,405	1.85	1.3801	
0.6526	5,263	1.90	1.3796	
0.6358	5,128	1.95	1.3791	
0.6199	5,000	2.0	1.3787	
0.5904	4,762	2.1	1.3777	
0.5636	4,545	2.2	1.3766	
0.5391	4,348	2.3	1.3755	
0.5166	4,167	2.4	1.3744	
0.4959	4,000	2.5	1.3731	
0.4769	3,846	2.6	1.3719	
0.4592	3,704	2.7	1.3706	
0.4428	3,571	2.8	1.3693	
0.4275	3,448	2.9	1.3679	
0.4133	3,333	3.0	1.3665	
0.4000	3,226	3.1	1.3650	
0.3875	3,125	3.2	1.3635	
0.3757	3,030	3.3	1.3619	
0.3647	2,941	3.4	1.3602	
0.3542	2,857	3.5	1.3585	
0.3444	2,778	3.6	1.3568	
0.3351	2,703	3.7	1.3550	
0.3263	2,632	3.8	1.3531	
0.3179	2,564	3.9	1.3512	
0.3100	2,500	4.0	1.3493	
0.3024	2,439	4.1	1.3473	
0.2952	2,381	4.2	1.3452	
0.2883	2,326	4.3	1.3431	
0.2852	2,300	4.348		2.1×10^{-7} [14]
0.2818	2,273	4.4	1.3409	
0.2755	2,222	4.5	1.3387	
0.2728	2,200	4.545		4.3
0.2695	2,174	4.6	1.3364	
0.2638	2,128	4.7	1.3340	
0.2604	2,100	4.762		8.0×10^{-7}
0.2583	2,083	4.8	1.3316	
0.2530	2,041	4.9	1.3291	
0.2480	2,000	5.0	1.3266	

(*continued*)

TABLE VI (*Continued*)

Lithium Fluoride

eV	cm^{-1}	μm	n	k
0.2480	2,000	5.000		1.8×10^{-6}
0.2431	1,961	5.1	1.3240	
0.2384	1,923	5.2	1.3213	
0.2356	1,900	5.263		3.6
0.2339	1,887	5.3	1.3186	
0.2296	1,852	5.4	1.3158	
0.2254	1,818	5.5	1.3130	
0.2232	1,800	5.556		7.5×10^{-6}
0.2214	1,786	5.6	1.3101	
0.2175	1,754	5.7	1.3071	
0.2138	1,724	5.8	1.3041	
0.2108	1,700	5.882		1.5×10^{-5}
0.2101	1,695	5.9	1.3010	
0.2066	1,667	6.0	1.2978	
0.2033	1,639	6.1	1.2946	
0.2000	1,613	6.2	1.2912	
0.1984	1,600	6.250		3.1
0.1968	1,587	6.3	1.2879	
0.1937	1,563	6.4	1.2844	
0.1907	1,538	6.5	1.2809	
0.1879	1,515	6.6	1.2773	
0.1860	1,500	6.667		6.9×10^{-5}
0.1851	1,493	6.7	1.2736	
0.1823	1,471	6.8	1.2698	
0.1797	1,449	6.9	1.2660	
0.1771	1,429	7.0	1.2621	
0.1746	1,408	7.1	1.2581	
0.1736	1,400	7.143		1.4×10^{-4}
0.1722	1,389	7.2	1.2541	
0.1698	1,370	7.3	1.2499	
0.1675	1,351	7.4	1.2457	
0.1653	1,333	7.5	1.2414	
0.1631	1,316	7.6	1.2369	
0.1612	1,300	7.692		2.9
0.1610	1,299	7.7	1.2325	
0.1590	1,282	7.8	1.2279	
0.1569	1,266	7.9	1.2232	
0.1550	1,250	8.0	1.2184	6.0 [18]
0.1531	1,235	8.1	1.2136	
0.1512	1,220	8.2	1.2086	
0.1494	1,205	8.3	1.2036	
0.1488	1,200	8.333		6.0×10^{-4} [14]
0.1476	1,190	8.4	1.1984	
0.1459	1,176	8.5	1.1931	
0.1442	1,163	8.6	1.1878	
0.1425	1,149	8.7	1.1823	
0.1409	1,136	8.8	1.1768	

TABLE VI (*Continued*)

Lithium Fluoride

eV	cm^{-1}	μm	n	k
0.1393	1,124	8.9	1.1711	
0.1378	1,111	9.0	1.1653	1.5×10^{-3} [18]
0.1364	1,100	9.091		1.2 [14]
0.1362	1,099	9.1	1.1594	
0.1348	1,087	9.2	1.1533	
0.1333	1,075	9.3	1.1472	
0.1319	1,064	9.4	1.1409	
0.1305	1,053	9.5	1.1345	
0.1292	1,042	9.6	1.1280	
0.1278	1,031	9.7	1.1213	
0.1265	1,021	9.8	1.1145	
0.1252	1,010	9.9	1.1076	
0.1240	1,000	10.0	1.1005	2.6
			1.11 [19]	8.10 [19]
				3.3×10^{-3} [18]
0.1216	980.4	10.2	1.0859 [12]	
0.1192	961.5	10.4	1.0706	
0.1178	950	10.53	1.07 [19]	1.02×10^{-2} [19]
0.1170	943.4	10.6	1.0547 [12]	
0.1148	925.9	10.8	1.0381	
0.1127	909.1	11.0	1.0208	8.0×10^{-3} [18]
0.1116	900	11.11	1.01 [19]	1.31×10^{-2} [19]
				6.2×10^{-3} [14]
0.1054	850	11.76	0.947	1.76×10^{-2} [19]
0.1033	833.3	12.0		1.9 [18]
0.09919	800	12.50	0.856	2.49 [19]
0.09671	780	12.82	0.810	2.84
0.09537	769.2	13		3.7 [18]
0.09423	760	13.16	0.755	3.53 [19]
0.09184	740.7	13.5		5.0 [18]
0.09175	740	13.51	0.691	4.36 [19]
0.08927	720	13.89	0.611	5.61
0.08679	700	14.29	0.508	7.74
0.08555	690	14.49	0.443	9.54×10^{-2}
0.08431	680	14.71	0.367	0.124
0.08307	670	14.93	0.279	0.177
0.08183	660	15.15	0.201	0.268
0.08059	650	15.38	0.157	0.373
0.07935	640	15.63	0.137	0.471
0.07811	630	15.87	0.127	0.561
0.07687	620	16.13	0.122	0.645
0.07563	610	16.39	0.121	0.725
0.07439	600	16.67	0.124	0.804
0.07315	590	16.95	0.128	0.881
0.07191	580	17.24	0.136	0.957
0.07067	570	17.54	0.146	1.03

(*continued*)

TABLE VI (*Continued*)

Lithium Fluoride

eV	cm^{-1}	μm	n	k
0.06943	560	17.86	0.161	1.11
0.06819	550	18.18	0.179	1.18
0.06695	540	18.52	0.203	1.26
0.06571	530	18.87	0.233	1.33
0.06447	520	19.23	0.265	1.39
0.06323	510	19.61	0.293	1.43
0.06199	500	20.00	0.306	1.47
0.06075	490	20.41	0.297	1.51
0.05951	480	20.83	0.270	1.57
0.05827	470	21.28	0.237	1.65
0.05703	460	21.74	0.210	1.76
0.05579	450	22.22	0.191	1.88
0.05455	440	22.73	0.180	2.01
0.05331	430	23.26	0.177	2.16
0.05207	420	23.81	0.181	2.32
0.05083	410	24.39	0.191	2.50
0.04959	400	25.00	0.208	2.71
0.04835	390	25.64	0.234	2.94
0.04711	380	26.32	0.269	3.21
0.04587	370	27.03	0.325	3.53
0.04463	360	27.78	0.407	3.93
0.04401	355	28.17	0.465	4.16
0.04339	350	28.57	0.539	4.43
0.04277	345	28.99	0.637	4.75
0.04215	340	29.41	0.772	5.12
0.04154	335	29.85	0.964	5.57
0.04092	330	30.30	1.25	6.10
0.04030	325	30.77	1.71	6.77
0.03968	320	31.25	2.51	7.57
0.03906	315	31.75	3.98	8.37
0.03844	310	32.26	6.43	8.35
0.03782	305	32.79	8.58	6.35
0.03720	300	33.33	8.76	3.91
0.03658	295	33.90	8.05	2.43
0.03596	290	34.48	7.32	1.62
0.03534	285	35.09	6.70	1.16
0.03472	280	35.71	6.22	0.875
0.03410	275	36.36	5.82	0.687
0.03348	270	37.04	5.50	0.554
0.03286	265	37.74	5.23	0.458
0.03224	260	38.46	5.00	0.386
0.03162	255	39.22	4.81	0.331
0.03100	250	40.00	4.64	0.287
				0.26 [21]
0.02976	240	41.67	4.36	0.222 [19]
0.02852	230	43.48	4.14	0.177
0.02728	220	45.45	3.96	0.145

TABLE VI (*Continued*)

Lithium Fluoride

eV	cm^{-1}	μm	n	k
0.02604	210	47.62	3.81	0.120
0.02480	200	50.00	3.69	0.102
				0.12 [21]
0.02066	166.7	60	3.39	0.105
0.01771	142.9	70		0.101
0.01550	125.0	80	3.17	0.101
0.01378	111.1	90		0.103
0.01240	100.0	100	3.067 [21]	0.106
			3.09 [19]	
0.01033	83.33	120		9.6×10^{-2}
0.08266	66.67	150	3.067 [21]	6.5
0.06199	50.00	200	3.067	4.0
			2.99 [19]	
0.04959	40.00	250	3.067 [21]	2.2
0.04133	33.33	300	3.067	1.4×10^{-2}
0.03875	31.25	320		8.66×10^{-3} [23]
0.03100	25.00	400	3.067	8.5 [21]
			2.96 [19]	
0.02480	20.00	500	3.067 [21]	6.3
0.02066	16.67	600	3.067	5.0
0.01771	14.29	700		4.1
0.01550	12.50	800		3.5
0.01378	11.11	900		3.1
4.798×10^{-4}	3.870	2,584	3.023 [24]	1.19×10^{-3} [24]
1.464×10^{-4}	1.181	8,469	3.023	6.20×10^{-4}
4.053×10^{-5}	0.3269	30,590	3.023	2.63×10^{-4}
1.861×10^{-7}	1.501×10^{-3}	6.662×10^{6}	3.018 [26]	1.6×10^{-5} [26]
3.718×10^{-8}	2.999×10^{-4}	3.335×10^{7}	3.018	1.6

[a] References are given in brackets.

Lithium Niobate ($LiNbO_3$)

EDWARD D. PALIK
Naval Research Laboratory
Washington, D.C.

Lithium niobate is a uniaxial, trigonal crystal useful for second-harmonic-generation applications of laser radiation. Index matching at ω and 2ω in the near IR–visible region is accomplished by temperature tuning of the ordinary (o) refractive index $n_o(\omega)$ ($E \perp c$ axis) and the extraordinary (e) refractive index $n_e(2\omega)$ ($E \parallel c$ axis). Two types of material are considered stoichiometric and congruent. A mole ratio of $Li_2O/(LiO_2 + Nb_2O_5) = 0.500$ corresponds to stoichiometric material. This is grown from a melt containing excess Li. A congruently melting composition crystal grows from a melt of the *same* composition, corresponding to a mole ration of $Li_2O/(LiO_2 + Nb_2O_5) = 0.486$. This material is used in most applications.

The UV data are taken from the reflection data of Wiesendanger and Güntherodt [1] obtained at 293 K on cleaved surfaces; stoichiometry was not specified. Kramers–Kronig (KK) analyses for both polarizations ($E\|$ and $\perp$ to the c axis) were performed. Above ~ 7 eV, the difference in $R_{\|}$ and $R_{\perp}$ is negligible. An analysis by Barner *et al.* [2] from 4 to 14.5 eV with unpolarized light and their subsequent KK analysis is not used here because of the large differences with Wiesendanger and Güntherodt [1]. It is not obvious that n, k (unpolarized) are indeed averages of n_o, n_e and k_o, k_e. Since $n_{o,e}$ and $k_{o,e}$ were calculated from values of ε_1 and ε_2 as read from a graph, the numbers are probably good to two figures, although three figures are listed in Table VII. Table VII is plotted in Fig. 7 for both o and e rays.

The absorption edge of congruent material has been studied by Redfield and Burke [3] over a wide temperature range. A series of samples were mechanically polished. This produced spurious absorption in the small-absorption region when compared to the transmission of the next thicker sample. The c axis was in the plane of the sample, so that dichroism might be measured. However, very little difference was observed, so that only $E \parallel c$ data are given. The tabulated data are for 300 K.

The refractive index in the transparent region has been measured for various materials, MgO doped [4], stoichiometric [5], and congruent [6]. Generally, the minimum-deviation technique has been used with the optic axis

HANDBOOK OF OPTICAL CONSTANTS OF SOLIDS ISBN 0-12-544420-6

parallel to both faces of the prism. We tabulate the data from Boyd *et al.* [5] and Nelson and Mikulyak [6]. Boyd *et al.* [5] do not state room temperature explicitly. Nelson and Mikulyak [6] used 24.5°C and state an accuracy of ± 0.0002. Differences in n in the two sets of data are due to the slight differences in stoichiometry in the two kinds of materials.

In the infrared, the lattice vibration bands have been studied in reflection by Barker and Loudon [7], Axe and O'Kane [8], and Poplavko *et al.* [9]. The refractive indices at 300 K have been provided by Barker and Loudon [7] in the transparent region by analysis of reflectivity directly as $R = (\sqrt{\varepsilon_1} - 1)^2/(\sqrt{\varepsilon_1} + 1)^2$. Barker and Loudon [7] fit oscillator models through the data of Boyd *et al.* [5] and through their own data by using one band-gap oscillator and eight lattice oscillators for $E \parallel c$ and one band-gap oscillator and five lattice oscillators for $E \perp c$. Since the given numbers did not reproduce the long-wavelength values for $n_o(\perp)$ and $n_e(\parallel)$ given in a graph by Barker and Loudon [7], we chose to read the given graph of experimental data directly. The results are tabulated from 5 to 11 μm.

In Barker and Loudon [7], Axe and O'Kane [8], and Poplavko [9], the reflectivity was measured and KK analyzed. As an example of the differences, the vibration mode near 150 cm^{-1} has an imaginary peak $\varepsilon_{02} = 230$, 158, and 200, respectively.

We tabulate the data of Axe and O'Kane [8] at longer wavelength because it is more complete. The samples were probably stoichiometric material polished with 0.05-μm alumina and etched with $HF–HNO_3$ until certain reflection features present in mechanically polished surfaces cleared up or became sharper. Reflectivity was measured with an aluminized reference surface. Temperature was not stated but was no doubt near 300 K. Dispersion-relation analysis yielded graphs of ε_1 and ε_2 that we read and then converted to n and k. While two decimal places are given, the numbers are probably good to the first significant figure.

In the far infrared, Bosomworth [10] and Sakai [11] have measured n_o and n_e by utilizing channel spectra, and the former has also measured the absorption coefficient, all at 300 K. We tabulate the refractive indices of Sakai [11] because they cover a somewhat wider spectral range and are virtually identical to the value of Bosomworth [10] (both read off graphs). We read the values from a smooth line put through the data points that scatter by ± 0.05. The extinction coefficients of Bosomworth [10] are tabulated for a Czochralski-grown sample polished with diamond grit. In the 60-cm^{-1} region, k_o and k_e from the KK analysis [8] are much larger than measured in transmission [10], suggesting that dispersion-relation analysis is poor when $n \gg k$.

Poplavko *et al.* [9] found that $n_o = 7.19$, $k_o = 0.8$ and $n_e = 5.48$, $k_e = 0.2$ at 300 μm. These n values are significantly larger than those of Barker and Loudon [7] and Axe and O'Kane [8]; the k values are one to two orders of magnitude larger, which is troublesome. Permittivity measurements at

3000 μm using a waveguide-resonance reflection method yielded ε_1 and $\tan\delta = \varepsilon_2/\varepsilon_1$; then $n_o = 7.21$, $k_o = 0.04$ and $n_e = 5.66$, $k_e = 0.01$, but the variation in ε_{01} from sample to sample was typically 52–48 due to differences in stoichiometry and structure defects in the crystals. Measurements of ε_1 and ε_2 down to ~ 50 Hz with standard bridge and resonance measurements methods showed a piezoelectric resonance near 10^6–10^7 Hz. In the frequency range 126–132 GHz (2380–2270 μm), Vinogradov *et al.* [12] determined $n_o = 7.2 \pm 0.2$ and $\tan\delta = (2.5 \pm 0.5) \times 10^{-3}$. This gave $\varepsilon_{01} = 51.8$, $\varepsilon_{02} = 0.13$, so that $n_o = 7.20$ and $k_o = 9 \times 10^{-3}$. Again we see the large variation in the data of Barker and Loudon [7], Axe and O'Kane [8], Poplavko *et al.* [9], Bosomworth [10], and Sakai [11], which is probably sample dependent.

REFERENCES

1. E. Wiesendanger and G. Güntherodt, *Solid State Commun.* **14**, 303 (1974).
2. K. Barner, R. Braunstein, and H. A. Weakliem, *Phys. Stat. Solidi B* **68**, 525 (1975).
3. D. Redfield and W. J. Burke, *J. Appl. Phys.* **45**, 4566 (1974).
4. G. D. Boyd, W. L. Bond, and H. L. Carter, *J. Appl. Phys.* **38**, 1941 (1967).
5. G. D. Boyd, R. C. Miller, K. Nassau, W. L. Bond, and A. Savage, *Appl. Phys. Lett.* **5**, 934 (1964).
6. D. F. Nelson and R. M. Mikulyak, *J. Appl. Phys.* **45**, 3688 (1974).
7. A. S. Barker and R. Loudon, *Phys. Rev.* **158**, 433 (1967).
8. J. D. Axe and D. F. O'Kane, *Appl. Phys. Lett.* **9**, 58 (1966).
9. Y. M. Poplavko, V. V. Meriakri, V. N. Aleshechkin, V. G. Tsykalov, E. F. Ushatkin, and A. S. Knyazev, *Sov. Phys. Solid State* **15**, 991 (1973); Y. M. Poplavko, V. V. Meriakri, V. N. Aleshechkin, V. G. Tsykalov, E. F. Ushatkin, and A. S. Knyazev, *Fiz. Tverd. Tela.* **15**, 1473 (1973).
10. D. R. Bosomworth, *Appl. Phys. Lett.* **9**, 330 (1966).
11. K. Sakai, *Appl. Opt.* **11**, 2894 (1972).
12. P. N. Vinogradov, N. A. Prisova, and G. V. Kozlov, *Sov. Phys. Solid State* **12**, 605 (1970); P. N. Vinogradov, N. A. Prisova, and G. V. Kozlov, *Fiz. Tverd. Tela.* **12**, 781 (1970).

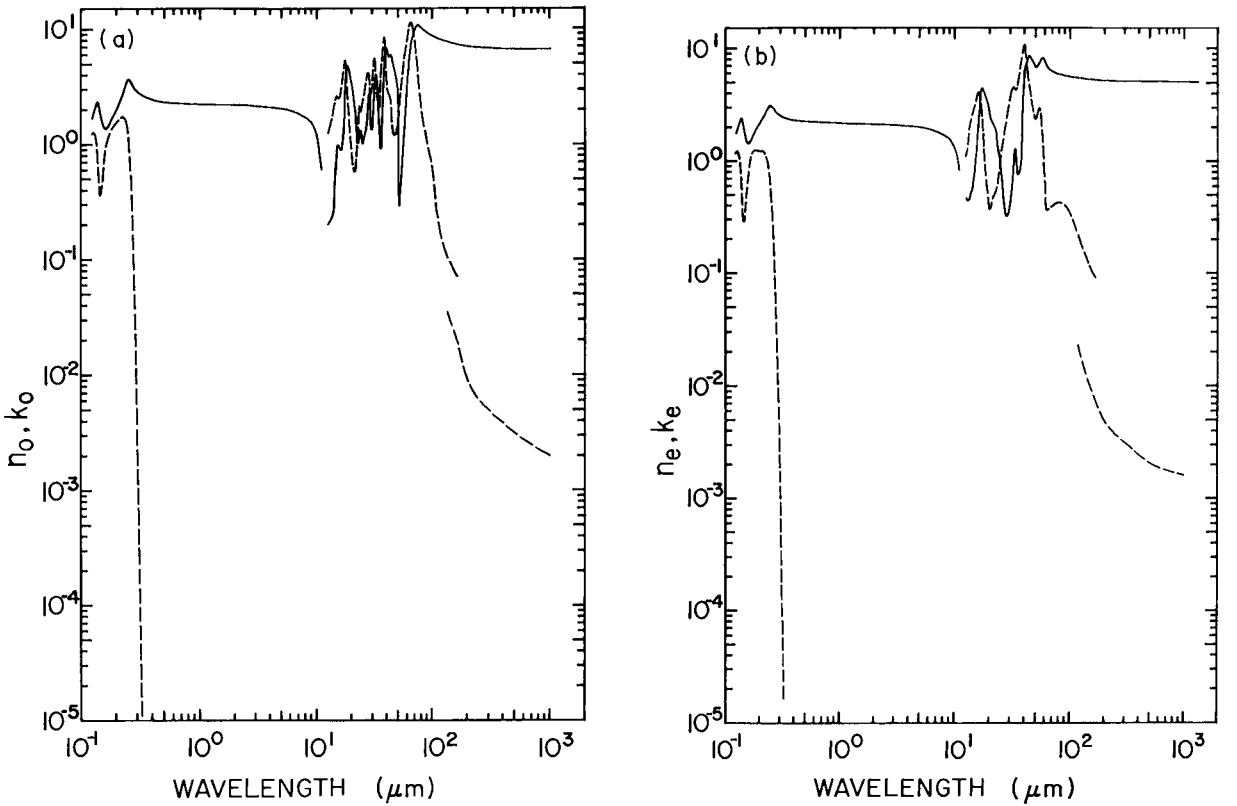

Fig. 7. (a) Log–log plot of n_o (——) and k_o (– – –) versus wavelength in micrometers for lithium niobate. (b) Log–log plot of n_e (——) and k_e (– – –) versus wavelength in micrometers for lithium niobate.

TABLE VII
Values of n and k for Lithium Niobate Obtained from Various References[a]

eV	cm^{-1}	μm	$n_o(\perp)$	$k_o(\perp)$	$n_e(\parallel)$	$k_e(\parallel)$
10.0	80,650	0.1240	1.67 [1]	1.22 [1]	1.73 [1]	1.18 [1]
9.75	78,640	0.1272	1.88	1.28	1.97	1.22
9.5	76,620	0.1305	2.04	1.17	2.14	1.12
9.25	74,610	0.1340	2.19	1.09	2.32	1.03
9.0	72,590	0.1378	2.32	0.75	2.42	0.72
8.75	70,570	0.1417	2.12	0.45	2.17	0.34
8.5	68,560	0.1459	1.82	0.36	1.89	0.29
8.25	66,540	0.1503	1.58	0.46	1.63	0.40
8.0	64,520	0.1550	1.43	0.59	1.48	0.57
7.5	60,490	0.1653	1.38	0.98	1.48	0.94
7.0	56,460	0.1771	1.54	1.30	1.75	1.24
6.5	52,430	0.1907	1.82	1.48	2.07	1.26
6.0	48,390	0.2066	2.16	1.60	2.30	1.22
5.75	46,380	0.2156	2.36	1.67	2.46	1.22
5.5	44,360	0.2254	2.68	1.75	2.76	1.16
5.25	42,340	0.2362	3.22	1.60	2.98	1.00
5.0	40,330	0.2480	3.62	1.27	3.10	0.64
4.75	38,310	0.2610	3.52	0.43	2.99	0.25
4.5	36,290	0.2755	3.19	0.11	2.79	0.06
4.25	34,280	0.2917	2.91	0.00	2.59	0.00
						1.02×10^{-2} [3]
4.2	33,880	0.2952				5.87×10^{-3}
4.15	33,470	0.2988				3.09
4.1	33,070	0.3024				1.71×10^{-3}
4.05	32,670	0.3061				9.01×10^{-4}
4.0	32,260	0.3100	2.76		2.49	4.19
3.95	31,860	0.3139				2.12×10^{-4}
3.9	31,460	0.3179				7.84×10^{-5}
3.85	31,050	0.3220				3.33
3.8	30,650	0.3263				1.69×10^{-5}
3.75	30,250	0.3306				8.16×10^{-6}
3.7	29,840	0.3351				5.07

eV	cm^{-1}	μm	$n_o(\perp)$	$n_e(\parallel)$	$n_o(\perp)$	$n_e(\parallel)$
3.0642	24,714	0.40463	2.4317 [6]	2.3260 [6]		
2.952	23,810	0.42			2.4089 [5]	2.3025 [5]
2.8447	22,944	0.43584	2.3928	2.2932		
2.755	22,220	0.45			2.3780	2.2772
2.6503	21,376	0.46782	2.3634	2.2683		
2.5831	20,834	0.47999	2.3541	2.2605		
2.480	20,000	0.50			2.3410	2.2457
2.4379	19,663	0.50858	2.3356	2.2448		
2.2705	18,313	0.54607	2.3165	2.2285		
2.254	18,180	0.55			2.3132	2.2237
2.1489	17,332	0.57696	2.3040	2.2178		
2.1415	17,272	0.57897	2.3032	2.2171		
2.1102	17,019	0.58756	2.3002	2.2147		

(*continued*)

TABLE VII (*Continued*)

Lithium Niobate

eV	cm^{-1}	μm	$n_o(\perp)$	$n_e(\parallel)$	$n_o(\perp)$	$n_e(\parallel)$
2.066	16,670	0.60			2.2967	2.2082
1.9257	15,532	0.64385	2.2835	2.2002		
1.8566	14,974	0.66782	2.2778	2.1953		
1.771	14,290	0.70			2.2716	2.1874
1.7549	14,154	0.70652	2.2699	2.1886		
1.550	12,500	0.80			2.2571	2.1745
1.5321	12,357	0.80926	2.2541	2.1749		
1.4224	11,472	0.87168	2.2471	2.1688		
1.378	11,110	0.90			2.2448	2.1641
1.3251	10,688	0.93564	2.2412	2.1639		
1.2915	10,417	0.95998	2.2393	2.1622		
1.240	10,000	1.00			2.2370	2.1567
1.2227	9,961.9	1.0140	2.2351	2.1584		
1.1352	9,156.34	1.09214	2.2304	2.1545		
1.0745	8,666.11	1.15392	2.2271	2.1517		
1.0707	8,636.03	1.15794	2.2269	2.1515		
1.033	8,333	1.20			2.2269	2.1478
0.96284	7,765.78	1.28770	2.2211	2.1464		
0.8856	7,143	1.40			2.2184	2.1417
0.86103	6,944.59	1.43997	2.2151	2.1413		
0.7749	6,250	1.60			2.2113	2.1361
0.75683	6,104.22	1.63821	2.2083	2.1356		
0.6888	5,556	1.80			2.2049	2.1306
0.64871	5,232.18	1.91125	2.1994	2.1280		
0.6199	5,000	2.00			2.1974	2.1250
0.56762	4,578.17	2.18428	2.1912	2.1211		
0.5636	4,545	2.20			2.1909	2.1183
0.51662	4,166.75	2.39995	2.1840	2.1151		
0.5166	4,167	2.40			2.1850	2.1129
0.4769	3,846	2.60			2.1778	2.1071
0.47412	3,824.03	2.61504	2.1765	2.1087		
0.45410	3,662.53	2.73035	2.1724	2.1053		
0.4428	3,571	2.80			2.1703	2.1009
0.42793	3,451.45	2.89733	2.1657	2.0999		
0.4133	3,333	3.00			2.1625	2.0945
0.40631	3,277.10	3.05148	2.1594	2.0946		
0.3875	3,125	3.20			2.1543	2.0871
0.3647	2,941	3.40			2.1456	2.0804
0.3444	2,778	3.60			2.1363	2.0725
0.3263	2,632	3.80			2.1263	2.0642
0.3100	2,500	4.00			2.1155	2.0553

eV	cm^{-1}	μm	$n_o(\perp)$	$k_o(\perp)$	$n_e(\parallel)$	$k_e(\parallel)$
0.2480	2,000	5.0	2.05 [7]		2.00 [7]	
0.2066	1,667	6.0	1.97		1.93	
0.1771	1,429	7.0	1.84		1.83	
0.1550	1,250	8.0	1.71		1.72	
0.1378	1,111	9.0	1.52		1.55	
0.1240	1,000	10	1.20		1.30	

TABLE VII (*Continued*)

Lithium Niobate

eV	cm^{-1}	μm	$n_o(\perp)$	$k_o(\perp)$	$n_e(\parallel)$	$k_e(\parallel)$
0.1127	909.1	11	0.60		0.81	
0.09919	800	12.50	0.20 [8]	1.24 [8]	0.46 [8]	1.10 [8]
0.09671	780	12.82	0.21	1.43	0.44	1.48
0.09423	760	13.16	0.22	1.56	0.45	1.78
0.09175	740	13.51	0.23	1.74	0.46	2.17
0.08927	720	13.89	0.26	1.94	0.53	2.34
0.08679	700	14.29	0.54	2.30	0.56	2.67
0.08431	680	14.71	0.90	2.51	0.75	3.01
0.08307	670	14.93	0.90	2.60		
0.08183	660	15.15	0.99	2.52	1.05	3.33
0.07935	640	15.63	0.95	2.52	1.44	3.83
0.07811	630	15.87			1.85	4.05
0.07687	620	16.13	0.90	2.88	2.52	4.16
0.07563	610	16.39			3.42	4.09
0.07439	600	16.67	1.10	3.63	4.02	3.48
0.07315	590	16.95			4.24	2.83
0.07191	580	17.24	1.83	4.62	4.47	2.12
0.07067	570	17.54	3.01	5.30		
0.06943	560	17.86	4.77	4.55	4.17	1.20
0.06819	550	18.18	4.88	2.97		
0.06695	540	18.52	4.51	2.10	3.67	0.68
0.06447	520	19.23	4.00	1.24	3.20	0.47
0.06199	500	20.00	3.27	0.84	2.67	0.37
0.05951	480	20.83	2.52	0.59	2.28	0.44
0.05703	460	21.74	1.78	0.62	2.06	0.48
0.05455	440	22.73	1.03	1.44	1.82	0.55
0.05331	430	23.26	1.20	2.11		
0.05207	420	23.81	1.30	1.92	1.27	0.79
0.04959	400	25.00	1.01	2.45	0.83	1.09
0.04711	380	26.32	1.33	3.36	0.48	1.65
0.04587	370	27.03	1.73	3.74		
0.04463	360	27.78	2.61	4.10	0.32	2.47
0.04339	350	28.57	2.64	2.83		
0.04215	340	29.41	1.34	2.96	0.37	3.34
0.04092	330	30.30	1.89	4.75		
0.03968	320	31.25	3.39	5.52	0.70	4.30
0.03844	310	32.26	4.09	3.04	1.16	4.51
0.03720	300	33.33	2.80	1.96	1.20	4.35
0.03596	290	34.48			0.75	4.64
0.03472	280	35.71	0.92	4.34	0.80	5.62
0.03348	270	37.04	2.19	6.84	0.94	6.91
0.03286	265	37.74	4.19	8.34		
0.03224	260	38.46	5.71	7.91	3.04	9.86
0.03100	250	40.00	6.79	2.94	6.58	10.4
0.02976	240	41.67	5.76	2.68	7.48	7.34
0.02852	230	43.48	5.82	2.31	8.55	4.91
0.02728	220	45.45	4.94	1.21	8.32	3.36

(*continued*)

TABLE VII (*Continued*)

Lithium Niobate

eV	cm^{-1}	μm	$n_o(\perp)$	$k_o(\perp)$	$n_e(\parallel)$	$k_e(\parallel)$
0.02604	210	47.62			7.66	2.60
0.02480	200	50.00	2.54	1.57	6.78	2.35
0.02356	190	52.63			7.08	2.85
0.02232	180	55.56	0.98	5.09	7.86	2.41
0.02108	170	58.82	2.04	7.36	8.03	0.75
0.01984	160	62.50	5.43	10.1	6.93	0.36
0.01860	150	66.67	7.96	9.92	6.33	0.38
0.01736	140	71.43	10.1	5.68	6.17	0.40
0.01612	130	76.92	10.6	3.06	6.01	0.43
0.01488	120	83.33	9.83	1.67	5.84	0.43
0.01240	100	100	8.57	0.70	5.66	0.35
0.01054	85	117.6				2.3×10^{-2} [10]
0.009919	80	125	7.87	0.13	5.52	0.18 [8]
						1.8×10^{-2} [10]
0.009299	75	133.3		3.5×10^{-2} [10]		
0.008679	70	142.9		3.0		1.1
0.007439	60	166.7	7.34	7 [8]	5.38	9×10^{-2} [8]
			7.06 [11]	1.9×10^{-2} [10]	5.22 [11]	8.0×10^{-3} [10]
0.006199	50	200	6.90	9.5×10^{-3}	5.165	4.8
0.004959	40	250	6.85 [8]	6.0		3.6
			6.80 [11]		5.125	
0.003720	30	333.3	6.70	4.5	5.10	2.9
0.002480	20	500	6.64	3.2	5.07	2.0
0.001240	10	1000	6.61	2.0	5.06	1.6

[a] The reference is given in brackets at the beginning of the tabulation of n and k and is understood to refer to all n's or all k's below it until a new reference appears. When an exponent of 10 is given, all numbers below it have the same exponent until the power of 10 changes or the next number has 10^{-1}, which is usually written as a decimal. Boyd *et al.* [5] n values are for stoichiometric material and Nelson and Mikulyak [6] n values are for congruent material. We specify $n_o(\perp)$ and $n_e(\parallel)$ for redundancy.

Potassium Chloride (KCl)

EDWARD D. PALIK
Naval Research Laboratory
Washington, D.C.

The optical constants n and k are collected in Table VIII and plotted in Fig. 8.

The spectral region 3000–300 μm primarily contains absorption due to two- and three-phonon absorption processes. Here, k has been determined by transmission measurements of slabs. The data of Genzel *et al.* [1] are tabulated in Table VIII. Measurement was with a grating monochromator utilizing an Hg lamp and the harmonics of a 12-mm Klystron as sources. The tabulated numbers were read off a wavelength graph with a smooth line drawn through the data points, which scattered by $\lesssim 10\%$. The more-limited results of Stolen and Dransfeld [2] at 300 K were in good agreement, with the temperature dependence studied in detail.

The spectral region 200–30 μm has beeen studied by Johnson and Bell [3] by asymmetric Fourier-transform spectroscopy. This technique yields the phase and amplitude of the reflectivity experimentally, thus circumventing Kramers–Kronig (KK) analysis of R or oscillator-model fits. At the rest-strahlen minimum, a power reflectance of 0.0004 was measured, which suggests little polishing damage. Resolution was 2 cm^{-1}. An accuracy of 0.005 in amplitude reflectance was stated. Shoulders on the high-frequency side of ν_T are due to multiple-phonon absorption processes. We have read graphs to obtain n and k. Bravo to workers who put fiduciary marks on all four sides of a graph and include all the digits from 2 to 9 on the log scales! We typically give three figures, but our reading ability is probably somewhat less than this.

For the region 50–12.5 μm, Deutsch [4] has collected values of absorption coefficient α from several sources all more or less at room temperature. Transmission of slab samples was used. On semilog paper these form a straight line to within the scatter, and we have read the values on the line. Boyer *et al.* [5] treat the temperature dependence of such absorption in numerous materials including KCl.

ISBN 0-12-544420-6

Calorimetry measurements at single laser wavelengths have been carried out in the transparent region [5–7] and the k values are listed. These represent bulk values with uncertainties of factors of 2 from sample to sample and lab to lab. Surface preparation included chemical polishing.

In the transparent region 35–0.18 μm, Li [8] has assembled and analyzed a great deal of n data from many references. Minimum deviation was the experimental method in most cases. He has fitted a Sellmeier-type equation with nine adjustable parameters to represent the data to the fifth decimal place. The dispersion formula has the form

$$n^2 = 1.26486 + \frac{0.30523\lambda^2}{\lambda^2 - (0.100)^2} + \frac{0.41620\lambda^2}{\lambda^2 - (0.131)^2} + \frac{0.18870\lambda^2}{\lambda^2 - (0.162)^2} + \frac{2.6200\lambda^2}{\lambda^2 - (70.42)^2} \quad (1)$$

at 293 K. This indicates that $\lambda_T = 70.42$ μm ($\nu_T = 142.0$ cm^{-1}). Li [8] has provided a temperature-dependence formula of the form

$$2n\frac{dn}{dT} = -11.13(n^2 - 1) + 0.19 + \frac{3.393\lambda^4}{(\lambda^2 - 0.02624)^2} + \frac{142.56\lambda^4}{(\lambda^2 - 4958.98)^2}. \quad (2)$$

where dn/dT is in units of 10^{-5} K^{-1}. Thus, a 3-K difference in room temperature between labs begins to affect the fourth decimal place. For the spectral region 0.24–21 μm, Li [8] states that the fourth decimal place is meaningful, with estimated uncertainties in the range 0.0001–0.0005. To either side, the uncertainty moves to the third decimal place.

At and above the fundamental band gap, a variety of n and k data have been assembled. Some overlap is provided to show discrepancies and variations. For 295 K, Tomiki [9] has measured transmission of thin slabs to determine k in the region 6.8–7.9 eV, including the Urbach tail and exciton effects. Two discharge lamps (hydrogen and CO_2) were utilized. Much attention was given to the growth and preparation of pure samples to minimize impurity absorption effects.

For the region 6.4–11.6 eV, reflectivity of cleaved samples has been fitted by KK analysis to yield n and k as listed [10]. A great deal of temperature data was obtained by Tomiki *et al.* [11]. In this region absorption is due primarily to a number of interband transitions between lower-lying valence and higher-lying conduction bands.

In the spectral region 5–26 eV, R was measured by Roessler and Walker [12] with KK analysis. More recent measurements have been performed [13] that we choose to emphasize. As usual, differences of 20% in n and k appear in overlap regions, although the features seem the same. Antinori *et al.* [13] used a continuum He discharge as a source. Reflectivity was

reproducible among various cleaved samples to within 5%. As Table II in Antinori *et al.* [13] emphasizes, the reflectivity at 18.4 eV varied by a factor of 2 among seven different references. As Fig. 5 in Antinori *et al.* [13] indicates, spectra in this region are also affected by resolution; two examples of spectra of 1.5 and 3 Å resolution are shown to differ significantly. More structure was resolved in room-temperature spectra than previously had been seen. Absorption in this region is due primarily to plasma oscillations of the 6p electrons of Cl^- filling the valence-band states ($\sim$14 eV) and to transitions of 3p electrons of K^+ to the bottom of the conduction band ($\sim$20 eV).

Balzarotti *et al.* [14] have measured reflectivity in the region from 20 to 44 eV by utilizing synchrotron radiation. Kramers–Kronig analysis values of n and k are listed. Peaks in this spectral region are primarily due to electron transitions from 3p levels of K^+ and 3s levels of Cl^- into the conduction band. No doubt, cleaved samples were used.

Above this energy, absolute values of k become sparse, although a great deal of work has been done at the various L and K absorption edges. The work is collected by Haelbich *et al.* [15], and it proved very useful as a starting point for the present work. They give a figure summarizing absorption coefficient α in inverse centimeters for the range 50–280 eV. However, some of the original references contain only relative values. Therefore, we have found some other references to supplement these. For the spectral region 50–200 eV, the data of Lukirskii and Zimkina [16] as given in Haelbich *et al.* [15] indicated a featureless decrease in k to high energy. Lukirskii *et al.* [17] report measurements of n and k at two x-ray wavelengths. The k values are about a factor of 2 smaller than those given in Haelbich *et al.* [15], but we list them along with the n values since they seem to join the high-energy data better.

For the spectral region 200–240 eV, the data of Brown *et al.* [18], obtained with synchrotron radiation, are only relative in the original paper. We use the work of Aita *et al.* [19], who used an x-ray tube as a continuous source to study the $L_{2,3}$ edge of Cl^- in evaporated films. Iguchi *et al.* [20] used synchrotron radiation to measure relative absorption in the 200–280 eV region.

Finally, the K absorption edge of Cl^- near 2823 eV has been studied by Parratt *et al.* [21] with an x-ray source spectrometer, and k is tabulated. They pointed out a resolution (spectral window) problem that distorted the measurement of α as a function of sample thickness near the absorption edge. Kiyono and Sugiura [22] also measured relative absorption in this region.

The K absorption edge of potassium near 3610 eV has been studied by Sugiura [23]. It is not clear that the L edges of potassium have been measured in the 290–300 eV region.

REFERENCES

1. L. Genzel, H. Happ, and R. Weber, *Z. Physik* **154**, 13 (1959).
2. R. Stolen and K. Dransfeld, *Phys. Rev.* **139A**, 1295 (1965).
3. K. W. Johnson and E. E. Bell, *Phys. Rev.* **187**, 1044 (1969).
4. T. F. Deutsch, *J. Phys. Chem. Solids* **34**, 209 (1973).
5. L. L. Boyer, J. A. Harrington, M. Hass, and H. R. Rosenstock, *Phys. Rev.* **11B**, 1665 (1975).
6. S. D. Allen and J. A. Harrington, *Appl. Opt.* **17**, 1679 (1978).
7. J. A. Harrington, B. L. Bobbs, M. Braunstein, R. K. Kim, R. Stearns, and R. Braunstein, *Appl. Opt.* **171**, 541 (1978).
8. H. H. Li, *J. Phys. Chem. Ref. Data* **5**, 329 (1976).
9. T. Tomiki, *J. Phys. Soc. Jpn.* **23**, 1280 (1967).
10. T. Tomiki, *J. Phys. Soc. Jpn.* **22**, 463 (1967).
11. T. Tomiki, T. Miyata, and H. Tsukamoto, *J. Phys. Soc. Jpn.* **35**, 495 (1973).
12. D. M. Roessler and W. C. Walker, *J. Opt. Soc. Am.* **58**, 279 (1968).
13. M. Antinori, A. Balzarotti, and M. Piacentini, *Phys. Rev. B* **7**, 1541 (1973); M. Antinori, A. Balzarotti, and M. Piacentini, private communication (1982).
14. A Balzarotti, A. Bianconi, E. Burattini, and G. Strinati, *Solid State Commun.* **15**, 1431 (1974).
15. R. P. Haelbich, M. Iwan, and E. E. Koch, "Physik Daten, Physics Data." Fach-information Zentrum, Karlsruhe, 1977.
16. A. P. Lukirskii and T. M. Zimkina, *in* "Rontgen Spektren und Chemische Bindung," p. 187. Karl-Marx Universitat, Leipzig, 1966.
17. A. P. Lukirskii, E. P. Savinov, O. A. Ershov, and Y. F. Shepelev, *Opt. Spectrosc.* **16**, 168 (1964); A. P. Lukirskii, E. P. Savinov, O. A. Erskov, and Y. F. Shepelev, *Opt. Specktrosk.* **16**, 310 (1964).
18. F. C. Brown, C. Gahwiller, H. Fujita, A. B. Kunz, W. Scheifley, and N. Carrera, *Phys. Rev. B* **2**, 2126 (1970).
19. O. Aita, I. Nagakura, and T. Sagawa, *J. Phys. Soc. Jpn.* **30**, 1414 (1971).
20. Y. Iguchi, T. Sagawa, S. Sato, M. Watanabe, H. Yamashita, A. Ejiri, M. Sasanuma, S. Nakai, M. Nakamura, S. Yamaguchi, Y. Nakai, and Y. Oshio, *Solid State Commun.* **6**, 575 (1968).
21. L. G. Parratt, C. F. Hempstead, and E. L. Jossem, *Phys. Rev.* **105**, 1228 (1957).
22. S. Kiyono and C. Sugiura, *Tech. Repts. Tohoku Univ.* **30**, 9 (1965).
23. C. Sugiura, *Sci. Repo. Tohoku Univ.* **45**, 248 (1961).

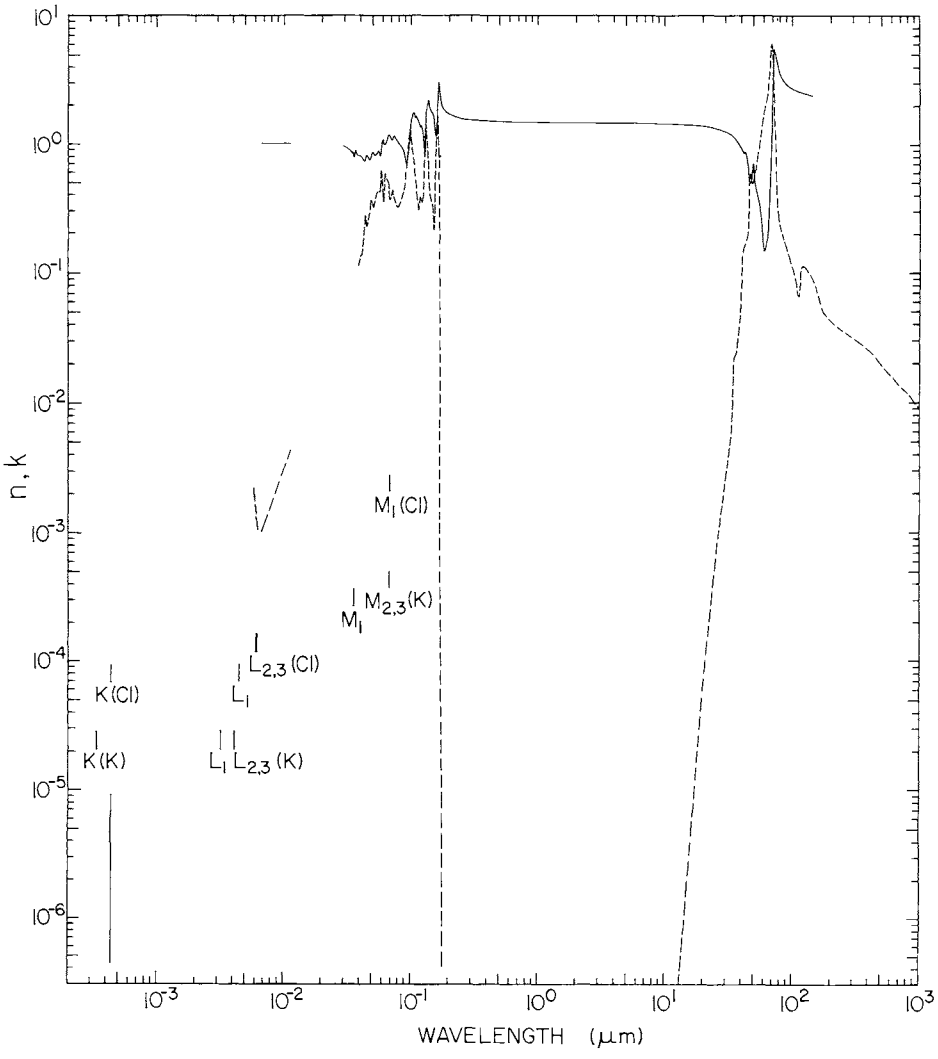

Fig. 8. Log–log plot of n (——) and k (– – –) versus wavelength in micrometers for potassium chloride.

TABLE VIII

Values of n and k for Potassium Chloride Obtained from Various References[a]

eV	Å	n	k
2860.3	4.3347		3.93×10^{-6} [21]
2859.3	4.3362		3.83
2858.3	4.3377		3.73
2857.3	4.3392		3.63
2856.3	4.3408		3.52
2855.3	4.3423		3.39

(*continued*)

TABLE VIII (*Continued*)

Potassium Chloride

eV	Å	n	k
2854.3	4.3438		3.32
2853.3	4.3453		3.60
2852.3	4.3468		3.91
2851.3	4.3484		4.36
2850.3	4.3499		4.74
2849.3	4.3514		4.61
2848.3	4.3530		4.16
2847.3	4.3545		4.09
2846.3	4.3560		4.13
2845.3	4.3575		4.20
2844.3	4.3590		4.06
2843.3	4.3606		3.82
2842.8	4.3614		3.71
2842.3	4.3621		3.71
2841.8	4.3629		3.82
2841.3	4.3637		3.89
2840.8	4.3644		3.54
2840.3	4.3652		2.54
2839.8	4.3660		2.08
2839.3	4.3668		1.95
2838.8	4.3675		2.09
2838.3	4.3683		2.57
2837.8	4.3691		3.65
2837.3	4.3698		4.80
2836.8	4.3706		4.94
2836.3	4.3714		4.87
2835.8	4.3721		5.85
2835.3	4.3729		5.95
2834.8	4.3737		5.85
2834.3	4.3745		4.53
2833.8	4.3752		3.55
2833.3	4.3760		3.66
2832.8	4.3768		4.53
2832.3	4.3775		5.85
2831.8	4.3783		7.49
2831.3	4.3791		9.34
2830.8	4.3799		9.06
2830.3	4.3806		6.45
2829.8	4.3814		1.57
2829.3	4.3822		1.05×10^{-6}
2828.8	4.3830		6.98×10^{-7}
2828.3	4.3837		4.19×10^{-7}
219	56.61		1.82×10^{-3} [19]
218.5	56.74		1.82
218	56.87		1.85
217.5	57.00		1.88
217	57.13		1.87
216.5	57.27		1.89
216	57.40		1.92
215.5	57.53		1.91

TABLE VIII (*Continued*)

Potassium Chloride

eV	Å	n	k
215	57.67		1.84
214.5	57.80		1.84
214	57.94		1.84
213.5	58.07		1.85
213	58.21		2.02
212.5	58.34		2.19
212	58.48		2.14
211.5	58.62		1.87
211	58.76		1.82
210.5	58.90		1.91
210	59.04		1.71
209.5	59.18		1.48
209	59.32		1.45
208.5	59.46		1.42
208	59.61		1.46
207.5	59.75		1.55
207	59.89		1.56
206.5	60.04		1.51
206	60.19		1.55
205.5	60.33		1.56
205	60.48		1.52
204.5	60.63		1.40
204	60.78		1.23
203.5	60.92		1.31
203	61.07		1.46
202.5	61.23		1.15
202	61.38		1.13
201.5	61.53		1.22
201	61.68		1.04
200.5	61.84		1.03
200	61.99		1.03
185.1	67	0.99874 [17]	1.01 [17]
109.7	113	0.99578	4.22×10^{-3}

eV	cm^{-1}	μm	n	k
43		0.02883	0.96 [13, 14]	3.0×10^{-2} [13, 14]
42		0.02952	0.955	2.5
41		0.03024	0.945	2.0
40		0.03099	0.925	1.8
39		0.03179	0.91	2.0
38		0.03263	0.89	3.0
37		0.03351	0.87	5.0
36.5		0.03397	0.845	7.04
36		0.03444	0.86	8.0
35.5		0.03493	0.830	9.16×10^{-2}
35		0.03542	0.87	0.115
34.5		0.03594	0.851	0.105
34		0.03646	0.89	0.12

(*continued*)

TABLE VIII (*Continued*)

Potassium Chloride

eV	cm^{-1}	μm	n	k
33.5		0.03701	0.854	7.83×10^{-2}
33.1		0.03746	0.821	6.77
32.7		0.03792	0.800	9.24×10^{-2}
32.3		0.03839	0.797	0.111
31.9		0.03887	0.795	0.121
31.5		0.03936	0.797	0.131
31.1		0.03987	0.799	0.134
30.7		0.04039	0.795	0.134
30.3		0.04092	0.779	0.134
29.9		0.04147	0.756	0.145
29.5		0.04203	0.743	0.175
29.1		0.04261	0.730	0.207
28.9		0.04290	0.729	0.234
28.7		0.04320	0.743	0.265
28.5		0.04350	0.785	0.275
28.3		0.04381	0.805	0.261
28.1		0.04412	0.816	0.245
27.9		0.04444	0.814	0.228
27.5		0.04509	0.789	0.230
27.1		0.04575	0.775	0.241
26.7		0.04644	0.755	0.263
26.3		0.04714	0.745	0.302
26.1		0.04750	0.750	0.335
25.9		0.04787	0.779	0.359
25.7		0.04824	0.805	0.362
25.5		0.04862	0.824	0.358
25.3		0.04901	0.836	0.357
25.1		0.04940	0.851	0.346
24.7		0.05020	0.849	0.317
24.3		0.05102	0.813	0.328
23.9		0.05188	0.806	0.363
23.5		0.05276	0.819	0.388
23.1		0.05367	0.834	0.413
22.9		0.05414	0.849	0.418
22.7		0.05462	0.860	0.420
22.5		0.05510	0.868	0.420
22.3		0.05560	0.872	0.418
21.9		0.05661	0.814	0.416
21.7		0.05714	0.790	0.488
21.5		0.05767	0.820	0.569
21.3		0.05821	0.918	0.612
21.1		0.05876	1.01	0.587
20.9		0.05932	1.06	0.530
20.7		0.05990	1.07	0.449
20.5		0.06048	1.02	0.355
20.3		0.06108	0.926	0.411
20.1		0.06168	0.910	0.495

TABLE VIII (*Continued*)

Potassium Chloride

eV	cm^{-1}	μm	n	k
19.9		0.06230	0.982	0.584
19.7		0.06294	1.00	0.497
19.5		0.06358	1.01	0.533
19.1		0.06491	1.09	0.525
18.7		0.06630	1.17	0.489
18.3		0.06775	1.15	0.387
17.9		0.06927	1.11	0.367
17.7		0.07005	1.07	0.382
17.5		0.07085	1.07	0.411
17.3		0.07167	1.09	0.428
17.1		0.07251	1.13	0.420
16.9		0.07336	1.14	0.376
16.7		0.07424	1.13	0.357
16.3		0.07606	1.09	0.322
15.9		0.07798	1.05	0.317
15.5		0.07999	1.01	0.328
15.1		0.08211	0.965	0.344
14.7		0.08434	0.931	0.367
14.3		0.08670	0.883	0.415
13.9		0.08920	0.791	0.441
13.5		0.09184	0.690	0.731
13.1		0.09465	0.841	0.950
12.9		0.09611	0.914	1.04
12.7		0.09763	1.04	1.22
12.5		0.09919	1.34	1.29
12.3		0.1008	1.57	1.12
12.1		0.1025	1.67	0.959
11.9		0.1042	1.74	0.767
11.7		0.1060	1.73	0.640
11.6		0.1069	1.67 [10]	0.58 [10]
11.5		0.1078	1.66	0.53
			1.69	0.520 [13]
11.4		0.1088	1.65	0.49 [10]
11.3		0.1097	1.63	0.45
			1.62	0.425 [13]
11.2		0.1107	1.60	0.41 [10]
11.1		0.1117	1.57	0.38
			1.55	0.374 [13]
11.0		0.1127	1.54	0.35 [10]
10.9		0.1137	1.50	0.325
			1.50	0.363 [13]
10.8		0.1148	1.47	0.31 [10]
10.7		0.1159	1.42	0.315
			1.40	0.336 [13]
10.6		0.1170	1.38	0.36 [10]
10.55		0.1175	1.36	0.38

(*continued*)

TABLE VIII (*Continued*)

Potassium Chloride

eV	cm^{-1}	μm	n	k
10.5		0.1181	1.37	0.385
10.4		0.1192	1.395	0.38
10.3		0.1204	1.35	0.37
10.2		0.1216	1.30	0.35
10.1		0.1228	1.24	0.355
10.0		0.1240	1.16	0.38
9.9		0.1252	1.05	0.41
9.8		0.1265	0.87	0.58
9.75		0.1272		0.71
9.7		0.1278	0.80	0.90
9.65		0.1285		1.1
9.6		0.1291	0.94	1.27
9.55		0.1298		1.41
9.5		0.1305	1.38	1.495
9.45		0.1312		1.48
9.4		0.1319	1.81	1.38
9.35		0.1326		1.28
9.3		0.1333	2.07	1.13
9.2		0.1348	2.18	0.85
9.1		0.1362	2.12	0.64
9.0		0.1378	1.99	0.50
8.9		0.1393	1.90	0.43
8.8		0.1409	1.85	0.40
8.7		0.1425	1.81	0.39
8.6		0.1442	1.79	0.37
8.5		0.1459	1.75	0.345
8.4		0.1476	1.73	0.34
8.3		0.1494	1.68	0.265
8.2		0.1512	1.54	0.215
8.1		0.1531	1.36	0.25
8.0		0.1550	1.15	0.46
7.95		0.1560		0.67
7.9		0.1569	1.13	0.90
7.85		0.1579		1.12
7.8		0.1589	1.30	1.36
7.75		0.1600		1.54
7.7		0.1610	1.92	1.64
				1.67 [9]
7.65		0.1621		1.6 [10]
7.6		0.1631	2.63	1.34
				1.43 [9]
7.55		0.1642	2.92	1.1 [10]
7.5		0.1653	3.0	0.51
				0.494 [9]
7.45		0.1664	2.8	0.2 [10]
7.4		0.1675	2.61	6×10^{-2}
				5.60×10^{-2} [9]

TABLE VIII (*Continued*)

Potassium Chloride

eV	cm^{-1}	μm	n	k
7.3		0.1698	2.34	3.11×10^{-3}
7.2		0.1722	2.19	1.78×10^{-4}
7.1		0.1746	2.08	7.96×10^{-6}
7.0		0.1771	2.0	8.46×10^{-7}
6.9		0.1797	1.94	2.29×10^{-7}
6.888		0.180	1.89324 [8]	
6.812		0.182	1.86392	
6.8		0.1823	1.89 [10]	1.45×10^{-7}
6.738		0.184	1.83883 [8]	
6.7		0.1850	1.85 [10]	
6.666		0.186	1.81705 [8]	
6.6		0.1879	1.82 [10]	
6.595		0.1888	1.79789 [8]	
6.525		0.190	1.78087	
6.5		0.1907	1.80 [10]	
6.4		0.1937	1.78	
6.199	50,000	0.20	1.71739 [8]	
5.904	47,620	0.21	1.67539	
5.636	45,450	0.22	1.64517	
5.391	43,480	0.23	1.62226	
5.166	41,670	0.24	1.60426	
4.959	40,000	0.25	1.58972	
4.769	38,460	0.26	1.57775	
4.592	37,040	0.27	1.56772	
4.428	35,710	0.28	1.55921	
4.275	34,480	0.29	1.55191	
4.133	33,330	0.30	1.54558	
3.999	32,260	0.31	1.54005	
3.874	31,250	0.32	1.53518	
3.757	30,300	0.33	1.53087	
3.647	29,410	0.34	1.52703	
3.542	28,570	0.35	1.52358	
3.473	28,010	0.357		5.1×10^{-10} [7]
3.444	27,780	0.36	1.52049	
3.351	27,030	0.37	1.51769	
3.263	26,320	0.38	1.51515	
3.179	25,640	0.39	1.51283	
3.100	25,000	0.40	1.51072	
2.952	23,810	0.42	1.50701	
2.818	22,730	0.44	1.50386	
2.695	21,740	0.46	1.50115	
2.616	21,100	0.474		7.6×10^{-11}
2.583	20,830	0.48	1.49882	
2.480	20,000	0.50	1.49679	
2.384	19,230	0.52	1.49501	
2.296	18,520	0.54	1.49344	

(*continued*)

TABLE VIII (*Continued*)

Potassium Chloride

eV	cm^{-1}	μm	n	k
2.214	17,860	0.56	1.49205	
2.138	17,240	0.58	1.49081	
2.066	16,670	0.60	1.48969	
2.000	16,130	0.62	1.48869	
1.937	15,630	0.64	1.48779	
1.879	15,150	0.66	1.48697	
1.823	14,710	0.68	1.48623	
1.771	14,290	0.70	1.48555	
1.722	13,890	0.72	1.48493	
1.675	13,510	0.74	1.48436	
1.631	13,160	0.76	1.48384	
1.590	12,820	0.78	1.48336	
1.550	12,500	0.80	1.48291	
1.512	12,200	0.82	1.48250	
1.476	11,900	0.84	1.48212	
1.442	11,630	0.86	1.48176	
1.409	11,360	0.88	1.48143	
1.378	11,110	0.90	1.48111	
1.348	10,870	0.92	1.48082	
1.319	10,640	0.94	1.48055	
1.291	10,420	0.96	1.48030	
1.265	10,200	0.98	1.48006	
1.240	10,000	1.00	1.47983	
1.127	9,091	1.1	1.47887	
1.033	8,333	1.2	1.47813	
0.9537	7,692	1.3	1.47755	
0.8856	7,143	1.4	1.47708	
0.8265	6,667	1.5	1.47668	
0.7749	6,250	1.6	1.47634	
0.7293	5,882	1.7	1.47605	
0.6888	5,556	1.8	1.47580	
0.6525	5,263	1.9	1.47557	
0.6199	5,000	2.0	1.47536	
0.5636	4,545	2.2	1.47498	
0.5166	4,167	2.4	1.47464	
0.4769	3,046	2.6	1.47433	
0.4428	3,571	2.8	1.47403	1.27×10^{-10} [6]
0.4133	3,333	3.0	1.47374	
0.3874	3,125	3.2	1.47345	
0.3647	2,941	3.4	1.47315	
0.3444	2,778	3.6	1.47285	
0.3263	2,632	3.8	1.47254	1.97×10^{-10}
0.3100	2,500	4.0	1.47223	
0.2952	2,381	4.2	1.47190	
0.2818	2,273	4.4	1.47156	
0.2695	2,174	4.6	1.47122	
0.2583	2,083	4.8	1.47085	

TABLE VIII (*Continued*)

Potassium Chloride

eV	cm^{-1}	μm	n	k
0.2480	2,000	5.0	1.47048	
0.2384	1,923	5.2	1.47010	
0.2339	1,887	5.3		2.11×10^{-11}
0.2296	1,852	5.4	1.46970	
0.2214	1,786	5.6	1.46928	
0.2138	1,724	5.8	1.46886	
0.2066	1,667	6.0	1.46842	
0.2000	1,613	6.2	1.46796	
0.1937	1,563	6.4	1.46749	
0.1879	1,515	6.6	1.46701	
0.1823	1,471	6.8	1.46651	
0.1771	1,429	7.0	1.46600	
0.1722	1,389	7.2	1.46547	
0.1675	1,351	7.4	1.46493	
0.1631	1,316	7.6	1.46437	
0.1590	1,282	7.8	1.46379	
0.1550	1,250	8.0	1.46290	
0.1512	1,220	8.2	1.46260	
0.1476	1,190	8.4	1.46198	
0.1442	1,163	8.6	1.46134	
0.1409	1,136	8.8	1.46069	
0.1378	1,111	9.0	1.46002	
0.1348	1,087	9.2	1.45934	
0.1319	1,064	9.4	1.45864	
0.1291	1,042	9.6	1.45792	
0.1265	1,020	9.8	1.45719	
0.1240	1,000	10.0	1.45644	
0.1216	980.4	10.2	1.45567	
0.1192	961.5	10.4	1.45489	
0.1170	943.4	10.6	1.45409	2.53×10^{-8} [5]
0.1148	925.9	10.8	1.45327	
0.1127	909.1	11.0	1.45244	
0.1107	892.9	11.2	1.45159	
0.1088	877.2	11.4	1.45072	
0.1069	862.1	11.6	1.44984	
0.1051	847.5	11.8	1.44893	
0.1033	833.3	12.0	1.44801	
0.1016	819.7	12.2	1.44707	
0.09999	806.5	12.4	1.44611	
0.09919	800	12.50		1.49×10^{-7} [4]
0.09840	793.7	12.6	1.44514	
0.09686	781.3	12.8	1.44415	
0.09537	769.2	13.0	1.44313	
0.09393	757.6	13.2	1.44210	
0.09252	746.3	13.4	1.44105	
0.09116	735.3	13.6	1.43999	

(*continued*)

TABLE VIII (*Continued*)

Potassium Chloride

eV	cm^{-1}	μm	n	k
0.08984	724.6	13.8	1.43890	
0.08856	714.3	14.0	1.43779	
0.08731	704.2	14.2	1.43667	
0.08679	700	14.29		1.14×10^{-6}
0.08610	694.4	14.4	1.43552	
0.08492	684.9	14.6	1.43343	
0.08377	675.7	14.8	1.43317	
0.08265	666.7	15.0	1.43197	
0.08157	657.9	15.2	1.43074	
0.08051	649.4	15.4	1.42950	
0.07948	641.0	15.6	1.42823	
0.07847	632.9	15.8	1.42694	
0.07749	625.0	16.0	1.42563	
0.07653	617.3	16.2	1.42	
0.07560	609.8	16.4	1.42295	
0.07469	602.4	16.6	1.42158	
0.07439	600	16.67		8.76×10^{-6}
0.07380	595.2	16.8	1.42018	
0.07293	588.2	17.0	1.41877	
0.07208	581.4	17.2	1.41733	
0.07125	574.7	17.4	1.41587	
0.07044	568.2	17.6	1.41438	
0.06965	561.8	17.8	1.41287	
0.06888	555.6	18.0	1.41134	
0.06812	549.4	18.2	1.40979	
0.06738	543.5	18.4	1.40821	
0.06666	537.6	18.6	1.40661	
0.06595	531.9	18.8	1.40498	
0.06525	526.3	19.0	1.40333	
0.06457	520.8	19.2	1.40165	
0.06391	515.5	19.4	1.39995	
0.06326	510.2	19.6	1.39822	
0.06262	505.1	19.8	1.39647	
0.06199	500.0	20.0	1.39469	7.64×10^{-5}
0.06048	487.8	20.5	1.39012	
0.05904	476.2	21.0	1.38538	
0.05767	465.1	21.5	1.38047	
0.05636	454.5	22.0	1.37537	
0.05510	444.4	22.5	1.37009	
0.05391	434.8	23.0	1.36461	
0.05276	425.5	23.5	1.35892	
0.05166	416.7	24.0	1.35303	
0.05060	408.2	24.5	1.34692	
0.04959	400.0	25.0	1.34059	6.57×10^{-4}
0.04862	392.2	25.5	1.33402	
0.04769	384.6	26.0	1.32721	
0.04679	377.4	26.5	1.32014	

TABLE VIII (*Continued*)

Potassium Chloride

eV	cm^{-1}	μm	n	k
0.04592	370.4	27.0	1.31281	
0.04508	363.6	27.5	1.30520	
0.04428	357.1	28.0	1.29731	
0.04350	350.9	28.5	1.28911	
0.04275	344.8	29.0	1.28060	
0.04215	340	29.41	1.30 [3]	
0.04203	339.0	29.5	1.27175 [8]	
0.04133	333.3	30.0	1.2626	
0.04065	327.9	30.5	1.2530	
0.03999	322.6	31.0	1.2431	
0.03967	320	31.25	1.28 [3]	
0.03936	317.5	31.5	1.2327 [8]	
0.03874	312.5	32.0	1.2220	
0.03843	310	32.26	1.25 [3]	
0.03815	307.7	32.5	1.2108 [8]	
0.03757	303.0	33.0	1.1991	
0.03719	300	33.33	1.20 [3]	6.63×10^{-3}
0.03701	298.5	33.5	1.8669 [8]	
0.03647	294.1	34.0	1.1741	
0.03595	290	34.48	1.15 [3]	
0.03594	289.9	34.5	1.1608 [8]	
0.03542	285.7	35.0	1.1469	
0.03471	280	35.71	1.10 [3]	2.3×10^{-2} [3]
0.03409	275	36.36		2.5
0.03348	270	37.04	1.05	2.8
0.03268	265	37.74		3.2
0.03224	260	38.46	0.99	4.2
0.03100	250	40.00	0.93	8.3×10^{-2}
0.02976	240	41.67	0.85	0.16
0.02914	235	42.55	0.86	0.17
0.02852	230	43.48	0.80	0.18
0.02790	225	44.44	0.70	0.20
0.02728	220	45.45	0.53	0.35
0.02666	215	46.51	0.61	0.58
0.02604	210	47.62	0.70	0.52
0.02542	205	48.78		0.50
0.02480	200	50.00	0.57	0.53
0.02356	190	52.63	0.41	0.77
0.02232	180	55.56	0.31	1.05
0.02170	175	57.14	0.23	
0.02108	170	58.82	0.17	1.5
0.02046	165	60.61	0.15	
0.01984	160	62.50	0.17	2.2
0.01922	155	64.52	0.24	2.9
0.01860	150	66.67	0.44	4.0
0.01798	145	68.97	1.1	5.5

(*continued*)

TABLE VIII (*Continued*)

Potassium Chloride

eV	cm^{-1}	μm	n	k
0.01736	140	71.43	5.3	4.0
0.01674	135	74.07	5.0	0.80
0.01612	130	76.92	4.1	0.32
0.01550	125	80.00	3.5	0.23
0.01488	120	83.33	3.2	0.20
0.01364	110	90.91	2.9	0.15
0.01240	100	100.0	2.7	0.11
0.01178	95	105.3		9.0×10^{-2}
0.01116	90	111.1	2.6	6.6×10^{-2}
0.01054	85	117.6		0.11
0.009919	80	125.0	2.5	0.11
0.009299	75	133.3		
0.008679	70	142.9	2.4	9.2×10^{-2}
0.007439	60	166.7	2.3	5.3
0.006199	50	200.0	2.2	
0.004133	33.33	300		3.1×10^{-2} [1]
0.003874	31.25	320		2.65 [2]
0.003100	25.00	400		2.5 [1]
0.002480	20.00	500		1.9
				1.83 [2]
0.002066	16.67	600		1.6 [1]
0.001771	14.29	700		1.3
0.001550	12.50	800		1.2
0.001378	11.11	900		1.0
				1.07 [2]
0.001240	10.00	1,000		9.0×10^{-3} [1]
0.0008265	6.667	1,500		5.5
0.0006199	5.000	2,000		3.7
0.0004133	3.333	3,000		2.0

[a] The original references for the n and k data are indicated in brackets. A given reference applies down the column until a new one appears. The smaller values of k are given in powers of 10 until 10^{-2}, whereupon we revert to decimals only.

Silicon Dioxide (SiO_2), Type α (Crystalline)

H. R. PHILIPP
General Electric Research and Development Center
Schenectady, New York

The room-temperature optical properties of type α, crystalline SiO_2 have been the subject of numerous studies. In the infrared spectral region, this information is reasonably detailed. In the vacuum ultraviolet, however, few attempts have been made to obtain a self-consistent set of optical constants n and k for this material. These parameters are generally obtained by Kramers–Kronig (KK) analysis of reflectance data, which are difficult to measure with high accuracy. In addition, the analysis in the case of SiO_2 requires extrapolation of the reflectance into spectral regions in which no data exist. This introduces considerable uncertainty in the derived n and k values. In the region of low absorption between the infrared and vacuum ultraviolet bands, the index of refraction can be evaluated from prism data, and this has been accomplished with great precision. The measured k values, on the other hand, can be strongly influenced by the presence of impurity and defect absorption, and for this reason no k values are given in the wavelength range $6.0\ \mu m \geq \lambda \geq 0.1476\ \mu m$, although some data are available for the users' consideration and will be referenced.

A set of optical parameters n and k are given in Table IX and plotted in Fig. 9 for the wavelength region $333.3\ \mu m \geq \lambda \geq 0.04768\ \mu m$. They were obtained from a variety of sources. The wavelength λ, index of refraction n and extinction coefficient k are given to four places in most of the table entries. The accuracy of these values does not, in general, warrant this precision. This is done to show the possible presence of weak structure in the optical properties that can often be discerned by comparison of precise, but not necessarily accurate, values over small wavelength ranges. The n_o and k_o values refer to the ordinary (o) ray (electric field perpendicular to the optic axis), and n_e and k_e refer to the extraoridinary (e) ray (electric field parallel to the optic axis).

Copyright © 1985 by Academic Press, Inc.
All rights of reproduction in any form reserved.
ISBN 0-12-544420-6

In the sub-millimeter-wave region from 1000 to 200 μm the n_o results of several workers have been combined and fitted by Simonis† with a frequency-squared dependence. This fit gives values in agreement with all these experiments to ± 0.0015, except for the results of Loewenstein *et al.* [1], which are consistently 0.005 higher. Most of these results were obtained by analysis of channel spectra. In the far infrared $333 \geq \lambda \geq 50$ μm the optical constants determined by Loewenstein *et al.* [1] are used. The estimated experimental error in n is ± 0.001, but at least in the region 333–200 μm it is considerably more. The error in k is considerably larger than the error in n. Their data extend to shorter wavelength ($\lambda = 30.3$ μm) for temperature $T = 1.5$ K but were not evaluated at room temperature. Because of the strong temperature dependence of the absorption in this region and the presence of a resonance absorption at $\lambda \approx 37.88$ μm, considerable caution should be taken in using the low-temperature data to estimate room-temperature values.

In the infrared, 32.00 μm $\geq \lambda \geq 2.000$ μm, the values were obtained from the analysis of Spitzer and Kleinman [2]. They carefully measured the reflectance and fitted the results to classical dispersion theory. Their n and k values reproduce the measured reflectance and independently obtained transmission curves in detail over most of the spectral range. They also compare their results with values derived by KK analysis of the same reflectance data. They find that the agreement in k is quite good for $k > 0.1$ but is poor for $k \lesssim 0.1$. We believe that this inconsistency is due, at least in part, to the lack of adequate precision in the reflectance data that is necessary to evaluate accurately small k values by KK analysis. We note in this connection that in the regions of very low reflectance, the measured values are generally appreciably higher (on a relative basis) than those calculated from the n and k values. This could result from a small scattered-light component in the measuring beam.

The n and k values given in the table were computed from the dispersion parameters of Spitzer and Kleinman [2] that do not consider absorption processes (resonances) above $\lambda \approx 35$ μm. The results for the e ray join, more or less smoothly, in the region 32 μm $\leq \lambda \leq 50$ μm with the results of Loewenstein *et al.* [1], while those for the o ray, which show the presence of a resonance near 38 μm, do not. At the shorter wavelengths, the results of Spitzer and Kleinman [2] agree very well with index of refraction data for SiO_2 obtained from prism measurements [3]. For the o ray, the precise prism measurements extend as high as 4 μm, while for the e ray, they extend only to 2 μm. It should be noted here that less precise index of refraction values given in the American Institute of Physics Handbook [3] for the range 4.2 μm $\leq \lambda \leq 7.0$ μm do not agree very closely with the dispersion analysis results [2] that are given in the table.

No k values are given in the table for infrared wavelengths below 6.00 μm. Both Saksena [4] and Drummond [5] have examined the absorption spectra

† See Chapter 8 of this handbook.

of α-SiO_2 for $\lambda \leq 6.00$ μm, and the results show a variety of features. It is difficult to determine which of these features are intrinsic to SiO_2, and, hence, these results are not considered further here, although they do contain a wealth of information.

In the wavelength region $2.00\ \mu m \geq \lambda \geq 0.185\ \mu m$, the precise index of refraction values of the American Institute of Physics Handbook [3] are given in table. Some time ago Sosman [6] prepared a list of most probable values of the refraction indices of SiO_2, and these values are also given in the table, in which they are denoted by brackets. These latter values are generally more precise than those of the American Institute of Physic Handbook [3]; however, I cannot comment on their accuracy.

For $\lambda < 0.185\ \mu m$, the optical constants given in the table were obtained from the reflectance measurements of Philipp [7] augmented by the transmission measurements of Appleton *et al.* [8] and Philipp [9] in the tail of the fundamental absorption edge. Both Lamy [10] and Philipp [7] have measured the reflectance and determined n and k by KK analysis. The analysis of Lamy [10] uses the reflectance values of Philipp [7] for $\lambda \leq 0.10\ \mu m$. The n values from these two sources agree very closely for wavelengths down to $\sim 0.11\ \mu m$. The k values show very good agreement for $\lambda \lesssim 0.08\ \mu m$. The differences found below these wavelengths of $\sim 10\%$ must be attributed to the extrapolation procedures used in the KK analysis. The choice of using Philipp's [7] values over those of Lamy [10] was an arbitrary one. Care should be exercised in using the table results, especially for $\lambda < 0.08\ \mu m$, until data are available for $\lambda \lesssim 0.05\ \mu m$, which more specifically details the reflectance extrapolation.

The k values determined from the KK analysis of Phillipp [7] are tabulated for wavelengths of 0.1278 μm and below. Above this wavelength, where they become small, they are unreliable as determined by this technique. In the range $0.1476\ \mu m \geq \lambda \geq 0.1409\ \mu m$, they are obtained from the absorption measurements of Appleton *et al.* [8] and Philipp [9], which agree reasonably closely. A smooth curve was drawn between the absorption data and the KK results, and the values so determined are given in the table, in which they are delineated by brackets; they are not reliable. No k values are given for $\lambda > 0.1476\ \mu m$ because they may have a component associated with a defect or impurity absorption.

It is recommended that anyone who uses the table carefully examine the material and references cited in the above-named references [1–10] as well as other references [11–15].

REFERENCES

1. E. V. Loewenstein, D. R. Smith, and R. L. Morgan, *Appl. Opt.* **12**, 398 (1973).
2. W. G. Spitzer and D. A. Kleinman, *Phys. Rev.* **121**, 1324 (1961).
3. "American Institute of Physics Handbook," 3rd ed., Chapter 6, p. 27. McGraw-Hill, New York, 1972.

4. B. D. Saksena, *Proc. Phys. Soc. London* **72**, 9 (1958).
5. D. G. Drummond, *Proc. R. Soc. London* **153**, 328 (1935).
6. R. B. Sosman, "The Properties of Silica," p. 591. Chem. Catalog Co. (Tudor), New York, 1927.
7. H. R. Philipp, *Solid State Commun.* **4**, 73 (1966).
8. A. Appleton, T. Chiranjivi, and M. Jafaripour-Ghazvini, *in* "The Physics of SiO_2 and Its Interfaces" (S. T. Pantelides, ed.), p. 94. Pergamon, New York, 1978.
9. H. R. Philipp, *J. Phys. Chem. Solids* **32**, 1935 (1971).
10. P. L. Lamy, *Appl. Opt.* **16**, 2212 (1977).
11. I. Simon and H. O. McMahon, *J. Chem. Phys.* **21**, 23 (1953).
12. J. Reitzel, *J. Chem. Phys.* **23**, 2407 (1955).
13. E. Loh, *Solid State Commun.* **2**, 269 (1964).
14. S. Roberts and E. Coon, *J. Opt. Soc. Am.* **53**, 1023 (1962).
15. D. E. McCarthy, *Appl. Opt.* **2**, 591 (1963).

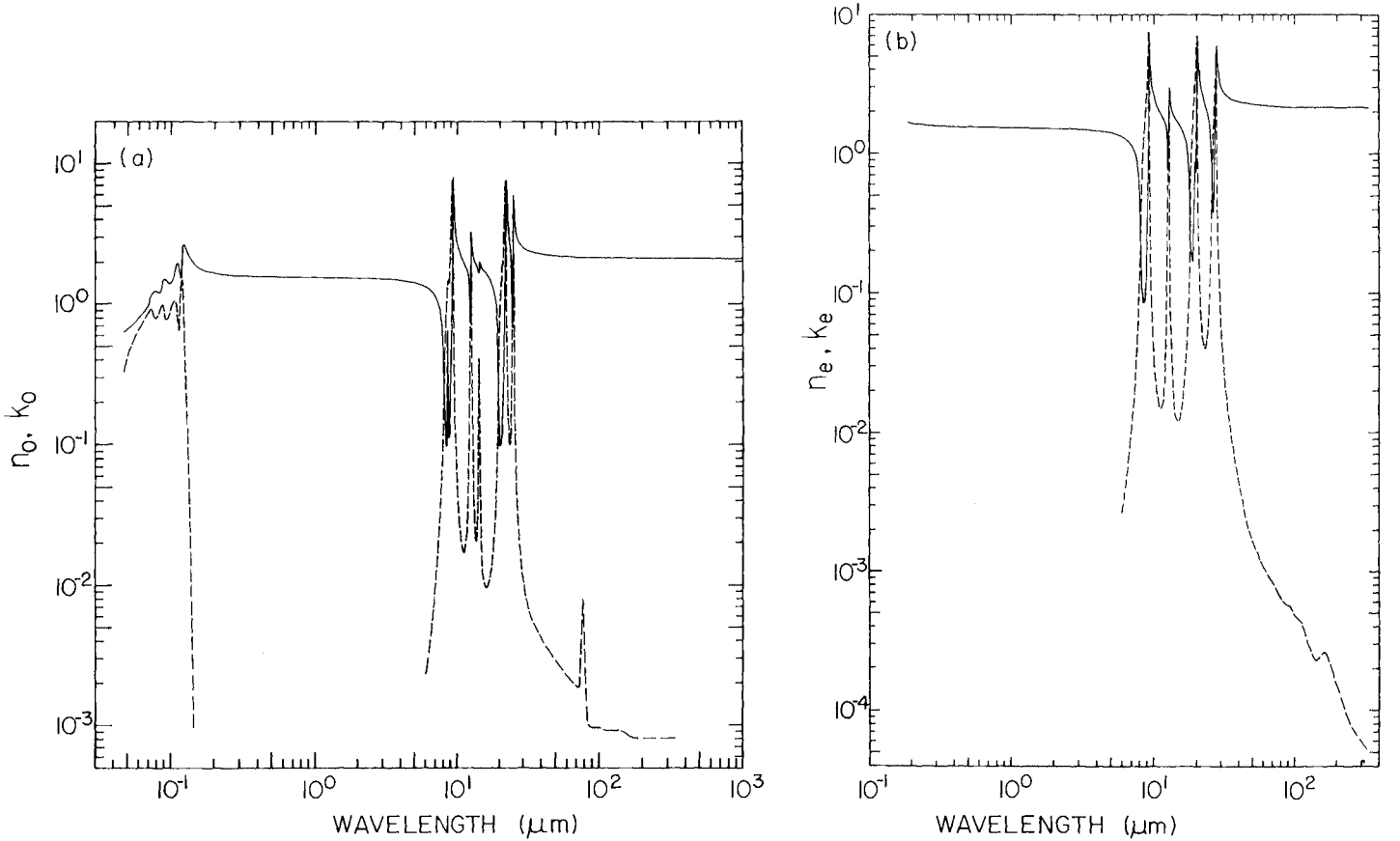

Fig. 9. (a) Log–log plot of n_o (——) and (– – – –) k_o versus wavelength in micrometers for silicon dioxide (type α, crystalline). (b) Log–log plot of n_e (——) and (– – – –) k_e versus wavelength in micrometers for silicon dioxide (type α, crystalline).

TABLE IX

Values of n and k for Silicon Dioxide (Type α, Crystalline) from Various References[a]

eV	cm^{-1}	μm	n_o	k_o	n_e	k_e
26		0.04769	0.6285 [7]	0.3243 [7]		
25.5		0.04862	0.6432	0.3609		
25		0.04959	0.6517	0.3907		
24.5		0.05061	0.6591	0.4231		
24		0.05166	0.6723	0.4540		
23.5		0.05276	0.6862	0.4822		
23		0.05391	0.6998	0.5097		
22.5		0.05510	0.7138	0.5387		
22		0.5636	0.7304	0.5667		
21.5		0.05767	0.7470	0.5959		
21		0.05904	0.7664	0.6272		
20.5		0.06048	0.7900	0.6559		
20		0.06199	0.8131	0.6844		
19.5		0.06358	0.8371	0.7154		
19		0.06526	0.8642	0.7488		
18.5		0.06702	0.8949	0.7847		
18		0.06888	0.9289	0.8273		
17.75		0.06985	0.9499	0.8619		
17.5		0.07085	0.9894	0.8987		
17.4		0.07125	1.013	0.9108		
17.25		0.07187	1.052	0.9236		
17		0.07293	1.118	0.9153		
16.75		0.07402	1.169	0.8917		
16.5		0.07514	1.205	0.8599		
16.25		0.07629	1.224	0.8223		
16		0.07749	1.221	0.7896		
15.75		0.07872	1.210	0.7848		

15.5	0.07999	1.202	0.7841
15.25	0.08130	1.191	0.7968
15	0.08266	1.184	0.8265
14.8	0.08377	1.187	0.8694
14.6	0.08492	1.217	0.9290
14.4	0.08610	1.285	0.9724
14.3	0.08670	1.335	0.9829
14.2	0.08731	1.386	0.9709
14	0.08856	1.457	0.9187
13.8	0.08984	1.484	0.8462
13.6	0.09116	1.469	0.7910
13.4	0.09252	1.447	0.7761
13.2	0.09392	1.430	0.7715
13	0.09537	1.410	0.7753
12.8	0.09686	1.394	0.8017
12.6	0.09839	1.390	0.8406
12.4	0.09998	1.400	0.8908
12.2	0.1016	1.435	0.9573
12	0.1033	1.504	1.015
11.9	0.1042	1.551	1.035
11.8	0.1051	1.602	1.048
11.7	0.1060	1.661	1.056
11.6	0.1069	1.722	1.046
11.5	0.1078	1.782	1.027
11.4	0.1088	1.839	0.9939
11.3	0.1097	1.892	0.9452
11.2	0.1107	1.924	0.8730
11.1	0.1117	1.925	0.7958
11	0.1127	1.891	0.7210
10.9	0.1137	1.805	0.6597
10.85	0.1143	1.738	0.6418

(*continued*)

TABLE IX (*Continued*)

Silicon Dioxide (Type α, Crystalline)

eV	cm^{-1}	μm	n_o	k_o	n_e	k_e
10.83		0.1145	1.688	0.6356		
10.8		0.1148	1.626	0.6732		
10.75		0.1153	1.569	0.7594		
10.7		0.1159	1.528	0.8463		
10.65		0.1164	1.506	0.9666		
10.6		0.1170	1.521	1.114		
10.55		0.1175	1.607	1.289		
10.5		0.1181	1.769	1.400		
10.45		0.1186	1.959	1.454		
10.4		0.1192	2.159	1.452		
10.37		0.1196	2.289	1.423		
10.35		0.1198	2.373	1.378		
10.3		0.1204	2.515	1.229		
10.25		0.1210	2.590	1.072		
10.2		0.1215	2.619	0.9326		
10.1		0.1227	2.621	0.7123		
10		0.1240	2.581	0.5441		
9.9		0.1252	2.529	0.4161		
9.8		0.1265	2.464	0.3148		
9.7		0.1278	2.397	0.2402		
9.6		0.1291	2.335	(0.17)		
9.5		0.1305	2.275	(0.12)		
9.4		0.1319	2.222	(0.082)		
9.3		0.1333	2.174	(0.056)		
9.2		0.1348	2.133	(0.036)		
9.1		0.1362	2.095	(0.023)		
9		0.1378	2.060	(0.013)		

8.9		0.1393	2.028	(7.0×10^{-3})		
8.8		0.1409	1.999	3.1×10^{-3} [8, 9]		
8.7		0.1425	1.971	1.0×10^{-3}		
8.6		0.1442	1.946	2.3×10^{-4}		
8.5		0.1459	1.922	3.5×10^{-5}		
8.4		0.1476	1.899	2.7×10^{-6}		
8.3		0.1494	1.877			
8.2		0.1512	1.856			
8.1		0.1531	1.838			
8		0.1550	1.820			
7.8		0.1590	1.789			
7.6		0.1631	1.761			
7.4		0.1675	1.737			
7.2		0.1722	1.716			
7		0.1771	1.698			
6.75		0.1837	1.679			
6.7		0.1851	1.6775 [3]		1.68988 [3]	
6.68484	53,917.9	0.185467	(1.67578) [6]		(1.68997) [6]	
6.40458	51,657.4	0.193583	(1.65999)		(1.67343)	
6.262	50,510	0.1980	1.65087 [3]		1.66394 [3]	
6.1972	49,985	0.20006	(1.64927) [6]		(1.66227) [6]	
6.1210	49,371	0.20255	(1.64557)		(1.65842)	
6.06422	48,912.2	0.204448	(1.64288)		(1.65562)	
5.8740	47,378	0.21107	(1.63432)		(1.64671)	
5.78168	46,633.3	0.214439	(1.63039)		(1.64262)	
5.64935	45,566.0	0.219462	(1.62497)		(1.63698)	
5.47374	44,149.5	0.226503	(1.61818)		(1.62992)	
5.367	43,290	0.2310	1.61395 [3]		1.62555 [3]	
5.36049	43,236.1	0.231288	(1.61401)		(1.62559)	
5.10642	41,186.8	0.242796	(1.60525)		(1.61650)	
4.95275	39,947.4	0.250329	(1.60032)		(1.61139)	

(*continued*)

TABLE IX (*Continued*)

Silicon Dioxide (Type α, Crystalline)

eV	cm^{-1}	μm	n_o	k_o	n_e	k_e
4.81849	38,864.5	0.257304	(1.59622)		(1.60714)	
4.71136	38,000.4	0.263155	(1.59309)		(1.60389)	
4.51061	36,381.2	0.274867	(1.58752)		(1.59813)	
4.25531	34,322.0	0.291358	(1.58098)		(1.59136)	
4.08625	32,958.5	0.303412	(1.57955)		(1.58720)	
3.97023	32,022.6	0.312279	(1.57433)		(1.584485)	
3.81186	30,745.3	0.325253	(1.570915)		(1.58095)	
3.647	29,410	0.3400	1.56747 [3]		1.57737 [3]	
3.64261	29,380.2	0.340365	(1.56747) [6]		(1.577385) [6]	
3.4566	27,880	0.35868	(1.563915)		(1.573705)	
3.147	25,380	0.3940	1.55846 [3]		1.56805 [3]	
3.12416	25,198.6	0.396848	(1.55813) [6]		(1.56772) [6]	
3.06388	24,712.3	0.404656	(1.557156)		(1.56671)	
3.02266	24,379.9	0.410174	(1.556502)		(1.566031)	
2.857	23,040	0.4340	1.55396 [3]		1.56339 [3]	
2.85641	23,093.0	0.434047	(1.553963) [6]		(1.563405) [6]	
2.84470	22,944.5	0.435834	(1.553790)		(1.563225)	
2.65023	21,376.0	0.467815	(1.551027)		(1.560368)	
2.58300	20,833.7	0.479991	(1.550118)		(1.559428)	
2.55037	20,570.5	0.486133	(1.549683)		(1.558979)	
2.441	19,685	0.5080	1.54822 [3]		1.55746 [3]	
2.43779	19,662.5	0.508582	(1.548229) [6]		(1.557475) [6]	
2.39180	19,291.5	0.518362	(1.547651)		(1.556877)	
2.32241	18,731.9	0.53385	(1.546799)		(1.555996)	
2.27043	18,312.6	0.546072	(1.546174)		(1.555350)	
2.14107	17,269.2	0.579066	(1.544667)		(1.553791)	
2.11010	17,019.5	0.587563	(1.544316)		(1.553428)	

2.1039	16,970	0.58929	(1.544246)	(1.553355)
2.104	16,970	0.5893	1.54424 [3]	1.55335 [3]
1.9748	15,928	0.62782	(1.542819) [6]	(1.551880) [6]
1.92564	15,531.6	0.643847	(1.542288)	(1.551332)
1.88917	15,237.4	0.656278	(1.541899)	(1.550929)
1.85653	14,974.2	0.667815	(1.541553)	(1.550573)
1.84831	14,907.9	0.670786	(1.541466)	(1.550483)
1.75482	14,153.9	0.706520	(1.540488)	(1.549472)
1.70273	13,733.7	0.728135	(1.539948)	(1.548913)
1.61752	13,046.4	0.766494	(1.539071)	(1.548005)
1.614	13,020	0.7680	1.53903 [3]	1.54794 [3]
1.55998	12,582.4	0.794763	(1.538478) [6]	(1.547392) [6]
1.489	12,010	0.8325	1.53773 [3]	1.54661 [3]
1.4678	11,839	0.84467	(1.537525) [6]	(1.54640) [6]
1.251	10,090	0.9914	1.53514 [3]	1.54392 [3]
1.23982	10,000.0	1.00000	(1.53503) [6]	(1.54381) [6]
1.22263	9,861.35	1.01406	(1.53483)	(1.54360)
1.14477	9,233.35	1.08303	(1.53387)	(1.54260)
1.0695	8,626.6	1.1592	1.53283 [3]	1.54152 [3]
1.03318	8,333.33	1.20000	(1.53232) [6]	(1.54098) [6]
0.953706	7,692.31	1.30000	(1.53102)	(1.53962)
0.94860	7,651.1	1.3070	1.53090 [3]	1.53951 [3]
0.88825	7,164.4	1.3958	1.52977	1.53832
0.885584	7,142.86	1.40000	(1.52972) [6]	(1.53826) [6]
0.83817	6,760.4	1.4792	1.52865 [3]	1.53716 [3]
0.810545	6,537.61	1.52961	(1.52800) [6]	(1.53646) [6]
0.80435	6,487.6	1.5414	1.52781 [3]	1.53630 [3]
0.774886	6,250.00	1.60000	(1.52703) [6]	(1.53545) [6]
0.73733	5,947.1	1.6815	1.52583 [3]	1.53422 [3]
0.70388	5,677.3	1.7614	1.52468	1.53301
0.688788	5,555.55	1.80000	(1.52413) [6]	(1.53242) [6]

(*continued*)

TABLE IX (*Continued*)

Silicon Dioxide (Type α, Crystalline)

eV	cm^{-1}	μm	n_o	k_o	n_e	k_e
0.63721	5,139.5	1.9457	1.52184 [3]		1.53004 [3]	
0.60388	4,870.7	2.0531	1.52005		1.52823	
0.602362	4,858.47	2.05820	(1.51998) [6]		(1.52814) [6]	
0.5391	4,348	2.300	1.51561 [3]			
0.495927	4,000.00	2.50000	(1.51156) [6]		(1.5195)	
0.4769	3,846	2.600	1.50986 [3]			
0.4133	3,333	3.000	1.49953		1.507 [2]	
0.3542	2,857	3.500	1.48451		1.492	
0.3100	2,500	4.000	1.46617		1.473	
0.2952	2,381	4.200	1.457 [2]		1.465	
0.2818	2,273	4.400	1.448		1.455	
0.2695	2,174	4.600	1.437		1.444	
0.2583	2,083	4.800	1.425		1.432	
0.2480	2,000	5.000	1.412		1.419	
0.2384	1,923	5.200	1.398		1.404	
0.2296	1,852	5.400	1.382		1.388	
0.2214	1,786	5.600	1.364		1.369	
0.2138	1,724	5.800	1.343		1.348	
0.2066	1,667	6.000	1.320	2.270×10^{-3} [2]	1.325	2.672×10^{-3} [2]
0.2033	1,639	6.100	1.307	2.545	1.311	3.000
0.2000	1,613	6.200	1.294	2.862	1.297	3.378
0.1968	1,587	6.300	1.279	3.229	1.282	3.816
0.1937	1,563	6.400	1.263	3.657	1.266	4.328
0.1907	1,538	6.500	1.245	4.160	1.248	4.928
0.1879	1,515	6.600	1.226	4.755	1.229	5.639
0.1851	1,493	6.700	1.206	5.467	1.207	6.486
0.1823	1,471	6.800	1.183	6.328	1.184	7.507

0.1797	1,449	6.900	1.158	7.380	1.159	8.747×10^{-3}
0.1771	1,429	7.000	1.130	8.683	1.130	1.027×10^{-2}
0.1759	1,418	7.050	1.115	9.455×10^{-3}	1.115	1.117
0.1746	1,408	7.100	1.099	1.032×10^{-2}	1.099	1.217
0.1734	1,399	7.150	1.083	1.131	1.081	1.330
0.1722	1,389	7.200	1.065	1.243	1.063	1.457
0.1710	1,379	7.250	1.046	1.370	1.043	1.601
0.1698	1,370	7.300	1.025	1.517	1.023	1.764
0.1687	1,361	7.350	1.004	1.687	1.000	1.951
0.1675	1,351	7.400	0.9801	1.885	0.9764	2.166
0.1664	1,342	7.450	0.9549	2.117	0.9505	2.413
0.1653	1,333	7.500	0.9277	2.391	0.9226	2.700
0.1642	1,325	7.550	0.8982	2.717	0.8923	3.035
0.1631	1,316	7.600	0.8660	3.108	0.8592	3.430
0.1621	1,307	7.650	0.8308	3.583	0.8230	3.899
0.1610	1,299	7.700	0.7921	4.163	0.7829	4.462
0.1600	1,290	7.750	0.7492	4.883	0.73383	5.150
0.1590	1,282	7.800	0.7013	5.788	0.6881	6.007
0.1579	1,274	7.850	0.6472	6.949	0.6308	7.112
0.1569	1,266	7.900	0.5953	8.487×10^{-2}	0.5642	8.609×10^{-2}
0.1560	1,258	7.950	0.5132	0.1063	0.4850	0.1081
0.1550	1,250	8.000	0.4276	0.1391	0.3885	0.1450
0.1540	1,242	8.050	0.3274	0.1962	0.2767	0.2179
0.1531	1,235	8.100	0.2318	0.2958	0.1890	0.3399
0.1521	1,227	8.150	0.1728	0.4190	0.1454	0.4685
0.1512	1,220	8.200	0.1410	0.5380	0.1230	0.5857
0.1503	1,212	8.250	0.1216	0.6504	0.1094	0.6947
0.1494	1,205	8.300	0.1088	0.7599	0.1003	0.7992
0.1485	1,198	8.350	0.1005	0.8699	0.09390	0.9019
0.1476	1,190	8.400	0.0965	0.9842	0.08950	1.005

(*continued*)

TABLE IX (*Continued*)

Silicon Dioxide (Type α, Crystalline)

eV	cm^{-1}	μm	n_o	k_o	n_e	k_e
0.1467	1,183	8.450	0.09826	1.109	0.08671	1.110
0.1459	1,176	8.500	0.1136	1.255	0.08538	1.218
0.1450	1,170	8.550	0.1913	1.459	0.08549	1.331
0.1442	1,163	8.600	0.6590	1.421	0.08711	1.450
0.1433	1,156	8.650	0.2427	1.178	0.09042	1.578
0.1425	1,149	8.700	0.1309	1.408	0.09570	1.717
0.1417	1,143	8.750	0.1115	1.591	0.1034	1.868
0.1409	1,136	8.800	0.1102	1.763	0.1143	2.038
0.1401	1,130	8.850	0.1167	1.941	0.1296	2.230
0.1393	1,124	8.900	0.1290	2.134	0.1513	2.453
0.1385	1,117	8.950	0.1478	2.352	0.1828	2.719
0.1378	1,111	9.000	0.1757	2.606	0.2308	3.047
0.1370	1,105	9.050	0.2178	2.911	0.3092	3.470
0.1362	1,099	9.100	0.2846	3.296	0.4518	4.050
0.1355	1,093	9.150	0.4006	3.808	0.7618	4.924
0.1348	1,087	9.200	0.6330	4.546	1.689	6.406
0.1340	1,081	9.250	1.230	5.733	5.862	7.634
0.1333	1,075	9.300	3.583	7.566	7.460	2.497
0.1326	1,070	9.350	7.929	4.184	5.808	0.9409
0.1319	1,064	9.400	6.336	1.331	4.868	0.5056
0.1312	1,058	9.450	5.180	0.6460	4.291	0.3239
0.1305	1,053	9.500	4.497	0.3920	3.899	0.2293
0.1298	1,047	9.550	4.048	0.2685	3.614	0.1732
0.1292	1,042	9.600	3.727	0.1982	3.395	0.1367
0.1285	1,036	9.650	3.485	0.1539	3.221	0.1116
0.1278	1,031	9.700	3.295	0.1240	3.079	9.335×10^{-2}
0.1272	1,026	9.750	3.142	0.1027	2.961	7.968

0.1265	1,020	9.800	3.014	8.691×10^{-2}	2.860	6.913
0.1259	1,015	9.850	2.907	7.485	2.773	6.078
0.1252	1,010	9.900	2.814	6.540	2.697	5.405
0.1246	1,005	9.950	2.734	5.785	2.631	4.854
0.1240	1,000	10.00	2.663	5.170	2.571	4.396
0.1234	995.0	10.05	2.600	4.662	2.518	4.011
0.1228	990.1	10.10	2.544	4.238	2.469	3.684
0.1221	985.2	10.15	2.493	3.879	2.425	3.403
0.1216	980.4	10.20	2.447	3.573	2.385	3.161
0.1210	975.6	10.25	2.405	3.310	2.348	2.950
0.1204	970.9	10.30	2.366	3.083	2.314	2.766
0.1198	966.2	10.35	2.330	2.885	2.282	2.603
0.1192	961.5	10.40	2.297	2.712	2.253	2.460
0.1186	956.9	10.45	2.266	2.560	2.225	2.333
0.1181	952.4	10.50	2.237	2.427	2.199	2.220
0.1175	947.9	10.55	2.210	2.309	2.175	2.120
0.1170	943.4	10.60	2.184	2.205	2.151	2.030
0.1164	939.0	10.65	2.159	2.114	2.129	1.949
0.1159	934.6	10.70	2.136	2.033	2.108	1.878
0.1153	930.2	10.75	2.113	1.962	2.088	1.814
0.1148	925.9	10.80	2.092	1.901	2.069	1.757
0.1143	921.7	10.85	2.071	1.847	2.051	1.707
0.1137	917.4	10.90	2.051	1.802	2.033	1.662
0.1132	913.2	10.95	2.032	1.764	2.016	1.623
0.1127	909.1	11.00	2.013	1.734	1.999	1.590
0.1122	905.0	11.05	1.995	1.710	1.983	1.561
0.1117	900.9	11.10	1.977	1.694	1.967	1.538
0.1112	896.9	11.15	1.959	1.685	1.952	1.519
0.1107	892.9	11.20	1.941	1.683	1.937	1.505
0.1102	888.9	11.25	1.924	1.690	1.922	1.496
0.1097	885.0	11.30	1.906	1.706	1.907	1.492

(*continued*)

TABLE IX (*Continued*)

Silicon Dioxide (Type α, Crystalline)

eV	cm^{-1}	μm	n_o	k_o	n_e	k_e
0.1092	881.1	11.35	1.888	1.730	1.892	1.493
0.1088	877.2	11.40	1.870	1.766	1.878	1.499
0.1083	873.4	11.45	1.852	1.814	1.863	1.511
0.1078	869.6	11.50	1.833	1.877	1.849	1.530
0.1073	865.8	11.55	1.814	1.956	1.834	1.556
0.1069	862.1	11.60	1.794	2.055	1.819	1.590
0.1064	858.4	11.65	1.773	2.180	1.804	1.632
0.1060	854.7	11.70	1.751	2.335	1.789	1.685
0.1055	851.1	11.75	1.727	2.530	1.773	1.751
0.1051	847.5	11.80	1.701	2.775	1.756	1.830
0.1046	843.9	11.85	1.672	3.088	1.739	1.927
0.1042	840.3	11.90	1.641	3.491	1.721	2.044
0.1038	836.8	11.95	1.605	4.021	1.702	2.187
0.1033	833.3	12.00	1.564	4.732	1.682	2.363
0.1029	829.9	12.05	1.516	5.715	1.660	2.579
0.1025	826.4	12.10	1.457	7.123	1.637	2.848
0.1020	823.0	12.15	1.384	9.241×10^{-2}	1.611	3.188
0.1016	819.7	12.20	1.289	0.1265	1.581	3.622
0.1012	816.3	12.25	1.162	0.1868	1.548	4.187
0.1008	813.0	12.30	0.9858	0.3097	1.510	4.940
0.1004	809.7	12.35	0.7844	0.5904	1.466	5.971
0.09999	806.5	12.40	0.7289	1.072	1.412	7.434
0.09958	803.2	12.45	0.9288	1.655	1.345	9.608×10^{-2}
0.09919	800.0	12.50	1.587	2.269	1.260	0.1304
0.09879	796.8	12.55	2.900	2.106	1.148	0.1896
0.09840	793.7	12.60	3.236	1.105	0.9971	0.3041

0.09801	790.5	12.65	2.956	0.4893	0.8281	0.5464
0.09762	787.4	12.70	2.718	0.2805	0.7711	0.9621
0.09724	784.3	12.75	2.552	0.1823	0.9404	1.473
0.09686	781.3	12.80	2.433	0.1291	1.482	1.990
0.09648	778.2	12.85	2.344	9.703×10^{-2}	2.539	1.968
0.09611	775.2	12.90	2.275	7.628	3.011	1.099
0.09574	772.2	12.95	2.220	6.208	2.834	0.5529
0.09537	769.2	13.00	2.174	5.194	2.625	0.3183
0.09501	766.3	13.05	2.136	4.446	2.469	0.2061
0.09464	763.4	13.10	2.102	3.879	2.355	0.1451
0.09429	760.5	13.15	2.073	3.441	2.269	0.1085
0.09393	757.6	13.20	2.047	3.098	2.202	8.480×10^{-2}
0.09357	754.7	13.25	2.024	2.825	2.148	6.861
0.09322	751.9	13.30	2.002	2.607	2.104	5.705
0.09287	749.1	13.35	1.983	2.433	2.066	4.851
0.09253	746.3	13.40	1.964	2.296	2.034	4.201
0.09218	743.5	13.45	1.947	2.189	2.006	3.696
0.09184	740.7	13.50	1.930	2.109	1.981	3.295
0.09150	738.0	13.55	1.915	2.055	1.959	2.972
0.09117	735.3	13.60	1.899	2.026	1.939	2.708
0.09083	732.6	13.65	1.884	2.022	1.920	2.489
0.09050	729.9	13.70	1.869	2.047	1.903	2.305
0.09017	727.3	13.75	1.854	2.107	1.887	2.151
0.08984	724.6	13.80	1.839	2.208	1.873	2.019
0.08952	722.0	13.85	1.823	2.366	1.859	1.906
0.08920	719.4	13.90	1.807	2.601	1.846	1.809
0.08888	716.8	13.95	1.789	2.953	1.833	1.725
0.08856	714.3	14.00	1.769	3.484	1.821	1.651
0.08825	711.7	14.05	1.746	4.311	1.810	1.587
0.08793	709.2	14.10	1.719	5.665	1.799	1.531

(continued)

TABLE IX (*Continued*)

Silicon Dioxide (Type α, Crystalline)

eV	cm^{-1}	μm	n_o	k_o	n_e	k_e
0.08762	706.7	14.15	1.686	8.025×10^{-2}	1.788	1.482
0.08731	704.2	14.20	1.649	0.1246	1.778	1.439
0.08701	701.8	14.25	1.621	0.2119	1.768	1.401
0.08670	699.3	14.30	1.670	0.3539	1.758	1.368
0.08640	696.9	14.35	1.867	0.4101	1.749	1.339
0.08610	694.4	14.40	1.999	0.2820	1.740	1.314
0.08580	692.0	14.45	1.998	0.1644	1.730	1.292
0.08551	689.7	14.50	1.964	0.1016	1.721	1.273
0.08521	687.3	14.55	1.931	6.871×10^{-2}	1.713	1.257
0.08492	684.9	14.60	1.903	5.016	1.704	1.243
0.08463	682.6	14.65	1.881	3.885	1.695	1.231
0.08434	680.3	14.70	1.861	3.150	1.687	1.222
0.08406	678.0	14.75	1.845	2.646	1.678	1.215
0.08377	675.7	14.80	1.831	2.287	1.670	1.210
0.08349	673.4	14.85	1.818	2.022	1.661	1.206
0.08321	671.1	14.90	1.806	1.821	1.653	1.204
0.08293	668.9	14.95	1.795	1.664	1.644	1.204
0.08266	666.7	15.0	1.785	1.540	1.636	1.205
0.08238	664.5	15.05	1.776	1.439	1.628	1.208
0.08211	662.3	15.10	1.767	1.358	1.619	1.213
0.08184	660.1	15.15	1.758	1.290	1.611	1.218
0.08157	657.9	15.20	1.750	1.234	1.602	1.226
0.08130	655.7	15.25	1.742	1.186	1.594	1.234
0.08103	653.6	15.30	1.734	1.146	1.585	1.245
0.08077	651.5	15.35	1.726	1.112	1.576	1.256
0.08051	649.4	15.40	1.719	1.083	1.568	1.269
0.08025	647.2	15.45	1.711	1.059	1.559	1.284

0.07999	645.2	15.50	1.704	1.037	1.550	1.300
0.07973	643.1	15.55	1.697	1.019	1.541	1.317
0.07948	641.0	15.60	1.690	1.004×10^{-2}	1.532	1.336
0.07922	639.0	15.65	1.683	9.912×10^{-3}	1.522	1.357
0.07897	636.9	15.70	1.676	9.805	1.513	1.379
0.07872	634.9	15.75	1.669	9.716	1.504	1.404
0.07847	632.9	15.80	1.663	9.644	1.494	1.429
0.07822	630.9	15.85	1.656	9.588	1.484	1.457
0.07798	628.9	15.90	1.649	9.546	1.474	1.487
0.07773	627.0	15.95	1.642	9.518	1.464	1.519
0.07749	625.0	16.00	1.635	9.501	1.453	1.553
0.07725	623.1	16.05	1.629	9.497	1.443	1.589
0.07701	621.1	16.10	1.622	9.503	1.432	1.628
0.07677	619.2	16.15	1.615	9.520	1.421	1.670
0.07653	617.3	16.20	1.608	9.547	1.410	1.714
0.07630	615.4	16.25	1.601	9.583	1.398	1.761
0.07606	613.5	16.30	1.594	9.629	1.386	1.811
0.07583	611.6	16.35	1.587	9.683	1.374	1.865
0.07560	609.8	16.40	1.580	9.747	1.361	1.923
0.07537	607.9	16.45	1.573	9.820	1.349	1.984
0.07514	606.1	16.50	1.566	9.901	1.335	2.050
0.07491	604.2	16.55	1.559	9.991×10^{-3}	1.322	2.121
0.07469	602.4	16.60	1.551	1.009×10^{-2}	1.308	2.196
0.07446	600.6	16.65	1.544	1.020	1.293	2.278
0.07424	598.8	16.70	1.537	1.031	1.278	2.365
0.07402	597.0	16.75	1.529	1.044	1.263	2.459
0.07380	595.2	16.80	1.521	1.058	1.247	2.561
0.07358	593.5	16.85	1.514	1.072	1.230	2.671
0.07336	591.7	16.90	1.506	1.087	1.213	2.790
0.07315	590.0	16.95	1.498	1.104	1.195	2.919
0.07293	588.2	17.00	1.490	1.121	1.175	3.060

(*continued*)

TABLE IX (*Continued*)

Silicon Dioxide (Type α, Crystalline)

eV	cm^{-1}	μm	n_o	k_o	n_e	k_e
0.07272	586.5	17.05	1.481	1.140	1.157	3.213
0.07250	584.8	17.10	1.473	1.159	1.136	3.382
0.07229	583.1	17.15	1.464	1.180	1.115	3.567
0.07208	581.4	17.20	1.456	1.202	1.093	3.771
0.07187	579.7	17.25	1.447	1.225	1.069	3.997
0.07167	578.0	17.30	1.438	1.249	1.045	4.249
0.07146	576.4	17.35	1.429	1.275	1.019	4.532
0.07126	574.7	17.40	1.420	1.302	0.9913	4.850
0.07105	573.1	17.45	1.410	1.331	0.9620	5.211
0.07085	571.4	17.50	1.400	1.361	0.9309	5.623
0.07065	569.8	17.55	1.390	1.393	0.8976	6.100
0.07045	568.2	17.60	1.380	1.427	0.8619	6.655
0.07025	566.6	17.65	1.370	1.462	0.8234	7.313
0.07005	565.0	17.70	1.359	1.500	0.7817	8.102
0.06985	563.4	17.75	1.348	1.540	0.7361	9.068×10^{-2}
0.06965	561.8	17.80	1.337	1.581	0.6860	0.1028
0.06946	560.2	17.85	1.326	1.626	0.6307	0.1184
0.06927	558.7	17.90	1.314	1.672	0.5689	0.1394
0.06907	557.1	17.95	1.302	1.722	0.5001	0.1689
0.06888	555.6	18.00	1.289	1.774	0.4251	0.2123
0.06869	554.0	18.05	1.277	1.830	0.3501	0.2764
0.06850	552.5	18.10	1.263	1.889	0.2886	0.3607
0.06831	551.0	18.15	1.250	1.951	0.2481	0.4527
0.06812	549.5	18.20	1.236	2.018	0.2243	0.5420
0.06794	547.9	18.25	1.221	2.089	0.2109	0.6256
0.06775	546.4	18.30	1.207	2.165	0.2037	0.7034
0.06757	545.0	18.35	1.191	2.245	0.2003	0.7763

0.06738	543.5	18.40	1.175	2.332	0.1990	0.8449
0.06720	542.0	18.45	1.159	2.424	0.1983	0.9101
0.06702	540.5	18.50	1.142	2.524	0.1972	0.9728
0.06684	539.1	18.55	1.124	2.631	0.1950	1.034
0.06666	537.6	18.60	1.105	2.746	0.1913	1.096
0.06648	536.2	18.65	1.086	2.871	0.1865	1.160
0.06630	534.8	18.70	1.066	3.006	0.1814	1.226
0.06612	533.3	18.75	1.045	3.153	0.1768	1.295
0.06595	531.9	18.80	1.023	3.313	0.1733	1.367
0.06577	530.5	18.85	1.000	3.489	0.1713	1.442
0.06560	529.1	18.90	0.9761	3.682	0.1712	1.520
0.06543	527.7	18.95	0.9507	3.896	0.1730	1.601
0.06526	526.3	19.00	0.9239	4.134	0.1768	1.685
0.06508	524.9	19.05	0.8955	4.401	0.1827	1.773
0.06491	523.6	19.10	0.8654	4.701	0.1911	1.866
0.06474	522.2	19.15	0.8333	5.044	0.2023	1.963
0.06457	520.8	19.20	0.7989	5.438	0.2169	2.065
0.06441	519.5	19.25	0.7620	5.897	0.2359	2.174
0.06424	518.1	19.30	0.7221	6.441	0.2608	2.291
0.06407	516.8	19.35	0.6786	7.099	0.2941	2.417
0.06391	515.5	19.40	0.6308	7.915	0.3398	2.552
0.06374	514.1	19.45	0.5777	8.963×10^{-2}	0.4042	2.695
0.06358	512.8	19.50	0.5180	0.1037	0.4971	2.841
0.06342	511.5	19.55	0.4501	0.1240	0.6278	2.971
0.06326	510.2	19.60	0.3723	0.1558	0.7847	3.044
0.06310	508.9	19.65	0.2879	0.2097	0.8957	3.037
0.06293	507.6	19.70	0.2149	0.2924	0.8839	3.033
0.06278	506.3	19.75	0.1696	0.3862	0.8042	3.144
0.06262	505.1	19.80	0.1439	0.4746	0.7526	3.371
0.06246	503.8	19.85	0.1284	0.5554	0.7629	3.673
0.06230	502.5	19.90	0.1183	0.6300	0.8405	4.035

(*continued*)

TABLE IX (*Continued*)

Silicon Dioxide (Type α, Crystalline)

eV	cm^{-1}	μm	n_o	k_o	n_e	k_e
0.06215	501.3	19.95	0.1113	0.69998	0.9974	4.464
0.06199	500.0	20.00	0.1065	0.7665	1.270	4.976
0.06184	498.8	20.05	0.1030	0.8304	1.743	5.589
0.06168	497.5	20.10	0.1006	0.8924	2.597	6.267
0.06153	496.3	20.15	9.894×10^{-2}	0.9530	4.127	6.707
0.06138	495.0	20.20	9.794	1.013	6.142	5.987
0.06123	493.8	20.25	9.747	1.072	7.094	4.070
0.06107	492.6	20.30	9.746	1.130	6.818	2.521
0.06092	491.4	20.35	9.786	1.189	6.247	1.643
0.06078	490.2	20.40	9.863	1.247	5.724	1.149
0.06063	489.0	20.45	9.976×10^{-2}	1.306	5.296	0.8527
0.06048	487.8	20.50	0.1012	1.365	4.951	0.6618
0.06033	486.6	20.55	0.1031	1.425	4.669	0.5316
0.06019	485.4	20.60	0.1052	1.486	4.435	0.4386
0.06004	484.3	20.65	0.1078	1.548	4.238	0.3697
0.05989	483.1	20.70	0.1107	1.611	4.069	0.3171
0.05975	481.9	20.75	0.1140	1.676	3.923	0.2759
0.05961	480.8	20.80	0.1177	1.742	3.795	0.2430
0.05946	479.6	20.85	0.1219	1.811	3.682	0.2162
0.05932	478.5	20.90	0.1266	1.881	3.581	0.1941
0.05918	477.3	20.95	0.1319	1.954	3.490	0.1756
0.05904	476.2	21.00	0.1379	2.030	3.408	0.1600
0.05890	475.1	21.05	0.1446	2.108	3.334	0.1466
0.05876	473.9	21.10	0.1521	2.191	3.265	0.1351
0.05862	472.8	21.15	0.1606	2.277	3.203	0.1251
0.05848	471.7	21.20	0.1703	2.368	3.145	0.1164
0.05834	470.6	21.25	0.1812	2.464	3.091	0.1087

0.05821	469.5	21.30	0.1937	2.565	3.041	0.1020
0.05807	468.4	21.35	0.2081	2.673	2.994	9.592×10^{-2}
0.05794	467.3	21.40	0.2248	2.789	2.950	9.054
0.05780	466.2	21.45	0.2442	2.914	2.909	8.571
0.05767	465.1	21.50	0.2670	3.048	2.870	8.137
0.05753	464.0	21.55	0.2941	3.195	2.834	7.745
0.05740	463.0	21.60	0.3267	3.356	2.799	7.390
0.05727	461.9	21.65	0.3664	3.533	2.766	7.068
0.05713	460.8	21.70	0.4154	3.731	2.734	6.776
0.05700	459.8	21.75	0.4773	3.955	2.704	6.509
0.05687	458.7	21.80	0.5569	4.209	2.676	6.265
0.05674	457.7	21.85	0.6622	4.502	2.648	6.043
0.05661	456.6	21.90	0.8059	4.846	2.622	5.839
0.05648	455.6	21.95	1.010	5.253	2.596	5.651
0.05636	454.5	22.00	1.314	5.742	2.572	5.480
0.05623	453.5	22.05	1.793	6.326	2.548	5.323
0.05610	452.5	22.10	2.595	6.983	2.526	5.178
0.05597	451.5	22.15	3.966	7.519	2.504	5.046
0.05585	450.5	22.20	5.976	7.259	2.482	4.924
0.05572	449.4	22.25	7.562	5.603	2.462	4.812
0.05560	448.4	22.30	7.753	3.682	2.441	4.710
0.05547	447.5	22.35	7.250	2.412	2.422	4.617
0.05535	446.4	22.40	6.658	1.671	2.403	4.532
0.05523	445.4	22.45	6.139	1.225	2.384	4.454
0.05510	444.4	22.50	5.709	0.9407	2.366	4.384
0.05498	443.5	22.55	5.354	0.7490	2.348	4.320
0.05486	442.5	22.60	5.058	0.6136	2.330	4.264
0.05474	441.5	22.65	4.807	0.5142	2.313	4.213
0.05462	440.5	22.70	4.593	0.4390	2.296	4.168
0.05450	439.6	22.75	4.406	0.3806	2.279	4.129
0.05438	438.6	22.80	4.243	0.3343	2.263	4.095

(continued)

TABLE IX (*Continued*)

Silicon Dioxide (Type α, Crystalline)

eV	cm^{-1}	μm	n_o	k_o	n_e	k_e
0.05426	437.6	22.85	4.098	0.2969	2.247	4.067
0.05414	436.7	22.90	3.968	0.2663	2.231	4.044
0.05402	435.7	22.95	3.851	0.2408	2.215	4.025
0.05391	434.8	23.00	3.745	0.2195	2.199	4.012
0.05379	433.8	23.05	3.648	0.2015	2.184	4.004
0.05367	432.9	23.10	3.558	0.1861	2.169	4.000
0.05356	432.0	23.15	3.475	0.1728	2.153	4.001
0.05344	431.0	23.20	3.398	0.1614	2.138	4.007
0.05333	430.1	23.25	3.325	0.1515	2.123	4.018
0.05321	429.2	23.30	3.257	0.1429	2.108	4.034
0.05310	428.3	23.35	3.192	0.1354	2.093	4.054
0.05298	427.4	23.40	3.131	0.1289	2.077	4.079
0.05287	426.4	23.45	3.072	0.1233	2.062	4.110
0.05276	425.5	23.50	3.015	0.1184	2.047	4.145
0.05265	424.6	23.55	2.961	0.1142	2.032	4.186
0.05253	423.7	23.60	2.908	0.1106	2.017	4.232
0.05242	422.8	23.65	2.857	0.1076	2.001	4.284
0.05231	421.9	23.70	2.806	0.1052	1.986	4.341
0.05220	421.1	23.75	2.757	0.1033	1.970	4.405
0.05209	420.2	23.80	2.708	0.1020	1.954	4.475
0.05198	419.3	23.85	2.659	0.1012	1.938	4.552
0.05188	418.4	23.90	2.610	0.1009	1.922	4.635
0.05177	417.5	23.95	2.651	0.1012	1.906	4.727
0.05166	416.7	24.00	2.512	0.1020	1.889	4.826
0.05155	415.8	24.05	2.461	0.1036	1.872	4.933
0.05144	414.9	24.10	2.409	0.1059	1.855	5.049
0.05134	414.1	24.15	2.355	0.1090	1.838	5.175

0.05123	413.2	24.20	2.300	0.1131	1.820	5.311
0.05113	412.4	24.25	2.241	0.1184	1.802	5.458
0.05102	411.5	24.30	2.179	0.1252	1.783	5.617
0.05092	410.7	24.35	2.112	0.1336	1.764	5.789
0.05081	409.8	24.40	2.041	0.1444	1.744	5.975
0.05070	409.0	24.45	1.962	0.1581	1.724	6.176
0.05061	408.2	24.50	1.876	0.1757	1.703	6.393
0.05050	407.3	24.55	1.779	0.1988	1.682	6.629
0.05040	406.5	24.60	1.668	0.2298	1.660	6.885
0.05030	405.7	24.65	1.540	0.2730	1.637	7.163
0.05020	404.9	24.70	1.390	0.3360	1.614	7.465
0.05009	404.0	24.75	1.214	0.4336	1.589	7.795
0.04999	403.2	24.80	1.015	0.5932	1.564	8.155
0.04989	402.4	24.85	0.8305	0.8431	1.537	8.550
0.04979	401.6	24.90	0.7156	1.161	1.510	8.984
0.04969	400.8	24.95	0.6717	1.502	1.481	9.461
0.04959	400.0	25.00	0.6787	1.853	1.451	9.989×10^{-2}
0.04949	399.2	25.05	0.7284	2.224	1.419	0.1058
0.04940	398.4	25.10	0.8260	2.630	1.386	0.1123
0.04930	397.6	25.15	0.9915	3.087	1.350	0.1196
0.04920	396.8	25.20	1.270	3.618	1.313	0.1279
0.04910	396.0	25.25	1.759	4.233	1.273	0.1372
0.04900	395.3	25.30	2.661	4.854	1.231	0.1479
0.04891	394.5	25.35	4.194	5.028	1.186	0.1602
0.04881	393.7	25.40	5.689	3.971	1.137	0.1745
0.04872	392.9	25.45	5.982	2.469	1.085	0.1914
0.04862	392.2	25.50	5.633	1.515	1.029	0.2116
0.04853	391.4	25.55	5.220	0.9975	0.9678	0.2362
0.04843	390.6	25.60	4.872	0.7043	0.9017	0.2665
0.04834	389.9	25.65	4.595	0.5253	0.8305	0.3047
0.04824	389.1	25.70	4.373	0.4086	0.7547	0.3537

(*continued*)

TABLE IX (*Continued*)

Silicon Dioxide (Type α, Crystalline)

eV	cm^{-1}	μm	n_o	k_o	n_e	k_e
0.04815	388.3	25.75	4.193	0.3284	0.6769	0.4168
0.04805	387.6	25.80	4.044	0.2708	0.6020	0.4962
0.04796	386.8	25.85	3.919	0.2280	0.5364	0.5907
0.04787	386.1	25.90	3.812	0.1954	0.4845	0.6952
0.04778	385.4	25.95	3.720	0.1698	0.4465	0.8037
0.04769	384.6	26.00	3.639	0.1494	0.4198	0.9127
0.04759	383.9	26.05	3.568	0.1328	0.4018	1.020
0.04750	383.1	26.10	3.505	0.1191	0.3905	1.127
0.04741	382.4	26.15	3.448	0.1077	0.3842	1.232
0.04732	381.7	26.20	3.397	9.810×10^{-2}	0.3820	1.337
0.04723	381.0	26.25	3.350	8.988	0.3833	1.442
0.04714	380.2	26.30	3.308	8.280	0.3878	1.548
0.04705	379.5	26.35	3.269	7.666	0.3952	1.656
0.04696	378.8	26.40	3.233	7.129	0.4055	1.765
0.04687	378.1	26.45	3.199	6.656	0.4189	1.877
0.04679	377.4	26.50	3.168	6.237	0.4345	1.992
0.04670	376.6	26.55	3.140	5.865	0.4554	2.112
0.04661	375.9	26.60	3.113	5.531	0.4793	2.236
0.04652	375.2	26.65	3.087	5.230	0.5078	2.367
0.04644	374.5	26.70	3.063	4.959	0.5416	2.504
0.04635	373.8	26.75	3.041	4.713	0.5818	2.649
0.04626	373.1	26.80	3.020	4.489	0.6297	2.803
0.04618	372.4	26.85	2.999	4.284	0.6873	2.968
0.04609	371.7	26.90	2.980	4.096	0.7569	3.145
0.04600	371.1	26.95	2.962	3.924	0.8419	3.336
0.04592	370.4	27.00	2.945	3.764	0.9469	3.544
0.04583	369.7	27.05	2.928	3.617	1.078	3.770

0.04575	369.0	27.10	2.913	3.480	1.246	4.015
0.04567	368.3	27.15	2.898	3.353	1.461	4.279
0.04558	367.6	27.20	2.883	3.235	1.744	4.559
0.04550	367.0	27.25	2.869	3.125	2.119	4.843
0.04541	366.3	27.30	2.856	3.021	2.618	5.099
0.04533	365.6	27.35	2.843	2.924	3.263	5.267
0.04525	365.0	27.40	2.831	2.833	4.043	5.246
0.04517	364.3	27.45	2.819	2.748	4.854	4.934
0.04509	363.6	27.50	2.808	2.667	5.509	4.327
0.04500	363.0	27.55	2.797	2.591	5.870	3.574
0.04492	362.3	27.60	2.786	2.519	5.951	2.855
0.04484	361.7	27.65	2.776	2.451	5.855	2.263
0.04476	361.0	27.70	2.766	2.386	5.677	1.809
0.04468	360.4	27.75	2.756	2.325	5.473	1.467
0.04460	359.7	27.80	2.747	2.267	5.270	1.209
0.04452	359.1	27.85	2.738	2.212	5.079	1.012
0.04444	358.4	27.90	2.729	2.159	4.905	0.8598
0.04436	357.8	27.95	2.720	2.108	4.748	0.7397
0.04428	357.1	28.00	2.712	2.060	4.607	0.6437
0.04420	356.5	28.05	2.704	2.014	4.479	0.5657
0.04412	355.9	28.10	2.696	1.971	4.364	0.5016
0.04404	355.2	28.15	2.689	1.929	4.260	0.4482
0.04397	354.6	28.20	2.681	1.888	4.166	0.4033
0.04389	354.0	28.25	2.674	1.850	4.080	0.3651
0.04381	353.4	28.30	2.667	1.813	4.002	0.3323
0.04373	352.7	28.35	2.660	1.777	3.930	0.3040
0.04366	352.1	28.40	2.653	1.743	3.863	0.2794
0.04358	351.5	28.45	2.647	1.710	3.802	0.2578
0.04350	350.9	28.50	2.641	1.678	3.745	0.2388
0.04343	350.3	28.55	2.634	1.647	3.692	0.2220
0.04335	349.7	28.60	2.628	1.618	3.643	0.2069

(continued)

TABLE IX (*Continued*)

Silicon Dioxide (Type α, Crystalline)

eV	cm^{-1}	μm	n_o	k_o	n_e	k_e
0.04327	349.0	28.65	2.622	1.589	3.597	0.1935
0.04320	348.4	28.70	2.617	1.562	3.554	0.1814
0.04312	347.8	28.75	2.611	1.535	3.514	0.1705
0.04305	347.2	28.80	2.605	1.510	3.476	0.1607
0.04297	346.6	28.85	2.600	1.485	3.440	0.1517
0.04290	346.0	28.90	2.595	1.461	3.407	0.1435
0.04283	345.4	28.95	2.589	1.438	3.375	0.1360
0.04275	344.8	29.00	2.584	1.415	3.345	0.1291
0.04246	342.5	29.20	2.565	1.332	3.238	0.1066
0.04217	340.1	29.40	2.547	1.258	3.151	8.996×10^{-2}
0.04189	337.8	29.60	2.530	1.192	3.077	7.722
0.04160	335.6	29.80	2.515	1.132	3.013	6.724
0.04133	333.3	30.00	2.500	1.079×10^{-2}	2.959	5.926
0.04065	327.9	30.50	2.468	9.643×10^{-3}	2.849	4.508
0.04000	322.6	31.00	2.440	8.721	2.766	3.590
0.03936	317.5	31.50	2.416	7.962	2.701	2.957
0.03875	312.5	32.00	2.395	7.326	2.648	2.500
0.02480	200.0	50.00	2.214 [1]	2.86 [1]	2.262 [1]	1.71×10^{-3} [1]
0.02356	190.0	52.63	2.200	2.68	2.248	1.47
0.02232	180.0	55.56	2.188	2.48	2.237	1.28
0.02108	170.0	58.82	2.178	2.29	2.226	1.12×10^{-3}
0.01984	160.0	62.50	2.169	2.14	2.217	9.95×10^{-4}
0.01860	150.0	66.67	2.161	1.91	2.208	9.02
0.01736	140.0	71.43	2.154	1.82	2.200	7.96
0.01705	137.5	72.73	2.152	1.85		
0.01674	135.0	74.07	2.150	2.36		
0.01643	132.5	75.47	2.148	3.60		

0.01612	130.0	76.92	2.147	6.18	2.193	6.73
0.01581	127.5	78.43	2.147	6.74		
0.01550	125.0	80.00	2.148	3.69		
0.01519	122.5	81.63	2.146	1.56		
0.01488	120.0	83.33	2.144	1.06×10^{-3}	2.187	5.97
0.01364	110.0	90.91	2.136	9.40×10^{-4}	2.182	5.79
0.01240	100.0	100.0	2.132	9.55	2.176	4.77
0.01116	90.0	111.1	2.128	8.84	2.172	4.42
0.009919	80	125.0	2.124	8.95	2.168	2.98
0.008679	70	142.9	2.121	9.10	2.164	2.27
0.007439	60	166.7	2.119[b]	7.96	2.162	2.65
0.006199	50	200.0	2.1114	7.96	2.159	1.59×10^{-4}
0.004959	40	250.0	2.1096	7.96	2.157	7.96×10^{-5}
0.003720	30	333.3	2.1081	7.96	2.156	5.30
0.002480	20	500.0	2.1070			
0.001240	10	1000	2.1063			

[a] Optical constants n and k for both the ordinary and extraordinary rays are listed. References from which the data were obtained are listed in brackets. Values of k enclosed by brackets in the wavelength region $0.1291\ \mu m \leq \lambda \leq 0.1378\ \mu m$ were obtained from a smooth curve drawn between absorption data and KK results. Therefore, no reference is applicable to these results. Values of n enclosed by brackets in the wavelength region $0.185467\ \mu m \leq \lambda \leq 2.50000\ \mu m$ were taken from Sosman [6].

[b] Data from George J. Simonis in Chapter 8 of this handbook.

Silicon Dioxide (SiO_2) (Glass)

H. R. PHILIPP
General Electric Research and Development Center
Schenectady, New York

The room-temperature optical properties of SiO_2 glass have been the subject of numerous studies; however, few attempts have been made to analyze this information to obtain a self-consistent set of optical constants, n and k, for this material, especially in the regions of strong absorption in the infrared and vacuum ultraviolet. Considering the technological importance of this material, it is somewhat surprising that this information is not presently available in precise detail. There are, of course, reasons for this. When the absorption is high, the optical constants are usually obtained by Kramers–Kronig (KK) analysis of reflectance data that are difficult to measure with high accuracy. The KK analysis itself may require extrapolations into spectral regions for which no data exist, thereby introducing additional uncertainties in the derived n and k values. In the region of low absorption, the index of refraction can be evaluated from prism data, and this has been accomplished with great precision for SiO_2. However the measured k values can be strongly affected by impurity and defect absorption. For SiO_2, the presence of water or OH absorption in the samples makes the determination of the intrinsic k values extremely difficult (if not impossible) in certain parts of the infrared and vacuum ultraviolet spectral regions. The importance of SiO_2 in fiber-optical applications may give people a strong incentive to clean up this material as much as possible.

A set of optical parameters n and k are given in Table X and plotted in Fig. 10 for the wavelength region $500\ \mu m \geq \lambda \geq 0.05\ \mu m$. They were obtained from a variety of sources. The wavelength λ and index of refraction n values are given to four places, and the extinction coefficient k values are given to three places in most of the table entries. The accuracy of these values does not, in general, warrant this precision. This is done to show the possible presence of weak structure in the optical properties that can often be discerned by comparison of precise, but not necessarily accurate, values over small wavelength ranges.

Copyright © 1985 by Academic Press, Inc.
All rights of reproduction in any form reserved.
ISBN 0-12-544420-6

In the far infrared, 500 μm $\geq \lambda \geq$ 100 μm, the values given in the table were obtained from Randall and Rawcliffe [1], who used an interferometric technique. The n values appear to be reasonably precise, while the k values may be in error by as much as $\pm 30\%$.

In the infrared 40.00 μm $\geq \lambda \geq$ 3.846 μm, the values given in the table were taken from Philipp [2]. They were obtained by KK analysis of reflectance data augmented by absorption measurements. His reflectance values are similar to those of Miller [3] but generally slightly lower in absolute magnitude. While Miller also performed a KK analysis on his data, his computing technique leads to nonphysical results in certain parts of the spectrum and hence are not used in this documentation. Miller correctly points out that on the short-wavelength side of the 9-μm absorption peak, the reflectance shows a deep minimum whose absolute value is difficult to evaluate. Philipp [2] used absorption measurements and a KK analysis on n and α (absorption coefficient $\alpha = 4\pi k/\lambda$) parameters in addition to that on reflectance R and phase ϕ to evaluate R in this region.

In the regions of strong infrared absorption ($k \gtrsim 0.5$), the values for n and k given in the table should be reasonably good ($\pm 15\%$), although there is certainly room for improvement, and further optical studies should be undertaken to improve their accuracy. In the regions of weak infrared absorption, the k values as given by KK analysis are not reliable. Hence, a second set of k values determined from absorption data [2] are given in the table for certain wavelength ranges. They are listed under the heading k_{ABS}. While they are perhaps better than the KK derived values, they should also be treated as unreliable. This is mainly due to the possible presence of impurities and defects in the samples used. In fact, k values must be carefully examined for wavelengths below 7.634 μm, where impurity absorption, especially that associated with OH bonding, can mask intrinsic SiO_2 absorption. Drummond [4] has examined the absorption spectrum of SiO_2 for $\lambda \lesssim 7.5$ μm, and his results show a variety of features (some multiphonon bands) that have been duplicated for the most part by Galeener and Lucovsky [5] in the 3.7–7.5-μm region, with α roughly 20% larger. Therefore, we include some of these k values.

For wavelengths in the range 3.7067 μm $\geq \lambda \geq$ 0.213856 μm, the index of refraction of SiO_2 has been determined with great precision by Malitson [6], who used prism data. His results have been fitted to three- and four-term Sellmeier equations, and the values generated by Brixner [7] are given in the table. It should be pointed out that the very precise Sellmeier-equation fits to index of refraction data are not very reliable for wavelengths outside the fitted range. This is probably related to the fact that these fits tend to be purely mathematical and do not necessarily relate to the actual physical absorption processes that determine the spectral dependence of the index of refraction.

No k values are given in this wavelength range. For $\lambda \gtrsim 0.6$ μm, the measured absorption is dominated by the presence of OH impurity bands. For $\lambda \lesssim 0.6$ μm, the ultimate lower limit to the intrinsic absorption has been estimated by Keck *et al.* [8]; however, the reliability of their values are questionable, especially at the shorter wavelengths.

For $\lambda < 0.2139$ μm, the optical constants given in the table were obtained from a variety of sources. Both Philipp [9] and Lamy [10] have evaluated n and k down to $\lambda = 0.05$ μm from KK analysis of reflectance data. Lamy's [10] results make use of reflectance data by Platzoder and Steinmann [11] for $\lambda \leq 0.1$ μm. For $\lambda > 0.11$ μm, the n and k values of Philipp [9] and Lamy [10] differ somewhat, while for $\lambda < 0.11$ μm they are in reasonably good agreement. The decision to use the results of Philipp [9] (n values) rather than those of Lamy [10] for $\lambda > 0.11$ μm was based on the close agreement of Philipp's k values in the region from 0.11 to 0.12 μm with the results of Weinberg *et al.* [12], who made very careful transmission measurements on thin layers of SiO_2 prepared by thermal oxidation of silicon. This agreement was accomplished with a slight modification of Philipp's results as described in Weinberg *et al.* [12]. The k values given in the table for 0.11 μm $\leq \lambda \leq$ 0.13 μm are taken from this work [12]. For $\lambda > 0.13$ μm, where absorption in SiO_2 is weak, the k values were obtained from a smooth curved drawn through the transmission results of Weinberg *et al.* [12], their thickest sample, those of Appleton *et al.* [13] and those of Kaminow *et al.* [14], sample B_2. Care should be taken in using the k values for $\lambda \gtrsim 0.13$ μm because they may have a component of impurity absorption (especially OH) and defect absorption in them. For this reason, no k values are given for $\lambda \geq 0.163$ μm.

For $\lambda \leq 0.11$ μm, where the results of Philipp [9] and Lamy [10] are in reasonably good agreement, the n and k values given in the table were obtained from a smooth curve drawn through both sets of data. The deviations of each set of data points from the smoothed curve is generally less than 5%. This does not attest to their absolute accuracy, however, because in both cases the KK evaluations are based on somewhat arbitrary extrapolations of the reflectance for $\lambda < 00.5$ μm as required by the analysis. In addition, the reflectance values themselves may be in error.

Hunter [15] has determined n and k for fused silica in the region from 0.3 to 0.03 μm by measuring reflectivity versus angle of incidence. We use these data from 600 to 300 Å, which show good overlap with the data of Philipp [9] and Lamy [10]. For the region 300–82 Å, data of Rife and Osantowski [16] for a high-silica glass with 7.5% TiO_2 were used. They measured reflectivity as a function of angle of incidence utilizing synchrotron radiation.

Since there are no experimental data at shorter wavelengths, we have calculated n and k based on the results of Henke *et al.* [17] in the region 80.5–6.1 Å by assuming the atomic scattering factors of Si and O in appropriate mixture. (See the section by Lynch and Hunter for metals in this

handbook.) The agreement in the overlap region near 82 Å with data of Rife and Osantowski [16] is remarkable. The same calculated n and k would be obtained for α-quartz, assuming that the density of fused silica and α-quartz are the same. These calculated values are at least a starting point for the optical properties of glass in the far-UV and x-ray regions.

It is recommended that anyone who uses the table carefully examine the material and references cited in the above-named references as well as other references [18–25] listed.

REFERENCES

1. C. M. Randall and R. D. Rawcliffe, *Appl. Opt.* **6**, 1889 (1967).
2. H. R. Philipp, *J. Appl. Phys.* **50**, 1053 (1979).
3. M. Miller, *Czech. J. Phys. B* **18**, 354 (1968).
4. D. G. Drummond, *Proc. R. Soc. London* **153**, 328 (1935).
5. F. L. Galeener and G. Lucovsky, *Proc. Int. Conf. Light Scat. Solids, 3rd, Campenas*, 1975 (M. Balkanski, R. C. C. Leite, and S. P. S. Porto, eds.), p. 641. Flammarion Sciences, Paris, 1976.
6. I. H. Malitson, *J. Opt. Soc. Am.* **55**, 1205 (1965).
7. B. Brixner, *J. Opt. Soc. Am.* **57**, 674 (1967).
8. D. B. Keck, R. D. Maurer, and P. C. Schultz, *Appl. Phys. Lett.* **22**, 307 (1973).
9. H. R. Philipp, *Solid State Commun.* **4**, 73 (1966); H. R. Philipp, *J. Phys. Chem. Solids* **32**, 1935 (1971).
10. P. L. Lamy, *Appl. Opt.* **16**, 2212 (1977).
11. K. Platzoder and W. Steinmann, *J. Opt. Soc. Am.* **58**, 588 (1968).
12. Z. A. Weinberg, G. W. Rubloff, and E. Bassous, *Phys. Rev. B* **19**, 3107 (1979).
13. A. Appleton, T. Chiranjivi, and M. Jafaripour-Ghazvini, *in* "The Physics of SiO_2 and Its Interfaces" (S. T. Pantelides, ed.), p. 94. Pergamon, New York, 1978.
14. I. P. Kaminow, B. G. Bagley, and C. G. Olson, *Appl. Phys. Lett.* **32**, 98 (1978).
15. W. R. Hunter, private communication of unpublished data (1983).
16. J. Rife and J. Osantowski, *J. Opt. Soc. Am.* **70**, 1513 (1980).
17. B. L. Henke, P. Lee, T. J. Tanaka, R. L. Shimabukuro, and B. K. Fujikawa, "Low Energy X-Ray Diagnostics–1981" (D. T. Attwood and B. L. Henke, eds.). AIP Conference Proc., No. 75, American Institute of Physcis, New York, 1981.
18. I. Simon and H. O. McMahon, *J. Chem. Phys.* **21**, 23 (1953).
19. J. Reitzel, *J. Chem. Phys.* **23**, 2407 (1955).
20. P. E. Jellyman and J. P. Procter, *J. Soc. Glass Technol.* **39**, 173 (1955).
21. Gouq-Jen Su, N. F. Borrelli, and A. R. Miller, *Phys. Chem. Glasses* **3**, 167 (1962).
22. D. Crozier and R. W. Douglas, *Phys. Chem. Glasses* **6**, 240 (1965).
23. J. E. Diai, R. E. Gong, and J. N. Fordemwalt, *J. Electrohem. Soc.* **115**, 327 (1968).
24. J. F. Osantowski, *J. Opt. Soc. Am.* **64**, 834 (1974).
25. R. J. Powell and M. Morad, *J. Appl. Phys.* **49**, 2499 (1978).

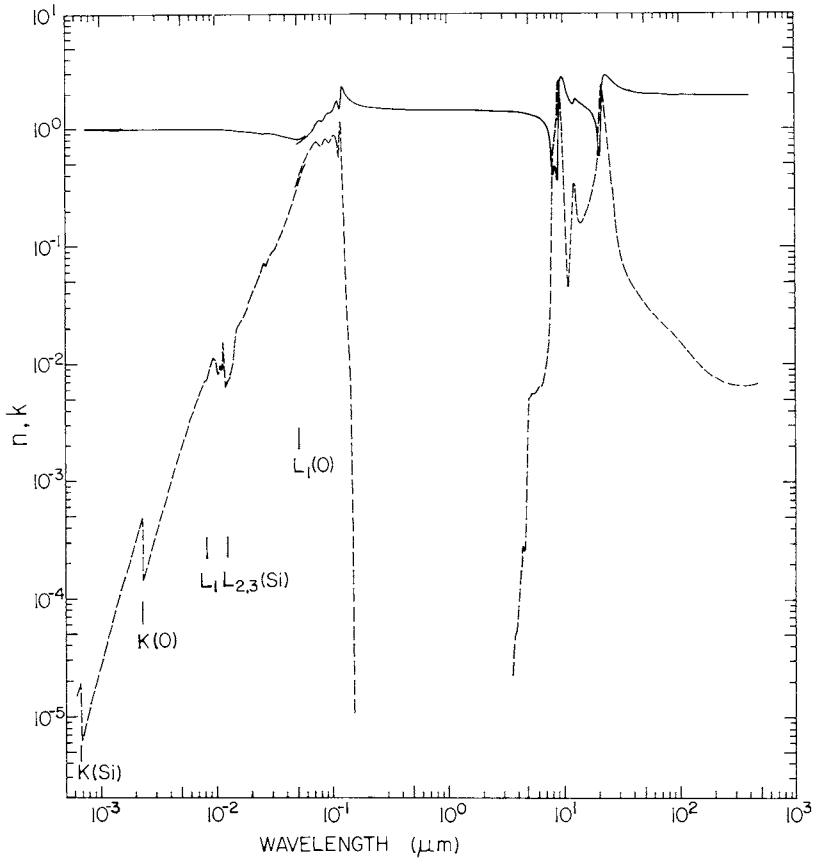

Fig. 10. Log–log plot of n (——) and k (– – – –) versus wavelength in micrometers for silicon dioxide (glass).

TABLE X

Values of n and k for Silicon Dioxide Glass Obtained from Various References[a]

eV	cm^{-1}	Å	n	k
2000		6.199	0.99993 [17]	1.503×10^{-5} [17]
1952		6.351	0.99992	1.636
1905		6.508	0.99992	1.781
1860		6.665	0.99991	1.936×10^{-5}
1815		6.831	0.99991	6.300×10^{-6}
1772		6.997	0.99991	6.904
1730		7.166	0.99990	7.564
1688		7.345	0.99990	8.298
1648		7.523	0.99989	9.083
1609		7.705	0.99989	9.941×10^{-6}

(*continued*)

TABLE X (*Continued*)

Silicon Dioxide (Glass)

eV	cm^{-1}	Å	n	k
1570		7.897	0.99988	1.090×10^{-5}
1533		8.087	0.99987	1.193
1496		8.287	0.99987	1.308
1460		8.492	0.99986	1.432
1426		8.694	0.99985	1.562
1392		8.906	0.99985	1.708
1358		9.129	0.99984	1.872
1326		9.350	0.99983	2.044
1294		9.581	0.99982	2.238
1263		9.816	0.99981	2.447
1233		10.05	0.99981	2.673
1204		10.30	0.99980	2.916
1175		10.55	0.99979	3.189
1147		10.81	0.99978	3.483
1119		11.08	0.99976	3.812
1093		11.34	0.99975	4.155
1067		11.62	0.99974	4.537
1041		11.91	0.99973	4.965
1016		12.20	0.99971	5.423
992		12.50	0.99970	5.915
968		12.81	0.99968	6.468
945		13.12	0.99967	7.061
923		13.43	0.99965	7.686
901		13.76	0.99964	8.364
879		14.10	0.99962	9.121
858		14.45	0.99960	9.928×10^{-5}
838		14.79	0.99958	1.080×10^{-4}
818		15.16	0.99956	1.179
798		15.54	0.99954	1.289
779		15.92	0.99951	1.407
760		16.31	0.99949	1.535
742		16.71	0.99946	1.671
725		17.10	0.99944	1.813
707		17.54	0.99941	1.981
690		17.97	0.99938	2.149
674		18.39	0.99935	2.326
658		18.84	0.99932	2.536
642		19.31	0.99928	2.771
627		19.77	0.99925	3.009
612		20.26	0.99921	3.270
597		20.77	0.99917	3.560
583		21.27	0.99913	3.862
569		21.79	0.99909	4.199
555		22.34	0.99904	4.578
542		22.87	0.99899	4.971
529		23.44	0.99894	1.486
516		24.03	0.99889	1.621

TABLE X (*Continued*)

Silicon Dioxide (Glass)

eV	cm^{-1}	Å	n	k
504		24.60	0.99884	1.76
492		25.20	0.99878	1.91
480		25.83	0.99872	2.08
469		26.43	0.99866	2.26
458		27.07	0.99859	2.45
447		27.74	0.99852	2.67
436		28.44	0.99845	2.90
426		29.10	0.99837	3.15
415		29.87	0.99828	3.44
406		30.54	0.99821	3.71
396		31.31	0.99812	4.04
386		32.12	0.99802	4.40
377		32.89	0.99792	4.77
368		33.69	0.99782	5.18
359		34.53	0.99771	5.63
351		35.32	0.99760	6.07
342		36.25	0.99747	6.62
334		37.12	0.99735	7.17
326		38.03	0.99722	7.77
318		38.99	0.99708	8.44
311		39.86	0.99695	9.09
303		40.92	0.99678	9.91×10^{-4}
296		41.88	0.99663	1.07×10^{-3}
289		42.90	0.99646	1.16
282		43.96	0.99629	1.25
275		45.08	0.99609	1.36
269		46.09	0.99592	1.46
262		47.32	0.99570	1.59
256		48.43	0.99549	1.71
250		49.59	0.99527	1.85
244		50.81	0.99504	2.00
238		52.09	0.99478	2.16
232		53.44	0.99451	2.34
227		54.62	0.99427	2.50
221		56.10	0.99395	2.72
216		57.40	0.99367	2.92
211		58.76	0.99336	3.14
206		60.18	0.99304	3.37
201		61.68	0.99269	3.63
196		63.25	0.99231	3.90
191		64.91	0.99190	4.21
187		66.30	0.99155	4.47
182		68.12	0.99108	4.82
178		69.65	0.99068	5.11
174		71.25	0.99024	5.44
170		72.93	0.9898	5.80

(*continued*)

TABLE X (*Continued*)

Silicon Dioxide (Glass)

eV	cm^{-1}	Å	n	k
166		74.69	0.9893	6.19
162		76.53	0.9887	6.62
158		78.47	0.9882	6.99
154		80.51	0.9875	7.30
151.2		82	0.9871 [16]	7.3 [16]
147.6		84	0.9865	7.6
144.2		86	0.986	8.1
140.9		88	0.9855	8.9
137.8		90	0.9853	9.9×10^{-3}
134.8		92	0.9854	1.07×10^{-2}
131.9		94	0.9858	1.14
129.2		96	0.9868	1.11
126.5		98	0.9872	1.11×10^{-2}
124.0		100	0.9874	9.7×10^{-3}
121.6		102	0.9865	8.5
119.2		104	0.9851	8.3
117.0		106	0.9841	9.6
114.8		108	0.9848	9.9
112.7		110	0.9844	9.0
110.7		112	0.9822	9.3×10^{-3}
108.8		114	0.9828	1.59×10^{-2}
106.9		116	0.9867	1.06×10^{-2}
105.1		118	0.9858	7.5×10^{-3}
103.3		120	0.9839	6.5
101.6		122	0.9823	6.8
99.99		124	0.9813	7.0
98.40		126	0.9803	7.3
96.86		128	0.9794	7.6
95.37		130	0.9789	7.6
93.93		132	0.9778	8.3
92.53		134	0.977	8.7
91.17		136	0.9761	9.3×10^{-3}
89.84		138	0.9747	1.03×10^{-2}
82.66		150	0.9634	1.99
77.49		160	0.9608	2.26
72.93		170	0.9562	2.44
68.88		180	0.9509	2.81
65.26		190	0.9458	3.35
61.99		200	0.9416	3.74
59.04		210	0.9386	4.37
56.36		220	0.9328	4.62
53.91		230	0.9271	5.2
51.66		240	0.9222	5.78
49.59		250	0.9164	6.5
47.69		260	0.9105	7.26
45.92		270	0.9207	6.8
44.28		280	0.9175	7.5

TABLE X (*Continued*)

Silicon Dioxide (Glass)

eV	cm^{-1}	Å	n	k
42.75		290	0.9137	8.2
41.33		300	0.913 [15]	9.0 [15]
40.00		310	0.907	9.2
38.75		320	0.901	9.4
37.57		330	0.895	9.8×10^{-2}
36.47		340	0.888	0.107
35.42		350	0.882	0.113
34.44		360	0.877	0.120
33.51		370	0.870	0.128
32.63		380	0.866	0.137
31.79		390	0.858	0.144
31.00		400	0.851	0.156
30.24		410	0.845	0.169
29.52		420	0.839	0.180
28.83		430	0.833	0.190
28.18		440	0.827	0.202
27.55		450	0.822	0.218
26.95		460	0.817	0.233
26.38		470	0.813	0.250
25.83		480	0.808	0.270
25.30		490	0.804	0.282
eV	cm^{-1}	μm	n	k
25		0.04959	0.733 [9, 10]	0.325 [9, 10]
24.80		0.0500	0.803 [15]	0.300 [15]
24.31		0.0510	0.804	0.322
24		0.05166	0.753 [9, 10]	0.375 [9, 10]
23.84		0.0520	0.806 [15]	0.343 [15]
23.39		0.0530	0.811	0.366
23		0.05391	0.774 [9, 10]	0.434 [9, 10]
22.96		0.540	0.817 [15]	0.385 [15]
22.54		0.0550	0.822	0.408
22.14		0.0560	0.829	0.430
22		0.05636	0.797 [9, 10]	0.480 [9, 10]
21.75		0.0570	0.833 [15]	0.450 [15]
21.38		0.0580	0.843	0.470
21.01		0.0590	0.851	0.482
21		0.05904	0.827 [9, 10]	0.530 [9, 10]
20.66		0.0600	0.862 [15]	0.497 [15]
20		0.06199	0.859 [9, 10]	0.585 [9, 10]
19.5		0.06358	0.879	0.613
19		0.06526	0.902	0.645
18.5		0.06701	0.927	0.677
18		0.06888	0.957	0.712
17.75		0.06985	0.975	0.731

(*continued*)

TABLE X (*Continued*)

Silicon Dioxide (Glass)

eV	cm^{-1}	μm	n	k
17.5		0.07085	0.999	0.750
17.25		0.07187	1.030	0.763
17		0.07293	1.072	0.768
16.75		0.07402	1.124	0.765
16.5		0.07514	1.137	0.755
16.25		0.07630	1.156	0.737
16		0.07749	1.172	0.717
15.75		0.07872	1.178	0.703
15.5		0.07999	1.172	0.696
15.25		0.08130	1.167	0.699
15		0.08266	1.168	0.711
14.75		0.08405	1.175	0.739
14.5		0.08551	1.195	0.771
14.25		0.08700	1.225	0.799
14		0.08856	1.265	0.808
13.75		0.09017	1.320	0.795
13.5		0.09184	1.363	0.775
13.25		0.09357	1.371	0.755
13		0.09537	1.368	0.747
12.75		0.09724	1.372	0.766
12.5		0.09919	1.383	0.793
12.25		0.1012	1.410	0.824
12		0.1033	1.475	0.861
11.8		0.1051	1.554	0.874
11.6		0.1069	1.635	0.859
11.4		0.1088	1.716	0.810
11.2		0.1107	1.766 [9]	0.718 [12]
11		0.1127	1.739	0.569
10.9		0.1137	1.687	0.565
10.8		0.1148	1.587	0.618
10.7		0.1159	1.513	0.725
10.6		0.1170	1.492	0.914
10.5		0.1181	1.567	1.11
10.45		0.1187	1.645	1.136
10.4		0.1192	1.772	1.13
10.35		0.1198	1.919	1.045
10.3		0.1204	2.048	0.925
10.25		0.1210	2.152	0.810
10.2		0.1215	2.240	0.715
10.1		0.1228	2.332	0.460
10		0.1240	2.330	0.323
9.9		0.1252	2.292	0.236
9.8		0.1265	2.243	0.168
9.7		0.1278	2.190	0.119
9.6		0.1291	2.140	0.077
9.5		0.1305	2.092	0.0561 [12–14]
9.4		0.1319	2.047	0.0430

TABLE X (*Continued*)

Silicon Dioxide (Glass)

eV	cm^{-1}	μm	n	k
9.3		0.1333	2.006	0.0339
9.2		0.1348	1.969	0.0271
9.1		0.1362	1.935	0.0228
9.0		0.1378	1.904	1.89×10^{-2}
8.9		0.1393	1.876	1.56
8.8		0.1409	1.850	1.32
8.7		0.1425	1.825	1.09×10^{-2}
8.6		0.1442	1.803	8.38×10^{-3}
8.5		0.1459	1.783	5.57
8.4		0.1476	1.764	3.17
8.3		0.1494	1.747	1.40×10^{-3}
8.2		0.1512	1.730	4.63×10^{-4}
8.1		0.1531	1.716	1.22×10^{-4}
8.0		0.1550	1.702	3.2×10^{-5}
7.8		0.1590	1.676	4.7×10^{-6}
7.6		0.1631	1.653	
7.4		0.1675	1.633	
7.2		0.1722	1.616	
7.0		0.1771	1.600	
6.75		0.1837	1.582	
6.5		0.1907	1.567	
6.25		0.1984	1.554	
6.0	48,390	0.2066	1.543	
5.7976	46,760.4	0.213856	1.53429 [7]	
5.7819	46,633.5	0.214438	1.53371	
5.4680	44,102.0	0.226747	1.52276	
5.3858	43,438.8	0.230209	1.52009	
5.2131	42,046.3	0.237833	1.51474	
5.1674	41,677.4	0.239938	1.51338	
4.9939	40,278.4	0.248272	1.50841	
4.6751	37,706.8	0.265204	1.50004	
4.5940	37,052.8	0.269885	1.49805	
4.5040	36,326.9	0.275278	1.49592	
4.4226	35,670.1	0.280347	1.49404	
4.2848	34,559.0	0.289360	1.49099	
4.1784	33,700.9	0.296728	1.48873	
4.1034	33,096.1	0.302150	1.48719	
3.7542	30,279.3	0.330259	1.48053	
3.7105	29,926.9	0.334148	1.47976	
3.6427	29,380.2	0.340365	1.47858	
3.5770	28,850.0	0.346620	1.47746	
3.4340	27,696.9	0.361051	1.47512	
3.3967	27,396.1	0.365015	1.47453	
3.0640	24,712.3	0.404656	1.46961	
2.8448	22,944.5	0.435835	1.46669	
2.6503	21,375.9	0.467816	1.46429	

(*continued*)

TABLE X (*Continued*)

Silicon Dioxide (Glass)

eV	cm^{-1}	μm	n	k	
2.5504	20,570.5	0.486133	1.46313		
2.4379	19,662.5	0.508582	1.46187		
2.2705	18,312.5	0.546074	1.46008		
2.1489	17,332.3	0.576959	1.45885		
2.1411	17,269.2	0.579065	1.45877		
2.1102	17,019.5	0.587561	1.45847		
2.1041	16,970.4	0.589262	1.45841		
1.9257	15,531.6	0.643847	1.45671		
1.8892	15,237.6	0.656272	1.45637		
1.8566	14,974.2	0.667815	1.45608		
1.7549	14,153.9	0.706519	1.45515		
eV	cm^{-1}	μm	n	k	k_{ABS}
1.4550	11,735.6	0.852111	1.45248		
1.3863	11,181.3	0.894350	1.45185		
1.2228	9,862.13	1.01398	1.45025		
1.1449	9,233.87	1.08297	1.44941		
1.0985	8,860.06	1.12866	1.44888		
0.91018	7,341.1	1.3622	1.44621		
0.88874	7,168.15	1.39506	1.44584		
0.84372	6,805.0	1.4695	1.44497		
0.81061	6,538.00	1.52952	1.44427		
0.74663	6,021.9	1.6606	1.44267		
0.7376	5,949	1.681	1.44241		
0.73225	5,906.0	1.6932	1.44226		
0.72543	5,850.93	1.70913	1.44205		
0.68384	5,515.51	1.81307	1.44069		
0.62934	5,075.91	1.97009	1.43851		
0.60243	4,858.9	2.0581	1.43722		
0.57598	4,645.5	2.1526	1.43576		
0.53317	4,300.30	2.32542	1.43292		
0.50868	4,102.7	2.4374	1.43095		
0.38221	3,082.7	3.2439	1.41314		
0.37953	3,061.1	3.2668	1.41253		
0.37542	3,027.9	3.3026	1.41155		
0.3623	2,922	3.422	1.40819		
0.35354	2,851.4	3.5070	1.40568		
0.34863	2,811.8	3.5564	1.40418		
0.3410	2,750	3.636			2.25×10^{-5} [4]
0.3348	2,700	3.704			3.39
0.33449	2,697.8	3.7067	1.39936		
0.3286	2,650	3.774			3.93
0.3224	2,600	3.846	1.395 [2]		4.96
0.3162	2,550	3.922			5.18
0.3100	2,500	4.000			5.79
0.3038	2,450	4.082			7.99×10^{-5}
0.2976	2,400	4.167	1.383		1.07×10^{-4}

TABLE X (*Continued*)

Silicon Dioxide (Glass)

eV	cm^{-1}	μm	n	k	k_{ABS}
0.2914	2,350	4.255			1.32
0.2852	2,300	4.348			2.13
0.2821	2,275	4.396			2.65
0.2790	2,250	4.444			2.84
0.2759	2,225	4.494			2.84
0.2728	2,200	4.545	1.365		2.56
0.2666	2,150	4.651			2.62
0.2604	2,100	4.762			4.85×10^{-4}
0.2542	2,050	4.878			1.82×10^{-3}
0.2480	2,000	5.000	1.342		3.98
0.2449	1,975	5.063			5.12
0.2418	1,950	5.128			5.18
0.2356	1,900	5.263			5.49
0.2325	1,875	5.333			5.69
0.2294	1,850	5.405			5.72
0.2232	1,800	5.556	1.306		5.63
0.2170	1,750	5.714			
0.2108	1,700	5.882	1.278		5.94
0.2046	1,650	6.061			6.32
0.2015	1,625	6.154			6.46
0.1984	1,600	6.250	1.239		6.52
0.1922	1,550	6.452	1.212		6.57
0.1860	1,500	6.667	1.175		7.16
0.1835	1,480	6.757	1.158		
0.1810	1,460	6.849	1.135		
0.1798	1,450	6.897			8.51×10^{-3}
0.1785	1,440	6.944	1.107		
0.1761	1,420	7.042	1.084		
0.1736	1,400	7.143	1.053		1.06×10^{-2}
0.1711	1,380	7.246	1.014		
0.1686	1,360	7.353	0.9702		
0.1674	1,350	7.407	0.9488		1.48
0.1661	1,340	7.463	0.9175		
0.1649	1,330	7.519	0.8897		
0.1637	1,320	7.576	0.8600		
0.1624	1,310	7.634	0.8213		
0.1612	1,300	7.692	0.7719 [2]	3.72×10^{-2} [2]	4.0×10^{-2} [2]
0.1599	1,290	7.752	0.7037	4.74	5.2
0.1587	1,280	7.813	0.6232	7.68×10^{-2}	7.3
0.1575	1,270	7.874	0.5456	0.132	
0.1562	1,260	7.937	0.4677	0.216	
0.1550	1,250	8.000	0.4113	0.323	
0.1537	1,240	8.065	0.3931	0.446	
0.1525	1,230	8.130	0.4020	0.553	
0.1513	1,220	8.197	0.4329	0.635	
0.1500	1,210	8.265	0.4530	0.704	

(*continued*)

TABLE X (*Continued*)

Silicon Dioxide (Glass)

eV	cm^{-1}	μm	n	k	k_{ABS}
0.1488	1,200	8.333	0.4600	0.771	
0.1475	1,190	8.403	0.4730	0.840	
0.1463	1,180	8.475	0.4746	0.903	
0.1451	1,170	8.547	0.4656	0.978	
0.1438	1,160	8.621	0.4563	1.07	
0.1426	1,150	8.696	0.4309	1.17	
0.1413	1,140	8.772	0.3915	1.32	
0.1401	1,130	8.850	0.3563	1.53	
0.1389	1,120	8.929	0.3705	1.85	
0.1376	1,110	9.009	0.5846	2.27	
0.1364	1,100	9.091	1.043	2.55	
0.1351	1,090	9.174	1.616	2.63	
0.1333	1,075	9.302	2.250	2.26	
0.1302	1,050	9.524	2.760	1.65	
0.1271	1,025	9.756	2.839	0.962	
0.1240	1,000	10.00	2.694	0.509	
0.1209	975	10.26	2.448	0.231	6.8×10^{-2}
0.1178	950	10.53	2.224	0.102	3.1
0.1147	925	10.81	2.038	4.60×10^{-2}	2.3
0.1116	900	11.11	1.869	5.06	2.2
0.1091	880	11.36	1.784	7.75×10^{-2}	2.6
0.1066	860	11.63	1.690	0.116	7.7×10^{-2}
0.1054	850	11.76	1.652	0.152	0.12
0.1041	840	11.90	1.619	0.204	0.17
0.1029	830	12.05	1.615	0.267	
0.1017	820	12.20	1.658	0.323	
0.1004	810	12.35	1.701	0.341	
0.09919	800	12.50	1.753	0.343	
0.09795	790	12.66	1.789	0.314	
0.09671	780	12.82	1.811	0.275	0.16
0.09547	770	12.99	1.810	0.227	0.11
0.09423	760	13.16	1.779	0.192	8.5×10^{-2}
0.09299	750	13.33	1.756	0.177	8.0
0.08989	725	13.79	1.698	0.157	7.5
0.08679	700	14.29	1.643	0.157	7.2
0.08369	675	14.81	1.598	0.168	7.7
0.08059	650	15.38	1.555	0.182	8.8×10^{-2}
0.07749	625	16.00	1.502	0.202	0.11
0.07439	600	16.67	1.450	0.235	0.14
0.07191	580	17.24	1.401	0.264	0.16
0.06943	560	17.86	1.337	0.298	0.18
0.06695	540	18.52	1.235	0.341	0.21
0.06534	527	18.97	1.161	0.377	0.25
0.06447	520	19.23	1.050	0.415	0.32
0.06323	510	19.61	0.8857	0.524	
0.06199	500	20.00	0.6616	0.822	

TABLE X (*Continued*)

Silicon Dioxide (Glass)

eV	cm^{-1}	μm	n	k	k_{ABS}
0.06075	490	20.41	0.5777	1.28	
0.05951	480	20.83	0.7517	1.86	
0.05889	475	21.05	1.002	2.22	
0.05827	470	21.28	1.484	2.39	
0.05703	460	21.74	2.308	2.29	
0.05455	440	22.73	2.936	1.29	
0.05207	420	23.81	2.912	0.738	
0.04959	400	25.00	2.739	0.397	
0.04649	375	26.67	2.537	0.199	0.20
0.04339	350	28.57	2.388		0.13
0.04030	325	30.77	2.284		9.2×10^{-2}
0.03720	300	33.33	2.210		6.7
0.03410	275	36.36	2.147		5.6
0.03100	250	40.00	2.100		4.6
0.01240	100	100.0	1.967 [1]	1.59×10^{-2} [1]	
0.009919	80	125.0	1.962	1.19×10^{-2}	
0.007439	60	166.7	1.959	8.62×10^{-3}	
0.004959	40	250.0	1.957	6.96	
0.002480	20	500.0	1.955	7.96	

[a] References are indicated in brackets. Data marked k_{ABS} were obtained from transmission measurements.

Silicon Monoxide (SiO) (Noncrystalline)

H. R. PHILIPP
General Electric Research and Development Center
Schenectady, New York

Silicon monoxide (SiO) is used as a protective layer and antireflecting coating in optical applications and as the dielectric material in certain microelectronic devices. These layers are generally prepared by the rapid evaporation of silicon monoxide under high-vacuum conditions. If the deposition is carried out slowly in the presence of a partial pressure of oxygen, the condensate acquires excess oxygen and the O-to-Si-atom ratio rises above unity. These materials are often labeled SiO_x ($x > 1.0$). The optical properties of SiO and SiO_x are different, and the values given here should only be applied to materials of stoichiometry SiO. For completeness, references will be given that also describe the optical behavior of SiO_x materials.

Although SiO has some important applications, it is a rather dull material from an optical point of view. For this and other reasons, there is not very much information available on its optical properties. However, in the visible and near-ultraviolet spectral regions in which data from several sources can be compared, the results agree with one another quite well. This would indicate that SiO is a reasonably well defined material, when prepared in the absence of oxygen, with definitive optical properties.

A set of optical parameters n and k for noncrystalline SiO are given in Table XI and plotted in Fig. 11 for the wavelength region $14.0\ \mu m \geq \lambda \geq 0.050\ \mu m$. The wavelength λ, index of refraction n, and extinction coefficient k are given to four places in most of the table entries. The accuracy of the values does not warrant this precision. This is done to show the possible presence of weak structure in the optical properties that can often be discerned by comparison of precise, but not necessarily accurate, values over small wavelength ranges.

In the infrared, $14.0\ \mu m \geq \lambda \geq 1.00\ \mu m$, the values given in the table were obtained from Hass and Salzberg [1]. The values were derived through analysis of transmittance and reflectance measurements on a series of SiO layers

HANDBOOK OF OPTICAL CONSTANTS OF SOLIDS

Copyright © 1985 by Academic Press, Inc.
All rights of reproduction in any form reserved.
ISBN 0-12-544420-6

of various thicknesses. Although the overall accuracy of these values cannot be simply specified, they fit the measured transmittance and reflectance to within $\pm 2\%$.

In the region $1.00\ \mu m \geq \lambda \geq 0.049\ \mu m$, the values are taken from Philipp [2]. They were derived from Kramers–Kronig (KK) analysis of reflectance data augmented by transmission measurements in the region of low absorption. These results agree reasonably well with those of Hass and Salzberg [1], whose measurements extend to $0.24\ \mu m$, as well as with the absorption data of Cremer *et al.* [3]. The results of Philipp are given in the table because they cover a wider wavelength range and more explicitly evaluate the extinction coefficient in the region of low absorption compared to the other measurements. They are not necessarily more accurate than those of Hass and Salzberg [1] and Cremer [3]. The differences that are found in these measurements [1–3], $\pm 5\%$ or less in n and slightly larger in k, may be due in part to sample preparation (evapoaration rate, vacuum conditions, substrate temperature, etc.), and as stated earlier, it is encouraging that they agree as well as they do. It should also be pointed out that the table values at the shorter wavelengths, especially those below $0.100\ \mu m$, depend somewhat on the extrapolation used in the KK analysis and should be treated with caution until more definitive measurements are made for $\lambda \leq 0.05\ \mu m$, which more clearly delineate the proper reflectance extrapolation.

It is recommended that anyone who uses the table carefully examine the measurements and references cited in the references discussed [1–3] as well as other references [4–7] that also describe the optical behavior of materials of stoichiometry SiO_x ($x > 1$).

REFERENCES

1. G. Hass and C. D. Salzberg, *J. Opt. Soc. Am.* **44**, 181 (1954).
2. H. R. Philipp, *J. Phys. Chem. Solids* **32**, 1935 (1971).
3. E. Cremer, T. Kraus, and E. Ritter, *Z. Elektrochem.* **62**, 939 (1958).
4. E. Ritter, *Opt. Acta* **9**, 197 (1962).
5. A. P. Bradford and G. Hass, *J. Opt. Soc. Am.* **53**, 1096 (1963).
6. G. Hass, *J. Am. Ceramic Soc.* **33**, 353 (1950).
7. A. P. Bradford, G. Hass, M. McFarland, and E. Ritter, *Appl. Opt.* **4**, 971 (1965).

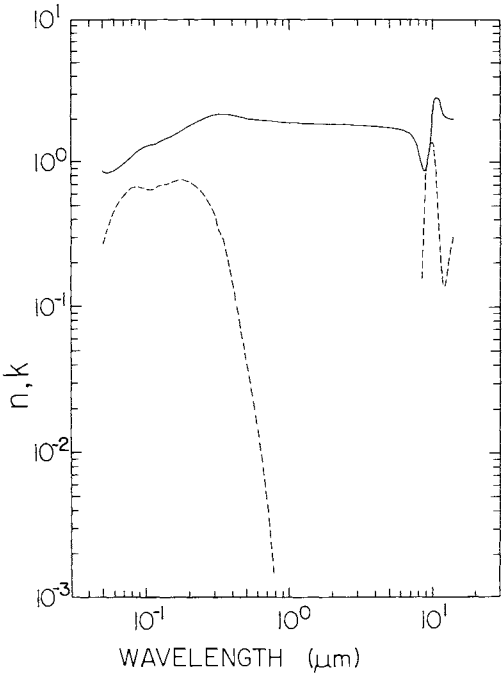

Fig. 11. Log–log plot n (——) and k (– – – –) versus wavelength in micrometers for silicon monoxide (noncrystalline).

TABLE XI
Values of n and k for Silicon Monoxide (Noncrystalline) from Various References[a]

eV	cm^{-1}	μm	n	k
25		0.04959	0.8690 [2]	0.2717 [2]
24		0.05166	0.8444	0.3060
23		0.05391	0.8371	0.3505
22.5		0.05510	0.8391	0.3761
22		0.05636	0.8454	0.3987
21.5		0.05767	0.8519	0.4222
21		0.05904	0.8610	0.4456
20.5		0.06048	0.8721	0.4688
20		0.06199	0.8853	0.4919
19.5		0.06358	0.9007	0.5140
19		0.06526	0.9178	0.5362
18.5		0.06702	0.9376	0.5578
18		0.06888	0.9596	0.5771
17.5		0.07085	0.9825	0.5961
17		0.07293	1.008	0.6147
16.5		0.07514	1.036	0.6309
16		0.07749	1.066	0.6453
15.5		0.07999	1.098	0.6566

(*continued*)

TABLE XI (*Continued*)

Silicon Monoxide (Noncrystalline)

eV	cm^{-1}	μm	n	k
15		0.08266	1.132	0.6651
14.5		0.08551	1.166	0.6692
14		0.08856	1.199	0.6698
13.5		0.09184	1.231	0.6666
13		0.09537	1.259	0.6602
12.5		0.09919	1.283	0.6523
12		0.1033	1.307	0.6464
11.5		0.1078	1.311	0.6293
11		0.1127	1.320	0.6529
10.5		0.1181	1.345	0.6701
10		0.1240	1.378	0.6843
9.5		0.1305	1.412	0.6920
9		0.1378	1.445	0.7002
8.5		0.1459	1.482	0.7153
8		0.1550	1.530	0.7333
7.5		0.1653	1.593	0.7473
7		0.1771	1.667	0.7479
6.5		0.1907	1.746	0.7348
6	48,390	0.2066	1.829	0.7084
5.75	46,380	0.2156	1.871	0.6890
5.5	44,360	0.2254	1.914	0.6663
5.25	42,340	0.2362	1.957	0.6383
5	40,330	0.2480	2.001	0.6052
4.8	38,710	0.2583	2.034	0.5723
4.6	37,100	0.2695	2.066	0.5364
4.4	35,490	0.2818	2.094	0.4948
4.2	33,880	0.2952	2.119	0.4499
4	32,260	0.3100	2.141	0.4006
3.8	30,650	0.3263	2.157	0.3453
3.6	29,040	0.3444	2.162	0.2872
3.4	27,420	0.3647	2.160	0.2287
3.2	25,810	0.3875	2.144	0.1706
3	24,200	0.4133	2.116	0.1211
2.8	22,580	0.4428	2.085	0.08374
2.6	20,970	0.4769	2.053	0.05544
2.4	19,360	0.5166	2.021	0.03533
2.2	17,740	0.5636	1.994	0.02153
2	16,130	0.6199	1.969	0.01175
1.8	14,520	0.6888	1.948	0.00523
1.6	12,900	0.7749	1.929	0.00151
1.4	11,290	0.8856	1.913	
1.240	10,000	1.000	1.87 [1]	
0.6199	5,000	2.000	1.84	
0.4133	3,333	3.000	1.82	
0.3100	2,500	4.000	1.80	
0.2480	2,000	5.000	1.75	

TABLE XI (*Continued*)

Silicon Monoxide (Noncrystalline)

eV	cm^{-1}	μm	n	k
0.2066	1,667	6.000	1.70	
0.1771	1,492	7.000	1.60	
0.1653	1,333	7.500	1.42	
0.1550	1,250	8.000	1.15	
0.1459	1,176	8.500	0.90	0.18 [1]
0.1378	1,111	9.000	0.91	0.75
0.1305	1,053	9.500	1.20	1.20
0.1240	1,000	10.00	2.00	1.38
0.1181	952.4	10.50	2.85	0.90
0.1153	930.2	10.75	2.86	0.58
0.1127	909.1	11.00	2.82	0.40
0.1078	869.6	11.50	2.50	0.20
0.1033	833.3	12.00	2.13	0.14
0.09537	769.2	13.00	2.04	0.20
0.08856	714.3	14.00	2.01	0.30

[a] References are indicated in brackets.

Silicon Nitride (Si_3N_4) (Noncrystalline)

H. R. PHILIPP
General Electric Research and Development Center
Schenectady, New York

Noncrystalline silicon nitride (Si_3N_4) is an important material in integrated-circuit technology. In this application it is used in thin-film form and can be prepared by a variety of deposition techniques, including (a) pyrolytic decomposition of a mixture of gases containing silicon and nitrogen (for example, SiH_4 and NH_3), (b) sputtering, and (c) rf glow-discharge techniques. Silicon oxynitride (SiO_xN_y) films can also be readily formed by adding small amounts of NO or O_2 to the reactive gases. The optical properties of these films are strongly dependent on the deposition temperature and the Si-to-N- and Si-to-O-atom ratios. Other studies also indicate the presence of chemically bound hydrogen in the film. Thus, the stoichiometry of an arbitrary film can be more accurately indicated by $SiO_xN_yH_z$, and the refractive index and other optical properties will be a function of x, y, and z. Samples prepared by high-temperature pyrolysis are generally considered to have, or come close to, the ideal stoichiometry, Si_3N_4 (exclusive of hydrogen content).

While there have been a number of studies on the optical properties of silicon nitride materials, the data have generally been limited to the evaluation of the index of refraction in the visible region of the spectrum [1–14] and to infrared measurements of the lattice absorption bands near 11 μm and other bands, particularly those which show up N–H and Si–H bonding [1–7, 9, 12, 15–20]. The infrared measurements have been used mainly for structural and chemical evaluation purposes. While Taft [12] measured the absorption coefficient of silicon nitride films prepared by several different techniques in the region of 11-μm wavelength, no attempt has been made to determine a self-consistent set of optical parameters for this material in the infrared.

In the region of strong electronic absorption, both Philipp [21] and Bauer [22] have evaluated n and k from the visible into the vacuum ultraviolet region. The results of Philipp [21], which extend to 24 eV, were determined by Kramers–Kronig analysis of reflectance and absorption data. The films

HANDBOOK OF OPTICAL CONSTANTS OF SOLIDS

Copyright © 1985 by Academic Press, Inc.
All rights of reproduction in any form reserved.
ISBN 0-12-544420-6

he used were prepared by pyrolytic decomposition at 1000°C of a mixture of SiH_4 and NH_3 gases in the ratio 1 to 40,000. Bauer's [22] measurements extend to only 7.5 eV but were obtained on samples prepared by a variety of deposition techniques including pyrolysis of a mixture of SiO_4 and NH_3 gases at substrate temperatures in the range 720 to 1000°C. His n and k values were evaluated by error-function analysis of reflectance and transmission data. For pyrolytic silicon nitride films, the results of Philipp [21] and Bauer [22] show reasonable but not precise agreement.

A set of optical parameters n and k for noncrystalline silicon nitride are given in Table XII and are plotted in Fig. 12 for the energy range 1–24 eV (1.24–0.0517-μm wavelength). They are taken entirely from the work of Philipp [21]. These results are not necessarily more accurate than other data but were primarily chosen because they cover the widest energy range. In addition, Theeten *et al.* [23] in a study of Si_3N_4 in the region from 1.5 to 5.8 eV using spectroscopic ellipsometry found good agreement with the values of Philipp [21] (and it is in this energy range that the largest differences occur between the results of Philipp [21] and Bauer [22]). In most of the table entries, the index of refraction n values are given to four places and the extinction coefficient k values are given to three places. The accuracy of these values does not warrant this precision. This is done to show the possible presence of weak structure in the optical properties that can often be discerned by comparison of precise, but not necessarily accurate, values over small energy ranges. It is also recommended that anyone who uses the table carefully examine the material and references cited in the references. Since the optical properties of silicon nitride depend on the method and temperature of deposition, care must be taken in using the table values for materials prepared by using techniques other than high-temperature pyrolysis of gases with a high N-to-Si ratio.

REFERENCES

1. V. Doo, D. Nichols, and G. Silvey, *J. Electrochem. Soc.* **133**, 1279 (1966).
2. K. Bean, P. Gleim, R. Yeakley, and W. Runyan, *J. Electrochem. Soc.* **114**, 733 (1967).
3. T. Chu, C. Lee, and G. Gruber, *J. Electrochem. Soc.* **114**, 717 (1967).
4. V. Doo, D. Kerr, and D. Nichols, *J. Electrochem. Soc.* **115**, 61 (1968).
5. D. Brown, P. Gray, F. Heumann, H. Philipp, and E. Taft, *J. Electrochem. Soc.* **115**, 311 (1968).
6. M. Grieco, F. Worthing, and B. Schwartz, *J. Electrochem. Soc.* **115**, 525 (1968).
7. R. Levitt and W. Zwicker, *J. Electrochem. Soc.* **114**, 1192 (1967).
8. B. Deal, P. Fleming, and P. Castro, *J. Electrochem. Soc.* **115**, 300 (1968).
9. G. Brown, W. Robinette, Jr., and H. Carlson, *J. Electrochem. Soc.* **115**, 948 (1968).
10. E. V. Shitova, I. A. Yasneva, and N. A. Genkina, *Opt. Spectrosc.* **43**, 140 (1977); E. V. Shitova, I. A. Yasneva, and N. A. Genkina, *Opt. Spektrosk.* **43**, 244 (1977).
11. Y. N. Volgin, O. P. Borisov, Y. I. Ukhanov, and N. I. Sukhanova, *J. Appl. Spectrosc.* **24**, 115 (1976); Y. N. Volgin, O. P. Borisov, Y. I. Ukhanov and N. I. Sukhanova, *Zh. Priklad. Spektrosk.* **24**, 164 (1976).
12. E. A. Taft, *J. Electrochem. Soc.* **118,** 1341 (1971).
13. M. J. Rand and D. R. Wonsidler, *J. Electrochem. Soc.* **125**, 99 (1978).

14. T. Wittberg, J. Hoenigman, W. Moddeman, C. Cothern, and M. Gulett, *J. Vac. Sci. Technol.* **15**, 348 (1978).
15. S. Yoshioka and S. Takayanagi, *J. Electrochem. Soc.* **114**, 962 (1967).
16. H. J. Stein, *Appl. Phys. Lett.* **32**, 379 (1978).
17. S. M. Hu, *J. Electrochem. Soc.* **113**, 693 (1966).
18. H. J. Stein and H. A. R. Wagener, *J. Electrochem. Soc.* **124**, 908 (1977).
19. P. S. Peercy, H. J. Stein, B. L. Doyle, and S. T. Picraux, *J. Electron. Mater.* **8**, 11 (1979).
20. L. F. Cordes, *Appl. Phys. Lett.* **11**, 383 (1967).
21. H. R. Philipp, *J. Electrochem. Soc.* **120**, 295 (1973).
22. J. Bauer, *Phys. Status. Solidi A* **39**, 411 (1977).
23. J. B. Theeten, D. E. Aspnes, F. Simondet, M. Errman, and P. C. Mürau, *J. Appl. Phys.* **52**, 6788 (1981).

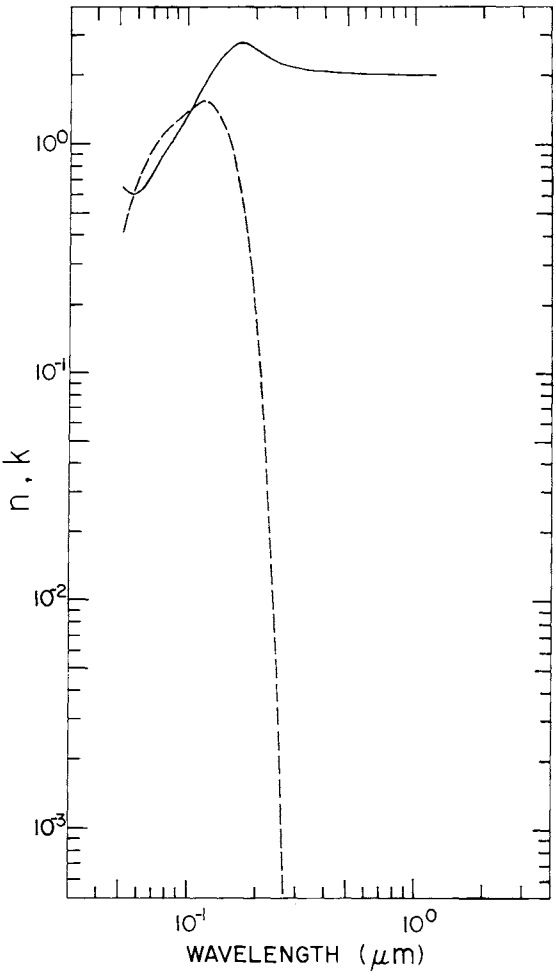

Fig. 12. Log–log plot of n (——) and k (– – – –) versus wavelength in micrometers for silicon nitride (noncrystalline).

TABLE XII

Values of n and k for Silicon Nitride (Noncrystalline) from Various References[a]

eV	cm^{-1}	μm	n	k
24		0.05166	0.655 [21]	0.420 [21]
23		0.05391	0.625	0.481
22		0.05636	0.611	0.560
21		0.05904	0.617	0.647
20		0.06199	0.635	0.743
19		0.06526	0.676	0.841
18		0.06888	0.735	0.936
17		0.07293	0.810	1.03
16		0.07749	0.902	1.11
15		0.08266	1.001	1.18
14		0.08856	1.111	1.26
13		0.09537	1.247	1.35
12	96,790	0.1033	1.417	1.43
11	88,720	0.1127	1.657	1.52
10.5	84,690	0.1181	1.827	1.53
10	80,650	0.1240	2.000	1.49
9.5	76,620	0.1305	2.162	1.44
9	72,590	0.1378	2.326	1.32
8.5	68,560	0.1459	2.492	1.16
8	64,520	0.1550	2.651	0.962
7.75	62,510	0.1600	2.711	0.866
7.5	60,490	0.1653	2.753	0.750
7.25	58,470	0.1710	2.766	0.612
7	56,460	0.1771	2.752	0.493
6.75	54,440	0.1837	2.724	0.380
6.5	52,430	0.1907	2.682	0.273
6.25	50,410	0.1984	2.620	0.174
6	48,390	0.2066	2.541	0.102
5.75	46,380	0.2156	2.464	5.7×10^{-2}
5.5	44,360	0.2254	2.393	2.9
5.25	42,340	0.2362	2.331	1.1×10^{-2}
5	40,330	0.2480	2.278	4.9×10^{-3}
4.75	38,310	0.2610	2.234	1.2×10^{-3}
4.5	36,290	0.2755	2.198	2.2×10^{-4}
4.25	34,280	0.2917	2.167	
4	32,260	0.3100	2.141	
3.5	28,230	0.3542	2.099	
3	24,200	0.4133	2.066	
2.5	20,160	0.4959	2.041	
2	16,130	0.6199	2.022	
1.5	12,100	0.8266	2.008	
1	8,065	1.240	1.998	

[a] Data obtained from Philipp [21].

Sodium Chloride (NaCl)

J. E. ELDRIDGE
Department of Physics
University of British Columbia
Vancouver, British Columbia, Canada

EDWARD D. PALIK
Naval Research Laboratory
Washington, D.C.

The room-temperature values of n and k tabulated here were obtained from the following works and references therein: The centimeter–millimeter-wave-region results, 0.33 cm^{-1} (30 mm) to 5 cm^{-1} (2 mm), are from Owens [1]; the 3.1-cm^{-1} (3200-μm) to 10-cm^{-1} (1000-μm) results are from Stolen and Dransfeld [2], Genzel *et al.* [3], and Dianov and Irisova [4]; the far-infrared reststrahlen results, 10 cm^{-1} (1000 μm) to 500 cm^{-1} (20 μm), are from Eldridge and Staal [5]; the multiphonon-tail data, 500 cm^{-1} (20 μm) to 900 cm^{-1} (11.1 μm), are from Harrington *et al.* [6]; values of k in the transparent region, 943 cm^{-1} (10.6 μm) to 3571 cm^{-1} (2.8 μm), are from Allen and Harrington [7]; while those in the visible, 19,430 cm^{-1} (0.5145 μm) to 28,489 cm^{-1} (0.3511 μm), are from Harrington *et al.* [8]; values of n from 500 cm^{-1} (20 μm) to 50,000 cm^{-1} (0.2 μm), also in the transparent region, are from Li [9], who consolidated various data [10–13]; the visible and ultraviolet values are from Miyata and Tomiki [14] and Roessler and Walker [15]; $L_{2,3}$ absorption-edge data for Cl^- are from Aita *et al.* [16]. A composite smooth-curve plot of $\log n$ and $\log k$ versus log wavelength is given in Fig. 13. Numerical values are given in Table XIII.

In the centimeter–millimeter-wave region a filled resonant-cavity method was used [1] to measure the real part of the dielectric function ε' and the loss tangent, $\tan\delta = \varepsilon''/\varepsilon'$. From these, n and k could be extracted. Other results in the millimeter-wave region were obtained with transmission measurements made on slab samples of different thicknesses to determine n and k [2–4].

While not listed in the table, Breckenridge [17] gives 85°C data over a wide range of frequencies, 10^2–10^{10} Hz by measuring the capacitance and

Copyright © 1985 by Academic Press, Inc.
All rights of reproduction in any form reserved.
ISBN 0-12-544420-6

susceptance of blocks of NaCl. Generally, k is less than the last value given in the table, as was noted by Owens [1].

Above 10 cm^{-1} the far-infrared results were obtained mainly by the technique of dispersive-reflection spectroscopy [5]. In this technique a flat-polished (to within 0.3 μm) crystal of the material under investigation replaces the mirror in one of the arms of a Michelson interferometer. The temperature was 290 K. The resulting interferogram is asymmetric and contains information on both the reflectance amplitude r and phase change θ where $\hat{r} = re^{i\theta}$ for the crystal. When ratioed with a background spectrum, obtained when the usual mirror is in place, both r and θ, and consequently *all* of the real and imaginary optical properties, can be obtained simultaneously and directly.

This obviates the need for a Kramers–Kronig (KK) analysis of power reflectivity measurements, which has serious and well-known limitations [18]. For instance, the KK analysis will give poor values of n or k if either one is much smaller than the other. It works best when the values are comparable, since they both then have an effect of the power reflectivity. Of course, one also has to measure this power reflectivity over a large range for the integral to be at all valid. Furthermore, the power reflectivity becomes extremely small following a strong resonance such as the transverse-optic lattice mode in alkali halides. This occurs in the region of the longitudinal-optic frequency. All of the fine structure in the optical properties at this frequency is therefore usually lost. Another difficult region is the reststrahlen peak when the reflectivity can be very close to unity and an accurate value for k difficult to obtain. One has then to resort to measurements of transmission through thin films, with their concomitant dependence on interference effects and the quality and properties of the surfaces.

The dispersive-reflection technique is therefore obviously superior, but it is not without its difficulties. The main one of these is the physical interchange of reference mirror and sample in exactly the same position (either that or the exact relative position must be known). In Eldridge and Staal [5] this problem was overcome by aluminizing a portion of the large NaCl crystal, which would then act as the reference surface. (A correction must be made to the reflectivity and phase change of aluminum, depending on the film thickness.) In order to avoid the other main problem of ratioing spectra taken subsequent to one another, with the associated errors due to micrometer mirror-drive backlash, thermal drift, and component drift, a mask was placed in front of the aluminized sample and switched from background to sample at each step of the moving mirror. Dual interferograms were therefore simultaneously obtained. The eight-sector design of the mask and aluminized sample also relaxed the condition of flatness required of the polished sample, since both sample and reference were equally affected.

The results obtained cover the reststrahlen region between 100 cm^{-1} (100 μm) and 340 cm^{-1} (29.4 μm). Below this, and up to 500 cm^{-1} (20 μm),

the results were supplemented with transmission measurements through thin, wedge-shaped, polished single crystals.

One can see in Fig. 13 that there is structure after the resonance, between 200 and 300 cm^{-1} (50 to 33 μm), and a distinct shoulder at 20 cm^{-1} (500 μm). In the past a multioscillator model has been used to fit reflection and transmission data [3]. However, there is only one oscillator, the TO mode, but it has an extremely frequency-dependent damping. The primary component of this damping is the coupling of the TO mode, through cubic anharmonicity, to two phonons. Energy and crystal momentum are conserved. This accounts for most of the structure in the damping. Three-phonon and higher-order processes also contribute strongly, depending on the temperature and the frequency, but they contain little structure, especially at room temperature. There is also some damping around the resonance due to the isotopic disorder of the chlorine ion, although this is extremely small at room temperature. All of the damping contributions mentioned can now be calculated with high accuracy, by use of the theories that have been developed, in conjunction with good lattice-dynamical data, which are obtained by inelastic neutron scattering (see Eldridge and Staal [5]). The agreement between experiment and theory is excellent. The similarities in the optical-phonon spectra of many alkali halides are discussed by Bilz [19].

Beyond the reststrahlen peak, in the "transparent" region (20–0.2 μm), the refractive index n has been determined by Li [9], who has fitted a multitude of experimental data [10–13] with a dispersion formula of the Sellmeier type, assuming $k = 0$. Temperature no doubt varied from 293 to 298 K for various laboratories. The formula for 293 K is

$$n^2 = 1.00055 + \frac{0.198\lambda^2}{\lambda^2 - (0.05)^2} + \frac{0.48398\lambda^2}{\lambda^2 - (0.1)^2} + \frac{0.38693\lambda^2}{\lambda^2 - (0.128)^2} + \frac{0.25998\lambda^2}{\lambda^2 - (0.158)^2} + \frac{0.08796\lambda^2}{\lambda^2 - (40.5)^2} + \frac{3.17064\lambda^2}{\lambda^2 - (60.98)^2} + \frac{0.30028\lambda^2}{\lambda^2 - (120.34)^2}. \quad (1)$$

The 15 adjustable parameters were first chosen as input parameters for least-square fitting based on previous fits of more restricted data. The first 5 terms constitute the dispersion due to all interband oscillators above the band gap. Note that Li [9] used three far-IR classical oscillators to account for dispersion well above the TO phonon frequency (60.98 μm). This choice is based on earlier work of Genzel *et al.* [3] and Geick [18], who measured and collected n and k data, interpreting them as indicating oscillators at these frequencies.

Li's [9] fit agrees with the experiment generally to a few units in the fourth decimal place ($\pm 0.03\%$). We have therefore used this fit in the table for the region from 0.2 to 20 μm as representative of experimental data. Typical measurements of n were done with a prism utilizing the angle of minimum deviation [10–13, 20, 21] with four to five decimal places quoted.

Interestingly, even present-day determinations of n for laser-window materials use this technique and achieve an accuracy of several parts in 10^6, quoting five decimal places [22]. Since the temperature dependence of n is -3.27×10^{-5} K^{-1} at 2000 cm^{-1}, one sees that control of room temperature (293 K) is important, since a variation of 1 K from laboratory to laboratory leads to changes of three units in the fifth decimal place [9].

The values of k between 550 cm^{-1} (18.2 μm) and 900 cm^{-1} (11.1 μm) in Table XIII were taken from Harrington *et al.* [6] and are the average transmission results through single crystals, taken at two laboratories with different spectrometers. Corrections for the low-temperature emittance of the sample were also employed. Sample temperature was 300 K. These agree at the 500-cm^{-1} end with the infrared results of Eldridge and Staal [5] and at the high-energy end with the laser-calorimetry results of Allen and Harrington [7]. These authors obtained values at five distinct laser wavelengths between 10.6 and 2.8 μm. Here the values of k are so small that the calorimetry method is essential. Up to 1000 cm^{-1} or so (i.e., above 10 μm), the absorption is multiphonon damping of the TO resonance as previously mentioned, and agreement between experiment and theory is good. Beyond 1000 cm^{-1}, the absorption is greater than predicted by the theory, and one must assume that much of it is extrinsic and due to impurity levels in the gap [7, 8]. Certainly, as materials are purified, this absorption decreases. One also has a sizable contribution from surface absorption, which can, however, be dynamically separated from the bulk absorption in the laser-calorimetric technique. Surface polish is still very important. The bulk values are quoted in Table XIII.

In the UV region near the band gap, there are two detailed measurements [14, 15]. Thin transmission samples at 298 K have been used to determine n and k in the Urbach tail [14], while in the exciton region (0.158 μm) and above the band gap, near-normal-incidence reflectance measurements of cleaved samples have been made followed by KK analysis. In Miyata and Tomiki [14] the reflectance at wavelengths shorter than 0.092 μm has been approximated by extrapolation to zero, while the contribution of the reststrahlen region at long wavelength has been added in performing the KK integrals. The experimentally determined values of k in the Urbach tail are fitted smoothly to the values of k above the band gap, since KK values determined below the gap are erratic. There is no reliable oscillator model for interband absorption to give the detailed values and structure shown in Fig. 13, although in Eq. (1) lossless oscillators are assumed above the fundamental band gap to account for the dispersion below the band gap.

The second set of data [15] was measured over a wider range from 0.048 to 0.247 μm (at a temperature of 300 K) and a method of KK analysis used that utilized a restricted data range (as justified in Roessler [23]). Far-infrared contributions were neglected. The two sets of data differ by as much as 20% at peaks and valleys in n and k. Perusal of the reflectance data

indicates that the reflectance of Miyata and Tomiki [14] was higher at peaks than the Roessler and Walker [15] data, although not always at the valleys. Each work quotes experimental uncertainties in R to $\pm 3\%$ in the range 0.2479–0.1033 μm with Roessler and Walker [15] giving $\pm 10\%$ for 0.1033–0.0476 μm. Such variations are enough to account for the differences in n and k. At low temperature adsorbed gases were a serious problem affecting R; this did not seem to be a problem at room temperature, although pressures of about 3×10^{-7} torr were reported in Miyata and Tomiki [14]. This suggests that monolayers of absorbed molecules such as water and hydrocarbons form within minutes after cleaving. Each work is presumably an absolute reflectance measurement involving comparison of the direct intensity with the reflected intensity with no additional mirror reflection involved. The use of refractive-index data in the transparent region by Miyata and Tomiki [14] as a secondary standard seems to be reasonable.

In the interband spectral region from 0.04 to 0.16 μm, the structure in k is intrinsic due to a series of excitions associated with various interband transitions [15, 24]. The Urbach tail at wavelengths slightly longer than 0.16 μm is due to intrinsic rather than impurity excitons, as temperature dependence shows [14]. Extrapolation of this tail to longer wavelength yields values of k much smaller than observed experimentally [8], which suggests absorption due to color centers or metal-ion impurities.

Since we have a classic case of two reflectance measurements differing slightly with the subsequent differences in n and k upon KK analysis, we elect to display both sets of data for this one material.

Above 25 eV there are few data giving any sort of absolute values for n and k. The available data have been reviewed by Haelbich *et al.* [25].

Relative absorption in the 25–72 eV region has been measured by Le Comte *et al.* [26] for samples at 80 K.

The room-temperature, $L_{2,3}$ absorption edge of Cl^- in NaCl has been measured on an absolute scale by Aita *et al.* [16] in the 200–210-eV region at 300 K and is tabulated. The samples were evaporated polycrystalline films on transparent substrate films. The source was an x-ray tube emitting continuous radiation. Brown *et al.* [27], using synchrotron radiation, have made measurements in a somewhat wider spectral region but only in arbitrary units.

The absorption in arbitrary units has been measured in the region 200–280 eV by Iguchi *et al.* [28]. The K absorption edge of Na^+ near 1076 eV has been measured by Rule [29], and the K absorption edge of Cl^- near 2825 eV has been measured by Sugiura [30].

REFERENCES

1. J. C. Owens, *Phys. Rev.* **181**, 1228 (1969).
2. R. Stolen and K. Dransfeld, *Phys. Rev.* **139A**, 1295 (1965).
3. L. Genzel, H. Happ, and R. Weber, *Z. Physik* **154**, 13 (1959).

4. E. M. Dianov and N. A. Irisova, *J. Appl. Spectros.* **5**, 187 (1966); E. M. Dianov and N. A. Irisova, *Zhur. Prikl. Spektrosk.* **5**, 251 (1966).
5. J. E. Eldridge and P. R. Staal, *Phys. Rev. B* **16**, 4608 (1977).
6. J. A. Harrington, C. J. Duthler, F. W. Patten, and M. Hass, *Solid State Commun.* **18**, 1043 (1976).
7. S. Allen and J. A. Harrington, *Appl. Opt.* **17**, 1679 (1978).
8. J. A. Harrington, B. L. Bobbs, M. Braunstein, R. K. Kim, R. Stearns, and R. Braunstein, *Appl. Opt.* **17**, 1541 (1978).
9. H. H. Li, *J. Phys. Chem. Refer. Data* **5**, 329 (1976).
10. H. Rubens and E. F. Nichols, *Ann. Phys. Chem.* **60**, 418 (1897).
11. H. Rubens and A. Trowbridge, *Ann. Phys. Chem.* **60**, 724 (1897).
12. F. Paschen, *Ann. Physik* **26**, 120 (1908).
13. F. F. Martens, *Ann. Physik* **6**, 603 (1901); F. F. Martens, *Ann. Physik* **8**, 459 (1902).
14. T. Miyata and T. Tomiki, *J. Phys. Soc. Jpn.* **24**, 1286 (1968); T. Miyata and T. Tomiki, *J. Phys. Soc. Jpn.* **22**, 209 (1967); T. Miyata and T. Tomiki, private communication (1981).
15. D. M. Roessler and W. C. Walker, *J. Opt. Soc. Am.* **58**, 279 (1968); D. M. Roessler and W. C. Walker, *Phys. Rev.* **166**, 599 (1968).
16. O. Aita, I. Nagakura, and T. Sagawa, *J. Phys. Soc. Jpn.* **30**, 1414 (1971).
17. R. G. Breckenridge, *J. Chem. Phys.* **16**, 959 (1948).
18. R. Geick, *Z. Physik* **166**, 122 (1962).
19. H. Bilz, *in* "Correlation Functions and Quasiparticle Interactions in Condensed Matter" (J. W. Halley ed.), p. 531. Plenum, New York, 1978.
20. S. P. Langley, *Ann. Astrophy. Obs. Smithsonian Inst.* **1**, 219 (1902).
21. W. W. Coblentz, *J. Opt. Soc. Am.* **4**, 443 (1920).
22. A. Feldman, D. Horowitz, R. M. Waxler, and M. J. Dodge, NBA Technical Note 933, Optical Materials Characterization. U.S. Department of Commerce, National Bureau of Standards, Washington, D.C., February 1979.
23. D. M. Roessler, *Brit. J. Appl. Phys.* **16**, 1119 (1965); D. M. Roessler, *Brit. J. Appl. Phys.* **17**, 1313 (1966).
24. T. Tomiki, T. Miyata, and H. Tsukamoto, *Z. Naturforsch*, **29**, 145 (1974).
25. R. P. Haelbich, M. Iwan, and E. E. Koch, "Physik Daten-Physics Data", p. 57. Fachinformation Zentrum, Karlsruhe, 1977.
26. A. Le Comte, A. Savary, M. Morlais, and S. Robin, *Opt. Commun.* **4**, 296 (1971).
27. F. C. Brown, C. Gähwiller, H. Fujita, A. B. Kunz, W. Scheifley, and N. Carrera, *Phys. Rev. B* **2**, 2126 (1970).
28. Y. Iguchi, T. Sagawa, S. Sato, M. Watanabe, H. Yamashita, A. Ejiri, M. Sasanuma, S. Nakai, M. Nakamura, S. Yamaguchi, Y. Nakai, and T. Oshio, *Solid State Commun.* **6**, 575 (1968).
29. K. C. Rule, *Phys. Rev.* **66**, 199 (1944).
30. C. Sugiura, *Phys. Rev. B* **6**, 170 (1972).

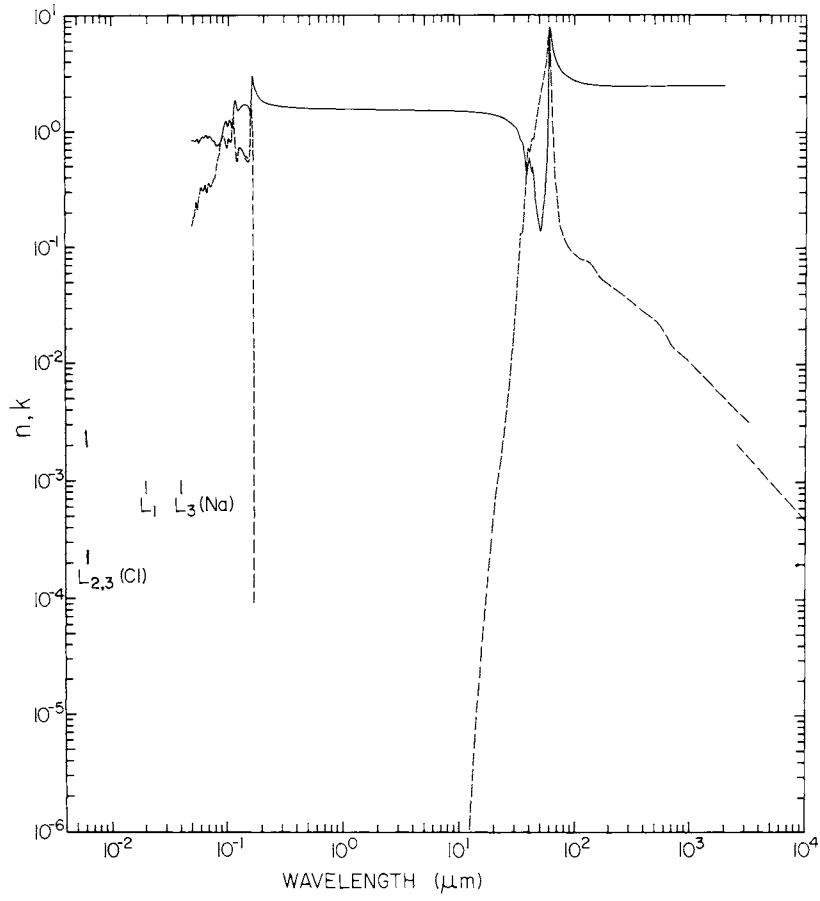

Fig. 13. Log–log plot of n (——) and k (----) versus wavelength in micrometers for sodium chloride.

TABLE XIII

Values of n and k for Sodium Chloride from Various References[a]

eV	cm^{-1}	Å	n	k	n	k
209.5		59.18	2.54×10^{-3} [16]			
209		59.32	2.56			
208.5		59.46	2.58			
208		59.61	2.55			
207.5		59.75	2.56			
207		59.89	2.59			
206.5		60.04	2.64			
206		60.19	2.62			

(*continued*)

TABLE XIII (*Continued*)

Sodium Chloride

eV	cm^{-1}	Å	n	k	n	k
205.75		60.26		2.57		
205.5		60.33		2.45		
205.25		60.41		2.48		
205		60.48		2.53		
204.75		60.55		2.60		
204.5		60.63		2.68		
204.25		60.70		2.65		
204		60.78		2.64		
203.75		60.85		2.52		
203.5		60.92		2.38		
203.25		61.00		2.14		
203		61.07		2.08		
202.75		61.15		2.04		
202.5		61.23		2.06		
202.25		61.30		2.24		
202		61.38		2.22		
201.5		61.53		1.96		
201		61.68		1.91		
200.5		61.84		1.91		
200		61.99		1.92		

eV	cm^{-1}	μm	n	k	n	k
26.0		0.04769	0.83 [15]	0.15 [15]		
25.6		0.04842	0.82	0.17		
25.4		0.04880	0.83	0.17		
25.2		0.04919	0.83	0.18		
25.0		0.04959	0.83	0.18		
24.9		0.04979	0.82	0.18		
24.7		0.05019	0.82	0.18		
24.3		0.05101	0.81	0.21		
24.1		0.05144	0.81	0.22		
24.0		0.05166	0.82	0.23		
23.9		0.05187	0.82	0.23		
23.8		0.05209	0.83	0.24		
23.4		0.05298	0.85	0.23		
23.3		0.05320	0.85	0.22		
23.2		0.05343	0.85	0.21		
23.1		0.05366	0.83	0.21		
23.0		0.05391	0.82	0.21		
22.8		0.05437	0.80	0.23		
22.6		0.05485	0.79	0.26		
22.5		0.05510	0.80	0.27		
22.4		0.05534	0.80	0.28		
22.3		0.05559	0.81	0.29		
22.2		0.05584	0.82	0.30		
22.0		0.05636	0.83	0.31		

TABLE XIII (*Continued*)

Sodium Chloride

eV	cm^{-1}	μm	n	k	n	k
21.9		0.05661	0.84	0.32		
21.8		0.05687	0.85	0.32		
21.5		0.05766	0.87	0.32		
21.1		0.05875	0.88	0.31		
20.9		0.05931	0.88	0.30		
20.8		0.05960	0.88	0.30		
20.6		0.06018	0.88	0.30		
20.5		0.06048	0.87	0.31		
20.2		0.06137	0.87	0.33		
20.1		0.06168	0.88	0.33		
20.0		0.06199	0.88	0.34		
19.9		0.06230	0.89	0.34		
19.8		0.06261	0.91	0.34		
19.6		0.06325	0.92	0.32		
19.5		0.06358	0.92	0.31		
19.4		0.06390	0.91	0.30		
19.3		0.06423	0.90	0.29		
19.2		0.06457	0.88	0.29		
19.1		0.06490	0.87	0.30		
18.9		0.06559	0.86	0.33		
18.8		0.06594	0.86	0.34		
18.7		0.06629	0.87	0.35		
18.6		0.06666	0.88	0.35		
18.5		0.06702	0.89	0.35		
18.4		0.06737	0.90	0.35		
18.3		0.06774	0.90	0.34		
18.2		0.06811	0.90	0.33		
18.0		0.06888	0.89	0.33		
17.5		0.07085	0.85	0.33		
17.3		0.07166	0.84	0.34		
17.1		0.07250	0.82	0.36		
17.0		0.07293	0.82	0.37		
16.9		0.07335	0.82	0.38		
16.8		0.07379	0.82	0.38		
16.7		0.07423	0.82	0.38		
16.5		0.07514	0.80	0.38		
16.4		0.07559	0.79	0.39		
16.3		0.07601	0.77	0.40		
16.2		0.07652	0.74	0.43		
16.1		0.07700	0.74	0.45		
15.9		0.07797	0.74	0.49		
15.7		0.07896	0.74	0.53		
15.5		0.07999	0.75	0.57		
15.4		0.08050	0.76	0.59		
15.3		0.08103	0.76	0.60		
15.2		0.08156	0.77	0.62		

(*continued*)

TABLE XIII (*Continued*)

Sodium Chloride

eV	cm^{-1}	μm	n	k	n	k
14.9		0.08320	0.77	0.67		
14.8		0.08376	0.76	0.71		
14.7		0.08433	0.78	0.75		
14.65		0.08460	0.79	0.77		
14.6		0.08491	0.81	0.78		
14.55		0.08520	0.82	0.79		
14.5		0.08551	0.84	0.80		
14.45		0.08570	0.85	0.81		
14.4		0.08609	0.86	0.82		
14.3		0.08669	0.88	0.84		
14.25		0.08700	0.89	0.85		
14.2		0.08730	0.91	0.86		
14.1		0.08792	0.94	0.88		
14.0		0.08856	0.98	0.89		
13.9		0.08919	1.02	0.90		
13.8		0.08983	1.06	0.90		
13.7		0.09049	1.10	0.89		
13.5		0.09184	1.16	0.85		
13.40		0.09255			1.096 [14]	0.916 [14]
13.30		0.09322	1.20 [15]	0.81 [15]		
13.20		0.09390			1.197	0.868
13.1		0.09464	1.21	0.74		
13.05		0.09500			1.169	0.759
13.0		0.09537	1.19	0.71		
12.95		0.09574	1.17	0.70		
12.93		0.09587			1.104	0.765
12.90		0.09611	1.16	0.70		
12.88		0.09626			1.088	0.794
12.85		0.09648	1.14	0.71		
12.8		0.09686	1.12	0.71		
12.76		0.09712			1.083	0.834
12.7		0.09762	1.10	0.75		
12.65		0.09802			1.082	0.896
12.60		0.09840	1.10	0.81		
12.55		0.09879	1.14	0.83		
12.51		0.09907			1.119	0.967
12.45		0.09958	1.15	0.84		
12.40		0.09998	1.17	0.85		
12.36		0.1003			1.197	1.02
12.35		0.1004	1.19	0.85		
12.31		0.1007			1.230	1.02
12.30		0.1008	1.21	0.85		
12.20		0.1016	1.24	0.83	1.304	0.999
12.10		0.1025	1.24	0.79		
12.09		0.1025			1.320	0.940
12.0		0.1033	1.22	0.79		
11.99		0.1034			1.290	0.921

TABLE XIII (*Continued*)

Sodium Chloride

eV	cm^{-1}	μm	*n*	*k*	*n*	*k*
11.92		0.1040			1.272	0.931
11.90		0.1042	1.20	0.79		
11.84		0.1047			1.234	0.937
11.80		0.1051	1.16	0.80		
11.78		0.1052			1.209	0.987
11.71		0.1058			1.204	1.05
11.70		0.1060	1.12	0.86		
11.65		0.1064	1.10	0.89		
11.64		0.1065			1.219	1.14
11.60		0.1069	1.07	0.96		
11.58		0.1071			1.255	1.205
11.55		0.1073	1.09	1.06		
11.51		0.1077			1.338	1.28
11.50		0.1078	1.15	1.14		
11.46		0.1082			1.422	1.34
11.45		0.1083	1.24	1.19		
11.43		0.1085			1.491	1.36
11.40		0.1088	1.32	1.21		
11.38		0.1090			1.588	1.35
11.35		0.1092	1.40	1.23		
11.32		0.1095			1.682	1.34
11.30		0.1097	1.49	1.22		
11.25		0.1102	1.57	1.19	1.809	1.29
11.23		0.1104			1.864	1.27
11.20		0.1107	1.64	1.15	1.918	1.21
11.10		0.1117	1.75	1.04		
11.08		0.1119			2.002	1.02
11.03		0.1124			2.003	0.938
11.00		0.1127	1.82	0.93		
10.94		0.1133			1.990	0.834
10.90		0.1137	1.82	0.78		
10.82		0.1146			1.975	0.706
10.77		0.1151			1.947	0.650
10.68		0.1161			1.873	0.569
10.63		0.1166			1.821	0.543
10.60		0.1170	1.67	0.56		
10.55		0.1175			1.730	0.546
10.50		0.1181	1.58	0.53	1.707	0.563
10.45		0.1186	1.54	0.54		
10.42		0.1189			1.654	0.575
10.40		0.1192	1.51	0.56		
10.35		0.1198	1.49	0.59	1.637	0.623
10.29		0.1205			1.637	0.645
10.20		0.1216			1.640	0.673
10.15		0.1221	1.50	0.70		
10.13		0.1224			1.664	0.694

(*continued*)

TABLE XIII (*Continued*)

Sodium Chloride

eV	cm^{-1}	μm	n	k	n	k
10.10		0.1227	1.52	0.71		
10.08		0.1230			1.673	0.687
10.06		0.1232	1.54	0.71		
10.00		0.1240	1.55	0.71	1.678	0.697
9.908		0.1251			1.711	0.715
9.825		0.1262			1.742	0.700
9.80		0.1265	1.59	0.70		
9.757		0.1271			1.751	0.681
9.662		0.1283			1.764	0.670
9.60		0.1291	1.63	0.68		
9.586		0.1293			1.770	0.658
9.557		0.1297			1.779	0.655
9.539		0.1300			1.776	0.647
9.444		0.1313			1.787	0.623
9.40		0.1319	1.65	0.65		
9.356		0.1325			1.780	0.617
9.214		0.1345			1.792	0.597
9.20		0.1348	1.66	0.63		
9.093		0.1363			1.791	0.585
9.00		0.1378	1.67	0.60		
8.947		0.1386			1.804	0.564
8.90		0.1393	1.66	0.59		
8.894		0.1394			1.792	0.549
8.840		0.1402			1.789	0.552
8.80		0.1409	1.66	0.60		
8.775		0.1413			1.789	0.546
8.75		0.1417	1.66	0.59		
8.70		0.1425	1.66	0.59		
8.652		0.1433			1.776	0.529
8.60		0.1442	1.65	0.58	1.765	0.521
8.550		0.1450			1.749	0.534
8.50		0.1459	1.64	0.58		
8.490		0.1460			1.745	0.539
8.45		0.1467	1.64	0.58	1.746	0.539
8.409		0.1474			1.735	0.531
8.40		0.1476	1.63	0.58		
8.367		0.1482			1.719	0.531
8.35		0.1485	1.61	0.57		
8.325		0.1489			1.695	0.534
8.30		0.1494	1.59	0.58		
8.290		0.1496			1.682	0.542
8.267		0.1500			1.665	0.542
8.25		0.1503	1.55	0.58		
8.238		0.1505			1.638	0.550
8.20		0.1512	1.50	0.60	1.604	0.567
8.169		0.1517			1.547	0.598
8.15		0.1521	1.44	0.65		

TABLE XIII (*Continued*)

Sodium Chloride

eV	cm^{-1}	μm	n	k	n	k
8.127		0.1525			1.483	0.691
8.10		0.1531	1.38	0.74		
8.091		0.1532			1.461	0.784
8.08		0.1534	1.36	0.80	1.451	0.829
8.062		0.1538			1.446	0.878
8.05		0.1540	1.33	0.89		
8.040		0.1542			1.470	0.974
8.03		0.1544	1.34	0.99		
8.024		0.1545			1.490	1.01
8.00		0.1550	1.38	1.10		
7.98		0.1554	1.42	1.18	1.550	1.20
7.95		0.1560	1.51	1.29		
7.93		0.1563	1.60	1.36	1.727	1.40
7.918		0.1566			1.809	1.45
7.90		0.1569	1.74	1.43	1.929	1.51
7.885		0.1572			2.025	1.53
7.88		0.1573	1.84	1.46		
7.859		0.1577			2.206	1.52
7.85		0.1579	2.00	1.49		
7.83		0.1583	2.12	1.49		
7.802		0.1589			2.563	1.45
7.78		0.1594	2.42	1.41	2.695	1.39
7.767		0.1596			2.778	1.37
7.75		0.1600	2.59	1.33	2.911	1.31
7.738		0.1602			3.019	1.21
7.73		0.1604	2.72	1.26	3.078	1.12
7.710		0.1608			3.161	0.991
7.70		0.1610	2.91	1.05		
7.684		0.1613			3.252	0.737
7.65		0.1621	2.90	0.59	3.180	0.383
7.613		0.1628			3.019	0.151
7.60		0.1631	2.69		2.974	0.126
7.588		0.1634			2.902	8.67×10^{-2}
7.567		0.1638			2.827	2.76×10^{-2}
7.55		0.1642	2.55			
7.50		0.1653	2.46		2.636	
7.45		0.1664	2.40			
7.419		0.1671				5.67×10^{-4}
7.40		0.1675	2.34			
7.353		0.1686				1.11×10^{-7}
7.30		0.1698	2.25			
7.276		0.1704				1.37×10^{-5}
7.27		0.1704				1.37×10^{-5}
7.205		0.1721				2.02×10^{-6}
7.20		0.1722	2.17			2.02×10^{-6}
7.112		0.1743			2.081	4.43×10^{-7}

(*continued*)

TABLE XIII (*Continued*)

Sodium Chloride

eV	cm^{-1}	μm	n	k	n	k
7.00		0.1771	2.03			
6.996		0.1772				1.83
6.75		0.1837	1.91			
6.50		0.1907	1.84			
6.23		0.1990			1.792	
6.199	50,000	0.20	1.7899 [9]			
6.00	48,390	0.2066	1.75 [15]			
5.904	47,620	0.21	1.74676 [9]			
5.636	45,450	0.22	1.71499			
5.50	44,360	0.2254	1.69 [15]			
5.391	43,480	0.23	1.69056 [9]			
5.166	41,670	0.24	1.67118			
5.00	40,330	0.2480	1.65 [15]			
4.959	40,000	0.25	1.65537 [9]			
4.769	38,460	0.26	1.64227			
4.592	37,040	0.27	1.63124			
4.428	35,710	0.28	1.62184			
4.275	34,480	0.29	1.61374			
4.133	33,330	0.30	1.60669			
3.875	31,250	0.32	1.59506			
3.647	29,410	0.34	1.58590			
3.531	28,480	0.3511		6.4×10^{-10} [8]		
3.444	27,780	0.36	1.57852			
3.408	27,490	0.3638		4.3		
3.263	26,320	0.38	1.57248			
3.100	25,000	0.40	1.56746			
2.952	23,810	0.42	1.56324			
2.818	22,730	0.44	1.55965			
2.708	21,840	0.4579		2.9		
2.695	21,740	0.46	1.55657			
2.583	20,830	0.48	1.55390			
2.541	20,490	0.4880		1.1×10^{-10}		
2.480	20,000	0.50	1.55157			
2.410	19,440	0.5145		4.9×10^{-11}		
2.384	19,230	0.52	1.54953			
2.296	18,520	0.54	1.54773			
2.214	17,860	0.56	1.54613			
2.138	17,240	0.58	1.54471			
2.066	16,670	0.60	1.54343			
2.000	16,130	0.62	1.54228			
1.937	15,630	0.64	1.54124			
1.879	15,150	0.66	1.54030			
1.823	14,710	0.68	1.53944			
1.771	14,290	0.70	1.53865			
1.722	13,890	0.72	1.53794			
1.675	13,510	0.74	1.53728			
1.631	13,160	0.76	1.53667			

TABLE XIII (*Continued*)

Sodium Chloride

eV	cm^{-1}	μm	n	k	n	k
1.590	12,820	0.78	1.53611			
1.550	12,500	0.80	1.53560			
1.512	12,200	0.82	1.53512			
1.476	11,900	0.84	1.53467			
1.442	11,630	0.86	1.53426			
1.409	11,360	0.88	1.53387			
1.378	11,110	0.90	1.53351			
1.348	10,870	0.92	1.53317			
1.319	10,640	0.94	1.53285			
1.292	10,420	0.96	1.53255			
1.265	10,200	0.98	1.53227			
1.240	10,000	1.0	1.53200			
1.127	9,091	1.1	1.53088			
1.033	8,333	1.2	1.53000			
0.9537	7,692	1.3	1.52930			
0.8856	7,143	1.4	1.52873			
0.8266	6,667	1.5	1.52824			
0.7749	6,250	1.6	1.52782			
0.7293	5,882	1.7	1.52745			
0.6888	5,556	1.8	1.52712			
0.6526	5,263	1.9	1.52682			
0.6199	5,000	2.0	1.52654			
0.5904	4,762	2.1	1.52627			
0.5636	4,545	2.2	1.52602			
0.5391	4,348	2.3	1.52578			
0.5166	4,167	2.4	1.52554			
0.4959	4,000	2.5	1.52531			
0.4769	3,846	2.6	1.52509			
0.4592	3,704	2.7	1.52486			
0.4428	3,571	2.8	1.52463	$(1.3 \pm 0.1) \times 10^{-9}$ [7]		
0.4275	3,448	2.9	1.52441			
0.4133	3,333	3.0	1.52418			
0.4000	3,226	3.1	1.52395			
0.3875	3,125	3.2	1.52372			
0.3757	3,030	3.3	1.52349			
0.3647	2,941	3.4	1.52325			
0.3542	2,857	3.5	1.52301			
0.3444	2,778	3.6	1.52277			
0.3351	2,703	3.7	1.52252			
0.3263	2,632	3.8	1.52226	$(1.8 \pm 0.2) \times 10^{-9}$		
0.3179	2,564	3.9	1.52201			
0.3100	2,500	4.0	1.52174			
0.3024	2,439	4.1	1.52148			
0.2952	2,381	4.2	1.52121			
0.2883	2,326	4.3	1.52093			
0.2818	2,273	4.4	1.52065			

(*continued*)

TABLE XIII (*Continued*)

Sodium Chloride

eV	cm^{-1}	μm	n	k	n	k
0.2755	2,222	4.5	1.52036			
0.2695	2,174	4.6	1.52006			
0.2638	2,128	4.7	1.51977			
0.2583	2,083	4.8	1.51946			
0.2530	2,041	4.9	1.51915			
0.2480	2,000	5.0	1.51883			
0.2431	1,961	5.1	1.51851			
0.2384	1,923	5.2	1.51818			
0.2339	1,887	5.3	1.51785	$(1.7 \pm 0.5) \times 10^{-9}$		
0.2296	1,852	5.4	1.51751			
0.2254	1,818	5.5	1.51716			
0.2214	1,786	5.6	1.51681			
0.2175	1,754	5.7	1.51645			
0.2138	1,724	5.8	1.51609			
0.2101	1,695	5.9	1.51572			
0.2066	1,667	6.0	1.51534			
0.2000	1,613	6.2	1.51457			
0.1937	1,563	6.4	1.51377			
0.1879	1,515	6.6	1.51294			
0.1823	1,471	6.8	1.51209			
0.1771	1,429	7.0	1.51122			
0.1722	1,389	7.2	1.51031			
0.1675	1,351	7.4	1.50938			
0.1631	1,316	7.6	1.50842			
0.1590	1,282	7.8	1.50744			
0.1550	1,250	8.0	1.50643			
0.1512	1,220	8.2	1.50539			
0.1476	1,190	8.4	1.50432			
0.1442	1,163	8.6	1.50322			
0.1409	1,136	8.8	1.50210			
0.1378	1,111	9.0	1.50094			
0.1348	1,087	9.2	1.49996			
0.1337	1,079	9.27		$(2 \pm 1.5) \times 10^{-8}$		
0.1319	1,064	9.4	1.49855			
0.1292	1,042	9.6	1.49731			
0.1265	1,020	9.8	1.49604			
0.1240	1,000	10.0	1.49473			
0.1216	980.4	10.2	1.49340			
0.1192	961.5	10.4	1.49204			
0.1170	943.4	10.6	1.49065	$(8 \pm 0.8) \times 10^{-8}$		
0.1148	925.9	10.8	1.48922			
0.1127	909.1	11.0	1.48776			
0.1116	900.0	11.11		1.5×10^{-7} [6]		
0.1107	892.9	11.2	1.48628			
0.1088	877.2	11.4	1.48476			
0.1069	862.1	11.6	1.48320			
0.1054	850.0	11.76		4.5×10^{-7}		

TABLE XIII (*Continued*)

Sodium Chloride

eV	cm^{-1}	μm	n	k	n	k
0.1051	847.5	11.8	1.48162			
0.1033	833.3	12.0	1.48000			
0.1016	819.7	12.2	1.47834			
0.09999	806.5	12.4	1.47665			
0.09919	800.0	12.50		1.4×10^{-6}		
0.09840	793.7	12.6	1.47493			
0.09686	781.3	12.8	1.47318			
0.09537	769.2	13.0	1.47138			
0.09393	757.6	13.2	1.46956			
0.09299	750.0	13.33		3.8×10^{-6}		
0.09252	746.3	13.4	1.46769			
0.09116	735.3	13.6	1.46579			
0.08984	724.6	13.8	1.46385			
0.08856	714.3	14.0	1.46188			
0.08731	704.2	14.2	1.45986			
0.08679	700.0	14.29		1.1×10^{-5}		
0.08670	699.3	14.3				
0.08610	694.4	14.4	1.45781			
0.08492	684.9	14.6	1.45572			
0.08377	675.7	14.8	1.45359			
0.08266	666.7	15.0	1.4514			
0.08157	657.9	15.2	1.4492			
0.08059	650.0	15.38		3.6×10^{-5}		
0.08051	649.4	15.4	1.4469			
0.07948	641.0	15.6	1.4446			
0.07847	632.9	15.8	1.4423			
0.07749	625.0	16.0	1.4399			
0.07653	617.3	16.2	1.4375			
0.07560	609.8	16.4	1.4351			
0.07469	602.4	16.6	1.4325			
0.07439	600.0	16.67		8.6×10^{-5}		
0.07380	595.2	16.8	1.4300			
0.07293	588.2	17.0	1.4274			
0.07208	581.4	17.2	1.4247			
0.07125	574.7	17.4	1.4220			
0.07044	568.2	17.6	1.4193			
0.06965	561.8	17.8	1.41649			
0.06888	555.5	18.0	1.41364			
0.06819	550.0	18.18		2.2×10^{-4}		
0.06812	549.4	18.2	1.41074			
0.06738	543.5	18.4	1.40779			
0.06666	537.6	18.6	1.40478			
0.06595	531.9	18.8	1.40173			
0.06526	526.3	19.0	1.39861			
0.06457	520.8	19.2	1.39544			
0.06391	515.5	19.4	1.39222			

(*continued*)

TABLE XIII (*Continued*)

Sodium Chloride

eV	cm^{-1}	μm	n	k	n	k
0.06326	510.2	19.6	1.38893			
0.06262	505.0	19.8	1.38559			
0.06199	500.0	20.0	1.3822			
			1.41 [5]	6.2×10^{-4} [5]		
0.05951	480	20.83	1.38	8.7×10^{-4}		
0.05703	460	21.74	1.35	1.1×10^{-3}		
0.05455	440	22.73	1.33	1.5		
0.05207	420	23.81	1.32	2.3		
0.04959	400	25.00	1.27	3.5		
0.04711	380	26.32	1.23	5.3		
0.04463	360	27.78	1.17	9.8		
0.04215	340	29.41	1.12	1.7×10^{-2}		
0.03967	320	31.25	1.01	4.5×10^{-2}		
0.03720	300	33.33	0.85	0.11		
0.03658	295	33.90	0.83	0.13		
0.03596	290	34.48	0.80	0.13		
0.03534	285	35.09	0.78	0.14		
0.03472	280	35.71	0.69	0.17		
0.03410	275	36.36	0.59	0.22		
0.03348	270	37.04	0.49	0.31		
0.03286	265	37.74	0.42	0.50		
0.03224	260	38.46	0.45	0.66		
0.03162	255	39.22	0.57	0.71		
0.03124	252	39.68	0.59	0.67		
0.03100	250	40.00	0.58	0.66		
0.03038	245	40.82	0.51	0.69		
0.02976	240	41.67	0.46	0.81		
0.02938	237	42.19	0.44	0.87		
0.02914	235	42.55	0.46	0.87		
0.02889	233	42.92	0.49	0.87		
0.02852	230	43.48	0.43	0.87		
0.02790	225	44.44	0.30	1.00		
0.02728	220	45.45	0.25	1.15		
0.02666	215	46.51	0.20	1.36		
0.02604	210	47.62	0.18	1.56		
0.02542	205	48.78	0.16	1.74		
0.02480	200	50.00	0.14	1.99		
0.02418	195	51.28	0.15	2.29		
0.02356	190	52.63	0.19	2.63		
0.02294	185	54.05	0.24	3.02		
0.02232	180	55.56	0.35	3.72		
0.02170	175	57.14	0.59	4.57		
0.02108	170	58.82	1.35	6.03		
0.02046	165	60.61	6.17	7.41		
0.02021	163	61.35	7.76	6.03		
0.01984	160	62.50	6.92	2.14		
0.01922	155	64.52	5.50	0.87		

TABLE XIII (*Continued*)

Sodium Chloride

eV	cm^{-1}	μm	n	k	n	k
0.01860	150	66.67	4.52	0.380		
0.01798	145	68.97	4.07	0.309		
0.01736	140	71.43	3.72	0.219		
0.01674	135	74.07	3.47	0.145		
0.01612	130	76.92	3.31	0.135		
0.01488	120	83.33	3.02	0.110		
0.01364	110	90.91	2.85	0.095		
0.01240	100	100.0	2.74	0.087		
0.01116	90	111.1	2.63	0.078		
0.009919	80	125.0	2.57	0.077		
0.008679	70	142.9	2.52	0.068		
0.007439	60	166.7	2.48	0.055		
0.006199	50	200.0	2.45	0.047		
0.005579	45	222.2	2.44	0.045		
0.004959	40	250.0	2.44	0.041		
0.004339	35	285.7	2.43	0.036		
0.004132	33.3	300		0.030 [2]		
0.003720	30	333.3	2.43	0.032 [5]		
0.003100	25	400.0	2.43	0.027		
0.002480	20	500.0	2.43	0.024		
				0.024 [2]		
0.001860	15	666.7	2.43	0.014 [5]		
0.001240	10	1000	2.43	0.006 [5]		
				0.01 [3]		
0.001215	9.8	1020		8.1×10^{-3} [2]		
0.001127	9.091	1100		9.5 [3]		
0.001033	8.333	1200		8.8		
0.0008856	7.143	1400		6.5		
0.0007872	6.349	1575		5.76		
0.0006888	5.556	1800		5.4		
0.0006199	5.000	2000	2.43 [4]			
0.0005904	4.762	2100		4.3		
0.0004959	4.000	2500		4.4		
0.0004797	3.869	2584	2.43 [1]	2.1 [1]		
0.0003875	3.125	3200		3.3×10^{-3} [3]		
0.0001464	1.181	8469	2.43	5.8×10^{-4} [1]		
0.00004053	0.3269	30590	2.43	2.5		

[a] Tabulation of n and k as a function of photon energy (electron volts), wave number (inverse centimeters), and wavelength (micrometers). References for the data are given in brackets and apply to all data below the brackets until a new reference appears; k is often very small and exponents often are given for numbers smaller than 10^{-2}. The power of 10 applies for all data below the exponent until a new exponent appears or the exponent becomes 10^{-1}, whereupon the number is given in decimal form.

Titanium Dioxide (TiO_2) (Rutile)

M. W. RIBARSKY
School of Physics
Georgia Institute of Technology
Atlanta, Georgia

Titanium dioxide exists in three crystal structures: rutile, brookite, and anatase. The work reported here is all on rutile (tetragonal) single crystals. Rutile is easily reduced, and the crystal will have some oxygen vacancies or titanium interstitials. Since the structure cannot be treated as a slightly perturbed cubic crystal, there are pronounced polarization effects. It is therefore necessary to measure the optical constants for $E \| c$ axis and $E \perp c$ axis.

Compiled in Table XIV and plotted in Fig. 14 are room-temperature values of n and k for wavelengths between 36 and 0.11 μm.

There are evidently very few reports of optical constants for single-crystal TiO_2 in the ultraviolet above 20 eV. In the far infrared, Smith and Loewenstein [1] measured n_o ($\perp$) at 1.5 K from channeled spectra in the range 400–100 μm. Meriakri and Ushatkin [2] measured n at 1030 μm at an unspecified room temperature. The technique involved the use of a millimeter-wave source whose frequency could be varied periodically over a short range and a Michelson interferometer in which the path length could be varied. A beating fringe pattern was obtained from which an average n could be obtained. Parker [3] measured the susceptability of oriented rutile in a capacitor at low frequency and determined dc values of $n_{\|}^2 = 170$ and $n_{\perp}^2 = 86$ at 300 K.

The infrared results of 36.4 to 11.1 μm are from Gervais and Piriou [4]; the results in the near infrared and visible 1.5 to 0.425 μm are from Devore [5], and overlapping sets of results for the visible to ultraviolet regions are from Cardona and Harbeke [6] (1.2–0.11 μm) and from Vos and Krusemeyer [7] (0.413–0.207 μm). Cardona and Harbeke [6] have also taken the reflectivity from 0.11 to 0.056 μm with unpolarized light.

All the results were obtained from power reflectivity measurements. In the case of Cardona and Harbeke [6] and Vos and Krusemeyer [7] a Kramers–

Copyright © 1985 by Academic Press, Inc.
All rights of reproduction in any form reserved.
ISBN 0-12-544420-6

Kronig (KK) analysis was used to obtain the optical constants. The uncertainty due to truncation of the reflectivity to a finite frequency range was somewhat relieved by extrapolation to previous measurements at frequencies below the measured region. Above the measured region, a standard power-law fit to the reflectivity [7] was used, or a fit of the expansion coefficients in an approximate expression for the phase of the complex reflectivity was made [6]. Neither procedure took account of the higher interband transitions in any direct way. Such uncertainties introduce errors in the magnitudes of the optical constants and in the positions of peaks and other features [8]. These errors are more pronounced near the boundaries of the spectrum.

Most of the spectra were derived from reflectivity measurements. All the experiments used single crystals with the orientation of the c axis determined by x-ray diffraction. The infrared reflectivity spectra were taken with a single-beam monochromator on optically polished rutile crystals [4]. Errors were of the order $\Delta R/R = 2\%$ and $\Delta E = 2$–$5\ \mathrm{cm}^{-1}$. The very near-infrared refractive-index results [5] were taken directly from the measured amount of refraction of light from a mercury arc by a single-crystal rutile prism. Cardona and Harbeke [6] measured the reflectivity spectra below 6 eV with a grating spectrometer and used a vacuum-UV spectrometer at higher energies. Vos and Krusemeyer [7] took the absolute specular reflectance with a relative uncertainty of less than 0.5%. They cut their samples from flame-fusion-grown boules of rutile that were polished and etched in NaOH.

The optical constants in the infrared were tabulated by using the following four-parameter semiquantum model [4] for the dielectric function

$$\tilde{\varepsilon} = \varepsilon_1 \pm i\varepsilon_2 = \varepsilon_\infty \prod_j \frac{\Omega_{j\mathrm{LO}}^2 - \omega^2 \pm i\gamma_{j\mathrm{LO}}\omega}{\Omega_{j\mathrm{TO}}^2 - \omega^2 \mp i\gamma_{j\mathrm{TO}}\omega}. \tag{1}$$

Each TO (LO) phonon mode is assumed to be an oscillator with frequency Ω_{TO} (Ω_{LO}) and damping γ_{TO} (γ_{LO}). In general, the parameters are frequency and time dependent, but tests of Eq. (1) for realistic cases have shown that the parameters vary slowly with frequency even for wide reflectivity bands [9]. The temperature dependences of γ_{TO} and γ_{LO} for $E \| c$ indicate large anharmonicities due perhaps to sixth-order coupling at higher temperatures. The model dielectric function was used in the expression for the power reflectivity, and the resulting fit to the reflectivity data was within the experimental error. The results tabulated here use this model with the parameters given in Tables I and II of Gervais and Piriou [4].

The data show that there are only one TO mode and one LO mode in the A_{2u} ($E \| c$) spectrum but that there is also a secondary mode at $592\ \mathrm{cm}^{-1}$. This could be a two-phonon peak since high phonon densities exist at energies about half the secondary oscillator energy [10]. However, it could also be a forbidden mode, such as the A_{1g} mode, activated by substitutional impurities

[4]. The E_u ($E \perp c$) spectrum has three TO and LO modes and a secondary peak near the same energy as the A_{2u} peak.

There are apparently no recent measurements of the optical constants in the range 1.5–11.1 μm. However, in 1921 Liebisch and Rubens [11] measured the index of refraction of a rutile prism in this range. For the region in which their measurements overlap those of Devore [5] (0.7–1.5 μm), Liebisch and Rubens's [11] results are in agreement with Devore's [5] for $E \perp c$. However, for $E \parallel c$ the refractive-index curve of Liebisch and Rubens [11] has the same shape as Devore's [5] but is offset by approximately -0.1. A similar offset for $E \parallel c$ exists between the curves of Devore [5] and Cronemeyer [12] in the range 0.4–0.6 μm. However, Devore's [5] values are quite close to the original measurements of Baerwald [13]. There are no measurements of the extinction coefficient in the range 0.45–1.5 μm, but it is presumably quite small and structureless.

Devore has fit his refractive-index results with the equations

$$\begin{aligned} n_\perp^2 &= 5.913 + 2.441 \times 10^7/(\lambda^2 - 0.803 \times 10^7), \\ n_\parallel^2 &= 7.197 + 3.322 \times 10^7/(\lambda^2 - 0.843 \times 10^7), \end{aligned} \tag{2}$$

where λ is in angstroms. These equations give results within 0.001–0.003 of the experimental results, and they are used here to obtain the tabulated results from 0.425 to 1.5 μm. At 0.405 μm Cronemeyer [12] gives $k = 0.086$.

The data of Cardona and Harbeke [6] and of Vos and Krusemeyer [7] are significantly different in the region of overlap (0.21–0.41 μm). Vos and Krusemeyer [7] ascertain that bulk pretreatment of their samples did not affect the reflectivity and that there were no errors in their measuring procedure. Gupta and Ravindra [14] point out that the values of ε_∞ obtained by integrating ε_2 over the spectral range are in better agreement with experiment for the results of Cardona and Harbeke [6] than for those of Vos and Krusemeyer [7]. However, the Vos and Krusemeyer [7] results are over a more limited energy range and the truncated KK analysis can introduce shifts in the optical-constant spectra [8] that would affect the evaluation of ε_∞. We have therefore elected to present both the results of Cardona and Harbeke [6] and of Vos and Krusemeyer [7].

There is a rapid rise in all the spectra above the fundamental edge at 3.05 eV (0.405 μm). Comparison with a semiempirical band structure [15] indicates that the rise is due to nearly parallel conduction and valence bands. The calculations also show that the structures in ε_2 for both directions of polarization are due to transitions to two groupings of conduction bands, one from 3 to 6 eV and the other from 6 to 9 eV above the valence bands. The calculated ε_2 for $E \perp c$ is not as close to experiment as for $E \parallel c$ [15]. The shift to lower energy of the main peak in the experimental spectrum may indicate the presence of excitonic effects.

REFERENCES

1. D. R. Smith and E. V. Loewenstein, *Appl. Opt.* **15**, 859 (1976).
2. V. V. Meriakri and E. F. Ushatkin, *Prib. Tekh. Eksp.* **16**, 143 (1973); V. V. Meriakri and E. F. Ushatkin, *Instrum. Exp. Tech.* **16**, 498 (1973).
3. R. A. Parker, *Phys. Rev.* **124**, 1719 (1961).
4. F. Gervais and B. Piriou, *Phys. Rev. B* **10**, 1642 (1974).
5. J. R. Devore, *J. Opt. Soc. Am.* **41**, 416 (1951).
6. M. Cardona and G. Harbeke, *Phys. Rev.* **137A**, 1467 (1965).
7. K. Vos and H. J. Krusemeyer, *J. Phys. C* **10**, 3893 (1977).
8. W. E. Wall, M. W. Ribarsky, and J. R. Stevenson, *J. Appl. Phys.* **51**, 661 (1980).
9. F. Gervais and B. Piriou, *J. Phys. C* **7**, 2374 (1974).
10. G. A. Samara and P. S. Peercy, *Phys. Rev. B* **7**, 1131 (1973).
11. T. Liebisch and H. Rubens, *Sitzungsber. Preuss. Akad. Wiss. Phys.-Math. Kl.* 211 (1921).
12. D. C. Cronemeyer, *Phys. Rev.* **87**, 876 (1952).
13. C. Baerwald, *Z. Krist.* **7**, 167 (1883).
14. V. P. Gupta and N. M. Ravindra, *Phys. Chem. Solids* **41**, 591 (1980).
15. K. Vos, *J. Phys. C* **10**, 3917 (1977).

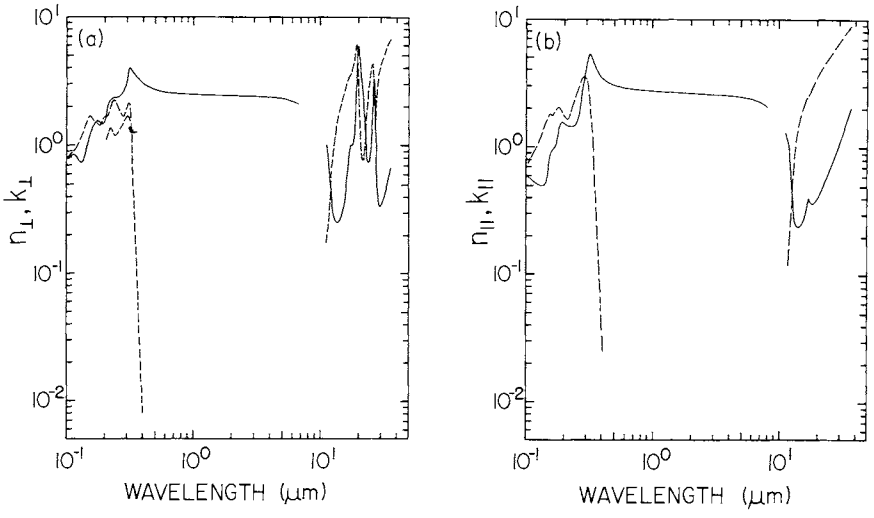

Fig. 14. (a) Log–log plot of $n_\perp$ (——), $k_\perp$ (– – – –) versus wavelength in micrometers for titanium dioxide. (b) Log–log plot of $n_{||}$ (——), $k_{||}$ (– – – –) versus wavelength in micrometers for titanium dioxide. The $\perp$ and $||$ symbols refer to radiation electric field E perpendicular and parallel to the c axis of the crystal. The values of n at 1030 μm given in Meriakri and Ushatkin [2] are not shown.

TABLE XIV

Values of n and k for Titanium Dioxide Obtained from Various References[a]

eV	cm^{-1}	μm	$n(\parallel)$	$n(\perp)$	$k(\parallel)$	$k(\perp)$
12.04		0.103	0.590 [6]	0.790 [6]	0.760 [6]	0.820 [6]
11.07		0.112	0.510	0.854	0.908	0.893
10.25		0.121	0.560	0.816	1.05	0.947
9.116		0.136	0.490	0.740	1.42	1.31
8.377		0.148	0.670	1.07	1.74	1.67
8.051		0.154			1.81	
7.798		0.159	0.950	1.32	1.77	1.57
7.293		0.170	1.04	1.51	1.94	1.50
7.167		0.173			2.01	
6.965		0.178	1.31	1.54	2.03	1.38
6.391		0.194	1.55	1.46	1.77	1.65
6.048	48,780	0.205		1.98 [7]		1.10 [7]
5.904	47,620	0.210	1.46	1.46 [6]	1.65	1.68 [6]
				2.02 [7]		1.20 [7]
5.713	46,080	0.217	1.82 [7]		0.971 [7]	
5.610	45,250	0.221		2.26		1.35
5.510	44,440	0.225				2.21 [6]
5.438	43,860	0.228	1.81		1.17	
5.344	43,100	0.232	1.45 [6]	2.31 [6]	2.15 [6]	2.29
5.188	41,840	0.239		2.36 [7]		1.19 [7]
4.940	39,840	0.251	2.01 [7]		1.71 [7]	
4.862	39,220	0.255		2.37		1.29
4.661	37,590	0.266	1.97 [6]	2.44 [6]	3.36 [6]	1.67 [6]
4.592	37,040	0.270	2.53 [7]		2.09 [7]	
4.558	36,760	0.272	2.59 [6]	2.49 [6]	3.47 [6]	1.65 [6]
4.541	36,630	0.273	2.92	2.50	3.49	1.65
4.492	36,230	0.276		2.59 [7]		1.41 [7]
4.350	35,090	0.285	3.03 [7]		2.21 [7]	
					3.56 [6]	
4.305	34,720	0.288	3.56 [6]	2.83 [6]	3.55	1.82 [6]
4.217	34,010	0.294	4.23	3.02	3.48	1.97
4.174	33,670	0.297		3.00 [7]		1.68 [7]
4.105	33,110	0.302				2.13 [6]
4.052	32,680	0.306	3.84 [7]		1.95 [7]	
4.038	32,570	0.307		3.42		1.61 [7]
3.899	31,450	0.318	5.38 [6]	4.00 [6]	2.18 [6]	1.79 [5]
3.827	30,870	0.324			1.44	1.44
3.791	30,580	0.327		3.87 [7]		0.810 [7]
3.701	29,850	0.335	4.22 [7]		0.788 [7]	
3.604	29,070	0.344	4.36 [6]	4.30 [6]		
3.463	27,930	0.358		3.38 [7]		0.117 [7]
3.444	27,780	0.360	3.87 [7]		0.251	
3.195	25,770	0.388	3.49	2.88		
3.100	25,000	0.400	3.40 [5]	3.00 [5]		
3.084	24,870	0.402		3.00 [7]		0.008

(*continued*)

TABLE XIV (*Continued*)

Titanium Dioxide

eV	cm^{-1}	μm	$n(\|\|)$	$n(\perp)$	$k(\|\|)$	$k(\perp)$
3.009	24,270	0.412	3.24 [7]		0.022	
2.952	23,810	0.420	3.29 [5]	2.91 [5]		
2.818	22,730	0.440	3.20	2.84		
2.817	22,670	0.441			0.080 [6]	0.040 [6]
2.695	21,740	0.460	3.13	2.79		
2.583	20,830	0.480	3.08	2.75		
2.480	20,000	0.500	3.03	2.71		
2.384	19,230	0.520	3.00	2.68		
2.300	18,550	0.539	2.95 [6]			
2.296	18,520	0.540	2.97 [5]	2.66 [5]		
2.214	17,860	0.560	2.94	2.64		
2.138	17,240	0.580	2.92	2.62		
2.066	16,670	0.600	2.90	2.60		
2.000	16,130	0.620	2.88	2.59		
1.937	15,630	0.640	2.87	2.58		
1.879	15,150	0.660	2.85	2.57		
1.823	14,710	0.680	2.84	2.56		
1.771	14,290	0.700	2.83	2.55		
1.722	13,890	0.720	2.82	2.54		
1.675	13,510	0.740	2.81	2.54		
1.631	13,160	0.760	2.81	2.53		
1.590	12,820	0.780	2.80	2.52		
1.550	12,500	0.800	2.79	2.52		
1.512	12,200	0.820	2.79	2.52		
1.476	11,900	0.840	2.78	2.51		
1.442	11,630	0.860	2.78	2.51		
1.409	11,360	0.880	2.77	2.50		
1.378	11,110	0.900	2.77	2.50		
1.348	10,870	0.920	2.76	2.50		
1.319	10,640	0.940	2.76	2.49		
1.291	10,420	0.960	2.76	2.49		
1.265	10,200	0.980	2.75	2.49		
1.240	10,000	1.00	2.75	2.49		
1.216	9,804	1.02	2.75	2.48		
1.192	9,615	1.04	2.74	2.48		
1.170	9,434	1.06	2.74	2.48		
1.148	9,259	1.08	2.74	2.48		
1.127	9,091	1.10	2.74	2.48		
1.107	8,929	1.12	2.74	2.47		
1.088	8,772	1.14	2.73	2.47		
1.069	8,621	1.16	2.73	2.47		
1.051	8,475	1.18	2.73	2.47		
1.033	8,333	1.20	2.73	2.47		
1.016	8,197	1.22	2.73	2.47		
0.9999	8,065	1.24	2.72	2.47		
0.9840	7,937	1.26	2.72	2.46		

TABLE XIV (*Continued*)

Titanium Dioxide

eV	cm^{-1}	μm	$n(\parallel)$	$n(\perp)$	$k(\parallel)$	$k(\perp)$
0.9686	7,813	1.28	2.72	2.46		
0.9537	7,692	1.30	2.72	2.46		
0.9393	7,576	1.32	2.72	2.46		
0.9252	7,463	1.34	2.72	2.46		
0.9116	7,353	1.36	2.72	2.46		
0.8984	7,246	1.38	2.72	2.46		
0.8856	7,143	1.40	2.72	2.46		
0.8731	7,042	1.42	2.71	2.46		
0.8610	6,944	1.44	2.71	2.46		
0.8492	6,849	1.46	2.71	2.46		
0.8377	6,757	1.48	2.71	2.46		
0.8265	6,667	1.50	2.71	2.45		
0.5123	4,132	2.42	2.59 [12]	2.40 [12]		
0.3668	2,959	3.38	2.58	2.41		
0.3271	2,639	3.79	2.57	2.39		
0.2897	2,336	4.28	2.51	2.34		
0.2535	2,045	4.89	2.49	2.32		
0.2164	1,745	5.73	2.43	2.24		
0.1839	1,484	6.74		2.11		
0.1729	1,395	7.17	2.27			
0.1542	1,244	8.04	2.06			
0.1107	892.9	11.2	1.30 [4]	1.01 [4]	0.075 [4]	0.176 [4]
0.1088	877.2	11.4	1.21	0.905	0.091	0.209
0.1069	862.1	11.6	1.11	0.784	0.111	0.256
0.1051	847.5	11.8	1.01	0.649	0.136	0.328
0.1033	833.3	12.0	0.882	0.513	0.171	0.440
0.1016	819.7	12.2	0.743	0.406	0.224	0.591
0.09999	806.5	12.4	0.587	0.340	0.310	0.751
0.09840	793.7	12.6	0.441	0.301	0.450	0.902
0.09686	781.2	12.8	0.345	0.278	0.625	1.04
0.09537	769.2	13.0	0.296	0.264	0.791	1.17
0.09393	757.6	13.2	0.269	0.255	0.940	1.30
0.09252	746.3	13.4	0.254	0.250	1.07	1.42
0.09116	735.3	13.6	0.245	0.249	1.20	1.53
0.08984	724.6	13.8	0.241	0.250	1.31	1.65
0.08856	714.3	14.0	0.239	0.253	1.42	1.76
0.08731	704.2	14.2	0.239	0.258	1.52	1.87
0.08610	694.4	14.4	0.240	0.265	1.62	1.98
0.08492	684.9	14.6	0.243	0.275	1.72	2.09
0.08377	675.7	14.8	0.247	0.287	1.81	2.21
0.08265	666.7	15.0	0.253	0.303	1.90	2.32
0.08157	657.9	15.2	0.259	0.322	1.98	2.44
0.08051	649.4	15.4	0.268	0.347	2.07	2.56
0.07948	641.0	15.6	0.278	0.378	2.15	2.69
0.07847	632.9	15.8	0.290	0.418	2.24	2.81

(*continued*)

TABLE XIV (*Continued*)

Titanium Dioxide

eV	cm^{-1}	μm	$n(\|\|)$	$n(\perp)$	$k(\|\|)$	$k(\perp)$
0.07749	625.0	16.0	0.306	0.468	2.32	2.94
0.07653	617.3	16.2	0.326	0.533	2.39	3.07
0.07560	609.8	16.4	0.351	0.614	2.46	3.19
0.07469	602.4	16.6	0.377	0.710	2.52	3.30
0.07380	595.2	16.8	0.398	0.814	2.57	3.39
0.07293	588.2	17.0	0.406	0.908	2.61	3.45
0.07208	581.4	17.2	0.401	0.972	2.66	3.49
0.07125	574.7	17.4	0.389	1.00	2.71	3.54
0.07044	568.2	17.6	0.378	1.00	2.77	3.62
0.06965	561.8	17.8	0.370	1.00	2.84	3.76
0.06888	555.6	18.0	0.366	1.02	2.91	3.94
0.06812	549.5	18.2	0.364	1.06	2.98	4.16
0.06738	543.5	18.4	0.365	1.15	3.05	4.43
0.06666	537.6	18.6	0.368	1.31	3.12	4.74
0.06595	531.9	18.8	0.372	1.56	3.19	5.10
0.06525	526.3	19.0	0.377	1.96	3.25	5.51
0.06457	520.8	19.2	0.382	2.62	3.32	5.91
0.06391	515.5	19.4	0.389	3.64	3.39	6.12
0.06326	510.2	19.6	0.395	4.96	3.45	5.72
0.06262	505.1	19.8	0.403	5.88	3.52	4.51
0.06199	500.0	20.0	0.410	5.95	3.59	3.17
0.06138	495.0	20.2	0.418	5.53	3.65	2.21
0.06078	490.2	20.4	0.427	5.01	3.72	1.63
0.06019	485.4	20.6	0.435	4.51	3.78	1.27
0.05961	480.8	20.8	0.444	4.06	3.84	1.05
0.05904	476.2	21.0	0.453	3.66	3.91	0.909
0.05848	471.7	21.2	0.463	3.29	3.97	0.826
0.05794	467.3	21.4	0.472	2.96	4.04	0.783
0.05740	463.0	21.6	0.482	2.64	4.10	0.772
0.05687	458.7	21.8	0.492	2.33	4.16	0.792
0.05636	454.5	22.0	0.502	2.03	4.23	0.846
0.05585	450.5	22.2	0.513	1.73	4.29	0.941
0.05535	446.4	22.4	0.524	1.45	4.35	1.09
0.05486	442.5	22.6	0.535	1.21	4.42	1.28
0.05438	438.6	22.8	0.546	1.03	4.48	1.51
0.05391	434.8	23.0	0.557	0.904	4.54	1.75
0.05344	431.0	23.2	0.569	0.822	4.60	1.98
0.05298	427.4	23.4	0.581	0.772	4.67	2.19
0.05253	423.7	23.6	0.593	0.744	4.73	2.40
0.05209	420.2	23.8	0.605	0.733	4.79	2.59
0.05166	416.7	24.0	0.617	0.737	4.85	2.78
0.05123	413.2	24.2	0.630	0.756	4.92	2.96
0.05081	409.8	24.4	0.643	0.790	4.98	3.14
0.05040	406.5	24.6	0.656	0.841	5.04	3.32
0.04999	403.2	24.8	0.670	0.916	5.11	3.51
0.04959	400.0	25.0	0.683	1.02	5.17	3.70

TABLE XIV (*Continued*)

Titanium Dioxide

eV	cm^{-1}	μm	$n(\|)$	$n(\perp)$	$k(\|)$	$k(\perp)$
0.04920	396.8	25.2	0.697	1.17	5.23	3.90
0.04881	393.7	25.4	0.711	1.39	5.29	4.09
0.04843	390.6	25.6	0.726	1.70	5.36	4.26
0.04805	387.6	25.8	0.740	2.15	5.42	4.33
0.04769	384.6	26.0	0.755	2.70	5.48	4.18
0.04732	381.7	26.2	0.771	3.18	5.55	3.67
0.04696	378.8	26.4	0.786	3.30	5.61	2.93
0.04661	375.9	26.6	0.802	3.02	5.67	2.26
0.04626	373.1	26.8	0.818	2.52	5.74	1.84
0.04592	370.4	27.0	0.834	1.95	5.80	1.66
0.04558	367.6	27.2	0.851	1.40	5.87	1.72
0.04525	365.0	27.4	0.867	0.968	5.93	1.95
0.04492	362.3	27.6	0.885	0.704	5.99	2.24
0.04460	359.7	27.8	0.902	0.553	6.06	2.51
0.04428	357.1	28.0	0.920	0.465	6.12	2.75
0.04397	354.6	28.2	0.938	0.411	6.19	2.95
0.04366	352.1	28.4	0.956	0.377	6.25	3.13
0.04335	349.7	28.6	0.975	0.356	6.32	3.30
0.04305	347.2	28.8	0.994	0.344	6.38	3.44
0.04275	344.8	29.0	1.01	0.336	6.45	3.58
0.04246	342.5	29.2	1.03	0.333	6.51	3.71
0.04217	340.1	29.4	1.05	0.332	6.58	3.83
0.04189	337.8	29.6	1.07	0.334	6.64	3.94
0.04160	335.6	29.8	1.09	0.336	6.71	4.05
0.04133	333.3	30.0	1.12	0.341	6.78	4.15
0.04105	331.1	30.2	1.14	0.346	6.84	4.25
0.04078	328.9	30.4	1.16	0.351	6.91	4.35
0.04052	326.8	30.6	1.18	0.358	6.98	4.45
0.04025	324.7	30.8	1.20	0.365	7.04	4.54
0.03999	322.6	31.0	1.23	0.372	7.11	4.63
0.03974	320.5	31.2	1.25	0.380	7.18	4.72
0.03948	318.5	31.4	1.28	0.389	7.25	4.81
0.03923	316.5	31.6	1.30	0.398	7.31	4.90
0.03899	314.5	31.8	1.33	0.407	7.38	4.98
0.03874	312.5	32.0	1.35	0.416	7.45	5.07
0.03850	310.6	32.2	1.38	0.426	7.52	5.16
0.03827	308.6	32.4	1.40	0.436	7.59	5.24
0.03803	396.7	32.6	1.43	0.446	7.66	5.33
0.03780	304.9	32.8	1.46	0.457	7.73	5.41
0.03757	303.0	33.0	1.48	0.468	7.79	5.49
0.03734	301.2	33.2	1.51	0.480	7.86	5.58
0.03712	299.4	33.4	1.54	0.491	7.93	5.66
0.03690	297.6	33.6	1.57	0.503	8.00	5.75
0.03668	295.9	33.8	1.60	0.516	8.08	5.83
0.03647	294.1	34.0	1.63	0.528	8.15	5.92

(*continued*)

TABLE XIV (*Continued*)

Titanium Dioxide

eV	cm^{-1}	μm	$n(\|)$	$n(\perp)$	$k(\|)$	$k(\perp)$
0.03625	292.4	34.2	1.66	0.541	8.22	6.00
0.03604	290.7	34.4	1.69	0.555	8.29	6.09
0.03583	289.0	34.6	1.73	0.569	8.36	6.17
0.03563	287.4	34.8	1.76	0.583	8.43	6.26
0.03542	285.7	35.0	1.79	0.598	8.50	6.34
0.03522	284.1	35.2	1.83	0.613	8.58	6.43
0.03502	282.5	35.4	1.86	0.628	8.65	6.52
0.03483	280.9	35.6	1.90	0.644	8.72	6.60
0.03463	279.3	35.8	1.93	0.661	8.79	6.69
0.03444	277.8	36.0	1.97	0.678	8.87	6.78
0.03425	276.2	36.2	2.01	0.695	8.94	6.87
0.03406	274.7	36.4	2.05	0.713	9.01	6.96
0.00120	9.71	1,030	12.85	9.15 [2]		

[a] References are indicated in brackets. While we use the notation $\|$, $\perp$, these are the same as e, o and *c*, *a* used by others.



Handbook of Optical Constants of Solids II

edited by

Edward D. Palik

Copyrighted material

Handbook of Optical Constants of Solids II

This book is printed on acid-free paper. ♾

Copyright © 1998, 1991, Elsevier Science (USA).

All Rights Reserved.
No part of this publication may be reproduced or transmitted in any form or by any means, electronic or mechanical, including photocopy, recording, or any information storage and retrieval system, without permission in writing from the publisher.

Permissions may be sought directly from Elsevier's Science & Technology Rights Department in Oxford, UK: phone: (+44) 1865 843830, fax: (+44) 1865 853333, e-mail: permissions@elsevier.com.uk. You may also complete your request on-line via the Elsevier Science homepage (http://elsevier.com), by selecting "Customer Support" and then "Obtaining Permissions."

Academic Press
An imprint of Elsevier Science
525 B Street, Suite 1900, San Diego, California 92101-4495, USA
http://www.academicpress.com

Academic Press
84 Theobald's Road, London WC1X 8RR, UK
http://www.academicpress.com

Library of Congress Cataloging-in-Publication Data

Handbook of optical constants of solids II / edited by Edward D. Palik.
p. cm.
Includes bibliolographical references.
International Standard Book Number: 0-12-544422-2
1. Solids. 2. Optical properties. 3. Handbooks, manuals, etc.
I. Palik, Edward D.
QC176.8.06H63 1991 90-826
530.4'12 CIP

PRINTED IN THE UNITED STATES OF AMERICA
03 04 05 06 07 9 8 7 6 5 4 3

Contents

List of Contributors xv

Part I DETERMINATION OF OPTICAL CONSTANTS

Chapter 1 **Introductory Remarks** 3
EDWARD D. PALIK

I. Introduction 3
II. The Chapters 3
III. The Critiques 5
IV. The Tables 6
V. The Figures of the Tables 7
VI. General Remarks 7
VII. Errata 8
References 11

Chapter 2 **Convention Confusions** 21
R. T. HOLM

I. Introduction 21
II. Units 22
III. Wave Equation 22
IV. Polarization 26
V. Fresnel's Amplitude Reflection Coefficients 37
VI. Nomenclature 50
VII. Concluding Remarks 51
Acknowledgments 52
References 52

Chapter 3 **Methods for Determining Optical Parameters of Thin Films** 57
E. PELLETIER

I. Introduction 57
II. An Example of Comparison between the Different Techniques of Index Determination 58
III. Principle Methods of Index Determination 60
IV. Sensitivity and Accuracy of the Determination Methods 64
V. Overlapping and Tests of Validity of the Model 67
VI. Results and Conclusion 71
References 71

Chapter 4 **The Attenuated Total Reflection Method** 75
G. J. SPROKEL AND J. D. SWALEN

I. Introduction 75
II. Surface-Plasmon Oscillations 77
III. Optical Analysis of ATR Structures 81
IV. Guided Modes 84
V. Applications of ATR 87
VI. Conclusion 94
References 94

Chapter 5 **Optical Properties of Superlattices** 97
P. APELL AND O. HUNDERI

I. Introduction 97
II. The Classical Optical Response of a Multilayer System 98
III. Semiconductor Superlattices 101
IV. Amorphous Superlattices 109
V. Collective Excitations 112
VI. Lattice Disorder 118
VII. The Effect of Nonlocal Dielectric Functions 120
VIII. Concluding Remarks 122
References 122

Chapter 6 **Calculation of the Refractive Index of Compound Semiconductors below the Band Gap** 125
B. JENSEN

I. Introduction 125
II. The Quantum-Density-Matrix Formulation of the Complex Dielectric Constant 128
III. Comparison with Experimental Results 138
IV. Summary 147
References 148

Chapter 7 **Calculation of Optical Constants, *n* and *k*, in the Interband Region** 151
A. R. FOROUHI AND I. BLOOMER

I. Introduction 151
II. The Extinction Coefficient, $k(E)$, and the Refractive Index, $n(E)$ 154
III. Discussion 163
IV. Examples 166
V. Summary 174
References 175

Chapter 8 **Temperature Dependence of the Complex Index of Refraction** 177
MICHAEL E. THOMAS

I. Introduction 177
II. Temperature Dependence of n and k 179

III. Conclusions 199
References 199

Chapter 9 **Measurement of *n* and *k* in the XUV by the Angle-of-Incidence Total-External-Reflectance Method** 203

MARION L. SCOTT

I. Introduction 203
II. General Considerations 204
III. Aluminum Reflectance versus Angle in UHV 206
IV. Determination of *n* and *k* 207
V. Comparison with Other Results 210
References 212

Chapter 10 **Spectroscopic Ellipsometry in the 6–35 eV Region** 213

J. BARTH, R. L. JOHNSON, AND M. CARDONA

I. Introduction 213
II. The Bessy VUV Ellipsometer 217
III. Theory 226
IV. Results and Comparison with Reflectance Spectra 237
V. Summary 244
Acknowledgment 245
References 245

Chapter 11 **Methods Based on Multiple-Slit Fourier Transform Interferometry for Determining Thin-Film Optical Constants in the VUV/Soft X-Ray Range** 247

ROMAN TATCHYN

I. Introduction to MSFTI 247
II. Fundamental Dimensional Constraints and Inequalities 253
III. Relationship of MSFTI to Alternative Metrological Techniques 254
IV. General Experimental Equations and Sensitivity Analysis 258
V. A Characterization of the Optical Constants of Au Using MSFTI in the 280–640 eV Range 265
VI. Problems and Prospects in Sample Preparation 270
VII. Prospects for MSFTI in Other Spectral Regimes 272
VIII. Summary 273
Acknowledgments 274
References 274

Chapter 12 **Determination of Optical Constants from Angular-Dependent, Photoelectric-Yield Measurements** 279

H.-G. BIRKEN, C. BLESSING, AND C. KUNZ

I. Introduction 279
II. Theoretical Background 280
III. Experimental Details 285

IV. Examples 286
V. Conclusions and Future Prospects 289
References 292

Chapter 13 **Determination of Optical Constants by High-Energy, Electron-Energy-Loss Spectroscopy (EELS)** 293
J. PFLÜGER AND J. FINK

I. Introduction 293
II. Description of an EELS Experiment 295
III. Scattering Cross-Section 297
IV. Exact Determination of the Loss Function 298
V. Kramers–Kronig Analysis 299
VI. Brief Summary of the Evaluation Procedure 300
VII. Comparison with Reflectivity Measurements 300
VIII. Optical Properties of TiC, VC, TiN, and VN 303
References 310

Chapter 14 **Optical Parameters for the Materials in *HOC I* and *HOC II*** 313
EDWARD D. PALIK

I. Introduction 313
II. The Parameters 313
References 334

Part II CRITIQUES

Subpart 1 Metals

An Introduction to the Data for Several Metals 341
DAVID W. LYNCH AND W. R. HUNTER

I. Introduction 341
References 341
II. Alkali Metals 342
References 344
III. Lithium (Li) 345
References 347
IV. Sodium (Na) 354
References 357
V. Potassium (K) 364
References 367
VI. Chromium (Cr) 374
References 376
VII. Iron (Fe) 385
References 387
VIII. Niobium (Nb) 396
References 397
IX. Tantalum (Ta) 408
References 409

Beryllium (Be)
E. T. ARAKAWA, T. A. CALLCOTT, AND YUN-CHING CHANG 421
References 425

Cobalt (Co) 435
L. WARD
References 440

Graphite (C) 449
A. BORGHESI AND G. GUIZZETTI
References 453

Liquid Mercury (Hg) 461
E. T. ARAKAWA AND T. INAGAKI
References 465

Palladium (Pd) 469
A. BORGHESI AND A. PIAGGI
References 472

Vanadium (V) 477
G. GUIZZETTI AND A. PIAGGI
References 480

Subpart 2 Semiconductors

Aluminum Arsenide (AlAs) 489
EDWARD D. PALIK, O. J. GLEMBOCKI, AND KENICHI TAKARABE
Acknowledgments 492
References 492

Aluminum Antimonide (AlSb) 501
DAVID F. EDWARDS AND RICHARD H. WHITE
References 505

Aluminum Gallium Arsenide ($Al_xGa_{1-x}As$) 513
O. J. GLEMBOCKI AND K. TAKARABE
Acknowledgments 515
References 515

Cadmium Selenide (CdSe) 559
H. PILLER

References 563

Cadmium Sulphide (CdS) 579
L. WARD

References 586

Gallium Antimonide (GaSb) 597
DAVID F. EDWARDS AND RICHARD H. WHITE

References 601

Silicon–Germanium Alloys (Si_xGe_{1-x}) 607
J. HUMLÍČEK, F. LUKEŠ, AND E. SCHMIDT

References 611

Lead Tin Telluride (PbSnTe) 637
H. PILLER

References 639

Mercury Cadmium Telluride ($Hg_{1-x}Cd_xTe$) 655
P. M. AMIRTHARAJ

Acknowledgments 666
References 667

Selenium (Se) 691
EDWARD D. PALIK

Acknowledgments 693
References 694

Cubic Silicon Carbide (β-SiC) 705
SAMUEL A. ALTEROVITZ AND JOHN A. WOOLLAM

References 706

Tellurium (Te) 709
EDWARD D. PALIK

Acknowledgments 713
References 713

Tin Telluride (SnTe) 725
H. PILLER

References 727

Zinc Selenide (ZnSe)
Zinc Telluride (ZnTe) 737
L. WARD
References 747

Subpart 3 Insulators

Aluminum Oxide (Al_2O_3) 761
FRANÇOIS GERVAIS
References 764

Aluminum Oxynitride (ALON) Spinel 777
WILLIAM J. TROPF AND MICHAEL E. THOMAS
References 780
Notes Added in Proof 781

Barium Titanate ($BaTiO_3$) 789
CHUEN WONG, YE YUNG TENG, J. ASHOK, AND P. L. H. VARAPRASAD
Acknowledgments 793
References 793

Beryllium Oxide (BeO) 805
DAVID F. EDWARDS AND RICHARD H. WHITE
References 807

Calcium Fluoride (CaF_2) 815
D. F. BEZUIDENHOUT
References 825

Amorphous Hydrogenated "Diamondlike" Carbon Films and Arc-Evaporated Carbon Films 837
SAMUEL A. ALTEROVITZ, N. SAVVIDES, F. W. SMITH, AND JOHN A. WOOLLAM
References 840

Cesium Iodide (CsI) 853
JOHN E. ELDRIDGE
References 857

Copper Oxides (Cu_2O, CuO) 875
CARL G. RIBBING AND ARNE ROOS
References 878

Magnesium Aluminium Spinel ($MgAl_2O_4$) 883
WILLIAM J. TROPF AND MICHAEL E. THOMAS

References 887

Magnesium Fluoride (MgF_2) 899
THOMAS M. COTTER, MICHAEL E. THOMAS, AND WILLIAM J. TROPF

References 903

Magnesium Oxide (MgO) 919
DAVID M. ROESSLER AND DONALD R. HUFFMAN

Acknowledgments 939
References 939

Polyethylene $(C_2H_4)_n$ 957
J. ASHOK, P. L. H. VARAPRASAD, AND J. R. BIRCH

References 968

Potassium Bromide (KBr) 989
EDWARD D. PALIK

References 992

Potassium Dihydrogen Phosphate (KH_2PO_4, KDP) and Three of Its Isomorphs 1005
DAVID F. EDWARDS AND RICHARD H. WHITE

References 1008

Sodium Fluoride (NaF) 1021
I. OHLÍDAL AND K. NAVRÁTIL

References 1024

Strontium Titanate ($SrTiO_3$) 1035
FRANÇOIS GERVAIS

References 1037

Thorium Fluoride (ThF_4) 1049
I. OHLÍDAL AND K. NAVRÁTIL

References 1054

Water (H_2O) 1059

MARTIN R. QUERRY, DAVID M. WIELICZKA, AND DAVID J. SEGELSTEIN

References 1063

Yttrium Oxide (Y_2O_3) 1079

WILLIAM J. TROPF AND MICHAEL E. THOMAS

References 1084
Notes Added in Proof 1086

List of Contributors

Numbers in parentheses indicate the pages on which the authors' contributions begin.

SAMUEL A. ALTEROVITZ (705, 837), Space Electronics Division, NASA Lewis Research Center, Cleveland, Ohio 44135
P. M. AMIRTHARAJ (655), U.S. Army Center for Night Vision and Electro-Optics, Mail Code AMSEL-NV-IT, Ft. Belvoir, Ft. Belvoir, Virginia 22060
P. APELL (97), Institute of Theoretical Physics, Chalmers University of Technology, S-412 96 Göteborg, Sweden
E. T. ARAKAWA (421, 461), P.O. Box 2008, Oak Ridge National Laboratory, Oak Ridge, Tennessee 37831
J. ASHOK (789, 957), Department of Applied Physics, Andhra University, Visakhapatnam 530 003, India
J. BARTH (213), Elktro-Optik GmbH, Fördestr. 35, D-2392 Glücksburg, Federal Republic of Germany
D. F. BEZUIDENHOUT (815), Division of Production Technology, P.O. Box 395, Council for Scientific and Industrial Research, Pretoria, South Africa
J. R. BIRCH (957), Division of Electrical Science, National Physical Laboratory, Teddington, Middlesex TW11 0LW, United Kingdom
H.-G. BIRKEN (279), Institute für Experimentalphysik, Universität Hamburg, Luruper Chausee 149, D-2000 Hamburg 50, Federal Republic of Germany
C. BLESSING (279), Institut für Experimentalphysik, Universität Hamburg, Luruper Chausee 149, D-2000 Hamburg 50, Federal Republic of Germany
I. BLOOMER (151), Department of Physics, San José University, One Washington Square, San José, California 95192
A. BORGHESI (449, 469), Dipartimento di Fisica "A. Volta," Università di Pavia, Via A. Bassi, 6, 27100 Pavia, Italy
T. A. CALLCOTT (421), Physics Department, The University of Tennessee, Knoxville, Tennessee 37933
M. CARDONA (213), Max-Planck Institut für Festkörperforschung, Heisenbergstrasse 1, D-7000 Stüttgart 80, Federal Republic of Germany
YUN-CHING CHANG (421), Physics Department, The University of Tennessee, Knoxville, Tennessee 37933

T. M. COTTER (899), Applied Physics Laboratory, The Johns Hopkins University, Johns Hopkins Road, Laurel, Maryland 20707
DAVID F. EDWARDS (501, 597, 805, 1005), University of California, Lawrence Livermore National Laboratory, P.O. Box 808, Livermore, California 94550
J. E. ELDRIDGE (853), Department of Physics, 6224 Agriculture Road, The University of British Columbia, Vancouver, British Columbia V6T 2A6, Canada
J. FINK (293), Kernforschungszentrum Karlsruhe, Institute für Nukleare Festkörperphysik, P.O. Box 3640, D-7500 Karlsruhe, Federal Republic of Germany
A. R. FOROUHI (151), Loral Fairchild Imaging Sensors, 1801 McCarthy Boulevard, Milpitas, California 95035
FRANÇOIS GERVAIS (761, 1035), Centre de Recherches sur la Physique des Hautes Températures, 1D Avenue de la Recherche Scientifique, 45071 Orléans Cedex, France
O. J. GLEMBOCKI (489, 513), Code 6833, Naval Research Laboratory, Washington, D.C. 20375
G. GUIZZETTI (449, 477), Dipartimento di Fisica "A. Volta," Università di Pavia, Via A. Bassi, 6, 27100 Pavia, Italy
R. T. HOLM (21), Code 6833, Naval Research Laboratory, Washington, D.C. 20375
DONALD R. HUFFMAN (921), Physics Department, University of Arizona, Tucson, Arizona 85721
J. HUMLÍČEK (607), Department of Solid State Physics, Masaryk University, Kotlářská 2, 611 37 Brno, Czechoslovakia
O. HUNDERI (97), Division of Physics, NTH, N 7034 Trondheim, Norway
W. R. HUNTER (341), S.F.A., Inc., 1401 McCormick Dr., Landover, Maryland 20785
T. INAGAKI (341, 461), P.O. Box 2008, Oak Ridge National Laboratory, Oak Ridge, Tennessee 37831
B. JENSEN (125), Department of Physics and Applied Physics, College of Pure and Applied Science, University of Lowell, Lowell, Massachusetts 01854
R. L. JOHNSON (213), Institut für Experimentalphysik, Universität Hamburg, Luruper Chausee 149, D-2000 Hamburg 50, Federal Republic of Germany
C. KUNZ (279), Institut für Experimentalphysik, Universität Hamburg, Luruper Chausee 149, D-2000 Hamburg 50, Federal Republic of Germany
F. LUKEŠ (607), Department of Solid State Physics, Masaryk University, Kotlářská 2, 611 37 Brno, Czechoslovakia
DAVID W. LYNCH (341), Department of Physics, 12 Physics Building, Iowa State University, Ames, Iowa 50011

K. NAVRÁTIL (1021, 1049), Department of Solid State Physics, Masaryk University, Kotlářská 2, 611 37 Brno, Czechoslovakia
L. OHLÍDAL (1021, 1049), Department of Solid State Physics, Masaryk University, Kotlářská 2, 611 37 Brno, Czechoslovakia
EDWARD D. PALIK (3, 313, 489, 691, 709, 989), Institute of Physical Sciences and Technology, University of Maryland, College Park, Maryland 20742
E. PELLETIER (57), Laboratoire d'Optique des Surfaces et des Couches Minces, Unité Associée au CNRS, Ecole Nationale Supérieure de Physique de Marseille, Domaine Universitaire de St. Jérôme, 13397 Marseille Cedex 13, France
J. PFLÜGER (293), Synchrotronstrahlungslabor, HASYLAB at DESY, Notkestrasse 85, D-2000 Hamburg 52, Federal Republic of Germany
A. PIAGGI (469, 477), Dipartimento di Fisica "A. Volta," Università di Pavia, Via A. Bassi, 6, 27100 Pavia, Italy
H. PILLER (559, 637, 725), Department of Physics and Astronomy, Louisiana State University, Baton Rouge, Louisiana 70803
MARVIN R. QUERRY (1059), Department of Physics, University of Missouri-Kansas City, Kansas City, Missouri 64110
CARL G. RIBBING (875), School of Engineering, Department of Technology, Uppsala University, Box 534, S-751 21 Uppsala, Sweden
DAVID M. ROESSLER (921), Physics Department, General Motors Research Laboratories, 30500 Mound Road, Warren, Michigan 48089
ARNE ROOS (875), School of Engineering, Department of Technology, Uppsala University, Box 534, S-751 21 Uppsala, Sweden
N. SAVVIDES (837), CSIRO Division of Applied Physics, National Measurements Laboratory, Sydney, Australia 2070
E. SCHMIDT (607), Department of Solid State Physics, Masaryk University, Kotlářská 2, 611 37 Brno, Czechoslovakia
MARION L. SCOTT (203), E 549, Los Alamos National Laboratory, Los Alamos, New Mexico 87545
DAVID J. SEGELSTEIN (1059), Bell Communications Research, Red Bank, New Jersey 07701
F. W. SMITH (837), Department of Physics, City College of CUNY, New York, New York 10031
G. J. SPROKEL (75), IBM Almaden Research Center, Department K33, 650 Harry Road, San Jose, California 95120
J. D. SWALEN (75), IBM Almaden Research Center, Department K33, 650 Harry Road, San Jose, California 95120
KENICHI TAKARABE (489, 513), Department of Natural Science, Faculty of Science, Okayama University of Science, 1-1 Ridai-cho, Okayama City, Okayama 700, Japan
ROMAN TATCHYN (247), Stanford Electronics Laboratory, Stanford University, Stanford, California 94305

YE YUNG TENG (789), Department of Physics and Applied Physics, University of Lowell, 1 University Avenue, Lowell, Massachusetts 01854
MICHAEL E. THOMAS (177, 777, 883, 899, 1079), The Johns Hopkins University, Applied Physics Laboratory, Johns Hopkins Road, Laurel, Maryland 20707
WILLIAM J. TROPF (777, 883, 899, 1079), The Johns Hopkins University, Applied Physics Laboratory, Johns Hopkins Road, Laurel, Maryland 20707
P. L. H. VARAPRASAD (789), Department of Applied Physics, Andhra University, Visakhapatnam 530 003, India
L. WARD (435, 579, 737), Department of Applied Physical Science, Coventry (Lanchester) Polytechnic, Coventry CV1 5FB, United Kingdom
RICHARD H. WHITE (501, 597, 805, 1005), University of California, Lawrence Livermore National Laboratory, P.O. Box 808, Livermore, California 94550
DAVID M. WIELICZKA (1059), Department of Physics, University of Missouri-Kansas City, Kansas City, Missouri 64110
JOHN A. WOOLLAM (705, 837), Center for Microelectronic and Optical Materials Research and Department of Electrical Engineering, University of Nebraska, Lincoln, Nebraska 68588
CHUEN WONG (789), Department of Physics and Applied Physics, University of Lowell, 1 University Avenue, Lowell, Massachusetts 01854

Chapter 1
Introductory Remarks

EDWARD D. PALIK
Institute for Physical Science and Technology
University of Maryland
College Park, Maryland

I. Introduction 3
II. The Chapters 3
III. The Critiques 5
IV. The Tables 6
V. The Figures of the Tables 7
VI. General Remarks 7
VII. Errata 8
References 11

INTRODUCTION I

The original list of materials prepared for the *Handbook of Optical Constants of Solids (HOC I)* [1] contained about 60 materials, but because of a lack of critiquers, the published handbook contained only 37 materials, more or less evenly divided among metals, semiconductors, and insulators. Useful, important materials had to be omitted. More than three years after the publication of *HOC I*, I approached Academic Press about a second volume to cover these additional materials. Having now added another 48 materials to the list, I can see another 30 materials that might be of interest also.

THE CHAPTERS II

As with *HOC I* the first part of the *Handbook of Optical Constants of Solids II (HOC II)* consists of short topics dealing with the determination of optical constants.

In Chapter 2, R. T. Holm discusses sign and polarization conventions

Copyright © 1991 by Academic Press.
All rights of reproduction in any form reserved.
ISBN 0-12-544422-2

starting with the form of the electromagnetic wave used to solve Maxwell's equations. It seems that in many optics books and papers I read, the authors have not stated this wave form and used it consistently; they sometimes change wave forms. Although this does not affect the final calculated answers, it surely confuses the student with + and − signs and sines and cosines.

In Chapter 3, E. Pelletier discusses the problems involved in determining the optical constants of a film on a substrate (a common sample in this day and age of epitaxial layers, and reflection and antireflection coatings). Also, the improvement in deposition processes is now providing thin-film samples, which look more and more like bulk material (except for strain, perhaps).

In Chapter 4, G. J. Sprokel and J. D. Swalen discuss the determination of n and k by the technique of attenuated total reflection. This is a powerful technique of examining deposited, single or multiple thin films; oxide layers on substrates; bulk material; and surface properties such as surface plasmons and phonons.

In Chapter 5, P. Apell and O. Hunderi extend thin-film structures to superlattice structures, discussing how fundamental optical properties are changed and how we can treat a superlattice as a new material with new, effective n and k values different from the parent materials. This should be very important as multiple-quantum wells, and so forth, become routine optical samples in the future, and as the field of textured surfaces and textured bulk becomes optically more interesting in the context of photonic band structure.

In Chapter 6, Barbara Jensen calculates the index of refraction at and below the fundamental band gap of semiconductors from quantum mechanics principles, stressing the ternary and quaternary materials of widespread interest. This gives a calculational way of determining n for $Al_xGa_{1-x}As$ for any value of x, for example.

In Chapter 7, A. R. Forouhi and I. Bloomer develop a model for electronic transitions across the band gaps, which accounts for n and k in the interband region. They assign the several peaks in k to transitions with strengths and widths, fitting the experimental k spectrum and then Kramers–Kronig analyzing it to get the n spectrum. Thus, one has an analytical form for n and k in the interband region.

In Chapter 8, Michael E. Thomas develops a model to account for multiphonon absorption as a function of temperature in the region straddling the fundamental transverse optical phonon resonance. This is useful in determining the intrinsic (versus extrinsic) absorption coefficient, especially in studies of laser-window materials in the IR.

The next three chapters concentrate on the determination of n and k in the UV–X-Ray regions. Because of the advent of synchrotron radiation sources, this is a very active spectral region.

In Chapter 9, Marion L. Scott discusses the use of total external reflection to determine n and k in the UV–X-Ray region. All materials eventually have $n<1$ above the interband region where this technique applies, and variable-angle-of-incidence measurements can yield n and k.

In Chapter 10, J. Barth, R. L. Johnson, and M. Cardona describe spectroscopic ellipsometry, extending it beyond the usual region of 1.5–6 eV to as high as 35 eV. Linear polarization is not so good at these higher photon energies, and the data must be analyzed in terms of partially linearly polarized radiation.

In Chapter 11 Roman Tatchyn describes the interference effects of a microfabricated Au transmission grating in the soft x-ray region and how the complex index of refraction can be extracted from such interference patterns by comparing relative intensities of interference orders.

There now follow two chapters describing "nonoptical" techniques for determining n and k in the interband region. Although in the critiques we do not often use the numbers obtained from such techniques, they are still of interest.

In Chapter 12, H.-G. Birken, C. Blessing, and C. Kunz describe the angular-resolved photoemission process as a probe of optical constants in the interband region. Although light is used to produce the electrons, it is the electron currents emitted by a crystalline sample (proportional to k) that are of interest.

In Chapter 13, J. Pflüger and J. Fink describe how n and k are obtained from a truly nonoptical experiment, electron-energy-loss spectroscopy. This technique has been used for many years as a way of determining $\mathrm{Im}(-1/\varepsilon)$ for unsupported thin films.

Finally, in Chapter 14, I have attempted to collect many optical parameters for the 86 materials in *HOC I* and *II* and display them in a gigantic table. Again, these are parameters that I have often needed but could not find in one place, things like crystal symmetry, lattice constant, irreducible representation, TO and LO resonant frequencies, plasma frequency ω_p, fundamental band gap E_g, d.c. dielectric constant ε_0, and so on.

In regards to Chapter 2, which discusses conventions, it is interesting to note that in three of the chapters $n-ik$ is used, whereas in four others $n+ik$ is used. The other chapter writers have avoided making the choice. In the critiques both conventions are also used.

THE CRITIQUES III

The critiques are meant to be the critiquer's own judgment of the best values of n and k over the widest spectral range. Some spectral-region

values can overlap slightly to indicate typical differences among laboratories and methods. When possible, estimates of uncertainties are stated, but a rule of thumb is that n is good to two figures and k is good to a factor of two. Beyond this, one has to examine the experimental methods; n can be good to five figures for minimum-deviation techniques, and k can be good to two figures if one measures transmittance carefully.

In a few cases, data such as reflectance R and transmittance T are found in the literature, but no determination of n and k has been made; in such cases we can only cite the work. This happens most often in the UV interband region and in the IR reststrahlen region.

A good review and source of references for properties of many materials (including optical) is "Landolt–Börnstein Numerical Data and Functional Relationships in Science and Technology," (K.-H. Hellwege, ed.), Springer-Verlag, Berlin, 1983. This series consists of 23 volumes, which cover quite a few of the materials discussed in *HOC I* and *II*.

IV THE TABLES

The biggest change from *HOC I* is in the use of camera-ready tables of n and k. Although uniformity could not be achieved in every case, the tables should be more free of typographical errors. We have given the various critiquers more leeway in the format. The eV, cm^{-1}, and μm units may not run continously from X-ray to mm-wave regions, but may "back up" for another author's values to overlap, and then continue on. The exponential form of k varies; sometimes $\times 10^{-5}$ runs down to $\times 10^{-4}$ line by line. (This is because it is easier for the critiquers than the typesetter to include every single $\times 10^{-5}$. Other critiquers leave the intermediate lines blank and $\times 10^{-5}$ is understood until a change takes place at $\times 10^{-4}$. Although we try to continue exponents down to $\times 10^{-2}$, then switch to decimals for $\times 10^{-1}$, $\times 10^{0}$, $\times 10^{1}$, this is not done consistently. Sometimes 4.6 E − 03 is used, and sometimes a star indicates the multiplication sign ($4.6 * 10^{-2}$). Some authors have carried cm^{-1} up into the millions; we usually stop mentioning it above 50,000 cm^{-1}. Always keep in mind the conversion factor 8065.48 cm^{-1}/eV. Although we have used this conversion factor to move among the units in most cases, some critiquers have used values differing by one digit in the fourth significant figure. This should cause no problems in an experiment until the fourth figure is reached in the eV, cm^{-1} or μm units, which is not frequently. Values of n and k are identified by a reference number in brackets, which is understood to apply in that particular column until a new reference appears.

Several alloy semiconductors have been included, such as $Al_xGa_{1-x}As$,

$Pb_{1-x}Sn_xTe$, $Hg_{1-x}Cd_xTe$, Si_xGe_{1-x}. Although it would be nice to list x in tenths from zero to one, these are not necessarily available from UV to IR, so in most instances we have taken what the literature supplies for a few representative values of x. Hopefully, the dependence of band gap and optical-phonon frequencies on x can be obtained from the cited literature.

Values of n and k have been read from expanded graphs, from tables in the original papers, original reports, and data kindly supplied by the investigators in private communications, and in at least one or two cases, the critiquers have made additional measurements for their particular critiques.

THE FIGURES OF THE TABLES V

Log–log plots of n, k versus μm have been prepared in a uniform format. The details are often lost in the thickness of the pen line, but the reader can always return to the tables to interpolate values. The figures give an instant bird's-eye view of n and k.

We also cannot plot all the data for every x tabulated for an alloy semiconductor, for example, so we have chosen only a few examples, where hopefully there is a wide spectrum of data for one or two values of x.

GENERAL REMARKS VI

In *HOC I*, we had concentrated on room-temperature (often not stated in the original papers) values of n and k. Some critiquers have included temperature dependence of n at various wavelengths and commented on what raising or lowering the temperature does to k. Of special interest is the fact that lowering the temperature significantly widens the spectral windows in the optic-phonon regions, and materials that are optical windows on dewars at room temperature invariably become much better windows when used as low-temperature windows inside the dewar (sapphire is a good example).

We cannot hope to tabulate every useful optical parameter for these materials, although in Chapter 14 there is a table listing some of the parameters for each material.

Of some interest is the effort that has gone into a material like $BaTiO_3$ (for physics and technology), but its UV properties have not been

measured to 30 eV. Also, a material like Cu_2O is very prominent in solar research and is used as an example in a book on IR and Raman selection rules for optic phonons, but again no UV data are available. Even a material of great interest for quantum-well studies and superlattices in general, like $Al_xGa_{1-x}As$, has not been studied from UV to far IR for $x = 0, 0.1, 0.2, \ldots, 1.0$ in detail. Only bits and pieces seem to be done with existing or readily grown materials for a few values of x. The uncertainty in x is also a problem, often being ± 0.01.

Our knowledge of deposited films improves steadily. Ion-beam-assisted layer growth is producing samples that look more and more like bulk materials (either single crystal or polycrystal). Variations in n from the substrate to outer surface, related to the columnar growth process, are now seen; the strain effects in films on substrates are not yet optically clear.

I proposed the title of this volume to be *Handbook of Optical Functions of Solids* because n and k are not constant, and physicists use the term often. However, to relate to *HOC I* better, we retain the use of optical constants in the title and in most of the critiques and chapters.

We have stretched the truth a little in the title, in that two liquids are discussed: Hg (as a classic liquid metal) and water (because H_2O surrounds us). Also, we have included polyethylene because it is a prototype plastic and has been widely used in IR spectroscopy. In addition, it shows scattering in the visible because of its structure and therefore provides a tricky task for the experimentalist to characterize it. Also, a-C:H (amorphous hydrogenated carbon) is of considerable interest (as is a-Si:H), so we touch upon this material.

Among the materials offered but not claimed by critiquers are AgCl, CsBr, NaBr, KI, BaO, NiO, PbF_2, HgS, HgSe, GaN, Mg, Cd, Pb, Mn, Ti, Teflon, Plexiglas, mica, and liquid nitrogen (the only material not at room temperature). The high-temperature superconductors were considered for inclusion, but at this date, the optical properties have not "stabilized."

VII ERRATA

In using *HOC I*, I have found mistakes and typographical errors; a few readers have also pointed out mistakes.

p. 6, line 18: insulators

p. 7, line 5: for the choice $n + ik$ the wave form is $\exp[i(-\omega t \pm \mathbf{q} \cdot \mathbf{r})]$; for $n - ik$ the wave form is $\exp[i(\omega t \pm \mathbf{q} \cdot \mathbf{r})]$. The $\pm$ on the term $\mathbf{q} \cdot \mathbf{r}$ pertains to propagation in the $\pm r$ direction for $n + ik$, and to propagation in the $\mp r$ direction for $n - ik$. The variations used in the chapters and critiques testify

to the fact that we will never agree on one convention, and it behooves us to learn how to switch back and forth between them. See Chapter 2, Table 1 in this volume to sort out the ± signs.

p. 15, line 7: $f = \ln(\hat{m}) = \ln(\hat{\xi}\hat{\gamma})$
$g = \ln(\hat{m}/\hat{\gamma}^2) = \ln(\hat{\xi}/\hat{\gamma})$

p. 19, in denominator in two lines after Eq. (22):

$1 + \hat{r}_{0f}\hat{r}^*_{0f} + 2\,\mathrm{Re}(\hat{r}_{0f})$

$1 + \hat{R}_{0f} + 2\,\mathrm{Re}\,(\hat{r}_{0f})$

p. 21, numerator in last line: $\hat{t}'_f\hat{t}'^*_f\,\mathrm{Re}(1/\zeta_{fo})$

p. 23, denominator of Eq. (36):

$1 - \{R_{01}R_{12}(1-W^2) + 2(1-W)\,\mathrm{Re}(\hat{r}_{01}\hat{r}_{12})$

$+ 4W\sin\delta[\sin\delta\,\mathrm{Re}(\hat{r}_{01}\hat{r}_{12}) - \cos\delta\,\mathrm{Im}(\hat{r}_{01}\hat{r}_{12})\}/D$

with

$D = 1 + R_{01}R_{12} + 2\,\mathrm{Re}(\hat{r}_{01}\hat{r}_{12}),$

p. 24, denominator of Eq. (38):

$1 - 4\{\beta d[R_{01}R_{12} + \mathrm{Re}(\hat{r}_{01}\hat{r}_{12})] - \delta\,\mathrm{Im}(\hat{r}_{01}\hat{r}_{12})\}/D$

p. 25, denominator of Eq. (31): $1 - R'_fR_bE^2$

p. 27, line 9 up from bottom:

$g_{jk} = [(P_j^2P_k^2 - S^4)(P_k^2 - P_j^2) - 4S^2(\alpha_j^2\beta_k^2 - \alpha_k^2\beta_j^2)]/D_{jk}$

$h_{jk} = 2[(\varepsilon'_j\varepsilon'_k + \varepsilon''_j\varepsilon''_k)(\alpha_j\beta_k - \alpha_k\beta_j) + \cdots$

p. 28, line 2 below Fig. 1: $T_f = (1 + R_{02} + 2g_{02})\dfrac{W}{D_f}\,\mathrm{Re}\left(\dfrac{\zeta_0}{\zeta_2}\right),$

p. 28, line 3: $T'_f = (1 + R_{02} - 2g_{02})\dfrac{W}{D_f}\,\mathrm{Re}^{-1}\left(\dfrac{\zeta_0}{\zeta_2}\right);$

p. 28, line 4: $\dfrac{T_b(1-R_{02})}{1+R_{02}-2g_{02}}\,\mathrm{Re}\left(\dfrac{\zeta_0}{\zeta_2}\right) = T_{02}$

p. 28, line 7: $T_f = (1-R_{02}),\ T'_f = (1-R_{02})\left(1 + \left(\dfrac{2\,h_{02}}{1-R_{02}}\right)^2\right)$

p. 28, line 10:

$$T_f=(1+R_{02}+2g_{02})\frac{W}{D_f}\mathrm{Re}\left(\frac{\zeta_0}{\zeta_2}\right),\ T'_f=(1+R_{02}-2g_{02})\frac{W}{D_f}\mathrm{Re}^{-1}\left(\frac{\zeta_0}{\zeta_2}\right)$$

p. 28, line 11: $T_fT'_f=T_fT_b$

p. 31, line 6: $2(S^2-n_1^2)^{1/2}d_1=2\beta_1 d_1$

p. 31, denominator in line 7: $h_{01}^2+(S^2-n_1^2)d_1^2$

p. 38, line 14: advantage

p. 62, line 7: arithmetic

p. 70, lines 20, 21: the term $(n^2-k^2-\sin^2\phi)$ in brackets [ ] should be squared

p. 310, 16.8 eV − 0.07380 μm

p. 429, last line: is given by Bennett

p. 466, line 9: $D\lambda^2/(\lambda^2-E)$

p. 470, Fig. 4: k curve should be dashed between 3×10^{-3} and 6×10^{-3} μm

p. 480, line 13: subtracted

p. 480, line 21: footnote b

p. 623, $ReAs_2Se_3$: Room-temperature data for α and ε_2 in the 2–12 eV region can be obtained from R. E. Drews, R. L. Emerald, M. L. Slade, and R. Zallen, *Solid State Commun.* **10**, 293 (1972).

p. 704, Eq. (2): dn/dT is in units of 10^{-5} K^{-1}

p. 704, line 15 up from bottom: Tomiki

p. 704, line 8 up from bottom: Tomiki

p. 706, Refs. 9, 10, 11: Tomiki

p. 719, line 9 up from bottom: The wavelength λ, index

p. 731, on 0.1579 eV − 1,274 cm^{-1} line: $k_0=6.949$

p. 778, line 15 up from bottom: Miyata

p. 798, Ref. 9: (1974)

In the critiques for ZnS (cubic), LiF, and SiO_2 (glass) in *HOC I*, the Henke model was used to calculate n and k in the X-ray region. The densities used in this calculation are: ZnS (cubic), 4.1; LiF, 2.635; SiO_2 (glass), 2.648. In the critiques for AlAs and $Al_xGa_{1-x}As$ in *HOC II*, the densities used were calculated from the density equation $g=5.36-1.6x$

given in the $Al_xGa_{1-x}As$ critique: AlAs, 3.76; $Al_{0.3}Ga_{0.7}As$, 4.88. Since slightly different densities can be found in various handbooks for the same material, it is important to know the value used.

Regarding the LiF, ZnS, and SiO_2 critiques in *HOC I*:

Since the publication of *HOC I*, it has been brought to our attention that the k values for LiF calculated using the scattering factors reported by Henke *et al.* [2] do not agree with experiment and appear to be too small by approximately a factor of two. This discrepancy was discovered by Powell and Tanuma [3] during an investigation of mean free paths of photoelectrons in LiF. On closer scrutiny of our calculations, and in consultation with Mark Thomas of Lawrence Berkeley Laboratory, we found that indeed the formulas converting scattering factors to n, k had been misinterpreted. The consequence is that the calculated n, k values for LiF, ZnS, and SiO_2 reported in *HOC I* are too small. Using the corrected formulas the difference in n is small, but the new k is larger by about a factor of two for the binary compounds and about 30% larger for the ternary compound. Calculations for the elements are not changed. We take this opportunity to present the newly calculated values for these three materials in Table I at the end of this chapter. These values are calculated from a new set of scattering factors disseminated by Henke *et al.* [4] and cover a wider range of wavelengths, 1.24–240 Å. We regret any inconvenience that may have been caused through use of the older values.

REFERENCES

1. Edward D. Palik, ed., "Handbook of Optical Constants of Solids," Academic Press, Orlando (1985).
2. B. L. Henke, P. Lee, T. J. Tanaka, R. L. Shimabukuro, and B. K. Fujikawa, "Low Energy X-ray Diagnostics—1981" (D. T. Attwood and B. L. Henke, eds.), p. 340, *AIP Conf. Proc.* No. 75, American Institute of Physics, New York, 1981.
3. C. J. Powell, National Institutes of Science and Technology, Gaithersburg, MD 20899, USA, and S. Tanuma, Central Research Laboratories, Nippon Mining Company, Ltd., 3-17-35 Niizo-Minami, Toda, Saitama 335, Japan, private communication.
4. B. L. Henke, J. C. Davis, E. M. Gullikson, and R. C. C. Perera, "A preliminary report on x-ray photoabsorption coefficients and atomic scattering factors for 92 elements in the 10–10000 eV region," Lawrence Berkeley Laboratory Report 26259, Nov. 1988, Berkeley, CA.

TABLE 1

Optical Constants of LiF, ZnS, and SiO_2 Obtained from Reference [3]

		LiF		ZnS		SiO_2	
eV	Å	*n*	*k*	*n*	*k*	*n*	*k*
10000.0	1.240	0.9999949	1.48E-08	0.9999928	7.09E-07	0.9999945	4.68E-08
9772.4	1.269	0.9999947	1.63E-08	0.9999925	7.69E-07	0.9999942	5.13E-08
9549.9	1.298	0.9999944	1.79E-08	0.9999919	1.75E-07	0.9999939	5.62E-08
9332.5	1.329	0.9999942	1.97E-08	0.9999913	1.91E-07	0.9999936	6.16E-08
9120.1	1.359	0.9999939	2.16E-08	0.9999908	2.09E-07	0.9999933	6.75E-08
8912.5	1.391	0.9999936	2.38E-08	0.9999903	2.28E-07	0.9999930	7.40E-08
8709.6	1.424	0.9999933	2.61E-08	0.9999897	2.50E-07	0.9999927	8.10E-08
8511.4	1.457	0.9999930	2.87E-08	0.9999893	2.73E-07	0.9999923	8.88E-08
8317.6	1.491	0.9999926	3.16E-08	0.9999887	2.98E-07	0.9999920	9.73E-08
8128.3	1.525	0.9999923	3.47E-08	0.9999881	3.26E-07	0.9999916	1.07E-07
7943.3	1.561	0.9999919	3.81E-08	0.9999875	3.56E-07	0.9999912	1.17E-07
7762.5	1.597	0.9999915	4.19E-08	0.9999869	3.88E-07	0.9999908	1.28E-07
7585.8	1.634	0.9999911	4.60E-08	0.9999863	4.24E-07	0.9999903	1.40E-07
7413.1	1.673	0.9999907	5.05E-08	0.9999856	4.63E-07	0.9999899	1.53E-07
7244.4	1.711	0.9999903	5.55E-08	0.9999849	5.06E-07	0.9999894	1.68E-07
7079.5	1.751	0.9999898	6.09E-08	0.9999842	5.52E-07	0.9999889	1.84E-07
6918.3	1.792	0.9999893	6.69E-08	0.9999834	6.03E-07	0.9999884	2.01E-07
6760.8	1.834	0.9999889	7.35E-08	0.9999826	6.58E-07	0.9999878	2.20E-07
6606.9	1.877	0.9999883	8.06E-08	0.9999818	7.18E-07	0.9999872	2.41E-07
6456.5	1.920	0.9999877	8.85E-08	0.9999809	7.83E-07	0.9999866	2.64E-07
6309.6	1.965	0.9999872	9.71E-08	0.9999800	8.55E-07	0.9999860	2.89E-07
6166.0	2.011	0.9999865	1.07E-07	0.9999790	9.32E-07	0.9999853	3.16E-07
6025.6	2.058	0.9999859	1.17E-07	0.9999780	1.02E-06	0.9999846	3.46E-07
5888.4	2.106	0.9999852	1.28E-07	0.9999769	1.11E-06	0.9999839	3.79E-07
5754.4	2.155	0.9999846	1.41E-07	0.9999758	1.21E-06	0.9999831	4.14E-07
5623.4	2.205	0.9999838	1.54E-07	0.9999747	1.32E-06	0.9999823	4.53E-07
5495.4	2.256	0.9999831	1.69E-07	0.9999735	1.44E-06	0.9999815	4.96E-07
5370.3	2.309	0.9999822	1.86E-07	0.9999722	1.57E-06	0.9999806	5.42E-07

5248.1	2.362	0.9999814	2.04E-07	0.9999709	1.71E-06	0.9999797	5.93E-07
5128.6	2.418	0.9999805	2.24E-07	0.9999694	1.87E-06	0.9999787	6.48E-07
5011.9	2.474	0.9999796	2.45E-07	0.9999680	2.03E-06	0.9999777	7.09E-07
4897.8	2.531	0.9999786	2.69E-07	0.9999664	2.22E-06	0.9999766	7.75E-07
4786.3	2.590	0.9999776	2.95E-07	0.9999648	2.42E-06	0.9999755	8.47E-07
4677.4	2.651	0.9999765	3.23E-07	0.9999632	2.63E-06	0.9999744	9.26E-07
4570.9	2.712	0.9999754	3.54E-07	0.9999614	2.87E-06	0.9999731	1.01E-06
4466.8	2.776	0.9999743	3.88E-07	0.9999596	3.12E-06	0.9999719	1.11E-06
4365.2	2.840	0.9999730	4.25E-07	0.9999577	3.40E-06	0.9999705	1.21E-06
4265.8	2.906	0.9999717	4.66E-07	0.9999557	3.71E-06	0.9999691	1.32E-06
4168.7	2.974	0.9999704	5.10E-07	0.9999536	4.04E-06	0.9999676	1.44E-06
4073.8	3.043	0.9999689	5.59E-07	0.9999514	4.40E-06	0.9999661	1.58E-06
3981.1	3.114	0.9999675	6.12E-07	0.9999491	4.79E-06	0.9999645	1.72E-06
3890.5	3.187	0.9999660	6.70E-07	0.9999467	5.21E-06	0.9999629	1.88E-06
3801.9	3.261	0.9999643	7.34E-07	0.9999442	5.68E-06	0.9999611	2.05E-06
3715.4	3.337	0.9999626	8.03E-07	0.9999416	6.18E-06	0.9999592	2.24E-06
3630.8	3.415	0.9999608	8.79E-07	0.9999389	6.72E-06	0.9999573	2.44E-06
3548.1	3.494	0.9999590	9.62E-07	0.9999360	7.32E-06	0.9999554	2.67E-06
3467.4	3.576	0.9999570	1.05E-06	0.9999331	7.96E-06	0.9999532	2.91E-06
3388.4	3.659	0.9999550	1.15E-06	0.9999300	8.66E-06	0.9999510	3.17E-06
3311.3	3.744	0.9999529	1.26E-06	0.9999268	9.42E-06	0.9999487	3.46E-06
3235.9	3.832	0.9999506	1.38E-06	0.9999235	1.02E-05	0.9999464	3.77E-06
3162.3	3.921	0.9999482	1.50E-06	0.9999201	1.11E-05	0.9999439	4.11E-06
3090.3	4.012	0.9999458	1.65E-06	0.9999165	1.21E-05	0.9999412	4.48E-06
3020.0	4.105	0.9999431	1.80E-06	0.9999128	1.32E-05	0.9999385	4.89E-06
2951.2	4.201	0.9999405	1.97E-06	0.9999090	1.43E-05	0.9999356	5.32E-06
2884.0	4.299	0.9999376	2.15E-06	0.9999050	1.55E-05	0.9999326	5.80E-06
2818.4	4.399	0.9999346	2.35E-06	0.9999011	1.69E-05	0.9999296	6.32E-06
2754.2	4.502	0.9999315	2.56E-06	0.999897	1.83E-05	0.9999263	6.88E-06
2691.5	4.607	0.9999282	2.80E-06	0.999893	1.99E-05	0.9999230	7.49E-06
2630.3	4.714	0.9999248	3.06E-06	0.999889	2.16E-05	0.9999195	8.15E-06
2570.4	4.824	0.9999213	3.34E-06	0.999885	2.35E-05	0.9999159	8.86E-06
2511.9	4.936	0.9999175	3.65E-06	0.999883	2.55E-05	0.9999121	9.64E-06
2454.7	5.051	0.9999136	3.98E-06	0.999890	1.68E-05	0.9999082	1.05E-05

(*continued*)

TABLE 1 (*Continued*)

		LiF		ZnS		SiO_2	
eV	Å	*n*	*k*	*n*	*k*	*n*	*k*
2398.8	5.169	0.9999095	4.35E-06	0.999871	1.82E-05	0.9999042	1.14E-05
2344.2	5.289	0.9999051	4.74E-06	0.999863	1.98E-05	0.9999000	1.24E-05
2290.9	5.412	0.9999006	5.18E-06	0.999855	2.15E-05	0.999896	1.35E-05
2238.7	5.538	0.999896	5.65E-06	0.999848	2.34E-05	0.999891	1.46E-05
2187.8	5.667	0.999891	6.17E-06	0.999840	2.55E-05	0.999887	1.59E-05
2138.0	5.799	0.999886	6.73E-06	0.999832	2.77E-05	0.999882	1.72E-05
2089.3	5.934	0.999880	7.34E-06	0.999824	3.00E-05	0.999878	1.87E-05
2041.7	6.073	0.999875	8.01E-06	0.999816	3.26E-05	0.999873	2.03E-05
1995.3	6.214	0.999869	8.73E-06	0.999807	3.54E-05	0.999869	2.20E-05
1949.8	6.359	0.999862	9.52E-06	0.999798	3.84E-05	0.999865	2.38E-05
1905.5	6.507	0.999856	1.04E-05	0.999789	4.17E-05	0.999861	2.58E-05
1862.1	6.658	0.999849	1.13E-05	0.999779	4.52E-05	0.999863	2.80E-05
1819.7	6.813	0.999842	1.23E-05	0.999769	4.91E-05	0.999858	9.04E-06
1778.3	6.972	0.999834	1.35E-05	0.999758	5.33E-05	0.999843	9.87E-06
1737.8	7.135	0.999827	1.47E-05	0.999748	5.78E-05	0.999833	1.08E-05
1698.2	7.301	0.999819	1.60E-05	0.999736	6.26E-05	0.999823	1.18E-05
1659.6	7.471	0.999810	1.74E-05	0.999725	6.78E-05	0.999813	1.28E-05
1621.8	7.645	0.999801	1.90E-05	0.999713	7.35E-05	0.999802	1.40E-05
1584.9	7.823	0.999792	2.07E-05	0.999701	7.96E-05	0.999792	1.53E-05
1548.8	8.005	0.999782	2.25E-05	0.999688	8.62E-05	0.999781	1.66E-05
1513.6	8.191	0.999772	2.46E-05	0.999676	9.34E-05	0.999770	1.81E-05
1479.1	8.382	0.999762	2.67E-05	0.999663	1.01E-04	0.999758	1.98E-05
1445.4	8.578	0.999750	2.91E-05	0.999649	1.10E-04	0.999746	2.15E-05
1412.5	8.778	0.999739	3.17E-05	0.999636	1.19E-04	0.999734	2.35E-05
1380.4	8.982	0.999727	3.45E-05	0.999622	1.28E-04	0.999721	2.55E-05
1349.0	9.191	0.999714	3.75E-05	0.999609	1.39E-04	0.999707	2.78E-05
1318.3	9.405	0.999701	4.08E-05	0.999596	1.51E-04	0.999693	3.03E-05
1288.2	9.625	0.999688	4.43E-05	0.999583	1.63E-04	0.999678	3.30E-05

1258.9	9.849	0.999674	4.82E-05	0.999572	1.76E-04	0.999662	3.59E-05
1230.3	10.08	0.999659	5.23E-05	0.999561	1.89E-04	0.999646	3.91E-05
1202.3	10.31	0.999644	5.69E-05	0.999552	2.02E-04	0.999629	4.25E-05
1174.9	10.55	0.999628	6.17E-05	0.999542	2.15E-04	0.999611	4.62E-05
1148.2	10.80	0.999612	6.70E-05	0.999535	2.30E-04	0.999593	5.03E-05
1122.0	11.05	0.999595	7.28E-05	0.999530	2.45E-04	0.999573	5.47E-05
1096.5	11.31	0.999578	7.90E-05	0.999531	2.62E-04	0.999553	5.95E-05
1071.5	11.57	0.999560	8.57E-05	0.999540	2.79E-04	0.999532	6.48E-05
1047.1	11.84	0.999541	9.30E-05	0.999570	2.98E-04	0.999510	7.05E-05
1023.3	12.12	0.999522	1.01E-04	0.999644	3.18E-04	0.999487	7.66E-05
1000.0	12.40	0.999502	1.10E-04	0.999572	7.60E-05	0.999464	8.29E-05
977.2	12.69	0.999483	1.19E-04	0.999485	8.21E-05	0.999439	9.00E-05
955.0	12.98	0.999462	1.29E-04	0.999427	8.87E-05	0.999413	9.80E-05
933.3	13.28	0.999442	1.40E-04	0.999376	9.59E-05	0.999386	1.07E-04
912.0	13.59	0.999421	1.51E-04	0.999327	1.04E-04	0.999358	1.16E-04
891.3	13.91	0.999400	1.64E-04	0.999281	1.13E-04	0.999329	1.25E-04
871.0	14.23	0.999380	1.77E-04	0.999234	1.22E-04	0.999299	1.36E-04
851.1	14.57	0.999359	1.91E-04	0.999187	1.32E-04	0.999268	1.47E-04
831.8	14.91	0.999340	2.07E-04	0.999138	1.43E-04	0.999235	1.60E-04
812.8	15.25	0.999322	2.24E-04	0.999089	1.55E-04	0.999202	1.74E-04
794.3	15.61	0.999306	2.42E-04	0.999038	1.68E-04	0.999167	1.89E-04
776.3	15.97	0.999294	2.61E-04	0.99899	1.82E-04	0.999132	2.06E-04
758.6	16.34	0.999286	2.83E-04	0.99893	1.97E-04	0.999096	2.23E-04
741.3	16.73	0.999288	3.06E-04	0.99888	2.13E-04	0.999059	2.42E-04
724.4	17.12	0.999310	3.30E-04	0.99882	2.30E-04	0.999021	2.63E-04
708.0	17.51	0.999394	3.57E-04	0.99876	2.49E-04	0.99898	2.85E-04
691.8	17.92	0.999465	2.56E-05	0.99869	2.68E-04	0.99895	3.08E-04
676.1	18.34	0.999278	2.82E-05	0.99863	2.88E-04	0.99891	3.33E-04
660.7	18.77	0.999180	3.11E-05	0.99856	3.12E-04	0.99887	3.62E-04
645.7	19.20	0.999102	3.43E-05	0.99849	3.38E-04	0.99883	3.93E-04
631.0	19.65	0.999031	3.78E-05	0.99841	3.65E-04	0.99879	4.26E-04
616.6	20.11	0.99896	4.16E-05	0.99834	3.94E-04	0.99876	4.61E-04
602.6	20.57	0.99889	4.56E-05	0.99826	4.25E-04	0.99874	4.99E-04
588.8	21.06	0.99883	4.99E-05	0.99817	4.58E-04	0.99872	5.40E-04

(*continued*)

TABLE 1 (*Continued*)

		LiF		ZnS		SiO_2	
eV	Å	*n*	*k*	*n*	*k*	*n*	*k*
575.4	21.55	0.99876	5.47E-05	0.99808	4.95E-04	0.99871	5.85E-04
562.3	22.05	0.99868	5.99E-05	0.99799	5.34E-04	0.99874	6.33E-04
549.5	22.56	0.99861	6.55E-05	0.99790	5.77E-04	0.99890	6.86E-04
537.0	23.09	0.99853	7.16E-05	0.99780	6.24E-04	0.99887	2.04E-04
524.8	23.63	0.99845	7.83E-05	0.99769	6.74E-04	0.99862	2.21E-04
512.9	24.17	0.99837	8.56E-05	0.99759	7.29E-04	0.99848	2.39E-04
501.2	24.74	0.99828	9.35E-05	0.99748	7.88E-04	0.99835	2.58E-04
489.8	25.31	0.99819	1.02E-04	0.99736	8.52E-04	0.99824	2.79E-04
478.6	25.91	0.99810	1.12E-04	0.99724	9.22E-04	0.99812	3.02E-04
467.7	26.51	0.99800	1.22E-04	0.99712	9.97E-04	0.99801	3.26E-04
457.1	27.12	0.99790	1.34E-04	0.99700	1.08E-03	0.99789	3.52E-04
446.7	27.76	0.99779	1.46E-04	0.99688	1.16E-03	0.99778	3.80E-04
436.5	28.40	0.99768	1.60E-04	0.99674	1.25E-03	0.99765	4.11E-04
426.6	29.06	0.99756	1.75E-04	0.99661	1.34E-03	0.99753	4.44E-04
416.9	29.74	0.99743	1.91E-04	0.99647	1.44E-03	0.99740	4.80E-04
407.4	30.43	0.99731	2.09E-04	0.99633	1.55E-03	0.99727	5.18E-04
398.1	31.14	0.99717	2.29E-04	0.99618	1.67E-03	0.99713	5.60E-04
389.0	31.87	0.99703	2.50E-04	0.99603	1.80E-03	0.99698	6.05E-04
380.2	32.61	0.99688	2.73E-04	0.99589	1.93E-03	0.99683	6.53E-04
371.5	33.37	0.99673	2.96E-04	0.99574	2.06E-03	0.99667	7.06E-04
363.1	34.15	0.99657	3.22E-04	0.99558	2.20E-03	0.99651	7.64E-04
354.8	34.94	0.99640	3.51E-04	0.99541	2.35E-03	0.99634	8.26E-04
346.7	35.76	0.99622	3.81E-04	0.99524	2.51E-03	0.99616	8.93E-04
338.8	36.60	0.99603	4.15E-04	0.99507	2.68E-03	0.99598	9.65E-04
331.1	37.45	0.99584	4.51E-04	0.99489	2.86E-03	0.99579	1.04E-03
323.6	38.31	0.99563	4.91E-04	0.99471	3.05E-03	0.99559	1.13E-03
316.2	39.21	0.99542	5.34E-04	0.99453	3.26E-03	0.99539	1.22E-03
309.0	40.12	0.99520	5.81E-04	0.99435	3.48E-03	0.99518	1.32E-03
302.0	41.05	0.99496	6.32E-04	0.99417	3.71E-03	0.99496	1.43E-03

295.1	42.01	0.99472	6.86E-04	0.99399	3.96E-03	0.99473	1.54E-03
288.4	42.99	0.99446	7.45E-04	0.99381	4.22E-03	0.99450	1.66E-03
281.8	44.00	0.99419	8.09E-04	0.99364	4.50E-03	0.99426	1.79E-03
275.4	45.02	0.99391	8.78E-04	0.99349	4.78E-03	0.99401	1.92E-03
269.1	46.07	0.99362	9.52E-04	0.99334	5.04E-03	0.99375	2.07E-03
263.0	47.14	0.99331	1.03E-03	0.99317	5.32E-03	0.99348	2.22E-03
257.0	48.24	0.99299	1.12E-03	0.99299	5.61E-03	0.99320	2.39E-03
251.2	49.36	0.99265	1.21E-03	0.99281	5.92E-03	0.99291	2.57E-03
245.5	50.50	0.99229	1.32E-03	0.99263	6.24E-03	0.99260	2.77E-03
239.9	51.68	0.99192	1.43E-03	0.99245	6.59E-03	0.99229	2.98E-03
234.4	52.89	0.99154	1.55E-03	0.99226	6.95E-03	0.99197	3.21E-03
229.1	54.12	0.99113	1.68E-03	0.99208	7.34E-03	0.99165	3.46E-03
223.9	55.37	0.99071	1.82E-03	0.99190	7.76E-03	0.99131	3.72E-03
218.8	56.67	0.99027	1.97E-03	0.99174	8.21E-03	0.99097	4.01E-03
213.8	57.99	0.9898	2.13E-03	0.99161	8.69E-03	0.99063	4.32E-03
208.9	59.35	0.9893	2.31E-03	0.99152	9.17E-03	0.99028	4.66E-03
204.2	60.72	0.9888	2.50E-03	0.99143	9.67E-03	0.9899	5.02E-03
199.5	62.15	0.9883	2.71E-03	0.99137	1.02E-02	0.9896	5.41E-03
195.0	63.58	0.9878	2.93E-03	0.99134	1.08E-02	0.9892	5.83E-03
190.6	65.05	0.9872	3.17E-03	0.99136	1.13E-02	0.9889	6.28E-03
186.2	66.59	0.9866	3.43E-03	0.99146	1.19E-02	0.9886	6.78E-03
182.0	68.12	0.9860	3.71E-03	0.99164	1.26E-02	0.9884	7.30E-03
177.8	69.73	0.9853	4.01E-03	0.99194	1.32E-02	0.9882	7.76E-03
173.8	71.34	0.9847	4.33E-03	0.99237	1.38E-02	0.9881	8.21E-03
169.8	73.02	0.9840	4.68E-03	0.99310	1.44E-02	0.9879	8.61E-03
166.0	74.69	0.9832	5.06E-03	0.99454	1.51E-02	0.9878	8.92E-03
162.2	76.44	0.9825	5.46E-03	0.99827	9.47E-03	0.9875	9.18E-03
158.5	78.22	0.9817	5.90E-03	0.99434	9.90E-03	0.9872	9.48E-03
154.9	80.04	0.9809	6.37E-03	0.99289	1.04E-02	0.9868	9.79E-03
151.4	81.89	0.9800	6.87E-03	0.99203	1.08E-02	0.9863	1.02E-02
147.9	83.83	0.9791	7.41E-03	0.99142	1.13E-02	0.9859	1.08E-02
144.5	85.80	0.9782	8.00E-03	0.99103	1.18E-02	0.9855	1.15E-02
141.3	87.75	0.9772	8.63E-03	0.99059	1.19E-02	0.9853	1.23E-02
138.0	89.84	0.9763	9.32E-03	0.9899	1.20E-02	0.9853	1.29E-02

(*continued*)

TABLE 1 (*Continued*)

		LiF		ZnS		SiO_2	
eV	Å	*n*	*k*	*n*	*k*	*n*	*k*
134.9	91.91	0.9752	1.01E-02	0.9890	1.25E-02	0.9853	1.34E-02
131.8	94.07	0.9742	1.09E-02	0.9883	1.31E-02	0.9854	1.38E-02
128.8	96.26	0.9731	1.17E-02	0.9878	1.38E-02	0.9854	1.41E-02
125.9	98.48	0.9720	1.26E-02	0.9873	1.45E-02	0.9854	1.43E-02
123.0	100.8	0.9709	1.36E-02	0.9869	1.51E-02	0.9855	1.44E-02
120.2	103.1	0.9697	1.46E-02	0.9864	1.57E-02	0.9853	1.41E-02
117.5	105.5	0.9685	1.57E-02	0.9860	1.63E-02	0.9849	1.39E-02
114.8	108.0	0.9672	1.69E-02	0.9855	1.69E-02	0.9843	1.37E-02
112.2	110.5	0.9659	1.82E-02	0.9850	1.76E-02	0.9834	1.38E-02
109.7	113.0	0.9646	1.95E-02	0.9844	1.82E-02	0.9827	1.39E-02
107.2	115.7	0.9631	2.10E-02	0.9840	1.89E-02	0.9819	1.42E-02
104.7	118.4	0.9616	2.27E-02	0.9835	1.96E-02	0.9813	1.45E-02
102.3	121.2	0.9601	2.45E-02	0.9830	2.03E-02	0.9809	1.48E-02
100.0	124.0	0.9588	2.67E-02	0.9824	2.10E-02	0.9821	1.52E-02
97.7	126.9	0.9575	2.88E-02	0.9818	2.17E-02	0.9792	1.09E-02
95.5	129.8	0.9562	3.12E-02	0.9812	2.24E-02	0.9762	1.16E-02
93.3	132.9	0.9550	3.37E-02	0.9806	2.32E-02	0.9740	1.24E-02
91.2	135.9	0.9542	3.65E-02	0.9800	2.40E-02	0.9721	1.32E-02
89.1	139.2	0.9536	3.92E-02	0.9793	2.48E-02	0.9702	1.40E-02
87.1	142.3	0.9531	4.16E-02	0.9786	2.56E-02	0.9683	1.49E-02
85.1	145.7	0.9526	4.39E-02	0.9779	2.65E-02	0.9665	1.59E-02
83.2	149.0	0.9518	4.63E-02	0.9771	2.75E-02	0.9646	1.69E-02
81.3	152.5	0.9511	4.88E-02	0.9763	2.85E-02	0.9627	1.80E-02
79.4	156.2	0.9503	5.12E-02	0.9755	2.96E-02	0.9608	1.92E-02
77.6	159.8	0.9492	5.38E-02	0.9747	3.06E-02	0.9588	2.04E-02
75.9	163.4	0.9479	5.67E-02	0.9740	3.18E-02	0.9568	2.18E-02
74.1	167.3	0.9466	6.00E-02	0.9732	3.29E-02	0.9547	2.32E-02
72.4	171.2	0.9453	6.39E-02	0.9724	3.41E-02	0.9525	2.46E-02
70.8	175.1	0.9444	6.84E-02	0.9716	3.53E-02	0.9503	2.62E-02

69.2	179.2	0.9438	7.35E-02	0.9708	3.65E-02	0.9481	2.79E-02
67.6	183.4	0.9444	7.96E-02	0.9700	3.77E-02	0.9457	2.97E-02
66.1	187.6	0.9464	8.48E-02	0.9691	3.90E-02	0.9434	3.16E-02
64.6	191.9	0.9492	8.97E-02	0.9682	4.03E-02	0.9409	3.37E-02
63.1	196.5	0.9525	9.35E-02	0.9673	4.16E-02	0.9384	3.59E-02
61.7	200.9	0.9558	9.65E-02	0.9664	4.29E-02	0.9359	3.82E-02
60.3	205.6	0.9593	9.94E-02	0.9654	4.43E-02	0.9333	4.07E-02
58.9	210.5	0.9632	0.102	0.9646	4.58E-02	0.9307	4.33E-02
57.5	215.6	0.9680	0.103	0.9637	4.70E-02	0.9279	4.61E-02
56.2	220.6	0.9738	0.104	0.9626	4.82E-02	0.9252	4.91E-02
55.0	225.4	0.9891	0.104	0.9614	4.95E-02	0.9224	5.23E-02
53.7	230.9	0.9741	8.02E-02	0.9602	5.08E-02	0.9196	5.56E-02
52.5	236.2	0.9650	8.37E-02	0.9589	5.21E-02	0.9168	5.92E-02
51.3	241.7	0.9600	8.74E-02	0.9576	5.35E-02	0.9140	6.31E-02

Chapter 2

Convention Confusions

R. T. HOLM
Naval Research Laboratory
Washington, D.C.

I. Introduction 21
II. Units 22
III. Wave Equation 22
IV. Polarization 26
A. Linear Polarization 28
B. Circular Polarization 30
V. Fresnel's Amplitude Reflection Coefficients 37
A. *s* Polarization 38
B. *p* Polarization 40
C. Phase Change 41
VI. Nomenclature 50
VII. Concluding Remarks 51
Acknowledgments 52
References 52

INTRODUCTION I

As with other scientific fields, optics has its own genre of conventions. The general subject of conventions includes units, symbols, definitions, nomenclature, and sign choices. One of the criticisms of *HOC I* was a lack of a consistent set of conventions by the contributing authors. This criticism can also be voiced about optics literature in general. Almost everyone, even "old hands," has experienced that frustrating feeling of trying to reconcile differences caused by conventions. However, most authors (for whatever reasons) sidestep the convention issue completely.

We do not intend to advocate any particular set of conventions. Instead, we present different conventions that are in general use and discuss conflicts that result because of their differences. We also include reasons that are put forward to justify a particular convention. Here and there, we weave in some history. For a detailed account of the beginnings of the wave theory of light, see the book by Buchwald [1].

Copyright © 1991 by Academic Press.
All rights of reproduction in any form reserved.
ISBN 0-12-544422-2

In this chapter we discuss the plane-wave solutions to the electromagnetic wave equation. The solution of choice dictates which of the two forms of the complex refractive index ($n + ik$ or $n - ik$) is used. We point out that opposite terms are used to label the same polarization state. The different sign conventions used in Fresnel's reflection equations and the subsequent misunderstandings that this leads to are discussed. The various definitions for the expressions *phase change, in phase,* and *out of phase*, and the resulting ambiguities, are presented. Finally, the meanings of *reflection*, *reflectance*, and *reflectivity* are given. We assume the reader has some familiarity with optic and electromagnetic theory.

The actual set of conventions that one uses is completely arbitrary—the physics, after all, has to be independent of convention. As far as we know, Muller has provided the most extensive discussion of different conventions that are used in optics [2]. At the Second International Conference on Ellipsometry, held at the University of Nebraska in 1968, he proposed a standard set of conventions, which have become known as the Nebraska conventions. Bennett and Bennett have also commented on the convention issue [3]. Although the comments and recommendations by Muller and by Bennett and Bennett are addressed primarily to the ellipsometric community, they are relevant to anyone working with electromagnetic waves.

II UNITS

Since 1960, the single convention in optics that should be standard is electromagnetic units. The *International System of Units*, abbreviated SI units, has been adopted nearly worldwide [4–6]. The SI system is based on the rationalized MKSA (meter, kilogram, second, ampere) system of units. Although most journals request that SI units be used, many authors continue to use one of the other systems (Gaussian, practical [7], and so on). Jackson [8] and Frankl [9] provide enlightening comparisons of the common systems of units and conversion tables between systems. We use SI units in this chapter.

III WAVE EQUATION

The wave equations for the electric and magnetic fields, as developed in any electromagnetic textbook, are

$$\nabla^2 \mathbf{E} = \varepsilon\varepsilon_0\mu_0 \frac{\partial^2 \mathbf{E}}{\partial t^2} + \sigma\mu_0 \frac{\partial \mathbf{E}}{\partial t} \tag{1a}$$

$$\nabla^2\mathbf{H} = \varepsilon\varepsilon_0\mu_0\frac{\partial^2\mathbf{H}}{\partial t^2} + \sigma\mu_0\frac{\partial\mathbf{H}}{\partial t}, \tag{1b}$$

where **E** is the electric field strength in volt/meter (V/m), **H** is the magnetic field strength in ampere/meter (A/m), ε_0 is the permittivity of free space in coulomb^2/newton meter^2 (C^2/N m^2), μ_0 is the permeability of free space in weber/ampere meter (Wb/A m), ε is the dielectric constant (relative permittivity), and σ is the conductivity in siemens/meter (S/m). The wave equations shown above are applicable to media that are homogeneous, isotropic, linear, and nonmagnetic. For simplicity, one usually establishes a right-handed Cartesian coordinate system in which the wave propagates along one axis, say the z axis. For layered media, the z axis is chosen to be perpendicular to the interfaces.

Whether the wave equation is for an electromagnetic wave, a stretched string, or a sound wave, the same four well-known plane-wave solutions apply [10, 11]. These four solutions for the electric field of an electromagnetic wave may be formally expressed in complex form as

$$\mathbf{E} = \mathbf{E}_0 e^{c_1 i(c_2 qz - \omega t)}, \tag{2}$$

where c_1 and c_2 are sign coefficients and can take the values of ± 1; $q(=2\pi/\lambda)$ is the wave number [12] and is the magnitude of the wave or propagation vector, **q**; λ is the vacuum wavelength; $\omega(=2\pi f)$ is the angular frequency; f is the frequency; and $\mathbf{E}_0$ is a vector representing the direction and maximum amplitude of **E**.

In Eq. 2 the coefficient c_2 determines the direction of propagation. Time, t, is inherently positive and always increasing. When $c_2 = +1$, z must increase so that the phase term $qz - \omega t$ remains constant. Thus, the wave propagates toward increasing $z(+z$ direction). When $c_2 = -1$, the phase term $-qz - \omega t$ remains constant for decreasing z, that is, propagation toward decreasing $z(-z$ direction).

As will be discussed shortly, the choice of c_1 determines the form in which complex numbers have to be expressed. If $c_1 = +1$, complex numbers take the form $a' + ia''$, whereas if $c_1 = -1$, complex numbers take the form $a' - ia''$, where prime and double prime denote the real and imaginary parts of a complex quantity, respectively. The effects of the values of c_1 and c_2 are summarized in Table I.

We have now reached the point at which the first arbitrary choice must be made. One has to decide to use either $c_1 = +1$ or $c_1 = -1$, that is, to use either a minus sign or a plus sign in front of ωt. However, whichever choice is made for c_1, both values of c_2 are admissible. A general solution consists of a linear superposition of two waves propagating in opposite directions.

In the early days of electromagnetic theory, the $\exp[i(\omega t \pm qz)]$ solution was commonly used. Today, most opticists still prefer that solution. However, physicists (at least since the advent of quantum mechanics)

TABLE I

Possible Forms of Solution to Wave Equation, with Corresponding Propagation Direction and Form for Complex Numbers

c_1	c_2	$e^{c_1 i(c_2 qz - \omega t)}$	Propagation direction	Complex numbers
1	1	$e^{i(qz-\omega t)}$	$+z$	$a'+ia''$
1	−1	$e^{i(-qz-\omega t)}$	$-z$	$a'+ia''$
−1	1	$e^{i(\omega t-qz)}$	$+z$	$a'-ia''$
−1	−1	$e^{i(\omega t+qz)}$	$-z$	$a'-ia''$

$$(n+ik)^2=\tilde{\varepsilon}=\varepsilon_\infty\left(1-\frac{\omega_p^2}{\omega(\omega+i\gamma)}+\frac{\omega_L^2-\omega_T^2}{\omega_T^2-\omega^2-i\Gamma\omega}\right)$$

$$(n-ik)^2=\tilde{\varepsilon}=\varepsilon_\infty\left(1-\frac{\omega_p^2}{\omega(\omega-i\gamma)}+\frac{\omega_L^2-\omega_T^2}{\omega_T^2-\omega^2+i\Gamma\omega}\right)$$

Included is the infrared dielectric function for polar semiconductors expressed in the two complex-number forms.

prefer to use the $\exp[i(\pm qz-\omega t)]$ solution. The one-dimensional form of the Schrödinger wave equation for a free particle of mass m is [13]

$$i\hbar\frac{\partial\psi}{\partial t}=-\frac{\hbar^2}{2m}\frac{\partial^2\psi}{\partial z^2}. \tag{3}$$

Note that the Schrödinger equation contains a first derivative with respect to time rather than a second derivative as the electromagnetic wave equation does. As a result, the kinetic energy of the particle is positive [13] only if the $\exp[i(\pm qz-\omega t)]$ solution is used. Being comfortable with this form, physicists carry this solution from quantum mechanics to other fields, such as optics.

Other reasons have been proffered for picking one choice of c_1 over the other. One consideration is whether one is dealing with temporal or spatial phenomena. For temporal effects, it is the damping in time at a fixed point in space that is important. In this situation, the angular frequency, ω, is taken as complex [14], so that the imaginary term accounts for damping in time. Hence, it is convenient to choose $\exp(i\omega t)$ and discard the spatial terms.

Circuit theory primarily deals with temporal phenomena, so electrical engineers are usually reared on $\exp(\mathrm{i}\omega t)$. Then, when they study wave propagation, they continue to use the $\exp(i\omega t)$ formalism because that is what they are comfortable with.

Spatial phenomena are primarily concerned with steady-state effects.

For a wave propagating in the z direction, for example, it is the spatial damping that is important. Thus, q is complex, and it is convenient to use $\exp(iqz)$ and to discard the temporal terms. In either case, a positive exponent is chosen, so that one does not continually have to carry a minus sign along when writing equations (laziness).

Many textbooks simply state a solution to the wave equation without discussing reasons for their choice or even mentioning that another possibility exists. Several textbooks first give an abstract solution of the form $f(qz-\omega t)+g(qz+\omega t)$. Then without any explanation, however, they say that it is "convenient" to use the $\exp[i(\omega t \pm qz)]$ solution. An otherwise excellent optics book actually uses both conventions throughout the book. Although each section is consistent within itself, it becomes confusing when comparing sections.

Before leaving this section, let us have that talk about complex numbers. In a lossy material the wave number is complex and given by

$$\tilde{q}=\frac{\omega}{c}\tilde{n}, \tag{4}$$

where $\tilde{n}$ is the complex refractive index and a tilde ($\tilde{}$) signifies complex numbers. All complex quantities must be expressed in the form

$$\tilde{a}=a'+ic_1a'', \tag{5}$$

so that

$$\tilde{q}=q'+ic_1q'', \tag{6a}$$

and

$$\tilde{n}=n+ic_1k, \tag{6b}$$

where n is the refractive index, k is the extinction coefficient [15], and c_1 takes the value chosen in Eq. 2. Note that q', q'', n, and k are all positive. The factor c_1 in Eq. 5 assures that a wave decays (rather than grows) exponentially as it propagates; see Table I. To reiterate, if one uses the $\exp[i(\pm qz-\omega t)]$ solution, the complex refractive index must be written $\tilde{n}=n+ik$. For the $\exp[i(\omega t \pm qz)]$ solution, the $\tilde{n}=n-ik$ form is required.

An equation expressed in one form of complex number can be converted to the other form by taking its complex conjugate [16]. As an example, we

have included in Table I the equation for the classical dielectric function, $\tilde{\varepsilon}$, which describes the optical properties of a polar semiconductor in the infrared [17]. Free carriers (second term) and phonons (third term) are formulated in terms of the Drude and Lorentz models, respectively. In the dielectric function ε_∞ is the high-frequency dielectric constant; ω_p is the bulk plasma frequency; γ is the free-carrier damping constant; ω_L and ω_T are the longitudinal and transverse optic-phonon frequencies, respectively; and Γ is the phonon damping constant.

One must exercise caution when programming reflectance (and other) formulas that contain complex variables [18]. When taking the square root of a complex number, whether it be in the $(a'+ia'')$ or the $(a'-ia'')$ form, most (all?) compilers will return the answer in the correct form. However, when taking the square root of a negative real number, compilers return a positive imaginary number; for example, $(-4)^{1/2}=+2i$. This is the correct answer for the $(a'+ia'')$ form, but for the $(a'-ia'')$ form, the correct answer is $-2i$.

If one writes one's own programs and uses formulas that require the $(a'-ia'')$ form, it is easy to test complex variables before taking a square root. Just insert a line of code that sets (square root) $=-$(square root) if a complex number has only a negative real part. Such situations arise when calculating internal reflection spectra (IRS) [19], in which terms like $[1-(n_i\sin\theta_i)^2/n_t^2]^{1/2}$, with $n_i\sin\theta_i > n_t$, are encountered. As Spiller [18] points out, commercial computer programs may not offer any provision for setting the form of complex numbers. To obtain the correct answer, either assign negative values to the thicknesses of those films whose extinction coefficients are zero, or set k to some small value that does not significantly affect the results.

Before those who use the $(n-ik)$ form panic, we point out that reflectance programs that do not test complex numbers yield the correct results most of the time. We had used an IRS program successfully for over a year before it gave reflectances greater than unity for a particular IRS configuration. It takes a long time to find such a "bug." To be on the safe side, put in a test.

Finally, let us give a gentle reminder. The form for $\tilde{n}$ (and other complex variables) has nothing to do with the direction of propagation. The form is determined solely by the sign of ωt in Eq. 2.

IV POLARIZATION

In addition to its amplitude, frequency, and direction of propagation, an electromagnetic wave is characterized by the orientation of its field vectors,

E and **H**. Since, in an isotropic medium, an electromagnetic wave is transverse rather than longitudinal, its field vectors are normal to its wave vector. The temporal behavior of the orientation of the electric field, **E**, as observed at a fixed location along the propagation direction, determines the *polarization state* of the wave [20–22]. The polarization state is represented by the curve traced out by the tip of the instantaneous **E** vector. The electric field is chosen as the descriptor of the polarization state because it exerts a much stronger force on electrons than the magnetic field [23].

Polarization terminology and even the word *polarization* itself [24–26] are perplexing, if not downright contradictory. The first reported observation of an effect arising directly from polarization was by Erasmus Bartholinus [27, 28]. In 1670 he described double refraction, in which two images are seen, in calcite (Iceland spar) [29]. It was not until 1808 that Etienne Louis Malus discovered polarization by reflection. While looking through a calcite crystal at the reflection of the setting sun from a window of a nearby building, he saw only one image, rather than two, for certain orientations of the crystal [30, 31]. Malus introduced the term *polarization* to distinguish the two light beams that emerge from a calcite crystal. We shall now present the various ways that polarization terms are defined and used.

When a phase term δ is included, four different forms can be found in the literature to express the electric-field strength of a monochromatic wave propagating in the $+z$ direction [2]:

$$\mathbf{E} = \mathbf{E}_0 e^{i(\omega t - qz + \delta)} \tag{7a}$$

$$\mathbf{E} = \mathbf{E}_0 e^{i(\omega t - qz - \delta)} \tag{7b}$$

$$\mathbf{E} = \mathbf{E}_0 e^{i(qz - \omega t + \delta)} \tag{7c}$$

$$\mathbf{E} = \mathbf{E}_0 e^{i(qz - \omega t - \delta)}. \tag{7d}$$

Most authors, when describing polarization, revert to the real form. The real parts of Eq. 7 are

$$\mathbf{E} = \mathbf{E}_0 \cos(\omega t - qz + \delta) \tag{8a}$$

$$\mathbf{E} = \mathbf{E}_0 \cos(\omega t - qz - \delta) \tag{8b}$$

$$\mathbf{E} = \mathbf{E}_0 \cos(qz - \omega t + \delta) = \mathbf{E}_0 \cos(\omega t - qz - \delta) \tag{8c}$$

$$\mathbf{E} = \mathbf{E}_0 \cos(qz - \omega t - \delta) = \mathbf{E}_0 \cos(\omega t - qz + \delta). \tag{8d}$$

Thus, we see that Eqs. 8a and 8d are mathematically equivalent, as are Eqs. 8b and 8c. We shall refer to Eqs. 8a and 8d as the $(\omega t + \delta)$ form, and to Eqs. 8b and 8c as the $(\omega t - \delta)$ form. What is important is the relative sign of the time and phase terms [2, 22, 32]. If the phase term has the same sign as ωt (that is, $\delta > 0$ with the $(\omega t + \delta)$ form and $\delta < 0$ with the $(\omega t - \delta)$ form), then δ represents an increase in time, or a phase advance (leading). Likewise, if the sign of the phase term is opposite that of ωt (that is, $\delta < 0$ with the $(\omega t + \delta)$ form and $\delta > 0$ with the $(\omega t - \delta)$ form), then δ represents a phase retardation (lagging).

An arbitrary wave, **E**, propagating in the $+z$ direction can be treated as a superposition of two orthogonal waves, E_x and E_y, expressed in the $(\omega t - \delta)$ form by

$$\begin{aligned} E_x &= E_{x0} \cos(\omega t - qz - \delta_x) \\ E_y &= E_{y0} \cos(\omega t - qz - \delta_y), \end{aligned} \tag{9a}$$

and in the $(\omega t + \delta)$ form by

$$\begin{aligned} E_x &= E_{x0} \cos(\omega t - qz + \delta_x) \\ E_y &= E_{y0} \cos(\omega t - qz + \delta_y), \end{aligned} \tag{9b}$$

such that

$$\mathbf{E} = \hat{\imath} E_x + \hat{\jmath} E_y, \tag{10}$$

where $\hat{\imath}$ and $\hat{\jmath}$ are unit vectors in the $+x$ and $+y$ directions, respectively, of an (again arbitrary) right-handed Cartesian coordinate system. However, practical considerations based on the experimental system ultimately dictate the selection of a coordinate system. The actual polarization state of the wave depends on the relative values of E_{x0} and E_{y0} and of δ_x and δ_y. For arbitrary values of E_{x0}, E_{y0}, δ_x, and δ_y, the wave is *elliptically polarized*. Two special cases result: (A) when $\delta \equiv \delta_y - \delta_x = 0$ or $\pm\pi$; and (B) when $E_{x0} = E_{y0}$ and in addition $\delta = \pm\pi/2$. (Almost every author defines δ as $\delta_y - \delta_x$, rather than as $\delta_x - \delta_y$.)

A Linear Polarization

Even though polarization is referenced to the temporal variation of the orientation of **E**, many authors provide a spatial visualization of the

component (E_x and E_y) and resultant (**E**) waves at an instant of time. Such a snapshot [22, 33] is shown in Fig. 1 for $\delta = 0$. A sinusoidal curve is an expedient representation of a monochromatic light wave. If we fixed our attention at some point on the z axis, we would see that **E** oscillates, with time, along a fixed line that is normal to the z axis. **E** would change direction every half cycle, having maximum extensions of $\pm E_0$ $[= (E_{x0}^2 + E_{y0}^2)^{1/2}]$. The curve is drawn by connecting the tips of the instantaneous **E** vectors along the z axis at an instant of time. The resultant wave lies in a plane inclined at an angle $\alpha[= \tan^{-1}(E_{y0}/E_{x0})]$ to the x axis. Such a wave is said to be *linearly polarized*. Sometimes a linearly polarized wave is referred to as being *plane polarized* because the wave lies in a plane, as in Fig. 1; however, many authors discourage the use of this term [24, 26].

Three points are worth noting. First, both E_x and E_y in Fig. 1 are also linearly polarized. Second, if $\delta = \pm\pi$, then E_y inverts, which means that **E** lies on the other side of the x axis. Third, both the $(\omega t - \delta)$ and $(\omega t + \delta)$ forms (Eq. 9) give the same description of linear polarization.

Another expression that has long been in disfavor [24, 26] is *plane of polarization*. The plane of polarization, as originally defined by Malus [27], is the plane that is normal to the crystal surface and contains the light ray polarized by reflection. That plane is nothing more than the plane of incidence. Malus' definition was more closely tied to the procedure of producing polarized light than to the physical nature of light. About forty years later, people discovered the vector (**E** and **H**) nature of light, and they figured out that it is actually the **H** field, rather than the **E** field, that lies in Malus' plane of polarization. As a result, some authors have tried to redefine the plane of polarization to be the plane containing **E** and the wave vector **q**; such are the ways that ambiguity raises its evil head.

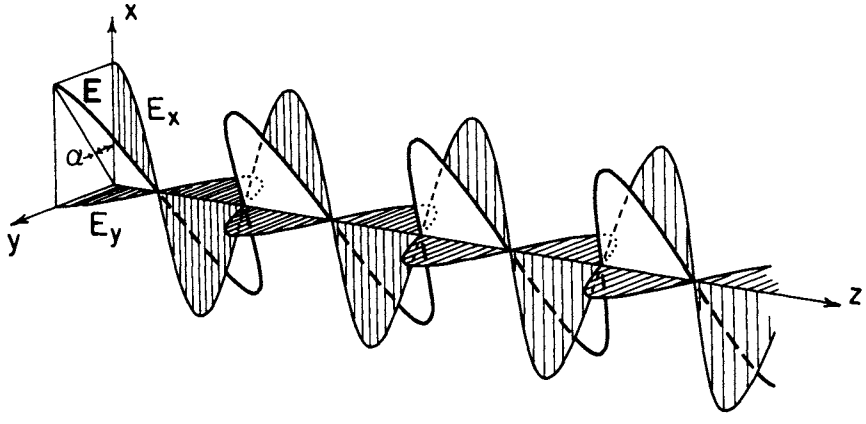

Fig. 1. Snapshot of a linearly polarized wave propagating in the $+z$ direction. E_x and E_y are the component fields; **E** is the resultant field inclined at an angle α to the x axis.

To make matters worse, the IEEE has defined the plane of polarization [34] to be the plane containing **E** and **H**. Thus, the IEEE plane of polarization is perpendicular to that of opticists.

Several authors [24, 25] have pointed out that a plane of polarization does not define a unique wave (although a particular wave does have a unique plane of polarization). As an alternative, many authors prefer to prescribe a linearly polarized wave by the direction of its wave vector and the direction of vibration of the **E** field. Clark [26] suggests that azimuth (rather than direction) of vibration is a better term to describe the orientation of the **E** field.

B Circular Polarization

When $E_{x0} = E_{y0}$ and $\delta = \pm \pi/2$, electromagnetic waves are *circularly polarized*. The sense of rotation depends on the sign of δ and which form of Eq. 9 is used. Since it is the *difference* between the phases of E_x and E_y that is important, we let $\delta_x = 0$ so that $\delta = \delta_y$. Initially, circular polarization will be described from a strictly mathematical point of view. Then the contradictory ways in which various disciplines label circular polarization will be presented.

1 $(\omega t - \delta)$ Form

First, consider the $(\omega t - \delta)$ form with $E_{x0} = E_{y0} = E_0$. The component field equations from Eq. 9a for $\delta = -\pi/2$ are

$$\begin{aligned} E_x &= E_0 \cos(\omega t - qz) \\ E_y &= -E_0 \sin(\omega t - qz), \end{aligned} \tag{11a}$$

and the equations for $\delta = +\pi/2$ are

$$\begin{aligned} E_x &= E_0 \cos(\omega t - qz) \\ E_y &= E_0 \sin(\omega t - qz). \end{aligned} \tag{11b}$$

Figure 2a shows a plot of the E_x and E_y components as a function of ωt for $\delta = -\pi/2$, and Fig. 2b shows a similar plot for $\delta = +\pi/2$. It can be seen that when $\delta = -\pi/2$, E_y leads E_x by $\pi/2$ (Fig. 2a), whereas when $\delta = +\pi/2$, E_y lags E_x by $\pi/2$ (Fig. 2b).

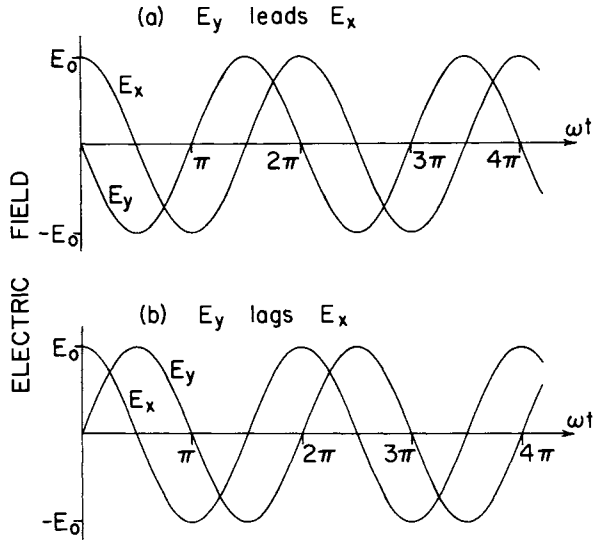

Fig. 2. The orthogonal components of circularly polarized waves as a function of time. In (a) E_y leads E_x, and in (b) E_y lags E_x.

Recall that the resultant field, **E**, is the vectorial sum (Eq. 10) of E_x and E_y and that polarization is related to the time variation of **E** at a fixed location along z. Figures 3a and 3b show the position (orientation) of **E** in the x–y plane located at $z=0$, at several values of ωt, for $\delta=-\pi/2$ and $\delta=+\pi/2$, respectively. In Fig. 3a, **E** rotates, with constant amplitude and angular frequency ω, from the positive x axis toward the negative y axis. In

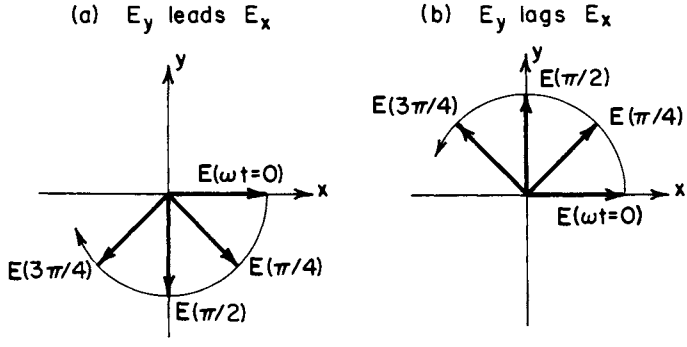

Fig. 3. Orientation of the field vector, **E**, of circularly polarized waves at several values of ωt, with the sense of rotation indicated. In (a) E_y leads E_x (right-handed, traditional optics), and in (b) E_y lags E_x (left-handed).

contrast, **E** rotates from the positive x axis toward the positive y axis in Fig. 3b.

2 $(\omega t+\delta)$ Form

Let us now repeat the above procedure for the $(\omega t+\delta)$ form. The component field equations from Eq. 9b for $\delta=-\pi/2$ are

$$\begin{aligned} E_x &= E_0\cos(\omega t-qz) \\ E_y &= E_0\sin(\omega t-qz), \end{aligned} \tag{12a}$$

and the equations for $\delta=+\pi/2$ are

$$\begin{aligned} E_x &= E_0\cos(\omega t-qz) \\ E_y &= -E_0\sin(\omega t-qz). \end{aligned} \tag{12b}$$

We see that Eq. 12a is identical to Eq. 11b and that Eq. 12b is identical to Eq. 11a. Thus, it is apparent that Fig. 2b (E_y lags E_x) and Fig. 3b are applicable to the $(\omega t+\delta)$ form when $\delta=-\pi/2$. Likewise, Fig. 2a (E_y leads E_x) and Fig. 3a are applicable to the $(\omega t+\delta)$ form when $\delta=+\pi/2$.

We suspect that the reader feels befuddled by now. The crux of the analysis can be summarized in two statements.

(1) If the phase term has the same (opposite) sign as ωt, then E_y leads (lags) E_x (see the discussion between Eqs. 8 and 9).

(2) If E_y leads (lags) E_x, then the sense of rotation of **E** is from the positive x axis toward the negative (positive) y axis [35].

3 Spatial Visualization

In addition to the temporal pictures given in Figs. 2 and 3, many authors also present a spatial visualization. Let us do so at $\omega t=0$. Rather than depicting in detail the four combinations obtained from the $(\omega t\pm\delta)$ forms with $\delta=\pm\pi/2$, it will suffice to consider only one combination, let us say the $(\omega t-\delta)$ form with $\delta=-\pi/2$.

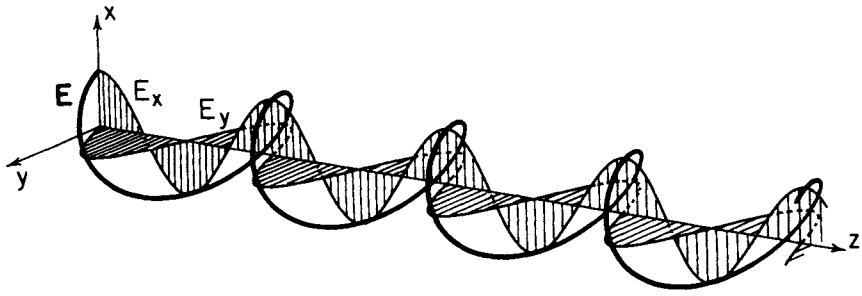

Fig. 4. Spatial representation (snapshot) of a circularly polarized wave propagating in the $+z$ direction. E_x and E_y are the component fields; **E** is the resultant field, in the form of a right-handed helix.

The component fields are

$$E_x = E_0 \cos(qz)$$
$$E_y = E_0 \sin(qz). \tag{13}$$

The tip of the vector representing the resultant field, **E**, traces out a helix whose axis coincides with the z axis. The helix, along with the component fields, is shown in Fig. 4. The helix has the same pitch direction as a right-handed screw. The $(\omega t - \delta)$ form with $\delta = +\pi/2$ gives a left-handed helix. As one would expect (by now, we hope), the $(\omega t + \delta)$ form with $\delta = +\pi/2$ and $\delta = -\pi/2$ results in right-handed and left-handed helices, respectively. Note that the handedness of a helix is independent of an observer's viewpoint—a right-handed screw looks like a right-handed screw, no matter from what direction you look at it.

The temporal behavior of the helix has been the subject of some confusion. Several authors [36–38] have stated that the helix rotates as time increases, whereas others [39–41] point out that the helix moves forward without rotating. Since both scenarios cannot be correct, which one is?

Figure 5 shows six snapshots of a right-handed helix at $\omega t = \pi$ for the first snapshot and incrementing by $\pi/4$ for each succeeding snapshot. The spatial patterns of the component and resultant waves are shown between $z = 0$ and $z = 2\lambda$. In addition, the resultant **E** vector lying in the x–y plane at $z = (9/8)\lambda$ is shown. If the helix were to rotate as it moved forward, then the resultant **E** vector at a fixed point (say, at $z = (9/8)\lambda$) would remain fixed in space. Any ***E*** vector in front of the x–y plane at $z = (9/8)\lambda$ would rotate into the position shown in the top picture in Fig. 5 as it passed through that plane. The helix would appear to be passing through a hole, located at the tip of the **E** vector, in the x–y plane. Therefore, in order for

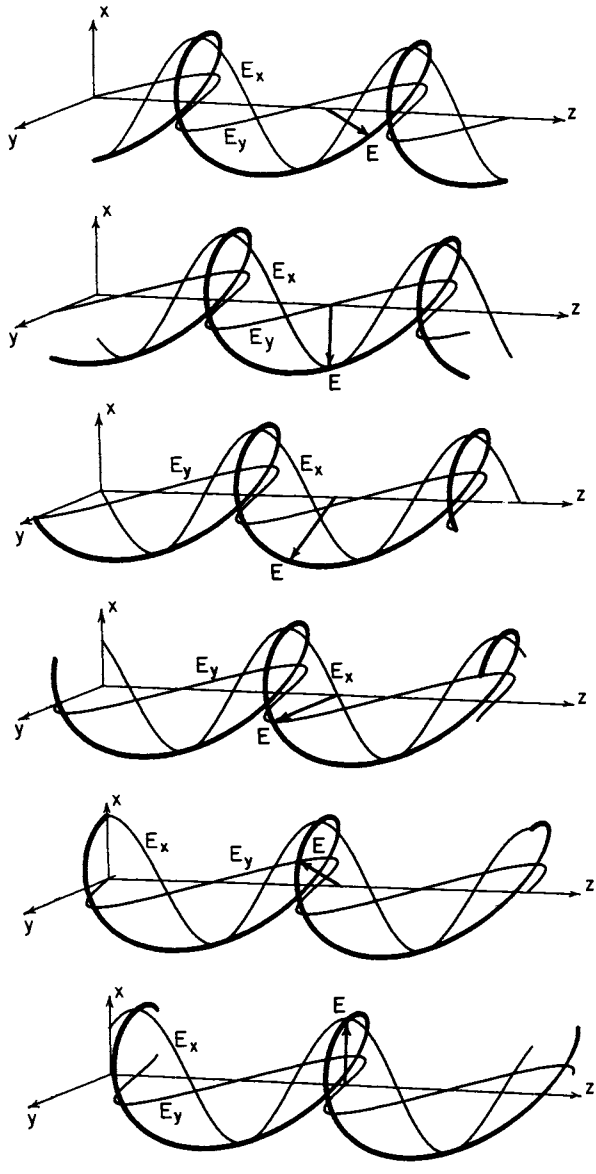

Fig. 5. Snapshots of a propagating circularly polarized wave and its components. The snapshots, taken every $\pi/4\omega$ of a second, show the wave between $z=0$ and $z=2\lambda$. The field vector, **E**, at $z=9\lambda/8$ rotates clockwise, as viewed by looking toward the source ($-z$ direction).

the resultant **E** vector to rotate in a plane, the helix must move forward without rotating, as demonstrated in Fig. 5. As the helix moves forward a distance of λ, it scribes out a complete circle in any x–y plane.

Terminology 4

The terminology used to classify circular polarization varies with country and field of science and has changed with time [42]. To begin with, there are two ways to view a circularly polarized wave: opticists and physicists prefer to look into the oncoming wave (that is, toward the source); and radio and microwave engineers usually look at the receding wave (that is, in the direction of propagation). Thus, opticists and physicists say that **E** is rotating clockwise in Fig. 3a and counterclockwise in Fig. 3b, whereas engineers say just the opposite. As the reader looks at Fig. 3, the $+z$ axis is normal to the page and pointing toward the reader. Therefore, the view corresponds to the optics convention of looking toward the source. Engineers would be behind the figure looking out at the reader.

When explaining the convention you use to define clockwise and counterclockwise, it is important to be specific and to avoid ambiguous phrases, such as "as seen looking down the beam." Which direction is down?

The traditional optics convention refers to the clockwise (counterclockwise) rotating field **E** as being right (left) circularly polarized. One reason for this is that the spatial pattern for a right-handed (left-handed) wave would then be a right-handed (left-handed) helix, even though polarization is supposed to be referenced to the temporal variation. Of course, the helix serves as a good mnemonic, since its sense of inclination is invariant to the point of observation.

Engineers usually reverse the definitions for the handedness of circularly polarized waves [34, 43–45]. For them, the **E** vector of a right-handed wave rotates clockwise (as seen looking in the direction of propagation), but has a left-handed helix. This definition is appropriate for a right-handed, helical-beam antenna, which receives right circular (left-handed helix) polarization [45].

As everyone knows, a light wave has a linear momentum **p**. In addition, a circularly polarized wave also carries an angular momentum **L** [46–51]. The direction of angular momentum is obtained from the right-hand rule. When the right hand curls around the direction of propagation with the fingers pointing in the direction that **E** is rotating (see Fig. 3), the thumb points in the direction of the angular momentum. Thus, the linear and angular momenta of a left circularly polarized wave (traditional optics definition) point in the same direction, whereas they point in opposite directions for a right circularly polarized wave. The direction that the angular momentum of the wave points determines whether electron or

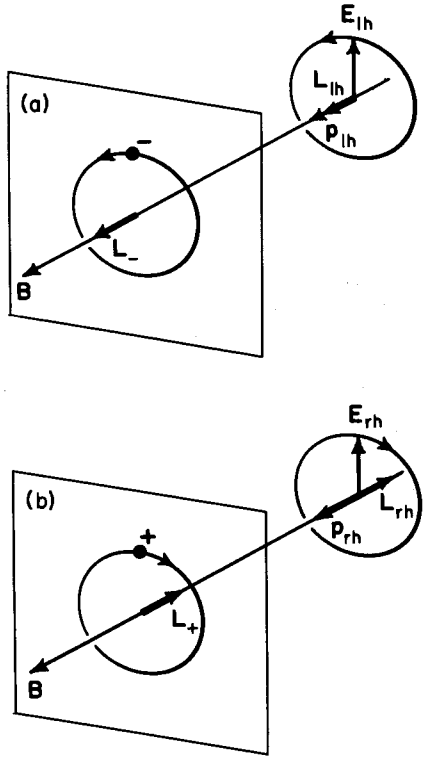

Fig. 6. Schematic representation of (a) electron and (b) hole cyclotron resonance. The charge carriers revolve in a plane normal to the applied dc magnetic induction, **B**. The election and hole angular momenta are $\mathbf{L}_-$ and $\mathbf{L}_+$, respectively. The angular momenta of the left and right circularly polarized waves are $\mathbf{L}_{lh}$ and $\mathbf{L}_{rh}$, respectively, and the linear momenta are $\mathbf{p}_{lh}$ and $\mathbf{p}_{rh}$.

hole cyclotron resonance is excited in a semiconductor [52]. As depicted schematically in Fig. 6, left and right circularly polarized waves are propagating in the direction of the applied dc magnetic induction, **B**. In Fig. 6a, electrons revolve counterclockwise around **B** (looking against **B**), and in Fig. 6b, holes revolve clockwise around **B**. Electron and hole angular momenta are parallel and antiparallel to **B**, respectively. In order to satisfy selection rules [52], the angular momentum of a circularly polarized wave must point in the same direction as that of the charge carrier. Therefore, electrons absorb left circular polarization, and holes absorb right circular polarization.

Modern physics has also seen fit to reverse the meaning of right-handed from that of traditional optics. The convention of particle physics is that both the linear momentum and the angular momentum of a right-handed

wave point in the same direction. Thus, the wave represented in Fig. 3b is right-handed in modern physics.

FRESNEL'S AMPLITUDE REFLECTION COEFFICIENTS V

Augustin Fresnel's derivation in 1823 of the amplitude reflection coefficients of light waves is a classic case of knowing the answer and working backwards [53]. Working nearly fifty years before Maxwell published his electromagnetic theory, Fresnel was fettered by a bogus concept known as the *luminiferous ether (aether)*. Making an analogy between sound and light, early scientists had postulated the existence of the ether. Since sound could not propagate in vacuum, it seemed logical that light could not either, that it needed some medium which filled all space out to the farthermost star [54]. Even though common sense (at that time) dictated the existence of the ether, common sense was noticeably absent when the ether was endowed with some rather remarkable properties [55]: it must be millions of times more rigid than steel to transmit waves having the frequency and velocity of light; it offers no resistance to the passage of the earth and planets around the sun; and it is composed of extremely minute particles, far smaller than atoms.

Working within the *elastic-solid theory*, Fresnel adjusted his concept of the ether until he was able to derive reflection formulas that agreed with experiment [56]. Fresnel knew that something was vibrating, and whatever it was, the vibration was transverse to the direction of propagation. He also assumed that the vibration was normal to the plane of polarization (the $\mathbf{q} - \mathbf{H}$ plane). He finally based his concept of the elastic-solid theory on the following three tenets [57]:

(1) Conservation of energy—the energy of the incident wave is equal to the sum of the energies of the reflected and transmitted waves.

(2) Uniform elasticity—the densities of the ether in each medium could be different, but not the elasticity (the ether is incompressible).

(3) Continuity of displacement—there is no tangential slipping of the ether across the interface.

Using these principles and without any knowledge of the electromagnetic character of light waves, Fresnel was able to derive the correct formulas.

Since Maxwell's time, however, Fresnel's reflection coefficients have been derived in the more familiar way of using the **E** and **H** fields and their associated boundary conditions. In 1890, Otto Wiener demonstrated that a node in the electric field exists at the surface of a mirror, indicating that the electric field reverses phase upon reflection at normal incidence [58, 59].

Thus, the reflection coefficients are usually derived in terms of the electric field. The standard procedure is to resolve the electric field of the incident wave into two orthogonal, linearly polarized components, one normal to the plane of incidence (E_s), and the other parallel (E_p). These two components are then treated as independent cases.

For both the normal case and the parallel case, three waves are involved—incident, reflected, and transmitted—and each of the three waves can be represented by an **E** vector that can point in one of two opposite directions. The first step is to pick the direction for the **E** vector of the incident wave. This choice may depend on many factors, including type of experiment, personal preference, academic heritage, and so on. The second step is to select the direction for the reflected (and transmitted) **E** vector. Hindsight usually influences this choice. We do not know a priori in which direction the **E** field of the reflected wave will point; indeed, its direction depends on the relative refractive indices of the two contiguous media at the interface. It does not matter which direction we choose because the reflection coefficient will ultimately provide the correct direction for the reflected **E** field relative to that of the incident wave. Since each field can point in one of two opposite directions, there are eight possible arbitrary ways to arrange the three electric fields at the interface for both the normal and parallel cases. Fortunately, all eight configurations of each case have not been used; but those used have been enough to cause confusion. Luckily, some are redundant in that they give the same expressions for the reflection coefficients [60].

In general, reflection must be treated as a three-dimensional problem. Thus, an orthographiclike drawing aids the reader in visualizing the field vectors in relation to the plane of incidence and the reflecting surface. Over the past forty years or so, several excellent variations [61–68] have been presented. Figure 7 is typical of the type presented to depict the relative orientations of the field vectors of the incident, reflected, and transmitted waves. The coordinate system has been chosen so that the reflecting surface is in the x–y plane and the plane of incidence is in the y–z plane. The angles of incidence and transmission, related by Snell's law, are θ_i and θ_t, respectively.

A *s* Polarization

In Fig. 7a, the electric fields are normal to the plane of incidence. Such waves are usually denoted as s-polarized, transverse electric (TE), or $\perp$ waves. Almost every author has chosen E_{is}, E_{rs}(FC), and E_{ts} to point in the same direction [69, 70], which is usually the $+x$ direction. The subscripts, is, rs, and ts, designate the incident, reflected, and transmitted waves,

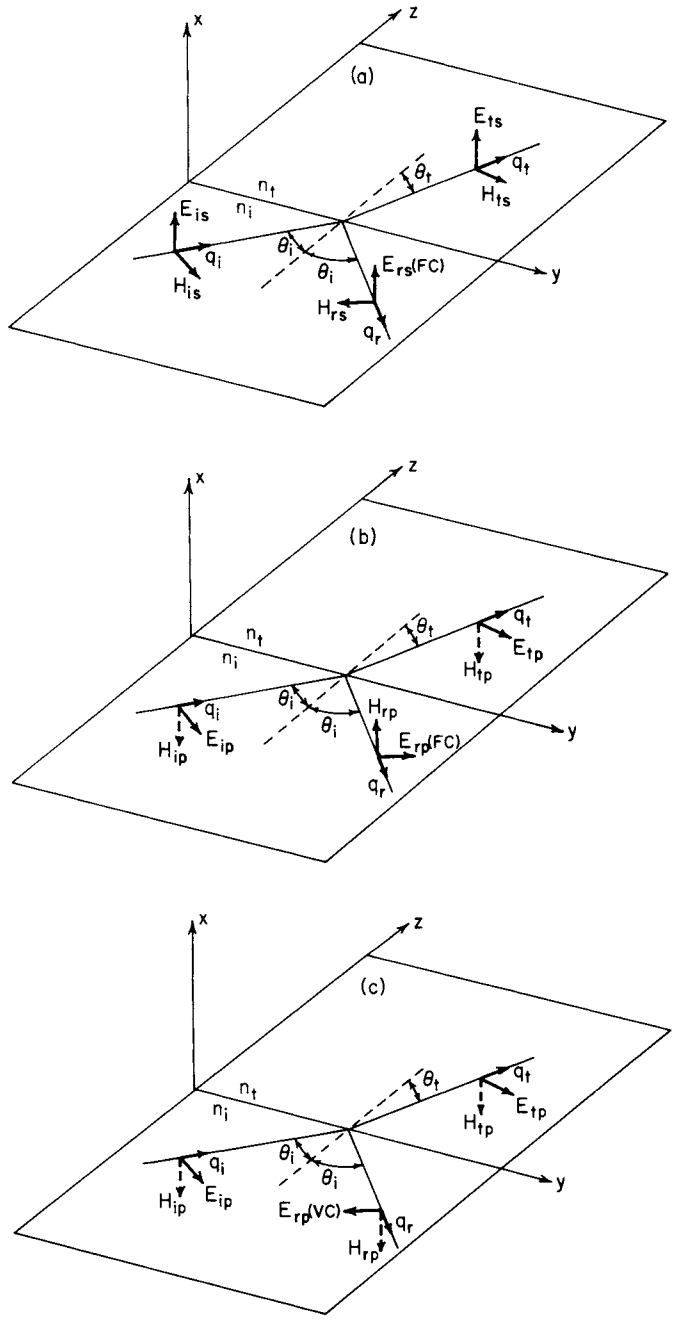

Fig. 7. The conventions used to derive the Fresnel reflection coefficients. The field (**E** and **H**) and wave (**q**) vectors of the incident (i), reflected (r), and transmitted (t) waves are shown for (a) *s* polarization, (b) *p* polarization, Fresnel convention, and (c) *p* polarization, Verdet convention.

respectively, for *s* polarization. The FC label attached to the reflected wave in Fig. 7a signifies the Fresnel convention. We use this label to emphasize that $E_{rs}(FC)$ is an arbitrarily selected vector from which one derives the Fresnel reflection coefficient. The actual reflected field may point in the same direction as the convention vector in Fig. 7a or in the opposite direction. Once the direction of **E** is chosen, the direction of **H** is determined by $\mathbf{q} \times \mathbf{E} = \omega\mu_0 \mathbf{H}$.

It must be pointed out that Fig. 7 is just a schematic representation of the actual situation. Although it is the field vectors located at the interface that satisfy the boundary conditions, the field vectors are drawn some distance from the interface for clarity [71]. In addition, the vectors represent peak values, rather than instantaneous values, and the direction each vector points is defined as the positive direction for that vector [72]. The Fresnel amplitude reflection coefficient for *s* polarization is [73]

$$\tilde{r}_s \equiv \frac{E_{rs}(FC)}{E_{is}} = \frac{\tilde{n}_i \cos\theta_i - \tilde{n}_t \cos\theta_t}{\tilde{n}_i \cos\theta_i + \tilde{n}_t \cos\theta_t} = -\frac{\sin(\theta_i - \theta_t)}{\sin(\theta_i + \theta_t)}, \tag{14}$$

where $\tilde{n}_i$ and $\tilde{n}_t$ are the complex refractive indices of the incident and transmission media, respectively.

B *p* Polarization

For the other case in which the electric field is parallel to the plane of incidence, a wave is denoted as a *p*-polarized, transverse magnetic (TH), or ∥ wave. One of the oldest (and continuing) controversies in optics is associated with the sign of the reflection coefficient for *p* polarization. Fresnel felt that the tangential component of the displacement associated with the reflected wave should point in the same direction as that of the incident wave [74]. This means, in electromagnetic terms, that the tangential components of E_{ip} and $E_{rp}(FC)$ point in the same direction, as shown in Fig. 7b. For this situation, the Fresnel amplitude reflection coefficient for *p* polarization is [75]

$$\tilde{r}_p(F) \equiv \frac{E_{rp}(FC)}{E_{ip}} = \frac{\tilde{n}_i \cos\theta_t - \tilde{n}_t \cos\theta_i}{\tilde{n}_i \cos\theta_t + \tilde{n}_t \cos\theta_i} = -\frac{\tan(\theta_i - \theta_t)}{\tan(\theta_i + \theta_t)}. \tag{15}$$

Fresnel argued for this form because at normal incidence ($\theta_i = 0°$), $r_s = r_p(F)$. It was intuitively consistent because at normal incidence there

is no distinction between s and p polarizations. However, and herein lies the root of the controversy, at glancing incidence ($\theta_i \to 90°$), $r_s = -r_p(F)$.

When Verdet published Fresnel's work, he changed the sign of r_p because he felt that r_s should equal r_p at glancing incidence rather than at normal incidence [76]. This is equivalent to reversing the direction of the **E** vector of the reflected wave, as shown by $E_{rp}(VC)$ in Fig. 7c, where the VC label signifies the Verdet convention. Thus, in this case, the form of the reflection coefficient for p polarization is [73]

$$\tilde{r}_p(V) \equiv \frac{E_{rp}(VC)}{E_{ip}} = \frac{\tilde{n}_t \cos\theta_i - \tilde{n}_i \cos\theta_t}{\tilde{n}_t \cos\theta_i + \tilde{n}_i \cos\theta_t} = \frac{\tan(\theta_i - \theta_t)}{\tan(\theta_i + \theta_t)}. \tag{16}$$

There is nothing wrong with $r_s = -r_p(V)$ at normal incidence. Figures 7a and 7c do not correspond to the same convention at $\theta_i = 0°$, so why should r_s necessarily equal r_p?

The reasons for choosing either Fig. 7b or 7c have changed over time. Now they are related to whether one relates the field vectors to a coordinate system tied to the sample surface or to a coordinate system localized with the field vectors themselves [77].

Fresnel's reflection formula for p polarization was not universally accepted in the beginning because it did not completely agree with experiment. (Presumably, the data were in error.)

Phase Change C

Everyone knows that an electromagnetic wave "suffers a phase change" upon reflection. As expected, the various conventions discussed so far result in different phase changes. However, as we shall show, they all yield the same reflected $\mathbf{E}_r$ field in the final analysis. There is, in addition, no consensus on the meanings of the expressions *in phase* and *out of phase*. We shall first give the pertinent mathematical expressions for reflection phase change. Next, we shall summarize some of the ideas about phase change that are encountered in the literature. Finally, we shall discuss the physical significance of phase change.

The Fresnel reflection coefficients may be formally expressed in the form

$$\tilde{r}_s \equiv r_s' + ir_s'' = |r_s| e^{i\delta_s} \tag{17a}$$

$$\tilde{r}_p \equiv r_p' + ir_p'' = |r_p| e^{i\delta_p}, \tag{17b}$$

where

$$|r_{s,p}| = [(r'_{s,p})^2 + (r''_{s,p})^2]^{1/2} \tag{18a}$$

$$\delta_{s,p} = \tan^{-1}\left(\frac{r''_{s,p}}{r'_{s,p}}\right). \tag{18b}$$

The corresponding electric fields for the reflected waves are given by

$$E_{rs}(F) = |r_s| e^{i\delta_s(F)} E_{is} \tag{19a}$$

$$E_{rp}(F, V) = |r_p| e^{i\delta_p(F,V)} E_{ip}, \tag{19b}$$

where E_{is} and E_{ip} point as shown in Fig. 7. $E_{rs}(F)$ and $E_{rp}(F,V)$ are the actual reflected fields for s and p polarization, respectively, and are distinguished from the fields $E_{rs}(FC)$ and $E_{rp}(FC,VC)$ used to establish the reflection conventions in Fig. 7.

The reflection phase changes (shifts), δ_s and δ_p, are usually thought of as the difference between the phases of the incident and reflected waves. However, this thought is somewhat misleading. Electric field, being a vector, has a magnitude and a direction. Equations like Eq. 19 account for the magnitude. The direction is implicit through the conventions expressed in Fig. 7. Therefore, it is more apropos to think of δ_p as the difference between the phases of $E_{rp}(F,V)$ and $E_{rp}(FC,VC)$, with $E_{rp}(FC,VC)$ related to E_{ip} through Fig. 7. $E_{rp}(FC,VC)$ acts as an intermediary between $E_{rp}(F,V)$ and E_{ip}. In other words, $E_{rp}(F,V)$ is what $E_{rp}(FC,VC)$ looks like after $r_p(F,V)$ is taken into account. Similar points of view hold for δ_s. Since the phase change also depends on whether one uses $(n+ik)$ or $(n-ik)$, there are two expressions for δ_s and four expressions for δ_p. From Eqs. 14–18, one finds

$$\begin{array}{lll} & \underline{n+ik \text{ form}} & \underline{n-ik \text{ form}} \\ \delta_s = & \tan^{-1}\left(\dfrac{-s_{num}}{s_{den}}\right) & \tan^{-1}\left(\dfrac{s_{num}}{s_{den}}\right) \\ \delta_p(V) = & \tan^{-1}\left(\dfrac{p_{num}}{p_{den}}\right) & \tan^{-1}\left(\dfrac{-p_{num}}{p_{den}}\right) \\ \delta_p(F) = & \tan^{-1}\left(\dfrac{-p_{num}}{-p_{den}}\right) & \tan^{-1}\left(\dfrac{p_{num}}{-p_{den}}\right), \end{array} \tag{20}$$

where

$$s_{\text{num}} = 2\beta \cos \theta_i \tag{21a}$$

$$s_{\text{den}} = \cos^2 \theta_i - \alpha^2 - \beta^2 \tag{21b}$$

$$p_{\text{num}} = 2 \cos \theta_i [2n_t k_t \alpha - (n_t^2 - k_t^2)\beta] \tag{21c}$$

$$p_{\text{den}} = (n_t^2 + k_t^2)^2 \cos^2 \theta_i - \alpha^2 - \beta^2 \tag{21d}$$

$$\alpha^2 = \tfrac{1}{2}\{[(n_t^2 - k_t^2 - \sin^2 \theta_i)^2 + (2n_t k_t)^2]^{1/2} + n_t^2 - k_t^2 - \sin^2 \theta_i\} \tag{21e}$$

$$\beta^2 = \tfrac{1}{2}\{[(n_t^2 - k_t^2 - \sin^2 \theta_i)^2 + (2n_t k_t)^2]^{1/2} - n_t^2 + k_t^2 + \sin^2 \theta_i\}, \tag{21f}$$

where num and den refer to numerator and denominator, respectively [78], and assuming $n_i = 1$. Note that the equation for $\delta_p(\text{F}, n + ik)$ has a minus sign in both the numerator and the denominator. As we shall show, one must not inadvertently cancel out these minus signs.

There is another, equivalent expression for the numerator of the reflection phase shift for p polarization; this alternative form was derived by Abelès and is used by some authors [79–81]. Abelès expressed the reflection coefficients in terms of effective refractive indices. For p polarization these are $n_i^{\text{eff}} = 1/\cos \theta_i$ and $\tilde{n}_t^{\text{eff}} = \tilde{n}_t/\cos \theta_t$, with $n_i = 1$. In the Abelès method, p_{num} (Abelès), which is equivalent to p_{num} in Eq. 21c, is given by

$$p_{\text{num}}(\text{Abelès}) = 2 \cos \theta_i \beta(\alpha^2 + \beta^2 - \sin^2 \theta_i). \tag{22}$$

Figure 8 presents the phase changes as a function of the angle of incidence, θ_i, calculated from Eq. 20 for steel ($\lambda = 589.3$ nm, $n_t = 2.485$, $k_t = 3.432$) [82, 83]. The $(n + ik)$ forms are in Fig. 8a and the $(n - ik)$ forms in Fig. 8b. Note that the four δ_p curves are different, as are the two δ_s curves. Figures 8a and 8b are mirror images of each other, and the δ_p curves in Fig. 8a differ by 180°, as do those in Fig. 8b.

Care must be exercised to place δ_s and δ_p in the correct quadrant of the complex r_s and r_p planes, especially when calculating phase changes with a computer. By convention, angles are measured positive in a counterclockwise direction starting from the positive real axis [84]. One must test separately the signs of the numerator and denominator to determine proper placement. If both r' and r'' are positive (negative), δ lies in quadrant I (III). If r' is positive (negative) and r'' is negative (positive), δ lies in quadrant IV (II). Thus, $\tan^{-1}(a/b)$ and $\tan^{-1}(-a/-b)$ differ by

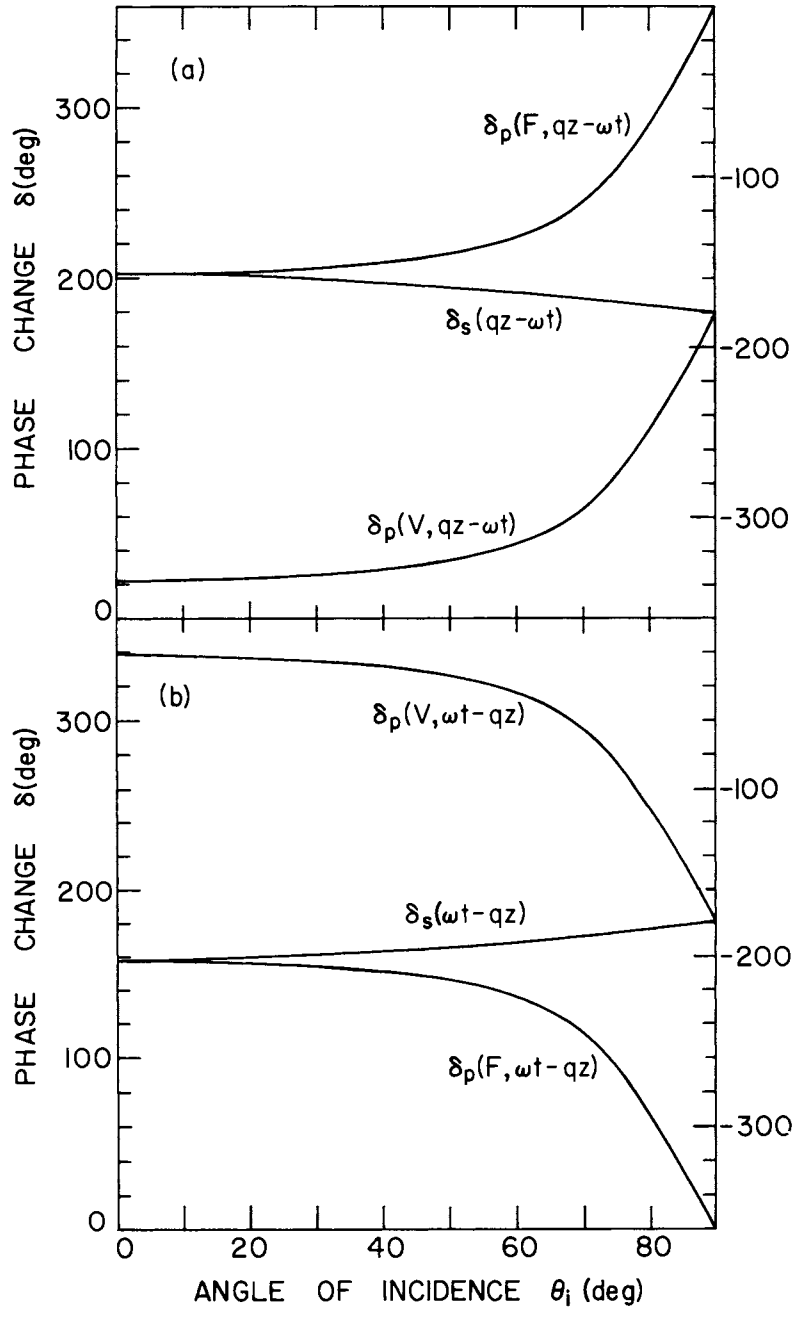

Fig. 8. Reflection phase change for steel as a function of the angle of incidence for (a) the $(n+ik)$ form and (b) the $(n-ik)$ form.

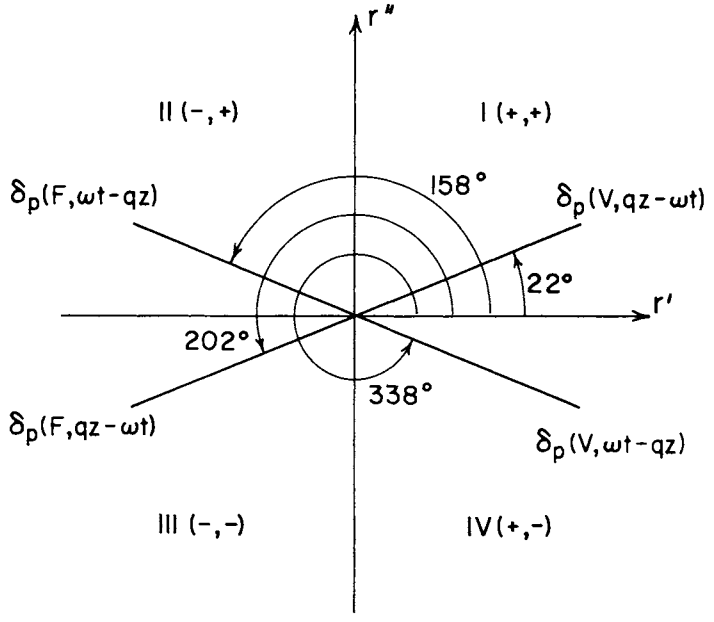

Fig. 9. The four values of δ_p at $\theta_i = 0°$ from Fig. 7, located in the complex $\tilde{r}$ plane.

180°. As an example, Fig. 9 shows the four δ_p phase changes from Fig. 8 for $\theta_i = 0°$.

Even though the four values of δ_p in Fig. 9 are different, each is correct within its own convention. It is easy to show that they all yield the identical reflected field, E_r (as they must!). For example, from Eq. 19b,

$$\begin{aligned} E_{rp}(F, n+ik) &= |r_p| e^{i202°} E_{ip0} e^{-i\omega t} \\ &= |r_p| E_{ip0} e^{i(360° - 158° - \omega t)} \\ &= |r_p| E_{ip0} e^{-i(158° + \omega t)} \\ &= E_{rp}(F, n-ik), \end{aligned} \tag{23}$$

remembering to take the real parts [85]. Likewise, $E_{rp}(V, n-ik) = E_{rp}(F, n-ik)$ when one takes into account the fact that the p-polarized reflected E fields in Fig. 7 point in opposite directions for the Fresnel and Verdet conventions.

There is a nitpicking point (which we have never seen discussed) that a purist might raise concerning Eq. 17 when $\tilde{n} = n - ik$ is used. Since complex quantities must then be expressed in an $(a' - ia'')$ form, why is Eq. 17 not

written as

$$\tilde{r}_s \equiv r'_s - ir''_s = |r_s| e^{-i\delta_s} \tag{24a}$$

$$\tilde{r}_p \equiv r'_p - ir''_p = |r_p| e^{-i\delta_p}, \tag{24b}$$

where again

$$\delta_{s,p} = \tan^{-1}\left(\frac{r''_{s,p}}{r'_{s,p}}\right)? \tag{25}$$

Equation 24 is the complex conjugate of Eq. 17. If one rederives the expressions for the $(n-ik)$ form of $\delta_{s,p}$ from Fresnel's reflection coefficients using Eqs. 24 and 25, one finds that they are the same as those in Eq. 20 for the $(n+ik)$ form. In other words, the same numeric values are obtained for $\delta_{s,p}$ whether $\tilde{n} = n + ik$ or $\tilde{n} = n - ik$ is used.

The expressions *phase change, in phase*, and *out of phase* convey a sense of comparison or relation. The meanings of these expressions are a matter of definition and, of course, different people prescribe different definitions. Essentially, there are two approaches in defining *in phase* and *out of phase*. In one approach, positive phase is associated with some particular direction [86]. The other approach is concerned with the superposition of the incident and reflected waves. The relevant points can be made by considering reflection from a dielectric ($k_t = 0$).

Figure 10 shows incident and reflected electric-field vectors, $\mathbf{E}_i$ and $\mathbf{E}_r$, respectively, for reflection from a more dense optical medium (that is, $n_i < n_t$). The angle of incidence, θ_i, is less than Brewster's angle in Fig. 10a and greater in Fig. 10b. The incident and reflected waves are resolved into their *s* and *p* polarized components, with E_{rs} and E_{rp} pointing in the correct directions after reflection [87]. As is commonly done [88–90], separate coordinate systems are attached to the incident and reflected waves. The coordinate systems are oriented so that they are right-handed as the viewer looks into the oncoming wave [91, 92], with E_{ip} and E_{is} pointing in the positive *x* and *y* directions, respectively. (Note that in Fig. 7 the coordinate system is attached to the sample). The coordinate system for the reflected wave has the same relative orientation as that of the incident wave [93]. For *s* polarization, everything is fairly straightforward. Incident and reflected fields are colinear. In Fig. 10, E_{rs} points in the opposite direction as E_{is} and is π out of phase with respect to E_{is}. If r_s is positive (reflection from a less optically dense medium), E_{rs} and E_{is} point in the same direction and are in phase. The above two statements are true for all angles of incidence (except above the critical angle for the latter statement [94]).

The situation is not as clear-cut for *p* polarization, in which electric-field

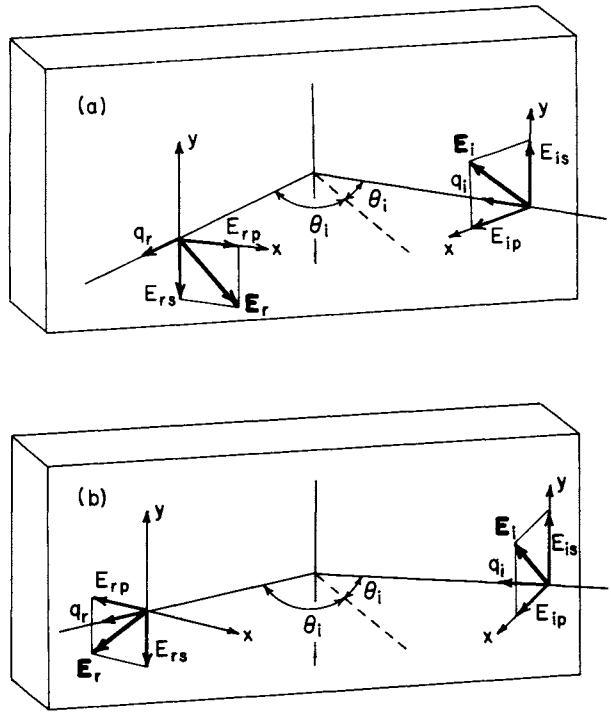

Fig. 10. Reflection of a linearly polarized wave (a) above and (b) below Brewster's angle for $n_i < n_t$. The rs and rp components point in their true directions.

vectors for incident and reflected waves are coplanar but not colinear (except at $\theta_i = 0$ and 90°). In Fig. 10a, the components of E_{ip} and E_{rp} that are parallel to the surface point in opposite directions, whereas the components that are normal to the surface point in the same direction. Are E_{ip} and E_{rp} in phase or out of phase? According to the first approach, if E_{ip} and E_{rp} point in the same direction relative to their individual coordinate systems, they are in phase. In Fig. 10a, they both point in the $+x$ direction, so they are in phase by definition. In Fig. 10b, E_{rp} points in the $-x$ direction, so it is π out of phase with respect to E_{ip}. According to this definition, E_{rp} is in phase with E_{ip} at near-normal incidence ($\theta_i \approx 0°$), but π out of phase at glancing incidence ($\theta_i \approx 90°$), even though E_{ip} and E_{rp} are antiparallel in both limits. This apparent incongruity is not as bad as it seems because one is usually more concerned with the phase of $\mathbf{E}_r$ relative to the experimental setup rather than to $\mathbf{E}_i$.

The above definitions of *in phase* and *out of phase* for *p* polarization are incompatible with the concept of superposition [95]. As we have mentioned, there is a node in the electric field at the surface of a mirror at

normal incidence. In the Lloyd's mirror experiment [96], a node (dark fringe) also occurs at the point of contact of the mirror and screen for grazing incidence. Thus, from this point of view, E_{rp} is π out of phase with respect to E_{ip} for all angles of incidence as long as $n_i < n_t$.

In the general case, the s and p reflection coefficients and phase changes vary with the angle of incidence. In addition, the reflection coefficients are not equal, nor are the phase changes. Thus, if the incident wave is linearly polarized and inclined 45° to the x axis (that is, $E_{x0} = E_{y0}$), the reflected wave is elliptically polarized. (This is the working principle of ellipsometry [89]). To be consistent, one should use the Verdet convention for the p-polarized component when analyzing the polarization state of the reflected wave. In Fig. 7, the three vectors $\mathbf{E}_{is}$, $\mathbf{E}_{ip}$, and $\mathbf{q}_i$ (in that order) form a right-handed triad for the incident wave. For the reflected wave, $\mathbf{E}_{rs}$(FC), $\mathbf{E}_{rp}$(VC), and $\mathbf{q}_r$ form a commensurate right-handed triad. Some authors (for example, [65]) use a different layout for the s and p components and the wave vector from that presented in Fig. 7. In those cases, right-handed triads are formed by $\mathbf{E}_{ip}$, $\mathbf{E}_{is}$, $\mathbf{q}_i$ and by $\mathbf{E}_{rp}$(VC), $\mathbf{E}_{rs}$(FC), $\mathbf{q}_r$. Balanis derives r_p in the Fresnel convention. Then, when he discusses polarization changes upon reflection, he draws the incident and reflected field vectors for p polarization in the Verdet convention. To account for this, he introduces a minus sign into the equation for $\mathbf{E}_{rp}$ [97].

When an elliptically polarized wave reflects from a metallic surface, the handedness of the wave reverses, independent of the angle of incidence [98–101]. When the reflection surface is a dielectric, the handedness reverses if the angle of incidence is less than Brewster's angle and remains the same for angles of incidence greater than Brewster's angle.

To grasp the physical significance of phase change, consider a fictitious surface for which $|r| = 1$ at normal incidence. The incident and reflected waves form a standing wave in front of the surface [102–105]. The nodal positions in front of the surface depend on the phase change. If we assume the Fresnel convention and the $(n - ik)$ form, the incident and reflected waves can be expressed as

$$\begin{aligned} E_i &= E_0 \cos(\omega t - qz) \\ E_r &= E_0 \cos(\omega t + qz + \delta). \end{aligned} \tag{26}$$

The superposition of these two waves yields

$$E = E_i + E_r = 2E_0 \cos(\omega t + \delta/2) \cos(qz + \delta/2). \tag{27}$$

The envelope (maximum curve) of the standing wave obtains when

$\cos(\omega t + \delta/2) = \pm 1$. Then

$$E_{\max} = \pm 2E_0 \cos(qz + \delta/2). \tag{28}$$

Thus, it is clear that nodes occur when

$$qz = (2m+1)\pi/2 - \delta/2, \tag{29}$$

for those integral values of m that place qz in front of the reflecting surface.

Figure 11 shows several periods of a standing wave envelope. As can be seen, when δ equals 0° and 180°, an antinode and a node, respectively, occur at the surface. If δ is less than 180°, it is as if the node appears behind

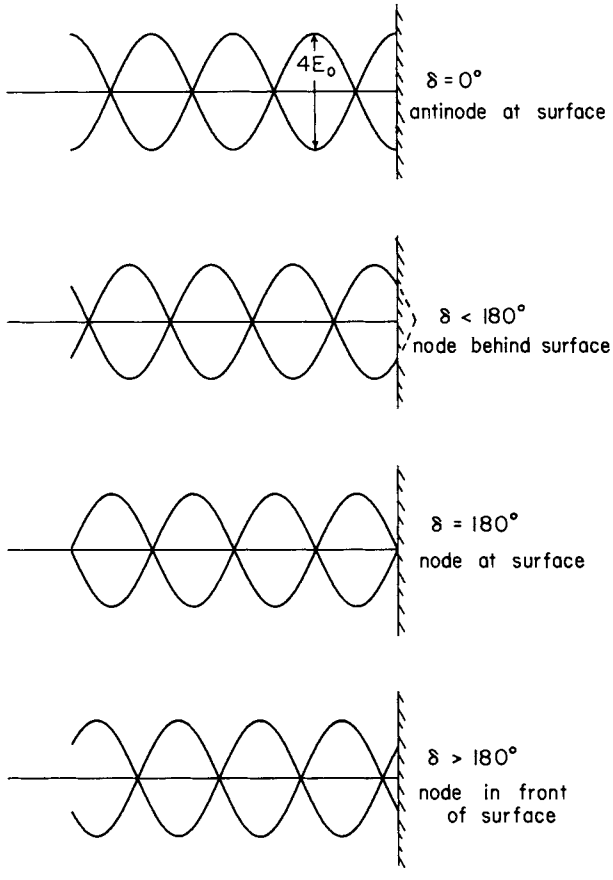

Fig. 11. Standing wave pattern in front of a surface with $|r| = 1$. The dependence of the nodal position on δ is shown. The values of δ are for the Fresnel convention with the $(n - ik)$ form.

the surface, whereas if δ were greater than 180°, the node would occur in front of the surface. Once again, we point out that Eqs. 26–29 are applicable only for the Fresnel convention and the $(n-ik)$ form. For the other cases in Fig. 8, Eqs. 26–29 have to be adjusted accordingly. However, all conventions result in the same standing wave pattern.

The preceding discussion is mathematically rigorous, but does not completely comply with physical reality. First of all, $|r|$ never equals unity so that the nodes are minima in the standing wave pattern, rather than zeros. Second, phase shift does not vary over the entire range from 0 to 2π. Thus, in Fig. 10, an antinode occurs at the surface when reflection is from a less optically dense dielectric ($k=0$); a node occurs when reflection is from a more optically dense dielectric. When the incident medium is transparent and the transmission medium is lossy ($k\neq 0$), the phase shift will lie between 0 and π (Fresnel convention, $(n-ik)$ form, normal incidence). Therefore, the node would appear to be behind the surface. Since phase shift cannot exceed π, a node will not occur in front of the surface (within a distance of $\lambda/4$).

Before proceeding to the next section, four points are worth making. First, reflection coefficients are characterized by two parameters: a magnitude and a phase. It is difficult to express meaningfully the values of both these parameters in an orthographic figure of the type shown in Fig. 7. A drawing such as in Fig. 9, in which E_i is drawn along the positive real axis and E_r has the appropriate magnitude and phase angle, is more informative [106].

The second point is that some authors express phase changes as negative values. In other words, they measure phase change clockwise from the positive real axis. Thus, if everything is done correctly, δ(clockwise) = δ(counterclockwise) − 360°. The right-hand ordinate in Fig. 8 measures the phase changes as negative quantities. The final E_r field is the same—just the intermediate steps are different.

The third point concerns phase change when $k_t=0$. As might be surmised from Fig. 8, when the angle of incidence is less than the Brewster angle (and for $n_i<n_t$) [83, 107], $\delta_p(V, n-ik)=360°$, not 0° as most books state. Likewise, above the Brewster angle, $\delta_p(F, n+ik)=360°$.

Finally, an interesting optical morsel. Abelès [108–110] showed that at $\theta_i=45°$, $|r_p|=|r_s|^2$. In addition, for the Verdet form of r_p, $\delta_p=2\delta_s$. This is true in general for reflection from any semi-infinite medium.

VI NOMENCLATURE

Nomenclature is not a burning issue, but is worthy of mention. The distinctions between *reflection*, *reflectance*, and *reflectivity* are subtle [111–

115] but are favored by many authors. Reflection is the act or process by which the incident wave is redirected back into the incident medium. Reflectance is a measured value. It is the fractional amount of the incident energy or intensity that is reflected from the surface. Reflectivity refers to a fundamental or characteristic property of a material. It is the theoretical reflectance that a semi-infinite medium would have. Applying the *-ion, -ance,* and *-ity* suffixes to the words *transmit* and *absorb* yields *transmission*, *transmittance*, and *transmissivity*, and *absorption, absorptance*, and *absorptivity*. These words have the same usage as the corresponding words derived from *reflect.*

CONCLUDING REMARKS VII

Although we did not cover such specific topics as Jones matrices, Poincaré sphere, ψ and Δ in ellipsometry, and so forth [2], we have presented the fundamental conventions dealing with electromagnetic wave propagation. It is important to recognize that conventions are a matter of definition or convenience. One must be able to separate physics from conventions and one convention from another. An amusing example of the misunderstandings that can arise is presented by a series of papers (and counter-papers), which discusses the "proper way" to account for reflection phase changes in interferometric measurements [116–122]. Since the various authors involved were using different conventions, they did not agree on the proper way and made scathing comments about each other. Finally, in an effort to end the controversy, the editors of *Optics and Spectroscopy* stated that they ". . . consider the discussion of phase shifts during reflection of light to be closed [117]." Of course, the controversy continues.

Even though we do not advocate a particular set of conventions, we do have one recommendation. Textbook authors should devote more time to the convention issue. They should point out the various conventions that a student is likely to encounter.

How can you determine which conventions an author uses if he fails to mention them? Look for obvious clues. Try to find equations, figures, tables, and so on, in which either $\exp(i\omega t)$ or $\exp(-i\omega t)$ is used. Are optical constants listed as $n-ik$ or $n+ik$? Is r_p given in the Fresnel or Verdet convention? Review papers may by their very nature contain mixed conventions, especially when they quote from the original papers. For example, Weinberg [123] states that a metal is characterized by $\tilde{n}=n-ik$ but then presents phase changes in an $(n+ik)$ form. Also, he presents dielectric constants in the $(a'+ia'')$ form.

The two watchwords are convention and consistency. When you write a paper, either state your conventions explicitly or refer to a paper that does. Regardless of which set of conventions you choose, use them consistently throughout [3].

ACKNOWLEDGMENTS

The author wishes to express his thanks and appreciation to J. M. Bennett, D. M. Roessler, E. D. Palik, A. S. Glass, W. R. Hunter, and P. J. McMarr for valuable comments and suggestions. It is a pleasure to acknowledge the effort by M. E. Dixon in typing the manuscript.

REFERENCES

1. J. Z. Buchwald, "The Rise of the Wave Theory of Light," University of Chicago Press, Chicago (1989).
2. R. H. Muller, *Surf. Sci.* **16**, 14 (1969); P. S. Hauge, R. H. Muller, and C. G. Smith, *Surf. Sci.* **96**, 81 (1980).
3. J. M. Bennett and H. E. Bennett in "Handbook of Optics," (W. G. Driscoll, ed.), McGraw-Hill, New York, 10-1 (1978).
4. "The International System of Units (SI)," NBS Special Publication 330 (1986).
5. "Units of Measure," ISO Standards Handbook 2, 1st ed., International Organization for Standardization, Switzerland (1979).
6. R. A. Nelson, "SI: The International System of Units," American Association of Physics Teachers, Stony Brook, New York (1981).
7. M. Abraham, "The Classical Theory of Electricity and Magnetism," 2nd ed., Blackie & Son, London, 158 (1950).
8. J. D. Jackson, "Classical Electrodynamics," 2nd ed., John Wiley and Sons, New York, 811 (1975).
9. D. R. Frankl, "Electromagnetic Theory," Prentice-Hall, Englewood Cliffs, N.J., 147 (1986).
10. J. B. Marion and S. T. Thornton, "Classical Dynamics of Particles and Systems," 3rd ed., Harcourt Brace Jovanovich, New York, 476 (1988).
11. See Ref. 9, p. 260.
12. Many books use k for both the wave number and the imaginary part of the refractive index. Be careful.
13. L. I. Schiff, "Quantum Mechanics," 3rd ed., McGraw-Hill, New York, 20 (1968).
14. A. V. Sokolov, "Optical Properties of Metals," English ed., Elsevier, New York, 20 (1967).
15. Some authors define the refractive index as $\tilde{n}=n(1+i\kappa)$ or $n(1-i\kappa)$, where κ is the index of absorption (not to be confused with the absorption coefficient, $\alpha=2\omega k/c$). Also, n and k are referred to as the optical constants, even though neither is constant.
16. H. C. Chen, "Theory of Electromagnetic Waves," McGraw-Hill, New York, xiii (1983).
17. S. S. Mitra in "Handbook of Optical Constants of Solids," (E. D. Palik, ed.), Academic Press, New York, 213 (1985).
18. E. Spiller, *Appl. Opt.* **23**, 3036 (1984).
19. N. J. Harrick, "Internal Reflection Spectroscopy," John Wiley and Sons, New York, (1967); F. M. Mirabella and N. J. Harrick, "Internal Reflection Spectroscopy: Review and Supplement," Harrick Scientific Corp., Ossining, N.Y. (1985).
20. See Ref. 16, p. 93.
21. P. Yeh, "Optical Waves in Layered Media," John Wiley and Sons, New York, 14 (1988).

22. E. Hecht, "Optics," 2nd ed., Addison-Wesley, Reading, Mass., 270 (1987).
23. M. Born and E. Wolf, "Principles of Optics," 6th ed., Pergamon Press, London, 28 (1980).
24. W. A. Shurcliff, "Polarized Light: Production and Use," Harvard University Press, Cambridge, Mass., 6 (1962).
25. D. Clark and J. F. Grainger, "Polarized Light and Optical Measurement," Pergamon, Oxford, 173 (1971).
26. D. Clark, *Appl. Opt.* **13**, 3 (1974); ibid. **13**, 222 (1974).
27. E. Mach, "The Principles of Physical Optics," republication of 1926 English translation, Dover Publications, 186 (1953).
28. T. Preston, "The Theory of Light," 4th ed., Macmillan and Co., London, 25 (1944).
29. See Fig. 8.21 in Ref. 22.
30. See Ref. 27, p. 190.
31. See Ref. 1, p. 41.
32. F. L. Pedrotti and L. S. Pedrotti, "Introduction to Optics," Prentice-Hall, Englewood Cliffs, N.J., 341 (1987).
33. For an algorithm to generate perspective drawings, see R. E. Myers, "Microcomputer Graphics," Addison-Wesley, Reading, Mass., Chapter 6 (1982).
34. "IEEE Standard 145-1983, IEEE Standard Definitions of Terms for Antennas," *IEEE Trans. Antenna Propagat.* **AP-31**, Part II, 1 (1983).
35. The sense of rotation is determined by rotating the phase-leading component toward the phase-lagging component. See C. A. Balanis, "Advanced Engineering Electromagnetics," John Wiley and Sons, New York, 163 (1989).
36. M. V. Klein, "Optics," John Wiley and Sons, New York, 487 (1970).
37. R. F. Harrington, "Time-Harmonic Electromagnetic Fields," McGraw-Hill, New York, 46 (1961).
38. J. Strong, "Concepts of Classical Optics," W. H. Freeman and Company, San Francisco, 28 (1958).
39. See Ref. 24, p. 5.
40. See Ref. 25, p. 19.
41. J. A. Kong, "Electromagnetic Wave Theory," John Wiley and Sons, New York, 37 (1986).
42. S. Shibuya, "A Basic Atlas of Radio-Wave Propagation," John Wiley and Sons, New York, 14 (1987).
43. J. D. Kraus, "Electromagnetics," 3rd ed., McGraw-Hill, New York, 497 (1984).
44. P. A. Rizzi, "Microwave Engineering," Prentice-Hall, Englewood Cliffs, N.J., 36 (1988).
45. See Ref. 35, p. 158.
46. See Ref. 22, p. 275.
47. R. H. Webb, "Elementary Wave Optics," Academic Press, New York, 80 (1969).
48. R. W. Ditchburn, "Light," 3rd ed., Academic Press, New York, 638 (1976).
49. R. P. Feynman, R. B. Leighton, and M. Sands, "The Feynman Lectures on Physics," Vol. 1, Addison-Wesley, Reading, Mass., 33-10 (1963).
50. See Ref. 36, p. 488.
51. F. H. Read, "Electromagnetic Radiation," John Wiley and Sons, New York, 37 (1980).
52. B. D. McCombe and R. J. Wagner in "Advances in Electronics and Electron Physics," (L. Marton, ed.), Vol. 37, Academic Press, New York, 1 (1975).
53. E. Whittaker, "A History of the Theories of Aether and Electricity," Vol. 1, Philosophical Library, New York, 125 (1951).
54. See Ref. 28, p. 29.
55. R. W. Wood, "Physical Optics," 3rd ed., Macmillan, New York, 4 (1934).

56. A. Schuster, "An Introduction to the Theory of Optics," 3rd ed., Longmans, Green, and Co., New York, 241 (1924).
57. See Ref. 28, p. 360.
58. F. A. Jenkins and H. E. White, "Fundamentals of Optics," 4th ed., McGraw-Hill, New York, 244 (1976).
59. See Ref. 55, p. 211.
60. G. Friedmann and H. S. Sandhu, *Am. J. Phys.* **33**, 135 (1965).
61. F. W. Sears, "Optics," 3rd ed., Addison-Wesley, Reading, Mass., Fig. 7-3 (1958).
62. B. Rossi, "Optics," Addison-Wesley, Reading, Mass., Figs. 8-9, 8-10 (1957).
63. See Ref. 22, Figs. 4.20 and 4.21.
64. W. N. Hansen, *J. Opt. Soc. Am.* **58**, 380 (1968).
65. D. T. Paris and F. K. Hurd, "Basic Electromagnetic Theory," McGraw-Hill, New York, Fig. 8-5 (1969).
66. See Ref. 32, Figs. 23-1 and 23-2.
67. R. I. Sarbacher and W. A. Edson, "Hyper and Ultrahigh Frequency Engineering," 8th printing, John Wiley and Sons, New York, Figs. 4-4, 4-5 (1950).
68. D. R. Corson and P. Lorrain, "Introduction to Electromagnetic Fields and Waves," W. H. Freeman and Co., San Francisco, Figs. 11-4, 11-5 (1962).
69. Three books (Refs. 61, 67, 70) present figures in which E_{rs} points in the opposite direction. However, the expression for the reflection coefficient given by Refs. 61 and 70 corresponds with the convention of Fig. 7a.
70. A. B. Winterbottom, "Optical Studies of Metal Surfaces," Kgl. Norske Vedenskab. Selskabs Skrifter, Trondheim, Norway, 15 (1955).
71. See how much easier it is to visualize Fig. 7-3 than Fig. 7-4 in Ref. 61.
72. See Ref. 61, p. 167.
73. See Ref. 22, p. 94.
74. See Ref. 28, p. 361.
75. See Ref. 68, p. 363.
76. See Ref. 25, p. 55.
77. See Ref. 14, p. 31.
78. L. Ward, "The Optical Constants of Bulk Materials and Films," Adam Hilger, Bristol, 10 (1988).
79. F. Abelès, in "Progress in Optics," (E. Wolf, ed.), Vol. 2, North-Holland, Amsterdam, 251 (1963).
80. See Ref. 3, p. 10-10.
81. P. H. Berning, in "Physics of Thin Films," (G. Hass and R. E. Thun, eds.), Vol. 1, Academic Press, New York, 69, (1963).
82. F. A. Jenkins and H. E. White, "Fundamentals of Physical Optics," 1st ed., McGraw-Hill, New York, 402 (1937). Note that Fig. 18O and Eqs. (18n) and (18o) do not appear in later editions.
83. See Ref. 3, p. 10-12.
84. Typically, x is chosen to be the real axis and counterclockwise rotation is from the positive x axis toward the positive y axis.
85. In a calculation, phase angles must be expressed in radians, not degrees. See H. Anders, "Thin Films in Optics," English ed., The Focal Press, London, 24, footnote (1967).
86. R. S. Longhurst, "Geometrical and Physical Optics," 2nd ed., John Wiley and Sons, New York, 471 (1967).
87. Since we are showing the actual reflected field vectors, we have dropped the F and V labels.
88. See Ref. 48, p. 514.
89. R. M. A. Azzam and N. M. Bashara, "Ellipsometry and Polarized Light," North-Holland, Amsterdam, 67 (1977).

90. See Ref. 3, p. 10-20.
91. See Ref. 58, p. 528.
92. H. E. Bennett and J. M. Bennett, in "Physics of Thin Films," (G. Hass and R. E. Thun, eds.), Vol. 4, Academic Press, New York, 66 (1967).
93. A trivial but not necessarily inconsequential point is that no author (that we know of) tells the reader where to put his feet when looking into the oncoming wave. Left and right, as well as up and down, are relative to the body's orientation. Thus, the reader must be able to position (in his mind, at least) his body correctly to a sample surface, plane of incidence, optical element, or whatever. If the viewer stands on a plane parallel to the plane of incidence in Fig. 10 and looks into the wave, either incident or reflected, the y axis points up and the x axis points to the right.
94. See Ref. 22, p. 100.
95. See Ref. 25, p. 44.
96. See Ref. 58, p. 268.
97. See Ref. 35, Fig. 5-22 and Eq. (5-90a).
98. See Ref. 25, p. 48.
99. See Ref. 35, p. 236.
100. See Ref. 43, p. 519.
101. See Ref. 42, pp. 18 and 53.
102. G. W. DeBell, *SPIE Proc.* **140**, 2 (1978).
103. See Ref. 43, p. 439.
104. E. E. Wahlstrom, "Optical Crystallography," 5th ed., John Wiley and Sons, New York, 154 (1979).
105. See Ref. 58, p. 242.
106. J. M. Bennett, *J. Opt. Soc. Am.* **54**, 612 (1964).
107. R. H. Muller, in "Advances in Electrochemistry and Electrochemical Engineering," (R. H. Muller, ed.), Vol. 9, John Wiley and Sons, New York, 167 (1973).
108. F. Abclès, *C.R. Acad. Sci.* **230**, 1942 (1950).
109. R. M. A. Azzam, *Opt. Acta* **26**, 113 (1979); ibid. **26**, 301 (1979).
110. See Ref. 3, p. 10-86.
111. J. F. Snell, in "Handbook of Optics," (W. G. Driscoll, ed.), McGraw-Hill, New York, 1-1 (1978).
112. D. L. MacAdam, *J. Opt. Soc. Am.* **57**, 854 (1967).
113. G. Hass, J. B. Heaney, and W. R. Hunter, in "Physics of Thin Films," (G. Hass, M. H. Francombe, and J. L. Vossen, eds.), Vol. 12, Academic Press, New York, 1 (1982).
114. E. D. Palik and J. K. Furdyna, *Rept. Prog. Phys.* **33**, 1193 (1970).
115. J. D. Rancourt, "Optical Thin Films," Macmillan, New York, 12 (1987).
116. I. N. Shklyarevskii and N. A. Nosulenko, *Opt. Spec.* **14**, 127 (1963).
117. I. N. Shklyarevskii and V. K. Miloslavskii, *Opt. Spec.* **12**, 449 (1962).
118. L. Dunajsky, *Opt. Spec.* **12**, 448 (1962).
119. I. N. Shklyarevskii, N. A. Vlasenko, V. K. Miloslavskii, and N. A. Noculenko, *Opt. Spec.* **9**, 337 (1960).
120. N. Y. Gorban and I. A. Shaikevich, *Opt. Spec.* **11**, 404 (1961).
121. P. E. Ciddor, *Opt. Acta* **7**, 399 (1960).
122. I. N. Shklyarevskii, *Sov. Phys. Tech. Phys.* **1**, 327 (1956).
123. W. H. Weinberg, in "Solid State Physics: Surfaces," (R. L. Park and M. G. Lagally, eds.), Vol. 22, Academic Press, New York, 22, Fig. 26b (1985).

Chapter 3

Methods for Determining Optical Parameters of Thin Films

E. PELLETIER
Laboratoire d'Optique des Surfaces et des Couches Minces
Unité Associeé au CNRS
Ecole Nationale Supérieure de Physique de Marseille
Domaine Universitaire de St. Jérôme
Marseille, France

I. Introduction 57
II. An Example of Comparison between the Different Techniques of Index Determination 58
III. Principle Methods of Index Determination 60
IV. Sensitivity and Accuracy of the Determination Methods 64
V. Overlapping and Tests of Validity of the Model 67
VI. Results and Conclusion 71
References 71

I INTRODUCTION

The aim of this chapter is to give an overview of the different methods used for determining the parameters that optically characterize a thin film. We limit ourselves to the case of a single layer deposited on a substrate, the properties of which are well known, and the materials involved are exclusively those generally used for optical multilayer coatings. Practically, these coatings can be used in the ultraviolet, visible, or infrared regions of the spectrum (100 nm to 100 μm). In a filter some wavelengths are transmitted, and others are completely reflected, according to the characteristics of the layers that constitute this optical filter.

In a general way, each layer is characterized by its refractive index n, its extinction coefficient k, and its thickness d [1].

For the production of optical filters, we will deal more precisely with the materials in their transparent region, that is, the spectral range in which the extinction coefficient is very weak.

Copyright © 1991 by Academic Press.
All rights of reproduction in any form reserved.
ISBN 0-12-544422-2

Concerning the optical characterization of a single film, we can find in the literature numerous references with particularly exhaustive review articles. It is impossible to give an analysis of these works in a short chapter. However, it seems useful to display the evolution of the problems and the techniques used to solve them for some decades. In 1963, Abelès [2] gave a general review of the work done by different groups in the world. Some years later, with the introduction of computers, data processing greatly improved, and numerous ways were found to ease the acquisition of experimental results and the characterization of thin films. On this subject, we can refer to Liddell's book in which a complete chapter is devoted to the question of index determination [3]. At present, with the development of very high-performing optical filters, a more precise determination of the index values is of great importance.

What kinds of methods can meet these requirements? What progress has been made recently and how can we go further? We will try to give answers to these questions.

II AN EXAMPLE OF COMPARISON BETWEEN THE DIFFERENT TECHNIQUES OF INDEX DETERMINATION

To have access to the values of refractive indices of thin layers, we will attempt to exploit directly the optical measurements made on these layers. Different techniques can be of potential use according to the transparency or nontransparency of the material. According to each case, measurements of transmission and reflection parameters or ellipsometric measurements of Δ, Ψ angles can be used [4].

Each author has his preferred method, and it is not possible to distinguish clearly the advantages and disadvantages of each without a detailed study, at least from the point of view of accuracy. We are indebted to the Optical Materials and Thin Films technical group of the Optical Society of America, with J. A. Dobrowolski as leader, for an attempt to address this question [5]. Seven laboratories were given films of different thicknesses of ScO_2 and Rh. The substrates used for the coatings were commercially polished fused silica (Dynasil). All the samples of each material were prepared in a single deposition run; the aim of the panelists (R. M. Azzam, J. M. Bennett, W. E. Case, C. K. Carniglia, J. A. Dobrowolski, U. J. Gibson, H. A. Macleod, and E. Pelletier) was to compare the optical constants obtained.

The results are meaningful: Table I gives the optical constants for scandium oxide. We give here only the values and variances of refractive index for different wavelengths in the 400–750 nm spectral range. Two

TABLE I

From Results in Arndt *et al.* [5], Concerning Index Measurements on Two Scandium Oxide Layers d_1 and d_2 in the Spectral Range 400–750 nm (Substrate: Fused Silica)

Method	R, T and d	Reflection ellipsometry	Wide-band spectrophotometric	Modified Valeev turing point	Algebraic inversion	Inverse synthesis	Envelope	
d_1 (nm)	224.5	228.2	217.6	219.0	225.0	221.2	219.4	222.2±3.9
d_2 (nm)	452.5	462.6	447.8	447.4	450.0	450.3	449.6	451.5±5.2
	A	B	C	D	E	F	H	
λ (nm)								Mean values
400 d_1	—	2.07	1.89	1.91	—	1.87	1.90	1.93
d_2	—		1.89	1.90	—		1.89	±0.08
450 d_1	1.70	2.01	1.88	1.89	1.84	1.86	1.88	1.88
d_2	1.86		1.87	1.88	1.87		1.89	±0.07
500 d_1	1.86	1.93	1.87	1.88	—	1.85	1.86	1.87
d_2	1.85		1.86	1.87	1.86		1.87	±0.03
550 d_1	1.84	1.85	1.87	1.86	1.87	1.85	1.85	1.86
d_2	1.87		1.85	1.85	—		1.86	±0.01
600 d_1	1.84	1.82	1.87	1.85	1.84	1.84	1.83	1.84
d_2	1.86		1.85	1.84	1.87		1.85	±0.02
650 d_1	1.84	1.81	1.86	1.84	1.82	1.84	1.82	1.83
d_2	1.82		1.84	1.83	1.82		1.84	±0.01
700 d_1	1.83	—	1.86	1.84	1.81	1.84	1.81	1.83
d_2	1.84	—	1.84	1.83	1.83		1.83	±0.01
750 d_1	1.82	—	—	1.83	—	1.84	—	1.83
d_2	1.84	—	—	1.82	—		—	±0.01

Seven measurement techniques (referenced from A to H in [5]) are compared.

layers of different thicknesses were studied, and here the problem is thickness measurement. The thicknesses determined by different methods were remarkably close to the average values 222.2±3.9 and 451.5±5.2 nm. The refractive index agreement is not bad—on the order of 0.01 for the 550–750 nm wavelength range. The extinction coefficient is very low; the methods were not able to determine significant values for it. Some panelists assumed that the Sc_2O_3 layers were nonabsorbing, and this assumption was not disturbing.

The results of determination of the optical constants of the Rh films are less satisfactory (Table II). The average variances in the determination of n and k in the 400–750 nm spectral region were 0.35 and 0.26, respectively, or 13% and 8%. The disparity of the thickness measurement results is of the same order. However, we must note Dobrowolski's important observation: compared with the optical properties of the bulk material, the values found for the optical constants of the material in thin-film form are sometimes disconcerting, but this may be the reason why the field of thin-film physics is so fascinating! And our attempt to compare the different techniques of index determination is not simplified, either.

At this stage, it is necessary to investigate the detail of the different methods compared; we will begin by examining the principles behind these methods, before approaching more technical aspects.

III Principle Methods of Index Determination

For a first approach, we will consider two extreme cases as above.

In the first case, we will consider a transparent layer, and our problem is the determination of $n(\lambda)$, the refractive index for each of the wavelengths, together with the thickness d of the layer, assuming that $k(\lambda) = 0$ is valid at all wavelengths.

In the second case, the layer is absorbing and the values $n(\lambda)$, $k(\lambda)$, and d have to be determined.

We have to consider three steps.

- measuring of optical properties;
- choosing of a technique to calculate the optical properties with a model of the layer included in it; and
- the numerical treatment used for the compiling of data.

We must note that except for very particular cases, the value of the refractive index is not obtained by a rapid calculation. We must generally proceed with successive approximations to fit n in order to obtain good agreement between the calculated and the measured optical properties.

TABLE II

From results in Arndt *et al.* [5], Concerning Index and Thickness Measurements on Two Rhodium Thin Layers d_1 and d_2 in the Spectral Range 400–750 nm (Substrate: Fused Silica)

Method	R, T and d Method		Reflection Ellipsometry		Nestell and Christy		Algebraic Inversion		Inverse Synthesis		Bennett and Booty			
d_1 (nm)	14.2		15.5		17.2		12.0		16.9		17.0		15.5±2.1	
d_2 (nm)	27.1		31.6		30.1		27.5		31.7		—		29.6±2.2	
	A	B	D	E	F	G								
	n	*k*	*n*	*k*	*n*	*k*	*n*	*k*	*n*	*k*	*n*	*k*	*n*	*k*
λ (nm)													Mean	values
400 d_1	—	—	2.10	3.00	1.86	2.88	2.50	3.45	1.80	2.85	3.16	2.15	2.18	2.91
d_2	—	—			1.86	2.97	2.40	3.00			—	—	±0.45	±0.34
450 d_1	2.40	3.29	2.35	3.12	2.04	3.02	2.75	3.55	2.11	3.00	3.19	2.34	2.38	3.08
d_2	2.27	3.25			1.96	3.12	2.75	3.15			—	—	±0.38	±0.29
500 d_1	2.60	3.40	2.56	3.25	2.18	3.14	3.10	3.55	2.20	3.15	3.22	2.54	2.55	3.21
d_2	2.39	3.42			2.04	3.27	3.00	3.15			—	—	±0.40	±0.26
550 d_1	2.78	3.53	2.74	3.41	2.32	3.28	3.20	3.75	2.40	3.25	3.19	2.79	2.68	3.36
d_2	2.51	3.58			2.13	3.43	3.10	3.30			—	—	±0.37	±0.24
600 d_1	2.95	3.65	2.92	3.54	2.46	3.40	3.30	3.90	2.55	3.35	3.15	3.03	2.81	3.50
d_2	2.62	3.75			2.23	3.59	3.30	3.40			—	—	±0.36	±0.23
650 d_1	3.11	3.77	3.08	3.68	2.61	3.52	3.35	4.15	2.75	3.50	3.13	3.26	2.94	3.65
d_2	2.75	3.89			2.36	3.74	3.35	3.50			—	—	±0.32	±0.24
700 d_1	3.23	3.91	—	—	2.75	3.63	3.60	4.20	2.90	3.60	3.07	3.47	3.03	3.77
d_2	2.87	4.04			2.47	3.88	3.50	3.60			—	—	±0.36	±0.25
750 d_1	3.35	4.03	—	—	2.88	3.74			3.00	3.75	3.07	3.61	2.99	3.86
d_2	3.01	4.16			2.60	4.01					—	—	±0.22	±0.20

One of these steps cannot be solved without taking account of the other two, which can simultaneously affect the efficiency of the method of characterization.

Let us now consider the first point: What optical properties must be measured?

The answer is not the same for the different authors. Dobrowolski [5] is very explicit on this subject. In this paper we find

- measurement of normal incidence reflectance R and transmittance T for a single wavelength;
- measurement of polarization states of collimated monochromatic light before and after reflection from a surface to obtain the ratio $\rho = R_p/R_s = \tan \psi \exp(i\Delta)$ of the complex p and s reflection coefficients;
- measurement of normal-incidence reflectance and transmittance over a wide spectral range; and
- measurement of R and T for normal and oblique angles of incidence (45°; 60°) for the polarizations T_E and T_M, over a wide spectral range.

The second point we consider is calculation of optical properties. Determination (with a computer) of the optical properties is easy only if we accept some hypotheses, mainly related to the model of the layer. In a classical way, it is assumed that the layer is optically homogeneous and isotropic with plane and parallel surfaces. With Maxwell equations, parameters n, k and d describe theoretically the optical properties of the layer. However, a comparison between theory and experiment requires some precautions.

(1) Illumination conditions: angle of incidence and wavelength must be specified. In monochromatic or wide-spectral-range methods, R and T must be measured for the same angle of incidence. In the calculations, we consider a monochromatic plane wave. What about the spectrophotometer set up, with respect to aperture, angle of incidence, and monochromaticity of the measurement beam?

(2) In the calculations, we assume that the layer is deposited on a substrate of well-determined index $n_s(\lambda)$ and of infinite thickness. In other words, the layer is inserted between two semi-infinite media of index n_0 and n_s. Very often, the experimental conditions are different, because the substrate has a finite thickness, relatively large with respect to the layer thickness, so that the interference effects in the substrate are not resolved; but—and this is an essential problem—the back face of the substrate does give rise to a reflected and a transmitted beam, which can perturb the reflectance and transmittance measurements. To this must be added the surface of the substrate itself, whose quality determines the quality of the two interfaces of the layer, which are never absolutely plane.

Different techniques have been proposed to minimize these undesirable

experimental conditions; the solutions are more or less successful, depending mainly on the experimental conditions used.

When comparing the results, we observed systematic differences between the authors, probably due to these problems of measurement. A more complete analysis of this subject can be found elsewhere [3, 5, 6].

Finally, we consider the numerical treatment used for compilation of the data. We compare the experimental results with the theory to determine the values of the optical constants. The mathematical solution is not obvious. However, knowing that the optical properties at wavelength λ_i can be described with the three parameters n_i, k_i, and d, we can find a solution by simplifying the problem. For example, for an absorbing material, d can be determined with a complementary method (interferometry or mechanical stylus [7]), thus reducing the problem to two unknown quantities, n and k. In the case of a transparent material, the first approximation $k=0$ makes the work easier, especially if we note that transmittance and reflectance are functions of the variable $2\pi nd/\lambda$. So, if we consider two measurements, we can determine two unknowns. From 3, 4, or even L measurements, we could determine the same number of unknowns, such as n and k, for a series of different wavelengths. And if L is large, we can verify the results by cross-checking. It is obvious that the problem of data compilation will require a powerful computer, if we want to exploit these data better.

We can give a quick presentation of the methods of index determination, the common base of which is as follows: we will consider the case of a layer of refractive index greater than the substrate index. First, we exploit the values of the extrema of $R(\lambda)$ (Fig. 1). Neglecting the effects of index dispersion for the values of λ corresponding to these extrema, the layer has an optical thickness, which is an odd multiple of $\lambda/4$, and we can find that the reflectance is maximum and given by

$$R=\left(\frac{n^2-n_0n_s}{n^2+n_0n_s}\right)^2.$$

With low-index layers, the minima of $R(\lambda)$ are used because for the same optical thickness, the reflection is minimum, and the reflectance is given by the same formula. We can find many papers in the literature that exploit the turning-point method [8].

To determine n for other wavelengths, two methods can be followed. The first consists of plotting the two curves enveloping the extrema of the profile of $R(\lambda)$ and analyzing these envelopes [9]. The second directly uses the profile of $R(\lambda)$ and synthesizes the spectrum to determine the parameters that account for the effective optical properties of the layer. The more sophisticated synthesis methods, such as Dobrowolski's, are easily

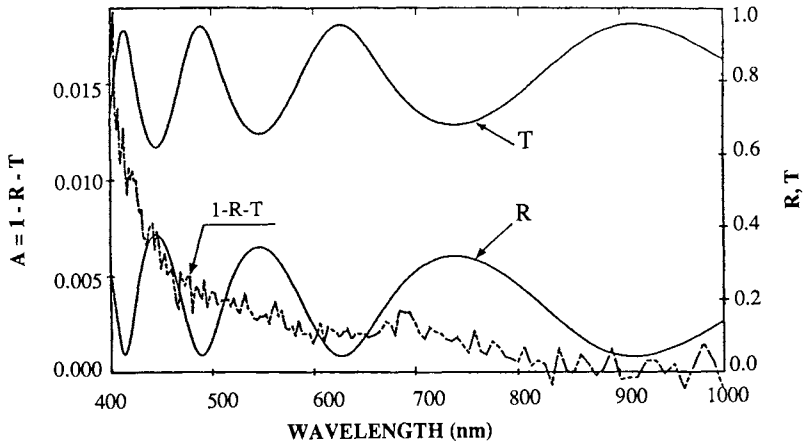

Fig. 1. TiO_2 layer, after J. P. Borgogno *et al.* [6]. From the measurement of reflection, $R(\lambda)$, and transmission, $T(\lambda)$, coefficients, we have plotted the variations of the absorption $A(\lambda) = 1 - R(\lambda) - T(\lambda)$ versus wavelength λ. Maximums of $R(\lambda)$ lead to a rapid determination of d and $n(\lambda)$.

applied here, since they involve a single layer and not a multilayer [10].

Either process, by successive approximations, results in a determination of the parameters' values, giving better interpretation of the measured values of the optical properties. A figure of merit is used, and a convergence process drives the cycle of approximations. The difficulties of this technique are well-known: the solution is not necessarily unique, and the efficiency of the convergence process essentially depends on the values assigned at the beginning of the iteration process.

The completely automatic programs of index determination must avoid these difficulties [11], and great precautions must be taken at the beginning of the synthesis calculation, in particular for determining initial d and k values, even before n values [12]. For highly absorbing materials, the efficiency of these programs is not so obvious.

IV SENSITIVITY AND ACCURACY OF THE DETERMINATION METHODS

We get a preliminary idea of the accuracy of the methods of index determination by examining the results of data processing. As an illustration, we present in Fig. 2 the amplitude of errors on n, when measurements of R and T are affected by an error $\Delta R = \Delta T = \pm 0.003$. We note the well-known result [13]: the precision of Δn is strongly dependent on the particular wavelength. To continue in our investigation, it is interesting to compare systematically the agreement obtained between the optical

properties measured and those calculated from the determined values of parameters n, k, and d. The result is very often surprising, particularly if we consider a sampling of wavelengths different from that used for the measurements. On this subject, it is interesting to recall the technique of representing the law of index dispersion by a limited equation such as Cauchy's [14]:

$$n = A + \frac{B}{\lambda^2} + \frac{C}{\lambda^4}$$

under the express condition that its validity is well verified.

There appears a systematic disagreement between calculation and experiment, at least for particular spectral ranges (Fig. 3). Discontinuities can also be seen on the graph (Fig. 2) of the curve $n(\lambda)$, for particular regions of the spectrum. It can be shown that it is not sufficient just to blame the measurement techniques and the numerical techniques of convergence. We have here a more fundamental difficulty in the problem of index determination, which concerns the validity of the model used to account for the effective properties of the layers. We have assumed in the simple model that the layer was homogeneous and isotropic with plane and parallel surfaces. At a given degree of perfection, it is no longer possible to assume these three hypotheses. The problems of inhomogeneity and anisotropy will prevent us from using these methods to their maximum

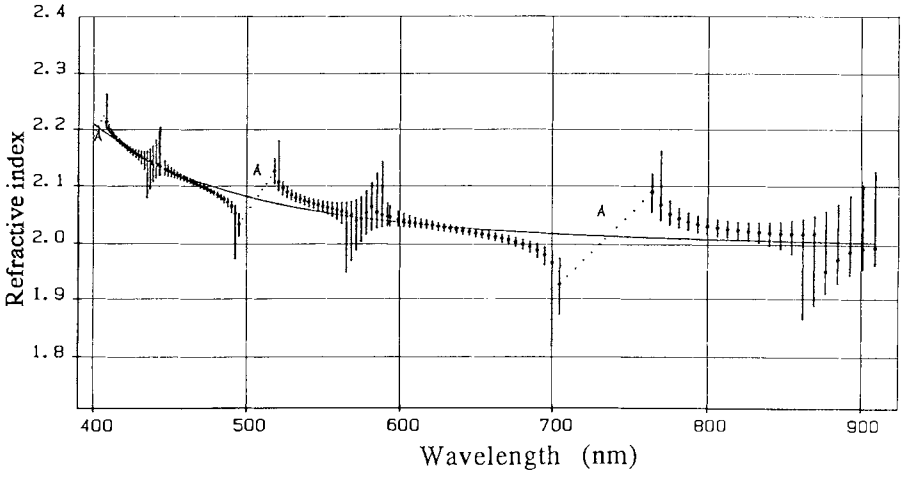

Fig. 2. Refractive index of a titanium oxide layer using the classical model of homogeneous layer. Note the parts of the graph deviating from the mean-value curve and the two ranges (A) where index determination is impossible.

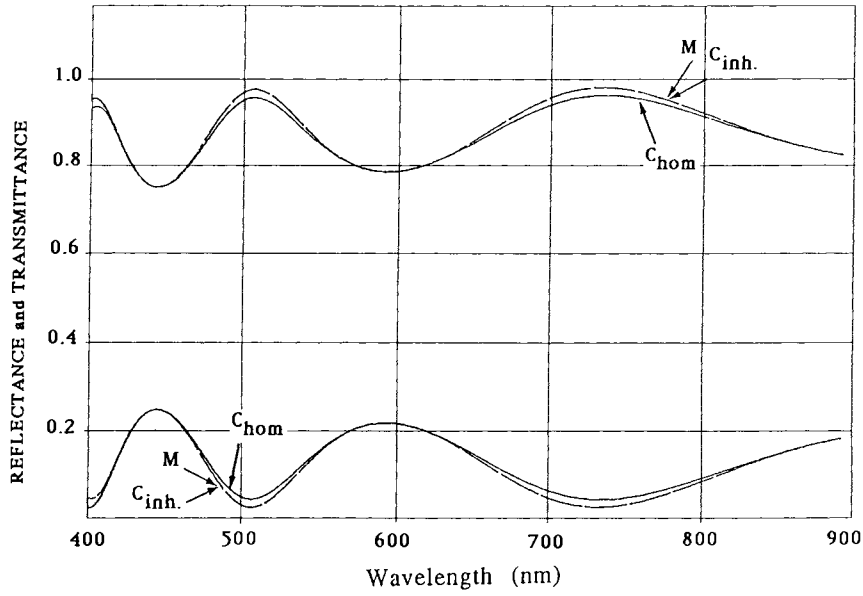

Fig. 3. For the TiO_2 layer of Fig. 2, disagreement between calculation and experiment. M indicates measurements of reflectance and transmittance for normal incidence. C_{hom} is the calculated result using a nonclassical homogeneous model. A better agreement, C_{inh}, can be obtained by introducing inhomogeneity in the model (after Borgogno *et al.* [11]).

potential. Planarity and roughness of the surfaces, from which light scattering originates, are hopefully negligible for substrates of good optical quality [15].

Numerous authors agree to the obvious presence of inhomogeneity in transparent layers [11, 16]. We can take advantage of the fact that a layer with optical thickness of $\lambda/2$ or a multiple of $\lambda/2$ is *absent*, that is, it does not modify, for this wavelength, the reflectance of the substrate. From the experimental results concerning the values of R for these wavelengths, we can deduce information about the global variation of refractive index in the volume of the layer. So we often give the value $\Delta n/n$ with $\Delta n = n_0 - n_i$, where n_0 and n_i represent the refractive index at the interfaces on the air or on the substrate side, respectively. The form of the gradation of n inside the layer is not of great importance, and a linear variation seems a reasonably good approximation (Fig. 4). Other forms of gradation can be used, depending essentially on the layers considered, since the structure of the coatings depends in great part on the deposition technique [17].

Some results of $n(\lambda)$ with measurements of inhomogeneity $(\Delta n/n)(\lambda)$ have been published [18] (see Fig. 5). We can consider that the introduction of the parameter $\Delta n/n$ has a decisive role here in the improvement of accuracy of the method of index determination.

We can understand the differences observed among the results of the different authors, such as those presented in Section II. Three difficulties are simultaneously involved: accuracy of the measurements, efficiency of calculations, and validity of the layer model. For a well-characterized yttrium oxide layer, Daugy *et al.* [19] have shown how divergences can appear as soon as we neglect absorption and inhomogeneity in the analysis techniques already mentioned [8, 9, 11]. Figure 6 displays the results, including the result of ellipsometric measurements. In addition, the values of bulk yttrium oxide from Nigara [20] are reported, but the comparison between the optical constants of the material in the bulk and thin-film form cannot be of much help in corroborating the results for the methods of index determination of the layers. Only a systematic cross-checking of the different techniques applied to a thin film can give us a clue for obtaining better accuracy. We will now give a short overview of this subject.

V OVERLAPPING AND TESTS OF VALIDITY OF THE MODEL

The optical measurements are, unfortunately, never perfect, and this sometimes prevents the calculations from converging toward a good

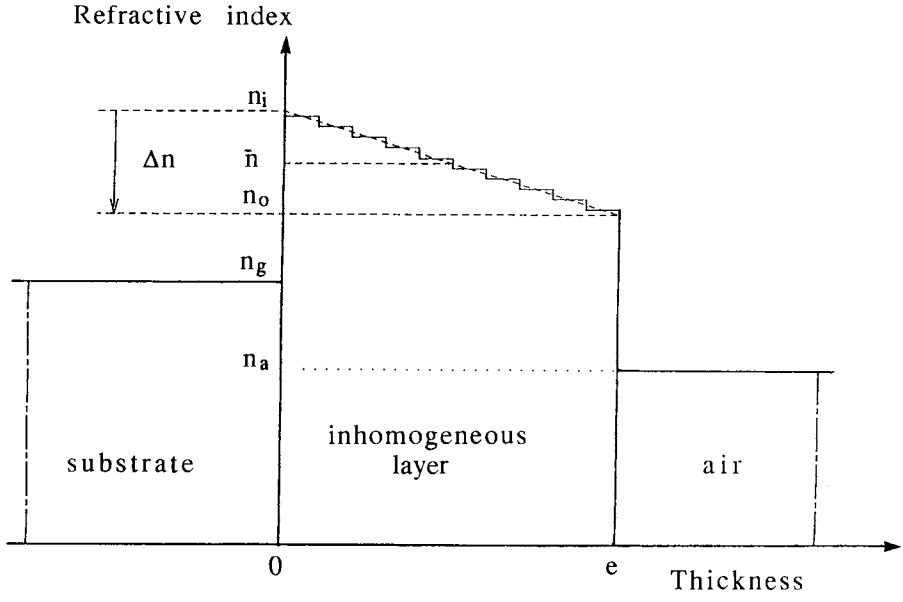

Fig. 4. Model of inhomogeneous layer used in the calculation: $\Delta n = n_0 - n_i$. The value Δn is negative for index decreasing from the substrate (after Borgogno *et al.* [11]).

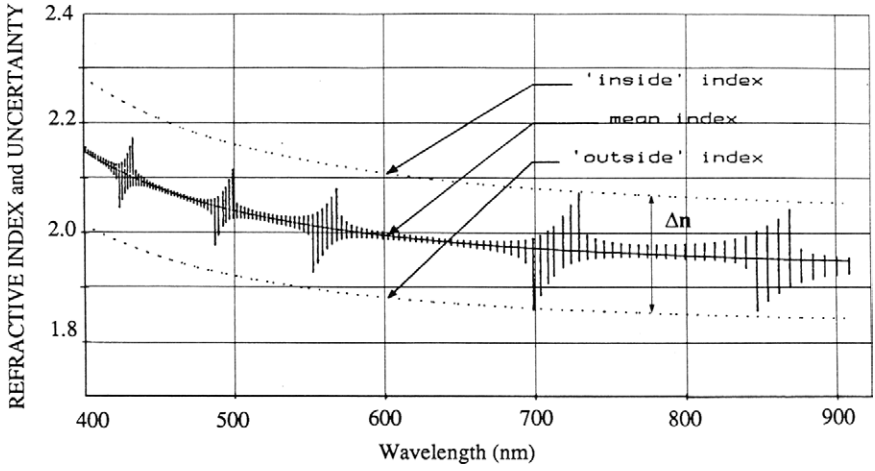

Fig. 5. Determination of $n(\lambda)$ and $\Delta n(\lambda)$ for a TiO_2 layer with the model of Fig. 4. The results can be easily described by a Cauchy equation.

solution. A priori, under these conditions, it is always interesting to add some complementary measurements to help in searching for the solution, and especially to remove any ambiguity.

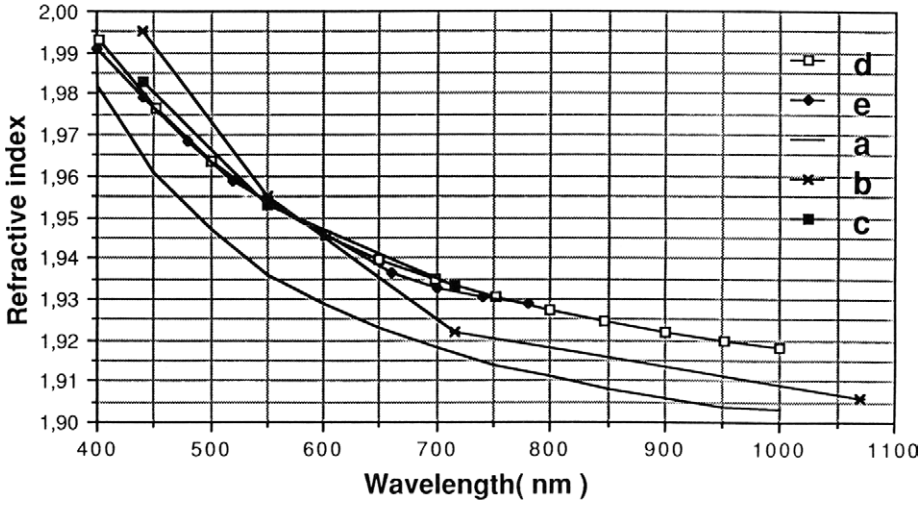

Fig. 6. Study of a Y_2O_3 layer. Refractive-index values given by different techniques: (a) bulk material, after Nigara [20]; (b) from T measurements, after Daugy *et al.* [19]; (c) from T and R, after Daugy *et al.* [19]; (d) after T and R measurements, from Borgogno *et al.* [11, 12]; (e) ellipsometric measurements of Sté SOPRA, France (see Daugy *et al.* [19]).

In this way, the use of oblique incidence can be of great assistance, mainly for absorbing materials [10, 21]. The same principle leads authors to measure both the values of R measured "on the air side" and R' measured "on the substrate side," either for dielectrics [22] or for metals on substrates [23]. In fact, this technique allows the quality of the spectrophotometric measurements to be tested and eventually reveals structure defects in the layer. If we want to go further in this analysis, we must consider that, far from being competitive, spectrophotometric and ellipsometric methods are rather complementary [24].

Until now, we have limited ourselves to the classical methods of index determination, but we must note that in the last few years, complementary characterization methods have been proposed for very particular applications. Improving the accuracy of n and especially of k is of great interest for transparent layers. And for absorbing materials, an unambiguous determination of k is essential.

For studying highly transparent materials, guided-wave techniques are particularly interesting. Following Ulrich and Torge [25], one can exploit the idea of using the layer as a light guide, by coupling light with a prism of known refractive index.

Basically, parameters n and d of the layer are the unknowns: it is sufficient to study the propagating conditions of two different modes to determine these two values. Given the accuracy obtained for angular measurements, the refractive index value can be measured to within almost the third decimal place.

With three modes, the overlapping can be exploited to test the validity of the layer model used in the calculation. This technique has been used to show an optical anisotropy induced by the particular microstructure of dielectric materials evaporated under vacuum. We know that they condense in a columnar form, the orientation of which depends on the incidence angle of the flux emitted by the crucible and arriving on the surface being coated.

From ellipsometric and absorption measurements, Hodgkinson *et al.* and Horowitz have developed a layer model to account for the optical anisotropy induced by this columnar structure [26] (Fig. 7). Measurements with guided waves [27] allow a complete validation of the model proposed. Table III is an illustration of the results obtained.

Coupling light into metallic layers gives rise to more difficult problems. Known as *surface-plasmon effect*, it can lead to index measurements in some particular cases. Macleod has shown how to exploit this phenomenon, well-known by the optical scientists [28].

Concerning the determination of extinction coefficients $k(\lambda)$ of dielectrics, we must note the measurements of propagation attenuation: they give access to the value of k, at least in the case where scattering losses can be neglected.

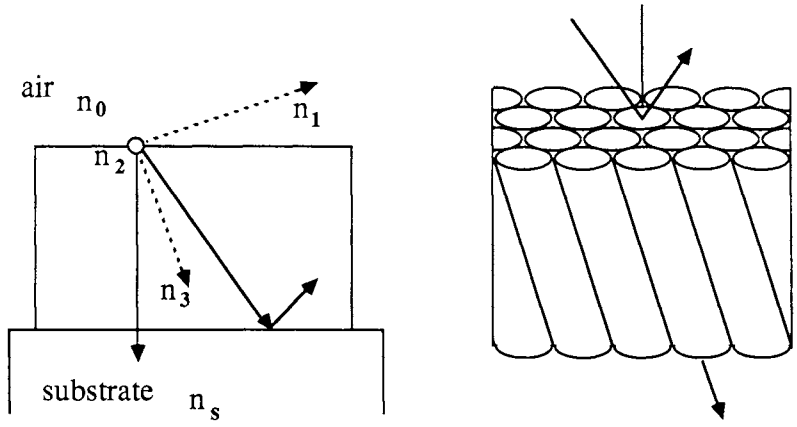

Fig. 7. Columnar structure model (after Horowitz [26]). For the calculation of anisotropy, the three principal indices of refraction are n_1, n_2, and n_3. With this model, in the columnar growth direction, the index value is n_3.

For some years, works on acousto-optical and mainly photothermal methods have also led to the measurement of absorption in thin layers. It is probable that the method of Boccara *et al.* [29] will be more widely utilized, under conditions of good calibration of the measurements, either for very low values of k [30] or for specific absorptions [31].

TABLE III

Measurement of Anisotropy: TiO_2, ZnS, Ta_2O_5 Layers Produced by Evaporation and Ta_2O_5 Layers Produced by Ion Assisted Deposition

	TiO_2	ZnS	Ta_2O_5	Ta_2O_5
n_1	2.320	2.349	2.119	2.151
n_2	2.321	2.351	2.115	2.151
n_3	2.357	2.356	2.127	2.155

The angle between the normal to the substrate and the direction of the material flux is 19°. Macleod and Horowitz model (Fig. 7): measurements with guided waves of the values of the three principal indices n_1, n_2, and n_3 (which corresponds to the columnar growth direction) [27].

VI RESULTS AND CONCLUSION

Some amount of humor is necessary to use the expression *optical constant* in referring to the complex refractive index of a thin layer. In this chapter, we have shown that an accurate measurement implies taking account of the dependence of n and k on a series of parameters, which are wavelength, layer thickness, angle of incidence, and so forth. It remains to introduce the dependence with time: the layers are in equilibrium with the surrounding medium, and the amount of absorbed water or contaminants is a function of the hydroscopic character of this medium, of the void-fraction of the deposited material, and of the temperature. A comparison of the results obtained in air and in vacuum gives significant differences [32], which can be explained as absorption–desorption phenomena.

For relatively thick transparent layers (several $\lambda/4$) deposited on transparent substrates, we can determine n in a transparent region with a precision no better than 1%.

Concerning k (except for photothermal measurements), the precision is very limited for values of $k < 1 \times 10^{-3}$. Outside the transparent region, the conclusions are still more pessimistic. All numerical extrapolation for wavelengths outside the measurement range can lead to nonreliable results.

Often, when we plot the graphs $n(\lambda)$ and $k(\lambda)$ on a wide spectral range (as is done in this handbook), we often observe discontinuities between two ranges where the techniques used were different.

So, should we give up determining the layer index to more than two decimals? Certainly not; the need for all the applications is much too important. But we must take account of the detail of the technique of fabrication of the layers; it determines the microstructure of the materials. It is interesting to note that with a classical evaporation, a repeatability better than 1% in the index cannot be guaranteed. It is the order of magnitude of the accuracy of the classical methods of index determination. Modern technologies of layer production, particularly those using ion bombardment, lead to coatings with a more compact structure, similar to that of bulk material, resulting in a clear improvement of the validity of the theoretical models; the methods of index determination are then more reliable.

REFERENCES

1. H. A. Macleod, "Thin Film Optical Filters," Adam Hilger, Bristol, 1986.
2. F. Abelès, "Methods for determining optical parameters of thin films," in "Progress in Optics," (E. Wolf, ed.) vol. 2, North-Holland, Amsterdam, 250 (1963).
3. M. Liddell, "Computer Aided Techniques for Design of Multilayer Filters," Adam Hilger, Bristol, 1981.

4. R. M. A. Azzam and N. M. Bashara "Ellipsometry and Polarized Light," North-Holland, Amsterdam, 1977.
5. D. P. Arndt, R. M. A. Azzam, J. M. Bennett, J. P. Borgogno, C. K. Carniglia, W. E. Case, J. A. Dobrowolski, U. J. Gibson, T. Tuttlehart, F. C. Ho, V. A. Hodgkin, W. P. Klapp, H. A. Macleod, E. Pelletier, M. K. Purvis, D. M. Quinn, D. H. Strome, R. Swenson, P. A. Temple, and T. F. Thonn, Multiple determination of the optical constants of thin-film coating materials," *Appl. Opt.* **23**, 3571 (1984).
6. J. Lafait, "Goniospectrophotomètre à polarisation de 0,25 à 1 μm," *Optica Acta* **20**, 365 (1973); J. P. Borgogno and E. Pelletier, "Determination of the extinction coefficient of dielectric thin films from spectrophotometric measurements," *Appl. Opt.* **28**, 2895 (1989).
7. H. E. Bennett and J. M. Bennett, "Precision measurements in thin film optics," in "Physics of Thin Films," (G. Hass and R. E. Thun, eds.) vol. 4, Academic Press, New York, 1 (1967).
8. J. F. Hall and W. F. C. Fergusson, "Optical properties of cadmium sulphide and zinc sulphide from 0.6 micron to 14 microns," *J. Opt. Soc. Am.* **45**, 714 (1955); A. S. Valeev, "Constants of thin weakly absorbing layers," *Opt. Spectrosc. USSR* **18**, 498 (1965).
9. J. C. Manifacier, J. Gasiot, and J. D. Fillard, "A simple method for the determination of the optical constants n, k, and the thickness of a weakly absorbing thin film," *J. Phys. E.* **9**, 1002 (1976).
10. J. A. Dobrowolski, F. C. Ho, and A. Waldorf, "Determination of optical constants of thin film coating materials based on inverse synthesis," *Appl. Opt.* **22**, 3191 (1983).
11. J. P. Borgogno, B. Lazaridès, and E. Pelletier, "Automatic determination of the optical constants of inhomogeneous thin films," *Applied Optics* **21**, 4020 (1982).
12. J. P. Borgogno, B. Lazaridès, and P. Roche, "An improved method for the determination of the extinction coefficient of thin film materials," *Thin Solid Films* **102**, 209 (1983).
13. C. Bazin, "Influence des erreurs commises lors des mesures expérimentales sur la détermination de l'indice d'une couche mince absorbante," *Compt. Rend. Acad. Sc.* **260**, 83 (1965).
14. D. J. Schroeder, "Interference transmission filters for the far ultraviolet," *J. Opt. Soc. Am.* **52**, 1380 (1962).
15. P. Baumeister, "Reflectance and transmission measurements," *Proc. Soc. Photo-Opt. Instrum. Eng.* **50**, 37 (1974).
16. R. Jacobsson, "Inhomogeneous and coevaporated homogeneous films for optical applications," in "Physics of Thin Films," (G. Hass, ed.), vol. 8, Publisher, City, 51 (1975).
17. H. A. Macleod, "Microstructure of optical thin films," *Proc. Soc. Photo-Opt. Instrum. Eng.* **325**, 21 (1982).
18. J. P. Borgogno, F. Flory, P. Roche, B. Schmitt, G. Albrand, E. Pelletier, and H. A. Macleod, "Refractive index and inhomogeneity of thin films," *Appl. Opt.* **23**, 3567 (1984); J. M. Bennett, E. Pelletier, G. Albrand, J. P. Borgogno, B. Lazaridès, C. K. Carniglia, R. A. Schmell, T. H. Allen, T. Tuttle-Hart, K. H. Guenther, and A. Saxer, "Comparison of the properties of titanium dioxide films prepared by various techniques," *Appl. Opt.* **28**, 3303 (1989).
19. E. Daugy, B. Pointu, C. Audry, and C. Hervo, "Correlations entre les caractéristiques optiques et physico-chimiques de couches minces de Y_2O_3 et ZrO_2 obtenues par pulvérisation par canon à ions," paper presented at "Horizons de l'Optique," Jouy en Josas, August 1989. *J. of Optics* **21**, 99 (1990).
20. Y. Nigara, "Measurements of the Optical Constants of Yttrium Oxide," *Jap. J. Appl. Phys.* **7**, 404 (1967).
21. J. E. Nestell, Jr. and R. W. Christy, "Derivation of optical constants of metals from thin-film measurements at oblique incidence," *Appl. Opt.* **11**, 643 (1972).

22. E. Pelletier, P. Roche, and B. Vidal, "Détermination automatique des constantes optiques et de l'épaisseur de couches minces: application aux couches diélectriques," *Nouv. Rev. Optique* **7**, 353 (1976).
23. P. Rouard, "Etude des propriétés optiques des lames métalliques très minces," *Ann. Phys.* **7**, 291 (1937).
24. D. E. Aspnes, "The characterization of materials by spectroscopic ellipsometry," *Proc. Soc. Photo-Opt. Instrum. Eng.* **452**, 60 (1983).
25. R. Ulrich and R. Torge, "Measurement of thin film parameters with a prism coupler," *Appl. Opt.* **12**, 2901 (1973).
26. F. Horowitz, "Structure Induced Optical Anisotropy in Thin Film," Ph.D., diss. University of Arizona, Optical Sciences Center (1983); I. J. Hodgkinson, F. Horowitz, H. A. Macleod, M. Sikkens, and J. J. Wharton, "Measurement of the principal refractive indices of thin films deposited at oblique incidence," *J. Opt. Soc. Am. A* **2**, 1693 (1985).
27. E. Pelletier, F. Flory, and Y. Hu, "Optical characterization of thin films by guided waves. *Appl. Opt.* **28**, 2918 (1989).
28. H. A. Macleod, "Surface plasmon resonance effects and the admittance diagram," *Proc. Soc. Photo-Opt. Instrum. Eng.* **777**, 300 (1987); H. Raether, "Surface plasma oscillations and their applications," *Phys. Thin Films* **9**, 145 (1977).
29. A. C. Boccara, D. Fournier, W. Jackson, and N. M. Amer, "Sensitive photothermal deflection technique for measuring absorption in optically thin media," *Opt. Letters* **5**, 377 (1980).
30. M. Commandré, L. Bertrand, G. Albrand, and E. Pelletier, "Measurement of absorption losses of optical thin film components by Photothermal Deflection Spectroscopy," *Proc. Soc. Photo-Opt. Instrum. Eng.* **805**, 128 (1987).
31. N. M. Amer, W. Jackson, in "Semiconductors and Semimetals," (J. I. Pankore, ed.), vol. 21B, Academic Press, New York, 83 (1984).
32. B. Schmitt, J. P. Borgogno, G. Albrand, and E. Pelletier, "In situ and air index measurements: influence of the deposition parameters on the shift of TiO_2/SiO_2 Fabry-Perot filters," *Appl. Opt.* **25**, 3909 (1986).
33. P. J. Martin, "Ion-based methods for optical thin film deposition," *J. Mat. Sci.* **21**, 1 (1986).

Chapter 4

The Attenuated Total Reflection Method

G. J. SPROKEL and J. D. SWALEN
IBM Research Division
Almaden Research Center
San Jose, California

I. Introduction 75
II. Surface-Plasmon Oscillations 77
III. Optical Analysis of ATR Structures 81
IV. Guided Modes 84
V. Applications of ATR 87
A. Optical Constants of Metals 87
B. Molecular Films 87
C. Organic Dyes 89
D. Dielectric Films 90
E. Surface Tilt Angle of Nematic Liquid Crystals 90
F. Tutorial Demonstration of ATR 93
G. Guided Modes and ATR 93
H. Long-Range Surface-Plasmon Waves 93
VI. Conclusion 94
References 94

I INTRODUCTION

Attenuated total reflection (ATR) is a technique for determining the optical constants of thin-film samples, that is, the refractive index and the absorption coefficient. It differs from other, perhaps better-known procedures, such as ellipsometry and reflectometry, in that ATR probes the sample with an evanescent wave rather than a collimated beam of light. As is well-known, evanescent waves near an interface decay away exponentially over a distance comparable to the wavelength. There is no energy transport across the interface, and thus the reflectivity is unity. However, for very specific conditions, an evanescent wave can be made to interact

Copyright © 1991 by Academic Press.
All rights of reproduction in any form reserved.
ISBN 0-12-544422-2

with material in its field and energy can be transported. Then the reflectivity will be less than unity and hence the term *attenuated total reflectivity*. In practice, a light beam is directed through a prism or rhomb such that the angle of incidence at the base exceeds the critical angle, and the sample is placed within the evanescent field either in contact with the prism or separated by a narrow gap, which must be smaller than one wavelength. Evanescent waves can also be generated by gratings, and historically the use of gratings preceded that of prisms; however, the prism technique is simpler by far. The prism geometry has been employed in internal reflection spectroscopy (IRS) for many years. The light enters a prism, and the sample is pressed to its base. It is well detailed by Harrick [1].

Here ATR is taken to encompass such widely differing phenomena as plasmon waves on metal surfaces and certain organic dyes, guided modes in dielectric films, and surface waves on diffraction gratings. In ATR experiments, the probe is an evanescent wave rather than the incident beam itself, and resonance is observed by measuring reflectivity as a function of the angle of incidence or the wavelength. It is more common to scan the angle of incidence. In IRS, as in all spectroscopy, the wavelength is scanned.

ATR evolved as a technique in 1968 mostly through the work of Otto in Munich [2–5] and Raether and Kretschmann in Hamburg [6–10]. Although surface-plasmon waves were known since the work of Sommerfeld [2] in radio-wave propagation (1909), they received little attention in optics until the work of Fano in 1941 [11]. Fano's paper dealt with anomalies in the diffraction spectra of metal gratings known as Wood's anomalies. He recognized that surface electromagnetic (EM) waves are evanescent waves with wave vectors larger than that of the incident beam, and that the grating increased the incident wave vector. Much later (1967–1968) this was again taken up by Teng and Stern [12] and by Ritchie *et al.* [13], who used coupling by gratings to excite surface-plasmon waves.

Otto [4, 5], Raether [9], and Burstein *et al.* [14] all published review papers between 1974 and 1977 discussing the physical optics of ATR. Palik and Holm [15] reviewed IRS in 1978. Later papers have dealt more with specific topics. Swalen [16] reviewed the optics of Langmuir–Blodgett films (1986). Rabolt and Swalen [17] discussed integrated optics and its application to Raman scattering (1988). Debe [18] made an extensive review on the optics of organic thin films (1987). The following is a brief discussion of physical optics applied to ATR and outlines the calculation of the dielectric function of the sample. Surface-plasmon oscillations (SPO) and guided modes are discussed. Gratings could not be included because of space limitations. Next, some recent papers are reviewed, selected to exemplify both the versatility and limitations of ATR.

SURFACE-PLASMON OSCILLATIONS II

Surface-plasmon waves are EM waves propagating along the interface of a metal and a dielectric (or air). The conditions for their existence can be derived from Maxwell equations. Take a coordinate system such that the interface is the xy plane, the x axis is the propagation direction and z is the normal. Let the index 0 refer to the dielectric and 1 to the metal. Superscript + indicates the direction into the metal (0→1).

First consider *p*-polarization (E_z, E_x, H_y, k_x, and k_z). The continuity equations for E, D, and H are

$$E_{0x}^{+} = E_{1x}^{+} \tag{1}$$

$$H_{0y}^{+} = H_{1y}^{+} \tag{2}$$

$$D_{0z}^{+} = D_{1z}^{+}. \tag{3}$$

The Maxwell relation for harmonic waves is

$$\mathbf{k} \times \mathbf{H} = \left(\frac{\omega}{c}\right)\mathbf{D}. \tag{4}$$

Substitution of Eqs. 1, 2, and 3 into Eq. 4 yields the following relations between the **k** vectors:

$$\frac{k_{0z}}{\varepsilon_0} + \frac{k_{1z}}{\varepsilon_1} = 0 \tag{5}$$

$$k_{0x} = k_{1x}. \tag{6}$$

By inserting this into the dispersion equation, the result is

$$k_{0x}^2 = k_{1x}^2 = \left(\frac{\omega}{c}\right)^2 \frac{\varepsilon_0 \varepsilon_1}{\varepsilon_0 + \varepsilon_1}. \tag{7}$$

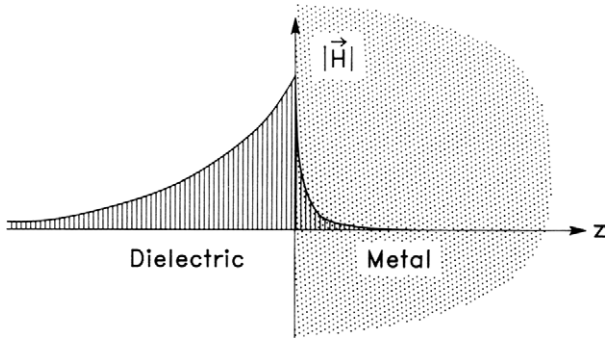

Fig. 1. Schematic showing the optical field at an interface that supports surface plasmons. $\mathbf{E}_z$, $\mathbf{E}_x$, $\mathbf{H}_y$, $\mathbf{k}_x$, and $\mathbf{k}_z$ define a surface plasmon propagating down the x axis (into the page); see the discussion of Eqs. 1–7.

Following the same sequence for s-polarization (E_y, H_x, H_z), the relation for the k vectors is

$$k_{0z} + k_{1z} = 0 \tag{8}$$

$$k_{0x} = k_{1x}. \tag{9}$$

Inserting this in the dispersion equation leads to

$$k_0^2 = \left(\frac{\omega}{c}\right)^2 \varepsilon_0 = k_1^2 = \left(\frac{\omega}{c}\right)^2 \varepsilon_1, \tag{10}$$

but this is an inconsistency, which means that the boundary conditions have solutions only for p-polarized waves; s-polarized surface-plasmon waves do not exist.

Inside the metal, the amplitude of the normal component of the plasmon wave decreases, as shown schematically in Fig. 1 and according to the expression

$$\exp(-2ik_{1z}z) \approx \exp\left(-4\pi \operatorname{Im}\sqrt{\varepsilon_1}\frac{z}{\lambda}\right) \tag{11}$$

for small k_{0x}. The wave penetrates much less than one wavelength. The tangential component, k_{0x}, is also complex; however, the imaginary part is

small compared with the real part, and the wave can be regarded as a damped oscillation propagating some distance along the surface.

In the visible spectrum, the propagation distance is small compared with the width of the incident beam, whereas in the infrared (IR), propagation attains macroscopic dimensions, although it is still a damped wave. Thus, the plasmon wave is limited to the surface region and is said to be *nonradiative*. Radiative surface plasmons do exist, but they are beyond the scope of this discussion. Nonradiative plasmon waves cannot be excited by light incident on a metal surface in vacuum or air because the vacuum wave vector is always smaller than that of the plasmon. There are two ways to excite plasmon waves on smooth surfaces.

Historically, Otto [2, 3] was the first to show that if a prism is used in total reflection, the wave vector of the evanescent wave outside the reflecting surface can match that of the plasmon.

The tangential component of the evanescent wave is

$$k_{\parallel}=\frac{\omega}{c}\sqrt{\varepsilon_p}\sin\phi_i \tag{12}$$

where ε_p is the permittivity of the prism and ϕ_i is the incidence angle inside the prism. At the critical incidence angle, $\sqrt{\varepsilon_p}\sin\phi_i=1$ and $k_{\parallel}=\omega/c$. At normal incidence, $k_{\parallel}=\omega/c\sqrt{\varepsilon_p}$. Thus, $k_{\parallel}$ increases from ω/c to $\omega/c\sqrt{\varepsilon_p}$ as ϕ_i is increased beyond total reflection.

If a metal surface is brought close to the prism, a surface-plasmon wave is generated when $k_{\parallel}$ equals the plasmon wave vector k_{0x}. The plasmon dissipates energy, and the reflected intensity decreases. The normal component of the evanescent wave in the gap is

$$k_{\perp}=\frac{\omega}{c}\sqrt{1-\varepsilon_p\sin^2\phi_i}, \tag{13}$$

and the intensity decreases as

$$\exp\left(-4\pi\,\mathrm{Im}\sqrt{1-\varepsilon_p\sin^2\phi_i}\,\frac{z}{\lambda}\right). \tag{14}$$

Thus, the gap between the prism and the metal surface must be of the order of the wavelength, which requires care in the visible region, but which is easier in the IR.

A second method was suggested in a paper submitted about four months later. Kretschmann and Raether [7] showed that a thin metal film evaporated directly onto the prism can serve to excite plasmon waves at the *metal/dielectric* (air) interface, provided the index of refraction of the prism is larger than the index of the dielectric (air). In addition, there are some restrictions on the dielectric function of the metal. Optically, the system now has two interfaces: prism/metal and metal/dielectric (air) and there are four boundary equations:

$$E_{0x}^{-} = E_{1x}^{+} + E_{1x}^{-} \tag{15}$$

$$H_{0y}^{-} = H_{1y}^{+} + H_{1y}^{-} \tag{16}$$

$$E_{1x}^{+} \exp(-ik_{1z}d) + E_{1x}^{-} \exp(+ik_{1z}d) = E_{2x}^{+} \exp(-ik_{2z}d) \tag{17}$$

$$H_{1y}^{+} \exp(-ik_{1z}d) + H_{1y}^{-} \exp(+ik_{1z}d) = H_{2y}^{+} \exp(-ik_{2z}d), \tag{18}$$

where index 0 refers to the prism, 1 to the metal, and 2 to the dielectric (air). The 0/1 interface is at z_0, the 1/2 surface at z_1 and $d = z_1 - z_0$. Superscript + indicates the direction prism→metal→dielectric.

On eliminating H, the relation for the incident and reflected E vectors is

$$\begin{bmatrix} \dfrac{k_{1z}}{\varepsilon_1} + \dfrac{k_{0z}}{\varepsilon_0} & \dfrac{k_{1z}}{\varepsilon_1} - \dfrac{k_{0z}}{\varepsilon_0} \\ \left(\dfrac{k_{1z}}{\varepsilon_1} - \dfrac{k_{2z}}{\varepsilon_2}\right) \exp(-ik_{1z}d) & \left(\dfrac{k_{1z}}{\varepsilon_1} + \dfrac{k_{2z}}{\varepsilon_2}\right) \exp(ik_{1z}d) \end{bmatrix} \begin{pmatrix} E_{0x}^{+} \\ E_{0x}^{-} \end{pmatrix} = 0. \tag{19}$$

Solutions exist only if the determinant is zero:

$$\left(\frac{k_{0z}}{\varepsilon_0} + \frac{k_{1z}}{\varepsilon_1}\right)\left(\frac{k_{1z}}{\varepsilon_1} + \frac{k_{2z}}{\varepsilon_2}\right) \exp(ik_{1z}d)$$

$$+ \left(\frac{k_{0z}}{\varepsilon_0} - \frac{k_{1z}}{\varepsilon_1}\right)\left(\frac{k_{1z}}{\varepsilon_1} - \frac{k_{2z}}{\varepsilon_2}\right) \exp(-ik_{1z}d) = 0, \tag{20}$$

which then is the condition for the existence of a plasmon wave in the metal

film. Equation 20 is the form used by Raether [9]. It can be condensed by introducing the Fresnel coefficients for p-polarization:

$$r_{01} = \left(\frac{k_{0z}}{\varepsilon_0} - \frac{k_{1z}}{\varepsilon_1}\right) \Big/ \left(\frac{k_{0z}}{\varepsilon_0} + \frac{k_{1z}}{\varepsilon_1}\right) \tag{21}$$

$$r_{12} = \left(\frac{k_{1z}}{\varepsilon_1} - \frac{k_{2z}}{\varepsilon_2}\right) \Big/ \left(\frac{k_{1z}}{\varepsilon_1} + \frac{k_{2z}}{\varepsilon_2}\right) \tag{22}$$

$$r_{01} r_{12} \exp(-2ik_{1z}d) + 1 = 0. \tag{23}$$

Although the analysis is more complicated, the Kretschmann configuration relies on the same principle as the Otto scheme. The wave vector of the light in the prism has increased to $\omega/c\sqrt{\varepsilon_p}$ and at some angle of incidence can equal k_{0x} for the plasmon. Since this experimental arrangement is more manageable, it is now widely used. The metal film on the prism is usually about 50 nm of Ag or Au, these metals having optimum permittivities in the visible spectrum; Al has been used at short wavelengths. The film to be examined is deposited on the metal film. Analysis of this structure is discussed below. It is of interest here that nine years before the Kretschmann paper, Turbadar [19, 20] reported that thin Al films deposited on a prism have near-zero reflectivity for an incident angle slightly above total reflection and for p-polarization. He showed this to be in agreement with thin-film theory. However, surface-plasmon oscillations were not mentioned, and seemingly, the work did not receive further attention.

OPTICAL ANALYSIS OF ATR STRUCTURES III

Samples are prepared and measured in steps. First, a 50 nm Ag or Au film is evaporated onto a prism or half-cylinder of high-index glass. The reflectivity is measured for p-polarized light as a function of the angle of incidence starting near the angle of total reflection. The reflectivity versus angle curve will show a sharp minimum at a certain angle depending on the index of the prism. Typically, the minimum will be at about 0.05, the width at half-height about 1°. From the angle, the minimum, and the width, one obtains the exact thickness and the permittivity of the layer. Next, the layer to be analyzed is deposited. This can take many forms, from evaporated

films of a dielectric or a metal, to molecular layers deposited by the Langmuir–Blodgett technique, and even operating liquid-crystal cells and metal electrodes in an electrolytic cell. Examples are discussed in the next section. However, the analysis is applicable to all cases. The new layer will change the critical angle and thus the position of the minimum. It may also impose more damping, and thus the curve will be wider. More than one layer can be applied but for each layer one must obtain the ATR curve. The total thickness of all layers should not be larger than the wavelength of the evanescent wave in the sample, typically a fraction of a micron in the visible.

An ATR sample, then, is a stratified multilayer structure. The optical analysis of such structures has been well documented in textbooks [21, 22] and papers [23, 24]. It is based on the continuity of the tangential components of the E and H fields and the normal components of D at each interface as was exemplified in Eqs. 1–3. Also in each layer there are the Maxwell relations between the tangential components of E and H. Thus, the entire structure is described by a set of linear equations, which can become rather large, because there are 12 equations for each interface. Only the external values of E are observable quantities (reflectance and transmittance); all others can be eliminated algebraically. Eliminating H for each layer results in a relation for the E vectors on the two sides of each interface, which is conveniently written as a Jones 2×2 matrix. Next, the two matrices for each layer are combined, and one obtains a new matrix, called the *characteristic matrix*, which relates the E vectors on the two sides of each layer. The structure is then described by the product of these matrices taken in succession.

Take—as before—all interfaces in consecutive xy planes at $z_0, z_1 \ldots z_n$ and the plane of incidence xz so that the plasmon propagates in the x direction. The result of this vectorization is

$$\begin{pmatrix} E_{0x}^{+} \\ E_{0x}^{-} \end{pmatrix} = [M_0][M_1] \ldots [M_{n-1}] \begin{pmatrix} E_{nx}^{+} \exp(-ik_{nz}z_n) \\ 0 \end{pmatrix} \tag{24}$$

$$[M_i] = \frac{\dfrac{k_{iz}}{\varepsilon_i} + \dfrac{k_{i+1,z}}{\varepsilon_{i+1}}}{2\dfrac{k_{i+1,z}}{\varepsilon_{i+1}}} \exp(ik_{iz}d_i) \begin{bmatrix} 1 & r_{\mathrm{pi}} \\ r_{\mathrm{pi}}Ex & Ex \end{bmatrix}, \tag{25}$$

where E_{0x}^{+} is the x-component of the incident wave; E_{0x}^{-} is the x-component of the reflected wave; r_{pi} is the Fresnel coefficient at interface i; $Ex = \exp(-2ik_{iz}d_i)$; $d_i = z_{i+1} - z_i$ is the thickness of layer i.

The product of the matrices M_i is again a 2×2 matrix. If c_{ij} denotes the matrix terms, then the Fresnel reflectance is the ratio of c_{21} and c_{11}:

$$\begin{pmatrix} E_{0x}^{+} \\ E_{0x}^{-} \end{pmatrix} = \begin{bmatrix} c_{11} & c_{12} \\ c_{21} & c_{22} \end{bmatrix} \begin{pmatrix} E_{nx}^{+} \exp(-ik_{nz}z_n) \\ 0 \end{pmatrix} \tag{26}$$

$$r \equiv \frac{E_{0x}^{-}}{E_{0x}^{+}} = \frac{c_{21}}{c_{11}} \tag{27}$$

and the calculated reflectance is

$$R = rr^{*}. \tag{28}$$

To obtain the observed values, this has to be corrected by the reflections at the two prism surfaces.

The phase difference between the reflected and incident beam is

$$E_{0x}^{-} = E_{0x}^{+} r = E_{0x}^{+}(r' + ir'') = E_{0x}^{+} \sqrt{R} \exp i\phi \tag{29}$$

$$\phi = \tan^{-1} \frac{r''}{r'}. \tag{30}$$

Note that only ratios of matrix terms are involved. The factors outside the matrix brackets need not be evaluated. This saves computer time, but much more important, it avoids accumulation of round-off errors. Retaining the exponential terms in the matrices can lead to instabilities [25].

It will now be clear why it is necessary to obtain an ATR curve for each layer. Then all previous parameters are known, and there is only one set of d and ε values to be determined. The procedure is entirely iterative, but programming details will not be discussed here.

For a two-interface system, for example, prism/Ag/air, the $[c_{ij}]$ matrix is readily evaluated:

$$\begin{bmatrix} 1 & r_{01} \\ r_{01} & 1 \end{bmatrix} \begin{bmatrix} 1 & r_{12} \\ r_{12}E_x & E_x \end{bmatrix} = \begin{bmatrix} 1 + r_{01}r_{12}E_x & r_{12} + r_{01}E_x \\ r_{01} + r_{12}E_x & r_{01}r_{12} + E_x \end{bmatrix}, \tag{31}$$

and one obtains the well-known expression,

$$r=\frac{r_{01}+r_{12}\exp(-2ik_{1z}d)}{1+r_{01}r_{12}\exp(-2ik_{1z}d)}. \tag{32}$$

Kretschmann [8] analyzed Eq. 32 analytically and compared the theory and his experimental results. The paper presents graphs of the reflectivity versus wavelength for constant film thickness and for the reflectivity versus film thickness at constant wavelength for Ag films deposited on a prism. At longer wavelength the damping increases and the curves are wider. The optimum film thickness is about 50 nm for Ag. For thinner films the minimum decreases, and the curves flatten out.

Pockrand [26] studied damping by thin transparent and absorbing coatings. The coating changes the field at the interface. The net result is that for transparent coatings the ATR resonance minimum shifts to larger angles, and the half-width of the curve increases, but the minimum itself remains unaffected. For absorbing coatings the resonance minimum shifts, the curves become wider and asymmetric, and the reflectivity minimum is less pronounced. These results are reproduced in Fig. 2. Optimum thickness of the metal is that for which radiative losses equal the internal loss. Thus, if $|\varepsilon''|$ is larger, the film thickness must be decreased.

For a multilayer system the algebraic expressions for the matrix terms become unwieldy, but numerical techniques can be used to extend these results.

IV GUIDED MODES

Thin-film waveguides were first discussed in a series of papers by Tien and Ulrich [27–29] in 1969 and 1970. Shortly thereafter, Marcuse [30] published a monograph on the theory of dielectric optical waveguides (1974). Tien [31] published a comprehensive tutorial paper in 1977. Swalen [32] reviewed optical-wave spectroscopy in 1979. Rabolt and Swalen [33] reviewed integrated optics for Raman spectroscopy in 1988.

Tien *et al.* [27, 28] showed that a thin dielectric film deposited on a substrate that has a lower index of refraction can form a perfect waveguide. A wave propagating through the film is then totally reflected at both interfaces; outside the film only evanescent waves exist. The light is coupled in by the evanescent wave of a prism in the Otto configuration. The essential difference with the Otto experiment lies in the permittivity of the film. Otto used a metal with $\varepsilon'<0$, $\varepsilon''\gg 0$. Tien and Ulrich used a dielectric with $\varepsilon'>0$, $\varepsilon''\approx 0$.

A wave can propagate in a light guide only if the phase difference after one cycle is a multiple of 2π; otherwise, there will be destructive interference. In addition, the imaginary part of the permittivity must be very small.

By using the matrix method, the amplitude after one cycle is

$$E_{1x}^{+2} = E_{1x}^{+0} r_{10} r_{12} \exp(-2ik_{1z}d), \tag{33}$$

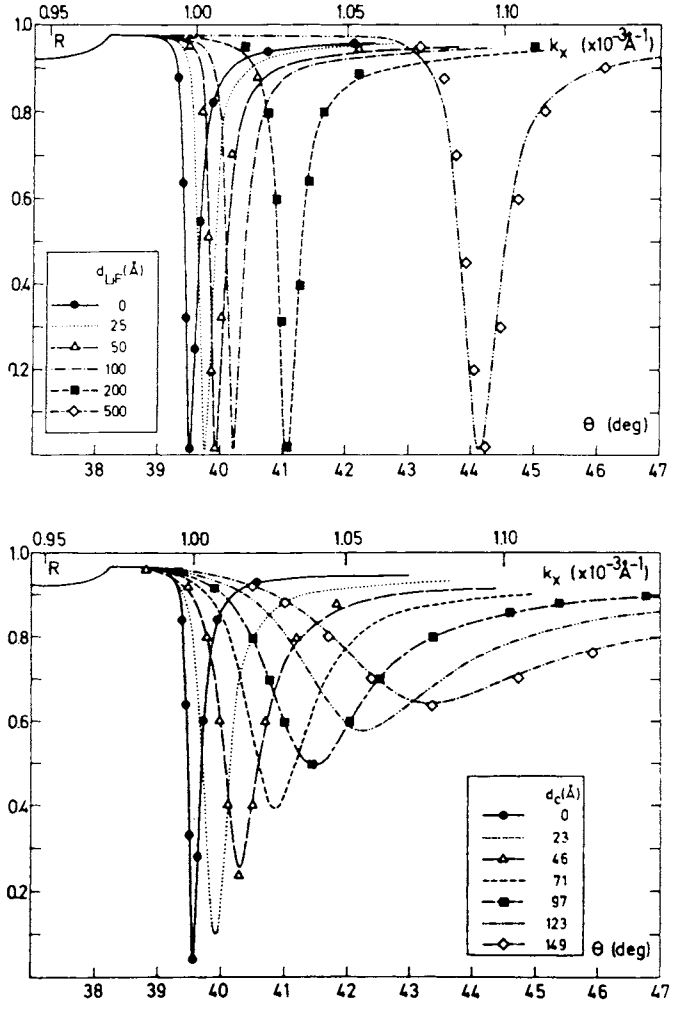

Fig. 2. Measured and calculated SPO resonance curves for Ag films with LiF coatings (top) of various thicknesses and carbon coatings (bottom) of various thicknesses. From I. Pockrand, *Surf. Sci.* **72**, 577 (1978). With permission from the publisher.

where r_{12} is the Fresnel coefficient at the film-substrate interface and r_{10} the coefficient at the film-air surface. The phase shift is obtained as in Eq. 30 from the ratio of the imaginary and real parts.

Thus, for a given film structure there exist only a discrete set of values for k_{1z} for which the phase shift will be an integral value of 2π. The tangential component of the wave vector in the prism equals k_{1x} in the film, and thus, propagating waves are generated only if the angle of incidence is such that

$$k_{\parallel}^2 + k_{1z}^2 = \left(\frac{\omega}{c}\right)^2 \varepsilon_1. \tag{34}$$

Tien and Ulrich considered the special case k_{1z} real, k_{0z} and k_{2z} purely imaginary. Then the Fresnel coefficients have the form

$$r_{10} = \exp iQ_{10} \rightarrow \tan Q_{10}/2 = \frac{k_{0z}}{\varepsilon_0}\frac{\varepsilon_1}{k_{1z}} \tag{35}$$

$$r_{12} = \exp iQ_{12} \rightarrow \tan Q_{12}/2 = \frac{k_{2z}}{\varepsilon_2}\frac{\varepsilon_1}{k_{1z}}, \tag{36}$$

and the mode equation can be written as

$$Q_{10} + Q_{12} - 2k_{1z}d = 2\pi m. \tag{37}$$

Notice that the mode equation is the Bragg equation with terms added to account for the phase shift caused by total reflection. Equations 34 and 37 impose no restrictions on the polarization of the incident beam. Of course, the Fresnel coefficients are different, as will be the positions of the guided modes. For ε real and scalar, the film thickness d and ε can be obtained if at least two modes can be observed. Many films are not isotropic and ε is a tensor. Then the film must be scanned in two mutually perpendicular directions. A four-sided pyramid can be used instead of a prism; examples of this are given in the next section. However, even if sufficient data are available, the problem is still undetermined: an *a priori* assumption must be made for the tilt angle of the optic axis.

ATR and guided modes are often combined by using an ATR prism, that is, by first evaporating about 50 nm of Ag. At a certain angle a plasmon wave is excited at the Ag surface. At other angles the evanescent wave at the Ag surface can excite guided waves in the waveguide. For *s*-polarization there is of course no ATR minimum.

From Eq. 34 or 37, tables or graphs for the function with the mode number as parameter can be made as a guide for the design of the waveguide (for examples, see [27, 53]).

APPLICATIONS OF ATR V

We review here a number of papers selected to demonstrate the versatility and the limits of ATR and integrated optics.

Optical Constants of Metals A

Gugger *et al.* [34, 35] determined the dielectric function for Ag from 441.6 nm to 676.4 nm using the Kretschmann configuration, prism/Ag/air. Data for two samples agreed to about 1%. If the air is replaced by hexane or carbon tetrachloride, slightly larger values for the dielectric function were obtained. This was attributed to a surface modification of the dielectric function of silver.

Bradberry *et al.* [36] measured n and k for W and Mo at 3.39 μm using the Otto configuration with gap spacings in the order of 10 μm. For all metals, n and k are larger in the IR than in the visible part of the spectrum. Thus, there is more damping. The minimum ATR reflectivity is larger, and the resonance is wider. For Ag, for example, at 0.6328 μm $n=0.14$, $k=4.4$, and the ATR minimum is typically 0.04. At 3.26 μm $n=1.54$, $k=19.8$, and the observed minimum is only 0.8. Recently [37] the work was extended to include Ni, Pd, and Pt. The gap was varied between 5 μm and 10 μm, and the results agree to about 2%.

Molecular Films B

The Langmuir–Blodgett (LB) technique allows repetitive deposition of a single molecular layer of a fatty-acid salt (thickness 25Å–30Å, approxi-

mately equal to the chain length). An ATR curve can be made readily after each deposition, which makes it an elegant way to study ATR molecular layers. In 1986, Swalen [16] reviewed the extensive literature on optical properties of LB films. Here we summarize only the important ATR papers leading to the more recent work.

Gordon and Swalen [38] obtained ATR curves for the system Cd-arachidate on Au. Up to four monolayers were deposited. The peak shift is of the order of 0.5° per layer, much larger than the angular resolution 0.02°.

Pockrand *et al.* [40] extended the work, using Ag as the ATR metal, and calculated the index for Cd-arachidate for each monolayer deposited. The film is obviously anisotropic. However, one cannot determine the complete ε tensor from a single SPO resonance curve. Assuming a constant difference, $n_0 - n_e = 0.043$, n_0 and n_e were calculated. Later [41], the work was extended to include dyes having a strong absorption band in the visible region. The dyes chosen had C18 hydrocarbon chains, as in arachidic acid. As it turned out for one dye, the molecular alignment in the film is identical with that of Cd-arachidate. Thus, the film is anisotropic, and again the dielectric function is a tensor. It was assumed that the permittivity perpendicular to the film plane is the same as that of Cd-arachidate (real), whereas the parallel component is complex. The inplane permittivity was determined from surface-plasmon resonance curves at different wavelengths.

Swalen *et al.* [42, 43] determined the indices of Cd-arachidate films using the guided-mode techniques (1978). The films were deposited on glass or on PMMA, and mode patterns were obtained for both *s*- and *p*-polarization at three wavelenghts. The film thickness was obtained from the number of monolayers for each run (30–40), and the ordinary and extraordinary indices were calculated. These results are reproduced in Fig. 3.

Barnes and Sambles [44, 45] used much thicker LB films, about 1.1 microns. The light was coupled in by the evanescent wave from an Ag film deposited on the base of a four-sided pyramid. From the ATR curves combined with the guided-mode resonances in the xz and yz planes, there was enough information to determine the complete tensor if the tilt angle was known. As it turned out, the sample used, 22-tricosenoic acid, is best described as a biaxial birefringent film.

Loulergue *et al.* [46] used ATR to study the effect of a static electric field on an LB film of an azo dye. The dye (DPNA) has a C12 aliphatic chain and can be deposited on an Ag film on a slide using the technique. A second Ag-coated slide is mounted with spacers onto the first, so that a field can be applied across the film. Light is coupled in through a prism and an index-matching oil. Curves are shown for the ATR reflectivity and the differential reflectivity versus applied electric field.

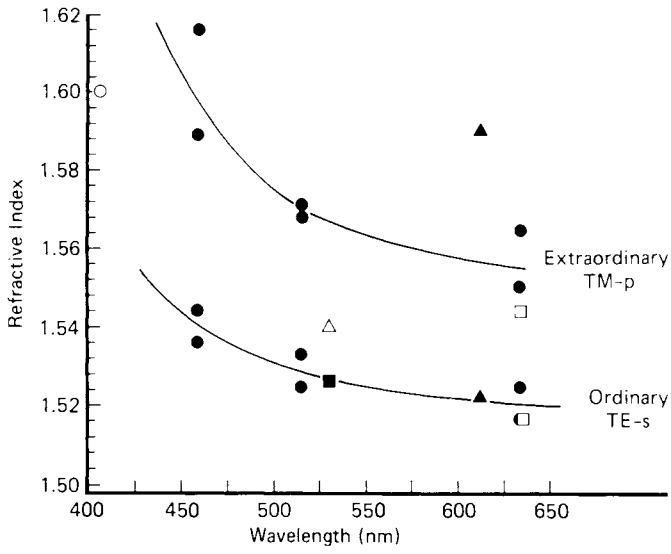

Fig. 3. Dispersion curves for the optical constants of Cd-arachidate. From J. D. Swalen, K. E. Rieckhoff, and M. Tacke, *Opt. Commun.* **24**, 146 (1978). With permission from the publisher.

Organic Dyes C

Philpott *et al.* [47–48] obtained ATR curves for three organic dyes at wavelengths within the absorption bands. The dyes chosen all reflect light with a metallic luster although they are insulators. The reflection is, of course, quite different from metallic reflection, and a new name, *exciton surface polaritons*, was introduced to distinguish this effect from *plasmon surface polaritons* at metal surfaces. The dyes are anisotropic, and the permittivity is a tensor. The dielectric function is assumed to be given by a Lorentz–Lorenz expression, and practical formulas are given to calculate ATR spectra. Again, the criterion is that within the exciton band $|\varepsilon'| < -1$ (Otto configuration). The important difference from metals is that for exciton surface polaritons, the ATR minimum can occur at either side of the critical angle. One of the dyes (TCNQ) indeed has ATR minima below the critical angle.

The ratio of the imaginary and real parts of the permittivity for these dyes is much larger than it is for Ag or Au, and thus, the damping is much larger. Half-widths are typically 4°.

D Dielectric Films

Levy *et al.* [49] were probably first in using a four-sided pyramid instead of a prism to analyze anisotropic films. The dielectric is a thick (570 nm) film of angularly deposited SiO_x. Angular deposition is used to produce liquid-crystal (LC) cells with large surface tilt angle. (For LC cells, much thinner layers (20 nm) are used, but thin films cannot be examined by SEM.)

For thin films only surface-plasmon oscillations are observed. For thick films both SPO and guided modes were observed, the SiO_x film acting as the waveguide (see Fig. 4). The calculated indices for the SiO_x film were $n_0 = 1.253$ and $n_e = 1.239$, well below the value for SiO_x glass. Reflectivity curves obtained with the film immersed in hexane showed a large shift in the SPO minimum, and it was concluded that void areas surrounded the SiO_2 columns. By applying effective-media theory, it was shown that the columns have an index of about 1.47 but occupy only 0.54 of the film's volume.

E Surface Tilt Angle of Nematic Liquid Crystals

Thin layers of nematic liquid crystals will align uniformly between two specially prepared glass surfaces. The liquid layer then is uniaxial birefringent. A thin SiO_2 film obtained by oxidizing silane in an Ar-O_2 plasma will produce parallel alignment; that is, the optic axis of the cell is parallel with the substrate surface, and its direction is determined by the deposition geometry. A polyfluorocarbon film produced from tetrafluoroethylene in an RF plasma will produce cells in which the optic axis is perpendicular to the surface [50]. Swalen and Sprokel [51] used ATR prisms of the Kretschmann configurations as one of the substrates of an aligned LC cell and determined n_0 and n_e for the LC.

A gold film (approximately 50 nm) was evaporated onto a prism cut from glass having an index larger than n_0 of the liquid crystal. The ATR curve was obtained, and d and ε for the Au film were calculated. Next, the aligning layer was deposited and from the new ATR curve, d and ε for the aligning layer were obtained. Finally, the LC cell was assembled, and the index for the aligned LC was obtained. Thus, n_0 and n_e are obtained independently and without *ad hoc* assumptions for the orientation of the optic axis. The results were in good agreement with the bulk data.

Since ATR probes about 100 nm into a 6 μm LC cell, it can be used to obtain the surface tilt angle of the LC molecules. This is an important parameter in the theory for the deformation of an LC in an electric field.

Sprokel *et al.* [52] obtained ATR curves for an operating LC cell initially aligned with the optic axis parallel to the surface and in the plane of incidence. The parameters were determined as described above, then ATR

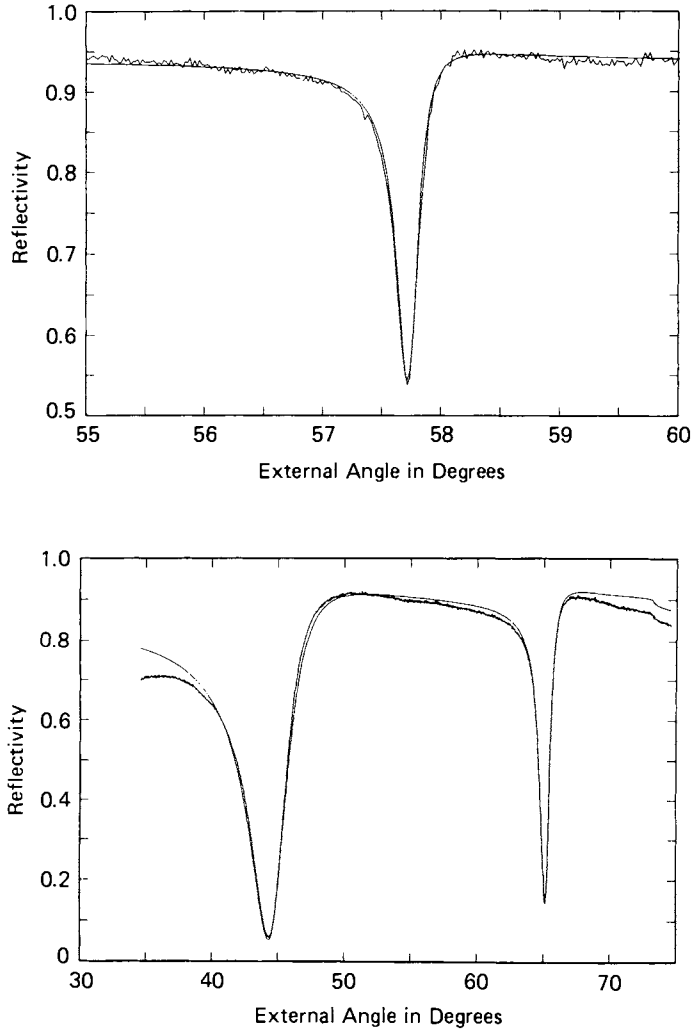

Fig. 4. Measured and calculated ATR reflectivity curves for thick SiO_x films on Au. Top: *s*-polarized incident wave, guided-mode resonance at 57.7 nm. Bottom: *p*-polarized incident wave, guided-mode resonance at 44.32 nm, SPO resonance at 65.2 nm. From Y. Levy, M. Jurich, and J. D. Swalen, *J. Appl. Phys.* **57**, 2601 (1985). With permission from the publisher.

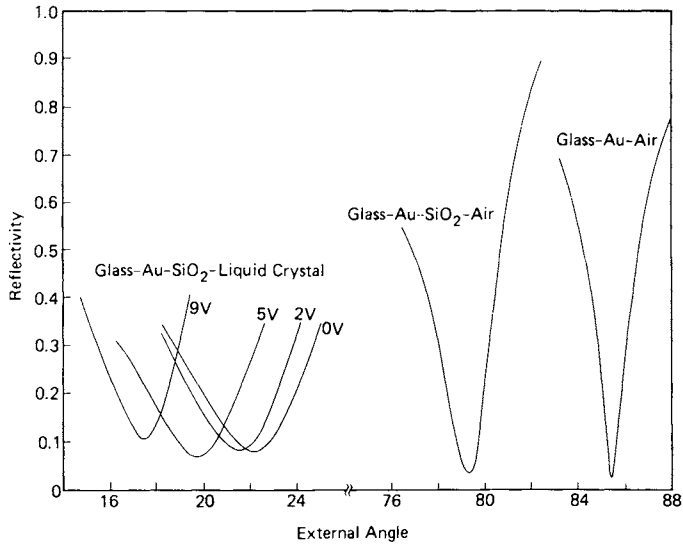

Fig. 5. ATR reflectivity curves on an operating liquid-crystal cell. Initially the optic axis is parallel with the surface and in the plane of incidence. The tilt angle at the surface can be calculated from the observed index. From G. J. Sprokel, R. Santo, and J. D. Swalen, *Mol. Cryst. Liq. Cryst.* **68**, 29 (1981). With permission from the publisher.

curves were obtained as a voltage was applied across the cell. Since the indices for parallel and perpendicular orientation are known, the tilt angle near the surface can be calculated from the ATR curves at each applied voltage without introducing new assumptions. It was found that liquid crystals bent away from the surface much faster than indicated by the Frank–Oseen theory and the standard boundary conditions. Figure 5 exemplifies the ATR resonance curves as a square-wave voltage is applied to the cell.

Starting in 1987, the group at Exeter University, U.K., has published extensively on ATR experiments with LC cells [53, 54]. Their method is identical: the cell has the Kretschmann configuration; parameters of the successive layers are determined one at a time as in the original work. Of interest is the fact that guided modes appear near the ATR minimum, which was not observed in the earlier work. An important difference is in the aligning layers used by the two groups. The IBM group used a smooth and dense SiO_2 film (it had the same index as SiO_2 glass, $n = 1.457$). The Exeter group used an SiO_x film deposited by angle evaporation. Such films are rough and porous because of columnar growth and can couple to a surface plasmon as a grating as well as through the evanescent wave.

The aligning layers in both experiments are too thin to support guided modes. However, the alignment of the liquid crystal near the surface is quite different. The overall effect of a field on parallel and tilted aligned

cells was studied in some detail [54]. Information about the change in surface tilt for tilted aligned cells by an external field is not available.

Tutorial Demonstration of ATR F

Swalen *et al.* [57] demonstrated ATR using a Kretschmann prism, a cylindrical lens, a prism, and a light source available in any optics lab. The prism produces a continuous spectrum that is focused by the lens onto the base of the Kretschmann prism. The projected light is in effect a display of wavelength versus incident angle, and it consists of the continuous spectrum except for the angles where surface-plasmon resonance occurs, reducing the reflectivity to almost zero. Similarly, using a stepped LB wedge, the effect of each step can be shown.

Guided Modes and ATR G

If an Ag-coated prism is used to excite guided modes in a waveguide, the ATR resonance will probably occur at an angle different from those for the guided modes. However, by choosing the proper thickness of the waveguide, it should be possible to match the ATR resonance with one of the guided modes.

Nakagawa *et al.* [58] showed experimentally that this is feasible by using a waveguide of the correct thickness to excite a plasmon-surface-polariton wave in an Ag film deposited on the waveguide. The cavity was a Ta_2O_5 film on a quartz substrate. The light was coupled in and out by TiO_2 prisms. The Ag film is deposited on an SiO_2 film on the Ta_2O_5. The mode chosen to excite the plasmon resonance is sharply attenuated (10 dB), whereas other modes show very little attenuation.

Long-Range Surface-Plasmon Waves H

In his review paper, Raether [9] discussed coupling of the modes at the two interfaces of a thin metal film as in the Kretschmann configuration. The topic was later taken up by Sarid *et al.* [59–61], Stegeman *et al.* [62], and others, and this led eventually to a proposal for electro-optic modulators [63].

If the metal film is bounded by identical dielectric layers, the surface-plasmon oscillations on both sides are also identical. If the film is thin enough, the evanescent waves extending into the metal overlap and split into symmetric and antisymmetric modes [9]. If the dielectric layers have slightly different indices, each of the two modes will split in two branches.

The metal film can be regarded as a waveguide, and the standard Eq. 37 can be used to obtain the propagation constants. The antisymmetric mode carries most of its intensity in the dielectric layers; hence, the damping is smaller and the propagation distance is longer. Craig *et al.* [60] obtained 0.25 mm on a 10 nm Ag film. Schildkraut replaced the lower dielectric with an electro-optic film. As a voltage is applied across the film, its index will change, and the coupling between the modes will change. Operated in the antisymmetric mode (*long-range surface-plasmon mode*), a potential of 100V changes the reflectivity from 0 to 0.84, whereas in the *normal surface-plasmon mode* the reflectivity changes from 0 to 0.12.

VI CONCLUSION

The ATR method was described using classical physical optics. The technique is useful not only to obtain the optical constants of thin films, but more generally to study a variety of surface phenomena. Examples from recent literature were given to exemplify its versatility and its limitations.

REFERENCES

1. N. J. Harrick, "Internal Reflection Spectroscopy," Wiley, New York, (1967).
2. A. Otto, *Z. Physik* **216**, 398 (1968).
3. A. Otto, *Z. Angew. Physik* **27**, 207 (1969).
4. A. Otto, *Festkörperprobleme*, **XIV**, 1 (1974).
5. A. Otto, in "Optical Properties of Solids," Elsevier, Amsterdam, chapter 13 (1976).
6. E. Kretschmann and H. Raether, *Z. Naturforschung*, **22a**, 1623 (1976).
7. E. Kretschmann and H. Raether, *Z. Naturforschung*, **23a**, 3135 (1968).
8. E. Kretschmann, *Z. Physik* **241**, 313 (1971).
9. H. Raether in *Physics of Thin Films*, Vol. 9, (G. Hass, M. H. Francombe, and R. W. Hoffman, eds.), Academic Press, New York, 145 (1977).
10. K. Holst and H. Raether, *Opt. Commun.* **2**, 313 (1970).
11. U. Fano, *J. Opt. Soc. Am.* **31**, 213 (1941).
12. Y. Y. Teng and E. A. Stern, *Phys. Rev. Lett.* **19**, 511 (1967).
13. R. H. Ritchie, E. T. Arakawa, J. J. Cowan, and R. N. Hamm, *Phys. Rev. Lett.* **21**, 1530 (1968).
14. E. Burstein, W. P, Chen, Y. J. Chen, and A. Hartstein, *J. Vac. Sci. Technol.* **11**, 1004 (1974).
15. E. D. Palik and R. T. Holm, *Opt. Eng.* **17**, 512 (1978).
16. J. D. Swalen, *J. Mol. Electronics* **2**, 155 (1986).
17. J. F. Rabolt and J. D. Swalen, in "Spectroscopy of Surfaces," (R. J. H. Clark and R. E. Hester, eds.), Wiley, New York, chapter 1 (1988).
18. M. K. Debe, *Prog. Surf. Sci.* **24**, 1 (1987).
19. T. Turbadar, *Proc. Phys. Soc. London* **73**, 41 (1959).
20. T. Turbadar, *Opt. Acta* **11**, 207 (1964).
21. H. Wolter, in "Handbuch der Physik," Vol. XXIV, (S. Flugge, ed.), Springer-Verlag, Berlin, 461 (1956).

22. O. S. Heavens, "Optical Properties of Thin Solid Films," Dover Publications, New York, 1965.
23. D. W. Berreman, *J. Opt. Soc. Am.* **62**, 502 (1972).
24. G. J. Sprokel, *Mol. Cryst. Liq. Cryst.* **68**, 39 (1981).
25. D. Y. K. Ko and J. R. Sambles, *J. Opt. Soc. Am. A* **5**, 1863 (1988).
26. I. Pockrand, *Surf. Sci.* **72**, 577 (1978).
27. P. K. Tien, R. Ulrich, and R. J. Martin, *Appl. Phys. Lett.* **14**, 291 (1969).
28. P. K. Tien and R. Ulrich, *J. Opt. Soc. Am.* **60**, 1325 (1970).
29. R. Ulrich, *J. Opt. Soc. Am.* **60**, 1337 (1970).
30. D. Marcuse, "Theory of Dielectric Optical Waveguides," Academic Press, New York, (1974).
31. P. K. Tien, *Rev. Mod. Phys.* **49**, 361 (1977).
32. J. D. Swalen, *J. Phys. Chem.* **83**, 1438 (1979).
33. J. F. Rabolt and J. D. Swalen, in "Spectroscopy of Surfaces," (R. J. H. Clark and R. E. Hester, eds.) Wiley, New York (1988).
34. H. Gugger, M. Jurich, J. D. Swalen, and A. J. Sievers, *Phys. Rev. B* **30**, 4189 (1984).
35. H. Gugger, M. Jurich, J. D. Swalen, and A. J. Sievers, *Phys. Rev. B* **34**, 1322 (1986).
36. G. W. Bradberry and J. R. Sambles, *Opt. Commun.* **67**, 404 (1988).
37. Y. Fuzi, G. W. Bradberry, and J. R. Sambles, *J. Mod. Opt.* **36**, 1405 (1989).
38. J. G. Gordon and J. D. Swalen, *Opt. Commun.* **22**, 374 (1977).
39. I. Pockrand, *Opt. Commun.* **13**, 311 (1975).
40. I. Pockrand, J. D. Swalen, J. G. Gordon, and M. R. Philpott, *Surf. Sci.* **74**, 237 (1977).
41. I. Pockrand, J. D. Swalen, R. Santo, A. Brillante, and M. R. Philpott, *J. Chem. Phys.* **69**, 4001 (1978).
42. J. D. Swalen, M. Tacke, R. Santo, and J. Fischer, *Opt. Commun.* **18**, 387 (1976).
43. J. D. Swalen, K. E. Rieckhoff, and M. Tacke, *Opt. Commun.* **24**, 146 (1978).
44. W. L. Barnes and J. R. Sambles, *Surf. Sci.* **177**, 399 (1986).
45. W. L. Barnes and J. R. Sambles, *Surf. Sci.* **187**, 144 (1987).
46. J. C. Loulergue, M. Dumont, Y. Levy, P. Robin, J. P. Pocholle and M. Papuchon, *Thin Solid Films* **160**, 399 (1988).
47. M. R. Philpott and J. D. Swalen, *J. Chem. Phys.* **69**, 2912 (1978).
48. M. R. Philpott, A. Brillante, I. R. Pockrand, and J. D. Swalen, *Mol. Cryst. Liq. Cryst.* **50**, 139 (1979).
49. Y. Levy, M. Jurich, and J. D. Swalen, *J. Appl. Phys.* **57**, 2601 (1985).
50. G. J. Sprokel and R. M. Gibson, *J. Electrochem. Soc.* **124**, 557 (1977).
51. J. D. Swalen and G. J. Sprokel, "The Physics and Chemistry of Liquid Crystal Devices," (G. J. Sprokel, ed.), Plenum, New York, (1979).
52. G. J. Sprokel, R. Santo, and J. D. Swalen, *Mol. Cryst. Liq. Cryst.* **68**, 29 (1981).
53. K. R. Welford and J. R. Sambles, *Appl. Phys. Lett.* **50**, 871 (1987).
54. K. R. Welford, J. R. Sambles, and M. G. Clark, *Liquid Crystals* **2**, 91 (1987).
55. R. A. Innes, K. R. Welford, and J. R. Sambles, *Liquid Crystals* **2**, 843 (1987).
56. G. J. Sprokel and N. Chou, *Liq. Cryst. Ordered Fluids*, Vol. 4, (A. G. Griffin and J. E. Johnson, eds.), Plenum, New York, 865 (1982).
57. J. D. Swalen, J. G. Gordon, M. R. Philpott, A. Brillante, I. Pockrand, and R. Santo, *Am. J. Phys.* **48**, 669 (1980).
58. Y. Nakagawa, M. Kaneko, and N. Terunuma, *Appl. Phys. Lett.* **53**, 2141 (1988).
59. D. Sarid, *Phys. Rev. Lett.* **47**, 1927 (1981).
60. A. E. Craig, G. A. Olson, and D. Sarid, *Opt. Lett.* **8**, 380 (1983).
61. D. Sarid, R. T. Deck, and J. J. Fasano, *J. Opt. Soc. Am. A* **72**, 1345 (1982).
62. G. I. Stegeman, J. J. Burke, and D. G. Hall, *Appl. Phys. Lett.* **41**, 906 (1982).
63. J. S. Schildkraut, *Appl. Opt.* **27**, 4587 (1988).

Chapter 5

Optical Properties of Superlattices

P. APELL
Institute of Theoretical Physics
Chalmers University of Technology
S-412 96 Göteborg, Sweden
and
O. HUNDERI
Division of Physics
Norwegian Institute of Technology
and
SINTEF, Applied Physics
N 7034 Trondheim, Norway

I. Introduction 97
II. The Classical Optical Response of a Multilayer System 98
III. Semiconductor Superlattices 101
A. Excitons and Single-Particle Excitations 102
B. Phonons 108
IV. Amorphous Superlattices 109
V. Collective Excitations 112
VI. Lattice Disorder 118
VII. The Effect of Nonlocal Dielectric Functions 120
VIII. Concluding Remarks 122
References 122

I INTRODUCTION

The first GaAs/GaAlAs superlattice (SL), made by Chang *et al.* [1], realizing ideas put forward by Esaki and Tsu [2], represents a milestone in "material engineering" through the use of MBE technology. It consists of a periodic repetition of alternating layers of lattice-matched GaAs and $Ga_{1-x}Al_xAs$. The properties of the bulk materials are retained in the direction perpendicular to the stacking, whereas if the layer width is less than the Bohr radius (a_0^*) for the bulk material, novel quantum-mechanical confinement effects are obtained. These are to a certain extent

Copyright © 1991 by Academic Press.
All rights of reproduction in any form reserved.
ISBN 0-12-544422-2

controllable, leading to a wide range of applicabilities of such a material, especially in linear and nonlinear optical engineering. We refer the interested reader to the excellent textbook by M. Jaros [3]. In what follows we will discuss the new or modified optical characteristics that the SL shows, and that differ from the properties of the constituent materials. Our discussion will be in terms of the elementary excitations of such structures, especially their characteristics in the SL environment and most important, the new elementary excitations having origins in the SL construction, while being absent in the constituents. Our survey will basically cover single-particle excitations, excitons, phonons, and collective excitations such as plasmons and polaritons. Before starting, we notice that the original proposal by Esaki and Tsu was rejected for publication for being "too speculative" and invoking "no new physics" [4].

We will start this review by a discussion of the classical optical response of a superlattice in terms of the macroscopic dielectric functions of its constituents. This will be followed by a more detailed description of the elementary excitations in the SL, including collective excitations such as plasmons and polaritons. We conclude the review by a brief look at the effect of nonlocal dielectric functions.

II THE CLASSICAL OPTICAL RESPONSE OF A MULTILAYER SYSTEM

When the layers in the superlattice are sufficiently thin, we can describe the optical properties of the SL on the average as those of a uniaxial material. Expressions for the effective dielectric constants can be derived for an ideal superlattice in the limit of infinitely thin, individual layers, and can be extended to finite layer thicknesses. If the lattice is aperiodic, if nonlocal effects are included, or if quantum-size effects are important, this effective-medium theory breaks down. However, we will illustrate by model calculations the effects of aperiodicity and nonlocality on the properties of metal-insulator superlattices. These show strong resonant excitation in the region above the bulk plasmon frequency. The existence of interfaces and potential steps at these lead to the creation of narrow quantum wells in such structures. This has a profound influence on band structure and band gaps even in the case of amorphous semiconductors.

The effective-medium response of a multilayer superlattice system of thin films may be derived in several ways; see [5, 6] and references therein. The most fruitful approach seems to be by way of transfer matrices. In this approach one considers a two- or multicomponent superlattice of materials a, b, c . . . , a, b, c, . . . with dielectric constants ε_a, ε_b, ε_c . . . and thicknesses d_a, d_b, d_c and total stack thickness D. The structure a, b, c . . .

represents the unit cell in a periodic structure. The transfer matrix of the total system is given by the product $M_a M_b M_c \ldots M_a M_b M_c \ldots$. Taking the limit $d_a, d_b, d_c \to 0$, $N \to \infty$, where N is the total number of periods in the stack, in such a way that the total stack thickness is kept constant, leads to a transfer matrix, which is a function of four parameters only [5], namely $\langle\varepsilon\rangle$, $\langle 1/\varepsilon\rangle$, D, and the angle of incidence. Furthermore, this transfer matrix is identical in form to the transfer matrix of a single uniaxial film. This allows us to draw the following conclusion: a superlattice is optically equivalent to a uniaxial material with optic axis normal to the surface and with optical constants given by

$$\begin{aligned} \varepsilon_o &= \langle\varepsilon\rangle \\ 1/\varepsilon_e &= \langle 1/\varepsilon\rangle. \end{aligned} \tag{1}$$

Here ε_o is the ordinary and ε_e is the extraordinary dielectric constant, and the average is taken over one unit cell of the superlattice. These equations in the form given here are correct irrespective of the number of layers in the unit cell of the superlattice, as long as the total thickness of the unit cell is small compared to the wavelength of light in the material. These values for the effective constants are the same as the Wiener bounds. The superlattice thus exhibits the maximum optical anisotropy possible for a multicomponent mixture.

To illustrate the uniaxial nature of superlattices, we have calculated the effective dielectric constant for a hypothetical metal/insulator superlattice [5]. The metal was assumed to have a Drudelike, frequency-dependent dielectric constant; the insulator was assumed to have a frequency-independent dielectric constant, ε_i, equal to 2.25. Figure 1a shows the imaginary part of the calculated dielectric constants. The ordinary dielectric constant is that of a Drude metal with an electron density equal to the average electron density in the superlattice. The extraordinary spectrum is the same as that of a single bound oscillator shifted from $\omega_0 = 0$, characteristic of a metal, to

$$\omega_o = \omega_p / \sqrt{1 + \varepsilon_i f/(1-f)}, \tag{2}$$

where ω_p is the plasmon frequency, and f is the filling factor of metal; $f = 1$ corresponds to only metal. The corresponding reflectivity at 60° for $\omega_p = 10$ eV and $f = 0.5$ is shown in Fig. 1b. At short wavelengths it behaves like a typical metal and it becomes transparent at roughly 5.5 eV. The high reflectivity around the plasmon frequency of the Drude metal is somewhat reminiscent of the reststrahlen band in insulators. In our case, the high

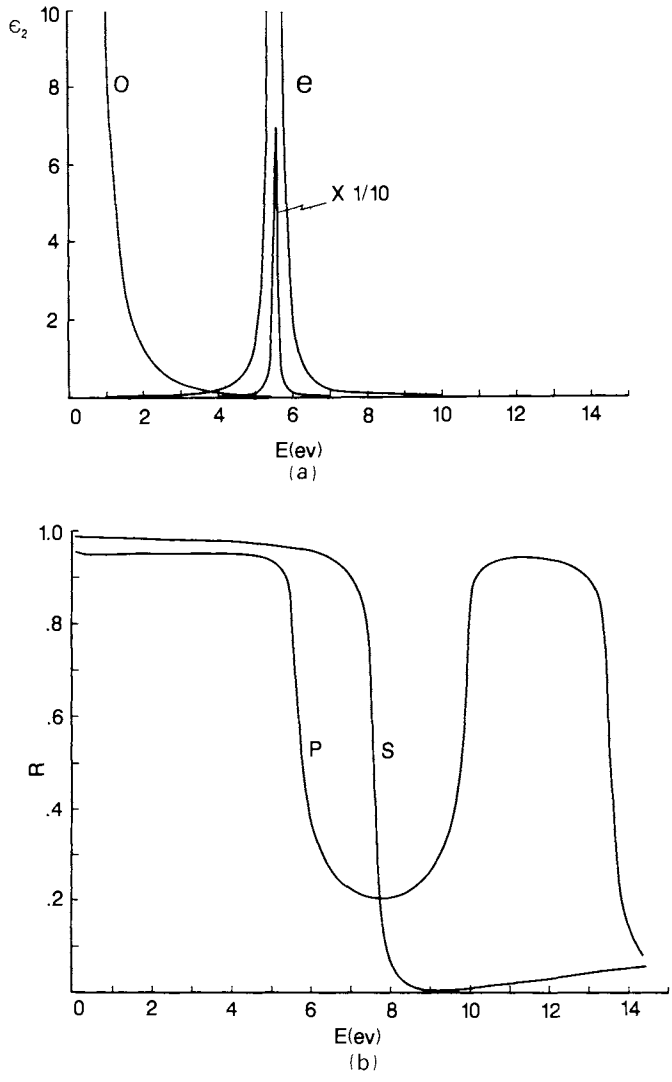

Fig. 1. (a) Imaginary parts of the ordinary (o) and extraordinary (e) dielectric constants, ε_{o2} and ε_{e2}, versus energy, and (b) the corresponding reflectivity R for both s- and p-polarized light at 60° angle of incidence. The parameters used in the calculation are $\hbar\omega_p = 10\,\text{eV}$, $\hbar/\tau = 0.1\,\text{eV}$ and filling factor $f = 0.5$.

reflectivity is caused by evanescent bulk-polariton excitation in the superlattice.

An effective-medium dielectric constant is meaningful and can be derived in the case of finite-layer-thickness superlattices if the unit cell is

symmetric. Consider, for example, the structure *b/2ababababab . . . bab/2*. This notation represents a stack where the two outermost layers have half the thickness that they have in the rest of the stack. A symmetric unit cell can then be defined, leading to a total transfer matrix with $M_{11} = M_{22}$. This transfer matrix allows one to extract a unique set of effective dielectric constants, but these are, in principle, dependent on both thickness and angle of incidence. Further details are given elsewhere in [5].

When the layer thickness becomes comparable to the wavelength of the light in the medium, new effects arise. Bragg reflection gives rise to forbidden-frequency bands or stopgaps where optical propagation cannot occur, in much the same way as band gaps occur when electrons propagate in the periodic potential of a crystal. In the stopgaps the effective dielectric constant is purely imaginary, resulting in an electromagnetic wave that decays exponentially with distance into the medium; in a pass band it is real, and the wave is a propagating wave. The concept of photonic band structure has been introduced and concepts such as gaps, dispersion, density of states, and localization are as relevant for photons as they are for electrons, but the vector character adds a new component to the problem, which shows itself, for instance, in the importance of the polarization of the waves [7, 8]. We will return briefly to localization in a disordered superlattice below. The concept of stopgaps is an important part of optical-filter design, but will not be treated further here.

We have described the general optical features of a multilayer system in terms of macroscopic dielectric functions of the materials in the SL. We now turn a more detailed description of the elementary excitations, giving the structure of the dielectric function. Before doing so, we note that the simplest modification of the macroscopic response in a superlattice is caused by the scattering at the interfaces in the SL. If the scattering of electrons at the interfaces is diffuse, the mean free path of electrons will be reduced from the value in the bulk to something of the order of the layer thickness. In the case of metals, this effect can be incorporated through a modification of the Drude part of the dielectric constant, and may alter considerably the dielectric response in the layers.

SEMICONDUCTOR SUPERLATTICES III

The GaAlAs SL is a so-called type I SL, where the band-gap energy difference between GaAs and $Ga_{1-x}Al_xAs$ is shared by potential steps in both the valence (ΔE_v) and conduction (ΔE_c) bands of the GaAs, which leads to holes and electrons being confined to the GaAs layers, thus making up quantum-mechanical wells. The $Ga_{1-x}Al_xAs$ layers in between

provide the barriers between these wells (see Fig. 2). We can approach the SL from two directions. One way is to start from one quantum well being characterized by a few discrete levels in accordance with the confining potential and having bulklike dispersion in the perpendicular direction. When many of those are assembled to a so-called multiple-quantum-well (MQW) material, they retain their discrete energy level character as long as they are separated by a reasonable distance. Bringing them closer leads to electronic well–well coupling, and the levels broaden into narrow bands: we have reached what one usually means by an SL. We can also reach this limit by going in the other direction from the bulk materials introducing a periodicity equal to the one for the SL, and we then expect, on general grounds from band-structure arguments, that the Brillouin zone opens up into mini-zones having subbands and subgaps. In what follows, we will see results pertaining both to SL and MQW materials. In Fig. 3a, we show a comparison between the absorption spectrum for a thick GaAs sample and a 77-period SL with 102 Å GaAs layers alternating with 207 Å AlGaAs layers at room temperature [9]; in Fig. 3b we show a similar comparison at 2 K, [10] (50 layers of 140 Å GaAs/ > 250 Å $Ga_{0.8}Al_{0.2}As$). An SL absorption spectrum is shown on a more expanded energy scale in Fig. 4 [11] with the characteristic plateaus of a material having two-dimensional character.

A Excitons and Single-Particle Excitations

There are four major, more or less interrelated, differences between the SL absorption spectrum and the absorption spectrum for the corresponding bulk material (in practice, the low-gap material): (i) stronger excitonic features, (ii) split excitons due to the new symmetry in the SL, (iii)

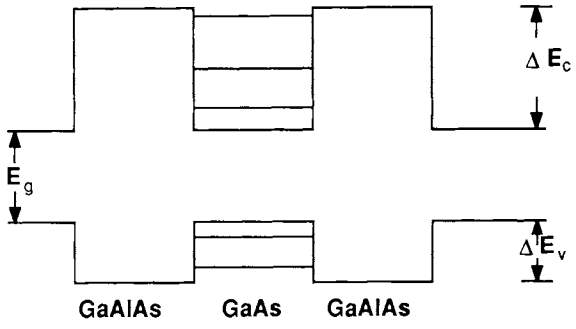

Fig. 2. Schematic band structure of GaAlAs superlattice. Electrons and holes are confined to the GaAs layers due to the different band gaps of the constituent materials.

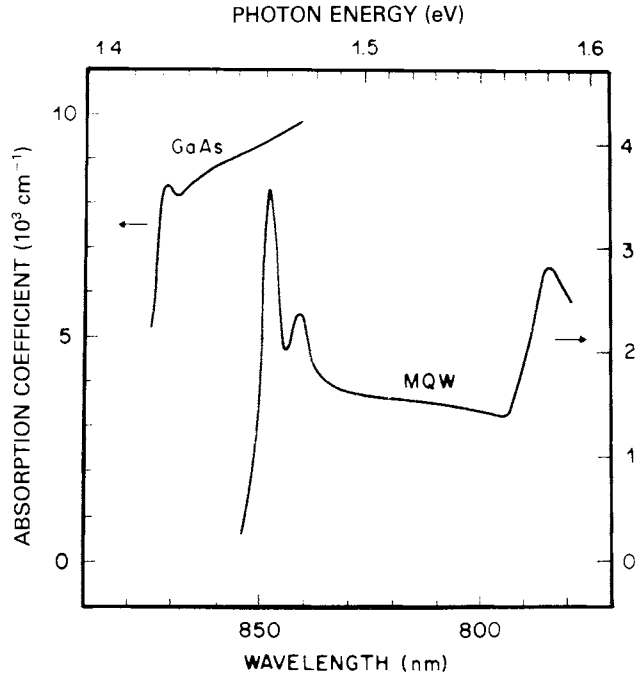

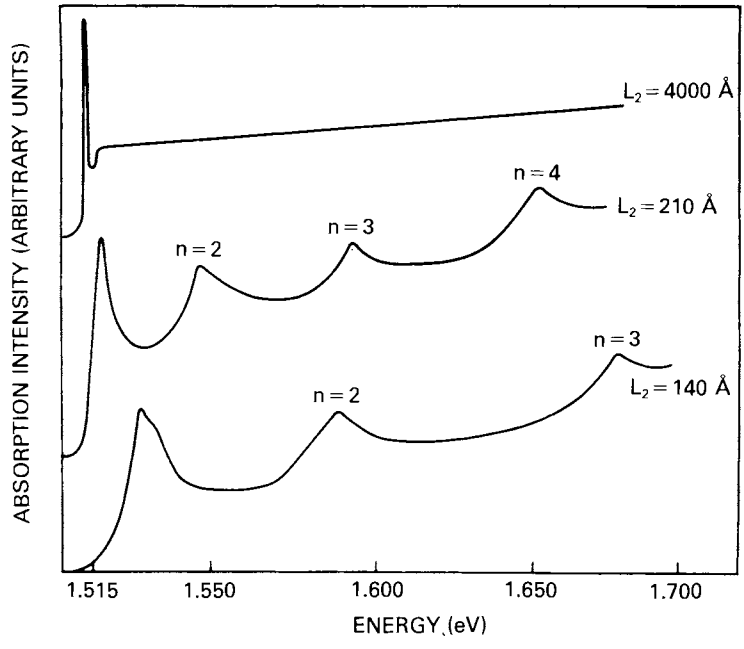

Fig. 3. (a) Comparison between absorption spectrum of bulk GaAs and SL GaAlAs at room temperature [9]. (b) Same comparison as in (a) but at 2 *K* [10].

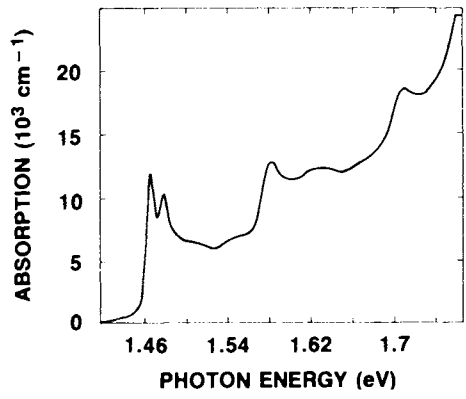

Fig. 4. Room-temperature absorption spectrum of GaAlAs showing excitonic resonances and two-dimensional plateaus [11].

different selection rules affecting possible peaks, and (iv) less than three-dimensional characteristics appearing as a result of the confinement. We now discuss these differences in turn:

1 *Stronger Excitonic Features*

As for the bulk semiconductors, the excitons play a major role in the absorption spectrum for an SL also. The exciton, which is created in the excitation process, should be distinguished from the single-particle excitation, which is a particle already present, but which of course will also be affected by the SL environment. The confinement effect present in an SL turns the three-dimensional excitons into quasi-two-dimensional ones, increasing the binding energy of the exciton and increasing the exciton absorption strength relative to the continuum absorption strength. Both effects lead to more visible excitons for an SL, as Figs. 3 and 4 show, where the SL exciton at room temperature (Fig. 3a) is as visible as the bulk exciton at 2 K (Fig. 3b). It is not only this visibility effect that is responsible for this. The new symmetry introduced by the confinement reduces the interaction with polar phonons, which are usually responsible for ionizing the excitons by the strong electric fields they produce. The major source of thermal broadening, the LO phonons, give an exciton linewidth of approximately 7 meV in bulk (3D) GaAs [12] and 5 meV in an SL ($\approx$2D) [13]. However, the excitonic transitions in SL are, in general, broader than the ones observed in their component materials. The reason for this is that the excitonic resonance is not only a function of temperature but also of the well width, the quality of the interfaces, structural disorder in the constit-

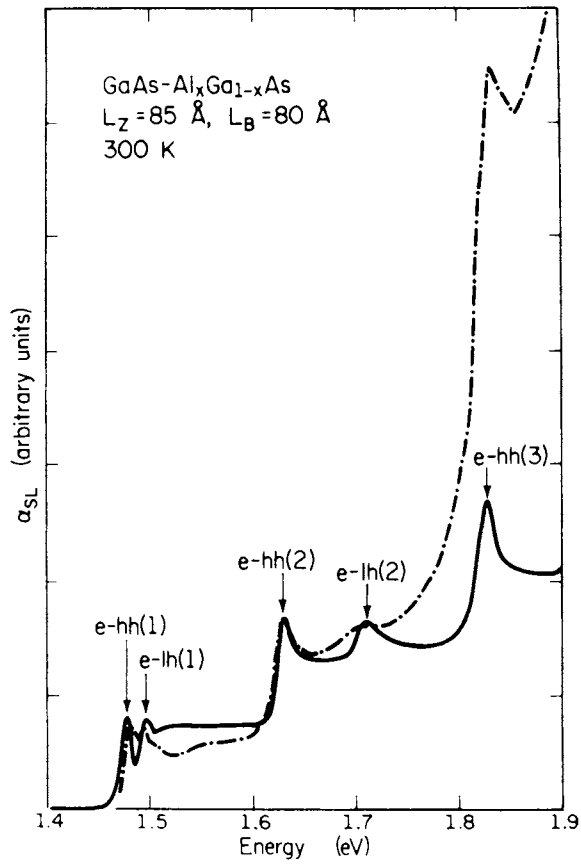

Fig. 5. Comparison between experimental (dashed) and theoretical (full) absorption in GaAs-$Al_{0.5}Ga_{0.5}As$ SL [17].

uents, and so on. This means that the low-temperature exciton features can be used as fairly reliable measures of the quality of the microstructure product [14, 15]. For a GaAs well with thickness $L > a_0^*$ ($\approx$300 Å; bulk exciton radius), the excitons are, in general, three-dimensional with bulk broadening, whereas if $L < 50$ Å the material-quality factors dominate the broadening. The best value of L is therefore around 100 Å and gives sharp excitons with two dimensional character [16], provided the well–well distance is larger than on the order of 100 Å to minimize the well–well coupling. In Fig. 5 we show a theoretical calculation [17] for the experimental absorption spectrum of a GaAlAs SL, which shows the relatively good account one can achieve in the modeling of the essential features for the absorption process. It is specifically demonstrated in [17] that the anisotropy and structure-dependence of the dielectric function, and hence,

the index of refraction, come from the Γ region, while the X and L regions of the Brillouin zone give contributions very much like the compositional-alloy values. The reason for this is the difference in conduction-band effective masses.

2 Split Excitons

A comparison between the bulk and SL absorption curves in Fig. 3a shows clearly how the bulk exciton is split in the SL, which is demonstrated even more clearly in Fig. 6 [18]. The reason for the split exciton peak is that the degeneracy in bulk GaAs between the valence heavy- and light-hole bands is lifted by the perturbation introduced when constructing the SL, affecting the light- and heavy-hole energies differently.

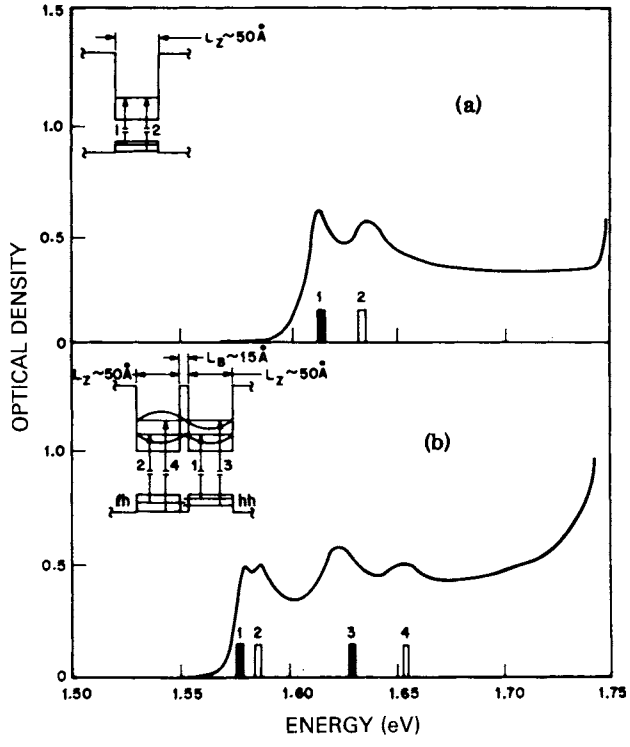

Fig. 6. Comparison between single-well and double-well SL, illustrating the effect of well–well coupling. Notice the lowest split exciton [18].

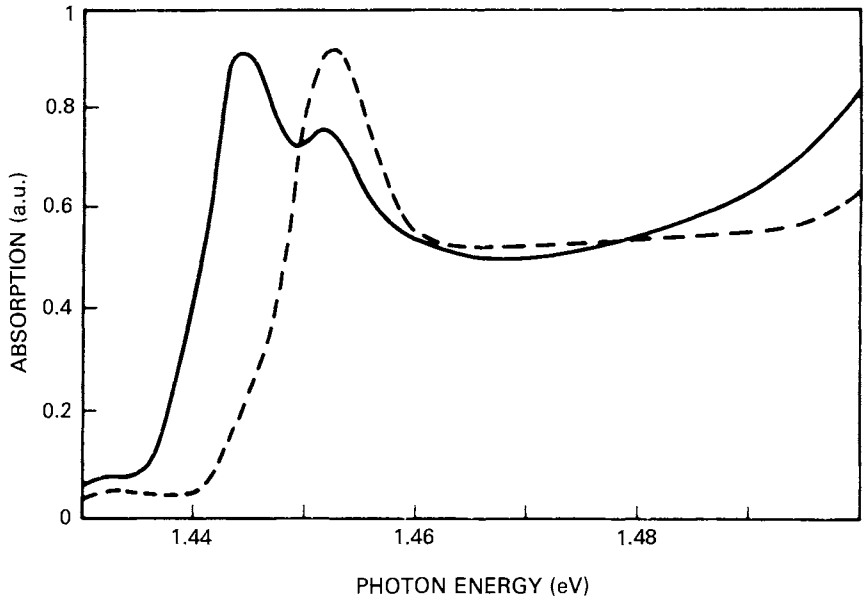

Fig. 7. Room-temperature absorption with light polarization parallel to the layers (solid) and perpendicular to them (dashed) [11].

Selection Rules 3

As soon as we introduce a stacking, a high degree of anisotropy is introduced in a system, and this can be used to design novel optical properties, as already mentioned above. The main effect is to give an absorption that is depending very sensitively on whether the incident light is parallel or perpendicular to the barriers [19]. Let M_{nm} (k, q) denote the matrix element between two levels n and m in the valence and conduction bands, respectively (interband transition), and where k is the SL wave vector along the stacking and q is perpendicular to it. For type I SL, for light having its propagation vector along the stacking, one finds that M_{nm} is almost independent of k and q, and is parity-forbidden if $n-m$ is odd and parity-allowed if $n-m$ is even. The $n=m$ transition is by far the most intense. As a general illustration, we show in Fig. 7 the absorption spectrum close to threshold, when the electric field is parallel and perpendicular to the stacking, respectively. Light polarized parallel to the layers involves both light- and heavy-hole excitons, whereas the other polarization involves only one of them as a result of the specific selection rules for this configuration. The absorption for an optical field polarized normal to the layer is in general difficult to investigate for thin-film samples due to the strong refraction at the interface of the sample. A waveguide configuration, however, enabled polarizations both parallel and perpendicular to the layers to be studied. Further details are given elsewhere [11].

4 Two-Dimensional Density of States

As is seen in Figs. 4 and 5, the general absorption characteristic of the SL is that of a two-dimensional electron gas, whose constant density of states generates a staircase of absorption features with superimposed excitonic transitions. By properly designing well parameters, including the possibility of doping, one can tune the absorption features from less than 5 μm to more than 100 μm [20]. From measurements on such designed systems, one finds very large dipole matrix elements $\langle z \rangle \approx 21$ Å, corresponding to large spatial separations between the ground and first excited states, leading to large oscillator strength and, therefore, to potential technological applications. It should be stressed that the strength and energies of these transitions, and especially the *unconfined* ones, that is, those above the conduction band or below the valence band, are strong functions of the barrier widths. The reason is that the states penetrate far into the neighboring wells [21]. Effects of confinement and interlayer coupling on the optical interband transitions (1.5–5.5 eV) of $(GaAs)_m(AlAs)_m$ superlattices with m ranging from 1 to 15 and with SL periods from 0.6–9 nm are summarized in the work by Garriga *et al.* [22].

Apart from absorption, there are many other optical probes that are useful when investigating SL systems. Here we shall mention only luminescence [23, 24]. The main finding when using this probe is that the SL luminescence spectrum is dominated by so-called intrinsic luminescence (free-exciton recombination processes) in contrast to the bulk GaAs, which is dominated by extrinsic luminescence (recombination with neutral acceptors, that is; impurities, such as carbon). Another often-used probe is Raman scattering, which we will discuss in the next section about phonons in SL.

B Phonons

With the help of Raman scattering and especially resonant Raman scattering, one can utilize the relatively sharp excitonic transitions in the form of a derivative spectrum, and the signal of interest is then not swamped by a large background as with the absorption spectrum. In this way the phonon spectrum of SL can be studied. Of the different kinds of phonons in a material, one finds for a GaAlAs SL that the dominating phonon is the GaAs LO phonon (36.5 meV) [25], the TO phonons being absent because of the usual Raman selection rules. The phonons associated with the $Ga_{1-x}Al_xAs$ layers are not seen, since the electrons and holes involved are confined to the GaAs regions. Phonons are also affected by the periodicity in the SL construction leading to Brillouin-zone folding and

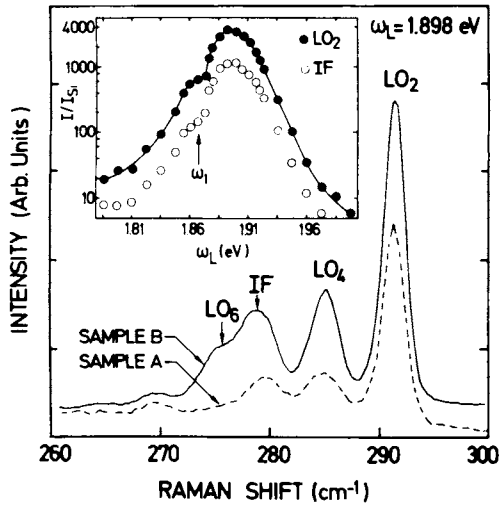

Fig. 8. Raman spectrum showing confined LO phonons and GaAs-like interface mode (IF). Insert shows resonant behavior of LO_2 and IF mode [28].

the appearance of gaps in the phonon spectrum for wave vectors satisfying the Bragg condition [26]. This is most important for LA phonons, since the acoustical branches in different materials overlap energetically, leading to propagation of vibrations and folding. The optical branches, however, are usually separated in energy, and they show confinement effects in the individual slabs [27]. On top of this, we have the possibility of interface vibrational modes [28], (see Fig. 8). These are in nature very similar in structure to the coupled plasmon modes that we will discuss in Section V, showing both band effects and folding. Using a photoelastic continuum model [29], one can give a good account for the observed features in the resonant Raman scattering spectra. Raman scattering spectroscopy also has the potential to provide structural information similar to that obtained by X-ray diffraction [29, 30]. The relative intensities of the folded-acoustic-phonon peaks give a measure of the interface sharpness and layer widths. In this context we shall discuss a related SL construction: the amorphous SL, which still shows sharp interfaces.

AMORPHOUS SUPERLATTICES IV

Semiconductor superlattices and, in particular, crystalline semiconductor superlattices exhibit many interesting transport and optical properties that are associated with the periodic nature of the superlattices and with

the repeat distance in the structure, for example, quantum size effects. The production of crystalline superlattice structures requires lattice matching, and this considerably limits the choice of material and the number of systems that can be produced. Amorphous superlattices, on the other hand, do not require lattice matching and epitaxy. It has been demonstrated that uniform multilayers of amorphous semiconductors can be grown with interfaces that are sharp and essentially defect-free down to very small individual layer thickness [31–37]. This allows for a much larger variety in the systems to be studied. The amorphous superlattice will, therefore, offer an attractive alternative to crystalline superlattices, since amorphous superlattices will exhibit many of the effects seen in crystalline superlattices with the obvious exception of effects associated with the existence of a long mean free path of the carriers.

Quantum size effects on the band gap have been seen in the optical properties of amorphous semiconductors [31–37]. Optical studies will thus constitute an important base for the understanding of quantum size effects on the band structure and effective mass in these systems. We will illustrate this by the studies of Bittar *et al.* [36] on the Si/SiO_x superlattices. This is an attractive system to study, since the band gaps in the two materials are quite different, and for such systems, theories based on an effective-medium approach are expected to be valid. The samples were made by evaporation onto room-temperature substrates. High-resolution transmission electron microscopy and small-angle electron diffraction indicated that the multilayers indeed constituted superlattices with sharp interfaces and well-defined periods.

The optical properties of the samples were studied by means of normal-incidence reflection and transmission measurements in the range 0.9–4 eV. At this stage it is appropriate to discuss the validity of an effective absorption coefficient for a multilayer sample. Can the optical properties of a superlattice be described in a way that allows the extraction of a value for the optical gap? We have outlined above an effective-medium theory for superlattices. This approach assumes a localized response in each layer, that is, electron wavefunctions, which are localized to one layer. This is the case for amorphous superlattices. Therefore, extracting effective constants from optical measurements gives information about the response in the individual layers. Also, normal-incidence reflectance and transmission are determined by the ordinary dielectric constant ε_0 only. Furthermore, in the region below the SiO_x absorption edge, the absorption is, in the absence of long-range interactions and long mean free paths, determined by the Si layers only. For semiconductors the band shapes near the absorption edge are often parabolic. In these cases the optical gap can be determined from the equation

$$(\alpha\hbar\omega)^{1/2} = B(\hbar\omega - E_g), \tag{3}$$

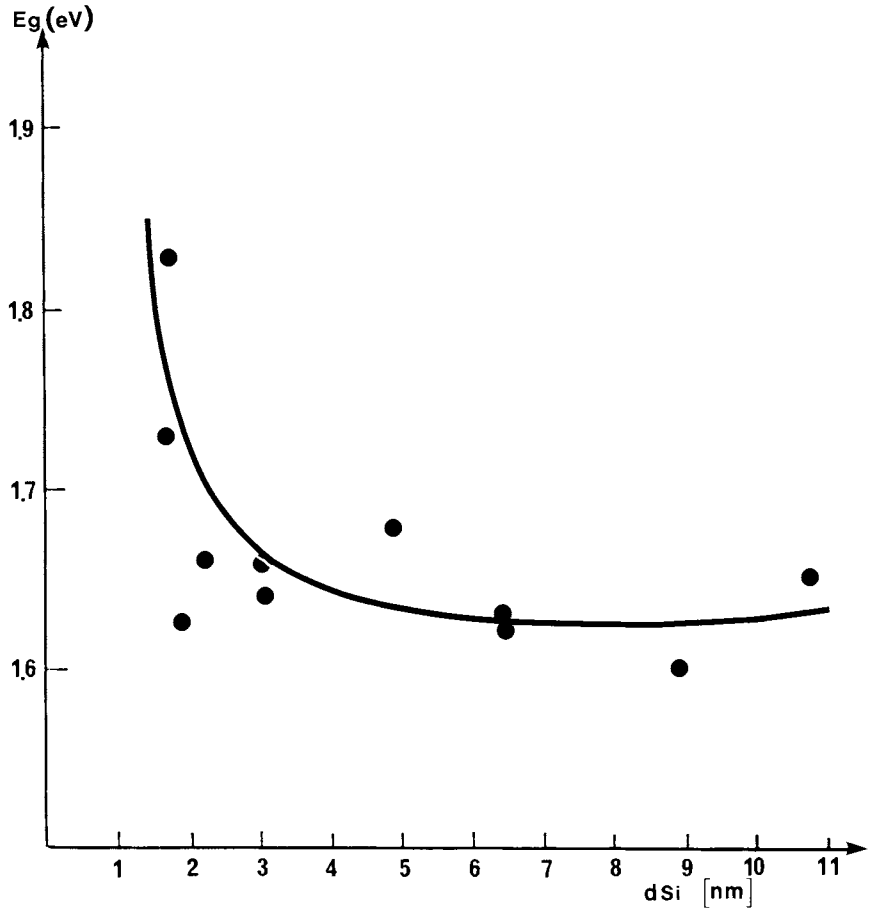

Fig. 9. Experimental band gap, E_g, as a function of silicon layer thickness, d_{Si}, for the Si/SiO_x system [36].

in the region of photon energies above the gap E_g. Thus, by plotting the measured absorption coefficient α in a so-called Tauc plot given by Eq. 3, values for the band gap in the Si layers can be obtained.

The results of these studies are summarized in Fig. 9, where values of the band gap E_g are plotted as a function of Si layer thickness. The figure shows band-gap values that are influenced by quantum-well confinement for layer thicknesses below 3 nm. The absence of any firm information about the modulation profiles of the valence- and conduction-band edges, or about electron and hole effective masses, prevents an exact comparison of the measured gap with calculations. Nonetheless, the magnitude of the

shift, and the layer-thickness value at which it sets in, can be modeled with a square-wave modulation of band edges [37]. This modeling demonstrates that the variation in bandgap with layer thickness is indeed a quantum size effect.

V COLLECTIVE EXCITATIONS

So far we have said very little about the coherent motion of single-particle excitations in the form of collective excitations such as plasmons and polaritons. The very nature of the SL makes it possible to have or construct collective modes of almost any frequency and dispersion. Lately, this has been an intense field of research, where we would particularly like to mention the theoretical contributions by Bloss and Brody [38], Tselis and Quinn [39], Das Sarma and Quinn [40], and the very condensed presentation by Camley and Mills [41]. Experimentally the first confirmation of collective modes in layered structures, which were in-between those for two- and three-dimensional systems, came about at the same time by Olego and co-workers [42], using inelastic light scattering. In this section we will give a simple description of how to analyze the SL response with respect to collective modes as seen in elastic light scattering. The interested reader should consult Rytov [43] and Brekhovskikh [44] to get some flavor of the original work being done on the optical properties of SL. It should be mentioned, however, that during recent years there have appeared two very powerful methods for the optical-response description of SL; one is based on a continued fraction-approach by Lambin *et al.* [45] and the other is a very useful transfer-matrix formulation by Mocha'n *et al.* [46]. The latter actually goes back to a description of the optical properties of thin films by Jones *et al.* [47] in terms of the surface-impedance concept. The surface impedance is defined as the ratio between the parallel-field components of the electric and magnetic fields at an interface (the conserved quantities). It turns out that when relating the field components at the two sides of a layer in an SL through a transfer matrix, its elements can be expressed in terms of surface impedances for field components that are symmetric and antisymmetric with respect to the layer in question. We will return to this in a following section; right now we will outline the simplest way of analyzing the possibility of having collective modes in a two-component, semi-infinite SL using the surface-impedance construction.

The optically equivalent medium of the ideal superlattice is fully specified by giving the surface impedance of the uniaxial crystal found earlier:

$$Z_{ep} = p_e / q\varepsilon_o \tag{4}$$

for p-polarized light, where p_e is the perpendicular wave-vector component of the bulk "extraordinary" polariton with

$$p_e^2 = (q^2 - k_\parallel^2/\varepsilon_e)\varepsilon_o, \qquad q = \omega/c, \tag{5}$$

and

$$Z_{es} = p_o/q, \tag{6}$$

with $p_o^2 = q^2\varepsilon_o - k_\parallel^2$ for s-polarized light. Notice how s-polarized light only involves ε_o. This is because s-polarized light does not have any field component perpendicular to the surface, as is also the case for p-polarized light at normal incidence ($k_\parallel = 0$ yields p_e, independent of ε_e, *cf.* Eq. 5).

With the surface impedance, a number of interesting physical quantities can be calculated [6]. For a semi-infinite medium with surface impedance Z (which is calculated classically from bulk quantities) adjacent to vacuum, with p-polarized light c incident at an angle θ with the surface normal, we have the following reflection coefficient:

$$r_p = \frac{\cos\theta - Z_p}{\cos\theta + Z_p}, \tag{7}$$

which yields our superlattice reflection coefficient r_{ep} simply by replacing Z_p with Z_{ep}, the surface impedance for the infinite medium being equivalent to our superlattice. The general behavior of r_{ep} is easily found from an inspection of Eq. 5. Since whenever $p_e^2 < 0$, Z_{ep} becomes imaginary, the reflectance $|r_{ep}|^2$ from this system approaches unity. This occurs provided the imaginary part from $p_e^2 < 0$ dominates the imaginary parts in the component dielectric constants ε_a and ε_b describing the Drude damping (τ). In the optical regime this is a good approximation, since usually $1/\tau \sim (10^{-3} - 10^{-2})\omega_p << 1$ eV, for typical plasma frequencies on the order of 10 eV and where 1 eV is the typical energy for $|p_e|\, c$. Using this form for p_e thus facilitates an easy inspection of the reflective properties of a superlattice.

When the denominator of Eq. 7 vanishes, we have a situation with a divergent reflection coefficient; we can have a reflected field without any incoming one. This is characteristic of an eigenmode of the coupled vacuum-superlattice system and corresponds to what is called a *surface polariton*. Whereas the dispersion relation of the bulk polariton is obtained from Eq. 5, yielding $\omega = \omega(k_\parallel, p_e)$, the surface-polariton dispersion relation, which is a solution to $\cos\theta + Z_{ep} = 0$, yields $\omega = \omega(k_\parallel)$ with $\cos\theta =$

$\sqrt{1-(k_\parallel c/\omega)^2}$. Using Z_{ep} from Eq. 4 and a little algebra, we arrive at the following dispersion relation for the surface polariton in a superlattice with the "optical axis" perpendicular to the stacking:

$$k_\parallel^2 = q^2 \frac{\varepsilon_o - 1}{\varepsilon_o - 1/\varepsilon_e}, \tag{8}$$

which goes over to the appropriate limit $k_\parallel^2 = q^2\varepsilon_a/(1+\varepsilon_a)$ if medium b is absent ($\varepsilon_o = \varepsilon_e = \varepsilon_a$). When solving Eq. 8, it should be complemented with the condition that only (ω, $k_\parallel$) values that make $p_e^2 < 0$ are physical solutions, that is, that correspond to decaying (localized) solutions. This automatically ensures that we find no mode to the left of the light line in vacuum ($\omega = k_\parallel c$).

Letting $c \to \infty$, we reach the electrostatic regime ($p_e \to ik_\parallel$), where the dispersion relation in Eq. 8 goes over to its short-wavelength limit ($k_\parallel \gg \omega/c$):

$$\varepsilon_e \varepsilon_o = 1. \tag{9}$$

The surface mode is now called a *surface plasmon*, since it no longer has any photon character, and for a semi-infinite medium of material a only, Eq. 9 goes over to $\varepsilon_a + 1 = 0$. However, for the superlattice, which has a unit cell with two components, we will actually find two possible solutions (modes).

For a metal–metal superlattice described by Drude dielectric functions $\varepsilon_{a,b} = 1 - \omega^2_{a,b}/\omega^2$, with $\omega_a = 2\omega_b$ and $f = 1/2$, we show in Fig. 10 the possible surface-polariton modes. The lower mode follows the photon line for small $k (= k_\parallel c/\omega_a)$ and approaches $\omega_i^2 = \omega_a^2\omega_b^2/(\omega_a^2 + \omega_b^2)$ for large k (a solution of Eq. 9). The other mode is unphysical; it stays outside the dotted area that corresponds to a solution which is confined to the surface ($p_e^2 < 0$), until it reaches the light line $\omega = k_\parallel c$ and then goes rapidly towards the interface plasmon frequency for a bimetallic junction: $\omega_s^2 = (\omega_a^2 + \omega_b^2)/2$. Notice that this mode measures the average electron density in the superlattice, since $\omega^2_{a,b} \propto n_{a,b}$, n being the electron density. On the other hand, the lower mode is a measure of the sum of the inverse electron densities.

Our second example, shown in Fig. 11, is for a metal–insulator system with $\varepsilon_a = 1 - \omega_p^2/\omega^2$, $\varepsilon_b = \varepsilon_i = 9/4$, and $f = 1/2$. Again we have a lower mode starting out following the light line, and it approaches the surface plasmon for a metal in contact with an insulator having dielectric function ε_i, namely, $\omega_0^2 = \omega_p^2/(1+\varepsilon_i)$. The upper mode is very different compared to the metal–metal case, both in absolute frequency and dispersion. It starts out

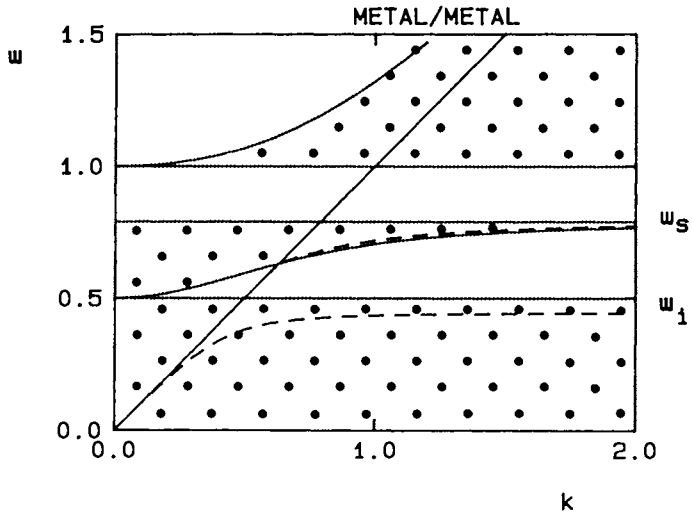

Fig. 10. Surface polariton dispersion relation for a metal–metal superlattice, with $\omega_a = 2\omega_b$ and $f = 1/2$, adjacent to vacuum. Only solutions within dotted areas satisfy the criterion for being surface localized ($p_c^2 < 0$) and are retained. The two physical modes are to the right of the light line (full curve) and soon approach $\omega_s^2 = (\omega_a^2 + \omega_b^2)/2$ and $\omega_i^2 = \omega_a^2\omega_b^2/(\omega_a^2 + \omega_b^2)$, respectively. k is in units of ω_a/c and ω in units of ω_a.

from the light line $\omega = k_\parallel c$ exactly at the point where the border line corresponding to a decaying solution (dotted area) cuts the light line (full curve). It stays within the allowed region and approaches $\omega_i^2 = \omega_p^2\varepsilon_i/(\varepsilon_i - 1)$ for large $k_\parallel c/\omega_p$.

As we have just seen, the presence of interfaces allows for the propagation of interface polaritons, and this can have a dominating influence on the optical response for a metal–metal or a metal–insulator superlattice. The most prominent aspect of the optical properties of an insulator is the reststrahlen band in the infrared. The reflectance of a semi-infinite medium increases sharply near the pole in $\varepsilon(\omega)$ caused by the resonance of the transverse-optical-phonon polariton and decreases again at the longitudinal-optical-phonon polariton. For a thin film the reflectance at normal incidence continues to exhibit a structure at the TO resonance, but no structure is seen at the LO resonance. At oblique incidence a structure is, however, seen for p-polarized light, but not for s-polarized light. This phenomenon was first discussed by Berreman [48]. In the case of free electrons discussed previously, the same effect occurs at the frequency of the bulk plasmon. The Berreman effect in the case of a single thin insulating film has been studied in detail by Harbecke *et al.* [49]. The effect can be very prominent, particularly for an insulating film on a metallic backing. This is illustrated in Fig. 12, which in a three-dimensional plot

shows how the reflectance varies with frequency and layer thickness [49]. The Berreman effect shows a maximum at a particular layer thickness given by

$$d_B = \frac{\lambda \cos\theta}{2\pi \sin^2\theta}[\mathrm{Im}\{-1/\varepsilon\}]^{-1}, \tag{10}$$

which is called the *Berreman thickness*.

In the case of superlattices, the effect may again be strongly enhanced due to the presence of many interfaces. This is the case for an insulator–insulator superlattice if one of the materials is transparent at the LO frequency of the other material. This is illustrated in Fig. 13, which shows the reflectance of such a system [50]. The model superlattice has been calculated for two values of the damping parameter $\Gamma = \omega_0\tau$. Here ω_0 is the TO phonon frequency and τ is the corresponding lifetime. The parameters for the material showing the Berreman effect are typical for those of SiO_2 in curve 2, whereas curve 1 shows the same superlattice for a value of Γ, which is roughly three times larger.

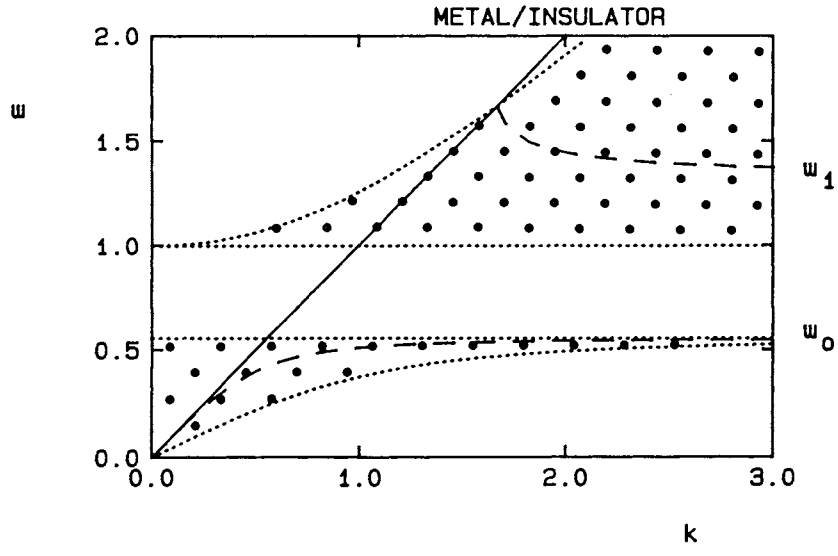

Fig. 11. Surface polariton dispersion relations for a metal–insulator superlattice, in contact with vacuum. $f = 1/2$, $\varepsilon_a = 1 - \omega_p^2/\omega^2$, and $\varepsilon_b = 9/4$. ω is in units of ω_p and $k_\parallel$ is in units of ω_p/c. The lower mode starts out from the light line (full curve) and approaches the electrostatic result $\omega_0^2 = \omega_p^2/(1+\varepsilon_b)$. The upper mode starts out from the light line and is surface-confined immediately, since the dotted areas in the figure correspond to physical surface solutions. The upper mode approaches $\omega_1^2 = \omega_p^2\varepsilon_b/(\varepsilon_b - 1)$ for large k.

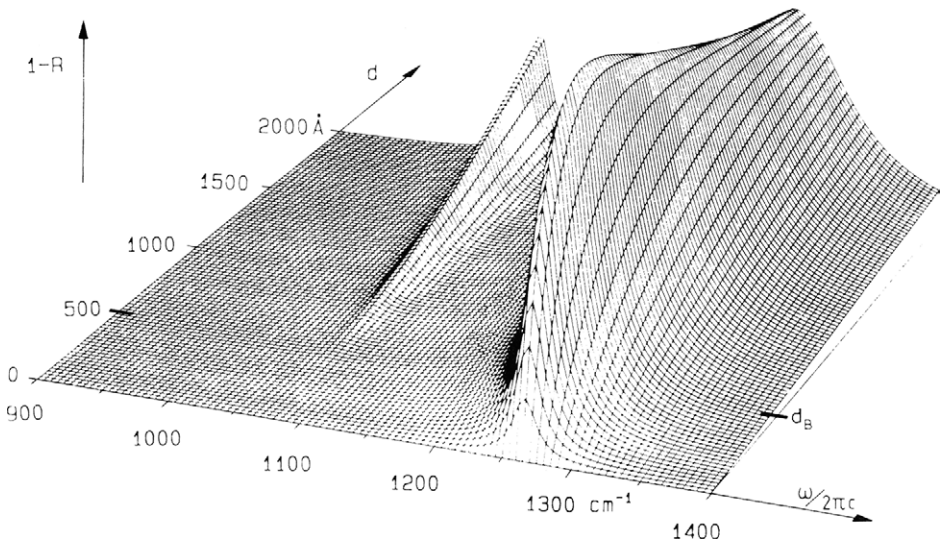

Fig. 12. Three-dimensional plot of the dependence of the absorptance 1-R of an SiO_2 film on a metal substrate against frequency and thickness. The parameters used in the calculation are given elsewhere [49].

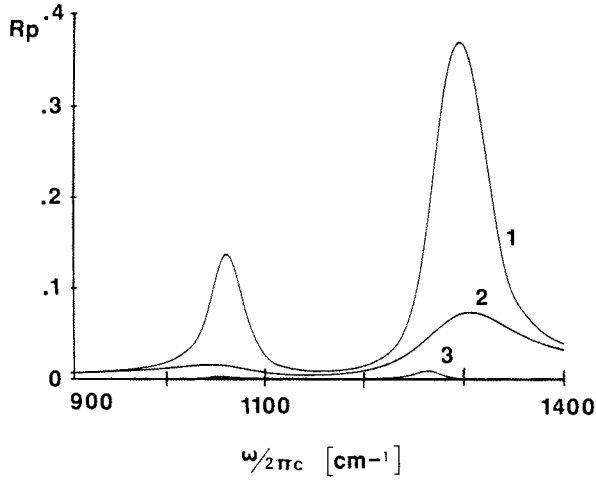

Fig. 13. Model calculation for the reflectance of a single SiO_2 film, (3); and two insulator–insulator superlattices, (1 and 2), versus frequency. The filling factor of SiO_2 in the superlattice is 0.5. Curves 2 and 3 have $\Gamma = 30$; curve 1 has $\Gamma = 100$. The angle of incidence was 70°. The other parameters used in the calculation are given elsewhere [50].

Grosse *et al.* [51] have studied the optical properties of GaAs heterostructures in the infrared (70–2500 cm^{-1}). The main structures in the spectra are due to phonon reststrahlen bands (TO), Fabry–Perot interferences, and Berreman modes. A fit to data allows one to extract carrier concentration and thickness of the epitaxial films as well as carrier concentration of the GaAs substrate. The films in this study were thick, and no quantum-well effects were expected, but they demonstrate that the reststrahlen region provides a powerful tool for nondestructive profiling of the heterostructure.

Maslin *et al.* [52] have studied a superlattice in the reststrahlen region. The superlattice consisted of 150 periods, each period composed of two monolayers of GaAs and two monolayers of AlAs with cladding layers of 0.1 μm of $Al_{0.7}Ga_{0.3}As$ on each side, and the complete structure was grown on a GaAs substrate. The effective-medium description, which the same authors found to be adequate for relatively long-period superlattices, cannot describe the structures observed in the reststrahlen region. Account must be taken of the contribution to the dielectric susceptibility of the zone-folded optic phonons and of the way in which long-range electrostatic interactions responsible for the LO–TO splitting are modified by the periodicity of the superlattice. The spectrum also shows a pronounced structure below about 250 cm^{-1}, which most probably arises from the free-carrier response.

In the case of a metal–insulator superlattice, the optical properties are very much dominated by those of the metal. For somewhat thicker films in the superlattice the response also depends strongly on whether the outer layer is metal or insulator. If the outer layer is metal the incoming light is damped through the metal layer, and the effect is weak. If the outer layer is an insulator, the effect is similar to an insulator on a metallic backing. The Berreman effect is still prominent in a metal insulator superlattice. We have a balance between the damping due to the metal layers and an enhancement due to the presence of many interfaces. This effect has been studied experimentally for a Pt/Al_2O_3 multilayer system [50]. The samples were made by sequentially sputtering Pt and Al in a reactive atmosphere. The experimental results were in reasonable agreement with model calculations based on macroscopic dielectric functions.

VI LATTICE DISORDER

Up to now, all our discussion has been based on the assumption of a perfect superlattice. It is of interest to study the effect of deviations from

this assumption, that is, to study realistic superlattices. This can be done by introducing a statistical variation in the thickness of the individual layers. It is only in the limit of thin individual layers or a symmetric unit cell that the total transfer matrix will have equal diagonal elements, and thus allows the extraction of effective dielectric constants. Therefore, the effect of lattice disorder was studied by simulation, using the exact transfer matrix formalism [53]. A Drude metal–insulator superlattice was taken as a model system. The film consisted of 1000 layers. The layer thicknesses were generated by means of a Gaussian distributed random-number generator. The average layer thickness was 2 nm, and the standard deviation was 0.5 nm.

The resulting reflectance in the 5–8 eV range, where the absorption coefficient is small so that the light penetrates many layers in the superlattice, is shown in Fig. 14. The effect of finite layer thickness on the reflectance is small for 4 nm unit-cell size, for an ideal superlattice. If we let the layer thickness vary, however, the difference between the effective-medium theory and the exact theory may be large indeed (see Fig. 14). The strong variations seen in the reflectance are the result of the statistical variations in the phases of the waves reflected from the various interfaces.

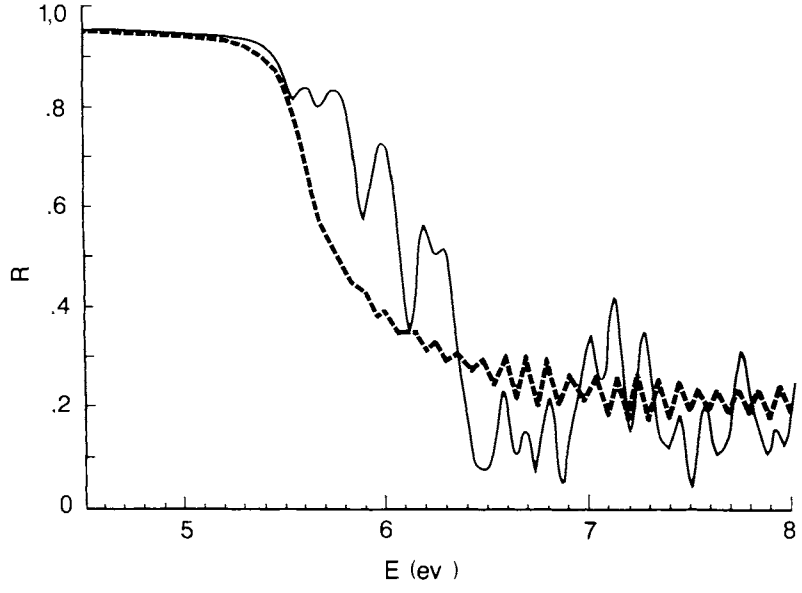

Fig. 14. Reflectance for *p*-polarized light at a 60-degree angle of incidence for an ideal superlattice (dashed) and with a statistical variation in the layer thicknesses (solid). The rms variation in layer thickness was 25%. The parameters are otherwise as in Fig. 1.

In the absence of absorption, these fluctuations would be reminiscent of the speckle pattern in the reflection from a rough object. There, the highest frequency is given by the size of the object; here, the highest frequency would be given by the total thickness of the sample. Another way of looking at these structures is to compare them to the Anderson localization in a random potential in solid-state physics. Here we have a localization of an electromagnetic wave in a random superlattice. Such localization, for example, has been observed experimentally by Genack [54] in a dense random packing of microspheres and is also predicted in quasiperiodic media [55].

For superlattices with finite thickness *and* where the unit cell is not symmetric, *or* if we include a statistical variation in the layer thickness, the total transfer matrix of the system will not have equal diagonal elements. In this case the system is not equal to a simple film, and we cannot extract effective dielectric constants. It has been stated in the literature that a transfer matrix with unequal diagonal elements is equivalent to a double film [56]. It takes a total of six parameters to characterize a double film, two complex dielectric constants and two thicknesses, and these could in principle be extracted from the transfer matrix.

VII THE EFFECT OF NONLOCAL DIELECTRIC FUNCTIONS

For nonnormal incidence onto a metal surface, the electromagnetic wave propagating into the metal is no longer purely transverse; it also has a longitudinal component. A description of the interaction of the wave with the electrons will then involve both the transverse dielectric function, ε_T, and the longitudinal dielectric function, ε_L. Furthermore, the field varies very rapidly near the surface, and the usual dipole approximation is no longer valid. A common name for all these effects in optics is *nonlocal*. Several authors have studied the effect of nonlocal transverse and longitudinal dielectric functions on the optical properties of a single slab. A superlattice consists of a very large number of slabs, and the effect of nonlocality can be important. We therefore include a review of the effect of nonlocality. A fruitful approach is as follows: one uses the expansion of the surface impedance in terms of waves of even and odd parity, which was first derived by Jones *et al.* [47]. Then one expresses the transfer matrix of a single film in terms of the surface impedance Z_0 for odd waves and Z_e for even waves. We have shown that this leads to the following transfer matrix [5]:

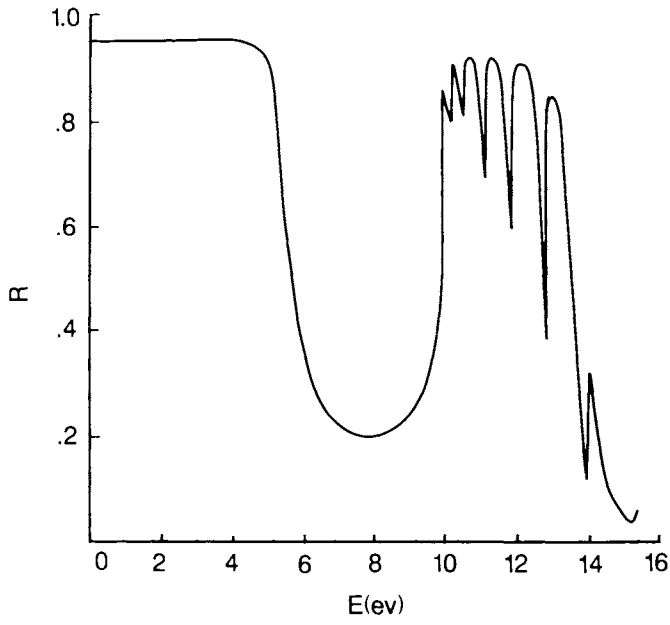

Fig. 15. Reflectance for p-polarized light at a 60 degree angle of incidence with nonlocal dielectric constants. The other parameters used in the calculation are given elsewhere [5].

$$M_u = \begin{vmatrix} \dfrac{Z_e + Z_o}{Z_e - Z_o} & \dfrac{2Z_eZ_o}{Z_e - Z_o} \\ \dfrac{2}{Z_e - Z_o} & \dfrac{Z_e + Z_o}{Z_e - Z_o} \end{vmatrix}. \tag{11}$$

Explicit expressions for Z_o and Z_e were given by Jones *et al.* Those expressions have been used to calculate the reflectance from a stack of the form $b/2ab \ldots ab/2$. Here b represents thin layers of an insulating material; a represents the metallic slabs. For the transfer matrix of the insulating slabs, we use the usual expressions for the transfer matrix. The layer thicknesses are sufficiently small for the effective-medium expressions to apply if a local dielectric constant is used for the metal. Figure 15 shows the reflectance for p-polarized light with nonlocal dielectric functions. These were obtained from the Boltzman equation for a free-electron gas. We used the Fermi velocity $v/c = 2.8 \times 10^{-3}$, and the metallic-layer thickness was chosen to be 2 nm. The parameters are otherwise the same as those in Fig. 1. The structure associated with the excitation of bulk plasmons is much more pronounced in the superlattice than in a single film [5]. These calculations indicate that nonlocal effects can play a role in the

optical properties of metal–metal and metal–insulator superlattices. The position and strength of the longitudinal-plasmon peaks are, however, exceedingly sensitive to the thickness of the metal layers. Sample quality is therefore important for the overall optical spectrum.

VIII CONCLUDING REMARKS

The engineering of SL semiconducting materials with novel physical properties has been extensively studied over the last decade. Because of the important optoelectronic applications of these structures, large emphasis has been placed on determining their optical properties. These may, as we have seen in this review, be strongly modified by localization and quantum-confinement effects. Much less effort has been expended to produce and to study the properties of metallic superlattices, although such superlattices can be made [57, 58]. The emphasis there has been on magnetic properties, and no study of the optical properties of metallic superlattices has to our knowledge been carried out yet. It is clear that the band structure of a metallic SL will be very different from those of the constituents if the layer thickness is only one or a few atomic layers thick. Such a material would in many respects be an "ordinary" uniaxial material, and the optical properties would be an important tool to study the band structure of the material. There has again been little or no experimental effort to make and study the optical properties of metal–insulator or insulator–insulator superlattices. The superlattice phenomenon to be studied are in particular collective modes: plasmons and polaritons. These have been studied extensively theoretically; the lack of experimental data is, in part, related to difficulties in sample preparation, but it should also be recognized that the industrial emphasis has been on semiconductor superlattices due to their vast potential applications.

REFERENCES

1. L. L. Chang, L. Esaki, W. E. Howard and R. Ludeke, *J. Vac. Sci. Technol.* **10**, 11 (1973).
2. L. Esaki and R. Tsu, IBM Research Note RC-2418 (1969).
3. M. Jaros, "Physics and Applications of Semiconductor Microstructures," Clarendon Press, Oxford (1989).
4. L. Esaki, "Science Citation Index," number 28, July (1987).
5. O. Hunderi, *J. Wave-Mat. Int.* **2**, 29 (1987).
6. P. Apell, R. Monreal, and O. Hunderi, *Physica Scripta* **34**, 348 (1986).
7. A. Yariv and P. Yeh, "Optical Waves in Crystals," Wiley, New York, (1984).
8. S. John, *Phys. Rev. Lett.* **58**, 2486 (1987).

9. D. S. Chemla, D. A. B. Miller, and P. W. Smith, *Opt. Eng.* **24**, 556 (1985).
10. R. Dingle, W. Wiegmann, and C. H. Henry, *Phys. Rev. Lett.* **33**, 827 (1974).
11. D. S. Chemla and D. A. B. Miller, *J. Opt. Soc.* **B2**, 1155 (1985).
12. V. I. Alperowich, V. M. Zal, A. F. Kranchinko and A. S. Terekhev, *Phys. Stat. Solidi* **b77**, 466 (1976).
13. D. S. Chemla, D. A. B. Miller, P. W. Smith, A. C. Gossard, and W. Wiegmann, *IEEE J. Quantum Electron.* **QE-20**, 265 (1984).
14. K. K. Bajaj and D. C. Reynolds, Proceedings of Advances in Semiconductors and Semiconductor Structures, *SPIE* **794**, 2 (1987).
15. D. C. Reynolds, K. K. Bajaj, C. W. Litton, Jasprit Singh, P. W. Yu, P. Pearah, J. Klem, and H. Morkoc, *Phys. Rev.* **B33**, 5931 (1986).
16. J. E. Zucker, A. Pinczuk, D. S. Chemla, A. Gossard, and W. Wiegmann, *Phys. Rev. Lett.* **51**, 1293 (1983).
17. K. B. Kahen and J. P. Leburton, *Phys. Rev.* **B33**, 5465 (1986).
18. R. Dingle, A. C. Gossard, and W. Wiegmann, *Phys. Rev. Lett.* **34**, 1327 (1975).
19. P. Voisin, *Surf. Sci.* **142**, 460 (1984).
20. B. F. Levine, R. J. Malik, J. Walker, K. K. Choi, and C. G. Bethea, Proceedings of Advances in Semiconductors and Semiconductor Structures, *SPIE* **792**, 157 (1987).
21. J. J. Song, Y. S. Yoon, P. S. Jung, A. Fedotowsky, and Y. B. Kim, Proceedings of Advances in Semiconductors and Semiconductor Structures, *SPIE* **794**, 55 (1987).
22. M. Garriga, M. Cardona, N. E. Christensen, P. Lautenschlager, T. Isu, and K. Ploog, *Phys. Rev.* **B36**, 3254 (1987).
23. R. C. Miller, A. C. Gossard, W. T. Tsang, and O. Munteanu, *Phys. Rev.* **B25**, 3871 (1982).
24. C. Weisbuch, R. C. Miller, R. Dingle, A. C. Gossard and W. Wiegmann, *Solid State Commun.* **37**, 219 (1981).
25. P. Manuel, G. A. Sai-Halasz, L. L. Chang, Chin-An Chang, and L. Esaki, *Phys. Rev. Lett.* **37**, 1701 (1976).
26. C. Colvard, R. Merlin, M. V. Klein, and A. C. Gossard, *Phys. Rev. Lett.* **45**, 298 (1980).
27. A. K. Sood, J. Menéndez, M. Cardona, and K. Ploog, *Phys. Rev. Lett.* **54**, 2111 (1985).
28. A. K. Sood, J. Menéndez, M. Cardona, and K. Ploog, *Phys. Rev. Lett.* **54**, 2115 (1985).
29. C. Colvard, T. A. Gant, M. V. Klein, R. Merlin, R. Fischer, H. Morkoc, and A. C. Gossard, *Phys. Rev.* **B31**, 2080 (1985).
30. C. Colvard, Proceedings of Advances in Semiconductors and Semiconductor Structures, *SPIE* **794**, 209 (1987).
31. B. Abeles and T. Tiedje, *Phys. Rev. Lett.* **51**, 2003 (1983).
32. N. Ibaraki and H. Fritsche, *Phys. Rev.* **B30**, 5791 (1984).
33. T. Tiedje, B. Abeles, P. D. Persans, B. G. Brooks, and G. D. Cody, *J. Non-Cryst. Solids* **66**, 339 (1984).
34. H. Munekata, M. Mizuta, and H. Kukimoto, *J. Non-Cryst. Solids* **59 & 60**, 1167 (1983).
35. H. J. Trodahl and M. W. Wright, *Solid State Commum.* **59**, 699 (1986).
36. A. Bittar, O. Hunderi, and H. J. Trodahl, Proceedings of Advances in Semiconductors and Semiconductor Structures, *SPIE* **792**, 249 (1987).
37. A. Bittar, G. V. M. Williams, and H. J. Trodahl, *Physica* **A157**, 411 (1989).
38. See, for example, W. L. Bloss and E. M. Brody, *Solid State Commun.* **43**, 523 (1982); ibid. **44**, 363 (1982) and ibid. **48**, 927 (1983).
39. See, for example, A. C. Tselis and J. J. Quinn, *Phys. Rev.* **B29**, 2021 (1984); ibid. 2318 (1984).
40. See, for example, S. Das Sarma and J. J. Quinn, *Phys. Rev.* **B25**, 7603 (1982).
41. R. E. Camley and D. L. Mills, *Phys. Rev.* **B29**, 1625 (1984).
42. D. Olego, A. Pinczuk, A. C. Gossard, and W. Wiegmann, *Phys. Rev.* **B25**, 7867 (1982).
43. S. M. Rytov, *Sov. Phys. JETP* **2**, 466 (1956).

44. L. M. Brekhovskikh, "Waves in Layered Media," 2nd edition, Academic Press, New York (1980).
45. Ph. Lambin, J. P. Vigneron, and A. A. Lucas, *Solid State Commun.* **54**, 257 (1985).
46. W. L. Mocha'n, M. del Castillo-Mussot, and R. G. Barrera, *Phys. Rev.* **B35**, 1088 (1987).
47. W. E. Jones, K. L. Kliewer, and R. Fuchs, *Phys. Rev.* **178**, 1201 (1969); R. Fuchs and K. L. Kliewer, *Phys. Rev.* **185**, 905 (1969).
48. D. W. Berreman, *Phys. Rev.* **130**, 2193 (1963).
49. B. Harbecke, B. Heinz, and P. Grosse, *Appl. Phys.* **A38**, 263 (1985).
50. O. Hunderi, *Physica* **A157**, 309 (1989).
51. P. Grosse, B. Harbecke, B. Heinz, W. Jantz, and M. Maier, *Appl. Phys.*, in press.
52. K. A. Maslin, T. J. Parker, N. Raj, D. R. Tilley, P. J. Dobson, D. Hilton, and C. T. B. Foxton, *Solid State Commun.* **60**, 461 (1986).
53. O. Hunderi and K. Johannessen, *Superlatt. and Microstruct.* **3**, 193 (1987).
54. A. Genack, *Phys. Rev. Lett.* **58**, 2043 (1987).
55. M. Kohmoto, B. Sutherland, and K. Iguchi, *Phys. Rev. Lett.* **58**, 2436 (1987).
56. A. Herpin, *Comptes Rendus des Sciences* **225**, 182 (1947).
57. I. K. Schuller, *Phys. Rev. Lett.* **24**, 1597 (1980).
58. C. M. Falco, *Journal de Physique, Coll C5*, **45**, 499 (1984).

Chapter 6

Calculation of the Refractive Index of Compound Semiconductors below the Band Gap

B. JENSEN
Department of Physics
University of Lowell
Lowell, Massachusetts

I. Introduction 125
II. The Quantum-Density-Matrix Formulation of the Complex Dielectric Constant 128
III. Comparison with Experimental Results 138
IV. Summary 147
References 148

I INTRODUCTION

The interaction of the radiation field with the free carriers and bound electrons in a compound semiconductor can be described in terms of a complex dielectric constant

$$e = \varepsilon_1 - i\varepsilon_2 = N^2, \tag{1}$$

where the real and imaginary parts of the complex dielectric constant ε_1 and ε_2 are functions of the complex refractive index N as follows:

$$N = n - ik \tag{2}$$

$$\varepsilon_1 = n^2 - k^2 \tag{3}$$

$$\varepsilon_2 = 2nk = 4\pi\sigma/\omega. \tag{4}$$

Copyright © 1991 by Academic Press.
All rights of reproduction in any form reserved.
ISBN 0-12-544422-2

In Eq. 2, n is the real and k the imaginary part of the complex refractive index, and σ is the optical conductivity, which is proportional to ε_2 and to the absorption coefficient α with

$$n\alpha = 4\pi\sigma/c = (\omega/c)\varepsilon_2. \tag{5}$$

The classical Drude model may be used to extract the mobility and the free-carrier density n_e from an analysis of the reflection and the transmission data in the far infrared. The Drude model gives the complex dielectric constant in terms of a high-frequency lattice dielectric constant ε_∞, the plasma frequency $\bar{\omega}_p$, and the electron scattering time τ as

$$\varepsilon_1 = \varepsilon_\infty[1 - (\bar{\omega}_p^2/\omega^2\eta)] \tag{6}$$

$$\varepsilon_2 = (\omega_p^2/\omega^2\eta)(1/\omega\tau), \tag{7}$$

where

$$\eta = 1 + (1/\omega^2\tau^2) \rightarrow 1, \qquad \omega\tau \gg 1 \tag{8}$$

$$\omega_p^2 = 4\pi n_e e^2/m_n \tag{9}$$

$$\bar{\omega}_p^2 = \omega_p^2/\varepsilon_\infty. \tag{10}$$

The real and imaginary parts of the complex refractive index are obtained from ε_1 and ε_2 as follows:

$$\varepsilon = (\varepsilon_1^2 + \varepsilon_2^2)^{1/2} = n^2 + k^2 \tag{11}$$

$$n = [(\varepsilon + \varepsilon_1)/2]^{1/2} \tag{12}$$

$$k = \varepsilon_2/2n = [(\varepsilon - \varepsilon_1)/2]^{1/2}. \tag{13}$$

The experimental determination of n and k involves measuring the reflectivity of a bulk, opaque sample and the transmittance of a slab from which values of n and k can be obtained.

The absorption of radiation by free carriers is represented by ε_2 or α, and is a function of the plasma frequency and the electron scattering rate $1/\tau$ for an n-type material. The high-frequency lattice dielectric constant arises from the interaction of the radiation field with the bound electrons. It is

assumed, in writing Eqs. 6 and 7, that the photon energy is small compared with the band gap energy, G, of the semiconductor. This is the condition for the validity of the quasi-classical Boltzmann transport equation, or Drude theory, in terms of the frequency-independent electron scattering rate $1/\tau$. It is expected that deviations from the quasi-classical Boltzmann equation should occur when photon energies become large compared with electron energies. The latter are of the order of k_0T or e_f for nondegenerate or degenerate materials, respectively, where e_f is the electron Fermi energy measured relative to the conduction-band edge. In particular, quantum effects may be expected to occur when the photon energy is of the order of the band-gap energy in materials such as InP and GaAs. In this case, a generalized Boltzmann equation is obtained, which reduces to the quasi-classical Boltzmann transport equation when the wave vector of the driving field tends to zero and ω is small [1–4]. When ω is large, a solution of the Boltzmann equation in terms of a frequency-dependent relaxation time is obtained under certain conditions [1, 4]. This relaxation rate has been tabulated as a function of frequency and carrier concentration for various materials, [5–7], and can be used in the usual expressions of the classical Drude theory in Eq. 7 to obtain the quantum result for k from Eq. 13 as

$$k = \varepsilon_2/2n = (1/2n)(\omega_p^2/\omega^2)(1/\omega\tau), \qquad \omega\tau \gg 1. \tag{14}$$

This problem has been discussed in some detail for the imaginary part of the complex dielectric constant, or the absorption coefficient, to which it is proportional. In the case of k or ε_2, the quantum effects are notable. The low-frequency limit of the result for τ gives a good estimate for the dc electron mobility when used to calculate this quantity from the usual formula; at high frequencies, it predicts the change in wavelength dependence observed in k or the absorption coefficient α when used in Eq. 14. The exact wavelength dependence of the observed high-frequency absorption coefficient depends on the dominant scattering mechanism, which is polar-optical-mode scattering at low carrier concentrations, or charged-impurity (ionic) scattering in highly doped materials [6, 8].

One also expects quantum effects to occur in the real part of the dielectric constant near the fundamental absorption edge. When the imaginary part of the complex refractive index, that is, the extinction coefficient k, is small, a change in ε_1 is essentially a change in n^2, and hence, a change in the real part of the refractive index. Although this change is small, and less dramatic than the change in k, it is of technological importance, and its study provides insight into how to effect variations in n in this important spectral region, which is also the region of operation of a double-heterostructure, semiconductor diode laser. It is this subject to which this chapter is addressed. We will outline the calculation of $\varepsilon_1 \cong n^2$

for $\hbar\omega \leqslant G$ and identify the parameter ε_∞ in the Drude theory with the value of ε_1 at $\hbar\omega = G$, when the carrier concentration and hence the plasma frequency are zero.*

The usual method of calculation of ε_1 near the band edge involves the calculation of ε_2 due to direct interband transitions and subsequent integration of this result to obtain ε_1 via the Kramers–Kronig relations [9]. Here, ε_1 is determined directly by calculating the interaction energy of the lattice polarization due to valence electrons and the radiation field. One obtains from this the real part of the susceptibility, which is then related to ε_1 and hence to n.

II THE QUANTUM-DENSITY-MATRIX FORMULATION OF THE COMPLEX DIELECTRIC CONSTANT

We consider a system consisting of a number of dynamically independent electrons, a scattering system taken to be optical- or acoustical-mode phonons or charged impurities, and an equilibrium radiation field. A perturbing field is then applied. The system is described by a quantum density matrix R with the equation of motion [4, 10]

$$\begin{aligned} i\hbar\dot{p} = i\hbar sp = [H, R] \\ R = R^o + p, \end{aligned} \tag{15}$$

where R^o is the equilibrium density matrix, and p is the deviation from equilibrium. The total Hamiltonian of the system, denoted by H, is given by

$$H = H^o + H^i \tag{16}$$

$$H^o = H^e(n) + H^s(\nu) + H^r(\gamma), \tag{17}$$

where H^o is the sum of the Hamiltonians of the noninteracting subsystems consisting of electrons (n), phonons (ν), and photons (γ). The interaction between subsystems is specified by

$$H^i = H' + H^{er}, \tag{18}$$

* The calculation of n for $\hbar\omega \geqslant G$ is treated in a forthcoming publication; B. Jensen, W. D. Jensen, *IEEE J. Quant. Electron.*, in press.

where H' is the scattering interaction of the electrons with the phonon field, and H^{er} is the interaction of the electrons with the radiation field:

$$H^{er} = -(e/mc)\mathbf{A} \cdot \mathbf{P}. \tag{19}$$

The form of H' depends on the scattering mechanism. Various cases are given in Refs. [4] and [8].

In the occupation-number representation, H^o is diagonal and the eigenstate $|N\rangle$ of H^o is the product of the eigenstates of H^e, H^s, and H',

$$|N\rangle = |n\rangle|\nu\rangle|\gamma\rangle. \tag{20}$$

The coulomb gauge is used, which implies that the vector potential of the radiation field $\mathbf{A}$ and the electric field $\mathbf{E}$ are related as follows:

$$\mathbf{E} = -(1/c)\dot{\mathbf{A}}. \tag{21}$$

We let q denote the wave vector of the applied radiation field.

In Eq. 19, $\mathbf{P}$ denotes the momentum operator for the electron system. In the occupation-number representation, H_q^{er} has no diagonal elements,

$$H_{N'N}^{cr} = \langle N'|H_q^{cr}|N\rangle = \begin{cases} 0 & |N\rangle = |N'\rangle \\ H_{N'N}^{cr} & |N\rangle \neq |N'\rangle. \end{cases} \tag{22}$$

The derivation of the perturbation energy $\langle \delta H_q \rangle$, arising from the interaction of the electron–photon system, is given in Ref. [10]. The perturbation energy is proportional to the real part of the susceptibility χ_1 and is found on taking the trace of p_N and $E_N^{(2)}$:

$$E_N^{(2)} = \sum_{N'} \frac{H_{NN'}^{cr} H_{N'N}^{er}}{E_N - E_{N'}}, \qquad p_N = (N|p|N) = 2F_N \tag{23}$$

$$\langle \delta H_q \rangle = \sum_N p_N E_N^{(2)} = \chi_1 \langle E_q^2 \rangle, \tag{24}$$

where p is found from the solution of Eq. 15. In the derivation, the Bloch

functions of the electrons in the crystal lattice are taken to be

$$|k\rangle = |n, k, s\rangle = e^{i\mathbf{k}\cdot\mathbf{r}} U_{nks}, \tag{25}$$

where k denotes the electron wave vector, s the spin index, and n the band index. These wave functions and the corresponding electron energies are given by the Kane theory [11], and are useful in calculating a number of properties of electrons in compound semiconductors [12, 13, 8].

The real part of the susceptibility is the ratio of the perturbation energy $\langle \delta H_q \rangle$ to $\langle E_q^2 \rangle$, and the real part of the complex dielectric constant is obtained as $\varepsilon_1 = 1 + 4\pi\chi_1$ [10, 14]:

$$\varepsilon_1 = 1 + (4\pi e^2/\omega^2) \sum_{v_i, k} \hat{\mathbf{e}} \cdot \mathbf{V}_{v_i, k; c, k+q} \mathbf{V}_{c, k+q; v_i, k} \cdot \hat{\mathbf{e}} \frac{(f^0_{v_i, k} - f^0_{c, k+q})}{E_{c, k+q} - E_{v_i, k} - \hbar\omega}, \tag{26}$$

where $\hat{\mathbf{e}}$ is the photon polarization vector and

$$\mathbf{V}_{c, k+q; v_i k} = (1/m)\langle c, k+q, s' | \mathbf{p} | v_i, k, s \rangle \tag{27}$$

is the matrix element of the single-electron momentum operator $\mathbf{p}$ between states $|v_i, k, s\rangle$ in the ith valence band and $|c, k+q, s'\rangle$ in the conduction band, and is calculated using the band structure of the Kane theory. In Eq. 26, q denotes the wave vector of the photon, which is negligible for vertical transitions in k space, and hence is neglected. The energies $E_{c,k}$ and $E_{v_i,k}$ are the positive energy of an electron in the conduction band with wave vector k and the negative energy of an electron in band v_i with the same wave vector. The sum over valence bands v_i, $i = 1, 2, 3$ is taken over the heavy-hole band, the light-hole band, and the spin-orbit split-off valence band. The quantities $f^0_{c,k}$ and $f^0_{v_i,k}$ are the occupation probabilities for electrons in states $|c, k, s'\rangle$ and $|v_i, k, s\rangle$, respectively. We now consider unpolarized radiation and cubic crystals.

Using the results of Ref. [8], Table 1, one can show that the following result is obtained on summing over final and averaging over initial electron spins,

$$\frac{1}{2} \sum_{ss'} |\langle v_i, k, s | \mathbf{p} | c, k, s' \rangle|^2 \Big|_{k=0} = m^2 \mathcal{P}^2/\hbar^2 \tag{28}$$

for $i = 1, 2, 3$, where G is the direct-band-gap energy, m_n is the effective

electron mass and

$$\frac{m^2\mathcal{P}^2}{\hbar^2} = (3/2)m^2(G/2m_n)\frac{(1+r)}{(\frac{3}{2}+r)}. \tag{29}$$

Defining

$$\bar{\eta} = \frac{1}{2}\frac{(1+r)}{(\frac{3}{2}+r)} \rightarrow \begin{cases} 1/3, & r \rightarrow 0 \\ 1/2, & r \rightarrow \infty, \end{cases} \tag{30}$$

where r is the ratio of the spin-orbit-splitting energy to the direct-band-gap energy, one has for the angle average in a cubic crystal

$$(1/3m^2)\left[\frac{1}{2}\sum_{ss'}|\langle v_i, k, s'|\mathbf{p}|c, k, s\rangle|^2\right]\Bigg|_{k=0} = \bar{\eta}(G/2m_n). \tag{31}$$

We use the fact that the term

$$(f^0_{v_i,k} - f^0_{c,k})/(E_{c,k} - E_{v_i,k} - \hbar\omega) \tag{32}$$

falls off rapidly with k to evaluate the coefficient of this term in Eq. 26 at $k=0$, as in Eq. 31, and remove it from the integration over k space. We consider the case of arbitrary spin-orbit splitting and define

$$r = \Delta/G \tag{33}$$

$$X = \hbar\omega/G \tag{34}$$

$$1/m_{r_i} = (1/m_n) + (1/m_{p_i}), \qquad i = 1, 2, 3 \tag{35}$$

$$\lambda^2_{r_i} = \hbar^2/2m_{r_i}G. \tag{36}$$

Summing over photon polarizations, Eq. 26 may then be written

$$\varepsilon_1 = 1 + \frac{(4\pi e^2/m_n)}{\omega^2}\bar{\eta}\sum_{\substack{v_i,k \\ i=1,2,3}}\frac{(f^0_{v_i,k} - f^0_{c,k})}{(1 + r\delta_{i3} - X) + \lambda^2_{r_i}k^2}. \tag{37}$$

In Eq. 35, m_n and m_{p_i} are the effective electron mass in the conduction band and the effective hole mass at the band edge of the ith valence band, and m_{r_i} is the corresponding reduced mass. The quantity δ_{i3} is the Kroneker delta. To recover the Drude theory from Eq. 37, neglect the term $\hat{\lambda}_{ri}^2 k^2$ in the denominator of the summation over k, the sum over v_2, and v_3, and set $r=0$, $X \ll 1$, and $\bar{\eta}=1$. On defining

$$\varepsilon_\infty = 1 + \frac{4\pi e^2/m_n}{\omega^2} \sum_k f^0_{v_1,k}$$

$$n_e = \sum_k f^0_{c,k},$$

one recovers Eq. 6 as

$$\varepsilon_1 = \varepsilon_\infty - [\omega_p^2/\omega^2] = \varepsilon_\infty[1 - (\bar{\omega}_p^2/\omega^2)], \qquad \frac{1}{\tau} \ll \omega \ll \frac{G}{\hbar},$$

which gives the Drude-theory result. We note that ε_∞ is the value of ε_1 obtained when there are no electrons in the conduction band and $f^0_{c,k}=0$.

Returning to the evaluation of Eq. 37 and defining

$$\begin{aligned} z_i &= (1 + r\delta_{ik} - X)^{1/2} \\ z &= (1-X)^{1/2}, \end{aligned} \tag{38}$$

and converting from summation to integration in the usual fashion, one has

$$\varepsilon_1 = 1 + \frac{4\pi e^2}{m_n \omega^2} \bar{\eta} \frac{8\pi}{(2\pi)^3} \sum_{i=1}^{3} \int_0^{k_B} \frac{k^2\, dk}{z_i^2 + \hat{\lambda}_{r_i}^2 k^2} [f^0_{v_i,k} - f^0_{c,k}]. \tag{39}$$

We define the following quantities:

$$N_v^* = 1/3\pi^2 \hat{\lambda}_{r_1}^3 \tag{40}$$

$$e^*_{v_i,k} = \frac{\hbar^2 k^2}{2m_{p_i}} + rG\delta_{i3} \tag{41}$$

$$e_{c,k} \cong \hbar^2 k^2 / 2m_n \tag{42}$$

$$f^0_{c,k} = 1/[e^{\beta(e_{c,k}+G/2-E_F)}+1], \qquad \beta = 1/k_0T \tag{43}$$

$$f^0_{v_i,k} = 1/[e^{-\beta(e^*_{v_i,k}+G/2+E_F)}+1]. \tag{44}$$

In Eqs. 43 and 44, E_F is the Fermi energy, measured relative to the center of the band gap, and $e_{c,k}$ and $e^*_{v_i,k}$ are the absolute values of the electron energy measured relative to the conduction-band edge, and the hole in the ith valence band measured relative to the edge of the valence band v_1, (that is, the heavy-hole band). The (negative) energy of the electron in the ith valence band, measured relative to the center of the band gap, is $E_{v_i,k}$ in Eq. 26.

Expanding ω to lowest order around $\omega_g = G/\hbar$ in the coefficient of the integral and defining a new variable of integration $y = \lambda_{r_i} k$, Eq. 39 can be written

$$\varepsilon_1 = 1 + \frac{[4\pi N^*_v e^2]}{m_n \omega_g^2}(3\bar{\eta}) \sum_{i=1}^{3} \frac{[1+(m_n/m_{p_1})]^{3/2}}{[1+(m_n/m_{p_i})]^{3/2}} \times \int_0^{y_B} \frac{y^2\,dy}{z_i^2+y^2}[f^0_{v_i,k} - f^0_{c,k}] \tag{45}$$

To proceed further, one must specify the type of material (n-type or p-type), which then specifies the E_F in Eqs. 43 and 44. Treating a degenerate semiconductor as a poor metal, we consider several cases in the limit $T \to 0$. The lower limit of the integrand in Eq. 45 is then determined by E_F, and hence, by the type and carrier concentration of the material. For n-type materials, this dependence is due to the exclusion principle. The dielectric constant decreases from that of the pure material as free electrons are added and fewer conduction-band states are available for virtual transitions. The upper limit y_B of the integrand is a function of the lattice constant, and its determination will be discussed.

Case 1: Degenerate n-Type Material

$$E_F = G/2 + e_F, \qquad e_F \gg k_o T \to 0,$$

$$f^0_{v_i,k} \cong 1$$

$$f^0_{c,k} \cong \begin{cases} 1, & e_{c,k} \le e_F, \quad y \le y_F \\ 0, & e_{c,k} > e_F, \quad y > y_F. \end{cases}$$

$$\varepsilon_1 = 1 + [4\pi N^*_v e^2/m_n\omega_g^2](3\bar{\eta}) \sum_{i=1}^{3} \left[\frac{(1+(m_n/m_{p_1})}{(1+(m_n/m_{p_i})}\right]^{3/2} \times [(y_B - y_F) - z_i(\tan^{-1}(y_B/z_i) - \tan^{-1}(y_F/z_i))]. \tag{46}$$

In the limit of small spin-orbit splitting, $r \ll 1$, $z_i = z$, and Eq. 46 assumes the simple form

$$\varepsilon_1 = 1 + 2C_o[(y_B - y_F) - z \tan^{-1}(y_B/z) - \tan^{-1}(y_F/z))], \tag{47}$$

where

$$C_o = (3/2)\eta(\omega_v^2/\omega_g^2) \tag{48}$$

$$\omega_v^2 = 4\pi N_v^* e^2/m_n \tag{49}$$

$$\eta = \bar{\eta} S \tag{50}$$

$$S = \sum_{i=1}^{3} [(1 + (m_n/m_{p_1}))/(1 + (m_n/m_{p_i}))]^{3/2}. \tag{51}$$

In practice, $m_{p_1} > m_{p_2}, m_{p_3}$ and hence, S lies between the limits of one for $m_{p_2} \ll m_n \ll m_{p_1}$, $m_{p_3} \ll m_n \ll m_{p_1}$, and three for $m_{p_2} = m_{p_1}$, $m_{p_3} = m_{p_1}$.

The quantity y_F is related to the Fermi level of the n-type material and hence to the carrier concentration n_e. Because $m_n \ll m_{p_1}$, y_F is determined mainly by the electron Fermi level. For high carrier concentrations, we also note that the dispersion relation of the conduction band becomes hyperbolic at large values of k [8]. We therefore define $y_F = \lambda\!\!\!^{-}_c k_F$, where k_F is the electron wave vector at the Fermi surface and

$$\lambda\!\!\!^{-}_c = \hbar/m_n \alpha_o c \tag{52}$$

$$\alpha_o = (G/2m_n c^2)^{1/2} \tag{53}$$

$$N_v = (8/3\pi^2 \lambda\!\!\!^{-3}_c). \tag{54}$$

One then has, for the relation between y_F and the carrier concentration n_e,

$$y_F = 2(n_e/N_v)^{1/3}, \quad \text{high carrier concentrations.} \tag{55}$$

At low carrier concentrations, a parabolic dispersion relation can be used to give the relation between y_F and n_e as $y_F = (1/2)(m_n/m_{r_1})^{1/2} \lambda\!\!\!^{-}_c k_F$, where $k_F = (3\pi^2 n_e)^{1/3}$.

Case 2: Degenerate p-Type Material:

$$E_F = -G/2 - e_F, \quad e_F \gg k_0 T \to 0.$$

In this case, the second term in brackets in the integrand of Eq. 45 may be neglected, while the first term in brackets may be written

$$f^0_{v,k} = 1 - f^0_{v,k}(p) = 1 - [1/(e^{\beta(e^*_{v,k} - e_F)} + 1)], \tag{56}$$

where $f^0_{v,k}(p)$ is the hole occupation probability for a hole in the valence band v. We consider the case of $m_{p_1} \gg m_{p_2}$, $m_{p_3} \to 0$, so that only the heavy-hole valence band contributes in Eq. 45. Under the conditions of case 2, $f^0_{v,k}(p)$ is approximately unity for $e^*_{v,k} < e_F$ and negligible for $e^*_{v,k} > e_F$. Therefore, defining $y_F = \hat{\lambda}_{r_1} k_F$, where k_F is the wave vector at the Fermi surface and the Fermi level lies inside the valence band, and where p is the hole concentration in the heavy-hole valence band, one has

$$\begin{aligned} k_F &= (3\pi^2 p)^{1/3} \\ \hat{\lambda}^2_{r_1} &= \hbar^2/2m_{r_1} G \\ y_F &= \hat{\lambda}_{r_1} k_F. \end{aligned} \tag{57}$$

Hence, Eqs. 47–50 apply to p-type materials with S replaced by 1 and with y_F given by Eq. 57.

Case 3: Inversion

In the case of inversion, we express the electron- and hole-occupation probabilities in terms of the electron quasi-Fermi level μ_e and the hole quasi-Fermi level μ_h. We again consider that $m_{p_1} \gg m_{p_2}$, $m_{p_3} \to 0$, so that only the heavy-hole band contributes. In the limit $T \to 0$, one has

$$f^0_{c,k} = \frac{1}{e^{\beta(e_{c,k} - \mu_e)} + 1} = \begin{cases} 1, & e_{c,k} \le \mu_e \\ 0, & e_{c,k} > \mu_e \end{cases} \tag{58}$$

$$f^0_{v_1,k} = 1 - \frac{1}{e^{\beta(e^*_{v_1,k} - \mu_h)} + 1} = \begin{cases} 0, & e^*_{v_1,k} \le \mu_h \\ 1, & e^*_{v_1,k} > \mu_h \end{cases}. \tag{59}$$

Using Eqs. 58 and 59 in Eq. 45, one obtains

$$\varepsilon_1 \cong n^2 = 1 + (\omega_v^2/\omega_g^2)(3\bar{\eta})[[y_B - y_F(p) - y_F(n_e)] - z[\tan^{-1}(y_B/z) - \tan^{-1}(y_F(p)/z) - \tan^{-1}(y_F(n_e)/z)]], \quad (60)$$

where $y_F(n_e)$ and $y_F(p)$ are the quantities defined for n-type and p-type materials, respectively. In the case of an undoped material, the requirement $n_e = p$ implies $y_F(n_e) = y_F(p)$ if the parabolic dispersion relation, Eq. 57, is used for both types of material. If Eq. 55 is used for $y_F(n)$ and Eq. 57 for $y_F(p)$, the requirement $n_e = p$ implies

$$y_F(p) = \tfrac{1}{2}(m_n/m_{r_1})^{1/2} y_F(n_e). \quad (61)$$

The quantity y_B in Eq. 47 is a function of the lattice constant a, and can be expanded as a Taylor series in a (for a cubic crystal) as

$$y_B(a) = y_B(a_0) + \left.\frac{dy_B}{da}\right|_{a=a_o} (a - a_o) + \frac{1}{2!}\left.\frac{d^2 y_B}{d^2 a}\right|_{a=a_o} (a - a_o)^2 + \ldots \quad (62)$$

Comparison with experimental results on a given series of compounds, such as III-V or II-IV materials, indicates that only the linear term is significant, and y_B can be written to a good approximation as

$$y_B = M(a_o - a) \quad (63)$$

$$M = \begin{cases} 3.04 \pm 0.08\ \text{Å}^{-1}, & \text{III-V compounds} \\ 0.346 \pm 0.020\ \text{Å}^{-1}, & \text{II-VI compounds} \end{cases} \quad (64)$$

$$a_o = \begin{cases} 7.49 \pm 0.04\ \text{Å}, & \text{III-V compounds} \\ 17.37 \pm 0.88\ \text{Å}, & \text{II-VI compounds.} \end{cases} \quad (65)$$

We note that y_B is related to the linear coefficient of thermal expansion as follows:

$$\frac{dy_B}{dT} = -M\frac{da}{dT} = -Ma\alpha_T \quad (66)$$

$\alpha_T = (1/a)\, da/dT =$ linear thermal coefficient of expansion.

The thermo-optic coefficient dn/dT, which can be obtained from Eq. 46 or 47 when $\varepsilon_1 \cong n^2$, is important in the design of optical components [14].

If higher conduction bands, which have not been considered here, make a contribution to n at $\hbar\omega \cong G$, they may be shown to appear as a contribution to the constant term in Eq. 63. It is necessary to consider higher-conduction-band contributions explicitly in order to calculate n for $\hbar\omega > G$, where the approximation $\varepsilon_1 = n^2$ no longer holds, because the imaginary part of the refractive index is not negligible.*

Two useful limiting cases of n^2 will now be obtained from Eq. 46 and used for comparison of theoretical and experimental results in the following section. In the limit that $m_{p_1} \gg m_{p_2}$, $m_{p_3} \to 0$, the contribution of the light-hole band and the split-off band are negligible, and one obtains from Eq. 46

$$n^2(z, y_F) = 1 + 2C_o[(y_B - y_F) - z \times (\tan^{-1}(y_B/z) - \tan^{-1}(y_F/z))] \tag{67}$$

$$C_o = (3/2)\bar{\eta}[\omega_v^2/\omega_g^2] \to (1/2)[\omega_v^2/\omega_g^2],$$

$r \to 0$ small spin-orbit-splitting limit.

If the spin-orbit splitting is small compared with G, so that $z_3 \cong z$, but m_{p_2} and m_{p_3} are not small enough so that the contributions of bands v_2 and v_3 can be neglected, one has, from Eq. 46,

$$n^2(z, y_F) = 1 + 2C_o[(y_B - y_F) - z(\tan^{-1}(y_B/z) - \tan^{-1}(y_F/z))] \tag{68}$$

$$C_o = (3/2)\bar{\eta}[\omega_v^2/\omega_g^2]S < (3^2/2)\bar{\eta}[\omega_v^2/\omega_g^2] = C_{o_{max}}.$$

An upper bound on $C_{0_{max}}$ is obtained by setting $\bar{\eta} = 1/2$. Hence, one can say

$$(1/2)[\omega_v^2/\omega_g^2] \leq C_o < (3/2)^2[\omega_v^2/\omega_g^2]. \tag{69}$$

The exact expression for n^2 may be obtained from Eq. 46 as

$$n^2(z, y_F) = 1 + (3\bar{\eta})[\omega_v^2/\omega_g^2] \sum_i S_i \left[(y_B - y_F) - z_i \left[\tan^{-1}\frac{y_B}{z_i} - \tan^{-1}\frac{y_F}{z_i} \right] \right], \tag{70}$$

* See footnote page 128. The refractive index is continuous at $\hbar\omega = G$, but changes its functional form for $\hbar\omega > G$.

where

$$S_i = [(1 + (m_n/m_{p_1}))/(1 + (m_n/m_{p_i}))]^{3/2}. \tag{71}$$

The refractive index is therefore a function of measurable material parameters only. These are the band-gap energy G, the effective electron mass m_n, the effective hole masses m_{p_i}, the lattice constant a (Å), and the spin-orbit-splitting energy Δ. In the limit that $m_{p_1} \gg m_{p_2}$, $m_{p_3} \to 0$, these reduce to five material parameters: G, m_n, m_{p_1}, a, and Δ.

III COMPARISON WITH EXPERIMENTAL RESULTS

The result calculated for n in the previous section will now be applied to the ternary III-V compound $Al_xGa_{1-x}As$, the quaternary III-V compound $In_{1-x}Ga_xAs_yP_{1-y}$ lattice matched to InP (which requires that $x = 0.466\,y$), and the ternary II-VI compound $Hg_xCd_{1-x}Te$. Formulas specific to each compound and room-temperature values of band-structure parameters will be given, so that n may be calculated for any value of x.

Case 1: $In_{1-x}Ga_xAs_yP_{1-y}$ (lattice matched, $x = 0.466\,y$) [15]

The calculation of n for this compound requires an accurate expression relating the experimental parameters to the mole fraction x of Ga and the mole fraction y of As. The experimental parameters are the band-gap energy G, the electron and heavy-hole effective mass, the lattice constant a, and the spin-orbit splittir⁻, or equivalently η. In the limit that $m_{p_1} > m_{p_2}$, m_{p_3} and $r \ll 1$, one has $z_i \cong z$, $i = 1, 2, 3$ and Eq. 46 becomes

$$n^2 = 1 + 2C_o[(y_B - y_F) - z(\tan^{-1}(y_B/z) - \tan^{-1}(y_F/z))] \tag{72}$$

$$2C_o = [\omega_v^2/\omega_g^2](3\eta), \qquad \eta = \bar{\eta}S \tag{73}$$

$$z = [1 - (\hbar\omega/G)]^{1/2}. \tag{74}$$

Table I lists the values of y_B, G, C_o, and lattice constant a as a function of y, with $x = 0.466y$. The values of C_o have been calculated using the following expressions for G, m_n, and m_p (where $m_p = m_{p_1}$):

$$G(\text{eV}) = 1.35 - 0.72y + 0.12y^2 \quad \text{(Ref. [16])} \tag{75}$$

TABLE I

The Numerical Values of G (eV), C_0, a (Å), and y_B as a Function of y for $In_{1-x}Ga_xAs_yP_{1-y}$ with $x = 0.466y$ (Lattice Matched to InP)

y	G (eV)	a (Å)	C_0	y_B
0.0	1.350	5.86960	1.113	4.9246
0.1	1.279	5.86910	1.143	4.9261
0.2	1.211	5.86872	1.171	4.9273
0.3	1.145	5.86847	1.199	4.9280
0.4	1.081	5.86834	1.224	4.9284
0.5	1.020	5.86832	1.247	4.9285
0.6	0.961	5.86843	1.270	4.9282
0.7	0.905	5.86866	1.289	4.9275
0.8	0.851	5.86901	1.306	4.9264
0.9	0.799	5.86949	1.320	4.9249
1.0	0.750	5.87008	1.330	4.9231

$$m_n = xym_n(\text{GaAs}) + x(1-y)m_n(\text{GaP}) + y(1-x)m_n(\text{InAs}) + (1-x)(1-y)m_n(\text{InP}) \tag{76}$$

$$m_p = xym_p(\text{GaAs}) + x(1-y)m_p(\text{GaP}) + y(1-x)m_p(\text{InAs}) + (1-x)(1-y)m_p(\text{InP}). \tag{77}$$

The values of m_n and m_p that have been used for GaAs, GaP, InP, and InAs are listed in Table II.

Figure 1 shows the refractive index of $In_{1-x}Ga_xAs_yP_{1-y}$ as a function of photon energy and mole fraction y, assuming that $x = 0.466y$. The numerical values of Table I have been used. The refractive index increases as y

TABLE II

Values of m_n/m and m_p/m

Material	m_n/m	m_p/m
GaAs	0.07	0.5
GaP	0.13	0.8
InP	0.07	0.4
InAs	0.028	0.33

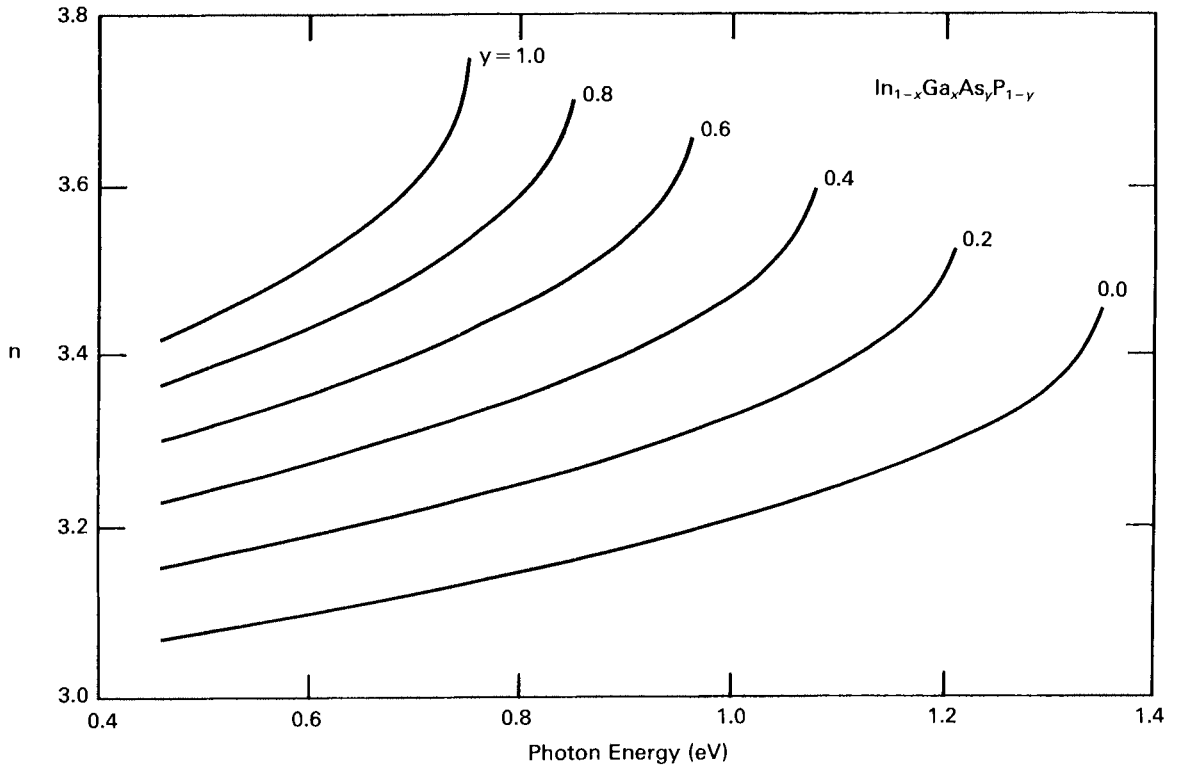

Fig. 1. Theoretical values of the refractive index n for the quaternary compound $In_{1-x}Ga_xAs_yP_{1-y}$ as a function of photon energy (eV) and y increments of 0.2. We assume the sample to be intrinsic with no carrier concentration. The requirement of lattice matching to InP implies $x = 0.466y$.

increases, due mainly to the dependence of G on y in Eq. 75. This behavior has been verified experimentally. Figure 2 compares theory and experiment [17].

Case 2: $Al_xGa_{1-x}As$ [18]

In the ternary III-V compound $Al_xGa_{1-x}As$, the AlAs concentration can be changed continuously, thus changing the refractive index without substantially altering the lattice constant. $Al_xGa_{1-x}As$ has a refractive index less than that of GaAs for x greater than zero at all wavelengths [19]. Hence, it is possible to design waveguides on $Al_xGa_{1-x}As$ substrates by varying the parameter x.

Using the limit of n^2 in Eq. 67 or Eq. 68, one requires values of G, m_n, and $m_{p_l} = m_p$ as functions of x. Various expressions given in the literature are as follows.

$$\begin{aligned} G(\text{eV}) &= 1.424 + 1.247x \text{ [20]} \\ &\quad 1.435 + 1.209x + 0.386x^2 \text{ [21]} \\ &\quad 1.424 + 1.59x + x(1-x)(0.127 - 1.310x) \text{ [22]} \end{aligned} \tag{78}$$

$$\begin{aligned} m_p/m &= 0.48 + 0.81x \text{ [20]} \\ &\quad 0.45 + 0.302x \text{ [23]} \end{aligned} \tag{79}$$

$$\begin{aligned} m_n/m &= 0.067 + 0.083x \text{ [20]} \\ &\quad 0.0775 + 0.0830x \text{ [23]}. \end{aligned} \tag{80}$$

Values of G, m_n/m, and m_p/m calculated from Eqs. 78–80 are used to calculate C_0, y_B, and the index of refraction of a pure material $n(0, 0)$ at $\hbar\omega = G$ in Table III, where

$$n(z, y_F)\Big|_{\substack{z=0 \\ y_F=0}} = n(0, 0) = [1 + 2C_o y_B]^{1/2}. \tag{81}$$

Since y_B, which depends on the lattice constant, and C_o remain approximately constant as x is varied, $n(0, 0)$ is also slowly varying. Theoretical and experimental values of n versus $\hbar\omega$ are given in Fig. 3 for various values of x.

Case 3: $Hg_{1-x}Cd_xTe$ [24]

The ternary II-VI compound $Hg_{1-x}Cd_xTe$ is of importance as a detector

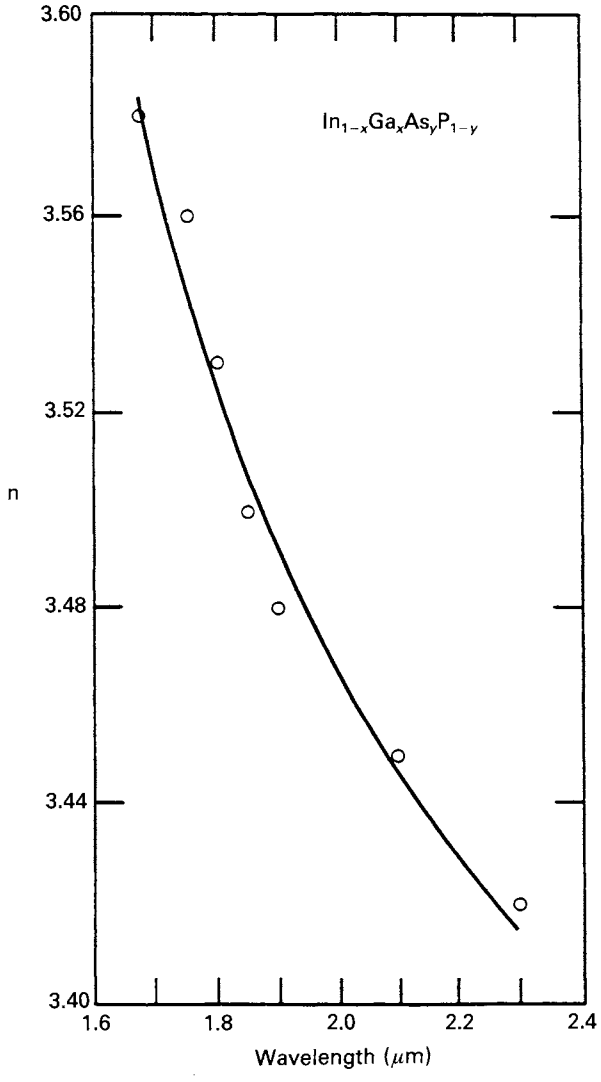

Fig. 2. Theoretical (solid lines) and experimental (open circles) values of the refractive index of $In_{1-x}Ga_xAs_yP_{1-y}$ versus wavelength (μm). The experimental results of Ref. [17] for the case of $y = 1.0$ and $x = 0.415$ have been used. The fit of data to the theoretical refractive index n gives the carrier concentration as $n_e = (1.26 \pm 0.60) \times 10^{17}$ (cm^{-3}).

TABLE III

Values of G (eV) Calculated for Direct Gap $Al_xGa_{1-x}As$ from Expressions Given in Refs. [19–22] and Calculated Results for C_o and y_B.

	G (eV)	C_o	y_B	$n(0,0)$
$x=0.07$	1.467 [19][a]	1.13	5.48	3.66
	1.511 [20]	1.11		3.63
	1.522 [21]	1.11		3.62
	1.538 [22]	1.10		3.61
$x=0.10$	1.533	1.12	5.54	3.66
	1.549	1.12		3.66
	1.560	1.12		3.66
	1.583	1.11		3.64
$x=0.15$	1.592	1.13	5.47	3.66
	1.611	1.12		3.64
	1.625	1.12		3.63
	1.654	1.11		3.62
$x=0.20$	1.650	1.13	5.44	3.65
	1.673	1.12		3.65
	1.692	1.11		3.62
	1.721	1.10		3.61
$x=0.24$	1.700	1.13	5.40	3.63
	1.723	1.12		3.62
	1.747	1.11		3.61
	1.772	1.10		3.60
$x=0.29$	1.788	1.13	5.41	3.64
	1.785	1.13		3.64
	1.818	1.12		3.62
	1.834	1.12		3.61

[a] Estimated from Fig. 1 of Ref. [19].

The index of refraction for a pure material is given by $n(0,0)=(1+2C_oy_B)^{1/2}=(\varepsilon_\infty)^{1/2}$, and ε_∞ is identified as the lattice dielectric constant in the Drude theory. Since y_B, which depends on the lattice constant, and C_o remain approximately constant as x is varied, n (0,0) is also slowly varying.

in infrared technology, since its band gap can be continuously varied from 0–1.5 eV by variation of the mole fraction x of cadmium. The calculation of the refractive index for II–VI compounds is discussed in Ref. [24]. One calculates the value for y_B as specified for II-VI compounds in Eqs. 63–65. Values of the lattice constants a(Å) and y_B as a function of x are given in Table IV for $Hg_{1-x}Cd_xTe$. The calculation also requires an accurate expression relating the band-gap energy G, and the effective electron and heavy-hole masses m_n and m_p to the mole fraction x of cadmium. The

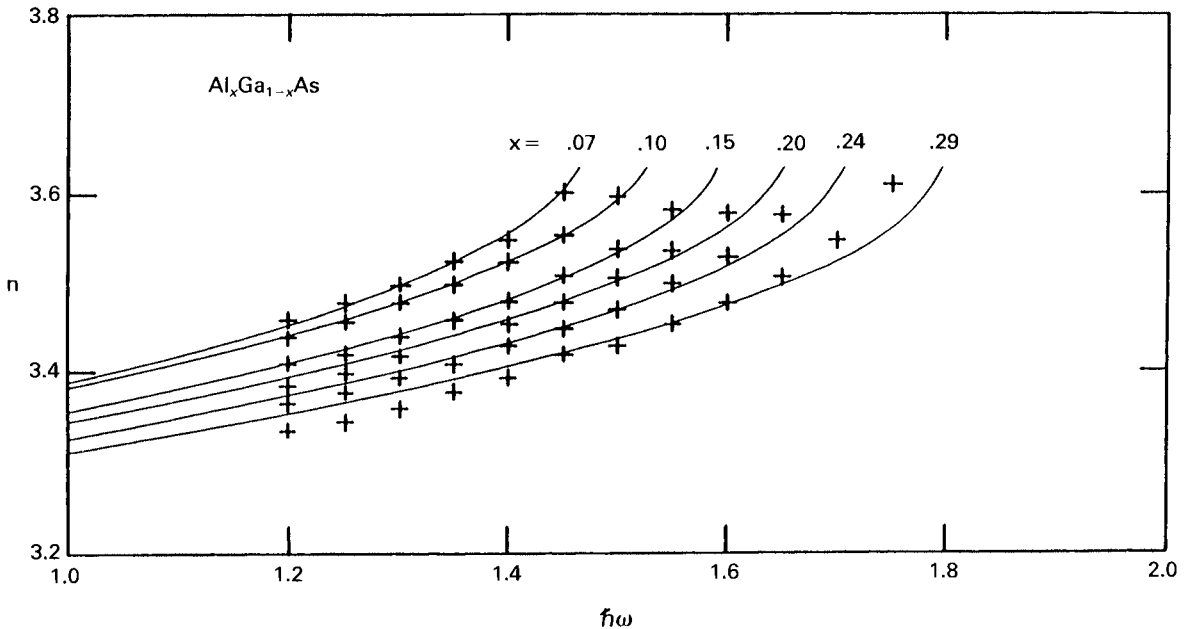

Fig. 3. Theoretical (————) and experimental (+ + + + + + +) values of the refractive index of $Al_xGa_{1-x}As$ versus photon energy. The band-gap energy of Ref. [21] given in Eq. 78 has been used, and a carrier concentration of $n_e = 10^{16}$ cm^{-3} has been assumed. Experimental results of Ref. [19] have been used. Agreement is best at smaller x. There is an experimental uncertainty in x of ± 0.02, and the best fit at higher x is obtained by choosing the smallest value for x consistent with the uncertainty involved. For example, one obtains a better fit of the curve marked $x = 0.29$ to the experimental data by taking $x = 0.27$ instead, which is still within the limits of the uncertainty involved in x. Other difficulties in the comparison of theoretical and experimental results are that no exact information on the carrier concentration of the experimental samples is given, and it has been reported that at a constant doping level, the carrier concentration varies as x is varied [36]. Also, the refractive index is a sensitive function of the dependence of G on x, and a precise determination of this dependence needs to be made, so that one may better choose from the various expressions given in the literature.

values of G, m_n, m_p, and C_o given in Table IV can be calculated as a function of x using the following expressions [25, 26].

$$G\,(\text{eV}) = 6.006 \times 10^{-4} T(1 - 1.89x) + 1.948x - 0.337 \text{ [25]} \tag{82}$$

$$G(x, T) = G(x, 0) + dG/dT|_x T$$

$$G(x, 0) = 1.948x - 0.337$$

$$dG/dT| = 6.006 \times 10^{-4}(1 - 1.89x)$$

TABLE IV

Values of Lattice Constants a (Å) and y_B as a Function of x for $Hg_{1-x}Cd_xTe$

x	a (Å)	y_B
0.35	6.464	3.7765
0.50	6.469	3.7748
0.65	6.473	3.7734
0.75	6.475	3.7727
0.85	6.477	3.7720

Values of y_F and C_o Using the Band Gap of Ref. [25] with $n_e = 1.0 \times 10^{17}$ cm^{-3}.

x	G (eV)	y_F	C_o
0.35	0.3581	0.391	1.942
0.50	0.5645	0.283	1.634
0.65	0.7906	0.209	1.439
0.75	0.9606	0.191	1.336
0.85	1.1518	0.167	1.245

Values of y_F and C_o Using the Band Gap Calculated from Eq. 82 with $n_e = 1.0 \times 10^{17}$ cm^{-3}.

x	G (eV)	y_F	C_o
0.35	0.4057	0.368	1.825
0.50	0.6469	0.264	1.526
0.65	0.8880	0.208	1.358
0.75	1.0487	0.183	1.279
0.85	1.2095	0.163	1.215

$$m_n/m = 0.11x + 0.029(1-x) \tag{83}$$

$$m_p/m = 0.35x + 0.3(1-x). \tag{84}$$

In Eq. 82, T is the temperature in degrees Kelvin. We assume the sample to be n-type with a carrier concentration of $n_e = 1.0 \times 10^{17}\,\mathrm{cm}^{-3}$. The quantities C_0 and y_F calculated using these expressions are given in Table IV.

Figure 4 shows the refractive index of $Hg_{1-x}Cd_xTe$ as a function of photon energy and different mole fractions x. The numerical values of Table IV and Eq. 82 have been used. The reduction of refractive index as one increases x is noticeable and is similar to that observed in the

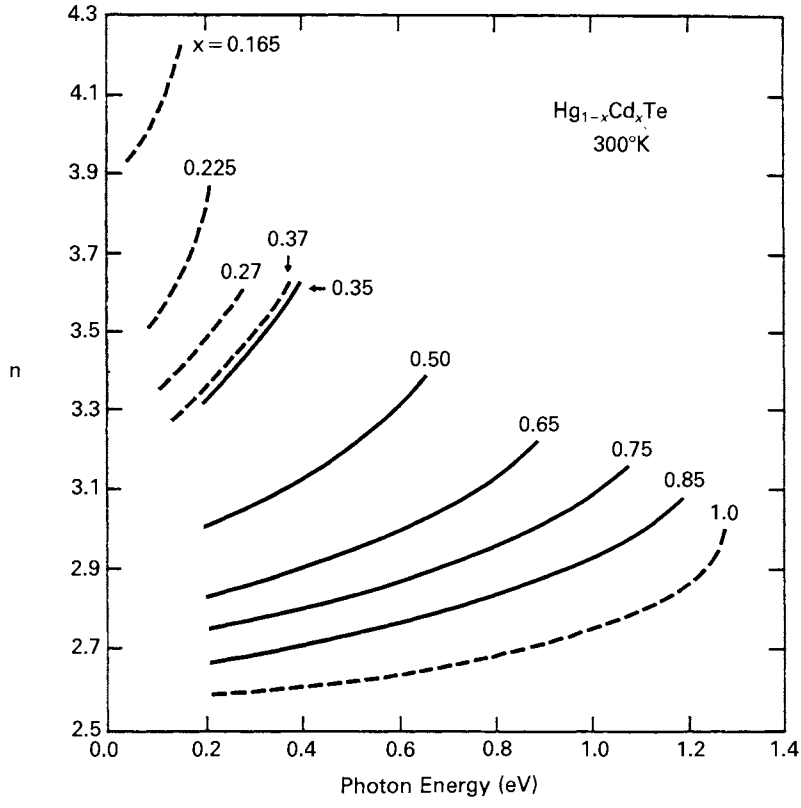

Fig. 4. Theoretical refractive index n (solid lines) along with the experimental refractive index (dashed lines) for the compound $Hg_{1-x}Cd_xTe$ as a function of photon energy (eV) and mole fraction x. The sample is assumed to be n-type with a carrier concentration of $n_e = 1.0 \times 10^{17}\,\mathrm{cm}^{-3}$ in the theoretical calculation. Results are taken from Ref. [24].

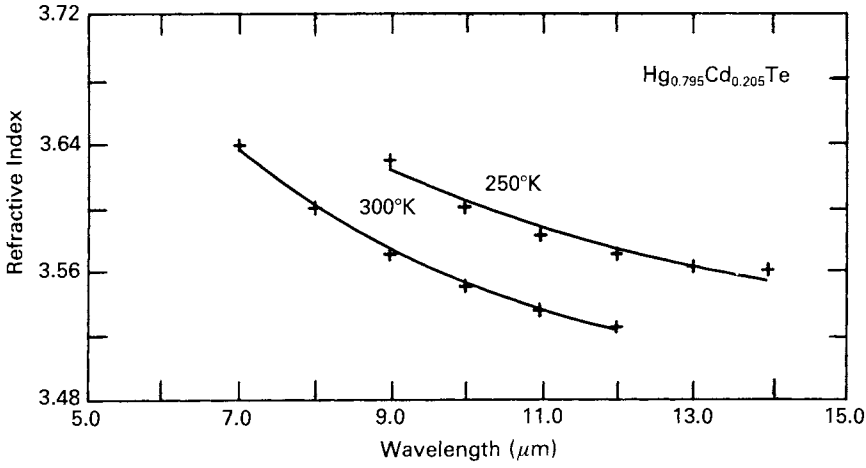

Fig. 5. Theoretical refractive index n (solid lines) and experimental refractive index [37] (crosses) as functions of temperature for $Hg_{0.795}Cd_{0.205}Te$. Numerical results are given and discussed in Ref. [24].

compound $Al_xGa_{1-x}As$, as one increases the Al mole fraction at frequencies just below the fundamental absorption edge [18, 19]. Numerical results for theoretical and experimental values of n are given in Ref. [24]. Theoretical and experimental values of n are given in Fig. 5 for a specific material $Hg_{0.795}Cd_{0.205}Te$ at two temperatures.

SUMMARY IV

The calculation of the real part of the complex refractive index from the quantum-density-matrix formulation of the complex dielectric constant has been outlined and the result given for the refractive index in terms of measurable material parameters only. These material parameters are the band-gap energy G, the effective electron mass m_n, the effective hole masses of the three valence bands m_{p_i}, $i=1, 2, 3$, the lattice constant a (Å), and the spin-orbit-splitting energy Δ. Under certain simplifying assumptions enumerated in the text, the number of material parameters can be reduced to G, m_n, $m_{p_1}=m_p$, a (Å), and Δ. The refractive index is also a function of frequency and of carrier concentration. The major contribution to the refractive index at $\hbar\omega=G$ arises from valence band electrons

making virtual transitions with intermediate states lying in the conduction band. When free carriers (electrons) are added, their role is considered as blocking possible intermediate states through the exclusion principle, and they would also block possible final states for direct transitions and hence shift the absorption edge (that is, the Burstein–Moss effect). The process of an electron *in* the conduction band absorbing and re-emitting a photon and the corresponding contribution to ε_1 is neglected for $\hbar\omega = G$, because it is a small contribution at these frequencies. The value of n^2 at $\hbar\omega = G$ for a pure material with no free carriers, denoted by $n^2(0, 0)$, is identified as the high-frequency lattice dielectric constant ε_∞ appearing in the Drude theory.

The result obtained for n has been applied to the III-V quaternary $In_{1-x}Ga_xAs_yP_{1-y}$ lattice matched to InP ($x = 0.466y$), the III-V ternary $Al_xGa_{1-x}As$, and the II-VI ternary compound $Hg_{1-x}Cd_xTe$. The necessary parameters for the calculation of the refractive index as a function of frequency, carrier concentration, and mole fraction x are given. Results are given for n in the literature for the II-VI compounds CdSe, CdS, and $CdSe_xS_{1-x}$ [27], ZnTe [28, 10], ZnSe [29, 10], CdTe [10], and $Cd_xZn_{1-x}Te$ [30]. Results are also given for the III-V compounds InP [28, 10], GaAs [10], and InSb [10]. The refractive index is calculated for the IV-VI binary compounds PbS, PbSe, and PbTe in Ref. [31], and for the IV-VI ternary compound $Pb_{1-x}Sn_xTe$ in Ref. [32]. The accuracy of the theoretical result calculated for n is limited by the accuracy with which G, m_n, m_p, a (Å), and Δ are known as functions of mole concentration x, by experimental uncertainty in the value of x itself, and by the fact that carrier concentration is often unknown or unspecified. It is hoped that future experimental work will improve matters in this respect. An analytical model for n for various materials in terms of experimental parameters is a useful result to have as an aid in the design of electro-optic devices and components, and in the fabrication of materials with desirable optical properties. In addition, one gains insight into the physical mechanism of how the variation of the carrier concentration affects the variation in the refractive index, which is a topic of considerable interest [33]. An extension of the above theory to two-dimensional, quantum-well structures, and a study of carrier concentration as a function of applied voltage and the resultant effect on the refractive index [34, 35] would be interesting areas for future investigation, as would be a study of n at photon energies greater than G.

REFERENCES

1. P. J. Price, *IBM J. Res. Dev.* **10**, 395 (1966).
2. W. Kohn and J. M. Luttinger, *Phys. Rev.* **108**, 590 (1957); W. Kohn and J. M. Luttinger, *Phys. Rev.* **109**, 1892 (1958).
3. P. N. Argyres, *J. Phys. Chem. Solids* **19**, 66 (1961).
4. B. Jensen, *Ann. Phys.* **95**, 229 (1975).

5. B. Jensen, in "Handbook of Optical Constants of Solids," (E. D. Palik, ed.), Vol. 1, Academic Press, Orlando, (1985).
6. B. Jensen, in "Infrared and Submillimeter Waves," (K. J. Button, ed.), Vol. 8, Academic Press, New York (1983).
7. B. Jensen, *Phys. Status Solidi* **86**, 291 (1978); *Solid State Commun.* **24**, 853 (1977); *J. Appl. Phys.* **50**, 5800 (1979).
8. B. Jensen, *Ann. Phys.* **80**, 284 (1973).
9. S. Adachi, *J. Appl. Phys.* **53**, 5863 (1982); *J. Appl. Phys.* **58**, R1 (1985).
10. B. Jensen, *IEEE J. Quant. Electron.* **QE-18**, 1361 (1982); B. Jensen, A. Torabi, *IEEE J. Quant. Electron.* **QE-19**, 448 (1983).
11. E. O. Kane, *J. Phys. Chem. Solids* **1**, 249 (1957).
12. H. Ehrenreich, *J. Phys. Chem. Solids* **2**, 131 (1957).
13. M. Asada, A. Kameyama, and Y. Suematsu, *IEEE J. Quant. Electron.* **QE-20**, 745 (1984).
14. B. Jensen and A. Torabi, *J. Opt. Soc. Am. B*, **2**, 1395 (1985).
15. B. Jensen and A. Torabi, *J. Appl. Phys.* **54**, 3623 (1983).
16. R. E. Nahory, N. A. Pollack, W. D. Johnson, Jr., and R. L. Barns, *Appl. Phys. Lett.* **33**, 659 (1978).
17. P. Chandra, L. A. Colden, and K. E. Strege, *Electron. Lett.* **17**, 6 (1981).
18. B. Jensen and A. Torabi, *IEEE J. Quant. Electron.* **QE-19**, 877 (1983).
19. H. C. Casey, D. D. Sell and M. B. Panish, *Appl. Phys. Lett.* **24**, 63 (1974).
20. H. C. Casey, *J. Appl. Phys.* **49**, 3684 (1978).
21. J. C. Dyment, Y. C. Cheng, and A. J. Springthorpe, *J. Appl. Phys.* **46**, 1739 (1975).
22. D. E. Aspnes, S. M. Kelso, R. A. Logan and R. Bhat, *J. Appl. Phys.* **60**, 754 (1986).
23. M. D. Camras, *Appl. Phys. Lett.* **41**, 317 (1982).
24. B. Jensen and A. Torabi, *J. Appl. Phys.* **54**, 5945 (1983).
25. G. L. Hansen, J. L. Schmit, and T. N. Casselman, *J. Appl. Phys.* **53**, 7099 (1982).
26. J. Calas, J. Allgre, and C. Fau, *Phys. Status Solidi B* **107**, 275 (1981).
27. B. Jensen and A. Torabi, *J. Opt. Soc. Am. B* **6**, 857 (1986).
28. B. Jensen and A. Torabi, *J. Appl. Phys.* **54**, 2030 (1983).
29. B. Jensen and A. Torabi, *Infrared Physics* **23**, 359 (1983).
30. B. Jensen and A. Torabi, *IEEE J. Quant. Electron.* **QE-19**, 1362 (1983).
31. B. Jensen and A. Torabi, *IEEE J. Quant. Electron.* **QE-20**, 618 (1984).
32. B. Jensen and A. Torabi, *Appl. Phys. Lett.* **45**, 266 (1984).
33. H. Yamamoto, M. Asada and Y. Suematsu, *J. Lightwave Technol.* **6**, 1831 (1988).
34. Y. Arakawa and A. Yariv, *IEEE J. Quant. Electron* **QE-21**, 1666 (1985).
35. P. J. Price, *Phys. Rev. B* **38**, 1994 (1988).
36. T. Ishibashi, S. Tarucha, and H. Okamoto, *Japan J. Appl. Phys.* **21**, 1476 (1982).
37. E. Finkman and Y. Nemirovsky, *J. Appl. Phys.* **50**, 4356 (1979).

Chapter 7

Calculation of Optical Constants, *n* and *k*, in the Interband Region

A. R. FOROUHI
Actel Corporation
Sunnyvale, California

and

I. BLOOMER
Physics Department
San José State University
San José, California

I. Introduction 151
II. The Extinction Coefficient, $k(E)$, and the Refractive Index, $n(E)$ 154
A. Derivation of $k(E)$ 154
B. Derivation of $n(E)$ 160
III. Discussion 163
A. The Parameters Involved in the Equations for $k(E)$ and $n(E)$ 163
B. k(E) and n(E) in the Limit E Approaches Infinity 164
IV. Examples 166
A. Amorphous Semiconductors and Dielectrics 166
B. Crystalline Semiconductors and Dielectrics 169
C. Metals 171
V. Summary 174
References 175

I INTRODUCTION

In this chapter we present a unified formulation of optical properties of materials. This formulation is applicable to amorphous semiconductor and dielectrics, crystalline semiconductors and dielectrics, and metals, throughout the fundamental optical energy range, that is, the interband region.

We use the complex index of refraction, $N = n - ik$, to describe optical properties. The real and imaginary parts of N are termed refractive index

Copyright © 1991 by Academic Press.
All rights of reproduction in any form reserved.
ISBN 0-12-544422-2

and extinction coefficient, respectively. n and k are referred to as the optical constants of the medium. Optical constants depend on photon energy, $E = \hbar\omega$, and exhibit structure in the interband region where bound-electron transitions are dominant.

Optical constants are related to each other through the Kramers–Kronig dispersion relation. The Kramers–Kronig relation provides a simple integral formula, giving $n(E)$ as the Hilbert transform of $k(E)$. This relation is a consequence of the principle of causality, which states that no signal travels faster than the speed of light in vacuum. Therefore, any complete derivation of optical constants should be consistent with the Kramers–Kronig relation.

There are numerous other formulations of optical properties in the fundamental optical regime [1–10]. They fall into one of four categories: (1) empirical formulas; (2) harmonic-oscillator models; (3) quantum-mechanical treatments; (4) point-by-point analyses of the Brillouin zone.

Optical constants determined from empirical formulas (such as the Sellmeier dispersion equations for the refractive index and Urbach's rule for the absorption coefficient [1–4]) are not related through the Kramers–Kronig dispersion relation and are valid only over a very limited energy range.

The harmonic-oscillator model [1, 2, 10] does not incorporate the concept of an optical energy band gap, E_g. Thus, the optical energy band gap of semiconductors and dielectrics cannot be directly determined from this approach. Furthermore, many fitting parameters are needed to describe $n(E)$ and $k(E)$ in the fundamental energy range [10].

Quantum-mechanical treatments [1–9] involve either a quantized electromagnetic (photon) interaction where an infinite lifetime for the excited electron state is assumed, or a semiclassical (nonquantized) electromagnetic interaction where lifetime broadening assumptions are sometimes incorporated [9]. These approaches provide optical constants that are effective over only a small energy range.

Point-by-point analyses of the Brillouin zone [5, 6] do not provide equations for optical constants in closed algebraic form. Using these analyses, peaks in the optical spectra cannot be explained except by assuming the occurrence of simultaneous transitions from two singularities, that is, from two critical points, which accidentally have the same energy. Agreement with experimental results is often poor.

The formulation in this chapter is based on the quantum-mechanical theory of absorption, from which we deduce a general expression for the extinction coefficient, k. A finite lifetime is incorporated for the excited state to which the electron transfers, due to photon absorption. The optical energy band gap, E_g, is identified to be that energy for which $k(E)$ has its absolute minimum.

From the deduced equation for $k(E)$, we then derive an expression for

the refractive index, $n(E)$, via the Kramers–Kronig dispersion relation.

For particular photon energies, peaks occur in the optical spectra. We attribute these peaks to transitions of electrons from one distinguishable state to another. We define distinguishable states as either the bonding, $|\sigma\rangle$, and antibonding, $|\sigma^*\rangle$, states in the valence and conduction bands of amorphous materials [11] or critical-point, $|\mathbf{k}_{\text{crit}}\rangle$, states in the valence and conduction bands of crystalline semiconductors, dielectrics, and metals. The symbol $\mathbf{k}$ represents electron wave vector.

In the simplest case of amorphous semiconductors and dielectrics, a single peak is exhibited in the optical spectra, implying only one possible type of distinguishable transition, from $|\sigma\rangle$ to $|\sigma^*\rangle$.

For crystalline semiconductors and dielectrics, several peaks are apparent, thus indicating several possible types of distinguishable transitions, from $|\mathbf{k}^{\text{v}}_{\text{crit}}\rangle_i$ to $|\mathbf{k}^{\text{c}}_{\text{crit}}\rangle_i$. The subscript i denotes the ith type of critical-point state and ranges over the number of observable peaks, that is, the number of types of critical-point transitions responsible for the peaks in the energy range under consideration. The superscripts v and c denote valence and conduction band, respectively.

For metals, unlike semiconductors and dielectrics, the strongest photon absorption occurs outside the fundamental range in the far- and near-infrared regime. Optical constants of metals are structureless in this energy range. Interactions involving free electrons in the partially filled conduction band contribute for the most part to their optical properties at these low energies. However, beyond the infrared regime, metals do exhibit several peaks in their optical spectra. In the fundamental optical regime, similar structure in optical constants is apparent for metals, semiconductors, and dielectrics. Therefore, we expect that optical interactions involve the same physical processes for all three types of materials. In fact we have found, as will be discussed, that in the interband region, metals can be treated as a subcase of crystalline semiconductor and dielectric materials with E_g equal to zero, that is, with zero optical energy band gap.

In Section II.A we derive closed algebraic equations for $k(E)$ applicable to amorphous semiconductors and dielectrics as well as to crystalline semiconductors, dielectrics, and metals. In Section II.B we use the Kramers–Kronig dispersion relation to obtain $n(E)$ as the Hilbert transform of $k(E)$. In Section III.A we show how to determine the parameters involved in the equations that we derive, by making use of the physical significance of these parameters. In Section III.B we discuss the high energy limit of $k(E)$ and $n(E)$. In Section IV, we apply the equations that we derive for $k(E)$ and $n(E)$ to different materials to show the excellent agreement obtained with experimental data throughout the entire interband region and to show that this agreement depends on far fewer parameters in comparison to other treatments. In Section V, a summary of this chapter is presented.

II THE EXCTINCTION COEFFICIENT, $k(E)$, AND THE REFRACTIVE INDEX, $n(E)$

A Derivation of $k(E)$

In the fundamental optical regime, interband transitions of bound electrons are mostly responsible for optical properties. Therefore, we need to consider the relationship between photon absorption and electron transitions. Time-dependent perturbation theory provides the relation between probability per unit time that a photon is removed from an incident beam and that an electron transfers to an excited state. If we take this transition probability rate and multiply it by photon energy, $\hbar\omega$, we obtain the rate at which photon energy is absorbed from the incident intensity in the frequency range from ω to $\omega + d\omega$, which we denote by the symbol $\Phi(\omega)$.

We define the absorption coefficient, α, as proportional to $\Phi(\omega)$. The absorption coefficient is directly related to the extinction coefficient, k, that is, $\alpha = (2\omega/c)k$, where c is the speed of light. In addition to Φ, we define the absorption coefficient as depending on the total number of ways a photon, of energy $\hbar\omega$, can be removed from the incident intensity, per unit volume in a layer of infinitesimal thickness, which we denote by the symbol Θ. Thus, our definition for α is

$$\alpha(\omega) = \Theta\Phi/I_0, \tag{1}$$

where I_0 represents the incident photon intensity.

Recently, we showed [12] that the rate of energy absorbed, $\Phi(\omega)$, in the frequency range ω to $\omega + \mathrm{d}\omega$, associated with an electron transition between two arbitrary states $|a\rangle$ to $|b\rangle$ (where $E_b > E_a$), when the excited state $|b\rangle$ has a finite lifetime, $\tau = 1/\gamma$, is given by

$$\Phi(\omega) = \frac{4\pi\hbar}{3c} e^2 \omega I_0 |\langle b|\mathbf{x}|a\rangle|^2 \left\{ \frac{\gamma}{(E_b - E_a - \hbar\omega)^2 + \dfrac{\hbar^2\gamma^2}{4}} \right\}, \tag{2}$$

where e stands for electron charge, $\mathbf{x}$ is the electron position vector, and $\langle b\,|\mathbf{x}|\,a\rangle$ is the dipole matrix element between initial and final states. I_0, the incident photon intensity, is given by

$$I_0 = (\hbar\omega)\mathcal{N}\rho c, \tag{3}$$

where $\mathcal{N}$ is photon occupation number and ρ is the number of allowed photon states in the frequency range from ω to $\omega + d\omega$. All physical quantities used in Eqs. 1, 2, and 3, including I_0 and c, are taken to be at the site of the absorbing electron.

Equation 2 is based on first-order time-dependent perturbation theory, so that the electron transitions are direct; that is, there are no intermediate states involved in the transition from $|a\rangle$ to $|b\rangle$.

The finite-lifetime assumption leads to a new way of accounting for peaks in the optical spectra. It gives a Lorentzian dependence on energy in the equation for $\Phi(\omega)$ (the term in curly brackets in Eq. 2). This Lorentzian energy dependence produces a maximum in $\Phi(\omega)$ when $\hbar\omega = E_b - E_a$. Thus, the maximum probability that a photon of energy $\hbar\omega$ is removed from the incident beam occurs when $\hbar\omega = E_b - E_a$. This condition for a maximum in $\Phi(\omega)$ is analogous to resonance excitations in atomic systems [13]. And, as in the case of atomic systems, photons can still be removed from the incident beam even when the "resonant" condition is not satisfied; that is, $\Phi(\omega)$ is nonzero, even when $\hbar\omega = E_b - E_a$.

We assume that direct transitions from distinguishable states lead to peaks in optical constants. Therefore, we take $|a\rangle$ and $|b\rangle$ to be $|\sigma\rangle$ and $|\sigma^*\rangle$, with associated energies E_σ and E_{σ^*}, respectively, in the amorphous case; we take $|a\rangle$ and $|b\rangle$ to be $|\mathbf{k}^{\mathrm{v}}_{\mathrm{crit}}\rangle_i$ and $|\mathbf{k}^{\mathrm{c}}_{\mathrm{crit}}\rangle_i$, with associated energies $E_{\mathrm{v}}(\mathbf{k}_{\mathrm{crit}})_i$ and $E_{\mathrm{c}}(\mathbf{k}_{\mathrm{crit}})_i$ in the crystalline semiconductor, dielectric, and metal case [12, 14, 15]. Accordingly, when $\hbar\omega = E_{\sigma^*} - E_\sigma$, or $\hbar\omega = E_{\mathrm{c}}(\mathbf{k}_{\mathrm{crit}})_i - E_{\mathrm{v}}(\mathbf{k}_{\mathrm{crit}})_i$, a peak in $\Phi(\omega)$ (and therefore a peak in optical constants) is expected to occur.

There is only one peak in the optical constants of amorphous semiconductors and dielectrics, indicating only one possible type of distinguishable transition. For these materials, $\Phi(\omega)$ will consist of a single term. (Amorphous materials whose optical constants exhibit more than one peak, such as amorphous silicon dioxide [1], are not discussed in this work, although the present formulation can be applied to them.) Since more than one peak occurs in the optical constants of crystalline semiconductors, dielectrics, and metals suggesting more than one type of distinguishable transition for these materials, we take $\Phi(\omega)$ to be a sum over the number of types of distinguishable transitions.

Thus, for the amorphous case,

$$\Phi(\omega) = \frac{4\pi\hbar}{3c} e^2 \omega I_0 |\langle \sigma^* | \mathbf{x} | \sigma \rangle|^2 \left\{ \frac{\gamma}{(E_{\sigma^*} - E_\sigma - \hbar\omega)^2 + \dfrac{\hbar^2\gamma^2}{4}} \right\}, \tag{4}$$

and for crystalline semiconductors, dielectrics, and metals,

$$\Phi(\omega)=\frac{4\pi\hbar}{3c}e^2\omega I_0\sum_{i=1}^{q}|\langle\mathbf{k}_{\text{crit}}^{\text{c}}|\mathbf{x}|\mathbf{k}_{\text{crit}}^{\text{v}}\rangle|^2\left\{\frac{\gamma_i}{\{[E_c(\mathbf{k}_{\text{crit}})-E_{\text{v}}(\mathbf{k}_{\text{crit}})]_i-\hbar\omega\}^2+\dfrac{\hbar^2\gamma_i^2}{4}}\right\}. \tag{5}$$

In Eq. 4 the term $|\langle\sigma^*|\mathbf{x}|\sigma\rangle|^2$ represents the dipole matrix element squared between bonding, $|\sigma\rangle$, and antibonding, $|\sigma\rangle$, states; the term $|\langle\mathbf{k}_{\text{crit}}^{\text{c}}|\mathbf{x}|\mathbf{k}_{\text{crit}}^{\text{v}}\rangle|_i^2$ represents the dipole matrix element squared between the ith critical-point state in the valence band and the ith critical-point state in the conduction band. In Eq. 5, the integer q is equal to the number of observed peaks associated with the critical-point transitions.

With Φ given by either Eq. 4 or 5, part of our task in determining the extinction coefficient, k, is accomplished. That is, since

$$k=\frac{c}{2\omega}\alpha=\frac{c}{2\omega}\frac{1}{I_0}\Phi\Theta, \tag{6}$$

we have, so far,

$$k_\alpha(\omega)=\Theta_\alpha\frac{2\pi\hbar}{3}e^2|\langle\sigma^*|\mathbf{x}|\sigma\rangle|^2\left\{\frac{\gamma}{(E_{\sigma^*}-E_\sigma-\hbar\omega)^2+\dfrac{\hbar^2\gamma^2}{4}}\right\}, \tag{7}$$

or

$$k_\chi(\omega)=\Theta_\chi\frac{2\pi\hbar}{3}e^2\sum_{i=1}^{q}|\langle\mathbf{k}_{\text{crit}}^{\text{c}}|\mathbf{x}|\mathbf{k}_{\text{crit}}^{\text{v}}\rangle|_i^2\left\{\frac{\gamma_i}{\{[E_{\text{c}}(\mathbf{k}_{\text{crit}})-E_{\text{v}}(\mathbf{k}_{\text{crit}})]_i-\hbar\omega\}^2+\dfrac{\hbar^2\gamma_i^2}{4}}\right\}, \tag{8}$$

or

$$k_\mu(\omega)=\Theta_\mu\frac{2\pi\hbar}{3}e^2\sum_{i=1}^{q}|\langle\mathbf{k}_{\text{crit}}^{\text{c}}|\mathbf{x}|\mathbf{k}_{\text{crit}}^{\text{v}}\rangle|_i^2\left\{\frac{\gamma_i}{\{[E_{\text{c}}(\mathbf{k}_{\text{crit}})-E_{\text{v}}(\mathbf{k}_{\text{crit}})]_i-\hbar\omega\}^2+\dfrac{\hbar^2\gamma_i^2}{4}}\right\}. \tag{9}$$

The subscripts α, χ, and μ in Eqs. 7, 8, and 9 stand for amorphous

semiconductors and dielectrics, crystalline semiconductors and dielectrics, and metals, respectively.

Our next task is to determine Θ. This parameter represents the total number of ways a photon of energy $\hbar\omega$ can be removed from the incident intensity, per unit volume in an infinitesimal layer of thickness. Thus, Θ is proportional to the number of possible transitions for a given photon energy, $\hbar\omega$.

In addition to counting the number of direct transitions, we will also include the number of indirect (second-order) transitions when determining Θ. Although we neglected the probability for second-order processes in our determination of $\Phi(\omega)$, we do not neglect the number of possible second-order transitions for a given $\hbar\omega$. This is because we are interested in the product of $\Phi\Theta$, which may be approximated as $\Phi\Theta \approx [\Phi_{\text{first order}} + \Phi_{\text{second order}}] \times [\Theta_{\text{first order}} + \Theta_{\text{second order}}]$. However, we assume that the probability for photon absorption via second-order processes is much smaller than the probability for photon absorption via first-order processes; that is, $\Phi_{\text{second order}} \ll \Phi_{\text{first order}}$. On the other hand, the number of possible second-order transitions for a given $\hbar\omega$ is not assumed negligible, compared with the number of first-order transitions.

Thus, Θ depends on the product of the number of occupied electron states in the valence band in the energy range dE_v, that is, $\eta_v(E_v)f_v(E_v)dE_v$, times the number of unoccupied electron states per energy in the conduction band, that is, $\eta_c(E_c) \times (1 - f_c(E_c))$, which are separated by an energy, $\hbar\omega$, from states in the valence band [3]. The expression $\eta_v(E_v)$ represents the density of states in the valence band, $E_v(\mathbf{k})$, and $\eta_c(E_c)$ represents the density of states in the conduction band, $E_c(\mathbf{k})$. The expression $f(E)$ represents the Fermi function. Therefore,

$$\Theta \propto \int \eta_v(E_v) f_v(E_v) \eta_c(E_v + \hbar\omega)[1 - f_c(E_v + \hbar\omega)]\, dE_v. \tag{10}$$

We assume that $f_v(E_v)$ is of order unity and $f_c(E_v + \hbar\omega)$ is of order zero. This assumption is valid for temperatures that are not too high. Then

$$\Theta \propto \int \eta_v(E_v) \eta_c(E_v + \hbar\omega)\, dE_v. \tag{11}$$

In the case of amorphous and crystalline semiconductors and dielectrics, the limits of integration range from $(E_c^{\text{bottom}} - \hbar\omega)$ to E_v^{top}, where E_c^{bottom} and E_v^{top} represent the bottommost and topmost energies of the conduction and valence bands, respectively. Then the minimum energy above which a

transition can occur, is equal to $(E_c^{\text{bottom}} - E_v^{\text{top}})$. We take the optical energy band gap, E_g, equal to this minimum energy, that is,

$$E_g = E_c^{\text{bottom}} - E_v^{\text{top}}. \tag{12}$$

Since Θ represents the total number of direct or indirect ways a photon can be removed, E_g gives the minimum energy required for the onset of absorption.

In the case of metals, $E_c^{\text{bottom}} = E_v^{\text{top}}$, since metals are distinguished from semiconductors and dielectrics by the absence of a band gap in their electronic band structure. Therefore, we take E_g equal to zero and assume that the free-electron contributions are negligible in the interband region.

In order to evaluate the integral for Θ given by Eq. 11, we need to know $\eta_v(E_v)$ and $\eta_c(E_c)$. Exact algebraic expressions for $\eta_v(E_v)$ and $\eta_c(E_c)$, however, are unknown. We will assume a parabolic approximation in all cases for these functions such that $E_v(\mathbf{k})$ and $E_c(\mathbf{k})$ are a maximum and a minimum, respectively, when $E = E_v^{\text{top}}$ and $E = E_c^{\text{bottom}}$. Accordingly, $\eta_v(E_v)$ and $\eta_c(E_c)$ are determined to be [5]

$$\eta_v(E) = \text{const}(E_v^{\text{top}} - E)^{1/2} \tag{13}$$

and

$$\eta_c(E) = \text{const}(E - E_c^{\text{bottom}})^{1/2}. \tag{14}$$

Equation 11 can then be evaluated as

$$\Theta_\alpha = \Theta_\chi = \text{const}(\hbar\omega - E_g)^2 \tag{15}$$

for amorphous and crystalline semiconductors and dielectrics. We see from Eq. 15 that Θ is a minimum, and hence k is a minimum when $E = E_g$.

For metals, with $E_v^{\text{top}} = E_c^{\text{bottom}}$,

$$\Theta_\mu = \text{const}(\hbar\omega)^2. \tag{16}$$

Surprisingly, the parabolic approximation produces excellent agreement with experimental results for all cases [12, 14, 15] (see Section IV).

For the amorphous case, we insert Eq. 15 into Eq. 7:

$$k_\alpha(\omega) = \text{const}|\langle\sigma^*|\mathbf{x}|\sigma\rangle|^2 \times \left\{ \frac{\gamma}{(E_{\sigma^*} - E_\sigma - \hbar\omega)^2 + \frac{\hbar^2\gamma^2}{4}} \right\} (\hbar\omega - E_g)^2. \quad (17)$$

For crystalline semiconductors and dielectrics, we insert Eq. 15 into Eq. 8:

$$k_\chi(\omega) = \text{const} \sum_{i=1}^{q} |\langle \mathbf{k}_{\text{crit}}^{\text{c}} | \mathbf{x} | \mathbf{k}_{\text{crit}}^{\text{v}} \rangle|_i^2 \times \left\{ \frac{\gamma_i}{\{[E_c(\mathbf{k}_{\text{crit}}) - E_v(\mathbf{k}_{\text{crit}})]_i - \hbar\omega\}^2 + \frac{\hbar^2\gamma_i^2}{4}} \right\} (\hbar\omega - E_g)^2. \quad (18)$$

For metals, we insert Eq. 16 into Eq. 9:

$$k_\mu(\omega) = \text{const} \sum_{i=1}^{q} |\langle \mathbf{k}_{\text{crit}}^{\text{c}} | \mathbf{x} | \mathbf{k}_{\text{crit}}^{\text{v}} \rangle|_i^2 \left\{ \frac{\gamma_i}{\{[E_c(\mathbf{k}_{\text{crit}}) - E_v(\mathbf{k}_{\text{crit}})]_i - \hbar\omega\}^2 + \frac{\hbar^2\gamma_i^2}{4}} \right\} (\hbar\omega)^2. \quad (19)$$

The extinction coefficient in each case can be written more compactly in the following way:

$$k_\alpha(E) = \frac{A(E - E_g)^2}{E^2 - BE + C}, \quad (20)$$

$$k_\chi(E) = \left[\sum_{i=1}^{q} \frac{A_i}{E^2 - B_i E + C_i} \right] (E - E_g)^2, \quad (21)$$

$$k_\mu(E) = \left[\sum_{i=1}^{q} \frac{A_i}{E^2 - B_i E + C_i} \right] (E)^2. \quad (22)$$

In the amorphous case, the parameters are given by

$$A = \text{const}|\langle\sigma^*|\mathbf{x}|\sigma\rangle|^2 \times \gamma, \quad (23)$$

$$B = 2(E_{o^*} - E_o), \tag{24}$$

$$C = (E_{o^*} - E_o)^2 + \frac{\hbar^2\gamma^2}{4}. \tag{25}$$

For crystalline semiconductors, dielectrics, and metals, the parameters are given by

$$A_i = \text{const}|\langle \mathbf{k}^{\text{c}}_{\text{crit}}|\mathbf{x}|\mathbf{k}^{\text{v}}_{\text{crit}}\rangle|_i^2 \times \gamma_i, \tag{26}$$

$$B_i = 2[E_{\text{c}}(\mathbf{k}_{\text{crit}}) - E_{\text{v}}(\mathbf{k}_{\text{crit}})]_i, \tag{27}$$

$$C_i = [E_{\text{c}}(\mathbf{k}_{\text{crit}}) - E_{\text{v}}(\mathbf{k}_{\text{crit}})]_i^2 + \frac{\hbar^2\gamma_i^2}{4}. \tag{28}$$

B Derivation of $n(E)$

The refractive index, $n(E)$, and the extinction coefficient, $k(E)$, are related by the Kramers–Kronig dispersion relations. These relations are a consequence of the analytic behavior of the complex index of refraction, $N(E) = n(E) - ik(E)$. In turn, the analytic behavior of $N(E)$ stems from the principle of causality, which states that no signal can be transmitted through a medium at a speed greater than that of light in vacuum [16, 17].

Specifically, the necessary and sufficient condition for $N(E)$ to be a causal function is that $N(E)$ must be analytic in the lower half of the complex E plane [17]. As indicated in Ref. [12], this will be the case because $A > 0$, $B > 0$, $C > 0$, and $4C - B^2 > 0$ and likewise, $A_i > 0$, $B_i > 0$, $C_i > 0$, and $4C_i - B_i^2 > 0$ (see Eqs. (23–28)).

The Kramers–Kronig dispersion relation gives $n(E)$ as the Hilbert transform of $k(E)$, that is,

$$n(E) - n(\infty) = \frac{1}{\pi} P \int_{-\infty}^{\infty} \frac{k(E') - k(\infty)}{E' - E}\, dE', \tag{29}$$

where $n(\infty) = \lim_{E\to\infty} n(E)$, and $k(\infty) = \lim_{E\to\infty} k(E)$.

In Eq. 29, P denotes the Cauchy's principle-value integral, defined by

$$P\int_{-\infty}^{\infty} Z(E')\,dE' = -\sum_j (2\pi i R_j + \pi i S_j), \tag{30}$$

where Z represents a general function of the complex variable E', and where R_j is the jth residue of the integrand at the jth pole located in the lower half of the complex E' plane, and S_j is the jth residue evaluated at the jth pole located along the real axis [17].

We first consider $k_\alpha(E)$, Eq. 20, consisting of a single term, and insert it into the Kramers–Kronig relation, Eq. 29:

$$n_\alpha(E) - n_\alpha(\infty) = \frac{1}{\pi} P\int_{-\infty}^{\infty} \frac{A[(B-2E_g)E' + E_g^2 - C]}{(E'^2 - BE' + C)(E' - E)}\,dE'. \tag{31}$$

The pole in the integrand of Eq. 31, located in the lower half of the complex E' plane, is at $E' = B/2 - iQ$, since $Q = 1/2(4C - B^2)^{1/2} > 0$. The pole along the real axis is at $E' = E$. Applying Eq. 30 to Eq. 31, we obtain

$$n_\alpha(E) = n_\alpha(\infty) + \frac{B_\alpha E + C_\alpha}{E^2 - BE + C}, \tag{32}$$

where

$$B_\alpha = \frac{A}{Q}\left(-\frac{B^2}{2} + E_g B - E_g^2 + C\right), \tag{33}$$

$$C_\alpha = \frac{A}{Q}\left[\left(E_g^2 + C\right)\frac{B}{2} - 2E_g C\right]. \tag{34}$$

The expressions $k_\chi(E)$ and $k_\mu(E)$ consist of a sum of terms, each one having the same form as $k_\alpha(E)$. Therefore, $n_\chi(E)$ and $n_\mu(E)$ consist of a sum of terms, with each term having the same form as $n_\alpha(E)$. Inserting $k_\chi(E)$, Eq. 21, and $k_\mu(E)$, Eq. 22, into the Kramers–Kronig relation, Eq. 29,

gives

$$n_\chi(E) = n_\chi(\infty) + \sum_{i=1}^{q} \frac{B_{\chi i}E + C_{\chi i}}{E^2 - B_i E + C_i} \tag{35}$$

and

$$n_\mu(E) = n_\mu(\infty) + \sum_{i=1}^{q} \frac{B_{\mu i}E + C_{\mu i}}{E^2 - B_i E + C_i}. \tag{36}$$

The parameters $B_{\mu i}$ and $C_{\mu i}$ in the equation for $n_\mu(E)$ differ from $B_{\chi i}$ and $C_{\chi i}$ in the equation for $n_\chi(E)$ by the absence of E_g. Thus, for crystalline semiconductors and dielectrics,

$$B_{\chi i} = \frac{A_i}{Q_i}\left(-\frac{B_i^2}{2} + E_g B_i - E_g^2 + C_i\right) \tag{37}$$

$$C_{\chi i} = \frac{A_i}{Q_i}\left[(E_g^2 + C_i)\frac{B_i}{2} - 2E_g C_i\right]. \tag{38}$$

For metals,

$$B_{\mu i} = \frac{A_i}{Q_i}\left(-\frac{B_i^2}{2} + C_i\right) \tag{39}$$

$$C_{\mu i} = \frac{A_i B_i C_i}{2Q_i}. \tag{40}$$

Q_i is the same in both cases:

$$Q_i = \tfrac{1}{2}(4C_i - B_i^2)^{1/2}. \tag{41}$$

This completes the derivation of optical constants $k_\alpha(E)$ and $n_\alpha(E)$ for amorphous semiconductors and dielectrics, Eqs. 20 and 32; $k_\chi(E)$ and $n_\chi(E)$ for crystalline semiconductors and dielectrics, Eqs. 21 and 35; and

$k_\mu(E)$ and $n_\mu(E)$ for metals, Eqs. 22 and 36. In the next section, we discuss the practical applications of these equations.

DISCUSSION III

The Parameters Involved in the Equations for $k(E)$ and $n(E)$ A

In the amorphous case, the energy dependence of both $k_\alpha(E)$ and $n_\alpha(E)$, given by Eqs. 20 and 32, can be fully and simultaneously determined by five parameters, A, B, C, E_g, and $n(\infty)$. Note that B_α and C_α are not independent parameters.

For crystalline semiconductors and dielectrics, each term in the sum for $k_\chi(E)$, Eq. 21, contributes either a peak or a shoulder to the k spectrum and a corresponding structure to $n_\chi(E)$, Eq. 35—likewise for $k_\mu(E)$, Eq. 22, and $n_\mu(E)$, Eq. 36, for metals. Thus, the number of terms equals the number of discernible peaks and shoulders in the energy range in question.

We have found that for the most part, four terms, that is, fourteen parameters (including E_g and $n(\infty)$), are sufficient to describe $k_\chi(E)$ and $n_\chi(E)$ over the interband region, indicating four types of critical-point transitions that produce spectral peaks. In the case of metals, with $E_g = 0$, we have found that three terms, that is, ten parameters (including $n(\infty)$), give an excellent fit in this region. Nevertheless, in some cases, more terms may be required to bring out the details of the spectra [14].

An important point about these parameters is that they all have physical significance, and consequently, can almost be determined by glancing at the experimental values of $k(E)$ and $n(E)$.

E_g, the optical energy band gap, is simply the measured energy for which $k(E)$ has its absolute minimum value. This is consistent with the experimental findings that the absolute minimum of $k(E)$ occurs at the onset of the "fundamental" absorption edge. By contrast, the values of E_g quoted in the literature are obtained, usually, by extrapolating the "linear portion" of the plot of $(\alpha\hbar\omega)^{1/m}$ or $(\alpha\hbar\omega n)^{1/m}$ versus $\hbar\omega$, where $m = 1/2$, $3/2$, or 2, depending on the assumed mode of optical transition (direct, forbidden, or indirect, respectively). Examples are given in Refs. [12] and [14].

In all cases, $n(\infty)$ is approximately equal to but always greater than one, as discussed in the following section. However, if $n(\infty)$ is assumed equal to unity, reasonable agreement to experimental data is still obtained.

An uncomplicated determination of the other parameters, A, B, and C, associated with their physical significance, can readily be appreciated by considering the amorphous case. The value of $B/2$ is approximately equal

to the energy at which $k_\alpha(E)$ is a maximum. This is because $k_\alpha(E)$ is close to a maximum when $h\omega \approx E_{\sigma'} - E_\sigma = B/2$. The parameter C depends on the energy difference between distinguishable states and on the lifetime of a distinguishable transition. To a first approximation, the lifetime contribution can be ignored so that $C \approx B^2/4$, assuming $B/2$ is equal to the peak energy (see Eqs. 24 and 25). Thus, position of the peak in the experimental $k_\alpha(E)$ spectrum provides knowledge of B and C. The parameter A is related to the dipole matrix element squared and essentially gives the strength of the peak in $k_\alpha(E)$.

Analogous statements can be made for the parameters A_i, B_i and C_i connected with crystalline semiconductors, dielectrics, and metals.

The overall fit of the equations for $k(E)$ and $n(E)$ to experimental data can be refined by means of a nonlinear, least-square, curve-fitting program, where the required preliminary values of the parameters are determined as outlined above. The values of the parameters for the crystalline materials presented in Tables I, III, IV, V, were obtained in this way. However, for the amorphous case, we used an algebraic scheme, described in Ref. [12], to determine the parameters presented in Table II.

B $k(E)$ and $n(E)$ in the Limit E Approaches Infinity

According to Eqs. 20, 21, and 22, $k(\infty)$ is a nonzero constant. Classically, (for instance, in the harmonic-oscillator model), it is expected that $k(\infty) = 0$. However, there are processes that do occur at high energies [15] that remove photons from the incident intensity and that therefore lead to a nonzero $k(\infty)$. Although our equations for $k(E)$ (as well as those based on classical models) do not describe these high-energy events, we regard $k(\infty) \neq 0$ as indicating that these events do take place.

Furthermore, in our treatment we find that $n(\infty) > 1$ for all cases, in contrast to classical dispersion theory. The values that we obtain for $n(\infty)$ and that depend on the particular material, are close to but always greater than one. Nevertheless, it should be noted that agreement with experimental results provided by our equations is not very much dependent on taking $n(\infty) > 1$. That is, if we take $n(\infty) = 1$ in our equations, we get a very slight alteration (for the worse) in our agreement with experiment. This is shown in Fig. 1a and b, for crystalline Si. The difference in fitting the experimental data to Eqs. 21 and 35 is depicted, where $n(\infty)$ is taken either as a constant equal to unity (Fig. 1a), or as a fitting parameter, determined to be 1.95 (Fig. 1b). As seen in this figure, better agreement is attained when $n(\infty)$ is not assumed a priori equal to unity. Details concerning the fit are discussed in Section IV.B.

However, we have stronger reasons (other than obtaining better agree-

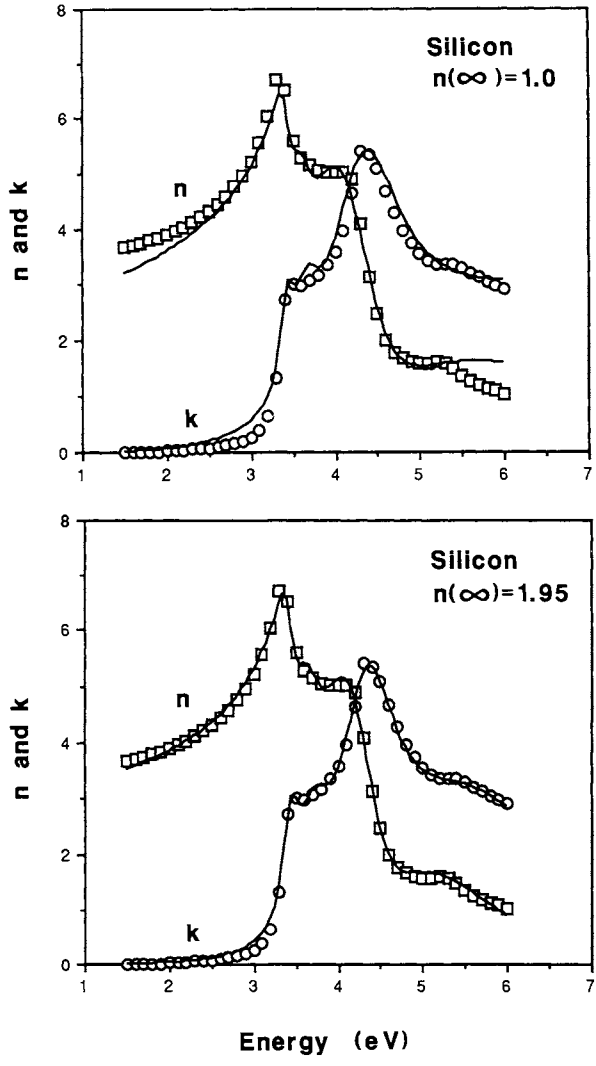

Fig. 1. The solid lines are the theoretical plots of $k_\chi(E)$ and $n_\chi(E)$ given by Eqs. 21 and 35 with the parameters specified in Table I for crystalline Si. Experimental data are by Aspnes and Studna [1, 21]. In (a), $n(\infty)$ is taken equal to unity, whereas in (b), $n(\infty)$ is equal to 1.95, as determined by least-square fitting of experimental data.

ment with experiment) for not assuming $n(\infty)$ equal to unity. The first reason is that J. S. Toll [16] has established mathematically that as a consequence of causality, $n(\infty) > 1$. His proof applies to the case $k(\infty) = 0$ and can trivially be extended to our case where $k(\infty) = \text{constant}$ [14]. Moreover, there is a multitude of published papers [1] by other

TABLE I

	A_i	B_i (eV)	C_i (eV^2)	$n(\infty)$	E_g (eV)
Si	0.00280	6.873	11.820	1.00	1.06
	0.00769	7.319	13.429		
	0.10213	8.589	18.705		
	0.75064	10.159	33.183		
	0.00405	6.885	11.864	1.950	1.06
	0.01427	7.401	13.754		
	0.06830	8.634	18.812		
	0.17488	10.652	29.841		

Two separate sets of parameters describing the theoretial equations $k_\chi(E)$ and $n_\chi(E)$, Eqs. 21 and 35, with four terms in the sums, for crystalline Si. In both sets, values of the parameters A_i, B_i, and C_i are obtained by least-square fitting of experimental data [1, 21] to the theoretical equations. However, in the first set, $n(\infty)$ is taken equal to unity, whereas in the second set, $n(\infty)$ is determined by the least-square fitting program. The optical energy band gap E_g, is taken as the energy at which the experimental k spectrum has its absolute minimum. The corresponding plots are shown in Fig. 1a and b.

researchers, which show that $\varepsilon_1(\infty) > 1$ when experimental data are fitted to a harmonic-oscillator model or variations of a harmonic-oscillator model (where $\varepsilon_1(\infty) = n^2(\infty)$ and $k(\infty) = 0$). Finally, since the electromagnetic interaction takes place within the medium and not in a vacuum, we expect that $n_{\text{medium}}(\infty) \neq n_{\text{vacuum}}(\infty)$; that is, the presence of matter is "sensed" by electromagnetic radiation, even at high energies.

IV EXAMPLES

As seen in the following examples, the present formulation requires far fewer parameters compared with other formulations, and at the same time it provides better agreement with experimental data. As previously noted, this approach is consistent with Kramers–Kronig analysis, and directly incorporates the concept of optical energy band gap, E_g.

A Amorphous Semiconductors and Dielectrics

Our formulation for $k_\alpha(E)$ and $n_\alpha(E)$ was successfully applied to the published data of a wide class of amorphous materials, including a variety

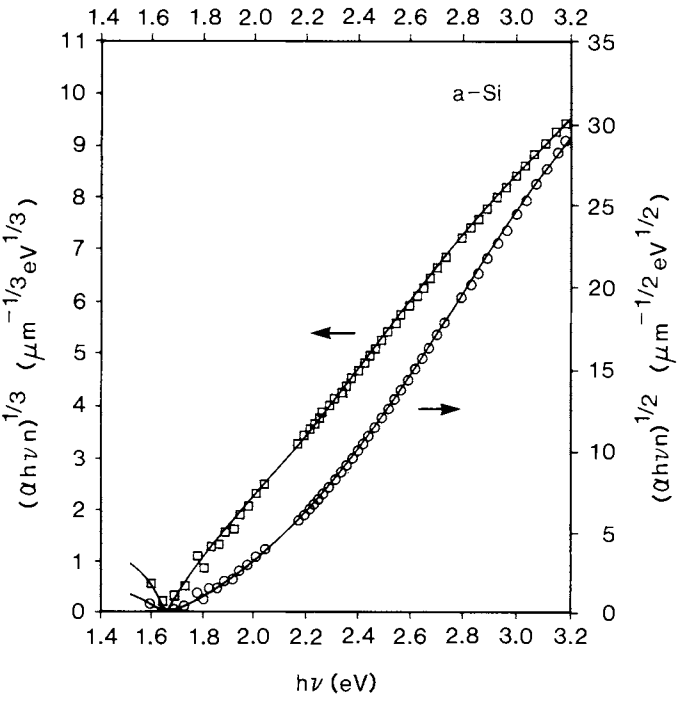

Fig. 2. The solid lines are the theoretical plots for a-Si representing $(\alpha h\nu n)^{1/2}$ versus $h\nu$ and $(\alpha h\nu n)^{1/3}$ versus $h\nu$, where $E = h\nu$ and $\alpha = (2\omega/c)k = 4\pi kE/hc$, with $k = k_a(E)$ given by Eq. 20 and $n = n_a(E)$ given by Eq. 32. The parameters are specified in Table II. The experimental data are from Klazes *et al.* [19] for a-Si produced by glow-discharge decomposition of SiH_4. (From Forouhi and Bloomer [12]).

of amorphous silicon, a-Si, and hydrogenated amorphous silicon, a-Si:H, prepared by different methods under different processing conditions [12, 18], as well as a-Si_3N_4 and a-TiO_2 [12].

TABLE II

	A	B (eV)	C (eV^2)	$n(\infty)$	E_g (eV)
a-Si	1.5690	5.5311	9.6390	2.4330	1.65
a-TiO_2	0.5189	8.1605	17.5291	1.7614	2.8

Values of the parameters describing the theoretical equations $k_a(E)$ and $n_a(E)$, Eqs 20 and 32, for amorphous silicon, a-Si, and amorphous titanium dioxide, a-TiO_2. The parameters are obtained by an algebraic method described in Ref. [12]. Experimental data for a-Si and a-TiO_2 are taken from Refs. [19] and [20], respectively. The corresponding plots are shown in Figs. 2 and 3.

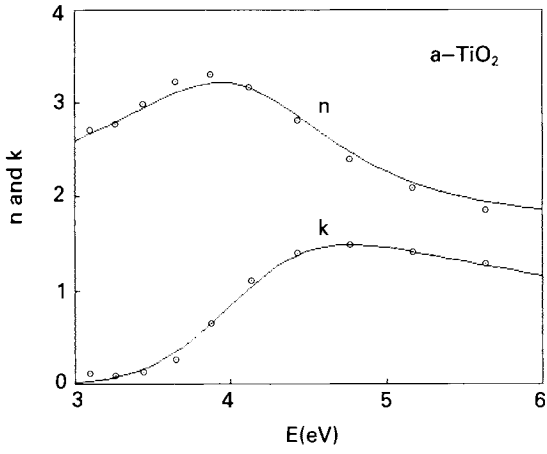

Fig. 3. The solid lines are the theoretical plots of $k_\alpha(E)$ and $n_\alpha(E)$ given by Eqs. 20 and 32 with the parameters specified in Table II for a-TiO_2. The experimental data are from Joseph [20]. (From Forouhi and Bloomer [12].)

As an example, in Fig. 2 the theoretical and experimental plots are displayed for $(\alpha h\nu n)^{1/3}$ and $(\alpha h\nu n)^{1/2}$ versus $h\nu$ for an a-Si film, where α denotes absorption coefficient and $h\nu$ denotes photon energy. Experimental data are from Klazes *et al.* [19]. The film was produced by capacitance rf glow-discharge decomposition of silane (SiH_4) diluted in argon. It was deposited on a fused-silica substrate at a deposition temperature of 370°C. Although the film is considered as a-Si in the original reference, it may be more appropriately presented as a-Si:H, since films prepared by glow-discharge decomposition of SiH_4 incorporate hydrogen.

The reason that consideration is given to the functions $(\alpha h\nu n)^{1/3}$ and $(\alpha h\nu n)^{1/2}$ is that Klazes *et al.* [19] argued that $(\alpha h\nu n)^{1/3} \propto (h\nu - E_g)$ provides a better fit to their experimental data than $(\alpha h\nu n)^{1/2} \propto (h\nu - E_g)$, from which they deduced E_g, using a linear extrapolation of $(\alpha h\nu n)^{1/3}$ as a function of $h\nu$.

The theoretical curves presented in Fig. 2 are obtained by using Eqs. 20 and 32 for $k_\alpha(E)$ and $n_\alpha(E)$ in the expressions $(\alpha h\nu n)^{1/3}$ and $(\alpha h\nu n)^{1/2}$ with the parameters A, B, C, n (∞), and E_g given in Table II. As seen in this figure, a remarkably good fit is found between the experimental data and the corresponding theoretical curves. This result is in line with taking E_g simply as the energy for which $k(E)$ has its absolute minimum; that is, E_g need not be determined via a linear extrapolation of experimental data.

Experimental data of a-TiO_2 presented in Fig. 3 are from Joseph and Gagnaire [20]. The film was produced by an anodic oxidation of titanium sample. The optical constants were determined from analysis of ellipsometric measurements on a set of samples with different film thicknesses in

the wavelength range 220–720 nm, corresponding to 5.6–1.8 eV. Theoretical and experimental plots of $k_\alpha(E)$ and $n_\alpha(E)$ are shown in Fig. 3, and the parameters A, B, C, $n(\infty)$, and E_g are given in Table II.

These two examples, as well as those given in Refs. [12] and [18], point to the fact $k_\alpha(E)$ and $n_\alpha(E)$, specified by a total of only five parameters, provide an excellent fit to measured data throughout the interband regime. As discussed in Ref. [12], this is distinctive from previous formulations, which require nine parameters to specify simultaneously $k_\alpha(E)$ and $n_\alpha(E)$ just at the absorption edge, and which furthermore do not relate $n_\alpha(E)$ to $k_\alpha(E)$ according to the Kramers–Kronig dispersion relation.

Crystalline Semiconductors and Dielectrics B

Our formulation for $k_\chi(E)$ and $n_\chi(E)$, Eqs. 21 and 35, has been successfully applied to group IV semiconductors (Si and Ge), group III-V semiconductors (GaP, GaAs, GaSb, InP, InAs, and InSb), group IV-IV semiconductor (SiC), and crystalline insulators (cubic C and SiO_2) [14].

As an example, the theoretical and experimental plots of $k_\chi(E)$ and $n_\chi(E)$ for crystalline Si are shown in Fig. 1a and b. We have taken the number of terms in Eqs. 21 and 35 equal to four, corresponding to three discernable peaks and one shoulder in the experimental k-versus-E spectrum of Si in the 1.5–6 eV range. The experimental data are by Aspnes and Studna [1, 21]. Values of the parameters, obtained by least-square fitting, are given in Table I. As discussed in Section III.B, in Fig. 1a, $n(\infty)$ is taken equal to unity, whereas in Fig. 1b, $n(\infty)$ is taken as a fitting parameter, determined equal to 1.95.

Furthermore, it should be noted that the value of the optical energy band gap, E_g, presented in Table I is taken as equal to 1.06 eV, corresponding to the position of the absolute minimum in the experimental values of $k(E)$. (It is not necessary to consider E_g as a fitting parameter). The values that we obtain for the critical-point transition energies, $[E_c(\mathbf{k}_{crit}) - E_\gamma(\mathbf{k}_{crit})]_i = B_i/2$, are essentially the same as previously identified values of these transition energies. For example, for Si we obtain $B_1/2 \approx 3.4$ eV, $B_2/2 \approx 3.7$ eV, $B_3/2 \approx 4.3$ eV, and $B_4/2 \approx 5.3$ eV. On the other hand, from reflectance measurements, these energies are determined as $E_1 \approx 3.4$ eV, $E_0 \approx 4.0$ eV, $E_2 \approx 4.4$ eV, and $E_1' \approx 5.5$ eV [6]. (Reported values differ by a few tenths of an electron volt from one reference to another. See, for example, Refs. [5] and [6].) The notations E_0, E_1, E_1', and E_2 refer to an identification of the critical points involved and are described in Ref. [6].

Another example is shown in Fig. 4 for crystalline SiO_2. Experimental data are by Philipp [1, 22]. Again, the number of terms in equations for

$k_\chi(E)$ and $n_\chi(E)$ is taken equal to four, corresponding to four distinct peaks in the experimental $k(E)$ in the 2–18 eV range. E_g is taken equal to 7.0 eV, corresponding to the position of the absolute minimum in $k(E)$. We have found that the values of the parameters initially determined from the position of the peaks in the experimental k versus E spectrum are very close to the values obtained by a least-square, curve-fitting program (Section III.A). Experimentally, the peaks in k occur at 10.45 eV, 11.7 eV, 14.3 eV, and 17.25 eV [22], whereas the least-squares fit yields $B_1/2 \approx 10.36$ eV, $B_2/2 \approx 11.64$ eV, $B_3/2 \approx 14.08$ eV, and $B_4/2 \approx 17.15$ eV. Values of the parameters are given in Table III.

These examples, as well as those given in Ref. [14], indicate that four terms in the sum for $k_\chi(E)$ and $n_\chi(E)$ are sufficient to specify simultaneously the extinction coefficient and the refractive index of crystalline semiconductors and dielectrics in the fundamental optical regime. In some cases, however, more terms may be required to bring out the details of the optical spectra [14]. Conversely, when the number of terms is reduced, fine structural details are lost and eventually one peak remains, resembling the amorphous case. This is shown for SiC in Fig. 5a, b, and c, with the number of terms equal to one, two, and four. The experimental data presented in Fig. 5 are by Leveque and Lynch [23]. Values of the parameters are given in Table IV. In the examples given in this section, as well as those in Ref.

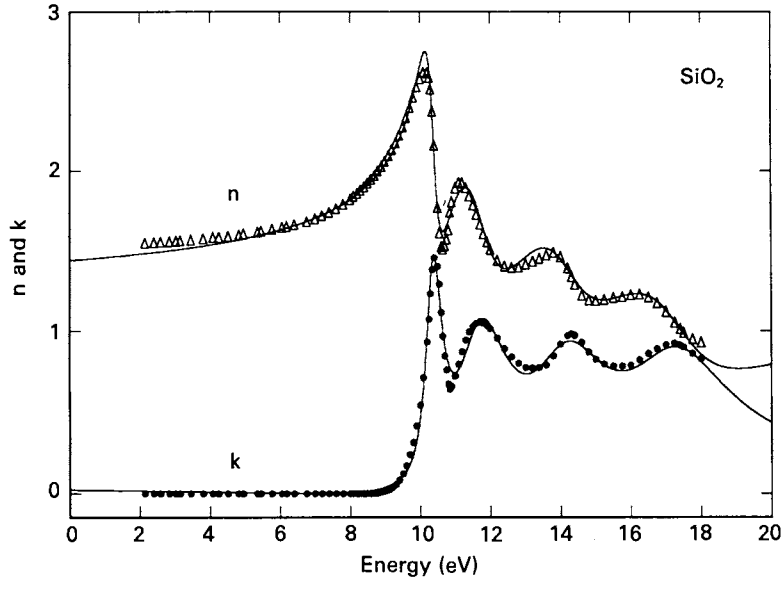

Fig. 4. The solid lines are the theoretical plots of $k_\chi(E)$ and $n_\chi(E)$ given by Eqs. 21 and 35 with the parameters specified in Table III for crystalline SiO_2. Experimental data are by Philipp [1, 22]. (From Forouhi and Bloomer [14].)

TABLE III

	A_i	B_i (eV)	C_i (eV^2)	$n(\infty)$	E_g (eV)
SiO_2	0.00867	20.729	107.499	1.226	7.00
	0.02948	23.273	136.132		
	0.01908	28.163	199.876		
	0.01711	34.301	297.062		

The parameters describing the theoretical equations $k_\chi(E)$ and $n_\chi(E)$, Eqs. 21 and 35, with four terms in the sums, for crystalline SiO_2. Values of the parameters A_i, B_i, C_i, and $n(\infty)$ are obtained by least-suqare fitting of the experimental data [1, 22] to the theoretical equations. E_g is taken as the energy at which the experimental k spectrum has its absolute minimum. The corresponding plots are shown in Fig. 4.

[14], the number of parameters (14, including E_g and $n(\infty)$) used to specify simultaneously $k_\chi(E)$ and $n_\chi(E)$, is much less than that required by other approaches. For example, the harmonic-oscillator model requires 22 parameters to fit experimental data of Si [10] in essentially the same energy range without the benefit of providing E_g.

C Metals

In the case of metals, we use the example of Cu to demonstrate the applicability of $k_\mu(E)$, Eq. 22, and $n_\mu(E)$, Eq. 36. (Preliminary results indicate that they apply to other metals, such as Al and Au.) These equations, with three terms included in the sum, are fitted to the experimental values of $k_\mu(E)$ and $n_\mu(E)$ obtained by Hagemann *et al.* [24] for the energy range where interband transitions of bound electrons are predominant (see next paragraph), namely, 1.7–10 eV. Theoretical and experimental plots of $k_\mu(E)$ and $n_\mu(E)$ are shown in Fig. 6 with values of the parameters given in Table V; excellent agreement with the experimental data is achieved.

Contribution of bound electrons for $E < 1.7$ eV is overshadowed by the strength of free-electron transitions. Thus, the measured reflectance spectrum, $R(E)$, exhibits a flat, structureless plateau for $E < 1.7$ eV [25]. For $E > 1.7$ eV, bound-electron contributions prevail. Experimentally, $R(E)$ decreases sharply between 1.7 and 2.1 eV and thereafter exhibits several peaks [25].

We have extended the theoretical plots of $k_\mu(E)$ and $n_\mu(E)$ down to $E = 0$ in order to determine the interband contributions in the far-infrared regime. It should be emphasized that free-electron interactions are not

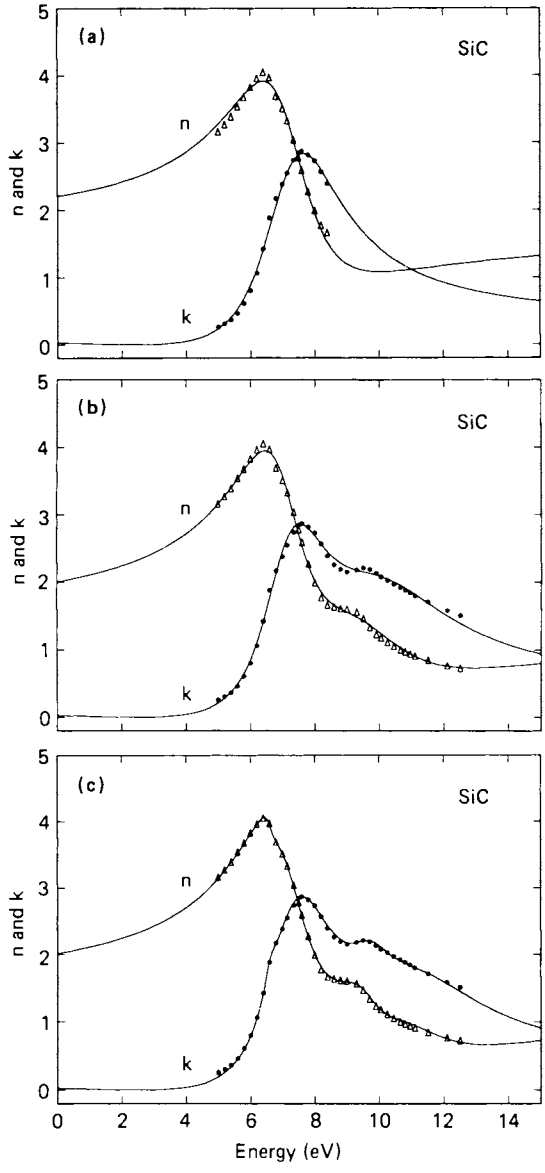

Fig. 5. The solid lines are the theoretical ploits of $k_\chi(E)$ and $n_\chi(E)$ given by Eqs. 21 and 35 with the parameters specified in Table IV for crystalline SiC, taking the number of terms in these equations equal to 1, 2, and 4 in (a), (b), and (c), respectively. In (a), only experimental data in the 5–8.5 eV energy range are considered. Experimental data are by Leveque and Lynch [1, 23]. (From Forouhi and Bloomer [14].)

TABLE IV

	A_i	B_i (eV)	C_i (eV^2)	$n(\infty)$	E_g (eV)
SiC					
1 term	0.25926	14.359	53.747	1.680	2.50
2 terms	0.18028	14.222	52.148	1.337	2.50
	0.10700	19.397	99.605		
4 terms	0.00108	13.227	43.798	1.353	2.50
	0.19054	14.447	53.860		
	0.00646	19.335	94.105		
	0.05366	21.940	125.443		

Three separate sets of parameters describing the theoretical equations $k_\chi(E)$ and $n_\chi(E)$, Eqs. 21 and 35, for crystalline SiC. The number of terms in the sums for these equations is taken equal to one, two, or four, as indicated. In all three sets, values of the parameters A_i, B_i, C_i, and $n(\infty)$ are obtained by least-square fitting of the experimental data [1, 23] to the theoretical equations. E_g is taken as the energy at which the experimental k spectrum has its absolute minimum. The corresponding plots are shown in Fig. 5a, b and c.

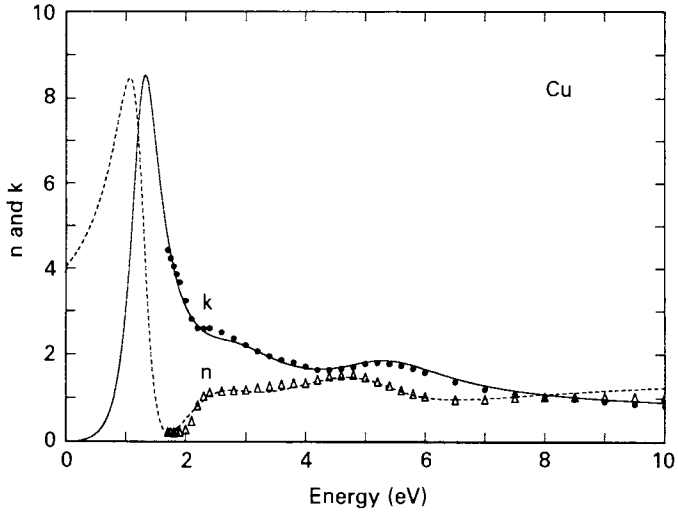

Fig. 6. The solid and dashed lines represent, respectively, the theoretical plots of $k_\mu(E)$ and $n_\mu(E)$ given by Eqs. 22 and 36 with the parameters specified in Table V for Cu. Experimental data are by Hagemann *et al.* [1, 24]. (From Forouhi and Bloomer [15].)

TABLE V

	A_i	B_i (eV)	C_i (eV^2)	$n(\infty)$
Cu	0.46531	2.499	1.652	1.711
	0.07489	5.390	8.010	
	0.03872	10.396	28.393	

The parameters describing the theoretical equations $k_\mu(E)$ and $n_\mu(E)$, Eqs. 22 and 36, with three terms in the sums, for Cu. Values of the parameters A_i, B_i, C_i, and $n(\infty)$ are obtained by least-square fitting of experimental data [1, 24] to the theoretical equations. The corresponding plots are shown in Fig. 6.

included in the present treatment. As expected, $k(E)\rightarrow 0$ when $E\rightarrow 0$, since bound-electron transitions are negligible at low energies where free-electron interactions dominate. (Free-electron transitions do not give rise to structure in optical constants of metals [1]). As seen in Fig. 6, a sharp peak in the theoretical curve of $k_\mu(E)$ occurs at $E\approx 1.7$ eV, indicative of a sharp peak in reflectance, $R(E)$, near this energy. This is consistent with strong reflectance of red-orange frequencies, producing the characteristic copper color. Thus, we infer that the color of Cu can be attributed to direct interband critical-point transitions of bound electrons. In fact, this was concluded by Mott and Jones [26] nearly thirty years ago.

V SUMMARY

We have deduced equations for the extinction coefficient, $k(E)$, (Eqs. 20, 21, 22) and the refractive index, $n(E)$, (Eqs. 32, 35, 36) applicable to amorphous semiconductors and dielectrics, crystalline semiconductors and dielectrics, and metals. Amorphous semiconductors and dielectrics are distinguished from crystalline semiconductors and dielectrics and metals by the number of terms in the equations for $k(E)$ and $n(E)$, which in turn is equal to the number of spectral peaks. Metals are distinguished from crystalline semiconductors and dielectrics by the absence of E_g. The equations that we derive for $k(E)$ are based on direct interband transitions of bound electrons and lead to structure in optical constants through transitions of electrons from one distinguishable state to another. Distinguishable states are defined to be either the bonding and antibonding states associated with the valence and conduction bands of amorphous materials, or critical-point states associated with the valence and conduc-

tion bands of crystalline materials. The expression $n(E)$ is determined according to the Kramers–Kronig dispersion relation from the corresponding $k(E)$. These equations are applicable throughout the fundamental optical energy range. Thus, the present formulation furnishes a unified treatment of optical constants of materials in the interband region.

REFERENCES

1. E. D. Palik, ed., "Handbook of Optical Constant Solids," Academic Press, New York (1985).
2. T. S. Moss, G. J. Burrell, and B. Ellis, "Semiconductor Opto-Electronics," Wiley, New York (1973).
3. N. F. Mott and E. A. Davis, "Electronic Processes in Non-Crystalline Materials," 2nd ed., Clarendon, Oxford (1979).
4. J. I. Pankove, "Optical Processes in Semiconductors," Dover, New York (1971).
5. D. L. Greenaway and G. Harbeke, "Optical Properties and Band Structure of Semiconductors," Pergamon, Oxford (1968).
6. J. C. Phillips, "Bonds and Bands in Semiconductors," Academic Press, New York (1973).
7. F. Stern, in "Solid State Physics" (F. Seitz and D. Turnbull, eds.), Vol. 15, Academic Press, New York, 299 (1963).
8. J. Tauc, R. Grigorovici, and A. Vancu, *Phys. Status Solidi* **15**, 627 (1966).
9. H. Ehrenreich and M. Cohen, *Phys. Rev.* **115**, 786 (1959).
10. H. W. Verleur, *J. Opt. Soc. Am.* **58**, 1356 (1968).
11. R. Zallen, "The Physics of Amorphous Solids," Wiley, New York (1983).
12. A. R. Forouhi and I. Bloomer, *Phys. Rev. B* **34**, 7018 (1986).
13. W. Heitler, "The Quantum Theory of Radiation," 3rd ed., Dover, New York (1984).
14. A. R. Forouhi and I. Bloomer, *Phys. Rev. B* **38**, 1865 (1988).
15. A. R. Forouhi and I. Bloomer, unpublished.
16. J. S. Toll, Ph.D. thesis, Princeton University, New Jersey (1952).
17. P. Roman, "Advanced Quantum Theory," Addison-Wesley, Reading, Mass. (1965).
18. A. R. Forouhi, in "Properties of Amorphous Silicon," 2nd ed., EMIS Datareview Series No. 1, INSPEC, The Institution of Electrical Engineers, London, Chapter 9, 309 (1989).
19. R. H. Klazes, M. H. L. M. van den Broek, J. Bezemer, and S. Radelaar, *Philos. Mag. B* **45**, 377 (1982).
20. J. Joseph and A. Gagnaire, *Thin Solid Films* **103**, 257 (1983).
21. D. E. Aspnes and A. A. Studna, *Phys. Rev. B* **27**, 985 (1983).
22. H. R. Philipp, *Solid State Commun.* **4**, 73 (1966); quoted in tabulated form by H. R. Philipp in Ref. 1, p. 719.
23. G. Leveque and D. A. Lynch, private communication with W. J. Choyke and E. D. Palik. See Ref. 1, p. 587.
24. H. J. Hagemann, W. Gudat, and C. Kunz, DEZY Report SR-74/7, Hamburg, (1974); H. J. Hagemann, W. Gudat, and C. Kunz, *J. Opt. Soc. Am.* **65**, 742 (1975); quoted in tabulated form by D. W. Lynch and W. R. Hunter in Ref. 1, p. 275.
25. H. Ehrenreich and H. R. Philipp, *Phys. Rev.* **128**, 1622 (1962).
26. N. F. Mott and H. Jones, "The Theory of the Properties of Metals and Alloys," Dover, New York (1958).

Chapter 8

Temperature Dependence of the Complex Index of Refraction

MICHAEL E. THOMAS
Applied Physics Laboratory
The Johns Hopkins University
Laurel, Maryland

I. Introduction 177
II. Temperature Dependence of n and k 179
A. General Remarks 179
B. One-Phonon Temperature Dependence 181
C. Absorption near Transparency 185
III. Conclusions 199
References 199

I INTRODUCTION

Although the emphasis of *HOC I* and *HOC II* is room-temperature optical properties of materials, a discussion of temperature dependence is imperative for many current applications. A good example is thermal lensing by high-power laser windows, which requires knowledge of both absorption and index of refraction as a function of temperature. Also, the range of window materials transparency is temperature dependent. Transparency is improved by lowering temperature. For maximum sensitivity, thermal emission from a window in front of a detector must be considered. Imaging through a nonuniform hot window requires compensation of the distortions caused by the temperature-dependent index of refraction.

The intrinsic optical properties of a material are determined by three basic physical processes: free carriers, lattice vibrations, and electronic transitions. These processes were described in *HOC I*. However, the dominant physical process depends on the material. All materials have contributions to the complex index of refraction from electronic transitions. Metals and semiconductors are additionally influenced by free-

Copyright © 1991 by Academic Press.
All rights of reproduction in any form reserved.
ISBN 0-12-544422-2

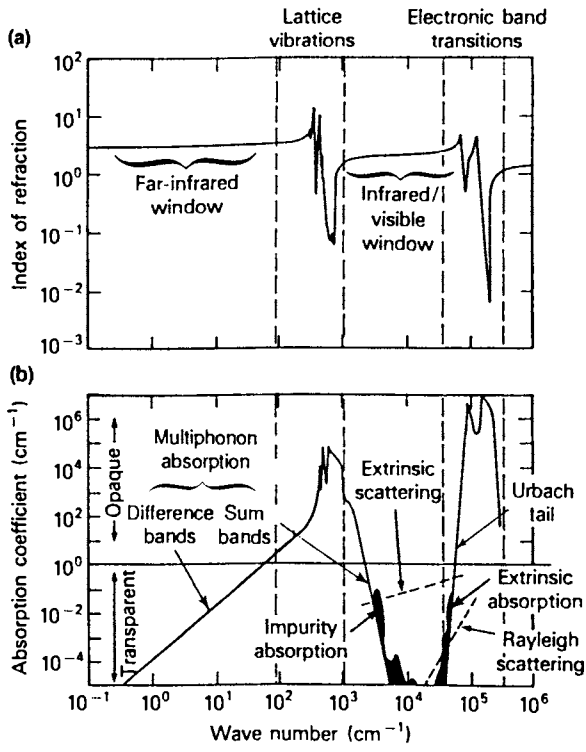

Fig. 1. Optical properties of a typical polar crystalline insulator.

carrier effects. The strength of this effect depends on the carrier concentration; thus, it is very important in metals. Insulators and semiconductors also require the characterization of the lattice vibrations (or phonons) to understand fully the optical properties.

In the range of transparency, more subtle processes such as impurities, defects, and scattering become important. Intrinsic Rayleigh scattering is a very weak effect, but is important in long-path optical fibers and UV transparent materials. Extrinsic scattering, caused by defects or grains in polycrystalline solids, is typically much larger than Rayleigh scattering. Impurity and defect absorption features can be of great concern depending on the spectral region, incident radiation intensity, and material temperature.

The temperature, T, and frequency, ν (in wave numbers), dependence of the real part of the index of refraction, $n(\nu, T)$ (index of refraction), is determined by the dominant physical processes previously mentioned. Figure 1a illustrates this point for the case of an insulating polar crystal. The value of $n(\nu, T)$ is essentially the sum of the strengths of all oscillators

with fundamental oscillation frequencies above ν. Thus, the temperature dependence of those oscillations must be known to characterize $n(\nu, T)$ fully at any frequency.

The temperature and frequency dependence of the imaginary part of the index of refraction, $k(\nu, T)$ (index of extinction), is more involved and requires consideration of not only the dominant physical processes but also higher-order processes, impurities, and defects. The spectral regions of the fundamental oscillations are opaque. Transparency of an insulator is determined by three different absorption edges as illustrated in Figure 1b. Far-infrared transparency ends in the region of two-phonon difference bands and the one-phonon red wing (the low-frequency side of the absorption band). Infrared transparency begins in the region of three-phonon sum bands (essentially the third harmonic of the one-phonon bands). Visible/ultraviolet transparency ends at the Urbach tail, which can be phenomenologically interpreted as thermal fluctuations in the band-gap energy [1]. (A formula representing the Urbach tail, including temperature dependence, was given in *HOC I*, Chapter 10, by Lynch [2]). A detailed discussion of the temperature dependence of one- and multiphonon processes extends the work of Mitra in *HOC I* and is the central topic of this chapter.

The temperature dependence of intrinsic Rayleigh scattering will not be considered because it is usually too small to be of concern. Extrinsic scatter in polycrystalline materials has been observed to be constant with temperature for low-expansion materials [3], and also will not be discussed further. Impurity and defect absorption, which may be significant, are highly material and manufacturing-process dependent and will not be properly treated within the limits of this chapter.

The emphasis of this chapter is on the temperature-dependence of optical phonons. Insulators are the primary examples to be compared to the models presented.

TEMPERATURE DEPENDENCE OF *n* AND *k* II

General Remarks A

As an introduction to the temperature dependence of the complex index of refraction, $n^*(\nu, T) = n(\nu, T) - jk \leftarrow (\nu, T)$, consider the Lorentz–Lorenz formula,

$$\frac{n^2-1}{n^2+2} = \frac{1}{3\varepsilon_0}\rho(T)\alpha_p(\rho, T), \tag{1}$$

where ρ is the number density of oscillators per unit volume and α_p is the polarizability. The derivative of n with respect to T becomes [4]

$$2n\varepsilon_0\frac{dn}{dT}=(n^2+2)(n^2-1)\left[\frac{1}{3\rho}\frac{\partial\rho}{\partial T}+\frac{1}{3\alpha_p}\left\{\left(\frac{\partial\alpha_p}{\partial\rho}\right)_T\frac{\partial\rho}{\partial T}+\left(\frac{\partial\alpha_p}{\partial T}\right)_\rho\right\}\right]. \quad (2)$$

The number density, ρ, is

$$\rho=N/V,$$

where N is the number of oscillators per unit volume V. Further, the derivative of volume with respect to temperature can be written in terms of the linear coefficient of expansion, α_e, as

$$\frac{dV}{dT}=3V\alpha_e. \quad (3)$$

Now, Eq. 2 can be rewritten in a more meaningful form

$$2n\varepsilon_0\frac{dn}{dT}=-(n^2+2)(n^2-1)\alpha_e\left[1-\frac{V}{\alpha_p}\left(\frac{\partial\alpha_p}{\partial V}\right)_T\right] + \frac{(n^2+2)(n^2-1)}{3\alpha_p}\left(\frac{\partial\alpha_p}{\partial T}\right)_V. \quad (4)$$

The first term depends on changes in volume with respect to temperature. Thermal expansion is the dominant contributor. The second term represents the temperature changes in the polarizability. Many optical materials, such as the alkali halides and the fluorides, have negative values for dn/dT in the visible and infrared. Thus, for these materials, volume expansion dominates over polarizability temperature dependence. Li [5] is able to show a direct proportionality between the expansion coefficient and dn/dT for the alkali halides.

The polarizability is determined by two fundamental processes in an insulating material: electronic transitions and vibrational transitions. The electronic transitions contribute to the index of refraction from the ultraviolet/visible region to DC. The vibrational transitions also contribute to the index of refraction from the far-infrared to DC. They are more

temperature sensitive than the electronic transitions; thus, dn/dT in the far infrared below the optical phonons is usually positive and greater than dn/dT in the visible/IR.

A more detailed discussion of the temperature dependence is given in the following sections.

One-Phonon Temperature Dependence B

The optical properties of an insulating material can be completely specified by the complex index of refraction, $n^*(\nu, T)$, or the complex permittivity, $\varepsilon^*(\nu, T)$, where ν is the wave number (reciprocal wavelength). The relationship between n^* and ε^* is

$$n^*(\nu, T) = \sqrt{\varepsilon^*(\nu, T)}, \tag{5}$$

where

$$\varepsilon^*(\nu) = (n^2 - k^2) - 2jnk = \varepsilon_1 - j\varepsilon_2. \tag{6}$$

The absorption coefficient is defined by

$$\beta_a(\nu, T) = 4\pi\nu k(\nu, T). \tag{7}$$

In the following, only intrinsic absorption losses will be considered. The magnitude of the single-surface reflectance, $|R|$, of a medium (at normal incidence) is

$$|R| = \frac{(n-1)^2 + k^2}{(n+1)^2 + k^2}. \tag{8}$$

Generally, a measurement of $|R|$ is not sufficient to determine ε^* (for example, both n and k). Hence, it is necessary to describe the relationship between n and k. The "classical pole-fit model" (see Mitra, *HOC I*)

represents ε^* in terms of the lattice vibrations:

$$\varepsilon^*(\nu, T) = \varepsilon_\infty(T) + \sum_i \frac{\Delta\varepsilon_i(T)\nu_i^2(T)}{\nu_i^2(T) - \nu^2 + j\gamma_i(\nu, T)\nu}, \tag{9}$$

where $\Delta\varepsilon_i$, γ_i and ν_i are the jth mode strength, line width, and long-wavelength transverse optical frequency, respectively. The sum on i is over all transverse optical modes. This model is well-known to describe n adequately in the infrared and radar-frequency regions [1]. Using Eq. 9, the static dielectric constant, $\varepsilon_s(T) = \varepsilon_1(0, T)$, becomes

$$\varepsilon_s(T) = \varepsilon_\infty(T) + \sum_i \Delta\varepsilon_i(T) \tag{10}$$

The implied frequency dependence of γ_i represents a cutoff beyond the one-phonon region caused by anharmonicities of the potential. The cutoff is empirically represented by the formula [6]

$$\gamma_i(\nu, T) = \gamma_i(T) \left\{ \begin{array}{ll} 1; & \nu \leq \tilde{\nu} \\ \exp\left\{ -\alpha \left[\left(\frac{\nu}{\tilde{\nu}} \right)^2 - 1 \right] \right\}; & \nu \geq \tilde{\nu} \end{array} \right\}, \tag{11}$$

where α and $\tilde{\nu}$ are arbitrary parameters. We have been most successful in this effort by choosing $\alpha = 4$ and $\tilde{\nu}$ as the highest infrared-allowed longitudinal-optical-mode frequency. Although those values for α and $\tilde{\nu}$ are not unique, they are adequate for the present purpose.

This model satisfies the Kramers–Kronig relationship and therefore provides the correct relationship between ε_1 and ε_2. It also allows for the construction of a physically meaningful representation of ε^*, using only the magnitude of R as input. This point has been extremely useful in modeling efforts.

Another commonly used pole-fit model features four parameters per transition, as given by the expression [7]

$$\varepsilon^*(\nu, T) = \varepsilon_\infty(T) \prod_i \frac{\nu_{iLO}^2(T) - \nu^2 + j\nu\gamma_{iLO}(\nu, T)}{\nu_i^2(T) - \nu^2 + j\nu\gamma_i(\nu, T)}, \tag{12}$$

where the additional subscript LO indicates longitudinal-optical-mode parameters. A product instead of a sum is now used. Equation 12 in the

static limit reduces to the Lyddane–Sachs–Teller relation [8]

$$\frac{\varepsilon_s}{\varepsilon_\infty} = \prod_i \frac{\nu_{iLO}^2}{\nu_i^2}. \tag{13}$$

This is a similar statement to Eq. 10, now in the form of a product.

As Eq. 9 suggests, the reflectance is a function not only of frequency but also of temperature. Experiments reported by Jasperse *et al.* [9] have demonstrated that the optical parameters $\Delta\varepsilon_i$ and ν_i have a linear temperature dependence, and calculations by Maradudin and coworkers [10] have successfully utilized a quadratic temperature dependence for γ_i at high temperatures. A theoretical calculation by Wallis and Maradudin [11] has shown that the temperature dependence of ν_i and γ_i comes from cubic anharmonic terms in the lattice potential energy. The origin of the temperature dependence of the mode strengths, $\Delta\varepsilon_i$, is not well established but can be understood by considering the static dielectric constant. Szigeti [12] has shown that not only do anharmonic terms in the lattice potential energy contribute to the temperature dependence of $\varepsilon_s(T)$, but also a contribution arises from terms in the dipole moments that are of higher order in the displacement coordinates. These latter higher-order terms have their origin in the deformation of the electronic shells.

The temperature dependence of the transverse-mode frequencies, ν_i, and the mode strengths, $\Delta\varepsilon_i$, can be represented by linear equations of the form

$$\nu_i(T) = \nu_i(T_0) - a_i[T - T_0] \tag{14a}$$

and

$$\Delta\varepsilon_i(T) = \Delta\varepsilon_i(T_0) + b_i[T - T_0], \tag{14b}$$

where T_0 is a reference temperature (typically room temperature) and a_i and b_i are mode- and material-specific constant coefficients. The dependence of the linewidth on temperature can be described by a quadratic equation in T as

$$\frac{\gamma_i}{\nu_i}(T) = \frac{\gamma_i}{\nu_i}(T_0) + c_i[T - T_0] + d_i[T - T_0]^2, \tag{14c}$$

where T_0 is again a reference temperature and c_i and d_i are also mode- and

material-specific constant coefficients. The high-frequency permittivity, ε_∞, is temperature dependent and is represented by

$$\varepsilon_\infty(T) = \varepsilon_\infty(T_0) + e_i[T - T_0]. \tag{14d}$$

Note that $e_i = d\varepsilon_\infty/dT = 2n_\infty(dn_\infty/dT)$; thus, in most cases, e_i can be determined from visible dn/dT measurements.

Table I lists the optical constants of Y_2O_3 based on the previously discussed formulas. The parameters are determined from reflection spectra as shown in Fig. 2. A comparison is made between the experimental data and the one-phonon-model representation. Other examples can be found in *HOC I*, Chapter 11. This model is important for spectral-emissivity calculations and index-of-refraction calculations from microwave to ultraviolet over a wide range of temperatures.

Differentiating Eq. 9 with respect to temperature gives an explicit formula for dn/dT, replacing Eq. 4 [5]. The value $\Delta\varepsilon$ depends linearly on the oscillator density and will lead to the term representing volume change with respect to temperature. Now the details of the polarizability term can be understood. For materials with strong polarizability and small volume expansion (for example, the oxides), the values of dn/dT in the visible and

TABLE I

Optical Constants of Y_2O_3

Mode	ν_i (T_0) (cm^{-1})	a_i ($cm^{-1}\,K^{-1}$)	$\Delta\varepsilon_i(T_0)$	b_i (K^{-1})	$\gamma_i/\nu_i(T_0)$	c_i (K^{-1})	d_i (K^{-1})
1	120.0	~0.01	0.2	—	0.035	—	—
2	172.0	~0.01	0.1	—	0.025	—	—
3	182.0	~0.01	0.15	—	0.025	—	—
4	241.0	0.0072	0.200	7.10×10^{-5}	0.025	1.46×10^{-5}	—
5	303.0	0.0144	2.600	6.24×10^{-4}	0.0135	3.35×10^{-5}	—
6	335.0	0.0109	1.749	-3.55×10^{-4}	0.0115	2.38×10^{-5}	—
7	371.0	0.0109	2.651	6.38×10^{-5}	0.021	2.51×10^{-5}	—
8	415.0	0.0109	0.040	3.55×10^{-5}	0.011	3.24×10^{-5}	—
9	461.0	0.0144	0.050	3.55×10^{-5}	0.015	1.80×10^{-5}	—
10	490.0	0.0180	0.005	3.55×10^{-6}	0.018	2.12×10^{-5}	—
11	555.0	0.0210	0.095	9.36×10^{-5}	0.025	1.21×10^{-5}	—
12[b]	72,100.0	—	2.579	1.40×10^{-4}	—	—	—

[a] $T_0 = 295$ K.
[b] Electronic transition.
$\varepsilon_\infty(T) = 1.00$.

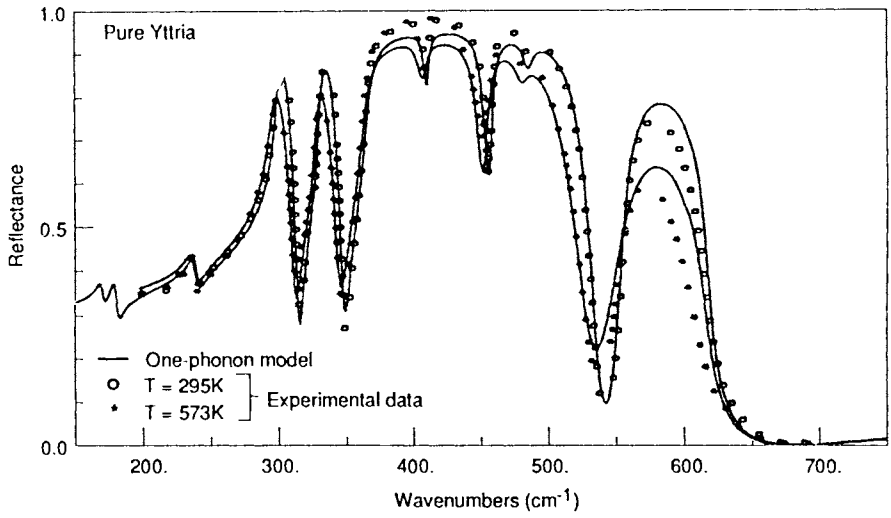

Fig. 2. Reflection spectra of pure yttria at two temperatures.

IR are small and positive. This is in contrast to previously discussed results for the alkali-halides and the fluorides. In the microwave region the static dielectric constant is used (see Eq. 10), which includes the contributions from the lattice vibrations. Thus, the value of the net polarizability can greatly increase, and $d\varepsilon_s/dT$ is usually positive. Figure 3 illustrates the experimental temperature dependence of $\varepsilon_s(T)$ for the ordinary-ray of sapphire [13–16]. The dashed curve shows the range of validity of the linear approximations used in obtaining Eq. 14b.

Absorption near Transparency C

The classical pole-fit model represents the fundamental lattice vibrations or one-phonon transitions in a material. But the absorption coefficient obtained from the model is valid only in the vicinity of the one-phonon frequencies. The absorption coefficient needs to be known in the regions of transparency as well, requiring a description of multiphonon absorption bands in which more than one-phonon excitation occurs upon the absorption of a single photon. The mm-wave region is dominated by the one-phonon red wing and multiphonon difference bands. The IR region is dominated by multiphonon sum bands.

The absorption coefficient is expressed, in general, as

$$\beta_a(\nu, T) = \sum_{l} S_{lu}(T; \nu_{lu}) g(\nu, T; \nu_{lu}), \tag{15}$$

where ν_{lu} is the transition center frequency, $S_{lu}(T)$ is the transition strength, $g(\nu, T)$ is the spectral distribution function, and the sum is over all initial states. Based on the work of Kubo [17] and Van Vleck and Huber [18], the strength and shape functions are expressed as

$$S_{lu} = \frac{8\pi^3 \nu_{lu}}{3hn} \rho \frac{e^{-E_l/k_B T}}{Z(T)} (1 - e^{-hc\nu_{lu}/k_B T}) |\bar{M}|^2 \tag{16}$$

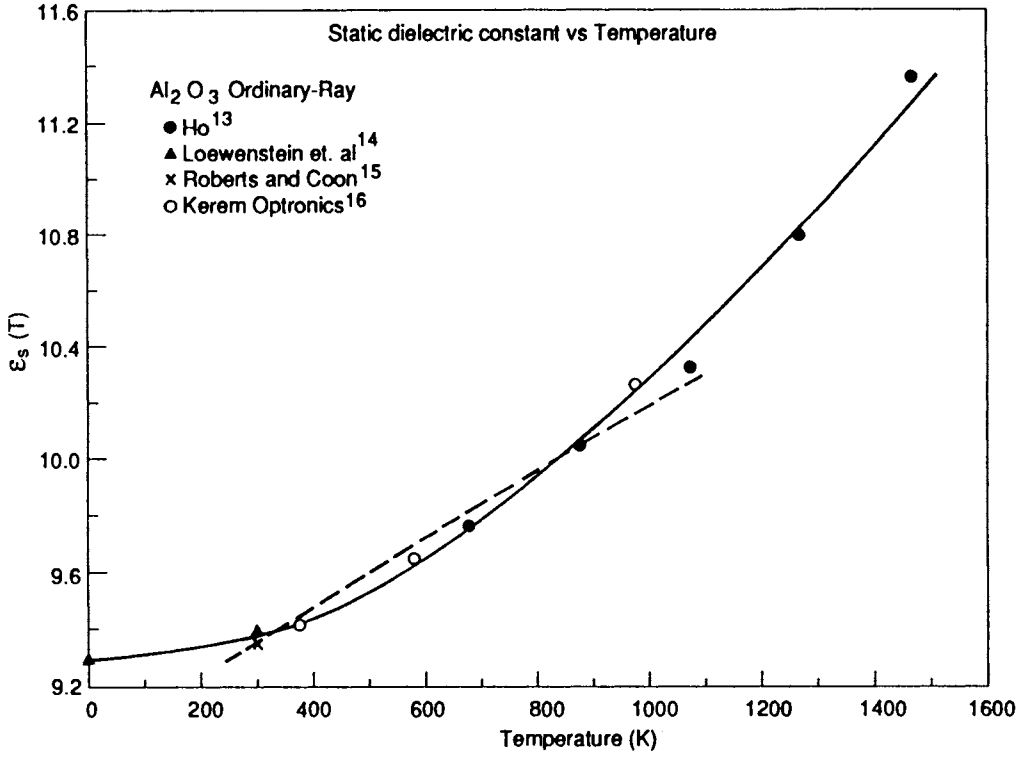

Fig. 3. The temperature dependence of the static dielectric constant of the ordinary-ray of Al_2O_3. The dash curve represents a linear approximation to the experimental data.

TABLE II

The Far-Infrared Absorption-Coefficient Parameters for $T_0 = 295$ K

Material	$A(T_0)$ [cm]	$A_{1p}(T_0)$ [cm]	A_{2p} [cm K^{-1}]	A_{3p} [cm K^{-2}]
MgO	—	6.1×10^{-4}		
SiO_2 o-ray	1.07×10^{-4}	8.9×10^{-5}		
e-ray	8.2×10^{-5}	1.39×10^{-4}		
Al_2O_3 o-ray	9.15×10^{-4}	2.2×10^{-4}	4.7×10^{-4}	2.2×10^{-4}
e-ray	1.28×10^{-3}	8.6×10^{-4}		
Y_2O_3	2.1×10^{-3}	8.4×10^{-4}		
$MgAl_2O_4$	2.2×10^{-3}	1.6×10^{-4}		
ALON	1.1×10^{-3}	—		
ZnS	5.8×10^{-4}	9.8×10^{-4}		
NaCl	1.2×10^{-2}	3.0×10^{-3}	9.0×10^{-3}	

and

$$g(\nu, T) = \frac{\nu}{\nu_{lu}} \frac{(1 - e^{-hc\nu/k_B T})}{(1 - e^{-hc\nu_{lu}/k_B T})} j(\nu), \tag{17}$$

where h is Planck's constant, ρ is the density of dipoles per unit volume, E_l is the lower energy of the transition, $Z(T)$ is the partition function, k_B is Boltzmann's constant, $|\bar{M}|^2$ is the dipole matrix element, and $j(\nu)$ is the Fourier transform of the dipole autocorrelation function. On the basis of this theory, the low-frequency (that is, ≤ 50 cm^{-1}) absorption coefficient is ν^2 multiplied by the line-shape function. A simple ν^2 falloff will dominate in two cases. The first is the far red wing of an absorption band and the second is for broad line-shape functions featuring very little frequency dependence throughout a band. These conditions are met for many materials of interest in the far infrared, because the absorption is dominated by intrinsic processes. Thus, the simple formula

$$\beta_a(\nu) = A\nu^2 \tag{18}$$

can be used to represent experimental data of these materials.

Based on Eq. 9, the one-phonon red wing ($\nu \to 0$) becomes

$$\beta_{1p}(\nu \to 0, T) = \left[\frac{2\pi}{n(0, T)} \sum_i \frac{\Delta\varepsilon_i(T)\gamma_i(\nu, T)}{\nu_i^2(T)} \right] \nu^2. \tag{19}$$

Even though Eq. 9 comes from a phenomenological model, this extrapolation to the red wing works for many materials (see Table II). In addition to the one-phonon contributions, difference bands of two and three phonons must also be included. Detailed models are extremely difficult to obtain, and thus only empirical formulas are used. It is straightforward to show, however, in the high-temperature limit ($hc\nu \ll k_B T$) that the n-phonon difference-band temperature dependence goes as [19]

$$\beta_{np} = A_{np} T^{n-1} \nu^2. \tag{20}$$

Thus, experimental data in this high-temperature limit can be represented by the formula

$$\beta_a(\nu, T) = \sum_n \beta_{np}(\nu, T) \tag{21}$$

and

$$\beta_a(\nu, T) \underset{\nu \to 0}{=} \left[\frac{2\pi}{n(0, T)} \sum_i \frac{\Delta\varepsilon_i(T)\gamma_i(\nu, T)}{\nu_i^2(T)} + A_{2p}T + A_{3p}T^2 \right] \nu^2 \tag{22}$$

$$= A(T)\nu^2.$$

Based on Eq. 22, the far-infrared absorption coefficient increases with increasing temperature. Temperature-dependent data are needed to determine the contributions from two-phonon and three-phonon difference bands. Figure 4 compares experimental data for sapphire [14, 15, 20] to the model based on the parameters given in Table II [14, 15, 20–22] and Eq. 22. A good fit is obtained from above 200K to 1000K for a variety of wave numbers. The fact that the absorption coefficient does not go to zero as the temperature goes to zero is a clear indication of the existence of the one-phonon red wing. The one-phonon red wing is frequently ignored in interpreting far-infrared absorption data [19], and this is not correct. Extrapolation to lower frequencies more typical of mm-wave frequencies

work reasonably well at room temperature [23]. However, the temperature dependence may change because three-phonon contributions will be greater at frequencies below two-phonon absorption than this simple model represents. This fact is demonstrated in Fig. 4; the model underestimates the experimental absorption coefficients at $50\,cm^{-1}$ at elevated temperatures. A more rapid temperature dependence is needed at $50\,cm^{-1}$ than is observed at $100\,cm^{-1}$ or $200\,cm^{-1}$. This is consistent with an increasing contribution to the absorption from three-phonon difference bands with decreasing frequency.

The absorption coefficient also increases with increasing temperature at the infrared edge of transparency. This region is dominated by multipho-

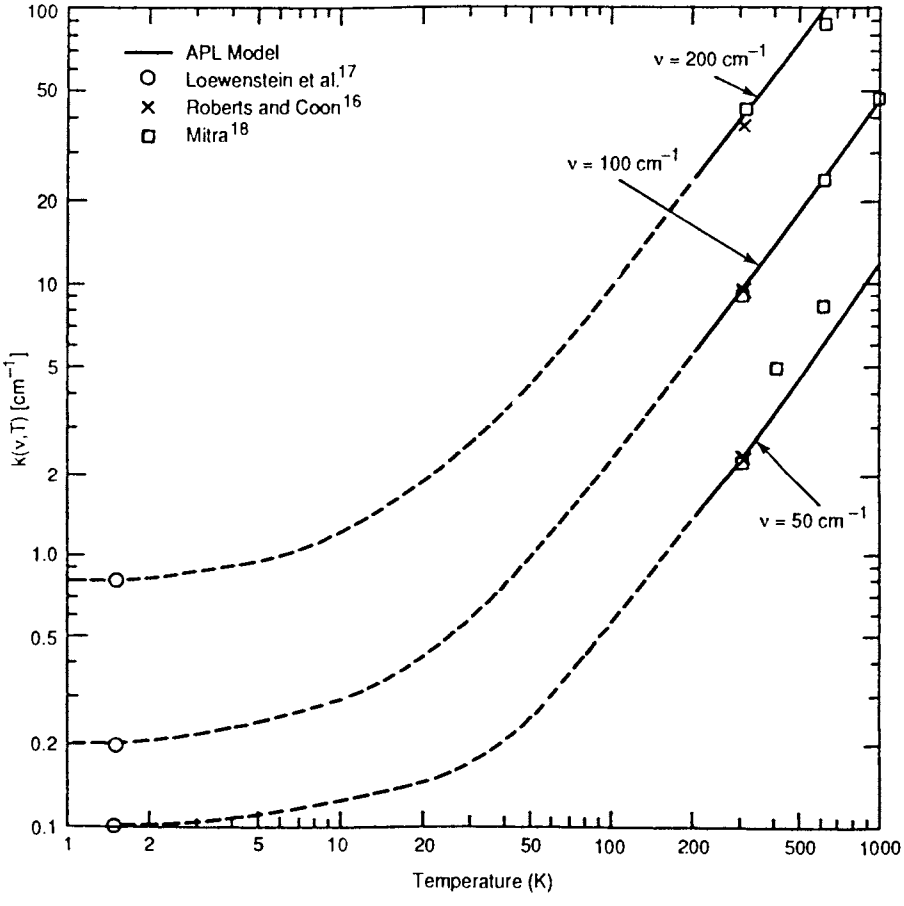

Fig. 4. Comparison of experimental data to the APL model for the far-infrared absorption coefficient as a function of temperature and frequency, for the ordinary-ray of Al_2O_3.

non sum bands. Fortunately, in this case, there are theoretical models that accurately characterize the absorption loss, and one such model requires only a few material-dependent parameters.

There are several models that have been developed to describe multiphonon absorption [24–28]. Criteria of simplicity, minimum number of parameters, and general applicability have led to models based on the Morse interatomic potential, which is given by

$$V(r) = D(1 - \exp[-a(r - r_0)])^2. \tag{23}$$

D is the dissociation energy, r_0 is the location of the equilibrium position, $a = \omega_0(\mu/2D)^{1/2}$, ω_0 is the fundamental lattice-vibration frequency, and μ is the reduced mass. Both classical [24, 25] and quantum-mechanical [26–28] models exist. The Morse potential leads to an exact solution of the Schrödinger equation and includes anharmonic effects to all orders. These characteristics greatly simplify the model. The strong anharmonic nature of the true potential means that the harmonic-oscillator perturbational approaches have questionable validity and require major correction factors.

A brief discussion of the quantum-mechanical, Morse-potential, multiphonon model is presented in the following. Assumptions used in the model, besides use of the Morse potential, are as follows:

(1) A single generalized dissociation energy is sufficient.
(2) No impurities and defects are considered.
(3) Phonon density-of-state functions quickly approach the Gaussian form dictated by the central-limit theorem as the order of the harmonic increases.

The solution of the stationary-state Schrödinger wave equation using the Morse potential results in the following energy eigenvalues [26]:

$$E_m = \hbar\omega_0\left[\left(m + \frac{1}{2}\right) - \frac{1}{J}\left(m + \frac{1}{2}\right)^2\right], \tag{24}$$

where $\hbar = h/2\pi$, $J = (4D/\hbar\omega_0)$, and m is an integer, so that $m = 0, 1, 2, \ldots,$ $m_{\max} \leqslant 1/2\ (J - 1)$.

Based on Eqs. 15–17, the absorption coefficient β_a as a function of temperature T and wave number ν is

$$\beta_a(\nu, T) = \frac{8\pi^3 \rho \nu}{3hZn}[1 - \exp(-hc\nu/k_B T)]$$

$$\times \sum_{n=1}^{\infty} \sum_{m=0}^{m_{\max}-n} \exp(-E_m/k_B T)|M_{m(n+m)}|^2 j(\nu - \nu_{nm}), \qquad (25)$$

where

$$\nu_{nm} = \frac{E_{n+m} - E_m}{hc} = \nu_0 \left[n - \frac{1}{J}(n^2 + 2nm + n) \right] = N\nu_0. \qquad (26)$$

For the case of $m \ll J$ (that is, below the material melting temperature),

$$|M_{m(n+m)}|^2 \approx \frac{e^2 h}{8\pi^2 c \nu_0 \mu} \frac{(m+n)!}{m! n^2 J^{(n-1)}}. \qquad (27)$$

Substituting this result into Eq. 25 produces

$$\beta_a(\nu, T) = K \frac{\nu[1 - \exp(-\beta)]}{\nu_0 Z'} \sum_{n=1}^{\infty} \frac{1}{n^2} J^{-(n-1)} \sum_{m=0}^{m_{\max}-n}$$

$$\times \frac{(m+n)!}{m!} \exp(-\gamma M) j(\nu - \nu_{nm}), \qquad (28)$$

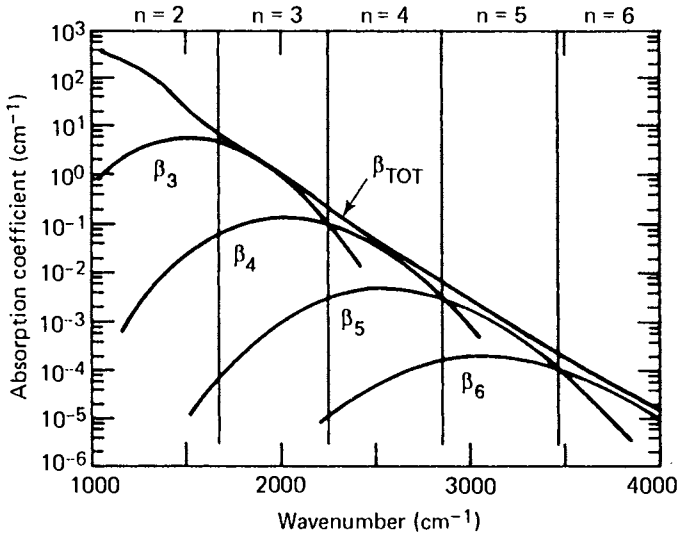

Fig. 5. The n-phonon absorption regions for room-temperature sapphire.

where

$$\beta = \frac{hc\nu}{k_B T},$$

$$Z' = \sum_{m=0}^{m_{\max}} \exp(-\gamma M),$$

$$\gamma = \frac{hc\nu_0}{k_B T},$$

$$K = \frac{\pi \rho e^2}{3c\mu n},$$

$$M = m\left(1 - \frac{1}{J}\right) - \frac{m^2}{J}.$$

In the continuum limit $J \to \infty$ ($hc\nu \ll 4D$) and for T large ($\gamma \ll 1$), the

absorption coefficient reduces to

$$\beta_a(n\nu_0, T) \simeq Kn! \left(\frac{k_B T}{4D}\right)^{n-1} j(0), \tag{29}$$

which agrees with the classical result [24].

Following the development of Boyer *et al.* [26], the transition line shape $[j(\nu - \nu_{nm})]$ is considerably narrower than the density-of-states distribution and is approximated by a delta function. The net absorption is the integration over all appropriately weighted oscillators.

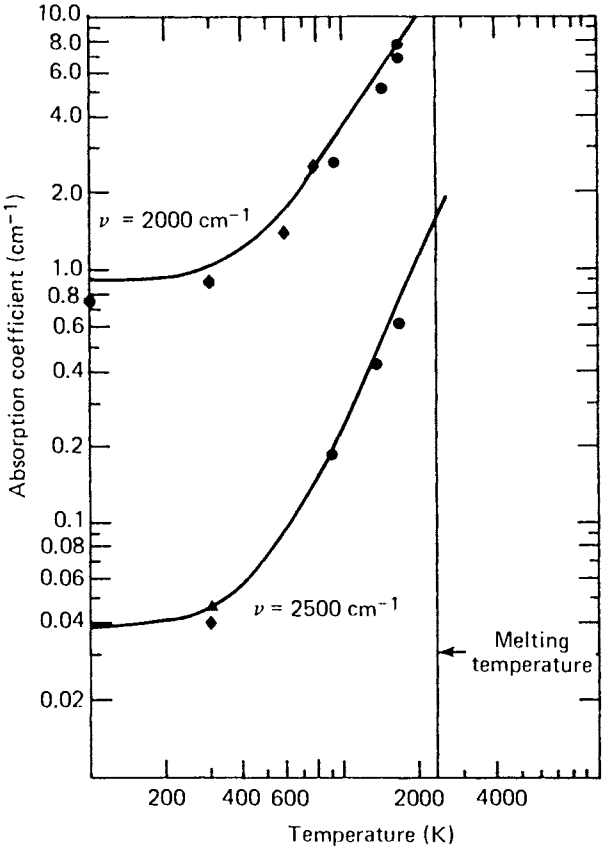

Fig. 6. Temperature dependence of the multiphonon absorption coefficient at fixed wave numbers for Al_2O_3 (▲ Deutsch [32], ● Billard *et al.* [29] and ◆ Thomas *et al.* [3]).

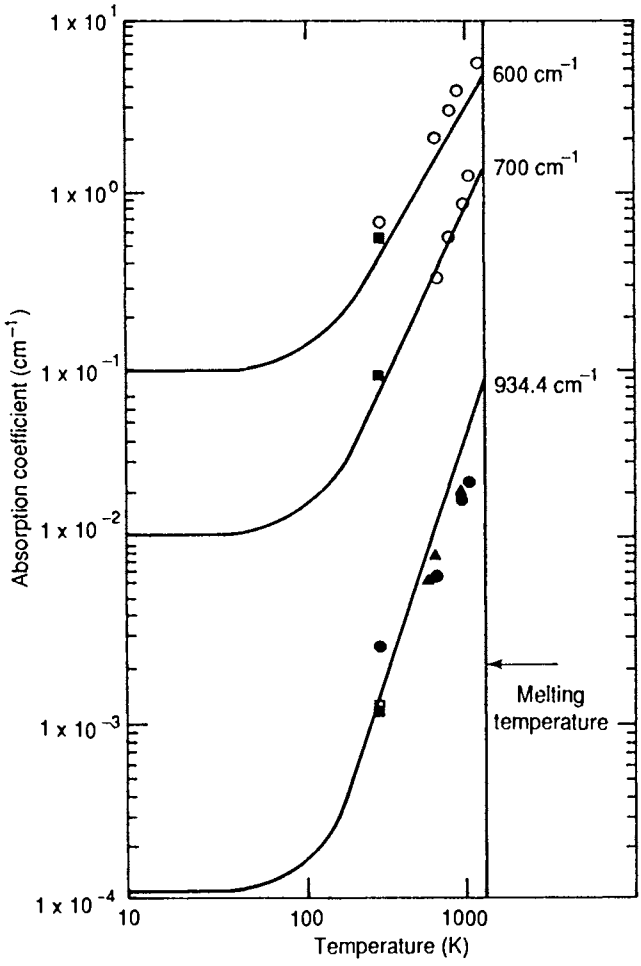

Fig. 7. Temperature dependence of the multiphonon absorption coefficient at fixed wave numbers for NaCl (□ Boyer *et al.* [26], ● Namjoshi and Mitra [20], ■ Deutsch [32], ○ Barker [33], and ▲ Harrington and Hass [34]).

$$\beta_{\text{tot}}(\nu, T) = \int_0^\infty d\nu_0 \beta(\nu_0, T)\rho_n(\nu_{nm})$$

$$= K[1-\exp(-\beta)] \sum_{n=1}^{\infty} \frac{\rho_n(\nu)}{n^2 Z'} \sum_{m=0}^{m_{\max}-n} \frac{(m+n)!}{m!} \frac{\exp[-\beta(M/N)}{J^{(n-1)}} \tag{30}$$

$$= \sum_{n=1}^{\infty} k_n(\nu, T),$$

where

$$Z' = \sum_{m=0}^{m_{\max}} \exp\left[-\beta\left(\frac{M}{N}\right)\right], \qquad J = \frac{4DN}{hc\nu},$$

and $\rho_n(\nu)$, the n-phonon density of states, is given by

$$\rho_n(\nu) = \int_0^\infty d\nu'' \int_0^\infty d\nu' \, \rho_{n-1}(\nu')\rho_1(\nu'')\delta(\nu - \nu' - \nu''), \tag{31}$$

where $\delta(\ )$ is the delta function. The value $\rho_n(\nu)$ is the probability of finding n-phonons in the lattice whose energies add up to $hc\nu$. It is required

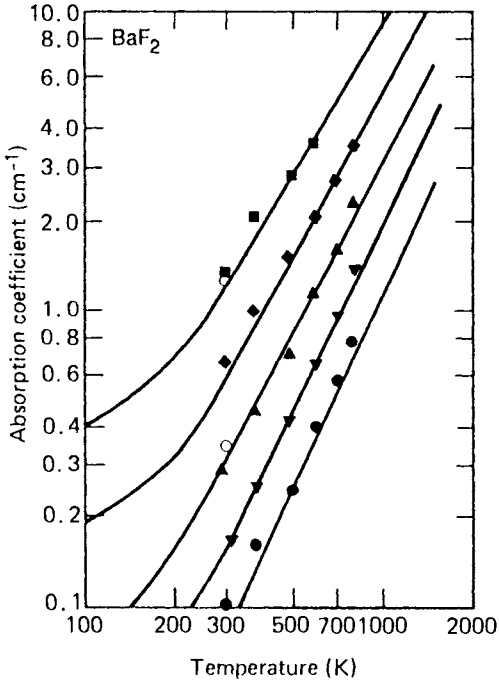

Fig. 8. Temperature dependence of the multiphonon absorption coefficient at fixed wave numbers for BaF_2 [34, 35] (○ Deutsch [32], ● $\nu = 1000\,cm^{-1}$, ▼ $\nu = 950\,cm^{-1}$, ▲ $\nu = 900\,cm^{-1}$, ◆ $\nu = 850\,cm^{-1}$, ■ $\nu = 800\,cm^{-1}$, and — multiphonon model [6]).

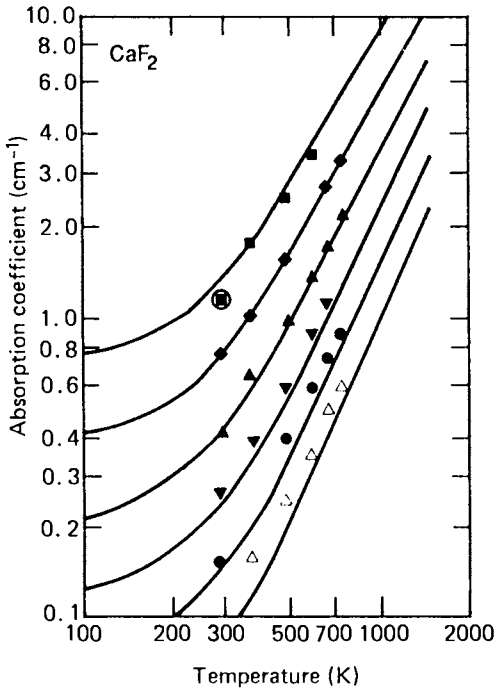

Fig. 9. Temperature dependence of the multiphonon absorption coefficient at fixed wave numbers for CaF_2 [34, 35] (○ Deutsch [32], △ $\nu = 1300\,cm^{-1}$, ● $\nu = 1050\,cm^{-1}$, ▼ $\nu = 1200\,cm^{-1}$, ▲ $\nu = 1150\,cm^{-1}$, ◆ $\nu = 1100\,cm^{-1}$, ■ $\nu = 1050\,cm^{-1}$ and — multiphonon model [6]).

that

$$\int_0^\infty \rho_1(\nu)\, d\nu = 1. \tag{32}$$

Using Eq. 31, it can be shown that all $\rho_n(\nu)$ values normalize to unity. As n increases, $\rho_n(\nu)$ rapidly becomes Gaussian. This is a manifestation of the central-limit theorem. (For sapphire, even $\rho_2(\nu)$ can be somewhat approximated by a Gaussian profile [29].) Based on the results of Boyer *et al.* [26], Sparks and Sham [28], and the asymptotic expansion of the central-limit theorem [30], $\rho_n(\nu)$ can be represented by the form

$$\rho_n(\nu) = \frac{1}{\sigma'\sqrt{2\pi}}\left[1 - \frac{\alpha_3}{\sqrt{n}}(3x - x^3)\right]\exp(-x^2/2);\ n \geq 3, \tag{33}$$

where

$$x = \frac{\nu - n\alpha_1 \nu_m}{\sigma'},$$

$$\sigma' = \alpha_2 \nu_m \sqrt{n},$$

$$\alpha_1 = \frac{\langle \nu \rangle}{\nu_m},$$

$$\alpha_2 = \frac{(\langle \nu^2 \rangle - \langle \nu \rangle^2)^{1/2}}{\nu_m},$$

$$\alpha_3 = \frac{\langle \nu^3 \rangle - 3\langle \nu^2 \rangle \langle \nu \rangle + 2\langle \nu \rangle^3}{6(\langle \nu^2 \rangle - \langle \nu \rangle^2)^{3/2}},$$

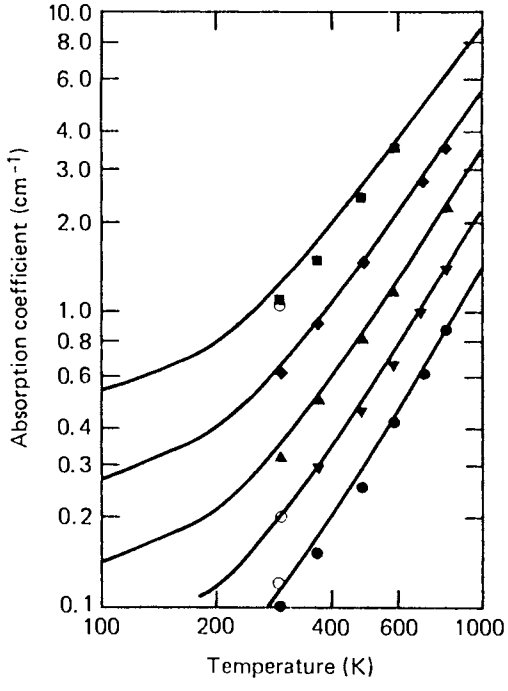

Fig. 10. Temperature dependence of the multiphonon absorption coefficient at fixed wave numbers for SrF_2 [34, 35] (○ Deutsch [32], ● $\nu = 1100\,cm^{-1}$, ▼ $\nu = 1050\,cm^{-1}$, ▲ $\nu = 1000\,cm^{-1}$, ◆ $\nu = 950\,cm^{-1}$, ■ $\nu = 900\,cm^{-1}$ and — multiphonon model [6]).

and

$$\langle \nu^r \rangle = \int_0^\infty d\nu \, \rho_1(\nu) \nu^r, \qquad r = 1, 2, 3.$$

Here ν_m is the maximum fundamental lattice-vibration frequency. It is taken to be the maximum longitudinal-optical-mode frequency of the crystal. The value of ν_m is determined experimentally for each material from the reflection spectrum. A derivative reflection-spectroscopy technique developed at The Johns Hopkins University/Applied Physics Laboratory [31] has been used to determine the values.

The shape of the distribution is determined by three parameters: α_1, the distribution mean normalized by ν_m; α_2, the distribution standard deviation normalized by ν_m; and α_3, the distribution skewness divided by six. The parameters α_1, α_2, and α_3 are directly determined from $\rho_1(\nu)$ as indicated by Billard *et al.* [29] for sapphire. The results are $\alpha_1 = 0.537$, $\alpha_2 = 0.213$, and $\alpha_3 = 0.052$. However, in practice the α_2 parameter requires modification, because the true phonon distribution function, $\rho_n(\nu)$, goes to zero at $n\nu_m$. Thus, the value for α_2 is too large and can artificially produce steps in the net absorption coefficient caused by the assumption of a Gaussian phonon-distribution function. Based on sapphire absorption data, a simple but effective empirical correction is used. Let $\alpha_2 = 0.153$ and multiply the strength by N to correct for the increased slope in β_a caused by the narrower $\rho_n(\nu)$. In this way, a smooth and realistic representation of the absorption coefficient is obtained.

Figure 5 illustrates the structure of $\beta_{\text{tot}}(\nu, T)$ in terms of $\beta_n(\nu, T)$, the absorption coefficient of a single n-phonon process. There are spectral regions in which a single n-phonon absorption process dominates. The individual β_n values are nearly Gaussian in shape, yet the sum produces a nearly exponential curve for β_{tot}, as observed in experiment.

Now the temperature dependence of the multiphonon sum-band edge can be understood in a straightforward way. From very low temperature to roughly room temperature, the absorption coefficient is nearly constant, because the population of the majority of oscillators are in the ground state ($m = 0$). At high temperature, when the upper levels achieve enough population, then photon absorption for $m > 0$ becomes important. Also, the dipole matrix element increases with increasing m. Thus, the absorption coefficient increases with temperature basically as Eq. 29 dictates in this high-temperature regime. Figures 6–10 illustrate this point by comparing model predictions against experimental data for Al_2O_3 [3, 29, 32], NaCl [6, 26, 20, 32, 33, 34], BaF_2, CaF_2, and SrF_2 [32, 35, 36], respectively. This multiphonon sum-band model has been applied to a variety of window

materials [6]. Three parameters are needed to specify a material; K, the scaling constant representing the dipole density; D, the dissociation energy; and ν_m, the maximum longitudinal-optical-mode frequency. All of these parameters can be determined from room-temperature measurements. Thus, the model provides a means of predicting $\beta_a(\nu, T)$ as a function of temperature for a material with known $\beta_a(\nu, T_0)$ at a fixed temperature T_0.

CONCLUSIONS III

The previously presented models provide more than physical insight into the optical properties of materials. Because of the physical basis for the theories, meaningful interpolations and extrapolations can be made as a function of frequency and temperature. Furthermore, the models provide a precise and convenient means of communicating optical-properties data and represent an improvement over conventional figures and tables. The formulas are easily programmed on a computer, providing quick and easy access to the complex index of refraction. These results can be used further to calculate transmittance, reflectance, absorptance and emittance of bulk materials and thin films.

Efforts at JHU/APL, utilizing this approach to optical properties characterization, have resulted in the FORTRAN-based computer code PHONONB. This work is continuing and more comprehensive versions will be available in the future.

REFERENCES

1. T. Skettrup, "Urbach's Rule Derived From Thermal Fluctuations in the Band Gap Energy," *Phys. Rev. B* **18**, 2622 (1978).
2. E. D. Palik, ed., "Handbook of Optical Constants of Solids," Academic Press, New York, (1985).
3. M. E. Thomas, R. I. Joseph, and W. J. Tropf, "Infrared Transmission Properties of Sapphire, Spinel, Yttria and ALON as a Function of Temperature and Frequency," *Appl. Opt.* **27**, 239 (1988).
4. A. J. Bosman and E. E. Havinga, "Temperature Dependence of Dielectric Constants of Cubic Ionic Compounds," *Phys. Rev.* **129**, 1593 (1963).
5. H. H. Li, "Refractive Index of Alkali Halides," *J. Phys. Chem. Ref. Data,* **5**, 329 (1976).
6. M. E. Thomas and R. I. Joseph, "A Comprehensive Model for the Intrinsic Transmission Properties of Optical Windows," in *Infrared Optical Materials, Proc. SPIE* **929**, 87 (1988).
7. F. Gervais and B. Piriou, "Temperature Dependence of Transverse- and Longitudinal-Optic Modes in TiO_2 (Rutile)," *Phys. Rev. B* **10** 1642 (1974).
8. R. H. Lyddane, R. G. Sachs, and E. Teller, "On the Polar Vibrations of Alkali Halides," *Phys. Rev.* **59**, 673 (1941).

9. J. R. Jasperse, A. Kahan, J. N. Plendly, and S. S. Mitra, "Temperature Dependence of Infrared Dispersion in Ionic Crystals LiF and MgO," *Phys. Rev.* **146**, 526–542 (1966).
10. A. A. Maradudin, J. P. Ipatoua, and R. F. Wallis, "Temperature Dependence of the Width of the Fundamental Lattice-Vibration Absorption Peak in Ionic Crystals II. Approximate Numerical Results," *Phys. Rev.* **155**, 882 (1967).
11. R. F. Wallis and A. A. Maradudin, "Lattice Anharmonicity and Optical Absorption in Polar Crystals: III. Quantum Mechanical Treatment in the Linear Approximation," *Phys. Rev.* **125**, 1277 (1962).
12. B. Szigeti, "Higher-Order Terms in the Dielectric Constant of Ionic Crystals," *Proc. Roy. Soc. A* **252**, 217 (1959).
13. W. W. Ho, "High-Temperature Dielectric Properties of Polycrystalline Ceramics," MRS Symposium M, April 6, 1988.
14. E. V. Loewenstein, D. R. Smith, and R. L. Morgan, "Optical Constants of Far-Infrared Materials 2: Crystalline Solids," *Appl. Opt.* **12**, 398 (1973).
15. S. Roberts and D. D. Coon, "Far-Infrared Properties of Quartz and Sapphire," *J. Opt. Soc. Am.*, **52**, 1023 (1962).
16. Kerem Optronics, Manufacturer's data sheet.
17. Kubo, R., "Lectures in theoretical physics," Vol. I, (W. E. Britten and L. G. Dunham, eds.), Interscience, New York, 151 (1959).
18. J. H. Van Vleck and D. L. Huber, "Absorption Emission and Linebreadths: A Semihistorical Perspective," *Rev. Mod. Phys.*, **49**, 939 (1977).
19. R. Stolen and K. Dransfedl, "Far-Infrared Lattice Absorption in Alkali Halide Crystals," *Phys. Rev.* **139**, 3A1295 (1965).
20. S. S. Mitra, in "Optical Properties of Nonmetallic Solids for Photon Energies Below the Fundamental Band Gap," in "Handbook of Optical Constants," (E. D. Palik, ed.), Academic Press, New York, 213 (1985).
21. M. Stead and G. Simonis, "Near Millimeter Wave Characterization of Dual Mode Materials," *Appl. Opt.* **28**, 1874 (1989).
22. J. R. Hardy and A. M. Karo, "Theoretical Study of the Long-Wavelength Optical Properties of NaCl, KCl, KBr and KI," *Phys. Rev. B* **26**, 3327 (1982).
23. M. E. Thomas, R. I. Joseph, G. J. Simonis, and M. Stead, "Characterization of the Infrared and Far-Infrared Properties of Sapphire and Quartz," in "13th International Conf. on Infrared and Millimeter Waves," (R. J. Temkin, ed.), *SPIE Conf. Digest* **1039**, 339 (1988).
24. D. L. Mills and A. A. Maradudin, "Theory of Infrared Absorption by Crystals in the High Frequency Wing of Their Fundamental Lattice Absorption," *Phys. Rev. B* **8**, 1617 (1973).
25. A. A. Maradudin and D. L. Mills, "Temperature Dependence of the Absorption Coefficient of Alkali Halides in the Multiphonon Regime," *Phys. Rev. Lett.* **31**, 718 (1973).
26. L. L. Boyer, J. A. Harrington, M. Hass, and H. B. Rosenstock, "Multiphonon Absorption in Ionic Crystals," *Phys. Rev. B* **11**, 1665–1679 (1975).
27. H. B. Rosenstock, "Multiphonon Absorption in Alkali Halides: Quantum Treatment of Morse Potential," *Phys. Rev. B* **9**, 1963 (1974).
28. M. Sparks and L. J. Sham, "Theory of Multiphonon Absorption in Insulating Crystals," *Phys. Rev. B* **8**, 3037 (1973).
29. D. Billard, F. Gervais, and B. Piriou, "Analysis of Multiphonon Absorption in Corundum," *Phys. Status Solidi B* **75**, 117 (1976).
30. H. Cramer, "Random Variables and Probability Distributions," Cambridge University Press, London (1970).
31. R. I. Joseph and M. E. Thomas, "Differential Reflection Spectroscopy: A Direct Determination of Long Wavelength Optical Mode Frequencies in Polar Crystals," *Phys. Status Solidi B* **141**, K163 (1987).

32. T. F. Deutsch, "Absorption Coefficient of Infrared Laser Window Materials," *J. Phys. Chem. Solids* **34**, 2091 (1973).
33. A. J. Barker, "The Effect of Melting on the Multiphonon Infrared Absorption Spectra of KBr, NaCl, and LiF," *J. Phys. C* **5**, 2276 (1972).
34. J. A. Harrington and M. Hass, "Temperature Dependence of Multiphonon Absorption," *Phys. Rev. Lett.* **31**, 710 (1973).
35. H. G. Lipson, B. Bendow, N. E. Massa, and S. S. Mitra, "Multiphonon Infrared Absorption in the Transparent Regime of Alkaline-Earth Fluorides," *Phys. Rev. B* **13**, 2614 (1976).
36. M. E. Thomas, "A Computer Code for Modeling Optical Properties of Window Materials," in Window and Dome Technologies and Materials, *Proc. of SPIE*, **1112**, 260–267 (1989).

Chapter 9

Measurement of n and k in the XUV by the Angle-of-Incidence, Total-External-Reflectance Method

MARION L. SCOTT
Los Alamos National Laboratory
Los Alamos, New Mexico

I. Introduction 203
II. General Considerations 204
A. Contamination and Surface Roughness 204
B. Vacuum Deposition and In Situ Reflectance Measurement 205
C. Potential Errors 206
III. Aluminum Reflectance versus Angle in UHV 206
IV. Determination of n and k 207
A. Thin-Film Thickness 208
B. Sensitivity to n and k 208
C. Results at 58.4 nm and 30.4 nm 210
V. Comparison with Other Results 210
A. Aluminum at 58.4 nm 210
B. Aluminum at 30.4 nm 211
C. Drude Free-Electron Model 211
D. Discussion 212
References 212

I INTRODUCTION

Many methods have been developed and employed over the years to determine the optical constants of materials. Not all of these methods are useful in the extreme ultraviolet (XUV) due to the lack of appropriate optics such as quarterwave plates; the high absorption of materials; and the extreme dispersion in both n and k typical of this spectral region. Another complication inherent in making measurements in the XUV is the absorption of air in this spectral region, which necessitates the use of vacuum chambers for any optical measurements to be performed.

Copyright © 1991 by Academic Press.
All rights of reproduction in any form reserved.
ISBN 0-12-544422-2

The phenomenon of total external reflectance, although not unique to the XUV spectrum, is encountered in many materials in this wavelength range. This effect is analogous to total internal reflectance observed in the visible spectrum when light propagating in a dense medium (such as glass) is obliquely incident at an interface between this dense medium and a less dense medium (such as vacuum). Since the light in the less dense medium refracts away from the normal to the interface, there exists an incident angle, called the critical angle, where the refracted angle is 90 degrees. Light incident at any angle greater than this critical angle cannot be transmitted into the second medium, and in the absence of absorption, total internal reflectance is observed at the interface. If the incident-medium index of refraction is n_1 and the exit-medium index of refraction is n_2, the critical angle, θ_c, is given by

$$\theta_c = \sin^{-1}[n_2/n_1]. \tag{1}$$

Total external reflectance generally occurs when light is incident in a vacuum onto a material that has the real part of its index of refraction, n, less than unity. The imaginary part of the complex index of refraction, k, which represents absorption, is never zero for these materials, but is sometimes quite small. In these cases, the critical angle is still defined by Eq. 1, but the reflectance at the interface rises to a value less than 100% at incidence angles greater than the critical angle, due to the presence of absorption. The existence of total external reflectance at a given wavelength for a specific material then implies that the complex index of refraction can be determined quite accurately by making measurements of reflectance versus angle of incidence and performing the necessary analysis. In this chapter, aluminum will be used as a specific example of this technique for the determination of n and k.

II GENERAL CONSIDERATIONS

There are several general considerations concerning the determination of the optical constants of a material in the XUV that should be discussed prior to a discussion of this particular method.

A Contamination and Surface Roughness

One of the complications in using any reflection or transmission method for the determination of the optical constants of a material in the XUV is

the potential presence of contamination layers on the surface of the material. Any analysis of the reflectance data to obtain optical constants for this material must accurately include this surface contamination layer or the surface layer must be removed before measurements are attempted. The principal contamination layer on vacuum-deposited aluminum films is aluminum oxide, and a method of dealing with this oxide layer will be discussed in Section II.B.

Surface roughness of the material to be measured should be minimized for two reasons. First, surface roughness leads to optical scattering losses, which will effectively reduce the measured reflectance from the material with subsequent errors in the determination of n and k for the material. Second, surface roughness can cause coupling to surface plasmons in the material being measured at a characteristic wavelength. In the vicinity of this characteristic wavelength, the reflectance measurements of this material can be considerably lower than that expected from a simple interface, resulting in errors in the data analysis. Both of these effects are negligible for a thin film of material deposited on a highly polished (smooth) substrate with an rms roughness of 0.7 nm or less. These effects are discussed in detail in Ref. [1].

B Vacuum Deposition and In Situ Reflectance Measurement

Simple vacuum deposition of a material is no guarantee that the material will not have a surface contamination layer. In particular, a monolayer of oxide will form on a freshly deposited aluminum layer exposed to 2×10^{-8} torr of oxygen in one hour [2]. Thus, to avoid oxide formation, aluminum must be deposited in an ultrahigh-vacuum (UHV) system and maintained in this UHV environment during measurement. The system utilized in Ref. [2] for making reflectance measurements on aluminum had a base pressure of 2×10^{-10} torr. In addition, the vacuum system should be pumped with oil-free pumps (sorption, ion, cryo) to avoid surface contamination by carbon layers.

The requirement for surface-contamination control and the consequent requirement for the maintenance of the sample in a UHV environment implies the need for an in situ XUV reflectometer to perform the reflectance measurements. This in situ reflectometer requires an XUV source, monochromator, and detector, as well as appropriate sample and detector manipulators. One method of accomplishing this would be to attach a deposition and analysis chamber to a synchrotron source, such as the SURF facility at NIST, Gaithersburg. The method utilized in Ref. [2] was to attach a capillary gas-discharge source and monochromator to a UHV deposition and analysis chamber.

C Potential Errors

There are potential systematic errors in the measurement of n and k using the angle-of-incidence, total-external-reflectance (AOITER) method. An example of one of these potential errors arises from changes in beam intensity during the course of making a complete set of angular reflectance measurements. This error is minimized if the beam is measured before *and* after the angular reflectance measurements, so that a suitable average can be used to normalize the reflectance data.

The polarization of the XUV beam (if unknown) is also a potential source of error in analyzing the AOITER data for values of n and k. In the case of a synchrotron source, the XUV beam starts out as a linearly polarized beam, and this polarization can be maintained in a carefully designed transport and monochromator system. In the case of gas-discharge sources, the XUV beam starts out as unpolarized, and some polarizing effects may be introduced by the beam-transport or monochromator system. This effect is less pronounced when the beam is incident at grazing angles on all optics.

Another example of a potential error that can occur is a spatially nonuniform detector sensitivity. This error can be minimized by always requiring that the reflected beam strike the same spot on the detector. This requirement is greatly simplified if an imaging microchannel-plate detector is used. Similarly, maintaining the same beam spot size during all measurements by keeping the source-to-detector distance the same is very important. Other potential error sources include angular misalignments, inadequate vacuum level, impurities in the evaporated material, and so on. Careful control of these potential errors will allow the measurement error to be determined primarily by the repeatability of the measurement.

III ALUMINUM REFLECTANCE VERSUS ANGLE IN UHV

In order to describe adequately the AOITER method of determining n and k for a material in the XUV, aluminum will be used as an example. The reflectance versus angle of incidence for an aluminum film freshly deposited in a UHV system has been measured in situ at XUV wavelengths of 58.4 nm [2] and 30.4 nm [3]. These measurements were accomplished by rotating the coated sample and a microchannel-plate detector in synchronism to achieve an angular incidence from 10° to 85° with an interval of 5°. The sample is manipulated out of the XUV beam in order to measure the incident beam intensity. The resulting reflectance versus angle-of-

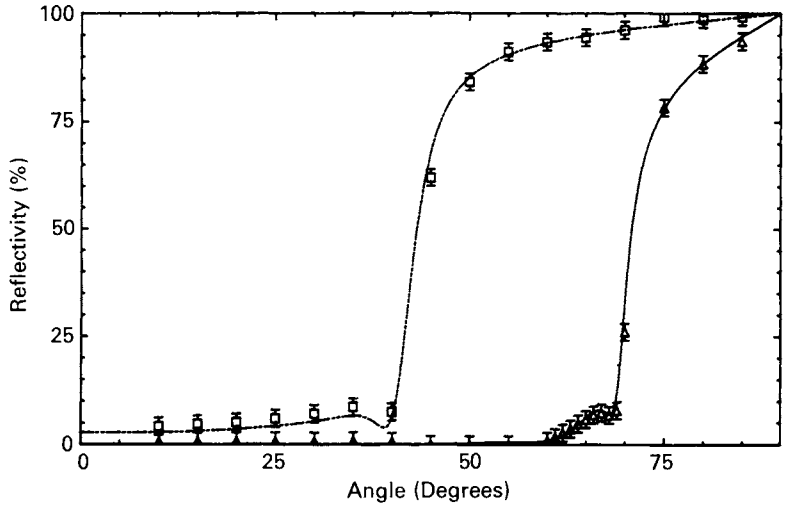

Fig. 1. Reflectance versus incidence angle for UHV aluminum film at 58.4 nm (squares) and at 30.4 nm (triangles). Note the rapid rise in reflectance at the critical angles (44.4 degrees for 58.4 nm and 70.7 degrees for 30.4 nm). The aluminum film thickness in these fits is 70 nm.

incidence curves for aluminum at 58.4 nm and 30.4 nm are shown in Fig. 1. The 1° increments between 60° and 70° for the 30.4 nm data clearly outline the interference "bump" that occurs with this highly transmissive sample due to the coherent addition of the reflection from the vacuum–film interface with the reflection from the film–substrate interface.

The 58.4 nm aluminum reflectance data shown in Fig. 1 clearly indicate the total-external-reflectance phenomenon that has been described here. The critical angle at which the high-reflectance onset occurs is given by Eq. 1 for a vacuum-incident medium ($n_1 = 1$),

$$\theta_c = \sin^{-1}[0.7/1] = 44.4°. \tag{2}$$

The rapid rise of the aluminum reflectance at this angle gives an unambiguous indication of the real part of the index of refraction for this wavelength. Similarly, the 30.4 nm aluminum reflectance data indicate a much greater critical angle given by

$$\theta_c = \sin^{-1}[0.944/1] = 70.7°. \tag{3}$$

DETERMINATION OF n AND k IV

The actual determination of n and k from reflectance data such as that shown in Fig. 1 proceeds in the following manner: a computer algorithm

for the calculation of the reflectance of a substrate overcoated with one or more thin-film layers is utilized to generate reflectance curves that can be fitted to the data. This algorithm is based on the characteristic-matrix method [4] and will not be elaborated here. The n and k values for the substrate (silicon) must be inserted into the algorithm and previously published values [5] are available over a wide wavelength range. The thickness of the thin-film layer must also be included in the algorithm, but this value is monitored during the aluminum deposition.

A Thin-Film Thickness

A secondary check on the accuracy of the thin-film thickness is available in the reflectance data of Fig. 1 due to the presence of interference "bumps" in the data near the onset of high reflectance. The position of these bumps is dependent on the thickness of the film, since this thickness affects the constructive and destructive interference between light reflected from the film and substrate surfaces versus angle of incidence. The appearance of these interference effects is an indication that the absorption of the thin film is very low, since the beam reflected from the second surface must traverse the thin film twice in order to interfere with the first surface reflection. The aluminum film thickness for the measurements in Fig. 1 was 70 nm.

B Sensitivity to n and k

The AOITER method of determining the optical constants of a thin-film coating material is very useful, when conditions allow its use, due to the separation in the effects on the angular reflectance spectrum caused by changes in n and k. The analytical formulation for the relationship between changes in the critical angle, $\Delta\theta_c$, and fractional changes in the index of refraction, $\Delta n/n$, is obtained from the derivative of Eq. 1,

$$\frac{\Delta n}{n} = \frac{\sqrt{1-n^2}}{n} \Delta\theta_c. \tag{4}$$

In Fig. 2, the relative changes in n, caused by critical-angle uncertainties, from Eq. 4, are shown for three values of n. It is clear from Fig. 2 that the accuracy of AOITER is better for smaller values of n. Using Eq. 4, we find that an index of 0.7, and a $\Delta\theta_c = \pm 0.4°$ gives a $\Delta n/n = \pm 0.007$.

For a material with $n = 0.7$, the reflectance beyond the critical angle for various values of k is shown in Fig. 3. The lower values of k lead to higher

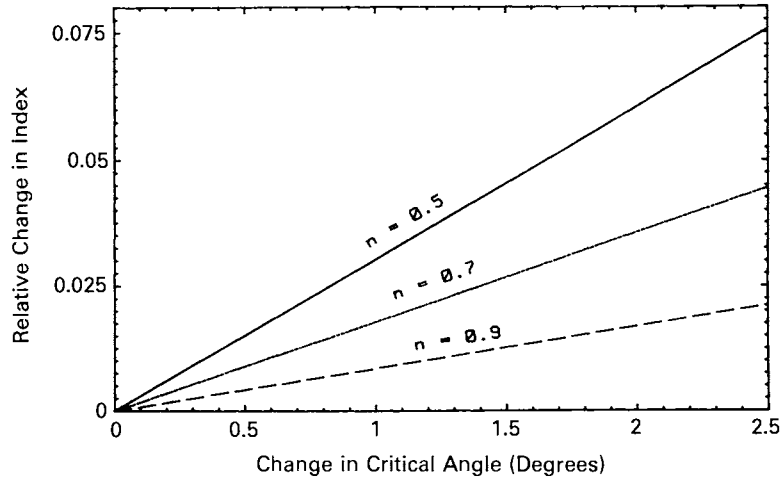

Fig. 2. Relative change in index of refraction, $\Delta n/n$, versus critical-angle uncertainty, $\Delta\theta_c$, for three different values of n.

reflectance values as one would expect. Calculations with the computer algorithm indicate that a change in k of ± 0.003 from a nominal value of 0.01 leads to changes in reflectance values that vary from zero to $\pm 7\%$ depending on the incidence angle. The fact that the effects due to variations in n and k are essentially separate means that it is very unlikely that ambiguities will occur in determining n and k values with AOITER.

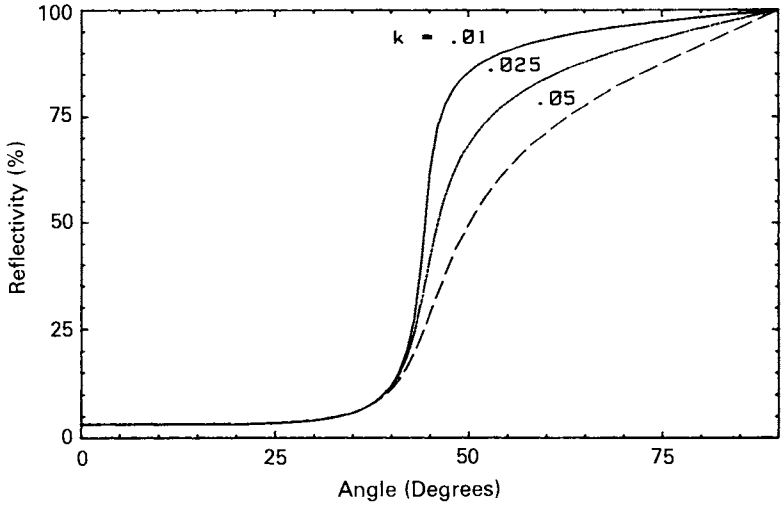

Fig. 3. Reflectance versus incidence angle for $n = 0.7$ and three values of k, the absorption index.

C Results at 58.4 nm and 30.4 nm

With the above inputs to the reflectance calculation, the n and k of the aluminum thin film can be varied to get the best fit to the measured XUV reflectance data. The error in the n and k determined from reflectance data can be estimated from the $\pm 2\%$ reflectance error in the following way: one adds 2% to each reflectance data point to generate a new (higher) reflectance curve. This new curve is again fit to determine n and k. One then subtracts from the original reflectance data points to generate a new (lower) reflectance curve, which is also fitted to determine n and k. The excursion of n and k from the original data fit is used as the error bar on n and k. The results of this fitting procedure for aluminum are given as the AOITER entries in Table I. In situ UHV-AOITER measurements on aluminum at other XUV wavelengths have not yet been performed.

V COMPARISON WITH OTHER RESULTS

Other methods exist to determine the optical constants of materials in the XUV. Typically, these methods utilize reflection and/or transmission values measured at normal incidence or at more than one incident angle, to infer the optical constants of the material.

A Aluminum at 58.4 nm

Using a combination of transmission and reflection measurements, Ditchburn and Freeman [6] determined the n and k of aluminum at various wavelengths. A linear interpolation of their values gives $n = 0.69$ and $k = 0.023$ at 58.4 nm. Madden, Canfield, and Hass [7] used a reflection versus time method to minimize the effects of oxidation in determining the optical constants of aluminum. The values quoted in this reference are $n = 0.71$ and $k = 0.018$ for 58.4 nm. In early work [8], Hunter used reflection measurements and determination of the critical angle to deduce the optical constants of aluminum to be $n = 0.72$ and $k = 0.018$ at 58.4 nm. In later work [9, 10], Hunter used transmission measurements to find k values between 0.018 and 0.023 with a best-fit curve for multiple-wavelength data passing through $k = 0.023$ at 58.4 nm. Hass and Tousey [11] indicate that interference-fringe analysis gives $n = 0.7$ at 58.4 nm. They state that the k value for aluminum at this wavelength is less than 0.04; however, the aluminum reflectance calculations in this paper were performed with

$n = 0.7$ and $k = 0.018$. The extensive compilation and analysis of aluminum optical constant data by Smith *et al.* [12] indicates that $n = 0.715$ and $k = 0.0237$ at 58.4 nm.

Aluminum at 30.4 nm B

Fomichev and Lukirskii [13] measured absorption coefficients of thin aluminum films in the wavelength range from 2.36 nm to 41 nm. The value of k linearly interpolated from this reference at 30.4 nm is $k = 0.009$. Hunter [9, 10] used the critical-angle method to determine n and transmission measurements to determine k at wavelengths between 10 nm and 80 nm. The approximate values from these references at 30.4 nm are $n = 0.94$ nm and $k = 0.009$ (these values were taken from the best-fit line on a graphical presentation of this multiple-wavelength data). The aluminum optical-constant data from the compilation by Smith *et al.* [12] indicates that $n = 0.943$ and $k = 0.0079$ at 30.4 nm.

Drude Free-Electron Model C

This model utilizes only two parameters, the plasma critical wavelength and the electronic relaxation time, to characterize the optical constants of a

TABLE I

A Comparison of the Optical Constants of Aluminum[a]

Source of data	n	k
58.4 nm		
AOITER	0.700 ± 0.005	0.010 ± 0.002
Ref. [6]	0.69 ± 0.02	0.023 ± 0.012
Ref. [7]	0.71 ± 0.02	0.018 ± 0.009
Ref. [8]	0.72 ± 0.015	0.018 ± 0.009
Ref. [9, 10]	0.72 ± 0.02	0.023 ± 0.01
Ref. [11]	0.70 ± 0.02	0.018 ± 0.020
Ref. [12]	0.715 ± 0.02	0.0237 ± 0.01
Drude model	0.72	0.010
30.4 nm		
AOITER	0.944 ± 0.002	0.0055 ± 0.0008
Ref. [13]	—	0.009 ± 0.004
Ref. [9, 10]	0.94 ± 0.03	0.009 ± 0.004
Ref. [12]	0.943 ± 0.03	0.0079 ± 0.004
Drude model	0.93	0.001

[a] Errors have been estimated by the author.

given material over a wide range of wavelengths. The values of these two parameters that give the best fit [14] to available data on aluminum (in the UV and visible spectral regions) are $\lambda_{crit} = 83.7$ nm and $\tau = 1.1 \times 10^{-15}$ sec. The optical constants can be calculated in the Drude model by means of

$$\varepsilon_1 = n^2 - k^2 = 1 - [\omega_{crit}^2 \tau^2/(1+\omega^2\tau^2)], \tag{5}$$

$$\varepsilon_2 = 2nk = (\omega\tau)^{-1}[\omega_{crit}^2 \tau^2/(1+\omega^2\tau^2)], \tag{6}$$

$$\omega_{crit}^2 = 4\pi Ne^2/m = (2\pi c/\lambda_{crit})^2, \tag{7}$$

where c is the speed of light, N is the effective valence-electron density, e is the charge of an electron and m is its mass. The values for n and k calculated with the simple Drude model at 58.4 nm and 30.4 nm using the above values for the parameters are given in Table I along with a comparison of the various measured values discussed above.

D Discussion

The AOITER results given in Table I are very similar to previous results, except that the AOITER values obtained for k and the error bars on n and k are significantly smaller. The larger previous values of k are presumed to arise from the presence of some oxide deposited in the coating, surface-oxide layers, surface contamination, or impurities in the starting material.

REFERENCES

1. J. G. Endriz and W. E. Spicer, *Phys. Rev. B* **4**, 4144 (1971).
2. M. L. Scott, P. N. Arendt, B. J. Cameron, J. M. Saber, and B. E. Newnam, *Appl. Opt.* **27**, 1503 (1988).
3. M. L. Scott (unpublished).
4. M. Born and E. Wolf, "Principles of Optics," Macmillan, New York, 57 (1964).
5. D. F. Edwards, in "Handbook of Optical Constants of Solids," (E. D. Palik, ed.), Academic Press, Orlando, 547 (1985).
6. R. W. Ditchburn and G. H. C. Freeman, *Proc. R. Soc. London, Ser. a* **294**, 20 (1966).
7. R. P. Madden, L. R. Canfield, and G. Hass, *J. Opt. Soc. Am.* **53**, 620 (1963).
8. W. R. Hunter, *J. Opt. Soc. Am.* **54**, 15 (1964).
9. W. R. Hunter, *Appl. Opt.* **21**, 2103 (1982).
10. W. R. Hunter, in "Proceedings, International Colloquium on Optical Properties and Electronics Structure of Metals and Alloys," (F. Abeles, ed.), North-Holland, Amsterdam, 136 (1966).
11. G. Hass and R. Tousey, *J. Opt. Soc. Am.* **49**, 593 (1959).
12. D. Y. Smith, E. Shiles, and M. Inokuti, in "Handbook of Optical Constants of Solids," (E. D. Palik, ed.), Academic Press, Orlando, 369 (1985).
13. V. A. Fomichev and A. P. Lukirskii, *Opt. Spectrosc.* **22**, 432 (1967).
14. W. R. Hunter, *J. Appl. Phys.* **34** 1565 (1963).

Chapter 10

Spectroscopic Ellipsometry in the 6–35 eV Region

J. BARTH,* R. L. JOHNSON,† and M. CARDONA
Max-Planck-Institut für Festkörperforschung
D-7000 Stuttgart 80
Federal Republic of Germany

I. Introduction 213
II. The BESSY VUV Ellipsometer 217
A. Basic Experimental Considerations 217
B. Optimum Geometry 218
C. Design of the Ellipsometer 221
D. VUV Polarizers 224
E. Photodiodes as VUV-Detectors 225
III. Theory 226
A. Basic Formulas 226
B. Calibration 231
C. Error Analysis 232
IV. Results and Comparison with Reflectance Spectra 237
A. III-V Semiconductors 237
B. II-VI Compounds 238
C. Calcium Fluoride 242
V. Summary 244
Acknowledgment 245
References 245

I INTRODUCTION

The technique of ellipsometry has experienced a renaissance recently driven by the ever-increasing demand for rapid, nondestructive analysis of surfaces and thin films. Ellipsometry enables the optical constants of

* Present address: Elektro-Optik GmbH, Fördestraße. 35, D-2392 Glücksburg, Federal Republic of Germany.
† Present address: II. Institut für Experimentalphysik, Universität Hamburg, Luruper Chaussee 149, D-2000 Hamburg 50, Federal Republic of Germany.

Copyright © 1991 by Academic Press.
All rights of reproduction in any form reserved.
ISBN 0-12-544422-2

materials to be determined with high accuracy and can therefore help to solve a wide variety of problems in different disciplines. The fact that ellipsometric measurements can be performed without a vacuum environment in the visible and near-UV regions is a definite advantage over other surface-science techniques for industrial applications. Ellipsometry is widely used in assessing the quality of semiconductor materials and oxide coatings and to characterize such diverse systems as polymers, liquid crystals, and Langmuir–Blodgett films.

There are now a number of commercial ellipsometers available that exploit recent advances in detection systems and computer technology and allow precise and rapid measurement of the optical properties of thin films and surfaces in the IR–VIS–near-UV spectral region (1.5–6.0 eV). The microscopic-imaging ellipsometer described by Beaglehole [1] is a particularly interesting instrument that enables ellipsometric measurements to be performed with a lateral resolution of about 3 μm. Given these developments and the incontestable advantages of ellipsometry for determining the optical constants of materials, it seems obvious to extend the spectral range for ellipsometry into the vacuum-ultraviolet (VUV) region. This expands the number of systems accessible for ellipsometric studies to include large-band-gap insulators and excitations from deeper valence bands and also from shallow core levels into the conduction bands.

The best light source for spectroscopic ellipsometry in the VUV region is without doubt monochromatized synchrotron radiation because of its tunability, high intensity, and natural collimation. It is also highly polarized, although the degree of linear polarization is not as high as that which can be achieved in the visible region. The possibility of carrying out ellipsometry with synchrotron radiation was demonstrated by Schledermann and Skibowski in 1970 [2, 3] at the DESY synchrotron in Hamburg. Apparently, since then no further attempts have been made despite recent advances in the development of high brightness storage rings as much more powerful sources of synchrotron radiation.

At present, reflectometry is the best-established technique for determining the optical constants in the VUV region. A detailed description of the method and data analysis has been presented by Hunter [4]. To perform such measurements, one simply measures the specularly reflected intensity from the sample using a collimated monochromatic beam of light, which has a well-defined state of polarization. Reflectometry can be performed throughout the entire VUV and X-ray regions, and by scanning the photon energy, a wealth of spectroscopic information can be obtained. The greatest uncertainty in such measurements is usually caused by variations in the intensity and spectral purity of the primary photon flux. At high energies diffuse scattering and geometrical-shadowing effects can introduce significant errors; however, by taking suitable precautions and using highly monochromatic synchrotron radiation, excellent data can be

obtained. In order to calculate the optical constants from reflectance data, it is necessary to make use of the Kramers–Kronig relation, which implies that data over a very wide energy range should be available. It is difficult to estimate the amount of uncertainty in the absolute values of the dielectric function introduced by the unavoidable extrapolation necessary for Kramers–Kronig analysis. A more complete discussion of these aspects can be found in the article by Smith [5]. The alternative method of multiple-angle reflectivity measurements is a time-consuming and laborious exercise [6].

In ellipsometry one measures the change in polarization state of the beam of light after nonnormal reflection from the sample. The polarization state is defined by two parameters, for example, the relative phase and relative amplitude of the orthogonal electric-field components of the polarized light wave. On reflection both electric-field components are modified in a linear way, so a single ellipsometric measurement provides two independent parameters. The name *ellipsometry* derives from the fact that linearly polarized light after oblique reflection becomes elliptically polarized due to the different reflection coefficients for *s*- and *p*-polarized light. By measuring the polarization ellipse, one can determine the complex dielectric function of the sample. The principles of ellipsometry were established about 100 years ago [7], but the technique only became practical with the development of the rotating-analyzer ellipsometer (RAE) [8], which makes use of digital computers to handle the rather unwieldy equations. The RAE measures continuously, so wavelength scanning or spectroscopic ellipsometry can be performed.

A conventional ellipsometer consists of a light source and a rotatable polarizer, so that the plane of polarization can be inclined to the plane of incidence. The measurement geometry is shown in Fig. 1. Polarized light falls on the sample at an angle of incidence of about 70° typically, and the reflected light is analyzed using a second rotatable polarizer and a suitable detector. The simplest ellipsometers use a single-wavelength light source and manual determination of the ellipsometric angles Δ and ψ (where Δ corresponds to the phase shift and $\tan \psi = |\tilde{r}_p/\tilde{r}_s|$, the amplitude ratio of the reflected components). The measurement procedure is to locate the minimum transmission through the optical system by alternately rotating polarizer and analyzer (or equivalently polarizer and compensator). The extinction condition determines both of the ellipsometric angles; thus, a single ellipsometric measurement provides two parameters. Furthermore, since it is the polarization state and not the intensity which is being measured, the results are unaffected by source intensity fluctuations. The fact that ellipsometry simultaneously determines the relative phases and amplitudes accounts for the high sensitivity of this technique. In particular, the direct measurement of the phase changes makes ellipsometry highly surface-sensitive, and it is possible to detect extremely thin adsorbed films

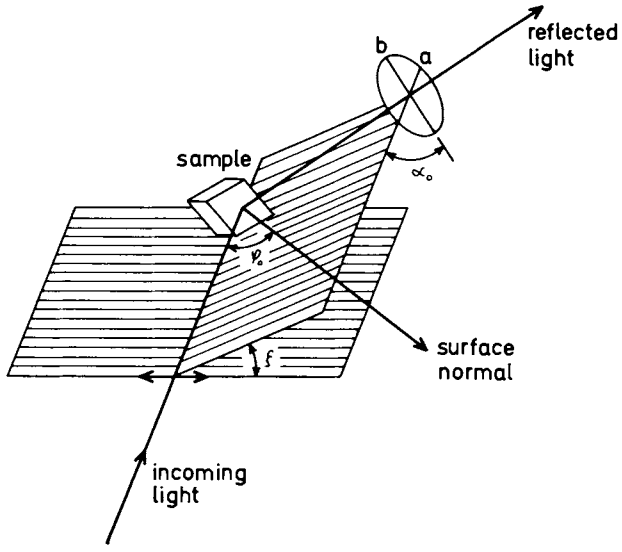

Fig. 1. Measurement geometry for ellipsometry: the angle of incidence is ϕ_0, and the angle between the plane of incidence and the plane of polarization is ξ. The polarization ellipse of the reflected light is characterized by the ratio of the axes and the angle α_0.

(down to 0.01 monolayer, with a good instrument). By assuming an appropriate model, the measured ellipsometric parameters can be evaluated in terms of a macroscopic refractive index with real and imaginary components. Alternatively, a single ellipsometric measurement can be used to determine the thickness and refractive index of transparent films.

The interpretation of the measured changes in polarization in terms of optical functions is a problematic aspect of ellipsometry. The simplest approach is to apply the Fresnel equations and a two-phase model to the vacuum–solid interface. The Fresnel equations are strictly applicable only to an abrupt interface between homogeneous isotropic media. In reality, no materials are perfectly isotropic and, on a microscopic scale, no interfaces are abrupt; however, the two-phase model generally provides the most useful basis for interpreting ellipsometric data. The application of the two-phase model to anisotropic media enables a "pseudodielectric function" to be calculated, which allows anisotropic samples to be characterized. A full determination of all the components of the dielectric tensor in anisotropic media is, in principle, possible by performing measurements at multiple angles of incidence for different orientations of the sample. Measurement of optical anisotropies is a challenging field of current research [9].

So far we have outlined some of the salient aspects of ellipsometry, which we can summarize as follows: spectroscopic ellipsometry is now a

well-established technique for determining the optical constants of bulk materials and thin films in the IR–VIS–near-UV spectral region over the photon-energy range 1.5–6.0 eV. It is generally accepted to be a technique with high intrinsic precision and accuracy, which allows both real and imaginary parts of the dielectric function to be measured simultaneously. In the visible, conventional instruments can yield information on samples with absorption coefficients down to typically $10^4\,\mathrm{cm}^{-1}$, and extinction indices ~0.1. More details about conventional ellipsometry can be found in review articles [10, 11] and the proceedings of the ellipsometry conferences [12].

The purpose of this article is to introduce the concepts of VUV ellipsometry and to demonstrate that it is a viable technique to determine the optical constants of solids. There are important differences between ellipsometry in the visible and VUV regions. The fact that there are no perfect polarizers for the VUV means that all four components of the Stokes vector have to be considered in the data analysis. This, in turn, means that the full Mueller matrix notation has to be used in the theoretical description. On the experimental side it was necessary to develop new instrumentation and procedures to calibrate the imperfect polarizers and also to measure the polarization of the incident light. By making use of synchrotron radiation with its high degree of linear polarization and triple-reflection polarizers, we built an automated instrument that extends the spectral range of spectroscopic ellipsometry up to 35 eV [13]. We present data that demonstrate the usefulness of our instrument for measuring the optical constants of solids. By combining the data with theoretical calculations, new insights about the band structure of wide-band-gap semiconductors and insulators have been gained.

THE BESSY VUV ELLIPSOMETER II

Basic Experimental Considerations A

There are a number of different optical configurations that can be used for ellipsometry. A typical system consists of a collimated unpolarized monochromatic light source, a polarizer, a compensator, the reflecting sample under investigation, the polarization analyzer, and a detector. The modern rotating-analyzer ellipsometer has a great advantage over the older null technique in that it can be readily automated to allow the wavelength to be scanned continuously, yielding dielectric-function spectra. In a rotating-analyzer ellipsometer, the state of polarization of the

reflected light (ellipticity and orientation of the ellipse) is measured with a photodetector behind an analyzer, which rotates at a fixed frequency. Thus, the intensity at the detector has, as a function of analyzer rotation angle, α, the form of a sinusoidal curve on a dc background, which can be written as

$$I_{\text{det}} = \text{const}(1 + a_1 \cos 2\alpha + a_2 \sin 2\alpha). \tag{1}$$

Fourier analysis yields the coefficients a_1 and a_2, which are used to determine numerically $\varepsilon_1(\hbar\omega)$ and $\varepsilon_2(\hbar\omega)$. The detected intensity is a function of 2α because the optical cycle of the rotating analyzer corresponds to half a mechanical cycle.

The rotating analyzer is advantageous because of its higher speed of data collection, its high precision, and the fact that a compensator is not necessary. Practically all aspects of rotating-analyzer ellipsometry have been described by Aspnes [8, 10, 11, 14, 15], and our present VUV ellipsometer is based on his pioneering work.

One obstacle to performing ellipsometric measurements in the VUV is the lack of suitably intense laboratory light sources. The brightest tunable VUV light is provided by specially constructed synchrotron radiation facilities. Synchrotron radiation (SR) has the additional advantage of being highly polarized. SR extends over a broad continuum from the IR to X-ray regions, so a monochromator has to be used to filter out a narrow bandwidth. The present VUV ellipsometer at the dedicated light source BESSY in Berlin is installed on the 2m Seya–Namioka beam line, which nominally covers the photon-energy range from 5–35 eV using two gratings. The photon flux falls off rapidly near the ends of the spectral range, so it is primarily the monochromator that limits the range of the ellipsometer. In spectroscopic ellipsometry the monochromator plays a particularly important role, since alignment has to be maintained while scanning the monochromator. The present system dispenses with a polarizer before the sample and uses the fact that synchrotron radiation is linearly polarized in the plane of orbit and that the optical components in the beam line enhance the degree of polarization.

B Optimum Geometry

In ellipsometry, linearly polarized light is incident at an oblique angle on the surface under investigation. The reflected light is in general elliptically polarized due to the differences in the complex $\tilde{r}_s$ and $\tilde{r}_p$ reflection coefficients. The complex reflection ratio can be obtained di-

rectly from the ellipsometric angles ψ and Δ since, by definition, $\rho = \tilde{r}_p/\tilde{r}_s = \tan\psi \exp(i\Delta)$. The reflection coefficients depend on the angle of incidence, the photon energy, and the material properties, so it is clear that different geometrical arrangements are required to obtain the best sensitivity in ellipsometry in different spectral regions. Furthermore, different optimum geometries are to be expected for such different samples as wide-band-gap semiconductors or adsorbates on metals. A versatile instrument could be conceived with a variable angle of incidence, but it would be difficult and expensive to attain the necessary precision in ultra-high vacuum. A theoretical analysis of the optimum experimental geometry is, therefore, a prerequisite for establishing a practical design of a VUV ellipsometer.

General equations for optimizing the precision of rotating-analyzer ellipsometers have been given by Aspnes [14]. He found that for rotating-analyzer systems with an ideal detector, the angle of incidence should be as close as possible to the "principal angle." At this angle of incidence, for which $\Delta = \pm\pi/2$, linearly polarized light is generally reflected as elliptically polarized light, but when the angle between the plane of polarization and the plane of incidence is equal to ψ, the reflected light is circularly polarized. For spectroscopic measurements over a given spectral range, minimum uncertainty is obtained as a compromise between the conditions that yield circularly polarized light and those that maximize the transmitted flux. It is interesting to note that the optimum precision in the ideal-detector case is achieved when the measured Fourier coefficients a_1 and a_2 are zero, so the complex-reflectance ratio ρ is determined purely by instrument settings. The angle of incidence is one of the most important parameters in ellipsometry and has to be determined with at least the same accuracy as the ellipsometric angles. In the principal-angle-of-incidence ellipsometer [16, 17], the rotating analyzer is used as a null detector seeking circularly polarized light. The dielectric function of the sample is determined solely by the angle of incidence and the polarizer position. The best accuracy in the determination of the optical constants is obtained at the principal angle of incidence; the linearity of the detector becomes unimportant. Hence, accurate determination of the dielectric function requires high angular precision and good mechanical stability of the ellipsometer.

Aspnes [14] applied the theory to the practical cases of silicon and gold surfaces measured with a rotating-analyzer ellipsometer and shot-noise-limited detector without using a compensator. He found that for an angle of incidence of 68 degrees, the optimum polarizer azimuth was 30 degrees over the energy range 2.5–5.5 eV.

In general, the optimum sensitivity is obtained for an angle of incidence close to the principal angle ($\Delta = \pm\pi/2$) and an optimum polarizer azimuth equal to ψ (where $\tan\psi = |\rho|$). We can make use of the fact that at high photon energies $\varepsilon_1 \simeq 1$ and $\varepsilon_2 \simeq 0$ to derive the optimum experimental

geometry in the X-ray limit. In this case the optimum angle of incidence is 45°, and the optimum polarizer azimuth tends toward zero. Thus, we see that the optimum angle of incidence decreases from about 70° in the visible region to 45° in the XUV. Unfortunately, the reflectivity of the sample is reduced at the smaller angle of incidence, and this constitutes a fundamental limitation to performing ellipsometry in the soft X-ray region.

The strong dependence of the precision obtainable in ellipsometry on the measurement geometry is interesting and in some ways nonintuitive. It is somewhat paradoxical that it is necessary to know the dielectric function of the sample before one can measure it with the greatest precision by ellipsometry. It is also difficult to appreciate that the same sample will require different geometries in different wavelength regions. It is instructive to plot the variation of ε_1 and ε_2 with energy as shown in Fig. 2 and Fig. 3 for InAs. The curve A-B in Fig. 2 corresponds to photon energies from 1.5–9 eV and the curve in Fig. 3 corresponds to photon energies 14–25 eV. The optimum sensitivity is obtained when the dielectric-function curve lies in the vicinity of the principal-angle curves shown as semicircles for angles of incidence of 67.5°, 56.25°, and 45°. These figures demonstrate clearly that for InAs, the optimum angle of incidence tends rapidly toward 45°

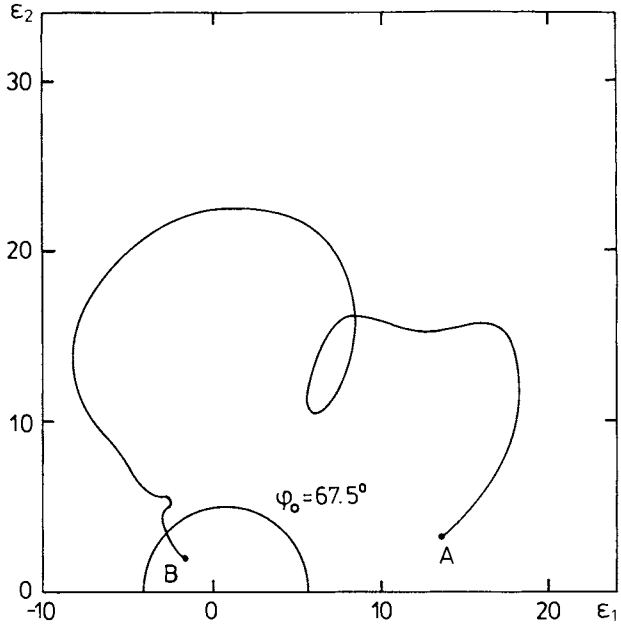

Fig. 2. The dielectric function of InAs from 1.5 eV (A) to 9 eV (B) plotted in the complex plane (Argand diagram). The semicircle corresponds to the values of $\varepsilon_1 + i\varepsilon_2$ for which $\Delta = -90°$ at an angle of incidence $\phi_0 = 67.5°$.

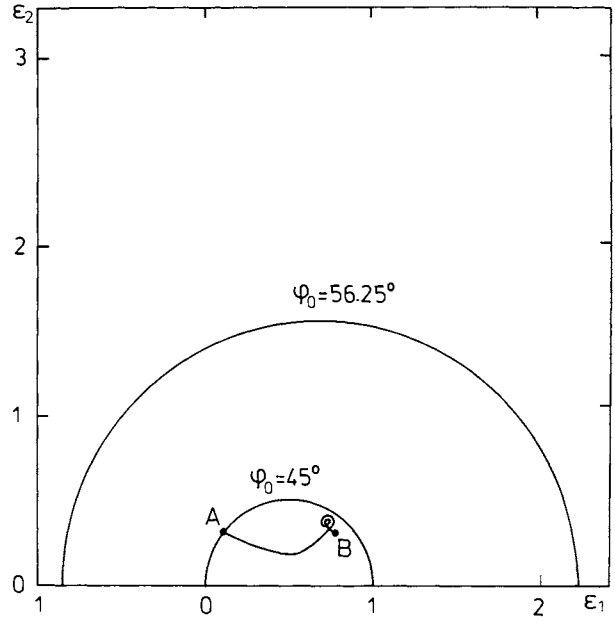

Fig. 3. Argand diagram for the dielectric function of InAs from 14 eV (A) to 25 eV (B). The semicircles correspond to the values of $\varepsilon_1 + i\varepsilon_2$ for which $\Delta = -90°$ at angles of incidence of 56.25° and 45°.

with increasing photon energy. Although the magnitudes of ε_1 and ε_2 become smaller at higher energies, it is important to note that good precision can be achieved by measuring with the optimum geometry.

As a compromise between optimum precision and mechanical stability, our ellipsometer provides two different angles of incidence. In the energy region 5–10 eV, the incidence angle is 67.5°, and a MgF_2 Rochon polarizer is used. Above 10 eV, a 45° incidence angle produces better results for most materials and only triple-reflection polarizers can be used at these energies. In practice, the two fixed angles of incidence have been found to be quite adequate, since the optimum conditions do not have to be fulfilled stringently. The two angles also provide complementary information, which is useful when studying thin films and adsorbates.

Design of the Ellipsometer C

The basic design of the VUV ellipsometer is modular, which enables functions to be separated and individually modified and upgraded as the

system evolves. The present ellipsometer comprises of three vacuum chambers: the main UHV chamber (base pressure 10^{-10} mbar) around the sample manipulator, the analyzer chamber, and a preparation chamber with load-lock. In order to tilt the plane of polarization with respect to the plane of incidence, usually accomplished by turning the polarizer, the whole ellipsometer has to be rotated about the axis of the incoming light. As shown in Fig. 4, the sample is mounted on the precision manipulator in the center of the main UHV chamber. Samples are introduced via a rapid load-lock and exchanged with a transfer system and can be heated or cooled on the manipulator (77–900 K). Facilities are provided for cleaving samples and for evaporation *in situ*.

The analyzer chamber can be readily removed and positioned at ports corresponding to angles of incidence of either 67.5° or 45°. It contains the most important parts of the ellipsometer, that is, the rotating analyzer and the detector. The prealigned standardized polarizer assemblies can be easily interchanged and fit snugly inside a rotating drum, which is driven via a friction wheel by a tachogenerator-stabilized dc motor. The angular orientation of the analyzer is measured with an angle encoder (1000 pulses per revolution) mounted directly on the drum. The pulses from the angle

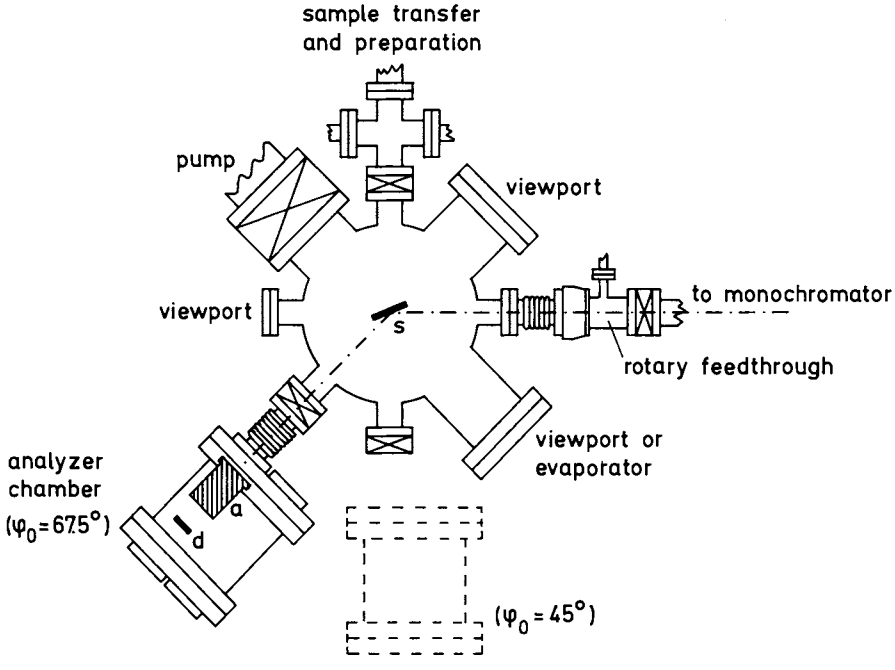

Fig. 4. Schematic diagram of the VUV-ellipsometer (s = sample, a = rotating analyzer, d = photodiode detector).

encoder trigger the readout of the detector 50 times per optical cycle. Two photodiode detectors—one for lower energies and one for higher energies—are mounted on a linear-motion feedthrough perpendicular to the axis of the analyzer. This enables the detector to be moved out of the optical path and allows direct visual adjustment of the polarizer by viewing the zero-order light through a window on the end of the analyzer chamber. The mounting of the analyzer chamber allows precision adjustment of the axis of the analyzer onto the beam reflected from the sample. For triple-reflection polarizers the adjustment is extremely critical and requires experience. The visual adjustment is essential to obtain correct prealignment; the final adjustment is performed using the photodiode signal at a convenient photon energy. The adjustment is optimal when the signal is sinusoidal, as a function of analyzer angle with equal intensity in both optical cycles. The photodiode signal is continuously displayed on both an oscilloscope and the computer terminal.

The ellipsometer at BESSY is installed on the 2m Seya–Namioka beamline, which contains three mirrors in addition to the spherical diffraction grating. The light from the ring is focused by a Pt-coated toroidal mirror and an Au-cylindrical mirror before being dispersed using either a 610 l/mm mechanically ruled grating coated with $Al + MgF_2$, or a Pt-coated 1200 l/mm holographic grating. The monochromatic light is brought to a stigmatic focus with an additional Au-coated cylindrical mirror. The grating can be masked down in both vertical and horizontal directions to enhance the degree of linear polarization. The monochromator can achieve high resolution ($\lambda/\delta\lambda = 4000$ at 180 nm with 50 μm slits and 610 l/mm grating), but for ellipsometry a high photon flux and linearly polarized light are the primary requirements.

Although the light from the 2 m Seya–Namioka monochromator is highly linearly polarized, it may still contain components of elliptically and unpolarized light at the level of a few percent. The proportion of these components can vary as the monochromator is scanned, and this should be taken into account when evaluating the data. Similarly, the triple-reflection analyzer has nonideal polarization characteristics, so the experimental Fourier coefficients have to be corrected for the polarization properties of the analyzer before accurate values of the dielectric function can be obtained. By mounting the analyzer chamber at the exit of the monochromator, we can directly characterize the polarization properties of the monochromator. Figure 5 shows three results of such measurements performed at different times on two different 610 l/mm gratings coated with $Al + MgF_2$. The lowest curve was recorded from the grating originally installed in the monochromator and exhibits a pronounced dip near 12 eV and a steady decline above 16 eV. A new grating was installed and the measurement was repeated, yielding the upper curve with a higher polarization and a smaller dip at 12 eV, but still with a decrease at higher photon

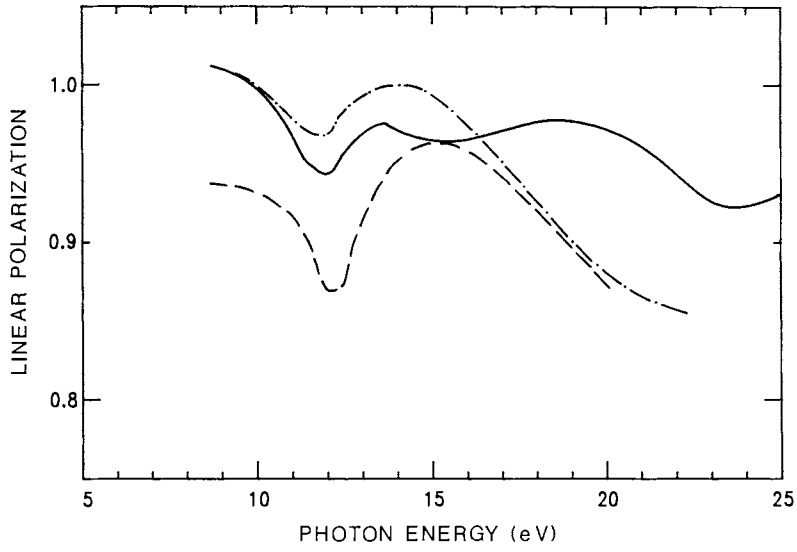

Fig. 5. Degree of linear polarization of light from the monochromator. The three curves were recorded at different times: the dashed line was recorded when grating was originally installed in monochromator; the dash-dot line was recorded after replacement of grating; the solid line indicates measurement with new reflection polarizer five months later.

energies. The characterization was repeated five months later with a new analyzer. The dip at 12 eV had increased again, and we attribute this to radiation-induced degradation of the monochromator grating. The decrease in the polarization at higher photon energies is no longer apparent with the new analyzer. Thus, it is clear that the optical elements in both the monochromator and the ellipsometer deteriorate with time.

D VUV Polarizers

Rochon polarizers made from MgF_2 are the best polarizers to use in the photon energy range 5–10 eV. The upper limit is determined by the quality of the MgF_2. The long optical path through the prism (~27 mm) means that the absorption due to impurities can be significant. Since the ordinary beam passes undeviated along the axis, the Rochon polarizer is achromatic. The extraordinary beam is refracted away from the axis of rotation and is absorbed in a mask placed before the photodiode. The extinction coefficient of Rochon polarizers that we use is 10^5, which means they can be treated as being essentially perfect.

From the considerations about the optimum geometry for ellipsometry, it is clear that reflection polarizers can only be optimized for high transmission and good polarization over a limited photon-energy range. However, for spectroscopic measurements a wide range is necessary. As shown by Hamm *et al.* [18, 19] a triple-reflection polarizer with gold-coated mirrors represents a suitable compromise. The triple-reflection polarizer we use consists of a 135° prism and a plane mirror with gold coatings [20]. A minimum of three reflections is necessary to avoid a net deviation of the transmitted light beam from the optical axis. Using literature values for the optical constants of gold [21], we have calculated the transmission and degree of polarization that we expect from our reflection polarizer. The results are shown in Fig. 6.

Photodiodes as VUV-Detectors E

Semiconductor photodiodes have numerous advantages over other detectors. They are inexpensive, compact, easy to use, highly linear (over 10 orders of magnitude), UHV-compatible and insensitive to contamination. For ellipsometry, the good linearity, lack of polarization dependence, and uniform response over the active area make these detectors particularly attractive. The stability, quantum efficiency, and responsivity of

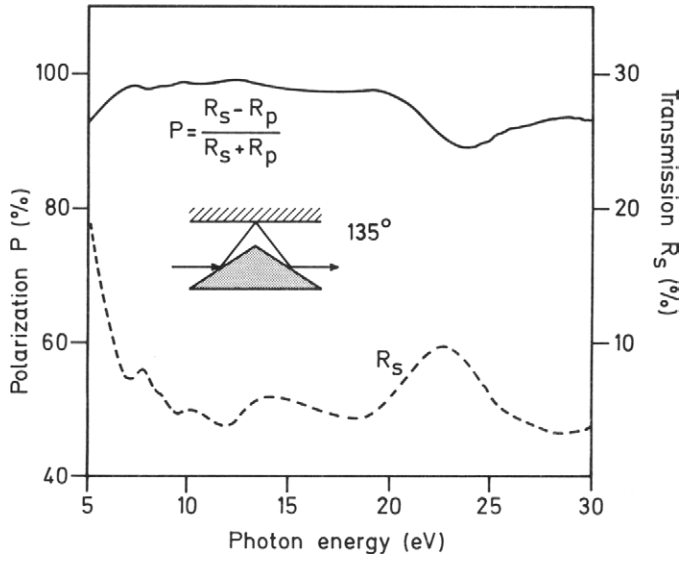

Fig. 6. Calculated degree of polarization and transmission of the triple-reflection polarizer.

various photodiodes have already been reported [22, 23]. In the ellipsometer, we use diffused silicon diodes with a thin oxide overlayer in conjunction with the MgF_2 polarizer. The standard silicon diodes have a high quantum efficiency, but are not as stable as GaAsP or GaP Schottky diodes. A particular problem with the Si diodes is charge-trapping in the silicon-dioxide layer, which can lead to a complete loss in sensitivity if the diode is inadvertently exposed to high-energy radiation (for example, zero-order light from the monochromator). Recently, a new type of inversion-layer silicon photodiode has been developed [24], which has good stability and an extremely high quantum efficiency. These are the best detectors for VUV ellipsometry. In the past, we used GaP Schottky diodes and Si diodes covered only with a thin natural-oxide layer for photon energies above 10 eV.

The rapid increase in the quantum efficiency of photodiodes with increasing photon energy enhances the contributions of higher harmonics from the monochromator. Unfortunately, there are very few filters available for the photon-energy region 5–35 eV, so it is not always easy to eliminate unwanted higher harmonics.

III THEORY

A Basic Formulas

Compared with conventional ellipsometry, the conditions under which we perform our measurements in the VUV are significantly less than ideal in two respects. First, the light emerging from the monochromator may contain elliptically polarized and unpolarized components at the level of a few percent, which vary as the monochromator is scanned. In principle, these unwanted components may be suppressed by an additional reflection polarizer but only at the expense of intensity. We decided to measure the complete state of polarization of the incident light and to use these reference data to evaluate $\varepsilon_1(\hbar\omega)$ and $\varepsilon_2(\hbar\omega)$ with the "Mueller matrix formalism" [29], which is a more general formalism than that usually applied. Second, for the analyzer we can use only conventional birefringent transmission polarizers for the very near VUV range. Rochon-type MgF_2 polarizers can be obtained with a cutoff energy between 9 eV and 10 eV depending on the optical quality. At higher photon energies, reflection polarizers have to be used, which are less ideal. Consequently, a careful characterization of these polarizers is necessary for a correct data evaluation.

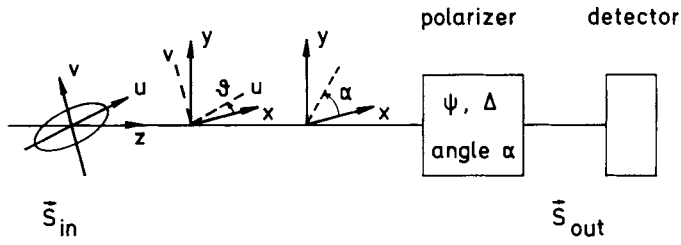

Fig. 7. Schematic drawing of system for analyzing polarized light.

Only very few polarimetry experiments have been conducted previously in the VUV region. The obvious difficulty is to measure the polarization of the light with a polarizer of unknown characteristics (which need to be determined at the same time). Without relying on other input parameters such as the optical constants of the polarizer surfaces, such a measurement requires the use of two sequential polarizers, which can be rotated independently [3, 25, 26, 27]. In the present experiment, however, the sample itself may be regarded as a polarizer, and by using all the mechanical degrees of freedom of our ellipsometer, we are able to perform all characterization measurements without any additional optical elements. To understand the measurement procedure, it is necessary first to deduce some relations between the measured detector signal and the parameters of the light, sample, and polarizer in the Mueller matrix formalism.

Consider the situation of Fig. 7, where light is incident on a polarizer and the intensity of the transmitted fraction is detected. The polarization of the incoming light is conveniently described by its Stokes vector in the u, v, z coordinate frame with the z-axis being the direction of propagation and the u, v-axes coincident with the main axes a and b of the polarization ellipse [28]:

$$\mathbf{S}_{in} = \begin{pmatrix} I \\ IP\cos 2\varepsilon \\ 0 \\ IP\sin 2\varepsilon \end{pmatrix}. \tag{2}$$

Here I denotes the light intensity, P the degree of total polarization, and ε the ellipticity with $\tan \varepsilon = b/a$. In Fig. 7, θ defines a tilt angle of the u, v, z frame with respect to an x, y, z laboratory frame, and α is the angle of rotation of the polarizer; both rotations are about the (common) z-axis.

The Stokes vector of the transmitted light in the laboratory frame is then calculated by multiplication of the Stokes vector of the incoming light with

4×4 real Mueller matrices [29],

$$\mathbf{S}_{\text{out}} = R_{-\alpha} M_{\text{pol}} R_{\alpha} R_{-\theta} \mathbf{S}_{\text{in}}, \tag{3}$$

where R represents a rotation by an angle indicated as a subscript and M_{pol} represents a polarizer. Since our detector is insensitive to polarization, we measure only the intensity of the outgoing light, which is given by the first component of the Stokes vector. This component remains unchanged under rotation of the vector about the z-axis, so we can omit the rotation matrix $R_{-\alpha}$ and calculate the intensity using

$$\mathbf{S}_{\text{out}} = M_{\text{pol}} R_{\alpha-\theta} \mathbf{S}_{\text{in}}$$

$$\mathbf{S}_{\text{out}} = \text{const} \begin{pmatrix} 1 & \cos 2\psi_A & 0 & 0 \\ \cos 2\psi_A & 1 & 0 & 0 \\ 0 & 0 & \sin 2\psi_A \cos \Delta_A & \sin 2\psi_A \sin \Delta_A \\ 0 & 0 & -\sin 2\psi_A \sin \Delta_A & \sin 2\psi_A \cos \Delta_A \end{pmatrix}$$

$$\times \begin{pmatrix} 1 & 0 & 0 & 0 \\ 0 & \cos 2(\alpha-\theta) & \sin 2(\alpha-\theta) & 0 \\ 0 & -\sin 2(\alpha-\theta) & \cos 2(\alpha-\theta) & 0 \\ 0 & 0 & 0 & 1 \end{pmatrix} \begin{pmatrix} I \\ IP \cos 2\varepsilon \\ 0 \\ IP \sin 2\varepsilon \end{pmatrix} \tag{4}$$

and further,

$$I_{\text{det}} = I_0(1 + P \cos 2\varepsilon \cos 2\psi_A \cos 2\theta \cos 2\alpha + P \cos 2\varepsilon \cos 2\psi_A \sin 2\theta \sin 2\alpha). \tag{5}$$

The parameters ψ_A and Δ_A are related to the complex transmittance of the polarizer for the electric-field vector of the light in s and p geometry [28]:

$$\tan \psi_A e^{i\Delta_A} = (t_p/t_s) e^{i(\delta_p - \delta_s)} \tag{6}$$

Note that frequently used "polarization" or "fractional polarization" of the polarizer follows as

$$\frac{T_s - T_p}{T_s + T_p} = \frac{1 - \tan^2 \psi_A}{1 + \tan^2 \psi_A} = \cos 2\psi_A, \tag{7}$$

with $T_{s,p}=t_{s,p}^2$ as the transmittance of the polarizer for the light intensity in s and p geometry. By comparison of Eqs. 1 and 5, we find the following relations using the Fourier coefficients a_1 and a_2:

$$P\cos 2\varepsilon\cos 2\psi_A=\sqrt{a_1^2+a_2^2}$$

$$\tan 2\theta=a_2/a_1. \tag{8}$$

Thus, the angle θ of the polarization plane is determined directly from a_2/a_1, but no independent information on the total polarization, ellipticity, and polarization of the polarizer is obtained.

Figure 8 illustrates the situation for an ellipsometry experiment. The incoming light is now incident on a sample with angle ξ between the plane of incidence and the plane of polarization. The reflected light passes through a reflection polarizer and is subsequently detected. The measured intensity may be calculated from

$$\mathbf{S}_{\text{out}}=M_{\text{pol}}R_{\alpha}M_{\text{sample}}R_{-(\xi-\theta)}\mathbf{S}_{\text{in}}. \tag{9}$$

The Mueller matrix M_{sample} represents the reflection at the sample and is

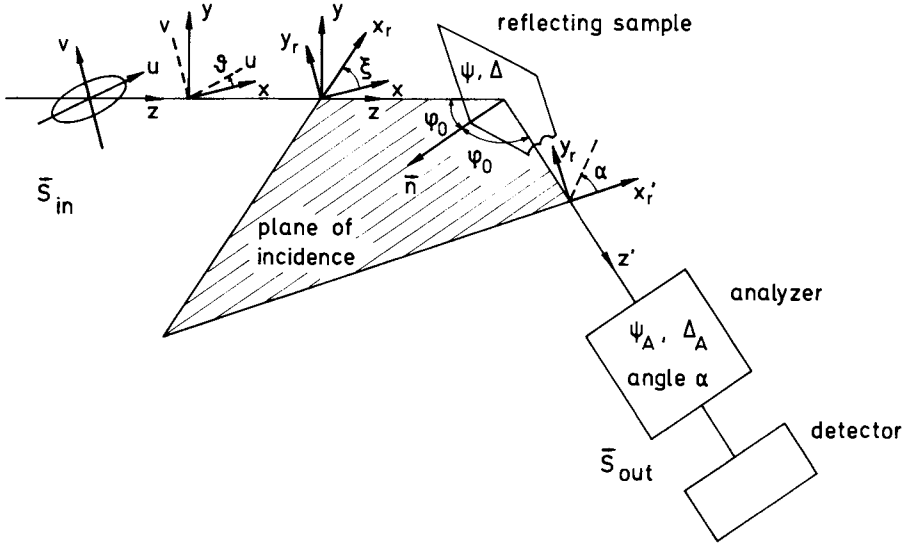

Fig. 8. Diagram showing coordinate systems and parameters of ellipsometer.

analogous to that of the reflection polarizer [28],

$$M_{\text{sample}} = \begin{pmatrix} 1 & -\cos 2\psi & 0 & 0 \\ -\cos 2\psi & 1 & 0 & 0 \\ 0 & 0 & \sin 2\psi \cos \Delta & \sin 2\psi \sin \Delta \\ 0 & 0 & -\sin 2\psi \sin \Delta & \sin 2\psi \cos \Delta \end{pmatrix}. \quad (10)$$

The first component of the Stokes vector $\mathbf{S}_{\text{out}}$ gives the detected intensity again, which has the general form of Eq. 1 with the Fourier coefficients

$$a_1 = \frac{P \cos 2\varepsilon \cos 2(\xi - \theta) - \cos 2\psi}{1 - P \cos 2\varepsilon \cos 2(\xi - \theta) \cos 2\psi} \cos 2\psi_A$$

$$a_2 = \frac{P \sin 2\varepsilon \sin \Delta + P \cos 2\varepsilon \sin 2(\xi - \theta) \cos \Delta}{1 - P \cos 2\varepsilon \cos 2(\xi - \theta) \cos 2\psi} \sin 2\psi \cos 2\psi_A. \quad (11)$$

From these two expressions the complex reflectance, $\rho = \tan \psi e^{i\Delta}$, of the sample can be calculated, provided we know the total polarization, P, ellipticity, ε, and orientation of the polarization plane, θ, of the input light, and the polarization, $\cos 2\psi_A$, of the analyzer. We may then proceed to calculate the complex dielectric constant, for example, using Fresnel's formula for the two-phase model [28]:

$$\tilde{\varepsilon}_s = \tilde{\varepsilon}_0 (\sin^2 \phi_0 + \left(\frac{1-\rho}{1+\rho}\right)^2 \sin^2 \phi_0 \tan^2 \phi_0), \quad (12)$$

with $\tilde{\varepsilon}_0$ as the dielectric constant of the ambient and ϕ_0 as the angle of incidence.

Some remarks are in order regarding the relation between the Fourier coefficients and the complex reflectivity ρ of the sample, Eq. 11. Under ideal conditions, that is, $P = 1$, $\varepsilon = 0$, $\cos 2\psi_A = 1$, we obtain the magnitude and phase of the complex reflectance as

$$\tan \psi = \sqrt{\frac{1 + a_1}{1 - a_1}} |\tan(\xi - \theta)|$$

$$\cos \Delta = \frac{a_2}{\sqrt{1 - a_1^2}} \operatorname{sgn}(\xi - \theta), \quad (13)$$

which are the well-known formulas from conventional ellipsometry [8]. The correction for an ellipticity ε gives only a second-order contribution to the Fourier coefficient a_1 and hence also to tan ψ, but may influence the coefficient a_2 drastically depending on the value of Δ. The polarization of the analyzer enters as a multiplicative parameter in both Fourier coefficients and can thus be taken into account in exactly the same manner as the electronic attenuation factor for the difference in amplification of the ac versus the dc part of the signal [8]. Observe further that a_1 is an even function of the effective tilt angle $(\xi - \theta)$ of the ellipsometer; a_2 is an odd function of $(\xi - \theta)$ only if the ellipticity is zero, and otherwise it contains an offset.

B Calibration

The calibration procedure is performed to establish the reference azimuthal angles for the plane of polarization of the incident light and for the analyzer. The procedure has been described in detail by Aspnes [8] and relies on the fact that linearly polarized light, reflected at an oblique angle, remains linearly polarized only if the plane of polarization is either parallel or perpendicular to the plane of incidence. The plane of polarization is determined accurately by measuring the Fourier coefficients for a range of angles about the horizontal, and then fitting a parabola to the residuals of the polarization. The minimum of the parabola gives the plane of polarization, and the analyzer azimuth and electronic attenuation factor can then be readily determined from the Fourier coefficients.

In practice, the calibration defines the condition for p-polarization, and the reflected light is linearly polarized, so from Eqs. 1 and 8 the Fourier coefficients are given by

$$1 - a_1^2 - a_2^2 = 0 \tag{14}$$

$$1/2 \arctan(a_2/a_1) = 0. \tag{15}$$

The residuum given by Eq. 14, when plotted as a function of the ellipsometer tilt angle, ξ, can be approximated by a parabola for small values of ξ. Equation 15, which determines the analyzer offset angle, is linear in ξ [8].

The sum of the squared Fourier coefficients may deviate from unity even for exactly linear-polarized light due to electronic attenuation of the ac component relative to the dc component of the signal. However, the

"zero" position for the ellipsometer tilt angle is unambiguously identified by the minimum value of the residuum. At this position, the "zero" of the analyzer angle is fixed also, and the electronic attenuation factor can be determined [8].

Under nonideal polarization conditions, we have to analyze the expressions in Eqs. 14 and 15 using Eq. 11 for the Fourier coefficients. To simplify the calculation, only first-order terms of the ellipticity ε and the fraction of unpolarized light, $1-P$, are taken into account. A power-series expansion in the effective ellipsometer tilt angle, $\xi-\theta$, then leads to the expressions

$$\begin{aligned} 1-a_1^2-a_2^2 &= 1-\cos^2 2\psi_A + 2(1-P)\cot^2\psi\cos^2 2\psi_A \\ &\quad + 8\varepsilon\cot^2\psi\sin\Delta\cos\Delta\cos^2 2\psi_A(\xi-\theta) \\ &\quad + 4\cot^2\psi(\sin^2\Delta-(1-P)\cot^2\psi)\cos^2 2\psi_A(\xi-\theta)^2 \\ 1/2\arctan(a_2/a_1) &= \varepsilon\cot\psi\sin\Delta+\cot\psi\cos\Delta(\xi-\theta). \end{aligned} \tag{16}$$

The minimum of the residuum is obtained at

$$\xi_0=\theta+\varepsilon\cot\Delta, \tag{17}$$

and the measured analyzer offset angle at this position is

$$\frac{1}{2}\arctan\frac{a_2}{a_1}=\varepsilon\frac{\cot\psi}{\sin\Delta}. \tag{18}$$

For $P=1$ and $\cos 2\psi_A=1$, Eqs. 17 and 18 are identical with those given by Aspnes for totally polarized light containing ellipticity [15]. We find that the angular position of the minimum of the residuum is displaced by the ellipticity, and its value at the minimum is changed by unpolarized light and nonideal polarization of the polarizer.

C Error Analysis

Figure 9 shows the variation of the Fourier coefficients a_1 and a_2 as a function of the angle ξ between the plane of polarization and the plane of reflection (polarizer angle). The sample is a ZnS single crystal, the photon energy is set to 5 eV, and the angle of incidence is 67.5°. The crosses

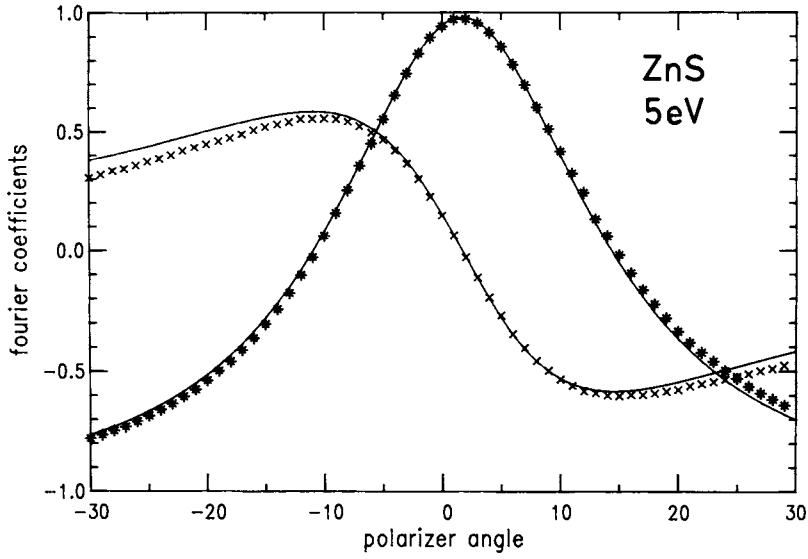

Fig. 9. Variation of the Fourier coefficients a_1 (stars) and a_2 (crosses) versus polarizer angle at fixed photon energy ($\hbar\omega = 5$ eV, $\phi_0 = 67.5°$).

indicate the Fourier coefficients measured with a conventional laboratory ellipsometer corrected with the appropriate analyzer and polarizer offset angles from the calibration. The solid lines are fits to the experimental values according to Eq. 11. Such measurements are extremely useful in estimating the accuracy of the experiment. In this particular case there is a significant discrepancy between the experimental data and the fit at large angles, which cannot be eliminated by varying the parameters of Eq. 11. Fitting the data separately for positive or negative ξ changes the fit parameters ψ by 0.3° and Δ by 0.5°. This difference can be compensated by a change in the angle of incidence on the sample of $\pm 0.2°$ as the polarizer is rotated, to yield approximately the same values of ε_1 and ε_2 as for the fit in Fig. 9.

This example demonstrates that in addition to the statistical variations in the measured Fourier coefficients, systematic errors in the angles which determine the experimental geometry set limits on the accuracy of the measured dielectric function. Now we will examine the influence of these errors, assuming that we have the optimum geometry so $\xi = \psi$ and $\Delta = -90°$. The variation of the dielectric function due to changes in the Fourier coefficients is then given by

$$\delta\tilde{\varepsilon} = \left(\frac{\partial\tilde{\varepsilon}}{\partial\psi}\bigg|_{\substack{\Delta=-90° \\ \psi=\xi}}\right)\left(\frac{\partial\psi}{\partial a_1}\delta a_1\right) + \left(\frac{\partial\tilde{\varepsilon}}{\partial\Delta}\bigg|_{\substack{\Delta=-90° \\ \psi=\xi}}\right)\left(\frac{\partial\Delta}{\partial a_2}\delta a_2\right) \tag{19}$$

$$\delta\varepsilon_1 = \left(\frac{\sin 2\psi}{4} - 4\sin^2\psi\cos^2 2\psi\right)\delta a_1 + \left(\frac{1}{2} + \sin 2\psi\cos 4\psi\right)\delta a_2 \quad (20)$$

$$\delta\varepsilon_2 = \sin 2\psi(\cos^2 2\psi - \sin^2 2\psi)\delta a_1 + 2\sin^2 2\psi\cos 2\psi\delta a_2. \quad (21)$$

For a value of $\psi = 15°$, we obtain

$$\delta\varepsilon_1 = -0.08\delta a_1 + 0.75\delta a_2, \qquad \delta\varepsilon_2 = 0.25\delta a_1 + 0.43\delta a_2.$$

Thus, an uncertainty in the measured Fourier coefficients introduces an error of the same absolute magnitude in the dielectric function. The experimental error is typically of the order of 0.01, and is therefore negligible, provided the dielectric function is large. In the VUV region, this is usually not the case and furthermore, for samples with low reflectance, the limited primary intensity can lead to an adverse signal-to-noise ratio.

Errors in the analyzer angle and polarizer angle are directly related to uncertainties in the Fourier coefficients, but are typically lower than the statistical uncertainty. The variation of the dielectric function with the uncertainty in the angle of incidence can be calculated from Eq. 12 to be

$$\delta\tilde{\varepsilon} = \frac{2}{\sin\phi_0\cos\phi_0}[(1+\cos^2\phi_0)\tilde{\varepsilon} - \sin^2\phi_0]\delta\phi_0. \quad (22)$$

This error depends on the magnitude of the dielectric function and the angle of incidence. If we assume typical values in the visible and near-UV region of $\tilde{\varepsilon} = 5 + i10$ and $\phi_0 = 67.5°$, we obtain

$$\delta\varepsilon_1 = 30\delta\phi_0; \qquad \delta\varepsilon_2 = 60\delta\phi_0.$$

Typical values for the VUV range ($\tilde{\varepsilon} = 1 + i0.2$ and $\phi_0 = 45°$) yield

$$\delta\varepsilon_1 = 4\delta\phi_0; \qquad \delta\varepsilon_2 = 1.2\delta\phi_0.$$

Thus, the absolute magnitude of this systematic error is reduced by about the same amount as the change in the absolute magnitude of the dielectric function. We conclude that the systematic errors limit the accuracy of ellipsometry at low photon energies, whereas statistical errors

due to diminishing reflected signal limit the accuracy at high photon energies.

Figure 10 shows the Fourier coefficients plotted against polarizer angle ξ for ZnS at 8 eV measured with the synchrotron-radiation ellipsometer. Note that Δ is close to $-90°$ in this example, so the optimum angle of incidence is 67.5°. The quality of the fit indicates that it is in fact possible to obtain accuracies with this UHV system comparable to those routinely achieved with standard ellipsometers. It is necessary, however, to perform a rather time-consuming adjustment procedure to establish all the angular settings to an accuracy of a few tenths of a degree, and the storage ring must operate stably over this period of time.

Figure 11 shows results obtained at higher photon energies using a reflection polarizer. These measurements can be used not only to determine the ellipsometric angles with good accuracy, but can also be used to determine the polarization of the incoming light and the polarization properties of the polarizer. The data analysis indicates that the output of the monochromator contains negligible contributions of elliptically polarized light, but unpolarized light must be taken into account at high photon energies. In the energy range below 12 eV it was not possible to obtain satisfactory fits for measurements with the reflection polarizer, most probably due to second-order light from the monochromator grating. At higher energies, the second-order radiation is adequately suppressed by

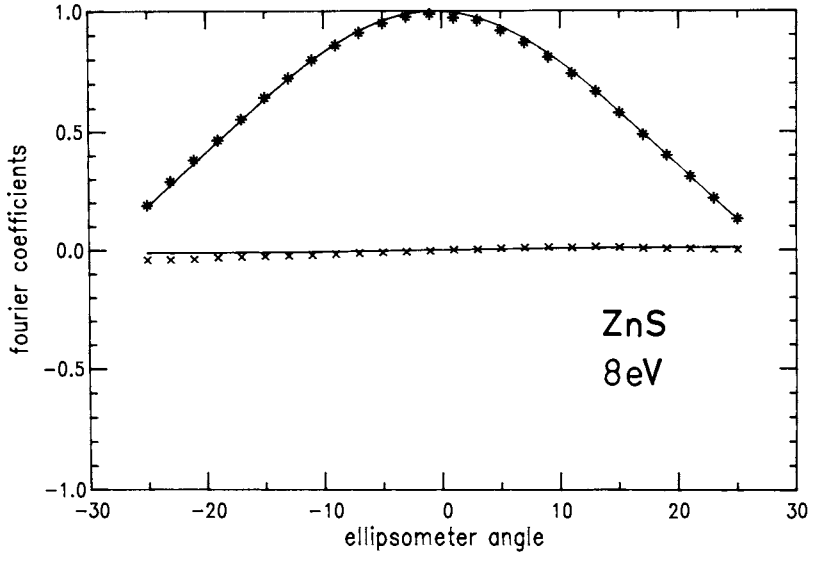

Fig. 10. Variation of the Fourier coefficients a_1 (stars) and a_2 (crosses) versus polarizer angle at fixed photon energy ($\hbar\omega = 8$ eV, $\phi_0 = 67.5°$).

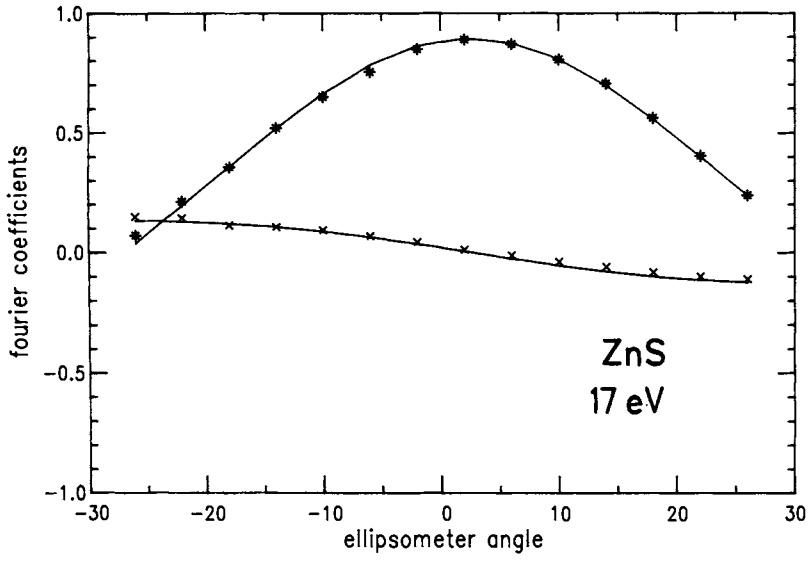

Fig. 11. Variation of the Fourier coefficients a_1 (stars) and a_2 (crosses) versus polarizer angle at fixed photon energy ($\hbar\omega = 17$ eV, $\phi_0 = 45°$).

the monochromator, and below 10 eV we use a MgF_2 Rochon polarizer, which absorbs all radiation above 11.2 eV, so second-order light is transmitted only for $\hbar\omega < 5.6$ eV.

The results of all the fits of the Fourier coefficients versus polarizer angle for ZnS are compiled in Table I. The sample was cleaved in air and

TABLE I

The Dielectric Function of Cleaved ZnS(110) at Room Temperature, Determined by Stepwise Rotation of the Plane of Polarization at Fixed Photon Energies

$\hbar\omega$	ε_1	ε_2	$\hbar\omega$	ε_1	ε_2
4.0	7.06	3.16	9.5	−1.47	3.74
5.0	7.04	5.58	12.0	0.46	0.43
6.5	3.32	7.36	14.0	0.08	0.82
7.0	−0.57	10.13	15.0	−0.06	0.66
8.0	−1.17	4.31	17.0	0.19	0.55
9.0	−0.55	4.35	20.0	0.45	0.38

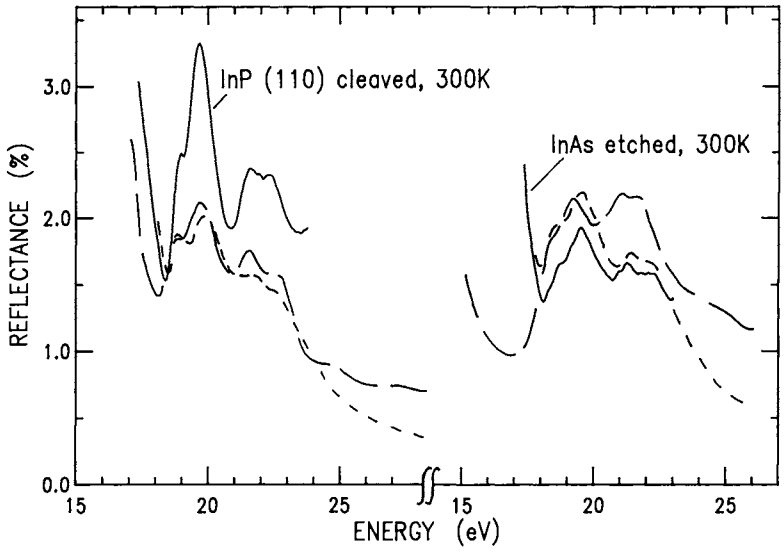

Fig. 12. Reflectance of InP and InAs at the In 4d edge, calculated from ellipsometric data (solid curves). For comparison the reflectance calculated by Kramers–Kronig analysis of absorption data (short dashed lines) and directly measured (long dashed lines) are included from Ref. [31].

subsequently introduced into the UHV system. The data at 4 eV and 5 eV were obtained on the same sample using a rotating-analyzer ellipsometer at our institute in Stuttgart. We estimate the uncertainty in the dielectric function to be about 0.5 for measurements below 10 eV and 0.1 for $\hbar\omega > 10$ eV in both ε_1 and ε_2.

RESULTS AND COMPARISON WITH REFLECTANCE SPECTRA IV

III-V Semiconductors A

The optical constants of the III-V compounds in the energy range of about 20 eV are interesting because the threshold for core *d*-level excitation lies in this region. Reflectance spectra have been reported in Refs. [31] and [32], and the data for InP and InAs are shown in Fig. 12 together with the reflectance calculated from our ellipsometrically determined dielectric function. The InAs sample was chemically etched to strip off the surface oxides following the recipe described by Aspnes [32] and was introduced into the UHV chamber after etching. The InP sample was

cleaved in situ along the (110) plane. All the reflectance spectra in [32] were measured on chemically etched samples. The absolute reflectances all compare very well; however, the spectral features at the In 3d edge are much more pronounced for the sample that was cleaved in situ. It is our experience that the structures are most clearly observed from single crystals cleaved in situ. It is important to note that ellipsometry can be carried out with a reasonable signal-to-noise ratio even when the absolute reflectivity of the sample is only about 1%.

Figures 13, 14, and 15 show the dielectric function of GaP, GaAs, and InP in the photon energy region 15–30 eV. All the samples are single crystals cleaved in situ and cooled to liquid-nitrogen temperature to enhance the weak structures at the Ga 3d and In 4d edges. These results are summarized in Ref. [30], which should be consulted for more details.

B II-VI Compounds

1 *ZnS*

Figures 16 and 17 show the dielectric function of cubic ZnS at room temperature over the photon-energy range 3–22 eV, with the data from

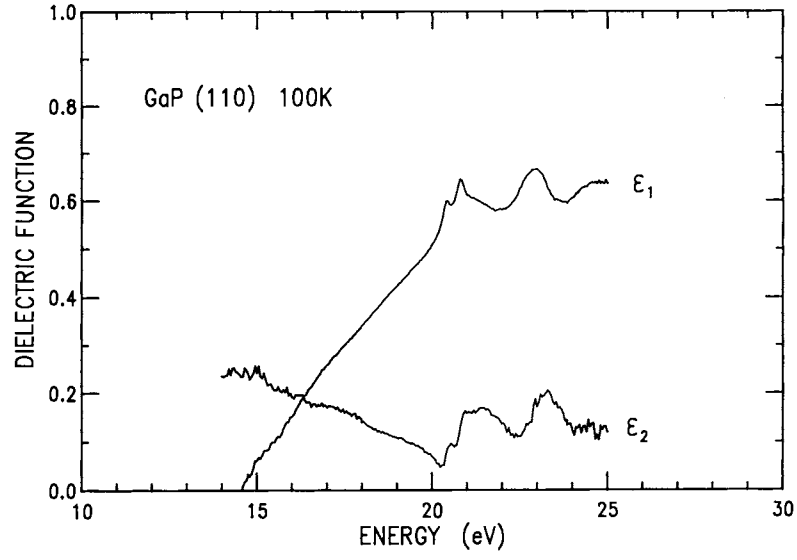

Fig. 13. Dielectric function of cleaved GaP(110) at 100 K.

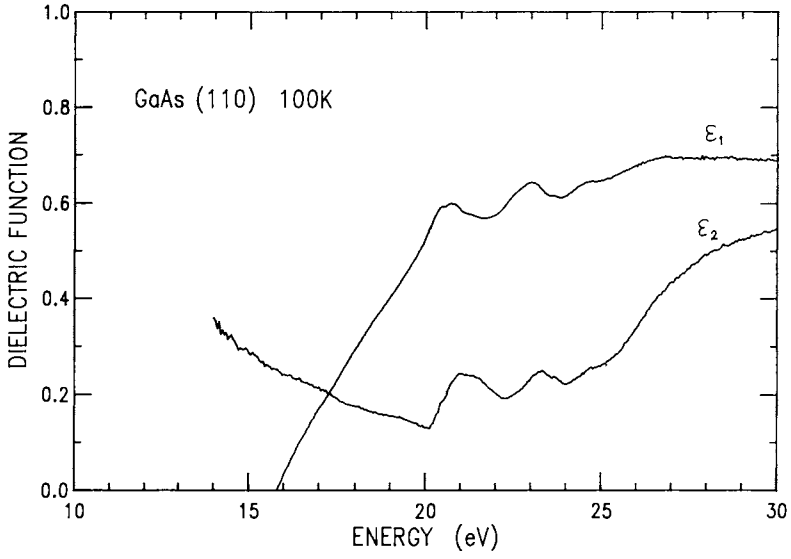

Fig. 14. Dielectric function of cleaved GaAs(110) at 100 K.

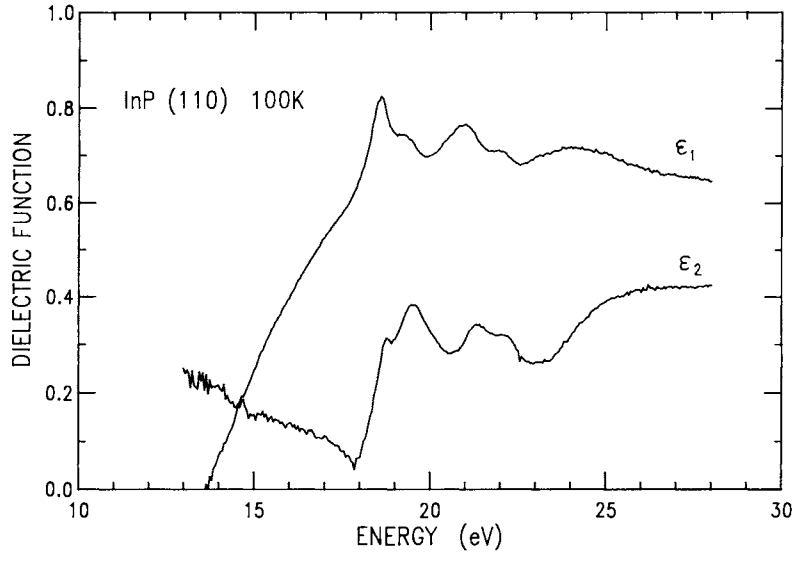

Fig. 15. Dielectric function of cleaved InP(110) at 100 K.

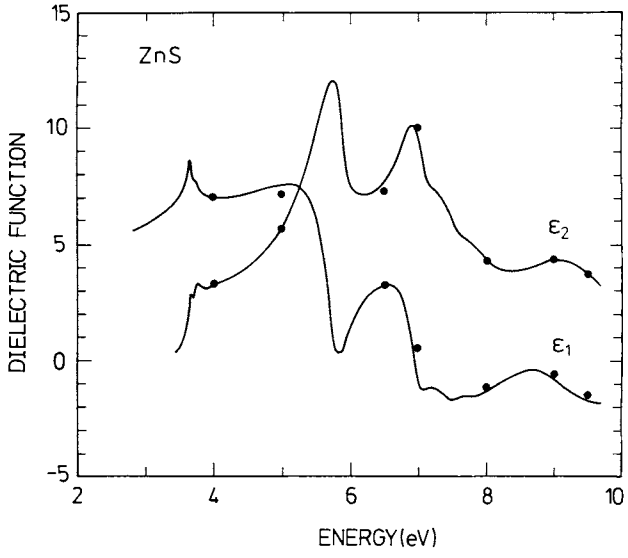

Fig. 16. Dielectric function of cleaved ZnS(110) at room temperature. The dots are the data from Table I.

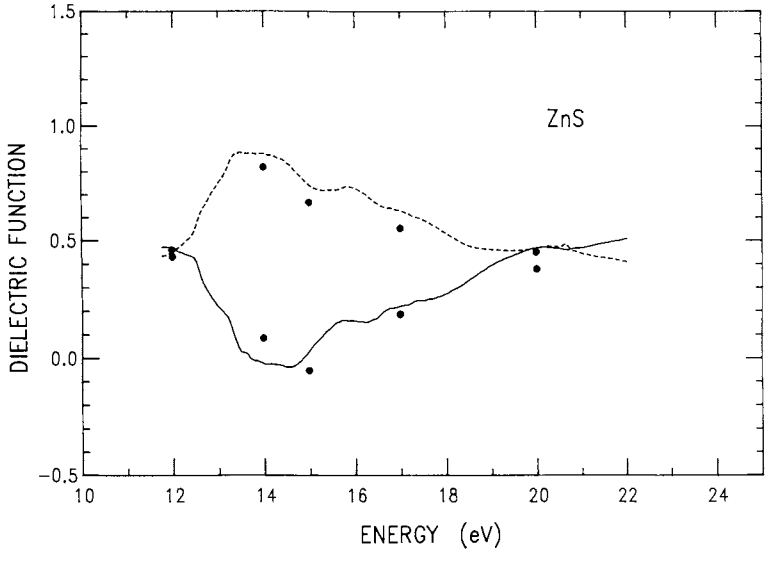

Fig. 17. Dielectric function of cleaved ZnS(110) at room temperature. (ε_1, solid line; ε_2, dashed line). The dots are the data from Table I.

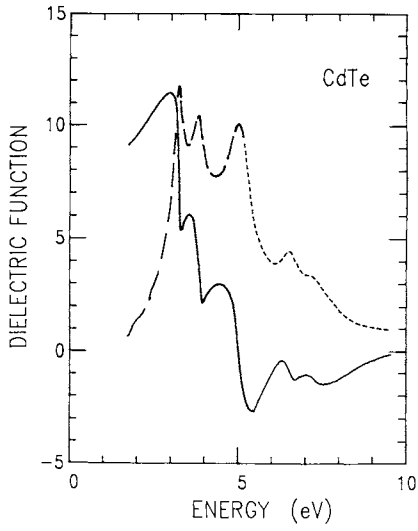

Fig. 18. Dielectric function of cleaved CdTe(110) at room temperature. (ε_1, solid line; ε_2, dashed line).

Table I included for comparison. The data below 5.6 eV were obtained with an ellipsometer at the Max-Planck-Institute in Stuttgart on samples previously measured at BESSY. Both natural ZnS and laboratory-grown single crystals were measured, some of which were cleaved in air and some in situ. In the photon-energy region below 10 eV, no significant differences were observed between different samples. Above 12 eV, the structures in the dielectric function were most pronounced for the natural crystal cleaved in situ. The structures in this energy range originate from transitions of Zn 3d electrons into the conduction band. By differentiating such spectra, the energies of conduction-band critical points can be readily determined. It is interesting to note that although the magnitudes of ε_1 and ε_2 are greatly reduced in the VUV compared with the visible region, detailed information can be derived from the ellipsometric data.

CdTe 2

Figures 18 and 19 show the dielectric function of CdTe with the data from Lautenschlager *et al.* [34] included below $\hbar\omega = 5.6$ eV. In this case the samples are all etched single crystals measured at room temperature, so it is likely that the data in the energy range above 12 eV are influenced by a surface layer on the sample. The fine structures in the high-energy spectrum are due to transitions of Cd 4d electrons into the conduction band.

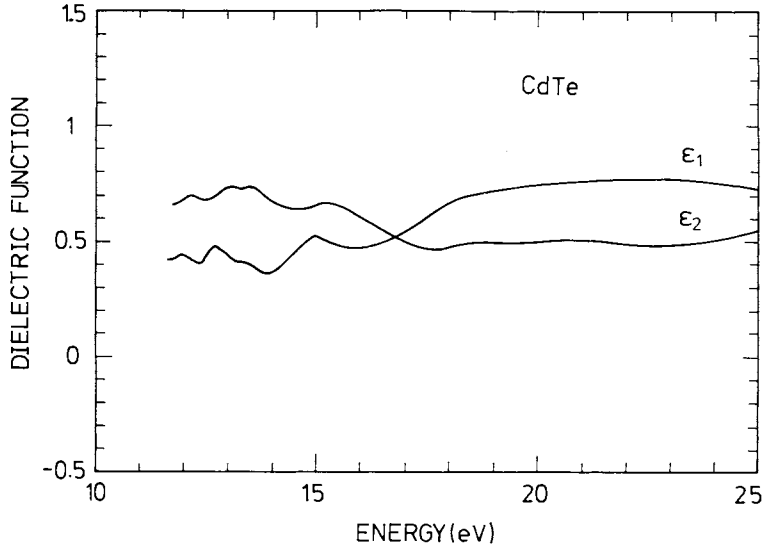

Fig. 19. Dielectric function of cleaved CdTe(110) at room temperature for energies above the Cd 4d threshold.

From our ellipsometrically determined dielectric-function data, it is straightforward to calculate a reflectance curve, which can be directly compared with experimental reflectivity data. In Fig. 20 we compare our calculated reflectance with the data measured by Jung [35], and the agreement is excellent. The Kramers–Kronig analysis of the reflectance data, however, yields values for ε_2 that differ by about 25% from the ellipsometrically measured value. In view of the excellent agreement of the reflectivity calculated from the dielectric function and the directly measured reflectance data, the discrepancy in ε_2 can probably be attributed to incorrect extrapolation of the reflectance when performing the Kramers–Kronig analysis. This example demonstrates nicely how ellipsometric measurements can augment reflectivity data. In the VUV region, where sample surface conditions play a particularly important role, it is advantageous to be able to compare data from two independent measurement techniques.

C Calcium Fluoride

Another example of the type of data that can be obtained from the VUV ellipsometer is the dielectric function from a cleaved CaF_2 (111) crystal at

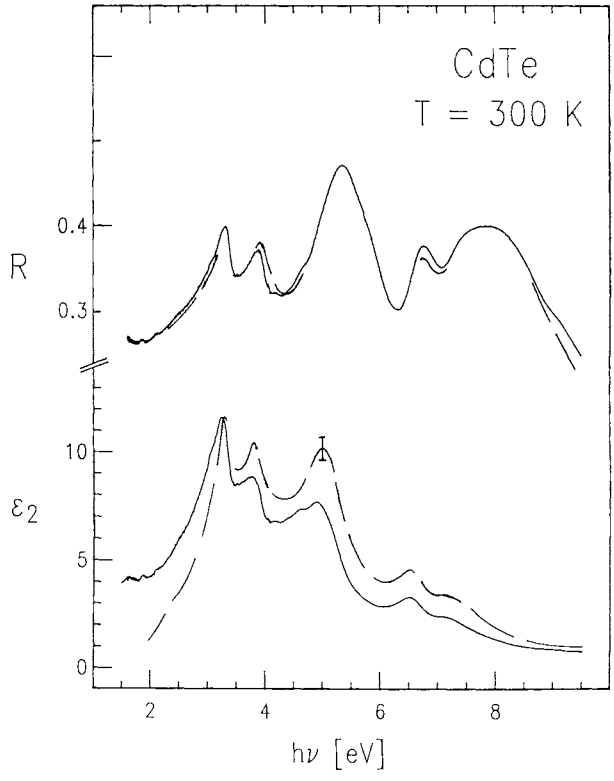

Fig. 20. Reflectance spectrum of CdTe and imaginary part of the dielectric function obtained by Kramers–Kronig analysis [35] (solid curves), compared to the reflectivity calculated from ellipsometric data (dashed curve) and the directly measured ε_2 spectrum (dashed curve).

room temperature, shown in Fig. 21. This spectrum covers the photon-energy range 10–35 eV and indicates the power of spectroscopic ellipsometry using synchrotron radiation for studying the optical properties of insulators. Considerable structure is observed throughout the entire energy range due to interband transitions between the F 2p derived valence and the Ca 4s and 3d derived conduction bands, but the threshold structures at 11.2 eV are obscured by second-order light from the monochromator grating. Above 27 eV, excitation of the 3p core electrons dominate the spectrum. In the lower energy region the spectrum is fairly well described by a recent band-structure calculation [36]. At higher energies, there is a plethora of excitonic lines associated with transitions from the Ca 3p core level; a more complete data analysis can be found in Ref. [37].

There are discrepancies of up to a factor of two between previous reflectance and energy-loss measurements on CaF_2, so we also performed

reflectance measurements in our ellipsometer. In Fig. 22 the direct measurement is compared to the reflectance calculated from our dielectric-function data, and it can be seen that the results agree to within the experimental error.

V SUMMARY

Ellipsometry has developed into a standard technique for studying the optical constants of solids in the NIR-VIS-UV spectral region with high precision. With our present instrument we have demonstrated the feasibility of performing ellipsometry in the VUV and have obtained useful data from a range of samples. The examples shown here illustrate the variety of optical excitations in solids that can be studied in this spectral range. Valence excitations can be followed to energies far above the absorption threshold, and structures due to core-level excitations can be resolved in detail. For insulators with large band gaps, VUV ellipsometry is a very promising technique for band-structure investigations.

The accuracy of our results is comparable to the best reflectance data, but ellipsometry has the advantage of directly determining both real and imaginary parts of the dielectric function, and thus avoids the uncertainty

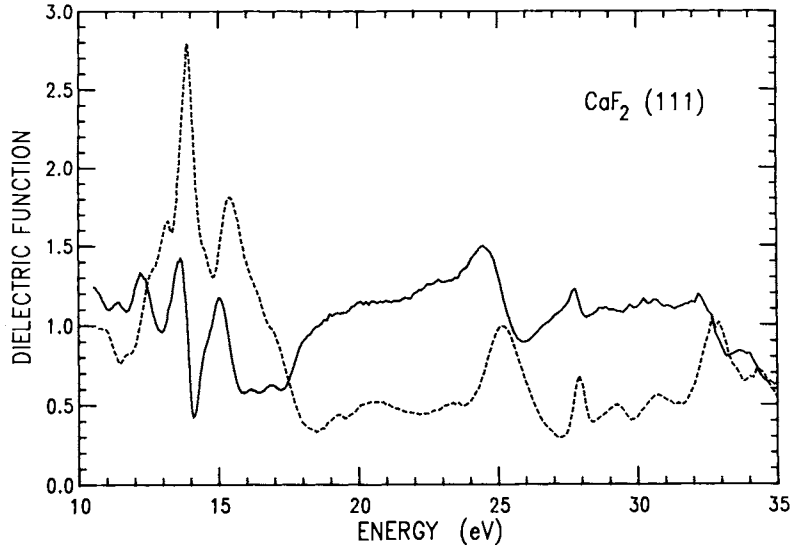

Fig. 21. The dielectric function of cleaved $CaF_2(111)$ at room temperature (ε_1, solid line, ε_2, dashed line).

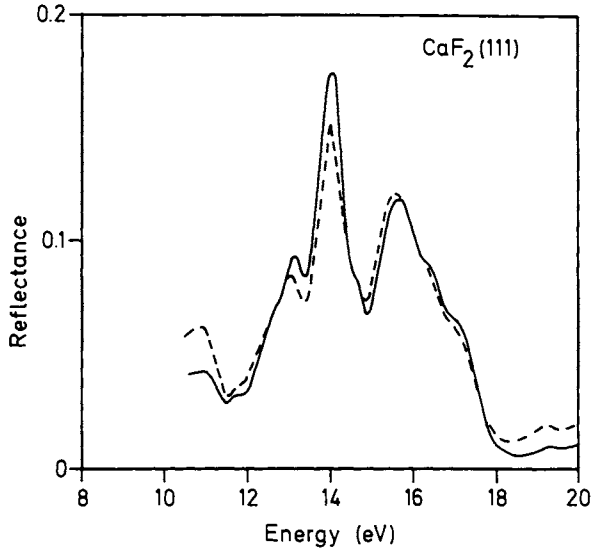

Fig. 22. Reflectance of CaF_2 at room temperature: the dashed line indicates directly measured reflectance; the solid line indicates reflectivity calculated from ellipsometric dielectric function.

associated with a Kramers–Kronig analysis. Ellipsometry is therefore potentially a more powerful technique for determining the optical constants of solids. It is to be expected that instruments with higher mechanical precision and stability, using improved polarizers and monochromators with better spectral purity, will be constructed in the near future, which will be able to obtain optical constants with enhanced precision up to even higher photon energies.

ACKNOWLEDGEMENT

This work was supported under project no. 05 490CAB by the German Federal Minister for Research and Technology (BMFT).

REFERENCES

1. D. Beaglehole, *Rev. Sci. Instr.* **59**, 2557 (1988).
2. M. Schledermann, DESY Internal Report 70/28 (1970).
3. M. Schledermann and M. Skibowski, *Appl. Opt.* **10**, 321 (1971).
4. W. R. Hunter in "Handbook of Optical Constants of Solids," (E. D. Palik, ed.), Academic Press, Orlando (1985).
5. D. Y. Smith in "Handbook of Optical Constants of Solids," (E. D. Palik, ed.), Academic Press, Orlando (1985).
6. D. W. Lynch in "Handbook on Synchrotron Radiation," Vol. 2, (G. V. Marr, ed.), North-Holland, Amsterdam (1987).

7. P. Drude, *Ann. d. Phys. u. Chem.* **36**, 532 (1889); **39**, 481 (1890).
8. D. E. Aspnes and A. A. Studna, *Appl. Opt.* **14**, 220 (1975).
9. S. Logothetidis, L. Viña, and M. Cardona, *Phys. Rev.* **31**, 2180 (1985).
10. D. E. Aspnes in "Optical Properties of Solids: New Developments," (B. O. Seraphin, ed.), North-Holland, Amsterdam (1976).
11. D. E. Aspnes in "Handbook of Optical Constants of Solids," (E. D. Palik, ed.), Academic Press, Orlando (1985).
12. Proc. Int. Conf. on Ellipsometry, published as Vols. 16, 56, 96 of *Surf. Sci.*
13. R. L. Johnson, J. Barth, M. Cardona, D. Fuchs, and A. M. Bradshaw, *Rev. Sci. Instr.* **60**, 2209 (1989).
14. D. E. Aspnes, *J. Opt. Soc. Am.* **64**, 639 (1974).
15. D. E. Aspnes, *J. Opt. Soc. Am.* **64**, 812 (1974).
16. M. Yamamoto and O. S. Heavens, *Surf. Sci.* **96**, 202 (1980).
17. D. Chandler-Horowitz and G. A. Candela, *Appl. Opt.* **21**, 2972 (1982).
18. R. N. Hamm, R. A. MacRae, and E. T. Arakawa, *J. Opt. Soc. Am.* **55**, 1460 (1965).
19. V. G. Horton, E. T. Arakawa, R. N. Hamm, and M. W. Williams, *Appl. Opt.* **8**, 667 (1969).
20. The triple-reflection polarizers were supplied by B. Halle Nachfolger GmbH, Berlin.
21. C. G. Olson and D. W. Lynch, tabulated optical data for Au in "Optical Properties of Metals II," (J. H. Weaver, C. Krafka, D. W. Lynch, and E. E. Koch, eds.), Fachinformationszentrum, Karlsruhe (1981).
22. J. Barth, E. Tegeler, M. Krisch, and R. Wolf in "Soft X-ray Optics and Technology," (E. E. Koch and G. Schmahl, eds.), *Proc. SPIE* **733**, 481 (1986).
23. M. Krumrey, E. Tegeler, J. Barth, M. Krisch, F. Schaefers, and R. Wolf, *Appl. Opt.* **27**, 4336 (1988).
24. R. Korde, L. R. Canfield, and B. Wallis, in "Ultraviolet Technology II," *Proc. SPIE* **932**, 153 (1988).
25. W. B. Westerveld, K. Becker, P. W. Zetner, J. J. Corr and J. W. McConkey, *Appl. Opt.* **24**, 2256 (1985).
26. A. Gaupp and W. B. Peatman in "Soft X-ray Optics and Technology," (E. E. Koch and G. Schmahl, eds.), *Proc. SPIE* **733**, 272 (1986).
27. J. Barth, R. L. Johnson, S. Logothetidis, M. Cardona, D. Fuchs and A. M. Bradshaw in "Soft X-ray Optics and Technology," (E. E. Koch and G. Schmahl, eds.), *Proc. SPIE* **733**, 265 (1986).
28. R. M. A. Azzam and N. M. Bashara, "Ellipsometry and Polarized Light," North-Holland, Amsterdam (1977).
29. H. Mueller, *J. Opt. Soc. Am.* **38**, 661 (1948).
30. J. Barth, R. L. Johnson, M. Cardona, D. Fuchs and A. M. Bradshaw, *Proc. 19th Int. Conf. Phys. of Semicond.*, Warsaw, 1988, (W. Zawadski, ed.), Institute of Physics, Polish Academy of Sciences, Warsaw, 885 (1988).
31. W. Gudat, E. E. Koch, P. Y. Yu, M. Cardona, and C. M. Penchina, *Phys. Status Solidi (b)* **52**, 505 (1972).
32. D. E. Aspnes, M. Cardona, V. Saile, M. Skibowski, and G. Sprüssel, *Solid State Commun.* **31**, 99 (1979).
33. D. E. Aspnes and A. A. Studna, *Phys. Rev. B* **27**, 985 (1983).
34. P. Lautenschlager, S. Logothetidis, L. Viña, and M. Cardona, *Phys. Rev. B* **32**, 3811 (1985).
35. C. Jung, private communication.
36. R. A. Heaton and C. C. Lin, *Phys. Rev. B* **22**, 3629 (1980).
37. J. Barth, R. L. Johnson, M. Cardona, D. Fuchs and A. M. Bradshaw, *Phys. Rev. B* **41**, 3291 (1990).

Chapter 11

Methods Based on Multiple-Slit Fourier Transform Interferometry for Determining Thin-Film Optical Constants in the VUV/Soft X-Ray Range

ROMAN TATCHYN*
Stanford Synchrotron Radiation Laboratory
Stanford University
Stanford, California
and
Institute of Theoretical Science
University of Oregon
Eugene, Oregon

I. Introduction to MSFTI 247
II. Fundamental Dimensional Constraints and Inequalities 253
III. Relationship of MSFTI to Alternative Metrological Techniques 254
IV. General Experimental Equations and Sensitivity Analysis 258
V. A Characterization of the Optical Constants of Au Using MSFTI in the 280–640 eV Range 265
VI. Problems and Prospects in Sample Preparation 270
VII. Prospects for MSFTI in Other Spectral Regimes 272
VIII. Summary 273
Acknowledgments 274
References 274

I. INTRODUCTION TO MSFTI

We begin with an elementary discussion of the physical principles on which the metrological technique of multiple-slit Fourier transform

* Affiliate Member, Center for X-Ray Optics, Lawrence Berkeley Laboratory, Berkeley, California 94720.

Copyright © 1991 by Academic Press.
All rights of reproduction in any form reserved.
ISBN 0-12-544422-2

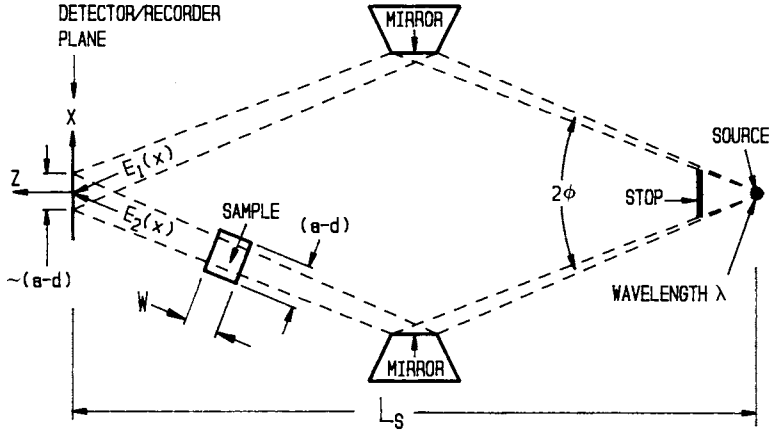

Fig. 1. Elementary split-beam interferometer configuration excited by a monochromatic point source. The mirrors are symmetrically positioned midway between the source and detector planes. For sufficiently small λ, $\lambda/(a-d)$, and sufficiently long beam path lengths, the wave fronts impinging on the detector can be assumed to be planar.

interferometry (MSFTI), or transmission-diffraction interferometry [1–3], is based. This will provide a foundation for the more detailed discussions to follow, and will also enable us to classify this still relatively new method with reference to the large number of alternative or complementary techniques reviewed elsewhere [4–8].

As a starting point, we consider the basic configuration of a symmetric split-beam interferometer of the direct-field type [9], shown schematized in Fig. 1. The depicted source is assumed to be monochromatic with wavelength λ. An isotropic, homogeneous, and uniformly thick sample characterized by the complex index of refraction $\hat{n}(\lambda) = (1 - \delta(\lambda)) + ik(\lambda)$, where δ and k are the λ-dependent phase and absorption components [10, 11], intercepts the lower beam at normal incidence. Approximating both beams by plane waves of unit amplitude and assuming complete cancellation of surface phase shifts and negligible multiple scattering (that is, reflection) [12] within the sample, we can straightforwardly determine the intensity distribution generated on the recorder–detector plane by the two interfering wavefronts to be

$$|E_1(x) + E_2(x)|^2 = (1 + e^{-4\pi Wk}) + 2e^{-2\pi Wk} \cos(2\pi[2x \sin\phi + W\delta]). \quad (1)$$

Here all the length dimensions have been normalized into units of

"numbers of wavelengths λ," a convention to be used throughout this chapter. From Eq. 1 it is evident that by interchanging two or more samples with different Ws, δ and k can be recovered from measurements of the interference pattern's fringe-shift, $W\delta/2 \sin\phi$, and contrast ratio $[2\exp(-2\pi Wk)/(1+\exp(-2\pi Wk)]^2$.

Now consider the case depicted in Fig. 2, in the limit where the two mirrors are removed and the beam stop height is reduced to zero, allowing the adjacent beam boundaries to just touch each other. It is clear that in this limit the two independent wavefronts can at best be made to illuminate *contiguous* regions on the detector plane, apparently leaving no direct way to discern a measurable interference pattern.

We note, in passing, that the removal of the mirrors from the apparatus in Fig. 1 has resulted in a configuration of utmost simplicity, that is to say, the precisely configured interferometer has been reduced to nothing more than a point source, a sample, and an aperture in the detector plane. As indicated, the sample has been advanced forward to the original detector plane, since in the eikonal[1] approximation [13] (which is conventionally assumed for the direct-field interferometric technique under discussion), the sample's distance from the detector plane does not alter the amplitude or phase modulation of the transmitted light reaching the plane. We will henceforth refer to the plane at which the sample is located as the *sample plane*.

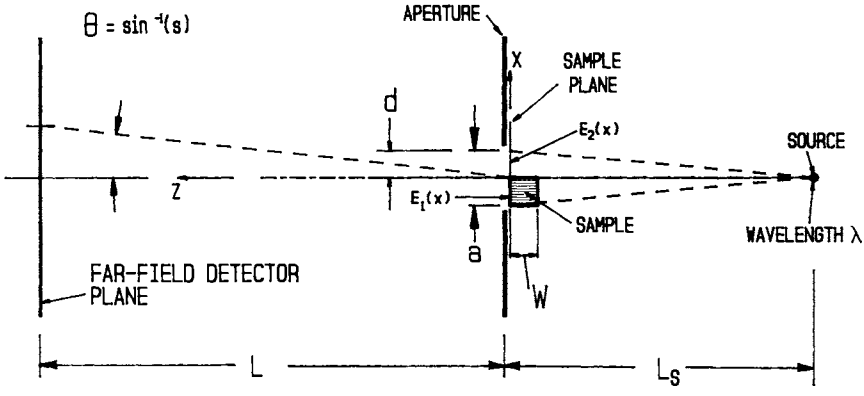

Fig. 2. Elementary configuration for Fourier transform interferometry viewed as a limiting case of a conventional split-beam interferometer. The width of the sample in the x direction is $(a-d)$.

[1] The meaning of this term, as we use it here and throughout this chapter, is that diffraction is assumed to be negligible *over the limited distance of light travel through the medium in question*. In the far field, we assume that diffraction will *always* manifest itself. In quantitative terms, we do not actually take the wavelength limit to zero, but simply assume it to be sufficiently smaller than the minimum lateral dimension of the optical neighborhood in question.

The configuration of Fig. 2 in fact provides a convenient starting point for implementing techniques based on Fourier transform interferometry (FTI). To wit, we simply move into the far field [14], away from the sample plane, and the two apparently disparate electrical-field distributions, $E_1(x)$ and $E_2(x)$, will generate an interference pattern given by the absolute value squared of the Fourier transform of their sum. Under the restriction (which will be relaxed later) that the sample width be equal to the aperture width, that is, that $a = 2d$, this far-field intensity pattern is straightforwardly found to be

$$|\overline{E_1(x) + E_2(x)}|^2 = \left| \int_0^d dx e^{-2\pi i s x} + \int_{-d}^0 dx e^{-2\pi i W[\delta - ik]} e^{-2\pi i s x} \right|^2$$

$$= (d)^2 \operatorname{sinc}^2(ds)[(1 + e^{-4\pi k W}) + 2e^{-2\pi k W} \cos(2\pi[ds - W\delta])]. \tag{2}$$

In Eq. 2 we have utilized the notation $\operatorname{sinc}(x)$ to represent the quantity $\sin(\pi x)/\pi x$, and an overbar to represent the Fourier transformation. We point out (with reference to Fig. 2) that s can be interpreted as the sine of the angle with respect to the axis of symmetry of the system (the z axis) [15].

We now systematically compare Eq. 2 with Eq. 1. First, apart from the sinc^2 factor in Eq. 2 and an inessential sign reversal, the expression in square brackets is identical in form to the right-hand side of Eq. 1. In this sense, we have established that the basic FTI approach allows us to regain valid analytical terms from which the optical constants of the sample material can in principle be unfolded. Second, we note that even for the simple configuration being considered, the FTI technique already exhibits certain decisive advantages over the direct-field method. The first of these is the greatly simplified physical arrangement upstream of the sample plane in Fig. 2. The second stems from the fact that we can now place our detector at arbitrarily large distances from the sample in the far field, and provided we do not lose sensitivity to the transmitted signal altogether, we can in principle resolve the measured features of the intensity spectrum with superior precision.

Having isolated these two evident advantages, we are now in turn forced to recognize that the sinc^2 factor in Eq. 2 constitutes a potentially troublesome difference with respect to Eq. 1. By virtue of possessing a period comparable to the half-width of the cos term on its right, this factor is capable of distorting both the shapes and locations of the salient intensity maxima associated with the term in square brackets. It is clear that this "damping" modulation (whose direct-field analog is ordinarily negligible

[16]), can render the unambiguous characterization of the far-field spectrum problematical. In this fashion we come face-to-face with essentially two basic possibilities for mitigating this problem. In both instances, the basic idea is to sharpen the salient maxima of the intensity pattern with respect to the fixed sinc^2 pattern: in the first case by greatly reducing the period of the cos term in Eq. 2, and in the second by greatly compressing, or sharpening, the angular width of its intensity peaks.

The first approach is readily implemented by introducing an axially centered displacement D' between the two contiguous illuminated strips at the sample plane in Fig. 2. This modification is trivially incorporated into Eq. 2 by suitably changing the integral limits, and the resulting expression for the intensity assumes the same form as Eq. 2, with the period of the cos term replaced by $[1/(d+D')]$, QED. This approach, which was in fact originally employed for measuring optical phase constants by Rayleigh [17], is in many respects analogous to Young's original double-slit configuration [18]. Its primary disadvantage is that it greatly increases the number of fringes in the far field without significantly adding to the information content associated with any fringe pair. In this respect it is highly wasteful of source light, a potentially limiting factor under certain circumstances.

A second drawback, especially troublesome in the soft X-ray range, is that even a significant attenuation of either beam will only weakly affect the contrast ratio of the intensity pattern. In fact, as may be verified by applying the sensitivity operator defined in Section IV, the sensitivities of the contrast ratio and the intensity peaks to incremental changes in Wk actually vanish when the two beams become equal (that is, when $Wk \dot{\to} 0$), mandating the accurate measurement of the (nearly evanescent) intensity minima for the determination of k. In view of fundamental signal-to-noise limitations, this tends to make split-beam configurations significantly less flexible for measuring absorption than for phase delay.

A schematized version of the second approach is depicted in Fig. 3. The basic idea is to set up an alternating periodic array of N samples and open apertures, that is to say, to configure a diffraction grating out of the material to be measured. This multiplicity of (nominally identical) periods and open apertures underlies our addition of the *multiple-slit* qualifier to the name of the basic FTI method. From elementary Fourier theory, we observe that the N-fold increase in the number of periods will indeed compress the angular widths of the far-field intensity peaks in inverse proportion to N, making the identification and measurement of the sharpened maxima highly insensitive to the attenuating sinc^2 factor. In addition, two other significant advantages can be shown to accrue [1, 2]:

(i) By selecting the dimensions and the number of periods of the grating structure properly, the effects of both δ and k on the far-field intensity maxima can be individually controlled. MSFTI can consequently

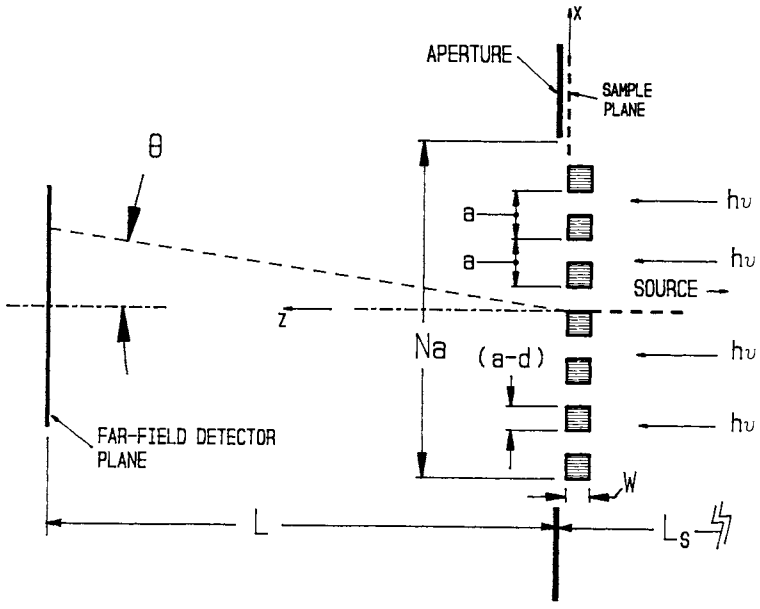

Fig. 3. Simplified version of the full MSFTI configuration. The incoming light waves are assumed to be planar.

be optimized for measuring both parts of the complex index of refraction with flexible accuracy.

(ii) Small-scale imperfections in the grating (sample) material, by virtue of generating much more spread-out spectra than the grating lattice, exert a proportionally diluted effect on the salient intensity peaks in the far field, minimizing the effect of such imperfections on the measured accuracy of $\hat{n}$.[2]

It is instructive to assess the basic principles underlying the MSFTI technique from the point of view of physical optics. Perhaps the most natural interpretation of the method is to view the periodic sample array as two interleaved diffraction gratings, one consisting of opaque apertures alternating with bars composed of the sample material and the other consisting of opaque bars alternating with open apertures. In this picture, each grating generates its own diffracted amplitude pattern in the far field,

[2] This phenomenon, which also helps in suppressing the effects of edge imperfections in the grating bars, can be interpreted as an illustrative case of Ernst Abbe's diffractive imaging theory [19].

and since these patterns are shift-invariant with respect to the grating's lateral positions, they interfere additively (that is, as if the gratings were situated on top of one another at the sample plane). Thus, to the extent that all the grating bars are identical, MSFTI can be viewed as being analogous to the direct-field (that is, split-beam) interferometric techniques cited above. From an alternative point of view, the radiation passing through the open apertures can be regarded as constituting a reference beam, and the resulting far-field pattern as an in-line (Gabor) hologram [20] of the sample structure. This picture becomes the more orthodox one as the number of bars and slits in the grating is reduced to one (Fig. 2).

FUNDAMENTAL DIMENSIONAL CONSTRAINTS AND INEQUALITIES II

It will be of interest at this point to analyze the dimensional constraints on the MSFTI configuration that are required to make its practical performance consistent with the analysis in Section I. In allowing for minimal complexity in the soft X-ray range, no focusing or collimating optics are assumed.

We first note, in view of the assumption that the radiation emanates from an effective point source, that the wavefronts impinging on the sample will have the divergence angle Na/L_s (see Figs. 2 and 3). To enforce a significant peak separation, our first requirement on this angle is that it leads to a peak width at the detector plane significantly smaller than L/a. If the natural $1/aN$ width of the peak profiles needs to be preserved, the tighter constraint $(1 + L/L_s)Na \ll L/Na$ must be established. As an intermediate criterion, we can specify a marginal restriction of

$$L_s \gg a^2 N^{3/2}. \tag{3}$$

If the source has a height Δ_s in the plane of dispersion such that $\Delta_s \geq Na$, the above restriction should be tightened to

$$L_s \gg aN^{1/2}(\Delta_s + Na). \tag{4}$$

The next constraint on L_s is dictated by our approximation of the wavefronts by plane waves. Given the assumed point source, we can require the maximum phase variation of the light irradiating the sample to

be significantly less than one equivalent wavelength over its surface. This leads to

$$L_s > N^2 a^2, \tag{5}$$

an inequality that will typically dominate the lower bounds of the "intermediate" cases (Eqs. 3 and 4).

Moving downstream of the sample plane, the establishment of "far-field" conditions on L for Fraunhofer diffraction can readily be shown [14] to be equivalent to the physical argument underlying Eq. 5; thus, we obtain a constraint of

$$L > N^2 a^2 \tag{6}$$

on the distance of the detector plane from the sample.

These relations, while explicitly restricting L and L_s in terms of N and a, also strongly indicate the motivation for keeping the product Na as small as possible. In this regard, we note that a is restricted from below by the eikonal assumption (as outlined in Section I) and the applicability of scalar diffraction formalism. If we conservatively assume these two conditions to be very well fulfilled by the inequality $a > 100$, we can use the constraint given in Eq. 6 to define a dimensional range for nominally acceptable values of a, namely,

$$100 < a < L^{1/2}/N. \tag{7}$$

This inequality is useful in estimating the allowable period and size of a sample grating when L is defined by extraneous factors.

III RELATIONSHIP OF MSFTI TO ALTERNATIVE METROLOGICAL TECHNIQUES

In view of the background concepts developed in Section I, multiple-slit Fourier transform interferometry can be characterized as a photometric [21] technique that is based on normal-incidence[3] transmission and multiple-beam interference. In its usual application to nominally isotropic and homogeneous materials, it is insensitive to polarization effects and is

[3] See, however, Ref. [22].

therefore unrelated to ellipsometric [7] or polarimetric methods. In attempting to assess its range of utility within contemporary optical metrology, several issues that have a bearing on the suitability of any experimental technique need to be considered. Among these are: requirements on sample preparation; the spectral range of interest; physical properties of available light sources; requirements on detectors; experimental complexity with respect to available technology; and the merits of competing techniques. We will begin by enumerating some of the experimental requirements for MSFTI, most of which follow from the elementary analyses in Sections I and II:

(1) In the soft X-ray range ($\simeq$4–120 Å), sample structures will ordinarily be characterized by small dimensions and laterally microscopic features. This need not necessarily be the case in the visible, where lenses and collimators can be employed.

(2) In order to ensure effective planarity of the incoming wave fronts, the sample has to be located at a sufficiently far distance from the source, particularly in spectral ranges where compact optical collimators or lenses are unavailable.

(3) The detector has to be in the far field with respect to the sample, which in the soft X-ray range typically translates into distances of several to several tens of meters.

(4) In view of requirement 2, and more particularly requirement 3, which can reduce effective light flux by as much as the square of the distance from the sample (see Fig. 3), highly collimated and intense light sources are required.

(5) Additional requirements for high intensity and collimation can arise when the samples are mounted on substrates whose marginal absorption is significant.

(6) Depending on the spectral range, operation of the entire MSFTI apparatus within a hard vacuum may be required. In the soft X-ray range, operation inside a vacuum is unavoidable.

With these prolegomena, we can now systematically compare the respective merits of MSFTI with those of other metrological techniques that are used, or that could in principle be adopted, for characterizing the optical constants of thin-film samples in the VUV–soft X-ray range. In the discussions to follow, it is worthwhile to keep in mind that even very thin films in the 100–3000 eV range can exhibit high absorption [6, 23], and that naturally occurring Bragg or Laue diffractors are unavailable over large spectral regions.

As MSFTI is an interferometric method, we have listed it, along with a selected set of alternative techniques of the same class, in Table I. The configurations identified as "direct-field, split-beam" are known to be well-suited for the visible range, in which they have in fact evolved. Beginning

with Lloyd's mirror, perhaps the simplest of all direct-field interferometers, the remaining instruments become progressively more sophisticated, with the Mach–Zehnder interferometer requiring precise beam-splitters and lenses, elements that have as yet no equally viable or efficient analogs in the soft X-ray range [24, 25]. Even if Lloyd's mirror (or Fresnel's mirrors) by virtue of their simplicity could be considered as potential competitors in the soft X-ray range at a given wavelength, spanning more than a limited wavelength range would in all likelihood necessitate the eventual manipulation of their reflecting facets, leading back to an increase in system complexity (exacerbated by operation inside a vacuum). Apart from this, existing soft X-ray sources such as conventional undulators [26] are still much too limited in terms of coherent output power to give split-beam configurations [27]—which, as was pointed out in Section I, are much more wasteful of interfering photons than the multiple-slit configuration—any significant advantage in comparison to MSFTI.

Irrespective of these observations, it is noteworthy that interferometers of the split-beam type shown in Fig. 1 have nevertheless been developed for the hard X-ray range,[4] where absorption is much less severe, and diffracting-crystal arrays instead of mirrors can be used to steer the beams. These hybrid configurations, ably pioneered in the metrology of X-ray optical constants by Bonse *et al.* [4, 28] and Hart [5], can utilize diffraction to maintain the angles of the intersecting beams constant, minimizing configurational complexity. Inasmuch, however, as they employ diffracting crystals, their range of operation cannot at present be extended downward to fully encompass the soft X-ray range.

Next, the alternative multiple-beam, direct-field configurations in the visible range, typified, for example, by the Fabry–Perot interferometer, cannot be employed in the 100–3000 eV range with anywhere near the efficiency or finesse [29] that they exhibit in the visible. This is due primarily to the practically unavoidable confinement of the interfering light within media that exhibit relatively high absorption at soft X-ray wavelengths. Again, however, we note that multilayer analogs of the Fabry–Perot etalon for the lower end of the hard X-ray range (Table I) have been developed [30] and indeed proposed for characterizing optical constants. However, in view of the fact that such systems are composed of at least two different materials, and inasmuch as the dynamics of multiple scattering are highly sensitive to the sample quality and absorptance [31], the associated experimental schemes would in general need to be more intricate than for MSFTI, and therefore inferior to it.

Concluding, on the basis of Section I and the above discussions, that MSFTI in fact exhibits a number of advantages in the soft X-ray range with

[4] At energies in excess of 3–5 KeV, operation inside a vacuum is not obligatory, a simplifying factor in high-precision experimental work.

respect to alternative interferometric techniques, we next contrast it with the purely photometric method of normal-incidence absorption measurement, a technique applied in recent years to the characterizations of thin films in the VUV and soft X-ray ranges [32]. This method, based on measuring the transmittance of thin films [33], depends on accurate total-flux measurements of beams impinging on, and then passing through, a sample. The necessity for integrating all the flux, including that *scattered* by both sample surfaces, places stringent requirements on the detector quality and configuration, factors that can lead to a heightened susceptibility to systematic errors. In contrast to MSFTI, which is to a significant extent self-filtering against the presence of small-scale imperfections (see Sections I and IV), integrated absorption measurements can also be extremely sensitive to small-scale imperfections in the sample's thickness profile for

TABLE I

A Classification of Selected Interferometric Configurations Used in Optical Metrology

	Interferometer	
Types	Split-beam[a]	Multiple-beam[b]
Direct field[c] (*specular reflection, refraction*)	Lloyd's Mirror[f] Fresnel's Mirrors[f] Mach–Zehnder[f]	Fabry-Perot[f]
Fourier transform[d] (diffraction)	**Rayleigh**[f,g]	**Multiple-Slit FT**[h]
Hybrid[e]	Bonse–Hart[i]	Multilayer Etalon[j]

[a] Configurations based on interference between two beams.
[b] Configurations based on interference among more than two beams.
[c] Based on interference of deflected beams for which diffraction can be disregarded. Configurations utilize reflection (and refraction in the visible and infrared ranges) to steer the beams.
[d] Based on interference of diffracted beams. Configurations utilize diffraction through slits. The diffractive metrological techniques in boldface are typified by unmatched systemic simplicity, a critical consideration in certain spectral ranges.
[e] Based on direct-field interference of beams that have been steered by Bragg or Laue diffraction.
[f] Described in Ref. [9], Chapter 7.
[g] According to Rayleigh [17], first explored by Fraunhofer.
[h] Multiple-slit Fourier Transform configuration, described in Refs. [1–3] and this chapter.
[i] Used primarily from the hard X-ray range down to the higher end of the soft X-ray range.
[j] X-ray analog of Fabry–Perot etalon with multilayer (Bragg-diffracting) facets.

unfavorable values of k and W. The latter parameter in particular tends to be unfavorable in the soft X-ray range, as the typically acceptable thicknesses ($\simeq$500–5000 Å) in that region are conducive to the generation of small-scale bulk and surface asperities during the preparation of samples [33, 34]. Additionally, only the absorption constant gets measured; the phase constant must subsequently be unfolded from a typically discrete set of k values via Kramers–Kronig analysis [35], an abstraction that is not always comparable in validity to a direct measurement [2, 36].

In view of these observations, we can underscore the following two potential advantages in addition to those itemized in Section I:

(iii) In contrast to alternative techniques, MSFTI apparently requires by far the least complex experimental arrangement in the soft X-ray range. Apart from the detector and source, all the high-precision aspects of the configuration inhere in the sample, which is small, accepts the probe radiation at normal incidence, and requires no manipulation in a vacuum environment.

(iv) With respect to the detector, no absolute *or* total-flux measurements are required. All that is required is a detector that is *linear* over the typically small [2] dynamic range represented by the ratios of the first to zeroth orders.

In contrast to these favorable conditions, however, it is evident that the requirement of a precisely fabricated, high-quality sample grating with microscopic features represents a significantly more demanding requirement for MSFTI than for competing techniques. This fact perhaps provides a clue as to the apparent absence of MSFTI from the soft X-ray scene prior to the relatively recent advent of reliable microfabrication technology [37, 38, 39]. Indeed, as will be discussed in Section VI, the requirement for high-quality microstructures is still perhaps the central issue in determining the future status of MSFTI in soft X-ray metrology. The second necessary requirement for MSFTI, namely, intense and highly collimated X-ray sources, has undoubtedly been fulfilled to a certain extent by the relatively recent advent of synchrotron storage rings and insertion devices [26]. Assuming the continued evolution of these two technological underpinnings, as well as the validity of the advantages (i–iv) posited above, the characterization of soft X-ray optical constants of thin films would seem to represent an optimal niche for MSFTI within the realm of optical metrology.

IV GENERAL EXPERIMENTAL EQUATIONS AND SENSITIVITY ANALYSIS

In this section we present the basic experimental equations of the MSFTI method, including expressions for evaluating the sensitivities of the experi-

mental quantities with respect to $\delta(\lambda)$ and $k(\lambda)$. These expressions are not the most general ones possible and are based on the following simplifying assumptions:

(1) No support structure is assumed for the free-standing diffracting bars in Fig. 3.

(2) The bars are assumed to be plane-parallel, congruent, homogeneous, and isotropic samples of the test material.

(3) The surfaces of the bars are assumed to be perfectly planar.

(4) Surface phase shifts and multiple reflections are ignored.

(5) The source radiation is assumed to be monochromatic and planar at the sample plane.

(6) The aperture and bar dimensions d and $(a\text{-}d)$ are assumed to be large enough for the eikonal approximation to apply in transmission through the grating bars. Additionally, all the conditions for the validity of scalar diffraction theory are assumed to hold [40]. As opposed to assumptions 1–5, these idealizations are to be considered as prerequisites for all valid MSFTI implementations.

Although this is evidently a large set of idealizations, departures from most of the listed assumptions have been analyzed in prior work and the results are available in the literature [1–3]. In most practical cases the corresponding corrections in the soft X-ray range can be expressed quantitatively as simple correcting terms or factors in the basic equations. In view of the referential purpose of this handbook chapter, some of the more important of these will be included in this section.

We begin by quantifying the notion of sensitivity, whose physical meaning can be interpreted as the "fractional change in a parameter x induced by a fractional change in a parameter y." Analytically, the differential form of this quantity is given by

$$S_y^x = \frac{y}{x}\left(\frac{\partial x}{\partial y}\right) \equiv \frac{\partial(\ln x)}{\partial(\ln y)}. \tag{8}$$

Referring to Fig. 3, we can now write out the expression for the magnitude squared of the Fourier transform of the electric field x-distribution along the sample plane in direct analogy to Eq. 2. For the intensity of the mth peak in the far field, this expression reduces to [41]

$$I^{(m)} = \left(\frac{\sin(\pi m N)}{\sin(\pi m)}\right)^2 |\bar{M} + e^{\pi i m}\bar{A}|^2, \qquad m = 0, \pm 1, \pm 2, \ldots, \tag{9}$$

where $\bar{M}$ and $\bar{A}$ are, respectively, the Fourier transforms of the electric

field distributions across a bar surface and an open aperture. For a given period a and an arbitrary aperture dimension d, we obtain the following expression for the ratio of the mth order peak intensity to the zeroth order peak intensity:

$$\frac{I^{(m)}}{I^{(0)}} = \frac{[1 - 2e^{-2\pi W k(\lambda)} \cos 2\pi W \delta(\lambda) + e^{-4\pi W k(\lambda)}] \operatorname{sinc}^2(md/a)}{[1 + 2(a/d - 1)e^{-2\pi W k(\lambda)} \cos 2\pi W \delta(\lambda) + (a/d - 1)^2 e^{-4\pi W k(\lambda)}]}, \qquad m \neq 0. \tag{10}$$

This expression demonstrates that for the assumed rectangular bar cross-section, the peak intensity ratios among orders other than the first will be independent of $k(\lambda)$ and $\delta(\lambda)$, and that the entire effect of $\hat{n}$ on the far-field intensity spectrum can be deduced solely from the ratio $I^{(1)}/I^{(0)}$. The establishment of the experimental equations based on Eq. 10 is immediate. If we choose two gratings of the same material and of parameters a_1, d_1, W_1, and a_2, d_2, W_2 and denote the corresponding intensity ratios by

$$I_i^{(1)}/I_i^{(0)} = R_i, \qquad i = 1, 2, \tag{11}$$

we get

$$\cos 2\pi W_i \delta(\lambda) - \frac{1}{1 + A_i} \cosh 2\pi W_i k(\lambda) + \frac{A_i}{1 + A_i} \cosh[2\pi W_i k(\lambda) + r_i] = 0, \tag{12}$$

where

$$A_i = R_i \tfrac{1}{4}\pi^2 [\sin(\pi\eta_i) \cosh(\tfrac{1}{2} r_i)]^{-2}, \tag{13}$$

$$\eta_i = d_i / a_i, \tag{14}$$

and

$$r_i = \ln\left(\frac{\eta_i}{1 - \eta_i}\right), \tag{15}$$

It is evident that accurate measurements of the *lengths* a_i, d_i, W_i and the far-field *intensities* $I_i^{(0)}$ and $I_i^{(1)}$ constitute, in principle, a sufficient data set for iterating the values of k and $|\delta|$ out of Eq. 12.

The sensitivities of the measured peak-intensity ratios R_i to the sample grating parameters are straightforwardly derived by directly applying Eq. 8 to Eq. 12. The results are

$$S_\delta^{R_i} = \left(\frac{2\pi W_i\delta \sin 2\pi W_i\delta}{\cosh 2\pi W_i k - \cos 2\pi W_i\delta}\right)\left(\frac{\cosh 2\pi W_i k + \cosh(2\pi W_i k + r_i)}{\cosh(2\pi W_i k + r_i) + \cos 2\pi W_i\delta}\right), \quad (16)$$

$$S_k^{R_i} = \left(\frac{2\pi W_i k \sinh 2\pi W_i k}{\cosh 2\pi W_i k - \cos 2\pi W_i\delta}\right)$$

$$\times \left(\frac{2\cos 2\pi W_i\delta + \cosh(2\pi W_i k + r_i) - \cosh 2\pi W_i k}{\cosh(2\pi W_i k + r_i) + \cos 2\pi W_i\delta}\right), \quad (17)$$

$$S_{W_i}^{R_i} = [2\pi W_i\delta \sin 2\pi W_i\delta(\cosh(2\pi W_i k + r_i) + \cosh 2\pi W_i k)$$

$$+ 2\pi W_i k \cosh 2\pi W_i\delta(\sinh(2\pi W_i k + r_i)$$

$$+ \sinh 2\pi W_i k) - 2\pi W_i k \sinh 2\pi W_i k]$$

$$\div [(\cosh(2\pi W_i k + r_i) + \cos 2\pi W_i\delta)(\cosh 2\pi W_i k - \cos 2\pi W_i\delta)], \quad (18)$$

and

$$S_{\eta_i}^{R_i} = 2([\pi\eta_i \cot \pi\eta_i] - 1)$$

$$+ \left[\frac{2\eta_i(e^{-2\pi W_i k} + (\eta_i^{-1} - 1)^{-1}\cos 2\pi W_i\delta)}{((\eta_i^{-1} - 1)^{-1}e^{2\pi W_i k} + (\eta_i^{-1} - 1)e^{-2\pi W_i k} + 2\cos 2\pi W_i\delta)}\right]. \quad (19)$$

Equations 11–15 constitute the basic experimental relations for a minimal set of two gratings. Utilizing more than two gratings in an experimental determination will, as expected, result in the statistical reduction of the uncertainties stemming from random errors. For example, if M' gratings are used, there will be $M'(M'-1)/2$ cross-correlated calculations of δ and k, and the sensitivity equations must then be employed in an iterative rondo with Eqs. 11–15 to make all the calculated values of δ and k consistent with each other and the known systematic errors [2]. The second, evident use of the sensitivity equations is to help choose optimal parameters or parameter ranges for sample gratings to be fabricated for an experiment, provided some initial knowledge of the actual values of the constants exists.

We next turn to the question of corrections to the basic experimental

equations, which can arise from departures from the ideal conditions assumed at the outset of this section. We will focus on those corrections liable to be of immediate concern for preliminary evaluations of MSFTI experiments. More complete treatments of nonideal experimental conditions have been cited above. The first important modification arises when multiple reflections in the grating bars have to be taken into account (as in the visible and UV [6] ranges), or when the phase shifts induced by the sample surfaces do not all cancel (as can happen, for instance, when the sample bars are deposited on a plane–parallel substrate). If we can represent all these effects by applying a complex factor, $\tau \exp(i\Phi)$, to $\bar{M}$ in Eq. 9, we arrive at the following modified version of Eq. 10, wherein we have introduced the quantity $\Omega = -\frac{1}{2}\ln(\tau)$ and utilized the (unindexed) Eq. 15:

$$\frac{I'^{(1)}}{I'^{(0)}} = e^{r}\,\mathrm{sinc}^2\left(\frac{d}{a}\right)\frac{\cosh(2\pi Wk+\Omega)-\cos(2\pi W\delta-\Phi)}{\cosh(2\pi Wk+r+\Omega)+\cos(2\pi W\delta-\Phi)}. \qquad (20)$$

We see immediately that since both τ and Φ depend on both δ and k [2, 10], the establishment of an equation separable in δ and k (such as Eq. 15) will not in general be possible when τ differs from 1 and/or Φ from 0. This can in certain instances lead to an enhanced sensitivity of the experimental results to systematic errors, thereby degrading the validity and reliability of computed results. This fact highlights one of the more important potential advantages of MSFTI in the 100–3000 eV region, which we herewith add to those already listed in Sections I and III:

(v) For many materials throughout broad portions of the VUV–soft X-ray range, Ω and Φ are often close enough to zero to be ignored, a factor underlying the simplicity of the basic experimental formalism of MSFTI. This in effect can reduce the number of physical variables influencing measurements, enhancing the validity of MSFTI in the corresponding spectral region.

The following modifications of the ideal experimental equations are based on the statistical departure of real-life sample bars from cross-sectional rectangularity, dimensional congruency, and surface perfection. To generate readily interpreted worst-case corrections, we assume that the bars' total thickness W varies randomly in the x–y plane over a range $[-b, b]$; the bars' positions in the x direction vary randomly over a range $[-g, g]$; and the bars' widths vary randomly over a range $[-c, c]$, all with associated uniform probability density functions.[5] Under a broad range of

[5] The general case based on arbitrary probability density functions is treated in Ref. [2].

circumstances, the primary effect of the variability of W will be to alter the ratio $I^{(1)}/I^{(0)}$ *by adding the terms*

$$[e^{-2\pi\langle W\rangle k}(Q_4-1)-2(Q_1-1)\cos 2\pi\langle W\rangle\delta+2Q_3\sin 2\pi\langle W\rangle\delta] \tag{21}$$

and

$$(\eta^{-1}-1)[e^{-2\pi\langle W\rangle k}(\eta^{-1}-1)(Q_4-1)+2(Q_1-1)\cos 2\pi\langle W\rangle\delta-Q_3\sin 2\pi\langle W\rangle\delta] \tag{22}$$

into, respectively, the bracketed numerator and denominator of the right side of Eq. 10. Here we have utilized the unindexed Eq. 14, represented the average bar thickness by $\langle W\rangle$, and employed shorthand symbols Q_j $(j=1,3,4)$ for

$$Q_1=\frac{k\cos 2\pi\delta b\sinh 2\pi kb+\delta\sin 2\pi\delta b\cosh 2\pi kb}{2b\pi(k^2+\delta^2)}, \tag{23}$$

$$Q_3=\frac{\delta\cos 2\pi\delta b\sinh 2\pi kb-k\sin 2\pi\delta b\cosh 2\pi kb}{2b\pi(k^2+\delta^2)}, \tag{24}$$

$$Q_4=\frac{(\cos 2\pi\delta b\sinh 2\pi kb)^2+(\sin 2\pi\delta b\cosh 2\pi kb)^2}{4b^2\pi^2(k^2+\delta^2)}. \tag{25}$$

Equations 21–25 are useful in estimating acceptable limits on both the large- and small-scale surface roughness of a sample material for use in an MSFTI experiment, particularly when prior estimates of its actual optical constants are available.

The effect of the laterally random variations is primarily to modulate the diffracted nonzero orders [1]. If we express g and c as fractional lengths of the grating period a, the ideal $I^{(1)}/I^{(0)}$ ratio in Eq. 10 is transformed into

$$\frac{I^{(1)}}{I^{(0)}}\rightarrow\left(\frac{I^{(1)}}{I^{(0)}}\right)\left[\operatorname{sinc}^2\left(\frac{2g}{a}\right)\operatorname{sinc}^2\left(\frac{c}{a}\right)\right]. \tag{26}$$

The sinc^2 factors can be used to estimate acceptable limits on the lateral mechanical distortions that will be present, to a greater or lesser degree, in all sample grating structures. Conversely, accurate characterizations of the

lateral distortions of a sample grating can be used to correct the measured intensity ratios.

The final important departure from ideality that should be taken into account is the effect of nonrectangular bar edges. The issues to be covered in a comprehensive treatment are detailed, covering a wide range of cases and assumptions [2], and we must consequently restrict ourselves here to the brief derivation of an approximate worst-case criterion. We first assign a length parameter Δ_E to the grating structure in the x direction, which we center on the nominally ideal edge locations of each bar. We then assume that over the extent of this length, each edge can assume an arbitrary thickness profile, and we represent the effect of its shape by adding the decremental electric field profile transmitted through it to the ideal field distribution in the sample plane. This procedure generates two periodic field distributions, one associated with each set of (imperfect) edges of the grating bars. Clearly, as $\Delta_E \to 0$, the ideal field distribution is recovered. We now assume that each edge-transmitted field has twice the amplitude of the field transmitted by the ideal bars. Next, we appeal to elementary diffraction theory [19] and Eq. 10 to postulate that the angular spread of the edge spectra in the far field will be greater than the primary spectral spread by the approximate factor Δ_E/d. In this picture, the field amplitude transmitted by the ideal grating is taken to be proportional to $[d+(a-d)\exp(-2\pi Wk)]$ and the corresponding amplitude from the edges to $[2\Delta_E \exp(-\pi Wk)]$. A factor describing the worst-case relative intensity perturbation of, say, the first order can then be approximated by the expression

$$\left(\frac{2\Delta_E e^{-\pi Wk}(\Delta_E/d)+[d+(a-d)e^{-2\pi Wk}]}{[d+(a-d)e^{-2\pi Wk}]}\right)^2. \tag{27}$$

Assuming the representative conditions $2\pi Wk \simeq 1$ and $a \simeq 2d$, we find the perturbation on the first order to be given approximately by $[4\Delta^2{}_E/(d^2(1+\sqrt{e}))]$, and assuming (again as a worst case) an equal perturbation of the zeroth order, we arrive at a maximal perturbation on the unindexed ratio R (defined by Eq. 11) of

$$\Delta R \simeq 3\left(\frac{\Delta_E}{d}\right)^2. \tag{28}$$

Perhaps the most important practical implication of Eq. 28 is that real-life experimental grating bars in the MSFTI technique should be chosen with

aspect ratios $(a-d)/W$ as large as possible, since for most fabrication techniques this will be naturally conducive to the minimization of Δ_E/d.

V A CHARACTERIZATION OF THE OPTICAL CONSTANTS OF Au USING MSFTI IN THE 280–640 eV RANGE

In this section we will augment the predominantly theoretical discussions of the prior sections by briefly reviewing the implementation and results of an actual MSFTI experiment performed on Au [3] in the 280–640 eV range.

The radiation source employed for the experiment was a bending magnet on SPEAR,[6] the storage ring at the Stanford Synchrotron Radiation Laboratory (SSRL) [42]. The radiation, which is characterized by a broad and smooth spectrum [43], was monochromatized with a 1m Rowland-circle monochromator, whose details and performance characteristics are described elsewhere [44]. For our present purposes we require the fact that this single-grating instrument, when tuned to a given photon energy, is also capable of transmitting the higher diffracted orders of shorter-wavelength radiation emanating from a broadband source.

The sample gratings for the experiment were fabricated at IBM's Thomas J. Watson Research Center, using combinations of wet and dry etching and vacuum deposition techniques. Several of the technical aspects and developments associated with this work have been described in the literature [45]. In particular, in view of the generation of the initial grating pattern as a holographic interferogram, the grating period a is defined with exceptional precision. A micrograph of a typical sample grating is shown in Fig. 4. As can be seen, the grating bars are supported on a grid structure constituted of much thicker bars, and that support grid is itself supported on a tertiary grid (not shown) with proportionately coarser features. Apart from the micrographs, which were taken *following* the MSFTI experiment, the gratings' dimensional parameters were initially characterized with an inverse application of the formulas in Section IV. To wit, a set of values of δ and k was selected in the 100–160 eV range that had earlier been found to corroborate the measured performance of other well-characterized Au gratings at SSRL [46, 47], and applied to unfold d and W from the measured intensity ratios R. The basic parameters of the final set of three gratings selected to measure $\hat{n}$ are listed in Table II. To be noted are the fairly high values of $(a-d)/W$, stipulated by the analytical results of Section IV.

[6] Stanford Positron Electron Asymmetric Ring.

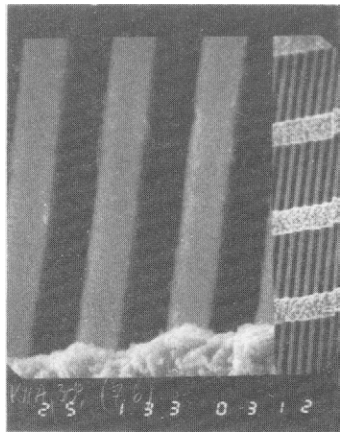

Fig. 4. Electromicrograph of an Au sample grating structure used in an initial version of an MSFTI experiment. The period of the free-standing bars is 2.5 μ and their width-to-thickness ratio $(a-d)/W$ is approximately 10. Portions of the supporting structure for the sample bars are visible in the demagnified structure on the right. During the experiment, the support structures face the source and intercept a significant fraction of the probe light.

A typical MSFTI spectrum, drawn from the prior characterization of the gratings' dimensions, is shown in Fig. 5. The profile reveals both spectral and line-shape anomalies, both of which typify the kinds of systematic errors that can arise in an actual experiment. In the example shown, the anomalous peaks between the zeroth and first orders stem from the harmonics transmitted by the monochromator, and it is apparent that the spectral components with which they are associated contribute to both the zeroth and first orders of the primary spectrum. The peak shape distortions are related to the shadowing effects of the structural grids sup-

TABLE II

Selected Parameters of Sample Au Gratings Used in an MSFTI Experiment

Grating	W (Å)	d/a	a (μm)
K12A[a]	969.5	0.312	2.5
13F[a]	1774.6	0.565	2.5
K4[a]	1067.0	0.350	2.5

[a] Grating identification codes.

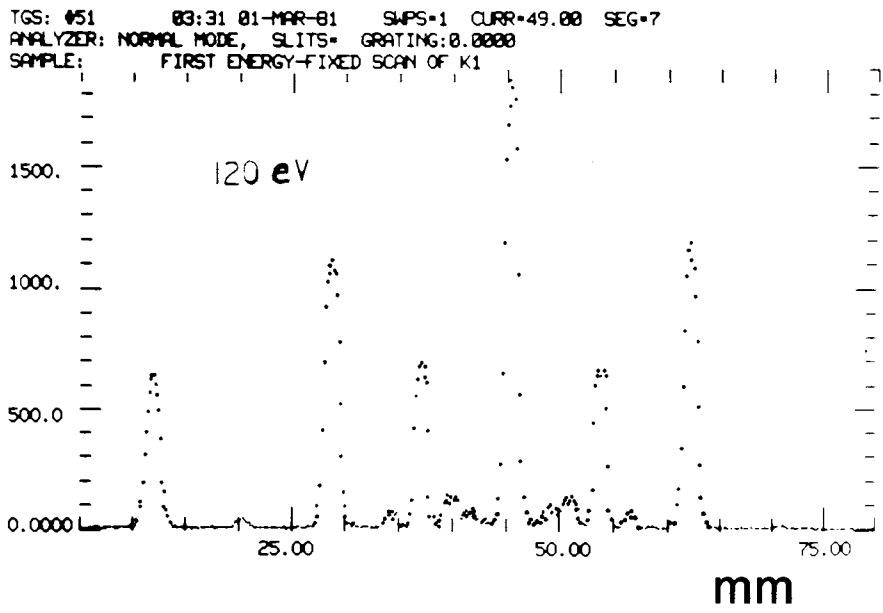

Fig. 5. Experimental transmission diffraction spectrum generated by an Au sample grating structure. The source radiation is monochromatized synchrotron light from a bending magnet. The 120 eV first and negative first orders are located at 28 mm and 62.5 mm.

porting the grating bars, and the slight asymmetry in the peak values is traceable in part to misalignments in detector motion [2].

Following measurements of the diffracted spectra, the data were analyzed and corrected for systematic errors, including those associated with the imperfections of the grating structures and their support grids, and the values of δ and k were generated as described in Section IV. Particularly troublesome was the task of numerically separating the spectra of interest from the anomalous higher-energy diffraction patterns, which are themselves model-dependent. In all these calculations the sensitivity expressions (Eqs. 16–19) were utilized to converge on self-consistent values of $\hat{n}$ among the three sets of grating pairs, and to estimate the final error limits. A set of sensitivity curves based on the final computed constants for one of the gratings is displayed in Fig. 6. Above 640 eV and below 280 eV, the curves are smoothly adjusted to optical constants reported elsewhere [32]. The final experimental values of δ and k are listed in the fourth and sixth columns of Table III.

A brief assessment of the displayed constants is in order. In the literature, Au has been particularly noted for the significant variation in the values of both its measured and calculated constants [48, 49]. These discrepancies have been associated with the apparently wide variability in the physical parameters of thin gold films prepared via different techniques

[50], or with postulated physical differences between the surface and interior regions of ordinary samples [51]. In view of these considerations, it is of interest to contrast the MSFTI constants with those measured or derived by alternative techniques.

In the fifth and seventh columns of Table III we have listed the corresponding optical constants for Au compiled by Henke *et al.* [23]. These values, based on first-principle calculations fitted to available (and very sparse) experimental data, can be used as an arbitrary referent for our purposes. We note fairly good agreement for k, with the exception of 640 eV and the 280–360 eV interval. Regarding these discrepancies, partial corroboration is available for the MSFTI results in the theoretical *atomic* absorption cross-sections compiled by Plechaty, Cullen, and Howerton [52], who identify strong resonances both at $\simeq$320 eV and 600 eV, the latter being clearly associated with Au's N edge. A corresponding interpretation for the large discrepancy with Henke's δ, however, which is based largely on Kramers–Kronig analysis of the absorption data, has proved elusive. The technique most closely related to MSFTI in terms of sample penetration, that of thin-film absorption, has been utilized by Hagemann, Gudat, and Kunz [32] to measure k for Au over this region. Their films were prepared by evaporation from resistance-heated crucibles onto mesh-supported polymer substrates, which were subsequently etched away outside of the vacuum. Their measured k values, interpolated, agree with both Henke's and MSFTI's to within the cited error bounds. Their primary

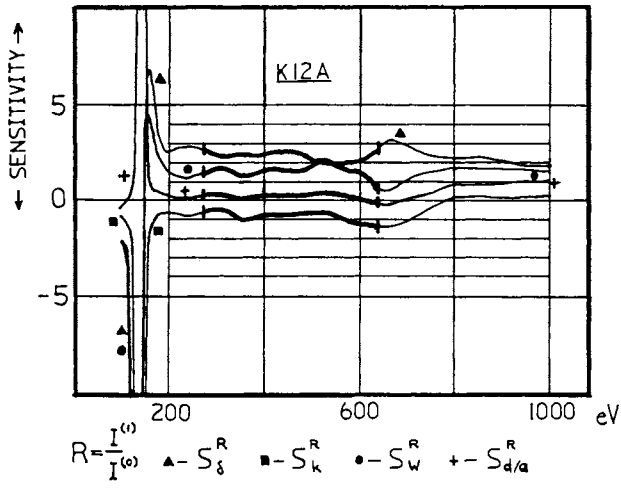

Fig. 6. Sensitivity curves for a typical sample grating (code number K12A) used to measure optical constants via MSFTI. Bold curve segments denote the 280–640 eV measurement interval. For this particular grating, the diffracted order ratio R is seen to be minimally sensitive to the aperture-to-period ratio d/a.

TABLE III

Optical Constants of Gold (Au) as Determined by the MSFTI Method and by Henke *et al.* [23].

eV	cm^{-1}	μm	$1-n$ (MSFTI)	$1-n$ (Henke)	k (MSFTI)	k (Henke)
280	—	0.00443	0.0119	0.00732	0.00762	0.101
320	—	0.00389	0.0109	0.00649	0.00790	0.00892
360	—	0.00344	0.00959	0.00592	0.00762	0.00797
400	—	0.00310	0.00872	0.00580	0.00672	0.00710
440	—	0.00282	0.00798	0.00552	0.00574	0.00594
480	—	0.00258	0.00729	0.00514	0.00506	0.00501
520	—	0.00238	0.00695	0.00472	0.00427	0.00426
560	—	0.00241	0.00648	0.00430	0.00378	0.00361
600	—	0.00207	0.00596	0.00385	0.00329	0.00328
640	—	0.00194	0.00500	0.00365	0.00463	0.00294

The average error bounds for the MSFTI values, dominated in large part by systematic errors, are estimated to be about ±18% for k and ±10% for δ ($\delta \equiv 1-n$).

data points, however, are too sparse for resolving the two absorption anomalies observed with MSFTI. With respect to δ, Hagemann *et al.*'s Kramers–Kronig analysis produces values that are closer to MSFTI's than to Henke *et al.*'s in the 280–400 eV range, but closer to Henke *et al.*'s from 400–640 eV. A set of characterizations of δ and k for Au based on multiple-reflectivity measurements in the soft X-ray range has recently been reported by Windt *et al.* [53]. Their sample surfaces were prepared by *e*-beam evaporation of Au onto polished Si wafers, and their measurements extended up to ≈520 eV, with only three data points reported in the 280–520 eV interval. Their k value of 0.0042 at 385 eV is noticeably lower than in all the previous compilations cited, and their δ values of 0.0069 at 280 eV and 0.00418 at 385 eV are also significantly lower than Henke *et al.*'s. On the other hand, their values compare, by and large, favorably with Lukirskii *et al.* [51], who also employed a reflectivity-based technique (at virtually the same three energy points) in an experiment reported in 1964. In still other compilations reviewed for this chapter, for example, Zombeck [54], data for the 280–640 eV range are either drawn from some of the above sources or generally fall within the same range of values.

This wide-ranging spectrum of results clearly underscores the still-unsettled status of current experimental knowledge of the optical constants of Au in the soft X-ray range, and of their systematic relationship to the surface or bulk properties of samples. Whereas some degree of correlation is perhaps apparent among the *measured* constants acquired with reflection- versus transmission-dependent techniques, the sparseness of actual measurements of *both* components of $\hat{n}$, by whatever technique, is clearly still too inhibitive to permit reliable conclusions to be drawn. This

state of affairs is no doubt partially due to the enhanced difficulty of optical experimentation in ultra-high vacuum, and to the still-extant lack of instrumentation comparable in quality or sophistication to that available in other spectral regions. In this respect, the development of a technique such as MSFTI, which is both experimentally simple and can measure both δ and k directly with optimal sensitivity, could prove essential in helping to identify and resolve the issues involved.

VI PROBLEMS AND PROSPECTS IN SAMPLE PREPARATION

Perhaps the most pertinent question that can be raised at this point concerning the present and future utility of multiple-slit Fourier transform interferometry is whether high-quality samples constructed out of materials other than Au can be prepared. It is clear that the long-term import of this metrological technique will depend directly on its ability to accommodate a wide variety of elements and materials, enabling intercomparisons and correlations with data taken by other methods.

From our present perspective, we can remark that the preparation of samples of the type used in the first experiments, namely, free-standing, grid-supported diffraction gratings, out of a wide variety of materials other than Au, does not appear overly promising. This is due in large part to the complexity of the associated fabrication processes [37, 45], which utilize sequences of several in- and out-of-vacuum procedures of both a chemical and mechanical nature. Thus, the quality and integrity of the bars in the final grating structure can strongly depend on the chemical and mechanical properties of the element or material being used, necessitating the programmatic exploration of various fabrication procedures for virtually each material of interest. To date, for example, successful results have been reported for Ag [55], whereas preliminary attempts with Ni and Cu have been inconclusive [56].

Based on this state of affairs, it seems apparent that samples of less complex construction must be made amenable to the MSFTI technique if it is to become widely applied. To this end, we can consider two simpler alternatives. First, we consider the structure in Fig. 7a [57]. Its preparation is based on the deposition of a thin film onto a substrate, and a subsequent inscription of a periodic groove structure into its surface. Due to the mechanical support of the substrate and the reduced number of fabrication steps, it can be expected that a much larger class of materials could be prepared for MSFTI in this way. Indeed, this expectation is corroborated by ongoing work in associated areas of microfabrication technology [58]. We note that the analytical formalism developed in this chapter is entirely

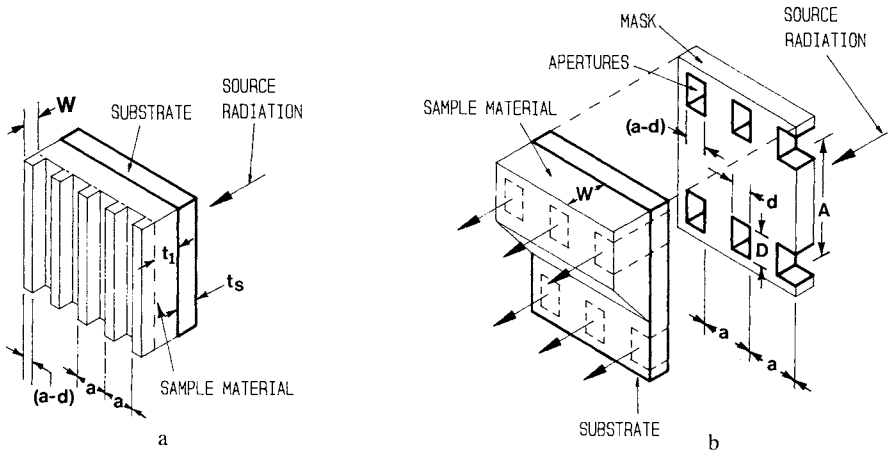

Fig. 7. Two alternative sample configurations (a and b) for probing the optical constants of a wide range of metallic and nonmetallic thin films in the soft X-ray range with the technique of MSFTI. The essential notion behind both configurations is to bypass the potentially problematical fabrication of free-standing diffraction gratings out of unsuitable materials. In configuration b, all microfabrication or micromachining of the sample material can in principle be avoided.

applicable to the depicted configuration, since the plane-parallel substrate (thickness t_s) and subsequent sample slab (thickness t_1) modulate the probe wavefronts homogeneously. Experimentally, the configuration is superior in avoiding the systematic errors introduced by a support grid; on the other hand, it will in general place significantly higher demands on the intensity of the radiation source.

An alternative technique that would demand an even greater source intensity, but that would in principle allow the MSFTI characterization of any material that can be deposited in thin-film form—and this includes most of the elements—is shown in Fig. 7b. Here the periodic sample bars are defined by a sequence of channels of width $a-d$ and height D cut or etched into an opaque mask; the apertures are defined by a second sequence of width d located at a distance A below. A must be chosen large enough to occlude the edge region of the thin film to ensure the homogeneity of both the defined bars and apertures. During operation, the mask is adjoined to the substrate and the two grating structures are defined (in the eikonal approximation) by the radiation passing through the apertures. With regard to the viability of this approach, we note that Si structures such as the depicted mask have recently been implemented, with smoothnesses approaching the *atomic* level [59]. This suggests that spectra of the highest quality could be generated with such configurations. Feasibility studies of sample preparation using this approach, as well as the develop-

ment of the analytical formalism for the mask/thin-film geometry, which in certain respects differs from that outlined in Sections I and IV, are currently in progress.

VII PROSPECTS FOR MSFTI IN OTHER SPECTRAL REGIMES

It is of interest to inquire into the applicability of MSFTI in spectral regimes outside of the VUV/soft X-ray range. Just as in the comparisons drawn in Section II, the central issue is whether alternative techniques can produce superior results, and at what cost. As a specific example, consider the sensitivities defined in Section IV (Eqs. 16–18), in the limits $r \to 0$ and $W \to 0$. These become $[1+(k/\delta)^2]^{-1}$, $[1+(\delta/k)^2]^{-1}$, and $\{1+[1+(k/\delta)^2]^{-1}\}$, respectively. As opposed to the corresponding sensitivities of a split-beam interferometer, they are all seen to be independent of W. Thus, in regions where k is of the same order of magnitude as δ, and where surface phase-shift and reflectivity effects can be accounted for, MSFTI would appear to offer advantages for the testing of even extremely thin films in transmission. Based on existing tabulations of k and δ [60–62], we can consequently infer that this form of MSFTI could in principle be applied to a significant number of materials in regions of the IR–visible–UV range. A practical factor that could enhance the applicability of MSFTI at these lower energies is the ready selection of focusing and collimating optics (namely, lenses), the judicious use of which would permit significantly shorter source/sample/detector lengths and coarser gratings. Such structures could consequently be imbued with higher quality, enhancing the experimental reliability even further. On the other hand, in cases where only δ was required, ordinary split-beam interferometry, or even the FTI scheme employed by Rayleigh, would probably remain preferable, since—as was discussed earlier—the simpler sample structures and the ready availability of highly intense and tunable coherent photon sources in the lower energy regimes would more than compensate for their relative inefficiency.

At energies well in excess of 3–5 KeV, the natural crystal structures of most materials begin imposing their own modulation on the light transmitted into the far-field (via Bragg or Laue diffraction), and numerous higher-energy scattering mechanisms (for example, Compton) start manifesting themselves [63]. In view of this, the additional modulation of a high-energy diffraction pattern by an array of bars of the material in question might not necessarily prove to be of value. One possibly useful interpretation of MSFTI in this regime would be to view the individual atomic planes as the "bars" of a grating, and the interplane spacings (with their lower electron densities) as the "apertures". Such a configuration could conceivably be

employed to help characterize inner-shell scattering coefficients at the appropriate absorption edges in the 10 KeV–1 MeV range, and even of nuclear cross-sections at absorption edges in the 100 KeV+ energy domain. Although the quality, alignment, and photon flux requirements for a sample structure of this type would evidently be severe, recent technological developments have shown that both of these requirements could in fact be duly met [64, 65].

A final question, of possible importance at sub-VUV energies, is whether MSFTI configurations based on reflection could be implemented. A general assessment of the analytical formalism of MSFTI clearly shows that this would indeed be possible. On the other hand, configurational problems such as the copositioning of a reference interference pattern, or the variation of the incidence and reflection angles to establish multiple equations in δ and k (when only one material is being used), would seem to imply a considerably higher degree of experimental complexity. In view of the complicated dependence of the reflectivity on $\hat{n}$ (see the discussion in Sections I and IV), the analytical complexity of the experimental equations could in general be expected to be greater as well. As in all proposed applications of MSFTI (reflection- or transmission-based), the bottom-line question of whether the anticipated complexity is justified for a given material would need to be answered with a careful case-by-case analysis of the attainable precision in comparison to alternative techniques.

SUMMARY VIII

The VUV/soft X-ray range is currently perhaps the least developed in terms of versatile coherence techniques and a broad range of sophisticated optical instrumentation. An inhibiting factor to progress in these two areas has undoubtedly been our limited knowledge and understanding of the optical constants of candidate materials. In this chapter we have reviewed MSFTI, a method for determining optical constants that is based on the interference of multiple diffracted beams following transmission. It was shown to feature a number of advantages for characterizing the complex index of refraction $\hat{n}$ of thin films in the 0.1–3 KeV range; in particular, certain troublesome errors associated with alternative techniques in this region can be minimized or avoided. In broad terms, the technique has been made possible only recently due to significant advances in high-brightness, soft X-ray sources and the advent of reliable microfabrication technology. With additional directed development of these two resources, such as was outlined in Section VI, it is expected that the method could eventually be made applicable to a wide variety of materials, enabling the

programmatic characterization of their optical constants in thin-film form. Such an experimental program would provide data complementary to that acquired with reflectivity-based techniques, enabling us, perhaps for the first time, to begin systematizing our knowledge and understanding of $\hat{n}$ in the soft X-ray range.

ACKNOWLEDGMENTS

The author would like to acknowledge critical support from Elisabeth Källne, Ingolf Lindau, and Eberhard Spiller during the initial experimental implementations of the MSFTI technique. The tabulated optical constants were characterized at the Stanford Synchrotron Radiation Laboratory (SSRL), which is operated by the Department of Energy, Office of Basic Energy Research, Division of Chemical Sciences. That office's Division of Materials Science is acknowledged for support for this undertaking.

REFERENCES

1. R. Tatchyn, I. Lindau, and E. Källne, "Analysis of a new method for determining optical constants in the soft x-ray region," *Optica Acta* **27**, 1505 (1980).
2. R. Tatchyn, "The Introduction and Development of a New Method for Measuring the Optical Constants of Metals in the Soft X-Ray Range," Doctoral thesis, Stanford University, SSRL Report No. 82/02 (1982).
3. R. Tatchyn, I. Lindau, E. Källne, and E. Spiller, "Derivation of the Optical Constants of Gold from Transmission Diffraction Measurements in the 280–640 eV Range," *Phys. Rev. Lett.* **53**, 1264 (1984).
4. U. Bonse and W. Graeff, "X-Ray and Neutron Interferometry," in "X-Ray Optics," (H.-J. Queisser, ed.), *Topics in Applied Physics*, Vol. 22, Springer-Verlag, Berlin, 93 (1977).
5. M. Hart, "The Application of Synchrotron Radiation to X-Ray Interferometry," *Nucl. Instr. Meth.* **172**, 209 (1980).
6. W. R. Hunter, "Measurements of Optical Constants in the Vacuum Ultraviolet Spectral Region," in "Handbook of Optical Constants of Solids," (E. D. Palik, ed.), Academic Press, New York, Chap. 4 (1985).
7. D. E. Aspnes, "The Accurate Determination of Optical Properties by Ellipsometry," op. cit., Chap. 5.
8. J. Shamir, "Interferometric Methods for the Determination of Thin-Film Parameters," op. cit., Chap. 6.
9. M. Born and E. Wolf, "Principles of Optics," Pergamon, Oxford, Chap. 7.3.2 (1980).
10. op. cit., Chap. 13.
11. B. L. Henke, "Low Energy X-Ray Interactions: Photoionization, Scattering, Specular and Bragg Reflection," in *AIP Proceedings No. 75*, (D. T. Attwood and B. L. Henke, eds.), 146 (1981).
12. Born and Wolf, op. cit. Chap. 7.6.
13. op. cit. Chap. 3.
14. op. cit. Chap. 8.3.3.
15. R. Bracewell, "The Fourier Transform and Its Applications," McGraw-Hill, New York, Chap. 13 (1965).
16. Born and Wolf, op. cit. Chap. 7.2.
17. Lord Rayleigh, "On some Physical Properties of Argon and Helium," *Proc. Roy. Soc. London* **59**, 198 (1896).
18. Born and Wolf, op. cit. Chap. 7.3.

19. Born and Wolf, op. cit. Chap. 8.6.
20. H. M. Smith, "Principles of Holography," Wiley-Interscience, New York, Chap. 6.1 (1969).
21. J. H. Weaver, C. Krafka, D. W. Lynch, and E. E. Koch, "Physik Daten, Physics Data," "Optical Properties of Metals," Vol. 18-2, Fach-informations-zentrum, Karlsruhe, 12 (1981).
22. R. Tatchyn and I. Lindau, "An Extended Maximization Technique for Measuring Optical Constants Using Transmission Gratings in the Soft X-Ray Range," in *AIP Proceedings No. 75*, (D. T. Attwood and B. L. Henke, eds.), 323 (1981).
23. B. L. Henke, P. Lee, T. J. Tanaka, R. L. Shimabukuro, and B. K. Fujikawa, "The Atomic Scattering Factor, $f_1 + if_2$, for 94 Elements and for the 100 to 2000 eV Photon Energy Region," (Appendix), in *AIP Proceedings No. 75*, (D. T. Attwood and B. L. Henke, eds.), 340 (1981).
24. A. G. Michette, "Optical Systems for X-Rays," Plenum, New York, 28 (1986).
25. A. M. Hawryluk, N. M. Ceglio, D. G. Stearns, K. Danzmann, M. Kühne, P. Müller, and B. Wende, "Soft x-ray beamsplitters and highly dispersive multilayer mirrors for use as soft x-ray laser cavity components," *SPIE Proceedings* **688**, 81 (1987).
26. H. Winick and J. E. Spencer, "Wiggler Magnets at SSRL—Present Experience and Future Plans," *Nucl. Instr. Meth.* **172**, 45 (1980).
27. R. Tatchyn, E. Källne, A. Toor, T. Cremer, and P. Csonka, "Operation of a normal-incidence transmission grating monochromator at ALLADIN," *Rev. Sci. Instrum.* **60**, 1579 (1989).
28. U. Bonse, P. Spieker, J.-T. Hein, and G. Materlik, "Measurement of K-Edge Dispersion Anomalies with the New X-Ray Interferometer at DORIS," *Nucl. Instr. Meth.* **172**, 223 (1980).
29. G. R. Fowles, "Introduction to Modern Optics," Holt, Rhinehart and Winston, New York, Chap. 4.1 (1975).
30. T. Barbee, Jr., and J. Underwood, "Solid Fabry-Perot Etalons for X-Rays," *Opt. Commun.* **48**, 161 (1983).
31. A. E. Rosenbluth and J. M. Forsyth, "The Reflecting Properties of Soft X-Ray Multilayers," in *AIP Proceedings No. 75*, (D. T. Attwood and B. L. Henke, eds.), 280 (1981).
32. H.-J. Hagemann, W. Gudat, and C. Kunz, "Optical Constants from the Far Infrared to the X-Ray Region: Mg, Al, Cu, Ag, Au, Bi, C, and Al_2O_3," *J. Opt. Soc. Am.* **65**, 742 (1975); DESY-Report SR-74/77, DESY, Hamburg, Federal Republic of Germany, (1974).
33. Hunter, op. cit. p. 81*ff*.
34. Aspnes, op. cit. p. 96*ff*.
35. D. Y. Smith, "Dispersion Theory, Sum Rules, and Their Application to the Analysis of Optical Data," in "Handbook of Optical Constants of Solids," (E. D. Palik, ed.), Academic Press, New York, Chap. 3 (1985).
36. Barbee and Underwood, op. cit. pp. 17–18.
37. H. I. Smith, "Fabrication Techniques for Surface-Acoustic-Wave and Thin-Film Optical Devices," *Proc. IEEE* **62**, 1361 (1974).
38. J. Dijkstra, "X-Ray Transmission Optics," *Space Sci. Instrum.* **2**, 363 (1976).
39. K. P. Beuermann, R. Lenzen, and H. Bräuninger, "Properties of a transmission grating behind a grazing incidence telescope for cosmic x-ray spectroscopy," *Appl. Opt.* **16**, 1425 (1977).
40. Born and Wolf, op. cit. Chap. 11.
41. H. W. Schnopper, L. P. Van Speybroeck, J. P. Delvaille, A. Epstein, E. Källne, R. Z. Bachrach, J. Dijkstra, and L. Lantward, "Diffraction grating transmission efficiencies for XUV and soft x-rays," *Appl. Opt.* **16**, 1088 (1977).

42. A. Bienenstock, "An Overview of the Stanford Synchrotron Radiation Laboratory," *Nucl. Instr. Meth.* **172**, 13 (1980).
43. S. Krinsky, M. L. Perlman, and R. E. Watson, "Characteristics of Synchrotron Radiation and of Its Sources," in "Handbook on Synchrotron Radiation," (E.-E. Koch, ed.), Vol. 1A, North-Holland, Amsterdam, 65 (1983).
44. F. C. Brown, R. Z. Bachrach, and N. Lien, "The SSRL Ultrahigh Vacuum Grazing Incidence Monochromator: Design Considerations and Operating Experience," *Nucl. Instr. Meth.* **152**, 73 (1978).
45. Y. Vladimirsky, E. Källne, and E. Spiller, "Fabrication of free-standing x-ray transmission gratings and zone plates," *SPIE Proceedings* **44**, 25 (1984).
46. R. Tatchyn, "*Planar Transmission Gratings Compatible with Synchrotron Radiation Sources: Analysis, Computer Modelling, Testing, and Design*," Engineer's thesis, Stanford University, 1980.
47. J. P. Delvaille, H. W. Schnopper, E. Källne, I. Lindau, R. Tatchyn, R. A. Gutcheck, R. Z. Bachrach, and J. H. Dijkstra, "Diffraction Efficiencies of Holographic Transmission Gratings in the Region 80 eV–1300 eV," *Nucl. Instr. Meth.* **172**, 281 (1980).
48. H.-J. Hagemann, W. Gudat, and C. Kunz, "Optical Constants from the Far Infrared to the X-Ray Region: Mg, Al, Cu, Ag, Au, Bi, C, and Al_2O_3," DESY-Report SR-74/77, DESY, Hamburg, Federal Republic of Germany 17 (1974).
49. D. W. Lynch and W. R. Hunter, "Comments on the Optical Constants of Metals and an Introduction to the Data for Several Metals," in "Handbook of Optical Constants of Solids," (E. D. Palik, ed.) Academic Press, New York, 286 (1985).
50. D. E. Aspnes, E. Kinsbron, and D. D. Bacon, "Optical properties of Au: Sample effects," *Phys. Rev.* **B21**, 3290 (1980).
51. A. P. Lukirskii, E. P. Savinov, O. A. Ershov, and Yu. F. Shepelev, "Reflection Coefficients of Radiation in the Wavelength Range from 23.6 to 113 Å for a Number of Elements and Substances and the Determination of the Refractive Index and Absorption Coefficient," *Opt. and Spectrosc.* **16**, 168 (1964).
52. E. F. Plechaty, D. E. Cullen, and R. J. Howerton, "Tables and Graphs of Photon-Interaction Cross Sections from 0.1 keV to 100 MeV Derived from the LLL Evaluated-Nuclear-Data Library," University of California Research Report UCRL-50400, **6**, Rev. 3, 398 (1981).
53. David L. Windt, Webster C. Cash, Jr., M. Scott, P. Arendt, B. Newnam, R. F. Fisher, and A. B. Swartzlander, "Optical Constants for thin films of Ti, Zr, Nb, Mo, Ru, Rh, Pd, Ag, Hf, Ta, W, Re, Ir, OS, Pt, and Au from 24 Å to 1216 Å," *Appl. Opt.* **27**, 246 (1988).
54. M. V. Zombeck, "Optical Constants and Reflectivities for Nickel, Gold, and Platinum in the X-Ray Region of the Spectrum (0.1–10 KeV)," AXAF Interim Report, Nos. SAO-AXAF-83-015 and SAO-AXAF-83-016, Smithsonian Institution Astrophysical Observatory, Cambridge, Mass., January–March (1983).
55. N. M. Ceglio, "Recent Advances in X-Ray Optics," in "X-Ray Microscopy," (G. Schmahl and D. Rudolph, eds.), *Springer Series in Optical Sciences*, Vol. 43, Berlin, 97 (1984).
56. E. Källne, private communication.
57. R. Tatchyn, unpublished, (1984).
58. H. I. Smith, E. H. Anderson, A. M. Hawryluk, and M. L. Schattenburg, "Planar Techniques for Fabricating X-Ray Diffraction Gratings and Zone Plates," in "X-Ray Microscopy," (G. Schmahl and D. Rudolph, eds.), *Springer Series in Optical Sciences*, Vol. 43, Berlin, 51 (1984).
59. D. Ciarlo and D. E. Miller, "Silicon diffraction gratings for multilayer structures," *SPIE Proceedings* **688**, 163 (1987).
60. Lynch and Hunter, op. cit. pp. 275–367. Energy ranges over which $|\delta| < k$ are tabulated for Cu, Au, Ir, Mo, Ni, Os, Pt, Rh, Ag, and W.

61. D. Y. Smith, E. Shiles, and M. Inokuti, "The Optical Properties of Aluminum," in "Handbook of Optical Constants of Solids," (E. D. Palik, ed.), Academic Press, New York, 369 (1985).
62. E. D. Palik, "Cadmium Telluride (CdTe)," in "Handbook of Optical Constants of Solids," (E. D. Palik, ed.), Academic Press, New York, 409 (1985).
63. Plechaty *et al.*, op. cit. pp. vii–xii.
64. R. Coisson and H. Winick, eds., "Workshop on PEP as a Synchrotron Radiation Source," SSRL, 10/20–21/87.
65. R. Tatchyn, P. Csonka, and A. Toor, "Perspectives on micropole undulators in synchrotron radiation technology," *Rev. Sci. Instrum.* **60**, 1796 (1989).

Chapter 12

Determination of Optical Constants from Angular-Dependent, Photoelectric-Yield Measurements

H.-G. BIRKEN, C. BLESSING, and C. KUNZ
II. Institut für Experimentalphysik
Universität Hamburg
D-2000 Hamburg 50
Federal Republic of Germany

I. Introduction 279
II. Theoretical Background 280
III. Experimental Details 285
IV. Examples 286
V. Conclusions and Future Prospects 289
References 292

INTRODUCTION I

Although optical constants ordinarily are determined by measuring the primary interaction of photons with matter, we describe here a method that relies on the measurement of a secondary process, namely photoemission. The determination of the total photoelectric yield as a function of the angle of incidence on a mirror made of a conducting material, or of a thin film of such a material on a well-defined substrate, is sufficiently specific to obtain accurate optical constants. Pepper [1] has given a simple but very successful model, which yields an analytic expression for the photoelectric yield of a bulk conductor and also of a thin conducting film on a substrate if the optical constants of the materials involved, the film thickness, and the average escape depth of the photoelectrons are known. This model is based on the description of photoemission as a four-step process: primary excitation, multiplication by inelastic scattering, migration to the surface,

Copyright © 1991 by Academic Press.
All rights of reproduction in any form reserved.
ISBN 0-12-544422-2

and penetration through the surface into the vacuum. The factor that describes the penetration of photoelectrons through the surface barrier and some other constant factors cancel out if only the relative photoelectric yield for different angles of incidence is of interest. This model can be used in reverse to fit experimental angular-dependent, photoelectric-yield measurements and to determine optical constants, film thickness, and electron escape depth as fitting parameters.

Although the method is applicable only at photon energies above the photoemission threshold, no limitations other than practical ones appear to exist for higher photon energies. This method gives excellent results in those cases that have been investigated up to now. It was originally applied by Arakawa *et al.* [2, 3] with the primary interest of obtaining electron escape depths of Al at 21.1 eV and of C at 20–64 eV photon energy. In addition, the real part of the index of refraction was obtained. There are also some other investigations based on Pepper's [1] and similar formalisms [4]. In combination with synchrotron radiation, the method was explored thoroughly by Birken *et al.* [5] with Al films evaporated in ultra-high vacuum. In this case, a measurement of multiangle reflectances was performed on the same films without breaking the vacuum. Both methods yielded optical constants in excellent agreement with each other. The method was extended later at the HASYLAB reflectometer [7, 8] to copper, platinum, and Kanigen, a nickel alloy used as a polishable mirror material. Some of these unpublished results are included in this chapter. In Section II, the theoretical background is presented in detail, then the fairly simple experimental setup is described in Section III, taking as a model case the arrangement as it was used at HASYLAB. Section IV gives the examples, and finally, Section V points out future prospects of the method.

II THEORETICAL BACKGROUND

We consider a linearly polarized light wave incident on a film of thickness d, which is supported by a substrate. The angle of incidence is measured relative to the normal to the film surface, and the optical properties of the film (1) and the substrate (2) are characterized by the complex dielectric functions ε_1 and ε_2, respectively, Fig. 1. ε is related to the complex index of refraction by $N = n + i\kappa = \sqrt{\varepsilon}$. The central assumption in describing the photoelectric yield is that the contribution of an infinitesimal volume element of the film to the total number of escaping electrons is proportional to the photon energy absorbed within that volume element. The electromagnetic-field distribution inside the film is thus responsible for the primary excitation of photoelectrons. On the other hand, the dielectric functions ε_1 and ε_2, together with the boundary conditions, determine this field.

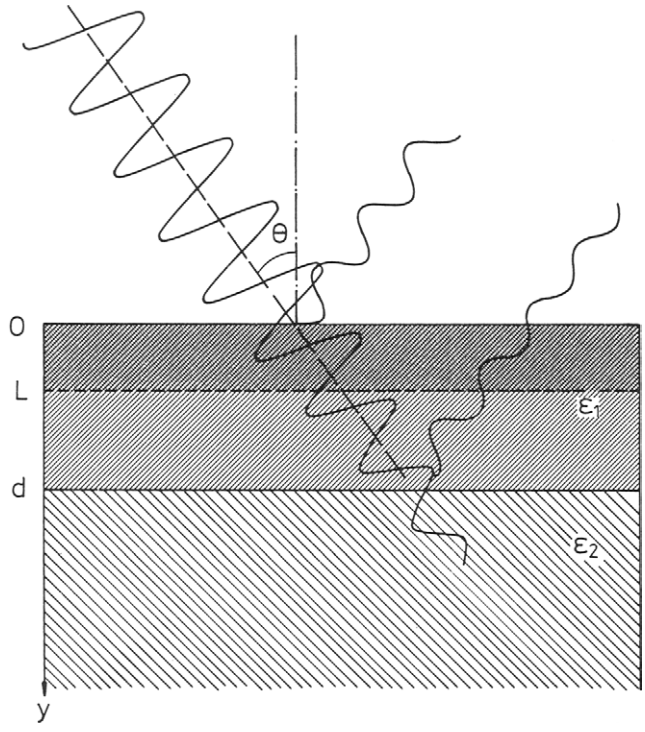

Fig. 1. Schematic representation of the optical system composed of a film (1) with thickness d, which is supported by a substrate (2). θ is the angle of incidence of the incoming light beam, and $\varepsilon_{1,2}$ denote the dielectric functions of the film and the substrate, respectively. The vacuum dielectric function ε_0 is unity. L is the mean electron escape length.

In calculating the photoelectric yield, diffusion of the primarily excited photoelectron to the surface, multiplication due to electron–electron scattering along its path, and escape through the surface potential barrier are all condensed in the simple function $Ce^{-y/L}$. The factor C takes into account the multiplication of the primary electron through electron–electron scattering and the probability of penetration through the surface potential barrier for the secondary electrons. $L(\hbar\omega)$ denotes the photon-energy-dependent electron escape depth. This is a complicated function of the mean-free paths for both elastic electron–phonon and inelastic electron–electron scattering averaged over the whole spectrum of kinetic energies. The introduction of such an exponential escape function is a simple approximation, which cannot be expected to describe perfectly this intricate escape and multiplication mechanism. Nevertheless, for our present application it turns out to be adequate.

If the contribution of the substrate to the total yield is negligible, that is,

$L \ll d$, the expression for the total yield may be written as

$$Y = C \int_0^d e^{-y/L} \eta(y)\, dy = CF(L), \tag{1}$$

where $\eta(y)$ is the volume absorptance, which is proportional to the negative divergence of the Poynting vector. This approximation, however, is no longer applicable if the film thickness becomes comparable to the electron escape depth, since then the photoelectrons arising from the substrate region must also be taken into account. This holds even in the case where the substrate is an insulating material. For electrons excited within the substrate, an analogous escape probability function $C_s e^{-y/Ls}$ may be assumed, but the values of C_s and L_s might be very different from those pertaining to the film. Within the frame of this chapter, we do not wish to expand Pepper's model further for such a case. In principle, however, this appears to be possible with the disadvantage that electron escape will require two (or more) additional parameters.

Defining the quantity $G(\theta) = Y(\theta)/Y(0)$ as the relative angular-dependent total yield and neglecting electrons from the substrate, the factor C cancels out, since it does not depend on the angle of incidence θ of the incoming photons. Pepper has calculated analytic expressions for the absorption of energy per unit volume as well as for the reflectance and the transmittance for a system, which is composed of a film on a substrate [1]. The film and the substrate are allowed to be absorbing, homogeneous, and uniaxially anisotropic media, with their optical axes in the direction normal to the boundaries. Here, Pepper's equations for the case of a film on a substrate with homogeneous, isotropic, optical properties are reproduced for completeness:

$$\begin{aligned}
F_s(L) = {} & \frac{(1-|r_{1,s}|^2)\alpha}{|1+r_{1,s}\exp(2id\xi_1)|^2}\left\{\frac{1-\exp(-(\alpha+1/L)d)}{\alpha+1/L}\right. \\
& + |r_{2,s}|^2 \exp(-2\alpha d)\frac{1-\exp(-(1/L-\alpha)d)}{1/L-\alpha} \\
& \left. + 2\exp(-\alpha d)\,\mathrm{Re}\left[\frac{r_{2,s}(\exp(2i\xi_1' d)-\exp(-d/L))}{2i\xi_1'+1/L}\right]\right\} \\
F_p(L) = {} & \frac{(1-|r_{1,p}|^2)\alpha}{|1+r_{1,p}r_{2,p}\exp(2id\xi_1)|^2}\left\{\frac{1-\exp(-(\alpha+1/L)d)}{\alpha+1/L}\right. \\
& + |r_{2,p}|^2 \exp(-2\alpha d)\frac{1-\exp(-(1/L-\alpha)d)}{1/L-\alpha} \\
& \left. + 2\exp(-\alpha d)\,\mathrm{Re}\left[\frac{r_{2,p}(\exp(2i\xi_1' d)-\exp(-d/L))}{2i\xi_1'+1/L}\right]\frac{\xi_1'\,\mathrm{Im}(\varepsilon_1^*\xi_1)}{\xi_1''\,\mathrm{Re}(\varepsilon_1^*\xi_1)}\right\}
\end{aligned} \tag{2}$$

$$r_{j,s}=\frac{\xi_{j-1}-\xi_j}{\xi_{j-1}+\xi_j}, \qquad r_{j,p}=\frac{\varepsilon_j\xi_{j-1}-\varepsilon_{j-1}\xi_j}{\varepsilon_j\xi_{j-1}+\varepsilon_{j-1}\xi_j}, \qquad (j=1,2),$$

where $\xi_j=2\pi/\lambda\sqrt{\varepsilon_j-\sin^2\theta}(j=0,1,2)$ are the y components of the wave vector within the three media. The indices s and p refer to incident light with s- and p-polarization, respectively, and $r_j(j=1,2)$ are the Fresnel amplitude reflectance coefficients of the two boundaries. ξ_1' and ξ''_1 are abbreviations for the real and imaginary parts of ξ_1, respectively, and * denotes complex conjugate. The quantity $\alpha=2\xi''_1$ is the effective absorption coefficient of the film that depends on the angle of incidence. If the film thickness approaches infinity, these equations reduce to those which describe the relative total yield from a bulk system:

$$F_i(L)=(1-|r_{1,i}|^2)\frac{\alpha}{\alpha+1/L}, \qquad (i=s,p). \tag{3}$$

Eqs. 2 and 3 may be used in a least-squares-fit procedure in order to determine the optical constants, film thickness, and the electron escape depth. Therefore, a χ^2 function

$$\chi^2=\sum_{i=1}^{n}\frac{1}{\sigma_i^2}[G_{\text{exp}}(\theta_i)-G_{\text{theo}}(\theta_i,\varepsilon_1,\varepsilon_2,d,L)]^2, \tag{4}$$

has to be minimized, while the optical constants, the film thickness, and the escape depth serve as fit parameters. σ_i denotes the statistical error of each experimental point.

In the following, the sensitivity of $G(\theta)$ spectra to changes in $\varepsilon=\varepsilon'+i\varepsilon''$ is analyzed. Since by definition $G=1$ at normal incidence, the information on $\varepsilon=\varepsilon'+i\varepsilon''$ is contained mainly in the angular region around the critical angle of incidence of the material under investigation. In the XUV spectral range, the values $|1-\varepsilon'|$ and ε'' typically are less than 0.1 for many materials. Critical angles therefore are close to $\theta=90°$, mostly above $\theta=80°$. The individual shapes of the $G(\theta)$ spectra are due to two competing mechanisms:

(1) Since $n<1$, the penetrating wave is always refracted away from the surface normal. At the critical angle $\theta=\theta_c$, the refracted wave propagates parallel to the surface, and the power deposited in the material is concentrated in a small layer below the surface. Consequently, the total yield is

much higher than at normal incidence, where the energy is deposited in deeper regions of the sample.

(2) As the angle of incidence is further increased, the energy flux into the sample decreases at the expense of the increasing reflectance of the sample, which is unity at $\theta = 90°$. Thus, as θ approaches 90°, the total yield vanishes. The shape of the $G(\theta)$ curve is mainly determined by ε'', whereas the position of the maximum in $G(\theta)$ yields information predominantly on ε'.

The left upper part of Fig. 2 shows calculated $G(\theta)$ spectra between 60° and 90° angles of incidence for three different values of ratio L/λ and *s*-polarized light. The arrows indicate the maximum of each $G(\theta)$ curve.

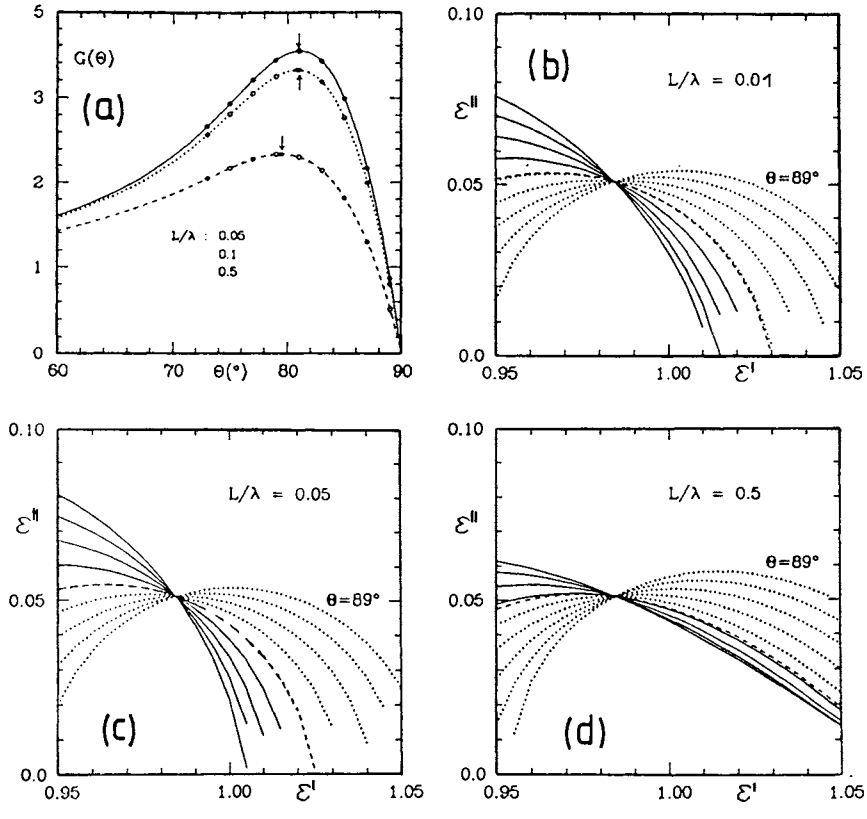

Fig. 2. Calculated relative angular-dependent total photoelectron yield from a bulk system for three different ratios L/λ (a) and curves of constant $G(\theta)$ (b, c, d), corresponding to the $G(\theta)$ points in (a) as marked by circles. The dashed curves of constant $G(\theta)$ in (b, c, d) correspond to the maxima of the $G(\theta)$ spectra in (a). Consecutive curves of constant $G(\theta)$ differ from each other by $\Delta\theta = -2°$.

Also plotted in Fig. 2 are curves of constant $G(\theta)$ within the complex-ε plane corresponding to the marked points on the angular-dependent $G(\theta)$ curves. Consecutive curves of constant $G(\theta)$ differ from each other by $\Delta\theta = -2°$, and the dashed lines correspond to the points at the maximum of the $G(\theta)$ curves. In principle, the point of intersection of two curves of constant $G(\theta)$ determines a value for $\varepsilon = \varepsilon' + i\varepsilon''$. An indication of the sensitivity of $G(\theta)$ spectra to changes in ε is the angle of intersection of the curves of constant $G(\theta)$. Usually the $G(\theta)$ values have an uncertainty due to experimental errors. As a consequence, the curves of constant $G(\theta)$ will be shifted parallel to themselves by an amount that depends on the magnitude as well as on the sign of the error. From this it follows that the uncertainty of the value of ε determined from $G(\theta)$ spectra increases with decreasing angle of intersection of different curves of constant $G(\theta)$. As long as the wavelength λ is much larger than the electron escape depth $L(\hbar\omega)$, the curves fan out equally on both sides of the critical angle. If the wavelength becomes comparable to the electron escape depth or smaller, the curves of constant $G(\theta)$ for angles smaller than the critical angle are less separated than those for larger angles of incidence. In this case, the decrease of $G(\theta)$ above the critical angle of incidence, which originates from the loss of penetrating intensity due to the increasing reflectance, is decisive in determining the optical constants. Although surface roughness strongly influences reflectance measurements, its influence on total-yield measurements may be less important. This conjecture stems from the fact that in the case of not-too-large surface roughness and a large correlation length of the roughness profile, the sum of the specularly and diffusely reflected light is practically equal to the specularly reflected light from the corresponding perfectly smooth sample [6].

EXPERIMENTAL DETAILS III

The principle of the setup of a sample holder for measuring angular-dependent total yield is shown in Fig. 3. The sample, either a film prepared on a substrate or a bulk material, is mounted (electrically insulated) on a holder, which allows precise rotations around an axis that lies in the surface of the sample. An anode, which is fixed to the sample holder and has slits for the incoming and reflected radiation, surrounds the sample. In this way, the anode is moved rigidly with the rotating sample, and the collection efficiency for the photoelectrons is independent of the angle of rotation. A potential difference of 15 V between the anode and the photoemitter has been shown to suffice to extract practically all photoelectrons. Thus, the signal-to-noise ratio is kept high, although the measured currents through the samples are typically on the order of 0.1 nA or less. A

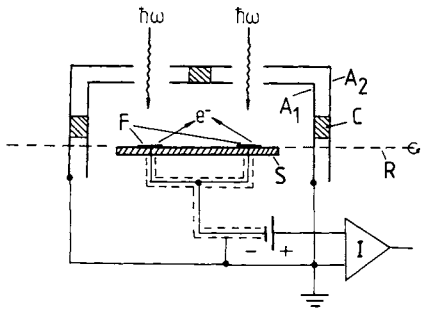

Fig. 3. Schematic diagram of the total-yield sample holder and electron collector ($A1$ anode, $A2$ shield anode, F film, S substrate, R axis of rotation, C insulating ceramics).

second shield is used to prevent the collection of electrons not resulting from photoemission from the sample. This setup permits total yield as well as reflectance measurements as a function of the angle of incidence of the incoming light.

The measurements described in this chapter have been performed at the UHV reflectometer at HASYLAB (DORIS II). The reflectometer [7] is equipped with 360° rotatable feedthroughs for sample and detector with rotational increments of 0.005° and an uncertainty of 0.03°. An adequate angular resolution and accuracy of the measurements is essential considering the importance of fast changes in intensity in the region around the maximum of the yield spectrum for the determination of the optical constants. In addition, the sample and the detector can be translated axially by up to 70 mm, allowing for measurements on two different samples.

An electron-beam gun and an oscillating quartz thickness monitor for *in situ* evaporation of films are installed in the reflectometer chamber. After baking, a base pressure of less than 3×10^{-8} Pa is reached. The experiment is supplied with monoenergetic radiation from the monochromator "Bumble Bee" in the energy range 40–1000 eV. More details on the monochromator can be found in Ref. [8].

IV EXAMPLES

Photoelectric-yield measurements have been performed with a 770 Å-thick Al film on borosilicate glass at 40–600 eV photon energy [5]. Fig. 4 shows a plot of the measured $G(\theta)$ curve of the Al film at 65.3 eV photon energy together with the fitted theoretical $G(\theta)$ curve. The strong interference pattern of the $G(\theta)$ curve, which allows the determination of the film

thickness d from the fit with high accuracy, is typical of photon energies below the Al–$L_{2,3}$ edge. The theoretical expression of $G(\theta)$ depends on six adjustable parameters, the optical constants ε_{Al} and the thickness d of the Al film, the optical constants ε_{Sub} of the substrate, and the electron escape depth L. Values for the optical constants of the substrate, determined from multiple-angle reflectance measurements of the substrate before evaporating the Al film, were treated as fixed fit parameters. Above the Al–$L_{2,3}$ edge, the interferences in the $G(\theta)$ spectra vanished, and the theoretical expression of $G(\theta)$ for a bulk system according to Eq. 3 was used to determine ε_{Al} and the electron escape length L of the Al film. As an example, Fig. 5 shows a plot of the measured $G(\theta)$ curve of the same sample as in Fig. 4 at 122.9 eV photon energy, together with the fitted theory. In addition, the reflectance versus angle of incidence for a large number of angles of the same Al film was measured. Fitting of these reflectance spectra to Fresnel's equations yielded values for ε_{Al} and the thickness of the Al film, and therefore enabled a direct comparison of the two methods applied to the same sample. Figures 6 and 7 summarize the fit results of ε_{Al} obtained by both the total yield and the reflectance measure-

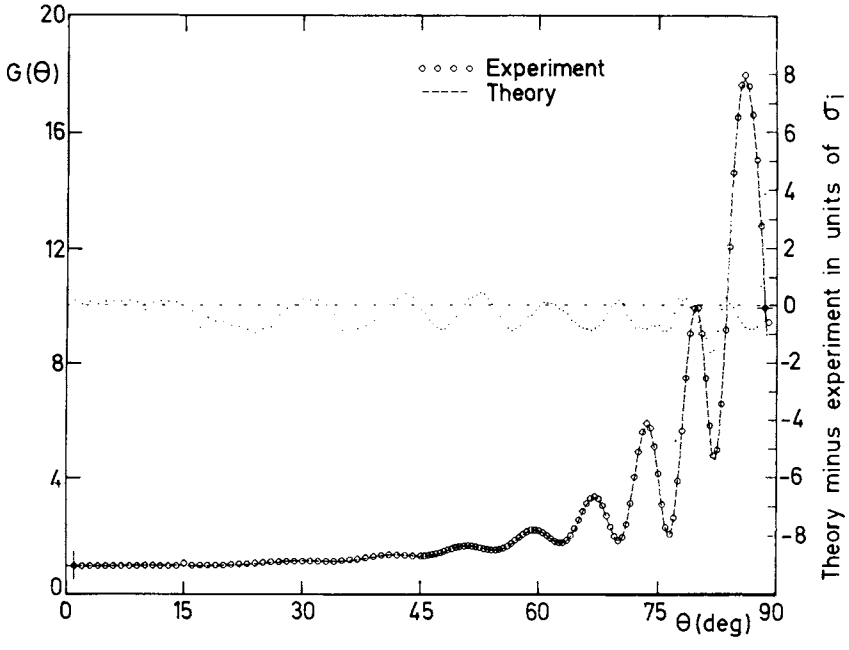

Fig. 4. Total yield versus angle of incidence normalized to the yield at normal incidence at 65.3 eV photon energy of an 770 Å-thick Al film. At this energy, strong interference patterns are visible in the $G(\theta)$ spectra. The dotted line in the middle of the figure shows the deviation of theory and experiment in units of the experimental error σ_i, which was estimated to be 1% of the experimental $G(\theta)$ value. For more details, see text.

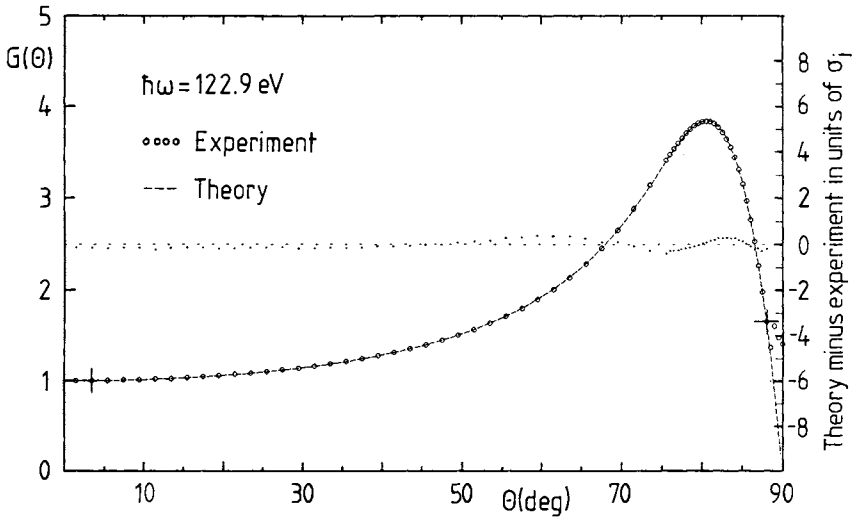

Fig. 5. Relative total photoelectric-yield $G(\theta)$ versus angle of incidence θ at $\hbar\omega = 122.9$ eV. This spectrum was obtained from the same Al film as the spectrum in Fig. 4. The fitted curve (dashed line) is based on the assumption of a bulk material, because the film appears to be opaque above the Al-$L_{2,3}$ edge.

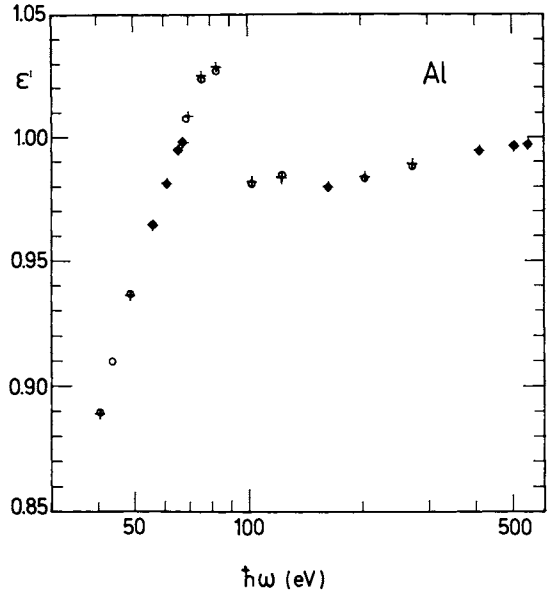

Fig. 6. Real part ε' of the dielectric function ε_{Al} versus photon energy $\hbar\omega$. The crosses denote the fit results of the total-yield method, whereas the circles refer to the reflectance measurements.

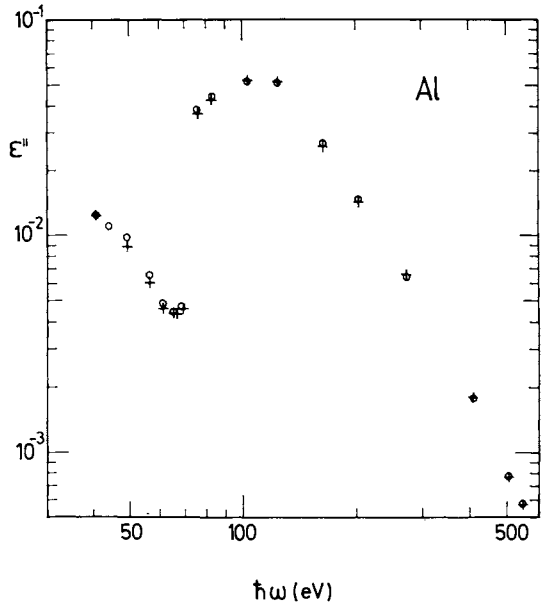

Fig. 7. Imaginary part ε'' of the dielectric function ε_{Al} versus photon energy $\hbar\omega$ (compare with Fig. 6).

ments. The value of the film thickness determined from the yield method is $d = 773 \pm 9$ Å, whereas the reflectance measurements yielded $d = 768 \pm 10$ Å. The error is determined by averaging results over a range of photon energies. The smallness of the statistical spread is an additional indication of the applicability of the whole procedure.

Similar investigations have been performed on thin copper films on glass substrates in the range of 50–900 eV [10]. An example of a measurement on Cu at 644 eV photon energy is given in Fig. 8. Figures 9 and 10 show the optical constants of two films as determined from reflectance (open symbols) and total-yield measurements (closed symbols). The thicknesses of the films have been determined to be 225 ± 5 Å (circles) and 317 ± 6 Å (diamonds) from both types of measurements. For comparison, values of ε_{Cu} have been calculated from atomic scattering factors given by Henke *et al.* [9] and are included in Figs. 9 and 10.

CONCLUSIONS AND FUTURE PROSPECTS V

In this chapter it is demonstrated that angular-dependent photoelectric yield contains sufficiently detailed information, at least in the spectral

range $\hbar\omega = 20$–1000 eV, to extract accurate values for the optical constants. Up to now the method was applied only to a few substances, all of them metals, and in most cases they were supported by a glass substrate. The measurement of a thin layer on a substrate has the advantage of producing very pronounced interference structures, by which the sensitivity of the fits appears to be considerably increased. On the other hand, a fairly powerful computer system is needed to calculate the best fit in a reasonable time. For bulk materials the mathematical procedure is much simpler.

At first glance, the method appears to be applicable only to conducting materials, including doped semiconductors. If films are used, their thicknesses have to be so large that practically no electrons emerging from the substrate penetrate the film and contribute to the yield. The reason is that such a contribution is not included in the theory, as outlined in Section II. With materials such as metals, having mean-free paths of the order of 20 Å, a film thickness on the order of 100 Å suffices. As a matter of fact, we even had good results with a 51 Å Pt film on glass [11].

Would it also be possible to measure optical constants of insulating materials in this way? It is well-known that films with thicknesses on the order of a few hundred angstroms show no serious charging problems. Actually, CsI is used above 1000 Å as a photocathode material. In this case, the problem arises from the very large mean-free paths for slow secondary electrons. Since electron–electron scattering is not possible when the kinetic energy of the electrons is less than roughly the band gap above the conduction-band minimum, only inelastic impurity scattering

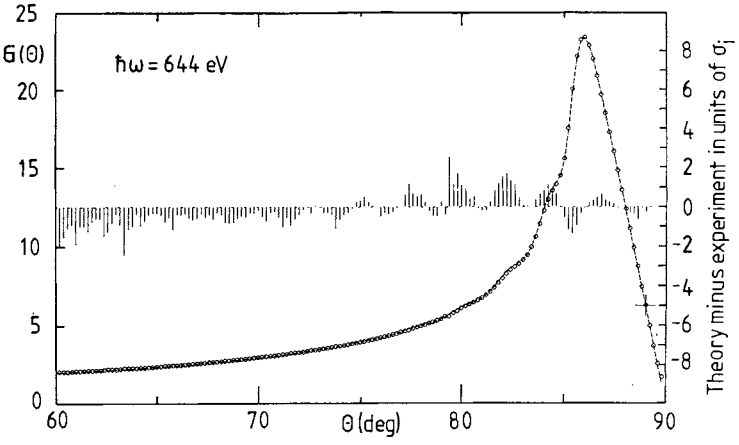

Fig. 8. Relative total yield $G(\theta)$ of a Cu film of 225 Å thickness on white crown glass at $\hbar\omega = 644$ eV. In addition to the experimental $G(\theta)$ spectrum (open circles), the fitted theoretical curve (dashed line) and the deviation between the theoretical and the measured spectra in units of $\sigma_i = 0.01 \times G_{\text{exp}}(\theta_i)$ (vertical bars) are plotted.

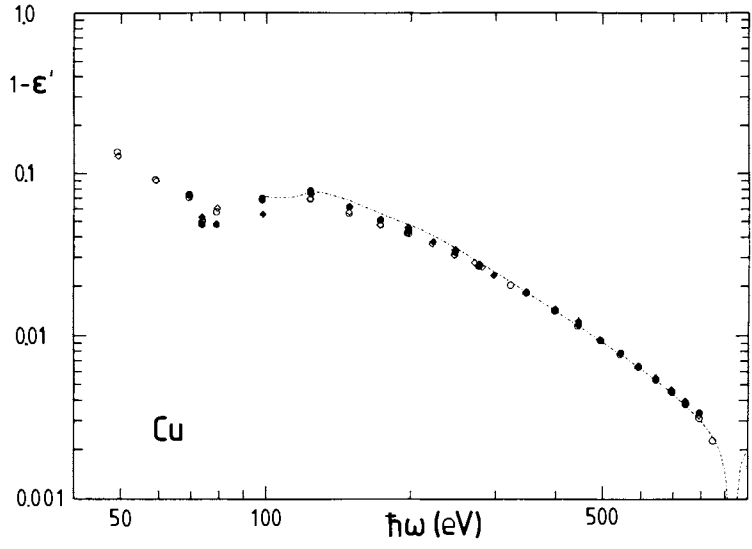

Fig. 9. Real part of the dielectric function ε_{Cu} plotted as $1-\varepsilon'$ versus photon energy $\hbar\omega$. Full symbols result from reflectance measurements, open symbols from total-yield measurements on two samples of 225±5 Å (circles) and 317±6 Å (diamonds). The dash-dotted line represents values calculated from atomic scattering factors according to Henke *et al.* [9].

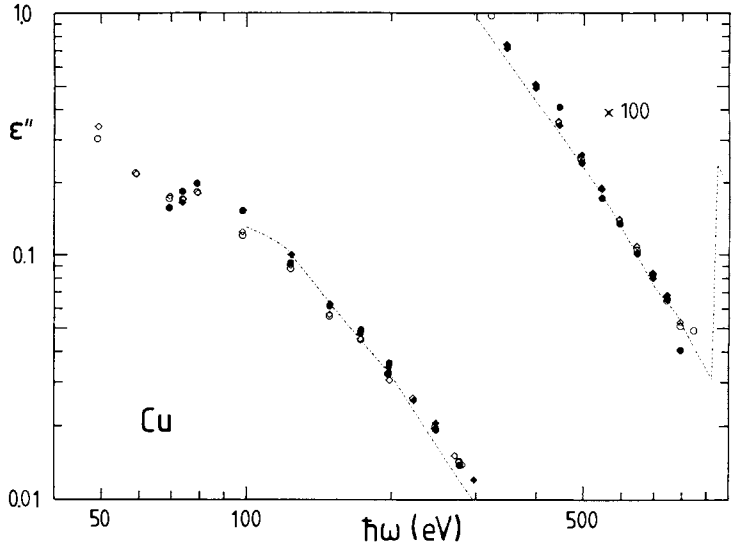

Fig. 10. Imaginary part ε'' of the dielectric function ε_{Cu}. Symbols are as in Fig. 9.

and a slow energy loss due to electron–phonon scattering remains. As a consequence, electrons originating from the substrate, which needs to be a conductor, can contribute to the total yield. A fairly realistic theoretical treatment of such a system appears to be possible. One or two additional parameters for the electron transport would enter the equations. They would have to be fitted together with the other parameters. Their correlation with the other parameters (optical constants) might not be very large, since the characteristic shape of the $G(\theta)$ curves close to the peak would be determined, to a large extent, by the optical constants of the insulator under investigation. Therefore, such a program could yield satisfactory results for this class of materials also. In this case, the method would be expanded beyond its present limitations.

REFERENCES

1. S. V. Pepper, *J. Opt. Soc. Amer.* **60**, 805 (1970).
2. T. F. Gesell and E. T. Arakawa, *Phys. Rev. Lett.* **26**, 377 (1971).
3. E. T. Arakawa, R. N. Hamm, and M. W. Williams, *J. Opt. Soc. Amer.* **63**, 1131 (1973); E. T. Arakawa, M. W. Williams, R. N. Hamm, R. D. Birkhoff, and A. J. Braundmeier, "Proc. IV Int. Conf. on VUV Radiation Physics, Hamburg 1974," (E. E. Koch, R. Haensel, C. Kunz, eds.), Pergamon/Vieweg, Braunschweig, 580 (1974).
4. P. J. Vernier, J. P. Goudonnet, G. Chabrier, and J. Cornaz, *J. Opt. Soc. Amer.* **53**, 620 (1971); J. Peisner, A. Quemerais, M. Priol and S. Robin, *J. Phys. (France)* **34**, C6 (1973); A. Quemerais, J. Peisner, M. Priol, and S. Robin, *Comp. Rend. (Paris)* **276B**, 753 (1973).
5. H.-G. Birken, W. Jark, C. Kunz, and R. Wolf, *Nucl. Instr. and Meth. A* **253**, 166 (1986).
6. J. M. Elson, J. P. Rahn, and J. M. Bennett, *Appl. Opt.* **22**, 3207 (1983).
7. H. Hogrefe, D. Giesenberg, R. P. Haelbich, and C. Kunz, *Nucl. Instr. and Meth.* **208**, 415 (1983).
8. W. Jark and C. Kunz, *Nucl. Instr. and Meth. A* **246**, 320 (1986).
9. B. L. Henke, P. Lee, T. J. Tanaka, R. L. Shimabukuro, and B. K. Fujikawa, *At. Data Nucl. Data Tables* **27**, 1 (1982).
10. H.-G. Birken, C. Blessing, C. Kunz, and R. Wolf, *Rev. Sci. Instrum.* **60**, 2226 (1989).
11. C. Blessing, H.-G. Birken, C. Kunz, and R. Wolf, to be published; C. Blessing, diploma thesis, Hamburg (1988).

Chapter 13

Determination of Optical Constants by High-Energy, Electron-Energy-Loss Spectroscopy (EELS)

J. PFLÜGER
Hamburger Synchrotronstrahlungslabor HASYLAB at DESY
D-2000 Hamburg 52
Federal Republic of Germany

and

J. FINK
Kernforschungszentrum Karlsruhe
Institut für Nukleare Festkörperphysik
D-7500 Karlsruhe
Federal Republic of Germany

I. Introduction 293
II. Description of an EELS Experiment 295
III. Scattering Cross-Section 297
IV. Exact Determination of the Loss Function 298
V. Kramers–Kronig Analysis 299
VI. Brief Summary of the Evaluation Procedure 300
VII. Comparison with Reflectivity Measurements 300
VIII. Optical Properties of TiC, VC, TiN, and VN 303
References 310

I INTRODUCTION

Optical properties of solids are important in the design of optical elements such as mirrors, prisms, multilayers, and so on. Optical quantities such as the complex refractive index, the reflectivity, or the absorption coefficient are also important for the investigation of the electronic structure of solids. These quantities are most commonly determined by optical

Copyright © 1991 by Academic Press.
All rights of reproduction in any form reserved.
ISBN 0-12-544422-2

methods such as reflection or absorption of light by suitable samples. The electric-field vector of a light wave is perpendicular to its **k** vector. So the electronic system is displaced transversely as a whole, and as a consequence, the electron density is not changed. Today, optical measurements are widely used and with the help of modern synchrotron-radiation sources, a very large energy range can be covered, from the far infrared up to the hard X-ray region.

A completely different method for determining optical constants is the measurement of energy losses suffered by fast electrons, with a kinetic energy of typically 50–300 keV when they are transmitted through thin solid films. In this case the electronic density is modulated longitudinally. The situation resembles the propagation of sound waves through air. The probability for energy losses is determined by the imaginary part of $-1/\varepsilon_L$, which is called the *loss function*. $\varepsilon_L(q,\omega)$ is the longitudinal q- and ω-dependent dielectric function, which in general is different from the transverse function, which is measured by experiments involving transverse light waves. However, for $q \to 0$, ε_T and ε_L become identical, and thus, EELS and optical experiments give the same results. Since this contribution deals with EELS results only, we implicitly assume that only the longitudinal dielectric function ε_L is involved in the formulas and drop the corresponding suffix.

Maxima in the loss function are determined by $\varepsilon_1 \simeq 0$ and ε_2 being "small." Such an excitation is called a plasmon [1].

More than 20 years ago, Raether's group in Hamburg [2, 3] demonstrated that dielectric properties determined by EELS can agree well with those obtained by optical methods. A compilation of older work is given in Refs. [1–4]; more recent work is reviewed in Ref. [5]. These investigations demonstrated the advantages of EELS:

1. Quite a large energy range is available starting at about 0.2 eV. The upper limit is about 2000 eV. It is, however, important to note that the accuracy of optical constants determined by EELS is reduced more and more, starting at about 30 eV, due to multiple-scattering events, which can be corrected only within a limited accuracy. This energy range is available with the help of a laboratory-scale instrument; optical methods at these energies require the use of a large synchrotron-radiation facility.
2. Only bulk properties are measured using EELS. The results are independent of surface preparation or contamination. EELS might be an alternative to optical techniques, when the preparation of an optically good surface is difficult or even impossible.
3. Since EELS is a scattering experiment, it can be performed with a momentum transfer $\hbar q$. This allows the determination of $\mathrm{Im}(-1/\varepsilon\,(q,\omega))$, which contains information about the dispersion of the electronic band structure and electron–electron correlation effects. For the determination

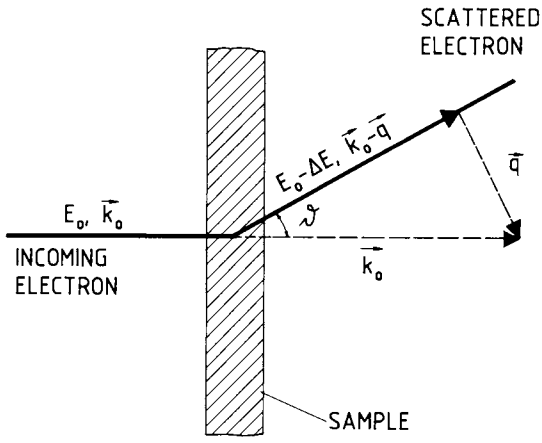

Fig. 1. Scattering geometry of an EELS experiment. An electron with a kinetic energy of typically 50–300 keV penetrating a sample of thickness 500–1000 Å is scattered by an angle ϑ and suffers an energy loss ΔE. The scattering angles are very small, typically several mrad.

of optical constants, however, only the limit $q \rightarrow 0$ is important.

A severe problem is sample preparation, since thin self-supporting samples with a thickness of 500–2000 Å and an area of roughly 1 mm^2 are needed. Many techniques have been applied. A comprehensive overview of many preparation techniques is given in Ref. [5]. However, as experience shows, there is a preparation method for almost every problem. In this chapter we will restrict ourselves to the optical limit ($q \rightarrow 0$), so that the data obtained are comparable to those obtained using optical methods. The determination of optical constants from EELS data will be described in detail. The optical properties of the refractory compounds TiC, VC, TiN, and VN are discussed in detail, and for TiC, a comparison of EELS data with optical data is performed.

DESCRIPTION OF AN EELS EXPERIMENT

The scattering geometry is shown in Fig. 1. A highly collimated beam of monochromatized electrons with a kinetic energy E_o of 50–300 keV and an angular spread $\Delta\vartheta \simeq 0.3$–$0.5$ mrad penetrates a thin sample, typically 500–2000 Å thick. On its passage through the sample, the electron may be scattered inelastically by an angle ϑ and loses an amount of energy ΔE.

Energy and momentum conservation require

$$\Delta E = (\hbar^2/2m)(k_o^2 - k_n^2) \tag{1}$$

$$\hbar q = \hbar(k_o - k_n). \tag{2}$$

Here, k_o and k_n are the wave vector of the unscattered and the scattered electrons, $\hbar$ is Planck's constant divided by 2π, and m is the electron mass. The transferred momentum $\hbar q$ can be decomposed into a parallel and a perpendicular component, to k_o, $q_\parallel$ and $q_\perp$, respectively:

$$\hbar q_\parallel = \hbar k_o \vartheta_E \tag{3}$$

with

$$\vartheta_E = \Delta E/2E_o. \tag{4}$$

This longitudinal momentum transfer is related to the energy loss only.

Similarly, the transverse momentum transfer is given by

$$\hbar q_\perp = \hbar k_o \vartheta, \tag{5}$$

which is independent of the energy loss and depends on the scattering angle only, so that the total momentum transfer is given by

$$\hbar q = \hbar k_o (\vartheta^2 + \vartheta_E^2)^{1/2}. \tag{6}$$

For scattering angles somewhat larger than ϑ_E, the momentum transfer is practically determined by ϑ only. As an example, some numerical values for an electron-energy-loss experiment, used to study the optical properties of a number of refractory compounds, are given [6, 7]. The kinetic energy of the electrons was 170 keV corresponding to $k_o = 228.4$ Å^{-1}. At a characteristic energy loss of $\Delta E = 20$ eV, $\vartheta_E = 0.059$ mrad, which corresponds to $q_\parallel = 0.012$ Å^{-1}. This is, by the way, roughly the same momentum carried by a 20 eV photon (0.01 Å^{-1}).

SCATTERING CROSS-SECTION III

The double-differential scattering cross-section per atom for high-energy electrons in an (infinite) solid is treated in the Born approximation and can be written as [4, 5]

$$\frac{d^2\sigma}{d\omega\, d\Omega} = \frac{4\hbar\gamma^2}{a_o^2 q^4} S(q,\omega) = \frac{\hbar\gamma^2}{(\pi e a_o)^2 N}\frac{1}{q^2}\,\mathrm{Im}(-1/\varepsilon(q,\omega)). \tag{7}$$

Here, in addition, the electron charge e, Bohr's radius a_o and the number density of electrons N per unit volume has been introduced. The factor $\gamma = 1 + E_o/m_o c^2$ makes the result relativistically invariant, where $m_o c^2 =$ 511 keV is the rest mass energy of the electron.

$S(q,\omega)$ is the dynamic structure factor originally derived by van Hove [8]. The second identity of Eq. 7, correlating the dynamic structure factor with the loss function, is derived in Ref. [9]. A derivation of the right-hand side from dielectric theory is given in Ref. [10]. Since the loss function is typically of order unity, the scattering cross-section given by Eq. 7 falls off like $1/q^2$. Using Eq. 6 gives

$$\frac{d^2\sigma}{d\omega\, d\Omega} = \frac{\hbar\gamma^2}{(\pi e a_o)^2 k_o^2}\frac{1}{\vartheta^2 + \vartheta_E^2}\,\mathrm{Im}(-1/\varepsilon(q,\omega)). \tag{8}$$

Thus, measuring the cross-section for inelastic electron scattering gives information on the loss function $\mathrm{Im}(-1/\varepsilon(q,\omega))$.

There are, however, two other contributions that might influence the accuracy of the determination of the volume loss function.

1. In a sample of finite thickness D, excitation of surface modes, also called *surface plasmons*, may take place, which contributes to the scattered intensity. The cross-section for surface-plasmon generation is proportional to

$$\frac{d^2\sigma}{d\omega\, d\Omega} \cong (1/q^3)\,\mathrm{Im}(-1/(\varepsilon+1)). \tag{9}$$

The function $\mathrm{Im}(-1(\varepsilon+1))$ is also called the *surface loss function*.

Surface losses are easily verified, since their cross-section varies like $1/q^3$. On the other hand, their contribution to the observed intensity decreases

as the sample thickness is increased. It was already shown by Raether [2] that even for momentum transfer $q \simeq 0.2\,\text{Å}^{-1}$, the ratio of volume-to-surface losses can be made negligibly small.

2. Radiation losses due to the emission of Cerenkov radiation can take place when the electron velocity exceeds the phase velocity of light. This might occur in highly polarizable materials. It was shown by Kröger [11] that radiation losses, like surface losses, contribute only at very small angles.

The usual way to suppress contributions from surface and radiation losses is to perform the measurements at a finite momentum transfer q, which is small enough so that the optical limit $q \to 0$ is still valid, but which is large enough so that only volume losses contribute. In the case of refractory compounds reported later in this article, $q = 0.1$–$0.15\,\text{Å}^{-1}$ was found sufficiently small.

IV EXACT DETERMINATION OF THE LOSS FUNCTION

To determine the exact loss function from a spectrum measured at small q, as described in the preceeding section, corrections for finite spectrometer resolution and multiple scattering have to be applied. Both energy and angular resolution of a spectrometer are finite, and therefore the observed intensity at some energy and angle is a convolution of Eq. 8 with the energy- and angular-resolution function. The problem is simplified on assuming that $\text{Im}(-1/\varepsilon(q,\omega))$ is constant over the resolution interval. This assumption is fulfilled, since energy resolution typically is of the order of 0.1 eV, and the momentum transfer resolution is typically $<0.05\,\text{Å}^{-1}$. Then the convolution problem leads to a correction factor $F(\Delta E)$, which depends on the energy loss only. The whole procedure has already been described in detail in Ref. [3]. To make all corrections properly, the energy and angular resolution are recorded before each measurement, in order to calculate $F(\Delta E)$ exactly. For the spectrometer resolution given previously, the correction by $F(\Delta E)$ is below 10% and does not vary much with the energy loss.

The scattering cross-section for highly energetic electrons in solids is very high, and mean free paths are of the order of a few hundred angstroms. Therefore, there exists a probability that an electron undergoes more than one scattering event on traversing the sample. In the range of roughly twice the plasma energy, up to energy losses of 40–50 eV, only double scattering events contribute significantly and therefore have to be corrected for.

Double scattering can be described as a convolution of a "true" single-scattering spectrum with itself. In this way dominant structures like volume plasmons are also found at twice the single-energy loss. Triple losses lead to losses at three times the single-loss energy, and so on.

Several numerical deconvolution schemes have been developed [12] and applied to EELS data [3, 4, 13, 14]. Following Ref. [3], double scattering can be calculated starting at low-energy losses up to about 1–2 eV, where double scattering is negligibly small. Then, the double-scattering contribution can be calculated at slightly higher energies and subtracted from the uncorrected spectrum. By this step-by-step method, the whole spectrum can be corrected. At the end of the procedure, the loss function is determined experimentally except for a multiplicative constant. It is possible to measure the absolute value of the loss function experimentally [2, 3] but this method is not very accurate. Instead, it is preferable to use a suitable sum rule derived from the Kramers–Kronig relations for normalization.

KRAMERS–KRONIG ANALYSIS V

The causality principle connects imaginary and real parts of a complex function via the Kramers–Kronig (K–K) integrals. Many optical spectroscopies make use of these relations. In the case of EELS at small momentum transfer ($q \rightarrow 0$), the K–K transform is given by

$$\mathrm{Re}(-1/\varepsilon(\omega)) - 1 = \frac{2}{\pi} P \int_0^\infty \mathrm{Im}(-1/\varepsilon(\omega')) \frac{\omega' \, d\omega'}{\omega'^2 - \omega^2}. \tag{10}$$

where P denotes the Cauchy principal value of the integral. Two extrapolations are necessary in order to perform the integral form zero to infinity. From zero to about 0.5 eV the loss function is interpolated linearly starting at zero, since in the original data this region is obscured by the primary beam. At higher energies, above 40–50 eV, the loss function is extrapolated proportional to ω^{-3}, which is the loss function of a free-electron gas. The proper normalization of the loss function can be obtained from Eq. 10 by setting $\omega = 0$:

$$\mathrm{Re}(-1/\varepsilon(\omega = 0)) - 1 = \frac{2}{\pi} P \int_0^\infty \mathrm{Im}(-1/\varepsilon(\omega')) \frac{d\omega'}{\omega'}. \tag{11}$$

For metals, $1/\varepsilon(\omega=0)=0$. For insulators and semiconductors ε is real below the band gap and can be obtained from the refractive index by $\varepsilon_1=n^2$. The advantage of using Eq. 11 for normalization is this: the measured spectrum is weighted inversely proportional to the energy loss. Thus, the energy region is weighted most where multiple losses contribute only little and the loss function is therefore determined with the highest accuracy. The well-known *f*-sum rule,

$$\int_0^\infty \mathrm{Im}(-1/\varepsilon)\omega \, d\omega = \pi/2\omega_p^2. \tag{12}$$

which in principle can also be used for normalization of $\mathrm{Im}(-1/\varepsilon)$, weights the loss function proportional to ω. In addition, an assumption for the electron density N, which enters into the plasma frequency

$$\omega_p = (4\pi Ne^2/m)^{1/2} \tag{13}$$

has to be made. This can be avoided by using Eq. 11.

VI BRIEF SUMMARY OF THE EVALUATION PROCEDURE

To give an overview over the evaluation procedure, the five steps leading to readily evaluated data from EELS measurements will be briefly summarized.

(1) Measurement of the angular- and energy-resolution functions.
(2) Measurement of the loss spectrum.
(3) Angular and energy deconvolution.
(4) After correction for double scattering, the unnormalized loss function $\mathrm{Im}(-1/\varepsilon)$ is obtained.
(5) Kramers–Kronig analysis and normalization of the loss function using Eq. 11. Calculation of ε_1, ε_2, n, k, and so on.

VII COMPARISON WITH REFLECTIVITY MEASUREMENTS

During the last years, EELS has been used by the Karlsruhe group in a number of experiments to elucidate the dielectric properties in the energy

range 0.5–40 eV. Examples include the study of the binding states in amorphous hydrogenated carbon coatings [15], conducting polymers [16–22], carbides and nitrites of 3d and 4d transition metals [6, 7], A-15 superconductors [23], and, most recently, ceramic superconductors [24–26].

As an illustrative and representative example, the dot-dashed curve in Fig. 2 shows the measured loss function of TiN after the elastic line has been subtracted, and the energy and angular deconvolution was performed. The energy range extends from 0–40 eV. The solid line shows the influence of the double-scattering correction as described in Ref. [3]. It is seen that at higher energies this correction is quite substantial, whereas below about 20 eV it is less important. The maximum of the curves is arbitrarily normalized to 25. The solid curve is the input spectrum for the K–K analysis. The normalization of the loss function is then performed using Eq. 11.

In Fig. 3, optical data are shown for TiC obtained with different methods. A comparison is made between the optical constants derived by the procedure described above taken from Pflüger *et al.* [6] with data from Lynch *et al.* [27] deduced from reflectivity measurements using synchrotron radiation in the energy range 0.1–30 eV. To our knowledge, these are the only available optical measurements on refractory compounds over a large energy range comparable to that covered by EELS. The upper part of Fig. 3 shows the measured reflectance from Ref. [27] versus reflectance derived

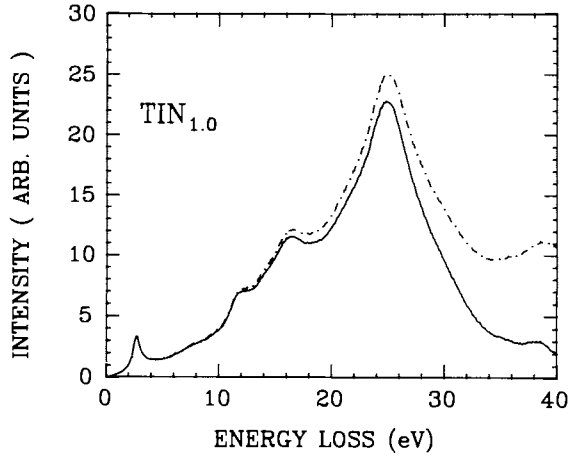

Fig. 2. Energy-loss intensity of TiN after the elastic line has been subtracted and angular deconvolution has been applied. The dot-dashed curve is without correction for double scattering. The solid curve is corrected for double scattering. Above about 20 eV, the correction becomes substantial.

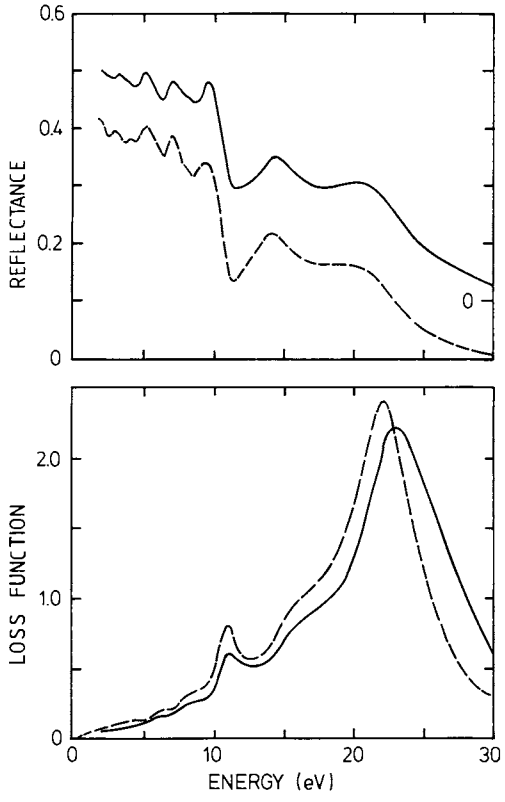

Fig. 3. Comparison of optical constants obtained with EELS taken from Ref. [6] with those obtained with reflectance measurements from Ref. [27]. Solid lines indicate data derived from EELS measurements. Dashed lines indicate data derived from reflectance measurements. Note the 0.1 upward shift of the solid-line curve in the upper figure.

from EELS data. Note that the scale of the EELS curve is shifted upward by one tick mark. The lower part of Fig. 3 shows the opposite comparison. The loss function calculated from reflectivity data, reproduced in Ref. [27], is compared to the loss function measured by EELS.

The data obtained by the two methods agree remarkably well. Generally the reflectance obtained by EELS differs less than reflectance data for TiC published earlier [28, 29].

Each method shows its particular strength and weakness. At about 25 eV, the EELS reflectivity seems to be too high compared with the optical data, whereas the EELS volume plasmon, at 23.5 eV, is slightly higher than that derived from optical data. Also, some structures in the EELS spectra are broader and less pronounced than in the optical curves. One possible explanation for this is the completely different method of

sample preparation. Large, carefully polished zone-melted single crystals were used by Lynch *et al.* Thin, self-supported 770 Å-thick polycrystalline films of TiC were prepared by reactive sputtering for the EELS measurements. In both groups great care was taken for a good characterization of the samples.

VIII OPTICAL PROPERTIES OF TiC, VC, TiN, AND VN

In this section we briefly review the dielectric properties of the refractory compounds TiC, VC, TiN, and VN as determined by EELS [6]. Similar experiments were also performed on ZrN, NbC, and NbN [7]. For a complete description the reader is referred to these references.

The properly normalized loss functions together with the real and imaginary parts of the dielectric function are shown in Fig. 4 for TiC, VC, TiN, and VN. One realizes that maxima in the loss functions correspond to $\varepsilon_1 \simeq 0$ and small ε_2. The better this condition is fulfilled, the more pronounced is the structure of the loss function. The real and the imaginary part of the refractive index of these compounds is given in Tables I–IV.

The dominant feature in all loss spectra is the volume plasmon, the collective oscillation of all valence electrons, found at 23.5, 24.9, 24.9, and 26.3 eV for TiC, VC, TiN, and VN, respectively. These values might be compared to the plasma energy defined by Eq. 13 taking into account the metal 4s and 3d and the nonmetal 2s and 2p orbitals. One obtains 23.3, 25.5, 25.5, and 28.0 eV, which is in quite satisfactory agreement.

Apart from the main plasmon peak, there are other excitations that are caused by interband transitions, and therefore might be termed interband plasmons. Spectra of the carbides and nitrides look quite different, but there is some similarity between TiC and VC and between TiN and VN. These differences between carbides and nitrides are, however, closely related to the electronic structure of these compounds.

In the vicinity of the Fermi level, the electronic states of the refractory compounds consist of bonding nonmetal p orbitals strongly hybridized with metal d orbitals below, and antibonding d orbital hybridized with nonmetal orbitals above E_F [30]. Hybridization is stronger for the carbides than for the nitrides. The Fermi level is determined by the number of available valence electrons. For TiC it lies in the very minimum between p and d states, whereas for VC, TiN, and VN it is shifted more and more upward into the d bands.

Many features of the loss spectra can be understood from details of the electronic structure. For a comparison with calculated band-structure data,

the optical joint density of states (OJDS), which is defined as [31]

$$I_1(\omega) = 2\omega\varepsilon_2(\omega)/\pi\omega_p^2 \tag{14}$$

was calculated from ε_2 as derived from the K–K analysis.

Fig. 5 shows a comparison between the OJDS (solid curve) and joint densities of states (dashed curve) derived from self-consistent Gaussian LCAO band-structure data [32]. The joint density of states gives a measure for the probability of interband transitions when matrix elements as well as lifetime effects are neglected. Many structures seen in the OJDS are also reflected by the calculations. The maximum (around 7 eV), which is present in all compounds, can be attributed to transitions between the

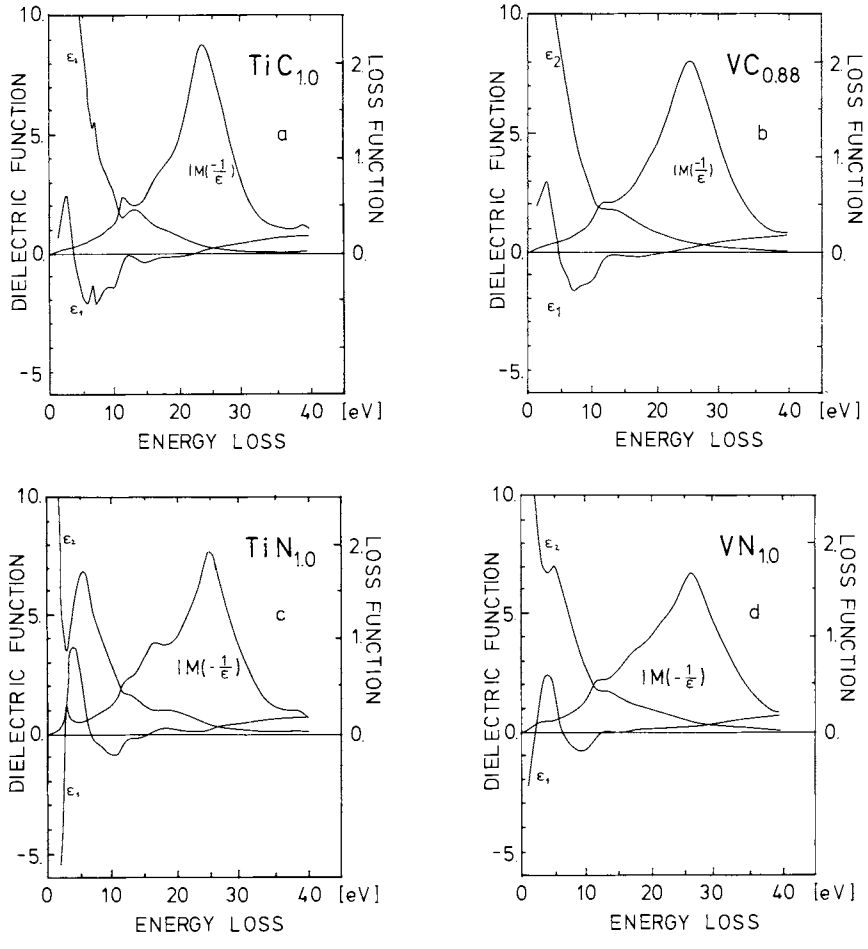

Fig. 4. Loss functions and Kramers–Kronig-derived real and imaginary parts of the dielectric function ε_1, ε_2 for (a) $TiC_{1.0}$, (b) $VC_{0.88}$, (c) $TiN_{1.0}$, (d) $VN_{1.0}$.

TABLE I

Values of n and k for TiC Obtained by EELS

eV	cm^{-1}	Å	n	k
0.5	4032.7	24797	5.44×10^{0}	5.54×10^{0}
1.0	8065.5	12399	3.97	3.78
1.5	12098	8266	3.51	3.07
2.0	16131	6199	3.05	2.67
2.5	20164	4959	2.95	2.38
3.0	24169	4133	2.78	2.43
3.5	28229	3542	2.57	2.34
4.0	32262	3100	2.30	2.33
4.5	36295	2755	2.16	2.31
5.0	40327	2480	1.96	2.25
5.5	44360	2254	1.74	2.20
6.0	48393	2066	1.52	2.02
6.5	52426	1907	1.43	1.86
7.0	56458	1771	1.42	1.89
7.5	60491	1653	1.21	1.84
8.0	64524	1550	1.12	1.69
8.5	68557	1459	1.07	1.63
9.0	72589	1378	1.00×10^{0}	1.55
9.5	76622	1305	9.55×10^{-1}	1.50
10.0	80655	1240	8.01	1.44
10.5	84688	1181	7.25	1.25
11.0	88720	1127	7.45	1.06
11.5	92753	1078	8.67	0.96
12.0	96785	1033	9.42	0.98
13.0		953.7	9.59	1.02
14.0		885.6	8.70	1.03×10^{0}
15.0		826.6	7.47	9.62×10^{-1}
16.0		774.9	7.23	8.59
17.0		729.3	7.06	8.01
18.0		688.8	6.88	7.50
19.0		652.6	6.57	7.29
20.0		619.9	6.03	6.75
21.0		590.4	5.51	6.04
22.0		563.6	5.23	5.16
23.0		539.1	5.23	4.21
24.0		516.6	5.47	3.44
25.0		495.9	5.79	2.91
26.0		476.9	6.03	2.48
27.0		459.2	6.27	2.10
28.0		442.8	6.54	1.74
29.0		427.5	6.79	1.45
30.0		413.3	7.09	1.23
31.0		400.0	7.34	1.07×10^{-1}
32.0		387.5	7.62	8.92×10^{-2}
33.0		375.7	7.85	8.30
34.0		364.7	8.08	8.10
35.0		354.2	8.26	7.95
36.0		344.4	8.39	7.97
37.0		335.1	8.53	8.41
38.0		326.3	8.63	8.96
39.0		317.9	8.53	1.01
39.9		310.7	8.40	5.05

TABLE II

Values of n and k for VC Obtained by EELS

eV	cm^{-1}	Å	n	k
0.5	4032.7	24797	4.86×10^{0}	5.34×10^{0}
1.0	8065.5	12399	3.66	3.42
1.5	12098	8266	3.37	2.88
2.0	16131	6199	3.01	2.51
2.5	20164	4959	2.84	2.21
3.0	24196	4133	2.77	2.16
3.5	28229	3542	2.59	2.12
4.0	32262	3100	2.47	2.15
4.5	36295	2755	2.27	2.18
5.0	40327	2480	2.04	2.13
5.5	44360	2254	1.86	2.04
6.0	48393	2066	1.74	2.00
6.5	52426	1907	1.62	1.97
7.0	56458	1771	1.42	1.92
7.5	60491	1653	1.32	1.83
8.0	64524	1550	1.22	1.73
8.5	68557	1459	1.13	1.64
9.0	72589	1378	1.07×10^{0}	1.59
9.5	76622	1305	9.58×10^{-1}	1.51
10.0	80655	1240	8.65	1.41
10.5	84688	1181	8.27	1.28
11.0	88720	1127	8.20	1.14
11.5	92753	1078	8.58	1.04
12.0	96785	1033	9.17	0.99
13.0		953.7	9.56	1.00×10^{0}
14.0		885.6	9.04	9.96×10^{-1}
15.0		826.6	8.57	9.58
16.0		774.9	8.03	9.33
17.0		729.3	7.28	8.72
18.0		688.8	6.89	7.99
19.0		652.6	6.65	7.30
20.0		619.9	6.37	6.86
21.0		590.4	6.06	6.33
22.0		563.6	5.78	5.68
23.0		539.1	5.61	4.99
24.0		516.6	5.60	4.33
25.0		495.9	5.64	3.71
26.0		476.9	5.82	3.16
27.0		459.2	6.01	2.68
28.0		442.8	6.23	2.31
29.0		427.5	6.45	1.99
30.0		413.3	6.68	1.72
31.0		400.0	6.87	1.52
32.0		387.5	7.06	1.29
33.0		375.7	7.25	1.13×10^{-1}
34.0		364.7	7.42	9.82×10^{-2}
35.0		354.2	7.60	8.57
36.0		344.4	7.76	7.27
37.0		335.1	7.95	6.33
38.0		326.3	8.14	5.76
39.0		317.9	8.30	5.89
39.9		310.7	8.37	6.42

TABLE III

Values of n and k for TiN Obtained by EELS

eV	cm^{-1}	Å	n	k
0.5	4032.7	24797	4.52×10^{0}	8.25×10^{0}
1.0	8065.5	12399	2.69	5.04
1.5	12098	8266	1.82	3.81
2.0	16131	6199	1.32	2.69
2.5	20164	4959	1.20	1.65
3.0	24196	4133	1.74	1.04
3.5	28229	3542	2.14	1.06
4.0	32262	3100	2.27	1.23
4.5	36295	2755	2.31	1.38
5.0	40327	2480	2.25	1.54
5.5	44360	2254	2.06	1.64
6.0	48393	2066	1.85	1.71
6.5	52426	1907	1.69	1.66
7.0	56458	1771	1.55	1.64
7.5	60491	1653	1.46	1.58
8.0	64524	1550	1.38	1.53
8.5	68557	1459	1.28	1.49
9.0	72589	1378	1.19	1.49
9.5	76622	1305	1.09	1.43
10.0	80655	1240	1.00×10^{0}	1.38
11.0	88720	1127	8.23×10^{-1}	1.17×10^{0}
12.0	96785	1033	8.55	9.76×10^{-1}
13.0		953.7	8.60	9.48
14.0		885.6	7.93	8.74
15.0		826.6	7.59	7.95
16.0		774.9	7.47	6.89
17.0		729.3	7.91	6.34
18.0		688.8	8.11	6.28
19.0		652.6	7.93	6.27
20.0		619.9	7.49	6.22
21.0		590.4	7.02	5.87
22.0		563.6	6.67	5.45
23.0		539.1	6.28	4.97
24.0		516.6	5.89	4.31
25.0		495.9	5.83	3.48
26.0		476.9	6.02	2.78
27.0		459.2	6.33	2.31
28.0		442.8	6.58	2.00
29.0		427.5	6.81	1.72
30.0		413.3	6.98	1.48
31.0		400.0	7.15	1.24
32.0		387.5	7.37	1.02×10^{-1}
33.0		375.7	7.60	8.63×10^{-2}
34.0		364.7	7.81	7.67
35.0		354.2	8.01	7.39
36.0		344.4	8.15	7.07
37.0		335.1	8.31	7.03
38.0		326.3	8.34	7.31
39.0		317.9	8.31	6.49
39.9		310.7	8.40	5.05

TABLE IV

Values of n and k for VN Obtained by EELS

eV	cm^{-1}	Å	n	k
0.5	4032.7	24797	4.23×10^{0}	6.13×10^{0}
1.0	8065.5	12399	3.19	3.66
1.5	12098	8266	2.73	2.92
2.0	16131	6199	2.35	2.47
2.5	20164	4959	2.17	1.98
3.0	24196	4133	2.13	1.70
3.5	28229	3542	2.18	1.58
4.0	32262	3100	2.20	1.54
4.5	36295	2755	2.19	1.56
5.0	40327	2480	2.10	1.64
5.5	44360	2254	1.98	1.70
6.0	48393	2066	1.82	1.74
6.5	52426	1907	1.66	1.68
7.0	56458	1771	1.56	1.65
7.5	60491	1653	1.46	1.60
8.0	64524	1550	1.36	1.57
8.5	68557	1459	1.25	1.51
9.0	72589	1378	1.17	1.46
9.5	76622	1305	1.07×10^{0}	1.39
10.0	80655	1240	9.82×10^{-1}	1.31
10.5	84688	1181	9.22	1.20
11.0	88720	1127	8.96	1.10
11.5	92753	1078	9.03	1.00×10^{0}
12.0	96785	1033	9.31	9.46×10^{-1}
13.0		953.7	9.73	9.24
14.0		885.6	9.22	9.02
15.0		826.6	8.73	8.65
16.0		774.9	8.29	8.06
17.0		729.3	8.03	7.34
18.0		688.8	7.97	6.91
19.0		652.6	7.82	6.67
20.0		619.9	7.59	6.35
21.0		590.4	7.36	5.98
22.0		563.6	7.14	5.60
23.0		539.1	6.95	5.30
24.0		516.6	6.63	4.95
25.0		495.9	6.34	4.43
26.0		476.9	6.19	3.81
27.0		459.2	6.28	3.18
28.0		442.8	6.44	2.70
29.0		427.5	6.65	2.35
30.0		413.3	6.83	2.09
31.0		400.0	6.96	1.86
32.0		387.5	7.12	1.62
33.0		375.7	7.27	1.40
34.0		364.7	7.41	1.22
35.0		354.2	7.58	1.06×10^{-1}
36.0		344.4	7.72	9.26×10^{-2}
37.0		335.1	7.88	7.90
38.0		326.3	8.05	7.22
39.0		317.9	8.23	6.49
39.9		310.7	8.33	6.71

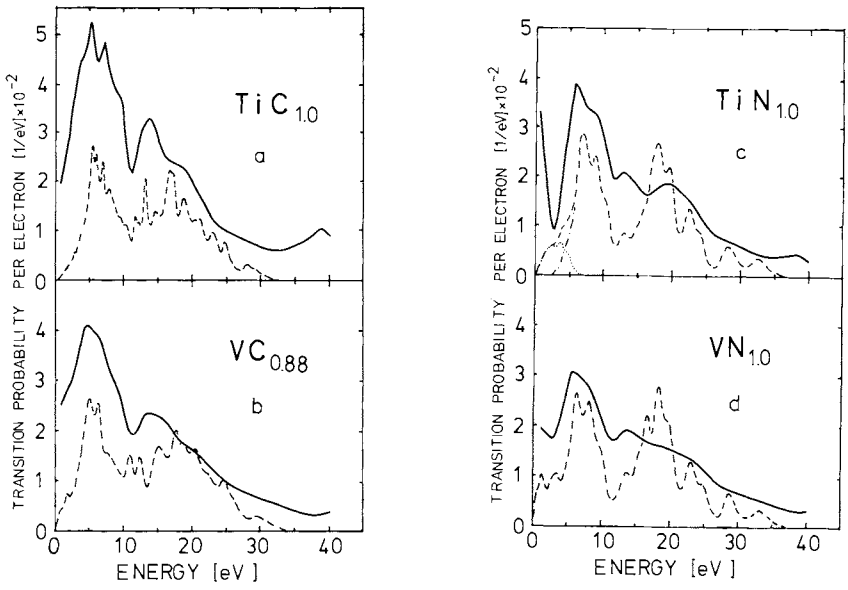

Fig. 5. Kramers–Kronig-derived optical joint densities of states of the stochiometric compounds (solid lines) and joint densities of states from our band-structure calculation (dashed lines) for (a) $TiC_{1.0}$, (b) $VC_{0.88}$, (c) $TiN_{1.0}$, (d) $VN_{1.0}$. In the TiN curves, the joint density of states for transitions between d bands and without d-d transitions are shown separately (dotted and dotted-dashed lines, respectively).

occupied p to unoccupied d states. Especially in the nitrites, the Fermi level lies well within the d bands. Transitions between these d states are dipole-forbidden. Thus, up to about 2.5–3 eV, interband damping is very weak. This is most clearly seen in the TiN curve. To emphasize this, the contribution of d-d transitions to the joint density of states for TiN in Fig. 5 is also shown (dotted curve in Fig. 5c). The onset of strong p-d transitions is observed above 2.8 eV. Below 2.8 eV the OJDS in Fig. 5 is dominated by intraband transitions. The strong minimum at 2.8 eV is, of course, also seen in ε_2. This weak interband damping (small ε_2) at this energy therefore ensures that the Drude plasmon (the collective oscillation of the free electrons, which is shifted down by strong interband transitions at higher energies) can be observed at 2.8 eV in TiN, and from the OJDS curve, Drude parameters that agree well with other published data can also be obtained [6, 33–35]. This low-energy plasma excitation is also observed in VN, but there much more damping occurs.

Since in the carbides E_F lies in the middle between p and d states, interband transitions down to very low energies are possible. Therefore, ε_2 is high in that energy range so that collective oscillations are strongly damped. The same observation was also made by Lynch *et al.* on TiC [27].

This example shows how optical properties determined by EELS can be

used for a detailed comparison with theoretical band-structure data and thus can help to understand the electronic structure of these compounds.

REFERENCES

1. H. Raether, "Excitation of Plasmons and Interband Transitions by Electrons," Springer Tracts in Modern Physics, Vol. 38, Springer, Berlin (1980).
2. H. Raether, in "Springer Tracts in Modern Physics," Vol. 28, Springer, Berlin (1965).
3. J. Daniels, C. V. Festenberg, H. Raether, and K. Zeppenfeld, in "Springer Tracts in Modern Physics," Vol. 54, Springer, Berlin (1970).
4. S. E. Schnatterly, in "Solid State Physics," Vol. 34, Academic Press, New York (1979).
5. J. Fink, "Electronics and Electron Physics," Vol. 75, Academic Press, Orlando, 121 (1988).
6. J. Pflüger, J. Fink, W. Weber, K. P. Bohnen, and G. Crecelins, *Phys. Rev. B* **30**, 1155 (1984).
7. J. Pflüger, J. Fink, W. Weber, K. P. Bohnen, and G. Crecelins, *Phys. Rev. B* **31**, 1244 (1985).
8. L. van Hove, *Phys. Rev.* **95**, 249 (1954).
9. P. M. Platzmann and P. A. Wolf, "Waves and Interactions in Solid State Plasmas," Academic Press, New York (1982).
10. J. Geiger, "Elektronen und Festkörper," Vieweg und Sohn, Braunschweig (1968).
11. E. Kröger, *Z. Physik* **216**, 115 (1968).
12. A. F. Corley and R. W. Joyner, *J. Electr. Spectroscopy and Related Phenomena* **16**, 1 (1979).
13. P. Schattschneider, F. Foedermayer, and D. S. Su, *Scanning Microscopy*, Suppl. 2, 255 (1988).
14. P. Livius, T. Aton, and S. E. Schnatterly, *Phys. Rev. B* **38**, 5511 (1989).
15. J. Fink, T. Müller-Heinzerling, J. Pflüger, B. Scheerer, B. Dischler, P. Koidl, A. Bubenzer, and R. E. Sah, *Phys. Rev. B* **30**, 4713 (1984).
16. J. J. Ritsko, G. Crecelius, and J. Fink, *Phys. Rev. B* **27**, 4902 (1983).
17. J. Fink, B. Scheerer, M. Stamm, B. Thicke, B. Kanellakopulos, and E. Dornberger, *Phys. Rev. B* **30**, 4867 (1984).
18. J. Fink, B. Scheerer, W. Wernet, M. Monkenbusch, G. Wegner, H.-J. Freund, and H. Gonska, *Phys. Rev. B* **34**, 1101 (1986).
19. J. Fink and G. Leising, *Phys. Rev. B* **34**, 5320 (1986).
20. J. Fink, *Synth. Metals* **21**, 87 (1987).
21. H. Fritzsche, N. Nücker, B. Scheerer, J. Fink, and G. Leising, *Synth. Metals* **28**, D237 (1989).
22. H. Fritzsche, J. Fink, N. Nücker, B. Scheerer, and G. Leising, to be published.
23. T. Müller-Heinzerling, J. Fink, and W. Weber, *Phys. Rev. B* **32**, 1850 (1985).
24. J. Fink, J. Pflüger, T. Müller-Heinzerling, N. Nücker, B. Scheerer, H. Romberg, M. Alexander, R. Manzke, T. Buslaps, R. Claessen, and M. Skibowski, Proc. of the Internat. Conf. of Materials Science and Technology, July 4–16, 1989. To be published in "Earlier and Recent Aspects of Superconductivity," (K. A. Müller and G. Bednorz, eds.), Springer Series in Solid-State Science, Springer, Berlin (1990).
25. N. Nücker, H. Romberg, S. Nakai, B. Scheerer, J. Fink, Y. F. Yan, and Z. X. Zhao, *Phys. Rev. B* **39**, 12379 (1989).
26. H. Romberg, N. Nücker, J. Fink, T. Wolf, X. X. Xi, B. Koch, H. P. Geserich, M. Durrler, W. Assmus, and B. Gegenheimer, *Z. Phys.*, submitted.
27. D. W. Lynch, C. G. Olsen, and D. J. Peterman, *Phys. Rev. B* **22**, 3991 (1980).
28. R. Lye, E. M. Logothetis, *Phys. Rev.* **147**, 622 (1966).

29. J. F. Alward, C. Y. Fong, M. El-Batanouny, and F. Wooten, *Phys. Rev. B* **12**, 1105 (1974).
30. A. Neckel, *Int. J. Quantum Chem.* **23**, 1317 (1983).
31. W. Y. Liang and A. R. Beal, *J. Phys. C* **9**, 2823 (1976).
32. J. A. Appelbaum and D. R. Hamann, in "Proc. of the Internat. Conf. on the Physics of Transition Metals, Toronto 1977," (M. J. G. Lee, J. M. Perz, E. Fawcett, eds.), IOP, London, 111 (1978).
33. J. Rivory, J. M. Behaghel, S. Berthier, and J. Lafait, *Thin Solid Films* **78**, 161 (1981).
34. A. Schlegel, P. Wachter, J. J. Nicke, and H. Lingh, *J. Phys. C* **10**, 4889 (1977).
35. B. Karlsson, J.-E. Sundgren, and B.-O. Johansson, *Thin Solid Films* **87**, 181 (1982).

Chapter 14

Optical Parameters for the Materials in *HOC I* and *HOC II*

EDWARD D. PALIK
Institute for Physical Science and Technology
University of Maryland
College Park, Maryland

I. Introduction 313
II. The Parameters 313
References 334

INTRODUCTION I

We have collected several optical parameters that are useful in characterizing the materials in *HOC I* and *HOC II*. Some of these parameters were obtained directly from the critiques; others were found in references given in the critiques; still others were found in other references, in review articles, and in other general references such as handbooks. Some of these articles, review articles, and handbook articles are listed in the references [1–11]. Especially useful has been Ref. [4]. It was not feasible to list the many specific original references for each material, although a few have been included as Refs. [13–35].

THE PARAMETERS II

The column headings in Table I are as follows:

(1) *Chemical formula of material.*

(2) *Most common crystallographic form of the material at room temperature.* The materials fall into many of the 32 point groups (crystal classes) and the 14 Bravais lattice classifications shown in Fig. 1.

(3) and (4) *The space group in the X-ray and spectroscopic notation.*

Copyright © 1991 by Academic Press.
All rights of reproduction in any form reserved.
ISBN 0-12-544422-2

(5) *The dimensions of the unit cell.* This will include an angle when it is not 90°. Figure 1 will suggest if the angle is not 90°.

(6) The number of molecular units in the unit cell.

(7) *The number of molecular units in the primitive (Bravais) cell.* This number is important in determining the total number of optic modes, $3N$-3, where N is the number of atoms in the primitive cell. We will generally use the term *optic* mode to rhyme with *acoustic* mode.

(8) *The irreducible representation.* Each term designates one of the

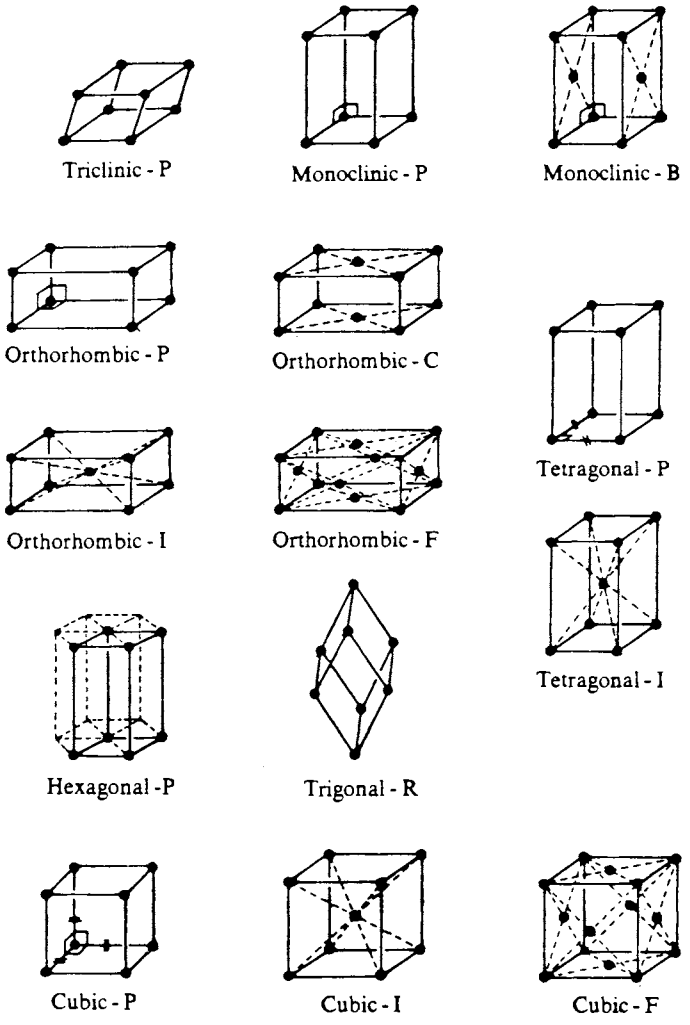

Fig. 1. The unit cell for each of the 14 Bravais lattices (from Burns and Glazer [5], copyright 1978, Academic Press).

types of optic modes allowed; IR, R, and O represent infrared, Raman, and silent activity. A and B have single degeneracy, E has double degeneracy, and F has triple degeneracy. In most cases subscripts u and g specify IR and R activity, respectively. The three acoustic modes have already been subtracted off.

(9) *Total number of optic modes in the crystal as obtained from* $3N$-3 *or from examination of the irreducible representation.*

(10) *Transverse optic* (TO) *phonon frequencies with their species and ordinary (o)/extraordinary (e) designations.* Generally, group-theory analysis is done on the basis of the symmetry transformation properties of the e_x, e_y, and e_z displacements of the atoms from their equilibrium positions. The members of the irreducible representation that are IR-active are associated with the transverse optic phonons with displacements in the x, y, z directions, but the directions of propagation are not necessarily specified.

(11) *Longitudinal optic* (LO) *phonon frequencies with their species and ordinary (o)/extraordinary (e) designations.* The radiation electric field is $\|$ to the optic axis (e) or $\perp$ to the optic axis (o). In the irreducible representation for a cubic material, we can associate any particular IR term (F, for example) with two TO modes and one LO mode, thinking of them as propagating in the same direction as the direction of the EM wave with which we measure them. This suggests that the LO mode should be IR active. But it does not produce absorption, except in a special case of a thin sample measured at nonnormal incidence with p-polarization [12]. In this case the component of E$\perp$ to the film can drive (couple to) the long-wavelength LO phonons (propagating $\perp$ to the film surface), and an absorption line appears. This is related to the fact that the dipole matrix element for LO phonons in bulk materials is zero, although the mode (or rather its displacement direction) is IR-active. The activity becomes apparent in the nonnormal-incidence case. For nonpolar crystals such as Si, all three modes are degenerate, IR-inactive and R-active. For polar cubic crystals such as GaAs, the LO mode is raised slightly in frequency above the two still-degenerate TO modes; the two TO and one LO modes are IR-active and R-active, also. (Notice that the LO mode is not seen directly in IR as an absorption line for the reasons discussed above.)

For some simple cubic crystals, large anharmonic effects produce multiple structure in the reststrahlen spectrum above TO, which precludes a Lorentz-oscillator fit and obscures the LO frequency. We can still choose the $n = k$ wavelength farthest above TO (but not to the band gap yet) as the definition of LO and list this number in parentheses in Table I. Otherwise, the LO frequency is directly obtained from a simple Lorentz-oscillator fit (where $n = k$) or from Raman measurement (if selection rules permit). In studying the literature, we have found that values of TO and LO from R and IR data often vary by 5 cm^{-1} from lab to lab. This is disquieting, suggesting poor spectroscopic calibration for R and IR experiments and/or

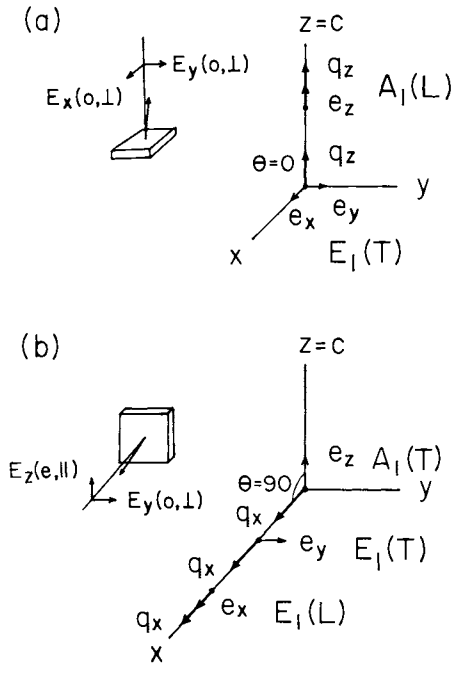

Fig. 2. (a) Wave vector q_z for a transverse optic mode $E_1(T)$ with its accompanying lattice displacement e_x and e_y; and wave vector q_z for a longitudinal optic mode $A_1(L)$ and its accompanying lattice displacement e_z. The inset shows the sample with $E_x(o, \perp)$ and $E_y(o, \perp)$ electric fields. Direction of phonon propagation is parallel to the $z=c$ optic axis for $\theta=0$. (b) Wave vector q_x for a transverse optic mode $A_1(T)$ with its accompanying lattice displacement e_z; wave vector q_x for a transverse optic mode $E_1(T)$ with its lattice displacement e_y; wave vector q_x for a longitudinal optic mode $E_1(L)$ with its lattice displacement e_x. The inset shows the sample with E_x $(e, \|)$ and $Ey(o, \perp)$ electric fields. Direction of phonon propagation is perpendicular to the $z=c$ axis for $\theta=90°$.

poor material or poor model analysis for IR. It is not obvious that recent data are calibrated any better than older data.

For a uniaxial crystal (all noncubic crystals in Table I are uniaxial except for As_2S_3, As_2Se_3, ThF_4 and CuO), the situation is more complicated. For wurtzite structure for phonon wave vector $q(z)$ parallel to the $z=c$ optic axis ($\theta=0$), the degenerate TO modes ($E_1(T)$, lattice displacement $e\|x, \|y$) and the LO mode ($A_1(L)$, lattice displacement $e\|z$) appear in the Raman experiment when the appropriate polarizations for incident and scattered light are used. They also appear in the IR experiment with the proper polarization (Fig. 2a). They are designated as $E_1(T)$, $E_1(T)$ and $A_1(L)$. For phonon wave vector $q(x)$ perpendicular to the $z=c$ axis ($\theta=90°$), the nondegenerate TO mode ($E_1(T)$, $e\|y$) and the LO mode ($E_1(L)$, $e\|x$) can

appear in R, as well as the TO mode ($A_1(T)$, $e\|z$). They also appear in the IR experiment with the proper polarization (Fig. 2b). They are designated as $E_1(L)$, $E_1(T)$, $A_1(T)$. A number of uniaxial materials have been studied for wave vectors varying from $\theta = 0$ to $\theta = 90°$. Such a measurement reveals how the modes shift in frequency and symmetry as the direction of phonon propagation changes. In the Tables a–p accompanying Table I, we have tried to indicate this behavior by listing the TO and LO frequencies of each symmetry for $\theta = 0$ and $\theta = 90°$. An arrow then indicates how a given mode shifts in frequency and symmetry as the direction of propagation changes. This is relatively simple for wurtzite crystals but complicated for x-SiO_2, for example. Luckily, most wurtzite crystals have small force-constant anisotropies for directions of vibration $\|$ and $\perp$ to the c axis, and the symmetry-species designations in Table d hold. For large force-constant anisotropies, the assignment of symmetry species can be quite different. This hinges on whether as the **q** vector is "tipped" from $\theta = 0$ to $\theta = 90°$, the lattice displacement can also "tip," or remains along the same direction.

Modes only R-active or O-silent are listed at the bottom of the TO column (they do not affect the optical constants). These are often TO modes not accompanied by an LO mode (as are the polar modes discussed above), but LO modes are often Raman-active, also.

If the modes are both R- and IR-active, the pertinent reststrahlen reflection spectrum can be "constructed" approximately from the TO and LO frequencies (and their line widths) determined from Raman scattering. For wurtzite crystals, the $\theta = 0$, $E_1(T)$ mode has an accompanying $\theta = 90°$, $E_1(L)$ mode forming the reststrahlen peak for the $E \perp c$ ordinary-ray polarization with sample plane $\perp c$. This LO mode is to the right and one line down from the TO mode in the Table d listing. Of course, an $E \perp c$ spectrum can also be obtained from a sample cut with the c axis in the plane of the sample. Such a sample then allows the $E\|c$ spectrum to be measured, also. Now the $\theta = 90°$, $A_1(T)\|$ mode has an accompanying $\theta = 0$, $A_1(L)\|$ mode (one column to the right and one row down) forming the reststrahlen peak for the $E\|c$ extraordinary-ray polarization. Thus, a Lorentz-model analysis of the reflection spectrum gives $A_1(T)\|$ with $e\|z$ (direction of vibration of the transverse mode) and $A_1(L)\|$ with $e\|z$ (now the direction of vibration of the longitudinal mode). Of course, no absorption line is seen at ω_L where $\varepsilon_1 = n^2 - k^2 = 0$. By and large, independent measurements of R and IR spectra in various labs give results in agreement within $10\,cm^{-1}$. This again indicates the wide variations in measured frequencies from lab to lab.

In more complicated systems such as x-SiO_2 (Table m) for the pairs of T and L modes, the L mode is adjacent to the T mode on the same line or the L mode is one line down, depending on the pairing scheme.

Some types of uniaxial crystals have not been studied in detail by Raman scattering for wave vectors varying from $\theta = 0$ to $\theta = 90°$, perhaps because

TABLE I

Collected Optical Parameters

Material	Crystal structure	Space group		Unit cell dimensions (Å)	Molecular units per Unit cell	Molecular units per Primative cell	No. of optic modes	Total irreducible representation	ω_T (cm^{-1})	ω_L (cm^{-1})	ω_P Drude (eV)	$n=k$ (eV)	E_g (eV)	ε_0
Cu	fcc	Fm3m	O_h^5	3.6149	4	1	0	None	None	None	7.4	8.0	None	−65000
Au				4.0782							9.0	5.5		−110000
Ir				3.8394								7.8		
												20.5		
Ni				3.5238							4.9	9.4		−13000
Pt				3.9231							5.1	6.1		−5500
												19.6		
												24.9		
Rh				3.8031								8.5		
Ag				4.0862							3.8	3.8		−250000
											9.0	4.8		
												7.3		
Al				4.0495							14.8	15		−34000
Pd				3.8898							5.5	7.7		−150000
PbS	cubic NaCl	Fm3m	O_h^5	5.936	4	1	3	F_{1u}(IR)	71 IR	212		3.25	0.41(d)	169
												14		
PbSe				6.124					39	111		2.5	0.278(d)	210
												7.0		
PbTe				6.46					32	112		1.7	0.31(d)	414
												9		
SnTe				6.313								1.7	0.19(d)	1770
												5.5		
												12.0		
												12.4		
NaCl				5.64					164	(266)		----	8.6	5.90
KCl				6.2929					142	(213)		7.8	8.5	4.4
												9.45		
												9.75		
												12.6		
LiF				4.0263					307	501		12.8	14.2(d)	9.06

KBr				6.6000					113	(155)		----	7.8	4.8
NaF				4.620					246	(420)			10.5	~5.7
MgO				4.215					396	729		13.2	7.8(d)	9.8
												13.9		
												17.5		
												21.6		
CaF_2	cubic fluorite	Fm3m	O_h^5	5.4629	4	1	6	$F_{1u}(IR) + F_{2g}(R)$	258 IR 322 R	473		----	~11	6.7
Mo	bcc	Im3m	O_h^9	3.1473	2	1	0	None	None	None	7.5	2.3	None	−21000
												10.4		
W				3.1646							6.4	1.3		−13000
												5.2		
												24.7		
Fe				2.8665							4.1	0.99		−50000
Cr				2.8839								1.51		
												9.05		
												10.3		
Nb				3.3004								1.32		
												2.43		
												3.32		
												4.38		
												9.76		
												14.6		
												19.1		
K				5.2							4.25	3.8		
Na				4.2906							5.91	~5.9		
Li				3.5902								6.66		
Ta				3.3058							6.2	2.04		
												5.27		
												19.9		
V				3.0240							5.2	1.24		−7200
												2.63		
Y_2O_3	bcc	Ia3	T_h^7	10.604	16	8	117	$4A_g(R) + 5A_u(O) + 4E_g(R) + 5E_u(O) + 14F_g(R) + 16F_u(IR)$	See Table a				12.4 14.2	~6	11.4
Si	cubic diamond	Fd3m	O_h^7	5.4307	4	1	3	$F_{2g}(R)$	521 R	521 R		4.22 16.3	1.1(i)	11.6

(continued)

TABLE I (continued)

Collected Optical Parameters

Material	Crystal structure	Space group		Unit cell dimensions (Å)	Molecular units per Unit cell	Molecular units per Primative cell	No. of optic modes	Total irreducible representation	ω_T (cm^{-1})	ω_L (cm^{-1})	ω_P Drude (eV)	$n=k$ (eV)	E_g (eV)	ϵ_σ
Ge				5.6573					301	301		4.14 9.5	0.66(i)	16.0
C				3.5667					1332	1332		11.8 30	5.2(i)	5.6
Al_2MgO_4	cubic	Fd3m	Oh^7	8.0800	8	2	39	$A_{1g}(R) + 2A_{2u}(O) + Eg(R) + 2Eu(O) + F_{1g}(O) + 4F_{1u}(IR) + 3F_{2g}(R) + 2F_{2u}(O)$	See Table b					~8	8.29
ZnS	cubic zincblende	$F\bar{4}3m$	Td^2	5.4093	4	1	3	$F_2(R, IR)$	279 IR, R	351 R		7 15	3.68(d)	8.35
ZnSe				5.6676					206	252			2.83(d)	9.0
ZnTe				6.089					179	206		4.96	2.3(d)	9.8
CdTe				6.480					141	169			1.5(d)	10.2
GaAs				5.6535					269	292		4.7 10.7	1.42(d)	13.0
GaP				5.4506					367	403		5.0 13.5	2.27(i)	11.1
InAs				6.0585					218	240		4.47 11.9	0.35(d)	14.1
InSb				6.4782					179	190		3.82 9.5	0.18(d)	17.7
InP				5.8688					304	345		4.73 14.3	1.34(d)	12.4
SiC β				4.348					796	972			2.86	9.72
GaSb				6.118					227	237			0.75	15.7
AlSb				6.1347					318	340			1.61(i)	11.2
AlAs				5.62					362	404		4.7	2.15(i)	10.06
HgTe				6.460					116	139			0	
CsI	cubic CsCl	Pm3m	O_h^1	4.5667	1	1	3	$F_{1u}(IR)$	62 IR	93		----	6.4(d)	6.54

$SrTiO_3$	cubic perovskite	Pm3m	O_h^1	3.9051	1	1	12	$3F_{1u}(IR) + F_{2u}(IR)$	See Table c			26.4 28.8	3.4	311
Cu_2O	cubic	Pn3m	O_h^1	4.2696	2	2	15	$A_{2u}(O) + E_u(O) + F_{2u}(O) +$ $2F_{1u}(IR) + F_{2g}(R)$	613 IR 146 IR 110 R E_u 300 R A_{2u}	638 149			2.17(d)	~7.5
$Al_{23}O_{27}N_5$	cubic			7.948										
ZnS	hexagonal wurzite	$P6_3mc$	C_{6v}^4	a = 3.811 c = 6.234	2	2	9	$A_1(R, IR\|) + 2B_1(O) +$ $E_1(R, IR\perp) + 2E_2(R)$	See Table d			× × × ×	3.91	
CdS				a = 4.1348 c = 6.7490								× × × ×	2.55(d)	9.6(o) 10.7(e)
CdSe				a = 4.2999 c = 7.0109									1.75(d)	9.29(o) 10.16(e)
BeO				a = 2.698 c = 4.380									9.4	6.94(o) 7.65(e)
SiC 6H, αII				a = 3.076 c = 5.048								7.45 21.7	3.1	9.7(o) 10.0(e)
Os	hcp	$P6_3/mmc$	D_{6h}^4	a = 2.7352 c = 4.3190	2	2	3	$A_{1u}(O) + E_{2g}(R)$				9.6 17.5	None	
Co				a = 2.5071 c = 4.0686							4.0	7.75		− 12000
Be				a = 2.2866 c = 3.5833					463 R					
C graphite	hexagonal	$P6_3/mmc$	D_{6h}^4	2.456 6.696	4	4	9	$2B_{2g}(O) + A_{2u}(IR\|) +$ $E_1(IR\perp) + 2E_{2g}(R)$	See Table e			4.5(o) 6.8(o) 14.4(o) 25.0(o) 6.85(e) 25(e)		5.7(e)
TiO_2	tetragonal SnO_2	$P4_2/mnm$	D_{4h}^{14}	a = 4.5937 c = 2.9581	2	2	15	$A_{1g}(R) + A_{2g}(O) + 2A_{2u}(IR\|) +$ $B_{1g}(R) + 2B_{1u}(O) + B_{2g}(R) +$ $E_g(R) + 3E_u(IR\perp) +$	See Table f			6.5(o) 7.3(o) 4.3(e)	3.06(d,o) 4.3(d, e)	83.7(o) 165(e)

(*continued*)

TABLE I (continued)

Collected Optical Parameters

Material	Crystal structure	Space group		Unit cell dimensions (Å)	Molecular units per Unit cell	Molecular units per Primative cell	No. of optic modes	Total irreducible representation	ω_T (cm^{-1})	ω_L (cm^{-1})	ω_P Drude (eV)	$n=k$ (eV)	E_g (eV)	ϵ_0
MgF_2				a = 4.623 c = 3.052								----	11	5.47(o) 4.62(e)
$BaTiO_3$	tetragonal	P4mm	C_{4v}^1	a = 3.9920 c = 4.0361	1	1	12	$3A_1(R, IR\|) + B_1(R) + 4E(R, IR\perp)$	See Table g			22.1 25.4	~3.5	31.5(e)
KH_2PO_4	tetragonal	$I\bar{4}2d$	D_{2d}^{12} V_d^{12}	a = 7.448 c = 6.977	4	2	45	$4A_1(R) + 5A_2(O) + 6B_1(R) +$ $6B_2(R, IR\|) + 12E(R, IR\perp)$	See Table h				4.96	~44(o) ~21(e)
$NH_4H_2PO_4$	tetragonal	$I\bar{4}2d$	D_{2d}^{12} V_d^{12}	a = 7.510 c = 7.564	4	2	69	$7A_1(R) + 7A_2(O) + 9B_1(R) +$ $8B_2(R, IR\|) + 19E(R, IR\perp)$	See Table i				9.92	~56(o) ~15(e)
$LiNbO_3$	trigonal	R3c	C_{3v}^6	a = 5.47 $\alpha = 55°43'$	2	2	27	$4A_1(R, IR\|) + 5A_2(O) + 9E(R, IR\perp)$	See Table j				~4.2	43.7(o) 25.6(e)
Al_2O_3	trigonal	$R\bar{3}c$	D_{3d}^6	a = 5.128 $\alpha = 55°20'$	2	2	27	$2A_{1g}(R) + 3A_{2g}(O) + 2A_{1u}(O) +$ $2A_{2u}(IR\|) + 5E_g(R) + 4E_u(IR\perp)$	See Table k			----	8.3	9.49(o) 11.4(e)
Se	trigonal	$P3_121$	$_1D_3^4$	a = 4.3551 c = 4.9494	3	3	6	$A_1(R) + A_2(IR\|) + 2E(R, IR\perp)$	See Table l				~1.6(i)	7.40(o) 12.2(e)
Te		$P3_221$	$_1D_3^6$	a = 4.4469 c = 5.9149								2.5(o) 4.5(o) 2.0(e) 5.0(e)	0.33(d)	30(o) 43(e)
SiO_2	trigonal	$P3_121$	$_1D_3^4$	a = 4.9130 c = 5.4046	3	3	24	$4A_1(R) + 4A_2(IR\|) + 8E(R, IR\perp)$	See Table m			----	~9	4.41(o) 4.62(e)
As_2S_3	monoclinic (unit cell)	$P2_1/b,c$	C_{2h}^5	a = 11.475 b = 9.577 c = 4.256 $\beta = 90°41'$	4	4	57	$15A_g(R) + 15B_g(R) +$ $14A_u(IR) + 13B_u(IR)$	See Table n				2.43(a, d) 2.45(c, d)	15.2(a) 6.25(b) 13.0(c)

As_2Se_3	orthorhombic (layer)	$Pnm2_1$	C_{2v}^7	a = 12.053 b = 9.890 c = 4.277 $\beta = 90°28'$	2	2	27	$7A_1(R, IRc) + 6B_2(R, IRa) + 7A_2(R) + 7B_1(R, IRb)$			~2	14.4(a) 13.0(c)
CuO	monoclinic	B2/b C2/c	C_{2h}^6	a = 4.6837 b = 3.4226 C = 5.1288 $\beta = 99°29'$	4	2	9	$A_g(R) + 3A_u(IR) + 2B_g(R) + 3B_u(IR)$	See Table o		~1.3i	
ThF_4	monoclinic	B2/b	C_{2h}^6	a = 12.90 b = 10.93 c = 8.58 $\beta = 126.4°$	12	6	87					
$(CH_2)_n$	orthorhombic	Pnam	V_h^{16} D_{2h}^{16}	a = 7.40 b = 4.93 c = 2.534	4	4	33	$6A_g(R) + 3A_u(O) + 3B_{1g}(R) + 5B_{1u}(IRc) + 3B_{2g}(R) + 5B_{2u}(IRb) + 6B_{3g}(R) + 2B_{3u}(IRa)$	See Table p			2.29(b) 2.32(c)
(AlGaAs) (HgCdTe) (PbSnTe) (Ge-Si)	alloy											
(a-Si)	amorphous									3.9	1.77	13.7
(a-SiO_2)									469 800 1094		~9	3.8
(a-SiO)									1020		~6	4.0
(a-Si_3N_4)												3.6
(a-As_2S_3)												7.45
(a-As_2Se_3)												9.0
(a-ThF_4)												
(a-C:H)												
Hg	liquid											
H_2O												78.3

TABLE a

Y_2O_3

F_{1u}(T)(IR)	F_{1u}(L)(IR)
120	121
172	173
182	183
241	242
303	315
335	359
371	412
415	456
461	486
490	535
555	620

331 E_g (R)
431 F_g
469 F_g
595 F_g
830 E_g
948 E_g
1184 A_g

TABLE b

Al_2MgO_4

F_{1u}(T)(IR)	F_{1u}(L)(IR)
307	311
482	497
675	800

311 F_{2g} (R)
492 F_{2g}
611 F_{2g}
410 E_g
772 A_{1g}

TABLE c

$SrTiO_3$

F_{1u}(T)(IR)	F_{1u}(L)(IR)
88	173
178	473
544	804

No (R)

TABLE d

ZnS [2]

$\theta = 0$	90°	90°	0
$E_1(T)(R, IR \perp)$	$E_1(L)(R, IR \perp)$	$A_1(T)(R, IR\|\|)$	$A_1(L)(R, IR\|\|)$
274 →		→ 274	
	352 ←		← 352

55 E_2 (R)
280 E_2

CdS [2]

243 →		→ 234	
	307 ←		← 305

43 E_2 (R)
170 B_1 (O)
256 E_2 (R)

CdSe [2]

171 →		→ 165	
	←		← 208

34 E_2 (R)

BeO [2]

722 →		→ 678	
	1095 ←		← 1085

340 E_2 (R)
684 E_2

SiC (6H): Because of polytype structure, the 6H crystal stacks up in 6-atomic-layer sequences. See Ref. [28] for complicated Raman spectrum due to effective zone folding.

794 →		→ 785	
	~970 ←		← 970

TABLE e

C Graphite [21]

$\theta = 0$	90°	90°	0
$E_{1u}(T)(IR \perp)$	$E_{1u}(L)(IR \perp)$	$A_{2u}(T)(IR\|\|)$	$A_{2u}(L)(IR\|\|)$
1587.0	1587.5	867.8	868.1

42 E_{2g} (R)
127 B_{2g} (O)
1575 E_{2g} (R)

TABLE f

TiO_2 [2, 20]

$\theta = 0$	90°	90°	0
$E_u(T)(IR \perp)$	$E_u(L)(IR \perp)$	$A_{2u}(T)(IR\|\|)$	$A_{2u}(L)(IR\|\|)$
183	373	167	811
388	458		
500	806		

113 B_{1u} (O)
143 B_{1g} (R)
447 E_g (R)
612 A_{1g} (R)
653 A_{2g} (O)
826 B_{2g} (R)

MgF_2 [2,20]

247	303	399	625
410	415		
450	617		

92 B_{1g} (R)
295 E_g (R)
326 A_{2g} (O)
410 A_{1g} (R)
515 B_{2g} (R)

TABLE g

$BaTiO_3$ [14]

$\theta = 0$	90°	90°	0
E(T)(R, IR ⊥)	E(L)(R, IR ⊥)	A_1(T)(R, IR‖)	A_1(L)(R, IR‖)
38 →	→	→ 179	
180 →	→ 180		
		276 ←	← 189
308 →	→ 308		
	466 ←	←	← 471
498 →	→	→ 515	
	722 ←	←	← 725
305B_1 (R)			

TABLE h

KH_2PO_4; R and IR Values from Three References for Comparison

A_1 (R)		B_1 (R)		B_2 (R)		(IR‖)		E(R)		(IR ⊥)	
[29]	[30]	[29]	[30]	[29]	[30]	[30]	[31]	[29]	[30]	[30]	[31]
360	365	156	155	80	100	60	52	75		86	90
514		479	473	174	183	178	185	95	96	102	106
918	918	570	540	*				113	116	122	123
										152	152
2700		1366		386				190	192	206	200
		1806		510			470	320			
		2390		1350				490			
								530	533	526	540
								568			
								960			
								1145			
								*			
								1325			

Above the Curie temperature (123 K), the crystal is paraelectric (tetragonal); below T_c, it is ferroelectric (orthorhombic).

TABLE i

$NH_4H_2PO_4$; R and IR Values from Two References for Comparison

A_1 (R)		B_1 (R)		B_2 (R)		(IR‖)	E(R)	(IR ⊥)	
[29]	[30]	[29]	[30]	[29]	[30]	[30]	[29]	[30]	[30]
337	341	178	182	80	100	76	100	68	51
									70
520		474	476	185	204	198	120	125	
								140	150
918	922	541		*			172	175	164
2700		1298		397	401	450	268		
		1750		547			390		350
		2370		1320			470		
							538	542	540
							568		
							960		
							1106		
							*		
							1338		

Above the Curie temperature (148K), the crystal is paraelectric (tetragonal); below T_c, it is antiferroelectric (orthorhombic).

TABLE j

$LiNbO_3$[18]

$\theta = 0$	90°	90°	0
E(T)(R, IR ⊥)	E(L)(R, IR ⊥)	A_1(T)(R, IR‖)	A_1(L)(R, IR‖)
155 →	→ 198		
238 →	→ 243		
265 →		→ 255	
		276 ←	← 275
325 →	→ 295		
		334 ←	← 333
371 →	→ 371		
431 →	→ 428		
	454 ←		← 436
582 →		→ 633	
668 →	→ 668		
743 →	→ 739		
	880 ←		← 876

TABLE k

Al_2O_3 [22]

$\theta = 0$	90°	90°	0
$E_u(T)(IR \perp)$	$E_u(L)(IR \perp)$	$A_{2u}(T)(IR\|)$	$A_{2u}(L)(IR\|)$
385 442 569 635	388 480 625 900	400 583	512 871

378 E_g (R)
418 A_{1g}
432 E_g
451 E_g
578 E_g
645 A_{1g}
751 E_g

TABLE l

Se [2, 23]

$\theta = 0$	90°	90°	0
$E(T)(R, IR \perp)$	$E(L)(R, IR \perp)$	$A_2(T)(IR\|)$	$A_2(L)(IR\|)$
144 225	150 225	102	106

237 A_1 (R)

Te

92 144	106 145	90	96

120 A_1 (R)

TABLE m

SiO_2 [17]

$\theta = 0$	90°	90°	0
E(T)(R, IR ⊥)	E(L)(R, IR ⊥)	A_2(T)(IR∥)	A_2(L)(IR∥)
127 →	129		
265 →	270		
		364 ←	387
394 →	403		
450 →		489	
	510 ←		547
697 →	699		
		777 ←	789
796 →	809		
1076 →		1080	
1161 →	1161		
	1236 ←		1240

207 A_1 (R)
356 A_1
464 A_1
1085 A_1

TABLE n

As_2S_3; The Layer Symmetry Properties Dominate the *R* and IR Spectra [27]

E∥a		E∥b		E∥c	
T	L	T	L	T	L
182	189	186		140	148
246		386	392	159	165
279				185	189
293	328			201	203
348	354			260	
354	369			278	
369	370			307	326
384	390			355	368
				385	390
As_2Se_3					
106	108			94	97
132	134			105	108
201	209			132	136
224	238			217	232
249				248	250
				268	

TABLE o

CuO: Spectra Were Not Necessarily Obtained for *E*-field Polarization (IR) and/or Wave Vector (*R*) Parallel to the *a*, *b*, *c* Axes [25]

A_u(T)(IR)	(L)	B_u(T)(IR)	(L)
164	165	145	147
355		480	593
(421)		603	624

296 A_g (R)
346 B_g
636 B_g

TABLE p

$(CH_2)n$: The Formula for Polyethylene Is Designated by the Molecular Unit CH_2, Four of Which Are in the Unit Cell and in the Primitive Cell

	(IR)		(R)
Translation *x*	0 B_{3u}	Libration	101 B_{3g}
Translation *y*	0 B_{2u}	Libration	141 A_g
Translation *z*	0 B_{1u}	Optical skeletal	1066 B_{1g}
Translatory	86 B_{1u}	Optical skeletal	1070 B_{2g}
Translatory	109 B_{2u}	Optical skeletal	1137 B_{3g}
CH_2 rocking	721 B_{2u}	Optical skeletal	1138 A_g
CH_2 rocking	736 B_{1u}	CH_2 rocking	1175 A_g
CH_2 twisting	1043 B_{3u}	CH_2 rocking	1176 B_{3g}
CH_2 wagging	1177 B_{3u}	CH_2 twisting	1293 B_{2g}
CH_2 scissors	1472 B_{2u}	CH_2 twisting	1297 B_{1g}
CH_2scissors	1478 B_{1u}	CH_2 wagging	1371 B_{1g}
C-H sym stretch	2851 B_{1u}	CH_2 wagging	1373 B_{2g}
C-H sym stretch	2853 B_{2u}	CH_2 scissors	1445 A_g
C-H asym stretch	2921 B_{1u}	CH_2 scissors	1458 B_{3g}
C-H asym stretch	2922 B_{2u}	C-H sym stretch	2850 B_{3g}
		C-H sym stretch	2855 A_g
	(O)	C-H asym stretch	2885 A_g
Translatory	55 A_u	C-H asym stretch	2889 B_{3g}
CH_2 twisting	1041 A_u		
CH_2 wagging	1181 A_u		

These calculated frequencies are usually within 5 cm^{-1} of the observed frequencies. The translation modes (acoustic phonons) $B_{3u} + B_{2u} + B_{1u}$ are included in this example but not in the irreducible representation. While the acoustic-phonon modes are not IR-active, they are included in the IR column because of the *u* subscript. They should be active in Brillouin scattering, however. Most of the other observed modes in the IR are combination bands of these fundamentals [32–34].

the IR-active modes are not also R-active. In this case we state only the T and L modes omitting the arrows.

It is interesting to note the differences in R and IR experiments. Raman measurements are very specific as to which phonon mode is being measured because of the constraints on wave vector and energy. Infrared measurements do not have the constraint of wave-vector conservation. Therefore, for the configuration of Fig. 2b, many TO phonons traveling in many directions in the x, y plane (and for that matter, other directions having a component of dipole moment $\|E$) contribute to the absorption line seen for $E\|c$ (they may not all have the same frequency). The imaginary part of the IR transverse dielectric function ($\varepsilon_2 = 2nk$) has a peak at ω_T. The real part of the transverse dielectric function ($\varepsilon_1 = n^2 - k^2$) usually has a zero very near here, and it usually has a second zero above ω_T at ω_L. This zero is presumably at the frequency of the LO phonon propagating $\|c$.

If the unit cell has a center of symmetry, modes are mutually exclusive; an R-active mode is not also IR-active and vice versa.

In the optic frequency Tables a–p, a notation such as $E(L)(\text{IR}\perp)$, $A(L)(\text{IR}\|)$ indicates that the E and A modes are IR-active (their transverse members are seen; the longitudinal members are not seen because of dipole-moment, matrix-element considerations, but we can obtain their values from an oscillator fit of the reststrahlen reflectivity by finding where $\varepsilon_1 = 0$).

(12) and (13) *Plasma frequency.* Metals have plasma frequencies typically in the VIS–UV because of their large free-carrier (usually electron) densities (10^{22}–$10^{23}\,\text{cm}^{-1}$). Since semiconductors can be doped with controlled amounts of impurities, their free-carrier plasma frequencies can be varied. We therefore omit this parameter for semiconductors. The Drude plasma frequency ω_P^2 (rad/s) is given by the formula $\omega_P^2 = 4\pi Ne^2/m^*\varepsilon$ with N in cm^{-3}; $e = 4.77 \times 10^{-10}$ esu; m^* is the effective mass compared to the free-electron mass of 9.10×10^{-28} gm; ε is the background lattice dielectric constant at the plasma frequency. The values of ω_P for a given material obtained from different laboratories often vary by tens of percent, so we use the fewest possible number of significant figures, namely two. A polariton composed of a coupled EM wave and the plasmon can exist in the region where ε_1 is negative (from 0 to ω_P) and is measurable by a total internal reflection technique in ω–q space, where q is the polariton wave vector.

Three ways of determining ω_P are fitting the reflectivity with a Drude model; measuring the energy loss of an electron beam passing through a thin layer; and determining where the real part of the dielectric function is zero ($\varepsilon_1 = n^2 - k^2 = 0$). This last criterion is easy to determine for the metals in the Tables in *HOC I* and *HOC II*. When interband absorption effects are small, n crosses k at only one point in the VIS–UV and this point often agrees with a Drude-model fit (which ignores interband effects). However,

for some metals, $n = k$ occurs at two, three, or four wavelengths, and the definition is obscured. This is usually due to strong interband transitions giving strong absorption/dispersion effects.

For metals, semiconductors, and insulators the valence (bound) electrons also produce a plasma effect in the interband region usually at a frequency higher than the free-electron plasma frequency for a metal. For a metal the first zero should locate the free-electron plasma frequency and the third should locate the valence plasma frequency. Between the second and third zeros, ε_1 is negative and a valence plasma polariton should be definable just as a free-electron plasma polariton in ω–q space is definable from 0 to ω_P. Ideally for a semiconductor or insulator, this valence plasma frequency is at the second zero (above the band gap). The polariton mode is confined between the first and second zeros in ε_1 above the band gap in the spectral region where ε_1 is negative. These frequencies are listed in the $n = k$ column, although with overlapping interband effects, the valence plasma frequency may not be pinpointed by the second zero (higher-energy zero) of each pair of zeros. In Table I, in the $n = k$ column for some of the materials, there is no crossing (dashed line); in other cases there are two sets of data that differ, and the crossing cannot be pinpointed (crosses); in still other cases, no data are available in the interband region, and the space is left blank.

In addition to a phonon resonance producing a zero in ε_1 very close to ω_T for a semiconductor and insulator, the zero somewhat above the resonance allows a longitudinal mode to exist: ω_L, for example. This idea is straightforward for lattice vibrations. It also holds for the free-carriers in metals and doped semiconductors, which have a resonant frequency at $\omega = 0$ and an ω_P (a longitudinal propagating plasmon) at $\varepsilon_1 = 0$. However, the interband region (especially at the second of each pair of zeros) and the nature of the longitudinal mode are not so clear.

(14) *The fundamental band gap E_g of semiconductors and insulators.* The analysis of the absorption coefficient to extract E_g is model-dependent for indirect (i) and direct (d) energy gaps. In lieu of a model fit, some investigators just define E_g as the point at which the absorption coefficient $\alpha = 4\pi k/\lambda = 100$–$1000\ \mathrm{cm}^{-1}$.

(15) *The dc dielectric constant ε_0.* The real part of ε_0 near $\omega = 0$ for insulators is a positive number, which is straightforwardly determined from low-frequency optical or capacity experiments. However, for doped semiconductors and metals ε_0 tends to large, negative values because of the free-carrier dispersion. According to the Drude model, $\varepsilon = \varepsilon_1 + i\varepsilon_2$ contains components $\varepsilon_1 = \varepsilon_\infty\,[1 - \omega_P^2/(\omega^2 + w_\tau^2)]$ and $\varepsilon_2 = \varepsilon_\infty\,\omega_P^2\,\omega_\tau/\omega(\omega^2 + \omega_\tau^2)$ with $\omega_\tau(s^{-1}) = 1/\tau$, where $\tau(s)$ is the free-carrier lifetime and ω_τ is the damping constant. However, ε_2 approaches infinity as $\omega \to 0$. To escape this "dilemma," we can switch our attention to the real part of the electrical conductivity. Since $\sigma = -i\varepsilon\omega/4\pi$, then $\sigma_1 = \varepsilon_2\,\omega/4\pi = \varepsilon_\infty\,\omega_P^2\,\omega_\tau/4\pi(\omega^2 + \omega_\tau^2)$. The dc conductivity is given by $\sigma_0(s^{-1}) = \varepsilon_\infty\,\omega_P^2/4\pi\omega_\tau$, a finite num-

ber. The resistivity $\rho_0(s) = 1/\sigma_0$; $\rho_0(\text{ohm cm}) = 9 \times 10^{11}\ \rho_0(s)$. For metals $\varepsilon_\infty = 1$; for semiconductors $\varepsilon_\infty \simeq 4 - 16$.

We do not include the high-frequency dielectric constant ε_∞. The real part of ε_∞ for a metal is generally taken as unity in the X-ray region. For a semiconductor or insulator it is usually defined in connection with the Lorentz-model fit to reststrahlen reflectivity data; it is the value of ε_1 below the fundamental band gap where ε_1 is nearly a constant before the lattice-vibration dispersion begins to decrease ε_1 significantly.

REFERENCES

1. H. P. R. Frederikse, in "AIP Handbook," (D. E. Gray, ed.), 3rd ed., McGraw-Hill, New York, 9–56 (1972).
2. G. R. Wilkinson, in "Raman Effect," (A. Anderson, ed.), Marcel Dekker, New York, 811 (1973).
3. G. F. Koster, J. O. Dimmock, R. G. Wheeler, and H. Statz, "Properties of the Thirty-Two Point Groups," MIT Press, Cambridge, Mass. (1963).
4. K.-H. Hellewege and D. O. Madelung, eds. "Landolt–Börnstein Numerical Data and Functional Relationships in Science and Technology," Springer-Verlag, New York (1985).
5. G. Burns and A. M. Glazer, "Space Groups for Solid State Scientists," Academic Press, New York (1978).
6. R. W. G. Wyckoff, "Crystal Structures," Vols. 1–4, Interscience, New York, (1965).
7. R. Loudon, *Adv. Phys.* **13**, 423 (1964).
8. W. G. Fateley, F. R. Dollish, N. T. McDevitt, and F. F. Bentley, "Infrared and Raman Selection Rules for Molecular and Lattice Vibrations: The Correlation Method," Wiley-Interscience, New York (1972).
9. H. Poulet and J. P. Mathieu, "Vibration Spectrum and Symmetry of Crystals," Gordon and Breach, Paris (1976).
10. W. Hayes and R. Loudon, "Scattering of Light by Crystals," Wiley-Interscience, New York (1978).
11. S. S. Mitra and S. Nudelman, eds., "Far-Infrared Properties of Solids," Plenum, New York (1970).
12. D. W. Berreman, *Phys. Rev.* **130**, 2193 (1963).
13. R. Dalven, *Infrared Phys.* **9**, 141 (1969); PbS, PbSe, PbTe.
14. A. Scalabrin, A. S. Chaves, D. S. Shin, and S. P. S. Porto, *Phys. Stat. Sol. B* **79**, 731 (1977); $BaTiO_3$.
15. M. A. Ordal, R. J. Bell, R. W. Alexander, Jr., L. L. Long, and M. R. Querry, *Appl. Opt.* **26**, 744 (1987); several metals.
16. J. L. Servoin, R. Gervais, A. M. Quittet and Y. Luspin, *Phys. Rev. B* **21**, 2038 (1980); Ref. [2], p. 872; $SrTiO_3$.
17. S. M. Shapiro and J. D. Axe, *Phys. Rev.* **B6**, 2420 (1972); SiO_2.
18. R. Claus, *Z. Naturforsch.* **27A**, 1187 (1972); $LiNbO_3$.
19. Ref. [7], p. 172; Ref. [2], p. 861; wurzite semiconductors.
20. S. P. S. Porto, P. A. Fleury, and T. C. Damen, *Phys. Rev.* **154**, 522 (1967); Ref. [2], p. 878; TiO_2, MgF_2.
21. F. Tuinstra and J. L. Koenig, *J. Chem. Phys.* **53**, 1126 (1970); graphite.
22. S. P. S. Porto and R. S. Krishnan, *J. Chem. Phys.* **47**, 1009 (1967); Ref. [2], p. 894; Al_2O_3.
23. G. Lucovsky, A. Mooradian, W. Taylor, G. B. Wright, and R. C. Keezer, *Solid State Commun.* **5**, 113 (1967); Ref. [2], p. 851; Se.

24. P. Dawson, M. M. Hargreave, and G. R. Wilkinson, *J. Phys. Chem. Solids* **34**, 2201 (1973); Cu_2O.
25. S. Guha, D. Peebles, and T. J. Wieting, *Bull. Amer. Phys. Soc.* **35**, 293, 782 (1990); *Phys. Rev.* (in press), *Bull. Mater. Sci.* (in press); CuO.
26. Ref. [2], p. 859; Zinc blende semiconductors.
27. R. Zallen, M. L. Slade, and A. T. Ward, *Phys. Rev.* **B3**, 4257 (1971); As_2S_3, As_2Se_3.
28. D. W. Feldman, J. H. Parker, W. J. Choyke, and L. Patrick, *Phys. Rev.* **170**, 698 (1968); *Phys. Rev.* **173**, 787 (1968); SiC.
29. D. K. Agrawal and C. H. Perry, in "Proc. 2nd Inter. Conf. Light Scattering in Solids," (M. Balkanski, ed.), Flammarion, Paris, 429 (1971); KDP, ADP.
30. T. Kawamura and A. Mitsuishi, *Technology Reports, Osaka University* **23**, 365 (1973); KDP, ADP.
31. F. Onyango, W. Smith, and J. F. Angress, *J. Phys. Chem. Solids* **36**, 309 (1975); KDP.
32. J. R. Nielsen and A. H. Wollett, *J. Chem. Phys.* **26**, 1391 (1957); $(CH_2)_n$.
33. R. Zbinden, "Infrared Spectroscopy of High Polymers," Academic Press, New York (1964); $(CH_2)_n$.
34. P. C. Painter, M. M. Coleman, and J. L. Koenig, "The Theory of Vibrational Spectroscopy and its Application to Polymer Materials," Wiley, New York, 1982; $(CH_2)_n$.
35. L. M. Fraas and S. P. S. Porto, *Solid State Commun.* **8**, 803 (1970); Be.

An Introduction to the Data for Several Metals

DAVID W. LYNCH
Department of Physics and Ames Laboratory
Institue for Physical Research and Technology
Iowa State University
Ames, Iowa
and
W. R. HUNTER
SFA, Inc.
Landover, Maryland

INTRODUCTION I

We present data below for several metals: the alkali metals Li, Na, and K, and the transition metals Cr, Fe, Nb, and Ta. There are some other data compilations that it may be useful to consult. Weaver *et al.* [1] present optical data for noble metals, transition metals, lanthanides, actinides, and a few other metals. They present plots that show the agreement, or lack thereof, of data from many investigators. The spectral region covered is usually up to 200 eV or less. Henke *et al.* [2, 3] present calculated atomic scattering factors, and derive an empirical set of data based on experimental results. The spectra range is 10–10,000 eV. Actual data do not exist over most of this range, and some of the data presented were taken on atoms (vapor samples) and some on solids.

REFERENCES

1. J. H. Weaver, C. Krafka, D. W. Lynch, and E.-E. Koch, "Optical Properties of Metals," Parts I and II (Physics Data Series No. 18-1 and 18-2, Fachinformationszentrum Energie Physik Mathematik, Karlsruhe, 1981).
2. B. L. Henke, P. Lee, T. J. Tanaka, R. L. Shimabukuro, and B. K. Fujikawa, *Atomic Data and Nucl. Data Tables* **27**, 1 (1982).
3. B. L. Henke, J. C. Davis, E. M. Gullikson, and R. C. C. Perera, Lawrence Berkeley Laboratory Report No. LBL-26259 (1988).

Copyright © 1991 by Academic Press.
All rights of reproduction in any form reserved.
ISBN 0-12-544422-2

II ALKALI METALS

The alkali metals are the simplest of all metals, and their dielectric functions the simplest and best understood. The nearly-free-electron model should be valid. The Fermi level should lie about in the middle of the lowest conduction band, and the gap between the bands at the zone boundaries should be small. The Fermi surface should be spherical, and all interband optical transitions should occur in a central spherical region of the Brillouin zone. The interband optical properties should be accurately calculable by perturbation theory [1–3]. Indeed this might be the case for all alkali metals except Li. Li has only three electrons per atom, with a $1s^2 2s$ configuration. In a pseudopotential approach, there are no core p electrons to which the 2p part of the valence electrons can be orthogonalized. Consequently, the pseudopotential is not as small as for other alkali metals, and the band gap is larger. The Fermi level then comes closer to the zone boundary, and the Fermi surface is distorted from a sphere. Another view is that the screening of the core potential by the single 2s valence electron of the atom is less effective in Li than by the corresponding electrons in the other alkali metals, and the gap is consequently larger. Thus, Li is expected to be somewhat different from the other alkali metals, and this is borne out by experiment.

In fact, however, recent photoemission measurements [4, 5] show that the apparent filled region of the valence band in Na and K (and presumably other alkali metals) is narrower than band-structure calculations show. This is an effect of the response of the conduction electrons to the photohole, that is, one should not interpret photoelectron spectra (or optical spectra) on the basis of the one-electron density of states, but rather the spectral density of the interacting system of electrons. An equivalent picture is to augment the calculated one-electron band structure by the (complex) self energy, which shifts bands nonuniformly and broadens them [6–9].

The experimental situation is complicated by several factors. The alkali metals are reactive. They have low melting points, and relatively high diffusion rates at room temperature, leading to surfaces that are possibly rough. A number of measurements were taken not at free metal surfaces, but at quartz–alkali metal interfaces to avoid contamination, even in ultra-high vacuum, and to yield a smooth interface. The roles of interfacial grain structure, reactions, and strain are unknown. A number of years ago, a significant peak in the optical conductivity was reported for several alkali metals, with potassium being the most studied [10, 11]. The peak occurred at an energy lower than the threshold for interband absorption. Many theoretical explanations were proposed in the ensuing years, but that peak was not found in many subsequent measurements, especially, but not

exclusively, those made on the quartz–metal interface. The best early explanation was that it arose because of roughness at the alkali metal–vacuum interface [12]. Some experiments showed that it may be present only when water is adsorbed on the alkali metal surface [13]. This led to a new interpretation, that it arose from charge-density waves, at least in potassium [14, 15]. Subsequent measurements did not confirm the predicted optical structures [16]. A final complication is the fact that at low temperatures both Na and Li undergo a structural phase transition from their normal body-centered cubic structure.

There are not many measurements in the infrared on alkali metals. They should behave as free-electron gases in this region, for there is a threshold energy of the order of 1 eV for direct interband absorption. The measurements are difficult, for the reflectance is very high, and one needs great precision and accuracy, of the order of four decimal places in the reflectance. Ellipsometry, using several reflections, has often been used for metals in the infrared, but again the measurement is difficult, for the real part of the ratio of p- to s-polarized electric-field reflection coefficients is very close to one, and the phase shift is very close to 180°. One really needs the difference between the optical properties of the metal and those of a perfect conductor in such cases, and few measurements have been made at wavelengths longer than 2.5 μm for any alkali metal. Intrinsic surface states have been calculated to be present on alkali metals, and to contribute significantly to the infrared optical properties [17–21], in contrast to their contribution in noble metals, for example Ag, where such states contribute effects of only about a part in 10^4. The large predicted effects have not been seen, but there are really no data in the right spectral region on clean samples.

Since there may be interest in infrared optical properties, and the only such measurements do not tie in well with those in the visible, the only option is to use a nearly-free-electron (Drude) model. The parameters in this model may be obtained from data in the near infrared. In the discussion of each alkali metal, we give those parameters that have been extracted from experimental data, but there is considerable scatter in them. The real and imaginary parts of the refractive indices can be obtained from the real and imaginary parts of the Drude dielectric function from

$$2n^2 = +\varepsilon_1 + (\varepsilon_1^2 + \varepsilon_2^2)^{1/2}$$

$$2k^2 = -\varepsilon_1 + (\varepsilon_1^2 + \varepsilon_2^2)^{1/2},$$

with

$$\varepsilon_1 = 1 + \varepsilon_{xx} - \omega_p^2 \tau^2/(1 + (\omega\tau)^2)$$

$$\varepsilon_2 = \omega_p^2 \tau/\omega(1 + (\omega\tau)^2).$$

ε_{xx} is the contribution of high-energy interband transitions to the low-frequency dielectric function, ω_p is the plasma frequency, given in cgs units

by $\omega_p^2 = 4\pi Ne^2/m^*$, with N the number density of electrons and m^* their effective mass. τ is the relaxation time. However, to obtain a good fit to data, τ must be frequency-dependent, in the form

$$1/\tau = 1/\tau_0 + \beta\omega^2.$$

Thus, to characterize the infrared optical properties, we must know four parameters. Note that ω_p and τ_o should give the correct static conductivity, $\omega_p\tau_o/4\pi$. (Sometimes data taken above the lowest interband absorption are fit to a Drude expression. However, in such cases the relaxation time will be different, and the plasma frequency should contain the free-electron mass, or an effective mass closer to it than the infrared value.)

The following critiques, tables, and graphs contain what we consider to be the most useful n and k values for the chosen metals. One of the steps in producing the tables containing E (energy), λ (wavelength), n (index of refraction), and k (extinction coefficient) is to convert E (usually the experimental units in eV) to λ by means of the formula $E\,(\text{eV})\lambda\,(\text{Å}) = 12{,}398.42$. This was done and the values subsequently rounded to those found in the table (usually to four figures). After rounding, however, $E\lambda$ may not give the original conversion factor to four significant figures. Thus, if E from the table is converted to λ using the above conversion factor, the result may not equal the wavelength value in the table and vice versa. This slight discrepancy happens most often in the data taken from Henke *et al.* but should produce no practical problems.

REFERENCES

1. A. H. Wilson, "The Theory of Metals," Cambridge University Press, Cambridge, 133 (1936).
2. P. N. Butcher, *Proc. Phys. Soc. (London)* **A64**, 50 (1951).
3. N. W. Ashcroft and K. Sturm, *Phys. Rev.* **B3**, 1898 (1971).
4. E. Jensen and E. W. Plummer, *Phys. Rev. Lett.* **55**, 1912 (1985).
5. I.-W. Lyo and E. W. Plummer, *Phys. Rev. Lett.* **60**, 1558 (1988).
6. J. E. Northrup, M. S. Hybertsen, and S. G. Louie, *Phys. Rev. Lett.* **59**, 819 (1987).
7. K. W. Shung, B. E. Sernelius, and G. D. Mahan, *Phys. Rev.* **B36**, 4499 (1987).
8. K. W. Shung and G. D. Mahan, *Phys. Rev.* **B38**, 3856 (1988).
9. J. E. Northrup, M. S. Hybertsen, and S. G. Louie, *Phys. Rev.* **B39**, 8198 (1989).
10. H. Mayer and M. H. El Naby, *Z. Physik* **174**, 269 (1963).
11. H. Mayer and B. Heitel in "Optical Properties of Solids," (F. Abeles, ed.), North-Holland, Amsterdam, 47 (1972).
12. J. P. Marton, *Appl. Phys. Lett.* **18**, 140 (1971).
13. P. Harms, dissertation, Clausthal, 1972.
14. A. W. Overhauser and N. R. Butler, *Phys. Rev.* **B14**, 3371 (1976).
15. F. E. Fragachan and A. W. Overhauser, *Phys. Rev.* **B31**, 4802 (1985).
16. L. H. Dubois and N. V. Smith, *J. Phys. F Met. Phys.* **17**, L7 (1987).
17. R. Garron, *Surf. Sci.* **79**, 489 (1979).
18. R. Garron, *Surf. Sci.* **91**, 358 (1980).
19. R. Garron and H. Roubaud, *Surf. Sci.* **92**, 593 (1980).

20. R. Garron and H. Roubaud, *Surf. Sci.* **146**, 527 (1984).
21. R. Garron, *Appl. Opt.* **20**, 1747 (1981).

LITHIUM (Li) III

Lithium is a reactive material, and generally only data taken under ultrahigh-vacuum conditions will be mentioned. Li is normally body-centered cubic, but at low temperatures there is a transition to a phase often reported to be hexagonal, a phase with different optical properties. It is the stable phase below about 80 K. However, the phase transition is sluggish, and a low-temperature sample may be a mixture of phases. In fact, the early reports of this transition stated the low-temperature phase was hexagonal close packed [1, 2], but more recent descriptions [3] are 9*R*, a closed-packed stacking that is mixed fcc and hcp. We report only data on the bcc phase. We do not consider data taken in arbitrary units, for example, optical density of a film or electron-energy-loss spectra without suitable normalization, unless those are the only data available in a particular wavelength region. In such a case, we give only a reference to the original work.

The first modern measurements on Li are those of Hodgson [4]. Although the films were not prepared in ultrahigh vacuum, the ellipsometric measurements were made on an Li-silica interface, which remained stable for about a day. The data, taken in the 0.22–2 μm region and at two temperatures, were fit to a free-electron model in the longer-wavelength region. To obtain a good fit, the relaxation time had to depend on frequency. The interband-absorption threshold was not well-defined. Bösenberg [5, 6] made attenuated-total-reflectance measurements on films deposited in better vacuum, using the Li-sapphire interface. His data, covering the range of 2–3.8 eV, are not in good agreement with Hodgson's, but agree better with data taken later by other groups.

Myers and coworkers [7–9] made ellipsometric measurements at the vacuum–metal interface in the range 0.6–4 eV. They evaporated films on several substrates at several temperatures, obtaining different results. There were changes in the spectra with time after deposition. Others (see below) also observed time-dependence. For what was believed to be bcc Li, the first interband threshold was at 2.6 eV. At lower energies, the data were fitted to a free-electron model, but to obtain a fit it was necessary that the relaxation time depend on frequency. Table I lists Drude parameters from several references. Table II lists values of n and k. Figure 1 plots n and k versus μm. Myers and Sixtensson [9] also reported the optical constants of hexagonal Li. Rasigni and Rasigni [10] measured the transmittance of Li films of varying thickness, from which measurements they

extracted the optical conductivity. They covered the 1–6 eV region and found two interband peaks. The one with a threshold at about 2.6 eV was the expected interband peak, whereas the anomalous one peaked between 1.5 and 2.6 eV. Films giving the latter were found to be grainier, either discontinuous grains on the substrate or a distribution of grains on a smoother Li film on the substrate. They made additional studies of the nature of the surfaces of films evaporated on substrates at different temperatures, correlating them with optical spectra [11–15]. They were able to eliminate the anomalous peak in later work [16], in which they give optical constants in the 0.15–10.7 eV range, obtained by Kramers–Kronig analysis of their reflectance measurements in the range 0.5–6 eV [13], and the reflectance of Callcott and Arakawa [17] from 3–10.7 eV. Inagaki *et al.* [18] measured the optical properties of Li in the 0.6–3.8 eV region by ellipsometry on the Li–silica interface. They obtained the anomalous absorption mentioned earlier after allowing their films to stand for a day in UHV, even though their measurements were at the Li–silica interface. The data that they took before the growth of this peak do not agree well with those of Myers *et al.*, but the reflectance calculated from their data agrees with that of Rasigni and Rasigni [13].

The spectra of k from the papers mentioned earlier agree reasonably well, but there are large differences in the n spectra. n has a minimum near 0.5 μm, and the values at this minimum range from 0.13 to 0.21. The data of Rasigni and Rasigni exhibit a local maximum in n at about 0.33 μm not apparent in the other spectra (which end at about 0.33 μm). There are also discrepancies at both ends of the range of these measurements, either in the magnitudes of n, the slopes $dn/d\lambda$, or both. There are no data further into the infrared, and the only data at shorter wavelengths are described in the next paragraph. Of the measurements described in the previous paragraph, only those of Rasigni and Rasigni [16] are close to matching the only data set to shorter wavelengths, and this matching was part of their own data analysis. This does not mean these are the best data, but this matching is the only criterion we can use for having selected them for the table. The data sets are too limited in range to test for consistency by sum rules. Moreover, not all authors report the frequency-dependence of the relaxation time necessary for an extrapolation of their data to longer wavelengths. The discrepancies probably result from differences in samples, either the possible occurrence of two phases, differences in surface roughness, or both. (There may be voids at the Li–substrate interface, which would appear as roughness in measurements made on that interface.)

Callcott and Arakawa [17] determined the optical constants of Li films in the 3–10.7 eV region by multiple-angle reflectance measurements. They worked on the Li–vacuum interface and the Li–substrate (MgF_2) interface, getting agreement in the optical constants only for energies above 6 eV.

Discrepancies below 6 eV were assigned to substrate roughness and structural effects in the film. Below 6 eV, they chose no best set of data, and only results above 6 eV are tabulated.

There are no absolute measurements at energies above 10.7 eV. Haensel *et al.* [19] presented the results of transmission measurements in the 60–149 eV region. They show considerable structure at and above the Li 1s absorption edge, structure that will appear prominently in the k spectrum, but very weakly in that of n.

Extrapolation to the infrared may be made from the Drude parameters, but in the case of Li, those reported are not in good agreement with each other. We list many of them in Table I. (The fact that the effective-mass values are considerably larger than unity is a consequence of the distortion of the Fermi surface mentioned earlier). The first interband transition begins at about 2.6 eV. The Drude parameters may be used to obtain ε_2 for energies below this, but the interband contribution to ε_2 will persist several tenths of an eV below 2.6 eV. Thus, Drude values of n and k would be reliable below about 2 eV, except that a reliable set of parameters cannot be chosen rationally. (Values of the Drude parameters determined from data in the spectral region above the interband absorption are not given in Table I. Such data yield a smaller effective mass, not suitable for extrapolation in the infrared).

We have calculated n and k in the 1.24–240 Å (10,000–51.5 eV) region using the model of Henke *et al.* [20]. The atomic absorption edge is K (55 eV) [21].

We used 8065.48 cm^{-1}/eV to convert among the units of [20], whereas the conversion factor varies by a digit or so for [16]. This should give no problems among the units until the fourth figure.

REFERENCES

1. C. S. Barrett, *Phys. Rev.* **72**, 245 (1947).
2. C. S. Barrett, *Acta. Cryst.* **9**, 671 (1956).
3. References to the recent structural literature may be found in R. J. Gooding and J. A. Krumhansl, *Phys. Rev.* **B38**, 1695 (1988).
4. J. N. Hodgson in "Optical Properties and Electronic Structure of Metals and Alloys," (F. Abeles, ed.), North-Holland, Amsterdam, 60 (1966).
5. J. Bösenberg, *Phys. Lett.* **41A**, 185 (1972).
6. J. Bösenberg, *Z. Physik B* **22**, 261 (1975).
7. A. G. Mathewson and H. P. Myers, *Physica Scripta* **4**, 291 (1971).
8. A. G. Mathewson and H. P. Myers, *Phil. Mag.* **25**, 853 (1972).
9. H. P. Myers and P. Sixtensson, *J. Phys. F* **6**, 2023 (1976).
10. M. Rasigni and G. Rasigni, *J. Opt. Soc. Am.* **63**, 775 (1973).
11. M. Rasigni and G. Rasigni, *J. Opt. Soc. Am.* **62**, 1033 (1972).
12. M. Rasigni, G. Rasigni, and J. P. Palmari, *Phil. Mag.* **31**, 1307 (1975).
13. M. Rasigni and G. Rasigni, *J. Opt. Soc. Am.* **66**, 826 (1976).
14. M. Rasigni, J. P. Gasparini, G. Rasigni, and R. Fraisse, *Solid State Commun.* **18**, 629 (1976).

15. M. Rasigni, G. Rasigni, J. P. Gasparini, and R. Fraisse, *J. Appl. Phys.* **47**, 1757 (1976).
16. M. Rasigni and G. Rasigni, *J. Opt. Soc. Am.* **67**, 54 (1977).
17. T. A. Callcott and E. T. Arakawa, *J. Opt. Soc. Am.* **64**, 839 (1974).
18. T. Inagaki, L. C. Emerson, E. T. Arakawa, and M. W. Williams, *Phys. Rev.* **B13**, 2305 (1976).
19. R. Haensel, G. Keitel, B. Sonntag, C. Kunz, and P. Schreiber, *Phys. Stat. Solidi (a)* **2**, 85 (1970).
20. B. L. Henke, J. C. Davis, E. M. Gullikson, and R. C. C. Perera, Lawrence Berkeley Laboratory Report No. LBL-26259 (1988).
21. K. Siegbahn, C. Nordling, A. Fahlman, R. Nordberg, K. Hamrin, J. Hedman, G. Johansson, T. Bergmark, S.-E. Karlsson, I. Lindgren, and B. Lindberg, in "Nova Acta Regiae Societatis Scientiarum Upsaliensis," Ser. IV, Vol. 20, Almqvist and Wiksells Boktryckeri, Uppsala, (1967).

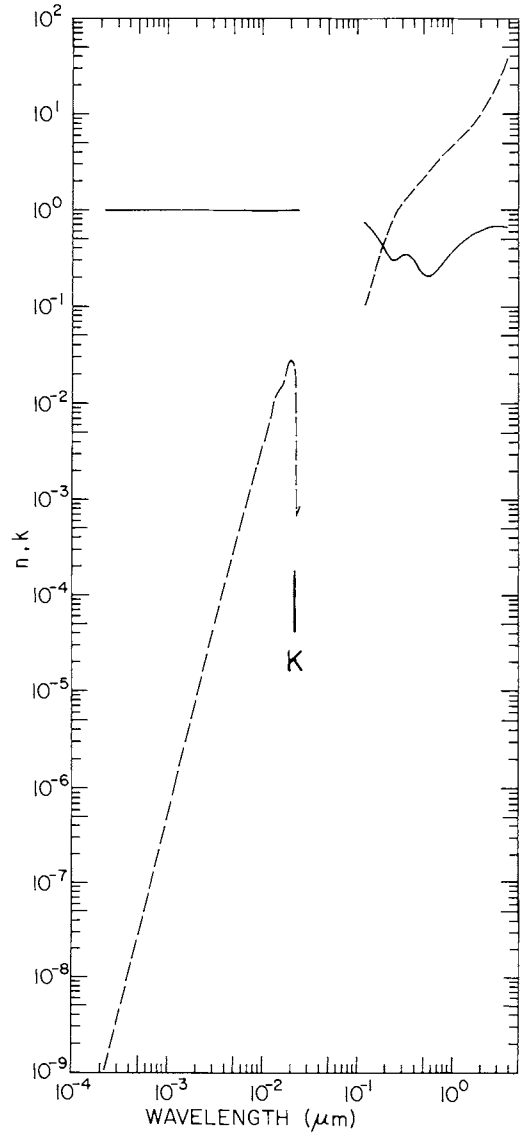

Fig. 1. Log–log plot of n (solid line) and k (dashed line) versus wavelength in micrometers for lithium.

TABLE I

Drude-Model Parameters from Various References

Ref.	ε_∞	τ (10^{-14} sec)	β (10^{-14} sec eV^{-2})	ω_p (eV)	m^*/m
[4]	1.0			6.4	1.57
[5]	0.8				1.47
[6]	0.75			6.2	1.68
[8]				6.94	1.33
[9]	<1	2.06	0.285	6.58	1.52
[16]	0				1.80
[18]					1.61

TABLE II

Values of n and k Obtained from Various References for Lithium[a]

eV	cm^{-1}	Å	n	k
10000		1.240	0.9999990 [20]	1.14E-10 [20]
9549		1.298	0.9999989	1.35E-10
9117		1.360	0.9999989	1.60E-10
8706		1.424	0.9999987	1.90E-10
8313		1.492	0.9999986	2.28E-10
7937		1.562	0.9999985	2.75E-10
7579		1.636	0.9999983	3.31E-10
7237		1.713	0.9999982	3.94E-10
6910		1.794	0.9999980	4.67E-10
6598		1.879	0.9999978	5.55E-10
6300		1.968	0.9999976	6.59E-10
6015		2.061	0.9999974	7.82E-10
5744		2.159	0.9999971	9.29E-10
5484		2.261	0.9999968	1.11E-09
5237		2.368	0.9999965	1.34E-09
5000		2.480	0.9999962	1.61E-09
4775		2.597	0.9999958	1.94E-09
4559		2.720	0.9999954	2.35E-09
4353		2.848	0.9999949	2.83E-09
4157		2.983	0.9999945	3.41E-09
3969		3.124	0.9999939	4.12E-09
3790		3.272	0.9999933	4.96E-09
3619		3.426	0.9999927	5.98E-09
3455		3.588	0.9999920	7.21E-09
3299		3.758	0.9999912	8.69E-09
3150		3.936	0.9999903	1.05E-08
3008		4.122	0.9999894	1.26E-08
2872		4.317	0.9999884	1.52E-08
2742		4.521	0.9999872	1.84E-08
2619		4.735	0.9999860	2.24E-08
2500		4.959	0.9999846	2.71E-08
2387		5.193	0.9999831	3.28E-08
2280		5.439	0.9999815	3.98E-08
2177		5.696	0.9999797	4.82E-08
2078		5.965	0.9999777	5.84E-08
1985		6.248	0.9999755	7.08E-08
1895		6.543	0.9999731	8.56E-08
1809		6.852	0.9999705	1.01E-07
1728		7.176	0.9999676	1.22E-07
1650		7.516	0.9999645	1.48E-07
1575		7.871	0.9999610	1.80E-07
1504		8.244	0.9999572	2.18E-07
1436		8.633	0.9999530	2.65E-07
1371		9.041	0.9999484	3.21E-07

[a]The references from which the values were extracted are given in brackets.

TABLE II (*Continued*)

Lithium

eV	cm^{-1}	Å	*n*	*k*
1309		9.469	0.9999434	3.88E-07
1250		9.917	0.9999379	4.70E-07
1194		10.39	0.9999318	5.68E-07
1140		10.88	0.9999251	6.87E-07
1088		11.39	0.9999177	8.30E-07
1039		11.93	0.9999097	1.00E-06
992.3		12.49	0.9999008	1.21E-06
947.5		13.09	0.999891	1.46E-06
904.7		13.70	0.999880	1.77E-06
863.9		14.35	0.999869	2.14E-06
824.9		15.03	0.999856	2.58E-06
787.7		15.74	0.999841	3.12E-06
752.1		16.49	0.999825	3.76E-06
718.1		17.27	0.999808	4.54E-06
685.7		18.08	0.999789	5.45E-06
654.7		18.94	0.999768	6.59E-06
625.1		19.83	0.999745	7.98E-06
610.9		20.30	0.999733	8.75E-06
596.9		20.77	0.999720	9.61E-06
583.3		21.26	0.999706	1.05E-05
570.0		21.75	0.999692	1.16E-05
544.0		22.78	0.999661	1.39E-05
519.7		23.86	0.999627	1.67E-05
496.2		24.99	0.999590	2.01E-05
473.8		26.17	0.999549	2.42E-05
452.4		27.41	0.999504	2.92E-05
432.9		28.70	0.999454	3.50E-05
412.5		30.06	0.999399	4.20E-05
393.8		31.48	0.999339	5.04E-05
376.1		32.97	0.999273	6.03E-05
359.1		34.53	0.999200	7.21E-05
342.9		36.16	0.999120	8.61E-05
327.4		37.87	0.999031	1.03E-04
312.6		39.66	0.99893	1.23E-04
298.5		41.54	0.99883	1.47E-04
285.0		43.50	0.99871	1.76E-04
272.1		45.56	0.99858	2.10E-04
259.9		47.71	0.99844	2.49E-04
248.1		49.97	0.99828	2.96E-04
236.9		52.33	0.99811	3.52E-04
226.2		54.81	0.99793	4.19E-04
216.0		57.40	0.99772	4.98E-04
206.2		60.12	0.99750	5.89E-04
196.9		62.96	0.99726	6.96E-04
188.0		65.94	0.99699	8.24E-04

(*Continued*)

TABLE II (*Continued*)

Lithium

eV	cm^{-1}	Å	n	k
179.6		69.05	0.99671	9.75E-04
171.4		72.32	0.99640	1.14E-03
163.7		75.74	0.99607	1.35E-03
156.3		79.32	0.99571	1.58E-03
149.3		83.07	0.99532	1.86E-03
142.5		87.00	0.99489	2.18E-03
136.1		91.11	0.99444	2.57E-03
129.9		95.42	0.99398	3.02E-03
124.1		99.94	0.99349	3.53E-03
118.5		104.7	0.99297	4.13E-03
113.1		109.6	0.99245	4.81E-03
108.0		114.8	0.99181	5.58E-03
103.1		120.2	0.99108	6.63E-03
98.47		125.9	0.99057	8.05E-03
94.03		131.9	0.99025	9.81E-03
89.78		138.1	0.99065	1.18E-02
85.73		144.6	0.99152	1.31E-02
81.85		151.5	0.99210	1.40E-02
78.16		158.6	0.99233	1.47E-02
74.63		166.1	0.99202	1.60E-02
71.26		174.0	0.99169	1.85E-02
68.04		182.2	0.99257	2.28E-02
64.97		190.8	0.99707	2.66E-02
62.04		199.9	1.003	2.74E-02
59.24		209.3	1.019	2.66E-02
56.56		219.2	1.017	2.36E-02
55.27		224.3	1.026	2.18E-02
54.01		229.6	1.021	6.86E-04
52.77		234.9	1.014	7.23E-04
51.57		240.4	1.010	7.91E-04
eV	cm^{-1}	μm	n	k
10.6	85897	0.1164	0.753 [16]	8.00E-02 [16]
10.4	83478	0.1198	0.743	0.102
10.1	81058	0.1234	0.726	0.108
9.75	78638	0.1272	0.708	0.119
9.45	76219	0.1312	0.680	0.130
9.15	73799	0.1355	0.657	0.144
8.85	71379	0.1401	0.624	0.163
8.55	68960	0.1450	0.601	0.189
8.25	66540	0.1503	0.572	0.214
7.95	64121	0.1560	0.545	0.246
7.65	61701	0.1621	0.517	0.282
7.35	59281	0.1687	0.492	0.320

(*Continued*)

TABLE II (*Continued*)

Lithium

eV	cm^{-1}	μm	*n*	*k*
7.95	64121	0.1560	0.545	0.246
7.65	61701	0.1621	0.517	0.282
7.35	59281	0.1687	0.492	0.320
7.05	56862	0.1759	0.466	0.364
6.75	54442	0.1837	0.440	0.407
6.45	52022	0.1922	0.408	0.460
6.15	49603	0.2016	0.376	0.522
5.85	47183	0.2119	0.342	0.594
5.55	44763	0.2234	0.310	0.688
5.25	42344	0.2362	0.299	0.795
4.95	39924	0.2505	0.302	0.906
4.65	37504	0.2666	0.317	1.01
4.35	35085	0.2850	0.333	1.11
4.05	32665	0.3061	0.346	1.21
3.75	30246	0.3306	0.345	1.32
3.45	27826	0.3594	0.334	1.45
3.15	25406	0.3936	0.304	1.60
2.85	22987	0.4350	0.247	1.82
2.55	20567	0.4862	0.217	2.11
2.25	18147	0.5510	0.206	2.48
1.95	15728	0.6358	0.221	2.94
1.65	13308	0.7514	0.265	3.55
1.35	10888	0.9184	0.338	4.36
1.05	8469	1.181	0.448	5.58
0.750	6049	1.653	0.561	7.68
0.540	4355	2.296	0.661	12.6
0.140	1129	8.856	0.659	38.0

IV SODIUM (Na)

The optical properties of sodium have been measured with more consistency than those of Li, but the agreement among measurements is still not satisfying. Na is normally body-centered cubic, but it also has a low-temperature hexagonal phase. However, the phase transition sets in at 51 K if aided by plastic deformation, and at 36 K upon simply cooling [1]. This means that evaporated-film samples of Na condensed on substrates at liquid-nitrogen temperatures are probably single-phase films, unlike films of Li condensed under similar circumstances. Na films are similarly likely to be rough, however, and Na is a reactive material.

The first modern measurements on Na were those of Hodgson [2, 3] and Mayer and Heitel [4]. Hodgson made ellipsometric measurements from 0.65 μm to 2.5 μm on the Na–silica interface of films evaporated in less than ultrahigh-vacuum conditions. He reported that his spectra of the optical

conductivity (hence, in this case, of k) were not reproducible from sample to sample, whereas those of ε_1 (essentially n^2) were. This is a similar problem to that encountered in Li. Mayer and Heitel made ellipsometric measurements from 0.3 μm to 2.5 μm on the Na–vacuum interface in ultrahigh vacuum. The real part of the dielectric function was fit to a Drude expression. The imaginary part of the dielectric function, or the optical conductivity, or the k spectrum, exhibited a Drude region and the expected weak interband-absorption threshold at about 2 eV, but there was a lower-energy, temperature-dependent absorption threshold and peak, at about 1.2 and 1.8 eV, respectively. This anomalous peak has proven to be only intermittently reproducible over the years. For example, Payan and Roux [5] found such a peak in Na films, and the peak position depended on film thickness and temperature. Many of the references cited here did not find this peak, although not all carried their measurements to long-enough wavelengths. This peak is discussed in a previous section on alkali metals in general, and we view it here as anomalous, and possibly spurious, despite the extensive theoretical effort it engendered.

Althoff and Hertz [6] made the only measurements to date at wavelengths longer than 2.5 μm, using an ellipsometric method on the Na–NaCl interface over the 2.5–10 μm region. However, their samples were evaporated in vacua of 10^{-6} torr, and their spectra do not agree well with any spectra measured at shorter wavelengths on samples prepared in ultrahigh vacuum.

Smith [7] measured the optical properties of Na films at the Na–silica interface by ellipsometry in the 0.5–4.0 eV spectral region. The interband-absorption threshold was found to be 2.0 eV. Drude parameters were obtained at lower energies. There was no anomalous absorption structure, but the fit to the Drude parameters required a scattering rate that had a term that increased with photon energy, but when plotted as a function of the square of the energy, the expected straight line did not result. Drude parameters are listed in Table I.

Palmer and Schnatterly [8] also used an ellipsometric method on films condensed on sapphire substrates at 77 K. (Other substrates gave rough surfaces that obviously scattered incident light.) They covered the spectral range 1.75–4.5 eV. They also fit ε_1 data to the Drude model. Their optical-conductivity data resembled those of Smith, but agreement was not good in both the Drude and interband regions. They made some measurements at the Na–glass interface. The resultant conductivity spectrum resembled that of Smith more closely in both spectral shape and magnitude. The difference between data at the Na–vacuum and Na–silica or glass interface thus appears to be real, and the explanation is likely to be found in an effective-medium approach to both sets of data. The free surface may be rough to a degree depending on the substrate materials and temperature. The Na–substrate interface may have regions of low density or even

voids between grains nucleated at separate sites.

Monin and Boutry [9] made ellipsometric measurements between 0.24 μm and 0.63 μm on the vacuum–Na interface of films that were condensed at 77 K. They found that upon warming to room temperature, then cooling to 77 K, the optical properties at this temperature had changed irreversibly, evidently due to annealing at room temperature, which led to increased grain size. Their results for both n and k are quite close to those of Smith, although they used the Na–vacuum interface, unlike Smith.

Bösenberg [10] made measurements on the Na–silica interface by attenuated total reflection in the 2–3.8 eV region. His optical-conductivity spectrum does not show much evidence for the expected interband transitions beginning at about 2 eV. Inagaki *et al.* [11] also made ellipsometric measurements on the Na–silica interface in the 0.6–3.8 eV region. Their results are close to those of Smith. Their interband peak in the optical conductivity is somewhat higher and narrower than Smith's.

Sutherland *et al.* [12, 13] made measurements in the vacuum ultraviolet. They first measured spectra of n on the Na–vacuum interface in the region 420–2000 Å by fitting the reflected radiation near the critical angle (n is less than unity in this spectral region) as a function of angle to the Fresnel equations and by using interference fringes in the reflected signal [12]. These data do not scatter much about a curve drawn through them. They then determined the k spectrum of semitransparent Na films from transmission measurements in the region of 2.8–11 eV [13]. At the longer wavelengths, their data are significantly lower than those of Smith and the later data of Inagaki *et al.* Above 6 eV, there is a great deal of scatter in the k spectrum, and its general shape does not interpolate well between the spectra of Smith and Inagaki *et al.* at longer wavelengths, and of Sato *et al.* [14] at shorter.

Sato *et al.* [14] measured the absorption coefficient of Na films in the 10–35 eV region. By assuming n is unity throughout this region, an assumption good to within a few percent in this region [12], they obtained an optical-conductivity spectrum, hence a spectrum of k. We reproduce their values in our tables, but with one exception. Between 30 and 31 eV, there is a sharp absorption edge terminating in two sharp peaks arising from the excitation of the spin-orbit-split $2p$ electrons. We do not reproduce these narrow features in Table II and Fig. 1.

The infrared data of Althoff and Hertz do not match any of the other data in the region of overlap around 2 μm. In particular, at 2 μm there is a jump in the value of k from about 9 in the data of Smith and of Inagaki *et al.* to 11 in the data of Althoff and Hertz. Thus, there are no recommended infrared data, and one must resort to the Drude parameters of Table I. These do not scatter badly, but at increasing wavelength the optical constants calculated from different sets will diverge somewhat. No reliable

values of the scattering time exist, for these have been sample-dependent. Without such data one can calculate only $\varepsilon_1 = n^2 - k^2$. Since $k \gg n$ in this region, one can calculate k but not n from the parameters in Table I. As with Li, Drude parameters determined from data in the ultraviolet are not given below.

In the visible region, we believe the data of Smith and Inagaki *et al.* are the most reliable and physically reasonable. They differ primarily in the height and width of the weak interband-absorption peak in the optical conductivity. We list those of Smith. At shorter wavelengths, the n data of Sutherland *et al.* are listed, but not their k values, which scatter considerably and do not match with other data at either end of their spectral range. At the shortest wavelengths, the k data of Sato *et al.* are listed, assuming n is within a few percent of unity. There are no data at all in the 2000–3000 Å region, and the data sets listed do not extrapolate toward each other satisfactorily across this gap, especially the n spectrum, which has a minimum in the region for which no data exist.

We have calculated n and k in the 1.24–240 Å (10,000–51.5 eV) region using the model of Henke *et al.* [15]. The atomic absorption edges are K (1072 eV), L_1 (63 eV), $L_{2,3}$ (31 eV). Some of these features are indicated in Fig. 1.

We used 8065.48 cm^{-1}/eV to convert between units in [15]. Note that the conversion factors for [7], [12], [14] are slightly different by a digit or two in the fourth significant figure.

REFERENCES

1. C. S. Barrett, *Acta Cryst.* **9**, 671 (1956).
2. J. N. Hodgson, *J. Phys. Chem. Solids* **24**, 1213 (1963).
3. J. N. Hodgson, *Phys. Lett.* **7**, 300 (1963).
4. H. Mayer and B. Heitel, in "Proceedings of the International Colloquium on the Optical Properties and Electronic Structure of Metals and Alloys," (F. Abeles, ed.), North-Holland, Amsterdam, 47 (1966).
5. R. Payan and D. Roux, *Opt. Commun.* **1**, 37 (1969).
6. R. Althoff and J. H. Hertz, *Infrared Physics* **7**, 11 (1967).
7. N. V. Smith, *Phys. Rev.* **183**, 634 (1969).
8. R. E. Palmer and S. E. Schnatterly, *Phys. Rev.* **B4**, 2329 (1971).
9. J. Monin and G.-A. Boutry, *Phys. Rev.* **B9**, 1309 (1974).
10. J. Bösenberg, *Z. Physik* **22**, 261 (1975).
11. T. Inagaki, L. T. Emerson, E. T. Arakawa, and M. W. Williams, *Phys. Rev.* **B13**, 2305 (1976).
12. J. C. Sutherland, E. T. Arakawa, and R. Hamm, *J. Opt. Soc. Am.* **57**, 645 (1967).
13. J. C. Sutherland, R. N. Hamm, and E. T. Arakawa, *J. Opt. Soc. Am.* **59**, 1581 (1969).
14. S. Sato, T. Miyahara, T. Hanyu, S. Yamaguchi, and T. Ishii, *J. Phys. Soc. Japan* **47**, 846 (1979).
15. B. L. Henke, J. C. Davis, E. M. Gullikson and R. C. C. Perera, Lawrence Berkeley Laboratory Report No. LBL-26259 (1988).

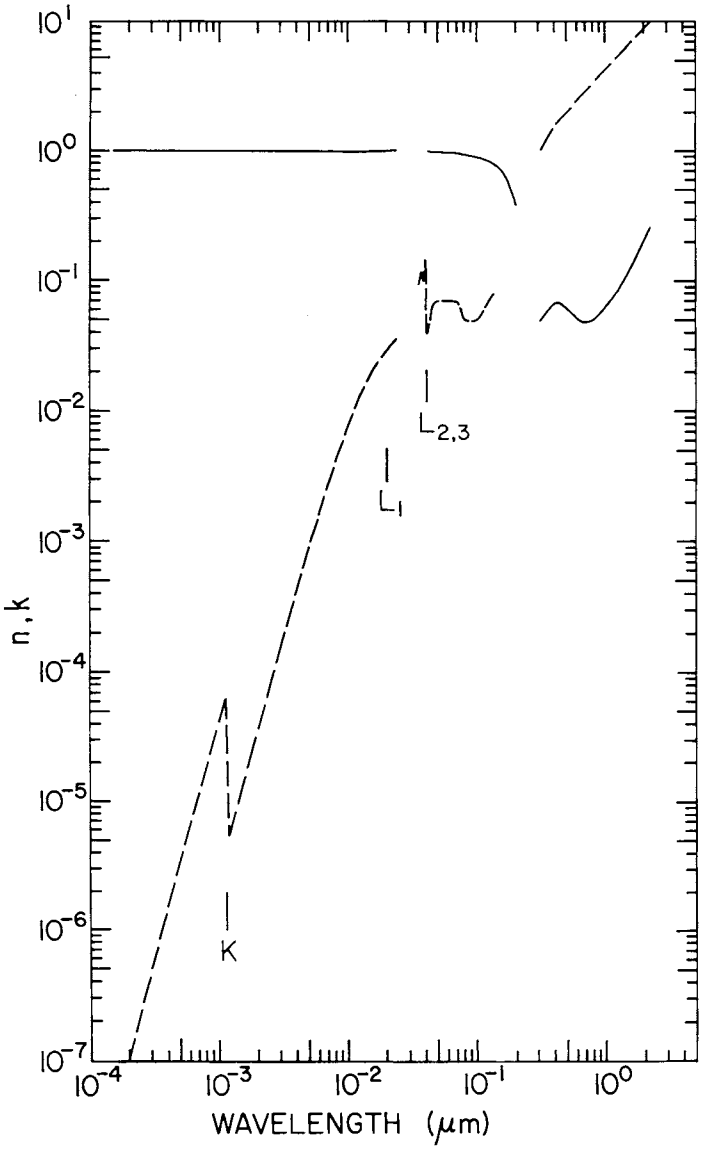

Fig. 1. Log–log plot of n (solid line) and k (dashed line) versus wavelength in micrometers for sodium.

TABLE I

Drude-Model Parameters from Various References

Ref.	ε_∞	τ (10^{-14} sec)	β (10^{-14} sec eV^{-2})	ω_p (eV)	m^*/m
[2,3]	0.1	2.45		5.94	1.08
[4]	0.15				1.27
[6]		1.85			0.99
[7]	0	2.4	[a]	5.65	1.13
[8]	0.34	2.4		5.4	1.00
[9]	0.04			5.61	1.07
[10]	0.15			5.77	1.09
[11]	0.1			5.6	1.07

[a] A plot of τ versus ω is given, but replotting shows that the scattering rate does not increase as the square of the frequency, but somewhat faster.

TABLE II

Values of n and k Obtained from Various References for Sodium[a]

eV	cm^{-1}	Å	n	k
10000		1.240	0.9999980 [15]	1.38E-08 [15]
9549		1.298	0.9999979	1.66E-08
9117		1.360	0.9999977	2.00E-08
8706		1.424	0.9999974	2.41E-08
8313		1.492	0.9999972	2.91E-08
7937		1.562	0.9999969	3.50E-08
7579		1.636	0.9999966	4.21E-08
7237		1.713	0.9999962	5.07E-08
6910		1.794	0.9999959	6.09E-08
6598		1.879	0.9999955	7.33E-08
6300		1.968	0.9999951	8.81E-08
6015		2.061	0.9999946	1.06E-07
5744		2.159	0.9999940	1.27E-07
5484		2.261	0.9999934	1.53E-07
5237		2.368	0.9999928	1.83E-07
5000		2.480	0.9999921	2.20E-07
4775		2.597	0.9999914	2.64E-07
4559		2.720	0.9999905	3.16E-07
4353		2.848	0.9999896	3.79E-07
4157		2.983	0.9999885	4.54E-07
3969		3.124	0.9999874	5.44E-07
3790		3.272	0.9999862	6.52E-07
3619		3.426	0.9999848	7.80E-07
3455		3.588	0.9999833	9.32E-07
3299		3.758	0.9999816	1.12E-06
3150		3.936	0.9999799	1.33E-06
3008		4.122	0.9999779	1.59E-06
2872		4.317	0.9999757	1.90E-06
2742		4.521	0.9999734	2.26E-06
2619		4.735	0.9999708	2.70E-06
2500		4.959	0.9999680	3.22E-06
2387		5.193	0.9999649	3.83E-06
2280		5.439	0.9999616	4.55E-06
2177		5.696	0.9999579	5.41E-06
2078		5.965	0.9999539	6.43E-06
1985		6.248	0.9999496	7.62E-06
1895		6.543	0.9999450	9.02E-06
1809		6.852	0.9999400	1.07E-05
1728		7.176	0.9999346	1.26E-05
1650		7.516	0.9999289	1.49E-05
1575		7.871	0.9999228	1.76E-05
1504		8.244	0.9999164	2.08E-05
1436		8.633	0.9999099	2.45E-05
1371		9.041	0.9999032	2.88E-05

[a]The references from which the values were extracted are given in brackets.

TABLE II (*Continued*)

Sodium

eV	cm^{-1}	Å	*n*	*k*
1309		9.469	0.999897	3.40E-05
1250		9.917	0.999891	4.01E-05
1194		10.39	0.999887	4.73E-05
1140		10.88	0.999888	5.58E-05
1114		11.13	0.999893	6.06E-05
1088		11.39	0.9999092	6.58E-05
1064		11.66	0.9999223	4.76E-06
1039		11.93	0.999891	5.20E-06
1016		12.21	0.999874	5.68E-06
992.3		12.49	0.999861	6.21E-06
947.5		13.09	0.999838	7.42E-06
904.7		13.70	0.999816	8.84E-06
863.9		14.35	0.999793	1.05E-05
824.9		15.03	0.999769	1.25E-05
787.7		15.74	0.999743	1.48E-05
752.1		16.49	0.999715	1.76E-05
718.1		17.27	0.999684	2.09E-05
685.7		18.08	0.999651	2.47E-05
654.7		18.94	0.999614	2.93E-05
625.1		19.83	0.999574	3.47E-05
596.9		20.77	0.999530	4.07E-05
570.0		21.75	0.999482	4.80E-05
544.0		22.78	0.999429	5.65E-05
519.7		23.86	0.999371	6.66E-05
496.2		24.99	0.999306	7.85E-05
473.8		26.17	0.999236	9.25E-05
452.4		27.41	0.999159	1.09E-04
432.9		28.70	0.999074	1.29E-04
412.5		30.06	0.99898	1.52E-04
393.8		31.48	0.99888	1.80E-04
376.1		32.97	0.99877	2.12E-04
359.1		34.53	0.99865	2.50E-04
342.9		36.16	0.99851	2.95E-04
327.4		37.87	0.99837	3.46E-04
312.6		39.66	0.99821	4.06E-04
298.5		41.54	0.99804	4.77E-04
285.0		43.50	0.99785	5.60E-04
272.1		45.56	0.99765	6.58E-04
259.9		47.71	0.99744	7.71E-04
248.1		49.97	0.99720	8.98E-04
236.9		52.33	0.99695	1.04E-03
226.2		54.81	0.99667	1.22E-03
216.0		57.40	0.99638	1.41E-03
206.2		60.12	0.99607	1.64E-03
196.9		62.96	0.99575	1.91E-03

(*Continued*)

TABLE II (*Continued*)

Sodium

eV	cm^{-1}	Å	*n*	*k*
188.0		65.94	0.99540	2.20E-03
179.6		69.05	0.99503	2.53E-03
171.4		72.32	0.99463	2.91E-03
163.7		75.74	0.99422	3.35E-03
156.3		79.32	0.99380	3.85E-03
149.3		83.07	0.99339	4.43E-03
142.5		87.00	0.99298	5.03E-03
136.1		91.11	0.99254	5.69E-03
129.9		95.42	0.99209	6.45E-03
124.1		99.94	0.99163	7.31E-03
118.5		104.7	0.99119	8.27E-03
113.1		109.6	0.99076	9.35E-03
108.0		114.8	0.99040	1.06E-02
103.1		120.2	0.99012	1.20E-02
98.47		125.9	0.99009	1.34E-02
94.03		131.9	0.99008	1.48E-02
89.78		138.1	0.99011	1.64E-02
85.73		144.6	0.99037	1.81E-02
81.85		151.5	0.99082	1.96E-02
78.16		158.6	0.99122	2.12E-02
74.63		166.1	0.99173	2.29E-02
71.26		174.0	0.99247	2.48E-02
68.04		182.2	0.99376	2.65E-02
64.97		190.8	0.99485	2.78E-02
62.04		199.9	0.99591	2.92E-02
59.24		209.3	0.99705	3.05E-02
56.56		219.2	0.99825	3.21E-02
54.01		229.6	0.999606	3.36E-02
51.57		240.4	1.001	3.52E-02
34.0		364.7		1.0E-02 [14]
33.0		375.7		1.0E-02
32.5		381.5		1.1E-02
32.3		383.9		1.2E-02
32.0		387.5		1.0E-02
31.6		392.4		1.0E-02
31.5		393.6		1.0E-02
31.0		399.9		1.2E-02
30.9		401.2		1.4E-02
30.8		402.5		1.2E-02
30.6		405.2		1.0E-02
30.0		413.3		4E-03
29.5		420.3		5E-03
29.0		427.5		5E-03
28.0		443.0		5E-03
27.0		459.2		6E-03

(*Continued*)

TABLE II (*Continued*)

Sodium

eV	cm^{-1}	Å	*n*	*k*
26.5		467.9		7E-03
26.0		476.9		7E-03
25.0		495.9		7E-03
24.0		516.6		7E-03
23.0		539.1		7E-03
22.0		563.6		7E-03
21.0		590.4		7E-03
20.0		619.9		7E-03
19.0		652.5		7E-03
18.0		688.8		7E-03
17.0		729.3		7E-03
16.5		751.4		7E-03
16.0		774.9		6E-03
15.0		826.6		5E-03
14.0		885.6		5E-03
13.0		953.7		5E-03
eV	cm^{-1}	μm	*n*	*k*
12.0	96786	0.1033		5E-03
11.0	88720	0.1127		6E-03
10.0	80655	0.1240		7E-03
9.00	72589	0.1378		8E-03
29.52		0.0420	1.02 [12]	
28.37		0.0437	1.01	
27.68		0.0448	1.01	
26.95		0.0460	1.00	
25.51		0.0486	0.993	
21.12		0.0587	0.979	
18.10		0.0685	0.964	
16.21		0.0765	0.948	
15.46		0.0802	0.942	
15.05		0.0824	0.936	
14.83		0.0836	0.934	
14.07		0.0881	0.922	
13.73		0.0903	0.917	
13.42		0.0924	0.914	
13.05		0.0950	0.913	
12.73		0.0974	0.907	
11.83	95420	0.1048	0.887	
11.08	89366	0.1119	0.870	
10.20	82237	0.1216	0.843	
9.709	78309	0.1277	0.819	
9.143	73746	0.1357	0.800	
8.634	69638	0.1437	0.762	

(*Continued*)

TABLE II (*Continued*)

Sodium

eV	cm^{-1}	μm	*n*	*k*
8.015	64641	0.1548	0.710	
7.847	63291	0.1579	0.700	
7.583	61162	0.1636	0.674	
7.328	59102	0.1691	0.641	
7.130	57504	0.1739	0.616	
6.888	55555	0.1799	0.574	
6.702	54054	0.1851	0.533	
6.526	52632	0.1899	0.485	
6.358	51282	0.1949	0.454	
6.199	50000	0.2000	0.390	
3.97	32020	0.3123	0.49E-01 [7]	1.01 [7]
3.71	29923	0.3342	0.55E-01	1.13
3.40	27423	0.3647	0.61E-01	1.33
3.20	25810	0.3875	0.65E-01	1.47
3.06	24680	0.4052	0.69E-01	1.54
2.95	23793	0.4203	0.68E-01	1.63
2.82	22745	0.4397	0.68E-01	1.76
2.64	21293	0.4696	0.66E-01	1.88
2.45	19760	0.5061	0.63E-01	2.07
2.27	18309	0.5462	0.59E-01	2.23
2.07	16696	0.5990	0.53E-01	2.48
1.87	15082	0.6630	0.49E-01	2.76
1.65	13308	0.7514	0.50E-01	3.22
1.44	11614	0.8610	0.53E-01	3.72
1.23	9921	1.008	0.64E-01	4.35
1.05	8469	1.181	0.78E-01	5.11
0.920	7420	1.348	0.99E-01	5.82
0.810	6533	1.531	0.123	6.67
0.730	5888	1.698	0.147	7.42
0.670	5404	1.851	0.175	8.09
0.630	5081	1.968	0.207	8.80
0.580	4678	2.138	0.241	9.45
0.550	4436	2.254	0.262	9.97

V POTASSIUM (K)

Potassium is a reactive metal that does not have a phase transition at low temperature. However, it has a low melting point. Room temperature is adequate for significant atomic motion to take place, which reduces strains at the surface, but may roughen the surface.

The first modern measurements on K were those of Hodgson [1], Mayer and El Naby [2, 3], and Mayer and Heitel [4]. Hodgson made ellipsometric measurements between 0.6 μm and 2.5 μm on the K–silica interface. He

fitted the real part of the dielectric function to a Drude model. The imaginary part varied by about a factor of two from film to film. He did not see the anomalous, low-energy, interband peak reported by Mayer *et al.*, who made ellipsometric measurements on the K-vacuum interface of bulk K samples. Mayer *et al.* fitted the real part of the dielectric function to a Drude expression. The imaginary part, or the optical conductivity, became well-known for many years because of a strong anomalous structure, an apparent interband-absorption peak beginning at about 1 eV, in addition to the expected one, which begins near 2.5 eV. Further discussion appears in the section on alkali metals. We consider the peak anomalous.

Althoff and Hertz [5] made the only measurements to date at wavelengths longer than 2.5 μm, using an ellipsometric method on K–NaCl and K–KBr interfaces over the 2.5–10 μm region. However, their samples were evaporated in vacua of 10^{-6} torr, and their spectra do not agree well with any spectra measured at shorter wavelengths on samples prepared in ultrahigh vacuum.

Smith [6] made ellipsometric measurements between 0.5 and 4.0 eV on the K–silica interface and obtained no anomalous peak. The interband threshold was at 1.3 eV, and the interband-absorption spectrum was in accord with theoretical expectations. Drude parameters were obtained from the data at lower energy. A frequency-dependent scattering rate resulted, but it increased with increasing photon energy faster than the expected second power.

Palmer and Schnatterly [7] also used an ellipsometric method between 1.75 and 4.5 eV on the K–vacuum interface. Their data do not agree well with those of Smith. They did not go to low enough energy to see the interband-absorption threshold.

Yamaguchi and Hanyu [8] made photometric measurements in the 2.07–6.2 eV region on semitransparent films. They measured the transmission and the reflectance from both the K–vacuum and K–silica sides, using polarized radiation and several angles of incidence. Their Drude parameters are listed here. The optical conductivity depended somewhat on sample thickness, but generally was close to that of Smith. The low-energy limit did not permit measurements at the interband threshold.

Harms [9] repeated the measurements of El Naby [3], using essentially the same techniques. The measurements spanned the 0.25–2.5 μm range. He did not find the anomalous peak in most of his measurements, but did detect it when some water vapor had been admitted to the vacuum. His and others' Drude parameters are listed in Table I. The interband conductivity was close to that of Smith; Harm's interband peak was a bit less sharp.

Monin and Boutry [10] made ellipsometric measurements on the K–silica interface in the 2500–6300 Å range. Their lowest energy is not low enough to allow observing the interband threshold, but their data appear

to have a threshold, and certainly a peak, in the interband region much higher in energy than expected and much higher than in Smith's data.

Sutherland and Arakawa [11] measured n in the 3.96–9.69 eV region by the critical-angle method on the K–quartz and K–fluorite interfaces. Sutherland *et al.* [12] measured the k spectrum from transmission measurements of K films on quartz of LiF substrates. They report only a few points between 3.9 eV and 7.1 eV. Their work was superseded by that of Whang *et al.* [13], who covered the 3.3–10.7 eV range. They measured reflectance versus angle of incidence on the K–MgF_2 interface, and transmission of semitransparent films. Their optical-conductivity spectrum matches Smith's fairly well and lies generally somewhat below those of Palmer and Schnatterly, Sutherland, and Yamaguchi and Hanyu. A second interband-absorption structure begins at about 4 eV, and peaks at 8 eV. Its origin is likely to be transitions to d-like states several eV above the Fermi level, but convincing proof is lacking.

Garron [14] showed that surface states may be responsible for some of the discrepancies in the near-infrared data, in particular for differences between data on K–vacuum and K–quartz interfaces. More discussion of these surface states appears in the general section on alkali metals.

Sato *et al.* [15] measured transmission spectra, which give spectra of k under the assumption that n is unity, an assumption valid in the 9.5–32 eV spectral region covered. We tabulate them in Table II, but do not list points close enough together to give a good representation of the $3p$ absorption edge just above 18 eV. The n and k spectra are plotted in Fig. 1.

The data for wavelengths longer than 2.5 μm do not match any data at shorter wavelengths, so for this region it is necessary to extrapolate with the Drude parameters given in Table I. As with Na, this is fairly reliably done for ε_1, which means that the k spectrum can be reliably obtained, but the n spectrum cannot because of the imprecise and sample-dependent values of ε_2 (and, hence, the relaxation time). For the near infrared, visible, and near ultraviolet, we list Smith's data in Table II, which are close to several other spectra reported, as noted above. Further in the ultraviolet, we list the data of Whang *et al.* and Sato *et al.* Unfortunately, Smith's and Whang *et al.*'s data do not overlap. They both end at about 3250 Å, where there is a peak in k and a minimum in n, and there are no data points at these structures.

We have calculated n and k in the 1.24–240 Å (10,000–51.5 eV) region using the model of Henke *et al.* [16]. The atomic absorption edges are K (3608 eV), L_1 (377 eV), $L_{2,3}$ (297, 294 eV), M_1 (34 eV), $M_{2,3}$ (18 eV). Some of these features are indicated in Fig. 1.

We used 8065.48 cm^{-1}/eV to convert among the units of [16], whereas the conversion factor is slightly different for other data in Table II (usually by a digit or two in the fourth figure). This should not present any problems among the units until the fourth figure.

REFERENCES

1. J. Hodgson, *Phys. Lett.* **7**, 300 (1963).
2. H. Mayer and M. H. El Naby, *Z. Physik* **174**, 269 (1963).
3. M. H. El Naby, *Z. Physik* **174**, 280 (1963).
4. H. Mayer and B. Heitel, in "Proceedings of the International Colloquium on the Optical Properties and Electronic Structure of Metals and Alloys," (F. Abeles, ed.) North-Holland, Amsterdam, 47 (1966).
5. R. Althoff and J. H. Hertz, *Infrared Phys.* **7**, 11 (1967).
6. N. V. Smith, *Phys. Rev.* **183**, 634 (1969).
7. R. E. Palmer and S. E. Schnatterly, *Phys. Rev.* **B4**, 2329 (1971).
8. S. Yamaguchi and T. Hanyu, *J. Phys. Soc. Japan* **31**, 1431 (1971).
9. P. Harms, dissertation, Technische Universitaet Clausthal, 1972.
10. J. Monin and G.-A. Boutry, *Phys. Rev.* **B9**, 1309 (1974).
11. J. C. Sutherland and E. T. Arakawa, *J. Opt. Soc. Am.* **58**, 1080 (1968).
12. J. C. Sutherland, R. N. Hamm, and E. T. Arakawa, *J. Opt. Soc. Am.* **59**, 1581 (1969).
13. U. S. Whang, E. T. Arakawa, and T. A. Callcott, *Phys. Rev.* **B6**, 2109 (1972).
14. R. Garron, *Appl. Opt.* **20**, 1747 (1981).
15. S. Sato, T. Miyahara, T. Hanyu, S. Yamaguchi, and T. Ishii, *J. Phys. Soc. Japan* **47**, 836 (1979).
16. B. L. Henke, J. C. Davis, E. M. Gullikson, and R. C. C. Perera, Lawrence Berkeley Laboratory Report No. LBL-26259 (1988).

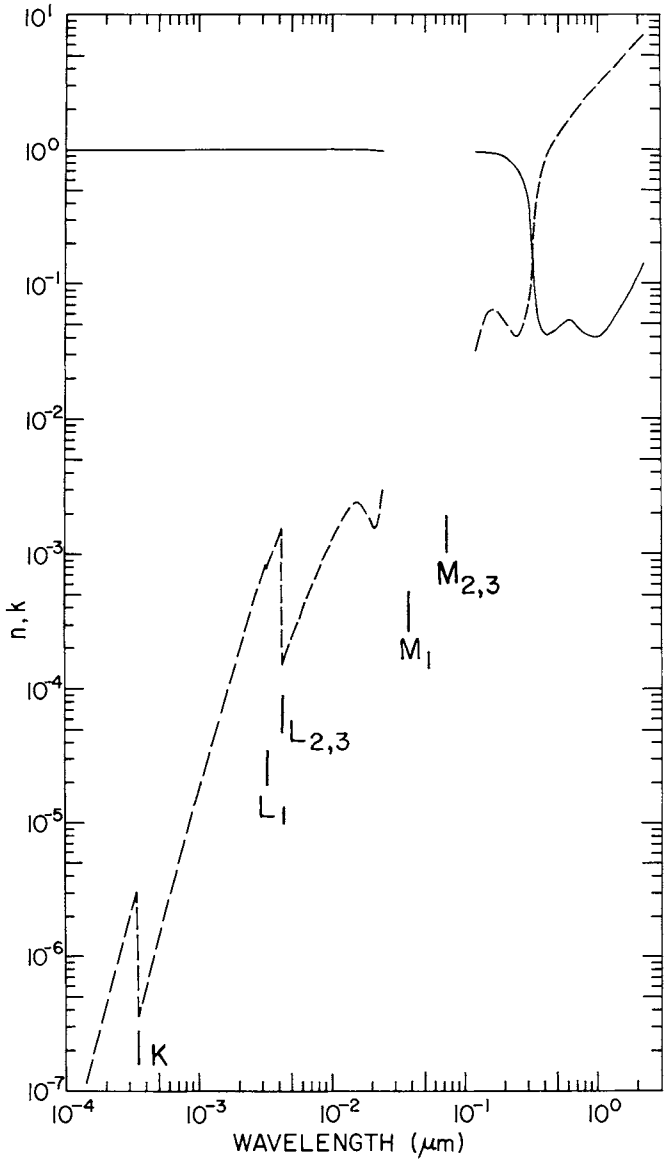

Fig. 1. Log–log plot of n (solid line) and k (dashed line) versus wavelength in micrometers for potassium.

TABLE I

Drude-Model Parameters from Various References

Ref.	ε_∞	τ (10^{-14} sec)	β (10^{-14} sec eV^{-2})	ω_p (eV)	m^*/m
[1]	0	1.58			1.16
[3]	0.11				1.00
[5]		1.55			1.17
[6]	0.20	3.3	[a]	3.80	1.16
[7]		3.2		3.8	1.08
[8]	0.14			4.15	1.05
[9]	0.15	4.4		3.87	1.11
[10]	0.20			3.79	1.08

[a] A plot of τ vs. ω is given, but replotting shows that the scattering rate does not increase as the square of the freqeuncy, but somewhat faster.

TABLE II

Values of n and k Obtained from Various References for Potassium[a]

eV	cm^{-1}	Å	n	k
10000		1.240	0.9999982 [16]	7.02E-08 [16]
9549		1.298	0.9999980	8.10E-08
9117		1.360	0.9999979	9.63E-08
8706		1.424	0.9999977	1.15E-07
8313		1.492	0.9999974	1.38E-07
7937		1.562	0.9999972	1.65E-07
7579		1.636	0.9999969	1.97E-07
7237		1.713	0.9999966	2.34E-07
6910		1.794	0.9999963	2.78E-07
6598		1.879	0.9999959	3.30E-07
6300		1.968	0.9999955	3.92E-07
6015		2.061	0.9999951	4.66E-07
5744		2.159	0.9999946	5.53E-07
5484		2.261	0.9999942	6.57E-07
5237		2.368	0.9999936	7.80E-07
5000		2.480	0.9999931	9.25E-07
4775		2.597	0.9999924	1.10E-06
4559		2.720	0.9999918	1.30E-06
4353		2.848	0.9999911	1.55E-06
4157		2.983	0.9999905	1.83E-06
3969		3.124	0.9999899	2.18E-06
3790		3.272	0.9999895	2.58E-06
3703		3.348	0.9999896	2.81E-06
3619		3.426	0.9999905	3.06E-06
3536		3.506	0.9999891	3.50E-07
3455		3.588	0.9999880	3.81E-07
3299		3.758	0.9999862	4.52E-07
3150		3.936	0.9999844	5.35E-07
3008		4.122	0.9999827	6.34E-07
2872		4.317	0.9999808	7.54E-07
2742		4.521	0.9999787	8.96E-07
2619		4.735	0.9999765	1.07E-06
2500		4.959	0.9999741	1.27E-06
2387		5.193	0.9999714	1.51E-06
2280		5.439	0.9999685	1.79E-06
2177		5.696	0.9999653	2.12E-06
2078		5.965	0.9999618	2.52E-06
1985		6.248	0.9999579	2.99E-06
1895		6.543	0.9999537	3.55E-06
1809		6.852	0.9999490	4.21E-06
1728		7.176	0.9999440	5.00E-06
1650		7.516	0.9999384	5.92E-06
1575		7.871	0.9999322	7.00E-06

[a]The references from which the values were extracted are given in brackets.

TABLE II (*Continued*)

Potassium

eV	cm^{-1}	Å	n	k
1504		8.244	0.9999255	8.27E-06
1436		8.633	0.9999181	9.77E-06
1371		9.041	0.9999100	1.15E-05
1309		9.469	0.9999011	1.36E-05
1250		9.917	0.999891	1.61E-05
1194		10.39	0.999881	1.90E-05
1140		10.88	0.999869	2.23E-05
1088		11.39	0.999857	2.63E-05
1039		11.93	0.999843	3.09E-05
992.3		12.49	0.999828	3.64E-05
947.5		13.09	0.999812	4.23E-05
904.7		13.70	0.999794	4.89E-05
863.9		14.35	0.999774	5.64E-05
824.9		15.03	0.999752	6.66E-05
787.7		15.74	0.999728	7.86E-05
752.1		16.49	0.999703	9.27E-05
718.1		17.27	0.999677	1.09E-04
685.7		18.08	0.999649	1.29E-04
654.7		18.94	0.999619	1.50E-04
625.1		19.83	0.999587	1.75E-04
596.9		20.77	0.999553	2.04E-04
570.0		21.75	0.999518	2.38E-04
544.0		22.78	0.999482	2.78E-04
519.7		23.86	0.999447	3.24E-04
496.2		24.99	0.999411	3.76E-04
473.8		26.17	0.999378	4.38E-04
452.4		27.41	0.999352	5.08E-04
432.9		28.70	0.999331	5.81E-04
412.5		30.06	0.999317	6.64E-04
393.8		31.48	0.999319	7.59E-04
376.1		32.97	0.999388	7.84E-04
359.1		34.53	0.999331	9.01E-04
342.9		36.16	0.999361	1.04E-03
327.4		37.87	0.999454	1.19E-03
312.6		39.66	0.999676	1.36E-03
305.5		40.59	0.999883	1.45E-03
298.5		41.54	1.000338	1.54E-03
291.7		42.51	1.001052	1.53E-04
285.0		43.50	1.000136	1.63E-04
278.5		44.52	0.999882	1.74E-04
272.1		45.56	0.999709	1.85E-04
259.9		47.71	0.999460	2.10E-04
248.1		49.97	0.999259	2.38E-04
236.9		52.33	0.999077	2.70E-04
226.2		54.81	0.99890	3.06E-04

(*Continued*)

TABLE II (*Continued*)

Potassium

eV	cm^{-1}	Å	*n*	*k*
216.0		57.40	0.99872	3.46E-04
206.2		60.12	0.99854	3.91E-04
196.9		62.96	0.99834	4.41E-04
188.0		65.94	0.99814	4.96E-04
179.6		69.05	0.99792	5.55E-04
171.4		72.32	0.99769	6.21E-04
163.7		75.74	0.99745	6.96E-04
156.3		79.32	0.99718	7.76E-04
149.3		83.07	0.99690	8.60E-04
142.5		87.00	0.99659	9.52E-04
136.1		91.11	0.99625	1.05E-03
129.9		95.42	0.99589	1.17E-03
124.1		99.94	0.99551	1.29E-03
118.5		104.7	0.99510	1.41E-03
113.1		109.6	0.99464	1.53E-03
108.0		114.8	0.99414	1.67E-03
103.1		120.2	0.99359	1.82E-03
98.47		125.9	0.99301	1.98E-03
94.03		131.9	0.99236	2.12E-03
89.78		138.1	0.99170	2.30E-03
85.73		144.6	0.99096	2.38E-03
81.85		151.5	0.99011	2.44E-03
78.16		158.6	0.9891	2.44E-03
74.63		166.1	0.9880	2.40E-03
71.26		174.0	0.9866	2.26E-03
68.04		182.2	0.9849	2.08E-03
64.97		190.8	0.9828	1.91E-03
62.04		199.9	0.9803	1.68E-03
59.24		209.3	0.9772	1.57E-03
56.56		219.2	0.9733	1.61E-03
54.01		229.6	0.9685	1.97E-03
51.57		240.4	0.9624	2.97E-03
32.0		387.5		4.8E-02 [15]
31.0		399.9		5.2E-02
30.0		413.3		5.9E-02
29.0		427.5		6.8E-02
28.0		442.8		7.9E-02
27.0		459.2		9.2E-02
26.0		476.9		9.9E-02
25.0		495.9		0.100
24.0		516.6		9.7E-02
23.0		539.1		8.5E-02
22.5		551.0		7.9E-02
22.0		563.6		7.5E-02
21.5		576.7		7.5E-02

(*Continued*)

TABLE II (*Continued*)

Potassium

eV	cm^{-1}	Å	*n*	*k*
21.0		590.4		6.8E-02
20.0		619.9		5.4E-02
19.0		652.5		4.3E-02
18.8		659.5		4.3E-02
18.5		670.2		5.1E-02
18.4		673.8		4.2E-02
18.3		677.5		4.7E-02
18.0		688.8		1.4E-02
17.5		708.5		1.2E-02
17.0		729.3		1.2E-02
16.0		774.9		1.4E-02
15.0		826.6		1.8E-02
14.0		885.6		2.5E-02
13.0		953.7		2.3E-02
eV	cm^{-1}	μm	*n*	*k*
12.0	96786	0.1033		2.8E-02
11.0	88720	0.1127		3.1E-02
10.33	83333	0.120	0.94 [13]	3E-02 [13]
9.919	80000	0.125	0.94	4E-02
9.537	76923	0.130	0.94	4E-02
9.50	76622	0.1305		5.0E-02 [15]
9.184	74074	0.135	0.94 [13]	5E-02 [13]
8.856	71429	0.140	0.94	5E-02
8.551	68966	0.145	0.94	6E-02
8.26	66667	0.150	0.94	6E-02
7.999	64516	0.155	0.94	6E-02
7.749	62500	0.160	0.94	6E-02
7.514	60606	0.165	0.93	6E-02
7.293	58824	0.170	0.93	6E-02
7.085	57143	0.175	0.92	6E-02
6.888	55555	0.180	0.92	6E-02
6.702	54054	0.185	0.91	6E-02
6.526	52632	0.190	0.90	6E-02
6.358	51282	0.195	0.88	5E-02
6.199	50000	0.200	0.87	5E-02
6.048	48780	0.205	0.85	5E-02
5.767	46512	0.215	0.83	5E-02
5.637	45455	0.220	0.81	5E-02
5.510	44444	0.225	0.79	5E-02
5.391	43478	0.230	0.78	4E-02
5.276	42553	0.235	0.76	4E-02
5.166	41667	0.240	0.74	4E-02
5.061	40816	0.245	0.72	4E-02

(*Continued*)

TABLE II (*Continued*)

Potassium

eV	cm^{-1}	μm	*n*	*k*
4.959	40000	0.250	0.70	4E-02
4.862	39216	0.255	0.68	4E-02
4.769	38462	0.260	0.66	4E-02
4.679	37736	0.265	0.64	4E-02
4.592	37037	0.270	0.61	5E-02
4.509	36364	0.275	0.58	5E-02
4.428	35714	0.280	0.55	5E-02
4.350	35088	0.285	0.52	5E-02
4.275	34483	0.290	0.48	6E-02
4.203	33898	0.295	0.45	6E-02
4.133	33333	0.300	0.41	7E-02
4.065	32787	0.305	0.38	7E-02
4.000	32258	0.310	0.34	8E-02
3.97	32020	0.3123	0.287 [6]	9.10E-02 [6]
3.71	29923	0.3342	8.9E-02	0.288
3.40	27423	0.3647	5.2E-02	0.549
3.06	24680	0.4052	4.1E-02	0.799
2.95	23793	0.4203	4.1E-02	0.898
2.82	22745	0.4397	4.3E-02	1.02
2.64	21293	0.4696	4.3E-02	1.14
2.45	19760	0.5061	4.6E-02	1.28
2.27	18309	0.5462	4.9E-02	1.43
2.07	16696	0.5990	5.3E-02	1.62
1.87	15082	0.6630	5.0E-02	1.84
1.65	13308	0.7514	4.4E-02	2.19
1.44	11614	0.8610	4.0E-02	2.56
1.23	9921	1.008	4.0E-02	3.04
1.05	8469	1.181	4.4E-02	3.58
0.92	7420	1.348	5.6E-02	4.19
0.81	6533	1.531	6.6E-02	4.75
0.73	5889	1.698	7.9E-02	5.30
0.67	5404	1.851	9.1E-02	5.79
0.63	5081	1.968	0.106	6.32
0.58	4678	2.138	0.119	6.72
0.55	4436	2.254	0.139	7.10

VI CHROMIUM (Cr)

Chromium is a body-centered cubic metal. It is antiferromagnetic below 312 K. The magnetic ordering, the spatial period of which is incommensurate with the period of the crystal lattice, introduces structure in the spectra of the optical constants in the infrared [1–4]. Since the room-temperature phase of Cr is antiferromagnetic, our data include such structure. The ordering is usually multidomained, so bulk anisotropy does not develop. A single domain of antiferromagnetic Cr is slightly tetragonal, not cubic, but the anisotropy is small. Optical anisotropies due to the ordering [2] are

neglected here. One should also note that the type of antiferromagnetism (commensurate or incommensurate) may vary with the content of impurities, especially of other transition metals, and impurity concentrations of the order of 1% may raise or lower the transition temperature by many degrees [2, 3, and references therein].

Cr oxidizes readily, but the overlayer of Cr_2O_3 is continuous and impermeable to Cr or O after a thickness of about 30 Å is reached, and further oxidation does not occur at room temperature. Such an overlayer may affect optical constants in the visible and near infrared obtained by ellipsometry, and by any technique in the vacuum ultraviolet. There have been few studies in which the sample was both prepared and measured in ultrahigh vacuum.

In the visible, near infrared, and near ultraviolet, we report in Table 1 and Fig. 1 the data of Bos and Lynch [3], the result of a Kramers–Kronig analysis of low-temperature absorptance data on bulk samples. They agree well with the room-temperature data of Barker and Ditzenberger [2]. The data of Johnson and Christy [5] are often quoted. They were obtained from reflectance and transmittance measurements on semitransparent films. However, later work [6] showed that these films were rather fine-grained and porous, and new data were obtained on denser, larger-grained films [7]. The reflectance spectrum calculated from these new data agrees well with that derived from the data we quote below, but there are shifts in the individual spectra of n and k.

In the vacuum ultraviolet, we list the data of Olson and Lynch [8]. These data and others in this spectral region [9] may be affected by the presence of an oxide overlayer, but data taken in this spectral region under UHV conditions do not yet exist. In the soft X-ray region, transmission data [10–12] give spectra of k under the assumption that n is unity. The region of the $3p$ absorption edge has been measured. We list the data of Sonntag *et al.* [12].

The measurements of Bos and Lynch extend to 13 μm in the infrared, although their Kramers–Kronig analysis extends further. A number of measurements extend to longer wavelengths [2, 13–21]. These measurements do not agree well with each other, and some of them show weak structures which are probably spurious. Because of this, it is not possible to select long-wavelength data that are reliable. Since Cr is a transition metal, interband transitions occur at arbitrarily long wavelengths, although their strength eventually becomes negligible with respect to the Drude (interband) contribution at wavelengths longer than some value. This appears to be about 20 μm or even longer [22] and makes fits to the Drude model suspect at shorter wavelengths.

We have calculated n and k in the 1.24–240 Å (10,000–51.5 eV) region using the model of Henke *et al.* [23]. The atomic absorption edges are K (5989 eV), L_1 (695 eV), $L_{2,3}$ (584, 575 eV), M_1 (74 eV), $M_{2,3}$ (43 eV), $M_{4,5}$

(2 eV). These features, especially at the lower energies, will be shifted due to the bonding properties of the crystal.

We used 8065.48 cm^{-1}/eV to convert among the units of [23], whereas the conversion factor may be different by one or two digits in the fourth figure for the other data in Table I.

We list below several other reports of quantitative optical spectra for Cr [24–28].

REFERENCES

1. A. S. Barker, B. I. Halperin, and T. M. Rice, *Phys. Rev. Lett.* **20**, 384 (1968).
2. A. S. Barker and J. A. Ditzenberger, *Phys. Rev.* **B1**, 4378 (1970).
3. L. W. Bos and D. W. Lynch, *Phys. Rev.* **B2**, 4567 (1970).
4. M. A. Lind and J. L. Stanford, *Phys. Lett.* **39A**, 5 (1972).
5. P. B. Johnson and R. W. Christy, *Phys. Rev.* **B9**, 5056 (1974).
6. J. E. Nestell, R. W. Christy, M. Cohen, and G. C. Ruben, *J. Appl. Phys.* **51**, 655 (1980).
7. J. E. Nestell and R. W. Christy, *Phys. Rev.* **B21**, 3173 (1980).
8. C. G. Olson and D. W. Lynch, unpublished (1980).
9. P. Girault, A. Seignac, M. Priol, and S. Robin, *Compt. Rend.* **266**, 688 (1968).
10. A. P. Lukirskii, E. P. Savinov, O. A. Ershov, and Y. F. Shepelev, *Opt. Spectrosc. (USSR)* **16**, 168 (1964); *Opt. Spektrosk.* **16**, 310 (1964).
11. E. P. Savinov, L. I. Lyakhovskaya, O. A. Ershov, and E. A. Kovalyeva, *Opt. Spectrosc. (USSR)* **27**, 179 (1969); *Opt. Spektrosk.* **27**, 342 (1969).
12. B. Sonntag, R. Haensel, and C. Kunz, *Solid State Commun.* **7**, 597 (1969).
13. A. P. Lenham and D. M. Treherne, *J. Opt. Soc. Am.* **56**, 1137 (1966).
14. A. P. Lenham and D. M. Treherne, in "Optical Properties and Electronic Structure of Metals and Alloys," (F. Abeles, ed.), North-Holland, Amsterdam, 196 (1966).
15. A. P. Lenham, *J. Opt. Soc. Am.* **57**, 473 (1967).
16. R. H. W. Graves and A. P. Lenham, *J. Opt. Soc. Am.* **58**, 884 (1968).
17. M. M. Kirillova and M. M. Noskov, *Phys. Met. Metall.* **26**, 189 (1969); *Fiz. Met. Metalloved.* **26**, 592 (1968).
18. A. S. Siddiqui and D. M. Treherne, *Infrared Phys.* **17**, 33 (1975).
19. N. Fuschillo, B. Lalevic, W. Suslark, and A. Delahoy, *J. Vac. Sci. Tech.* **12**, 84 (1975).
20. M. M. Kirillova and L. V. Nomerovannaya, *Phys. Met. Metall.* **40**, 69 (1975); *Fiz. Met. Metalloved.* **40**, 983 (1975).
21. M. M. Kirillova and L. V. Nomerovannaya, *Opt. Spectrosc. (USSR)* **39**, 303 (1975); *Opt. Spektrosk.* **39**, 540 (1975).
22. J. C. Jones, D. C. Palmer, and C. L. Tien, *J. Opt. Soc. Am.* **62**, 353 (1972).
23. B. L. Henke, J. C. Davis, E. M. Gullikson, and R. C. C. Perera, Lawrence Berkeley Laboratory Report No. LBL-26259 (1988).
24. Y. P. Udoev, *Opt. Spectrosc. (USSR)* **33**, 185 (1972); *Opt. Spektrosk.* **33**, 350 (1972).
25. M. R. Steel, *J. Phys. F* **4**, 783 (1974).
26. C. Wehenkel and B. Gauthé, *Phys. Lett.* **47A**, 253 (1974).
27. C. Wehenkel and B. Gauthé, *Phys. Stat. Solidi (b)* **64**, 515 (1974).
28. P. Gravier, G. Chassaing, and M. Sigrist, *Thin Solid Films* **57**, 93 (1979).

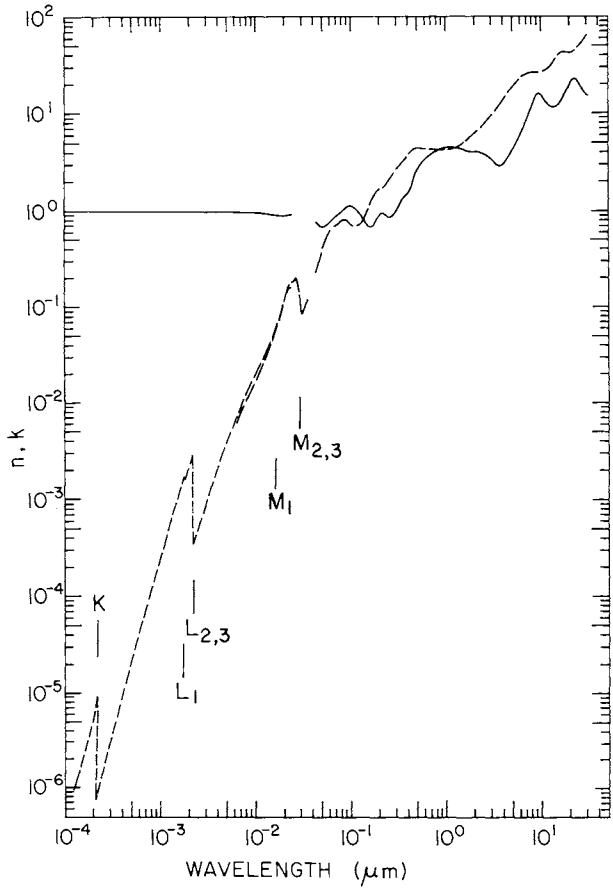

Fig. 1. Log–log plot of n (solid line) and k (dashed line) versus wavelength in micrometers for chromium.

TABLE I

Values of n and k Obtained from Various References for Chromium[a]

eV	cm^{-1}	Å	n	k
10000		1.240	0.9999862 [28]	9.71E-07 [28]
9549		1.298	0.9999847	1.15E-06
9117		1.360	0.9999833	1.37E-06
8706		1.424	0.9999818	1.62E-06
8313		1.492	0.9999802	1.92E-06
7937		1.562	0.9999783	2.27E-06
7579		1.636	0.9999764	2.69E-06
7237		1.713	0.9999744	3.17E-06
6910		1.794	0.9999723	3.74E-06
6598		1.879	0.9999703	4.40E-06
6300		1.968	0.9999686	5.17E-06
6156		2.014	0.9999682	5.60E-06
6015		2.061	0.9999723	6.06E-06
5878		2.109	0.9999663	8.00E-07
5744		2.159	0.9999633	8.71E-07
5613		2.209	0.9999608	9.49E-07
5484		2.261	0.9999585	1.03E-06
5237		2.368	0.9999537	1.23E-06
5000		2.480	0.9999486	1.46E-06
4775		2.597	0.9999432	1.73E-06
4559		2.720	0.9999374	2.05E-06
4353		2.848	0.9999309	2.44E-06
4157		2.983	0.9999238	2.90E-06
3969		3.124	0.9999161	3.45E-06
3790		3.272	0.9999076	4.10E-06
3619		3.426	0.999898	4.87E-06
3455		3.588	0.999888	5.80E-06
3299		3.758	0.999877	6.89E-06
3150		3.936	0.999865	8.20E-06
3008		4.122	0.999851	9.75E-06
2872		4.317	0.999836	1.16E-05
2742		4.521	0.999820	1.38E-05
2619		4.735	0.999802	1.64E-05
2500		4.959	0.999782	1.95E-05
2387		5.193	0.999760	2.32E-05
2280		5.439	0.999737	2.75E-05
2177		5.696	0.999711	3.27E-05
2078		5.965	0.999682	3.88E-05
1985		6.248	0.999651	4.60E-05
1895		6.543	0.999616	5.45E-05
1809		6.852	0.999579	6.46E-05
1728		7.176	0.999538	7.65E-05
1650		7.516	0.999493	9.05E-05
1575		7.871	0.999445	1.07E-04

[a]The references from which the values were extracted are given in brackets.

TABLE I (*Continued*)

Chromium

eV	cm^{-1}	Å	n	k
1504		8.244	0.999392	1.26E-04
1436		8.633	0.999335	1.49E-04
1371		9.041	0.999273	1.75E-04
1309		9.469	0.999206	2.06E-04
1250		9.917	0.999133	2.43E-04
1194		10.39	0.999055	2.85E-04
1140		10.88	0.99897	3.34E-04
1088		11.39	0.99888	3.93E-04
1039		11.93	0.99879	4.61E-04
992.3		12.49	0.99869	5.42E-04
947.5		13.09	0.99859	6.39E-04
904.7		13.70	0.99849	7.48E-04
863.9		14.35	0.99839	8.83E-04
824.9		15.03	0.99831	1.04E-03
787.7		15.74	0.99825	1.20E-03
752.1		16.49	0.99820	1.38E-03
734.9		16.87	0.99819	1.48E-03
718.1		17.27	0.99820	1.59E-03
701.7		17.67	0.99827	1.71E-03
685.7		18.08	0.99828	1.62E-03
670.0		18.51	0.99822	1.73E-03
654.7		18.94	0.99822	1.84E-03
639.8		19.38	0.99824	1.97E-03
610.9		20.30	0.99846	2.33E-03
596.9		20.77	0.99879	2.55E-03
583.3		21.26	0.999636	2.78E-03
570.0		21.75	1.000161	3.41E-04
557.0		22.26	0.999117	3.68E-04
544.2		22.78	0.99862	3.97E-04
531.8		23.31	0.99828	4.27E-04
519.7		23.86	0.99800	4.58E-04
507.8		24.42	0.99775	4.91E-04
484.9		25.57	0.99728	5.63E-04
463.0		26.78	0.99683	6.45E-04
442.1		28.04	0.99638	7.37E-04
422.1		29.37	0.99590	8.42E-04
403.0		30.77	0.99538	9.71E-04
384.8		32.22	0.99484	1.12E-03
367.5		33.74	0.99426	1.31E-03
350.9		35.33	0.99365	1.53E-03
335.0		37.01	0.99301	1.76E-03
319.9		38.76	0.99232	2.02E-03
305.5		40.58	0.99157	2.31E-03
291.7		42.50	0.99078	2.64E-03
278.5		44.52	0.9899	3.00E-03

(*Continued*)

TABLE I (*Continued*)

Chromium

eV	cm^{-1}	Å	*n*	*k*
265.9		46.63	0.9890	3.39E-03
253.9		48.83	0.9880	3.83E-03
242.5		51.15	0.9870	4.32E-03
231.5		53.56	0.9858	4.87E-03
221.1		56.08	0.9846	5.49E-03
211.1		58.73	0.9833	6.15E-03
201.5		61.53	0.9818	6.86E-03
192.4		64.44	0.9802	7.66E-03
183.7		67.49	0.9785	8.63E-03
175.5		70.69	0.9767	9.77E-03
167.5		74.02	0.9749	1.11E-02
160.0		77.49	0.9730	1.23E-02
152.7		81.19	0.9710	1.36E-02
145.8		85.04	0.9687	1.51E-02
139.3		89.01	0.9662	1.67E-02
133.0		93.22	0.9637	1.86E-02
127.0		97.63	0.9611	2.05E-02
121.2		102.3	0.9583	2.25E-02
115.8		107.1	0.9553	2.45E-02
110.5		112.2	0.9518	2.64E-02
105.5		117.5	0.9476	2.88E-02
100.8		123.0	0.9431	3.15E-02
96.22		128.9	0.9380	3.48E-02
91.88		134.9	0.9326	3.88E-02
87.73		141.4	0.9270	4.34E-02
83.77		148.0	0.9209	4.84E-02
79.99		155.0	0.9139	5.43E-02
78.16		158.5	0.9104	5.79E-02
76.37		162.3	0.9068	6.17E-02
74.63		166.2	0.9030	6.58E-02
72.92		170.1	0.8990	7.08E-02
71.26		173.9	0.8954	7.62E-02
69.63		178.1	0.8918	8.21E-02
68.04		182.3	0.8886	8.91E-02
64.97		190.7	0.8850	0.104
62.04		200.0	0.8841	0.120
59.24		209.4	0.8882	0.136
56.56		219.1	0.8970	0.150
54.01		229.6	0.9077	0.157
51.57		240.3	0.9207	0.159
200		61.99		6.0E-03 [12]
150		82.66		1.2E-02
140		88.56		1.3E-02
130		95.37		1.6E-02

(*Continued*)

TABLE I (*Continued*)

Chromium

eV	cm^{-1}	Å	*n*	*k*
125		99.19		1.7E-02
120		103.3		1.9E-02
115		107.8		2.0E-02
110		112.7		2.3E-02
105		118.1		2.60E-02
100		124.0		2.90E-02
95.0		130.5		3.20E-02
90.0		137.8		3.60E-02
85.0		145.9		4.30E-02
80.0		155.0		5.10E-02
75.0		165.3		6.20E-02
70.0		177.1		7.80E-02
65.0		190.7		0.100
60.0		206.6		0.132
59.0		210.1		0.139
58.0		213.8		0.148
57.0		217.5		0.159
56.0		221.4		0.167
55.0		225.4		0.172
54.0		229.6		0.177
53.0		233.9		0.182
52.0		238.4		0.182
51.0		243.1		0.182
50.0		248.0		0.184
49.0		253.0		0.189
48.0		258.3		0.195
47.0		263.8		0.197
46.0		269.5		0.195
45.0		275.5		0.182
44.0		281.8		0.164
43.0		288.3		9.2E-02
42.0		295.2		8.2E-02
41.0		302.4		8.3E-02
40.0		310.0		8.6E-02
35.0		354.2		0.121
29.5		420.3	0.78 [3,8]	0.21 [3,8]
28.8		430.5	0.77	0.22
28.2		439.7	0.75	0.23
27.6		449.2	0.73	0.25
27.0		459.2	0.72	0.26
26.4		469.6	0.71	0.28
25.8		480.6	0.70	0.31
25.3		490.1	0.68	0.33
24.8		499.9	0.68	0.36
24.3		510.2	0.67	0.39

(*Continued*)

TABLE I (*Continued*)

Chromium

eV	cm^{-1}	Å	*n*	*k*
23.9		518.8	0.68	0.43
23.4		529.9	0.68	0.45
23.0		539.1	0.69	0.48
22.5		551.0	0.70	0.50
22.1		561.0	0.71	0.52
21.8		568.7	0.72	0.54
21.4		579.4	0.73	0.56
21.0		590.4	0.74	0.58
20.7		599.0	0.74	0.60
20.3		610.8	0.75	0.62
20.0		619.9	0.77	0.64
19.7		629.4	0.78	0.65
19.4		639.1	0.80	0.67
19.1		649.1	0.82	0.68
18.8		659.5	0.83	0.68
18.5		670.2	0.84	0.69
18.2		681.2	0.85	0.70
18.0		688.8	0.87	0.70
17.7		700.5	0.87	0.71
17.5		708.5	0.88	0.72
17.2		720.8	0.89	0.72
17.0		729.3	0.90	0.73
16.8		738.0	0.90	0.74
16.5		751.4	0.91	0.75
16.3		760.6	0.92	0.76
16.1		770.1	0.92	0.77
15.7		789.7	0.95	0.79
15.5		799.9	0.96	0.80
15.3		810.4	0.97	0.80
14.9		832.1	1.00	0.82
14.8		837.7	1.01	0.82
14.6		849.2	1.03	0.82
14.3		867.0	1.06	0.82
13.9		892.0	1.09	0.82
13.8		898.4	1.10	0.82
13.5		918.4	1.12	0.80
13.3		932.2	1.13	0.80
13.1		946.5	1.15	0.77
12.8		968.6	1.15	0.75
12.5		991.9	1.15	0.73
eV	cm^{-1}	μm	*n*	*k*
12.3	99205	0.1008	1.14	0.71
12.0	96786	0.1033	1.13	0.70

(*Continued*)

TABLE I (*Continued*)

Chromium

eV	cm^{-1}	μm	n	k
11.7	94366	0.1060	1.10	0.69
11.5	92753	0.1078	1.09	0.69
11.3	91140	0.1097	1.07	0.69
11.1	89527	0.1117	1.05	0.69
10.8	87107	0.1148	1.03	0.70
10.5	84688	0.1181	1.01	0.72
10.3	83074	0.1204	1.00	0.72
10.0	80655	0.1240	0.98	0.73
9.76	78719	0.1270	0.95	0.730
9.54	76945	0.1300	0.92	0.740
9.25	74606	0.1340	0.86	0.770
9.05	72993	0.1370	0.83	0.810
8.92	71944	0.1390	0.81	0.830
8.73	70412	0.1420	0.78	0.870
8.61	69444	0.1440	0.76	0.890
8.49	68476	0.1460	0.74	0.920
8.32	67105	0.1490	0.72	0.970
8.21	66218	0.1510	0.71	1.00
8.10	65330	0.1531	0.69	1.04
8.00	64524	0.1550	0.68	1.07
7.90	63717	0.1569	0.68	1.11
7.80	62911	0.1590	0.67	1.15
7.70	62104	0.1610	0.67	1.19
7.61	61378	0.1629	0.66	1.23
7.52	60652	0.1649	0.67	1.27
7.38	59523	0.1680	0.69	1.33
7.29	58797	0.1701	0.70	1.36
7.21	58152	0.1720	0.71	1.39
7.13	57507	0.1739	0.72	1.42
7.01	56539	0.1769	0.74	1.45
6.89	55571	0.1799	0.76	1.49
6.81	54926	0.1821	0.75	1.51
6.70	54039	0.1851	0.78	1.57
6.60	53232	0.1879	0.80	1.59
6.49	52345	0.1910	0.82	1.63
6.39	51538	0.1940	0.85	1.66
6.29	50732	0.1971	0.88	1.68
6.20	50006	0.2000	0.89	1.69
6.11	49280	0.2029	0.92	1.72
5.99	48312	0.2070	0.94	1.73
5.90	47586	0.2101	0.96	1.73
5.79	46699	0.2141	0.97	1.74
5.71	46054	0.2171	0.97	1.75
5.61	45247	0.2210	0.95	1.74
5.51	44441	0.2250	0.94	1.76

(*Continued*)

TABLE I (*Continued*)

Chromium

eV	cm^{-1}	μm	n	k
5.39	43473	0.2300	0.93	1.80
5.30	42747	0.2339	0.90	1.83
5.21	42021	0.2380	0.87	1.87
5.10	41134	0.2431	0.86	1.94
5.00	40327	0.2480	0.85	2.01
4.90	39521	0.2530	0.86	2.07
4.80	38714	0.2583	0.86	2.13
4.70	37908	0.2638	0.86	2.21
4.60	37101	0.2695	0.88	2.28
4.50	36295	0.2755	0.89	2.35
4.40	35488	0.2818	0.90	2.42
4.32	34843	0.2870	0.91	2.49
4.22	34036	0.2938	0.94	2.58
4.13	33310	0.3002	0.98	2.67
4.03	32504	0.3077	1.02	2.76
3.92	31617	0.3163	1.06	2.85
3.83	30891	0.3237	1.12	2.95
3.72	30004	0.3333	1.18	3.04
3.63	29278	0.3416	1.26	3.12
3.53	28471	0.3512	1.33	3.18
3.42	27584	0.3625	1.39	3.24
3.33	26858	0.3723	1.43	3.31
3.22	25971	0.3850	1.44	3.40
3.13	25245	0.3961	1.48	3.54
3.03	24438	0.4092	1.54	3.71
2.92	23551	0.4246	1.65	3.89
2.83	22825	0.4381	1.80	4.06
2.72	21938	0.4558	1.99	4.22
2.63	21212	0.4714	2.22	4.36
2.53	20406	0.4901	2.49	4.44
2.42	19518	0.5123	2.75	4.46
2.33	18793	0.5321	2.98	4.45
2.22	17905	0.5585	3.18	4.41
2.13	17179	0.5821	3.34	4.38
2.03	16373	0.6108	3.48	4.36
1.77	14276	0.7005	3.84	4.37
1.52	12260	0.8157	4.23	4.34
1.50	12098	0.8266	4.27	4.33
1.46	11776	0.8492	4.31	4.32
1.44	11615	0.8610	4.33	4.32
1.40	11292	0.8856	4.38	4.31
1.36	10969	0.9116	4.42	4.30
1.32	10646	0.9393	4.47	4.29
1.28	10324	0.9686	4.49	4.28
1.24	10001	0.9999	4.50	4.28

(*Continued*)

TABLE I (*Continued*)

Chromium

eV	cm^{-1}	μm	n	k
1.20	9679	1.033	4.52	4.29
1.16	9356	1.069	4.53	4.30
1.12	9033	1.107	4.53	4.31
1.08	8711	1.148	4.53	4.34
1.04	8388	1.192	4.51	4.36
1.00	8065	1.240	4.47	4.43
0.96	7743	1.292	4.47	4.50
0.92	7420	1.348	4.45	4.56
0.90	7259	1.378	4.43	4.60
0.86	6936	1.442	4.35	4.66
0.82	6614	1.512	4.24	4.81
0.78	6291	1.590	4.13	5.03
0.74	5968	1.675	4.06	5.30
0.70	5646	1.771	4.01	5.59
0.66	5323	1.879	3.96	5.95
0.62	5001	2.000	4.01	6.31
0.58	4678	2.138	4.01	6.65
0.54	4355	2.296	3.92	7.06
0.50	4033	2.480	3.83	7.58
0.46	3710	2.695	3.72	8.20
0.42	3388	2.952	3.47	8.97
0.38	3065	3.263	3.09	10.2
0.34	2742	3.647	2.89	12.0
0.30	2420	4.133	3.15	14.3
0.26	2097	4.769	3.91	17.1
0.22	1774	5.636	5.30	20.6
0.18	1452	6.888	8.73	25.4
0.14	1129	8.856	15.3	26.4
0.10	806.5	12.40	11.8	29.8
0.09	725.9	13.78	11.8	33.9
0.08	645.2	15.50	13.6	42.2
0.06	483.9	20.66	21.2	42.0
0.04	322.6	31.00	14.9	65.2

IRON (Fe) VII

Iron is a bcc metal. It has an fcc phase at high temperatures, but we ignore that here. A single domain of cubic Fe that is magnetized is optically anisotropic; the optical dielectric function is a tensor with three independent complex components. However, the anisotropy is small, and we neglect it here. The off-diagonal anisotropy is proportional to the magnetization (M) and the diagonal anisotropy is proportional to its square. Iron is not a highly reactive material, but it is not inert. Several different oxides grow at rates dependent on surface quality, impurities, and ambient conditions.

We do not discuss all of the optical studies on Fe. By and large, the data in the visible and near ultraviolet are in relatively good mutual agreement. The soft X-ray data (k spectrum, since $n \approx 1$) generally agree in shape above the $3p$ absorption edge, but the magnitudes do not, and the discrepancy with the longer-wavelength bulk data is in the wrong direction to be explained by a lower film density.

Values of n and k are given in Table I and plotted in Fig. 1. In the infrared and visible, we list the data of Weaver *et al.* [1]. These were obtained by a Kramers–Kronig analysis of absorptance data on bulk samples. They agree well, where they overlap, with the data of Johnson and Christy [2], obtained from reflectance and transmittance measurements on semitransparent films, which data we report in the ultraviolet. In the vacuum ultraviolet we use the data of Moravec *et al.* [3] obtained from Kramers–Kronig analysis of reflectance data on opaque, thin-film samples. These data show a higher reflectance, and presumably are less affected by oxides. They also match better with the soft X-ray data. At higher energies, we list k spectra obtained from absorption-coefficient measurements on thin films by Sonntag *et al.* [4], using the assumption that n is unity. Their data cover the region of the $3p$ absorption edge, as do those of Wehenkel and Gauthé [5, 6].

Because of the partially filled $3d$ band, interband transitions exist to arbitrarily low photon energies, although at some point they become weak. Jones *et al.* [7] showed that for wavelengths longer than about 10 μm, the interband transitions were negligible. The only infrared measurements that yield spectra of n and k, however, appear to be those of Weaver *et al.* [1], of Lenham and Treherne [8–10], of Siddiqui and Treherne [11], and of Ordal *et al.* [12], from which we list data here. Ordal *et al.* made reflectance measurements to 55.6 μm, although details are not reported, then compared their spectra with others for consistency and fit to a set of Drude parameters. Ordal *et al.* [13] later made measurements in the 33.3–333 μm region, using a resonant cavity. This gives only one measured quantity at each point, but a reasonable approximation allows n and k to be extracted. We list their data in this spectral region.

We have calculated n and k in the 1.24–240 Å (10,000–51.5 eV) region using the model of Henke *et al.* [14]. The atomic absorption edges are K (7114 eV), L_1 (846 eV), $L_{2,3}$ (723, 710 eV), M_1 (95 eV), $M_{2,3}$ (56 eV), $M_{4,5}$ (6 eV). At the lower energies these atomic features may be perturbed by the bonding properties of the crystal.

We used 8065.48 cm^{-1}/eV to convert among the units of [14], whereas the conversion factor may be different by one or two digits in the fourth figure for the other data of Table I.

Finally, we list other references to optical constants of Fe [15–18]. We do not include those that give data only in arbitrary units.

REFERENCES

1. J. H. Weaver, E. Colavita, D. W. Lynch, and R. Rosei, *Phys. Rev.* **B19**, 3850 (1979).
2. P. B. Johnson and R. W. Christy, *Phys. Rev.* **B9**, 5056 (1974).
3. T. J. Moravec, J. C. Rife, and D. L. Dexter, *Phys. Rev.* **B13**, 3297 (1976).
4. B. Sonntag, R. Haensel, and C. Kunz, *Solid State Commun.* **7**, 597 (1969).
5. C. Wehenkel and B. Gauthé, *Phys. Lett.* **47A**, 253 (1974).
6. C. Wehenkel and B. Gauthé, *Phys. Stat. Solidi (b)* **64**, 515 (1974).
7. J. C. Jones, D. C. Palmer, and C. L. Tien, *J. Opt. Soc. Am.* **62**, 353 (1972).
8. A. P. Lenham and D. M. Treherne, *J. Opt. Soc. Am.* **56**, 1137 (1966).
9. A. P. Lenham and D. M. Treherne, in "Optical Properties and Electronic Structure of Metals and Alloys," (F. Abeles, ed.), North-Holland, Amsterdam, 196 (1966).
10. A. P. Lenham, *J. Opt. Soc. Am.* **57**, 473 (1967).
11. A. S. Siddiqui and D. M. Treherne, *Infrared Phys.* **17**, 33 (1977).
12. M. A. Ordal, R. J. Bell, R. W. Alexander, L. L. Long, and M. R. Querry, *Appl. Opt.* **24**, 4493 (1985).
13. M. A. Ordal, R. J. Bell, R. W. Alexander, L. A. Newquist, and M. R. Querry, *Appl. Opt.* **27**, 1203 (1988).
14. B. L. Henke, J. C. Davis, E. M. Gullikson, and R. C. C. Perera, Lawrence Berkeley Laboratory Report No. LBL-26259 (1988).
15. H. T. Yolken and J. Kruger, *J. Opt. Soc. Am.* **55**, 842 (1965).
16. A. J. Blodgett and W. E. Spicer, *Phys. Rev.* **158**, 514 (1967).
17. G. A. Bolotin, M. M. Kirillova, and V. M. Mayevskiy, *Phys. Met. Metall.* **27**, 31 (1969); *Fiz. Met. Metalloved.* **27**, 224 (1969).
18. V. P. Shirokovskii, M. M. Kirillova, and N. A. Shilkova, *Sov. Phys. JETP* **55**, 464 (1982); *Zh. Eksp. Teor. Fiz.* **82**, 784 (1982).

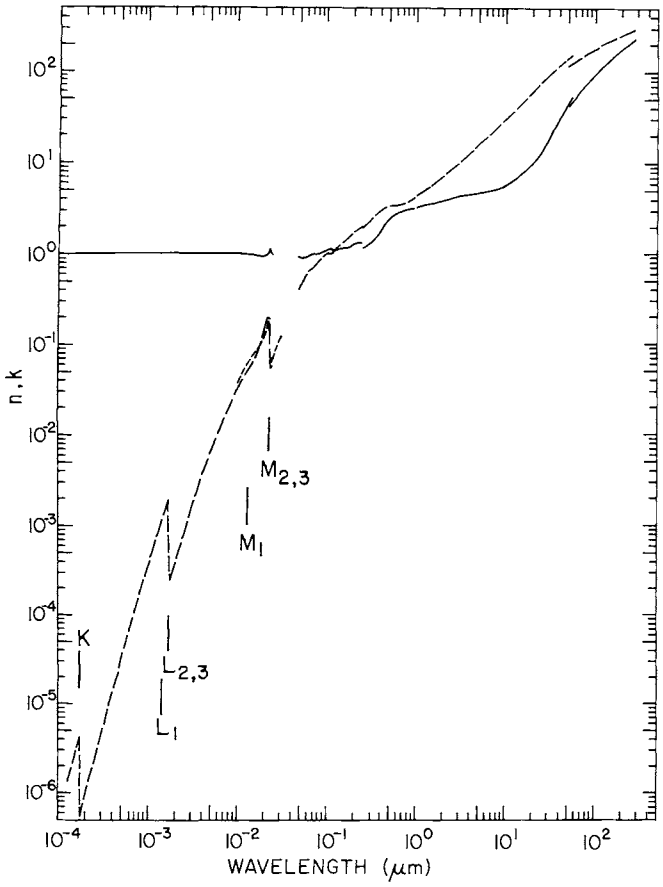

Fig. 1. Log–log plot of n (solid line) and k (dashed line) versus wavelength in micrometers for iron.

TABLE I

Values of n and k Obtained from Various References for Iron[a]

eV	cm^{-1}	Å	n	k
10000		1.240	0.9999849 [18]	1.32E-06 [18]
9549		1.298	0.9999834	1.57E-06
9117		1.360	0.9999819	1.86E-06
8706		1.424	0.9999803	2.19E-06
8313		1.492	0.9999787	2.59E-06
7937		1.562	0.9999771	3.04E-06
7579		1.636	0.9999755	3.58E-06
7406		1.674	0.9999750	3.88E-06
7237		1.713	0.9999750	4.20E-06
7071		1.753	0.9999753	5.70E-07
6910		1.794	0.9999721	6.21E-07
6752		1.836	0.9999701	6.77E-07
6598		1.879	0.9999682	7.38E-07
6300		1.968	0.9999645	8.77E-07
6015		2.061	0.9999607	1.04E-06
5744		2.159	0.9999565	1.24E-06
5484		2.261	0.9999520	1.47E-06
5237		2.368	0.9999471	1.75E-06
5000		2.480	0.9999416	2.08E-06
4775		2.597	0.9999357	2.48E-06
4559		2.720	0.9999293	2.94E-06
4353		2.848	0.9999222	3.50E-06
4157		2.983	0.9999144	4.16E-06
3969		3.124	0.9999058	4.95E-06
3790		3.272	0.999896	5.88E-06
3619		3.426	0.999886	6.99E-06
3455		3.588	0.999875	8.30E-06
3299		3.758	0.999862	9.86E-06
3150		3.936	0.999848	1.17E-05
3008		4.122	0.999834	1.39E-05
2872		4.317	0.999817	1.65E-05
2742		4.521	0.999799	1.96E-05
2619		4.735	0.999779	2.32E-05
2500		4.959	0.999757	2.76E-05
2387		5.193	0.999733	3.27E-05
2280		5.439	0.999707	3.87E-05
2177		5.696	0.999679	4.58E-05
2078		5.965	0.999647	5.42E-05
1985		6.248	0.999614	6.41E-05
1895		6.543	0.999576	7.57E-05
1809		6.852	0.999536	8.94E-05
1728		7.176	0.999492	1.06E-04
1650		7.516	0.999445	1.24E-04
1575		7.871	0.999393	1.46E-04

[a]The references from which the values were extracted are given in brackets.

TABLE I (*Continued*)

Iron

eV	cm^{-1}	Å	*n*	*k*
1504		8.244	0.999337	1.72E-04
1436		8.633	0.999278	2.03E-04
1371		9.041	0.999214	2.38E-04
1309		9.469	0.999146	2.79E-04
1250		9.917	0.999075	3.28E-04
1194		10.39	0.99900	3.84E-04
1140		10.88	0.99892	4.49E-04
1088		11.39	0.99884	5.26E-04
1039		11.93	0.99876	6.15E-04
992.3		12.49	0.99869	7.19E-04
947.5		13.09	0.99862	8.38E-04
904.7		13.70	0.99857	9.80E-04
884.1		14.02	0.99856	1.06E-03
863.9		14.35	0.99858	1.15E-03
844.2		14.69	0.99863	1.10E-03
824.9		15.03	0.99857	1.19E-03
806.0		15.38	0.99856	1.28E-03
787.7		15.74	0.99858	1.38E-03
769.7		16.11	0.99864	1.50E-03
752.1		16.49	0.99875	1.62E-03
734.9		16.87	0.99897	1.75E-03
718.1		17.27	0.999579	1.89E-03
701.7		17.67	0.999763	2.40E-04
685.7		18.08	0.999100	2.57E-04
670.0		18.51	0.99876	2.76E-04
654.7		18.94	0.99851	2.98E-04
639.8		19.38	0.99831	3.22E-04
610.9		20.30	0.99794	3.71E-04
583.3		21.26	0.99759	4.29E-04
557.0		22.26	0.99724	4.99E-04
531.8		23.31	0.99687	5.80E-04
507.8		24.42	0.99649	6.75E-04
484.9		25.57	0.99608	7.85E-04
463.0		26.78	0.99564	9.13E-04
442.1		28.05	0.99517	1.06E-03
422.1		29.37	0.99465	1.23E-03
403.0		30.76	0.99411	1.43E-03
384.8		32.22	0.99351	1.65E-03
367.5		33.74	0.99286	1.93E-03
350.9		35.34	0.99218	2.25E-03
335.0		37.01	0.99147	2.63E-03
319.9		38.76	0.99072	3.01E-03
305.5		40.59	0.9899	3.44E-03
291.7		42.51	0.9890	3.94E-03
278.5		44.52	0.9881	4.51E-03

(*Continued*)

TABLE I (*Continued*)

Iron

eV	cm^{-1}	Å	n	k
265.9		46.63	0.9872	5.07E-03
253.9		48.83	0.9862	5.68E-03
242.5		51.14	0.9850	6.35E-03
231.5		53.56	0.9838	7.11E-03
221.1		56.09	0.9823	8.00E-03
211.1		58.74	0.9809	9.09E-03
201.5		61.52	0.9794	1.03E-02
192.4		64.43	0.9779	1.18E-02
183.7		67.48	0.9765	1.31E-02
175.5		70.67	0.9749	1.45E-02
167.5		74.01	0.9732	1.61E-02
160.0		77.51	0.9713	1.78E-02
152.7		81.17	0.9694	1.97E-02
145.8		85.01	0.9674	2.18E-02
139.3		89.03	0.9653	2.40E-02
133.0		93.24	0.9631	2.64E-02
127.0		97.66	0.9609	2.91E-02
121.2		102.3	0.9587	3.17E-02
115.8		107.1	0.9561	3.45E-02
110.5		112.2	0.9534	3.75E-02
105.5		117.5	0.9505	4.08E-02
100.8		123.0	0.9474	4.43E-02
98.47		125.9	0.9457	4.61E-02
96.22		128.9	0.9440	4.81E-02
94.03		131.9	0.9422	5.01E-02
91.88		134.9	0.9403	5.22E-02
89.78		138.1	0.9383	5.44E-02
87.73		141.3	0.9363	5.67E-02
85.73		144.6	0.9341	5.92E-02
81.85		151.5	0.9295	6.44E-02
78.16		158.6	0.9243	7.02E-02
74.63		166.1	0.9172	7.70E-02
71.26		174.0	0.9102	8.77E-02
68.04		182.2	0.9034	0.100
64.97		190.8	0.8969	0.121
62.04		199.9	0.9013	0.149
59.24		209.3	0.9252	0.179
56.56		219.2	0.9751	0.191
55.27		224.3	1.012	0.185
54.01		229.6	1.109	0.175
52.77		234.9	1.004	5.36E-02
51.57		240.4	0.9695	5.44E-02
250		49.59		5.0E-03 [4]
200		61.99		1.0E-02

(*Continued*)

TABLE I (*Continued*)

Iron

eV	cm^{-1}	Å	*n*	*k*
150		82.66		2.3E-02
120		103.3		3.8E-02
115		107.8		4.1E-02
110		112.7		4.5E-02
105		118.1		5.0E-02
100		124.0		5.4E-02
95.0		130.5		6.0E-02
90.0		137.8		6.5E-02
85.0		145.9		7.0E-02
80.0		155.0		7.6E-02
75.0		165.3		8.4E-02
70.0		177.1		9.4E-02
65.0		190.7		0.108
60.0		206.6		0.130
56.0		221.4		0.176
52.0		238.4		6.0E-02
50.0		248.0		6.5E-02
45.0		275.5		9.2E-02
40.0		310.0		0.118
26.0		476.9	0.890 [3]	0.376 [3]
25.8		480.6	0.887	0.383
25.6		484.3	0.886	0.395
25.4		488.1	0.884	0.402
25.2		492.0	0.881	0.408
25.0		495.9	0.877	0.411
24.8		499.9	0.874	0.418
24.6		504.0	0.876	0.434
24.4		508.1	0.872	0.436
24.2		512.3	0.870	0.443
24.0		516.6	0.867	0.450
23.8		520.9	0.865	0.468
23.6		525.4	0.859	0.477
23.4		529.8	0.861	0.482
23.2		534.4	0.862	0.493
23.0		539.1	0.863	0.504
22.8		543.8	0.861	0.511
22.6		548.6	0.863	0.515
22.4		553.5	0.862	0.522
22.2		558.5	0.865	0.537
22.0		563.6	0.872	0.556
21.8		568.7	0.874	0.561
21.6		574.0	0.875	0.571
21.4		579.4	0.875	0.571
21.2		584.8	0.878	0.575
21.0		590.4	0.882	0.590

(*Continued*)

TABLE I (*Continued*)

Iron

eV	cm^{-1}	Å	n	k
20.8		596.1	0.892	0.605
20.6		601.9	0.898	0.613
20.4		607.8	0.903	0.620
20.2		613.8	0.905	0.624
20.0		619.9	0.910	0.632
19.8		626.2	0.919	0.636
19.6		632.6	0.924	0.644
19.4		639.1	0.927	0.647
19.2		645.8	0.933	0.648
19.0		652.5	0.936	0.652
18.8		659.5	0.938	0.656
18.6		666.6	0.938	0.656
18.4		673.8	0.941	0.659
18.2		681.2	0.941	0.659
18.0		688.8	0.939	0.665
17.8		696.5	0.944	0.672
17.6		704.5	0.946	0.682
17.4		712.6	0.945	0.688
17.2		720.8	0.947	0.697
17.0		729.3	0.948	0.707
16.8		738.0	0.952	0.719
16.6		746.9	0.955	0.723
16.4		756.0	0.951	0.731
16.2		765.3	0.944	0.742
16.0		774.9	0.940	0.750
15.8		784.7	0.941	0.765
15.6		794.8	0.943	0.774
15.4		805.1	0.945	0.783
15.2		815.7	0.949	0.791
15.0		826.6	0.952	0.798
14.8		837.7	0.959	0.824
14.6		849.2	0.974	0.847
14.4		861.0	0.988	0.870
14.2		873.1	0.993	0.881
14.0		885.6	1.00	0.889
13.8		898.4	1.00	0.898
13.6		911.6	1.01	0.911
13.4		925.3	1.02	0.925
13.2		939.3	1.03	0.935
13.0		953.7	1.05	0.951
12.8		968.6	1.06	0.964
12.6		984.0	1.08	0.972
12.4		999.9	1.09	0.968

(*Continued*)

TABLE I (*Continued*)

Iron

eV	cm^{-1}	μm	n	k
12.2	98399	0.1016	1.10	0.971
12.0	96786	0.1033	1.10	0.969
11.8	95173	0.1051	1.11	0.967
11.6	93560	0.1069	1.12	0.968
11.4	91946	0.1088	1.11	0.958
11.2	90333	0.1107	1.11	0.953
11.0	88720	0.1127	1.11	0.950
10.8	87107	0.1148	1.10	0.959
10.6	85494	0.1170	1.07	0.991
10.4	83881	0.1192	1.07	1.02
10.2	82268	0.1216	1.06	1.06
10.0	80655	0.1240	1.05	1.09
9.80	79042	0.1265	1.08	1.13
9.60	77429	0.1292	1.09	1.15
9.40	75816	0.1319	1.10	1.17
9.20	74202	0.1348	1.12	1.19
9.00	72589	0.1378	1.12	1.20
8.80	70976	0.1409	1.13	1.22
8.60	69363	0.1442	1.13	1.24
8.40	67750	0.1476	1.13	1.26
8.20	66137	0.1512	1.13	1.28
8.00	64524	0.1550	1.13	1.32
7.80	62911	0.1590	1.15	1.32
7.60	61298	0.1631	1.15	1.37
7.40	59684	0.1675	1.15	1.40
7.20	58071	0.1722	1.13	1.45
7.00	56458	0.1771	1.15	1.49
6.80	54845	0.1823	1.20	1.54
6.60	53232	0.1879	1.22	1.61
6.40	51619	0.1937	1.23	1.67
6.20	50006	0.2000	1.28	1.71
6.00	48393	0.2066	1.30	1.73
5.80	46780	0.2138	1.32	1.75
5.60	45167	0.2214	1.32	1.78
5.40	43554	0.2296	1.31	1.82
5.20	41940	0.2384	1.32	1.88
5.00	40327	0.2480	1.31	1.95
1.240	10000	1.000	3.23 [12]	4.35 [12]
1.116	9000	1.111	3.32	4.65
0.9919	8000	1.250	3.42	5.04
0.8679	7000	1.429	3.53	5.54
0.7439	6000	1.667	3.67	6.21
0.6199	5000	2.000	3.84	7.16
0.5889	4750	2.105	3.92	7.50
0.5579	4500	2.222	3.98	7.80

(*Continued*)

TABLE I (*Continued*)

Iron

eV	cm^{-1}	μm	n	k
0.5269	4250	2.353	4.04	8.18
0.4959	4000	2.500	4.13	8.59
0.4649	3750	2.667	4.22	9.02
0.4339	3500	2.857	4.30	9.55
0.4030	3250	3.077	4.39	10.1
0.3720	3000	3.333	4.45	10.8
0.3410	2750	3.636	4.51	11.6
0.3100	2500	4.000	4.54	12.6
0.2790	2250	4.444	4.59	13.8
0.2480	2000	5.000	4.59	15.4
0.2356	1900	5.263	4.60	16.2
0.2232	1800	5.555	4.63	17.1
0.2108	1700	5.882	4.66	18.1
0.1984	1600	6.250	4.96	19.2
0.1860	1500	6.667	4.75	20.5
0.1736	1400	7.143	4.89	22.0
0.1612	1300	7.692	5.10	23.7
0.1488	1200	8.333	5.37	25.6
0.1364	1100	9.091	5.59	27.8
0.1240	1000	10.00	5.81	30.4
0.1178	950	10.53	5.95	32.0
0.1116	900	11.11	6.12	33.7
0.1054	850	11.76	6.31	35.7
0.09919	800	12.50	6.48	37.7
0.09299	750	13.33	6.88	40.3
0.08679	700	14.29	7.30	43.2
0.08059	650	15.38	7.71	46.5
0.07439	600	16.67	8.38	50.3
0.06819	550	18.18	9.04	54.7
0.06199	500	20.00	9.87	60.1
0.05951	480	20.83	10.3	62.6
0.05703	460	21.74	10.7	65.4
0.05455	440	22.73	11.3	68.6
0.05207	420	23.81	12.0	71.9
0.04959	400	25.00	13.0	75.7
0.04711	380	26.32	14.2	79.8
0.04463	360	27.78	15.7	84.5
0.04215	340	29.41	17.7	89.3
0.03968	320	31.25	19.9	94.5
0.03720	300	33.33	22.5	100
0.03472	280	35.71	25.2	106
0.03224	260	38.46	29.1	114
0.02976	240	41.67	33.6	122
0.02728	220	45.45	38.6	130
0.02480	200	50.00	45.7	141

(*Continued*)

TABLE I (*Continued*)

Iron

eV	cm^{-1}	μm	*n*	*k*
			43.2 [13]	115 [13]
0.02232	180	55.55	54.2 [12]	152 [12]
0.02170	175	57.14	51.2 [13]	126 [13]
0.01860	150	66.67	61.3	140
0.01550	125	80.00	75.2	158
0.01240	100	100.0	95.4	182
0.009919	80	125.0	120	207
0.008059	65	153.8	147	230
0.006199	50	200.0	183	260
0.004339	35	285.7	238	306

VIII NIOBIUM (Nb)

Niobium is a body-centered cubic metal. It is not highly reactive, but a thin oxide film does form at room temperature, a film that may effect ellipsometric measurements in the visible and near ultraviolet, and all measurements further in the ultraviolet.

There are many sets of near-infrared, visible, and near-ultraviolet data [1–16]. Most of them agree in the number and position of structures in the spectra in the visible and ultraviolet, but there are large discrepancies in the magnitudes of the optical constants. Data taken on films condensed on room-temperature substrates are suspect; heated substrates must be used, and high evaporation rates are necessary to reduce surface roughness [14]. Some measurements were carried out on films prepared in UHV, but the measurements were not made in UHV. There are two vacuum-ultraviolet measurements [8, 17]. The only all-UHV studies were those of Truong *et al.* [17], and of Carroll *et al.* [18]. The former used foil samples heavily annealed in UHV. Unfortunately, their data do not match well at longer wavelengths with any other measurements, although they may be the most reliable to date at shorter wavelengths because of the possible influence of oxides on the other data. Carroll *et al.* worked with an atomically clean single-crystal surface in UHV, but their data are at only seven wavelengths in the 0.40 μm to 0.63 μm region. In this range their *n* spectrum is about 10% higher than that of Weaver *et al.* [8], and their *k* spectrum lies about 4% lower. It is not clear that these differences can be attributed exclusively to surface cleanliness. There is one measurement [19] of optical absorption in the soft X-ray region, the region of the 4*p* excitation, from which a spectrum of *k* can be obtained with the assumption that *n* is unity. However, the sample was a film condensed on a room-temperature

substrate, and its density was probably lower than bulk. The resultant k spectrum is lower than expectations based on longer-wavelength data [8, 17]. Windt *et al.* [20] made multiple-angle reflectance measurements on films to obtain optical constants in the 24–1216 Å region, but all the films were produced *ex situ*.

There are discrepancies in the number and strength of interband transitions in the infrared. In the region below 1 eV, Weaver *et al.* [8] found no peaked structures, although that does not necessarily mean interband absorption is negligible. Golovashkin *et al.* [7] and Kirillova and Nomerovannaya [12] find a number of structures in ε_2 below 1 eV. Rashkeev *et al.* [21] calculated that there is an interband peak at 0.09 eV and a weaker one at 0.3 eV. The calculated peaks were at about the correct positions, but were considerably weaker than the experimental ones.

In Table I we list Weaver *et al.*'s data [8] for the near infrared, visible, ultraviolet, and vacuum ultraviolet. The data of Nestell and Christy [14] and of Lluesma and Aspnes [15] cover a smaller spectral region, but they result in larger values of ε_2, indicative of data less affected by overlayers and granularity or roughness of the sample. We do not list them, for they do not match well with the extant infrared data [7, 8, 12], which should be less sensitive to some of the problems mentioned above. The k spectra we list, then, may be somewhat low in the visible, ultraviolet, and vacuum ultraviolet. We also list the soft X-ray data of Weaver and Olson [19]. Values of n and k are plotted in Fig. 1.

We have calculated n and k in the 1.24–240 Å (10,000–51.5 eV) region using the model of Henke *et al.* [22]. The absorption edges are K (18 986 eV), L_1 (2698 eV), $L_{2,3}$ (2465, 2371 eV), M_1 (469 eV), $M_{2,3}$ (379, 363 eV), $M_{4,5}$ (208, 205 eV), N_1 (58 eV), $N_{2,3}$ (34 eV), $N_{4,5}$ (4 eV). At lower frequencies these features are perturbed by the bonding properties of the crystal.

REFERENCES

1. M. M. Kirillova and B. A. Charikov, *Phys. Met. Metall.* **15**, 13 (1965); *Fiz. Met. Metalloved.* **15**, 495 (1965).
2. B. T. Barnes, *J. Opt. Soc. Am.* **56**, 1546 (1966).
3. A. P. Lenham and D. M. Treherne, *J. Opt. Soc. Am.* **56**, 1137 (1966).
4. A. P. Lenham and D. M. Treherne, in "Optical Properties and Electronic Structure of Metals and Alloys," (F. Abeles, ed.), North-Holland, Amsterdam, 196 (1966).
5. A. P. Lenham, *J. Opt. Soc. Am.* **57**, 473 (1967).
6. M. M. Kirillova, L. V. Nomerovannaya, G. A. Bolotin, V. M. Mayevskiy, M. M. Noskov, and M. L. Bolotina, *Phys. Met. Metall.* **25**, 81 (1968); *Fiz. Met. Metalloved.* **25**, 459 (1968).
7. A. I. Golovashkin, I. E. Leksina, G. P. Motulevich, and A. A. Shubin, *Soviet Phys. JETP* **29**, 27 (1969); *Zh. Eksp. Teor. Fiz.* **56**, 51 (1969).
8. J. H. Weaver, D. W. Lynch, and C. G. Olson, *Phys. Rev.* **B7**, 4311 (1973).
9. M. Sigrist, G. Chessaing, and P. Gravier, *Solid State Commun.* **17**, 647 (1975).

10. M. Sigrist, G. Chessaing, P. Gravier, and R. Pierrisnard, *Compt. Rend. Acad.* **280**, 413 (1975).
11. G. Chessaing, P. Gravier, and M. Sigrist, *Thin Solid Films* **35**, L25 (1976).
12. M. M. Kirillova and L. V. Nomerovannaya, *Sov. Phys. Solid State* **20**, 568 (1978); *Fiz. Tverd. Tela* **20**, 984 (1978).
13. P. Gravier, G. Chassaing, and M. Sigrist, *Thin Solid Films* **57**, 93 (1979).
14. J. E. Nestell and R. W. Christy, *Phys. Rev.* **B21**, 3173 (1980).
15. E. Lluesma and D. E. Aspnes, unpublished.
16. A. I. Golovashkin and A. L. Shelekhov, *Sov. Phys. JETP* **57**, 1246 (1983); *Zh. Eksp. Teor. Fiz.* **84**, 2141 (1983).
17. V. V. Truong, L. J. LeBlanc, and G. J. Turpin, *J. Opt. Soc. Am.* **68**, 1017 (1978).
18. J. J. Carroll, C. T. Ceyer, and A. J. Melmed, *J. Opt. Soc. Am.* **72**, 668 (1982).
19. J. H. Weaver and C. G. Olson, *Phys. Rev.* **B14**, 3251 (1976).
20. D. L. Windt, W. C. Cash, M. Scott, P. Arendt, B. Newnam, R. F. Fisher, and A. B. Swartzlander, *Appl. Opt.* **27**, 246 (1988).
21. S. N. Rashkeev, Y. A. Uspenskii, and I. I. Mazin, *Soviet Phys. JETP* **61**, 1004 (1985); *Zh. Eksp. Teor. Fiz.* **88**, 1687 (1985).
22. B. L. Henke, J. C. Davis, E. M. Gullikson, and R. C. C. Perera, Lawrence Berkeley Laboratory Report No. LBL-26259 (1988).

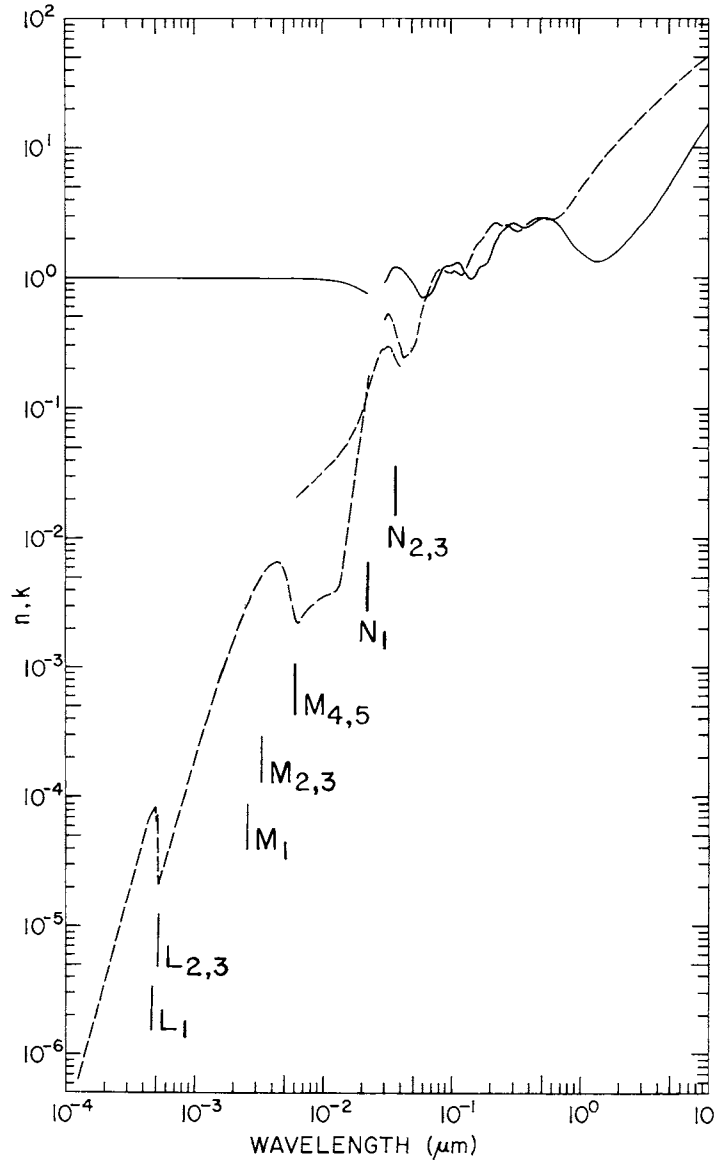

Fig. 1. Log–log plot of n (solid line) and k (dashed line) versus wavelength in micrometers for niobium.

TABLE I

Values of n and k Obtained from Various References for Niobium[a]

eV	cm^{-1}	Å	n	k
10000		1.240	0.9999845 [22]	6.55E-07 [22]
9549		1.298	0.9999829	7.80E-07
9117		1.360	0.9999812	9.28E-07
8706		1.424	0.9999794	1.10E-06
8313		1.492	0.9999774	1.31E-06
7937		1.562	0.9999751	1.56E-06
7579		1.636	0.9999726	1.86E-06
7237		1.713	0.9999700	2.21E-06
6910		1.794	0.9999670	2.62E-06
6598		1.879	0.9999638	3.11E-06
6300		1.968	0.9999602	3.70E-06
6015		2.061	0.9999564	4.39E-06
5744		2.159	0.9999521	5.21E-06
5484		2.261	0.9999475	6.18E-06
5237		2.368	0.9999425	7.34E-06
5000		2.480	0.9999370	8.70E-06
4775		2.597	0.9999310	1.03E-05
4559		2.720	0.9999245	1.22E-05
4353		2.848	0.9999175	1.44E-05
4157		2.983	0.9999099	1.71E-05
3969		3.124	0.9999018	2.02E-05
3790		3.272	0.999893	2.38E-05
3619		3.426	0.999884	2.81E-05
3455		3.588	0.999874	3.31E-05
3299		3.758	0.999864	3.90E-05
3150		3.936	0.999854	4.59E-05
3008		4.122	0.999845	5.39E-05
2872		4.317	0.999836	6.32E-05
2807		4.418	0.999833	6.84E-05
2742		4.521	0.999832	7.40E-05
2680		4.627	0.999832	7.02E-05
2619		4.735	0.999826	7.59E-05
2559		4.846	0.999825	8.21E-05
2500		4.959	0.999831	8.88E-05
2443		5.075	0.999835	6.97E-05
2387		5.193	0.999839	7.57E-05
2333		5.315	0.999822	2.21E-05
2280		5.439	0.999795	2.38E-05
2228		5.566	0.999775	2.58E-05
2177		5.696	0.999757	2.79E-05
2078		5.965	0.999723	3.26E-05
1985		6.248	0.999688	3.83E-05
1895		6.543	0.999651	4.49E-05

[a]The references from which the values were extracted are given in brackets.

TABLE I (*Continued*)

Niobium

eV	cm^{-1}	Å	*n*	*k*
1809		6.852	0.999613	5.27E-05
1728		7.176	0.999570	6.19E-05
1650		7.516	0.999525	7.29E-05
1575		7.871	0.999475	8.58E-05
1504		8.244	0.999422	1.01E-04
1436		8.633	0.999364	1.18E-04
1371		9.041	0.999301	1.38E-04
1309		9.469	0.999232	1.61E-04
1250		9.917	0.999157	1.88E-04
1194		10.39	0.999076	2.20E-04
1140		10.88	0.99899	2.56E-04
1088		11.39	0.99889	2.99E-04
1039		11.93	0.99879	3.47E-04
992.3		12.49	0.99868	4.05E-04
947.5		13.09	0.99856	4.70E-04
904.7		13.70	0.99843	5.49E-04
863.9		14.35	0.99830	6.47E-04
824.9		15.03	0.99817	7.50E-04
787.7		15.74	0.99803	8.58E-04
752.1		16.49	0.99787	9.82E-04
718.1		17.27	0.99772	1.12E-03
685.7		18.08	0.99755	1.27E-03
654.7		18.94	0.99737	1.44E-03
625.1		19.83	0.99719	1.64E-03
596.9		20.77	0.99700	1.86E-03
570.0		21.75	0.99682	2.11E-03
544.2		22.78	0.99666	2.40E-03
519.7		23.86	0.99651	2.67E-03
496.2		24.99	0.99635	2.96E-03
484.9		25.57	0.99627	3.12E-03
473.8		26.17	0.99620	3.29E-03
463.0		26.78	0.99613	3.47E-03
452.4		27.41	0.99608	3.65E-03
442.1		28.05	0.99602	3.82E-03
432.0		28.70	0.99596	4.00E-03
412.5		30.06	0.99587	4.38E-03
403.0		30.76	0.99585	4.59E-03
393.8		31.48	0.99585	4.77E-03
384.8		32.22	0.99584	4.93E-03
376.1		32.97	0.99582	5.10E-03
367.5		33.74	0.99581	5.28E-03
359.1		34.53	0.99580	5.46E-03
350.9		35.34	0.99580	5.65E-03
342.9		36.16	0.99584	5.83E-03
335.0		37.01	0.99590	5.97E-03

(*Continued*)

TABLE I (*Continued*)

Niobium

eV	cm^{-1}	Å	n	k
319.9		38.76	0.99597	6.22E-03
305.5		40.58	0.99612	6.48E-03
291.7		42.50	0.99628	6.48E-03
278.5		44.52	0.99637	6.48E-03
265.9		46.63	0.99663	6.28E-03
253.9		48.83	0.99658	5.77E-03
242.5		51.13	0.99645	5.06E-03
231.5		53.56	0.99586	4.12E-03
221.1		56.08	0.99472	3.23E-03
216.0		57.40	0.99400	2.87E-03
211.1		58.73	0.99322	2.62E-03
206.2		60.13	0.99238	2.41E-03
201.5		61.53	0.99149	2.30E-03
196.9		62.97	0.99060	2.26E-03
192.4		64.44	0.98970	2.29E-03
188.0		65.95	0.9888	2.34E-03
179.6		69.03	0.9871	2.55E-03
171.4		72.34	0.9853	2.70E-03
163.7		75.74	0.9834	2.86E-03
156.3		79.32	0.9814	3.01E-03
149.3		83.04	0.9791	3.16E-03
142.5		87.01	0.9767	3.27E-03
136.1		91.10	0.9740	3.40E-03
129.9		95.45	0.9709	3.51E-03
124.1		99.91	0.9676	3.60E-03
118.5		104.6	0.9638	3.69E-03
113.1		109.6	0.9595	3.75E-03
108.0		114.8	0.9546	3.78E-03
103.1		120.3	0.9490	3.87E-03
98.47		125.9	0.9424	4.03E-03
94.03		131.9	0.9348	4.69E-03
89.78		138.1	0.9263	5.74E-03
85.73		144.7	0.9164	7.34E-03
81.85		151.5	0.9054	9.92E-03
78.16		158.6	0.8929	1.35E-02
74.63		166.1	0.8791	1.87E-02
71.26		174.0	0.8643	2.57E-02
68.04		182.2	0.8478	3.45E-02
64.97		190.8	0.8299	4.62E-02
63.49		195.3	0.8206	5.36E-02
62.04		199.8	0.8113	6.20E-02
60.62		204.5	0.8021	7.10E-02
59.24		209.3	0.7926	8.12E-02
57.88		214.2	0.7828	9.27E-02
56.56		219.2	0.7732	0.106

(*Continued*)

TABLE I (*Continued*)

Niobium

eV	cm^{-1}	Å	*n*	*k*
54.01		229.6	0.7559	0.138
51.57		240.4	0.7451	0.178
200		61.99		2.0E-02 [19]
150		82.66		2.6E-02
100		124.0		3.9E-02
95.0		130.5		4.2E-02
90.0		137.8		4.4E-02
85.0		145.9		4.7E-02
80.0		155.0		5.2E-02
75.0		165.3		5.7E-02
70.0		177.1		6.5E-02
65.0		190.7		7.7E-02
60.0		206.6		9.4E-02
55.0		225.4		0.126
50.0		248.0		0.180
45.0		275.5		0.243
44.0		281.8		0.258
43.0		288.3		0.275
42.0		295.2		0.277
41.0		302.4		0.279
40.5		306.1	0.920 [8]	0.47 [8]
40.0		310.0		0.284 [19]
39.5		313.9	0.950 [8]	0.50 [8]
39.0		317.9		0.291 [19]
38.5		322.0	1.00 [8]	0.53 [8]
38.0		326.3		0.293 [19]
37.5		330.6	1.07 [8]	0.53 [8]
37.0		335.1		0.291 [19]
36.8		336.9	1.11 [8]	0.52 [8]
36.4		340.6	1.13	0.51
36.0		344.4	1.15	0.50
				0.288 [19]
35.6		348.3	1.16 [8]	0.49 [8]
35.2		352.2	1.17	0.47
35.0		354.2		0.268 [19]
34.8		356.3	1.19 [8]	0.46 [8]
34.4		360.4	1.20	0.44
34.0		364.7	1.20	0.42
33.8		366.8	1.21	0.41
33.6		369.0	1.21	0.41
33.4		371.2	1.21	0.40
33.2		373.4	1.21	0.39
33.0		375.7	1.21	0.38
32.8		378.0	1.21	0.37

(*Continued*)

TABLE I (*Continued*)

Niobium

eV	cm^{-1}	Å	*n*	*k*
32.6		380.3	1.21	0.36
32.4		382.7	1.21	0.35
32.2		385.0	1.21	0.35
32.0		387.5	1.20	0.34
31.8		389.9	1.20	0.33
31.6		392.4	1.20	0.32
31.4		394.9	1.19	0.32
31.2		397.4	1.18	0.31
31.0		399.9	1.18	0.31
30.8		402.5	1.17	0.31
30.6		405.2	1.18	0.31
30.4		407.8	1.18	0.30
30.2		410.5	1.18	0.29
30.0		413.3	1.18	0.28
				0.207 [19]
29.8		416.1	1.17 [8]	0.27 [8]
29.6		418.9	1.16	0.26
29.4		421.7	1.15	0.25
29.2		424.6	1.14	0.25
29.0		427.5	1.13	0.25
28.8		430.5	1.12	0.25
28.6		433.5	1.11	0.24
28.4		436.6	1.10	0.24
28.2		439.7	1.09	0.24
28.0		442.8	1.08	0.24
27.8		446.0	1.07	0.25
27.6		449.2	1.06	0.25
27.4		452.5	1.05	0.25
27.2		455.8	1.05	0.25
27.0		459.2	1.04	0.25
26.8		462.6	1.03	0.25
26.6		466.1	1.03	0.25
26.4		469.6	1.02	0.26
26.2		473.2	1.01	0.26
26.0		476.9	1.00	0.26
25.8		480.6	0.99	0.26
25.6		484.3	0.99	0.26
25.4		488.1	0.98	0.27
25.2		492.0	0.97	0.27
25.0		495.9	0.96	0.27
24.8		499.9	0.95	0.28
24.6		504.0	0.94	0.28
24.4		508.1	0.93	0.28
24.2		512.3	0.92	0.29
24.0		516.6	0.91	0.29

(*Continued*)

TABLE I (*Continued*)

Niobium

eV	cm^{-1}	Å	n	k
23.8		520.9	0.90	0.30
23.6		525.4	0.88	0.30
23.4		529.8	0.87	0.31
23.2		534.4	0.86	0.32
23.0		539.1	0.85	0.33
22.8		543.8	0.83	0.34
22.6		548.6	0.82	0.35
22.4		553.5	0.81	0.36
22.2		558.5	0.79	0.38
22.0		563.6	0.78	0.40
21.8		568.7	0.77	0.41
21.6		574.0	0.75	0.43
21.4		579.4	0.74	0.45
21.2		584.8	0.73	0.47
21.0		590.4	0.72	0.50
20.8		596.1	0.72	0.52
20.6		601.9	0.71	0.55
20.4		607.8	0.72	0.57
20.2		613.8	0.72	0.60
20.0		619.9	0.72	0.62
19.8		626.2	0.72	0.64
19.6		632.6	0.72	0.66
19.4		639.1	0.73	0.68
19.2		645.8	0.73	0.69
19.0		652.5	0.72	0.72
18.8		659.5	0.73	0.74
18.6		666.6	0.73	0.77
18.4		673.8	0.73	0.79
18.2		681.2	0.73	0.82
18.0		688.8	0.74	0.85
17.8		696.5	0.75	0.87
17.6		704.5	0.76	0.90
17.4		712.6	0.77	0.93
17.2		720.8	0.79	0.96
17.0		729.3	0.80	0.99
16.8		738.0	0.82	1.02
16.6		746.9	0.85	1.04
16.4		756.0	0.87	1.06
16.2		765.3	0.89	1.09
16.0		774.9	0.92	1.11
15.8		784.7	0.95	1.13
15.6		794.8	0.99	1.14
15.4		805.1	1.02	1.15
15.2		815.7	1.05	1.16
15.0		826.6	1.08	1.16

(*Continued*)

TABLE I (*Continued*)

Niobium

eV	cm^{-1}	Å	n	k
14.8		837.7	1.11	1.16
14.6		849.2	1.14	1.15
14.4		861.0	1.16	1.15
14.2		873.1	1.18	1.14
14.0		885.6	1.20	1.13
13.8		898.4	1.22	1.13
13.6		911.6	1.23	1.12
13.4		925.3	1.24	1.10
13.2		939.3	1.24	1.09
13.0		953.7	1.24	1.09
12.8		968.6	1.24	1.09
12.6		984.0	1.24	1.09
12.4		999.9	1.24	1.10
eV	cm^{-1}	μm	n	k
12.2	98399	0.1016	1.25	1.11
12.0	96786	0.1033	1.25	1.12
11.8	95173	0.1051	1.27	1.13
11.6	93560	0.1069	1.28	1.13
11.4	91946	0.1088	1.30	1.13
11.3	91140	0.1097	1.31	1.12
11.2	90333	0.1107	1.31	1.12
11.1	89527	0.1117	1.32	1.11
11.0	88720	0.1127	1.32	1.10
10.9	87914	0.1137	1.32	1.09
10.8	87107	0.1148	1.32	1.08
10.7	86301	0.1159	1.31	1.07
10.6	85494	0.1170	1.30	1.06
10.5	84688	0.1181	1.29	1.05
10.4	83881	0.1192	1.27	1.04
10.3	83074	0.1204	1.25	1.04
10.2	82268	0.1216	1.23	1.04
10.1	81461	0.1228	1.20	1.04
10.0	80655	0.1240	1.18	1.05
9.9	79848	0.1252	1.15	1.06
9.8	79042	0.1265	1.13	1.09
9.7	78235	0.1278	1.11	1.11
9.6	77429	0.1292	1.10	1.13
9.5	76622	0.1305	1.08	1.15
9.4	75816	0.1319	1.07	1.18
9.3	75009	0.1333	1.06	1.19
9.2	74202	0.1348	1.04	1.22
9.1	73396	0.1362	1.02	1.25
9.0	72589	0.1378	1.01	1.29

(*Continued*)

TABLE I (*Continued*)

Niobium

eV	cm^{-1}	μm	n	k
8.9	71783	0.1393	1.00	1.32
8.8	70976	0.1409	1.00	1.36
8.7	70170	0.1425	0.99	1.39
8.6	69363	0.1442	0.99	1.43
8.4	67750	0.1476	0.99	1.51
8.2	66137	0.1512	1.00	1.60
8.0	64524	0.1550	1.02	1.69
7.8	62911	0.1590	1.07	1.78
7.6	61298	0.1631	1.14	1.85
7.4	59684	0.1675	1.20	1.88
7.2	58071	0.1722	1.22	1.91
7.0	56458	0.1771	1.23	1.96
6.8	54845	0.1823	1.24	2.04
6.6	53232	0.1879	1.26	2.14
6.4	51619	0.1937	1.31	2.25
6.2	50006	0.2000	1.38	2.38
6.0	48393	0.2066	1.49	2.49
5.8	46780	0.2138	1.63	2.60
5.6	45167	0.2214	1.81	2.67
5.4	43554	0.2296	2.00	2.68
5.2	41940	0.2384	2.16	2.62
5.0	40327	0.2480	2.26	2.57
4.8	38714	0.2583	2.32	2.52
4.6	37101	0.2695	2.39	2.56
4.4	35488	0.2818	2.53	2.56
4.2	33875	0.2952	2.64	2.42
4.0	32262	0.3100	2.64	2.33
3.9	31455	0.3179	2.62	2.29
3.8	30649	0.3263	2.59	2.28
3.7	29842	0.3351	2.56	2.27
3.6	29036	0.3444	2.52	2.29
3.5	28229	0.3542	2.48	2.33
3.4	27423	0.3647	2.46	2.38
3.3	26616	0.3757	2.44	2.45
3.2	25810	0.3875	2.45	2.53
3.1	25004	0.3999	2.48	2.60
3.00	24197	0.4133	2.51	2.68
2.85	22987	0.4350	2.58	2.80
2.75	22181	0.4509	2.66	2.86
2.65	21374	0.4679	2.74	2.90
2.55	20568	0.4862	2.83	2.92
2.45	19761	0.5061	2.89	2.90
2.35	18954	0.5276	2.92	2.88
2.25	18148	0.5510	2.93	2.87
2.15	17341	0.5767	2.92	2.87

(*Continued*)

TABLE I (*Continued*)

Niobium

eV	cm^{-1}	μm	n	k
2.05	16535	0.6048	2.89	2.87
1.95	15728	0.6358	2.82	2.86
1.85	14922	0.6702	2.69	2.89
1.75	14115	0.7085	2.54	2.99
1.65	13308	0.7514	2.36	3.13
1.55	12502	0.7999	2.15	3.37
1.45	11695	0.8551	1.95	3.68
1.35	10889	0.9184	1.76	4.13
1.25	10082	0.9919	1.65	4.63
1.15	9276	1.078	1.55	5.18
1.05	8469	1.181	1.44	5.86
0.95	7662	1.305	1.35	6.70
0.85	6856	1.459	1.35	7.74
0.75	6049	1.653	1.41	9.00
0.65	5243	1.907	1.57	10.6
0.55	4436	2.254	1.83	12.7
0.45	3630	2.755	2.28	15.6
0.35	2823	3.542	3.11	20.0
0.28	2258	4.428	4.26	25.0
0.24	1936	5.166	5.47	28.9
0.20	1613	6.199	7.25	34.1
0.16	1290	7.749	10.2	41.7
0.12	967.9	10.33	16.0	53.2

IX TANTALUM (Ta)

Tantalum is a body-centered cubic metal. It is relatively nonreactive, but a thin oxide layer forms at room temperature, which may affect ellipsometric measurements in the visible and near ultraviolet and all measurements further in the ultraviolet. Very few measurements have been carried out in ultrahigh vacuum, and as for other refractory transition metals, it is difficult to make large-grained films that are of bulk density without condensation on a hot substrate. In common with other transition metals, Ta has interband transitions extending to arbitrarily low energies, making the determination of Drude parameters unreliable.

The near-infrared, visible, and near-ultraviolet data reported to date [1–11] do not agree well qualitatively, although there is agreement on structures. There are only three sets of VUV data [5, 6, 12]. They agree in magnitude, but disagree on the occurrence of a peak in ε_2 at about 8.5 eV. Two transmission studies have been made in the soft X-ray region [13, 14], from which k spectra can be obtained. However, these spectra do not match well any of the spectra from longer wavelengths. The data listed

below for the 20–40 eV region must be considered less reliable than the other data. Finally, Windt *et al.* [15] measured multiple-angle reflectance on thin-film samples prepared ex situ, from which optical constants were derived for the 24–1216 Å region. Ordal *et al.* [16] measured the far-infrared optical properties in the 41.3–413 μm region using a cavity technique. Both optical constants were obtained from a single measurement at each wavelength by using an approximation that should be valid in this spectral region.

We list in Table I the data of Weaver *et al.* [6] for the infrared, visible, ultraviolet, and vacuum ultraviolet. These data were taken on bulk electropolished samples, and were derived by Kramers–Kronig analysis of absorptance measurements at low temperature (longer wavelengths) and room-temperature reflectance measurements (shorter wavelengths). We list the k spectrum in the soft X-ray region derived from absorption (transmission) measurements [14] under the assumption that n is unity. This spectrum does not join well with the higher-energy end of the data from Ref. [6], however. The discrepancy may be ascribable to the effect of an oxide overlayer on the high-energy region of the data of Ref. [6]. The spectra of n and k are given in Fig. 1.

We have calculated n and k in the 1.24–240 Å (10,000–51.5 eV) region using the model of Henke *et al.* [17]. The absorption edges are K (67,417 eV), L_1 (11,680 eV), $L_{2,3}$ (11,156, 9881 eV), M_1 (2708 eV), $M_{2,3}$ (2469, 2194 eV), $M_{4,5}$ (1793, 1735 eV), N_1 (566 eV), $N_{2,3}$ (465, 405 eV), $N_{4,5}$ (242, 230 eV), $N_{6,7}$ (27, 25 eV), O_1 (71 eV), $O_{2,3}$ (45, 37 eV), $O_{4,5}$ (6 eV). At lower frequencies these atomic features are perturbed by the bonding properties of the crystal.

REFERENCES

1. B. T. Barnes, *J. Opt. Soc. Am.* **56**, 1546 (1966).
2. A. P. Lenham and D. M. Treherne, *J. Opt. Soc. Am.* **56**, 1137 (1966).
3. A. P. Lenham, *J. Opt. Soc. Am.* **57**, 473 (1967).
4. A. P. Lenham and D. M. Treherne, in "Optical Properties and Electronic Properties of Metals and Alloys," (F. Abeles, ed.), North-Holland, Amsterdam, 196 (1966).
5. D. W. Juenker, L. J. LeBlanc, and C. R. Martin, *J. Opt. Soc. Am.* **58**, 164 (1968).
6. J. H. Weaver, D. W. Lynch, and C. G. Olson, *Phys. Rev.* **B10**, 501 (1974).
7. M. M. Kirillova, L. V. Nomerovannaya, and M. M. Noskov, *Sov. Phys. Solid State* **16**, 1425 (1975); *Fiz. Tverd. Tela* **16**, 2181 (1974).
8. L. K. Thomas and S. Thurm, *J. Phys. F* **6**, 279 (1976).
9. B. U. Habedank, L. K. Thomas and S. Thurm, *J. Phys. F* 7, 2217 (1977).
10. P. Gravier, G. Chassaing, and M. Sigrist, *Thin Solid Films* **57**, 93 (1979).
11. J. E. Nestell and R. W. Christy, *Phys. Rev.* **B21**, 3173 (1980).
12. L. J. LeBlanc, J. S. Farrell, and D. W. Juenker, *J. Opt. Soc. Am.* **54**, 956 (1964).
13. P. Jaegle, F. Combet-Farnoux, P. Dhez, M. Cremonese, and G. Onori, *Phys. Lett.* **26A**, 364 (1968).

14. R. Haensel, K. Radler, B. Sonntag, and C. Kunz, *Solid State Commun.* **7**, 1495 (1969).
15. D. L. Windt, W. C. Cash, M. Scott, P. Arendt, B. Newnam, R. F. Fisher, and A. B. Swartzlander, *Appl. Opt.* **27**, 246 (1988).
16. M. A. Ordal, R. J. Bell, R. W. Alexander, L. A. Newquist, and M. R. Querry, *Appl. Opt.* **27**, 1203 (1988).
17. B. L. Henke, J. C. Davis, E. M. Gullikson, and R. C. C. Perera, Lawrence Berkeley Laboratory Report No. LBL-26259 (1988).

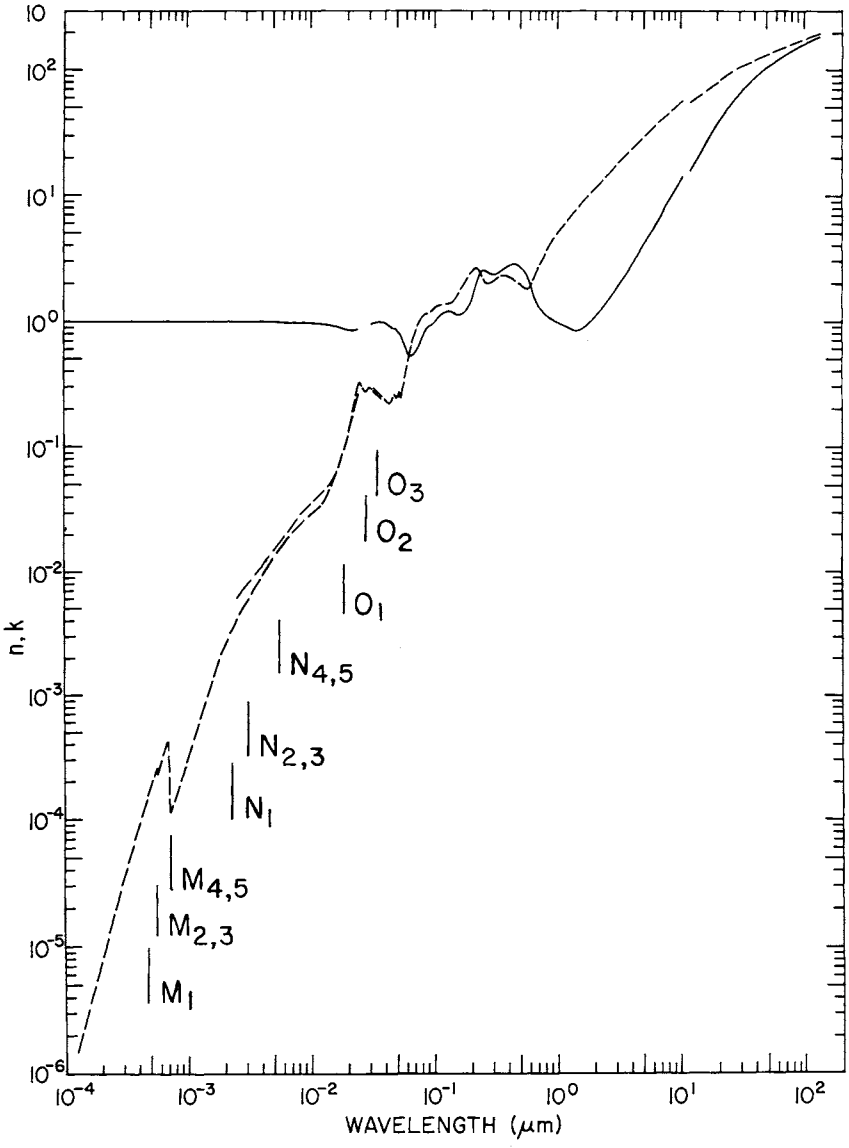

Fig. 1. Log–log plot of n (solid line) and k (dashed line) versus wavelength in micrometers for tantalum.

TABLE I

Values of n and k Obtained from Various References for Tantalum[a]

eV	cm^{-1}	Å	n	k
10000		1.240	0.9999766 [17]	1.49E-06 [17]
9772		1.269	0.9999748	1.62E-06
9549		1.298	0.9999730	1.75E-06
9117		1.360	0.9999697	2.07E-06
8706		1.424	0.9999664	2.44E-06
8313		1.492	0.9999628	2.88E-06
7937		1.562	0.9999589	3.39E-06
7579		1.636	0.9999548	4.00E-06
7237		1.713	0.9999501	4.72E-06
6910		1.794	0.9999451	5.56E-06
6598		1.879	0.9999396	6.55E-06
6300		1.968	0.9999336	7.72E-06
6015		2.061	0.9999270	9.10E-06
5744		2.159	0.9999198	1.07E-05
5484		2.261	0.9999120	1.26E-05
5237		2.368	0.9999033	1.48E-05
5000		2.480	0.999894	1.75E-05
4775		2.597	0.999884	2.06E-05
4559		2.720	0.999873	2.42E-05
4353		2.848	0.999861	2.84E-05
4157		2.983	0.999847	3.34E-05
3969		3.124	0.999833	3.92E-05
3790		3.272	0.999818	4.60E-05
3619		3.426	0.999801	5.40E-05
3455		3.588	0.999784	6.33E-05
3299		3.758	0.999765	7.42E-05
3150		3.936	0.999745	8.69E-05
3008		4.122	0.999725	1.02E-04
2872		4.317	0.999704	1.19E-04
2807		4.418	0.999694	1.28E-04
2742		4.521	0.999685	1.39E-04
2680		4.627	0.999673	1.44E-04
2619		4.735	0.999661	1.56E-04
2559		4.846	0.999650	1.70E-04
2500		4.959	0.999644	1.84E-04
2443		5.075	0.999634	1.87E-04
2387		5.193	0.999619	2.03E-04
2280		5.439	0.999601	2.40E-04
2228		5.566	0.999602	2.60E-04
2127		5.829	0.999577	2.62E-04
2177		5.696	0.999603	2.42E-04
2078		5.965	0.999563	2.84E-04
1985		6.248	0.999552	3.32E-04
1895		6.543	0.999569	3.90E-04

[a]The references from which the values were extracted are given in brackets.

TABLE I (*Continued*)

Tantalum

eV	cm^{-1}	Å	*n*	*k*
1852		6.696	0.999604	4.22E-04
1809		6.852	0.999696	4.21E-04
1768		7.013	0.999757	3.20E-04
1728		7.176	0.999723	1.14E-04
1688		7.344	0.999592	1.23E-04
1650		7.516	0.999516	1.32E-04
1575		7.871	0.999405	1.53E-04
1504		8.244	0.999307	1.78E-04
1436		8.633	0.999212	2.05E-04
1371		9.041	0.999114	2.37E-04
1309		9.469	0.999012	2.74E-04
1250		9.917	0.99890	3.16E-04
1194		10.39	0.99879	3.64E-04
1140		10.88	0.99867	4.19E-04
1088		11.39	0.99854	4.82E-04
1039		11.93	0.99840	5.54E-04
992.3		12.49	0.99825	6.36E-04
947.5		13.09	0.99809	7.28E-04
904.7		13.70	0.99792	8.31E-04
863.9		14.35	0.99774	9.48E-04
824.9		15.03	0.99756	1.08E-03
787.7		15.74	0.99736	1.23E-03
752.1		16.49	0.99715	1.39E-03
718.1		17.27	0.99693	1.58E-03
685.7		18.08	0.99671	1.78E-03
654.7		18.94	0.99646	2.01E-03
625.1		19.83	0.99623	2.27E-03
596.9		20.77	0.99600	2.56E-03
583.3		21.26	0.99591	2.71E-03
570.0		21.75	0.99583	2.84E-03
557.0		22.26	0.99571	2.90E-03
544.2		22.78	0.99551	3.03E-03
519.7		23.86	0.99521	3.38E-03
496.2		24.99	0.99491	3.74E-03
473.8		26.17	0.99462	4.14E-03
463.0		26.78	0.99449	4.35E-03
452.4		27.41	0.99438	4.56E-03
442.1		28.04	0.99427	4.73E-03
432.0		28.70	0.99413	4.89E-03
412.5		30.06	0.99379	5.22E-03
403.0		30.77	0.99359	5.39E-03
393.8		31.48	0.99334	5.59E-03
384.8		32.22	0.99309	5.83E-03
376.1		32.97	0.99286	6.09E-03
359.1		34.53	0.99238	6.65E-03

(*Continued*)

TABLE I (*Continued*)

Tantalum

eV	cm^{-1}	Å	*n*	*k*
342.9		36.16	0.99191	7.26E-03
327.4		37.87	0.99142	7.93E-03
312.6		39.66	0.99092	8.66E-03
298.5		41.54	0.99044	9.46E-03
285.0		43.50	0.9900	1.03E-02
272.1		45.56	0.9897	1.12E-02
259.9		47.71	0.9893	1.19E-02
248.1		49.97	0.9888	1.27E-02
242.5		51.14	0.9885	1.31E-02
236.9		52.33	0.9882	1.36E-02
231.5		53.56	0.9879	1.40E-02
226.2		54.81	0.9876	1.45E-02
221.1		56.09	0.9873	1.50E-02
216.0		57.40	0.9870	1.54E-02
206.2		60.12	0.9865	1.64E-02
196.9		62.96	0.9858	1.73E-02
188.0		65.94	0.9852	1.82E-02
179.6		69.05	0.9843	1.90E-02
171.4		72.32	0.9832	1.99E-02
163.7		75.74	0.9820	2.10E-02
156.3		79.32	0.9807	2.21E-02
149.3		83.07	0.9793	2.32E-02
142.5		87.00	0.9777	2.45E-02
136.1		91.11	0.9760	2.57E-02
129.9		95.42	0.9740	2.70E-02
124.1		99.94	0.9719	2.82E-02
118.5		104.7	0.9693	2.92E-02
113.1		109.6	0.9660	3.03E-02
108.0		114.8	0.9621	3.19E-02
103.1		120.2	0.9579	3.36E-02
98.47		125.9	0.9524	3.55E-02
94.03		131.9	0.9462	3.89E-02
89.78		138.1	0.9398	4.27E-02
85.73		144.6	0.9329	4.71E-02
81.85		151.5	0.9250	5.20E-02
78.16		158.6	0.9151	5.82E-02
74.63		166.1	0.9047	6.71E-02
71.26		174.0	0.8937	7.77E-02
68.04		182.2	0.8814	9.22E-02
64.97		190.8	0.8714	0.110
62.04		200.0	0.8623	0.131
59.24		209.3	0.8546	0.156
56.56		219.2	0.8508	0.188
54.01		229.6	0.8567	0.225
51.57		240.4	0.8744	0.256

(*Continued*)

TABLE I (*Continued*)

Tantalum

eV	cm^{-1}	Å	*n*	*k*
500		24.80		6.0E-03 [14]
400		31.00		8.0E-03
300		41.33		1.2E-02
200		61.99		2.0E-02
190		65.25		2.1E-02
780		15.90		5.0E-03
170		72.93		2.4E-02
160		77.49		2.6E-02
150		82.66		2.9E-02
140		88.56		3.1E-02
130		95.37		3.4E-02
120		103.3		3.7E-02
110		112.7		4.0E-02
100		124.0		4.4E-02
90.0		137.8		5.0E-02
80.0		155.0		6.0E-02
70.0		177.1		8.0E-02
60.0		206.6		0.148
55.0		225.4		0.233
50.0		248.0		0.322
45.0		275.5		0.268
44.0		281.8		0.269
41.0		302.4		0.296
40.0		310.0		0.291
			0.95 [6]	0.29 [6]
39.5		313.9	0.96	0.29
39.0		317.9	0.97	0.29
38.5		322.0	0.97	0.29
38.0		326.3	0.98	0.28
37.5		330.6	0.98	0.28
37.0		335.1	0.99	0.28
36.5		339.7	0.99	0.27
36.0		344.4	0.99	0.27
35.5		349.3	0.99	0.27
35.0		354.2	0.99	0.26
				0.248 [14]
34.5		359.4	0.99 [6]	0.26 [6]
34.0		364.7	0.99	0.25
33.5		370.1	0.98	0.25
33.0		375.7	0.98	0.25
				0.239 [14]
32.5		381.5	0.98 [6]	0.24 [6]
32.0		387.5	0.98	0.24
31.5		393.6	0.97	0.24
31.0		399.9	0.97	0.23

(*Continued*)

TABLE I (*Continued*)

Tantalum

eV	cm^{-1}	Å	n	k
30.5		406.5	0.96	0.23
30.0		413.3	0.95	0.22
				0.313 [14]
29.8		416.1	0.95 [6]	0.22 [6]
29.6		418.9	0.94	0.22
29.4		421.7	0.94	0.22
29.2		424.6	0.93	0.22
29.0		427.5	0.92	0.22
28.8		430.5	0.92	0.22
28.6		433.5	0.91	0.22
28.4		436.6	0.91	0.22
28.2		439.7	0.90	0.22
28.0		442.8	0.90	0.23
27.8		446.0	0.89	0.23
27.6		449.2	0.89	0.23
27.4		452.5	0.88	0.24
27.2		455.8	0.88	0.24
27.0		459.2	0.87	0.25
26.8		462.6	0.87	0.25
26.6		466.1	0.87	0.26
26.4		469.6	0.87	0.26
26.2		473.2	0.88	0.26
26.0		476.9	0.88	0.25
25.8		480.6	0.87	0.25
25.6		484.3	0.86	0.24
25.4		488.1	0.85	0.24
25.2		492.0	0.84	0.25
25.0		495.9	0.83	0.25
24.8		499.9	0.83	0.25
24.6		504.0	0.82	0.25
24.4		508.1	0.81	0.25
24.2		512.3	0.80	0.26
24.0		516.6	0.80	0.26
23.9		518.8	0.79	0.27
23.8		520.9	0.80	0.27
23.7		523.1	0.80	0.27
23.6		525.4	0.80	0.26
23.5		527.6	0.79	0.25
23.4		529.8	0.79	0.25
23.2		534.4	0.76	0.24
23.0		539.1	0.73	0.24
22.8		543.8	0.71	0.26
22.6		548.6	0.69	0.27
22.4		553.5	0.68	0.29
22.2		558.5	0.66	0.30

(*Continued*)

TABLE I (*Continued*)

Tantalum

eV	cm^{-1}	Å	*n*	*k*
22.0		563.6	0.64	0.32
21.8		568.7	0.64	0.34
21.6		574.0	0.64	0.34
21.4		579.4	0.61	0.35
21.2		584.8	0.59	0.37
21.0		590.4	0.57	0.39
20.8		596.1	0.56	0.42
20.6		601.9	0.55	0.44
20.4		607.8	0.55	0.47
20.2		613.8	0.54	0.50
20.0		619.9	0.54	0.52
19.8		626.2	0.53	0.55
19.6		632.6	0.53	0.57
19.4		639.1	0.53	0.60
19.2		645.8	0.52	0.63
19.0		652.5	0.53	0.65
18.8		659.5	0.53	0.68
18.6		666.6	0.53	0.71
18.4		673.8	0.54	0.73
18.2		681.2	0.54	0.76
18.0		688.8	0.55	0.79
17.8		696.5	0.56	0.81
17.6		704.5	0.56	0.84
17.4		712.6	0.57	0.87
17.2		720.8	0.58	0.89
17.0		729.3	0.60	0.92
16.8		738.0	0.61	0.94
16.6		746.9	0.63	0.97
16.4		756.0	0.64	0.99
16.2		765.3	0.66	1.02
16.0		774.9	0.68	1.04
15.8		784.7	0.70	1.06
15.6		794.8	0.72	1.08
15.4		805.1	0.75	1.10
15 2		815.7	0.77	1.12
15.0		826.6	0.80	1.13
14.8		837.7	0.82	1.14
14.6		849.2	0.85	1.15
14.4		861.0	0.87	1.15
14.2		873.1	0.89	1.15
14.0		885.6	0.90	1.15
13.8		898.4	0.91	1.16
13.6		911.6	0.91	1.16
13.4		925.3	0.91	1.18
13.2		939.3	0.92	1.20

(*Continued*)

TABLE I (*Continued*)

Tantalum

eV	cm^{-1}	Å	*n*	*k*
13.0		953.7	0.93	1.22
12.8		968.6	0.94	1.24
12.6		984.0	0.96	1.26
12.4		999.9	0.98	1.28
eV	cm^{-1}	μm	*n*	*k*
12.2	98399	0.1016	1.00	1.29
12.0	96786	0.1033	1.02	1.31
11.8	95173	0.1051	1.05	1.32
11.6	93560	0.1069	1.07	1.33
11.4	91946	0.1088	1.09	1.34
11.2	90333	0.1107	1.11	1.35
11.0	88720	0.1127	1.13	1.35
10.8	87107	0.1148	1.15	1.36
10.6	85494	0.1170	1.16	1.36
10.4	83881	0.1192	1.18	1.37
10.2	82268	0.1216	1.19	1.37
10.0	80655	0.1240	1.20	1.37
9.8	79042	0.1265	1.21	1.37
9.6	77429	0.1292	1.21	1.38
9.4	75816	0.1319	1.21	1.38
9.2	74202	0.1348	1.21	1.38
9.0	72589	0.1378	1.19	1.40
8.8	70976	0.1409	1.17	1.41
8.6	69363	0.1442	1.14	1.45
8.4	67750	0.1476	1.13	1.50
8.2	66137	0.1512	1.12	1.55
8.0	64524	0.1550	1.11	1.61
7.8	62911	0.1590	1.11	1.68
7.6	61298	0.1631	1.12	1.75
7.4	59684	0.1675	1.13	1.82
7.2	58071	0.1722	1.15	1.91
7.0	56458	0.1771	1.18	2.01
6.8	54845	0.1823	1.23	2.11
6.6	53232	0.1879	1.29	2.22
6.4	51619	0.1937	1.37	2.33
6.2	50006	0.2000	1.48	2.45
6.0	48393	0.2066	1.63	2.56
5.8	46780	0.2138	1.83	2.63
5.6	45167	0.2214	2.06	2.67
5.4	43554	0.2296	2.31	2.61
5.2	41940	0.2384	2.52	2.44
5.0	40327	0.2480	2.58	2.20
4.8	38714	0.2583	2.53	2.06

(*Continued*)

TABLE I (*Continued*)

Tantalum

eV	cm^{-1}	μm	*n*	*k*
4.6	37101	0.2695	2.45	2.06
4.4	35488	0.2818	2.39	2.01
4.2	33875	0.2952	2.35	2.06
4.0	32262	0.3100	2.36	2.14
3.8	30649	0.3263	2.40	2.22
3.6	29036	0.3444	2.49	2.30
3.4	27423	0.3647	2.61	2.33
3.2	25810	0.3875	2.73	2.31
3.0	24196	0.4133	2.81	2.24
2.9	23390	0.4275	2.84	2.20
2.8	22583	0.4428	2.85	2.14
2.7	21777	0.4592	2.84	2.08
2.6	20970	0.4769	2.80	2.02
2.5	20164	0.4959	2.75	1.98
2.4	19357	0.5166	2.68	1.92
2.3	18551	0.5391	2.56	1.86
2.2	17744	0.5636	2.36	1.81
2.1	16938	0.5904	2.10	1.84
2.0	16131	0.6199	1.83	1.99
1.9	15324	0.6525	1.57	2.24
1.8	14518	0.6888	1.35	2.60
1.7	13711	0.7293	1.24	2.95
1.6	12905	0.7749	1.15	3.33
1.5	12098	0.8266	1.09	3.73
1.4	11292	0.8856	1.04	4.15
1.3	10485	0.9537	1.00	4.62
1.2	9679	1.033	0.980	5.14
1.1	8872	1.127	0.930	5.75
1.0	8065	1.240	0.890	6.47
0.98	7904	1.265	0.880	6.64
0.94	7582	1.319	0.860	6.99
0.90	7259	1.378	0.840	7.38
0.86	6936	1.442	0.850	7.81
0.82	6614	1.512	0.860	8.27
0.78	6291	1.590	0.890	8.77
0.74	5968	1.675	0.920	9.32
0.70	5646	1.771	0.960	9.92
0.66	5323	1.879	1.00	10.6
0.62	5001	2.000	1.06	11.4
0.58	4678	2.138	1.15	12.2
0.54	4355	2.296	1.25	13.1
0.50	4033	2.480	1.37	14.3
0.46	3710	2.695	1.54	15.6
0.42	3388	2.952	1.75	17.1
0.38	3065	3.263	2.03	18.9

(*Continued*)

TABLE I (*Continued*)

Tantalum

eV	cm^{-1}	μm	*n*	*k*
0.34	2742	3.647	2.40	21.1
0.30	2420	4.133	2.87	23.9
0.28	2258	4.428	3.23	25.6
0.26	2097	4.769	3.67	27.5
0.24	1936	5.166	4.20	29.8
0.22	1774	5.636	4.88	32.4
0.20	1613	6.199	5.77	35.5
0.19	1533	6.525	6.29	37.2
0.18	1452	6.888	6.91	39.2
0.16	1290	7.749	8.45	43.7
0.15	1210	8.266	9.45	46.4
0.14	1129	8.856	10.6	49.4
0.13	1049	9.537	12.1	52.9
0.12	967.9	10.33	14.0	56.8
0.1116	900	11.11	15.6 [16]	54.6 [16]
0.09919	800	12.50	19.1	59.9
0.08679	700	14.29	24.2	66.4
0.07439	600	16.67	31.5	73.9
0.06199	500	20.00	41.7	82.8
0.05579	450	22.22	48.4	93.1
0.04959	400	25.00	56.4	98.9
0.04339	350	28.57	66.1	105
0.03720	300	33.33	77.9	111
0.03100	250	40.00	92.0	119
0.02790	225	44.44	100	127
0.02480	200	50.00	109	137
0.02170	175	57.14	119	143
0.01860	150	66.67	131	151
0.01550	125	80.00	146	162
0.01240	100	100.0	164	178
0.009919	80	125.0	184	197

Beryllium* (Be)

E. T. ARAKAWA, T. A. CALLCOTT,† and YUN-CHING CHANG†
Health and Safety Research Division
Oak Ridge National Laboratory
Oak Ridge, Tennessee

Beryllium has many unique properties that make it of both theoretical and practical interest. As a metal, it is strikingly different both from lithium, its neighbor in the periodic table, and the higher Z alkaline-earth metals magnesium and calcium, which occupy the same column of the periodic table. The density of beryllium is not only 3.5 times larger than that of lithium, but is greater than that of magnesium and calcium. Its compressibility is very low, its Debye temperature is among the highest in the periodic table, its melting temperature is much higher than the other alkaline earths, and its electronic specific heat is very low. These properties, and its hexagonal crystalline structure, have generated much theoretical interest in its electronic properties. Several authors have discussed the optical properties of Be expected from theoretical band-structure calculations [1–3].

Beryllium also has many properties that recommend it for exotic optical applications. It is relatively light compared with other metals of optical importance, offers a very high specific stiffness (ratio of Young's modulus to density), a low thermal expansion at cryogenic temperatures, a low Z number, high thermal conductivity, and high reflectivity in the infrared. These properties make it particularly attractive for optical components that are intended for use in space.

In view of its many unique properties, it is surprising that no careful survey of the optical properties of Be has yet been published. In fact, only a few studies have been made, and they have produced widely different results, particularly in the visible region of the spectrum, where the methodology and instrumentation are best developed, and results are

* This research was sponsored jointly by the Office of Health and Environmental Research, U.S. Department of Energy, under contract DE-AC05-840R21400 with Martin Marietta Energy Systems, Inc. and by the Optics-MODIL under USDOE-DOD Interagency Agreement No. 1855-1562-A1.
† Also from The University of Tennessee, Physics Department, Knoxville, Tennessee

Copyright © 1991 by Academic Press.
All rights of reproduction in any form reserved.
ISBN 0-12-544422-2

normally most consistent. The variability of results may be traced to the difficulty of sample preparation. Bulk samples are usually produced by high-pressure sintering of microcrystalline powder, which results in the incorporation of significant amounts of BeO in the sample.

For many metals, oxidation problems may be overcome readily by vacuum evaporation, in which the metal evaporates, leaving the more stable oxide behind. In practice, Be is easily evaporated by subliming from the solid state at temperatures of about 900°C, well below its melting temperature at 1278°C. Our own studies suggest that the optical properties depend critically on the evaporation procedure used, and that much of the variability of the results reported in the literature can be traced to sample-preparation problems.

Published studies on the optical properties of Be date from about 50 years ago. Table I summarizes relevant facts about the more significant studies including photon-energy range, sample type, method of measurement, date of publication, and reference number. Note that all the samples in Table I except that listed as single crystal are polycrystalline.

We will discuss the available experimental data in four spectral regions. They are the soft X-ray range (SXR, $\hbar\omega > 50$ eV), the vacuum ultraviolet (VUV, $10\text{ eV} < \hbar\omega < 50$ eV), the infrared–visible–ultraviolet (IR–V–UV, $1\text{ eV} < \hbar\omega < 10$ eV), and the far infrared (FIR, $\hbar\omega < 1$ eV). These regions are chosen not to match the standard definitions of these regions, which in any case are very vague, but for convenient discussion of the available results.

Normal-incidence reflectance data for the three lowest-energy spectral regions are shown in Fig. 1. The wide range of results in the available literature is apparent, and will be the subject of further discussion. The reason for the above division into four spectral regions is also apparent. Above 10 eV, the reflectance makes the transition from reflecting to transmitting behavior at the plasmon energy. Between 1 and 10 eV, absorption by interband transitions reduces the reflectance and introduces prominent structure. Below 1 eV, the rising reflectance indicates a transition to free-electron metallic behavior.

In the SXR spectral region (>50 eV), the photon energy is above the plasmon energy (18.4 eV), and most of the interband oscillator strength is exhausted. Consequently, Be is weakly absorbing so that $n \cong \sqrt{\varepsilon_1} \approx 1$ and $\varepsilon_2 \simeq 2k \ll 1$. The only important physical process affecting the optical properties is the onset of absorption at the Be K-edge at 109 eV. The data available in this region are from thin-film transmittances that provide a measure of the linear absorption coefficient, $\mu = 4\pi k/\lambda_0$, where λ_0 is the wavelength of the incident radiation. The available measurements are reported in Refs. [4–7]. The measurements reported by Henke and Elgin [5] and Barstow *et al.* [6] are consistent with each other.

In the VUV spectral range (10–50 eV), the major feature of the spec-

trum is the transition from reflecting to transmitting behavior at the plasma energy (18.4 eV). Reflectance data from Seignac and Robin [8] and Toots *et al.* [9] are plotted in Fig. 1. Both sets of data were obtained on films with thickness 300–1000 Å evaporated on glass substrates and measured in vacua of 10^{-7} to 10^{-10} torr.

The reflectance data in the 1–10 eV range from Seignac and Robin [8], Hunderi and Myers [10], Weaver *et al.* [11], and Hull [12] are also plotted in Fig. 1. The most striking feature in this region is the wide range of reflectances obtained from careful studies in a spectral region where the procedures of optical measurements are usually most reliable. The two reflectance curves reported by Weaver *et al.* for the electric-field vector parallel ($E \| c$) and perpendicular ($E \perp c$) to the c-axis direction, were obtained on single-crystal surfaces prepared by mechanical polishing, with a subsequent chemical etch. These values are represented by the symbols (+) and (□), respectively. The reflectance data of Hull [12] were taken on the carefully polished surface of a polycrystalline mirror blank prepared by pressure sintering a low-oxygen-content (<0.5%) Be powder. This surface, intended for use as a reflector in the infrared, gives one of the highest reflectances for Be reported to date in the FIR region. However, this surface shows lower reflectance than the best evaporated films in this spectral region.

The highest reflectances reported in the visible were obtained by Seignac and Robin on Be films prepared by slow evaporation in ultrahigh vacuum (UHV). Because of the careful UHV-preparation techniques used, and because most sample preparation problems tend to reduce the measured reflectance, our initial assessment was that these data were the best available. A series of experiments performed in our laboratory confirm this initial judgment. We have been able to identify film-preparation procedures that result in lower reflectances. Thus, we adopt the reflectance values of Seignac and Robin as the best available in this spectral region. It should be noted that the reflectance values of Hunderi and Myers are substantially the same in the region of overlap. Hunderi and Myers' results are for evaporated films on sapphire prepared and measured in a vacuum of 10^{-10} torr.

Values of n and k in the visible region have been obtained by Seignac and Robin and Hunderi and Myers. Although the reflectances are very similar, there are substantial differences in the values of n and k. Of particular significance is the crossing in the values of n and k in the spectral region between 1.7 eV and 3 eV in the data of Seignac and Robin, which results in the value of ε_1 exceeding zero over this range. Our own ellipsometric measurements on evaporated films in this spectral range confirm the crossing of the n and k values reported by Seignac and Robin.

The large range of reflectance values observed for samples in the visible and ultraviolet is not unprecedented. An equally large range of reflec-

tances has been reported for aluminum, depending on the method of film preparation (evaporation in UHV or normal vacuum, sputtering or mechanical polishing) [13]. It is well-known that rough surfaces not only scatter, but can couple incident light to surface-plasmon modes and reduce the reflectance [14]. It seems probable that the sensitivity of the reflectance to surface structure, and perhaps to bulk grain size, is related to coupling of light to surface- and/or bulk-plasmon modes in these samples.

In the FIR spectral region (<1 eV), Shklyarevskii and Yarovaya [15] report a full set of optical constants, and other workers [12, 16, 17] have obtained normal-incidence reflectance data. The reflectances obtained by Shklyarevskii and Yarovaya are low, which we believe to be evidence for poor film structure. The reflectances of Hull's polished bulk samples [12] are among the highest reported for this spectral region. We have measured the optical constants by ellipsometry for a number of samples in the transition region from 3 eV to 0.6 eV, and normal-incidence reflectance from 3 eV to 0.1 eV. In general, it appears that in the FIR, as in the visible region, the best samples have the highest reflectance.

From the sources described in previous paragraphs, optical constants are available that span the spectral region up to 26 eV, although only normal-incidence reflectance data are available for most of the far-infrared region. We have obtained a consistent set of optical response functions for the entire spectral range by assembling a normal-incidence reflectance $R(0)$ curve for energies of $0.06\text{ eV} < \hbar\omega < 26\text{ eV}$ from published results, extending it to zero and infinite energies using appropriate analytic functions, and performing a Kramers–Kronig (K–K) analysis on $R(0)$. The reflectance values used were obtained by drawing a smooth curve through the following data sets:

$$0.06 < \hbar\omega < 0.8\text{ eV}\ [12];$$

$$0.8 < \hbar\omega < 5.0\text{ eV}\ [10];$$

$$1.5 < \hbar\omega < 14\text{ eV}\ [8];$$

$$14 < \hbar\omega < 26\text{ eV}\ [9].$$

In regions of overlap, higher reflectance values were favored. These data sets are shown along with the fitted $R(\hbar\omega)$ curve in Fig. 1.

Below 0.06 eV, the reflectance was extrapolated to zero energy using a linear extrapolation of Hull's data. Above 26 eV the reflectance was extrapolated to infinite energy as $\hbar\omega^{-4}$, in accordance with the behavior of nearly-free-electron metal above the plasma edge. Reliable n and k values

could be obtained only up to 25 eV from this analysis. To obtain the optical constants above 25 eV, a second K–K analysis was carried out using the k values from zero to 25 eV derived above, together with the experimental k values of Henke (60–250 eV) and Barstow (41–705 eV). The structural features from 110 eV to 130 eV just above the K edge were derived from the absorption data of Sagawa [18]. The k values from 15 eV to 25 eV together with the experimental values from 60 eV to 190 eV were found to fit the relation $k \propto E^{-3.3}$. This relationship was used in the region of 25–60 eV where no values were available. The k values above 160 eV were found to fit the relation $k \propto \hbar\omega^{-3.33}$. This analytic function was used in the high-energy extrapolation required for the K–K analysis. Finally, the initial K–K analysis on the normal-incidence reflectance $R(0)$ was refined slightly by using a high-energy extrapolation of $R(0) \propto \hbar\omega^{-4.7}$ as found from the behavior of $R(0)$ derived in the second K–K analysis of k. The results of these analyses are likely to be least reliable in the FIR spectral region. For example, an error of ± 0.005 in the measured reflectance in this region changes the k values by only a few percent but changes the n values by 20–30%.

The n and k values derived from the K–K analysis are plotted in Fig. 2 and a numerical printout is given in Table II. These values are a combination of the results from the two types of K–K analyses. The values from 0.02 eV to 20 eV and from 26 eV to 300 eV were those derived in the analyses of $R(0)$ and k, respectively. The k values from 20 eV to 26 eV are the same in both sets of data, whereas the n values are a smooth joining of the two data sets.

The n and k values derived from the K–K analyses agree well with the values given by Seignac and Robin for 2–26 eV and those given by Toots *et al.* for 10–28 eV. The k values from 0.6 eV to 2.5 eV agree with Hunderi and Myers' values, while the n values differ somewhat. In general, the optical constants derived here for polycrystalline Be are believed to be accurate to $\pm 20\%$ over the whole energy region.

Also included here as Table III are the n and k values from 299 eV to 10,000 eV derived from the latest Henke-model scattering data [19]. Henke *et al.*'s values agree well with those in Table II in the region of overlap from 200 eV to 300 eV.

REFERENCES

1. P. O. Nilsson, G. Arbman, and T. Gustafsson, *J. Phys. F: Metal Phys.* **4**, 1937 (1974).
2. M. Taut, *Phys. Status Solidi* **77**, 165 (1976); also *Phys. Status Solidi* **77**, 543 (1976).
3. P. Sinha and S. Chatterjee, *Indian J. Phys.* **52A**, 503 (1978).
4. R. W. Johnston and D. H. Tomboulian, *Phys. Rev.* **94**, 1585 (1954).
5. B. L. Henke and R. L. Elgin, *Adv. X-ray Anal.* **13**, 639 (1970).
6. M. A. Barstow, M. Lewis, and R. Petre, *J. Opt. Soc. Am.* **73**, 1220 (1983).
7. B. J. Muldar and J. J. Vrakking, *J. Phys. E: Sci. Instrum.* **11**, 743 (1978).

8. A. Seignac and S. Robin, *Solid State Commun.* **19**, 343 (1976).
9. J. Toots, H. A. Fowler, and L. Marton, *Phys. Rev.* **172**, 670 (1968).
10. O. Hunderi and H. P. Myers, *J. Phys. F: Metal Phys.* **4**, 1088 (1974).
11. J. H. Weaver, D. W. Lynch, and R. Rosei, *Phys. Rev.* **B7**, 3537 (1973).
12. Anthony B. Hull, Perkin-Elmer/Applied Optics Operations, Box 3115, Garden Grove, Calif. 92641 (private communication).
13. D. Y. Smith, E. Shiles, and Mitio Inokuti, in "Handbook of Optical Constants of Solids," (E. D. Palik, ed.), Academic Press, Orlando, 389 (1985).
14. R. H. Ritchie and R. E. Wilems, *Phys. Rev.* **178**, 372 (1969); J. Crowell and R. H. Ritchie, *J. Opt. Soc. Am.* **60**, 794 (1970); J. M. Elson and R. H. Ritchie, *Phys. Rev.* **B4**, 4129 (1971).
15. I. N. Shklyarevskii and R. G. Yarovaya, *Opt. Spect. (USSR)* **11**, 355 (1960); *Opt. Spekt.* **11**, 661 (1961).
16. H. M. O'Bryan, *J. Opt. Soc. Am.* **26**, 122 (1936).
17. R. Blickensderfer, D. K. Deardorff, and R. L. Lincoln, *J. Less Common Metals* **51**, 13 (1977).
18. T. Sagawa, in "Soft X-Ray Band Spectra," (D. J. Fabian, ed.), Academic Press, New York, 29 (1968).
19. B. L. Henke, J. C. Davis, E. M. Gullickson, and R. C. C. Perera, Lawrence Berkeley Lab Report LBL-26259 (1988).

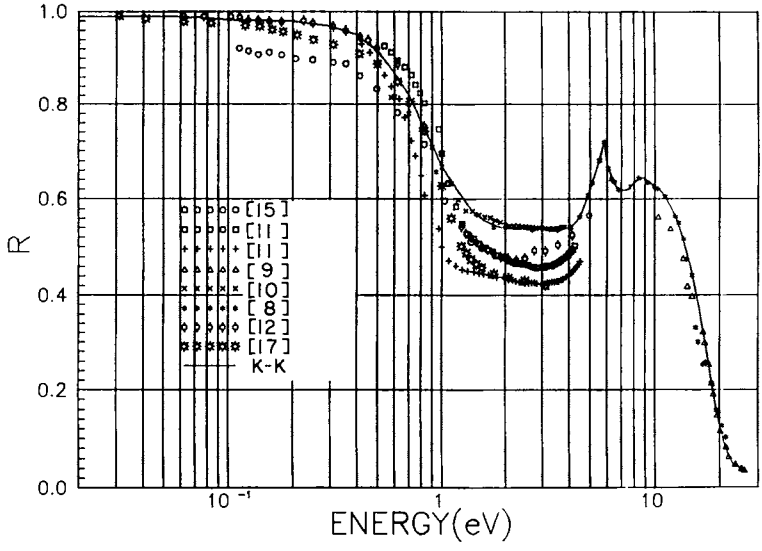

Fig. 1. Normal-incidence reflectances reported in the literature and reflectance data used as input for the K–K analysis.

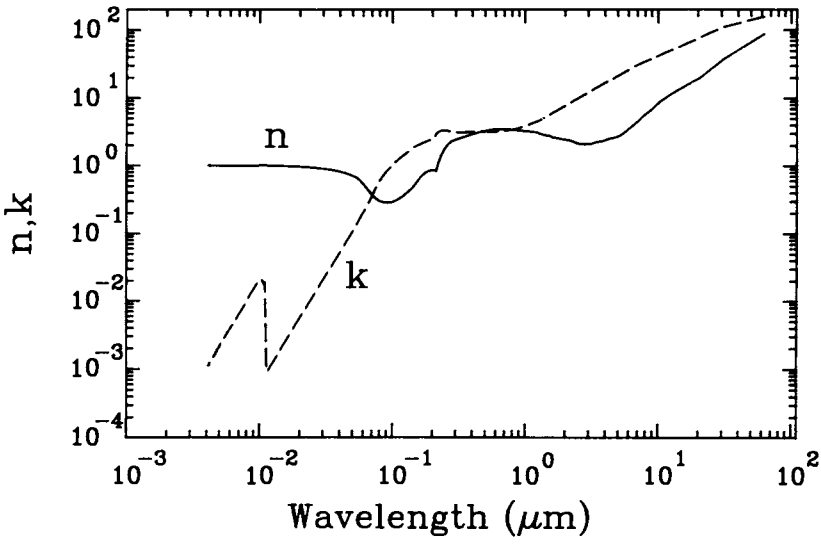

Fig. 2. Log–log plot of n (solid line) and k (dashed line) versus wavelength in micrometers for beryllium.

TABLE I

Summary of Experimental Information for Significant Studies of the Optical Properties of Be

Ref. (date)	Range (eV)	Method	Preparation	Temp. (K)
[5] (1970)	60–250	Transmission	Evap. film	298
[6] (1983)	41–705	Transmission	Evap. film	298
[9] (1968)	10–26	$R(\Theta)$	Evap. film	298
[8] (1976)	2–25	$R(0)$ and K–K	Evap. film	298
[10] (1974)	0.5–3.8	Ellipsometry	Evap. film	298; 20
[11] (1973)	0.12–4.5	Abs. and K–K	Single crystal	4
[15] (1961)	0.11–1.5	Ellipsometry	Evap. film	298; 82
[17] (1977)	0.03–3.1	$R(0)$ only	Polished bulk	298; 82
[12] (1989)	0.06–4.8	$R(0)$ only	Polished bulk	298

$R(\Theta)$ denotes reflectance as a function of incidence angle and $R(0)$ is normal-incidence reflectance.

TABLE II

Values of n and k for Beryllium

eV	cm^{-1}	μm	n	k
0.02	161.3	6.199E+01	8.61E+01	1.57E+02
0.03	242.0	4.133E+01	5.19E+01	1.32E+02
0.04	322.6	3.100E+01	3.74E+01	1.10E+02
0.05	403.3	2.480E+01	2.47E+01	9.17E+01
0.06	483.9	2.066E+01	1.99E+01	7.71E+01
0.07	564.6	1.771E+01	1.70E+01	6.76E+01
0.08	645.2	1.550E+01	1.46E+01	6.04E+01
0.09	725.9	1.378E+01	1.27E+01	5.08E+01
0.1	806.5	1.240E+01	1.13E+01	5.01E+01
0.2	1,613	6.199E+00	3.66E+00	2.67E+01
0.3	2,420	4.133E+00	2.43E+00	1.73E+01
0.4	3,226	3.099E+00	2.07E+00	1.26E+01
0.5	4,033	2.480E+00	2.14E+00	9.67E+00
0.6	4,839	2.066E+00	2.41E+00	7.88E+00
0.7	5,646	1.771E+00	2.55E+00	6.64E+00
0.8	6,452	1.550E+00	2.74E+00	5.66E+00
0.9	7,259	1.378E+00	2.87E+00	5.02E+00
1.0	8,066	1.240E+00	3.09E+00	4.51E+00
1.2	9,679	1.033E+00	3.26E+00	3.96E+00
1.4	11,292	8.856E-01	3.35E+00	3.55E+00
1.6	12,905	7.749E-01	3.44E+00	3.35E+00
1.8	14,518	6.888E-01	3.47E+00	3.23E+00
2.0	16,132	6.199E-01	3.46E+00	3.18E+00
2.2	17,745	5.635E-01	3.39E+00	3.17E+00
2.4	19,358	5.166E-01	3.30E+00	3.18E+00
2.6	20,971	4.768E-01	3.19E+00	3.16E+00
2.8	22,584	4.428E-01	3.07E+00	3.16E+00
3.0	24,198	4.133E-01	2.95E+00	3.14E+00
3.2	25,811	3.874E-01	2.84E+00	3.12E+00
3.4	27,424	3.646E-01	2.73E+00	3.10E+00
3.6	29,037	3.444E-01	2.64E+00	3.08E+00
3.8	30,650	3.263E-01	2.55E+00	3.08E+00
4.0	32,263	3.100E-01	2.47E+00	3.08E+00
4.2	33,876	2.952E-01	2.39E+00	3.10E+00
4.4	35,490	2.818E-01	2.30E+00	3.15E+00
4.6	37,103	2.695E-01	2.17E+00	3.22E+00
4.8	38,716	2.583E-01	1.99E+00	3.29E+00
5.0	40,329	2.480E-01	1.78E+00	3.32E+00
5.2	41,942	2.384E-01	1.54E+00	3.30E+00
5.4	43,555	2.296E-01	1.31E+00	3.23E+00
5.6	45,169	2.214E-01	1.08E+00	3.11E+00
5.8	46,780	2.138E-01	8.21E-01	2.90E+00
6.0	48,393	2.066E-01	8.49E-01	2.64E+00
6.2		2.000E-01	8.44E-01	2.52E+00
6.4		1.937E-01	8.37E-01	2.42E+00
6.6		1.878E-01	8.25E-01	2.34E+00
6.8		1.823E-01	8.05E-01	2.28E+00

TABLE II (*Continued*)

Beryllium

eV	cm^{-1}	μm	n	k
7.0		1.771E-01	7.78E-01	2.23E+00
7.2		1.722E-01	7.44E-01	2.18E+00
7.4		1.675E-01	7.07E-01	2.13E+00
7.6		1.631E-01	6.71E-01	2.08E+00
7.8		1.589E-01	6.28E-01	2.04E+00
8.0		1.550E-01	5.88E-01	1.98E+00
8.2		1.512E-01	5.51E-01	1.92E+00
8.4		1.476E-01	5.18E-01	1.87E+00
8.6		1.442E-01	4.90E-01	1.81E+00
8.8		1.409E-01	4.63E-01	1.75E+00
9.0		1.378E-01	4.45E-01	1.69E+00
9.2		1.348E-01	4.27E-01	1.64E+00
9.4		1.319E-01	4.12E-01	1.59E+00
9.6		1.291E-01	3.98E-01	1.54E+00
9.8		1.265E-01	3.85E-01	1.50E+00
10.0		1.240E-01	3.73E-01	1.45E+00
10.5		1.181E-01	3.45E-01	1.35E+00
11.0		1.127E-01	3.24E-01	1.25E+00
11.5		1.078E-01	3.09E-01	1.16E+00
12.0		1.033E-01	2.98E-01	1.07E+00
12.5		9.918E-02	2.87E-01	9.91E-01
13.0		9.537E-02	2.84E-01	9.13E-01
13.5		9.184E-02	2.83E-01	8.41E-01
14.0		8.856E-02	2.84E-01	7.72E-01
14.5		8.550E-02	2.87E-01	7.07E-01
15.0		8.265E-02	2.93E-01	6.45E-01
15.5		7.999E-02	3.00E-01	5.85E-01
16.0		7.749E-02	3.12E-01	5.27E-01
16.5		7.514E-02	3.26E-01	4.73E-01
17.0		7.293E-02	3.42E-01	4.21E-01
17.5		7.085E-02	3.61E-01	3.72E-01
18.0		6.888E-02	3.82E-01	3.25E-01
18.5		6.702E-02	4.07E-01	2.95E-01
19.0		6.525E-02	4.36E-01	2.70E-01
19.5		6.358E-02	4.68E-01	2.42E-01
20.0		6.199E-02	4.96E-01	2.20E-01
20.5		6.048E-02	5.26E-01	2.03E-01
21.0		5.904E-02	5.55E-01	1.90E-01
21.5		5.767E-02	5.83E-01	1.72E-01
22.0		5.635E-02	6.11E-01	1.60E-01
22.5		5.510E-02	6.32E-01	1.47E-01
23.0		5.390E-02	6.53E-01	1.35E-01
23.5		5.276E-02	6.68E-01	1.22E-01
24.0		5.166E-02	6.84E-01	1.15E-01
24.5		5.060E-02	6.97E-01	1.08E-01
25.0		4.959E-02	7.10E-01	1.02E-01
25.5		4.862E-02	7.22E-01	9.50E-02

TABLE II (*Continued*)

Beryllium

eV	cm^{-1}	μm	n	k
26		4.769E-02	7.34E-01	8.95E-02
27		4.592E-02	7.53E-01	8.00E-02
28		4.428E-02	7.70E-01	7.05E-02
29		4.275E-02	7.86E-01	6.35E-02
30		4.133E-02	8.00E-01	5.65E-02
35		3.542E-02	8.54E-01	3.47E-02
40		3.100E-02	8.89E-01	2.24E-02
45		2.755E-02	9.14E-01	1.54E-02
50		2.480E-02	9.32E-01	1.10E-02
55		2.254E-02	9.45E-01	8.08E-03
60		2.066E-02	9.55E-01	6.09E-03
65		1.907E-02	9.63E-01	4.72E-03
70		1.771E-02	9.69E-01	3.71E-03
75		1.653E-02	9.74E-01	2.98E-03
80		1.550E-02	9.79E-01	2.42E-03
85		1.459E-02	9.83E-01	2.00E-03
90		1.378E-02	9.86E-01	1.66E-03
95		1.305E-02	9.89E-01	1.39E-03
100		1.240E-02	9.93E-01	1.18E-03
105		1.181E-02	9.97E-01	1.01E-03
110		1.127E-02	1.00E+00	9.43E-04
111		1.117E-02	1.01E+00	1.49E-03
112		1.107E-02	1.01E+00	4.87E-03
113		1.097E-02	1.01E+00	1.32E-02
114		1.088E-02	1.01E+00	1.88E-02
115		1.078E-02	1.01E+00	1.74E-02
116		1.069E-02	1.00E+00	1.79E-02
117		1.060E-02	1.00E+00	1.85E-02
118		1.051E-02	1.00E+00	1.99E-02
119		1.042E-02	1.00E+00	2.04E-02
120		1.033E-02	9.99E-01	2.04E-02
121		1.025E-02	9.98E-01	2.05E-02
122		1.016E-02	9.97E-01	2.05E-02
123		1.008E-02	9.96E-01	2.04E-02
124		9.998E-03	9.95E-01	2.02E-02
125		9.918E-03	9.95E-01	2.00E-02
126		9.840E-03	9.94E-01	1.99E-02
127		9.762E-03	9.93E-01	1.95E-02
128		9.686E-03	9.93E-01	1.90E-02
129		9.611E-03	9.93E-01	1.84E-02
130		9.537E-03	9.91E-01	1.80E-02
140		8.856E-03	9.89E-01	1.41E-02
150		8.265E-03	9.89E-01	1.12E-02
160		7.749E-03	9.89E-01	9.02E-03
170		7.293E-03	9.90E-01	7.37E-03
180		6.888E-03	9.91E-01	6.09E-03
190		6.525E-03	9.91E-01	5.09E-03

TABLE II (*Continued*)

Beryllium

eV	cm^{-1}	μm	n	k
200		6.199E-03	9.92E-01	4.29E-03
210		5.904E-03	9.92E-01	3.65E-03
220		5.636E-03	9.93E-01	3.12E-03
230		5.390E-03	9.94E-01	2.69E-03
240		5.166E-03	9.94E-01	2.34E-03
250		4.959E-03	9.94E-01	2.04E-03
260		4.769E-03	9.95E-01	1.79E-03
270		4.592E-03	9.95E-01	1.58E-03
280		4.428E-03	9.95E-01	1.40E-03
290		4.275E-03	9.96E-01	1.24E-03
300		4.133E-03	9.96E-01	1.11E-03

TABLE III

Optical Constants for Be from Henke Model

eV	Å	n	k
299	4.154E+03	0.99586	1.11E-03
313	3.966E+03	0.99622	9.36E-04
327	3.787E+03	0.99655	7.92E-04
343	3.616E+03	0.99686	6.71E-04
359	3.453E+03	0.99713	5.68E-04
376	3.297E+03	0.99739	4.81E-04
394	3.148E+03	0.99762	4.06E-04
413	3.006E+03	0.99783	3.41E-04
432	2.870E+03	0.99802	2.86E-04
452	2.741E+03	0.99820	2.40E-04
474	2.617E+03	0.99836	2.01E-04
496	2.499E+03	0.99851	1.69E-04
520	2.386E+03	0.99865	1.42E-04
574	2.278E+03	0.99877	1.19E-04
570	2.175E+03	0.99888	9.94E-05
583	2.126E+03	0.99893	9.09E-05
597	2.077E+03	0.99898	8.32E-05
611	2.030E+03	0.999030	7.61E-05
625	1.983E+03	0.999075	6.96E-05
655	1.894E+03	0.999159	5.79E-05
686	1.808E+03	0.999236	4.82E-05
718	1.727E+03	0.999305	4.05E-05
752	1.649E+03	0.999368	3.37E-05
788	1.574E+03	0.999425	2.81E-05
825	1.503E+03	0.999477	2.34E-05
864	1.435E+03	0.999525	1.95E-05
905	1.370E+03	0.999568	1.63E-05
948	1.308E+03	0.999607	1.35E-05
992	1.249E+03	0.999642	1.13E-05
1039	1.193E+03	0.999674	9.34E-06
1088	1.139E+03	0.999704	7.75E-06
1140	1.088E+03	0.999730	6.42E-06
1194	1.039E+03	0.999755	5.33E-06
1250	9.917E+02	0.999777	4.42E-06
1309	9.469E+02	0.999797	3.66E-06
1371	9.041E+02	0.999815	3.04E-06
1436	8.633E+02	0.999832	2.52E-06
1504	8.244E+02	0.999847	2.10E-06
1575	7.871E+02	0.999860	1.78E-06
1650	7.516E+02	0.999873	1.52E-06
1728	7.176E+02	0.999884	1.29E-06
1809	6.852E+02	0.999895	1.09E-06
1895	6.543E+02	0.9999039	9.18E-07
1985	6.248E+02	0.9999125	7.70E-07
2078	5.965E+02	0.9999203	6.46E-07
2177	5.696E+02	0.9999273	5.42E-07
2280	5.439E+02	0.9999338	4.50E-07

TABLE III (*Continued*)

Optical Constants for Be from Henke Model

eV	Å	n	k
2387	5.193E+02	0.9999397	3.74E-07
2500	4.959E+02	0.9999450	3.11E-07
2619	4.735E+02	0.9999499	2.58E-07
2742	4.521E+02	0.9999544	2.14E-07
2872	4.317E+02	0.9999585	1.77E-07
3008	4.122E+02	0.9999621	1.46E-07
3150	3.936E+02	0.9999655	1.20E-07
3299	3.758E+02	0.9999685	9.89E-08
3455	3.588E+02	0.9999713	8.15E-08
3619	3.426E+02	0.9999739	6.71E-08
3790	3.272E+02	0.9999762	5.53E-08
3969	3.124E+02	0.9999783	4.57E-08
4157	2.983E+02	0.9999802	3.79E-08
4353	2.848E+02	0.9999819	3.14E-08
4559	2.720E+02	0.9999835	2.60E-08
4775	2.597E+02	0.9999850	2.15E-08
5000	2.479E+02	0.9999864	1.78E-08
5237	2.368E+02	0.9999875	1.48E-08
5484	2.261E+02	0.9999887	1.22E-08
5744	2.159E+02	0.9999896	1.01E-08
6015	2.061E+02	0.9999060	8.34E-09
6300	1.968E+02	0.99999140	6.89E-09
6598	1.879E+02	0.99999220	5.68E-09
6910	1.794E+02	0.99999280	4.64E-09
7237	1.713E+02	0.99999350	3.78E-09
7579	1.636E+02	0.99999400	3.09E-09
7937	1.562E+02	0.99999460	2.52E-09
8313	1.492E+02	0.99999510	2.06E-09
8706	1.424E+02	0.99999550	1.68E-09
9117	1.360E+02	0.99999590	1.37E-09
9549	1.298E+02	0.99999620	1.12E-09
10000	1.240E+02	0.99999660	9.12E-10

Cobalt (Co)

L. WARD
Coventry Polytechnic
Coventry, England

Cobalt is an element with an atomic number of 27 and is one of the group of transition metals; it can readily be obtained in the form of blocks, rods, or powder, and its most common impurities are iron, nickel, sodium, and potassium. There are two allotropic forms of cobalt: close-packed hexagonal, which is stable at room temperature, and face-centered cubic, which is stable above 417 °C and which can be produced from the hexagonal form by a suitable annealing procedure. Much of the published work on solid cobalt refers to the hexagonal close-packed crystal structure, which implies that the optical properties should be different along different crystal directions. However, in most cases, authors have dealt with polycrystalline material, where the optical properties are independent of direction; only one set of results has been published for single-crystal bulk cobalt in which the optical properties along both the main crystal axes are considered. In addition, several papers have reported measurements on thin films, again mostly in the polycrystalline form.

Being metallic, cobalt, at long wavelengths in the infrared region, may be expected to behave according to the classical Drude formulas for free-electron materials, namely,

$$\varepsilon_1 = n^2 - k^2 = 1 - A\nu_c/2\pi(\nu^2 + \nu_c^2)$$

$$\varepsilon_2 = 2nk = A\nu_c^2/2\pi\nu(\nu^2 + \nu_c^2),$$

where A is a constant, proportional to the dc electrical conductance, ν is the frequency and ν_c is the electron collision frequency. These formulas predict that in the infrared the optical constants n and k should have large values with both increasing with wavelength. This behavior is in fact observed at all wavelengths longer than about 6 μm, but below that point, there is a marked departure from the Drude equation in the form of increases in the values of both n and k as the wavelength decreases, producing maxima in each at about 3 μm. It is generally regarded that this

Copyright © 1991 by Academic Press.
All rights of reproduction in any form reserved.
ISBN 0-12-544422-2

anomaly is caused by the onset of interband electron transitions due to the very small energy gap (0.20 eV) between the Fermi level in the almost full d-band and the next higher s-band. However, as the wavelength continues to decrease below 1 μm, n and k resume their downward trend in values and ultimately n becomes equal to k, which is the condition for plasma oscillations; this plasma resonance occurs at a frequency of $18.6 \times 10^{14}\, s^{-1}$ (0.16 μm). At very short wavelengths, n becomes asymptotic to unity, while k continues to fall, reaching extremely low values below 0.01 μm. However, there are further maxima in k, one at 0.020 μm and a second at 0.011 μm. These are due to additional electron transitions between inner levels, the first at the $M_{II,III}$ point and the second at the M_I point. Beyond this wavelength, there is little published experimental optical information on cobalt, so further interband transitions have not been recorded, although X-ray data indicate L-edges at 0.0016 μm and 0.0013 μm and a K-edge at 0.00016 μm [1].

Much of the work on the optical properties of metals published before about 1950 is now regarded as unreliable because of the uncertain state of the surfaces used. Not only does mechanical polishing produce an atypical surface layer in which the crystal structure is broken down and much dislocated, but many crystals rapidly become oxidized or contaminated when exposed to air; this produces a surface layer having unknown optical properties, of which it is consequently difficult to take account when calculating n and k. Two developments since 1950 have led to the production of reliable, clean, and reproducible crystalline surfaces, suitable for optical work: ultrahigh-vacuum conditions can be generated, which almost eliminate oxidation problems and at the same time create the conditions under which epitaxial films can be deposited; and mechanical polishing can be carefully controlled or replaced by electrochemical polishing, so that deep-seated mechanical damage may be avoided. Archard [2] has given a review of modern polishing techniques.

There have been two major reviews covering the optical constants of the transition metals, including cobalt. The first, by Weaver *et al.* [3], surveyed a large number of papers including those by Kirillova and Charikov [4], Lenham and Treherne [5], Yu *et al.* [6], Sonntag *et al.* [7], Johnson and Christy [8], Weaver *et al.* [9] and Wehenkel and Gauthe [10]. Making use mainly of their own results on single-crystal hcp cobalt, Weaver *et al.* [3] have presented sets of data of n and k over the wavelength range 0.15–12.44 μm for the two cases of the electric field vector of the incident radiation parallel to and perpendicular to the c axis of the crystal, that is, the axis at right angles to the base of the hexagon. In the second review, Ordal *et al.* [11] collected data for cobalt over a wide range of wavelengths from 0.20–20 μm, mainly in the infrared region. The main sources of their data were Johnson and Christy [8], Weaver *et al.* [9], and Kirillova and Charikov [4]. As well as giving tables of values of n and k between 0.19 μm

and 20.0 μm, they have graphed ε_1 and ε_2 against wave number. A further, later review by Ordal *et al.* [12] continued the same work in the infrared and showed graphically a Drude-model fit to the various experimental results.

Values of n and k for cobalt from various sources are given in Table I and graphed in Fig. 1; the wavelength range covered is 6×10^{-4}–12.4 μm and, wherever possible, slight wavelength overlaps have been included between the different sets of results.

Results for X-ray Region

For extremely short wavelengths in the X-ray region (6–120 Å), there are no direct experimental results for the optical constants of cobalt. However, Henke [13] has shown that n and k in this wavelength region may be calculated from the X-ray scattering coefficients of the atoms involved. Thus, for cobalt:

$$k = 40.0\lambda^2 f_2$$

$$n = 1 - 40.0\lambda^2 f_1,$$

where λ is the wavelength in microns and f_1 and f_2 are the appropriate scattering factors. Henke *et al.* [14] have published tables of f_1 and f_2 for many values of wavelength and photon energy for some of the atoms in the periodic table, from which the values of n and k for cobalt at these wavelengths have been calculated; these are tabulated at the end of this article in Table I. As expected, n in this region of the spectrum is close to unity, whereas k shows a definite peak at 16 Å (0.0016 μm) due to the $L_{2,3}$ transitions, and a much smaller peak at 0.00134 μm due to the L_1 transition.

Results for Cobalt Films

At slightly longer wavelengths (0.004–0.06 μm) experimental values of the absorption coefficient, α, equal to $4\pi k/\lambda$, have been published by Sonntag *et al.* [7] and also by Wehenkel and Gauthe [10, 26]. Sonntag *et al.* used synchrotron radiation in a direct measurement of the absorption coefficient; k may be easily deduced from the graphs they provide. It is assumed that n is approximately equal to unity in this spectral region. Wehenkel and Gauthe measured the electron-energy-loss spectrum by bombarding thin films of cobalt by 35 keV electrons; a Kramers–Kronig summation technique was then used to calculate ε_1 and ε_2, from which n and k can be extracted. Both these studies revealed a maximum in k at 0.020 μm and a shoulder at 0.011 μm (62.3 eV and 107 eV); these are due to the transitions $M_{II,III}$ and M_I, respectively. The values of k deduced from

Wehenkel and Gauthe are larger than those from Sonntag *et al.*, particularly at the shorter wavelength end. Values of k from both sources are presented in Table I, those of Sonntag *et al.* from 0.006–0.03 μm and the ones from Wehenkel and Gauthe between 0.035 μm and 0.31 μm. There is some wavelength overlap between these results and those calculated by Henke's method, and the agreement in the values of the optical constants is considered to be satisfactory. Fanfoni *et al.* [15], studying the electron-energy-loss spectrum up to 240 eV (0.005 μm), confirmed the $M_{II,III}$ edge at 0.018 μm but did not discover any further edges beyond that point, although a peak might have been expected at 0.011 μm.

A set of results produced by Yu *et al.* [6] is considered to be very reliable; they used specimens of polycrystalline cobalt prepared by electron-beam evaporation under ultrahigh-vacuum conditions. The optical parameter measured was the reflectance near normal incidence, and the optical constants were extracted by Kramers–Kronig analysis over the range 0.1–25 μm, although they give useful graphs only for energies greater than 0.25 eV, that is, wavelengths less than 5.0 μm; these values of n and k have also been tabulated in Table I and link reasonably well with those of Wehenkel and Gauthe.

Johnson and Christy [8] give a set of values of n and k between 0.64 eV and 6.60 eV (0.2–2.0 μm), their results being obtained from measurements of the reflectance and transmittance of thin evaporated films having thicknesses between 200 Å and 500 Å. In general, their values of both n and k, which are presented in Table I, were smaller than those reported by Yu, possibly either because of the vacuum conditions prevailing in their equipment or the different substrate temperature used during evaporation.

Viguier *et al.* [16], using both ellipsometric and reflectance measurements, have produced values of ε_1 and ε_2 for polycrystalline cobalt films 1000 Å thick between 1 eV and 5 eV (0.25–1.25 μm). There were no distinctive optical features over this region; ε_2 was positive and increased steadily with wavelength, whereas ε_1 was negative and became more so as the wavelength increased. An accuracy of 0.2% was claimed for measurements in the visible spectrum, the greatest uncertainty being due to the surface roughness. However, the calculated values of n and k from this work are both at least 10% smaller than those given by Johnson and Christy. A set of their results is included in Table I, since this is one of the most recent determinations of the optical constants of cobalt.

Kudryavtsev and Lezhnenko [17] investigated cobalt films between 1 μm and 13 μm in both the hcp and the fcc crystal forms, changing from one form to the other by suitable annealing above 400 °C. Experimentally, Beattie's method [18] was used, in which the phase change on reflection was measured for several angles of incidence, which in this case were greater than 80°. The authors noted significant differences between the optical properties of the two forms of cobalt in both the intra- and

interband transition regions. In the interband region ($\lambda > 6$ μm) n increased while k decreased on changing from hexagonal to cubic, whereas in the interband region ($1 < \lambda < 6$ μm) both n and k decreased for a similar change. Because their set of results for the cubic form of cobalt is virtually unique, it has been included in Table I.

Clemens and Jaumann [19] measured the optical constants of evaporated layers of cobalt having thicknesses of about 0.03 μm and deposited on glass substrates; the wavelength range covered was 0.42–2.5 μm. The special feature of this work was that the films were magnetically saturated at right angles to their plane, and measurements were made of the reflectances and transmittances from both sides of the substrate. Both n and k turned out to be different as determined from the two sides, but those from the air side agreed well with the results of Weaver *et al.* [3] for the extraordinary ray. Over the spectral region investigated, both sets of optical constants increased steadily with wavelength; from the published graphs, n and k can be read to about ± 0.01.

Results for Bulk Cobalt

Kirillova *et al.* [20] measured the reflectance of polycrystalline solid specimens between 0.1 μm and 0.25 μm and then used Kramers–Kronig analysis to extract ε_1 and ε_2. They noted the effects of the first quantum absorption band between 0.2 μm and 1.2 μm due to electron transitions in various directions within the Brillouin zone. However, the graphs they give are not suitable for the accurate reading of n and k values. Kirillova and Charikov [4] studied bulk polycrystalline cobalt by a polarimetric technique between 2.5 μm and 20.0 μm, noting the contribution from interband transitions in this region even up to 6 or 7 μm. They calculated the plasma frequency to be $18.6 \times 10^{14} s^{-1}$ (that is, the plasma wavelength = 0.162 μm) and the electron relaxation frequency as $2.5 \times 10^{14} s^{-1}$. Bolotin *et al.* [21] obtained the optical constants for a mechanically polished and then annealed polycrystalline specimen of cobalt using the method of Beattie [18]; values of n and k were tabulated between 0.3 μm and 17.0 μm. The classical free-electron theory provided a satisfactory model between 6 μm and 17 μm, but at shorter wavelengths the anomalous behavior described above was observed, there being a peak in the electrical conductivity at 1.5 μm. The values of k reported by this group were in approximate agreement with those of Yu, but those for n were considerably lower, particularly at the shorter wavelengths investigated, again probably because of the damage to the surface layer by the mechanical-polishing technique employed. However, because they are still one of the few sets of data covering this wide wavelength band, they are quoted in Table I. Afanasyeva and Kirillova [22] give data measured on polycrystalline cobalt between 0.8 μm and 3.5 μm. Using mechanically polished specimens, the measured parameter was the electrical conductivity, which as shown above

is closely related to the optical constants. They also paid particular attention to the spectral region where n increased as the wavelength decreased. Their values for k were comparable with those of Bolotin *et al.*, but the data for n were significantly smaller, particularly at the shorter wavelengths, perhaps due to their polishing technique. Other sets of data for the infrared region (0.3–12.5 μm) have been obtained by Lenham and his collaborators [5, 23], who used an ellipsometric technique in conjunction with mechanically polished polycrystalline specimens. Their published graphs, however, are not generally suitable for the extraction of accurate values. A set of values of n and k for bulk cobalt at different temperatures has been published by Gushchin *et al.* [24]. Beattie's method was again the experimental method used, and the measurements were carried out between 0.4 and 3.3 μm and at temperatures of 20, 1400 and 1600 °C. The results at 20 °C are in fair agreement with those of Bolotin *et al.* taken at the same temperature, and it was also observed that both n and k increased with temperature up to 1400 °C. The optical constants at 1400 °C are included in Table I. Kulikov and Kulatov [25] report an interesting theoretical study of the variation of the optical properties of cobalt with pressure.

Results for Cobalt Using Polarized Radiation

Weaver *et al.* [9] present detailed tables of the optical constants of single-crystal cobalt between 0.15 and 12.4 μm for radiation polarized with its **E** vector parallel to and perpendicular to the c axis, that is, the axis at right angles to the base of the crystalline hexagon; these being the only data to deal with both states of polarization, they are quoted extensively in Table I. Their measurements were made on electrolytically polished specimens employing reflectance for wavelengths below 0.3 μm and calorimetry for wavelengths greater than 0.3 μm. The two sets of values exhibit their greatest differences at the longer wavelengths investigated (1–6.5 μm), where n for $\mathbf{E}_{\parallel c}$ (n_e) is smaller than that for $\mathbf{E}_{\perp c}$ (n_o); the opposite applies to the values of k where k_e is larger than k_o. For wavelengths below 0.6 μm, the separate values of n and k converge. At this point, the values of the optical constants are also in good agreement with those produced by Yu *et al.* and Bolotin *et al.* for the polycrystalline form of cobalt, as would be expected to happen. The results of Weaver *et al.* for the cases of polarization both parallel and perpendicular to the c axis indicate maxima in n at 1.7 μm and corresponding minima at 6 μm. For k there is a maximum at 1.35 μm (perpendicular c axis) and a much less well-defined maximum at 1.40 μm (parallel c axis).

REFERENCES

1. J. R. Beardon and A. F. Burr, *Rev. Mod. Phys.* **39**, 125 (1967).

2. J. F. Archard, *Phys. Bull.* **36**, 212 (1985).
3. J. H. Weaver, C. Krafta, D. W. Lynch, and E. E. Koch, "Physics Data, Optical Properties of Metals, Part 2," Fachsinformazionszentrum, Karlsruhe (1981).
4. M. M. Kirillova and B. A. Charikov, *Opt. and Spectros.* **17**, 134 (1964).
5. A. P. Lenham and D. M. Treherne, *J. Opt. Soc. Am.* **56**, 1076 (1966).
6. A. Y.-C. Yu, T. M. Donovan, and W. E. Spicer, *Phys. Rev.* **167**, 670 (1968).
7. B. Sonntag, R. Haensel, and C. Kunz, *Solid State Commun.* **7**, 597 (1969).
8. P. B. Johnson and R. W. Christy, *Phys. Rev.* **B9**, 5056 (1974).
9. J. H. Weaver, E. Colevita, D. W. Lynch and R. Rossi, *Phys. Rev.* **B19**, 3850 (1979).
10. C. Wehenkel and B. Gauthe, *Phys. Stat. Solidi. B* **64**, 515 (1974).
11. M. R. Ordal, L. L. Long, R. J. Bell, S. E. Bell, R. R. Bell, R. W. Alexander, and C. R. Ward, *Appl. Opt.* **22**, 1099 (1983).
12. M. R. Ordal, R. J. Bell, R. W. Alexander, L. L. Long, and M. R. Quarry, *Appl. Opt.* **24**, 4493 (1985).
13. B. L. Henke, *A.I.P. Conf. Proc. No. 75*, 146 (1981).
14. B. L. Henke, P. Lee, T. J. Tanaka, R. Shimabukaro and B. K. Fujikawa, *Atomic Data and Nuclear Data Tables* **27**, 1 (1982).
15. M. Fanfoni, S. Modesti, R. Motta, N. de Cresenta, and R. Rossi, *Phys. Rev.* **B32**, 7826 (1985).
16. C. Viguier, R. Cros, A. Humbert, C. Ferrien, O. Thomas, R. Mader, and J. P. Senateur, *Solid State Commun.* **60**, 923 (1986).
17. V. Y. Kudryavtsev and I. V. Lezhnenko, *Sov. Phys. Solid State* **21**, 249 (1981).
18. J. R. Beattie, *Phil. Mag.* **46**, 222 (1955).
19. K. H. Clemens and J. Jaumann, *Z. Physik* **173**, 135 (1963).
20. M. M. Kirillova, L. V. Nomerovannya, G. A. Bolotin, V. M. Mayevskiy, M. M. Noskov, and M. S. Bolotin, *Phys. Met. Metallog.* **25**, 81 (1969).
21. G. A. Bolotin, M. M. Noskov, and I. I. Sasovshaya, *Phys. Met. Metallog.* **35**, 24 (1973).
22. L. A. Afanasyeva and M. M. Kirillova, *Phys. Met. Metallog.* **23**, 80 (1967).
23. A. P. Lenham, *J. Opt. Soc. Am.* **57**, 473 (1967).
24. V. S. Gushchin, K. M. Shararev, B. A. Baum, and P. V. Geld, *Sov. Phys. Dokl.* **23**, 344 (1978).
25. N. I. Kulatov and E. T. Kulakov, *J. Phys. F* **12**, 2267 (1982).
26. C. Wehenkel and R. Gauthe, *Phys. Lett.* **47A**, 253 (1974).

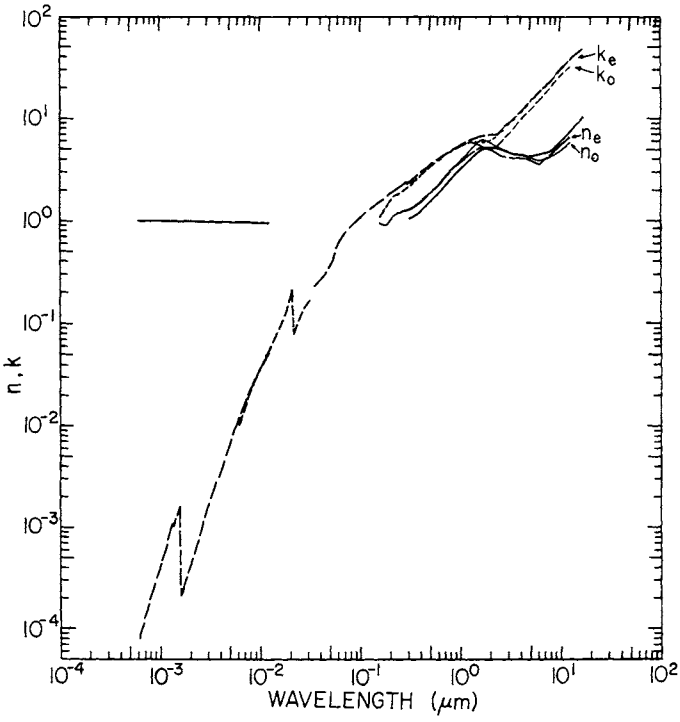

Fig. 1. Log–log plot of n (solid line) and k (dashed line) versus wavelength in micrometers for cobalt (unpolarized radiation unless specified otherwise).

TABLE I

Values of *n* and *k* for Hexagonal Cobalt from Various Refs.[a]

eV	cm^{-1}	μm	n	k
2000	16,131,000	0.00062	0.9996 [13]	$8.0*10^{-5}$ [13]
1850	14,921,000	0.00067	0.9996	$1.0*10^{-4}$
1688	13,615,000	0.00073	0.9994	1.4
1609	12,977,000	0.00077	0.9994	1.6
1550	12,500,000	0.00080	0.9992	2.0
1358	10,953,000	0.00091	0.9992	3.0
1240	10,000,000	0.00100	0.9990	4.2
1148	9,259,300	0.00108	0.9988	5.2
1016	8,194,500	0.00122	0.9988	8.0
946.5	7,633,900	0.00131	0.9992	10.4
925.3	7,463,000	0.00134	0.9992	10.8
898.4	7,246,000	0.00138	0.9992	10.6
879.3	7,092,000	0.00141	0.9992	11.6
855.1	6,896,700	0.00145	0.9988	12.6
815.7	6,579,000	0.00152	0.9990	14.6
800.0	6,452,400	0.00155	0.9992	15.6
775.0	6,250,000	0.00160	1.0006	17.0
760.6	6,134,600	0.00163	0.9994	2.2
729.3	5,882,100	0.00170	0.9988	2.4
725.1	5,848,200	0.00171	0.9986	2.6
620.0	5,000,000	0.00200	0.9976	4.2
529.0	4,273,700	0.00234	0.9964	7.0
413.3	3,333,300	0.00300	0.9938	15.0
368.0	2,968,100	0.00337	0.9920	22.0
310.0	2,500,000	0.00400	0.9810	34.0
269.0	2,169,600	0.00461	0.9858	52.0
248.0	2,000,000	0.00500	0.9838	64.0
227.1	1,831,700	0.00546	0.9810	$84.0*10^{-4}$
206.6	1,666,700	0.00600	0.9770	$10.8*10^{-3}$
190.7	1,538,100	0.00650	0.9748	13.2
177.1	1,428,400	0.00700	0.9720	15.6
155.0	1,250,000	0.00800	0.9656	21.8
137.8	1,111,100	0.00900	0.9586	29.0
124.0	1,000,000	0.0100	0.9550	35.2
111.7	900,900	0.0111	0.9492	42.8
104.2	840,400	0.0119	0.9492	49.0
100.0	806,500	0.0124	0.9414	52.8

Values of *n* and *k* for Hexagonal Cobalt Films

eV	cm^{-1}	μm	n	k
200	1,612,900	0.006200	1.00 [7]	$1.0*10^{-2}$ [7]
172	1,388,900	0.007209	1.00	1.5
149	1,205,000	0.008322	1.00	2.3
120	971,100	0.01033	1.00	3.8
110	887,200	0.01127	1.00	4.7
106	854,900	0.01170	1.00	5.0
100	806,500	0.01240	1.00	5.5
94.7	763,400	0.01309	1.00	6.1
89.8	724,600	0.01381	1.00	7.0
80.0	645,200	0.01550	1.00	$8.7*10^{-2}$

TABLE I (*Continued*)

Hexagonal Cobalt

eV	cm^{-1}	μm	n	k
70.1	565,000	0.01769	1.00 [7]	$1.2*10^{-1}$ [7]
62.0	500,000	0.02000	1.00	1.8
56.4	454,600	0.02199	1.00	0.8
49.6	400,000	0.02500	1.00	1.1
44.3	357,100	0.02805	1.00	1.4
38.8	312,500	0.03196	1.00	$1.7*10^{-1}$
35.4	285,700	0.03503	1.00 [10]	0.23 [10]
31.0	250,000	0.04000	1.00	0.26
24.8	200,000	0.05000	1.00	0.35
20.7	166,300	0.05990	1.00	0.65
17.7	142,800	0.07006	1.00	0.77
15.5	125,000	0.08000	1.00	0.90
12.4	100,000	0.1000	1.00	1.08
10.0	80,650	0.1240	1.00	1.31
7.01	56,500	0.1769	1.00	1.68
4.00	32,260	0.3100	1.00	2.48
11.46	90,430	0.1080	1.096 [6]	0.775 [6]
9.69	78,130	0.1280	1.088	0.827
7.75	62,500	0.1600	1.049	1.049
5.99	48,310	0.2070	1.210	1.570
3.94	31,750	0.3150	1.298	2.118
3.00	24,210	0.4133	2.153	3.484
2.00	16,130	0.6200	2.486	4.022
1.00	8,065	1.240	3.639	6.184
0.600	4,839	2.067	4.708	8.495
0.400	3,226	3.100	5.301	11.318
6.60	53,230	0.1879	1.16 [8]	1.59 [8]
6.22	50,170	0.1993	1.29	1.71
5.85	47,180	0.2119	1.38	1.82
5.36	43,230	0.2313	1.47	1.87
4.98	40,170	0.2490	1.45	1.93
4.61	37,180	0.2689	1.44	2.04
4.24	34,200	0.2924	1.44	2.19
3.99	32,190	0.3107	1.44	2.31
3.74	30,160	0.3315	1.46	2.44
3.50	28,230	0.3542	1.49	2.61
3.25	26,710	0.3815	1.53	2.82
3.00	24,200	0.4133	1.61	3.05
2.75	22,180	0.4509	1.74	3.28
2.50	20,160	0.4959	1.88	3.55
2.26	18,180	0.5486	2.05	3.82
2.13	17,240	0.5821	2.13	3.96
2.01	16,130	0.6168	2.19	4.11
1.88	15,160	0.6595	2.25	4.27
1.76	14,280	0.7045	2.31	4.45
1.64	13,160	0.7560	2.40	4.64
1.51	12,200	0.8211	2.53	4.88
1.39	11,240	0.8920	2.65	5.16
1.26	10,200	0.9840	2.78	5.50

TABLE I (*Continued*)

Hexagonal Cobalt

eV	cm^{-1}	μm	n	k
1.14	9,170	1.088	2.94	5.88
1.02	8,295	1.216	3.17	6.31
0.892	7,194	1.390	3.42	6.77
0.771	6,211	1.592	3.61	7.26
0.641	5,146	1.937	3.87	7.79
4.59	37,040	0.2702	0.87 [16]	1.85 [16]
4.00	32,260	0.3100	0.89	2.02
3.54	28,570	0.3543	0.96	2.31
3.02	24,390	0.4106	1.08	2.68
2.48	20,000	0.5000	1.34	3.23
2.00	16,130	0.6200	1.83	3.71
1.49	12,050	0.8322	2.34	4.38

f.c.c. Cobalt Films

eV	cm^{-1}	μm	n	k
1.240	10,000	1.00	2.30 [17]	5.27 [17]
1.033	8,333	1.20	2.90	6.77
0.8856	7,143	1.40	3.36	7.39
0.7749	6,250	1.60	6.20	9.46
0.6888	5,555	1.80	7.80	8.46
0.6199	5,000	2.00	6.10	7.06
0.5636	4,545	2.20	4.96	6.75
0.5166	4,167	2.40	4.60	6.80
0.4769	3,846	2.60	4.68	7.17
0.4428	3,571	2.80	4.60	7.68
0.4133	3,333	3.00	4.39	8.13
0.3875	3,125	3.20	4.50	8.51
0.3647	2,941	3.40	4.77	9.08
0.3444	2,778	3.60	4.56	9.66
0.3263	2,632	3.80	4.74	10.16
0.3100	2,500	4.00	5.01	10.61
0.2818	2,273	4.40	5.45	11.58
0.2583	2,083	4.80	5.45	12.11
0.2384	1,923	5.20	5.61	13.48
0.2214	1,786	5.60	5.67	14.42
0.2067	1,667	6.00	6.13	15.38
0.1937	1,563	6.40	6.52	16.26
0.1771	1,429	7.00	6.76	17.22
0.1675	1,351	7.40	7.03	18.15
0.1550	1,250	8.00	7.36	19.56
0.1476	1,190	8.40	7.62	20.41
0.1376	1,111	9.00	7.97	21.64
0.1292	1,042	9.60	8.18	22.84
0.1240	1,000	10.00	8.42	23.63
0.1181	952	10.50	8.77	24.47
0.1127	909	11.00	9.09	25.16
0.1078	870	11.50	9.39	25.88
0.1033	833	12.00	9.70	26.47

TABLE I (*Continued*)

f.c.c. Cobalt Films

eV	cm^{-1}	μm	n	k
0.09919	800	12.50	10.03	26.91
0.09537	769	13.00	10.30	27.38

Bulk Hexagonal Cobalt

eV	cm^{-1}	μm	n	k
4.133	33,330	0.300	1.06 [21]	2.29 [21]
3.397	27,400	0.365	1.10	2.76
3.100	25,000	0.400	1.25	3.05
2.755	22,220	0.450	1.40	3.22
2.480	20,000	0.500	1.56	3.43
2.254	18,180	0.550	1.71	3.66
2.067	16,670	0.600	1.86	4.02
1.908	15,390	0.650	2.00	4.23
1.771	14,290	0.700	2.18	4.47
1.550	12,500	0.800	2.56	4.92
1.378	11,111	0.900	2.93	5.28
1.240	10,000	1.00	3.21	5.57
1.033	8,333	1.20	3.77	6.12
0.8866	7,151	1.40	4.45	6.52
0.7751	6,250	1.60	5.03	6.63
0.6898	5,564	1.80	5.25	6.69
0.6048	4,878	2.05	5.15	6.96
0.5391	4,348	2.30	5.13	6.90
0.4960	4,000	2.50	4.96	7.34
0.4509	3,636	2.75	4.75	8.23
0.4000	3,226	3.10	4.60	9.03
0.3543	2,857	3.50	4.49	10.06
0.3179	2,564	3.90	4.36	10.91
0.2818	2,273	4.40	4.25	12.73
0.2583	2,083	4.80	4.25	13.89
0.2384	1,923	5.20	4.25	15.13
0.2296	1,852	5.40	4.26	15.68
0.2175	1,754	5.70	4.37	16.44
0.2033	1,639	6.10	4.70	17.35
0.1907	1,538	6.50	4.69	18.71
0.1746	1,408	7.10	4.66	20.93
0.1550	1,250	8.00	4.89	23.73
0.1377	1,111	9.00	5.34	26.66
0.1240	1,000	10.0	5.88	29.37
0.1127	909.1	11.0	6.55	32.34
0.1033	833.3	12.0	7.20	35.13
0.09537	769.2	13.0	7.75	37.83
0.08856	714.3	14.0	8.49	40.81
0.08266	666.7	15.0	9.16	43.47
0.07749	625.0	16.0	10.11	46.31
0.07293	588.2	17.0	10.44	48.55

TABLE I (*Continued*)

Bulk Hexagonal Cobalt

eV	cm^{-1}	μm	n	k
3.100	25,000	0.400	1.60 [24]	3.30 [24]
2.480	20,000	0.500	2.15	3.70 1400°C
2.066	16,670	0.600	2.55	4.05
1.771	14,290	0.700	2.93	4.38
1.550	12,500	0.800	3.30	4.70
1.377	11,110	0.900	3.70	4.90
1.240	10,000	1.00	3.95	5.28
1.025	8,264	1.21	4.40	6.00
0.8266	6,667	1.50	5.00	7.00
0.7293	5,882	1.70	5.34	7.35
0.5990	4,831	2.07	5.50	7.80
0.4679	3,774	2.65	6.40	8.90
0.3657	2,950	3.39	8.03	10.28

TABLE I (*Continued*)

Bulk Hexagonal Cobalt

eV	cm^{-1}	μm	n_e (‖)	k_e (‖)	n_o (⊥)	k_o (⊥)
8.00	64,520	0.1550	0.95[3]	1.09[3]	0.95[3]	1.09 [3]
7.60	61,350	0.1631	0.93	1.17	0.93	1.17
7.20	58,140	0.1722	0.91	1.26	0.91	1.26
7.00	56,490	0.1771	0.91	1.32	0.91	1.32
6.60	53,220	0.1879	0.91	1.46	0.91	1.46
6.20	50,000	0.2000	0.97	1.62	0.98	1.62
6.00	48,400	0.2066	1.03	1.68	1.04	1.69
5.50	44,370	0.2254	1.18	1.76	1.19	1.77
5.00	40,230	0.2480	1.22	1.83	1.24	1.84
4.50	36,300	0.2755	1.24	1.98	1.26	1.99
4.10	33,070	0.3024	1.25	2.15	1.30	2.17
3.80	30,650	0.3263	1.28	2.33	1.33	2.33
3.50	28,230	0.3542	1.34	2.56	1.39	2.54
3.30	26,620	0.3757	1.42	2.72	1.46	2.70
3.10	25,000	0.4000	1.51	2.88	1.55	2.86
2.80	22,580	0.4428	1.66	3.13	1.72	3.11
2.70	21,770	0.4592	1.73	3.24	1.79	3.19
2.48	20,000	0.5000	1.88	3.40	1.90	3.34
2.30	18,550	0.5391	2.01	3.59	1.99	3.56
2.10	16,940	0.5904	2.13	3.85	2.13	3.89
1.90	15,320	0.6526	2.31	4.18	2.41	4.27
1.75	14,120	0.7085	2.56	4.50	2.72	4.54
1.65	13,310	0.7514	2.74	4.66	2.93	4.66
1.55	12,500	0.8000	2.96	4.87	3.14	4.83
1.40	11,290	0.8856	3.37	5.09	3.55	5.05
1.35	10,890	0.9184	3.49	5.14	3.67	5.09
1.25	10,080	0.9919	3.70	5.28	3.90	5.25
1.10	8,873	1.127	4.07	5.61	4.31	5.60
1.00	8,065	1.240	4.46	5.86	4.83	5.94
0.90	7,258	1.378	4.94	5.95	5.57	5.93
0.80	6,452	1.550	5.17	5.89	6.08	5.61
0.70	5,645	1.771	5.24	5.85	6.15	5.12
0.65	5,242	1.908	5.12	5.93	5.99	5.10
0.60	4,839	2.067	4.91	6.13	5.77	5.17
0.55	4,435	2.255	4.65	6.56	5.50	5.36
0.50	4,032	2.480	4.41	7.19	5.17	5.75
0.45	3,629	2.756	4.24	8.12	4.86	6.46
0.40	3,226	3.100	4.24	9.13	4.66	6.46
0.35	2,826	3.543	4.18	10.38	4.54	8.47
0.30	2,419	4.133	4.04	12.16	4.34	10.01
0.25	2,000	5.000	3.98	14.59	4.19	12.12
0.20	1,613	6.200	3.55	18.78	3.87	15.53
0.17	1,371	7.294	4.14	21.81	4.02	18.08
0.15	1,210	8.267	4.66	25.47	4.24	21.37
0.13	1,048	9.538	5.38	30.52	4.78	25.88
0.10	806.5	12.400	6.71	37.87	5.83	32.36

[a] References are given in brackets.

Graphite (C)

A. BORGHESI and G. GUIZZETTI
Dipartimento di Fisica "A. Volta"
and
Gruppo Nazionale di Struttura della Materia del CNR
Università di Pavia
Pavia, Italy

Graphite is a semimetal with uniaxial layered crystalline structure and is characterized by two different dielectric functions, $\tilde{\varepsilon}_\perp$ and $\tilde{\varepsilon}_\parallel$. They correspond to the electric-field vector **E** perpendicular ($\tilde{\varepsilon}_\perp$) and parallel ($\tilde{\varepsilon}_\parallel$), respectively, to the c axis (symmetry axis, perpendicular to the basal plane). Therefore, $\tilde{\varepsilon}_\perp$ measures the ordinary (o) while $\tilde{\varepsilon}_\parallel$ the extraordinary (e) ray properties. Since the cleavage plane is perpendicular to the c axis, $\tilde{\varepsilon}_\perp$ can easily be determined, for example, by normal-incidence reflectance measurements. $\tilde{\varepsilon}_\parallel$ cannot be obtained in a similar way, because of the difficulty of preparing suitable optical surfaces parallel to the c axis.

Small, soft flakes of natural graphite are found in various rock formations, but relatively little work has been done on these crystals, since they are generally quite impure, highly twinned, and rather difficult to handle [1, 2]. After 1958, it was established that massive coherent deposition of carbon can be produced by the pyrolysis of carbonaceous vapor on a suitable substrate at temperatures of the order of 2000°C. This material, called pyrolytic graphite, consists of many small crystallites with random orientation about the c axes, but with varying degrees of misorientation of c axes. Successively, it was found that highly oriented (HO) material (c axes aligned to within 0.2°) could be obtained if pyrolytic graphite was annealed at very high temperatures (~3000°C), particularly under applied stress [3]. HO pyrolytic graphite exhibits characteristics very similar to high-purity, natural, single crystals: in particular, their reflectance spectra coincide within experimental accuracy [3, 4]. This fact allowed the optical functions of graphite to be obtained mainly on HO pyrolytic material.

Graphite has aroused great interest from both fundamental and technological points of view, and various attempts have been made to study, experimentally and theoretically, its optical and dielectric functions [4–26]. Nevertheless, the experimental data are not yet complete and show

Copyright © 1991 by Academic Press.
All rights of reproduction in any form reserved.
ISBN 0-12-544422-2

disagreement among themselves. Overlooking the differences inherent in the techniques used (optical, photoemission, EELS), this disagreement is due to the aforesaid difficulty in obtaining good surfaces parallel to the c axis, and to the fact that all optical data have been derived from reflectivity (R) measurements (at near-normal incidence, with subsequent Kramers–Kronig (K–K) analysis, or as a function of angle of incidence, using the Fresnel relations). Therefore, the scattering among data can be explained by errors connected to K–K analysis; the difficulty of obtaining absolute values of reflectivity, particularly at large angles of incidence; and the different surface conditions affecting R. The room-temperature values of n_o, k_o and n_e, k_e tabulated in Table I and shown in Fig. 1, were obtained from the following works and references therein: Klucker [17] from 40 eV to 5 eV; Venghaus [21] for n_e and k_e obtained by EELS, in the 18–2 eV range, where they substantially differ from optical data; Greenaway *et al.* [5] from 5 eV to 2 eV; Guizzetti and Piaggi [26] who K–K-transformed R spectra from Refs. [5, 17, 22] from 2 to 0.02 eV for n_o and k_o only.

Klucker *et al.* [17, 18] measured R of freshly cleaved samples (c axis perpendicular to the surface) of pyrolytic graphite between 3 eV and 40 eV for different angles of incidence. The synchrotron radiation was polarized either parallel or perpendicular to the plane of incidence, with a degree of polarization between 0.9 and 0.97. The spectral resolution was better than 6 Å. Relative and absolute R measurements were performed. The ratios of the reflectances for nine angles between 15° and 75°, in steps of 7.5°, were determined in the relative measurements. $\tilde{\varepsilon}_\perp$ and $\tilde{\varepsilon}_\parallel$ were then derived simultaneously by least-squares fitting R with Fresnel's formula for anisotropic uniaxial crystals. Absolute R at near-normal incidence (15°) was used to determine $\tilde{\varepsilon}$ by K–K analysis. The asymptotic behavior $R(\omega) \propto \omega^{-4}$ was assumed for energies above 40 eV, whereas the R data from Greenaway *et al.* [5], Boyle and Nozières [6], and Sato [10] were used below 3 eV. Absolute R was in good agreement with R calculated from relative measurements. Moreover, the gross features in the R spectrum for $E \perp c$ generally agreed well with previous spectra in [4, 5, 8] and those derived from EELS [13, 14, 21]. Two major differences were observed above 8 eV. First, the extrapolated reflectance of Taft and Philipp [4] above 25 eV, which is important for K–K analysis, was significantly lower. Second, the reflectance calculated by Zeppenfeld [14] and Venghaus [21] from EELS was lower and did not show the sharp structure between 15 and 16 eV. These differences obviously were manifested in the spectra of $\tilde{\varepsilon}_\perp$, mainly in their absolute magnitudes and in some fine structures. More significant differences occur in $\tilde{\varepsilon}_\parallel$ among results from optical measurements, EELS, and theoretical calculations, in both the overall spectral behavior and the absolute magnitude below 15 eV. In particular, EELS data [14, 21] produce a peak at 11.4 eV in $\tilde{\varepsilon}_\parallel$, which is totally absent in the Klucker *et al.* [18] spectrum. This peak is several times larger than the

estimated uncertainty in the optical spectra, which is relatively large in this region, due to uncertainty in the degree of polarization.

The electron-energy-loss spectrum was measured by Venghaus [21] on stripped pyrolytic-graphite samples about 1000 Å in thickness. The experimental conditions were as follows: 60 keV energy of the primary electrons, with 0.4 keV halfwidth in the energy distribution; 10^{-3} rad scattering angle; 70° angle between the c axis and the direction of incoming electrons to determinate $\mathrm{Im}(-1/\tilde{\varepsilon}_{\parallel})$. Corrections for double-scattering and for $\tilde{\varepsilon}_{\perp}$ were included in the calculation of $\tilde{\varepsilon}_{\parallel}$. The resulting $\tilde{\varepsilon}_{\parallel}$ was in very good agreement with that obtained by Zeppenfeld [14]. In particular, a detailed discussion of uncertainties in the energy-loss function and in the K–K analysis led Venghaus [21] to conclude that the maximum in $\varepsilon_{2\parallel}$ near 11 eV was established beyond experimental and computational errors. No conclusive evidence in favor of or against a strong transition at ~11 eV has been provided by band-structure calculations [5, 13, 19], due to uncertainty in the calculated gaps and to the difficulty in correlating structures in the loss spectrum to specific interband transitions. Due to a lack of other evidence that could resolve the problem, we have tabulated $n_{\parallel}$ and $k_{\parallel}$, in the 2–18 eV range, both from optical and EELS measurements.

Greenaway *et al.* [5] measured reflectance of both natural and pyrolytic-graphite single crystals in the visible and UV regions. Samples of pyrolytic graphite, annealed at 3600 K, were prepared with a polished face perpendicular to the cleavage planes, by careful cutting and mechanical-polishing techniques. No etching procedure were attempted. The surface area of these samples (>1 cm^2) and the high degree of flatness permitted accurate R measurements with incidence angle as high as 88°. Laser light at three different wavelengths (4579 Å, 5145 Å, 6328 Å) yielded good absolute R values, to be used as reference and to check that no significant differences existed between the optical properties of natural and pyrolytic graphite. The reflectance R_s and R_p, corresponding to the electric field perpendicular or parallel to the plane of incidence, respectively, were measured from 1.9 to 5.15 eV at incidence angles from 10° to 80° in steps of 10°, as well as at 75°, 85°, and 87°. For small angles the results agreed well with those of Refs. [4, 18] taken at near-normal incidence. The same excellent agreement was obtained in [5] from 0.3 to 11.5 eV R on cleaved natural graphite. In addition, Greenaway *et al.* [5] measured R in the 2–9 eV range at near-normal incidence on polished surfaces both parallel and perpendicular to the c axis. R spectra of polished surfaces were not suited for deriving the optical constants through K–K transforms due to their inferior quality with respect to the cleaved surfaces; they are useful only in comparing data for $E \perp c$ and $E \| c$ under identical surface conditions. The optical constants $n_{\perp}$, $k_{\perp}$ and $n_{\parallel}$, $k_{\parallel}$ from 0.9 to 5.15 eV were obtained by a least-squares fit of R_s and R_p at different incidence angles with the Fresnel relations for uniaxial materials. The values of $n_{\perp}$ and $k_{\perp}$ were in close agreement (±10%) with

those of Taft and Phillip [4] obtained from K–K analysis, and with those of Klucker *et al.* [18]. We note that $n_{\parallel}$ and $k_{\parallel}$ show no structures in this region ($k_{\parallel} \approx 0$), in agreement with data of Ergun [9]. However, this is in contrast with optical properties of graphite calculated by Johnson and Dresselhaus [15], who predict a lower reflectivity with a peak near 4.3 eV. They attributed this discrepancy to experimental difficulties, for example, a slight depolarization of the light in both Greenaway *et al.*'s and Ergun's experiments [5, 9].

Guizzetti and Piaggi [26] derived $n_{\perp}$ and $k_{\perp}$ below 2 eV by K–K transforming R spectra, at near-normal incidence, of Klucker [17], Greenaway *et al.* [5], and Nemanich *et al.* [22], which showed the best agreement among themselves. Moreover, the infrared R values of Nemanich *et al.* [22] were much higher than those reported by Boyle and Nozières [6], Sato [10], Misu *et al.* [23], and Bowers *et al.* [24]. The extrapolation $R(\omega) \propto \omega^{-p}$ was used above 40 eV. Two different values of the exponent p were used. In one case the usual value $p = 4$ was assumed. In the other case p was adjusted to reproduce the values of $n_{\perp} = 2.91$ and $k_{\perp} = 1.71$, measured with an ellipsometer working at $\lambda = 6328$ Å. Although the resulting value of p is 3.4, $n_{\perp}$ and $k_{\perp}$ values below 2 eV differ only by 1% from the previous ones, which are tabulated here.

Nemanich *et al.* [22] measured IR reflectivity of HO pyrolytic graphite for $E \perp c$ on a cleaved surface parallel to the layers and for $E \| c$ on a polished surface cut perpendicular to the layers. The surface damage incurred in the polishing step was accounted for by scaling the $E \| c$ spectrum with the ratio of two $E \perp c$ spectra, obtained from a cleaved and a polished surface, respectively. The $E \perp c$ spectrum exhibits a sharp weak structure at 1587 cm^{-1} (attributed to the "in-plane" E_{1u} symmetry vibrational mode), superimposed on a background reflectance rising slowly with decreasing frequency. The $E \| c$ spectrum displays a sharp weak structure at 868 cm^{-1} (attributed to the "out-of-plane" A_{2u} symmetry mode) on a constant background. These structures were well fitted by the classical oscillator model, which yields the complex dielectric function

$$\tilde{\varepsilon} = \tilde{\varepsilon}_{\infty} + \frac{S\omega_T^2}{(\omega_T^2 - \omega^2 - i\Gamma\omega)},$$

where ω_T is the phonon frequency, Γ is the phenomenological damping constant, S is the oscillator strength, and $\tilde{\varepsilon}_{\infty}$ is the complex dielectric function resulting from electronic transitions. In the range of measurement (500–4000 cm^{-1}) $\tilde{\varepsilon}_{\infty\parallel}$ is real with a constant value of 5.78, although theoretical calculations [15] predicted a free-carrier absorption, corresponding to a plasma frequency of ~0.1 eV. On the contrary, $\tilde{\varepsilon}_{\infty\perp}$ is really complex due

to both interband and intraband electronic transitions, which produce a positive divergence in ε_2 at low frequencies. The values of the real and imaginary parts of $\tilde{\varepsilon}_{\infty\perp}$ have been obtained from Table I as $\varepsilon_{1\perp} = n_\perp^2 - k_\perp^2$ and $\varepsilon_{2\perp} = 2n_\perp k_\perp$, respectively. The other oscillator parameters were as follows: for $\tilde{\varepsilon}_\parallel$, $\omega_T = 867.8\,\text{cm}^{-1}$, $\Gamma = 0.001\,\text{cm}^{-1}$, and $S = 0.004$; for $\tilde{\varepsilon}_\perp$, $\omega_T = 1587.0\,\text{cm}^{-1}$, $\Gamma = 0.003\,\text{cm}^{-1}$, and $S = 0.031$. The resulting calculated values of n_o, k_o, n_e, and k_e are reported in Table I.

REFERENCES

1. C. A. Klein, *Rev. Mod. Phys.* **34**, 56 (1962).
2. C. A. Klein, W. D. Straub, and R. J. Diefendorf, *Phys. Rev.* **125**, 468 (1962).
3. A. W. Moore, A. R. Ubbelohde, and D. A. Young, *Proc. Roy. Soc. (London)* **A280**, 153 (1964).
4. E. A. Taft and H. R. Philipp, *Phys. Rev.* **138**, A197 (1965).
5. D. L. Greenaway, G. Harbeke, F. Bassani, and E. Tosatti, *Phys. Rev.* **178**, 1340 (1969).
6. W. S. Boyle and P. Nozières, *Phys. Rev.* **111**, 782 (1958).
7. J. R. Nelson, *Bull. Am. Phys. Soc.* **7**, 332 (1962).
8. J. G. Carter, R. H. Huebner, R. N. Hamm, and R. D. Birkhoff, *Phys. Rev.* **137**, A639 (1965).
9. S. Ergun, *Nature* **14**, 135 (1967); S. Ergun, in "Chemistry and Physics of Carbon," (P. L. Walker, Jr., ed.), Vol. 3, M. Dekker, New York, 45 (1968).
10. Y. Sato, *J. Phys. Soc. Jpn.* **24**, 489 (1968).
11. K. Zeppenfeld, *Z. Physik* **211**, 391 (1968).
12. F. Bassani and E. Tosatti, *Phys. Lett.* **27A**, 446 (1968); *Il Nuovo Cimento* **LXV B**, 161 (1970).
13. G. S. Painter and D. E. Ellis, *Phys. Rev.* **B1**, 4747 (1970).
14. K. Zeppenfeld, *Z. Physik* **243**, 229 (1971).
15. L. G. Johnson and G. Dresselhaus, *Phys. Rev.* **B7**, 2275 (1973).
16. G. Guizzetti, L. Nosenzo, E. Reguzzoni, and G. Samoggia, *Phys. Rev. Lett.* **31**, 154 (1973).
17. R. Klucker, Interner Bericht, DESY F41-72/1 (1972).
18. R. Klucker, M. Skibowski, and W. Steinmann, *Phys. Stat. Solidi. (b)* **65**, 703 (1974).
19. R. F. Willis, B. Fitton, and G. S. Painter, *Phys. Rev.* **B9**, 1926 (1974).
20. G. Bellodi, A. Borghesi, G. Guizzetti, L. Nosenzo, E. Reguzzoni, and G. Samoggia, *Phys. Rev.* **B12**, 5951 (1975).
21. H. Venghaus, *Phys. Stat. Solidi. (b)* **71**, 609 (1975).
22. R. J. Nemanich, G. Lucovsky, and S. A. Solin, *Solid State Commun.* **23**, 117 (1977).
23. A. Misu, E. E. Mendez, and M. S. Dresselhaus, *J. Phys. Soc. Jpn.* **47**, 199 (1979).
24. C. W. Bowers, R. B. Culver, W. A. Solberg, and I. L. Spain, *Appl. Opt.* **26**, 4625 (1987).
25. N. B. Brandt, S. M. Chudinov, and Y. G. Ponomarev, in "Modern Problems in Condensed Matter Sciences, Semimetals," (V. M. Agranovich and A. A. Maradudin, eds.), Vol. 20.1, North-Holland, Amsterdam, 129 (1988).
26. G. Guizzetti and A. Piaggi, private communication (1988).

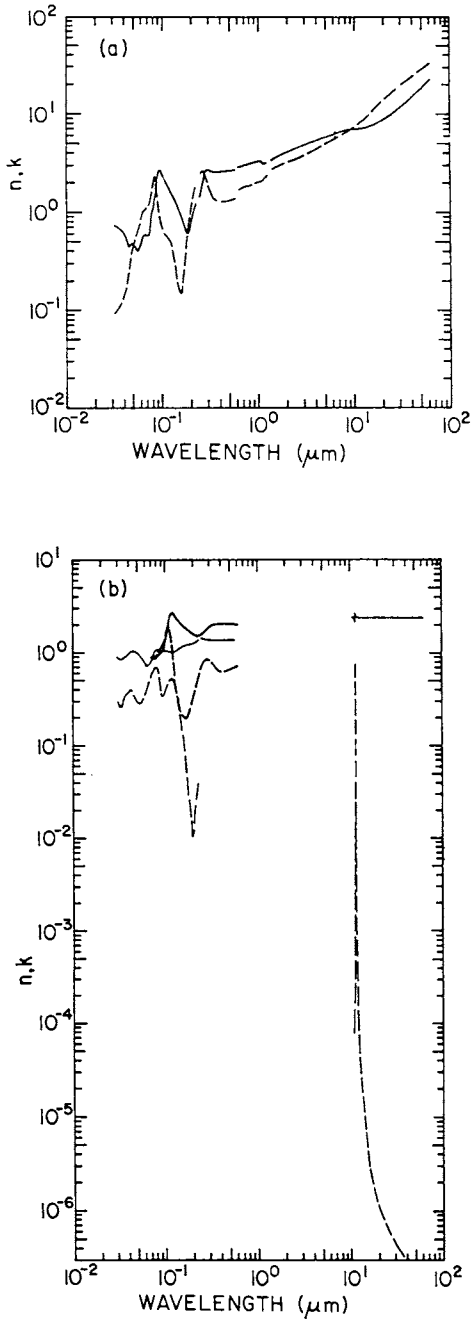

Fig. 1. (a) Log–log plot of n_o (solid line) and k_o (dashed line) versus wavelength in micrometers for graphite. (b) Log–log plot of n_e (solid line) and k_e (dashed line) versus wavelength in micrometers.

TABLE I

Values of n and k for Graphite from Various References[a]

eV	cm^{-1}	Å	n_e	n_e	k_e	k_e	n_o	k_o
40.0		309.96	0.91 [17]		0.30 [17]		0.75 [17]	0.10 [17]
39.5		313.89	0.89		0.29		0.75	0.10
39.0		317.91	0.88		0.28		0.75	0.10
38.5		322.04	0.86		0.27		0.74	0.10
38.0		326.28	0.85		0.26		0.74	0.10
37.5		330.63	0.85		0.26		0.72	0.10
37.0		335.10	0.85		0.27		0.72	0.10
36.5		339.69	0.85		0.27		0.72	0.10
36.0		344.40	0.84		0.28		0.71	0.10
35.5		349.25	0.85		0.30		0.70	0.10
35.0		354.24	0.86		0.31		0.68	0.10
34.5		359.38	0.88		0.33		0.68	0.10
34.0		364.66	0.89		0.34		0.67	0.12
33.5		370.11	0.90		0.35		0.67	0.12
33.0		375.71	0.91		0.36		0.66	0.12
32.5		381.49	0.92		0.36		0.66	0.12
32.0		387.45	0.93		0.37		0.64	0.13
31.5		393.60	0.94		0.37		0.61	0.13
31.0		399.95	0.95		0.38		0.60	0.14
30.5		406.51	0.97		0.38		0.58	0.16
30.0		413.28	0.99		0.39		0.57	0.16
29.5		420.29	1.01		0.40		0.55	0.17
29.0		427.54	1.02		0.40		0.52	0.19
28.5		435.04	1.04		0.39		0.49	0.21
28.0		442.80	1.05		0.38		0.47	0.24
27.5		450.86	1.06		0.37		0.45	0.27

(continued)

TABLE I (*Continued*)

Graphite

eV	cm^{-1}	μm	n_e	n_e	k_e	k_e	n_o	k_o
27.0		459.20	1.07		0.35		0.46	0.31
26.5		467.87	1.06		0.33		0.47	0.35
26.0		476.87	1.05		0.32		0.48	0.38
25.5		486.20	1.03		0.31		0.47	0.43
25.0		495.94	1.02		0.30		0.47	0.47
24.5		506.06	1.00		0.29		0.46	0.51
24.0		516.60	0.99		0.28		0.46	0.54
23.5		527.60	0.97		0.28		0.44	0.56
23.0		539.07	0.95		0.28		0.41	0.60
22.5		551.05	0.93		0.28		0.40	0.66
22.0		563.57	0.91		0.29		0.41	0.70
21.5		576.68	0.88		0.31		0.43	0.76
21.0		590.41	0.84		0.33		0.45	0.82
20.5		604.81	0.81		0.35		0.51	0.92
20.0		619.93	0.77		0.38		0.55	1.01
19.5		635.82	0.74		0.42		0.58	1.05
19.0		652.55	0.71		0.47		0.58	1.07
18.5		670.19	0.71		0.51		0.58	1.10
18.0		688.81	0.77	0.77 [21]	0.53	0.75 [21]	0.58	1.12
17.5		708.49	0.85	0.81	0.56	0.81	0.58	1.15
17.0		729.32	0.92	0.86	0.60	0.86	0.61	1.25
16.5		751.43	0.99	0.90	0.65	0.87	0.75	1.36
16.0		774.91	1.05	0.91	0.68	0.87	0.98	1.63
15.5		799.90	1.10	0.87	0.71	0.91	1.09	1.92
15.0		826.57	1.10	0.86	0.69	0.97	1.33	2.15
14.5		855.07	1.10	0.91	0.61	1.04	1.84	2.25
14.0		885.61	1.06	0.98	0.48	1.09	2.31	1.50
13.5		918.41	1.02	1.02	0.34	1.14	2.72	1.03
13.0		953.73	1.02	1.02	0.33	1.24	2.67	0.83
12.5		991.88	1.04	1.07	0.37	1.36	2.48	0.70

12.0		0.1033	1.06	1.34	0.42	1.66	2.25	0.63
11.5		0.1078	1.05	1.63	0.47	1.86	2.03	0.58
11.0		0.1127	1.03	2.30	0.52	1.78	1.81	0.57
10.5		0.1181	1.02	2.54	0.53	1.34	1.65	0.53
10.0		0.1240	0.98	2.68	0.50	0.73	1.52	0.46
9.5		0.1305	1.01	2.46	0.39	0.43	1.38	0.37
9.0		0.1378	1.05	2.27	0.29	0.31	1.25	0.27
8.5		0.1459	1.10	2.13	0.20	0.23	1.10	0.18
8.0		0.1550	1.15	1.99	0.12	0.21	0.96	0.15
7.5		0.1653	1.18	1.87	0.06	0.19	0.82	0.20
7.0		0.1771	1.20	1.73	0.03	0.22	0.65	0.44
6.5		0.1907	1.23	1.67	0.01	0.26	0.66	0.84
6.0	48,393	0.2066	1.27	1.55	0.02	0.34	0.94	1.35
5.5	44,360	0.2254	1.31	1.48	0.04	0.48	1.25	1.85
5.0	40,327	0.2480	1.46 [12]	1.51		0.71	1.39 [12]	2.48 [12]
4.9	39,521	0.2530	1.44				1.66	2.56
4.8	38,714	0.2583	1.43				1.95	2.65
4.7	37,908	0.2638	1.42				2.18	2.64
4.6	37,101	0.2695	1.41				2.38	2.54
4.5	36,295	0.2755	1.40	1.70		0.84	2.53	2.41
4.4	35,488	0.2818	1.40				2.64	2.26
4.3	34,681	0.2883	1.39				2.71	2.10
4.2	33,875	0.2952	1.38				2.75	1.94
4.1	33,068	0.3024	1.37				2.75	1.79
4.0	32,262	0.3100	1.37	1.94		0.83	2.73	1.66
3.9	31,455	0.3179	1.36				2.69	1.56
3.8	30,649	0.3263	1.36				2.66	1.49
3.7	29,842	0.3351	1.36				2.64	1.43
3.6	29,036	0.3444	1.36				2.63	1.39
3.5	28,229	0.3542	1.36	2.02		0.69	2.62	1.36
3.4	27,423	0.3647	1.35				2.62	1.33
3.3	26,616	0.3757	1.35				2.61	1.31
3.2	25,809	0.3875	1.35				2.61	1.29
3.1	25,003	0.4000	1.35				2.62	1.29

(continued)

TABLE I (*Continued*)

Graphite

eV	cm^{-1}	μm	n_e	n_e	k_e	k_e	n_o	k_o
3.0	24,196	0.4133	1.35	2.04		0.62	2.62	1.28
2.9	23,390	0.4275	1.35				2.63	1.28
2.8	22,583	0.4428	1.36				2.63	1.28
2.7	21,777	0.4592	1.36				2.64	1.28
2.6	20,970	0.4769	1.36				2.64	1.30
2.5	20,164	0.4959	1.36	2.03		0.64	2.65	1.31
2.4	19,357	0.5166	1.36				2.66	1.33
2.3	18,551	0.5391	1.36				2.67	1.34
2.2	17,744	0.5636	1.36				2.68	1.36
2.1	16,937	0.5904	1.37				2.70	1.39
2.00	16,131	0.6199		2.01		0.72	2.86 [26]	1.73 [26]
1.90	15,324	0.6526					2.91	1.77
1.80	14,518	0.6888					2.96	1.81
1.70	13,711	0.7293					3.01	1.84
1.60	12,905	0.7749					3.06	1.86
1.50	12,098	0.8266					3.10	1.90
1.40	11,292	0.8856					3.14	1.95
1.30	10,485	0.9537					3.20	2.02
1.20	9,679	1.033					3.25	2.07
1.16	9,356	1.069					3.33	2.07
1.12	9,033	1.107					3.19	2.07
1.08	8,711	1.148					3.16	2.17
1.04	8,388	1.192					3.16	2.28
1.00	8,065	1.240					3.18	2.40
0.90	7,259	1.378					3.39	2.70
0.80	6,452	1.550					3.69	2.91
0.70	5,646	1.771					3.94	3.02
0.60	4,839	2.066					4.24	3.25
0.50	4,033	2.480					4.50	3.41
0.40	3,226	3.100					4.83	3.82

0.30	2,420	4.133			5.36	4.48
0.2294	1,850	5.405			5.866 [22]	5.124 [22]
0.2232	1,800	5.555			5.923	5.217
0.2170	1,750	5.714			6.000	5.318
0.2108	1,700	5.882			6.070	5.420
0.2046	1,650	6.061			6.129	5.520
0.2002	1,615	6.192			6.150	5.597
0.1996	1,610	6.211			6.145	5.611
0.1990	1,605	6.230			6.135	5.627
0.1984	1,600	6.250			6.120	5.656
0.1977	1,595	6.269			6.097	5.721
0.1971	1,590	6.289			6.131	5.948
0.1970	1,589	6.293			6.212	6.036
0.1969	1,588	6.297			6.378	6.094
0.1967	1,587	6.301			6.590	6.016
0.1966	1,586	6.305			6.687	5.813
0.1965	1,585	6.309			6.646	5.644
0.1959	1,580	6.329			6.371	5.498
0.1952	1,575	6.349			6.291	5.515
0.1946	1,570	6.369			6.258	5.530
0.1922	1,550	6.452			6.217	5.560
0.1860	1,500	6.666			6.205	5.600
0.1798	1,450	6.896			6.238	5.663
0.1736	1,400	7.143			6.323	5.775
0.1674	1,350	7.407			6.476	5.955
0.1612	1,300	7.692			6.712	6.218
0.16	1,290	7.749			6.77 [26]	6.29 [26]
0.14	1,129	8.856			6.91	6.63
0.12	968	10.33			6.96	7.38
0.1165	940	10.64	2.399 [22]	3.00×10^{-5} [22]		
0.1153	930	10.75	2.398	4.05		
0.1141	920	10.87	2.397	5.75		
0.1128	910	10.99	2.395	8.10×10^{-5}		
0.1115	900	11.11	2.393	1.51×10^{-4}		
0.1103	890	11.23	2.388	3.19×10^{-4}		

(continued)

TABLE I (*Continued*)

Graphite

eV	cm^{-1}	μm	n_e	n_e	k_e	k_e	n_o	k_o
0.1091	880	11.36	2.374		1.06×10^{-3}			
0.1085	875	11.43	2.353		3.07			
0.1084	874	11.44	2.345		4.15			
0.1082	873	11.45	2.334		5.92			
0.1081	872	11.47	2.317		9.11×10^{-3}			
0.1080	871	11.48	2.291		0.015			
0.1079	870	11.49	2.241		0.033			
0.1077	869	11.51	2.124		0.108			
0.1076	868	11.52	2.196		0.750			
0.1075	867	11.53	2.735		0.166			
0.1074	866	11.55	2.587		0.042			
0.1071	864	11.57	2.496		0.010			
0.1069	862	11.60	2.465		4.51×10^{-3}			
0.1066	860	11.63	2.450		2.52×10^{-3}			
0.1054	850	11.76	2.424		4.90×10^{-4}			
0.1041	840	11.90	2.417		2.01×10^{-4}			
0.10	806	12.40	2.410		4.08×10^{-5}		7.14	8.75
0.08	645	15.50	2.406		3.08×10^{-6}		7.68	10.80
0.06	484	20.66	2.405		9.77×10^{-7}		8.86	14.02
0.04	323	30.99	2.405		4.17		11.75	20.00
0.02	161	61.99	2.404		1.65×10^{-7}		22.42	33.49

[a] The references from which the values were extracted are given in brackets.

Liquid Mercury (Hg)*

E. T. ARAKAWA and T. INAGAKI†
Oak Ridge National Laboratory
Oak Ridge, Tennessee

The optical constants of liquid Hg at room temperature in the near infrared to the near UV have been measured extensively [1–11] by spectroscopic ellipsometry. The measurements were made both on a free surface under vacuum or inert gases [1, 4–7, 9, 10] and on a surface in contact with solid [2, 6, 8, 10, 11] or liquid [3] dielectrics. Except for the results of [2], the values of n and k obtained from these measurements agree in general with one another. However, the scatter of the data is far larger than the stated accuracies of individual results, which are reported with three or four significant figures. A careful recent study [11] finds no systematic difference between data obtained on a free surface and on a surface in contact with dielectrics. The measurements at wavelengths below 0.25 μm are very limited, with only two reflectance measurements at normal incidence, one on a free surface under vacuum from 0.06–0.6 μm [12] and one on a surface in contact with MgF_2 from 0.15–2.5 μm [8].

The room-temperature values of n and k are tabulated in Table I and plotted in Fig. 1. The data above 0.31 μm are from those determined by Inagaki *et al.* [11] as the mean values from the various ellipsometric measurements [1, 3–11]. The data below 0.31 μm are from the Kramers–Kronig (K–K) analysis made [11] on the normal-incidence reflectance data taken by Wilson and Rice [12] combined with the reflectance values above 0.31 μm calculated from the ellipsometric data of n and k. We believe that the n and k values given in Table I are accurate to ±0.2% on an absolute scale.

As with other liquid metals, the n and k spectra from the infrared to the UV are nearly free-electron-like up to the plasma wavelength at 0.177 μm. However, in contrast with some other liquid metals, the n and k values are significantly higher in the visible region than those given by the simple Drude expressions. Two absorption features at 0.149 μm and 0.124 μm

* Sponsored by the Office of Health and Environmental Research, U.S. Department of Energy, under Contract DE-AC05-840R21400 with Martin Marietta Energy Systems, Inc.
† Permanent address: Physics Department, Osaka Kyoiku University, Osaka, Japan.

Copyright © 1991 by Academic Press.
All rights of reproduction in any form reserved.
ISBN 0-12-544422-2

were assigned to excitations from the spin-orbit split 5d band to the valence band [12]. In addition, a weak structure was noticed at 0.191 μm, for which the possibility of an exciton or a surface plasmon was suggested [8, 12].

Liquid Hg is one of the easiest metals on which an ideally smooth surface can be made in a reproducible manner. Surface contamination due to oxidation has also been believed to be less severe than for any other metal except for a few inert metals such as gold. On the other hand, many metals dissolve readily in liquid Hg, forming an amalgam. In most measurements, therefore, the sample was distilled under vacuum or under a reduced pressure [1, 3–7, 9, 10], and in some cases, directly into the sample dish [4, 9, 10]. Prior to distillation, the sample was washed in dilute solutions of KOH and/or H_2NO_3 and then in distilled water to remove oxides [3, 5].

For measurements on a free surface, surface oxidation was the major source of error in the measured values of n and k. Most measurements were made under vacuum without exposing the surface to the atmosphere [1, 4–7, 9, 10]. It was reported [1], however, that the values of the optical constants in air did not change appreciably for up to 30 minutes and the changes in 60 minutes were still only of the order of the probable error. Since oxide and impurities tend to float to the surface, the overflow method was used [1, 11] to obtain clean surfaces.

Measurements on a surface in contact with dielectrics [2, 3, 6, 8, 10, 11] were relatively free from surface contamination. These measurements were also free from vibration of the liquid surface. However, two possible sources of error arose with this method. The first was due to imperfect optical contact of liquid Hg with the dielectric prism or window, and the second was due to strain in the dielectric overlayer. Schulz [13] employed the Ag-precoat method to obtain good optical contact of liquid Hg with several solid dielectrics. The liquid dielectrics used by Smith and Stromberg [3] avoided the contact and strain problems encountered with solid dielectrics.

Hodgson [1] measured a free surface by ellipsometry for the first time in an extended region from 0.365–2.40 μm using the rotating-polarizer method. The results showed unambiguously that the optical constants of liquid Hg did not agree with those given by the simple Drude formula for a nearly-free-electron metal. Lelyuk *et al.* [2] measured a sample in contact with a glass prism in the region from 0.45–1.54 μm. Multiple-reflection ellipsometry was used, and the angle of incidence was varied so that linear polarization of the incident light was restored in the reflected beam. The values of n and k obtained were much higher than those from the other ellipsometric measurements. This was later interpreted by Smith [5] as arising from imperfect contact between liquid Hg and the glass prism, and was reproduced experimentally by Faber and Smith [6].

Smith and Stromberg [3] measured liquid Hg in contact with three

different liquid dielectrics—cyclohexane, benzene, and distilled water—at 0.5461 μm. They used the conventional null method. The liquid Hg sample was immersed directly into the liquid dielectrics after vacuum distillation without exposure to the atmosphere. No difference was found in the n and k values measured under the different immersion liquids beyond the experimental accuracy of four significant figures. They analyzed theoretically the effects of surface layers, misalignment, and window birefringence on the measured values of n and k, and evaluated the limit of accuracy of their measurements.

Smith [4] and Faber and Smith [6] measured two different surfaces, a free surface under vacuum and a surface in contact with a quartz prism, in the region from 0.4–0.7 μm. They used a variant of the null method using three polarizers, one of which rotated continuously. The n and k values obtained for the two different surfaces were in good agreement. The Ag-precoat method was employed to obtain good optical contact of liquid Hg with the quartz prism. They attempted to clean the free surface using argon glow discharge. This increased the n and k values slightly. They also measured the effects of surface contamination during several days' exposure to atmosphere.

Smith [5] measured free surfaces under vacuum and He atmosphere at 0.5461 μm. The null method was employed with a commercial ellipsometer. The surface was cleaned by moving a stainless-steel barrier along the surface. Along with the ellipsometric measurement, surface tension and contact potential were measured to ensure that the surface was free of contamination. Ellipsometric measurements were made on a free surface by Busch and Guggenheim [7] in the region from 0.47–2.32 μm and on a surface in contact with a quartz prism by Choyke *et al.* [8] at three wavelengths in the visible.

Comins [9] extended the measurement on a free surface in the infrared up to 6.3 μm. A variant of Beattie and Conn's method [14] was employed. The n and k values obtained were in good agreement with those given by the semiempirical formulas of Smith [15]. The formulas were derived to explain the deviations of the optical constants of liquid Hg from the simple Drude theory in terms of backscattering of the electrons. Crozier and Murphy [10] extended the measurements on a free surface down to 0.25 μm. The method of Beattie and Conn [14] was used with an ellipsometer whose entire optical assembly was enclosed in a vacuum chamber. They also measured surfaces in contact with a quartz and a glass prism. The values of n and k obtained for these surfaces were slightly higher than those obtained for a free surface. For the surfaces in contact with a quartz and a glass prism, n and k values were obtained from reflectances measured with p- and s-polarized light. The values obtained were in a good agreement with those from the ellipsometric data in the case of the quartz prism, but not in the case of the glass prism.

Inagaki *et al.* [11] measured a surface in contact with a quartz prism in the region from 0.335–2.0 μm using a method similar to the one used by Crozier and Murphy [10]. Good consistency was obtained between the n and k values obtained from the ellipsometric data and the reflectance data taken simultaneously on the same surface. The earlier ellipsometric values of n and k obtained using various contact media were analyzed and shown to be consistent with each other within the experimental accuracies. They were also shown to be internally consistent using a K–K analysis of the ellipsometric n and k data combined with reflectance data in the shorter-wavelength region.

Wilson and Rice [12] measured normal-incidence reflectance of a free surface under vacuum in an extended region from 0.06–0.6 μm. A K–K analysis was performed on these data to deduce n and k values. However, extrapolation of the reflectance data into the shorter-wavelength region was made to give agreement of the optical-constant values at 0.6 μm with those given by the simple Drude expressions. Choyke *et al.* [8] measured normal-incidence reflectance of a surface in contact with MgF_2 in the region from 0.15–2.5 μm. Values of n and k were derived from these data by a curve-fitting method [16] using classical oscillators. The results were subject to a large uncertainty.

The temperature dependences of the optical constants were measured by Hodgson [1] at three different temperatures—22°, 124° and 230 °C—in the region from 0.6–2.4 μm. Smith [5] measured n and k values at 0.5461 μm at a number of different temperatures between 23° and 115 °C. From these measurements he derived

$$n = [1.593 + 0.00036T] \pm 0.004$$

$$k = [4.771 - 0.00155T] \pm 0.031,$$

where T was in degrees Celsius.

A few values of the optical constants have been reported [13, 17] which differ significantly from those obtained by ellipsometry. Schulz [13] reported values of n and k that agreed quite well with those given by the simple Drude theory in the region from 0.4–0.87 μm. However, it has been shown by the K–K analysis [11] and sum-rule calculations [7] that those values of the optical constants were questionable. The values were derived from reflectance data measured on a surface in contact with a quartz prism with unpolarized light incident at 45° and phase-shift data measured by an interferometric method for normal-incidence reflection from a surface in contact with mica. Mueller [17] also reported optical constants in the region from 0.26–2.48 μm, which were in good agreement above 0.38 μm with the simple Drude theory. The values were derived from reflectance

data measured with *s*-polarized light on a surface in contact with sapphire at normal incidence and at 45°. It was shown [11] that the precision of these reflectance measurements was far too low to permit an accurate determination of the optical constants. In addition to these two reports [13, 17], a few measurements [18, 19] of normal-incidence reflectances have been reported, which deviate slightly from those given by the n and k values determined by ellipsometry [1, 3–11]. The deviations were less than 0.02 in the absolute reflectance values. Bloch and Rice [19] have taken this discrepancy to be real, and proposed a model of the surface-transition zone to reconcile the discrepancy. Several papers [10, 20–24] have been developed along this line. A recent measurement made in our laboratory [25] with laser beams and with an Xe lamp at several wavelengths show that the measured values of reflectance agree well with those calculated from the optical constants determined by ellipsometry [11].

REFERENCES

1. J. N. Hodgson, *Phil. Mag.* **4**, 183 (1959).
2. L. G. Lelyuk, I. N. Shklyarevskii, and R. G. Yarovaya, *Opt. Spect. (U.S.S.R)* **16**, 263 (1964).
3. L. E. Smith and R. R. Stromberg, *J. Opt. Soc. Am.* **56**, 1539 (1966).
4. N. V. Smith, *Adv. Phys.* **16**, 629 (1967).
5. T. Smith, *J. Opt. Soc. Am.* **57**, 1207 (1967).
6. T. E. Faber and N. V. Smith, *J. Opt. Soc. Am.* **58**, 102 (1968).
7. G. Busch and J. Guggenheim, *Helv. Phys. Acta* **41**, 401 (1968).
8. W. J. Choyke, S. H. Vosko, and T. W. O'Keeffe, *Solid State Commun.* **9**, 361 (1971).
9. N. R. Comins, *Phil. Mag.* **25**, 817 (1972).
10. E. D. Crozier and E. Murphy, *Can. J. Phys.* **50**, 1914 (1972).
11. T. Inagaki, E. T. Arakawa, and M. W. Williams, *Phys. Rev. B* **23**, 5246 (1981).
12. E. G. Wilson and S. A. Rice, *Phys. Rev.* **145**, 55 (1966).
13. L. G. Schulz, *J. Opt. Soc. Am.* **47**, 64 (1957).
14. J. R. Beattie and G. K. T. Conn, *Phil. Mag.* **46**, 222 (1955).
15. N. V. Smith, *Phys. Lett.* **26A**, 126 (1968).
16. H. W. Verleur, *J. Opt. Soc. Am.* **58**, 1356 (1968).
17. W. E. Mueller, *J. Opt. Soc. Am.* **59**, 1246 (1969).
18. J. Boiani and S. A. Rice, *Phys. Rev.* **185**, 931 (1969).
19. A. N. Bloch and S. A. Rice, *Phys. Rev.* **185**, 933 (1969).
20. H. L. Lemberg, S. A. Rice, P. H. Naylor, and A. N. Bloch, *Solid State Commun.* **14**, 1097 (1974).
21. H. L. Lemberg, S. A. Rice, and D. Guidotti, *Phys. Rev. B* **10**, 4079 (1974).
22. D. Guidotti and S. A. Rice, *Phys. Rev. B* **15**, 3796 (1977).
23. A. Tadjeddine, G. Piazza, and M. Costa, *Europhys. Lett.* **5**, 87 (1988).
24. W. L. Schaich, *Phys. Rev. B* **37**, 6193 (1988).
25. E. T. Arakawa, T. Inagaki, and P. S. Tuminello, *Bull. Am. Phys. Soc.* **33**, 422 (1988).
26. P. S. Yuminello, E. T. Arakawa, T. Inagaki, and J. E. Parks, II, *Phys. Rev. B* **40**, 11994 (1989).

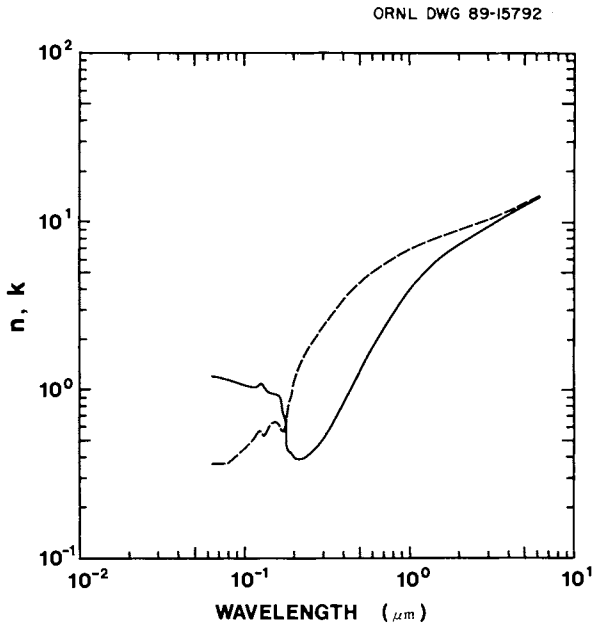

Fig. 1. Log–log plot of n (solid line) and k (dashed line) versus wavelength in micrometers for liquid mercury.

TABLE I

Values of n and k for Liquid Mercury from Various References

eV	cm^{-1}	μm	n	k
19.5		0.06358	1.208 [11]	0.364 [11]
19.0		0.06526	1.200	0.366
18.5		0.06702	1.195	0.367
18.0		0.06888	1.191	0.367
17.5		0.07085	1.184	0.366
17.0		0.07293	1.177	0.367
16.5		0.07514	1.170	0.367
16.0		0.07749	1.159	0.368
15.5		0.07999	1.146	0.374
15.0		0.08266	1.135	0.383
14.5		0.08551	1.125	0.394
14.0		0.08856	1.115	0.404
13.5		0.09184	1.104	0.416
13.0		0.09537	1.092	0.430
12.5		0.09919	1.078	0.445
12.0		0.1033	1.064	0.467
11.5		0.1078	1.050	0.491
11.0		0.1127	1.039	0.523
10.8		0.1148	1.039	0.537
10.6		0.1170	1.041	0.550
10.4		0.1192	1.045	0.561
10.2		0.1216	1.054	0.569
10.0		0.1240	1.062	0.567
9.8		0.1265	1.061	0.557
9.6		0.1292	1.044	0.541
9.4		0.1319	1.009	0.548
9.2		0.1348	0.988	0.568
9.0		0.1378	0.975	0.588
8.8		0.1409	0.965	0.607
8.6		0.1442	0.956	0.624
8.4		0.1476	0.953	0.638
8.2		0.1512	0.952	0.645
8.0		0.1550	0.946	0.639
7.8		0.1590	0.929	0.623
7.6		0.1631	0.893	0.597
7.5		0.1653	0.860	0.580
7.4		0.1675	0.817	0.574
7.3		0.1698	0.769	0.575
7.2		0.1722	0.717	0.584
7.1		0.1746	0.663	0.589
7.0		0.1771	0.585	0.617
6.9		0.1797	0.510	0.676
6.8		0.1823	0.459	0.756

(continued)

TABLE I (*Continued*)

Values of n and k for Liquid Mercury from Various References

eV	cm^{-1}	μm	n	k
6.7		0.1851	0.438 [11]	0.836 [11]
6.6		0.1879	0.436	0.898
6.5		0.1907	0.428	0.949
6.4		0.1937	0.412	1.002
6.3		0.1968	0.399	1.058
6.2		0.2000	0.390	1.118
6.1	49,199	0.2033	0.388	1.176
6.0	48,393	0.2066	0.386	1.232
5.9	47,586	0.2101	0.385	1.287
5.8	46,780	0.2138	0.386	1.341
5.7	45,973	0.2175	0.386	1.396
5.6	45,167	0.2214	0.386	1.454
5.5	44,360	0.2254	0.390	1.512
5.4	43,554	0.2296	0.394	1.569
5.2	41,940	0.2384	0.401	1.687
5.0	40,327	0.2480	0.414	1.806
4.8	38,714	0.2583	0.431	1.929
4.6	37,101	0.2695	0.452	2.058
4.4	35,488	0.2818	0.477	2.195
4.2	33,875	0.2952	0.507	2.341
4.0	32,262	0.3100	0.542	2.502
3.8	30,649	0.3263	0.589	2.665
3.6	29,036	0.3444	0.644	2.860
3.4	27,423	0.3647	0.713	3.074
3.2	25,810	0.3875	0.798	3.294
3.0	24,196	0.4133	0.898	3.538
2.8	22,583	0.4428	1.027	3.802
2.6	20,970	0.4769	1.186	4.090
2.4	19,357	0.5166	1.384	4.407
2.2	17,744	0.5636	1.620	4.751
2.0	16,131	0.6199	1.910	5.150
1.8	14,518	0.6888	2.284	5.582
1.6	12,905	0.7749	2.746	6.054
1.4	11,292	0.8856	3.324	6.558
1.2	9,679	1.0332	4.050	7.082
1.0	8,065	1.240	4.962	7.643
0.8	6,452	1.550	6.086	8.312
0.6	4,839	2.066	7.574	9.195
0.5	4,0329	2.480	8.528	9.805
0.4	3,226	3.100	9.741	10.65
0.3	2,4197	4.133	11.37	11.95
0.2	1,613	6.199	13.99	14.27

Palladium (Pd)

A. BORGHESI and A. PIAGGI
Dipartimento di Fisica "A. Volta"
and
Gruppo Nazionale di Struttura della Materia del CNR
Università di Pavia
Pavia, Italy

The optical properties of Pd have been studied under a variety of experimental conditions and by several techniques [1–28]. Unfortunately, many results disagree as to the actual magnitude of optical structures, although the structure energies agree in almost every case. This depends on sample preparation, accuracy of the optical measurements, and on the method by which the experimental data are analyzed.

Experimentally, Pd is difficult to study in bulk samples, since it is readily contaminated and does not electropolish easily [19]. Vacuum deposition is relatively easy, but aging effects have been shown to be significant [13]. Although Pd does not oxidize as rapidly in air as other transition metals, Pd films show a critical dependence on thickness and evaporation rate [15].

The room-temperature values of n and k tabulated here (Table I and Fig. 1) were obtained from the following works and references therein: Windt *et al.* [27] from 525–12.5 eV; Vehse *et al.* [13] from 12.5–6.0 eV; Johnson and Christy [15] from 6.0–0.6 eV; Weaver and Benbow and Weaver *et al.* [18, 29] from 0.6–0.1 eV. Although the optical response in the visible–UV region has been clarified by Johnson and Christy [15], experimental differences and doubts regarding higher energies and the IR region still remain to be resolved. We chose the results that were in major agreement and were reported to have comparable experimental accuracy.

Windt *et al.* [27] evaporated Pd of unknown purity with an electron-beam current of 100 mA, at a rate of 10–12 Å/s onto polished silicon (111) wafers. The pressure in the deposition system was $\sim 5 \times 10^{-6}$ torr, and the substrate temperature was 80 °C. The film thickness chosen was 1000 Å, verified using a quartz-crystal monitor during deposition. Surface roughness was 18±3 Å, measured with an optical profilometer. The Auger-electron-spectroscopy profile indicated that oxidation was confined to the film surface. Absolute-reflectance (R) measurements were performed at thirty-six wavelengths (λ) from 24 Å to 1216 Å, using a

Copyright © 1991 by Academic Press.
All rights of reproduction in any form reserved.
ISBN 0-12-544422-2

computer-controlled reflectometer at several incidence angles (usually sixteen angles between 10° and 85°). The incident-beam polarization was measured for $\lambda > 200$ Å using a rhodium-mirror polarization analyzer; for $\lambda \leqslant 200$ Å, the beam was assumed to be unpolarized. Although higher in overall magnitude, the shape of normal-incidence R agreed with the curve of Vehse *et al.* [13], showing the characteristic peak near 600 Å and the minimum near 700 Å. Using a nonlinear, least-squares, curve-fitting technique based on the χ^2 test, the values of n and k with their probable errors were determined from R versus incidence angle. The fitting procedure accounted for the effects of beam polarization, film thickness, and surface roughness in the calculation of the model reflectance [30]. The soft X-ray data of Henke *et al.* [22], the data of Vehse *et al.* [13], and the absorptivity of Weaver and Olson [20] are in moderate agreement with Windt *et al.* [27] optical constants in the range of overlap.

In Vehse *et al.* [13], Pd films were obtained by evaporation of Pd wire of 99.9995% purity in a vacuum of 10^{-8} torr. The deposition rate was ~150 Å/s, and the film thickness, measured by multiple-beam interferometry, ranged from 1600–2200 Å. The near-normal-incidence R was measured from 2–24 eV; in addition, R was measured as a function of the angle of incidence for a few selected photon energies. Even though the measurements were made *in situ*, R data were found to vary somewhat from sample to sample and to deteriorate with time; the data presented concern films with the highest R measured immediately after deposition. The prevalent conditions during evaporation and the history of the sample after its preparation must account for some discrepancies in the R values extending into the VUV [1–3, 7, 11]; such discrepancies occurred for all the opaque films evaporated on smooth substrates. Some scatter among data exists even for samples prepared *in situ* [11], mainly from 4 eV up to the region of the surface-plasma resonance at 7.3 eV. This probably results from surface-quality differences: the highest R values of Vehse *et al.* could indicate a better surface than in Ref. [27], even though their R is lower in the 10–24 eV range. In the low-energy range (4–6.5 eV) where experimental spectra overlap, R agrees well with that calculated from n and k measured on thin semitransparent films by Johnson and Christy [15] (see below). For multiangle measurements at selected energies, n and k were determined by a least-squares fit to Fresnel's equations. n and k were determined by the Kramers–Kronig analysis of the normal-incidence R spectrum from 2–24 eV. In the K–K integrals, the contribution $\Delta\theta$ to the phase change θ from the region above 24 eV was determined by interpolating the known values of $\Delta\theta$ at the selected energies mentioned above with a smoothly varying function. The results from the two methods agree within experimental error (±5%). Despite the good agreement of R values, n and k do not agree well with Johnson and Christy's values [15] in the 4–6.5 eV range, probably due to K–K interpolations.

Johnson and Christy [15] deposited Pd onto fused-quartz substrates at room temperature by vacuum evaporation of high-purity (99.97%) material. The evaporation was performed at pressure below 3×10^{-6} torr and at a fast rate (50 Å/s) to ensure the surface smoothness of the films. Several additional films were formed by sublimation at a rate of 0.3 Å/s. The reflectance was much higher for the quickly evaporated rather than for the sublimated films, so the optical constants determined from the former type were preferred. Moreover, annealing of the films in a nitrogen atmosphere indicated that quickly evaporated films were smooth and homogeneous, since they did not change after annealing like noble metals, whereas sublimated films changed. n and k as well as thickness d of the films were determined at eight selected wavelengths by inverting normal-incidence R and T functions simultaneously with the T function for p-polarized light incident at 60°. A three-parameter fit was used, and the resulting eight values of d (which presented a scatter of ±4 Å) were averaged. Then n and k were determined throughout the entire 0.5–6.5 eV spectral range using only normal-incidence R and T. The accuracy of the spectrophotometer in R (or T) was ±0.005, ±0.001 and ±0.0005, for the ranges $R>0.2$, $0.1 \leqslant R \ll 0.2$, and $R<0.1$, respectively. R spectra are in very good agreement (±0.01 in R) with those derived by Weaver and Benbow [18] (see below) from optical absorptivity between 0.15 and 4.4 eV. The optical constants exhibited a thickness dependence when the films were excessively thin (~100 Å). This behavior is qualitatively predicted by the Maxwell–Garnett theory [31]. n and k values listed are the averages of experiments on 277 and 375 Å films, which yielded results in agreement within the estimated error (less than ±1.5% in R and ±4% in n). As stated above, R processing (K–K transform) is exclusively responsible for moderate agreement of n and k values with those of Ref. [13]. R measured by Yu and Spicer [11] on opaque films from 2.2–11.6 eV was lower, because their slowly evaporated films were probably similar in structure to slowly sublimed films. This, with additional error introduced by K–K analysis, can account for most of the differences in their n and k values.

Weaver and Benbow [18] Pd samples were cut from a high-purity rod, mechanically polished to obtain a specular surface, then etched in boiling aqua regia. They were then annealed at 800 °C in vacuum (10^{-8} torr), followed by a high-temperature anneal under a partial pressure of He (1020 °C at 10^{-3} torr) to promote grain growth. Microscopic examination showed large grain (~4 mm) and an excellent work-free surface. Immediately prior to measurement, the sample was flashed in high vacuum to thermal-desorb any surface contamination. The absorptivity $A = 1 - R$ was measured at 4.2 K between 0.15 and 4.4 eV by a calorimetric technique. A K–K analysis was used to determine the optical constants [29]. For the extrapolations, a Drude form was used below 0.15 eV, and the data of Johnson and Christy [15], Vehse *et al.* [13] and Robin [7] were used from

4–50 eV. A power-law approximation $R(E) = R_o E^{-\beta}$ was used above 50 eV, with β adjusted to fit the independently determined dielectric function of Johnson and Christy [15], whose reflectance was in very good agreement in the overlap range. Although the optical spectra of Duisebaeva *et al.* [14] also present a structure near 0.46 eV, it is approximately three times stronger than that in [18]; moreover, another structure reported in [14] between 1.5 and 3 eV was not observed in [15] and [18]. Lafait *et al.* [21] also determined the infrared optical constants of Pd, from 0.1–0.5 eV, by means of surface-plasmon excitation. Unfortunately, their data were in disagreement with those of Refs. [14] and [18]. Furthermore, their conventional measurements of near-normal R and T from 0.5–6 eV also disagreed with those of Refs. [15] and [18], corresponding to a systematically lower reflectance.

Very recently, Fuzi *et al.* [32] used a prism-coupling (ATR) technique to measure the surface-plasmon properties of electron-beam-evaporated Pd on a glass slide. The ATR data as a function of angle of incidence at the He/Ne laser wavelength of 3.391 μm gave average values of $\varepsilon_R = 82.6$ and $\varepsilon_I = 109.3$ for several different prism-air space thicknesses. This gives $n = 5.21$ and $k = 10.48$, compared with values interpolated from Table I of $n = 4.08$ and $k = 14.05$. Fuzi *et al.* discuss variations of ε_R and ε_I for different kinds of metallic thin-film samples.

REFERENCES

1. G. B. Sabine, *Phys. Rev.* **55**, 1064 (1939).
2. D. Malé and J. Trompette, *J. de Physique et le Radium* **18**, 128 (1957).
3. P. Lostis, *J. de Physique* **25**, 118 (1964).
4. B. Dold and R. Mecke, *Optik* **22**, 435 (1965).
5. A. P. Lenham and D. M. Treherne, *J. Opt. Soc. Am.* **56**, 1137 (1966).
6. A. P. Lenham and D. M. Treherne, in "Optical Properties and Electronic Structure of Metals and Alloys," (F. Abelès ed.), North-Holland, Amsterdam, 196 (1966).
7. S. Robin, in "Optical Properties and Electronic Structure of Metals and Alloys," (F. Abelès ed.), North-Holland, Amsterdam, 202 (1966).
8. G. A. Bolotin, M. M. Kirillova, L. V. Nomerovannaya, and M. M. Noskov, *Fiz. Metal. Metalloved* **23**, 72 (1967).
9. F. I. Vilesov, A. A. Azgrubskii, and M. M. Kirillova, *Opt. Spectrosc.* **23**, 79 (1967); *Opt. Spektrosk.* **23**, 153 (1967).
10. A. P. Lenham, *J. Opt. Soc. Am.* **57**, 473 (1967).
11. A. Y-C. Yu and W. E. Spicer, *Phys. Rev.* **169**, 497 (1968).
12. J. Daniels, *Z. Physik* **227**, 234 (1969).
13. R. C. Vehse, E. T. Arakawa, and M. W. Williams, *Phys. Rev.* **B1**, 517 (1970).
14. Z. Duisebaeva, M. I. Korsunskii and G. P. Motulevich, *Opt. Spectrosc.* **34**, 307 (1973); *Opt. Spektrosk.* **34**, 535 (1973).
15. P. B. Johnson and R. W. Christy, *Phys. Rev.* **B9**, 5056 (1974).
16. Z. Duisabaeva, M. I. Korsunskii, and G. P. Motulevich, *Opt. Spectrosc.* **37**, 82 (1974); *Opt. Spektrosk.* **37**, 149 (1974).
17. C. Wehenkel and B. Gauthé, *Optics Commun.* **11**, 62 (1974).
18. J. H. Weaver and R. L. Benbow, *Phys. Rev.* **12**, 3509 (1975).

19. J. H. Weaver, *Phys. Rev.* **B11**, 1416 (1975).
20. J. H. Weaver and C. G. Olson, *Phys. Rev.* **B14**, 3251 (1976).
21. J. Lafait, F. Abelès, M. L. Theye, and G. Vuye, *J. Phys. F: Metal Phys.* **8**, 1597 (1978).
22. B. L. Henke, P. Lee, T. J. Tanaka, R. L. Shimabukuro and B. K. Fujikawa, *AIP Conf. Proc.* **75**, 340 (1981).
23. R. Riedinger and M. A. Khan, *Philos. Mag. B* **44**, 547 (1981).
24. M. A. Ordal, L. L. Long, R. J. Bell, S. E. Bell, R. W. Alexander, Jr., and C. A. Ward, *Appl. Opt.* **22**, 1099 (1983).
25. M. A. Ordal, R. J. Bell, R. W. Alexander, Jr., L. L. Long, and M. R. Querry, *Appl. Opt.* **24**, 4493 (1985).
26. G. N. Zhizhin, V. I. Silin and V. A. Yakovlev, *Sov. Phys. Solid State* **29**, 1224 (1987); *Fiz. Tverd. Tela* **29**, 231 (1987).
27. D. L. Windt, W. C. Cash, Jr., M. Scott, P. Arendt, B. Newnam, R. F. Fisher, and A. B. Swartzlander, *Appl. Opt.* **27**, 246 (1988).
28. H. Chen, N. E. Brener, and J. Callaway, *Phys. Rev.* **B40**, 1443 (1989).
29. J. H. Weaver, C. Krafka, D. W. Lynch, and E. E. Koch, in "Physik Daten, Physics Data, Optical Properties of Metals," Vol. 18-1, Fach-information zentrum, Karlsruhe, 179 (1981).
30. D. L. Windt, W. C. Cash, Jr., M. Scott, P. Arendt, B. Newnam, R. F. Fisher, A. B. Swartzlander, P. Z. Takacs, and J. M. Pinneo, *Appl. Opt.* **27**, 279 (1988).
31. O. S. Heavens, in "Optical Properties of Thin Solid Films," Dover, New York, 177 (1965).
32. Y. Fuzi, G. W. Bradberry, and J. R. Sambles, *J. Mod. Opt.* **36**, 1405 (1989).

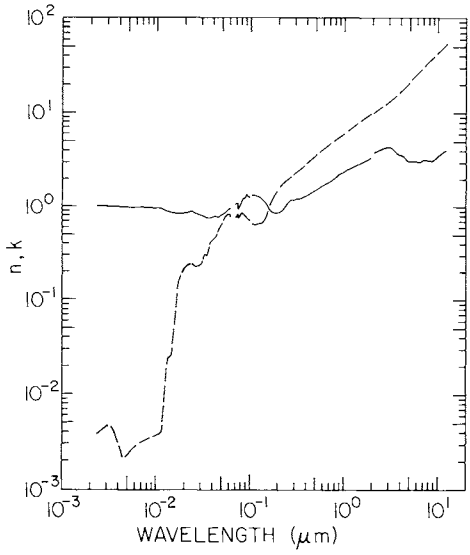

Fig. 1. Log–log plot of n (solid line) and k (dashed line) versus wavelength in micrometers for palladium.

TABLE I

Values of n and k for Palladium from Various References[a]

eV	cm^{-1}	Å	n	k
525.36		23.6	0.996 [27]	3.8×10^{-3} [27]
392.36		31.6	0.998	4.8
330.63		37.5	0.995	3.5
277.37		44.7	0.993	2.1
247.97		50.0	0.992	2.3
206.64		60.0	0.986	2.8
183.41		67.6	0.982	3.1
165.31		75.0	0.980	3.3
123.99		100.0	0.960	3.7
108.76		114.0	0.938	3.9
99.19		125.0	0.910	9.0×10^{-3}
91.50		135.5	0.871	0.025
82.66		150.0	0.851	0.072
72.34		171.4	0.835	0.148
61.99		200.0	0.850	0.22
51.02		243.0	0.879	0.244
48.38		256.3	0.851	0.224
40.81		303.8	0.821	0.247
37.92		327.0	0.799	0.310
34.75		356.8	0.758	0.307
32.69		379.3	0.763	0.420
30.55		405.9	0.794	0.451
27.69		447.8	0.780	0.495
26.91		460.7	0.765	0.547
25.33		489.5	0.809	0.625
23.00		539.1	0.853	0.763
21.22		584.3	0.913	0.850
20.12		616.3	0.990	0.790
18.48		670.9	1.03	0.766
17.26		718.5	1.06	0.778
16.85		735.9	1.07	0.824
16.67		743.7	0.94	0.744
14.86		834.5	1.24	0.877
14.12		878.0	1.23	0.815
13.48		919.8	1.36	0.796
13.30		932.1	1.30	0.749
12.54		988.8	1.28	0.733
eV	cm^{-1}	μm	n	k
12.0		0.1033	1.34 [13]	0.66 [13]
11.5		0.1078	1.33	0.65
11.0		0.1127	1.31	0.65
10.5		0.1181	1.30	0.66
10.0		0.1240	1.28	0.66

[a] The references from which the values were extracted are given in brackets.

TABLE I (*Continued*)

Palladium

eV	cm^{-1}	μm	n	k
9.5		0.1305	1.25	0.66
9.0		0.1378	1.19	0.68
8.5		0.1459	1.10	0.72
8.0		0.1550	0.98	0.84
7.5		0.1653	0.89	1.02
7.0		0.1771	0.85	1.23
6.5		0.1907	0.86	1.44
5.98	48,232	0.2073	0.87 [15]	1.60 [15]
5.85	47,183	0.2119	0.89	1.65
5.73	46,215	0.2164	0.91	1.70
5.60	45,167	0.2214	0.92	1.76
5.48	44,199	0.2263	0.94	1.81
5.36	43,231	0.2313	0.97	1.86
5.23	42,182	0.2371	1.00	1.91
5.11	41,215	0.2426	1.04	1.95
4.98	40,166	0.2490	1.08	1.99
4.86	39,198	0.2551	1.11	2.03
4.74	38,230	0.2616	1.13	2.07
4.61	37,182	0.2689	1.16	2.10
4.49	36,214	0.2761	1.19	2.13
4.36	35,165	0.2844	1.18	2.18
4.24	34,198	0.2924	1.18	2.23
4.12	33,230	0.3009	1.20	2.29
3.99	32,181	0.3107	1.21	2.35
3.87	31,213	0.3204	1.21	2.42
3.74	30,165	0.3315	1.20	2.50
3.62	29,197	0.3425	1.22	2.57
3.50	28,229	0.3542	1.23	2.65
3.37	27,181	0.3679	1.24	2.74
3.25	26,213	0.3815	1.26	2.83
3.12	25,164	0.3974	1.30	2.93
3.00	24,196	0.4133	1.33	3.03
2.88	23,229	0.4305	1.37	3.14
2.75	22,180	0.4509	1.41	3.26
2.63	21,212	0.4714	1.46	3.39
2.50	20,164	0.4959	1.52	3.54
2.38	19,196	0.5209	1.57	3.68
2.26	18,228	0.5486	1.64	3.84
2.13	17,179	0.5821	1.68	4.02
2.01	16,212	0.6168	1.75	4.21
1.88	15,163	0.6595	1.80	4.42
1.76	14,195	0.7045	1.86	4.65
1.64	13,227	0.7560	1.95	4.89
1.51	12,179	0.8211	2.06	5.19
1.39	11,211	0.8920	2.33	5.50

(continued)

TABLE I (*Continued*)

Palladium

eV	cm^{-1}	μm	n	k
1.26	10,162	0.9840	2.34	5.89
1.14	9,195	1.088	2.52	6.33
1.02	8,227	1.215	2.66	6.90
0.89	7,178	1.393	2.80	7.65
0.77	6,210	1.610	3.01	8.59
0.64	5,162	1.937	3.34	9.89
0.60	4,839	2.066	3.80 [31]	9.96 [31]
0.58	4,678	2.138	3.85	10.23
0.56	4,517	2.214	3.92	10.49
0.54	4,355	2.296	3.97	10.79
0.52	4,194	2.384	4.03	11.10
0.50	4,033	2.480	4.10	11.44
0.48	3,871	2.583	4.20	11.77
0.46	3,710	2.695	4.27	12.11
0.44	3,549	2.818	4.31	12.46
0.42	3,387	2.952	4.31	12.85
0.40	3,226	3.100	4.27	13.27
0.38	3,065	3.263	4.17	13.77
0.36	2,904	3.444	3.98	14.41
0.34	2,742	3.647	3.80	15.18
0.32	2,581	3.875	3.56	16.21
0.30	2,420	4.133	3.56	17.27
0.28	2,258	4.428	3.30	18.52
0.26	2,097	4.769	3.11	20.15
0.24	1,936	5.166	3.15	21.97
0.22	1,774	5.636	3.10	24.06
0.20	1,613	6.199	3.07	26.59
0.19	1,532	6.526	3.07	28.09
0.18	1,452	6.888	3.15	29.71
0.17	1,371	7.293	3.20	31.46
0.16	1,290	7.749	3.17	33.45
0.15	1,210	8.266	3.13	35.82
0.14	1,129	8.856	3.11	38.48
0.13	1,048	9.537	3.36	41.52
0.12	968	10.33	3.60	45.08
0.11	887	11.27	3.85	49.21
0.10	806	12.40	4.13	54.15

Vanadium (V)

G. GUIZZETTI and A. PIAGGI
Dipartimento di Fisica "A. Volta"
and
Gruppo Nazionale di Struttura della Materia del CNR
Università di Pavia
Pavia, Italy

There have been many measurements of the optical properties of V [1–23]. Although in the 1960s they were generally obtained on bulk samples mechanically polished, in later years films were preferentially used. The optical properties of the V films are strongly dependent on the preparation technique and the physical-chemical conditions (in particular, deposition rate and substrate temperature). To some degree this can explain scatter among the data. Moreover, V is particularly sensitive to oxide, but no author has quantitatively estimated the oxide-coating effect on the optical response. In any case, the best films give a response very similar to the bulk.

The room-temperature values of n and k tabulated here (Table I and Fig. 1) were obtained from the following works and references therein: Sonntag *et al.* [7] from 300–120 eV, Wehenkel and Gauthé [13] from 120–40 eV; Seignac and Robin [8] from 40–6 eV; Nestell and Christy [19] from 6–0.5 eV; Weaver *et al.* [12] from 0.5–0.1 eV. As a general rule we preferred data that were obtained "directly," for example, from R and T by inverting the Fresnel relations or from ellipsometry, which do not rely on extrapolations outside the measured spectrum. However, we also considered values derived from Kramers–Kronig analysis of reflectance [12] or electron-energy-loss spectra [13], based on a very wide energy range and accurate measurements: This ensured reliable results, which were in good agreement with the others in the overlapping regions. We have disregarded data that were insufficient and ambiguous, in terms of either the sample preparation and characterization or the measurement accuracy, especially when inexplicable or in clear disagreement with other researchers. This is particularly true in the IR region, where despite numerous ellipsometric measurements, we preferred the results of calorimetry [12], although limited to 0.1 eV.

Copyright © 1991 by Academic Press.
All rights of reproduction in any form reserved.
ISBN 0-12-544422-2

In Table I we have retained three significant figures, but it is probably too generous for optical constants obtained from photometric or ellipsometric techniques.

Sonntag *et al.* [7] evaporated films onto substrates of zapon and aluminum using an electron gun. The optical absorption coefficient α was determined with an absolute accuracy of $\pm 20\%$, but the relative accuracy of adjacent regions was much better, about $1 \times 10^4\,\mathrm{cm}^{-1}$. The wavelength resolution in the continuous spectrum between 40 eV and ~300 eV of synchrotron light (of DESY accelerator) was better than 1 Å (0.1 eV at 40 eV, 8 eV at 300 eV). The α spectrum only showed an appreciable rise at 47.7 eV, while the strong oscillations reported by previous investigators [24, 25] appear to have been spurious. Above 200 eV, α quasi-linearly decreases to the value of $0.9 \times 10^5\,\mathrm{cm}^{-1}$ at 300 eV. The absolute magnitude of α was checked by performing oscillator sums to produce the expected value of $N_{\mathrm{eff}} \approx 8$ electrons.

Wehenkel and Gauthé [13] deposited V films by clean-vacuum (10^{-8}–10^{-7} torr) evaporation from bulk material on freshly cleaved rocksalt and floated off on distilled water. Film thicknesses from 200–400 Å were determined with an accuracy of about $\pm 10\%$, by weighing the substrate before and after evaporation. Electron-energy-loss spectra were obtained by transmission of 35 keV electrons in the 2–120 eV range with an accuracy better or equal to ± 0.5 eV and constant through the whole spectral range. To achieve statistical accuracy, a large number of spectra were recorded, using different specimens of different thicknesses. Through Ritchie's formula [26], the single-scattering volume losses were separated from the surface losses. Then ε_1, ε_2, and thickness were calculated by means of Kramers–Kronig relations. The energy-loss function was extrapolated by setting $\mathrm{Im}(-1/\tilde{\varepsilon}) = 0$ at $E = 0$ and assuming that it varies as $E^{-2.5}$ at high energies. In the superposition region (40–120 eV), the α spectrum derived is in good accord with that directly measured by Sontagg *et al.* [7]. In particular the peak at 47.7 eV differs only 3% in the energy position, although it is ~30% higher. So we report Kramers–Kronig-derived n values in the range 40–120 eV.

Seignac and Robin [8] evaporated V buttons of high purity (99.98%) with an electron gun onto mica and pyrex substrates, heated to a temperature between 350 and 400 °C. The films, grown at a rate of ≈5 Å/s, had thicknesses of 900–1400 Å. The optical constants were determined by both R measurements at two angles of incidence in the 4–50 eV range, and by Kramers–Kronig transforms; as far as the structure positions are concerned, the results were equivalent. The optical spectra in [8] are comparable with those of Ref. [7, 12, 19] in the respective superposition ranges; in particular, R is lower than in Ref. [19], and the α spectrum at high energy is flatter than in [7].

Nestell and Christy [19] evaporated polycrystalline thin films in a

vacuum system (the pressure was in the range $2–5 \times 10^{-7}$ torr) onto fused-quartz substrates heated to high temperature (550–700 °C). The evaporation rates were 200–800 Å/s for opaque films, and 20 Å/s for thin films of ~200 Å. X-ray analysis showed that the films were well crystallized with a lattice constant approximately 1% smaller than bulk value (due to uniform strain) and a grain size of 150 Å. Transmittance and absolute reflectance measurements were made in the 0.5–6.5 eV range with a double-beam spectrophotometer. The accuracy was about ± 0.005 in R. The reflectance of opaque films showed a strong evaporation-rate dependence; high rates avoid surface roughness, producing the most highly reflecting films (for example, at 6 eV, R increased ~6% when the evaporation rate was increased from 21 to 317 Å/s). The reflectance of rapidly evaporated opaque films was in quite good agreement with bulk-sample results [12], but it was much higher above 5 eV and lower below 1 eV. In the UV this discrepancy is attributed to surface roughness of the bulk samples, resulting from etching; in the IR it may be due to the different measurement technique used (calorimetry; see in the following). The optical constants n and k as well as the film thickness were determined by inverting the normal-incidence R and T along with the p-polarized T at a 60° angle of incidence, with R measured from opaque films. The estimate of instrumental error was ~1% in k and ~2% in n over most of the spectral range. The aforesaid differences in R between [19] and [8, 12] involve discontinuities in n and k at 0.5 eV and 6 eV, respectively.

In Weaver *et al.* [12], samples of V were spark-cut from electron-beam-melted buttons of high-purity material; then they were successively macroetched, mechanically polished, carefully electropolished, and finally very slightly polished with 0.3 μm diameter Al_2O_3. An X-ray Laue-gram indicated an unstrained surface. Although the samples were not single crystals, most or all of the illuminated surface was a single crystallite. A calorimetric method was used between 0.1 and 4.88 eV to determine the absorptivity $A = 1 - R$ at 4.2 K and a 15° angle of incidence. Room-temperature R measurements were made at 10°, 45°, and 60° for s- and p-polarized synchrotron radiation from 3.1–35 eV. A comparison of low-energy absorptivities with those calculated from the n and k values of Bolotin *et al.* [1] show good qualitative agreement, although A values are considerably lower in magnitude (that is, R was higher). Instead, above 5–6 eV R was lower than that of Seignac and Robin [8], probably due to an oxide layer. Optical constants were determined by Kramers–Kronig analysis: at low energy a Drudelike behavior was introduced; at high-energy, Sonntag *et al.* [10] absorption measurements were used to 300 eV; the range was extended up to 1000 eV (where $R = 1.4 \times 10^{-8}$) assuming $R(E) = R_o E^{-\beta}$ (with $\beta = 4.1$, from fitting R at 190 and 300 eV). The very wide energy range used in Kramers–Kronig analysis and the quite good agreement below 5 eV with the data of Nestell and Christy [19] make the n and k

values here reported in the 0.1–0.5 eV range more reliable than those obtained by ellipsometry [1–6, 22].

REFERENCES

1. G. A. Bolotin, A. N. Voloshinskii, M. M. Kirillova, M. M. Noskov, A. V. Solokov, and B. A. Charikov, *Phys. Met. Metall.* **13**, 24 (1962).
2. M. M. Kirillova and B. A. Charikov, *Phys. Met. Metall.* **19**, 13 (1965).
3. A. P. Lenham and D. M. Treherne, in "Optical Properties and Electronic Structures of Metals and Alloys," (F. Abelès, ed.), North-Holland, Amsterdam, 196 (1966).
4. A. P. Lenham and D. M. Treherne, *J. Opt. Soc. Am.* **56**, 1076 (1966).
5. A. P. Lenham and D. M. Treherne, *J. Opt. Soc. Am.* **56**, 1137 (1966).
6. A. P. Lenham, *J. Opt. Soc. Am.* **57**, 473 (1967).
7. B. Sonntag, R. Haensel, and C. Kunz, *Solid State Commun.* **7**, 597 (1969).
8. A. Seignac and S. Robin, *C. R. Acad. Sc. Paris* **B271**, 919 (1970).
9. G. W. Simmons and E. J. Scheibner, *J. Appl. Phys.* **43**, 693 (1972).
10. P. B. Johnson and R. W. Christy, *Phys. Rev.* **B9**, 5056 (1974).
11. C. Wehenkel and B. Gauthé, *Phys. Lett.* **47A**, 253 (1974).
12. J. H. Weaver, D. W. Lynch, and C. G. Olson, *Phys. Rev.* **B10**, 501 (1974).
13. C. Wehenkel and B. Gauthé, *Phys. Status Solidi* **B64**, 515 (1974).
14. G. Chassaing, P. Gravier, M. Sigrist, and R. Pierrisnard, *Solid State Commun.* **15**, 1613 (1974).
15. M. R. Steel, *J. Phys. F: Metal Phys.* **4**, 783 (1974).
16. G. Chassaing, P. Gravier, and M. Sigrist, *Thin Solid Films* **35**, L25 (1976); *Thin Solid Films* **57**, 93 (1979).
17. R. Blickensderfer, D. K. Deardorff, and R. L. Lincoln, *J. Less Common Metals* **51**, 13 (1977).
18. J. E. Nestell, R. W. Christy, M. Cohen, and G. C. Ruben, *J. Appl. Phys.* **51**, 655 (1980).
19. J. E. Nestell and R. W. Christy, *Phys. Rev.* **B21**, 3173 (1980).
20. T. G. Lanskaya, R. I. Lyubinskaya, S. N. Svitasheva, K. K. Svitashev, *Sov. Phys. Tech. Phys.* **26**, 1115 (1981).
21. M. A. Ordal, R. J. Bell, R. W. Alexander, Jr., L. L. Long, M. R. Querry, *Appl. Opt.* **24**, 4493 (1985).
22. S. Mahmoud and Z. S. El Mandouh, *J. Mat. Sci.* **22**, 2852 (1987).
23. G. N. Zhizhin, V. I. Silin, and V. A. Yakovlev, *Sov. Phys. Solid State* **29**, 1224 (1987).
24. B. K. Agarwal and M. P. Givens, *Phys. Rev.* **108**, 658 (1957).
25. N. N. Axelrod and M. P. Givens, *Phys. Rev.* **120**, 1205 (1960).
26. R. H. Ritchie, *Phys. Rev.* **106**, 874 (1957).

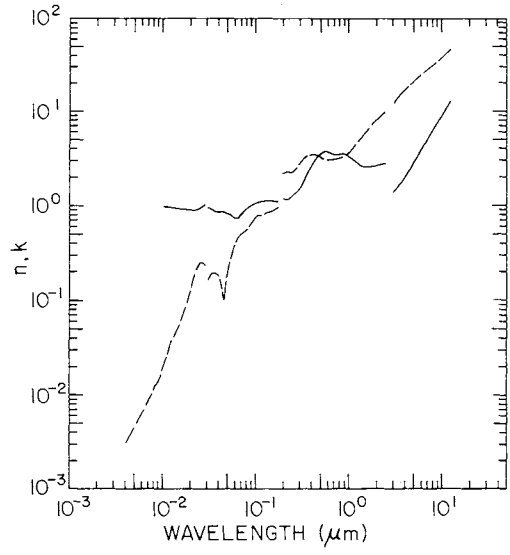

Fig. 1. Log–log plot of n (solid line) and k (dashed line) versus wavelength in micrometers for vanadium.

TABLE I

Values of n and k for Vanadium from Various References[a]

eV	cm^{-1}	Å	n	k
300		41.33		3.0×10^{-3} [7]
275		45.08		3.9
250		49.59		4.8
225		55.10		5.7
200		61.99		6.6
195		63.58		6.9
190		65.26		7.2
185		67.02		7.6
180		68.88		8.0
175		70.85		8.5
170		72.93		8.9
165		75.14		9.5×10^{-3}
160		77.49		1.00×10^{-2}
155		79.99		1.08
150		82.66		1.14
145		85.51		1.22
140		88.56		1.29
135		91.84		1.38
130		95.37		1.46
125		99.19		1.67
120.0		103.32	0.96 [13]	1.96 [13]
117.5		105.52	0.96	2.09
115.0		107.81	0.95	2.36
112.5		110.21	0.95	2.50
110.0		112.71	0.95	2.63
107.5		115.34	0.95	2.77
105.0		118.08	0.94	2.91
102.5		120.96	0.94	3.19
100.0		123.99	0.94	3.33
97.5		127.16	0.94	3.74
95.0		130.51	0.93	3.88
92.5		134.04	0.93	4.04
90.0		137.76	0.93	4.32
87.5		141.70	0.92	4.60
85.0		145.86	0.92	4.90
82.5		150.29	0.92	5.19
80.0		154.98	0.91	5.48
77.5		159.98	0.91	6.06
75.0		165.31	0.90	6.65
72.5		171.01	0.90	7.24
70.0		177.12	0.90	8.07
67.5		183.68	0.89	9.29×10^{-2}
65.0		190.75	0.88	0.10
62.5		198.38	0.88	0.12
60.0		206.64	0.87	0.14

[a] The references from which the values were extracted are given in brackets.

TABLE I (*Continued*)

Vanadium

eV	cm^{-1}	Å	n	k
57.5		215.63	0.86	0.16
55.0		225.43	0.87	0.19
52.5		236.16	0.89	0.22
50.0		247.97	0.91	0.24
47.5		261.02	0.94	0.25
45.0		275.52	0.98	0.25
42.5		291.73	1.01	0.23
40		309.96	0.94 [8]	0.16 [8]
39		317.91	0.93	0.17
38		326.28	0.92	0.18
36		344.40	0.89	0.19
35		354.24	0.88	0.19
34		364.66	0.86	0.19
33		375.71	0.83	0.19
32		387.45	0.83	0.18
31		399.95	0.84	0.18
30		413.28	0.84	0.16
29		427.54	0.84	0.15
28		442.80	0.84	0.12
27		459.20	0.83	0.10
26		476.87	0.83	0.13
25		495.94	0.81	0.17
24		516.60	0.80	0.22
23		539.07	0.78	0.25
22		563.57	0.76	0.29
21		590.41	0.71	0.35
20		619.93	0.71	0.42
19		652.55	0.72	0.44
18		688.81	0.78	0.48
17		729.32	0.83	0.51
16		774.91	0.87	0.52
15		826.57	0.92	0.56
14		885.61	0.97	0.61
13		953.73	1.02	0.67
eV	cm^{-1}	μm	n	k
12		0.1033	1.04	0.72
11		0.1127	1.08	0.76
10		0.1240	1.10	0.80
9		0.1378	1.11	0.83
8		0.1550	1.10	0.87
7		0.1771	1.09	0.95
6.0	48,393	0.2066	1.14 [19]	2.18 [19]
5.9	47,586	0.2101	1.14	2.20

(continued)

TABLE I (*Continued*)

Vanadium

eV	cm^{-1}	μm	n	k
5.8	46,780	0.2138	1.13	2.21
5.7	45,973	0.2175	1.12	2.22
5.6	45,167	0.2214	1.12	2.22
5.5	44,360	0.2254	1.13	2.21
5.4	43,554	0.2296	1.14	2.21
5.3	42,747	0.2339	1.16	2.21
5.2	41,940	0.2384	1.17	2.21
5.1	41,134	0.2431	1.20	2.18
5.0	40,327	0.2480	1.23	2.19
4.9	39,521	0.2530	1.26	2.20
4.8	38,714	0.2583	1.30	2.20
4.7	37,908	0.2638	1.30	2.29
4.6	37,101	0.2695	1.32	2.35
4.5	36,295	0.2755	1.34	2.42
4.4	35,488	0.2818	1.39	2.50
4.3	34,682	0.2883	1.41	2.57
4.2	33,875	0.2952	1.46	2.65
4.1	33,068	0.3024	1.51	2.73
4.0	32,262	0.3100	1.56	2.81
3.9	31,455	0.3179	1.64	2.89
3.8	30,649	0.3263	1.73	2.97
3.7	29,842	0.3351	1.84	3.06
3.6	29,036	0.3444	1.96	3.14
3.5	28,230	0.3542	2.07	3.22
3.4	27,423	0.3647	2.18	3.26
3.3	26,616	0.3757	2.30	3.31
3.2	25,809	0.3875	2.42	3.33
3.1	25,003	0.4000	2.55	3.38
3.0	24,196	0.4133	2.71	3.38
2.9	23,390	0.4275	2.84	3.42
2.8	22,583	0.4428	3.03	3.40
2.7	21,777	0.4592	3.19	3.38
2.6	20,970	0.4769	3.36	3.33
2.5	20,164	0.4959	3.53	3.26
2.4	19,357	0.5166	3.63	3.15
2.3	18,551	0.5391	3.68	3.05
2.2	17,744	0.5636	3.68	2.98
2.1	16,937	0.5904	3.65	2.94
2.0	16,131	0.6199	3.55	2.93
1.9	15,324	0.6526	3.50	2.99
1.8	14,518	0.6888	3.43	3.05
1.7	13,711	0.7293	3.41	3.08
1.6	12,905	0.7749	3.42	3.14
1.5	12,098	0.8266	3.47	3.18
1.4	11,292	0.8856	3.43	3.22

(continued)

TABLE I (*Continued*)

Vanadium

eV	cm^{-1}	μm	n	k
1.3	10,485	0.9537	3.38	3.31
1.2	9,679	1.0332	3.19	3.54
1.1	8,872	1.1271	2.95	3.87
1.0	8,065	1.2399	2.69	4.43
0.9	7,259	1.3776	2.56	5.02
0.8	6,452	1.5498	2.52	5.77
0.7	5,646	1.7712	2.56	6.83
0.6	4,840	2.0664	2.62	8.19
0.5	4,033	2.4797	2.72	9.73
0.40	3,226	3.100	1.38 [12]	11.90 [12]
0.36	2,904	3.440	1.57	13.32
0.32	2,581	3.875	1.79	15.08
0.28	2,258	4.428	2.13	17.35
0.24	1,936	5.166	2.82	20.32
0.20	1,613	6.199	3.90	24.30
0.16	1,290	7.749	5.77	30.03
0.12	968	10.332	9.51	38.97
0.10	806	12.400	12.83	45.89

Aluminum Arsenide (AlAs)

EDWARD D. PALIK
Institute for Physical Science and Technology
University of Maryland
College Park, Maryland

O. J. GLEMBOCKI
Naval Research Laboratory
Washington, D.C.
and

KENICHI TAKARABE
Department of Natural Science
Okayama University of Science
Okayama-City
Okayama 700, Japan

Although AlAs is one end of the important superlattice material $Al_xGa_{1-x}As$, it has not been investigated nearly as much because of its hydroscopic nature. This has necessitated some care in experiment often with a thin capping of GaAs, especially for superlattice structures containing alternate layers of AlAs and GaAs. Such a multilayer sample is more complicated to analyze if one wishes to extract n and k from spectroscopic ellipsometry or reflection–transmission experiments. The data chosen for this critique are listed in Table I and plotted in Fig. 1. Because there are several sources of data in a given energy range, we have chosen to list these separately rather than interspersing the data. Thus, in Table I the eV scale does not run consecutively but sometimes backs up to introduce new data with a bracket reference. This is usually indicated with a space.

At high energy we have used values of n and k obtained from a Henke-model calculation [1, 2] in the range 10,000–51.57 eV (1.240–240.4 Å). The atomic absorption edges are found at $K(\mathrm{Al}) = 1559.8$ eV, $K(\mathrm{As}) = 11{,}865$ eV, $L_1(\mathrm{Al}) = 87.01$ eV, $L_1(\mathrm{As}) = 1529.3$ eV, $L_{2,3}(\mathrm{Al}) = 72.78$ eV, $L_2(\mathrm{As}) = 1358.7$ eV, $L_3(\mathrm{As}) = 1323.5$ eV.

A gap appears to exist in experimental reflectivity data between 51 and ~6 eV, so no n and k data are available.

The region 5.6–1.7 eV has been studied with spectroscopic ellipsometry by Garriga *et al.* [3]. The AlAs sample was 1 μm thick, grown on a GaAs

Copyright © 1991 by Academic Press.
All rights of reproduction in any form reserved.
ISBN 0-12-544422-2

(100) substrate; it was capped with a 17 Å GaAs layer. A multilayer model was used to extract the optical constants. A 6 Å oxide layer was assumed on top of the GaAs capping layer. We have read an expanded graph of ε_1 and ε_2 and calculated n and k using the equations

$$2n^2 = \varepsilon_1 + \sqrt{\varepsilon_1^2 + \varepsilon_2^2}$$

$$2k^2 = -\varepsilon_1 + \sqrt{\varepsilon_1^2 + \varepsilon_2^2}.$$

We carry three figures, but the data are surely not that good. The direct gap at 3.0 eV was defined in a fit of the absorption coefficient α versus eV, assuming a lineshape of a broadened two-dimensional interband minimum. These data are significantly different from data of Yim [4], who measured the transmission of bulk platelets of AlAs and determined both the indirect gap at 2.14 and the direct gap at 3.14 eV; this latter value is significantly different from that of Garriga *et al.*, and the k values are over an order of magnitude different; $k = 6.38 \times 10^{-2}$ at 3.0 eV [3] and $k = 1.79 \times 10^{-3}$ at 3.0 eV [4]. We have not found other measurements of k at the direct gap for comparison. To interpret the systematic variation of photoluminescence peak energies of GaAs/AlAs short-period superlattices, Nakayama *et al.* [5] cited values of 2.223 eV for the indirect gap and 3.125 eV for the direct gap of AlAs at 77 K.

An example of accuracy in reading two different graphs in the same paper is given for the values of k at 3.0 eV [3]: 5.3×10^{-2} from a graph of ε_1, ε_2 and 6.38×10^{-2} from a graph of α. This represents a 20% variation.

The 300 K values of index of refraction for energies below the direct gap has been measured by Fern and Onton [6] using the minimum-deviation method and a wedge-shaped sample (20°) of multigrained material. The experimental data were fit with the equation

$$\varepsilon = \varepsilon_r - i\varepsilon_i = \varepsilon_x + \frac{S_1 E_1^2}{E_1^2 - E^2 + iE\gamma_1} + \frac{S_2 E_2^2}{E_2^2 - E^2 + iE\gamma_2},$$

where ε_x represents the contribution to the dielectric constant by higher energy processes above the E_1 and E_2 interband transitions, and S_i and γ_i are the oscillator strength and damping constant of the E_1 and E_2 "oscillators." Finally, n is determined from $n = \mathrm{Re}[\varepsilon^{1/2}]$. This approximation is possible because in the spectral range of the measurements (<2.218 eV) the contribution from ε_i is very small. The fitting process reproduced the experimental data for n to ± 0.008 by using $E_1 = 3.9$ eV, $E_2 = 4.54$ eV, $S_1 = 3.019$, $S_2 = 3.030$, $\gamma_1 = 0.503$ eV, $\gamma_2 = 2.101$ eV, and $\varepsilon_x = 2.114$.

Monemar [7] used interference fringes to obtain 300 K values of n below the band gap for bulk samples. However, these values are considerably smaller (about -0.06) than those of Fern and Onton. A model of Adachi [8] for the system $Al_xGa_{1-x}As$ gives values of n much closer to Fern and Onton (presumably because the adjustable constants were chosen to fit these data) as does an extrapolation of the values for $Al_xGa_{1-x}As$ by Aspnes *et al.* [9]; for example, at 1.5 eV $n=2.995$ [6], 2.936 [7], 3.01 [8], and ~3.01 [9]. We elect to stress the experimental data of Fern and Onton but also show the calculated data [8] over a somewhat wider spectral range. Lorenz [10] measured $n=3.3$ at 2.2 eV, this number being about $+0.1$ larger than that of Fern and Onton at 2.2 eV. Such variations are probably due to the quality of the various samples.

In the lattice-vibration region, the reststrahlen spectrum has been measured by Rheinlander and Neumann [11] for bulk thin plates, but no optical constants were obtained by fitting an oscillator model to the data. The data of Minden [12] do not appear to be consistent with the results of Ref. [11], which we must attribute to the quality of the epilayers used in Ref. [12]. Minden measured R and T in the 1300–1400 cm^{-1} region for an epitaxial layer of AlAs grown on a GaAs substrate. The sample oxidized rapidly when brought out into the laboratory, and the data, which took several hours to obtain, surely contained effects of this layer. Although we expect an oxidation layer to be thin and transparent and not to perturb the results in the long-wave infrared, it is not clear what sort of material the hydroscopic nature of AlAs will produce on the surface.

Perkowitz *et al.* and Sudharsanan *et al.* [13, 14] have measured a heterostructure consisting of several layers of GaAs and AlAs. The substrate was 350 μm of undoped GaAs; on this were a 1 μm epitaxial layer of GaAs, a 0.2 μm layer of undoped AlAs, a 1 μm layer of Si-doped AlAs (the sample) and a capping layer of 250 Å of undoped GaAs. Measurements of reflectivity were performed from 200–450 cm^{-1} with reststrahlen peaks of AlAs and GaAs appearing along with interference fringes. Although the fit with a multilayer model was qualitatively good, the magnitudes were not matched very well except at the reststrahlen peaks. The parameters for GaAs were assumed to be known. The parameters for AlAs for a Lorentz-oscillator model of the form

$$\varepsilon = \varepsilon_\infty + \frac{S\nu_T^2}{\nu_T^2 - \nu^2 - i\nu\gamma}$$

were determined to be $\nu_T = 361.8\ cm^{-1}$, $S = 1.9$, $\gamma = 8.0\ cm^{-1}$, $\varepsilon_\infty = 8.2$. At low frequency, the dc dielectric constant is $\varepsilon_o = 10.1$.

Interestingly, the Raman spectrum yields most of the parameters needed

to calculate the IR spectrum. From Raman data, Onton [15] determined $\nu_T = 361.8\,\text{cm}^{-1}$, $S = 1.90$, and $\gamma = 0.97\,\text{cm}^{-1}$, and chose $\varepsilon_\infty = 7.8$. These can be used in the above formula to determine n and k also. The only drastic difference in the two sets of parameters is in the values of γ; the line width $0.97\,\text{cm}^{-1}$ seems too small [15], while the line width $8.0\,\text{cm}^{-1}$ seems too large [13, 14] for typical semiconductors. We calculated the reflectivity with both sets and found that the parameters of Perkowitz *et al.* give a better fit to the reflectivity in Ref. [11], agreeing with the experimental R within a few reflectivity percentage units almost everywhere; this assumes an uncertainty of a few cm^{-1} in the wave number axis as well. We did not attempt to refit the R data to obtain independent values of n and k, however. Therefore, we have listed these values [13, 14] in Table I.

Experimental transmission data for the two-phonon spectrum above ν_T were not found.

ACKNOWLEDGMENTS

We thank W. R. Hunter for providing the n and k values calculated from the Henke model.

REFERENCES

1. B. L. Henke, P. Lee, T. J. Tanaka, R. L. Shimabukuro, and B. K. Fujikama, *At. Data Nucl. Data Tables* **27**, 1 (1982).
2. B. L. Henke, J. C. Davis, E. M. Gullickson, and R. C. C. Perera, Lawrence Berkeley Laboratory Report No. LBL-26259 (1988).
3. M. Garriga, P. Lautenschlager, M. Cardona, and K. Ploog, *Solid State Commun.* **61**, 157 (1987).
4. W. M. Yim, *J. Appl. Phys.* **42**, 2854 (1971).
5. M. Nakayama, I. Tanaka, I. Kimura, and H. Nishimura, *Jpn. J. Appl. Phys.* **29**, 41 (1990).
6. R. E. Fern and A. Onton, *J. Appl. Phys.* **42**, 3499 (1971).
7. B. Monemar, *Solid State Commun.* **8**, 2121 (1970).
8. S. Adachi, *J. Appl. Phys.* **58**, R1 (1985).
9. D. E. Aspnes, S. M. Kelso, R. A. Logan and R. Bhat, *J. Appl. Phys.* **60**, 754 (1986).
10. M. R. Lorenz, R. Chicotka, and G. D. Pettit, *Solid State Commun.* **8**, 693 (1970).
11. B. Rheinlander and H. Neumann, *Phys. Status Solidi* **(b)45**, K9 (1971).
12. H. T. Minden, *Appl. Phys. Lett.* **17**, 358 (1970).
13. S. Perkowitz, R. Sudharsanan, S. S. Yom, and T. J. Drummond, *Solid State Commun.* **62**, 645 (1987).
14. R. Sudharsanan, S. Perkowitz, S. S. Yom, and T. J. Drummond, *Proc. SPIE* **794**, 197 (1987).
15. A. Onton, in "Proc. 10th Intern. Conf. on the Physics of Semiconductors," U.S. Atomic Energy Commission, Washington, 107 (1970).

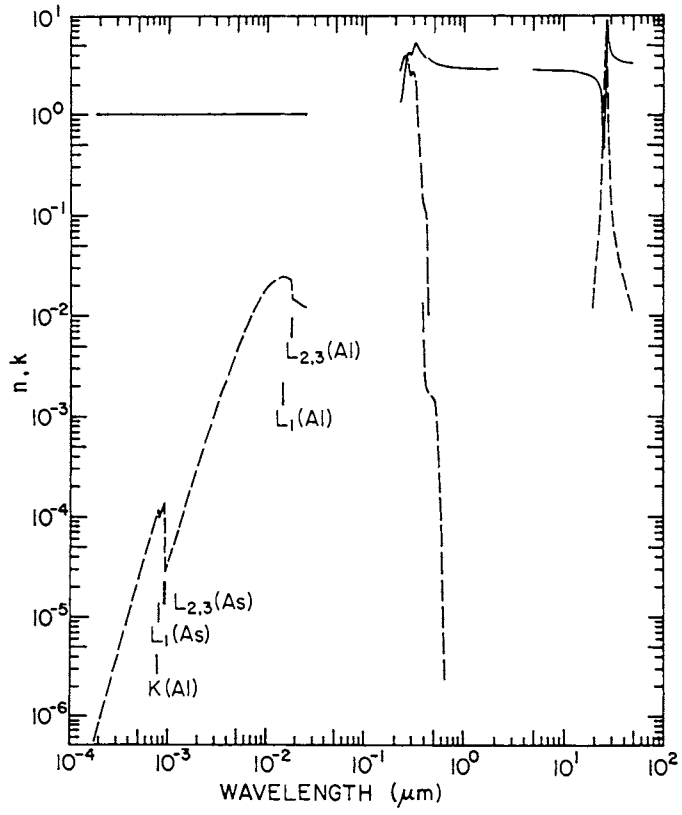

Fig. 1. Log–log plot of n (solid line) and k (dashed line) versus wavelength in micrometers for aluminum arsenide.

TABLE I

Values of n and k for Aluminum Arsenide Obtained from Various References[a]

eV	cm^{-1}	Å	n	k
10000		1.240	0.99999320[1]	1.33×10^{-7}[1]
9772		1.269	0.99999280	1.45
9331		1.329	0.99999210	1.73
8909		1.392	0.99999130	2.07
8507		1.458	0.99999050	2.47
8123		1.526	0.9999895	2.94
7756		1.599	0.9999884	3.50
7406		1.674	0.9999873	4.18
7072		1.753	0.9999861	4.97
6752		1.836	0.9999846	5.92
6447		1.923	0.9999831	7.05
6156		2.014	0.9999815	8.40
5878		2.109	0.9999796	9.99×10^{-7}
5613		2.209	0.9999776	1.19×10^{-6}
5359		2.314	0.9999754	1.41
5117		2.423	0.9999730	1.68
4886		2.538	0.9999703	2.00
4665		2.658	0.9999674	2.38
4455		2.783	0.9999642	2.83
4254		2.915	0.9999607	3.36
4062		3.053	0.9999568	3.99
3878		3.197	0.9999526	4.74
3703		3.348	0.9999480	5.63
3536		3.506	0.9999429	6.67
3376		3.672	0.9999374	7.92
3224		3.846	0.9999313	9.39×10^{-6}
3078		4.028	0.9999248	1.11×10^{-5}
2939		4.218	0.9999176	1.32
2807		4.418	0.9999099	1.56
2680		4.627	0.9999015	1.84
2559		4.846	0.999893	2.18
2443		5.075	0.999883	2.58
2333		5.315	0.999872	3.04
2228		5.566	0.999861	3.59
2127		5.829	0.999850	4.22
2031		6.105	0.999838	4.97
1939		6.394	0.999825	5.83
1852		6.696	0.999813	6.85
1768		7.013	0.999802	8.03
1688		7.344	0.999792	9.40×10^{-5}
1650		7.516	0.999789	1.02×10^{-4}
1612		7.691	0.999788	1.10
1575		7.871	0.999796	1.19
1539		8.055	0.999794	1.03×10^{-4}
1504		8.244	0.999782	9.80×10^{-5}
1470		8.436	0.999771	1.06×10^{-4}
1436		8.633	0.999766	1.14
1403		8.835	0.999765	1.22

TABLE I (*Continued*)

Aluminumn Arsenide

eV	cm^{-1}	Å	n	k
1371		9.041	0.999772	1.32
1340		9.253	0.999811	1.42×10^{-4}
1309		9.469	0.999801	2.76×10^{-5}
1280		9.690	0.999749	2.99
1250		9.917	0.999716	3.23
1222		10.15	0.999688	3.50
1167		10.63	0.999639	4.10
1114		11.13	0.999590	4.80
1064		11.66	0.999539	5.62
1016		12.21	0.999486	6.58
969.7		12.79	0.999429	7.70
925.9		13.39	0.999367	9.01×10^{-5}
884.1		14.02	0.999299	1.05×10^{-4}
844.2		14.69	0.999226	1.23
806.0		15.38	0.999147	1.44
769.7		16.11	0.999060	1.68
734.9		16.87	0.99897	1.95
701.7		17.67	0.99886	2.27
670.0		18.51	0.99875	2.63
639.8		19.38	0.99863	3.08
610.9		20.30	0.99850	3.58
583.3		21.26	0.99836	4.16
557.0		22.26	0.99820	4.83
531.8		23.31	0.99803	5.59
507.8		24.42	0.99785	6.47
484.9		25.57	0.99766	7.47
463.0		26.78	0.99745	8.63
442.1		28.05	0.99722	9.95×10^{-4}
422.1		29.37	0.99699	1.14×10^{-3}
403.0		30.76	0.99673	1.32
384.8		32.22	0.99646	1.51
367.5		33.74	0.99617	1.71
350.9		35.34	0.99585	1.96
335.0		37.01	0.99552	2.23
319.9		38.76	0.99516	2.55
305.5		40.59	0.99479	2.92
291.7		42.51	0.99441	3.34
278.5		44.52	0.99404	3.81
265.9		46.63	0.99368	4.33
253.9		48.83	0.99330	4.87
242.5		51.14	0.99289	5.48
231.5		53.56	0.99250	6.16
221.1		56.09	0.99210	6.95
211.1		58.74	0.99182	7.83
201.5		61.52	0.99156	8.65
192.4		64.43	0.99126	9.58×10^{-3}
183.7		67.48	0.99106	1.06×10^{-2}
175.5		70.67	0.99101	1.17
167.5		74.01	0.99093	1.26

TABLE I (*Continued*)

Aluminumn Arsenide

eV	cm^{-1}	Å	n	k
160.0		77.51	0.99087	1.37
152.7		81.17	0.99086	1.48
149.3		83.07	0.99092	1.54
145.8		85.01	0.99102	1.60
142.5		87.00	0.99112	1.65
139.3		89.03	0.99119	1.71
136.1		91.11	0.99128	1.76
133.0		93.24	0.99139	1.82
129.9		95.42	0.99153	1.88
127.0		97.66	0.99176	1.94
124.1		99.94	0.99212	2.00
121.2		102.3	0.99248	2.04
118.5		104.7	0.99273	2.07
115.8		107.1	0.99294	2.10
113.1		109.6	0.99312	2.14
110.5		112.2	0.99330	2.17
108.0		114.8	0.99349	2.20
105.5		117.5	0.99368	2.24
103.1		120.2	0.99389	2.27
100.8		123.0	0.99411	2.30
98.47		125.9	0.99435	2.33
96.22		128.9	0.99461	2.36
94.03		131.9	0.99484	2.38
91.88		134.9	0.99506	2.40
89.78		138.1	0.99532	2.42
87.73		141.3	0.99567	2.44
85.73		144.6	0.99627	2.44
83.77		148.0	0.99664	2.41
81.85		151.5	0.99686	2.38
79.99		155.0	0.99704	2.35
78.16		158.6	0.99726	2.32
76.37		162.3	0.99762	2.29
74.63		166.1	0.99847	2.26
72.92		170.0	1.00073	2.23
71.26		174.0	0.99803	1.43
69.63		178.1	0.99493	1.43
68.04		182.2	0.99292	1.42
66.49		186.5	0.99125	1.41
64.97		190.8	0.98960	1.39
63.49		195.3	0.98799	1.37
62.04		199.9	0.98635	1.35
60.62		204.5	0.98469	1.32
59.24		209.3	0.98292	1.30
57.88		214.2	0.98103	1.27
56.56		219.2	0.97903	1.25
55.27		224.3	0.97692	1.23
54.01		229.6	0.97470	1.21
52.77		234.9	0.97236	1.20
51.57		240.4	0.96977	1.18×10^{-2}

TABLE I (*Continued*)

Aluminumn Arsenide

eV	cm^{-1}	μm	n	k
5.6	45,167	0.2214	1.36[3]	2.75[3]
5.5	44,360	0.2254	1.36	2.89
5.4	43,554	0.2296	1.36	3.12
5.3	42,747	0.2339	1.53	3.40
5.2	41,940	0.2384	1.77	3.65
5.1	41,134	0.2431	2.16	3.86
5.0	40,327	0.2480	2.48	3.95
4.9	39,521	0.2630	2.92	4.04
4.8	38,714	0.2583	3.48	4.02
4.7	37,908	0.2638	3.96	3.70
4.6	37,101	0.2695	4.22	3.09
4.5	36,295	0.2755	4.18	2.63
4.4	35,088	0.2818	4.04	2.52
4.3	34,682	0.2883	4.01	2.52
4.2	33,875	0.2952	4.11	2.63
4.1	33,068	0.3024	4.47	2.68
4.0	32,262	0.3100	4.92	2.49
3.9	31,455	0.3179	5.35	2.15
3.8	30,649	0.3263	5.39	1.30
3.7	29,842	0.3351	4.99	0.752
3.6	29,036	0.3444	4.72	0.519
3.5	28,229	0.3542	4.48	0.334
3.4	27,423	0.3647	4.30	0.233
3.3	26,616	0.3757	4.13	0.139
3.2	25,810	0.3875	3.93	0.115
3.1	25,003	0.4000	3.77	0.113
3.0	24,196	0.4133	3.77	5.3×10^{-2}
3.15	25,406	0.3936		0.119[3]
3.12	25,205	0.3968		0.115
3.10	25,003	0.4000		0.113
3.075	24,801	0.4032		0.110
3.05	24,600	0.4065		0.106
3.025	24,398	0.4099		9.98×10^{-2}
3.00	24,196	0.4133		6.38
2.975	23,995	0.4168		3.15
2.95	23,793	0.4203		1.89
2.925	23,592	0.4239		1.18
2.90	23,390	0.4275		1.05
2.875	23,188	0.4313		1.03×10^{-2}
2.85	22,987	0.4305		9.93×10^{-3}
3.35	27,019	0.3701		1.38×10^{-2}[4]
3.3	26,616	0.3757		3.81×10^{-3}
3.25	26,213	0.3815		3.21
3.2	25,810	0.3875		2.43
3.1	25,003	0.4000		1.94
3.0	24,196	0.4133		1.79
2.9	23,390	0.4275	3.919[8]	1.67

TABLE I (*Continued*)

Aluminumn Arsenide

eV	cm^{-1}	μm	n	k
2.8	22,583	0.4428	3.703	1.61
2.7	21,777	0.4592	3.570	1.56
2.6	20,970	0.4769	3.472	1.53
2.5	20,164	0.4959	3.394	1.25×10^{-3}
2.4	19,357	0.5166	3.329	6.82×10^{-4}
2.3	18,551	0.5391	3.273	2.75×10^{-4}
2.2	17,744	0.5636	3.225	4.04×10^{-5}
2.1	16,938	0.5904	3.183	2.30×10^{-6}
2.0	16,131	0.6199	3.145	
1.9	15,324	0.6526	3.112	
1.8	14,518	0.6888	3.082	
1.7	13,711	0.7293	3.056	
1.6	12,905	0.7749	3.032	
1.5	12,098	0.8266	3.010	
1.4	11,292	0.8856	2.990	
1.3	10,485	0.9537	2.973	
1.2	9,679	1.033	2.957	
1.1	8,872	1.127	2.943	
1.0	8,065	1.157	2.930	
0.9	7,259	1.378	2.919	
0.8	6,452	1.550	2.909	
0.7	5,646	1.771	2.901	
0.6	4,839	2.066	2.894	
0.5	4,033	2.480	2.888	
2.218	17,889	0.5590	3.201[6]	
2.187	17,639	0.5669	3.189	
2.053	16,558	0.6039	3.139	
1.934	15,599	0.6411	3.102	
1.831	14,768	0.6771	3.072	
1.741	14,042	0.7121	3.049	
1.660	13,389	0.7469	3.029	
1.583	12,768	0.7832	3.012	
1.573	12,687	0.7882	3.009	
1.550	12,501	0.7999	3.005	
1.517	12,235	0.8173	2.999	
1.506	12,147	0.8233	2.995	
1.447	11,671	0.8568	2.983	
1.374	11,082	0.9024	2.970	
1.312	10,582	0.9450	2.960	
1.256	10,130	0.9871	2.951	
1.240	10,001	0.9999	2.948	
1.192	9,614	1.040	2.942	
1.033	8,332	1.200	2.919	
0.775	6,251	1.600	2.892	
0.620	5,001	2.000	2.876	
0.564	4,549	2.198	2.875	
0.2480	2,000	5.000	2.85[13,14]	
0.1860	1,500	6.667	2.84	

TABLE I (*Continued*)

Aluminumn Arsenide

eV	cm^{-1}	μm	n	k
0.1240	1,000	10.00	2.81	
0.1116	900	11.11	2.80	
0.09919	800	12.50	2.78	
0.08679	700	14.29	2.74	2.0×10^{-3} [13,14]
0.07439	600	16.67	2.67	4.3×10^{-3}
0.06199	500	20.00	2.47	1.4×10^{-2}
0.05579	450	22.22	2.18	4.0×10^{-2}
0.05331	430	23.26	1.90	7.7×10^{-2}
0.05207	420	23.81	1.67	0.12
0.05145	415	24.10	1.50	0.16
0.05083	410	24.39	1.27	0.23
0.05021	405	24.69	0.95	0.38
0.04959	400	25.00	0.60	0.78
0.04897	395	25.32	0.46	1.33
0.04835	390	25.64	0.45	1.87
0.04773	385	25.97	0.51	2.44
0.04711	380	26.32	0.63	3.12
0.04649	375	26.67	0.90	4.00
0.04587	370	27.03	1.57	5.25
0.04525	365	27.40	3.78	6.90
0.04486	361.8	27.64	6.87	6.25
0.04463	360	27.78	7.84	4.57
0.04401	355	28.17	6.99	1.59
0.04339	350	28.57	5.95	0.75
0.04215	340	29.41	4.90	0.29
0.04092	330	30.30	4.40	0.15
0.03968	320	31.25	4.11	9.5×10^{-2}
0.03844	310	32.26	3.91	6.5×10^{-2}
0.03720	300	33.33	3.78	4.7×10^{-2}
0.03100	250	40.00	3.44	1.5×10^{-2}
0.02480	200	50.00	3.31	7.3×10^{-3}

[a] References are indicated in brackets.

Aluminum Antimonide (AlSb)

DAVID F. EDWARDS and RICHARD H. WHITE
University of California
Lawrence Livermore National Laboratory
Livermore, California

The refractive index, n, and the extinction coefficient, k, of AlSb have been measured for a limited number of samples. The two main reasons for this are that large high-quality single crystals are difficult to grow, and the surface of AlSb reacts rapidly with the atmosphere to produce a relatively thick contaminated layer.

One method for measuring the optical properties (n and k) of semiconductors, especially for the UV and visible regions, is spectroscopic ellipsometry. However, as pointed out by Aspnes and Studna [1] and Zollner *et al.* [2], contamination-free surfaces are needed for precise ellipsometric measurements. Using the wet-chemical etching procedures of Ref. [1], Zollner *et al.* have obtained AlSb surfaces of sufficient quality for ellipsometric measurements at room temperature from 5.8–1.4 eV. They report n and k values calculated from the measured pseudo-dielectric function. This is called the pseudo-dielectric function because no corrections were made for any surface overlayers that may be present. For surfaces free of these overlayers or by making the appropriate corrections, the ellipsometric measurements would give the "true" dielectric function. In either case, the n and k values for the near UV and visible regions are calculated from the ellipsometric measurements.

Strossner *et al.* [3] have measured the dependence of the energy gap absorptance of AlSb at room temperature for hydrostatic pressures from atmospheric up to the phase change at about 8 GPa. We have extracted the extinction coefficient from the atmospheric-pressure absorption coefficient for the energy range 2.2–1.4 eV.

Oswald and Schade [4] were among the first to report n and k value for AlSb in the infrared region. They simultaneously measured the transmittance and reflectance of a 1 Ω-cm p-type sample from about 1–15 μm. From these data they calculated n and k. They make no report of surface contamination effects and give only a plot of n and k. Their k values increase monotonically with wavelength indicating free-carrier absorption.

Copyright © 1991 by Academic Press.
l rights of reproduction in any form reserved.
ISBN 0-12-544422-2

This, coupled with the small resistivity and possible surface contamination are reasons for excluding the Oswald–Schade data from the table that follows.

Turner and Reese [5] have measured the reflectance of room-temperature AlSb between 16 μm and 40 μm, which includes the infrared lattice reflectance band. By fitting their reflectance data to the classical dispersion theory [6], they calculated n and k values for the 20–38 μm spectral region. Their method is similar to that used by Spitzer, Kleinman, and Walsh [7] for SiC, and by Kleinman and Spitzer [8] for GaP. In the classical dispersion theory of solids [6], the susceptibility χ and conductivity σ in the neighborhood of a resonance frequency ν_o are given by

$$\chi = \rho \frac{1-\nu^2}{(1-\nu^2)^2+(\gamma\nu)^2} \tag{1}$$

and

$$\frac{\sigma}{\nu} = 2\pi\rho \frac{\gamma\nu}{(1-\nu^2)^2+(\gamma\nu)^2}, \tag{2}$$

where ν is the measured frequency divided by ν_o, σ is the conductivity divided by ν_o, and γ and ρ are dimensionless parameters. In the Lorentz theory, ρ is given by

$$\rho = \frac{Ne^2}{4\pi^2 m^* \nu_0^2}, \tag{3}$$

where N is the concentration of ion pairs, and m^* is their reduced mass. The dielectric constant is

$$\varepsilon = \varepsilon_0 + 4\pi\chi, \tag{4}$$

where ε_o is the high-frequency ($\nu >> 1$) dielectric constant. The four parameters (ε_o, ν_o, ρ, γ) were adjusted [5] for the best least-squares fit of the reflectance data to a single resonance. From these parameters the index of refraction and the extinction coefficient, n and k, are calculated from

$$n^2 = \tfrac{1}{2}[\varepsilon^2 + 4(\sigma/\nu)^2]^{1/2} + \varepsilon \tag{5}$$

and

$$k^2 = \tfrac{1}{2}[\varepsilon^2 + 4(\sigma/\nu)^2]^{12} - \varepsilon. \tag{6}$$

Turner and Reese [5] give the following values for their four parameters:

$$\nu_0 = (9.564 \pm 0.019) \times 10^{12}\ \text{sec}^{-1}$$

$$\rho = 0.1060 \pm 0.0005$$

$$\gamma = 0.0059 \pm 0.0005$$

$$\varepsilon_0 = 9.880 \pm 0.12.$$

Hass and Henvis [9] measured the fundamental reflection band of six III-V compound semiconductors at liquid helium-temperature. AlSb was one of the materials measured. They evaluated the oscillator parameters by comparing their measured reflectance with that calculated using the classical dispersion theory of Born and Huang [10]. The four parameters as found by Hass and Henvis are

$$\omega_0 = 318\ \text{cm}^{-1}$$

$$\varepsilon_\infty = 10.24$$

$$\varepsilon_0 - \varepsilon_\infty = 1.8$$

$$\gamma/\omega_0 = 0.02.$$

The n and k values are calculated using these parameters and the dispersion formulas of Ref. [10].

Pikhtin and Yas'kov [11] report a semiempirical method for calculating the dispersion of the refractive index using three adjustable parameters associated with the energy-band structure. For AlSb they use the data of Oswald and Schade [4] to evaluate the three adjustable parameters. Test calculations by one of us [12] and a comparison of their predictions to the data of Refs. [5] and [9] indicate that the indices are sensitively dependent on the values of the three parameters. It appears that indices over a spectral range broader than that of Ref. [4] are needed to improve the accuracy of the Pikhtin–Yas'kov calculated data for AlSb.

The indices of refraction and extinction coefficients for AlSb are given in

Table I and plotted in Fig. 1. Most of the data are for room temperature except those of Hass and Henvis [9], which are at liquid-helium temperature. The n and k values from 5.8 eV to 2.1 eV are the ellipsometrically measured data of Zollner *et al.* [2]. The k values for the absorption-edge region (2.2–1.4 eV) are calculated from the measured absorption coefficients of Strossner *et al.* [3]. The n values from 2.1 eV to 0.529 eV [0.5905 μm to 23 μm) were calculated from a Herzberger-type dispersion formula fit to the data of Refs. [2] and [5]. A total of 16 data points were used. As seen in Table I below, the index data in the 2.3–2.1 eV region has a slope discontinuity due to an interband critical point [2]. Data for energies greater than 2.1 eV were therefore not included in the dispersion-formula fit. The indices for wavelengths greater than 23 μm were also not included in the fit because of the onset of the infrared lattice band.

The Herzberger-type dispersion formula is [13]

$$n = A + BL + CL^2 + D\lambda^2 + E\lambda^4,$$

where $L = 1/(\lambda^2 - 2.8 \times 10^6)$ with the wavelength in angstroms. As explained by Herzberger and Salzberg [13], 2.8×10^6 is the square of the mean asymptote for the short-wavelength abrupt increase in the index for 14 materials (AlSb not included). For the 16 points from 0.5905 μm to 23 μm and at room temperature, the coefficients are

$$A = 3.204093$$

$$B = 1.874871 \times 10^7$$

$$C = 2.205306 \times 10^{14}$$

$$D = -4.144419 \times 10^{12}$$

$$E = -3.199325 \times 10^{-23}$$

The RMS error between the measured values and the dispersion-formula calculated indices is 0.179%.

For the reader's convenience, the same 16 indices were also fit to the modified Sellmeier-type dispersion formula [14]:

$$n^2 = 1 + A/(\lambda^2 - B) + C\lambda^2/(\lambda^2 - D),$$

where the wavelength λ is in angstroms. For the 16 data points, the coefficients are

$$A = 4.094753 \times 10^{-5}$$

$$B = -7.086745 \times 10^{-5}$$

$$C = 4.198623$$

$$D = 1.925813 \times 10^{-9}.$$

The RMS error is 0.371%.

The room-temperature n and k values of Table I from 25 μm to 100 μm were calculated from Eqs. 1–6 using the four parameters of Ref. [5]. These calculations were extended beyond the range of measurement to 100 μm in order to estimate ε_o ($=n^2$). The room-temperature measurements of Ref. [5] give $\varepsilon_o = 9.88$, compared with $n^2 = 11.36$ at 100 μm. At liquid-helium temperature (Ref. [9]) the parameter fit gives $\varepsilon_o = 12.04$, compared with $n^2 = 12.24$ at 100 μm.

Ghosh *et al.* [15] have developed a simple model for predicting the temperature and pressure coefficients of the refractive index of some zinc-blende semiconductors, AlSb included. They predict the temperature coefficient at constant pressure to be

$$\left(\frac{dn}{dT}\right)_p = 1.19 \times 10^{-4}\,\mathrm{K}^{-1}.$$

No wavelength or temperature range is given.

The pressure coefficient is predicted to be

$$-\left(\frac{dn}{dP}\right)_T = 34.10 \times 10^{-3}\,\mathrm{GPa}^{-1}.$$

No wavelength or pressure range is given. They have no measured data with which they can evaluate the accuracy of these predictions.

REFERENCES

1. D. E. Aspnes and A. A. Studna, "Dielectric Functions and Optical Parameters of Si, Ge, GaP, GaAs, GaSb, InP, InAs, and InSb from 1.5 to 6.0 eV," *Phys. Rev.* **B27**, 985 (1983).

2. S. Zollner, C. Lin, E. Schönherr, A. Böhringer, and M. Cardona, "The Dielectric Function of AlSb from 1.4 to 5.8 eV Determined by Spectroscopic Ellipsometry," *J. Appl. Phys.* **66**, 383 (1989).
3. K. Strossner, S. Ves, Chul Koo Kim, and M. Cardona, "Dependence of the Direct and Indirect Gap of AlSb on Hydrostatic Pressure," *Phys. Rev. B* **33** (6), 4044 (1986).
4. F. Oswald and R. Schade, "Über die Bestimmung der Optischen Kunstanten von Halbleitern des Typus $A^{III}B^{V}$ in Infraroten," *Z. Naturforsch.* **9a**, 611 (1954).
5. W. J. Turner and W. E. Reese, "Infrared Lattice Bands in AlSb," *Phys. Rev.* **127** (1), 126 (1962).
6. F. Seitz, "Modern Theory of Solids," McGraw-Hill, New York, Chap. 17 (1940).
7. W. G. Spitzer, D. Kleinman, and D. Walsh, "Infrared Properties of Hexagonal Silicon Carbide," *Phys. Rev.* **113** (1), 127 (1959).
8. D. A. Kleinman and W. G. Spitzer, "Infrared Lattice Absorption of GaP," *Phys. Rev.* **118** (1), 110 (1960).
9. M. Hass and B. W. Henvis, "Infrared Lattice Reflectance Spectra of III-V Compound Semiconductors," *J. Phys. Chem. Solids* **23**, 1099 (1962).
10. M. Born and K. Huang, "Dynamical Theory of Crystal Lattices," University Press, Oxford, Chap. II (1954).
11. A. N. Pikhtin and A. D. Yas'kov, "Dispersion of the Refractive Index of Semiconductors with Diamond and Zinc-blende Structures," *Sov. Phys. Semicond.* **12**, 622 (1978).
12. D. F. Edwards, 1989 (unpublished).
13. M. Herzberger and C. D. Salzberg, "Refractive Indices of Infrared Optical Materials and Color Correction of Infrared Lenses," *J. Opt. Soc. Am.* **52**, 420 (1962); M. Herzberger, "Colour Correction in Optical Systems and a New Dispersion Formula," *Opt. Acta* **6**, 197 (1959).
14. D. F. Edwards and R. H. White, see KDP in this volume.
15. D. K. Ghosh, L. K. Samanata, and G. C. Bahr, "The Temperature and Pressure Dependence of Refractive Indices of Some III-V and II-VI Binary Semiconductors," *Infrared Physics* **26**, 111 (1986).

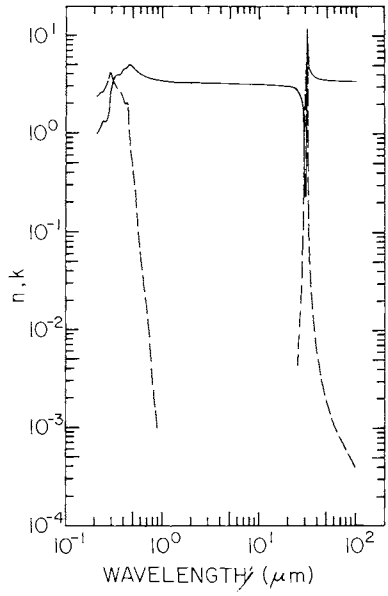

Fig. 1. Log–log plot of n (solid line) and k (dashed line) versus wavelength in micrometers for aluminum antimonide.

TABLE I

Values of *n* and *k* for Aluminum Antimonide at 300 K from Various References[a]

eV	cm^{-1}	μm	n	n_c	k	k
5.8	46,774	0.2138	1.00[2]		2.40[2]	
5.7	45,968	0.2175	1.01		2.42	
5.6	45,161	0.2214	1.04		2.46	
5.5	44,355	0.2255	1.09		2.52	
5.4	43,548	0.2296	1.17		2.58	
5.3	42,742	0.2340	1.26		2.59	
5.2	41,935	0.2385	1.31		2.58	
5.1	41,129	0.2431	1.31		2.59	
5.0	40,323	0.2480	1.30		2.64	
4.9	39,516	0.2531	1.29		2.72	
4.8	38,710	0.2583	1.30		2.84	
4.7	37,903	0.2638	1.33		2.99	
4.6	37,097	0.2696	1.38		3.16	
4.5	36,290	0.2756	1.45		3.39	
4.4	35,484	0.2818	1.59		3.70	
4.3	34,677	0.2884	1.96		4.07	
4.2	33,871	0.2952	2.60		4.22	
4.1	33,065	0.3024	3.15		4.00	
4.0	32,258	0.3100	3.50		3.71	
3.9	31,452	0.3179	3.71		3.40	
3.8	30,645	0.3263	3.81		3.16	
3.7	29,839	0.3351	3.93		2.97	
3.6	29,032	0.3444	3.96		2.81	
3.5	28,226	0.3543	3.95		2.69	
3.4	27,419	0.3647	3.97		2.64	
3.3	26,613	0.3758	4.14		2.69	
3.2	25,806	0.3875	4.51		2.47	
3.1	25,000	0.4000	4.57		2.12	

3.0	24,194	0.4133	4.52		1.97	
2.9	23,387	0.4276	4.66		2.06	
2.8	22,581	0.4429	5.27		1.58	
2.7	21,774	0.4593	5.08		0.92	
2.6	20,968	0.4769	4.81		0.63	
2.5	20,161	0.4960	4.61		0.46	
2.4	19,355	0.5167	4.44		0.33	
2.3	18,548	0.5391	4.31		0.24	
2.2	17,742	0.5636	4.20		1×10^{-2}	1.2×10^{-2} [3]
2.1	16,935	0.5905	4.01		6×10^{-3}	6.2×10^{-3}
2.0	16,129	0.6200		3.9036	4×10^{-3}	3.9×10^{-3}
1.9	15,323	0.6526		3.8143	3×10^{-3}	2.3×10^{-3}
1.8	14,516	0.6889		3.7343	2×10^{-3}	1.4×10^{-3}
1.7	13,710	0.7294		3.6626	1×10^{-3}	6.3×10^{-4}
1.6	12,903	0.7750		3.5985	3×10^{-4}	3.1×10^{-4}
1.5	12,097	0.8267		3.5412	2×10^{-4}	3.3×10^{-4}
1.4	11,290	0.8857		3.4901	1×10^{-4}	
1.3	10,484	0.9538		3.4447		
1.2	9,677	1.033		3.4044		
1.1	8,871	1.127		3.3687		
1.0	8,064	1.240		3.3373		
0.9	7,258	1.378		3.3099		
0.8	6,452	1.550		3.2860		
0.7	5,645	1.771		3.2654		
0.6	4,839	2.067		3.2477		
0.5	4,032	2.480		3.2327		
0.4	3,226	3.100		3.2199		
0.3	2,419	4.133		3.2080		
0.2	1,613	6.200		3.1926		
0.1	806.5	12.40		3.1340		
0.09	725.9	13.78		3.1149		
0.08	645.2	15.50		3.0868		
0.07	564.6	17.71		3.0431		
0.06	483.9	20.67		2.9692		
0.05	403.3	24.80		2.8285		

(continued)

TABLE I (*Continued*)

Aluminumn Antimonide

eV	cm^{-1}	μm	n	n_c	k	k
0.04959	400.0	25.0	2.75 [5]		5.4×10^{-3} [5]	
0.04769	384.6	26.0	2.64		8.7×10^{-3}	
0.04592	370.4	27.0	2.46	2.28 [9]	0.0151	0.0719 [9]
0.04558	367.6	27.2	2.42	2.22	0.0172	0.0824
0.04525	365.0	27.4	2.37	2.15	0.0197	0.0952
0.04492	362.3	27.6	2.31	2.06	0.0227	0.111
0.04460	359.7	27.8	2.24	1.96	0.0265	0.132
0.04428	357.1	28.0	2.16	1.85	0.0313	0.159
0.04397	354.6	28.2	2.07	1.72	0.0375	0.196
0.04336	352.1	28.4	1.96	1.55	0.0457	0.249
0.04347	359.7	28.6	1.83	1.35	0.0572	0.331
0.04305	347.2	28.8	1.66	1.11	0.0742	0.475
0.04275	344.8	29.0	1.44	0.840	0.102	0.740
0.04246	342.5	29.2	1.13	0.663	0.157	1.12
0.04217	340.1	29.4	0.633	0.594	0.344	1.53
0.04189	337.8	29.6	0.276	0.583	0.992	1.93
0.04161	335.6	29.8	0.225	0.610	1.56	2.34
0.04133	333.3	30.0	0.224	0.669	2.09	2.77
0.04106	331.1	30.2	0.247	0.769	2.64	3.24
0.04079	328.9	30.4	0.294	0.925	3.25	3.78
0.04052	326.8	30.6	0.382	1.18	4.01	4.41
0.04026	324.7	30.8	0.557	1.60	5.02	5.17
0.04013	323.6	30.9	0.718	1.93	5.70	5.62
0.04000	322.6	31.0	0.987	2.39	6.58	6.09
0.03987	321.5	31.1	1.50	3.04	7.80	6.58
0.03974	320.5	31.2	2.67	3.95	9.56	6.98
0.03962	319.5	31.3	6.13	5.16	11.7	7.12
0.03949	318.5	31.4	12.1	6.53	8.43	6.74
0.03937	317.5	31.5	11.3	7.62	3.37	5.75

0.03924	316.5	31.6	9.57	8.13	1.67	4.50
0.03912	315.5	31.7	8.39	8.13	1.00	3.39
0.03899	314.5	31.8	7.60	7.88	0.676	2.57
0.03887	313.5	31.9	7.02	7.55	0.491	1.98
0.03875	312.5	32.0	6.59	7.23	0.376	1.57
0.03757	303.0	33.0	4.86	5.40	0.0824	0.361
0.03647	294.1	34.0	4.34	4.75	0.0377	0.165
0.03542	285.7	35.0	4.08	4.42	0.0223	0.0977
0.03444	277.8	36.0	3.93	4.22	0.0150	0.0660
0.03351	270.3	37.0	3.82	4.09	0.0110	0.0484
0.03262	263.2	38.0	3.75	3.99	8.5×10^{-3}	0.0375
0.03100	250.0	40.0	3.65	3.87	5.7×10^{-3}	0.0250
0.02755	222.2	45.0	3.53	3.71	2.9×10^{-3}	0.0129
0.02480	200.0	50.0	3.48	3.64	1.9×10^{-3}	8.5×10^{-3}
0.02066	166.7	60.0	3.42	3.57	1.1×10^{-3}	5.0×10^{-3}
0.01771	142.9	70.0	3.40	3.53	8.1×10^{-4}	3.6×10^{-3}
0.01550	125.0	80.0	3.38	3.52	6.4×10^{-4}	2.8×10^{-3}
0.01378	111.1	90.0	3.38	3.51	5.2×10^{-4}	2.3×10^{-3}
0.01240	100.0	100.0	3.37	3.50	4.5×10^{-4}	2.0×10^{-3}

[a] The column headed n_c contains refractive index values calculated with the Herzberger-type formula. The bracketed numbers indicate the reference to the data.

Aluminum Gallium Arsenide ($Al_xGa_{1-x}As$)

O. J. GLEMBOCKI
Naval Research Laboratory
Washington, D.C.
and
KENICHI TAKARABE
Department of Natural Science
Okayama University of Science
Okayama-City
Okayama 700, Japan

The $Al_xGa_{1-x}As$ system is technologically one of the most important alloy systems, especially when combined with GaAs. It forms the basis of quantum-well, superlattice, and single-barrier device structures, which in turn have a significant effect on high-speed electro-optics. Because of this, it would be of the utmost importance to have the optical constants, n and k, over a wide spectral range and over the concentration range of $x=0$ to $x=1$, in as narrowly spaced x intervals as possible, preferably $\Delta x=0.1$. This, however, is not the case. In fact, we could find only bits and pieces of data at almost random values of x over narrow spectral ranges, except for $x=0.3$.

There is, however, a fair amount of information about other physical parameters such as lattice constant, density, band gap, and phonon frequency. Because these parameters are useful in many applications, we list Adachi's values [1] for these most commonly used ones:

1. Lattice constant (Å) $a=5.6533+0.0078x$;
2. Density (gm/cm^3) $g=5.36-1.6x$;
3. Band gap (eV) $E_g=1.424+1.247x \quad (0<x<0.45)$
$=1.900+0.125x+0.143x^2 \quad (0.45<x<1.0)$;
4. LO phonon energy (meV) $\hbar\omega(\text{GaAs})=36.25-6.55x+1.79x^2$
$\hbar\omega(\text{AlAs})=44.63+8.78x-3.32x^2$;
5. TO phonon energy (meV) $\hbar\omega(\text{GaAs})=33.29-0.64x-1.16x^2$
$\hbar\omega(\text{AlAs})=44.63+0.55x-0.30x^2$.

We were able to find only one value of $x=0.3$ (within a typical

Copyright © 1991 by Academic Press.
All rights of reproduction in any form reserved.
ISBN 0-12-544422-2

uncertainty of ±0.01) where UV, VIS, and IR data have been analyzed to give n and k. Otherwise, there are spectroscopic-ellipsometry data for n and k in the range of 6–1.5 eV for a number of x values near tenths [2], IR reststrahlen data for n and k from 1000–100 cm^{-1} for other values of x [3] and some measurements [4] and calculations [1, 5] of n from 2.5–0.5 eV. In Table I we display the values of x for which we found spectroscopic data in the various photon-energy ranges. It is clear that near $x = 0.3$, we have data for a wide wavelength range, but for other values of x, only data in the visible or IR are available.

In Table II we list n and k data for the values of x noted in Table I. In Fig. 1 we have plotted the values of the optical constants for $x = 0.3$. It is important to note that the end member GaAs ($x = 0$) was previously treated in *HOC I* [6], and that AlAs ($x = 1$) is discussed separately in this volume [7].

In the X-ray region from 10,000–51.5 eV (1.24–240 Å) there are no experimental data. The numbers for $x = 0.3$ listed in Table II were calculated using the Henke model [8, 9]. This model, based on calculated atomic scattering cross-sections, requires a knowledge of the density of $Al_{0.3}Ga_{0.7}As$, which is given by Adachi [1] to be $g(0.3) = 4.88$. The absorption edges of the atomic constituents are $K(Al) = 1559.88$ eV, $K(Ga) = 10368.2$ eV, $K(As) = 11865$ eV, $L_1(Al) = 87.01$ eV, $L_1(As) = 1529.3$ eV, $L_{2,3}(Al) = 72.78$ eV, $L_{2,3}(Ga) = 1145.0$, 1116.9 eV, $L_{2,3}(As) = 1358.7$, 1323.5 eV. The lower-lying energies may be perturbed by the bonding properties of the crystal material. It should be noted that this calculation can be used for any value of x provided that the parameters listed above are appropriately adjusted.

There appear to be no reflectivity data that would yield n and k in the ultraviolet down to 6 eV.

Aspnes *et al.* [2] measured n and k from 6–1.5 eV by spectroscopic ellipsometry from samples close to tenths in x. Values of x are usually determined by X-ray analysis to ±0.01. Care was taken to remove or account for the native oxide on the surface.

Interestingly, we find little data for the absorption coefficient at the band edge, presumably because the alloy samples are always on a GaAs substrate with a band gap smaller than the alloy film. This requires a reflection experiment or, for transmission, an etching process to remove the substrate but still support the film.

Below the fundamental band gap E_g, n has been measured for a number of x values [4]. Jensen [5] has developed a model to calculate n in the transparent region for ternary and quaternary semiconductors. Adachi [1] has used a different model to calculate n below the band gap. We have used both models for $x = 0.14$ to determine n and list the values in Table II. In the overlap region (1.2–1.5 eV) agreement is to ~1% at lower energies and increases to ~2% at higher energies. The Adachi calculation does not

seem to work well as E_g is neared, whereas the Jensen calculation is applicable much closer to E_g, even showing a plateauing of the n values. In addition, we have used the latter model [1] to calculate n below the respective band gaps for the tenth values of x, and we list them in Table II. It is also reported that the n values at 0.9 μm below all the band gaps vary linearly with x; $\Delta n = n(Al_xGa_{1-x}As) - n(GaAs) = 0.62x$ [10].

The n and k values in the far infrared for $Al_xGa_{1-x}As$ were obtained by fitting the reflectivity data [3] taken near normal incidence, that is, within approximately a 10° angle of incidence. The $Al_xGa_{1-x}As$ samples were grown by an isothermal liquid-phase-epitaxy (LPE) technique for x values ranging from 0 to 0.54. All materials had n-type carrier concentrations of less than $5 \times 10^{16}\,cm^{-3}$. The free-carrier plasma edge was not observed for $v > 50\,cm^{-1}$. The alloy compositions were evaluated by analysis of X-ray emission produced from the layer by the electron beam of an ARL model EMX-SM electron-probe microanalyzer. The accuracy of the composition measured was estimated to be within 2%; for example, $\Delta x = \pm 0.01$ for $x = 0.54$.

The optical phonons of the $Al_xGa_{1-x}As$ behave as the two-mode type [11–13]. The n and k values were calculated by the factorized form of the classical dispersion equation

$$(\nu) = (n + ik)^2 = \frac{(\nu_{11}^2 - \nu^2 - i\nu\gamma_{11})(\nu_{12}^2 - \nu^2 - i\nu\gamma_{12})}{(\nu_{t1}^2 - \nu^2 - i\nu\gamma_{t1})(\nu_{t2}^2 - \nu^2 - i\nu\gamma_{t2})}$$

where ν_{ti}, ν_{li}, γ_{ti}, and γ_{li} denote TO frequency, LO frequency, TO damping constant, and LO damping constant, respectively. The indexes $i = 1$ and $i = 2$ identify the parameters for the GaAs-like and the AlAs-like modes, respectively. Those values referred to are shown in Table III [10]. The n and k values are tabulated in the region of 5–100 μm in Table II.

ACKNOWLEDGMENTS

We thank W. R. Hunter for the calculation of n and k in the X-ray region with the Henke model.

REFERENCES

1. S. Adachi, *J. Appl. Phys.* **58**, R1 (1985).
2. D. E. Aspnes, S. M. Kelso, R. A. Logan, and R. Bhat, *J. Appl. Phys.* **60**, 754 (1986).
3. O. K. Kim and W. G. Spitzer, *J. Appl. Phys.* **50**, 4362 (1979).
4. H. C. Casey, Jr., D. D. Sell, and M. B. Panish, *Appl. Phys. Lett.* **24**, 63 (1974).
5. B. Jensen, chapter in this volume and references therein.
6. E. D. Palik, in "Handbook of Optical Constants of Solids," (E. D. Palik, ed.), Academic Press, Orlando, 429 (1985).

7. E. D. Palik, O. J. Glembocki, and K. Takarabe, AlAs critique in this volume.
8. B. L. Henke, P. Lee, T. J. Tanaka, R. L. Shimabukuro, and B. K. Fujikama, *At. Data Nucl. Data Tables* **27**, 1 (1982).
9. B. L. Henke, J. C. Davis, E. M. Gullikson, and R. C. C. Perera, Lawrence Berkeley Laboratory Report No. LBL-26259 (1988).
10. H. Kressel and J. K. Butler, in "Semiconductors Lasers and Heterojunction LED's," Academic Press, New York, 413 (1977).
11. D. W. Taylor, in "Optical Properties of Mixed Crystals," (R. J. Elliot and I. P. Ipotova, eds.), North-Holland, Amsterdam, 35 (1988).
12. R. Bonneville, *Phys. Rev.* **B29**, 907 (1984).
13. A. S. Barker, Jr., and A. J. Sievers, *Rev. Mod. Phys.* **47**, Suppl. No. 2, S143 (1975).

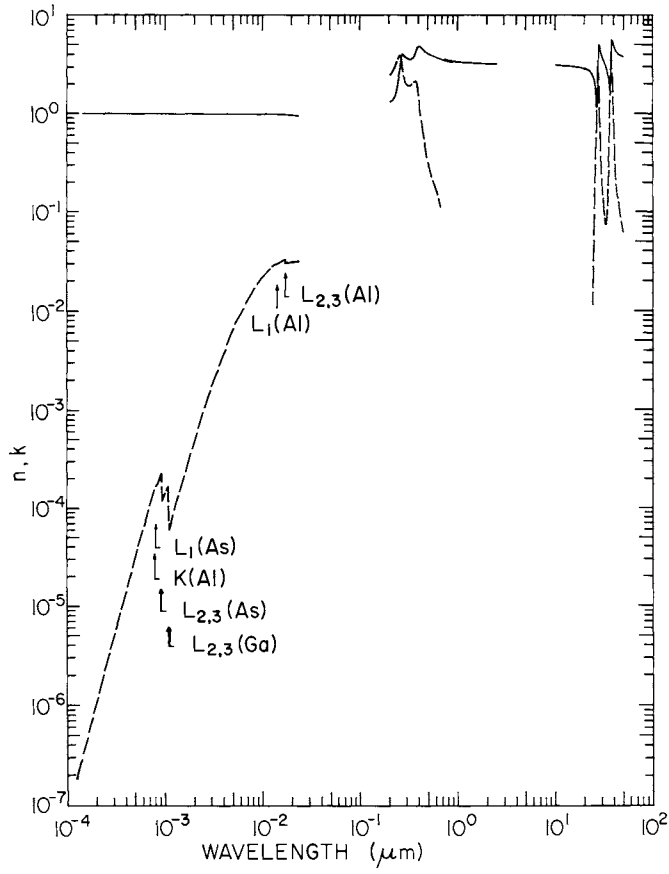

Fig. 1. Log–log plot of n (solid line) and k (dashed line) versus wavelength in micrometers for $Al_xGa_{1-x}As$ with $x = 0.31 \pm 0.01$.

TABLE I

Values of x for Which Spectroscopic Data for n and k Are Presented in the Various References

x	X-RAY–UV (10000–51 eV) n & k	UV–VIS (6–1.5 eV) n & k	Near IR (2.7–0.5 eV) n	Far IR (1000–200 cm^{-1}) n & k
0	[6]	[6]	[6]	[6] See *HOC I*
0.099		[2]		
0.1			[1]	
0.14			[1, 5]	[3]
0.18				[3]
0.198		[2]		
0.2			[1]	
0.30	[8, 9]		[1]	[3]
0.315		[2]		
0.36				[3]
0.4			[1]	
0.419		[2]		
0.44				[3]
0.491		[2]		
0.5			[1]	
0.54				[3]
0.590		[2]		
0.6			[1]	
0.700		[2]	[1]	
0.8			[1]	
0.804		[2]		
0.9			[1]	
1.0	[7]	[7]	[7]	[7] See *HOC II*

TABLE II

Value of n and k for $Al_{0.3}Ga_{0.7}As$ (X-RAY-UV) from Various References[a]

eV	cm^{-1}	Å	n	k
10000		1.240	0.99999150[8,9]	1.74×10^{-7}[8,9]
9772		1.269	0.99999110	1.90
9331		1.329	0.99999010	2.27
8909		1.392	0.9999891	2.71
8507		1.458	0.9999880	3.23
8123		1.526	0.9999868	3.85
7756		1.599	0.9999854	4.59
7406		1.674	0.9999840	5.46
7072		1.753	0.9999824	6.50
6752		1.836	0.9999806	7.73
6447		1.923	0.9999787	9.20×10^{-7}
6156		2.014	0.9999766	1.09×10^{-6}
5878		2.109	0.9999743	1.30
5613		2.209	0.9999717	1.55
5359		2.314	0.9999689	1.84
5117		2.423	0.9999658	2.18
4886		2.538	0.9999624	2.59
4665		2.658	0.9999587	3.08
4455		2.783	0.9999546	3.66
4254		2.915	0.9999501	4.34
4062		3.053	0.9999452	5.15
3878		3.197	0.9999399	6.11
3703		3.348	0.9999340	7.24
3536		3.506	0.9999275	8.59×10^{-6}
3376		3.672	0.9999205	1.02×10^{-5}
3224		3.846	0.9999128	1.21
3078		4.028	0.9999044	1.43
2939		4.218	0.999895	1.69
2807		4.418	0.999885	2.00
2680		4.627	0.999875	2.37
2559		4.846	0.999863	2.80
2443		5.075	0.999850	3.30
2333		5.315	0.999837	3.90
2228		5.566	0.999822	4.60
2127		5.829	0.999807	5.42
2031		6.105	0.999791	6.38
1939		6.394	0.999774	7.49
1852		6.696	0.999757	8.80×10^{-5}
1768		7.013	0.999739	1.03×10^{-4}
1688		7.344	0.999723	1.21
1612		7.691	0.999710	1.42
1575		7.871	0.999708	1.53
1539		8.055	0.999706	1.58
1504		8.244	0.999697	1.58
1470		8.436	0.999687	1.70
1436		8.633	0.999683	1.83
1403		8.835	0.999683	1.98
1371		9.041	0.999692	2.14
1340		9.253	0.999735	2.31

TABLE II (*Continued*)

$Al_{0.3}Ga_{0.7}As$ (X-RAY-UV)

eV	cm^{-1}	Å	n	k
1309		9.469	0.999732	1.23
1280		9.690	0.999684	1.21
1250		9.917	0.999652	1.29
1222		10.15	0.999629	1.38
1194		10.39	0.999612	1.47
1167		10.63	0.999601	1.57
1140		10.88	0.999603	1.67×10^{-4}
1114		11.13	0.999635	6.37×10^{-5}
1088		11.39	0.999554	6.88
1064		11.66	0.999503	7.43
1039		11.93	0.999461	8.02
1016		12.21	0.999421	8.66×10^{-5}
969.7		12.79	0.999342	1.01×10^{-4}
925.9		13.39	0.999261	1.18
884.1		14.02	0.999175	1.38
844.2		14.69	0.999083	1.61
806.0		15.38	0.99898	1.88
769.7		16.11	0.99888	2.21
734.9		16.87	0.99876	2.59
701.7		17.67	0.99863	3.03
670.0		18.51	0.99850	3.54
639.8		19.38	0.99835	4.12
610.9		20.30	0.99819	4.79
583.3		21.26	0.99802	5.55
557.0		22.26	0.99784	6.43
531.8		23.31	0.99764	7.45
507.8		24.42	0.99743	8.59
484.9		25.57	0.99720	9.89×10^{-4}
463.0		26.78	0.99695	1.14×10^{-3}
442.1		28.05	0.99669	1.31
422.1		29.37	0.99641	1.50
403.0		30.76	0.99611	1.73
384.8		32.22	0.99581	1.97
367.5		33.74	0.99548	2.24
350.9		35.34	0.99513	2.55
335.0		37.01	0.99476	2.90
319.9		38.76	0.99438	3.30
305.5		40.59	0.99401	3.75
291.7		42.51	0.99361	4.23
278.5		44.52	0.99321	4.77
265.9		46.63	0.99283	5.36
253.9		48.83	0.99243	6.00
242.5		51.14	0.99203	6.69
231.5		53.56	0.99163	7.44
221.1		56.09	0.99125	8.29
211.1		58.74	0.99096	9.20×10^{-3}
201.5		61.52	0.99069	1.01×10^{-2}
192.4		64.43	0.99035	1.10
183.7		67.48	0.99008	1.20
175.5		70.67	0.98988	1.31

TABLE II (*Continued*)

$Al_{0.3}Ga_{0.7}As$ (X-RAY-UV)

eV	cm^{-1}	Å	n	k
167.5		74.01	0.98966	1.41
160.0		77.51	0.98947	1.53
152.7		81.17	0.98931	1.65
149.3		83.07	0.98928	1.71
145.8		85.01	0.98930	1.78
142.5		87.00	0.98933	1.84
139.3		89.03	0.98937	1.90
136.1		91.11	0.98941	1.95
133.0		93.24	0.98942	2.01
129.9		95.42	0.98944	2.07
127.0		97.66	0.98948	2.13
124.1		99.94	0.98956	2.19
121.2		102.3	0.98967	2.24
118.5		104.7	0.98972	2.30
115.8		107.1	0.98978	2.35
113.1		109.6	0.98985	2.40
110.5		112.2	0.98994	2.45
108.0		114.8	0.98999	2.50
105.5		117.5	0.99001	2.54
103.1		120.2	0.99002	2.59
100.8		123.0	0.99003	2.64
98.47		125.9	0.99005	2.68
96.22		128.9	0.99007	2.72
94.03		131.9	0.99002	2.76
91.88		134.9	0.98995	2.80
89.78		138.1	0.98988	2.84
87.73		141.3	0.98983	2.89
85.73		144.6	0.98987	2.92
83.77		148.0	0.98978	2.95
81.85		151.5	0.98962	2.97
79.99		155.0	0.98942	3.00
78.16		158.6	0.98924	3.03
76.37		162.3	0.98909	3.06
74.63		166.1	0.98911	3.09
72.92		170.0	0.98957	3.12
71.26		174.0	0.98850	2.91
69.63		178.1	0.98727	2.94
68.04		182.2	0.98637	2.97
66.49		186.5	0.98554	2.99
64.97		190.8	0.98462	3.00
63.49		195.3	0.98370	3.01
62.04		199.9	0.98272	3.02
60.62		204.5	0.98162	3.02
59.24		209.3	0.98038	3.01
57.88		214.2	0.97898	3.01
56.56		219.2	0.97746	3.01
55.27		224.3	0.97582	3.02
54.01		229.6	0.97407	3.03
52.77		234.9	0.97221	3.03
51.57		240.4	0.970077	3.05×10^{-2}

TABLE II (*Continued*)

$Al_{0.099}Ga_{0.901}As$ (UV-VIS)

eV	cm^{-1}	μm	n	k
6.0	48393	0.2066	1.311[2]	2.457[2]
5.9	47586	0.2101	1.318	2.538
5.8	46780	0.2138	1.330	2.608
5.7	45973	0.2175	1.345	2.698
5.6	45167	0.2214	1.371	2.800
5.5	44360	0.2254	1.408	2.921
5.4	43554	0.2296	1.459	3.059
5.3	42747	0.2339	1.531	3.223
5.2	41940	0.2384	1.634	3.433
5.1	41134	0.2431	1.819	3.704
5.0	40327	0.2480	2.207	3.983
4.9	39521	0.2530	2.772	4.036
4.8	38714	0.2583	3.267	3.846
4.7	37908	0.2638	3.611	3.536
4.6	37101	0.2695	3.829	3.229
4.5	36295	0.2755	4.010	2.876
4.4	35488	0.2818	4.017	2.507
4.3	34682	0.2883	3.922	2.240
4.2	33875	0.2952	3.801	2.074
4.1	33068	0.3024	3.697	1.983
4.0	32262	0.3100	3.618	1.937
3.9	31455	0.3179	3.566	1.920
3.8	30649	0.3263	3.537	1.924
3.7	29842	0.3351	3.532	1.945
3.6	29036	0.3444	3.552	1.979
3.5	28229	0.3542	3.601	2.030
3.4	27423	0.3647	3.690	2.100
3.3	26616	0.3757	3.864	2.203
3.2	25810	0.3875	4.253	2.187
3.1	25003	0.4000	4.460	1.949
3.0	24196	0.4133	4.838	1.836
2.9	23390	0.4275	4.968	1.126
2.8	22583	0.4428	4.725	0.763
2.7	21777	0.4592	4.518	0.575
2.6	20970	0.4769	4.353	0.462
2.5	20164	0.4959	4.220	0.382
2.4	19357	0.5166	4.111	0.320
2.3	18551	0.5391	4.018	0.276
2.2	17744	0.5636	3.940	0.237
2.1	16938	0.5904	3.876	0.199
2.0	16131	0.6199	3.820	0.171
1.9	15324	0.6526	3.775	0.127
1.8	14518	0.6889	3.716	0.099
1.7	13711	0.7293	3.678	0.082
1.6	12905	0.7749	3.661	0.059
1.5	12098	0.8266	3.572	

TABLE II (*Continued*)

$Al_{0.198}Ga_{0.802}As$ (UV-VIS)

eV	cm^{-1}	μm	n	k
6.0	48393	0.2066	1.333[2]	2.457[2]
5.9	47586	0.2101	1.339	2.531
5.8	46780	0.2138	1.349	2.600
5.7	45973	0.2175	1.366	2.688
5.6	45167	0.2214	1.393	2.794
5.5	44360	0.2254	1.433	2.912
5.4	43554	0.2296	1.490	3.049
5.3	42747	0.2339	1.567	3.208
5.2	41940	0.2384	1.677	3.407
5.1	41134	0.2431	1.860	3.654
5.0	40327	0.2480	2.210	3.914
4.9	39521	0.2530	2.734	3.997
4.8	38714	0.2583	3.238	3.867
4.7	37908	0.2638	3.638	3.575
4.6	37101	0.2695	3.924	3.223
4.5	36295	0.2755	4.053	2.803
4.4	35488	0.2818	4.018	2.449
4.3	34682	0.2883	3.911	2.206
4.2	33875	0.2952	3.795	2.059
4.1	33068	0.3024	3.701	1.976
4.0	32262	0.3100	3.633	1.933
3.9	31455	0.3179	3.588	1.917
3.8	30649	0.3263	3.568	1.922
3.7	29842	0.3351	3.572	1.942
3.6	29036	0.3444	3.602	1.979
3.5	28229	0.3542	3.668	2.034
3.4	27423	0.3647	3.792	2.115
3.3	26616	0.3757	4.084	2.180
3.2	25810	0.3875	4.379	1.978
3.1	25003	0.4000	4.607	1.857
3.0	24196	0.4133	4.943	1.322
2.9	23390	0.4275	4.757	0.865
2.8	22583	0.4428	4.547	0.636
2.7	21777	0.4592	4.375	0.499
2.6	20970	0.4769	4.235	0.409
2.5	20164	0.4959	4.118	0.341
2.4	19357	0.5166	4.022	0.288
2.3	18551	0.5391	3.940	0.242
2.2	17744	0.5636	3.871	0.202
2.1	16938	0.5904	3.815	0.165
2.0	16131	0.6199	3.759	0.118
1.9	15324	0.6526	3.700	0.094
1.8	14518	0.6889	3.662	0.082
1.7	13711	0.7293	3.635	0.002
1.6	12905	0.7749	3.536	0.002
1.5	12098	0.8266	3.457	

TABLE II (*Continued*)

$Al_{0.315}Ga_{0.685}As$ (UV-VIS)

eV	cm^{-1}	μm	n	k
6.0	48393	0.2066	1.347[2]	2.443[2]
5.9	47586	0.2101	1.338	2.502
5.8	46780	0.2138	1.352	2.577
5.7	45973	0.2175	1.367	2.669
5.6	45167	0.2214	1.393	2.776
5.5	44360	0.2254	1.437	2.893
5.4	43554	0.2296	1.497	3.030
5.3	42747	0.2339	1.581	3.187
5.2	41940	0.2384	1.696	3.376
5.1	41134	0.2431	1.878	3.604
5.0	40327	0.2480	2.198	3.845
4.9	39521	0.2530	2.684	3.957
4.8	38714	0.2583	3.196	3.881
4.7	37908	0.2638	3.669	3.617
4.6	37101	0.2695	3.982	3.177
4.5	36295	0.2755	4.062	2.733
4.4	35488	0.2818	3.999	2.393
4.3	34682	0.2883	3.883	2.172
4.2	33875	0.2952	3.772	2.040
4.1	33068	0.3024	3.686	1.966
4.0	32262	0.3100	3.625	1.927
3.9	31455	0.3179	3.588	1.914
3.8	30649	0.3263	3.575	1.921
3.7	29842	0.3351	3.589	1.946
3.6	29036	0.3444	3.633	1.988
3.5	28229	0.3542	3.724	2.054
3.4	27423	0.3647	3.922	2.134
3.3	26616	0.3757	4.246	2.041
3.2	25810	0.3875	4.456	1.879
3.1	25003	0.4000	4.825	1.558
3.0	24196	0.4133	4.781	1.012
2.9	23390	0.4275	4.582	0.722
2.8	22583	0.4428	4.404	0.556
2.7	21777	0.4592	4.258	0.446
2.6	20970	0.4769	4.135	0.367
2.5	20164	0.4959	4.032	0.305
2.4	19357	0.5166	3.945	0.258
2.3	18551	0.5391	3.872	0.227
2.2	17744	0.5636	3.815	0.202
2.1	16938	0.5904	3.750	0.167
2.0	16131	0.6199	3.690	0.145
1.9	15324	0.6526	3.650	0.111
1.8	14518	0.6889	3.592	0.008
1.7	13711	0.7293	3.509	
1.6	12905	0.7749	3.456	
1.5	12098	0.8266	3.404	

TABLE II (*Continued*)

$Al_{0.419}Ga_{0.581}As$ (UV-VIS)

eV	cm^{-1}	μm	n	k
6.0	48393	0.2066	1.353[2]	2.440[2]
5.9	47586	0.2101	1.350	2.507
5.8	46780	0.2138	1.357	2.574
5.7	45973	0.2175	1.377	2.675
5.6	45167	0.2214	1.406	2.783
5.5	44360	0.2254	1.456	2.908
5.4	43554	0.2296	1.523	3.047
5.3	42747	0.2339	1.613	3.201
5.2	41940	0.2384	1.740	3.384
5.1	41134	0.2431	1.926	3.598
5.0	40327	0.2480	2.234	3.822
4.9	39521	0.2530	2.695	3.937
4.8	38714	0.2583	3.200	3.909
4.7	37908	0.2638	3.733	3.646
4.6	37101	0.2695	4.054	3.157
4.5	36295	0.2755	4.103	2.691
4.4	35488	0.2818	4.014	2.363
4.3	34682	0.2883	3.897	2.161
4.2	33875	0.2952	3.794	2.040
4.1	33068	0.3024	3.719	1.971
4.0	32262	0.3100	3.667	1.936
3.9	31455	0.3179	3.640	1.924
3.8	30649	0.3263	3.640	1.931
3.7	29842	0.3351	3.668	1.958
3.6	29036	0.3444	3.736	2.005
3.5	28229	0.3542	3.887	2.071
3.4	27423	0.3647	4.172	2.042
3.3	26616	0.3757	4.401	1.870
3.2	25810	0.3875	4.706	1.640
3.1	25003	0.4000	4.778	1.119
3.0	24196	0.4133	4.605	0.786
2.9	23390	0.4275	4.430	0.596
2.8	22583	0.4428	4.280	0.472
2.7	21777	0.4592	4.154	0.385
2.6	20970	0.4769	4.047	0.319
2.5	20164	0.4959	3.957	0.268
2.4	19357	0.5166	3.881	0.219
2.3	18551	0.5391	3.820	0.178
2.2	17744	0.5636	3.747	0.134
2.1	16938	0.5904	3.686	0.100
2.0	16131	0.6199	3.664	0.059
1.9	15324	0.6526	3.559	0.003
1.8	14518	0.6889	3.479	
1.7	13711	0.7293	3.422	
1.6	12905	0.7749	3.378	
1.5	12098	0.8266	3.341	

TABLE II (*Continued*)

$Al_{0.491}Ga_{0.509}As$ (UV-VIS)

eV	cm^{-1}	μm	n	k
6.0	48393	0.2066	1.366[2]	2.418[2]
5.9	47586	0.2101	1.363	2.490
5.8	46780	0.2138	1.364	2.572
5.7	45973	0.2175	1.379	2.666
5.6	45167	0.2214	1.412	2.780
5.5	44360	0.2254	1.462	2.903
5.4	43554	0.2296	1.532	3.045
5.3	42747	0.2339	1.632	3.199
5.2	41940	0.2384	1.763	3.378
5.1	41134	0.2431	1.951	3.579
5.0	40327	0.2480	2.250	3.787
4.9	39521	0.2530	2.686	3.904
4.8	38714	0.2583	3.187	3.899
4.7	37908	0.2638	3.731	3.645
4.6	37101	0.2695	4.072	3.147
4.5	36295	0.2755	4.107	2.668
4.4	35488	0.2818	4.009	2.351
4.3	34682	0.2883	3.894	2.159
4.2	33875	0.2952	3.798	2.046
4.1	33068	0.3024	3.730	1.980
4.0	32262	0.3100	3.688	1.945
3.9	31455	0.3179	3.671	1.933
3.8	30649	0.3263	3.680	1.942
3.7	29842	0.3351	3.724	1.969
3.6	29036	0.3444	3.822	2.017
3.5	28229	0.3542	4.034	2.049
3.4	27423	0.3647	4.294	1.922
3.3	26616	0.3757	4.525	1.748
3.2	25810	0.3875	4.753	1.340
3.1	25003	0.4000	4.654	0.926
3.0	24196	0.4133	4.483	0.684
2.9	23390	0.4275	4.328	0.534
2.8	22583	0.4428	4.195	0.429
2.7	21777	0.4592	4.081	0.355
2.6	20970	0.4769	3.985	0.292
2.5	20164	0.4959	3.903	0.245
2.4	19357	0.5166	3.838	0.205
2.3	18551	0.5391	3.761	0.164
2.2	17744	0.5636	3.696	0.133
2.1	16938	0.5904	3.665	0.088
2.0	16131	0.6199	3.558	0.002
1.9	15324	0.6526	3.477	
1.8	14518	0.6889	3.417	
1.7	13711	0.7293	3.368	
1.6	12905	0.7749	3.329	
1.5	12098	0.8266	3.283	

TABLE II (*Continued*)

$Al_{0.590}Ga_{0.410}As$ (UV-VIS)

eV	cm^{-1}	μm	n	k
6.0	48393	0.2066	1.385[2]	2.420[2]
5.9	47586	0.2101	1.370	2.485
5.8	46780	0.2138	1.370	2.565
5.7	45973	0.2175	1.389	2.669
5.6	45167	0.2214	1.422	2.785
5.5	44360	0.2254	1.475	2.915
5.4	43554	0.2296	1.553	3.059
5.3	42747	0.2339	1.661	3.217
5.2	41940	0.2384	1.805	3.392
5.1	41134	0.2431	2.007	3.581
5.0	40327	0.2480	2.304	3.772
4.9	39521	0.2530	2.740	3.881
4.8	38714	0.2583	3.221	3.866
4.7	37908	0.2638	3.762	3.617
4.6	37101	0.2695	4.120	3.107
4.5	36295	0.2755	4.127	2.616
4.4	35488	0.2818	4.015	2.318
4.3	34682	0.2883	3.903	2.142
4.2	33875	0.2952	3.815	2.038
4.1	33068	0.3024	3.758	1.978
4.0	32262	0.3100	3.729	1.947
3.9	31455	0.3179	3.725	1.935
3.8	30649	0.3263	3.750	1.944
3.7	29842	0.3351	3.822	1.973
3.6	29036	0.3444	3.977	2.002
3.5	28229	0.3542	4.224	1.924
3.4	27423	0.3647	4.429	1.754
3.3	26616	0.3757	4.665	1.450
3.2	25810	0.3875	4.649	1.028
3.1	25003	0.4000	4.497	0.754
3.0	24196	0.4133	4.343	0.584
2.9	23390	0.4275	4.208	0.468
2.8	22583	0.4428	4.092	0.384
2.7	21777	0.4592	3.992	0.317
2.6	20970	0.4769	3.909	0.262
2.5	20164	0.4959	3.837	0.205
2.4	19357	0.5166	3.758	0.157
2.3	18551	0.5391	3.690	0.126
2.2	17744	0.5636	3.658	0.063
2.1	16938	0.5904	3.546	0.005
2.0	16131	0.6199	3.467	
1.9	15324	0.6526	3.405	
1.8	14518	0.6889	3.354	
1.7	13711	0.7293	3.313	
1.6	12905	0.7749	3.274	
1.5	12098	0.8266	3.237	

TABLE II (*Continued*)

$Al_{0.700}Ga_{0.300}As$ (UV-VIS)

eV	cm^{-1}	μm	n	k
6.0	48393	0.2066	1.377[2]	2.426[2]
5.9	47586	0.2101	1.366	2.493
5.8	46780	0.2138	1.365	2.581
5.7	45973	0.2175	1.375	2.688
5.6	45167	0.2214	1.407	2.809
5.5	44360	0.2254	1.462	2.946
5.4	43554	0.2296	1.545	3.098
5.3	42747	0.2339	1.662	3.269
5.2	41940	0.2384	1.829	3.445
5.1	41134	0.2431	2.049	3.620
5.0	40327	0.2480	2.354	3.788
4.9	39521	0.2530	2.777	3.873
4.8	38714	0.2583	3.214	3.853
4.7	37908	0.2638	3.758	3.637
4.6	37101	0.2695	4.144	3.150
4.5	36295	0.2755	4.142	2.645
4.4	35488	0.2818	4.028	2.365
4.3	34682	0.2883	3.932	2.206
4.2	33875	0.2952	3.868	2.111
4.1	33068	0.3024	3.835	2.055
4.0	32262	0.3100	3.836	2.023
3.9	31455	0.3179	3.868	2.009
3.8	30649	0.3263	3.947	2.006
3.7	29842	0.3351	4.103	1.993
3.6	29036	0.3444	4.319	1.877
3.5	28229	0.3542	4.502	1.678
3.4	27423	0.3647	4.665	1.357
3.3	26616	0.3757	4.615	0.980
3.2	25810	0.3875	4.471	0.735
3.1	25003	0.4000	4.325	0.574
3.0	24196	0.4133	4.196	0.460
2.9	23390	0.4275	4.084	0.374
2.8	22583	0.4428	3.987	0.307
2.7	21777	0.4592	3.906	0.245
2.6	20970	0.4769	3.823	0.184
2.5	20164	0.4959	3.746	0.129
2.4	19357	0.5166	3.696	0.069
2.3	18551	0.5391	3.595	0.002
2.2	17744	0.5636	3.500	
2.1	16938	0.5904	3.425	
2.0	16131	0.6199	3.361	
1.9	15324	0.6526	3.306	
1.8	14518	0.6889	3.261	
1.7	13711	0.7293	3.225	
1.6	12905	0.7749	3.188	
1.5	12098	0.8266	3.153	

TABLE II (*Continued*)

$Al_{0.804}Ga_{0.196}As$ (UV-VIS)

eV	cm^{-1}	μm	n	k
6.0	48393	0.2066	1.368[2]	2.409[2]
5.9	47586	0.2101	1.360	2.473
5.8	46780	0.2138	1.354	2.560
5.7	45973	0.2175	1.370	2.667
5.6	45167	0.2214	1.399	2.792
5.5	44360	0.2254	1.447	2.935
5.4	43554	0.2296	1.528	3.104
5.3	42747	0.2339	1.661	3.293
5.2	41940	0.2384	1.857	3.475
5.1	41134	0.2431	2.110	3.635
5.0	40327	0.2480	2.426	3.763
4.9	39521	0.2530	2.833	3.815
4.8	38714	0.2583	3.233	3.765
4.7	37908	0.2638	3.751	3.582
4.6	37101	0.2695	4.107	3.128
4.5	36295	0.2755	4.112	2.639
4.4	35488	0.2818	4.004	2.389
4.3	34682	0.2883	3.928	2.256
4.2	33875	0.2952	3.893	2.183
4.1	33068	0.3024	3.904	2.144
4.0	32262	0.3100	3.962	2.119
3.9	31455	0.3179	4.078	2.092
3.8	30649	0.3263	4.267	2.013
3.7	29842	0.3351	4.462	1.820
3.6	29036	0.3444	4.613	1.561
3.5	28229	0.3542	4.667	1.199
3.4	27423	0.3647	4.562	0.890
3.3	26616	0.3757	4.413	0.685
3.2	25810	0.3875	4.277	0.541
3.1	25003	0.4000	4.155	0.437
3.0	24196	0.4133	4.050	0.353
2.9	23390	0.4275	3.961	0.276
2.8	22583	0.4428	3.872	0.205
2.7	21777	0.4592	3.787	0.161
2.6	20970	0.4769	3.738	0.104
2.5	20164	0.4959	3.635	0.013
2.4	19357	0.5166	3.519	0.004
2.3	18551	0.5391	3.440	0.003
2.2	17744	0.5636	3.378	
2.1	16938	0.5904	3.322	
2.0	16131	0.6199	3.277	
1.9	15324	0.6526	3.236	
1.8	14518	0.6889	3.202	
1.7	13711	0.7293	3.173	
1.6	12905	0.7749	3.147	
1.5	12098	0.8266	3.124	

TABLE II (*Continued*)

$Al_{0.1}Ga_{0.9}As$ (VIS-Near IR)

eV	cm^{-1}	μm	n
1.5	12098	0.8266	3.618[1]
1.4	11292	0.8856	3.531
1.3	10485	0.9537	3.484
1.2	9679	1.033	3.452
1.1	8872	**1.127**	3.428
1.0	8065	**1.240**	3.409
0.9	7259	**1.378**	3.395
0.8	6452	1.550	3.383
0.7	5646	1.771	3.373
0.6	4839	2.066	3.365
0.5	4033	2.480	3.359
	$Al_{0.14}Ga_{0.86}As$ (VIS- Near IR)		
1.5	12098	0.8266	3.570[1]
1.4	11292	0.8856	3.503
1.3	10485	0.9537	3.461
1.2	9679	1.033	3.431
1.1	8872	**1.127**	3.408
1.0	8065	**1.240**	3.390
0.9	7259	**1.378**	3.375
0.8	6452	1.550	3.363
0.7	5646	1.771	3.353
0.6	4839	2.066	3.345
0.5	4033	2.480	3.338
1.71	13792	0.7251	3.640[5]
1.70	13711	0.7293	3.642
1.69	13631	0.7336	3.642
1.68	13550	0.7380	3.642
1.67	13469	0.7424	3.643
1.66	13389	0.7469	3.643
1.65	13308	0.7514	3.643
1.64	13227	0.7560	3.644
1.63	13147	0.7606	3.606
1.62	13066	0.7653	3.591
1.61	12985	0.7701	3.579
1.60	12905	0.7749	3.569
1.55	12501	0.7999	3.532
1.50	12098	0.8266	3.505
1.45	11695	0.8551	3.482
1.40	11292	0.8856	3.463
1.35	10888	0.9184	3.445
1.30	10485	0.9537	3.429
1.25	10082	0.9919	3.414
1.20	9679	1.033	3.400

TABLE II (*Continued*)

eV	cm^{-1}	μm	n
		$Al_{0.2}Ga_{0.8}As$ (VIS-Near IR)	
1.6	12905	0.7749	3.603[1]
1.5	12098	0.8266	3.516
1.4	11292	0.8856	3.464
1.3	10485	0.9537	3.428
1.2	9679	1.033	3.400
1.1	8872	1.127	3.377
1.0	8065	1.240	3.359
0.9	7259	1.378	3.345
0.8	6452	1.550	3.333
0.7	5646	1.771	3.323
0.6	4839	2.066	3.314
0.5	4033	2.480	3.308
		$Al_{0.3}Ga_{0.7}As$ (VIS-Near IR)	
1.8	14518	0.6888	3.797[1]
1.7	13711	0.7293	3.580
1.6	12905	0.7749	3.498
1.5	12098	0.8266	3.443
1.4	11292	0.8856	3.403
1.3	10485	0.9537	3.372
1.2	9679	1.033	3.346
1.1	8872	1.127	3.326
1.0	8065	1.240	3.308
0.9	7259	1.378	3.294
0.8	6452	1.550	3.282
0.7	5646	1.771	3.271
0.6	4839	2.066	3.263
0.5	4033	2.480	3.256
		$Al_{0.4}Ga_{0.6}As$ (VIS-Near IR)	
1.9	15324	0.6526	3.693[1]
1.8	14518	0.6888	3.554
1.7	13711	0.7293	3.475
1.6	12905	0.7749	3.420
1.5	12098	0.8266	3.377
1.4	11292	0.8856	3.343
1.3	10485	0.9537	3.315
1.2	9679	1.033	3.292
1.1	8872	1.127	3.273
1.0	8065	1.240	3.256
0.9	7259	1.378	3.242
0.8	6452	1.550	3.230
0.7	5646	1.771	3.220
0.6	4839	2.066	3.212
0.5	4033	2.480	3.205

TABLE II (*Continued*)

eV	cm^{-1}	μm	n
		$Al_{0.5}Ga_{0.5}As$ (VIS-Near IR)	
2.0	16131	0.6199	3.635[1]
1.9	15324	0.6526	3.523
1.8	14518	0.6888	3.449
1.7	13711	0.7293	3.393
1.6	12905	0.7749	3.350
1.5	12098	0.8266	3.314
1.4	11292	0.8856	3.284
1.3	10485	0.9537	3.259
1.2	9679	1.033	3.238
1.1	8872	1.127	3.219
1.0	8065	1.240	3.190
0.9	7259	1.378	3.190
0.8	6452	1.550	3.178
0.7	5646	1.771	3.168
0.6	4839	2.066	3.160
0.5	4033	2.480	3.153
		$Al_{0.6}Ga_{0.4}As$ (VIS-Near IR)	
2.2	17744	0.5636	3.749[1]
2.1	16938	0.5904	3.585
2.0	16131	0.6199	3.489
1.9	15324	0.6526	3.419
1.8	14518	0.6888	3.365
1.7	13711	0.7293	3.320
1.6	12905	0.7749	3.284
1.5	12098	0.8266	3.252
1.4	11292	0.8856	3.226
1.3	10485	0.9537	3.202
1.2	9679	1.033	3.182
1.1	8872	1.127	3.165
1.0	8065	1.240	3.150
0.9	7259	1.378	3.137
0.8	6452	1.550	3.125
0.7	5646	1.771	3.116
0.6	4839	2.066	3.107
0.5	4033	2.480	3.101
		$Al_{0.7}Ga_{0.3}As$ (VIS-Near IR)	
2.4	19357	0.5166	3.918[1]
2.3	18551	0.5391	3.661
2.2	17744	0.5636	3.538
2.1	16938	0.5904	3.452
2.0	16131	0.6199	3.386
1.9	15324	0.6526	3.333
1.8	14518	0.6888	3.289
1.7	13711	0.7293	3.252
1.6	12905	0.7749	3.219
1.5	12098	0.8266	3.191

TABLE II (*Continued*)

eV	cm^{-1}	μm	n
		$Al_{0.7}Ga_{0.3}As$ (VIS-Near IR)	
1.4	11292	0.8856	3.167
1.3	10485	0.9537	3.146
1.2	9679	1.033	3.127
1.1	8872	1.127	3.110
1.0	8065	1.240	3.096
0.9	7259	1.378	3.083
0.8	6452	1.550	3.072
0.7	5646	1.771	3.063
0.6	4839	2.066	3.055
0.5	4033	2.480	3.048
		$Al_{0.8}Ga_{0.2}As$ (VIS-Near IR)	
2.5	20164	0.4959	3.746[1]
2.4	19357	0.5166	3.592
2.3	18551	0.5391	3.490
2.2	17744	0.5636	3.413
2.1	16938	0.5904	3.351
2.0	16131	0.6199	3.299
1.9	15324	0.6526	3.256
1.8	14518	0.6888	3.218
1.7	13711	0.7293	3.185
1.6	12905	0.7749	3.156
1.5	12098	0.8266	3.131
1.4	11292	0.8856	3.108
1.3	10485	0.9537	3.088
1.2	9679	1.033	3.071
1.1	8872	1.127	3.055
1.0	8065	1.240	3.041
0.9	7259	1.378	3.029
0.8	6452	1.550	3.018
0.7	5646	1.771	3.009
0.6	4839	2.066	3.002
0.5	4033	2.480	2.995
		$Al_{0.9}Ga_{0.1}As$ (VIS-Near IR)	
2.7	21777	0.4592	3.834[1]
2.6	20970	0.4769	3.649
2.5	20164	0.4959	3.531
2.4	19357	0.5166	3.442
2.3	18551	0.5391	3.372
2.2	17744	0.5636	3.313
2.1	16938	0.5904	3.263
2.0	16131	0.6199	3.220
1.9	15324	0.6526	3.183
1.8	14518	0.6888	3.149
1.7	13711	0.7293	3.120
1.6	12905	0.7749	3.094
1.5	12098	0.8266	3.070

TABLE II (*Continued*)

$Al_{0.9}Ga_{0.1}As$ (VIS-Near IR)

eV	cm^{-1}	μm	n
1.4	11292	0.8856	3.049
1.3	10485	0.9537	3.031
1.2	9679	1.033	3.014
1.1	8872	1.127	2.999
1.0	8065	1.240	2.986
0.9	7259	1.378	2.974
0.8	6452	1.550	2.964
0.7	5646	1.771	2.955
0.6	4839	2.066	2.948
0.5	4033	2.480	2.942

* References are indicated in brackets.

TABLE II (*Continued*)

Values of n and k for $Al_{0.14}Ga_{0.86}As$ from Various References[a]

eV	cm^{-1}	μm	n	k
0.2480	2000	5.00	3.244[3]	1.99×10^{-5}[3]
0.2066	1667	6.00	3.240	2.81
0.1771	1429	7.00	3.236	2.74
0.1550	1250	8.00	3.232	7.43×10^{-5}
0.1378	1111	9.00	3.226	1.43×10^{-4}
0.1240	1000	10.00	3.219	2.38
0.1227	990	10.10	3.219	2.49
0.1215	980	10.20	3.218	2.61
0.1203	970	10.31	3.217	2.74
0.1190	960	10.42	3.216	2.87
0.1178	950	10.53	3.215	3.01
0.1165	940	10.64	3.215	3.16
0.1153	930	10.75	3.214	3.32
0.1141	920	10.87	3.213	3.48
0.1128	910	10.99	3.212	3.66
0.1116	900	11.11	3.211	3.85
0.1103	890	11.24	3.210	4.04
0.1091	880	11.36	3.209	4.25
0.1079	870	11.49	3.208	4.47
0.1066	860	11.63	3.206	4.71
0.1054	850	11.76	3.205	4.96
0.1041	840	11.90	3.204	5.23
0.1029	830	12.05	3.203	5.51
0.1017	820	12.20	3.201	5.82
0.1004	810	12.35	3.200	6.14
0.0992	800	12.50	3.198	6.49
0.0979	790	12.66	3.197	6.87
0.0967	780	12.82	3.195	7.27
0.0955	770	12.99	3.193	7.70
0.0942	760	13.16	3.191	8.16
0.0930	750	13.33	3.189	8.66
0.0917	740	13.51	3.187	9.20
0.0905	730	13.70	3.185	9.78×10^{-4}
0.0893	720	13.89	3.183	1.04×10^{-3}
0.0880	710	14.08	3.180	1.11
0.0868	700	14.29	3.178	1.18
0.0855	690	14.49	3.175	1.27
0.0843	680	14.71	3.172	1.35
0.0831	670	14.93	3.169	1.45
0.0818	660	15.15	3.166	1.56
0.0806	650	15.38	3.163	1.68
0.0793	640	15.63	3.159	1.81
0.0781	630	15.87	3.155	1.95
0.0769	620	16.13	3.151	2.11
0.0756	610	16.39	3.146	2.29
0.0744	600	16.67	3.141	2.49
0.0731	590	16.95	3.136	2.71
0.0719	580	17.24	3.130	2.97
0.0707	570	17.54	3.124	3.26
0.0694	560	17.86	3.117	3.59

TABLE II (*Continued*)

$Al_{0.14}Ga_{0.86}As$

eV	cm^{-1}	μm	n	k
0.0682	550	18.18	3.110	3.97
0.0669	540	18.52	3.101	4.41
0.0657	530	18.87	3.092	4.92
0.0645	520	19.23	3.082	5.53
0.0632	510	19.61	3.071	6.25
0.0620	500	20.00	3.058	7.12
0.0608	490	20.41	3.044	8.17
0.0595	480	20.83	3.028	9.48×10^{-3}
0.0583	470	21.28	3.009	1.11×10^{-2}
0.0570	460	21.74	2.987	1.32
0.0558	450	22.22	2.961	1.60
0.0555	448	22.32	2.955	1.67
0.0553	446	22.42	2.949	1.74
0.0550	444	22.52	2.943	1.82
0.0548	442	22.62	2.936	1.90
0.0546	440	22.73	2.930	1.99
0.0543	438	22.83	2.922	2.08
0.0541	436	22.94	2.915	2.18
0.0538	434	23.04	2.907	2.29
0.0536	432	23.15	2.899	2.40
0.0533	430	23.26	2.891	2.53
0.0531	428	23.36	2.882	2.67
0.0528	426	23.47	2.872	2.81
0.0526	424	23.58	2.862	2.98
0.0523	422	23.70	2.852	3.15
0.0521	420	23.81	2.841	3.34
0.0518	418	23.92	2.829	3.56
0.0516	416	24.04	2.817	3.79
0.0513	414	24.15	2.803	4.05
0.0511	412	24.27	2.789	4.34
0.0508	410	24.39	2.774	4.66
0.0506	408	24.51	2.758	5.02
0.0503	406	24.63	2.741	5.43
0.0501	404	24.75	2.722	5.89
0.0498	402	24.88	2.702	6.42
0.0496	400	25.00	2.680	7.02
0.0493	398	25.13	2.656	7.73
0.0491	396	25.25	2.630	8.54
0.0488	394	25.38	2.601	9.51×10^{-2}
0.0486	392	25.51	2.569	1.07×10^{-1}
0.0484	390	25.64	2.533	1.20
0.0481	388	25.77	2.493	1.37
0.0479	386	25.91	2.448	1.58
0.0476	384	26.04	2.396	1.84
0.0474	382	26.18	2.337	2.18
0.0471	380	26.32	2.270	2.62
0.0469	378	26.46	2.191	3.22
0.0466	376	26.60	2.102	4.04
0.0464	374	26.74	2.002	5.21
0.0461	372	26.88	1.900	6.92

TABLE II (*Continued*)

$Al_{0.14}Ga_{0.86}As$

eV	cm^{-1}	μm	n	k
0.0459	370	27.03	1.819	$9.36x10^{-1}$
0.0456	368	27.17	1.805	$1.26x10^{0}$
0.0454	366	27.32	1.913	1.65
0.0451	364	27.47	2.194	2.05
0.0449	362	27.62	2.694	2.36
0.0446	360	27.78	3.380	2.41
0.0444	358	27.93	4.003	2.07
0.0441	356	28.09	4.291	1.52
0.0439	354	28.25	4.293	$1.05x10^{0}$
0.0436	352	28.41	4.177	$7.25x10^{-1}$
0.0434	350	28.57	4.037	5.19
0.0431	348	28.74	3.906	3.84
0.0429	346	28.90	3.791	2.94
0.0426	344	29.07	3.691	2.31
0.0424	342	29.24	3.604	1.86
0.0422	340	29.41	3.527	1.53
0.0419	338	29.59	3.459	1.29
0.0417	336	29.76	3.397	$1.10x10^{-1}$
0.0414	334	29.94	3.341	$9.55x10^{-2}$
0.0412	332	30.12	3.288	8.43
0.0409	330	30.30	3.238	7.56
0.0407	328	30.49	3.191	6.88
0.0404	326	30.67	3.144	6.37
0.0402	324	30.86	3.099	5.99
0.0399	322	31.06	3.054	5.73
0.0397	320	31.25	3.008	5.57
0.0394	318	31.45	2.962	5.51
0.0392	316	31.65	2.914	5.54
0.0389	314	31.85	2.864	5.67
0.0387	312	32.05	2.812	5.90
0.0384	310	32.26	2.756	6.24
0.0382	308	32.47	2.696	6.72
0.0379	306	32.68	2.630	7.35
0.0377	304	32.89	2.558	8.18
0.0374	302	33.11	2.478	$9.26x10^{-2}$
0.0372	300	33.33	2.388	$1.07x10^{-1}$
0.0369	298	33.56	2.283	1.25
0.0367	296	33.78	2.162	1.51
0.0365	294	34.01	2.017	1.87
0.0362	292	34.25	1.841	2.39
0.0360	290	34.48	1.620	3.23
0.0357	288	34.72	1.338	4.73
0.0355	286	34.97	1.013	$7.69x10^{-1}$
0.0352	284	35.21	0.786	$1.25x10^{0}$
0.0350	282	35.46	0.715	1.77
0.0347	280	35.71	0.734	2.31
0.0345	278	35.97	0.822	2.88
0.0342	276	36.23	0.992	3.51
0.0340	274	36.50	1.299	4.27
0.0337	272	36.76	1.882	5.18

TABLE II (*Continued*)

$Al_{0.14}Ga_{0.86}As$

eV	cm^{-1}	μm	n	k
0.0335	270	37.04	3.097	6.23
0.0332	268	37.31	5.523	6.60
0.0330	266	37.59	7.692	4.63
0.0327	264	37.88	7.611	2.49
0.0325	262	38.17	6.944	1.44×10^{0}
0.0322	260	38.46	6.375	9.23×10^{-1}
0.0320	258	38.76	5.947	6.45
0.0317	256	39.06	5.623	4.78
0.0315	254	39.37	5.371	3.70
0.0312	252	39.68	5.172	2.96
0.0310	250	40.00	5.009	2.43
0.0304	245	40.82	4.711	1.61
0.0298	240	41.67	4.507	1.16×10^{-1}
0.0291	235	42.55	4.360	8.78×10^{-2}
0.0285	230	43.48	4.247	6.92
0.0279	225	44.44	4.159	5.61
0.0273	220	45.45	4.087	4.66
0.0267	215	46.51	4.028	3.93
0.0260	210	47.62	3.978	3.37
0.0254	205	48.78	3.936	2.92
0.0248	200	50.00	3.899	2.56
0.0207	167	60.00	3.745	1.26×10^{-2}
0.0177	143	70.00	3.684	8.38×10^{-3}
0.0155	125	80.00	3.653	6.35
0.0138	111	90.00	3.634	5.14
0.0124	100	100.00	3.621	4.35

TABLE II (*Continued*)

Values of n and k for $Al_{0.18}Ga_{0.82}As$ from Various References[a]

eV	cm^{-1}	μm	n	k
0.2480	2000	5.00	3.228[3]	
0.2066	1667	6.00	3.225	
0.1771	1429	7.00	3.221	
0.1550	1250	8.00	3.216	
0.1378	1111	9.00	3.210	
0.1240	1000	10.00	3.203	
0.1227	990	10.10	3.202	
0.1215	980	10.20	3.202	
0.1203	970	10.31	3.201	
0.1190	960	10.42	3.200	
0.1178	950	10.53	3.199	
0.1165	940	10.64	3.198	
0.1153	930	10.75	3.197	
0.1141	920	10.87	3.196	
0.1128	910	10.99	3.195	
0.1116	900	11.11	3.194	
0.1103	890	11.24	3.193	
0.1091	880	11.36	3.192	
0.1079	870	11.49	3.191	
0.1066	860	11.63	3.190	
0.1054	850	11.76	3.188	
0.1041	840	11.90	3.187	
0.1029	830	12.05	3.186	
0.1017	820	12.20	3.184	
0.1004	810	12.35	3.183	
0.0992	800	12.50	3.181	
0.0979	790	12.66	3.179	
0.0967	780	12.82	3.178	
0.0955	770	12.99	3.176	
0.0942	760	13.16	3.174	
0.0930	750	13.33	3.172	
0.0917	740	13.51	3.170	
0.0905	730	13.70	3.168	
0.0893	720	13.89	3.165	
0.0880	710	14.08	3.163	
0.0868	700	14.29	3.160	
0.0855	690	14.49	3.157	
0.0843	680	14.71	3.154	
0.0831	670	14.93	3.151	
0.0818	660	15.15	3.147	
0.0806	650	15.38	3.144	
0.0793	640	15.63	3.140	
0.0781	630	15.87	3.136	
0.0769	620	16.13	3.131	
0.0756	610	16.39	3.126	
0.0744	600	16.67	3.121	
0.0731	590	16.95	3.115	
0.0719	580	17.24	3.109	
0.0707	570	17.54	3.103	
0.0694	560	17.86	3.095	

TABLE II (*Continued*)

$Al_{0.18}Ga_{0.82}As$

eV	cm^{-1}	μm	n	k
0.0682	550	18.18	3.087	
0.0669	540	18.52	3.078	
0.0657	530	18.87	3.069	
0.0645	520	19.23	3.058	
0.0632	510	19.61	3.045	
0.0620	500	20.00	3.031	
0.0608	490	20.41	3.016	
0.0595	480	20.83	2.997	
0.0583	470	21.28	2.976	
0.0570	460	21.74	2.951	
0.0558	450	22.22	2.921	
0.0555	448	22.32	2.915	
0.0553	446	22.42	2.908	
0.0550	444	22.52	2.900	
0.0548	442	22.62	2.893	
0.0546	440	22.73	2.885	
0.0543	438	22.83	2.876	
0.0541	436	22.94	2.868	
0.0538	434	23.04	2.859	
0.0536	432	23.15	2.849	
0.0533	430	23.26	2.839	
0.0531	428	23.36	2.828	
0.0528	426	23.47	2.817	
0.0526	424	23.58	2.805	
0.0523	422	23.70	2.792	
0.0521	420	23.81	2.779	
0.0518	418	23.92	2.764	
0.0516	416	24.04	2.749	
0.0513	414	24.15	2.733	
0.0511	412	24.27	2.716	
0.0508	410	24.39	2.697	
0.0506	408	24.51	2.677	
0.0503	406	24.63	2.655	
0.0501	404	24.75	2.631	
0.0498	402	24.88	2.605	
0.0496	400	25.00	2.576	1.56×10^{-2} [3]
0.0493	398	25.13	2.545	2.29
0.0491	396	25.25	2.511	3.17
0.0488	394	25.38	2.472	4.26
0.0486	392	25.51	2.429	5.59
0.0484	390	25.64	2.380	7.27
0.0481	388	25.77	2.325	9.40×10^{-2}
0.0479	386	25.91	2.262	1.21×10^{-1}
0.0476	384	26.04	2.189	1.58
0.0474	382	26.18	2.105	2.07
0.0471	380	26.32	2.007	2.75
0.0469	378	26.46	1.895	3.72
0.0466	376	26.60	1.772	5.15
0.0464	374	26.74	1.653	7.25×10^{-1}
0.0461	372	26.88	1.576	1.02×10^{0}

TABLE II (*Continued*)

$Al_{0.18}Ga_{0.82}As$

eV	cm^{-1}	μm	n	k
0.0459	370	27.03	1.589	1.38
0.0456	368	27.17	1.726	1.78
0.0454	366	27.32	2.012	2.16
0.0451	364	27.47	2.471	2.47
0.0449	362	27.62	3.090	2.60
0.0446	360	27.78	3.731	2.41
0.0444	358	27.93	4.165	1.96
0.0441	356	28.09	4.321	1.47
0.0439	354	28.25	4.299	$1.08x10^{0}$
0.0436	352	28.41	4.203	$8.01x10^{-1}$
0.0434	350	28.57	4.089	6.06
0.0431	348	28.74	3.978	4.70
0.0429	346	28.90	3.876	3.72
0.0426	344	29.07	3.785	2.99
0.0424	342	29.24	3.704	2.44
0.0422	340	29.41	3.632	2.01
0.0419	338	29.59	3.566	1.68
0.0417	336	29.76	3.506	1.41
0.0414	334	29.94	3.451	1.19
0.0412	332	30.12	3.400	$1.00x10^{-1}$
0.0409	330	30.30	3.351	$8.51x10^{-2}$
0.0407	328	30.49	3.304	7.22
0.0404	326	30.67	3.259	6.13
0.0402	324	30.86	3.216	5.20
0.0399	322	31.06	3.172	4.40
0.0397	320	31.25	3.129	3.72
0.0394	318	31.45	3.085	3.14
0.0392	316	31.65	3.040	2.66
0.0389	314	31.85	2.994	2.26
0.0387	312	32.05	2.946	1.96
0.0384	310	32.26	2.895	1.75
0.0382	308	32.47	2.841	1.63
0.0379	306	32.68	2.782	1.64
0.0377	304	32.89	2.719	1.78
0.0374	302	33.11	2.649	2.09
0.0372	300	33.33	2.571	2.63
0.0369	298	33.56	2.482	3.46
0.0367	296	33.78	2.380	4.72
0.0365	294	34.01	2.261	6.59
0.0362	292	34.25	2.119	$9.43x10^{-2}$
0.0360	290	34.48	1.944	$1.39x10^{-1}$
0.0357	288	34.72	1.724	2.12
0.0355	286	34.97	1.439	3.48
0.0352	284	35.21	1.089	$6.36x10^{-1}$
0.0350	282	35.46	0.840	$1.16x10^{0}$
0.0347	280	35.71	0.802	1.74
0.0345	278	35.97	0.889	2.31
0.0342	276	36.23	1.079	2.90
0.0340	274	36.50	1.409	3.53
0.0337	272	36.76	1.971	4.20

TABLE II (*Continued*)

$Al_{0.18}Ga_{0.82}As$

eV	cm^{-1}	μm	n	k
0.0335	270	37.04	2.919	4.79
0.0332	268	37.31	4.321	4.91
0.0330	266	37.59	5.634	4.13
0.0327	264	37.88	6.135	2.94
0.0325	262	38.17	6.049	2.02
0.0322	260	38.46	5.795	1.44
0.0320	258	38.76	5.534	1.08×10^{0}
0.0317	256	39.06	5.307	8.41×10^{-1}
0.0315	254	39.37	5.117	6.80
0.0312	252	39.68	4.959	5.65
0.0310	250	40.00	4.826	4.79
0.0304	245	40.82	4.574	3.41
0.0298	240	41.67	4.397	2.61
0.0291	235	42.55	4.267	2.09
0.0285	230	43.48	4.167	1.73
0.0279	225	44.44	4.088	1.47
0.0273	220	45.45	4.023	1.27
0.0267	215	46.51	3.970	1.11×10^{-1}
0.0260	210	47.62	3.924	9.87×10^{-2}
0.0254	205	48.78	3.886	8.85
0.0248	200	50.00	3.853	7.99
0.0207	167	60.00	3.710	4.58
0.0177	143	70.00	3.654	3.30
0.0155	125	80.00	3.625	2.62
0.0138	111	90.00	3.607	2.19
0.0124	100	100.00	3.595	1.89

TABLE II (*Continued*)

Values of n and k for $Al_{0.30}Ga_{0.70}As$ from Various References[a]

eV	cm^{-1}	μm	n	k
0.2480	2000	5.00	3.179[3]	
0.2066	1667	6.00	3.175	
0.1771	1429	7.00	3.170	
0.1550	1250	8.00	3.164	
0.1378	1111	9.00	3.157	
0.1240	1000	10.00	3.150	
0.1227	990	10.10	3.149	
0.1215	980	10.20	3.148	
0.1203	970	10.31	3.147	
0.1190	960	10.42	3.146	
0.1178	950	10.53	3.145	
0.1165	940	10.64	3.144	
0.1153	930	10.75	3.143	
0.1141	920	10.87	3.142	
0.1128	910	10.99	3.140	
0.1116	900	11.11	3.139	
0.1103	890	11.24	3.138	
0.1091	880	11.36	3.137	
0.1079	870	11.49	3.135	
0.1066	860	11.63	3.134	
0.1054	850	11.76	3.132	
0.1041	840	11.90	3.131	
0.1029	830	12.05	3.129	
0.1017	820	12.20	3.127	
0.1004	810	12.35	3.126	
0.0992	800	12.50	3.124	
0.0979	790	12.66	3.122	
0.0967	780	12.82	3.120	
0.0955	770	12.99	3.117	
0.0942	760	13.16	3.115	
0.0930	750	13.33	3.113	
0.0917	740	13.51	3.110	
0.0905	730	13.70	3.107	
0.0893	720	13.89	3.104	
0.0880	710	14.08	3.101	
0.0868	700	14.29	3.098	
0.0855	690	14.49	3.095	
0.0843	680	14.71	3.091	
0.0831	670	14.93	3.087	
0.0818	660	15.15	3.083	
0.0806	650	15.38	3.079	
0.0793	640	15.63	3.074	
0.0781	630	15.87	3.069	
0.0769	620	16.13	3.063	
0.0756	610	16.39	3.057	
0.0744	600	16.67	3.051	
0.0731	590	16.95	3.044	
0.0719	580	17.24	3.036	
0.0707	570	17.54	3.028	
0.0694	560	17.86	3.018	

TABLE II (*Continued*)

$Al_{0.30}Ga_{0.70}As$

eV	cm^{-1}	μm	n	k
0.0682	550	18.18	3.008	
0.0669	540	18.52	2.997	
0.0657	530	18.87	2.984	
0.0645	520	19.23	2.970	
0.0632	510	19.61	2.954	
0.0620	500	20.00	2.936	
0.0608	490	20.41	2.915	
0.0595	480	20.83	2.891	
0.0583	470	21.28	2.862	
0.0570	460	21.74	2.828	
0.0558	450	22.22	2.786	
0.0555	448	22.32	2.777	
0.0553	446	22.42	2.767	
0.0550	444	22.52	2.757	
0.0548	442	22.62	2.746	
0.0546	440	22.73	2.734	
0.0543	438	22.83	2.722	
0.0541	436	22.94	2.710	
0.0538	434	23.04	2.696	
0.0536	432	23.15	2.682	
0.0533	430	23.26	2.668	
0.0531	428	23.36	2.652	
0.0528	426	23.47	2.635	
0.0526	424	23.58	2.617	
0.0523	422	23.70	2.598	
0.0521	420	23.81	2.578	
0.0518	418	23.92	2.557	
0.0516	416	24.04	2.533	1.12×10^{-2} [3]
0.0513	414	24.15	2.508	1.50
0.0511	412	24.27	2.481	1.95
0.0508	410	24.39	2.452	2.46
0.0506	408	24.51	2.420	3.06
0.0503	406	24.63	2.385	3.76
0.0501	404	24.75	2.346	4.59
0.0498	402	24.88	2.304	5.58
0.0496	400	25.00	2.257	6.78
0.0493	398	25.13	2.205	8.24×10^{-2}
0.0491	396	25.25	2.146	1.00×10^{-1}
0.0488	394	25.38	2.080	1.23
0.0486	392	25.51	2.005	1.51
0.0484	390	25.64	1.918	1.89
0.0481	388	25.77	1.818	2.38
0.0479	386	25.91	1.702	3.06
0.0476	384	26.04	1.567	4.03
0.0474	382	26.18	1.418	5.44
0.0471	380	26.32	1.270	7.52×10^{-1}
0.0469	378	26.46	1.158	1.03×10^{0}
0.0466	376	26.60	1.114	1.37
0.0464	374	26.74	1.144	1.72
0.0461	372	26.88	1.246	2.10

TABLE II (*Continued*)

$Al_{0.30}Ga_{0.70}As$

eV	cm^{-1}	μm	n	k
0.0459	370	27.03	1.427	2.49
0.0456	368	27.17	1.712	2.89
0.0454	366	27.32	2.142	3.27
0.0451	364	27.47	2.761	3.56
0.0449	362	27.62	3.560	3.62
0.0446	360	27.78	4.356	3.28
0.0444	358	27.93	4.869	2.65
0.0441	356	28.09	5.025	2.00
0.0439	354	28.25	4.964	1.48
0.0436	352	28.41	4.820	1.11×10^{0}
0.0434	350	28.57	4.658	8.59×10^{-1}
0.0431	348	28.74	4.505	6.79
0.0429	346	28.90	4.367	5.49
0.0426	344	29.07	4.245	4.53
0.0424	342	29.24	4.137	3.80
0.0422	340	29.41	4.042	3.23
0.0419	338	29.59	3.957	2.78
0.0417	336	29.76	3.880	2.42
0.0414	334	29.94	3.811	2.12
0.0412	332	30.12	3.748	1.88
0.0409	330	30.30	3.689	1.68
0.0407	328	30.49	3.634	1.51
0.0404	326	30.67	3.583	1.36
0.0402	324	30.86	3.534	1.24
0.0399	322	31.06	3.486	1.13
0.0397	320	31.25	3.441	1.04×10^{-1}
0.0394	318	31.45	3.396	9.66×10^{-2}
0.0392	316	31.65	3.352	9.02
0.0389	314	31.85	3.308	8.49
0.0387	312	32.05	3.263	8.06
0.0384	310	32.26	3.218	7.74
0.0382	308	32.47	3.171	7.52
0.0379	306	32.68	3.122	7.41
0.0377	304	32.89	3.071	7.43
0.0374	302	33.11	3.017	7.59
0.0372	300	33.33	2.958	7.91
0.0369	298	33.56	2.894	8.44
0.0367	296	33.78	2.823	9.24×10^{-2}
0.0365	294	34.01	2.743	1.04×10^{-1}
0.0362	292	34.25	2.653	1.21
0.0360	290	34.48	2.548	1.44
0.0357	288	34.72	2.425	1.78
0.0355	286	34.97	2.277	2.29
0.0352	284	35.21	2.094	3.09
0.0350	282	35.46	1.868	4.41
0.0347	280	35.71	1.598	6.77×10^{-1}
0.0345	278	35.97	1.347	1.09×10^{0}
0.0342	276	36.23	1.247	1.66
0.0340	274	36.50	1.334	2.28
0.0337	272	36.76	1.606	2.94

TABLE II (*Continued*)

$Al_{0.30}Ga_{0.70}As$

eV	cm^{-1}	μm	n	k
0.0335	270	37.04	2.134	3.62
0.0332	268	37.31	3.055	4.18
0.0330	266	37.59	4.381	4.22
0.0327	264	37.88	5.496	3.42
0.0325	262	38.17	5.831	2.36
0.0322	260	38.46	5.705	1.60
0.0320	258	38.76	5.467	$1.13x10^{0}$
0.0317	256	39.06	5.237	$8.40x10^{-1}$
0.0315	254	39.37	5.042	6.53
0.0312	252	39.68	4.879	5.25
0.0310	250	40.00	4.744	4.34
0.0304	245	40.82	4.492	2.95
0.0298	240	41.67	4.320	2.19
0.0291	235	42.55	4.194	1.72
0.0285	230	43.48	4.099	1.40
0.0279	225	44.44	4.025	1.18
0.0273	220	45.45	3.964	$1.01x10^{-1}$
0.0267	215	46.51	3.914	$8.80x10^{-2}$
0.0260	210	47.62	3.872	7.78
0.0254	205	48.78	3.836	6.94
0.0248	200	50.00	3.805	6.25
0.0207	167	60.00	3.671	3.57
0.0177	143	70.00	3.618	2.57
0.0155	125	80.00	3.590	2.04
0.0138	111	90.00	3.573	1.70
0.0124	100	100.00	3.561	1.47

TABLE II (*Continued*)

Values of n and k for $Al_{0.36}Ga_{0.64}As$ from Various References[a]

eV	cm^{-1}	μm	n	k
0.2480	2000	5.00	3.160[3]	
0.2066	1667	6.00	3.155	
0.1771	1429	7.00	3.150	
0.1550	1250	8.00	3.144	
0.1378	1111	9.00	3.137	
0.1240	1000	10.00	3.129	
0.1227	990	10.10	3.128	
0.1215	980	10.20	3.127	
0.1203	970	10.31	3.126	
0.1190	960	10.42	3.125	
0.1178	950	10.53	3.124	
0.1165	940	10.64	3.123	
0.1153	930	10.75	3.122	
0.1141	920	10.87	3.121	
0.1128	910	10.99	3.120	
0.1116	900	11.11	3.118	
0.1103	890	11.24	3.117	
0.1091	880	11.36	3.116	
0.1079	870	11.49	3.114	
0.1066	860	11.63	3.113	
0.1054	850	11.76	3.111	
0.1041	840	11.90	3.109	
0.1029	830	12.05	3.108	
0.1017	820	12.20	3.106	
0.1004	810	12.35	3.104	
0.0992	800	12.50	3.102	
0.0979	790	12.66	3.100	
0.0967	780	12.82	3.098	
0.0955	770	12.99	3.095	
0.0942	760	13.16	3.093	
0.0930	750	13.33	3.090	
0.0917	740	13.51	3.088	
0.0905	730	13.70	3.085	
0.0893	720	13.89	3.082	
0.0880	710	14.08	3.079	
0.0868	700	14.29	3.075	
0.0855	690	14.49	3.071	
0.0843	680	14.71	3.068	
0.0831	670	14.93	3.063	
0.0818	660	15.15	3.059	
0.0806	650	15.38	3.054	
0.0793	640	15.63	3.049	
0.0781	630	15.87	3.044	
0.0769	620	16.13	3.038	
0.0756	610	16.39	3.032	
0.0744	600	16.67	3.025	
0.0731	590	16.95	3.017	
0.0719	580	17.24	3.009	
0.0707	570	17.54	3.000	
0.0694	560	17.86	2.990	

TABLE II (*Continued*)

$Al_{0.36}Ga_{0.64}As$

eV	cm^{-1}	μm	n	k
0.0682	550	18.18	2.979	
0.0669	540	18.52	2.967	
0.0657	530	18.87	2.954	
0.0645	520	19.23	2.939	
0.0632	510	19.61	2.921	
0.0620	500	20.00	2.902	
0.0608	490	20.41	2.879	
0.0595	480	20.83	2.853	
0.0583	470	21.28	2.822	
0.0570	460	21.74	2.784	
0.0558	450	22.22	2.738	
0.0555	448	22.32	2.728	
0.0553	446	22.42	2.717	
0.0550	444	22.52	2.706	
0.0548	442	22.62	2.694	
0.0546	440	22.73	2.681	
0.0543	438	22.83	2.668	
0.0541	436	22.94	2.654	
0.0538	434	23.04	2.639	
0.0536	432	23.15	2.623	
0.0533	430	23.26	2.607	
0.0531	428	23.36	2.589	
0.0528	426	23.47	2.570	
0.0526	424	23.58	2.550	
0.0523	422	23.70	2.529	
0.0521	420	23.81	2.506	
0.0518	418	23.92	2.482	
0.0516	416	24.04	2.455	
0.0513	414	24.15	2.427	
0.0511	412	24.27	2.396	
0.0508	410	24.39	2.362	
0.0506	408	24.51	2.325	
0.0503	406	24.63	2.285	
0.0501	404	24.75	2.241	1.53×10^{-2} [3]
0.0498	402	24.88	2.191	2.56
0.0496	400	25.00	2.136	3.84
0.0493	398	25.13	2.075	5.42
0.0491	396	25.25	2.005	7.41
0.0488	394	25.38	1.925	9.96×10^{-2}
0.0486	392	25.51	1.834	1.33×10^{-1}
0.0484	390	25.64	1.727	1.78
0.0481	388	25.77	1.602	2.41
0.0479	386	25.91	1.456	3.32
0.0476	384	26.04	1.290	4.70
0.0474	382	26.18	1.121	6.82
0.0471	380	26.32	0.995	9.74×10^{-1}
0.0469	378	26.46	0.946	1.31×10^{0}
0.0466	376	26.60	0.967	1.67
0.0464	374	26.74	1.049	2.03
0.0461	372	26.88	1.191	2.40

TABLE II (*Continued*)

$Al_{0.36}Ga_{0.4}As$

eV	cm^{-1}	μm	n	k
0.0459	370	27.03	1.411	2.79
0.0456	368	27.17	1.736	3.19
0.0454	366	27.32	2.213	3.56
0.0451	364	27.47	2.887	3.83
0.0449	362	27.62	3.733	3.84
0.0446	360	27.78	4.545	3.44
0.0444	358	27.93	5.043	2.76
0.0441	356	28.09	5.182	2.08
0.0439	354	28.25	5.109	1.55
0.0436	352	28.41	4.955	1.17×10^{0}
0.0434	350	28.57	4.787	9.04×10^{-1}
0.0431	348	28.74	4.627	7.15
0.0429	346	28.90	4.483	5.77
0.0426	344	29.07	4.355	4.74
0.0424	342	29.24	4.243	3.95
0.0422	340	29.41	4.143	3.33
0.0419	338	29.59	4.055	2.83
0.0417	336	29.76	3.975	2.43
0.0414	334	29.94	3.903	2.09
0.0412	332	30.12	3.837	1.81
0.0409	330	30.30	3.776	1.58
0.0407	328	30.49	3.720	1.37
0.0404	326	30.67	3.667	1.20
0.0402	324	30.86	3.617	1.04×10^{-1}
0.0399	322	31.06	3.569	9.11×10^{-2}
0.0397	320	31.25	3.523	7.93
0.0394	318	31.45	3.478	6.88
0.0392	316	31.65	3.434	5.95
0.0389	314	31.85	3.390	5.12
0.0387	312	32.05	3.347	4.39
0.0384	310	32.26	3.303	3.74
0.0382	308	32.47	3.258	3.18
0.0379	306	32.68	3.211	2.71
0.0377	304	32.89	3.163	2.33
0.0374	302	33.11	3.112	2.04
0.0372	300	33.33	3.057	1.87
0.0369	298	33.56	2.998	1.84
0.0367	296	33.78	2.934	2.00
0.0365	294	34.01	2.863	2.38
0.0362	292	34.25	2.782	3.10
0.0360	290	34.48	2.691	4.28
0.0357	288	34.72	2.584	6.14
0.0355	286	34.97	2.457	9.06×10^{-2}
0.0352	284	35.21	2.303	1.37×10^{-1}
0.0350	282	35.46	2.113	2.14
0.0347	280	35.71	1.875	3.49
0.0345	278	35.97	1.590	6.03×10^{-1}
0.0342	276	36.23	1.346	1.06×10^{0}
0.0340	274	36.50	1.306	1.67
0.0337	272	36.76	1.485	2.30

TABLE II (*Continued*)

$Al_{0.36}Ga_{0.64}As$

eV	cm^{-1}	μm	n	k
0.0335	270	37.04	1.879	2.90
0.0332	268	37.31	2.539	3.41
0.0330	266	37.59	3.473	3.63
0.0327	264	37.88	4.436	3.33
0.0325	262	38.17	5.024	2.65
0.0322	260	38.46	5.187	1.98
0.0320	258	38.76	5.132	1.48
0.0317	256	39.06	5.005	1.14×10^{0}
0.0315	254	39.37	4.869	9.03×10^{-1}
0.0312	252	39.68	4.743	7.38
0.0310	250	40.00	4.632	6.18
0.0304	245	40.82	4.414	4.30
0.0298	240	41.67	4.259	3.25
0.0291	235	42.55	4.144	2.58
0.0285	230	43.48	4.056	2.13
0.0279	225	44.44	3.986	1.81
0.0273	220	45.45	3.929	1.56
0.0267	215	46.51	3.882	1.37
0.0260	210	47.62	3.842	1.22
0.0254	205	48.78	3.808	1.10×10^{-1}
0.0248	200	50.00	3.779	9.92×10^{-2}
0.0207	167	60.00	3.651	5.77
0.0177	143	70.00	3.599	4.19
0.0155	125	80.00	3.572	3.34
0.0138	111	90.00	3.555	2.80
0.0124	100	100.00	3.544	2.42

TABLE II (*Continued*)

Values of n and k for $Al_{0.44}Ga_{0.56}As$ from Various References[a]

eV	cm^{-1}	μm	n	k
0.2480	2000	5.00	3.127[3]	
0.2066	1667	6.00	3.122	
0.1771	1429	7.00	3.117	
0.1550	1250	8.00	3.110	
0.1378	1111	9.00	3.102	
0.1240	1000	10.00	3.093	
0.1227	990	10.10	3.092	
0.1215	980	10.20	3.091	
0.1203	970	10.31	3.090	
0.1190	960	10.42	3.089	
0.1178	950	10.53	3.088	
0.1165	940	10.64	3.086	
0.1153	930	10.75	3.085	
0.1141	920	10.87	3.084	
0.1128	910	10.99	3.082	
0.1116	900	11.11	3.081	
0.1103	890	11.24	3.080	
0.1091	880	11.36	3.078	
0.1079	870	11.49	3.076	
0.1066	860	11.63	3.075	
0.1054	850	11.76	3.073	
0.1041	840	11.90	3.071	
0.1029	830	12.05	3.069	
0.1017	820	12.20	3.067	
0.1004	810	12.35	3.065	
0.0992	800	12.50	3.063	
0.0979	790	12.66	3.060	
0.0967	780	12.82	3.058	
0.0955	770	12.99	3.055	
0.0942	760	13.16	3.053	
0.0930	750	13.33	3.050	
0.0917	740	13.51	3.047	
0.0905	730	13.70	3.044	
0.0893	720	13.89	3.040	
0.0880	710	14.08	3.037	
0.0868	700	14.29	3.033	
0.0855	690	14.49	3.029	
0.0843	680	14.71	3.024	
0.0831	670	14.93	3.020	
0.0818	660	15.15	3.015	
0.0806	650	15.38	3.009	
0.0793	640	15.63	3.004	
0.0781	630	15.87	2.997	
0.0769	620	16.13	2.991	
0.0756	610	16.39	2.984	
0.0744	600	16.67	2.976	
0.0731	590	16.95	2.967	
0.0719	580	17.24	2.958	
0.0707	570	17.54	2.948	
0.0694	560	17.86	2.936	

TABLE II (*Continued*)

$Al_{0.44}Ga_{0.56}As$

eV	cm^{-1}	μm	n	k
0.0682	550	18.18	2.924	
0.0669	540	18.52	2.910	
0.0657	530	18.87	2.895	
0.0645	520	19.23	2.877	
0.0632	510	19.61	2.857	
0.0620	500	20.00	2.834	
0.0608	490	20.41	2.808	
0.0595	480	20.83	2.777	
0.0583	470	21.28	2.741	
0.0570	460	21.74	2.697	
0.0558	450	22.22	2.642	
0.0555	448	22.32	2.630	
0.0553	446	22.42	2.617	
0.0550	444	22.52	2.603	
0.0548	442	22.62	2.589	
0.0546	440	22.73	2.574	
0.0543	438	22.83	2.558	
0.0541	436	22.94	2.541	
0.0538	434	23.04	2.523	
0.0536	432	23.15	2.504	
0.0533	430	23.26	2.484	
0.0531	428	23.36	2.463	1.07×10^{-2} [3]
0.0528	426	23.47	2.440	1.34
0.0526	424	23.58	2.415	1.64
0.0523	422	23.70	2.389	1.98
0.0521	420	23.81	2.361	2.37
0.0518	418	23.92	2.331	2.81
0.0516	416	24.04	2.298	3.31
0.0513	414	24.15	2.263	3.89
0.0511	412	24.27	2.224	4.57
0.0508	410	24.39	2.182	5.35
0.0506	408	24.51	2.135	6.27
0.0503	406	24.63	2.084	7.37
0.0501	404	24.75	2.027	8.68×10^{-2}
0.0498	402	24.88	1.963	1.03×10^{-1}
0.0496	400	25.00	1.891	1.22
0.0493	398	25.13	1.809	1.47
0.0491	396	25.25	1.715	1.79
0.0488	394	25.38	1.607	2.21
0.0486	392	25.51	1.480	2.79
0.0484	390	25.64	1.331	3.63
0.0481	388	25.77	1.160	4.90
0.0479	386	25.91	0.983	6.84
0.0476	384	26.04	0.844	9.53×10^{-1}
0.0474	382	26.18	0.770	1.26×10^{0}
0.0471	380	26.32	0.751	1.58
0.0469	378	26.46	0.774	1.91
0.0466	376	26.60	0.832	2.25
0.0464	374	26.74	0.930	2.61
0.0461	372	26.88	1.077	3.01

TABLE II (*Continued*)

$Al_{0.44}Ga_{0.56}As$

eV	cm^{-1}	μm	n	k
0.0459	370	27.03	1.297	3.44
0.0456	368	27.17	1.632	3.92
0.0454	366	27.32	2.156	4.43
0.0451	364	27.47	2.984	4.89
0.0449	362	27.62	4.188	5.02
0.0446	360	27.78	5.463	4.43
0.0444	358	27.93	6.135	3.28
0.0441	356	28.09	6.146	2.24
0.0439	354	28.25	5.884	1.55
0.0436	352	28.41	5.578	1.11×10^{0}
0.0434	350	28.57	5.299	8.23×10^{-1}
0.0431	348	28.74	5.060	6.32
0.0429	346	28.90	4.859	4.99
0.0426	344	29.07	4.689	4.03
0.0424	342	29.24	4.543	3.31
0.0422	340	29.41	4.417	2.76
0.0419	338	29.59	4.307	2.32
0.0417	336	29.76	4.210	1.98
0.0414	334	29.94	4.124	1.69
0.0412	332	30.12	4.046	1.46
0.0409	330	30.30	3.975	1.27
0.0407	328	30.49	3.910	1.10×10^{-1}
0.0404	326	30.67	3.850	9.61×10^{-2}
0.0402	324	30.86	3.793	8.41
0.0399	322	31.06	3.740	7.37
0.0397	320	31.25	3.690	6.47
0.0394	318	31.45	3.642	5.69
0.0392	316	31.65	3.595	5.01
0.0389	314	31.85	3.550	4.42
0.0387	312	32.05	3.506	3.91
0.0384	310	32.26	3.461	3.48
0.0382	308	32.47	3.417	3.12
0.0379	306	32.68	3.372	2.84
0.0377	304	32.89	3.326	2.64
0.0374	302	33.11	3.279	2.52
0.0372	300	33.33	3.229	2.50
0.0369	298	33.56	3.177	2.59
0.0367	296	33.78	3.121	2.83
0.0365	294	34.01	3.060	3.25
0.0362	292	34.25	2.993	3.90
0.0360	290	34.48	2.919	4.89
0.0357	288	34.72	2.834	6.32
0.0355	286	34.97	2.737	8.43×10^{-2}
0.0352	284	35.21	2.623	1.15×10^{-1}
0.0350	282	35.46	2.486	1.63
0.0347	280	35.71	2.320	2.37
0.0345	278	35.97	2.114	3.59
0.0342	276	36.23	1.868	5.75
0.0340	274	36.50	1.628	9.58×10^{-1}
0.0337	272	36.76	1.533	1.52×10^{0}

TABLE II (*Continued*)

$Al_{0.44}Ga_{0.56}As$

eV	cm^{-1}	μm	n	k
0.0335	270	37.04	1.674	2.16
0.0332	268	37.31	2.068	2.79
0.0330	266	37.59	2.770	3.30
0.0327	264	37.88	3.761	3.46
0.0325	262	38.17	4.695	3.03
0.0322	260	38.46	5.156	2.29
0.0320	258	38.76	5.211	1.64
0.0317	256	39.06	5.100	1.20×10^{0}
0.0315	254	39.37	4.951	9.11×10^{-1}
0.0312	252	39.68	4.808	7.16
0.0310	250	40.00	4.682	5.80
0.0304	245	40.82	4.439	3.80
0.0298	240	41.67	4.271	2.74
0.0291	235	42.55	4.149	2.12
0.0285	230	43.48	4.057	1.70
0.0279	225	44.44	3.985	1.42
0.0273	220	45.45	3.927	1.21
0.0267	215	46.51	3.878	1.04×10^{-1}
0.0260	210	47.62	3.838	9.18×10^{-2}
0.0254	205	48.78	3.803	8.16
0.0248	200	50.00	3.773	7.32
0.0207	167	60.00	3.644	4.09
0.0177	143	70.00	3.591	2.92
0.0155	125	80.00	3.563	2.30
0.0138	111	90.00	3.547	1.92
0.0124	100	100.00	3.535	1.65

TABLE II (*Continued*)

Values of n and k for $Al_{0.54}Ga_{0.46}As$ from Various References[a]

eV	cm^{-1}	μm	n	k
0.2480	2000	5.00	3.088[3]	
0.2066	1667	6.00	3.083	
0.1771	1429	7.00	3.078	
0.1550	1250	8.00	3.071	
0.1378	1111	9.00	3.062	
0.1240	1000	10.00	3.053	
0.1227	990	10.10	3.052	
0.1215	980	10.20	3.051	
0.1203	970	10.31	3.049	
0.1190	960	10.42	3.048	
0.1178	950	10.53	3.047	
0.1165	940	10.64	3.046	
0.1153	930	10.75	3.044	
0.1141	920	10.87	3.043	
0.1128	910	10.99	3.042	
0.1116	900	11.11	3.040	
0.1103	890	11.24	3.039	
0.1091	880	11.36	3.037	
0.1079	870	11.49	3.035	
0.1066	860	11.63	3.033	
0.1054	850	11.76	3.032	
0.1041	840	11.90	3.030	
0.1029	830	12.05	3.028	
0.1017	820	12.20	3.025	
0.1004	810	12.35	3.023	
0.0992	800	12.50	3.021	
0.0979	790	12.66	3.018	
0.0967	780	12.82	3.016	
0.0955	770	12.99	3.013	
0.0942	760	13.16	3.010	
0.0930	750	13.33	3.007	
0.0917	740	13.51	3.004	
0.0905	730	13.70	3.000	
0.0893	720	13.89	2.997	
0.0880	710	14.08	2.993	
0.0868	700	14.29	2.989	
0.0855	690	14.49	2.985	
0.0843	680	14.71	2.980	
0.0831	670	14.93	2.975	
0.0818	660	15.15	2.970	
0.0806	650	15.38	2.964	
0.0793	640	15.63	2.958	
0.0781	630	15.87	2.951	
0.0769	620	16.13	2.944	
0.0756	610	16.39	2.936	
0.0744	600	16.67	2.928	
0.0731	590	16.95	2.919	
0.0719	580	17.24	2.908	
0.0707	570	17.54	2.897	
0.0694	560	17.86	2.885	

TABLE II (*Continued*)

$Al_{0.54}Ga_{0.46}As$

eV	cm^{-1}	μm	n	k
0.0682	550	18.18	2.871	
0.0669	540	18.52	2.856	
0.0657	530	18.87	2.839	
0.0645	520	19.23	2.820	
0.0632	510	19.61	2.798	
0.0620	500	20.00	2.772	
0.0608	490	20.41	2.743	
0.0595	480	20.83	2.708	
0.0583	470	21.28	2.667	
0.0570	460	21.74	2.616	
0.0558	450	22.22	2.553	$1.10x10^{-2}$[3]
0.0555	448	22.32	2.539	1.25
0.0553	446	22.42	2.524	1.41
0.0550	444	22.52	2.508	1.59
0.0548	442	22.62	2.491	1.78
0.0546	440	22.73	2.473	2.00
0.0543	438	22.83	2.454	2.23
0.0541	436	22.94	2.434	2.48
0.0538	434	23.04	2.413	2.77
0.0536	432	23.15	2.391	3.08
0.0533	430	23.26	2.367	3.43
0.0531	428	23.36	2.341	3.81
0.0528	426	23.47	2.313	4.24
0.0526	424	23.58	2.284	4.73
0.0523	422	23.70	2.252	5.27
0.0521	420	23.81	2.218	5.89
0.0518	418	23.92	2.180	6.60
0.0516	416	24.04	2.140	7.41
0.0513	414	24.15	2.096	8.34
0.0511	412	24.27	2.047	$9.43x10^{-2}$
0.0508	410	24.39	1.994	$1.07x10^{-1}$
0.0506	408	24.51	1.934	1.23
0.0503	406	24.63	1.868	1.41
0.0501	404	24.75	1.793	1.64
0.0498	402	24.88	1.709	1.92
0.0496	400	25.00	1.612	2.28
0.0493	398	25.13	1.501	2.76
0.0491	396	25.25	1.372	3.41
0.0488	394	25.38	1.224	4.35
0.0486	392	25.51	1.061	5.74
0.0484	390	25.64	0.905	$7.76x10^{-1}$
0.0481	388	25.77	0.790	$1.03x10^{0}$
0.0479	386	25.91	0.728	1.31
0.0476	384	26.04	0.707	1.60
0.0474	382	26.18	0.717	1.90
0.0471	380	26.32	0.753	2.20
0.0469	378	26.46	0.815	2.53
0.0466	376	26.60	0.910	2.88
0.0464	374	26.74	1.047	3.27
0.0461	372	26.88	1.249	3.70

TABLE II (*Continued*)

$Al_{0.54}Ga_{0.46}As$

eV	cm^{-1}	μm	n	k
0.0459	370	27.03	1.552	4.20
0.0456	368	27.17	2.028	4.75
0.0454	366	27.32	2.802	5.32
0.0451	364	27.47	4.038	5.69
0.0449	362	27.62	5.623	5.32
0.0446	360	27.78	6.702	4.02
0.0444	358	27.93	6.825	2.66
0.0441	356	28.09	6.500	1.74
0.0439	354	28.25	6.105	1.19×10^{0}
0.0436	352	28.41	5.751	8.54×10^{-1}
0.0434	350	28.57	5.454	6.35
0.0431	348	28.74	5.208	4.86
0.0429	346	28.90	5.003	3.81
0.0426	344	29.07	4.831	3.04
0.0424	342	29.24	4.684	2.46
0.0422	340	29.41	4.557	2.00
0.0419	338	29.59	4.446	1.65
0.0417	336	29.76	4.348	1.36
0.0414	334	29.94	4.261	1.12×10^{-1}
0.0412	332	30.12	4.183	9.28×10^{-2}
0.0409	330	30.30	4.112	7.63
0.0407	328	30.49	4.047	6.24
0.0404	326	30.67	3.987	5.03
0.0402	324	30.86	3.932	3.99
0.0399	322	31.06	3.880	3.08
0.0397	320	31.25	3.831	2.29
0.0394	318	31.45	3.785	1.58×10^{-2}
0.0392	316	31.65	3.741	9.54×10^{-3}
0.0389	314	31.85	3.699	3.97×10^{-3}
0.0387	312	32.05	3.658	9.83×10^{-4}
0.0384	310	32.26	3.617	5.38×10^{-3}
0.0382	308	32.47	3.578	9.25×10^{-3}
0.0379	306	32.68	3.539	1.26×10^{-2}
0.0376	304	32.89	3.499	1.55
0.0374	302	33.11	3.460	1.78
0.0372	300	33.33	3.419	1.95
0.0369	298	33.56	3.377	2.05
0.0367	296	33.78	3.333	2.07
0.0365	294	34.01	3.286	1.98
0.0362	292	34.25	3.237	1.76
0.0360	290	34.48	3.183	1.36×10^{-2}
0.0357	288	34.72	3.123	7.14×10^{-3}
0.0355	286	34.97	3.057	2.81×10^{-3}
0.0352	284	35.21	2.982	1.78×10^{-2}
0.0350	282	35.46	2.896	4.03
0.0347	280	35.71	2.795	7.45×10^{-2}
0.0345	278	35.97	2.674	1.27×10^{-1}
0.0342	276	36.23	2.531	2.12
0.0340	274	36.50	2.362	3.51
0.0337	272	36.76	2.183	5.86

TABLE II (*Continued*)

$Al_{0.54}Ga_{0.46}As$

eV	cm^{-1}	μm	n	k
0.0335	270	37.04	2.056	9.63×10^{-1}
0.0332	268	37.31	2.104	1.46×10^{0}
0.0330	266	37.59	2.407	1.96
0.0327	264	37.88	2.949	2.30
0.0325	262	38.17	3.606	2.33
0.0322	260	38.46	4.145	2.05
0.0320	258	38.76	4.430	1.64
0.0317	256	39.06	4.514	1.27×10^{0}
0.0315	254	39.37	4.495	9.91×10^{-1}
0.0312	252	39.68	4.436	7.88
0.0310	250	40.00	4.367	6.42
0.0304	245	40.82	4.208	4.20
0.0298	240	41.67	4.084	3.02
0.0291	235	42.55	3.991	2.32
0.0285	230	43.48	3.919	1.86
0.0279	225	44.44	3.862	1.54
0.0273	220	45.45	3.815	1.30
0.0267	215	46.51	3.775	1.12×10^{-2}
0.0260	210	47.62	3.742	9.82
0.0254	205	48.78	3.713	8.70
0.0248	200	50.00	3.688	7.77
0.0207	167	60.00	3.578	4.26
0.0177	143	70.00	3.532	3.01
0.0155	125	80.00	3.508	2.37
0.0138	111	90.00	3.493	1.96
0.0124	100	100.00	3.483	1.69

[a]References are indicated in brackets.

TABLE III

Oscillator Parameters Obtained from the Curve Fitting by Using a Factorized Form of a Dielectric Function; ν and γ in cm^{-1}

x	ν_{t1}	ν_{l1}	γ_{t1}	γ_{l1}	ν_{t2}	ν_{l2}	γ_{t2}	γ_{l2}	ε
0.14	267.1	285.7	5.67	4.85	358.8	369.0	10.56	11.31	10.57
0.18	266.9	283.4	8.76	4.24	360.1	372.4	12.20	10.24	10.47
0.30	265.2	278.3	8.64	6.15	360.2	379.1	12.10	9.42	10.16
0.36	264.5	276.5	10.69	5.58	360.4	381.3	12.23	8.08	10.04
0.44	262.9	273.7	10.05	6.44	360.2	385.4	9.55	7.90	9.84
0.54	261.8	269.8	12.43	7.97	361.5	390.1	8.75	8.68	9.60

Cadmium Selenide (CdSe)

H. PILLER
Louisiana State University
Baton Rouge, Louisiana

Cadmium selenide is a tetrahedral semiconductor with wurtzite structure in the hexagonal modification. CdSe is an optically uniaxial semiconductor with two components of the dielectric function. Measurements of the reflectivity spectra of CdSe crystals with polarized light have shown strong differences for the electric vector parallel ($\mathbf{E}\|c$) and perpendicular ($\mathbf{E}\perp c$) to the hexagonal axis. The room-temperature reflectivity of hexagonal CdSe was measured by Cardona and Harbeke [1] in the 0.8–12 eV region with linearly polarized light. Measurements were performed with the electric vector parallel and perpendicular to the c axis of the crystal. From these reflection measurements, extended with unpolarized light to the region between 11.3 and 22.5 eV, the optical constants were determined by means of the Kramers–Kronig technique. The crystals were polished in a crystal plane containing the hexagonal axis; however, no satisfactory etchant was found. The measurements were performed on polished, unetched surfaces; hence, the spectra obtained must be somewhat smeared out. The orientation of the c axis was determined by X-ray diffraction. The optical constants n and k, as read from the graph, are listed in Table I and plotted in Fig. 1 for both the ordinary (o) and extraordinary (e) rays. The numbers are probably correct to two figures.

Logothetidis *et al.* [2] investigated the real and imaginary parts of the ordinary and extraordinary dielectric functions of CdSe as a function of temperature with a scanning rotating-analyzer ellipsometer in the spectral range 1.3–5.5 eV. The measurements were made at 15, 210, 400, and 550 K. Automatic spectroscopic ellipsometry is an excellent technique to measure the real and imaginary parts of the dielectric function. On-line digitization of the data permits a fast and efficient analysis of the optical response of the semiconductor crystal. Ellipsometry is a sensitive technique used to investigate the optical response as it yields information on both the amplitude and the phase of the reflected polarized light beam. The data show strong structures in the optical spectra in the 4–5.5 eV region. For $\mathbf{E}\|c$ only one peak is seen, whereas three peaks are observed for $\mathbf{E}\perp c$. The absorption edge of CdSe exhibits three excitonic structures.

Copyright © 1991 by Academic Press.
All rights of reproduction in any form reserved.
ISBN 0-12-544422-2

The lowest excitation energy is 1.741 eV at 295 K. These peaks have been interpreted in terms of interband transitions modified by excitonic interaction. The spectra of the dielectric function were obtained using the two-phase model (ambient and uniaxially anisotropic substrate) of the interface. No additional corrections for possible surface overlayers or roughness were made (for the edge excitons, three-phase models were used to take exciton-free layers into account). All measurements were made at an angle of incidence of 67.5°. The sample surface treatment included mechanical lapping and polishing with Syton (Monsanto Chemical Co.) in a plane surface parallel to the c axis. Chemical etching was used to remove the distorted layer produced by the mechanical polishing. The maximization of the real part of the complex dielectric constant, ε_1, around the E_1 structure (in the 4–5.5 eV region) was used as a criterion of quality of the surface. The method of surface preparation involved the cleaning of a surface growth with methanol and distilled water, while the sample was kept under the flow of dry nitrogen. This method gave the highest values of ε_1. No systematic investigation of the effect of a possible residual oxide layer was made. The values of $n_{o,e}$ and $k_{o,e}$ were calculated from the values of ε_1 and ε_2 as read from the graphs. The tabulated data are for 210 K (except the n_o and k_o values in the photon-energy range 1.3–2 eV, which were measured at 330 K). The numbers are listed in Table I and are plotted in Fig. 1 for both o and e rays.

The absorption spectra of undoped semi-insulating CdSe were measured from 0.6–1.8 eV by Rosen *et al.* [3]. The absorption spectra showed indirect absorption from energy levels of the shallow-acceptor defect, including a possible deep level at 1.3 eV. The absorption (of sample H_1) was fitted with the following expression for the absorption coefficient α:

$$\alpha(\hbar\omega) = A + B(\hbar\omega - E_0),$$

where $\hbar\omega$ is the photon energy, $T = 293$ K, $A = 2.5\,\mathrm{cm}^{-1}$, $B = 6.1 \times 10^{-3}\,\mathrm{meV}^{-2}\,\mathrm{cm}^{-1}$, and $E_0 = 110$ meV. E_0 is the threshold energy, A is the deep-state absorption near E_0, and B is an indirect absorption parameter. The slopes of the absorption components were nearly temperature-independent. The deep-level absorption changed with temperature, indicating association with the shallow acceptor. The undoped samples of CdSe were made semi-insulating by treatment with Se vapor. The thickness of the samples were in the 1.55–2 mm. The c axis of the samples was perpendicular to the surface. The absorption coefficient was calculated at each wavelength and corrected for reflection at the two surfaces. We calculated the imaginary part of the complex refractive index k from the absorption data given in the graph [3, Fig. 7]. The results are listed in Table I and are plotted in Fig. 1.

Beserman [4] measured the infrared absorption by pure CdSe platelets

in the range of frequencies $300\,cm^{-1}$–$465\,cm^{-1}$. The experiments were performed at room temperature with an experimental resolution of approximately $1\,cm^{-1}$. The observed main absorption peaks in the range of combination of optical modes are at 329, 354, 365, and $371\,cm^{-1}$. Raman-scattering measurements were made on the same platelets. The following phonon frequencies (cm^{-1}) were obtained from the infrared absorption and Raman data: $TA = 43.5$, $LO_\Gamma = 210$, $TO_\Gamma = 168$. Table I lists k as calculated from the data given in the graph in Beserman [4, Fig. 1]. Fig. 1 shows k.

The spectral dependence of the refractive index and birefringence of CdSe single crystals was investigated in a wide temperature and wavelength range by Lisita *et al.* [5]. The single crystals were grown by sublimation from the gaseous phase and had a conductivity in the range 10^{-10}–$10^{-11}\,\Omega^{-1}\,cm^{-1}$. The direction of the c axis was determined by using X-ray analysis with an accuracy of 20 min. In the spectral region between the fundamental absorption edge and $\nu = 5000\,cm^{-1}$, the refractive index was determined by the prism method. Prisms were cut in such a way that the optical axis of the crystal was parallel to the refracting edge. The absolute error in determining n was about 5×10^{-4}. In the spectral region $\nu < 5000\,cm^{-1}$, the interference method was used to determine the refractive index n_o of the ordinary beam. The corresponding values of n_e were calculated according to the equation $n_e = n_o + \Delta n$. The absolute error in determining n_o using the interference method was about 5×10^{-3}. The dispersion of the birefringence was measured by the method of interference of polarized beams. The absolute error in determining Δn was between 2×10^{-5} and 4×10^{-5}. The measurements were performed in a temperature interval between 100 and 600 K. The room-temperature measurements show that $n_e > n_o$ for all crystals. The numerical values of n_o and n_e are in good agreement with the data by Bond [6]. We have listed the values of n_o and n_e in Table I. Pikhtin and Yas'kov [7] have refitted the data with an oscillator-model formula obtained from the Kramers–Kronig dispersion relations. Additional data points listed in Table I and plotted in Fig. 1 were calculated using these analytic expressions [7].

Transmission and reflection spectra were measured on CdSe single crystals in the region of 3.6–5.9 eV at 109 K and at room temperature by Lange and Iliev [8]. The optical constants were calculated from these data and agree well with the data of Ludeke and Paul [9] on CdSe thin films and agree semiquantitatively with those obtained by ellipsometry [2]. The plate-shaped, single-crystal samples were grown from the vapor phase. Thickness of the samples was measured by means of an interference microscope and ranged between 100 and 150 nm. The in-out technique was used in the optical experiments. The multiple internal reflections in the sample were neglected in calculating the absorption coefficient and the refractive index from experimental spectra.

Polarized synchrotron radiation was used by Freeouf [10] to measure the reflectance spectra for photon energies between 0.6 and 30 eV at temperatures between 90 and 400 K. The optical constants were determined by Kramers–Kronig analysis. Synchrotron radiation provides an intense polarized continuum spectrum of light throughout the ultraviolet spectral region. The reflectance was measured by the rotating-light-pipe, scanning-reflectometer technique. The precision of the reflectance measurements was lower for photon energies larger than 8 eV. The single crystals of CdSe were cleaved just prior to mounting in the experimental system.

Terekhova *et al.* [11] measured the ordinary and extraordinary refractive index in the photon-energy region of 1.88–1.76 eV using two-beam interferometry at 5 K. The observed dispersion in the refractive indices was interpreted in terms of exciton states.

Beserman and Balkanski [12] measured the vibrational properties of CdSe at room temperature. The reflectivity was measured on a single crystal of CdSe containing 0.5% S, for $\mathbf{E} \perp \mathbf{c}$ and $\mathbf{E} \| \mathbf{c}$, in the frequency range 100–350 cm^{-1}. The resolution was 1 cm^{-1} in the entire range studied. The real and imaginary parts of the dielectric constant were deduced from the reflectance data by means of the Kramers–Kronig relations in the frequency range 100–300 cm^{-1}. The optical-mode frequencies were calculated from the following equations:

$$\omega_{TO} = \varepsilon_{i\,\max} = 2nk_{\max}$$

$$\omega_{\mathrm{LO}} = \mathrm{Im}(-1/\varepsilon)_{\max} = [2nk/(n^2+k^2)]_{\max}$$

For each polarization two types of oscillators were observed: the TO mode of pure CdSe, whose frequencies are; for $\mathbf{E} \| c$, $\omega_{\mathrm{TO}} = 166.5\ cm^{-1}$, and for $\mathbf{E} \perp c$, $\omega_{\mathrm{TO}} = 169\ cm^{-1}$; and the localized-mode frequencies of S in CdSe. In both polarizations, two localized modes were observed: for $\mathbf{E} \| \mathbf{c}$, 262 cm^{-1} and 266.5 cm^{-1}; for $\mathbf{E} \perp c$, 263 cm^{-1} and 269 cm^{-1}. The LO-mode frequencies were calculated either from $\varepsilon_r = 0$ (ε_r is the real part of the dielectric constant) or from $\mathrm{Im}(-1/\varepsilon) = \max$. Two sets of LO modes were observed: for pure CdSe, $\omega_{\mathrm{LO}} = 210\ cm^{-1}$ ($\mathbf{E} \| c$) and $\omega_{\mathrm{LO}} = 212\ cm^{-1}$ ($\mathbf{E} \perp c$); for *S* in CdSe, $\omega_{\mathrm{LO}} = 262.5\ cm^{-1}$, $268.5\ cm^{-1}$ ($\mathbf{E} \| c$), and $\omega_{\mathrm{LO}} = 263.5\ cm^{-1}$, $270.5\ cm^{-1}$ ($\mathbf{E} \perp c$). We calculated the real and imaginary parts of the complex refractive index from the corresponding real and imaginary parts of the dielectric constant for the ordinary and extraordinary rays from the experimental data given in the graphs [12, Figs. 2 and 3]. The results are listed in Table I and plotted in Fig. 1.

Geick, Perry, and Mitra [13] measured the reflectivity of single-crystal CdSe with linearly polarized light at room temperature and at liquid-nitrogen temperature. The reflectivity was measured in the spectral region

from 70 cm^{-1} to 375 cm^{-1}. Transmission measurements were made with unpolarized light on polycrystalline samples. The extinction coefficient k was determined from the experimental results for the spectral region from 80 cm^{-1} to 500 cm^{-1}. The spectra were analyzed by means of an optimum fit with a classical dispersion formula. The transmission measurements showed several multiphonon peaks, which were interpreted in terms of four representative phonon energies for the edge of the Brillouin zone.

Verleur and Barker [14] measured the infrared reflectivity over the frequency range from 100 cm^{-1} to 400 cm^{-1} at 15 and 300 K with polarized light. A resolution of 2.5 cm^{-1} was maintained over the entire frequency range. Agreement between different runs on the same specimen was within 1%. "Pure" CdSe was found to contain up to 2% S. A single-crystal specimen containing 1.5% sulphur was used in the reflectivity measurements. Classical oscillator fits of the reflectivity spectrum were used to determine the mode parameters and related constants.

REFERENCES

1. M. Cardona and G. Harbeke, *Phys. Rev.* **137**, 1467 (1965).
2. S. Logothetidis, M. Cardona, P. Lautenschlager, and M. Garriga, *Phys. Rev. B* **34**, 2458 (1986).
3. D. L. Rosen, Q. X. Li, and R. R. Alfano, *Phys. Rev. B* **31**, 2396 (1985).
4. R. Beserman, *Solid State Commun.* **23**, 323 (1977).
5. M. P. Lisita, L. F. Gudymenko, V. N. Malinko, and S. F. Terekhova, *Phys. Status Solidi* **31**, 389 (1969).
6. W. L. Bond, *J. Appl. Phys.* **36**, 1674 (1965).
7. A. N. Pikhtin and A. D. Yas'kov, *Sov. Phys. Semicond.* **15**, 8 (1981).
8. H. Lange and I. A. Iliev, *Phys. Status Solidi B* **84**, 569 (1977).
9. R. Ludeke and W. Paul, *Phys. Status Solidi* **23**, 413 (1967); "Proc. 7th Internat. Conf. II-VI Compounds," (D. G. Thomas ed.) Benjamin, New York, Providence, 123 (1967).
10. J. L. Freeouf, *Phys. Rev. B* **7**, 3810 (1973).
11. S. F. Terekhova, N. A. Onishchenko, O. N. Talenskii, S. A. Pendur, *Phys. Status Solidi B* **131**, 207 (1985).
12. R. Beserman and M. Balkanski, *Phys. Rev. B* **1**, 608 (1970).
13. R. Geick, C. H. Perry, and S. S. Mitra, *J. Appl. Phys.* **37**, 1994 (1966).
14. H. W. Verleur and A. S. Barker, Jr., *Phys. Rev.* **155**, 750 (1967).

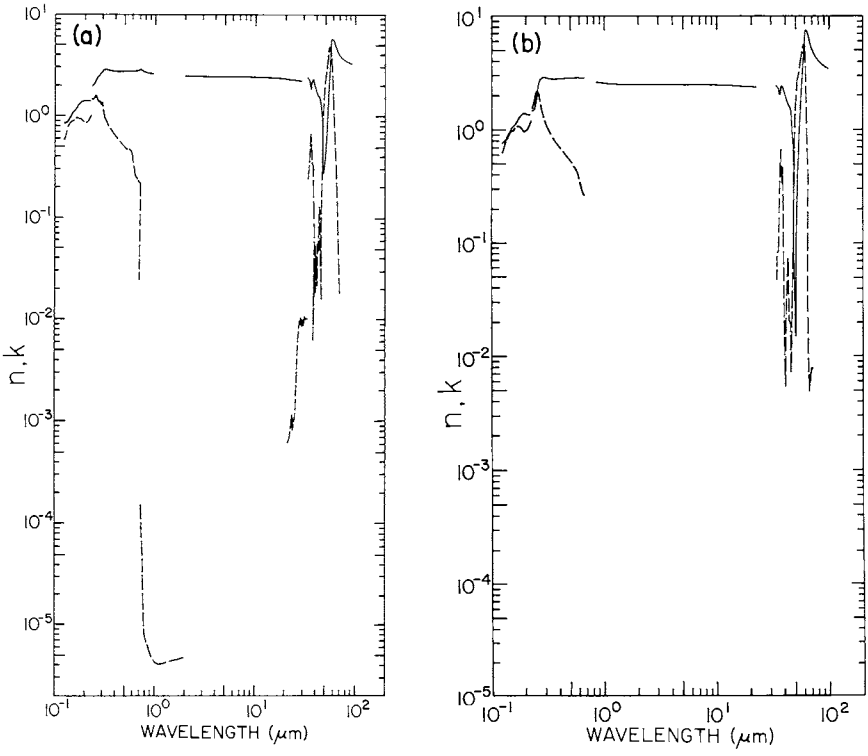

Fig. 1. (a) Log–log plot of n_o (solid line) and k_o (dashed line) versus wavelength in micrometers for cadmium selenide. (b) Log–log plot of n_e (solid line) and k_e (dashed line) versus wavelength in micrometers.

TABLE I

Values of n and k for Cadmium Selenide Obtained from Various References[a]

eV	μm	$n_\perp$	$k_\perp$	$n_\parallel$	$k_\parallel$
10.000	0.1240		0.591 [1]		0.625 [1]
9.959	0.1245	0.862 [1]		0.771 [1]	
9.867	0.1257			0.774	0.650
9.848	0.1259		0.599		
9.800	0.1265	0.848			
9.794	0.1266			0.781	
9.747	0.1272	0.847			0.675
9.738	0.1273		0.624		
9.710	0.1277			0.787	
9.651	0.1285				0.698
9.628	0.1288		0.650		
9.585	0.1293			0.793	
9.582	0.1294	0.846			
9.537	0.1300		0.678		
9.482	0.1308			0.792	
9.463	0.1310				0.747
9.431	0.1315		0.715		
9.364	0.1324	0.851		0.805	
9.311	0.1332		0.746		0.788
9.258	0.1339			0.811	
9.201	0.1348		0.769		
9.183	0.1350	0.865			
9.130	0.1358				0.835
9.102	0.1362		0.793	0.833	
8.999	0.1378			0.849	
8.984	0.1380		0.819		
8.962	0.1384				0.885
8.943	0.1386	0.901			
8.861	0.1399		0.840		
8.840	0.1403			0.880	
8.809	0.1407				0.923
8.735	0.1419		0.859	0.910	
8.709	0.1424				0.950
8.632	0.1436		0.877		
8.622	0.1438	0.968			
8.615	0.1439				0.974
8.575	0.1446			0.956	
8.512	0.1457		0.897		
8.499	0.1459				0.977
8.463	0.1465			0.988	
8.400	0.1476	1.016	0.907		
8.308	0.1492				0.972
8.301	0.1494		0.910	1.034	
8.263	0.1500	1.058			
8.201	0.1512		0.903		

TABLE I (*Continued*)

Cadmium Selenide

eV	μm	n_o	k_o	n_e	k_e
8.166	0.1518				0.971
8.163	0.1519			1.069	
8.101	0.1531	1.092			
8.088	0.1533		0.900		
8.045	0.1541			1.076	
7.972	0.1555		0.910		
7.968	0.1556				0.980
7.945	0.1561	1.111			
7.930	0.1564			1.082	
7.852	0.1579				1.014
7.849	0.1580		0.935		
7.814	0.1587			1.082	
7.802	0.1589	1.120			
7.771	0.1596			1.088	
7.758	0.1598		0.955		
7.748	0.1600				1.050
7.705	0.1609			1.096	
7.687	0.1613		0.967		
7.630	0.1620	1.148			
7.629	0.1622				1.066
7.608	0.1630			1.119	
7.583	0.1635		0.976		
7.527	0.1647			1.158	
7.506	0.1652				1.080
7.499	0.1653		0.968		
7.437	0.1667	1.213			
7.403	0.1675			1.217	
7.300	0.1699	1.256			1.084
7.266	0.1706		0.949		
7.225	0.1716			1.278	
7.184	0.1726	1.288			
7.108	0.1744				1.070
7.066	0.1755		0.942		
7.053	0.1758			1.326	
7.031	0.1763	1.325			
6.907	0.1795		0.947		
6.862	0.1807				1.046
6.797	0.1824		0.924		
6.782	0.1828			1.364	
6.692	0.1853			1.380	
6.665	0.1860		0.904		
6.604	0.1877	1.394			
6.589	0.1882			1.427	
6.551	0.1893				0.988

TABLE I (*Continued*)

Cadmium Selenide

eV	cm^{-1}	μm	n_o	k_o	n_e	k_e
6.501		0.1907			1.435	
6.428		0.1929	1.420	0.882		
6.402		0.1937			1.423	
6.367		0.1947				0.957
6.268		0.1978			1.419	
6.244		0.1986				0.957
6.233		0.1989	1.419			
6.192		0.2002		0.865		
6.162		0.2012			1.380	
6.153		0.2015				0.978
6.111		0.2029				1.001
6.090		0.2036	1.418			
6.063		0.2045				1.018
6.040		0.2053			1.368	
6.001		0.2066				1.012
5.988	48299	0.2070		0.870		
5.971	48162	0.2076			1.374	
5.946	47960	0.2085				1.011
5.912	47684	0.2097	1.414			
5.888	47490	0.2106				1.028
5.865	47306	0.2114			1.371	
5.801	46786	0.2137		0.898		
5.781	46627	0.2145	1.401			
5.775	46577	0.2147				1.065
5.753	46401	0.2155			1.357	
5.697	45948	0.2176			1.352	
5.694	45923	0.2178			1.354	
5.691	45898	0.2179				1.098
5.658	45637	0.2191		0.932		
5.631	45420	0.2202	1.392			
5.620	45324	0.2206				1.141
5.590	45089	0.2218		0.958		
5.557	44817	0.2231			1.358	
5.545	44724	0.2236				1.170
5.506	44411	0.2252				1.201
5.497	44333	0.2256			1.506 [2]	1.544 [2]
5.480	44202	0.2262		0.989		
5.444	43912	0.2277			1.505	1.566
5.432	43811	0.2283	1.399			
5.406	43600	0.2294			1.499	1.594
5.361	43237	0.2313		1.028		
5.353	43174	0.2316	1.943 [2]	1.497 [2]		
5.350	43152	0.2317			1.499	1.631
5.318	42894	0.2331			1.487	1.679
5.291	42676	0.2343			1.481	1.712
5.279	42574	0.2349	1.957	1.491		

TABLE I (*Continued*)

Cadmium Selenide

eV	cm^{-1}	μm	n_o	k_o	n_e	k_e
5.259	42418	0.2358			1.490	1.763
5.231	42188	0.2370			1.487	1.829
5.216	42068	0.2377	1.969	1.482		
5.190	41862	0.2389			1.526	1.914
5.170	41699	0.2398			1.555	1.959
5.145	41495	0.2410	1.967	1.481		
5.130	41373	0.2417			1.600	2.020
5.080	40975	0.2441	1.976	1.480		
5.035	40613	0.2462			1.812	2.178
5.021	40496	0.2469	1.991	1.528		
5.013	40436	0.2473			1.886	2.196
4.998	40314	0.2481			1.939	2.208
4.976	40136	0.2492	2.020	1.580		
4.965	40042	0.2497			2.046	2.214
4.941	39852	0.2509			2.096	2.217
4.931	39771	0.2514			2.121	2.215
4.922	39696	0.2519	2.062	1.623		
4.910	39603	0.2525	2.084	1.639		
4.874	39309	0.2544			2.269	2.198
4.857	39173	0.2553			2.320	2.187
4.842	39051	0.2561			2.364	2.178
4.828	38942	0.2568			2.399	2.169
4.826	38923	0.2569	2.229	1.647		
4.822	38888	0.2572			2.425	2.152
4.811	38807	0.2577			2.449	2.143
4.800	38712	0.2583			2.486	2.129
4.798	38698	0.2584			2.490	2.126
4.786	38603	0.2591			2.515	2.113
4.768	38454	0.2601			2.556	2.088
4.756	38359	0.2607	2.344	1.590	2.581	2.070
4.751	38318	0.2610			2.593	2.063
4.734	38182	0.2619			2.626	2.040
4.729	38141	0.2622			2.639	2.027
4.710	37992	0.2632			2.675	1.999
4.695	37870	0.2641			2.694	1.983
4.690	37829	0.2644			2.705	1.972
4.673	37693	0.2653			2.714	1.956
4.666	37631	0.2657	2.436	1.491		
4.663	37612	0.2659			2.745	1.930
4.646	37476	0.2668			2.774	1.889
4.635	37381	0.2675			2.787	1.869
4.625	37299	0.2681			2.808	1.858
4.613	37204	0.2688			2.817	1.833
4.600	37098	0.2696	2.443	1.434		
4.588	37001	0.2703			2.834	1.773
4.571	36865	0.2713			2.850	1.745

TABLE I (*Continued*)

Cadmium Selenide

eV	cm^{-1}	μm	n_o	k_o	n_e	k_e
4.562	36791	0.2718	2.438	1.408		
4.556	36743	0.2722			2.870	1.708
4.530	36539	0.2737			2.885	1.664
4.525	36498	0.2740	2.421	1.392		
4.512	36390	0.2748			2.892	1.631
4.502	36308	0.2754			2.910	1.609
4.478	36118	0.2769			2.919	1.571
4.474	36085	0.2771	2.435	1.429		
4.443	35832	0.2791	2.462	1.454		
4.441	35819	0.2792			2.914	1.502
4.407	35548	0.2813			2.915	1.450
4.375	35285	0.2834	2.575	1.419		
4.365	35208	0.2840			2.911	1.392
4.335	34965	0.2860	2.624	1.370		
4.318	34828	0.2871			2.904	1.337
4.299	34672	0.2884	2.621	1.332		
4.266	34407	0.2906			2.897	1.274
4.251	34286	0.2917	2.607	1.302		
4.216	34006	0.2941	2.593	1.313		
4.195	33833	0.2956	2.616	1.349		
4.192	33810	0.2958			2.885	1.203
4.173	33659	0.2971	2.673	1.370		
4.147	33446	0.2990	2.735	1.381		
4.140	33389	0.2995			2.865	1.163
4.124	33260	0.3007	2.779	1.322		
4.091	32993	0.3031	2.837	1.260		
4.066	32791	0.3050			2.845	1.109
4.063	32767	0.3052	2.854	1.201		
4.010	32340	0.3092	2.870	1.114		
3.992	32194	0.3106			2.830	1.069
3.965	31980	0.3127	2.871	1.054		
3.935	31741	0.3151	2.869	1.010		
3.916	31583	0.3166			2.813	1.027
3.904	31487	0.3176	2.864	0.981		
3.869	31208	0.3204	2.854	0.952		
3.831	30901	0.3236	2.843	0.922		
3.797	30621	0.3266	2.834	0.893		
3.795	30605	0.3267			2.793	0.964
3.740	30168	0.3315	2.818	0.859		
3.715	29967	0.3337			2.787	0.936
3.691	29768	0.3359	2.804	0.838		
3.640	29355	0.3407	2.791	0.809		
3.635	29315	0.3411			2.777	0.902
3.567	28769	0.3476	2.778	0.782		
3.540	28555	0.3502			2.767	0.850
3.511	28316	0.3532	2.764	0.760		

TABLE I (*Continued*)

Cadmium Selenide

eV	cm^{-1}	μm	n_o	k_o	n_e	k_e
3.434	27700	0.3610			2.765	0.817
3.423	27610	0.3622	2.751	0.736		
3.364	27130	0.3686	2.740	0.714		
3.335	26899	0.3718			2.763	0.781
3.258	26277	0.3806	2.724	0.682		
3.256	26260	0.3808			2.763	0.761
3.165	25527	0.3917			2.762	0.731
3.131	25251	0.3960	2.710	0.649		
3.089	24916	0.4014			2.762	0.709
3.046	24571	0.4070	2.704	0.630		
3.019	24346	0.4108			2.764	0.688
2.977	24012	0.4165	2.703	0.615		
2.966	23925	0.4180			2.763	0.675
2.919	23545	0.4247	2.698	0.602		
2.879	23219	0.4307			2.764	0.649
2.842	22919	0.4363	2.695	0.581		
2.822	22757	0.4394			2.771	0.635
2.774	22372	0.4470	2.696	0.566		
2.758	22241	0.4496			2.773	0.619
2.695	21733	0.4601	2.694	0.546		
2.677	21589	0.4632			2.780	0.596
2.594	20924	0.4779			2.785	0.583
2.586	20853	0.4796	2.703	0.523		
2.503	20191	0.4953			2.796	0.551
2.465	19881	0.5030	2.708	0.496		
2.429	19593	0.5104			2.802	0.524
2.362	19050	0.5249			2.812	0.506
2.331	18801	0.5319	2.728	0.478		
2.269	18303	0.5464			2.829	0.482
2.234	18015	0.5551	2.760	0.481		
2.202	17760	0.5631			2.853	0.440
2.196	17708	0.5647	2.765	0.459		
2.175	17543	0.5700			2.866	0.402
2.163	17448	0.5731			2.885	0.422
2.131	17189	0.5818	2.758	0.427		
2.125	17136	0.5836			2.874	0.391
2.076	16742	0.5973			2.853	0.344
2.022	16307	0.6132			2.837	0.311
1.972	15904	0.6288	2.740	0.275		
1.934	15599	0.6411	2.733	0.257		
1.916	15452	0.6472			2.834	0.268
1.891	15253	0.6556	2.733	0.242		
1.877	15140	0.6605	2.739	0.247		
1.861	15010	0.6662	2.741	0.250		
1.840	14841	0.6738			2.862	0.270
1.827	14737	0.6786	2.755	0.231		

TABLE I (*Continued*)

Cadmium Selenide

eV	cm^{-1}	μm	n_o	k_o	n_e	k_e
1.811	14608	0.6846	2.765	0.233		
1.799	14507	0.6893	2.778	0.231		
1.783	14383	0.6953	2.797	0.230		
1.768	14257	0.7014	2.812	0.230		
1.756	14166	0.7059	2.832	0.228		
1.750	14115	0.7085	2.845	0.217		
1.738	14016	0.7135	2.856	0.162		
1.727	13926	0.7181	2.864	0.025		
1.716	13838	0.7226	2.856			
1.706	13758	0.7269	2.841			
1.697	13689	0.7306	2.821			
1.691	13641	0.7331		1.55E-04 [3]		
1.690	13632	0.7336	2.807			
1.683	13571	0.7369		1.24E-04		
1.677	13526	0.7393	2.780			
1.676	13514	0.7400		1.00E-04		
1.667	13447	0.7437		7.88E-05		
1.665	13425	0.7449	2.761			
1.659	13384	0.7472		6.21E-05		
1.655	13348	0.7492	2.746			
1.652	13324	0.7505		5.04E-05		
1.649	13297	0.7520	2.660	[5]		
1.647	13286	0.7527	2.738			
1.640	13229	0.7559		3.67E-05		
1.639	13216	0.7567	2.727			
1.633	13172	0.7592		2.96E-05		
1.632	13164	0.7596	2.721			
1.626	13112	0.7627		2.35E-05		
1.623	13092	0.7638	2.712			
1.614	13017	0.7682		1.74E-05		
1.603	12927	0.7736	2.691			
1.602	12922	0.7739		1.32E-05		
1.593	12852	0.7781		9.93E-06		
1.590	12822	0.7799		8.58E-06		
1.584	12777	0.7826		7.50E-06		
1.573	12689	0.7881	2.673			
1.567	12642	0.7910	2.635			
1.560	12580	0.7949		7.07E-06		
1.552	12514	0.7991	2.659			
1.530	12341	0.8103	2.646			
1.528	12325	0.8113		6.69E-06		
1.497	12075	0.8282	2.634			
1.494	12051	0.8298		6.33E-06		
1.475	11897	0.8406	2.625			
1.459	11765	0.8500	2.608		2.626 [5]	
1.453	11719	0.8534		5.83E-06		

TABLE I (*Continued*)

Cadmium Selenide

eV	cm^{-1}	μm	n_o	k_o	n_e	k_e
1.442	11633	0.8596	2.612			
1.418	11435	0.8746	2.602			
1.417	11427	0.8752		5.51E-06		
1.386	11182	0.8943	2.592			
1.379	11122	0.8991		5.16E-06		
1.354	10921	0.9157	2.583			
1.352	10905	0.9171		4.94E-06		
1.328	10709	0.9338	2.576			
1.321	10655	0.9386		4.67E-06		
1.314	10600	0.9434	2.573			
1.293	10425	0.9592		4.47E-06		
1.265	10205	0.9799		4.23E-06		
1.248	10066	0.9935		4.15E-06		
1.240	10000	1.000	2.547		2.566	
1.229	9916	1.009		4.11E-06		
1.195	9641	1.037		4.14E-06		
1.164	9389	1.065		4.10E-06		
1.127	9089	1.100		4.11E-06		
1.080	8712	1.148		4.13E-06		
1.069	8619	1.160	2.524			
1.044	8423	1.187		4.12E-06		
1.010	8143	1.228		4.13E-06		
0.9659	7791	1.284		4.17E-06		
0.9269	7476	1.338		4.20E-06		
0.9239	7452	1.342	2.500			
0.8811	7107	1.407		4.26E-06		
0.8396	6772	1.477		4.31E-06		
0.8266	6667	1.500	2.484		2.504	
0.8019	6467	1.546		4.36E-06		
0.7647	6168	1.621		4.41E-06		
0.7421	5986	1.671	2.469			
0.7238	5838	1.713		4.51E-06		
0.6864	5536	1.806		4.60E-06		
0.6790	5477	1.826	2.465			
0.6551	5284	1.893		4.70E-06		
0.6328	5104	1.959		4.77E-06		
0.6199	5000	2.000	2.468		2.488	
0.5298	4273	2.340	2.459			
0.4623	3728	2.682	2.453			
0.3997	3223	3.102	2.451			
0.3519	2839	3.523	2.448			
0.3040	2452	4.000	2.449		2.469	
0.2679	2161	4.627	2.443			
0.2292	1848	5.410	2.441			
0.2066	1666	6.000	2.445		2.466	
0.1764	1422	7.030	2.438			

TABLE I (*Continued*)

Cadmium Selenide

eV	cm^{-1}	μm	n_o	k_o	n_e	k_e
0.1544	1245	8.033	2.432			
0.1353	1091	9.164	2.429			
0.1240	1000	10.00	2.431		2.452	
0.1072	864.6	11.57	2.413			
0.09733	785.0	12.74	2.419			
0.08860	714.6	13.99	2.410		2.431	
0.07750	625.1	16.00	2.399		2.419	
0.06874	554.4	18.04	2.385			
0.06200	500.1	20.00	2.376		2.389	
0.05763	464.8	21.52		6.35E-04 [4]		
0.05687	458.7	21.80		6.51E-04		
0.05630	454.1	22.02	2.339		2.351	
0.05627	453.8	22.04		6.61E-04		
0.05495	443.2	22.57		6.77E-04		
0.05422	437.3	22.87		7.94E-04		
0.05359	432.2	23.14		9.39E-04		
0.05311	428.4	23.34		1.12E-03		
0.05274	425.4	23.51		1.20E-03		
0.05254	423.8	23.60		1.18E-03		
0.05241	422.7	23.66		1.11E-03		
0.05210	420.2	23.80		9.74E-04		
0.05182	417.9	23.93		8.43E-04		
0.05157	415.9	24.04		8.08E-04		
0.05120	412.9	24.22		8.21E-04		
0.05099	411.3	24.32	2.291			
0.05075	409.3	24.43		8.37E-04		
0.05035	406.1	24.62		8.35E-04		
0.05008	403.9	24.76		9.25E-04		
0.04987	402.2	24.86		1.07E-03		
0.04956	399.7	25.00		1.31E-03		
0.04914	396.3	25.23		1.71E-03		
0.04876	393.3	25.43		2.10E-03		
0.04832	389.7	25.66		2.64E-03		
0.04799	387.1	25.84		3.28E-03		
0.04773	384.9	25.98		3.86E-03		
0.04757	383.7	26.06		4.59E-03		
0.04741	382.4	26.15		5.13E-03		
0.04727	381.2	26.23		5.76E-03		
0.04705	379.5	26.35		6.41E-03		
0.04688	378.1	26.45		6.96E-03		
0.04678	377.3	26.51		7.51E-03		
0.04655	375.5	26.63		8.11E-03		
0.04646	374.7	26.69		8.50E-03		
0.04641	374.3	26.72		8.69E-03		
0.04630	373.4	26.78	2.280			
0.04618	372.5	26.85		8.78E-03		

TABLE I (*Continued*)

Cadmium Selenide

eV	cm^{-1}	μm	n_o	k_o	n_e	k_e
0.04603	371.2	26.94		8.87E-03		
0.04600	371.0	26.95		8.96E-03		
0.04591	370.3	27.01		9.30E-03		
0.04580	369.4	27.07		9.66E-03		
0.04570	368.6	27.13		9.86E-03		
0.04555	367.4	27.22		9.96E-03		
0.04544	366.5	27.28		9.90E-03		
0.04541	366.2	27.31		9.84E-03		
0.04529	365.3	27.38		9.71E-03		
0.04518	364.4	27.44		9.55E-03		
0.04497	362.7	27.57		9.48E-03		
0.04480	361.3	27.68		9.67E-03		
0.04461	359.8	27.79		1.00E-02		
0.04448	358.8	27.87		1.04E-02		
0.04431	357.4	27.98		1.07E-02		
0.04413	355.9	28.10		1.09E-02		
0.04397	354.6	28.20		1.08E-02		
0.04387	353.9	28.26		1.07E-02		
0.04370	352.5	28.37		1.06E-02		
0.04361	351.7	28.43		1.02E-02		
0.04350	350.9	28.50		9.66E-03		
0.04343	350.2	28.55		9.15E-03		
0.04331	349.3	28.63		8.70E-03		
0.04300	346.8	28.83		8.63E-03		
0.04275	344.8	29.00		8.78E-03		
0.04269	344.3	29.05	2.253			
0.04267	344.2	29.06		8.95E-03		
0.04258	343.4	29.12		9.26E-03		
0.04248	342.6	29.19		9.55E-03		
0.04241	342.1	29.24		9.87E-03		
0.04228	341.0	29.33		1.02E-02		
0.04211	339.6	29.45		1.04E-02		
0.04196	338.4	29.55		1.03E-02		
0.04187	337.7	29.61		1.02E-02		
0.04178	336.9	29.68		1.01E-02		
0.04172	336.5	29.72	2.239			
0.04170	336.3	29.74		9.81E-03		
0.04156	335.2	29.83		9.31E-03		
0.04151	334.8	29.87		9.03E-03		
0.04126	332.8	30.05		9.34E-03		
0.04120	332.3	30.10		9.68E-03		
0.04118	332.2	30.11		1.01E-02		
0.04112	331.6	30.16		1.05E-02		
0.04110	331.5	30.17		1.08E-02		
0.04106	331.2	30.19		1.12E-02		
0.04098	330.6	30.25		1.16E-02		

TABLE I (*Continued*)

Cadmium Selenide

eV	cm^{-1}	μm	n_e	k_e	n_e	k_e
0.04079	329.0	30.40		1.08E-02		
0.04067	328.0	30.49		1.06E-02		
0.04055	327.0	30.58		1.04E-02		
0.04047	326.4	30.64		1.05E-02		
0.04046	326.3	30.65		1.06E-02		
0.04040	325.9	30.69		1.09E-02		
0.04035	325.4	30.73		1.12E-02		
0.04011	323.5	30.91		1.14E-02		
0.04001	322.7	30.99		1.12E-02		
0.03992	321.9	31.06		1.10E-02		
0.03988	321.6	31.09		1.08E-02		
0.03978	320.9	31.17		1.05E-02		
0.03974	320.6	31.20		1.03E-02		
0.03953	318.8	31.36		1.02E-02		
0.03940	317.8	31.47		1.03E-02		
0.03920	316.2	31.63		1.05E-02		
0.03895	314.2	31.83		1.07E-02		
0.03885	313.3	31.92		1.04E-02		
0.03870	312.1	32.04		1.04E-02		
0.03856	310.9	32.16		1.05E-02		
0.03825	308.5	32.41		1.07E-02		
0.03811	307.4	32.54		1.07E-02		
0.03800	306.5	32.63		1.07E-02		
0.03784	305.2	32.76		1.06E-02		
0.03750	302.5	33.06		1.05E-02		
0.03625	292.4	34.21			2.384[12]	4.64E-02[12]
0.03623	292.2	34.22	2.411[12]	2.40E-01[12]		
0.03586	289.2	34.58			2.386	4.66E-02
0.03577	288.5	34.67	2.400	2.98E-01		
0.03539	285.5	35.03	2.394	3.54E-01		
0.03539	285.4	35.04			2.369	8.25E-02
0.03500	282.3	35.43			2.287	8.73E-02
0.03498	282.2	35.44	2.288	5.13E-01		
0.03461	279.1	35.83			2.185	2.07E-01
0.03452	278.4	35.92	2.160	6.74E-01		
0.03419	275.8	36.26			2.017	4.18E-01
0.03413	275.3	36.33	1.961	6.27E-01		
0.03381	272.7	36.67			2.078	6.99E-01
0.03379	272.6	36.69	1.887	4.09E-01		
0.03343	269.6	37.09			2.245	4.80E-01
0.03341	269.5	37.11	2.006	3.38E-01		
0.03306	266.6	37.51			2.399	3.44E-01
0.03304	266.5	37.53	2.215	3.42E-01		
0.03263	263.2	38.00	2.268	3.30E-01	2.447	4.67E-01
0.03220	259.7	38.51			2.556	2.69E-01

TABLE I (*Continued*)

Cadmium Selenide

eV	cm^{-1}	μm	$n_\perp$	$k_\perp$	$n_\parallel$	$k_\parallel$
0.03214	259.2	38.58	2.341	2.16E-01		
0.03182	256.6	38.96			2.366	1.38E-01
0.03176	256.1	39.04	2.363	7.55E-03		
0.03133	252.7	39.58			2.220	2.55E-03
0.03132	252.6	39.59	2.221	7.16E-03		
0.03102	250.2	39.97			2.144	3.83E-03
0.03099	249.9	40.01	2.134	3.23E-02		
0.03065	247.2	40.45			2.047	1.00E-03
0.03064	247.1	40.47	2.052	5.67E-02		
0.03033	244.6	40.88			1.995	2.97E-02
0.03031	244.5	40.90	1.993	1.88E-02		
0.02996	241.6	41.39			1.883	5.35E-03
0.02990	241.1	41.47	1.909	4.23E-02		
0.02956	238.4	41.95	1.806	3.01E-02		
0.02955	238.3	41.96			1.837	2.30E-02
0.02911	234.7	42.59	1.704	2.21E-02		
0.02909	234.6	42.62			1.736	3.34E-02
0.02879	232.2	43.07			1.721	4.90E-02
0.02874	231.8	43.14	1.685	5.54E-02		
0.02832	228.4	43.77			1.649	7.44E-02
0.02829	228.2	43.82	1.590	4.79E-02		
0.02795	225.4	44.37			1.628	4.08E-02
0.02787	224.8	44.48	1.612	7.60E-02		
0.02752	221.9	45.05			1.581	2.05E-02
0.02749	221.7	45.09	1.555	9.72E-02		
0.02715	218.9	45.68			1.481	2.01E-02
0.02712	218.7	45.72	1.442	1.36E-01		
0.02675	215.8	46.35			1.329	1.96E-02
0.02674	215.7	46.37	1.343	4.59E-02		
0.02642	213.1	46.93			1.298	7.12E-03
0.02640	212.9	46.97	1.203	1.59E-02		
0.02599	209.6	47.71			0.801	3.33E-02
0.02596	209.4	47.75	0.714	1.83E-01		
0.02559	206.4	48.45			0.159	2.82E-01
0.02555	206.0	48.53	0.274	7.53E-01		
0.02518	203.1	49.23			0.095	9.81E-01
0.02515	202.8	49.30	0.298	1.34E+00		
0.02483	200.3	49.93			0.023	1.41E+00
0.02479	200.0	50.01	0.285	1.78E+00		
0.02449	197.5	50.63			0.015	1.91E+00
0.02447	197.4	50.66	0.381	2.08E+00		
0.02412	194.5	51.41	0.401	2.40E+00		
0.02411	194.4	51.43			0.110	2.24E+00
0.02375	191.5	52.21			0.333	2.65E+00
0.02371	191.3	52.29	0.582	2.72E+00		
0.02348	189.3	52.81			0.624	2.95E+00

TABLE I (*Continued*)

Cadmium Selenide

eV	cm^{-1}	μm	n_o	k_o	n_e	k_e
0.02341	188.8	52.97	0.655	3.07E+00		
0.02295	185.1	54.03	1.168	3.61E+00		
0.02294	185.0	54.05			0.934	3.54E+00
0.02261	182.3	54.85	1.696	4.12E+00		
0.02257	182.0	54.94			1.244	3.95E+00
0.02217	178.8	55.93	2.308	4.65E+00		
0.02212	178.4	56.06			1.662	4.53E+00
0.02179	175.7	56.90			2.314	4.98E+00
0.02174	175.3	57.03	3.238	4.74E+00		
0.02142	172.8	57.87	4.858	3.89E+00		
0.02137	172.4	58.01			3.081	5.38E+00
0.02125	171.4	58.34			3.664	5.66E+00
0.02124	171.3	58.38	5.439	3.75E+00		
0.02101	169.5	59.00	5.702	3.34E+00		
0.02100	169.3	59.05			4.396	5.60E+00
0.02076	167.4	59.73	5.964	2.75E+00		
0.02075	167.3	59.74			5.724	5.75E+00
0.02055	165.8	60.32	5.848	2.17E+00		
0.02052	165.6	60.41			6.554	5.19E+00
0.02035	164.1	60.92	5.682	1.68E+00		
0.02030	163.7	61.09			7.307	4.01E+00
0.02012	162.3	61.61	5.719	1.35E+00		
0.02008	162.0	61.73			7.633	3.05E+00
0.01998	161.1	62.07	5.667	1.07E+00		
0.01990	160.5	62.31			7.413	1.45E+00
0.01976	159.4	62.75	5.414	8.70E-01		
0.01966	158.6	63.06			7.389	6.18E-01
0.01940	156.5	63.91	5.062	5.47E-01		
0.01929	155.6	64.28			6.926	1.61E-01
0.01897	153.0	65.36	4.711	3.69E-01		
0.01893	152.7	65.49			5.903	1.65E-02
0.01863	150.2	66.56	4.484	2.50E-01		
0.01860	150.0	66.68			5.506	4.90E-03
0.01826	147.2	67.92	4.282	1.54E-01		
0.01822	146.9	68.05			5.257	5.97E-03
0.01788	144.2	69.36	4.136	7.89E-02		
0.01782	143.7	69.56			4.999	7.09E-03
0.01750	141.2	70.84	4.016	4.05E-02		
0.01748	140.9	70.95			4.800	7.97E-03
0.01710	137.9	72.49	3.877	1.78E-02		
0.01705	137.5	72.70			4.624	
0.01670	134.7	74.26	3.791			
0.01664	134.2	74.51			4.430	
0.01631	131.6	76.01	3.708			
0.01629	131.4	76.10			4.327	
0.01589	128.2	78.02	3.630			

TABLE I (*Continued*)

Cadmium Selenide

eV	cm^{-1}	μm	n_o	k_o	n_e	k_e
0.01587	128.0	78.12			4.178	
0.01555	125.4	79.76	3.576			
0.01549	124.9	80.05			4.063	
0.01515	122.2	81.84	3.532			
0.01511	121.8	82.06			3.967	
0.01471	118.6	84.29	3.469			
0.01464	118.1	84.69			3.838	
0.01437	115.9	86.27	3.416			
0.01433	115.6	86.54			3.745	
0.01395	112.5	88.86	3.405			
0.01394	112.4	88.94			3.688	
0.01359	109.6	91.25	3.377			
0.01355	109.3	91.49			3.609	
0.01321	106.6	93.82	3.352			
0.01314	106.0	94.33			3.538	
0.01278	103.1	97.03	3.340			
0.01275	102.8	97.26			3.474	
0.01245	100.4	99.55	3.335		3.474	

[a] References are indicated in brackets.

Cadmium Sulphide (CdS)

L. WARD
Coventry Polytechnic
Coventry, England

Cadmium sulphide is a member of the II-VI group of semiconducting compounds formed by alloying one element from group II of the periodic table with another from group VI. The energy gap between the valence and conduction bands is about 2.4 eV and CdS has been used extensively in photoconducting cells, being effective in the ultraviolet and blue parts of the spectrum. In addition, there is a strong absorption band in the infrared due to lattice vibrations (phonons). At short wavelengths there are also absorption bands due to electron transitions involving inner energy levels. The normal crystal structure is hexagonal close-packed (wurtzite), which is in space group C6mc, and most of the reported values of the optical constants of CdS have been for this form of the compound. However, a face-centered cubic form of CdS can also be prepared (zinc-blende structure, space group $F\bar{4}3m$), and a few results for this material are also available. In dealing with hexagonal CdS, the optical properties of the single crystals depend on whether the electric vector of the incident radiation is vibrating perpendicular to or parallel to the c axis, that is, the axis at a right angle to the crystal hexagon. The main impurities occurring in CdS are iron, potassium, and sodium; it is possible to obtain material where all the impurities total less than 0.01%. Values of n and k for CdS are given in Table I and graphed in Fig. 1; the wavelength range covered is 6×10^{-4} to 1000 μm and, wherever possible, slight wavelength overlaps have been included between the different sets of results.

Hexagonal Cadmium Sulphide

Henke [1] has described a method of calculating optical constants at X-ray wavelengths (0.0006–0.0124 μm) from X-ray scattering data; the scattering coefficients f_1 and f_2 for all elements are given in detail by Henke *et al.* [2]. For CdS, the following relationships apply;

$$n = 1 - 4.45\lambda^2(f_{1\mathrm{Cd}} + f_{1\mathrm{S}})$$
$$k = 4.45\lambda^2(f_{2\mathrm{Cd}} + f_{2\mathrm{S}}),$$

where λ is the wavelength in μm.

Copyright © 1991 by Academic Press.
All rights of reproduction in any form reserved.
ISBN 0-12-544422-2

The calculated values of n in this region, which are given in Table I, were generally just less than unity, whereas peaks in k were produced at 0.0075 μm ($L_{II,III}$ transition in S) and 0.0028 μm (M_V in Cd). Cardona and Haensel [3] made a direct measurement of the absorption coefficient, α, between 36 and 120 eV (0.01–0.34 μm) of evaporated thin films of CdS; k may then be calculated from the relationship, $k = \alpha\lambda/4\pi$, a peak being observed at 0.0225 μm (55 eV). Where overlap occurs, there is reasonably good agreement between the values of k from Henke and those of Cardona and Haensel.

Cardona and Harbeke [4] measured the reflectances R_p and R_s between 2 and 12 eV (0.1–0.62 μm) of platelets of CdS grown from the vapor phase, although they claimed that similar results could be obtained from etched solid material; they used a Kramers–Kronig (K–K) analysis to calculate n and k for the cases of both $\mathbf{E}_{\parallel c}$ and $\mathbf{E}_{\perp c}$. Peaks were observed in n at 0.490, 0.264, and 0.143 μm (both states of polarization) and at 0.234 μm ($\mathbf{E}_{\perp c}$) and 0.175 μm ($\mathbf{E}_{\parallel c}$); there were peaks in k at 0.490, 0.225, 0.155, and 0.136 μm (both) and at 0.200 μm ($\mathbf{E}_{\parallel c}$) and 0.253 μm ($\mathbf{E}_{\perp c}$); the peaks at 0.490 μm correspond to the main energy gap (2.53 eV). The authors were able to correlate all these peaks with different electron transitions within the energy-band structure of cadmium sulphide. Their values of n and k for both states of polarization are included in Table I. Balkanski and Petroff [5] determined ε_1 and ε_2 between 1 and 20 eV (0.06–1.24 μm) using measurements of reflectance from the natural faces of CdS crystals. They found a similar set of absorption peaks to those of Cardona and Harbeke with the addition of a further peak at 14.5 eV (0.0855 μm). Freeout [6] used synchrotron radiation to measure the reflectance of the natural faces of CdS crystals between 0.04 and 2.0 μm using a rotating-light-pipe scanning reflectometer originally devised by Gerhardt and Rubloff [7]. He presented graphs of ε_1 and ε_2 versus wavelength, finding a strong absorption doublet at 13.5 eV (0.092 μm), which is close to the M_1 transition in sulphur; he suggested that this doublet was produced by spin-orbit splitting of this transition.

In the region around 0.5 μm, which includes the main absorption band due to electron transitions between the valence and conduction bands, Brodin and his collaborators have made important contributions. Brodin and Strashnikova [8] determined n for single-crystal CdS films by an interference technique; for radiation polarized with the E vector perpendicular to the c axis, there was a single absorption peak at about 0.48 μm, whereas for the E vector parallel to the c axis, there were two close peaks centered about the same wavelength. In addition, there was also a wide absorption band near 0.28 μm, present in both states of polarization. Brodin *et al.* [9] also measured the reflectance of single-crystal material but at a temperature of 4.2 K; for E vibrations that were polarized parallel to the c axis, a single absorption maximum was found at 0.483 μm; for

polarization at right angles to the c axis, two maxima were discovered at 0.487 and 0.463 μm. Brodin [10] has published values of n versus wavelength between 0.5 and 0.65 μm for monocrystals of CdS at temperatures of 20 K and 290 K. He measured the reflectance and used K–K analysis to find n for **E** both parallel and perpendicular to the c axis; over the range of wavelengths studied, n_e ($\|$) was always about 2% larger than n_o ($\perp$).

Kreisel *et al.* [11] studied CdS in the range of 0.5–0.7 μm under different levels of light excitation and at low temperatures (5 K). At low excitation levels, excitons (see below) were observed, but at high levels of excitation, an electron-hole plasma was produced. n_o was larger than n_e up to 0.510 μm, but at the longer wavelengths this situation was reversed. When the CdS contained free-carrier impurities ($2 \times 10^{18}\,cm^{-3}$), the value of n at the absorption peak was reduced from 5.0 to 3.5. Lampicki [12] found three peaks in his reflectance curves at 0.4874, 0.4844, and 0.4731 μm, which he identified with electron transitions between the valence and conduction bands in the Γ direction in the Brillouin zone. All three peaks were present for $\mathbf{E}_{\perp c}$ but only the two at lower wavelengths for $\mathbf{E}_{\|c}$; these results are similar to those found by Brodin. Gobrecht and Bartschat [13] determined n and k by Denton's method [14], which required a knowledge of both the reflectance and transmittance and yielded values for both the *o*- and *e*-rays between 0.49 and 0.65 μm at both 20°C and −180°C. For the longer wavelengths, n_o was smaller than n_e, but there was a crossover at about 0.51 μm. They concluded that just beyond the absorption edge at 0.485 μm, CdS shows evidence of direct electron transitions between the valence and conduction bands. At higher photon energies, the form of the absorption curve was probably determined by the combined effects of indirect transitions and direct transitions between nonparabolic energy bands.

Bienewski and Czyzek [15] and also Czyzek *et al.* [16] have made measurements of n between 0.5 and 1.4 μm at 298 K using the minimum-deviation method reported by Czyzek *et al.* [17] in which the chopped radiation was detected by a thermocouple; tables of values for both the *o*- and *e*-rays ($\mathbf{E}_{\perp c}$ and $\mathbf{E}_{\|c}$) were produced in which n is quoted to three decimal places. These values are reproduced in Table I. Using a nonlinear regression technique, Sanchez-Gomez *et al.* [18] claimed to have refined these results of Bienewski and Czyzek for the dispersion of CdS and were also able to calculate the residuals for each wavelength. However, this process made little difference to the original values of n, causing only small alterations in the third decimal place. Another investigator in this part of the spectrum was Devore [19] who also used the prism technique and was able to produce Sellmeier-type equations for both the *e*- and *o*-rays. Reynolds *et al.* [20] have also published graphs of n and α against wavelength between 0.5 and 1.0 μm for single-crystal cadmium sulphide.

Francis and Carlson [21] have published a set of results for n measured

on polycrystalline cadmium sulphide between 1 and 14 μm determined by the minimum-deviation method involving a narrow-angled prism of the material. They did not distinguish between the *o*- and *e*-rays, but their values of n link well with those of Bienewski and Czyzek for *e*-rays; they have been quoted extensively in Table I.

Vitrikhovskii *et al.* [22], using single crystals of CdS, have investigated the variation of n with temperature over the range 100–600 K. The refractive index was measured between 0.5 and 1.6 μm by the prism technique and by an interference method; there was good agreement between their published values and those of Bienewski and Czyzek at 300 K. Both n_o and n_e increased with temperature, dn/dT being about 8×10^{-5}/°C.

Thin Films

Gottesmann and Ferguson [23] measured the reflectance of thin films of CdS between 0.4 and 0.75 μm finding an absorption edge at 0.52 μm. The most rapid deposition rate that they used (90 Å/min) produced the highest values of n, but these were still less than those for bulk material, presumably because of the low packing density of the film particles. Hall [24], who measured the reflectance and transmittance of thin films on quartz substrates between 0.2 and 0.6 μm at different deposition rates, observed peaks in n at 0.25 and 0.5 μm and in k at 0.23 μm. The absorption maximum occurred close to the s–p transition wavelength of sulphur at 0.229 μm. n was found to be proportional to the deposition rate up to 0.40 μm but not at the higher wavelengths, whereas k did not appear to be affected by the deposition rate. There was a region of anomalous dispersion between 0.40 and 0.50 μm due to the excitation of electrons from the valence to the conduction band; the absorption edge was measured at 0.51 μm.

De la Plaza *et al.* [25] studied RF sputtered films of CdS and published values of n versus wavelength over the narrow range 0.5–0.7 μm for different sputtering pressures. The largest values of n were obtained at the lowest deposition pressure, but again these were less than those for crystalline cadmium sulphide. Strashnikova *et al.* [26] using a prism of very small angle (0.75×10^{-4} rad), noted that n increased slightly with the thickness of the prism up to 4 μm thick at wavelengths between 0.46 and 0.49 μm. In another paper, Strashnikova *et al.* [27] studied the variation of the wavelength of the inversion point (where n is the same for both *o*- and *e*-rays) with film thickness. The inversion wavelength decreased from 0.510 μm for films thicker than 1.5 μm, to 0.498 μm at a thickness of 0.5 μm, the authors claiming that this effect was due to the decreasing oscillator strength of the exciton.

Khawaja and Tomlin [28] measured both the reflectance and transmittance of thin films deposited on quartz wedges with 3° angles to eliminate

reflection from the back of the substrate. The wavelength range covered was 0.3–2.0 μm and three substrate temperatures were used: 20, 140, and 180°C. The highest substrate temperature generated the largest values of n and k, presumably because the higher mobilities of the deposited particles produced a more densely packed film, but the values of n were still lower than those for bulk materials. Wohlegemutt *et al.* [29] also measured the normal-incidence reflectance and transmittance up to a wavelength of 1.0 μm for both polycrystalline and amorphous CdS films deposited on sapphire; they compared their results with those of Cardona and Harbeke [4], Khawaja and Tomlin [28] and Kuwabara [34], noting a peak in n at about 0.5 μm in all the sets of results. However, the curves of n versus wavelength produced by Wohlegemutt *et al.* were at all points lower than those by the other authors; on the other hand, the values of k were in much better agreement. n initially fell as the wavelength decreased over the anomalous-dispersion region, but commenced to increase again as the wavelength approached 0.3 μm. The results of Khawaja and Tomlin are regarded as being the best in this region of the spectrum, and they are given in Table I.

Shklyarevskii *et al.* [30] working between 0.45 and 0.65 μm used ellipsometry to measure the optical constants of a thin film of CdS deposited on a chromium substrate. n was found to be a function of both the film thickness and the wavelength, but all the curves showed a maximum at about 0.485 μm; k, however, was independent of thickness and increased with decreasing wavelength. Czyzek *et al.* [17] have reported studies on synthetic CdS from the visible region up to 1.4 μm. Over this limited wavelength range, the following Sellmeier-type equations were derived for n_o and n_e:

$$n_0^2 = 5.235 + 1.819 \times 10^7/(\lambda^2 - 1.651 \times 10^7)$$

$$n_e^2 = 5.239 + 2.076 \times 10^7/(\lambda^2 - 1.651 \times 10^7).$$

Measurements on polycrystalline films of CdS have been made by Soera and Serdyuk [31]. A complicated structure in the reflectance curve near the absorption edge was attributed to layers of excitons and possibly also to lattice defects. Nolly *et al.* [32] have carried out an ellipsometric study of spray-pyrolized thin films of CdS over the visible spectrum. Hall and Ferguson [33] determined the optical constants of films of CdS from measurements of reflectance and transmittance between 0.6 and 14 μm; n was found to be independent of the deposition rate and also decreased monotonically with wavelength from 2.52 at 0.6 μm to 2.26 at 14.0 μm, whereas k showed a linear increase with wavelength and was also dependent on the deposition rate up to 7 μm, being largest for the highest rates. Their values of n agree reasonably well with those of Bienewski and

Czyzek. As examples of the optical constants of thin films in this spectral region, Hall and Ferguson's results are reproduced in Table I.

Kuwabara [34] worked with polycrystalline evaporated films between 0.4 and 1.0 μm finding a maximum in n of 2.65 at 0.5 μm where k was equal to 0.18; the absorption edge, corresponding to electron transitions from the valence to the conduction band, occurred at the same wavelength. He claimed that the optical properties of the films were similar to those for a single crystal, but his values for n were significantly smaller than those of Khawaja and Tomlin for similar films. Elizelde and Rueda [35] measured the reflectance and transmittance of thin-film specimens and, using the exact equations for these parameters produced by Bauer [36] (which take account of both faces of the substrate), calculated the optical constants between 0.5 and 2.5 μm. Between 0.5 and 10.0 μm, Miloslavski [37], working with layers of single-crystal CdS of thickness 2–3 μm deposited on a sodium-chloride substrate, measured the transmittance, from which n could be calculated. He was interested in the effect on n of the presence of impurities and noted that as the proportion of impurities was increased up to 1.2×10^{18} carriers/cm^{-3}, the values of n between 5 and 18 μm decreased by about 2.5%.

Infrared region

In the spectral region from 10–50 μm several studies of the optical properties of cadmium sulphide have been made. Collins [38] has reported reflectance values for unpolarized radiation measured on a single crystal between 20 and 48 μm; these showed a minimum reflectance at 32 μm followed by a peak at 38 μm. Taking the value of the dielectric constant at very long wavelengths, e_0, as 9.3, the value of e_∞ as 5.76, and the transverse optical phonon as 241 cm^{-1} (41.5 μm), the wave number of the longitudinal optical phonon was deduced from a Lorentz-type equation to be 305 cm^{-1} (37.8 μm). Balkanski and Besson [39] measured the reflectance between 15 and 30 μm at both 293 K and 80 K and found that their results could be explained in terms of multiple-phonon processes, that is, two or three phonons being excited by the absorption of a single photon. Values of k over this wavelength range calculated from their absorption-coefficient graph are incorporated in Table I. Deutsch [40] also studied the infrared absorption of CdS between 10 and 25 μm, finding bands at 22.55 and 23.15 μm when the **E** vector of the incident radiation was parallel to the c axis of the crystal, and at 19.95 μm when the **E** vector was perpendicular to the c axis; he needed four phonons to explain his results. As the absorption curves were determined in more detail, extra phonons had to be invoked to explain all the peaks; for example, Marshall and Mitra [41] needed six phonons, and Balkanski *et al.* [42] required ten. Balkanski *et al.* also measured the absorption coefficient α of CdS between 27 and 120 μm and have presented a graph of α against wave number from which values of k

over this spectral region have been calculated and are presented in Table I. Because a logarithmic scale was used for α, it is difficult to take precise readings from this graph, and the estimated accuracy in k is no better than the second decimal place. In their experiment CdS was deposited on silicon whose (111) axis was at right angles to the surface; the layers were then found to have their c axes also at right angles to the substrate. For radiation vibrating parallel to the c axis, the transverse optical phonon, ν_t, was at 233.5 cm^{-1} (42.8 μm) and the longitudinal optical phonon, ν_l, was at 305 cm^{-1} (32.8 μm); radiation vibrating at right angles to the c axis gave a transverse optical phonon at 242 cm^{-1} with the longitudinal phonon being unchanged.

Balkanski [43] has given a graph of n versus wave number covering the range of wavelengths between 27 and 60 μm. Values of n read from this graph are incorporated in Table I.

Manabe *et al.* [44] measured the reflectance of polished specimens of CdS at wavelengths between 20 and 100 μm and at temperatures of 100 and 300 K; they calculated n and k using the following version of the Lorentz dispersion formulas:

$$n^2 - k^2 = \varepsilon_\infty + N(\nu_t^2 - \nu^2)/((\nu_t^2 - \nu^2)^2 + \gamma^2\nu^2)$$

$$2nk = N(\gamma\nu)/((\nu_t^2 - \nu^2)^2 + \gamma^2\nu^2).$$

For $\mathbf{E}_{\parallel c}$, they used $\varepsilon_\infty = 5.4$, $N = 1.92 \times 10^5$ cm^{-2}, $\nu_t = 234$ cm^{-1}, $\nu_l = 300$ cm^{-1} and $\gamma = 3.98$ cm^{-1}; for $\mathbf{E}_{\perp c}$ the constants were 5.3, 1.82×10^5 cm^{-2}, 241 cm^{-1}, 306 cm^{-1}, and 5.54 cm^{-1} at 300 K. Their values for n and k are those quoted in Table I to represent this part of the spectrum; from their published graphs, it is just possible to read off the values to the second decimal place.

Barker and Summers [45] have reported values for the dielectric constants both parallel and perpendicular to the c axis of platelets of single-crystal CdS measured by an interference method between 70 and 330 μm. Their results are given in Table I.

The refractive index of CdS between 100 and 1000 μm was determined by Hattori *et al.* [46] using a channel-spectrum technique in conjunction with a Michelson interferometer coupled to a germanium bolometer. The refractive index was calculated from the transmission interference maxima and minima. n for CdS appeared to be constant over this range of wavelengths: 3.27±3% for $\mathbf{E}_{\parallel c}$ and 3.11±2% for $\mathbf{E}_{\perp c}$. Both these values were up to 10% higher than those produced by other authors such as Berlincourt *et al.* [47], Verleur and Barker [48], and Barker and Summers [45] who have also made measurements in this spectral region.

Excitons

Gross *et al.* [49] investigated the presence of excitons, that is, electron-hole pairs having energy levels within the energy gap, at 4.2 K, finding 13 narrow emission lines between 4853.5 and 4889.5 Å near the main absorption edge. They also found a series of equally spaced lines between 5150 and 5600 Å, which were ascribed to electron transitions involving phonons. From their results, an absorption peak could be predicted in the infrared at 47 μm, compared with the now-accepted value of 42.25 μm. Pevtsov and his colleagues [50, 51] carried out thorough investigations on two types of excitons, specified as type A and type B, due to the double degeneracy of the valence band. Another group that studied excitons was Henneberger *et al.* [52], who used artificially grown platelets of CdS and measured the transmission between crossed polaroids. Voigt *et al.* [53] studied the energy spectra of type A and B excitons by reflectance and transmittance measurements on very thin but highly perfect crystals at 1.8 K. Exciton studies were also carried out by Lambe *et al.* [54] and by Thomas and Hopfield 55, 56, 57]. The properties of excitons in semiconductors has been well-covered in a review article by Thomas and Timofiev [58].

Cubic Cadmium Sulphide

Cubic cadmium sulphide was studied by Cardona [59], who measured the normal-incidence reflectance of epitaxial films deposited onto the (111) face of GaAs. He noted that most of the peaks in the reflectance spectrum occurred at the same wavelengths as those for the hexagonal form, although the peak at 7.12 eV (0.174 μm) was missing, and the one at 5.49 eV (0.226 μm) was not split, as it was in the hexagonal case. No values of n and k are available for cubic cadmium sulphide.

REFERENCES

1. B. L. Henke, *A.I.P. Conf. Proc. No. 75*, 146 (1981).
2. B. L. Henke, P. Lee, T. J. Tanoka, R. Shimabukura and B. K. Fujikawa, *Atomic Data and Nuclear Data Tables* **27**, 1 (1982).
3. M. Cardona and R. Haensel, *Phys. Rev.* **B1**, 2605 (1970).
4. M. Cardona and G. Harbeke, *Phys. Rev.* **A137**, 1467 (1965).
5. M. Balkanski and Y. Petroff, in "Int. Conf. Phys. Semicond. Paris," Dunod, Paris, and Academic Press, New York, 245 (1964).
6. J. L. Freeout, *Phys. Rev.* **B7**, 3810 (1973).
7. U. Gerhardt and G. W. Rubloff, *Appl. Opt.* **8**, 305 (1969).
8. M. S. Brodin and M. I. Strashnikova, *Sov. Phys. Sol. State* **8**, 549 (1966).
9. M. S. Brodin, A. V. Kritskii, and M. I. Strasnikova, *Sov. Phys. Sol. State* **13**, 475 (1971).
10. M. S. Brodin, *Sov. Phys. Sol. State* **2**, 1926 (1960); 2292 (1961).
11. A. Kreisel, K. Bohnert, V. G. Lyssenko, and C. Klingsheim, *Phys. Stat. Solidi* **B114**, 537 (1982).
12. A. Lampicki, *Proc. Phys. Soc.* **74**, 138 (1959).

13. H. Gobrecht and A. Bartschat, in "*Int. Conf. Phys. Semicond., Paris*," Dunod, Paris, and Academic Press, New York, 245 (1964).
14. R. E. Denton, R. D. Campbell, and S. G. Tomlin, *J. Phys. D* **5**, 872 (1972).
15. T. M. Bienewski and S. J. Czyzek, *J. Opt. Soc. Am.* **53**, 496 (1963).
16. S. J. Czyzek, R. C. Crane, and T. M. Bienewski, *J. Opt. Soc. Am.* **49**, 485 (1959).
17. S. J. Czyzek, W. M. Baker, R. C. Crane, and J. B. Howe, *J. Opt. Soc. Am.* **47**, 240 (1957).
18. M. Sanchez-Gomez, J. M. Guerra, and F. Vitches, *Appl. Opt.* **24**, 1147 (1985).
19. J. R. Devore, *J. Opt. Soc. Am.* **41**, 416 (1951).
20. D. C. Reynolds, S. J. Crzyzek, R. C. Allen, and C. C. Reynolds, *J. Opt. Soc. Am.* **45**, 136 (1955).
21. A. B. Francis and A. J. Carlson, *J. Opt. Soc. Am.* **50**, 118 (1960).
22. N. I. Vitrikhovskii, L. F. Gudymenko, and A. F. Maznichenko, *Sov. Phys. Semicond.* **2**, 732 (1968).
23. J. Gottesmann and W. F. C. Ferguson, *J. Opt. Soc. Am.* **44**, 368 (1954).
24. J. F. Hall, *J. Opt. Soc. Am.* **46**, 1013 (1956).
25. I. M. De la Plaza, G. Gonzales-Diaz, E. Sanchez-Quesada, and M. Rodriguez-Vidal, *Thin Solid Films* **120**, 31 (1984).
26. M. I. Strashnikova, V. Y. Resnichenko, and V. V. Cherny, *Phys. Stat. Solidi* **141**, K153 (1987).
27. M. I. Strashnikova, V. Y. Resnichenko, and V. V. Cherny, *Solid State Commun.* **47**, 375 (1983).
28. E. E. Khawaja and S. G. Tomlin, *J. Phys. D* **8**, 581 (1975).
29. J. H. Wohlgemutt, D. E. Brodie, and P. C. Eastman, *Can. J. Phys.* **54**, 785 (1976).
30. I. N. Shklyarevskii, A. F. A. El Shazli, R. G. Yarovaya, and V. P. Kostyuk, *Opt. Spectrosc.* **36**, 116 (1974).
31. T. Y. Soera and V. V. Serdyuk, *Opt. Spectrosc.* **9**, 210 (1960).
32. J. Nolly, K. K. Abadullah and K. P. Vyayakumar, *Phys. Stat. Solidi A* **101**, K35 (1987).
33. J. F. Hall and W. F. C. Ferguson, *J. Opt. Soc. Am.* **45**, 714 (1955).
34. S. Kuwabara, *J. Phys. Soc. Japan* **9**, 97 (1954).
35. E. Elizelde and F. Rueda, *Thin Solid Films* **122**, 45 (1984).
36. J. Bauer, *Exp. Tech. Phys.* **25**, 105 (1972).
37. J. K. Miloslavski, *Opt. Spectrosc.* **14**, 280 (1963).
38. R. T. Collins, *J. Appl. Phys.* **30**, 1135 (1959).
39. M. Balkanski and J. M. Besson, *J. Appl. Phys.* **32**, 2292 (1961).
40. T. Deutsch, *J. Appl. Phys.* **33**, 751 (1962).
41. R. Marshall and S. S. Mitra, *Phys. Rev.* **134**, 1019 (1964).
42. M. Balkanski, J. M. Besson, and R. Le Toullec, in "Int. Conf. Phys. Semicond., Paris," Dunod, Paris, and Academic Press, New York, 1091 (1964).
43. M. Balkanski, in "Optical Properties of Solids," (F. Abèles, ed.), North-Holland, Amsterdam, 529 (1972).
44. A. Manabe, A. Mitsuishi, and H. Yoshinga, *Jap. J. Appl. Phys.* **6**, 593 (1967).
45. A. S. Barker and C. J. Summers, *J. Appl. Phys.* **41**, 3552 (1970).
46. T. Hattori, Y. Homma, A. Mitsuishi, and M. Tacke, *Opt. Comm.* **7**, 229 (1971).
47. D. Berlincourt, H. Jaffe, and L. R. Shiozawa, *Phys. Rev.* **129**, 1009 (1963).
48. H. W. Verleur and A. S. Barker, *Phys. Rev.* **155**, 750 (1967).
49. E. F. Gross, B. S. Razbirin, and M. A. Iacobson, *Sov. Phys. Tech. Phys.* **2**, 2014 (1957).
50. A. B. Pevtsov, S. A. Permogorov, S. R. Salfullnev, and A. V. Sel'kin, *Sov. Phys. Sol. State* **22**, 1396 (1980).
51. A. B. Pevtsov and A. V. Sel'kin, *Sov. Phys. Sol. State* **25**, 85 (1983).
52. F. Henneberger, J. Puls, H. Rossmann, and I. N. Uraltsov., *Phys. Stat. Solidi* **B121**, K191 (1984).

53. J. Voigt, F. Spiegelberg, and M. Senomer, *Phys. Stat. Solidi* **B91**, 189 (1979).
54. J. J. Lambe, C. C. Klick, and D. L. Dexter, *Phys. Rev.* **103**, 1715 (1956).
55. D. G. Thomas and J. J. Hopfield, *Phys. Rev.* **116**, 573 (1959).
56. D. G. Thomas, J. J. Hopfield, and M. Power, *Phys. Rev.* **119**, 570 (1960).
57. D. G. Thomas and J. J. Hopfield, *Phys. Rev.* **128**, 2135 (1969).
58. G. A. Thomas and V. B. Timofiev, "Handbook on Semiconductors," (T. S. Moss, ed.) Vol. 2, North-Holland, Amsterdam, 45 (1984).
59. M. Cardona, *Phys. Rev.* **129**, 1068 (1963).

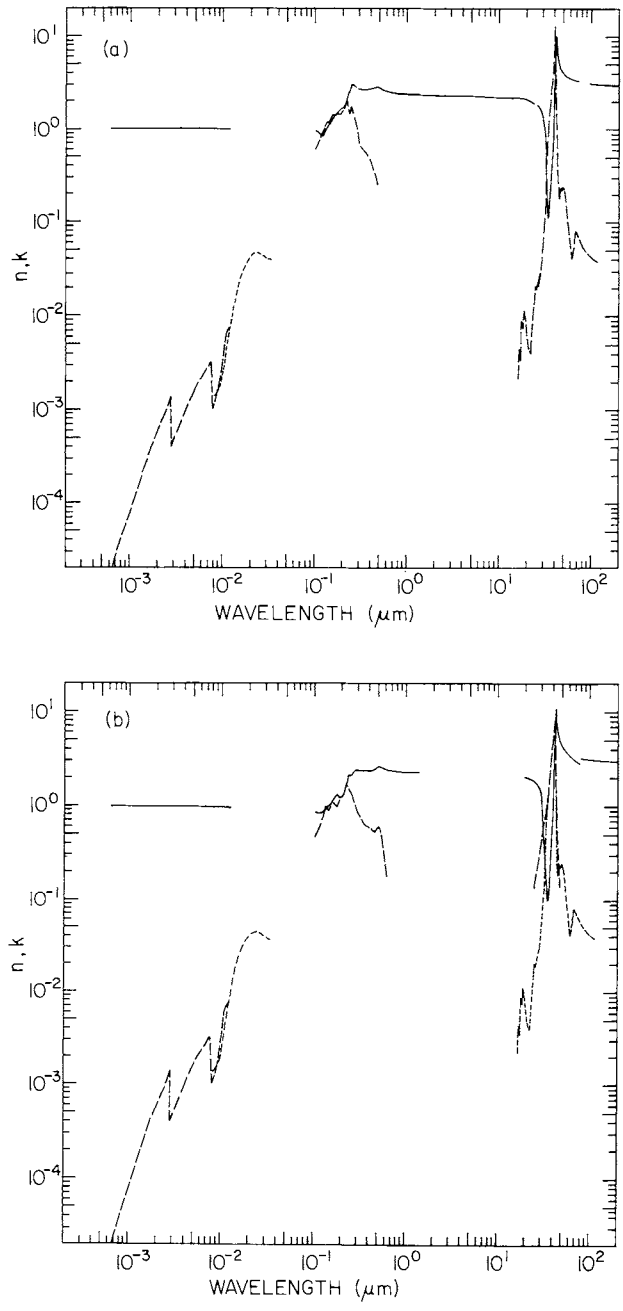

Fig. 1. (a) Log–log plot of n_o (solid line) and k_o (dashed line) versus wavelength in micrometers for cadmium sulphide. (b) Log–log plot of n_e (solid line) and k_e (dashed line) versus wavelength in micrometers.

TABLE I

Values of n and k for Hexagonal CdS from Various References[a]

eV	cm^{-1}	μm	n	k
2000	16,131,000	0.000620	0.9999 [1]	$2.0*10^{-5}$ [1]
1850	14,925,000	0.000670	0.9999	2.0
1688	13,614,000	0.000734	0.9999	3.0
1609	12,977,000	0.000771	0.9998	3.0
1358	10,953,000	0.000913	0.9998	6.0
1233	9,944,700	0.00100	0.9997	$8.0*10^{-5}$
1147	9,251,000	0.00108	0.9997	$1.0*10^{-4}$
946.5	7,634,000	0.00131	0.9996	1.8
855.1	6,896,800	0.00145	0.9995	2.5
826.6	6,666.700	0.00150	0.9995	2.8
815.7	6,579,000	0.00152	0.9995	2.9
760.6	6,134,600	0.00163	0.9994	3.6
725.1	5,848,300	0.00171	0.9994	4.0
620.0	5,000,000	0.00200	0.9993	6.0
529.9	4,273,900	0.00234	0.9992	$8.3*10^{-4}$
496.0	4,000,500	0.00250	0.9992	$1.0*10^{-3}$
469.6	3,787,900	0.00264	0.9993	1.2
447.6	3,613,100	0.00277	0.9994	$1.4*10^{-3}$
436.6	3,516,100	0.00284	1.0002	$4.0*10^{-4}$
426.0	3,436,000	0.00291	0.9995	4.2
413.3	3,333,300	0.00300	0.9993	5.0
368.0	2,968,100	0.00337	0.9987	$6.3*10^{-4}$
310.0	2,500,000	0.00400	0.9981	$1.0*10^{-3}$
269.0	2,169,600	0.00461	0.9976	1.3
248.0	2,000,000	0.00500	0.9974	1.6
227.1	1,831,700	0.00546	0.9969	2.0
206.6	1,666,700	0.00600	0.9965	2.2
190.7	1,538,100	0.00650	0.9949	2.6
177.1	1,428,400	0.00700	0.9960	2.9
165.3	1,333,300	0.00750	0.9975	3.3
162.1	1,307,200	0.00765	0.9963	0.94
155.0	1,250,000	0.00800	0.9946	1.0
136.3	1,099,300	0.00910	0.9910	1.7
124.0	1,000,000	0.0100	0.9885	3.4
118.1	951,530	0.0105	0.9870	5.7
111.7	900,910	0.0111	0.9852	7.0
104.2	833,330	0.0120	0.9833	7.5
100.0	806,550	0.0124	0.9823	8.0
149	1,201,800	0.008321	1.0000 [3]	$1.4*10^{-3}$ [3]
139	1,121,100	0.008920	1.0000	1.5
135	1,088,400	0.009184	1.0000	1.6
131	1,056,600	0.009469	1.0000	1.7
125	1,008,200	0.009919	1.0000	2.0
115	927,530	0.01078	1.0000	3.9
110	887,200	0.01127	1.0000	5.0
100	806,550	0.01240	1.0000	$8.9*10^{-3}$
90.0	725,890	0.01378	1.0000	$1.5*10^{-2}$
80.0	645,240	0.01550	1.0000	2.4
70.0	564,840	0.01771	1.0000	3.4

TABLE I (*Continued*)

Hexagonal Cadmium Sulphide

eV	cm^{-1}	μm	n	k
65.0	524,260	0.01908	1.0000 [3]	$3.8*10^{-2}$ [3]
60.0	483,930	0.02067	1.0000	4.1
55.0	443,600	0.02254	1.0000	4.5
50.0	403,270	0.02480	1.0000	4.3
40.0	322,620	0.03100	1.0000	3.8
37.5	302,460	0.03306	1.0000	$3.8*10^{-2}$

eV	cm^{-1}	μm	n_e (∥)	k_e (∥)
12.0	96,786	0.1033	0.88 [4]	0.48 [4]
11.0	88,720	0.1127	0.84	0.56
10.0	80,655	0.1240	0.76	0.75
9.3	75,010	0.1333	0.92	1.00
9.1	72,990	0.1362	0.95	0.96
8.7	69,940	0.1425	1.00	0.92
8.0	64,524	0.1550	1.10	1.12
7.6	60,610	0.1631	1.28	1.08
7.2	58,070	0.1722	1.29	1.04
7.0	56,460	0.1771	1.36	1.00
6.5	52,426	0.1907	1.22	1.18
6.0	48,390	0.2066	1.26	1.30
5.5	44,360	0.2254	1.72	1.76
5.4	43,551	0.2216	1.83	1.68
5.3	42,750	0.2339	1.96	1.66
5.2	41,940	0.2384	2.20	1.56
5.1	41,134	0.2431	2.20	1.52
5.0	40,330	0.2480	2.16	1.44
4.7	37,910	0.2638	2.34	1.24
4.4	35,490	0.2818	2.48	1.04
4.0	32,260	0.3100	2.40	0.81
3.75	30,245	0.3306	2.38	0.74
3.5	28,230	0.3542	2.38	0.65
3.25	26,213	0.3815	2.36	0.61
3.0	24,196	0.4133	2.37	0.56
2.7	21,780	0.4592	2.47	0.54
2.5	20,164	0.4959	2.62	0.60
2.25	18,147	0.5510	2.53	0.26
2.0	16,130	0.6199	2.44	0.18
1.5	12,098	0.8266	2.36	

eV	cm^{-1}	μm	n_o (⊥)	k_o (⊥)
12.0	96,786	0.1033	0.95 [4]	0.60 [4]
11.0	88,720	0.1127	0.87	0.72
10.0	80,655	0.1240	0.82	0.92
9.0	72,589	0.1377	1.00	1.19
8.7	70,170	0.1425	1.08	1.15
8.0	64,524	0.1550	1.20	1.40
7.5	60,490	0.1653	1.40	1.36

TABLE I (*Continued*)

Hexagonal Cadmium Sulphide

eV	cm^{-1}	μm	n_o (⊥)	k_o (⊥)
7.1	57,265	0.1746	1.44 [4]	1.47 [4]
7.0	56,460	0.1771	1.50	1.45
6.5	52,450	0.1907	1.60	1.40
6.0	48,390	0.2067	1.74	1.56
5.5	44,360	0.2254	1.84	1.96
5.4	43,550	0.2296	2.30	1.83
5.3	42,750	0.2339	2.49	1.68
5.2	41,940	0.2384	2.40	1.52
5.1	41,130	0.2431	2.48	1.48
5.0	40,330	0.2480	2.57	1.60
4.9	39,530	0.2530	2.92	1.73
4.8	38,760	0.2583	3.04	1.64
4.0	32,260	0.3100	2.64	0.64
3.75	30,245	0.3306	2.64	0.62
3.5	28,230	0.3542	2.62	0.56
3.25	26,213	0.3815	2.62	0.49
3.0	24,196	0.4133	2.63	0.44
2.75	22,180	0.4509	2.70	0.41
2.5	20,164	0.4959	2.81	0.36
2.25	18,147	0.5510	2.57	0.04
2.0	16,130	0.6199	2.48	0.02
1.5	12,098	0.8206	2.40	

eV	cm^{-1}	μm	n_o (⊥)	n_e (∥)
2.408	19,420	0.515	2.726 [15]	2.743 [15]
2.255	18,190	0.550	2.593	2.580
2.067	16,670	0.600	2.511	2.493
1.908	15,390	0.650	2.463	2.446
1.771	14,280	0.700	2.432	2.414
1.653	13,330	0.750	2.409	2.390
1.550	12,500	0.800	2.392	2.374
1.459	11,770	0.850	2.378	2.361
1.378	11,110	0.900	2.368	2.350
1.305	10,530	0.950	2.359	2.341
1.240	10,000	1.00	2.352	2.334
1.181	9,525	1.05	2.346	2.328
1.127	9,091	1.10	2.340	2.324
1.078	8,696	1.15	2.336	2.320
1.033	8,333	1.20	2.332	2.316
0.9919	8,000	1.25	2.329	2.312
0.9538	7,694	1.30	2.326	2.309
0.9184	7,408	1.35	2.323	2.306
0.8856	7,143	1.40	2.321	2.304

eV	cm^{-1}	μm	n(polycryst)	k
1.550	12,500	0.80	2.38 [21]	
1.240	10,000	1.00	2.33	
0.8266	6,667	1.50	2.29	

TABLE I (*Continued*)

Hexagonal Cadmium Sulphide

eV	cm^{-1}	μm	n	k(both axes)
0.6200	5,000	2.00	2.280 [21]	
0.4959	4,000	2.50	2.275	
0.4133	3,333	3.00	2.270	
0.3100	2,500	4.00	2.265	
0.2480	2,000	5.00	2.260	
0.2067	1,667	6.00	2.255	
0.1771	1,429	7.00	2.250	
0.1550	1,250	8.00	2.245	
0.1378	1,111	9.00	2.235	
0.1240	1,000	10.00	2.230	
0.1127	909.1	11.00	2.215	
0.1033	823.3	12.00	2.205	
0.09537	769.3	13.00	2.190	
0.08856	714.3	14.00	2.175	
0.08266	666.7	15.00	2.175	
0.07438	600	16.67		0.0022[39]
0.07290	588	17.01		0.0044
0.07191	580	17.24		0.0034
0.06993	564	17.73		0.0067
0.06894	556	17.86		0.0087
0.06670	538	18.59		0.0074
0.06532	526	19.00		0.011
0.06199	500	20.00		0.0080
0.05889	475	21.05		0.0047
0.05579	450	22.22		0.0039
0.05269	425	23.53		0.0075
0.04959	400	25.00		0.020
0.04811	388	25.77		0.019
0.04339	350	28.57		0.029

eV	cm^{-1}	μm	n_e ($\parallel$)	k_e ($\parallel$)	n_o ($\perp$)	k_o ($\perp$)
0.06200	500.1	20.0	2.10[44]		2.10[44]	
0.04959	400.0	25.0	1.90	0.14[44]	1.85	0.10[44]
0.04133	333.3	30.0	1.33	0.43	1.33	0.43
0.03542	285.7	35.0	0.10	1.28	0.10	1.78
0.03100	250.0	40.0	0.58	4.35	2.03	6.03
0.03024	243.9	41.0	1.55	5.95	3.10	8.99
0.02988	241.0	41.5	2.00	6.70	4.28	8.35
0.02931	236.6	42.3	5.50	8.12	9.71	5.90
0.02870	231.5	43.2	11.16	3.20	7.20	3.10
0.02818	227.3	44.0	7.85	1.22	5.65	1.05
0.02755	222.2	45.0	6.67	0.64	5.07	0.23
0.02638	212.8	47.0	5.23	0.14	4.30	
0.02480	200.0	50.0	4.29		3.77	
0.02067	166.7	60.0	3.48		3.19	
0.01771	142.8	70.0	3.04		3.04	
0.01653	133.3	75.0	2.90		2.90	
0.01550	125.0	80.0	2.90		2.90	

TABLE I (*Continued*)

Hexagonal Cadmium Sulphide

eV	cm^{-1}	μm	n_e (∥)	n_o (⊥)
0.01550	125	80.00	3.27 [45]	3.14 [45]
0.01240	100	100.0	3.18	3.06
0.009300	75.0	133.3	3.11	3.00
0.006199	50.0	200.0	3.07	2.97
0.01240	100.0	100	3.27 [46]	3.11 [46]
0.001240	10.00	1000	3.27	3.11
		>1000	3.00 [47]	3.09 [47]
		>1000	2.90 [48]	2.90 [48]

eV	cm^{-1}	μm	n_o (⊥)	k(both)
0.04563	368	27.17	1.78 [43]	0.02 [42]
0.04377	353	28.35	1.68	0.03
0.04104	331	30.21	1.37	0.05
0.03968	320	31.25	1.16	0.08
0.03831	309	32.36	0.96	0.13
0.03794	306	32.68	0.82	0.16
0.03769	304	32.89	0.77	0.26
0.03695	298	33.56	0.33	0.53
0.03596	290	34.48	0.14	0.82
0.03434	277	36.10	0.15	1.44
0.03174	256	39.01	0.55	3.11
0.03062	247	40.49	1.12	6.45
0.03025	244	40.98	2.03	9.77
0.03000	242	41.33	3.42	13.15
0.02963	239	41.84	4.45	10.01
0.02950	238	42.02	6.16	6.69
0.02926	236	42.37	10.0	3.38
0.02901	234	42.74	7.81	1.70
0.02889	233	42.92	7.29	1.02
0.02876	232	43.10	6.84	0.69
0.02814	227	44.05	5.82	0.35
0.02690	217	46.08	4.62	0.18
0.02591	209	47.85	4.10	0.23
0.02542	205	48.78	4.04	0.22
0.02505	202	49.51	4.10	0.23
0.02443	197	50.76	3.73	0.24
0.02368	191	52.36	3.70	0.21
0.02219	179	55.87	3.63	0.13
0.02182	176	56.82	3.49	0.09
0.01947	157	63.69	3.42	0.04
0.01798	145	68.97	3.34	0.08
0.01624	131	76.34	3.29	0.06
0.01277	103	97.09		0.04
0.01030	83	120.3		0.04

TABLE I (*Continued*)

Cadmium Sulphide (Thin Films)

eV	cm^{-1}	μm	n	k
4.133	33,330	0.30	2.68[28]	>0.70 [28]
3.543	28,580	0.35	2.58	>0.70
3.100	25,000	0.40	2.55	>0.70
2.480	20,000	0.50	2.72	0.70
2.067	16,670	0.60	2.40	0.54
1.771	14,280	0.70	2.35	0.47
1.550	12,500	0.80	2.32	0.43
1.378	11,110	0.90	2.30	0.40
1.240	10,000	1.0	2.28	0.37
1.127	9,091	1.1	2.28	0.33
1.033	8,333	1.20	2.27	0.28
0.9538	7,693	1.30	2.27	0.15
0.8856	7,143	1.40	2.26	0.04
0.8266	6,667	1.50	2.25	
0.7749	6,250	1.60	2.25	
0.6888	5,556	1.80	2.24	
0.6200	5,000	2.00	2.23	
0.6200	5,000	2.00	2.300 [33]	
0.4133	3,333	3.00	2.284	
0.3100	2,500	4.00	2.277	
0.2067	1,667	6.00	2.271	
0.1550	1,250	8.00	2.267	
0.1240	1,000	10.00	2.263	
0.1033	833.3	12.00	2.260	
0.08856	714.3	14.00	2.255	

[a] References are indicated in brackets.

Gallium Antimonide (GaSb)

DAVID F. EDWARDS and RICHARD H. WHITE
University of California
Lawrence Livermore National Laboratory
Livermore, California

Few reports can be found in the literature of the fundamental optical properties of GaSb. Research-sized crystals are relatively easy to grow, but GaSb has developed little technical interest. Aspnes and Studna [1] report n and k values calculated from pseudo-dielectric functions measured by spectroscopic ellipsometry. They call this the pseudo-dielectric function because no corrections were made for possible surface overlayers or subsurface damage effects. For surfaces free of these defects or by making the appropriate corrections, the ellipsometric measurements would give the "true" dielectric function. In either case they calculate the n and k values from the ellipsometric measurements.

As pointed out by Aspnes and Studna [1], three recent technical advances have been made that allow for more accurate determination of the optical properties of semiconductors, GaSb included. The first and most important is the development of their new etching and cleanup procedures [2]. These procedures minimize the thickness of the undesirable surface layer that forms on semiconductors. As a result, their ellipsometric measurements and calculated pseudo-dielectric functions more accurately represent the intrinsic bulk values. The second advance is the development of the automatic spectroscopic ellipsometer. This instrument determines both components of the complex pseudo-dielectric function over a broad spectral range. No wavelength extrapolations are needed as in the Kramers–Kronig analysis of reflectance data. The third is the development of unambiguous criteria for optically determining the best surfaces. These "best" surfaces are the ones most free of roughness, unintentional overlayers, absorbed contaminants, and subsurface damage. Aspnes and Studna have been leaders in this field of the ellipsometric determination of the optical properties of solids.

Several reports have been made of the reflectance in the near-UV and visible regions. Seraphin and Bennett [3] list the reflectance data of Cardona [4] for the 4–0.5 eV spectral range. Tauc and Abraham [5] report reflectance for the same spectral region. The objective of both reports was

Copyright © 1991 by Academic Press.
All rights of reproduction in any form reserved.
ISBN 0-12-544422-2

an investigation of the band structure of GaSb, and no extraction of n and k values was made.

Johnson, Filinski, and Fan [6] measured the absorption coefficient in a p-type undoped GaSb sample at 1.7 K in the region of the intrinsic energy gap. ($E_g = 0.8100$ eV at 1.7 K). They observed three sharp bands. The highest energy band (0.8100 eV) they identify as due to an exciton absorption. The two bands of lower energy (0.8049 eV and 0.7958 eV) they attribute to exciton-impurity complexes. They report their data in a curve of absorption coefficient (cm^{-1}) as a function of photon energy. From their curve we have extracted the k values. The three exciton peaks are designated α, β, and γ in Table I.

Edwards and Hayne [7], using the angle-of-minimum-deviation technique, measured the near-IR index of refraction from 1.8–2.5 μm (about 0.7–0.5 eV). Oswald and Schade [8] were among the first to report n and k values for the infrared region. They calculated n and k values from the measured reflectance and transmittance for a GaSb sample with a resistivity of only 0.08 Ω cm. This small resistivity and the monotonically increasing k values with wavelength indicate free-carrier absorption. As a result, the Oswald and Schade data are not given in the table that follows. Wynne and Bloembergen [9] calculated the indices of refraction at 5.3 μm and 10.6 μm from the measured transmittance and coherence length for second-harmonic generation in GaSb with a CO_2 laser. These data are not included in our tabulation because of the inconsistencies with the data of other sources and the lack of precision of their method for extracting index values.

Hass and Henvis [10] measured the fundamental lattice reflection bands of several III-V compound semiconductors including GaSb. These measurements were made at liquid-helium temperature using a grating spectrometer for increased spectral resolution. By comparing the observed reflectance spectrum with that calculated using a single classical oscillator [11], they obtained the "best" values of the oscillator parameters. From these parameters we calculated the n and k values for the 29–100 μm spectral region.

Pikhtin and Yas'kov [12] report a semi-empirical method for calculating the dispersion of the refractive index using three adjustable parameters associated with the energy-band structure. For those materials where extensive data are available, their predictions accurately fit the indices. For GaSb they use the data of Refs. [7] and [8], which do not have the spectral breadth necessary for the accurate determination of their three parameters. Test calculations [13] for wavelengths longer than those of Ref. [7] indicate the values of the indices are sensitively dependent on the values of these adjustable parameters. It appears that indices over a broad spectral range are needed to improve the accuracy of the Pikhtin–Yas'kov calculated data for GaSb.

The indices of refraction and extinction coefficients for GaSb are given in Table I and plotted in Fig. 1. Most of the data are for room temperature except where noted. The n and k values from 6.0 eV to 2.1 eV are the measured data of Aspnes and Studna [1]. The k values for the absorption-edge region are calculated from the measured absorption coefficients of Johnson *et al.* [6]. The n values from 2.0 eV to 0.0443 eV (0.62–28 μm) were calculated from a Herzberger-type dispersion formula fit to the measured data of various references [1, 7, 10]. These same data were also fit to a modified Sellmeier-type dispersion formula. This was done for convenience to the reader, but the Sellmeier values are not given in Table I. A total of 28 data points were used for these fittings. As seen in Fig. 1, the indices between 6.0 eV and 2.1 eV (0.2067 μm and 0.5905 μm) do not lend themselves to Herzberger- or Sellmeier-type, curve-fitting routines.

The Herzberger-type dispersion formula [14] is

$$n = A + BL + CL^2 + D\lambda^2 + E\lambda^4,$$

where $L = 1/(\lambda^2 - 2.8 \times 10^6)$ with the wavelength λ in Å, and 2.8×10^6 is the square of the mean asymptote for the short-wavelength abrupt rise in index for 14 materials (GaSb not included) [14]. For the 28 points from 0.62 μm to 28 μm, and room temperature, the coefficients are

$$A = 3.850787$$

$$B = 2.024481 \times 10^7$$

$$C = 1.079226 \times 10^{15}$$

$$D = -4.397689 \times 10^{-11}$$

$$E = 3.527494 \times 10^{-19}.$$

The RMS error between the reported indices and the values calculated from the dispersion formula is 0.192%.

For the reader's convenience, the modified Sellmeier-type dispersion formula [15] is

$$n^2 = 1 + A/(\lambda^2 - B) + C\lambda^2/(\lambda^2 - D),$$

where the wavelength λ is in Å. For the 28 data points, the coefficients are

$$A = 3.779678 \times 10^{-8}$$

$$B = 1.558825 \times 10^{-9}$$

$$C = 1.266738 \times 10^{1}$$

$$D = -1.013537 \times 10^{-9}.$$

The RMS error is 0.226%.

In Table I the n and k values from 29 μm to 100 μm were calculated from the lattice band parameters of Ref. [10] and are for liquid-helium temperature. These calculations were extended beyond the range of measurement to 100 μm, in order to estimate ε_0, the low frequency dielectric constant. Hass and Henvis [10] report $\varepsilon_o = 15.69$ compared with $n^2 = 15.98$ at 100 μm.

Cardona [16] reports the measured temperature coefficient of the refractive index of GaSb to be

$$\frac{1}{n}\frac{\mathrm{d}n}{\mathrm{d}T} = 8.1 \pm 0.2 \times 10^{-5}\,\mathrm{K}^{-1}$$

for the 5–10 μm spectral region. This coefficient was determined from changes in the interference patterns produced by multiple internal reflections in single crystals with low impurity concentrations. He reports that the results are independent of free-carrier effects for the temperature range of about 85–415 K.

Ghosh *et al.* [17] have developed a simple model for predicting the temperature and pressure coefficients of the refractive index of some zinc-blende semiconductors, GaSb included. They predict the temperature coefficient at constant pressure to be

$$\left(\frac{\mathrm{d}n}{\mathrm{d}T}\right)_{\mathrm{P}} = 1.47 \times 10^{-4}\,\mathrm{K}^{-1}$$

at 3.7 μm for the range −173–127 °C. They compare this with experimental values of $3.11\text{–}3.05 \times 10^{-4}\,\mathrm{K}^{-1}$. Their predicted pressure coefficient is

$$-\left(\frac{\mathrm{d}n}{\mathrm{d}P}\right)_{\mathrm{T}} = 44.5 - 52.8 \times 10^{-3}\,\mathrm{GPa}^{-1}.$$

They have no experimental data for comparison nor do they give a wavelength or pressure range.

REFERENCES

1. D. E. Aspnes and A. A. Studna, "Dielectric Functions and Optical Parameters of Si, Ge, GaP, GaAs, GaSb, InP, InAs, and InSb from 1.5 to 6.0 eV," *Phys. Rev. B* **27**, 985 (1983).
2. D. E. Aspnes and A. A. Studna, *SPIE Proc.* **276**, 227 (1981); *Appl. Phys. Lett.* **39**, 316 (1981).
3. B. O. Seraphin and H. E. Bennett, in "Optical Properties of III-V Compounds," (R. K. Willardson and A. C. Beer, eds.), Academic Press, New York, 499 (1967).
4. M. Cardona, "Optical Investigation of the Band Structure of GaSb," *Z. Phys.* **161**, 99 (1961); "Fundamental Reflectivity Spectrum of Semiconductors with Zinc-Blende Structure," *J. Appl. Phys.* **32**, Suppl., 2151 (1961).
5. J. Tauc and A. Abraham, "Reflection Spectra of Semiconductors with Diamond and Sphalerite Structures," "Proc. Int. Conf. Semicond. Phys., Prague, 1960," (K. Zaveta, ed.), Czech. Acad. Sci., Prague, and Academic Press, New York, 375 (1961).
6. E. J. Johnson, I. Filinski, and H. Y. Fan, "Absorption and Emission of Excitons and Impurities in GaSb," "Proc. Intern. Conf. Phys. Semicond. 6th, Exeter, 1962," The Institute of Physics and the Physical Society, London, 375 (1962).
7. D. F. Edwards and G. S. Hayne, "Optical Properties of Gallium Antimonide," *J. Opt. Soc. Am.* **49**, 414 (1959).
8. F. Oswald and R. Schade, "Uber die Bestimmung der Optischen Konstanten von Halbleitern des Typus $A^{III}B^{V}$ in Infraroten," *Z. Naturforschg.* **9a**, 611 (1954).
9. J. J. Wynne and N. Bloembergen, Measurement of the Lowest Order Nonlinear Susceptibility in III-V Semiconductors by Second-Harmonic Generation with a CO_2 Laser," *Phys. Rev.* **188**, 1211 (1969); Erratum, *Phys. Rev.* **B2**, 4306 (1970).
10. M. Hass and B. W. Henvis, "Infrared Lattice Refraction Spectra of III-V Compound Semiconductors," *J. Phys. Chem. Solids* **23**, 1099 (1962).
11. M. Born and K. Huang, "Dynamical Theory of Crystal Lattices," University Press, Oxford, Chap. 2 (1954).
12. A. N. Pikhtin and A. D. Yas'kov, "Dispersion of the Refractive Index of Semiconductors with Diamond and Zinc-blende Structures," *Sov. Phys. Semicond.* **12**, 622 (1978).
13. D. F. Edwards, 1989 (unpublished).
14. M. Herzberger and C. D. Salzberg, "Refractive Indices of Infrared Optical Materials and Color Correction of Infrared Lens," *J. Opt. Soc. Am.* **52**, (4), 420 (1962); M. Herzberger, "Colour Corrections in Optical Systems and a New Dispersion Formula," *Opt. Acta* **6**, 197 (1959).
15. D. F. Edwards and R. H. White, see KDP in this volume.
16. M. Cardona, "Temperature Dependence of the Refractive Index and the Polarizability of Free Carriers in Some III-V Semiconductors, "Proc. Intern. Conf. Semicond. Phys., Prague, 1960," Czech. Acad. Sci., Prague, and Academic Press, New York, 388 (1961).
17. D. K. Ghosh, L. K. Samanta, and G. C. Bhar, "The Temperature and Pressure Dependence of Refractive Indices of Some III-V and II-VI Binary Semiconductors," *Infrared Physics* **26**, 111 (1986).

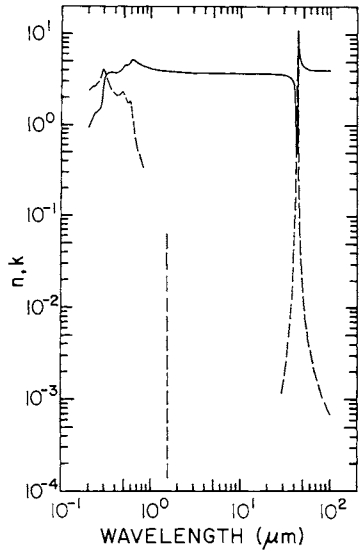

Fig. 1. Log–log plot of n (solid line) and k (dashed line) versus wavelength in micrometers for gallium antimonide.

TABLE I

Values of n and k for Gallium Antimonide Obtained from Various References[a]

eV	cm^{-1}	μm	n	n_c	k
6.00	48,387	0.2067	0.935 [1]		2.416 [1]
5.90	47,581	0.2102	0.985		2.444
5.80	46,774	0.2138	1.022		2.479
5.70	45,968	0.2175	1.062		2.535
5.60	45,161	0.2214	1.127		2.602
5.50	44,355	0.2255	1.212		2.645
5.40	43,548	0.2296	1.299		2.653
5.30	42,742	0.2340	1.345		2.638
5.20	41,935	0.2385	1.356		2.645
5.10	41,129	0.2431	1.358		2.685
5.00	40,323	0.2480	1.369		2.751
4.90	39,516	0.2531	1.387		2.829
4.80	38,710	0.2583	1.408		2.928
4.70	37,903	0.2638	1.444		3.055
4.60	37,097	0.2696	1.503		3.208
4.50	36,290	0.2756	1.586		3.392
4.40	35,484	0.2818	1.723		3.628
4.30	34,677	0.2884	1.989		3.923
4.20	33,871	0.2952	2.522		4.130
4.10	33,065	0.3024	3.100		3.976
4.00	32,258	0.3100	3.450		3.643
3.90	31,452	0.3179	3.620		3.323
3.80	30,645	0.3263	3.701		3.069
3.70	29,839	0.3351	3.748		2.862
3.60	29,032	0.3444	3.774		2.690
3.50	28,226	0.3543	3.785		2.545
3.40	27,419	0.3647	3.794		2.430
3.30	26,613	0.3758	3.808		2.319
3.20	25,806	0.3875	3.800		2.210
3.10	25,000	0.4000	3.766		2.134
3.00	24,194	0.4133	3.732		2.109
2.90	23,387	0.4276	3.728		2.121
2.80	22,581	0.4429	3.760		2.157
2.70	21,774	0.4593	3.836		2.211
2.60	20,968	0.4769	3.984		2.280
2.50	20,161	0.4960	4.312		2.285
2.40	19,355	0.5167	4.513		1.962
2.30	18,548	0.5391	4.492		1.789
2.20	17,742	0.5636	4.521		1.747
2.10	16,935	0.5905	4.705		1.803
2.000	16,129	0.620		5.2496	1.378
1.938	15,625	0.640		5.1058	
1.900	15,323	0.6526			0.829
1.879	15,152	0.660		4.9812	
1.824	14,706	0.680		4.8724	
1.800	14,516	0.6889			0.611
1.771	14,286	0.700		4.7771	

TABLE I (*Continued*)

Gallium Antimonide

eV	cm^{-1}	μm	n	n_c	k
1.722	13,889	0.720		4.6929	
1.700	13,710	0.7294			0.485
1.676	13,514	0.740		4.6184	
1.632	13,158	0.760		4.5521	
1.600	12,903	0.7750			0.416
1.590	12,821	0.780		4.4928	
1.550	12,500	0.800		4.4396	
1.512	12,195	0.820		4.3916	
1.500	12,096	0.8267			0.344
1.476	11,905	0.840		4.3483	
1.442	11,628	0.860		4.3090	
1.409	11,364	0.880		4.2733	
1.378	11,111	0.900		4.2406	
1.348	10,870	0.920		4.2108	
1.319	10,638	0.940		4.1834	
1.292	10,417	0.960		4.1583	
1.265	10,204	0.980		4.1351	
1.240	10,000	1.000		4.1137	
0.6199	5,000	2.0		3.7883	
0.4133	3,333	3.0		3.7421	
0.3100	2,500	4.0		3.7285	
0.2480	2,000	5.0		3.7241	
0.2066	1,667	6.0		3.7236	
0.1771	1,429	7.0		3.7251	
0.1550	1,250	8.0		3.7278	
0.1378	1,111	9.0		3.7313	
0.1240	1,000	10.0		3.7352	
0.1127	909.1	11.0		3.7395	
0.1033	833.3	12.0		3.7438	
0.09537	769.2	13.0		3.7481	
0.08856	714.3	14.0		3.7521	
0.08266	666.7	15.0		3.7557	
0.07749	625.0	16.0		3.7586	
0.07293	588.2	17.0		3.7608	
0.06889	555.6	18.0		3.7620	
0.06526	526.3	19.0		3.7620	
0.06199	500.0	20.0		3.7605	
0.05904	476.2	21.0		3.7574	
0.05636	454.5	22.0		3.7524	
0.05391	434.8	23.0		3.7453	
0.05166	416.7	24.0		3.7357	
0.04959	400.0	25.0		3.7235	
0.04769	384.6	26.0		3.7083	
0.04592	370.4	27.0		3.6898	
0.04428	357.1	28.0		3.6677	
0.04275	344.8	29.0		3.66 [10]	1.2×10^{-3} [10]
0.04133	333.3	30.0		3.65	1.5×10^{-3}

TABLE I (*Continued*)

Gallium Antimonide

eV	cm^{-1}	μm	n	n_c	k
0.04000	322.6	31.0		3.62	1.8×10^{-3}
0.03875	312.5	32.0		3.60	2.3×10^{-3}
0.03757	303.0	33.0		3.57	3.0×10^{-3}
0.03647	294.1	34.0		3.53	4.0×10^{-3}
0.03542	285.7	35.0		3.48	5.4×10^{-3}
0.03444	277.8	36.0		3.42	7.5×10^{-3}
0.03351	270.3	37.0		3.33	1.09×10^{-2}
0.03263	263.2	38.0		3.21	1.69×10^{-2}
0.03179	256.4	39.0		3.03	2.85×10^{-2}
0.03100	250.0	40.0		2.71	5.61×10^{-2}
0.03024	243.9	41.0		2.02	0.160
0.02952	238.1	42.0		0.484	2.06
0.02945	237.5	42.1		0.485	2.39
0.02938	237.0	42.2		0.502	2.73
0.02931	236.4	42.3		0.531	3.08
0.02924	235.8	42.4		0.575	3.45
0.02917	235.3	42.5		0.637	3.86
0.02910	234.7	42.6		0.723	4.31
0.02904	234.2	42.7		0.844	4.82
0.02897	233.6	42.8		1.02	5.41
0.02890	233.1	42.9		1.28	6.12
0.02883	232.6	43.0		1.70	6.98
0.02877	232.0	43.1		2.43	8.07
0.02870	231.5	43.2		3.84	9.36
0.02863	230.9	43.3		6.65	10.3
0.02857	230.4	43.4		10.3	8.56
0.02850	229.9	43.5		11.2	5.04
0.02844	229.4	43.6		10.4	2.87
0.02837	228.8	43.7		9.39	1.81
0.02831	228.3	43.8		8.62	1.24
0.02824	227.8	43.9		8.03	0.907
0.02818	227.3	44.0		7.57	0.694
0.02755	222.2	45.0		5.66	0.148
0.02695	217.4	46.0		5.07	6.64×10^{-2}
0.02638	212.8	47.0		4.78	3.85×10^{-2}
0.02583	208.3	48.0		4.61	2.56×10^{-2}
0.02530	204.1	49.0		4.50	1.84×10^{-2}
0.02480	200.00	50.0		4.42	1.41×10^{-2}
0.02066	166.67	60.0		4.13	3.4×10^{-3}
0.01771	142.86	70.0		4.058	1.8×10^{-3}
0.01550	125.00	80.0		4.026	1.2×10^{-3}
0.01378	111.11	90.0		4.008	8.9×10^{-4}
0.01240	100.00	100.0		3.997	7.2×10^{-4}
0.8166	6,585.5	1.5185			5.08×10^{-2} [6]
0.8145	6,568.5	1.5224			4.85
0.8128	6,554.8	1.5256			4.86
0.8120	6,548.4	1.5271			5.10
0.8112	6,541.9	1.5286			5.11

TABLE I (*Continued*)

Gallium Antimonide

eV	cm^{-1}	μm	n	n_c	k
0.8109	6,539.5	1.5292			5.35
0.8105	6,536.3	1.5299			5.84
0.8100	6,532.3	1.5309			α 6.33
0.8095	6,528.2	1.5318			5.73
0.8094	6,527.4	1.5320			4.88
0.8087	6,521.8	1.5333			2.5
0.8085	6,520.2	1.5337			1.35
0.8080	6,516.1	1.5347			1.07×10^{-2}
0.8075	6,512.1	1.5356			9.65×10^{-3}
0.8068	6,506.5	1.5369			9.05
0.8061	6,500.8	1.5383			9.06
0.8055	6,496.0	1.5394			9.80×10^{-3}
0.8053	6,494.4	1.5398			1.10×10^{-2}
0.8049	6,491.1	1.5406			β 1.23
0.8045	6,487.9	1.5413			1.03×10^{-2}
0.8040	6,483.9	1.5423			8.10×10^{-3}
0.8036	6,480.6	1.5431			5.16
0.8034	6,479.0	1.5434			3.93
0.8030	6,475.8	1.5442			2.70
0.8022	6,469.4	1.5457			1.66
0.8016	6,464.5	1.5469			1.23
0.8012	6,461.3	1.5477			1.05×10^{-3}
0.8005	6,455.6	1.5490			8.63×10^{-4}
0.7996	6,448.4	1.5508			6.54
0.7990	6,443.5	1.5519			5.31
0.7980	6,435.5	1.5339			3.59
0.7970	6,427.4	1.5558			3.10
0.7965	6,423.4	1.5568			3.34
0.7964	6,422.6	1.5570			4.09
0.7962	6,421.0	1.5574			4.71
0.7958	6,417.7	1.5582			γ 4.96
0.7957	6,416.9	1.5584			4.34
0.7954	6,414.5	1.5590			2.73
0.7950	6,411.3	1.5597			2.23
0.7946	6,408.1	1.5605			1.74
0.7940	6,403.2	1.5617			1.49
0.7932	6,396.8	1.5633			1.49
0.7922	6,388.7	1.5653			1.5
0.7906	6,375.8	1.5684			1.4×10^{-4}

[a] The column headed n_c contains refractive-index values calculated with the Herzberger-type formula. The bracketed numbers indicate the reference to the data. Near 1.54 μm excitonic peaks are designated α, β, γ.

Silicon–Germanium Alloys (Si_xGe_{1-x})

J. HUMLÍČEK, F. LUKEŠ, and E. SCHMIDT
Department of Solid State Physics
Masaryk University
Brno, Czechoslovakia

Silicon and germanium form a continuous series of crystalline alloys, Si_xGe_{1-x}, from $x=0$ to $x=1$. Optical constants of both constituents have been critiqued extensively by Potter [1] and Edwards [2] in *HOC I*. Optical response of the alloy varies continuously over the entire range of compositions x, providing a suitable degree of freedom in tailoring the material for possible optical applications. On the other hand, the alloy is a very good object for physical studies of disorder-induced effects in electron and phonon structure of crystalline solids. It has also been studied in order to understand better the electron band structure of the pure constituents. In spite of numerous studies devoted to this alloy system, the number of papers allowing reasonable extraction of the optical constants is somewhat limited.

In the present critique, we compile the optical data for three compositions, representative of Si-rich ($x\approx0.80$), Ge-rich ($x\approx0.25$), and nearly-equal-content ($x\approx0.50$) alloys. This particular choice was influenced by the requirement of nearly coinciding compositions for data available from various sources. With one exception, we did not interpolate the composition dependence at fixed wavelengths to match the chosen values of x; instead, we have tabulated the original data obtained for slightly different compositions. It should be pointed out that the three spectra are a rather limited data base with respect to possible accurate interpolation for other alloy compositions. Data are listed in Table I and plotted in Fig. 1.

Early measurements of the energy position of the intrinsic optical absorption edge were reported in 1954 by Johnson and Christian [3]. The near-infrared absorption spectra were subsequently studied in detail by Braunstein *et al.* [4] in wide ranges of composition and temperature. Bulk samples were single crystals in the range of 0–20% and 90–100% Si;

Copyright © 1991 by Academic Press.
All rights of reproduction in any form reserved.
ISBN 0-12-544422-2

intermediate compositions were polycrystals. The alloy composition was determined by spectrographic techniques to ±5% of the content of silicon (for 0–70% Si) or germanium (for 70–100% Si). Fluctuations in composition between slices from the same ingot are mentioned; consequently, the spectra of absorption coefficient α were taken on the same sample thinned progressively from 500 to 5 μm. Higher values of α might be influenced by the inferior quality reported for some of the thinnest alloy samples. Special care was taken to ensure that all the light transmitted through the sample was collected on the detector. This indicates problems with scattered light, which we also mention below in the discussion of phonon spectra. Room temperature was specified to be 296 K; this is fairly important, since the band edge shifts strongly with temperature. The refractive index needed for calculations of α from measured transmittances was obtained from the transmission at long wavelengths.

The extensive work of Braunstein *et al.* [4] provides no spectra for the representative compositions of 25%, 50%, and 80% Si; therefore, we used their results in the following interpolation scheme. The absorption coefficient was fitted in Ref. [4] to the Macfarlane–Roberts expression:

$$\alpha(E, T) = A\left[\frac{(E - E_g - k\theta)^2}{1 - \exp(-\theta/T)} + \frac{(E - E_g + k\theta)^2}{\exp(\theta/T) - 1}\right], \tag{1}$$

where E is the photon energy, $k\theta$ the phonon energy (k is the Boltzmann constant, not to be confused with the extinction coefficient), E_g the energy gap, T the temperature, and A a temperature-independent factor. The first term in square brackets of Eq. 1 is to be included for $E > E_g + k\theta$, the second for $E > E_g - k\theta$; $\alpha = 0$ below $E_g - k\theta$. A detailed compositional dependence of the best-fit values of $E_g(x)$ and the phonon equivalent temperature $\theta(x)$ is given by Braunstein *et al.* [4]. We have read their room-temperature spectra from graphs and determined the remaining parameter A that fits them best with appropriate values of E_g and θ. Interpolated values of all of the three parameters were inserted in Eq. 1 to generate the $\alpha(E)$ spectra for $T = 296$ K. We have limited the spectral range so as to obtain the α values from 1 to 1000 cm^{-1}. The corresponding extinction coefficient is shown in the tables. The results of the interpolation procedure agree to about ±20% with values obtained by interpolating the experimental spectra either in compositions for fixed photon energies or vice versa. Because of the smoothing action of Eq. 1, the precision of the tabular data is limited only by the three decimals shown. The accuracy, however, is probably much lower. A factor-of-two difference, which is rather typical of various sources for pure Si and Ge [1, 2], is probably hard to achieve in the case of an alloy.

Reflectance measurements in the spectral range of strong absorption above the band gap, aiming at the identification of several interband thresholds, were performed by Tauc and Abrahám [5]. Schmidt [6] measured the reflectance in the energy region from 1–13 eV on a number of alloy samples. Three of them had compositions suitable for our tabulation. The compositions were determined by X-ray diffraction; the mean error of x was ± 0.004. The polycrystalline samples were mechanically polished and chemically etched. The thickness of surface oxides was estimated ellipsometrically to be between 2 and 4 nm. No correction was performed for the overlayers. The optical constants were computed from Kramers–Kronig (K–K) relations, using a combination of exponential (13–18 eV) and constant (above 18 eV) extrapolation of the reflectance. The K–K analysis of these data was repeated with a modified extrapolation, and the accuracy of the dielectric functions was tested for pure Si and Ge by Humlíček *et al.* [7]. We tabulate the room-temperature (300 K) results of the latter K–K computations for selected photon energies. Since the low values of the extinction coefficient k at the red side of the spectral region are very unreliable, only values where $k>0.4$ are given.

Very recently, ellipsometry has been used to measure the optical response from 1.66–5.7 eV by Humlíček *et al.* [8]. Two series of samples were studied. Bulk polycrystals were Syton-polished; no polishing was used for single-crystal epitaxial layers. The epilayers were strain-free; the lattice mismatch was relaxed by misfit dislocations extending less than about 100 nm into the layers of total thickness of several micrometers. All samples were measured under flowing dry nitrogen, after a wet chemical treatment was used to remove the surface overlayers. The alloy compositions were determined from the energy position of the strong E_1 interband threshold; the mean error of x was about ± 0.003. The accuracy of the dielectric functions was estimated by examining trends in the data at fixed wavelengths as a function of alloy composition for 20 different samples. In spite of the care taken to avoid both surface damage and overlayers, the surface quality was found to be the limiting factor in the accuracy. In the nine spectra selected for tabulation in Ref. [8], the errors of both real and imaginary parts of the dielectric function are estimated to be a few tenths throughout the whole composition and spectral range. We have not tabulated the uncertain values of k less than 0.3 on the low-energy side of the ellipsometric spectra, because of the poor accuracy and precision of the method in this case [8].

There is a fairly good agreement of the reflectance and ellipsometric results in the energy position of all spectral structures. In particular, the E_1 absorption edge shifts from 2.1 eV in Ge to 3.4 eV in Si; this offers a convenient way to determine accurately the alloy composition, provided the bowing of the concentration dependence is taken into account [8]. A slight blue shift of the reflectance spectrum of Table I b with respect to the

ellipsometric one in the region around 2.7 eV is due to the difference of the compositions. The systematic trends in the differences of both sets of n and k are obviously due to the thicker surface films in the reflectance measurements. The refractive indices agree to two figures in the near infrared. The agreement of extinction coefficients above 5 eV is also satisfactory. The most pronounced failure of the reflectance data is the systematically lower values of n on the high-energy side of the overlap with the ellipsometric spectra. The discrepancy becomes more pronounced for Ge-rich alloys, in accordance with increasing optical thickness of the overlayers with increasing Ge content.

For both Ge and Si, refractive indices in the transparent region below the intrinsic absorption gap were measured with high precision by angle of minimum-deviation and channel-spectra techniques [1, 2]. We have not found analogous data for the alloys, obviously because of the problems in obtaining sufficiently homogeneous crystals of high optical quality. We have chosen the values based on the reflectance measured by Schmidt [6]. The R values were fitted with refractive coefficients given by the polynomial

$$n(E) = n_0 + n_1 E^2 \tag{2}$$

for the photon energy E from 1–1.5 eV, neglecting extinction indices k. The two coefficients n_0 and n_1 were determined from the least-squares fit for each alloy composition. The extrapolation of Eq. 2 below 1 eV is tabulated here. The values are probably accurate to a few hundredths, as indicated by a reasonable agreement of the results for pure Si and Ge.

Infrared lattice absorption in the alloys has been measured by Braunstein [9] throughout the whole range of compositions. However, most of his spectra for a silicon content of 22–81% showed a strong background absorption due to free carriers. Cosand and Spitzer [10] studied the lattice modes for Ge-rich ($x \leqslant 0.12$) and Si-rich ($x \geqslant 0.88$) alloys in the wavenumber region from 100–700 cm^{-1}. They identified two-phonon bands analogous to those of pure Si and Ge. In addition, several temperature-independent bands are interpreted as being due to single-phonon processes. The latter are not seen in perfect homopolar lattices of Si and Ge, since the single-phonon excitations produce no dipole moment. Unpublished spectra of Humlíček [11] were measured in the 180–1500 cm^{-1} range at 300 K. The samples were of p-type conductivity with about 10^{15} free holes per cm^3. No Drude-like background is observable for this low level of doping. The alloy compositions (determined from spectral positions of the E_1 interband thresholds [8]) are fairly close to the three target values of the present tabulation. The observed transmission in the transparent region above 1500 cm^{-1} was found to be lower than the

value predicted by reflection losses of the thick slab of nonabsorbing material:

$$T|_{k=0} = \frac{1-R}{1+R}, \qquad R = \left(\frac{n-1}{n+1}\right)^2, \tag{3}$$

where n is the refractive index. This is obviously due to the scattering of the probing beam by inhomogeneities in the composition, which prevents a part of the transmitted light from reaching the detector. The tabular k values were obtained from the transmittances normalized to the maximum value of Eq. 3 in the region above 1500 cm^{-1}. For $x = 0.8$, two strong peaks near 400 and 480 cm^{-1} emerge; they are related to the analogous bands observed for Si-rich alloys by Cosand and Spitzer [10]. For higher Ge content, the band near 400 cm^{-1} dominates the absorption spectrum with peak values of the absorption coefficient, $\alpha = 4\pi k/\lambda$, above 10 cm^{-1}. The phonon absorption is related to inevitable spectral variations of the refractive index. However, the magnitude of the changes from any smooth dispersion curve of the Eq. 2 type is expected to be less than a few thousandths, as found for silicon by Humlíček and Vojtěchovský [12]. Because of the rich spectral structure changing strongly with the composition, this spectral region is most difficult for dealing with the wavenumber- and composition-dependent extinction coefficients.

REFERENCES

1. R. F. Potter, in "Handbook of Optical Constants of Solids," (E. D. Palik, ed.), Academic Press, Orlando, 465 (1985).
2. D. F. Edwards, ibid., p. 547.
3. E. R. Johnson and S. M. Christian, *Phys. Rev.* **95**, 560 (1954).
4. R. Braunstein, A. R. Moore, and F. Herman, *Phys. Rev.* **109**, 695 (1958).
5. J. Tauc and A. Abrahám, *J. Phys. Chem. Solids* **20**, 190 (1961).
6. E. Schmidt, *Phys. Status Solidi* **27**, 57 (1968).
7. J. Humlíček, F. Lukeš, E. Schmidt, M. G. Kekoua, and E. Khoutsishvili, *Phys. Rev.* **B33**, 1092 (1986).
8. J. Humlíček, M. Garriga, M. I. Alonso, and M. Cardona, *J. Appl. Phys.* **65**, 2827 (1989).
9. R. Braunstein, *Phys. Rev.* **130**, 879 (1963).
10. A. E. Cosand and W. G. Spitzer, *J. Appl. Phys.* **42**, 5241 (1971).
11. J. Humlíček, unpublished data (1989).
12. J. Humlíček and K. Vojtěchovský, *Phys. Status Solidi (a)* **92**, 249 (1985).

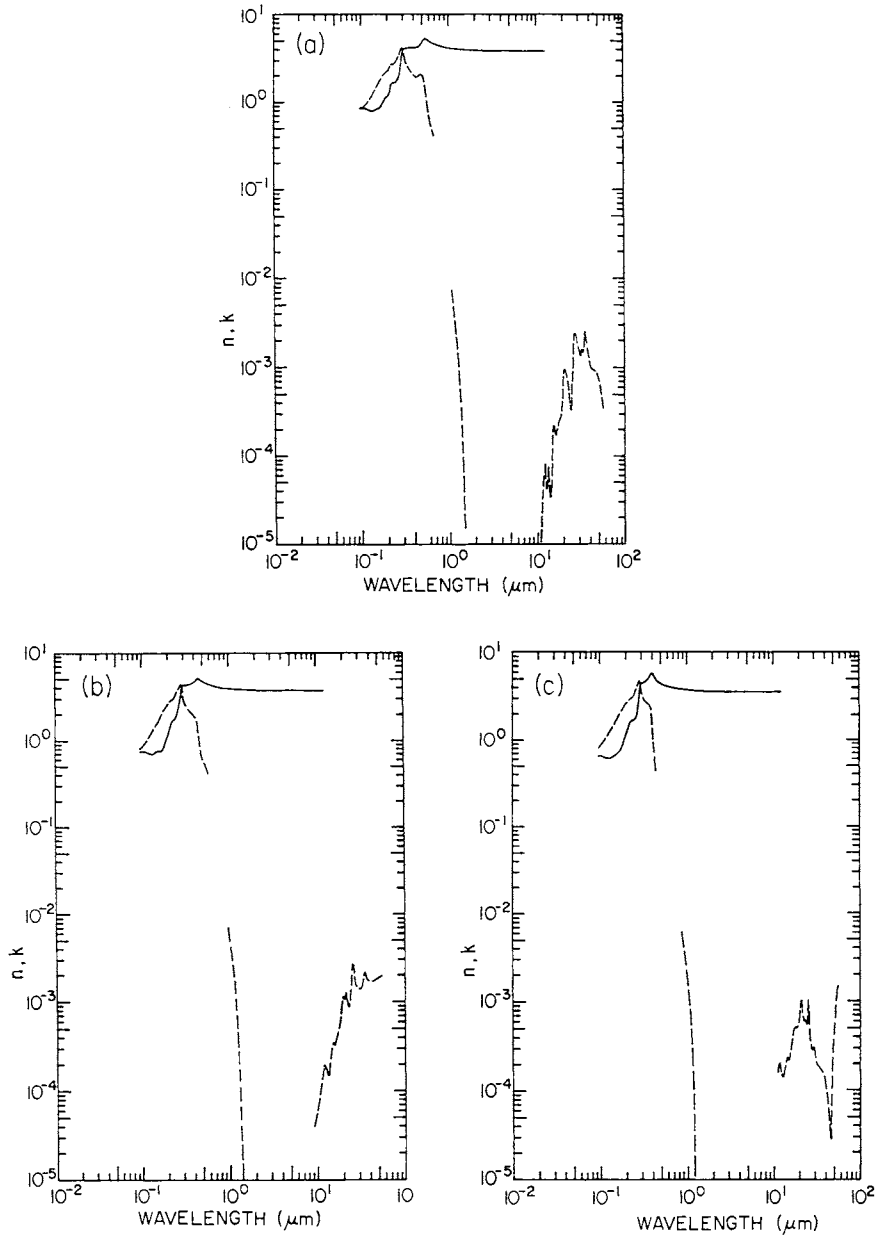

Fig. 1. Log–log plot of n (solid line) and k (dashed line) versus wavelength in micrometers. (a) For Si_xGe_{1-x}, $x = 0.25$. (b) For Si_xGe_{1-x}, $x = 0.50$. (c) For Si_xGe_{1-x}, $x = 0.80$.

TABLE I(a)

Values of n and k for Si_xGe_{1-x}, $x=0.25$, from Various References[a]

eV	cm^{-1}	μm	n	n	k	k
12.8		0.09686	0.85 [6]		0.84 [6]	
12.6		0.09840	0.85		0.85	
12.2		0.1016	0.85		0.88	
12.0		0.1033	0.85		0.90	
11.8		0.1051	0.85		0.92	
11.4		0.1088	0.85		0.95	
11.0		0.1127	0.84		0.99	
10.6		0.1170	0.83		1.02	
10.2		0.1216	0.81		1.09	
10.0		0.1240	0.80		1.13	
9.80		0.1265	0.79		1.17	
9.40		0.1319	0.79		1.26	
9.00		0.1378	0.80		1.36	
8.80		0.1409	0.81		1.40	
8.60		0.1442	0.82		1.45	
8.40		0.1476	0.82		1.50	
8.20		0.1512	0.82		1.57	
8.00		0.1550	0.83		1.64	
7.90		0.1569	0.83		1.68	
7.80		0.1590	0.84		1.72	
7.70		0.1610	0.85		1.77	
7.60		0.1631	0.87		1.81	
7.50		0.1653	0.89		1.85	
7.40		0.1675	0.91		1.90	
7.30		0.1698	0.93		1.95	
7.20		0.1722	0.96		1.99	
7.10		0.1746	0.99		2.03	
7.00		0.1771	1.03		2.08	
6.90		0.1797	1.08		2.10	
6.80		0.1823	1.11		2.11	
6.70		0.1851	1.12		2.12	
6.60		0.1879	1.12		2.15	
6.50		0.1907	1.12		2.20	
6.40		0.1937	1.13		2.26	
6.30		0.1968	1.15		2.32	
6.20		0.2000	1.17		2.39	
6.10	**49,200**	0.2033	1.20		2.48	
6.00	**48,390**	0.2066	1.27		2.58	
5.90	47,580	0.2101	1.36		2.66	
5.80	46,780	0.2138	1.48		2.70	
5.70	45,970	0.2175	1.58		2.69	
5.60	45,160	0.2214	1.64	1.28 [8]	2.66	2.89 [8]
5.50	44,360	0.2254	1.65	1.33	2.66	2.87
5.40	43,550	0.2296	1.65	1.34	2.68	2.87
5.30	42,740	0.2339	1.64	1.33	2.74	2.90
5.20	**41,940**	0.2384	1.66	1.33	2.83	2.96
5.18	**41,780**	0.2394		1.32		2.98

TABLE I(a) (*Continued*)

Si_xGe_{1-x}, $x = 0.25$

eV	cm^{-1}	μm	n	n	k	k
5.16	41,610	0.2403		1.33		3.00
5.14	41,450	0.2412		1.33		3.01
5.12	41,290	0.2422		1.33		3.04
5.10	41,130	0.2431	1.69	1.33	2.93	3.06
5.08	40,970	0.2441		1.33		3.08
5.06	40,810	0.2450		1.34		3.10
5.04	40,650	0.2460		1.34		3.12
5.02	40,480	0.2470		1.35		3.15
5.00	40,320	0.2480		1.35		3.17
4.98	40,160	0.2490		1.36		3.20
4.96	40,000	0.2500		1.37		3.22
4.94	39,840	0.2510		1.37		3.25
4.92	39,680	0.2520		1.38		3.28
4.90	39,520	0.2530	1.80	1.40	3.19	3.31
4.88	39,360	0.2541		1.40		3.34
4.86	39,190	0.2551		1.42		3.37
4.84	39,030	0.2562		1.43		3.40
4.82	38,870	0.2572		1.44		3.44
4.80	38,710	0.2583	1.89	1.45	3.34	3.47
4.78	38,550	0.2594		1.47		3.50
4.76	38,390	0.2605		1.48		3.54
4.75	38,310	0.2610	1.95		3.43	
4.74	38,230	0.2616		1.50		3.58
4.72	38,060	0.2627		1.52		3.62
4.70	37,900	0.2638	2.02	1.54	3.51	3.66
4.68	37,740	0.2649		1.56		3.70
4.66	37,580	0.2661		1.58		3.74
4.65	37,500	0.2666	2.09		3.61	
4.64	37,420	0.2672		1.61		3.79
4.62	37,260	0.2684		1.64		3.84
4.60	37,100	0.2695	2.19	1.67	3.72	3.89
4.58	36,940	0.2707	2.23	1.71	3.77	3.94
4.56	36,770	0.2719	2.28	1.74	3.82	3.99
4.54	36,610	0.2731	2.33	1.79	3.87	4.05
4.52	36,450	0.2743	2.39	1.84	3.92	4.10
4.50	36,290	0.2755	2.47	1.89	3.97	4.16
4.48	36,130	0.2768	2.55	1.95	4.03	4.23
4.46	35,970	0.2780	2.64	2.02	4.07	4.29
4.44	35,810	0.2792	2.74	2.10	4.12	4.35
4.42	35,640	0.2805	2.85	2.19	4.15	4.41
4.40	35,480	0.2818	2.97	2.30	4.18	4.46
4.38	35,320	0.2831	3.11	2.42	4.18	4.51
4.36	35,160	0.2844	3.24	2.54	4.17	4.54
4.34	35,000	0.2857	3.38	2.68	4.14	4.55
4.32	34,840	0.2870	3.52	2.81	4.09	4.54
4.30	34,680	0.2883	3.64	2.95	4.02	4.51
4.28	34,520	0.2897	3.75	3.08	3.93	4.48

TABLE I(a) (*Continued*)

Si_xGe_{1-x}, $x = 0.25$

eV	cm^{-1}	μm	n	n	k	k
4.26	34,350	0.2910		3.19		4.42
4.25	34,270	0.2917	3.87		3.79	
4.24	34,190	0.2924		3.29		4.35
4.22	34,030	0.2938	3.96	3.38	3.65	4.29
4.20	33,870	0.2952		3.46		4.21
4.19	33,790	0.2959	4.02		3.51	
4.18	33,710	0.2966		3.52		4.14
4.16	33,550	0.2980	4.05	3.58	3.38	4.06
4.14	33,390	0.2995		3.62		3.99
4.13	33,310	0.3002	4.07		3.27	
4.12	33,230	0.3009		3.67		3.92
4.10	33,060	0.3024	4.09	3.70	3.17	3.85
4.08	32,900	0.3039		3.72		3.79
4.06	32,740	0.3054		3.75		3.73
4.05	32,660	0.3061	4.09		3.02	
4.04	32,580	0.3069		3.77		3.68
4.02	32,420	0.3084		3.79		3.63
4.00	32,260	0.3100	4.09	3.80	2.91	3.58
3.98	32,100	0.3115		3.82		3.53
3.96	31,930	0.3131		3.83		3.49
3.95	31,850	0.3139	4.09		2.81	
3.94	31,770	0.3147		3.84		3.45
3.92	31,610	0.3163		3.86		3.41
3.90	31,450	0.3179	4.09	3.87	2.72	3.37
3.88	31,290	0.3195		3.88		3.34
3.86	31,130	0.3212		3.89		3.30
3.85	31,050	0.3220	4.08		2.64	
3.84	30,970	0.3229		3.90		3.27
3.82	30,810	0.3246		3.92		3.24
3.80	30,640	0.3263	4.08	3.92	2.58	3.22
3.78	30,480	0.3280		3.93		3.19
3.76	30,320	0.3297		3.95		3.16
3.75	30,240	0.3306	4.08		2.53	
3.74	30,160	0.3315		3.96		3.13
3.72	30,000	0.3333		3.96		3.11
3.70	29,840	0.3351	4.08	3.98	2.48	3.09
3.68	29,680	0.3369		3.99		3.06
3.66	29,520	0.3388		4.00		3.04
3.65	29,430	0.3397	4.09		2.43	
3.64	29,350	0.3406		4.01		3.02
3.62	29,190	0.3425		4.02		3.00
3.60	29,030	0.3444	4.10	4.03	2.39	2.98
3.58	28,870	0.3463		4.04		2.96
3.56	28,710	0.3483		4.05		2.94
3.55	28,630	0.3493	4.11		2.35	
3.54	28,550	0.3502		4.06		2.93
3.52	28,390	0.3522		4.08		2.91

TABLE I(a) (*Continued*)

Si_xGe_{1-x}, $x=0.25$

eV	cm^{-1}	μm	n	n	k	k
3.50	28,220	0.3542	4.13	4.09	2.31	2.89
3.48	28,060	0.3563		4.11		2.87
3.46	27,900	0.3583		4.13		2.85
3.45	27,820	0.3594	4.14		2.27	
3.44	27,740	0.3604		4.14		2.84
3.42	27,580	0.3625		4.16		2.82
3.40	27,420	0.3647	4.16	4.18	2.24	2.80
3.38	27,260	0.3668		4.20		2.78
3.36	27,100	0.3690		4.21		2.76
3.35	27,010	0.3701	4.19		2.19	
3.34	26,930	0.3712		4.23		2.75
3.32	26,770	0.3734		4.25		2.72
3.30	26,610	0.3757	4.21	4.27	2.14	2.70
3.28	26,450	0.3780		4.28		2.68
3.26	26,290	0.3803		4.30		2.65
3.25	26,210	0.3815	4.23		2.09	
3.24	26,130	0.3827		4.31		2.62
3.22	25,970	0.3850		4.32		2.60
3.20	25,810	0.3875	4.24	4.34	2.03	2.57
3.18	25,640	0.3899		4.35		2.55
3.16	25,480	0.3924		4.35		2.52
3.15	25,400	0.3936	4.23		1.98	
3.14	25,320	0.3949		4.36		2.49
3.12	25,160	0.3974		4.36		2.47
3.10	25,000	0.4000	4.21	4.36	1.94	2.45
3.08	24,840	0.4025		4.36		2.43
3.06	24,680	0.4052		4.36		2.41
3.05	24,600	0.4065	4.19		1.92	
3.04	24,510	0.4078		4.36		2.40
3.02	24,350	0.4105		4.36		2.39
3.00	24,190	0.4133	4.17	4.36	1.91	2.38
2.98	24,030	0.4161		4.36		2.38
2.96	23,870	0.4189		4.37		2.38
2.95	23,790	0.4203	4.16		1.92	
2.94	23,710	0.4217		4.38		2.38
2.92	23,550	0.4246		4.38		2.38
2.90	23,390	0.4275	4.17	4.40	1.94	2.39
2.88	23,220	0.4305		4.42		2.39
2.86	23,060	0.4335		4.43		2.40
2.85	22,980	0.4350	4.19		1.97	
2.84	22,900	0.4366		4.45		2.41
2.82	22,740	0.4397		4.48		2.41
2.80	22,580	0.4428	4.23	4.50	2.01	2.42
2.78	22,420	0.4460		4.54		2.42
2.76	22,260	0.4492		4.57		2.43
2.75	22,180	0.4509	4.30		2.04	
2.74	22,090	0.4525		4.62		2.44

TABLE I(a) (*Continued*)

Si_xGe_{1-x}, $x = 0.25$

eV	cm^{-1}	μm	n	n	k	k
2.72	21,930	0.4558		4.66		2.45
2.70	21,770	0.4592	4.38	4.72	2.07	2.45
2.68	21,610	0.4626		4.78		2.45
2.66	21,450	0.4661		4.85		2.45
2.65	21,370	0.4679	4.50		2.09	
2.64	21,290	0.4696		4.92		2.44
2.62	21,130	0.4732		5.00		2.42
2.60	20,970	0.4769	4.64	5.07	2.09	2.39
2.58	20,800	0.4806	4.72	5.15	2.08	2.35
2.56	20,640	0.4843	4.79	5.23	2.05	2.30
2.54	20,480	0.4881	4.86	5.30	2.02	2.24
2.52	20,320	0.4920	4.92	5.37	1.97	2.18
2.50	20,160	0.4959	4.97	5.45	1.92	2.11
2.48	20,000	0.4999	5.03	5.53	1.87	2.03
2.46	19,840	0.5040	5.08	5.59	1.83	1.93
2.44	19,680	0.5081	5.14	5.65	1.77	1.82
2.42	19,510	0.5123	5.20	5.70	1.71	1.70
2.40	19,350	0.5166	5.28	5.72	1.64	1.57
2.38	19,190	0.5209	5.33	5.74	1.53	1.43
2.36	19,030	0.5254	5.37	5.72	1.41	1.30
2.34	18,870	0.5299	5.37	5.69	1.30	1.17
2.32	18,710	0.5344	5.37	5.65	1.18	1.08
2.30	18,550	0.5391	5.34	5.60	1.07	0.98
2.28	18,380	0.5438	5.30	5.55	0.98	0.89
2.26	18,220	0.5486	5.25	5.49	0.91	0.81
2.24	18,060	0.5535	5.20	5.44	0.84	0.75
2.22	17,900	0.5585		5.39		0.67
2.20	17,740	0.5636	5.11	5.33	0.74	0.64
2.18	17,580	0.5687		5.29		0.58
2.16	17,420	0.5740		5.23		0.54
2.15	17,340	0.5767	5.00		0.65	
2.14	17,260	0.5794		5.19		0.49
2.12	17,090	0.5848		5.15		0.46
2.10	16,930	0.5904	4.91	5.11	0.58	0.43
2.08	16,770	0.5961		5.07		0.38
2.06	16,610	0.6019		5.03		0.37
2.05	16,530	0.6048	4.82		0.53	
2.04	16,450	0.6078		5.00		0.35
2.02	16,290	0.6138		4.96		0.33
2.00	16,130	0.6199	4.77	4.93	0.50	
1.98	15,970	0.6262		4.90		0.30
1.96	15,800	0.6326		4.87		
1.95	15,720	0.6358	4.72		0.46	
1.94	15,640	0.6391		4.83		
1.92	15,480	0.6458		4.81		
1.90	15,320	0.6526	4.67	4.78	0.41	
1.88	15,160	0.6595		4.75		

TABLE I(a) (*Continued*)

Si_xGe_{1-x}, $x = 0.25$

eV	cm^{-1}	μm	n	n	k	k
1.86	15,000	0.6666		4.72		
1.85	14,920	0.6702	4.62			
1.84	14,840	0.6738		4.69		
1.82	14,670	0.6812		4.67		
1.80	14,510	0.6888	4.58	4.65		
1.78	14,350	0.6965		4.63		
1.76	14,190	0.7045		4.60		
1.74	14,030	0.7126		4.58		
1.72	13,870	0.7208		4.56		
1.70	13,710	0.7293	4.49	4.54		
1.68	13,550	0.7380		4.51		
1.66	13,380	0.7469		4.49		
1.60	12,900	0.7749	4.42			
1.50	12,090	0.8266	4.36			
1.40	11,290	0.8856	4.30			
1.30	10,480	0.9537	4.23			
1.22	9,840	1.016				7.69E-03 [4]
1.21	9,759	1.024				7.29E-03
1.20	9,679	1.033	4.17			6.91E-03
1.19	9,598	1.041				6.53E-03
1.18	9,517	1.050				6.16E-03
1.17	9,437	1.059				5.80E-03
1.16	9,356	1.068				5.45E-03
1.15	9,275	1.078				5.11E-03
1.14	9,195	1.087				4.77E-03
1.13	9,114	1.097				4.44E-03
1.12	9,033	1.107				4.13E-03
1.11	8,953	1.116				3.82E-03
1.10	8,872	1.127	4.12			3.52E-03
1.09	8,791	1.137				3.23E-03
1.08	8,711	1.148				2.95E-03
1.07	8,630	1.158				2.68E-03
1.06	8,549	1.169				2.43E-03
1.05	8,469	1.180				2.18E-03
1.04	8,388	1.192				1.95E-03
1.03	8,307	1.203				1.72E-03
1.02	8,227	1.215				1.51E-03
1.01	8,146	1.227				1.31E-03
1.00	8,065	1.239	4.06			1.13E-03
0.99	7,985	1.252				9.55E-04
0.98	7,904	1.265				7.96E-04
0.97	7,824	1.278				6.51E-04
0.96	7,743	1.291				5.21E-04
0.95	7,662	1.305				4.06E-04
0.94	7,582	1.318				3.06E-04
0.93	7,501	1.333				2.22E-04
0.92	7,420	1.347				1.54E-04

TABLE I(a) (*Continued*)

Si_xGe_{1-x}, $x = 0.25$

eV	cm^{-1}	μm	n	n	k	k
0.91	7,340	1.362				1.04E-04
0.90	7,259	1.377	4.02			7.04E-05
0.89	7,178	1.393				4.75E-05
0.88	7,098	1.408				2.89E-05
0.87	7,017	1.425				1.48E-05
0.80	6,452	1.549	3.97			
0.70	5,646	1.771	3.94			
0.60	4,839	2.066	3.90			
0.50	4,033	2.479	3.88			
0.40	3,226	3.099	3.86			
0.30	2,420	4.132	3.84			
0.20	1,613	6.199	3.83			
0.1239	1,000	10.00				8.35E-06 [11]
0.1178	950	10.52				1.10E-05
0.1147	925	10.81				1.83E-05
0.1116	900	11.11				3.34E-05
0.1091	880	11.36				4.96E-05
0.1066	860	11.62				7.28E-05
0.1041	840	11.90				7.74E-05
0.1017	820	12.19				4.21E-05
0.1000	807	12.39	3.82			
0.09919	800	12.49				4.88E-05
0.09671	780	12.82				7.41E-05
0.09423	760	13.15				5.75E-05
0.09175	740	13.51				3.46E-05
0.08927	720	13.88				3.56E-05
0.08679	700	14.28				8.94E-05
0.08431	680	14.70				2.09E-04
0.08307	670	14.92				2.21E-04
0.08183	660	15.15				2.07E-04
0.07935	640	15.62				1.78E-04
0.07687	620	16.12				1.75E-04
0.07439	600	16.66				2.27E-04
0.07191	580	17.24				2.55E-04
0.06943	560	17.85				2.64E-04
0.06695	540	18.51				3.66E-04
0.06447	520	19.23				6.90E-04
0.06323	510	19.60				8.96E-04
0.06199	500	20.00				9.58E-04
0.06075	490	20.40				8.90E-04
0.05951	480	20.83				8.05E-04
0.05703	460	21.74				7.04E-04
0.05455	440	22.72				4.34E-04
0.05331	430	23.25				3.37E-04
0.05207	420	23.81				3.81E-04
0.05083	410	24.39				5.14E-04
0.04959	400	25.00				1.62E-03

TABLE I(a) (*Continued*)

Si_xGe_{1-x}, $x=0.25$

eV	cm^{-1}	μm	n	n	k	k
0.04835	390	25.64				2.25E-03
0.04711	380	26.31				2.34E-03
0.04587	370	27.02				2.35E-03
0.04463	360	27.78				2.11E-03
0.04339	350	28.57				1.72E-03
0.04215	340	29.41				1.55E-03
0.04092	330	30.29				1.35E-03
0.03968	320	31.24				1.46E-03
0.03906	315	31.74				1.63E-03
0.03844	310	32.25				1.62E-03
0.03782	305	32.78				1.46E-03
0.03720	300	33.33				1.92E-03
0.03596	290	34.47				2.50E-03
0.03472	280	35.70				2.11E-03
0.03348	270	37.03				1.54E-03
0.03224	260	38.45				1.18E-03
0.02976	240	41.66				9.36E-04
0.02728	220	45.44				9.28E-04
0.02480	200	50.00				7.10E-04
0.02232	180	55.54				3.48E-04

[a]The reference from which the values were extracted is given in brackets next to the first value. The nominal alloy compositions are: x=0.246 [6], x=0.250 [8], x=0.250 obtained by interpolating the data of Braunstein et al. [4], x=0.260 [11].

TABLE I(b)

Values of n and k for Si_xGe_{1-x}, $x = 0.50$, from Various References[a]

eV	cm^{-1}	μm	n	n	k	k
12.8		0.09686	0.75 [6]		0.81 [6]	
12.4		0.09999	0.75		0.85	
12.0		0.1033	0.75		0.88	
11.6		0.1069	0.75		0.92	
11.2		0.1107	0.74		0.96	
10.8		0.1148	0.73		1.01	
10.4		0.1192	0.72		1.07	
10.0		0.1240	0.70		1.15	
9.80		0.1265	0.70		1.19	
9.60		0.1292	0.70		1.23	
9.20		0.1348	0.71		1.32	
8.80		0.1409	0.72		1.42	
8.40		0.1476	0.74		1.53	
8.00		0.1550	0.76		1.63	
7.80		0.1590	0.75		1.70	
7.60		0.1631	0.75		1.78	
7.40		0.1675	0.76		1.88	
7.20		0.1722	0.77		2.00	
7.00		0.1771	0.82		2.13	
6.90		0.1797	0.86		2.19	
6.80		0.1823	0.90		2.24	
6.70		0.1851	0.95		2.29	
6.60		0.1879	0.99		2.33	
6.50		0.1907	1.02		2.38	
6.40		0.1937	1.05		2.42	
6.30		0.1968	1.08		2.48	
6.20		0.2000	1.11		2.55	
6.10	49,200	0.2033	1.16		2.62	
6.00	48,390	0.2066	1.22		2.70	
5.90	47,580	0.2101	1.29		2.77	
5.80	46,780	0.2138	1.37		2.83	
5.70	45,970	0.2175	1.47		2.88	
5.60	45,160	0.2214	1.56	1.32 [8]	2.91	2.87 [8]
5.50	44,360	0.2254	1.64	1.37	2.91	2.88
5.40	43,550	0.2296	1.70	1.39	2.91	2.88
5.30	42,740	0.2339	1.71	1.39	2.93	2.91
5.28	42,580	0.2348		1.39		2.91
5.26	42,420	0.2357		1.39		2.93
5.24	42,260	0.2366		1.39		2.93
5.22	42,100	0.2375		1.40		2.95
5.20	41,940	0.2384	1.72	1.40	3.00	2.96
5.18	41,780	0.2394		1.40		2.98
5.16	41,610	0.2403		1.40		2.99
5.14	41,450	0.2412		1.39		3.01
5.12	41,290	0.2422		1.40		3.03
5.10	41,130	0.2431	1.75	1.40	3.11	3.05
5.08	40,970	0.2441		1.41		3.07

TABLE I(b) (*Continued*)

Si_xGe_{1-x}, $x = 0.50$

eV	cm^{-1}	μm	n	n	k	k
5.06	40,810	0.2450		1.41		3.09
5.04	40;650	0.2460		1.41		3.11
5.02	40,480	0.2470		1.42		3.13
5.00	40,320	0.2480	1.81	1.43	3.24	3.16
4.98	40,160	0.2490		1.43		3.19
4.96	40,000	0.2500		1.44		3.21
4.94	39,840	0.2510		1.45		3.24
4.92	39,680	0.2520		1.46		3.26
4.90	39,520	0.2530	1.90	1.47	3.36	3.30
4.88	39,360	0.2541		1.48		3.32
4.86	39,190	0.2551		1.49		3.36
4.84	39,030	0.2562		1.51		3.39
4.82	38,870	0.2572		1.52		3.42
4.80	38,710	0.2583	2.00	1.54	3.51	3.46
4.78	38,550	0.2594		1.55		3.49
4.76	38,390	0.2605		1.57		3.52
4.75	38,310	0.2610	2.07		3.59	
4.74	38,230	0.2616		1.59		3.56
4.72	38,060	0.2627		1.60		3.60
4.70	37,900	0.2638	2.14	1.63	3.67	3.64
4.68	37,740	0.2649		1.66		3.68
4.66	37,580	0.2661		1.68		3.72
4.65	37,500	0.2666	2.22		3.78	
4.64	37,420	0.2672		1.71		3.77
4.62	37,260	0.2684		1.74		3.82
4.60	37,100	0.2695	2.33	1.77	3.89	3.87
4.58	36,940	0.2707	2.38	1.81	3.93	3.91
4.56	36,770	0.2719	2.44	1.85	3.98	3.97
4.54	36,610	0.2731	2.50	1.89	4.03	4.02
4.52	36,450	0.2743	2.57	1.95	4.07	4.07
4.50	36,290	0.2755	2.64	2.00	4.12	4.13
4.48	36,130	0.2768	2.72	2.06	4.16	4.18
4.46	35,970	0.2780	2.81	2.13	4.20	4.23
4.44	35,810	0.2792	2.91	2.21	4.24	4.29
4.42	35,640	0.2805	3.02	2.30	4.27	4.34
4.40	35,480	0.2818	3.14	2.40	4.29	4.39
4.38	35,320	0.2831	3.27	2.51	4.30	4.43
4.36	35,160	0.2844	3.41	2.63	4.31	4.46
4.34	35,000	0.2857	3.56	2.76	4.27	4.47
4.32	34,840	0.2870	3.70	2.90	4.22	4.46
4.30	34,680	0.2883	3.83	3.02	4.15	4.44
4.28	34,520	0.2897	3.94	3.15	4.05	4.40
4.26	34,350	0.2910	4.03	3.26	3.96	4.34
4.24	34,190	0.2924	4.11	3.36	3.87	4.28
4.22	34,030	0.2938	4.17	3.45	3.78	4.21
4.20	33,870	0.2952	4.25	3.53	3.70	4.14
4.18	33,710	0.2966	4.33	3.59	3.58	4.06

TABLE I(b) (*Continued*)

Si_xGe_{1-x}, $x = 0.50$

eV	cm^{-1}	μm	n	n	k	k
4.16	33,550	0.2980	4.34	3.65	3.41	3.99
4.14	33,390	0.2995	4.29	3.70	3.32	3.92
4.12	33,230	0.3009	4.30	3.74	3.31	3.85
4.10	33,060	0.3024	4.33	3.77	3.24	3.79
4.08	32,900	0.3039		3.80		3.73
4.06	32,740	0.3054		3.82		3.67
4.05	32,660	0.3061	4.34		3.06	
4.04	32,580	0.3069		3.84		3.61
4.02	32,420	0.3084		3.86		3.56
4.00	32,260	0.3100	4.34	3.87	2.92	3.52
3.98	32,100	0.3115		3.89		3.47
3.96	31,930	0.3131		3.90		3.42
3.95	31,850	0.3139	4.32		2.81	
3.94	31,770	0.3147		3.92		3.39
3.92	31,610	0.3163		3.93		3.35
3.90	31,450	0.3179	4.31	3.94	2.72	3.31
3.88	31,290	0.3195		3.95		3.28
3.86	31,130	0.3212		3.97		3.25
3.85	31,050	0.3220	4.30		2.64	
3.84	30,970	0.3229		3.98		3.22
3.82	30,810	0.3246		3.99		3.19
3.80	30,640	0.3263	4.30	4.00	2.57	3.16
3.78	30,480	0.3280		4.01		3.14
3.76	30,320	0.3297		4.02		3.11
3.75	30,240	0.3306	4.29		2.51	
3.74	30,160	0.3315		4.04		3.09
3.72	30,000	0.3333		4.04		3.06
3.70	29,840	0.3351	4.30	4.06	2.46	3.04
3.68	29,680	0.3369		4.07		3.02
3.66	29,520	0.3388		4.08		3.00
3.65	29,430	0.3397	4.30		2.41	
3.64	29,350	0.3406		4.10		2.98
3.62	29,190	0.3425		4.11		2.96
3.60	29,030	0.3444	4.31	4.12	2.37	2.94
3.58	28,870	0.3463		4.14		2.93
3.56	28,710	0.3483		4.15		2.91
3.55	28,630	0.3493	4.32		2.34	
3.54	28,550	0.3502		4.16		2.89
3.52	28,390	0.3522		4.19		2.88
3.50	28,220	0.3542	4.34	4.20	2.30	2.87
3.48	28,060	0.3563		4.22		2.85
3.46	27,900	0.3583		4.24		2.83
3.45	27,820	0.3594	4.37		2.27	
3.44	27,740	0.3604		4.26		2.82
3.42	27,580	0.3625		4.28		2.81
3.40	27,420	0.3647	4.40	4.31	2.24	2.79
3.38	27,260	0.3668		4.33		2.77

TABLE I(b) (*Continued*)

Si_xGe_{1-x}, $x=0.50$

eV	cm^{-1}	μm	n	n	k	k
3.36	27,100	0.3690		4.35		2.76
3.35	27,010	0.3701	4.44		2.20	
3.34	26,930	0.3712		4.38		2.74
3.32	26,770	0.3734		4.41		2.72
3.30	26,610	0.3757	4.48	4.43	2.15	2.69
3.28	26,450	0.3780		4.46		2.67
3.26	26,290	0.3803		4.48		2.65
3.25	26,210	0.3815	4.52		2.10	
3.24	26,130	0.3827		4.51		2.62
3.22	25,970	0.3850		4.53		2.60
3.20	25,810	0.3875	4.55	4.55	2.05	2.57
3.18	25,640	0.3899		4.56		2.55
3.16	25,480	0.3924		4.58		2.52
3.15	25,400	0.3936	4.57		2.00	
3.14	25,320	0.3949		4.60		2.50
3.12	25,160	0.3974		4.61		2.48
3.10	25,000	0.4000	4.61	4.63	1.97	2.46
3.08	24,840	0.4025	4.62	4.64	1.96	2.45
3.06	24,680	0.4052	4.64	4.66	1.95	2.44
3.04	24,510	0.4078	4.66	4.68	1.94	2.43
3.02	24,350	0.4105	4.69	4.71	1.94	2.42
3.00	24,190	0.4133	4.73	4.74	1.93	2.42
2.98	24,030	0.4161	4.77	4.78	1.91	2.41
2.96	23,870	0.4189	4.80	4.82	1.89	2.41
2.94	23,710	0.4217	4.85	4.87	1.87	2.40
2.92	23,550	0.4246	4.90	4.92	1.84	2.39
2.90	23,390	0.4275	4.95	4.98	1.80	2.38
2.88	23,220	0.4305	5.01	5.05	1.75	2.35
2.86	23,060	0.4335		5.12		2.32
2.84	22,900	0.4366	5.09	5.19	1.62	2.28
2.82	22,740	0.4397	5.13	5.27	1.55	2.23
2.80	22,580	0.4428	5.16	5.34	1.46	2.16
2.78	22,420	0.4460		5.42		2.09
2.76	22,260	0.4492		5.48		2.00
2.75	22,180	0.4509	5.17		1.24	
2.74	22,090	0.4525		5.55		1.90
2.72	21,930	0.4558		5.60		1.79
2.70	21,770	0.4592	5.10	5.64	1.04	1.66
2.68	21,610	0.4626		5.65		1.53
2.66	21,450	0.4661		5.65		1.40
2.65	21,370	0.4679	5.01		0.89	
2.64	21,290	0.4696		5.63		1.28
2.62	21,130	0.4732		5.59		1.17
2.60	20,970	0.4769	4.91	5.55	0.79	1.07
2.58	20,800	0.4806		5.50		0.99
2.56	20,640	0.4843		5.45		0.91
2.55	20,560	0.4862	4.82		0.72	

TABLE I(b) (*Continued*)

Si_xGe_{1-x}, $x = 0.50$

eV	cm^{-1}	μm	n	n	k	k
2.54	20,480	0.4881		5.40		0.83
2.52	20,320	0.4920		5.34		0.77
2.50	20,160	0.4959	4.74	5.29	0.66	0.72
2.48	20,000	0.4999		5.24		0.66
2.46	19,840	0.5040		5.19		0.61
2.45	19,760	0.5061	4.67		0.62	
2.44	19,680	0.5081		5.15		0.58
2.42	19,510	0.5123		5.10		0.52
2.40	19,350	0.5166	4.61	5.06	0.58	0.49
2.38	19,190	0.5209		5.01		0.46
2.36	19,030	0.5254		4.97		0.44
2.35	18,950	0.5276	4.56		0.55	
2.34	18,870	0.5299		4.93		0.41
2.32	18,710	0.5344		4.89		0.40
2.30	18,550	0.5391	4.52	4.85	0.52	0.35
2.28	18,380	0.5438		4.81		0.36
2.26	18,220	0.5486		4.77		0.34
2.25	18,140	0.5510	4.47		0.49	
2.24	18,060	0.5535		4.74		0.30
2.22	17,900	0.5585		4.71		
2.20	17,740	0.5636	4.44	4.67	0.46	
2.18	17,580	0.5687		4.64		
2.16	17,420	0.5740		4.61		
2.15	17,340	0.5767	4.41		0.44	
2.14	17,260	0.5794		4.58		
2.12	17,090	0.5848		4.55		
2.10	16,930	0.5904	4.38	4.52	0.41	
2.08	16,770	0.5961		4.50		
2.06	16,610	0.6019		4.47		
2.05	16,530	0.6048	4.35			
2.04	16,450	0.6078		4.45		
2.02	16,290	0.6138		4.42		
2.00	16,130	0.6199	4.32	4.40		
1.98	15,970	0.6262		4.38		
1.96	15,800	0.6326		4.36		
1.95	15,720	0.6358	4.29			
1.94	15,640	0.6391		4.34		
1.92	15,480	0.6458		4.32		
1.90	15,320	0.6526	4.26	4.30		
1.88	15,160	0.6595		4.28		
1.86	15,000	0.6666		4.26		
1.85	14,920	0.6702	4.24			
1.84	14,840	0.6738		4.25		
1.82	14,670	0.6812		4.23		
1.80	14,510	0.6888	4.21	4.21		
1.78	14,350	0.6965		4.20		
1.76	14,190	0.7045		4.18		

TABLE I(b) (*Continued*)

Si_xGe_{1-x}, $x = 0.50$

eV	cm^{-1}	μm	n	n	k	k
1.74	14,030	0.7126		4.16		
1.72	13,870	0.7208		4.14		
1.70	13,710	0.7293	4.16	4.13		
1.68	13,550	0.7380		4.11		
1.66	13,380	0.7469		4.09		
1.60	12,900	0.7749	4.11			
1.50	12,090	0.8266	4.06			
1.40	11,290	0.8856	4.01			
1.30	10,480	0.9537	3.96			7.24E-03 [4]
1.29	10,400	0.9611				6.91E-03
1.28	10,320	0.9686				6.59E-03
1.27	10,240	0.9763				6.27E-03
1.26	10,160	0.9840				5.96E-03
1.25	10,080	0.9919				5.66E-03
1.24	10,000	0.9999				5.36E-03
1.23	9,921	1.008				5.07E-03
1.22	9,840	1.016				4.78E-03
1.21	9,759	1.024				4.50E-03
1.20	9,679	1.033	3.92			4.23E-03
1.19	9,598	1.041				3.96E-03
1.18	9,517	1.050				3.70E-03
1.17	9,437	1.059				3.44E-03
1.16	9,356	1.068				3.20E-03
1.15	9,275	1.078				2.96E-03
1.14	9,195	1.087				2.73E-03
1.13	9,114	1.097				2.51E-03
1.12	9,033	1.107				2.29E-03
1.11	8,953	1.116				2.08E-03
1.10	8,872	1.127	3.88			1.88E-03
1.09	8,791	1.137				1.69E-03
1.08	8,711	1.148				1.51E-03
1.07	8,630	1.158				1.34E-03
1.06	8,549	1.169				1.18E-03
1.05	8,469	1.180				1.02E-03
1.04	8,388	1.192				8.81E-04
1.03	8,307	1.203				7.48E-04
1.02	8,227	1.215				6.26E-04
1.01	8,146	1.227				5.14E-04
1.00	8,065	1.239	3.84			4.14E-04
0.99	7,985	1.252				3.25E-04
0.98	7,904	1.265				2.47E-04
0.97	7,824	1.278				1.82E-04
0.96	7,743	1.291				1.30E-04
0.95	7,662	1.305				9.07E-05
0.94	7,582	1.318				6.48E-05
0.93	7,501	1.333				4.67E-05
0.92	7,420	1.347				3.14E-05

TABLE I(b) (*Continued*)

Si_xGe_{1-x}, $x = 0.50$

eV	cm^{-1}	μm	n	n	k	k
0.91	7,340	1.362				1.90E-05
0.90	7,259	1.377	3.80			9.66E-06
0.80	6,452	1.549	3.77			
0.70	5,646	1.771	3.75			
0.60	4,839	2.066	3.72			
0.50	4,033	2.479	3.70			
0.40	3,226	3.099	3.69			
0.30	2,420	4.132	3.67			
0.20	1,613	6.199	3.67			
0.1363	1,100	9.091				3.92E-05 [11]
0.1301	1,050	9.524				4.84E-05
0.1239	1,000	10.00				5.87E-05
0.1178	950	10.52				8.49E-05
0.1116	900	11.11				1.29E-04
0.1091	880	11.36				1.54E-04
0.1066	860	11.62				1.89E-04
0.1041	840	11.90				1.97E-04
0.1017	820	12.19				1.81E-04
0.1000	807	12.39	3.66			
0.09919	800	12.49				1.77E-04
0.09671	780	12.82				1.73E-04
0.09423	760	13.15				1.45E-04
0.09175	740	13.51				1.32E-04
0.08927	720	13.88				1.61E-04
0.08679	700	14.28				2.32E-04
0.08431	680	14.70				3.26E-04
0.08183	660	15.15				3.49E-04
0.07935	640	15.62				3.28E-04
0.07687	620	16.12				3.33E-04
0.07439	600	16.66				3.84E-04
0.07191	580	17.24				4.55E-04
0.06943	560	17.85				5.20E-04
0.06695	540	18.51				6.31E-04
0.06447	520	19.23				9.62E-04
0.06323	510	19.60				1.13E-03
0.06199	500	20.00				1.16E-03
0.06075	490	20.40				1.02E-03
0.05951	480	20.83				1.24E-03
0.05827	470	21.27				1.30E-03
0.05703	460	21.74				1.15E-03
0.05455	440	22.72				9.01E-04
0.05207	420	23.81				8.89E-04
0.05083	410	24.39				1.12E-03
0.04959	400	25.00				2.30E-03
0.04835	390	25.64				2.62E-03
0.04711	380	26.31				2.26E-03
0.04587	370	27.02				1.87E-03

TABLE I(b) (*Continued*)

Si_xGe_{1-x}, $x=0.50$

eV	cm^{-1}	μm	n	n	k	k
0.04463	360	27.78				1.47E-03
0.04215	340	29.41				1.43E-03
0.03968	320	31.24				1.39E-03
0.03720	300	33.33				1.57E-03
0.03596	290	34.47				2.11E-03
0.03472	280	35.70				2.13E-03
0.03348	270	37.03				1.80E-03
0.03224	260	38.45				1.71E-03
0.02976	240	41.66				1.70E-03
0.02728	220	45.44				1.70E-03
0.02480	200	50.00				1.81E-03
0.02232	180	55.54				1.95E-03

[a]The reference from which the values were extracted is given in brackets next to the first value. The nominal alloy compositions are: x=0.551 [6], x=0.487 [8], x=0.500 obtained by interpolating the data of Braunstein et al. [4], x=0.450 [11].

TABLE I(c)

Values of n and k for Si_xGe_{1-x}, $x = 0.80$, from Various References[a]

eV	cm^{-1}	μm	n	n	k	k
12.8		0.09686	0.64 [6]		0.78 [6]	
12.6		0.09840	0.65		0.80	
12.2		0.1016	0.65		0.84	
11.8		0.1051	0.64		0.88	
11.4		0.1088	0.63		0.92	
11.0		0.1127	0.62		0.98	
10.6		0.1170	0.61		1.04	
10.2		0.1216	0.60		1.11	
9.80		0.1265	0.60		1.20	
9.40		0.1319	0.60		1.29	
9.00		0.1378	0.60		1.40	
8.60		0.1442	0.63		1.51	
8.20		0.1512	0.65		1.63	
7.90		0.1569	0.67		1.73	
7.80		0.1590	0.67		1.76	
7.40		0.1675	0.69		1.95	
7.00		0.1771	0.77		2.18	
6.90		0.1797	0.82		2.25	
6.80		0.1823	0.87		2.30	
6.70		0.1851	0.91		2.34	
6.60		0.1879	0.95		2.38	
6.50		0.1907	0.99		2.42	
6.40		0.1937	1.02		2.45	
6.30		0.1968	1.05		2.51	
6.20		0.2000	1.08		2.57	
6.10	49,200	0.2033	1.12		2.64	
6.00	48,390	0.2066	1.18		2.71	
5.90	47,580	0.2101	1.24		2.78	
5.70	45,970	0.2175	1.40		2.89	
5.60	45,160	0.2214	1.48	1.28 [8]	2.92	3.06 [8]
5.50	44,360	0.2254	1.56	1.35	2.95	3.11
5.40	43,550	0.2296	1.62	1.43	2.96	3.13
5.30	42,740	0.2339	1.66	1.47	2.98	3.14
5.28	42,580	0.2348		1.47		3.15
5.26	42,420	0.2357		1.48		3.15
5.24	42,260	0.2366		1.48		3.16
5.22	42,100	0.2375		1.48		3.17
5.20	41,940	0.2384	1.67	1.48	3.01	3.18
5.18	41,780	0.2394		1.48		3.20
5.16	41,610	0.2403		1.48		3.21
5.14	41,450	0.2412		1.48		3.23
5.12	41,290	0.2422		1.48		3.25
5.10	41,130	0.2431	1.67	1.45	3.08	3.27
5.08	40,970	0.2441		1.48		3.29
5.06	40,810	0.2450		1.48		3.31
5.04	40,650	0.2460		1.49		3.34
5.02	40,480	0.2470		1.49		3.37

TABLE I(c) (*Continued*)

Si_xGe_{1-x}, $x = 0.80$

eV	cm^{-1}	μm	n	n	k	k
5.00	40,320	0.2480	1.67	1.50	3.19	3.39
4.98	40,160	0.2490		1.50		3.42
4.96	40,000	0.2500		1.51		3.45
4.94	39,840	0.2510		1.51		3.48
4.92	39,680	0.2520		1.52		3.52
4.90	39,520	0.2530	1.69	1.53	3.36	3.55
4.88	39,360	0.2541		1.54		3.59
4.86	39,190	0.2551		1.55		3.62
4.84	39,030	0.2562		1.57		3.66
4.82	38,870	0.2572		1.58		3.70
4.80	38,710	0.2583	1.75	1.60	3.56	3.74
4.78	38,550	0.2594		1.61		3.78
4.76	38,390	0.2605		1.63		3.83
4.75	38,310	0.2610	1.81		3.68	
4.74	38,230	0.2616		1.65		3.88
4.72	38,060	0.2627		1.68		3.93
4.70	37,900	0.2638	1.88	1.70	3.80	3.98
4.68	37,740	0.2649		1.73		4.03
4.66	37,580	0.2661		1.76		4.08
4.65	37,500	0.2666	1.95		3.95	
4.64	37,420	0.2672		1.79		4.14
4.62	37,260	0.2684		1.83		4.20
4.60	37,100	0.2695	2.07	1.87	4.10	4.26
4.58	36,940	0.2707	2.12	1.92	4.16	4.33
4.56	36,770	0.2719	2.19	1.97	4.23	4.39
4.54	36,610	0.2731	2.25	2.03	4.29	4.46
4.52	36,450	0.2743	2.33	2.10	4.35	4.52
4.50	36,290	0.2755	2.41	2.18	4.41	4.59
4.48	36,130	0.2768	2.51	2.26	4.47	4.66
4.46	35,970	0.2780	2.60	2.35	4.52	4.72
4.44	35,810	0.2792	2.71	2.45	4.58	4.78
4.42	35,640	0.2805	2.83	2.56	4.62	4.84
4.40	35,480	0.2818	2.96	2.68	4.66	4.90
4.38	35,320	0.2831	3.10	2.81	4.70	4.94
4.36	35,160	0.2844	3.25	2.96	4.72	4.98
4.34	35,000	0.2857	3.41	3.13	4.72	5.00
4.32	34,840	0.2870	3.59	3.30	4.70	5.00
4.30	34,680	0.2883	3.76	3.48	4.64	4.97
4.28	34,520	0.2897	3.92	3.64	4.54	4.91
4.26	34,350	0.2910	4.04	3.80	4.44	4.83
4.24	34,190	0.2924	4.15	3.93	4.34	4.73
4.22	34,030	0.2938	4.23	4.03	4.23	4.62
4.20	33,870	0.2952	4.32	4.13	4.14	4.51
4.18	33,710	0.2966	4.40	4.20	4.03	4.40
4.16	33,550	0.2980	4.45	4.25	3.89	4.30
4.14	33,390	0.2995	4.47	4.29	3.78	4.21
4.12	33,230	0.3009	4.49	4.33	3.69	4.11

TABLE I(c) (*Continued*)

Si_xGe_{1-x}, $x = 0.80$

eV	cm^{-1}	μm	n	n	k	k
4.10	33,060	0.3024	4.51	4.36	3.60	4.03
4.08	32,900	0.3039	4.52	4.38	3.52	3.95
4.06	32,740	0.3054	4.52	4.40	3.45	3.88
4.04	32,580	0.3069	4.53	4.41	3.38	3.81
4.02	32,420	0.3084	4.53	4.43	3.32	3.75
4.00	32,260	0.3100	4.53	4.44	3.26	3.69
3.98	32,100	0.3115		4.45		3.64
3.96	31,930	0.3131		4.46		3.59
3.95	31,850	0.3139	4.54		3.13	
3.94	31,770	0.3147		4.47		3.55
3.92	31,610	0.3163		4.48		3.50
3.90	31,450	0.3179	4.54	4.50	3.03	3.46
3.88	31,290	0.3195		4.51		3.42
3.86	31,130	0.3212		4.52		3.39
3.85	31,050	0.3220	4.54		2.95	
3.84	30,970	0.3229		4.53		3.36
3.82	30,810	0.3246		4.54		3.32
3.80	30,640	0.3263	4.55	4.56	2.88	3.30
3.78	30,480	0.3280		4.57		3.27
3.76	30,320	0.3297		4.59		3.24
3.75	30,240	0.3306	4.57		2.81	
3.74	30,160	0.3315		4.60		3.21
3.72	30,000	0.3333		4.62		3.19
3.70	29,840	0.3351	4.60	4.64	2.76	3.16
3.68	29,680	0.3369		4.65		3.14
3.66	29,520	0.3388		4.67		3.12
3.65	29,430	0.3397	4.63		2.71	
3.64	29,350	0.3406		4.69		3.10
3.62	29,190	0.3425		4.71		3.08
3.60	29,030	0.3444	4.66	4.73	2.67	3.06
3.58	28,870	0.3463		4.75		3.05
3.56	28,710	0.3483		4.77		3.03
3.55	28,630	0.3493	4.71		2.64	
3.54	28,550	0.3502		4.81		3.05
3.52	28,390	0.3522		4.82		3.01
3.50	28,220	0.3542	4.77	4.86	2.61	3.00
3.48	28,060	0.3563	4.80	4.90	2.61	2.99
3.46	27,900	0.3583	4.84	4.94	2.60	2.98
3.44	27,740	0.3604	4.88	4.98	2.59	2.97
3.42	27,580	0.3625	4.92	5.03	2.58	2.96
3.40	27,420	0.3647	4.98	5.09	2.57	2.95
3.38	27,260	0.3668	5.03	5.15	2.55	2.93
3.36	27,100	0.3690	5.10	5.21	2.53	2.91
3.34	26,930	0.3712	5.17	5.29	2.50	2.89
3.32	26,770	0.3734	5.24	5.37	2.46	2.86
3.30	26,610	0.3757	5.32	5.46	2.42	2.82
3.28	26,450	0.3780	5.40	5.55	2.36	2.76

TABLE I(c) (*Continued*)

Si_xGe_{1-x}, $x = 0.80$

eV	cm^{-1}	μm	n	n	k	k
3.26	26,290	0.3803	5.48	5.64	2.28	2.70
3.24	26,130	0.3827	5.55	5.73	2.19	2.61
3.22	25,970	0.3850	5.62	5.82	2.10	2.52
3.20	25,810	0.3875	5.68	5.89	1.99	2.41
3.18	25,640	0.3899	5.73	5.96	1.87	2.30
3.16	25,480	0.3924	5.76	6.01	1.75	2.17
3.14	25,320	0.3949	5.79	6.06	1.62	2.03
3.12	25,160	0.3974	5.80	6.10	1.48	1.88
3.10	25,000	0.4000	5.79	6.11	1.34	1.73
3.08	24,840	0.4025		6.11		1.58
3.06	24,680	0.4052		6.08		1.44
3.05	24,600	0.4065	5.66		1.03	
3.04	24,510	0.4078		6.04		1.30
3.02	24,350	0.4105		5.99		1.17
3.00	24,190	0.4133	5.49	5.92	0.81	1.06
2.98	24,030	0.4161		5.86		0.95
2.96	23,870	0.4189		5.78		0.87
2.95	23,790	0.4203	5.32		0.65	
2.94	23,710	0.4217		5.71		0.79
2.92	23,550	0.4246		5.64		0.73
2.90	23,390	0.4275	5.15	5.57	0.55	0.66
2.88	23,220	0.4305		5.50		0.60
2.86	23,060	0.4335		5.44		0.56
2.85	22,980	0.4350	5.00		0.47	
2.84	22,900	0.4366		5.38		0.51
2.82	22,740	0.4397		5.32		0.48
2.80	22,580	0.4428	4.88	5.26	0.43	0.44
2.78	22,420	0.4460		5.21		0.42
2.76	22,260	0.4492		5.16		0.39
2.75	22,180	0.4509	4.76			
2.74	22,090	0.4525		5.11		0.37
2.72	21,930	0.4558		5.06		0.34
2.70	21,770	0.4592	4.65	5.02		0.32
2.68	21,610	0.4626		4.97		0.30
2.66	21,450	0.4661		4.93		
2.65	21,370	0.4679	4.56			
2.64	21,290	0.4696		4.89		
2.62	21,130	0.4732		4.85		
2.60	20,970	0.4769	4.50	4.82		
2.58	20,800	0.4806		4.78		
2.56	20,640	0.4843		4.75		
2.55	20,560	0.4862	4.44			
2.54	20,480	0.4881		4.71		
2.52	20,320	0.4920		4.68		
2.50	20,160	0.4959	4.39	4.65		
2.48	20,000	0.4999		4.62		
2.46	19,840	0.5040		4.59		

TABLE I(c) (*Continued*)

Si_xGe_{1-x}, $x=0.80$

eV	cm^{-1}	μm	n	n	k	k
2.45	19,760	0.5061	4.35			
2.44	19,680	0.5081		4.57		
2.42	19,510	0.5123		4.54		
2.40	19,350	0.5166	4.30	4.51		
2.38	19,190	0.5209		4.49		
2.36	19,030	0.5254		4.46		
2.34	18,870	0.5299		4.44		
2.32	18,710	0.5344		4.41		
2.30	18,550	0.5391	4.23	4.39		
2.28	18,380	0.5438		4.37		
2.26	18,220	0.5486		4.35		
2.24	18,060	0.5535		4.33		
2.22	17,900	0.5585		4.31		
2.20	17,740	0.5636	4.16	4.29		
2.18	17,580	0.5687		4.27		
2.16	17,420	0.5740		4.25		
2.14	17,260	0.5794		4.23		
2.12	17,090	0.5848		4.21		
2.10	16,930	0.5904	4.11	4.19		
2.08	16,770	0.5961		4.18		
2.06	16,610	0.6019		4.16		
2.04	16,450	0.6078		4.14		
2.02	16,290	0.6138		4.13		
2.00	16,130	0.6199	4.05	4.11		
1.98	15,970	0.6262		4.10		
1.96	15,800	0.6326		4.08		
1.94	15,640	0.6391		4.07		
1.92	15,480	0.6458		4.05		
1.90	15,320	0.6526	4.00	4.04		
1.88	15,160	0.6595		4.03		
1.86	15,000	0.6666		4.01		
1.84	14,840	0.6738		4.00		
1.82	14,670	0.6812		3.99		
1.80	14,510	0.6888	3.96	3.98		
1.78	14,350	0.6965		3.97		
1.76	14,190	0.7045		3.95		
1.74	14,030	0.7126		3.94		
1.72	13,870	0.7208		3.93		
1.70	13,710	0.7293	3.91	3.92		
1.68	13,550	0.7380		3.91		
1.66	13,380	0.7469		3.90		
1.60	12,900	0.7749	3.87			
1.50	12,090	0.8266	3.84			
1.49	12,010	0.8321				6.43E-03 [4]
1.48	11,930	0.8377				6.19E-03
1.47	11,850	0.8434				5.96E-03
1.46	11,770	0.8492				5.73E-03

TABLE I(c) (*Continued*)

Si_xGe_{1-x}, $x = 0.80$

eV	cm^{-1}	μm	n	n	k	k
1.45	11,690	0.8551				5.50E-03
1.44	11,610	0.8610				5.28E-03
1.43	11,530	0.8670				5.06E-03
1.42	11,450	0.8731				4.84E-03
1.41	11,370	0.8793				4.63E-03
1.40	11,290	0.8856	3.80			4.42E-03
1.39	11,210	0.8920				4.21E-03
1.38	11,130	0.8984				4.01E-03
1.37	11,050	0.9050				3.81E-03
1.36	10,960	0.9117				3.61E-03
1.35	10,880	0.9184				3.42E-03
1.34	10,800	0.9253				3.23E-03
1.33	10,720	0.9322				3.05E-03
1.32	10,640	0.9393				2.87E-03
1.31	10,560	0.9465				2.70E-03
1.30	10,480	0.9537	3.76			2.53E-03
1.29	10,400	0.9611				2.36E-03
1.28	10,320	0.9686				2.20E-03
1.27	10,240	0.9763				2.04E-03
1.26	10,160	0.9840				1.89E-03
1.25	10,080	0.9919				1.74E-03
1.24	10,000	0.9999				1.60E-03
1.23	9,921	1.008				1.47E-03
1.22	9,840	1.016				1.33E-03
1.21	9,759	1.024				1.21E-03
1.20	9,679	1.033	3.73			1.09E-03
1.19	9,598	1.041				9.73E-04
1.18	9,517	1.050				8.64E-04
1.17	9,437	1.059				7.61E-04
1.16	9,356	1.068				6.64E-04
1.15	9,275	1.078				5.74E-04
1.14	9,195	1.087				4.90E-04
1.13	9,114	1.097				4.13E-04
1.12	9,033	1.107				3.42E-04
1.11	8,953	1.116				2.79E-04
1.10	8,872	1.127	3.69			2.22E-04
1.09	8,791	1.137				1.74E-04
1.08	8,711	1.148				1.32E-04
1.07	8,630	1.158				9.89E-05
1.06	8,549	1.169				7.34E-05
1.05	8,469	1.180				5.63E-05
1.04	8,388	1.192				4.55E-05
1.03	8,307	1.203				3.61E-05
1.02	8,227	1.215				2.76E-05
1.01	8,146	1.227				2.02E-05
1.00	8,065	1.239	3.65			1.39E-05
0.99	7,985	1.252				8.76E-06

TABLE I(c) (*Continued*)

Si_xGe_{1-x}, $x = 0.80$

eV	cm^{-1}	μm	n	n	k	k
0.90	7,259	1.377	3.63			
0.80	6,452	1.549	3.60			
0.70	5,646	1.771	3.58			
0.60	4,839	2.066	3.56			
0.50	4,033	2.479	3.55			
0.40	3,226	3.099	3.53			
0.30	2,420	4.132	3.52			
0.20	1,613	6.199	3.52			
0.1487	1,200	8.333				1.05E-05 [11]
0.1463	1,180	8.474				1.48E-05
0.1438	1,160	8.620				1.92E-05
0.1413	1,140	8.772				2.53E-05
0.1388	1,120	8.928				3.18E-05
0.1363	1,100	9.091				3.85E-05
0.1339	1,080	9.259				3.77E-05
0.1314	1,060	9.434				3.36E-05
0.1289	1,040	9.615				2.78E-05
0.1264	1,020	9.804				2.51E-05
0.1239	1,000	10.00				3.22E-05
0.1215	980	10.20				6.47E-05
0.1190	960	10.41				9.31E-05
0.1165	940	10.63				1.05E-04
0.1141	920	10.86				1.27E-04
0.1116	900	11.11				1.53E-04
0.1091	880	11.36				1.91E-04
0.1066	860	11.62				2.06E-04
0.1041	840	11.90				1.84E-04
0.1017	820	12.19				1.52E-04
0.1000	807	12.39	3.51			
0.09919	800	12.49				1.41E-04
0.09671	780	12.82				1.45E-04
0.09423	760	13.15				1.59E-04
0.09175	740	13.51				1.80E-04
0.08927	720	13.88				2.15E-04
0.08679	700	14.28				2.37E-04
0.08555	690	14.49				2.37E-04
0.08431	680	14.70				2.28E-04
0.08183	660	15.15				2.21E-04
0.07935	640	15.62				2.63E-04
0.07687	620	16.12				3.63E-04
0.07439	600	16.66				4.46E-04
0.07191	580	17.24				5.00E-04
0.07067	570	17.54				5.13E-04
0.06943	560	17.85				5.17E-04
0.06695	540	18.51				5.16E-04
0.06447	520	19.23				5.30E-04
0.06199	500	20.00				7.53E-04

TABLE I(c) (*Continued*)

Si_xGe_{1-x}, $x=0.80$

eV	cm^{-1}	μm	n	n	k	k
0.06075	490	20.40				9.45E-04
0.05951	480	20.83				1.01E-03
0.05827	470	21.27				9.21E-04
0.05703	460	21.74				6.81E-04
0.05579	450	22.22				6.06E-04
0.05455	440	22.72				6.33E-04
0.05331	430	23.25				5.97E-04
0.05207	420	23.81				5.61E-04
0.05145	415	24.09				5.55E-04
0.05083	410	24.39				6.93E-04
0.05021	405	24.69				9.63E-04
0.04959	400	25.00				1.06E-03
0.04897	395	25.31				8.23E-04
0.04835	390	25.64				6.58E-04
0.04711	380	26.31				4.42E-04
0.04587	370	27.02				3.16E-04
0.04463	360	27.78				2.91E-04
0.04339	350	28.57				3.11E-04
0.04215	340	29.41				2.85E-04
0.03968	320	31.24				1.98E-04
0.03720	300	33.33				1.88E-04
0.03472	280	35.70				1.64E-04
0.03224	260	38.45				1.24E-04
0.02976	240	41.66				7.93E-05
0.02728	220	45.44				2.84E-05
0.02604	210	47.61				2.68E-04
0.02480	200	50.00				4.28E-04
0.02356	190	52.62				1.24E-03
0.02232	180	55.54				1.49E-03

[a]The reference from which the values were extracted is given in brackets next to the first value. The nominal alloy compositions are: x=0.803 [6], x=0.782 [8], x=0.800 obtained by interpolating the data of Braunstein et al. [4], x=0.800 [11].

Lead Tin Telluride (PbSnTe)

H. PILLER
Louisiana State University
Baton Rouge, Louisiana

There are many alloys of $Pb_{1-x}Sn_xTe$. We can tabulate data only for a very few on the Pb-rich side. Also, it is not possible to find the same x value over a wide spectral range. The reflectivity of the lead-salt narrow-gap alloy PbSnTe was studied by Korn and Braunstein [1, 2]. Measurements of near-normal reflectivity were made at room temperature in the photon-energy range of 0.5–13 eV. Czochralski-grown p-type bulk samples were used in the measurements. Samples were cut, ground, and hand-polished to produce optical-quality surfaces. After an electrochemical etch, samples were immediately placed in a vacuum (at least 10^{-5} torr), and spectral scans were begun. Consistent results were obtained upon repreparation of sample surfaces. The maximum estimated absolute reflectance error throughout the spectral range was at most 2%. The optical constants n and k were obtained through a Kramers–Kronig computation. $Pb_{1-x}Sn_xTe$ can be grown throughout the range $0 \leqslant x \leqslant 1$. PbTe and SnTe both crystallize in the rocksalt structure, and both have interband optical transitions at the L point in the Brillouin zone. The width of the direct energy gap changes with the composition of the alloy; as x increases, the band gap first decreases and then increases. The optical constants are listed in Table II. Columns 4 and 5 show n and k for $x = 0.17$ and columns 6 and 7 for $x = 0.09$. Both samples were p-type single crystals. Values of n and k for $x = 0.19 \pm 0.02$ are plotted in Fig. 1.

Drabkin *et al.* [3] measured the variation of the absorption coefficient in $Pb_{1-x}Sn_xTe$ for $x = 0.2$ and $x = 0.1$ with carrier densities $n_e = 8 \times 10^{17}$ and $n_p = 2.5 \times 10^{18}\ cm^{-3}$, respectively. The measurements were made in the photon-energy region 0.2–0.8 eV. The data were obtained from epitaxial films at 300 K. The films were single crystals. The lattice constants of the films were identical with the constants of the bulk samples, which shows that the evaporation did not alter the composition. The thicknesses of the samples were 1.92 and 1.48 μm, respectively. The k data were calculated from the absorption coefficients given in the graph [3], which are readable to three figures. The corresponding k values for $x = 0.2$ and $x = 0.1$ are

Copyright © 1991 by Academic Press.
All rights of reproduction in any form reserved.
ISBN 0-12-544422-2

listed in Table II (columns 5 and 7) and k for $x=0.2$ is plotted in Fig. 1. Good agreement with experiment was found by calculating the data from a two-band Kane model. The following energy gaps were used in the calculations: 0.207 eV for $x=0.2$ and 0.25 eV for $x=0.1$.

McKnight and El-Rayess [4] measured the far-infrared reflectivity of films of indium-doped $Pb_{1-x}Sn_xTe$ from 40–240 cm^{-1}. The films were grown from sources with $x=0.21$ and 0.25 on BaF_2 substrates. The measurements were made at 300, 150, 80, 25, 20, 15, and 8 K. Both samples were doped with In at levels above 0.5 atomic percent. In "sufficiently doped" samples, the indium centers pin the Fermi level by binding carriers usually present because of deviations from metal-chalcogenide stochiometry. The sample with $x=0.21$ was estimated to be 15 μm thick and the sample with $x=0.25$ was 19 μm thick. Data were ratioed versus a coin-silver mirror of near-unit reflectivity. Multiple runs were made and the data averaged to achieve a standard deviation of about 1%. A fit to the reflectivity of the $x=0.21$ sample at 300 K was made assuming a film dielectric function, based on a classical two-oscillator (plasmon–phonon) model of the following form:

$$\varepsilon(\omega)=\varepsilon_\infty\left[\frac{(\omega_L^2-\omega^2)}{(\omega_T^2-\omega^2-i\Gamma\omega)}\right]-\frac{\omega_P^2}{\omega(\omega+i/\tau)}.$$

Here ω_T and ω_L are the transverse and longitudinal optical phonon frequencies, respectively. ω_P is the plasma frequency. A very good fit to the experimental reflectivity was obtained with the following parameters: $\omega_T=32\ cm^{-1}$, $\omega_L=111\ cm^{-1}$, $\omega_P=402\ cm^{-1}$, $1/\tau=88.4\ cm^{-1}$, $\Gamma=17.2\ cm^{-1}$, $\varepsilon_\infty=42.5$. The carrier concentration was estimated to be below $10^{17}\ cm^{-3}$. We calculated the optical constants n and k from the dielectric constant using the parameters given above. These data are listed in Table II. A smooth plot of the n and k data is given in Fig. 1.

McKnight and El-Rayess [5] measured also the far-infrared reflectivity of indium-doped $Pb_{1-x}Sn_xTe$ films with $x=0.25$ and $x=0.21$ under high hydrostatic pressure. The measurements were made in the region 50–200 cm^{-1}. The primary effect of the hydrostatic pressure is to decrease the band gap by about 7.4 meV/kbar. An increase in the plasma frequency was observed with increasing hydrostatic pressure. This is consistent with the observed large relative decrease in the narrow band gap and hence the effective mass. Carrier freeze-out and semi-insulating behavior was observed at low temperatures.

Takaoka *et al.* [6] measured the far-infrared magnetoplasma spectra in 1 at.% indium-doped $Pb_{1-x}Sn_xTe$ single crystals across the band-inversion region between $x=0.15$ and 0.40 at temperatures between 4.2 and 20 K. They observed that the band-edge masses and the energy gaps seem not to reach zero at the band-inversion tin composition ($x=0.35$) [7].

Takaoka and Murase [8] observed the local vibration mode of indium atoms in $Pb_{1-x}Sn_xTe$ at 160 cm^{-1} by far-infrared absorption measurements.

Dornhaus *et al.* [9] reviewed the optical properties, including dielectric properties and phonon spectra. The dielectric properties of the mixed-crystal $Pb_{1-x}Sn_xTe$ were extensively investigated. They are characterized by large static and optical dielectric constants. Lehmann *et al.* [10] measured the dielectric properties of epitaxial $Pb_{1-x}Sn_xTe$ layers in a range between $x=0$ and 0.225 at 9 GHz. Their results show that the static dielectric constant (ε_s) does not depend on the effective band gap. The authors measured $\varepsilon_s=230$ in an n-type sample with $x=0.2$ with a carrier concentration of 2×10^{17} cm^{-3} at 300 K and $\varepsilon_s=1850$ with a carrier concentration of 0.14×10^{17} cm^{-3} at 77 K. The temperature dependence of the static dielectric constant and of the TO phonon energy was investigated in many experiments, including neutron scattering experiments [9].

Table I is a summary of the n and k data for various values of x. We have plotted n and k only for $x=0.19\pm0.02$ over the widest possible spectral range, thus omitting plots for other x values in Table II.

REFERENCES

1. D. M. Korn, thesis (UCLA, 1971) (unpublished).
2. D. M. Korn and R. Braunstein, *Phys. Rev. B* **5**, 4837 (1972).
3. I. A. Drabkin, L. Ya. Morgovsky, I. V. Nelson, Yu. I. Ravich, *Sov. Phys. Semicond.* **6**, 1156 (1973).
4. S. W. McKnight and M. K. El-Rayess, *Solid State Commun.* **49**, 1001 (1984).
5. S. W. McKnight and M. K. El-Rayess, "Proc. Int. Conf. Semicond. Phys., San Francisco," 1984, Springer-Verlag, New York, 1389 (1984).
6. S. Takaoka, S. Shimomura, H. Takahashi, and K. Murase, *Phys. Rev. B* **40**, 5642 (1989).
7. J. F. Butler, *Solid State Commun.* **7**, 909 (1969).
8. S. Takaoka and K. Murase, *J. Phys. Soc. Jpn.* **52**, 25 (1983).
9. R. Dornhaus, G. Nimtz, and B. Schlicht, in "Narrow-Gap Semiconductors," Springer-Verlag, Berlin, (1983).
10. H. Lehmann, G. Nimtz, L. D. Haas, and T. Jakobus, *Appl. Phys.* **25**, 291 (1981).

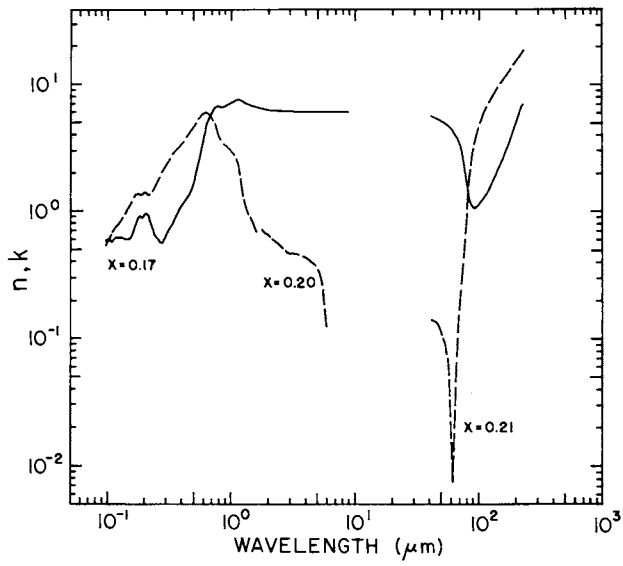

Fig. 1. Log–log plot of n (solid line) and k (dashed line) versus wavelength in micrometers for $Pb_{1-x}Sn_xTe$ with $x = 0.19 \pm 0.02$.

TABLE I

Values of x for Which Data for n and k Are Presented in Table II

x	UV–VIS (13–0.5 eV) n & k	Near IR (0.8–0.2 eV) k	Far IR (240–40 cm^{-1}) n & k
0	See PbTe *HOC I*		
0.09	*X*		
0.1		*X*	
0.17[a]	*X*		
0.2[a]		*X*	
0.21[a]			*x*
1	See SnTe *HOC II*		

[a] Plotted in Fig. 1.

TABLE II

Values of n and k for $Pb_{1-x}Sn_xTe$ Obtained from Various References[a]

eV	μm	n	k	n	k
		x = 0.17		x = 0.09	
12.86	0.0964			0.597 [1]	
12.84	0.0966		0.531 [1]		
12.82	0.0967	0.606 [1]			0.461 [1]
12.75	0.0972		0.527	0.598	
12.74	0.0973	0.608			
12.71	0.0975				0.462
12.66	0.0980		0.528		
12.64	0.0981	0.574			
12.62	0.0982				0.495
12.59	0.0985			0.600	
12.50	0.0992				0.497
12.43	0.0998	0.578	0.566		
12.41	0.0999			0.602	
12.30	0.1008	0.580			
12.27	0.1010				0.505
12.25	0.1012			0.589	
12.20	0.1016		0.597		
12.12	0.1023	0.583			
12.07	0.1027				0.530
12.03	0.1031		0.618	0.572	
11.92	0.1040	0.603			
11.91	0.1041				0.532
11.83	0.1048		0.613	0.574	
11.79	0.1052				0.562
11.76	0.1055	0.606			
11.62	0.1067			0.577	0.557
11.55	0.1073		0.648		
11.54	0.1074	0.574			
11.45	0.1083				0.583
11.43	0.1085		0.650		
11.39	0.1089			0.579	
11.33	0.1095	0.578			
11.23	0.1104				0.610
11.21	0.1106			0.581	
11.19	0.1108		0.683		
11.12	0.1115	0.582			
11.04	0.1124				0.645
11.02	0.1125		0.716		
10.96	0.1131			0.600	
10.93	0.1135	0.585			
10.89	0.1139				0.675
10.86	0.1142		0.741		
10.81	0.1146	0.617			

TABLE II (*Continued*)

$Pb_{1-x}Sn_xTe$

eV	μm	n	k	n	k
10.78	0.1151			0.625	
10.71	0.1157		0.760		
10.67	0.1162	0.619			0.678
10.58	0.1172			0.659	
10.54	0.1176		0.762		
10.49	0.1182	0.623			0.665
10.41	0.1192			0.674	
10.33	0.1200		0.785		
10.32	0.1202				0.658
10.31	0.1203	0.607			
10.22	0.1213			0.659	
10.15	0.1222				0.662
10.12	0.1225	0.610			
10.10	0.1228		0.788		
9.973	0.1243			0.660	
9.970	0.1244	0.613			
9.930	0.1249				0.665
9.898	0.1253		0.818		
9.789	0.1267	0.626			
9.750	0.1272			0.630	
9.706	0.1277		0.834		
9.706	0.1278				0.668
9.593	0.1292	0.606			
9.549	0.1298			0.600	
9.509	0.1304				0.671
9.455	0.1311	0.613			
9.454	0.1312		0.865		
9.328	0.1329				0.705
9.303	0.1333			0.556	
9.284	0.1336		0.901		
9.270	0.1338	0.616			
9.158	0.1354				0.756
9.101	0.1362		0.927		
9.089	0.1364	0.619			
9.059	0.1369			0.531	
8.996	0.1378				0.786
8.948	0.1386		0.954		
8.866	0.1398	0.593			
8.861	0.1399			0.508	
8.765	0.1415		1.005		
8.746	0.1418				0.819
8.670	0.1430	0.596			
8.602	0.1441			0.494	
8.575	0.1446		1.033		
8.525	0.1454				0.878
8.449	0.1467	0.600			

TABLE II (*Continued*)

$Pb_{1-x}Sn_xTe$

eV	μm	n	k	n	k
8.405	0.1475			0.496	
8.398	0.1476		1.095		
8.336	0.1487				0.961
8.298	0.1494	0.601			
8.274	0.1498		1.093		
8.246	0.1504			0.492	
8.155	0.1520				1.001
8.149	0.1522	0.604			
8.079	0.1535		1.157		
8.041	0.1542				1.062
8.025	0.1545			0.495	
7.990	0.1552	0.619			
7.915	0.1566		1.219		
7.894	0.1571			0.530	
7.875	0.1574				1.105
7.821	0.1585	0.658			
7.736	0.1603		1.259		
7.730	0.1604				1.141
7.648	0.1621	0.695			
7.632	0.1625			0.553	
7.544	0.1644				1.212
7.509	0.1651		1.325		
7.465	0.1661	0.743			
7.406	0.1674			0.619	1.244
7.356	0.1686		1.370		
7.310	0.1696	0.800			
7.262	0.1707				1.266
7.199	0.1722			0.653	
7.162	0.1731	0.823			
7.133	0.1738		1.382		
7.088	0.1749				1.269
7.038	0.1762			0.702	
6.997	0.1772	0.890			
6.954	0.1783		1.369		
6.903	0.1796			0.737	
6.895	0.1798	0.903			
6.871	0.1805				1.292
6.774	0.1830		1.325		
6.718	0.1846			0.739	
6.714	0.1847	0.910			
6.673	0.1858				1.291
6.611	0.1875		1.327		
6.543	0.1895	0.886			
6.533	0.1898			0.741	
6.496	0.1909				1.353
6.467	0.1917		1.355		

TABLE II (*Continued*)

$Pb_{1-x}Sn_xTe$

eV	cm^{-1}	μm	n	k	n	k
6.368		0.1947	0.889			
6.355		0.1951			0.743	1.344
6.342		0.1955		1.394		
6.202		0.1999		1.390		
6.198		0.2000	0.939			
6.186		0.2004			0.752	
6.180		0.2006				1.410
6.059		0.2046	0.955			
6.037		0.2054			0.802	
6.019		0.2060		1.407		
5.976	48197	0.2075				1.386
5.945	47949	0.2086			0.803	
5.941	47915	0.2087	0.947			
5.850	47184	0.2119		1.359		
5.796	46751	0.2139	0.916			
5.757	46436	0.2154			0.779	
5.752	46396	0.2155				1.344
5.683	45839	0.2182		1.327		
5.663	45678	0.2189	0.900			
5.582	45025	0.2221			0.706	
5.549	44754	0.2235				1.369
5.534	44635	0.2240		1.361		
5.492	44296	0.2258	0.819			
5.393	43494	0.2299				1.444
5.379	43388	0.2305			0.644	
5.357	43206	0.2315	0.752	1.395		
5.216	42071	0.2377			0.616	
5.209	42010	0.2380				1.548
5.174	41733	0.2396	0.704			
5.139	41452	0.2413		1.504		
5.062	40829	0.2449			0.582	
5.046	40698	0.2457	0.631			
5.017	40466	0.2471				1.642
4.967	40060	0.2496		1.613		
4.867	39258	0.2547			0.584	
4.859	39189	0.2552	0.614			
4.848	39103	0.2557				1.743
4.764	38428	0.2602		1.739		
4.727	38128	0.2623				1.797
4.678	37732	0.2650			0.586	
4.632	37359	0.2677	0.569			
4.629	37339	0.2678		1.862		
4.597	37079	0.2697				1.871
4.498	36280	0.2756		1.982		
4.489	36206	0.2762			0.588	
4.467	36031	0.2775	0.553			

TABLE II (*Continued*)

$Pb_{1-x}Sn_xTe$

eV	cm^{-1}	μm	n	k	n	k
4.434	35763	0.2796				1.987
4.346	35056	0.2853	0.584			
4.337	34982	0.2859		2.130		
4.304	34711	0.2881			0.590	
4.295	34641	0.2887				2.083
4.245	34238	0.2921		2.224		
4.184	33744	0.2964				2.159
4.168	33616	0.2975	0.634			
4.106	33119	0.3019		2.355		
4.082	32923	0.3037				2.246
4.077	32882	0.3041			0.581	
4.038	32569	0.3070	0.688			
3.982	32119	0.3114				2.346
3.971	32032	0.3122		2.491		
3.907	31509	0.3174			0.609	
3.864	31162	0.3209				2.434
3.860	31129	0.3213	0.735			
3.821	30821	0.3245		2.602		
3.766	30378	0.3292			0.633	
3.760	30327	0.3297				2.532
3.729	30079	0.3325	0.767			
3.690	29762	0.3360		2.719		
3.641	29363	0.3406				2.687
3.623	29218	0.3423			0.670	
3.598	29021	0.3446		2.855		
3.590	28958	0.3453	0.833			
3.526	28443	0.3516				2.832
3.468	27968	0.3576			0.717	
3.465	27947	0.3578		2.977		
3.461	27912	0.3583	0.897			
3.413	27524	0.3633				2.989
3.360	27099	0.3690		3.096		
3.331	26869	0.3722			0.773	
3.296	26587	0.3761				3.125
3.294	26570	0.3764	0.999			
3.240	26132	0.3827		3.230		
3.186	25697	0.3892	1.091			3.266
3.182	25668	0.3896			0.857	
3.098	24983	0.4003		3.355		
3.074	24790	0.4034				3.400
3.017	24330	0.4110			0.941	
2.982	24049	0.4158		3.514		
2.959	23869	0.4190	1.185			
2.954	23827	0.4197				3.570
2.877	23207	0.4309		3.693		
2.867	23121	0.4325				3.739

TABLE II (*Continued*)

$Pb_{1-x}Sn_xTe$

eV	cm^{-1}	μm	n	k	n	k
2.845	22945	0.4358			0.995	
2.817	22718	0.4402	1.255			
2.788	22486	0.4447		3.874		
2.772	22354	0.4474				3.901
2.729	22009	0.4544				4.066
2.720	21941	0.4558			1.100	
2.715	21897	0.4567		4.021		
2.690	21695	0.4609	1.373			
2.662	21472	0.4657				4.263
2.642	21312	0.4692		4.203		
2.607	21030	0.4755			1.223	
2.599	20958	0.4771	1.493			
2.597	20948	0.4774				4.441
2.569	20719	0.4827		4.455		
2.519	20318	0.4922				4.621
2.498	20150	0.4963	1.635	4.641		
2.484	20033	0.4992			1.396	
2.482	20021	0.4995				4.808
2.444	19711	0.5073		4.791		
2.434	19630	0.5094	1.798			
2.407	19410	0.5152				5.024
2.394	19312	0.5178			1.632	
2.379	19188	0.5212	1.978			
2.374	19147	0.5223		5.030		
2.364	19070	0.5244				5.226
2.342	18891	0.5294		5.182		
2.340	18874	0.5298			1.812	
2.324	18742	0.5336				5.402
2.317	18687	0.5351	2.167			
2.279	18383	0.5440		5.382		
2.278	18376	0.5442			2.000	
2.275	18347	0.5451	2.430			
2.261	18232	0.5485				5.579
2.245	18107	0.5523			2.205	
2.236	18037	0.5544				5.728
2.229	17978	0.5562		5.565		
2.218	17890	0.5590	2.613			
2.195	17707	0.5648			2.477	5.865
2.183	17603	0.5681	2.823			
2.170	17500	0.5715		5.754		
2.158	17407	0.5745	3.033			
2.150	17340	0.5767				5.980
2.142	17273	0.5790			2.705	
2.126	17150	0.5831	3.242			
2.125	17141	0.5834			2.932	
2.113	17045	0.5867		5.884		

TABLE II (*Continued*)

$Pb_{1-x}Sn_xTe$

eV	cm^{-1}	μm	n	k	n	k
2.104	16972	0.5892				6.064
2.103	16963	0.5895			3.145	
2.098	16918	0.5911	3.419			
2.073	16720	0.5981	3.618			
2.071	16705	0.5986			3.315	
2.071	16704	0.5987				6.100
2.070	16692	0.5991			3.513	
2.064	16646	0.6008		5.963		
2.062	16627	0.6014	3.814			
2.026	16337	0.6121	4.004			
2.017	16271	0.6146		5.986		
2.014	16241	0.6157			3.722	
2.000	16130	0.6200				6.101
1.986	16022	0.6242	4.226			
1.986	16018	0.6243			3.940	
1.982	15985	0.6256		5.992		
1.972	15908	0.6286			4.249	
1.962	15823	0.6320	4.420			
1.954	15758	0.6346	4.601			
1.946	15693	0.6372		5.942		
1.939	15641	0.6394				6.042
1.937	15619	0.6403	4.795			
1.919	15478	0.6461			4.521	
1.908	15386	0.6500	4.960			
1.907	15383	0.6501				5.893
1.892	15259	0.6554			4.786	
1.891	15249	0.6558	5.168			
1.858	14984	0.6674		5.784		
1.855	14959	0.6685	5.358			
1.851	14929	0.6698			4.996	
1.845	14878	0.6722				5.683
1.824	14712	0.6797			5.285	
1.824	14710	0.6798	5.512			
1.815	14642	0.6830	5.672			
1.809	14590	0.6854				5.532
1.801	14522	0.6886		5.546		
1.791	14446	0.6922			5.533	
1.788	14425	0.6933	5.845			
1.784	14385	0.6952				5.316
1.770	14275	0.7006		5.333		
1.747	14089	0.7098	6.027			
1.745	14072	0.7106			5.755	
1.728	13934	0.7177		5.094		
1.725	13912	0.7188				5.128
1.723	13896	0.7196	6.269			
1.698	13693	0.7303				4.920

TABLE II (*Continued*)

$Pb_{1-x}Sn_xTe$

eV	cm^{-1}	μm	n	k	n	k
1.688	13613	0.7346		4.900		
1.686	13602	0.7352			5.915	
1.673	13490	0.7413	6.486			
1.660	13385	0.7471				4.724
1.650	13306	0.7515	6.574			
1.646	13275	0.7533		4.685		
1.633	13168	0.7595	6.661			
1.632	13162	0.7598		4.464		
1.612	12998	0.7694			6.099	
1.602	12918	0.7741		4.283		
1.594	12858	0.7777	6.710			
1.591	12831	0.7794				4.480
1.570	12659	0.7900		4.106		
1.569	12655	0.7902	6.660			
1.545	12461	0.8025		3.942		
1.531	12348	0.8099				4.339
1.520	12256	0.8159			6.259	
1.512	12197	0.8199		3.714		
1.486	11985	0.8344	6.609			
1.468	11841	0.8445				4.260
1.437	11589	0.8629		3.516		
1.432	11551	0.8657			6.496	
1.421	11465	0.8722	6.661			
1.403	11315	0.8838				4.137
1.390	11211	0.8920		3.354		
1.379	11125	0.8989	6.710			
1.371	11059	0.9043			6.744	
1.338	10789	0.9269			6.951	
1.335	10770	0.9285				3.985
1.326	10692	0.9353	6.848			
1.303	10513	0.9512		3.164		
1.297	10460	0.9560				3.777
1.295	10442	0.9577			7.131	
1.274	10274	0.9734			7.285	
1.262	10178	0.9825	7.051			
1.251	10091	0.9910		3.014		
1.246	10049	0.9952				3.598
1.240	10004	0.9997			7.486	
1.231	9929	1.007			7.674	
1.208	9743	1.026				3.419
1.197	9652	1.036				3.278
1.190	9599	1.042	7.221			
1.190	9598	1.042				3.054
1.187	9574	1.044		2.822		
1.183	9543	1.048			7.933	
1.179	9511	1.051			8.094	

TABLE II (*Continued*)

$Pb_{1-x}Sn_xTe$

eV	cm^{-1}	μm	n	k	n	k
1.174	9472	1.056				2.873
1.172	9456	1.058				2.716
1.147	9247	1.081			8.190	
1.146	9243	1.082				2.563
1.143	9220	1.085				2.356
1.138	9178	1.090			8.260	
1.134	9145	1.093	7.423			
1.132	9130	1.095		2.602		
1.119	9022	1.108				2.198
1.117	9008	1.110				2.069
1.097	8850	1.130		2.374		
1.096	8842	1.131	7.517			
1.093	8813	1.135				1.795
1.087	8763	1.141			8.183	
1.075	8667	1.154		2.198		
1.074	8659	1.155	7.609			
1.061	8558	1.168			8.080	
1.061	8554	1.169		1.972		
1.060	8549	1.170			7.972	
1.043	8415	1.188				1.607
1.040	8387	1.192		1.813		
1.037	8368	1.195	7.570			
1.033	8330	1.201				1.373
1.023	8252	1.212	7.496			
1.017	8202	1.219			7.803	
1.011	8156	1.226		1.467		
1.006	8114	1.232		1.649		
0.9968	8040	1.244	7.382			
0.9949	8024	1.246				1.202
0.9739	7855	1.273			7.624	
0.9713	7834	1.277		1.256		
0.9696	7820	1.279				0.990
0.9545	7699	1.299	7.206			
0.9419	7597	1.316			7.439	
0.9363	7552	1.324		1.004		
0.9199	7419	1.348			7.298	
0.9089	7330	1.364				0.787
0.9005	7263	1.377	6.998			
0.8766	7070	1.414			7.106	
0.8596	6933	1.442		0.850		
0.8543	6890	1.451	6.811			
0.8330	6718	1.488			6.876	
0.8221	6631	1.508				0.600
0.7769	6266	1.596		0.660		
0.7732	6237	1.603			6.717	
0.7537	6079	1.645	6.612			

TABLE II (*Continued*)

$Pb_{1-x}Sn_xTe$

eV	cm^{-1}	μm	n	k	n	k
0.7417	5982	1.672				0.463
				x = 0.2		x = 0.1
0.7119	5742	1.741				0.607 [3]
0.7052	5688	1.758		0.718 [3]		
0.6990	5638	1.774	6.476 [1]			
0.6913	5575	1.794		0.672		
0.6909	5573	1.794				0.633
0.6849	5524	1.810			6.514 [1]	
0.6750	5444	1.837		0.665		
0.6744	5439	1.838				0.632
0.6582	5308	1.884		0.676		
0.6554	5286	1.892				0.621
0.6433	5189	1.927		0.659		
0.6429	5185	1.929				0.636
0.6287	5071	1.972		0.638		
0.6270	5057	1.978				0.619
0.6255	5045	1.982	6.332			
0.6119	4935	2.026				0.656
0.6116	4933	2.027		0.632		
0.6022	4857	2.059			6.312	
0.5993	4834	2.069				0.623
0.5970	4815	2.077		0.610		
0.5857	4724	2.117				0.624
0.5798	4677	2.138		0.601		
0.5738	4628	2.161	6.258			
0.5703	4600	2.174				0.602
0.5644	4552	2.197		0.590		
0.5579	4499	2.222				0.591
0.5472	4414	2.266				0.587
0.5457	4401	2.272		0.570		
0.5309	4282	2.335				0.591
0.5207	4200	2.381				0.564
0.5183	4180	2.392		0.558		
0.5149	4153	2.408			6.204	
0.5110	4121	2.427				0.574
0.5014	4044	2.473				0.557
0.4989	4024	2.485		0.548		
0.4902	3954	2.529				0.574
0.4812	3881	2.576				0.585
0.4772	3849	2.598		0.519		
0.4715	3803	2.630				0.551
0.4684	3777	2.647				0.507
0.4676	3772	2.651	6.171			

TABLE II (*Continued*)

$Pb_{1-x}Sn_xTe$

eV	cm^{-1}	μm	n	k	n	k
0.4617	3724	2.685		0.495		
0.4569	3685	2.714		0.472		
0.4547	3668	2.727				0.570
0.4458	3595	2.781				0.478
0.4367	3522	2.839		0.470		
0.4319	3484	2.871				0.565
0.4225	3408	2.935		0.470		
0.4222	3405	2.937				0.482
0.4164	3359	2.977			6.100	
0.4109	3314	3.017				0.498
0.4074	3286	3.044		0.464		
0.4013	3236	3.090				0.486
0.3920	3162	3.163				0.483
0.3908	3152	3.172		0.459		
0.3830	3089	3.237				0.474
0.3758	3031	3.299				0.461
0.3745	3021	3.310		0.464		
0.3645	2940	3.401				0.446
0.3615	2916	3.430		0.454		
0.3543	2858	3.500				0.465
0.3486	2812	3.557	6.095			
0.3480	2806	3.563				0.426
0.3451	2783	3.593		0.448		
0.3411	2751	3.635				0.432
0.3319	2677	3.736				0.417
0.3281	2647	3.779		0.441		
0.3215	2593	3.856				0.423
0.3154	2543	3.932		0.433		
0.3143	2535	3.945				0.393
0.3046	2457	4.071				0.383
0.3009	2427	4.121		0.421		
0.2993	2414	4.143			6.004	
0.2897	2336	4.280		0.408		
0.2853	2301	4.346				0.322
0.2794	2253	4.438		0.400		
0.2764	2229	4.486				0.323
0.2734	2205	4.535				0.288
0.2705	2182	4.583		0.386		
0.2683	2164	4.621				0.256
0.2644	2132	4.689				0.229
0.2634	2124	4.707			5.976	
0.2609	2104	4.752				0.210
0.2596	2094	4.777				0.194
0.2545	2053	4.872		0.367		
0.2542	2050	4.877				0.167
0.2476	1997	5.008		0.351		

TABLE II (*Continued*)

$Pb_{1-x}Sn_xTe$

eV	cm^{-1}	μm	n	k	n	k
0.2408	1942	5.149		0.317		
0.2325	1875	5.334		0.286		
0.2283	1841	5.431	6.052			
0.2265	1827	5.475		0.252		
0.2220	1791	5.584		0.215		
0.2189	1766	5.664		0.177		
0.2175	1754	5.701		0.157		
0.2138	1725	5.799		0.135		
0.2123	1712	5.841		0.123		
0.1349	1088	9.190	6.053			
0.08708	702	14.24			5.956	
			x = 0.21			
0.02976	240	41.67	5.602 [4]	0.139 [4]		
0.02926	236	42.37	5.568	0.138		
0.02876	232	43.10	5.533	0.137		
0.02827	228	43.86	5.495	0.135		
0.02777	224	44.64	5.456	0.133		
0.02728	220	45.46	5.413	0.131		
0.02678	216	46.30	5.368	0.128		
0.02628	212	47.17	5.320	0.125		
0.02579	208	48.08	5.269	0.121		
0.02529	204	49.02	5.214	0.117		
0.02480	200	50.00	5.156	0.111		
0.02430	196	51.02	5.093	0.106		
0.02381	192	52.08	5.025	0.0989		
0.02331	188	53.19	4.952	0.0911		
0.02281	184	54.35	4.873	0.0820		
0.02232	180	55.56	4.788	0.0715		
0.02182	176	56.82	4.695	0.0592		
0.02133	172	58.14	4.593	0.0448		
0.02083	168	59.52	4.482	0.0280		
0.02033	164	60.98	4.360	0.0080		
0.01984	160	62.50	4.224	0.0157		
0.01934	156	64.10	4.074	0.0442		
0.01885	152	65.79	3.905	0.0789		
0.01835	148	67.57	3.714	0.122		
0.01785	144	69.45	3.497	0.176		
0.01736	140	71.43	3.247	0.246		
0.01686	136	73.53	2.955	0.341		
0.01637	132	75.76	2.608	0.478		
0.01587	128	78.13	2.194	0.691		
0.01537	124	80.65	1.731	1.055		
0.01488	120	83.33	1.345	1.622		

TABLE II (*Continued*)

$Pb_{1-x}Sn_xTe$

eV	cm^{-1}	μm	n	k	n	k
0.01438	116	86.21	1.145	2.264		
0.01389	112	89.29	1.066	2.876		
0.01339	108	92.59	1.047	3.455		
0.01289	104	96.16	1.062	4.015		
0.01240	100	100.0	1.100	4.570		
0.01190	96	104.2	1.156	5.129		
0.01141	92	108.7	1.229	5.702		
0.01091	88	113.6	1.321	6.299		
0.01041	84	119.0	1.432	6.928		
0.009919	80	125.0	1.566	7.600		
0.009423	76	131.6	1.730	8.325		
0.008927	72	138.9	1.930	9.118		
0.008431	68	147.1	2.180	9.997		
0.007935	64	156.2	2.498	10.984		
0.007439	60	166.7	2.912	12.109		
0.006943	56	178.6	3.471	13.409		
0.006447	52	192.3	4.253	14.934		
0.005951	48	208.3	5.405	16.735		
0.005465	44	227.3	7.195	18.840		

The references are given in brackets.

Mercury Cadmium Telluride ($Hg_{1-x}Cd_xTe$)

P. M. AMIRTHARAJ
U.S. Army Center for Night Vision and Electro-Optics
Fort Belvoir, Virginia

Mercury cadmium telluride is a II-VI ternary alloy semiconductor that belongs to the zinc-blende family and hence has much in common with other, better known semiconductors such as GaAs and InP. The overall shape of the dielectric functions ε_1 and ε_2 are similar for most of the materials of the same family, but the precise energy positions of the various spectroscopic features vary from one material to the other. The uniqueness of $Hg_{1-x}Cd_xTe$ arises from the fact that the direct gap can be varied all the way from $0(x \simeq 0.15)$ to 1.6 eV ($x = 1$). The band gap can therefore be reduced below the lowest limit attainable within the III-V family. Hence, $Hg_{1-x}Cd_xTe$ has found widespread use in the fabrication of quantum infrared detectors and is currently the leading candidate. In order of technological importance, it is perhaps next only to Si and GaAs.

The optical properties of $Hg_{1-x}Cd_xTe$ has been investigated by many investigators ever since the very first reported study by Lawson *et al.* [1]. However, the main thrust of the early work was in using spectroscopic features for obtaining information regarding the electronic band structure. Hence, the photometric accuracy available in the reports on the measurement of reflection and transmission spectra was limited, and consequently, the precision of the optical constants determined is not completely satisfactory. More recent investigations, particularly using scanning ellipsometry, have yielded optical data with substantially improved accuracy.

One must also take note of the advances in materials technology. The more recent reports of absorption measurements performed on epitaxial films with well-controlled properties, in particular x and its uniformity, are clearly more dependable than the earliest reports. Hence, values compiled in this review are weighted toward the more recent papers and those that are expected to possess greater intrinsic accuracy. Comparisons to earlier work are made where warranted; the remaining earlier studies are referenced without an evaluation of the dependability and accuracy of the data.

Copyright © 1991 by Academic Press.
All rights of reproduction in any form reserved.
ISBN 0-12-544422-2

The review by Dornhaus and Nimtz [2], the compilation of several parameter values by Brice and Capper [3], and the comprehensive collection of n and k values of CdTe by Palik [4] are earlier works to which the reader is referred for additional information. Table I displays a summary of the data included in this review, and Fig. 1 shows a graphical plot of the variation of n and k for one representative alloy composition, namely $x = 0.2 \pm 0.01$. The complex forms of the dielectric function, ε, and the refractive index, $\mathbf{n}$, the absorption coefficient α and the reflectivity R are reproduced below for later reference:

$$\varepsilon = \varepsilon_1 + i\varepsilon_2 \tag{1}$$

$$\mathbf{n} = n + ik \tag{2}$$

$$\mathbf{n} = \sqrt{\varepsilon} = \sqrt{(\varepsilon_1 + i\varepsilon_2)} \tag{3}$$

$$R = |(\mathbf{n}-1)/(\mathbf{n}+1)|^2 = \{(n-1)^2 + k^2\}/\{(n+1)^2 + k^2\} \tag{4}$$

$$\alpha = 4\pi k/\lambda. \tag{5}$$

The units of energy (E), frequency (ω), and wavelength (λ) throughout this review will be eV, cm^{-1}, and μm, respectively.

The Ultraviolet, Visible, and Near-Infrared Range (6–1.5 eV)

The most complete and dependable set of ellipsometric measurements in the near-ultraviolet, visible, and near-infrared region on $Hg_{1-x}Cd_xTe$ have been reported by Arwin and Aspnes [5] and Viña *et al.* [6]. Arwin and Aspnes [5] measured ε_1 and ε_2 in the visible and near-visible energy region from 6–1.5 eV of crystalline HgTe, $Hg_{0.8}Cd_{0.2}Te$, $Hg_{0.71}Cd_{0.29}Te$ and CdTe. The samples were prepared by zone refining and were n-type. A detailed investigation was undertaken of the surface modifications introduced by the most commonly used chemical treatment, namely etching in a solution of Br_2/CH_3OH as well as other etching procedures. A residual layer of amorphous Te (α-Te), approximately 7 Å thick, was observed to be present on the Br_2/CH_3OH-treated surfaces. Figures 1 and 2 in Ref. [5] display the values of ε_1 and ε_2 corrected for the presence of the overlayers; an electronic computer record provided by Aspnes [7] was used to calculate the n and k values shown in Table II. The presented values are rounded off to three decimal places. Some variation can be seen in the last significant digit due to random noise. The overall absolute accuracy is ~2%. However, the ability to calculate third derivatives (to simulate electroreflectance data) suggests that the precision or relative accuracy is significantly better than that.

The ellipsometric measurements of Viña *et al.* [6] reported the ε_1 and ε_2 values for seven values of x: 0, 0.2, 0.43, 0.76, 0.86, 0.91, and 1.0. The samples were grown by the traveling-heater method using Te as a solvent, and sample surfaces were prepared using a chemomechanical polish of Br_2/CH_3OH. ε_1 and ε_2 were measured in the 5.5–1.7 eV energy region. Large figures provided by Cardona [8] were digitized using an electronic digitizer, the n and k values were computed, and they are displayed in Table III for all except the $x = 0.2$ sample. The digitization error in ε_1 and ε_2 is expected to be $\pm 1\%$ or ± 0.02, whichever is greater. The worst errors are likely to occur in the vicinity of the zero crossing of ε_1 and at the smallest values of k. Values for the endpoint binaries, HgTe and CdTe, are included for completeness as well as to provide the reader with a standard of comparison. The numerical procedures for correcting the data for the presence of the α-Te overlayer has been discussed by Aspnes and Arwin [9] and may be carried out where warranted.

For HgTe, the n and k values presented in Table III agree with those in Table II to better than ~3%, except for the k values at the lowest energies, which deviate by ~10%. The CdTe values, on the other hand, display a maximum deviation of ~10% for both n and k. In addition, a comparison of the values of Viña *et al.* [6] with those obtained from Arwin *et al.* [10] that were not corrected for the presence of the surface α-Te layer indicates a deviation of only ~5%, half of that for the previous comparison. Hence, at least part of the disagreement between the values quoted in Table II and III is probably due to the ~7 Å-thick surface α-Te layer. The n and k values in Table III are both more accurate for HgTe than for CdTe. For x values of 0.43, 0.76, 0.86, and 0.91, the values presented in Table III are likely to be reliable to better than ~3% for the low-x value; however, the error for the high-x samples may be as high as ~10% in the worst case.

The first scanning ellipsometric measurements for HgTe were reported by Moritani *et al.* [11]. Their uncorrected n and k values deviate approximately 10% from those in Table II; the corrections attempted by them to account for a thin overlayer actually make the deviation much larger. The n and k values for CdTe were compiled earlier by Palik [4]. The values for the 1.5–4.9 eV range were obtained from the ellipsometric results of Marple and Ehrenreich [12] and the reflection and transmission investigation of Myers *et al.* [13]. Marple and Ehrenreich's [12] results agree to within ~3% of those in Table II for n in the near-infrared and visible range of 1.5–3.2 eV but deviate by as much as 15% in the higher energy ultraviolet region, that is, 3.2–4.9 eV; the opposite seems to hold for k, with the UV values agreeing to better than ~10% but deviating much more for the visible and near IR. Both the n and k values of Myers *et al.* fall within 10% of those of Table II.

Single-wavelength measurements of ε_1 and ε_2 have been reported by Korsak *et al.* [14] for the He–Ne laser wavelength of 0.6328 μm for the

following x values: 0, ~0.16, 0.2, ~0.29, ~0.65, and 1.0. These measurements were conducted using ellipsometry with chemomechanically polished samples; allowance was made for a naturally occurring native-oxide layer. The graphs presented in the paper were digitized and n and k values calculated for all but the $x = 0.2$ sample, whose values were quoted in the paper; they are presented in Table IV. The n values, where a direct comparison could be made, agree to better than ~3% with those in Table II; the k values for the endpoint binaries, HgTe and CdTe, agree within ~10%, but those for the alloys indicate large differences, being greater than a factor of two for $x = 0.29$.

The dominant shape of the variation of ε_1 and ε_2 with the energy is determined by transitions between the various electronic bands. The main spectroscopic features in the 6–1.5 eV range are labeled E_1, $E_1 + \Delta_1$ and E_2. The variation of these transitions with the Cd mole fraction, x, have been investigated by Viña *et al.* [6] and are reproduced below:

$$E_1\,(\text{eV}) = (2.147 \pm 0.005) + (0.44 \pm 0.02)x + (0.7 \pm 0.1)x^2 \tag{6}$$

$$E_1 + \Delta_1\,(\text{eV}) = (2.778 \pm 0.005) + (0.47 \pm 0.02)x + (0.6 \pm 0.1)x^2 \tag{7}$$

$$E_2\,(\text{eV}) = \pm(4.468 \pm 0.003) + (0.66 \pm 0.01)x - (0.06 \pm 0.08)x^2. \tag{8}$$

The E_2 feature has been shown to comprise four transitions [5]. However, these can be resolved only in the derivative spectra [5] and not directly in the shape of ε_1 and ε_2.

Reflectivity measurements have been conducted for both the endpoint binaries and the alloy for energies above 6 eV, but no published results of Kramers–Kronig analysis exists. As noted earlier, the driving force behind the reflectivity measurements was the understanding of the electronic band structure, and hence the photometric accuracy of the results is less than that required to extract reliable n and k values. However, a short review of the reflectivity analysis is presented in the interest of completeness.

Room-temperature reflectivity measurements up to 22 eV have been reported by Cardona and Greenaway [15]. The measurements were performed on cleaved bulk crystals of CdTe and HgTe; the difficulty of obtaining crystals that were of sufficient size and flatness in the case of HgTe led to an error that could be as large ±10%. Shay and Spicer [16] have reported reflectivity measurements on CdTe in the 6–10 eV range. Low-temperature reflectivity for HgTe and CdTe measured at 10 and 15 K, respectively, in the 2.5–8 eV range has been published by Chadi *et al.* [17]. For the alloy, reflectivity measurements have been performed by Rodzik and Kisiel [18] in the energy range of 2–8.5 eV for the following thirteen alloy x values: 0, 0.02, 0.04, 0.095, 0.12, 0.155, 0.35, 0.37, 0.47, 0.5, 0.58,

0.62, and 1.0; the measurements were conducted in the 115–300 K temperature range, and the temperature coefficients of the various critical-point energies were computed.

The Band-Edge and Subband-Gap Region (~1.5 E_g–0.1 eV)

The energy region in the vicinity of the direct gap has, by far, commanded the most attention due to its obvious importance in electro-optic device applications. The dependence of the energy gap, E_g, on the alloy composition x has been reviewed by Hansen *et al.* [19], and more recently by Seiler *et al.* [20]. The relationship between E_g and x from Ref. [19], which is valid for the entire range of x for the temperature range 4.2–300 K, is given below:

$$E_g(x) = -0.302 + 1.93x + 5.35(1-2x)(10^{-4})T - 0.81x^2 + 0.832x^3. \quad (9)$$

The standard error in the calculation was estimated to be 0.013 eV [19]. A modification of the above equation that more accurately represents $E_g(x)$ for $0.2 \leqslant x \leqslant 0.3$ for low temperatures has been proposed in Ref. [20] and is shown below:

$$E_g(x) = -0.302 + 1.93x + 5.35(1-2x)(10^{-4})[(-1822 + T^3)/(255.2 + T^2)]$$
$$- 0.81x^2 + 0.832x^3. \quad (10)$$

A large number of infrared absorption measurements have been reported for the alloy beginning with the first report by Lawson *et al.* [1]. This review is limited to the more recent efforts, particularly those that report n and k and those for which a reasonable estimate of n can be carried out using the interpolation procedure described in the next section.

Many of the infrared optical studies in $Hg_{1-x}Cd_xTe$ have been limited to an analysis of the details of the absorption mechanisms and consequently report only the absorption coefficient, $\alpha(E)$. Fortunately, however, some exceptions exist. Kucera [21] has measured the value of n in the subband-gap energy region extending down to ~0.045 eV for x values of 0.18, 0.292, 0.39, 0.397, 0.459, 0.461, 0.522, and 1.0 at 80 and 300 K using the spacing of the interference fringes. Samples used in the study were grown using the Bridgman technique and annealed in Hg vapor to produce n-type conductivity except for the endpoint binary, CdTe, which was p-type and grown using a directional-freezing procedure. The observed n values at 300 K

were computer-fitted to the Sellmeier form with two resonances as shown:

$$n^2(\lambda) = a_0 + a_1/(1-(a_2/\lambda)^2) + a_3/(1-(a_4/\lambda)^2), \tag{11}$$

where λ is the wavelength in μm.

The parameters determined from the computer fit are presented in Table V. An interpolation procedure was also established to express the empirical x dependence of each of the parameters in Eq. 12 as shown below:

$$a_i = A_i + B_i x + C_i x^2. \tag{12}$$

The values of A_i, B_i, and C_i determined from a computer fit are presented in Table VI. In addition, Kucera [21] has measured the dispersion of n at 80 K and analyzed both the 80 and 300 K data using the semiempirical theory of Pikhtin and Yaskov [22]. Jensen and Torabi [23] have calculated the value of n from first principles for the whole alloy range, $0 \leqslant x \leqslant 1$. The calculations agree with the interpolated values of Kucera [21] to within ~3% for both high x values and low energies but deviate by 10% for energies close to the band gap for the low x alloys. The reader is referred to Refs. [21–23] for further details.

The behavior of n and k has been investigated by Finkman and Nemirovsky [24] for $0.205 \leqslant x \leqslant 0.220$ and by Finkman and Schacham [25] for $x = 0.29$ and 1.0. The refractive index was established using the interference fringes at energies below E_g, and the absorption coefficient in the vicinity of E_g was measured using straightforward reflection and transmission studies. The samples used were grown using the solid-state recrystallization method or the Bridgman technique and were n-type with carrier concentrations in the range of 1×10^{15} to 3×10^{15} cm^{-3} and mobilities in the range of 0.3×10^5 to 1×10^5 cm^2/Vs; the CdTe sample was semi-insulating. The x value was measured to an accuracy of better than ± 0.005.

The values of n were computer-fitted to a modified Sellmeier form with a λ^2 and a λ^4 correction term as shown below:

$$n^2(\lambda) = a_0 + a_1/(1-(a_2/\lambda)^2) + c\lambda^2 + d\lambda^4, \tag{13}$$

where λ is the wavelength in μm. The values of the parameters a_0, a_1, a_2, c, and d for $x = 0.205$, 0.29, and 1 are presented in Table V. The authors estimate the error in Eq. 13 to be less than ±2% and ±0.5%, respectively, for the absolute and relative values. The change in n when the temperature was reduced from 300 K to 80 K is estimated to be less than 3% [24, 25]. A comparison between the values reported by Finkman and Schacham [25]

and those obtained from Kucera [21] for $x = 0.29$ shows that the latter is systematically lower by ~1% for energies up to $\sim 0.75E_g$, above which it is lower by as much as 3%.

The dispersion of n is less than ±1% for the energy range $\sim 0.75E_g \leqslant E \leqslant 0.1$ eV for $0.29 \leqslant x \leqslant 0.522$ and for the energy range $\sim 0.5E_g \leqslant E \leqslant 0.1$ eV for CdTe. Hence, a consideration of the mean value of n in this region, namely n_{av}, is appropriate. A computation of n using the results from Refs. [21] and [25] and a computer fit, with the condition that the variation with x be monotonic, leads to the following simple empirical relationship:

$$n_{av} = 2.65 + 1.17(1-x)^2 \qquad 0.29 \leqslant x \leqslant 1. \tag{14}$$

The estimated errors are approximately ±2%. Values calculated using Eq. 14 for x ranging from 0.3–1 are displayed in Table VII; these values are lower by 5–8% than $\sqrt{\varepsilon_\infty}$ determined from the far-infrared measurements of Baars and Sorger [26].

Absorption measurements for HgTe, the endpoint binary, which is semimetallic with a band gap of ~ -0.3 eV, have been reported by Szuszkiewicz [27] in the 0.05–0.625 eV region. Optical measurements were conducted at 10 K using thin sample plates 10 μm thick, obtained by crystallization of HgTe on an Hg solution. The samples were further thinned using chemical etching. Figures provided in Ref. [27] were digitized, and the k values calculated are displayed in Table VIII; a constant value of 3.74 was assumed for n in calculating the absorption coefficient from the measured reflection and transmission spectra.

The absorption coefficient, $\alpha(E)$, in the vicinity of E_g was also studied by Finkman and Nemirovsky [24], Finkman and Schacham [25], and Schacham and Finkman [28] in the temperature range of ~85–300 K for the same samples used for determining n. The behavior of $\alpha(E)$ below the band gap was described by a modified form of the Urbach rule [24, 25] as shown:

$$\alpha(E) = \alpha_0 \exp[\sigma(E - E_0)/w] \tag{15}$$

$$w = T + T_0. \tag{16}$$

T is the lattice temperature of the specimen, and the parameters α_0, σ, E_0, and T_0 were determined using a computer fit to the measured $\alpha(E)$. For $x = 0.205$, the values of α_0, σ, E_0, and T_0 are 4×10^{-5} cm^{-1}; 5.65 K/cm^{-1}; 263.3 cm^{-1}, and 80.5 K, respectively [24]. A simultaneous computer fit to

two samples with $x = 0.215$ and 0.29 led to the following empirical dependence of the various parameters on the alloy composition, x [25]:

$$\alpha_0 = \exp(53.61.x - 18.88) \tag{17a}$$

$$E_0\,(\text{eV}) = 1.838.x - 0.3434\ \text{eV} \tag{17b}$$

$$\sigma(K/\text{eV}) = 3.267 \times 10^4 (1+x) K/\text{eV} \tag{17c}$$

$$T_0(K) = 81.9K. \tag{17d}$$

At energy values exceeding the band gap, direct optical transitions will occur between the valence and conduction bands. The large values of $\alpha(E)$ exceeding $10^3\,\text{cm}^{-1}$ require the use of very thin samples, and hence, relatively few results have been reported [28, 30]. However, Schacham and Finkman [28] have established the following approximate simple relationship to describe the behavior of $\alpha(E)$:

$$\alpha(E) = \beta(E - E_g)^{1/2} \tag{18a}$$

$$\beta = 2.109 \times 10^5 [(1+x)/(T+81.9)] \tag{18b}$$

with the band gap, E_g, being defined as that energy at which $\alpha(E) = 500\,\text{cm}^{-1}$ with Eq. 18a valid for $\alpha(E) > 800\,\text{cm}^{-1}$. The estimated values compared favorably for $E_g = 0.15$ eV with the theoretical calculation based on the Kane model by Anderson [29]. The values of E_g from $\alpha(E) = 500\,\text{cm}^{-1}$ deviate by ~10 meV from those calculated using Eq. 9 [25]. The values of $\alpha(E)$, and hence k, were calculated for $x = 0.205$ and 0.29 using the appropriate parameter values for the Urbach region and estimated for the band-to-band region up to $1.5E_g$ using the relationship shown in Eq. 18a. These k values along with the value of n for $x = 0.205$ and $x = 0.29$ are displayed in Tables IX and X, respectively, for temperatures of ~80 and 300 K; the values of E_g given in Refs. [24, 25] are indicated in the tables.

In the case of p-type samples and samples at high temperatures with a significant hole density, the intervalence-band transitions between the light- and the heavy-hole bands will cause additional absorption and hence a larger value of k. The values of k for $E \geqslant E_g$ and n are not likely to be affected significantly. Mroczkowski and Nelson [31] and Mroczkowski *et al.* [32] have reported $\alpha(E)$ for p-type samples with x values of 0.2 and 0.3 and acceptor density in the range of 1.2×10^{17} to $2.8 \times 10^{17}\,\text{cm}^{-3}$. Bulk samples grown using a quench-anneal process were thinned and transmission and reflection measurements made to establish the absorption

coefficient. Figures provided in Ref. [31] were digitized and interpolated to determine the appropriate values of k; they are presented in Tables IX and X for $x=0.2$ and 0.3, respectively. For energies below the fundamental gap, E_g, the k values in p-type samples are significantly larger than those in n-type samples.

Chu *et al.* [30] have also reported $\alpha(E)$ results for the $x=0.2$ value at 300 K. Compared with the values from Ref. [24], their values of $\alpha(E)$, and hence k, are twice as large for $E>E_g$ and nearly an order of magnitude greater at 0.12 eV. The lack of well-defined standards for measuring x and E_g as well as sample differences make it difficult to explain the disagreement. However, the k values presented in Tables IX and X are probably reliable only up to a factor of two. As indicated earlier, a comparison between the n values reported by Finkman and Schacham [25] and those obtained from Kucera [21] for $x=0.29$ shows that the latter is systematically lower by ~1% for energies up to $\sim 0.75E_g$, above which it is lower by as much as 3%.

The absorption behavior for $E \leqslant E_g$ can also be affected significantly by other sample-dependent properties: the presence of a large density of free electrons will affect the band edge through the Burstein–Moss shift [33], which is particularly important in small-band-gap $Hg_{1-x}Cd_xTe$. Chu *et al.* [33] have investigated the influence of the Burstein–Moss effect in samples with $0.165 \leqslant x \leqslant 0.194$ and electron density in the range of 0.4×10^{17} to $7 \times 10^{17}\ cm^{-3}$. For energies lower than E_g, free-carrier absorption will also play a part as shown by Qian *et al.* [34]; their absorption coefficient for a sample with $x=0.19$ and free-electron density of $7 \times 10^{17}\ cm^{-3}$ and impurity density of $3.4 \times 10^{18}\ cm^{-3}$ ranged from ~30 to ~200 cm^{-1} in the 9–15 μm wavelength region. Optical transitions between energy levels associated with impurity levels may also influence the k values in the subband-gap region.

The n values are not likely to change significantly with the electronic properties. For high temperatures approaching 300 K and above, the intrinsic carriers are likely to dominate [2], and hence, the optical absorption will be influenced by both the Burstein–Moss effect and the intervalence-band mechanisms.

The n and k values obtained at 300 K for $x=0.443$ are presented in Table XI. The k values were obtained by digitizing the appropriate $\alpha(E)$ curve provided in Ref. [30], and the value of n was calculated using the interpolation procedure established by Kucera [21].

Far-Infrared and Reststrahlen Region (0.05–0.0001 eV)

The optical behavior in the far-infrared (FIR) and reststrahlen region is determined by the lattice oscillations, free-carrier properties, impurity transitions, and band-to-band transitions in the narrow-gap alloys. Of these, the free-carrier and impurity-related behavior are extrinsic and can

vary significantly from sample to sample. Hence, the optical constants reported are confined to those determined at low temperatures using reflection spectroscopy, where the free-carrier and impurity contributions are expected to be small. Methods of estimating the free-carrier contribution and references to both free-carrier and impurity-related FIR investigations are provided for further information.

The FIR reflectivity spectrum of HgTe was studied by Grynberg *et al.* [35] in the frequency range extending from 80–250 cm^{-1} at temperatures ranging from 8–300 K. The samples were crystalline slabs, approximately 60 μm in thickness and were fabricated using liquid-phase deposition by slow cooling of Te in an Hg bath. At 4.2 K the samples were *n*-type with free-carrier densities and mobilities of $\sim 6 \times 10^{15}$ cm^{-3} and $\sim 6 \times 10^{5}$ cm^2/Vs, respectively. The dielectric function was determined using the Kramers–Kronig (K–K) analysis. The low-temperature values of n and k reported in Table XII were determined from digitized values of the $\mathrm{Im}(\varepsilon)$ and $\mathrm{Im}(-1/\varepsilon)$ curves presented in Ref. [35]. The approximate positions of the zeros in $\mathrm{Re}(\varepsilon)$ were estimated from the theory and the values of various parameters provided in Ref. [35]. The limited accuracy available in the procedure described confines the range of n and k to 110–161 cm^{-1} which overlaps the reststrahlen region extending from the transverse optical (TO) phonon frequency at ~ 118 cm^{-1} to the longitudinal optical (LO) phonon frequency at ~ 139 cm^{-1} [36]. Grynberg *et al.* have described the FIR behavior using a model of $\varepsilon(\omega)$ that accounts for the band-to-band transitions in addition to the well-known free-carrier and lattice-oscillation contributions. The functional form of the latter two are discussed in the following paragraphs.

The FIR reflectivity spectrum measured at a temperature of ~5 K and the associated K–K analysis results for *n*- and *p*-type samples with $x \simeq 0.21$ have recently been reported by Amirtharaj *et al.* [37]. The samples were grown using the solid-state recrystallization method, which usually yields *p*-type crystals; conversion to *n*-type was induced using an Hg vapor annealing procedure. The free-carrier densities were $\sim 4 \times 10^{17}$ and 3×10^{14} cm^{-3} in the *p*- and *n*-type samples, respectively, at low temperatures. The reflectivity spectrum measured in the 10–400 cm^{-1} frequency range was analyzed using the K–K procedure to determine the optical constants n and k presented in Table XII. The large differences in the values of n and k between the *n*- and *p*-type samples are expected to be due to the presence of the hole plasma, intervalence-band transitions, as well as possible impurity transitions in the *p*-type samples.

In samples with a large value of x and low impurity and hole density, the band-to-band and intervalence band transitions as well as impurity-related transitions can be neglected. In this case, the FIR behavior can be satisfactorily described using the well-known classical form shown below [38]:

$$\varepsilon(\omega) = \varepsilon_\infty + \Sigma_j\{S_j(\omega_j)^2\}/\{(\omega_j)^2 - \omega^2 - i\omega\Gamma_j\} - (\omega_p)^2\varepsilon_\infty/\{\omega(\omega + i/\tau)\}, \quad (19)$$

where ω is the frequency and the lattice oscillations are treated as damped oscillators with strength S_j, frequency ω_j, and damping Γ_j, and ε_∞ is the value of $\varepsilon(\omega)$ at frequencies much larger than the lattice oscillations in the absence of free carriers. The last term describes the contribution of the free carriers, where ω_p is the plasma frequency and τ is the scattering time. ω_p and τ are related to the free carrier density, N, and mobility, μ, through the following relations:

$$\omega_p = 4\pi Ne^2/m^*\varepsilon_\infty \quad (20a)$$

$$\tau = \mu m^*/e, \quad (20b)$$

where m^* is the effective mass of the charge carrier and e its electronic charge.

Shen and Chu [39] have analyzed the FIR reflectivity of an $x = 0.45$ sample using the classical form of $\varepsilon(\omega)$ shown in Eq. 19. The reflection spectrum was measured at a temperature of 35 K in the frequency range of 50–210 cm^{-1}. Seven lattice oscillators with the following parameters were used to computer fit the spectrum with all the observed fine structure: ω_j, S_j, Γ_j,

(1) 110 cm^{-1}, 0.3, 10 cm^{-1}
(2) 123 cm^{-1}, 5.6, 2.8 cm^{-1}
(3) 134 cm^{-1}, 0.7, 9 cm^{-1}
(4) 141 cm^{-1}, 0.15, 6 cm^{-1}
(5) 149 cm^{-1}, 0.9, 4 cm^{-1}
(6) 153 cm^{-1}, 0.35, 6 cm^{-1}
(7) 157 cm^{-1}, 0.15, 4 cm^{-1}.

The 110 cm^{-1} feature has been assigned to a two-phonon process. The HgTe- and the CdTe-like TO phonons occur at 123 and 149 cm^{-1}, respectively. The fine structure in the measured spectrum described by the remaining oscillators has been tentatively assigned to originate in optically active vibrational modes of the various combinations of anions and cations in the alloy lattice. The value of ε_∞ needed to fit the measurements is ~16. The values of n and k determined using Eq. 19 and the parameters mentioned above are displayed in Table XIII along with $\sqrt{\varepsilon_\infty}$ reported by Baars and Sorger [26].

The values of n and k for alloy compositions where the band gap occurs above the FIR region can be estimated if the lattice-oscillator and free-

carrier parameters are known. The two main optical phonons, namely the CdTe- (TO_1 and LO_1) and the HgTe-like (TO_2 and LO_2) phonons, have been investigated using both FIR reflectivity and Raman scattering by many investigators [2, 26, 40–43]. The variation of the optical phonons with x, the Cd mole fraction, is nearly linear. The CdTe-like phonons, TO_1 and LO_1 converge to $\sim 152\ \text{cm}^{-1}$ as x approaches 0, which is the frequency of the local vibrational mode of Cd in HgTe; and the HgTe-like modes, TO_2 and LO_2, converge to $\sim 131\ \text{cm}^{-1}$ at $x = 1$, which is the gap mode related to Cd oscillations in HgTe [40]. Talwar and Vandevyer [40] have used a random-element isodisplacement model to describe the x dependence of the optical phonons, and the fitted values of the various parameters may be found in Ref. [40].

Absorption due to electronic transitions associated with impurities at energies below the reststrahlen region has been reported by Scott [44] and Dornhaus [45]. Impurity-related vibrational features have been investigated by Talwar and Vandevyer [40], and Shen and Chu [46] have measured low-frequency absorption and interpreted it as originating in impurity- and disorder-activated phonons.

Conclusion

The optical constants, n and k, of the semiconducting alloy, $Hg_{1-x}Cd_xTe$, have been reviewed. Since $Hg_{1-x}Cd_xTe$ has been known and investigated only since 1959, the relevant published literature is less extensive and thorough than that of Si and GaAs. However, the technological importance of $Hg_{1-x}Cd_xTe$ is well recognized, and hence, it is hoped that this review is timely and will be helpful to researchers as well as engineers who are mainly concerned with the design and production of electro-optic devices.

The values of n and k included have been confined to the more recent reports and those that are, in the author's opinion, more reliable. Although a reasonable effort was made to study and evaluate all the published literature, inadvertent omissions are possible, particularly with papers published in languages other than English. The lack of measurements in the 1.5 eV to $\sim 1.5\ E_g$ energy region is a significant absence and needs to be addressed.

ACKNOWLEDGMENTS

The author wishes to thank Dr. D. E. Aspnes of Bellcore, Redbank, N.J., U.S.A. for the electronic record of ε_1 and ε_2 data and Prof. M. Cardona of the Max Planck Institute,

Stuttgart, Germany, for the expanded figures from Ref. [6]. The assistance provided by Mr. E. Kelso of the U.S. Army Center for Night Vision and Electro-Optics with the literature search is gratefully acknowledged.

REFERENCES

1. W. D. Lawson, S. Nielsen, E. H. Putley, and A. S. Young, *J. Phys. Chem. Solids* **9**, 325 (1959).
2. R. Dornhaus and G. Nimtz, "Narrow-Gap Semiconductors, Springer Tracts in Modern Physics," (G. Hohler and E. A. Niekisch, eds.), Vol. 98, Springer-Verlag, Berlin, 119 (1983).
3. J. Brice and P. Capper, eds., "Properties of Mercury Cadmium Telluride," Inst. of Electrical Engineers, London, 1987.
4. E. D. Palik, in "Handbook of Optical Constants of Solids," (E. D. Palik, ed.), Academic Press, New York, 409 (1985).
5. H. Arwin and D. E. Aspnes, *J. Vac. Sci. Technol. A* **2**, 1316 (1984).
6. L. Viña, C. Umbach, M. Cardona, and L. Vodopyanov, *Phys. Rev. B* **29**, 6752 (1984).
7. D. E. Aspnes, private communication.
8. M. Cardona, private communication.
9. D. E. Aspnes and H. Arwin, *J. Vac. Sci. Technol. A* **2**, 1309 (1984).
10. H. Arwin, D. E. Aspnes, and D. R. Rhiger, *J. Appl. Phys.* **54**, 7132 (1983).
11. A. Moritani, H. Sekiya, K. Taniguchi, C. Hamaguchi, J. Nakai, and R. Makabe, *Jpn. J. Appl. Phys.* **10**, 1410 (1971).
12. D. T. F. Marple and H. Ehrenreich, *Phys. Rev. Lett.* **8**, 87 (1962).
13. T. H. Myers, S. W. Edwards, and J. F. Schetzina, *J. Appl. Phys.* **52**, 4231 (1981).
14. T. E. Korsak, N. P. Sysoeva, B. M. Ayupov, V. V. Antonov, A. V. Voltsekhovskii, and E. F. Tivota, *Sov. Phys. Semicond.* **19**, 222 (1985).
15. M. Cardona and D. L. Greenaway, *Phys. Rev.* **131**, 98 (1963).
16. J. L. Shay and W. E. Spicer, *Phys. Rev.* **161**, 799 (1967).
17. D. J. Chadi, J. P. Walter, M. L. Cohen, Y. Petroff, and M. Balkanski, *Phys. Rev.* **5**, 3058 (1972).
18. A. Rodzik and A. Kisiel, *J. Phys. C.* **16**, 203 (1983).
19. G. L. Hansen, J. L. Schmit, and T. N. Casselman, *J. Appl. Phys.* **53**, 7099 (1982).
20. D. G. Seiler, J. R. Lowney, C. L. Littler, and M. R. Loloee, *J. Vac. Sci. Technol. A.* **8**, 1237 (1990).
21. Z. Kucera, *Phys. Status Solidi (a)* **100**, 659 (1987).
22. A. N. Pikhtin and A. D. Yaskov, *Sov. Phys. Semicond.* **15**, 8 (1981). See also V. G. Sredin, *Sov. Phys. Semicond.* **17**, 328 (1983).
23. B. Jensen and A. Torabi, *J. Appl. Phys.* **54**, 5945 (1983). See also chapter by B. Jensen, this volume.
24. E. Finkman and Y. Nemirovsky, *J. Appl. Phys.* **50**, 4356 (1979).
25. E. Finkman and S. E. Schacham, *J. Appl. Phys.* **56**, 2896 (1984).
26. J. Baars and F. Sorger, *Solid State Commun.* **10**, 875 (1972). See also Ref. [2].
27. W. Szuszkiewicz, *Phys. Status Solidi (b)* **79**, 691 (1977).
28. S. E. Schacham and E. Finkman, *J. Appl. Phys.* **57**, 2001 (1985).
29. W. W. Anderson, *Infrared Phys.* **20**, 363 (1980).
30. J. Chu, S. Xu, H. Ji, W. Zhang, C. Shiwei, and R. Jiang, *Chinese J. Infrared Res.* **4**, 255 (1985).
31. J. A. Mroczkowski and D. A Nelson, *J. Appl. Phys.* **54**, 2041 (1983).
32. J. A. Mroczkowski, D. A. Nelson, R. Murosako, and P. H. Zimmermann, *J. Vac. Sci. Technol. A* **1**, 1756 (1983).
33. J. Chu, D. Qian, and D. Tang, *Physica Scripta* **T14**, 37 (1986).

34. D. Qian, W. Tang, J. Shen, J. Chu, and G. Zheng, *Solid State Commun.* **56**, 813 (1985).
35. M. Grynberg, R. Le Toullec, and M. Balkanski, *Phys. Rev. B* **9**, 517 (1974).
36. P. M. Amirtharaj, K. K. Tiong, P. Parayanthal, F. H. Pollak, and J. K. Furdyna, *J. Vac. Sci. Technol. A* **3**, 226 (1985).
37. P. M. Amirtharaj, N. K. Dhar, J. Baars, and H. Seelewind, *Semiconductor Sci. Technol.* **5**, S68 (1990).
38. S. Perkowitz, "Infrared and Millimeter Waves," (K. J. Button, ed.), Vol. 8, Academic Press, New York, 71 (1983).
39. X. C. Shen and J. H. Chu, *Acta Physica Sinica* **34**, 56 (1985).
40. D. N. Talwar and M. Vandevyer, *J. Appl. Phys.* **56**, 1601 (1984).
41. S. P. Kozyrev, L. D. Vodopyanov, and R. Triboulet, *Solid State Commun.* **45**, 383 (1983).
42. A. Ksendzov, F. H. Pollak, P. M. Amirtharaj, and J. A. Wilson, *Semiconductor Sci. Technol.* **5**, S78 (1990).
43. A. Lusson and J. Wagner, *Phys. Rev. B* **38**, 10064 (1988).
44. W. Scott, E. L. Stelzer and R. J. Hager, *J. Appl. Phys.* **47**, 1408 (1976).
45. R. Dornhaus, G. Nimtz, W. Schlabitz, and H. Burkhard, *Solid State Commun.* **17**, 837 (1975).
46. S. C. Shen and J. H. Chu, *Solid State Commun.* **48**, 1017 (1983).

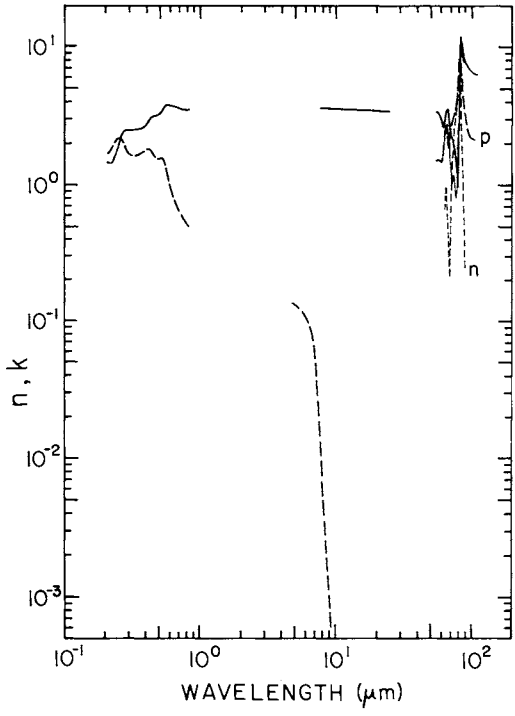

Fig. 1. Log–log plot of n (solid line) and k (dashed line) versus wavelength in μm are for $Hg_{1-x}Cd_xTe$ with $x=0.2$. The ultraviolet, visible, and near-infrared data are for $x=0.2$, n-type at room temperature. The IR data in the vicinity of E_g and lower energies are for $x\simeq 0.2$, n-type at room temperature. The far-infrared data are for $x=0.21$ at 5 K, n- and p-type. Free-carrier effects appear minimal in the n-type data.

TABLE I

Values of n and k of $Hg_{1-x}Cd_xTe$ – Synopsis of x values included in this review

x	UV, Visible and Near IR (6 - 1.5 eV)	Band Edge and Subband gap (~$1.5E_g$ - 0.1 eV)	Far Infrared and Reststrahlen (~0.05 - ~0.001 eV)
0	X	X	X
0.16	X[a]		
0.18		X[b]	
0.20	X	X	
0.205		X	
0.21			X
0.29	X	X	
0.292		X[b]	
0.3		X	
0.39		X[b]	
0.397		X[b]	
0.4		X[c]	
0.43	X		
0.443		X	
0.45			X
0.459		X[b]	
0.5		X[c]	
0.522		X[b]	
0.6		X[c]	
0.65	X[a]		
0.7		X[c]	
0.76	X		
0.8		X[c]	
0.86	X		
0.9		X[c]	
0.91	X		
1.0	X	X[c], Ref. [4]	Ref. [4]

[a] Measurements were made at the He-Ne laser wavelength of 0.6328 μm.
[b] n was measured in the subband gap region and computer fitted to the Sellmeier equation [21].
[c] Average values of n for the subband gap region ($0.75E_g$ to 0.1 eV) computed using an interpolation routine are presented.

TABLE II

Values of n and k for $Hg_{1-x}Cd_xTe$ (Ref. [5])

			x=0		0.20		0.29		1.0	
eV	cm^{-1}	μm	n	k	n	k	n	k	n	k
6.000	48395	0.2066	1.435	1.747	1.450	1.702	1.384	1.712	1.191	1.831
5.982	48249	0.2073	1.437	1.704	1.413	1.722	1.383	1.710	1.250	1.842
5.964	48103	0.2079	1.433	1.717	1.438	1.691	1.409	1.717	1.259	1.821
5.946	47958	0.2085	1.435	1.716	1.418	1.707	1.380	1.729	1.240	1.860
5.928	47812	0.2092	1.434	1.706	1.437	1.706	1.390	1.722	1.269	1.883
5.910	47666	0.2098	1.437	1.708	1.429	1.721	1.396	1.729	1.270	1.906
5.892	47520	0.2104	1.440	1.709	1.420	1.713	1.386	1.736	1.265	1.920
5.873	47375	0.2111	1.426	1.709	1.413	1.728	1.384	1.744	1.265	1.945
5.855	47229	0.2117	1.427	1.713	1.419	1.724	1.383	1.752	1.273	1.957
5.837	47083	0.2124	1.431	1.712	1.414	1.735	1.382	1.761	1.278	1.977
5.819	46937	0.2131	1.426	1.710	1.413	1.740	1.377	1.775	1.279	1.998
5.801	46791	0.2137	1.424	1.713	1.411	1.742	1.376	1.775	1.295	2.011
5.783	46646	0.2144	1.416	1.721	1.413	1.757	1.378	1.788	1.298	2.035
5.765	46500	0.2151	1.415	1.724	1.409	1.759	1.379	1.800	1.310	2.054
5.747	46354	0.2157	1.421	1.730	1.409	1.768	1.377	1.808	1.319	2.065
5.729	46208	0.2164	1.416	1.734	1.410	1.781	1.380	1.819	1.327	2.091
5.711	46063	0.2171	1.416	1.740	1.411	1.786	1.382	1.833	1.334	2.113
5.693	45917	0.2178	1.411	1.749	1.413	1.797	1.382	1.843	1.345	2.133
5.675	45771	0.2185	1.413	1.756	1.413	1.812	1.386	1.855	1.356	2.145
5.657	45625	0.2192	1.410	1.765	1.413	1.822	1.391	1.870	1.364	2.168
5.639	45480	0.2199	1.409	1.772	1.419	1.834	1.395	1.885	1.378	2.186
5.620	45334	0.2206	1.412	1.779	1.421	1.843	1.400	1.895	1.387	2.210
5.602	45188	0.2213	1.413	1.788	1.429	1.856	1.408	1.913	1.403	2.233
5.584	45042	0.2220	1.414	1.799	1.432	1.867	1.414	1.926	1.414	2.254
5.566	44896	0.2227	1.415	1.808	1.438	1.881	1.421	1.939	1.428	2.282
5.548	44751	0.2235	1.417	1.820	1.444	1.892	1.430	1.953	1.450	2.307
5.530	44605	0.2242	1.420	1.829	1.450	1.905	1.439	1.967	1.464	2.336
5.512	44459	0.2249	1.424	1.839	1.457	1.916	1.449	1.980	1.490	2.365
5.494	44313	0.2257	1.426	1.849	1.465	1.930	1.459	1.994	1.513	2.389
5.476	44168	0.2264	1.431	1.860	1.473	1.942	1.471	2.008	1.544	2.416
5.458	44022	0.2272	1.434	1.871	1.483	1.953	1.482	2.020	1.572	2.447
5.440	43876	0.2279	1.441	1.882	1.491	1.966	1.495	2.034	1.608	2.470
5.422	43730	0.2287	1.445	1.892	1.504	1.978	1.510	2.046	1.646	2.494
5.404	43585	0.2294	1.453	1.904	1.515	1.989	1.525	2.058	1.688	2.515
5.386	43439	0.2302	1.459	1.916	1.530	2.002	1.540	2.068	1.729	2.536
5.367	43293	0.2310	1.467	1.928	1.541	2.013	1.557	2.079	1.772	2.552
5.349	43147	0.2318	1.475	1.939	1.555	2.023	1.572	2.088	1.821	2.567
5.331	43001	0.2326	1.483	1.949	1.569	2.033	1.589	2.097	1.870	2.576
5.313	42856	0.2333	1.493	1.960	1.584	2.042	1.606	2.106	1.921	2.585
5.295	42710	0.2341	1.502	1.972	1.596	2.050	1.621	2.114	1.973	2.587
5.277	42564	0.2349	1.513	1.981	1.611	2.058	1.638	2.122	2.022	2.587
5.259	42418	0.2357	1.524	1.992	1.626	2.066	1.656	2.130	2.070	2.583
5.241	42273	0.2366	1.534	2.001	1.640	2.074	1.672	2.138	2.122	2.578
5.223	42127	0.2374	1.544	2.011	1.654	2.083	1.691	2.145	2.169	2.568

TABLE II (*Continued*)

			x=0		0.20		0.29		1.0	
eV	cm^{-1}	μm	n	k	n	k	n	k	n	k
5.205	41981	0.2382	1.555	2.019	1.668	2.090	1.707	2.152	2.217	2.556
5.187	41835	0.2390	1.566	2.029	1.683	2.098	1.726	2.158	2.264	2.542
5.169	41690	0.2399	1.577	2.037	1.699	2.106	1.745	2.166	2.310	2.525
5.151	41544	0.2407	1.587	2.047	1.715	2.113	1.764	2.172	2.356	2.507
5.133	41398	0.2416	1.598	2.057	1.731	2.120	1.783	2.176	2.400	2.483
5.114	41252	0.2424	1.610	2.067	1.749	2.128	1.802	2.181	2.446	2.458
5.096	41107	0.2433	1.622	2.079	1.766	2.136	1.822	2.185	2.487	2.430
5.078	40961	0.2441	1.635	2.089	1.785	2.142	1.842	2.188	2.527	2.399
5.060	40815	0.2450	1.649	2.101	1.803	2.149	1.862	2.191	2.562	2.362
5.042	40669	0.2459	1.664	2.112	1.822	2.153	1.882	2.194	2.598	2.325
5.024	40523	0.2468	1.680	2.123	1.843	2.157	1.903	2.196	2.627	2.285
5.006	40378	0.2477	1.697	2.134	1.862	2.164	1.923	2.198	2.655	2.242
4.988	40232	0.2486	1.715	2.145	1.881	2.166	1.943	2.200	2.675	2.201
4.970	40086	0.2495	1.734	2.154	1.902	2.170	1.965	2.201	2.692	2.160
4.952	39940	0.2504	1.754	2.162	1.922	2.173	1.987	2.201	2.704	2.116
4.934	39795	0.2513	1.774	2.171	1.942	2.175	2.008	2.202	2.714	2.076
4.916	39649	0.2522	1.795	2.177	1.964	2.177	2.031	2.202	2.721	2.038
4.898	39503	0.2531	1.817	2.184	1.985	2.178	2.054	2.201	2.724	2.002
4.880	39357	0.2541	1.838	2.188	2.007	2.179	2.077	2.199	2.725	1.966
4.861	39212	0.2550	1.860	2.193	2.029	2.180	2.100	2.197	2.723	1.936
4.843	39066	0.2560	1.882	2.196	2.051	2.180	2.121	2.194	2.722	1.904
4.825	38920	0.2569	1.904	2.199	2.074	2.179	2.146	2.190	2.718	1.875
4.807	38774	0.2579	1.926	2.201	2.097	2.177	2.169	2.185	2.713	1.849
4.789	38628	0.2589	1.949	2.203	2.121	2.174	2.194	2.180	2.709	1.825
4.771	38483	0.2599	1.971	2.204	2.144	2.170	2.218	2.173	2.702	1.802
4.753	38337	0.2608	1.994	2.203	2.168	2.166	2.243	2.164	2.696	1.780
4.735	38191	0.2618	2.017	2.202	2.191	2.160	2.267	2.155	2.689	1.762
4.717	38045	0.2628	2.041	2.201	2.215	2.153	2.291	2.145	2.681	1.742
4.699	37900	0.2639	2.065	2.198	2.239	2.145	2.315	2.132	2.675	1.725
4.681	37754	0.2649	2.088	2.194	2.262	2.136	2.338	2.117	2.668	1.710
4.663	37608	0.2659	2.111	2.189	2.286	2.125	2.361	2.101	2.659	1.696
4.645	37462	0.2669	2.135	2.183	2.309	2.114	2.381	2.084	2.653	1.682
4.627	37317	0.2680	2.158	2.177	2.332	2.101	2.400	2.066	2.645	1.670
4.608	37171	0.2690	2.180	2.169	2.353	2.086	2.418	2.047	2.638	1.659
4.590	37025	0.2701	2.203	2.161	2.373	2.070	2.435	2.028	2.630	1.649
4.572	36879	0.2712	2.225	2.151	2.393	2.054	2.449	2.008	2.624	1.640
4.554	36733	0.2722	2.246	2.141	2.409	2.036	2.462	1.988	2.617	1.632
4.536	36588	0.2733	2.267	2.130	2.427	2.018	2.475	1.969	2.611	1.625
4.518	36442	0.2744	2.287	2.117	2.441	1.999	2.485	1.948	2.604	1.619
4.500	36296	0.2755	2.307	2.104	2.454	1.980	2.494	1.928	2.598	1.613
4.482	36150	0.2766	2.325	2.089	2.466	1.961	2.502	1.908	2.592	1.608
4.464	36005	0.2777	2.343	2.075	2.477	1.942	2.508	1.888	2.586	1.605
4.446	35859	0.2789	2.360	2.059	2.487	1.923	2.513	1.870	2.582	1.602
4.428	35713	0.2800	2.375	2.043	2.495	1.904	2.517	1.852	2.576	1.599
4.410	35567	0.2812	2.388	2.026	2.503	1.886	2.519	1.835	2.571	1.596
4.392	35422	0.2823	2.401	2.009	2.508	1.867	2.520	1.818	2.566	1.596

TABLE II (*Continued*)

			x=0		0.20		0.29		1.0	
eV	cm^{-1}	μm	n	k	n	k	n	k	n	k
4.373	35276	0.2835	2.413	1.992	2.513	1.849	2.521	1.803	2.562	1.595
4.355	35130	0.2847	2.423	1.975	2.517	1.831	2.521	1.789	2.558	1.596
4.337	34984	0.2858	2.433	1.959	2.519	1.814	2.522	1.775	2.555	1.596
4.319	34839	0.2870	2.441	1.942	2.521	1.798	2.521	1.762	2.551	1.598
4.301	34693	0.2882	2.449	1.926	2.521	1.783	2.521	1.751	2.548	1.600
4.283	34547	0.2895	2.456	1.910	2.521	1.768	2.520	1.740	2.546	1.603
4.265	34401	0.2907	2.462	1.894	2.521	1.756	2.520	1.729	2.543	1.607
4.247	34255	0.2919	2.467	1.879	2.519	1.743	2.519	1.719	2.541	1.612
4.229	34110	0.2932	2.472	1.864	2.518	1.732	2.519	1.710	2.539	1.617
4.211	33964	0.2944	2.475	1.848	2.517	1.722	2.518	1.701	2.539	1.623
4.193	33818	0.2957	2.478	1.834	2.516	1.712	2.518	1.693	2.538	1.630
4.175	33672	0.2970	2.479	1.820	2.514	1.703	2.516	1.685	2.538	1.638
4.157	33527	0.2983	2.481	1.807	2.513	1.695	2.516	1.678	2.537	1.647
4.139	33381	0.2996	2.481	1.794	2.512	1.687	2.515	1.671	2.537	1.658
4.120	33235	0.3009	2.481	1.782	2.511	1.680	2.514	1.664	2.538	1.670
4.102	33089	0.3022	2.480	1.771	2.510	1.673	2.514	1.658	2.540	1.685
4.084	32944	0.3035	2.479	1.761	2.509	1.666	2.513	1.653	2.543	1.703
4.066	32798	0.3049	2.478	1.752	2.508	1.661	2.513	1.647	2.548	1.724
4.048	32652	0.3063	2.476	1.744	2.507	1.655	2.512	1.642	2.557	1.748
4.030	32506	0.3076	2.475	1.736	2.506	1.650	2.512	1.638	2.571	1.776
4.012	32360	0.3090	2.474	1.729	2.506	1.645	2.511	1.634	2.593	1.806
3.994	32215	0.3104	2.473	1.722	2.505	1.641	2.510	1.630	2.624	1.834
3.976	32069	0.3118	2.471	1.716	2.504	1.637	2.511	1.626	2.665	1.859
3.958	31923	0.3133	2.470	1.711	2.503	1.633	2.510	1.622	2.715	1.876
3.940	31777	0.3147	2.470	1.706	2.503	1.629	2.510	1.619	2.768	1.881
3.922	31632	0.3161	2.469	1.701	2.502	1.626	2.510	1.617	2.822	1.875
3.904	31486	0.3176	2.468	1.697	2.502	1.623	2.510	1.614	2.873	1.860
3.886	31340	0.3191	2.468	1.693	2.502	1.621	2.510	1.612	2.917	1.838
3.867	31194	0.3206	2.467	1.690	2.502	1.619	2.511	1.610	2.956	1.809
3.849	31049	0.3221	2.467	1.687	2.502	1.617	2.511	1.609	2.988	1.778
3.831	30903	0.3236	2.467	1.684	2.502	1.615	2.511	1.607	3.015	1.745
3.813	30757	0.3251	2.467	1.681	2.502	1.614	2.511	1.606	3.035	1.712
3.795	30611	0.3267	2.467	1.679	2.502	1.613	2.512	1.605	3.052	1.679
3.777	30465	0.3282	2.466	1.677	2.502	1.612	2.512	1.606	3.063	1.648
3.759	30320	0.3298	2.467	1.675	2.503	1.612	2.513	1.606	3.071	1.618
3.741	30174	0.3314	2.467	1.674	2.503	1.612	2.514	1.606	3.077	1.591
3.723	30028	0.3330	2.467	1.673	2.504	1.612	2.515	1.607	3.080	1.566
3.705	29882	0.3346	2.467	1.672	2.505	1.613	2.517	1.608	3.082	1.542
3.687	29737	0.3363	2.468	1.672	2.506	1.614	2.518	1.609	3.081	1.521
3.669	29591	0.3379	2.469	1.671	2.508	1.614	2.520	1.611	3.080	1.503
3.651	29445	0.3396	2.470	1.671	2.509	1.616	2.522	1.613	3.077	1.486
3.633	29299	0.3413	2.470	1.671	2.511	1.617	2.525	1.615	3.074	1.472
3.614	29154	0.3430	2.472	1.672	2.513	1.619	2.527	1.617	3.070	1.459
3.596	29008	0.3447	2.473	1.673	2.515	1.621	2.530	1.619	3.066	1.448
3.578	28862	0.3465	2.474	1.674	2.517	1.624	2.533	1.622	3.060	1.439
3.560	28716	0.3482	2.476	1.675	2.519	1.626	2.536	1.625	3.054	1.434

TABLE II (*Continued*)

			x=0		0.20		0.29		1.0	
eV	cm^{-1}	μm	n	k	n	k	n	k	n	k
3.542	28570	0.3500	2.478	1.677	2.522	1.629	2.540	1.629	3.047	1.430
3.524	28425	0.3518	2.480	1.679	2.525	1.633	2.544	1.632	3.040	1.430
3.506	28279	0.3536	2.481	1.681	2.529	1.636	2.548	1.636	3.032	1.434
3.488	28133	0.3555	2.484	1.683	2.532	1.640	2.553	1.640	3.023	1.445
3.470	27987	0.3573	2.487	1.686	2.536	1.644	2.557	1.645	3.016	1.463
3.452	27842	0.3592	2.489	1.689	2.540	1.648	2.563	1.649	3.013	1.490
3.434	27696	0.3611	2.492	1.692	2.545	1.652	2.568	1.654	3.019	1.528
3.416	27550	0.3630	2.495	1.696	2.549	1.657	2.574	1.659	3.040	1.575
3.398	27404	0.3649	2.499	1.699	2.555	1.662	2.580	1.665	3.085	1.626
3.380	27259	0.3669	2.502	1.703	2.560	1.667	2.587	1.670	3.158	1.667
3.361	27113	0.3688	2.506	1.707	2.566	1.673	2.595	1.676	3.251	1.683
3.343	26967	0.3708	2.510	1.712	2.572	1.679	2.603	1.682	3.350	1.668
3.325	26821	0.3728	2.515	1.716	2.579	1.685	2.612	1.689	3.441	1.625
3.307	26676	0.3749	2.520	1.722	2.586	1.691	2.621	1.696	3.515	1.561
3.289	26530	0.3769	2.525	1.727	2.594	1.697	2.630	1.703	3.569	1.489
3.271	26384	0.3790	2.530	1.732	2.602	1.704	2.641	1.710	3.605	1.416
3.253	26238	0.3811	2.536	1.738	2.610	1.711	2.652	1.717	3.627	1.345
3.235	26092	0.3833	2.542	1.743	2.620	1.718	2.664	1.725	3.639	1.277
3.217	25947	0.3854	2.548	1.750	2.630	1.726	2.676	1.732	3.643	1.213
3.199	25801	0.3876	2.555	1.756	2.640	1.733	2.691	1.741	3.641	1.154
3.181	25655	0.3898	2.563	1.763	2.652	1.742	2.706	1.749	3.634	1.101
3.163	25509	0.3920	2.570	1.770	2.664	1.750	2.723	1.758	3.625	1.051
3.145	25364	0.3943	2.578	1.777	2.677	1.759	2.741	1.766	3.613	1.007
3.127	25218	0.3965	2.587	1.784	2.691	1.767	2.761	1.774	3.600	0.9661
3.108	25072	0.3989	2.596	1.792	2.706	1.776	2.782	1.781	3.587	0.9297
3.090	24926	0.4012	2.606	1.800	2.722	1.785	2.806	1.788	3.572	0.8963
3.072	24781	0.4035	2.616	1.808	2.740	1.794	2.832	1.793	3.558	0.8639
3.054	24635	0.4059	2.627	1.816	2.759	1.804	2.861	1.795	3.543	0.8345
3.036	24489	0.4083	2.639	1.825	2.781	1.813	2.891	1.795	3.528	0.8078
3.018	24343	0.4108	2.651	1.834	2.804	1.822	2.922	1.790	3.513	0.7819
3.000	24197	0.4133	2.664	1.844	2.831	1.829	2.953	1.782	3.498	0.7588
2.982	24052	0.4158	2.678	1.853	2.860	1.835	2.983	1.770	3.484	0.7362
2.964	23906	0.4183	2.694	1.863	2.891	1.838	3.010	1.756	3.470	0.7148
2.946	23760	0.4209	2.710	1.873	2.923	1.837	3.034	1.740	3.457	0.6955
2.928	23614	0.4235	2.727	1.883	2.957	1.833	3.056	1.722	3.444	0.6762
2.910	23469	0.4261	2.746	1.893	2.991	1.823	3.075	1.703	3.430	0.6589
2.892	23323	0.4288	2.768	1.904	3.023	1.810	3.091	1.684	3.418	0.6419
2.873	23177	0.4315	2.790	1.914	3.052	1.793	3.105	1.666	3.405	0.6252
2.855	23031	0.4342	2.816	1.924	3.078	1.774	3.118	1.648	3.393	0.6105
2.837	22886	0.4370	2.844	1.933	3.101	1.754	3.129	1.631	3.381	0.5956
2.819	22740	0.4398	2.874	1.940	3.120	1.734	3.138	1.616	3.369	0.5824
2.801	22594	0.4426	2.908	1.945	3.136	1.713	3.146	1.602	3.358	0.5690
2.783	22448	0.4455	2.945	1.946	3.150	1.694	3.154	1.589	3.347	0.5552
2.765	22302	0.4484	2.983	1.942	3.162	1.675	3.161	1.576	3.336	0.5428
2.747	22157	0.4513	3.020	1.932	3.172	1.658	3.167	1.566	3.326	0.5306
2.729	22011	0.4543	3.056	1.917	3.181	1.642	3.174	1.555	3.315	0.5192

TABLE II (*Continued*)

			x=0		0.20		0.29		1.0	
eV	cm^{-1}	μm	n	k	n	k	n	k	n	k
2.711	21865	0.4573	3.088	1.898	3.190	1.627	3.181	1.546	3.305	0.5089
2.693	21719	0.4604	3.115	1.877	3.197	1.613	3.187	1.539	3.296	0.4995
2.675	21574	0.4635	3.138	1.856	3.203	1.601	3.193	1.533	3.286	0.4895
2.657	21428	0.4667	3.159	1.833	3.210	1.590	3.201	1.527	3.276	0.4800
2.639	21282	0.4699	3.175	1.812	3.216	1.581	3.207	1.524	3.269	0.4702
2.620	21136	0.4731	3.190	1.791	3.222	1.572	3.216	1.520	3.259	0.4607
2.602	20991	0.4764	3.203	1.771	3.229	1.564	3.225	1.517	3.252	0.4507
2.584	20845	0.4797	3.214	1.753	3.236	1.558	3.236	1.515	3.243	0.4421
2.566	20699	0.4831	3.223	1.736	3.242	1.554	3.246	1.516	3.237	0.4337
2.548	20553	0.4865	3.231	1.721	3.251	1.549	3.259	1.517	3.230	0.4248
2.530	20407	0.4900	3.239	1.707	3.259	1.546	3.274	1.518	3.223	0.4169
2.512	20262	0.4935	3.245	1.695	3.268	1.545	3.290	1.522	3.217	0.4080
2.494	20116	0.4971	3.252	1.683	3.278	1.544	3.310	1.525	3.211	0.3978
2.476	19970	0.5007	3.259	1.674	3.290	1.545	3.333	1.530	3.204	0.3900
2.458	19824	0.5044	3.265	1.665	3.303	1.546	3.360	1.534	3.197	0.3789
2.440	19679	0.5082	3.272	1.658	3.318	1.549	3.393	1.537	3.190	0.3681
2.422	19533	0.5120	3.279	1.653	3.335	1.553	3.433	1.536	3.182	0.3574
2.404	19387	0.5158	3.287	1.647	3.355	1.558	3.479	1.529	3.174	0.3475
2.386	19241	0.5197	3.294	1.644	3.379	1.564	3.527	1.514	3.165	0.3390
2.367	19096	0.5237	3.303	1.641	3.407	1.570	3.576	1.487	3.157	0.3315
2.349	18950	0.5277	3.313	1.641	3.442	1.576	3.621	1.450	3.148	0.3244
2.331	18804	0.5318	3.324	1.640	3.485	1.579	3.658	1.406	3.139	0.3189
2.313	18658	0.5360	3.335	1.642	3.536	1.574	3.688	1.358	3.131	0.3134
2.295	18513	0.5402	3.349	1.645	3.591	1.559	3.709	1.309	3.123	0.3080
2.277	18367	0.5445	3.364	1.649	3.648	1.530	3.724	1.261	3.116	0.3024
2.259	18221	0.5488	3.382	1.653	3.699	1.488	3.733	1.213	3.108	0.2970
2.241	18075	0.5532	3.402	1.660	3.741	1.437	3.738	1.167	3.102	0.2917
2.223	17929	0.5577	3.425	1.668	3.772	1.383	3.739	1.125	3.095	0.2854
2.205	17784	0.5623	3.454	1.677	3.794	1.328	3.738	1.085	3.089	0.2813
2.187	17638	0.5670	3.488	1.687	3.808	1.275	3.734	1.047	3.083	0.2734
2.169	17492	0.5717	3.532	1.696	3.816	1.224	3.729	1.011	3.076	0.2708
2.151	17346	0.5765	3.586	1.700	3.819	1.175	3.722	0.9776	3.070	0.2682
2.133	17201	0.5814	3.650	1.694	3.818	1.131	3.714	0.9480	3.064	0.2651
2.114	17055	0.5863	3.719	1.670	3.814	1.090	3.706	0.9190	3.059	0.2608
2.096	16909	0.5914	3.785	1.626	3.809	1.050	3.696	0.8924	3.054	0.2600
2.078	16763	0.5965	3.838	1.569	3.803	1.014	3.688	0.8664	3.048	0.2576
2.060	16618	0.6018	3.876	1.507	3.795	0.9795	3.678	0.8430	3.044	0.2508
2.042	16472	0.6071	3.901	1.443	3.786	0.9476	3.669	0.8201	3.040	0.2497
2.024	16326	0.6125	3.917	1.382	3.776	0.9175	3.659	0.7979	3.035	0.2450
2.006	16180	0.6180	3.925	1.325	3.766	0.8887	3.649	0.7780	3.031	0.2403
1.988	16034	0.6237	3.929	1.272	3.756	0.8630	3.641	0.7573	3.027	0.2338
1.970	15889	0.6294	3.929	1.222	3.745	0.8380	3.631	0.7401	3.023	0.2314
1.952	15743	0.6352	3.924	1.176	3.735	0.8145	3.621	0.7218	3.019	0.2249
1.934	15597	0.6411	3.919	1.134	3.724	0.7936	3.612	0.7053	3.016	0.2201
1.916	15451	0.6472	3.911	1.094	3.714	0.7725	3.603	0.6901	3.013	0.2182
1.898	15306	0.6534	3.903	1.058	3.703	0.7530	3.594	0.6745	3.009	0.2186

TABLE II (*Continued*)

			x=0		0.20		0.29		1.0	
eV	cm^{-1}	μm	n	k	n	k	n	k	n	k
1.880	15160	0.6596	3.892	1.024	3.691	0.7356	3.584	0.6616	3.005	0.2171
1.861	15014	0.6660	3.882	0.9923	3.682	0.7181	3.576	0.6486	3.002	0.2144
1.843	14868	0.6726	3.870	0.9642	3.671	0.7025	3.566	0.6368	3.000	0.2138
1.825	14723	0.6792	3.860	0.9358	3.661	0.6860	3.558	0.6253	2.997	0.2109
1.807	14577	0.6860	3.848	0.9107	3.652	0.6733	3.550	0.6136	2.995	0.2085
1.789	14431	0.6930	3.837	0.8863	3.643	0.6568	3.541	0.6022	2.994	0.2025
1.771	14285	0.7000	3.826	0.8633	3.633	0.6429	3.534	0.5914	2.992	0.1972
1.753	14139	0.7072	3.815	0.8419	3.624	0.6307	3.527	0.5802	2.990	0.1984
1.735	13994	0.7146	3.805	0.8226	3.617	0.6157	3.520	0.5703	2.990	0.1908
1.717	13848	0.7221	3.795	0.8024	3.608	0.6026	3.514	0.5586	2.989	0.1865
1.699	13702	0.7298	3.786	0.7828	3.600	0.5915	3.508	0.5512	2.989	0.1808
1.681	13556	0.7377	3.776	0.7644	3.593	0.5792	3.500	0.5415	2.989	0.1780
1.663	13411	0.7457	3.767	0.7474	3.585	0.5691	3.498	0.5344	2.990	0.1747
1.645	13265	0.7539	3.756	0.7351	3.576	0.5594	3.491	0.5229	2.991	0.1718
1.627	13119	0.7622	3.747	0.7225	3.570	0.5502	3.484	0.5147	2.992	0.1727
1.608	12973	0.7708	3.738	0.7097	3.562	0.5423	3.478	0.5073	2.997	0.1761
1.590	12828	0.7796	3.729	0.6957	3.554	0.5344	3.473	0.5019	3.004	0.1650
1.572	12682	0.7885	3.719	0.6864	3.548	0.5273	3.465	0.4966	3.012	0.1578
1.554	12536	0.7977	3.711	0.6716	3.541	0.5197	3.462	0.4845	3.021	0.1506
1.536	12390	0.8071	3.702	0.6600	3.533	0.5062	3.451	0.4905	3.033	0.1249
1.518	12244	0.8167	3.691	0.6552	3.524	0.5078	3.446	0.4793	3.037	0.1475
1.500	12099	0.8265	3.685	0.6382	3.518	0.4999	3.442	0.4716	3.037	0.0998

TABLE III

Values of n and k for $Hg_{1-x}Cd_xTe$ (Ref. [6])

			x=0		0.43		0.76		0.86		0.91		1.0	
eV	cm^{-1}	μm	n	k	n	k	n	k	n	k	n	k	n	k
5.50	44362	0.2254	1.42	1.75	1.41	1.94	1.39	2.06	1.41	2.05	1.41	2.10	1.35	2.12
5.46	44039	0.2271	1.42	1.77	1.43	1.96	1.40	2.09	1.42	2.08	1.43	2.13	1.40	2.18
5.42	43717	0.2287	1.43	1.79	1.46	1.99	1.44	2.12	1.47	2.11	1.46	2.16	1.44	2.22
5.38	43394	0.2304	1.44	1.81	1.49	2.01	1.49	2.15	1.51	2.13	1.50	2.19	1.50	2.26
5.34	43071	0.2322	1.45	1.83	1.53	2.04	1.54	2.18	1.56	2.16	1.57	2.22	1.58	2.29
5.30	42749	0.2339	1.46	1.85	1.57	2.06	1.58	2.20	1.62	2.18	1.62	2.24	1.65	2.32
5.26	42426	0.2357	1.48	1.87	1.61	2.06	1.63	2.21	1.68	2.21	1.68	2.25	1.73	2.33
5.22	42104	0.2375	1.50	1.88	1.65	2.08	1.68	2.23	1.74	2.22	1.75	2.25	1.84	2.32
5.18	41781	0.2393	1.51	1.91	1.70	2.09	1.76	2.26	1.81	2.21	1.85	2.25	1.94	2.31
5.14	41458	0.2412	1.54	1.94	1.74	2.11	1.82	2.25	1.91	2.23	1.95	2.23	2.03	2.29
5.10	41136	0.2431	1.56	1.95	1.78	2.12	1.90	2.25	1.99	2.22	2.03	2.21	2.10	2.29
5.06	40813	0.2450	1.58	1.97	1.82	2.12	1.97	2.26	2.06	2.22	2.10	2.20	2.18	2.27
5.02	40490	0.2470	1.61	1.99	1.87	2.13	2.06	2.22	2.14	2.19	2.19	2.14	2.26	2.22
4.98	40168	0.2490	1.65	2.01	1.92	2.13	2.14	2.18	2.21	2.14	2.28	2.08	2.34	2.15
4.94	39845	0.2510	1.69	2.03	1.97	2.13	2.20	2.14	2.25	2.11	2.33	2.04	2.38	2.10
4.90	39523	0.2530	1.72	2.05	2.01	2.13	2.24	2.10	2.29	2.06	2.37	1.99	2.42	2.04
4.86	39200	0.2551	1.76	2.06	2.07	2.11	2.27	2.05	2.32	2.01	2.40	1.94	2.44	1.98
4.82	38877	0.2572	1.81	2.07	2.14	2.11	2.30	2.00	2.33	1.95	2.42	1.89	2.45	1.93
4.78	38555	0.2594	1.86	2.07	2.20	2.08	2.31	1.95	2.35	1.90	2.43	1.85	2.45	1.87
4.74	38232	0.2616	1.90	2.07	2.24	2.05	2.33	1.91	2.36	1.87	2.44	1.82	2.44	1.83
4.70	37909	0.2638	1.94	2.07	2.29	2.01	2.34	1.87	2.36	1.84	2.45	1.79	2.44	1.79
4.66	37587	0.2661	2.00	2.07	2.32	1.98	2.34	1.84	2.37	1.80	2.45	1.76	2.43	1.75
4.62	37264	0.2684	2.05	2.05	2.35	1.94	2.35	1.81	2.37	1.77	2.45	1.74	2.42	1.72
4.58	36941	0.2707	2.10	2.04	2.38	1.90	2.36	1.78	2.37	1.75	2.45	1.72	2.41	1.70
4.54	36619	0.2731	2.13	2.03	2.38	1.87	2.36	1.76	2.37	1.73	2.44	1.70	2.40	1.69
4.50	36296	0.2755	2.17	2.01	2.40	1.83	2.36	1.75	2.36	1.71	2.44	1.69	2.40	1.67
4.46	35974	0.2780	2.21	1.98	2.41	1.80	2.36	1.72	2.37	1.69	2.44	1.67	2.39	1.66
4.42	35651	0.2805	2.24	1.95	2.41	1.77	2.37	1.71	2.37	1.68	2.43	1.66	2.38	1.66
4.38	35328	0.2831	2.27	1.92	2.41	1.74	2.37	1.70	2.38	1.67	2.43	1.66	2.37	1.65
4.34	35006	0.2857	2.29	1.89	2.42	1.73	2.37	1.69	2.38	1.67	2.43	1.65	2.37	1.65
4.30	34683	0.2883	2.31	1.86	2.42	1.71	2.37	1.68	2.38	1.66	2.43	1.65	2.36	1.65
4.26	34360	0.2910	2.33	1.83	2.42	1.69	2.38	1.67	2.39	1.66	2.43	1.66	2.36	1.66
4.22	34038	0.2938	2.34	1.81	2.42	1.67	2.38	1.66	2.39	1.65	2.44	1.66	2.36	1.67
4.18	33715	0.2966	2.35	1.78	2.42	1.67	2.38	1.66	2.40	1.65	2.44	1.66	2.35	1.68
4.14	33392	0.2995	2.35	1.76	2.42	1.66	2.38	1.66	2.40	1.65	2.44	1.67	2.35	1.69
4.10	33070	0.3024	2.35	1.73	2.43	1.65	2.39	1.66	2.41	1.65	2.45	1.68	2.34	1.72
4.06	32747	0.3054	2.35	1.71	2.43	1.64	2.40	1.66	2.42	1.66	2.47	1.69	2.35	1.76
4.02	32425	0.3084	2.35	1.70	2.43	1.64	2.40	1.66	2.42	1.66	2.48	1.70	2.36	1.79
3.98	32102	0.3115	2.35	1.68	2.43	1.63	2.41	1.66	2.43	1.67	2.49	1.72	2.39	1.85
3.94	31779	0.3147	2.35	1.67	2.43	1.63	2.42	1.66	2.45	1.67	2.51	1.73	2.51	1.89
3.90	31457	0.3179	2.35	1.66	2.44	1.62	2.43	1.67	2.47	1.68	2.56	1.74	2.66	1.90
3.86	31134	0.3212	2.36	1.66	2.44	1.62	2.45	1.67	2.49	1.69	2.60	1.76	2.75	1.88
3.82	30811	0.3246	2.36	1.65	2.44	1.62	2.46	1.68	2.51	1.70	2.63	1.77	2.82	1.84
3.78	30489	0.3280	2.36	1.65	2.45	1.62	2.48	1.68	2.53	1.71	2.68	1.78	2.87	1.79

TABLE III (*Continued*)

			x=0		0.43		0.76		0.86		0.91		1.0	
eV	cm^{-1}	μm	n	k	n	k	n	k	n	k	n	k	n	k
3.74	30166	0.3315	2.36	1.65	2.45	1.62	2.50	1.69	2.56	1.72	2.75	1.77	2.90	1.74
3.70	29844	0.3351	2.37	1.65	2.46	1.62	2.52	1.71	2.60	1.73	2.81	1.74	2.91	1.68
3.66	29521	0.3387	2.37	1.65	2.47	1.62	2.55	1.72	2.64	1.73	2.84	1.72	2.92	1.64
3.62	29198	0.3425	2.38	1.65	2.47	1.63	2.57	1.72	2.67	1.74	2.88	1.69	2.92	1.60
3.58	28876	0.3463	2.38	1.66	2.48	1.64	2.61	1.73	2.73	1.73	2.91	1.65	2.92	1.58
3.54	28553	0.3502	2.39	1.66	2.50	1.65	2.66	1.74	2.79	1.70	2.94	1.62	2.91	1.56
3.50	28230	0.3542	2.39	1.67	2.51	1.66	2.71	1.75	2.82	1.68	2.96	1.60	2.89	1.56
3.46	27908	0.3583	2.39	1.68	2.53	1.67	2.75	1.73	2.86	1.65	2.98	1.58	2.87	1.58
3.42	27585	0.3625	2.40	1.68	2.55	1.69	2.80	1.71	2.88	1.62	3.00	1.56	2.85	1.62
3.38	27262	0.3668	2.41	1.69	2.57	1.70	2.84	1.68	2.91	1.59	3.01	1.55	2.94	1.72
3.34	26940	0.3712	2.42	1.70	2.60	1.72	2.87	1.65	2.94	1.57	3.04	1.55	3.18	1.76
3.30	26617	0.3757	2.43	1.71	2.63	1.74	2.90	1.61	2.96	1.55	3.07	1.55	3.39	1.73
3.26	26295	0.3803	2.44	1.73	2.66	1.75	2.93	1.59	2.98	1.53	3.11	1.54	3.50	1.62
3.22	25972	0.3850	2.46	1.74	2.71	1.76	2.95	1.56	3.00	1.52	3.16	1.53	3.54	1.50
3.18	25649	0.3899	2.48	1.76	2.78	1.76	2.98	1.54	3.03	1.50	3.24	1.50	3.56	1.31
3.14	25327	0.3948	2.50	1.78	2.85	1.76	3.00	1.53	3.07	1.49	3.31	1.46	3.55	1.20
3.10	25004	0.3999	2.51	1.79	2.89	1.74	3.02	1.52	3.09	1.48	3.36	1.42	3.54	1.12
3.06	24681	0.4052	2.54	1.81	2.93	1.71	3.04	1.51	3.13	1.47	3.42	1.33	3.52	1.04
3.02	24359	0.4105	2.57	1.84	2.98	1.67	3.07	1.50	3.18	1.45	3.47	1.22	3.50	0.965
2.98	24036	0.4160	2.60	1.86	3.01	1.64	3.10	1.50	3.26	1.41	3.50	1.12	3.48	0.893
2.94	23714	0.4217	2.64	1.89	3.03	1.61	3.14	1.49	3.31	1.35	3.50	1.04	3.45	0.839
2.90	23391	0.4275	2.67	1.91	3.06	1.58	3.18	1.47	3.35	1.29	3.49	0.981	3.43	0.793
2.86	23068	0.4335	2.72	1.93	3.08	1.56	3.25	1.43	3.38	1.21	3.48	0.923	3.41	0.747
2.82	22746	0.4396	2.79	1.95	3.10	1.54	3.33	1.36	3.41	1.12	3.47	0.857	3.39	0.702
2.78	22423	0.4460	2.89	1.95	3.11	1.53	3.37	1.27	3.44	1.04	3.45	0.799	3.36	0.654
2.74	22100	0.4525	2.96	1.93	3.13	1.52	3.39	1.20	3.45	0.983	3.44	0.770	3.34	0.621
2.70	21778	0.4592	3.01	1.90	3.15	1.52	3.42	1.12	3.45	0.918	3.43	0.731	3.33	0.585
2.66	21455	0.4661	3.07	1.85	3.19	1.52	3.43	1.05	3.45	0.864	3.41	0.688	3.31	0.547
2.62	21132	0.4732	3.11	1.80	3.25	1.53	3.43	0.974	3.43	0.807	3.39	0.644	3.29	0.510
2.58	20810	0.4805	3.15	1.76	3.31	1.53	3.42	0.917	3.42	0.759	3.38	0.611	3.28	0.476
2.54	20487	0.4881	3.17	1.73	3.37	1.51	3.41	0.875	3.41	0.714	3.36	0.582	3.26	0.447
2.50	20165	0.4959	3.19	1.70	3.47	1.47	3.40	0.828	3.40	0.672	3.35	0.547	3.25	0.418
2.46	19842	0.5040	3.21	1.68	3.54	1.36	3.39	0.780	3.38	0.629	3.33	0.516	3.23	0.390
2.42	19519	0.5123	3.23	1.67	3.60	1.25	3.37	0.731	3.37	0.590	3.31	0.485	3.21	0.357
2.38	19197	0.5209	3.25	1.66	3.63	1.17	3.36	0.696	3.35	0.558	3.29	0.455	3.20	0.338
2.34	18874	0.5298	3.28	1.66	3.65	1.08	3.35	0.662	3.34	0.529	3.28	0.429	3.19	0.313
2.30	18551	0.5390	3.30	1.67	3.64	1.00	3.33	0.629	3.33	0.498	3.26	0.405	3.18	0.290
2.26	18229	0.5486	3.34	1.68	3.63	0.923	3.32	0.598	3.32	0.461	3.24	0.379	3.16	0.271
2.22	17906	0.5585	3.39	1.70	3.62	0.864	3.31	0.571	3.30	0.431	3.23	0.353	3.15	0.252
2.18	17583	0.5687	3.45	1.72	3.60	0.814	3.30	0.545	3.29	0.404	3.21	0.333	3.14	0.238
2.14	17261	0.5793	3.54	1.74	3.59	0.763	3.29	0.522	3.28	0.376	3.20	0.314	3.13	0.226
2.10	16938	0.5904	3.68	1.69	3.56	0.711	3.27	0.497	3.27	0.343	3.19	0.298	3.11	0.210
2.06	16616	0.6018	3.77	1.52	3.54	0.664	3.26	0.469	3.25	0.313	3.18	0.285	3.10	0.196
2.02	16293	0.6138	3.84	1.39	3.52	0.637	3.24	0.444	3.24	0.287	3.16	0.279	3.09	0.186
1.98	15970	0.6262	3.89	1.27	3.51	0.607	3.23	0.421	3.23	0.268	3.15	0.272	3.08	0.177
1.94	15648	0.6391	3.90	1.16	3.49	0.580	3.22	0.400	3.22	0.251	3.14	0.263	3.08	0.171

TABLE III (*Continued*)

			x=0		0.43		0.76		0.86		0.91		1.0	
eV	cm^{-1}	μm	n	k	n	k	n	k	n	k	n	k	n	k
1.90	15325	0.6525	3.88	1.09	3.47	0.553	3.21	0.377	3.21	0.239	3.12	0.260	3.06	0.169
1.86	15002	0.6666	3.86	1.05	3.45	0.534	3.20	0.362	3.19	0.238	3.12	0.259	3.05	0.170
1.82	14680	0.6812	3.84	1.02	3.44	0.519	3.19	0.351	3.18	0.239	3.11	0.258	3.04	0.173
1.78	14357	0.6965	3.82	0.989	3.42	0.508	3.18	0.346	3.17	0.241	3.09	0.260	3.03	0.178
1.74	14035	0.7125	3.80	0.969	3.40	0.498	3.17	0.341	3.16	0.244	3.08	0.263	3.03	0.184
1.70	13712	0.7293	3.77	0.951	3.39	0.487	3.16	0.336	3.16	0.246	3.07	0.266	3.02	0.189

TABLE IV

Values of n and k for $Hg_{1-x}Cd_xTe$ (Ref. [14])

			x=0		~0.16		0.2		~0.29		~0.65		1.0	
eV	cm^{-1}	μm	n	k	n	k	n	k	n	k	n	k	n	k
1.959	15803	0.6328	4.00	1.06	3.94	0.74	3.87	0.66	3.34	0.32	3.30	0.28	3.14	0.24

TABLE V

Sellmeier Parameters for $Hg_{1-x}Cd_xTe - 300K$

x	a_0	a_1	$a_2(\mu m)$	a_3	$a_4(\mu m)$	c	d
0.18[a]	13.337.	0.3890	8.628	10.067	65.63		
0.292	10.539	0.4792	3.75	6.063	74.29		
0.390	8.600	0.6029	2.333	3.698	77.97		
0.397	8.595	0.5954	2.304	3.785	75.20		
0.459	7.919	0.6816	1.843	3.414	75.80		
0.461	7.802	0.6968	1.820	3.418	76.14		
0.522	7.310	0.8223	1.413	2.209	67.74		
0.205[b]	12.33	0.2167	6.568			-1.102×10^{-3}	-3.065×10^{-7}
0.29	10.91	0.3437	3.752			-9.661×10^{-4}	-1.956×10^{-8}
1.0	5.304	1.899	0.5713			-4.188×10^{-4}	-2.391×10^{-7}

[a] The first seven values for $0.18 \leq x \leq 0.522$ are from Ref. [21].
[b] The next three values for x=0.205, 0.29 and 1.0 are from Ref. [26].

TABLE VI

Quadratic Interpolation Sellmeier Coefficients

	A_i	B_i	C_i
a_0	19.76	-41.82	34.5
a_1	0.373	-0.281	2.153
$a_2(\mu m)$	-200.0	2.841	1.897
a_3	18.79*	-58.4*	52.41*
$a_4(\mu m)$	73.25*	73.25*	73.25*

* The mean value of 73.25 μm was used.

TABLE VII

n_{av} – Mean Value of n for the Subband-Gap Region in $Hg_{1-x}Cd_xTe$ – 300K[a]

x	0.3	0.4	0.5	0.6	0.7	0.8	0.9	1.0
n_{av}	3.22	3.07	2.94	2.84	2.76	2.70	2.66	2.72

[a] n_{av} values are computed using interpolation procedure described in the section on the visible and near visible behavior and are valid for the energy range $0.75E_g \leq E \leq 0.1$ eV for $0.3 \leq x \leq 0.5$ and for $0.5E_g \leq E \leq 0.1$ eV for $0.5 \leq x \leq 1$

TABLE VIII

Values of n and k for HgTe – 10K (Ref. [27])

eV	cm^{-1}	μm	n	k
0.60	4839	2.066	3.74[a]	0.258
0.59	4759	2.101		0.261
0.58	4678	2.138		0.264
0.57	4598	2.175		0.267
0.56	4517	2.214		0.270
0.55	4436	2.254		0.269
0.54	4356	2.296		0.273
0.53	4275	2.339		0.277
0.52	4194	2.384		0.280
0.51	4114	2.431		0.284
0.50	4033	2.480		0.287
0.49	3952	2.530		0.291
0.48	3872	2.583		0.296
0.47	3791	2.638		0.299
0.46	3710	2.695		0.304
0.45	3630	2.755		0.309
0.44	3549	2.818		0.313
0.43	3468	2.883		0.316
0.42	3388	2.952		0.321
0.41	3307	3.024		0.325
0.40	3226	3.100		0.331
0.39	3146	3.179		0.335
0.38	3065	3.263		0.341
0.37	2984	3.351		0.344
0.36	2904	3.444		0.350
0.35	2823	3.542		0.351
0.34	2742	3.646		0.358
0.33	2662	3.757		0.357
0.32	2581	3.874		0.358
0.31	2500	3.999		0.354
0.30	2420	4.133		0.350*
0.29	2339	4.275		0.358
0.28	2258	4.428		0.364
0.27	2178	4.592		0.371
0.26	2097	4.768		0.378
0.25	2016	4.959		0.385
0.24	1936	5.166		0.390
0.23	1855	5.390		0.399
0.22	1774	5.635		0.410
0.21	1694	5.904		0.420
0.20	1613	6.199		0.430
0.19	1533	6.525		0.440
0.18	1452	6.888		0.449
0.17	1371	7.293		0.461
0.16	1291	7.749		0.477

TABLE VIII (*Continued*)

eV	cm^{-1}	μm	n	k
0.15	1210	8.265		0.487
0.14	1129	8.856		0.506
0.13	1049	9.537		0.524
0.12	967.9	10.33		0.545
0.11	887.2	11.27		0.574
0.10	806.6	12.40		0.600
0.09	725.9	13.78		0.633
0.08	645.3	15.50		0.668
0.07	564.6	17.71		0.712
0.06	483.9	20.66		0.763
0.05	403.3	24.77	3.74[a]	0.860

[a] A constant value was assumed to calculate $\alpha(E)$ in Ref. [27].

* The approximate position of the band-gap, E_g is indicated. Note that the value of E_g is negative in HgTe

TABLE IX

Values of n and k for $Hg_{1-x}Cd_xTe - x \simeq 0.2$ (Ref. [25] and [31])

eV	cm^{-1}	μm	n	n-type (x=0.205) k (300K)	n-type (x=0.205) k (80K)	p-type (x=0.2) k (295K)	p-type (x=0.2) k (90K)
0.260	2097	4.768		0.134			
0.255	2057	4.862		0.133			
0.250	2016	4.959		0.131			
0.245	1976	5.060		0.130			
0.240	1936	5.166		0.128			
0.235	1895	5.276		0.126			
0.230	1855	5.390		0.123			
0.225	1815	5.510		0.121			
0.220	1774	5.635		0.117			
0.215	1734	5.767		0.114			
0.210	1694	5.904		0.110			
0.205	1653	6.048		0.105			
0.200	1613	6.199		0.992×10^{-1}			
0.195	1573	6.358		0.924			
0.190	1533	6.525		0.843			
0.185	1492	6.702		0.741			
0.180	1452	6.888		0.607			
0.175	1412	7.085		0.408			
0.170	1371	7.293		0.324*		- * -	
0.165	1331	7.514		0.183			
0.160	1291	7.749	3.610	0.104			
0.155	1250	7.999	3.595	0.589×10^{-2}		0.155×10^{-1}	
0.150	1210	8.265	3.583	0.334		0.127	
0.145	1170	8.550	3.574	0.190		0.102	
0.140	1129	8.856	3.567	0.108	0.280	0.899×10^{-2}	
0.135	1089	9.184	3.561	0.616×10^{-3}	0.275	0.832	
0.130	1049	9.537	3.555		0.268	0.797	
0.125	1008	9.918	3.550		0.260	0.760	
0.120	967.9	10.33	3.546		0.249	0.773	
0.115	927.6	10.78	3.542		0.235	0.787	
0.110	887.2	11.27	3.537		0.216	0.803	
0.105	846.9	11.81	3.533		0.191	0.843	
0.100	806.6	12.40	3.529		0.155	0.899	- * -
0.095	766.3	13.05	3.525		0.935×10^{-1}	0.961	
0.090	725.9	13.78	3.520		0.519*	0.103×10^{-1}	
0.085	685.6	14.59	3.515		0.133	0.112	0.259×10^{-1}
0.080	645.3	15.50	3.509		0.341×10^{-2}	0.123	0.274
0.075	604.9	16.53	3.502		0.880×10^{-3}	0.141	0.297
0.070	564.6	17.71	3.494			0.164	0.323
0.065	524.3	19.07	3.483			0.186	0.352
0.060	483.9	20.66	3.471			0.215	0.390
0.055	443.6	22.54	3.454			0.258	0.441
0.050	403.3	24.80	3.431			0.311	

* The position of the band-gap, E_g, estimated in Ref. [25] and [31] is indicated.

TABLE X

Values of n and k for $Hg_{1-x}Cd_xTe - x \simeq 0.3$ (Ref. [26] and [31])

eV	cm^{-1}	μm	n	n-type (x=0.29) k (300K)	n-type (x=0.29) k (85K)	p-type (x=0.3) k (295K)	p-type (x=0.3) k (90K)
0.420	3388	2.952		0.108			
0.415	3347	2.987		0.108			
0.410	3307	3.024		0.107			
0.405	3267	3.061		0.106			
0.400	3226	3.100		0.106			
0.395	3186	3.139		0.105			
0.390	3146	3.179		0.104			
0.385	3105	3.220		0.103			
0.380	3065	3.263		0.102			
0.375	3025	3.306		0.100			
0.370	2984	3.351		0.991×10^{-1}			
0.365	2944	3.397		0.977			
0.360	2904	3.444		0.962			
0.355	2863	3.492		0.945			
0.350	2823	3.542		0.927			
0.345	2783	3.594		0.907			
0.340	2742	3.646		0.886	0.179		
0.335	2702	3.701		0.862	0.177		
0.330	2662	3.757		0.836	0.176		
0.325	2621	3.815		0.807	0.174		
0.320	2581	3.874		0.775	0.172		
0.315	2541	3.936		0.739	0.170		
0.310	2500	3.999		0.698	0.167	- * -	
0.305	2460	4.065		0.652	0.165		
0.300	2420	4.133		0.598	0.162		
0.295	2379	4.203		0.535	0.159		
0.290	2339	4.275		0.458	0.155		
0.285	2299	4.350		0.357	0.151		
0.280	2258	4.428	3.480	0.241*	0.147		- * -
0.275	2218	4.508	3.465	0.142	0.142		
0.270	2178	4.592	3.453	0.830×10^{-2}	0.136		
0.265	2137	4.678	3.443	0.487	0.130		
0.260	2097	4.768	3.434	0.286	0.123	0.336×10^{-2}	
0.255	2057	4.862	3.426	0.168	0.115	0.337	
0.250	2016	4.959	3.419	0.987×10^{-3}	0.105	0.339	
0.245	1976	5.060	3.413	0.580	0.933×10^{-1}	0.345	
0.240	1936	5.166	3.407	0.341	0.785	0.356	
0.235	1895	5.276	3.403		0.584	0.368	
0.230	1855	5.390	3.398		0.319*	0.380	
0.225	1815	5.510	3.394		0.921×10^{-2}	0.393	
0.220	1774	5.635	3.391		0.267	0.407	0.624×10^{-2}
0.215	1734	5.767	3.387		0.772×10^{-3}	0.421	0.645
0.210	1694	5.904	3.384			0.435	0.668
0.205	1653	6.048	3.381			0.451	0.695

TABLE X (*Continued*)

eV	cm^{-1}	μm	n	n-type (x=0.29 k (300K)	n-type (x=0.29 k (85K)	p-type (x=0.3) k (295K)	p-type (x=0.3) k (90K)
0.200	1613	6.199	3.379			0.468	0.727
0.195	1573	6.358	3.376			0.486	0.762
0.190	1533	6.525	3.374			0.505	0.798
0.185	1492	6.702	3.372			0.525	0.835
0.180	1452	6.888	3.369			0.546	0.875
0.175	1412	7.085	3.367			0.568	0.918
0.170	1371	7.293	3.365			0.591	0.963
0.165	1331	7.514	3.364			0.616	0.101×10^{-1}
0.160	1291	7.749	3.362			0.643	0.106
0.155	1250	7.999	3.360			0.671	0.112
0.150	1210	8.265	3.358			0.712	0.120
0.145	1170	8.550	3.356			0.755	0.128
0.140	1129	8.856	3.355			0.801	0.138
0.135	1089	9.184	3.353			0.851	0.148
0.130	1049	9.537	3.351			0.904	0.159
0.125	1008	9.918	3.349			0.962	0.170
0.120	967.9	10.33	3.347			0.102×10^{-1}	0.183
0.115	927.6	10.78	3.345			0.109	0.197
0.110	887.2	11.27	3.343			0.117	0.212
0.105	846.9	11.81	3.340			0.125	0.228
0.100	806.6	12.40	3.338			0.135	0.251
0.095	766.3	13.05	3.335			0.148	0.280
0.090	725.9	13.78	3.331			0.163	0.313
0.085	685.6	14.59	3.327			0.179	0.349
0.080	645.3	15.50	3.323			0.200	0.388
0.075	604.9	16.53	3.318			0.227	0.431
0.070	564.6	17.71	3.311			0.257	0.481
0.065	524.3	19.07	3.304			0.287	0.538
0.060	483.9	20.66	3.294			0.319	
0.055	443.6	22.54	3.281			0.357	
0.050	403.3	24.80	3.265				

* The position of the band-gap, E_g estimated in Ref. [26] and [31] is indicated.

TABLE XI

Values of n and k for $Hg_{1-x}Cd_xTe - x = 0.443$, 300K (Ref. [21] and [30])

eV	cm^{-1}	μm	n	k
0.625	5041	1.984		0.147
0.620	5001	2.000		0.144
0.615	4960	2.016		0.141
0.610	4920	2.032		0.138
0.605	4880	2.049		0.135
0.600	4839	2.066		0.133
0.595	4799	2.084		0.131
0.590	4759	2.101		0.130
0.585	4719	2.119		0.128
0.580	4678	2.138		0.125
0.575	4638	2.156		0.122
0.570	4598	2.175		0.120
0.565	4557	2.194		0.119
0.560	4517	2.214		0.117
0.555	4477	2.234		0.113
0.550	4436	2.254		0.110
0.545	4396	2.275		0.105
0.540	4356	2.296		0.101
0.535	4315	2.317		0.953×10^{-1}
0.530	4275	2.339		0.885
0.525	4235	2.362		0.815
0.520	4194	2.384		0.660
0.515	4154	2.407		0.574
0.510	4114	2.431		0.456
0.505	4073	2.455		0.308
0.500	4033	2.480	3.107	0.225*
0.495	3993	2.505	3.101	0.155
0.490	3952	2.530	3.092	0.941×10^{-2}
0.485	3912	2.556	3.085	0.620
0.480	3872	2.583	3.080	0.349
0.470	3791	2.638	3.068	
0.460	3710	2.695	3.057	
0.450	3630	2.755	3.048	
0.440	3549	2.818	3.040	
0.430	3468	2.883	3.033	
0.420	3388	2.952	3.026	
0.410	3307	3.024	3.020	
0.400	3226	3.100	3.013	
0.380	3065	3.263	3.003	
0.360	2904	3.444	2.995	
0.340	2742	3.646	2.987	
0.320	2581	3.874	2.980	
0.300	2420	4.133	2.975	

TABLE XI (*Continued*)

eV	cm^{-1}	μm	n	k
0.250	2016	4.959	2.963	
0.200	1613	6.199	2.953	
0.150	1210	8.265	2.945	
0.100	806.6	12.40	2.932	
0.050	403.3	24.80	2.875	

* The position of the band-gap, E_g estimated in Ref. [30] is indicated.

TABLE XII

Values of n and k for $Hg_{1-x}Cd_xTe - x = 0$ (Ref. [35]) and $x \simeq 0.21$ (Ref. [37])

			x=0		x≃0.21			
					n-type		p-type	
eV	cm^{-1}	μm	n	k	n	k	n	k
			(8K)		(~5K)		(~5K)	
0.02256	,182	54.95					3.42	1.52
0.02219	179	55.87					3.39	1.51
0.02182	176	56.82					3.36	1.54
0.02145	173	57.80					3.32	1.55
0.02108	170	58.82					3.28	1.52
0.02070	167	59.88					3.18	1.53
0.02033	164	60.98					2.96	1.51
0.01996	161	62.11	3.22	0.350			2.66	1.69
0.01959	158	63.29	3.17	0.376	1.91	0.672	2.76	2.15
0.01922	155	64.52	3.18	0.431	2.60	0.958	3.28	2.49
0.01884	152	65.79	3.15	0.491	2.72	0.722	3.41	2.48
0.01847	149	67.11	3.12	0.567	2.79	0.369	3.54	2.11
0.01810	146	68.49	3.05	0.660	2.10	0.219	3.06	1.89
0.01773	143	69.93	2.96	0.786	1.75	0.558	2.68	2.07
0.01736	140	71.43	2.85	0.935	1.03	1.53	2.23	2.74
0.01699	137	72.99	2.74	1.15	1.19	1.65	2.20	2.92
0.01661	134	74.63	2.64	1.40	1.01	2.14	1.96	3.28
0.01624	131	76.34	2.51	1.79	0.809	3.09	1.69	3.74
0.01587	128	78.13	2.09	3.04	1.08	4.56	1.26	4.52
0.01550	125	80.00	2.19	4.25	1.93	6.63	0.967	6.27
0.01513	122	81.97	3.26	6.33	5.60	10.2	1.83	10.3
0.01475	119	84.03	7.95	7.95	11.5	2.47	11.3	8.47
0.01438	116	86.21	9.97	2.49	9.52	0.595	9.43	4.63
0.01401	113	88.50	8.97	0.868	7.77	0.247	8.42	3.55
0.01364	110	90.91	9.61	0.503			7.70	2.81
0.01327	107	93.46					7.33	2.62
0.01289	104	96.15					7.07	2.37
0.01252	101	99.01					6.78	2.18
0.01215	98	102.0					6.51	2.18
0.01178	95	105.3					6.45	2.18
0.01141	92	108.7					6.34	2.11

TABLE XIII

Values of n and k for $Hg_{1-x}Cd_xTe - x = 0.45$ (Ref. [39])

eV	cm^{-1}	μm	n	k
0.04959	400	25.00	3.42[a]	
0.02703	218	45.87	3.41	0.197×10^{-1}
0.02666	215	46.51	3.38	0.215×10^{-1}
0.02628	212	47.17	3.35	0.235×10^{-1}
0.02591	209	47.85	3.31	0.259×10^{-1}
0.02554	206	48.54	3.27	0.286×10^{-1}
0.02517	203	49.26	3.23	0.318×10^{-1}
0.02480	200	50.00	3.18	0.356×10^{-1}
0.02442	197	50.76	3.13	0.402×10^{-1}
0.02405	194	51.55	3.07	0.456×10^{-1}
0.02368	191	52.36	3.00	0.524×10^{-1}
0.02331	188	53.19	2.93	0.609×10^{-1}
0.02294	185	54.05	2.83	0.718×10^{-1}
0.02256	182	54.95	2.73	0.862×10^{-1}
0.02219	179	55.87	2.60	0.106
0.02182	176	56.82	2.44	0.134
0.02145	173	57.80	2.23	0.178
0.02108	170	58.82	1.96	0.254
0.02070	167	59.88	1.58	0.410
0.02033	164	60.98	1.07	0.839
0.01996	161	62.11	0.807	1.68
0.01959	158	63.29	0.923	2.59
0.01922	155	64.52	1.49	3.54
0.01884	152	65.79	2.44	4.06
0.01847	149	67.11	4.65	4.17
0.01810	146	68.49	4.38	1.70
0.01773	143	69.93	3.09	1.59
0.01736	140	71.43	2.58	2.07
0.01699	137	72.99	2.17	2.79
0.01661	134	74.63	2.29	3.45
0.01624	131	76.34	1.88	4.17
0.01587	128	78.13	1.78	6.31
0.01550	125	80.00	4.04	10.3
0.01513	122	81.97	13.4	6.20
0.01475	119	84.03	10.1	1.43
0.01438	116	86.21	8.36	0.696
0.01401	113	88.50	7.47	0.519
0.01364	110	90.91	7.01	0.473
0.01327	107	93.46	6.73	0.353
0.01289	104	96.15	6.46	0.236
0.01252	101	99.01	6.23	0.166
0.01215	98	102.0	6.04	0.124
0.01178	95	105.3	5.89	0.977×10^{-1}
0.01141	92	108.7	5.76	0.793×10^{-1}
0.01103	89	112.4	5.66	0.660×10^{-1}

TABLE XIII (*Continued*)

eV	cm^{-1}	μm	n	k
0.01066	86	116.3	5.57	0.559×10^{-1}
0.01029	83	120.5	5.49	0.480×10^{-1}
0.00992	80	125.0	5.42	0.416×10^{-1}
0.000124	10	1000.0	4.91[b]	

[a] $\sqrt{\epsilon_\infty}$, from Ref. [26].
[b] $\sqrt{\epsilon_0}$, where $\epsilon_0 = \epsilon_\infty + \Sigma_j S_j$, from Ref. [39].

Selenium (Se)

EDWARD D. PALIK
Institute for Physical Science and Technology
University of Maryland
College Park, Maryland

The trigonal form of Se is birefringent with an optical c axis. Light polarized perpendicular to c is termed ordinary (o), and light polarized parallel to c is termed extraordinary (e). This leads to one of the applications of Se for second-harmonic generation of IR light [1, 2]. Se is a direct-band-gap semiconductor ($E_{g\perp} = 1.98$ eV; $E_{g\parallel} = 2.11$ eV). In addition to the IR spectrum (to be discussed), the Raman spectrum has been studied in some detail [3, 4]. A good collection of many of the properties of Se is given in Ref. [5].

The room-temperature n and k values chosen in this critique are listed in Table II. These are plotted in Fig. 1.

Starting at the long wavelength of 3.3 cm, permittivity measurements have been done by Sicha *et al.* [6] using a cavity-resonance method. A rectangular resonator with a TE_{101} mode had a resonance frequency of $\sim 9.1 \times 10^9$ Hz ($\sim$3.3 cm). A needle-shaped Se crystal with c along the long direction was inserted at a point of maximum electric-field intensity, and the change of resonant frequency was measured. Some analysis of the resonant frequency as a function of electric field across the cavity, depolarization factor for $\mathbf{E} \| c$, and ε for polycrystalline material, finally yielded $\varepsilon_\parallel = 9.3$ and $\varepsilon_\perp = 8.0$. These numbers prove to be in poor agreement with reststrahlen-data analysis and extrapolation ($\varepsilon_{o\parallel} = 12.2$, $\varepsilon_{o\perp} = 7.4$), and we do not weight them heavily. Other data of Salo *et al.* [7] give $\varepsilon_\parallel = 21$ and $\varepsilon_\perp = 11$, also much different. It seems that reflectivity to long wavelength (100–1000 μm) is a better way to determine ε_o as long as the free-carrier concentration is low. This question of the free-carrier contribution to the low-frequency dielectric function is important to consider and should be answered, based on the measured free-carrier concentration and conductivity.

Danielewicz and Coleman [8] have collected several sets of data in the spectral range 10–10^4 cm^{-1}, and we have used these as a basis set of data, adding other data for comparison and overlap. The extinction-coefficient

Copyright © 1991 by Academic Press.
All rights of reproduction in any form reserved.
ISBN 0-12-544422-2

data are extracted from absorption-constant data for the multiphonon region [9]. The fundamental transverse optic phonon absorption was obtained from a Lorentz-oscillator fit of the reststrahlen reflectivity. Similar results were obtained by Lucovsky *et al.* [10] and Geick *et al.* [9]. All these workers used equivalent models, except that Danielewicz and Coleman used UV interband oscillators to account for ε_∞ better. In their notation,

$$\varepsilon = \varepsilon_1 - i\varepsilon_2 = (n - ik)^2 = 1 + \sum \frac{Se_j ve_j^2}{ve_j - \nu^2} + \sum \frac{So_j vo_j^2}{vo_j - \nu^2 + i\gamma_j \nu},$$

but we have omitted their free-carrier term. Note that they have chosen the negative sign in defining ε. Se_j and So_j are the strengths for electronic and vibrational oscillators, respectively, for each polarization. ve_j and vo_j are the resonant frequencies for the electronic and vibrational oscillators, respectively, for each polarization. γ_j is the phonon line width (damping constant) for each polarization. We list these parameters in Table I.

The oscillator fit was used to calculate n from 10,000–10 cm^{-1}, but the near-IR data of Gampel and Johnson [11] are implicit in the tabulation. This fit also provided the k values in the vicinity of the phonon frequencies $v_T(\perp) = 140$ and $v_T(\|) = 102\ cm^{-1}$ but did not consider the multiphonon absorption.

Measurements of the IR refractive index by minimum-deviation and interference-fringe techniques yielded values from 3.2–3.7 for $n_\|$ and 2.5–2.9 for $n_\perp$, suggesting material and sample-preparation problems. We accept the values given by the fit of Danielewicz and Coleman, which are essentially those of Gampel and Johnson [11]; the results of Caldwell and Fan [12] are in reasonable agreement to one unit in the first decimal place; the results of Gobrecht and Tausend [13] are within two units in the first decimal place. Although the data of Ref. [13] fill in a gap from 1.0–0.7 μm, we have not tabulated it because it fails to join on to n values at either end. Gampel and Johnson discuss such variations in n among several groups.

Henrion [14] has measured the transmission of thin-plate samples at various temperatures between 400 K and 90 K. Analysis of α versus hv yielded a straight line indicating a direct band gap $E_{g\|} = 2.11$ eV and $E_{g\perp} = 1.98$ eV at 300 K. Exponential tail absorption at lower energy was shown to be due to charged impurities.

Several reflection experiments have been performed at and above the fundamental band gap [15, 16]. Absorption peaks have been correlated to band-structure calculation. The Kramers–Kronig (K–K) analysis of such data in the 4–14 eV region by Leiga [15] and in the 2–5 eV region by Tutihasi *et al.* [16] have been combined for Table II. Tutihasi *et al.*

performed standard reflection experiments from cleaved/acid-etched surfaces using Glan-prism linear polarizers. Prisms of silica and flint glass were used in the monochromator. The reflection standard was an Al mirror.

Leiga used a vacuum UV monochromator with hydrogen, neon, or helium discharges as the light source. Only cleaved or as-grown surfaces were used because chemical etching affected the reflectivity results. The angle of incidence was 20°. Two types of samples were used: one with the c axis perpendicular to the surface and one with the c axis in the surface. Measurements (with the partially polarized light from the monochromator) on both kinds of samples for two positions of each sample 90° apart (about the incident-beam direction) could be algebraically unsorted to give $R_\perp$ and $R_\parallel$. K–K analysis involved some assumptions and use of other researchers' data to cover the entire spectrum.

Bammes *et al.* [17] used synchrotron radiation to measure reflectivity from 3–30 eV for samples with the c axis in the plane. Since the synchrotron radiation was nearly linearly polarized to start, and further linearly polarized by a premirror and grating, the sample/detector could be rotated to change the angle of incidence and the sample could be rotated to measure $\mathbf{E} \perp c$ and $\mathbf{E} \parallel c$. This, along with the work of Liega, dramatically illustrates how to do polarization experiments when there are no polarizers at high photon energies!

The ε_1 and ε_2 dielectric-function data were plotted in small figures, which had to be expanded in order to read the values. Therefore, in addition to the errors in measuring R and performing K–K analysis, there are now errors due to graph reading. Since peaks are well-defined in the ε versus eV plots, however, we keep two to three significant figures for n and k to show the peaks in most instances.

We have found no data above 30 eV until the absorption edges are reached. Since X-ray scattering cross-sections have been determined for many elemental materials, we have used the model of Henke *et al.* [18] to calculate n and k from 4–250 Å. The X-ray absorption edges as listed in Ref. [19] are K(12.654 keV), L_1(1.652 keV), L_2(1.474 keV), L_3(1.434 keV), M_5(0.05443 keV), and most of these appear in Fig. 1 (remember the conversion factor 8065.48 cm^{-1}/eV). Still-lower-energy transitions are merged into the band structure. Although there is no overlap with the data of Bammes *et al.*, extrapolation of both sets of data toward each other seems to be feasible.

ACKNOWLEDGMENTS

We thank W. R. Hunter for calculating optical constants in the X-ray region. V. Saile kindly provided unpublished data in the visible–UV regions.

REFERENCES

1. G. W. Day, *Appl. Phys. Lett.* **18**, 347 (1971).
2. G. H. Sherman and P. D. Coleman, *J. Appl. Phys.* **44**, 238 (1973).
3. G. Lucovsky, A. Mooradian, W. Taylor, G. B. Wright, and R. C. Keezer, *Solid State Comm.* **5**, 113 (1967).
4. A. Mooradian and G. B. Wright, in "Physics of Selenium and Tellurium," (W. C. Cooper, ed.), Pergamon, New York, 296 (1969).
5. G. Weiser, in "Landolt–Börnstein Numerical Data and Functional Relationships in Science and Technology," (K.-H. Hellewege, ed.), Vol. 17, Springer-Verlag, Berlin, 86 (1983).
6. M. Sicha, J. Studnicka, V. Prosser, and B. Gruber, *Phys. Stat. Solidi* **7**, 1045 (1964).
7. T. Salo, T. Stubb, and E. Suosara, in "The Physics of Selenium and Tellurium," (W. C. Cooper, ed.), Pergamon, New York, 335 (1969).
8. E. J. Danielewicz and P. D. Coleman, *Appl. Opt.* **13**, 1164 (1974).
9. R. Geick, U. Schröder, and J. Stuke, *Phys. Stat. Solidi* **24**, 99 (1967).
10. G. Lucovsky, R. C. Keezer, and E. Burstein, *Solid State Comm.* **5**, 439 (1967).
11. L. Gampel and F. M. Johnson, *J. Opt. Soc. Am.* **59**, 72 (1969).
12. R. S. Caldwell and H. Y. Fan, *Phys. Rev.* **114**, 664 (1959).
13. H. Gorbrecht and A. Tausend, *Z. Physik* **161**, 205 (1961).
14. W. Henrion, in "Physics of Selenium and Tellurium," (W. C. Cooper, ed.), Pergamon, New York, 75 (1969); *Phys. Stat. Solidi* **12,** K113 (1965).
15. A. G. Leiga, *J. Opt. Soc. Am.* **58**, 880 (1968).
16. S. Tutihasi and I. Chen, *Phys. Rev.* **158**, 623 (1967).
17. P. Bammes, R. Klucker, E. E. Koch, and T. Tuomi, *Phys. Stat. Solidi (b)* **49**, 561 (1972); private communication from V. Saile.
18. B. L. Henke, P. Lee, T. J. Tanaka, R. L. Shimabukuro, and B. K. Fujikama, *At. Data Nucl. Data Tables* **27**, 1 (1982).
19. D. E. Gray, ed. "American Institute of Physics Handbook," Third Edition, McGraw-Hill, New York, 7–120 (1982).

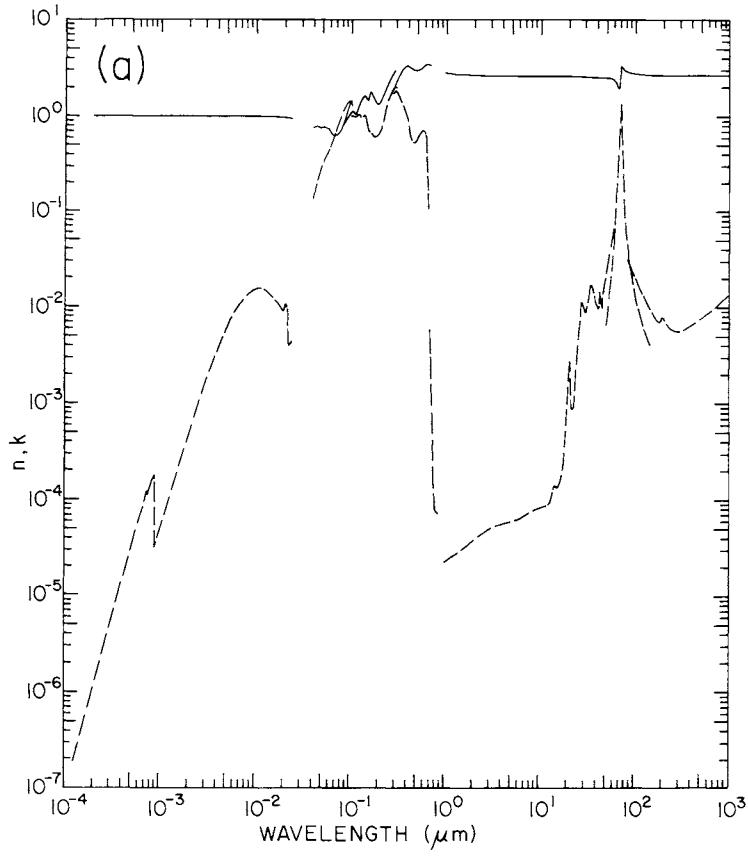

Fig. 1. (a) Log–log plot of n_o (solid line) and k_o (dashed line) versus wavelength in micrometers for selenium. (b) Log–log plot of n_e (solid line) and k_e (dashed line) versus wavelength in micrometers.

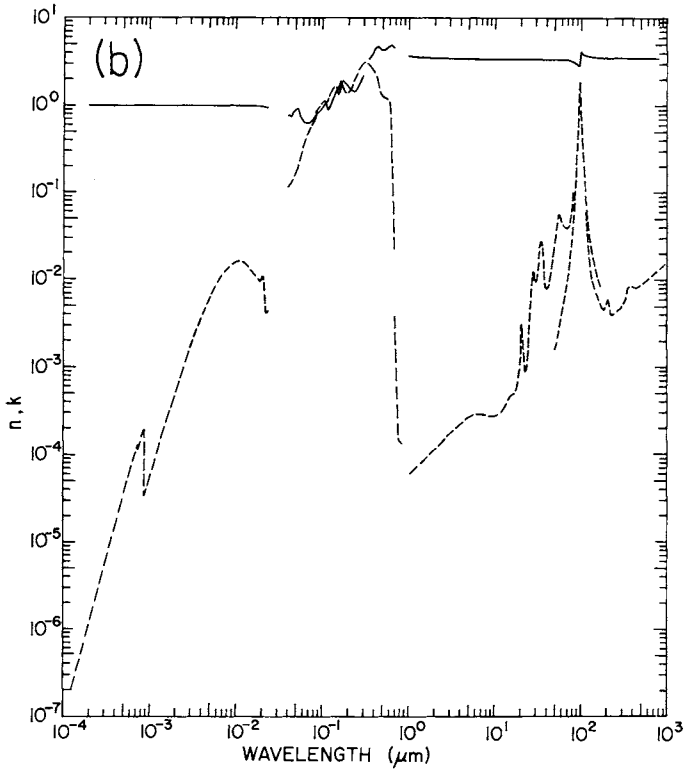

TABLE I

Oscillator Parameters for Se at 300 K

	$ve_j(cm^{-1})$	Se_j	$vo_j(cm^{-1})$	So_j	$\gamma_j(cm^{-1})$
∥	27,422.6	10.62	102.0	0.62	7.15
⊥	30,648.7	5.79	231.0	0.01	9.0
	12,904.8	0.18	140.0	0.45	8.0

TABLE II

Values of n and k for Selenium from Various References[a]

eV	cm^{-1}	Å	n	k
9972		1.243	0.99999190[18]	1.90×10^{-7}[18]
9331		1.329	0.99999110	2.47×10^{-7}
8909		1.392	0.99999020	2.94×10^{-7}
8507		1.458	0.9999892	3.50×10^{-7}
8123		1.526	0.9999881	4.17×10^{-7}
7756		1.599	0.9999869	4.96×10^{-7}
7406		1.674	0.9999856	5.90×10^{-7}
7072		1.753	0.9999841	7.02×10^{-7}
6752		1.836	0.9999826	8.34×10^{-7}
6447		1.923	0.9999809	9.92×10^{-7}
6156		2.014	0.9999790	1.18×10^{-6}
5878		2.109	0.9999769	1.41×10^{-6}
5613		2.209	0.9999746	1.67×10^{-6}
5359		2.314	0.9999720	1.98×10^{-6}
5117		2.423	0.9999693	2.35×10^{-6}
4886		2.538	0.9999663	2.79×10^{-6}
4665		2.658	0.9999630	3.32×10^{-6}
4455		2.783	0.9999593	3.94×10^{-6}
4254		2.915	0.9999554	4.67×10^{-6}
4062		3.053	0.9999509	5.54×10^{-6}
3878		3.197	0.9999462	6.57×10^{-6}
3703		3.348	0.9999410	7.79×10^{-6}
3536		3.506	0.9999353	9.23×10^{-6}
3376		3.672	0.9999290	1.09×10^{-5}
3324		3.846	0.9999223	1.29×10^{-5}
3078		4.028	0.9999149	1.53×10^{-5}
2939		4.218	0.9999070	1.81×10^{-5}
2807		4.418	0.999898	2.14×10^{-5}
2680		4.627	0.999889	2.53×10^{-5}
2559		4.846	0.999879	2.98×10^{-5}
2443		5.075	0.999869	3.52×10^{-5}
2333		5.315	0.999857	4.14×10^{-5}
2228		5.566	0.999846	4.88×10^{-5}
2127		5.829	0.999834	5.73×10^{-5}
2031		6.105	0.999821	6.73×10^{-5}
1939		6.394	0.999809	7.87×10^{-5}
1852		6.696	0.999798	9.22×10^{-5}
1768		7.013	0.999789	1.08×10^{-4}
1728		7.176	0.999787	1.17×10^{-4}
1688		7.344	0.999788	1.26×10^{-4}
1650		7.516	0.999817	1.20×10^{-4}
1612		7.691	0.999779	1.29×10^{-4}
1575		7.871	0.999778	1.39×10^{-4}
1539		8.055	0.999781	1.50×10^{-4}
1504		8.244	0.999791	1.62×10^{-4}
1470		8.436	0.999818	1.74×10^{-4}
1436		8.633	0.9999337	1.88×10^{-4}
1403		8.835	0.999811	3.29×10^{-5}

TABLE II (*Continued*)

Selenium

eV	cm^{-1}	Å	n	k
1371		9.041	0.999767	3.55×10^{-5}
1340		9.253	0.999736	3.84×10^{-5}
1280		9.690	0.999684	4.49×10^{-5}
1222		10.15	0.999637	5.25×10^{-5}
1167		10.63	0.999588	6.13×10^{-5}
1114		11.13	0.999538	7.17×10^{-5}
1064		11.66	0.999485	8.38×10^{-5}
1016		12.21	0.999427	9.76×10^{-5}
969.7		12.77	0.999366	1.14×10^{-4}
925.9		13.39	0.999299	1.34×10^{-4}
884.1		14.02	0.999226	1.55×10^{-4}
844.2		14.69	0.999148	1.81×10^{-4}
806.0		15.38	0.999063	2.10×10^{-4}
769.7		16.11	0.99897	2.44×10^{-4}
734.9		16.87	0.99887	2.84×10^{-4}
701.7		17.67	0.99876	3.28×10^{-4}
670.0		18.51	0.99864	3.79×10^{-4}
639.8		19.38	0.99852	4.41×10^{-4}
610.9		20.30	0.99838	5.10×10^{-4}
583.3		21.26	0.99823	5.89×10^{-4}
557.0		22.26	0.99808	6.80×10^{-4}
531.8		23.31	0.99791	7.83×10^{-4}
507.8		24.42	0.99773	8.99×10^{-4}
484.9		25.57	0.99753	1.03×10^{-3}
463.0		26.78	0.99733	1.19×10^{-3}
442.1		28.05	0.99711	1.36×10^{-3}
422.1		29.37	0.99689	1.56×10^{-3}
403.0		30.76	0.99665	1.78×10^{-3}
384.8		32.22	0.99642	2.02×10^{-3}
367.5		33.74	0.99616	2.29×10^{-3}
350.9		35.34	0.99589	2.59×10^{-3}
335.0		37.01	0.99561	2.92×10^{-3}
319.9		38.76	0.99533	3.30×10^{-3}
305.5		40.59	0.99505	3.74×10^{-3}
291.7		42.51	0.99478	4.22×10^{-3}
278.5		44.52	0.99455	4.76×10^{-3}
265.9		46.63	0.99437	5.27×10^{-3}
253.9		48.83	0.99415	5.81×10^{-3}
242.5		51.14	0.99392	6.40×10^{-3}
231.5		53.56	0.99371	7.05×10^{-3}
221.1		56.09	0.99353	7.76×10^{-3}
211.1		58.74	0.99343	8.54×10^{-3}
201.5		61.52	0.99339	9.30×10^{-3}
192.4		64.43	0.99347	1.01×10^{-2}
183.7		67.48	0.99354	1.08×10^{-2}
175.5		70.67	0.99359	1.15×10^{-2}
167.5		74.01	0.99373	1.22×10^{-2}
160.0		77.51	0.99385	1.28×10^{-2}

TABLE II (*Continued*)

Selenium

eV	cm^{-1}	Å	n	k
152.7		81.17	0.99397	1.35×10^{-2}
145.8		85.01	0.99418	1.41×10^{-2}
139.3		89.03	0.99435	1.46×10^{-2}
133.0		93.24	0.99464	1.51×10^{-2}
127.0		97.66	0.99481	1.55×10^{-2}
121.2		102.3	0.99493	1.58×10^{-2}
115.8		107.1	0.99515	1.60×10^{-2}
110.5		112.2	0.99517	1.61×10^{-2}
105.5		117.5	0.99513	1.61×10^{-2}
100.8		123.0	0.99522	1.59×10^{-2}
96.22		128.9	0.99486	1.53×10^{-2}
91.88		134.9	0.99427	1.48×10^{-2}
88.73		141.3	0.99351	1.40×10^{-2}
83.77		148.0	0.99218	1.31×10^{-2}
79.99		155.0	0.99042	1.24×10^{-2}
76.37		162.3	0.98843	1.18×10^{-2}
72.92		170.0	0.98618	1.12×10^{-2}
69.63		178.1	0.98358	1.04×10^{-2}
66.49		186.5	0.98040	9.68×10^{-3}
64.97		190.8	0.97851	9.35×10^{-3}
63.49		195.3	0.97636	9.33×10^{-3}
62.04		199.9	0.97419	9.66×10^{-3}
60.62		204.5	0.97294	1.06×10^{-2}
59.24		209.3	0.97252	1.07×10^{-2}
57.88		214.2	0.97257	9.39×10^{-3}
56.56		219.2	0.97010	5.25×10^{-3}
55.27		224.3	0.96510	4.06×10^{-3}
54.01		229.6	0.96089	4.10×10^{-3}
52.77		234.9	0.95714	4.23×10^{-3}
51.57		240.4	0.95339	4.42×10^{-3}

eV	cm^{-1}	μm	n_o (⊥)	k_o (⊥)	n_e (∥)	k_e (∥)
30		0.04133	0.79[17]	0.14[17]	0.87[17]	0.11[17]
29		0.04275	0.79	0.16	0.86	0.12
28		0.04428	0.80	0.19	0.85	0.13
27		0.04592	0.78	0.23	0.85	0.14
26		0.04769	0.78	0.26	0.86	0.15
25		0.04959	0.77	0.29	0.88	0.17
24		0.05166	0.78	0.32	0.91	0.18
23		0.05391	0.79	0.35	0.92	0.19
22		0.05636	0.78	0.39	0.81	0.25
21		0.05904	0.76	0.43	0.74	0.31
20		0.06199	0.73	0.48	0.69	0.36
19		0.06526	0.65	0.57	0.64	0.40
18		0.06888	0.61	0.65	0.65	0.48
17		0.07293	0.66	0.76	0.66	0.53

TABLE II (*Continued*)

Selenium

eV	cm^{-1}	μm	n_o (⊥)	k_o (⊥)	n_e (∥)	k_e (∥)
16		0.07749	0.68	0.96	0.65	0.61
15		0.08266	0.78	1.10	0.70	0.71
14.5		0.08551	0.80	1.18	0.60	0.92
					0.80[15]	0.85[15]
14		0.08856	0.90	1.30	0.76[17]	0.82[17]
			0.98[15]	0.92[15]	0.81[15]	0.91[15]
13.5		0.0918	1.04[17]	1.40[17]	0.81[17]	0.87[17]
			1.06[15]	0.97[15]	0.86[15]	0.96[15]
13		0.09537	1.23[17]	1.47[17]	0.88[17]	0.91[17]
			1.13[15]	1.00[15]	0.89[15]	1.02[15]
12.5		0.09919	1.45[17]	1.48[17]	0.98[17]	0.95[17]
			1.19[15]	1.01[15]	0.92[15]	1.06[15]
12		0.1033	1.66[17]	1.25[17]	1.09[17]	0.92[17]
			1.25[15]	1.02[15]	1.00[15]	1.10[15]
11.5		0.1078	1.71[17]	1.08[17]	1.05[17]	0.86[17]
			1.33[15]	1.01[15]	1.04[15]	1.10[15]
11		0.1127	1.69[17]	1.02[17]	0.95[17]	0.90[17]
			1.36[15]	1.00[15]	1.03[15]	1.08[15]
10.7		0.1153	1.37	1.04	0.90	1.16
10.5		0.1181	1.71[17]	0.99[17]	0.92[17]	0.98[17]
			1.43[15]	1.06[15]	0.91[15]	1.28[15]
10.0		0.1240	1.72[17]	0.95[17]	0.92[17]	1.07[17]
			1.56[15]	1.03[15]	1.03[15]	1.46[15]
9.7		0.1272	1.57	0.97	1.11	1.51
9.5		0.1305	1.57	0.97	1.18	1.54
9.2		0.1340	1.58	1.00	1.25	1.60
9.0		0.1378	1.66	1.02	1.35	1.64
8.7		0.1417	1.75	1.02	1.46	1.59
8.5		0.1459	1.82	0.92	1.48	1.52
8.25		0.1503	1.84	0.80	1.38	1.48
8.0		0.1550	1.81	0.69	1.35	1.68
7.75		0.1600	1.73	0.69	1.58	1.82
7.5		0.1653	1.71	0.67	1.84	1.83
7.25		0.1710	1.69	0.64	1.96	1.60
7.0		0.1771	1.62	0.61	1.84	1.45
6.75		0.1837	1.57	0.62	1.83	1.43
6.5		0.1907	1.51	0.63	1.72	1.35
6.25		0.1984	1.41	0.67	1.62	1.38
6.0	48393	0.2066	1.32	0.73	1.57	1.49
5.75	46377	0.2156	1.28	0.87	1.51	1.62
5.5	44360	0.2254	1.22	1.03	1.47	1.75
5.25	42344	0.2362	1.21	1.25	1.43	2.00
5.0	40327	0.2480	1.25	1.50	1.50	2.31
4.75	38311	0.2610	1.41	1.75	1.69	2.53
4.5	36295	0.2755	1.75	1.94	1.92	2.78
4.4	35488	0.2817	1.89[16]	1.72[16]		
4.25	34278	0.2917	2.01[15]	2.07[15]	2.22	3.06
4.2	33875	0.2952	2.18[16]	1.83[16]		

TABLE II (*Continued*)

Selenium

eV	cm^{-1}	μm	$n_o(\perp)$	$k_o(\perp)$	$n_e(\parallel)$	$k_e(\parallel)$
4.0	32261	0.3100	2.67[15]	1.99[15]		
			2.51[16]	1.81[16]		
3.8	30648	0.3262	2.84	1.66		
3.6	29035	0.3444	3.06	1.47	3.39[16]	3.01[16]
3.4	27422	0.3646	3.22	1.24	3.69	2.76
3.2	25809	0.3874	3.35	1.01	3.92	2.59
3.0	24196	0.4132	3.30	0.70	4.44	2.29
2.8	22583	0.4428	3.12	0.58	4.59	1.70
2.6	20970	0.4769	3.00	0.53	4.40	1.32
2.4	19357	0.5166	2.93	0.61	4.28	1.21
2.2	17744	0.5635	3.07	0.73	4.49	1.19
2.0	16130	0.6199	3.38	0.65	4.79	0.76
1.8	14517	0.6888	3.32	0.11	4.46	2.2×10^{-2}
				5.48×10^{-3}[14]		
1.78	14356	0.6965		3.49×10^{-3}		3.66×10^{-3}[14]
1.76	14195	0.7045		1.96×10^{-3}		2.41×10^{-3}
1.74	14034	0.7126		1.02×10^{-3}		1.44×10^{-3}
1.72	13873	0.7208		6.31×10^{-4}		9.75×10^{-4}
1.70	13711	0.7293		3.60×10^{-4}		6.27×10^{-4}
1.68	13550	0.7380		2.23×10^{-4}		4.23×10^{-4}
1.66	13389	0.7469		1.55×10^{-4}		2.85×10^{-4}
1.64	13227	0.7560		1.16×10^{-4}		2.17×10^{-4}
1.62	13066	0.7653		9.44×10^{-5}		1.83×10^{-4}
1.60	12905	0.7749		8.63×10^{-5}		1.59×10^{-4}
1.58	12743	0.7847		8.18×10^{-5}		1.44×10^{-4}
1.56	12582	0.7948		7.78×10^{-5}		1.36×10^{-4}
1.54	12421	0.8051		7.69×10^{-5}		1.36×10^{-4}
1.52	12259	0.8157		7.40×10^{-5}		1.35×10^{-4}
1.50	12098	0.8266		7.37×10^{-5}		1.33×10^{-4}
1.48	11937	0.8377		7.33×10^{-5}		1.31×10^{-4}
1.46	11775	0.8429		7.30×10^{-5}		1.30×10^{-4}
1.240	10000	1.000	2.816[8]	2.31×10^{-5}[8]	3.640[8]	5.81×10^{-5}[8]
1.116	9000	1.111	2.772	2.48×10^{-5}	3.592	6.37×10^{-5}
0.9919	8000	1.250	2.739	2.69×10^{-5}	3.551	7.11×10^{-5}
0.8679	7000	1.429	2.713	2.96×10^{-5}	3.516	8.07×10^{-5}
0.7439	6000	1.667	2.692	3.32×10^{-5}	3.486	9.42×10^{-5}
0.6199	5000	2.000	2.675	3.82×10^{-5}	3.462	1.12×10^{-4}
0.4959	4000	2.500	2.654	4.58×10^{-5}	3.442	1.41×10^{-4}
0.3720	3000	3.333	2.652	5.44×10^{-5}	3.427	1.90×10^{-4}
0.3100	2500	4.000	2.648	5.73×10^{-5}	3.422	2.26×10^{-4}
0.2480	2000	5.000	2.645	5.97×10^{-5}	3.417	2.67×10^{-4}
0.1860	1500	6.667	2.642	6.90×10^{-5}	3.413	2.81×10^{-4}
0.1550	1250	8.000	2.641		3.411	
0.1240	1000	10.00	2.639	8.51×10^{-5}	3.410	2.71×10^{-4}
0.1116	900	11.11	2.638	8.84×10^{-5}	3.409	2.87×10^{-4}
0.09919	800	12.50	2.637	8.95×10^{-5}	3.409	3.23×10^{-4}
0.09299	750	13.33		1.04×10^{-4}		2.44×10^{-4}
0.08679	700	14.29	2.636	1.42×10^{-4}	3.408	4.32×10^{-4}

TABLE II (*Continued*)

Selenium

eV	cm^{-1}	μm	$n_o(\perp)$	$k_o(\perp)$	$n_e(\parallel)$	$k_e(\parallel)$
0.08059	650	15.38		1.35×10^{-4}		4.41×10^{-4}
0.07439	600	16.67	2.635	1.59×10^{-4}	3.407	4.44×10^{-4}
0.06819	550	18.18		2.89×10^{-4}		5.79×10^{-4}
0.06199	500	20.00	2.632	2.07×10^{-3}	3.405	1.35×10^{-3}
0.05951	480	20.83		2.16×10^{-3}		2.98×10^{-3}
0.05703	460	21.74		8.65×10^{-4}		1.56×10^{-3}
0.05455	440	22.73		9.04×10^{-4}		9.04×10^{-4}
0.05207	420	23.81		1.52×10^{-3}		1.02×10^{-3}
0.04959	400	25.00	2.627	3.58×10^{-3}	3.403	2.79×10^{-3}
0.04711	380	26.32		7.33×10^{-3}		5.24×10^{-3}
0.04463	360	27.78		1.17×10^{-2}		1.13×10^{-2}
0.04215	340	29.41		9.36×10^{-3}		9.36×10^{-3}
0.03968	320	31.25		9.95×10^{-3} [9]		9.20×10^{-3} [9]
0.03720	300	33.33	2.613	1.54×10^{-2}	3.397	1.72×10^{-2}
0.03472	280	35.71	2.607	1.68×10^{-2}		2.70×10^{-2}
0.03224	260	38.46	2.598	1.16×10^{-2}		8.57×10^{-3}
0.03100	250	40.00			3.391	6.26×10^{-4} [8]
0.02976	240	41.67	2.576	9.95×10^{-3}		7.96×10^{-3} [9]
0.02914	235	42.55	2.568			
0.02876	232	43.10		1.51×10^{-2}		
0.02852	230	43.48	2.600			
0.02790	225	44.44	2.610			
0.02728	220	45.45	2.600	1.01×10^{-2}		1.16×10^{-2}
0.02604	210	47.62	2.582			
0.02480	200	50.00	2.550	2.39×10^{-2}	3.377	2.39×10^{-2}
				6.73×10^{-3} [8]		1.56×10^{-3} [8]
0.02418	195	51.28	2.555	7.96×10^{-3}		
0.02356	190	52.63	2.543	9.66×10^{-3}	3.372	1.96×10^{-3}
0.02294	185	54.05	2.530	1.20×10^{-2}		
0.02232	180	55.56	2.502	4.42×10^{-2} [9]	3.366	5.31×10^{-2} [9]
				1.53×10^{-2} [8]		2.54×10^{-3} [8]
0.02170	175	57.14	2.491	2.01×10^{-2}		
0.02108	170	58.82	2.462	2.76×10^{-2}	3.358	3.40×10^{-3}
0.02046	165	60.61	2.422	4.02×10^{-2}		
0.01984	160	62.50	2.356	7.46×10^{-2} [9]	3.346	4.23×10^{-2} [9]
				6.37×10^{-2} [8]		4.75×10^{-3} [8]
0.01922	155	64.52	2.270	0.114		
0.01860	150	66.67	2.111	0.255	3.330	7.04×10^{-3}
0.01798	145	68.97	1.964	0.771		
0.01736	140	71.43	2.959	1.33	3.306	3.81×10^{-2} [9]
						1.41×10^{-2} [8]
0.01674	135	74.07	3.342	0.466		
0.01612	130	76.92	3.140	0.175	3.263	2.13×10^{-3}
0.01550	125	80.00	3.013	8.71×10^{-2}		
0.01488	120	83.33	2.932	3.25×10^{-2} [9]	3.175	9.95×10^{-2} [9]
				5.16×10^{-2} [8]		5.22×10^{-2} [8]
0.01364	110	90.90	2.854	2.39×10^{-2}	2.914	0.248

TABLE II (*Continued*)

Selenium

eV	cm^{-1}	μm	$n_o(\perp)$	$k_o(\perp)$	$n_e(\parallel)$	$k_e(\parallel)$
0.01302	105	95.24			2.862	0.891[b]
0.01277	103	97.09			3.754	1.57
0.01265	102	98.04			3.676	1.70[b]
0.01252	101	99.01			3.884	1.07
0.01240	100	100.0	2.805	2.31×10^{-2}[9]	4.026	0.477[9]
				1.36×10^{-2}[b][8]		0.849[b][8]
0.01215	98	102.0			3.885	0.514[b]
0.01116	90	111.1	2.783	1.59×10^{-2}[9]	3.772	0.128[9]
				8.60×10^{-3}[b][8]		9.62×10^{-2}[b][8]
0.009919	80	125.0	2.761	1.29×10^{-2}[9]	3.633	1.69×10^{-2}[9]
				5.86×10^{-3}[b][8]		3.10×10^{-2}[b][8]
0.008679	70	142.9	2.753	1.05×10^{-2}[9]	3.575	8.07×10^{-3}
				4.15×10^{-3}[b][8]		1.48×10^{-2}[b]
0.007439	60	166.7	2.740	7.83×10^{-3}	3.545	5.31×10^{-3}
						8.40×10^{-3}[b]
0.007191	58	172.4				5.08×10^{-3}
0.006943	56	178.6				4.69×10^{-3}
0.006819	55	181.8		7.23×10^{-3}		
0.006695	54	185.2				4.49×10^{-3}
0.006447	52	192.3				4.67×10^{-3}
0.006199	50	200.0	2.737	8.12×10^{-3}	3.526	5.57×10^{-3}
0.005951	48	208.3				5.80×10^{-3}
0.005703	46	217.4				4.15×10^{-3}
0.005579	45	222.2		6.54×10^{-3}		
0.005455	44	227.3				3.89×10^{-3}
0.005207	42	238.1				4.02×10^{-3}
0.004959	40	250.0	2.729	5.97×10^{-3}	3.515	4.18×10^{-3}
0.004339	35	285.7				4.55×10^{-3}
0.003720	30	333.3	2.729	5.89×10^{-3}	3.507	5.84×10^{-3}
0.003410	27.5	363.6				8.10×10^{-3}
0.003100	25	400.0		6.84×10^{-3}		8.28×10^{-3}
0.002790	22.5	444.4				7.96×10^{-3}
0.002480	20	500.0	2.727	7.84×10^{-3}	3.502	8.55×10^{-3}
0.001860	15	666.7		9.71×10^{-3}		1.09×10^{-2}
0.001240	10	1000	2.724	1.43×10^{-2}	3.499	1.59×10^{-2}

[a] Various references are indicated in brackets.
[b] Values obtained from oscillator model in Ref. [8].

Cubic Silicon Carbide (β-SiC)

SAMUEL A. ALTEROVITZ
NASA Lewis Research Center
Cleveland, Ohio
and
JOHN A. WOOLLAM
Center for Microelectronic and Optical Materials Research
and Department of Electrical Engineering
University of Nebraska
Lincoln, Nebraska

The optical constants of 6H SiC were presented by Choyke and Palik in *HOC I* [1]. The purpose of the present critique is to present optical constants of high-quality, large-area, cubic β-SiC epitaxially grown films on (100) polished silicon wafers. This epitaxy and the advance in associated technology is a relatively recent development [2, 3] and permits electronic application using these materials. Optical-properties measurements taken so far include those in Refs. [4] and [5].

There are early references to properties of various polymorphs of SiC including bulk-grown cubic SiC that may interest the reader. Most of the references were given in [1], with additional ones listed elsewhere [6–10].

Cubic SiC films were grown on silicon substrates by S. Nishino, J. A. Powell, and others using the technique described in Refs. [2–4]. Briefly, buffer layers were formed on heated Si substrates by flowing hydrocarbon gas and hydrogen over the surface. Then crystalline SiC was grown by flowing silane, hydrocarbon, and hydrogen. Table I contains original, unpublished data, taken by variable-angle spectroscopic ellipsometry (VASE) on samples grown by J. A. Powell. Measurements at up to five angles of incidence were used for each wavelength. A model of a single film on a substrate was used, thus ignoring the possibility of an interface between the film and the substrate or of an overlayer. The refractive index of these (cubic) materials was assumed to be isotropic.

Results on two samples are reported here: a thick film (of order 10 μm), and a film approximately 6000 Å thick. For the spectral range given, the

Copyright © 1991 by Academic Press.
All rights of reproduction in any form reserved.
ISBN 0-12-544422-2

extinction coefficient, $|k|$, <0.02, which is the lower limit measurable by ellipsometry. Cubic SiC has an indirect optical band gap of approximately 2.3 eV. At 3500 Å the absorption coefficient is $3 \times 10^3\,\text{cm}^{-1}$ [5], corresponding to an extinction coefficient of <0.01, below the limit of reliable measurement by ellipsometry. Thus, the data in the table below are given down to 3500 Å.

Errors in index of refraction of the thick film were ±0.01, whereas for the 6000 Å film, errors were ±0.03. The results generally agree with the data reported for n_O of the 6H phase in Ref. [1]. The values of n reported for the thick film were lower than n_O [1] by 1%; the results for the 6000 Å film were higher than n_O in [1] by 1 to 3%. The 6000 Å film results for n were nearer to the values of n_e reported in [1].

The growth of polycrystalline β-SiC films on Si was accomplished by Spitzer *et al.* [11, 12] as early as 1959. They deposited the films on Si (heated to 1300 °C) from a gas mixture. The infrared properties were determined by study of transmittance and reflectance. Although data were obtained from 1–15 μm, we stress only the lattice-vibration region 10.5–15 μm. An oscillator fit [11, 12] yielded the parameters $\rho = 0.263 = (\omega_L^2 - \omega_T^2)\varepsilon_\infty / 4\pi\omega_T^2$, $\gamma = 0.0107 = \Gamma/\omega_T$, $\nu_O = 2.38 \times 10^{13}$ cycles/sec (12.60 μm, $\omega_T = 793.6\,\text{cm}^{-1}$), $\varepsilon_\infty = 6.7$; these are essentially the same as those obtained for αII-SiC (hexagonal) [12, 13] for reststrahlen reflection fits only. While the value of γ given here for β-SiC differs substantially from the one given in HOC I for αII-SiC ($\gamma = 0.006$, $\Gamma = 4.75\,\text{cm}^{-1}$), the effect on n and k is small except within $\omega_T \pm 5\,\text{cm}^{-1}$, where it can be as large as +30%. Therefore, the optical constants given by Choyke and Palik [1] for the ordinary ray (virtually the same as for the extraordinary ray) should suffice as a good first approximation for β-SiC. Note the definitions of the oscillator model parameters in Refs. [1, 11, 13].

REFERENCES

1. W. J. Choyke and E. D. Palik, in "Handbook of Optical Constants of Solids," (E. D. Palik, ed.), and references therein, Academic Press, Orlando, 587, (1985).
2. S. Nishino, V. Hazuki, H. Matsunami, and T. Tanaka, *J. Electrochem. Soc.* **127**, 2674 (1980).
3. S. Nishino, J. A. Powell, and H. A. Will, *Appl. Phys. Lett.* **42**, 460 (1983).
4. R. T. Holm, P. H. Klein, and P. E. R. Nordquist, Jr., *J. Appl. Phys.* **60**, 1479 (1986).
5. W. L. Choyke, L. C. Feng, and J. A. Powell, *J. Appl. Phys.* **64**, 3163 (1988).
6. M. Neuberger, in "Handbook of Electronic Materials," Vol. 5, IFI/Plenum, New York, 1971.
7. R. C. Marshall, J. W. Faust, Jr. and C. E. Ryan, eds., "Silicon Carbide 1973," University of South Carolina Press, Columbia, South Carolina, (1974).
8. J. A. Powell, *J. Opt. Soc. Amer.* **62**, 3411 (1972).
9. P. T. B. Shaffer and R. G. Naum, *J. Opt. Soc. Am.* **59**, 1498 (1969).
10. G. Derst, C. Wilbertz, K. L. Bhatia, W. Kratschmer, and S. Kalbitger, *Appl. Phys. Lett.* **54**, 1722 (1989).

11. W. G. Spitzer, D. A. Kleinman, and C. J. Frosch, *Phys. Rev.* **113**, 133 (1959).
12. W. G. Spitzer, D. A. Kleinman, C. J. Frosch, and D. J. Walsh, in "Silicon Carbide, A High Temperature Semiconductor," (J. R. O'Connor and J. Smiltens, eds.), Pergamon, New York, 347 (1960).
13. W. G. Spitzer, D. A. Kleinman, and D. Walsh, *Phys. Rev.* **113**, 127 (1959).

TABLE I

Index of Refraction of Epitaxially Grown Cubic SiC

E (eV)	cm^{-1}	μm	n (10 μm film)	n (6100 Å film)
3.543	28,576	0.350	2.828	2.83
3.444	27,777	0.360	2.800	2.89
3.351	27,027	0.370	2.780	2.85
3.263	26,318	0.380	2.763	2.77
3.179	25,640	0.390	2.749	2.81
3.100	25,003	0.400	2.738	2.74
3.024	24,390	0.410	2.727	2.78
2.952	23,809	0.420	2.719	2.80
2.884	23,261	0.430	2.710	2.78
2.818	22,729	0.440	2.702	2.77
2.756	22,228	0.450	2.693	2.72
2.696	21,745	0.460	2.687	2.72
2.638	21,277	0.470	2.680	2.73
2.583	20,833	0.480	2.673	2.72
2.531	20,414	0.490	2.664	2.73
2.480	20,000	0.500	2.664	2.72
2.431	19,607	0.510	2.658	2.63
2.385	19,236	0.520	2.654	2.67
2.340	18,873	0.530	2.650	2.69
2.296	18,518	0.540	2.645	2.71
2.255	18,188	0.550	2.640	2.70
2.214	17,857	0.560	2.636	2.68
2.175	17,542	0.570	2.632	2.69
2.138	17,244	0.580	2.630	2.67
2.102	16,954	0.590	2.621	2.69
2.067	16,667	0.600	2.621	2.71
2.033	16,397	0.610	2.617	2.64
2.000	16,131	0.620	2.613	2.66
1.968	15,873	0.630	2.613	2.66
1.938	15,631	0.640	2.608	2.65
1.908	15.389	0.650	2.604	2.66
1.879	15,155	0.660	2.605	2.68
1.851	14,929	0.670	2.606	2.65
1.826	14,728	0.680	2.599	2.66
1.797	14,494	0.690	2.594	2.67
1.771	14,286	0.700	2.588	2.66

$k < 0.01$ over the entire spectral range.

Tellurium (Te)

EDWARD D. PALIK
Institute for Physical Science and Technology
University of Maryland
College Park, Maryland

Te has been studied in some detail because
(1) it has a small band gap (0.335 eV, comparable to that of InAs, 0.35 eV, and PbS, 0.45 eV);
(2) this trigonal crystal is birefringent, making it useful as a nonlinear crystal for producing second-harmonic generation by orientation of the index ellipsoid, so that the ordinary index ($\perp$) at the fundamental (say 10.6 μm) can be matched to the extraordinary index ($\parallel$) at 5.3 μm [1];
(3) its band structure is similar to the "classic" III-V compound semiconductor InSb.

Te is a direct-band-gap semiconductor ($E_g = 0.33$ eV), which can be doped to produce free-carrier absorption. When p-doped, interband transitions between the split-off valence band and the heavy- and light-hole bands can be seen peaked at 900 cm^{-1} but covering a broad region of the near IR from 5–20 μm. Good collections of many of the properties of Te are given in Refs. [2, 3].

The room-temperature n and k values chosen in this critique are listed in Table II. These numbers are plotted in Fig. 1. The data were obtained by reading expanded graphs or tables in the original literature or from private-communication data. The references indicated in brackets in the n and k columns pertain down the column until a new reference appears.

Wagner [4] measured the dielectric constants of Te at two wavelengths, 3.2 cm and 8.5 mm, between -170 °C and room temperature. At 3.2 cm a standing-wave, node method was used in which the Te sample was placed at one end of the expandable microwave arm, sandwiched between a crystal-quartz plate and a shorting plate. At 8.5 mm a smaller, more detailed sample holder was used. After some analysis, the following low-temperature values were obtained: at 3.2 cm, $\varepsilon_\parallel = 53$ and $\varepsilon_\perp = 33$; at 8.5 mm, $\varepsilon_\parallel = 55$ and $\varepsilon_\perp = 32.5$. At 3.2 cm there seems to be a slight decrease in ε as the temperature is lowered from room temperature (~13 °C is the highest value from the graphs), then a flattening out. At 8.5 mm there is a

Copyright © 1991 by Academic Press.
All rights of reproduction in any form reserved.
ISBN 0-12-544422-2

slight rise, then a plateauing or decrease in ε. The conductivity is observed to decrease at the same time. We must conclude that the stated hole concentration of $N = 5 \times 10^{14}\,\mathrm{cm}^{-3}$ puts the plasma frequency $\omega_p = 4\pi Ne^2/\varepsilon m^*$ near 3.6 cm, and these slight variations in ε are indications that the free carriers are freezing out, revealing the dielectric constant of the lattice. (We used $e = 4.77 \times 10^{-10}$ esu, $\varepsilon_\parallel = 55$, $m^* = 0.11(9.1 \times 10^{-28}\,\mathrm{gm.})$) Subsequent use of these (low-temperature, hole-free) $\varepsilon_{\parallel,\perp}$ values as room-temperature data must be kept in mind. All subsequent Te samples in this collection of data will have comparable or larger free-carrier concentrations.

The lattice-vibration region in the far IR from 60–500 cm^{-1} has been measured in reflection and transmission by Geick *et al.* [5] with a Perkin–Elmer Model 301 grating spectrometer (sample at 300 K). Similar work over a shorter spectral range has been done by Lucovsky *et al.* [6], who concentrated on the reststrahlen reflectivity. Both groups fitted their reflectivities with the same type of Lorentz-oscillator model. Although the numbers are similar, some differences occur. More recently, Rautenberg [7] has measured the far-infrared reflectivity at 300 K with a Fourier transform infrared spectrometer. We choose these more recent data as analyzed with the same oscillator model, namely

$$(n - ik)^2 = \varepsilon_1 - i\varepsilon_2 = \varepsilon = \varepsilon_\infty + \frac{\Delta\varepsilon_j \nu_{Tj}^2}{\nu_{Tj}^2 - \nu^2 + i\Gamma_j \nu}$$

for each polarization. ε_∞ is the high-frequency dielectric constant at ~8 μm, ν_T is the transverse optic phonon frequency (cm^{-1}), $\Delta\varepsilon$ is the change in dielectric function upon passing through the resonant frequency from near IR to dc (oscillator strength), and Γ is the phonon damping constant (cm^{-1}). These are listed in Table I. The corresponding parameters of Geick *et al.* and Lucovsky *et al.* ($4\pi\rho = \Delta\varepsilon$ and $\gamma\nu_T = \Gamma$) vary significantly from these in some cases, and we list all three sets of parameters just to illustrate typical differences between laboratories.

The difference in the corresponding parameters indicates that we cannot hope to know n and k to better than one or, at most, two significant figures. Such large differences suggest crystal misorientation, poor polish, or filtering problems for grating spectrometers, all of which would affect R.

We are also confused by the different values of ε_∞ obtained by the three groups, since presumably these numbers are well known in the 5–10 μm region [8, 9], and they should have been used in the fitting process by all the groups. Caldwell and Fan [9] determined $n_\perp = 4.81$ ($\varepsilon_\perp = 23.1$) and $n_\parallel = 6.25$ ($\varepsilon_\parallel = 39.0$) at 8 μm. The fact that $\varepsilon_\parallel$ is as low as 36 suggests that the measured high-frequency reflectivity was too low.

Also of note is the dc dielectric constant obtained from each model: $\varepsilon_{o\parallel}=54.0$ and $\varepsilon_{o\perp}=34.7$ for Geick *et al.*; $\varepsilon_{o\parallel}=45.2$ and $\varepsilon_{o\perp}=30.6$ for Lucovsky *et al.*, and $\varepsilon_{o\parallel}=43.2$ and $\varepsilon_{o\perp}=30.1$ for Rautenberg. These values are to be compared with the values of Wagner: $\varepsilon_{\parallel}=54$ and $\varepsilon_{\perp}=33$. Measurement of reflectivity to 1000 μm is surely the easiest way to determine ε_o.

The region of multiphonon absorption above the fundamental TO frequency has been measured by Grosse and Richter [10] and Geick *et al.* [5]. Both sets of data are similar, but we chose the latter, more complete data as obtained with a Perkin–Elmer spectrophotometer Model 301 at 300 K. Polarization was obtained with polyethylene wire-grid polarizers. The k data as listed in Table II have somewhat less detail than the figures of Ref. [5] because of the coarse grid we used to read the values of the absorption coefficient from expanded graphs. Since the index of refraction was not determined in these measurements, the values listed are from a Lorentz-oscillator fit [7], which ignored this small amount of multiphonon absorption. Note that the values of k for the oscillator fit near ν_T are always less than the measured values of Geick *et al.*, as is to be expected.

The index of refraction has been measured in the near IR from 4–14 μm by Caldwell and Fan [9] using the minimum angle-of-deviation method for a collimated beam passing through an 8°16′ Te prism. However, it was not a single crystal but consisted of several crystallites with boundaries parallel to the c axis. Since the c axis was perpendicular to both the refracting edge and the base of the prism, light could be polarized $\parallel$ and $\perp$ to c for the measurement. Similar prism measurements were done earlier by Hartig and Loferski [8] with Te doped to $p=10^{17}\,\mathrm{cm}^{-3}$. These values, measured to two decimal places, were about 0.04 larger for $n_\perp$ and about 0.05 smaller for $n_\parallel$. This sort of difference could be due to a slight variation of the direction of the c axis, which was supposedly perpendicular to the refracting edge and the base. Note in Fig. 1 that the measured values of n [9] do not join smoothly with the calculated values obtained from the oscillator model [7].

p-Te with $1.25\times10^{17}\,\mathrm{cm}^{-3}$ holes at 300 K shows interband hole absorption (split-off valence band to light- and heavy-hole bands) peaked near $900\,\mathrm{cm}^{-1}$ for $\mathbf{E}\parallel c$ ($\alpha_\parallel=110\,\mathrm{cm}^{-1}$) and much less absorption ($\alpha_\perp=3\,\mathrm{cm}^{-1}$) for $\mathbf{E}\perp c$. We usually would not include such structure because it is extrinsic. However, for $1.7\times10^{15}\,\mathrm{cm}^{-3}$ at 297 K the peak is much smaller and data of Caldwell and Fan are included in Table II because the hole absorption is located just between the multiphonon absorption (which is decreasing to higher frequency) and the band gap absorption (which is increasing to higher frequency). n-Te would not show such absorption.

The absorption in the 5–3 μm region reaches a minimum at 5 μm and begins to increase rapidly at 4 μm as the band gap is neared. The values in this minimum of absorption at 5 μm vary considerably in the literature

depending on whether the material is *n*- or *p*-type; lightly doped *n*-type or *p*-type material with less than $1\times10^{15}\,cm^{-3}$ is desirable to obtain intrinsic results. With such a small band gap, pure Te is expected to be slightly intrinsic at 300 K with electrons as the electrical conductors. As an example, at 5 μm $k_{\|}=4.4\times10^{-4}$ [2], 7.2×10^{-5} [9], 3.7×10^{-4} [11], $<1.1\times10^{-5}$ [12].

The band-edge and higher-energy regions have been studied by several groups by transmission of thin plates [2, 12] and by reflectivity and Kramers–Kronig analysis by Tutihasi *et al.* [12], Merdy [13], and Bammes *et al.* [14]. We have used the data of Tutihasi *et al.* as the basis data (because it represents the lowest free-carrier concentration) over the range 0.3–12 eV, and we have added other sets of data for comparison and overlap. We read expanded graphs of absorption coefficient $\alpha=4\pi k/\lambda$ and ε_1 and ε_2 [12] and calculated *n* and *k*. At the fundamental edge between 0.37 and 0.45 eV, the data of Refs. [2] and [12] obtained from transmission measurements of thin plates are in good agreement. In Ref. [2] there is a table of *n* and *k* over a part of this spectral region (1.4–3.0 eV), presumably obtained from Ref. [12], but it is not exhibited in Ref. [12]. We include both sets of data to illustrate how two separate determinations agree (or disagree). The IR data were obtained with a Leiss monochromator equipped with a LiF prism and a double-plate Si transmission polarizer utilizing Brewster's angle. The UV reflectivity data were obtained with a McPherson 0.5 m monochromator with a 600 line/mm grating blazed at 1500 Å and a biotite plate used as a Brewster-angle reflection polarizer. In the various papers there is considerable discussion of excitons, and direct and indirect gaps; since we are only interested in optical constants, these interpretations are not of primary interest.

Bammes *et al.* have made synchrotron-radiation measurements of reflectivity from 3–30 eV. However, to determine absolute reflectivity, they had to normalize their measurements between 3.5 and 6 eV to the spectra of Tutihasi *et al.* For this reason, we still stress the Tutihasi *et al.* data in Table II. The sample was cleaved with the *c* axis in the sample plane. Since the synchrotron, premirror, and grating each tended to polarize the light linearly, the sample was rotated 90° in its near-normal-incidence position to change from ∥ to ⊥. Peaks in *k* appear to be more clear-cut in the data of Tutihasi *et al.* The overlap of the data of Refs. [7] and [13] is poor, principally in the vicinity of 6 eV.

Since X-ray scattering cross-sections have been determined for many elemental materials above 30 eV, we have used the model of Henke *et al.* [15] to calculate *n* and *k* from 4–250 Å. Since the model takes into account only the number of atoms/cm^3 and not the lattice structure, there is no ∥ and ⊥ designation. The absorption edges of Te [16] are found at *K* (31.811 keV), L_1(4.939 keV), L_2(4.612 keV), L_3(4.341 keV) and most of these appear in Fig. 1. Other broader peaks are made up of many M_3N_1,

$M_4O_{2,3}$, M_3M_5 transitions. Other lower-energy transitions are merged into the band structure. Although there is no overlap with the Bammes *et al.* data, extrapolation of both sets of data until they meet seems to be feasible.

ACKNOWLEDGMENTS

We thank W. R. Hunter for calculating the optical constants in the X-ray region. P. Grosse and V. Saile kindly provided unpublished data in the far IR and VIS–UV regions, respectively.

REFERENCES

1. G. H. Sherman and P. D. Coleman, *J. Appl. Phys.* **44**, 238 (1973).
2. P. Grosse and W. Richter, in "Landolt–Börnstein Numerical Data and Functional Relationships in Science and Technology," (K.-H. Hellwege, ed.), Vol. 17, Springer-Verlag, Berlin, 106 (1983).
3. P. Grosse, in "Springer Tracts in Modern Physics," (G. Höhler, ed.), Vol. 48, Springer, Berlin, (1969).
4. H. Wagner, *Z. Physik* **193**, 218 (1966).
5. R. Geick, P. Grosse, and W. Richter, in "Physics of Selenium and Tellurium," (W. C. Cooper, ed.), Pergamon, New York, 309 (1969).
6. G. Lucovsky, R. C. Keezer, and E. Burstein, *Solid State Comm.* **5**, 439 (1967).
7. M. Rautenberg, Ph.D. thesis, Der Rheinisch-Westfäleschen Technischen Hochschule Aachen, (1977); private communication from P. Grosse.
8. P. A. Hartig and J. J. Loferski, *J. Opt. Soc. Am.* **44**, 17 (1954).
9. R. S. Caldwell and H. Y. Fan, *Phys. Rev.* **114**, 664 (1959).
10. P. Grosse and W. Richter, *Phys. Stat. Solidi* **41**, 239 (1970).
11. J. J. Loferski, *Phys. Rev.* **93**, 707 (1954).
12. S. Tutihasi, G. G. Roberts, R. C. Keezer, and R. E. Drews, *Phys. Rev.* **177**, 1143 (1969).
13. H. Merdy, *Ann. Phys. Paris* **1**, 289 (1966).
14. P. Bammes, R. Klucker, E. E. Koch, and T. Tuomi, *Phys. Stat. Solidi (b)* **49**, 561 (1972); private communication from T. Saile.
15. B. L. Henke, P. Lee, T. J. Tanaka, R. L. Shimabukuro, and B. K. Fujikama, *At. Data Nucl. Data Tables* **27**, 1 (1982).
16. D. E. Gray, ed., "American Institute of Physics Handbook," Third Edition, McGraw-Hill, New York, 7 (1982).

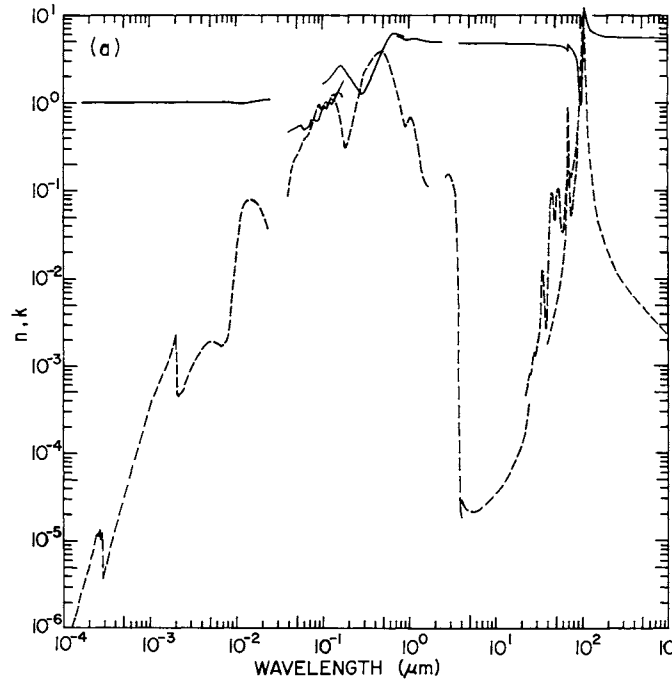

Fig. 1. (a) Log–log plot of n_o (solid line) and k_o (dashed line) versus wavelength in micrometers for tellurium. (b) Log–log plot of n_e (solid line) and k_e (dashed line) versus wavelength in micrometers.

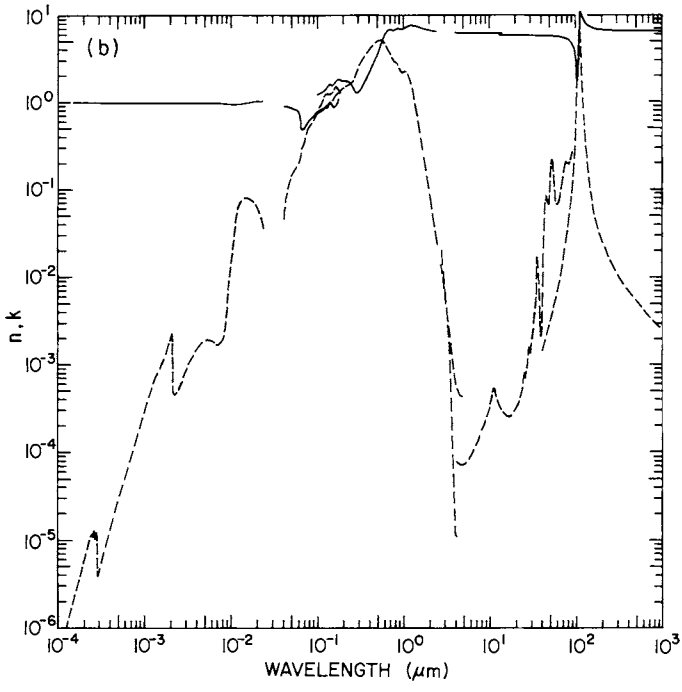

TABLE I

Parameters Obtained from Fitting an Oscillator Model to Reflectivity

	$\Delta\varepsilon$			$\nu_\Gamma(\mathrm{cm}^{-1})$			$\Gamma(\mathrm{cm}^{-1})$			ε_∞		
	[7]	[5]	[6]	[7]	[5]	[6]	[7]	[5]	[6]	[7]	[5]	[6]
∥	7.2	18	5.6	88.1	86.5	90	3.5	4.0	3.6	36	36	39.5
⊥	7.0	11	7.5	92.4	92	92	3.0	4.0	3.2	23	23	22.9
	0.14	0.73	0.25	141.1	142	144	2.7	6.5	5.8			

TABLE II

Values of *n* and *k* for Tellurium from Various References[a]

eV	Å	n	k
9972	1.243	0.9999889[15]	1.04x10^{-6}[15]
9331	1.329	0.9999878	1.23x10^{-6}
8909	1.392	0.9999866	1.46x10^{-6}
8507	1.458	0.9999853	1.73x10^{-6}
8123	1.526	0.9999840	2.05x10^{-6}
7756	1.599	0.9999825	2.43x10^{-6}
7406	1.674	0.9999809	2.87x10^{-6}
7072	1.753	0.9999791	3.40x10^{-6}
6752	1.836	0.9999720	4.01x10^{-6}
6447	1.923	0.9999752	4.73x10^{-6}
6156	2.014	0.9999731	5.58x10^{-6}
5878	2.109	0.9999709	6.57x10^{-6}
5613	2.209	0.9999860	7.73x10^{-6}
5359	2.314	0.9999640	9.08x10^{-6}
5117	2.423	0.9999645	1.07x10^{-5}
5000	2.480	0.9999640	1.15x10^{-5}
4886	2.538	0.9999635	1.10x10^{-5}
4775	2.597	0.9999621	1.19x10^{-5}
4665	2.658	0.9999622	1.30x10^{-5}
4559	2.720	0.9999619	1.03x10^{-5}
4455	2.783	0.9999603	1.12x10^{-5}
4353	2.848	0.9999635	1.21x10^{-5}
4254	2.915	0.9999568	3.84x10^{-6}
4157	2.983	0.9999523	4.17x10^{-6}
4062	3.053	0.9999486	4.53x10^{-6}
3878	3.197	0.9999417	5.34x10^{-6}
3703	3.348	0.9999347	6.30x10^{-6}
3536	3.506	0.9999273	7.42x10^{-6}
3376	3.672	0.9999194	8.75x10^{-6}
3224	3.846	0.9999108	1.03x10^{-5}
3078	4.028	0.9999015	1.22x10^{-5}
2939	4.218	0.999891	1.43x10^{-5}
2807	4.418	0.999880	1.69x10^{-5}
2680	4.627	0.999868	1.98x10^{-5}
2559	4.846	0.999855	2.34x10^{-5}
2443	5.075	0.999840	2.75x10^{-5}
2333	5.315	0.999825	3.23x10^{-5}
2228	5.557	0.999807	3.80x10^{-5}
2127	5.829	0.999789	4.46x10^{-5}
2031	6.105	0.999768	5.24x10^{-5}
1939	6.394	0.999745	6.13x10^{-5}
1852	6.696	0.999722	7.18x10^{-5}
1768	7.013	0.999696	8.42x10^{-5}
1688	7.344	0.999668	9.84x10^{-5}
1612	7.691	0.999637	1.15x10^{-4}
1539	8.055	0.999605	1.34x10^{-4}
1470	8.436	0.999570	1.56x10^{-4}
1403	8.835	0.999533	1.82x10^{-4}

TABLE II (*Continued*)

Tellurium

eV	Å	n	k
1340	9.253	0.999494	2.11×10^{-4}
1280	9.690	0.999452	2.45×10^{-4}
1222	10.15	0.999408	2.85×10^{-4}
1167	10.63	0.999363	3.31×10^{-4}
1114	11.13	0.999318	3.85×10^{-4}
1064	11.66	0.999274	4.48×10^{-4}
1016	12.21	0.999240	5.20×10^{-4}
969.7	12.79	0.999209	5.82×10^{-4}
925.9	13.39	0.999167	6.57×10^{-4}
884.1	14.02	0.999139	7.46×10^{-4}
844.2	14.69	0.999141	8.34×10^{-4}
806.0	15.38	0.999114	8.63×10^{-4}
769.7	16.11	0.999035	9.58×10^{-4}
734.9	16.87	0.998983	1.10×10^{-3}
701.7	17.67	0.998973	1.27×10^{-3}
670.0	18.51	0.999018	1.46×10^{-3}
639.8	19.38	0.999111	1.66×10^{-3}
610.9	20.30	0.999339	1.96×10^{-3}
596.9	20.77	0.999620	2.14×10^{-3}
583.3	21.26	1.000231	2.33×10^{-3}
570.0	21.75	1.001085	5.00×10^{-4}
557.0	22.26	1.000177	4.59×10^{-4}
531.8	23.31	0.999560	4.53×10^{-4}
507.8	24.42	0.999210	4.89×10^{-4}
484.9	25.57	0.99893	5.37×10^{-4}
463.0	26.78	0.99867	6.01×10^{-4}
442.1	28.05	0.99843	6.73×10^{-4}
422.1	29.37	0.99818	7.57×10^{-4}
403.0	30.76	0.99794	8.66×10^{-4}
384.8	32.22	0.99770	9.89×10^{-4}
367.5	33.74	0.99748	1.09×10^{-3}
350.9	35.34	0.99723	1.19×10^{-3}
335.0	37.01	0.99696	1.31×10^{-3}
319.9	38.76	0.99669	1.41×10^{-3}
305.5	40.59	0.99639	1.51×10^{-3}
291.7	42.51	0.99605	1.61×10^{-3}
278.5	44.52	0.99568	1.71×10^{-3}
265.9	46.63	0.99530	1.80×10^{-3}
253.9	48.83	0.99486	1.86×10^{-3}
242.5	51.14	0.99436	1.91×10^{-3}
231.5	53.56	0.99378	1.94×10^{-3}
221.1	56.09	0.99312	1.96×10^{-3}
211.1	58.74	0.99236	1.93×10^{-3}
201.5	61.52	0.99144	1.90×10^{-3}
192.4	64.43	0.99037	1.84×10^{-3}
183.7	67.48	0.9891	1.76×10^{-3}
175.5	70.67	0.9874	1.71×10^{-3}
167.5	74.01	0.9856	1.73×10^{-3}

TABLE II (*Continued*)

Tellurium

eV	Å	n	k
160.0	77.51	0.9833	1.79×10^{-3}
152.7	81.17	0.9805	1.94×10^{-3}
145.8	85.01	0.9768	2.43×10^{-3}
142.5	87.00	0.9747	2.88×10^{-3}
139.3	89.03	0.9724	3.64×10^{-3}
136.1	91.11	0.9699	4.62×10^{-3}
133.0	93.24	0.9673	5.87×10^{-3}
129.9	95.42	0.9644	7.45×10^{-3}
127.0	97.66	0.9614	9.45×10^{-3}
124.1	99.94	0.9581	1.20×10^{-2}
121.2	102.3	0.9547	1.55×10^{-2}
118.5	104.7	0.9515	2.00×10^{-2}
115.8	107.1	0.9493	2.57×10^{-2}
113.1	109.6	0.9483	3.11×10^{-2}
108.0	114.8	0.9469	4.34×10^{-2}
103.1	120.2	0.9522	5.68×10^{-2}
98.47	125.9	0.9600	6.60×10^{-2}
94.03	131.9	0.9680	7.26×10^{-2}
89.78	138.1	0.9767	7.67×10^{-2}
85.73	144.6	0.9854	7.99×10^{-2}
81.85	151.5	0.99376	8.03×10^{-2}
78.16	158.6	1.00126	7.98×10^{-2}
74.63	166.1	1.00741	7.82×10^{-2}
71.26	174.0	1.0140	7.63×10^{-2}
68.04	182.2	1.0193	7.33×10^{-2}
64.97	190.8	1.0250	6.85×10^{-2}
62.04	199.9	1.0278	6.29×10^{-2}
59.24	209.3	1.0311	5.65×10^{-2}
56.56	219.2	1.0302	4.92×10^{-2}
54.01	229.6	1.0286	4.35×10^{-2}
51.57	240.4	1.0265	3.59×10^{-2}

eV	cm^{-1}	μm	$n_o(\perp)$	$k_o(\perp)$	$n_e(\parallel)$	$k_e(\parallel)$
30		0.04133	0.46[14]	0.088[14]	0.90[14]	0.045[14]
29		0.04275	0.47	0.13	0.90	0.067
28		0.04428	0.48	0.17	0.89	0.090
27		0.04592	0.48	0.19	0.88	0.10
26		0.04769	0.50	0.20	0.87	0.12
25		0.04959	0.52	0.23	0.86	0.14
24		0.05166	0.54	0.25	0.85	0.15
23		0.05391	0.54	0.26	0.84	0.16
22		0.05636	0.56	0.29	0.83	0.18
21		0.05904	0.55	0.33	0.82	0.18
20		0.06199	0.50	0.38	0.74	0.20
19		0.06526	0.51	0.40	0.49	0.30
18		0.06888	0.52	0.41	0.48	0.31

TABLE II (*Continued*)

Tellurium

eV	cm^{-1}	μm	n_o (⊥)	k_o (⊥)	n_e (∥)	k_e (∥)
17		0.07293	0.56	0.46	0.51	0.39
16		0.07749	0.64	0.55	0.59	0.49
15		0.08266	0.62	0.70	0.64	0.55
14.5		0.08551	0.62	0.76	0.65	0.57
14		0.08856	0.59	0.87	0.67	0.59
13.5		0.09184	0.61	0.93	0.71	0.64
13		0.09537	0.69	0.94	0.73	0.69
12.5		0.09919	0.85	0.85	0.75	0.72
12	96,786	0.1033	0.87	0.87	0.79	0.76
			1.64[12]	0.70[12]	1.22[12]	0.82[12]
11.5	92,753	0.1078	1.70	0.83	1.24	0.89
			0.84[14]	0.90[14]	0.79[14]	0.75[14]
11	88,720	0.1127	0.84	1.01	0.80	0.77
			1.74[12]	0.92[12]	1.26[12]	0.95[12]
10.5	84,688	0.1181	1.84	1.04	1.33	1.09
			0.98[14]	0.98[14]	0.83[14]	0.80[14]
10.0	80,655	0.1240	0.99	1.04	0.86	0.86
			1.93[12]	1.06[12]	1.36[12]	1.21[12]
9.5	76,622	0.1305	2.08	1.11	1.47	1.25
			0.96[14]	1.20[14]	0.84[14]	0.95[14]
9.0	72,589	0.1378	1.11	1.24	0.99	0.93
			2.27[12]	1.12[12]	1.60[12]	1.25[12]
8.75	70,573	0.1417	2.35	1.06	1.59	1.23
8.5	68,557	0.1459	2.39	1.00	1.55	1.23
			1.25[14]	1.25[14]	0.96[14]	0.96[14]
8.25	66,540	0.1503	2.45[12]	0.96[12]	1.54[12]	1.30[12]
8.0	64,524	0.1550	2.59	0.91	1.54	1.37
			1.40[14]	1.36[14]	0.85[14]	1.06[14]
7.75	62,507	0.1600	2.61[12]	0.77[12]	1.60[12]	1.47[12]
7.5	60,491	0.1653	2.60	0.69	1.72	1.51
			1.66[14]	1.29[14]	0.92[14]	1.20[14]
7.25	58,475	0.1710	2.57[12]	0.55[12]	1.81[12]	1.44[12]
7.0	56,458	0.1771	2.48	0.40	1.83	1.36
			1.81[14]	1.18[14]	1.08[14]	1.29[14]
6.75	54,442	0.1837	2.35[12]	0.32[12]	1.79[12]	1.34[12]
6.5	52,426	0.1907	2.19	0.32	1.78	1.36
6.25	50,409	0.1984	2.04	0.36	1.73	1.41
6.0	48,393	0.2066	1.94	0.39	1.73	1.45
5.75	46,377	0.2156	1.82	0.47	1.72	1.51
5.5	44,360	0.2254	1.74	0.51	1.72	1.57
5.25	42,344	0.2362	1.59	0.69	1.71	1.58
5.0	40,327	0.2480	1.47	0.82	1.63	1.60
4.75	38,311	0.2610	1.39	1.01	1.49	1.71
4.5	36,295	0.2755	1.28	1.28	1.32	1.96
4.25	34,278	0.2917	1.27	1.65	1.25	2.31
4.0	32,262	0.3100	1.32	2.01	1.33	2.64
3.75	30,246	0.3306	1.50	2.37	1.44	3.06
3.5	28,229	0.3542	1.72	2.70	1.69	3.44

TABLE II (*Continued*)

Tellurium

eV	cm^{-1}	μm	$n_o(\perp)$	$k_o(\perp)$	$n_e(\parallel)$	$k_e(\parallel)$
3.25	26,213	0.3815	2.02	3.03	1.92	3.78
3.069	24,750	0.4040	2.37[2]	3.29[2]	2.22[2]	3.96[2]
3.0	24,196	0.4133	2.51[12]	3.39[12]	2.30[12]	4.16[12]
2.976	24,000	0.4167	2.56[2]	3.39[2]	2.35[2]	4.15[2]
2.883	23,250	0.4301	2.77	3.47	2.54	4.27
2.8	22,583	0.4428	3.03[12]	3.63[12]	2.73[12]	4.42[12]
2.790	22,500	0.4444	3.01[2]	3.57[2]	2.76[2]	4.39[2]
2.697	21,750	0.4598	3.27	3.66	2.98	4.52
2.604	21,000	0.4762	3.55	3.72	3.21	4.71
2.6	20,970	0.4769	3.57[12]	3.75[12]	3.25[12]	4.77[12]
2.534	20,440	0.4892	3.76[2]	3.76[2]	3.46[2]	4.85[2]
2.487	20,060	0.4985	3.91	3.77	3.63	4.93
2.441	19,690	0.5079	4.07	3.77	3.81	5.01
2.4	19,357	0.5166	4.24[12]	3.77[12]	3.94[12]	5.08[12]
2.394	19,310	0.5179	4.25[2]	3.78[2]	3.99[2]	5.08[2]
2.348	18,940	0.5280	4.43	3.76	4.20	5.16
2.301	18,560	0.5388	4.62	3.69	4.39	5.20
2.255	18,190	0.5498	4.81	3.63	4.65	5.21
2.209	17,820	0.5612	5.01	3.57	4.91	5.20
2.2	17,744	0.5636	5.10[12]	3.61[12]	4.94[12]	5.16[12]
2.162	17,440	0.5734	5.26[2]	3.52[2]	5.17[2]	5.16[2]
2.166	17,070	0.5858	5.49	3.37	5.45	5.06
2.069	16,690	0.5992	5.67	3.16	5.76	4.92
2.023	16,320	0.6127	5.82	2.94	6.00	4.77
2.0	16,131	0.6199	5.94[12]	2.69[12]	4.67[12]	4.67[12]
1.976	15,940	0.6274	5.97[2]	2.70[2]	6.21[2]	4.60[2]
1.930	15,570	0.6423	6.07	2.45	6.40	4.36
1.883	15,190	0.6583	6.11	2.25	6.58	4.10
1.837	14,820	0.6748	6.12	2.02	6.77	3.86
1.8	14,518	0.6888	6.10[12]	1.80[12]	6.89[12]	3.70[12]
1.790	14,440	0.6925	6.09[2]	1.72[2]	6.85[2]	3.65[2]
1.744	14,070	0.7107	6.04	1.52	6.86	3.47
1.697	13,690	0.7305	5.95	1.36	6.80	3.18
1.651	13,320	0.7508	5.87	1.26	6.78	3.03
1.604	12,940	0.7728	5.86	1.17	6.74	2.93
1.6	12,905	0.7749	5.88[12]	1.15[12]	6.75[12]	2.91[12]
1.557	12,560	0.7962	5.84[2]	1.06[2]	6.73[2]	2.89[2]
1.511	12,190	0.8203	5.78	0.895	6.81	2.86
1.464	11,810	0.8467	5.68	0.760	6.95	2.80
1.418	11,440	0.8741	5.59	0.659	7.14	2.56
1.4	11,292	0.8856	5.56[12]	0.63[12]	7.11[12]	2.46[12]
1.3	10,485	0.9537	5.36	0.54	6.87	2.16
1.2	9,679	1.033	5.17	0.63	6.99	2.22
1.1	8,872	1.127	5.33	0.68	7.51	2.10
1.0	8,065	1.240	5.35	0.45	7.70	1.56
0.9	7,259	1.378	5.22	0.22	7.48	0.94
0.8	6,452	1.550	5.10	0.13	7.23	0.48
0.7	5,646	1.771	4.95	0.11	7.00	0.24

TABLE II (*Continued*)

Tellurium

eV	cm^{-1}	μm	n_o (⊥)	k_o (⊥)	n_e (∥)	k_e (∥)
0.6	4,839	2.066	4.93		6.71	7.5×10^{-2}
0.5	4,033	2.480	4.90		6.53	2.3×10^{-2}
0.45	3,629	2.755		0.145[12]		2.02×10^{-2}[12]
0.44	3,549	2.818		0.150		1.52×10^{-2}
0.43	3,468	2.883		0.151		1.15×10^{-2}
0.42	3,388	2.952		0.150		8.69×10^{-3}
0.41	3,307	3.024		0.149		6.74×10^{-3}
0.40	3,226	3.100		0.148		5.18×10^{-3}
0.39	3,146	3.179		0.139		3.79×10^{-3}
0.38	3,065	3.263		0.125		2.60×10^{-3}
0.37	2,984	3.351		0.115		1.65×10^{-3}
0.365	2,944	3.397				1.35×10^{-3}
0.36	2,904	3.444		0.104		1.07×10^{-3}
0.355	2,863	3.493				7.64×10^{-4}
0.35	2,823	3.542		7.89×10^{-2}		4.93×10^{-4}
0.345	2,783	3.594		6.86×10^{-2}		3.15×10^{-4}
0.34	2,742	3.647		5.51×10^{-2}		1.68×10^{-4}
0.335	2,702	3.701		2.65×10^{-2}		9.13×10^{-5}
0.33	2,662	3.757		5.98×10^{-3}		5.08×10^{-5}
0.325	2,621	3.815		1.28×10^{-3}		2.79×10^{-5}
0.32	2,581	3.875		2.78×10^{-4}		1.88×10^{-5}
0.315	2,541	3.936		8.77×10^{-5}		1.45×10^{-5}
0.31	2,500	4.000	4.929[9]	3.18×10^{-5}	6.372[9]	1.18×10^{-5}
0.305	2,460	4.065		1.94×10^{-5}		1.10×10^{-5}
0.30	2,420	4.133		1.81×10^{-5}		1.09×10^{-5}
0.2976	2,400	4.167		2.92×10^{-5}[9]		7.96×10^{-5}[9]
0.2728	2,200	4.545		2.35×10^{-5}		7.23×10^{-5}
0.2480	2,000	5.000	4.864	2.19×10^{-5}	6.316	7.48×10^{-5}
0.2232	1,800	5.556		2.03×10^{-5}		7.60×10^{-5}
0.2066	1,667	6	4.838		6.286	
0.1984	1,600	6.250		2.09×10^{-5}		9.10×10^{-5}
0.1771	1,429	7	4.821		6.257	
0.1736	1,400	7.143		2.27×10^{-5}		1.31×10^{-4}
0.1550	1,250	8	4.809		6.253	
0.1488	1,200	8.333		2.59×10^{-5}		1.82×10^{-4}
0.1240	1,000	10.00	4.796	3.18×10^{-5}	6.246	3.34×10^{-4}
0.1116	900	11.11		3.63×10^{-5}		5.31×10^{-4}
0.1033	833.3	12	4.789		6.237	
0.09919	800	12.50		4.28×10^{-5}		3.68×10^{-4}
0.09299	750	13.33	4.78[7]		5.99[7]	
0.08856	714.3	14	4.785[9]		6.230[9]	
0.08679	700	14.29		5.34×10^{-5}		2.96×10^{-4}
0.07439	600	16.67		7.23×10^{-5}		2.52×10^{-4}
0.06199	500	20.00	4.77[7]	1.16×10^{-4}	5.98[7]	3.09×10^{-4}
0.05579	450	22.22		1.59×10^{-4}		3.89×10^{-4}
0.05455	440	22.73		4.52×10^{-4}[5]		4.16×10^{-4}[5]
0.05331	430	23.26		5.37×10^{-4}		4.81×10^{-4}
0.05207	420	23.81		6.06×10^{-4}		5.87×10^{-4}

TABLE II (*Continued*)

Tellurium

eV	cm^{-1}	μm	n_o (⊥)	k_o (⊥)	n_e (∥)	k_e (∥)
0.05083	410	24.39		6.79×10^{-4}		7.38×10^{-4}
0.04959	400	25.00		7.66×10^{-4}		8.16×10^{-4}
			4.75	3.58×10^{-4} [9]	5.97	7.36×10^{-4} [9]
0.04835	390	25.64		7.96×10^{-4} [5]		7.14×10^{-4} [5]
0.04711	380	26.32		8.38×10^{-4}		7.85×10^{-4}
0.04587	370	27.03		1.12×10^{-3}		1.03×10^{-3}
0.04463	360	27.78		1.35×10^{-3}		1.41×10^{-3}
0.04339	350	28.57	4.74	1.41×10^{-3}	5.96	1.59×10^{-3}
0.04215	340	29.41		1.29×10^{-3}		1.40×10^{-3}
0.04092	330	30.30		1.47×10^{-3}		1.93×10^{-3}
0.03968	320	31.25		1.89×10^{-3}		2.44×10^{-3}
0.03844	310	32.26		2.31×10^{-3}		3.08×10^{-3}
0.03720	300	33.33	4.71	2.65×10^{-3}	5.94	3.71×10^{-3}
0.03596	290	34.48		8.78×10^{-3}		5.76×10^{-3}
0.03472	280	35.71		1.25×10^{-2}		1.71×10^{-2}
0.03348	270	37.04		1.03×10^{-2}		8.84×10^{-3}
0.03224	260	38.46		3.06×10^{-3}		2.14×10^{-3}
0.03100	250	40.00		3.50×10^{-3}		2.86×10^{-3}
			4.67	1.76×10^{-3} [7]	5.91	1.38×10^{-3} [7]
0.02976	240	41.67		2.32×10^{-2} [5]		1.49×10^{-2} [5]
0.02852	230	43.48		7.09×10^{-2}		5.19×10^{-2}
0.02728	220	45.45		8.86×10^{-2}		8.32×10^{-2}
0.02604	210	47.62		9.28×10^{-2}		6.82×10^{-2}
0.02480	200	50.00		4.58×10^{-2}		7.16×10^{-2}
			4.58	4.36×10^{-3} [7]	5.85	3.21×10^{-3} [7]
0.02356	190	52.63		8.80×10^{-2} [5]		0.222[5]
0.02232	180	55.56		0.106		0.190
0.02170	175	57.14	4.48	7.48×10^{-3} [7]		
0.02108	170	58.82		4.21×10^{-2} [5]		7.49×10^{-2}
0.01984	160	62.50		3.43×10^{-2}		6.96×10^{-2}
0.01860	150	66.67		0.117		7.96×10^{-2}
			4.20	3.59×10^{-2} [7]	5.71	9.54×10^{-3} [7]
0.01835	148	67.57	4.15	5.03×10^{-2}		
0.01810	146	68.49	4.06	8.31×10^{-2}		
0.01785	144	69.44	3.92	0.188		
0.01761	142	70.42	3.87	0.676		
0.01749	141.1	70.87	4.30	0.873		
0.01736	140	71.43	4.63	0.499	5.59	1.74×10^{-2}
				0.171[5]		0.142[5]
0.01711	138	72.46	4.48	0.156[7]		
0.01686	136	73.53	4.34	8.35×10^{-2}		
0.01612	130	76.92	4.10	5.35×10^{-2}	5.47	2.78×10^{-2} [7]
				0.141[5]		0.208[5]
0.01550	125	80.00	3.90	6.35×10^{-2} [7]		
0.01488	120	83.33	3.65	8.94×10^{-2}	5.26	5.05×10^{-2} [7]
				0.206[5]		0.199[5]
0.01426	115	86.96	3.28	0.145[7]		
0.01364	110	90.90	2.61	0.298	4.82	0.118[7]

TABLE II (*Continued*)

Tellurium

eV	cm^{-1}	μm	$n_o(\perp)$	$k_o(\perp)$	$n_e(\parallel)$	$k_e(\parallel)$
				0.383[5]		0.268[5]
0.01333	107.5	93.02			4.63	0.156[7]
0.01302	105	95.24	1.16	1.30[7]	4.38	0.218
0.01271	102.5	97.56			4.01	0.326
0.01240	100	100.0	0.980	4.11	3.46	0.552
						0.446[5]
0.01215	98	102.0	1.30	5.52	2.77	0.986[7]
0.01190	96	104.2	2.12	7.48	2.00	2.11
0.01165	94	106.4	4.86	0.3	1.88	3.88
0.01146	92.4	108.2	11.0	9.84		
0.01141	92	108.7	12.1	8.34	2.51	6.00
0.01116	90	111.1	11.4	2.68	4.75	8.66
0.01092	88.1	113.5			10.5	8.62
0.01091	88	113.6	9.61	1.17[7]	10.8	8.38
0.01066	86	116.3	8.57	0.657	11.7	3.20
0.01041	84	119.0	7.91	0.422	10.3	1.37
0.01017	82	122.0	7.46	0.294	9.30	0.744
0.009819	80	125.0	7.13	0.218	8.69	0.466
				0.308[5]		0.597[5]
0.009671	78	128.2			8.28	0.319[7]
0.009423	76	131.6			7.98	0.232
0.009175	74	116.3			7.76	0.176
0.008927	72	138.9			7.58	0.138
0.008679	70	142.9	6.29	7.53×10^{-2}[7]	7.44	0.112
				0.250[5]		0.330[5]
0.007439	60	166.7		0.265		0.259
			5.94	3.72×10^{-2}[7]	7.03	4.81×10^{-2}[7]
0.006199	50	200.0	5.75	2.14×10^{-2}	6.83	2.58×10^{-2}
				0.382[5]		0.302[5]
0.004959	40	250.0		0.657		0.477
			5.64	1.32×10^{-2}[7]	6.71	1.53×10^{-2}[7]
0.003720	30	333.3	5.56	8.34×10^{-3}	6.64	9.38×10^{-3}
0.002480	20	500.0	5.52	4.94×10^{-3}	6.60	5.47×10^{-3}
0.001240	10	1000	5.50	2.31×10^{-3}	6.58	2.53×10^{-3}

[a] References are indicated in brackets.

Tin Telluride (SnTe)

H. PILLER
Louisiana State University
Baton Rouge, Louisiana

The binary compound semiconductor SnTe was found to be isomorphous with rock salt. The nature of chemical binding is mixed ionic–covalent. SnTe has direct interband optical transitions at the L point in the Brillouin zone. The band structure near the fundamental gap is more complicated than in the lead salts. For large hole concentrations one should observe a positive temperature coefficient of the fundamental gap. Optical experiments by Murase *et al.* [1] have shown that the temperature coefficient of the gap changes its sign from negative to positive with increasing hole concentration in the temperature region between 50 and 150 K.

The first detailed study of the reflectivity of SnTe was performed by Cardona and Greenaway [2]. The measurement of reflectivity and absorption of a semiconductor provides a direct method of studying the band structure. Epitaxial layers of SnTe on KCl were used for the reflection and transmission measurements. The SnTe layers were evaporated onto KCl single-crystal substrates, cleaved in air, and held at a temperature of approximately 573 K. X-ray results showed all the films to be single-crystal and to have the crystal orientation of the substrate: (100). No attempt was made to determine the impurity level in the samples. The thickness of the films was determined by the Tolansky interference method. The room-temperature reflectivity should be accurate to a few percent. An analysis of the reflectivity data for SnTe, using the Kramers–Kronig relation, made it possible to make a detailed comparison of the optical constants obtained from both the reflection and transmission results. The absorption constants obtained from the reflection analysis were compared with values obtained from transmission measurements on thin epitaxial films of SnTe. The agreement was shown to be excellent. The quasi-free electron region (plasma region) was also investigated. It was shown that the phenomenological scattering time required to fit the optical constants with the Drude formula [3] is 1.3×10^{-16} sec. The plasma frequency was calculated by taking the density of the valence electrons equal to five electrons per atom.

Copyright © 1991 by Academic Press.
All rights of reproduction in any form reserved.
ISBN 0-12-544422-2

The room-temperature reflectivity measurements were made over the photon energy range 0.5–20 eV. Measurements of transmission were made in the photon energy range below 4 eV. The optical constants n and k are listed in the first two columns of Table I (n and k). Figure 1 shows a plot of the data.

Korn and Braunstein [4, 5] measured the near-normal reflectivity of polycrystalline SnTe over the photon-energy range 0.5–21 eV at room temperature. The optical constants n and k were determined through a Kramers–Kronig computation. The samples were cut, ground, and hand-polished to produce optical-quality surfaces. After an electrochemical etch, samples were immediately placed in a vacuum (at least 10^{-5} torr) and spectral scans were begun. Consistent results were obtained upon repreparation of sample surfaces. The maximum absolute reflectance error throughout the spectral range was estimated to be at most 2%. The optical constants n and k are listed in Table I (columns 3 and 4). Figure 1 shows a plot of the data.

Burke and Riedl [6] measured the absorption coefficient and the index of refraction of SnTe at 300 K over the photon-energy range between 0.14 and 0.64 eV. The sample was a single-crystal film with a hole concentration of $3.6 \times 10^{19}\,\mathrm{cm}^{-3}$. The single crystal was epitaxially deposited to a thickness of 1.2 μm on an NaCl substrate. The room-temperature data are in good agreement with those obtained by Schoolar and Dixon [7], who measured the optical constants of p-type SnTe at room temperature over the spectral range from 0.1–3.8 eV. The indices of refraction and absorption coefficients were obtained from analysis of normal reflectance and transmittance measurements on epitaxial films ranging in carrier concentration from 3.6×10^{19} to $6.8 \times 10^{20}\,\mathrm{cm}^{-3}$. At photon energies greater than 1.0 eV, the absorption spectrum agrees with the results of Cardona and Greenaway [2]. Electrical, X-ray, and optical data indicate that the films are high quality, single crystals. A "sample in, sample out" procedure was used for taking the data. The error of reflectance and transmittance is estimated to be less than ±3%. The film thickness was determined from analysis of the interference fringes. Such spectra were also used to determine the carrier concentration p from the position of the plasma reflectance minimum. It was estimated that the carrier concentrations determined in this way are accurate to within ±10%. The homogeneity of the films was checked by measuring the reflectance of different areas of the films on both the front and back surfaces. Variations were less than ±3% for all the samples studied. The n and k values determined by Burke and Riedl [6] and Schoolar and Dixon [7] are listed in Table I and plotted in Fig. 1. These, of course, contain the effects of free holes.

Potter [8] made an ellipsometry study of SnTe in the infrared and visible spectral regions. Fukui *et al.* [9] measured the absorption spectra of crystalline SnTe films in the 2–120 eV region using synchrotron radiation at

liquid-nitrogen temperature. In the *in situ* measurements, an SnTe film was evaporated onto a collodion film cooled to about 80 K at a pressure below 10^{-8} torr before the absorption measurements were made. Then the film was annealed at room temperature and then again cooled to 80 K when the measurements were repeated. The absorption spectrum of SnTe in the amorphous and in the crystalline phase was measured. The structure in the absorption spectrum in the crystalline SnTe below 20 eV is in good agreement with previous results [2]. No absorption coefficient was determined from these measurements.

REFERENCES

1. K. Murase, S. Sugai, T. Higuchi, S. Takaoka, T. Fukunaga, and H. Kawamura, "Proc. 14th Internat. Conf. Phys. Semicond.," (B. L. H. Wilson, ed.), Institute of Physics, Edinburgh, 437 (1979).
2. M. Cardona and D. L. Greenaway, *Phys. Rev.* **133**, A1685 (1964).
3. H. R. Philipp and H. Ehrenreich, *Phys. Rev.* **129**, 1550 (1963).
4. D. M. Korn, thesis, UCLA, unpublished, (1971).
5. D. M. Korn and R. Braunstein, *Phys. Rev. B* **5**, 4837 (1972).
6. J. Richard Burke, Jr., and H. R. Riedl, *Phys. Rev.* **184**, 830 (1969).
7. R. B. Schoolar and J. R. Dixon, *J. Opt. Soc.* **58**, 119 (1968).
8. R. Potter, thesis, Brown University, unpublished, (1970).
9. K. Fukui, J. Yamazaki, T. Saito, S. Kondo, and M. Watanabe, *J. Phys. Soc. Japan* **56**, 4196 (1987).

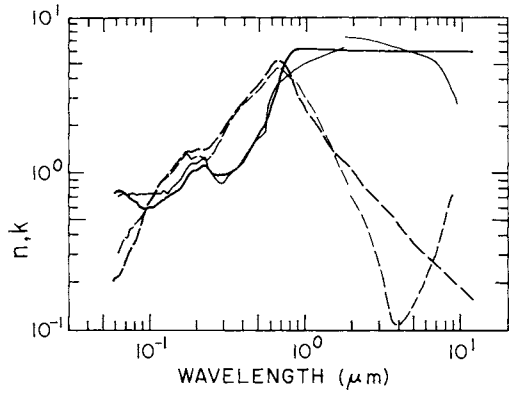

Fig. 1. Log–log plot of n (solid line) and k (dashed line) versus wavelength in micrometers for tin telluride.

TABLE I

Values of *n* and *k* for Tin Telluride Obtained from Various References[a]

eV	μm	n	k	n	k
21.203	0.05848			0.748 [4]	
21.195	0.05850				0.200 [4]
20.949	0.05919				0.215
20.824	0.05954			0.764	
20.652	0.06004				0.216
20.411	0.06074				0.216
20.400	0.06078			0.759	
20.204	0.06137				0.217
20.021	0.06193			0.771	
19.979	0.06206	0.725 [2]			
19.979	0.06206		0.312 [2]		
19.869	0.06240				0.217
19.645	0.06311			0.781	
19.561	0.06339				0.218
19.537	0.06347	0.730			
19.393	0.06394		0.342		
19.354	0.06406			0.768	
19.261	0.06437				0.219
19.035	0.06514			0.747	
19.033	0.06515	0.750			
18.961	0.06540		0.357		
18.948	0.06544				0.246
18.710	0.06627				0.235
18.644	0.06650			0.771	
18.478	0.06711	0.735			
18.394	0.06741				0.236
18.306	0.06773			0.729	
18.252	0.06794		0.393		
18.101	0.06850				0.278
17.902	0.06926			0.749	
17.860	0.06942				0.252
17.707	0.07003	0.735			
17.596	0.07046			0.734	
17.512	0.07081		0.383		
17.485	0.07091				0.269
17.215	0.07202			0.729	
17.119	0.07243				0.308
17.008	0.07291	0.740			
16.925	0.07326		0.448		
16.803	0.07379			0.705	
16.702	0.07424				0.309
16.504	0.07513	0.745			
16.476	0.07526			0.686	
16.391	0.07565		0.443		
16.375	0.07572				0.324

TABLE I (*Continued*)

Tin Telluride

eV	μm	n	k	n	k
16.033	0.07733				0.342
16.002	0.07748			0.671	
15.907	0.07795	0.750			
15.695	0.07900				0.345
15.650	0.07923		0.488		
15.537	0.07980			0.665	
15.352	0.08077	0.730			
15.306	0.08101				0.370
15.189	0.08163			0.650	
15.054	0.08236				0.370
14.951	0.08294		0.498		
14.883	0.08331			0.657	
14.789	0.08384				0.429
14.694	0.08439	0.745			
14.537	0.08529			0.610	
14.498	0.08552				0.430
14.293	0.08676		0.539		
14.254	0.08699			0.614	
14.190	0.08738				0.431
13.902	0.08919	0.740			
13.815	0.08975				0.512
13.808	0.08979			0.596	
13.635	0.09094		0.569		
13.474	0.09202				0.556
13.382	0.09265			0.590	
13.382	0.09265			0.590	
13.213	0.09384	0.745			
13.189	0.09401				0.574
13.112	0.09456			0.606	
13.028	0.09518		0.634		
12.920	0.09596				0.584
12.680	0.09778			0.619	
12.655	0.09798				0.612
12.627	0.09820	0.735			
12.411	0.0999		0.700		
12.397	0.1000			0.610	
12.392	0.1001				0.662
12.087	0.1026				0.683
12.043	0.1030			0.623	
11.959	0.1037	0.745			
11.754	0.1055				0.718
11.743	0.1056		0.775		
11.721	0.1058			0.619	
11.420	0.1086			0.630	
11.343	0.1093				0.775
11.177	0.1109	0.745			

TABLE I (*Continued*)

Tin Telluride

eV	μm	n	k	n	k
11.097	0.1117			0.645	
11.092	0.1118				0.819
11.064	0.1121		0.841		
10.842	0.1144			0.662	
10.770	0.1151				0.838
10.684	0.1161	0.740			
10.560	0.1174		0.901		
10.488	0.1182			0.680	
10.474	0.1184				0.869
10.247	0.1210			0.681	
10.174	0.1219				0.907
10.170	0.1219	0.780			
9.995	0.1241		0.941		
9.898	0.1253			0.709	
9.842	0.1260				0.942
9.589	0.1293			0.712	
9.542	0.1299	0.740			
9.514	0.1303				0.974
9.481	0.1308		1.002		
9.176	0.1351			0.747	
9.137	0.1357				1.024
9.039	0.1372	0.816			
8.936	0.1388		1.047		
8.876	0.1397			0.743	
8.813	0.1407				1.077
8.603	0.1441			0.783	
8.474	0.1463				1.144
8.452	0.1467	0.866			
8.452	0.1467		1.108		
8.286	0.1496			0.788	
8.133	0.1524				1.205
8.051	0.1540		1.223		
7.979	0.1554	0.916			
7.924	0.1565			0.810	
7.840	0.1582				1.243
7.733	0.1604		1.299		
7.642	0.1623			0.857	
7.572	0.1638				1.313
7.506	0.1652	1.012			
7.445	0.1666		1.354		
7.348	0.1687			0.913	
7.290	0.1701		1.354		
7.272	0.1705				1.377
7.208	0.1720	1.108			
7.105	0.1745			0.991	
7.054	0.1758		1.269		

TABLE I (*Continued*)

Tin Telluride

eV	cm^{-1}	μm	n	k	n	k
6.993		0.1773				1.369
6.941		0.1787	1.153			
6.810		0.1821			1.026	
6.787		0.1827		1.239		
6.663		0.1861	1.168			
6.618		0.1874				1.385
6.591		0.1881		1.254		
6.537		0.1897			1.049	
6.406		0.1936	1.163			
6.324		0.1961		1.299		
6.271		0.1977				1.432
6.239		0.1987			1.074	
6.057	48846	0.2047	1.188			
5.995	48349	0.2068		1.304		
5.909	47661	0.2098			1.128	
5.793	46720	0.2140				1.433
5.707	46026	0.2173		1.259		
5.676	45777	0.2184			1.155	
5.645	45529	0.2197	1.228			
5.450	43953	0.2275		1.223		
5.443	43899	0.2278				1.434
5.419	43704	0.2288	1.153			
5.319	42898	0.2331			1.081	
5.213	42046	0.2379	1.052			
5.183	41797	0.2393		1.284		
5.060	40811	0.2450				1.519
4.987	40223	0.2486			1.008	
4.925	39724	0.2518	0.977			
4.905	39558	0.2528		1.369		
4.791	38643	0.2588			0.990	
4.786	38603	0.2590				1.618
4.617	37236	0.2686		1.556		
4.599	37095	0.2696				1.721
4.555	36738	0.2722	0.881			
4.469	36042	0.2775			0.986	
4.350	35080	0.2851		1.752		
4.281	34529	0.2896				1.895
4.211	33960	0.2945			0.993	
4.144	33421	0.2992	0.876			
4.061	32752	0.3053				2.046
4.031	32509	0.3076		2.019		
3.979	32094	0.3116	0.967			
3.916	31580	0.3167			1.013	
3.888	31359	0.3189				2.195
3.763	30353	0.3295		2.261		
3.733	30104	0.3322	1.007			

TABLE I (*Continued*)

Tin Telluride

eV	cm^{-1}	μm	n	k	n	k
3.640	29357	0.3406				2.361
3.496	28194	0.3547			1.085	
3.486	28113	0.3557		2.502		
3.439	27739	0.3605				2.553
3.434	27699	0.3610	1.103			
3.275	26415	0.3786				2.756
3.229	26040	0.3840		2.749		
3.209	25884	0.3863			1.199	
3.177	25626	0.3903	1.228			
3.069	24753	0.4040				2.962
2.992	24133	0.4144	1.364			
2.958	23857	0.4192				3.127
2.935	23673	0.4224			1.375	
2.879	23221	0.4307		3.086		
2.800	22579	0.4429				3.349
2.771	22347	0.4475			1.542	
2.735	22060	0.4533	1.551			
2.666	21504	0.4650				3.555
2.577	20786	0.4811			1.745	
2.571	20733	0.4824		3.378		
2.488	20069	0.4983	1.702			
2.488	20069	0.4983				3.805
2.401	19362	0.5165			1.943	
2.386	19241	0.5197				3.980
2.375	19157	0.5220		3.685		
2.324	18742	0.5336	1.813			
2.317	18684	0.5352				4.177
2.265	18265	0.5475				4.420
2.262	18245	0.5481	1.878			
2.252	18162	0.5506	1.989			
2.242	18079	0.5532	2.135			
2.231	17997	0.5556			2.183	
2.221	17913	0.5583	2.442			
2.221	17913	0.5583		4.043		
2.190	17664	0.5662	2.719			
2.185	17620	0.5675				4.678
2.160	17423	0.5740			2.427	
2.129	17167	0.5826	2.991			
2.087	16835	0.5940		4.375		
2.086	16825	0.5943			2.673	
2.080	16774	0.5962				4.977
2.070	16692	0.5991			2.863	
2.056	16580	0.6031		4.496		
2.046	16503	0.6060	3.273			
2.019	16287	0.6140			3.059	
2.011	16216	0.6167				5.144

TABLE I (*Continued*)

Tin Telluride

eV	cm^{-1}	μm	n	k	n	k
2.003	16153	0.6191				5.266
1.995	16089	0.6216	3.479			
1.970	15885	0.6295		4.677		
1.961	15813	0.6324			3.257	
1.932	15585	0.6417			3.472	
1.928	15547	0.6432				5.372
1.921	15497	0.6453			3.664	
1.919	15474	0.6462		4.741		
1.913	15425	0.6483	3.701			
1.877	15135	0.6607			3.868	
1.874	15116	0.6615		4.749		
1.863	15025	0.6655			4.056	
1.834	14790	0.6761		4.754		
1.829	14748	0.6781			4.286	
1.824	14710	0.6798				5.295
1.822	14697	0.6804			4.516	
1.820	14679	0.6813	3.912			
1.795	14474	0.6909		4.687		
1.790	14439	0.6926			4.660	
1.785	14399	0.6945			4.839	
1.767	14254	0.7016				5.175
1.766	14243	0.7021		4.621		
1.739	14022	0.7132		4.560		
1.722	13887	0.7201				5.032
1.719	13865	0.7212			5.001	
1.714	13824	0.7234			5.190	
1.705	13748	0.7274		4.492		
1.688	13612	0.7346				4.912
1.684	13579	0.7364		4.402		
1.682	13562	0.7373			5.450	
1.667	13442	0.7440			5.586	
1.656	13352	0.7490	4.285			
1.651	13316	0.7510		4.334		
1.636	13194	0.7579			5.784	
1.622	13085	0.7643				4.690
1.620	13064	0.7655		4.251		
1.610	12987	0.7700				4.493
1.597	12880	0.7764			5.977	
1.587	12801	0.7812		4.156		
1.564	12617	0.7926				4.256
1.556	12548	0.7969		4.078		
1.552	12519	0.7988				4.049
1.542	12440	0.8039	4.541			
1.526	12306	0.8126		4.006		
1.520	12260	0.8156			6.221	
1.512	12192	0.8202			6.327	

TABLE I (*Continued*)

Tin Telluride

eV	cm^{-1}	μm	n	k	n	k
1.495	12058	0.8293				3.790
1.494	12053	0.8297		3.945		
1.480	11937	0.8377				3.574
1.462	11790	0.8482		3.898		
1.430	11531	0.8672			6.450	
1.429	11527	0.8676	4.803			
1.429	11522	0.8679				3.343
1.428	11516	0.8683		3.861		
1.407	11347	0.8813		3.724 [7]		
1.390	11214	0.8917			6.449	
1.373	11070	0.9033		3.566		
1.368	11033	0.9064				2.948
1.333	10751	0.9301			6.396	
1.320	10643	0.9396		3.322		
1.306	10532	0.9495	5.070			
1.277	10302	0.9706				2.721
1.271	10251	0.9756				2.542
1.269	10238	0.9768		3.126		
1.203	9706	1.030		2.886		
1.203	9703	1.031	5.312			
1.194	9634	1.038				2.341
1.174	9467	1.056			6.372	
1.150	9279	1.078		2.677		
1.126	9085	1.101				2.167
1.091	8801	1.136		2.446		
1.069	8625	1.160	5.573			
1.044	8424	1.187				1.971
1.028	8291	1.206			6.370	
1.026	8273	1.209		2.199		
0.980	7907	1.265		2.018		
0.946	7630	1.311	5.865			
0.937	7556	1.323				1.694
0.935	7541	1.326		1.815		
0.888	7165	1.396				1.509
0.887	7152	1.398		1.617		
0.864	6966	1.436	6.102			
0.837	6753	1.481		1.409		
0.822	6632	1.508			6.302	
0.798	6432	1.555		1.257		
0.784	6322	1.582				1.295
0.781	6303	1.587	6.314			
0.754	6085	1.644		1.097		
0.718	5794	1.726		0.984		
0.710	5722	1.748	6.545			
0.692	5583	1.791	7.681 [6]			
0.678	5468	1.829		0.864		

TABLE I (*Continued*)

Tin Telluride

eV	cm^{-1}	μm	n	k	n	k
0.674	5438	1.839			6.280	
0.650	5242	1.908		0.731 [6]		
0.646	5209	1.920				1.100
0.612	4938	2.025	7.550			
0.606	4891	2.045		0.669		
0.569	4588	2.180		0.572		
0.555	4477	2.234				0.843
0.548	4422	2.262	7.442			
0.528	4256	2.350		0.505		
0.493	3979	2.513	7.304			
0.487	3926	2.547		0.415		
0.447	3606	2.773		0.316		
0.427	3444	2.904		0.272		
0.425	3426	2.919	7.106			
0.406	3272	3.057		0.230		
0.400	3226	3.100		0.216		
0.396	3192	3.133	6.873			
0.382	3082	3.245		0.182		
0.366	2955	3.384		0.150		
0.366	2954	3.385	6.824			
0.363	2926	3.418		0.141		
0.346	2791	3.583		0.113		
0.342	2759	3.625			6.225	
0.341	2750	3.636				0.529
0.337	2719	3.678	6.628			
0.329	2657	3.764		0.109		
0.318	2562	3.903		0.109		
0.308	2481	4.031	6.447			
0.296	2388	4.188		0.116		
0.278	2240	4.465	6.255			
0.270	2176	4.595		0.131		
0.253	2044	4.892				0.351
0.250	2016	4.960		0.149		
0.249	2007	4.982	6.007			
0.226	1825	5.481		0.182		
0.214	1728	5.786	5.759			
0.206	1660	6.022		0.224		
0.187	1508	6.632	5.301			
0.182	1471	6.799		0.305		
0.164	1324	7.550		0.436		
0.163	1314	7.608	4.575			
0.157	1265	7.904		0.537		
0.143	1152	8.680	3.483			
0.142	1147	8.722		0.740		

TABLE I (*Continued*)

Tin Telluride

eV	cm^{-1}	μm	n	k	n	k
0.135	1088	9.187	2.863			
0.105	847	11.80			6.173	
0.104	841	11.89				0.15

[a] References are indicated in brackets.

Zinc Selenide (ZnSe)
Zinc Telluride (ZnTe)

L. WARD
Coventry Polytechnic
Coventry, England

In optical terms these two materials have many points in common, and it is therefore proposed to deal with both in the same critique. They are both semiconductors and are members of the II-VI group formed by alloying one element from group II of the periodic table with another from group VI. Their normal crystal structure is face-centered cubic, the zinc-blende or sphalerite type ($F\bar{4}3m$), although it is also possible to grow hexagonal forms of each material (wurtzite structure, C6mc). These materials may be produced synthetically by alloying the two elements in the correct proportions; by chemical vapor deposition (CVP); or by evaporation in vacuum. In making these materials from the basic elements, there is often a tendency for the resulting compound to be zinc-ion deficient and several investigators (for example, Horikoshi *et al.* [1]) have found that this situation may be partially remedied by soaking the boule for several hours in a bath of molten zinc.

In broad terms these two materials each exhibit two main absorption bands. The first of these is in the near-ultraviolet region and arises as a result of electron excitations across the energy gap (about 2 eV) between the broad valence band and the conduction band; the second occurs in the infrared at a wavelength between 40 and 50 μm and is caused by photon resonance with lattice vibrations (transverse phonons). Through the visible spectrum and into the near-infrared region, both ZnSe and ZnTe behave as normally dispersive materials, the refractive indices decreasing monotonically with wavelength; the mean value of n in this region for ZnSe is 2.5, and, that for ZnTe is 2.8. Over the same region, the extinction coefficient, k, is very small for each of the compounds. Consequently, both materials have been used extensively for high-refractive-index optical components and windows. In addition, many of the sets of values of the optical constants that have been published for the visible and near-infrared regions

Copyright © 1991 by Academic Press.
All rights of reproduction in any form reserved.
ISBN 0-12-544422-2

can be fitted into dispersion equations of the Sellmeier type; over the infrared absorption band, Lorentz equations for $\varepsilon_1 = (n^2 - k^2)$ and $\varepsilon_2 = 2nk$ have also been used successfully. At very short wavelengths there are further absorption bands due to the L and M transitions of electrons in both the elements within each of the compounds. In the X-ray region, the refractive indices approach a value of unity, whereas at very long wavelengths, n is asymptotic to about 3.0 for ZnSe and to 2.9 for ZnTe.

A comprehensive review (up until 1984) of the optical properties of both these materials as well as of zinc sulphide has been given by Li [2], who also presents the results in a variety of graphical forms. In addition, Li lists some of the Sellmeier and Lorentz equations derived by different authors. Tauc [3] has also reviewed the optical properties of semiconductors in the visible and ultraviolet regions and presents tables of the main absorption peaks and their identification with various electron transitions within the Brillouin zone.

Optical Properties of Zinc Selenide

The n and k data selected in this critique are listed in Table I and graphed in Fig. 1. At wavelengths in the X-ray region, 0.0006–0.012 μm, values of n and k may be calculated by the method described by Henke [4] based on the X-ray scattering coefficients, f_1 and f_2, for each element; values of these coefficients are presented in another paper by Henke *et al.* [5]. For ZnSe, $n = 1 - 9.90\lambda^2 (f_{1zn} + f_{1se})$ and $k = 9.90\lambda^2 (f_{2zn} + f_{2se})$, where λ is the wavelength in μm. Over this region, the calculated value of n is close to unity, whereas k shows maxima due to the $L_{II,III}$ transition in Zn (0.0012 μm) and the $L_{II,III}$ transition in Se (0.00085 μm). Values of n and k calculated by Henke's method are listed in Table I.

At short wavelengths (0.01–0.1 μm) the work of Freeout [6], Gautron *et al.* [7] and Cardona and Haensel [8] may be quoted. Cardona and Haensel used evaporated films and made a direct measurement of the absorption coefficient α using radiation from an electron synchrotron, which was dispersed by a Rowland grazing-incidence monochromator and detected by a photomultiplier. k may then be found from the relationship $\alpha = 4\pi k/\lambda$, and n is assumed to be equal to unity; their values of n and k between 0.008 and 0.033 μm are presented in Table I. They found a sharp absorption doublet at 90.6 and 93.35 eV (0.0133 and 0.0137 μm) corresponding to electron transits from the $3p$ level to the conduction band (L) in zinc. A less pronounced peak was caused by the $3d$ to conduction band transition (M) in selenium at 59 eV (0.021 μm). Where there is an overlap in wavelengths, their results are in reasonably good agreement with those calculated by the Henke method. Freeout used synchrotron radiation and a rotary light-pipe scanning reflectometer due to Gerhardt and Rubloff [9] to measure the polarization-dependent reflectance of cleaved single crystals of ZnSe. Analysis by the Kramers–Kronig (K–K) technique enabled him to

produce a graph of ε_2 versus energy, which showed strong structures in the valence-to-conduction-band transition region. Gautron *et al.*, using polished and etched single crystals of ZnSe, measured both the reflectance and the electrolyte electroreflectance; they also employed K–K analysis to extract ε_1 and ε_2, from which n and k may then be calculated over the wavelength range 0.04–1.24 μm. In their experimental technique (see Cardona *et al.* [10]), the specimen is immersed in an electrolyte and dc biased in the blocking direction; a modulating ac voltage is also applied. Monochromatic radiation is then reflected by the specimen to a photomultiplier and both the dc and ac components of the output are recorded. The dc output is proportional to the reflectance; the ratio of ac to dc outputs gives the quantity dR/R, which can be related to ε_1 and ε_2. Their results for n and k, which are also quoted in Table I, match well at the shortest wavelengths with those of Cardona and Haensel, but thereafter and up to 0.02 μm, n remains below 1.0, which behavior differs from that observed by other investigators, for example, Balkanski and Petroff [11]. They were also able to confirm the existence of excitons at room temperature and to correlate features in the reflectance spectrum with different band-to-band transitions within the Brillouin zone. Cardona [12] reported a series of eight peaks in the reflectance spectrum of ZnSe at room temperature between 2.0 and 14.0 eV (0.09–0.62 μm); he was able to correlate all of them with various electron transitions within the Brillouin zone.

Published results over the region of the main energy gap (0.1–0.5 μm) differ among themselves more than those for other wavelength regions; in particular, it is experimentally difficult to make accurate measurements of n and k at the actual absorption edge. Measuring reflectances, Balkanski and Petroff [11] obtained a peak in n of 3.61 at 0.28 μm followed by a minimum of 0.80 at 0.124 μm and then a second maximum of 1.42 at 0.095 μm; k showed peaks at 0.25, 0.18, and 0.13 μm. Aven *et al.* [13] made measurements of the reflectance of single-crystal zinc selenide from 0.1–0.5 μm and used K–K analysis to extract n and k. They found a maximum in n (3.24) also at 0.28 μm with peaks in k at 2.7, 3.15, 4.75, and 5.1 eV (0.459, 0.394, 0.261, and 0.243 μm). The work of Gautron *et al.* [7], which has already been discussed, also extended over the energy gap and up to 1.24 μm. Their peak value for n (2.68) was much smaller than that obtained by other investigators and was found at 0.41 μm, followed by a second maximum (2.57) at 0.31 μm, together with minima at 0.177 and 0.124 μm; k showed maxima at 0.25 and 0.19 μm. The results of Balkanski and Petroff [11] measured between 0.06 and 1.24 μm are considered to be the most reliable of this group and have been chosen to represent this spectral region in Table I.

Over the visible and near-infrared region (0.5–10.0 μm), there have been a large number of measurements of the refractive index, and there is very

good agreement among the various results. The work of Aven *et al.* [13] with single-crystal zinc selenide was extended up to 2.5 μm, and they presented values of ε_1 and ε_2, these being determined from a K–K analysis of the reflectance taken at a temperature of 296 K. From their results, they were able to determine ν_t, the transverse-optical-phonon energy, as 0.026 eV (48.5 μm) and ν_l, the longitudinal-optical-phonon energy as 0.031 eV (40.0 μm); the very-long-wavelength limit of n was calculated to be 2.85.

Thutupalli and Tomlin [14] have also published work in this region (0.3–2.0 μm), where they determined n for films of ZnSe from measurements of reflectance and transmittance at room temperature and also at 400 °C. At room temperature, only cubic crystals were observed in the films; the hexagonal form began to appear at 100 °C becoming more prominent as the temperature increased. Both n and k increased with temperature, and the values of n at 400 °C were in good agreement with those of Marple [15]. Ahmed and Khawaja [16] determined n between 2.5 and 14 μm using a technique due to Khawaja [17], in which the transmittance at normal incidence was measured; an iteration process was then used to produce a dispersion curve and when an acceptable version of this was obtained, it yielded both n and the specimen thickness. Over this region n fell monotonically from 2.42 to 2.40, in good agreement with Thutupalli and Tomlin's results. Marple [15] measured the refractive index of a prism by the minimum-deviation method between 0.5 and 2.5 μm for material containing less than 30 ppm of impurities, the chief ones being phosphorus, arsenic, and cadmium. The optical material was grown as single-crystal boules by sublimation in an argon-filled quartz tube. Marple claimed an experimental error of ±0.002 and was able to fit his experimental data over this wavelength region with a Sellmeier-type dispersion equation:

$$n^2 = 4.0 + 1.90\lambda^2/(\lambda^2 - 0.113),$$

where λ is the wavelength in μm.

An investigation covering the visible spectrum was made by Rambauske [18] using the minimum-deviation technique and Avery's method [19], in which the reflectance ratio (R_p/R_s) is measured. Two quite different dispersion curves were produced from two specimens of ZnSe, which had been obtained from different sources. For one specimen, the dispersion curve peaked at 0.50 μm ($n = 2.72$) and then fell rapidly as the wavelength decreased. The curve due to the second specimen closely followed those by Aven *et al.* and Thutupalli and Tomlin between 0.65 and 0.45 μm, where it peaked at $n = 2.82$. At shorter wavelengths, this curve was very different from theirs in that it fell to a value of n of 2.25 at 0.40 μm, whereas theirs, after a shoulder at 0.45 μm, went on to peak at 0.30 μm. There is some

evidence that the specimens used by Rambauske were not of high purity, and the displacement of the maximum may have been caused by the presence of impurity energy levels in the energy gap. Zholkevich [20] has determined directly the absorption coefficient of ZnSe between 0.45 and 0.65 μm; the derived values of k were very small, and they have been included in Table I with the values for n due to Balkanski and Petroff [11]. Another set of results covering a narrow range (0.476–0.633 μm) in the visible spectrum, which did not include the absorption edge, was produced by Wunderlich and De Shazer [21] also using the minimum-deviation prism technique. Their values of n, which had errors of ±0.002, were very similar to those of Rambauske over the same wavelength range.

Feldman *et al.* [22] also used the minimum-deviation method to measure n at room temperature for two specimens between 0.5 and 18.0 μm. Their values of n were quoted to five decimal places, but the results for the two specimens were not identical, and it is considered by Li that ±0.0004 is a more realistic error. A set of mean values for n calculated from the three-term dispersion formulas given by Feldman *et al.* is included in Table I, the fifth figure being given in brackets.

Measurements of n and k at wavelengths in the range 20–1000 μm have been performed by Manabe *et al.* [23] and by Hattori *et al.* [24]. Manabe *et al.* measured the reflectance of polished specimens between 20 and 85 μm at an angle of incidence of 12 degrees and determined n and k by the use of the following Lorentz-oscillator equations;

$$n^2 - k^2 = \varepsilon_\infty + N(\nu_t^2 - \nu^2)/((\nu_t^2 - \nu^2)^2 + \gamma^2\nu^2)$$

$$2nk = N\gamma\nu/((\nu_t^2 - \nu^2)^2 + \gamma^2\nu^2).$$

At 300 K, the transverse-optical-phonon frequency, $\nu_t = 207\ \text{cm}^{-1}$ (48.3 μm), the longitudinal-optical-phonon frequency, $\nu_l = 246\ \text{cm}^{-1}$ (40.7 μm), $\varepsilon_\infty = 5.4$, $N = 8.94 \times 10^5\ \text{cm}^{-2}$, and $\gamma = 3.73\ \text{cm}^{-1}$. They also produced another set of results at 100 K, where the corresponding values were $211\ \text{cm}^{-1}$, $250\ \text{cm}^{-1}$, 5.4, $9.25 \times 10^4\ \text{cm}^{-2}$, and $2.11\ \text{cm}^{-1}$. Their value of n at 20 μm and at 300 K compares well with that of Feldman *et al.* [22] at 18 μm. Hattori *et al.* [24] used transmission interferometry for their measurements taken between 100 and 1000 μm and at temperatures of 2, 80, and 300 K. Specimens were grown by Bridgman's technique and ranged in thickness between 500 and 1000 μm. Again, a simple dispersion formula was used to evaluate the optical constants. Their results agreed to within a few percent with those of Manabe *et al.* in the wavelength overlap region. They found the transverse optical phonon to be at $203\ \text{cm}^{-1}$ at 300 K, $207\ \text{cm}^{-1}$ at 80 K, and $210\ \text{cm}^{-1}$ at 2 K; the extreme long-wavelength value of n was 3.00 at

300 K and 2.96 at 80 K. Sets of results read from the graphs given by both Manabe *et al.* and Hattori *et al.* are quoted in Table I.

Miles [25] has published a graph of absorption coefficient versus wave number between 300 and 900 cm^{-1} (11–33 μm). This shows structure attributable to multiphonon absorption, the main peaks being at 360, 415, 430, 570, and 610 cm^{-1} with a shoulder at 800 cm^{-1}. The derived values of k are small (between 0.02 and 1×10^{-7}) and do not exhibit the structure clearly. Nevertheless, some values have been included in Table I. Aven *et al.* [13] have also reported results for the absorption coefficient in this region (0.02–0.08 eV, 15.5–62 μm); these had peaks at 0.026, 0.0375, 0.046, 0.0525, and 0.073 eV. (47.7, 33.1, 27.0, 23.6, and 17.0 μm). Over the main peak at 47.7 μm, the values for k agree well with those of Manabe *et al.*; other values of k, covering the regions of 30–40 μm and 50–60 μm are given in Table I.

At very low frequencies (20 Hz–1 mHz) Strzalkowski *et al.* [26] have measured the dielectric constant ε of ZnSe by the capacitance method. At 296 K, ε was equal to 9.25; that is, $n = 3.10$; ε varied linearly with temperature and, when extrapolated to 0 K, $\varepsilon_o = 8.80 \pm 0.04$; that is, $n_o = 2.97 \pm 0.02$. ε, and therefore n, were independent of wavelength out to 300 m.

Thompson *et al.* [27] measured n as a function of temperature at two discrete wavelengths, 3.8 and 10.8 μm, making use of the minimum-deviation method; it is possible to read values from their graphs to three decimal places. At 300 K and 3.8 μm, $n = 2.435$, whereas at 10.8 μm $n = 2.405$, both values being in very good agreement with those of Feldman *et al.* In each case, n fell by 0.010 when the temperature was reduced to 75 K, giving a temperature coefficient of 1.9×10^{-5}/°C. Another investigation of the effect of temperature was carried out by Tubota *et al.* [28], who studied the variation of the position of the absorption edge over the range 295–496 K. The energy gap was found to change from 2.59 eV (0.479 μm) at 293 K to 2.47 eV at 398 K and then to 2.38 eV at 496 K.

Excitons in ZnSe

At low temperatures (5 K), the presence of excitons has been detected in ZnSe crystals. These are electron-hole pairs that occupy energy levels inside the fundamental energy gap just below the conduction band; some excitons are free, and others are bound to impurity atoms. Spectroscopically, they may be represented by a simple hydrogenlike energy level series. Absorption lines are observed at energies just below the main band due to the breakup of the excitons by photons of the correct energy. This dissociation may also be brought about by thermal energy, and so it is more difficult to observe excitons at higher temperatures. An account of the properties of excitons has been given by Thomas and Timofiev [29]. Hite *et al.* [30] also found evidence for the presence of

excitons in ZnSe even though the absorption spectrum they observed was dominated by the defects in their crystals. Another group that observed the presence of excitons in ZnSe for temperatures below 60 K was Tokura *et al.* [31], who used attenuated total reflection to study the coupling of photons to excitons at the semiconductor surface. Jiang *et al.* [32] found evidence for the presence of excitons in ZnSe, bound to deep impurity levels or defects.

Irtran 4

Commercial synthetic zinc selenide, produced by hot sintering of the polycrystalline material and known as Irtran 4, has been investigated by McCarthy [33] between 2 and 50 μm using measurements of reflectance and transmittance. He produced curves of reflectance and transmittance versus wavelength but, unfortunately, did not evaluate n and k. Another study of Irtran 4 was made by Hilton and Jones [34] using a prism minimum-deviation technique to measure n between 3 and 13 μm and at temperatures of 198 and 295 K. Both values of n were presented graphically, and those for 198 K were lower by approximately 0.005 over the whole of the wavelength range covered. The temperature coefficient of n at 5 μm was found to be $2.0 \times 10^{-5}\,\mathrm{K}^{-1}$. Hadni *et al.* [35] measured the reflectance and transmittance of a thin plate of Irtran 4 and also of films of ZnSe on quartz at 290 K and at liquid-nitrogen temperature. They found that their results could be explained by postulating a single Lorentzian-type oscillator with ν_t equal to $204\,\mathrm{cm}^{-1}$ (49.0 μm) and ν_l, the longitudinal-optical-phonon frequency, equal to $254\,\mathrm{cm}^{-1}$ (39.4 μm) at 300 K. Their values for n and k were considerably smaller than those obtained by Manabe *et al.* for bulk material possibly because of the structural properties of their films. Their value of n extrapolated to very long wavelengths was 3.10 at 290 K.

There is some evidence that n for Irtran 4 may be sample dependent; nevertheless, results due to Hilton and Jones and to Hadni *et al.* are included in Table I.

Optical Properties of Zinc Telluride

The n and k data selected in this critique are listed in Table II and graphed in Fig. 2. Many of the authors who investigated zinc sellenide have also extended their work to cover the closely related material zinc telluride.

At wavelengths in the X-ray region, n and k may again be calculated by the method of Henke [4] described earlier. For ZnTe,

$$n = 1 - 7.88\lambda^2(f_{1zn} + f_{1te}),$$

where the wavelength λ is in μm. As with ZnSe, the values of n in this

region are very close to unity, and peaks in k are obtained at 0.0012 μm (the $L_{II,III}$ transition point in Zn) and 0.0021 μm (the $M_{IV,V}$ transition point in Te).

In direct measurements of the absorption coefficient, Cardona and Haensel [8] found a doublet of absorption lines for ZnTe at 89.4 and 93.0 eV (0.0133 and 0.0139 μm) corresponding to the M-transition in Zn. However, no peak for Te was discovered right up to a wavelength of 0.3 μm. Values of k for ZnTe between 0.008 and 0.033 μm, derived from α, are presented in Table II; n is assumed to be close to unity in this spectral region.

At wavelengths between 0.05 and 1.0 μm, Cardona and Greenaway [36] measured the reflectance of cleaved single-crystal ZnTe. In the region of 0.10 μm, the reflectance spectrum exhibited a number of structures that could be assigned to various electron transitions from the d-band to the conduction band in zinc (0.071 and 0.153 μm). The temperature coefficient of reflectance was approximately 6×10^{-4}/°C at all the wavelengths investigated. Cardona himself [37] measured the normal-incidence reflectance up to 20 eV at 300 and 77 K. He then calculated ε_1, ε_2, n, and k by K–K analysis and determined the dielectric constant at infinite wavelength using Penn's model [38]. His values for n and k are included in Table II.

Cardona [12] has also reported measurements of the reflectance of ZnTe at room temperature in the ultraviolet spectrum between 0.06 and 0.59 μm where 12 peaks were observed between 2.35 and 14.6 eV, all of which were accounted for in terms of electron transitions within the Brillouin zone. Freeout [6] used synchrotron radiation to measure the reflectance of cleaved ZnTe at wavelengths in the range 0.04–2.0 μm, analyzing the results by the K–K technique. He was able to correlate the structures in the reflectance spectrum with excitations of the core electrons.

Gauthe [39] studied the energy losses in 30 keV electrons on transmission through thin evaporated films of ZnTe. He found that the loss spectra were significantly different from a simple superposition of the loss spectra due to the component elements, the main loss peaks being at 4.6 and 16.3 eV and the plasmon energy at 14 eV. Tomoda and Mannami [40] also plotted the energy-loss spectrum of thin ZnTe films, which had been deposited on cubic rock salt, thus giving the zinc-blende lattice, and then dissolving away the substrate; using 40 keV electrons, they found a series of peaks ranging from 2.5–15.3 eV and also determined the plasmon energy as 12.3 eV. Walter *et al.* [41] measured the reflectance of ZnTe specimens cleaved in air along the (110) plane and subsequently maintained in a cryostat at low pressure. Taking into account the spin–orbit interactions, they were also able to make calculations of the reflectance from the band structure and claimed good agreement between the two sets of values.

Near the fundamental energy gap, the results from various studies are

again inconsistent. Loh and Newman [42] measured the transmittance of crystals of ZnTe near the fundamental edge and deduced the absorption coefficient, which was then plotted against wavelength. It was found that the absorption edge shifted upwards by about 0.1 eV as the temperature was reduced from 300 to 77 K. By measuring the absorption coefficient of hand-polished specimens of different thicknesses, it was possible to obtain estimates for the separate bulk and surface absorptions. Brown and Brodie [43] measured the reflectance and absorption spectra of amorphous ZnTe deposited on both glass and sapphire substratres; these showed only one broad maximum centered at 4.4 eV, which was associated with electron transitions near the center of the Brillouin zone in the [111] direction, that is, L direction. Their values of k between 0.35 and 0.61 μm are in reasonable agreement with those of Cardona [12] over the same spectral range.

The visible and near-infrared region has been well covered in a number of publications. Sliker and Jost [44] confirmed Cardona's results [37] and also gave tabulated values of n between 0.5 and 1.5 μm at 300 K. They used a single-crystal prism of undoped ZnTe cut from a boule grown by sublimation of high-purity zinc and tellurium; one face was polished using 0.3 μm alumina but because the material was cubic in structure, no attempt was made to align it crystallographically when making minimum-deviation measurements. Shiozawa *et al.* [45], also using the method of minimum deviation, have reported results in this same region (0.57–1.5 μm) for synthetic ZnTe. Aten *et al.* [46] used this particular experimental technique to produce a smooth curve of n versus photon energy at 300 K; at this temperature they measured the indirect energy gap as 2.164 eV. However, it is difficult to make accurate readings from the graphs they give, and their results have not been included. Working with thin films, Marple [15] used very pure ZnTe (containing less than 30 ppm of impurities) at wavelengths up to 2.0 μm and claimed an accuracy of ±0.003 in n from his minimum-deviation technique. He fitted his results into the following Sellmeier-type formula:

$$n^2 = 4.27 + 3.61/(\lambda^2 - 0.142).$$

Jensen and Torabi [47] derived a theoretical expression for the real part of the refractive index near the fundamental band edge and claimed that it gave a good fit with Marple's results. In addition, Horikoshi *et al.* [1] have reported values of n between 1.6 and 2.3 eV and at temperatures of 97 and 300 K, these being determined from their spectrophotometric measurements of transmittance. There is good agreement between this set of results and those of Marple, Shiozaka *et al.*, and Sliker and Jost. Horikoshi *et al.* also presented a graph of absorption coefficient versus energy

between 0.1 and 0.6 eV (2.0–12.0 μm) from which values of k may be calculated; k is very small (<0.01) over this range. In Table II, the values of n from Sliker and Jost and from Jensen and Torabi are presented for 300 K; Horikoshi *et al.*'s values of k between 2 and 12 μm are also included, as well as those of Zholkevich [20] between 0.5 and 0.7 μm.

Miloslavskii *et al.* [48] measured the transmittance of thin films of ZnTe and used the K–K method of analysis to calculate the phase change on transmission and hence to determine n and k. They produced a graph of n and k versus wave number between 10,000 and 22,500 cm^{-1} (0.44 and 1.0 μm), a peak in n being found at 0.526 μm. Chu *et al.* [49] also worked with films of ZnTe deposited on glass, ceramic, and tungsten, substrates at temperatures of 500–600 °C. They present a graph of the absorption coefficient squared versus energy between 2.20 and 2.28 eV for ZnTe on polished glass, and this was linear for energies just above the band gap. When extrapolated, the line intersected the energy axis at 2.25 eV, the optical band gap. Thutupalli and Tomlin's work [14] on thin films deposited at room temperature and between the wavelengths of 0.3 and 2.0 μm produced values of n that were in general smaller than those quoted in Table II, but when deposition took place at a substrate temperature of 325 °C, the values of n became very similar to those for the bulk material. A set of data in the near-infrared has also been published by Masso and Turner [50]. Where overlap of wavelength occurs, these data are in good agreement with those of Thutupalli and Tomlin for room-temperature deposition. For this wavelength region, Table II gives values of n due to Jensen and Torabi and also a set of values due to Masso and Turner, read off from the graph given by Li.

At long wavelengths (20–85 μm), Manabe *et al.* [23] again used the Lorentz-oscillator dispersion relationship quoted earlier to calculate n and k from their reflectance measurements on ZnTe. At 300 K, $\nu_t = 177\ cm^{-1}$, $\nu_l = 206\ cm^{-1}$, $\varepsilon_\infty = 6.7$, $N = 7.26 \times 10^4\ cm^{-2}$, and $\gamma = 3.01\ cm^{-1}$. At 100 K, the corresponding values were $180\ cm^{-1}$, $210\ cm^{-1}$, 6.7, $7.52 \times 10^4\ cm^{-2}$, and $2.34\ cm^{-1}$. Hadni *et al.* [35] measured the reflectance and transmittance of a pellet of ZnTe in the far infrared, explaining their results in terms of a single Lorentz-oscillator; this also produced values of $177\ cm^{-1}$ for ν_t and $205\ cm^{-1}$ for ν_l at 300 K. Hattori *et al.* [24] used their transmission interference technique to make measurements of n and k in the range 100–1000 μm and at temperatures of 300, 80, and 2 K; they were able to express their results in the form of a simple Sellmeier dispersion formula. Extrapolated to infinitely long wavelengths, the value of n became 3.15 at 300 K, 3.11 at 80 K, and 3.10 at 2 K. The corresponding values of the transverse-optical-phonon frequency were 180, 190, and $192\ cm^{-1}$, respectively. Nahory and Fan [51] presented graphs of the absorption coefficient of single crystals of ZnTe at wavelengths between the visible and 50 μm and at temperatures of 295 and 10 K. Most of the room-temperature

absorption was due to free holes, but there was some wavelength-related structure caused by lattice vibrations. Their values of k at room temperature are used in Table II, which also includes the optical constants due to Manabe *et al.*, Hadni *et al.*, and Hattori *et al.*

Excitons in ZnTe

Kurik and Manzhara [52] studied the exciton reflectance spectra of ZnTe single crystals, also noting the effects produced by the crystal defects. Pevtsov and Sel'kin [53] obtained the spectrum of excitons at 2 K by measurements of the reflectance and the phase change on reflection in both the s and p states of polarization. Their results appeared to fit well with the theoretical model of Thomas and Hopfield [54].

REFERENCES

1. Y. Horikoshi, A. Ebina, and T. Takahashi, *Japan. J. Appl. Phys.* **11**, 992 (1972).
2. H. H. Li, *J. Phys. Chem. Ref. Data* **13**, 103 (1984).
3. J. Tauc, in "Prog. in Semiconductors," (A. F. Gibson and R. E. Burgess, eds.), Vol. 9, Temple Press, London, 87 (1965).
4. B. L. Henke, *A.I.P. Conf. Proc. No 75*, 146 (1981).
5. B. L. Henke, P. Lee, T. J. Tanoka, R. Shimabukura, and B. K. Fujikawa, *Atomic Data and Nuclear Data Tables* **27**, 1, (1982).
6. J. L. Freeout, *Phys. Rev.* **B7**, 3810 (1973).
7. J. Gautron, C. Raisin, and P. Lemasson, *J. Phys. D* **15**, 153 (1982).
8. M. Cardona and R. Haensel, *Phys. Rev.* **B1**, 2605 (1970).
9. U. Gerhardt and G. W. Rubloff, *Appl. Opt.* **8**, 305 (1969).
10. M. Cardona, K. L. Shaklee, and F. H. Pollak, *Phys. Rev.* **154**, 696 (1967).
11. M. Balkanski and Y. Petroff, in "Int. Conf. Phys. Semicond., Paris, 1964," Dunod, Paris, and Academic Press, New York, 245 (1964).
12. M. Cardona, in "Int. Conf. Phys. Semicond., Paris, 1964,"Dunod, Paris, and Academic Press, New York, 181 (1964).
13. M. Aven, D. T. F. Marple, and B. Segall, *J. Appl. Phys.* **32**, 2261 (1961).
14. G. K. M. Thutupalli and S. G. Tomlin, *J. Phys. D* **9**, 1639 (1976).
15. D. T. F. Marple, *J. Appl. Phys.* **25**, 539 (1964).
16. S. Ahmed and E. E. Khawaja, *Thin Solid Films* **112**, L1 (1984).
17. E. E. Khawaja, *J. Phys. D* **9**, 1939 (1976).
18. M. R. Rambauske, *J. Appl. Phys.* **35**, 2958 (1964).
19. D. G. Avery, *Phil. Mag.* **41**, 1028 (1950).
20. G. A. Zholkevich, *Sov. Phys. Sol. State* **2**, 1009 (1960).
21. J. A. Wunderlich and L. G. De Shazer, *Appl. Opt.* **16**, 1584 (1977).
22. A. Feldman, I. Malitson, D. Horwitz, R. M. Waxler, and M. J. Dodge, Nat. Bur. Stand. (U.S.), Tech. Note 993, 63 (1979).
23. A. Manabe, A. Mitsuishi, and H. Yoshinga, *Japan J. Appl. Phys.* **6**, 593 (1967).
24. T. Hattori, Y. Homma, and A. Mitsuishi, *Opt. Commun.* **7**, 229 (1973).
25. P. A. Miles, *Appl. Opt.* **16**, 2891 (1977).
26. I. Strzalkowski, S. Joshi, and C. R. Crowell, *App. Phys. Lett.* **28**, 350 (1976).
27. C. I. C. Thompson, R. G. de Bell and W. L. Wolfe, *Appl. Opt.* **18**, 2085 (1979).
28. H. Tubota, H. Suzaki, and O. Motumba, *J. Phys. Soc. Japan* **11**, 610 (1956).
29. G. A. Thomas and V. B. Timofiev, in "Handbook on Semiconductors," (T. S. Moss, ed), North-Holland, Amsterdam, 45 (1980).

30. G. E. Hite, D. T. F. Marple, M. Aven, and B. Segall, *Phys. Rev.* **156**, 850 (1967).
31. Y. Tokura, T. Koda, I. Hirabayashi, and S. Nakada, *J. Phys. Soc. Japan* **50**, 145 (1981).
32. X. J. Jiang, T. Hisamura, Y. Nosua, and T. Goto, *J. Phys. Soc. Japan* **52**, 4008 (1983).
33. D. E. McCarthy, *Appl. Opt.* **4**, 317 (1965).
34. A. R. Hilton and C. E. Jones, *Appl. Opt.* **6**, 1513 (1967).
35. A. Hadni, J. Claudel, and P. Strimer, *Phys. Stat. Solidi* **26**, 241 (1968).
36. M. Cardona and D. L. Greenaway, *Phys. Rev.* **131**, 98 (1963).
37. M. Cardona, *J. Appl. Phys.* **36**, 2181 (1965).
38. D. R. Penn, *Phys. Rev.* **128**, 2093 (1962).
39. B. Gauthe, *Phys. Rev.* **114**, 1265 (1959).
40. T. Tomoda and M. Mannami, *J. Phys. Soc. Japan* **27**, 1204 (1969).
41. J. P. Walter, M. L. Cohen, Y. Petroff, and M. Balkanski, *Phys. Rev.* **B1**, 2261 (1970).
42. E. Loh and R. Newmann, *J. Phys. Chem. Solids* **21**, 324 (1961).
43. H. M. Brown and D. E. Brodie, *Can. J. Phys.* **50**, 2502 (1972).
44. T. Sliker and J. M. Jost, *J. Opt. Soc. Amer.* **56**, 130 (1966).
45. L. R. Shiozawa, J. L. Barrett, J. M. Jost, C. P. Chotkevys, and S. S. Devlin, "Research on II-VI Compound Semiconductors," Clevite Corp., Cleveland, Ohio, Final Report on the Office of Aerospace Research, U.S. Air Force Contract AF.33(616)-6865, (1962) [AD 287 718].
46. A. C. Aten, C. Z. Van Doorn and A. T. Vink, in "Proc. Int. Conf. Phys. Semicond. Exeter, 1962," (A. C. Stickland, ed.), Institute of Physics, London, 696 (1962).
47. B. Jensen and A. Torabi, *J. Appl. Phys.* **54**, 2030 (1983).
48. V. K. Miloslavskii and E. N. Nabockina, *Opt. and Spectros.* **38**, 565 (1975).
49. T. L. Chu, S. S. Chu, F. Firszt, and C. Herrington, *J. App. Phys.* **59**, 1259 (1986).
50. J. Masso and A. F. Turner, Bausch and Lomb Inc., Final Report on Development of Army Contract DA-44-009-AMC 124(T) (AD 600 264) (1964).
51. R. E. Nahory and H. Y. Fan, *Phys. Rev.* **156**, 825 (1967).
52. M. V. Kurik and V. S. Manzhara, *Sov. Phys. Sol. State* **18**, 1445 (1976).
53. A. B. Pevtsov and A. V. Sel'kin, *Sov. Phys. Sol. State* **23**, 1644 (1981).
54. D. G. Thomas and J. J. Hopfield, *Phys. Rev.* **128**, 2135 (1969).

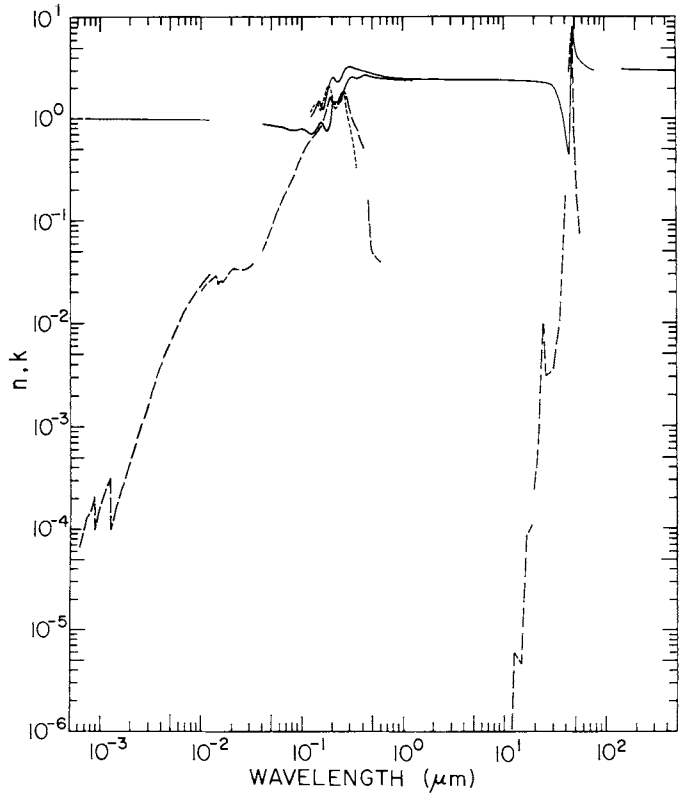

Fig. 1. Log–log plot of n (solid line) and k (dashed line) versus wavelength in micrometers for zinc selenide.

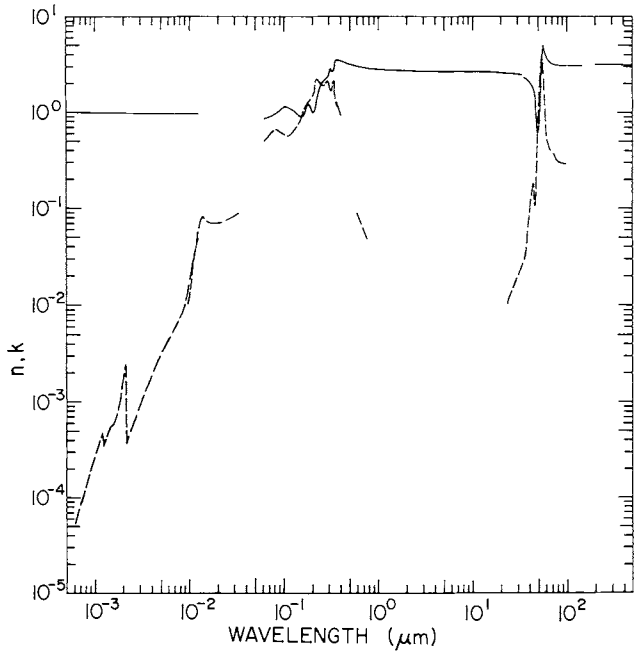

Fig. 2. Log–log plot of n (solid line) and k (dashed line) versus wavelength in micrometers for zinc telluride.

TABLE I

Values of *n* and *k* for Cubic ZnSe from Various References[a]

eV	cm^{-1}	μm	n	k
2000	16,131,000	0.00062	0.9998 [4]	7.0*10-5 [4]
1851	14,929,000	0.00067	0.9998	9.6*10-5
1698	13,695,000	0.00073	0.9998	1.32*10-4
1610	12,985,000	0.00077	0.9998	1.44
1459	11,768,000	0.00085	0.9998	2.00
1425	11,493,000	0.00087	0.9998	0.98
1393	11,235,000	0.00089	0.9996	1.22
1363	10,993,000	0.00091	0.9996	1.32
1240	10,000,000	0.00100	0.9996	1.80
1147	9,251,100	0.00108	0.9996	2.24
1033	8,333,300	0.00120	0.9996	3.00
991.9	8,000,000	0.00125	0.9994	1.00
946.5	7,634,000	0.00131	0.9992	1.22
826.6	6,666,700	0.00150	0.9990	2.00
815.7	6,579,000	0.00152	0.9990	2.02
760.7	6,135,400	0.00163	0.9988	2.54
725.1	5,848,300	0.00171	0.9986	2.96
673.9	5,435,300	0.00184	0.9984	3.69
620.0	5,000,000	0.00200	0.9982	4.80
529.9	4,273,900	0.00234	0.9974	7.96*10-4
413.3	3,333,300	0.00300	0.9960	1.69*10-3
367.9	2,967,300	0.00337	0.9952	2.36
310.0	2,500,000	0.00400	0.9938	3.74
269.0	2,169,600	0.00461	0.9924	5.48
248.0	2,000,000	0.00500	0.9918	6.62
227.1	1,831,700	0.00546	0.9908	8.12*10-3
206.7	1,666,700	0.00600	0.9900	1.00*10-2
190.8	1,538,900	0.0065	0.9898	1.18
177.1	1,428,400	0.0070	0.9890	1.36
155.0	1,250,000	0.0080	0.9886	1.71
136.3	1,099,300	0.0091	0.9882	2.02
124.0	1,000,000	0.0100	0.9876	2.28
109.7	884,780	0.0113	0.9872	2.68
103.3	833,330	0.0120	0.9870	2.88
100.0	806,550	0.01240	0.9872	2.98
150	1,209,800	0.008226	1.00 [8]	1.5*10-2 [8]
140	1,129,200	0.008856	1.00	1.6
136	1,096,900	0.009116	1.00	2.0
130	1,048,500	0.009537	1.00	2.0
125	1,008,200	0.009919	1.00	2.1
120	967,860	0.01033	1.00	2.2
115	927,530	0.0108	1.00	2.3
110	887,200	0.0113	1.00	2.4
100	806,550	0.0124	1.00	2.6
93.0	750,090	0.0133	1.00	2.8
90.0	725,890	0.0138	1.00	2.9
85.0	685,570	0.0146	1.00	2.4
80.0	645,240	0.0155	1.00	2.6
75.0	604,910	0.01653	1.00	2.6
70.0	564,580	0.01771	1.00	2.7*10-2

TABLE I (*Continued*)

ZnSe

eV	cm^{-1}	μm	n	k
60.0	483,930	0.02066	1.00 [8]	$3.4*10^{-2}$
50.0	403,270	0.02480	1.00	3.3
40.0	322,620	0.03100	1.00	3.5
37.5	302,460	0.03306	1.00	$3.8*10^{-2}$
30.0	241,960	0.04133	0.90 [7]	0.05 [7]
25.0	201,640	0.04959	0.86	0.08
20.0	161,310	0.06199	0.84	0.15
15.0	120,980	0.08266	0.76	0.25
12.5	100,820	0.09919	0.81	0.43
10.0	80,655	0.1240	0.70	0.65
8.00	64,524	0.1550	0.92	0.81
7.00	56,458	0.1771	0.76	1.28
6.50	52,426	0.1907	0.89	1.65
6.00	48,393	0.2066	1.40	1.40
5.50	44,360	0.2254	1.46	1.41
5.00	40,327	0.2480	1.43	1.86
4.50	36,295	0.2755	2.16	1.73
4.00	32,262	0.3100	2.57	1.00
3.50	28,229	0.3542	2.43	0.82
3.00	24,196	0.4133	2.68	0.50
2.00	16,131	0.6199	2.49	
1.00	8,065	1.240	2.38	
10.00	80,655	0.1240	1.03 [11]	1.19 [11]
8.99	72,509	0.1379	1.26	1.39
8.38	67,588	0.1480	1.48	1.35
8.00	64,524	0.1550	1.38	1.21
7.52	60,652	0.1649	1.25	1.60
7.01	56,539	0.1769	1.56	1.92
6.29	50,731	0.1971	2.45	2.00
5.99	48,312	0.2070	2.58	1.39
5.51	44,444	0.2250	2.38	1.29
5.30	42,747	0.2339	2.33	1.39
4.96	40,000	0.2500	2.54	1.57
4.77	38,472	0.2599	2.74	1.82
4.43	35,730	0.2800	3.24	1.23
4.30	34,682	0.2883	3.26	0.91
4.00	32,262	0.3100	3.24	0.70
3.54	28,551	0.3503	3.09	0.32
2.82	22,744	0.4397	2.83 [11]	0.16 [20]
2.70	21,777	0.4592	2.90	0.16
2.48	20,000	0.5000	2.78	0.05
2.00	16,131	0.6199	2.61	0.04
1.50	12,097	0.8266	2.51	
1.00	8,065	1.2400	2.45	
2.480	20,000	0.500	2.742(0) [22]	
1.653	13,333	0.750	2.578(2)	
1.240	10,000	1.00	2.489(0)	
0.9918	8,000	1.25	2.468(1)	
0.8266	6,667	1.50	2.457(1)	

TABLE I (*Continued*)

ZnSe

eV	cm^{-1}	μm	n	k
0.7085	5,714	1.75	2.450(6) [22]	
0.6199	5,000	2.00	2.446(2)	
0.5510	4,444	2.25	2.443(2)	
0.4959	4,000	2.50	2.440(9)	
0.4509	3,636	2.75	2.439(1)	
0.4133	3,333	3.00	2.437(6)	
0.3542	2,857	3.50	2.435(2)	
0.3100	2,500	4.00	2.433(1)	
0.2755	2,222	4.50	2.431(3)	
0.2480	2,000	5.00	2.429(5)	
0.2254	1,818	5.50	2.427(7)	
0.2066	1,667	6.00	2.425(8)	
0.1908	1,538	6.50	2.423(9)	
0.1771	1,429	7.00	2.421(8)	
0.1653	1,333	7.50	2.419(6)	
0.1550	1,250	8.00	2.417(3)	
0.1459	1,176	8.50	2.414(8)	
0.1378	1,111	9.00	2.412(2)	
0.1305	1,053	9.50	2.409(3)	
0.1240	1,000	10.00	2.406(5)	
0.1181	952.5	10.50	2.403(4)	
0.1127	909.0	11.00	2.400(1)	$1.1*10^{-7}$ [25]
0.1078	869.5	11.50	2.396(6)	
0.1033	833.2	12.00	2.392(9)	
0.09919	800.0	12.50	2.389(0)	$6.0*10^{-6}$
0.09538	769.3	13.00	2.384(9)	
0.09184	740.7	13.50	2.380(6)	
0.08856	714.3	14.00	2.376(1)	
0.08551	689.7	14.50	2.371(3)	$4.6*10^{-6}$
0.08266	666.7	15.00	2.366(3)	
0.08000	645.2	15.50	2.361(0)	
0.07749	625.0	16.00	2.355(5)	
0.07515	606.1	16.50	2.349(6)	$8.5*10^{-5}$
0.07294	588.3	17.00	2.343(5)	
0.07085	571.4	17.50	2.337(1)	
0.06888	555.6	18.00	2.330(3)	$1.1*10^{-4}$
0.06199	500.0	20.00	2.33 [23]	$4.8*10^{-4}$
0.05703	460.0	21.74	2.30	$1.7*10^{-3}$
0.05145	415.0	24.10	2.28	$2.0*10^{-2}$
0.04959	400.0	25.00	2.25	$6.0*10^{-3}$
0.04133	333.3	30.00	2.15	$7.0*10^{-3}$
0.03542	285.7	35.00	1.60	$2.1*10^{-2}$
0.03100	250.0	40.00	1.01	$3.2*10^{-1}$
0.02755	222.2	45.00	0.43	2.90 [23]
0.02695	217.4	46.00	0.58	3.62
0.02638	212.8	47.00	1.16	4.93
0.02610	210.5	47.50	2.10	6.10
0.02583	208.3	48.00	3.19	6.67
0.02556	206.2	48.50	3.20	6.20

TABLE I (*Continued*)

ZnSe

eV	cm^{-1}	μm	n	k	
0.02530	204.1	49.00	7.54	3.62	
0.02525	203.7	49.10	7.68	2.52	
0.02505	202.0	49.50	6.75	1.83	
0.02480	200.0	50.00	6.09	0.87	
0.02431	196.1	51.00	5.07	0.58	
0.02384	192.3	52.00	4.64	0.43	
0.02339	188.7	53.00	4.29	0.23	
0.02296	185.2	54.00	4.00	0.18	[23]
0.02254	181.8	55.00	3.83	0.14	
0.02156	173.9	57.50	3.71	0.11	
0.02066	166.7	60.00	3.54	0.08	
0.01771	142.8	70.00	3.04		
0.01550	125.0	80.00	2.90		
0.008257	66.67	150	3.07	[24]	
0.006199	50.00	200	3.04		
0.004959	40.00	250	3.03		
0.004133	33.33	300	3.02		
0.003542	28.57	350	3.02		
0.003100	25.00	400	3.01		
0.002755	22.22	450	3.01		
0.002480	20.00	500	3.01		
0.0	0	>99999.99	3.00		

Irtran 4

eV	cm^{-1}	μm	n	k	
0.4133	3,333	3.0	2.445	[34]	
0.3100	2,500	4.0	2.438		
0.2480	2,000	5.0	2.434		
0.2066	1,667	6.0	2.430		
0.1771	1,429	7.0	2.425		
0.1550	1,250	8.0	2.422		
0.1378	1,111	9.0	2.417		
0.1240	1,000	10.0	2.410		
0.1127	909.0	11.0	2.405		
0.1033	833.3	12.0	2.398		
0.09517	769.2	13.0	2.390		
0.08856	714.3	14.0	2.380		
0.04339	350	28.57	2.00	[35]	
0.03720	300	33.33	2.00		
0.03100	250	40.00	0.20	1.5	[35]
0.02790	225	44.44	0.50	2.8	
0.02604	210	47.62	2.50	7.9	
0.02542	205	48.78	5.00	4.8	
0.02480	200	50.00	8.42	3.2	
0.02170	175	57.14	3.50	0.4	
0.01860	150	66.67	3.40	0.5	

[a] References are indicated in brackets.

TABLE II

Values of *n* and *k* for Cubic ZnTe from Various References[a]

eV	cm^{-1}	μm	n	k
2000	16,131,000	0.00062	0.9998 [4]	$5.2*10^{-5}$ [4]
1850	14,929,000	0.00067	0.9998	7.2
1698	13,695,000	0.00073	0.9996	$9.8*10^{-5}$
1610	12,985,000	0.00077	0.9996	$1.18*10^{-4}$
1459	11,768,000	0.00085	0.9996	1.64
1363	10,993,000	0.00091	0.9996	2.00
1147	9,251,100	0.00108	0.9994	3.60
1033	8,333,300	0.00120	0.9994	4.80
991.9	8,000,000	0.00125	0.9994	3.60
855.1	6,896,800	0.00145	0.9992	5.40
826.6	6,666,700	0.00150	0.9990	5.80
815.7	6,579,000	0.00152	0.9990	5.80
760.7	6,135,400	0.00163	0.9990	6.40
725.1	5,848,300	0.00171	0.9988	$7.40*10^{-4}$
673.9	5,435,300	0.00184	0.9988	$1.02*10^{-3}$
620.0	5,000,000	0.00200	0.9988	1.82
582.1	4,694,900	0.00213	1.0000	2.44
563.6	4,545,700	0.00220	1.0012	0.38
529.9	4,273,900	0.00234	0.9990	0.48
413.3	3,333,300	0.00300	0.9976	0.92
367.9	2,967,400	0.00337	0.9968	1.24
310.0	2,500,000	0.00400	0.9954	1.90
269.0	2,169,600	0.00461	0.9940	2.60
248.0	2,000,000	0.00500	0.9932	3.20
227.1	1,831,700	0.00546	0.9920	3.80
206.7	1,666,700	0.0060	0.9904	4.60
190.8	1,538,900	0.0065	0.9892	5.40
177.1	1,428,400	0.0070	0.9876	6.20
155.0	1,250,000	0.0080	0.9832	$7.80*10^{-3}$
136.3	1,099,300	0.0091	0.9762	$1.08*10^{-2}$
124.0	1,000,000	0.0100	0.9688	1.66
112.7	909,090	0.0110	0.9626	3.02
103.3	833,330	0.0120	0.9638	4.28
100.0	806,550	0.0124	0.9666	4.96
150	1,209,800	0.008266	1.00 [8]	$3.8*10^{-3}$ [8]
140	1,129,200	0.008856	1.00	6.0
135	1,088,800	0.009184	1.00	7.4
130	1,048,500	0.009538	1.00	$9.8*10^{-3}$
125	1,008,200	0.009919	1.00	$1.2*10^{-2}$
120	967,860	0.01032	1.00	1.7
110	887,200	0.01127	1.00	3.2
100	806,550	0.01240	1.00	5.5
90.0	725,890	0.01378	1.00	8.2
80.0	645,240	0.01550	1.00	7.4
70.0	564,580	0.01771	1.00	7.2
60.0	483,930	0.02066	1.00	7.0
50.0	403,270	0.02480	1.00	7.4
37.5	302,460	0.03306	1.00	$9.0*10^{-2}$

TABLE II (*Continued*)

ZnTe

eV	cm^{-1}	μm	n	k
20.0	161,310	0.06200	0.87 [37]	0.50 [37]
15.0	120,980	0.08266	1.00	0.67
12.0	96,786	0.1033	1.17	0.60
11.0	88,720	0.1127	1.13	0.57
10.0	80,653	0.1240	1.07	0.64
9.0	72,589	0.1378	1.00	0.70
8.0	64,524	0.1550	0.90	0.83
7.5	60,491	0.1653	0.97	1.07
7.0	56,458	0.1771	1.20	1.20
6.0	48,393	0.2066	1.00	1.47
5.5	44,360	0.2254	1.43	2.17
5.0	40,327	0.2480	2.00	2.00
4.6	37,101	0.2695	2.20	1.90
4.3	34,682	0.2883	2.27	2.13
4.0	32,262	0.3100	2.80	2.00
3.85	31,052	0.3220	2.73	1.73
3.6	29,036	0.3444	3.00	2.10
3.5	28,229	0.3542	3.47	1.33
3.0	24,196	0.4133	3.40	0.95
2.18	17,583	0.5687	3.10 [15]	
2.00	16,130	0.6199	3.00	
1.72	13,873	0.7208	2.90	
1.30	10,485	0.9537	2.80	
1.00	8,065	1.240	2.75	
0.50	4,033	2.480	2.70	
2.179	17,580	0.569	3.111 [44]	
2.149	17,330	0.577	3.085	0.09 [20]
2.141	17,270	0.579	3.079	0.09
2.105	16,980	0.589	3.054	0.09
2.066	16,670	0.600	3.035	0.09
2.013	16,230	0.616	3.005	0.08
1.908	15,390	0.650	2.962	0.07
1.771	14,290	0.700	2.912	0.06
1.710	13,800	0.725	2.893	0.06
1.653	13,330	0.750	2.879	0.05
1.610	12,990	0.770	2.866	
1.550	12,500	0.800	2.853	
1.240	10,000	1.000	2.790	
1.033	8,333	1.200	2.758	
0.8856	7,143	1.400	2.741	
0.8266	6,667	1.500	2.734	
0.8194	6,609	1.513	2.734	
2.066	16,667	0.60	3.00 [47]	
1.240	10,000	1.0	2.82	
0.6200	5,000	2.0	2.73	$2.0*10^{-4}$ [1]
0.4133	3,333	3.0	2.69	4.0
0.3100	2,500	4.0	2.68	$8.0*10^{-4}$
0.2480	2,000	5.0	2.67	$1.6*10^{-3}$

TABLE II (*Continued*)

ZnTe

eV	cm^{-1}	μm	n	k
0.2067	1,667	6.0	2.67 [47]	$2.0*10^{-3}$ [1]
0.1771	1,429	7.0	2.66	3.0
0.1240	1,000	10.0	2.65	$7.0*10^{-3}$
0.06199	500.0	20.0	2.64	
0.04133	333.3	30.0	2.638	
0.03100	250.0	40.0	2.635	
0.02480	200.0	50.0	2.634	
0.9465	7,634	1.31	2.66 [50]	
0.5299	4,274	2.34	2.65	
0.3757	3,030	3.30	2.65	
0.2566	2,070	4.83	2.64	
0.1885	1,520	6.58	2.64	
0.1406	1,334	8.82	2.64	
0.1150	927.6	10.78	2.63	
0.09770	788.0	12.69	2.63	
0.08293	668.9	14.95	2.62	
0.06508	524.9	19.05	2.59	
0.05344	431.0	23.20	2.56	0.01 [51]
0.04521	364.6	27.43	2.53	0.02
0.03887	313.6	31.90	2.49	0.02
0.03591	298.6	34.53	2.47	0.03
0.03546	286	34.97	2.26 [35]	0.03 [51]
0.03224	260	38.46	2.19	0.03
0.03100	250	40.00	2.07	0.09
0.02914	235	42.55	1.92	0.15
0.02790	225	44.44	1.90	0.18
0.02728	220	45.45	1.68	0.11
0.02604	210	47.62	0.75	0.18
0.02480	200	50.00	0.70	1.0 [35]
0.02356	190	52.63	1.10	1.9
0.02294	185	54.05	1.46	3.1
0.02232	180	55.55	3.72	3.6
0.02207	178	56.18	4.00	3.0
0.02170	175	57.14	4.94	2.3
0.02070	167	59.88	3.95	0.6
0.01860	150	66.67	3.29	0.4
0.01773	143	69.93	3.14	0.4
0.01550	125	80.00	3.07	0.3
0.01376	111	90.09	3.06	0.3
0.01240	100	100.0	3.05	0.3
0.01116	90	111.1	3.04	0.3
0.009919	80	125.0	3.02	0.2
0.008307	67	150.0	3.01	0.2
0.06199	500.0	20.0	2.20 [25]	0.01 [51]
0.04133	333.3	30.0	2.10	0.03
0.03543	285.7	35.0	2.03	0.03
0.03100	250.0	40.0	1.74	–
0.02755	222.2	45.0	1.59	–

TABLE II (*Continued*)

ZnTe

eV	cm^{-1}	μm	n	k
0.02480	200.0	50.0	0.23 [23]	1.30 [23]
0.02431	196.1	51.0	0.14	1.74
0.02384	192.3	52.0	0.14	2.46
0.02339	188.7	53.0	0.23	3.48
0.02296	185.2	54.0	0.58	4.35
0.02254	181.8	55.0	1.45	6.09
0.02214	178.6	56.0	3.48	6.96
0.02175	175.4	57.0	7.97	2.90
0.02156	173.9	57.5	9.57	2.32
0.02138	172.4	58.0	7.54	1.88
0.02102	169.5	59.0	5.80	0.87
0.02067	166.7	60.0	5.16	0.35
0.01771	142.9	70.0	3.19	
0.01550	125.0	80.0	2.90	
0.006199	50.00	200	3.20	0.02 [24]
0.004959	40.00	250	3.18	0.02
0.004132	33.33	300	3.17	0.017
0.003100	25.00	400	3.16	

[a] References are indicated in brackets.

Aluminum Oxide (Al_2O_3)

FRANÇOIS GERVAIS
Centre de Recherches sur la Physique des Hautes Températures
Centre National de la Recherche Scientifique
45071 Orléans, France

Aluminum oxide crystallizes in the corundum (α-Al_2O_3) rhombohedral structure. It is also known as sapphire. The system is uniaxial and optical properties measured on a single crystal are therefore anisotropic. The structure of the oxygen sublattice is close-packed. As a result, the anisotropy of the refractive index in the visible region, mainly related to the anisotropy of the oxygen polarizability is small (less than 2%). In the millimeter-wave range, the anisotropy reaches 10%. The optical constants selected are listed in Table I and plotted in Fig. 1.

A study including original measurements and a compilation of previous data, which extends over a wide energy range, from 6 eV up to 1.6×10^3 eV, has been performed at the Deutsches Elektronen-synchrotron DESY [1]. The compilation concerns Refs. [2–5]. Although measurements have been performed on evaporated amorphous Al_2O_3 such that information related to anisotropy is lost, they are of practical interest. Results agree well with previous measurements at low energies but extend over a much wider energy range. Optical absorption measurements performed on single-crystal samples, but restricted to the 1–6 eV range, were reported in Refs. [6, 7]. Some anisotropy of the spectra is displayed in [6]. However, these spectra are of little practical interest, since it is difficult to extract n and k from the UV edge by Kramers–Kronig analysis in a too-narrow energy range where there is strong dispersion. Results of [1] are given in Table I.

The indexes of refraction of a synthetic sapphire prism measured over its entire range of transmission (0.2–6 μm) is reported in Ref. [8]. The optic axis of the prism was oriented parallel to the base and perpendicular to the apex, so that measurements refer to the ordinary ray (electric field perpendicular to the c axis of the corundum structure). Results are listed in Table I.

Measurements in the infrared were reported in the literature at the beginning of this century. However, the quantitative exploitation of

Copyright © 1991 by Academic Press.
All rights of reproduction in any form reserved.
ISBN 0-12-544422-2

infrared reflectivity spectra started with the availability of computers in the 1960s. The most complete set of measurements in the infrared complemented by data processing was performed by Barker [9]. Several single crystals from different origins were compared. Measurements were performed with a prism spectrometer. Barker emphasized the large differences that may appear from one sample to another in specific spectral regions. The forbidden modes disappear after etching of the surface. Measurements analyzed in Refs. [11] and [12] were performed on a single crystal previously annealed at 1775 K, thus above 3/4 of the temperature of the melting point, to regenerate the surface partially altered by the polishing. The spectra then consist of normal vibrational modes only, and no extra modes are visible.

Surprisingly, the literature is short of data concerning n and k in alumina ceramics. A study of this type was published only recently [12], performed with a grating spectrometer. The hot-pressed alumina sample was as-fired. The spectrum mainly resembles that for the ordinary ray of a single crystal but of course also contains features related to the extraordinary ray. Again, the authors emphasize the influence of polishing on the appearance of forbidden modes. The authors seem to have been surprised by the existence of a weak band at approximately $500\,\mathrm{cm}^{-1}$. This is simply the signature of the presence of the longitudinal optical mode at $514\,\mathrm{cm}^{-1}$ for the electric field polarized parallel to the c axis (extraordinary ray) in the vicinity of the LO mode at $482\,\mathrm{cm}^{-1}$ for the ordinary ray. In randomly oriented materials, a reflection band necessarily develops between the two values that cancel the real part of the dielectric response. In other words, there is necessarily a maximum between two minima of the dielectric response. In Ref. [12], the optical constants are calculated by Kramers–Kronig relations.

In single crystals, the dielectric function can be modeled. As soon as a dielectric function model fits the infrared reflectivity, one may deduce the optical constants more accurately than with a Kramers–Kronig analysis. The absorption coefficient is found to be extremely high. The penetration depth of the infrared radiation is found currently smaller than 1 μm at a peak corresponding to a normal vibrational mode. As a result, the infrared beam in these spectral regions probes the surface of the sample rather than the bulk. The result is then very sensitive to the alterations of the crystal surface, as shown by various authors. Conversely, in the vicinity of vibrational-mode frequencies, the results reflect bulk properties on etched surfaces or annealed crystals. This is also true far from normal modes, because then the penetration depth of the infrared beam is much larger. Disorder or alteration of the sample surface increases mode damping and therefore lowers the reflectivity level. The higher the reflectivity, the better is the sample quality generally. Note that fitting the spectra minimizes the spurious effects of the surface (by comparison with a Kramers–Kronig

analysis) because the damping is averaged over a wide spectral range (with larger penetration depth on average) in the former case, instead of being determined too near the mode frequency where disorder may alter the result.

Barker [9] fitted his spectra with the dielectric-function model

$$\varepsilon = \varepsilon_\infty + \sum_j \Delta\varepsilon_j \frac{\Omega_{j\mathrm{TO}}^2}{\Omega_{j\mathrm{TO}}^2 - \omega^2 + i\gamma_{j\mathrm{TO}}\omega}. \tag{1}$$

Here ε stands for the dielectric function, ε_∞ is the high-frequency dielectric constant, $\Delta\varepsilon$, Ω, and γ are the oscillator strength, the frequency, and the damping of the jth TO (transverse optic) mode, respectively. Results have been used to calculate the n and k data given in Table I.

A factorization over poles and zeros of the dielectric response in the form

$$\varepsilon = \varepsilon_\infty \prod_j \frac{\Omega_{j\mathrm{LO}}^2 - \omega^2 + i_{j\mathrm{LO}}\omega}{\Omega_{j\mathrm{TO}}^2 - \omega^2 + i\gamma_{j\mathrm{TO}}\omega} \tag{2}$$

was preferred in Refs. [10] and [11]. Here the index LO refers to longitudinal optic modes. The reason invoked by the authors is that in highly polar systems where the coulombic field splits the polar modes into transverse and longitudinal components (one being possibly twice more energetic than the other), phonons have very different decays, and mode damping is possibly very different. Conversely, identical dampings are implicitly assumed for the TO and LO components by the model in Eq. 1. Results deduced from the fit to the reflectivity data with the dielectric-function model in Eq. 2 are compared with those of Barker [9] in Table I. Data are given for the electric field of infrared radiation polarized perpendicular (ordinary ray) and parallel (extraordinary ray) to the crystal c axis. The overall agreement is good. Discrepancies appear in the regions of poor fitting in Eq. 1 and mainly near highly polar TO modes, where surface effects limit the penetration depth of the infrared radiation, thus giving less-sharp peaks for n and k. Note that this fitting procedure yields better agreement to the data near the normal vibrational modes, but results far from the resonances are less reliable than those calculated with Eq. (1).

Also included in Table I are the data given in [12] for a polycrystalline sample of hot-pressed 99.9% alumina. These data have been deduced by the author of the measurements via a Kramers–Kronig analysis of his reflectivity data.

REFERENCES

1. H. J. Hagemann, W. Gudat, and C. Kunz, *J. Opt. Soc. Am.* **65**, 742 (1975); DESY SR-74/7 (Hamburg, 1974).
2. G. Hass, W. R. Hunter, and R. Tousey, *J. Opt. Soc. Am.* **47**, 1070 (1957).
3. W. R. Hunter, *J. Opt. Soc. Am.* **54**, 15 (1964).
4. W. A. Fomichev and A. S. Parobets, *Opt. Spectrosc.* **21**, 419 (1966).
5. V. A. Fomichev, *Sov. Phys.-Solid State* **8**, 2312 (1967).
6. E. W. J. Mitchell, J. D. Ridgen, and P. D. Townsend, *Phil. Mag.* **5**, 1013 (1960).
7. P. W. Levy, *Phys. Rev.* **123**, 1226 (1961).
8. I. H. Malitson, F. V. Murphy, and W. S. Rodeny, *J. Opt. Soc. Am.* **48**, 72 (1958).
9. A. S. Barker, *Phys. Rev.* **132**, 1474 (1963).
10. F. Gervais and B. Piriou, *J. Phys. C.-Solid St. Phys.* **7**, 2374 (1974).
11. F. Gervais, D. Billard, and B. Piriou, *Revue Internationale des Hautes Températures et des Réfractaires* **12**, 58 (1975).
12. C. A. Worrell, *J. Mat. Science* **21**, 781 (1986).

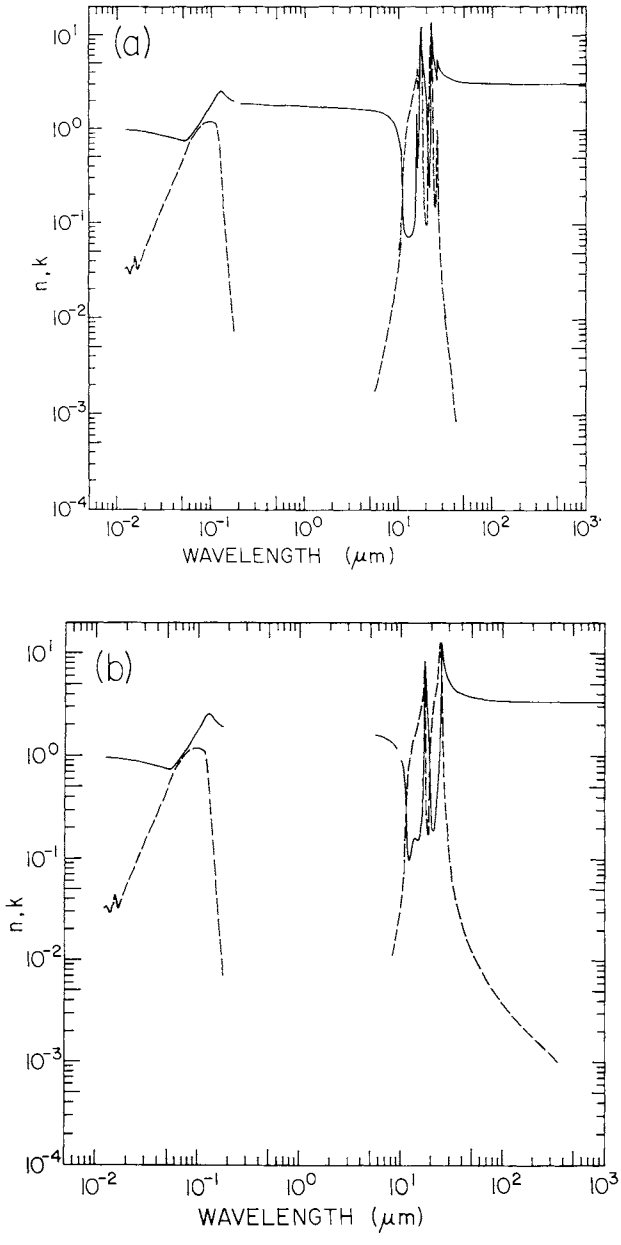

Fig. 1. (a) Log–log plot of n_o (solid line) and k_o (dashed line) versus wavelength in micrometers for aluminum oxide. (b) Log–log plot of n_e (solid line) and k_e (dashed line) versus wavelength in micrometers.

TABLE I

Values of n and k for Aluminum Oxide Obtained from Various References[a]

eV	cm^{-1}	μm	n	k	$n_\perp$	$k_\perp$	$n_\perp$	$k_\perp$	$n_\parallel$	$k_\parallel$	$n_\parallel$	$k_\parallel$
100.0	806,452	0.01240	0.967	0.033[1]								
99.0	798,387	0.01252	0.968	0.034								
98.0	790,323	0.01265	0.968	0.034								
97.0	782,258	0.01278	0.968	0.034								
96.0	774,194	0.01292	0.969	0.033								
95.0	766,129	0.01305	0.969	0.033								
94.0	758,065	0.01319	0.970	0.032								
93.0	750,000	0.01333	0.969	0.032								
92.0	741,935	0.01348	0.968	0.031								
91.0	733,871	0.01363	0.968	0.030								
90.0	725,806	0.01378	0.967	0.029								
89.0	717,742	0.01393	0.966	0.029								
88.0	709,677	0.01409	0.965	0.030								
87.0	701,613	0.01425	0.963	0.031								
86.0	693,548	0.01442	0.962	0.032								
85.0	685,484	0.01459	0.961	0.033								
84.0	677,419	0.01476	0.960	0.034								
83.0	669,355	0.01494	0.959	0.035								
82.0	661,290	0.01512	0.958	0.035								
81.0	653,226	0.01531	0.955	0.037								
80.0	645,161	0.01550	0.956	0.044								
79.0	637,097	0.01570	0.958	0.042								
78.0	629,032	0.01590	0.960	0.040								
77.0	620,968	0.01610	0.961	0.038								
76.0	612,903	0.01632	0.963	0.035								
75.0	604,839	0.01653	0.960	0.030								
74.0	596,774	0.01676	0.957	0.032								
73.0	588,710	0.01700	0.954	0.033								
72.0	580,645	0.01722	0.952	0.034								
71.0	572,581	0.01746	0.949	0.036								

TABLE I (*Continued*)

Aluminum Oxide

eV	cm^{-1}	μm	n	k	$n_\perp$	$k_\perp$	$n_\perp$	$k_\perp$	$n_{\|\|}$	$k_{\|\|}$	$n_{\|\|}$	$k_{\|\|}$
70.0	564,516	0.01771	0.946	0.037								
69.0	556,452	0.01797	0.944	0.038								
68.0	548,387	0.01824	0.941	0.040								
67.0	540,323	0.01851	0.938	0.041								
66.0	532,258	0.01879	0.935	0.042								
65.0	524,194	0.01908	0.933	0.044								
64.0	516,129	0.01937	0.930	0.046								
63.0	508,065	0.01968	0.928	0.048								
62.0	500,000	0.02000	0.925	0.049								
61.0	491,935	0.02033	0.923	0.051								
60.0	483,871	0.02067	0.920	0.053								
59.0	475,806	0.02102	0.917	0.056								
58.0	467,742	0.02138	0.914	0.060								
57.0	459,677	0.02175	0.911	0.063								
56.0	451,613	0.02214	0.908	0.067								
55.0	443,548	0.02255	0.905	0.070								
54.0	435,484	0.02296	0.902	0.074								
53.0	427,419	0.02340	0.899	0.077								
52.0	419,355	0.02385	0.895	0.081								
51.0	411,290	0.02431	0.892	0.085								
50.0	403,226	0.02480	0.889	0.088								
49.0	395,161	0.02531	0.886	0.092								
48.0	387,097	0.02583	0.883	0.095								
47.0	379,032	0.02638	0.879	0.102								
46.0	370,968	0.02696	0.875	0.109								
45.0	362,903	0.02756	0.871	0.115								
44.0	354,839	0.02818	0.866	0.122								
43.0	346,774	0.02884	0.862	0.129								
42.0	338,710	0.02952	0.858	0.136								
41.0	330,645	0.03024	0.854	0.143								

TABLE I (*Continued*)

Aluminum Oxide

eV	cm^{-1}	μm	n	k	$n_\perp$	$k_\perp$	$n_\perp$	$k_\perp$	$n_{\|\|}$	$k_{\|\|}$	$n_{\|\|}$	$k_{\|\|}$
40.0	322,581	0.03100	0.850	0.150								
39.0	314,516	0.03179	0.845	0.159								
38.0	306,452	0.03263	0.839	0.171								
37.0	298,387	0.03351	0.834	0.182								
36.0	290,323	0.03444	0.828	0.194								
35.0	282,258	0.03543	0.823	0.205								
34.0	274,194	0.03647	0.817	0.217								
33.0	266,129	0.03758	0.812	0.229								
32.0	258,065	0.03875	0.805	0.248								
31.0	250,000	0.04000	0.798	0.266								
30.0	241,935	0.04133	0.791	0.285								
29.0	233,871	0.04276	0.782	0.307								
28.0	225,806	0.04429	0.774	0.330								
27.0	217,742	0.04593	0.762	0.362								
26.0	209,677	0.04769	0.750	0.395								
25.0	201,613	0.04960	0.737	0.436								
24.0	193,548	0.05167	0.730	0.500								
23.0	185,484	0.05391	0.737	0.574								
22.0	177,419	0.05636	0.764	0.651								
21.0	169,355	0.05905	0.805	0.725								
20.0	161,290	0.06200	0.856	0.774								
19.0	153,226	0.06526	0.896	0.832								
18.0	145,161	0.06889	0.953	0.916								
17.0	137,097	0.07294	1.037	0.998								
16.0	129,032	0.07750	1.149	1.078								
15.0	120,968	0.08267	1.297	1.135								
14.0	112,903	0.08857	1.465	1.166								
13.0	104,839	0.09538	1.657	1.179								
12.0	96,774	0.1033	1.885	1.171								
11.0	88,710	0.1127	2.231	1.109								

TABLE I (*Continued*)

Aluminum Oxide

eV	cm^{-1}	μm	n	k	$n_\perp$	$k_\perp$	$n_\perp$	$k_\perp$	$n_\parallel$	$k_\parallel$	$n_\parallel$	$k_\parallel$
10.0	80,645	0.1240	2.519	0.629								
9.0	72,581	0.1378	2.338	0.108								
8.0	64,516	0.1550	2.074	0.032								
7.0	56,452	0.1771	1.939	0.007								
6.0	48,387	0.2067			1.834[8]							
5.9	47,581	0.2102			1.834							
5.8	46,774	0.2138			1.834							
5.7	45,968	0.2175			1.834							
5.6	45,161	0.2214			1.834							
5.5	44,355	0.2255			1.834							
5.4	43,548	0.2296			1.834							
5.3	42,742	0.2340			1.834							
5.2	41,935	0.2385			1.834							
5.1	41,129	0.2431			1.834							
5.0	40,323	0.2480			1.834							
4.9	39,516	0.2531			1.834							
4.8	38,710	0.2583			1.834							
4.7	37,903	0.2638			1.834							
4.6	37,097	0.2696			1.831							
4.5	36,290	0.2756			1.827							
4.4	35,484	0.2818			1.823							
4.3	34,677	0.2884			1.820							
4.2	33,871	0.2952			1.817							
4.1	33,065	0.3024			1.813							
4.0	32,258	0.3100			1.810							
3.9	31,452	0.3179			1.807							
3.8	30,645	0.3263			1.804							
3.7	29,839	0.3351			1.801							
3.6	29,032	0.3444			1.799							
3.5	28,226	0.3543			1.796							

TABLE I (*Continued*)

Aluminum Oxide

eV	cm^{-1}	μm	n	k	$n_{\perp}$	$k_{\perp}$	$n_{\perp}$	$k_{\perp}$	$n_{\parallel}$	$k_{\parallel}$	$n_{\parallel}$	$k_{\parallel}$
3.4	27,419	0.3647			1.794							
3.3	26,613	0.3758			1.791							
3.2	25,806	0.3875			1.789							
3.1	25,000	0.4000			1.787							
3.0	24,194	0.4133			1.784							
2.9	23,387	0.4276			1.782							
2.8	22,581	0.4429			1.780							
2.7	21,774	0.4593			1.779							
2.6	20,968	0.4769			1.777							
2.5	20,161	0.4960			1.775							
2.4	19,355	0.5167			1.773							
2.3	18,548	0.5391			1.771							
2.2	17,742	0.5636			1.770							
2.1	16,935	0.5905			1.768							
2.0	16,129	0.6200			1.767							
1.9	15,323	0.6526			1.765							
1.8	14,516	0.6889			1.764							
1.7	13,710	0.7294			1.762							
1.6	12,903	0.7750			1.761							
1.5	12,097	0.8267			1.759							
1.4	11,290	0.8857			1.758							
1.3	10,484	0.9538			1.757							
1.2	9,677	1.033			1.755							
1.1	8,871	1.127			1.753							
1.0	8,065	1.240			1.751							
0.9	7,258	1.378			1.749							
0.8	6,452	1.550			1.746							
0.7	5,645	1.771			1.742							
0.6	4,839	2.067			1.736							
0.5	4,032	2.480			1.726							

TABLE I (*Continued*)

Aluminum Oxide

eV	cm^{-1}	μm	n	k	$n_\perp$	$k_\perp$	$n_\perp$	$k_\perp$	$n_{\|\|}$	$k_{\|\|}$	$n_{\|\|}$	$k_{\|\|}$
0.48	3,900	2.564			1.723							
0.47	3,800	2.632			1.721							
0.46	3,700	2.703			1.719							
0.45	3,600	2.778			1.716							
0.43	3,500	2.857			1.714							
0.42	3,400	2.941			1.712							
0.41	3,300	3.030			1.709							
0.40	3,200	3.125			1.707							
0.38	3,100	3.226			1.705							
0.37	3,000	3.333			1.701							
0.36	2,900	3.448			1.697							
0.35	2,800	3.571			1.692							
0.33	2,700	3.704			1.687							
0.32	2,600	3.846			1.681							
0.31	2,500	4.000			1.674							
0.30	2,400	4.167			1.667							
0.29	2,300	4.348			1.658							
0.27	2,200	4.545			1.647							
0.26	2,100	4.762			1.636							
0.25	2,000	5.000			1.624							
0.24	1,900	5.263			1.607							
0.2232	1,800	5.556			1.624[9]	0.002[9]			1.594[9]	0.002[9]		
0.2108	1,700	5.882			1.600	0.002			1.571	0.003		
0.1984	1,600	6.250			1.571	0.003			1.542	0.004		
0.1860	1,500	6.667			1.534	0.004			1.506	0.004		
0.1736	1,400	7.143			1.485	0.005			1.459	0.006		
0.1612	1,300	7.692			1.419	0.007			1.396	0.008		
0.1488	1,200	8.333			1.325	0.011			1.307	0.011		
0.1364	1,100	9.091			1.181	0.017			1.174	0.018		
0.1240	1,000	10.00	0.907[12]	0.003[12]	0.925	0.034	0.877[10]	0.053[10]	0.950	0.033	0.935[11]	0.037[11]

TABLE I (*Continued*)

Aluminum Oxide

eV	cm^{-1}	μm	n	k	$n_{\perp}$	$k_{\perp}$	$n_{\perp}$	$k_{\perp}$	$n_{\parallel}$	$k_{\parallel}$	$n_{\parallel}$	$k_{\parallel}$
0.1228	990	10.10	0.875	0.003	0.888	0.037	0.839	0.057	0.918	0.035	0.904	0.039
0.1215	980	10.20	0.831	0.003	0.847	0.041	0.796	0.062	0.884	0.038	0.869	0.042
0.1203	970	10.31	0.770	0.003	0.801	0.045	0.749	0.068	0.846	0.042	0.832	0.045
0.1190	960	10.42	0.709	0.003	0.750	0.051	0.696	0.075	0.805	0.046	0.791	0.049
0.1178	950	10.53	0.648	0.021	0.693	0.058	0.636	0.084	0.759	0.051	0.745	0.054
0.1166	940	10.64	0.576	0.041	0.627	0.067	0.566	0.097	0.709	0.057	0.694	0.061
0.1153	930	10.75	0.499	0.088	0.550	0.081	0.484	0.117	0.651	0.066	0.636	0.069
0.1141	920	10.87	0.423	0.145	0.456	0.103	0.384	0.153	0.585	0.077	0.569	0.081
0.1128	910	10.99	0.344	0.228	0.340	0.147	0.270	0.224	0.507	0.093	0.489	0.098
0.1116	900	11.11	0.263	0.339	0.213	0.249	0.182	0.344	0.413	0.121	0.392	0.128
0.1104	890	11.24	0.180	0.449	0.143	0.393	0.138	0.468	0.298	0.176	0.276	0.192
0.1091	880	11.36	0.125	0.541	0.115	0.522	0.116	0.579	0.193	0.288	0.181	0.312
0.1079	870	11.49	0.109	0.629	0.101	0.634	0.103	0.680	0.140	0.419	0.136	0.440
0.1066	860	11.63	0.113	0.717	0.093	0.737	0.094	0.774	0.117	0.535	0.116	0.553
0.1054	850	11.77	0.114	0.797	0.088	0.834	0.087	0.864	0.104	0.639	0.106	0.655
0.1042	840	11.91	0.115	0.877	0.085	0.927	0.083	0.951	0.096	0.734	0.101	0.750
0.1029	830	12.05	0.116	0.957	0.083	1.017	0.079	1.037	0.092	0.825	0.099	0.840
0.1017	820	12.20	0.116	1.036	0.083	1.107	0.077	1.122	0.089	0.912	0.100	0.927
0.1004	810	12.35	0.117	1.116	0.083	1.197	0.075	1.208	0.087	0.998	0.103	1.011
0.09920	800	12.50	0.118	1.197	0.084	1.287	0.074	1.294	0.086	1.083	0.108	1.095
0.09796	790	12.66	0.119	1.278	0.085	1.379	0.073	1.383	0.086	1.167	0.115	1.177
0.09672	780	12.82	0.119	1.360	0.088	1.473	0.072	1.473	0.087	1.253	0.124	1.258
0.09548	770	12.99	0.120	1.441	0.090	1.571	0.072	1.567	0.089	1.340	0.134	1.338
0.09424	760	13.16	0.121	1.537	0.094	1.672	0.072	1.664	0.091	1.430	0.143	1.417
0.09300	750	13.33	0.121	1.637	0.099	1.778	0.073	1.766	0.094	1.523	0.152	1.495
0.09176	740	13.51	0.122	1.736	0.104	1.890	0.074	1.873	0.098	1.620	0.157	1.575
0.09052	730	13.70	0.122	1.836	0.111	2.010	0.076	1.988	0.102	1.721	0.159	1.659
0.08928	720	13.89	0.124	1.947	0.120	2.138	0.078	2.110	0.108	1.830	0.159	1.749
0.08804	710	14.09	0.126	2.058	0.131	2.278	0.080	2.243	0.116	1.946	0.156	1.848
0.08680	700	14.29	0.129	2.169	0.145	2.433	0.083	2.389	0.127	2.073	0.154	1.958

TABLE I (*Continued*)

Aluminum Oxide

eV	cm^{-1}	μm	n	k	$n_\perp$	$k_\perp$	$n_\perp$	$k_\perp$	$n_{\|\|}$	$k_{\|\|}$	$n_{\|\|}$	$k_{\|\|}$
0.08556	690	14.49	0.131	2.296	0.165	2.607	0.088	2.552	0.141	2.214	0.153	2.080
0.08432	680	14.71	0.142	2.441	0.192	2.807	0.094	2.739	0.164	2.375	0.153	2.216
0.08308	670	14.93	0.167	2.585	0.236	3.047	0.102	2.961	0.211	2.568	0.156	2.371
0.08184	660	15.15	0.192	2.811	0.317	3.350	0.118	3.243	0.358	2.782	0.163	2.547
0.08060	650	15.39	0.251	3.175	0.516	3.761	0.164	3.657	0.465	2.722	0.175	2.754
0.07936	640	15.63	0.807	3.642	1.222	4.181	0.580	4.557	0.329	2.951	0.194	3.004
0.07812	630	15.87	0.502	3.040	1.718	3.157	1.482	2.767	0.350	3.298	0.227	3.319
0.07688	620	16.13	0.361	3.479	0.852	3.306	0.474	3.564	0.449	3.720	0.286	3.740
0.07564	610	16.39	0.377	4.082	0.698	4.006	0.410	4.284	0.662	4.287	0.405	4.359
0.07440	600	16.67	0.516	4.784	0.841	4.789	0.491	5.099	1.178	5.123	0.725	5.428
0.07316	590	16.95	2.155	5.601	1.298	5.810	0.747	6.301	2.818	6.198	2.371	7.855
0.07192	580	17.24	4.935	7.345	2.636	7.240	1.690	8.614	5.915	4.426	8.501	3.269
0.07068	570	17.54	6.713	5.552	6.570	7.320	10.257	11.277	5.185	1.755	5.363	0.678
0.06944	560	17.86	7.407	0.816	7.683	3.150	9.100	1.534	4.066	0.949	3.959	0.313
0.06820	550	18.18	5.406	0.487	6.256	1.432	6.548	0.507	3.265	0.673	3.106	0.206
0.06696	540	18.52	4.391	0.378	5.206	0.865	5.280	0.255	2.631	0.580	2.449	0.174
0.06572	530	18.87	3.526	0.350	4.455	0.635	4.456	0.158	2.061	0.595	1.837	0.186
0.06448	520	19.23	2.722	0.357	3.856	0.545	3.817	0.115	1.488	0.738	1.126	0.278
0.06324	510	19.61	2.089	0.584	3.318	0.544	3.243	0.099	0.959	1.121	0.342	0.932
0.06200	500	20.00	1.674	1.002	2.774	0.642	2.636	0.106	0.680	1.660	0.213	1.644
0.06076	490	20.41	1.035	1.366	2.170	0.930	1.830	0.163	0.582	2.161	0.187	2.168
0.05952	480	20.83	0.312	1.879	1.620	1.635	0.380	1.028	0.563	2.627	0.186	2.636
0.05828	470	21.28	0.255	2.826	1.521	2.697	0.241	2.622	0.591	3.091	0.201	3.103
0.05704	460	21.74	0.337	3.910	1.989	3.903	0.323	4.155	0.663	3.586	0.229	3.606
0.05580	450	22.22	0.765	5.591	3.501	5.065	0.730	6.677	0.792	4.145	0.279	4.186
0.05456	440	22.73	5.581	8.162	6.125	4.255	10.079	14.014	1.016	4.813	0.363	4.906
0.05332	430	23.26	6.676	4.919	6.386	2.025	8.570	0.764	1.422	5.654	0.522	5.881
0.05208	420	23.81	6.185	2.747	5.683	1.057	6.356	0.257	2.247	6.738	0.889	7.382
0.05084	410	24.39	5.710	1.893	5.102	0.699	5.356	0.152	4.148	7.894	2.161	10.225
0.04960	400	25.00	5.366	1.769	4.677	0.612	4.635	0.156	7.599	7.167	11.820	12.959

TABLE I (*Continued*)

Aluminum Oxide

eV	cm^{-1}	μm	n	k	$n_{\perp}$	$k_{\perp}$	$n_{\perp}$	$k_{\perp}$	$n_{\parallel}$	$k_{\parallel}$	$n_{\parallel}$	$k_{\parallel}$
0.04836	390	25.64	5.454	2.034	4.482	0.719	3.533	0.732	8.708	3.874	11.359	2.261
0.04712	380	26.32	5.443	0.381	4.589	0.634	5.644	0.552	7.807	1.991	8.541	0.804
0.04588	370	27.03	4.942	0.213	4.485	0.378	4.774	0.097	6.927	1.180	7.178	0.422
0.04464	360	27.78	4.635	0.183	4.302	0.245	4.438	0.045	6.279	0.782	6.364	0.264
0.04340	350	28.57	4.362	0.164	4.144	0.178	4.229	0.028	5.800	0.560	5.816	0.182
0.04216	340	29.41	4.152	0.144	4.015	0.139	4.075	0.020	5.436	0.422	5.417	0.133
0.04092	330	30.30	3.985	0.125	3.908	0.113	3.953	0.015	5.149	0.331	5.112	0.101
0.03968	320	31.25	3.863	0.105	3.818	0.095	3.852	0.011	4.918	0.267	4.871	0.080
0.03844	310	32.26	3.758	0.089	3.740	0.082	3.767	0.009	4.727	0.221	4.674	0.064
0.03720	300	33.33	3.661	0.074	3.672	0.071	3.693	0.007	4.568	0.185	4.510	0.053
0.03596	290	34.48	3.603	0.059	3.611	0.062	3.629		4.431	0.158	4.371	0.044
0.03472	280	35.71	3.545	0.043	3.558	0.055	3.572		4.314	0.136	4.253	0.037
0.03348	270	37.04	3.501	0.028	3.510	0.049	3.521		4.212	0.119	4.150	0.032
0.03224	260	38.46	3.460	0.013	3.467	0.044	3.475		4.123	0.104	4.060	0.027
0.03100	250	40.00	3.422	0.009	3.428	0.040	3.434		4.044	0.092	3.980	0.024
0.02976	240	41.67			3.393	0.036	3.397		3.973	0.082	3.910	0.021
0.02852	230	43.48			3.361	0.033	3.363		3.911	0.073	3.847	0.018
0.02728	220	45.46			3.331	0.030	3.332		3.854	0.066	3.791	0.016
0.02604	210	47.62			3.304	0.027	3.304		3.804	0.059	3.741	0.014
0.02480	200	50.00			3.280	0.025	3.279		3.758	0.053	3.695	0.012
0.02356	190	52.63			3.258	0.023	3.255		3.717	0.048	3.654	0.011
0.02232	180	55.56			3.237	0.021	3.234		3.680	0.043	3.617	0.010
0.02108	170	58.82			3.218	0.019	3.214		3.646	0.039	3.583	0.009
0.01984	160	62.50			3.201	0.017	3.196		3.615	0.036	3.553	0.008
0.01860	150	66.67			3.185	0.016	3.180		3.588	0.032	3.525	0.007
0.01736	140	71.43			3.171	0.014	3.165		3.562	0.029	3.501	0.006
0.01612	130	76.92			3.158	0.013	3.151		3.540	0.026	3.478	0.006
0.01488	120	83.33			3.146	0.012	3.139		3.519	0.023	3.458	0.005
0.01364	110	90.91			3.135	0.011	3.128		3.501	0.021	3.440	0.004
0.01240	100	100.0			3.126	0.009	3.118		3.485	0.019	3.424	0.004

TABLE I (*Continued*)

Aluminum Oxide

eV	cm^{-1}	μm	n	k	$n_\perp$	$k_\perp$	$n_\perp$	$k_\perp$	$n_{\|\|}$	$k_{\|\|}$	$n_{\|\|}$	$k_{\|\|}$
0.01116	90	111.1			3.117	0.008	3.109		3.470	0.016	3.409	0.003
0.009920	80	125.0			3.110	0.007	3.101		3.458	0.014	3.397	0.003
0.008680	70	142.9			3.103	0.006	3.095		3.447	0.012	3.386	0.002
0.007440	60	166.7			3.097	0.005	3.089		3.437	0.010	3.376	0.002
0.006200	50	200.0			3.093	0.004	3.084		3.429	0.009	3.369	0.002
0.004960	40	250.0			3.089	0.004	3.080		3.423	0.007	3.362	0.001
0.003720	30	333.3			3.086	0.003	3.077		3.418	0.005	3.357	0.001
0.002480	20	500.0			3.084	0.002	3.075		3.415	0.003	3.354	0.001
0.001240	10	1000.0			3.083	0.001	3.073		3.412	0.002	3.352	

[a] References are indicated in brackets.

Aluminum Oxynitride (ALON) Spinel

WILLIAM J. TROPF and MICHAEL E. THOMAS
Applied Physics Laboratory
The Johns Hopkins University
Laurel, Maryland

Aluminum oxynitride, or ALON, is a crystal made of various amounts of aluminum oxide and aluminum nitride, with the aluminum-nitride content between 27 and 40 mole-percent. The resulting material, a nitrogen-stabilized cubic aluminum oxide, is face-centered cubic with spinel structure (see "Magnesium Aluminum Spinel," this volume). The lattice parameter of ALON varies from 7.938 (30 mole-percent AlN) to 7.951 (38 mole-percent AlN) [1]. Of particular interest is the composition of ≈35.7 mole-percent, which is equivalent to the composition $5AlN9Al_2O_3$ or $Al_{23}O_{27}N_5$. This composition has a unit cell with lattice parameter of 0.7948 nm [1]. Theoretical density of this composition is 3.71 g/cm^3 and melting point is 2323 K [1] to 2438±15 K [2].

Aluminum oxynitride is termed a nonstoichiometric spinel because some cation sites are occupied by vacancies. McCauley [3] proposed a formula of the form

$$Al_{(64+X)/3}\square_{(8-X)/3}O_{32-X}N_X \qquad 0 \leqslant x \leqslant 8, \tag{1}$$

where $x = 0$ corresponds to γ-alumina, and $x = 8$ is the unstable stoichiometric oxynitride Al_3O_3N. The symbol □ denotes cation vacancies. Since ALON exists over the range 27–40 mole-percent AlN, values of x for ALON range from approximately 3.5 to 5.8. When the composition is 35.7 mole-percent AlN ($x = 5$), there is one cation vacancy per unit cell. Neutron-diffraction studies (see [2]) confirm that oxygen and nitrogen occupy the anion sites of the spinel lattice and that aluminum cations occupy both the octahedral and tetrahedral sites of the spinel ($Fd3m$) structure. Corbin [2] implies that the vacancies occur at the octahedral cation sites.

ALON can be produced by a variety of methods, including reaction sintering of alumina and aluminum nitride, simultaneous reduction and nitridation of alumina, combustionlike reaction of aluminum metal with

Copyright © 1991 by Academic Press.
All rights of reproduction in any form reserved.
ISBN 0-12-544422-2

oxygen and nitrogen, and reaction of gases [2]. Commercial optical ALON is made by reacting the raw materials, pressing into near-finished shape, and firing at high temperature to produce a fully dense, transparent ceramic [4]. The resulting high-temperature, high-strength ceramic is used for windows and optical elements where hardness and resistance to harsh environments is important. Property data for ALON are given in the literature [4–7].

ALON is transparent at 0.230 to 5.0 μm. The band gaps of the constituent materials, alumina and aluminum nitride, are 9.9 and 6.0 eV, respectively [8]. From this information we surmise a band gap of 6–7 eV.

Index-of-refraction data for ALON are very sparse. Hartnett and Gentilman give a measured value of 1.793 at 0.589 μm and an estimated value of 1.66 at 4 μm based on reflection loss [4]. Corbin [2] and Hartnett *et al.* [9] give an index of refraction from 1.770 (also see [1]) to 1.785 in the visible (0.55 μm) as the composition increases from 30% to 37.5% AlN.

Precision room-temperature index-of-refraction measurements have also been made by Scheller [10] using a prism supplied by Raytheon. These values were used to construct the following Sellmeier formula:

$$n^2 - 1 = \frac{20.32 \times 10^9}{(97{,}500)^2 - \nu^2} + \frac{1.287 \times 10^6}{(530)^2 - \nu^2}, \tag{2}$$

where ν is the frequency in wave numbers. This formula is applicable to bulk polycrystalline ALON (37.5% AlN) in the range of 0.4–2.3 μm and duplicates measurements to within ±0.0002.

The dominant loss mechanism in the visible and near-IR transparent region of polycrystalline ALON is scatter. Bulk scatter in polycrystalline ALON is low and decreases with increasing wavelength [4, 5].

Absorption at the IR edge of transparency is dominated by multiphonon absorption. A model of multiphonon absorption for ALON has been developed and validated with experimental data over a wide temperature range [11]. ALON exhibits a two-phonon structure in the 1700–1950 cm^{-1} region that is not adequately represented by this multiphonon model. The fundamental (one-phonon) lattice vibrations occur in the 350–970 cm^{-1} spectral region.

Table I gives the transverse and longitudinal optical frequencies of ALON [12] as determined by reflectance measurements. The transverse optical frequencies are the mode locations, and the maximum longitudinal frequency is an important parameter in the multiphonon model [11], since it designates the maximum phonon frequency.

At frequencies below the lowest fundamental optical mode, absorption decreases, and the material becomes transparent. The magnitude of absorption is thought to be a combination of contributions from both the

tail of the fundamental lattice vibrations and various multiphonon difference bands. The index of refraction now also includes the effect of lattice vibrations.

The low-frequency real index of refraction (dielectric constant) of ALON is given as 2.93 by McCauley and Corbin [1] for a composition of 30% AlN and as 3.06 by Stead and Simonis [13] for ALON with 37.5% AlN. Temperature dependence of the low-frequency index of refraction is given by Ho [14] as 2.2×10^{-4}/K (average, 23–300 °C), 2.7×10^{-4}/K (average, 23–1000 °C), and 3.0×10^{-4}/K (average, 23–1200 °C). Stead and Simonis [13] give values for the imaginary index of refraction (k) in the 7–16 cm^{-1} region. Estimates made from the red wing of the fundamental modes (Table I) are three to four times greater than the experimental imaginary index-of-refraction value determined by Stead and Simonis [13] at 10 and 15 cm^{-1}. Corbin [2] also gives absorption coefficient data in the 5–40 cm^{-1} range for ALON of an unreported composition. These values agree well with model predictions of k, but tend to have lower values at low frequency.

The high-temperature electrical conductivity of ALON was measured by Kim and Richards [15] and found to be typical of oxides. They found a correlation between the number of vacancies (see Eq. [1]) and conductivity and interpret the conductivity as ionic.

Table II was constructed from measurements reported in the literature as well as model predictions. Real-index data (n) in the visible and near IR are taken from the measurements by Scheller [10]. Lattice-vibration-model results [12] are used to calculate real-index data from 0–10,000 cm^{-1} and imaginary-index data from 5–3300 cm^{-1}. Laser-calorimetry results for k at 2.9 and 3.9 μm by Detrio and Greason [16] give measurements of the imaginary part of the index of refraction, based on thin samples with the lowest absorption coefficients. Note that the value at 3.9 μm agrees well with the multiphonon-absorption-model prediction [11, 12]. The measured value at 2.9 μm is much higher than the multiphonon model value because of the presence of an OH^- impurity vibrational band.

Measurements of Stead and Simonis [13] are used to represent the low-frequency characteristics of ALON (37.5% AlN). In this region, one-phonon model predictions [12] of k are several times the measured values [13], probably because a few wide fundamental modes are used to represent many narrower modes, and the broadness of these modes gives excessive low-frequency-wing absorption. Values of k for ALON of unknown composition are also given [2]. Low-frequency index predictions are virtually the same as measurements [13]. At very low frequency, ALON exhibits considerable free-carrier absorption that increases rapidly with temperature [9]. Extrapolation of this low-frequency absorption (in the region dominated by free-carrier effects) to 100 GHz (3 cm^{-1}) gives a value for k of 3×10^{-4} for ALON (30 mole-percent AlN) [9], consistent

with the data given in Table II. ALON with 30 mole-percent AlN has a low-frequency index of refraction of 2.9 [9].

Index measurements by Scheller [10] are accurate to ± 0.00001. Calculated index data are probably accurate to ± 0.01 for n (outside the range of measured values) and $\pm 5\%$ for k down to 350 cm^{-1}. Calculated values of k below 350 cm^{-1} are too high, ultimately by a factor of four at low frequency. In all data, except k below 350 cm^{-1}, the uncertainty in the values is probably in the least significant digit reported in Table II.

Figure 1 shows a composite of the complex index of refraction based on the data of Table II.

Table III gives temperature dependence for the real part of the index of refraction. Our measurements of dn/dT in the visible and those of Ho [14] at low frequency are given.

Temperature-dependent absorption computed from optical models of ALON [12] have been used to estimate total hemispherical emissivity of pure, transparent ALON over the temperature range 200–1000 K, where the models are expected to give the best results and defect absorption is believed to be insignificant. These results were obtained by estimating complex refractive index at a given temperature, calculating directional emittance for a specific slab thickness, integrating over angle, and convolving the resulting spectral hemispherical emittances with the Planck function.

Table IV gives the resulting total hemispherical emittance for semi-infinite slabs as a function of slab thickness. Since total hemispherical emissivity is an important function for radiation-relief calculations and may be needed to correct property measurements such as thermal conductivity, we have included this calculated result.

REFERENCES

1. J. W. McCauley and N. D. Corbin, "Phase Relations and Reaction Sintering of Transparent Cubic Aluminum Oxynitride (ALON)," *J. Am. Ceram. Soc.* **62**, 476 (1979).
2. N. D. Corbin, "Aluminum Oxynitride Spinel (ALON): A Review," U.S. Army Materials Technology Laboratory Report MTL MS 87-3, July (1987).
3. J. W. McCauley, "A Simple Model for Aluminum Oxynitride Spinels," *J. Am. Ceram. Soc.* **61**, 372 (1978).
4. T. M. Hartnett and R. L. Gentilman, "Optical and Mechanical Properties of Highly Transparent Spinel and ALON Domes," *Proc. SPIE* **505**, 15 (1984).
5. R. Gentilman, E. Maguire, T. Kohane, and D. B. Valentine, "Comparison of Large ALON and Sapphire Windows," *Proc. SPIE* **1112**, 31 (1989).
6. G. D. Quinn, N. D. Corbin, and J. W. McCauley, "Thermomechanical Properties of Aluminum Oxynitride Spinel," *Bull. Am. Ceram. Soc.* **64**, 723 (1984).
7. E. K. Graham, W. C. Munly, J. W. McCauley, and N. D. Corbin, "Elastic Properties of Polycrystalline Aluminum Oxynitride Spinel and Their Dependence on Pressure, Temperature, and Composition," *J. Am. Ceram. Soc.* **71**, 807 (1988).
8. J. Bauer, L. Biste, and D. Bolze, "Optical Properties of Aluminum Nitride Prepared by Chemical and Plasmachemical Vapour Deposition," *Phys. Stat. Solidi (a)* **39**, 173 (1977).

9. T. M. Hartnett, E. A. Maguire, and R. L. Gentilman, "Aluminum Oxynitride Spinel (ALON)-A New Optical and Multimode Window Material," in "Ceramic Engineer and Science Proceedings," Vol. 3, American Ceramic Society, Columbus, Ohio, 67 (1982).
10. R. J. Scheller, Schott Glass Technologies, Inc., personal communication (Oct. 2, 1989).
11. M. E. Thomas, R. I. Joseph, and W. J. Tropf, "Infrared Transmission Properties of Sapphire, Spinel, Yttria, and ALON as a Function of Temperature and Frequency," *Appl. Opt.* **27**, 239 (1988).
12. M. E. Thomas, "A Computer Code for Modeling Optical Properties of Window Materials," *Proc. SPIE* **1112**, 260 (1989).
13. M. Stead and G. Simonis, "Near Millimeter Wave Characterization of Dual Mode Materials," *Appl. Opt.* **28**, 1874 (1989).
14. W. W. Ho, "High-Temperature Dielectric Properties of Polycrystalline Ceramics," in "MRS Symposium M," Reno, April 6 (1988).
15. I.-U. Kim and V. L. Richards, "High-Temperature Electrical Conductivity of Aluminum Oxynitride Spinel," *J. Am. Ceram. Soc.* **68**, C210 (1985).
16. J. A. Detrio and P. Greason, University of Dayton, personal communication (April 8, 1988).

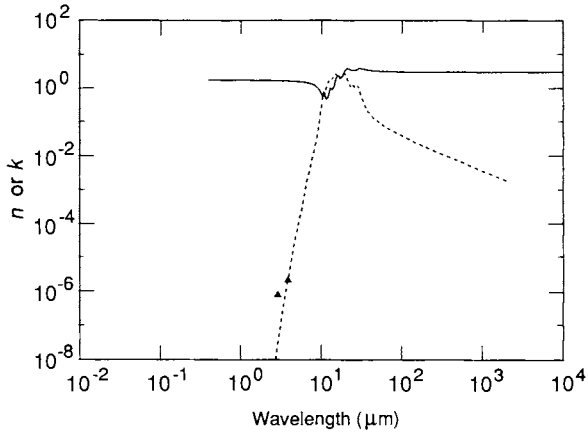

Fig. 1. Log–log plot of n (solid line) and k (dashed line) versus wavelength in micrometers for aluminum oxynitride spinel. Symbols are laser-calorimetry measurements of k.

NOTES ADDED IN PROOF

The electronic structure and bang gap of ALON was recently measured by French [17]. The first UV absorption peak occurs at 7.3 eV and bandgap is approximately 6.2 eV.

Details of the measurement of dn/dT at 0.6328 μm in Table III are given in [18]. Spectral and directional scatter measurement of commercial ALON are given in [19].

17. R. H. French, "Electronic Band Structure of Al_2O_3 with Comparison to ALON and AlN," *J. Am. Ceram. Soc.* **73**, 477–489 (1990).
18. C. H. Lange and D. D. Duncan, "Temperature Coefficient of Refractive Index for Candidate Optical Windows," *SPIE Proc.* **1326**, 71–78 (1990).
19. C. H. Lange, D. D. Duncan, and D. G. Fischer "Imaging Performance of Crystalline and Polycrystalline Oxides," *SPIE Proc.* **1326**, 59–70 (1990).

TABLE I

Fundamental Infrared Lattice Vibration Parameters of ALON[a]

Mode	Transverse optical frequency (cm^{-1})	Strength	Normalized width	Longitudinal optical frequency (cm^{-1})	Refs.
1	346	1.0	0.16	—	[12]
2	395	0.4	0.13	—	[12]
3	495	3.33	0.20	551	[12]
4	634	1.32	0.15	718	[12]
5	768	0.16	0.085	869	[12]
6	920	0.03	0.050	969	[12]
	Total = 6.24				

[a]The transverse optical frequency (ν_j) is the location of the mode. The strength ($\Delta\epsilon_j$) is the contribution of the mode to the dielectric constant. The normalized width (γ_j) is the mode width divided by the mode frequency. The complex dielectric constant (ϵ) is then modeled as a function of frequency (ν) by:

$$\epsilon(\nu) = \epsilon_\infty + \sum_j \frac{\Delta\epsilon_j \, \nu_j^2}{\nu_j^2 - \nu^2 + i\gamma_j \nu_j \nu} ,$$

where the ϵ_∞ term (= 3.1375) represents the electronic contributions to the dielectric constant (plus one). This model has a static dielectric constant of 9.38.

TABLE II

Values of n and k Obtained from Various References for ALON[a]

eV	cm^{-1}	μm	n		k		n	k
3.064	24710	0.40466	1.81167	[10]				
2.845	22944.7	0.43583	1.80562					
2.270	18312	0.54601	1.79218					
2.104	16969	0.5893	1.793	[8]				
1.455	11735.6	0.85211	1.77758	[10]				
1.240	10000	1.0000	1.776	[12]				
1.223	9862.13	1.01398	1.77375	[10]				
1.215	9800	1.0204	1.776	[12]				
1.190	9600	1.0417	1.775					
1.165	9400	1.0638	1.774					
1.141	9200	1.0870	1.774					
1.116	9000	1.1111	1.773					
1.091	8800	1.1364	1.773					
1.066	8600	1.1628	1.772					
1.041	8400	1.1905	1.771					
1.017	8200	1.2195	1.771					
0.9919	8000	1.2500	1.770					
0.9671	7800	1.2821	1.769					
0.9423	7600	1.3158	1.769					
0.9175	7400	1.3514	1.768					
0.8927	7200	1.3889	1.767					
0.8679	7000	1.4286	1.766					
0.8431	6800	1.4706	1.766					
0.8183	6600	1.5152	1.765					
0.8106	6537.74	1.52958	1.76543	[10]				
0.7935	6400	1.5625	1.764	[12]				
0.7687	6200	1.6129	1.763					
0.7439	6000	1.6667	1.762					
0.7191	5800	1.7241	1.761		$3.9 \cdot 10^{-13}$	[12]		
0.6943	5600	1.7857	1.759		$1.5 \cdot 10^{-12}$			
0.6695	5400	1.8519	1.758		$4.9 \cdot 10^{-12}$			
0.6447	5200	1.9231	1.756		$1.4 \cdot 10^{-11}$			
0.6293	5075.91	1.97009	1.75838	[10]				
0.6199	5000	2.0000	1.755	[12]	$3.5 \cdot 10^{-11}$			
0.6075	4900	2.0408	1.754		$5.5 \cdot 10^{-11}$			
0.5951	4800	2.0833	1.753		$8.4 \cdot 10^{-11}$			
0.5827	4700	2.1277	1.752		$1.3 \cdot 10^{-10}$			
0.5703	4600	2.1739	1.751		$1.9 \cdot 10^{-10}$			
0.5579	4500	2.2222	1.750		$2.9 \cdot 10^{-10}$			
0.5455	4400	2.2727	1.749		$4.4 \cdot 10^{-10}$			
0.5332	4300.30	2.32542	1.75268	[10]				
0.5331	4300	2.3256	1.747	[12]	$6.7 \cdot 10^{-10}$			
0.5207	4200	2.3810	1.746		$1.0 \cdot 10^{-9}$			
0.5083	4100	2.4390	1.745		$1.6 \cdot 10^{-9}$			

(*continued*)

TABLE II *(Continued)*

ALON

eV	cm^{-1}	μm	n	k	n	k
0.4959	4000	2.5000	1.743	$2.4 \cdot 10^{-9}$		
0.4835	3900	2.5641	1.741	$3.7 \cdot 10^{-9}$		
0.4711	3800	2.6316	1.740	$5.7 \cdot 10^{-9}$		
0.4587	3700	2.7027	1.738	$9.0 \cdot 10^{-9}$		
0.4463	3600	2.7778	1.735	$1.4 \cdot 10^{-8}$		
0.4339	3500	2.8571	1.733	$2.3 \cdot 10^{-8}$		
0.4275	3448	2.9000				$7.8 \cdot 10^{-7}$ [16]
0.4215	3400	2.9412	1.731	$3.6 \cdot 10^{-8}$		
0.4092	3300	3.0303	1.728	$5.8 \cdot 10^{-8}$		
0.3968	3200	3.1250	1.725	$9.3 \cdot 10^{-8}$		
0.3844	3100	3.2258	1.722	$1.5 \cdot 10^{-7}$		
0.3720	3000	3.3333	1.718	$2.5 \cdot 10^{-7}$		
0.3596	2900	3.4483	1.714	$4.2 \cdot 10^{-7}$		
0.3472	2800	3.5714	1.709	$7.1 \cdot 10^{-7}$		
0.3348	2700	3.7037	1.704	$1.2 \cdot 10^{-6}$		
0.3224	2600	3.8462	1.698	$2.0 \cdot 10^{-6}$		
0.3179	2564	3.9000				$2.1 \cdot 10^{-6}$ [16]
0.3100	2500	4.0000	1.702	$3.3 \cdot 10^{-6}$		
0.2976	2400	4.1667	1.68	$5.8 \cdot 10^{-6}$		
0.2852	2300	4.3478	1.68	$1.0 \cdot 10^{-5}$		
0.2728	2200	4.5455	1.67	$1.9 \cdot 10^{-5}$		
0.2604	2100	4.7619	1.65	$3.4 \cdot 10^{-5}$		
0.2480	2000	5.0000	1.64	$6.0 \cdot 10^{-5}$		
0.2418	1950	5.1282	1.63	$9.0 \cdot 10^{-5}$ [11][b]		
0.2356	1900	5.2632	1.62	$1.7 \cdot 10^{-4}$		
0.2294	1850	5.4054	1.62	$3.1 \cdot 10^{-4}$		
0.2232	1800	5.5556	1.60	$3.6 \cdot 10^{-4}$		
0.2170	1750	5.7143	1.59	$4.3 \cdot 10^{-4}$		
0.2108	1700	5.8824	1.58	$4.9 \cdot 10^{-4}$		
0.2046	1650	6.0606	1.57	$5.0 \cdot 10^{-4}$ [12]		
0.1984	1600	6.2500	1.55	$7.4 \cdot 10^{-4}$		
0.1922	1550	6.4516	1.53	$1.1 \cdot 10^{-3}$		
0.1860	1500	6.6667	1.51	$1.6 \cdot 10^{-3}$		
0.1798	1450	6.8966	1.49	$2.4 \cdot 10^{-3}$		
0.1736	1400	7.1429	1.46	$3.6 \cdot 10^{-3}$		
0.1674	1350	7.4074	1.43	$5.2 \cdot 10^{-3}$		
0.1612	1300	7.6923	1.39	$7.5 \cdot 10^{-3}$		
0.1550	1250	8.0000	1.34	0.011		
0.1488	1200	8.3333	1.29	0.017		
0.1426	1150	8.6957	1.21	0.026		
0.1364	1100	9.0909	1.12	0.045		
0.1302	1050	9.5238	0.99	0.088		
0.1240	1000	10.000	0.80	0.21		
0.1215	980	10.204	0.71	0.33		

(continued)

TABLE II *(Continued)*
ALON

eV	cm^{-1}	μm	n	k	n	k
0.1190	960	10.417	0.63	0.49		
0.1165	940	10.638	0.62	0.69		
0.1141	920	10.870	0.77	0.78		
0.1116	900	11.111	0.74	0.70		
0.1091	880	11.364	0.59	0.79		
0.1066	860	11.628	0.51	0.98		
0.1041	840	11.905	0.50	1.2		
0.1017	820	12.195	0.54	1.4		
0.0992	800	12.500	0.65	1.6		
0.0967	780	12.821	0.87	1.7		
0.0942	760	13.158	1.04	1.7		
0.0917	740	13.514	0.98	1.6		
0.0893	720	13.889	0.92	1.8		
0.0868	700	14.286	1.00	2.1		
0.0843	680	14.706	1.21	2.4		
0.0818	660	15.152	1.57	2.6		
0.0794	640	15.625	2.04	2.6		
0.0769	620	16.129	2.36	2.3		
0.0744	600	16.667	2.34	2.0		
0.0719	580	17.241	2.16	1.9		
0.0694	560	17.857	2.06	2.1		
0.0670	540	18.519	2.19	2.5		
0.0645	520	19.231	2.63	2.7		
0.0620	500	20.000	3.28	2.7		
0.0608	490	20.408	3.58	2.5		
0.0595	480	20.833	3.79	2.2		
0.0583	470	21.277	3.89	1.9		
0.0570	460	21.739	3.90	1.7		
0.0558	450	22.222	3.84	1.4		
0.0546	440	22.727	3.75	1.3		
0.0533	430	23.256	3.63	1.2		
0.0521	420	23.810	3.52	1.1		
0.0508	410	24.390	3.45	1.2		
0.0496	400	25.000	3.46	1.2		
0.0484	390	25.641	3.51	1.2		
0.0471	380	26.316	3.51	1.1		
0.0459	370	27.027	3.48	1.1		
0.0446	360	27.778	3.51	1.2		
0.0434	350	28.571	3.67	1.2		
0.0422	340	29.412	3.86	1.1		
0.0409	330	30.303	3.95	0.87		
0.0397	320	31.250	3.93	0.66		
0.0384	310	32.258	3.86	0.51		
0.0372	300	33.333	3.78	0.41		

(continued)

TABLE II *(Continued)*

ALON

eV	cm^{-1}	μm	n	k	n	k	
0.0360	290	34.483	3.70	0.33			
0.0347	280	35.714	3.63	0.28			
0.0335	270	37.037	3.56	0.24			
0.0322	260	38.462	3.51	0.21			
0.0310	250	40.000	3.46	0.19			
0.0298	240	41.667	3.42	0.16			
0.0285	230	43.478	3.38	0.15			
0.0273	220	45.455	3.34	0.13			
0.0260	210	47.619	3.31	0.12			
0.0248	200	50.000	3.28	0.11			
0.0236	190	52.632	3.26	0.10			
0.0223	180	55.556	3.23	0.090			
0.0211	170	58.824	3.21	0.082			
0.0198	160	62.500	3.19	0.075			
0.0186	150	66.667	3.18	0.068			
0.0174	140	71.429	3.16	0.062			
0.0161	130	76.923	3.15	0.056			
0.0149	120	83.333	3.13	0.050			
0.0136	110	90.909	3.12	0.045			
0.0124	100	100.00	3.11	0.040			
0.0112	90	111.11	3.10	0.036			
0.0099	80	125.00	3.09	0.031			
0.0087	70	142.86	3.09	0.027			
0.0074	60	166.67	3.08	0.023			
0.0062	50	200.00	3.075	0.019			
0.0050	40	250.00	3.071	0.015		0.012	[2]
0.0037	30	333.33	3.067	0.011		$8.8 \cdot 10^{-3}$	
0.0025	20	500.00	3.065	$7.5 \cdot 10^{-3}$		$5.9 \cdot 10^{-3}$	
0.0019	15	666.67	3.064	$5.6 \cdot 10^{-3}$		$1.5 \cdot 10^{-3}$	[13]
0.0012	10	1000.0	3.064	$3.7 \cdot 10^{-3}$	3.06 [13]	$8.8 \cdot 10^{-4}$	
0.0006	5	2000.0	3.063	$1.9 \cdot 10^{-3}$			
0.0000	0	∞	3.063	0.0			

[a]References are indicated in brackets.

[b]Values in the two-phonon region from 1700–1950 cm^{-1} are taken from our measurements.

TABLE III

Values of dn/dT Obtained from Various References for ALON

eV	cm^{-1}	μm	dn/dT (1/K)	Notes
1.959	15803	0.6328	$1.5 \cdot 10^{-5}$	Our measurement
0.310	2500	4.0000	$2.8 \cdot 10^{-6}$	Model [12]
0.0	0	∞	$2.2 \cdot 10^{-4}$	Average, 23–300°C [14]

TABLE IV

Calculated Total Hemispherical Emissivity for ALON

Temperature (K)	Thickness (cm)			
	0.10	0.25	0.50	1.25
200.0	0.62	0.62	0.62	0.62
300.0	0.65	0.66	0.66	0.67
400.0	0.64	0.67	0.69	0.71
500.0	0.59	0.64	0.67	0.70
600.0	0.53	0.58	0.62	0.66
700.0	0.46	0.52	0.56	0.61
800.0	0.40	0.46	0.50	0.55
900.0	0.35	0.41	0.45	0.50
1000.0	0.31	0.36	0.40	0.45

Barium Titanate ($BaTiO_3$)

CHUEN WONG and YE YUNG TENG
Department of Physics and Applied Physics
University of Lowell
Lowell, Massachusetts
and
J. ASHOK and P. L. H. VARAPRASAD
Applied Physics Department
Andhra University
Visakhapatnam, India

The barium titanate crystal is ferroelectric at room temperature. The crystal structure is perovskite, cubic above the Curie temperature, and tetragonal below the Curie temperature. At room temperature, the *c* axis is longer than the *a* axis by 1% [1]. Practically all the barium titanate samples described in the literature were fabricated by either the flux-grown or the melt-grown method. The process of growing large single crystals of barium titanate by the top-seeded melt growth was developed by a group headed by A. Linz at MIT [2] and later transferred to Sanders Associates [3], which is presently a major commercial supplier of this crystal. The Curie temperature of melt-grown barium titanate is about 133 °C, while that of flux-grown is 120 °C. The lower Curie temperature of flux-grown barium titanate is believed to be a result of the higher impurity content, which also affects the optical constants. Recently, there has been increased interest in barium titanate, mainly due to its photorefractive properties and other associated effects and applications, such as phase conjugation, volume holography for optical storage, two-beam coupling, and optical computing.

The UV data in Table II are the result of Kramers–Kronig (K–K) analysis of reflectivity measurement on unpoled multiple-domain samples. They represent a certain weighted average of the optical constants for the ordinary (o) and extraordinary (e) rays. The o-ray is expected to dominate because it has an entire plane of polarization, whereas the e-ray has only one direction of polarization [4]. We read the n and k values from the graphs of Bäuerle *et al.* [5], who measured the reflectivity from 10–32 eV at room temperature, and did a K–K analysis of a combination of their own reflectivity data and Cardona's [6] 2–22 eV, room-temperature data. At 2.94 eV, these graphs give $n = 2.67$, $k = 0.05$, whereas Table II lists

Copyright © 1991 by Academic Press.
All rights of reproduction in any form reserved.
ISBN 0-12-544422-2

$n_o = 2.644$, $n_e = 2.541$ from minimum deviation and $k_o = 5.84 \times 10^{-6}$, $k_e = 6.51 \times 10^{-6}$ from absorption measurements. There is significant disagreement in the k values. The reflectivity measurement of Bäuerle *et al.* [5] involved the polarized synchrotron radiation from the DORIS storage ring at Hamburg together with a modified special UHV version of the McPherson Model 225.3 monochromator with a resolution of 0.03 Å. The sample was a polished single crystal with (100) faces in the cubic phase. Cardona [6] used unpolarized light from various arc lamps, and a 1-m McPherson monochromator. The unpoled sample was polished, etched, and had random orientation for the ferroelectric domains.

For the visible region, we tabulate the room-temperature index of refraction data from Wemple *et al.* [7], covering the range 0.42–0.68 μm. Their sample was melt-grown. The method of measurement was minimum deviation. The sample was poled to a single domain, then cut with a string saw to minimize surface damage and polished with 6 and 3 μm diamond paste on a flat tin lap. The data can be represented by the following single-oscillator Sellmeier equations:

$$n_o^2 = 1 + \frac{4.219}{1 - (0.2231/\lambda)^2}$$
$$n_e^2 = 1 + \frac{4.064}{1 - (0.2109/\lambda)^2}, \tag{1}$$

where λ is wavelength in μm. Discrepancy between Eq. 1 and the data is within 0.003 for wavelengths shorter than 0.45 μm, higher for shorter wavelengths. We read the data from the graphs in Fig. 4 of Ref. [7]. The measurements by Deshpande *et al.* [8, 9] at the wavelength of the sodium D line using two different methods agree well with the data of Wemple *et al.* [7]. The first method [8] is a refinement of Duc de Chaulnes' method of image displacement. The second method [9] uses the phenomenon of polarization by reflection, and the results are $n_o = 2.428 \pm 0.002$, $n_e = 2.371 \pm 0.0045$. According to Deshpande *et al.* [8, 9], these methods can achieve accuracy better than or comparable to that of minimum deviation in the case of ferroelectric barium titanate. As for flux-grown samples, the data of Johnston [10] agree well with those of Wemple *et al.* [7] for the o-ray, although the e-ray data are slightly larger. The explanation is in the difference in polarization of the flux-grown and melt-grown samples. Johnston [10] used the method of minimum deviation and analyzed his data with a two-oscillator Sellmeier equation.

The extinction coefficient k in the UV–VIS range was calculated using

the absorption coefficient data from DiDomenico and Wemple [11] and Schunemann *et al.* [12]. Both their samples were melt-grown. Schunemann *et al.* [12] prepared a particularly pure sample and made absorption measurements between 0.4 and 0.85 μm. Temperature was not mentioned, but must be room temperature. DiDomenico and Wemple [11] made their measurements at 33 °C, between 2.95 and 3.27 eV (0.38–0.42 μm), near the absorption edge. Their absorption coefficient data exhibit an exponential Urbach tail, and there is a large difference between the o- and e-rays. At about 0.4 μm, where measurements of DiDomenico and Wemple [11] and Schunemann *et al.* [12] overlap, their data agree to within 50%. The absorption coefficient was found to be very sensitive to small amounts of impurities [13]. Klein and Schwartz [14] measured the absorption coefficient between 0.44 and 0.64 μm of four samples grown by Sanders Associates [3] and obtained results from 0.16 to 2.2 cm^{-1} at 0.5 μm. Flux-grown barium titanate was found to have higher absorption coefficients than those of melt-grown [11, 15].

In the near-IR region, the index of refraction between 0.85 and 2 μm was calculated using Eq. 1. Equation 1 is probably valid in this region because the value of n_o at 2 μm calculated from this equation agrees with the reflectivity data of Spitzer *et al.* [16]. Furthermore, the absorption in this region is very low according to Schunemann [17] and Hilsum [18]. Schunemann [17] measured the absorption coefficient between 0.85 and 3 μm on the same very pure sample [12] using unpolarized light. The absorption coefficient reaches a minimum at about 2 μm where the extinction coefficient k is about 10^{-7}. Hilsum [18] reported transmission and absorption data between 1 and 12 μm, and the minimum absorption also occurs around 2 μm with k about 10^{-5}. Hilsum's [18] sample is a yellowish plate several millimeters square and 0.1 mm thick. Temperature was not mentioned. A plot of α versus wavelength from 7 to 12 μm has been used to determine k as listed in Table II. No crystal orientation was specified, so we assume $k_o(\perp)$.

The index of refraction below the band gap for many covalent and ionic materials has been discussed by Wemple and DiDomenico [19], who developed a model equation of the form

$$n^2 = \frac{1 + E_d E_o}{E_o^2 - (\hbar\omega)^2}$$

to fit many materials. For $BaTiO_3$, $E_d = 24.0$ eV and $E_o = 5.63$ eV. Although this does not take into account the birefringence, it gives values closely approaching $n_o(\perp)$, so we have included these values (three significant figures) in Table II.

For the region between 10 and 1000 μm, Servoin *et al.* [20] measured the reflectivity with a Fourier-transform scanning interferometer, on a small, natural, single domain in the surface of a crystal. They fitted their data with the four-parameter factorized form of the dielectric function

$$\varepsilon = \varepsilon' \pm i\varepsilon'' = \varepsilon_\infty \prod_j \frac{\Omega_{j\mathrm{LO}}^2 - \omega^2 \mp i\gamma_{j\mathrm{LO}}\omega}{\Omega_{j\mathrm{TO}}^2 - \omega^2 \mp i\gamma_{j\mathrm{TO}}\omega}, \tag{2}$$

where ω is the frequency, Ω and γ are the mode frequency and damping constant, respectively, and ε_∞ is the high-frequency dielectric constant. Preliminary values of the mode frequencies and damping constants were obtained from Raman spectra and then fine-tuned to fit the reflectivity data. The fit is very good. In Table II, the n and k values from 2 to 1000 μm were calculated using Eq. 2 and the values of mode frequencies and damping constants given by Servoin *et al.* [20]. These parameters are listed in Table I. To fit the reflectivity data of Servoin *et al.* [20], we chose 5.3 to be the high-frequency dielectric constant for the o-ray, and 5.1 for the e-ray. We have extended the use of Eq. 2 to obtain the n and k values in the 2–10 μm region. Results from Eq. 2 in this region agree with the data of Spitzer *et al.* [16] who measured the o-ray reflectivity at room temperature from 5000 to 70 cm^{-1} using a double-pass prism spectrometer between 5000 and 333 cm^{-1} and a single-pass grating monochromator below 333 cm^{-1}. The reflectivity data of Servoin *et al.* [20] agree with those of Spitzer *et al.* [16] to within 2–3%, and Sanjurjo *et al.* [4], except at low frequencies.

Sanjurjo *et al.* [21] fitted their room-temperature (not defined) reflectivity data for $\mathbf{E}\|c$ with a coupled-mode model, noting that real coupling (in contrast to imaginary coupling and independent oscillators) provided the best fit. They displayed graphs of $\varepsilon_1(\|)$ and $\varepsilon_2(\|)$ in a coarser grid than the calculated values of Servoin *et al.* [20], also given in Table II. We have displayed these data in a separate block at the end of Table II. Although most values of n and k are well within a factor of two of each other, it is interesting to note where large differences occur. Sanjurjo *et al.* [21] also performed a K–K analysis of their reflectivity data demonstrating a good qualitative agreement with the coupled-oscillator-model fit. They displayed only $\varepsilon_2(\|)$ in this case.

Ballantyne [22] measured the reflectivity of the o-ray only, from 4000 to 5 cm^{-1} and between 24 and 200 °C using various spectrometers, an interferometer, and a Carcinotron system, and permittivities were obtained from K–K analysis. The n values, calculated from Ballantyne's [22] permittivities, agree with those of Servoin *et al.* [20] at the ends of the spectral region: within 1% at 10 cm^{-1} and 6% at 900 cm^{-1}. The discrepancy increases to 24% at 600 cm^{-1} and 90% at 200 cm^{-1}. There is better

agreement for the k values, especially when they are larger than unity. Barker [23] measured the reflectivity between 400 and 100 cm^{-1} at 300 K and 475 K on a multiple-domain sample, and the spectra resemble closely the o-ray spectra of Servoin *et al.* [20].

It is interesting to observe that an "antiresonance" occurs at 780 cm^{-1} (12.82 μm) where $n_o = 1.01$ and $k_o = 9.18 \times 10^{-4}$ as shown in Table II. A similar antiresonance occurs at 800 cm^{-1} (12.50 μm), where $n_e = 1.03$ and $k_e = 6.18 \times 10^{-3}$. At antiresonances, an incident ray will suffer very small reflection and absorption. Antiresonance is a quantum effect occurring when two electronic levels attempt to cross each other. The integrated absorption remains constant, but the absorption is redistributed. When two phonon levels (frequencies) attempt to cross (couple), the effect also occurs. The factorized form of Eq. 2 leads to such effects. Note that the model predicts much too much absorption in the 2.5–10 μm region compared with the measurement of Hilsum [18].

In the microwave region at a wavelength of 12 mm, we have $n_o = 39$ and $k_o = 4.7$, calculated from Ballantyne's [22] permittivity data (accuracy 20%) measured with a microwave dielectrometer. As a comparison, Eq. 2 gives, at 12.5 mm, $n_o = 46$ and $k_o = 1.6$.

Turik and Shevchenko [24] measured the permittivity along the c axis in the 1×10^3 to 3×10^8 Hz frequency range using a bridge and various Q meters. They found piezoelectric resonance at 10^6–10^7 Hz. Permittivity data from other authors [25] were also presented. At 10^{10} Hz, we have $\varepsilon_{33} = 44.9$ and the loss tangent $\tan \delta = 0.24$, from which we obtain $n_e = 6.74$ and $k_e = 0.798$. At 10^4–10^5 Hz, $\varepsilon_{33} = 188$, $\tan \delta = 0.027$, $n_e = 13.7$, and $k_e = 0.187$.

Papers dealing with optical properties of powders and small particles include Ruppin [26], Mara *et al.* [27], Last [28] and Demeshina and Murzin [29].

Although we have stressed room-temperature measurements, there has been much work (both IR and Raman) through the Curie temperature at 133 °C. IR data are found in Luspin *et al.* [30]. Some of the Raman data are found in DiDomenico *et al.* [31], Vogt *et al.* [32], Pinczuk *et al.* [33], and references therein.

ACKNOWLEDGMENTS

We would like to thank the editor for valuable suggestions, D. Bäuerle for providing a larger-size graph of n and k, and P. G. Schunemann for a copy of his thesis. The assistance of C. H. Lin, L. Li, and M. Villani in the preparation of the tables is greatly appreciated.

REFERENCES

1. W. J. Merz, *Phys. Rev.* **76**, 1221 (1949).
2. A. Linz, V. Belruss, and C. S. Naiman, *J. Electrochem. Soc.* **112**, 60C (1965).

3. Sanders Associates, 130 Daniel Webster Highway, Merrimack, N. H., 03054, U.S.A.
4. J. A. Sanjurjo, S. P. S. Porto, and E. Silberman, *Solid State Commun.* **30**, 55 (1979).
5. D. Bäuerle, W. Braun, V. Saile, G. Sprüssel, and E. E. Koch, *Z. Physik B* **29**, 179, (1978).
6. M. Cardona, *Phys. Rev.* **140**, A651 (1965).
7. S. H. Wemple, M. DiDomenico, Jr., and I. Camlibel, *J. Phys. Chem. Solids* **29**, 1797 (1968).
8. L. V. Deshpande, M. B. Joshi, and R. B. Mishra, *J. Opt. Soc. Am.* **70**, 1160 (1980).
9. L. V. Deshpande, M. B. Joshi, and R. B. Mishra, *J. Opt. Soc. Am.* **70**, 1163 (1980).
10. A. R. Johnston, *J. Appl. Phys.* **42**, 3501 (1971).
11. M. DiDomenico, Jr., and S. H. Wemple, *Phys. Rev.* **166**, 565 (1968).
12. P. G. Schunemann, D. A. Temple, R. S. Hathcock, H. L. Tuller, H. P. Jenssen, D. R. Gabbe, and C. Ward, *J. Opt. Soc. Am. B* **5**, 1685 (1988).
13. P. G. Schunemann and T. M. Pollak, Y. Yang, Y. Y . Teng, and C. Wong, *J. Opt. Soc. Am. B* **5**, 1702 (1988).
14. M. B. Klein and R. N. Schwartz, *J. Opt. Soc. Am. B* **3**, 293 (1986).
15. R. C. Casella and S. P. Keller, *Phys. Rev.* **116**, 1469 (1959).
16. W. G. Spitzer, R. C. Miller, I. A. Kleinman, and L. E. Howarth, *Phys. Rev.* **126**, 1710 (1962).
17. P. G. Schunemann, master's thesis, Massachusetts Institute of Technology, May 8, 1987.
18. C. Hilsum, *J. Opt. Soc. Am.* **45**, 771 (1955).
19. S. H. Wemple and M. DiDomenico, Jr., *Phys. Rev. B* **3**, 1338 (1971).
20. J. L. Servoin, F. Gervais, A. M. Quittet, and Y. Luspin, *Phys. Rev. B* **21**, 2038 (1980).
21. J. A. Sanjurjo, R. S. Katiyar, and S. P. S. Porto, *Phys. Rev. B* **22**, 2396 (1980).
22. J. M. Ballantyne, *Phys. Rev.* **136**, A 429 (1964).
23. A. S. Barker, Jr., *Phys. Rev.* **145**, 391 (1966).
24. A. V. Turik and N. B. Shevchenko, *Sov. Phys. Solid State* **19**, 1644 (1977).
25. A. V. Turik and K. R. Chernyshev, *Izv. Akad. Nauk SSSR Ser. Fiz* **31**, 1775 (1967); A. V. Turik, E. N. Sidorenko, B. F. Proskuryakov, V. F. Zhestkov, and N. B. Shevchenko, in "Crystallization and Properties of Crystals" (Inter-University Collection) [in Russian], No. 2, Novocherkassk, 72 (1975).
26. R. Ruppin, *Phys. Stat. Sol. b* **64**, 701 (1974).
27. R. T. Mara, G. B. B. M. Sutherland, and H. V. Tyrell, *Phys. Rev.* **96**, 801 (1954).
28. J. T. Last, *Phys. Rev.* **105**, 1740 (1957).
29. A. I. Demeshina and V. N. Murzin, *Solid State Phys. (USSR)* **4**, 2185 (1963); *Fiz. Tverd. Tela* **4**, 2980 (1962).
30. Y. Luspin, J. L. Servoin, and F. Gervais, *J. Phys. C: Solid State Phys.* **13**, 3761 (1980).
31. M. DiDomenico, Jr., S. H. Wemple, S. P. S. Porto, and R. P. Bauman, *Phys. Rev.* **174**, 522 (1968).
32. H. Vogt, J. A. Sanjurjo, and G. Rossbroich, *Phys. Rev. B* **26**, 5904 (1982).
33. A. Pinczuk, W. Taylor, E. Burstein, and I. Lefkowitz, *Solid State Commun.* **5**, 429 (1967).

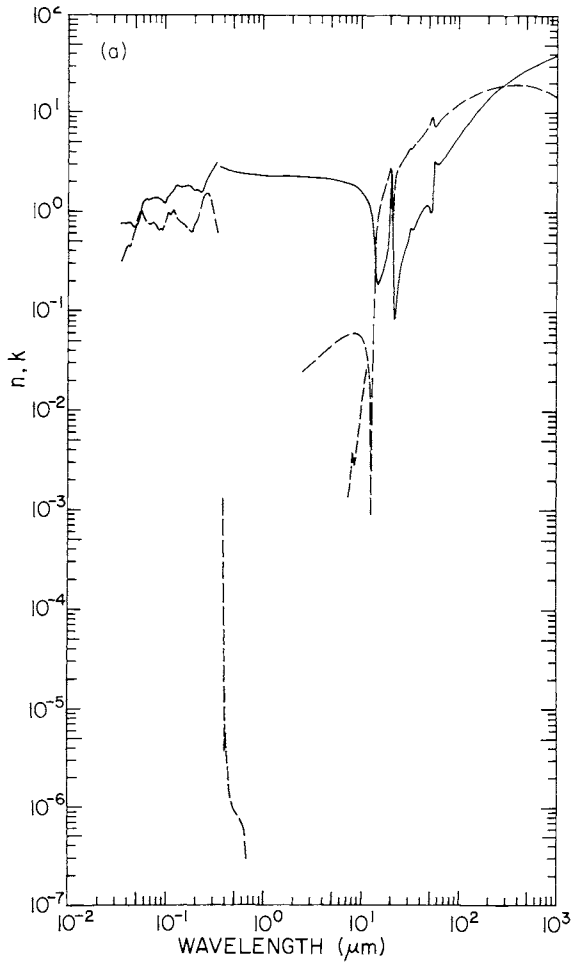

Fig. 1. (a) Log–log plot of n_o (solid line) and k_o (dashed line) versus wavelength in micrometers for barium titanate. (b) Log–log plot of n_e (solid line) and k_e (dashed line) versus wavelength in micrometers.

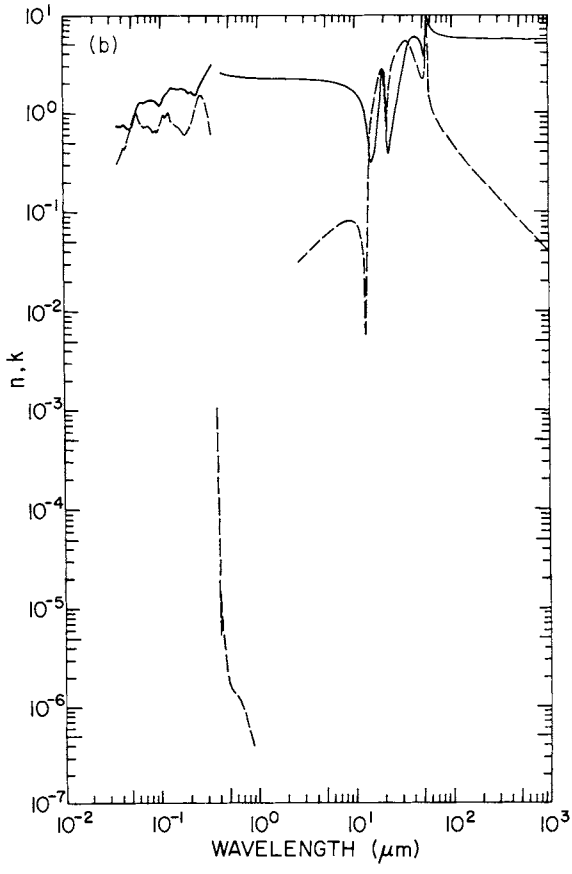

TABLE I

Values of Mode Frequencies and Damping Constants for Barium Titanate[a]

j	Ω_{jLO}	γ_{jLO}	Ω_{jTO}	γ_{jTO}
1	180	9	34	100
2	305.6	9	181.8	2.8
3	465	5	306	9
4	706	22	482	21
1	187	9	180	4
2	469	12	280	120
3	729	34	507	45

[a]The data were obtained from Ref. [20]. The unit is cm^{-1}. The first four rows are for the ordinary ray and the last three rows are for the extraordinary ray.

TABLE II

Values of n and k for Barium Titanate Obtained from Various References[a]

eV	cm^{-1}	μm	n	k
33.8		0.03668	0.761[5]	0.326[5]
32.5		0.03815	0.753	0.370
31.3		0.03968	0.745	0.420
30.0		0.04133	0.782	0.450
29.4		0.04217	0.786	0.444
28.1		0.04412	0.741	0.449
27.4		0.04533	0.720	0.494
26.6		0.04670	0.700	0.548
25.7		0.04867	0.679	0.667
24.6		0.05040	0.720	0.770
24.0		0.05166	0.741	0.839
22.9		0.05414	0.872	0.956
22.3		0.05560	0.975	1.002
21.7		0.05714	1.09	1.020
20.9		0.05947	1.26	0.914
19.3		0.06424	1.32	0.790
18.3		0.06794	1.29	0.741
17.3		0.07167	1.32	0.765
16.3		0.07618	1.36	0.763
15.3		0.08091	1.39	0.723
14.1		0.08794	1.36	0.672
13.4		0.09236	1.32	0.654
12.6		0.09880	1.21	0.751
11.7	94,370	0.1060	1.39	0.985
11.1	89,530	0.1117	1.48	0.938
10.2	82,270	0.1216	1.65	1.05
9.45	76,220	0.1312	1.84	0.839
8.50	68,560	0.1459	1.77	0.760
7.68	61,940	0.1616	1.82	0.704
6.75	54,440	0.1837	1.78	0.617
6.33	51,050	0.1960	1.63	0.720
5.75	46,380	0.2156	1.65	0.844
5.25	42,340	0.2362	1.54	1.28
5.08	40,930	0.2443	1.72	1.30
4.93	39,760	0.2518	1.91	1.51
4.58	36,940	0.2707	2.40	1.40
4.00	32,262	0.3110	3.10[19]	
3.98	32,100	0.3115	2.81 [5]	1.07
3.83	30,890	0.3237	2.98	0.86
3.63	29,280	0.3420	3.20	0.62

(continued)

TABLE II (*Continued*)

Barium Titanate

eV	cm^{-1}	μm	$n_o(\perp)$	$k_o(\perp)$	$n_e(\|\|)$	$k_e(\|\|)$
3.500	28,229	0.3542	2.82[19]			
3.270	26,347	0.3792				1.08×10^{-3}[11]
3.180	25,648	0.3899		1.33×10^{-3}[11]		1.68×10^{-4}
3.150	25,406	0.3936		6.42×10^{-4}		7.11×10^{-5}
3.100	25,003	0.4000		1.91		1.91
						1.49 [12]
3.050	24,600	0.4065		5.53×10^{-5}		5.53×10^{-6}[11]
3.000	24,196	0.4133	2.64	1.38		
2.950	23,793	0.4203		3.68×10^{-6}		
2.938	23,697	0.422	2.645[7]	5.84×10^{-6}[12]	2.541[7]	6.51×10^{-6}[12]
2.755	22,222	0.450	2.578	1.86	2.492	2.51
2.610	21,053	0.475	2.534	1.25	2.461	1.70
2.500	20,164	0.4959	2.51[19]			
2.480	20,000	0.500	2.500[7]	1.03	2.436	1.55
2.362	19,048	0.525	2.478	9.6×10^{-7}	2.416	1.46
2.254	18,182	0.550	2.459	8.8	2.400	1.44
2.156	17,391	0.575	2.442	7.8	2.385	1.37
2.066	16,667	0.600	2.430	7.2	2.372	1.29
2.000	16,131	0.6199	2.42[19]			
1.984	16,000	0.625	2.416[7]	7.0	2.362	1.14
1.907	15,385	0.650	2.405	6.2	2.352	1.03
1.837	14,815	0.675	2.396	3.8	2.344	1.02
1.797	14,493	0.690	2.390	2.8	2.340	9.6×10^{-7}
1.710	13,793	0.725	2.379		2.332	7.5
1.653	13,333	0.750	2.372		2.327	6.0
1.600	12,903	0.775	2.366		2.321	5.6
1.550	12,500	0.800	2.361		2.317	5.1
1.503	12,121	0.825	2.356		2.313	4.8
1.500	12,098	0.8266	2.36[19]			
1.459	11,765	0.850	2.352[7]		2.309	4.1
1.417	11,429	0.875	2.348		2.305	
1.378	11,111	0.900	2.344		2.302	
1.305	10,526	0.950	2.338		2.297	
1.240	10,000	1.00	2.332		2.292	
1.181	9,524	1.05	2.328		2.288	
1.127	9,091	1.10	2.324		2.284	
1.078	8,696	1.15	2.320		2.281	
1.033	8,333	1.20	2.317		2.279	
1.000	8,065	1.240	2.32[19]			
0.9919	8,000	1.25	2.314[7]		2.277	

(continued)

TABLE II (*Continued*)

Barium Titanate

eV	cm^{-1}	μm	$n_o(\perp)$	$k_o(\perp)$	$n_e(\|\|)$	$k_e(\|\|)$
0.9537	7,692	1.30	2.312[7]		2.275[7]	
0.9184	7,407	1.35	2.310		2.273	
0.8856	7,143	1.40	2.308		2.271	
0.8551	6,897	1.45	2.307		2.270	
0.8266	6,667	1.50	2.305		2.268	
0.7999	6,452	1.55	2.304		2.267	
0.7749	6,250	1.60	2.303		2.266	
0.7514	6,061	1.65	2.301		2.265	
0.75	6,049	1.653	2.31[19]			
0.7293	5,882	1.70	2.300[7]		2.264	
0.7085	5,714	1.75	2.300		2.264	
0.6888	5,556	1.80	2.299		2.263	
0.6702	5,405	1.85	2.298		2.262	
0.6526	5,263	1.90	2.297		2.262	
0.6358	5,128	1.95	2.297		2.261	
0.6199	5,000	2.00	2.296		2.260	
0.5	4,033	2.480	2.30[19]			
0.4960	4,000	2.50	2.27[20]	2.48×10^{-2}[20]	2.21[20]	3.15×10^{-2}[20]
0.4092	3,300	3.03	2.25	2.97	2.19	3.79
0.3472	2,800	3.57	2.23	3.46	2.18	4.42
0.3100	2,500	4.00	2.22	3.83	2.16	4.91
0.2728	2,200	4.55	2.19	4.28	2.14	5.51
0.2480	2,000	5.00	2.16	4.62	2.11	5.99
0.2356	1,900	5.26	2.15	4.82	2.10	6.25
0.2232	1,800	5.56	2.13	5.02	2.08	6.54
0.2108	1,700	5.88	2.10	5.23	2.06	6.84
0.1984	1,600	6.25	2.08	5.45	2.04	7.16
0.1860	1,500	6.67	2.04	5.67	2.00	7.48
0.1736	1,400	7.14	2.00	5.88×10^{-2}	1.97	7.81
0.1653	1,333	7.5		1.37×10^{-3}[18]		
0.1612	1,300	7.69	1.95	6.06×10^{-2}[20]	1.92	8.11
0.1600	1,290	7.75		2.03×10^{-3}		
0.1550	1,250	8.0		2.93[18]		
0.1503	1,212	8.25		3.87		
0.1488	1,200	8.33	1.88	6.18×10^{-2}[20]	1.85	8.33
0.1459	1,176	8.5		3.38×10^{-3}[18]		
0.1417	1,143	8.75		2.85		
0.1378	1,111	9.0		3.58		
0.1364	1,100	9.09	1.78	6.15×10^{-2}[20]	1.76	8.35
0.1305	1,053	9.5		5.74×10^{-3}[18]		

(continued)

TABLE II (*Continued*)

Barium Titanate

eV	cm^{-1}	μm	$n_o(\perp)$	$k_o(\perp)$	$n_e(\|\|)$	$k_e(\|\|)$
0.1240	1,000	10.00	1.65[20]	5.81×10^{-2}[20] 8.75×10^{-3}[18]	1.63[20]	7.89×10^{-2}[20]
0.1215	980	10.20	1.61	5.68×10^{-2}[20]	1.59	7.68
0.1181	952.4	10.5		1.33×10^{-2}[18]		
0.1203	970	10.31	1.60	5.60 [20]	1.57	7.56
0.1190	960	10.42	1.58	5.51	1.55	7.42
0.1178	950	10.53	1.56	5.41	1.54	7.26
0.1116	940	10.64	1.54	5.30	1.51	7.09
0.1153	930	10.75	1.52	5.18	1.49	6.89
0.1141	920	10.87	1.50	5.05	1.47	6.66
0.1128	910	10.99	1.47	4.90	1.44	6.40
0.1127	909.1	11.0		1.88 [18]		
0.1160	900	11.11	1.45	4.73 [20]	1.42	6.11
0.1104	890	11.24	1.42	4.54	1.39	5.78
0.1091	880	11.36	1.40	4.34	1.36	5.41
0.1079	870	11.49	1.37	4.10	1.33	4.98
0.1078	869.6	11.5		2.74 [18]		
0.1066	860	11.63	1.34	3.84 [20]	1.30	4.50
0.1054	850	11.76	1.30	3.55	1.26	3.94
0.1042	840	11.90	1.27	3.22	1.22	3.29
0.1029	830	12.05	1.23	2.84	1.18	2.54
0.1017	820	12.20	1.20	2.41	1.14	1.67
0.1004	810	12.35	1.15	1.92	1.09	6.27×10^{-3}
0.0992	800	12.50	1.11	1.36	1.03	6.18
0.0980	790	12.66	1.06	6.92×10^{-3}	0.976	2.14×10^{-2}
0.0967	780	12.82	1.01	9.18×10^{-4}	0.911	4.03
0.0955	770	12.99	0.946	1.04×10^{-2}	0.837	6.45
0.0942	760	13.16	0.880	2.20	0.754	9.69×10^{-2}
0.0930	750	13.33	0.807	3.68	0.659	0.143
0.0918	740	13.51	0.723	5.65	0.552	0.212
0.0905	730	13.70	0.625	8.46	0.447	0.319
0.0893	720	13.89	0.508	0.130	0.372	0.459
0.0880	710	14.08	0.372	0.215	0.335	0.605
0.0868	700	14.29	0.262	0.364	0.321	0.741
0.0856	690	14.49	0.214	0.523	0.320	0.867
0.0843	680	14.71	0.197	0.662	0.326	0.987
0.0831	670	14.93	0.191	0.785	0.338	1.10
0.0818	660	15.15	0.192	0.898	0.354	1.21
0.0806	650	15.38	0.196	1.00	0.374	1.32
0.0794	640	15.63	0.202	1.11	0.399	1.43

(continued)

TABLE II (*Continued*)

Barium Titanate

eV	cm^{-1}	μm	$n_o(\perp)$	$k_o(\perp)$	$n_e(\parallel)$	$k_e(\parallel)$
0.0781	630	15.87	0.210[20]	1.20[20]	0.427[20]	1.55[20]
0.0769	620	16.13	0.220	1.30	0.461	1.66
0.0756	610	16.39	0.232	1.40	0.501	1.77
0.0744	600	16.67	0.246	1.50	0.550	1.89
0.0732	590	16.95	0.262	1.59	0.608	2.02
0.0719	580	17.24	0.281	1.69	0.681	2.15
0.0707	570	17.54	0.304	1.79	0.773	2.29
0.0694	560	17.86	0.331	1.89	0.893	2.44
0.0682	550	18.18	0.366	2.01	1.06	2.59
0.0670	540	18.52	0.410	2.12	1.29	2.73
0.0657	530	18.87	0.471	2.26	1.63	2.83
0.0645	520	19.23	0.561	2.40	2.11	2.77
0.0632	510	19.61	0.709	2.58	2.60	2.36
0.0620	500	20.00	0.994	2.76	2.71	1.62
0.0608	490	20.41	1.63	2.81	2.32	0.99
0.0595	480	20.83	2.32	1.80	1.65	0.68
0.0583	470	21.28	1.35	0.69	0.849	0.81
0.0570	460	21.74	0.165	1.26	0.428	1.42
0.0558	450	22.22	8.56×10^{-2}	1.85	0.374	1.91
0.0546	440	22.73	0.111	2.17	0.408	2.27
0.0533	430	23.26	0.148	2.40	0.472	2.58
0.0521	420	23.81	0.185	2.60	0.555	2.85
0.0508	410	24.39	0.220	2.76	0.652	3.10
0.0496	400	25.00	0.254	2.92	0.763	3.34
0.0484	390	25.64	0.287	3.07	0.890	3.58
0.0471	380	26.32	0.320	3.22	1.04	3.83
0.0459	370	27.03	0.354	3.37	1.21	4.07
0.0446	360	27.78	0.389	3.52	1.41	4.32
0.0434	350	28.57	0.425	3.68	1.66	4.56
0.0422	340	29.41	0.464	3.84	1.95	4.81
0.0409	330	30.30	0.507	4.01	2.29	5.04
0.0397	320	31.25	0.563	4.20	2.70	5.23
0.0384	310	32.26	0.700	4.41	3.18	5.38
0.0372	300	33.33	0.691	4.41	3.72	5.44
0.0360	290	34.48	0.688	4.65	4.30	5.38
0.0347	280	35.71	0.736	4.88	4.88	5.17
0.0335	270	37.04	0.793	5.11	5.38	4.83
0.0322	260	38.46	0.855	5.35	5.77	4.39
0.0310	250	40.00	0.922	5.60	6.01	3.90
0.0298	240	41.67	0.993	5.87	6.11	3.42

(continued)

TABLE II (*Continued*)

Barium Titanate

eV	cm^{-1}	μm	$n_o(\perp)$	$k_o(\perp)$	$n_e(\|\|)$	$k_e(\|\|)$
0.0285	230	43.48	1.07[20]	6.18[20]	6.08[20]	2.99[20]
0.0273	220	45.45	1.14	6.52	5.94	2.62
0.0260	210	47.62	1.19	6.92	5.67	2.34
0.0248	200	50.00	1.19	7.46	5.16	2.22
0.0242	195	51.28	1.14	7.86	4.68	2.33
0.0236	190	52.63	1.00	8.57	3.86	2.91
0.0231	186	53.76	0.88	9.96	3.14	4.62
0.0228	184	54.35	1.33	11.7	3.35	6.32
0.0227	183	54.64	2.57	13.1	3.88	7.42
0.0226	182	54.95	5.61	13.5	5.01	8.63
0.0224	181	55.25	7.82	10.8	7.10	9.46
0.0223	180	55.56	7.29	8.41	9.81	8.78
0.0221	178	56.18	5.41	6.95	11.3	4.56
0.0218	176	56.82	4.35	6.84	10.1	2.65
0.0211	170	58.82	3.28	7.32	8.19	1.44
0.0205	165	60.61	3.07	7.70	7.54	1.21
0.0198	160	62.50	3.04	8.03	7.17	1.09
0.0186	150	66.67	3.17	8.63	6.74	0.928
0.0174	140	71.43	3.44	9.22	6.48	0.811
0.0161	130	76.92	3.81	9.84	6.29	0.712
0.0149	120	83.33	4.28	10.5	6.16	0.627
0.0136	110	90.91	4.87	11.2	6.04	0.550
0.0124	100	100.0	5.59	12.0	5.95	0.482
0.0112	90	111.1	6.48	12.8	5.88	0.419
0.0099	80	125.0	7.59	13.8	5.81	0.362
0.0087	70	142.9	9.00	14.8	5.76	0.309
0.0074	60	166.7	10.8	15.9	5.72	0.259
0.0062	50	200.0	13.2	17.0	5.68	0.212
0.0050	40	250.0	16.4	18.1	5.65	0.167
0.0037	30	333.3	20.9	19.1	5.63	0.124
0.0025	20	500.0	27.7	19.0	5.61	8.20×10^{-2}
0.0012	10	1000.0	37.8	15.0	5.61	4.08×10^{-2}
0.0744	600	16.67			0.44[21]	2.05[21]
0.0719	580	17.24			0.48	2.29
0.0694	560	17.86			0.67	2.82
0.0670	540	18.52			0.99	3.24
0.0657	530	18.87			1.34	3.43
0.0645	520	19.23			2.05	3.42
0.0632	510	19.61			2.93	2.93
0.0620	500	20.00			3.60	1.39

(continued)

TABLE II (*Continued*)

Barium Titanate

eV	cm^{-1}	μm	$n_o(\perp)$	$k_o(\perp)$	$n_e(\|\|)$	$k_e(\|\|)$
0.0595	480	20.83			1.39[21]	0.65[21]
0.0570	460	21.74			0.13	1.88
0.0546	440	22.73			0.091	2.74
0.0521	420	23.81			0.24	3.17
0.0496	400	25.00			0.27	3.75
0.0471	380	26.32			0.28	4.48
0.0446	360	27.78			0.44	5.12
0.0422	340	29.41			0.77	5.88
0.0397	320	31.25			1.35	7.06
0.0384	310	32.26			1.82	7.70
0.0372	300	33.33			2.60	8.47
0.0360	290	34.48			3.70	9.34
0.0347	280	35.71			5.36	9.79
0.0335	270	37.04			8.09	8.97
0.0322	260	38.46			9.81	7.44
0.0298	240	41.67			9.33	3.48
0.0273	220	45.45			6.08	2.24
0.0260	210	47.62			7.15	2.03
0.0248	200	50.00			5.68	2.29
0.0236	190	52.63			3.42	4.67
0.0223	180	55.55			7.52	13.3
0.0211	170	58.82			10.9	0.0046
0.0198	160	62.50			9.11	0.082
0.0186	150	66.67			8.37	0.11
0.0174	140	71.43			7.75	0.13
0.0149	120	83.33			7.07	0.13
0.0124	100	100.0			6.71	0.097

[a] The references are given in brackets at the beginning of the tabulation of n and k and are understood to refer to all n's or all k's below it until a new reference appears. When an exponent of 10 is given, all numbers below it have the same exponent until the power of 10 changes or the next number has 10^{-1}, which is usually written as a decimal. The samples used in Refs. [7], [11] and [12] were melt-grown. Method of sample growth were not mentioned in Refs. [5] and [20]. The optical constants from Ref. [5] are for unpoled samples.

Beryllium Oxide (BeO)

DAVID F. EDWARDS and RICHARD H. WHITE
University of California
Lawrence Livermore National Laboratory
Livermore, California

The optical properties of crystalline synthetic beryllium oxide, BeO, have been reported for a very limited number of samples. The main reasons for this lack of data are probably the toxic properties of the material and the difficulty of growing large optical-quality crystals [1]. As pointed out by Peterson and Palma [2], BeO is a useful new optical material for the vacuum UV because of its high transmittance down to about 9.4 eV (1320 Å) and its apparent resistance to UV radiation damage. In their report they show only the transmittance and, unfortunately, not enough data to estimate the n and k values for the 3–10 eV region. Calculations by White, Edwards, and Rathkopf [3] predict that overlayers of BeO on metallic reflectors should significantly enhance their hardness to X-ray radiation.

Natural bromellite (BeO) and synthetically grown BeO crystals are uniaxially positive. Newkirk *et al.* [4], using the angle-of-minimum-deviation technique, have measured the ordinary and extraordinary refractive indices and their dependence on temperature from 0.430 μm to 0.690 μm.

Loh [5] has evaluated the ordinary and extraordinary infrared refractive indices and extinction coefficients for BeO from their polarized reflectance spectra. The n and k values were derived from parameters used to fit the classical oscillator dispersion formula to the reflectance spectra. The well-known formula, as used by Loh, is

$$\varepsilon(\omega) - n_\infty^2 = (\varepsilon_0 - n_\infty^2)\omega_0^2/(\omega_0^2 - \omega^2 + i\gamma\omega),$$

where ε_0 is the static dielectric constant, and n_∞^2 is the high-frequency dielectric constant. γ is a phenomenological damping term, and ω_0 is the transverse optical resonance frequency. These classical dispersion parameters are given in Table I. The n and k values were determined from the

Copyright © 1991 by Academic Press.
All rights of reproduction in any form reserved.
ISBN 0-12-544422-2

complex dielectric constant and are included in Table II (and Fig. 1) for the infrared region 100 to 1400 cm^{-1} (100 to 7.14 μm). These calculations were extended beyond the measurement range (up to 400 cm^{-1}) to 100 cm^{-1} in order to estimate the static dielectric constant, ε_o. From the classical dispersion analysis of Loh, $\varepsilon_o(\|) = 7.65$ and $\varepsilon_o(\perp) = 6.94$. From Table II, $n(\|)^2 = 7.765$ and $n(\perp)^2 = 6.96$ at 100 cm^{-1}.

The indices of refraction between 0.440 μm and 7.0 μm have been fit to both a Herzberger-type and a modified Sellmeier-type dispersion formula. A total of 31 and 29 wavelengths were used for fitting the ordinary and extraordinary indices, respectively. The indices for wavelengths greater than 7.0 μm are from the lattice band spectra of Loh [5] and are not included in the dispersion formulas.

The Herzberger-type dispersion formula for the index is [6]

$$n = A + BL + CL^2 + D\lambda^2 + E\lambda^4,$$

where $L = 1/(\lambda^2 - 2.80 \times 10^6)$ with λ in angstroms. As explained by Herzberger [6], the 2.80×10^6 is the square of the mean asymptote for the short-wavelength abrupt increase in the index for 14 materials (BeO not included). The coefficients for the room-temperature ordinary indices, evaluated by least squares, are $A = 1.699773$, $B = 7.451288 \times 10^2$, $C = -4.331397 \times 10^{12}$, $D = -8.194535 \times 10^{-12}$, and $E = -1.659630 \times 10^{-20}$. The RMS error between the measured values and the dispersion formula calculated indices is 0.355% for the 0.440 to 7.0 μm range. The coefficients for the extraordinary indices are $A = 1.715140$, $B = 7.871215 \times 10^5$, $C = -4.782711 \times 10^{12}$, $D = -2.139439 \times 10^{-11}$, and $E = -1.390880 \times 10^{-20}$. The RMS error is 0.263%. The calculated n_o and n_e values are included in Table II.

The modified Sellmeier-type dispersion formula [7] is

$$n^2 = 1 + A/(\lambda^2 - B) + C\lambda^2/(\lambda^2 - D),$$

where the wavelength λ is in angstroms. For the 31 ordinary and 29 extraordinary data points, the coefficients are as follows. For the ordinary index of refraction, $A = 3.698124 \times 10^{-6}$, $B = -1.878147 \times 10^{-6}$, $C = 1.953730$, and $D = 1.472502 \times 10^{-6}$. The extraordinary coefficients are $A = 3.257604 \times 10^{-6}$, $B = -1.609457 \times 10^{-6}$, $C = 1.997330$, and $D = 1.548286 \times 10^{-6}$. The RMS errors are 0.228% and 0.216% for the ordinary and extraordinary indices, respectively. The Sellmeier-calculated indices are not tabulated here but the equation and coefficients are included for completeness.

Worrell [8] has determined the infrared optical constants for commer-

cially available ceramic beryllia, BeO. He evaluated n and k from a Kramers–Kronig analysis of the reflectance spectrum at near normal incidence. His results for one of the two measured samples are tabulated in Table III. The data for the second sample are not listed here but have the same general features with some variation in detail. Comparisons have been made of these ceramic data with those of Loh [5] for the crystalline BeO. The ceramic beryllia is optically isotropic compared with the uniaxial crystalline BeO. Plots of the ceramic data are not shown here but a comparison with the Loh data shows that the reststrahlen band is the same for the two materials: 1200 to 600 cm^{-1}. The maximum reflectance at the center of this band (around 800 cm^{-1}) is less than that of the crystalline BeO: approximately, 84% versus 96%. This lower reflectance is attributed to a lower density and the polycrystalline nature of the ceramic relative to the crystal. Differences in band profile are noted with the appearance of shoulder bands at approximately 1070 cm^{-1} and 710 cm^{-1} in the ceramic materials. The peak values of the index and extinction coefficient are about 10 to 13 for the crystal and about half that for the ceramic. The n and k values outside of the reststrahlen band show greater variation with the Loh data. The reason is that corrections were not applied by Worrell [8] to the Kramers–Kronig analysis to account for truncations.

Newkirk *et al.* [4] measured the ordinary and extraordinary indices at five different temperatures from -12.06 ± 0.01°C to 44.85 ± 0.01°C, at five different wavelengths from 0.450 to 0.670 μm. They found the temperature coefficient of refractive index (dn/dT) to be essentially wavelength independent and linear with temperature. They report the ordinary coefficient to be $+8.18\times10^{-6}$/°C and $+13.40\times10^{-6}$/°C for the extraordinary index.

REFERENCES

1. S. B. Austerman, "Growth of Beryllia Crystals," *J. Am. Ceram. Soc.* **46**, 6 (1963).
2. C. W. Peterson and G. E. Palma, "BeO as a Window in the Vacuum UV," *J. Opt. Soc. Am.* **63**, 387 (1973).
3. R. H. White, D. F. Edwards, and J. A. Rathkopf, "Hardening of Optical Coatings to the Effects of X-Rays," *J. Appl. Phys.* (in press).
4. H. W. Newkirk, D. K. Smith, and J. S. Kahn, "Synthetic Bromellite III. Some Optical Properties," *Am. Mineral.* **51**, 141 (1966).
5. E. Loh, "Optical Phonons in BeO Crystals," *Phys. Rev.* **166**, 673 (1968).
6. M. Herzberger and C. D. Salzberg, "Refractive Indices of Infrared Optical Materials and Color Correction of Infrared Lenses," *J. Opt. Soc. Am.* **52** 420 (1962); M. Herzberger, "Colour Correction in Optical Systems and a New Dispersion Formula," *Opt. Acta* **6**, 197 (1959).
7. D. F. Edwards and R. H. White, see KDP in this volume.
8. C. A. Worrell, "Infrared Optical Constants for CO_2 Laser Waveguide Materials," *J. Mater. Sci.* **21**, 781 (1986); private communication, (1990).

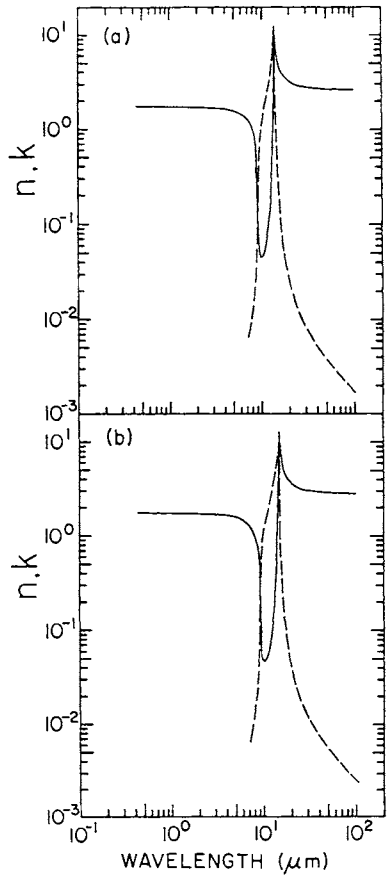

Fig. 1. (a) Log–log plot of n_o (solid line) and k_o (dashed line) versus wavelength in micrometers for beryllium oxide. (b) Log–log plot of n_e (solid line) and k_e (dashed line) versus wavelength in micrometers.

TABLE I

Classical Dispersion Parameters for Evaluating the Infrared Optical Properties of BeO

	Ordinary (⊥)	Extraordinary (‖)
$\omega_o(cm^{-1})$	680	724
λ	12.8	11.6
ε_o	7.65	6.94
n_∞^2	2.99	2.95

TABLE II

Values of *n* and *k* for Beryllium Oxide from Various References[a]

eV	cm^{-1}	μm	n_o (⊥)	k_o (⊥)	n_e (∥)	k_e (∥)
2.818	22,727	0.44	1.7288 [4]		1.7448 [4]	
2.696	21,739	0.46	1.7273		1.7434	
2.583	20,833	0.48	1.7258		1.7419	
2.480	20,000	0.50	1.7243		1.7403	
2.385	19,231	0.52	1.7229		1.7389	
2.296	18,519	0.54	1.7216		1.7375	
2.214	17,857	0.56	1.7203		1.7362	
2.138	17,241	0.58	1.7191		1.7349	
2.067	16,667	0.60	1.7180		1.7337	
2.000	16,129	0.62	1.7169		1.7326	
1.938	15,625	0.64	1.7160		1.7316	
1.879	15,152	0.66	1.7151		1.7306	
1.824	14,706	0.68	1.7142		1.7297	
1.771	14,286	0.70	1.7134 [6]		1.7289 [6]	
1.722	13,889	0.72	1.7127		1.7281	
1.676	13,514	0.74	1.7120		1.7273	
1.632	13,158	0.76	1.7114		1.7266	
1.590	12,821	0.78	1.7108		1.7259	
1.550	12,500	0.80	1.7102		1.7253	
1.378	11,111	0.90	1.7078		1.7226	
1.240	10,000	1.0	1.7060		1.7205	
0.6199	5,000	2.0	1.6957		1.7063	
0.4133	3,333	3.0	1.6798		1.6855	
0.3100	2,500	4.0	1.6446		1.6458	
0.2480	2,000	5.0	1.5759		1.5750	
0.2067	1,667	6.0	1.4554		1.4581	
0.1771	1,429	7.0	1.2613		1.2765	
0.1736	1,400	7.143	1.230 [5]	0.0076 [5]	1.247 [5]	0.007 [5]
0.1674	1,350	7.407	1.166	0.008	1.187	0.008
0.1612	1,300	7.692	1.086	0.011	1.113	0.011
0.1550	1,250	8.000	0.981	0.014	1.018	0.014
0.1488	1,200	8.333	0.834	0.021	0.890	0.019
0.1457	1,175	8.511	0.735	0.026	0.806	0.024
0.1426	1,150	8.696	0.604	0.036	0.701	0.030
0.1395	1,125	8.889	0.411	0.060	0.562	0.043
0.1364	1,100	9 091	0.105	0.267	0.348	0.078
0.1333	1,075	9.302	0.057	0.568	0.089	0.344

TABLE II (*Continued*)

Beryllium Oxide

eV	cm^{-1}	μm	n_o (⊥)	k_o (⊥)	n_e (∥)	k_e (∥)
0.1302	1,050	9.524	0.048	0.789	0.058	0.609
0.1271	1,025	9.756	0.045	0.986	0.050	0.816
0.1240	1,000	10.00	0.045	1.179	0.047	1.005
0.1209	975	10.26	0.047	1.375	0.047	1.189
0.1178	950	10.53	0.050	1.583	0.049	1.376
0.1147	925	10.81	0.056	1.810	0.052	1.573
0.1116	900	11.11	0.064	2.066	0.057	1.787
0.1085	875	11.43	0.076	2.365	0.065	2.024
0.1054	850	11.76	0.095	2.729	0.075	2.295
0.1023	825	12.12	0.126	3.196	0.091	2.617
0.09919	800	12.50	0.184	3.847	0.115	3.015
0.09609	775	12.90	0.321	4.879	0.157	3.537
0.09299	750	13.33	0.830	6.700	0.239	4.284
0.08989	725	13.79	10.089	11.834	0.444	5.523
0.08679	700	14.29	7.805	0.870	1.407	8.36
0.08369	675	14.81	5.725	0.296	13.180	7.050
0.08059	650	15.38	4.814	0.155	7.428	0.732
0.07749	625	16.00	4.287	0.097	5.715	0.289
0.07439	600	16.67	3.939	0.068	4.888	0.160
0.07129	575	17.39	3.689	0.050	4.389	0.103
0.06819	550	18.18	3.502	0.038	4.052	0.073
0.06509	525	19.05	3.355	0.030	3.807	0.054
0.06199	500	20.00	3.237	0.025	3.620	0.042
0.05889	475	21.05	3.141	0.020	3.474	0.034
0.05579	450	22.22	3.061	0.017	3.356	0.027
0.05269	425	23.53	2.993	0.014	3.259	0.023
0.04959	400	25.00	2.936	0.012	3.178	0.018
0.04339	350	28.57	2.845	9.1x10-3	3.052	0.0136
0.03720	300	33.3	2.776	6.9x10-3	2.960	0.010
0.03100	250	40	2.725	5.1x10-3	2.893	7.4x10-3
0.02480	200	50	2.686	3.8x10-3	2.843	5.4x10-3
0.01860	150	66.7	2.659	2.7x10-3	2.807	3.8x10-3
0.01240	100	100	2.639	1.7x10-3	2.783	2.4x10-3

[a] The n_o and n_e values for wavelength 7.0 μm and smaller were calculated with the Herzberger-type formula. The n and k values for wavelength greater than 7.0 μm were calculated from the reststrahlen data. The bracketed numbers indicate the reference to the data.

TABLE III

Values of n and k for Ceramic Beryllium Oxide [8]

eV	cm^{-1}	μm	n	k
0.02244	181.0	55.25	2.6208	0.0799
0.02360	190.3	52.55	2.6270	0.0779
0.02480	200.0	50.00	2.6336	0.0784
0.02606	210.2	47.57	2.6410	0.0798
0.02740	221.0	45.25	2.6491	0.0819
0.02852	230.0	43.48	2.6562	0.0841
0.02982	240.5	41.58	2.6650	0.0871
0.03104	250.3	39.95	2.6735	0.0903
0.03230	260.5	38.39	2.6828	0.0938
0.03346	269.8	37.06	2.6917	0.0973
0.03482	280.8	35.61	2.7027	0.1018
0.03605	290.7	34.40	2.7131	0.1061
0.03715	299.6	33.38	2.7227	0.1101
0.03846	310.2	32.25	2.7348	0.1151
0.03963	319.6	31.29	2.7459	0.1198
0.04104	331.0	30.21	2.7599	0.1255
0.04209	339.4	29.46	2.7707	0.1298
0.04357	351.4	28.46	2.7869	0.1360
0.04468	360.3	27.75	2.8009	0.1397
0.04581	369.4	27.07	2.8138	0.1457
0.04723	380.9	26.25	2.8327	0.1522
0.04838	390.2	25.63	2.8485	0.1564
0.04961	400.1	24.99	2.8683	0.1602
0.05086	410.2	24.38	2.8905	0.1665
0.05214	420.5	23.78	2.9165	0.1718
0.05320	429.0	23.31	2.9376	0.1801
0.05454	439.8	22.74	2.9683	0.1928
0.05591	450.9	22.18	2.9961	0.2071
0.05704	460.0	21.74	3.0179	0.2199
0.05819	469.3	21.31	3.0375	0.2277
0.05967	481.2	20.78	3.0734	0.2323
0.06086	490.8	20.37	3.1129	0.2375
0.06209	500.7	19.97	3.1595	0.2499
0.06335	510.8	19.57	3.2034	0.2701
0.06462	521.1	19.19	3.2464	0.2892
0.06592	531.6	18.81	3.2978	0.3091
0.06691	539.6	18.53	3.3361	0.3238
0.06826	550.5	18.17	3.3931	0.3382

TABLE III (*Continued*)

Beryllium Oxide

eV	cm^{-1}	μm	n	k
0.06964	561.6	17.81	3.4728	0.3566
0.07069	570.1	17.54	3.5387	0.3662
0.07212	581.6	17.19	3.6485	0.3993
0.07320	590.3	16.94	3.7442	0.4173
0.07467	602.2	16.61	3.9054	0.4786
0.07580	611.3	16.36	4.0367	0.5445
0.07694	620.5	16.12	4.1815	0.6166
0.07811	629.9	15.88	4.3584	0.7298
0.07929	639.4	15.64	4.5546	0.8448
0.08048	649.0	15.41	4.8086	1.0489
0.08169	658.8	15.18	5.1446	1.3233
0.08334	672.1	14.88	5.5384	2.0507
0.08459	682.2	14.66	5.6595	2.8332
0.08587	692.5	14.44	5.4389	3.7439
0.08673	699.4	14.30	5.1068	4.3753
0.08804	710.0	14.08	4.1266	5.1834
0.08937	720.7	13.88	2.9343	5.2651
0.09071	731.5	13.67	2.1243	4.8910
0.09208	742.6	13.47	1.6565	4.5246
0.09300	750.0	13.33	1.4092	4.3319
0.09440	761.3	13.14	1.0695	4.0385
0.09583	772.8	12.94	0.7918	3.7230
0.09678	780.5	12.81	0.6559	3.5065
0.09825	792.3	12.62	0.5184	3.2061
0.09922	800.2	12.50	0.4551	3.0236
0.1007	812.3	12.31	0.3912	2.7791
0.1017	820.4	12.19	0.3630	2.6336
0.1033	832.8	12.01	0.3359	2.4419
0.1043	841.2	11.89	0.3224	2.3282
0.1054	849.6	11.77	0.3125	2.2235
0.1069	862.4	11.60	0.2959	2.0818
0.1080	871.0	11.48	0.2872	1.9938
0.1091	879.8	11.37	0.2804	1.9097
0.1107	893.0	11.20	0.2704	1.7957
0.1118	902.0	11.09	0.2622	1.7242
0.1130	911.0	10.98	0.2525	1.6550
0.1141	920.2	10.87	0.2424	1.5876
0.1152	929.4	10.76	0.2320	1.5215
0.1170	943.4	10.60	0.2151	1.4235

TABLE III (*Continued*)

Beryllium Oxide

eV	cm^{-1}	μm	n	k
0.1182	952.9	10.49	0.2032	1.3580
0.1193	962.4	10.39	0.1911	1.2919
0.1205	972.1	10.29	0.1791	1.2248
0.1217	981.8	10.19	0.1669	1.1556
0.1230	991.7	10.08	0.1564	1.0832
0.1242	1001.6	9.984	0.1488	1.0080
0.1254	1011.6	9.885	0.1453	0.9309
0.1267	1021.8	9.787	0.1466	0.8535
0.1280	1032.0	9.690	0.1510	0.7783
0.1293	1042.4	9.593	0.1531	0.7041
0.1305	1052.8	9.498	0.1507	0.6246
0.1319	1063.4	9.404	0.1463	0.5277
0.1332	1074.0	9.311	0.1602	0.4103
0.1345	1084.8	9.218	0.2098	0.2794
0.1352	1090.2	9.173	0.2469	0.2173
0.1365	1101.2	9.081	0.3590	0.1216
0.1379	1112.2	8.991	0.4797	0.0777
0.1393	1123.3	8.902	0.5733	0.0678
0.1414	1140.3	8.770	0.6778	0.0587
0.1428	1151.7	8.683	0.7388	0.0555
0.1442	1163.3	8.596	0.7874	0.0523
0.1457	1174.9	8.511	0.8354	0.0505
0.1464	1180.8	8.469	0.8586	0.0512
0.1479	1192.6	8.385	0.8996	0.0553
0.1494	1204.6	8.302	0.9347	0.0604
0.1501	1210.6	8.260	0.9476	0.0632
0.1516	1222.7	8.179	0.9770	0.0623
0.1524	1228.9	8.137	0.9900	0.0633
0.1539	1241.2	8.057	1.0180	0.0607
0.1554	1253.6	7.977	1.0484	0.0621
0.1562	1259.9	7.937	1.0621	0.0638
0.1578	1272.5	7.859	1.0858	0.0695
0.1594	1285.3	7.780	1.1072	0.0760
0.1602	1291.7	7.742	1.1169	0.0786
0.1618	1304.6	7.665	1.1369	0.0802
0.1626	1311.2	7.627	1.1469	0.0822
0.1642	1324.3	7.551	1.1670	0.0916
0.1650	1330.9	7.514	1.1744	0.0969
0.1667	1344.3	7.439	1.1850	0.1058

TABLE III (*Continued*)

Beryllium Oxide

eV	cm^{-1}	μm	n	k
0.1675	1351.0	7.402	1.1900	0.1087
0.1692	1364.5	7.329	1.2002	0.1185
0.1701	1371.4	7.292	1.2040	0.1259
0.1718	1385.1	7.220	1.1972	0.1430
0.1726	1392.0	7.184	1.1838	0.1435
0.1735	1399.0	7.148	1.1714	0.1354
0.1752	1413.0	7.077	1.1636	0.1006
0.1761	1420.1	7.042	1.1711	0.0831
0.1779	1434.3	6.972	1.1968	0.0611
0.1787	1441.5	6.937	1.2132	0.0544
0.1823	1470.5	6.800	1.2617	0.0586
0.1917	1545.8	6.469	1.3150	0.0697
0.2015	1624.8	6.155	1.3571	0.0743
0.2226	1795.2	5.570	1.4255	0.0735
0.2460	1983.5	5.042	1.4726	0.1125

Calcium Fluoride (CaF_2)

D. F. BEZUIDENHOUT
Division of Production Technology
Council for Scientific and Industrial Research
Pretoria, Republic of South Africa

X-ray diffraction analysis of calcium fluoride (CaF_2) has shown it to belong to the cubic fluorite structure. The Ca^{2+} ions are arranged in a face-centered cubic lattice and the F^- ions in a cubic lattice. Each fluorine ion is surrounded by four calcium ions and each calcium ion by eight fluorine ions [1, 2, 3]. The lattice constant a_o is given as 0.546305 nm [4], which is slightly higher than $a_o = 0.545$ nm reported by Goldschmidt [5]. Based on symmetry considerations, CaF_2 is classified under the space group $Fm3m$ (O_h^5) [6].

An early account of the growth of "artificial" CaF_2 is given by Stockbarger [7]. At present, high-purity, synthetic CaF_2 material is readily available in cylindrical form up to 200 mm in diameter [8]. However, it has been reported that large crystals of optical quality CaF_2, 600 mm in diameter, have been grown by Sokolov *et al.* [9, 10]. In a more recent publication, Horowitz *et al.* gave a correlation between growth parameters and the chemical and structural quality of CaF_2 crystals [11]. Mechanical and thermal properties of synthetic CaF_2, which are relevant from an engineering point of view, are given by Combes *et al.* [12]. Because of the physical properties of calcium fluoride, both mechanical and thermal shock should be avoided during optical processing [7, 13, 14].

The wide transmission band (0.2–9 μm) of CaF_2 leads to a multitude of applications. These applications range from dispersive elements in infrared monochromators [15], filters for reducing stray light [16] and radiation-blocking elements [17, 18], to lenses and windows [19, 20]. When used as laser elements, the tendency of water to adsorb on CaF_2 surfaces should be kept in mind [21]. However, it has been found that laser-induced desorption treatment leads to passivated CaF_2 surfaces that are highly resistant to water adsorption at room temperature [22]. During the early 1940s, CaF_2 was used in thin-film form as antireflection coatings on glass lenses [23].

Copyright © 1991 by Academic Press.
All rights of reproduction in any form reserved.
ISBN 0-12-544422-2

More recent applications of CaF_2 include areas such as optical fibers [24] and laser host material [25].

Synthetic Calcium Fluoride

CaF_2, which is a highly ionic compound, has a wide band gap. The edge of the fundamental absorption band lies in the vacuum ultraviolet at about 12 eV [26]. Much of the X-ray and ultraviolet work has been centered on studies concerning the determination of the electronic structure of CaF_2 and on color-center phenomena [27, 28]. The forbidden energy band gap is formed by the F^- $2p$ state and the $3d$ and $4s$ states of the Ca^{2+} ions [26]. Rubloff [29] used the synchrotron radiation from a 240 MeV electron storage ring as a light source in the vacuum ultraviolet to investigate the reflectance spectrum of CaF_2 covering the photon energy range 6–36 eV. The characteristics of the reflection spectra above the fundamental absorption edge were divided into three regions. Peaks in region I (6–26 eV) arise from optical excitation of electrons in the valence band. The peaks at lower energy in the valence excitation region are caused by exciton absorption, whereas intraband transitions dominate at higher energies in region I. Although valence excitations may continue into regions II (26–30 eV) and III (30–36 eV) at higher photon energies, electrons are mainly excited from core states, which lie below the valence bands. A change to broader peaks occurs on passing from region II to III, where the spectral features are caused primarily by excitations of the core states of Ca^{2+}.

Cluster calculations on CaF_2 showed the influence of impurities on the position of the absorption edge: oxygen impurity caused transitions to appear in the region 4.3–5 eV [26]. However, the theoretical values for the excitation energies in CaF_2 associated with defects appear to be less than the experimental values [26]. The effect of impurities such as oxygen or hydroxyl ions is a sharp cutoff at 0.22 μm [30, 31].

Bontinck [32] reported on the formation of color centers in CaF_2. He identified a number of absorption bands in the visible and near-infrared regions after X-ray radiation or additive coloration at high temperatures. During investigation of the coloration and luminescence of CaF_2 crystals, Rauch *et al.* [33] found that crystals that differed relatively little as to UV absorption showed marked differences in their photoluminescence and thermoluminescence behavior. Exposure to an electric field or to X-rays also leads to a change in the absorption features of CaF_2 [34, 35]. De and Rao [35] subjected low-absorption CaF_2 crystals to a high AC (or DC) field. There seems to be a considerable interaction of the field with the crystal lattice, resulting in increased concentration of lattice defects, which increases the absorption at 0.2 μm. Furthermore, when these crystals were irradiated with X-rays, absorption bands were observed at 0.375 and 0.58 μm.

The importance of surface preparation for short-wavelength investi-

gations has been stated by two groups who have done reflectance and transmittance measurements over the absorption-edge region of CaF_2 (0.12–0.16 μm) [36, 37]. It was reported that as the surface polish is improved, the increase in transmission is greater at shorter rather than at longer wavelengths. Different types of abrasives did not play any significant role in the reflectance behavior of these surfaces at short wavelengths. However, it was suggested that fluorite powder be used for the final polishing step [36]. Furthermore, it was also stated that an adsorbed layer of water vapor might influence the reflective properties of a CaF_2 surface because the absorption of water is quite high in the 0.12–0.16 μm region.

The temperature dependence of the absorption tail was investigated over the temperature range 78–573 K [37, 38, 39]. Linear behavior was found in the shift of the absorption edge. The rate of thermal shift was expressed by Tomiki and Miyata [37] as $\Delta\lambda/\Delta T = 0.26$ Å/K at the $\alpha = 10\ cm^{-1}$ point, where α is the absorption coefficient. The transmission limit (that is, $T<1\%$) changed from 0.121 μm at 291 K to 0.1165 μm at 77 K, where the sample thicknesses ranged from 0.25–0.71 mm [38]. These facts should be kept in mind when CaF_2 is used as window material near its shortwave edge in thermal experiments. At wavelengths longer than 0.15 μm, the transmission of CaF_2 windows is not affected appreciably by temperatures up to 500 °C [40].

The reflecting power of a polished fluorite surface has been measured from 0.0927 μm to 0.1605 μm for angles of incidence varying from 45 to 85 degrees [41]. A vacuum spectrograph and a method of photographic photometry, using oil-sensitized photographic film were used. The oil layer on the surface of the film absorbs the incident extreme ultraviolet light completely and fluoresces in the near ultraviolet. It is this fluorescent radiation that exposes the film, and its intensity is proportional to that of the incident light reflected from the CaF_2 sample surface inside the spectrograph. Below 0.123 μm the reflection becomes metallic in character, and by applying the appropriate reflectance formula and a numerical method, the refractive index and extinction coefficient were determined over the 0.0927–0.119 μm region. The first absorption band below the cutoff edge of CaF_2 was identified in the vicinity of 0.1115 μm. This band corresponds to an energy of 11.12 eV, which is in good agreement with the results of later reports such as Rubloff [29], who found a reflection peak at 11.02 eV at 300 K.

The dispersion curve is anomalous from between 0.113 and 0.12 μm to about 0.109 μm, when crossing the center of the absorption band. It becomes normal again toward the shorter wavelengths, but appears to become anomalous again at 0.1 μm as the next absorption band is approached [41].

On the long-wave side of the cutoff edge, refractive-index values are given for wavelengths up to 0.1605 μm [41]. For longer wavelengths, the

publication by Malitson [42] is a most comprehensive report on the dispersive properties of CaF_2. He used a modified Gaertner precision spectrometer, fitted with reflecting optics, to measure at visible and nonvisible wavelengths. The method of minimum deviation was applied to determine refractive-index values from wavelengths of 0.2288–9.724 μm. The experimentally determined index values were fitted to a three-term Sellmeier dispersion equation of the form

$$n^2 - 1 = \sum A_j \lambda^2 / (\lambda^2 - \lambda_j^2). \tag{1}$$

The λ_j represents ultraviolet and infrared absorption wavelengths and the A_j is related to the strength of the absorption bands. The parameters of the equation are given in Table I. The dispersion formula was then used to compute the refractive index at 24 °C, at wavelengths separated by regular intervals (Table IV and Fig. 1).

Malitson [42] also investigated dispersion, chromatic abberation, and resolution. It was found that the dispersion decreases steadily with increasing wavelength, reaches a minimum at 1.5 μm, and then slowly increases again while approaching the long-wavelength cutoff. For the purpose of lens design, chromatism is therefore minimized in the region near 1.5 μm. Finally, CaF_2 was found to be an excellent choice as prism material in the wavelength range 4–9 μm.

The thermal coefficient of the refractive index was determined for the range 15–35 °C and for the range 35–55 °C [42]. The results can be summarized as follows:

(1) The value of dn/dT is negative.

(2) The dn/dT versus wavelength behavior shows a steeper slope in the ultraviolet than in the visible, indicating a shift of the ultraviolet bands toward longer wavelengths with an increase in temperature.

(3) In the visible region, increases in temperature lead to a decrease in refractive-index values.

(4) The absolute value of dn/dT tends to increase with increasing wavelength and temperature.

(5) A decrease of the absolute dn/dT values in the infrared indicates that the infrared absorption bands have also shifted toward longer wavelengths with increasing temperature.

(6) An average value of $-dn/dT$ for the temperature interval of 15–24 °C over the wavelength range 0.228–9.7 μm is 8.65×10^{-6}/°C.

The temperature coefficient of the refractive index was measured by Lipson *et al.* [43] using a laser interferometric method. The temperature

was varied over the 25–110 °C range, and the wavelengths used were those of He–Ne lasers radiating at 0.6328 μm, 1.15 μm, and 3.39 μm. The *dn/dT* behavior showed the same previously observed trends [42, 44]. The *dn/dT* data follow the theoretical model suggested by Tsay *et al.* [45], where *dn/dT* is given by an approximation of the form

$$\frac{dn}{dT}=\frac{\sqrt{\varepsilon_\infty}}{n(\omega)}\left[\left(\frac{dn}{dT}\right)_e+\left(\frac{dn}{dT}\right)_l\right].$$

$(dn/dT)_e$ and $(dn/dT)_l$ are the electronic and lattice contributions to *dn/dT*. Furthermore, it was demonstrated that the slight increase in the value of *dn/dT* is comparable to the variation of the thermal expansion coefficient with temperature.

Measurements at very high temperatures in the range 293–300 K showed that the refractive index at 0.6328 μm decreased according to the relationship

$$n_T=n_r[1-8.07\times10^{-6}(T-293)-4.27\times10^{-9}(T-293)^2],$$

where n_r is the refractive index at 293 K [46]. In the same experiment it was found that the short wavelength side of the infrared band edge shifted considerably toward higher frequencies as the temperature was increased from 293 K to 1600 K. This behavior is believed to originate from a temperature broadening of the absorption band. These measurements were carried out in argon-filled chambers.

Several processes can contribute to absorption in the transparent region of a material, between the absorption edge (due to electronic transitions) on the short-wavelength side, and the reststrahlen band (due to lattice vibrations characteristic of ionic materials) on the long-wavelength side. These processes include multiphonon absorption, where a photon is absorbed and generates two or more phonons; free-carrier absorption identified by the λ^2 dependence of the absorption coefficient on the wavelength λ; impurity absorptions, which are recognized by a sharp-line structure; and the short-wavelength tail of the reststrahlen band extending into the transparent region [47].

An explanation of what may be regarded as impurity bands in CaF_2 has been given by Wickersheim and Hanking [48]. Absorption bands were observed at 2.74, 2.79, 6.76, 7.07, and 11.36 μm after CaF_2 samples were heated in air. The band at 2.74 μm was termed the infrared OH-stretching fundamental of $Ca(OH)_2$ occurring in or on the crystal. The band at 2.79 μm was identified as the stretching vibration of hydroxyl ions occur-

ring substitutionally for fluorine in CaF_2. The bands at 6.76, 7.07, and 12.5 μm were ascribed to a surface layer of $CaCO_3$.

An exponential frequency dependence of the infrared absorption coefficient, α, was found at frequencies ω greater than several times the reststrahlen frequency ω_o [47, 49, 50]. In this region the value of α decreases from about $10\,cm^{-1}$ at a wavelength of 12.5 μm, to approximately $10^{-4}\,cm^{-1}$ at 5 μm [50]. These results were interpreted as being caused by intrinsic multiphonon absorption processes [49, 50].

Kaiser *et al.* [51] used reflection and transmission measurements to obtain information on lattice vibrations. The absorption coefficient α was calculated from the transmission according to the equation

$$T=(1-R)^2e^{-\alpha x}/(1-R^2e^{-2\alpha x}),$$

where R is the reflectivity and x the sample thickness. Over the wavelength range 16.67–8.89 μm, the value of α decreased from $200\,cm^{-1}$ to $0.4\,cm^{-1}$ at a temperature of 77 K.

The reflection band was analyzed using the classical dispersion theory [51]. According to this theory, the real and imaginary parts of the complex dielectric constant, ε' and ε'', are given by

$$\varepsilon' = n^2 - k^2 = \varepsilon_\infty + \sum_j 4\pi\rho_j\nu_j^2 \frac{\nu_j^2 - \nu^2}{(\nu_j^2-\nu^2)^2+\gamma_j^2\nu^2\nu_j^2} \tag{2}$$

and

$$\varepsilon'' = 2nk = \sum_j 4\pi\rho_j\nu_j^2 \frac{\gamma_j\nu\nu_j}{(\nu_j^2-\nu^2)^2+\gamma_j^2\nu^2\nu_j^2}, \tag{3}$$

where n is the refractive index, k the extinction coefficient, ε_∞ the high-frequency limiting value of the dielectric constant, $4\pi\rho_j$ the strength of the jth resonance, γ_j the damping constant for the jth resonance, and ν_j the resonance frequency. From this analysis a strong resonance was found at 38.91 μm ($257\,cm^{-1}$) and identified as the transverse optical phonon mode [51].

At longer wavelengths the refractive index was determined from transmission interference measurements over the range 280–600 μm [52]. An average value of n equal to 2.58 ± 0.06 was found with no indication of any dispersive behavior. The extinction coefficient was calculated from trans-

mission of a thick sample over the range 170–250 μm. Values obtained for k were around 0.034 at 170 μm and 0.017 at 320 μm.

The optical constants of CaF_2 were determined from transmittance measurements on plane-parallel slabs over the wavelength band 50–200 cm^{-1} [53]. Dispersion curves were found by fitting the expression

$$n(\omega) = (\varepsilon(\omega))^{1/2} = \{(\varepsilon_0 \nu_{TO}^2 - \varepsilon_\infty \omega^2)/(\omega_{TO}^2 - \omega^2)\}^{1/2} \tag{4}$$

to the experimentally obtained values. There are essentially two unknowns: ε_o, the static dielectric constant and ω_{TO}, the vibrational frequency at zero wave vector. The values used were $\varepsilon_\infty = 2.04$, $\varepsilon_o = 6.63$, and $\omega_{TO} = 257$ cm^{-1} at 300 K. Equation 4 was used to calculate n at 100 and 200 μm (Table IV); however, it should be noted that Eq. 4 does not take absorption into account. The absorption coefficient was found to be strongly temperature dependent. At a wavelength of 100 μm the absorption α decreases from approximate values of 50 cm^{-1} at 300 K to 4 cm^{-1} at 80 K and less than 1 cm^{-1} at 5 K [53].

Denham *et al.* [54] used a Kramers–Kronig analysis to determine the dielectric parameters ε' and ε'' from reflection-spectra measurements over the 20–100 μm range. At 200 μm an estimated reflectivity of 19.6% leads to a refractive index $n = 2.52$. In the mm range (0.4–3 mm) the absorption of CaF_2 decreases with increasing wavelength (at $\lambda = 1$ mm, $k = 5 \times 10^{-3}$) [55]. A constant refractive index $n = \sqrt{\varepsilon_o} = 2.61$ is found at wavelengths beyond 0.3 mm.

The lattice vibrations in a crystal can be classified into optic and acoustic branches. For each value of the wave vector **k** there are $3N$ branches, where N is the number of ions in the unit cell. Three of the $3N$ branches are acoustic and $3N$-3 are optic modes [56, 57, 58]. The minimal unit cell of CaF_2 is formed by two fluorine ions sitting at the center of two tetrahedra [59]. Since the unit cell contains three nonequivalent ions (one formula unit), there are nine branches in the phonon spectra of which six are due to optic modes.

A mode of vibration can absorb energy only if a mechanism exists for the coupling of vibrational motion to the electromagnetic radiation—the motion produces an oscillating dipole moment, which can be driven by the oscillating electric field of the radiation. Also, the requirements for the conservation of energy and momentum must hold [57]. To determine the optically active vibrational modes, a crystal factor group analysis [60] or the correlation method of Fately *et al.* can be used [61].

The factor group (O_h in the case of CaF_2) leads to an identification of the species of lattice vibrations in the crystal also allowing the prediction of infrared or Raman activity. The total irreducible representation for CaF_2

can be written as [61]

$$\Gamma_{CaF_2} = 2F_{1u} + 1F_{2g}.$$

Both the optic and acoustic vibrations are included in the irreducible representation given above. One of the F_{1u} modes represents the three acoustic branches and can be subtracted leading to [61]

$$\Gamma_{optical} = F_{iu}(ir) + F_{2g}(R).$$

The remaining F_{1u} representation can be classified as a doubly degenerate transverse optic mode ν_{TO}, which interacts with infrared radiation and a longitudinal mode ν_{LO} [54]. Therefore, only one (double degenerate) mode is infrared active, resulting from the sublattice of metal ions vibrating rigidly against the fluorine lattice [62]. From the measurements of Kaiser *et al.* [51], the transverse optic mode of vibration was found at $\nu_{TO} = 257\,cm^{-1}$. The frequency of the longitudinal phonon is related to the transverse vibrational mode by the Lyddane, Sacks, Teller relation [54]:

$$\nu_{LO} = \nu_{TO}(\varepsilon_0/\varepsilon_\infty)^{1/2}.$$

A value of $\upsilon_{LO} = 476 \pm 4\,cm^{-1}$ was suggested by Zernik [63].

The Raman scattering process involves the destruction of an incident photon of frequency ω_i, the creation of a scattered photon of frequency ω_s, and the creation or destruction of a phonon of frequency ω_p [57]. In wave-vector notation the Raman process can be expressed as $\mathbf{k}_i = \mathbf{k}_s \pm \mathbf{k}_p$. The mode of symmetry F_{2g} is triply degenerate and Raman-active [54]. This mode results from a stationary cation lattice with the anions undergoing displacements against each other [58]. Using shortwave (0.488–0.6328 μm) laser light to excite CaF_2 crystals, the Stokes shifted component of the Raman spectrum was found at $322\,cm^{-1}$ [59, 64, 65]. It has also been pointed out that impurities might lead to fluorescent lines, which could be misinterpreted as Raman scattering [64]. The temperature dependence of the one-phonon Raman bands has been investigated using argon-ion (0.488 μm and 0.5145 μm) and He–Cd (0.4416 μm) lasers as light sources. A shift was observed from $330\,cm^{-1}$ at 15 K to about $300\,cm^{-1}$ at 1200 K [59]. Raman spectra excited by surface polaritons were produced by 0.5145 μm light and investigated at different scattering angles θ_s [66]. The angle of incidence was 35 degrees and Raman peaks were observed from $324\,cm^{-1}$ ($\theta_s = 36.5°$) to $403\,cm^{-1}$ ($\theta_s = 38.25°$). The strongest peaks were found at $371.5\,cm^{-1}$ ($\theta_s = 37°$) and $391\,cm^{-1}$ ($\theta_s = 37.25°$).

Laser Applications

Calcium fluoride has been considered a prime candidate for use as laser windows at both short (249 nm) [67] and long wavelengths (2.8–5.3 μm) [68]. Its sensitivity to thermal and mechanical shock led to programs for

strengthening the material without degrading the optical performance over its transparent range [68, 69, 70]. A hot-forging process was developed to produce small-grain polycrystalline blanks. Forged CaF_2 has shown an increase in the crystal-fracture energy in excess of five times that of single crystals, but has the disadvantage of cloudy regions within the bulk, or so-called veiling. Microscopic investigation of a veiled area has shown it to be composed of needlelike defects, which are voids lying parallel to the boundaries of elongated grains. These defects are characteristic of the forging process [68]. A hot isostatic pressing (HIP) treatment can eliminate these voids. It was postulated that the veils migrated to the surface where the bulk material collapsed in on itself [69]. It was also concluded that HIP-processed CaF_2 showed slightly increased absorption at 2.7 and 3.8 μm, and although the optical inhomogeneity is increased at 633 nm, it is still very low. Furthermore, the visible-scattering levels are decreased by a factor of eight compared with pre-HIP material, and the infrared scatter (at 3.7 μm) was largely unaffected.

An early attempt to determine some of the optical properties of forged CaF_2 is that of Dodge [71]. The index of refraction was determined by means of the minimum-deviation method. Data were obtained at 20.8 °C and 33.6 °C from 0.25–8 μm. Each set of experimental values was fitted to a three-term Sellmeier dispersion equation (Eq. 1). Emphasis was placed on obtaining a mathematical fit of the measured data, and the λ_j and A_j values are not intended to have any physical significance. These values are given in Table III. A comparison of Dodge's results [71] with those of Malitson [42] shows a minimum difference between 0.7 and 0.9 μm ($\Delta n = 0.5 \times 10^{-5}$) and a maximum difference ($\Delta n = 6.6 \times 10^{-5}$) at 0.28 μm and 4.8 μm. The index variation at 0.28 μm is attributed to a weak absorption band near 0.3 μm in the forged CaF_2. A possible absorption band between 4 and 5 μm was considered to be the reason for the difference at 4.8 μm. It must also be stressed that Dodge's [71] investigation should be regarded as a case study of a specific piece of CaF_2 material.

A photoacoustic study of the absorption properties reveals that surface absorption was found to be strongly wavelength dependent [72]. In the 2.7 μm region the surface absorption becomes dominant over bulk absorption. In another experiment both a photoacoustical and a laser-calorimetry method were used to determine bulk and surface absorption values at 1.3 μm [73]. Photoacoustic values of $\alpha_{\text{bulk}} = 6.8 \times 10^{-4}\,\text{cm}^{-1}$, $\alpha_{\text{surface}} = 4.8 \times 10^{-5}\,\text{cm}^{-1}$ compared closely with calorimetry values $\alpha_{\text{bulk}} = 6.14 \times 10^{-4}\,\text{cm}^{-1}$ and $\alpha_{\text{surface}} = 8.36 \times 10^{-5}\,\text{cm}^{-1}$ [73]. The optical absorption coefficient α measured at DF (3.8 μm) and HF (2.7 μm) wavelengths showed that single-crystal material has a slightly lower absorption than the forged material; the results for the absorption obtained from a variety of commercial CaF_2 samples indicate a variation in α obtained from different suppliers [74]. An investigation into the surface spectral distribution of

extrinsic absorption in highly transparent solids revealed that the atmospheric contaminants identified on CaF_2 surfaces could be grouped as hydrocarbons (3–4 μm), CO_2 (4.2 μm), liquid water (around 6 μm), and carbides (6.8 μm) [75]. The results obtained by Fernelius *et al.* [73] (that $\alpha_{surface} < \alpha_{bulk}$) might be ascribed to the fact that atmospheric contaminants at 1.3 μm are much less absorbing than at other wavelengths, such as the excimer UV region or 2.7 μm in the infrared, for example. Also, surface preparation, that is, polishing and cleaning before the tests, plays an important role in the experimental results of surface absorption measurements. In an experiment in which the absorption of CaF_2 was measured by laser calorimetry, it was found that hydrofluoric-acid cleaning reduced the surface absorption of the samples substantially [76]. It was suggested that contamination from the polishing process or the presence of calcium oxides on the sample surfaces led to the relatively high precleaned absorption values [76]. The presence of smooth, undamaged surface layers (<20 nm thick), which cover the subsurface damage on polished CaF_2, was illustrated by Law *et al.* [77].

Damage in CaF_2 optics used at excimer wavelengths may manifest itself in bulk and surface damage or in the generation of color centers. A laser damage experiment was carried out using a 0.249 μm, 3 ns excimer laser with an output pulse energy of around 700 mJ [67]. Work on the surface finish of CaF_2 surfaces indicated that the damage threshold is not as dependent on surface topography as it is on surface cleanliness, which is by far the greatest factor affecting damage thresholds [67]. For instance, it was suggested that the most important role of cracks is to act as a trap for absorbing impurities. Work done on highly pure CaF_2 crystals and naturally occurring fluorspar led to the conclusion that the presence of rare earth 3^+ ions is crucial in the formation of color centers [67]. XeF laser-damage experiments were used to measure damage thresholds for bare polished crystals of CaF_2 [78]. Damage was induced by applying 1000 pulses ($\lambda = 0.35$ μm, 25 ns) to small sites (0.12×0.03 cm) on the surfaces of the samples. Fluorescence-free CaF_2 exhibited both surface and bulk damage at 10 J cm^{-2}, whereas UV-grade CaF_2 showed only surface damage at 10 J cm^{-2}. From the damage morphology on the UV grade samples, it was suggested that improved polishing methods could lead to higher surface-damage thresholds. Laidler and Emmony [79] demonstrated the effect of rare-earth impurities on the ultraviolet wavelength absorption (0.339 μm) of CaF_2. It was found by these authors that pulsed laser damage thresholds (at 0.248 μm) indicated that the impure crystals had a higher damage threshold than the pure ones at certain dopant levels. It was suggested that the impurities, which act as electron acceptors, or holes formed by these impurities, continually trap conduction electrons and therefore hinder the buildup of an efficient electron avalanche process [79].

At infrared wavelengths the laser-damage threshold of CaF_2 was investi-

gated using pulsed DF laser light with three dominant lines at 3.8 μm [80]. The temporal pulse width was approximately 75 ns and a single-shot, one-site method was used. The peak on-axis intensity that damages CaF_2 was 25 GW/cm^2. What is more important, though, are the conclusions that the surface-damage thresholds are much lower than the bulk-damage thresholds, and that the damage-site morphology suggests that inclusions or defects are responsible for the damaging interaction [80].

It is clear that special attention must be given to surface preparation such as polishing and cleaning, in order to obtain CaF_2 laser components that will withstand high laser power densities.

Thin Films

Films a few thousand angstroms thick, grown by physical vapor deposition, were investigated by X-ray diffraction for a number of different coating conditions [81, 82]. It was found that when the substrate temperature was maintained at 25 °C during evaporation, the (111) planes were orientated approximately parallel to the glass substrate surface. For a substrate temperature of 110 °C the (110) planes were strongly oriented parallel to the surface, and this orientation of the (110) planes persisted for temperatures up to 310 °C [81, 82]. Stress measurements showed a high initial tensile stress, which rapidly fell to a low value as the thickness increased [83].

When the substrate temperature was kept below 100 °C during coating, the film showed a refractive index as low as about 1.26 [23]. These films tended to be very soft. At substrate temperatures between 280 and 300 °C, hard, robust films were formed with an estimated refractive index of 1.4. When the substrate temperature was 330 °C, films with a refractive index of approximately 1.42 resulted [23]. In a review of ultraviolet coating materials the refractive index of CaF_2 was given as 1.23–1.46 at 0.55 μm [84].

Bousquet [85] found that the reflectances of CaF_2 films at the half-wave positions are invariably lower than those of the substrate, where $n_f < n_s$. This result has been interpreted by Heavens and Smith as being caused by films having a gradient of refractive index normal to the substrate surface, with the index decreasing as the air–film surface is approached [86].

The laser-damage threshold of CaF_2 films was found to increase with an increase in both wavelength and pulse width [87]. At 0.265 μm, threshold values of 2.29 J cm^{-2} (5 ns pulse width) and 3.55 J cm^{-2} (15 ns pulse width) were found. Corresponding threshold values at 1.06 μm are 20 J cm^{-2} and 33 J cm^{-2} (pulse width 5 ns and 15 ns, respectively). These results were obtained for $\lambda/4$ films ($\lambda = 1.06$ μm).

REFERENCES

1. W. L. Bragg, *Proc. Roy. Soc.* **A89**, 468 (1914).

2. H. Pealing, *Proc. Roy. Soc.* **33**, 297 (1920).
3. A. F. Wells, *Phil. Mag.* **37**, 217 (1946).
4. Powder Diffraction File (Joint Committee on Powder Diffraction Standards, International Centre for Diffraction Data, Swarthmore, PA) Card: 35-0816 (1986).
5. V. M. Goldschmidt, *Trans. Faraday Soc.* **25**, 253 (1929).
6. G. Burns and A. M. Glazer, "Space Groups for Solid State Scientists," Academic Press, New York, (1978).
7. D. C. Stockbarger, *J. Opt. Soc. Am.* **39**, 731 (1949).
8. J. A. Savage, "Infrared Optical Materials and their Antireflection Coatings," Adam Hilger, Bristol, (1988).
   C. W. King and O. H. Nestov, *SPIE Proceedings* **1047**, 80 (1989).
9. V. A. Sokolov, E. A. Simun, and A. N. Sinev, *Sov. J. Opt. Technol.* **46**, 279 (1979).
10. V. A. Sokolov, A. N. Sinev, I. B. Gusev, and V. I. Nikolaev, *Sov. J. Opt. Technol.* **51**, 530 (1984).
11. A. Horowitz, S. Biderman, G. Ben Amar, U. Laor, M. Weiss, and A. Stern, *J. Crystal Growth* **85**, 215 (1987).
12. L. S. Combes, S. S. Ballard, and K. A. McCarthy, *J. Opt. Soc. Am.* **41**, 215 (1951).
13. W. L. Wolfe and G. J. Zissis, "The Infrared Handbook," Environmental Research Institute of Michigan (1978).
14. G. W. Fynn and W. J. A. Powell, "The Cutting and Polishing of Electro-Optic Materials," Adam Hilger Ltd., Bristol, England, (1979).
15. R. C. Gore, R. S. McDonald, V. Z. Williams, and J. U. White, *J. Opt. Soc. Am.* **37**, 23 (1947).
16. E. K. Plyler, *Phys. Rev.* **72**, 165 (1947).
17. Y. Yamada, A. Mitsuishi, and H. Yoshinaga, *J. Opt. Soc. Am.* **52**, 17 (1962).
18. G. M. Ressler and K. D. Möller, *Appl. Opt.* **5**, 877 (1966).
19. M. Buback, E. U. Franck, and H. Lendle, *Z. Naturforsch.* **34a**, 1489 (1979).
20. D. Funnemann and H. Merz, *J. Phys. E: Sci. Instrum.* **19**, 554 (1986).
21. R. C. Estler, J. E. Anderson, E. C. Apel, and N. S. Nogar, *J. Vac. Sci. Technol.* **B5**, 1519 (1987).
22. S. D. Allen, J. O. Porteus, W. N. Faith, and J. B. Franck, *Appl. Phys. Lett.* **45**, 997 (1984).
23. J. Bannon, *Nature* **157**, 446 (1946).
24. R. S. Feigelson, W. L. Kway, and R. K. Route, *Opt. Eng.* **24**, 1102 (1985).
25. H. Marxer, B. Derighetti, and E. Brun, *Phys. Rev. Lett.* **50**, 958 (1983).
26. N. I. Medvedeva, V. A. Gubanov, A. I. Likhtenshtein, A. F. Golota, M. Y. Khodos, and F. I. Kosintsev, *J. Struct. Chem.* **25**, 649 (1984).
27. S. Muramatsu and C. Sugiura, *Phys. Rev. B.* **26**, 3092 (1982).
28. W. Hayes, A. B. Kunz, and E. E. Koch, *J. Phys. C* **4**, L 200 (1971).
29. G. W. Rubloff, *Phys. Rev. B.* **5**, 662 (1972).
30. W. Bontinck, *Physica* **24**, 650 (1958).
31. H. Bruch, P. Görlich, H. Karras, and R. Lehmann, *Phys. Stat. Solidi* **4**, 685 (1964).
32. W. Bontinck, *Physica* **24**, 639 (1958).
33. R. Rauch, R. Reimann, and G. Schwotzer, *Phys. Stat. Solidi (a)* **23**, 69 (1974).
34. F. Abba, Y. Marqueton, and E. A. Decamps, *Phys. Stat. Solidi* **35**, K129 (1969).
35. A. De and K. V. Rao, *Phys. Stat. Solidi (a)* **105**, 297 (1988).
36. W. M. Powell, *Phys. Rev.* **45**, 154 (1934).
37. T. Tomiki and T. Miyata, *J. Phys. Soc. Jap.* **27**, 658 (1969).
38. A. R. Knudson and J. E. Kupperian, *J. Opt. Soc. Am.* **47**, 440 (1957).
39. A. H. Laufer, J. A. Pirog, and J. R. McNesby, *J. Opt. Soc. Am.* **55**, 64 (1965).
40. A. Gilles and B. Vodar, *J. Opt. Soc. Am.* **42**, 783 (1952).
41. R. Tousey, *Phys. Rev.* **50**, 1057 (1936).

42. I. H. Malitson, *Appl. Opt.* **2**, 1103 (1963).
43. H. G. Lipson, Y. F. Tsay, B. Bendow, and P. A. Ligor, *Appl. Opt.* **15**, 2352 (1976).
44. T. Radhakrishnan, *Proc. Ind. Acad. Sci.* **A33**, 22 (1951).
45. Y. F. Tsay, B. Bendow, and S. S. Mitra, *Phys. Rev.* **B8**, 2688 (1973).
46. G. N. Vasil'chenko, I. E. Veneraki, A. M. Mikhal'chuk, and V. A. Sokolov, *Sov. J. Opt. Technol.* **49**, 226 (1982).
47. T. F. Deutsch, *J. Phys. Chem. Solids* **34**, 2091 (1973).
48. K. A. Wickersheim and B. M. Hanking, *Physica* **25**, 569 (1959).
49. M. Sparks and L. J. Sham, *Solid State Commun.* **11**, 1451 (1972).
50. K. V. Namjoshi, S. S. Mitra, B. Bendow, J. A. Harrington, and D. L. Stierwalt, *Appl. Phys. Lett.* **26**, 41 (1975).
51. W. Kaiser, W. G. Spitzer, R. H. Kaiser, and L. E. Howarth, *Phys. Rev.* **127**, 1950 (1962).
52. L. V. Berman and A. G. Zhukov, *Opt. Spectrosc.* **19**, 433 (1965).
53. D. R. Bosomworth, *Phys. Rev.* **157**, 709 (1967).
54. P. Denham, G. R. Field, P. L. R. Morse, and G. R. Wilkinson, *Proc. Roy. Soc. London A* **317**, 55 (1970).
55. H. Happ, H. W. Hofmann, E. Lux, and G. Seger, *Z. Physik* **166**, 510 (1962).
56. R. Loudon, *Advances in Physics* **13** (B. R. Coles ed.), 423 (1964).
57. J. T. Houghton and S. D. Smith, "Infra-red Physics," Oxford University Press, London, (1966).
58. W. Hayes and A. M. Stoneham, in "Crystals with the Fluorite Structure," (W. Hayes, ed.), Oxford University Press, London, (1974).
59. D. G. Mead and G. R. Wilkinson, *J. Phys. C: Solid State Phys.* **10**, 1963 (1977).
60. D. M. Adams and D. C. Newton, "Tables for Factor Group and Point Group Analysis," Beckman-RIII Ltd, Croydon, (1970).
61. W. G. Fateley, F. R. Dollish, N. T. McDevitt, and F. F. Bentley, "Infrared and Raman Selection Rules for Molecular and Lattice Vibrations: The Correlation Method," John Wiley, New York, (1972).
62. D. H. Martin, Advances in Physics, **14** (B. R. Coles, ed.), 39 (1965).
63. W. Zernik, *Rev. Mod. Phys.* **39**, 432 (1967).
64. A. R. Gee, D. C. O'Shea, and H. Z. Cummins, *Solid State Comm.* **4**, 43 (1965).
65. R. Srivastava, H. V. Lauer, Jr., L. L. Chase, and W. E. Bron, *Phys. Lett.* **36A**, 333 (1971).
66. Y. Q. Sheng, E. Rechnagel, A. Weidinger, Z. G. Gu, Z. Y. Lai, and Z. G. Zhurang, *Phys. Stat. Sol. (b)* **145**, 151 (1988).
67. I. Laidler and D. C. Emmony, *NBS Special Publication* **746**, 182 (1985).
68. R. H. Anderson, R. A. Skogman, J. F. Ready, and J. M. Bennett, *NBS Special Publication* **541**, 70 (1978).
69. A. K. Hopkins, R. H. Anderson, J. F. Ready, J. M. Bennett, P. C. Archibald, and D. K. Burge, *NBS Special Publication* **568**, 47 (1979).
70. C. B. Willingham, M. A. Spears, G. A. Graves, and W. L. Knecht, *NBS Special Publication* **688**, 101 (1983).
71. M. J. Dodge, *NBS Special Publication* **462**, 64 (1976).
72. A. Hordvik, B. Bendow, H. G. Lipson, L. H. Skolnik, and R. N. Brown, *NBS Special Publication* **462**, 50 (1976).
73. N. C. Fernelius, D. V. Dempsey, and D. B. O'Quinn, *NBS Special Publication* **620**, 58 (1980).
74. J. A. Harrington, D. A. Gregory, and W. F. Otto, *Appl. Opt.* **15**, 1953 (1976).
75. R. Braunstein, R. K. Kim, and M. Braunstein, *NBS Special Publication* **620**, 29 (1980).
76. D. J. Gallant, M. Law, and B. Pond, *NBS Special Publication* **752**, 159 (1986).
77. M. Law, J. Bender, and C. K. Carniglia, *NBS Special Publication* **752**, 532 (1986).

78. M. C. Staggs, D. Milam, I. M. Thomas, and J. G. Wilder, *NBS Special Publication* **746**, 404 (1985).
79. I. Laidler and D. C. Emmony, *NBS Special Publication* **752**, 151 (1986).
80. M. Bass, K. M. Leung, C. Tang, and M. J. Soileau, *NBS Special Publication* **462**, 136 (1976).
81. J. Bannon and C. E. Curnow, *Nature* **161**, 136 (1948).
82. J. Bannon and C. K. Coogan, *Nature* **163**, 62 (1949).
83. A. E. Ennos, *Appl. Opt.* **5**, 51 (1966).
84. M. L. Scott, *NBS Special Publication* **688**, 329 (1983).
85. P. Bousquet, *Compt. Rend.* **238**, 1485 (1954).
86. O. S. Heavens and S. D. Smith, *J. Opt. Soc. Am.* **47**, 469 (1957).
87. T. W. Walker, A. H. Guenther, C. G. Fray, and P. Nielson, *NBS Special Publication* **568**, 405 (1979).
88. G. Stephan, J. C. Lemonnier, Y. Le Calvez and S. Robin, *Compt. Rend.* **262** *Serie B*, 1272 (1966).
89. Landolt-Börnstein, "Physikalisch-Chemische Tabellen," (W. A. Roth and K. Scheel, eds.), Edwards Brothers, Inc., Berlin, 911 (1923).
90. F. F. Martens, *Ann. Phys.* **6**, 603 (1901).
91. J. C. Lemonnier, G. Stéphan, and S. Robin, *Compt. Rend.* **261**, 2463 (1965).

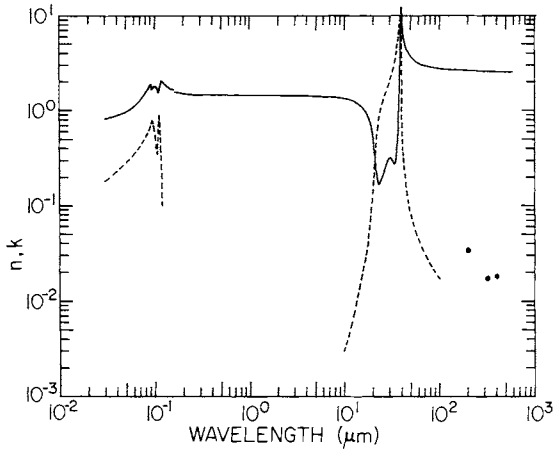

Fig. 1. Log–log plot of n (solid line) and k (dashed line) versus wavelength in micrometers for calcium fluoride.

TABLE I

Constants of the Dispersion Equation Used by Malitson [42]

$\lambda_1 = 0.050263605$	$A_1 = 0.5675888$
$\lambda_2 = 0.1003909$	$A_2 = 0.4710914$
$\lambda_3 = 34.64904$	$A_3 = 3.8484723$

TABLE II

A List of Parameters Used to Calculate the Dispersion Values in Table IV from 1000 cm^{-1} to 100 cm^{-1} [51]

Parameter	Value
ν_1	257 cm^{-1}
γ_1	0.018
$4\pi\rho_1$	4.2
ν_2	328 cm^{-1}
γ_2	0.35
$4\pi\rho_2$	0.4
ε_∞	2.045

TABLE III

Constants for Dispersion Equations Used by Dodge at a temperature of 20.8 °C [71]

$\lambda_1 = 0.07218116$	$A_1 = 0.98584551$
$\lambda_2 = 0.14114719$	$A_2 = 0.05290246$
$\lambda_3 = 36.465937$	$A_3 = 4.2816899$

TABLE IV

Values of n and k for Calcium Fluoride obtained from various references[a]

eV	Å	n	k
41.3285	300	0.814 [91][b]	0.148 [91][b]
		0.82 [88]	0.18 [88]
30.9964	400	0.917 [91]	0.284 [91]
24.7971	500	1.108	0.433
20.6643	600	1.074	0.335
		1.08 [88]	0.34 [88]
17.7122	700	0.908 [91]	0.353 [91]
15.4982	800	1.169	0.753
13.7762	900	1.630	0.675
		1.85 [88]	0.65 [88]
13.3749	927	1.640 [41]	0.768 [41]
12.6775	978	1.780	0.650
12.2153	1,015	1.775	0.540
12.0844	1,026	1.742	0.517
11.9793	1,035	1.732	0.473
11.8420	1,047	1.725	0.395
11.6200	1,067	1.615	0.344
11.3748	1,090	1.533	0.600
11.2714	1,100	1.570	0.785
11.1098	1,116	1.775	0.830
10.8190	1,146	2.000	0.631
10.6700	1,162	2.027	0.490
10.5520	1,175	1.996	0.390
10.4190	1,190	1.983	0.290
10.3321	1,200	2.05 [88]	0.1 [88]
9.8872	1,254	1.888 [41]	
9.7167	1,276	1.855	
9.3013	1,333	1.803	
8.6522	1,433	1.711	
7.7250	1,605	1.607	
		1.5547 [89]	

TABLE IV (*Continued*)

Calcium Fluoride

eV	Å	n	k
7.6914	1,612	1.5509	
7.5371	1,645	1.5438	
7.4199	1,671	1.5385	
7.1876	1,725	1.5289	
7.0287	1,764	1.5227	
6.8161	1,819	1.5152	
6.7019	1,850	1.51024 [90]	
6.6659	1,860	1.50930	
6.4241	1,930	1.50150	
6.2937	1,970	1.49755	
6.2619	1,980	1.49643	
6.1993	2,000	1.49547	
6.0777	2,040	1.49190	
5.9609	2,080	1.48907	
5.8761	2,110	1.48705	
5.7937	2,140	1.48480	
5.6614	2,190	1.48167	

eV	cm^{-1}	μm	n	k
5.6357	45,455	0.22	1.48110 [42]	
5.1661	41,666	0.24	1.47120	
4.7687	38,462	0.26	1.46391	
4.4281	35,714	0.28	1.45836	
4.1329	33,333	0.30	1.45402	
3.8746	31,250	0.32	1.45056	
3.6466	29,412	0.34	1.44775	
3.4440	27,778	0.36	1.44548	
3.2628	26,316	0.38	1.44349	
3.0996	25,000	0.40	1.44185	
2.9520	23,810	0.42	1.44045	
2.8179	22,727	0.44	1.43924	
2.6953	21,739	0.46	1.43820	

TABLE IV (*Continued*)

Calcium Fluoride

eV	cm^{-1}	μm	n	k
2.5830	20,833	0.48	1.43728	
2.4797	20,000	0.50	1.43647	
2.3843	19,231	0.52	1.43575	
2.2960	18,519	0.54	1.43512	
2.2140	17,857	0.56	1.43454	
2.1377	17,241	0.58	1.43403	
2.0664	16,667	0.60	1.43356	
1.9998	16,129	0.62	1.43313	
1.9373	15,625	0.64	1.43275	
1.8786	15,152	0.66	1.43239	
1.8233	14,706	0.68	1.43206	
1.7712	14,286	0.70	1.43176	
1.7220	13,889	0.72	1.43148	
1.6755	13,514	0.74	1.43121	
1.6314	13,158	0.76	1.43097	
1.5896	12,821	0.78	1.43074	
1.5498	12,500	0.80	1.43052	
1.5120	12,195	0.82	1.43032	
1.4760	11,905	0.84	1.43013	
1.4417	11,628	0.86	1.42995	
1.4089	11,364	0.88	1.42977	
1.3776	11,111	0.90	1.42961	
1.3477	10,870	0.92	1.42945	
1.3190	10,638	0.94	1.42930	
1.2915	10,417	0.96	1.42915	
1.2652	10,204	0.98	1.42901	
1.2399	10,000	1.00	1.42888	
1.0332	8,333	1.20	1.42771	
0.8856	7,143	1.40	1.42672	
0.7749	6,250	1.60	1.42579	
0.6888	5,555	1.80	1.42484	
0.6199	5,000	2.00	1.42385	
0.5636	4,545	2.20	1.42280	

TABLE IV (*Continued*)

Calcium Fluoride

eV	cm^{-1}	μm	n	k
0.5166	4,167	2.40	1.42168	
0.4769	3,846	2.60	1.42049	
0.4428	3,571	2.80	1.41921	
0.4133	3,333	3.00	1.41785	
0.3875	3,125	3.20	1.41639	
0.3647	2,941	3.40	1.41484	
0.3444	2,778	3.60	1.41320	
0.3263	2,632	3.80	1.41147	
0.3100	2,500	4.00	1.40963	
0.2952	2,381	4.20	1.40770	
0.2818	2,273	4.40	1.40567	
0.2695	2,174	4.60	1.40354	
0.2583	2,083	4.80	1.40130	
0.2480	2,000	5.00	1.39895	
0.2384	1,923	5.20	1.39650	
0.2296	1,852	5.40	1.39394	
0.2234	1,800	5.55		3.5×10^{-8} [50]
0.2214	1,786	5.60	1.39127	
0.2138	1,724	5.80	1.38849	
0.2066	1,667	6.00	1.38559	
0.2000	1,613	6.20	1.38258	
0.1984	1,600	6.25		3.5×10^{-7}
0.1937	1,563	6.40	1.37945	
0.1879	1,515	6.60	1.37620	
0.1823	1,471	6.80	1.37282	
0.1771	1,429	7.00	1.36932	
0.1737	1,400	7.14		3.4×10^{-6}
0.1722	1,389	7.20	1.36569	
0.1676	1,351	7.40	1.36193	
0.1631	1,316	7.60	1.35804	
0.1590	1,282	7.80	1.35401	
0.1550	1,250	8.00	1.34983	
0.1512	1,220	8.20	1.34552	

TABLE IV (*Continued*)

Calcium Fluoride

eV	cm^{-1}	μm	n	k
0.1488	1,200	8.33		3.3×10^{-5}
0.1476	1,190	8.40	1.34106	
0.1442	1,163	8.60	1.33645	
0.1409	1,136	8.80	1.33169	
0.1378	1,111	9.00	1.32677	
0.1348	1,087	9.20	1.32168	
0.1319	1,064	9.40	1.31643	
0.1292	1,042	9.60	1.31101	
0.1265	1,020	9.80	1.30541	
0.1240	1,000	10.000	1.306 [51][c]	0.0029 [51][c]
0.1178	950	10.526	1.289	0.0035
0.1116	900	11.111	1.269	0.004
0.1054	850	11.765	1.247	0.005
0.0992	800	12.500	1.218	0.007
0.0930	750	13.333	1.181	0.009
0.0868	700	14.286	1.133	0.012
0.0806	650	15.385	1.067	0.017
0.0744	600	16.667	0.971	0.027
0.0713	575	17.391	0.906	0.035
0.0682	560	18.182	0.821	0.047
0.0651	525	19.048	0.707	0.068
0.0620	500	20.000	0.539	0.115
0.0589	475	21.053	0.291	0.280
0.0558	450	22.222	0.182	0.609
0.0527	425	23.529	0.174	0.902
0.0496	400	25.000	0.196	1.187
0.0465	375	26.667	0.241	1.488
0.0434	350	28.571	0.298	1.818
0.0403	325	30.769	0.317	2.235
0.0372	300	33.333	0.276	3.011
0.0360	290	34.483	0.280	3.565
0.0347	280	35.714	0.346	4.430
0.0335	270	37.037	0.639	6.071

TABLE IV (*Continued*)

Calcium Fluoride

eV	cm^{-1}	μm	n	k
0.0322	260	38.462	3.909	11.146
0.0320	258	38.760	8.093	12.137
0.0319	257	38.911	10.876	10.750
0.0317	256	39.063	12.342	8.010
0.0315	254	39.370	11.463	3.831
0.0312	252	39.683	9.864	2.115
0.0310	250	40.000	8.673	1.352
0.0298	240	41.667	5.927	0.389
0.0285	230	43.478	4.867	0.206
0.0273	220	45.455	4.283	0.136
0.0260	210	47.619	3.907	0.100
0.0248	200	50.000	3.641	0.079
0.0223	180	55.556	3.289	0.053
0.0198	160	62.500	3.066	0.039
0.0174	140	71.429	2.914	0.029
0.0149	120	83.333	2.805	0.022
0.0124	100	100.00	2.726	0.017
			2.729 [53][d]	
0.0062	50	200.00	2.610	
				0.034 [52]
0.0042	34.01	294.0	2.57 [52]	
0.0040	31.85	314.0	2.55	
0.0039	31.25	320.0		0.017
0.0037	29.41	340.0	2.55	
0.0034	27.62	362.0	2.49	
0.0031	25.32	395.0	2.47	
0.0031	25.00	400.0		0.018
0.0027	22.08	453.0	2.55	
0.0021	17.24	580.0	2.54	

[a] References are given in brackets.

[b] Values obtained from Fig. 5 [91].

[c] Values obtained using Eqs. (2) and (3).

[d] Values obtained using Eq. (4).

Amorphous Hydrogenated "Diamondlike" Carbon Films and Arc-Evaporated Carbon Films

SAMUEL A. ALTEROVITZ
Space Electronics Division
NASA Lewis Research Center
Cleveland, Ohio

N. SAVVIDES
CSIRO Division of Applied Physics
National Measurements Laboratory
Sydney, Australia

F. W. SMITH
Department of Physics
City College of CUNY
New York, New York
and
JOHN A. WOOLLAM
Center for Microelectronic and Optical Materials Research
and Department of Electrical Engineering
University of Nebraska
Lincoln, Nebraska

There is considerable nomenclature confusion concerning these films, which various authors have attempted to rectify. Although there is no general consensus on terminology, they are often referred to as "a-C : H" or "diamondlike" carbon or "DLC." Here we will use the terms a-C : H and DLC interchangeably. Unfortunately, they are also being confused recently with diamond films. Amorphous hydrogenated carbon (a-C : H) has 20–55 percent hydrogen, and an optical band gap (determined from Tauc plots) between 0.5 and 3.0 eV. Diamond films nominally contain no hydrogen, are polycrystalline, and form only at high temperatures. a-C : H films are typically formed by plasma or ion-beam deposition (using hydrocarbon gas) onto substrates maintained at room temperature or slightly

Copyright © 1991 by Academic Press.
All rights of reproduction in any form reserved.
ISBN 0-12-544422-2

above room temperature. There are other preparation techniques as well [1–30]. There is considerable general literature on these films, including reviews [1, 2, 5, 6, 10, 17, 26, 27]. a-C : H (DLC) films graphitize above a few hundred degrees Celcius [31].

The properties of DLC, including optical constants, depend strongly on preparation conditions. Thus, the user can prepare samples with an optical gap anywhere in the 0.5–3.0 eV range, but most easily in the 1–2 eV range. Associated with this is the control of index of refraction from approximately 1.7 to 2.2, and a related extinction-coefficient dependence.

DLC is generally transparent for wavelengths greater than mid-visible. In the infrared there are resonant hydrogen absorptions in several spectral ranges, but with minimal absorption in other ranges [1–2].

Readers should carefully compare their preparation techniques and conditions before using data from the literature or from the table displayed in this critique. We have included the dependence of optical constants on substrate and/or annealing temperature, since this is a commonly varied parameter, which results in large property changes.

We have chosen to present the optical data of plasma-deposited DLC in tabular form, as well as the constants of a fit to the experimental data according to the theory given by Forouhi and Bloomer [24, 32]. Table I gives the constants in the following equations for index of refraction n and extinction coefficient k:

$$n(E) = n(\infty) + [B_0 E + C_0]/[E^2 - BE + C] \tag{1}$$

$$k(E) = A(E - E_g)^2/(E^2 - BE + C), \tag{2}$$

where E is photon energy, and E_g is the optical band gap, both in eV. Also,

$$B_0 = (A/Q)[-B^2/2 + E_g B - E_g^2 + C], \tag{3}$$

$$C_0 = (A/Q)[(E_g^2 + C)B/2 - 2E_g C], \tag{4}$$

and

$$Q = \tfrac{1}{2}(4C - B^2)^{1/2}. \tag{5}$$

The values of the constants in Table I are given for films prepared by

30 kHz plasma deposition from CH_4 on silicon substrates held at room temperature using powers of 50–200 W with subsequent annealing at 400, 600, and 750°C [24]. In all depositions the flowing CH_4 pressure was held at 315 m torr. Data were taken over the range 1.5–4.1 eV. Extensions of Eqs. 1 and 2 beyond this range should be done cautiously.

Table II gives the measured data for selected samples described above, but in tabular form. Fig. 1 is a plot of n and k. These data were taken by variable-angle spectroscopic ellipsometry (VASE) (for which no Kramers–Kronig analysis is required), assuming a model of a single film on a substrate. These results are highly reliable with the exception of very low values of k; it is difficult to measure k accurately by ellipsometry for values less than about 0.02.

Infrared optical-constant data for samples prepared in the same deposition system for data given in Tables I and II are given in Table III [6, 28].

For completeness, we also include optical constants of a-C:H in the 1.5–4.75 eV spectral range prepared in a dc glow discharge from C_2H_2 deposited on quartz held at 250°C with anneal at 350°C, as well as with no further anneal [3]. These are shown in Table IV. Fig. 2 is a plot of n and k. In the original reference the reader can find data for samples annealed to even higher temperatures [3]. These are not repeated here, due to the expected partial graphitic transformaton of the DLC films at higher than about 400°C [31].

In addition to data presented above on plasma-deposited films, we present data in Tables V and VI on diamondlike films made by a low-energy, ion-assisted deposition (IAD) technique based on unbalanced dc magnetron sputtering. Fig. 3 is a plot of n and k from Table VI. Details of the preparation technique are given in Refs. [5, 33–35]. The optical properties of these films are sensitive to both the ion energy per deposited carbon atom, and (as for all diamondlike carbon) the hydrogen content. These films were deposited at 300 K onto quartz substrates, and the optical constants were determined from transmittance and near-normal reflectance measurements in the photon energy range 0.5–7.3 eV. Measurements were made at room temperature (295 K). The relative measurement accuracy is about 1% except at the UV extreme (>6.5 eV) where it is a bit worse. Table V gives preparation parameters for nine different samples, but detailed data are given only for sample numbers 1, 5, and 9. These three were selected because they represent a range of hydrogen concentration and therefore a range of optical properties. Notice the trend toward increasing optical band gap with increasing hydrogen content C_H. The original references [5, 33–35] can be consulted for information on the remaining samples.

Finally, we present in Table VII the optical constants of arc-evaporated carbon films [36, 37]. These are amorphous and nominally contain no hydrogen; these are *not* called "a-C:H," "DLC," or "diamondlike"

carbon. The reader can see from the table that these films are very different from DLC, for example, in the lack of an optical absorption edge.

REFERENCES

1. J. C. Angus, P. Koidl, and S. Domitz, in "Plasma Deposited Thin Films," (J. Mort and F. Jansen, eds.), CRC Press, Cleveland (1986).
2. A. Bubenzer, B. Dischler, G. Brandt, and P. Koidl, *J. Appl. Phys.* **54**, 4590 (1983).
3. F. W. Smith, *J. Appl. Phys.* **55**, 764 (1984).
4. J. Fink, T. Muller-Heinzerling, J. Pfluger, B. Scheerer, B. Dischler, P. Koidl, A. Bubenzer, and R. E. Sah, *Phys. Rev.* **B30**, 4713 (1985).
5. N. Savvides, in "Properties and Characterization of Amorphous Carbon Films", (J. J. Pouch and S. A. Alterovitz, eds.), Materials Science Forum **52**, **53**, Trans Tech Publications, Zurich, Switzerland, 407 (1990).
6. J. A. Woollam, B. N. De, S. Orzeszko, N. J. Ianno, P. G. Snyder, S. A. Alterovitz, J. J. Pouch, R. L. C. Wu, and D. C. Ingram in "Properties and Characterization of Amorphous Carbon Films," (J. J. Pouch and S. A. Alterovitz, eds.), Materials Science Forum **52**, **53**, Trans Tech Publications, Zurich, Switzerland, 577 (1990).
7. B. Dischler, A. Bubenzer, and P. Koidl, *Appl. Phys. Letters* **42**, 636 (1983).
8. P. Coderc and Y. Catherine, *Thin Solid Films* **146**, 93 (1987).
9. B. Dischler, A. Bubenzer, and P. Koidl, *Solid State Commun.* **48**, 105 (1983).
10. P. Koidl, C. Wild, B. Dischler, J. Wagner, and M. Ramsteiner, in "Properties and Characterization of Amorphous Carbon Films," (J. J. Pouch and S. A. Alterovitz, eds.), Materials Science Forum **52**, **53**, Trans Tech Publications, Zurich, Switzerland, 41 (1990).
11. J. Wagner and P. Lautenschlager, *J. Appl. Phys.* **56**, 2044 (1986).
12. K. Mui, D. K. Basa, F. W. Smith, and R. Corderman, Phys. Rev. **B35**, 8089 (1987).
13. R. T. Moravec and J. C. Lee, *J. Vac. Sci. Technol.* **20**, 338, (1982).
14. D. A. Anderson, *Phil. Mag.* **35**, 17 (1977).
15. K. Fujii, N. Shohata, M. Mikami, and M. Yonezawa, *Appl. Phys. Lett.* **47**, 370 (1985).
16. V. Natarajan, J. D. Lamb, J. A. Woollam, D. C. Liu, and D. Gulino, *J. Vac. Sci. Technol.* **A3**, 681 (1985).
17. J. A. Woollam, G. H. Bu-Abbud, J. Oh, P. G. Snyder, J. D. Lamb, D. C. Ingram, and A. K. Rai, "Proc. of Symp. on Dielectric Films on Compound Semiconductors," (V. K. Kapoor, D. J. Connolly and Y. H. Wong, eds.), Electrochemical Society, Pennington, N.J., 289 (1986).
18. A. A. Khan, D. Mathine, J. A. Woollam, and Y. Chung, *Phys. Rev.* **B28**, 7229 (1983).
19. S. A. Alterovitz, J. D. Warner, D. C. Liu, J. J. Pouch, *J. Electrochem. Soc.* **133**, 2339 (1986).
20. E. Staryga, A. Lipinski, S. Mitura, and Z. Has, *Thin Solid Films* **145**, 17 (1986).
21. S. Lin and S. Chen, *J. Mater. Res.* **2**, 645 (1982).
22. S. Orzeszko, B. N. De, P. G. Snyder, J. A. Woollam, J. J. Pouch, and S. A. Alterovitz, *J. Chimie Physiq.* **84**, 1469 (1987).
23. S. A. Alterovitz, J. J. Pouch, J. D. Warner, *MRS Symp. Proc.* **92**, 311 (1987).
24. S. A. Alterovitz, R. M. Sieg, W. S. Shoemaker, and J. J. Pouch, *MRS Symp. Proc.* **152**, 21 (1989).
25. R. W. Collins, *Appl. Phys. Lett.* **52**, 2025 (1988).
26. R. W. Collins, in "Properties and Characterization of Amorphous Carbon Films," (J. J. Pouch and S. A. Alterovitz, eds.), Materials Science Forum **52**, **53**, Trans Tech Publications, Zurich, Switzerland, 341 (1990).
27. H. C. Tsai and B. D. Bogy, *J. Vac. Sci. Tech.* **A5**, 3287 (1988).
28. J. A. Woollam, B. N. De, L. Y. Chen, J. J. Pouch, S. A. Alterovitz, *Mat. Res. Soc. Symp. Proc.* **152**, 27 (1989).

29. B. N. De, S. Orzeszko, J. A. Woollam, D. C. Ingram, and A. J. McCormick, *Proc SPIE* **969**, 60 (1988).
30. J. A. Woollam, H. Chang, and V. Natarajan, *Appl. Phys. Commun.* **5**, 263 (1985).
31. R. O. Dillon, J. A. Woollam, and V. Katkanant, *Phys. Rev.* **B57**, 3482 (1984).
32. A. R. Forouhi and I. Bloomer, *Phys. Rev.* **B34**, 7018 (1986).
33. N. Savvides, in "Amorphous Hydrogenated Carbon Films," (P. Koidl and P. Oelhafen, eds.), Les Editions de Physique, Paris, 275 (1987); *E-MRS Symposia Proceedings* **XVII**.
34. N. Savvides, *J. Appl. Phys.* **59**, 4133 (1986).
35. N. Savvides, *Thin Solid Films* **163**, 13 (1988).
36. E. T. Arakawa, M. W. Williams, and T. Inagaki, *J. Appl. Phys.* **48**, 3176 (1977).
37. E. T. Arakawa, S. M. Dolfini, J. C. Ashley, and M. W. Williams, *Phys. Rev.* **B31**, 8097 (1985).

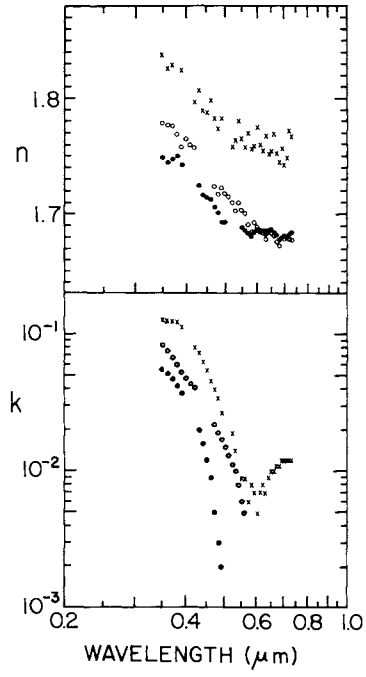

Fig. 1. Plot of n and k versus wavelength in micrometers for a-C:H. Experimental values are listed in Tables IIa (○), IIb (●), and IIc (x).

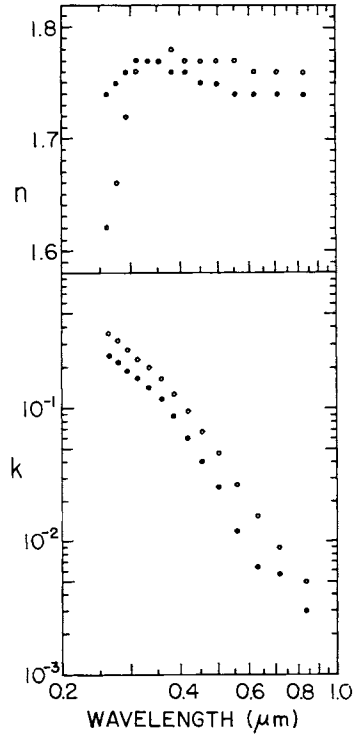

Fig. 2. Plot of n and k versus wavelength in micrometers for a-C : H. Experimental values are listed in Tables IVa (●), and IVb (○).

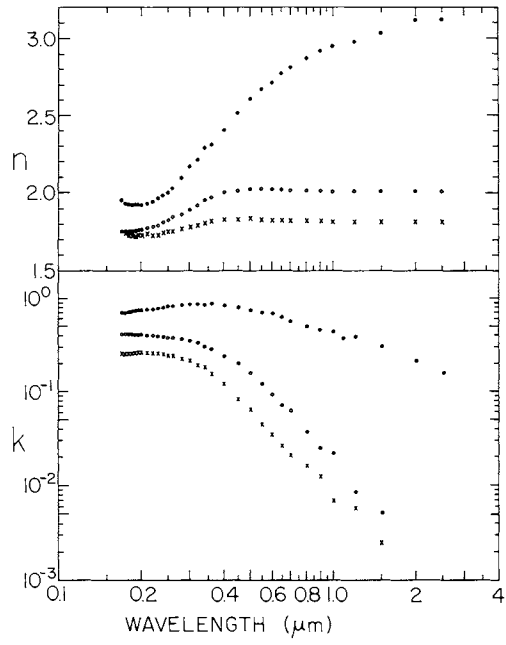

Fig. 3. Plot of n and k versus wavelength in micrometers for a-C:H. Experimental values are listed in Tables VIa (●), VIb (○), and VIc (x).

TABLE I

Dispersion-Relation Parameters for a-C:H Films (Eqs. 1–5) Prepared by Plasma Deposition on Silicon Wafer Substrates [24, 32]. T is the Annealing Temperature

P(W)	T(C)	A	B (eV)	C (eV^2)	E_g (eV)	$n(\infty)$
50	<25	.06	6.39	12.67	1.64	1.63
100	<25	.01	6.46	10.51	2.70	1.7
150	<25	.05	5.90	9.75	2.23	1.67
200	<25	.11	5.99	11.73	1.65	1.69
150	400	.06	5.10	7.20	1.90	1.70
150	600	.40	3.66	4.22	1.03	1.58
150	750	.85	1.21	1.85	0.39	1.71

TABLE IIa

Experimental Values of *n* and *k* for a-C:H. Deposition Conditions Are 50 W Plasma Power, Room Temperature Substrate, No Post-Deposition Anneal [24]

eV	cm^{-1}	μm	n	k
3.543	28,571	0.350	1.779	0.084
3.444	27,778	0.360	1.777	0.076
3.351	27,027	0.370	1.776	0.068
3.263	26,318	0.380	1.769	0.060
3.179	25,641	0.390	1.758	0.053
3.100	25,000	0.400	1.765	0.048
3.024	24,390	0.410	1.760	0.044
2.952	23,809	0.420	1.758	0.041
2.638	21,277	0.470	1.724	0.022
2.583	20,833	0.480	1.717	0.019
2.531	20,408	0.490	1.723	0.017
2.480	20,000	0.500	1.718	0.015
2.431	19,600	0.510	1.715	0.013
2.385	19,230	0.520	1.710	0.011
2.340	18,868	0.530	1.703	0.010
2.296	18,518	0.540	1.710	0.008
2.255	18,182	0.550	1.704	0.006
2.214	17,859	0.560	1.701	0.005
2.175	17,543	0.570	1.691	
2.138	17,244	0.580	1.685	
2.102	16,949	0.590	1.693	
2.067	16,667	0.600	1.689	
2.033	16,393	0.610	1.687	
2.000	16,129	0.620	1.684	
1.968	15,873	0.630	1.678	
1.938	15,625	0.640	1.686	
1.908	15,385	0.650	1.683	
1.879	15,151	0.660	1.681	
1.851	14,925	0.670	1.676	
1.824	14,706	0.680	1.672	
1.797	14,493	0.690	1.680	
1.771	14,285	0.700	1.678	
1.746	14,085	0.710	1.678	
1.722	13,889	0.720	1.678	
1.699	13,119	0.730	1.677	

TABLE IIb

Experimental Values of *n* and *k* for a-C:H. Deposition Conditions Are 150 W Plasma Power, Room Temperature Substrate, No Post-Deposition Anneal, [24]

eV	cm-1	μm	n	k
3.543	28,571	0.350	1.749	0.056
3.444	27,778	0.360	1.745	0.052
3.351	27,027	0.370	1.748	0.047
3.263	26,318	0.380	1.750	0.042
3.179	25,641	0.390	1.743	0.037
2.884	23,256	0.430	1.725	0.020
2.818	22,729	0.440	1.717	0.016
2.756	22,228	0.450	1.715	0.012
2.696	21,738	0.460	1.713	0.009
2.638	21,270	0.470	1.706	0.005
2.583	20,833	0.480	1.701	0.003
2.531	20,408	0.490	1.693	0.002
2.480	20,000	0.500	1.693	
2.255	18,182	0.550	1.689	
2.214	17,857	0.560	1.686	
2.175	17,541	0.570	1.684	
2.138	17,241	0.580	1.681	
2.102	16,949	0.590	1.684	
2.067	16,667	0.600	1.687	
2.033	16,393	0.610	1.685	
2.000	16,129	0.620	1.686	
1.968	15,893	0.630	1.683	
1.938	15,625	0.640	1.685	
1.908	15,385	0.650	1.687	
1.879	15,158	0.660	1.684	
1.851	14,925	0.670	1.682	
1.824	14,706	0.680	1.678	
1.797	14,490	0.690	1.680	
1.771	14,285	0.700	1.682	
1.746	14,085	0.710	1.680	
1.722	13,889	0.720	1.683	
1.699	13,699	0.730	1.685	

TABLE IIc

Experimental Values of *n* and *k* for a-C:H. Deposition Conditions Are 150 W Plasma Power, 400°C Post-Deposition Anneal [24]

eV	cm^{-1}	μm	n	k
3.543	28,571	0.350	1.838	0.129
3.444	27,778	0.360	1.826	0.127
3.351	27,027	0.370	1.829	0.126
3.263	26,316	0.380	1.845	0.124
3.179	25,641	0.390	1.825	0.113
2.952	23,810	0.420	1.797	0.082
2.884	23,256	0.430	1.807	0.074
2.818	22,727	0.440	1.789	0.064
2.756	22,222	0.450	1.788	0.055
2.696	21,739	0.460	1.798	0.046
2.638	21,277	0.470	1.782	0.040
2.583	20,833	0.480	1.774	0.034
2.531	20,108	0.490	1.783	0.027
2.385	19,231	0.520	1.758	0.019
2.340	18,868	0.530	1.764	0.014
2.296	18,519	0.540	1.780	0.008
2.255	18,182	0.550	1.765	0.009
2.214	17,857	0.560	1.758	0.009
2.175	17,543	0.570	1.770	0.006
2.138	17,244	0.580	1.756	0.008
2.102	16,949	0.590	1.759	0.007
2.067	16,667	0.600	1.775	0.005
2.033	16,393	0.610	1.760	0.007
2.000	16,129	0.620	1.755	0.008
1.968	15,873	0.630	1.768	0.007
1.938	15,625	0.640	1.752	0.009
1.908	15,385	0.650	1.754	0.010
1.879	15,152	0.660	1.769	0.010
1.851	14,925	0.670	1.752	0.011
1.824	14,906	0.680	1.745	0.011
1.797	14,492	0.690	1.757	0.012
1.771	14,286	0.700	1.743	0.012
1.746	14,085	0.710	1.749	0.012
1.722	13,889	0.720	1.771	0.012
1.699	13,699	0.730	1.767	0.012

TABLE III

Experimental Values of *n* and *k* for a-C:H. Deposition Conditions Are 150 W Plasma Power, Room Temperature Substrate, No Post-Deposition Anneal [6, 28]

eV	cm^{-1}	μm	n	k
0.3100	2,500	4	1.65+0.05	0.01
0.1240	1,000	10	1.75+0.15	0.01

TABLE IVa

Experimental Values of *n* and *k* for a-C:H. Deposition Conditions Are dc Glow Discharge, Substrate at 250°C, No Post-Deposition Anneal [3]

eV	cm^{-1}	μm	n	k
4.75	38,311	0.2611	1.74	0.246
4.50	36,295	0.2755	1.75	0.220
4.25	34,298	0.2918	1.76	0.195
4.00	32,262	0.3100	1.77	0.168
3.75	30,245	0.3307	1.77	0.144
3.50	28,229	0.3543	1.77	0.119
3.25	26,213	0.3815	1.76	0.089
3.00	24,196	0.4133	1.76	0.061
2.75	22,180	0.4509	1.75	0.041
2.50	20,164	0.4960	1.75	0.026
2.25	18,147	0.5511	1.74	0.0120
2.00	16,131	0.6200	1.74	0.0065
1.75	14,115	0.7086	1.74	0.0057
1.50	12,098	0.8267	1.74	0.0030

TABLE IVb

Experimental Values of n and k for a-C:H. Deposition Conditions Are dc glow Discharge, Substrate at 250°C, 350°C Post-Deposition Anneal [3]

eV	cm^{-1}	μm	n	k
4.75	38,311	0.2611	1.62	0.360
4.50	36,295	0.2755	1.66	0.320
4.25	34,278	0.2918	1.72	0.273
4.00	32,262	0.3100	1.76	0.234
3.75	30,246	0.3307	1.77	0.203
3.50	28,229	0.3543	1.77	0.168
3.25	26,213	0.3815	1.78	0.129
3.00	24,196	0.4133	1.77	0.096
2.75	22,180	0.4509	1.77	0.068
2.50	20,164	0.4960	1.77	0.047
2.25	18,147	0.5511	1.77	0.027
2.00	16,131	0.6200	1.76	0.0155
1.75	14,115	0.7036	1.76	0.0090
1.50	12,098	0.8267	1.76	0.0050

TABLE V

Deposition Parameters. (P_H = Partial Pressure of Hydrogen Gas; E_i = Ion Energy; Ar+/C = Ion to Condensing Carbon Atom Arrival Rate Ratio; E_t/C = Ion Energy per C Atom; the Partial Pressure of Argon Gas Was 1 Pa; C_H Is the Hydrogen Concentration [33–35])

Specimen	Power (W)	P_H (Pa)	C_H (at.%)	E_i (eV)	Ar/C	E_t/C (eV)
1	500	0	0	13	2.2	29
2	50	0	0	14	2.9	41
3	10	0	0	16	3.7	59
4	500	0.1	4	13	2.2	29
5	50	0.1	12	16	2.9	46
6	10	0.1	18	18	3.7	67
7	500	0.5	13	14	2.2	31
8	50	0.5	20	18	2.9	52
9	10	0.5	25	20	3.7	74

TABLE VIa

Experimental *n* and *k* for Ion Assisted Deposited a-C:H Specimen No. 1 [33–35]

eV	cm^{-1}	μm	n	k
7.294	58,824	0.170	1.957	0.705
7.086	57,143	0.175	1.938	0.713
6.889	55,555	0.180	1.930	0.722
6.703	54,054	0.185	1.924	0.730
6.526	52,638	0.190	1.929	0.744
6.359	51,282	0.195	1.928	0.748
6.200	50,000	0.20	1.918	0.750
5.905	47,619	0.21	1.932	0.767
5.636	45,455	0.22	1.948	0.777
5.391	43,478	0.23	1.969	0.790
5.167	41,666	0.24	1.986	0.801
4.960	40,000	0.25	2.004	0.825
4.769	38,462	0.26	2.032	0.835
4.429	35,714	0.28	2.100	0.851
4.133	33,333	0.30	2.171	0.866
3.875	31,250	0.32	2.217	0.875
3.647	29,412	0.34	2.292	0.865
3.444	27,778	0.36	2.312	0.881
3.100	25,000	0.40	2.408	0.853
2.756	22,222	0.45	2.518	0.805
2.480	20,000	0.50	2.610	0.754
2.255	18,182	0.55	2.672	0.717
2.067	16,667	0.60	2.715	0.692
1.908	15,385	0.65	2.773	0.641
1.771	14,286	0.70	2.815	0.579
1.550	12,500	0.80	2.875	0.505
1.378	11,111	0.90	2.926	0.462
1.240	10,000	1.0	2.951	0.442
1.033	8,333	1.2	2.982	0.390
0.827	6,666	1.5	3.037	0.309
0.620	5,000	2.0	3.123	0.217
0.496	4,000	2.5	3.125	0.160

TABLE VIb

Experimental n and k for Ion-Assisted Deposited a-C:H Specimen No. 5 [33–35]

eV	cm^{-1}	μm	n	k
7.294	58,824	0.170	1.750	0.415
7.086	57,143	0.175	1.750	0.414
6.889	55,555	0.180	1.753	0.412
6.703	54,054	0.185	1.756	0.410
6.526	52,638	0.190	1.758	0.409
6.359	51,282	0.195	1.766	0.405
6.200	50,000	0.20	1.767	0.405
5.905	47,619	0.21	1.780	0.401
5.636	45,455	0.22	1.787	0.400
5.391	43,478	0.23	1.796	0.393
5.167	41,666	0.24	1.813	0.388
4.960	40,000	0.25	1.828	0.379
4.769	38,462	0.26	1.848	0.376
4.429	35,714	0.28	1.868	0.368
4.133	33,333	0.30	1.897	0.352
3.875	31,250	0.32	1.925	0.336
3.647	29,412	0.34	1.958	0.304
3.444	27,778	0.36	1.975	0.287
3.100	25,000	0.40	2.007	0.242
2.756	22,222	0.45	2.016	0.201
2.480	20,000	0.50	2.028	0.160
2.255	18,182	0.55	2.029	0.121
2.067	16,664	0.60	2.026	0.093
1.908	15,385	0.65	2.022	0.071
1.771	14,286	0.70	2.019	0.062
1.550	12,500	0.80	2.018	0.037
1.378	11,111	0.90	2.017	0.025
1.240	10,000	1.0	2.013	0.022
1.033	8,333	1.2	2.017	0.008
0.827	6,666	1.5	2.013	0.005
0.620	5,000	2.0	2.013	<0.001
0.496	4,000	2.5	2.013	

TABLE VIc

Experimental *n* and *k* for Ion-Assisted Deposited a-C:H Specimen No. 9 [33–35]

eV	cm^{-1}	μm	n	k
7.294	58,824	0.170	1.741	0.259
7.086	57,143	0.175	1.735	0.257
6.889	55,555	0.180	1.730	0.259
6.703	54,054	0.185	1.724	0.259
6.526	52,638	0.190	1.718	0.261
6.359	51,282	0.195	1.725	0.263
6.200	50,000	0.20	1.728	0.264
5.905	47,619	0.21	1.737	0.261
5.636	45,455	0.22	1.727	0.260
5.391	43,478	0.23	1.730	0.256
5.167	41,666	0.24	1.743	0.251
4.960	40,000	0.25	1.749	0.246
4.769	39,462	0.26	1.753	0.242
4.429	35,714	0.28	1.772	0.226
4.133	33,333	0.30	1.783	0.218
3.875	31,250	0.32	1.798	0.193
3.647	29,412	0.34	1.809	0.185
3.444	27,778	0.36	1.820	0.156
3.100	25,000	0.40	1.831	0.121
2.756	22,222	0.45	1.830	0.083
2.480	20,000	0.50	1.836	0.065
2.255	18,182	0.55	1.830	0.045
2.067	16,667	0.60	1.826	0.035
1.908	15,385	0.65	1.822	0.027
1.771	14,286	0.70	1.822	0.021
1.550	12,500	0.80	1.821	0.016
1.378	11,111	0.90	1.819	0.013
1.240	10,000	1.0	1.820	0.007
1.033	8,333	1.2	1.82	0.006
0.827	6,666	1.5	1.819	0.002
0.620	5,000	2.0	1.819	<0.001
0.496	4,000	2.5	1.818	

TABLE VII

Experimental Values of *n* and *k* for Arc-Evaporated Carbon. After Arakawa *et al.* [36, 37]

eV	cm^{-1}	μm	n	k
10.00	80,655	0.1240	1.66	0.795
9.00	72,589	0.1378	1.70	0.713
8.00	64,524	0.1550	1.71	0.656
7.00	56,458	0.1771	1.70	0.628
6.00	48,393	0.2066	1.70	0.646
5.00	40,327	0.2480	1.73	0.712
4.00	32,262	0.3100	1.84	0.808
3.8	30,649	0.3263	1.90	0.91
3.6	29,036	0.3444	1.94	0.92
3.4	27,423	0.3647	2.00	0.92
3.2	25,810	0.3884	2.06	0.91
3.0	24,196	0.4133	2.11	0.90
2.8	22,583	0.4428	2.17	0.89
2.6	20,970	0.4789	2.24	0.88
2.4	19,357	0.5166	2.30	0.87
2.2	17,744	0.5636	2.38	0.82
2.0	16,131	0.6199	2.43	0.75
1.8	14,518	0.6888	2.43	0.70
1.6	12,905	0.7749	2.33	0.71
1.4	11,292	0.8856	2.24	0.80
1.2	9,679	1.033	2.26	1.09
1.0	8,065	1.240	2.63	1.47
0.8	6,452	1.550	3.34	1.63
0.7	5,646	1.771	3.67	1.60
0.6	4,839	2.066	3.73	1.54

Cesium Iodide (CsI)

JOHN E. ELDRIDGE
Department of Physics
University of British Columbia
Vancouver, British Columbia, Canada

The room-temperature values of n and k tabulated here (Table I, Fig. 1) were obtained from the following works and references therein: in the millimeter region, an individual measurement of n at 2 mm (5 cm^{-1}) is from Dianov and Irisova [1]; both n and k at selected points in the submillimeter region, 300 GH_z (10 cm^{-1}), 500 GH_z (16.7 cm^{-1}) and 700 GH_z (23.3 cm^{-1}) are from Bystrov *et al.* [2]; values of k in the far-infrared region at 14–56 cm^{-1} and at 94–200 cm^{-1} are from Beairsto and Eldridge [3]; over the reststrahlen peak, from just below 60 cm^{-1} to 94 cm^{-1}, n and k are given by Vergnat *et al.* [4], and values of n are continued into the wings by the same authors [4, 5]; in the transparent region, which covers the infrared and the visible from 67 μm (149 cm^{-1}) to 0.25 μm (40,000 cm^{-1}), values of n are from Li [6], who relied mainly on the data of Rodney [7]; in the vacuum ultraviolet from 5 eV (0.25 μm) to 11.4 eV (0.11 μm) n and k values are from Said and Green [8]; in the low-energy X-ray region from 100 eV (124 Å) to 2000 eV (6.2 Å), *calculated* values of n and k are from Henke *et al.* [9].

Cesium iodide has the lowest-energy reststrahlen band of all the alkali halides and common diatomic optical-window crystals, with a room-temperature peak in extinction coefficient, k, near 63 cm^{-1} (159 μm, 7.8 meV. Apart from the structure in this strong and relatively broad resonance, there is, of course, no other intrinsic absorption until electronic transitions in the vacuum ultraviolet. For this reason it is a common window material in infrared spectroscopy, providing the largest range to low energies in the far-infrared region, (for example, a window of 3 mm thickness will transmit down to approximately 150 cm^{-1}). Although it is very soft, with some care it can be used with indium O-rings for low-temperature studies. Since the absorption in the wings falls off very rapidly, the intrinsic absorption in the infrared region is extremely low, offering promise for CsI, as a low-loss, light-guide material and as windows for high-intensity laser beams.

Copyright © 1991 by Academic Press.
All rights of reproduction in any form reserved.
ISBN 0-12-544422-2

The reststrahlen band is due to the only optically active vibration in the crystal, the doubly degenerate, transverse-optic (TO) mode with zero wave vector, which has a frequency inversely proportional to the reduced mass of Cs and I. The structure in the wings is due to the frequency-dependence of the damping of this TO mode. This damping, in turn, is due to the two- and higher-phonon processes by which the TO mode can relax when energy and momentum are conserved. Calculations of this damping for CsI, and the resulting absorption through the reststrahlen band, give good agreement with the experiment data [10, 3]. The most accurate method of measuring n and k in this region would be that of dispersive-reflection spectroscopy (also known as asymmetric Fourier-transform spectroscopy), which was used in the investigations of NaCl and KCl, as well as some of the semiconductors reported in *HOC I.* In such a method n and k are measured directly, without the need for a Kramers–Kronig analysis or a fit to several fictitious Lorentzian oscillators. No such experiment has, however, been performed so far for CsI. The peak values of n and k reported here have therefore been obtained from a Kramers–Kronig analysis of the power reflectivity [4], which necessarily misses much of the two-phonon structure in n, above the resonance where n is small.

Starting at the lowest energy, Dianov and Irisova [1] measured n at 2 mm (5 cm^{-1}) at 300 K and 77 K with a Michelson interferometer. The room-temperature value agrees with that measured at 300 GH_z (10^{-1}) by Bystrov *et al.* [2] using an "Epsilon backward-wave-tube submillimeter spectrometer." They also reported n and k values at 500 GH_z (16.7 cm^{-1}) and 700 GH_z (23.3 cm^{-1}). The k values agree with those obtained by Beairsto and Eldridge [3] from transmission measurements through single crystals in a Michelson interferometer. Samples ranged in thickness from 0.007 cm to 0.8 cm. They were cut with a wire saw and then polished using jeweller's rouge in ethylene glycol. After polishing, they were cleaned in acetone and then trichloroethylene. k was obtained from $\alpha/4\pi\bar{\nu}$, and α was extracted from the expression for the transmitted intensity, I, given by

$$I=\frac{I_0(1-R)^2(1+k^2/n^2)e^{-\alpha d}}{1-R^2e^{-2\alpha d}}. \tag{1}$$

Measured values of R were used. The term $(1+k^2/n^2)$ is negligible except when close to the resonance on the high-frequency side. These results show k to be fairly smooth below the resonance, but Love *et al.*'s accurate low-temperature measurements on KI crystals up to 10 cm long [11] show that two-phonon structure can be observed in these materials.

The thinnest crystal used in Ref. [3] did not transmit between 56 cm^{-1} and 94 cm^{-1}. The two models used in the reflectivity analysis [4, 5] give n

and k values that can differ by up to 50%. The Kramers–Kronig values [4] are tabulated, since they are more directly obtained, but these are supplemented with Lorentz-model values [5] in the wings. The accuracy in the wings is poor and, as has been mentioned, structure is missing above the resonance. The reflectivity measurements were performed on a 15° wedged single crystal, and the authors report a 3% reproducibility.

In the wide transparent region from 67 μm (150 cm^{-1}) to 0.25 μm (40,000 cm^{-1}), Li [6] has tabulated very accurate values of n. Starting with the 297 K data of Rodney [7], which Li reduced to 293 K, and using the infrared absorption peak at 161.29 μm (detailed earlier [4]), together with the seven known absorption peaks in the vacuum ultraviolet, Li fitted the following dispersion equation of the Sellmeier type,

$$n^2 = 1.27587 + \frac{0.68689\lambda^2}{\lambda^2-(0.130)^2} + \frac{0.26090\lambda^2}{\lambda^2-(0.147)^2} + \frac{0.06256\lambda^2}{\lambda^2-(0.163)^2} + \frac{0.06527\lambda^2}{\lambda^2-(0.177)^2} + \frac{0.14991\lambda^2}{\lambda^2-(0.185)^2} + \frac{0.51818\lambda^2}{\lambda^2-(0.206)^2} + \frac{0.01918\lambda^2}{\lambda^2-(0.218)^2} + \frac{3.38229\lambda^2}{(\lambda^2-161.29)^2}, \quad (2)$$

where λ is in μm. Values from Eq. 2 are tabulated, although to greater accuracy than warranted by the experiment for the purpose of smoothness and internal comparison. Rodney's measurements of minimum deviation were performed on a 25° prism sample, loaned by the Harshaw Chemical Company, in two temperature-controlled spectrometers. The precision of the index measurements was reduced by the small wedge angle, since 60° is closer to the optimum, and instrumental factors reduced the wavelength accuracy when broad reference bands were used. Only the third decimal place is meaningful between 67 μm (150 cm^{-1}) and 50 μm (200 cm^{-1}), and the fourth decimal place elsewhere. The estimated uncertainty decreases from 1×10^{-3} at the low-energy limit to 1×10^{-4} near the high-energy limit. As an example of this accuracy, comparison may be made with the results of Selvarajan *et al.* [12], who later performed similar measurements at 300 K and 80 K over the smaller range from 30 μm^{-1} (333 cm^{-1}) to 2 μm (5000 cm^{-1}). After correcting for the temperature difference, these results agree to within $2–3 \times 10^{-4}$ with those of Li, the former being consistently higher.

No measurements of k beyond 200 cm^{-1} have been found. Measurements of the absorption in the transparent region have, however, been performed

using laser calorimetry, but these have all measured impurity absorption. Plotnichenko *et al.* [13] measured the volume absorption coefficient at several laser wavelengths, yielding k values of 7.6×10^{-10}, 4.4×10^{-10}, and 7.6×10^{-10} at $10.6\,\mu$m ($943\,\text{cm}^{-1}$), $5.54\,\mu$m ($1805\,\text{cm}^{-1}$), and $1.06\,\mu$m ($9433\,\text{cm}^{-1}$), respectively. Even though very small, and claimed by the authors to be the lowest value at $10\,\mu$m of any infrared material, these values are still orders of magnitude higher than the calculated intrinsic k due to the combination of multiphonon absorption and Mandel'shtam–Brillouin scattering.

In the vacuum ultraviolet, n and k are given by Said and Green [8] at 300 K and 25 K between 5 eV ($40{,}330\,\text{cm}^{-1}$, $0.248\,\mu$) and 11.4 eV ($91950\,\text{cm}^{-1}$, $0.11\,\mu$m). These were obtained by a Kramers–Kronig analysis of the power reflectivity. In this region the principal features of the reflectivity spectrum are due to excitons and the lower interband transitions, since the direct band gap between the valence-band maximum and the conduction-band minimum is calculated to be about 6.4 eV. There are seven discernible broad features, as mentioned in Li's fit to Eq. 2, which sharpen considerably at 25 K, revealing further structure. After unsuccessful attempts to cleave the samples *in situ*, Said and Green mechanically polished them with fine alumina in mineral oil, thoroughly cleaned them in an ultrasonic bath to remove the aluminum, and kept them in high vacuum until required. Prior to insertion in the reflectometer, the samples were annealed for several hours at 400 K to remove any surface damage. Their results have been read from the graphs at 0.1 eV intervals and have been tabulated. They differ considerably from the results of Lamatsch *et al.* [14] between 2500 Å (5 eV) and 2000 Å (6.2 eV). Lamatsch *et al.*'s results were obtained by analyzing the transmission and reflection spectra of a thin film. Although the two features in this interval are similar to those in Ref. [8], n and k values disagree by more than a factor of two. Lamatsch *et al.* also noticed discrepancies in magnitude between the reflection spectrum obtained from a bulk sample and that calculated from their thin-film values of n and k. They attributed these discrepancies to the different effect that localized excitons have on the absorption spectra of films and bulk samples. Only the bulk-sample data from Ref. [8] have therefore been tabulated here.

Beyond 11.4 eV, no values of n and k have been found. Many studies of total absorption have been performed, usually through thin films, which yield spectra of the absorption coefficient μ either in arbitrary or in absolute units. Those performed before 1977 have been summarized by Haelbich *et al.* [15]. These spectra are very similar to the k spectra, as may be seen by comparing the work above in Ref. [8] at 25 K with the 10 K μ spectra of Teegarden and Baldini [16], so that the structure in k, if not the absolute magnitude, may be found. In particular, Saito *et al.* [17] give μ in arbitrary units at room temperature between 12 eV and 24 eV; Cardona *et*

al. [18] give absolute values of μ between 50 eV and 190 eV; Lukirskii and Zimkina [19] give μ in arbitrary units between 50 eV and 500 eV; and Sugiura and Kiyono [20] give μ in arbitrary units at the Cs and I X-ray L edges around 5 kV.

For several materials, good agreement has been found previously in the soft X-ray region between experimental values and those calculated using the atomic-scattering factors of Henke *et al.* [9] (see, for instance, Ni, Ag, Au, and SiO_2 in *HOC I*). We have therefore tabulated the calculated values of n and k for CsI between 100 eV and 2000 eV, which includes the M absorption edges. In scattering theory, the refractive index is given as

$$n = 1 - \delta - i\beta, \tag{3}$$

where

$$\delta = \frac{r_0 \lambda^2}{2\pi} N \bar{f}_1$$

$$\beta = \frac{r_0 \lambda^2}{2\pi} N \bar{f}_2. \tag{4}$$

Here, $r_0 = e^2/mc^2$, the classical electron radius, equal to 2.814×10^{-13} cm; N is the density of atoms per unit volume; and $\bar{f}_1$ and $\bar{f}_2$ are the sum of the scattering factors, which are listed in [9].

REFERENCES

1. E. M. Dianov and N. A. Irisova, *Sov. Phys.-Solid State* **8**, 1807 (1967).
2. V. P. Bystrov, Y. G. Goncharov, G. V. Kozlov, and A. F. Kupriyanenko, *Sov. Phys.-Tech. Phys.* **31**, 1206 (1986).
3. J. A. B. Beairsto and J. E. Eldridge, *Can. J. Phys.* **51**, 2550 (1973).
4. P. P. Vergnat, J. Claudel, A. Hadni, P. Strimer, and F. Vermillard, *J. de Phys.* **30**, 723 (1969) (data obtained from a Kramers–Kronig analysis).
5. Ibid. (data obtained from a Lorentz analysis).
6. H. H. Li, *J. Phys. Chem. Refer. Data* **5**, 329 (1976).
7. W. S. Rodney, *J. Opt. Soc. Am.* **45**, 987 (1955).
8. K. I. Said and G. W. Green, *J. Phys.* **C10**, 479 (1977).
9. B. L. Henke, P. Lee, T. J. Tanaka, R. L. Shimabukuro, and B. K. Fujikawa, in "Low Energy X-Ray Diagnostics—1981," (D. T. Attwood and B. L. Henke, eds.), AIP Conf. Proc. no. 75, American Institute of Physics, New York, 340 (1981).
10. J. E. Eldridge, R. Howard, and P. R. Staal, *Can. J. Phys.* **55**, 227 (1977).
11. S. P. Love, W. P. Ambrose, and A. J. Sievers, *Phys. Rev.* **B39**, 10352 (1989).
12. A. Selvarajan, J. L. Swedberg, A. G. DeBell, and W. L. Wolfe, *Appl. Opt.* **18**, 3116 (1979).

13. V. G. Plotnichenko, V. K. Sysoev, and I. G. Firsov, *Sov. J. Opt. Technol.* **50**, 563, (1983).
14. H. Lamatsch, J. Rossel, and E. Saurer, *Phys. Stat. Solidi (b)* **49**, 311 (1972).
15. R. P. Haelbich, M. Iwan, and E. E. Koch, "Physik Daten-Physics Data," Fach-information Zentrum, Karlsruhe, 152 (1977).
16. K. Teegarden and G. Baldini, *Phys. Rev.* **155**, 896 (1967).
17. H. Saito, S. Saito, R. Onaka, and B. Ikeo, *J. Phys. Soc. Japan* **24**, 1095 (1968).
18. M. Cardona, R. Haensel, D. W. Lynch, and B. Sonntag, *Phys. Rev.* **B2**, 1117 (1970).
19. A. P. Lukirskii and T. M. Zimkina, "Röntgenspektren und chemische Bindung," Karl-Marx-Univ., Leipzig, 187 (1966).
20. C. Sugiura and S. Kiyono, Technology Reports, Tohoku Univ. **35**, 119 (1970); Ibid. **35**, 61 (1970).

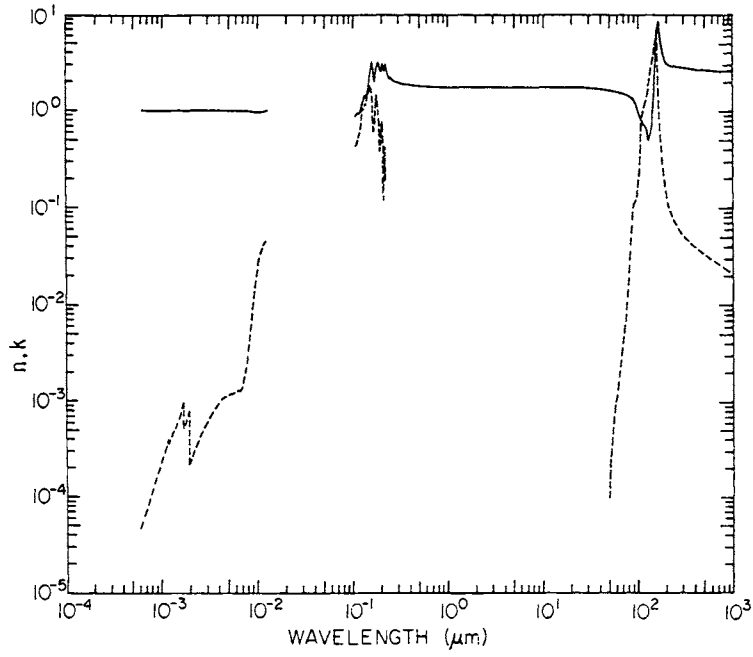

Fig. 1. Log–log plot of n (solid line) and k (dashed line) versus wavelength in micrometers for cesium iodide.

TABLE I

Values of n and k for Cesium Iodide from Various References[a]

eV	cm^{-1}	Å	n	k
2000		6.2	0.999822 [9]	4.71×10^{-5} [9]
1952		6.35	0.999814	5.11
1905		6.51	0.999804	5.55
1860		6.67	0.999795	6.02
1815		6.83	0.999786	6.52
1772		7.00	0.999776	7.07
1730		7.17	0.999765	7.67
1688		7.34	0.999755	8.29
1648		7.52	0.999744	8.98
1609		7.71	0.999732	9.74×10^{-5}
1570		7.90	0.999720	1.06×10^{-4}
1533		8.09	0.999709	1.14
1496		8.29	0.999696	1.24
1460		8.49	0.999683	1.34
1426		8.69	0.999671	1.45
1392		8.91	0.999657	1.57
1358		9.13	0.999643	1.70
1326		9.35	0.999630	1.83
1294		9.58	0.999616	1.98
1263		9.82	0.999602	2.15
1233		10.06	0.999589	2.32
1204		10.30	0.999576	2.49
1175		10.55	0.999563	2.68
1147		10.81	0.999551	2.89
1119		11.08	0.999540	3.12
1093		11.34	0.999530	3.35
1067		11.62	0.999527	3.61
1041		11.91	0.999533	3.90
1016		12.20	0.999527	3.69
992		12.50	0.999494	3.90
968		12.81	0.999473	4.22
945		13.12	0.999459	4.56
923		13.43	0.999455	4.86
901		13.76	0.999447	5.08
879		14.10	0.999434	5.32
858		14.45	0.999412	5.58
838		14.79	0.999390	6.00
818		15.16	0.999379	6.57
798		15.54	0.999389	7.20
779		15.92	0.999434	7.88
760		16.31	0.999525	8.65
742		16.71	0.999649	9.48
725		17.10	1.000202	5.23
707		17.54	0.999730	5.68
690		17.97	0.999633	6.15

(continued)

TABLE I (*Continued*)

Cesium Iodide

eV	cm^{-1}	Å	n	k
674		18.39	0.999605	6.64
658		18.84	0.999658	7.24
642		19.31	0.999781	7.91
627		19.77	1.000059	2.29
612		20.26	0.999702	2.43
597		20.77	0.999512	2.58
583		21.27	0.999403	2.74
569		21.79	0.999312	2.91
555		22.34	0.999230	3.09
542		22.87	0.999158	3.28
529		23.44	0.999082	3.47
516		24.03	0.999008	3.68
504		24.60	0.99894	3.88
492		25.20	0.99886	4.10
480		25.83	0.99879	4.33
469		26.4	0.99872	4.56
458		27.1	0.99863	4.83
447		27.7	0.99856	5.10
436		28.4	0.99848	5.37
426		29.1	0.99840	5.65
415		29.9	0.99831	5.97
406		30.5	0.99824	6.22
396		31.3	0.99814	6.56
386		32.1	0.99805	6.85
377		32.9	0.99795	7.15
368		33.7	0.99785	7.44
359		34.5	0.99775	7.72
351		35.3	0.99764	8.01
342		36.3	0.99751	8.36
334		37.1	0.99740	8.63
326		38.0	0.99728	8.92
318		39.0	0.99714	9.27
311		39.9	0.99701	9.55
303		40.9	0.99686	9.85×10^{-4}
296		41.9	0.99671	1.01×10^{-3}
289		42.9	0.99655	1.04
282		44.0	0.99637	1.07
275		45.1	0.99619	1.10
269		46.1	0.99602	1.11
262		47.3	0.99580	1.13
256		48.4	0.99559	1.14
250		49.6	0.99536	1.16
244		50.8	0.99510	1.17
238		52.1	0.99481	1.18
232		53.4	0.99451	1.19

(continued)

TABLE I (*Continued*)

Cesium Iodide

eV	cm^{-1}	Å	n	k
227		54.6	0.99421	1.19
221		56.1	0.99382	1.20
216		57.4	0.99347	1.21
211		58.8	0.99306	1.22
206		60.2	0.99262	1.23
201		61.7	0.99213	1.25
196		63.3	0.99158	1.28
191		64.9	0.99100	1.29
187		66.3	0.99041	1.28
182		68.1	0.9895	1.30
178		69.7	0.9888	1.40
174		71.3	0.9880	1.52
170		72.9	0.9871	1.68
166		74.7	0.9860	1.91
162		76.5	0.9848	2.20
158		78.5	0.9835	2.61
154		80.5	0.9820	3.17
150		82.7	0.9803	3.97
147		84.3	0.9790	4.71
143		86.7	0.9770	5.97
140		88.6	0.9752	7.37
136		91.2	0.9731	9.84×10^{-3}
133		93.2	0.9716	1.21×10^{-2}
130		95.4	0.9703	1.50
127		97.6	0.9696	1.81
124		100.0	0.9691	2.14
121		102.5	0.9691	2.50
118		105.1	0.9696	2.91
115		107.8	0.9714	3.34
112		110.7	0.9737	3.65
110		112.7	0.9755	3.84
107		115.9	0.9784	4.12
104		119.2	0.9818	4.36
102		121.5	0.9842	4.48
100		124.0	0.9869	4.62

(continued)

TABLE I (*Continued*)

Cesium Iodide

eV	cm^{-1}	μm	n	k
11.4	91950	0.1088		0.428 [8]
11.3	91140	0.1097	0.86 [8]	0.445
11.2	90330	0.1107	0.88	0.453
11.1	89530	0.1117	0.91	0.473
11.0	88720	0.1127	0.93	0.478
10.9	87910	0.1137	0.93	0.478
10.8	87110	0.1148	0.93	0.486
10.7	86300	0.1159	0.93	0.490
10.6	85490	0.1170	0.93	0.506
10.5	84690	0.1181	0.91	0.531
10.4	83880	0.1192	0.92	0.576
10.3	83070	0.1204	0.93	0.629
10.2	82270	0.1216	0.95	0.694
10.1	81460	0.1228	0.98	0.771
10.0	80650	0.1240	1.04	0.853
9.9	79850	0.1252	1.10	0.939
9.8	79040	0.1265	1.16	1.016
9.7	78240	0.1278	1.22	1.045
9.6	77430	0.1292	1.27	1.029
9.5	76620	0.1305	1.31	1.012
9.4	75820	0.1319	1.34	1.037
9.3	75010	0.1333	1.37	1.061
9.2	74200	0.1348	1.39	1.073
9.1	73400	0.1362	1.40	1.098
9.0	72590	0.1378	1.40	1.127
8.9	71780	0.1393	1.40	1.143
8.8	70980	0.1409	1.39	1.184
8.7	70170	0.1425	1.42	1.298
8.6	69360	0.1442	1.46	1.420
8.5	68560	0.1459	1.53	1.498
8.4	67750	0.1476	1.72	1.714
8.3	66940	0.1494	1.95	1.824
8.2	66140	0.1512	2.12	1.824
8.1	65330	0.1531	2.41	1.857
8.0	64520	0.1550	2.56	1.763
7.9	63720	0.1569	2.73	1.678
7.8	62910	0.1590	2.95	1.571
7.7	62100	0.1610	3.15	1.347
7.6	61300	0.1631	3.08	0.824
7.5	60490	0.1653	2.73	0.649
7.4	59680	0.1675	2.39	0.612
7.3	58880	0.1698	2.13	0.690
7.2	58070	0.1722	2.01	0.878
7.1	57260	0.1746	2.11	1.253
7.0	56460	0.1771	2.38	1.461

(continued)

TABLE I (*Continued*)

Cesium Iodide

eV	cm^{-1}	μm	n	k
6.9	55650	0.1797	2.81	1.376
6.8	54850	0.1823	2.84	1.139
6.7	54040	0.1851	3.05	1.102
6.6	53230	0.1879	3.18	0.922
6.5	52430	0.1907	2.96	0.514
6.4	51620	0.1937	2.79	0.371
6.3	50810	0.1968	2.66	0.404
6.2	50010	0.2000	2.55	0.424
6.1	49200	0.2033	2.53	0.543
6.0	48390	0.2066	2.86	0.784
5.9	47590	0.2101	3.05	0.490
5.8	46780	0.2138	2.81	0.118
5.7	45970	0.2175	2.59	0.208
5.6	45170	0.2214	2.99	0.408
5.5	44360	0.2254	2.97	0.196
5.4	43550	0.2296	2.76	
5.3	42750	0.2339	2.48	
5.2	41940	0.2384	2.33	
5.1	41130	0.2431	2.21	
5.0	40330	0.2480	2.14	
4.959	40000	0.250	2.20938 [6]	
4.920	39680	0.252	2.19248	
4.881	39370	0.254	2.17676	
4.843	39060	0.256	2.16208	
4.806	38760	0.258	2.14834	
4.769	38460	0.260	2.13545	
4.732	38170	0.262	2.12333	
4.696	37880	0.264	2.11190	
4.661	37590	0.266	2.10110	
4.626	37310	0.268	2.09089	
4.592	37040	0.270	2.08121	
4.558	36760	0.272	2.07202	
4.525	36500	0.274	2.06328	
4.492	36230	0.276	2.05496	
4.460	35970	0.278	2.04703	
4.428	35710	0.280	2.03946	
4.397	35460	0.282	2.03222	
4.366	35210	0.284	2.02530	
4.335	34970	0.286	2.01867	
4.305	34720	0.288	2.01232	
4.275	34480	0.290	2.00622	
4.246	34250	0.292	2.00037	
4.217	34010	0.294	1.99474	
4.189	33780	0.296	1.98932	
4.161	33560	0.298	1.98411	

(continued)

TABLE I (*Continued*)

Cesium Iodide

eV	cm^{-1}	μm	n	k
4.133	33330	0.300	1.97909	
4.065	32790	0.305	1.96731	
4.000	32260	0.310	1.95651	
3.936	31750	0.315	1.94658	
3.875	31250	0.320	1.93741	
3.815	30770	0.325	1.92893	
3.757	30300	0.330	1.92106	
3.701	29850	0.335	1.91373	
3.647	29410	0.340	1.90690	
3.594	28990	0.345	1.90051	
3.542	28570	0.350	1.89453	
3.493	28170	0.355	1.88891	
3.444	27780	0.360	1.88363	
3.397	27400	0.365	1.87866	
3.351	27030	0.370	1.87397	
3.306	26670	0.375	1.86954	
3.263	26320	0.380	1.86535	
3.220	25970	0.385	1.86138	
3.179	25640	0.390	1.85762	
3.139	25320	0.395	1.85404	
3.100	25000	0.40	1.85064	
3.024	24390	0.41	1.84433	
2.952	23810	0.42	1.83859	
2.883	23260	0.43	1.83336	
2.818	22730	0.44	1.82857	
2.755	22220	0.45	1.82417	
2.695	21740	0.46	1.82012	
2.638	21280	0.47	1.81637	
2.583	20830	0.48	1.81291	
2.530	20410	0.49	1.80970	
2.480	20000	0.50	1.80672	
2.431	19610	0.51	1.80393	
2.384	19230	0.52	1.80134	
2.339	18870	0.53	1.79891	
2.296	18520	0.54	1.79664	
2.254	18180	0.55	1.79451	
2.214	17860	0.56	1.79250	
2.175	17540	0.57	1.79062	
2.138	17240	0.58	1.78884	
2.101	16950	0.59	1.78717	
2.066	16670	0.60	1.78559	
2.000	16130	0.62	1.78268	
1.937	15630	0.64	1.78006	
1.879	15150	0.66	1.77770	
1.823	14710	0.68	1.77557	

(continued)

TABLE I (*Continued*)

Cesium Iodide

eV	cm^{-1}	μm	n	k
1.771	14290	0.70	1.77363	
1.722	13890	0.72	1.77186	
1.675	13510	0.74	1.77025	
1.631	13160	0.76	1.76877	
1.590	12820	0.78	1.76741	
1.550	12500	0.80	1.76615	
1.512	12200	0.82	1.76500	
1.476	11900	0.84	1.76392	
1.442	11630	0.86	1.76293	
1.409	11360	0.88	1.76201	
1.378	11110	0.90	1.76115	
1.348	10870	0.92	1.76035	
1.319	10640	0.94	1.75960	
1.292	10420	0.96	1.75890	
1.265	10200	0.98	1.75824	
1.240	10000	1.00	1.75736	
1.181	9524	1.05	1.75624	
1.127	9091	1.10	1.75505	
1.078	8696	1.15	1.75401	
1.033	8333	1.20	1.75310	
0.9919	8000	1.25	1.75230	
0.9537	7692	1.30	1.75160	
0.9184	7407	1.35	1.75097	
0.8856	7143	1.40	1.75040	
0.8551	6896	1.45	1.74990	
0.8267	6667	1.50	1.74944	
0.7999	6452	1.55	1.74903	
0.7749	6250	1.60	1.74866	
0.7514	6061	1.65	1.74832	
0.7293	5882	1.70	1.74801	
0.7085	5714	1.75	1.74772	
0.6888	5556	1.80	1.74746	
0.6702	5405	1.85	1.74721	
0.6526	5263	1.90	1.74699	
0.6358	5128	1.95	1.74678	
0.6199	5000	2.00	1.74659	
0.6048	4878	2.05	1.74641	
0.5904	4762	2.10	1.74625	
0.5767	4651	2.15	1.74609	
0.5636	4545	2.20	1.74594	
0.5510	4444	2.25	1.74581	
0.5391	4348	2.30	1.74568	
0.5276	4255	2.35	1.74555	
0.5166	4167	2.40	1.74544	
0.5061	4082	2.45	1.74533	

(continued)

TABLE I (*Continued*)

Cesium Iodide

eV	cm^{-1}	μm	n	k
0.4959	4000	2.50	1.74523	
0.4862	3922	2.55	1.74513	
0.4769	3846	2.60	1.74504	
0.4679	3774	2.65	1.74495	
0.4592	3704	2.70	1.74487	
0.4509	3636	2.75	1.74479	
0.4428	3571	2.80	1.74471	
0.4350	3509	2.85	1.74464	
0.4275	3448	2.90	1.74457	
0.4203	3390	2.95	1.74450	
0.4133	3333	3.00	1.74443	
0.4065	3279	3.05	1.74437	
0.4000	3226	3.10	1.74431	
0.3936	3175	3.15	1.74425	
0.3875	3125	3.20	1.74420	
0.3815	3077	3.25	1.74414	
0.3757	3030	3.30	1.74409	
0.3701	2985	3.35	1.74404	
0.3647	2941	3.40	1.74399	
0.3594	2899	3.45	1.74394	
0.3542	2857	3.50	1.74390	
0.3493	2817	3.55	1.74385	
0.3444	2778	3.60	1.74381	
0.3397	2740	3.65	1.74376	
0.3351	2703	3.70	1.74372	
0.3306	2667	3.75	1.74368	
0.3263	2632	3.80	1.74364	
0.3220	2597	3.85	1.74360	
0.3179	2564	3.90	1.74356	
0.3139	2532	3.95	1.74352	
0.3100	2500	4.00	1.74349	
0.3061	2469	4.05	1.74345	
0.3024	2439	4.10	1.74341	
0.2988	2410	4.15	1.74338	
0.2952	2381	4.20	1.74334	
0.2917	2353	4.25	1.74331	
0.2883	2326	4.30	1.74327	
0.2850	2299	4.35	1.74324	
0.2818	2273	4.40	1.74321	
0.2786	2247	4.45	1.74317	
0.2755	2222	4.50	1.74314	
0.2725	2198	4.55	1.74311	
0.2695	2174	4.60	1.74308	
0.2666	2151	4.65	1.74305	
0.2638	2128	4.70	1.74302	

(continued)

TABLE I (*Continued*)

Cesium Iodide

eV	cm^{-1}	μm	n	k
0.2610	2105	4.75	1.74298	
0.2583	2083	4.80	1.74295	
0.2556	2062	4.85	1.74292	
0.2530	2041	4.90	1.74289	
0.2505	2020	4.95	1.74286	
0.2480	2000	5.0	1.74283	
0.2431	1961	5.1	1.74277	
0.2384	1923	5.2	1.74271	
0.2339	1887	5.3	1.74265	
0.2296	1852	5.4	1.74260	
0.2254	1818	5.5	1.74254	
0.2214	1786	5.6	1.74248	
0.2175	1754	5.7	1.74242	
0.2138	1724	5.8	1.74236	
0.2101	1695	5.9	1.74231	
0.2066	1667	6.0	1.74225	
0.2033	1639	6.1	1.74219	
0.2000	1613	6.2	1.74213	
0.1968	1587	6.3	1.74207	
0.1937	1563	6.4	1.74202	
0.1908	1538	6.5	1.74196	
0.1879	1515	6.6	1.74190	
0.1851	1493	6.7	1.74184	
0.1823	1471	6.8	1.74178	
0.1797	1449	6.9	1.74172	
0.1771	1429	7.0	1.74166	
0.1746	1408	7.1	1.74160	
0.1722	1389	7.2	1.74154	
0.1698	1370	7.3	1.74147	
0.1675	1351	7.4	1.74141	
0.1653	1333	7.5	1.74135	
0.1631	1316	7.6	1.74129	
0.1610	1299	7.7	1.74122	
0.1590	1282	7.8	1.74116	
0.1569	1266	7.9	1.74109	
0.1550	1250	8.0	1.74103	
0.1531	1235	8.1	1.74096	
0.1512	1220	8.2	1.74090	
0.1494	1205	8.3	1.74083	
0.1476	1190	8.4	1.74076	
0.1459	1176	8.5	1.74069	
0.1442	1163	8.6	1.74063	
0.1425	1149	8.7	1.74056	
0.1409	1136	8.8	1.74049	
0.1393	1124	8.9	1.74042	

(continued)

TABLE I (*Continued*)

Cesium Iodide

eV	cm^{-1}	μm	n	k
0.1378	1111	9.0	1.74034	
0.1362	1099	9.1	1.74027	
0.1348	1087	9.2	1.74020	
0.1333	1075	9.3	1.74013	
0.1319	1064	9.4	1.74005	
0.1305	1053	9.5	1.73998	
0.1292	1042	9.6	1.73990	
0.1278	1031	9.7	1.73983	
0.1265	1020	9.8	1.73975	
0.1252	1010	9.9	1.73967	
0.1240	1000	10.0	1.73960	
0.1216	980.4	10.2	1.73944	
0.1192	961.5	10.4	1.73928	
0.1170	943.4	10.6	1.73911	
0.1148	925.9	10.8	1.73895	
0.1127	909.1	11.0	1.73878	
0.1107	892.9	11.2	1.73861	
0.1088	877.2	11.4	1.73843	
0.1069	862.1	11.6	1.73826	
0.1051	847.5	11.8	1.73808	
0.1033	833.3	12.0	1.73789	
0.1016	819.7	12.2	1.73771	
0.09999	806.5	12.4	1.73752	
0.09840	793.7	12.6	1.73732	
0.09686	781.3	12.8	1.73713	
0.09537	769.2	13.0	1.73693	
0.09393	757.6	13.2	1.73673	
0.09253	746.3	13.4	1.73653	
0.09117	735.3	13.6	1.73632	
0.08984	724.6	13.8	1.73611	
0.08856	714.3	14.0	1.73589	
0.08731	704.2	14.2	1.73568	
0.08610	694.4	14.4	1.73546	
0.08492	684.9	14.6	1.73524	
0.08377	675.7	14.8	1.73501	
0.08266	666.7	15.0	1.73478	
0.08157	657.9	15.2	1.73455	
0.08051	649.4	15.4	1.73431	
0.07948	641.0	15.6	1.73408	
0.07847	632.9	15.8	1.73383	
0.07749	625.0	16.0	1.73359	
0.07653	617.3	16.2	1.73334	
0.07560	609.8	16.4	1.73309	
0.07469	602.4	16.6	1.73284	
0.07380	595.2	16.8	1.73258	

(continued)

TABLE I (*Continued*)

Cesium Iodide

eV	cm^{-1}	μm	n	k
0.07293	588.2	17.0	1.73232	
0.07208	581.4	17.2	1.73206	
0.07126	574.7	17.4	1.73179	
0.07045	568.2	17.6	1.73152	
0.06965	561.8	17.8	1.73124	
0.06888	555.6	18.0	1.73097	
0.06812	549.5	18.2	1.73069	
0.06738	543.5	18.4	1.73041	
0.06669	537.6	18.6	1.73012	
0.06596	531.9	18.8	1.72983	
0.06526	526.3	19.0	1.72954	
0.06458	520.8	19.2	1.72924	
0.06391	515.5	19.4	1.72894	
0.06326	510.2	19.6	1.72864	
0.06262	505.1	19.8	1.72833	
0.06199	500.0	20.0	1.72802	
0.06048	487.8	20.5	1.72723	
0.05904	476.2	21.0	1.72642	
0.05767	465.1	21.5	1.72559	
0.05636	454.5	22.0	1.72474	
0.05510	444.4	22.5	1.72387	
0.05391	434.8	23.0	1.72298	
0.05276	425.5	23.5	1.72206	
0.05166	416.7	24.0	1.72112	
0.05061	408.2	24.5	1.72016	
0.04959	400.0	25.0	1.71918	
0.04862	392.2	25.5	1.71817	
0.04769	384.6	26.0	1.71715	
0.04679	377.4	26.5	1.71610	
0.04592	370.4	27.0	1.71502	
0.04509	363.6	27.5	1.71392	
0.04428	357.1	28.0	1.71281	
0.04350	350.9	28.5	1.71167	
0.04275	344.8	29.0	1.71050	
0.04203	339.0	29.5	1.70931	
0.04133	333.3	30.0	1.70810	
0.04065	327.9	30.5	1.70686	
0.04000	322.6	31.0	1.70560	
0.03936	317.5	31.5	1.70431	
0.03875	312.5	32.0	1.70300	
0.03815	307.7	32.5	1.70166	
0.03757	303.0	33.0	1.70030	
0.03701	298.5	33.5	1.69891	
0.03647	294.1	34.0	1.69750	
0.03594	289.9	34.5	1.69606	

(continued)

TABLE I (*Continued*)

Cesium Iodide

eV	cm^{-1}	μm	n	k
0.03542	285.7	35.0	1.69460	
0.03493	281.7	35.5	1.69310	
0.03444	277.8	36.0	1.69158	
0.03397	274.0	36.5	1.69004	
0.03351	270.3	37.0	1.68846	
0.03306	266.7	37.5	1.68686	
0.03263	263.2	38.0	1.68523	
0.03220	259.7	38.5	1.68358	
0.03179	256.4	39.0	1.68189	
0.03139	253.2	39.5	1.68017	
0.03100	250.0	40.0	1.67843	
0.03061	246.9	40.5	1.67666	
0.03024	243.9	41.0	1.67485	
0.02988	241.0	41.5	1.67302	
0.02952	238.1	42.0	1.67115	
0.02917	235.3	42.5	1.66926	
0.02883	232.6	43.0	1.66733	
0.02850	229.9	43.5	1.66537	
0.02818	227.3	44.0	1.66338	
0.02786	224.7	44.5	1.66136	
0.02755	222.2	45.0	1.65930	
0.02725	219.8	45.5	1.65721	
0.02695	217.4	46.0	1.65509	
0.02666	215.1	46.5	1.65293	
0.02638	212.8	47.0	1.65073	
0.02610	210.5	47.5	1.64851	
0.02583	208.3	48.0	1.64624	
0.02556	206.2	48.5	1.64394	
0.02530	204.1	49.0	1.64161	
0.02505	202.0	49.5	1.63923	
0.02480	200.0	50.0	1.63682	9.9×10^{-5} [3]
0.02455	198.0	50.5	1.63437	1.15×10^{-4}
0.02431	196.1	51.0	1.63188	
0.02430	196.0	51.0		1.43
0.02407	194.2	51.5	1.62935	
0.02405	194.0	51.5		1.78
0.02384	192.3	52.0	1.62679	
0.02381	192.0	52.1		2.22
0.02362	190.5	52.5	1.62418	
0.02356	190.0	52.6		2.76
0.02339	188.7	53.0	1.62153	
0.02331	188.0	53.2		3.21
0.02317	186.9	53.5	1.61884	
0.02306	186.0	53.8		3.72
0.02296	185.2	54.0	1.61610	

(continued)

TABLE I (*Continued*)

Cesium Iodide

eV	cm^{-1}	μm	n	k
0.02281	184.0	54.35		4.32
0.02275	183.5	54.5	1.61332	
0.02257	182.0	54.95		5.02
0.02254	181.8	55.0	1.61050	
0.02234	180.2	55.5	1.60764	
0.02232	180.0	55.56		5.83
0.02214	178.6	56.0	1.60473	
0.02207	178.0	56.18		6.78
0.02194	177.0	56.5	1.60177	
0.02182	176.0	56.82		7.35
0.02175	175.4	57.0	1.59877	
0.02157	174.0	57.47		8.0
0.02156	173.9	57.5	1.59572	
0.02138	172.4	58.0	1.59262	
0.02133	172.0	58.14		8.6
0.02119	170.9	58.5	1.58947	
0.02108	170.0	58.82		9.4×10^{-4}
0.02101	169.5	59.0	1.58628	
0.02084	168.1	59.5	1.58303	
0.02083	168.0	59.52		1.05×10^{-3}
0.02066	166.7	60.0	1.57973	
0.02058	166.0	60.24		1.18
0.02049	165.3	60.5	1.57637	
0.02033	164.0	60.98		1.37
0.02032	163.9	61.0	1.57297	
0.02016	162.6	61.5	1.56951	
0.02009	162.0	61.73		1.49
0.02000	161.3	62.0	1.56599	
0.01984	160.0	62.50	1.56242	1.62
0.01968	158.7	63.0	1.55879	
0.01959	158.0	63.29		1.76
0.01953	157.5	63.5	1.55510	
0.01937	156.2	64.0	1.55136	
0.01934	156.0	64.10		1.97
0.01922	155.0	64.5	1.54755	
0.01909	154.0	64.94		2.22
0.01907	153.8	65.0	1.54368	
0.01893	152.7	65.5	1.53974	
0.01885	152.0	65.79		2.41
0.01879	151.5	66.0	1.53575	
0.01864	150.4	66.5	1.53168	
0.01860	150.0	66.67		2.61
0.01851	149.2	67.0	1.52755	
0.01835	148	67.50		3.04
0.01810	146	68.49		3.30

(continued)

TABLE I (*Continued*)

Cesium Iodide

eV	cm^{-1}	μm	n	k
0.01798	145	69.0	1.52 [5]	
0.01785	144	69.44		3.72
0.01761	142	70.4		4.05
0.01736	140	71.4	1.51	4.6
0.01711	138	72.46		4.9
0.01686	136	73.53		5.8
0.01674	135	74.1	1.5	
0.01661	134	74.63		6.7
0.01637	132	75.76		7.3
0.01612	130	76.9	1.48	8.5×10^{-3}
0.01587	128	78.13		1.0×10^{-2}
0.01562	126	79.37		1.2
0.01550	125	80.0	1.45	
0.01537	124	80.65		1.6
0.01513	122	81.97		2.1
0.01488	120	83.3	1.40	2.8
0.01463	118	84.75		4.0
0.01438	116	86.21		5.4
0.01426	115	87.0	1.35	
0.01413	114	87.72		7.5×10^{-2}
0.01389	112	89.29		0.105
0.01364	110	90.9	1.3	0.110
0.01339	108	92.59		0.115
0.01314	106	94.34		0.119
0.01302	105	95.2	1.2	
0.01289	104	96.15		0.125
0.01265	102	98.04		0.142
0.01240	100	100.0	1.0	0.155
0.01215	98	102.0		0.188
0.01190	96	104.2		0.220
0.01165	94	106.4	0.85 [4]	0.287
				0.7 [4]
0.01134	91.5	109.2	0.79	
0.01121	90.4	110.6		0.8
0.01095	88.3	113.3	0.75	
0.01076	86.8	115.2		1.1
0.01055	85.1	117.5	0.72	
0.01033	83.3	120.0		1.2
0.01015	81.9	122.1	0.68	
9.968×10^{-3}	80.4	124.4		1.4
9.758	78.7	127.1	0.57	
9.621	77.6	128.9		1.8
9.448	76.2	131.2	0.50	
9.361	75.5	132.4		2.2
9.088	73.3	136.4	0.57	2.6

(continued)

TABLE I (*Continued*)

Cesium Iodide

eV	cm^{-1}	μm	n	k
8.828	71.2	140.4		3.0
8.741	70.5	141.8	0.64	
8.567	69.1	144.7		3.4
8.394	67.7	147.7	0.99	
8.344	67.3	148.6		3.8
8.208	66.2	151.1	1.42	4.4
8.121	65.5	152.7	1.91	5.1
8.034	64.8	154.3	2.55	5.6
7.947	64.1	156.0		6.3
7.898	63.7	157.0	3.26	
7.873	63.5	157.5	3.82	
7.861	63.4	157.7	4.53	6.7
7.836	63.2	158.2	5.24	
7.799	62.9	159.0	5.95	
7.774	62.7	159.5	6.66	6.4
7.749	62.5	160.0		5.9
7.724	62.3	160.5	7.79	5.2
7.699	62.1	161.0		4.7
7.687	62.0	161.3		4.1
7.637	61.6	162.3		3.6
7.600	61.3	163.1	8.36	2.9
7.563	61.0	163.9		2.2
7.501	60.5	165.3	8.78	1.5
7.464	60.2	166.1	8.22	0.82
7.414	59.8	167.2	7.65	
7.328	59.1	169.2	7.01	
7.241	58.4	171.2	6.51	
7.204	58.1	172.1	6.02	
7.104	57.3	174.5	5.45	
6.980	56.3	177.6	4.96	
6.943	56.0	178.6		0.48 [5]
				0.296 [3]
6.894	55.6	179.9	4.46	
6.695	54.0	185.2	4.00	0.250
6.534	52.7	189.8	3.54	
6.447	52.0	192.3		0.171
6.274	50.6	197.6	3.26	
6.199	50.0	200.0		0.144
				0.17 [5]
5.951	48.0	208.3		0.114 [3]
5.703	46.0	217.4		0.100
5.579	45.0	222.2	2.91	
5.455	44.0	227.3		0.088
5.207	42.0	238.1		0.077
4.959	40.0	250.0	2.87	0.071

(continued)

TABLE I (*Continued*)

Cesium Iodide

eV	cm^{-1}	μm	n	k
4.711	38.0	263.2		0.067
4.463	36.0	277.8		0.058
4.339	35.0	285.7	2.84	
4.215	34.0	294.1		0.053
3.968	32.0	312.5		0.049
3.720	30.0	333.3	2.81	0.046
3.472	28.0	357.1		0.042
3.224	26.0	384.6		0.043
2.976	24.0	416.7		0.038
2.889	23.3	429.2	2.63 [2]	0.039 [2]
2.728	22.0	454.5		0.036 [3]
2.480	20.0	500		0.032
2.232	18.0	556		0.031
2.071	16.7	599	2.59	0.031 [2]
1.984	16.0	625		0.028 [3]
1.736	14.0	714		0.026
1.240	10.0	1000	2.56	0.021 [2]
6.199×10^{-4}	5.0	2000	2.54 [1]	

[a]Tabulation of n and k as a function of photon energy (electron volts), wave number (inverse centimeters), and wavelength (Angstroms or micrometers). References for the data are given in brackets and apply to all data below the brackets until a new reference appears; k is often very small and exponents are given for numbers smaller than 10^{-2}. The power of 10 applies for all data below the exponent until a new exponent appears or the exponent becomes 10^{-1}, whereupon the number is given in decimal form.

Copper Oxides (Cu_2O, CuO)

CARL G. RIBBING and ARNE ROOS
Institute of Technology
Uppsala University
Uppsala, Sweden

The established stoichometric copper oxides, cuprous oxide, Cu_2O ("red") and cupric oxide, CuO ("black"), form cubic and monoclinic unit cells in their respective equilibrium crystalline forms [1]. Reports on the phase $CuO_{.67}$, described as a gross defect structure of Cu_2O, are found in the literature [2, 3], but will not be considered here. It has furthermore been claimed that Cu_2O is actually not an equilibrium structure at temperatures below 375 °C and therefore decomposes very slowly at room temperature into metallic copper and cupric oxide [4]. The Cu-O phase diagram is markedly pressure dependent, such that a CuO layer transforms into Cu_2O and eventually into metallic copper when placed in vacuum.

Cuprous oxide is a semiconductor with a direct band gap of 2.17 eV. It has been the object of several basic studies concerning optical-band-gap absorption, its temperature dependence, and the interpretation of the low-temperature absorption line spectrum below the gap as transitions to excitonic levels [5–7]. The partly ionic character of the bonding causes structures in the optical functions in the infrared spectral region. The strongest IR-active mode, corresponding to the residual-ray region, was located at 609 cm^{-1} (16.4 μm) [8]. A secondary lattice mode at 146 cm^{-1} (68 μm) is reported for polycrystalline samples [9]. Several other lattice modes have been identified in later work and attributed to defects, impurities, and nonstoichiometry, and somewhat varying positions of the major lattice mode are given in the literature, which also include several Raman studies [9–11]. The recent discovery of high-temperature superconductors in which a key role seems to be played by the copper oxide in the formation of Cooper pairs has renewed the interest in the infrared properties of the copper oxides [12].

Considerably less has been reported about the black cupric oxide CuO. It is also a semiconductor, obviously with a smaller optical band gap than the red oxide. The values reported in the literature vary within the range 1.2–1.5 eV. A wet photoelectrochemical technique was used to obtain an indirect energy gap of 1.35 eV [13]. Early measurements on a bulk,

Copyright © 1991 by Academic Press.
All rights of reproduction in any form reserved.
ISBN 0-12-544422-2

polycrystalline sample, sintered in an oxygen atmosphere, resulted in an absorption edge too shallow to define an energy gap [14]. Simultaneous measurements on reactively sputtered films were also used to derive the optical constants without specifying an energy gap [15]. Recent transmittance measurements versus thickness on thin films prepared by rf, reactive sputtering gave an energy gap value of $1.21 \pm .05$ eV [16].

Much of the work on the physical properties of the copper oxides has been motivated by various technical applications. Cuprous oxide was one of the very early model semiconductors, and the discovery of the Cu_2O–Cu rectifier dates back to 1920 [17]. The use of cupric oxide on copper as a photoelectric and/or photoconductive material was suggested even earlier [18]. It is still of technical interest [19] to utilize this metal–oxide system as a possible low-cost solar cell. Oxidizing copper has furthermore been one of the alternatives to prepare the selectively absorbing surface of a thermal solar collector [20]. In this application the black oxide results in higher efficiency owing to its higher absorption of solar radiation. Several methods have been used to oxidize a copper base giving optimum performance in terms of selectivity and stability [21], and the use of a warm mixture of acids has been commercialized [22]. It has been demonstrated that the wet-oxidation techniques result in a rough interface between the oxide and the metal, which significantly increases the solar absorption [23, 24].

The ease with which oxidation of copper can take place is partly a corrosion problem, but it is also one of the reasons for the technical interest in this system. Even relatively thick layers of copper can be transformed into either one of the stoichiometric oxides, merely by heating in air. The green hue of old copper roofs is often (but incorrectly) said to be due to copper oxide. Instead, this surface is formed in the presence of water together with some other substances. It consists mainly of copper hydroxysulfate or, especially in coastal areas, copper hydroxychloride. From a basic point of view, the fact that copper is an easily oxidized noble metal with the typical strong tendency for diffusion creates a strong incentive for careful studies of the oxidation mechanism, rate laws, temperature dependence, and so on. The literature on the oxidation of copper is therefore very rich [25–28]. Copper is also a suitable metal for the study of laser-oxidation techniques [29, 30].

The thermal oxidation of copper, in contrast to wet oxidation, produces a rough oxide–metal interface that is *not* absorbing, but causes strong light scattering in the visible and near-infrared regions. The amount of scattering and its conspicous spectral dependence was used to determine the RMS roughness amplitude of both the air–oxide and oxide–metal uncorrelated interfaces [31, 32]. Here the Cu_2O–Cu served as a model system because of the exceptional magnitude of the light scattering.

For reasons made obvious above, there is a wealth of published optical constants for the cuprous oxide in the visible and near-infrared spectral

regions and considerably less data for cupric oxide in the same spectral regions. It has not been possible to find published optical constants for either one of the copper oxides in the vacuum UV or soft X-ray regions, however. Tables I and II and Figs. 1 and 2 therefore cover only the near UV, down to 300 nm. The valence bands and the core-level positions have been determined by electron spectroscopy as part of basic investigations about satellite formation in photoelectron spectra [33, 34]. Without knowledge of the numerical values of the optical functions, we can predict that they will exhibit oscillator structures, in the case of CuO around the core levels: O(1s)-530 eV ($\lambda = 2.34$ nm), Cu($2p_{3/2}$) − 933 eV (1.33 nm) and Cu($2p_{1/2}$) − 954 eV (1.30 nm). In Cu_2O there is a 1.2 eV chemical shift in the copper levels toward lower binding energy whereas the O(1s) is unchanged.

For the cuprous oxide in the visible region, data have been selected for thermally oxidized copper films, which have been prepared in different thicknesses to allow combined R and T measurements. The optical thickness nd was calculated from the position of the interference fringes, and the refractive index was determined from their envelope function in the region of low absorption. The values from Ref. [35] cover the broadest region and are somewhat higher than the data from Refs. [36] (electrodeposited), [37], and [14]. The values given are also marginally higher than those obtained from the dispersion relation [36]

$$n^2(\lambda) = 1 + A\lambda^2/(\lambda^2 - B),$$

which can be used for wavelengths longer than 0.550 μm; here, $A = 4.81$ $(\mu m)^{-2}$ and $B = 0.125$ $(\mu m)^2$. At shorter wavelengths this relation gives values that are too high, however. The k values are significantly lower than those obtained for sintered powder [14] and slightly higher than those of Ref. [37].

The optical constants given here for cupric oxide have also been determined for thermally oxidized copper films [35]. In the visible part of the spectrum, the n and k values are in good agreement with those of Ref. [3]. In contrast, both functions are significantly lower than those of Refs. [2] and [14] as well as those for *rf* reactively sputtered films in Ref. [16].

For the cuprous oxide in the infrared, optical reflectance measurements on single crystals [8, 11] or polycrystalline films [9] were performed. Kramers–Kronig analysis of these spectra [11] or additional transmittance measurements on polycrystalline films [8, 9] were used to derive the optical constants in the vicinity of the resonance frequencies. It was found that the Lyddane–Sachs–Teller relation was valid for cuprous oxide, and the dielectric constant ε_0 is equal to 7.4 in the low-frequency region [11]. The ε_0 value given by O'Keeffe [8] ($\varepsilon_0 = 6.46$) does not take the low-frequency

resonance at 146 cm^{-1} into account, but is in excellent agreement with the ε_∞ value ($\varepsilon_\infty = 6.5$) for this resonance.

It has not been possible to find published values of n and k in the infrared region for cupric oxide. Poling [38] reports absorbance spectra for CuO without giving the n and k values. The oxide exhibits an intense single band around 510 cm^{-1}. This is the only significant band in the 230–4000 cm^{-1} region.

REFERENCES

1. M. Hansen, "Constitution of Binary Alloys," 2nd ed., McGraw Hill, New York, 604 (1958).
2. H. Wieder and A. W. Czanderna, *J. Appl. Phys.* **37**, 184 (1966).
3. P. C. Ladelfe, A. W. Czanderna, and J. R. Biegen, *Thin Solid Films* **10**, 403 (1972).
4. R. Vogel and W. Pocher, *Z. Metallkunde* **21**, 333 and 368 (1929).
5. Y. F. Gross, *Izvest, Akad. Nauk. S.S.S.R. Ser.* **84**, 261 and 471 (1952). Translated in *Bull. Acad. Sc. (USSR)* **20**, 79 (1956).
6. J. H. Apfel and L. N. Hadley, *Phys. Rev.* **100**, 1689 (1955).
7. P. W. Baumeister, *Phys. Rev.* **121**, 359 (1961).
8. M. O'Keeffe, *J. Chem. Phys.* **39**, 1789 (1963).
9. E. C. Heltemes, *Phys. Rev.* **141**, 803 (1966).
10. J. Reydellet, M. Balkanski, and D. Trivich, *Phys. Stat. Solidi (b)* **52**, 175 (1972).
11. P. Dawson, M. M. Hargreave, and G. R. Wilkinson, *J. Phys. Chem. Solids* **34**, 2201 (1973).
12. G. Wendin, *Physica Scripta* **T27**, 31 (1989).
13. F. P. Koffyberg and F. A. Benko, *J. Appl. Phys.* **53**, 1173 (1982).
14. T. Tanaka, *Jap. J. Appl. Phys.* **18**, 1043 (1979).
15. V. F. Drobny and D. L. Pulfrey, *Thin Solid Films* **61**, 89 (1979).
16. A. E. Rakhshani and F. K. Barakat, *Materials Lett.* **6**, 37 (1987).
17. L. O. Grondahl, *Rev. Mod. Phys.* **5**, 141 (1933).
18. A. H. Pfund, *Phys. Rev.* **3**, 289 (1916).
19. A. E. Rakhshani, *Solid-State Electr.* **29**, 7 (1986).
20. B. O. Seraphin, in "Solar Energy Conversion—Solid State Physics Aspects," (B. O. Seraphin, ed.), Springer-Verlag, Berlin, (1979).
21. D. J. Close, "Commonwealth Scientific and Industrial Research Organization," Australia, Engineering section, Report E. D. 7, (1962).
22. "Ebonol" of Enthone, Inc., New Haven, Conn.
23. A. Roos, T. Chibuye, and B. Karlsson, *Solar Energy Mat.* **7**, 453 (1983).
24. A. Roos and B. Karlsson, *Solar Energy Mat.* **7**, 467 (1983).
25. A. Rönnquist and H. Fischmeister, *J. Inst. Metals* **89**, 65 (1960–1961).
26. J. V. Cathcart, G. F. Petersen, and C. J. Sparks, in "Surfaces and Interfaces," Vol. 1, (J. J. Burke, ed.) Syracuse University Press, New York, 333 (1967).
27. C. Tsiranovits, J. G. Antonopoulos, and J. Stoemenos, *Thin Solid Films* **71**, 133 (1980).
28. S. K. Roy and C. Sircar, *Oxidation of Metals* **15**, 9 (1981).
29. L. Baufay, F. A. Houle, and R. J. Wilson, *J. Appl. Phys.* **61**, 4640 (1987).
30. M. Wautelet and R. Andrew, *Phil. Mag. B* **55**, 261 (1987).
31. A. Roos, M. Bergkvist, and C. G. Ribbing, *Appl. Opt.* **28**, 1360 (1989).
32. M. Bergkvist, A. Roos, C. G. Ribbing, J. M. Bennett, and L. Mattsson *Appl. Opt.*, **28**, 3902 (1989).
33. A. Rosencwaig and G. K. Wertheim, *J. Electron Spectrosc. Relat. Phenom.* **1**, 493 (1972/73).

34. H. Siegbahn and L. Karlsson, in "Handbuch der Physik," (W. Mehlhorn, ed), Vol. xxxi, Springer–Verlag, Berlin, 215 (1982).
35. B. Karlsson, C. G. Ribbing, A. Roos, E. Valkonen, and T. Karlsson, *Physica Scripta* **25**, 826 (1982).
36. A. E. Rakhshani, *J. Appl. Phys.* **62**, 1528 (1987).
37. K. Bärwinkel and H. J. Schmidt, *Thin Solid Films* **59**, 373 (1979).
38. G. W. Poling, *J. Electrochem. Soc.* **116**, 958 (1969).
39. Interpolated values of *n*.

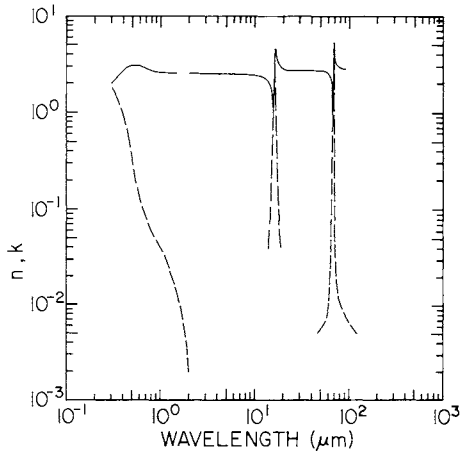

Fig. 1. Log–log plot of *n* (solid line) and *k* (dashed line) versus wavelength in micrometers for cuprous oxide (Cu_2O).

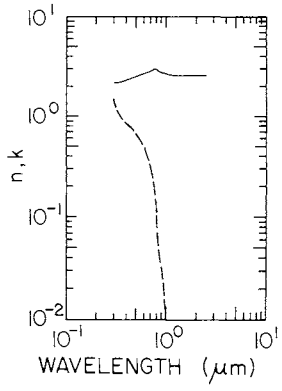

Fig. 2. Log–log plot of *n* (solid line) and *k* (dashed line) versus wavelength in micrometers for cupric oxide (CuO).

TABLE I

Values of n and k for Cuprous Oxide Obtained from Various References[a]

eV	cm^{-1}	μm	n	k
4.133	33,330	0.3	2.0 [35]	1.85 [35]
3.542	28,570	0.35	2.40	1.44
3.100	25,000	0.40	2.80	0.99
2.756	22,220	0.45	3.06	0.60
2.480	20,000	0.50	3.12	0.35
2.255	18,180	0.55	3.10	0.19
2.067	16,670	0.60	3.02	0.13
1.908	15,380	0.65	2.90	0.10
1.771	14,290	0.70	2.83	0.083
1.653	13,330	0.75	2.77	0.070
1.550	12,500	0.80	2.70	0.060
1.459	11,770	0.85	2.66	0.053
1.378	11,110	0.90	2.63	0.048
1.305	10,530	0.95	2.61	0.043
1.240	10,000	1.00	2.60	0.040
1.127	9,090	1.10	2.59	0.033
1.033	8,330	1.20	2.58	0.027
0.954	7,690	1.30	2.57	0.021
0.886	7,110	1.40	2.57	0.017
0.827	6,670	1.50	2.57	0.013
0.620	5,000	2.00	2.56	0.002
0.496	4,000	2.5	2.56	
0.413	3,333	3.0	2.55 [39]	
0.310	2,500	4.0	2.54	
0.248	2,000	5.0	2.53	
0.207	1,667	6.0	2.52	
0.177	1,429	7.0	2.51	
0.155	1,250	8.0	2.50 [8]	
0.138	1,111	9.0	2.48	
0.124	1,000	10.0	2.46	
0.113	909.1	11.0	2.42	
0.103	833.3	12.0	2.37	
0.0954	769.2	13.0	2.29	
0.0886	714.3	14.0	2.15	0.04 [8]
0.0827	666.7	15.0	1.79	0.13
0.0800	645.2	15.5	1.13	0.46
0.0785	632.9	15.8	0.92	1.68
0.0775	625.0	16.0	1.09	2.52
0.0761	613.5	16.3	2.94	3.49
0.0752	606.1	16.5	4.71	2.27
0.0729	588.2	17.0	3.78	0.42

[a] References are indicated in brackets

(continued)

TABLE I (*Continued*)

Cuprous Oxide (Cu_2O)

eV	cm^{-1}	μm	*n*	*k*
0.0709	571.4	17.5	3.42	0.17
0.0689	555.6	18.0	3.21	0.08
0.0653	526.3	19.0	2.98	0.04
0.0620	500.0	20.0	2.89	0
0.0590	476.2	21.0	2.82	
0.0564	454.5	22.0	2.79	
0.0539	434.7	23.0	2.77	
0.0517	416.7	24.0	2.76	
0.0496	400.0	25.0	2.75	
0.0413	333	30.0	2.75 [39]	
0.0354	286	35.0	2.75	
0.0310	250	40.0	2.75	
0.0273	220	45.5	2.75	0.005 [9]
0.0248	200	50.0	2.74	0.006
0.0223	180	55.56	2.72 [11]	0.006
0.0211	170	58.82	2.66	0.009
0.0198	160	62.50	2.42	0.017
0.0192	155	64.52	2.18	0.05 [11]
0.0188	152	65.79	1.81	0.10
0.0186	150	66.67	1.19	0.59
0.01844	148.7	67.25	0.89	1.88
0.01823	147	68.03	3.37	3.97
0.01819	146.7	68.17	4.56	4.37
0.01810	146	68.49	5.56	2.78
0.01786	144	69.44	3.97	0.20
0.01761	142	70.42	3.47	0.08
0.01736	140	71.43	3.21	0.04
0.0161	130	76.9	2.98	0.013 [9]
0.0149	120	83.3	2.92	0.010
0.0136	110	90.9	2.84	0.008
0.0124	100	100.0		0.007
0.00992	80	125.0		0.005

[a] References are indicated in brackets.

TABLE II

Values of n and k for Cupric Oxide Obtained from Various References[a]

eV	cm^{-1}	μm	n	k
4.133	33,330	0.30	2.18 [35]	1.50 [35]
3.542	28,570	0.35	2.24	1.03
3.100	25,000	0.40	2.34	0.87
2.756	22,220	0.45	2.45	0.77
2.480	20,000	0.50	2.54	0.68
2.255	18,180	0.55	2.58	0.59
2.067	16,670	0.60	2.65	0.50
1.908	15,380	0.65	2.72	0.40
1.771	14,290	0.70	2.88	0.31
1.653	13,330	0.75	2.97	0.22
1.550	12,500	0.80	2.94	0.11
1.459	11,770	0.85	2.81	0.04
1.378	11,110	0.90	2.74	0.03
1.305	10,530	0.95	2.69	0.02
1.240	10,000	1.00	2.65	0.01
1.127	9,090	1.10	2.61	
1.033	8,330	1.20	2.58	
0.954	7,690	1.30	2.57	
0.886	7,110	1.40	2.56	
0.827	6,670	1.50	2.56	
0.620	5,000	2.00	2.55	
0.496	4,000	2.5	2.55	

[a] References are indicated in brackets.

Magnesium Aluminum Spinel ($MgAl_2O_4$)

WILLIAM J. TROPF and MICHAEL E. THOMAS
Applied Physics Laboratory
The Johns Hopkins University
Laurel, Maryland

Magnesium aluminum spinel (the mineral spinel) is face-centered cubic material, the prototype for the spinel structural family, which includes binary oxides, sulfides, selenides, as well as many other materials (see ALON, this volume). The space group is O_h^7 or $Fd3m$, unit cell length is 0.8084 nm, and the unit cell has eight formula units (56 atoms). Theoretical density is 3.58 g/cm^3, and melting point is 2378 K [1] to 2408 K [2].

In the normal spinel structure, magnesium ions occupy tetrahedral sites with T_d symmetry, aluminum ions occupy distorted octrahedral sites with D_{3d} symmetry, and the oxygen ions are at sites with C_{3v} symmetry. The positions of the ions in the unit cell have been determined by both X-ray and neutron diffraction techniques [3–6].

There is also an "inverse" spinel structure, wherein the aluminum ions occupy both T_d and D_{3d} sites, and the magnesium ions occupy some of the D_{3d} sites. The occurrence of the normal, inverse, or in-between structure depends on ionic size, method of preparation, and composition. Natural magnesium aluminum spinel has the normal spinel structure, although there is evidence that synthetic forms of spinel prepared at high temperature have the inverse structure [5, 7]. Disordering in both natural and synthetic near-stoichiometric spinel crystals is apparently caused by heating [7, 8], the structural transition taking place at 750–800 °C. This transition is apparently irreversible.

The composition of magnesium aluminum spinel varies from near-stoichiometric to highly alumina-rich. The compositions have the general formula $MgO \times mAl_2O_3$, where m varies from 0.9 up to 4. All formulations have the spinel structure (with vacancies at octrahedral sites when $m \neq 1$), with the lattice constant continuously decreasing as m goes from 1 to 3.5 [3, 9]. As m increases above 1, cation vacancies appear and typically occupy octrahedral sites [5].

Copyright © 1991 by Academic Press.
All rights of reproduction in any form reserved.
ISBN 0-12-544422-2

Spinel is a naturally occurring mineral, sometimes with gem quality. Optical-quality spinel can be synthetically made with a variety of techniques, including growth using the Czochralski method [10], the gradient-furnace technique [11], as well as by hot pressing of powder [2, 12], press forging [13], flame fusion (Verneuil method) [3, 14], and fusion casting [15].

Little information on optical constants in the electronic region is available. Summers *et al.* [16] report an absorption edge (onset of significant electronic absorption) 7.75 eV. Woosley *et al.* [17] report a band gap of about 9 eV, with evidence of exciton formation in the 6–8 eV range, band-to-band transitions begining at 8–9 eV, and photoemission from the top of the valence band beginning at energies above 11 eV. The valance band is estimated by Woosley to be 8–9 eV wide.

Refractive-index measurements of natural spinels were made by Schlossmacher [18], who reported real and imaginary parts of the index of refraction for red-, blue-, and violet-colored crystals. Index data from the lowest absorption ("bright red") natural crystal agrees well with recent measurements (see below). Wickersheim and LaFever [19] report that the index of refraction increases with greater alumina content. They found an index of 1.708 for stoichiometric spinel and 1.717–1.720 for alumina-rich ($m=3.5$) commercial spinel using a blue filter. Roy and Hastert [2] reported visible and IR measurements made by Kodak on artificial spinel. Visible and near-IR measurements agree well with other data, but the accuracy of IR measurements above 1 μm is doubtful. Vadem *et al.* [20] measured the refractive index of stoichiometric and nonstoichiometric ($m\approx 2.7$) spinel at 0.5893 μm and obtained values of 1.718 and 1.724, respectively. They also measured the pressure and temperature dependence of their samples, obtaining dn/dT of 9.05×10^{-6} for stoichiometric and 9.34×10^{-6} for nonstoichiometric spinel.

Recent index-of-refraction measurements of Coors Optical Systems Company's stoichiometric spinel made in the UV and visible by General Dynamics [21] and the visible and near-IR by Schott Glass [22] are self-consistent and agree well with index data for low-absorption natural spinel [18].

Spinel refractive-index data for the visible and IR transparent region are summarized with a Sellmeier formula of the form

$$n^2-1=\frac{18.96\times 10^9}{(100,080)^2-\nu^2}+\frac{1.2234\times 10^6}{(527.18)^2-\nu^2}, \tag{1}$$

where ν is the frequency in wave numbers. This formula is applicable to bulk crystalline (or polycrystalline) stoichiometric spinel with low impurity and defect concentration and is accurate to ± 0.001. Figure 1 compares the

index-of-refraction data from several sources to Eq 1. Evaporated thin films made with spinel material have a wide index-of-refraction variation and nonstoichiometric composition [23].

Absorption in the transparent region (0.25–5 μm) is governed by impurities and defects. The structure and visible optical absorption of spinel with various amounts of chromium, cobalt, and iron have been widely studied [24–27]. Optical effects of X-ray, γ-ray [28, 29], electron [16], and neutron [16, 30] irradiation are well-known. An F center at 5.3 eV (234 nm), an F^+ center at 4.75 eV (261 nm), and a V center at 3.2 eV (387 nm) are known [16, 31]. The most prominent IR absorption feature is the OH^- absorption band that occurs at 3345 cm^{-1} [9, 15, 19, 32]. Nonstoichiometric spinel has an additional OH^- absorption band at 3528 cm^{-1} that grows with increasing alumina content [3, 9, 15, 19, 32].

The dominant loss mechanism in the visible and near-IR transparent region of polycrystalline spinel is scatter. Bulk scatter in polycrystalline spinel is low and decreases with increasing wavelength [2].

Absorption at the IR edge of transparency is dominated by multiphonon absorption. A model of multiphonon absorption for spinel has been developed and validated with experimental data over a wide temperature range [33]. The fundamental (one-phonon) lattice vibrations occur in the 300–800 cm^{-1} spectral region. Group theory predicts the following phonon modes for spinel [34–36]:

$$\Gamma = A_{1g} + E_g + F_{1g} + 3F_{2g} + 2A_{2u} + 2E_u + 4F_{1u} + 2F_{2u}. \quad (2)$$

The Raman-active modes are A_{1g}, E_g, and F_{2g}, and the F_{1u} modes are IR-active. Table I lists locations of the IR modes (transverse optical frequency) observed by several researchers [37–39]. There is good agreement on the location of three prominent modes; the fourth mode is either weak or masked by the other three. Also, other weak modes not predicted by group theory may be present because of disorder or lack of stoichiometry [35]. In particular, an absorption peak near 818 cm^{-1} becomes prominent as the alumina concentration is increased, as demonstrated by Hafner and Laves [8] and Wang and Zanzucchi [40]. Table II gives mode locations, widths, and strengths as determined by Thomas [39]. Temperature dependence of these modes has been measured over the range 290–775 K.

Table II also lists both the transverse and longitudinal optical frequencies of spinel. The transverse optical frequencies are the mode locations; the maximum longitudinal is an important parameter in the multiphonon model [33], since it designates the maximum phonon frequency.

At frequencies below the lowest fundamental optical mode, absorption decreases and the material becomes transparent. The magnitude of absorption is thought to be a combination of contributions from both the tail of

the fundamental lattice vibrations and various multiphonon difference bands. The index of refraction now also includes the effect of lattice vibrations.

The low-frequency real index of refraction (dielectric constant $\approx n^2$) of spinel was measured by Wang and Zanzucchi [40], Westphal and Iglesias [41], Stead and Simonis [42], and Ho [43]. These values lie between 2.88 and 2.90, which are slightly higher that the value of 2.86 determined from Table II. Wang [3] reported very little change in dielectric constant when m ranged from 1 to 3. Temperature dependence of the low-frequency index of refraction is given by Westphal and Iglesias [41] as 2.5×10^{-4}/K (average, 25–455 °C) and by Ho [43] as 2.3×10^{-4}/K (average, 23–300 °C), 2.8×10^{-4}/K (average, 23–1000 °C), and 3.0×10^{-4}/K (average, 23–1200 °C). Stead and Simonis [42] also give values for the imaginary index of refraction (k) in the 5–15 cm^{-1} region. Estimates of the imaginary index of refraction made from the low-frequency side (red wing) of the fundamental modes (Table II) are about 72% of the experimental value determined by Stead and Simonis [42] at 5 cm^{-1}, with better agreement at higher frequency.

Table III was constructed from measurements reported in the literature as well as model predictions. Real-index (n) data in the visible and near IR are taken from the measurements of Furutani [21] and Scheller [22].

Lattice-vibration-model results [39] are used to calculate real-index data from 0–9600 cm^{-1} and imaginary index data from 5–5000 cm^{-1}. Laser calorimetry results for k at 2.9 and 3.9 μm by Detrio and Greason [44] give extrinsic measurements of the imaginary part of the index of refraction, based on thin samples with the lowest absorption coefficients. Of particular note is the imaginary index of refraction at 2.9 μm, which lies on the OH^- absorption feature of spinel.

Measurements of Stead and Simonis [42] and others [40, 41, 43] are used to represent the low-frequency characteristics of spinel. In this region, one-phonon-model contributions [39] to k are 70 to 100% of measured values [42], and index predictions are 0.7 to 1.5% low compared with measured values [40–43]. Two- and three-phonon difference bands presumably account for the unaccounted portion of k.

The accuracy of available index data is unknown. In all data, the uncertainty in the values is probably in the least-significant digit reported in Table III. In spectral regions where several sources of data exist, there is a large disparity between references.

Figure 2 shows a composite of the complex index of refraction based on the data of Table III.

Table IV gives temperature dependence for the real part of the index of refraction. Measurements of dn/dT by Vadem *et al.* [20], Westphal and Iglesias [41], and Ho [43] are included.

Temperature-dependent absorption computed from optical models of

spinel [39] has been used to estimate total hemispherical emissivity of pure, transparent spinel over the range 200–1000 K, where the models are expected to give the best results, and defect absorption is believed to be insignificant. These results were obtained by estimating the complex refractive index at a given temperature, calculating directional emittance for a specific slab thickness, integrating over angle, and convolving the resulting spectral hemispherical emittances with the Planck function.

Table V gives the resulting total hemispherical emittance for semi-infinite slabs as a function of slab thickness. Since total hemispherical emissivity is an important function for radiation-relief calculations and may be needed to correct property measurements such as thermal conductivity, we have included this calculated result.

REFERENCES

1. A. M. Alper, R. N. McNally, P. G. Ribbe, and R. C. Doman, "The System MgO–$MgAl_2O_4$," *J. Am. Ceram. Soc.* **45**, 264 (1962).
2. D. W. Roy and J. L. Hastert, "Polycrystalline $MgAl_2O_4$ (Spinel) for Use as Windows and Domes from 0.3 to 6.0 Micrometers," *Proc. SPIE* **400**, 37 (1983).
3. C. C. Wang, "Growth and Characterization of Spinel Single Crystals for Substrate Use in Integrated Electronics," *J. Appl. Phys.* **40**, 3433 (1969).
4. G. E. Bacon, "A Neutron-Diffraction Study of Magnesium Aluminium Oxide," *Acta Cryst.* **5**, 684 (1952).
5. Von H. Jagodzinski and H. Saalfeld, "Cation Distribution and Structural Relations in Mg-Al-Spinel," *Z. Kristallogr.* **110**, 197 (1958).
6. P. Fischer, "Neutron Diffraction Investigation of the Structure of $MgAl_2O_4$ and $ZnAl_2O_4$ Spinel as a Function of Previous History," *Z. Kristallogr.* **124**, 275 (1967).
7. U. Schmocker, H. R. Boesch, and F. Waldner, "A Direct Determination of Cation Disorder in $MgAl_2O_4$ Spinel by ESR," *Phys. Lett.* **40A**, 237 (1972).
8. S. Hafner and F. Laves, "Order/Disorder and Infrared Absorption III. The Systems $MgAl_2O_4$-Al_2O_3 and $MgAl_2O_4$-$LiAl_5O_8$," *Z. Kristallogr.* **115**, 321 (1961).
9. J. S. Reed, "Optical Absorption Spectra of Cr^{3+} in $MgO \cdot Al_2O_3$-$MgO \cdot 3.5Al_2O_3$ Spinels," *J. Am. Ceram. Soc.* **54**, 202 (1971).
10. B. Cockayne and M. Chesswas, "The Vertical Pulling of $MgAl_2O_4$ Single Crystals," *J. Mater. Sci.* **2**, 498 (1967).
11. D. Viechnicki, F. Schmid, and J. W. McCauley, "Growth of Nearly Stoichiometric $MgAl_2O_4$ Spinel Single Crystals by a Gradient Furnace Technique," *J. Appl. Phys.* **43**, 4508 (1972).
12. T. M. Hartnett and R. L. Gentilman, "Optical and Mechanical Properties of Highly Transparent Spinel and ALON Domes," *Proc. SPIE* **505**, 15 (1984).
13. P. F. Becher, "Press-Forged Al_2O_3-Rich Spinel Crystals for IR Applications," *Bull. Am. Ceram. Soc.* **56**, 1015 (1977).
14. R. A. LaFever and G. W. Clark, "Multiple-Tube Flame Fusion Burner for the Growth of Oxide Single Crystals," *Rev. Sci. Instr.* **33**, 769 (1962).
15. R. L. Gentilman, "Fusion-Casting of Transparent Spinel," *Bull. Am. Ceram. Soc.* **60**, 906 (1981).
16. G. P. Summers, G. S. White, K. H. Lee, and J. H. Crawford, 'Radiation Damage in $MgAl_2O_4$," *Phys. Rev. B* **21**, 2578 (1980).
17. J. D. Woosley, C. Wood, E. Sonder, and R. A. Weeks, "Photoelectric Effects in Magnesium Aluminium Spinel," *Phys. Rev. B* **22**, 1065 (1980).

18. K. Schlossmacher, "Absorption and Refraction of the Red, Blue, and Violet Spinels of Ceylon," *Z. Kristallogr.* **72**, 447 (1930).
19. K. A. Wickersheim and R. A. LaFever, "Optical Properties of Synthetic Spinel," *J. Opt. Soc. Am.* **50**, 831 (1960).
20. K. Vadem, J. L. Kirk, and B. N. N. Achar, "Piezo- and Thermo-Optic Behavior of Spinel ($MgAl_2O_4$)," *J. Solid State Chem.* **12**, 213 (1975).
21. N. Furutani, General Dynamics, Valley Systems Division, personal communcation (Oct. 5, 1989).
22. R. J. Scheller, Schott Glass Technologies, Inc., personal communication (June 20, 1989).
23. J. B. Hearney, G. Hass, and M. McFarland, "Spinel (Al_2O_3:MgO): Refractive-Index Variations and Lack of Stoichiometry in Evaporated Films," *Appl. Opt.* **14**, 2335 (1981).
24. G. A. Slack, "$FeAl_2O_4$-$MgAl_2O_4$: Growth and Some Thermal, Optical, and Magnetic Properties of Mixed Single Crystals," *Phys. Rev.* **134A**, 1268 (1964).
25. P. K. Sharpe and J. C. Vickerman, "Solid State Properties of Copper Containing Spinel Solutions ($Cu_xMg_{1-x}Al_2O_4$)," *J. Chem. Soc. Faraday Trans. I* **73**, 505 (1977).
26. C. Angeletti, F. Pele, and P. Porta, "Structure and Catalytic Activity of $Co_xMg_{1-x}Al_2O_4$ Spinel Solid Solutions," *J. Chem. Soc. Faraday Trans. I* **73**, 1972 (1977).
27. W. Strek, P. Deren, and B. Jezowska-Trzebiatoeska, "Optical Properties of Cr^{3+} in $MgAl_2O_4$ Spinel," *Physica B* **152**, 379 (1988).
28. G. S. White, K. H. Lee, and J. H. Crawford, "Effects of λ-Irradiation upon the Optical Behavior of Spinel," *Phys. Stat. Solidi (a)* **42**, K137 (1977).
29. G. S. White, R. V. Jones, and J. H. Crawford, "Optical Spectra of $MgAl_2O_4$ Crystals Exposed to Ionizing Radiation," *J. Appl. Phys.* **53**, 265 (1982).
30. L. S. Cain, G. J. Pogatshnik, and Y. Chin, "Optical Transitions in Neutron-Irradiated $MgAl_2O_4$ Spinel Crystals," *Phys. Rev. B* **37**, 2645 (1988).
31. P. K. Bandyopadhyay and G. P. Summers, "Luminescence and Photoconductivity in Magnesium Aluminum Spinel," *Phys. Rev. B* **31**, 2422 (1985).
32. E. Sonder and R. A. Weeks, "Behavior of Electrical Conduction of Spinel and Other Insulating Oxides in Moderate Electric Fields at High Temperature," *J. Appl. Phys.* **56**, 2365 (1984).
33. M. E. Thomas, R. I. Joseph, and W. J. Tropf, "Infrared Transmission Properties of Sapphire, Spinel, Yttria, and ALON as a Function of Temperature and Frequency," *Appl. Opt.* **27**, 239 (1988).
34. H. D. Lutz, "Lattice Vibrational Spectra. III. Symmetry Coordinates and Vibrational Forms of Lattice Vibrations in Spinel," *Z. Naturforsch. A* **24**, 1417 (1969).
35. W. B. White and B. A. DeAngelis, "Interpretation of the Vibrational Spectra of Spinels," *Spectrochim. Acta* **23A**, 985 (1967).
36. J. Preudhomme and P. Tarte, "Infrared Studies of Spinels-III: The Normal II–III Spinels," *Spectrochim. Acta* **27A**, 1817 (1971).
37. M. P. O'Horo, A. L. Frisillo, and W. B. White, "Lattice Vibrations of $MgAl_2O_4$ Spinel, *J. Phys. Chem. Solids* **34**, 23 (1973).
38. M. E. Striefler and S. I. Boldish, "Transverse and Longitudinal Optic Frequencies of Spinel $MgAl_2O_4$," *J. Phys.* **C11**, L237 (1978).
39. M. E. Thomas, "A Computer Code for Modelling Optical Properties of Window Materials," *Proc. SPIE* **1112**, 260 (1989). Mode parameters in Tables I and II have been improved over the values given in the reference.
40. C. C. Wang and P. J. Zanzucchi, "Dielectric and Optical Properties of Stoichiometric Magnesium Aluminate Spinel Single Crystals," *J. Electrochem. Soc.* **118**, 586 (1971).
41. W. B. Westphal and J. Iglesias, Dielectric Spectroscopy of High-Temperature Materials, Air Force Materials Laboratory Report AFML-TR-71-66, April (1971). (Available from NTIS as AD 884597.)

42. M. Stead and G. Simonis, "Near Millimeter Wave Characterization of Dual Mode Maerials," *Appl. Opt.* **28**, 1874 (1989).
43. W. W. Ho, "High-Temperature Dielectric Properties of Polycrystalline Ceramics," in "MRS Symposium M," Reno (April 6, 1988).
44. J. A. Detrio and P. Greason, University of Dayton, personal communication (April 8, 1988).

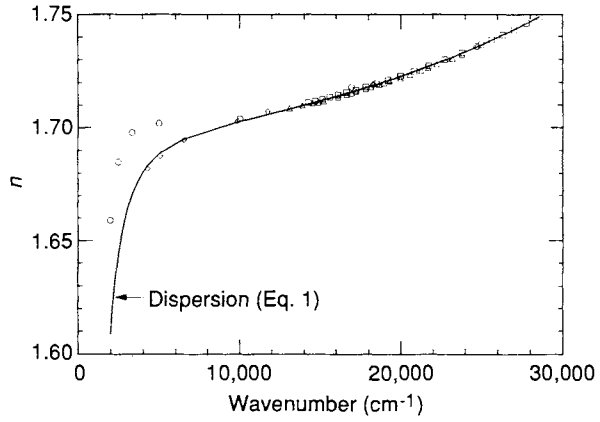

Fig. 1. Index of refraction (n) versus wave number in cm^{-1} for magnesium aluminum spinel. Data from Schlossmacher [18] (triangles), Furutani [21] (squares), Scheller [22] (diamonds), and Roy and Hastert [2] (circles) are compared with the dispersion equation (solid line) given in the text.

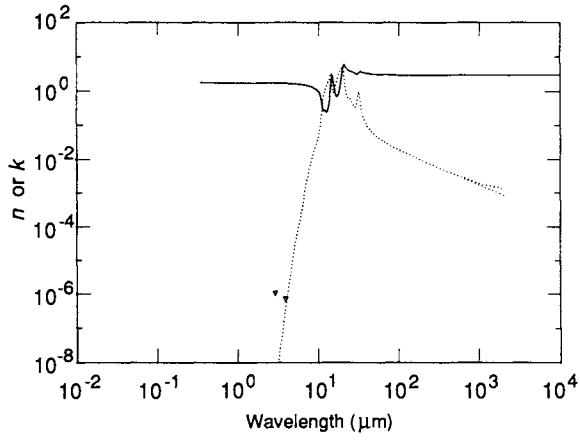

Fig. 2. Log–log plot of n (solid line) and k (dashed line) versus wavelength in micrometers for magnesium aluminum spinel. Data from various sources sometimes do not join together in overlap regions. Symbols are laser-colarimetry measurements of k.

TABLE I

Determination of Spinel Infrared Lattice-Vibration Frequencies (cm^{-1})[a]

O'Horo *et al.* [37]	Striefer [38]				Thomas [39]
	4-pole fits				
4-pole fit	#1	#2	#3	6-pole fit	7-pole fit
305	305	305	306	306	307
428(w)		416*(s)		363	400*
485(s)	490(s)	491(s)	490(s)	491(s)	482(s)
					505
	580(w)			581(w)	580*
670	670	676	674	674	675
			812(w)	812(w)	815(w)

[a]References are indicated in brackets. Letters in parentheses indicate mode strength: s = strong, w = weak. Asterisks indicate very broad modes (probably made of many modes and caused by defects). Modes at 305–308, 482–491, and 670–675 are three of the four spinel fundamental lattice vibrations. The mode at 812–815 is likely caused by nonstoichiometry (see [40]). O'Horo *et al.* [37] give the following Raman-active mode locations: 311, 492, 611 (F_{2g}); 410 (E_g); and 772 (A_{1g}).

TABLE II

Fundamental Infrared Lattice-Vibration Parameters of Spinel[a]

Mode	Transverse optical frequency (cm^{-1})	Strength	Normalized width	Longitudinal optical frequency (cm^{-1})	Refs.
1*	307	0.45	0.080	311	[37-39]
2	400	0.50	0.20	—	[39]
3*	482	2.70	0.065	497	[37-39]
4	505	0.80	0.080	—	[39]
5	580	0.15	0.30	603	[38,39]
6*	675	0.66	0.045	800	[37-39]
7	815	0.01	0.065	869	[38,39]
		Total = 5.27			

[a]The transverse optical frequency (ν_j) is the location of the mode. Modes marked with an asterisk are three of the four fundamental IR modes (F_{1u}). Frequently, one mode of greater strength (e.g., 3.5) is substituted for our modes 3 and 4 [36-38]. Preudhomme and Tarte [36] identified mode 5 as the fourth fundamental IR vibration by analogy to other spinels. The strength ($\Delta\epsilon_j$) is the contribution of the mode to the dielectric constant. The normalized width (γ_j) is the mode width divided by the mode frequency. The complex dielectric constant (ϵ) is then modeled as a function of frequency (ν) by

$$\epsilon(\nu) = \epsilon_\infty + \sum_j \frac{\Delta\epsilon_j \nu_j^2}{\nu_j^2 - \nu^2 + i\gamma_j \nu_j \nu} ,$$

where the ϵ_∞ term (= 2.892) represents the electronic contributions to the dielectric constant (plus one). This model has a static dielectric constant of 8.16.

TABLE III

Values of n and k Obtained from Various References for Spinel[a]

eV	cm^{-1}	μm	n	n	n	n
3.542	28571	0.350			1.7489 [21]	
3.444	27778	0.360			1.7461	
3.351	27027	0.370			1.7433	
3.263	26316	0.380			1.7409	
3.179	25641	0.390			1.7389	
3.100	25000	0.400			1.7368	
3.064	24710	0.40466	1.73574 [22]	1.736 [2]		
2.952	23810	0.420			1.7332	1.7324 [18]
2.878	23213	0.4308				1.7306
2.845	22944.7	0.43583	1.73054			
2.818	22727	0.440			1.7302	
2.755	22222	0.450				1.7281
2.695	21739	0.460			1.7273	
2.691	21701	0.4608				1.7264
2.638	21277	0.470				1.7252
2.583	20833	0.480			1.7250	
2.551	20572	0.4861				1.7234
2.480	20000	0.500			1.7229	1.7219
2.397	19331	0.5173				1.7207
2.384	19231	0.520			1.7211	
2.353	18975	0.527				1.7197
2.317	18688	0.5351				1.7191
2.296	18519	0.540			1.7195	
2.270	18312	0.54607	1.71896	1.719		
2.254	18182	0.550				1.7180
2.214	17857	0.560			1.7180	1.7172
2.138	17241	0.580			1.7167	1.7160
2.104	16969	0.5893		1.718 [20]		1.7154
2.066	16667	0.600			1.7156	1.7146
2.000	16129	0.620			1.7145	1.7135
1.937	15625	0.640			1.7135	
1.889	15237	0.6563				1.7118
1.879	15152	0.660			1.7126	
1.848	14908	0.6708				1.7112
1.823	14706	0.680			1.7119	
1.803	14543	0.6876				1.7109
1.771	14286	0.700			1.7111	
1.725	13912.1	0.7188				1.7099
1.625	13109.6	0.7628				1.7086
1.455	11735.6	0.85211	1.70728			
1.240	10000	1.0000		1.704 [2]		
1.223	9862.1	1.01398	1.70300	1.703		

(*continued*)

TABLE III (*Continued*)

Spinel

eV	cm^{-1}	μm	n	n	n	k	
1.190	9600	1.0417			1.702		[39]
1.165	9400	1.0638			1.701		
1.141	9200	1.0870			1.701		
1.116	9000	1.1111			1.700		
1.091	8800	1.1364			1.700		
1.066	8600	1.1628			1.700		
1.041	8400	1.1905			1.699		
1.017	8200	1.2195			1.699		
0.9919	8000	1.2500			1.698		
0.9671	7800	1.2821			1.698		
0.9423	7600	1.3158			1.697		
0.9175	7400	1.3514			1.697		
0.8927	7200	1.3889			1.696		
0.8679	7000	1.4286			1.695		
0.8431	6800	1.4706			1.695		
0.8183	6600	1.5152			1.694		
0.8106	6537.74	1.52958	1.69468				
0.7935	6400	1.5625			1.693		
0.7687	6200	1.6129			1.693		
0.7439	6000	1.6667			1.692		
0.7191	5800	1.7241			1.691		
0.6943	5600	1.7857			1.690		
0.6695	5400	1.8519			1.689		
0.6447	5200	1.9231			1.688		
0.6293	5075.91	1.97009	1.68763				
0.6199	5000	2.0000		1.702	1.686	$2.2 \cdot 10^{-13}$	[39]
0.6075	4900	2.0408			1.686	$4.4 \cdot 10^{-13}$	
0.5951	4800	2.0833			1.685	$8.6 \cdot 10^{-13}$	
0.5827	4700	2.1277			1.684	$1.6 \cdot 10^{-12}$	
0.5703	4600	2.1739			1.683	$2.9 \cdot 10^{-12}$	
0.5579	4500	2.2222			1.682	$5.2 \cdot 10^{-12}$	
0.5455	4400	2.2727			1.681	$9.0 \cdot 10^{-12}$	
0.5332	4300.30	2.32542	1.68194				
0.5331	4300	2.3256			1.680	$1.6 \cdot 10^{-11}$	
0.5207	4200	2.3810			1.679	$2.7 \cdot 10^{-11}$	
0.5083	4100	2.4390			1.678	$4.6 \cdot 10^{-11}$	
0.4959	4000	2.5000			1.677	$8.0 \cdot 10^{-11}$	
0.4835	3900	2.5641			1.675	$1.4 \cdot 10^{-10}$	
0.4711	3800	2.6316			1.674	$2.4 \cdot 10^{-10}$	
0.4587	3700	2.7027			1.672	$4.2 \cdot 10^{-10}$	
0.4463	3600	2.7778			1.671	$7.3 \cdot 10^{-10}$	
0.4339	3500	2.8571			1.669	$1.3 \cdot 10^{-9}$	
0.4275	3448	2.9000				$1.0 \cdot 10^{-6}$	[44]
0.4215	3400	2.9412			1.667	$2.3 \cdot 10^{-9}$	[39]

(*continued*)

TABLE III (*Continued*)

Spinel

eV	cm^{-1}	μm	n	k	n	k
0.1017	820	12.195			0.274	0.94
0.0992	800	12.500			0.259	1.1
0.0967	780	12.821			0.240	1.3
0.0942	760	13.158			0.255	1.6
0.0917	740	13.514			0.307	1.9
0.0893	720	13.889			0.431	2.2
0.0868	700	14.286			0.792	2.8
0.0843	680	14.706			2.150	3.2
0.0818	660	15.152			2.799	1.5
0.0794	640	15.625			1.943	0.87
0.0769	620	16.129			1.232	0.96
0.0744	600	16.667			0.805	1.4
0.0719	580	17.241			0.682	2.0
0.0694	560	17.857			0.718	2.6
0.0670	540	18.519			0.931	3.3
0.0645	520	19.231			1.576	4.1
0.0620	500	20.000			2.938	4.7
0.0608	490	20.408			4.040	4.9
0.0595	480	20.833			5.550	4.1
0.0583	470	21.277			5.904	2.5
0.0570	460	21.739			5.460	1.5
0.0558	450	22.222			4.967	1.1
0.0546	440	22.727			4.569	0.82
0.0533	430	23.256			4.264	0.69
0.0521	420	23.810			4.039	0.64
0.0508	410	24.390			3.888	0.62
0.0496	400	25.000			3.795	0.60
0.0484	390	25.641			3.730	0.55
0.0471	380	26.316			3.662	0.49
0.0459	370	27.027			3.576	0.42
0.0446	360	27.778			3.476	0.37
0.0434	350	28.571			3.363	0.34
0.0422	340	29.412			3.238	0.34
0.0409	330	30.303			3.097	0.40
0.0397	320	31.250			2.988	0.61
0.0384	310	32.258			3.242	0.95
0.0372	300	33.333			3.679	0.69
0.0360	290	34.483			3.634	0.37
0.0347	280	35.714			3.509	0.23
0.0335	270	37.037			3.408	0.16
0.0322	260	38.462			3.330	0.13
0.0310	250	40.000			3.267	0.10
0.0298	240	41.667			3.216	0.088
0.0285	230	43.478			3.172	0.077

(*continued*)

TABLE III (*Continued*)

Spinel

eV	cm^{-1}	μm	n	k	n	k
0.0273	220	45.455			3.134	0.067
0.0260	210	47.619			3.101	0.060
0.0248	200	50.000			3.071	0.054
0.0236	190	52.632			3.045	0.048
0.0223	180	55.556			3.022	0.044
0.0211	170	58.824			3.001	0.039
0.0198	160	62.500			2.982	0.036
0.0186	150	66.667			2.965	0.032
0.0174	140	71.429			2.949	0.029
0.0161	130	76.923			2.935	0.026
0.0149	120	83.333			2.923	0.024
0.0136	110	90.909			2.912	0.021
0.0124	100	100.00			2.902	0.019
0.0112	90	111.11			2.893	0.017
0.0099	80	125.00			2.885	0.015
0.0087	70	142.86			2.878	0.013
0.0074	60	166.67			2.873	0.011
0.0062	50	200.00			2.868	$8.8 \cdot 10^{-3}$
0.0050	40	250.00			2.864	$7.0 \cdot 10^{-3}$
0.0037	30	33.333			2.861	$5.2 \cdot 10^{-3}$
0.0025	20	500.00			2.859	$3.5 \cdot 10^{-3}$
0.0019	15	666.67		$2.4 \cdot 10^{-3}$ [42]	2.858	$2.6 \cdot 10^{-3}$
0.0012	10	1000.0	2.88 [42]	$1.8 \cdot 10^{-3}$	2.857	$1.7 \cdot 10^{-3}$
0.0006	5	2000.0		$1.2 \cdot 10^{-3}$	2.857	$8.6 \cdot 10^{-4}$
0.0000	0	∞	2.90 [40]		2.857	
			2.88 [41]			
			2.88–2.90 [43]			

[a]References are indicated in brackets.

TABLE V

Values of dn/dT Obtained from Various References for Spinel[a]

eV	cm^{-1}	μm	dn/dT (1/K)	Notes
2.104	16969	0.5893	$0.90_5 \cdot 10^{-5}$	Measurement [20]
1.959	15803	0.6328	$1.2 \cdot 10^{-5}$	Our measurement
0.310	2500	4.0000	$3.1 \cdot 10^{-6}$	Model [39]
0.0	0	∞	$2.5 \cdot 10^{-4}$	4 GHz, 25–455°C [41]
			$2.8 \cdot 10^{-4}$	35 GHz, 23–1000°C [43]

[a]References are indicated in brackets.

TABLE IV

Calculated Total Hemispherical Emissivity for Spinel

Temperature (K)	Thickness (cm)			
	0.10	0.25	0.50	1.25
200	0.56	0.57	0.57	0.57
300	0.59	0.60	0.61	0.62
400	0.59	0.62	0.64	0.66
500	0.54	0.59	0.62	0.65
600	0.48	0.53	0.57	0.61
700	0.42	0.47	0.51	0.55
800	0.36	0.41	0.45	0.49
900	0.31	0.36	0.40	0.44
1000	0.27	0.31	0.35	0.39

TABLE III *(Continued)*

Spinel

eV	cm^{-1}	μm	n	k	n	k
0.4133	3333	3.0000	1.698 [2]			
0.4092	3300	3.0303			1.664	$4.1 \cdot 10^{-9}$
0.3968	3200	3.1250			1.662	$7.5 \cdot 10^{-9}$
0.3844	3100	3.2258			1.659	$1.4 \cdot 10^{-8}$
0.3720	3000	3.3333			1.656	$2.4 \cdot 10^{-8}$
0.3596	2900	3.4483			1.653	$4.5 \cdot 10^{-8}$
0.3472	2800	3.5714			1.649	$8.4 \cdot 10^{-8}$
0.3348	2700	3.7037			1.645	$1.6 \cdot 10^{-7}$
0.3224	2600	3.8462			1.640	$3.1 \cdot 10^{-7}$
0.3179	2564	3.9000		$6.8 \cdot 10^{-7}$ [44]		
0.3100	2500	4.0000	1.685		1.635	$5.9 \cdot 10^{-7}$
0.2976	2400	4.1667			1.629	$1.1 \cdot 10^{-6}$
0.2852	2300	4.3478			1.622	$2.1 \cdot 10^{-6}$
0.2728	2200	4.5455			1.614	$4.1 \cdot 10^{-6}$
0.2604	2100	4.7619			1.605	$8.6 \cdot 10^{-6}$
0.2480	2000	5.0000	1.659		1.594	$1.8 \cdot 10^{-5}$
0.2418	1950	5.1282			1.587	$2.6 \cdot 10^{-5}$
0.2356	1900	5.2632			1.581	$3.7 \cdot 10^{-5}$
0.2294	1850	5.4054			1.573	$5.2 \cdot 10^{-5}$
0.2232	1800	5.5556			1.565	$7.1 \cdot 10^{-5}$
0.2170	1750	5.7143			1.556	$1.0 \cdot 10^{-4}$
0.2108	1700	5.8824			1.545	$1.4 \cdot 10^{-4}$
0.2046	1650	6.0606			1.534	$2.0 \cdot 10^{-4}$
0.1984	1600	6.2500			1.522	$2.9 \cdot 10^{-4}$
0.1922	1550	6.4516			1.507	$4.4 \cdot 10^{-4}$
0.1860	1500	6.6667			1.491	$6.9 \cdot 10^{-4}$
0.1798	1450	6.8966			1.473	$1.1 \cdot 10^{-3}$
0.1736	1400	7.1429			1.451	$1.8 \cdot 10^{-3}$
0.1674	1350	7.4074			1.427	$2.8 \cdot 10^{-3}$
0.1612	1300	7.6923			1.398	$4.4 \cdot 10^{-3}$
0.1550	1250	8.0000			1.363	$6.6 \cdot 10^{-3}$
0.1488	1200	8.3333			1.322	$9.8 \cdot 10^{-3}$
0.1426	1150	8.6957			1.271	0.014
0.1364	1100	9.0909			1.206	0.020
0.1302	1050	9.5238			1.122	0.028
0.1240	1000	10.000			1.006	0.041
0.1215	980	10.204			0.946	0.049
0.1190	960	10.417			0.875	0.061
0.1165	940	10.683			0.789	0.079
0.1141	920	10.870			0.680	0.11
0.1116	900	11.111			0.539	0.17
0.1091	880	11.364			0.377	0.32
0.1066	860	11.628			0.282	0.54
0.1041	840	11.905			0.255	0.76

(continued)

Magnesium Fluoride (MgF_2)

THOMAS M. COTTER, MICHAEL E. THOMAS,
and WILLIAM J. TROPF
Applied Physics Laboratory
The Johns Hopkins University
Laurel, Maryland

Magnesium fluoride is a tetragonal material with TiO_2 (rutile) structure. The space group is D_{4h}^{14} or $P4_2/mnm$. The unit cell contains two formula units (six atoms). Dimensions of the cell (at 27 °C) are 0.4623 nm along the a axis and 0.3052 nm along the c axis [1, also see 2]. Theoretical density is 3.177 g/cm^3 and melting point is 1528 ± 3 K [2]. A melting point of 1543 K is also reported [3].

Magnesium ions occupy octahedral sites with D_{2h} point symmetry. Six fluorine ions at sites with C_{2v} symmetry surround each magnesium ion. Fluorine-ion positions in the unit cell are known from X-ray diffraction measurements [1, 2].

A wide transparency range from 0.12 to 8 μm [2], good mechanical properties, and low optical index of refraction make magnesium fluoride a desirable material for coatings and interference filters. MgF_2 is a positive uniaxial material, with its highest birefringence in the UV. Except for lithium fluoride, MgF_2 has the shortest wavelength cutoff of any common optical material.

Magnesium fluoride occurs naturally as the mineral selliate [3]. Single-crystal MgF_2 [3, 4] is widely used for windows, lenses, polarizers, and other optical components. Optical-quality, hot-pressed polycrystalline MgF_2 is also used for optical components, particularly in the infrared. IRTRAN 1 [5] is a trade name for hot-pressed MgF_2 made by Kodak; KO-1 is an equivalent Soviet material [6]. Olsen and McBride [7] compare properties of IRTRAN 1 and single-crystal magnesium fluoride.

MgF_2 has been used as a divalent-ion host material for solid-state lasers. Vanadium, nickel, and cobalt have been used as dopants to produce tunable solid-state lasers in the infrared [8, 9].

The UV and IR transparency of magnesium fluoride lends itself to many applications. MgF_2 has been used as a window material for UV detectors in space applications [10, 11]. The birefringence is used to polarize light in the UV [12–14]. One such polarizer, operating from the UV to the IR, has

Copyright © 1991 by Academic Press.
All rights of reproduction in any form reserved.
ISBN 0-12-544422-2

been constructed [15]. The low index of MgF_2 in the IR led to its use as a Soleil compensator in the IR [16]. Magnesium fluoride is also used as a thin film to coat aluminum mirrors for enhanced reflectivity in the vacuum UV [17, 18]. Because of the relatively low index, magnesium fluoride is also used as an antireflection coating for lenses and as a low-index layer in dielectric interference filters.

Magnesium fluoride has a band gap of approximately 11.8 eV. Optical constants from the UV through the XUV have been measured for single-crystal magnesium fluoride [19–22]. The lowest-energy electronic feature of the magnesium fluoride spectrum is an exciton peak centered near 11.8 eV [20, 21]. This is due to an exciton peak at 11.6 eV for the extraordinary component and at 12.2 eV for the ordinary component [22]. The exciton peak obscures the UV absorption edge in this region, measured at 10.9 eV [20]. Although an absorption band beginning at 1320 Å has been observed, the transmission does not drop significantly until 1150 Å (10.8 eV) [2], which is close to the measured absorption edge. The interband transitions begin near 12.2 eV [21], at 12.4 eV for the extraordinary and 12.6 eV for the ordinary ray [22]. The extraordinary-ray absorption curve has structure at 18.6 eV and the ordinary ray at 15 and 20.5 eV [22]. Broad absorption structure near 20.8 eV is attributed to interband transitions [20]. These transitions are believed to arise from transitions from the upper valence band of fluorine ($2p^6$) to the conduction band of magnesium ($3s+3p$) [21]. A peak at 24.5 eV is attributed to a plasmon [20, 21]. The plasmon peak is composed of an extraordinary-ray component at 24.3 eV and an ordinary-ray component at 24.6 eV [22]. Structure seen in the absorption coefficient from 27–40 eV is attributed to interband transitions $2s^2$ level of the fluorine ion to the conduction band [19, 21]. In the 40–56 eV region, two absorption peaks exist: an absorption peak at 47.5 eV caused by a double plasmon and a peak at 54.6 eV attributed to an exciton [19]. Structure from 56–62 eV is attributed to transitions of $2p^6$ electrons of magnesium to the conduction band [19].

Refractive-index data for the MgF_2 transparent region from the UV through the IR are given by many sources [2, 12, 23–27]. Dodge [27] fitted index data (at 19°C) to a Sellmeier-type dispersion relationship of the form

$$n_o^2 - 1 = \frac{2.5903553 \times 10^{10}}{(230,499.30)^2 - \nu^2} + \frac{4.4543708 \times 10^9}{(105,692.13)^2 - \nu^2} + \frac{4.0838897 \times 10^5}{(420.28101)^2 - \nu^2} \tag{1a}$$

and

$$n_e^2 - 1 = \frac{3.0458725 \times 10^{10}}{(271,424.78)^2 - \nu^2} + \frac{6.1300694 \times 10^9}{(110,178.73)^2 - \nu^2} + \frac{4.4070997 \times 10^5}{(420.66305)^2 - \nu^2}, \tag{1b}$$

where ν is the frequency in wave numbers. Equation 1 represents electro-

nic resonances with the first two terms and all IR resonances with the third term. These terms fall in the middle of the measured electronic transitions and lattice vibrations, respectively. The overall accuracy of index calculated from Eq. 1 is quoted as better than 2×10^{-5} over the 1400–50,000 cm^{-1} range.

Change in the index of refraction with temperature, pressure, and stress is available. Thermo-optic data are given by many sources [2, 28–30] without good agreement; data from the National Bureau of Standards [28] are considered comprehensive, cover a wide temperature range, and agree well with recent measurements of the temperature dependence of optical dispersion [30]. The elastic properties of MgF_2 have been reported in the form of elastic constants, photoelastic constants, and piezoelectric constants [31, 32].

Optical properties of thin films of magnesium fluoride have been studied extensively. Much disparity exists between published data due to variations of the conditions and method of preparation of the sample under study [33–37]. In addition, thin-film properties usually do not match single-crystal properties [19, 20]. Consequently, this article concentrates on properties of single crystals.

Radiation damage of MgF_2 is described elsewhere [38]. Studies of radiation effects on the absorption of magnesium fluoride have revealed absorption bands in the UV. Three prominent absorption peaks at 117, 260, and 370 nm develop, which can be attributed to the creation of *F* centers by radiation [38]. No observations of IR absorption due to radiation have been reported [38]. The characterization of the fluorescence of MgF_2 has also been undertaken [38, 39].

Absorption at the IR edge of transparency is dominated by multiphonon absorption [40]. A model of multiphonon absorption [41] has been developed and confirmed with experimental data over a wide temperature range. Model constants for the ordinary ray of MgF_2 are given by Thomas and Joseph [42].

The fundamental (one-phonon) lattice vibrations occur in the 250–625 cm^{-1} spectral region. Group theory predicts the following phonon modes for MgF_2 [43–46]:

$$\Gamma = A_{1g} + A_{2g} + A_{2u} + B_{1g} + B_{2g} + 2B_{1u} + E_g + 3E_u, \tag{2}$$

where the A_{2g} and B_{1u} modes are optically inactive, the A_{2u} ($\mathbf{E}\|c$) and E_u ($\mathbf{E}\perp c$) modes are IR-active, and the remaining modes are Raman-active. Table I lists the IR modes as determined by Barker [44], Thomas and Joseph [42], and Giordano and Benoit [46]. Locations of the Raman modes are given by Porto *et al.* [45] as 92 (B_{1g}), 295 (E_g), 410 (A_{1g}), and 515 (B_{2g}) cm^{-1}.

Table I also lists both the transverse and longitudinal optical frequen-

cies. The transverse optical frequencies are the mode locations; the maximum longitudinal-mode frequency is an important parameter in the multiphonon-absorption model [41], since it designates the maximum phonon frequency.

At frequencies below the lowest-frequency transverse optical mode, absorption decreases and the material becomes transparent. The magnitude of absorption is thought to be a combination of contributions from both the tail of the fundamental lattice vibrations and various multiphonon difference bands. The index of refraction now also includes the effect of lattice vibrations. Estimates of low-frequency absorption made from the red wing of the fundamental modes (Table I) for MgF_2 are about 60% of the ordinary-ray imaginary index of refraction and 95% of the extraordinary-ray values determined by Bystrov *et al.* [47] in the 10–23 cm^{-1} region. Measurements of two different sintered samples of polycrystalline MgF_2 by Stead and Simonis [48] showed yet higher absorption.

The low-frequency index of refraction of magnesium fluoride is given by Fontanella *et al.* [49] at 1000 Hz and by Bystrov *et al.* [47] for the 300–700 GHz range. These data agree with each other and with the data in Table I except for the slightly higher extraordinary-ray value given by Fontanella *et al.* [49]. No temperature-dependent low-frequency index data were found, but pressure dependence is given by Link *et al.* [50].

Table II was constructed from measurements reported in the literature as well as model predictions [51]. Real-index data (n) from 10–83 eV and imaginary-index (k) data from 11–83 eV are taken from several sources [19–22]. The measurements by Hanson *et al.* [19], Williams *et al.* [20], and Stephan *et al.* [21] did not distinguish between ordinary- and extraordinary-ray components. These data can be considered to be an "average" for the crystal. Thomas *et al.*'s [22] measurement of ordinary- and extraordinary-ray optical constants for the 11–28 eV region are also included.

Ordinary-ray index data in the 0.115–0.200 μm region are taken from Williams and Arakawa [23], supplemented by measurements of Steinmetz *et al.* [12]. Extraordinary-ray data for this region are obtained by combining ordinary-ray data with the anomalous dispersion data of Chandrasekharan and Damany [24]. Both ordinary- and extraordinary-ray data in the 1400–50,000 cm^{-1} range are calculated from the Sellmeier dispersion relationships (Eq. 1) of Dodge [27]. One value of ordinary-ray absorption coefficient is given by Steinmetz *et al.* [12].

Single [51] and multiphonon [41] lattice-vibration models are used to estimate the complex index of refraction for wavelengths of 7.41 μm and longer. Measurements of Bystrov *et al.* [47], and Fontanella *et al.* [49] are the best available low-frequency index data.

The accuracy of index measurements in the electronic region is relatively poor; estimated errors are approximately 10%. Data from Hanson *et al.*

[19] and Williams *et al.* [20] agree well in the overlap region (20–27 eV). Data from Stephan *et al.* [21] have consistently lower n and higher k compared with other sources [19, 20]. Data from Thomas *et al.* [22] have precision on the order of ±5%.

The real-index data from 0.115–0.200 μm have a quoted accuracy of ±0.002; the dispersion formula of Dodge [27] represents the data from 0.2–7.0 μm within ±0.00002. The accuracy of complex-index data at longer wavelength is unknown, but uncertainty in the values is probably in the least-significant digit reported in Table II (that is, n accurate to ±0.01 and k to about 5%). Low-frequency real-index measurements of Fontanella *et al.* [49] are given an accuracy of ±0.001. Bystrov *et al.* [47] states the accuracy of n to be ±0.005 and k to be within ±5%.

Figures 1 and 2 show a composite of the complex index of refraction based on the data of Table II. Figure 1 gives the ordinary-ray index and Fig. 2 shows the extraordinary-ray properties. Complex index-of-refraction data for the electronic region (wavelengths below 0.05 μm) derived from unpolarized measurements with an unknown mix of ordinary- and extraordinary-ray index are included in Fig. 1.

Tables III and IV give temperature dependence for the real part of the index of refraction. Measurements of dn/dT by Feldman *et al.* [28] typically have a standard deviation to a linear temperature-dependence fit of 0.1×10^{-6}/K.

REFERENCES

1. R. W. G. Wyckoff, "Crystal Structures," Interscience Publishers, New York, 251 (1963).
2. A. Duncanson and R. W. H. Stevenson, "Some Properties of Magnesium Fluoride Crystallized from the Melt," *Proc. Phys. Soc. (London)* **72**, 1001 (1958).
3. W. A. Hargreaves, "Magnesium Fluoride Update and Summary of Optical Properties," *Laser focus* **18**, 86 (1982).
4. "Crystal Optics," Catalog OP 101, Harshaw/Filtrol, Solon, Ohio, 26 (1985).
5. "Kodak IRTRAN Infrared Optical Materials," Publication U-72, Eastman Kodak Company, Rochester, New York, (1971).
6. I. V. Men', F. K. Volynets, and Y. P. Smirnaya, "The Emissivity of KO-1 Optical Ceramic," *Sov. J. Opt. Tech.* **41**, 95 (1974).
7. A. L. Olsen and W. R. McBride, "Transmittance of Single-Crystal Magnesium Fluroide and IRTRAN-1 in the 0.2 to 15 μ Range," *J. Opt. Soc. Am.* **53**, 1003 (1963).
8. L. F. Johnson and H. J. Guggenheim, "Phonon-Terminated Optical Masers," *Phys. Rev.* **149**, 179 (1967).
9. P. F. Moulton, "Pulse-Pumped Operation of Divalent Transition-Metal Lasers," *IEEE J. Quantum Electro.* **QE-18**, 1185 (1982).
10. D. Gormly, M. Bottema, B. Darnell, W. Fowler, and W. Medenica, "Fabrication of MgF_2 and LiF Windows for the Hubble Space Telescope Imaging Spectrograph," *Proc. SPIE* **992**, 139 (1988).
11. W. Vishman, A. G. Eubanks, G. F. Pieper, and J. H. Bredekamp, "Photomultiplier Window Materials under Electron Irradiation: Fluorescence and Phosphorescence," *Appl. Opt.* **14**, 2104 (1975).

12. D. L. Steinmetz, W. G. Phillips, M. Wirick, and F. F. Forbes, "Polarizer for the Vacuum Ultraviolet," *Appl. Opt.* **6**, 1001 (1967).
13. G. Hass and W. R. Hunter, "Reflection Polarizers for the Vacuum Ultraviolet Using Al + MgF_2 Mirrors and an MgF_2 Plate," *Appl. Opt.* **17**, 76 (1978).
14. W. C. Johnson, Jr., "Magnesium Fluoride Polarizing Prism for the Vacuum Ultraviolet," *Rev. Sci. Instrum.* **35**, 1375 (1964).
15. G. C. Morris and A. S. Abramson, "Single Rochon Prisms for Light Polarization Between 1400–70,000 Å," *Appl. Opt.* **8**, 1249 (1969).
16. E. D. Palik, "A MgF_2 Soleil Compensator for the Near Infrared," *Appl. Opt.* **7**, 978 (1968).
17. W. R. Hunter, J. F. Osantowski, and G. Hass, "Reflectance of Aluminum Overcoated with MgF_2 and LiF in the Wavelength Region from 1600 Å to 300 Å at Various Angles of Incidence," *Appl. Opt.* **10**, 540 (1971).
18. B. Bates and D. J. McCartney, "Optical Properties of Multilayer Overcoated Aluminum Films in the UV (2000–2500 Å)," *Appl. Opt.* **15**, 2216 (1976).
19. W. F. Hanson, E. T. Arakawa, and M. W. Williams, "Optical Properties of MgO and MgF_2 in the Extreme Ultraviolet Region," *J. Appl. Phys.* **43**, 1661 (1972).
20. M. W. Williams, R. A. MacRae, and E. T. Arakawa, "Optical Properties of Magnesium Fluoride in the Vacuum Ultraviolet," *J. Appl. Phys.* **38**, 1701 (1967).
21. G. Stephan, Y. Le Calvez, J. C. Lemonier, and S. Robin, "Properties Optiques et Spectre Electronique du MgF_2 et du CaF_2 de 10 à 48 eV," *J. Phys. Chem. Solids* **30**, 601 (1969).
22. J. Thomas, G. Stephan, J. C. Lemonnier, M. Nisar, and S. Robin, "Optical Anisotropy of MgF_2 in Its UV Absorption Region," *Phys. Stat. Solidi B* **56**, 163 (1973).
23. M. W. Williams and E. T. Arakawa, "Optical Properties of Crystalline MgF_2 from 115 to 400 nm," *Appl. Opt.* **18**, 1477 (1979).
24. V. Chandrasekharan and H. Damany, "Anomalous Dispersion of Birefringence of Sapphire and Magnesium Fluoride in the Vacuum Ultraviolet," *Appl. Opt.* **8**, 671 (1969).
25. W. L. Wolfe, "Properties of Optical Materials," in "Handbook of Optics" (W. G. Driscoll, ed.), McGraw-Hill, New York, 7–95 (1978).
26. H. H. Li, "Refractive Index of Alkaline Earth Halides and Its Wavelength and Temperature Derivatives," *J. Phys. Chem. Ref. Data* **9**, 161 (1980).
27. M. J. Dodge, "Refractive Properties of Magnesium Fluoride," *Appl. Opt.* **23**, 1980 (1984).
28. A. Feldman, D. Horowitz, R. M. Waxler, and M. J. Dodge, "Optical Materials Characterization Final Technical Report, February 1, 1978–September 30, 1978," National Bureau of Standards Technical Note 993, 49 (February 1979).
29. P. H. Lissberger, A. K. Roy, I. W. Salter, and J. A. Shan, "Thermal and Structural Constraints of Magnesium Fluoride and Zinc Sulphide for Optical Coating Applications," *Opt. Acta* **33**, 925 (1986).
30. D. P. Belanger, A. R. King, and V. Jaccarine, "Temperature Dependence of the Optical Birefringence of MnF_2, MgF_2, and ZnF_2," *Phys. Rev. B* **29**, 2636 (1984).
31. S. Chung, "Photoelastic Properties of Magnesium Fluoride," in "Basic Optical Properties of Materials, Summaries of Papers," National Bureau of Standards Special Publication 574, 213 (May 1980).
32. I. I. Afranas'ev, L. K. Andrianova, I. Y. Mamontov, and V. M. Reiterov "Photoelastic Properties and Residual Stresses in Magnesium Fluoride Crystals," *Sov. Phys. Solid State* **17**, 2006 (1975).
33. D. Smith and P. Baumeister, "Refractive Index of Some Oxide and Fluoride Coating Materials," *Appl. Opt.* **18**, 111 (1979).
34. O. R. Wood II, H. G. Craighead, J. E. Sweeney, and P. J. Maloney, "Vacuum Ultraviolet Loss in Magnesium Fluoride Films," *Appl. Opt.* **23**, 3644 (1984).

35. P. J. Martin, W. G. Sainty, R. P. Netterfield, D. R. McKenzie, D. J. H. Cockayne, S. H. Sie, O. R. Wood, and H. G. Craighead, "Influence of Ion Assistance on the Optical Properties of MgF_2," *Appl. Opt.* **26**, 1235 (1987).
36. A. S. Barrière and A. Lachter, "Optical Transitions in Disordered Thin Films of the Ionic Compounds MgF_2 and AlF_3 as a Function of Their Conditions of Preparation," *Appl. Opt.* **16**, 2865 (1977).
37. J. M. Siqueiros, R. Machorro, and L. E. Regalado, "Determination of the Optical Constants of MgF_2 and ZnS from Spectrophotometric Measurements and the Classical Oscillator Method," *Appl. Opt.* **27**, 2549 (1988).
38. M. J. Weber, ed., "CRC Handbook of Laser Science and Technology, Volume 3: Optical Materials; Part 1: Nonlinear Optical Properties/Radiation Damage," CRC Press, Boca Raton, Fla., 304 (1988).
39. W. Viehmann, A. G. Eubanks, G. F. Pieper, and J. H. Bredekamp, "Photomultiplier Window Materials under Electron Irradiation: Fluroescence and Phosphoresence," *Appl. Opt.* **14**, 2104 (1975).
40. T. F. Deutsch, "Absorption Coefficient of Infrared Laser Window Materials," *J. Phys. Chem. Solids* **34**, 2091 (1973).
41. M. E. Thomas, R. I. Joseph, and W. J. Tropf, "Infrared Transmission Properties of Sappbire, Spinel, Yttria, and ALON as a Function of Frequency and Temperature," *Appl. Opt.* **27**, 239 (1988).
42. M. E. Thomas and R. I. Joseph, "A Comprehensive Model for the Intrinsic Transmission Properties of Optical Windows," *Proc. SPIE* **929**, 87 (1988).
43. G. R. Hunt and C. H. Perry, "Far-Infrared Reflectance and Transmittance of Potassium Magnesium Fluoride and Magnesium Fluoride," *Phys. Rev.* **134**, A688 (1964).
44. A. S. Barker, "Transverse and Longitudinal Optic Mode Study in MgF_2 and ZnF_2," *Phys. Rev.* **136**, A1290 (1964).
45. S. P. S. Porto, P. A. Fleury, and T. C. Damen, "Raman Spectra of TiO_2, MgF_2, ZnF_2, FeF_2, and MnF_2," *Phys. Rev.* **154**, 522 (1967).
46. J. Giordano and C. Benoit, "Infrared Spectra of Iron, Zinc, and Magnesium Fluorides: I. Analysis of Results," *J. Phys. C: Solid State Phys.* **21**, 2749 (1988).
47. V. P. Bystrov, Y. G. Goncharov, G. V. Kozlov, and A. F. Kupriyanenko, "Dielectric Properties of Optical Crystals at Submillimeter Wavelengths," *Sov. Phys. Tech. Phys.* **31**, 1206 (1986).
48. M. Stead and G. Simonis, "Near Millimeter Wave Characterization of Dual Mode Materials," *Appl. Opt.* **28**, 1874 (1989).
49. J. Fontanella, C. Andeen, and D. Schuele, "Low-Frequency Dielectric Constants of α-Quartz, Sapphire, MgF_2, and MgO," *J. Appl. Phys.* **45**, 2852 (1974).
50. J. Link, M. C. Wintersgill, J. J. Fontanella, V. E. Bean, and C. G. Andeen, "Pressure Variation of the Low Frequency Dielectric Constants of Some Anisotropic Crystals," *J. Appl. Phys.* **52**, 936 (1981).
51. M. E. Thomas, "A Computer Code for Modeling Optical Properties of Window Materials," *Proc. SPIE* **1112**, 260 (1989).

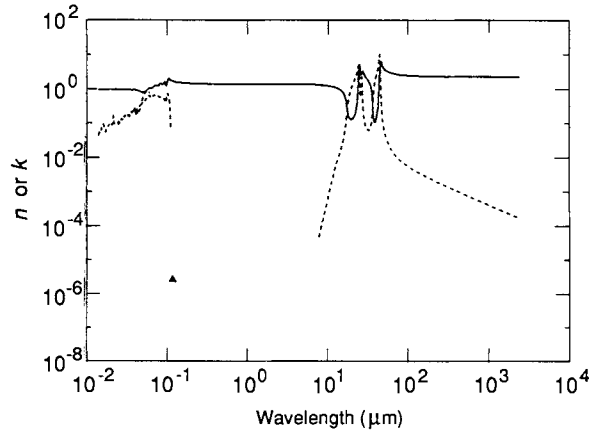

Fig. 1. Log–log plot of n_o (solid line) and k_o (dashed line) versus wavelength in micrometers for the ordinary ray of magnesium fluoride. Data below 0.05 μm (electronic region) are combined ordinary- and extraordinary-ray results.

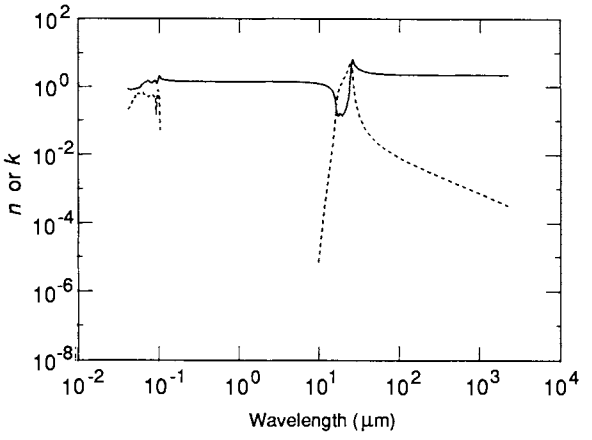

Fig. 2. Log–log plot of n_e (solid line) and k_e (dashed line) versus wavelength in micrometers for the extraordinary ray of magnesium fluoride.

TABLE I

Fundamental Infrared Lattice Vibration Parameters for MgF_2[a]

Mode	Transverse optical frequency (cm^{-1})	Strength	Normalized width	Longitudinal optical frequency (cm^{-1})	Refs.
		E ⊥ c axis (ordinary ray)			
1	247	2.22	0.014	303	[44]
2	410	0.19	0.033	415	[44]
3	450	1.14	0.058	617	[44]
	Total = 3.55				
1	248	2.23	0.0115	302	[51]
2	408.5	0.22	0.0165	414	[51]
3	447	1.10	0.025	621	[51]
4[b]	535	0.05	0.3		[51]
	Total = 3.60				
1	251			304	[46]
2	413			422	[46]
3	452			610	[46]
	Total = 3.38				
		E ∥ c axis (extraordinary ray)			
1	399	2.7	0.048	625	[44]
2[c]	556	0.01	0.08		
	Total = 2.71				
1	404	2.69		626	[46]

[a]The frequency (ν_j) is the location of the mode (transverse optical frequency). The strength ($\Delta\epsilon_j$) is the contribution of the mode to the dielectric constant. The normalized width (γ_j) is the mode width divided by the mode frequency. The complex dielectric constant (ϵ) is then modeled as a function of frequency (ν) by:

$$\epsilon(\nu) = \epsilon_\infty + \sum_j \frac{\Delta\epsilon_j \, \nu_j^2}{\nu_j^2 - \nu^2 + i\gamma_j \nu_j \nu} ,$$

where the ϵ_∞ term (= 1.886 for E ⊥ c and 1.918 for E ∥ c axis) represents the electronic contributions to the dielectric constant (plus one).

[b]Mode 4 (E ⊥ c) is probably caused by an impurity.

[c]Barker [44] identifies this as a weak forbidden mode.

TABLE II

Values of n and k Obtained from Various References for Magnesium Fluoride[a]

eV	cm^{-1}	μm	n	k	n	k
83.0	669608	0.0149	0.906 [19]	0.046 [19]		
78.5	633511	0.0158	0.912	0.070		
76.9	620336	0.0161	0.906	0.064		
75.5	608714	0.0164	0.906	0.081		
74.2	598809	0.0167	0.902	0.083		
72.3	583074	0.0172	0.918	0.095		
68.5	552191	0.0181	0.902	0.055		
66.0	532322	0.0188	0.915	0.073		
65.0	524256	0.0191	0.917	0.076		
64.0	516191	0.0194	0.919	0.079		
63.0	508125	0.0197	0.921	0.083		
62.0	500060	0.0200	0.923	0.090		
61.0	491994	0.0203	0.924	0.095		
60.0	483929	0.0207	0.926	0.096		
59.0	475863	0.0210	0.926	0.093		
58.0	467798	0.0214	0.925	0.090		
57.0	459732	0.0218	0.925	0.092		
56.0	451667	0.0221	0.913	0.094		
55.0	443601	0.0225	0.936	0.165		
54.0	435536	0.0230	0.940	0.103		
53.0	427470	0.0234	0.934	0.098		
52.0	419405	0.0238	0.930	0.098		
51.0	411339	0.0243	0.927	0.100		
50.0	403274	0.0248	0.925	0.103		
49.0	395209	0.0253	0.922	0.107		
48.0	387143	0.0258	0.920	0.111		
47.5	383110	0.0261	0.920	0.113	0.957 [21]	0.092 [21]
47.0	379078	0.0264	0.919	0.115	0.956	0.096
46.5	375045	0.0267	0.919	0.118	0.955	0.099
46.0	371012	0.0270	0.919	0.120	0.954	0.103
45.5	366979	0.0272	0.918	0.122	0.952	0.107
45.0	362947	0.0276	0.918	0.125	0.949	0.110
44.5	358914	0.0279	0.918	0.128	0.949	0.114
44.0	354881	0.0282	0.918	0.131	0.947	0.119
43.5	350848	0.0285	0.918	0.134	0.942	0.125
43.0	346816	0.0288	0.918	0.137	0.936	0.130
42.5	342783	0.0292	0.918	0.142	0.929	0.129
42.0	338750	0.0295	0.918	0.145	0.922	0.129
41.5	334717	0.0299	0.918	0.150	0.914	0.129
41.0	330685	0.0302	0.919	0.154	0.907	0.131
40.5	326652	0.0306	0.919	0.159	0.899	0.139
40.0	322619	0.0310	0.919	0.163	0.885	0.149
39.5	318586	0.0314	0.919	0.167	0.894	0.158
39.0	314554	0.0318	0.920	0.171	0.894	0.169

(*continued*)

TABLE II (*Continued*)

Magnesium Fluoride

eV	cm^{-1}	μm	n	k	n	k
38.5	310521	0.0322	0.921	0.172	0.898	0.170
38.0	306488	0.0326	0.922	0.173	0.902	0.168
37.5	302456	0.0331	0.923	0.174	0.901	0.165
37.0	298423	0.0335	0.924	0.175	0.900	0.162
36.5	294390	0.0340	0.921	0.175	0.899	0.160
36.0	290357	0.0344	0.925	0.175	0.896	0.159
35.5	286325	0.0349	0.925	0.175	0.897	0.159
35.0	282292	0.0354	0.925	0.175	0.898	0.162
34.5	278259	0.0359	0.918	0.177	0.899	0.166
34.0	274226	0.0365	0.904	0.179	0.893	0.176
33.5	270194	0.0370	0.898	0.183	0.890	0.188
33.0	266161	0.0376	0.893	0.190	0.888	0.206
32.5	262128	0.0381	0.891	0.200	0.887	0.224
32.0	258095	0.0387	0.897	0.210	0.880	0.221
31.5	254063	0.0394	0.904	0.219	0.867	0.199
31.0	250030	0.0400	0.910	0.228	0.858	0.200
30.5	245997	0.0407	0.910	0.232	0.857	0.235
30.0	241964	0.0413	0.907	0.228	0.865	0.283
29.5	237932	0.0420	0.898	0.224	0.876	0.273
29.0	233899	0.0428	0.885	0.221	0.873	0.184
28.5	229866	0.0435	0.875	0.234	0.850	0.164
28.0	225833	0.0443	0.865	0.254	0.842	0.200
27.5	221801	0.0451	0.855	0.264	0.841	0.232
27.0	217768	0.0459	0.842	0.272	0.822	0.227
26.5	213735	0.0468	0.824	0.282	0.812	0.246
26.0	209702	0.0477	0.805	0.308	0.801	0.267
25.5	205670	0.0486	0.789	0.336	0.787	0.294
25.0	201637	0.0496	0.779	0.384	0.771	0.324
24.5	197604	0.0506	0.769	0.443	0.758	0.361
24.0	193572	0.0517	0.788	0.524	0.736	0.410
23.5	189539	0.0528	0.816	0.610	0.742	0.445
23.0	185506	0.0539	0.856	0.666	0.765	0.475
22.5	181473	0.0551	0.900	0.729	0.820	0.546
22.0	177441	0.0564	0.946	0.771	0.849	0.564
21.5	173408	0.0577	1.012	0.807	0.898	0.624
21.0	169375	0.0590	1.102	0.819	0.891	0.616
20.5	165342	0.0605	1.184	0.805	0.965	0.643
20.0	161310	0.0620	1.266	0.767	0.981	0.646
19.8	159697	0.0626			0.995	0.642
19.6	158083	0.0633			1.000	0.645
19.4	156470	0.0639			0.996	0.615
19.2	154857	0.0646			1.001	0.605
19.0	153244	0.0653			1.012	0.615
18.8	151631	0.0659			1.021	0.618

(*continued*)

TABLE II (*Continued*)

Magnesium Fluoride

eV	cm^{-1}	μm	*n*	*k*	*n*	*k*
18.6	150018	0.0667			1.034	0.626
18.4	148405	0.0674			1.048	0.636
18.2	146792	0.0681			1.072	0.661
18.0	145179	0.0689	1.322 [20]	0.671 [20]	1.093	0.651
17.8	143566	0.0697	1.337	0.658	1.095	0.654
17.6	141952	0.0704	1.347	0.657	1.103	0.661
17.4	140339	0.0713	1.356	0.660	1.114	0.660
17.2	138726	0.0721	1.359	0.665	1.090	0.665
17.0	137113	0.0729	1.354	0.661	1.080	0.663
16.8	135500	0.0738	1.348	0.605	1.108	0.670
16.6	133887	0.0747	1.346	0.631	1.143	0.676
16.4	132274	0.0756	1.369	0.606	1.180	0.689
16.2	130661	0.0765	1.387	0.575	1.195	0.664
16.0	129048	0.0775	1.435	0.547	1.196	0.639
15.9	128241	0.0780	1.449	0.539	1.195	0.630
15.8	127435	0.0785	1.457	0.533	1.195	0.625
15.7	126628	0.0790	1.465	0.528	1.193	0.623
15.6	125821	0.0795	1.474	0.529	1.191	0.620
15.5	125015	0.0800	1.483	0.529	1.190	0.617
15.4	124208	0.0805	1.490	0.531	1.196	0.623
15.3	123402	0.0810	1.495	0.533	1.209	0.631
15.2	122595	0.0816	1.500	0.536	1.228	0.635
15.1	121789	0.0821	1.505	0.538	1.248	0.638
15.0	120982	0.0827	1.508	0.533	1.256	0.630
14.9	120176	0.0832	1.510	0.520	1.257	0.622
14.8	119369	0.0838	1.512	0.510	1.257	0.614
14.7	118563	0.0843	1.513	0.501	1.257	0.608
14.6	117756	0.0849	1.508	0.501	1.258	0.602
14.5	116949	0.0855	1.498	0.502	1.262	0.600
14.4	116143	0.0861	1.488	0.504	1.268	0.596
14.3	115336	0.0867	1.481	0.514	1.268	0.595
14.2	114530	0.0873	1.470	0.518	1.260	0.598
14.1	113723	0.0879	1.473	0.517	1.250	0.602
14.0	112917	0.0886	1.496	0.507	1.237	0.607
13.9	112110	0.0892	1.520	0.496	1.234	0.607
13.8	111304	0.0898	1.541	0.484	1.231	0.608
13.7	110497	0.0905	1.561	0.473	1.236	0.605
13.6	109691	0.0912	1.573	0.463	1.239	0.606
13.5	108884	0.0918	1.584	0.453	1.242	0.606
13.4	108077	0.0925	1.588	0.444	1.235	0.603
13.3	107271	0.0932	1.585	0.448	1.225	0.594
13.2	106464	0.0939	1.562	0.453	1.215	0.585
13.1	105658	0.0946	1.555	0.454	1.202	0.577
13.0	104851	0.0954	1.561	0.429	1.192	0.568

(*continued*)

TABLE II (*Continued*)

Magnesium Fluoride

eV	cm^{-1}	μm	n	k	n	k
12.9	104045	0.0961	1.566	0.393	1.192	0.553
12.8	103238	0.0969	1.579	0.357	1.240	0.530
12.7	102432	0.0976	1.574	0.332	1.297	0.526
12.6	101625	0.0984	1.501	0.329	1.272	0.558
12.5	100818	0.0992	1.409	0.364	1.258	0.593
12.4	100012	0.1000	1.330	0.409	1.232	0.636
12.3	99205	0.1008	1.269	0.451	1.212	0.676
12.2	98399	0.1016	1.231	0.491	1.194	0.717
12.1	97592	0.1025	1.207	0.542	1.177	0.758
12.0	96786	0.1033	1.351	0.723	1.176	0.790
11.9	95979	0.1042	1.603	0.953	1.235	0.828
11.8	95173	0.1051	1.759	1.073	1.343	0.834
11.7	94366	0.1060	1.872	1.024	1.477	0.831
11.6	93560	0.1069	2.201	0.807	1.573	0.822
11.5	92753	0.1078	2.258	0.683	1.617	0.826
11.4	91946	0.1088	2.245	0.524	1.645	0.793
11.3	91140	0.1097	2.219	0.332	1.689	0.640
11.2	90333	0.1107	2.123	0.220	1.671	0.478
11.1	89527	0.1117	2.010	0.110	1.590	0.341
11.0	88720	0.1127	1.956	0.058	1.519	0.197
10.9	87914	0.1137	1.904		1.490	0.028
10.8	87107	0.1148	1.883		1.480	
10.7	86301	0.1159	1.812		1.469	
10.6	85494	0.1170	1.773		1.463	
10.5	84688	0.1181	1.734		1.459	
10.4	83881	0.1192	1.694		1.456	
10.3	83074	0.1204	1.660		1.453	
10.2	82268	0.1216	1.630		1.449	
10.1	81461	0.1228	1.615		1.446	
10.0	80655	0.1240	1.601		1.443	

eV	cm^{-1}	μm	n_o	k_o	n_e	k_e
27.0	217768	0.0459	0.811 [22]	0.214 [22]	0.832 [22]	0.214 [22]
26.5	213735	0.0468	0.796	0.240	0.816	0.223
26.0	209702	0.0477	0.784	0.282	0.803	0.241
25.5	205670	0.0486	0.770	0.322	0.790	0.261
25.0	201637	0.0496	0.765	0.361	0.794	0.289
24.5	197604	0.0506	0.756	0.398	0.799	0.332
24.0	193572	0.0517	0.763	0.422	0.807	0.369
23.5	189539	0.0528	0.774	0.441	0.816	0.405
23.0	185506	0.0539	0.790	0.456	0.827	0.441
22.5	181473	0.0551	0.809	0.469	0.837	0.468
22.0	177441	0.0564	0.837	0.493	0.847	0.598

(*continued*)

TABLE II (*Continued*)

Magnesium Fluoride

eV	cm^{-1}	μm	n_o	k_o	n_e	k_e
21.5	173408	0.0577	0.886	0.545	0.866	0.588
21.0	169375	0.0590	0.959	0.600	0.881	0.614
20.5	165342	0.0605	1.003	0.607	0.894	0.612
20.0	161310	0.0620	1.010	0.610	0.905	0.607
19.5	157277	0.0636	1.006	0.541	0.919	0.607
19.0	153244	0.0653	1.000	0.540	0.983	0.623
18.5	149211	0.0670	1.008	0.572	1.117	0.652
18.0	145179	0.0689	1.080	0.604	1.151	0.652
17.5	141146	0.0708	1.180	0.627	1.264	0.620
17.0	137113	0.0729	1.189	0.632	1.317	0.575
16.5	133080	0.0751	1.186	0.626	1.353	0.561
16.0	129048	0.0775	1.184	0.608	1.416	0.556
15.5	125015	0.0800	1.192	0.581	1.513	0.496
15.0	120982	0.0827	1.354	0.555	1.387	0.508
14.5	116949	0.0855	1.342	0.548	1.299	0.550
14.0	112917	0.0886	1.257	0.529	1.272	0.520
13.5	108884	0.0918	1.343	0.514	1.348	0.538
13.0	104851	0.0954	1.546	0.467	1.449	0.504
12.8	103238	0.0969	1.281	0.386	1.423	0.463
12.6	101625	0.0984	1.162	0.405	1.419	0.485
12.4	100012	0.1000	1.222	0.545	1.470	0.224
12.2	98399	0.1016	1.465	0.709	1.346	0.151
12.0	96786	0.1033	1.693	0.714	1.223	0.462
11.8	95173	0.1051	1.923	0.620	1.343	0.752
11.6	93560	0.1069	1.943	0.515	1.636	0.777
11.4	91946	0.1088	1.834	0.380	1.911	0.612
11.2	90333	0.1107	1.701	0.241	1.988	0.401
11.0	88720	0.1127	1.538	0.063	1.931	0.054
10.9	87914	0.1137			1.892	
10.8	87107	0.1148			1.776	
10.781	86957	0.115	1.714 [23]		1.694[b]	
10.7	86301	0.1159			1.657 [22]	
10.332	83333	0.120	1.626		1.626[b]	
10.230	82508	0.1212		$3.3 \cdot 10^{-6}$ [12]		
9.919	80000	0.125	1.588		1.597[b]	
9.537	76923	0.130	1.555		1.567[b]	
8.856	71429	0.140	1.513		1.527[b]	
8.266	66667	0.150	1.484		1.498[b]	
7.749	62500	0.160	1.464		1.478[b]	
7.293	58824	0.170	1.451		1.465[b]	
6.965	56180	0.1780	1.43975 [12]		1.45365 [12]	
6.888	55556	0.180	1.440 [23]			
6.702	54054	0.1850	1.43424 [12]		1.44797	
6.526	52632	0.190	1.430 [23]			

(*continued*)

TABLE II (*Continued*)

Magnesium Fluoride

eV	cm^{-1}	μm	n_o	k_o	n_e	k_e
6.199	50000	0.200	1.42309 [27]		1.43657 [27]	
5.904	47619	0.210	1.41754		1.43085	
5.636	45455	0.220	1.41291		1.42608	
5.391	43478	0.230	1.40900		1.42204	
5.166	41667	0.240	1.40567		1.41859	
4.959	40000	0.250	1.40280		1.41562	
4.769	38462	0.260	1.40030		1.41303	
4.592	37037	0.270	1.39812		1.41077	
4.428	35714	0.280	1.39620		1.40877	
4.275	34483	0.290	1.39450		1.40700	
4.133	33333	0.300	1.39298		1.40543	
4.000	32258	0.310	1.39162		1.40402	
3.875	31250	0.320	1.39040		1.40275	
3.757	30303	0.330	1.38930		1.40160	
3.647	29412	0.340	1.38830		1.40056	
3.542	28571	0.350	1.38739		1.39961	
3.444	27778	0.360	1.38656		1.39875	
3.351	27027	0.370	1.38580		1.39796	
3.263	26316	0.380	1.38510		1.39723	
3.179	25641	0.390	1.38446		1.39656	
3.100	25000	0.400	1.38387		1.39594	
2.952	23810	0.420	1.38281		1.39484	
2.818	22727	0.440	1.38189		1.39389	
2.695	21739	0.460	1.38110		1.39306	
2.583	20833	0.480	1.38040		1.39233	
2.480	20000	0.500	1.37978		1.39168	
2.384	19231	0.520	1.37923		1.39111	
2.296	18519	0.540	1.37873		1.39059	
2.214	17857	0.560	1.37829		1.39013	
2.138	17241	0.580	1.37789		1.38971	
2.066	16667	0.600	1.37752		1.38932	
2.000	16129	0.620	1.37718		1.38897	
1.937	15625	0.640	1.37688		1.38865	
1.879	15152	0.660	1.37659		1.38835	
1.823	14706	0.680	1.37633		1.38808	
1.771	14286	0.700	1.37608		1.38782	
1.722	13889	0.720	1.37585		1.38758	
1.675	13514	0.740	1.37563		1.38735	
1.631	13158	0.760	1.37543		1.38714	
1.590	12821	0.780	1.37524		1.38693	
1.550	12500	0.800	1.37506		1.38674	
1.512	12195	0.820	1.37488		1.38656	
1.476	11905	0.840	1.37472		1.38639	
1.442	11628	0.860	1.37456		1.38622	

(*continued*)

TABLE II (*Continued*)

Magnesium Fluoride

eV	cm^{-1}	μm	n_o	k_o	n_e	k_e
1.409	11364	0.880	1.37440		1.38606	
1.378	11111	0.900	1.37426		1.38590	
1.348	10870	0.920	1.37411		1.38575	
1.319	10638	0.940	1.37398		1.38561	
1.292	10417	0.960	1.37384		1.38546	
1.265	10204	0.980	1.37371		1.38533	
1.240	10000	1.0000	1.37358		1.38519	
1.215	9800	1.0204	1.37346		1.38506	
1.190	9600	1.0417	1.37333		1.38492	
1.165	9400	1.0638	1.37319		1.38478	
1.141	9200	1.0870	1.37306		1.38464	
1.116	9000	1.1111	1.37292		1.38449	
1.091	8800	1.1364	1.37277		1.38434	
1.066	8600	1.1628	1.37263		1.38418	
1.041	8400	1.1905	1.37247		1.38402	
1.017	8200	1.2195	1.37231		1.38385	
0.9919	8000	1.2500	1.37215		1.38367	
0.9671	7800	1.2821	1.37197		1.38349	
0.9423	7600	1.3158	1.37179		1.38329	
0.9175	7400	1.3514	1.37160		1.38309	
0.8927	7200	1.3889	1.37140		1.38287	
0.8679	7000	1.4286	1.37118		1.38265	
0.8431	6800	1.4706	1.37096		1.38240	
0.8183	6600	1.5152	1.37071		1.38214	
0.7935	6400	1.5625	1.37045		1.38186	
0.7687	6200	1.6129	1.37017		1.38156	
0.7439	6000	1.6667	1.36986		1.38124	
0.7191	5800	1.7241	1.36953		1.38088	
0.6943	5600	1.7857	1.36917		1.38049	
0.6695	5400	1.8519	1.36877		1.38007	
0.6447	5200	1.9231	1.36833		1.37960	
0.6199	5000	2.0000	1.36784		1.37907	
0.6075	4900	2.0408	1.36757		1.37879	
0.5951	4800	2.0833	1.36729		1.37849	
0.5827	4700	2.1277	1.36699		1.37817	
0.5703	4600	2.1739	1.36667		1.37783	
0.5579	4500	2.2222	1.36633		1.37747	
0.5455	4400	2.2727	1.36597		1.37708	
0.5331	4300	2.3256	1.36559		1.37667	
0.5207	4200	2.3810	1.36518		1.37623	
0.5083	4100	2.4390	1.36474		1.37576	
0.4959	4000	2.5000	1.36426		1.37525	
0.4835	3900	2.5641	1.36375		1.37471	
0.4711	3800	2.6316	1.36320		1.37412	

(*continued*)

TABLE II (*Continued*)

Magnesium Fluoride

eV	cm^{-1}	μm	n_o	k_o	n_e	k_e
0.4587	3700	2.7027	1.36261		1.37348	
0.4463	3600	2.7778	1.36196		1.37279	
0.4339	3500	2.8571	1.36126		1.37204	
0.4215	3400	2.9412	1.36049		1.37122	
0.4092	3300	3.0303	1.35966		1.37033	
0.3968	3200	3.1250	1.35874		1.36934	
0.3844	3100	3.2258	1.35773		1.36827	
0.3720	3000	3.3333	1.35662		1.36707	
0.3596	2900	3.4483	1.35539		1.36575	
0.3472	2800	3.5714	1.35402		1.36429	
0.3348	2700	3.7037	1.35249		1.36265	
0.3224	2600	3.8462	1.35077		1.36080	
0.3100	2500	4.0000	1.34883		1.35873	
0.2976	2400	4.1667	1.34663		1.35637	
0.2852	2300	4.3478	1.34412		1.35369	
0.2728	2200	4.5455	1.34125		1.35060	
0.2604	2100	4.7619	1.33792		1.34704	
0.2480	2000	5.0000	1.33404	$4.2 \cdot 10^{-7}$ [51]	1.34288	
0.2418	1950	5.1282	1.33186	$6.0 \cdot 10^{-7}$	1.34054	
0.2356	1900	5.2632	1.32948	$8.5 \cdot 10^{-7}$	1.33799	
0.2294	1850	5.4054	1.32689	$1.2 \cdot 10^{-6}$	1.33521	
0.2232	1800	5.5556	1.32406	$1.7 \cdot 10^{-6}$	1.33217	
0.2170	1750	5.7143	1.32096	$2.5 \cdot 10^{-6}$	1.32885	
0.2108	1700	5.8824	1.31754	$3.6 \cdot 10^{-6}$	1.32518	
0.2046	1650	6.0606	1.31378	$5.1 \cdot 10^{-6}$	1.32114	
0.1984	1600	6.2500	1.30961	$7.4 \cdot 10^{-6}$	1.31666	
0.1922	1550	6.4516	1.30497	$1.1 \cdot 10^{-5}$	1.31168	
0.1860	1500	6.6667	1.29978	$1.6 \cdot 10^{-5}$	1.30611	
0.1798	1450	6.8966	1.29396	$2.4 \cdot 10^{-5}$	1.29986	
0.1736	1400	7.1429	1.28740	$3.7 \cdot 10^{-5}$	1.29280	
0.1674	1350	7.4074	1.281 [51]	$5.7 \cdot 10^{-5}$	1.288 [51]	
0.1612	1300	7.6923	1.273	$8.6 \cdot 10^{-5}$	1.279	
0.1550	1250	8.0000	1.264	$1.3 \cdot 10^{-4}$	1.269	
0.1488	1200	8.3333	1.252	$1.9 \cdot 10^{-4}$	1.257	
0.1426	1150	8.6957	1.240	$2.8 \cdot 10^{-4}$	1.243	
0.1364	1100	9.0909	1.224	$4.4 \cdot 10^{-4}$	1.227	
0.1302	1050	9.5238	1.206	$7.1 \cdot 10^{-4}$	1.208	
0.1240	1000	10.0000	1.18	$1.2 \cdot 10^{-3}$	1.18	
0.1215	980	10.204	1.17	$1.5 \cdot 10^{-3}$	1.17	
0.1190	960	10.417	1.16	$1.9 \cdot 10^{-3}$	1.16	
0.1165	940	10.638	1.15	$2.4 \cdot 10^{-3}$	1.15	
0.1141	920	10.870	1.14	$3.0 \cdot 10^{-3}$	1.13	
0.1116	900	11.111	1.12	$3.7 \cdot 10^{-3}$	1.12	
0.1091	880	11.364	1.11	$4.6 \cdot 10^{-3}$	1.10	

(*continued*)

TABLE II (*Continued*)

Magnesium Fluoride

eV	cm^{-1}	μm	n_o	k_o	n_e	k_e
0.1066	860	11.628	1.09	$5.7 \cdot 10^{-3}$	1.08	
0.1041	840	11.905	1.07	$6.9 \cdot 10^{-3}$	1.06	
0.1017	820	12.195	1.04	$8.4 \cdot 10^{-3}$	1.04	
0.0992	800	12.500	1.02	0.010	1.01	
0.0967	780	12.821	0.99	0.012	0.98	
0.0942	760	13.158	0.95	0.015	0.94	
0.0917	740	13.514	0.91	0.018	0.89	
0.0893	720	13.889	0.86	0.022	0.84	$7.2 \cdot 10^{-3}$ [51]
0.0868	700	14.286	0.79	0.029	0.78	0.012
0.0843	680	14.706	0.71	0.041	0.69	0.021
0.0818	660	15.152	0.61	0.062	0.58	0.039
0.0794	640	15.625	0.47	0.11	0.43	0.084
0.0769	620	16.129	0.28	0.24	0.22	0.26
0.0744	600	16.667	0.17	0.50	0.14	0.53
0.0719	580	17.241	0.14	0.73	0.14	0.76
0.0694	560	17.857	0.14	0.96	0.16	0.95
0.0670	540	18.519	0.14	1.2	0.15	1.1
0.0645	520	19.231	0.15	1.5	0.14	1.4
0.0620	500	20.000	0.17	1.9	0.15	1.7
0.0608	490	20.408	0.21	2.2	0.17	1.8
0.0595	480	20.833	0.27	2.5	0.19	2.0
0.0583	470	21.277	0.42	3.1	0.23	2.2
0.0570	460	21.739	0.86	4.0	0.27	2.5
0.0558	450	22.222	3.11	5.3	0.34	2.8
0.0546	440	22.727	4.97	1.8	0.46	3.2
0.0533	430	23.256	3.58	0.68	0.66	3.7
0.0521	420	23.810	2.59	0.58	1.08	4.4
0.0508	410	24.390	2.70	2.2	2.19	5.5
0.0496	400	25.000	3.30	0.39	5.09	5.5
0.0484	390	25.641	2.74	0.17	6.07	2.5
0.0471	380	26.316	2.43	0.12	5.15	1.1
0.0459	370	27.027	2.21	0.091	4.45	0.62
0.0446	360	27.778	2.02	0.078	3.98	0.40
0.0434	350	28.571	1.84	0.070	3.65	0.28
0.0422	340	29.412	1.66	0.068	3.41	0.21
0.0409	330	30.303	1.46	0.071	3.22	0.16
0.0397	320	31.250	1.20	0.083	3.07	0.13
0.0384	310	32.258	0.81	0.13	2.95	0.11
0.0372	300	33.333	0.18	0.64	2.85	0.090
0.0360	290	34.483	0.11	1.3	2.76	0.076
0.0347	280	35.714	0.11	2.0	2.69	0.065
0.0335	270	37.037	0.15	2.8	2.63	0.057
0.0322	260	38.462	0.32	4.3	2.57	0.050
0.0310	250	40.000	3.25	9.9	2.52	0.044

(*continued*)

TABLE II (*Continued*)

Magnesium Fluoride

eV	cm^{-1}	μm	n_o	k_o	n_e	k_e
0.0298	240	41.667	6.19	0.49	2.48	0.039
0.0285	230	43.478	4.43	0.14	2.44	0.034
0.0273	220	45.455	3.76	0.072	2.41	0.031
0.0260	210	47.619	3.40	0.045	2.38	0.027
0.0248	200	50.000	3.16	0.032	2.35	0.025
0.0236	190	52.632	2.99	0.024	2.33	0.022
0.0223	180	55.556	2.87	0.019	2.31	0.020
0.0211	170	58.824	2.78	0.015	2.29	0.018
0.0198	160	62.500	2.70	0.013	2.27	0.016
0.0186	150	66.667	2.64	0.011	2.25	0.015
0.0174	140	71.429	2.59	$9.3 \cdot 10^{-3}$	2.24	0.013
0.0161	130	76.923	2.54	$8.0 \cdot 10^{-3}$	2.22	0.012
0.0149	120	83.333	2.51	$7.0 \cdot 10^{-3}$	2.21	0.011
0.0136	110	90.909	2.48	$6.1 \cdot 10^{-3}$	2.20	$9.5 \cdot 10^{-3}$
0.0124	100	100.00	2.45	$5.2 \cdot 10^{-3}$	2.19	$8.5 \cdot 10^{-3}$
0.0112	90	111.11	2.43	$4.5 \cdot 10^{-3}$	2.18	$7.5 \cdot 10^{-3}$
0.0099	80	125.00	2.41	$3.9 \cdot 10^{-3}$	2.18	$6.5 \cdot 10^{-3}$
0.0087	70	142.86	2.39	$3.3 \cdot 10^{-3}$	2.17	$5.6 \cdot 10^{-3}$
0.0074	60	166.67	2.38	$2.8 \cdot 10^{-3}$	2.17	$4.7 \cdot 10^{-3}$
0.0062	50	200.00	2.37	$2.3 \cdot 10^{-3}$	2.16	$3.9 \cdot 10^{-3}$
0.0050	40	250.00	2.36	$1.8 \cdot 10^{-3}$	2.16	$3.1 \cdot 10^{-3}$
0.0037	30	333.33	2.35	$1.3 \cdot 10^{-3}$	2.15	$2.3 \cdot 10^{-3}$
0.0029	23.3	428.57	2.354 [47]	$2.4 \cdot 10^{-3}$ [47]	2.190 [47]	$2.8 \cdot 10^{-3}$ [47]
0.0025	20	500.0	2.35 [51]	$8.7 \cdot 10^{-4}$ [51]	2.15 [51]	$1.5 \cdot 10^{-3}$ [51]
0.0021	16.7	600.0	2.345 [47]	$1.4 \cdot 10^{-3}$ [47]	2.181 [47]	$1.7 \cdot 10^{-3}$ [47]
0.0019	15	666.67	2.34 [51]	$6.5 \cdot 10^{-4}$ [51]	2.15 [51]	$1.1 \cdot 10^{-3}$ [51]
0.0012	10	1000.0	2.335 [47]	$7.0 \cdot 10^{-4}$ [47]	2.173 [47]	$8.0 \cdot 10^{-4}$ [47]
			2.34 [51]	$4.3 \cdot 10^{-4}$ [51]	2.15 [51]	$7.6 \cdot 10^{-4}$ [51]
0.0006	5	2000.0	2.34	$2.2 \cdot 10^{-4}$	2.15	$3.8 \cdot 10^{-4}$
0.0000	≈0	—	2.34	0	2.15	0
			2.345 [49]		2.197 [49]	

[a]References are indicated in brackets.

[b]Ordinary data from Williams and Arakawa [23] and anomalous dispersion data from Chandrasekharan and Damany [24] are combined to estimate extraordinary-ray index.

TABLE III

Values of dn_o/dT Obtained from Various References for Magnesium Fluoride

eV	cm^{-1}	μm	dn_o/dT (1/K)	Notes
2.708	21839	0.4579	$1.47 \cdot 10^{-6}$	20°C [28]
1.959	15803	0.6328	$1.12 \cdot 10^{-6}$	20°C [28]
1.078	8696	1.15	$0.88 \cdot 10^{-6}$	20°C [28]
0.366	2950	3.39	$1.1 \cdot 10^{-6}$	20°C [28]
0.0	≈ 0	—	$1.0 \cdot 10^{-4}$	Our data [51]

TABLE IV

Values of dn_e/dT Obtained from Various References for Magnesium Fluoride

eV	cm^{-1}	μm	dn_e/dT (1/K)	Notes
2.708	21839	0.4579	$0.86 \cdot 10^{-6}$	20°C [28]
1.959	15803	0.6328	$0.58 \cdot 10^{-6}$	20°C [28]
1.078	8696	1.15	$0.32 \cdot 10^{-6}$	20°C [28]
0.366	2950	3.39	$0.6 \cdot 10^{-6}$	20°C [28]

Magnesium Oxide (MgO)

DAVID M. ROESSLER
General Motors Research Laboratories
Warren, Michigan
and
DONALD R. HUFFMAN
Physics Department
University of Arizona
Tucson, Arizona

Magnesium oxide is an ionic material, crystallizing in the rock-salt structure and cleaving on (100) and (111) planes. It is found in nature as periclase or β-magnesia. MgO has a molecular weight of 40.32, a density of 3.576 kg/m^3 at 25°C, and a lattice parameter of 4.215 Å. It is insoluble in water but atmospheric moisture reacts with the surface to form a thin film, which can be easily polished off. High physical strength and stability, a melting point near 2852°C, and excellent optical transparency (absorption coefficient less than 1 cm^{-1}) throughout the range 0.25 to 6.8 μm, combine to make the material of considerable interest.

Very pure, microcrystalline powders can be prepared in several ways and exhibit high (over 90%) diffuse reflectance throughout the visible region and extending into both the ultraviolet (UV) and infrared (IR). As such, they have been of interest as reference standards in optical work and as coatings in devices such as integrating spheres. Similar optical properties are exhibited by "smoked" or "fumed" MgO, produced by burning magnesium ribbon and collecting the smoke on a substrate. However, pressed, sintered material can be made to have optical properties close to those of the single crystal. It has been used for a variety of optical purposes, particularly as window and substrate material.

In the mid-1970s, one of us [1] presented a composite picture of the dielectric parameters, ε_1 and ε_2, of MgO in the range 0.02 to 28 eV. The present review includes more recent data, extends the spectral range, and focuses on the n and k values (Table I and Fig. 1).

X-Ray and Ultraviolet Range

The only quantitative data published on the optical properties of MgO at photon energies above about 120 eV appear to be those of Maeda *et al.* [2],

Copyright © 1991 by Academic Press.
All rights of reproduction in any form reserved.
ISBN 0-12-544422-2

in the range 500 to 590 eV. Using bremsstrahlung radiation from a tungsten target, in conjunction with an X-ray spectrometer, they were able to measure the transmission of MgO films deposited onto 350 nm-thick aluminum foil. From the spectra of films with thicknesses of 50 nm and 200 nm, they derived the absorption coefficient in the region of the oxygen K absorption edge. The absorption increases sharply near 535 eV, from a background level of about 5×10^3 cm^{-1} to a maximum value of 7×10^4 cm^{-1} at 539 eV. There are several smaller peaks to higher energies. Photoelectric-yield spectra [3] measured on powdered MgO show similar structure. The tabulated values of k (Table I) in the range 500 to 590 eV have been calculated from the absorption-coefficient data of Maeda *et al.* [2]. The data scatter indicates an uncertainty of at least $\pm 10\%$.

The region 30 to 100 eV has been explored more extensively. Townsend [4] explored the Mg $L_{2,3}$ edge in MgO, which occurs near 55 eV. He oxidized magnesium foils and measured their opacity in the range 80 to 350 Å, using a concave grating spectrograph and a spark-discharge light source. He assumed that the densities of the foils were the same as that of the bulk materials, in order to estimate the thickness of the MgO film. Taking his value of 171 nm for the thickness of one sample, we can calculate k from the opacity data. The resulting k values increase from less than 0.015 at a wavelength of 100 Å to about 0.06 at 320 Å. Superimposed on this background is the structure associated with the Mg L edges.

Fomichev *et al.* [5] used an X-ray spectrometer with a diffraction grating to examine the absorption spectra of MgO layers of unknown thickness. The material was prepared by burning magnesium in air and depositing the product onto a nitrocellulose substrate. Absorption data are shown on an arbitrary intensity scale in the range 50 to 68 eV but show the L edge structure, similar to that in Townsend's work. They were also able to measure the K absorption of oxygen, just above 535 eV. Their data, in arbitrary intensity units, cover the range 535 to 570 eV, and show similar features to those studied later in more detail by Maeda *et al.* [2]. The earlier work [5] is not quite as well resolved or sophisticated, and the absorption peaks are systematically displaced to higher energies by about 5 eV. A follow-up paper [6] presented more extensive data for the 35 to 100 eV region. In neither paper [5, 6] is film thickness quoted.

Although only optical density data are available in the literature for the range 80 to 120 eV, there are k data at lower energies. Further, in the overlap region below 80 eV, the primary spectral structure in both Townsend's data [4] and in those of Fomichev and Zhukova [6] replicates that in the work on single crystals to be described later. There are small displacements in peak energies, but the general agreement is good enough for us to calibrate the optical-density data and derive equivalent k values. We have therefore normalized both sets of optical-density data to give k values in agreement with the lower energy data, and used the resultant

values above 80 eV in Table I. The uncertainty in k is high, over $\pm 50\%$, because the MgO samples were prepared from burning magnesium rather than in the form of single crystals.

Hanson [7] was able to measure the optical properties of single crystals in the range 29 to 80 eV and provide quantitative data for both n and k. He used a high-voltage capillary discharge in air to provide a line-emission source. He then measured the reflectance of single-crystal MgO and the transmittance of amorphous thin films. The single crystals were cleaved along the (100) plane immediately before they were transferred to the vacuum chamber. Data were recorded for 12 angles of incidence in the range 20 to 75° and used to determine n and k from a least-squares fit to the Fresnel equations. However, data scatter, particularly in k, was rather large. The data were therefore used in conjunction with a Kramers–Kronig (K–K) analysis of 15° incidence reflectance data to provide final values. Transmittance data on two films, about 28 nm and 78 nm thick, respectively, were also used to derive k values.

As noted previously, the data published by Hanson and his coworkers [7, 8] show structural features similar to those of Townsend [4] and Fomichev *et al.* [5, 6], including the Mg L edge. The k values for his thin films are about a factor of two greater than those of Townsend, rising from 0.04 at 72 eV to about 0.12 at 29 eV. The single-crystal data for k show considerable scatter but are generally larger than those for the thin films. Values at 72 eV are in the range 0.06 to 0.1; at 29 eV, the values are in the range 0.17 to 0.25. The n values for the single crystal [8] show much less scatter. They are relatively flat, staying within the values 0.91 to 0.99 throughout the range 29 to 80 eV.

There are several sources of reflectance data on single-crystal MgO in the range 7 to 30 eV. Combining the best of these with the reflectance data of Hanson *et al.* [8] gives us a continuous spectrum for the range 6 to 72 eV. We can then use a K–K analysis to compute the corresponding values of n and k. Some of the published data are only on a relative reflectance scale, but there is general agreement regarding the primary spectral features. However, there are substantial variations in the absolute magnitude of the reflectance, especially in the 7.6 eV exciton region. The published data on the optical constants show corresponding variations, and we must therefore consider what reflectance data to use as a primary source for n and k.

Nelson [9] measured the relative reflectance of a cleaved, single crystal obtained from the Norton Research Corporation (Canada), Ltd., Niagara Falls, Ontario, in the wavelength range 90 to 175 nm. He observed three peaks: the one at 164 nm narrowed in measurements at 140 K, whereas the broad structure near 115 nm and the peak at 93 nm seemed to be temperature-insensitive. At room temperature, the three structures had comparable reflectance; at 140 K, the longest wavelength peak, assumed to be excitonic, was higher. Nelson believed that the absorption coefficient

for the exciton was of the order of 10^6 cm^{-1}. The value of k would therefore be of the order of unity.

Reiling and Hensley [10] measured the relative reflectance of freshly cleaved surfaces of several single crystals at 45° incidence, and the absorption of both thin cleaved samples and films evaporated onto LiF substrates. The main features resemble those in Nelson's data [9], the biggest difference being a sharp drop in reflectance on the high-energy side of the exciton peak. Some single crystals grown in their own University of Missouri laboratory showed both the sharpest exciton peak in reflection, and also the lowest absorption on the low-energy tail of this peak. The absorption coefficient was between 30 and 50 cm^{-1} throughout the range 5.8 to 7.0 eV for this material, whereas other crystals (Norton) had absorption coefficients of about 75 cm^{-1} at 5.8 eV, increasing to about 285 cm^{-1} at 7.0 eV. The k value for the Missouri material is about 5×10^{-5} from 5.8 eV to nearly 7 eV, even though there was some evidence of extrinsic structure in both the reflection and absorption low-energy tails of the exciton peak. The intrinsic absorption increased very rapidly beyond about 7.4 eV, being well above 500 cm^{-1} at 7.5 eV for all crystals examined (at room temperature).

Harris [11] was able to measure the absolute reflectance of MgO in the ultraviolet. He used a hydrogen discharge tube for a light source. This provides a strong continuum at energies below 7.5 eV and line emission at higher energies. A vertically mounted, rotatable, phosphor-coated light pipe coupled to a blue-sensitive photomultiplier enabled absolute measurements to be made. Roessler [12], using the same equipment, extended these data, made measurements at both 15° and 45° incidence, and also used the K–K relations to derive the dielectric parameters. The near-normal-incidence data in the range 4 to 14 eV show structure very similar to those of Reiling and Hensley [10] and Nelson [9]. The room-temperature reflectance at the exciton peak was over 22% and dropped sharply to just under 11% on the high-energy side (near 8 eV). The broad peak near 11 eV had a reflectance of about 17%, while the peak just above 13 eV had a reflectance of about 23%.

Roessler and Walker [13] made studies of the exciton reflectance at both room temperature and at 77 K. The crystal was cleaved in air but transferred to a vacuum system of the reflectometer within about two minutes. At 300 K, the exciton peak had a reflectance of about 25% at 7.60 eV, whereas crystal surfaces exposed to laboratory air for three days showed reflectances of 20–23%. Data on the best surface were reproducible to within 2% while the sample was maintained in the vacuum system. At 77 K, the exciton structure exhibits two peaks at 7.69 and 7.76 eV. Later, Whited and Walker [14] showed that additional structure can be seen at 25 K, reflectance peaks occurring at 7.689, 7.715, 7.752, and 7.768 eV.

Studies [15] over a more extended range (4 to 12 eV) confirmed earlier

findings that only the exciton structure showed strong temperature dependence, whereas the reflectance in the region 8 to 12 eV was virtually unchanged between room temperature and 77 K. It was again noted that surfaces exposed for several days to laboratory air deteriorated, as indicated by lowering of the exciton reflection peak and a slight broadening of the spectral features. The best surfaces had peak reflectances of about 27.5% at 7.6 eV, 23% at 11 eV, and 31.5% at 13.5 eV (all at room temperature).

Roessler and Walker [16] used a pulsed discharge in argon to provide line emission beyond the hydrogen-discharge limit, and were able to extend their reflectance data to 28 eV. A very broad composite structure was seen in the 16 to 23 eV region, peak reflectances being about 25%. The data were recorded at 8° incidence and repeated on several freshly cleaved, single-crystal samples (all from Semi-Elements, Inc., Saxonburg, Pennsylvania). Light-source emission lines exhibiting intensity fluctuations of more than 5% were not used in the final computation of the reflectance. A K–K inversion was used to generate n and k values from these reflectance data [17].

Williams and Arakawa [18] also measured the reflectance of cleaved, single crystals of MgO in the same energy range. Their samples were obtained from Muscle Shoals Minerals Company, Barton, Alabama, and from J. Burrow of Bristol University, U.K., and were cleaved in the (100) plane. They contained from 10 to 57 ppm of Fe. The data were recorded at 15° incidence and qualitatively very closely resemble the Roessler and Walker data [16] in spectral structure. However, the absolute reflectance was slightly less: their exciton-peak reflectance was only 22%, the 11 eV peak had a reflectance of 19%, the 13.5 eV peak had a reflectance of 27%, and the broad structure near 20 eV had maximum values near 20%. Thus, the peaks were about 0.04 to 0.05 lower in absolute reflectance than those of Roessler and Walker. Williams and Arakawa noted that there were variations in absolute reflectance between their own samples. They also used the K–K relation to compute n and k values from the reflectance.

Freehouf [19] measured the reflectance of a single-crystal sample of MgO over the range 4 to 30 eV, using synchrotron radiation. Data were recorded for sample temperatures in the range 100 to 400 K. The sample was cleaved in air just prior to being mounted in the vacuum system. Measurements were also made on a polished sample and showed considerable broadening of the exciton structure near 7.5 eV, but little difference at higher energies. He estimated the absolute values of reflectance to be correct to ± 0.03. The room-temperature data have almost identical structure to that revealed by the earlier work [16, 18], and the absolute magnitudes lie between the two previous sets of data over this range. These data are of particular interest because of the use of a continuum rather than a line source. In principle, this should provide more reliable details of

optical structure, especially above 20 eV, where there are often gaps of up to 0.5 eV between emission lines. Freehouf also used a K–K inversion of the reflectance to compute the optical constants, but shows the ε_2 data only at 100 K.

Mikhailin *et al.* [20] measured the relative reflectance at 15° incidence of cleaved single crystals in the range 15 to 40 eV, using the DESY synchrotron light source. There were only minor differences from earlier data, mainly in the 20 eV structure. Kuusmann and Fel'dbakh [21] measured the relative reflectance in the exciton region at 10 K, and saw fine structure similar to that observed in the 25 K data of Whited and Walker [14]. French and Coble [22] made preliminary measurements of the room-temperature reflectance of MgO in the range 7.5 to 14.5 eV. Details of the measurement, including crystal quality, were not given, but the absolute values of the reflectance are low. The exciton-peak reflectance, for example, was only 18.5%.

Summarizing the reflectance data, we find that reports of the value at the 7.6 eV exciton peak vary from as low as 18.5% to as high as 27.5%. The variations are slightly smaller at the higher-energy peaks: values for the peak near 21 eV range were from 19% to 25%. In general, we believe that the data corresponding most closely to intrinsic bulk MgO are those with the highest reflectance values and the sharpest spectral features. The exciton peak near 21 eV range from 19% to 25%. In general, we believe that the higher-energy features seem to be remarkably durable in terms of qualitative structure.

In this connection we note the results of Carden *et al.* [23] on the ion bombardment of an electropolished single crystal of magnesium. This process promotes rapid growth of an oxide layer, which can be monitored by optical reflectance measurements. They measured the reflectance in the range 8.3 to 41.3 eV, using the synchrotron radiation from the University of Wisconsin storage ring. The optical reflectance after bombardment was much lower than before in the range below 12 eV, but virtually unchanged at higher energies. The film was sufficiently like MgO to exhibit weak reflectance structure near 11 eV, 13 eV , and 20 eV, although the reflectance throughout this region was less than 4%.

The preferred reflectance data in the range 5 to 17 eV are those of Roessler and Walker [16]. They exhibit the highest and sharpest reflectance values; the low-energy tail of the exciton peak extrapolates smoothly onto values of the reflectance computed from reliable refractive-index data; and there is close agreement with the synchrotron data of Freehouf [19] in the 11 to 17 eV range. In the range 17 to 23 eV, we believe the reflectivity of single-crystal MgO is slightly lower than the Roessler and Walker data and closer to the values measured by Freehouf. The line emission from the spark discharge in argon [16] is not as stable in intensity as the light from the synchrotron source [19], and the data scatter is

significantly larger than in the hydrogen-discharge light-source range. Both sets of data [16, 19] differ by only about ±0.02 in absolute reflectance in this region, well within the estimated uncertainty. Above 23 eV, we extrapolated the reflectance to join the data of Hanson *et al.* [7, 8].

The final values of n and k used for Table I for the range 6 to 75 eV were obtained from a K–K inversion of the reflectance data selected as above. We took precautions to minimize computational errors introduced by integration of the reflectance data over a limited energy range. The low-energy tail was extrapolated smoothly to below 1 eV, using known values of the refractive index (discussed later), whereas the upper end of the spectrum was extrapolated to 800 eV on the assumption that the reflectance varied inversely with the fourth power of the energy. Further, we employed the correction technique described by Roessler [24] for dealing with K–K analysis in limited spectral regions. By varying the width of the spectral range, we estimate that our use of the K–K analysis contributes an uncertainty of less than ±0.003 to the tabulated values of n and k. However, the total uncertainty in the final values of n and k in the range 7 to 75 eV is at least ±0.05. This is primarily because the relative uncertainty in the original reflectance measurements is at least 3%. Three decimal places are used in Table I to emphasize the spectral structure in n and k rather than to denote true precision. Our present values of n and k in the range 20 to 30 eV are systematically lower than those reported by previous groups [8, 18, 19].

Several workers have measured the electron-energy-loss spectra (EELS) of MgO and compared the spectral features with those obtained optically. Venghaus [25] analyzed his 60 kV EELS spectrum with a K–K transformation and obtained the dielectric parameters, ε_1 and ε_2, in the range 0 to 80 eV. There is remarkable agreement with the optical data of Roessler and Walker [16] in the region of spectral range overlap, 5 to 28 eV. Every feature, with the obvious exception of the 7.6 eV exciton, is reproduced.

Reflection-electron-energy-loss spectra from excellent, cleaved surfaces of single-crystal MgO [26] also reproduce the optical structure in the range 5 to 28 eV. Kambe *et al.* [27] explored several spectral energy regions via EELS from MgO crystallites. Their data, in arbitrary intensity units, cover several ranges: 0 to 60 eV, showing the plasmon loss just above 20 eV; 40 to 120 eV, showing the Mg L edges; 500 to 750 eV, showing the oxygen K edge; and 1250 to 1500 eV, showing the Mg K edge. Where corresponding optical data exist, there is good agreement for the spectral structure. The EEL spectra in the region of the Mg L edges show peaks close to those seen in the optical data [4, 5, 6]; similarly, there is good agreement for the oxygen K edge [2, 5]. We do not know of any optical data in the region of the Mg K edge, but on the basis of the EEL spectra, the value of k should show a small increase above 1310 eV.

A derivation of both n and k from EELS in the range 15 to 40 eV has

been made for evaporated films of MgO [28]. The exciton structure is missing, as anticipated, and the spectra lack the fine detail of the optical data. However, there are some interesting similarities to the present values of n and k in terms of general spectral dependence, despite the differences in both material (thin film rather than bulk single crystal) and experimental probe (EELS rather than optical reflectance).

Absorption in the Near-UV through Near-IR Region

MgO has excellent transparency throughout the near UV, visible, and near IR. In good material the value of k is less than 10^{-4} throughout the wavelength region 0.17 to 7.3 μm, and less than 10^{-7} in part of this range. Impurities and other defects can significantly increase this absorption. For example, Hibben [29] did some early work on the absorption induced by UV irradiation. The present review will generally exclude discussion of extrinsic features, except insofar as the associated absorption is presumed to be greater than that of any intrinsic absorption.

Molnar and Hartman [30] reported the effect of 40 kV X-irradiation on the absorption in the 0.2 to 0.9 μm region. They induced at least three bands, with peaks at 0.22 μm, 0.285 μm, and 0.525 μm. Although they did not show the absorption of preirradiated crystals, their data can be regarded as upper bounds to the intrinsic absorption. The value of k is then less than 3×10^{-5} at 0.2 μm, less than 4×10^{-6} near 0.35 μm, and less than 10^{-6} beyond 0.85 μm. The crystals were obtained from the Norton Research Corporation (Canada) Ltd.; some were very clear, and others had a slight yellow or greenish tint. The absorption data reported were from clear samples, which, from spectrographic analysis, revealed no impurities other than about 0.1% of calcium.

Tyler and Sproull [31] measured the transmittance of three unpolished MgO crystals (Norton), in the wavelength range 0.2 to 0.4 μm. They showed comparable absorption: at 0.21 μm, the absorption coefficient was estimated to be about 15 cm^{-1} ($k = 2.5 \times 10^{-5}$), and to result partly from impurities.

Weber [32] measured the transmission of plates of MgO with thicknesses of 0.42 and 0.92 mm, which had been heated in various atmospheres of excess oxygen and excess metal. He derived the absorption coefficient in the range 1.5 to 8 eV and noted the treatment-senstive structure. For the least-absorbing samples, k was about 6.5×10^{-5} at 6.075 eV (0.204 μm), decreasing monotonically to 3.1×10^{-6} at 5.0 eV, and being too small to measure at 4.5 eV.

Johnson [33] obtained some very clear, synthetic single crystals from several sources and cleaved them to obtain plates with thicknesses of 0.27 to 0.75 mm. The purest samples, grown at the University of Missouri, contained only a few parts per million of Ca, Fe, Na, and Ni, as principal impurities. They had a blue-ultraviolet fluorescence under UV excitation,

whereas less pure samples (from Norton and from the Lamp Division of thue General Electric Company, Cleveland, Ohio (GE)) were nonluminescent. The absorption coefficient, uncorrected for surface reflection losses, was derived from transmission measurements in the range 0.16 to 0.35 μm. The GE and Missouri samples had very similar absorption; the Norton material had about twice as much absorption at wavelengths longer than 0.175 μm. All samples had absorption coefficients greater than 400 cm^{-1} at 0.16 μm. The absorption dropped to 20 cm^{-1} at 0.18 μm in the Missouri samples and to 6 cm^{-1} at 0.22 μm.

Johnson's data [33] provide the lowest values of k reported for the range 7.3 to 6.7 eV, and extrapolate smoothly to the values determined by K–K analysis at higher energies. We therefore use these in Table I.

Peria [34] examined the 3 to 6 eV UV absorption of MgO crystals from a wide variety of sources. The transmittance was measured on cleaved samples from 0.2 to 1 mm thick. Most showed extrinsic absorption features consisting of various admixtures of bands at 4.3, 4.8, and 5.7 eV. These could often be reduced if the samples were heated in vacuum. The k values in the least absorbing material decrease from about 2.5×10^{-5} at 5.8 eV to 3.3×10^{-6} at 5.1 eV, and are lower than found in any other work in the 5 to 5.5 eV range.

Ballesteros *et al.* [35, 36] recently made an extensive study of optical absorption in a variety of MgO crystals, with controlled metal impurities and subjected to various heat treatments. Absorption coefficients are given for the range 2 to 6.5 eV. The most transparent material is slightly more absorbing than that of Peria [34] below 5.5 eV but provides lower values of k at higher energies, joining smoothly onto Johnson's data [33] above 6.5 eV.

The few data that exist for k in the 2 to 5 eV range all exhibit structure indicating that extrinsic absorption is present. The most precise measurements are probably those of Harrington *et al.* [37], who used combined wavlength-modulation and laser-calorimetric techniques to measure the low absorption in the 2.4 to 3.6 eV range. The wavelength-modulation spectra give the derivative of the absorption coefficient. This is then integrated, the constant of integration being given via Ar-ion-laser calorimetric measurements at the discrete laser-line wavelengths. No details of the samples were given. The absorption coefficient decreased from about 0.3 cm^{-1} at 0.355 μm to about 0.02 cm^{-1} at 0.502 μm, the latter giving a k value of 8×10^{-8}.

A completely different technique was used by Sakhnovskii [38], who determined absorption coefficients from a detailed analysis of the diffuse reflection of powdered MgO in the range 0.24 to 1 μm. The powder was obtained by burning magnesium shavings on a steel plate, and the measurements were performed with an integrating photometer. The values of k derived from his data are within a factor of three of those derived from the

single-crystal data [32–37]. The earlier data of Molnar and Hartman [30] give values of k between five and ten times those of Sakhnovskii over the range 2 to 5 eV, but both show the same general spectral features, including a broad absorption minimum near 3 eV.

Most of the data for k that exist in the range 0.3 to 2 eV (4 to 0.6 μm) were made at discrete laser wavelengths: 1.319 μm (modified Nd:YAG), 2.7 μm (HF), and 3.8 μm (DF). There are strong impurity bands in this region, probably associated with oxygen or OH^-. Values of k derived from different sources range from about 2×10^{-8} to a few times 10^{-6}.

Harrington *et al.* [39] used standard laser-calorimetric methods and analysed their data from a single-crystal sample (Norton Company) to derive the absorption coefficients at 2.7 and 3.8 μm. They showed that the respective values of $4.0\times10^{-2}\,\mathrm{cm}^{-1}$ ($k=8.6\times10^{-7}$) and $5.4\times10^{-3}\,\mathrm{cm}^{-1}$ ($k=1.6\times10^{-7}$) indicate extrinsic absorption contributions.

Laser calorimetry was also used by Fernelius *et al.* [40] to measure the absorption of some polished Norton crystals at 1.319, 2.7, and 3.8 μm. Spectral traces indicated extrinsic absorption features in this wavelength range, and absorption measurements varied significantly with the sample at 2.7 μm. However, a sample that appeared slightly yellow-green in color was less absorbing at 2.7 μm than a very clear sample. The average value of k was 3×10^{-6}. At $\lambda=3.8$ μm, k varied from 2.8×10^{-7} to 3.2×10^{-7}. The absorption values originally reported for the 1.319 μm wavelength were revised later [41]. The k values for two samples were 7.1×10^{-8} and 9.2×10^{-8}, the tinted sample having lower absorption than the clear crystal, possibly because of its superior surface polish.

The lowest values of absorption at 2.7 and 3.8 μm were obtained by Hordvik and Skolnik [42], using a photoacoustic technique. They examined a mechanically polished MgO crystal supplied by Norton. The photoacoustic technique allows separation of the bulk and surface contributions. At 2.7 μm, the bulk absorption coefficient was $5.2\times10^{-3}\,\mathrm{cm}^{-1}$ ($k=1.1\times10^{-7}$), and the loss per surface was $9\times10^{-4}\,\mathrm{cm}^{-1}$. At 3.8 μm, the bulk value was $6.7\times10^{-4}\,\mathrm{cm}^{-1}$ ($k=2.0\times10^{-8}$), and the loss per surface was $1\times10^{-4}\,\mathrm{cm}^{-1}$. Hordvik and Skolnik also show bulk-absorption-coefficient data extending from 3.8 μm to 8.4 μm. The k values derived from these data are among those we consider most representative of intrinsic bulk material.

Infrared wavelength-modulation spectroscopy [43] of a Linde A polished single crystal of MgO from Optovac, North Brookfield, Massachusetts, shows extrinsic structure in the absorption coefficient throughout the region 2.5–5 μm. Although this changed slightly, depending on whether the sample was measured in normal laboratory air or in a dry-nitrogen atmosphere, the total absorption remained small. The data were normalized to a value of $7.6\times10^{-3}\,\mathrm{cm}^{-1}$ ($k=2.3\times10^{-7}$) at $\lambda=3.8$ μm. This results in k values of less than 3×10^{-7} throughout the range. These values

are lower than those of Hordvik and Skolnik near 5 μm and do not extrapolate as smoothly onto the available longer-wavelength data.

Refractive Index in and near the Visible Region

Early measurements of the refractive index of MgO in the visible region generally employed prisms, and were reported to three or four decimal places. References [44–49] describe some of this work, which was subsequently compiled and analyzed by Haase [50].

An extensive study was made by Strong and Brice [51], who cut two prisms from one of several very pure Norton MgO crystals and used a minimum-deviation method to measure the refractive index at 23°C in the range $\lambda = 0.2536$ μm to $\lambda = 0.7065$ μm. The corresponding values for n were quoted to four decimal places in the ultraviolet and to five decimal places in the visible region, and decreased from 1.8450 to 1.73126. Measurements were also made at 2°C and dn/dT was determined to be 1.47×10^{-5}/°C at $\lambda = 0.4861$ μm ($n = 1.74711$) and to be 1.14×10^{-5}/°C at $\lambda = 0.6563$ μm ($n = 1.73340$).

Radhakrishnan [52] found that the 23°C data of Strong and Brice could be fit to within ±0.003 over the range 0.2967 to 0.7065 μm by the formula

$$n^2 = 1.3224 + \frac{1.6294\lambda^2}{(\lambda^2 - 0.01387)}. \tag{1}$$

Peria [34] has a slightly different equation, which fits the whole spectral range with the same degree of fit.

Radhakrishnan also measured the temperature coefficient of the refractive index of a polished, strain-free crystal at the wavelengths 0.4358, 0.5461, and 0.5893 μm. He used an interferometric method from room temperature up to 400°C, and found that dn/dT decreased slightly with wavelength but did not vary with temperature. Later [53], he extended the wavelength coverage to 0.4047 μm and 0.3650 μm, confirming the trends seen earlier. His values for dn/dT decrease from 1.95×10^{-5}/°C at 0.3650 μm to 1.60×10^{-5}/°C at 0.5893 μm.

The most detailed refractive-index data for MgO are those of Stephens and Malitson at NBS [54]. Measurements were made on two prisms of magnesium oxide crystals of "excellent optical quality" by the minimum-deviation method in the wavelength range $\lambda = 0.36117$ μm to $\lambda = 5.35$ μm. In the visible region, measurements were made at temperatures near 20°C, 30°C, and 40°C, at each of nine wavelengths. These data were then averaged for the two prisms. The final values of the refractive index at 30°C were found to fit a four-constant dispersion equation:

$$n^2 = 2.957019 - 0.0101373\lambda^2 + \frac{0.0216485}{(\lambda^2 - 0.0158650)} \tag{2}$$

The computed values are within $\pm 6 \times 10^{-6}$ of the averaged, corrected values, throughout the visible region.

Stephens and Malitson fitted the 23.3°C refractive-index data for the whole wavelength range from 0.36117 to 5.35 μm to a five-constant dispersion equation:

$$n^2 = 2.956362 - 0.01062387\lambda^2 - 0.0000204968\lambda^4 + \frac{0.02195770}{(\lambda^2 - 0.01428322)}. \tag{3}$$

The values computed from this formula are systematically lower than those of Strong and Brice at the same temperature by about 3.7×10^{-4}.

Saksena and Viswanathan [55] have given a slightly different dispersion equation for the 23°C NBS data, but without improving the fit. Dodge [56] has fitted the 20 °C NBS data to the following equation:

$$n^2 = 1 + \frac{1.111033\lambda^2}{\lambda^2 - 0.005076} + \frac{0.8460085\lambda^2}{\lambda^2 - 0.018912} + \frac{7.808527\lambda^2}{\lambda^2 - 723.2345}. \tag{4}$$

More recent measurements confirm the results of Stephens and Malitson. For example, the compilation by Moses [57] includes data on a 99.7% pure single crystal (Norton) [58]. Values of n were measured at about 25 °C in the range 0.6907 to 5.35 μm and agree to five decimal places with the Stephens and Malitson values. Herzberger and Salzberg [59] measured several samples of MgO, found no significant differences from the NBS data, but provided a different dispersion equation:

$$n = 1.71960 + 0.006305L - 0.000090L^2 - 0.0031356\lambda^2 - 0.00000770\lambda^4, \tag{5}$$

where $L = 1/(\lambda^2 - 0.028)$.

They did not state the temperature: we assume it to be 20 ± 5°C. Stephens and Malitson [54] estimated dn/dT at 20°C to be 1.36×10^{-5}/°C at $\lambda = 0.7679$ μm, increasing to 1.89×10^{-5}/°C at $\lambda = 0.4047$ μm. An uncertainty of ±5°C therefore gives an uncertainty of about ±0.0001 in n.

The values of n tabulated over the range 5 to 0.21 eV (0.25 to 5.9 μm) are based primarily on the work of Stephens and Malitson [54]. We quote their experimental values to five decimal places, and use Eq. 3 to give

values of n to four decimal places at other wavelengths. The high-energy tail of their data was extrapolated smoothly onto the n values computed from the K–K analysis of the UV reflectance. Supplemental data are included from various references [56, 58, 59]. Although we quote the NBS data [54] to five decimal places, we believe the uncertainty in the tabulated values of n in the range 0.5 to 3.5 eV is ± 0.0001. It is about ± 0.002 in the range 3.5 to 7.3 eV, and about ± 0.0005 at energies below 0.5 eV.

Irtran 5 is a hot-pressed, polycrystalline compact of MgO and has been used extensively in much infrared work. The Eastman Kodak Company no longer manufacturers it. However, the company published index-of-refraction values for this material in the range 1 to 9 μm, and a convenient list appears in the *Handbook of Optics* [60]. These data were determined experimentally and fitted to an interpolation formula by a least-squares method. Despite the different form of MgO, the values of n differ by less than ± 0.001 from the single-crystal data of Stephens and Malitson in the overlapping range (1 to 5.35 μm).

Derivations of n from reflection methods are usually less precise than those obtained via transmission. An early example is the work of Barnes *et al.* [61], who measured the reflectance of a single crystal of MgO (Norton) in the wavelength range 1 to 15.5 μm. They assumed negligible absorption in the range 1 to 8 μm and derived n in this region from the Fresnel equation for normal incidence:

$$n = \frac{(1 - \sqrt{R})}{(1 + \sqrt{R})}. \tag{6}$$

Hanna [62] found little difference between the reflectance spectra of single-crystal and polycrystalline MgO in the range 4000 to 300 cm^{-1}. Using the Fresnel equation, he derived values of n that are systematically lower than those of Stephens and Malitson by at least 0.03.

A novel approach was adopted by Welber [63], who used an index-matching technique and measured the transmission of an alkali–halide matrix containing MgO powder. This enabled him to determine n in the wavelength range 5 to 8 μm. The data near 5 μm accord well with the NBS results [54] despite the difference in the nature of the samples.

Thin Films, UV–VIS

As noted previously, the optical properties of thin films often differ significantly from those of the bulk material. In spectral regions of nominal transparency, impurities and surface defects in the film may contribute additional absorption. However, if the films contain many voids, there may be spectral regions in which values of k are less than those of bulk material.

The following section discusses thin-film data in the near-UV through near-IR regions.

Reiling and Hensley [10] prepared thin (65 nm) films of MgO by evaporating magnesium metal onto polished, cleaved LiF substrates and baking them at 650°C in air. The transmission spectra showed only a weak exciton feature superimposed on the main absorption. However, this peak moved slightly to higher energy as the temperature decreased from 25 to −170°C. Absorption coefficients, uncorrected for reflection losses, were about $2\times10^5\,\mathrm{cm}^{-1}$ near the exciton structure at 7.8 eV, and reached a maximum value of about $3\times10^5\,\mathrm{cm}^{-1}$ near 10.5 eV. The corresponding values of k are about 0.25 and 0.28, respectively, or about a quarter of the value in single-crystal material.

Malherbe [64] used an electron beam to evaporate thin films of MgO in high vacuum. He baked the films at 450°C to decrease extrinsic absorption and tried to protect them from water-vapor contamination. However, his values of n decrease from 1.99 at 0.186 μm to 1.73 at 0.248 μm, considerably lower than the single-crystal values of about 2.10 and 1.86, respectively. His k values decrease from about 0.022 at 0.198 μm to 3×10^{-4} at 0.251 μm. By contrast, Johnson's single-crystal data [33] show k values of about 1.5×10^{-5} at 0.198 μm, and Weber's single-crystal data [32] show k to be below 3×10^{-6} at 0.251 μm. Thus, the thin-film absorption in this region is two to three orders of magnitude greater than that found in single crystals.

Bradford *et al.* [65] examined the optical properties of evaporated films, using both Irtran 5 and 99.9% pure MgO as starting material. The absorption was negligible throughout the 0.22 to 8.0 μm region, and values of the refractive index derived by three different techniques (interferometric and polarimetric) agreed within 1%. The films were crystalline, with the same cubic structure and lattice constant as the bulk material, whether deposited at 50°C or 300°C onto various substrates. The crystallites were larger at the higher deposition temperature and had refractive indices identical to those of single-crystal MgO in the visible region and identical to those of Irtran 5 in the infrared. However, the refractive index of the films deposited at 50°C was about 2.3% lower, a difference attributed to the presence of more boundary-layer material between the crystallites. For the 50°C films, $n=1.70$ at $\lambda=0.55$ μm, and $n=1.62$ at $\lambda=4$ μm. The corresponding values for the 300°C films were 1.74 and 1.66.

It was noted that a hazy, bluish, scattering coating formed on films exposed to normal air [65]. Deitch *et al.* [66] used RF sputtering to prepare MgO films and observed formation of a white haze on the films after exposure to air. They measured n at only one wavelength (0.6328 μm), and found that it varied from 1.72 to 1.75 as the sputtering atmosphere was varied from part oxygen/part argon to pure argon. These values are close

to the single-crystal value of 1.7346, whereas films that were electron-beam evaporated by Kersten *et al.* [67] had n values in the range 1.684 to 1.702, depending on the substrate. These authors deposited films at 50°C as dielectric planar waveguides and derived n from knowledge of the film thickness and the angle of coupling between the waveguide and a prism for He–Ne light at 0.6328 μm. Measurements of the absorption losses indicate a value of k of about 3×10^{-5}, at least two orders of magnitude greater than that assumed for single-crystal material.

Reale [68] studied the refractive index of electron-beam evaporated MgO films as a function of the temperature of deposition onto clean, flat, soda-lime glass substrates. Impurities were removed by heating the films at 400°C in vacuum for two hours. The refractive index was determined from interference structure in the reflectance and transmittance spectra obtained with a normal-incidence, double-beam spectrophotometer. No wavelength is given, but the data are claimed to be consistent with those of Bradford *et al.* [65]. The value of n increased from 1.70 for films deposited at 50°C, to about 1.74 for films deposited at 200°C. Increasing the deposition temperature to 300°C produced a further but negligible increase in n. The films were described as being polycrystalline and the change in n ascribed to a reduction in intergranular boundaries as deposition temperatures increased.

Harrington *et al.* [69] used a laser calorimeter to measure the aborption in electron-beam evaporated MgO films. They tried to minimize extrinsic absorption by using high-purity starting material. The films were deposited onto carefully cleaned, polished CaF substrates, at temperatures in the range 50 to 200°C. Thicknesses were from $\lambda/2$ to λ at 3.8 μm, in order to simplify the subsequent optical analysis. The values of k were 2.2×10^{-3} at $\lambda = 3.8$ μm, and 6.2×10^{-3} at 2.8 μm; these values are from three to four orders of magnitude higher than found in bulk crystals.

Blanc [70] presents both n and k values for evaporated films of thicknesses 50 to 250 nm in the range 0.170 to 0.250 μm. The refractive index of these films, evaporated onto silica substrates at 250°C, is about 7% lower than that of single-crystal bulk material. However, the absortion in these films is at least two orders of magnitude greater than that of bulk material: k is about 0.001 at $\lambda = 0.2026$ μm and increases to 0.01 at $\lambda = 0.1779$ μm.

Aboelfotoh and Ramsey [71] also examined the UV absorption of electron-beam evaporated films. Their films, about 300 nm thick, were deposited onto fused-silica substrates. Spectra were recorded in the range 3 to 7 eV with a Beckmann DK-2A spectrophotometer. A variety of extrinsic absorption features were seen, which varied with deposition temperature and subsequent heating of the films in air or under vacuum. Some of this structure closely resembles that seen by other workers in MgO, which has been subjected to treatments such as X-irradiation, UV-irradiation, additive coloration, or mechanical deformation, and variously ascribed to

Fe impurities, interstitial oxygen, and so on. All the films exhibited absorption coefficients greater than $6 \times 10^4\,\mathrm{cm}^{-1}$ at 7 eV, corresponding to k values above 0.08, almost an order of magnitude greater than those in single crystals.

Maclean and Duley [72, 73] measured the transmission of MgO films prepared by the laser evaporation of high-purity Norton MgO crystals. Data were recorded in the range 0.135 to 0.240 μm for films of thicknesses between 21 and 93 nm. These films were amorphous and showed no evidence of the strong exciton structure near 0.163 μm seen in single-crystal material. The absorption coefficient did not vary strongly with film thickness but was very much larger than that of single crystals for wavelengths longer than 0.17 μm. (At shorter wavelengths, that is, to the high-energy side of the exciton feature, the films were slightly *less* absorbing than single crystals.) Annealing films in air at temperatures up to 800°C did not decrease the absorption but did produce a weak exciton structure at 0.16 μm. Other structure seen on the absorption tail of both amorphous and partially recrystallized films was attributed to absorption by surface defects, and associated with O^{2-} ions in particular.

Infrared Region

In addition to the earlier compilation of the dielectric functions [1], there are three other surveys of the infrared properties of MgO that contain optical constants: one by DeWitt of the Thermophysical Properties Research Center at Purdue [74], that by Moses from Hughes Aircraft Company [57], and the other by Whitson of the Aerospace Corporation [75]. The last contains extensive tabulations of infrared data in digital form taken from the original papers, including tables of "representative" or "best" values of n and k. This part of Whitson's work thus has much in common with the present section of this work. However, we have done a completely independent evaluation of the published infrared results, supplemented by original measurements in the regions where adequate data were missing or were questionable. Only after the infrared part of Table I was assembled was a comparison made with the Aerospace handbook values, which overall showed rather good agreement at the higher infrared frequencies.

Many measurements of optical properties have been made on MgO particulate samples, especially MgO smoke, which is easily prepared by burning magnesium ribbon in air. Extensive infrared measurements have been performed to study small-particle optical properties, such as surface modes in these samples. For an introduction to this field, Section 12.3.5 of the monograph by Bohren and Huffman [76] is suggested reading. For the purpose of arriving at the most reliable optical constants of MgO, however, we have deliberately omitted work on powders and smoke because of the complex behavior they show, and have relied exclusively on measurements

taken from bulk single crystals. Similarly, measurements on Irtran 5 have been excluded, although some comments on comparisons are included. Emphasis is exclusively on the room-temperature region.

In the infrared region the absorption of MgO begins to rise toward a reststrahlen peak in absorption near 400 cm^{-1} (25 μm). In this spectral region the absorption is so high that reflectance techniques must be employed to derive optical constants, whether by a K–K analysis of the reflectance at one angle, multiangle reflectance analysis, or by means of an oscillator fit to specular reflectance spectra. On both the low- and high-frequency sides of the restsrahlen region, there occur spectral ranges where absorption is weak enough for transmission to be carried out on cut or cleaved and polished single-crystal samples.

In this review we proceed to discuss the infrared in three regions. The first ranges from about 2000 cm^{-1} to about 750 cm^{-1} (5 to 13 μm), where multiphonon processes apparently dominate the absorption and where transmission measurements can be made. The second is the reststrahlen region, stretching from about 750 cm^{-1} down to about 300 cm^{-1}: here, k is greater than 0.1 and reflectance measurements are employed. Below 300 cm^{-1} in the far infrared, k values again fall below 0.1, low enough for transmission measurements.

Workers reporting infrared transmission measurements on solids are not always interested in extracting optical constants from their measurements, so we have had to undertake this task. When only transmission or absorptance measurements are given, it is necessary to apply a correction for surface reflection. This can be based either on measured reflectance values or on values calculated from n via the Fresnel equations. Among several possible choices for this task we have chosen the work of Piriou and Cabannes [77], who fitted reflectance data with a classical oscillator model. These authors made a special effort to achieve agreement with the accurate n values of Stephens and Malitson in the near infrared [54]. The same calculations also agree quite well with results in Duesler's thesis of K–K analysis for n tabulated from 20 to 300 cm^{-1} [78]. In addition to providing the reflection coefficients, the n values provided by Piriou and Cabannes have been used in the tabulation. It was also found that their oscillator fit [77] produced excellent agreement, both with K–K results in the far infrared at wavelengths longer than 100 μm (100 cm^{-1}) and with analysis of interference fringes in our own transmission measurements. Because of these facts, we used the same classical oscillator fit to determine the reflection corrections in the far infrared.

There have been numerous transmission measurements on single-crystal samples of MgO in the multiphonon absorption region between about 2000 and 1050 cm^{-1} (5 to 9.5 μm). The earliest work was by Barnes and coworkers [61, 79]. Burstein *et al.* [80] were concerned about some anomalies in these early data and made both reflection and transmission measure-

ments on cleaved single crystals. They present a plot of the absorption coefficient, α, rising from a value of about $1\,cm^{-1}$ near $6\,\mu m$ to over $500\,cm^{-1}$ near $14\,\mu m$. Willmott [81] measured transmission for four thicknesses of cleaved MgO ranging from 0.076 to 0.468 mm, gave tabulated values of k for 10 wavelengths, and showed a curve of both n and k from about 7 to 25 μm, parts of which were based on smoked MgO. Despite the use of a single monochromator with a natural-rock-salt prism, these measurements agree quite well with more recent work with a later generation of commercial infrared monochromators. Other such measurements are reported in the papers by Oppenheim and Goldman [82], Billard *et al.* [83], Cabannes and Billard [84], and Hanna [62].

The values of k tabulated in the range 6 to 14 μm rely primarily on two papers, one by Gourley and Runciman [85] and the other by Piriou and Cabannes [86]. Gourley and Runciman measured the transmission of 0.037 to 5 mm-thick cleaved and ground platelets and presented their data in the form of absorption coefficient spectra at 35 and 305 K. Piriou and Cabannes [86] cleaved and polished samples to thicknesses ranging from 0.064 to 20 mm, and reported measurements at 77 and 273 K. They present transmission curves as far as $1700\,cm^{-1}$ and the corresponding absorption coefficient data over the spectral range 700 to $1500\,cm^{-1}$ (14.3 to 6.7 μm).

In the region from 2000 to about $1000\,cm^{-1}$, there are systematic differences between the two sets of data [85, 86]. The Piriou and Cabannes values become increasingly lower than those of Gourley and Runciman toward higher frequencies, but in agreement with Ref. [83]. The difference approaches a factor of two at $1700\,cm^{-1}$. We made an attempt to resolve this discrepancy by making our own measurements on cleaved MgO, with results intermediate between the two. The absorption in this spectral region is dominated by contributions from nonintrinsic proceses, and we believe that the differences in the data reflect differences between individual samples and between sample-preparation techniques. The values of k selected for Table I in the range 1700 to $1050\,cm^{-1}$ are based on the Piriou and Cabannes data [86], because of their lower values.

From 1050 to $750\,cm^{-1}$ there is excellent agreement between values of k derived from the absorption coefficients of Piriou and Cabannes and from the optical density curves (absorptance) of Gourley and Runciman [85]. Values in the table are taken from the smoothed curve of these data plots and therefore represent the average of these two sources.

The absorption rapidly rises in the region below $800\,cm^{-1}$, and it becomes impractical to produce samples from bulk single crystals that are sufficiently thin to make transmission techniques useful. Although some of the older works resorted to smoke or powder samples, it seems preferable to use reflectance techniques on single-crystal material, if one is interested in the intrinsic optical properties. One of the earliest analyses by reflectance techniques was by Häfele [87], who used reflectance at two different

angles to derive optical constants. Jasperse *et al.* [88] measured near-normal-incidence (11°) reflectance on single-crystal samples that had been cut, polished, and annealed. Measurements were made from 200 to 800 cm^{-1} at several temperatures in the range 8.5 to 1950 K. The data were analyzed by fitting the reflectance with a two-oscillator classical dispersion model, using the equations

$$\varepsilon_1 = n^2 - k^2 = \varepsilon_\infty + \sum_j \frac{4\pi\rho_j \nu_j^2(\nu_j^2 - \nu^2)}{(\nu_j^2 - \nu^2)^2 + (\gamma_j \nu)^2} \tag{7}$$

$$\varepsilon_2 = 2nk = \sum_j \frac{4\pi\rho_j \nu_j^2(\gamma_j \nu)}{(\nu_j^2 - \nu^2)^2 + (\gamma_j \nu)^2}. \tag{8}$$

Kachare *et al.* [89] reanalyzed these results and emphasized the superiority of using a K–K analysis of the reflectance data. Piriou and Cabannes [77] made similar specular-reflectance measurements between about 300 and 1000 cm^{-1} and analyzed the measurements with both a two-oscillator fit and a K–K analysis. These authors had previously made extensive studies of absorption in MgO outside of the reststrahlen region [86] and used the results in adjusting the oscillator parameters for proper fits to these accurate k values. It was for this reason that we adopted their model to calculate reflection corrections at both lower and higher frequencies than the reststrahlen region, as mentioned earlier. The oscillator parameters used by Piriou and Cabannes are

$$\varepsilon_\infty = 2.964,\ \nu_1 = 396\ cm^{-1},\ 4\pi\rho_1 = 6.80,\ \gamma_1/\nu_1 = 0.0192,$$

$$\nu_2 = 643\ cm^{-1},\ 4\pi\rho = 0.043,\ \text{and}\ \gamma_2/\nu_2 = 0.140.$$

Andermann and Duesler [90] paid considerable attention to factors affecting the K–K results for MgO, especially in the very low reflectance region near 840 cm^{-1} and in the shoulder region at about 720 cm^{-1}, where the reflectance is rapidly rising. These authors showed that even the position of the maximum absorption peak near 400 cm^{-1} can be affected by slight errors in these regions away from the peak. By taking special care in these regions they have analyzed a composite of their own reflectance data and those of Piriou and Cabannes [77] to obtain a revised set of optical constants derived from the K–K technique. The values are available in tabular form in the thesis of Duesler [78] and are those presented in Table I

for the range 740 to 320 cm^{-1}. There is, in fact, very little difference (averaging a few percent relative difference) in the range 740 to 400 cm^{-1} between the various k values taken from the oscillator fits of Piriou and Cabannes [77] and Jasperse *et al.* [88], and the K–K technique of Andermann and Duesler [90]. In the 400 to 300 cm^{-1} region, where k rapidly decreases, there are much greater differences (approaching a factor of two).

In the far infrared beyond the strong reststrahlen peak, there are some distinct gaps in the reported optical constants of single-crystal MgO. This situation is worse for the 100 to 300 cm^{-1} region than below 100 cm^{-1}. In the latter region, Rowntree [91] determined k values from measurements of transmission. Billard *et al.* [92] measured absorption in monocrystalline samples of several thicknesses in the 20 to 350 cm^{-1} spectral range, and at temperatures of 300 to 1350 K. Unfortunately, they plot absorption coefficient versus temperature at only three frequencies: 50, 70, and 90 cm^{-1}. At higher frequencies up to about 300 cm^{-1}, where we feel the K–K results become suitably accurate, we could find no pertinent measurements except for those of Hanna [62], used in Whitson's compilation [75]. However, these data were for hot-pressed powders of MgO, and not necessarily characteristic of bulk-single-crystal values.

Because of the inadequate information about the absorption in the spectral region between 100 and 300 cm^{-1}, one of us (DRH) collaborated with W. Kratschmer to fill this gap. A Fourier-transform infrared spectrophotometer was used to make transmission measurements at room temperature on cleaved slabs of MgO. The thicknesses were 0.0405, 2.55, and 6.12 mm. Further details of these measurements and a discussion of their physical implications will be published elsewhere [93], but we believe the k values themselves are useful enough to include in the present compilation. Our own recent measurements agree rather well with those of Rowntree [91] within the region of overlap up to 85 cm^{-1}, so we have used his values at lower wave numbers in Table I. Rowntree estimates the experimental uncertainty in his room-temperature measurements to be $\pm 20\%$. This may be on the conservative side; our independent determinations of k in the 50 to 85 cm^{-1} region agree with his to better than 10%. Above 85 cm^{-1}, however, measurements on our 0.0405 mm sample depart seriously from the high-frequency tail of the Rowntree curve. Our data rise to a peak at about 105 cm^{-1}, followed by a gentle decline toward higher frequencies. Billard *et al.* [92] qualitatively described a somewhat similar behavior as "absorption abruptly rises to a considerable level at 100 cm^{-1} and then stays at this level over about 100 cm^{-1} before increasing again." These authors did not give the spectral absorption curve. Our values for k quoted in Table I are probably accurate to within about 10% except toward the high-frequency end, where increasingly small transmission may limit the accuracy to about 30% at the last point. There remains the region 275 to

300 cm^{-1}, where there appears to be no good data, but a reasonable extrapolation now appears to be possible in this gap.

As noted earlier, the values of n in Table I in the region below 270 cm^{-1} are based on a classical oscillator fit to reflectance data [77]. However, Rowntree [91] made a more direct experimental determination of n from interference spectra in the range 100 to 10 cm^{-1}. His values agree to within about ± 0.01 with those in Table I.

For completeness, we note that the commonly accepted value of the static dielectric constant, ε_0, is 9.8. This was obtained experimentally by a capacitance technique by Højendahl [94] and later by analysis of optical data [91, 95].

ACKNOWLEDGMENTS

We thank Drs. N. C. Fernelius (Wright–Patterson Air Force Base, Dayton), J. L. Freehouf (IBM, Yorktown Heights), W. F. Hanson (University of Texas, Radiological Physics Center), D. R. McKenzie (University of Sydney, Australia), and E. T. Arakawa and Y. Chen (both of Oak Ridge National Laboratory, Tennessee), for providing us with further information, including digitized data, from their original research.

REFERENCES

1. D. R. Huffman, *Advances in Physics* **26**, 129 (1977).
2. K. Maeda, M. Uda, and Y. Hayasi, *Phys. Letters* **112A**, 431 (1985).
3. S. Nakai, T. Mitsuishi, H. Sugawara, H. Maezawa, T. Matsukawa, S. Mitani, K. Yamasaki, and T. Fujikawa, *Phys. Rev.* **B36**, 9241 (1987).
4. J. R. Townsend, *Phys. Rev.* **92**, 556 (1953).
5. V. A. Fomichev, T. M. Zimkina, and I. I. Zhukova, *Sov. Phys. Solid State* **10**, 2421 (1969).
6. V. A. Fomichev and I. I. Zhukova, *Sov. Phys. Solid State* **10**, 2992 (1969).
7. W. F. Hanson, Ph.D. Thesis, University of Tennessee, 1971.
8. W. F. Hanson, E. T. Arakawa, and M. W. Williams, *J. Appl. Phys.* **43**, 1661 (1972).
9. J. R. Nelson, *Phys. Rev.* **99**, 1902 (1955).
10. G. H. Reiling and E. B. Hensley, *Phys. Rev.* **112**, 1106 (1958).
11. P. V. Harris, Ph.D. Thesis, University of London, unpublished (1963).
12. D. M. Roessler, *Brit. J. Applied Phys.* **16**, 1359 (1965).
13. D. M. Roessler and W. C. Walker, *Phys. Rev. Letters* **17**, 319 (1966).
14. R. C. Whited and W. C. Walker, *Phys. Rev. Letters* **22**, 1428 (1969).
15. M. L. Cohen, P. J. Lin, D. M. Roessler, and W. C. Walker, *Phys. Rev.* **155**, 992 (1967).
16. D. M. Roessler and W. C. Walker, *Phys. Rev.* **159**, 733 (1967).
17. D. M. Roessler and W. C. Walker, *J. Opt. Soc. Am.* **57**, 835 (1967).
18. M. W. Williams and E. T. Arakawa, *J. Appl. Phys.* **38**, 5272 (1967).
19. J. L. Freehouf, *Phys. Rev.* **B7**, 3810 (1973).

20. V. Mikhailin, E. E. Koch, and M. Skibowski, in "Proc, 4th Int. Conf. Vac. Ultraviolet Radiation Phys.," (E. E. Koch, R. Haensel, and C. Kunz, eds.), Pergamon Press, Oxford, England, 401 (1974).
21. I. L. Kuusmann and E. K. Fel'dbakh, *Sov. Phys. Solid State* **23**, 259 (1981).
22. R. H. French and R. L. Coble, *Ann. Isr. Phys. Soc.* **6**, 261 (1984).
23. J. Carden, F. Ferrandino, J. Larsen, W. Wall, and J. R. Stevenson, in "Proc. 4th Int. Conf. Vac. Ultraviolet Radiation Phys.," (E. E. Koch, R. Haensel, and C. Kunz, eds.), Pergamon Press, Oxford, England, 572 (1974).
24. D. M. Roessler, *Brit. J. Appl. Phys.* **16**, 1119 (1965).
25. H. Venghaus, *Optics Comm.* **2**, 447 (1971).
26. V. E. Henrich, G. Dresselhaus, and H. J. Zeiger, *Phys. Rev.* **B22**, 4764 (1980).
27. K. Kambe, D. Krahl, and K.-H. Herrmann, *Ultramicroscopy* **6**, 157 (1981).
28. P. J. Martin, W. G. Sainty, R. P. Netterfield, D. R. McKenzie, D. J. H. Cockayne, S. H. Sie, O. R. Wood, and H. G. Craighead, *App. Opt.* **26**, 1235 (1987).
29. J. H. Hibben, *Phys. Rev.* **51**, 530 (1937).
30. J. P. Molnar and C. D. Hartman, *Phys. Rev.* **79**, 1015 (1950).
31. W. W. Tyler and R. L. Sproull, *Phys. Rev.* **83**, 548 (1951).
32. H. Weber, *Zeitschr. Physik* **130**, 392 (1951).
33. P. D. Johnson, *Phys. Rev.* **94**, 845 (1954).
34. W. T. Peria, *Phys. Rev.* **112**, 423 (1958).
35. C. Ballesteros, R. Gonzalez, and Y. Chen, *Phys. Rev.* **B37**, 8008 (1988).
36. C. Ballesteros, R. Gonzalez, S. J. Pennycook, and Y. Chen, *Phys. Rev.* **B38**, 4231 (1988).
37. J. A. Harrington, B. L. Bobbs, M. Braunstein, R. K. Kim, R. Stearns, and R. Braunstein, *Appl. Opt.* **17**, 1541 (1978).
38. M. Y. Sakhnovskii, *Opt. & Spectros.* **18**, 100 (1965).
39. J. A. Harrington, D. A. Gregory, and W. F. Otto, Jr., *Appl. Opt.* **15**, 1953 (1976).
40. N. C. Fernelius, G. S. Coble, D. V. Dempsey, J. A. Detrio, J. A. Fox, P. R. Greason, G. T. Johnston, and D. B. O'Quinn, *SPIE* **297**, 137 (1981).
41. N. C. Fernelius, R. J. Harris, D. B. O'Quinn, M. E. Gangl, D. V. Dempsey, and W. L. Knecht, *Opt. Eng.* **22**, 411 (1983).
42. A. Hordvik and L. Skolnik, *Appl. Opt.* **16**, 2919 (1977).
43. R. Braunstein, R. K. Kim, and M. Braunstein, NBS Special Publication 620, U.S. Government Printing Office, Washington, D.C., (1980).
44. E. S. Larsen, *Bull. Soc. Franc. Mineral.* **16**, 177 (1893).
45. E. Mallard, *Bull. Soc. Franc. Mineral.* **16**, 16 (1893).
46. E. Sommerfeldt, *Centralbl. Min. Geol. Pal.* 212 (1907).
47. F. E. Wright, *Anorg. Chemie* **68**, 410 (1910).
48. O. Westphal, *Centralbl. Min. Geol. Pal.* 516 (1913).
49. J. B. Ferguson and H. E. Merwin, *Amer. J. Science (Fourth Series)* **48**, no. 284, 81 (1919).
50. M. Haase, *Z. Kristallograph.* **65**, 509 (1927).
51. J. Strong and R. T. Brice, *J. Opt. Soc. Amer.* **25**, 207 (1935).
52. T. Radhakrishnan, *Proc. Indian Acad. Sci.* **31A**, 229 (1950).
53. T. Radhakrishnan, *Proc. Indian Acad. Sci.* **33A**, 22 (1951).
54. R. E. Stephens and I. H. Malitson, *J. Research Nat. Bur. Stand.* **49**, no. 4, 249 (1952).
55. B. D. Saksena and S. Viswanathan, *Proc. Phys. Soc.* **B69**, 129 (1956).
56. M. J. Dodge, in "CRC Handbook of Laser Science and Technology," (M. J. Weber, ed.), Vol. IV, CRC Press, Inc., Boca Raton, Florida, 31 (1986).
57. A. J. Moses, "Refractive Index of Optical Materials in the Infrared Region", EPIC Report DS-1966 (January 1970), Hughes Aircraft Company, Culver City, California; Government Report AD 704555 (1970).

58. Norton Company Refractories Division, Report #P-1.5-1, March 1, 1962.
59. M. Herzberger and C. D. Salzberg, *J. Opt. Soc. Amer.* **52**, 420 (1962).
60. "Handbook of Optics," (W. G. Driscoll and W. Vaughan, eds.), McGraw-Hill, New York, 7–93 (1978).
61. R. B. Barnes, R. R. Brattain, and F. Seitz, *Phys. Rev.* **48**, 582 (1935).
62. R. Hanna, *J. Amer. Ceram. Soc.* **48**, 376 (1965).
63. B. Welber, *Appl. Opt.* **6**, 925 (1967).
64. A. Malherbe, *Nouv. Rev. Opt. Appl.* **2**, 337 (1971).
65. A. P. Bradford, G. Hass, and M. McFarland, *Appl. Opt.* **11**, 2242 (1972).
66. R. H. Deitch, E. J. West, T. G. Giallorenzi, and J. F. Weller, *Appl. Opt.* **13**, 712 (1974).
67. R. T. Kersten, H. F. Mahlein, and W. Rauscher, *Thin Solid Films* **28**, 369 (1974).
68. C. Reale, *Comptes Rendus Acad. Bulgar. Sci. (Bulgaria)* **31**, 281 (1978).
69. J. A. Harrington, J. E. Rudisill, and M. Braunstein, *Appl. Opt.* **17**, 2798 (1978).
70. M. Blanc, *J. Optics (Paris)* **11**, 127 (1980).
71. M. O. Aboelfotoh and J. N. Ramsey, *Thin Solid Films* **91**, 191 (1982).
72. S. G. MacLean and W. W. Duley, *Astrophys. J.* **252**, L25 (1982).
73. S. G. MacLean and W. W. Duley, *J. Phys. Chem. Solids* **45**, 223 (1984).
74. D. P. DeWitt, "Handbook of the Optical, Thermal, and Mechanical Properties of Six Polycrystalline Dielectric Materials," Purdue Univ. Thermophysical Properties Research Center rept. #TPRC-19, Dec. 1972.
75. M. E. Whitson, Jr., "Handbook of the Infrared Optical Properties of Al_2O_3, Carbon, MgO, and ZrO_2," Vol. I & II, Govt. Doc. AD-A013 722/4G, June 4, 1975, Rept. TR-0075(5548)-2-Vol 1&2 SAMSO-TR-75-131-Vol-1&2.
76. C. F. Bohren and D. R. Huffman, "Absorption and Scattering of Light by Small Particles," Wiley, New York, (1983).
77. B. Piriou and F. Cabannes, *Optica Acta* **15**, 271, (1968).
78. E. Duesler, "The Kramers–Kronig Dispersion Analysis of MgO Infrared Reflectance Data," M. S. Thesis, University of Hawaii (1968).
79. R. B. Barnes and R. R. Brattain, *Phys. Rev.* **47**, 416 (1935).
80. E. Burstein, J. J. Oberly, and E. K. Plyler, *Proc. Indian Acad. Sci.* **28A**, 388 (1948).
81. J. C. Willmott, *Phys. Soc. Proc. (London)* **63A**, 389 (1950).
82. U. P. Oppenheim and A. Goldman, *J. Opt. Soc. Am.* **54**, 127 (1964).
83. D. Billard, J.-L. Servoin, F. Gervais, and B. Piriou, *High Temp. High Pressures* **11**, 415 (1979).
84. F. Cabannes and D. Billard, *Int. J. Thermophysics* **8**, 97 (1987).
85. J. T. Gourley and W. A. Runciman, *J. Phys. C: Solid State Phys.* **6**, 583 (1973).
86. B. Piriou and F. Cabannes, *C. R. Acad. Sci. Paris* **264B**, 630 (1967).
87. H. G. Häfele, *Ann. Phys.* **10**, 321 (1963).
88. J. R. Jasperse, A. Kahan, J. N. Plendl, and S. S. Mitra, *Phys. Rev.* **146**, 526 (1966).
89. A. Kachare, G. Andermann, and L. R. Brantley, *J. Phys. Chem, Solids* **33**, 467 (1972).
90. G. Andermann and E. Duesler, *J. Opt. Soc. Am.* **60**, 53 (1970).
91. R. F. Rowntree, "Measurements of the Optical Constants of Magnesium Oxide and Calcium Tungstate (spectral region between 10 cm^{-1} and 100 cm^{-1} at 300 K and 90 K)," Ph.D. Thesis, Ohio State University (1963); also Ohio State Univ. Sci. Report 4 (1963) and AFCRL-63-454.
92. D. Billard, F. Gervais, and B. Piriou, *Int. J. Infrared and Millimeter Waves* **1**, 641 (1980).
93. D. R. Huffman and W. Kratschmer, private communication (1989).
94. K. Højendahl, Det Kgl. Danske Videnskabernes Selskab., *Mathematisk-fysiske Meddelelser.* **16**, 3 (1938).
95. O. L. Anderson and P. Glyn, *J. Phys. Chem. Solids* **26**, 1961 (1965).
96. Based on present analysis of optical density data above 80 eV and a Kramers–Kronig analysis of composite reflectance spectra at lower energies (see text).

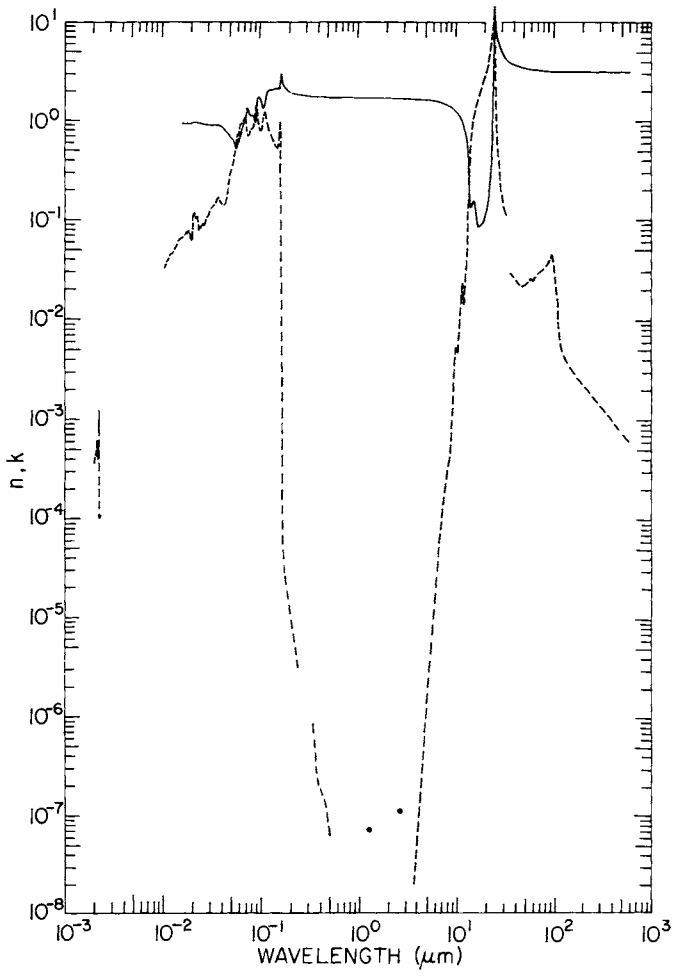

Fig. 1. Log–log plot of n (solid line) and k (dashed line) versus wavelength in micrometers for magnesium oxide.

TABLE I

Values of n and k for Magnesium Oxide Obtained from Various References[a]

eV	cm^{-1}	nm	n	k
586		2.116		3.69×10^{-4} [2]
584		2.123		3.86
582		2.130		4.06
580		2.138		4.25
579		2.141		4.35
578		2.145		4.42
576		2.153		4.48
575		2.156		4.47
574		2.160		4.41
573		2.164		4.31
572		2.168		4.23
571		2.171		4.29
570		2.175		4.40
569		2.179		4.44
568		2.183		4.39
567.5		2.185		4.37
567		2.187		4.40
565		2.194		4.50
563		2.202		4.66
562		2.206		4.85
561		2.210		5.27
560		2.214		5.89
559		2.218		6.29
558.2		2.221		6.35
558		2.222		6.35
557		2.226		6.13
556		2.230		5.53
555		2.234		4.99
554		2.238		4.63
553		2.242		4.27
552.5		2.244		4.20
552.4		2.245		4.19
552		2.246		4.20
551		2.250		4.35
550		2.254		4.57
549		2.258		4.97
548.5		2.260		5.75
548		2.262		6.18
547.5		2.265		6.51
547		2.267		6.36
546		2.271		5.26
545		2.275		4.32
544.5		2.277		4.10
544		2.279		4.00
543		2.283		4.62

TABLE I (*Continued*)

Magnesium Oxide

eV	cm^{-1}	nm	n	k
542		2.288		6.15×10^{-4}
541		2.292		8.19
540.5		2.294		9.50×10^{-4}
540		2.296		1.08×10^{-3}
539.5		2.298		1.20
539.3		2.299		1.24
539.2		2.300		1.26
539		2.300		1.25
538.5		2.302		1.18×10^{-3}
538		2.305		9.81×10^{-4}
537.5		2.307		8.48
537		2.309		7.41
536.5		2.311		6.37
536		2.313		5.32
535.5		2.315		4.28
535		2.317		3.23
534.5		2.320		2.30
534		2.322		1.75
533		2.326		1.40
530		2.339		1.18
527		2.353		1.08
524		2.366		1.04
517		2.398		1.03
513		2.417		1.02
507		2.445		1.06
503		2.465		1.09×10^{-4}

eV	cm^{-1}	μm	n	k
121		0.01025		0.033 [96]
118.5		0.01046		0.034
116		0.01069		0.035
114		0.01088		0.036
112		0.01107		0.037
110		0.01127		0.038
108		0.01148		0.040
106.5		0.01164		0.041
105		0.01181		0.043
104		0.01192		0.045
103.5		0.01198		0.045
101.5		0.01222		0.043
99.5		0.01246		0.045
98		0.01265		0.046
96.5		0.01285		0.045

TABLE I (*Continued*)

Magnesium Oxide

eV	cm^{-1}	μm	n	k
95		0.01305		0.045
93.5		0.01326		0.046
92		0.01348		0.048
90		0.01378		0.051
88.5		0.01401		0.052
86		0.01442		0.053
84.5		0.01467		0.054
82.5		0.01503		0.056
80.5		0.01540		0.060
80		0.01550		0.061
78.5		0.01579		0.065
76.5		0.01621		0.069
75		0.01653	0.951 [96]	0.070
74		0.01675	0.952	0.070
73		0.01698	0.954	0.069
72		0.01722	0.954	0.069
70		0.01771	0.952	0.074
68		0.01823	0.952	0.077
66		0.01879	0.958	0.076
65		0.01907	0.962	0.073
64		0.01937	0.964	0.064
63		0.01968	0.965	0.063
62		0.02000	0.960	0.064
61		0.02033	0.950	0.067
60		0.02066	0.938	0.071
59		0.02101	0.925	0.081
58		0.02138	0.926	0.113
57		0.02175	0.954	0.117
56		0.02214	0.964	0.105
55		0.02254	0.964	0.105
54.5		0.02275	0.965	0.104
54		0.02296	0.966	0.106
53		0.02339	0.975	0.109
52		0.02384	0.985	0.094
51.5		0.02407	0.981	0.082
51		0.02431	0.972	0.079
50		0.02480	0.963	0.084
49		0.02530	0.960	0.083
48		0.02583	0.955	0.085
47		0.02638	0.950	0.084
46		0.02695	0.943	0.090
45		0.02755	0.940	0.088
44		0.02818	0.930	0.094
43		0.02883	0.926	0.103
42		0.02952	0.924	0.106

TABLE I (*Continued*)

Magnesium Oxide

eV	cm^{-1}	μm	n	k
41		0.03024	0.918	0.113
40		0.03100	0.915	0.123
39		0.03179	0.916	0.129
38		0.03263	0.915	0.133
37		0.03351	0.912	0.138
36		0.03444	0.909	0.140
35.5		0.03493	0.903	0.143
35		0.03542	0.898	0.153
34		0.03647	0.902	0.165
33		0.03757	0.908	0.169
32		0.03875	0.913	0.166
31.5		0.03936	0.913	0.160
31		0.03999	0.909	0.153
30.5		0.04065	0.901	0.145
30		0.04133	0.887	0.142
29		0.04275	0.862	0.142
28		0.04428	0.830	0.142
27.5		0.04509	0.806	0.146
27		0.04592	0.781	0.155
26.5		0.04679	0.754	0.168
26		0.04769	0.724	0.188
25.5		0.04862	0.694	0.221
25.0		0.04959	0.677	0.264
24.9		0.04979	0.675	0.275
24.8		0.04999	0.675	0.287
24.5		0.05061	0.689	0.303
24.3		0.05102	0.692	0.304
24.1		0.05145	0.684	0.309
24.0		0.05166	0.680	0.313
23.9		0.05188	0.678	0.319
23.7		0.05231	0.677	0.325
23.5		0.05276	0.669	0.328
23.3		0.05321	0.658	0.334
23.0		0.05391	0.636	0.348
22.7		0.05462	0.612	0.365
22.5		0.05510	0.589	0.382
22.2		0.05585	0.553	0.423
22.0		0.05636	0.531	0.464
21.8		0.05687	0.522	0.511
21.6		0.05740	0.519	0.507
21.5		0.05767	0.522	0.586
21.4		0.05794	0.526	0.614
21.3		0.05821	0.535	0.642
21.2		0.05848	0.550	0.669

TABLE I (*Continued*)

Magnesium Oxide

eV	cm^{-1}	μm	n	k
21.1		0.05876	0.568	0.693
21.0		0.05904	0.592	0.716
20.9		0.05932	0.624	0.723
20.8		0.05961	0.645	0.720
20.7		0.05990	0.659	0.723
20.6		0.06019	0.676	0.710
20.5		0.06048	0.673	0.704
20.4		0.06078	0.669	0.704
20.3		0.06108	0.661	0.707
20.2		0.06138	0.651	0.716
20.0		0.06199	0.632	0.752
19.9		0.06230	0.625	0.786
19.8		0.06262	0.635	0.820
19.7		0.06294	0.652	0.847
19.6		0.06326	0.670	0.871
19.5		0.06358	0.691	0.892
19.4		0.06391	0.714	0.911
19.3		0.06424	0.743	0.930
19.2		0.06458	0.776	0.918
19.1		0.06491	0.780	0.929
19.05		0.06508	0.792	0.929
19.0		0.06525	0.798	0.929
18.9		0.06560	0.807	0.935
18.8		0.06595	0.817	0.944
18.7		0.06630	0.828	0.955
18.6		0.06666	0.842	0.969
18.5		0.06702	0.859	0.982
18.35		0.06757	0.887	0.996
18.2		0.06812	0.915	1.007
18.1		0.06850	0.931	1.014
18.0		0.06888	0.947	1.023
17.9		0.06926	0.964	1.034
17.8		0.06965	0.984	1.049
17.7		0.07005	1.009	1.064
17.65		0.07025	1.025	1.074
17.6		0.07045	1.046	1.082
17.5		0.07085	1.087	1.074
17.4		0.07126	1.119	1.081
17.3		0.07167	1.166	1.074
17.2		0.07208	1.203	1.043
17.1		0.07251	1.224	1.023
17.0		0.07293	1.241	1.001
16.95		0.07315	1.248	1.001
16.9		0.07336	1.265	1.000
16.8		0.07380	1.301	0.976

TABLE I (*Continued*)

Magnesium Oxide

eV	cm^{-1}	μm	n	k
16.7		0.07424	1.333	0.941
16.6		0.07469	1.341	0.883
16.5		0.07514	1.344	0.862
16.4		0.07560	1.346	0.810
16.3		0.07606	1.337	0.774
16.2		0.07653	1.301	0.714
16.1		0.07701	1.247	0.705
16.0		0.07749	1.214	0.724
15.9		0.07798	1.195	0.727
15.8		0.07847	1.173	0.736
15.7		0.07897	1.160	0.760
15.5		0.07999	1.149	0.773
15.4		0.08051	1.141	0.788
15.3		0.08104	1.135	0.798
15.2		0.08157	1.131	0.819
15.1		0.08211	1.139	0.835
15.0		0.08266	1.147	0.841
14.9		0.08321	1.149	0.843
14.8		0.08377	1.150	0.852
14.7		0.08434	1.149	0.847
14.6		0.08492	1.137	0.851
14.5		0.08551	1.120	0.864
14.4		0.08610	1.115	0.883
14.3		0.08670	1.110	0.903
14.2		0.08731	1.106	0.919
14.1		0.08793	1.094	0.929
14.0		0.08856	1.065	0.947
13.9		0.08920	1.023	0.994
13.8		0.08984	0.990	1.087
13.75		0.09017	0.984	1.133
13.7		0.09050	0.980	1.218
13.6		0.09116	1.054	1.350
13.55		0.09150	1.111	1.418
13.5		0.09184	1.191	1.471
13.45		0.09218	1.283	1.499
13.4		0.09253	1.374	1.507
13.35		0.09287	1.463	1.503
13.3		0.09322	1.549	1.479
13.25		0.09357	1.632	1.446
13.2		0.09393	1.702	1.380
13.15		0.09428	1.744	1.312
13.1		0.09464	1.768	1.248
13.05		0.09501	1.779	1.193
13.0		0.09537	1.786	1.147
12.95		0.09574	1.789	1.103

TABLE I (*Continued*)

Magnesium Oxide

eV	cm^{-1}	μm	n	k
12.9		0.09611	1.788	1.065
12.8		0.09686	1.779	0.997
12.6		0.09840	1.745	0.894
12.5		0.09919	1.723	0.858
12.4		0.1000	1.694	0.824
12.1		0.1025	1.603	0.770
12.0		0.1033	1.565	0.765
11.9		0.1042	1.520	0.767
11.8		0.1051	1.473	0.787
11.65		0.1064	1.397	0.839
11.6		0.1069	1.370	0.890
11.5		0.1078	1.371	1.000
11.4		0.1088	1.409	1.081
11.3		0.1097	1.468	1.161
11.2		0.1107	1.555	1.210
11.15		0.1112	1.601	1.220
11.1		0.1117	1.646	1.230
11.0		0.1127	1.735	1.228
10.9		0.1137	1.814	1.202
10.8		0.1148	1.877	1.166
10.5		0.1181	1.999	1.041
10.2		0.1216	2.045	0.921
10.0		0.1240	2.061	0.867
9.8		0.1265	2.074	0.819
9.7		0.1278	2.079	0.798
9.5		0.1305	2.091	0.761
9.3		0.1333	2.103	0.728
9.0		0.1378	2.130	0.679
8.8		0.1409	2.147	0.642
8.5		0.1459	2.160	0.587
8.2		0.1512	2.171	0.545
8.1		0.1531	2.168	0.532
8.0		0.1550	2.154	0.530
7.95		0.1560	2.145	0.539
7.90		0.1569	2.137	0.558
7.85		0.1579	2.127	0.589
7.83		0.1583	2.126	0.611
7.80		0.1590	2.132	0.651
7.75		0.1600	2.180	0.731
7.70		0.1610	2.270	0.813
7.68		0.1614	2.327	0.851
7.66		0.1619	2.389	0.885
7.64		0.1623	2.498	0.936
7.63		0.1625	2.574	0.949
7.62		0.1627	2.665	0.944
7.61		0.1629	2.753	0.912

TABLE I (*Continued*)

Magnesium Oxide

eV	cm^{-1}	μm	n	k
7.60		0.1631	2.839	0.866
7.59		0.1634	2.922	0.800
7.58		0.1636	2.994	0.711
7.57		0.1638	3.048	0.600
7.56		0.1640	3.061	0.474
7.55		0.1642	3.035	0.360
7.54		0.1644	2.999	0.272
7.53		0.1647	2.944	0.204
7.52		0.1649	2.892	0.149
7.50		0.1653	2.793	0.076
7.48		0.1658	2.701	0.039
7.45		0.1664	2.603	0.018
7.40		0.1675	2.494	0.002
7.35		0.1687	2.419	
7.30		0.1698	2.363	
7.28		0.1703	2.346	1.36×10^{-4} [33]
7.25		0.1710	2.319	
7.20		0.1722	2.281	7.6×10^{-5}
7.185		0.1726	2.269	6.87
7.15		0.1734	2.248	
7.14		0.1737	2.241	5.53
7.10		0.1746	2.220	
7.06		0.1757	2.198	4.19
7.05		0.1759	2.196	
7.00		0.1771	2.176	3.7
6.90		0.1797	2.141	
6.89		0.1800	2.138	2.86
6.80		0.1823	2.110	
6.70		0.1851	2.084	2.00
6.60		0.1879	2.060	
6.50		0.1907	2.039	1.39 [36]
6.40		0.1937	2.020	
6.20	50,000	0.2000	1.986	1.11
6.00	48,393	0.2066	1.958	1.0×10^{-5}
5.80	46,780	0.2138	1.933	8.5×10^{-6}
5.60	45,167	0.2214	1.911	7.0 [34]
5.50	44,360	0.2254	1.901	6.0
5.40	43,554	0.2296	1.892	5.0
5.20	41,941	0.2384	1.874	3.7
5.09	41,054	0.2436	1.865	3.2
5.00	40,328	0.2480	1.858	3.1×10^{-6} [32]
4.75	38,311	0.2610	1.840	
4.50	36,295	0.2755	1.824	
4.25	34,279	0.2917	1.810	
4.00	32,262	0.3100	1.798	
3.75	30,246	0.3306	1.785	

TABLE I (*Continued*)

Magnesium Oxide

eV	cm^{-1}	μm	n	k
3.531	28,482	0.3511	1.7768 [56]	
3.487	28,125	0.3556	1.7755 [54]	8.5×10^{-7} [37]
3.435	27,705	0.3609	1.7732	5.75
3.433	27,688	0.36117	1.77318	5.65
3.397	27,396	0.36502	1.77186	4.9
3.245	26,173	0.3821	1.7668	2.75
3.206	25,859	0.3867	1.7655	2.45
3.152	25,423	0.3934	1.7638	2.2
3.064	24,710	0.4047	1.76104	1.95
2.877	23,205	0.4310	1.7557	1.7
2.845	22,946	0.4358	1.75471	1.65
2.708	21,839	0.4579	1.7512	1.45
2.594	20,922	0.4780	1.7483	1.15
2.551	20,572	0.4861	1.74711	1.0×10^{-7}
2.541	20,492	0.4880	1.7469 [56]	9.75×10^{-8}
2.480	20,000	0.5	1.7454 [59]	8.25
2.468	19,906	0.5024	1.7453 [54]	8.0
2.438	19,666	0.5085	1.74446	7.0
2.410	19,436	0.5145	1.7439	6.55
2.270	18,312	0.5461	1.74077	
2.104	16,969	0.5893	1.73737	
1.959	15,803	0.6328	1.7346 [56]	
1.926	15,533	0.6438	1.73400 [54]	
1.889	15,237	0.6563	1.73335	
1.857	14,975	0.6678	1.73277	
1.795	14,478	0.6907	1.73191 [58]	
1.755	14,154	0.7065	1.73101 [54]	
1.615	13,023	0.7679	1.72872	
1.240	10,000	1.0	1.7229 [59]	
1.223	9,862	1.01398	1.72259 [58]	
1.170	9,434	1.06	1.7217 [56]	
1.099	8,860	1.12866	1.72059 [54]	
0.9400	7,582	1.319	1.7177	7.1×10^{-8} [41]
0.9068	7,314	1.36728	1.71715	
0.8266	6,667	1.5	1.7153 [59]	
0.8106	6,538	1.52952	1.71496 [54]	
0.7999	6,452	1.55	1.7147 [56]	
0.7322	5,906	1.6932	1.71281 [54]	
0.7254	5,851	1.7092	1.71258	
0.6838	5,516	1.81307	1.71108	
0.6293	5,076	1.97009	1.70885 [58]	
0.6199	5,000	2.0	1.7085 [59]	
0.5512	4,446	2.24929	1.70470 [54]	
0.5332	4,300	2.32542	1.70350	
0.4959	4,000	2.5	1.7007 [59]	
0.4592	3,704	2.7	1.6973 [54]	1.1×10^{-7} [42]

TABLE I (*Continued*)

Magnesium Oxide

eV	cm^{-1}	μm	n	k
0.4428	3,571	2.8	1.6954 [56]	
0.4133	3,333	3.0	1.6915 [59]	
0.3753	3,027	3.3033	1.68526 [58]	
0.3720	3,000	3.333	1.6846 [54]	
0.3596	2,900	3.448	1.6820	
0.3542	2,857	3.5	1.6806 [59]	
0.3535	2,851	3.5078	1.68055 [54]	
0.3472	2,800	3.571	1.6791	
0.3348	2,700	3.704	1.6758	
0.3263	2,632	3.8	1.6734	2.0×10^{-8} [42]
0.3224	2,600	3.846	1.6722	
0.3100	2,500	4.0	1.6679 [59]	3.7
0.2976	2,400	4.167	1.6634 [54]	7.4×10^{-8}
0.2912	2,349	4.258	1.66039 [58]	1.0×10^{-7}
0.2852	2,300	4.348	1.6581 [54]	1.5
0.2755	2,222	4.5	1.6533 [59]	2.5
0.2728	2,200	4.545	1.6520 [54]	2.9
0.2604	2,100	4.762	1.6450	5.8×10^{-7}
0.2480	2,000	5.0	1.6373	1.2×10^{-6}
0.2418	1,950	5.128	1.6328 [77]	1.63 [83]
0.2380	1,920	5.208	1.6299	2.0 [42]
0.2356	1,900	5.263	1.6278	2.3
0.2331	1,880	5.319	1.6256	2.7
0.2306	1,860	5.376	1.6233	3.1
0.2281	1,840	5.435	1.6210	3.5
0.2257	1,820	5.495	1.6186	4.0
0.2231	1,800	5.555	1.6161	4.6
0.2207	1,780	5.618	1.6135	5.3
0.2182	1,760	5.682	1.6108	6.1
0.2157	1,740	5.747	1.6080	7.1
0.2132	1,720	5.814	1.6051	8.1
0.2108	1,700	5.882	1.6021	9.0×10^{-6} [86]
0.2083	1,680	5.952	1.5989	1.1×10^{-5} [42]
0.2058	1,660	6.024	1.5957	1.2
0.2033	1,640	6.098	1.5922	1.4
0.2008	1,620	6.172	1.5887	1.6
0.1984	1,600	6.250	1.5849	1.83 [86]
0.1959	1,580	6.329	1.5811	2.2 [42]
0.1934	1,560	6.410	1.5770	2.5
0.1909	1,540	6.494	1.5727	2.9
0.1884	1,520	6.579	1.5683	3.3
0.1860	1,500	6.667	1.5636	4.60 [86]
0.1835	1,480	6.757	1.5510	5.38
0.1810	1,460	6.849	1.5536	5.98
0.1785	1,440	6.944	1.548	7.00

TABLE I (*Continued*)

Magnesium Oxide

eV	cm^{-1}	μm	n	k
0.1760	1,420	7.042	1.543	7.89×10^{-5}
0.1736	1,400	7.143	1.537	8.59
0.1711	1,380	7.246	1.530	9.30×10^{-5}
0.1686	1,360	7.352	1.524	1.03×10^{-4}
0.1661	1,340	7.463	1.517	1.15
0.1637	1,320	7.576	1.509	1.31
0.1612	1,300	7.692	1.502	1.54
0.1587	1,280	7.812	1.493	1.84
0.1562	1,260	7.936	1.485	2.11
0.1537	1,240	8.065	1.475	2.47
0.1513	1,220	8.197	1.465	2.73
0.1488	1,200	8.333	1.455	3.09
0.1463	1,180	8.475	1.443	3.26
0.1438	1,160	8.621	1.431	3.52
0.1413	1,140	8.772	1.418	4.14
0.1389	1,120	8.929	1.404	5.76
0.1364	1,100	9.091	1.389	6.27
0.1339	1,080	9.259	1.373	8.47×10^{-4}
0.1314	1,060	9.434	1.355	1.07×10^{-3}
0.1302	1,050	9.524	1.346	1.33
0.1289	1,040	9.615	1.336	1.58 [85,86]
0.1277	1,030	9.709	1.326	1.92
0.1265	1,020	9.804	1.315	2.44
0.1252	1,010	9.901	1.304	3.02
0.1240	1,000	10.00	1.292	3.90
0.1227	990	10.10	1.280	4.70
0.1215	980	10.20	1.267	5.13
0.1202	970	10.31	1.253	4.29
0.1190	960	10.42	1.239	3.55
0.1178	950	10.53	1.224	3.40
0.1165	940	10.64	1.209	3.70
0.1153	930	10.75	1.191	4.58
0.1141	920	10.87	1.174	5.91
0.1128	910	10.99	1.155	7.80×10^{-3}
0.1116	900	11.11	1.135	0.0102
0.1103	890	11.24	1.114	0.0137
0.1091	880	11.36	1.091	0.0162
0.1079	870	11.49	1.067	0.0196
0.1066	860	11.63	1.041	0.0223
0.1060	855	11.70	1.027	0.0229
0.1054	850	11.76	1.013	0.0227
0.1041	840	11.90	0.982	0.0205
0.1029	830	12.05	0.949	0.0171
0.1017	820	12.20	0.913	0.0147
0.1010	815	12.27	0.893	0.0143

TABLE I (*Continued*)

Magnesium Oxide

eV	cm^{-1}	μm	n	k
0.1004	810	12.35	0.873	0.0146
0.0992	800	12.50	0.829	0.0167
0.0979	790	12.66	0.780	0.0236
0.0967	780	12.82	0.724	0.0295
0.0955	770	12.99	0.660	0.0346
0.0930	750	13.33	0.503	0.0475
0.0918	740	13.51	0.393	0.0913 [78]
0.0905	730	13.70	0.267	0.172
0.0893	720	13.89	0.156	0.317
0.0880	710	14.08	0.139	0.478
0.0868	700	14.29	0.132	0.595
0.0856	690	14.49	0.134	0.692
0.0843	680	14.71	0.136 [78]	0.787
0.0831	670	14.93	0.143	0.877
0.0818	660	15.15	0.154	0.955
0.0806	650	15.38	0.155	1.03
0.0794	640	15.63	0.151	1.09
0.0781	630	15.87	0.135	1.17
0.0769	620	16.13	0.116	1.26
0.0756	610	16.39	0.108	1.35
0.0744	600	16.67	0.098	1.45
0.0732	590	16.95	0.086	1.56
0.0719	580	17.24	0.087	1.67
0.0707	570	17.54	0.086	1.78
0.0694	560	17.86	0.088	1.90
0.0682	550	18.18	0.089	2.03
0.0670	540	18.52	0.091	2.16
0.0657	530	18.87	0.093	2.31
0.0645	520	19.23	0.097	2.47
0.0632	510	19.61	0.102	2.64
0.0620	500	20.00	0.109	2.84
0.0608	490	20.41	0.119	3.06
0.0595	480	20.83	0.131	3.31
0.0583	470	21.28	0.148	3.60
0.0570	460	21.74	0.170	3.95
0.0558	450	22.22	0.207	4.39
0.0546	440	22.73	0.261	4.95
0.0533	430	23.26	0.362	5.71
0.0521	420	23.81	0.543	6.86
0.0508	410	24.39	1.01	8.97
0.0496	400	25.00	5.05	15.20
0.0484	390	25.64	13.50	4.06
0.0471	380	26.32	9.28	1.02
0.0459	370	27.03	7.44	0.56
0.0446	360	27.78	6.46	0.379
0.0434	350	28.57	5.83	0.266

TABLE I (*Continued*)

Magnesium Oxide

eV	cm^{-1}	μm	n	k
0.0425	340	29.41	5.35	0.208
0.0409	330	30.30	5.03	0.168
0.0397	320	31.25	4.74	0.129
0.0384	310	32.26	4.51	0.126
0.0372	300	33.33	4.36	0.113
0.0335	270	37.04	3.97 [77]	0.029 [93]
0.0322	260	38.46	3.87	0.0276
0.0310	250	40.00	3.78	0.0265
0.0298	240	41.67	3.71	0.0254
0.0285	230	43.47	3.64	0.0233
0.0273	220	45.46	3.58	0.0215
0.0260	210	47.62	3.53	0.0214
0.0248	200	50.00	3.48	0.0218
0.0236	190	52.63	3.44	0.0220
0.0223	180	55.56	3.40	0.0236
0.0211	170	58.82	3.37	0.0255
0.0198	160	62.50	3.34	0.0246
0.0186	150	66.67	3.31	0.0280
0.0174	140	71.43	3.28	0.0299
0.0161	130	76.92	3.26	0.0313
0.0149	120	83.33	3.24	0.0338
0.0136	110	90.91	3.22	0.0387
0.0130	105	95.24	3.21	0.0455
0.0124	100	100.00	3.20	0.0356
0.0118	95	105.2	3.20	0.0236
0.0112	90	111.1	3.19	0.0146
0.0105	85	117.6	3.18	6.2×10^{-3} [91]
0.0099	80	125.0	3.178	4.8
0.0093	75	133.3	3.172	3.9
0.0087	70	142.9	3.167	3.42
0.0081	65	153.8	3.162	3.15
0.0074	60	166.7	3.157	2.80
0.0068	55	181.8	3.153	2.53
0.0062	50	200.0	3.149	2.28
0.0056	45	222.2	3.146	2.00
0.0049	40	250.0	3.143	1.79
0.0043	35	285.7	3.140	1.51
0.0037	30	333.3	3.138	1.21×10^{-3}
0.0031	25	400.0	3.136	9.8×10^{-4}
0.0025	20	500.0	3.134	7.3
0.0020	16	625.0	3.133	5.8×10^{-4}

[a]References are given in brackets.

Polyethylene $(C_2H_4)_n$

J. ASHOK and P. L. H. VARAPRASAD
Applied Physics Department
Andhra University
Visakhapatnam, India
and
J. R. BIRCH
Division of Electrical Science
National Physical Laboratory
Teddington, Middlesex TW11 0LW, United Kingdom

In the papers to be discussed, a variety of polyethylenes have been studied, so one cannot hope to collect n and k over a wide spectral range for a given type of material. Luckily, the variations among materials are usually less than a factor of two where spectra overlap.

Ideal polyethylene forms a planar (zigzag) carbon chain constructed with C═C and C═H σ bonds only (see inset in Fig. 1). The unit cell contains two C_2H_4 molecules. Normal commercial low-density polyethylene is usually around 80% crystalline [1]. Partridge [2], however, reports a crystallinity of only 55%. The values of bond length and bond angle are 1.53 Å and 112°, respectively. The refractive index for amorphous specimens is given as 1.49 and for crystalline material as $\alpha \approx \beta = 1.52$ and $\gamma = 1.582$ at $\lambda = 5461$ Å (where α, β, and γ are the refractive indices along the a, b, and c crystallographic directions) [3–5].

Light-scattering experiments made by Partridge [6] have shown considerable scattering by thick polyethylene samples. A method of correcting for light scattering has been discussed in this paper.

Optical properties of polyethylene in the photon energy range 76–0.5 eV have been measured by Painter *et al.* [7]. Various transmission techniques were used over nearly the entire range; free-standing Glad Wrap (Union Carbide registered trade name); Dow Corning polyethylene pellets evaporated onto one half of a MgF_2 disk; polyethylene evaporated onto one half of a thick layer of *p*-terphenyl covering a glass slide. The *p*-terphenyl is fluorescent, so light passing through the polyethylene produces light emission in the *p*-terphenyl, which is measured through the glass slide. It is probable that the polyethylene was not highly crystalline (and perhaps it was even amorphous). The UV structure is primarily due to the chain carbon atoms and is probably similar for crystalline or amorphous polyethylene. We assume unpolarized light was used and that normal incidence

Copyright © 1991 by Academic Press.
All rights of reproduction in any form reserved.
ISBN 0-12-544422-2

was maintained with the Cary and Seya–Namioka monochromators used. The index of refraction was measured using a critical-angle measurement. A polyethylene film was deposited onto the flat side of sapphire hemicylinder. The angle of incidence was varied to detect the critical angle. Painter *et al.* extrapolated their k values to high energy and calculated the contribution of the C atomic scattering cross-section at 282 eV. Although there is concern about light scattering in polyethylene (samples are often not clear to the eye), this does not appear to have been a problem into the short-wavelength UV. The results for n and k obtained from tables and graphs in Ref. [7] are listed in Table I and plotted in Fig. 1.

Ritsko [1] reported measurements on films of polyethylene prepared from solvent evaporation. The thickness of the films was about 1000–2000 Å. They obtained values of the real and imaginary parts of the dielectric constants from measurements of energy-loss spectra and application of Kramers–Kronig analysis. The energy-loss spectra of an electron beam were recorded as a function of scattering angles θ or momentum transfer Φ. The samples were exposed to the incident beam for five minutes at $\theta = 0$. The energy-loss probability or differential scattering cross-section per unit energy loss E per unit solid angle Ω is a function of ε, the complex dielectric response function with real and imaginary parts ε_1 and ε_2, respectively [8].

Since the energy-loss spectrum is proportional to the energy-loss function $\mathrm{Im}(-1/\varepsilon)$, the constant of proportionality can be determined by normalizing the spectrum to the known value of the refractive index 1.4907 at 2.22 eV [9]. In addition, a correction for multiple inelastic scattering was made for the spectrum. Once the energy-loss function was normalized and multiple scattering eliminated, the function $\mathrm{Re}(-1/\varepsilon)$ was computed from the Kramers–Kronig relation, and hence, ε_1 and ε_2 could be calculated [10]. The complex refractive index $(n+ik) = \sqrt{\varepsilon}$ is listed in Table I. Where overlap occurs, these values agree well with those of Painter *et al.*

The n curve shows a peak near 7.2 eV. The peak was also reported by Tanaka [11]. This peak in n gives an approximate value for the optical band gap.

The values of the absorption edge show considerable variation as reported by different authors [12]. This is likely to have been caused by the choice of polyethylenes used (high density or low density) and the difference in the preparation of specimens. The drawn-film samples exhibit anisotropy.

The values of refractive index obtained for polyethylene depend critically on the method of film preparation. The density of the film depends on the method of preparation. It is possible to introduce methyl groups (CH_3) and vinyl groups (C_2H_3) into the regular $=CH_2=CH_2=CH_2=$ sequence. If the number of CH_3 groups per 1000 C atoms is 83, the refractive index

for the Na D line (5890 Å) is 1.5060; it increases to 1.5260 when 16 CH_3 groups are present per 1000 C atoms (see inset in Fig. 1).

The variation of refractive index with temperature for low-density polyethylene seems to be greater than that for high-density polyethylene. The variation for a temperature change from 70° to 124 °C is about 0.05 for low-density polyethylene, and from 130° to 154 °C it is about 0.07 for high-density polyethylene.

The properties of polyethylene films prepared by the solvent-evaporation technique are dependent on a number of parameters, such as the solvent used, the starting concentration, the temperatures, and speed in cases when the evaporation was effected by centrifugal rotation.

At a spin speed of 3000 RPM, a solution of 0.05% by weight of polyethylene in CCl_4 yields films of density 0.914 gm/cm^3 and refractive index $1.459 + i0.023$ at 2.254 eV; when the concentration is increased to 0.4% by weight, the refractive index changes to about 1.502. When the spin speed increases to 4000 RPM, the 0.4% concentration solution gives films of refractive index 1.457 [13].

A change in solvent also makes a difference. A starting solution of low-density polyethylene in xylene with 0.05% by weight at a spin speed of 1000 RPM yields films of density 0.923 gm/cm^3 and refractive index $1.464 + i0.021$ at 2.254 eV. When the concentration is increased to 0.4% by weight, the refractive index changes to $1.501 + i0.004$. When the specimen speed increases to 4000 RPM, the 0.4% by weight solution yields films of refractive index $1.495 + i0.011$ [13].

Although the vibrational absorption bands of polyethylene are well-known, we could not find a determination of the optical constants in the 2–20 μm region. The structure of crystalline polyethylene was determined long ago, and most spectroscopic efforts were directed towards assigning the many vibration modes of the various kinds of polyethylene (14–17). These include the orthorhombic crystal with two CH_2 groups repeating themselves in zigzag carbon skeleton chains throughout the crystal: $(C_2H_4)n$. However, various types of branching can occur, which lead to subtle additional features in the spectrum, and methyl and vinyl groups can occur along the chains. Although Krimm *et al.* [14] measured spectra of oriented crystal samples with polarized light, we have elected to use unpolarized spectra of Nielsen and Woollett [15] to determine approximate k values. They present transmittance spectra of a specific kind of polyethylene (Marlex 50) for three thicknesses. Marlex 50 is 95% crystalline with less than two methyl groups per 1000 carbon atoms and one vinyl group per molecule (for each C_2H_4 molecule, one H is missing). Nearly all the absorption lines (designated s (strong), m (medium) and w (weak)) are the same in a number of different polyethylenes [17].

We assumed $n = 1.5$ throughout the near IR and calculated k using the equation $T/T_o = (1 - R)^2 \exp(-\alpha x)$, where R is the single-surface reflecti-

vity $R=(n-1)^2/(n+1)^2$, since $k \ll n$ in the near IR; $\alpha=4\pi k/\lambda$ is the absorption coefficient, and x is the film thickness. This formula assumes that interference effects are averaged out, which is suggested by most of the spectra. Because k is small even at vibrational resonances, the dispersion should be small, and assuming that n is a constant is reasonable. The k values outside of resonances varied by as much as a factor of two among the three thicknesses, suggesting some scattering effects especially at shorter wavelengths. We suggest that the k values at resonances are probably good to $\pm 30\%$. In Fig. 1 the density of absorption lines is so great that it is not possible to resolve every line, although in Table I every line is defined by several data points. We have rounded off the k values to two significant figures; this loses only a few weak structures in the spectrum.

In the far-infrared region of the electromagnetic spectrum ($\lambda > 20$ μm), polyethylene is one of the most widely used materials for the fabrication of optical elements such as windows and lenses. This is due not only to its transparency, but also to its availability, low cost, machinability, and relative stability. As a consequence, its power transmission properties in this spectral region have been studied by many authors (see, for example, some reviews [18–20]). However, the optical properties of polyethylene, and indeed of many other polymers in the far infrared, are known to be specimen dependent, and can vary significantly depending on the past history of the specimen. In this spectral region, for example, it is not unusual to find differences of up to a factor of two between the absorption spectra of specimens with different histories. Some of the factors that affect this will include the particular manufacturing process used (extrusion, or vacuum- or injection-molding) and the density and degree of crystallinity achieved in the final material. The optical properties will also be varied by the presence in the material of impurities such as antioxidants, agents to improve flow during the manufacturing process, heavy-metal salts or oxides as residues of the catalysts used in polymerization, and microdroplets of water. Similarly, exposure of the material to environmental factors such as high temperatures, ultraviolet radiation, mechanical stress, and high-energy irradiation can significantly change the far-infrared optical constants of this material. It is therefore difficult to arrive at a unique set of intrinsic optical constants for polyethylene in the far-infrared. This problem is further aggravated by the fact that although there have been many measurements of the transmission properties of this material, there is little detailed quantitative information available on the spectral variation of both optical constants over this region. This critique will discuss, therefore, such data as are available with a view to providing typical values of the optical constants and their spectral variation across the far infrared. These values can be used to give reasonable calculations of the consequences of using a polyethylene-based optical element in an optical system. However, in applications where such calculations are critical to an evaluation of

system performance, it might well be best to measure the optical constants of the particular piece of polyethylene that is to be used. In most of the original publications the measurements have been made by Fourier-transform spectroscopy, so the independent spectral variable is given as wave number in reciprocal centimeters. Similarly, in most far-infrared measurements the dissipative part of the complex refractive index is usually described by the power absorption coefficient, α, rather than the extinction coefficient, k. The two parameters are related by

$$\alpha = 4\pi\nu k, \tag{1}$$

in which ν is the wave number.

The best optical-constant data for polyethylene in the far infrared are presently provided by the technique of dispersive Fourier-transform spectroscopy (DFTS) [21–23]. This is because of the measurement precision and accuracy that can be achieved, together with the wide broad-band spectral coverage available with the technique. Under the ideal conditions of a perfectly homogeneous, plane-parallel-sided specimen, measurements that are limited by random uncertainties of better than parts in 10^5 in the refractive index and better than a few percent in the extinction coefficient can readily be achieved for a low-loss material such as polyethylene. Ideal conditions, however, are rarely found for a mechanically soft material such as polyethylene. Nonetheless, some of the DFTS measurements on this material will be seen to provide the most representative optical-constant data set. In this technique both the attenuation and the phase shift imposed on an electromagnetic wave that propagates through a specimen are directly measured, and the optical constants calculated from these measured parameters via Fresnel's relations for the complex transmission and reflection coefficients of an interface between dissimilar media.

Most of the DFTS studies on polyethylene have been at near-millimeter wavelengths. The first of these [24, 25] covered the spectral region between 4 and 40 cm^{-1} (wavelengths from 2.5 mm to 250 μm) and reported the results of measurements at a temperature of 290 K on specimens of low- and high-density polyethylene, although density values were not given. These optical-constant spectra reveal the general behavior found in such measurements on polyethylene. The refractive index spectra (refraction spectra) are virtually wave number independent at the parts-in-10^3 level, taking mean values of 1.5138 for low-density polyethylene (LDPE) and 1.5246 for high-density polyethylene (HDPE). The power absorption coefficient spectra for the two densities both increase monotonically with increasing wave number, with that of LDPE being systematically some 0.002–0.006 cm^{-1} below that of HDPE. Typically, the random uncertainties in these measurements were estimated to be between ±0.002 and

$\pm 0.005\,\mathrm{cm}^{-1}$ in the absorption coefficient, corresponding to random uncertainties of a few times 10^{-5} in the extinction coefficient. In the refraction spectra the random variation was about 10^{-5}, increasing to a few times that at either end of the measured spectral range.

Other subsequent near-millimeter-wavelength DFTS measurements on HDPE [26, 27] at a temperature of 299 K with, again, an unspecified density, gave absorption spectra in broad agreement with the earlier studies, although the mean level of the refraction spectrum (~1.5184) fell between those of the earlier LDPE and HDPE measurements. DFTS measurements of the temperature variation of the refraction spectra of the same LDPE and HDPE specimens measured in the 290 K measurements of Birch *et al.* [24, 25] have been made between 4.2 and 300 K in the spectral region 10 to $30\,\mathrm{cm}^{-1}$ [28]. These showed the overall level of the refraction spectrum to increase with decreasing temperature between 300 and 40 K, as one would qualitatively expect on thermal-contraction grounds, and then to decrease slightly down to 4.2 K. At temperatures near 300 K the slope of both refraction temperature data sets varied at a rate of approximately $-2.5 \times 10^{-4}\,\mathrm{K}^{-1}$. In both LDPE and HDPE these measurements showed the overall level of the refraction spectra to increase by about 2.5% and 2.8%, respectively, between 300 and 40 K.

Moving away from the near millimeter into the far infrared, one finds DFTS measurements on polyethylene at a temperature of 298 K in the spectral range from ~30 to $200\,\mathrm{cm}^{-1}$ [29, 30]. Although the overall level of the refraction spectra in these works is consistent with that of the near-millimeter-wave studies, both the refraction spectrum and the corresponding absorption spectrum appear with quite large discrete features. One of these, the $73\,\mathrm{cm}^{-1}$ B_{1u} lattice mode [31, 32] is a well-known feature of the infrared spectrum of polyethylene, but the other features near 105 and $142\,\mathrm{cm}^{-1}$ are reported for the first time. It may be best to treat these as either measurement artifacts of some kind or as representing some extrinsic contribution to the optical constants from some unexpected impurity. There are two reasons for this, in addition to that of these measurements being the only observation of such structure in polyethylene spectra. First, in one case [29], the absorption spectrum is shown accompanied by that for a specimen of the polymer TPX, another widely studied far-infrared material. This also contains discrete features at similar wave numbers. One at $105\,\mathrm{cm}^{-1}$ has not been reported in other studies on TPX; one at $141.7\,\mathrm{cm}^{-1}$ has been seen in other measurements [33, 34], but only as a weak, rather narrow band, and not as prominent and as broad as shown in Afsar *et al.* [29]. The second reason for discounting these features as intrinsic features of the polyethylene spectrum cómes from the lack of consistent corresponding dispersion in the refraction spectra. The two features in the absorption spectrum are very similar in width and intensity, and one would therefore expect to observe similar dispersions in the

refraction spectrum, whereas one finds a region of dispersion across the 142 cm^{-1} position but none in the region of 105 cm^{-1}.

There have also been other, more recent, DFTS measurements on polyethylene in the far infrared [35] that do not show the discrete features found in Afsar *et al.* [29, 30]. These were on both LDPE and HDPE in the spectral region from 50 to 450 cm^{-1} at a temperature of 293 K. The densities of the two specimens were not given. The corresponding spectra for the two specimens are qualitatively similar in their larger-scale features. The random uncertainties in these spectra were estimated as about 10^{-5} in the refraction spectra and about 0.05 cm^{-1} in the absorption spectra, over most of the measured spectral range. Both absorption spectra clearly show the B_{1u} lattice mode in the region of 73 cm^{-1}, although it is nearly three times more intense in the HDPE spectrum, reflecting the higher degree of crystallinity in that specimen. The two refraction spectra similarly show the corresponding dispersion associated with the band. At higher wave numbers the HDPE absorption spectrum increases with increasing wave number to reach a broad maximum in the region of 200 cm^{-1}, before falling to a shallow minimum around 300 cm^{-1}, and then rising again. The HDPE refraction spectra falls to a shallow minimum between 200 and 250 cm^{-1}, and then rises with increasing wave number to be consistent with the increasing absorption. The LDPE spectra show similar overall behavior, although the broad band is present only as a shoulder in the absorption spectrum. Both refraction spectra show a clear but small localized region of dispersion in the region of 94 cm^{-1} with corresponding weak shoulders in the absorption spectra. Fleming *et al.* [36], in a study of temperature effects in the far-infrared absorption of polyethylene, assign a weak band at 94 cm^{-1} to the B_{2u} lattice band, which was first observed at 110 cm^{-1} at a temperature of 2 K [37].

There have been a considerable number of measurements of the power transmission spectrum of polyethylene in the far infrared using conventional Fourier-transform spectroscopy (FTS). Such measurements can be converted into optical-constant data in a number of ways. First, if the measurements are such that a channel spectrum due to multiple-beam interference between internally reflected rays is resolved, then various methods exist for deriving a refractive-index spectrum from the period of the channel spectrum. The measurements can then be repeated or the results reprocessed to give a spectrum with reduced spectral resolution and no channel spectrum. The refraction spectrum can then be used to derive the absorption spectrum from the transmission spectrum. If channel-spectra methods are not used, then a value for the refractive index could be taken from the literature, for example, and used to calculate the absorption spectrum from the transmission spectrum. Alternatively, measurements can be made on two specimens of different thicknesses of the material under investigation. The absorption spectrum is then calculated

from the ratio of the transmission spectra of the two specimens using an expression that assumes single-pass transmission through the specimens, with no contributions from internally reflected rays. In many of the FTS measurements on polyethylene the manner in which the absorption spectrum has been obtained is often not explicitly stated. It can be difficult, therefore, to assess such data, especially if they differ in a significant way from other results.

Loewenstein and Smith [38] developed a channel-spectrum method and published a number of papers on the far-infrared optical constants of a range of materials, including high-density polyethylene [39]. Over their measured wave number range of 50 to 250 cm^{-1} the derived refraction spectrum was virtually constant at a level of about 1.520 with an experimental uncertainty of 0.1% (~0.001), which is consistent with the DFTS results of Birch [35] on HDPE, given the absence of quoted density values. The measured absorption spectrum of the specimen of Smith and Loewenstein [39], however, is up to a factor of two greater than those of both the DFTS studies already discussed and of non-DFTS studies to be discussed subsequently. Their spectrum is presented with estimated uncertainties, presumably random, of about 10%. Again, given the uncertainties imposed by the lack of knowledge of specimen history, it is not possible to discuss such differences in the context of specimen-to-specimen variations or systematic measurement errors. However, the absorption measurements of Smith and Loewenstein [39] are certainly unusual in that they show no B_{1u} lattice mode in the vicinity of 73 cm^{-1}. Coleman *et al.* [40] have also used a channel spectrum approach to determine the optical constants of both LDPE and HDPE between 25 and 500 cm^{-1}. Although their absorption spectra are not dissimilar from those of the other measurements considered in this critique, their refraction spectra show overall dispersions across this spectral range (~0.03 for LDPE and ~0.08 for HDPE) that are more than an order of magnitude greater than those found by the various DFTS studies.

Measurements by Chantry *et al.* [41] are representative of what can be achieved by two-thickness FTS methods. They derived the absorption spectrum of both LDPE and HDPE in the region from 20 to 220 cm^{-1}. In addition to the broad-band FTS measurements, the coefficient at 29.7 cm^{-1} was also derived from transmission measurements made using a hydrogen-cyanide laser as a radiation source. The measurement temperature was not specified, but was clearly that of the ambient laboratory environment from the description of their apparatus. Specimen densities were not given. In the spectral region above 50 cm^{-1} their absorption spectra are in general agreement with other FTS and DFTS studies, with a clearly resolved B_{1u} band at 73 cm^{-1} superimposed on the increasing background absorption to higher wave numbers. In the region below 50 cm^{-1} Chantry *et al.* found little difference between the absorption spectra of LDPE and HDPE,

which is consistent with the DFTS data of Birch *et al.* [24, 25], which found differences of less than 0.006 cm^{-1} between the spectra of the two forms of the material in the region below 40 cm^{-1}. Chantry *et al.* were able to fit their absorption data to the following quadratic:

$$\alpha(\nu) = 8 \times 10^{-4}\nu + 1.4 \times 10^{-4}\nu^2 \tag{2}$$

in the wave number region between 2 and 50 cm^{-1}. Their HCN-laser determination of the absorption coefficient at 29.7 cm^{-1} was in good agreement with the value predicted by Eq. 2.

The spectrum calculated from Eq. 2 gives a reasonable fit to most of the published data on polyethylene in this spectral region, although it predicts values that are somewhat below the trend of some of the DFTS near-millimeter-wave measurements. It would not be unreasonable, therefore, to use it to provide a guide to expected absorption levels, although as discussed previously, for some applications it might be prudent to determine the absorption spectrum of the particular material to be used. Chantry *et al.* [41] proceeded to derive an equation for the spectral variation of the loss tangent of polyethylene from Eq. 2. One should note two things about this: first, that it was stated to have been derived using a value for the refractive index (1.461) that is lower than those generally associated with either LDPE or HDPE, and which may have been taken from earlier hydrogen-cyanide laser measurements at 891 GHz [42]); second, that the numerical constants of that equation are not consistent with that value of the refractive index. The correct values would be slightly different.

There have been a number of monochromatic determinations of the optical constants of polyethylene using coherent sources. Bicanic and Dymanus [43], for example, have determined the absorption coefficient at 29.7 cm^{-1} of a unspecified specimen 0.21 mm thick, at room temperature using an HCN laser to measure its power-transmission coefficient. They used a literature value of the refractive index to correct for reflection effects and found a value of 0.27 cm^{-1}, which is about twice the values given by DFTS studies and predicted by Eq. 2. If one were to assume the Eq. 2 value, the absorption loss for this specimen would be about 3% in the presence of a 7% reflection loss. Such a small loss could easily be obscured by systematic effects in a measurement with coherent radiation. This could well account for their relatively high value.

Llewellyn-Jones *et al.* [44] have determined the absorption coefficients of LDPE and HDPE specimens with densities of 0.89 and 0.93 $g\,cm^{-3}$, respectively, using an untuned cavity technique at 156 GHz (5.2 cm^{-1}). Their results of 0.013 and 0.012 cm^{-1}) (LDPE and HDPE) are somewhat higher than the prediction of Eq. 2 (0.008 cm^{-1}), but in good agreement

with DFTS results [24–27].

Monochromatic measurements can also be used to determine the refractive index. Early measurements by Chamberlain and Gebbie [42], for example, demonstrated how a Michelson interferometer and a laser source could be used to give such information, by placing the specimen within one arm of the interferometer and rotating it slightly to vary the optical path through the specimen. Such a measurement on polyethylene led to a value of 1.461 ± 0.023 at 337 μm wavelength, which is low in comparison with more recent values.

Stützel *et al.* [45], in a noninterferometric approach, used the Abbe method in which the refractive index is found from the angle of incidence that causes a right triangular prism to retro-reflect incident radiation. With this method Stützel *et al.* determined the refractive indices of polyethylene specimens of different, quoted, crystallinities at 296 K for wavelengths of 118 and 570 μm using an optically pumped gas laser. In addition, they determined the temperature variation of the refractive index of a 27% crystalline specimen between 5 and 290 K at an unspecified wavelength, but presumably either 118 or 570 μm. Their result showed the refractive index generally increasing with decreasing temperature in good agreement with previous DFTS results [28], although their finer temperature resolution revealed abrupt changes of slope at 50 and 110 K, whereas only the former had been seen in the DFTS study. Near to room temperature, Stützel *et al.* found the slope of their data to be approximately $-13 \times 10^{-4}\,K^{-1}$, which is larger than the $-2.5 \times 10^{-4}\,K^{-1}$ of the DFTS measurements [28], but this difference may again only reflect the finer temperature resolution of the former study. Alvarez *et al.* [46] have also measured the refraction spectrum of a Rigidex polyethylene between 50 and 200 cm^{-1} at 1.6 and 300 K. They found a 6% increase in the overall level of the refraction spectrum in going to 1.6 K, which is about twice that found in the other temperature-variation studies [28, 45].

In this next section the results of a number of papers are discussed to illustrate the extent to which the optical constants of polyethylene will depend on extrinsic factors, which prevent one from talking in terms of unique intrinsic data for this material. Davies and Haigh [47] and Ayers *et al.* [48], for example, describe the results of FTS absorption studies on both LDPE and HDPE specimens manufactured by a vacuum-melt extraction and casting technique, which produces bulk material from polymer powder free of additives. The processing avoids oxidation effects and removes volatile impurities and microscopic gas bubbles. Materials produced by this process were shown to have absorption spectra reduced by factors of up to two from those generally associated with this material in the far infrared. In addition, microwave bridge measurements [48] showed loss-angle reductions by a factor of three at 27.8 GHz. To the extent that this vacuum-melt extraction process yields purer material than that generally available

for far-infrared applications, these measurements of its absorption spectra [47, 48] may be taken as providing a close approach to the intrinsic-polyethylene absorption spectra.

There have been a number of studies of the variation in line position of the B_{1u} and B_{2u} lattice modes with various macroscopic parameters. Bank and Krimm [32], for example, used a grating spectrophotometer to make transmission measurements at temperatures of 103 and 303 K, which demonstrated the sensitivity of the line shape, line intensity, and line position of the B_{1u} mode to both temperature and degree of crystallinity. Similar FTS-based measurements have been reported by Zirke and Meissner [49]. These are the effects that cause significant changes to the optical constants only in the region within about 5 cm^{-1} of line center, and will not be relevant to many applications. Nonetheless, it is important to be aware of them. Other similar temperature-dependent studies have been reported by Fleming *et al.* [36], Stone and Williams [50], Frank *et al.* [51], and Goldstein *et al.* [52]. Frank *et al.* [53] report the appearance of an absorption band at 39 cm^{-1} in the absorption spectrum of high-pressure annealed specimens when the specimen temperature was below 170 K. The band intensified with decreasing temperature but did not shift its position.

There have also been some far-infrared studies of the effects of neutron and gamma-ray irradiation on the optical constants of polyethylene. Frank [54], for example, has demonstrated the effect that high-energy irradiation has on the absorption spectra of LDPE and HDPE in the region between 50 and 90 cm^{-1}. The intensity of the B_{1u} mode was not affected, whereas the overall level of the broad background absorption was almost doubled for radiation doses of 50 Mrad. Eberhagen and Fahrbach [55], working at much higher radiation doses, demonstrated an onset of radiation-induced transmission loss at doses above 10^9 rad, which led to a fourfold reduction in the transmission coefficient of a specimen 5 mm thick at 0.2 mm wavelength (50 cm^{-1}) by a dose of 10^{10} rad.

Finally, it is well-known that the application of stress to a polymer, either during its manufacture or subsequently, will yield material in which the molecular chain axes are preferentially aligned in certain directions. This will result in the optical constants exhibiting both birefringence and dichroism. Jacobsson and Hård [56], for example, using what was essentially a monochromatic version of DFTS, found birefringence, which varied with spatial position by between 0.01 and 0.025 at a wavelength of 70.5 μm in an injection-molded specimen of HDPE. Similarly, Read *et al.* [57] report the results of birefringence measurements on a LDPE sheet 0.33 mm thick, which had been stretched to a draw ratio of one to four; it was found to have a virtually constant in-plane birefringence of 0.016 from 0.546 μm wavelength in the visible, though the far infrared, and out to 8.6 mm wavelength in the microwave.

In conclusion, then, concerning the optical constants of polyethylene in

the far-infrared spectral region, one can see the difficulties of arriving at a definitive set of data that represents the intrinsic properties of this material. It is much easier instead to define a reasonably representative set of spectra for the real and imaginary parts of the complex refractive index, which one can use as a guide to expected, typical values. Thus, some of the DFTS results that have been discussed [24, 25, 35] have been used to supply such data, and these are presented in Fig. 1 and Table II. These references were chosen in part because they offer the widest spectral coverage combined with precise and accurate data, data with sufficiently low random uncertainties that the weak refractive-index dispersion associated with the intrinsic lattice modes is clearly resolved. They were chosen also because they were readily available to the author in a tabulated form and did not need to be read from a graph with the consequential loss of accuracy. This should not be taken as a claim for any special status for this data. Given the problem of specimen-to-specimen variation that this critique has discussed, these data should be taken only as typical of what might be found in a particular specimen. The far-infrared spectrum of Fig. 1 is not a definitive polyethylene spectrum. In Fig. 1 the featureless line labeled n represents the refractive index of both LDPE and HDPE material. The small differences between these spectra, and their dispersions, cannot be seen on the scale of the figure. The two curves labeled LDPE and HDPE represent the far-infrared k spectra [35]. The curve labeled a is a composite from the near-millimeter-wave k spectra of both LDPE and HDPE of Birch *et al.* [24, 25]; the curve labelled b is the k spectrum calculated from Eq. 2. Since the details of the refraction spectra are not resolved in Fig. 1, they are shown replotted on expanded scales in the linear–linear representation of Fig. 2. Now the dispersion due to the 73 cm^{-1} mode is seen clearly.

REFERENCES

1. J. J. Ritsko, *J. Chem. Phys.* **70**, 5343 (1979).
2. R. H. Partridge, *J. Chem. Phys.* **45**, 1685 (1966).
3. C. W. Bunn, *Trans. Faraday Soc.* **35**, 482 (1939).
4. A. Charlesby, *Proc. Phys. Soc. (London)* **57**, 496 (1945).
5. J. J. Trillat, *Compt. Rend. Acad. Sci.* **230**, 1522 (1950).
6. R. H. Partridge, *J. Chem. Phys.* **45**, 1679 (1966).
7. L. R. Painter, E. T. Arakawa, M. W. Williams, and J. C. Ashley, *Rad. Res.* **83**, 1 (1980).
8. J. Pflüger and J. Fink, "Determination of Optical Constants by High-Energy, Electron-Energy-Loss Spectroscopy (EELS)," this volume.
9. S. L. Aggarwal, "Polymer Handbook," Interscience, New York, PVI-41 (1967).
10. J. J. Ritsko, L. J. Brillson, R. W. Bigelow, and T. J. Fabish, *J. Chem. Phys.* **69**, 3931 (1978).
11. T. Tanaka, *J. Appl. Phys.* **44**, 2430 (1973).
12. S. Hashimoto, K. Seki, N. Sato, and H. Inokuchi, *J. Chem. Phys.* **76**, 163 (1982).
13. J. Ashok, P. Varaprasad, and S. Avadhani, unpublished data.

14. S. Krimm, C. Y. Liang, and G. B. B. M. Sutherland, *J. Chem. Phys.* **25**, 549 (1956).
15. J. R. Nielsen and A. H. Woollett, *J. Chem. Phys.* **26**, 1391 (1957).
16. R. Zbinden, "Infrared Spectroscopy of High Polymers," Academic Press, New York, Chap. II (1964).
17. P. C. Painter, M. M. Coleman, and J. L. Koenig, "The Theory of Vibrational Spectroscopy and its Application to Polymeric Materials," Wiley, New York, (1982).
18. G. W. Chantry and J. E. Chamberlain, in "Polymer Science," (A. D. Jenkins, ed.), North-Holland, Amsterdam, Ch. 20 (1972).
19. W. F. X. Frank and U. Leute, in "Infrared and Millimeter Waves," (K. J. Button, ed.), Vol. 8, Academic Press, New York, Ch. 2 (1983).
20. J. F. Rabolt, in "Infrared and Millimeter Waves," (K. J. Button, ed.), Vol. 12, Academic Press, New York, Ch. 2 (1984).
21. J. R. Birch and T. J. Parker, in "Infrared and Millimeter Waves," (K. J. Button, ed.), Vol. 2, Academic Press, New York, Ch. 3 (1979).
22. J.R. Birch, *Mikrochimica Acta [Wien]* **III**, 105 (1987).
23. G. J. Simonis, in "Handbook of Optical Constants of Solids," (E. D. Palik, ed.), Academic Press, Orlando, Ch. 8 (1985).
24. J. R. Birch, J. D. Dromey, and J. Lesurf, *NPL Report DES* **69**, (1981).
25. J. R. Birch, J. D. Dromey, and J. Lesurf, *Infrared Physics* **21**, 225 (1981).
26. M. N. Afsar, *IEEE Trans. Microwave Theory Tech.* **MTT-33**, 1410 (1985).
27. M. N. Afsar, *IEEE Trans. Instrumentation Meas.* **IM-33**, 530 (1987).
28. J. R. Birch and K. F. Ping, *Infrared Physics* **24**, 309 (1984).
29. M. N. Afsar, J. Chamberlain, and G. W. Chantry, *IEEE Trans. Instrumentation Meas.* **IM-25**, 290 (1976).
30. M. N. Afsar, *NPL Report DES* **42**, (1977).
31. S. Krimm and M. I. Bank, *J. Chem. Phys.* **42**, 4059 (1965).
32. M. I. Bank and S. Krimm, *J. App. Phys.* **39**, 4951 (1968).
33. G. W. Chantry, H. M. Evans, J. W. Fleming, and H. A. Gebbie, *Infrared Physics* **9**, 31 (1969).
34. J. R. Birch and E. A. Nicol, *Infrared Physics* **24**, 573 (1984).
35. J. R. Birch, *Infrared Physics* **30**, 195 (1990).
36. J. W. Fleming, G. W. Chantry, P. A. Turner, E. A. Nicol, H. A. Willis, and M. E. A. Cudby, *Chem. Phys. Lett.* **17**, 84 (1972).
37. G. D. Dean and D. H. Martin, *Chem. Phys. Lett.* **1**, 415 (1967).
38. E. V. Loewenstein and D. R. Smith, *Appl. Opt.* **10**, 577 (1971).
39. D. R. Smith and E. V. Loewenstein, *Appl. Opt.* **14**, 1335 (1975).
40. P. D. Coleman, G. Sherman, D. Parsons, and D. Akitt, in "Proc. Symposium on Submillimeter Waves," Polytechnic Press, New York, (1971).
41. G. W. Chantry, J. W. Fleming, P. M. Smith, M. Cudby and H. A. Willis, *Chem. Phys. Lett.* **10**, 473 (1971).
42. J. E. Chamberlain and H. A. Gebbie, *Nature* **206**, 602 (1965).
43. D. D. Bicanic and A. Dymanus, *Infrared Physics* **14**, 153 (1974).
44. D. T. Llewellyn-Jones, R. J. Knight, P. H. Moffat, and H. A. Gebbie, *IEE Proc.* **127**, 535 (1980).
45. P. Stützel, H. D. Tegtmeier, and M. Tacke, *Infrared Physics* **28**, 67 (1988).
46. J. A. Alvarez, R. E. Jennings, and A. F. M. Moorwood, *Infrared Physics* **15**, 45 (1975).
47. G. J. Davies and J. Haigh, *Infrared Physics* **14**, 183 (1974).
48. S. Ayers, G. J. Davies, J. Haigh, D. Marr and A. E. Parker, *Proc. IEE* **121**, 1447 (1974).
49. J. Zirke and M. Meissner, *Infrared Physics* **18**, 871 (1978).
50. N. W. B. Stone and D. Williams, *Appl. Opt.* **5**, 353 (1966).
51. W. Frank, H. Schmidt, and W. Wulff, *J. Polymer Sci.* **61**, 317 (1977).
52. M. Goldstein, D. Stephenson, and W. F. Maddams, *Polymer Comm.* **24**, 2459 (1983).

53. W. F. X. Frank, H. Schmidt, B. Heise, G. W. Chantry, E. A. Nicol, H. A. Willis and M. E. A. Cudby, *Polymer* **22**, 17 (1981).
54. W. Frank, *Polymer Letters* **15**, 679 (1977).
55. A. Eberhagen and H.-U. Fahrbach, *Intl. J. Infrared and Millimeter Waves* **3**, 297 (1982).
56. S. Jacobsson and S. Hård, *Rev. Sci. Instr.* **53**, 1012 (1982).
57. B. E. Read, J. C. Duncan, and D. E. Meyer, *Polymer Testing* **4**, 143 (1984).

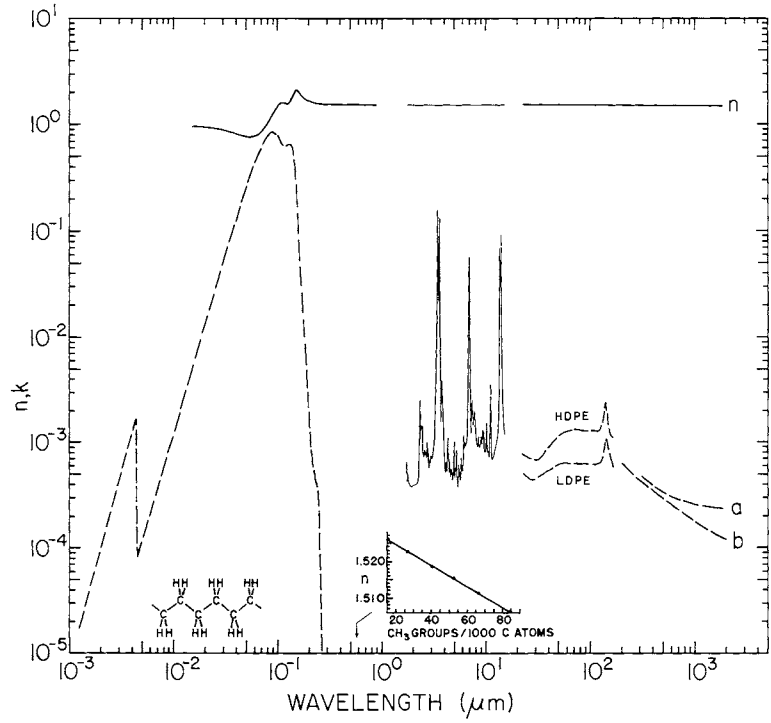

Fig. 1. Log–log plot of n (solid line) and k (dashed line) versus wavelength in micrometers for polyethylene. For the near IR, k is given by the thin solid line in order to show some of the detailed structure. The insets represent (1) the C-chain structure and (2) the variation of n with CH_3 groups at 0.589 μm.

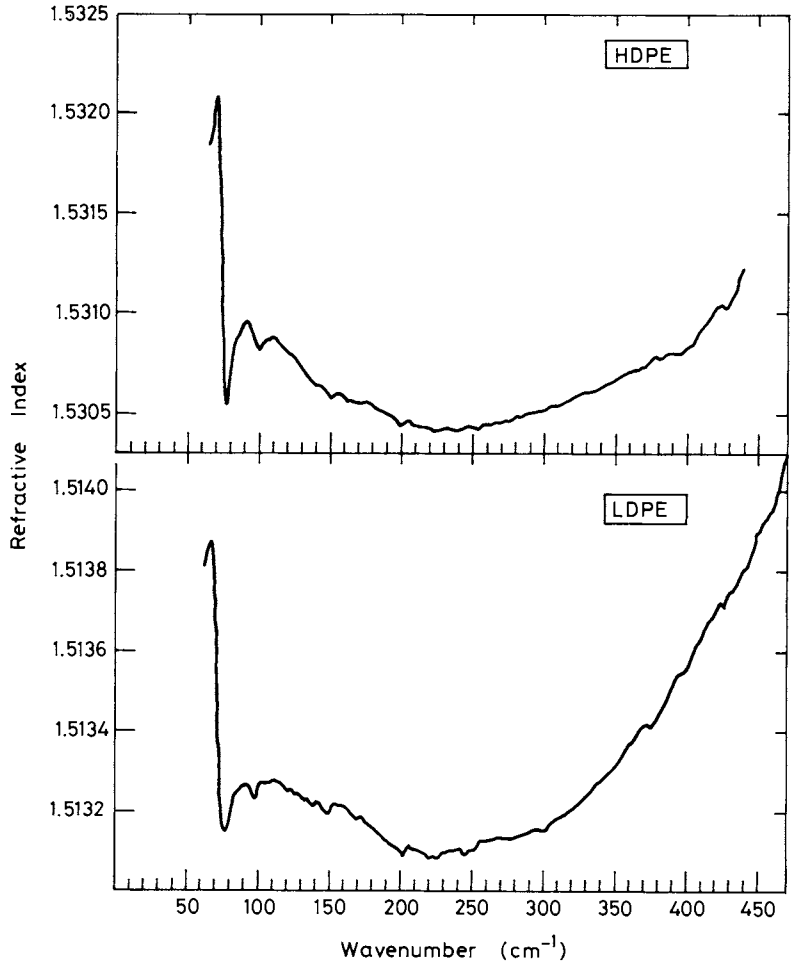

Fig. 2. Linear–linear plot of n versus wave number for high-density and low-density polyethylene showing dispersion of the low-frequency vibration mode.

TABLE I

Values of n and k for Polyethylene from Various References[a]

eV	cm^{-1}	μm	n	k	n	k
1000		0.001240		1.8×10^{-5} [7]		
900		0.001378		2.3		
800		0.001550		4.0		
700		0.001771		7.0×10^{-5}		
600		0.002066		1.1×10^{-4}		
500		0.002480		2.1		
400		0.003100		5.0×10^{-4}		
300		0.004133		1.4×10^{-3}		
282		0.004379		1.7×10^{-3}		
280		0.004428		8.6×10^{-5}		
200		0.006199		2.3×10^{-4}		
150		0.008266		6.0×10^{-4}		
100		0.01240		2.5×10^{-3}		
80		0.01550	0.97[7]			
70		0.01771	0.96			
60		0.02066	0.94	1.38×10^{-2}		
50		0.02480	0.92	2.5		
40		0.03100	0.89	5.5×10^{-2}		
35		0.03542	0.86			
33		0.03757			0.844[1]	0.113[1]
32		0.03875			0.839	0.119
31		0.04000			0.835	0.132
30		0.04133	0.805	0.130	0.825	0.145
29		0.04275	0.80		0.818	0.171
28		0.04428	0.79		0.809	0.185
27		0.04592	0.785		0.809	0.210
26		0.04769	0.78		0.804	0.236
25		0.04959	0.775	0.245	0.803	0.274
24		0.05166	0.77		0.788	0.317
23		0.05391	0.77		0.796	0.365
22		0.05636	0.77		0.795	0.403
21		0.05904	0.775		0.808	0.439
20		0.06199	0.78	0.440	0.818	0.489
19		0.06526	0.81	0.500	0.836	0.538
18		0.06888	0.83	0.565	0.868	0.594
17		0.07293	0.88	0.64	0.916	0.655
16		0.07749	0.96	0.720	0.981	0.723
15		0.08266	1.03	0.805	1.05	0.798
14		0.08856	1.18	0.860	1.24	0.887
13		0.09537	1.35	0.807	1.40	0.849
12	96786	0.1033	1.52	0.680	1.55	0.746
11	88720	0.1127	1.55	0.550	1.61	0.622
10	80655	0.1240	1.53	0.580	1.64	0.610
9.8	79042	0.1265		0.600		
9.6	77429	0.1292		0.615		
9.4	75816	0.1319		0.635		
9.2	74202	0.1348		0.650		
9.0	72589	0.1378	1.66	0.655	1.758	0.626
8.85	71379	0.1401			1.810	0.604

TABLE I (*Continued*)

Polyethylene

eV	cm^{-1}	μm	n	k	n	k
8.8	70976	0.1409		0.640		
8.7	70170	0.1425			1.934	0.565
8.6	69363	0.1442		0.620		
8.55	68960	0.1450			1.981	0.472
8.4	67750	0.1476		0.530	2.065	0.380
8.25	66540	0.1503			2.076	0.318
8.2	66137	0.1512		0.385		
8.10	65330	0.1531			2.067	0.252
8.0	64524	0.1550	2.08	0.240		
7.95	64121	0.1560			2.634	0.128
7.8	62911	0.1590		0.145	1.964	8.15×10^{-2}
7.65	61701	0.1621			1.924	4.67
7.6	61298	0.1631		8.4×10^{-2}		
7.5	60491	0.1653			1.877	3.73
7.4	59685	0.1675		4.5		
7.35	59281	0.1687			1.809	3.04
7.2	58071	0.1722		2.5	1.732	2.30
7.05	56862	0.1759			1.715	1.74×10^{-2}
7.0	56458	0.1771	1.76	1.35×10^{-2}		
6.9	55652	0.1797			1.694	8.8×10^{-3}
6.8	54845	0.1823		7.70×10^{-3}		
6.75	54442	0.1837			1.661	
6.6	53232	0.1879		4.20	1.643	
6.45	52022	0.1922			1.634	
6.4	51619	0.1937		2.35		
6.3	50813	0.1968			1.619	
6.2	50000	0.2000		1.40×10^{-3}		
6.15	49603	0.2016			1.608	
6.0	48393	0.2066	1.65	8.6×10^{-4}	1.597	
5.85	47183	0.2119			1.578	
5.8	46780	0.2138		6.3		
5.75	46377	0.2156			1.568	
5.6	45167	0.2214		5.1		
5.55	44763	0.2234			1.559	
5.4	43554	0.2296		4.4	1.549	
5.25	42344	0.2361			1.543	
5.2	41940	0.2384		3.8		
5.1	41134	0.2431			1.533	
5.0	40327	0.2480	1.6	2.5		
4.95	39924	0.2505			1.523	
4.9	39521	0.2530		1×10^{-4}		
4.8	38714	0.2583			1.517	
4.7	37908	0.2638		1×10^{-5}		
4.65	37504	0.2666			1.513	
4.5	36295	0.2755			1.510	
4.35	35085	0.2850			1.507	
4.20	33875	0.2952			1.505	
4.05	32665	0.3061			1.502	
3.90	31455	0.3179			1.500	

TABLE I (*Continued*)

Polyethylene

eV	cm^{-1}	μm	n	k	n	k
3.75	30245	0.3306			1.498	
3.60	29036	0.3444			1.498	
3.45	27826	0.3594			1.498	
3.30	26616	0.3757			1.498	
3.15	25406	0.3936			1.497	
3.00	24196	0.4133			1.495	
2.85	22987	0.4350			1.495	
2.70	21777	0.4592			1.493	
2.55	20567	0.4862			1.492	
2.40	19357	0.5166			1.490	
2.25	18147	0.5511			1.490	
			1.5260[9]		1.4590[13]	2.3×10^{-2}[13]
2.10	16935	0.5904			1.482[1]	
1.95	15728	0.6358			1.480	
1.80	14518	0.6888			1.478	
1.65	13308	0.7514			1.476	
1.50	12098	0.8266			1.471	
1.35	10888	0.9184			1.466	
0.7191	5800	1.724	1.5[15][b]	5.0×10^{-4}[15]		
0.7179	5790	1.727		5.3		
0.7166	5780	1.730		5.7		
0.7154	5770	1.733		6.2		
0.7142	5760	1.736		5.7		
0.7129	5750	1.739		4.8		
0.7117	5740	1.742		4.5		
0.7092	5720	1.748		4.1		
0.7067	5700	1.754		4.1		
0.7042	5680	1.761		4.3		
0.7030	5670	1.764		4.7		
0.7018	5660	1.767		4.8		
0.7005	5650	1.770		4.6		
0.6993	5640	1.773		4.4		
0.6968	5620	1.779		4.1		
0.6943	5600	1.786		4.1		
0.6819	5500	1.818		4.0		
0.6695	5400	1.852		3.8		
0.6571	5300	1.887		3.7		
0.6447	5200	1.923		3.7		
0.6323	5100	1.961		3.8		
0.6199	5000	2.000		3.8		
0.6075	4900	2.041		3.8		
0.5951	4800	2.083		3.8		
0.5827	4700	2.128		3.8		
0.5703	4600	2.174		3.9		
0.5579	4500	2.222		4.0		
0.5555	4480	2.232		4.2		
0.5530	4460	2.242		4.4		
0.5505	4440	2.252		4.6		

TABLE I (*Continued*)

Polyethylene

eV	cm^{-1}	μm	n	k
0.5480	4420	2.262		5.0
0.5455	4400	2.273		5.7
0.5431	4380	2.283		7.1
0.5406	4360	2.294		9.4×10^{-4}
0.5393	4350	2.299		1.2×10^{-3}
0.5381	4340	2.304		1.9
0.5369	4330	2.309		2.5
0.5356	4320	2.315		1.7
0.5344	4310	2.320		1.0
0.5331	4300	2.326		1.2
0.5307	4280	2.336		1.2
0.5294	4270	2.342		1.3
0.5282	4260	2.347		1.5
0.5269	4250	2.353		1.8
0.5257	4240	2.358		1.2
0.5232	4220	2.370		1.2
0.5207	4200	2.381		1.4
0.5183	4180	2.392		1.4
0.5170	4170	2.398		1.4
0.5158	4160	2.404		1.4
0.5145	4150	2.410		1.4
0.5133	4140	2.415		1.4
0.5121	4130	2.421		1.3
0.5108	4120	2.427		1.4
0.5096	4110	2.433		1.4
0.5083	4100	2.439		1.4
0.5071	4090	2.445		1.1
0.5059	4080	2.451		1.0×10^{-3}
0.5034	4060	2.463		9.4×10^{-4}
0.5009	4040	2.475		8.6
0.4984	4020	2.488		8.4
0.4959	4000	2.500		7.1
0.4947	3990	2.506		7.3
0.4935	3980	2.513		7.4
0.4922	3970	2.519		7.0
0.4910	3960	2.525		7.2
0.4885	3940	2.538		7.2
0.4860	3920	2.551		7.9
0.4835	3900	2.564		8.1
0.4811	3880	2.577		8.0
0.4786	3860	2.591		7.7
0.4761	3840	2.604		7.4
0.4736	3820	2.618		7.8
0.4711	3800	2.632		7.7
0.4687	3780	2.646		7.3
0.4662	3760	2.660		7.0
0.4637	3740	2.674		6.8
0.4612	3720	2.688		6.9
0.4587	3700	2.703		7.0

TABLE I (*Continued*)

Polyethylene

eV	cm^{-1}	μm	n	k
0.4563	3680	2.717		9.8
0.4538	3660	2.732		8.0
0.4525	3650	2.740		8.6
0.4513	3640	2.747		8.1
0.4501	3630	2.755		8.0
0.4488	3620	2.762		7.6×10^{-4}
0.4476	3610	2.770		1.0×10^{-3}
0.4463	3600	2.778		8.6×10^{-4}
0.4439	3580	2.793		6.4
0.4414	3560	2.809		5.8
0.4389	3540	2.825		5.5
0.4364	3520	2.841		5.5
0.4339	3500	2.857		5.5
0.4315	3480	2.874		5.9
0.4290	3460	2.890		6.2
0.4265	3440	2.907		6.6
0.4240	3420	2.924		6.4
0.4215	3400	2.941		6.4
0.4203	3390	2.950		6.8
0.4191	3380	2.959		7.2
0.4178	3370	2.967		7.3
0.4166	3360	2.976		7.1
0.4141	3340	2.994		6.8
0.4116	3320	3.012		6.8
0.4092	3300	3.030		6.8
0.4067	3280	3.049		6.8
0.4042	3260	3.067		7.1
0.4017	3240	3.086		7.3
0.3992	3220	3.106		7.6
0.3968	3200	3.125		7.7
0.3943	3180	3.145		7.9
0.3918	3160	3.165		8.6
0.3893	3140	3.185		9.5×10^{-4}
0.3868	3120	3.205		1.8×10^{-3}
0.3844	3100	3.226		1.5
0.3819	3080	3.247		2.3
0.3794	3060	3.268		2.7
0.3769	3040	3.289		3.1
0.3744	3020	3.311		3.8
0.3720	3000	3.333		4.5
0.3695	2980	3.356		6.1
0.3670	2960	3.378		9.5×10^{-3}
0.3645	2940	3.401		2.8×10^{-2}
0.3633	2930	3.413		7.3×10^{-2}
0.3620	2920	3.425		1.9×10^{-1}
0.3608	2910	3.436		8.8×10^{-2}
0.3596	2900	3.448		5.2
0.3583	2890	3.460		4.6
0.3571	2880	3.472		2.5

TABLE I (*Continued*)

Polyethylene

eV	cm^{-1}	μm	n	k
0.3558	2870	3.484		2.2
0.3546	2860	3.497		3.3×10^{-2}
0.3534	2850	3.509		1.5×10^{-1}
0.3521	2840	3.521		3.6×10^{-2}
0.3509	2830	3.534		1.5
0.3496	2820	3.546		1.1×10^{-2}
0.3472	2800	3.571		7.8×10^{-3}
0.3447	2780	3.597		3.6
0.3422	2760	3.623		2.9
0.3397	2740	3.650		2.6
0.3372	2720	3.676		2.4
0.3348	2700	3.703		2.1
0.3323	2680	3.731		1.8
0.3310	2670	3.745		2.3
0.3298	2660	3.759		3.8
0.3286	2650	3.774		2.4
0.3273	2640	3.788		2.8
0.3261	2630	3.802		2.5
0.3248	2620	3.817		2.5
0.3224	2600	3.846		1.8
0.3199	2580	3.876		1.5
0.3174	2560	3.906		1.4
0.3162	2550	3.922		1.0
0.3149	2540	3.937		1.1×10^{-3}
0.3137	2530	3.953		8.5×10^{-4}
0.3124	2520	3.968		1.1×10^{-3}
0.3100	2500	4.000		6.3×10^{-4}
0.3087	2490	4.016		6.1
0.3075	2480	4.032		6.4
0.3062	2470	4.049		5.8
0.3050	2460	4.065		5.1
0.3025	2440	4.098		5.0
0.3000	2420	4.132		6.3
0.2988	2410	4.149		6.3
0.2976	2400	4.167		5.7
0.2951	2380	4.202		5.2
0.2926	2360	4.237		6.7×10^{-4}
0.2914	2350	4.255		1.1×10^{-3}
0.2901	2340	4.274		1.1
0.2889	2330	4.292		1.1×10^{-3}
0.2876	2320	4.310		9.6×10^{-4}
0.2852	2300	4.348		6.8
0.2839	2290	4.367		6.6
0.2827	2280	4.386		7.0
0.2814	2270	4.405		6.3
0.2802	2260	4.425		5.1
0.2790	2250	4.444		5.0
0.2777	2240	4.464		6.2
0.2765	2230	4.484		4.5

TABLE I (*Continued*)

Polyethylene

eV	cm^{-1}	μm	n	k
0.2752	2220	4.505		5.2
0.2740	2210	4.525		4.6
0.2728	2200	4.545		4.6
0.2715	2190	4.566		4.9
0.2703	2180	4.587		4.9
0.2690	2170	4.608		4.9
0.2678	2160	4.630		5.4
0.2666	2150	4.651		5.7
0.2653	2140	4.673		5.3
0.2641	2130	4.695		4.5
0.2628	2120	4.717		4.2
0.2604	2100	4.762		4.3
0.2579	2080	4.808		4.4
0.2554	2060	4.854		5.0
0.2529	2040	4.902		6.9
0.2517	2030	4.926		8.3×10^{-4}
0.2505	2020	4.950		1.0×10^{-3}
0.2492	2010	4.975		6.2×10^{-4}
0.2480	2000	5.000		5.0
0.2455	1980	5.051		4.5
0.2430	1960	5.102		5.3
0.2418	1950	5.128		5.3
0.2405	1940	5.155		5.1
0.2381	1920	5.208		5.5
0.2368	1910	5.236		6.4
0.2356	1900	5.263		8.1
0.2343	1890	5.291		7.3
0.2331	1880	5.319		4.5
0.2306	1860	5.376		3.6
0.2281	1840	5.435		3.9
0.2269	1830	5.464		4.7
0.2257	1820	5.495		5.9
0.2244	1810	5.525		4.9
0.2232	1800	5.556		4.6
0.2219	1790	5.587		4.4
0.2207	1780	5.618		4.3
0.2195	1770	5.650		4.3
0.2182	1760	5.682		4.6
0.2170	1750	5.714		5.4
0.2157	1740	5.747		6.9
0.2145	1730	5.780		7.0
0.2133	1720	5.814		6.2
0.2120	1710	5.848		5.5
0.2108	1700	5.882		5.2
0.2095	1690	5.917		5.2
0.2083	1680	5.952		5.2
0.2071	1670	5.988		5.2
0.2058	1660	6.024		5.4
0.2046	1650	6.061		6.7×10^{-4}

TABLE I (*Continued*)

Polyethylene

eV	cm^{-1}	μm	n	k
0.2033	1640	6.098		1.2×10^{-3}
0.2021	1630	6.135		8.8×10^{-4}
0.2009	1620	6.173		8.3
0.1996	1610	6.211		8.7
0.1984	1600	6.250		9.2
0.1971	1590	6.289		9.9
0.1959	1580	6.329		9.7
0.1947	1570	6.369		9.0
0.1934	1560	6.410		9.0
0.1922	1550	6.452		9.7×10^{-4}
0.1909	1540	6.494		1.1×10^{-3}
0.1897	1530	6.536		1.2
0.1885	1520	6.579		1.3
0.1872	1510	6.623		1.6
0.1860	1500	6.667		2.9
0.1847	1490	6.711		5.4×10^{-3}
0.1841	1485	6.734		1.7×10^{-2}
0.1835	1480	6.757		4.5
0.1829	1475	6.780		3.5
0.1823	1470	6.803		3.0
0.1816	1465	6.826		5.5
0.1810	1460	6.849		2.8×10^{-2}
0.1798	1450	6.897		8.5×10^{-3}
0.1785	1440	6.944		5.9
0.1773	1430	6.993		4.1
0.1761	1420	7.042		3.0
0.1748	1410	7.092		2.4
0.1736	1400	7.143		2.1
0.1723	1390	7.194		1.2
0.1711	1380	7.246		1.6
0.1705	1375	7.273		2.2
0.1699	1370	7.299		2.9
0.1692	1365	7.326		2.8
0.1686	1360	7.353		2.5
0.1680	1355	7.380		2.4
0.1674	1350	7.407		2.4
0.1661	1340	7.463		2.1
0.1649	1330	7.519		1.5
0.1637	1320	7.576		1.5
0.1624	1310	7.634		1.9
0.1612	1300	7.692		2.0
0.1599	1290	7.752		1.8
0.1587	1280	7.813		1.6
0.1575	1270	7.874		1.3
0.1562	1260	7.937		1.2
0.1550	1250	8.000		1.1
0.1537	1240	8.065		1.0
0.1525	1230	8.130		1.0×10^{-3}
0.1513	1220	8.197		9.6×10^{-4}

TABLE I (*Continued*)

Polyethylene

eV	cm^{-1}	μm	n	k
0.1500	1210	8.264		9.2
0.1488	1200	8.333		8.9
0.1475	1190	8.403		9.3
0.1469	1185	8.439		9.1
0.1463	1180	8.475		9.4×10^{-4}
0.1457	1175	8.511		1.2×10^{-3}
0.1451	1170	8.547		9.9×10^{-4}
0.1444	1165	8.584		9.7
0.1438	1160	8.621		9.9
0.1426	1150	8.696		9.5
0.1413	1140	8.772		9.6
0.1401	1130	8.850		9.9×10^{-4}
0.1389	1120	8.929		1.1×10^{-3}
0.1376	1110	9.009		1.1×10^{-3}
0.1364	1100	9.091		9.4×10^{-4}
0.1351	1090	9.174		1.1×10^{-3}
0.1339	1080	9.259		1.3
0.1333	1075	9.302		1.3
0.1327	1070	9.346		1.2
0.1320	1065	9.390		1.2
0.1314	1060	9.434		1.1
0.1308	1055	9.479		1.1
0.1302	1050	9.524		1.1×10^{-3}
0.1296	1045	9.569		9.3×10^{-4}
0.1289	1040	9.615		9.2
0.1277	1030	9.709		8.2
0.1265	1020	9.804		8.1
0.1252	1010	9.901		8.3×10^{-4}
0.1240	1000	10.00		1.0×10^{-3}
0.1234	995	10.05		1.3
0.1227	990	10.10		1.5
0.1221	985	10.15		1.3
0.1215	980	10.20		1.1×10^{-3}
0.1209	975	10.26		8.0×10^{-4}
0.1203	970	10.31		8.4
0.1196	965	10.36		9.1
0.1190	960	10.42		8.5
0.1184	955	10.47		8.3
0.1178	950	10.53		8.2
0.1165	940	10.64		8.3
0.1153	930	10.75		8.7×10^{-4}
0.1141	920	10.87		1.0×10^{-3}
0.1134	915	10.93		1.6
0.1131	912.5	10.96		2.3
0.1128	910	10.99		3.5
0.1125	907.5	11.02		3.6
0.1122	905	11.05		2.7
0.1116	900	11.11		1.7×10^{-3}
0.1103	890	11.24		9.0×10^{-4}

TABLE I (*Continued*)

Polyethylene

eV	cm^{-1}	μm	n	k
0.1091	880	11.36		8.1
0.1079	870	11.49		6.7
0.1066	860	11.63		7.2
0.1054	850	11.76		7.6
0.1041	840	11.90		7.8
0.1029	830	12.05		8.2
0.1017	820	12.20		8.7
0.1004	810	12.35		9.5×10^{-4}
0.09919	800	12.50		1.0×10^{-3}
0.09795	790	12.66		1.1
0.09671	780	12.82		1.1
0.09547	770	12.99		1.3
0.09423	760	13.16		1.6
0.09299	750	13.33		2.3
0.09175	740	13.51		6.4×10^{-3}
0.09113	735	13.61		1.9×10^{-2}
0.09051	730	13.70		8.1
0.08989	725	13.79		2.9
0.08927	720	13.89		7.0
0.08865	715	13.99		1.9
0.08803	710	14.08		1.2×10^{-2}
0.08679	700	14.29		3.5×10^{-3}
0.08555	690	14.49		1.9
0.08431	680	14.71		1.5
0.08307	670	14.93		1.2

[a] References are given in square brackets.
[b] n = 1.5 was assumed constant down to 670 cm^{-1} for the calculation of k.

TABLE II

Values of *n* and *k* for Polyethylene Obtained from Various References[a]

eV	cm^{-1}	μm	n[b]	k[b]	n[c]	k[c]
0.05567	449.2	22.26	1.51390[35]	0.00050[35]	1.53119[35]	0.00077[35]
0.05542	447.3	22.36	1.51388	0.00050	1.53122	0.00079
0.05518	445.3	22.46	1.51384	0.00050	1.53123	0.00073
0.05494	443.4	22.56	1.51381	0.00050	1.53117	0.00075
0.05470	441.4	22.65	1.51380	0.00049	1.53104	0.00090
0.05446	439.4	22.76	1.51380	0.00049	1.53121	0.00075
0.05421	437.5	22.86	1.51378	0.00051	1.53119	0.00068
0.05397	435.6	22.96	1.51376	0.00051	1.53115	0.00070
0.05373	433.6	23.06	1.51375	0.00051	1.53110	0.00071
0.05349	431.6	23.17	1.51375	0.00053	1.53108	0.00071
0.05325	429.7	23.27	1.51374	0.00053	1.53104	0.00070
0.05300	427.7	23.38	1.51373	0.00051	1.53102	0.00069
0.05276	425.8	23.49	1.51371	0.00050	1.53104	0.00070
0.05252	423.8	23.59	1.51372	0.00049	1.53104	0.00071
0.05228	421.9	23.70	1.51371	0.00049	1.53103	0.00070
0.05203	419.9	23.81	1.51370	0.00050	1.53102	0.00067
0.05179	418.0	23.93	1.51369	0.00049	1.53100	0.00067
0.05155	416.0	24.04	1.51368	0.00047	1.53098	0.00069
0.05131	414.1	24.15	1.51367	0.00047	1.53095	0.00070
0.05107	412.1	24.27	1.51365	0.00046	1.53094	0.00069
0.05082	410.2	24.38	1.51364	0.00045	1.53093	0.00067
0.05058	408.2	24.50	1.51362	0.00045	1.53091	0.00067
0.05034	406.2	24.62	1.51361	0.00045	1.53089	0.00068
0.05010	404.3	24.73	1.51360	0.00045	1.53086	0.00068
0.04986	402.3	24.85	1.51358	0.00045	1.53083	0.00067
0.04961	400.4	24.98	1.51357	0.00045	1.53083	0.00065
0.04937	398.4	25.10	1.51355	0.00046	1.53083	0.00065
0.04913	396.5	25.22	1.51355	0.00046	1.53081	0.00066
0.04889	394.5	25.35	1.51354	0.00044	1.53080	0.00066
0.04865	392.6	25.47	1.51354	0.00044	1.53080	0.00067
0.04840	390.6	25.60	1.51352	0.00044	1.53080	0.00068
0.04816	388.7	25.73	1.51350	0.00044	1.53079	0.00068
0.04792	386.7	25.86	1.51349	0.00044	1.53079	0.00069
0.04768	384.8	25.99	1.51348	0.00044	1.53079	0.00071
0.04744	382.8	26.12	1.51346	0.00044	1.53078	0.00071
0.04719	380.9	26.26	1.51344	0.00044	1.53077	0.00069
0.04695	378.9	26.39	1.51343	0.00044	1.53078	0.00070
0.04671	376.9	26.53	1.51342	0.00044	1.53078	0.00071
0.04647	375.0	26.67	1.51341	0.00045	1.53077	0.00071
0.04623	373.0	26.81	1.51342	0.00045	1.53077	0.00070
0.04598	371.1	26.95	1.51342	0.00045	1.53074	0.00071
0.04574	369.1	27.09	1.51341	0.00044	1.53073	0.00071
0.04550	367.2	27.23	1.51341	0.00043	1.53073	0.00070
0.04526	365.2	27.38	1.51340	0.00043	1.53072	0.00069
0.04502	363.3	27.53	1.51339	0.00043	1.53071	0.00069
0.04477	361.3	27.68	1.51338	0.00042	1.53072	0.00069
0.04453	359.4	27.83	1.51337	0.00042	1.53072	0.00068
0.04429	357.4	27.98	1.51336	0.00042	1.53071	0.00067
0.04405	355.5	28.13	1.51334	0.00042	1.53070	0.00067
0.04381	353.5	28.29	1.51333	0.00042	1.53069	0.00067
0.04356	351.6	28.44	1.51332	0.00042	1.53068	0.00067

TABLE II (*Continued*)

Polyethylene

eV	cm^{-1}	μm	n^b	k^b	n^c	k^c
0.04332	349.6	28.60	1.51332	0.00042	1.53067	0.00066
0.04308	347.7	28.76	1.51331	0.00042	1.53067	0.00066
0.04284	345.7	28.93	1.51330	0.00042	1.53065	0.00066
0.04260	343.7	29.09	1.51329	0.00042	1.53065	0.00066
0.04235	341.8	29.26	1.51328	0.00042	1.53064	0.00066
0.04211	339.8	29.43	1.51328	0.00042	1.53064	0.00066
0.04187	337.9	29.60	1.51327	0.00043	1.53063	0.00066
0.04163	335.9	29.77	1.51327	0.00043	1.53062	0.00066
0.04139	334.0	29.94	1.51326	0.00043	1.53061	0.00066
0.04114	332.0	30.12	1.51325	0.00043	1.53061	0.00066
0.04090	330.1	30.30	1.51324	0.00043	1.53060	0.00065
0.04066	328.1	30.48	1.51323	0.00044	1.53060	0.00066
0.04042	326.2	30.66	1.51322	0.00044	1.53060	0.00066
0.04018	324.2	30.84	1.51322	0.00044	1.53060	0.00066
0.03993	322.3	31.03	1.51321	0.00044	1.53059	0.00066
0.03969	320.3	31.22	1.51321	0.00044	1.53058	0.00066
0.03945	318.4	31.41	1.51320	0.00044	1.53057	0.00066
0.03921	316.4	31.60	1.51320	0.00045	1.53057	0.00067
0.03897	314.4	31.80	1.51319	0.00045	1.53056	0.00067
0.03872	312.5	32.00	1.51319	0.00046	1.53055	0.00066
0.03848	310.6	32.20	1.51319	0.00046	1.53054	0.00066
0.03824	308.6	32.41	1.51318	0.00046	1.53054	0.00067
0.03800	306.6	32.61	1.51318	0.00046	1.53053	0.00068
0.03776	304.7	32.82	1.51317	0.00046	1.53054	0.00068
0.03751	302.7	33.03	1.51316	0.00046	1.53054	0.00068
0.03727	300.8	33.25	1.51315	0.00047	1.53053	0.00068
0.03703	298.8	33.46	1.51315	0.00047	1.53052	0.00069
0.03679	296.9	33.68	1.51315	0.00048	1.53051	0.00070
0.03655	294.9	33.91	1.51316	0.00048	1.53051	0.00070
0.03630	293.0	34.13	1.51316	0.00048	1.53051	0.00070
0.03606	291.0	34.36	1.51315	0.00048	1.53051	0.00071
0.03582	289.1	34.59	1.51315	0.00049	1.53050	0.00072
0.03558	287.1	34.83	1.51315	0.00049	1.53050	0.00072
0.03534	285.2	35.07	1.51314	0.00049	1.53050	0.00072
0.03509	283.2	35.31	1.51314	0.00050	1.53048	0.00073
0.03485	281.2	35.56	1.51314	0.00050	1.53048	0.00073
0.03461	279.3	35.80	1.51314	0.00050	1.53048	0.00074
0.03437	277.3	36.06	1.51313	0.00050	1.53047	0.00076
0.03413	275.4	36.31	1.51314	0.00050	1.53047	0.00077
0.03388	273.4	36.57	1.51314	0.00050	1.53046	0.00077
0.03364	271.5	36.83	1.51314	0.00050	1.53047	0.00078
0.03340	269.5	37.10	1.51314	0.00050	1.53046	0.00078
0.03316	267.6	37.37	1.51314	0.00050	1.53046	0.00079
0.03292	265.6	37.65	1.51314	0.00050	1.53046	0.00079
0.03267	263.7	37.93	1.51313	0.00050	1.53046	0.00080
0.03243	261.7	38.21	1.51313	0.00050	1.53045	0.00080
0.03219	259.8	38.50	1.51313	0.00050	1.53044	0.00081
0.03195	257.8	38.79	1.51313	0.00050	1.53044	0.00082
0.03171	255.9	39.08	1.51313	0.00051	1.53045	0.00083
0.03146	253.9	39.38	1.51312	0.00051	1.53044	0.00085
0.03122	251.9	39.69	1.51311	0.00051	1.53043	0.00086

TABLE II (*Continued*)

Polyethylene

eV	cm^{-1}	μm	n^b	k^b	n^c	k^c
0.03098	250.0	40.00	1.51311	0.00051	1.53043	0.00087
0.03074	248.0	40.31	1.51310	0.00051	1.53044	0.00088
0.03049	246.1	40.63	1.51310	0.00052	1.53044	0.00088
0.03025	244.1	40.96	1.51310	0.00052	1.53044	0.00089
0.03001	242.2	41.29	1.51310	0.00052	1.53043	0.00091
0.02977	240.2	41.63	1.51310	0.00052	1.53042	0.00092
0.02953	238.3	41.97	1.51310	0.00053	1.53041	0.00094
0.02928	236.3	42.31	1.51310	0.00053	1.53042	0.00095
0.02904	234.4	42.67	1.51310	0.00054	1.53043	0.00096
0.02880	232.4	43.03	1.51310	0.00054	1.53043	0.00096
0.02856	230.5	43.39	1.51310	0.00054	1.53043	0.00097
0.02832	228.5	43.76	1.51310	0.00054	1.53043	0.00098
0.02807	226.6	44.14	1.51309	0.00055	1.53042	0.00099
0.02783	224.6	44.52	1.51308	0.00055	1.53042	0.00099
0.02759	222.7	44.91	1.51309	0.00056	1.53041	0.00101
0.02735	220.7	45.31	1.51309	0.00056	1.53041	0.00102
0.02711	218.7	45.71	1.51309	0.00057	1.53042	0.00104
0.02686	216.8	46.13	1.51309	0.00058	1.53044	0.00107
0.02662	214.8	46.55	1.51310	0.00059	1.53044	0.00107
0.02638	212.9	46.97	1.51310	0.00059	1.53043	0.00106
0.02614	210.9	47.41	1.51310	0.00059	1.53044	0.00106
0.02590	209.0	47.85	1.51310	0.00060	1.53045	0.00106
0.02565	207.0	48.30	1.51311	0.00060	1.53044	0.00108
0.02541	205.1	48.76	1.51311	0.00060	1.53045	0.00111
0.02517	203.1	49.23	1.51310	0.00060	1.53047	0.00112
0.02493	201.2	49.71	1.51309	0.00060	1.53046	0.00114
0.02469	199.2	50.20	1.51310	0.00061	1.53045	0.00115
0.02444	197.3	50.69	1.51311	0.00061	1.53044	0.00115
0.02420	195.3	51.20	1.51311	0.00062	1.53045	0.00117
0.02396	193.4	51.72	1.51312	0.00062	1.53046	0.00119
0.02372	191.4	52.24	1.51313	0.00062	1.53048	0.00118
0.02348	189.4	52.78	1.51313	0.00062	1.53050	0.00116
0.02323	187.5	53.33	1.51313	0.00062	1.53051	0.00118
0.02299	185.5	53.89	1.51314	0.00062	1.53051	0.00120
0.02275	183.6	54.47	1.51315	0.00063	1.53052	0.00120
0.02251	181.6	55.05	1.51316	0.00063	1.53052	0.00119
0.02227	179.7	55.65	1.51316	0.00063	1.53053	0.00119
0.02202	177.7	56.26	1.51316	0.00063	1.53055	0.00120
0.02178	175.8	56.89	1.51317	0.00063	1.53056	0.00122
0.02154	173.8	57.53	1.51318	0.00062	1.53056	0.00124
0.02130	171.9	58.18	1.51319	0.00062	1.53057	0.00122
0.02106	169.9	58.85	1.51318	0.00062	1.53056	0.00122
0.02081	168.0	59.53	1.51318	0.00062	1.53056	0.00124
0.02057	166.0	60.24	1.51319	0.00062	1.53056	0.00125
0.02033	164.1	60.95	1.51320	0.00062	1.53057	0.00126
0.02009	162.1	61.69	1.51321	0.00062	1.53057	0.00126
0.01985	160.2	62.44	1.51321	0.00061	1.53056	0.00125
0.01960	158.2	63.21	1.51321	0.00061	1.53058	0.00125
0.01936	156.2	64.00	1.51321	0.00060	1.53060	0.00125
0.01912	154.3	64.81	1.51322	0.00060	1.53060	0.00126
0.01888	152.3	65.64	1.51322	0.00060	1.53060	0.00127

TABLE II (*Continued*)

Polyethylene

eV	cm^{-1}	μm	n^b	k^b	n^c	k^c
0.01864	150.4	66.49	1.51320	0.00060	1.53059	0.00128
0.01839	148.4	67.37	1.51319	0.00060	1.53058	0.00127
0.01815	146.5	68.27	1.51320	0.00060	1.53060	0.00129
0.01791	144.5	69.19	1.51321	0.00059	1.53063	0.00131
0.01767	142.6	70.14	1.51322	0.00059	1.53064	0.00131
0.01743	140.6	71.11	1.51322	0.00059	1.53064	0.00130
0.01718	138.7	72.11	1.51321	0.00059	1.53064	0.00130
0.01694	136.7	73.14	1.51322	0.00060	1.53065	0.00131
0.01670	134.8	74.20	1.51323	0.00060	1.53067	0.00132
0.01646	132.8	75.29	1.51323	0.00061	1.53067	0.00132
0.01622	130.9	76.42	1.51323	0.00061	1.53069	0.00134
0.01597	128.9	77.58	1.51324	0.00061	1.53072	0.00134
0.01573	126.9	78.77	1.51324	0.00061	1.53074	0.00133
0.01549	125.0	80.00	1.51324	0.00061	1.53076	0.00132
0.01525	123.0	81.27	1.51325	0.00061	1.53078	0.00130
0.01501	121.1	82.58	1.51325	0.00060	1.53079	0.00128
0.01476	119.1	83.93	1.51325	0.00060	1.53079	0.00127
0.01452	117.2	85.33	1.51326	0.00061	1.53081	0.00127
0.01428	115.2	86.78	1.51327	0.00061	1.53083	0.00126
0.01404	113.3	88.28	1.51328	0.00061	1.53084	0.00128
0.01380	111.3	89.82	1.51328	0.00061	1.53086	0.00127
0.01355	109.4	91.43	1.51327	0.00061	1.53088	0.00125
0.01331	107.4	93.09	1.51327	0.00061	1.53088	0.00124
0.01307	105.5	94.81	1.51327	0.00060	1.53087	0.00123
0.01283	103.5	96.60	1.51327	0.00060	1.53086	0.00123
0.01259	101.6	98.46	1.51327	0.00061	1.53085	0.00126
0.01234	99.6	100.4	1.51325	0.00060	1.53082	0.00129
0.01210	97.7	102.4	1.51323	0.00061	1.53083	0.00128
0.01186	95.7	104.5	1.51325	0.00061	1.53087	0.00127
0.01162	93.7	106.7	1.51326	0.00060	1.53091	0.00128
0.01138	91.8	108.9	1.51327	0.00059	1.53094	0.00128
0.01113	89.8	111.3	1.51327	0.00059	1.53096	0.00125
0.01089	87.9	113.8	1.51326	0.00060	1.53094	0.00123
0.01065	85.9	116.4	1.51325	0.00061	1.53091	0.00123
0.01041	84.0	119.1	1.51324	0.00062	1.53088	0.00123
0.01016	82.0	121.9	1.51322	0.00062	1.53083	0.00124
0.00992	80.1	124.9	1.51319	0.00062	1.53075	0.00130
0.00968	78.1	128.0	1.51315	0.00066	1.53063	0.00142
0.00944	76.2	131.3	1.51314	0.00072	1.53053	0.00159
0.00920	74.2	134.7	1.51315	0.00082	1.53073	0.00201
0.00895	72.3	138.4	1.51327	0.00098	1.53163	0.00232
0.00871	70.3	142.2	1.51358	0.00103	1.53207	0.00188
0.00847	68.4	146.3	1.51381	0.00088	1.53200	0.00150
0.00823	66.4	150.6	1.51387	0.00074	1.53188	0.00129
0.00799	64.4	155.1	1.51385	0.00065	1.53182	0.00115
0.00774	62.5	160.0	1.51381	0.00060	1.53186	0.00109
0.00750	60.5	165.2	1.51381	0.00057	1.53188	0.00109
0.00620	50.0	200.0		0.00062[41]		
0.00558	45.0	222.2		0.00056		
0.00496	40.0	250.0		0.00051		
0.00434	35.0	285.7		0.00045		

TABLE II (*Continued*)

Polyethylene

eV	cm^{-1}	μm	n^b	k^b	n^c	k^c
0.00372	30.0	333.3		0.00040		
0.00310	25.0	400.0		0.00034		
0.00248	20.0	500.0		0.00029		
0.00186	15.0	666.7		0.00023		
0.00124	10.0	1000		0.00017		
0.000620	5.0	2000		0.00012		
0.00399	32.2	310.3	1.51362[25]	0.00047[25]	1.52454[25]	0.00048[25]
0.00393	31.7	315.1	1.51363	0.00046	1.52458	0.00046
0.00387	31.2	320.0	1.51363	0.00045	1.52458	0.00045
0.00381	30.8	325.1	1.51363	0.00043	1.52460	0.00045
0.00375	30.3	330.4	1.51362	0.00044	1.52460	0.00043
0.00369	29.8	335.7	1.51362	0.00044	1.52462	0.00044
0.00363	29.3	341.3	1.51362	0.00043	1.52462	0.00042
0.00357	28.8	347.1	1.51363	0.00042	1.52465	0.00041
0.00351	28.3	353.1	1.51363	0.00041	1.52466	0.00040
0.00345	27.8	359.3	1.51361	0.00041	1.52465	0.00040
0.00339	27.3	365.8	1.51362	0.00041	1.52465	0.00041
0.00333	26.9	372.3	1.51362	0.00041	1.52466	0.00039
0.00327	26.4	379.2	1.51362	0.00040	1.52467	0.00040
0.00321	25.9	386.4	1.51362	0.00039	1.52467	0.00038
0.00315	25.4	393.9	1.51363	0.00039	1.52471	0.00038
0.00309	24.9	401.6	1.51364	0.00038	1.52458	0.00037
0.00302	24.4	409.7	1.51364	0.00037	1.52464	0.00036
0.00297	23.9	417.9	1.51364	0.00037	1.52467	0.00035
0.00290	23.4	426.6	1.51365	0.00037	1.52467	0.00034
0.00284	22.9	435.7	1.51365	0.00036	1.52468	0.00034
0.00278	22.5	445.2	1.51368	0.00036	1.52467	0.00033
0.00272	22.0	455.2	1.51371	0.00034	1.52467	0.00033
0.00266	21.5	465.6	1.51371	0.00034	1.52467	0.00032
0.00260	21.0	476.2	1.51370	0.00034	1.52467	0.00031
0.00254	20.5	487.6	1.51369	0.00035	1.52468	0.00029
0.00248	20.0	499.5	1.51371	0.00034	1.52469	0.00031
0.00242	19.5	512.0	1.51372	0.00032	1.52468	0.00030
0.00236	19.0	525.2	1.51373	0.00031	1.52473	0.00028
0.00230	18.5	539.1	1.51373	0.00029	1.52454	0.00030
0.00224	18.1	553.4	1.51373	0.00030	1.52461	0.00030
0.00218	17.6	568.8	1.51377	0.00031	1.52463	0.00030
0.00212	17.1	585.1	1.51380	0.00029	1.52465	0.00031
0.00206	16.6	602.4	1.51380	0.00028	1.52464	0.00030
0.00200	16.1	620.7	1.51382	0.00029	1.52462	0.00030
0.00194	15.6	640.2	1.51383	0.00029	1.52462	0.00031
0.00188	15.1	660.5	1.51386	0.00029	1.52464	0.00031
0.00182	14.6	682.6	1.51391	0.00029	1.52458	0.00032
0.00175	14.2	706.2	1.51395	0.00022	1.52459	0.00030
0.00169	13.7	731.5	1.51395	0.00029	1.52457	0.00030
0.00163	13.2	758.7	1.51391	0.00028	1.52462	0.00029
0.00157	12.7	787.4	1.51390	0.00027	1.52464	0.00029
0.00151	12.2	819.0	1.51397	0.00027	1.52471	0.00029
0.00145	11.7	853.2	1.51404	0.00023	1.52476	0.00029
0.00139	11.2	890.5	1.51406	0.00020	1.52476	0.00028

TABLE II (*Continued*)

Polyethylene

eV	cm^{-1}	μm	n^b	k^b	n^c	k^c
0.00133	10.7	931.1	1.51406	0.00021	1.52470	0.00028
0.00127	10.2	975.6	1.51407	0.00022	1.52468	0.00030
0.00121	9.8	1024	1.51407	0.00022	1.52472	0.00028
0.00115	9.3	1078	1.51404	0.00022	1.52472	0.00025
0.00109	8.8	1138	1.51399	0.00023	1.52473	0.00026
0.00103	8.3	1205	1.51395	0.00023	1.52473	0.00028
0.00097	7.8	1280	1.51402	0.00023	1.52475	0.00025
0.00091	7.3	1366	1.51409	0.00024	1.52479	0.00022
0.00085	6.8	1462	1.51407	0.00023	1.52476	0.00022
0.00079	6.3	1575	1.51408	0.00024	1.52468	0.00025
0.00073	5.9	1706	1.51410	0.00022	1.52463	0.00024
0.00067	5.4	1862	1.51405	0.00024	1.52461	0.00024

[a] References are given in square brackets.
[b] Low-density polyethylene data (LDPE).
[c] High-density polyethylene data (HDPE).

Potassium Bromide (KBr)

EDWARD D. PALIK
Institute for Physical Science and Technology
University of Maryland
College Park, Maryland

The selected optical constants n and k are collected in Table I and plotted in Fig. 1. There is some overlap of data to indicate the typical variations that occur from lab to lab. The eV, cm^{-1}, or μm units of the original data are usually listed with three or fewer significant figures (eV, for example, as read off a graph), and the other two units (cm^{-1} and μm) are listed with four figures. Although n and k are often listed with two decimal places (and at least three significant figures) in the IR and UV, the accuracy (absolute value) is probably poorer, but the precision is good enough to show structure in the original measurements (multiphonon peaks in the IR and peaks in interband absorption in the UV). In the transparent visible and near-IR regions, n is known to four or five figures.

Starting at low frequency, we note that a simple capacity measurement of the loss tangent, $\tan\delta = \varepsilon_2/\varepsilon_1$, and the real part of the dielectric function, ε_1, have been nearly forgotten. Breckenridge [1] measured these parameters from 10^2 to 10^8 Hz for KBr at 85 °C. However, to see an effect in ε_2, it was necessary to heat-treat the sample to produce defects; this gave rise to extrinsic absorption, which is not of particular interest here, and these numbers are not tabulated. The low-frequency (nearly dc) dielectric constant at 85 °C was found to be 4.90, which yields $n = 2.21$, in agreement with higher frequency, room-temperature values cited in Table I.

For somewhat higher frequencies, at 9.8, 35.4 and 116 GHz, Owens [2] has measured the capacity at 25 °C and cited several other values by other workers. These values of ε_1 and ε_2 along with far-IR values of Genzel *et al.* [3] and Stolen and Dransfeld [4] have been used by Sparks *et al.* [5] in a model invoking two-phonon difference processes in the range 0.5 to 33 cm^{-1}. We emphasize the calculated results for 293 K, since these fit the measured values over most of the range to better than ±50% (the largest deviation between theory and experiment); we list some other values also. Genzel *et al.* did not specify room temperature for their grating-spectrometer transmission measurements; Stolen and Dransfeld made

Copyright © 1991 by Academic Press.
All rights of reproduction in any form reserved.
ISBN 0-12-544422-2

transmission measurements with a grating spectrometer at three wavelengths (320, 500, and 900 μm) as a function of temperature from 15 to 420 K. Samples were presumably mechanically polished with conventional grits. Quality of surface is usually not an issue at these long wavelengths.

The spectral region 20 to 240 cm^{-1} has been covered by Johnson and Bell [6] using asymmetric Fourier-transform spectroscopy. This technique yielded the phase and amplitude of the reflectivity directly with no need for Kramers–Kronig analysis or a Lorentz-oscillator-model fit. The reststrahlen minimum was measured to be 0.0008, indicating little or no polishing damage. Resolution was 2 cm^{-1}. Sample temperature was 300 K. Shoulders on the low- and high-frequency sides of the transverse optical phonon frequency are due to difference and sum phonon absorption bands, respectively. We have read graphs to obtain n and k.

For the region 250 to 700 cm^{-1} Deutsch [7] has collected the absorption coefficient α from several sources all more or less at room temperature. Transmission measurements of slab samples were used in all cases. We have read an experimental curve to obtain α and converted to k with the equation $k = \alpha\lambda/4\pi$. McGill *et al.* [8] have developed a model for multiphonon absorption and used it to fit these experimental data.

Laser calorimetry has been performed in the CO_2-laser region by at least two groups [9, 10]. The temperature rise is measured with thermocouples upon irradiation of the sample with a specific laser wavelength. The technique is very sensitive and can be used to distinguish between surface absorption and bulk absorption. Surface absorption can occur due to surface properties such as roughness and adsorption of gaseous species from the air, such as water, hydrocarbons, and so on. Bulk absorption can occur due to intrinsic processes for the purest materials or extrinsic processes due to impurity molecules (SO_4, NO_2, $HCCO_3$, and so forth) "grown" into the materials. We chose the data of Ref. [9] because they showed the smallest absorption (indicating the purest material).

In the transparent region 42 to 0.2 μm, Li [11] has collected and analyzed a great deal of n data from many references. Prism minimum deviation was the experimental method in most cases. He has fitted a Sellmeier-type equation with eleven adjustable parameters to represent the data to the fifth decimal place. The dispersion formula for 293 K is

$$n^2 = 1.39408 + \frac{0.79221\lambda^4}{\lambda^2 - (0.146)^2} + \frac{0.01981\lambda^2}{\lambda^2 - (0.173)^2}$$

$$+ \frac{0.15587\lambda^2}{\lambda^2 - (0.187)^2} + \frac{0.17673\lambda^2}{\lambda^2 - (60.61)^2} + \frac{2.06217\lambda^2}{\lambda^2 - (87.72)^2}.$$

This indicates that $\lambda_T = 87.72$ μm (114.0 cm^{-1}). For the spectral range

0.25 to 26 μm, Li states that the fourth decimal place is meaningful, with estimated uncertainties in the range 0.0001 to 0.0005. To either side the uncertainty moves to the third decimal place.

Li has also provided a temperature-dependence formula of the form

$$2n\frac{dn}{dT} = -11.61(n^2-1) + 0.39 + \frac{3.944\lambda^4}{(\lambda^2-0.03497)^2} + \frac{182.88\lambda^2}{(\lambda^2-7694.80)^2},$$

where dn/dT is in units of 10^{-5}/K and λ is in μm. Note that a 3 K difference in room temperature between labs begins to affect the fourth decimal place.

The fundamental band gap of KBr is at ~6.6 eV, and there exists much data for the region 6 to 30 eV as discussed in Refs. [12–14]. We have usually selected the more recent measurements and/or those showing more structure in the reflectivity. Although much of the data involved electron-energy-loss measurements on thin films, we have ignored this nonoptical way of determining the imaginary part of the dielectric function, because thin films are deposited and usually represent defected, polycrystalline material with voids, not bulk material. Bulk crystals cleaved in UHV are presumably the best samples for reflectivity, so synchrotron data are to be preferred.

Tomiki *et al.* measured the optical constants in the range 5.5 to 12 eV using thin plates at the band edge [13] and reflectivity and Kramers–Kronig (K–K) analysis in the opaque region at 301 K [14]. Verification of Erbach's rule at the band edge was discussed in detail [13]. Small variations between eV and cm^{-1} occur between data of Refs. [13] and [14] because we read eV from a graph in [13] and converted to cm^{-1} using 8065.48 cm^{-1}/eV, whereas Tomiki supplied original data using 8066.0 cm^{-1}/eV.

Antinori *et al.* [15] used a continuum He discharge lamp as a source of radiation in the range 13.5 to 20.5 eV. A 1-m grating spectrometer gave a resolution of better than 1.8 Å at 990 Å. Samples were cleaved in air and then put into the sample chamber, which was pumped to 10^{-5} torr. The reflectivity was K–K analyzed using the data of Rubloff [12] and Blechschmidt *et al.* [16] to cover the lower and higher energy ranges, respectively, as is required by K–K analysis. We have read the values of ε_1, ε_2 from a graph and obtained the numbers listed from the equations

$$2n^2 = \varepsilon_1 + \sqrt{\varepsilon_1^2 + \varepsilon_2^2}$$

$$2k^2 = -\varepsilon_1 + \sqrt{\varepsilon_1^2 + \varepsilon_2^2}.$$

From 13 to 31 eV we have used data of Blechschmidt *et al.* [16]. The experiments were performed at the Deutsche Elektronen-Synchrotron with a normal-incidence monochromator in a modified Wadsworth mount. Single crystals were freshly cleaved and put into the vacuum of 5×10^{-8} torr. Angle of incidence was varied from 15 to 75° for both $\parallel(p)$ and $\perp(s)$ polarizations using angles on both sides of the normal for increased accuracy. R was then used to calculate ε_1 and ε_2. We then calculated n and k from graph values of ε_1 and ε_2.

From 25 to 40 eV we have chosen the ε_1, ε_2 data of Stephan *et al.* [17]; it shows a little more detail than the data of Blechschmidt *et al.* [16] and covers a wider spectral region. The data were obtained with a grating spectrometer with an 82° angle of incidence. The source was a spark discharge with a 15 Hz rate. Sample reflectivity was measured at three angles of incidence using polarized light. We have overlapped the above UV data to give an indication of the accuracy from lab to lab.

Above 40 eV absorption decreases steadily with little structure. The data of Brown *et al.* [18] cover the range 70 to 200 eV. A grating monochromator was used at an 86° angle of incidence. The source was the Stoughton, Wisconsin, synchrotron. The films were evaporated *in situ* onto Formvar, carbon, or gold substrates whose transmission had been previously measured. Thicknesses were determined by a crystal-quartz thickness monitor.

Far above these energies the L and K absorption edges of K and Br are reached. These features occur at K(K), 3608 eV; K(Br), 13470 eV; $L_{2,3}$ (K), 295 eV; L_1 (Br), 1781 eV; L_2 (Br), 1599 eV; L_3 (Br), 1553 eV; N_1(Br), 31.3 eV. The M absorption edges for atomic K and Br are not defined in Ref. [19]. Other atomic energy states are presumably mixed into the conduction-band structure seen in k in the lower-energy region [12].

REFERENCES

1. R. G. Breckenridge, *J. Chem. Phys.* **16**, 959 (1948).
2. J. C. Owens, *Phys. Rev.* **181**, 1228 (1969).
3. L. Genzel, H. Happ, and R. Weber, *Z. Physik* **154**, 13 (1959).
4. R. Stolen and K. Dransfeld, *Phys. Rev.* **139A**, 1295 (1965).
5. M. Sparks, D. F. King, and D. L. Mills, *Phys. Rev.* **B26**, 6987 (1982).
6. K. W. Johnson and E. E. Bell, *Phys. Rev.* **187**, 1044 (1969).
7. T. F. Deutsch, *J. Phys. Chem. Solids* **34**, 2091 (1973).
8. T. C. McGill, R. W. Hellwarth, M. Mangir, and H. V. Winston, *J. Phys. Chem. Solids* **34**, 2105 (1973).
9. J. M. Rowe and J. A. Harrington, *Proc. 5th IR Laser Window Conf.* (1976); and private communication.
10. T. Hidaka, T. Morikawa, and J. Shimada, *Appl. Opt.* **19**, 3763 (1980).
11. H. H. Li, *J. Phys. Chem. Ref. Data* **5**, 345 (1976).
12. G. W. Rubloff, *Phys. Rev.* **B5**, 662 (1972).
13. T. Tomiki, T. Miyata, and H. Tsukamoto, *Z. Naturforsch.* **29a**, 145 (1974).

14. T. Tomiki, T. Miyata, and H. Tsukamoto, *J. Phys. Soc. Japan* **35**, 495 (1973); and private communication.
15. M. Antinori, A. Balzarotti, and M. Piacentini, *Phys. Rev.* **B7**, 1541 (1973).
16. D. Blechschmidt, *Phys. Stat. Sol.* **B36**, 625 (1969).
17. G. Stephan, E. Garignon, and S. Robin, *Comp. Rend. Sci. Paris* **268C**, 408 (1969).
18. F. C. Brown, C. Gahwiller, H. Fujita, A. B. Kung, W. Scheifley, and N. Carrera, *Phys. Rev.* **B2**, 2126 (1970).
19. American Institute of Physics Handbook, (D. E. Gray, ed.), Third Edition, McGraw-Hill, New York, 7 (1982).

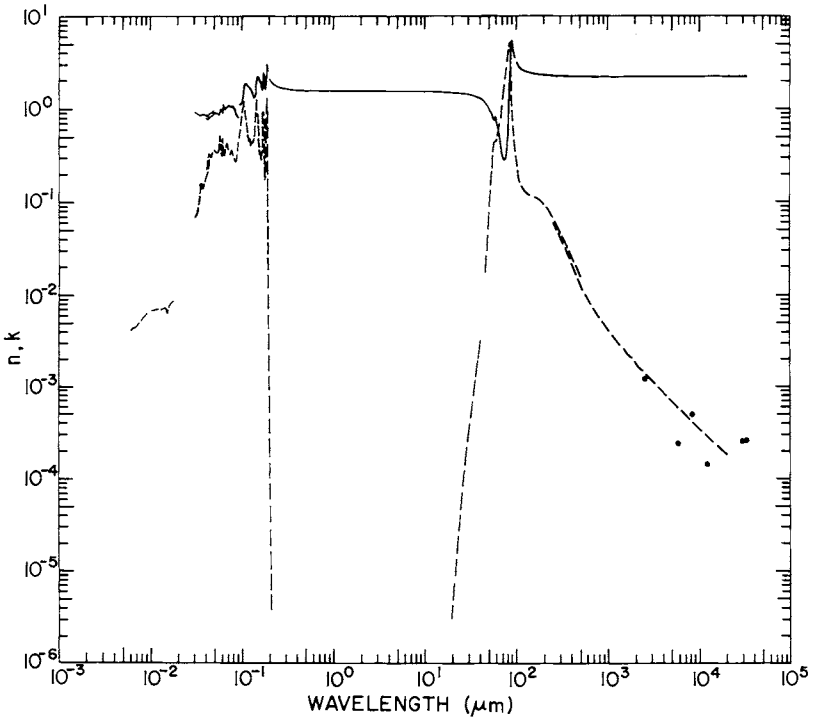

Fig. 1. Log–log plot of n (solid line) and k (dashed line) versus wavelength in micrometers for potassium bromide.

TABLE I

Values of *n* and *k* for Potassium Bromide from Various References[a]

eV	cm^{-1}	Å	n	k
200		61.99		4.17×10^{-3} [18]
195		63.58		4.40×10^{-3}
192.5		64.40		4.43×10^{-3}
190		65.26		4.52×10^{-3}
187.5		66.12		4.68×10^{-3}
185		67.02		4.47×10^{-3}
180		68.88		4.63×10^{-3}
175		70.85		4.79×10^{-3}
170		72.93		4.97×10^{-3}
165		75.14		5.14×10^{-3}
160		77.49		5.30×10^{-3}
155		79.99		5.51×10^{-3}
150		82.65		5.75×10^{-3}
145		85.51		6.00×10^{-3}
140		88.56		6.20×10^{-3}
135		91.84		6.35×10^{-3}
130		95.37		6.49×10^{-3}
125		99.19		6.59×10^{-3}
120		103.3		6.74×10^{-3}
115		107.8		6.82×10^{-3}
110		112.7		6.91×10^{-3}
105		118.1		6.95×10^{-3}
100		124.0		6.91×10^{-3}
95		130.5		6.91×10^{-3}
90		137.8		7.04×10^{-3}
89		139.3		7.12×10^{-3}
88		140.8		7.19×10^{-3}
87		142.5		7.26×10^{-3}
86		144.1		7.28×10^{-3}
85		145.9		7.20×10^{-3}
84		147.6		6.93×10^{-3}
83		149.3		6.66×10^{-3}
82		151.2		6.38×10^{-3}
81		153.0		6.33×10^{-3}
80.5		154.0		6.40×10^{-3}
80		155.0		7.03×10^{-3}
79.5		155.9		7.38×10^{-3}
79		156.9		7.80×10^{-3}
78.5		157.9		8.42×10^{-3}
78		158.9		8.22×10^{-3}
77.5		159.9		8.15×10^{-3}
77		161.0		8.04×10^{-3}
76.5		162.0		8.06×10^{-3}
76		163.1		7.98×10^{-3}
75.5		164.2		8.04×10^{-3}
75		165.3		8.09×10^{-3}
74.5		166.4		8.87×10^{-3}
74		167.5		9.60×10^{-3}

TABLE I (*Continued*)

Potassium Bromide

eV	cm^{-1}	Å	n	k
73.5		168.6		9.46×10^{-3}
73		169.8		9.87×10^{-3}
72.5		171.0		8.44×10^{-3}
72		172.2		7.54×10^{-3}
71.5		173.4		6.76×10^{-3}
71		174.6		6.67×10^{-3}
70.5		175.8		6.71×10^{-3}
70		177.1		6.76×10^{-3}

eV	cm^{-1}	μm	n	k
40		0.03099	0.91[17]	6.9×10^{-2}[17]
39.5		0.03138	0.90	7.1×10^{-2}
39		0.03179	0.90	7.2×10^{-2}
38.5		0.03220	0.89	7.6×10^{-2}
38		0.03262	0.88	8.0×10^{-2}
37.5		0.03306	0.87	8.6×10^{-2}
37		0.03350	0.86	9.3×10^{-2}
36.5		0.03396	0.84	0.11
36		0.03444	0.84	0.13
35.5		0.03492	0.85	0.14
35		0.03542	0.85	0.15
34.5		0.03593	0.86	0.15
34		0.03646	0.87	0.15
33.5		0.03701	0.88	0.15
33		0.03757	0.88	0.14
32.5		0.03814	0.86	0.14
32		0.03874	0.85	0.15
31.5		0.03936	0.85	0.16
31		0.03999	0.84	0.18
			0.80[16]	
30.5		0.04065	0.84[17]	0.18[17]
			0.80[16]	
30		0.04132	0.84[17]	0.19[17]
			0.78[16]	0.22[16]
29.5		0.04202	0.83[17]	0.20[17]
			0.77[16]	0.23[16]
29		0.04275	0.81[17]	0.22[17]
			0.76[16]	0.26[16]
28.5		0.04350	0.82[17]	0.29[17]
			0.76[16]	0.31[16]
28		0.04428	0.88[17]	0.32[17]
			0.79[16]	0.33[16]
27.5		0.04508	0.92[17]	0.29[17]
			0.84[16]	0.31[16]
27		0.04592	0.91[17]	0.26[17]
			0.84[16]	0.30[16]

TABLE I (*Continued*)

Potassium Bromide

eV	cm^{-1}	μm	n	k
26.5		0.04678	0.89[17]	0.27[17]
			0.83[16]	0.31[16]
26		0.04769	0.89[17]	0.30[17]
			0.82[16]	0.34[16]
25.5		0.04959	0.92[17]	0.33[17]
			0.85[16]	0.34[16]
25		0.04959	0.95[17]	0.33[17]
			0.88[16]	0.35[16]
24.5		0.05060	0.90	0.35
24		0.05166	0.90	0.34
23.5		0.05275	0.90	0.33
23		0.05391	0.89	0.33
22.5		0.05510	0.88	0.34
22		0.05636	0.87	0.35
21.75		0.05700	0.86	0.38
21.5		0.05766	0.85	0.40
21.25		0.05834	0.85	0.52
21		0.05904	0.98	0.47
20.75		0.05975	0.98	0.41
20.5		0.06048	0.97	0.34
20.4		0.06077	1.01[15]	0.31[15]
20.25		0.06122	0.95[16]	0.34[16]
20.2		0.06137	0.96[15]	0.34[15]
20.1		0.06168	0.92	0.36
20		0.06199	0.91[16]	0.38[16]
			0.94[15]	0.42[15]
19.95		0.06214	0.97	0.46
19.9		0.06230	1.01	0.49
19.85		0.06246	1.02	0.48
19.8		0.06261	1.04	0.46
19.75		0.06277	1.07	0.46
19.7		0.06293	1.09	0.44
19.6		0.06325	1.12	0.39
19.5		0.06358	1.10	0.34
19.4		0.06390	1.07	0.32
19.2		0.06457	1.03	0.32
19.0		0.06525	1.00	0.33
18.8		0.06594	0.98	0.36
18.6		0.06665	0.98	0.37
18.4		0.06737	0.99	0.41
18.2		0.06811	1.03	0.43
18.0		0.06888	1.05	0.43
17.8		0.06965	1.07	0.42
17.6		0.07044	1.09	0.41
17.4		0.07125	1.10	0.39
17.2		0.07208	1.10	0.37
17.0		0.07293	1.10	0.36
16.8		0.07380	1.09	0.32

TABLE I (*Continued*)

Potassium Bromide

eV	cm^{-1}	μm	n	k
16.6		0.07380	1.09	0.32
16.4		0.07560	1.09	0.32
16.2		0.07653	1.05	0.32
16.0		0.07749	1.03	0.36
15.8		0.07847	1.07	0.35
15.6		0.07947	1.07	0.34
15.4		0.08050	1.07	0.33
15.2		0.08156	1.06	0.30
15.0		0.08265	1.04	0.29
14.8		0.08377	1.01	0.28
14.6		0.08492	0.98	0.27
14.4		0.08610	0.95	0.27
14.2		0.08731	0.90	0.29
14.0		0.08856	0.86	0.33
13.8		0.08984	0.84	0.37
13.6		0.09116	0.82	0.40
13.4		0.09253	0.79	0.45
13.2		0.09393		0.50[15]
13.05		0.09500	1.133[14]	0.645[14]
13.0		0.09537		0.61[15]
12.83		0.09666	1.107	0.656[14]
12.60		0.09840	1.086	0.758
12.37		0.1002	1.113	0.854
12.20		0.1016	1.132	0.938
11.99		0.1034	1.207	1.058
11.84		0.1047	1.341	1.166
11.64		0.1065	1.621	1.192
11.43		0.1085	1.851	0.986
11.23		0.1104	1.859	0.838
11.00		0.1128	1.838	0.655
10.94		0.1133	1.824	0.634
10.82		0.1146	1.824	0.571
10.69		0.1160	1.760	0.532
10.63		0.1166	1.752	0.520
10.52		0.1178	1.719	0.494
10.42		0.1189	1.704	0.501
10.33		0.1200	1.687	0.504
10.20		0.1216	1.684	0.458
10.13		0.1223	1.635	0.473
9.890		0.1254	1.670	0.424
9.807		0.1264	1.606	0.413
9.712		0.1277	1.588	0.433
9.611		0.1290	1.569	0.432
9.520		0.1302	1.539	0.414
9.356		0.1325	1.488	0.434
9.294		0.1334	1.452	0.413
9.203		0.1347	1.369	0.449
9.093		0.1363	1.303	0.553

TABLE I (*Continued*)

Potassium Bromide

eV	cm^{-1}	μm	n	k
9.002		0.1377	1.282	0.698
8.894		0.1394	1.335	0.797
8.801		0.1409	1.341	0.879
8.712		0.1423	1.390	1.073
8.604		0.1441	1.702	1.267
8.504		0.1458	2.042	1.125
8.409		0.1474	2.150	0.929
8.291		0.1495	2.153	0.774
8.203		0.1511	2.195	0.650
8.091		0.1532	2.192	0.551
8.011		0.1548	2.158	0.437
7.899		0.1570	2.056	0.330
7.840		0.1581	1.990	0.297
7.790		0.1592	1.950	0.333
7.752		0.1599	1.953	0.334
7.710		0.1608	1.910	0.348
7.648		0.1621	1.946	0.312
7.613		0.1629	1.875	0.278
7.557		0.1640	1.808	0.303
7.506		0.1652	1.802	0.307
7.446		0.1665	1.713	0.347
7.402		0.1675	1.649	0.397
7.358		0.1685	1.613	0.480
7.293		0.1700	1.593	0.662
7.250		0.1710	1.650	0.809
7.208		0.1720	1.799	0.925
7.146		0.1735	2.142	0.983
7.105		0.1745	2.349	0.826
7.044		0.1760	2.433	0.486
7.004		0.1770	2.348	0.322
6.945		0.1785	2.174	0.179
6.907		0.1795	2.029	0.172
6.850		0.1810	1.863	0.229
6.793	54,790	0.1825	1.732	0.345
6.756	54,500	0.1835	1.669	0.473
6.701	54,050	0.1850	1.679	0.774
6.7	54,080	0.1850		0.780[13]
6.65	53,680	0.1864		0.564
6.648	53,620	0.1865	1.876	1.070[14]
6.6	53,280	0.1879		1.26[13]
6.595	53,190	0.1880	2.348	1.279[14]
6.55	52,870	0.1893		0.678[13]
6.542	52,770	0.1895	2.977	0.846[14]
6.508	52,490	0.1905	2.957	0.444
6.5	52,470	0.1907		0.334[13]
6.457	52,080	0.1920	2.761	0.131[14]
6.45	52,020	0.1922		6.12×10^{-2}[13]
6.407	51,680	0.1935	2.549	2.31×10^{-2}[14]

TABLE I (*Continued*)

Potassium Bromide

eV	cm^{-1}	μm	n	k
6.4	51,620	0.1937		1.70×10^{-2} [13]
6.35	51,220	0.1953		3.89×10^{-3}
6.3	50,810	0.1968		9.71×10^{-4}
6.25	50,410	0.1984		2.53×10^{-4}
6.2	50,010	0.2000		6.37×10^{-5}
6.199	50,000	0.20	2.09953[11]	
6.15	49,600	0.2016		3.05×10^{-5} [13]
6.1	49,200	0.2033		1.62×10^{-5}
6.05	48,800	0.2049		9.78×10^{-6}
6.0	48,390	0.2066		5.75×10^{-6}
5.95	47,990	0.2048		4.24×10^{-6}
5.904	47,620	0.21	1.93440[11]	
5.9	47,590	0.2101		3.68×10^{-6} [13]
5.636	45,450	0.22	1.85023[11]	
5.391	43,480	0.23	1.79622	
5.166	41,670	0.24	1.75773	
4.959	40,000	0.25	1.72863	
4.769	38,460	0.26	1.70575	
4.592	37,040	0.27	1.68725	
4.428	35,710	0.28	1.67197	
4.275	34,480	0.29	1.65915	
4.133	33,330	0.30	1.64825	
3.999	32,260	0.31	1.63886	
3.874	31,250	0.32	1.63071	
3.757	30,300	0.33	1.62357	
3.647	29,410	0.34	1.61727	
3.542	28,570	0.35	1.61167	
3.444	27,780	0.36	1.60668	
3.351	27,030	0.37	1.60220	
3.263	26,320	0.38	1.59816	
3.179	25,640	0.39	1.59450	
3.100	25,000	0.40	1.59117	
2.952	23,810	0.42	1.58537	
2.818	22,730	0.44	1.58048	
2.695	21,740	0.46	1.57632	
2.583	20,830	0.48	1.57274	
2.480	20,000	0.50	1.56964	
2.384	19,230	0.52	1.56694	
2.296	18,520	0.54	1.56456	
2.214	17,860	0.56	1.56247	
2.138	17,240	0.58	1.56060	
2.066	16,670	0.60	1.55894	
2.000	16,130	0.62	1.55744	
1.937	15,630	0.64	1.55610	
1.879	15,150	0.66	1.55488	
1.823	14,710	0.68	1.55378	
1.771	14,290	0.70	1.55278	
1.722	13,890	0.72	1.55186	

TABLE I (*Continued*)

Potassium Bromide

eV	cm^{-1}	μm	n	k
1.675	13,510	0.74	1.55102	
1.631	13,160	0.76	1.55025	
1.590	12,820	0.78	1.54954	
1.550	12,500	0.80	1.54888	
1.512	12,200	0.82	1.54828	
1.476	11,900	0.84	1.54772	
1.442	11,630	0.86	1.54720	
1.409	11,360	0.88	1.54671	
1.378	11,110	0.90	1.54626	
1.348	10,870	0.92	1.54584	
1.319	10,640	0.94	1.54544	
1.291	10,420	0.96	1.54507	
1.265	10,200	0.98	1.54472	
1.240	10,000	1.00	1.54440	
1.033	8,333	1.2	1.54198	
0.8856	7,143	1.4	1.54052	
0.7749	6,250	1.6	1.53955	
0.6888	5,556	1.8	1.53901	
0.6199	5,000	2.0	1.53833	
0.5636	4,545	2.2	1.53792	
0.5166	4,167	2.4	1.53758	
0.4769	3,046	2.6	1.53728	
0.4428	3,571	2.8	1.53702	
0.4133	3,333	3.0	1.53677	
0.3874	3,125	3.2	1.53655	
0.3647	2,941	3.4	1.53633	
0.3444	2,778	3.6	1.53611	
0.3263	2,632	3.8	1.53590	
0.3100	2,500	4.0	1.53569	
0.2952	2,381	4.2	1.53547	
0.2818	2,273	4.4	1.53526	
0.2695	2,174	4.6	1.53504	
0.2583	2,083	4.8	1.53482	
0.2480	2,000	5.0	1.53459	
0.2384	1,923	5.2	1.53435	
0.2296	1,852	5.4	1.53411	
0.2214	1,786	5.6	1.53386	
0.2138	1,724	5.8	1.53361	
0.2066	1,667	6.0	1.53335	
0.2000	1,613	6.2	1.53308	
0.1937	1,563	6.4	1.53281	
0.1879	1,515	6.6	1.53253	
0.1823	1,471	6.8	1.53224	
0.1771	1,429	7.0	1.53194	
0.1722	1,389	7.2	1.53163	
0.1675	1,351	7.4	1.53132	
0.1631	1,316	7.6	1.53100	
0.1590	1,282	7.8	1.53067	

TABLE I (*Continued*)

Potassium Bromide

eV	cm^{-1}	μm	n	k
0.1550	1,250	8.0	1.53033	
0.1512	1,220	8.2	1.52998	
0.1476	1,190	8.4	1.52962	
0.1441	1,163	8.6	1.52926	
0.1409	1,136	8.8	1.52889	
0.1378	1,111	9.0	1.52851	
0.1348	1,087	9.2	1.52812	
0.1319	1,064	9.4	1.52772	
0.1300	1,049	9.536		2.5×10^{-9} [9]
0.1291	1,042	9.6	1.52731	
0.1284	1,035	9.657		2.0×10^{-9}
0.1265	1,020	9.8	1.52689	
0.1240	1,000	10.0	1.52647	
0.1221	984.4	10.159		1.8×10^{-9}
0.1216	980.4	10.2	1.52603	
0.1203	970.5	10.303		1.2×10^{-9}
0.1192	961.5	10.4	1.52559	
0.1179	951.2	10.513		2.3×10^{-9}
0.1171	944.2	10.591		1.0×10^{-9}
0.1170	943.4	10.6	1.52514	
0.1148	925.9	10.8	1.52467	
0.1127	909.1	11.0	1.52420	
0.1107	892.9	11.2	1.52372	
0.1088	877.2	11.4	1.52323	
0.1069	862.1	11.6	1.52273	
0.1051	847.5	11.8	1.52222	
0.1033	833.3	12.0	1.52171	
0.1016	819.7	12.2	1.52118	
0.09999	806.5	12.4	1.52064	
0.09840	793.7	12.6	1.52009	
0.09686	781.3	12.8	1.51954	
0.09537	769.2	13.0	1.51897	
0.09393	757.6	13.2	1.51840	
0.09252	746.3	13.4	1.51781	
0.09116	735.3	13.6	1.51721	
0.08984	724.6	13.8	1.51661	
0.08856	714.3	14.0	1.51599	
0.08731	704.2	14.2	1.51536	
0.08610	694.4	14.4	1.51473	
0.08492	684.9	14.6	1.51408	
0.08377	675.7	14.8	1.51342	
0.08265	666.7	15.0	1.51275	
0.08157	657.9	15.2	1.51208	
0.08059	650	15.38		5.5×10^{-8} [7]
0.08051	649.4	15.4	1.51139	
0.07948	641.0	15.6	1.51069	
0.07847	632.9	15.8	1.50998	
0.07749	625.0	16.0	1.50926	

TABLE I (*Continued*)

Potassium Bromide

eV	cm^{-1}	μm	n	k
0.07653	617.3	16.2	1.50852	
0.07560	609.8	16.4	1.50778	
0.07469	602.4	16.6	1.50703	
0.07439	600	16.67		2.1×10^{-7}
0.07380	595.2	16.8	1.50626	
0.07293	588.2	17.0	1.50548	
0.07208	581.4	17.2	1.50470	
0.07125	574.7	17.4	1.50390	
0.07044	568.2	17.6	1.50309	
0.06965	561.8	17.8	1.50227	
0.06888	555.6	18.0	1.50143	
0.06819	550	18.18		7.8×10^{-7}
0.06812	549.4	18.2	1.50059	
0.06738	543.5	18.4	1.49973	
0.06666	537.6	18.6	1.49886	
0.06595	531.9	18.8	1.49798	
0.06525	526.3	19.0	1.49709	
0.06457	520.8	19.2	1.49618	
0.06391	515.5	19.4	1.49526	
0.06326	510.2	19.6	1.49433	
0.06262	505.1	19.8	1.49339	
0.06199	500.0	20.0	1.49243	
				3.0×10^{-6}
0.06048	487.8	20.5	1.48999	
0.05904	476.2	21.0	1.48746	
0.05767	465.1	21.5	1.48485	
0.05636	454.5	22.0	1.48215	
0.05579	450	22.22		1.2×10^{-5}
0.05510	444.4	22.5	1.47937	
0.05391	434.8	23.0	1.47650	
0.05276	425.5	23.5	1.47353	
0.05166	416.7	24.0	1.47047	
0.05060	408.2	24.5	1.46732	
0.04959	400.0	25.0	1.46406	
				4.8×10^{-5}
0.04862	392.2	25.5	1.46070	
0.04769	384.6	26.0	1.45723	
0.04679	377.4	26.5	1.45366	
0.04592	370.4	27.0	1.44998	
0.04508	363.6	27.5	1.44618	
0.04428	357.1	28.0	1.44226	
0.04350	350.9	28.5	1.43821	
0.04339	350	28.57		2.0×10^{-4}
0.04275	344.8	29.0	1.43404	
0.04203	339.0	29.5	1.42974	
0.04133	333.3	30.0	1.42531	
0.04065	327.9	30.5	1.42073	
0.03999	322.6	31.0	1.41601	

TABLE I (*Continued*)

Potassium Bromide

eV	cm^{-1}	μm	n	k
0.03936	317.5	31.5	1.41114	
0.03874	312.5	32.0	1.40611	
0.03815	307.7	32.5	1.40091	
0.03757	303.0	33.0	1.39555	
0.03720	300	33.33		8.5×10^{-4}
0.03701	298.5	33.5	1.39001	
0.03647	294.1	34.0	1.38429	
0.03594	289.9	34.5	1.37838	
0.03542	285.7	35.0	1.37227	
0.03493	281.7	35.5	1.36595	
0.03444	277.8	36.0	1.35941	
0.03397	274.0	36.5	1.35264	
0.03351	270.3	37.0	1.34563	
0.03306	266.7	37.5	1.33837	
0.03263	263.2	38.0	1.33084	
0.03220	259.7	38.5	1.32304	
0.03179	256.4	39.0	1.31494	
0.03139	253.2	39.5	1.30653	
0.03100	250.0	40.0	1.29779	
			1.35[6]	3.2×10^{-3}
0.03061	246.9	40.5	1.28870[11]	
0.03024	243.9	41.0	1.27924	
0.02988	241.0	41.5	1.26939	
0.02976	240	41.67	1.33[6]	
0.02952	238.1	42.0	1.25911[11]	
0.02852	230	43.48	1.30[6]	
0.02728	220	45.45	1.20	1.7×10^{-2}[6]
0.02604	210	47.62	1.10	2.9×10^{-2}
0.02480	200	50.00	1.00	6.0×10^{-2}
0.02418	195	51.28	0.93	0.11
0.02356	190	52.63	0.90	0.18
0.02294	185	54.05	0.89	0.20
0.02232	180	55.55	0.83	0.22
0.02170	175	57.14	0.76	0.39
0.02108	170	58.82	0.76	0.44
0.02046	165	60.61	0.80	0.44
0.01984	160	62.50	0.76	0.47
0.01922	155	64.52	0.60	0.58
0.01860	150	66.67	0.48	0.72
0.01798	145	68.97	0.39	0.90
0.01736	140	71.43	0.32	1.2
0.01674	135	74.07	0.29	2.0
0.01612	130	76.92	0.30	2.0
0.01550	125	80.00	0.33	2.9
0.01488	120	83.33	0.65	4.3
0.01426	115	86.96	3.00	5.3
0.01364	110	90.91	5.50	1.0
0.01302	105	95.24	3.90	0.54
0.01116	100	100.0	3.40	0.33

TABLE I (*Continued*)

Potassium Bromide

eV	cm^{-1}	μm	n	k
0.01177	95	105.3	3.10	0.20
0.01116	90	111.1	2.80	0.15
0.01054	85	117.6	2.60	0.13
0.00991	80	125.0	2.52	0.125
0.00867	70	142.8	2.40	0.12
0.00743	60	166.7	2.35	0.11
0.00619	50	200.0	2.30	9.3×10^{-2}
				9.5×10^{-2} [5]
0.00495	40	250.0	2.28	6.8×10^{-2} [6]
				6.2×10^{-2} [5]
0.00372	30	333.3	2.24	3.7×10^{-2} [6]
				3.4×10^{-2} [5]
0.00248	20	500.0	2.20	1.6×10^{-2} [6]
				1.2×10^{-2} [5]
0.001240	10	1000		4.2×10^{-3}
0.001116	9.0	1111		3.7×10^{-3}
0.000991	8.0	1250		3.1×10^{-3}
0.000867	7.0	1429		2.6×10^{-3}
0.000743	6.0	1667		2.3×10^{-3}
0.000619	5.0	2000		1.8×10^{-3}
0.000495	4.0	2500		1.4×10^{-3}
0.000479	3.87	2584	2.21[2]	1.18×10^{-3} [2]
0.000372	3.0	3333		1.1×10^{-3} [5]
0.000248	2.0	5000		6.8×10^{-4}
0.000207	1.67	6000	2.19	2.40×10^{-4} [2]
0.0001463	1.18	8500	2.21	4.99×10^{-4}
0.0001240	1.0	10000		3.4×10^{-4} [5]
0.0001116	0.9	11110		3.1×10^{-4}
0.00009919	0.8	12500		2.8×10^{-4}
			2.20	1.43×10^{-4} [2]
0.00008679	0.7	14290		2.4×10^{-4} [5]
0.00007439	0.6	16670		2.3×10^{-4}
0.00006199	0.5	20000		1.8×10^{-4}
0.00004141	0.334	30000	2.21	2.54×10^{-4} [2]
0.00003682	0.297	33200	2.22	2.61×10^{-4}

[a] References are indicated in brackets.

Potassium Dihydrogen Phosphate (KH_2PO_4, KDP) and Three of Its Isomorphs

DAVID F. EDWARDS and RICHARD H. WHITE
University of California
Lawrence Livermore National Laboratory
Livermore, California

Potassium dihydrogen phosphate (KDP) is perhaps the best known, most extensively studied, and most widely used crystal in laser technology. Crystals of KDP are used for frequency-upconversion operation in high-power laser systems. At the present time the NOVA laser at Lawrence Livermore National Laboratory uses KDP crystals for upconversion from the fundamental wavelength, 1.053 μm, to the second, third, and fourth harmonics, 0.527 μm, 0.351 μm, and 0.263 μm, respectively. KDP is also the primary nonlinear optical material being used at the major laser facilities in France, Great Britain, Japan, China, and the Soviet Union. Ammonium dihydrogen phosphate (ADP) and the deuterated crystals (labeled D*) AD*P and KD*P have also found use in state-of-the-art nonlinear optical devices.

For each application of these nonlinear crystals, a precise knowledge is required of the crystal's refractive index as a function of wavelength. In addition, crystal temperature has a sensitive effect on the indices within the precision range of interest. The first precise measurement of the indices of refraction of KDP and ADP for a broad wavelength range was that of Zernike [1]. He measured the indices at 25 wavelengths between 2138 Å and 1.529 μm and at 24.8°±0.2 °C. He reports his indices to be accurate to at least $\pm 3 \times 10^{-5}$. Zernike used the method of known incidence used by Rydberg [2] and Tilton *et al.* [3]. For this method a prism of the material to be measured is inserted into a Littrow-type mount monochromator. The deviation is measured for different wavelengths by measuring the angle over which the Littrow mirror had to be rotated to pass a particular wavelength to the exit slit. More recently, Kirby and DeShazer [4] reported the index measurements for KDP, KD*P, ADP, AD*P and

Copyright © 1991 by Academic Press.
All rights of reproduction in any form reserved.
ISBN 0-12-544422-2

several other nonlinear crystals isomorphic to KDP. Their measurements were at 16 wavelengths from 4046 Å to 1.06 μm and a sample temperature of 33.0°±0.4 °C. This slightly elevated temperature was used to remove any absorbed water vapor on the crystal faces owing to the hygroscopic nature of these crystals. The method of minimum deviation [5] was used to measure the indices. For the deuterated crystals the index values depend on the deuterium concentration. The KD*P and AD*P crystals of Kirby and DeShazer had 96% deuterium replacement for hydrogen. Phillips [6] and Yamazaki and Ogawa [7] report indices for partially deuterated (about 90%) KD*P.

Kirby and DeShazer show that the index values vary from about 6×10^{-5} to 60×10^{-5} in the visible region for KDP crystals from different crystal growers. They correlated these differences with deviations in the crystal-lattice parameters and speculate that crystalline defects incorporated during the crystal-growth process are the cause of the lattice-parameter variations.

The measured values of Zernike [1] and Kirby and DeShazer [4] were fit separately to both a Herzberger-type and a modified Sellmeier-type dispersion formula. These two measurements ([1] and [4]) were made at slightly different temperatures. The importance of the index sensitivity to temperature is the reason for reporting both fits. Given in Tables I–IV and plotted in Figs. 1–4 are the calculated indices of refraction for KDP, ADP, KD*P, and AD*P, respectively. The reported indices of other authors were not used in these fits for several reasons, including poorly defined sample temperatures, lack of precision, or untabulated data that could not be accurately read from their curves [6–9].

The Herzberger-type dispersion formula is [10]

$$n = A + BL + CL^2 + D\lambda^2 + E\lambda^4,$$

where $L = 1/(\lambda^2 - 2.80\times10^6)$ with λ in angstroms. As explained by Herzberger, the 2.80×10^6 is the square of the mean asymptote for the short-wavelength abrupt increase in the index for 15 materials (KDP, KD*P, ADP, and AD*P not included). The coefficients, evaluated by least squares, are given in Table V. Zernike did not measure deuterated samples so no coefficients are listed for KD*P or AD*P at 24.8 °C. The RMS errors between the measured values and the dispersion-formula calculated indices are given in the fourth column. These errors (%) range from about 2×10^{-5} to 4×10^{-4}.

The data of Zernike and of Kirby and DeShazer were also independently fit to a modified Sellmeier-type dispersion formula for the convenience of the reader. These Sellmeier values are not tabulated here. The modified Sellmeier-type formula used here is not the same as introduced by Zernike

[1] and used by Kirby and DeShazer [4]. Our dispersion formula is

$$n^2 = 1 + A/(\lambda^2 - B) + C\lambda^2/(\lambda^2 - D),$$

where the wavelength λ is in angstroms. This form is preferred to that of Zernike because of the rate and uniqueness of convergence of the regressive fit. The Zernike modified formula will converge to a local minimum depending on the initial guesses for the coefficients, and does not result in a unique coefficient set. This nonuniqueness of the Zernike modified formula can also be demonstrated by straightforward algebra. Zernike's modified formula is of the form

$$n^2 = A + B/(\lambda^2 - C) + D\lambda^2/(\lambda^2 - E).$$

Adding and subtracting $(-B/C + D)$ results in a formula of identical form but with the new coefficients in terms of the original coefficients.

The coefficient sets for our modified Sellmeier-type dispersion formula are given in Table VI. As before, coefficients are given for both 33.0° and 24.8 °C to demonstrate the temperature sensitivity of the indices. No data are given for the deuterated crystals at 24.8 °C because Zernike did not include these crystals in his measurements. The RMS error between the measured indices and the calculated values is given in Column 4, Table V. Overall, the fits for the two temperatures are within a few places in the fourth decimal with the one exception.

A comparison of the Zernike data at 24.8 °C with those of Kirby and DeShazer at 33.0 °C shows that the indices are sensitively dependent on sample temperature. The temperature dependence of the indices for KDP, KD*P, and ADP have been measured by several groups. Phillips [6] measured the indices of KDP, KD*P, and ADP at about nine wavelengths and three or four temperatures between the Curie point and room temperature. He estimates the data accuracy to be $\pm 10^{-4}$. Yamazaki and Ogawa [7] measured the temperature dependence for three wavelengths for these same materials and over the same temperature range as Phillips, and their results are similar. Likewise, similar results are reported by Onaka and Kawamura [8] for KDP, Onaka and Takeda [8] for ADP, and Barnes *et al.* [9] for KDP, KD*P, and ADP. An intercomparison of the predicted indices of Refs. [6–9] with the measured values of Refs. [1, 4] for small temperature intervals shows an internal consistency of 10^{-4} or smaller with the data of Onaka and Kawamura [8] having the greatest discrepancy. Phillips [6] has given the following empirical equation for the temperature change of index:

$$\Delta n = (n^2 + an + b)c(298 - T),$$

where T is the temperature in K. The values of the coefficients are given in Table VII.

Davis and Vedam [11] have measured the pressure dependence of the refractive indices at 5893 Å for KDP and ADP under hydrostatic conditions to 7 kbars. Both the ordinary and extraordinary indices were found to vary linearly with pressure for both materials. From their data the slopes of the index change with pressure curves are $+1.55 \times 10^3$/kbar and $+1.31 \times 10^3$/kbar for the KDP ordinary and extraordinary values, respectively. For ADP the values are 1.43×10^3/kbar and 1.12×10^3/kbar. They measured no deuterated crystals.

The reststrahlen spectrum of KDP and some of its isomorphs have been studied by several groups with emphasis on the low-frequency vibrational modes, one of which goes soft as the temperature is lowered below room temperature to the Curie temperature [12–22]. The coupling of these modes produces broad reflection peaks, which have been fitted with various models. Many of these references do not give information on all four parameters, ε' and ε'' for $(\mathbf{E} \perp c)$ and $(\mathbf{E} \| c)$, and the notation varies ($\| c \equiv c$, $\perp c \equiv a$). Often the graphs are too small to read. Raman-scattering studies of the phonon modes also abound [23–27].

In lieu of an extended study of this complicated IR spectral region to sort out the n and k values, we have listed in Table VIII various references with some pertinent information and leave it to the reader to examine the data directly. Much information about KDP and some of its isomorphs is given in Ref. [28].

REFERENCES

1. F. Zernike, "Refractive Indices of Ammonium Dihydrogen Phosphate and Potassium Dihydrogen Phosphate between 2000 Å and 1.5 μ," *J. Opt. Soc. Am.* **54**, 1215 (1964).
2. F. Rydberg, *Poggendorfs Ann.* **14**, 45 (1828).
3. L. W. Tilton, E. K. Plyler, and R. E. Stephens, *J. Res. Natl. Bur. Std. (U.S.)* **43**, 81 (1949).
4. K. W. Kirby and L. G. DeShazer, "Refractive Indices of 14 Nonlinear Crystals Isomorphic to KH_2PO_4," *J. Opt. Soc. Am.* **B4**, 1072 (1987).
5. L. W. Taylor, "College Manual of Optics," Ginn, Boston, (1924).
6. R. A. Phillips, "Temperature Variation of the Index of Refraction of ADP, KDP, and Deuterated KDP," *J. Opt. Soc. Am.* **56**, 629 (1966).
7. M. Yamazaki and T. Ogawa, "Temperature Dependence of the Refractive Indices of $NH_4H_2PO_4$, KH_2PO_4 and Partially Deuterated KH_2PO_4," *Appl. Opt.* **5**, 1407 (1966).
8. R. Onaka and T. Takeda, "Temperature Dependence of the Refractive Indices of KDP," *J. Phys. Soc. Jap.* **50**, 3695 (1981); R. Onaka and T. Takeda "Temperature Dependence of the Refractive Indices of ADP," *J. Phys. Soc. Jap.* **51**, 3258 (1982).
9. N. P. Barnes, D. J. Gettemy, and R. S. Adhav, "Variation of the Refractive Index with Temperature and the Tuning Rate for KDP Isomorphs," *J. Opt. Soc. Am.* **72**, 895 (1982).
10. M. Herzberger and C. D. Salzberg, "Refractive Indices of Infrared Optical Materials and Color Correction of Infrared Lenses," *J. Opt. Soc. Am.* **52**, 420 (1962); M. Herzberger,

"Color Correction in Optical Systems and a New Dispersion Formula," *Opt. Acta* **6**, 197 (1959).
11. T. A. Davis and K. Vedam, "Pressure Dependence of the Refractive Indices of the Tetragonal Crystals: ADP, KDP, $CaMoO_4$, $CaWO_4$, and Rutile," *J. Opt. Soc. Am.* **58**, 1446 (1968).
12. G. M. Murphy, G. Weiner, and J. J. Oberly, "Infrared Reflection Spectra of Phosphate and Arsenate Crystals," *J. Chem. Phys.* **22**, 1321 (1954).
13. A. S. Barker, Jr., and M. Tinkham, "Far-Infrared Dielectric Measurements on Potassium Dihydrogen Phosphate, Triglycerine Sulfate, and Rutile," *J. Chem. Phys.* **38**, 2257 (1963).
14. F. Sugawara and T. Nakamura, "Far-Infrared Reflectivity Spectra of KH_2PO_4 Crystal," *J. Phys. Soc. Jpn.* **28**, 158 (1970).
15. F. Bréhat and A. Hadni, "Transmission du phosphate diacide de potassium dans l'infrarouge lointain dans les phases para et ferroélectriques," *C.R. Acad. Sci. Paris* **271**, B1137 (1970).
16. E. Wiener-Arnear, S. Levin, and I. Pelah, "Proton Dynamics in KH_2PO_4 Type Ferroelectrics Studied by Infrared Absorption," *J. Chem. Phys.* **52**, 2881 (1970); "Antiferroelectric Transitions in $NH_4H_2PO_4$ and $NH_4H_2AsO_4$ Studied in Infrared Absorption," *J. Chem. Phys.* **52**, 2891 (1970).
17. T. Kawamura and A. Mitsuishi, "Raman and Far-Infrared Spectra of KH_2PO_4 and $NH_4H_2PO_4$," *Technology Reports Osaka University* **23**, 365 (1973); T. Kawamura, A. Mitsuishi, and H. Yoshinaga, Proc. 2nd Inter. Meeting on Ferroelectrics, *J. Phys. Soc. Jpn.* **28** Suppl., 227 (1970).
18. T. Kawamura, A. Mitsuishi, N. Furuya, and O. Shimomura, "Far-Infrared and Raman Spectra of KD_2PO_4," *Opt. Commum.* **10**, 337 (1974); T. Kawamura, A. Mitsuishi, N. Furuya, and O. Shimomura, "Optical Properties of KD_2PO_4 Crystal in the Low-Wavenumber Region," Technology Reports Osaka University **24**, 429 (1974).
19. F. Onyango, W. Smith, and J. F. Angress, "I. R. Reflection and Transmission Properties of KH_2PO_4," *J. Phys. Chem. Solids* **36**, 309 (1975).
20. K. E. Gauss, H. Happ, and G. Rother, "Millimeter Wave and Far-Infrared Investigation on KDP with Asymmetric Interferometers," *Phys. Stat. Solidi (b)* **72**, 623 (1975).
21. D. A. Ledsham, W. G. Chambers, and T. J. Parker, "Dispersive Reflection Spectroscopy in the Far Infrared Using a Polarising Interferometer," *Infrared Physics* **16**, 515 (1976).
22. D. A. Ledsham, W. G. Chambers, and T. J. Parker, "Far Infrared Measurements on KH_2PO_4 Using Dispersive Reflection Spectroscopy," *Infrared Physics* **17**, 165 (1977).
23. R. L. Reese, I. J. Fritz, and H. Z. Cummins, "Simultaneous Observation of the Soft Ferroelectric and Acoustic Modes of KD_2PO_4, *Solid State Commum.* **9**, 327 (1971).
24. D. K. Agrawal and C. H. Perry, "The Temperature Dependent Raman Spectra of KDP, KD*P, KDA and ADP," Proc. 2nd International Conference on Light Scattering in Solids, (M. Balkanski, ed.), Flammarion, Paris, 429 (1971).
25. H. Hammer, "Raman Spectra of Crystals of the KH_2PO_4-Type in Their Paraelectric and Low Temperature Phases," Proc. 2nd International Conference on Light Scattering in Solids," (M. Balkanski, ed.), Flammarion, Paris, 425 (1971).
26. C. Y. She, T. W. Broberg, L. S. Wall, and D. F. Edwards, "Effect of Proton-Photon Coupling on the Ferroelectric Mode in KH_2PO_4," *Phys. Rev.* **B6**, 1847 (1972).
27. N. Lagakos and H. Z. Cummins, "Preliminary Observation of a Central Peak in the Light-Scattering Spectrum of KH_2PO_4," *Phys. Rev.* **B10**, 1063 (1974).
28. K.-H. Hellwege, ed., "Landolt-Börnstein Numerical Data and Functional Relationships in Science and Technology," Vol. III/16b, Springer-Verlag, Berlin, (1983).

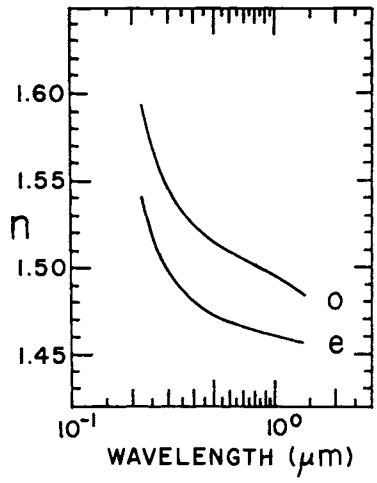

Fig. 1. Plot of n_o, n_e versus wavelength in micrometers for KDP.

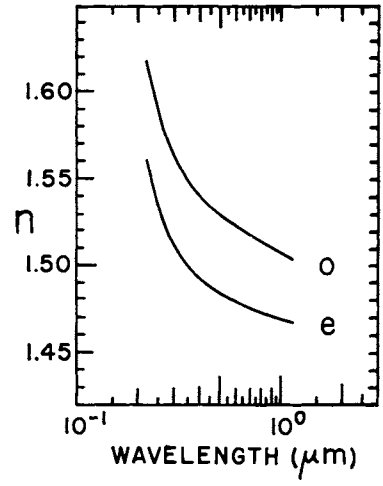

Fig. 2. Plot of n_o, n_e versus wavelength in micrometers for ADP.

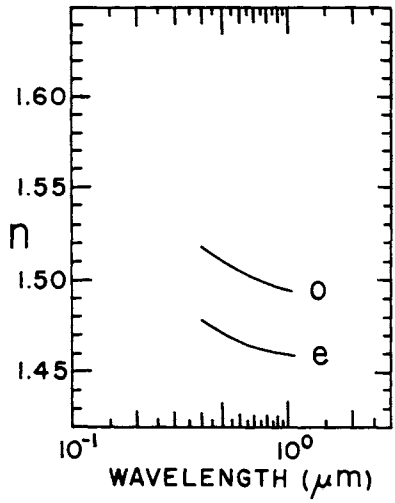

Fig. 3. Plot of n_o, n_e versus wavelength in micrometers for KD*P.

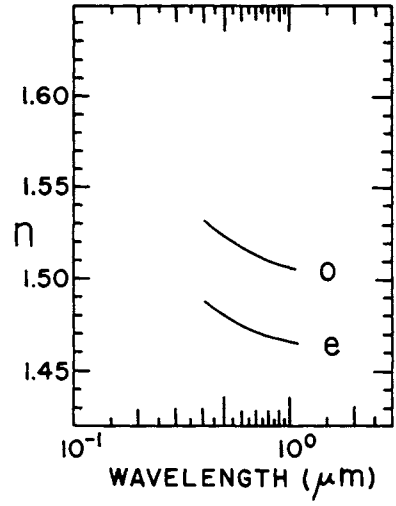

Fig. 4. Plot of n_o, n_e versus wavelength in micrometers for AD*P.

TABLE I

Values of n for KDP at 24.8°C and 33.0°C[a]

			24.8 ± 0.2 C		33.0 ± 0.4 C	
eV	cm^{-1}	μm	n_o	n_e	n_o	n_e
5.636	45,455	0.220	1.5951[1]	1.5413[1]		
5.167	41,667	0.240	1.5767	1.5257		
4.769	38,462	0.260	1.5626	1.5134		
4.429	35,714	0.280	1.5523	1.5044		
4.133	33,333	0.300	1.5444	1.4975		
3.875	31,250	0.320	1.5385	1.4923		
3.647	29,412	0.340	1.5337	1.4881		
3.444	27,778	0.360	1.5299	1.4848		
3.263	26,316	0.380	1.5267	1.4820		
3.100	25,000	0.400	1.5240	1.4797	1.5238[4]	1.4798[4]
2.952	23,810	0.420	1.5217	1.4778	1.5214	1.4777
2.818	22,727	0.440	1.5197	1.4761	1.5192	1.4760
2.696	21,739	0.460	1.5179	1.4747	1.5174	1.4745
2.583	20,833	0.480	1.5164	1.4735	1.5157	1.4731
2.480	20,000	0.500	1.5150	1.4724	1.5142	1.4720
2.385	19,231	0.520	1.5137	1.4714	1.5129	1.4710
2.296	18,519	0.540	1.5125	1.4705	1.5117	1.4700
2.214	17,857	0.560	1.5114	1.4697	1.5106	1.4692
2.138	17,241	0.580	1.5104	1.4690	1.5096	1.4685
2.067	16,667	0.600	1.5095	1.4683	1.5086	1.4678
2.000	16,129	0.620	1.5086	1.4677	1.5077	1.4672
1.938	15,625	0.640	1.5077	1.4671	1.5069	1.4666
1.879	15,152	0.660	1.5069	1.4666	1.5061	1.4661
1.824	14,706	0.680	1.5061	1.4661	1.5053	1.4656
1.771	14,286	0.700	1.5053	1.4656	1.5046	1.4651
1.722	13,889	0.720	1.5046	1.4652	1.5039	1.4647
1.676	13,514	0.740	1.5039	1.4648	1.5032	1.4643
1.632	13,158	0.760	1.5032	1.4644	1.5026	1.4639
1.590	12,821	0.780	1.5025	1.4640	1.5020	1.4635
1.550	12,500	0.800	1.5018	1.4636	1.5013	1.4632
1,512	12,195	0.820	1.5011	1.4633	1.5007	1.4628
1.476	11,905	0.840	1.5005	1.4629	1.5001	1.4625
1.442	11,628	0.860	1.4998	1.4626	1.4996	1.4622
1.409	11,364	0.880	1.4992	1.4623	1.4990	1.4619
1.378	11,111	0.900	1.4986	1.4620	1.4984	1.4617
1.348	10,870	0.920	1.4979	1.4617	1.4978	1.4614
1.319	10,638	0.940	1.4973	1.4614	1.4973	1.4612
1.292	10,417	0.960	1.4967	1.4611	1.4967	1.4609
1.265	10,204	0.980	1.4961	1.4608	1.4962	1.4607
1.240	10,000	1.000	1.4954	1.4606	1.4956	1.4605
1.216	9,804	1.020	1.4948	1.4603	1.4950	1.4603
1.192	9,615	1.040	1.4942	1.4600	1.4945	1.4601
1.170	9,434	1.060	1.4936	1.4598	1.4936	1.4599
1.148	9,259	1.080	1.4930	1.4595		
1.127	9,091	1.10	1.4924	1.4593		

TABLE I (*Continued*)

KDP

eV	cm^{-1}	μm	n_o	n_e	n_o	n_e
1.107	8,929	1.12	1.4918	1.4591		
1.088	8,772	1.14	1.4912	1.4588		
1.069	8,621	1.16	1.4906	1.4586		
1.051	8,475	1.18	1.4900	1.4584		
1.033	8,333	1.20	1.4895	1.4581		
1.016	8,197	1.22	1.4889	1.4579		
1.000	8,065	1.24	1.4883	1.4577		
0.9840	7,937	1.26	1.4877	1.4575		
0.9686	7,813	1.28	1.4872	1.4573		
0.9537	7,692	1.30	1.4866	1.4571		
0.9393	7,576	1.32	1.4861	1.4569		
0.9253	7,463	1.34	1.4855	1.4567		
0.9117	7,353	1.36	1.4850	1.4565		

[a] The indices were calculated with the Herzberger-type formula. The number in brackets indicates the data reference.

TABLE II

Values of n for ADP at 24.8°C and 33.0°C[a]

			24.8 ± 0.2 C		33.0 ± 0.4 C	
eV	cm^{-1}	μm	n_o	n_e	n_o	n_e
5.636	45,455	0.220	1.6186[1]	1.5609[1]		
5.167	41,667	0.240	1.5981	1.5429		
4.769	38,462	0.260	1.5827	1.5293		
4.429	35,714	0.280	1.5715	1.5193		
4.133	33,333	0.300	1.5630	1.5119		
3.875	31,250	0.320	1.5565	1.5062		
3.647	29,412	0.340	1.5513	1.5016		
3.444	27,778	0.360	1.5470	1.4979		
3.263	26,316	0.380	1.5435	1.4949		
3.100	25,000	0.400	1.5405	1.4923	1.5396[4]	1.4920[4]
2,952	23,810	0.420	1.5379	1.4901	1.5368	1.4897
2.818	22,727	0.440	1.5357	1.4882	1.5344	1.4877
2.696	21,739	0.460	1.5337	1.4865	1.5324	1.4860
2.583	20,833	0.480	1.5319	1.4851	1.5306	1.4845
2.480	20,000	0.500	1.5303	1.4837	1.5290	1.4832
2.385	19,231	0.520	1.5288	1.4825	1.5276	1.4820
2.296	18,519	0.540	1.5274	1.4814	1.5263	1.4810
2.214	17,857	0.560	1.5261	1.4804	1.5251	1.4800
2.138	17,241	0.580	1.5249	1.4795	1.5240	1.4791
2.067	16,667	0.600	1.5238	1.4786	1.5229	1.4783
2.000	16,129	0.620	1.5227	1.4778	1.5219	1.4776
1.938	15,625	0.640	1.5217	1.4770	1.5209	1.4769
1.879	15,152	0.660	1.5207	1.4763	1.5200	1.4763
1.824	14,706	0.680	1.5197	1.4756	1.5191	1.4757
1.771	14,286	0.700	1.5188	1.4749	1.5183	1.4751
1.722	13,889	0.720	1.5179	1.4743	1.5175	1.4746
1.676	13,514	0.740	1.5170	1.4737	1.5167	1.4741
1.632	13,158	0.760	1.5162	1.4732	1.5159	1.4736
1.590	12,821	0.780	1.5154	1.4726	1.5152	1.4731
1.550	12,500	0.800	1.5146	1.4721	1.5145	1.4727
1.512	12,195	0.820	1.5138	1.4716	1.5139	1.4722
1.476	11,905	0.840	1.5131	1.4712	1.5132	1.4718
1.442	11,628	0.860	1.5123	1.4707	1.5126	1.4714
1.409	11,364	0.880	1.5116	1.4703	1.5121	1.4710
1.378	11,111	0.900	1.5109	1.4699	1.5115	1.4707
1.348	10,870	0.920	1.5103	1.4695	1.5110	1.4703
1.319	10,638	0.940	1.5096	1.4692	1.5106	1.4700
1.292	10,417	0.960	1.5090	1.4688	1.5101	1.4696
1.265	10,204	0.980	1.5084	1.4685	1.5100	1.4693
1.240	10,000	1.000	1.5078	1.4683	1.5094	1.4689
1.216	9,804	1.020	1.5072	1.4680	1.5091	1.4686
1.192	9,615	1.040	1.5067	1.4678	1.5089	1.4683
1.170	9,434	1.060	1.5061	1.4676	1.5087	1.4680
1.148	9,259	1.080	1.5056	1.4674		
1.127	9,091	1.100	1.5052	1.4673		
1.107	8,929	1.120	1.5047	1.4672		

TABLE II (*continued*)

ADP

eV	cm^{-1}	μm	n_o	n_e	n_o	n_e
1.088	8,772	1.140	1.5043	1.4671		
1.069	8,621	1.160	1.5039	1.4670		

[a] The indices were calculated with the Herzberger-type formula. The numbers in brackets indicate the data reference.

TABLE III

Value of n for KD*P at 33.0°C[a]

eV	cm^{-1}	μm	n_o	n_e
3.100	25,000	0.400	1.5183[4]	1.4774[4]
2.952	23,810	0.420	1.5159	1.4755
2.818	22,727	0.440	1.5139	1.4738
2.696	21,739	0.460	1.5121	1.4723
2.583	20,833	0.480	1.5106	1.4710
2.480	20,000	0.500	1.5092	1.4699
2.385	19,231	0.520	1.5080	1.4689
2.296	18,519	0.540	1.5069	1.4680
2.214	17,857	0.560	1.5060	1.4672
2.138	17,241	0.580	1.5051	1.4664
2.067	16,667	0.600	1.5042	1.4658
2.000	16,127	0.620	1.5035	1.4652
1.938	15,625	0.640	1.5028	1.4646
1.879	15,152	0.660	1.5021	1.4641
1.824	14,706	0.680	1.5015	1.4636
1.771	14,286	0.700	1.5009	1.4632
1.722	13,889	0.720	1.5003	1.4628
1.676	13,514	0.740	1.4998	1.4624
1.632	13,158	0.760	1.4993	1.4620
1.590	12,821	0.780	1.4988	1.4617
1.550	12,500	0.800	1.4983	1.4614
1.512	12,195	0.820	1.4979	1.4611
1.476	11,905	0.840	1.4974	1.4608
1.442	11,628	0.860	1.4970	1.4605
1.409	11,364	0.880	1.4966	1.4602
1.378	11,111	0.900	1.4962	1.4600
1.348	10,870	0.920	1.4958	1.4597
1.319	10,638	0.940	1.4954	1.4595
1.292	10,417	0.960	1.4950	1.4593
1.265	10,204	0.980	1.4946	1.4591
1.240	10,000	1.000	1.4943	1.4589
1.216	9,804	1.020	1.4939	1.4587
1.192	9,615	1.040	1.4936	1.4585
1.170	9,434	1.060	1.4932	1.4583

[a] The indices were calculated with the Herzberger-type formula. The number in brackets indicates the data reference.

TABLE IV

Value of n for AD*P at 33.0°C[a]

eV	cm^{-1}	μm	n_o	n_e
3.100	25,000	0.400	1.5328[4]	1.4879[4]
2.952	23,810	0.420	1.5303	1.4857
2.818	22,727	0.440	1.5281	1.4839
2.696	21,739	0.460	1.5262	1.4822
2.583	20,833	0.480	1.5245	1.4808
2,480	20,000	0.500	1.5230	1.4795
2.385	19,231	0.520	1.5217	1.4784
2.296	18,519	0.540	1.5205	1.4774
2.214	17,857	0.560	1.5194	1.4765
2.138	17,241	0.580	1.5185	1.4756
2.067	16,667	0.600	1.5175	1.4749
2.000	16,127	0.620	1.5167	1.4742
1.938	15,625	0.640	1.5159	1.4736
1.879	15,152	0.660	1.5152	1.4730
1.824	14,706	0.680	1.5145	1.4724
1.771	14,286	0.700	1.5138	1.4719
1.722	13,889	0.720	1.5132	1.4715
1.676	13,514	0.740	1.5126	1.4710
1.632	13,158	0.760	1.5121	1.4706
1.590	12,821	0.780	1.5115	1.4702
1.550	12,500	0.800	1.5110	1.4698
1.512	12,195	0.820	1.5105	1.4695
1.476	11,905	0.840	1.5100	1.4691
1.442	11,628	0.860	1.5095	1.4688
1.409	11,364	0.880	1.5090	1.4685
1.378	11,111	0.900	1.5085	1.4682
1.348	10,870	0.920	1.5081	1.4679
1.319	10,638	0.940	1.5076	1.4676
1.292	10,417	0.960	1.5072	1.4673
1.265	10,204	0.980	1.5068	1.4670
1.240	10,000	1.000	1.5063	1.4668
1.216	9,804	1.020	1.5059	1.4665
1.192	9,615	1.040	1.5055	1.4662
1.170	9,434	1.060	1.5051	1.4660

[a] The indices were calculated with the Herzberger-type formula. The number in brackets indicates the data reference.

TABLE V

Herzberger-type Dispersion Formula Coefficients $n = A + BL + CL^2 + D\lambda^2 + E\lambda^4$

Material	Temp (C)		RMS error %	A	B	C	D	E
KDP	33.0	n_o	0.00326	1.503444	3.162307×10^{5}	-3.029850×10^{11}	$-1.152066 \times 10^{-10}$	4.545059×10^{-20}
		n_e	0.00376	1.462149	2.554564×10^{5}	-1.406152×10^{11}	$-5.962811 \times 10^{-11}$	1.701670×10^{-19}
	24.8	n_o	0.0375	1.507233	2.691571×10^{5}	-1.800594×10^{11}	$-1.655975 \times 10^{-10}$	2.017312×10^{-19}
		n_e	0.0218	1.463170	2.439193×10^{5}	-1.712637×10^{11}	$-6.011992 \times 10^{-11}$	9.221139×10^{-20}
KD*P	33.0	n_o	0.00166	1.499050	2.763783×10^{5}	-4.759414×10^{10}	$-9.103436 \times 10^{-11}$	1.482297×10^{-19}
		n_e	0.00167	1.458701	2.815843×10^{5}	-3.633300×10^{11}	$-3.235631 \times 10^{-11}$	5.360066×10^{-20}
ADP	33.0	n_o	0.00715	1.527573	1.635962×10^{5}	8.176341×10^{11}	$-3.372908 \times 10^{-10}$	1.379342×10^{-18}
		n_e	0.00137	1.472389	2.900877×10^{5}	-2.052917×10^{11}	$-7.730910 \times 10^{-11}$	1.326179×10^{-19}
	24.8	n_o	0.0285	1.523897	2.869378×10^{5}	-1.857597×10^{11}	$-2.660808 \times 10^{-10}$	7.551831×10^{-19}
		n_e	0.0269	1.476613	2.552032×10^{5}	-1.661894×10^{11}	$-1.792370 \times 10^{-10}$	6.965756×10^{-19}
AD*P	33.0	n_o	0.00404	1.510421	3.407679×10^{5}	-3.825237×10^{11}	$-7.869752 \times 10^{-11}$	3.167592×10^{-20}
		n_e	0.00251	1.467063	3.173115×10^{5}	-4.549975×10^{11}	$-3.729681 \times 10^{-11}$	2.002751×10^{-20}

TABLE VI

Modified Sellmeier-type Dispersion Formula Coefficients $n^2 = 1 + A/(\lambda^2 - B) + C\lambda^2/(\lambda^2 - D)$

Material	Temp (C)	Index	RMS error%	A	B	C	D
KDP	33.0	n_o	0.0356	2.140260×10^{-9}	-1.489486×10^{9}	1.209065	-1.489604×10^{-9}
		n_e	0.0107	4.503887×10^{-10}	$-2.879423 \times 10^{-10}$	1.121333	$-2.879296 \times 10^{-10}$
	24.8	n_o	0.190	1.724871×10^{-10}	$-1.288031 \times 10^{-11}$	1.221148	$-1.319929 \times 10^{-11}$
		n_e	0.0735	6.406553×10^{-11}	9.395038×10^{-11}	1.121184	3.414367×10^{-11}
KD*P	33.0	n_o	0.0248	1.087078×10^{-9}	$-7.256670 \times 10^{-10}$	1.215009	$-7.257061 \times 10^{-10}$
		n_e	0.00945	3.849747×10^{-10}	$-2.374996 \times 10^{-10}$	1.117103	$-2.374739 \times 10^{-10}$
ADP	33.0	n_o	0.0212	1.671714×10^{-9}	-1.085260×10^{-9}	1.251347	-1.085304×10^{-9}
		n_e	0.0208	8.937086×10^{-10}	$-6.214465 \times 10^{-10}$	1.141555	$-6.214699 \times 10^{-10}$
	24.8	n_o	0.164	1.572664×10^{-10}	1.510526×10^{-11}	1.265293	5.181578×10^{-12}
		n_e	0.0714	7.093846×10^{-11}	1.029798×10^{-10}	1.149624	3.790226×10^{-11}
AD*P	33.0	n_o	0.0288	1.312696×10^{-9}	$-8.562983 \times 10^{-10}$	1.248006	$-8.563000 \times 10^{-10}$
		n_e	0.0144	5.720224×10^{-10}	$-3.725013 \times 10^{-10}$	1.137827	$-3.725002 \times 10^{-10}$

TABLE VII

Values of the Coefficients for Determining the Temperature Change in Index of Refraction [6]

$\Delta n = (n^2 + an + b)c(298\text{-}T)$

		a	b	$c(K^{-1})$
KDP	n_o	0	−1.432	0.402×10^{-4}
	n_e	0	−1.105	0.221×10^{-4}
KD*P	n_o	0	−1.047	0.228×10^{-4}
	n_e	0	0	0.955×10^{-5}
ADP	n_o	−3.0297	2.3004	0.713×10^{-2}
	n_e	0	0	0.675×10^{-6}

TABLE VIII

Information about the Infrared Lattice Vibration Modes of KDP and Some of Its Isomorphs

Ref.	Technique	Temperature	Data	Spectrum	Material
[12]	IR refl.	25 °C & lower	reflection	400–10000 cm^{-1}	KDP
[13]	IR refl.	300 K	$\varepsilon''(a)$, $\varepsilon''(c)$	0–600	KDP
			$\varepsilon''(a)$, $\varepsilon''(c)$	70–330	KD*P
[14]	IR refl.	300 K & lower	$\varepsilon''(c)$	0–400	KDP
[15]	IR trans.	300 K & lower	$k(\|c)$	10–200	KDP
[16]	IR trans.	300 K & lower	absorption	250–4000	KDP, ADP
[17]	IR refl.	295 K & lower	$\varepsilon''(\|c)$, $\varepsilon''(\perp c)$	10–600	KDP, ADP
[18]	IR refl.	295 K & lower	$\varepsilon''(\|c)$	20–550	KD*P
[19]	IR refl.	290 K & lower	$\varepsilon'(a)$, $\varepsilon'(c)$	0–700	KDP
			$\varepsilon''(a)$	0–350	KDP
[20]	IR refl.	295 K & lower	$\varepsilon'(\|c)$, $\varepsilon''(\|c)$	0–350	KDP
			$\varepsilon'(\perp c)$, $\varepsilon''(\perp c)$	0–80	KDP
[21]	IR refl.	300 K & lower	$\varepsilon'(\|c)$, $\varepsilon''(\|c)$	10–210	KDP, ADP
			$\varepsilon'(\|a)$, $\varepsilon''(\|a)$		
[22]	IR refl.	300 K & lower	$\varepsilon'(\|c)$, $\varepsilon''(\|c)$	20–250	KDP

Sodium Fluoride (NaF)

I. OHLÍDAL and K. NAVRÁTIL
Department of Solid State Physics
Faculty of Science
Masaryk University Brno
Kotlářská 2
611 37 Brno, Czechoslovakia

The room-temperature values of the refractive index n and the extinction coefficient k tabulated here (see Table I and Fig. 1) were obtained from the following works: the 0.166 μm (7.56 eV) to 0.101 μm (12.4 eV) results are from the paper of Fabre *et al.* [1]; the 0.225 μm (5.5 eV) to 0.124 μm (10.0 eV) results are from the paper of Tomiki and Miyata [2]; the 2 μm (0.62 eV) to 0.25 μm (4.96 eV) values are from Navrátil and Ohlídal's measurements [3]; the 0.578 μm (2.15 eV) to 0.186 μm (6.7 eV) results are from the paper of Kublitzky [4]; the 1.1 μm (1.13 eV) to 0.238 μm (5.2 eV) values are presented by Harting [5]; the 24 μm (0.05 eV) to 0.546 μm (2.3 eV) data are from Hohls's measurements [6] and the 111.1 μm (90 cm^{-1}) to 21.1 μm (475 cm^{-1}) values were published by Pai *et al.* [7].

The values of n and k presented by Fabre *et al.* [1] were obtained by interpreting spectral dependences of the reflectance of NaF films corresponding to different thicknesses. These films were produced by vacuum evaporation using resistively heated sources. The substrates of the NaF films studied were formed by glass plates. In the formula for the reflectance, a roughness of the upper boundaries of the NaF films analyzed was handled in a certain way [1, 8], such that, in the spectral region mentioned, the influence of this roughness was eliminated in determining n and k for these films, at least in a first approximation. Absorption is caused by excitons in this region.

Tomiki and Miyata [2] determined the values of n and k characterizing sodium-fluoride plates by means of the values of the transmittance and the reflectance of these plates measured in the region $0.225\ \mu m \geq \lambda \geq 0.124\ \mu m$. In this region Tomiki and Miyata's values of n agree in a satisfactory way with those presented by Fabre *et al.* [1] for the NaF thin films (see Table I).

Copyright © 1991 by Academic Press.
All rights of reproduction in any form reserved.
ISBN 0-12-544422-2

However, in this region there are substantial differences between the values of k presented by Tomiki and Miyata and by Fabre *et al.* One can expect that the values of k determined by Tomiki and Miyata are more accurate than those determined by Fabre *et al.* The values of k characterizing the NaF film studied by Fabre *et al.* are apparently too great. These values are probably influenced by the light scattering caused by volume inhomogeneities not included in the formula for the reflectance of these films (for example, this scattering can be caused by microcrystals [1]). Moreover, the other structure defects can strongly affect the correctness of the data presented by Fabre *et al.* [1] (for example, some impurities occurring in the NaF films). These effects can evidently increase the values of k characterizing thin films.

In the region $2\,\mu m \geq \lambda \geq 0.25\,\mu m$, the values of the refractive index n were determined using the spectral dependences of the reflectance of the NaF films evaporated onto glass and single-crystal silicon substrates. In this region the NaF films are transparent, and therefore the thickness of these films was found by the Fizeau method, and the values of n were evaluated from the reflectance measured at the wavelengths of interest (the thickness of the NaF films was about 100 nm). The errors in n are ± 0.008 over the entire region mentioned. There is relatively good coincidence between the refractive index data of Fabre *et al.* [1] and Navrátil and Ohlídal [3]. (One can expect reasonable agreement of both sets of data after an extrapolation of the data of Fabre *et al.* [1] to longer wavelengths using a suitable dispersion formula; see Table I.) In Table I the value of n given by Pulker [9] for NaF films at the wavelength of $0.55\,\mu m$ is also listed. Taking into account the errors, we find that the values of n published by Pulker [9] agree very well with those determined by Navrátil and Ohlídal [3].

Kublitzky [4] measured the values of n characterizing sodium-fluoride prisms by the method of minimum deviation at selected wavelengths in the spectral region $0.578\,\mu m \geq \lambda \geq 0.186\,\mu m$. Harting [5] and Hohls [6] determined n by the same method in the regions $41\,\mu m \geq \lambda \geq 0.238\,\mu m$ and $10.9\,\mu m \geq \lambda \geq 0.8\,\mu m$, respectively. Moreover, in the region $19.7\,\mu m \geq \lambda \geq 8.8\,\mu m$, Hohls [6] evaluated the refractive-index data of NaF using interferometric methods based on determining positions of fringes of equal chromatic order for light reflected or transmitted by sodium-fluoride slabs. Furthermore, in the region $24\,\mu m \geq \lambda \geq 0.546\,\mu m$, Hohls determined the values of n and k for thinned plates of sodium fluoride by means of the values of the reflectance and the transmittance of these plates measured at selected wavelengths (the thickness of the thinnest plate was 0.024 mm). The thicknesses of the sodium-fluoride plates were determined independently [6].

Pai *et al.* [7] determined the spectral dependences of both n and k characterizing sodium-fluoride bulk samples using amplitude and phase-reflection measurements made by dispersive Fourier transform spectros-

copy in the region 111 μm $\geq \lambda \geq$ 21.2 μm. The errors of n and k determined in this way are dependent on wavelength. (The greatest and/or smallest errors in both n and k are equal to ± 0.56 and/or ± 0.005 at the wavelength of about 41 μm and/or 24 μm [7]). Spectral dependences of n and k in the vicinity of the maximum value of k at the wavelength $\lambda = 40.3$ μm are related to one-phonon absorption, corresponding to the TO phonon mode. The fine structure of the curve expressing the spectral dependence of n in the region 24–34 μm may be caused by multiple-phonon processes of absorption. However, a corresponding structure in k in this region is not observed (see Table I and Fig. 1). This discrepancy is probably caused by the fact that reflection techniques are not too sensitive to small changes of absorption. The structure in both the n and k curves in this region can be seen only when precision transmittance measurements of sufficiently thin NaF slabs are performed.

One can see that the values of n and k characterizing bulk NaF evaluated by the different authors at the same wavelengths agree very well (see Table I). This fact gives significant support for the correctness and reliability of the n and k values of bulk NaF presented here.

It should be also noted that the values of n describing the NaF thin films [3] in the region 2 μm $\geq \lambda \geq$ 0.25 μm are nearly identical with those characterizing bulk NaF [4–6]. This fact implies that the packing density p defined by $p = V_s/V$ (where V_s and V are the volume of the solid part of the film and the total volume of the film, respectively) is nearly equal to unity. This can be demonstrated if the value of p characterizing the NaF thin films studied [3] is calculated by means of the following formula for the mean refractive index of films with columnar structure [10–12]:

$$n = n_s p + n_o(1 - p), \tag{1}$$

where n, n_s, and n_o denote the mean refractive index, the columnar (bulk) refractive index of the film, and the refractive index of a substance filling the pores between columns. Assuming that $n_o = 1$, one obtains (using Eq. 1 and the values of n and n_s presented here) the value of $p = 0.98$. This means that the NaF films analyzed by Navrátil and Ohlídal [3] are formed by very close-packed columns [11, 13].

In conclusion, one can state that the refractive-index data summarized in this work represent the true values of n characterizing bulk NaF in the spectral regions under consideration (see Table I and Fig. 1). (In the region 0.124 μm $\geq \lambda \geq$ 0.101 μm, this conclusion is valid for the values of n determined by Fabre *et al.* [1], at least in a first approximation.) The same statement can be said for the extinction-index data, except for the region 0.124 μm $\geq \lambda \geq$ 0.101 μm. Namely, the values of k determined by Fabre *et al.* [1] in the region 0.166 μm $\geq \lambda \geq$ 0.101 μm can serve only as rough

information concerning the form of the spectral dependence of k of bulk NaF.

It should be noted that the refractive-index data corresponding to the region of transparency of NaF were also presented by Li [14].

REFERENCES

1. D. Fabre, J. Romand, and B. Vodar, *J. Phys. (Paris)* **25**, 55 (1964).
2. T. Tomiki and T. Miyata, *J. Phys. Soc. Japan* **27**, 658 (1969).
3. K. Navrátil and I. Ohlídal, unpublished results.
4. A. Kublitzky, *Ann. Phys.* **20**, 793 (1934).
5. H. Harting, *Sitzungsber. Deutsch. Akad. Wiss. Ber.* **4**, 1 (1948).
6. H. W. Hohls, *Ann. Phys.* **29**, 433 (1937).
7. K. F. Pai, T. J. Parker, N. E. Tornberg, R. P. Lowndes, and W. G. Chambers, *Infrared Physics* **18**, 199 (1978).
8. P. Bousquet, *J. Phys. (Paris)* **25**, 50 (1964).
9. H. K. Pulker, *Appl. Opt.* **18**, 1969 (1979).
10. K. Kinosita and M. Nishibori, *J. Vac. Sci. Technol.* **6**, 730 (1969).
11. M. Harris, H. A. Macleod, S. Ogura, E. Pelletier, and B. Vidal, *Thin Solid Films* **57**, 173 (1979).
12. S. Ogura, N. Sugawara, and R. Hiraga, *Thin Solid Films* **30**, 3 (1975).
13. I. Ohlídal and K. Navrátil, *Thin Solid Films* **74**, 51 (1980).
14. H. H. Li, *J. Phys. Chem. Ref. Data* **5**, 345 (1976).

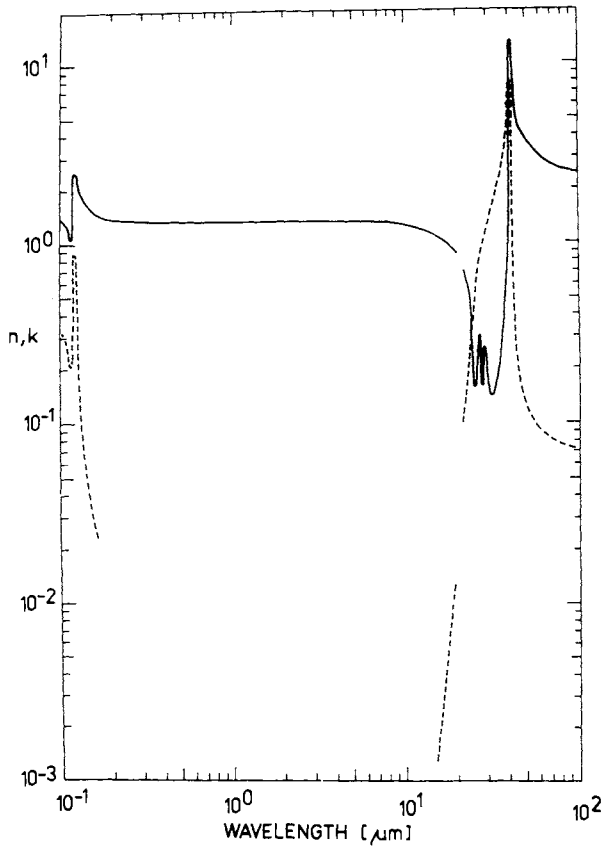

Fig. 1. Log–log plot of n (solid line) and k (dashed line) versus wavelength in micrometers for sodium fluoride.

TABLE I

Values of n and k for Sodium Fluoride from Various References[a]

eV	cm^{-1}	μm	n	k
12.28	99,010	0.101	1.360[1]	0.322[1]
12.16	98,039	0.102	1.359	0.321
12.04	97,087	0.103	1.358	0.316
11.92	96,154	0.104	1.358	0.307
11.81	95,238	0.105	1.351	0.297
11.70	94,340	0.106	1.333	0.280
11.59	93,458	0.107	1.320	0.254
11.48	92,593	0.108	1.289	0.227
11.38	91,743	0.109	1.247	0.213
11.27	90,909	0.110	1.204	0.205
11.17	90,090	0.111	1.128	0.204
11.07	89,286	0.112	1.093	0.209
10.97	88,496	0.113	1.138	0.272
10.88	87,719	0.114	1.269	0.342
10.78	86,957	0.115	1.567	0.578
10.69	86,207	0.116	1.822	0.784
10.60	85,470	0.117	2.167	0.900
10.51	84,746	0.118	2.404	0.833
10.42	84,034	0.119	2.511	0.629
10.33	83,333	0.120	2.493	0.491
10.25	82,645	0.121	2.360	0.382
10.16	81,967	0.122	2.230	0.308
10.08	81,300	0.123	2.122	0.236
10.0	80,653	0.1240	2.00[2] 2.044[1]	0.171[1]
9.919	80,000	0.125	1.958	0.140
9.9	79,846	0.1252	1.84[2]	9.9×10^{-4}[2]
9.84	79,365	0.126	1.911[1]	0.120[1]
9.8	79,040	0.1265	1.77[2]	1.0×10^{-4}[2]
9.763	78,740	0.127	1.866[1]	0.107[1]
9.687	78,125	0.128	1.822	0.096
9.611	77,519	0.129	1.800	0.087
9.6	77,427	0.1292	1.68[2]	2.9×10^{-5}[2]
9.538	76,923	0.130	1.756[1]	0.080[1]
9.465	76,336	0.131	1.736	0.076
9.4	75,814	0.1319	1.62[2]	2.6×10^{-5}[2]
9.393	75,758	0.132	1.717[1]	0.072[1]
9.322	75,188	0.133	1.700	0.069
9.253	74,627	0.134	1.683	0.064
9.2	74,201	0.1348	1.56[2]	2.4×10^{-5}[2]
9.184	74,074	0.135	1.667[1]	0.061[1]
9.117	73,529	0.136	1.652	0.058
9.050	72,993	0.137	1.638	0.056
9.0	72,588	0.1378	1.55[2]	2.2×10^{-5}[2]
8.985	72,464	0.138	1.625[1]	0.054[1]
8.920	71,942	0.139	1.613	0.052

(continued)

TABLE I (*Continued*)

Sodium Fluoride

eV	cm^{-1}	μm	n	k
8.856	71,429	0.140	1.601	0.049
8.793	70,922	0.141	1.591	0.048
8.732	70,423	0.142	1.580	0.047
8.670	69,930	0.143	1.571	0.045
8.610	69,444	0.144	1.562	0.044
8.551	68,966	0.145	1.554	0.042
8.5	68,555	0.1459	1.48[2]	1.2×10^{-5}[2]
8.492	68,493	0.146	1.546[1]	0.039[1]
8.435	68,027	0.147	1.539	0.038
8.378	67,568	0.148	1.532	0.036
8.321	67,114	0.149	1.526	0.035
8.266	66,667	0.150	1.520	0.033
8.211	66,225	0.151	1.514	0.032
8.157	65,790	0.152	1.509	0.031
8.104	65,360	0.153	1.505	0.030
8.051	64,935	0.154	1.500	0.028
8.0	64,516	0.155	1.497	0.027
			1.42[2]	2.7×10^{-6}[2]
7.948	64,103	0.156	1.493[1]	0.027[1]
7.897	63,694	0.157	1.490	0.027
7.847	63,291	0.158	1.487	0.026
7.798	62,893	0.159	1.848	0.026
7.749	62,500	0.160	1.482	0.023
7.701	62,112	0.161	1.479	0.023
7.654	61,728	0.162	1.477	0.023
7.607	61,350	0.163	1.476	0.023
7.560	60,976	0.164	1.474	0.023
7.5	60,490	0.1653	1.41[2]	
7.0	56,457	0.1771	1.40	
6.666	53,763	0.186	1.3930[4]	
6.5	52,424	0.1908	1.37[2]	
6.424	51,814	0.193	1.3850[4]	
6.231	50,251	0.199	1.3805	
6.108	49,261	0.203	1.3772	
6.019	48,544	0.206	1.3745	
6.0	48,392	0.2067	1.36[2]	
5.904	47,619	0.210	1.3718[4]	
5.794	46,729	0.214	1.3691	
5.662	45,662	0.219	1.3665	
5.5	44,359	0.2254	1.36[2]	
5.462	44,053	0.227	1.3630[4]	
5.367	43,290	0.231	1.3606	
5.232	42,194	0.237	1.3586	
5.209	42,017	0.238	1.35850[5]	
5.166	41,667	0.240	1.35792	
5.123	41,322	0.242	1.35717	

(continued)

TABLE I (*Continued*)

Sodium Fluoride

eV	cm^{-1}	μm	n	k
5.081	40,984	0.244	1.35644	
5.040	40,650	0.246	1.35574	
5.000	40,323	0.248	1.35506	
4.959	40,000	0.250	1.35440	
			1.342[3]	
4.920	39,683	0.252	1.35376[5]	
4.881	39,370	0.254	1.35314	
			1.3525[4]	
4.843	39,063	0.256	1.35254[5]	
4.824	38,929	0.257	1.3512[4]	
4.806	38,760	0.258	1.35197[5]	
4.769	38,462	0.260	1.35140	
			1.342[3]	
4.732	38,168	0.262	1.35084[5]	
4.697	37,879	0.264	1.35030	
4.688	37,736	0.265	1.3491[4]	
4.661	37,594	0.266	1.34987[5]	
4.626	37,313	0.268	1.34927	
4.592	37,037	0.270	1.34878	
			1.341[3]	
4.558	36,765	0.272	1.34830[5]	
4.525	36,496	0.274	1.34784	
4.509	36,363	0.275	1.3469[4]	
4.492	36,232	0.276	1.34738[5]	
4.460	35,971	0.278	1.34694	
4.428	35,714	0.280	1.34650	
			1.341[3]	
4.366	35,461	0.284	1.34567[5]	
4.335	34,965	0.286	1.34527	
4.305	34,722	0.288	1.34488	
4.275	34,483	0.290	1.34450	
			1.340[3]	
4.246	34,247	0.292	1.34413[5]	
4.218	34,014	0.294	1.34377	
4.189	33,784	0.296	1.34341	
4.161	33,357	0.298	1.34306	
4.133	33,333	0.300	1.34272	
			1.339[3]	
4.106	33,113	0.302	1.34293[5]	
			1.3417[4]	
4.079	32,895	0.304	1.34207[5]	
4.052	32,680	0.306	1.34175	
4.026	32,468	0.308	1.34144	
4.000	32,258	0.310	1.34114	
3.974	32,051	0.312	1.34084	
3.961	31,949	0.313	1.3401[4]	

(continued)

TABLE I (*Continued*)

Sodium Fluoride

eV	cm^{-1}	μm	n	k
3.949	31,847	0.314	1.34055[5]	
3.924	31,646	0.316	1.34027	
3.899	31,447	0.318	1.33999	
3.875	31,250	0.320	1.33972	
			1.337[3]	
3.851	31,056	0.322	1.33945[5]	
3.827	30,864	0.324	1.33919	
3.803	30,675	0.326	1.33894	
3.780	30,488	0.328	1.33869	
3.757	30,303	0.330	1.33844	
			1.336[3]	
3.735	30,121	0.332	1.33820[5]	
3.712	29,940	0.334	1.33779	
3.690	29,762	0.336	1.33774	
3.668	29,586	0.338	1.33751	
3.647	29,412	0.340	1.33729	
			1.335[3]	
3.625	29,240	0.342	1.33707[5]	
3.604	29,070	0.344	1.33686	
3.583	28,902	0.346	1.33665	
3.563	28,736	0.348	1.33644	
3.543	28,571	0.350	1.33624	
			1.334[3]	
3.522	28,409	0.352	1.33604[5]	
3.502	28,249	0.354	1.33585	
3.483	28,090	0.356	1.33566	
3.463	27,933	0.358	1.33547	
3.444	27,778	0.360	1.33529	
			1.334[3]	
3.425	27,624	0.362	1.33511[5]	
3.406	27,473	0.364	1.33493	
3.383	27,322	0.366	1.33476	
			1.3342[4]	
3.369	27,174	0.368	1.33459[5]	
3.351	27,028	0.370	1.33442	
			1.333[3]	
3.333	26,882	0.372	1.33426[5]	
3.315	26,738	0.374	1.33410	
3.298	26,596	0.376	1.33394	
3.280	26,455	0.378	1.33378	
3.263	26,316	0.380	1.33363	
			1.332[3]	
3.246	26,178	0.382	1.33348[5]	
3.229	26,042	0.384	1.33333	
3.212	25,907	0.386	1.33318	
3.196	25,773	0.388	1.33304	

(continued)

TABLE I (*Continued*)

Sodium Fluoride

eV	cm^{-1}	μm	n	k
3.179	25,641	0.390	1.33290 1.331[3]	
3.163	25,510	0.392	1.33276[5]	
3.147	25,381	0.394	1.33262	
3.131	25,253	0.396	1.33249	
3.115	25,126	0.398	1.33236	
3.100	25,000	0.400	1.33224 1.331[3]	
3.061	24,691	0.405	1.3314[4]	
3.024	24,390	0.41	1.33162[5]	
2.952	23,810	0.42	1.33105	
2.883	23,256	0.43	1.33053	
2.850	22,988	0.435	1.3300[4]	
2.818	22,727	0.44	1.33004[5]	
2.755	22,222	0.45	1.32959 1.327[3]	
2.695	21,739	0.46	1.32916[5]	
2.638	21,277	0.47	1.32876	
2.583	20,833	0.48	1.32839	
2.530	20,408	0.49	1.32805	
2.480	20,000	0.50	1.32772 1.325[3]	
2.431	19,608	0.51	1.32741[5]	
2.384	19,231	0.52	1.32712	
2.339	18,868	0.53	1.32684	
2.296	18,519	0.54	1.32658	
2.271	18,315	0.546	1.3260[4] 1.3258[6]	
2.254	18,182	0.55	1.32634[5] 1.321[3] 1.30[9]	
2.214	17,857	0.56	1.32611[5]	
2.175	17,544	0.57	1.32589	
2.145	17,301	0.578	1.3251[4]	
2.138	17,241	0.58	1.32567[5]	
2.101	16,949	0.59	1.32547	
2.067	16,667	0.60	1.32528 1.321[3]	
2.033	16,393	0.61	1.32510[5]	
2.000	16,129	0.62	1.32492	
1.968	15,873	0.63	1.32476	
1.937	15,625	0.64	1.32460	
1.908	15,385	0.65	1.32445	
1.879	15,152	0.66	1.32431	
1.851	14,925	0.67	1.32417	
1.823	14,706	0.68	1.32404	

(continued)

TABLE I (*Continued*)

Sodium Fluoride

eV	cm^{-1}	μm	n	k
1.797	14,493	0.69	1.32391	
1.771	14,286	0.70	1.32379	
			1.319[3]	
1.746	14,085	0.71	1.32367[5]	
1.722	13,889	0.72	1.32356	
1.698	13,699	0.73	1.32345	
1.676	13,514	0.74	1.32335	
1.653	13,333	0.75	1.32325	
1.631	13,158	0.76	1.32315	
1.610	12,987	0.77	1.32306	
1.590	12,821	0.78	1.32297	
1.569	12,658	0.79	1.32288	
1.550	12,500	0.80	1.32280	
			1.317[3]	
			1.3227[6]	
1.531	12,346	0.81	1.32272[5]	
1.512	12,195	0.82	1.32264	
1.494	12,048	0.83	1.32256	
1.476	11,905	0.84	1.32249	
1.459	11,765	0.85	1.32242	
1.442	11,628	0.86	1.32235	
1.425	11,494	0.87	1.32228	
1.409	11,364	0.88	1.32222	
1.393	11,236	0.89	1.32216	
1.378	11,111	0.90	1.32210	
			1.316[3]	
1.363	10,989	0.91	1.32204[5]	
1.348	10,870	0.92	1.32198	
1.333	10,753	0.93	1.32192	
1.319	10,638	0.94	1.32187	
1.305	10,526	0.95	1.32182	
1.292	10,417	0.96	1.32177	
1.278	10,309	0.97	1.32172	
1.265	10,204	0.98	1.32167	
1.252	10,101	0.99	1.32162	
1.240	10,000	1.00	1.32158	
			1.316[3]	
1.228	9,901	1.01	1.32154[5]	
1.216	9,804	1.02	1.32150	
1.204	9,709	1.03	1.32146	
1.192	9,615	1.04	1.32142	
1.181	9,524	1.05	1.32138	
1.170	9,434	1.06	1.32134	
1.159	9,346	1.07	1.32130	
1.148	9,259	1.08	1.32126	
1.138	9,174	1.09	1.32122	

(continued)

TABLE I (*Continued*)

Sodium Fluoride

eV	cm^{-1}	μm	n	k
1.127	9,091	1.10	1.32118	
0.9763	7,874	1.27	1.3202[6]	
0.8378	6,757	1.48	1.320	
0.8266	6,667	1.5	1.314[3]	
0.7424	5,988	1.67	1.318[6]	
0.6775	5,464	1.83	1.318	
0.6199	5,000	2.0	1.318	
			1.313[3]	
0.4769	3,846	2.6	1.316[6]	
0.4000	3,226	3.1	1.313	
0.3543	2,857	3.5	1.313	
0.3024	2,499	4.1	1.308	
0.2755	2,222	4.5	1.306	
0.2431	1,961	5.1	1.301	
0.2254	1,818	5.5	1.298	
0.2033	1,639	6.1	1.292	
0.1908	1,539	6.5	1.288	
0.1746	1,409	7.1	1.282	
0.1653	1,333	7.5	1.277	$5x10^{-6}$ [6]
0.1550	1,250	8.0	1.271	$1x10^{-5}$
0.1459	1,177	8.5	1.264	1.7
0.1378	1,111	9.0	1.262	2.3
0.1305	1,053	9.5	1.249	3.3
0.1240	1,000	10.0	1.241	4.3
0.1181	952.4	10.5	1.231	6.4
0.1127	909.1	11.0	1.214	$9.6x10^{-5}$
0.1078	869.6	11.5	1.20	$1.5x10^{-4}$
0.1033	833.3	12.0	1.19	2.1
0.09919	800.0	12.5	1.18	3.2
0.09538	769.2	13.0	1.17	4.7
0.09184	740.7	13.5	1.15	6.0
0.08856	714.3	14.0	1.14	7.9
0.08551	689.7	14.5	1.12	$9.9x10^{-4}$
0.08266	666.7	15.0	1.10	$1.3x10^{-3}$
0.08000	645.2	15.5	1.09	1.6
0.07749	625.0	16.0	1.07	2.2
0.07514	606.1	16.5	1.04	3.2
0.07293	588.2	17.0	1.02	4.7
0.07085	571.4	17.5	0.99	6.5
0.06888	555.6	18.0	0.97	8.7
0.06702	540.5	18.5	0.94	$8.7x10^{-3}$
0.06526	526.3	19.0	0.91	0.013
0.06358	512.8	19.5	0.87	0.019
0.06199	500.0	20.0	0.80	0.028
0.06048	487.8	20.5	0.80	0.036
0.05904	476.2	21.0	0.70	0.047

(continued)

TABLE I (*Continued*)

Sodium Fluoride

eV	cm^{-1}	μm	n	k
0.05889	475	21.05	0.691[7]	0.102[7]
0.05827	470	21.28	0.678	0.122
0.05765	465	21.51	0.646	0.116
			0.70[6]	0.06[6]
0.05703	460	21.74	0.616[7]	0.136[7]
0.05641	455	21.98	0.577	0.153
			0.60[6]	0.075[6]
0.05517	445	22.47	0.491[7]	0.139[7]
			0.50[6]	0.115[6]
0.05455	440	22.73	0.446[7]	0.147[7]
0.05393	435	22.99	0.43	0.201
			0.30[6]	0.140[6]
0.05331	430	23.26	0.405[7]	0.227[7]
0.05269	425	23.53	0.347	0.254
			0.30[6]	0.196[6]
0.05208	420	23.81	0.301[7]	0.296[7]
0.05166	416.7	24.0	0.20[6]	0.258[6]
0.05146	415	24.10	0.248[7]	0.339[7]
0.05084	410	24.39	0.215	0.400
0.05022	405	24.69	0.185	0.472
0.04960	400	25.00	0.158	0.545
0.04898	395	25.32	0.174	0.622
0.04836	390	25.64	0.198	0.679
0.04774	385	25.97	0.228	0.762
0.04712	380	26.32	0.266	0.825
0.04650	375	26.67	0.303	0.855
0.04588	370	27.03	0.282	0.864
0.04526	365	27.40	0.159	0.968
0.04464	360	27.78	0.26	1.00
0.04402	355	28.17	0.25	1.04
0.04340	350	28.57	0.24	1.05
0.04278	345	28.99	0.21	1.12
0.04216	340	29.41	0.18	1.20
0.04154	335	29.85	0.16	1.29
0.04092	330	30.30	0.16	1.39
0.04030	325	30.77	0.15	1.49
0.03968	320	31.25	0.14	1.57
0.03906	315	31.75	0.14	1.65
0.03844	310	32.26	0.14	1.77
0.00782	305	32.79	0.16	1.92
0.03720	300	33.33	0.17	2.04
0.03658	295	33.90	0.19	2.17
0.03596	290	34.48	0.21	2.33
0.03534	285	35.10	0.24	2.52
0.03472	280	35.71	0.27	2.71
0.03447	278	35.97	0.29	2.81

(continued)

TABLE I (*Continued*)

Sodium Fluoride

eV	cm^{-1}	μm	n	k
0.03422	276	36.23	0.31	2.93
0.03397	274	36.50	0.32	2.96
0.03372	272	36.77	0.36	3.02
0.03348	270	37.04	0.40	3.12
0.03323	268	37.31	0.43	3.29
0.03298	266	37.59	0.50	3.51
0.03273	264	37.88	0.56	3.69
0.03248	262	38.17	0.62	3.88
0.03224	260	38.46	0.64	3.99
0.03199	258	38.76	0.72	4.24
0.03174	256	39.06	0.81	4.52
0.03149	254	39.37	0.97	4.71
0.03125	252	39.68	1.50	5.26
0.03100	250	40.00	3.39	6.95
0.03075	248	40.32	8.69	7.90
0.03050	246	40.65	13.23	4.74
0.03025	244	40.98	13.22	1.31
0.03001	242	41.32	11.33	1.00
0.02976	240	41.68	9.91	0.69
0.02951	238	42.02	8.60	0.59
0.02926	236	42.37	7.26	0.45
0.02901	234	42.74	6.36	0.31
0.02877	232	43.10	5.63	0.25
0.02852	230	43.48	5.02	0.22
0.02827	228	43.86	4.78	0.21
0.02790	225	44.44	4.62	0.19
0.02728	220	45.46	4.22	0.16
0.02666	215	46.51	3.95	0.14
0.02604	210	47.62	3.86	0.13
0.02542	205	48.78	3.79	0.12
0.02480	200	50.00	3.67	0.12
0.02418	195	51.28	3.53	0.11
0.02356	190	52.63	3.39	0.11
0.02294	185	54.05	3.26	0.11
0.02232	180	55.56	3.13	0.09
0.02170	175	57.14	3.02	0.09
0.02108	170	58.82	2.95	0.09
0.02046	165	60.61	2.89	0.09
0.01984	160	62.50	2.84	0.09
0.01860	150	66.67	2.75	0.09
0.01736	140	71.43	2.68	0.09
0.01612	130	76.92	2.61	0.11
0.01488	120	83.33	2.56	0.10
0.01364	110	90.91	2.53	0.09
0.01240	100	100.0	2.50	0.07
0.01116	90	111.1	2.46	0.06

[a]The references from which the values were extracted are given in brackets.

Strontium Titanate ($SrTiO_3$)

FRANÇOIS GERVAIS
Centre de Recherches sur la Physique des Hautes Températures
Centre National de la Recherche Scientifique
45071 Orléans, France

Strontium titanate crystallizes in the cubic perovskite structure. Optical properties are therefore isotropic. Strontium titanate behaves like a ferroelectric material in the paraelectric phase. This property is referred to as *incipient ferroelectric*. The hypothetical Curie temperature would take place just below the absolute-zero temperature. As a result, the dielectric constant is strongly dependent on temperature and increases by a factor as large as 10 when the sample is cooled from room temperature to liquid-helium temperature [1]. Since the dielectric constant is the extrapolation down to zero frequency of the dielectric response, which itself is the square of the complex refractive index, optical constants also vary with temperature, but mainly in the far infrared. In addition, a phase transition related to alternate tilt of oxygen octahedra, which results in the formation of a tetragonal structure, takes place upon cooling below 105 K. The temperature dependence of data related to optical constants has been studied in various references; see Refs. [2, 3] for the UV range, Refs. [4, 5] in the visible and Refs. [6, 7] in the infrared.

Doping with Nb^{5+} or reduction of strontium titanate confers semiconducting properties to the material. Then the absorption related to free carriers may drastically modify the optical constants in the infrared depending on doping level [8]. Note also that heavily doped *n*-type strontium titanate has been reported to become a superconductor below 0.7 K [9].

All data compiled in Table I and Fig. 1 were obtained by measurements on undoped single crystals at room temperature. It should also be noted that in the infrared range, the reflectivity measurements performed on a sintered and polished strontium-titanate ceramic sample are practically indistinguishable from those performed on a single crystal [10], so that data compiled here, all obtained from studies on single crystals, are valid for ceramics also.

Reflectivity measurements in the ultraviolet energy range have been performed by various authors [11–14]. Among those studies, the one that

Copyright © 1991 by Academic Press.
All rights of reproduction in any form reserved.
ISBN 0-12-544422-2

extends over the widest energy range is the one by Baüerle *et al.* [13], thus allowing a Kramers–Kronig analysis of reflectivity data. Results of such an analysis are reported in Ref. [13] and reproduced in Table I. No n, k data were deduced from the experiments in other papers, but reflectance spectra shown in the three papers are in good agreement. Measurements of Ref. [13] were performed with the polarized synchrotron light from the storage ring DORIS at Hamburg coupled with a high-resolution monochromator.

The index of refraction in the transparent region is reported in Ref. [11] for wavelengths between 0.4 and 1.1 μm. They are in agreement with earlier measurements of Ref. [15], which were limited to a narrower wavelength range. Results of Ref. [11] determined by the angle-of-minimum-deviation method are given in Table I.

Early infrared reflectivity measurements of strontium titanate were reported by Barker and Tinkham [6]. The resolution of their measurement was not sufficient to detect a narrow infrared band observed three months later by Spitzer *et al.* [16] near 175 cm^{-1}, also with a prism monochromator. Spitzer *et al.* showed the failure of the usual dielectric function model,

$$\varepsilon = \varepsilon_\infty + \sum_j \Delta\varepsilon_j \frac{\Omega_{j\mathrm{TO}}^2}{\Omega_{j\mathrm{TO}}^2 - \omega^2 + i\gamma_{j\mathrm{TO}}\omega}, \tag{1}$$

expressed in terms of a sum over all the polar modes of the contributions of individual transverse optic modes, to fit the spectrum of strontium titanate. Later, Barker and Hopfield [17] introduced a mode-coupling formalism to fit the spectra of such highly polar incipient ferroelectric or ferroelectric crystals. An alternative model based on the factorized form of the dielectric response,

$$\varepsilon = \varepsilon_\infty \prod_j \frac{\Omega_{j\mathrm{LO}}^2 - \omega^2 + i\gamma_{j\mathrm{LO}}\omega}{\Omega_{j\mathrm{TO}}^2 - \omega^2 + i\gamma_{j\mathrm{TO}}\omega}, \tag{2}$$

was proposed subsequently [7] to palliate the weakness of the classical dielectric constant formula (Eq. 1) in such cases. The authors of this analysis also remeasured the infrared reflectivity spectrum with a modern Fourier-transform wide-band infrared spectrometer. Results for n and k obtained from a Kramers–Kronig analysis of data of Ref. [16] and from Ref. [7] by best fit of Eq. 2 to reflectivity data are compared in Table I. Both sets of data agree reasonably well.

REFERENCES

1. T. Mitsui and W. B. Westphal, *Phys. Rev.* **124**, 1354 (1961).
2. M. Capizzi and A. Frova, *Phys. Rev. Lett.* **25**, 1298 (1970).
3. K. W. Blazey, *Phys. Rev. Lett.* **27**, 146 (1971).
4. E. Schneider, P. J. Cressman, and R. L. Holman, *J. Appl. Phys.* **53**, 4054 (1982).
5. T. Toyoda and M. Yabe, *J. Phys. D: Appl. Phys.* **16**, L251 (1983).
6. A. S. Barker and M. Tinkham, *Phys. Rev.* **125**, 1527 (1962).
7. J. L. Servoin, Y. Luspin, and F. Gervais, *Phys. Rev. B* **22**, 5501 (1980).
8. W. S. Baer, *Phys. Rev.* **144**, 734 (1966).
9. F. F. Schooley, W. R. Hosler, and M. L. Cohen, *Phys. Rev. Letters* **12**, 474 (1964).
10. F. Gervais, B. Calès, and P. Odier, *Mat. Res. Bull.* **22**, 1629 (1987).
11. M. Cardona, *Phys. Rev.* **140**, A651 (1965).
12. M. I. Cohen and R. F. Blunt, *Phys. Rev.* **168**, 929 (1968).
13. D. Baüerle, W. Braun, V. Saile, G. Sprüssel, and E. E. Koch, *Z. Physik B* **29**, 179 (1978).
14. A. M. Mamedov, *Ferroelectrics* **45**, 55 (1982).
15. S. B. Levin, N. J. Field, F. M. Plock, and L. Merker, *J. Opt. Soc. Am.* **45**, 737 (1955).
16. W. G. Spitzer, R. C. Miller, D. A. Kleinman and L. E. Howarth, *Phys. Rev.* **126**, 1710 (1962).
17. A. S. Barker and J. J. Hopfield, *Phys. Rev.* **135**, A1732 (1964).

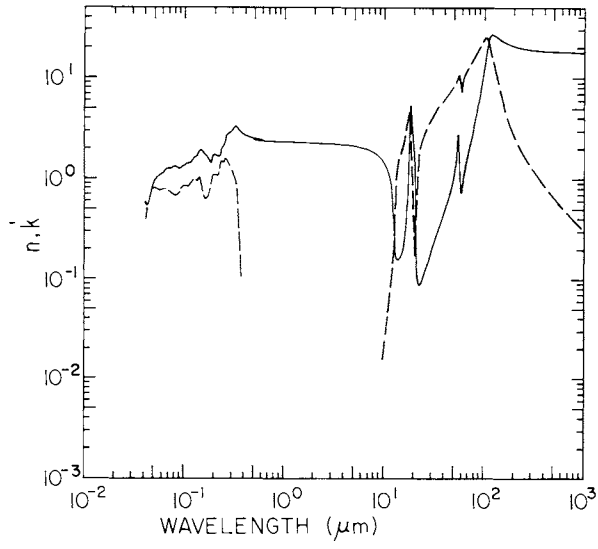

Fig. 1. Log–log plot of n (solid line) and k (dashed line) versus wavelength in micrometers for strontium titanate.

TABLE I

Values of n and k for Strontium Titanate Obtained from Various References[a]

eV	cm^{-1}	μm	n	k	n	k
30.0	241,935	0.04133	0.574[13]	0.383[13]		
29.9	241,129	0.04147	0.568	0.392		
29.8	240,323	0.04161	0.563	0.404		
29.7	239,516	0.04175	0.558	0.416		
29.6	238,710	0.04189	0.553	0.427		
29.5	237,903	0.04203	0.549	0.442		
29.4	237,097	0.04218	0.547	0.460		
29.3	236,290	0.04232	0.548	0.477		
29.2	235,484	0.04247	0.548	0.494		
29.1	234,677	0.04261	0.550	0.510		
29.0	233,871	0.04276	0.552	0.525		
28.9	233,065	0.04291	0.554	0.541		
28.8	232,258	0.04305	0.557	0.557		
28.7	231,452	0.04321	0.565	0.572		
28.6	230,645	0.04336	0.572	0.584		
28.5	229,839	0.04351	0.580	0.597		
28.4	229,032	0.04365	0.587	0.609		
28.3	228,226	0.04382	0.595	0.621		
28.2	227,419	0.04397	0.603	0.634		
28.1	226,613	0.04413	0.612	0.645		
28.0	225,806	0.04429	0.620	0.655		
27.9	225,000	0.04444	0.629	0.665		
27.8	224,194	0.04460	0.638	0.674		
27.7	223,387	0.04477	0.646	0.684		
27.6	222,581	0.04493	0.656	0.694		
27.5	221,774	0.04509	0.670	0.703		
27.4	220,968	0.04526	0.683	0.712		
27.3	220,161	0.04542	0.697	0.720		
27.2	219,355	0.04559	0.710	0.728		
27.1	218,548	0.04576	0.723	0.736		
27.0	217,742	0.04593	0.736	0.744		
26.9	216,935	0.04610	0.747	0.752		
26.8	216,129	0.04627	0.759	0.760		
26.7	215,323	0.04644	0.770	0.768		
26.6	214,516	0.04662	0.782	0.774		
26.5	213,710	0.04679	0.793	0.779		
26.4	212,903	0.04697	0.805	0.784		
26.3	212,097	0.04715	0.817	0.789		
26.2	211,290	0.04733	0.828	0.794		
26.1	210,484	0.04751	0.838	0.799		
26.0	209,677	0.04769	0.845	0.802		
25.9	208,871	0.04788	0.853	0.804		
25.8	208,065	0.04806	0.860	0.805		
25.7	207,258	0.04825	0.868	0.807		
25.6	206,452	0.04844	0.875	0.809		
25.5	205,645	0.04863	0.883	0.811		
25.4	204,839	0.04882	0.890	0.809		
25.3	204,032	0.04901	0.900	0.806		
25.2	203,226	0.04921	0.911	0.803		
25.1	202,419	0.04940	0.921	0.800		

TABLE I (*Continued*)

Strontium Titanate

eV	cm^{-1}	μm	n	k	n	k
25.0	201,613	0.04960	0.932	0.797		
24.9	200,806	0.04980	0.942	0.794		
24.8	200,000	0.05000	0.944	0.792		
24.7	199,194	0.05020	0.944	0.791		
24.6	198,387	0.05041	0.943	0.789		
24.5	197,581	0.05061	0.943	0.788		
24.4	196,774	0.05082	0.949	0.789		
24.3	195,968	0.05103	0.956	0.794		
24.2	195,161	0.05124	0.963	0.800		
24.1	194,355	0.05145	0.969	0.806		
24.0	193,548	0.05167	0.984	0.810		
23.9	192,742	0.05188	0.998	0.808		
23.8	191,935	0.05210	1.013	0.806		
23.7	191,129	0.05232	1.022	0.803		
23.6	190,323	0.05254	1.026	0.801		
23.5	189,516	0.05277	1.029	0.798		
23.4	188,710	0.05299	1.033	0.796		
23.3	187,903	0.05322	1.037	0.793		
23.2	187,097	0.05345	1.041	0.791		
23.1	186,290	0.05368	1.046	0.788		
23.0	185,484	0.05391	1.051	0.786		
22.9	184,677	0.05415	1.056	0.783		
22.8	183,871	0.05439	1.061	0.781		
22.7	183,065	0.05463	1.064	0.779		
22.6	182,258	0.05487	1.067	0.777		
22.5	181,452	0.05511	1.070	0.775		
22.4	180,645	0.05536	1.073	0.774		
22.3	179,839	0.05561	1.076	0.773		
22.2	179,032	0.05586	1.079	0.771		
22.1	178,226	0.05611	1.082	0.770		
22.0	177,419	0.05636	1.085	0.769		
21.9	176,613	0.05662	1.088	0.767		
21.8	175,806	0.05688	1.091	0.766		
21.7	175,000	0.05714	1.095	0.766		
21.6	174,194	0.05741	1.098	0.767		
21.5	173,387	0.05767	1.101	0.768		
21.4	172,581	0.05794	1.104	0.769		
21.3	171,774	0.05822	1.107	0.770		
21.2	170,968	0.05849	1.111	0.772		
21.1	170,161	0.05877	1.114	0.773		
21.0	169,355	0.05905	1.117	0.773		
20.9	168,548	0.05933	1.122	0.774		
20.8	167,742	0.05962	1.127	0.774		
20.7	166,935	0.05990	1.132	0.775		
20.6	166,129	0.06019	1.137	0.775		
20.5	165,323	0.06049	1.142	0.776		
20.4	164,516	0.06078	1.148	0.776		
20.3	163,710	0.06108	1.153	0.777		
20.2	162,903	0.06139	1.158	0.777		
20.1	162,097	0.06169	1.163	0.778		

TABLE I (*Continued*)

Strontium Titanate

eV	cm^{-1}	μm	n	k	n	k
20.0	161,290	0.06200	1.169	0.778		
19.9	160,484	0.06231	1.175	0.779		
19.8	159,677	0.06263	1.180	0.779		
19.7	158,871	0.06294	1.186	0.781		
19.6	158,065	0.06327	1.192	0.784		
19.5	157,258	0.06359	1.198	0.787		
19.4	156,452	0.06392	1.203	0.790		
19.3	155,645	0.06425	1.209	0.793		
19.2	154,839	0.06458	1.215	0.793		
19.1	154,032	0.06492	1.220	0.792		
19.0	153,226	0.06526	1.226	0.790		
18.9	152,419	0.06561	1.231	0.787		
18.8	151,613	0.06596	1.237	0.783		
18.7	150,806	0.06631	1.243	0.780		
18.6	150,000	0.06667	1.248	0.776		
18.5	149,194	0.06703	1.250	0.769		
18.4	148,387	0.06739	1.252	0.763		
18.3	147,581	0.06776	1.254	0.756		
18.2	146,774	0.06813	1.256	0.750		
18.1	145,968	0.06851	1.258	0.746		
18.0	145,161	0.06889	1.260	0.742		
17.9	144,355	0.06927	1.262	0.737		
17.8	143,548	0.06966	1.264	0.733		
17.7	142,742	0.07006	1.266	0.729		
17.6	141,935	0.07045	1.268	0.724		
17.5	141,129	0.07086	1.270	0.720		
17.4	140,323	0.07126	1.272	0.718		
17.3	139,516	0.07168	1.274	0.715		
17.2	138,710	0.07209	1.275	0.712		
17.1	137,903	0.07251	1.277	0.709		
17.0	137,097	0.07294	1.279	0.707		
16.9	136,290	0.07337	1.280	0.706		
16.8	135,484	0.07381	1.280	0.705		
16.7	134,677	0.07425	1.281	0.704		
16.6	133,871	0.07470	1.281	0.704		
16.5	133,065	0.07515	1.282	0.704		
16.4	132,258	0.07561	1.288	0.705		
16.3	131,452	0.07607	1.297	0.707		
16.2	130,645	0.07654	1.306	0.709		
16.1	129,839	0.07702	1.316	0.710		
16.0	129,032	0.07750	1.320	0.705		
15.9	128,226	0.07799	1.321	0.699		
15.8	127,419	0.07848	1.322	0.692		
15.7	126,613	0.07898	1.324	0.686		
15.6	125,806	0.07949	1.322	0.679		
15.5	125,000	0.08000	1.317	0.672		
15.4	124,194	0.08052	1.312	0.665		
15.3	123,387	0.08105	1.306	0.657		
15.2	122,581	0.08158	1.297	0.652		
15.1	121,774	0.08212	1.288	0.651		

TABLE I (*Continued*)

Strontium Titanate

eV	cm^{-1}	μm	n	k	n	k
15.0	120,968	0.08267	1.279	0.652		
14.9	120,161	0.08322	1.270	0.658		
14.8	119,355	0.08378	1.261	0.663		
14.7	118,548	0.08434	1.254	0.669		
14.6	117,742	0.08493	1.246	0.674		
14.5	116,935	0.08552	1.238	0.680		
14.4	116,129	0.08611	1.230	0.689		
14.3	115,323	0.08671	1.228	0.702		
14.2	114,516	0.08732	1.227	0.716		
14.1	113,710	0.08794	1.226	0.729		
14.0	112,903	0.08857	1.229	0.741		
13.9	112,097	0.08921	1.234	0.751		
13.8	111,290	0.08986	1.241	0.762		
13.7	110,484	0.09051	1.250	0.773		
13.6	109,677	0.09118	1.259	0.783		
13.5	108,871	0.09185	1.268	0.792		
13.4	108,065	0.09254	1.276	0.801		
13.3	107,258	0.09323	1.287	0.810		
13.2	106,452	0.09394	1.300	0.816		
13.1	105,645	0.09466	1.312	0.820		
13.0	104,839	0.09538	1.325	0.825		
12.9	104,032	0.09612	1.333	0.829		
12.8	103,226	0.09687	1.341	0.833		
12.7	102,419	0.09764	1.349	0.835		
12.6	101,613	0.09841	1.352	0.836		
12.5	100,806	0.09920	1.354	0.838		
12.4	100,000	0.1000	1.356	0.840		
12.3	99,194	0.1008	1.362	0.843		
12.2	98,387	0.1016	1.368	0.846		
12.1	97,581	0.1025	1.374	0.850		
12.0	96,774	0.1033	1.380	0.853		
11.9	95,968	0.1042	1.386	0.855		
11.8	95,161	0.1051	1.402	0.858		
11.7	94,355	0.1060	1.418	0.860		
11.6	93,548	0.1069	1.432	0.859		
11.5	92,742	0.1078	1.445	0.854		
11.4	91,935	0.1088	1.447	0.849		
11.3	91,129	0.1097	1.428	0.845		
11.2	90,323	0.1107	1.422	0.842		
11.1	89,516	0.1117	1.425	0.849		
11.0	88,710	0.1127	1.428	0.858		
10.9	87,903	0.1138	1.430	0.867		
10.8	87,097	0.1148	1.431	0.875		
10.7	86,290	0.1159	1.426	0.885		
10.6	85,484	0.1170	1.417	0.899		
10.5	84,677	0.1181	1.428	0.916		
10.4	83,871	0.1192	1.458	0.933		
10.3	83,065	0.1204	1.480	0.948		
10.2	82,258	0.1216	1.502	0.961		
10.1	81,452	0.1228	1.531	0.974		

TABLE I (*Continued*)

Strontium Titanate

eV	cm^{-1}	μm	n	k	n	k
10.0	80,645	0.1240	1.563	0.989		
9.9	79,839	0.1253	1.594	1.004		
9.8	79,032	0.1265	1.623	1.009		
9.7	78,226	0.1278	1.653	1.008		
9.6	77,419	0.1292	1.667	1.003		
9.5	76,613	0.1305	1.659	0.997		
9.4	75,806	0.1319	1.643	0.984		
9.3	75,000	0.1333	1.659	0.968		
9.2	74,194	0.1348	1.680	0.963		
9.1	73,387	0.1363	1.700	0.977		
9.0	72,581	0.1378	1.734	1.000		
8.9	71,774	0.1393	1.779	1.024		
8.8	70,968	0.1409	1.828	1.015		
8.7	70,161	0.1425	1.877	1.000		
8.6	69,355	0.1442	1.926	0.977		
8.5	68,548	0.1459	1.951	0.928		
8.4	67,742	0.1476	1.942	0.857		
8.3	66,935	0.1494	1.920	0.788		
8.2	66,129	0.1512	1.893	0.727		
8.1	65,323	0.1531	1.865	0.679		
8.0	64,516	0.1550	1.838	0.672		
7.9	63,710	0.1570	1.808	0.666		
7.8	62,903	0.1590	1.777	0.659		
7.7	62,097	0.1610	1.746	0.645		
7.6	61,290	0.1632	1.715	0.631		
7.5	60,484	0.1653	1.689	0.627		
7.4	59,677	0.1676	1.663	0.643		
7.3	58,871	0.1699	1.637	0.660		
7.2	58,065	0.1722	1.612	0.674		
7.1	57,258	0.1746	1.587	0.688		
7.0	56,452	0.1771	1.563	0.703		
6.9	55,645	0.1797	1.495	0.724		
6.8	54,839	0.1824	1.452	0.838		
6.7	54,032	0.1851	1.438	0.878		
6.6	53,226	0.1879	1.558	0.940		
6.5	52,419	0.1908	1.624	1.099		
6.4	51,613	0.1937	1.688	1.106		
6.3	50,806	0.1968	1.721	1.105		
6.2	50,000	0.2000	1.753	1.101		
6.1	49,194	0.2033	1.768	1.095		
6.0	48,387	0.2067	1.770	1.089		
5.9	47,581	0.2102	1.760	1.086		
5.8	46,774	0.2138	1.745	1.086		
5.7	45,968	0.2175	1.722	1.089		
5.6	45,161	0.2214	1.696	1.130		
5.5	44,355	0.2255	1.664	1.269		
5.4	43,548	0.2296	1.719	1.438		
5.3	42,742	0.2340	1.905	1.482		
5.2	41,935	0.2385	2.025	1.484		
5.1	41,129	0.2431	2.085	1.474		

TABLE I (*Continued*)

Strontium Titanate

eV	cm^{-1}	μm	n	k	n	k
5.0	40,323	0.2480	2.139	1.474		
4.9	39,516	0.2531	2.218	1.552		
4.8	38,710	0.2583	2.329	1.582		
4.7	37,903	0.2638	2.482	1.570		
4.6	37,097	0.2696	2.731	1.517		
4.5	36,290	0.2756	2.785	1.436		
4.4	35,484	0.2818	2.840	1.361		
4.3	34,677	0.2884	2.909	1.277		
4.2	33,871	0.2952	2.962	1.190		
4.1	33,065	0.3024	3.026	1.145		
4.0	32,258	0.3100	3.158	1.100		
3.9	31,452	0.3179	3.250	1.045		
3.8	30,645	0.3263	3.297	0.980		
3.7	29,839	0.3351	3.320	0.854		
3.6	29,032	0.3444	3.275	0.463		
3.5	28,226	0.3543	3.180	0.245		
3.4	27,419	0.3647	2.974	0.164		
3.3	26,613	0.3758	2.812	0.112		
3.2	25,806	0.3875	2.773	0.083		
3.1	25,000	0.4000	2.745	0.058		
3.0	24,194	0.4133	2.727	0.048	2.630[11]	
2.9	23,387	0.4276	2.712	0.038	2.587	
2.8	22,581	0.4429	2.669	0.028	2.558	
2.7	21,774	0.4593	2.610	0.019	2.528	
2.6	20,968	0.4769	2.581	0.015	2.504	
2.5	20,161	0.4960	2.552	0.011	2.481	
2.4	19,355	0.5167	2.524		2.462	
2.3	18,548	0.5391	2.495		2.443	
2.2	17,742	0.5636	2.475		2.426	
2.1	16,935	0.5905	2.456		2.410	
2.0	16,129	0.6200	2.437		2.394	
1.9	15,323	0.6526			2.382	
1.8	14,516	0.6889			2.369	
1.7	13,710	0.7294			2.358	
1.6	12,903	0.7750			2.348	
1.5	12,097	0.8267			2.339	
1.4	11,290	0.8857			2.330	
1.3	10,484	0.9538			2.321	
1.2	9,677	1.033			2.312	
1.1	8,871	1.127			2.305	
1.0	8,065	1.240			2.300	
0.9	7,258	1.378			2.291	
0.8928	7,200	1.389	2.268[7]			
0.8804	7,100	1.408	2.268			
0.8680	7,000	1.429	2.267			
0.8556	6,900	1.449	2.267			
0.8432	6,800	1.471	2.267			
0.8308	6,700	1.493	2.266			
0.8184	6,600	1.515	2.266			
0.8060	6,500	1.538	2.265			

TABLE I (*Continued*)

Strontium Titanate

eV	cm^{-1}	μm	n	k	n	k
0.7936	6,400	1.563	2.265			
0.7812	6,300	1.587	2.264			
0.7688	6,200	1.613	2.264			
0.7564	6,100	1.639	2.263			
0.7440	6,000	1.667	2.263			
0.7316	5,900	1.695	2.262			
0.7192	5,800	1.724	2.261			
0.7068	5,700	1.754	2.261			
0.6944	5,600	1.786	2.260			
0.6820	5,500	1.818	2.259			
0.6696	5,400	1.852	2.259			
0.6572	5,300	1.887	2.258			
0.6448	5,200	1.923	2.257			
0.6324	5,100	1.961	2.256			
0.6200	5,000	2.000	2.255			
0.6076	4,900	2.041	2.254			
0.5952	4,800	2.083	2.253			
0.5828	4,700	2.128	2.251			
0.5704	4,600	2.174	2.250			
0.5580	4,500	2.222	2.249			
0.5456	4,400	2.273	2.247			
0.5332	4,300	2.326	2.246			
0.5208	4,200	2.381	2.244			
0.5084	4,100	2.439	2.242			
0.4960	4,000	2.500	2.240			
0.4836	3,900	2.564	2.238			
0.4712	3,800	2.632	2.236			
0.4588	3,700	2.703	2.233			
0.4464	3,600	2.778	2.231			
0.4340	3,500	2.857	2.228			
0.4216	3,400	2.941	2.225			
0.4092	3,300	3.030	2.221			
0.3968	3,200	3.125	2.217			
0.3844	3,100	3.226	2.213			
0.3720	3,000	3.333	2.209			
0.3596	2,900	3.448	2.203			
0.3472	2,800	3.571	2.198			
0.3348	2,700	3.704	2.191			
0.3224	2,600	3.846	2.184			
0.3100	2,500	4.000	2.176			
0.2976	2,400	4.167	2.167			
0.2852	2,300	4.348	2.156			
0.2728	2,200	4.545	2.144			
0.2604	2,100	4.762	2.130			
0.2480	2,000	5.000	2.114			
0.2356	1,900	5.263	2.095			
0.2232	1,800	5.556	2.072			
0.2108	1,700	5.882	2.045			
0.1984	1,600	6.250	2.012			
0.1860	1,500	6.667	1.971			

TABLE I (*Continued*)

Strontium Titanate

eV	cm^{-1}	μm	n	k	n	k
0.1736	1,400	7.143	1.919			
0.1612	1,300	7.692	1.853			
0.1488	1,200	8.333	1.764			
0.1364	1,100	9.091	1.640			
0.1240	1,000	10.00	1.455	0.016[7]	1.419[17]	
0.1227	990	10.10	1.432	0.018	1.395	
0.1215	980	10.20	1.407	0.019	1.371	0.016[17]
0.1202	970	10.31	1.380	0.021	1.346	0.025
0.1190	960	10.42	1.353	0.023	1.327	0.033
0.1178	950	10.53	1.323	0.026	1.308	0.040
0.1166	940	10.64	1.292	0.028	1.289	0.044
0.1153	930	10.75	1.259	0.031	1.268	0.039
0.1141	920	10.97	1.223	0.035	1.241	0.043
0.1128	910	10.99	1.185	0.039	1.212	0.046
0.1116	900	11.11	1.144	0.043	1.183	0.030
0.1104	890	11.24	1.100	0.048	1.142	0.036
0.1091	880	11.36	1.052	0.054	1.080	0.050
0.1079	870	11.49	1.000	0.061	1.031	0.060
0.1066	860	11.63	0.942	0.069	0.982	0.068
0.1054	850	11.76	0.878	0.080	0.929	0.080
0.1042	840	11.90	0.805	0.093	0.880	0.089
0.1029	830	12.05	0.722	0.112	0.830	0.071
0.1017	820	12.20	0.626	0.139	0.681	0.053
0.1004	810	12.35	0.512	0.182	0.594	0.117
0.09920	800	12.50	0.383	0.263	0.522	0.105
0.09796	790	12.66	0.274	0.396	0.299	0.239
0.09672	780	12.82	0.215	0.545	0.217	0.397
0.09548	770	12.99	0.186	0.681	0.175	0.538
0.09424	760	13.16	0.170	0.805	0.139	0.689
0.09300	750	13.33	0.161	0.921	0.134	0.821
0.09176	740	13.51	0.157	1.030	0.134	0.941
0.09052	730	13.70	0.155	1.137	0.140	1.051
0.08928	720	13.89	0.155	1.241	0.146	1.155
0.08804	710	14.08	0.157	1.345	0.148	1.254
0.08680	700	14.29	0.161	1.449	0.146	1.357
0.08556	690	14.49	0.166	1.555	0.146	1.468
0.08432	680	14.71	0.172	1.664	0.150	1.580
0.08308	670	14.93	0.181	1.776	0.154	1.704
0.08184	660	15.15	0.191	1.894	0.172	1.833
0.08060	650	15.38	0.205	2.020	0.193	1.967
0.07936	640	15.63	0.222	2.154	0.221	2.106
0.07812	630	15.87	0.243	2.301	0.253	2.255
0.07688	620	16.13	0.272	2.465	0.291	2.422
0.07564	610	16.39	0.310	2.653	0.338	2.615
0.07440	600	16.67	0.364	2.873	0.405	2.849
0.07316	590	16.95	0.446	3.143	0.524	3.153
0.07192	580	17.24	0.580	3.490	0.758	3.528
0.07068	570	17.54	0.831	3.966	1.200	3.943
0.06944	560	17.86	1.405	4.653	1.938	4.328
0.06820	550	18.18	3.083	5.334	3.254	4.236

TABLE I (*Continued*)

Strontium Titanate

eV	cm^{-1}	μm	n	k	n	k
0.06696	540	18.52	5.333	3.250	4.663	2.963
0.06572	530	18.87	4.424	1.169	4.202	1.288
0.06448	520	19.23	3.407	0.538	3.427	0.552
0.06324	510	19.61	2.669	0.307	2.724	0.427
0.06200	500	20.00	2.069	0.208	2.110	0.342
0.06076	490	20.41	1.505	0.173	1.630	0.207
0.05952	480	20.83	0.847	0.217	1.079	0.224
0.05828	470	21.28	0.185	0.820	0.267	0.444
0.05704	460	21.74	0.108	1.342	0.094	1.127
0.05580	450	22.22	0.090	1.690	0.087	1.510
0.05456	440	22.73	0.087	1.965	0.086	1.781
0.05332	430	23.26	0.089	2.200	0.085	2.020
0.05208	420	23.81	0.094	2.412	0.089	2.231
0.05084	410	24.39	0.101	2.610	0.099	2.431
0.04960	400	25.00	0.109	2.799	0.113	2.615
0.04836	390	25.64	0.119	2.983	0.126	2.791
0.04712	380	26.32	0.130	3.165	0.136	2.961
0.04588	370	27.03	0.141	3.347	0.143	3.134
0.04464	360	27.78	0.154	3.532	0.150	3.314
0.04340	350	28.57	0.168	3.720	0.166	3.501
0.04216	340	29.41	0.184	3.914	0.186	3.686
0.04092	330	30.30	0.201	4.115	0.202	3.870
0.03968	320	31.25	0.219	4.325	0.214	4.067
0.03844	310	32.26	0.240	4.545	0.226	4.278
0.03720	300	33.33	0.264	4.777	0.247	4.503
0.03596	290	34.48	0.291	5.024	0.270	4.738
0.03472	280	35.71	0.321	5.287	0.297	4.988
0.03348	270	37.04	0.356	5.569	0.326	5.256
0.03224	260	38.46	0.397	5.875	0.359	5.545
0.03100	250	40.00	0.445	6.208	0.397	5.859
0.02976	240	41.67	0.503	6.574	0.440	6.204
0.02852	230	43.48	0.574	6.980	0.486	6.585
0.02728	220	45.45	0.665	7.438	0.534	7.028
0.02604	210	47.62	0.787	7.964	0.597	7.565
0.02480	200	50.00	0.972	8.595	0.728	8.248
0.02356	190	52.63	1.323	9.416	1.071	9.210
0.02232	180	55.56	2.750	10.69	3.220	10.99
0.02108	170	58.82	0.945	7.341	1.557	6.799
0.01984	160	62.50	0.930	10.22	0.985	9.612
0.01860	150	66.67	1.363	11.71	1.265	11.08
0.01736	140	71.43	1.896	13.22	1.941	12.81
0.01612	130	76.92	2.665	15.02	2.908	14.10
0.01488	120	83.33	3.934	17.32	4.429	16.25
0.01364	110	90.91	6.323	20.29	5.706	18.14
0.01240	100	100.0	11.44	23.59	10.51	21.94
0.01116	90	111.1	21.09	22.91	18.89	18.57
0.009920	80	125.0	26.59	13.93	20.28	13.67
0.008680	70	142.9	24.90	7.233	21.34	9.699
0.007440	60	166.7	22.47	4.133	20.44	7.169
0.006200	50	200.0	20.65	2.576	20.38	5.650

TABLE I (*Continued*)

Strontium Titanate

eV	cm^{-1}	μm	n	k	n	k
0.004960	40	250.0	19.38	1.675	20.26	3.933
0.003720	30	333.3	18.52	1.087	19.90	2.320
0.002480	20	500.0	17.97	0.658	19.23	0.998
0.001240	10	1000	17.65	0.311	18.46	0.185

a References are indicated in brackets.

Thorium Fluoride (ThF_4)

I. OHLÍDAL and K. NAVRÁTIL
Department of Solid State Physics
Faculty of Science
Masaryk University
Kotlářská 2
611 37 Brno, Czechoslovakia

Thorium fluoride possesses desirable optical properties including a broad range of transparency from the UV (0.2 μm) to the mid-IR (12 μm) regions, and low dispersion and low refractive index in the visible. Therefore, this material is widely used to form low-refractive-index thin films in non-absorbing multilayer systems employed for interference devices. For example, ThF_4 thin films together with ZnS thin films are utilized for producing interference coatings which can be used as broad-band laser mirrors in the visible [1].

ThF_4 is usually evaporated using resistively heated sources. Such ThF_4 thin films are soft, chemically very stable, and exhibit medium tensile stress [2]. The structure of the ThF_4 films was examined only by Heitmann and Ritter [3] using X-ray analysis. They found that these films were amorphous. However, X-ray analysis is less sensitive for the structure analysis of polycrystalline solids and thin films than methods of the electron analysis [4]. By means of X-ray analysis it is difficult, if not impossible, to reveal microcrystals whose linear dimensions are smaller than about 5 nm [4]. Thus, the results of X-ray analysis obtained by Heitmann and Ritter [3] show that the studied ThF_4 films can be amorphous or polycrystalline with very small microcrystals (smaller than about 5 nm in the linear dimensions). These films have optical properties, which are dependent on a number of effects:

(1) the columnar structure, and hence, the distribution of voids or low-density regions in the film

(2) the orientation of these columns with respect to the substrate normal and their dimensions

(3) environmental stability connected with capillary condensation taking place into the open voids (sometimes called pores)

Copyright © 1991 by Academic Press.
All rights of reproduction in any form reserved.
ISBN 0-12-544422-2

(4) the form of the columns and their variation with thickness, implying inhomogeneity of the film
(5) stress in the film, and hence, birefrigence and inhomogeneity
(6) surface roughness of the upper boundary of the film.

The most important of these effects is the columnar structure. The other effects are implied in principle by this structure (except the existence of the stress in the film). Thus, to describe in a true way, the optical properties of the ThF_4 and similar films, one has to express the optical constants of these films with formulas representing their columnar structure in a satisfactory manner. So far, this task has been solved primarily by using suitable formulas for the optical constants of the columnar films based on effective-medium theory [5–8]. For example, within this theory the following formula is often employed for evaluating the mean refractive index $\bar{n}$ of the film considered:

$$p\frac{n_s^2-\bar{n}^2}{n_s^2+2\bar{n}^2}+(1-p)\frac{n_v^2-\bar{n}^2}{n_v^2+2\bar{n}^2}=0, \tag{1}$$

where n_s and n_v denote the refractive indices of the columns and voids, respectively. p is the packing density defined by $p=V_s/V$, where V_s and V are the volume of the solid part of the film (columns) and the total volume of the film (including the voids), respectively. Equation 1, known as the Bruggeman [9] formula, is valid if the voids are filled with one nonabsorbing substance and the columns are formed by another nonabsorbing material. Of course, this equation can be generalized for an arbitrary number of materials forming the columns and the voids in the film [10] (for example, when the voids are partially filled with water and air).

So far, the values of the refractive index and the extinction coefficient of the ThF_4 thin films have been measured in the region $11\ \mu m \geq \lambda \geq 0.22\ \mu m$, that is, in the region of transparency of these films. The values of both optical constants of the ThF_4 films were primarily determined using an interpretation of experimental data (ellipsometric parameters, reflectance, and transmittance) based on single layers. The interpretation was performed within the framework of a model consisting of the single layer with ideally smooth and flat boundaries placed on a substrate. Furthermore, it was assumed that both the film and the substrate were formed by homogeneous and isotropic materials from the optical point of view. In this way either the mean optical constants of the films or the optical constants close to them were determined. These optical constants denoted by the symbols n (refractive index) and k (extinction coefficient) evaluated by Heitmann and Ritter [3] for the region 0.8–0.22 μm are collected in Table I and plotted in Fig. 1. Heitmann and Ritter analyzed the ThF_4 single layers

deposited by vacuum evaporation (molybdenum or platinum boat) onto quartz-glass substrates by using the values of reflectance of this system corresponding to the wavelengths λ at which the optical thicknesses of these films were equal to $m\lambda/4$ ($m = 1,3,5, \ldots$).

Table I shows that, in the visible, the refractive index of the ThF_4 thin films is roughly constant and lies in the range 1.52–1.53 (the error in the refractive indices was less than $\pm 1\%$). The values of n characterizing vacuum-evaporated ThF_4 single layers determined by Heisen [11] are outlined in Table I as well (Heisen evaluated the values of n for wedge-shaped ThF_4 films using an interferometric method for $\lambda = 0.546$ and 0.4358 μm). There is relatively good agreement between the values of n presented by Heitmann and Ritter [3] and Heisen [11] even when there were certain differences in preparation of the ThF_4 films. The values of k corresponding to the near-UV, the visible, and the near-IR regions can be considered to be zero for the majority of applications of ThF_4 films in optics. However, if multilayer systems with a great number of films are produced (for example, the mirrors for lasers with more than 30 films), the optical losses resulting from absorption and scattering must be considered inside of every film of this system [12]. Very small absorption losses in ThF_4 films can be measured. The method of Ahrens *et al.* [13] (based on measuring the temperature change caused by absorption of light by the film using a thin, gold-film resistance thermometer) was used to determine the values of the absorption coefficient for the wavelengths of 0.515 and 1.06 μm [12]. The values of the absorption coefficient determined by Pulker yield the following values of the extinction coefficient: $k = 3.3 \times 10^{-5}$ and 1.3×10^{-6} for $\lambda = 0.515$ and 1.06 μm, respectively [12].

Mouchart *et al.* [14] determined the values of both the refractive index and the extinction coefficient characterizing ThF_4 films in the mid-IR region $11\ \mu m \geq \lambda \geq 4\ \mu m$ by means of the spectral dependences of the transmittance (the ThF_4 films were deposited onto germanium substrates using electron bombardment in vacuum). They employed the method of Manifacier *et al.* [15] based on the use of the envelopes of the interference maxima and minima in the spectral dependences of the transmittance, since the ThF_4 films under investigation were relatively thick (2.2–4.9 μm). These authors also determined the coefficients of the following dispersion relations expressing the spectral dependences of n and k in the region considered:

$$n(\lambda) = A_0 + \frac{A_1}{\lambda} + \frac{A_2}{\lambda^2}, \tag{2}$$

$$k(\lambda) = B_0 + B_1\lambda + B_2\lambda^2, \tag{3}$$

The coefficients are as follows [14]: $A_0 = 1.118$, $A_1 = 2.46\ \mu m$, $A_2 = -$

2.98 μm^2, $B_0 = 0.00189$, $B_1 = -0.00015$ μm^{-1}, and $B_2 = 0.00001$ μm^{-2}. For the region 12 μm$\geq\lambda\geq$4 μm, the values of n and k calculated by Eqs. 2 and 3 are summarized in Table I and Fig. 1. It is interesting to note that the values of n for ThF_4 films placed on ZnS substrates as determined ellipsometrically at $\lambda = 10.6$ μm by Pedinoff *et al.* [16] agree very well with those found by Mouchart *et al.* [14] at the same wavelength, if the errors of n are taken into account (Pedinoff *et al.* determined the values of n with the accuracy of ±1.5%).

Kim and Vedam [17] determined the spectral dependence of the refractive index of ThF_4 films deposited on vitreous silica substrates using spectroscopic ellipsometry in the region 0.9–0.25 μm. These authors expressed the dispersion of the refractive index n by the formula

$$n^2(\lambda) = A + \frac{B\lambda^2}{\lambda^2 - \lambda_0^2}, \tag{4}$$

which represents a first approximation of the well-known Sellmeier dispersion equation,

$$n^2(\lambda) - 1 = a + \sum_{j=1} \frac{b_j\lambda^2}{\lambda^2 - \lambda_j^2}. \tag{5}$$

a, b_j, λ_j, A, B, and λ_o are constants (λ_o is the wavelength of the Sellmeier oscillator).

They used a three-layer model for interpreting the spectral dependences of the ellipsometric parameters [17]. Within the framework of this model, the columnar structure was assumed for both the upper and the lower layers (see Eq. 1), and therefore, eight parameters were needed. (That is, the values of A, B, and λ_o, the thicknesses characterizing all three layers, and the packing density of the upper and the lower layers must be evaluated.) From the values of A, B, and λ_o found, that is, $A = 1.665 \pm 0.005$, $B = 0.715 \pm 0.004$, and $\lambda_o = (0.149 \pm 0.001)$ μm [17], the values of n characterizing the ThF_4 films were calculated using Eq. 4 in the region 2 μm$\geq\lambda\geq$0.22 μm (see Table I and Fig. 1). The errors of these values are about ±0.005. The refractive index n determined in this way represents the columnar refractive index n_s of ThF_4 films.

Thus, the values of n found by Kim and Vedam [17] can be considered as those for the bulk refractive index of thorium fluoride. This statement is supported by the fact that the values of n determined using the results of Kim and Vedam are greater than those presented by Heitmann and Ritter at all wavelengths (see Table I). It should be noted that a spectral

dependence of the refractive index of a bulk sample of this material has not been measured yet. This means that the values of n presented by Kim and Vedam represent the best ones characterizing thorium fluoride in the region $2\ \mu m \geq \lambda \geq 0.22\ \mu m$ at present. However, the three-layer model of the ThF_4 films used by Kim and Vedam can be improved, so that even better values of n for ThF_4 can be obtained by reanalyzing the ellipsometric data of the ThF_4 films.

Dielectric [18] and metallic [19] thin films prepared by the ion-assisted deposition (IAD) process exhibit improved optical and mechanical properties; the environmental stability of these coatings is also improved. These improvements are caused by increasing the packing density of the films. The effect of IAD on the optical properties of the ThF_4 films deposited using a resistively heated source on unheated fused silica and sapphire substrates was examined also [20]. Bombardment of the growing ThF_4 films with 300 eV Ar ions was carried out during deposition. When the growing ThF_4 films were bombarded with an ion current density of $70\ \mu A/cm^2$, the value of n (the mean refractive index) was 1.56, compared with 1.53 for the unbombarded samples at the wavelength of $0.6\ \mu m$ [20]. The bombarded ThF_4 films exhibited high resistivity against the influence of moisture, which was demonstrated by very low absorption of these films in the water band near $3\ \mu m$. This fact implies that the packing density is close to unity. The refractive index value of 1.56 at $\lambda = 0.6\ \mu m$ agrees very well with that determined by Kim and Vedam [17], which also supports the conclusion concerning the good quality of Kim and Vedam's data.

Table I shows that the refractive-index values presented by Mouchart *et al.* [14] for the region $11\ \mu m \geq \lambda \geq 4\ \mu m$ do not correspond to those of Heitmann and Ritter [3] and Kim and Vedam [17]. Namely, the values of n found by Mouchart *et al.* at $\lambda = 4\ \mu m$ and the wavelengths close to that are relatively high compared with the refractive-index values published for the wavelengths of the visible in Refs. [3] and [17]. Moreover, dispersion of n presented by Mouchart *et al.* is rather pronounced. (An extrapolation of the data of Mouchart *et al.* to the visible and near-UV region gives values of n substantially higher than those presented in Refs. [3] and [17]). These discrepancies may be explained by the fact that the films analyzed by Mouchart *et al.* [14] were probably formed with a mixture of thorium fluoride and thorium oxide. For example, ThO_2 films are characterized by considerably higher values of the refractive index than the ThF_4 films in the visible and near-UV region: the values of n characterizing the ThO_2 films lie in the interval 1.75–1.9 from the visible to the near UV region [21]. Other, more reliable data of ThF_4 films are not available in the mid-IR region at present. Values of n and k of ThF_4 films for the far-IR region have not been presented yet, since spectrophotometric or Raman measurements have not been performed in this region (that is, optical-phonon frequencies of ThF_4 are not known).

In conclusion, it should be noted that thorium and its compounds are radioactive. In general, no risk of external radiation damage is present. However, incorporation of thorium compounds into the human organism does present danger. Recommended maximum permissible limits for thorium compounds in the body are outlined in Ref. [3].

REFERENCES

1. J. Ebert, H. Panhorst, H. Küster and H. Welling, *Appl. Opt.* **18**, 818 (1979).
2. H. K. Pulker, *Appl. Opt.* **18**, 1969 (1979).
3. W. Heitmann and E. Ritter, *Appl. Opt.* **7**, 307 (1968).
4. C. S. Barrett, "Structure of Metals," McGraw-Hill, New York, (1952).
5. D. E. Aspens, *Thin Solid Films* **89**, 249 (1982).
6. K. L. Chopra, S. K. Sharma, and V. N. Yadava, *Thin Solid Films* **20**, 209 (1974).
7. M. Harris, H. A. Macleod, S. Ogura, E. Pelletier, and B. Vidal, *Thin Solid Films* **57**, 173 (1979).
8. I. Ohlídal and K. Navrátil, *Thin Solid Films* **74**, 51 (1980).
9. D. A. G. Bruggeman, *Ann. Phys. (Leipzig)* **24**, 636 (1935).
10. D. E. Aspnes, J. B. Theeten, and F. Hottier, *Phys. Rev. B* **20**, 3292 (1979).
11. A. Heisen, *Optik* **18**, 59 (1961).
12. H. K. Pulker, *Thin Solid Films* **34**, 343 (1976).
13. H. Ahrens, H. Welling, and W. Scheel, *Appl. Phys.* **1**, 69 (1973).
14. J. Mouchart, G. Lagier, and B. Pointu, *Appl. Opt.* **24**, 1808 (1985).
15. J. C. Manifacier, J. Gasiot, and J. P. Fillard, *J. Phys. E* **9**, 1002 (1976).
16. M. E. Pedinoff, M. Braunstein, and O. M. Stafsudd, *Appl. Opt.* **16**, 1849 (1977).
17. S. Y. Kim and K. Vedam, *Thin Solid Films* **166**, 325 (1988).
18. P. J. Martin, H. A. Macleod, R. P. Netherfield, C. G. Pacey, and W. G. Sainty, *Appl. Opt.* **22**, 178 (1983).
19. G. A. Al-Jumaily, J. J. McNally, J. R. McNeil, and W. C. Herrmann, Jr., *J. Vac. Sci. Technol. A* **3**, 651 (1985).
20. G. A. Al-Jumaily, L. A. Yazlovitsky, T. A. Monney, and A. Smajikiewicz, *Appl. Opt.* **26**, 3752 (1987).
21. P. H. Lissberger, *Rep. Prog. Phys.* **39**, 197 (1970).

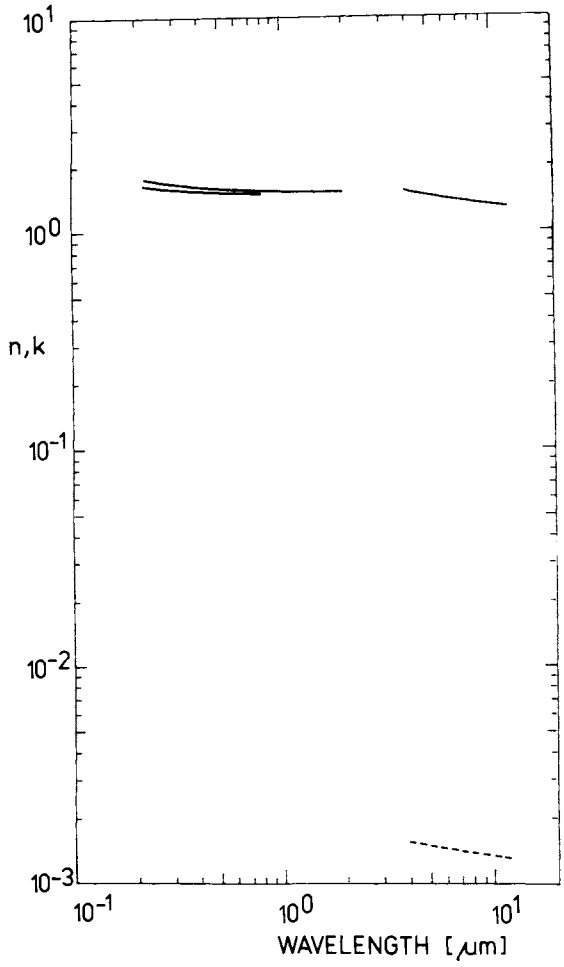

Fig. 1. Log–log plot of n (solid line) and k (dashed line) versus wavelength in micrometers for thorium fluoride.

TABLE I

Values of n and k for deposited Thorium Fluoride from Various References[a]

eV	cm^{-1}	μm	n	k	n	k
5.635	45,455	0.22	1.613[3]		1.728[17]	
5.391	43,478	0.23	1.599		1.702	
5.166	41,667	0.24	1.587		1.682	
4.959	40,000	0.25	1.577		1.664	
4.769	38,462	0.26	1.569		1.652	
4.592	37,037	0.27	1.563		1.642	
4.428	35,714	0.28	1.557		1.632	
4.275	34,483	0.29	1.553		1.624	
4.133	33,333	0.30	1.549		1.617	
4.000	32,258	0.31	1.545		1.611	
3.875	31,250	0.32	1.542		1.606	
3.757	30,303	0.33	1.540		1.601	
3.646	29,412	0.34	1.538		1.597	
3.543	28,571	0.35	1.536		1.593	
3.444	27,778	0.36	1.534		1.590	
3.351	27,027	0.37	1.532		1.587	
3.263	26,316	0.38	1.531		1.584	
3.179	25,641	0.39	1.530		1.582	
3.100	25,000	0.40	1.529		1.579	
3.024	24,390	0.41	1.528		1.577	
2.952	23,809	0.42	1.527		1.575	
2.883	23,256	0.43	1.526		1.574	
2.845	22,946	0.4358	1.533[11]			
2.818	22,727	0.44	1.526[3]		1.572	
2.755	22,222	0.45	1.525		1.571	

(continued)

TABLE I (*Continued*)

Thorium Fluoride

eV	cm^{-1}	μm	n	k	n	k
2.695	21,739	0.46	1.524		1.569	
2.638	21,277	0.47	1.524		1.568	
2.583	20,833	0.48	1.523		1.567	
2.530	20,408	0.49	1.523		1.566	
2.480	20,000	0.50	1.523		1.565	
2.431	19,608	0.51	1.522		1.564	
2.407	19,418	0.515		3.3×10^{-6}[12]		
2.384	19,231	0.52	1.522[3]		1.563	
2.296	18,519	0.54	1.521		1.561	
2.271	18,312	0.546	1.521[11]			
2.214	17,857	0.56	1.521[3]		1.560	
2.138	17,241	0.58	1.520		1.559	
2.066	16,667	0.60	1.520		1.558	
					1.560[21]	
2.000	16,129	0.62	1.520		1.557[17]	
1.937	15,625	0.64	1.519		1.556	
1.879	15,152	0.66	1.519		1.555	
1.771	14,286	0.70	1.519		1.554	
1.676	13,513	0.74	1.518		1.553	
1.590	12,821	0.78	1.518		1.552	
1.550	12,500	0.80	1.518		1.551	
1.378	11,111	0.90			1.550	
1.240	10,000	1.00			1.548	
1.170	9,434	1.06		1.3×10^{-6}[12]	1.548	
1.033	8,333	1.2			1.547	
0.8266	6,667	1.5			1.546	
0.6199	5,000	2.0			1.544	

(continued)

TABLE I (*Continued*)

Thorium Fluoride

eV	cm^{-1}	μm	n	k	n	k
0.3100	2,500	4.0	1.55[14]	$1.5x10^{-3}$[14]		
0.3024	2,439	4.1	1.54	1.4		
0.2883	2,326	4.3	1.53	1.4		
0.2755	2,222	4.5	1.52	1.4		
0.2638	2,128	4.7	1.51	1.4		
0.2480	2,000	5.0	1.49	1.4		
0.2384	1,923	5.2	1.48	1.4		
0.2296	1,852	5.4	1.47	1.4		
0.2214	1,786	5.6	1.46	1.4		
0.2138	1,724	5.8	1.45	1.4		
0.2067	1,667	6.0	1.45	1.4		
0.2001	1,613	6.2	1.44	1.3		
0.1937	1,563	6.4	1.43	1.3		
0.1879	1,515	6.6	1.42	1.3		
0.1771	1,429	7.0	1.41	1.3		
0.1653	1,333	7.5	1.39	1.3		
0.1550	1,250	8.0	1.38	1.3		
0.1459	1,177	8.5	1.37	1.3		
0.1378	1,111	9.0	1.35	1.4		
0.1292	1,042	9.6	1.34	1.4		
0.1240	1,000	10.0	1.33	1.4		
0.1170	943.4	10.6	1.32 1.35[16]	$1.4x10^{-3}$		
0.1127	909.1	11.0	1.32[14]	$1.4x10^{-3}$		
0.1078	869.6	11.5	1.31	1.4		
0.1033	833.3	12.0	1.30	$1.4x10^{-3}$		

[a]The references from which the values were extracted are given in brackets.

Water (H_2O)

MARVIN R. QUERRY and DAVID M. WIELICZKA
Department of Physics
University of Missouri-Kansas City
Kansas City, Missouri
and
DAVID J. SEGELSTEIN
Bell Communications Research
Red Bank, New Jersey

One could easily prepare a list of several hundred primary references to the scientific literature on spectral measurements of the optical properties of water and compilations of water's refractive index and absorption coefficient. In this critique, however, we only highlight such activities during the past century. Readers interested in more detail should consult bibliographies in the references cited here. To those who contributed to the scientific literature on the optical properties of water and are not explicitly acknowledged here, we apologize. We conclude the critique with two of our previously unpublished compilations of n and k for water.

In 1892, Rubens [1] presented refractometer measurements of the refractive index $n(\lambda)$ of water to a long-wavelength limit of 1.256 μm. These measurements of $n(\lambda)$ were extended to a new long-wavelength limit of 2.327 μm by Seegert's [2] doctoral work in 1908. In 1908 and 1909, Rubens and Ladenberg [3] published their measurements of the reflectance and absorption spectra, and determined what was later discovered to be incorrect dispersion $n(\lambda)$ of water out to a wavelength of 18 μm. Others who measured the infrared reflectance spectrum of water in 1906, 1915, 1918, and 1931, respectively, were Pfund [4], Gehrts [5], Brieger [6], and Weingeroff [7]. General reviews of the infrared absorption spectrum of water were published in 1917, 1929, 1930, and 1934 by Fowle [8], Lecompte [9], Schaefer and Matossi [10], and Dawson and Hulburt [11], respectively. Compilations of the optical properties of water were published in 1929 by Becquerel and Rossignol [12], and in 1940 by Dorsey [13].

One can gain a historical and technical perspective from Dorsey's thorough compilation of water's optical properties. He presented data, gleaned from about 320 references, that spanned the spectral range from low frequency (dielectric constants) to the X-ray region (absorption coefficients). For example, Dorsey's Table 137 provides values for $n(\lambda)$ in the

Copyright © 1991 by Academic Press.
All rights of reproduction in any form reserved.
ISBN 0-12-544422-2

wavelength range 0.154 nm–11 mm. For the visible and ultraviolet regions, Dorsey reviewed several dispersion relations for the refractive index of water at temperatures in the range of 0–80 °C. Of particular interest to Dorsey were the data of Martens [14], Duclaux and Jeantet [15], Chéneveau [16], and Tilton and Taylor [17].

Among those who also published works prior to 1941 on the optical properties of water were Paschen [18], 1894; Coblentz [19], 1905, 1906, and 1911; Goldhammer [20], 1913; Collins [21], 1922 and 1939; Plyler [22], 1924; Dreisch [23], 1924; Hulburt [24], 1928; Cartwright [25], 1935; Williams *et al.* [26], 1936; and Fox and Martin [27], 1940.

Centeno's [28] tabulation in 1941 of n and k for water, and the compilation previously published by Dorsey in 1940, were benchmarks for the future of such activity and were the standard of such compilations for nearly three decades. Centeno gleaned data from 59 articles, including all those previously noted here, to determine n and k for water in the 0.1151–18 μm and 1–18 μm wavelength regions, respectively. Centeno's values of $n(\lambda)$ in the ultraviolet, visible, and near infrared were from Refs. [13], [16], and [17]. Centeno corrected the infrared absorption spectrum of a 90% water and 10% glycerin mixture previously measured in 1909 by Rubens and Ladenburg [3], to obtain the absorption and extinction coefficients $\alpha(\lambda) = 4\pi k(\lambda)/\lambda$ and $k(\lambda)$ of water. Possessing corrected values for $k(\lambda)$ and the normal-incidence infrared reflectance spectrum $R(\lambda)$ [3] of water, he determined $n(\lambda)$ by use of

$$R = \frac{[(n-1)^2 + k^2]}{[(n+1)^2 + k^2]}.$$

The scientific literature on the optical properties of water fell silent through the 1940s. During the 1950s the following articles on the absorption and reflectance of water appeared in the literature: studying absorption were Curcio and Petty [29], 1951; Blout and Lenormant [30], 1953; Plyler and Aquista [31], 1954; Adams and Katz [32], Ceccaldi *et al.* [33], and Potts and Wright [34], 1956; Hyman *et al.* [35], 1957; Bocharov and Krutikov [36], and Waggener [37], 1958; and Goulden [38], 1959; Kislovskii [39], 1959, studied reflectance.

Kislovskii [39], who concluded his paper with a dateline of Christmas Day, 1958, measured the reflectance spectrum and determined the first fairly reliable values of n and k of water in the 2.1–3.4 μm wavelength range. He used semiempirical conceptual models to compute n in the 182.9 nm–1000 Km wavelength region. He also used the conceptual models to calculate k in the 2.0 μm–1000 Km wavelength region. Kislovskii's determinations of k, the measurements of $\alpha(\lambda)$ by Curcio and Petty [29] in the 0.7–2.5 μm wavelength region, and similar measurements of $\alpha(\lambda)$ by

Plyler and Aquista [31] in the 2–42 μm wavelength region, provided the standard values of k for the next six to nine years. A systematic error, however, was later discovered in the work of Plyler and Aquista. The error was corrected in part by measurement and publication of "Absolute Absorption Coefficients of Liquid Water at 2.95 μm, 4.7 μm, and 6.1 μm" by Plyler and Griff [40] in 1965.

The advent of the space age in 1957, the development of space technology in the 1960s and 1970s, and the consequent new opportunities for remote sensing of planetary atmospheres and surfaces created renewed interest in the optical properties of natural mineral materials. On Earth, water is a ubiquitous substance, and it was thus essential that some members of the scientific community again devote their interest to the optical properties of water. For the past three decades, an accurate compilation of $N = n + ik$ of liquid water and ice over the broadest possible range of frequency ν or wavelength λ has thus been a topic of considerable interest, particularly to those engaged in the endeavor and to those who used and continue to use the data in a host of varying theoretical constructs.

During the 1960s the following articles on the optical properties of water appeared in the literature: McDonald [41], 1960; Ackermann [42], 1961; Stanevich and Yaroslavskii [43], 1961; Bayly *et al.* [44], 1963; Kondratyev *et al.* [45], 1964; Plyler and Griff [40], 1965; Thompson [46], 1965; Bagdade and Tinkham [47], 1965; Draegert *et al.* [48], 1966; and Kondratyev [49], 1969, all studied absorption. Studying reflectance were McAlister [50], 1964; Pontier and Dechambenoy [51], 1965–1966; Painter *et al.* [52], 1968–1969; Querry *et al.* [53], 1969; and Zolotarev *et al.* [54], 1969.

Pontier and Dechambenoy [51] measured reflectance spectra of water for angles of incidence of 0 degrees (1965), and 50 and 60 degrees (1966), in the 1–38 μm and 1–28 μm regions, respectively. They also measured the absorption spectrum $\alpha(\lambda)$ in the 1–40 μm wavelength region (1966). The reflectance and absorption spectra, and the appropriate Fresnel equations, were used to determine n and k throughout the 1–40 μm wavelength region.

In 1968, Irvine and Pollack [55] published a more extensive tabulation of n and k for water and ice in the 0.2–200 μm wavelength region. Although they seemed to have overlooked the work by Pontier and Dechambenoy [51], Irvine and Pollack considered data from references [21, 23, 25, 27–48] to prepare their tabulation of the optical constants of water.

In 1969 and 1970, Zolotarev *et al.* [54, 56] presented a tabulation of $N(\lambda)$ for the $1\text{–}1 \times 10^6$ μm wavelength region. In the 1970 paper [56], they used four methods to determine n and k: measurements of absorption, reflectance, internal reflectance spectra, and Kramers–Kronig (K–K) analysis. Sources of spectral values of k used in the K–K analysis to determine n were the following:

Wavelength Region	Reference
$0.2 \leq \lambda \leq 1.0\ \mu m$	Lane and Saxton [57], 1952; Collie *et al.* [58], 1948; Gelebart and Johannin-Gillen [59], 1948;
$1.0 \leq \lambda \leq 2.0\ \mu m$	Kontratyev *et al.* [45], 1964;
$2.0 \leq \lambda \leq 40\ \mu m$	Zolotarev *et al.* [54, 56], 1969–70;
$40 \leq \lambda \leq 250\ \mu m$	Draegert *et al.* [48], 1966;
$250 \leq \lambda \leq 1000\ \mu m$	Stanevich and Yaroslavskii [43], 1961;
$l \geqslant 1000$ mm	Chamberlain *et al.* [60], 1966.

In the early 1970s several measurements were made of the optical properties of water [61–69]. In 1973, Hale and Querry [70] published a tabulation of $N(l)$ for water in the 200 nm–200 mm wavelength region based on a compilation and K–K analysis of $k(\lambda)$ to obtain $n(\lambda)$. Their compilation of $k(\lambda)$ was based on data selected from 58 references spanning 81 years of the scientific literature. Then, in 1975, Downing and Williams [71] presented a tabulation of $N(\nu)$ for the 10–5,000 cm^{-1} wave-number region, which also was based on a compilation and K–K analysis of $k(\nu)$ to determine $n(\nu)$.

In 1981, Segelstein [72] completed an extensive compilation of $k(\nu)$ for water throughout the 10^{-6} to $10^{8}\,cm^{-1}$ wave-number region. Beginning with the composite $k(\lambda)$ spectrum previously published by Hale and Querry, Segelstein incorporated data for $k(\nu)$ into the compilation for the frequency ranges and corresponding references listed below:

Wave Number Range	Reference
$0 \leq \nu \leq 5\ cm^{-1}$	Cole and Cole [73]
$5 \leq \nu \leq 500\ cm^{-1}$	Afsar and Hasted [74]
$500 \leq \nu \leq 1000\ cm^{-1}$	Robertson and Williams [62]
$3{,}300 \leq \nu \leq 4000\ cm^{-1}$	Robertson and Williams [62]
$14{,}400 \leq \nu \leq 24{,}400\ cm^{-1}$	Tam and Patel [75]
$24{,}400 \leq \nu \leq 50{,}000\ cm^{-1}$	Lenoble and Saint-Guilly [76], and Kopelevich [77]
$50{,}000 \leq \nu \leq 65{,}000\ cm^{-1}$	Painter *et al.* [78]
$65{,}000 \leq \nu \leq 200{,}000\ cm^{-1}$	Heller *et al.* [68]
$2 \times 10^{5} \leq n \leq 4.3 \times 10^{6}\ cm^{-1}$	$k(n) = An^{1.23}$ [72]
$n > 4.3 \times 10^{6}\ cm^{-1}$	$k(n) = An^{1.63}$ [72].

Segelstein used an electron sum rule to test the validity of the $k(\nu)$ spectrum. Kramers–Kronig analysis of $k(\nu)$ then provided $n(\nu)$ throughout the 10^{-3} to $10^{6}\,cm^{-1}$ wave-number region. More specific details of Segelstein's investigation of $N(\nu)$ for water will be presented elsewhere [79], but his tabulation of n and k for water is presented in Table I.

Graphical presentations of the n and k data in Table I appear in Fig. 1. The values of k in Table I are from work by several investigators, but are believed to represent n and k for water in a temperature range of 25°–35 °C.

The relatively large static dielectric constant $\varepsilon = n^2$ is due to the strong polar nature and polarizability of water. Also, the famous rotational absorption line at 1.26 cm wavelength, which hampered the development of radar in the early 1940s, occurs in water vapor and not in liquid water and is therefore not present in the data in Table I.

More recently Wieliczka *et al.* [80] used a wedge-shaped cell, which was an improved functional design of similar cells previously described by Robertson and Williams [62] and Tyler *et al.* [81], to determine accurate values of the Lambert absorption coefficient $\alpha(\nu)$ of water in the 500–8000 cm^{-1} region. Kramers–Kronig analysis of the $k(\nu)$ spectrum determined values for $n(\nu)$. Their values of n and k for water are presented in Table II. The sample was purified, deionized water. The temperature of the water was approximately 30 °C.

REFERENCES

1. H. Rubens, *Ann. Physik* **45**, 253 (1892).
2. B. Seegert, Dissertation, Berlin Universität (1908).
3. H. Rubens and E. Ladenberg, *Verh. Deut. Phys. Ges.* **10**, 227 (1908); *Verh. Deut. Phys. Ges.* **11**, 16 (1909).
4. A. H. Pfund, *Astrophys. J.* **24**, 19 (1906).
5. F. Gehrts, *Ann. Physik* **47**, 1059 (1915).
6. K. Brieger, *Ann. Physik* **57**, 287 (1918).
7. M. Weingeroff, *Z. Physik* **70**, 104 (1931).
8. F. E. Fowle, *Smith. Misc. Coll.* **68**, No. 8 (Publ. 2484) (1917).
9. J. Lecompte, *Trans. Faraday Soc.* **25**, 864 (1929).
10. C. Shaefer and F. Matossi, "Das Ultrarote Spectrum," Springer, Berlin, (1930).
11. L. H. Dawson and E. O. Hulburt, *J. Opt. Soc. Am.* **24**, 175 (1934).
12. J. Becquerel and J. Rossignol, *Int. Crit. Tab.* **5**, 268 (1929).
13. N. E. Dorsey, "Properties of the Ordinary Water Substance in all Its Phases," Reinhold, New York, 279 (1940).
14. F. F. Martens, *Ann. Physik (4)* **6**, 603 (1901).
15. J. Duclaux and P. Jeantet, *J. de Phys. (6)* **5**, 92 (1924).
16. C. Chéneveau, *Int. Nat. Crit. Tab.* **7**, 13 (1930).
17. L. W. Tilton and J. K. Taylor, *J. Res. Nat. Bur. Stand.* **20**, 419 (RP1085) (1938).
18. F. Paschen, *Wied. Ann.* **51**, 21; **52**, 216; **53**, 334 (1894).
19. W. W. Coblentz, *Bull. Bur. Stand.* **2**, No. 3, 457 (1906); **7**, No. 4, 619 (1911); *Phys. Rev.* [1] **20**, 252 (1905); [1] **23**, 125 (1906).
20. D. A. Goldhammer, "Dispersion und Absorption des Lichtes," Teubner, Leipzig, (1913).
21. J. R. Collins, *Phys. Rev.* **20**, 486 (1922); *Phys. Rev.* **55**, 470 (1939).
22. E. K. Plyler, *J. Opt. Soc. Am.* **9**, 545 (1924).
23. T. Dreisch, *Z. Physik* **30**, 200 (1924).
24. E. O. Hulburt, *J. Opt. Soc. Am.* **17**, 15 (1928).
25. C. H. Cartwright, *Nature* **135**, 872 (1935).

26. D. Williams, R. D. Weatherford, and E. K. Plyler, *J. Opt. Soc. Am.* **26**, 149 (1936).
27. J. J. Fox and A. E. Martin, *Proc. Roy. Soc. London* **174**, 234 (1940).
28. M. Centeno, V, *J. Opt. Soc. Am.* **31**, 244 (1941).
29. J. A. Curcio and C. C. Petty, *J. Opt. Soc. Am.* **41**, 302 (1951).
30. E. R. Blout and H. Lenormant, *J. Opt. Soc. Am.* **43**, 1093 (1953).
31. E. K. Plyler and N. Aquista, *J. Opt. Soc. Am.* **44**, 505 (1954).
32. R. M. Adams and J. J. Katz, *J. Opt. Soc. Am.* **46**, 895 (1956).
33. M. Ceccaldi, M. Goldman, and E. Roth, "Proceedings of the Sixth International Spectroscopy Colloquium," Pergamon, London, (1956).
34. W. J. Potts, Jr., and N. Wright, *Anal. Chem.* **28**, 1255 (1956).
35. H. H. Hyman, M. Kilpatrick, and J. J. Katz, *J. Am. Chem. Soc.* **79**, 3668 (1957).
36. Y. I. Bocharov and A. S. Krutikov, *Bull. Izv. Akad. Sci. USSR, Geophys. Ser., No. 7*, 528 (1958).
37. W. C. Waggener, *Anal. Chem.* **30**, 1569 (1958).
38. J. D. S. Goulden, *Spectrochem. Acta.* **15**, 657 (1959).
39. L. D. Kislovskii, *Opt. Spektrosk.* **7**, 201 (1959).
40. E. K. Plyler and N. Griff, *Appl. Opt.* **4**, 1663 (1965).
41. J. E. McDonald, *J. Meteorol.* **17**, 232 (1960).
42. T. Ackermann, *Z. Phys. Chem.* **27**, 253 (1961).
43. A. E. Stanevich and N. G. Yaroslavskii, *Opt. Spektrosk.* **10**, 278 (1961).
44. J. G. Bayly, V. B. Kartha, and W. H. Stevens, *Infrared Phys.* **3**, 211 (1963).
45. K. Kondratyev, M. P. Burgova, I. F. Gainulin, and G. F. Tomunova, "Problemy Fiziki Atmosfery," Sb. 2, Izd. Leningrad Univ., Leningrad, (1964).
46. W. K. Thompson, *Trans. Faraday Soc.* **61**, 2635 (1965).
47. W. Bagdade and M. Tinkham, *Bull. Am. Phys. Soc.* **10**, 1209 (1965).
48. D. A. Draegert, N. W. B. Stone, B. Curnutte, and D. Williams, *J. Opt. Soc. Am.* **56**, 64 (1966).
49. K. Kondratyev, "Radiation in the Atmosphere," Vol. 12, International Geophysical Series, Academic Press, New York, (1969).
50. E. D. McAlister, *Appl. Opt.* **3**, 609 (1964).
51. L. Pontier and C. Dechambenoy, *Ann. Geophys.* **21**, 462 (1965); **22**, 633 (1966).
52. L. R. Painter, R. N. Hamm, E. T. Arakawa, and R. D. Birkhoff, *Phys. Rev. Lett.* **21**, 282 (1968); *J. Chem. Phys.* **51**, 243 (1969).
53. M. R. Querry, B. Curnutte, and D. Williams, *J. Opt. Soc. Am.* **59**, 1299 (1969).
54. V. M. Zolotarev, B. A. Mikhailov, L. I. Alperovich, and S. I. Popov, *Opt. Spectrosc.* **27**, 430 (1969).
55. W. M. Irvine and J. B. Pollack, *Icarus* **8**, 324 (1968).
56. V. M. Zolotarev, B. A. Mikhailov, L. I. Alperovich, and S. I. Popov, *Opt. Commun.* **1**, 301 (1970).
57. J. Lane and J. A. Saxton, *Proc. Roy. Soc. (London)* **213A**, 400 (1952); Ibid. 473.
58. C. H. Collie, J. B. Hasted, D. M. Riston, *Proc. Phys. Soc.* **60**, 71 (1948); Ibid. 145.
59. F. Gelebart and A. Johannin-Gillen, *Compt. Rend. Acad. Sci. (Paris)* **262B**, 1509 (1966).
60. J. E. Chamberlain, G. W. Chantry, H. A. Gebbie, N. W. B. Stone, T. B. Taylor, and G. Wyllie, *Nature* **210**, 790 (1966).
61. A. N. Rusk, D. Williams, and M. R. Querry, *J. Opt. Soc. Am.* **61**, 895 (1971).
62. C. W. Robertson and D. Williams, *J. Opt. Soc. Am.* **61**, 1316 (1971).
63. G. M. Hale, M. R. Querry, A. N. Rusk, and D. Williams, *J. Opt. Soc. Am.* **62**, 1103 (1972).
64. G. D. Kerr, R. N. Hamm, M. W. Williams, R. D. Birkhoff, and L. R. Painter, *Phys. Rev.* **A5**, 2523 (1972).
65. B. L. Sowers, R. D. Birkhoff, and E. T. Arakawa, *J. Chem. Phys.* **57**, 583 (1972).
66. C. W. Robertson, B. Curnutte, and D. Williams, *Mol. Phys.* **26**, 183 (1973).

67. M. S. Zafar, J. B. Hasted, and J. Chamberlain, *Nature* **243**, 106 (1973).
68. J. M. Heller, Jr., R. N. Hamm, R. D. Birkhoff, and L. R. Painter, *J. Chem. Phys.* **60**, 3483 (1974).
69. K. F. Palmer and D. Williams, *J. Opt. Soc. Am.* **64**, 1107 (1974).
70. G. M. Hale and M. R. Querry, *Appl. Opt.* **12**, 555 (1973).
71. H. D. Downing and D. Williams, *J. Geophys. Res.* **80**, 1656 (1975).
72. D. J. Segelstein, "The Complex Refractive Index of Water," M. S. Thesis, University of Missouri-Kansas City (1981).
73. K. S. Cole and R. H. Cole, *J. Chem. Phys.* **9**, 341 (1941).
74. M. N. Afsar and J. B. Hasted, *J. Opt. Soc. Am.* **67**, 902 (1977).
75. A. C. Tam and C. K. N. Patel, *Appl. Opt.* **18**, 3348 (1979).
76. J. Lenoble and B. Saint-Guilly, *Compt. Rend.* **240**, 954 (1955).
77. O. V. Kopelevich, *Opt. Spektrosk.* **41**, 666 (1976); *Opt. Spectrosc.* **49**, 391 (1976).
78. L. R. Painter, R. D. Birkhoff, and E. T. Arakawa, *J. Chem. Phys.* **51**, 243 (1969).
79. D. J. Segelstein and M. R. Querry, *Appl. Opt.* (submitted).
80. D. M. Wieliczka, S. Weng, and M. R. Querry, *Appl. Opt.* **28**, 1714 (1989).
81. I. L. Tyler, G. Taylor, and M. R. Querry, *Appl. Opt.* **17**, 960 (1978).

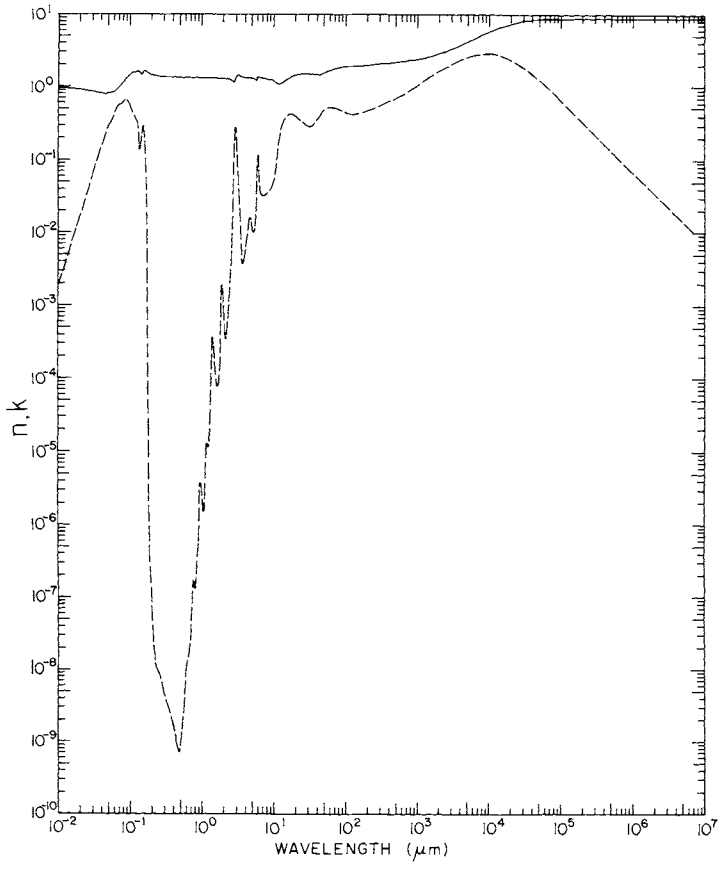

Fig. 1. Log–log plot of n (solid line) and k (dashed line) versus wavelength in micrometers for water.

TABLE I

Values of n and k for Water Obtained from Ref. [72][a]

eV	cm^{-1}	μm	n	k
1.2398×10^{-7}	1.000×10^{-3}	1.0000×10^{7}	8.849 [72]	6.931×10^{-3} [73]
1.3043	1.052	9.5057×10^{6}	8.849	7.291
1.3787	1.112	8.9928	8.849	7.688
1.4605	1.178	8.4890	8.849	8.124
1.5498	1.250	8.0000	8.849	8.626
1.6540	1.334	7.4963	8.849	9.200
1.7717	1.429	6.9979	8.849	9.858×10^{-3}
1.9069	1.538	6.5020	8.849	1.061×10^{-2}
2.0668	1.667	5.9988	8.849	1.148
2.2565	1.820	5.4945	8.849	1.250
2.4797	2.000	5.0000	8.849	1.373
2.7562	2.223	4.4984	8.849	1.523
3.0996	2.500	4.0000	8.849	1.713
3.5435	2.858	3.4990	8.849	1.953
4.1337	3.334	2.9994	8.849	2.274
4.9582	3.999	2.5006	8.849	2.721
6.1992	5.000	2.0000	8.848	3.395
8.2673×10^{-7}	6.668×10^{-3}	1.4997	8.848	4.506
1.2398×10^{-6}	1.000×10^{-2}	1.0000×10^{6}	8.848	6.727
1.3043	1.052	9.5057×10^{5}	8.848	7.076
1.3787	1.112	8.9928	8.847	7.461
1.4605	1.178	8.4890	8.847	7.885
1.5498	1.250	8.0000	8.847	8.391
1.6540	1.334	7.4963	8.847	8.929
1.7717	1.429	6.9979	8.847	9.567×10^{-2}
1.9069	1.538	6.5020	8.847	1.030×10^{-1}
2.0668	1.667	5.9988	8.846	1.114
2.2565	1.820	5.4945	8.846	1.213
2.4797	2.000	5.0000	8.845	1.333
2.7562	2.223	4.4984	8.844	1.478
3.0996	2.500	4.0000	8.843	1.659
3.5435	2.858	3.4990	8.841	1.891
4.1337	3.334	2.9994	8.838	2.202
4.9582	3.999	2.5006	8.833	2.634
6.1992	5.000	2.0000	8.824	3.277
8.2673×10^{-6}	6.668×10^{-2}	1.4997	8.804	4.337
1.2398×10^{-5}	1.000×10^{-1}	1.0000×10^{5}	8.743	6.409
1.3056	1.053	9.4967×10^{4}	8.732	6.730
1.3775	1.111	9.0009	8.720	7.083
1.4593	1.177	8.4962	8.705	7.476
1.5498	1.250	8.0000	8.689	7.914
1.6527	1.333	7.5019	8.670	8.406
1.7717	1.429	6.9979	8.648	8.960
1.9081	1.539	6.4977	8.620	9.589×10^{-1}
2.0656	1.666	6.0024	8.587	1.031×10^{0}
2.2540	1.818	5.5006	8.546	1.115
2.4797	2.000	5.0000	8.497	1.212
2.7549	2.222	4.5005	8.436	1.327
3.0996	2.500	4.0000	8.353	1.463

[a] References used in compilation of Ref. [72] given in brackets.

TABLE I (*Continued*)

Water

eV	cm^{-1}	μm	n	k	
3.5422	2.857	3.5002	8.238	1.627	
4.1324	3.333	3.0003	8.075	1.824	
4.9594	4.000	2.5000	7.831	2.064	
6.1992	5.000	2.0000	7.456	2.338	
8.2661×10^{-5}	6.667×10^{-1}	1.4999	6.867	2.630	
1.2398×10^{-4}	1.000×10^{0}	1.0000×10^{4}	5.879	2.830	
1.3056	1.053	9.4967×10^{3}	5.747	2.835	
1.3775	1.111	9.0009	5.607	2.832	
1.4581	1.176	8.5034	5.459	2.826	
1.5498	1.250	8.0000	5.305	2.811	
1.6527	1.333	7.5019	5.146	2.792	
1.7717	1.429	6.9979	4.980	2.766	
1.9081	1.539	6.4977	4.811	2.727	
2.0656	1.666	6.0024	4.631	2.685	
2.2540	1.818	5.5006	4.442	2.625	
2.4797	2.000	5.0000	4.248	2.551	
2.7549	2.222	4.5005	4.045	2.460	
3.0996	2.500	4.0000	3.829	2.360	
3.5422	2.857	3.5002	3.607	2.228	
4.1324	3.333	3.0003	3.375	2.079	
4.9594	4.000	2.5000	3.134	1.891	
6.1992	5.000	2.0000	2.882	1.670	[74]
8.2661×10^{-4}	6.667×10^{0}	1.4999	2.629	1.393	
1.2398×10^{-3}	1.000×10^{1}	1.0000×10^{3}	2.399	1.042×10^{0}	
1.6540	1.334	7.4963×10^{2}	2.290	8.725×10^{-1}	
2.2144	1.786	5.5991	2.220	7.359	
2.6942	2.173	4.6019	2.166	6.727	
3.4468	2.780	3.5971	2.099	5.967	
4.4300	3.573	2.7988	2.045	5.355	
5.3871	4.345	2.3015	2.001	4.964	
6.8923	5.559	1.7989	1.956	4.506	
9.5357×10^{-3}	7.691×10^{1}	1.3002×10^{2}	1.920	4.186	
1.2919×10^{-2}	1.042×10^{2}	9.5969×10^{1}	1.891	4.485	
1.4432	1.164	8.5911	1.860	4.773	
1.6304	1.315	7.6046	1.806	5.079	
1.8771	1.514	6.6050	1.729	5.233	
2.2144	1.786	5.5991	1.619	5.162	
2.5838	2.084	4.7985	1.520	4.579	
2.8864	2.328	4.2955	1.481	3.880	
3.2608	2.630	3.8023	1.481	3.190	
3.7530	3.027	3.3036	1.512	2.830	
4.4300	3.573	2.7988	1.546	2.991	
5.3871	4.345	2.3015	1.516	3.629	
6.2278	5.023	1.9908	1.467	3.952	[62]
6.3145	5.093	1.9635	1.460	4.016	
6.3877	5.152	1.9410	1.454	4.072	
6.4770	5.224	1.9142	1.446	4.110	
6.5675	5.297	1.8879	1.436	4.157	
6.6431	5.358	1.8664	1.428	4.196	

(*continued*)

TABLE I (*Continued*)

Water

eV	cm^{-1}	μm	n	k	
6.7361	5.433	1.8406	1.418	4.234	
6.8291	5.508	1.8155	1.407	4.254	
6.9246	5.585	1.7905	1.396	4.264	
7.0200	5.662	1.7662	1.386	4.283	
7.1180	5.741	1.7419	1.375	4.293	
7.2333	5.834	1.7141	1.361	4.293	
7.3349	5.916	1.6903	1.350	4.293	
7.4540	6.012	1.6633	1.335	4.283	
7.5569	6.095	1.6407	1.323	4.264	
7.6796	6.194	1.6145	1.309	4.244	
7.8048	6.295	1.5886	1.295	4.205	
7.9140	6.383	1.5667	1.283	4.176	
8.0417	6.486	1.5418	1.268	4.119	
8.1917	6.607	1.5135	1.254	4.053	
8.3243	6.714	1.4894	1.239	3.998	
8.4595	6.823	1.4656	1.226	3.934	
8.6169	6.950	1.4388	1.209	3.844	
8.7571	7.063	1.4158	1.196	3.757	
8.9195	7.194	1.3900	1.179	3.646	
9.0856	7.328	1.3646	1.162	3.514	
9.2542	7.464	1.3398	1.146	3.363	
9.4266	7.603	1.3153	1.131	3.183	
9.6026	7.745	1.2912	1.117	2.977	
9.8035×10^{-2}	7.907	1.2647	1.105	2.740	
1.0008×10^{-1}	8.072	1.2389	1.092	2.476	
1.0194	8.222	1.2162	1.087	2.177	
1.0409	8.395	1.1912	1.087	1.865	
1.0650	8.590	1.1641	1.096	1.570	
1.0873	8.770	1.1403	1.105	1.321	
1.1126	8.974	1.1143	1.119	1.083×10^{-1}	
1.1386	9.183	1.0890	1.134	8.970×10^{-2}	
1.1651	9.397	1.0642	1.150	7.359	
1.1922	9.616	1.0399	1.167	6.191	
1.2229	9.863×10^{2}	1.0139×10^{1}	1.184	5.380	
1.2510	1.009×10^{3}	9.9108×10^{0}	1.199	4.929	[70]
1.2832	1.035	9.6618	1.211	4.600	
1.3192	1.064	9.3985	1.223	4.333	
1.3564	1.094	9.1408	1.233	4.110	
1.3948	1.125	8.8889	1.241	3.916	
1.4333	1.156	8.6505	1.249	3.748	
1.4767	1.191	8.3963	1.257	3.604	
1.5213	1.227	8.1500	1.264	3.490	
1.5684	1.265	7.9051	1.270	3.395	
1.6192	1.306	7.6570	1.277	3.302	
1.6763	1.352	7.3964	1.284	3.242	
1.7358	1.400	7.1429	1.291	3.205	
1.7965	1.449	6.9013	1.298	3.220	
1.8635	1.503	6.6534	1.309	3.450	
1.9379	1.563	6.3980	1.325	4.485	

(*continued*)

TABLE I (*Continued*)

Water

eV	cm^{-1}	μm	n	k	
2.0011	1.614	6.1958	1.342	8.786	
2.0817	1.679	5.9559	1.232	8.646	
2.1747	1.754	5.7013	1.257	2.031	
2.2776	1.837	5.4437	1.282	1.078	
2.3842	1.923	5.2002	1.298	1.011	
2.5020	2.018	4.9554	1.307	1.312	
2.6384	2.128	4.6992	1.311	1.570	
2.7884	2.249	4.4464	1.315	1.140×10^{-2}	
2.9533	2.382	4.1982	1.324	6.883×10^{-3}	
3.1356	2.529	3.9541	1.337	4.157	
3.3526	2.704	3.6982	1.357	3.596×10^{-3}	
3.5918	2.897	3.4518	1.393	1.321×10^{-2}	
3.8758	3.126	3.1990	1.462	9.243×10^{-2}	
4.1535	3.350	2.9851	1.334	2.721×10^{-1}	
4.2204	3.404	2.9377	1.264	2.804	[62]
4.2787	3.451	2.8977	1.196	2.581	
4.3382	3.499	2.8580	1.145	2.060	
4.3990	3.548	2.8185	1.125	1.422×10^{-1}	
4.4597	3.597	2.7801	1.131	9.285×10^{-2}	
4.5230	3.648	2.7412	1.142	4.622	
4.5850	3.698	2.7042	1.175	1.640×10^{-2}	
4.6494	3.750	2.6667	1.199	7.325×10^{-3}	
4.7139	3.802	2.6302	1.218	4.016	
4.7796	3.855	2.5940	1.232	2.476	
4.8342	3.899	2.5648	1.240	2.266	
4.8565	3.917	2.5530	1.243	2.142	
4.9582	3.999	2.5006	1.253	1.900	[70]
5.0623	4.083	2.4492	1.261	1.348×10^{-3}	
5.1689	4.169	2.3987	1.268	9.095×10^{-4}	
5.2768	4.256	2.3496	1.273	6.365	
5.3871	4.345	2.3015	1.278	4.686	
5.5124	4.446	2.2492	1.282	3.739	
5.6413	4.550	2.1978	1.286	3.379	
5.7727	4.656	2.1478	1.289	3.705	
5.9066	4.764	2.0991	1.292	4.643	
6.0443	4.875	2.0513	1.294	6.742×10^{-4}	
6.1992	5.000	2.0000	1.297	1.101×10^{-3}	
6.3592	5.129	1.9497	1.298	1.848	
6.5216	5.260	1.9011	1.299	1.161×10^{-3}	
6.7051	5.408	1.8491	1.301	1.861×10^{-4}	
6.8923	5.559	1.7989	1.303	1.359	
7.0857	5.715	1.7498	1.305	1.000×10^{-4}	
7.3002	5.888	1.6984	1.307	7.743×10^{-5}	
7.5222	6.067	1.6483	1.308	7.591	
7.7515	6.252	1.5995	1.310	9.347×10^{-5}	
8.0057	6.457	1.5487	1.311	1.348×10^{-4}	
8.2673	6.668	1.4997	1.312	2.248	
8.5574	6.902	1.4489	1.313	3.637	
8.8587	7.145	1.3996	1.314	1.530×10^{-4}	

(*continued*)

TABLE I (*Continued*)

Water

eV	cm^{-1}	μm	n	k	
9.1910	7.413	1.3490	1.315	4.047×10^{-5}	
9.5357	7.691	1.3002	1.316	1.400	
9.9163×10^{-1}	7.998	1.2503	1.317	1.100	
1.0337×10^{0}	8.337	1.1995	1.318	1.199×10^{-5}	
1.0774	8.690	1.1507	1.319	9.306×10^{-6}	
1.1281	9.099	1.0990	1.320	1.708	
1.1813	9.528×10^{3}	1.0495	1.321	1.419	
1.2398	1.000×10^{4}	1.0000×10^{0}	1.322	3.000	
1.2721	1.026	9.7466×10^{-1}	1.322	3.480	
1.3043	1.052	9.5057	1.323	2.932	
1.3403	1.081	9.2507	1.323	1.060×10^{-6}	
1.3787	1.112	8.9928	1.324	4.862×10^{-7}	
1.4171	1.143	8.7489	1.324	3.907	
1.4605	1.178	8.4890	1.325	2.929	
1.5039	1.213	8.2440	1.325	1.819	
1.5498	1.250	8.0000	1.326	1.250	
1.6006	1.291	7.7459	1.327	1.478	
1.6540	1.334	7.4963	1.327	1.559×10^{-7}	
1.7110	1.380	7.2464	1.328	9.137×10^{-8}	
1.7717	1.429	6.9979	1.329	3.348	[75]
1.8387	1.483	6.7431	1.330	2.177	
1.9069	1.538	6.5020	1.331	1.674	
1.9838	1.600	6.2500	1.332	1.472×10^{-8}	
2.0668	1.667	5.9988	1.333	9.634×10^{-9}	
2.1549	1.738	5.7537	1.334	3.844	
2.2565	1.820	5.4945	1.336	2.442	
2.3619	1.905	5.2493	1.338	1.640×10^{-9}	
2.4797	2.000	5.0000	1.339	9.243×10^{-10}	
2.6086	2.104	4.7529	1.342	7.011	
2.7562	2.223	4.4984	1.344	8.087×10^{-10}	
2.9198	2.355	4.2463	1.347	1.169×10^{-9}	
3.0996	2.500	4.0000	1.350	1.580	[76], [77]
3.3067	2.667	3.7495	1.354	2.031	
3.5435	2.858	3.4990	1.358	2.528	
3.8138	3.076	3.2510	1.364	3.082	
4.1337	3.334	2.9994	1.371	4.148	
4.5118	3.639	2.7480	1.381	6.292	
4.9582	3.999	2.5006	1.395	9.307×10^{-9}	
5.5124	4.446	2.2492	1.416	1.158×10^{-8}	
5.9066	4.764	2.0991	1.435	3.844×10^{-8}	
6.1992	5.000	2.0000	1.452	1.101×10^{-7}	
6.5216	5.260	1.9011	1.475	3.622×10^{-7}	[78]
6.8923	5.559	1.7989	1.513	5.995×10^{-5}	
7.1180	5.741	1.7419	1.549	1.182×10^{-3}	
7.3002	5.888	1.6984	1.606	3.998×10^{-3}	
7.4713	6.026	1.6595	1.647	7.241×10^{-2}	
7.6449	6.166	1.6218	1.653	1.351×10^{-1}	
7.8408	6.324	1.5813	1.641	2.022	
8.0417	6.486	1.5418	1.597	2.581	

(*continued*)

TABLE I (*Continued*)

Water

eV	cm^{-1}	μm	n	k	
8.2673	6.668	1.4997	1.521	2.772	[68]
8.4992	6.855	1.4588	1.469	2.409	
8.7372	7.047	1.4190	1.462	1.927	
8.9815	7.244	1.3805	1.496	1.422	
9.2542	7.464	1.3398	1.586	1.489	
9.5357	7.691	1.3002	1.634	2.392	
9.8481×10^{0}	7.943	1.2590	1.606	3.220	
1.0172×10^{1}	8.204	1.2189	1.570	3.490	
1.0504	8.472	1.1804	1.553	3.705	
1.0873	8.770	1.1403	1.543	3.988	
1.1281	9.099	1.0990	1.529	4.303	
1.1705	9.441	1.0592	1.516	4.707	
1.2144	9.795×10^{4}	1.0209×10^{-1}	1.493	5.185	
1.2659	1.021×10^{5}	9.7943×10^{-2}	1.456	5.752	
1.3192	1.064	9.3985	1.388	6.292	
1.3787	1.112	8.9928	1.303	6.528	
1.4432	1.164	8.5911	1.215	6.573	
1.5114	1.219	8.2034	1.141	6.292	
1.5895	1.282	7.8003	1.088	5.981	
1.6763	1.352	7.3964	1.050	5.805	
1.7717	1.429	6.9979	0.982	5.791	
1.8771	1.514	6.6050	0.904	5.355	
2.0011	1.614	6.1958	0.841	4.558	
2.1400	1.726	5.7937	0.832	3.739	
2.2987	1.854	5.3937	0.835	3.310	
2.4797	2.000	5.0000	0.821	2.998	
2.6942	2.173	4.6019	0.797	2.414	
2.9533	2.382	4.1982	0.802	1.798	
3.2608	2.630	3.8023	0.820	1.303×10^{-1}	
3.6501	2.944	3.3967	0.842	9.074×10^{-2}	
4.1337	3.334	2.9994	0.867	6.064	
4.7685	3.846	2.6001	0.891	3.818	
5.6413	4.550	2.1978	0.914	2.227	
6.8923	5.559	1.7989	0.935	1.164×10^{-2}	
8.8587×10^{1}	7.145	1.3996	0.953	5.174×10^{-3}	
1.0337×10^{2}	8.337×10^{5}	1.1995	0.961	3.146	
1.2398	1.000×10^{6}	1.0000	0.968	1.745	

TABLE II

Values of n and k for Water Obtained from Ref. [80]

eV	cm^{-1}	μm	n	k
6.3009×10^{-2}	5.082×10^{2}	1.9677×10^{1}	1.521	4.007×10^{-1}
6.6282	5.346	1.8706	1.484	4.186
7.0039	5.649	1.7702	1.435	4.274
7.4193	5.984	1.6711	1.381	4.293
7.8954	6.368	1.5704	1.321	4.176
8.4409	6.808	1.4689	1.260	3.943
9.0447	7.295	1.3708	1.194	3.546
9.7576×10^{-2}	7.870	1.2706	1.131	2.791
1.0602×10^{-1}	8.551	1.1695	1.113	1.621
1.1159	9.000	1.1111	1.143	1.006×10^{-1}
1.1407	9.200	1.0870	1.154	8.515×10^{-2}
1.1655	9.400	1.0638	1.168	7.150
1.1903	9.600	1.0417	1.183	6.130
1.2151	9.800×10^{2}	1.0204	1.196	5.370
1.2398	1.000×10^{3}	1.0000×10^{1}	1.208	4.790
1.2646	1.020	9.8039×10^{0}	1.219	4.418
1.2894	1.040	9.6154	1.229	4.142
1.3142	1.060	9.4340	1.237	3.943
1.3390	1.080	9.2593	1.245	3.788
1.3638	1.100	9.0909	1.251	3.669
1.3886	1.120	8.9286	1.257	3.591
1.4134	1.140	8.7719	1.262	3.518
1.4382	1.160	8.6207	1.268	3.476
1.4630	1.180	8.4746	1.272	3.426
1.4878	1.200	8.3333	1.276	3.401
1.5126	1.220	8.1967	1.279	3.381
1.5374	1.240	8.0645	1.282	3.343
1.5622	1.260	7.9365	1.285	3.289
1.5870	1.280	7.8125	1.288	3.295
1.6118	1.300	7.6923	1.291	3.289
1.6366	1.320	7.5758	1.294	3.263
1.6614	1.340	7.4627	1.296	3.227
1.6862	1.360	7.3529	1.298	3.202
1.7110	1.380	7.2464	1.301	3.183
1.7358	1.400	7.1429	1.302	3.170
1.7606	1.420	7.0423	1.304	3.164
1.7854	1.440	6.9444	1.306	3.168
1.8102	1.460	6.8493	1.309	3.232
1.8350	1.480	6.7568	1.311	3.287
1.8598	1.500	6.6667	1.314	3.371
1.8846	1.520	6.5789	1.317	3.520
1.9094	1.540	6.4935	1.322	3.945
1.9342	1.560	6.4103	1.329	4.543
1.9590	1.580	6.3291	1.343	5.378
1.9838	1.600	6.2500	1.347	7.112×10^{-2}
2.0086	1.620	6.1728	1.337	1.110×10^{-1}
2.0334	1.640	6.0976	1.302	1.309
2.0581	1.660	6.0241	1.257	1.214×10^{-1}
2.0829	1.680	5.9524	1.240	9.140×10^{-2}

(continued)

TABLE II (*Continued*)

Water

eV	cm^{-1}	μm	n	k
2.1077	1.700	5.8824	1.235	5.394
2.1325	1.720	5.8140	1.248	3.635
2.1573	1.740	5.7471	1.261	2.636
2.1821	1.760	5.6818	1.270	1.770
2.2069	1.780	5.6180	1.275	1.448
2.2317	1.800	5.5556	1.284	1.274
2.2565	1.820	5.4945	1.289	1.166
2.2813	1.840	5.4348	1.294	1.083
2.3061	1.860	5.3763	1.298	1.037
2.3309	1.880	5.3191	1.301	1.032
2.3557	1.900	5.2632	1.304	1.042
2.3805	1.920	5.2083	1.307	1.049
2.4053	1.940	5.1546	1.310	1.076
2.4301	1.960	5.1020	1.312	1.136
2.4549	1.980	5.0505	1.314	1.219
2.4797	2.000	5.0000	1.315	1.291
2.5045	2.020	4.9505	1.316	1.353
2.5293	2.040	4.9020	1.318	1.434
2.5541	2.060	4.8544	1.318	1.500
2.5789	2.080	4.8077	1.319	1.549
2.6037	2.100	4.7619	1.320	1.558
2.6285	2.120	4.7170	1.319	1.551
2.6533	2.140	4.6729	1.319	1.524
2.6781	2.160	4.6296	1.319	1.481
2.7029	2.180	4.5872	1.319	1.398
2.7277	2.200	4.5455	1.319	1.315
2.7525	2.220	4.5045	1.320	1.232
2.7773	2.240	4.4643	1.321	1.151
2.8021	2.260	4.4248	1.322	1.065×10^{-2}
2.8269	2.280	4.3860	1.322	9.781×10^{-3}
2.8517	2.300	4.3478	1.323	9.127
2.8764	2.320	4.3103	1.324	8.544
2.9012	2.340	4.2735	1.325	7.862
2.9260	2.360	4.2373	1.327	7.274
2.9508	2.380	4.2017	1.329	6.813
2.9756	2.400	4.1667	1.330	6.389
3.0004	2.420	4.1322	1.332	5.984
3.0252	2.440	4.0984	1.334	5.557
3.0500	2.460	4.0650	1.335	5.155
3.0748	2.480	4.0323	1.337	4.912
3.0996	2.500	4.0000	1.339	4.636
3.1244	2.520	3.9683	1.342	4.334
3.1492	2.540	3.9370	1.344	4.076
3.1740	2.560	3.9063	1.346	3.911
3.1988	2.580	3.8760	1.349	3.781
3.2236	2.600	3.8462	1.352	3.669
3.2484	2.620	3.8168	1.354	3.588
3.2732	2.640	3.7879	1.355	3.624
3.2980	2.660	3.7594	1.358	3.712

(*continued*)

TABLE II (*Continued*)

Water

eV	cm^{-1}	μm	n	k
3.3228	2.680	3.7313	1.360	3.803
3.3476	2.700	3.7037	1.362	3.952
3.3724	2.720	3.6765	1.365	4.220
3.3972	2.740	3.6496	1.368	4.569
3.4220	2.760	3.6232	1.371	5.002
3.4468	2.780	3.5971	1.375	5.494
3.4716	2.800	3.5714	1.379	6.121
3.4964	2.820	3.5461	1.383	6.969
3.5212	2.840	3.5211	1.388	7.954
3.5460	2.860	3.4965	1.392	9.170×10^{-3}
3.5708	2.880	3.4722	1.396	1.064×10^{-2}
3.5956	2.900	3.4483	1.401	1.243
3.6204	2.920	3.4247	1.406	1.462
3.6452	2.940	3.4014	1.412	1.736
3.6700	2.960	3.3784	1.418	1.968
3.6947	2.980	3.3557	1.425	2.588
3.7195	3.000	3.3333	1.431	3.505
3.7443	3.020	3.3113	1.438	4.289
3.7691	3.040	3.2895	1.445	4.764
3.7939	3.060	3.2680	1.453	5.405
3.8187	3.080	3.2468	1.460	6.553
3.8435	3.100	3.2258	1.466	7.932
3.8683	3.120	3.2051	1.472	9.208×10^{-2}
3.8931	3.140	3.1847	1.478	1.058×10^{-1}
3.9179	3.160	3.1646	1.477	1.232
3.9427	3.180	3.1447	1.476	1.450
3.9675	3.200	3.1250	1.469	1.656
3.9923	3.220	3.1056	1.463	1.833
4.0171	3.240	3.0864	1.452	1.990
4.0419	3.260	3.0675	1.433	2.161
4.0667	3.280	3.0488	1.417	2.267
4.0915	3.300	3.0303	1.407	2.369
4.1163	3.320	3.0120	1.390	2.487
4.1411	3.340	2.9940	1.375	2.606
4.1659	3.360	2.9762	1.350	2.740
4.1907	3.380	2.9586	1.323	2.819
4.2155	3.400	2.9412	1.291	2.854
4.2403	3.420	2.9240	1.254	2.826
4.2651	3.440	2.9070	1.211	2.765
4.2899	3.460	2.8902	1.180	2.637
4.3147	3.480	2.8736	1.153	2.451
4.3395	3.500	2.8571	1.135	2.230
4.3643	3.520	2.8409	1.110	2.032
4.3891	3.540	2.8249	1.083	1.854
4.4139	3.560	2.8090	1.090	1.613
4.4387	3.580	2.7933	1.091	1.356
4.4635	3.600	2.7778	1.109	1.129×10^{-1}
4.4883	3.620	2.7624	1.115	9.598×10^{-2}
4.5130	3.640	2.7473	1.112	7.725

(*continued*)

TABLE II (*Continued*)

Water

eV	cm^{-1}	μm	n	k
4.5378	3.660	2.7322	1.131	4.909
4.5626	3.680	2.7174	1.150	2.388
4.5874	3.700	2.7027	1.164	1.248×10^{-2}
4.6122	3.720	2.6882	1.178	8.105×10^{-3}
4.6408	3.743	2.6717	1.190	5.456
4.6755	3.771	2.6518	1.204	3.943
4.7102	3.799	2.6323	1.214	3.163
4.7461	3.828	2.6123	1.222	2.647
4.7833	3.858	2.5920	1.229	2.316
4.8205	3.888	2.5720	1.236	2.158
4.8577	3.918	2.5523	1.241	2.099
4.8962	3.949	2.5323	1.245	2.065
4.9358	3.981	2.5119	1.249	1.984
4.9755	4.013	2.4919	1.253	1.824
5.0152	4.045	2.4722	1.256	1.586
5.0561	4.078	2.4522	1.259	1.353
5.0983	4.112	2.4319	1.262	1.156×10^{-3}
5.1404	4.146	2.4120	1.265	9.902×10^{-4}
5.1838	4.181	2.3918	1.267	8.574
5.2272	4.216	2.3719	1.270	7.381
5.2718	4.252	2.3518	1.272	6.365
5.3165	4.288	2.3321	1.274	5.513
5.3623	4.325	2.3121	1.276	4.806
5.4095	4.363	2.2920	1.278	4.244
5.4566	4.401	2.2722	1.279	3.805
5.5049	4.440	2.2523	1.281	3.501
5.5545	4.480	2.2321	1.283	3.304
5.6054	4.521	2.2119	1.284	3.217
5.6562	4.562	2.1920	1.286	3.205
5.7083	4.604	2.1720	1.287	3.324
5.7616	4.647	2.1519	1.288	3.510
5.8149	4.690	2.1322	1.289	3.817
5.8707	4.735	2.1119	1.291	4.283
5.9265	4.780	2.0921	1.292	4.919
5.9835	4.826	2.0721	1.293	5.732
6.0418	4.873	2.0521	1.294	6.780
6.1013	4.921	2.0321	1.295	8.087
6.1620	4.970	2.0121	1.296	9.765×10^{-4}
6.2240	5.020	1.9920	1.297	1.198×10^{-3}
6.2873	5.071	1.9720	1.297	1.477
6.3517	5.123	1.9520	1.298	1.785
6.4175	5.176	1.9320	1.298	1.997
6.4844	5.230	1.9120	1.298	1.849
6.5526	5.285	1.8921	1.298	1.069×10^{-3}
6.6233	5.342	1.8720	1.299	3.351×10^{-4}
6.6952	5.400	1.8519	1.301	1.674
6.7683	5.459	1.8318	1.301	1.326
6.8427	5.519	1.8119	1.302	1.267
6.9184	5.580	1.7921	1.303	1.252

(*continued*)

TABLE II (*Continued*)

Water

eV	cm^{-1}	μm	n	k
6.9965	5.643	1.7721	1.304	1.166×10^{-4}
7.0771	5.708	1.7519	1.304	9.999×10^{-5}
7.1589	5.774	1.7319	1.305	8.617
7.2420	5.841	1.7120	1.306	7.855
7.3275	5.910	1.6920	1.306	7.432
7.4155	5.981	1.6720	1.307	7.374
7.5048	6.053	1.6521	1.308	7.470
7.5966	6.127	1.6321	1.308	7.852
7.6908	6.203	1.6121	1.309	8.420
7.7875	6.281	1.5921	1.309	9.336×10^{-5}
7.8867	6.361	1.5721	1.310	1.083×10^{-4}
7.9883	6.443	1.5521	1.310	1.288
8.0925	6.527	1.5321	1.311	1.603
8.2004	6.614	1.5119	1.311	2.034
8.3095	6.702	1.4921	1.312	2.601
8.4223	6.793	1.4721	1.312	3.223
8.5388	6.887	1.4520	1.313	3.523
8.6579	6.983	1.4320	1.313	3.368
8.7806	7.082	1.4120	1.313	2.705
8.9071	7.184	1.3920	1.314	1.311×10^{-4}
9.0373	7.289	1.3719	1.314	5.043×10^{-5}
9.1699	7.396	1.3521	1.315	3.576
9.3088	7.508	1.3319	1.315	2.588
9.4501	7.622	1.3120	1.316	1.706
9.5964	7.740	1.2920	1.316	1.327
9.7477	7.862	1.2719	1.316	1.133
9.9027×10^{-1}	7.987	1.2520	1.317	1.170
1.0064×10^{0}	8.117	1.2320	1.317	1.263

Yttrium Oxide (Y_2O_3)

WILLIAM J. TROPF and MICHAEL E. THOMAS
Applied Physics Laboratory
The Johns Hopkins University
Laurel, Maryland

Yttrium sesquioxide (yttria) is a body-centered cubic material with bixbyite or cubic-C structure. The space group is T_h^7 or Ia3, unit cell length is 1.0604 nm, and the unit cell has 16 formula units (80 atoms). Theoretical density is 5.033 g/cm^3, melting point is 2710 K [1], and a phase change to a hexagonal form occurs at 2640 K [1].

Yttrium ions occupy two different sites, eight octahedral sites with C_{3i} point symmetry and 24 prismatic sites with C_2 symmetry. Six oxygen ions surround each yttrium ion. Ion positions in the unit cell are known from both X-ray and neutron-diffraction measurements [2, 3].

Optical-quality, single-crystal yttria is available, typically made by the flame-fusion technique [4], and optical-quality sintered polycrystalline yttria is available in a variety of window shapes [5]. Optical-grade cubic yttria stabilized with up to 10 mole-percent thoria ("Yttralox") was previously made [6], and cubic yttria with lanthanum oxide ("lanthana-strengthened yttria") is commercially available [7, 8]. Comprehensive properties of commercial, polycrystalline yttria and lanthana-doped yttria are given in the literature [9].

Yttria is an excellent trivalent-ion host material for solid-state lasers. A variety of candidate metal-ion dopants, particularly neodymium [10], as well as many other rare-earth metals [11, 12] have been investigated.

Yttria has a band gap of approximately 6.0 eV. Several investigators have measured the optical constants from the UV through the XUV [13–16]. Earlier measurements [13, 14] used poor-quality samples and obtained results that qualitatively match recent measurements of Abramov *et al.* [15] and Tomiki *et al.* [16]. The latter measurements are considered definitive because they show the most detail, give results over the widest spectral range (3–42 eV), and agree well with the best available value of refractive index at the UV edge of the transparent region [17].

The lowest-frequency electronic feature of the yttria spectrum is an exciton peak at 6.0 eV. The peak sits on the edge of a broad resonance

Copyright © 1991 by Academic Press.
All rights of reproduction in any form reserved.
ISBN 0-12-544422-2

structure extending from 6.5–15 eV at room temperature. This broad feature arises from interband transitions between the upper valence band of oxygen ($2p^6$) to the conduction band of yttrium (4d + 5s) [15, 16]. Weaker absorption in the 15–27 eV region may be caused by transitions from the upper valence band of oxygen to higher excited conduction bands of doubly ionized yttrium [16]. At energies between 27 and 35 eV, absorption is attributed to electronic transitions from the ground state ($4p^6$) of triply ionized yttrium and the $4p^54d$ and $4p^55s$ excited states, with additional transitions to the 60.6 eV ionization level of Y^{3+} postulated [16].

Tomiki *et al.* also give the temperature dependence of absorption at the UV edge of the transparent region (5.2–6.0 eV) for temperatures between 10 and 297 K and fit their measurements to an Urbach rule formulation

$$\alpha(E, T) = \alpha_0 \times \exp(-\sigma_s(T)(E_0 - E)/kT), \tag{1a}$$

where

$$\sigma_s(T) = \sigma_{s0} \times (2kT/E_{s0}) \tanh(E_{s0}/2kT). \tag{1b}$$

The constants of Eq. 1 are $\alpha_0 = 8.222 \times 10^6\ \text{cm}^{-1}$, $E_0 = 6.080$ eV, $\sigma_{s0} = 0.688$, and $E_{s0} = 0.0186$ eV. DeShazer *et al.* [18] report higher absorption values, and Nigara [17] gives even higher values.

Refractive-index data for the visible and IR transparent region of yttria are given in several sources. Wickersheim and LaFever [4] reported an index of refraction between 1.91 and 1.95 for yttria and mixed yttria–lanthana crystals. The most comprehensive data are provided by Nigara [17], who measured the index of crystals from 0.22–12 μm using different methods. His data were fitted to a Sellmeier-type dispersion relationship of the form

$$n^2 - 1 = \frac{13.4 \times 10^9}{(72{,}100)^2 - \nu^2} + \frac{7.48 \times 10^5}{(436)^2 - \nu^2}, \tag{2}$$

where ν is the frequency in wave numbers. This is the only available dispersion information for bulk yttria. Equation 2 represents electronic resonances at 72,100 cm^{-1} (8.9 eV) with the first term, and IR resonances at 436 cm^{-1} with the second term. These terms fall in the middle of the measured electronic transitions and lattice vibrations, respectively.

Tsukuda [19] also measured the refractive index of bulk transparent

yttria in the visible using an ellipsometry technique. His results are typically 0.5–1% below those of Nigara [17].

Smith and Baumeister [20] measured the refractive index of thin films of yttria over the 0.25–2 μm spectral range and found that the index was highly dependent on film preparation. Their measurements are significantly below those of Nigara (Eq. 2), typically by 10%, and the imaginary part of the refractive index (extinction coefficient) is much larger than is reported for bulk samples [16–18]. Thin-film refractive indices reported by Heitmann [21] are 2–3% below bulk index data [17], although more recent data by Arnon and Chou [22] also give index values 10% below that of bulk yttria.

Refractive indices of 1.92 at 0.589 μm for thoria-doped yttria (Yttralox, GE [23]) and 1.9699 at 0.546 μm for lanthana-doped yttria (an ellipsometer measurement [24]) have been reported. Equation 2 gives 1.930 and 1.937, respectively, at those two wavelengths.

Absorption in the transparent region (0.25–7 μm) is governed by impurities and defects. The most prominent absorption feature is the OH^- absorption, which occurs in a broad region between 2500 and 3500 cm^{-1} [4, 25, 26]. Various heat treatments can reduce the amount of OH^- impurity. Defect absorption in the transparent region is highly dependent on preparation environment. Several investigators show that partial pressure of oxygen is a critical factor in producing a low level of defect absorption [10, 24, 27]. The primary defect is believed to be oxygen vacancies or interstitials. When yttria is exposed to a reducing atmosphere (for example, hydrogen) at very high temperature (>2000 K), a black form of yttria is produced [28] with very high absorption in the visible. At high temperatures (>1200 K), absorption increases, likely caused by a greater concentration of oxygen vacancies and interstitials in equilibrium [24, 29].

The dominant loss mechanism in the visible and near-IR transparent region of polycrystalline yttria is scatter. Bulk scatter in polycrystalline yttria is low and decreases with increasing wavelength [8, 9, 29].

Absorption at the IR edge of transparency is dominated by multiphonon absorption. A model of yttria multiphonon absorption has been developed and confirmed with experimental data over a wide temperature range [30]. The fundamental (one-phonon) lattice vibrations occur in the 120–555 cm^{-1} spectral region. Group theory predicts the following phonon modes for yttria [31–33]:

$$\Gamma = 4E_g + 4A_g + 14F_g + 5E_u + 5A_u + 16F_u, \tag{3}$$

where all gerade modes are Raman-active, the E_u and A_u modes are inactive, and the 16 F_u modes are IR-active. Table I lists the 11 strongest modes as determined from McDevitt and Davidson [34] (modes 1–3, location only) and Thomas [35] (modes 4–11, as well as estimated widths

and strengths for modes 1–3). Thomas also gives the temperature dependence of modes 4–11 over the 290–775 K temperature range. Nigara *et al.* [32] also give parameters for modes 5–11. Bloor and Dean [33] observe an additional IR mode at 197 cm^{-1} in measurements made at 1.5 K.

Table I also lists both the transverse and longitudinal optical frequencies. The transverse optical frequencies are the mode locations; the maximum longitudinal mode frequency is an important parameter in the multiphonon absorption model [30], since it designates the maximum phonon frequency.

Characterization of the fundamental optical modes of yttria doped with 9 mole-percent lanthana [7, 8] shows similar lattice vibrational structures that are broader and red-shifted to lower frequency by 5–12 wave numbers. The multiphonon absorption edge is also red-shifted by a similar amount [30].

At frequencies below the last fundamental optical mode, absorption decreases and the material becomes transparent. The magnitude of absorption is thought to be a combination of contributions from both the tail of the fundamental lattice vibrations and various multiphonon difference bands. The index of refraction now also includes the effect of lattice vibrations. Estimates of low-frequency absorption made from the red wing of the fundamental modes (Table I) are about 40% of the imaginary index-of-refraction values determined by Stead and Simonis [36] in the 4–16 cm^{-1} region. Smith and Loewenstein [37] measured the absorption coefficient of Yttralox (yttria with 10 mole-percent thoria) in the 50–200 cm^{-1} region and found absorption similar to pure yttria.

The low-frequency index of refraction of yttria was measured by Stead and Simonis [36] at 3.43 (dielectric constant of 11.76), which agrees well with the measurements of Hyde [38] when corrected to full density and room temperature. The same value was obtained for Yttralox by Smith and Loewenstein [37], and a higher value of 3.49 (dielectric constant of 12.2) is given by Wei *et al.* [29] for yttria with 9 mole-percent lanthana. Westphal and Sils [39] report a room-temperature dielectric constant of 11.3 for 97% dense, 99.8% pure yttria.

Temperature dependence of the low-frequency index of refraction was measured by Hyde [38], who also found a resonance at very low frequencies (below 10^5 Hz). His dn/dT value of 1.05×10^{-4}/K ($d\varepsilon/dT = 7.2 \times 10^{-4}$/K) agrees well with the value predicted from the fundamental lattice-vibration model [35]. This model underpredicts the low-frequency index by 1.5%, probably because several weak vibrational modes have not been modelled (only 11 of the 16 modes predicted by group theory are observed and modeled).

Low-frequency dielectric constant data reported by Hyde [38] and Westphal and Sils [39] show a free-carrier effect that grows rapidly with temperature. Conductivity measurements by Tallan and Vest [27] also

indicate a growth in free carriers with temperature.

Table II was constructed from measurements reported in the literature as well as model predictions [30, 35]. Real-index (n) data from 2–40 eV, and imaginary-index (k) data from 5.2–40 eV are taken from the measurements of Tomiki *et al.* [16]. Real-index data below 6 eV (0.21–12 μm) are calculated from the Sellmeier dispersion relationship (Eq. 2) of Nigara [17]. Measurements of k (determined from absorption coefficients) reported by DeShazer *et al.* [18] are also shown. These data may include significant extrinsic absorption because the values are much higher than those in Tomiki *et al.* [16].

Lattice-vibration-model results [35], using Nigara's [17] representation of the electronic contribution to index, are used to calculate the index of refraction for wavelengths of 1 μm and longer. Laser-calorimetry results for k at 2.9 and 3.9 μm by Detrio and Greason [40] are also given to represent typical extrinsic absorption in the transparent region. Multiphonon absorption becomes important (greater than extrinsic absorption) at wavelengths beyond 4.5 μm. Values in the table up to 10 μm are calculated using the methods of Thomas *et al.* [30], which are validated by measurements. Beyond 10 μm, the fundamental (one-phonon) contributions become dominant. In this region, n and k are calculated using the parameters in Table I as described by Thomas [35]. The results are validated by comparing calculated reflection spectra to measurements.

Measurements of Stead and Simonis [36] and Hyde [38] best represent the low-frequency characteristics of yttria. In this region, one-phonon-model predictions [35] of k are only 40% of measurements [36], and real-index values are 1.5% low compared to measurements [36, 38].

The accuracy of available index data is unknown. In all data, the uncertainty in the values is probably in the least significant digit reported in Table II. In spectral regions where several sources of data exist, there is a large disparity between references.

Figure 1 shows a composite of the complex index of refraction based on the data of Table II.

Table III gives temperature dependence for the real part of the index of refraction. Measurements of dn/dT by Wei *et al.* [29] give 5.0×10^{-5}/K and 3.2×10^{-5}/K at wavelengths of 0.357 and 3.39 μm, respectively. Measurements made by A.P.L./J.H.U. at 0.633 μm give much lower values: 8.4×10^{-6} for pure yttria and 8.4×10^{-6} for lanthana-doped yttria. The temperature change in index of refraction at microwave frequencies remains nearly linear for most oxides up to 1000 K. This characteristic is likely to be true for yttria also, but has not been experimentally verified.

Temperature-dependent absorption predictions from optical models of yttria [30, 35] have been used to estimate total hemispherical emissivity of pure, transparent yttria over the 200 to 1000 K temperature range, where the models are expected to give the best results and intrinsic (temperature-

produced) defect absorption is believed to be insignificant [9]. These results were obtained by estimating the complex refractive index at a given temperature, calculating directional emittance for a specific slab thickness, integrating over angle, and convolving the resulting spectral hemispherical emittances with the Planck function.

Table IV gives the resulting total hemispherical emittance for semi-infinite slabs as a function of slab thickness. Since total hemispherical emissivity is an important function for radiation-relief calculations and is needed to correct property measurements such as thermal conductivity, we have included this calculated result.

REFERENCES

1. L. M. Lopato, B. S. Nigmanov, A. V. Shevchenko, and Z. A. Zaitseva, "Interaction between Lanthanum Oxide and Yttrium Oxide," *Inorg. Mater.* **22**, 678 (1986).
2. M. G. Paton and E. N. Maslen, "A Refinement of the Crystal Structure of Yttria," *Acta Crystallogr.* **19**, 307 (1965).
3. B. H. O'Conner and T. M. Valentine, "A Neutron Diffraction Study of the Crystal Structure of the C-form of Yttrium Sesquioxide," *Acta Crystallogr.* **B25**, 2140 (1960).
4. K. A. Wickersheim and R. A. LaFever, "Infrared Transmittance of Crystalline Yttrium Oxide and Related Compounds," *J. Opt. Soc. Am.* **51**, 1147 (1961).
5. R. L. Gentilman, "Current and Emerging Materials for 3–5 Micron IR Transmission," *Proc. SPIE* **683**, 2 (1986).
6. C. Greskovick and N. K. Woods, "Fabrication of Transparent ThO_2-Doped Y_2O_3," *Ceram. Bull.* **52**, 473 (1973).
7. W. H. Rhodes, "Controlled Transient Solid Second-Phase Sintering of Yttria," *J. Am. Ceram. Soc.* **64**, 13 (1981).
8. W. H. Rhodes, G. C. Wei, and E. A. Trickett, "Lanthana-Doped Yttria: A New Infrared Material," *Proc. SPIE* **683**, 12 (1986).
9. W. J. Tropf and D. C. Harris, "Mechanical, Thermal, and Optical Properties of Yttria and Lanthana-Doped Yttria," *Proc. SPIE* **1112**, 9 (1989).
10. H. Tsuiki, T. Masumoto, K. Kitazawa, and K. Fueki, "Effect of Point Defects on Laser Oscillation Properties of Nd-Doped Y_2O_3," *Jap. J. Appl. Phys.* **21**, 1017 (1982).
11. N. C. Chang, J. B. Gruber, R. P. Leavitt, and C. A. Morrison, "Optical Spectra, Energy Levels, and Crystal-Field Analysis of Positive Rare Earth Ions in Y_2O_3. I. Kramers Ions in C_2 Sites," *J. Chem. Phys.* **76**, 3877 (1982).
12. R. P. Leavitt, J. B. Gruber, N. C. Chang, and C. A. Morrison, "Optical Spectra, Energy Levels, and Crystal-Field Analysis of Positive Rare Earth Ions in Y_2O_3. II. Non-Kramers Ions in C_2 Sites," *J. Chem. Phys.* **76**, 4775 (1982).
13. V. N. Abramov and A. I. Kuznetsov, "Fundamental Absorption of Y_2O_3 and $YAlO_3$," *Sov. Phys. Solid State* **20**, 399 (1978).
14. K. S. Bagdasarov, V. P. Zhuze, M. G. Karin, K. K. Sidorin, and A. I. Shelykh, "Optical Properties of Rare-Earth Sesquioxides in the Fundamental Absorption Range," *Sov. Phys. Solid State* **26**, 687 (1984).
15. V. N. Abramov, A. N. Ermoshkin, and A. I. Kuznetsov, "Optical Properties and Electron Energy Structure of Y_2O_3 and Sc_2O_3," *Sov. Phys. Solid State* **25**, 981 (1983).
16. T. Tomiki, J. Tamashiro, Y. Tanahara, A. Yamada, H. Fukutani, T. Miyahara, H. Kato, S. Shin, and M. Ishigame, "Optical Spectra of Y_2O_3 Single Crystals in VUV," *J. Phys. Soc. Jap.* **55**, 4543 (1986).
17. Y. Nigara, "Measurement of the Optical Constants of Yttrium Oxide," *Jap. J. Appl. Phys.* **7**, 404 (1968).

18. L. G. DeShazer, S. C. Rand, and B. A. Wechsler, "Laser Crystals," in "CRC Handbook of Laser Science and Technology, Volume V: Optical Materials; Part 3: Applications, Coatings, and Fabrication," (M. J. Weber, ed.), CRC Press, Boca Raton, Florida, 288 (1988).
19. Y. Tsukuda, "Refractive and Reflective Indices of Y_2O_3 Sintered Bodies," *Nippon Kagaku Kaishi (8)*, 1106 (1979).
20. D. Smith and P. Baumeister, "Refractive Index of Some Oxide and Fluoride Coating Materials," *Appl. Opt.* **18**, 111 (1979).
21. W. Heitmann, "Reactively Evaporated Films of Scandia and Yttria," *Appl. Opt.* **12**, 394 (1973).
22. O. Arnon and T. J. Chou, "Wide Band Measurement of the Refractive Index of Optical Thin Films During Their Deposition," *Thin Solid Films* **91**, 23 (1982).
23. Yttralox data sheets, available from General Electric Research and Development Center, Schenectady, New York.
24. G. C. Wei, C. Brecher, and W. H. Rhodes, "Effect of Point Defects on High-Temperature Optical Properties in Transparent Polycrystalline Lanthana-Doped Yttria," *Proc. SPIE* **683**, 146 (1986).
25. G. C. Wei, "Extrinsic OH^- Absorption in Transparent Pollycrystalline Lanthana-Doped Yttria," *J. Am. Ceram. Soc.* **71**, C20 (1988).
26. J. A. Harrington and C. Greskovich, "Infrared Absorption in ThO_2-Doped Y_2O_3," *J. Appl. Phys.* **48**, 1585 (1977).
27. N. M. Tallan and R. W. Vest, "Electrical Properties and Defect Structure of Y_2O_3," *J. Am. Ceram. Soc.* **49**, 401 (1966).
28. Y. Tsukuda, "Properties of Black Y_2O_3 Sintered Bodies," *Mater. Res. Bull.* **16**, 453 (1981).
29. G. C. Wei, C. Brecher, M. R. Pascucci, E. A. Trickett, and W. H. Rhodes, "Characterization of Lanthana-Strengthened Yttria Infrared Transmitting Materials," *Proc. SPIE* **929**, 50 (1988).
30. M. E. Thomas, R. I. Joseph, and W. J. Tropf, "Infrared Transmission Properties of Sapphire, Spinel, Yttria, and ALON as a Function of Frequency and Temperature," *Appl. Opt.* **27**, 239 (1988).
31. N. V. Porotnikov, O. I. Kondratov, L. L. Kochergina, and K. I. Petrov, "Calculation of the Theoretical Vibrational Spectrum of Y_2O_3," *Russ. J. Inorg. Chem.* **29**, 954 (1984).
32. Y. Nigara, M. Ishigame, and T. Sakurai, "Infrared Properties of Yttrium Oxide," *J. Phys. Soc. Jap.* **30**, 453 (1971).
33. D. Bloor and J. R. Dean, "Spectroscopy of Rare Earth Oxide Systems: I. Far Infrared Spectra of the Rare Earth Sesquioxides, Cerium Oxide, and Nonstoichiometric Praseodymium and Terbium Oxides," *J. Phys. C.* **5**, 1237 (1972).
34. N. T. McDevitt and A. D. Davidson, "Infrared Lattice Spectra of Cubic Rare Earth Oxides in the Region 700 to 50 cm^{-1}," *J. Opt. Soc. Am.* **56**, 636 (1966).
35. M. E. Thomas, "A Computer Code for Modeling Optical Properties of Window Materials," *Proc. SPIE* **1112**, 260 (1989).
36. M. Stead and G. Simonis, "Near Millimeter Wave Characterization of Dual Mode Materials," *Appl. Opt.* **28**, 1874 (1989).
37. D. R. Smith and E. V. Loewenstein, "Optical Constants of Metal Oxides in the Far Infrared Region," *Appl. Opt.* **15**, 859 (1976).
38. G. R. Hyde, "Dielectric Properties of Sintered Yttrium Oxide," *J. Am. Ceram. Soc.* **54**, 535 (1971).
39. W. B. Westphal and A. Sils, "Dielectric Constant and Loss Data," Air Force Materials Laboratory, AFML-TR-72-39, Wright-Patterson AFB, Ohio, (April 1972).
40. J. A. Detrio and Paul Greason, University of Dayton, personal communication (April 8, 1988).

NOTES ADDED IN PROOF

A recent theoretical study of yttria electronic structure and bonding is given in [41]. Results agreed well with experiments.

A recent measurement of the index of refraction of 9% lanthana-doped yttria made by the minimum deviation method gave a value of 1.9294 ± 0.0001 at 546 nm [42]. This value, believed to be accurate, is considerably below the value given in [24], and much closer to the index of pure yttria. Other measurements between 0.4 and 2.3 μm show the same trend [42].

Details of the measurement of dn/dT at 0.6368 μm in Table III are given in [43]. Spectral and directional scatter measurements of commercial ALON are given in [44].

41. W. Y. Ching and Y.-N. Xu, "Electronic and Optical Properties of Yttria," *Phys. Rev. Lett.* **65**, 895–898 (1990).
42. R. J. Scheller, Schott Glass Technologies, Inc., personal communication (April 24, 1990).
43. C. H. Lange and D. D. Duncan, "Temperature Coefficient of Refractive Index for Candidate Optical Windows," *SPIE Proc.* **1326**, 71–78 (1990).
44. C. H. Lange, D. D. Duncan, and D. G. Fischer "Imaging Performance of Crystalline and Polycrystalline Oxides," *SPIE Proc.* **1326**, 59–70 (1990).

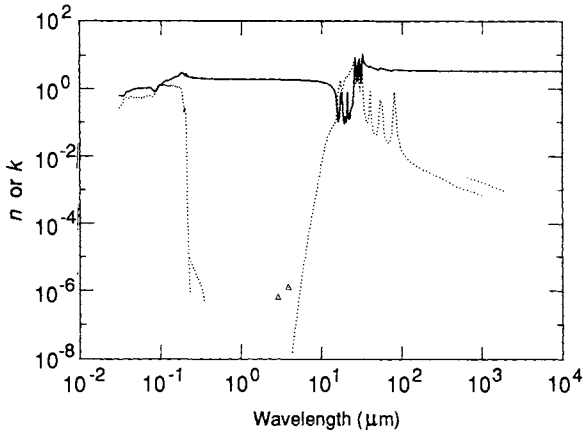

Fig. 1. Log–log plot of n (solid line) and k (dashed line) versus wavelength in micrometers for yttrium oxide. Data from various sources sometimes do not join together in overlap regions. Symbols are laser calorimetry measurements of k.

TABLE I

Fundamental Infrared Lattice-Vibration Parameters for Yttrium Oxide[a]

Mode	Transverse optical frequency (cm^{-1})	Strength	Normalized width	Longitudinal optical frequency (cm^{-1})	Refs.
1	120	0.20	0.035	121	[34,35]
2	172	0.10	0.025	173	[34,35]
3	182	0.15	0.025	183	[34,35]
4	241	0.20	0.025	242	[35]
5	303	2.60	0.0135	315	[35]
6	335	1.75	0.0115	359	[35]
7	371	2.65	0.021	412	[35]
8	415	0.04	0.011	456	[35]
9	461	0.05	0.015	486	[35]
10	490	0.005	0.018	535	[35]
11	555	0.095	0.025	620	[35]
		Total = 7.86			

[a]The transverse optical frequency (ν_j) is the location of the mode. The strength ($\Delta\epsilon_j$) is the contribution of the mode to the dielectric constant. The normalized width (γ_j) is the mode width divided by the mode frequency. The complex dielectric constant (ϵ) is then modeled as a function of frequency (ν) by

$$\epsilon(\nu) = \epsilon_\infty + \sum_j \frac{\Delta\epsilon_j \nu_j^2}{\nu_j^2 - \nu^2 + i\gamma_j \nu_j \nu} ,$$

where the ϵ_∞ term (= 3.579) represents the electronic contributions to the dielectric constant (plus one). Nigara *et al.* [32] also observed modes 5-11. Bloor and Dean [33] observed a mode at 197 cm^{-1} in measurements made at 1.5 K. Such a mode was not observed by McDevitt and Davidson [34].

TABLE II

Values of n and k Obtained from Various References for Yttrium Oxide[a]

eV	cm^{-1}	μm	n	k	n	k
40.0	322619	0.0310	0.624 [16]	0.272 [16]		
39.0	314554	0.0318	0.624	0.295		
38.0	306488	0.0326	0.624	0.314		
37.0	298423	0.0335	0.623	0.356		
36.0	290357	0.0344	0.621	0.388		
35.0	282292	0.0354	0.621	0.461		
34.0	274226	0.0365	0.671	0.535		
33.0	266161	0.0376	0.775	0.565		
32.0	258095	0.0387	0.823	0.535		
31.0	250030	0.0400	0.832	0.515		
30.0	241964	0.0413	0.834	0.543		
29.0	233899	0.0428	0.876	0.596		
28.0	225833	0.0443	0.942	0.567		
27.0	217768	0.0459	0.965	0.561		
26.0	209702	0.0477	0.985	0.551		
25.0	201637	0.0496	0.997	0.550		
24.5	197604	0.0506	1.000	0.554		
24.0	193572	0.0517	1.016	0.564		
23.5	189539	0.0528	1.025	0.563		
23.0	185506	0.0539	1.039	0.556		
22.5	181473	0.0551	1.048	0.547		
22.0	177441	0.0564	1.045	0.540		
21.5	173408	0.0577	1.044	0.545		
21.0	169375	0.0590	1.041	0.542		
20.5	165342	0.0605	1.040	0.543		
20.0	161310	0.0620	1.041	0.553		
19.5	157277	0.0636	1.042	0.560		
19.0	153244	0.0653	1.042	0.570		
18.5	149211	0.0670	1.042	0.584		
18.0	145179	0.0689	1.039	0.595		
17.5	141146	0.0708	1.051	0.618		
17.0	137113	0.0729	1.072	0.639		
16.5	133080	0.0751	1.084	0.631		
16.0	129048	0.0775	1.062	0.597		
15.5	125015	0.0800	0.979	0.578		
15.0	120982	0.0827	0.892	0.605		
14.5	116949	0.0855	0.819	0.702		
14.0	112917	0.0886	0.829	0.860		
13.9	112110	0.0892	0.843	0.900		
13.8	111304	0.0898	0.857	0.938		
13.7	110497	0.0905	0.875	0.971		
13.6	109691	0.0912	0.894	1.003		
13.5	108884	0.0918	0.917	1.035		
13.4	108077	0.0925	0.940	1.067		

(*continued*)

TABLE II (*Continued*)

Yttrium Oxide

eV	cm^{-1}	μm	n	k	n	k
13.3	107271	0.0932	0.973	1.101		
13.2	106464	0.0939	1.017	1.137		
13.1	105658	0.0946	1.043	1.169		
13.0	104851	0.0954	1.077	1.196		
12.9	104045	0.0961	1.143	1.220		
12.8	103238	0.0969	1.198	1.243		
12.7	102432	0.0976	1.247	1.265		
12.6	101625	0.0984	1.279	1.281		
12.5	100819	0.0992	1.287	1.295		
12.4	100012	0.1000	1.292	1.290		
12.3	99205	0.1008	1.296	1.282		
12.2	98399	0.1016	1.301	1.267		
12.1	97592	0.1025	1.305	1.250		
12.0	96786	0.1033	1.308	1.238		
11.9	95979	0.1042	1.323	1.234		
11.8	95173	0.1051	1.356	1.235		
11.7	94366	0.1060	1.390	1.246		
11.6	93560	0.1069	1.415	1.259		
11.5	92753	0.1078	1.440	1.273		
11.4	91946	0.1088	1.481	1.285		
11.3	91140	0.1097	1.520	1.291		
11.2	90333	0.1107	1.537	1.297		
11.1	89527	0.1117	1.543	1.292		
11.0	88720	0.1127	1.555	1.286		
10.9	87914	0.1137	1.575	1.276		
10.8	87107	0.1148	1.615	1.264		
10.7	86301	0.1159	1.643	1.258		
10.6	85494	0.1170	1.684	1.264		
10.5	84688	0.1181	1.704	1.262		
10.4	83881	0.1192	1.716	1.252		
10.3	83074	0.1204	1.721	1.237		
10.2	82268	0.1216	1.725	1.221		
10.1	81461	0.1228	1.730	1.208		
10.0	80655	0.1240	1.735	1.196		
9.9	79848	0.1252	1.741	1.192		
9.8	79042	0.1265	1.749	1.170		
9.7	78235	0.1278	1.757	1.163		
9.6	77429	0.1292	1.766	1.165		
9.5	76622	0.1305	1.782	1.173		
9.4	75816	0.1319	1.811	1.180		
9.3	75009	0.1333	1.857	1.185		
9.2	74202	0.1348	1.898	1.197		
9.1	73396	0.1362	1.908	1.216		
9.0	72589	0.1378	1.925	1.235		

(*continued*)

TABLE II (*Continued*)

Yttrium Oxide

eV	cm^{-1}	μm	n	k	n	k
8.9	71783	0.1393	1.946	1.266		
8.8	70976	0.1409	1.975	1.212		
8.7	70170	0.1425	2.021	1.211		
8.6	69363	0.1442	2.051	1.216		
8.5	68557	0.1459	2.089	1.221		
8.4	67750	0.1476	2.139	1.220		
8.3	66943	0.1494	2.181	1.217		
8.2	66137	0.1512	2.196	1.205		
8.1	65330	0.1531	2.209	1.188		
8.0	64524	0.1550	2.222	1.162		
7.9	63717	0.1569	2.240	1.136		
7.8	62911	0.1590	2.265	1.123		
7.7	62104	0.1610	2.294	1.124		
7.6	61298	0.1631	2.314	1.121		
7.5	60491	0.1653	2.334	1.110		
7.4	59685	0.1675	2.418	1.103		
7.3	58878	0.1698	2.468	1.110		
7.2	58071	0.1722	2.523	1.118		
7.1	57265	0.1746	2.592	1.118		
7.0	56458	0.1771	2.682	1.109		
6.9	55652	0.1797	2.820	1.093		
6.8	54845	0.1823	2.916	1.054		
6.7	54039	0.1851	2.952	0.926		
6.6	53232	0.1879	2.947	0.755		
6.5	52426	0.1907	2.891	0.590		
6.4	51619	0.1937	2.801	0.427		
6.3	50813	0.1968	2.682	0.276		
6.2	50006	0.2000	2.628	0.186		
6.1	49199	0.2033	2.583	0.249		
6.0	48393	0.2066	2.652	0.276	2.386 [17]	
5.9	47586	0.2101	2.726	0.129	2.359	
5.8	46780	0.2138	2.632	0.0113	2.335	
5.7	45973	0.2175	2.483	$8.74 \cdot 10^{-5}$	2.312	
5.6	45167	0.2214	2.360	$7.67 \cdot 10^{-5}$	2.290	
5.5	44360	0.2254	2.315	$9.49 \cdot 10^{-6}$	2.269	
5.4	43554	0.2296	2.266	$2.29 \cdot 10^{-6}$	2.249	$9.0 \cdot 10^{-6}$ [18]
5.3	42747	0.2339	2.233	$1.05 \cdot 10^{-6}$	2.230	$8.0 \cdot 10^{-6}$
5.2	41940	0.2384	2.199	$7.61 \cdot 10^{-7}$	2.213	$7.1 \cdot 10^{-6}$
5.1	41134	0.2431	2.176		2.196	$6.3 \cdot 10^{-6}$
5.0	40327	0.2480	2.155		2.180	$5.6 \cdot 10^{-6}$
4.9	39531	0.2530	2.127		2.164	$5.0 \cdot 10^{-6}$
4.8	38714	0.2583	2.115		2.150	$4.5 \cdot 10^{-6}$
4.7	37908	0.2638	2.106		2.136	$4.0 \cdot 10^{-6}$
4.6	37101	0.2695	2.096		2.123	$3.5 \cdot 10^{-6}$

(*continued*)

TABLE II (*Continued*)

Yttrium Oxide

eV	cm^{-1}	μm	n	k	n	k
4.5	36295	0.2755	2.085		2.110	$3.1 \cdot 10^{-6}$
4.4	35488	0.2818	2.073		2.098	$2.7 \cdot 10^{-6}$
4.3	34682	0.2883	2.062		2.086	$2.4 \cdot 10^{-6}$
4.2	33875	0.2952	2.052		2.075	$2.2 \cdot 10^{-6}$
4.1	33068	0.3024	2.042		2.065	$1.9 \cdot 10^{-6}$
4.0	32262	0.3100	2.034		2.055	$1.7 \cdot 10^{-6}$
3.9	31455	0.3179	2.025		2.045	$1.4 \cdot 10^{-6}$
3.8	30649	0.3263	2.017		2.036	$1.2 \cdot 10^{-6}$
3.7	29842	0.3351	2.010		2.027	$9 \cdot 10^{-7}$
3.6	29036	0.3444	2.004		2.019	$6 \cdot 10^{-7}$
3.5	28229	0.3542	1.998		2.011	$4 \cdot 10^{-7}$
3.4	27423	0.3647	1.992		2.003	
3.3	26616	0.3757	1.985		1.996	
3.2	25810	0.3875	1.978		1.989	
3.1	25003	0.4000	1.971		1.982	
3.0	24196	0.4133	1.964		1.976	
2.9	23390	0.4275	1.959		1.970	
2.8	22583	0.4428	1.953		1.964	
2.7	21777	0.4592	1.948		1.958	
2.6	20970	0.4769	1.944		1.953	
2.5	20164	0.4959	1.940		1.948	
2.48	20000	0.5000	1.939		1.947	
2.42	19500	0.5128	1.938		1.944	
2.4	19357	0.5166	1.938		1.943	
2.36	19000	0.5263	1.937		1.941	
2.3	18551	0.5391	1.936		1.939	
2.29	18500	0.5405	1.936		1.938	
2.23	18000	0.5556	1.935		1.936	
2.2	17744	0.5636	1.934		1.934	
2.17	17500	0.5714	1.933		1.933	
2.11	17000	0.5882	1.932		1.931	
2.1	16938	0.5904	1.932		1.930	
2.05	16500	0.6061	1.931		1.928	
2.0	16131	0.6199	1.930		1.926	
1.984	16000	0.6250			1.926	
1.922	15500	0.6452			1.923	
1.860	15000	0.6667			1.921	
1.798	14500	0.6897			1.919	
1.736	14000	0.7143			1.917	
1.674	13500	0.7407			1.915	
1.612	13000	0.7692			1.913	
1.550	12500	0.8000			1.911	
1.488	12000	0.8333			1.909	
1.426	11500	0.8696			1.908	

(*continued*)

TABLE II (*Continued*)

Yttrium Oxide

eV	cm^{-1}	μm	n	k	n	k
1.364	11000	0.9091			1.906	
1.302	10500	0.9524			1.904	
1.240	10000	1.0000	1.903 [35]		1.903	
1.215	9800	1.0204	1.902		1.902	
1.190	9600	1.0417	1.901		1.902	
1.165	9400	1.0638	1.901		1.901	
1.141	9200	1.0870	1.900		1.900	
1.116	9000	1.1111	1.900		1.900	
1.091	8800	1.1364	1.899		1.899	
1.066	8600	1.1628	1.898		1.899	
1.041	8400	1.1905	1.898		1.898	
1.017	8200	1.2195	1.897		1.897	
0.9919	8000	1.2500	1.896		1.897	
0.9671	7800	1.2821	1.896		1.896	
0.9423	7600	1.3158	1.895		1.896	
0.9175	7400	1.3514	1.895		1.895	
0.8927	7200	1.3889	1.894		1.895	
0.8679	7000	1.4286	1.893		1.894	
0.8431	6800	1.4706	1.893		1.893	
0.8183	6600	1.5152	1.892		1.893	
0.7935	6400	1.5625	1.891		1.892	
0.7687	6200	1.6129	1.891		1.891	
0.7439	6000	1.6667	1.890		1.891	
0.7191	5800	1.7241	1.889		1.890	
0.6943	5600	1.7857	1.888		1.889	
0.6695	5400	1.8519	1.888		1.889	
0.6447	5200	1.9231	1.887		1.888	
0.6199	5000	2.0000	1.886		1.887	
0.6075	4900	2.0408	1.885		1.886	
0.5951	4800	2.0833	1.885		1.886	
0.5827	4700	2.1277	1.884		1.885	
0.5703	4600	2.1739	1.883		1.885	
0.5579	4500	2.2222	1.883		1.884	
0.5455	4400	2.2727	1.882		1.884	
0.5331	4300	2.3256	1.881		1.883	
0.5207	4200	2.3810	1.881		1.882	
0.5083	4100	2.4390	1.880		1.882	
0.4959	4000	2.5000	1.879		1.881	
0.4835	3900	2.5641	1.878		1.880	
0.4711	3800	2.6316	1.877		1.879	
0.4587	3700	2.7027	1.876		1.879	
0.4463	3600	2.7778	1.875		1.878	
0.4339	3500	2.8571	1.874		1.877	
0.4275	3448	2.9000	1.873		1.876	$6.5 \cdot 10^{-7}$ [40]

(*continued*)

TABLE II (*Continued*)

Yttrium Oxide

eV	cm^{-1}	μm	n	k	n	k
0.4215	3400	2.9412	1.873		1.876	
0.4092	3300	3.0303	1.872		1.874	
0.3968	3200	3.1250	1.870		1.873	
0.3844	3100	3.2258	1.868		1.872	
0.3720	3000	3.3333	1.867		1.870	
0.3596	2900	3.4483	1.865		1.868	
0.3472	2800	3.5714	1.863		1.867	
0.3348	2700	3.7037	1.860		1.864	
0.3224	2600	3.8462	1.858		1.862	
0.3179	2564	3.9000	1.857		1.861	$1.3\cdot10^{-6}$
0.3100	2500	4.0000	1.855		1.859	
0.2976	2400	4.1667	1.851		1.856	
0.2852	2300	4.3478	1.847	$1.6\cdot10^{-8}$ [35]	1.853	
0.2728	2200	4.5455	1.843	$3.7\cdot10^{-8}$	1.849	
0.2604	2100	4.7619	1.838	$8.6\cdot10^{-8}$	1.845	
0.2480	2000	5.0000	1.832	$2.1\cdot10^{-7}$	1.8394	
0.2418	1950	5.1282	1.83	$3.3\cdot10^{-7}$	1.8364	
0.2356	1900	5.2632	1.82	$5.2\cdot10^{-7}$	1.8332	
0.2294	1850	5.4054	1.82	$8.2\cdot10^{-7}$	1.8298	
0.2232	1800	5.5556	1.82	$1.3\cdot10^{-6}$	1.8259	
0.2170	1750	5.7143	1.81	$2.0\cdot10^{-6}$	1.8218	
0.2108	1700	5.8824	1.81	$3.2\cdot10^{-6}$	1.8172	
0.2046	1650	6.0606	1.80	$5.0\cdot10^{-6}$	1.8121	
0.1984	1600	6.2500	1.80	$8.0\cdot10^{-6}$	1.8065	
0.1922	1550	6.4516	1.79	$1.3\cdot10^{-5}$	1.8002	
0.1860	1500	6.6667	1.78	$2.2\cdot10^{-5}$	1.7932	
0.1798	1450	6.8966	1.77	$3.7\cdot10^{-5}$	1.7854	
0.1736	1400	7.1429	1.76	$6.3\cdot10^{-5}$	1.7765	
0.1674	1350	7.4074	1.75	$1.0\cdot10^{-4}$	1.7665	
0.1612	1300	7.6923	1.74	$1.6\cdot10^{-4}$	1.7550	
0.1550	1250	8.0000	1.72	$2.7\cdot10^{-4}$	1.7417	
0.1488	1200	8.3333	1.71	$4.2\cdot10^{-4}$	1.7263	
0.1426	1150	8.6957	1.69	$7.0\cdot10^{-4}$	1.7082	
0.1364	1100	9.0909	1.67	$1.2\cdot10^{-3}$	1.6867	
0.1302	1050	9.5238	1.64	$2.3\cdot10^{-3}$	1.6609	
0.1240	1000	10.000	1.61	$4.5\cdot10^{-3}$	1.6293	
0.1215	980	10.204	1.59	$5.9\cdot10^{-3}$	1.6147	
0.1190	960	10.417	1.58	$7.9\cdot10^{-3}$	1.5986	
0.1165	940	10.638	1.56	$9.7\cdot10^{-3}$	1.5810	
0.1141	920	10.870	1.54	0.012	1.5615	
0.1116	900	11.111	1.52	0.015	1.5400	
0.1091	880	11.364	1.49	0.019	1.5159	
0.1066	860	11.628	1.47	0.024	1.4889	
0.1041	840	11.905	1.44	0.029	1.4584	

(*continued*)

TABLE II (*Continued*)

Yttrium Oxide

eV	cm^{-1}	μm	n	k	n	k
0.1017	820	12.195	1.41	0.035		
0.0992	800	12.500	1.37	0.041		
0.0967	780	12.821	1.33	0.048		
0.0942	760	12.158	1.28	0.055		
0.0917	740	13.514	1.22	0.063		
0.0893	720	13.889	1.15	0.070		
0.0868	700	14.286	1.07	0.078		
0.0843	680	14.706	0.97	0.086		
0.0818	660	15.152	0.83	0.096		
0.0794	640	15.625	0.62	0.12		
0.0769	620	16.129	0.22	0.26		
0.0744	600	16.667	0.10	0.78		
0.0719	580	17.241	0.15	1.2		
0.0694	560	17.857	0.73	1.8		
0.0670	540	18.519	0.66	0.65		
0.0645	520	19.231	0.12	1.2		
0.0620	500	20.000	0.09	1.7		
0.0608	490	20.408	0.15	1.9		
0.0595	480	20.833	0.10	2.1		
0.0583	470	21.277	0.15	2.4		
0.0570	460	21.739	0.77	2.3		
0.0558	450	22.222	0.15	2.4		
0.0546	440	22.727	0.12	2.7		
0.0533	430	23.256	0.13	3.1		
0.0521	420	23.810	0.22	3.6		
0.0508	410	24.390	0.28	3.7		
0.0496	400	25.000	0.29	4.4		
0.0484	390	25.641	0.50	5.4		
0.0471	380	26.316	1.38	7.4		
0.0459	370	27.027	8.44	7.1		
0.0446	360	27.778	5.36	1.4		
0.0434	350	28.571	1.94	1.8		
0.0422	340	29.412	1.68	6.6		
0.0409	330	30.303	7.48	1.5		
0.0397	320	31.250	3.47	0.86		
0.0384	310	32.258	1.53	5.4		
0.0372	300	33.333	10.88	2.9		
0.0360	290	34.483	6.89	0.38		
0.0347	280	35.714	5.72	0.17		
0.0335	270	37.037	5.10	0.11		
0.0322	260	38.462	4.67	0.095		
0.0310	250	40.000	4.26	0.15		
0.0298	240	41.667	4.65	0.82		
0.0285	230	43.478	4.38	0.099		

(*continued*)

TABLE II (*Continued*)

Yttrium Oxide

eV	cm^{-1}	μm	n	k	n	k
0.0273	220	45.455	4.13	0.052		
0.0260	210	47.619	3.96	0.041		
0.0248	200	50.000	3.80	0.043		
0.0236	190	52.632	3.56	0.095		
0.0223	180	55.556	4.04	0.47		
0.0211	170	58.824	4.09	0.30		
0.0198	160	62.500	3.79	0.040		
0.0186	150	66.667	3.67	0.025		
0.0174	140	71.429	3.57	0.024		
0.0161	130	76.923	3.43	0.048		
0.0149	120	83.333	3.63	0.80		
0.0136	110	90.909	3.67	0.041		
0.0124	100	100.00	3.57	0.016		
0.0112	90	111.11	3.51	0.010		
0.0099	80	125.00	3.48	$7.4 \cdot 10^{-3}$		
0.0087	70	142.86	3.45	$5.8 \cdot 10^{-3}$		
0.0074	60	166.67	3.43	$4.6 \cdot 10^{-3}$		
0.0062	50	200.00	3.41	$3.7 \cdot 10^{-3}$		
0.0050	40	250.00	3.40	$2.8 \cdot 10^{-3}$		
0.0037	30	333.33	3.39	$2.0 \cdot 10^{-3}$		
0.0025	20	500.00	3.38	$1.4 \cdot 10^{-3}$		
0.0019	15	666.67	3.38	$1.0 \cdot 10^{-3}$		$2.3 \cdot 10^{-3}$ [36]
0.0012	10	1000.0	3.38	$6.7 \cdot 10^{-4}$		$1.7 \cdot 10^{-3}$
0.0006	5	2000.0	3.38	$3.3 \cdot 10^{-4}$		$8.8 \cdot 10^{-4}$
0.0000	≈ 0	–	3.38	0.0	3.43 [36,38]	

[a]References are indicated in brackets.

TABLE III

Values of *dn/dT* Obtained from Various References for Yttrium Oxide[a]

eV	cm^{-1}	μm	dn/dT (1/K)	Notes
1.959	15803	0.6328	$8.1 \cdot 10^{-6}$	Our measurement
0.310	2500	4.0000	$7.6 \cdot 10^{-6}$	Model [35]
0.0	≈ 0	—	$1.05 \cdot 10^{-4}$	Measurement [38]
			$8.9 \cdot 10^{-5}$	Model [35]

[a]References are indicated in brackets.

TABLE IV

Calculated Total Hemispherical Emissivity for Yttrium Oxide

Temperature (K)	Thickness (cm)			
	0.10	0.25	0.50	1.25
200	0.49	0.50	0.50	0.51
300	0.53	0.56	0.58	0.60
400	0.48	0.52	0.56	0.59
500	0.40	0.45	0.49	0.53
600	0.33	0.38	0.41	0.45
700	0.27	0.31	0.35	0.39
800	0.22	0.26	0.29	0.33
900	0.19	0.22	0.25	0.28
1000	0.16	0.19	0.21	0.25



Handbook of Optical Constants of Solids

edited by

Edward D. Palik

This book is printed on acid-free paper.

Copyright © 1998 by Academic Press

All rights reserved.
No part of this publication may be reproduced or transmitted in any form or by any means, electronic or mechanical, including photocopy, recording, or any information storage and retrieval system, without permission in writing from the publisher.

ACADEMIC PRESS
525 B Street, Suite 1900, San Diego, CA 92101-4495, USA
1300 Boylston Street, Chestnut Hill, MA 02167, USA
http://www.apnet.com

Academic Press Limited
24–28 Oval Road, London NW1 7DX, UK
http://www.hbuk.co.uk/ap/

Library of Congress Cataloging-in-Publication Data

Library of Congress CIP data pending.

ISBN 0-12-544423-0

Printed in the United States of America
97 98 99 00 01 IC 9 8 7 6 5 4 3 2 1

Contents

List of Contributors xiii
Preface xvii

Part I DETERMINATION OF OPTICAL CONSTANTS

Chapter 1 **Introductory Remarks** 3
EDWARD D. PALIK

I. Introduction 3
II. The Chapters 4
III. The Critiques 5
IV. The Tables 5
V. The Figures of the Tables 5
VI. Corrections, Additions, and Comments 6
References 12

Chapter 2 **Determination of the Far-Infrared Optical Constants of Solids by Dispersive Fourier Transform Spectroscopy** 13
T. J. PARKER, K. A. MASLIN, and G. MIRJALILI

I. Introduction 13
II. The Materials 20
Acknowledgment 55
References 55

Chapter 3 **Photothermal/Photoacoustic Spectroscopic Measurements of Optical Absorption Coefficients in Semiconductors** 59
ANDREAS MANDELIS

I. Introduction 59
II. Photoacoustic Spectroscopy (PAS) 60
III. Photopyroelectric Spectroscopy (PPES) 67
IV. Measurements of $\alpha(\lambda)$ in Semiconductors using Photoacoustic/Photothermal Techniques 69
Acknowledgments 94
References 94

Chapter 4 **Photothermal Deflection Measurements of the Extinction Coefficient *k*** 99
MATTHEW E. BRIGGS

I. Introduction 99
II. Photothermal Deflection 103
III. Conclusions 116
Acknowledgments 117
References 117

Chapter 5 **Determination of Optical Constants by Brillouin Scattering** 121
HACÈNE BOUKARI and NICHOLAS LAGAKOS

I. Definition of Notation 121
II. Introduction 122
III. Background on Brillouin Scattering Technique 123
IV. Equations for Measurement of the Index of Refraction 125
V. Fabry-Perot Interferometers 128
VI. Discussion 128
VII. Brillouin Scattering in Thin Slabs and Optical Fibers 134
VIII. Special Case of Transparent Thin Slabs 135
IX. Brillouin Scattering in Optical Fibers 146
References 153

Chapter 6 **Doped n-Type Silicon (n-Si)** 155
MARK AUSLENDER and SHLOMO HAVA

I. Introduction 155
II. Contributions to Dielectric Function: Optical Properties versus Optical Constants 156
III. Semiclassical Theory of Free-Carrier Contribution to the Dielectric Function: The Drude Approximation 158
IV. Free-Carrier Contribution to the Dielectric Function in Quantum Absorption Regime: Generalized Drude Approach 159
V. Experimental Data Overview 162
VI. Generalized Drude Approximation for n-Si 166
VII. Tabulation of Optical Constants of Doped n-Si 171
References 185

Chapter 7 **Optical Parameters for the Materials in *HOC I, HOC II,* and *HOC III*** 187
EDWARD D. PALIK

I. Introduction 187
II. The Parameters 187
References 225

Part II CRITIQUES

Subpart 1 Metals

Introduction to the Data for Several Metals 233
DAVID W. LYNCH and W. R. HUNTER

I. Introduction 233
References 235
II. Magnesium (Mg) 235
References 235
III. Titanium (Ti) 240
References 241
IV. Manganese (Mn) 249
References 250
V. Ruthenium (Ru) 253
References 254
VI. Indium (In) 261
References 262
VII. Tin (Sn) 268
References 269
VIII. Antimony (Sb) 274
References 275
IX. Rhenium (Re) 278
References 279

Optical Constants of Eight Rare-Earth Elements 287
L. WARD

I. Introduction 287
II. Cerium (Ce) 292
III. Samarium (Sm) 293
IV. Gadolinium (Gd) 294
V. Terbium (Tm) 297
VI. Dysprosium (Dy) 298
VII. Erbium (Er) 300
VIII. Thulium (Tm) 301
IX. Ytterbium (Yb) 302
References 303

Cesium (Cs) 341
T. INAGAKI and E. T. ARAKAWA

References 344

Zirconium Nitride (ZrN), Hafnium Nitride (HfN) 351
CARL G. RIBBING and ARNE ROOS

References 358

Subpart 2 Semiconductors

Aluminum Nitride (AlN) 373
S. LOUGHIN and R. H. FRENCH

References 377

Bismuth Silicon Oxide ($Bi_{12}SiO_{20}$) and Bismuth Germanium Oxide ($Bi_{12}GeO_{20}$) 403
E. D. PALIK

References 408

Boron Nitride (BN) 425
GARY L. DOLL

References 429

Cadmium Germanium Arsenide ($CdGeAs_2$) 445
J. C. RIFE

References 448

Copper Gallium Sulfide ($CuGaS_2$) 459
J. C. RIFE

References 462

Gallium Selenide (GaSe) 473
DAVID F. EDWARDS

References 477

Gallium Telluride (GaTe) 489
DAVID F. EDWARDS

References 491

Iron Pyrite (FeS_2) 507
E. D. PALIK

References 511

Silicon (Si) Revisited (1.1–1.3 eV) 519
JON GEIST

References 524

Silicon (Si) Revisited (1.4–6.0 eV) 531
DAVID F. EDWARDS

References 533

Silicon–Germanium Alloys (Si_xGe_{1-x}) Revisited 537
J. HUMLÍČEK

References 538

Silver Chloride (AgCl), Silver Bromide (AgBr), Silver Iodide (AgI) 553
MASATO TAZAWA and ARMAND HADNI

References 556

Silver Gallium Selenide ($AgGaSe_2$) and Silver Gallium Sulfide ($AgGaS_2$) 573
LUIS ARTÚS

References 577

Zinc Arsenide (Zn_3As_2) 595
J. MISIEWICZ and K. JEZIERSKI

References 596

Zinc Phosphide (Zn_3P_2) 609
J. MISIEWICZ and K. JEZIERSKI

References 612

Zinc Germanium Phosphide ($ZnGeP_2$) 637
J. C. RIFE

References 640

Subpart 3 **Insulators**

Aluminum Oxide (Al_2O_3) Revisited 653
MICHAEL E. THOMAS and WILLIAM J. TROPF

References 657

Barium Fluoride (BaF_2) 683
MICHAEL E. THOMAS and WILLIAM J. TROPF

References 686

Calcium Carbonate, Calcite ($CaCo_3$) 701
WILLIAM J. TROPF

References 703

Cesium Bromide (CsBr) 717
W. J. MOORE

References 719

Cesium Chloride (CsCl) 731
JOHN E. ELDRIDGE

References 733

Cesium Fluoride (CsF) 743
JOHN E. ELDRIDGE

References 745

Beta-Gallium Oxide (β-Ga_2O_3) 753
DAVID F. EDWARDS

References 755

Lead Fluoride (PbF_2) 761
MÁRCIA A. F. DESTRO and ALVARO J. DAMIÃO

References 766

Lithium Tantalate ($LiTaO_3$) 777
FRANÇOIS GERVAIS and VICENTE FONSECA

References 780

Potassium Iodide (KI) 807
MICHAEL E. THOMAS

References 810

Potassium Niobate ($KNbO_3$) 821
IVAN BIAGGIO

References 825

Rubidium Bromide (RbBr) 845
IVAN OHLÍDAL and MILOSLAV OHLÍDAL

References 848

Rubidium Iodide (RbI) 857
IVAN OHLÍDAL and DANIEL FRANTA

References 861

Sodium Nitrate ($NaNO_3$) 871
EDWARD D. PALIK and R. KHANNA

References 873

Strontium Fluoride (SrF_2) 883
MICHAEL E. THOMAS

References 886

Orthorhombic Sulfur (α-S) 899
KIRK A. FULLER, HARRY D. DOWNING, and MARVIN R. QUERRY

References 905

Cubic Thallium(I) Halides 923
WILLIAM J. TROPF

References 931

Yttrium Aluminum Garnet ($Y_3Al_5O_{12}$) 963
WILLIAM J. TROPF

References 966

Zircon ($ZrSiO_4$) 987
EDWARD D. PALIK and R. KHANNA

References 989

List of Contributors

Numbers in parentheses indicate the pages on which the authors' contributions begin.

E. T. ARAKAWA (341), Life Sciences Division, Oak Ridge National Laboratory, Oak Ridge, Tennessee 37831

LUIS ARTÚS (573), Consejo Superior de Investigaciones Cientificas, Instituto Jaime Almera, Sole Sabaris s/n, 08028 Barcelona, Spain

MARK AUSLENDER (155), Department of Electrical and Computer Engineering, Ben-Gurion University of the Negev, Beer-Sheva 84105, Israel

IVAN BIAGGIO (821), Institute of Quantum Electronics, Swiss Federal Institute of Technology, ETH-Hönggerberg, CH-8093 Zürich, Switzerland

HACÈNE BOUKARI (121), Institute for Physical Science and Technology, University of Maryland, College Park, Maryland 20742

MATTHEW E. BRIGGS (99), Department of Physics, 201 James Fletcher Building, University of Utah, Salt Lake City, Utah 84112

ALVARO J. DAMIÃO (761), Centro Técnico Aeroespacial, Instituto de Estudos Avançados, São José dos Campos, São Paulo, Brasil

MÁRCIA A. F. DESTRO (761), Centro Técnico Aeroespacial, Instituto de Estudos Avancados, São José dos Campos, Sao Paulo, Brasil

GARY L. DOLL (425), Mail Code RES-04, The Timken Company, 1835 Dueber Avenue, S.W., Canton, Ohio 44706

HARRY D. DOWNING (899), Department of Physics and Astronomy, Stephen F. Austin State University, Nacogdoches, Texas 75962

DAVID F. EDWARDS (473, 489, 531, 753), 8820 W. Valpico Road, Tracy, California 95376

JOHN E. ELDRIDGE (731, 743), Department of Physics, 6224 Agriculture Road, The University of British Columbia, Vancouver, B. C. V6T 1Z1, Canada

VICENTE FONSECA (777), Centre de Recherches sur la Physique de Hautes Températures, 1D, Avenue de la Recherche Scientifique, 45071 Orléans Cedex, France

DANIEL FRANTA (857), Department of Solid State Physics, Faculty of Science, Masaryk University Brno, Kotlárská 2, 611 37 Brno, Czech Republic

ROGER H. FRENCH (373), DuPont Central Research and Development, Experimental Station Building E265-384, Wilmington, Delaware 19880-0356

KIRK A. FULLER (899), Department of Atmospheric Science, Colorado State University, Fort Collins, Colorado 80521
JON GEIST (519), 4008 Fulford Street, Olney, Maryland 20832
FRANÇOIS GERVAIS (777), Centre de Recherches sur la Physique de Hautes Temperatures, 1D, Avenue de la Recherche Scientifique, 45071 Orléans Cedex, France
ARMAND HADNI (553), Université Henri Poincaré, Nancy I, 54506 Vandoeuvre-les-Nancy Cedex, France
SHLOMO HAVA (155), Department of Electrical and Computer Engineering, Ben-Gurion University of the Negev, Beer-Sheva 84105, Israel
JOSEF HUMLÍČEK (537), Department of Solid State Physics, Faculty of Science, Masaryk University Brno, Kotlárská 2, 611 37 Brno, Czech Republic
W. R. HUNTER (233), SFA Inc., 1401 McCormack Drive, Largo, Maryland 20774
T. INAGAKI (341), Division of Natural Sciences, Osaka Kyoiku University, Osaka, Japan
K. JEZIERSKI (595, 609), Institute of Physics, Technical University of Wroclaw, Wybrzeze Wyspianskiego 27, 50-370 Wroclaw, Poland
R. KHANNA (871, 987), Department of Chemistry and Biochemistry, University of Maryland, College Park, Maryland 20742
NICHOLAS LAGAKOS (121), Code 7134, Naval Research Laboratory, Washington, D.C. 20375
STEPHEN LOUGHIN (373), Lockheed Martin Astro Space, Building B-29B12, P.O. Box 8555, Philadelphia, Pennsylvania 19101-8555
DAVID W. LYNCH (233), Department of Physics and Astronomy and Ames Laboratory, USDOE, Iowa State University, Ames, Iowa 50011
ANDREAS MANDELIS (59), Photothermal and Optoelectronic Diagnostics Laboratories, Department of Mechanical and Industrial Engineering, University of Toronto, 5 King's College Road, Toronto M5S3G8 Canada
K. A. MASLIN (13), Royal Holloway, University of London, Egham, Surrey TW20 OEX, United Kingdom
G. MIRJALILI* (13), Department of Physics, University of Essex, Colchester CO4 3SQ, United Kingdom
J. MISIEWICZ (595, 609), Institute of Physics, Technical University of Wroclaw, Wybrzeze Wyspianskiego 27, 50-370 Wroclaw, Poland
W. J. MOORE (717), Code 6870, Naval Research Laboratory, Washington, D.C. 20375
IVAN OHLÍDAL (845, 857), Department of Solid State Physics, Faculty of Science, Masaryk University Brno, Kotlárská 2, 611 37 Brno, Czech Republic
MILOSLAV OHLÍDAL (845), Institute of Physical Engineering, Technical University, Brno, Czech Republic

* Present address: Department of Physics, University of Yazd, Yazd, Iran

EDWARD D. PALIK (3, 187, 403, 507, 871, 987), Institute for Physical Science and Technology, University of Maryland, College Park, Maryland 20742

T. J. PARKER (13), Department of Physics, University of Essex, Colchester CO4 3SQ, United Kingdom

MARVIN R. QUERRY (899), Department of Physics, University of Missouri-Kansas City, Kansas City, Missouri 64110

CARL G. RIBBING (351), School of Engineering, Department of Technology, Uppsala University, Box 534, S-751 Uppsala, Sweden

J. C. RIFE (445, 459, 637), Code 6680, Naval Research Laboratory, 4555 Overlook Avenue, S.W., Washington, D. C. 20375

ARNE ROOS (351), School of Engineering, Department of Technology, Uppsala University, Box 534, S-751 Uppsala, Sweden

MASATO TAZAWA (553), National Industrial Research Institute of Nagoya, Nagoya 462, Japan

MICHAEL E. THOMAS (653, 683, 807, 883), The Johns Hopkins University, Applied Physics Laboratory, Johns Hopkins Road, Laurel, Maryland 20723-6099

WILLIAM J. TROPF (653, 683, 701, 923, 963), The Johns Hopkins University, Applied Physics Laboratory, Johns Hopkins Road, Laurel, Maryland 20723-6099

L. WARD (287), School of Natural and Environmental Sciences, Coventry University, Priory Street, Coventry CV1 5FB, United Kingdom

Preface

The *Handbook of Optical Constants of Solids* has now grown to three volumes. The publication of *HOC I* in 1985 and *HOC II* in 1991 has reduced but not exhausted the available materials of scientific and technological interest. One can ask what materials are left to critique. There are several candidates.

There is a trickle of recently published papers remeasuring "old" materials already critiqued in *HOC I* and *HOC II.* This is the case for Si, Al_2O_3, Si_xGe_{1-x}, which are revisited in *HOC III.* This will be worthwhile to do for several other materials from time to time.

We have not developed the courage to attack the III–V ternary and quaternary materials in detail except for $Al_xGa_{1-x}As$ *(HOC II),* so important in laser and electronic applications. We looked at the II–VI ternary compound $Hg_{1-x}Cd_xTe$ *(HOC II),* important in infrared-detector applications, as well as the IV-VI compound $Pb_{1-x}Sn_xTe$ *(HOC II).*

Our dream of critiquing all the alkali halides from LiF to CsBr is not yet fulfilled.

We have noticed a lack of data for the index of refraction n but not for the extinction coefficient k for gemstones. The gemologist only seems interested in n at the Na D line. We noticed from a scan of several gem books that n is not given throughout the visible. For most purposes, n is considered a constant. But to the physicist, n is not a constant. Since gemstones must be "full of impurities" to give them their wide variety of colors, the gemologist does measure the visible absorption spectrum to determine the impurity absorption bands. The physicist usually prefers pure crystals (at least insulators). We have previously critiqued diamond, sapphire, quartz, and spinel in pure form, the latter three being the starting point for several gemstones including ruby, amethyst, agate, opal, and chrysoberyl. In *HOC III* we add yttrium aluminum garnet and zircon. There are no n measurements in the visible except at 589.0 nm for zircon. We need to find more technology uses for gemstones which, in turn, will spur measurements of n and k! We could not find a critiquer for cubic zirconia, which to us is quite different from diamond in optical properties, but serves as "fake" diamond for many people.

As with *HOC I* and *HOC II,* I am indebted to the many scientists for their work in *HOC III,* writing chapters on still more ways to measure optical constants and writing critiques tabulating the optical constants of more than 60 additional materials.

June, 1997 EDWARD D. PALIK

Chapter 1

Introductory Remarks

EDWARD D. PALIK
Institute for Physical Science and Technology
University of Maryland
College Park, Maryland

I. Introduction 3
II. The Chapters 4
III. The Critiques 5
IV. The Tables 5
V. The Figures of the Tables 5
VI. Corrections, Additions, and Comments 6
A. Optical Constants of CdS 6
B. Optical Constants of Metal Films 6
C. Henke Model for the Elements 8
D. More-Recent Papers about Optical Constants 9
E. Optical Constants on Disk 12
References 12

INTRODUCTION I

The two previous volumes of *Handbook of Optical Constants of Solids (HOC I* and *HOC II)* contained about 85 materials. The present volume adds about 58 more materials, roughly divided into equal numbers of metals, semiconductors, and insulators. A long list of potential materials was circulated among possible critiquers. They chose and/or recommended the ones presented here. There are still some materials omitted because of a lack of critiquers. These include Bi, B, Ba, Ca, Cd, Pb, Zn, Zr, ZnO, HgS, HgSe, $Pb_xSn_{1-x}Se$, PbO, MoS_2, Cd_3As_2, GaS, LiOH, NaBr, NaI, KF, LiCl, LiBr, ZrO_2, BaO, and NiO. Note that 43 of the 92 chemical elements are done and 143 of the 100,000 (or more) chemical compounds. We have omitted glasses generally, which are covered to some extent by Efimov [1] and Tropf *et al.* [2].

There is some loose use of the words *semiconductor* and *insulator* in *HOC I* and *HOC II* based primarily on the band gap being less or greater than

HANDBOOK OF OPTICAL CONSTANTS OF SOLIDS III

Copyright © 1998 by Academic Press.
All rights of reproduction in any form reserved
ISBN 0-12-544423-0/$25.00.

3 eV. AgCl, AgBr, AgI, BSO, and BGO are considered as semiconductors because their electrical properties can be controlled by doping during growth of the crystals, but they may end up in either category. Diamond is invariably thought of as an insulator, although natural diamonds can be found with semiconducting properties.

II THE CHAPTERS

The chapters are meant to describe experimental techniques for measuring n and k.

In Chapter 2, Parker *et al.* discuss the determination of n and k by differential Fourier transform spectroscopy in the far infrared. This is an elegant way to obtain n and k from the reflection amplitude and phase and has been applied to many semiconductors and insulators. It is of interest to compare these newer optical constants with those in *HOC I* or *HOC II,* which have generally been obtained by Kramers-Kronig (K-K) analysis or classical oscillator fit.

In Chapter 3, Mandelis describes the use of photoacoustic spectroscopy to determine k. While this chapter stresses semiconductors, several variations of the technique have also found widespread use for other materials.

In Chapter 4, Briggs discusses photothermal deflection as a method of determining k. It is done with two intense beams, one to heat up a small spot on a sample and a second to detect bending of the sample as it expands locally.

In Chapter 5, Boukari and Lagakos describe the determination of n and k by Brillouin scattering. While not usually thought of as a technique for determining optical constants, there are novel ways to determine n an k in highly absorbing materials and n in transparent slabs and thin films.

In Chapter 6, Auslender and Hava develop models for calculating n and k in n-Si for the infrared region for free-electron concentrations from 10^{16} to 10^{20} cm^{-3}.

In Chapter 7, Palik collects a number of optical parameters for all the materials in *HOC I, HOC II,* and *HOC III* including crystal structure, space group symmetry, unit cell dimensions, number of molecules/unit cell, optic and acoustic irreducible representation, transverse and longitudinal lattice vibration frequencies, plasma frequency, band gap, and d.c. dielectric constant.

There were suggestions for chapters on the loss-tangent method at low frequencies and on the prism minimum-deviation technique (still the best way to determine n), but these could not be done at this time.

THE CRITIQUES III

The critiques are meant to be the critiquer's own judgment of the best room-temperature values of n and k over the widest spectral range. As the volumes have progressed, we have expanded the range a little with a few critiques including above and below room-temperature data. Sometimes there are two overlapping sets of data from two different laboratories which can be compared. This sometimes happens in the far infrared where reflectivity is K-K analyzed and/or a classical oscillator model is applied. Generally, it is not a good idea to give the reader a choice of data—it is the job of the critiquer to make the choice. Sometimes, however, a comparison sheds light on the problems arising in the measurement of optical constants such as wavelength calibration and determination of absolute reflectivity. Recently, spectroscopic ellipsometry has grown into a wide-spread technique for the 1.5–6 eV region, probably supplanting K-K analysis of reflectivity.

We have returned to a few materials done in previous volumes because more data have become available. Therefore, we revisit Al_2O_3, Si_xGe_{1-x} and Si.

THE TABLES IV

The tables of n and k have become more individual to meet the needs of the individual critiquers. We maintain the columns labeled eV, cm^{-1}, μm, n, k and proceed down the column in decreasing eV. Reference brackets [1] start at the top of a given data column and are understood down the column until a new data set occurs, which is then labeled [2], for example. We promoted exponential notation especially of k, ideally for every column, but have not yet reached that stage of uniformity.

To facilitate editing the tables for the Optical Society of America, we have requested that the exponential notation be used at every row, rather than omitting the exponent until it changes value somewhere down the column.

THE FIGURES OF THE TABLES V

The critiquers have taken more leeway with the figures, since they had to produce them with whatever graphics software they had available. In previous editions, all the figures were prepared by the same artist who kept the style uniform. Now critiquers can use data points (usually ○○○ for n and △△△ for k). Data points can be connected with lines, or just lines can be used (usually —— for n and --- for k). In the past, both n and k were plotted on the same

figure with the same log-log scale. Since the extent of k determined the number of decades of the log scale for the ordinate, ($10^{-7} < k < 10^{1}$), n was squeezed. Also, for solids with a lot of vibration bands, this region got very busy. Now some critiquers have separated n and k plots to show the structure more clearly.

The drawbacks in having each critiquer make his own figure are the many problems of font size, tick-mark position, and border thickness, remembering that the figure will be reduced in published form.

VI CORRECTIONS, ADDITIONS, AND COMMENTS

A Optical Constants of CdS

A correction and addition to the data for CdS from *HOC II* needs to be made according to the critiquer, L. Ward. Data of Dutton[1] near the band edge has been added. The extinction coefficient for both $\mathbf{E}_{\|c}$ and $\mathbf{E}_{\perp c}$ has been determined by transmission measurements of thin slabs of different thicknesses. These can be compared to data of Cardona and Harbeke[2] for bulk-oriented samples obtained from K-K analysis of reflectivity with polarized light. Data of Khawaja and Tomlin[3] for films deposited on quartz substrates (assumed to be polycrystalline) were obtained from transmittance and reflectance measurements; these data have been reassessed to correct an error in reading the wavelength scale. The results are presented in Table I. While above the band gap the results for k are comparable, below the band gap where absorption decreases orders of magnitude, the results differ drastically among the three data sets. We suspect that K-K analysis of reflectivity in Cardona and Harbeke gives poor results for $k \ll 1$ compared to transmittance of slabs in Dutton. For the polycrystalline films in Khawaja and Tomlin, it is not obvious why k is so much larger compared to the data of Dutton below the band gap. Perhaps there was significant light scattering from defected material, which was mistaken for absorption.

B Optical Constants of Metal Films

The optical constants of metals in *HOC I, II,* and *III* can be compared with those given in Optimatr, a computer program to calculate optical prop-

[1] D. Dutton, Fundamental absorption edge in cadmium sulfide. *Phys. Rev.* **112,** 785 (1958).

[2] M. Cardona and G. Harbeke, Optical properties and band structure in wurtzite-type crystals and rutile. *Phys. Rev.* **A137,** 1467 (1965).

[3] E. E. Khawaja and S. G. Tomlin, The optical constants of thin evaporated films of cadmium and zinc sulphide. *J. Phys. D: Appl. Phys.* **8,** 581 (1975).

TABLE I

Values of n and k for Cadmium Sulfide from Various References

eV	cm^{-1}	μm	n	k	$n\perp$	$k\perp$	$n\parallel$	$k\parallel$	$k\perp$	$k\parallel$
			[3]		[2]		[2]		[1]	
4.133	33333	0.30	2.68	0.70						
4.0	32260	0.3100			2.64	0.64	2.40	0.81		
3.75	30245	0.3306			2.64	0.62	2.38	0.74		
3.542	28571	0.35	2.58	0.47						
3.5	28230	0.3542			2.62	0.56	2.38	0.65		
3.25	26213	0.3815			2.62	0.49	2.36	0.61		
3.100	25000	0.40	2.55	0.37						
3.0	24196	0.4133			2.63	0.44	2.37	0.56		
2.755	22222	0.45	2.62	0.32						
2.75	22180	0.4509			2.70	0.41				
2.7	21777	0.4592					2.47	0.54		
2.6	20970	0.4769							0.32	0.32
2.575	20769	0.4815							0.32	0.32
2.55	20567	0.4862							0.32	0.32
2.525	20365	0.4910							0.29	0.22
2.5	20164	0.4959			2.81	0.36	2.62		0.28	0.16
2.475	19962	0.5009	2.72	0.15					0.25	0.15
2.45	19760	0.5061							0.081	0.022
2.425	19559	0.5113							0.014	0.0028
2.4	19357	0.5166							0.0016	0.00033
2.375	19155	0.5220							0.00019	
2.254	18182	0.55	2.45	0.01						
2.25	18147	0.5510			2.57	0.04	2.53	0.26		
2.066	16667	0.60	2.40							
2.0	16130	0.6199			2.48	0.02	2.44	0.18		

erties of materials. This software is available from ARSoftware, 8201 Corporate Dr., Suite 1110, Landover, MD 20785. It is copyrighted by the Johns Hopkins University/Applied Physics Laboratory and ARSoftware, Inc. The calculational procedures, based on several literature models for determining optical properties of solids, are based on the works of M. E. Thomas and W. J. Tropf. The data for metals in Optimatr were essentially that of Ordal *et al.*, who fitted a Drude model to many sets of existing data. In comparing the optical constants of metals from Optimatr and *HOC* in the visible and near-infrared regions, one finds for Au and Ag especially, significant variations in n and k (up to a factor of two). This is due to the fact that data from different laboratories were used. Where the data from the same laboratories were used, the agreement is much better, of course.

This general problem of the variation of optical constants of metal films deposited at different laboratories and with different deposition techniques, has been discussed by Aspnes *et al.* with regard to gold. They find that voids

and grain size in the films can account for significant variations in n and k, as demonstrated by their spectroscopic-ellipsometry measurements in the 1.5–6 eV spectral region. Therefore, it would appear that metal films (and especially Au and Ag) should be measured directly if the optical constants are needed for an application. Also, it would be good to measure the optical constants of single crystals of the metal, if polishing the surface can be accomplished with minimal damage. Since k is so large (generally > 1), the optical skin depth is typically less than a few hundred Angstroms. Native oxides can also pose a problem.

We list a number of papers about Au which trace this problem and may be of interest to the reader.

H. E. Bennett and J. M. Bennett, Validity of the Drude theory for silver, gold and aluminum in the infrared. *In* "Optical Properties and Electronic Structure of Metals and Alloys," (F. Abeles, ed.), p. 175. North-Holland, Amsterdam, 1966.

M.-L. Theye, Investigation of the optical properties of Au by means of thin semitransparent films. *Phys. Rev. B* **2,** 3060. (1970).

D. E. Aspnes, E. Kinsbron and D. D. Bacon, Optical properties of Au: Sample effects. *Phys. Rev. B* **21,** 3290 (1980), and references therein.

M. A. Ordal, L. L. Long, R. J. Bell, S. E. Bell, R. R. Bell, R. W. Alexander, Jr., and C. A. Ward, Optical properties of the metals Al, Co, Cu, Au, Fe, Pb, Ni, Pd, Pt, Ag, Ti, and W in the infrared and far infrared. *Appl. Opt.* **22,** 1099 (1983).

M. A. Ordal, R. J. Bell, R. W. Alexander, Jr., L. L. Long, and M. R. Querry, Optical properties of fourteen metals in the infrared and far infrared: Al, Co, Cu, Au, Fe, Pb, Mo, Ni, Pd, Pt, Ag, Ti, V, and W. *Appl. Opt.* **24,** 4493 (1985).

M. Yamamoto and T. Namioka, In situ ellipsometric study of optical properties of ultrathin films. *Appl. Opt.* **31,** 1612 (1992).

F. Xingwei, S. Yi, M. Hongzhou, C. Liangyao, and Q. Youhua, Precision of determination of optical constant of Au film by spectroscopic ellipsometry. *Chin. J. Infrared Millimeter Waves* **12,** 107 (1993).

C Henke Model for the Elements

The most recent update for the scattering factors of the chemical elements has appeared in B. L. Henke, E. M. Gullikson and J. C. Davis, X-Ray interactions: Photoabsorption, scattering, transmission, and reflection at E = 50–30000 eV, Z = 1–92. *At. Data Nucl. Data Tables* **54,** 181 (1993).

These data are also available by computer. In fact, the calculation of n and k can be carried out at

http://www-cxro.lbl.gov/optical_constants

Extension to compounds is also possible, although the values will not be correct at energies near bonding energies. Deep-lying K and L absorption edges are well approximated, however.

More-Recent Papers about Optical Constants D

Since 1985 for the materials in *HOC I,* and since 1991 for the materials in *HOC II,* more papers have appeared discussing optical constants. We list those papers below which we have noticed.

Occasionally, an older paper of interest, missed or omitted by the critiquer, has been included (without comment).

Metals 1

B. Henke, E. M. Gullikson and J. C. Davis, X-ray interactions; photoabsorption, scattering, transmission, and reflection at E = 50-30000 eV, Z = 1-92. *At. Data Nucl. Data Tables* **54,** 181 (1993).

M. Yamamoto and T. Namioka, In situ ellipsometric study of optical properties of ultrathin films. *Appl. Opt.* **31,** 1612 (1992). (C, Si, Ni, Nb, Mo, Ru, Rh, Pd, Ag, W, Re, Au.)

D. L. Windt, XUV optical constants of single-crystal GaAs and sputtered C, Si, Cr_3C_2, Mo, and W. *Appl. Opt.* **30,** 15 (1991).

D. L. Windt, W. C. Cash, Jr., M. Scott, P. Arendt, B. Newnam, R. F. Fisher, and A. B. Swartzlander, Optical constants for thin films of Ti, Zr, Nb, Mo, Ru, Rh, Pd, Ag, Hf, Ta, W, Re, Ir, Os, Pt, and Au from 24 Å to 1216 Å. *Appl. Opt.* **27,** 246 (1988).

D. L. Windt, W. C. Cash, Jr., M. Scott, P. Arendt, B. Newnam, R. F. Fisher, A. B. Swartzlander, P. Z. Takacs, and J.M. Pinneo, Optical constants for thin films of C, diamond, Al, Si and CVD SiC from 24 Å to 1216 Å. *Appl. Opt.* **27,** 279 (1988).

F. Xingwei, S. Yi, M. Hongzhou, C. Liangyao and Q. Youhua, Precision of determination of optical constants of Au film by spectroscopic ellipsometry. *Chin. J. Infrared Millimeter Waves* **12,** 107 (1993).

M. Yanagihara, J. Cao, M. Yamamoto, A. Arai, S. Nakayama, T. Mizuide, and T. Namioka, Optical constants of very thin gold films in the soft x-ray region. *Appl. Opt.* **30,** 2807 (1991).

J. Cao, M. Yanagihara, M. Yamamoto, Y. Goto, and T. Namioka, Simultaneous determination of the optical constants and thickness of very thin films by using soft-x-ray reflectance measurements. *Appl. Opt.* **33,** 2013 (1994). (Au, C.)

R. Wolf, H.-G. Birken, C. Blessing, and C. Kunz, Optical constants of gold in the soft-x-ray region from reflection and transmission measurements. *Appl. Opt.* **33,** 2683 (1994).

T. Maehara, M. Yanagihara, M. Yamamoto, and T. Namioka, Optical constants of very thin Pt and Rh films determined from soft-x-ray reflectance and photoelectric yield measurements. *Nucl. Instrum. Methods Phys. Res.* **B47,** 362 (1993).

B. T. Sullivan, Optical properties of palladium in the visible and near UV spectral regions. *Appl. Opt.* **29,** 1964 (1990).

J. I. Larruquert, J. A. Méndez, and J. A. Aznárez, Far-ultraviolet reflectance measurements and optical constants of unoxidized aluminum films. *Appl. Opt.* **34,** 4892 (1995).

J. I. Larruquert, J. A. Méndez, and J. A. Aznárez, Optical constants of aluminum films in the extreme ultraviolet interval of 82-77 nm. *Appl. Opt.* **35,** 5692 (1996).

Semiconductors 2

J. Geist, A. Migdall, and H. Baltes, Shape of the silicon absorption coefficient spectrum near 1.63 eV. *Appl. Opt.* **29,** 3548 (1990).

J. Geist, A. Migdall, and H. P. Baltes, Analytic representation of the silicon absorption coefficient in the indirect transition region. *Appl. Opt.* **27,** 3777 (1988).

H. A. Weakliem and D. Redfield, Temperature dependence of the optical properties of silicon *J. Appl. Phys.* **50,** 1491 (1979).

J. Geist, A. R. Schaefer, J.-F. Song, Y. H. Wang, and E. F. Zalewski, An accurate value for the absorption coefficient of silicon at 633 nm. *J. Res. Natl. Inst. Stand. Technol.* **95,** 549 (1990).

G. E. Jellison, Jr., and F. A. Modine, Optical functions of silicon at elevated temperatures. *J. Appl. Phys.* **76,** 3758 (1994).

G. E. Jellison, Jr., Optical functions of silicon determined by two-channel polarization modulation ellipsometry. *Opt. Mater.* **1,** 41, (1992).

G. E. Jellison, Jr., and F. A. Modine, Optical functions of silicon between 1.7 and 4.7 eV at elevated temperatures. *Phys. Rev.* **B27,** 7466 (1983); G. E. Jellison, Jr., and F. A. Modine, Optical absorption of silicon between 1.6 and 4.7 eV at elevated temperatures. *Appl. Phys. Lett.* **41,** 180 (1992).

J. F. Seely, W. R. Hunter, J. C. Rife, and M. P. Kowalski, Optical constants of thin silicon films near the silicon $L_{2,3}$ absorption edge. *Appl. Opt.* **31,** 7367 (1992).

G. E. Jellison, Jr., T. E. Haynes, and H. H. Burke, Optical functions of silicon-germanium alloys determined using spectroscopic ellipsometry. *Opt. Mater.* **2,** 105 (1993).

J. Humlíček and M. Garriga, Temperature dependence of the refractive index of crystalline germanium-silicon alloys. *Appl. Phys.* **A56,** 259 (1993).

J. Humlíček, A. Röseler, T. Zettler, M. G. Kekoua, and E. V. Khoutsishvili, Infrared refractive index of germanium-silicon alloy crystals. *Appl. Opt.* **31,** 90 (1992).

S. Chen, R. Jiang, and D. Mo, Ultraviolet-visible ellipsometric spectra and optical constants of sputtered amorphous silicon. *Acta Opt. Sin. (Guangxue Xuebao)* **4,** 49 (1984).

G. E. Jellison, Jr., Optical functions of GaAs, GaP, and Ge determined by two-channel polarization modulation ellipsometry. *Opt. Mater.* **1,** 151 (1992).

T. A. Kudykina, "Index of refraction of $A^{III}B^{V}$ compounds in the region of fundamental absorption. *Phys. Status Solidi B* **188,** K39 (1995).

C. M. Herzinger, H. Tao, P. G. Snyder, F. G. Celii, Y.-C. Kao, B. Johs, and J. A. Woollam, Determination of AlAs optical constants by variable angle spectroscopic ellipsometry and a multisample analysis. *J. Appl. Phys.* **77,** 4677 (1995).

C. M. Herzinger, P. G. Snyder, B. Johs and J. A. Woollam, InP optical constants between 0.7 and 5 eV determined by variable-angle spectroscopic ellipsometry. *J. Appl. Phys.* **77,** 1715 (1995).

C. M. Herzinger, P. G. Snyder, F. G. Celii, Y.-C Kao, D. Chow, B. Johs, and J. A. Woollam, Studies of thin stressed GaAs, AlAs and AlSb layers by spectroscopic ellipsometry. *J. Appl. Phys.* **79,** 2667 (1996).

W. J. Moore and R. T. Holm, Infrared dielectric constant of gallium arsenide. *J. Appl. Phys.* **80,** 6939 (1996).

L. Pajasová, P. Pajas, A. Šimunek, and O. A. Makarov, A study of the optical properties of semiconductors with synchrotron radiation from the VEPP-2M storage ring. *Nucl. Instrum. Methods Phys. Res.* **A261,** 131 (1987). (GaAs.)

V. Vaicikauskas, Far infrared surface electromagnetic waves propagation on A^3B^5 semiconductors. *Int. J. Infrared Millimeter Waves* **15,** 303 (1994). (InSb, InP, GaAs.)

J. A. McCaulley, T. W. M. Dommelly, M. Vernon, and I. Taha, Temperature dependence of the near-infrared refractive index of silicon, gallium arsenide, and indium phosphide. *Phys. Rev. B* **49,** 7408 (1994).

P. Martin, E. M. Skouri, L. Chusseau, and C. Milert, Accurate refractive index measurements of doped and undoped InP by a grating coupling technique. *Appl. Phys. Lett.* **67,** 881 (1995).

R. G. Kaufman, C. R. Hulse, D. J. Vezzetti, A. L. Moretti, K. A. Stair, G. P. Devane, and T. E. Bird, Measurement of the refractive index of $Al_xGa_{1-x}As$ and the mode indices of guided modes by a grating coupling technique. *J. Appl. Phys.* **75,** 8053 (1994).

R. J. Deri and M. A. Emanuel, Consistent formula for the refractive index of $Al_xGa_{1-x}As$ below the band edge. *J. Appl. Phys.* **77,** 4667 (1995).

C.-H. Lin and J. M. Meese, Optical properties of bulk $Al_xGa_{1-x}As$. *J. Appl. Phys.* **74,** 6341 (1993).
D. B. Chenault and R. A. Chipman, Infrared birefringence spectra for cadmium sulfide and cadmium selenide. *Appl. Opt.* **32,** 4223 (1993).
D. Dutton, Fundamental absorption edge in cadmium sulfide. *Phys. Rev.* **112,** 785 (1958).
P. Hofmann, K. Horn, A. M. Bradshaw, R. L. Johnson, D. Fuchs, and M. Cardona, Dielectric function of cubic and hexagonal CdS in the vacuum ultraviolet region. *Phys. Rev. B* **47,** 1639 (1993).
M. Schäffner, X. Bao, and A. Penzkofer, Principal optical constants measurement of uniaxial crystal CdSe in the wavelength region between 380 and 950 nm. *Appl. Opt.* **31,** 4546 (1992).
J. M. Hoffman and W. L. Wolfe, Cryogenic refractive indices of ZnSe, Ge, and Si at 10.6 μm. *Appl. Opt.* **30,** 4014 (1991).
C. A. Klein, R. P. Miller, and D. L. Stierwalt, Surface and bulk absorption characteristics of chemically vapor-deposited zinc selenide in the infrared. *Appl. Opt.* **33,** 4304 (1994).
E. N. Kotlikov, Analysis of absorption in zinc selenide and fluoride mirrors and films. *Opt. Spectrosc.* **70,** 490 (1991); *Opt. Spektrosk.* **70,** 838 (1991).
W. J. Moore, Errors in film refractive-index determinations from interference fringes. *Appl. Opt.* **33,** 4164 (1994). (3C-SiC films.)
W. J. Moore, R. T. Holm, M. J. Yang, and J. A. Freitas, Jr., Infrared dielectric constant of cubic SiC. *J. Appl. Phys.* **78,** 7255 (1995).
S. Ninomoya and S. Adachi, Optical constants of 6N-SiC single crystal. *Jpn. J. Appl. Phys.* **33,** 2479 (1994).
J. B. Kortright and D. L. Windt, Amorphous silicon carbide coatings for extreme ultraviolet optics. *Appl. Opt.* **27,** 2841 (1988).
M. Yanagihara, M. Niwano, T. Koide, S. Sata, T. Miyahara, Y. Iguchi, S. Yamaguchi, and T. Sasaki, Soft x-ray reflection from SiC, TiC, and WC mirrors. *Appl. Opt.* **25,** 4586 (1986).
C. Junhao and M. Zhengyu, Absorption and reflection spectra of HgCdTe *Chin. J. Infrared Millimeter Waves* **8,** 91 (1989).
A. I. Belogorokhov, A. G. Belov, and E. P. Rashevskaya, Effect of free charge carriers on $Cd_xHg_{1-x}Te$ solid-solution reflection spectra in the far infrared. *Opt. Spectrosc.* **69,** 86 (1990); *Opt. Spektrosk.* **69,** 139 (1990).
S. Farjami Shayesteh, T. Dumflow, T. J. Parker, T. I. Benushis, S. N. Ershov, and M. I. Vasilevskiy, Determination of the far infrared optical constants of n-doped bulk $Cd_xHg_{1-x}Te$ (CMT) by dispersive Fourier transform spectroscopy. *Int. J. Infrared Millimeter Waves* **16,** 763 (1995).
M. Nianxin, Y. Hongjuan, S. Xuechu, H. Zhihong, and L. Anxiang, Far-infrared reflectance spectra of naturally occuring PbS (galena). *Chin. J. Infrared Millimeter Waves* **13,** 91 (1994).

Insulators 3

J. M. Siqueiros, R. Machorro, and L. E. Regalado, Determination of the optical constants of MgF_2 and ZnS from spectrophotometric measurements and the classical oscillator method. *Appl. Opt.* **27,** 2549 (1988).
S. Cunsolo, P. Dore, and C. P. Varsamis, Refractive index of crystals from transmission and reflection measurements: MgO in the far-infrared region. *Appl. Opt.* **31,** 4554 (1992).
S. Cunsolo, P. Dore, S. Lupi, and P. Maselli, Complex refractive index of MgO in the far infrared from transmission and reflection measurements. *Infrared Phys.* **33,** 539 (1992).
X. Gerbaux, A. Hadni, M. Tazawa, and J. C. Villegier, Far-infrared spectra of magnesium oxide. *Appl. Opt.* **33,** 57 (1994).
J. Nithianandam and J. C. Rife, Synchrotron x-ray optical properties of natural diamond. *Phys. Rev. B* **47,** 3517 (1993).
G. Davies, A. T. Collins, and P. Spear, Sharp infrared absorption lines in diamond. *Solid State Commun.* **49,** 433 (1984).

Y. Pastol, G. Arjavalingam, G. V. Kopcsay, and J.-M. Halbout, Dielectric properties of uniaxial crystals measured with optoelectronically generated microwave transient radiation. *Appl. Phys. Lett.* **55,** 2277 (1989). (Al_2O_3, x-SiO_2.)

R. T. Swimm, Y. Xiao, and M. Bass, Calorimetric study of optical absorption of Suprasil W-1 fused quartz at visible, near-IR and near-UV wavelengths. *Appl. Opt.* **24,** 322 (1985).

M. L. Lang and W. L. Wolfe, Optical constants of fused silica and sapphire from 0.3 to 25 μm. *Appl. Opt.* **22,** 1267 (1983).

E. E. Khawaja and F. Bouamrane, Determination of the optical constants *(n, k)* of thin dielectric films. *Appl. Opt.* **32,** 1168 (1993). (deposited TiO_2.)

U. Schlarb and K. Betzler, Refractive indices of lithium niobate as a function of wavelength and composition. *J. Appl. Phys.* **73,** 3472 (1993).

A. V. Soldatov, I. E. Shtekhin, and A. Biankoni, Fine structure analysis of the L_2 edge of x-ray absorption by Ca in CaF_2 using multiple-scattering method. *Opt. Spectrosc.* **74,** 514 (1993); *Opt. Spektrosk.* **74,** 862 (1992).

A. B. Sushkov and E. A. Tishchenko, Ellipsometry of a convergent beam in the far infrared. *Opt. Spectrosc.* **72,** 265 (1992): *Opt. Spektrosk.* **72,** 491 (1992). ($SrTiO_3$.)

M. E. Thomas, W. J. Tropf, and S. L. Gilbert, Vacuum-ultraviolet characterization of sapphire, ALON, and spinel near the band gap. *Opt. Eng.* **32,** 1340 (1993).

M. E. Thomas, Optical properties of IR materials. *Thin Solid Films* **206,** 241 (1991). (MgO, SiO_2, Al_2O_3, Y_2O_3, $MgAl_2O_4$.)

G. Compagnini, Optical constants of hydrogenated and unhydrogenated amorphous carbon in the 0.5–12-eV range. *Appl. Opt.* **33,** 7377 (1994).

L. Kou, D. Labrie, and P. Chylek, Refractive indices of water and ice in the 0.65– to 2.5-μm spectral range. *Appl. Opt.* **32,** 3531 (1993).

V. M. Zoloratev and A. V. Demin, Optical constants of water over a broad range of wavelengths, 0.1Å–1m. *Opt. Spectrosc.* **43,** 157 (1977); *Opt. Spektrosk.* **43,** 271 (1977).

H. R. Zelsmann, Temperature dependence of the optical constants for liquid H_2O and D_2O in the far infrared region. *J. Mol. Struct.* **350,** 95 (1995).

M. E. Innocenzi, R. T. Swimm, M. Bass, R. H. French, A. B. Villaverde, and M. R. Kokta, Room-temperature optical absorption in undoped α-Al_2O_3. *J. Appl. Phys.* **67,** 7542 (1990).

M. Zukic, D. G. Torr, J. F. Spann, and M. R. Torr, Vacuum ultraviolet thin films. 1: Optical constants of BaF_2, CaF_2, LaF_3, MgF_2, Al_2O_3, HfO_2, and SiO_2 thin films. *Appl. Opt.* **29,** 4284 (1990).

E Optical Constants on Disk

The tables of *n* and *k* from *HOC I* and *HOC II* have been edited and put on disk by the Optical Society of America. One 3.5″ disk in MS DOS version in compressed format is available from Electronic Products, Optical Society of America, 2010 Massachusetts Ave., N.W., Washington, D.C. 20036. Hopefully, this can be expanded to include the materials in *HOC III* shortly.

REFERENCES

1. A. M. Efimov, "Optical Constants of Inorganic Glasses." CRC Press, Boca Raton, Florida, 1995.
2. W. J. Tropf, M. E. Thomas and T. J. Harris, Properties of crystals and glasses. *In* "Handbook of Optics, Volume II, Devices, Measurements and Properties," (M. Bass, E. W. Van Stryland, D. R. Williams and W. L. Wolfe, eds.), 2nd Ed. McGraw-Hill, New York, 1995.

Chapter 2

Determination of the Far-Infrared Optical Constants of Solids by Dispersive Fourier Transform Spectroscopy

T. J. PARKER[1], K. A. MASLIN[2], and G. MIRJALILI[1*]
[1]Department of Physics, University of Essex
Colchester, United Kingdom
[2]Royal Holloway, University of London
Egham, Surrey, United Kingdom

I. Introduction 13
II. The Materials 20
A. Alkali Halides 20
B. Semiconductors 32
C. II–VI Semiconductors 33
D. III–V Semiconductors 38
Acknowledgment 55
References 55

I INTRODUCTION

We present values of the far-infrared optical constants of a selection of alkali halide crystals (NaCl, KCl, KBr, KI, and RbCl), II–VI semiconductors (CdTe, ZnSe) and III–V semiconductors (GaP, GaAs, GaSb, InP, InAs, and InSb) determined by dispersive Fourier transform spectroscopy (DFTS). DFTS is a technique for determining the optical constants of materials in the solid, liquid, or gas phase from direct measurements of the amplitude and phase reflection or transmission coefficients of suitable samples as a function of frequency, $f = c/\lambda$, or wavenumber, $\nu = 1/\lambda$, where c is the speed of light in vacuo and λ is the wavelength. The technique was pio-

* Present address: Department of Physics, University of Yazd, Yazd, Iran

Copyright © 1998 by Academic Press.
All rights of reproduction in any form reserved
ISBN 0-12-544423-0/$25.00.

neered in the early 1960s by Chamberlain and colleagues [1–3] at the National Physical Laboratory in the United Kingdom, and by Bell and colleagues [4–6] at the Ohio State University in the United States. A number of extensive reviews of the applications of DFTS in solid, liquid, and gas state spectroscopy have been written over the past twenty years [7–10]; we shall not repeat that material here, but shall very briefly summarize the principles of the technique and then concentrate on aspects of the method which have a direct bearing on the accuracy of the determination of the optical constants.

In DFTS, a suitable sample, usually prepared with plane-parallel surfaces, is placed in one arm, usually the fixed arm, of a two-beam Michelson interferometer for measurements either in reflection or transmission; three geometrical arrangements have been described in the literature [8], and these are illustrated schematically in Fig. 1. Two interferograms are usually recorded, a sample interferogram $I_S(x)$, measured as a function of optical path difference, x, with the sample in place in the interferometer, and a reference, or background interferogram, $I_B(x)$, recorded after replacing the sample with a suitable reference material: in reflection DFTS, the reference material would be a reference mirror placed in the plane previously occupied by the sample; in transmission DFTS, the reference material would be the slab of vacuum left in the instrument after removing the sample. In either case, the information containing the frequency dependence of the amplitude and phase reflection or transmission coefficients is obtained by computing the ratio

$$L(\nu) = L_0(\nu)\exp i\phi_L(\nu) = \frac{FT[I_S(x)]}{FT[I_B(x)]} \tag{1}$$

of the complex Fourier transforms, $FT[I_S(x)]$ and $FT[I_B(x)]$, of the two recorded interferograms. The exact form of the relationship between $L(\nu)$, commonly known as the complex insertion loss, and the optical constants, (n, k), is determined by the details of the experimental arrangement.

In this article we shall review the optical constants of a selection of simple binary solids calculated from amplitude and phase reflection coefficients determined by reflection DFTS. In this geometry (Fig 1(c)), as already pointed out, the background interferogram is recorded after replacing the sample by a reference mirror. This is the simplest geometry encountered in DFTS, and the complex insertion loss is equal to the ratio of the complex amplitude reflection coefficients of the sample and the reference mirror. Thus, for reflection DFTS, or amplitude reflection spectroscopy as it is frequently known, the complex insertion loss is given by

$$L_0(\nu)\exp i\phi_L(\nu) = \frac{r_s(\nu)\exp i\phi_s(\nu)}{r_m(\nu)\exp i\phi_m(\nu)} \tag{2}$$

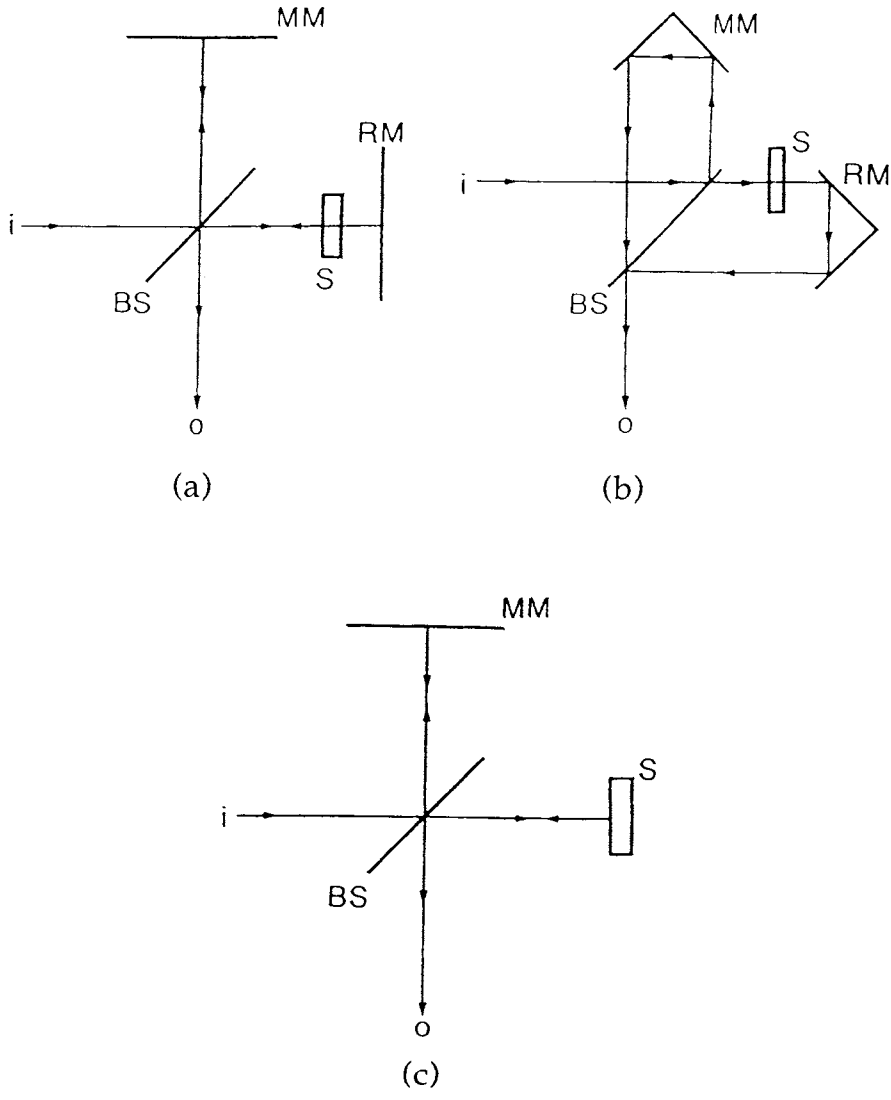

Fig. 1. Schematic drawing of the three experimental arrangements used in DFTS. (a) Double-pass transmission DFTS, (b) Single-pass transmission DFTS, and (c) Reflection DFTS, or amplitude-reflection spectroscopy. Key: *i*, input beam; *o*, output beam; *MM*, moving mirror; *RM*, reference mirror; *BS*, beam splitter; *S*, sample.

In DFTS in the far infrared, it is common practice to regard the reference mirror as a perfect mirror with a complex-amplitude reflection coefficient

$$r_m(\nu) \exp i\phi_m(\nu) = \exp i\pi. \tag{3}$$

Consequently, the amplitude and phase reflection coefficients of the sample are determined in a straightforward way from the measured interferograms, as

$$r_s(\nu) = L_0(\nu), \qquad \text{and} \qquad \phi_s(\nu) = \phi_L(\nu) + \pi. \tag{4}$$

In reflection DFTS, measurements are usually made at or at very nearly normal incidence, and samples are chosen with sufficient thickness to suppress all but the primary reflected partial wave from the front surface of the sample. Under these conditions, the simplest form of Fresnel's equations can be used, and the optical constants and amplitude and phase reflection coefficients are related by

$$n(\nu) + ik(\nu) = \frac{1 + r_s(\nu)\exp i\phi_s(\nu)}{1 - r_s(\nu)\exp i\phi_s(\nu)} \tag{5}$$

The intensity reflection coefficient, or reflectivity, $R_s(\nu)$, is related to the amplitude reflection coefficient by

$$R_s(\nu) = \boldsymbol{r}_s(\nu)\, \boldsymbol{r}_s{}^*(\nu), \qquad \text{where} \qquad \boldsymbol{r}_s(\nu) = r_s(\nu) \exp i\phi_s(\nu) \tag{6}$$

is the complex amplitude reflection coefficent, and $\boldsymbol{r}_s{}^*(\nu)$ is its complex conjugate.

DFTS has the advantage that both the amplitude and the phase are measured directly at all frequencies in the measured range; this eliminates uncertainties in $\phi_s(\nu)$ which arise due to truncation of the measured spectrum when the phase is calculated from the measured reflectivity using the Kramers-Kronig dispersion relations. As already mentioned, DFTS is invariably used at normal, or near-normal incidence, so that the simplest forms of the Fresnel equations can be used. Frequently a combination of reflection and transmission DFTS can be used very effectively to determine n and k at most frequencies. When R_s is small, as can be seen from Eq. (6), measuring r is an advantage; Johnson and Bell [11] have shown that values of R_s as small as 4×10^{-4} can be measured reliably by reflection DFTS. However, when R_s is large, this is a disadvantage because r_s for the sample then differs from the value for the reference mirror by even less than R_s. Finally, reflection DFTS cannot be used to determine reliable values of $k(\nu)$ in spectral regions where the sample is transparent, because the phase is then very small, as discussed further below.

In reflection DFTS, applicable here, it is convenient to consider uncertainties in the measured amplitude and phase reflection coefficients separately. Uncertainties in the amplitude arise in the same way as they do in

other forms of spectroscopy in which, usually, in reflection spectroscopy, it is the intensity, R_s, of the reflection coefficient which is measured. Provided that adequate precautions have been taken to eliminate systematic errors, uncertainties in r_s or R_s arise primarily from random uncertainties in the detector response. However, when using metal reference mirrors which are usually fabricated by metallizing optically flat glass blanks, systematic errors also arise due to lack of perfect reflection of the metal surface. This latter point has been discussed by Eldridge and Staal [12] and Staal and Eldridge [13] and corrections to both the amplitude and the phase reflection coefficient associated with such mirrors were taken into account in their determinations of the optical constants of NaCl by reflection DFTS. Comparisons of published data for NaCl, KCl, and KBr presented in this article indicate that such corrections are necessary if the technique is to be used to full advantage. Birch [14] has shown how, by using a thick transparent slab of a material such as silicon as a reference reflector, a combination of reflection and transmission DFTS can be used to determine absolute values of the amplitude and phase reflection coefficients of thin metal mirrors in the far infrared.

In the case of the phase reflection coefficient, a number of additional systematic errors can arise which are associated mainly with the way in which the comparatively small wavelengths encountered in the far infrared ($\lambda \sim 20$–500 μm) translate into a need for very precise technology for sampling the interferograms and handling optical components (such as the sample and reference mirror surfaces). In most reflection DFTS experiments, the sample and reference mirror surfaces must be precisely interchanged during the experiment. Let us first consider the possible sources of systematic phase error which are encountered in a far-infrared interferometer equipped with a mechanical step-drive mechanism for scanning the moving mirror. It will be convenient to begin by taking as the goal for our phase measurements a systematic error which is equal to the random phase error equivalent to the random error in the amplitude reflection coefficient. A convenient yardstick is a signal-to-noise ratio of 100, leading directly to an uncertainty in the amplitude reflection coefficient of $\delta r_s = 0.01$, or 1%. The equivalent uncertainty in the phase is $\delta\phi_s = 0.01 \times \pi$ radian, or $\delta\phi_s \sim 0.5°$. The most serious systematic phase errors are as follows.

1. Potentially most serious of all is the phase error resulting from failure to place the reference-mirror surface precisely in the same plane as the sample reflecting surface. If we consider measurements at 100 cm^{-1}, for instance, then a phase uncertainty of 0.5° would occur if the error in the positioning of the two optical components were $\delta x = (\lambda/2 \times 360)\,\delta\phi_s \sim 0.1$ μm. This is a very severe constraint indeed, bearing in mind that the limiting precision of most mechanical engineering work lies in the range between 2.5 and 25 μm.

2. Mechanical step drives for interferometers and, in particular, backlash errors which occur when such drives are operated over a sequence of scans, as required when recording background and sample interferograms in turn, can often introduce uncertainties in the position of the moving mirror of a magnitude $\delta x \sim 0.1$ μm.
3. Differential thermal expansion in the two arms of the interferometer can be the cause of significant systematic phase errors. If the optical components are at a distance L from the beam divider, then a relative change in the temperature of the two arms of the interferometer of δT will result in a differential change in the lengths of the two arms of the interferometer of $\delta L = \alpha L \delta T$, where α is the coefficient of thermal expansion of the material from which the interferometer is constructed. If we take $L = 30$ cm, and $\alpha = 2 \times 10^{-5}$ K^{-1}, corresponding to Al, then we must have $\delta T < 0.015$ K, if $\delta L < 0.1$ μm. Temperature control with this level of precision is fairly easily achievable, but the figure for δT does indicate that this aspect of instrument design cannot be ignored.
4. The flatness of the sample and reference mirror surfaces should also satisfy the criterion calculated in (1) above, i.e., the surface flatness should be within ~ 0.1 μm at all points across the surface. Apart from placing severe requirements on the quality of the flatness and the optical polish of these optical components, the two components must also be cut from material which is sufficiently thick to maintain the quality of the surface for the duration of the measurements. Usually, this means that for optical components of $\sim$ 10 mm in diameter, the thickness should not be less than $\sim$ 6 mm.

Fortunately, there are ways of avoiding most of these phase errors. Parker *et al.* [15] have described how the need for the accurate replacement of reflecting surfaces can be avoided by metallizing part of the sample surface for use as a reference mirror, and this technique has been used by a number of authors, including Pai *et al.* [16], Eldridge and Staal [12], Staal and Eldridge [13], and Plumb and Birch [17]. Maslin and Parker [18] have shown that by designing an interferometer with a subsidiary He-Ne laser beam running along the optical axis of the far-infrared beam and using laser fringe-counting techniques, the second and third of the systematic phase errors listed above can also be avoided. It has been shown by Wan Abdullah and Parker [19] that this method also significantly reduces noise in the measured spectrum arising from random errors in sampling the interferogram; such errors are often present when a mechanical step drive is used for the moving mirror. Burton and Parker [20, 21] have demonstrated that systematic phase errors arising from non-flatness of the sample surface can be reduced to the order of one degree when $\lambda > 0.4$ μm (i.e., for DFTS at all wavelengths exceeding those in the UV) by suitably coating the sample surface and reusing it as the reference surface; the method requires the use of four interferograms and has been demon-

strated with reflection DFTS measurements in the visible region of the spectrum, but it has not yet been used in the far-infrared. Birch [22, 23] has investigated these so-called pseudocoherence effects associated with nonflatness of optical components theoretically.

By far the greatest single difficulty in reflection DFTS is the need for the accurate mechanical replacement of the reference mirror and sample reflecting surfaces. However, careful consideration of the form of the Fresnel equations for reflection readily demonstrates that this difficult operation can often be avoided. In many materials of interest, and that applies to those considered in this article, there are frequency ranges in the measured range in which the extinction coefficient is very small compared with the real refractive index, i.e., $k(\nu) \ll n(\nu)$. In the limit of small k, it follows from Eq. (5) that n and k are given by

$$n(\nu) \sim \frac{1 + r_s(\nu)}{1 - r_s(\nu)} \text{ and } k(\nu) \sim \frac{2r_s(\nu)\phi_s(\nu)}{[1 - r_s(\nu)]^2}. \tag{7}$$

The smallest measurable value of $\phi_s(\nu)$, corresponding to the noise limit if the signal-to-noise ratio is 100, is 0.01 radian. For the semiconductors studied by Maslin *et al.* [24], $r_s(\nu) \sim 0.5$ well above the reststrahl region where $\phi_s(\nu)$ is small. From Eq. (7), the corresponding lower limit for the value of k which can be measured by reflection DFTS is then $k \sim 0.04$, and the associated experimental uncertainty would be $\sim$100%. In regions where k is much smaller and the sample is transparent, it follows from Eq. (7) that for practical purposes, $\phi_s(\nu)$ approaches zero. In the alkali-halide crystals where ϵ_∞ is smaller, smaller values of k are accessible to reflection DFTS, but the accuracy of the determination of k is still severely limited by the difficulty of measuring $\phi_s(\nu)$. At a suitable reference frequency, ν_H, sufficiently far above the reststrahl band of a binary solid, we can set $\phi_s(\nu_H) = 0$ on physical grounds. $\phi_s(\nu) = 0$ also at $\nu = 0$. It follows that we can dispense with the experimental requirement to mechanically locate the reference mirror and sample surfaces in precisely the same plane. Instead, a much simpler experimental requirement of placing them in precisely parallel planes will suffice; planes separated by $\delta x \sim$ a few microns are easily achievable experimentally and this will not introduce systematic errors in $r_s(\nu)$, even if the radiation is poorly collimated. Then, after recording the two interferograms and computing the sample phase reflection coefficient, $\phi_s(\nu)$, using Eq. (4), the value of $\delta x = \phi_s(\nu_H)/4\pi\nu$ required to correct the measured phase $\phi_s(\nu_H)$ at ν_H can be calculated and a linear phase correction

$$\delta\phi_s(\nu) = 4\pi\nu\ \delta x \tag{8}$$

applied throughout the phase spectrum. This procedure was followed by Maslin *et al.* [24] when they used reflection DFTS to determine the optical constants of the II–VI and III–V semiconductors presented here. The origi-

nal numerical data were lost when the group moved their laboratory from London to Colchester in 1991; computer-generated graphs of the numerical data for all samples were presented on paper 25 × 20 cm^2 in area in the Ph.D. thesis by Maslin [25], and the data for semiconductors presented here has been obtained by carrying out digital scans of those graphs. We consider that the errors introduced by this process have not significantly added to the spectroscopic errors of the original data.

A detailed statistical analysis of experimental uncertainties in reflection DFTS was carried out by Pai *et al.* [16]. They used a method in which part of the sample surface was metallized [15] and used to provide the reference phase measurement, thus obviating the need for the precise mechanical replacement of reflecting surfaces. They listed values of n and k, and of the associated experimental uncertainties Δn and Δk, throughout the reststrahl bands of eight alkali halide crystals: NaF, NaCl, KCl, KBr, KI, RbCl, RbBr, and RbI at 100 and 300 K. We reproduce their estimates of Δn and Δk in Tables I–V for five alkali-crystals here: NaCl, KCl, KBr, KI, and RbCl. Because of the similarity between the far-infrared optical properties of the alkali halides and the II–VI and III–V semiconductors, these experimental uncertainties provide a useful guide to the frequency dependence of the experimental uncertainties for the II–VI and III–V semiconductors listed here.

II THE MATERIALS

A Alkali Halides

1 *NaCl*

The far-infrared optical constants of NaCl determined by Pai *et al.* [16] at 300 K at a resolution of 2 cm^{-1} using DFTS are shown in Fig. 2 and listed in Table I, where they are compared with values measured by reflection DFTS by Eldridge and Staal [12], and listed numerically by Eldridge and Palik [26]. Pai *et al.* [16] also published numerical values for n and k for NaCl at 100 K. The two sets of values listed in Table I are generally in reasonable agreement, within the limits of the experimental errors listed by Pai *et al.*, differing at most by a few percent except in the region of high reflectivity where n and k have their highest values. Eldridge and Staal used aluminium as a reference surface and corrected for the fact that aluminium is not a perfect reflector and does not have a phase reflectivity of exactly π: this could account for the difference between the two sets of data in Table I where n and k are large. This is supported by the data presented below for

TABLE I

Values of *n* and *k* for Sodium Chloride from Various Sources

cm^{-1}	n	k	Δn, Δk	n	k
50	2.47	0.05	0.03 [16]	2.45	0.047 [12, 26]
60	2.51	0.06			
70	2.50	0.05			
80	2.52	0.06			
90	2.57	0.07			
100	2.62	0.09		2.74	0.087
110	2.76	0.06			
120	2.98	0.09			
130	3.21	0.15	0.04	3.31	0.135
135	3.37	0.17			
140	3.54	0.20			
144	3.85	0.24			
148	4.08	0.44			
152	4.46	0.47			
156	5.16	0.84	0.01		
160	6.16	1.31	0.13	6.92	2.14
162	6.73	2.45	0.16		
164	6.12	4.81	0.18		
166	3.84	5.79	0.14		
170	1.59	5.42	0.09	1.35	6.03
174	0.76	4.19	0.05		
178	0.59	3.46			
182	0.56	3.08	0.03		
186	0.45	2.79			
190	0.33	2.50		0.19	2.63
194	0.27	2.20	0.02		
198	0.28	1.99			
202	0.25	1.88			
206	0.23	1.69			
210	0.23	1.50		0.18	1.56
214	0.22	1.38			
218	0.24	1.16			
222	0.28	1.03			
226	0.32	0.90	0.01		
230	0.42	0.86		0.43	0.87
234	0.49	0.82			
238	0.43	0.78			
242	0.49	0.68			
246	0.53	0.64			
250	0.603	0.645		0.58	0.66
254	0.593	0.648			
258	0.487	0.616			
262	0.409	0.482	0.006		
266	0.433	0.359			

(continued)

TABLE I *(Continued)*

Sodium Chloride

cm^{-1}	n	k	Δn, Δk	n	k
270	0.482	0.208			
274	0.570	0.200			
278	0.652	0.199			
282	0.74	0.18			
286	0.78	0.15			
290	0.80	0.13			
294	0.83	0.12			
300	0.86	0.11	0.01	0.85	1.1 E-3
320	1.01	0.05			
340	1.10	0.02			
360	1.17	0.01			
380	1.22	0.01			
400	1.27		0.01	1.27	3.5 E-3

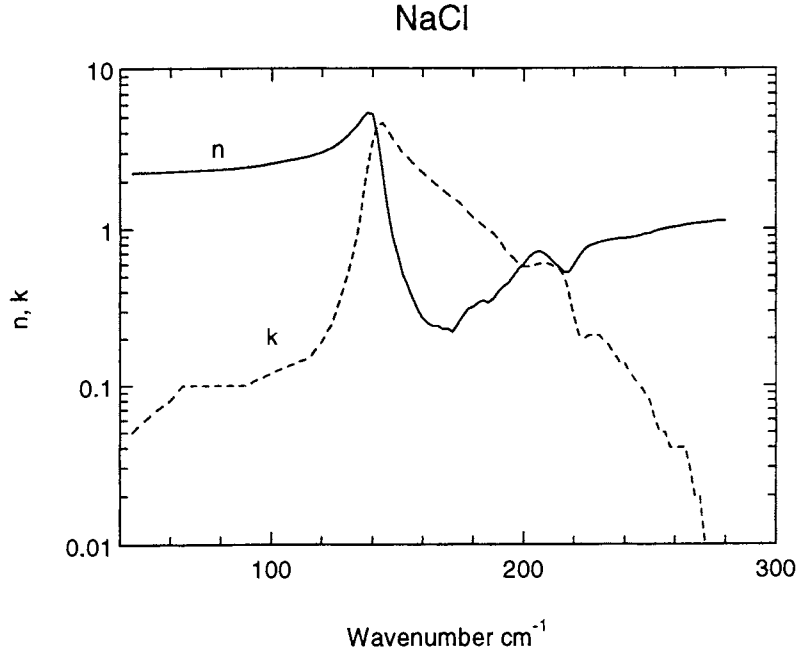

Fig. 2. Log-linear plot of the far-infrared optical constants, *n* and *k*, versus wavenumber for NaCl at 300 K. (From Pai *et al.* [16] with permission from the publisher.)

KCl and KBr; we can conclude that the corrections to the reference-mirror reflectivity carried out by Eldridge and Staal are worthwhile and to be recommended. Below 110 cm^{-1} and above 340 cm^{-1} where the phase reflection coefficient is very small, Eldridge and Staal [12] obtained the phase indirectly from transmission measurements on cleaved crystals, which yielded directly the absorption coefficient.

KCl 2

The far-infrared optical constants of KCl determined by Pai *et al.* [16] at 300 K at a resolution of 2 cm^{-1} using DFTS are shown in Fig. 3 and listed in Table II. They also published numerical values for n and k for KCl at 100 K. Johnson and Bell [11] also determined the optical constants of KCl at 300 K by reflection DFTS at 2 cm^{-1} resolution, and Palik [27] obtained numerical values by reading their graphs: a selection of these values is given in Table II, and it can be seen that there is very good agreement between the two sets of data, somewhat better than the agreement reported above between the data of Pai *et al.* [16] and Eldridge and Staal [12] for NaCl. Nei-

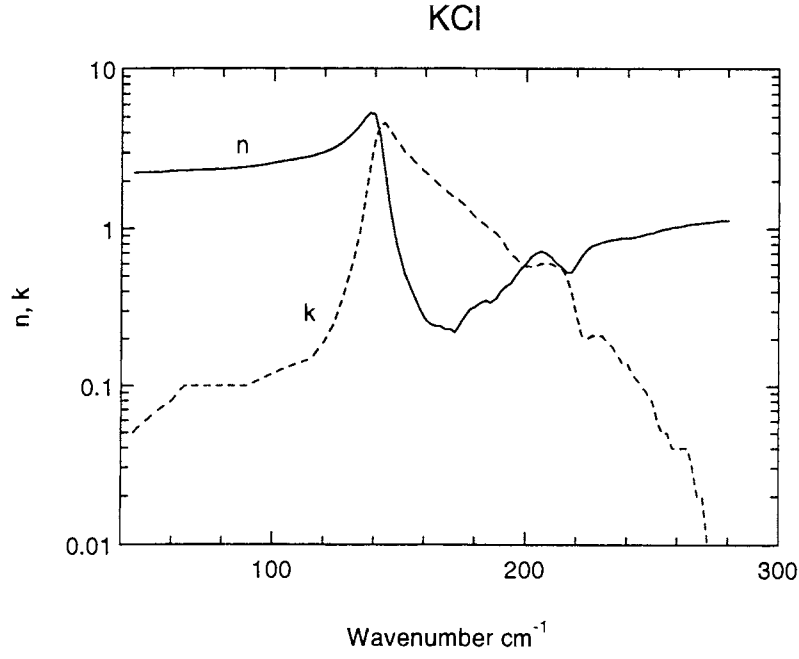

Fig. 3. Log-linear plot of the far-infrared optical constants, n and k, versus wavenumber for KCl at 300 K. (From Pai *et al.* [16] with permission from the publisher.)

TABLE II

Values of *n* and *k* for Potassium Chloride from Various Sources

cm^{-1}	n	k	Δn, Δk	n	k
50	2.27	0.06	0.03 [16]	2.2	[11, 27]
60	2.30	0.08		2.3	5.3 E-2
70	2.33	0.10		2.4	9.2 E-2
75	2.34	0.10			
80	2.37	0.10		2.5	0.11
85	2.40	0.10			
90	2.44	0.10		2.6	6.6 E-2
95	2.50	0.11			
100	2.57	0.12	0.03	2.7	0.11
110	2.75	0.14		2.9	0.15
120	3.02	0.19	0.04	3.3	0.20
124	3.22	0.25			
128	3.57	0.39			
132	4.09	0.66	0.07		
136	4.89	1.46	0.09		
140	5.20	3.47	0.13	5.3	4.0
144	2.36	4.58	0.08		
148	0.90	3.68	0.04		
152	0.52	3.01			
156	0.37	2.61			
160	0.27	2.27	0.02	0.17	2.2
164	0.24	1.99			
168	0.23	1.76			
172	0.22	1.56	0.01		
176	0.28	1.38			
180	0.32	1.18		0.31	1.05
190	0.40	0.86			
200	0.60	0.58			
204	0.70	0.59			
208	0.70	0.61			
212	0.61	0.58			
216	0.53	0.50			
220	0.59	0.28	0.01	0.53	0.35
224	0.74	0.20			
228	0.80	0.21			
232	0.84	0.19			
236	0.86	0.16			
240	0.87	0.14			
250	0.94	0.08			
260	1.03	0.04		0.99	4.2 E-2
264	1.06	0.04			
268	1.08	0.02			
272	1.10	0.01			
276	1.12	0.01			
280	1.13	0.01	0.01	1.10	2.3 E-2

ther set of data for KCl was corrected for the reference-mirror reflectivity; this supports the view that differences in the data of Pai *et al.* [16] and Eldridge and Staal [12] for NaCl can be attributed to the corrections which Eldridge and Staal made for the reflectivity of their Al reference mirror. Thus, for measurements with this accuracy, corrections for the imperfect reflectivity of metallized reference mirrors are to be recommended.

KBr 3

The far-infrared optical constants of KBr determined by Pai *et al.* [16] at 300 K at a resolution of 2 cm^{-1} using DFTS are shown in Fig. 4 and listed in Table III. They also published numerical values for n and k for KBr at 100 K. Johnson and Bell [11] also determined the optical constants of KBr at 300 K by reflection DFTS at 2 cm^{-1} resolution, and Palik [28] obtained numerical values by reading their graphs: a selection of these values is also given in Table III, and it can be seen that, as in the case of KCl, there is very good agreement between the two sets of data. Again, the agreement is significantly better than the agreement reported above between the data of Pai *et al.* [16] and Eldridge and Staal [12] for NaCl. Neither set of data for

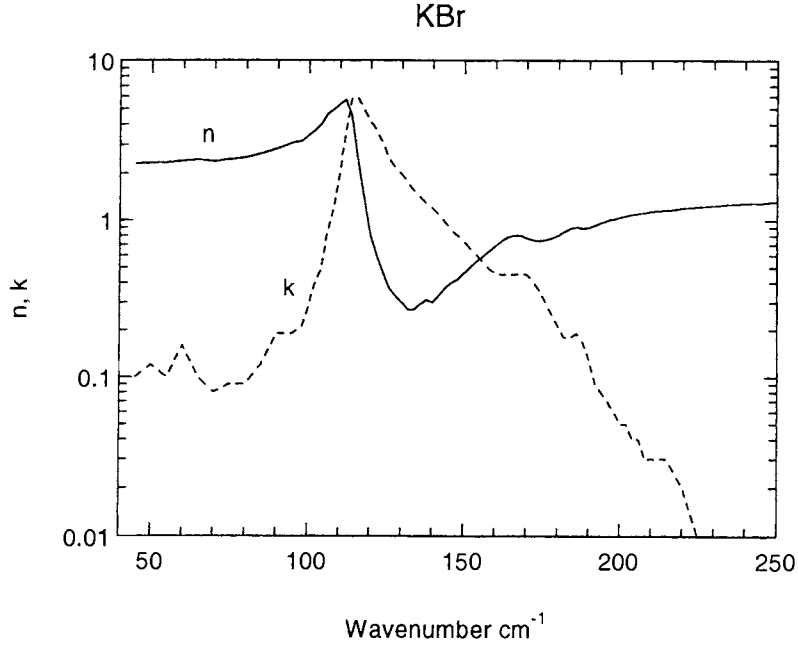

Fig. 4. Log-linear plot of the far-infrared optical constants, n and k, versus wavenumber for KBr at 300 K. (From Pai *et al.* [16] with permission from the publisher.)

TABLE III

Values of *n* and *k* for Potassium Bromide from Various Sources

cm^{-1}	n	k	Δn, Δk	n	k
50	2.30	0.12	0.03 [16]	2.30	9.3 E-2 [11, 28]
60	2.38	0.16		2.35	0.11
70	2.36	0.08		2.40	0.12
80	2.49	0.09	2.52	0.125	
85	2.65	0.12			
90	2.83	0.19		2.80	0.15
95	3.07	0.19	0.04		
98	3.17	0.21			
100	3.42	0.28		3.40	0.33
104	4.02	0.48			
110	5.35	1.98	0.11	5.50	1.0
114	4.55	5.84	0.16		
118	1.39	4.89	0.07		
122	0.60	3.64	0.04		
126	0.37	2.43	0.02		
130	0.30	1.97		0.30	2.0
134	0.27	1.54			
138	0.31	1.28	0.01		
142	0.33	1.08			
146	0.40	0.86			
150	0.46	0.73	0.01	0.48	0.72
154	0.55	0.60			
158	0.64	0.49			
162	0.74	0.45			
166	0.80	0.45			
170	0.77	0.45		0.76	0.44
174	0.74	0.36			
178	0.77	0.25			
182	0.85	0.18			
186	0.90	0.19			
190	0.90	0.13		0.90	0.18
194	0.97	0.08			
200	1.05	0.05	0.01		
210	1.14	0.03			
220	1.20	0.02			
230	1.25	0.01		1.30	
235	1.27	0.01			
240	1.29	0.01			
245	1.30	0.01			
250	1.32	0.01	0.01		
255	1.33				
260	1.35				
265	1.35				
270	1.36		0.01		

KBr was corrected for the reference-mirror reflectivity; this again supports the view that differences in the data of Pai *et al.* [16] and Eldridge and Staal [12] for NaCl can be attributed to the corrections which Eldridge and Staal made for the reflectivity of their Al reference mirror. Thus, for measurements with this accuracy, corrections for the imperfect reflectivity of metallized reference mirrors are to be recommended.

KI 4

The far-infrared optical constants of KI determined by Pai *et al.* [16] at 300 K at a resolution of 2 cm^{-1} using DFTS are shown in Fig. 5 and listed in Table IV. They also published numerical values for n and k for KI at 100 K. These values are generally in agreement, within the limits of the experimental uncertainties listed by Pai *et al.* [16], with other determinations of n and k for KI by DFTS reported by Berg and Bell [29] and Memon and Parker [30]. Thomas [31] has presented a critique of KI in this volume using the data in Refs. 16 and 29.

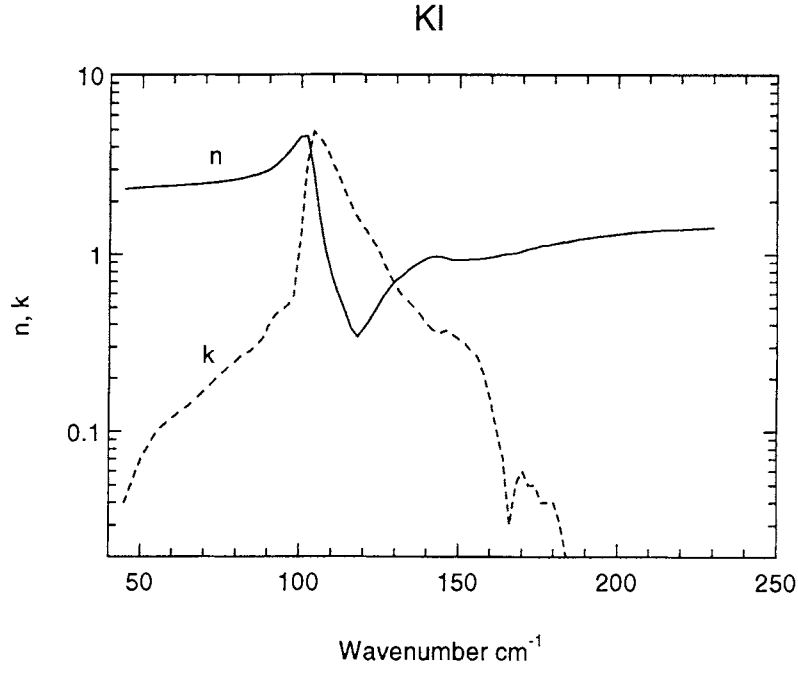

Fig. 5. Log-linear plot of the far-infrared optical constants, n and k, versus wavenumber for KI at 300 K. (From Pai *et al.* [16] with permission from the publisher.)

TABLE IV

Values of *n* and *k* for Potassium Iodide from Ref. [16]

cm^{-1}	n	k	Δn, Δk
45	2.33	0.04	0.03 [16]
50	2.38	0.07	
55	2.41	0.10	
60	2.44	0.12	
65	2.46	0.14	
70	2.51	0.17	
75	2.57	0.21	
80	2.65	0.25	
84	2.75	0.28	
88	2.88	0.33	0.04
92	3.16	0.45	
96	3.72	0.51	0.06
98	4.09	0.58	0.07
100	4.54	1.24	0.08
102	4.62	3.21	0.10
104	2.92	4.88	0.10
106	1.66	4.51	0.07
108	1.03	3.96	0.05
110	0.75	3.28	0.03
112	0.59	2.75	0.03
114	0.48	2.27	0.02
116	0.38	1.87	0.01
118	0.34	1.60	
120	0.38	1.42	
122	0.43	1.26	
124	0.49	1.11	
126	0.57	0.92	
128	0.64	0.77	
130	0.71	0.67	0.01
132	0.75	0.59	
134	0.81	0.54	
136	0.86	0.50	
138	0.91	0.45	
140	0.95	0.40	
142	0.97	0.37	
144	0.97	0.36	
146	0.95	0.37	
148	0.93	0.35	
150	0.93	0.33	0.01
160	0.96	0.15	
170	1.05	0.06	
180	1.16	0.04	
190	1.24	0.02	
200	1.31	0.02	0.01
210	1.37	0.01	
220	1.40	0.01	
230	1.43	0.01	
240	1.45		
250	1.47		0.01

RbCl 5

The far-infrared optical constants of RbCl determined by Pai *et al.* [16] at 300 K at a resolution of 2 cm^{-1} using DFTS are shown in Fig. 6 and listed in Table V. They also published numerical values for n and k for RbCl at 100 K. These are the only values of n and k determined by DFTS for RBCl reported in the literature. As in the case of all the alkali halide crystals studied by Pai *et al.*, the value of ν_{TO} determined from the peak in the conductivity, $\sigma(\nu) = \nu\epsilon''(\nu)/2$, calculated from these results is in good agreement with values reported by Jones *et al.* [32], Wilkinson [33], and Lowndes and Martin [34].

NaF, RbBr, and RbI 6

Pai *et al.* [16] also determined the optical constants of NaF, RbBr, and RbI in the optical phonon region at both 300 K and 100 K by DFTS at a resolution of 2 cm^{-1}. A critique of NaF was published by Ohlídal and Navrátil [35] in *HOC II* using the far-infrared data of Pai *et al.* [16]. The optical constants of RbBr and RbI are reviewed by Ohlídal and Ohlídal [36] and Ohlídal and Franta [37], respectively, elsewhere in this volume.

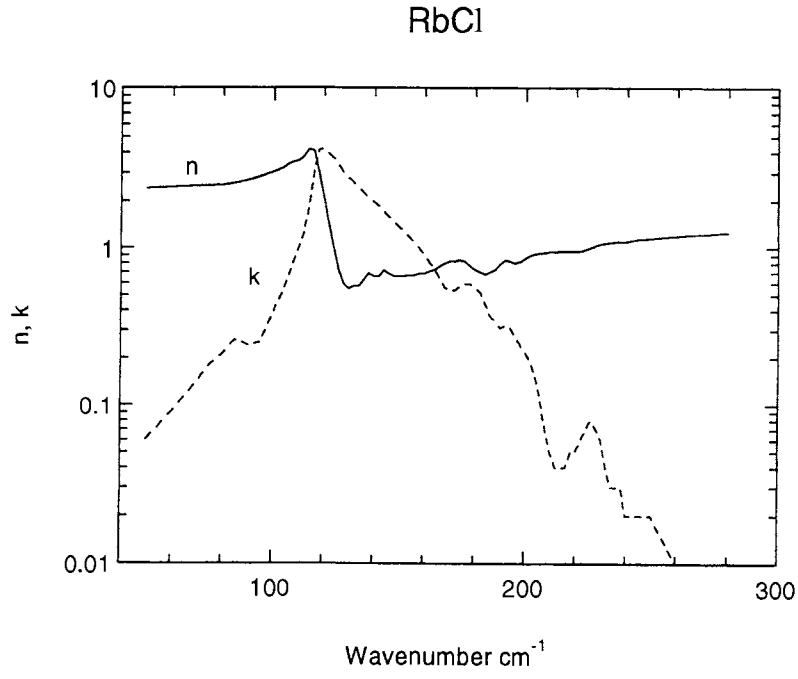

Fig. 6. Log-linear plot of the far-infrared optical constants, n and k, versus wavenumber for RbCl at 300 K. (From Pai *et al.* [16] with permission from the publisher.)

TABLE V

Values of *n* and *k* for Rubidium Chloride from Ref. [16]

cm^{-1}	n	k	Δn, Δk
50	2.40	0.06	0.03 [16]
60	2.44	0.09	
70	2.47	0.14	
75	2.50	0.18	
80	2.51	0.21	
85	2.58	0.26	
90	2.69	0.24	
95	2.85	0.25	
100	3.03	0.38	
102	3.12	0.45	
104	3.23	0.53	0.05
106	3.40	0.65	
108	3.52	0.81	
110	3.56	0.99	
112	3.76	1.22	
114	4.16	1.81	0.07
116	4.13	3.05	
118	3.04	4.15	
120	2.11	4.21	
122	1.48	3.93	
124	1.00	3.66	0.04
126	0.72	3.34	
128	0.59	2.99	
130	0.55	2.77	
132	0.57	2.59	
134	0.57	2.41	0.02
136	0.63	2.23	
138	0.69	2.07	
140	0.66	1.96	
142	0.66	1.86	
144	0.72	1.73	0.01
146	0.69	1.59	
148	0.66	1.48	
150	0.66	1.36	0.01
152	0.66	1.26	
154	0.67	1.18	
156	0.67	1.07	
158	0.69	0.99	
160	0.69	0.89	
162	0.71	0.81	
164	0.73	0.73	
166	0.77	0.64	
168	0.80	0.56	
170	0.83	0.54	
172	0.83	0.54	

(continued)

TABLE V *(Continued)*

Rubidium Chloride

cm^{-1}	n	k	Δn, Δk
174	0.84	0.57	
176	0.82	0.59	
178	0.77	0.59	
180	0.73	0.56	
182	0.70	0.52	
184	0.68	0.44	
186	0.70	0.37	
188	0.73	0.34	
190	0.79	0.31	
192	0.84	0.32	
194	0.82	0.31	
196	0.80	0.27	
198	0.82	0.24	
200	0.86	0.22	0.01
202	0.90	0.19	
204	0.92	0.15	
206	0.93	0.11	
208	0.94	0.07	
210	0.95	0.05	
212	0.95	0.04	
214	0.96	0.04	
216	0.96	0.04	
218	0.96	0.05	
220	0.96	0.05	
222	0.96	0.06	
224	0.98	0.07	
226	1.01	0.08	
228	1.04	0.07	
230	1.06	0.06	
232	1.08	0.04	
234	1.09	0.03	
236	1.10	0.03	
238	1.11	0.03	
240	1.11	0.02	
245	1.14	0.02	
250	1.16	0.02	0.01
260	1.20	0.01	
270	1.23	0.01	
280	1.26	0.01	
290	1.28		
300	1.30		0.01

B Semiconductors

Values of n and k measured by reflection DFTS in the far-infrared for the eight semiconductors CdTe, ZnSe, GaP, GaAs, GaSb, InP, InAs, and InSb are listed in Tables VII–XIV and log-linear graphs of the DFTS data are presented in Figs. 7–14. For each of these materials the phonon response has been modelled using a Lorentz model for a damped, simple harmonic oscillator:

$$\epsilon' + i\epsilon'' = (n + ik)^2 = \epsilon_\infty + \frac{\rho \nu_{TO}{}^2}{\nu_{TO}{}^2 - \nu^2 - i\nu\gamma}, \tag{9}$$

where ϵ' and ϵ'' are the real and imaginary parts of the complex dielectric response function, ϵ_∞ is the limiting high frequency value of the real part of the dielectric constant, ν_{TO} is the frequency of the transverse optic phonon mode at the center of the Brillouin zone, γ is the phonon damping parameter, ρ is the dipole strength defined by

$$\rho = \epsilon_0 - \epsilon_\infty, \tag{10}$$

and ϵ_0 is the static dielectric constant.

In the case of the four materials exhibiting free-carrier behavior at frequencies below their reststrahl bands, i.e., GaAs, GaSb, InAs, and InSb, a term has been added to Eq. (9) to account for the plasma response, i.e.,

$$\epsilon' + i\epsilon'' = (n + ik)^2 = \epsilon_\infty + \frac{\rho \nu_{TO}{}^2}{\nu_{TO}{}^2 - \nu^2 - i\nu\gamma} - \frac{\epsilon_\infty \nu_p{}^2}{\nu^2 + i\nu\gamma_p}, \tag{11}$$

where ν_p is the plasma frequency and γ_p is the plasmon damping parameter. The plasma frequency is given by

$$\nu_p{}^2 = \frac{ne^2}{\epsilon_\infty \epsilon_0 m^*}, \tag{12}$$

where n is the free-carrier concentration, e is the charge on the electron, and m^* is the effective mass of the free carriers. For fitting the experimental data, ν_p has been taken as the minimum in the measured amplitude reflectivity. In some cases the plasma frequency lies outside the range of data presented here [25].

The values of the parameters ϵ_0, ϵ_∞, ν_{TO}, γ, ν_p, and γ_p, which are needed to fit the spectra of each of the eight semiconductors, are listed in Table VI. The values of ϵ_0 and ϵ_∞, are taken from Kunc *et al.* [38]. Also listed are the values of the ratio m^*/m_0, where m_0 is the mass of the free-electron, taken from Gray [39] for the four samples which showed free-carrier effects at frequencies below the reststrahl bands.

TABLE VI

Parameters Used in Modelling the Contributions of the Lattice Resonance and the Free Carriers to the Far-Infrared Dielectric Response of Eight Semiconductor Crystals

	ϵ_0	ϵ_∞	ρ	ν_{TO} (cm^{-1})	γ (cm^{-1})	ν_P (cm^{-1})	γ_p (cm^{-1})	m^*/m_0
CdTe	10.2	7.10	3.10	141	6.63	—	—	—
ZnSe	8.80	5.9	2.9	207	6.50	—	—	—
GaP	11.01	9.07	1.945	367	9.0	—	—	—
GaAs	12.80	10.90	1.9	269	6.5	60	35	0.070
GaSb	15.80	14.44	1.36	227.5	3.0	30	25	0.047
InP	12.46	9.61	2.85	304	8.0	—	—	—
InAs	15.15	12.25	2.90	218.5	6.0	71	40	0.026
InSb	17.77	15.68	2.09	181.0	6.50	75	15	0.015

Numerical values for n and k calculated from Eq. (11) after fitting the model to the experimental data are quoted for comparison throughout each table. Doping has a very large effect on the far-infrared optical constants of semiconductors, not only in the region of the plasma resonance, but also throughout the reststrahl region because of the strong effect of plasmon-LO phonon coupling. This is likely to be the dominant reason for differences between the optical constants of (different) samples measured in different laboratories. The overall agreement between the calculated and measured values of n is generally quite fair throughout the spectrum for most materials. The most notable exceptions to this occur for GaP, InP, and to a lesser extent, GaAs, in the region between ν_{TO} and ν_{LO}, where n is small. In the case of k, reasonable agreement between calculated and measured values is generally found only in the reststrahl and free-carrier regions where k is large. In regions where k is small, a more sophisticated model is required to take account of the effects of additional absorption arising from anharmonicity and the non-linear dipole moment [40, 41]; apart from this, there is a large uncertainty in values of k determined by DFTS in regions where the phase reflection coefficient is small, as mentioned above.

II–VI Semiconductors C

CdTe 1

The far-infrared optical constants of CdTe determined by Maslin *et al.* [24] at 300 K using DFTS at a resolution of 2 cm^{-1} are shown in Fig. 7 and listed in Table VII, where they are compared with values calculated from the oscillator model, Eq. (11) [OM]. The optical constants of CdTe

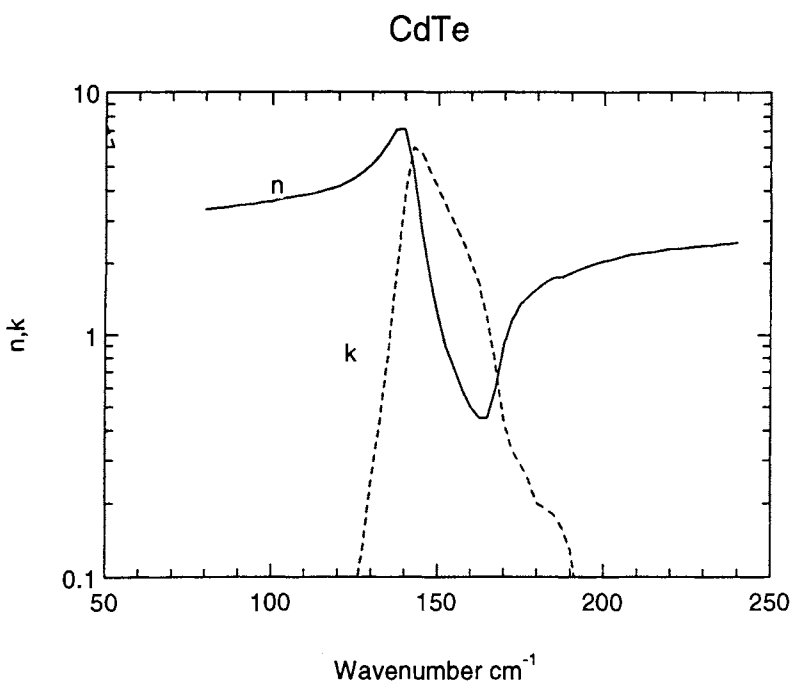

Fig. 7. Log-linear plot of the far-infrared optical constants, n and k, versus wavenumber for CdTe at 300 K.

have also been determined at 300 K using reflection DFTS by Birch and Murray [42] at a resolution of 1 cm^{-1}; their data contained much fine structure a little above the noise level and many features were later assigned by Mok *et al.* [43] as multi-phonon combination bands excited via lattice anharmonicity [40]. Numerical values of n and k read from Birch and Murray's graph by Palik [44] are also listed in Table VII. Differences in the values of n and k in the reststrahl region may be due to the differences in resolution. Apart from this, and poor agreement between the values of k outside the reststrahl region where DFTS is known to be unreliable for measuring k, the overall agreement is reasonable. The transverse optic phonon frequency determined from these data, $\nu_{TO} = 141$ cm^{-1}, is in excellent agreement with previous experimental values; 140.5 cm^{-1} determined by far-infrared reflection-DFTS [42], and 140 cm^{-1} determined by Raman spectroscopy [45] and near-infrared absorption spectroscopy [46]. The longitudinal optic phonon frequency, $\nu_{LO} = 167.5$ cm^{-1}, is in good agreement with previous experimental values for undoped CdTe: 167.5 cm^{-1}, determined by reflection-DFTS [42], and 171 cm^{-1}, determined by Raman spectroscopy [45]; Slack *et al.* [46] carried out an infrared investigation of substitutionally Fe^{2+}-doped CdTe and reported a value of $\nu_{LO} = 180$ cm^{-1}.

TABLE VII

Values of n and k for Cadmium Telluride from Various Sources

cm^{-1}	n	k		n	k	n	k	
80.0	3.34		[24]	3.42	2.6 E-2 [OM]	3.32	0.2	[42]
85.0	3.39							
90.0	3.47					3.45	0.2	
95.0	3.53							
100.0	3.61					3.62	0.2	
105.0	3.72							
110.0						3.9	0.25	
115.0	3.96	0.05						
120.0	4.16	0.03		4.26	0.19	4.4	0.3	
125.0	4.51	0.08				4.7	0.55	
130.0	5.10	0.25				5.1	0.8	
132.5	5.60	0.43						
135.0	6.23	0.83				6.75	2.2	
137.5	7.03	1.78						
140.0	7.07	3.86		6.76	4.50	5.5	5.5	
142.5	4.93	5.96						
145.0	2.81	5.70		2.41	5.50	1.8	5.2	
147.5	1.77	4.82						
150.0	1.20	4.06		1.02	3.81	0.8	3.7	
155.0	0.72	2.92						
160.0	0.50	2.03		0.51	1.89	0.2	1.81	
65.0	0.45	1.17						
170.0	0.91	0.43		0.80	0.52	0.8	0.5	
175.0	1.34	0.29						
180.0	1.56	0.20		1.50	0.16	1.5	0.1	
185.0	1.73	0.18						
190.0	1.81	0.13		1.82	8.0 E-2	1.9		
192.5	1.87	0.08						
195.0	1.93	0.06						
197.5	1.98	0.04						
200.0	2.03	0.03		2.01	5.0 E-2	2.05		
202.5	2.07	0.01						
205.0	2.11	0.01						
207.5	2.16	0.03						
210.0	2.18	0.01						
212.5	2.21	0.00						
215.0	2.23	0.00						
217.5	2.27	0.01						
220.0	2.30	0.01		2.22	2.5 E-2			
222.5	2.30	0.01						
225.0	2.32	0.02						
227.5	2.35	0.01						
230.0								
232.5	2.37	0.03						
235.0	2.40	0.05						
237.5	2.41	0.05						
240.0	2.44	0.04		2.34	1.5 E-2			

2 ZnSe

The far-infrared optical constants of ZnSe determined by Maslin *et al.* [24] at 300 K at a resolution of 4 cm^{-1} using DFTS are shown in Fig. 8 and listed in Table VIII, where they are compared with values calculated from the oscillator model, Eq. (11) [OM], and with values taken from the work of Feldman *et al.* [47], Cardona [48], and Thomas and Hopfield [49], and by Ward [50]. Values of the optical constants of ZnSe determined by transmission DFTS in the millimeter region have been reported by Afsar [51]. Previous data for n and k for ZnSe in the optical phonon region were listed by Ward [50] in *HOC II,* who tabulated the data of Manabe *et al.* [52] and Hattori *et al.* [53]. At frequencies up to about 200 cm^{-1}, i.e., up to the ZnSe transverse optic phonon frequency, the present data for n are in good agreement with the values listed by Ward. Between about 200 and 250 cm^{-1}, where the phase reflection coefficient has its largest values and $r_s(\nu)$ and $\phi_s(\nu)$ change most rapidly, the disagreement with the earlier data is largest, rising to about 60% in n. This is the region in which reflection DFTS is expected to have its greatest advantage. At higher frequencies, the DFTS and reflectivity data for n are again in relatively good agreement (i.e., within

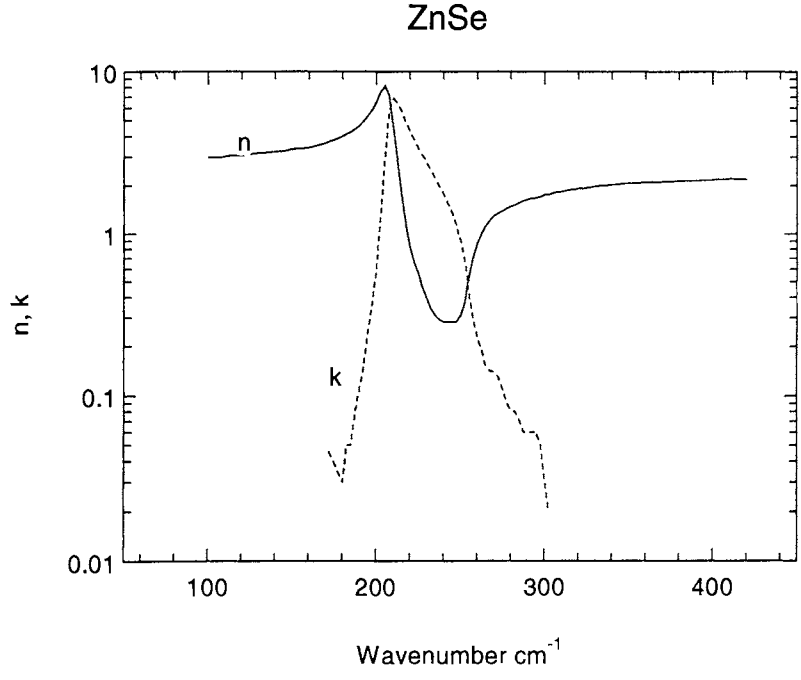

Fig. 8. Log-linear plot of the far-infrared optical constants, n and k, versus wavenumber for ZnSe at 300 K.

TABLE VIII

Values of n and k for Zinc Selenide from Various Sources

cm^{-1}	n	k	n	k	n	k
100.0	2.97	[24]	3.11	1.2 E-2 [OM]		
110.0	3.01					
120.0	3.06		3.20	1.9 E-2		
125.0	3.12				2.90 [47]	
130.0	3.17					
140.0	3.23		3.35	3.1 E-2		
150.0	3.34					
155.0	3.38					
160.0	3.43		3.62	6.0 E-2		
165.0	3.54					
166.7					3.54	0.08 [48]
170.0	3.66		3.84	9.1 E-2		
173.9					3.71	0.11
175.0	3.83					
180.0	4.04	0.03	4.2	0.16		
181.8					3.83	0.14
182.5	4.16	0.05				
185.0	4.30	0.05				
185.2					4.00	0.18
187.5	4.48	0.08				
188.7					4.29	0.23 [47]
190.0	4.69	0.11	4.88	0.33		
192.5	4.98	0.15				
192.3					4.64	0.43
195.0	5.36	0.24				
196.1					5.07	0.58
197.5	5.86	0.36				
200.0	6.56	0.59	6.60	1.25	6.09	0.87
202.0					6.75	1.83
202.5	7.55	1.26				
203.7					7.68	2.52
204.1					7.54	3.62
205.0	8.16	3.00	8.07	4.18		
206.2					3.20	6.20
207.5	7.22	5.74				
208.3					3.19	6.20
210.0	4.43	6.86	3.45	7.17		
210.5					2.10	6.10
212.5	2.81	6.44				
212.8					1.16	4.93
215.0	1.75	5.69	1.24	5.20		
217.4					0.58	3.62
217.5	1.14	4.90				
220.0	0.83	4.27	0.69	3.94		
222.2					0.43	2.90

(continued)

TABLE VIII *(Continued)*

Zinc Selenide

cm^{-1}	n	k	n	k	n	k
222.5	0.66	3.77				
225.0	0.56	3.37				
235.0	0.31	2.21				
240.0	0.28	1.75	0.28	1.58		
250.0	0.31	0.91			1.01	0.32 [49]
260.0	0.87	0.22				
270.0	1.30	0.14				
280.0	1.49	0.08				
285.7					1.60	2.1 E-2
287.5	1.62	0.06				
290.0	1.65	0.06				
300.0	1.75	0.03	1.81	3.0 E-2		
310.0	1.84	0.00				
320.0	1.92					
333.3					2.15	7.0 E-3
340.0	2.02					
360.0	2.09					
380.0	2.15	0.02				
400.0	2.18				2.25	6.0 E-3
420.0	2.19	0.03	2.23	4.3 E-3		

a few percent). The transverse and longitudinal optic phonon frequencies determined from these data, $\nu_{TO} = 207$ cm^{-1} and $\nu_{LO} = 253$ cm^{-1}, are in reasonable agreement with previous experimental values of 206 cm^{-1} and 250 cm^{-1}, respectively, determined by Raman spectroscopy [54]. Patel *et al.* [55] have analyzed fine structure and assigned features to phonon combination bands excited via lattice anharmonicity [40].

D III–V Semiconductors

1 GaP

The far-infrared optical constants of GaP determined by Maslin *et al.* [24] at 300 K at a resolution of 4 cm^{-1} using DFTS are shown in Fig. 9 and listed in Table IX, where they are compared with values calculated from the oscillator model, Eq. (11) [OM], and values listed by Borghesi and Guizzetti [56] taken from the work of Barker [57]. The transverse and longitudinal optic phonon frequencies determined from the data of Maslin *et al.*, $\nu_{TO} = 367$ cm^{-1} and $\nu_{LO} = 403$ cm^{-1}, are in good agreement with previ-

TABLE IX

Values of n and k for Gallium Phosphide from Various Sources

cm^{-1}	n	k	n	k	n	k
100.0	3.30	[24]	3.34	2.3 E-3 [OM]	3.3639	3.0 E-4 [56]
110.0	3.27					
120.0	3.32					
130.0	3.32					
140.0	3.37	0.02	3.37	3.7 E-3		
142.9					3.3947	5.2 E-4
150.0	3.38	0.00				
160.0	3.38	0.03				
170.0	3.43	0.02				
180.0	3.45	0.03	3.41	5.9 E-3		
190.0	3.46	0.03				
200.0	3.51	0.03			3.470	1.06 E-3
210.0	3.53	0.03				
220.0	3.57	0.03	3.48	1.0 E-2		
230.0	3.61	0.05				
240.0	3.65	0.05				
250.0	3.69	0.06			3.606	2.31 E-3
260.0	3.73	0.10	3.60	1.9 E-2		
270.0	3.80	0.10				
280.0	3.89	0.11				
285.7					3.809	5.18 E-3
290.0	3.99	0.13				
300.0	4.12	0.18	3.86	4.6 E-2		
310.0	4.28	0.21				
315.0	4.39	0.24				
320.0	4.50	0.30	4.14	8.7 E-2		
325.0	4.65	0.35				
330.0	4.86	0.42				
333.3					4.765	6.5 E-2
335.0	5.03	0.53				
340.0	5.29	0.69	4.74	0.23		
340.1					5.182	0.16
342.5	5.46	0.76				
344.8					5.578	0.31
345.0	5.62	0.86				
347.5	5.83	1.00				
350.0	6.12	1.19	5.43	0.48		
352.1					6.431	0.78
352.5	6.44	1.49				
355.0	6.77	1.93				
357.1					7.348	1.54
357.5	7.07	2.54				
360.0	7.35	3.50	6.96	1.67		
362.5	7.58	4.66				
365.0	7.14	6.79			10.314	8.62

(continued)

TABLE IX *(Continued)*

Gallium Phosphide

cm^{-1}	n	k	n	k	n	k
367.5	4.15	8.65				
370.0	1.84	8.08	4.11	6.64		
372.5	0.81	6.62				
373.1					0.515	5.86
375.0	0.43	5.49				
377.5	0.28	4.66				
378.8					0.208	4.05
380.0	0.21	3.98	1.06	4.01		
382.5	0.13	3.45				
385.0	0.11	3.02				
387.5	0.11	2.64				
387.6					0.103	2.52
390.0	0.11	2.30				
392.5	0.11	1.98				
395.0	0.13	1.70				
397.5	0.14	1.39				
400.0	0.17	1.05	0.60	1.20	0.108	0.89
402.5	0.29	0.65				
405.0	0.64	0.26				
407.5	0.96	0.16				
409.8					1.208	4.6 E-2
410.0	1.20	0.14				
412.5	1.38	0.11				
415.0	1.52	0.11				
416.7					1.585	2.6 E-2
420.0	1.76	0.11	1.69	0.17		
430.0	2.04	0.11				
440.0	2.27	0.16				
450.0	2.39	0.14				
460.0	2.55	0.16				
480.0	2.66	0.13				
500.0	2.74	0.22	2.61	1.7 E-2	2.606	

ous experimental values: $\nu_{TO} = 366\ cm^{-1}$ and $\nu_{LO} = 402\ cm^{-1}$ determined by far-infrared spectroscopy [58], and $\nu_{TO} = 367\ cm^{-1}$ and $\nu_{LO} = 403\ cm^{-1}$, determined by Raman spectroscopy [59]. No free-carrier response was observable in this sample at frequencies down to 20 cm^{-1} [25].

2 GaAs

The far-infrared optical constants of GaAs determined by Maslin *et al.* [24] at 300 K at a resolution of 4 cm^{-1} using DFTS are shown in Fig. 10

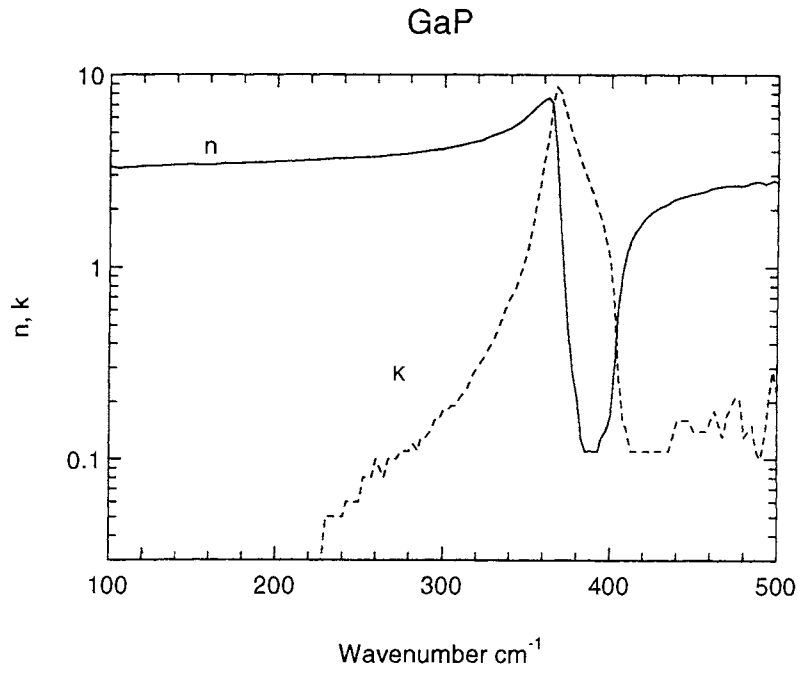

Fig. 9. Log-linear plot of the far-infrared optical constants, n and k, versus wavenumber for GaP at 300 K.

and listed in Table X, where they are compared with values calculated from Eq. (11) [OM] and values of n and k derived from the far-infrared reststrahl work of Kachare *et al.* [60] and Holm *et al.* [61], and values of k determined by Stolen [62], as listed by Palik [63]. Values of the millimeter-wave optical constants of GaAs determined by transmission DFTS have been reported by Afsar and Button [64] and Afsar [65]. The transverse and longitudinal optic phonon frequencies determined from the data of Maslin *et al.*, $\nu_{TO} = 269$ cm^{-1}, and $\nu_{LO} = 293$ cm^{-1}, are in reasonable agreement with previous experimental values, $\nu_{TO} = 269$ cm^{-1} and $\nu_{LO} = 291$ cm^{-1}, determined by Raman spectroscopy [66], and $\nu_{TO} = 271$ cm^{-1} and $\nu_{LO} = 295$ cm^{-1}, determined by far-infrared spectroscopy [67]. The sample was n-type and the onset of the free-carrier response can be seen at frequencies below 150 cm^{-1}. The plasma minimum in the reflectivity occurred at 60 cm^{-1} [25]; using $m^* = 0.07\ m_0$, Table VI [39], the free-carrier concentration is found to be 3.0×10^{16} cm^{-3}. Small differences in the LO frequencies may arise from differences in plasmon-LO phonon coupling for samples with different carrier concentrations.

TABLE X

Values of *n* and *k* for Gallium Arsenide from Various Sources

cm^{-1}	n	k	n	k	n	k
50.0	2.67	0.85 [24]	2.78	1.41 [OM]	3.615 [60, 61]	1.8 E-3 [62]
60.0	2.67	0.54				
70.0	2.85	0.34	2.90	0.67		
80.0	2.88	0.21				
90.0	3.09	0.07	3.10	0.35		
100.0	3.15	0.02			3.650	3.6 E-3
110.0	3.23		3.26	0.20		
120.0	3.33					
130.0	3.40		3.38	0.13		
140.0	3.45					
150.0	3.52					
160.0	3.57					
170.0	3.60		3.58	6.7 E-2		
180.0	3.66					
190.0	3.74		3.70	5.7 E-2		
200.0	3.81				3.93	8.49 E-3 [60, 61]
210.0	3.90		3.86	5.9 E-2	4.02	1.15 E-2
220.0	4.03				4.13	1.63 E-2
230.0	4.18		4.15	8.5 E-2	4.30	2.49 E-2
240.0	4.43	0.02			4.57	4.26 E-2
250.0	4.90	0.11	4.89	0.24	5.08	9.02 E-2
255.0	5.30	0.21			5.57	1.53 E-1
257.5	5.62	0.29				
260.0	6.01	0.41	6.05	0.76	6.47	0.323
262.5	6.56	0.60	6.62	1.20		
265.0	7.38	1.05			8.87	1.20
267.5	8.21	2.05				
270.0	7.84	4.92	5.52	6.49	4.66	11.0
272.5	4.42	7.09				
275.0	2.59	6.41			0.713	5.49
277.5	1.59	5.33				
280.0	1.03	4.40	0.95	3.37	0.358	3.48
282.5	0.71	3.64				
285.0	0.54	2.99			0.270	2.23
287.5	0.46	2.42				
290.0	0.43	1.88	0.77	1.25	0.323	1.09
292.5	0.48	1.37				
295.0	0.62	0.85			1.151	0.201
297.5	1.04	0.37				
300.0	1.40	0.22			1.707	9.59 E-2
305.0	1.82	0.11			2.020	6.02 E-2
310.0	2.06	0.10	2.18	0.13	2.229	4.21 E-2
315.0	2.24	0.06			2.380	3.14 E-2
320.0	2.38	0.03			2.495	2.43 E-2
330.0	2.58		2.61	5.3 E-2	2.659	1.59 E-2
340.0	2.70				2.7701	1.13 E-2

TABLE X *(Continued)*

Gallium Arsenide

cm^{-1}	n	k	n	k	n	k
342.5	2.72					
345.0	2.75					
347.5	2.78					
350.0	2.80		2.80	3.1 E-2	2.851	8.40 E-3
352.5	2.83					
355.0	2.85					
357.5	2.85					
360.0	2.86				2.913	6.50 E-3
362.5	2.88					
365.0	2.90					
367.5	2.91					
370.0	2.93		2.91	2.1 E-2		
372.5	2.94					
375.0	2.96					
377.5	2.98					
379.1					2.997	
380.0	2.98					
382.5	2.99					
385.0	2.99					
387.5	3.01					
390.0	3.01		2.99	1.5 E-2		
392.5	3.01					
395.0	3.01					
397.5	3.02					
399.2					3.058	
400.0	3.04					
402.5	3.04					
405.0	3.04	0.02				
407.5	3.04	0.02				
410.0	3.06	0.02	3.03	1.2 E-2		
412.5	3.07	0.02				
415.0	3.07	0.02				
417.5	3.09	0.02				
419.4					3.100	
420.0	3.09					
422.5	3.09					
425.0	3.09	0.01				
427.5	3.09	0.02				
430.0	3.09	0.03	3.077	9.3 E-2		
432.5	3.09	0.03				
435.0	3.09	0.03				
435.5					3.126	
437.5	3.09	0.03				
440.0	3.10	0.06				
442.5	3.10	0.10				
445.0	3.09	0.08				
447.5	3.09	0.05				
450.0	3.09	0.05	3.11	7.6 E-3		

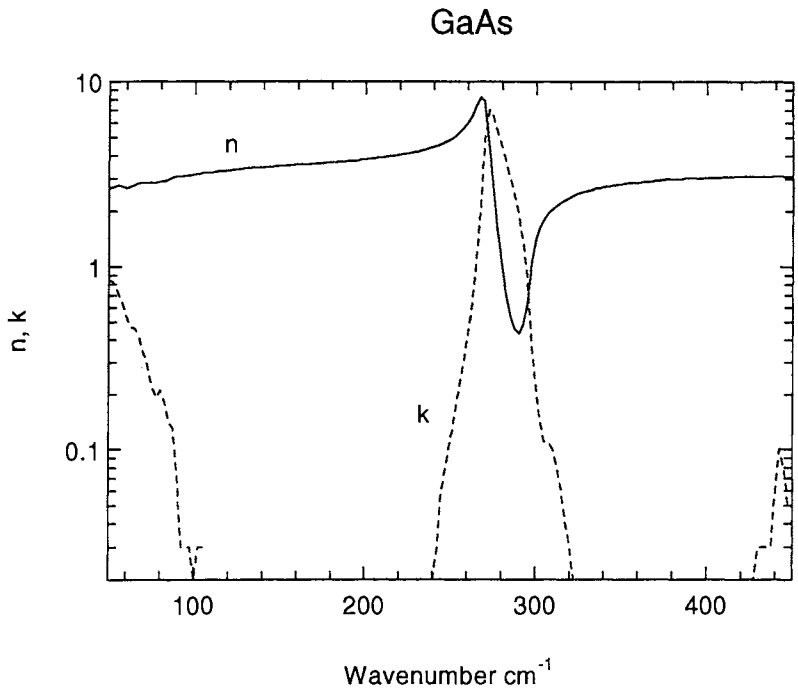

Fig. 10. Log-linear plot of the far-infrared optical constants, n and k, versus wavenumber for GaAs at 300 K.

3 GaSb

The far-infrared optical constants of GaSb determined by Maslin *et al.* [24] at 300 K at a resolution of 4 cm^{-1} using DFTS are shown in Fig. 11 and listed in Table XI, where they are compared with values calculated from the oscillator model, Eq. (11) [OM]. Hass and Henvis [68] measured the fundamental lattice reflection bands of several III-V semiconductors, including GaSb, at liquid-helium temperature and fitted a classical, damped harmonic oscillator model to their data. Edwards and White [69] have listed values of n and k for GaSb at liquid-helium temperature calculated from this model, but no previous numerical values for n and k for GaSb at 300 K have been found in the literature. The sample measured by Maslin *et al.* was n-type, and the onset of the free-carrier plasma response can be seen in Fig. 11 at frequencies below about 150 cm^{-1}. The presence of free carriers will modify the optical constants of the sample throughout the optical-phonon region, making it difficult to compare data for different samples. The transverse and longitudinal optic phonon frequencies determined from the data of Maslin *et al.*, ν_{TO} = 227.5 cm^{-1}, and ν_{LO} = 237.5 cm^{-1}, are in reason-

TABLE XI

Values of n and k for Gallium Antimonide from Various Sources

cm^{-1}	n	k	n	k
50.0	3.29	1.07 [24]	2.92	1.21 [OM]
60.0	3.33	0.81		
70.0	3.31	0.68	3.26	0.49
80.0	3.40	0.50		
90.0	3.56	0.34	3.52	0.24
100.0	3.61	0.24		
110.0	3.74	0.14	3.69	0.13
120.0	3.84	0.14		
130.0	3.90	0.08	3.81	8.2 E-2
140.0	3.99	0.08		
150.0	4.09	0.05	3.92	5.6 E-2
160.0	4.09	0.03		
170.0	4.17	0.03	4.04	4.3 E-2
180.0	4.30	0.02		
190.0	4.45	0.02	4.25	4.3 E-2
195.0	4.54	0.00		
200.0	4.63	0.04		
205.0	4.83	0.03		
210.0	5.03	0.06	4.80	9.8 E-2
212.5	5.19	0.09		
215.0	5.44	0.16		
217.5	5.78	0.22		
220.0	6.28	0.34		
222.5	7.11	0.59		
225.0	8.87	1.36		
227.5	5.34	8.32		
230.0	2.08	7.14	1.87	5.52
232.5	0.82	4.48		
235.0	0.66	2.60		
237.5	0.92	1.49		
240.0	1.62	0.47		
242.5	2.24	0.23		
245.0	2.54	0.17		
247.5	2.79	0.11		
250.0	2.92	0.11	2.74	0.10
252.5	3.03	0.10		
255.0	3.11	0.08		
257.5	3.19	0.06		
260.0	3.25	0.05		
262.5	3.32	0.05		
265.0	3.35	0.04		
267.5	3.42	0.03		
270.0	3.43	0.03	3.27	3.0 E-2
280.0	3.51	0.02		
290.0	3.59	0.01		
300.0	3.66			
310.0	3.69			

(continued)

TABLE XI *(Continued)*

Gallium Antimonide

cm^{-1}	n	k	n	k
320.0	3.72			
330.0	3.75		3.59	8.4 E-3
340.0	3.77			
350.0	3.79			
360.0	3.77			
370.0	3.79			
380.0	3.8			
390.0	3.80		3.68	4.4 E-3
400.0	3.79			
410.0	3.80			
420.0	3.80			
430.0	3.79			
440.0	3.71			
450.0	3.75		3.71	2.7 E-3

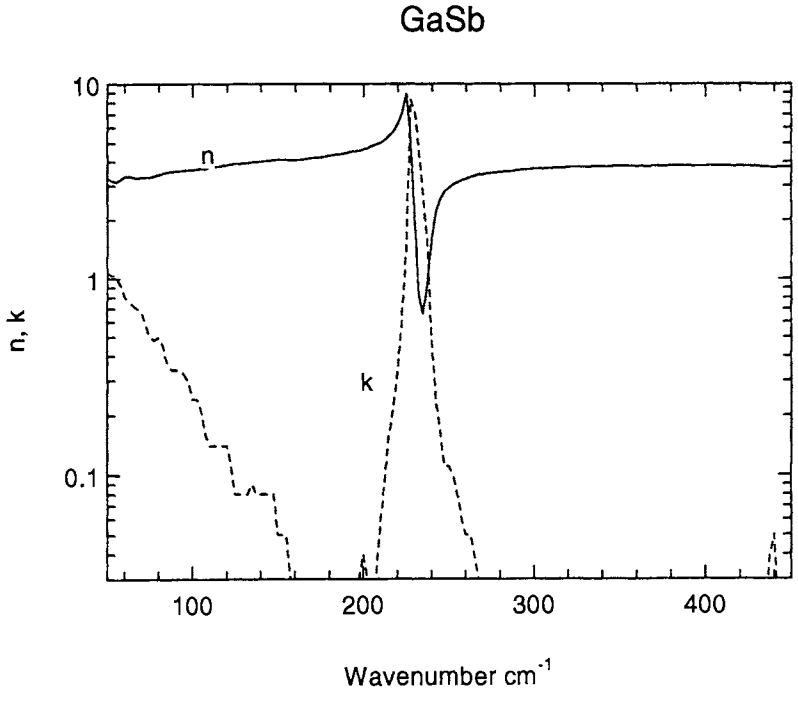

Fig. 11. Log-linear plot of the far-infrared optical constants, n and k, versus wavenumber for GaSb at 300 K.

able agreement with previous experimental values, $\nu_{TO} = 227$ cm^{-1} and $\nu_{LO} = 237$ cm^{-1}, determined by Raman spectroscopy [70], and $\nu_{TO} = 231$ cm^{-1} and $\nu_{LO} = 240$ cm^{-1}, determined by far-infrared spectroscopy [71]. The plasma minimum in the reflectivity occurred at 30 cm^{-1} [25]; using $m^* = 0.047\ m_0$ [39], the free-carrier concentration is found to be 6.7×10^{15} cm^{-3}. Small differences in the LO frequencies may arise from differences in plasmon-LO phonon coupling for samples with different carrier concentrations.

InP 4

The far-infrared optical constants of InP determined by Maslin *et al.* [24] at 300 K at a resolution of 2 cm^{-1} using DFTS are shown in Fig. 12 and listed in Table XII, where they are compared with values calculated from the oscillator model, Eq. (11) [OM], and values listed by Glembocki and Piller [72]. The values of n are the work of Pikhtin and Yas'kov [73], who fitted a lattice-vibration oscillator model to the refractive-index data of

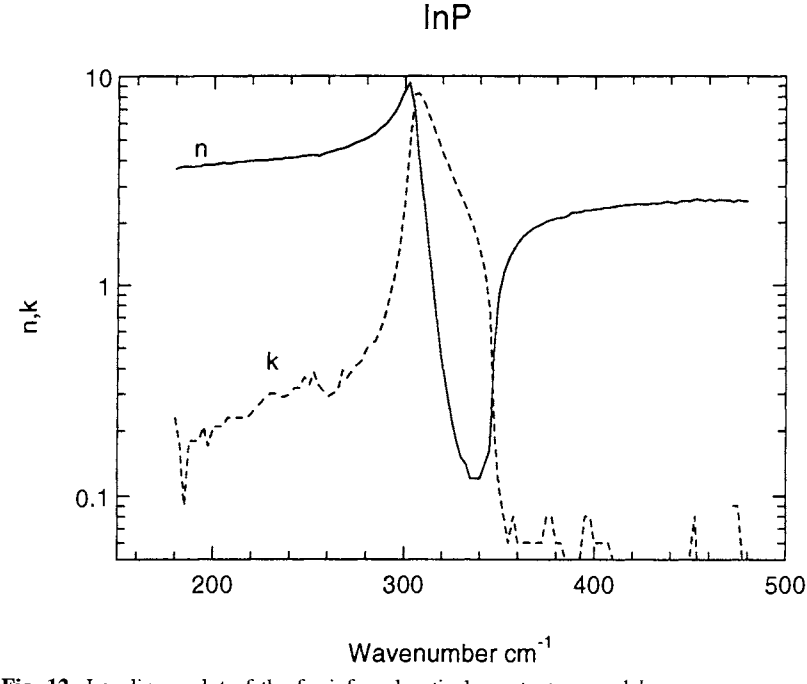

Fig. 12. Log-linear plot of the far-infrared optical constants, n and k, versus wavenumber for InP at 300 K.

TABLE XII

Values of *n* and *k* for Indium Phosphide from Various Sources

cm^{-1}	n	k	n	k	n	k
180.0	3.63	0.23 [24]	3.74	1.4 E-2 [OM]		
190.0	3.73	0.18				
200.0	3.82	0.21			3.81 [73]	8.7 E-3 [72]
210.0	3.88	0.23				
220.0	3.96	0.24	3.95	3.0 E-2		
225.0	3.99	0.27				
227.5	3.99	0.29				
230.0	4.02	0.30				
232.5	4.04	0.30				
235.0	4.05	0.29				
237.5	4.11	0.29				
240.0	4.10	0.30	4.14	5.0 E-2		
242.5	4.13	0.32				
245.0	4.17	0.32				
247.5	4.19	0.36				
250.0	4.20	0.33			4.27	3.0 E-2
252.5	4.23	0.38				
255.0	4.19	0.33				
257.5	4.28	0.31				
260.0	4.36	0.29	4.49	9.8 E-2		
262.5	4.42	0.30				
265.0	4.50	0.31				
267.5	4.56	0.39				
270.0	4.66	0.36			4.79	6.8 E-2
272.5	4.76	0.39				
275.0	4.87	0.41				
277.5	4.95	0.43				
280.0	5.08	0.49	5.29	0.28	5.31	0.124
282.5	5.24	0.52				
285.0	5.41	0.54				
287.5	5.66	0.61				
290.0	5.93	0.71	6.28	0.65		
292.5	6.31	0.88				
295.0	6.83	1.12				
297.5	7.60	1.49				
300.0	8.56	2.44	8.83	3.16	10.4	2.13
302.5	9.27	4.45				
305.0	7.02	8.14				
307.5	4.10	8.29				
310.0	2.52	7.50	2.45	6.75	1.81	7.32
312.5	1.62	6.60				
315.0	0.99	5.74				
317.5	0.61	5.00				
320.0	0.42	4.36	0.80	3.97	0.350	3.94
322.5	0.30	3.84				
325.0	0.22	3.36				

TABLE XII *(Continued)*

Indium Phosphide

cm^{-1}	n	k	n	k	n	k
327.5	0.18	3.00				
330.0	0.15	2.66			0.221	2.41
332.5	0.14	2.34				
335.0	0.12	2.05				
337.5	0.12	1.76				
340.0	0.12	1.46	0.49	1.35 [OM]	0.234	1.20
342.5	0.14	1.15				
345.0	0.16	0.78				
347.5	0.51	0.20				
350.0	0.90	0.11			1.069	0.16
352.5	1.15	0.08				
355.0	1.33	0.06				
357.5	1.48	0.08				
360.0	1.59	0.06	1.61	0.17	1.653	7.0 E-2
362.5	1.71	0.06				
365.0	1.79	0.06				
367.5	1.87	0.06				
370.0	1.92	0.06				
372.5	1.97	0.06				
375.0	2.03	0.08				
377.5	2.06	0.08				
380.0	2.11	0.06	2.14	6.9 E-2	2.163	2.9 E-3
382.5	2.12	0.06				
385.0	2.15	0.05				
387.5	2.23	0.05				
390.0	2.25	0.05				
392.5	2.26	0.05				
395.0	2.30	0.08				
397.5	2.31	0.08				
400.0	2.32	0.06	2.39	3.8 E-2	2.411	
402.5	2.34	0.06				
405.0	2.37	0.06				
407.5	2.37	0.06				
410.0	2.40	0.05				
415.0	2.43	0.03				
420.0	2.46	0.03	2.55	2.5 E-2		
430.0	2.49	0.02				
440.0	2.52					
450.0	2.55	0.05				
460.0	2.61	0.03	2.72	1.3 E-2		
470.0	2.58					
480.0	2.56		2.78	9.5 E-3		

Pettit and Turner [74], measured for an *n*-type sample with a carrier density of 5×10^{16} cm^{-3}. The values of k were calculated by Glembocki and Piller [72] using an oscillator model, with optical-phonon frequencies taken from Mooradian and Wright [75] and ϵ_∞ taken from Hass [76]. The transverse and longitudinal optic phonon frequencies determined from the data of Maslin *et al.*, $\nu_{TO} = 304$ cm^{-1}, and $\nu_{LO} = 346.5$ cm^{-1}, are in excellent agreement with previous experimental values, $\nu_{TO} = 304.5$ cm^{-1} and $\nu_{LO} = 346.4$ cm^{-1}, determined by Raman spectroscopy [77]. No free-carrier response was observable in this sample at frequencies down to 25 cm^{-1}, which puts an upper limit on the (*n*-type) free-carrier concentration of 7×10^{15} cm^{-3}.

5 InAs

The far-infrared optical constants of InAs determined by Maslin *et al.* [24] at 300 K at a resolution of 4 cm^{-1} using DFTS are shown in Fig. 13 and listed in Table XIII, where they are compared with values calculated from

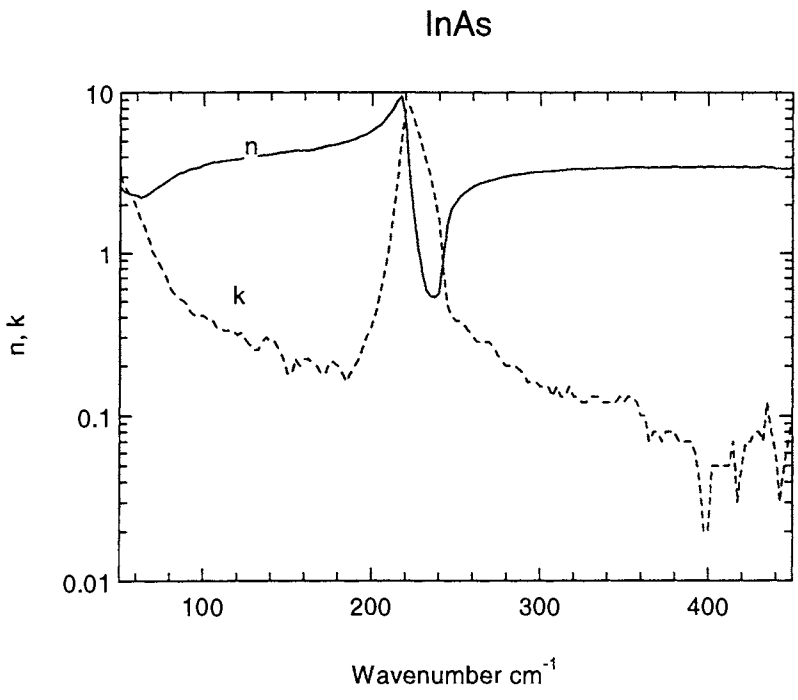

Fig. 13. Log-linear plot of the far-infrared optical constants, n and k, versus wavenumber for InAs at 300 K.

TABLE XIII

Values of n and k for Indium Arsenide from Various Sources

cm^{-1}	n	k	n	k	n	k
60.0	2.29	1.92 [24]	2.47	1.61 [OM]		
80.0	2.91	0.61				
100.0	3.54	0.41	3.27	0.33		
120.0	3.85	0.31				
140.0	4.14	0.28	3.78	0.13		
145.0	4.23	0.25				
150.0	4.31	0.18	3.90	0.11		
155.0	4.38	0.22			5.30	0.51 [80]
160.0	4.38	0.22	4.02	0.10		
165.0	4.42	0.21				
170.0	4.57	0.18	4.19	0.10		
175.0	4.70	0.21			5.58	0.20
180.0	4.80	0.20	4.41	0.12		
185.0	4.95	0.16				
190.0	5.19	0.20	4.73	0.16		
195.0	5.44	0.26			6.42	8 E-2
200.0	5.84	0.35	5.32	0.28		
205.0	6.35	0.57			7.48	0.48
210.0	7.33	1.04	6.76	0.89		
212					9.13	1.53
212.5	7.97	1.62				
216					9.24	3.50
215.0	8.83	2.75				
217.5	9.44	4.98				
220.0	6.82	8.13	5.43	7.76	7.50	6.40
222.5	3.09	8.15				
224					4.90	6.12
225.0	1.74	6.99				
227.5	1.08	5.63				
228					3.85	5.60
230.0	0.75	4.55	0.90	3.84		
232					2.79	5.17
232.5	0.59	3.71				
235.0	0.54	2.93				
236					1.27	4.20
237.5	0.53	2.21				
240.0	0.56	1.61	0.64	1.72	0.92	2.77
242.5	0.90	0.81				
244					1.24	1.44
245.0	1.53	0.48				
247.5	1.87	0.41				
248					1.88	0.97
250.0	2.07	0.38	1.46	0.38	2.03	0.83
252.5	2.26	0.38				
255.0	2.36	0.36			2.37	0.50
257.5	2.48	0.33				

(continued)

TABLE XIII *(Continued)*

Indium Arsenide

cm^{-1}	n	k	n	k	n	k
260.0	2.58	0.31	2.11	0.16	2.73	0.40
265.0	2.75	0.28			2.92	0.40
270.0	2.85	0.28			2.92	0.39
275.0	2.94	0.23				
280.0	3.01	0.20			3.00	0.17
285.0	3.09	0.20				
290.0	3.13	0.18	2.78	5.1 E-2	3.18	4 E-2
295.0	3.19	0.16				
300.0	3.22	0.15				
310.0	3.28	0.15	2.96	3.2		
320.0	3.36	0.13				
330.0	3.39	0.13				
340.0	3.40	0.12	3.11	2.0 E-2		
350.0	3.42	0.12				
360.0	3.46	0.10				
370.0	3.45	0.08				
380.0	3.47	0.08				
390.0	3.45	0.07	3.24	1.1 E-2		
400.0	3.47	0.02				
410.0	3.47	0.05				
420.0	3.44	0.05				
430.0	3.45	0.08				
440.0	3.40	0.06				
450.0	3.44	0.10	3.32	6.4 E-3		

the oscillator model, Eq. (11) [OM]. The far-infrared optical constants of InAs determined by reflection DFTS were previously reported by Gast and Genzel [78]. The transverse optic phonon frequency determined from these data, $\nu_{TO} = 218.5\ cm^{-1}$, is in good agreement with a previous experimental value, 217.3 cm^{-1}, determined by Raman spectroscopy [79]. The longitudinal optic phonon frequency, $\nu_{LO} = 242.5\ cm^{-1}$, is somewhat higher than a previous experimental value, 238.6 cm^{-1}, determined by Raman spectroscopy [79]. The plasma minimum in the reflectivity occurred at 71 cm^{-1} [25]; using $m^* = 0.026\ m_0$, Table VI [39], the free-carrier concentration is found from Eq. (12) to be $1.8 \times 10^{16}\ cm^{-3}$. Small differences in the LO frequencies may arise from differences in plasmon-LO phonon coupling for samples with different carrier concentrations. Also shown in the table are values of n and k determined by Memon *et al.* [80] for a different sample by DFTS. There are significant differences in the reststrahl region, particularly in the region of ν_{LO} which may also be due to different plasmon-phonon coupling in the two samples.

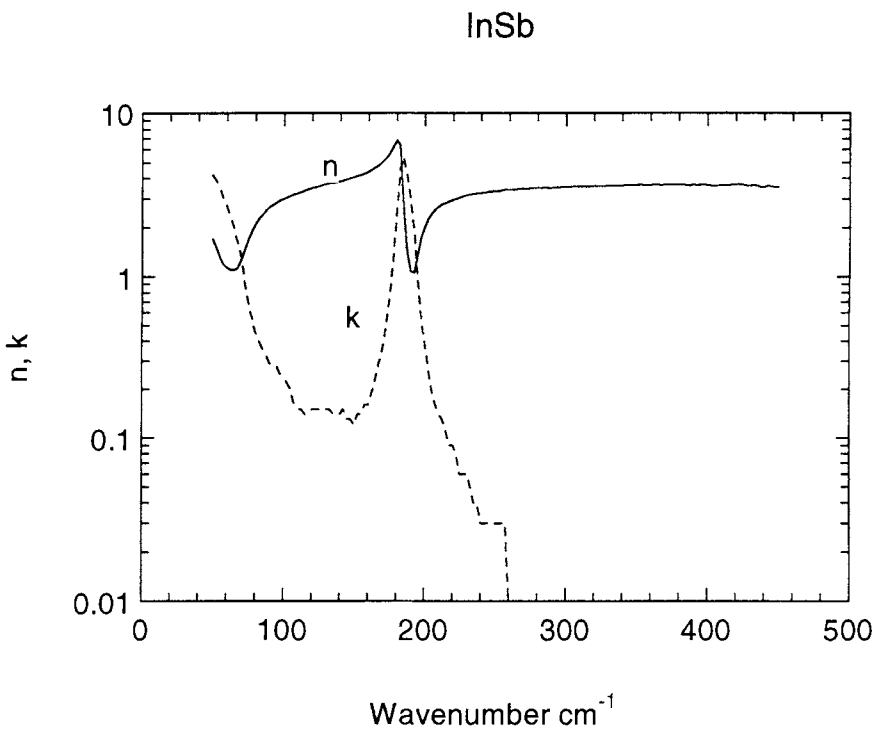

Fig. 14. Log-linear plot of the far-infrared optical constants, n and k, versus wavenumber for InSb at 300 K.

InSb 6

The far-infrared optical constants of InSb determined by Maslin *et al.* [24] at 300 K at a resolution of 4 cm^{-1} using DFTS are shown in Fig. 14 and listed in Table XIV where they are compared with values calculated from the oscillator model, Eq. (11) [OM], and the data of Sanderson [81] as listed by Holm [82]. Measurements of the far-infrared optical constants of InSb determined by reflection DFTS have also been reported by Gast and Genzel [78] and Afsar *et al.* [83]. The transverse optic and longitudinal optic phonon frequencies determined from the data of Maslin *et al.*, $\nu_{TO} = 181$ cm^{-1}, and $\nu_{LO} = 193$ cm^{-1}, are in excellent agreement with previous experimental values, $\nu_{TO} = 182.4$ cm^{-1}, and $\nu_{LO} = 193.0$ cm^{-1}, determined by Raman spectroscopy [84]. The plasma minimum in the reflectivity occurred at 75 cm^{-1} [25]; using $m^* = 0.015\ m_0$, Table VI [39], the free-carrier concentration is found from Eq. (12) to be 1.5×10^{16} cm^{-3}. Small differences in the LO frequencies may arise from differences in plasmon-LO phonon coupling for samples with different carrier concentrations.

TABLE XIV

Values of *n* and *k* for Indium Antimonide from Various Sources

cm^{-1}	n	k	n	k	n	k
50.0	1.70	4.20 [24]	1.22	3.99 [OM]	0.894	4.72 [81]
55.0	1.31	3.44				
60.0	1.13	2.67			0.771	3.21
65.0	1.10	1.98				
70.0	1.27	1.32	1.54	1.21	0.881	1.79
75.0	1.68	0.69				
80.0	2.10	0.45			1.68	0.633
85.0	2.40	0.36				
90.0	2.67	0.29	2.82	0.32	2.45	0.310
95.0	2.85	0.28				
100.0	3.01	0.24			2.92	0.193
105.0	3.13	0.20				
110.0	3.25	0.15	3.44	0.16	3.25	0.134
115.0	3.37	0.14				
120.0	3.50	0.15			3.51	0.100
125.0	3.57	0.15				
130.0	3.68	0.15	3.85	0.11	3.74	8.08 E-2
135.0	3.75	0.14				
140.0	3.83	0.14			3.96	7.15 E-2
145.0	3.93	0.13				
150.0	4.06	0.12	4.29	0.12	4.24	7.43 E-2
155.0	4.20	0.14				
160.0	4.37	0.16			4.66	0.105
162.5	4.49	0.19				
165.0	4.63	0.23				
167.5	4.80	0.29				
170.0	5.01	0.36	5.41	0.46	5.69	0.291
172.5	5.29	0.50				
175.0	5.67	0.76			7.32	0.963
177.5	6.22	1.26				
180.0	6.78	2.52			5.34	8.56
182.5	6.36	4.59				
185.0	2.74	5.40			0.884	4.10
187.5	1.44	4.22				
190.0	1.07	2.88	1.34	2.56	0.618	1.88
192.5	1.06	1.86				
195.0	1.35	0.94				
197.5	1.74	0.56				
200.0	2.02	0.39			2.22	0.165
205.0	2.43	0.20				
210.0	2.69	0.14	2.79	0.15	2.82	6.92 E-2
215.0	2.84	0.11				
220.0	2.96	0.09				
222.5	3.01	0.08				
225.0	3.06	0.06				
230.0	3.15	0.06	3.26	5.5 E-2		

TABLE XIV *(Continued)*

Indium Antimonide

cm^{-1}	n	k	n	k	n	k
235.0	3.21	0.04				
240.0	3.26	0.03				
250.0	3.35	0.03	3.46	3.0 E-2	3.45	1.75 E-2
260.0	3.41	0.01				
270.0	3.46	0.01	3.57	2.0 E-2		
280.0	3.49	0.01				
285.0	3.52	0.01				
290.0	3.51	0.01				
295.0	3.53	0.01				
300.0	3.55				3.662	7.84 E-3
302.5	3.55					
305.0	3.56					
310.0	3.57		3.70	1.1 E-2	320.0	3.59
330.0	3.61				3.708	
340.0	3.63				3.743	
350.0	3.64					
360.0	3.64					
370.0	3.65					
380.0	3.65					
400.0	3.64					
425.0	3.65					
450.0	3.54		3.85	2.8 E-3		

ACKNOWLEDGMENT

G. Mirjalili wishes to acknowledge the award of a scholarship by the Islamic Republic of Iran and the University of Yazd.

REFERENCES

1. J. E. Chamberlain, J. E. Gibbs, and H. A. Gebbie, *Nature (London)* **198**, 874 (1963).
2. J. E. Chamberlain and H. A. Gebbie, *Nature (London)* **208**, 480 (1965).
3. J. E. Chamberlain, F. D. Findlay, and H. A. Gebbie, *Appl. Opt.* **4**, 1382 (1965).
4. E. E. Bell, *Jpn. J. Appl. Phys.* **4**(Suppl. 1), 412 (1965).
5. E. E. Bell, *Infrared Phys.* **6**, 1382 (1965).
6. E. E. Russell and E. E. Bell, *Infrared Phys.* **6**, 75 (1966).
7. E. E. Bell, *Handb. Phys.* **25**, 1 (1967).
8. J. R. Birch and T. J. Parker, *in* "Infrared and Millimeter Waves" (K. J. Button, ed.), Vol. 2, Chap. 3. Academic Press, New York, 1979.
9. J. R. Birch, *Proc. SPIE* **289**, 362 (1981).
10. T. J. Parker, *Contemp. Phys.* **31**, 335 (1990).
11. K. W. Johnson and E. E. Bell, *Phys. Rev.* **187**, 1044 (1969).
12. J. E. Eldridge and P. R. Staal, *Phys. Rev. B* **16**, 4608 (1977).
13. P. R. Staal and J. E. Eldridge, *Can. J. Phys.* **57**, 1784 (1979).
14. J. R. Birch, *Infrared Phys.* **18**, 613 (1978).
15. T. J. Parker, W. G. Chambers, and J. F. Angress, *Infrared Phys.* **14**, 207 (1974).

16. K. F. Pai, T. J. Parker, N. E. Tornberg, R. P. Lowndes, and W. G. Chambers, *Infrared Phys.* **18**, 199 (1978).
17. G. O. Plumb and J. R. Birch, *Infrared Phys.* **24**, 315 (1984).
18. K. A. Maslin and T. J. Parker, *Proc. 14th Int. Conf. Infrared Millimeter. Waves, Wurzburg, October 2–6, 1989; Proc. SPIE* **1240**, 476 (1989).
19. A. K. Wan Abdullah and T. J. Parker, *Infrared Phys.* **29**, 799 (1989).
20. N. J. Burton and T. J. Parker, *Opt. Commun.* **45**, 367 (1983).
21. N. J. Burton and T. J. Parker, *Infrared Phys.* **24**, 291 (1984).
22. J. R. Birch, *Infrared Phys.* **28**, 345 (1988).
23. J. R. Birch, *Infrared Phys.* **28**, 425 (1988).
24. K. A. Maslin, C. Patel, and T. J. Parker, *Infrared Phys.* **18**, 199 (1978).
25. K. A. Maslin, Ph.D. Thesis, University of London, London (1986).
26. J. E. Eldridge and E. D. Palik, *in* "Handbook of Optical Constants of Solids" (E. D. Palik, ed.), p. 775. Academic Press, Orlando, Florida, 1985.
27. E. D. Palik, *in* "Handbook of Optical Constants of Solids," (E. D. Palik, ed.), p. 703. Academic Press, Orlando, Florida, 1985.
28. E. D. Palik, *in* "Handbook of Optical Constants of Solids II" (E. D. Palik, ed.), p. 989. Academic Press, Orlando, Florida, 1991.
29. J. I. Berg and E. E. Bell, *Phys. Rev. B* **10**, 3572 (1971).
30. A. Memon and T. J. Parker, *Int. J. Infrared Millim. Waves* **2**, 839 (1981).
31. M. E. Thomas, in this volume.
32. G. O. Jones, D. H. Martin, P. A. Mawer, and C. H. Perry, *Proc. R. Soc. London Ser. A* **261**, 10 (1961).
33. G. R. Wilkinson, *in* "Infrared Spectroscopy and Molecular Structure" (M. Davies, ed.), p. 85. Elsevier, Amsterdam, 1963.
34. R. P. Lowndes and D. H. Martin, *Proc. R. Soc. London Ser. A* **308**, 473 (1969).
35. I. Ohlídal and K. Navrátil, *in* "Handbook of Optical Constants of Solids II" (E. D. Palik, ed.), p. 1021. Academic Press, Orlando, Florida, 1991.
36. I. Ohlídal and M. Ohlídal, in this volume.
37. I. Ohlídal and D. Franta, in this volume.
38. K. Kunc, M. Balkanski, and M. A. Numisovici, *Phys. Status Solidi B* **72**, 229 (1975).
39. D. E. Gray, ed., "American Institute of Physics Handbook," 3rd Ed., pp. 9–59. McGraw-Hill, New York, 1972.
40. R. A. Cowley, *Adv. Phys.* **12**, 421 (1963).
41. R. Geick, *Phys. Rev.* **138**, 1495 (1965).
42. J. R. Birch and D. K. Murray, *Infrared Phys.* **18**, 283 (1978).
43. C. L. Mok, T. J. Parker, and J. R. Birch, *Solid State Commun.* **34**, 567 (1980).
44. E. D. Palik, *in* "Handbook of Optical Constants" (E. D. Palik, ed.), p. 409. Academic Press, Orlando, Florida 1985.
45. A. Mooradian and G. B. Wright, "Proceedings of The Ninth International Conference on The Physics of Semiconductors, Moscow," Vol. 2, p. 1020. Nauka, Leningrad, 1968.
46. G. A. Slack, F. S. Ham, and R. M. Chrenko, *Phys. Rev.* **152**, 376 (1971).
47. A. Feldman, I. Malitson, D. Horwitz, R. M. Waxler, and M. J. Dodge, *Natl. Bur. Stand. (U.S.), Tech. Note* **993**, 63 (1979).
48. M. Cardona, "Proceedings of the Seventh International Conference on The Physics of Semiconductors, Paris," p. 181. Dunod, Paris, and Academic Press, New York, 1964.
49. D. G. Thomas and J. J. Hopfield, *Phys. Rev.* **128**, 2135 (1969).
50. L. Ward, *in* "Handbook of Optical Constants of Solids II" (E. D. Palik, ed.), p. 737. Academic Press, Orlando, Florida, 1991.
51. M. N. Afsar, "Proceedings of the Third International Conference on Infrared Physics, Zurich" (W. Ruegsegger and F. K. Kneubuhl, eds.), p. 714. ETH, Zurich, 1984.
52. A. Manabe, A. Mitsuishi, and H. Yoshinaga, *Jpn. J. Appl. Phys.* **6**, 593 (1967).

53. T. Hattori, Y. Homma, and A. Mitsuishi, *Opt. Commun.* **7**, 229 (1973).
54. J. C. Irwin and J. La Combe, *Can. J. Phys.* **50**, 2596 (1972).
55. C. Patel, K. A. Maslin, and T. J. Parker, "Proceedings of the Second International Conference on Phonon Physics," p. 927. Phonon '85, Budapest, 1985.
56. A. Borghesi and G. Guizzetti, *in* "Handbook of Optical Constants of Solids" (E. D. Palik, ed.), p. 445. Academic Press, Orlando, Florida, 1985.
57. A. S. Barker, Jr., *Phys. Rev.* **165**, 917 (1968).
58. D. A. Kleinman and W. G. Spitzer, *Phys. Rev.* **118**, 110 (1960).
59. M. V. Hobden and J. P. Russell, *Phys. Lett.* **13**, 39 (1964).
60. A. H. Kachare, W. G. Spitzer, F. K. Euler, and A. Kahan, *J. Appl. Phys.* **45**, 2938 (1974).
61. R. T. Holm, J. W. Gibson, and E. D. Palik, *J. Appl. Phys.* **48**, 212 (1977).
62. R. H. Stolen, *Phys. Rev. B* **11**, 767 (1975); R. H. Stolen, *Appl. Phys. Lett.* **15**, 74 (1969).
63. E. D. Palik, *in* "Handbook of Optical Constants of Solids" (E. D. Palik, ed.), p. 429. Academic Press, Orlando, Florida, 1985.
64. M. N. Afsar and K. J. Button, *IEEE Trans. Microwave Theory Tech.* **MTT-31**, 217 (1983).
65. M. N. Afsar, *IEEE Trans. Microwave Theory Tech.* **MTT-32**, 1598 (1984).
66. T. Sekine, K. Uchinokura, and E. Matsuura, *J. Phys. Chem. Solids* **38**, 1091 (1977).
67. E. S. Koteles and W. R. Datars, *Can. J. Phys.* **54**, 1676 (1976).
68. M. Hass and B. W. Henvis, *J. Phys. Chem. Solids.* **23**, 1099 (1962).
69. D. F. Edwards and R. H. White, *in* "Handbook of Optical Constants of Solids II" (E. D. Palik, ed.), p. 597. Academic Press, Orlando, Florida, 1991.
70. T. Sekine, K. Uchinokura, and E. Matsuura, *Solid State Commun.* **18**, 1337 (1976).
71. S. S. Mitra, *Phys. Rev.* **132**, 986 (1963).
72. O. J. Glembocki and H. Piller, *in* "Handbook of Optical Constants of Solids" (E. D. Palik, ed.), p. 503. Academic Press, Orlando, Florida, 1985.
73. A. N. Pikhtin and A. D. Yas'kov, *Sov. Phys. Semicond. (Engl. Transl.)* **12**, 622 (1978); A. N. Pikhtin and A. D. Yas'kov, *Fiz. Tekh. Poluprovodu.* **12**, 1047 (1978).
74. G. D. Pettit and W. J. Turner, *J. Appl. Phys.* **36**, 2081 (1965).
75. A. Mooradian and G. B. Wright, *Solid State Commun.* **4**, 431 (1966).
76. M. Hass, *in* "Semiconductors and Semimetals" (R. K. Willardson and A. C. Beer, eds.), Vol. 3, p. 3. Academic Press, New York, 1967.
77. G. F. Alfrey and P. H. Borcherds, *J. Phys. C* **5**, 275 (1972).
78. J. Gast and L. Genzel, *Opt. Commun.* **8**, 26 (1973).
79. R. Carles, N. Saint-Cricq, J. B. Renucci, M. A. Renucci, and A. Zwick, *Phys. Rev. B* **22**, 4804 (1980).
80. A. Memon, T. J. Parker, and J. R. Birch, *Proc. 1981 Int. Conf. Fourier Transform Spectroscopy, Proc. SPIE* **289**, 20 (1981).
81. R. B. Sanderson, *J. Phys. Chem. Solids* **26**, 803 (1965).
82. R. T. Holm, *in* "Handbook of Optical Constants of Solids" (E. D. Palik, ed.), p. 491. Academic Press, Orlando, Florida 1985.
83. M. N. Afsar, J. R. Birch, and J. Chamberlain, *Proc. Conf. Dielectric Mater. Measurements Appl., IEE Conf. Publ.* **129**, 131 (1975).
84. W. Kiefer, W. Richter, and M. Cardona, *Phys. Rev. B* **12**, 2346 (1975).

Chapter 3

Photothermal/Photoacoustic Spectroscopic Measurements of Optical Absorption Coefficients in Semiconductors

ANDREAS MANDELIS
Photothermal and Optoelectronic Diagnostics Laboratories
Department of Mechanical and Industrial Engineering
University of Toronto
Toronto, ON, Canada

I. Introduction 59
II. Photoacoustic Spectroscopy (PAS) 60
III. Photopyroelectric Spectroscopy (PPES) 67
IV. Measurements of $\alpha(\lambda)$ in Semiconductors Using Photoacoustic/Photothermal Techniques 69
Acknowledgments 94
References 94

INTRODUCTION I

Photothermal- and photoacoustic-based spectroscopic techniques have proliferated in recent years as primary methodologies for measuring the optical absorption coefficient, α, in broad ranges of solids, which may, or may not, be easily measurable by other, more conventional spectroscopic techniques. An increasing body of literature concerning these measurements can be consulted by the interested reader, including a number of monographs, review books and treatises on the state-of-the-art in these fields [1–7]. It should be noted that the foregoing techniques are now widely used to measure *directly* the optical absorption coefficient $\alpha(\lambda)$ from a dynamic measurement of the heat released *via* the spatial rate of optical-to-thermal energy conversion in a material, rather than the extinction coefficient, $k(\lambda)$.

HANDBOOK OF OPTICAL CONSTANTS OF SOLIDS III

Copyright © 1998 by Academic Press.
All rights of reproduction in any form reserved
ISBN 0-12-544423-0/$25.00.

The two measurements are, of course, equivalent and are related through the defining equation of the former

$$\alpha(\lambda) = 4\pi k(\lambda)/\lambda \qquad [\text{cm}^{-1}]. \tag{1}$$

As a result of this peculiarity of the photoacoustic/photothermal techniques, all the spectroscopic plots and data to be discussed in this chapter will be given in terms of $\alpha(\lambda)$. The major α-measuring methodologies in this field include in order of historical sequence a) gas-cell and piezoelectric photoacoustic spectroscopy (PAS); various photothermal spectroscopies (PTS), such as b) photothermal beam-deflection spectroscopy (PDS), otherwise known as Mirage-Effect spectroscopy; c) Fourier-transform infrared photoacoustic (FTIR-PAS) spectroscopies; and d) photopyroelectric spectroscopy (PPES). The PDS family of techniques has been well described by Briggs in Chapter 4 and, therefore, will not be discussed further in this chapter, except where necessary for complementary measurements of α, especially with regard to semiconducting amorphous thin-films. Again, for historical reasons the presentation of the material in this chapter will be done as follows: i) technique description and instrumental implementation; and ii) applications to optical-property measurements of semiconductors, specifically of α at a single wavelength or within a spectral range.

II PHOTOACOUSTIC SPECTROSCOPY (PAS)

A Gas-Cell—Microphone Photoacoustics

The photoacoustic effect in solids was first described quantitatively by Parker [8] in 1973 and was later generalized by what has come to be known as the "Rosencwaig–Gersho (RG) Theory" [9]. Figure 1 shows a cross-section of a typical photoacoustic cell used for the measurement of α in sol-

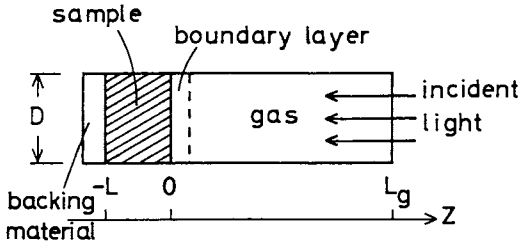

Fig. 1. Cross-sectional view of a simple cylindrical photoacoustic cell. (From Rosencwaig and Gersho [9] with permission from the publisher.)

ids. The gas-cell—microphone PA signal is generated as an acoustic disturbance in a hermetically sealed chamber equipped with a sensitive microphone, following the incidence and absorption of optical power by a solid sample inside the acoustic chamber. The incident radiation penetrates the cell through a transparent window, and the intensity is mechanically chopped or otherwise modulated at a constant frequency $f = \omega/2\pi$. The absorbed radiation is subsequently converted into heat through non-radiative relaxation mechanisms in the bulk and/or at the surface of the solid. Conduction heat transfer to the surrounding gaseous medium (air) at the frequency f is almost always the predominant energy-transport process and the one that generates the harmonic acoustic disturbance detected by the sensitive microphone. The absorption of photons by a solid followed by energy conversion and de-excitation pathways is described schematically in Fig. 2. Non-radiative conversion is but one such pathway, which, nevertheless, is usually the dominant de-excitation mechanism in solids, leading to production of heat. Other possible energy transformations and conversions are also shown in Fig. 2. The PA signal from the microphone is demodulated by a lock-in amplifier, and the amplitude and phase are stored and displayed on a computer screen for quantitative analysis. A typical experimental set-up is shown in Fig. 3.

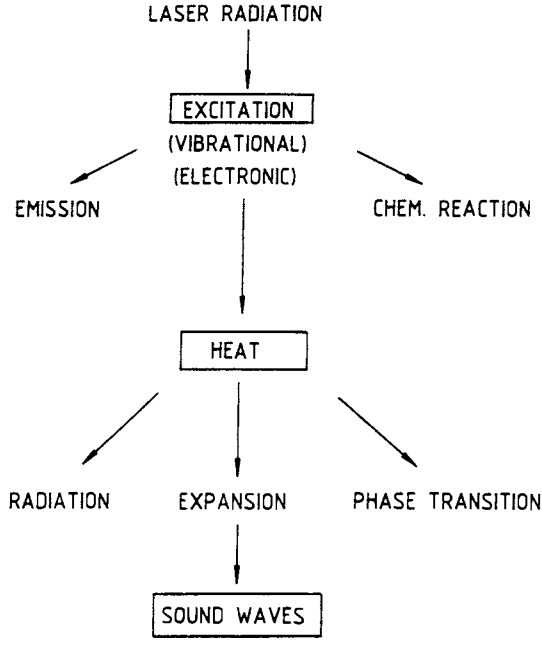

Fig. 2. Optical energy conversion pathways in a photoacoustic experiment.

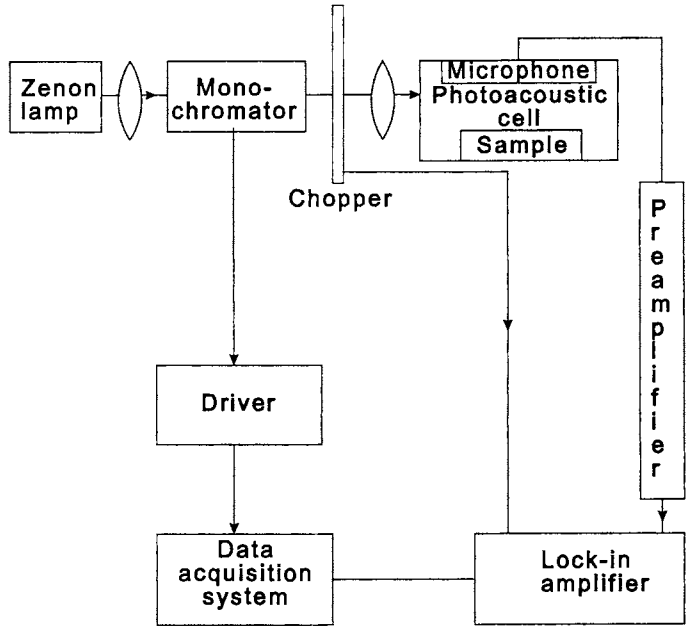

Fig. 3. Typical experimental set-up for gas-cell—microphone PAS of solids.

Assuming a spatially broad, homogeneous and isotropic, sinusoidally chopped/modulated monochromatic light source with wavelength, λ, impinging on an absorbing solid of optical absorption coefficient, $\alpha(\lambda)$, with intensity

$$I(t) = \frac{1}{2} I_0(1 + \cos\omega t) \qquad [\mathrm{W/cm^2}], \tag{2}$$

the heat density produced at depth x from the surface of the solid is given by

$$Q(x,t) = \frac{1}{2}\alpha I_0 e^{-\alpha x} Re(1 + e^{i\omega t}) \qquad [\mathrm{W/cm^3}]. \tag{3}$$

Coupled heat-diffusion equations in the gas, solid, and backing regions of Fig. 1 can be solved to give the a.c. temperature oscillation in the PA chamber [9]. This is the thermal-wave responsible for the acoustic oscillation (the pressure wave) detected by the microphone. From the real and imaginary parts of the complex thermal-wave signal *at the surface of the solid,* the PA signal expressions are worked out in the RG theory assuming the validity of the ideal gas law and the adiabatic gas law in the hermetically sealed

chamber/cell. The PA amplitude and phase can thus be calculated in the general case from the real and imaginary parts of the signal. These are complicated expressions, and they are generally non-linear in the parameter α. Nevertheless, substantial simplifications occur in a number of limiting cases of the RG theory:

Optically Transparent Solids ($\alpha^{-1} > L$)

Case 1a: Thermally Thin Solids ($\mu > L$; $\mu >$ or $< \alpha^{-1}$): The symbol μ, a function of the chopping frequency, stands for the thermal-wave penetration depth in the solid material of thickness L,

$$\mu(\omega) = \sqrt{2\beta/\omega}, \tag{4}$$

where β is the thermal diffusivity of the sample [cm^2/s]. In this limiting case, the optical radiation is assumed to obey the Beer-Lambert Law and is absorbed throughout the length of the solid. A fraction of it exits the back surface of the sample and impinges on the backing material, which is assumed to be transparent and of infinite thickness. In this limit, whether $\alpha >$ or $< \sqrt{2}/\mu(\omega)$, the complex magnitude of the PA signal is approximately given by

$$Q \approx Y\mu_g(\mu_b/\kappa_b)Y\frac{(1-i)\alpha L}{2}, \tag{5}$$

where the subscript *"b"* indicates the backing material, *"g"* indicates the surrounding gas (almost always air), κ stands for thermal conductivity [W/cm K], μ_j has the definition of Eq. (4) for $j = g$ or b. Y is a constant (real) pre-factor independent of the optical absorption coefficient of the sample, but generally dependent on wavelength through its linear dependence on the reflectivity in the form $[1 - R(\lambda)]$. Equation (5) shows that the PA signal in this limit is proportional to αL and inversely proportional to ω. Furthermore, the thermal properties of the backing play a role in this thermally thin situation.

Case 1b: Thermally Thick Solids ($\mu < L$; $\mu \ll \alpha^{-1}$): The complex magnitude of the PA signal is now approximated by

$$Q \approx -iY\mu_g(\mu/\kappa)\frac{\alpha\mu}{2}. \tag{6}$$

Here the signal is proportional to $\alpha\mu$, rather than αL, that is only the radiation that is absorbed within the optical absorption length α^{-1} contributes to the signal, even though optical absorption takes place throughout the thickness of the sample. Since the sample is now thermally "thick", the thermal properties of the backing material have been replaced by those of the solid, and the frequency dependence is $\omega^{-3/2}$.

Optically Opaque Solids ($\alpha^{-1} \ll L$)

Case 2a: Thermally Thin Solids ($\mu \gg L$, $\mu \gg \alpha^{-1}$): In this case the Beer-Lambert Law yields $e^{-\alpha L} \approx 0$, and the complex magnitude of the PA signal becomes

$$Q \approx Y(\mu/\kappa) \frac{(1-i)\mu_g}{2}. \tag{7}$$

In this case, the signal is independent of the optical absorption coefficient (*photoacoustic saturation*) and decreases with increasing frequency as ω^{-1}. No spectroscopic information can be derived in this limit.

Case 2b: Thermally Thick Solids ($\mu < L$, $\mu > \alpha^{-1}$): When the modulation/chopping frequency rises well above the limits represented in Case 2a, the PA signal becomes

$$Q \approx Y\mu_g(\mu/\kappa) \frac{(1-i)}{2}. \tag{8}$$

Again, this case lies within the range of photoacoustic saturation, and no spectroscopic information may be derived from experiments in this (intermediate) frequency range.

Case 2c: Thermally Thick Solids ($\mu \ll L$, $\mu < \alpha^{-1}$): This situation obtains at very high frequencies, so that the sample is entirely thermally thick, and the PA signal comes out of photoacoustic saturation with frequency dependence $\omega^{-3/2}$:

$$Q \approx -Y\mu_g(\mu/\kappa) \frac{\alpha\mu}{2}. \tag{9}$$

Even though theoretically this is a legitimate special case where PAS operates as an absorption spectroscopy, in practice the modulation frequencies required to satisfy the conditions of the case may be too high to yield an acceptable signal-to-noise ratio.

B Piezoelectric Photoacoustics

In the case of gas-microphone PA detection, the optically generated heat is coupled to the non-absorbing gas of the sample chamber, and the ensuing time-dependent pressure fluctuation is detected by a sensitive microphone. An alternative signal-transduction methodology is through coupling of the thermal energy released following optical absorption to the vibrational modes of the sample, i.e., through coupling to its acoustic phonon spectrum. In this

thermoelastic mode, the speed of energy transfer is governed by the speed of sound and is limited by the sample/transducer geometry and the boundary conditions at the sample-gas and sample-transducer interfaces. The thermoelastic theory of this PAS mode has been presented adequately by White [10]. The generated harmonic pressure pulse in the sample is communicated to an intimately attached piezoelectric transducer. This pressure pulse results in a harmonic electrical signal across the piezoelectric transducer, which may be demodulated by a lock-in amplifier (LIA) as in the case of gas-cell—microphone PAS. A more complete theory directly applicable to piezoelectric PAS of condensed matter was developed by Jackson and Amer [11], commonly known as the "Jackson–Amer (JA) model." A simple outline of this detection principle is shown in Fig. 4. The expansion of the central region causes displacement of the sample surface by two separate mechanisms. First, the enlargement of the central region causes the general expansion of both surfaces of the sample at $z = 0$ and $z = L$, Fig. 4(a). Second, in the case of strongly absorbing solids, the heat in the illuminated region decays spatially throughout the thickness of the sample; consequently, the front part of the sample expands more than the rear part, resulting in bending, Fig. 4(b). Such bending compresses the rear surface at $z = L$ and causes further expansion to the front surface, which adds to the general expansion. These displacements of the sample surfaces are sensed by a sufficiently thin piezoelectric transducer, the generated voltage being detected by appropriate electrodes.

The general expression of the piezoelectric PA signal is quite complicated

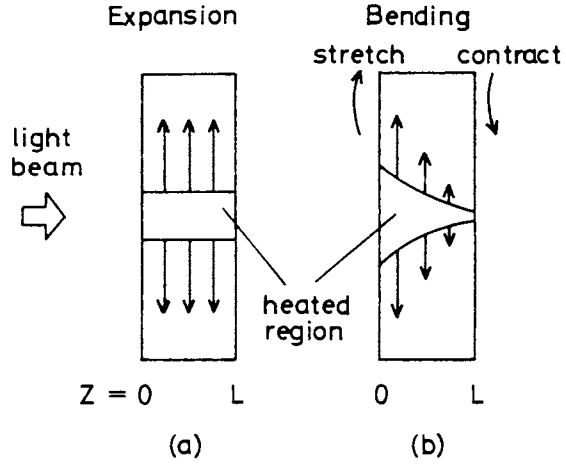

Fig. 4. Sources of surface strain for the average expansion (a) or bending (b) of an irradiated absorbing solid. The PA piezoelectric transducer may be attached to either side of the sample. (From Jackson and Amer [11] with permission from the publisher.)

and hard to interpret physically. For lucidity, Jackson and Amer [11] worked out a few special cases of the JA model, neglecting the surface thermal conduction of the solid to the surrounding gas and considering sample-parameter-limiting situations similar to those presented in the RG model. For front-surface illumination of a solid sample ($z = 0$) and the piezoelectric transducer at $z = L$, a convenient form of these special cases was given by Ikari *et al.* [12]

Optically opaque solids:

Case 1a: Thermally Thick Solid:

The complex magnitude of the PA signal is given by

$$Q \approx -\frac{2MPa_t}{i\omega L\rho_s C_s}, \tag{10}$$

where a_t is the linear expansion coefficient of the solid, P is the incident power corrected for the sample reflectivity $R(\lambda)$; M is a constant calculated by means of piezoelectric and dielectric constants; and ρ_s, C_s are the density and specific heat capacity of the solid, respectively.

Case 1b: Thermally Thin Solid: In this situation the complex signal is

$$Q \approx \frac{MPa_t}{i\omega L\rho_s C_s}. \tag{11}$$

Optically transparent solids:

In the thermally thick limit the expression for the PA signal is an explicit function of the optical absorption coefficient

$$Q \approx \frac{MPa_t}{i\omega L\rho_s C_s}\left[1 - e^{-\alpha L} \pm (6/L\alpha)[1 - (L\alpha/2) - e^{-\alpha L}(1 + L\alpha/2)]\right]. \tag{12}$$

The negative sign applies in the case where the transducer is away from the optical beam ($z = L$), and the positive sign is applicable when the transducer is toward the beam ($z = 0$).

In terms of the utility of piezoelectric PAS as a spectroscopic tool for the measurement of α, Eq. (12) shows that for small values of α the signal is directly proportional to this parameter. For high values of α, however, the position of the piezoelectric with respect to the incident beam yields significantly different results: In the position $z = L$, as α increases the signal decreases, eventually passing through zero and changing sign at higher values of α. In this limit, the bending compression exceeds the expansion due to heating. On the other hand, in the position $z = 0$, the signal shows little photoacoustic saturation up to some very high values of α. In this case the bending and the expansion terms add, thus increasing the observed signal.

From the foregoing discussion it is apparent that the mechanism generat-

ing the PA signal is greatly dependent on the position of the transducer, and the resulting spectra are frequently too complicated to understand quantitatively. The peaks and valleys in the spectra are sometimes inverted as well [13]. An alternative spectroscopic technique using a pyroelectric element [14] has been developed to detect photothermal waves in solids [15]. Photopyroelectric spectroscopy has distinct advantages over piezoelectric PAS, such as the simplicity of calibration, insensitivity to acoustic noise and mechanical resonances, a high potential for signal-to-noise-ratio improvement, and a flat response in the range 0.1 to 10^{-7} K/s. This technique has been useful for solids exhibiting complicated PA spectra.

PHOTOPYROELECTRIC SPECTROSCOPY (PPES) III

A one-dimensional geometry of a PPE system is shown in Fig. 5 [15]. The sample is in intimate contact with a pyroelectric transducer, most likely a thin polyvinylidene fluoride film (PVDF) of thickness ℓ. The pyroelectric

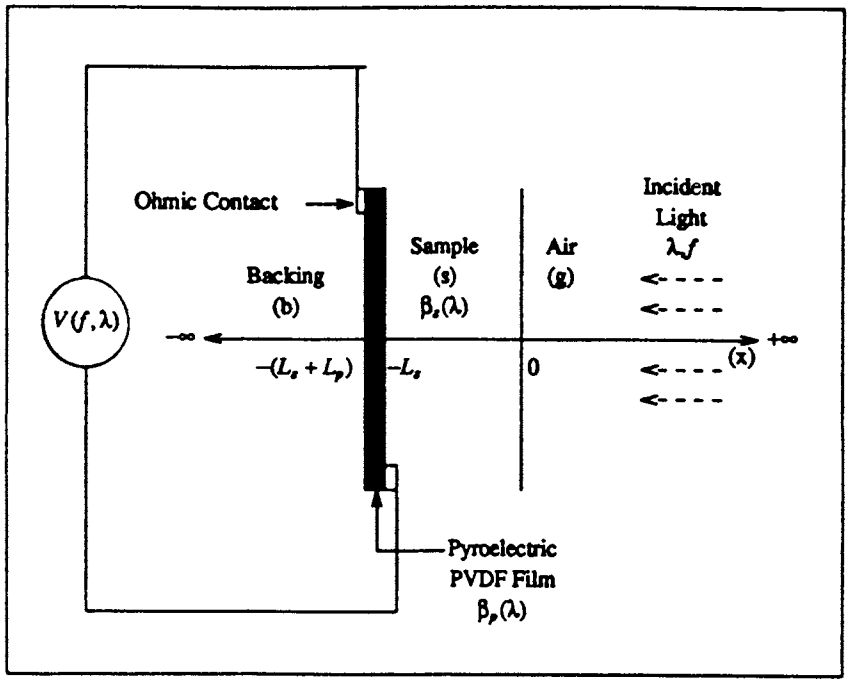

Fig. 5. One-dimensional geometry of a frequency-domain photopyroelectric system. (From Mandelis and Zver [15] with permission from the publisher.)

coefficient of the detector is p. The sample/transducer system is supported by a transparent (semi-infinite) backing material. The PPE cell, unlike the PA cell, does not require hermetic closure (open geometry). Light absorption by the sample and nonradiative energy conversion to heat increases the temperature of the pyroelectric thin-film transducer. This temperature increase results in a potential difference between the upper and lower surfaces of the transducer due to the pyroelectric effect [14]. This voltage $V[\omega, \alpha(\lambda)]$ amounts to an electrical signal, which is measured in the external circuit through the connection of Ohmic leads to the pyroelectric as shown in Fig. 5. The demodulation of the PPE voltage is done in a manner similar to that used for PAS, and the rest of the experimental system is also similar. The charge accumulated in the pyroelectric due to a change $T_p(t)$ in temperature is given by

$$q(t) = pT_p(t). \tag{13}$$

The PPE voltage across the transducer electrodes is

$$V(\omega,\alpha) = \frac{i\omega A < T_p(\omega,\alpha) > R}{(1 + i\omega\tau_E)}, \tag{14}$$

where A is the area of the pyroelectric exposed to temperature variation, R is the total resistance of the equivalent circuit, and τ_E is the RC time constant of the equivalent circuit [16]. The average value of the pyroelectric temperature oscillation is taken over the thickness of the pyroelectric element:

$$< T_p(\omega,\alpha) > = \frac{1}{\ell} \int_{\ell} T_p(x;\omega,\alpha)\, dx. \tag{15}$$

The expression for the average thermal-wave field across the pyroelectric is given by a treatment of coupled heat-diffusion equations similar to that derived for PAS [9]. For practical spectroscopic applications, Mandelis and Zver have developed a one-dimensional PPE model, valid for broad optical-excitation beams compared to both sample thickness and pyroelectric-element thickness, and known as the "Mandelis–Zver (MZ) model" [15]. In terms of the ability of the technique to measure optical absorption coefficients, a more extensive analysis of the signals has also been conducted by Chirtoc and Mihailescu [17]. According to the MZ model, the PPE signal depends linearly on the sample optical absorption coefficient

$$V(\omega,\alpha) \propto \alpha, \tag{16}$$

when *the sample is optically opaque,* $\alpha^{-1} \ll L$, *and thermally thick,* a case likely to occur at high modulation/chopping frequencies, such that $\mu << L$

and $\mu < \alpha^{-1}$. The signal magnitude, however, decreases exponentially with the square root of modulation frequency, $\exp(-L/\mu)$; therefore, the signal-to-noise ratio (SNR) is expected to be poor.

When the sample is *optically transparent,* $\alpha^{-1} > L$, *and thermally thick,* this case is of strong experimental interest, because the complex magnitude of the PPE signal is

$$V(\omega,\alpha) \propto 1 - \alpha L, \tag{17}$$

and the signal decreases only as ω^{-1}, so the SNR is expected to be satisfactory. This limit is achieved when $\mu < L$ and $\mu \ll \alpha^{-1}$. The two foregoing cases are the only ones which can yield direct spectroscopic information about the optical absorption coefficient of the sample material, as the result of thermal and optical transmission, respectively [18, 19].

IV MEASUREMENTS OF $\alpha(\lambda)$ IN SEMICONDUCTORS USING PHOTOACOUSTIC/PHOTOTHERMAL TECHNIQUES

In this section, several examples will be given of optical absorption spectra of simple semiconducting solids, which have been measured by means of photoacoustic or photothermal techniques. The selection of this particular family of solids is in order to keep the volume of material in this chapter within reason as a first photothermal/photoacoustic presentation in the *Handbook of Optical Constants of Solids* series, and reflects the extraordinary importance of these materials in science and technology in the 1990s. The major advantage of the methodologies discussed in Sects. I–III over their purely optical spectroscopic counterparts, is the superior dynamic range of the former, especially at low α ranges. This stems from the linear dependence of the photothermal signals on α (or αL in the case of thin layers), which renders the signal proportional to the thermal energy released following absorption, as opposed to optical reflectance or transmittance detection: in the former situation the transducer only registers the amount of converted thermal energy which is proportional to α; in the latter situation, two large optical signals must be subtracted (incident − transmitted energy) to calculate the amount absorbed and thus to estimate α. This subtraction procedure becomes increasingly less accurate as α decreases toward zero, and it is in this range where PAS, PPES, and PDS excel as zero-baseline spectroscopies. An excellent discussion of this crucial aspect of the photoacoustic/photothermal spectroscopies has been given by Boccara and Fournier [20]. Absolute measurements of α can be obtained using photoacoustic and photothermal methods, by normalizing sample spectra by the spectrum of a totally optically

opaque (reference) material. Such a spectrum is photothermally saturated [9, 19]; therefore, it is independent of the absorption coefficient of the reference and its spectral signature depends solely on the optical fluence of the source and on the thermal/acoustic and signal transduction characteristics of the sample chamber and the instrumentation. Quantitative $\alpha(\lambda)$ spectra of a material may be obtained from the ratio of the signal amplitude with that of the reference, and from the difference of the signal phase from the phase of the reference (normalization). Xerox toner is the usual reference material in the photoacoustic literature.

The PA or PT spectra in this section will be presented or discussed according to the following rules: 1) Quantitative spectra of α (cm^{-1}) will be presented from the original reference(s), whereas qualitative-only spectra will be briefly discussed and references will be given; 2) Spectra of semiconductors whose optical spectra (α, k, or n) have already appeared in the *HOC I, II,* or *III* will be given priority over other spectra. Historically, the complementary nature of PAS or PTS to optical spectroscopies has manifested itself through the measurement of spectra of materials in states complementary to those conventionally measured (e.g., powders instead of single crystals). Furthermore, the high dynamic range of the PAS or PTS signals has been taken advantage of in extending the low spectral (or α) ranges beyond those conventionally measured by optical techniques.

1 Si

Qualitative measurements of gas-cell microphonic PA spectra of Si in the 200–1200 nm region were performed by Tokumoto *et al.* [21]. The measurements were performed at low chopping frequencies so as to be in the thermally thin regime. An abrupt change was observed at 1100 nm (1.12 eV) which corresponds to the fundamental absorption edge, E_G. In the above-band-gap regime (photoacoustic saturation region) the only wavelength-dependent term of the PA signal is the $[1\text{-}R(\lambda)]$ factor embedded in Y, Eq. (7) or Eq. (8). Good correlation of the observed "dips" with optical reflectance spectra was found, thus verifying the origin of these features in the electronic band structure of Si. Ram *et al.* [22] recorded qualitative gas-cell—microphone PA spectra of powdered Si in the range 800–1300 nm and estimated the value of E_G to be 1.18 eV $\pm$ 0.01 eV. Quantitative $\alpha(\lambda)$ spectra of a 400 μm-thick crystalline Si wafer were obtained by Christofides *et al.* [23] using PPES. These authors used both PPE amplitude and phase data and the MZ theory to determine α from a single-modulation-frequency experiment in the range 1100–1400 nm: this procedure allowed the unambiguous determination of α at several frequencies in regimes intermediate between thermally thin and thick. The resulting spectra are shown in Fig. 6 [23–25].

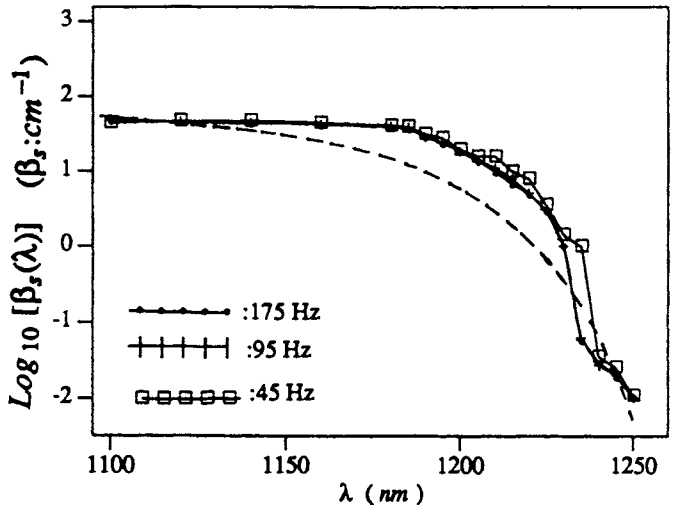

Fig. 6. Logarithm of the optical-absorption-spectrum calculation for Si. Data were taken from several PPE amplitude and phase data sets at 45, 95, and 175 Hz. Flatness in the short wavelength region is due to PPE saturation. The dashed curve is from Sze [24] and Kirev [25]. (From Christofides *et al.* [23] with permission from the publisher.)

Ge 2

Tokumoto *et al.* [21] presented a qualitative gas-cell PA spectrum of Ge in the 200–1000 nm region. Above-bandgap features due to the spectral variation of the reflectance were observed in the PA amplitude and were well correlated to optical reflectance spectra. Welsch *et al.* [26] used a thermoelastic variant of photothermal deflection spectroscopy (see Chapter 4), developed by Olmstead *et al.* [27] to obtain the absorption coefficient of a thin-film Ge sample at 10.6 μm, as characteristic of IR optical-component absorption. They found α_{Ge} (10.6 μm) = 0.0019 cm^{-1}. Fig. 7 shows quantitative $\alpha = \beta_s(\lambda)$ spectra of a wafer of crystalline Ge obtained using PPES at various chopping frequencies in the thermally thin limit of Eq. (17) [28]. Real-time spectrum normalization by the Xe-lamp throughput was employed. The high-energy flat regions are due to PPE saturation: this phenomenon sets in at ~ 1850 nm for the 14 Hz spectrum and at 1800 nm for the higher-chopping-frequency spectra. The very reproducible absorption feature centered at 1933 nm does not appear in the conventional optical transmission spectra of Ge [24,25]. It is believed to be a surface damage or contamination feature as a result of the fabrication and polishing process. This feature does not appear in the PPE phases corresponding to Fig. 7 (not shown), and such a correlation between amplitude and phase spectra would be expected from absorption features homogeneously distributed throughout the wafer

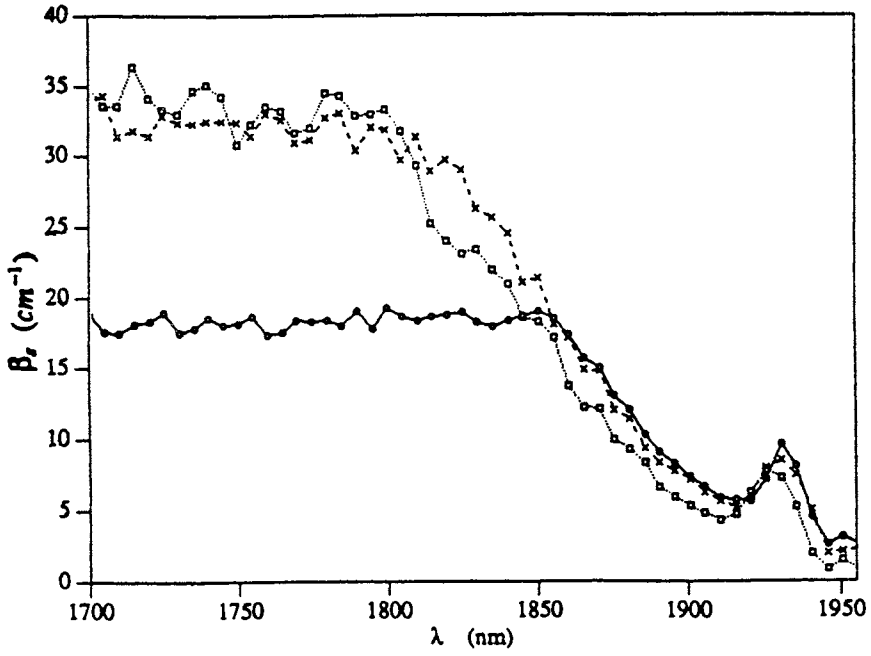

Fig. 7. Optical-absorption-coefficient $\alpha = \beta_s(\lambda)$ calculation for Ge as a function of wavelength. Data taken at various frequencies: - • - : 14 Hz; - x - : 41 Hz; - □ - : 75 Hz. (From Christofides *et al.* [28] with permission from the publisher.)

bulk according to the MZ theory [15]. Assuming a parabolic density-of-states approximation of the conduction-band structure of Ge, a plot of $\sqrt{\alpha h\nu}$ vs. photon energy E and a least-squares fit to the straight line obtained from the $f = 75$ Hz spectrum of Fig. 7, yielded an intercept which gave the energy-gap value for germanium [28] $E_G = 0.652$ eV. This value is in agreement with the one previously reported [24, 25].

3 AgCl

Low and Parodi [29] have used a home-made, single-beam, dispersive infrared PA spectrometer constructed from a Perkin-Elmer Model 421 bed and Model 421 or 621 interchange to obtain spectra of several inorganic solids, including AgCl in the 4000–800 cm^{-1} region. The spectra were normalized by that of carbon black and were presented in qualitative units as ratios of PA signals. Other IR spectra studied by these authors include aspirin, polyethylene, sucrose, siloxane, $BaI_2 \cdot 2H_2O$, KNO_4, $CaSO_4$, KBr, MgO, S, Cu_2O, and Ag_2S.

ZnS 4

Welsch *et al.* [26], using the thermoelastic variant of PDS developed by Olmstead *et al.* [27], measured the absorption coefficient of a thin-film of ZnS at 10.6 μm:

$$\alpha_{ZnS} = 0.18 \text{ cm}^{-1}$$

Rosencwaig [30] measured the qualitative gas-cell—microphonic PA spectrum of ZnS and obtained the band-gap value of 3.7 eV, compared with 3.6 eV from specular-reflectance measurements. Ram *et al.* [22] repeated those measurements with the same technique and estimated a value of 3.81 eV at room temperature. The *Handbook of Chemistry and Physics* value of E_G for ZnS is 3.67 eV [31].

ZnSe 5

The optical absorption coefficient of ZnSe has been measured at 10.6 μm by Welsch *et al.* [26] as discussed above, and by Fernelius [32] who fitted gas-cell—microphone PA frequency responses from a ZnSe window with an AR coating to a two-layer extension [33, 34] to the RG theory [9]. The results are

$$\alpha_{ZnSe} = 0.0055 \text{ cm}^{-1} \quad \text{(Thin-film; Welsch et al. [26])}$$

$$\alpha_{ZnSe} = 0.0064 \text{ cm}^{-1} \quad \text{(Bulk laser window; Fernelius [32]).}$$

Fernelius also measured an uncoated CVD ZnSe window [35] using the same technique. He found

$$\alpha_{CVD\text{-}ZnSe} = 4.06 \times 10^{-3} \text{ cm}^{-1}.$$

CdTe 6

The bandgap energy of this semiconductor at room temperature has been measured from the gas-cell microphonic PA spectrum by several investigators:

$$E_G = 1.58 \text{ eV} \quad \text{(Ram } et\ al. \text{ [22])}$$

$$E_G = 1.50 \text{ eV} \quad \text{(Nicolic and Todorovic [36]).}$$

These values compare well with the conventional value [31] of 1.50 eV.

7 GaAs

Microphonic PA measurements in the saturation region of III–V semiconducting GaAs samples lapped by alumina powder and etched by appropriate etchants, were measured by Tokumoto *et al.* [21]. This qualitative spectrum was shown to correlate well with the calculated $1 - R(\lambda)$ spectrum as expected in the optically opaque regime, and yielded the value $E_G = 1.43$ eV. Ikari *et al.* [37] performed piezoelectric PA measurements on 530–139 μm-thick samples of liquid-encapsulated-Czochralski-grown n-GaAs at room temperature. A continuous broad band below 1.35 eV and a peak at 1.383 eV were observed in the amplitude spectrum. The comparison with optical absorption spectra concluded that the broad band was due to the electronic transition involving the EL2 deep-level defect. The same group used the same technique [38] and investigated PA spectra of semi-insulating (SI) and n-type GaAs at 90 K. A distinctive peak at 0.92 eV and a hump near 1.2 eV were observed for these materials. Comparison with optical and electron photoionization spectra concluded that these features were due to electron transitions involving the EL2-level defect. Quantitative spectroscopic results at the 514.5 nm line of the Ar-ion laser photoexciting Si-implanted GaAs were obtained by Zammit *et al.* [39] by fitting their gas-cell—microphonic PA frequency data in the theory by Mandelis *et al.* [33]:

Si^+ implantation dose (cm^{-2})	$\alpha_{514.5}$ (cm^{-1})
5×10^{13}	$(1.17 \pm 0.04) \times 10^5$
1×10^{14}	$(1.23 \pm 0.04) \times 10^5$
1×10^{15}	$(1.42 \pm 0.04) \times 10^5$.

Figure 8 shows the near-bandgap (1.30–1.44 eV) $\alpha(\lambda)$ spectrum of GaAs immersed in cedar oil in order to produce a high signal-to-noise ratio by use of the PDS technique [40].

The optical absorption properties of Cr-doped GaAs crystals were measured at 1200 nm using gas-cell microphonic PAS at 40 Hz [41]. The fundamental absorption edge was found to be at 870 nm. The spectral peak at 1200 nm is well-known to be due to the Cr^{2+} center. The RG model was used for the quantitative results given in terms of α(1200 nm) vs. concentration. An increasing non-linearity with increased Cr content was thus found due to the presence of several Cr states, such as neutral Cr^{3+} and doubly-ionized Cr^+ states besides the Cr^{2+} state. Wasa *et al.* [42] used a piezoelectric ZnO transducer and obtained GaAs spectra in the 0.8–1.3 eV range. The bandgap was determined to be approximately at 0.88 eV and several peaks appeared which were ascribed to light absorption by non-radiative centers within the bandgap, formed by dislocations and Cr impurities. Qualitative piezoelectric PA spectra of molecular-beam-epitaxy (MBE)-grown GaAs lay-

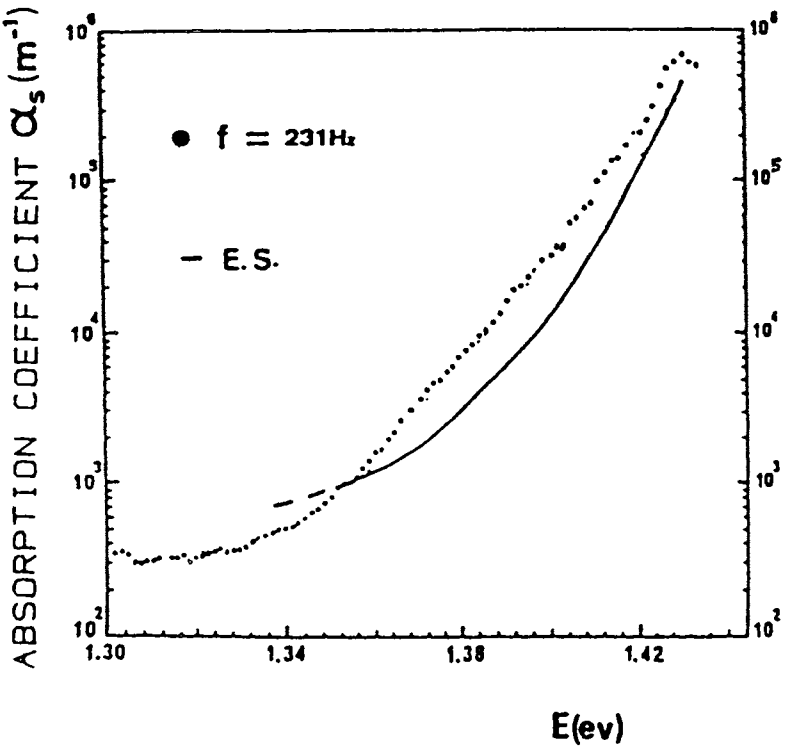

Fig. 8. Optical absorption spectrum of GaAs deduced from PDS data and compared with ellipsometry (E. S.). (From Fournier *et al.* [40] with permission from the publisher.)

ers on GaAs substrates in the photon energy range 1.1–1.5 eV and in the temperature range of 90 to 290 K were produced by Ikari *et al.* [43]. A broad (*D*) band ranging from 0.8 to 1.44 eV with a maximum near 1.3 eV, and a sharp (*Q*) peak at 1.485 eV were observed in the 90 K spectra. These features vanished under secondary illumination. The *D*-band was found to originate in electronic transitions involving EL2-level defects in the GaAs substrate. The *Q*-peak was attributed to electronic transitions from shallow acceptors such as carbon in GaAs.

GaP 8

Qualitative microphonic PA spectra in the saturation regime were obtained by Tokumoto *et al.* [21], showing abrupt changes at 540 nm, which corresponds to the fundamental absorption edge of GaP. This has led to a calculation of the indirect bandgap of GaP at 2.30 eV. For a coarse-powder sample, the indirect bandgap of GaP was measured by Rosencwaig [30] to be

approx. 2.80 eV. Pankove [44] reports 2.30 eV for the GaP bandgap. Fesquet *et al.* [45] used a method of measurement of $\alpha(\lambda)$ of thick GaP based on a simplified version of the RG model, which allowed them to deduce this parameter directly from the PA amplitude signal measurement, irrespective of the light-modulation frequency. The equation for the normalized gas-cell—microphonic PA signal (Cases 1b, 2b, and 2c of the RG model) valid for all optical-absorption-coefficient ranges becomes

$$Q = \frac{\alpha\mu}{[1 + (1 + \alpha\mu)^2]^{1/2}}. \tag{18}$$

Here, normalization is meant with respect to the maximum value Q_s of the PAS signal obtained for high values of α (PA saturation region). Application of Eq. (18) to the PA data yielded the absorption spectrum of Fig. 9. Along with the PAS-deduced spectrum Fig. 9 also shows data (solid line) obtained using ellipsometry in the range between 450 and 550 nm [46]. There is good agreement between the two sets of results in the overlap region 459 nm $\leq \lambda \leq$ 539 nm and for modulation frequencies 90 Hz $\leq f \leq$ 620 Hz. Complementary gas-cell—microphonic PA spectroscopic data were obtained from 0.2–1 mm-thick GaP crystals by Fathallah and Zouaghi [47], in the range 2.1–2.3 eV, and are shown in Fig. 10. These spectra correspond to optical absorption coefficients in the 15–200 cm^{-1} range and could not be obtained with the front-surface-illumination method. The authors used back-surface illumination with the microphone positioned to receive PA signals in the transmission mode, and used the modified RG theory relevant to this type of detection [48].

9 InSb

Tokumoto *et al.* [21] have reported a qualitative PA InSb spectrum obtained by the gas-cell—microphonic method in the PA saturation region, which correlates well with the complement of the conventional reflectance spectrum, $1\text{-}R(\lambda)$, and exhibits three minima corresponding to E_2, $E_1 + \Delta_1$ and E_1 transitions. Baltassare and Cingolani [49] obtained a reflectivity spectrum of InSb from the microphonic PA spectrum. The reflectivity was calculated from the PA signal $Q(\lambda)$ as

$$Q(\lambda)/I_0(\lambda) = 1 - R(\lambda), \tag{19}$$

where I_0 (λ) is the intensity of the incident radiation. These authors quantified the various electronic transitions in InSb at 2.42 eV (E_1'), 2.75 eV (E_1), 3.30 eV (E_2), 4.32 eV (E_3) and 4.80 eV (E_4), all corresponding with optical peaks identified by Piacentini *et al.* [50].

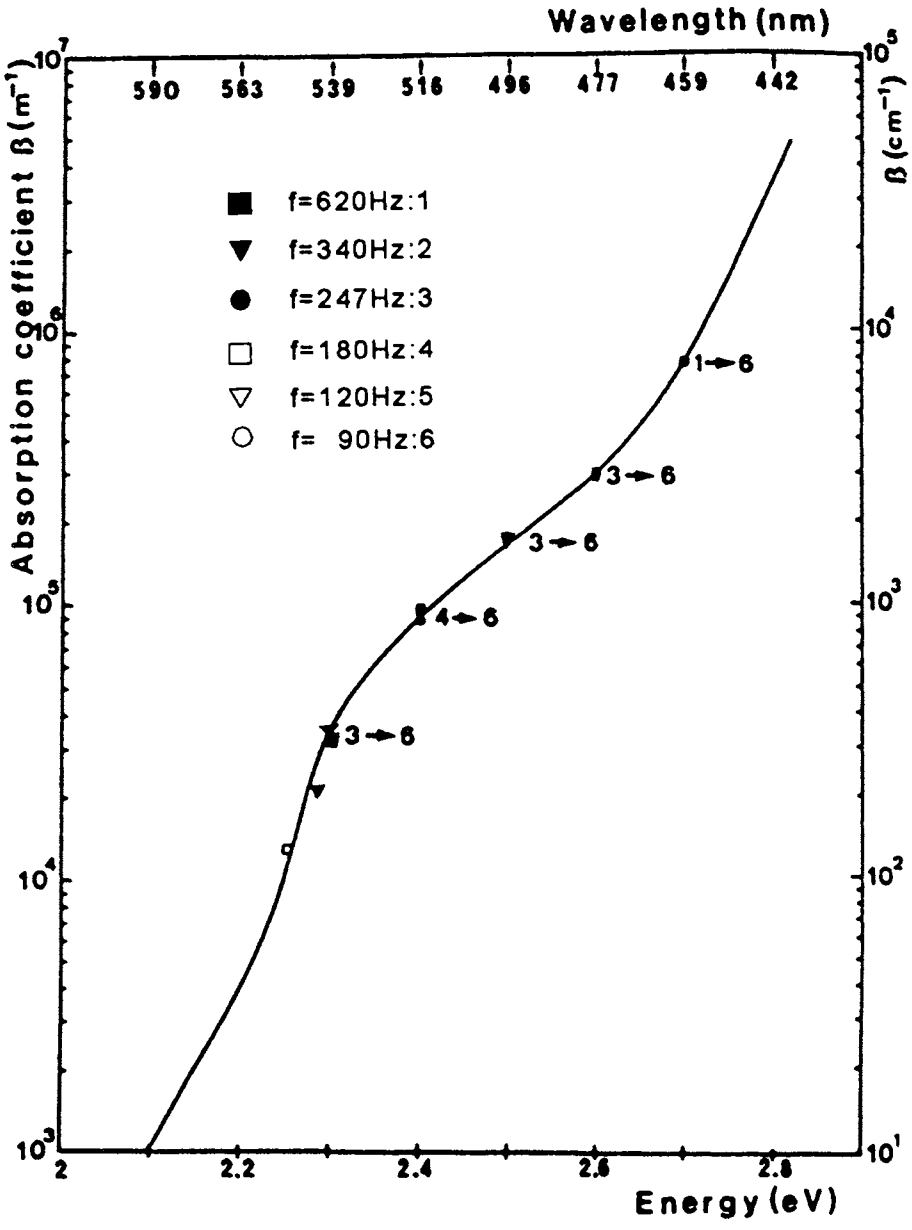

Fig. 9. Experimental results of $\alpha = \beta(\lambda)$ corresponding to various modulation frequencies (1–6) for GaP in the 2.1–2.9 eV range. The $\beta(\lambda)$ curve (solid line) was obtained from optical measurements using ellipsometry. The points on the curve correspond to two light-intensity-modulation frequencies, numbered as shown in the caption. The two unmarked, lowest-absorption-coefficient points correspond to 340 Hz (inverted triange) and 100 Hz (square). Both $\beta(\lambda)$ ordinates are PAS results: the left scale is graded in m^{-1}; the right scale is graded in cm^{-1}. (From Fesquet *et al.* [45] with permission from the publisher.)

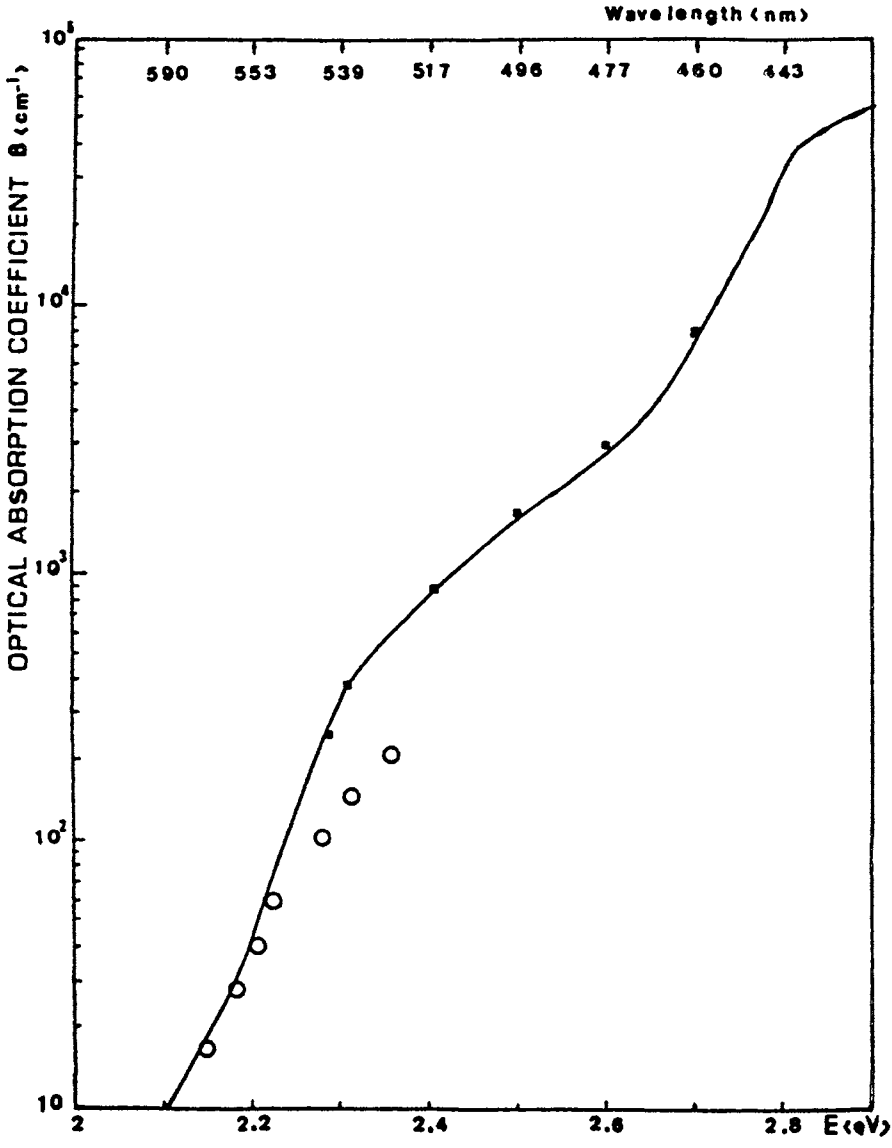

Fig. 10. Optical absorption spectrum $\alpha = \beta(\lambda)$ of GaP obtained by ellipsometry [46] (solid curve); front-side PA detection (■); and reverse-side PA detection (○). (From Fathallah and Zouaghi [47] with permission from the publisher.)

10 InP

Piezoelectric PAS with a PZT transducer was used by Yoshinaga *et al.* [51] to obtain spectra of InP in the range 400–1200 nm and various implantation fluences, including an unimplanted sample. The spectra were qualita-

tive and their shape depended on the optical reflectance as $1\text{-}R(\lambda)$ above the bandgap, where $\alpha \sim 10^4\ \text{cm}^{-1}$. The band edge yielded the PA value for the bandgap $E_G = 1.34$ eV.

GaSe 11

This material is characteristic of layered semiconductors. The gas-cell microphonic PA spectra of crystalline GaSe have been studied extensively in the neighborhood of the intrinsic absorption edge by Todorovic and Nicolic [36, 52]. The measurements were carried out at room temperature with 100 μm-thick samples. A peak appears in the PA spectrum at 2.02 eV, and the PA signal remains photon-energy independent above that peak. Comparing the results with optical absorption data, the authors concluded that the peak at 2.02 eV is due to formation of excitons. The RG theory was applied to experimental PA data with the absorption coefficient of GaAs given approximately by [52]

$$\alpha(E) = \alpha_0 \frac{\exp[\pi\sqrt{(E - E_G)/E_e}]}{2\sinh[\pi\sqrt{(E - E_G)/E_e}]}, \tag{20}$$

where E_e is the exciton binding energy, and α_0 is the absorption coefficient calculated neglecting Coulomb effects. This equation was fitted to the PA data with E_e being treated as a fitting parameter and E_G being defined by the position of the exciton peak, which is at $E_G - E_e$. The absorption profile of Fig. 11(a) was thus obtained with the following parameters:

$$\alpha_0 = 1430\ \text{cm}^{-1}; \qquad E_e = 17.5 \pm 0.5\ \text{meV}; \qquad E_G = 2.017 \pm 0.003\ \text{eV}.$$

Rochon and Racey [53] measured the optical transmission of two single-crystal GaSe specimens, and also used gas-cell microphonic PAS to measure the near-gap region photoacoustically and compare it to the optical spectrum. They observed that whereas the optical $\alpha(\lambda)$ spectra of the two samples were essentially identical around the band-gap edge, large differences appeared in the (thermally thin) PA spectra. They concluded that the PAS technique is not very appropriate for determining E_G for GaSe, but its usefulness centers around the study of near-gap phenomena, such as impurity states and the Urbach tail.

Ikari *et al.* [54] have studied the piezoelectric PA spectra of p-GaSe at 99, 113 and 295 K. The thickness of the sample was 350 μm, and a sputtered ZnO film transducer was used as the PA detector. A maximum was observed at 2.0 eV at 295 K, in good agreement with the direct-exciton formation [52]. The exciton ground-state ionization energy (Rydberg energy) was estimated to be 19.5 meV. A detailed discussion of low-temperature GaSe spectral features appears in Mandelis [2], Chapter 17, pp. 426–440.

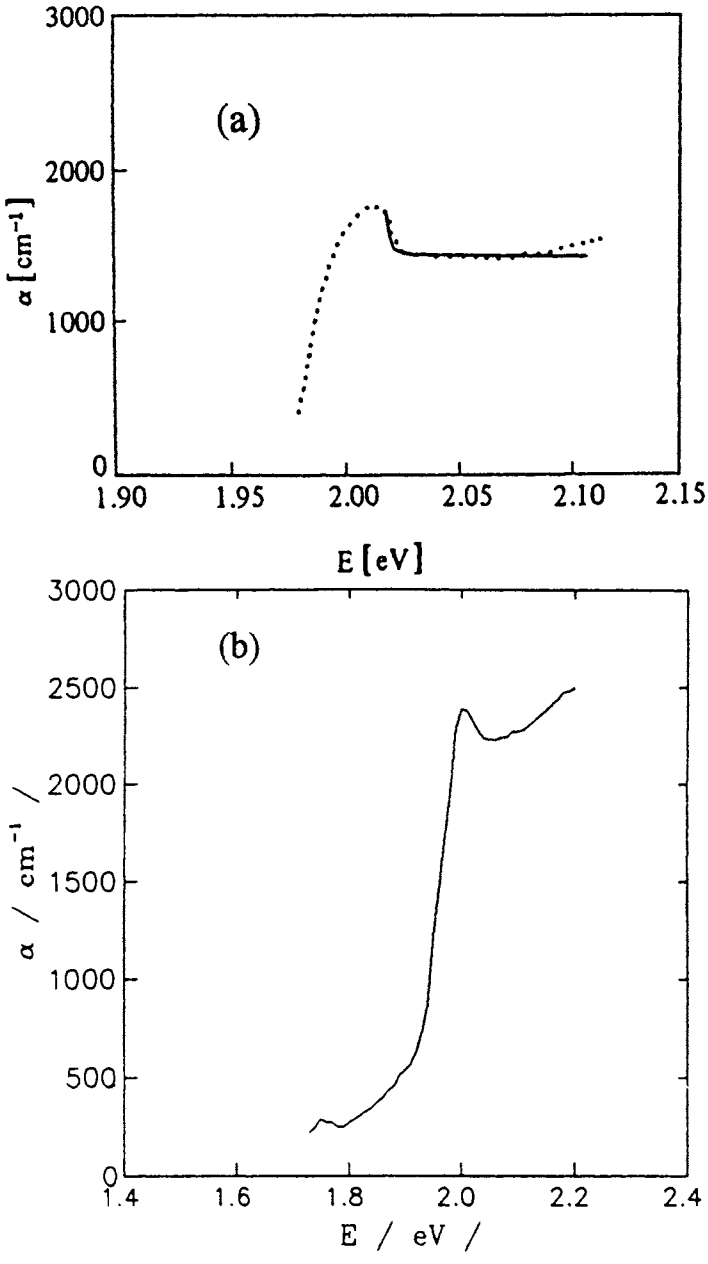

Fig. 11. a) Absorption edge of GaSe: experimental (.....) and theoretical (_____) absorption coefficients; b) Extended $\alpha(\lambda)$ spectrum of GaSe obtained from an analysis of PA amplitude and phase data. (From Todorovic and Nicolic [52] with permission from the publisher.)

CdS 12

Much PAS work has been done in measuring the band-gap energy of the direct semiconductor CdS:

E_G (eV)	T (°C)	Reference	Comments
2.4	Room	[30]	Powder
2.45	Room	[22]	Powder
2.40 ± 0.01	80	[55]	Polycrystalline films
2.35 ± 0.01	240	[55]	"
2.28 ± 0.01	300	[55]	"
2.34 ± 0.01	360	[55]	"
2.37 ± 0.01	470	[55]	"
2.38 ± 0.01	505	[55]	"

These values are to be compared to optically obtained data at room temperature: 2.42 eV [31]; and 2.48 eV [56]. Table I shows the spectral positions of seven states in CdS measured by gas-cell—microphone PAS compared to measurements made with photoconductivity and photoluminescence techniques. Table II shows the locations of the A-, B-, and C-exciton absorption in CdS measured by piezoelectric PAS in the transmission mode ("TPAS") with the transparent $LiNbO_3$ transducer contacting the back of the sample. Comparisons with optical absorption, electroreflectance, and photoconductivity measurements are also given. These tables and detailed discussions on CdS PAS can be found in Mandelis [57].

TABLE I[a]

The Values of Wavelength Corresponding to the Light Absorption Due to Seven States in CdS Measured by Various Methods (units:nm)

	Photoconductivity[b]	Photoluminescence[c]	PAS	Nature
P_1	507.5	—	509	nonradiative
P_2	513.5	514	513	radiative
P_3	517	—	518	nonradiative
P_4	522.5	524	523	radiative
P_5	532	531	534	radiative
P_6	542	—	544	nonradiative
P_7	555	—	554	radiative

[a] K. Wasa, K. Tsubouchi and N. Mikoshiba, *Jpn. J. Appl. Phys.* **19,** L475 (1980).
[b] I. Uchida, *J. Phys. Soc. Jpn.* **22,** 770 (1967).
[c] Obtained by the same sample as that used in PAS measurement.

TABLE II[a]

The Values of Wavelength Corresponding to A, B, C-exciton Absorption in CdS Measured by Various Methods (units:nm)

	Light absorption[b]	Electroreflectance[c]	Photoconductivity[d]	TPAS
A-exciton	501.5	505.7	501.5	506
B-exciton	498.5	502.8	498	503
C-exciton	486.1	491.0	485.5	490

[a] K. Wasa, K. Tsubouchi and N. Mikoshiba, *Jpn. J. Appl. Phys.* **19,** L475 (1980).
[b] E. Gutsche and I. Voigt, "II-VI Semiconducting Compounds," (D. G. Thomas, ed.), p. 337, Benjamin, New York, (1967).
[c] M. Cardona, K. L. Shaklee and F. H. Pollak, *Phys. Rev.* **154,** 696 (1967).
[d] I. Uchida, *J. Phys. Soc. Jpn.* **22,** 770 (1967).

13 CdSe

Powders of CdSe were examined using gas-cell—microphonic PAS [22]. The band gap was calculated to be $E_G = 1.88$ eV compared with 1.74 eV (optical) [31]; 1.75 eV (powder; PAS) [30]) and 1.8 eV (optical) [44].

14 CuO

Toyoda and co-workers have made extensive gas-cell—microphone PA spectroscopic measurements of Cu and its various oxides (including the semiconducting CuO) in the X-ray absorption, near-edge structure (XANES) regions using synchrotron radiation. These spectra are not directly comparable with existing data in *HOC I* or *II,* but they represent novel PAS applications in spectral regions hereto uncharted. These spectra were compared to optical-density X-ray spectroscopy in the 8.95–9.10 keV range [58]. The two sets of spectra were similar; however, the results showed that the increase and changes of the PAS-signal detailed structure at the XANES region were different from those of the X-ray absorption coefficient. Other Cu compounds studied by these authors included Cu_2O and pure Cu metal.

15 As_2S_3

Tanaka *et al.* [59] have utilized PPES in the thermally thin limit of the MZ model, with experimental data obtained using a PVDF thin-film transducer, thin-transparent CuI electrodes and an amorphous As_2S_3 film sample. The $\alpha(\lambda)$ spectrum thus obtained is shown in Fig. 12. A comparison with

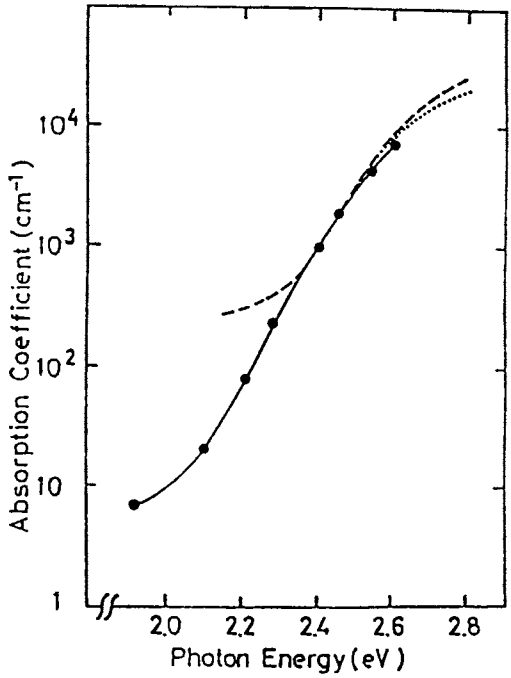

Fig. 12. Spectral dependence of the absorption coefficient of evaporated As_2S_3 films, measured with PPES (solid line). For comparison, results obtained by thermocouple photothermal spectroscopy (dashed line) and by conventional transmission spectroscopy (dotted line) are also shown. (From Mandelis [2] with permission from the publisher.)

conventional transmission spectroscopy and with thermocouple photothermal spectroscopy (PTS) is also shown in Fig. 12. It is seen that the dynamic range of PPES ($\sim$10 cm^{-1}) is superior to the conventional spectroscopies, giving reliable results down to 1.9 eV photon energy. The transmission technique yielded reproducible results for $\alpha \geq 5 \times 10^3$ cm^{-1}, and PTS had a higher dynamic range of $\alpha \geq 5 \times 10^2$ cm^{-1}. A qualitative gas-cell—microphone PA spectrum of a layered single-crystal As_2S_3 sample was also presented by Nicolic and Todorovic [36]. From the "knee" of the spectrum these authors calculated the bandgap energy $E_G = 2.65$ eV.

Tanaka *et al.* [60] employed a $LiTaO_3$ pyroelectric crystal transducer and CuI electrodes to produce the PPE absorption spectrum of the annealed amorphous semiconductor As_2S_3 shown in Fig. 13. This configuration was used instead of a PVDF transducer so as to withstand annealing temperatures of the samples at approximately 180°C. The difference in the absorption edge between the annealed and the illuminated state at 300 K corresponds to the so-called reversible photodarkening effect [60].

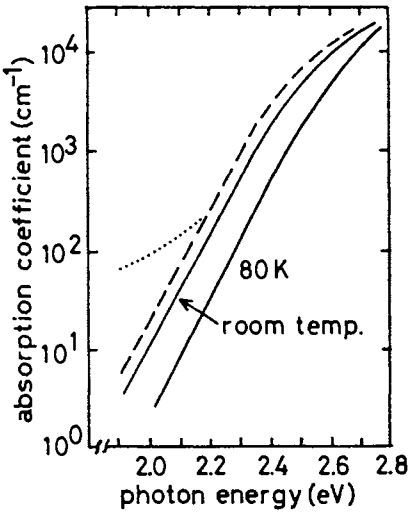

Fig. 13. The optical absorption edges of an annealed As_2S_3 film at room temperature and 80 K (solid lines). The characteristics at room temperature after illumination (dashed line) and under illumination (dotted line) are also shown. (From Tanaka *et al.* [60] with permission from the publisher.)

16 Se

Tanaka *et al.* [60] employed a 9-μm-thick PVDF film transducer to produce PPE spectra of amorphous Se. Figure 14 shows the resulting $\alpha(\hbar\omega)$ spectrum in the optical gap region, overlapping the Urbach tail represented by

$$\alpha \propto \exp(\Gamma\hbar\omega), \tag{21}$$

where Γ is the steepness parameter [61]. Figure 14 also shows the results obtained by Ceasar *et al.* [62] using the gas-cell—microphonic PAS technique. The high-energy end of the Urbach tails agree between these two sets of data, with the PPES technique exhibiting sensitivity of $\alpha L \geq 10^{-2}$. The PPE spectra in the $\leq$ 1.8 eV region deviate from the Urbach tail, because they are due to stray absorptions in the pyroelectric sensor.

Ram *et al.* [22] have measured qualitative PA spectra of powdered Se at room temperature. They found the bandgap energy to be E_G = 1.85 eV to be compared to the optical value of 1.80 eV [63].

17 $Ga_{1-x}Al_xAs$

In this case, and others involving multilayered structures, photothermal investigations have led to the determination of both the substrate *and* the film. The major rival methodology is ellipsometry, which is very convenient

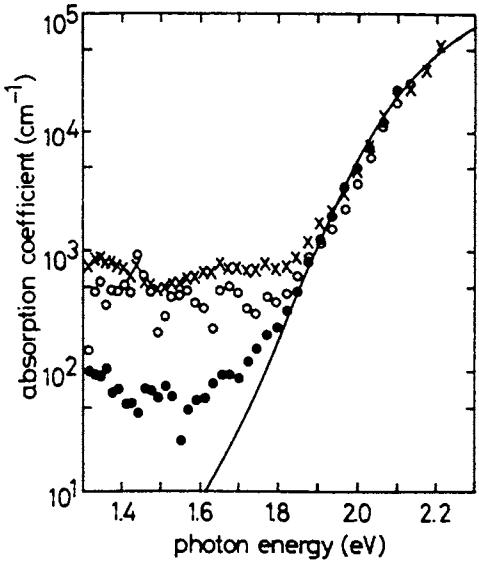

Fig. 14. The optical absorption edge of amorphous Se evaluated with PPES and from a PAS measurement (solid line). The PPES data are given for film thicknesses of 1.43 μm (•); 0.96 μm (○); and 0.74 μm (×). (From Tanaka *et al.* [60] with permission from the publisher.)

for monitoring the growth process of films, as polarized light is mainly sensitive to both the film thickness and the real part of the refractive index. Nevertheless, for low absorptions photothermal methods exhibit higher sensitivity [40]. Fournier and Boccara [40] and Yacoubi [64] utilized the two-layer theory of the PA/PT effect [33, 34] along with PDS-derived spectroscopic data from substrate GaAs to obtain the quantitative $\alpha(\lambda)$ spectrum of $Ga_{1-x}Al_xAs$ films deposited on GaAs. x is the mole-fraction of Al in the ternary GaAlAs alloy-semiconductor crystal matrix. The results are shown in Fig. 15.

Kubota *et al.* [65] measured the qualitative piezoelectric PA spectra of epitaxial layers (1.5 μm) of $Ga_{1-x}Al_xAs$ on GaAs wafers (300 μm). The incident light impinged on the epitaxial layer, and the PZT transducer was attached to the GaAs substrate. A steep rise of the PA signal at 1.42 eV due to the direct band-to-band transition of GaAs, as well as a less sharp decrease around 1.90 eV was observed. This energy is nearly equal to the indirect transition edge of $Ga_{1-x}Al_xAs$. Therefore, it was found by means of PZT PAS that $E_{G,GaAlAs}^{indirect} \approx 1.90$ eV for both $x = 0.25$ and 0.3.

a-Si 18

Quantitative $\alpha(\lambda)$ spectra of amorphous Si abound in the photothermal literature. Amer and Jackson [66] presented a detailed discussion on the appli-

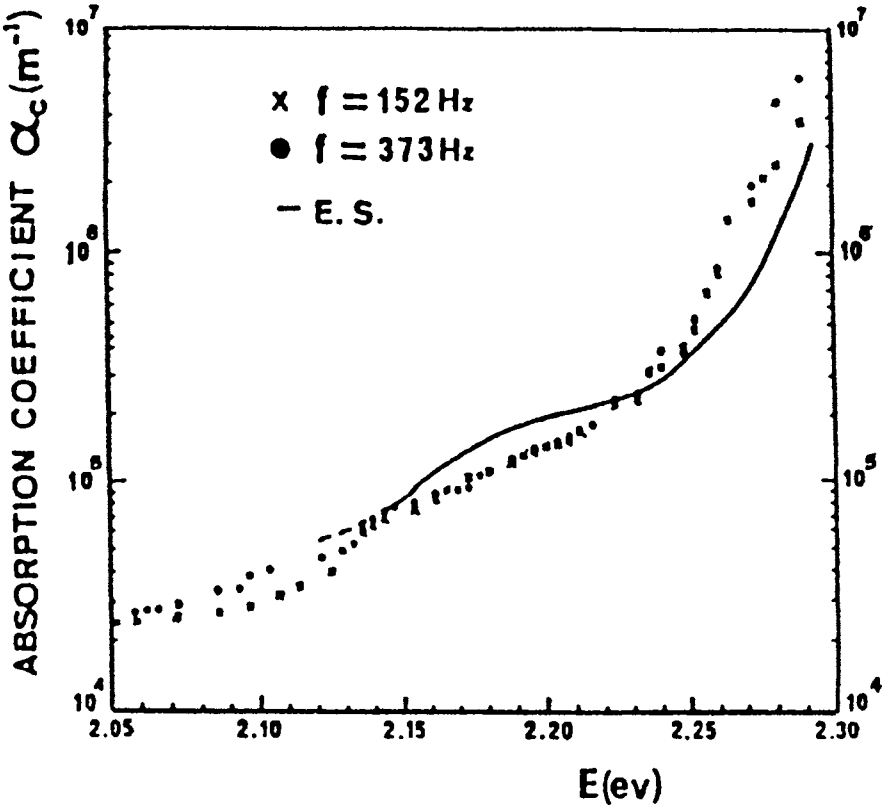

Fig. 15. Optical absorption spectrum of $Ga_{1-x}Al_xAs$ obtained using PDS data; x is the mole-fraction of Al in the ternary alloy semiconductor. The solid line is the spectrum obtained for comparison with the ellipsometric technique (E. S.). (From Fournier and Boccara [40] with permission from the publisher.)

cability of PDS to the measurement of the optical absorption coefficient of a-Si thin films under a variety of growth conditions. The advantage of photothermal techniques, such as PDS, is in the low-α region of the thin-film spectrum, where the film is entirely thermally thin and optically transparent: In this limit, the PDS signal is simply given by

$$< S(\lambda)/S_{\text{sat}} > = 1 - \exp[-\alpha_f(\lambda)\ell], \tag{22}$$

which gives the thin-film absorptance for an incoherent pump source. In Eq. (22) $< >$ denotes averaging of the interference fringes on a logarithmic scale, and S_{sat} is the saturated PDS signal obtained in the high-α region. Figures 16–20 are quantitative PDS spectra of a-Si in the 0.5 eV–2.0 eV range, measured by Amer and Jackson and their co-workers [67–70]. Figure 16 shows the effect of substrate temperature on the optical absorption spectrum: The sub-gap absorption is lowest for material deposited at 230°C and

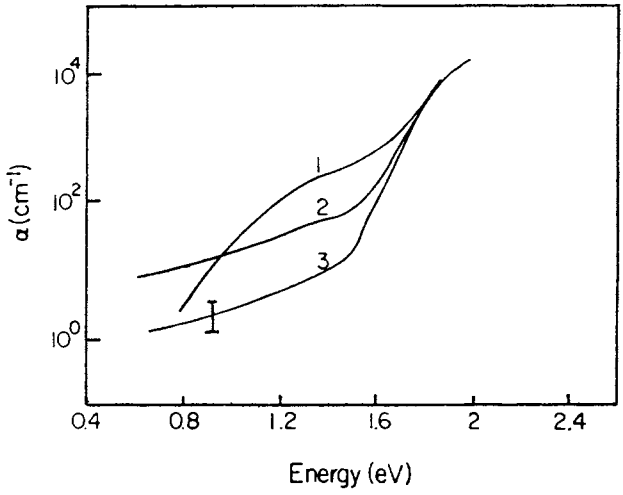

Fig. 16. The substrate temperature dependence of gap-state absorption (undoped a-Si): (1): 100°C; (2): 330°C; (3): 230°C. (From Jackson and Amer [67] with permission from the publisher.)

increases for both lower and higher deposition temperatures. The effect on $\alpha(\lambda)$ of increasing film-deposition power density on the sub-gap absorption for a constant substrate temperature is shown in Fig. 17. The shoulder which appears in the 1.25 eV range is due to large defect densities in the high-deposition power a-Si films. The effects of single doping are shown in Fig. 18. The $\alpha(\lambda)$ spectra for various phosphorus doping levels are shown in

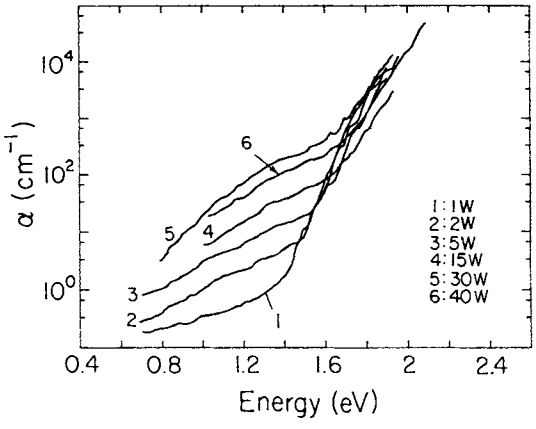

Fig. 17. The dependence of gap-state absorption on deposition power (undoped material). (1): 1 W; (2): 2 W; (3): 5 W; (4): 15 W; (5): 30 W; and (6): 40 W. (From Jackson and Amer [68] with permission from the publisher.)

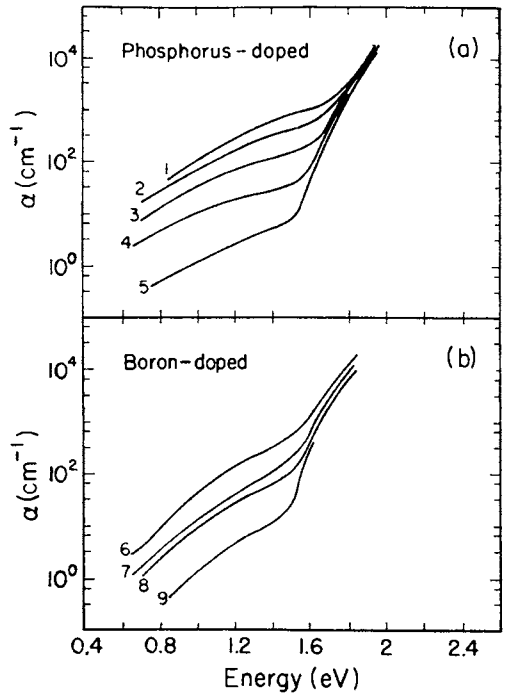

Fig. 18. The dependence of gap-state absorption on the type and level of doping. (a) PH_3 doping concentration: (1): 10^{-2}; (2): 10^{-3}; (3): 3×10^{-4}; (4): 10^{-5}; and (5): 10^{-6}. (b) B_2H_6 doping concentration: (6): 10^{-3}; (7): 3×10^{-4}; (8): 10^{-4}; and (9): 10^{-5}. All doping concentrations refer to gas-phase concentration. Substrate temperature is 230°C, and the rf deposition power is 2 W. (From Jackson and Amer [68] with permission from the publisher.)

Fig. 18a. The gap-state absorption increases and the Urbach edge broadens as the *P*-concentration is increased. Figure 18(b) shows that boron-doping has a similar qualitative effect on the absorption spectrum. The results of Figs. 16–18 demonstrate that the optical absorption coefficient of a-Si thin films is highly sensitive to doping and deposition conditions. The number of defects can be estimated by separating the sub-gap defect absorption from the exponential band-tail absorption [68]. The excess optical absorption α_{ex} due to gap-state defect absorption is given by:

$$\alpha_{ex}(E) = \alpha - \alpha_0 \exp\left(\frac{\hbar\omega}{E_0}\right), \tag{23}$$

where a_0 and E_0 are obtained from a fit to the exponential absorption. The defect number density is related to the sub-gap optical absorption by [66]:

$$N_s = 7.9 \times 10^{15} \int \alpha_{ex}(E)\, dE. \tag{24}$$

By combining Eq. (24) with the PDS results of a thickness-dependence study [69], it was found that for low-defect a-Si the film surface (or its interface with the substrate) has a defect density of $\sim 10^{22}$ cm^{-2} dangling bonds, (see Fig. 19). The absorption spectra are consistent with a defective surface layer of $\sim$ 5 nm thickness and is similar to that obtained from the highly defective bulk a-Si:H. Figure 20 shows the effect of illumination with broad-band light on the gap-state absorption of an undoped a-Si sample. The spectra show a clear and reproducible enhancement in the gap-state absorption coefficient after illumination. Annealing at 150°C in the dark restores the magnitude of $\alpha(\lambda)$ to its original value [70]. By using Eq. (24), the density and energy position of the optically induced defects can be determined.

Amato *et al.* [71] have introduced a new method for determining the surface-state absorption in a-Si thin films, based on the enhancement of the interference fringe amplitude in PDS spectra due to the presence of surface states in the region below 1.5 eV.

Ceasar *et al.* [72] have used gas-cell—microphone PAS to estimate the density of defect states responsible for the sub-gap tail of $\alpha(\lambda)$ of a-Si:H thin films prepared by ion-beam deposition. The values of α measured by PAS were found to be complimentary to those estimated by optical transmission and lay further toward the low-absorption, infrared region, down to

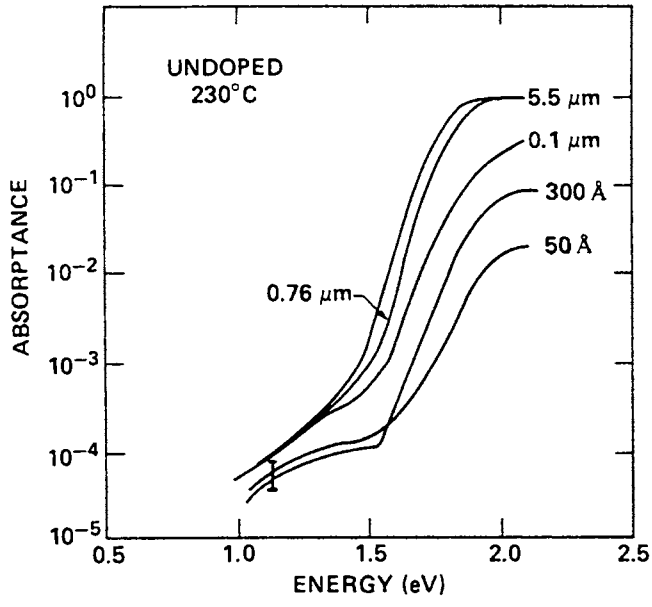

Fig. 19. Thickness dependence of the absorption coefficient in undoped a-Si at 230°C. (From Jackson *et al.* [69] with permission from the publisher.)

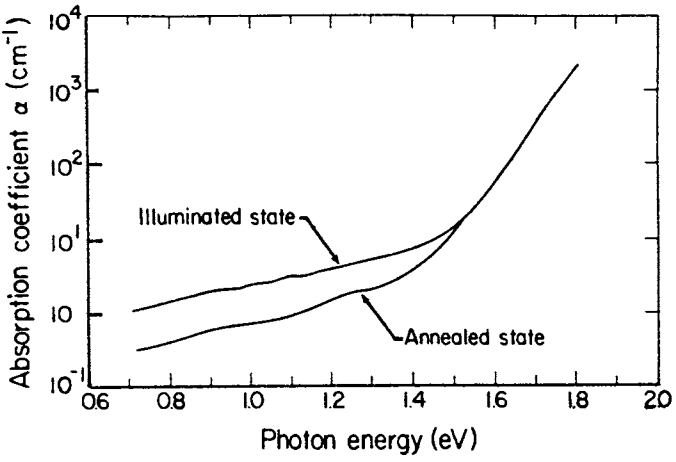

Fig. 20. The effect of illumination on the absorption spectrum of undoped a-Si:H. (From Amer *et al.* [70] with permission from the publisher.)

0.4 eV (see Fig. 21). The extension of the $\alpha(\hbar\omega)$ dynamic range to this sub-gap regime is a clear advantage of photothermal-based spectroscopies over purely optical techniques. Yamasaki [73] has also performed gas-cell—microphonic PAS studies of undoped hydrogenated a-Si as a function of the ambient temperature, the deposition temperature and the post-annealing temperature. The resulting absorption-coefficient spectra were determined between 2.0 and 0.6 eV and were of similar quality to those derived by Amer and Jackson [66]. Amato *et al.* [74] investigated the optical absorption coefficient of low-pressure, chemical-vapor-deposition (LPCVD) a-Si:H by using a combination of analytical techniques: Optical spectroscopy for the above-bandgap transitions, PAS in the sub-gap range, and the constant photocurrent method (CPM) in both regions. Differences in sensitivity to surface states and to inhomogeneities in the material along the growth axis were found. Figure 22 shows those differences between PAS and CPM spectroscopic measurements of $\alpha(\hbar\omega)$. Based on these spectra, a simple growth-kinetic model suggested that the growth kinetics could change during the film-deposition process. Ishiguro and Tokumoto [75] also reported on the improved resolution and accuracy of gas-cell—microphonic PA spectra from undoped and doped a-Si thin films over optical transmission data (see Fig. 23). The spectral photon-energy ranges were > 0.5 eV, similar to those studied by Ceasar *et al.* [72]. Tanaka [76] gives a detailed discussion on the physics behind the variations of the optical absorption coefficients of amorphous semiconductor thin-films as measured by photothermal spectroscopies.

More recently, PPES has been applied to the quantitative simultaneous measurement of two important spectroscopic parameters of amorphous Si thin-films: the optical absorption coefficient and the nonradiative quantum

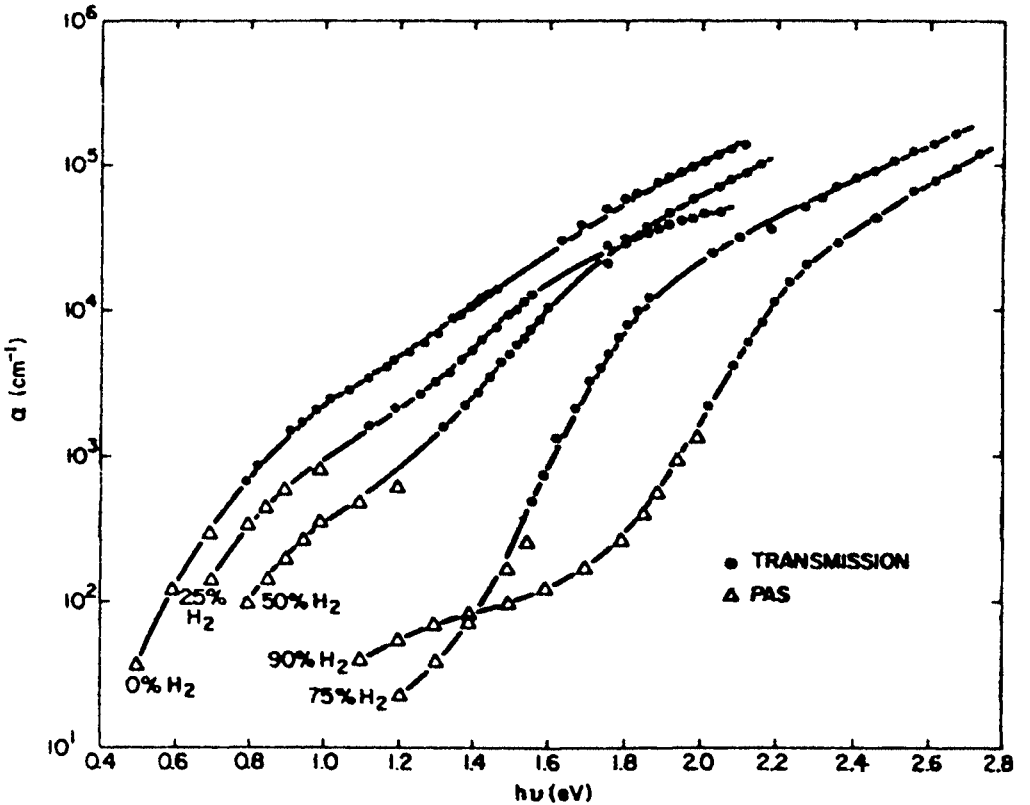

Fig. 21. Optical absorption-coefficient spectra for a-Si:H films made with ion beams of various H_2 compositions. (From Ceasar *et al.* [72] with permission from the publisher.)

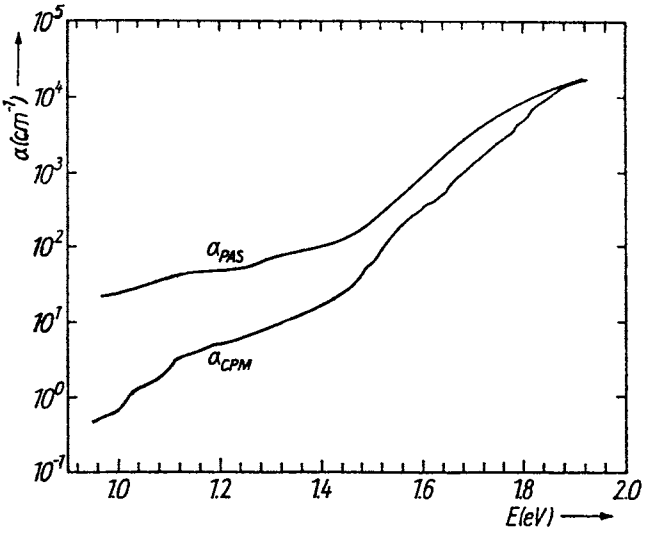

Fig. 22. Optical absorption-coefficient spectra obtained by means of PAS and CPM on a typical LPCVD a-Si:H sample. (From Amato *et al.* [74] with permission from the publisher.)

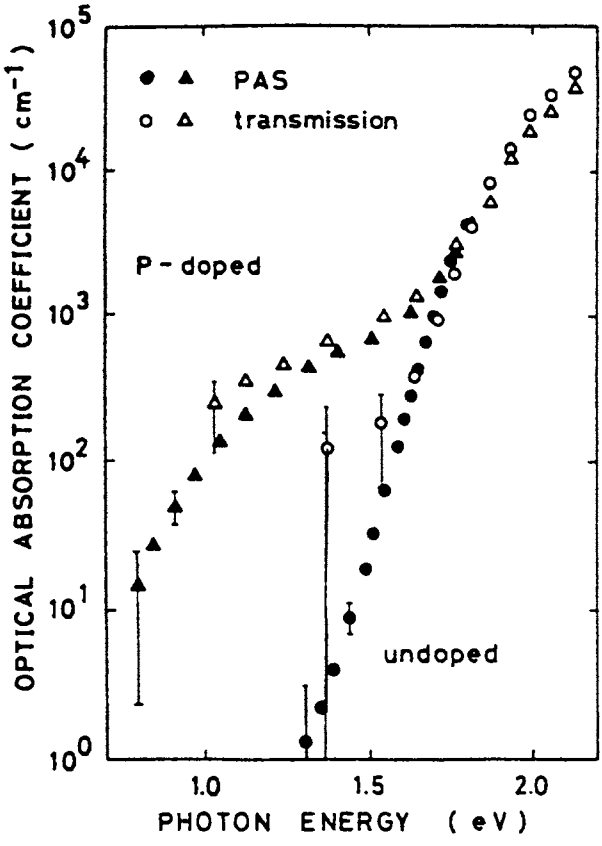

Fig. 23. Comparison of optical absorption-coefficient spectra obtained by the optical transmission method and PAS, for undoped and doped a-Si thin films. (From Ishiguro and Tokumoto [75] with permission from the publisher.)

efficiency [77]. As a back-surface (thermal-wave transmission) detection technique, PPES can be used to measure the absorption-coefficient spectrum in the thermally thick configuration of Eq. (17), whereas it can measure the optical-to-thermal energy conversion efficiency spectrum in the thermally thin configuration of Eq. (16). Based on this feature of PPES, Mandelis *et al.* [77] and Fan and Kakalios [78] obtained both spectra for a-Si:H samples for photon energies from 0.8 eV to 2.5 eV. This technique yielded a sensitivity of $\alpha\ell > 10^{-3}$, where ℓ is the thin-film thickness. This is of the same order as PDS with similar quality $\alpha(\hbar\omega)$ spectra. Unlike PDS, no coupling fluid is necessary (see Chapter 4 by Briggs in this volume), and the experimental geometry is simpler, enabling easy measurement of α as a function of temperature.

ZnO 19

Qualitative PA spectra of ZnO powders were measured by Ram *et al.* [22]. These authors reported the room-temperature bandgap energy of the powders as $E_G = 3.46$ eV, to be compared to 3.20 eV for the solid crystalline ZnO reported earlier [31] by means of optical spectroscopy. Toyoda *et al.* [79] measured the hard-X-ray spectrum of ZnO thin films in the EXAFS (extended X-ray absorption fine structure) region using synchrotron radiation (9.35–10.35 keV) and gas-cell—microphone PAS detection in the thermally thin limit (23–45 Hz). These spectra reflect the heat-production processes in radio-frequency-sputtered ZnO thin layers (~7 μm-thick), which exhibit oscillatory behavior with a peak at 9.95 keV. More work needs to be done to quantify these deep-energy-level features. The same group [80] performed photothermal studies of the optical spectral range, around the band-gap energy of ZnO thin films (2.6–3.4 eV). These spectra were obtained using a thermistor in contact with the sample (PTS). By ratioing the PTS signal to the absorptance 1-*T*-*R* (*T*: transmittance; *R*: reflectance) spectrum, Toyoda and Okonagi [80] showed that the mechanism for heat generation is different from the total rate of optical energy absorption below the fundamental absorption edge. It is this author's opinion that the interpretation of these phenomena may rest with the behavior of the nonradiative quantum-efficiency spectrum.

SnS 20

Nicolic and Todorovic [81] produced the microphonic PA spectrum of a prismatically shaped single crystal of SnS of 0.3 mm-thickness. The value of the bandgap energy was calculated from the spectrum to be $E_G \approx 1.24$ eV. A PA minimum at 0.85 μm (1.46 eV) was also observed, an ill-understood effect of the specific band structure of SnS. The fundamental direct energy gap of 1.5 eV was also measured from an abrupt drop of the PAS signal.

This feature was found to be in good agreement with a photovoltaic-effect spectrum [82].

21 InSe

This layered semiconductor belongs to the same family as GaSe; it is photosensitive, and is used for photovoltaic energy-converter device fabrication. Ikari *et al.* [83] have studied the piezoelectric PA spectra of 470-μm- and 115-μm- thick crystal of InSe extensively, both at room temperature and at 116 K, using a ZnO transducer. They discovered two peaks at 1.250 and at 1.212 eV at room temperature. The energy and the temperature variation of the 1.250 peak were well explained in terms of a free-exciton ($n = 1$) annihilation. The other peak was interpreted as a surface-state-related transition. These authors found that the optical absorption spectrum of InSe correlates well with the intensity of the PA spectrum in the near-band-gap region ($\sim$1.2 eV at room temperature), but no quantitative photoacoustic/photothermal measurement of $\alpha(\lambda)$ has been presented in the literature for InSe.

22 $GeSe_2$

This layered semiconductor can be grown in the form of a single crystal similar to GaSe and InSe. Nicolic and Todorovic [36] have estimated the bandgap energy from the gas-cell microphonic PA spectrum to be at $E_G \approx$ 2.53 eV.

ACKNOWLEDGMENTS

The author wishes to acknowledge the continuing support of the Natural Sciences and Engineering Research Council of Canada (NSERC) through multiple sustained Research Grants and an ongoing Collaborative Research Grant with Professor H. Ruda, which made partially possible his laboratories' contributions described in this chapter.

REFERENCES

1. A. Rosencwaig, "Photoacoustics and Photoacoustic Spectroscopy." Wiley, New York, 1980.
2. A. Mandelis, ed., "Photoacoustic and Thermal Wave Phenomena in Semiconductors." North-Holland Publ., New York, 1987.
3. J. A. Sell, ed., "Photothermal Investigations of Solids and Fluids." Academic Press, San Diego, 1989.
4. P. Hess, ed., "Photoacoustic, Photothermal and Photochemical Processes at Surfaces and Thin Films." Springer-Verlag, Heidelberg, 1989.
5. A. Mandelis, ed., "Progress in Photothermal and Photoacoustic Science and Technology, Volume I, Principles and Perspectives of Photothermal and Photoacoustic Phenomena." Elsevier, New York, 1992; A. Mandelis, ed., "Progress in Photothermal and Photoacoustic

Science and Technology, Volume II, Non-Destructive Evaluation." PTR Prentice-Hall, Englewood Cliffs, New Jersey, 1994; A. Mandelis and P. Hess, eds., "Progress in Photothermal and Photoacoustic Science and Technology, Volume III, Life and Earth Sciences." SPIE Publ., Bellingham, Washington, 1997.
6. D. P. Almond and P. M. Patel, "Photothermal Science and Techniques." Chapman & Hall, London, 1996.
7. S. E. Bialkowski, "Photothermal Spectroscopy Methods for Chemical Analysis." Wiley, New York, 1996.
8. J. G. Parker, *Appl. Opt.* **12**, 2974 (1973).
9. A. Rosencwaig and A. Gersho, *J. Appl. Phys.* **47**, 64 (1976).
10. R. M. White, *J. Appl. Phys.* **34**, 3559 (1963).
11. W. Jackson and N. M. Amer, *J. Appl. Phys.* **51**, 3343 (1980).
12. T. Ikari, S. Shigetomi, and Y. Koga, *in* "Photoacoustic and Thermal Wave Phenomena in Semiconductors," A. Mandelis, ed., Chap. 16, pp. 404–406. North-Holland Publ., New York, 1987.
13. T. Hata, Y. Sato, Y. Nagai, and T. Hada, *Jpn. J. Appl. Phys. Suppl.* **23-1**, 75 (1984).
14. J. Cooper, *Rev. Sci. Instrum.* **33**, 92 (1962).
15. A. Mandelis and M. M. Zver, *J. Appl. Phys.* **57**, 4421 (1985).
16. E. H. Putley, *in* "Semiconductors and Semimetals." (R. K. Willardson and A. C. Beer, eds.), Vol. 5, p. 259. Academic Press, New York, 1970.
17. M. Chirtoc and G. Mihailescu, *Phys. Rev. B* **40**, 9606 (1989).
18. H. Coufal, *Appl. Phys. Lett.* **45**, 516 (1984).
19. A. Mandelis, *Chem. Phys. Lett.* **108**, 388 (1984).
20. A. C. Boccara and D. Fournier, *in* "Progress in Photothermal and Photoacoustic Science and Technology, Volume I, Principles and Perspectives of Photothermal and Photoacoustic Phenomena," A. Mandelis, ed., Chap. 1. Elsevier, New York, 1992.
21. H. Tokumoto, M. Tokumoto, and T. Ishiguro, *J. Phys. Soc. Jpn.* **50**, 602 (1981).
22. R. S. Ram, O. M. Prakash, and A. N. Pandey, *Pramana* **28**, 293 (1987).
23. C. Christofides, A. Engel, and A. Mandelis, *Ferroelectrics* **118**, 411 (1991).
24. S. M. Sze, "Physics of Semiconductor Devices," Chap. 2. Wiley(Interscience), New York, 1969.
25. P. Kirev, "The Physics of Semiconductors," Chap. 8. Mir, Moscow, 1975.
26. E. Welsch, H.-G. Walther, K. Friedrich, and P. Eckardt, *J. Appl. Phys.* **67**, 6575 (1990).
27. M. A. Olmstead, N. M. Amer, S. Kohn, D. Fournier, and A. C. Boccara, *Appl. Phys. A* **32**, 141 1983.
28. C. Christofides, A. Mandelis, K. Ghandi, and R. Wagner, *Rev. Sci. Instrum.* **61**, 2360 (1990).
29. M. J. D. Low and G. A. Parodi, *J. Photoacoust.* **1**, 131 (1982).
30. A. Rosencwaig, *Anal. Chem.* **47**, 592A (1975).
31. R. C. Weast, ed., "CRC Handbook of Chemistry and Physics." CRC Press, Cleveland, Ohio, 1977.
32. N. C. Fernelius, "Proceedings on Laser Induced Damage in Optical Materials: 1979," p. 301. NIST, Gaithersburg, Maryland, 1980.
33. A. Mandelis, Y. C. Teng, and B. S. H. Royce, *J. Appl. Phys.* **50**, 7138 (1979).
34. N. C. Fernelius, *J. Appl. Phys.* **51**, 650 (1980).
35. N. C. Fernelius, "Proceedings on Laser Induced Damage in Optical Materials: 1981," p. 129. NIST, Gaithersburg, Maryland, 1983.
36. P. M. Nicolic and D. M. Todorovic, *Prog. Quantum Electron.* **13**, 107 (1989).
37. T. Ikari, K. Miyazaki, A. Fukuyama, H. Yokoyama, K. Maeda, and K. Futagami, *J. Appl. Phys.* **71**, 2408 (1992).
38. A. Fukuyama, T. Ikari, K. Miyazaki, K. Maeda, and K. Futagami, *Jpn. J. Appl. Phys. Suppl.* **31-1**, 20 (1992).
39. U. Zammit, M. Marinelli, F. Scudieri, and S. Martelucci, *Appl. Phys. Lett.* **50**, 830 (1987).

40. D. Fournier and A.C. Boccara, *in* "Photoacoustic and Thermal Wave Phenomena in Semiconductors," (A. Mandelis, ed.), Chap. 10, p. 247. North-Holland Publ., New York, 1987; D. Fournier and A. C. Boccara, *Mater. Sci. Eng.* **B5,** 83 (1990).
41. H. Tokumoto and T. Ishiguro, *Jpn. J. Appl. Phys. Suppl.* **22-3**, 202 (1983).
42. K. Wasa, K. Tsubouchi, and N. Mikoshiba, *Jpn. J. Appl. Phys.* **19**, L636 (1980).
43. T. Ikari, A. Fukuyama, K. Maeda, K. Futagami, S. Shigetomi, and Y. Akashi, *Phys. Rev. B* **46**, 10 173 (1992-II).
44. J. I. Pankove, "Optical Processes in Semiconductors." Prentice-Hall, New York, 1971.
45. J. Fesquet, B. Girault, and M. D. M. Razafindrandriatsimaniry, *Appl. Opt.* **23**, 2784 (1984).
46. D. E. Aspnes and A. A. Studna, *Phys. Rev. B* **27**, 123 (1983).
47. M. Fathallah and M. Zouaghi, *Solid State Commun.* **54**, 317 (1985).
48. R. Takaue, M. Matsunaga, and K. Hosokawa, *J. Appl. Phys.* **56**, 1543 (1984).
49. L. Baltassare and A. Cingolani, *Solid State Commun.* **44**, 705 (1982).
50. M. Piacentini, E. Doni, R. Girlanda, V. Grasso, and A. Balzarotti, *Nuovo Cimento B* **54**, 269 (1979).
51. H. Yoshinaga, J. Kawai, T. Agui, F. Uehara, and T. Matsumori, *Nucl. Instrum. Methods Phys. Res. B* **80/81**, 591 (1993).
52. D. M. Todorovic and P. M. Nicolic, *Appl. Opt.* **24**, 2252 (1985).
53. P. Rochon and T J. Racey, *J. Photoacoust.* **1**, 475 (1983–1984).
54. T. Ikari, S. Shigetomi, Y. Koga, and S. Shigetomi, *Rev. Sci. Instrum.* **57**, 17 (1986).
55. O. Zelaya-Angel, J. J. Alvarado-Gil, R. Lozada-Morales, H. Vargas, and A. Ferreira da Silva, *Appl. Phys. Lett.* **64**, 291 (1994).
56. A. F. Gibson, "Progress in Semiconductors," Vol. 3. Haywood, London, 1958.
57. A. Mandelis, *in* "Photoacoustic and Thermal Wave Phenomena in Semiconductors," A. Mandelis, ed., Chap. 15, pp. 353–395. North-Holland Publ., New York, 1987.
58. T. Toyoda, T. Masujima, H. Shiwaku, and M. Ando, *Jpn. J. Appl. Phys. Suppl.* **30-1**, 274 (1991); T. Toyoda, T. Masujima, H. Shiwaku, and M. Ando, *Appl. Phys. Lett.* **59**, 3657 (1991).
59. K. Tanaka, K. Sindoh, and A. Odajima, *Rep. Progr. Polymer Phys. Jpn.* **29**, 367 (1986).
60. K. Tanaka, Y. Ichimura, and K. Sindoh, *J. Appl. Phys.* **63**, 1815 (1988).
61. N. F. Mott and E. A. Davis, "Electronic Processes in Non-Crystalline Materials," Sections 6,9, and 10. Oxford Univ. Press (Clarendon), Oxford, 1979.
62. G. P. Ceasar, M. Abkowitz, and J. W.-P. Lin, *Phys. Rev. B* **29**, 2353 (1984).
63. R. A. Smith, "Semiconductors." Cambridge Univ. Press, London, 1968.
64. N. Yacoubi, Ph.D. Thesis, University of Montpellier, France (1986).
65. K. Kubota, H. Murai, and H. Nakatsu, *J. Appl. Phys.* **55**, 1520 (1984).
66. N. M. Amer and W. B. Jackson, *in* "Semiconductors and Semimetals: Hydrogenated Amorphous Silicon; Optical Properties," (J. I. Pankove, ed.), Vol. 21, Chap. 3. Academic Press, Orlando, Florida, 1984.
67. W. B. Jackson and N. M. Amer, *J. Phys. Colloq.* **42**, C4-293 (1981).
68. W. B. Jackson and N. M. Amer, *Phys. Rev. B* **25**, 5559 (1982).
69. W. B. Jackson, D. K. Biegelsen, R. J. Nemanich, and J. C. Knights, *Appl. Phys. Lett.* **42**, 105 (1983).
70. N. M. Amer, A. Skumanich, and W. B. Jackson, *Physica Utrecht* **117B & 118B**, 897 (1983).
71. G. Amato, G. Benedetto, L. Boarino, and R. Spagnolo, *Appl. Phys. A* **50**, 503 (1990).
72. G. P. Ceasar, K. Okumura, J. Lin, M. A. Machonkin, and L. Dudek, *J. Non-Cryst. Solids* **59 & 60**, 289 (1983).
73. S. Yamasaki, *Philos. Mag. B* **56**, 79 (1987).
74. G. Amato, G. Benedetto, F. Fizzotti, C. Manfredotti, and R. Spagnolo, *Phys. Status Solidi A* **119**, 169 (1990).
75. T. Ishiguro and H. Tokumoto, *Jpn. J. Appl. Phys. Suppl.* **21-3**, 11 (1982).
76. K. Tanaka, *in* "Photoacoustic and Thermal Wave Phenomena in Semiconductors," A. Mandelis, ed., Chap. 18, pp. 441–468. North-Holland Publ., New York, 1987.

77. A. Mandelis, R. E. Wagner, K. Ghandi, R. Baltman, and P. Dao, *Phys. Rev. B* **39**, 5254 (1989-I).
78. J. Fan and J. Kakalios, *Proc. MRS Meet.* **258** (1991).
79. T. Toyoda, T. Masujima, and M. Ando, *Jpn. J. Appl. Phys.* **32**, 2550 (1993).
80. T. Toyoda and K. Okonagi, *Proc. 2nd Int. Symp. Sputtering Plasma Processes (ISSP'93)*, 237 (1993).
81. P. M. Nicolic and D. M. Todorovic, *J. Phys. C: Solid State Phys.* **19**, L717 (1986).
82. D. Trbojevic, P. M. Nicolic, B. Perovic, and V. Cvekic, *Appl. Phys. Lett.* **38**, 362 (1981).
83. T. Ikari, S. Shigetomi, Y. Koga, and S. Shigetomi, *J. Phys. C: Solid State Phys.* **17**, L969 (1984).

Chapter 4

Photothermal Deflection Measurements of the Extinction Coefficient *k*

MATTHEW E. BRIGGS
Physics Department
University of Utah
Salt Lake City, Utah

I. Introduction 99
II. Photothermal Deflection 103
A. Advantages and Disadvantages 103
B. Examples of Deflection Techniques 104
C. Summary of Strengths and Weaknesses 105
D. Measurements of *k* Using Photothermal Deflection 106
E. Working Equations 114
III. Conclusions 116
Acknowledgments 117
References 117

INTRODUCTION I

The optical properties of a material can be studied using photothermal techniques when the energy absorbed from incident light dissipates mainly as heat. This is the case for most materials, so that photothermal techniques are used on a variety of materials to characterize thermal, optical, and surface properties. We will focus on one such technique, *photothermal deflection* [1], as shown in Fig. 1. A transparent material absorbs some light from a tightly focused heating-beam, and dissipates this energy as heat. This creates a hot spot in the material, and a laser probe-beam is deflected by gradients in the refractive index $\partial n/\partial r$ that arise from thermal expansion around the hot spot. The experimenter measures the deflection of the probe-beam, first calibrating the deflection with a standard sample in which the absorption is known, and then moving on to unkown samples. Such a measure-

HANDBOOK OF OPTICAL CONSTANTS OF SOLIDS III

Copyright © 1998 by Academic Press.
All rights of reproduction in any form reserved
ISBN 0-12-544423-0/$25.00.

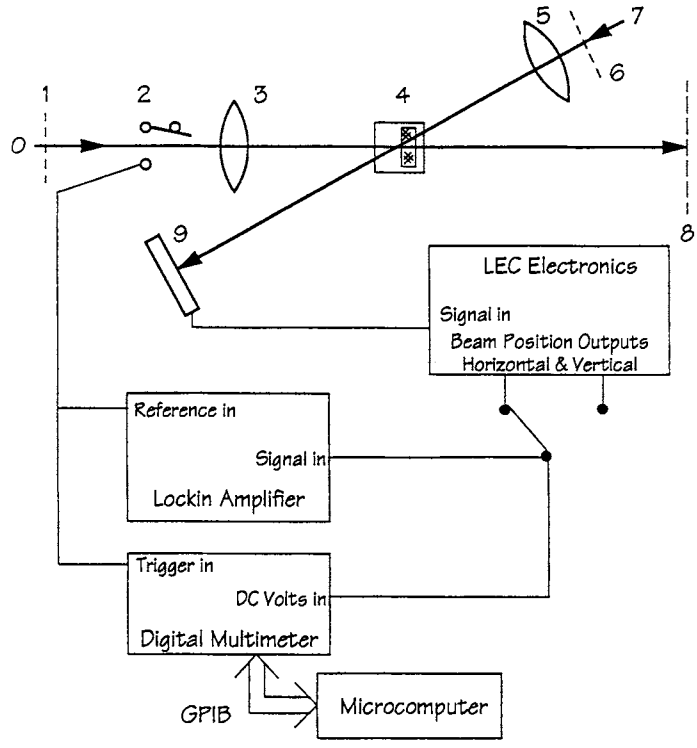

0 - pump laser 1 - attenuator (neutral density filter) 2 - shutter or chopper
3 - focusing lens for pump 4 - beams crossing in the fluid in front of a surface absorption
5 - focusing lens for the probe, on an x-z translation stage
6 - attenuator (neutral density filter) 7 - probe laser
8 - view -screen for pump (flows or lensing distortions) 9 - position sensor (lateral effects cell)

Fig. 1. A schematic of a collinear photothermal deflection apparatus used for measuring a surface absorption.

ment reveals the absorptance A of the material, which is the fraction of the power P that is travelling through the material which is absorbed,[1] and which is thus directly connected to the extinction coefficient k in the medium (see Section IID.)

We want to emphasize two features of photothermal deflection. First, it is a *localized* measurement—the effect relies on temperature *gradients* (Sec-

[1] P must take into account power lost to reflection (and scatter, if the material or its surface is highly scattering [2]), i.e., P must be given by the incident power P_i minus the reflected and scattered powers. Photothermal techniques have at best 10% accuracy and are usually (but not always) applied to transparent materials with polished surfaces. Under these conditions, the scatter and the $\approx 4\%$ reflection can be neglected, so that $P \approx P_i$, and the usual expression $A = P_a/P_i$ holds.

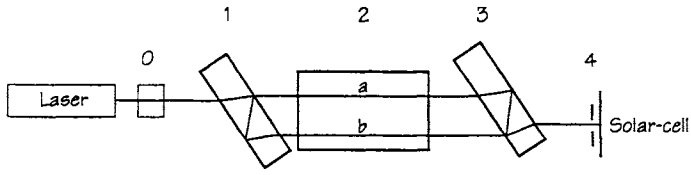

Fig. 2. An interferometer of the type used by Stone [8] to measure optical absorption in liquids.

tion IIE), and so is strongest at point sources such as the focused heating beam shown in Fig. 1. This first feature leads to two important capabilities: because the location of the region which the probe-beam senses is selected by where it crosses the heating-beam, surface and bulk absorptions can easily be separated in bulk samples (Sections IID1, IID13 give examples for bulk and film samples). For similar reasons, photothermal deflection finds widespread use as a form of microscopy, in which surface and sub-surface features of a material are found by scanning the sample and looking for changes in the deflection signal. The second feature we would like to emphasize is that photothermal deflection is *highly sensitive:* The high flux of a focused, laser heating-beam, the high sensitivity of photodiode-based beam-position sensors, and the use of a chopper to modulate the heating beam for lock-in detection combine to allow background levels equivalent to $A = 10^{-6}$ routinely [3], and $A = 10^{-9}$ more recently [4–6]. We should also mention a practical feature: the technique is simple to implement and inexpensive, if a laser source is already available with a power >100 mW.

We will finish the introduction with a few general comments about photothermal techniques, and then narrow the discussion to deflection techniques in Section II. We refer the reader to the reviews of Welsch [7] for a more detailed comparison and extensive bibliography. We divide photothermal techniques into two classes: *localized* measurements such as the deflection example just given, and *extended* measurements, typified by the interferometric measurement shown in Fig. 2 [8]. In photothermal interferometry, the experimenter places the sample in one leg of an interferometer, and detects the change in the fringe pattern that occurs when the heating beam is introduced into the sample. The difference between the classes is that the localized techniques detect the effect at a point in the sample, while the extended techniques *integrate* the thermal effect along the entire length in the material. Other examples of extended techniques include photothermal lensing (the first photothermal technique discovered) [9–11], and Fabry-Perot *etalon* work [12], as well as photoacoustic techniques, which can be adapted to both extended and localized measurements (see Chapter 3 by Mandelis, this

volume). The applications reflect the extendedness of the measurement, and include bulk optical-absorption measurements [8, 13], and trace detection of parts-per-billion impurities in bulk gases and liquids [14]. The two classes have much in common: it is the density change from heating which causes the signal, the source of the heating is usually the optical absorption from a focused heating beam, the heating beam is modulated to allow lock-in detection, and sensitivities are at least as good as $A = 10^{-6}$. In fact, photothermal techniques are the only means for detecting optical absorptions below 10^{-4} (Fig. 3); the traditional spectrophotometric approach is more appropriate for stronger absorbers because the absorption is found from the difference between large signals, the incident power minus the sum of the reflected and transmitted powers. Photothermal techniques now employ all the tools of modern optics—pulsed lasers, Fourier-transform techniques, microwave stimulation, to name a few, and have been applied to a wide range

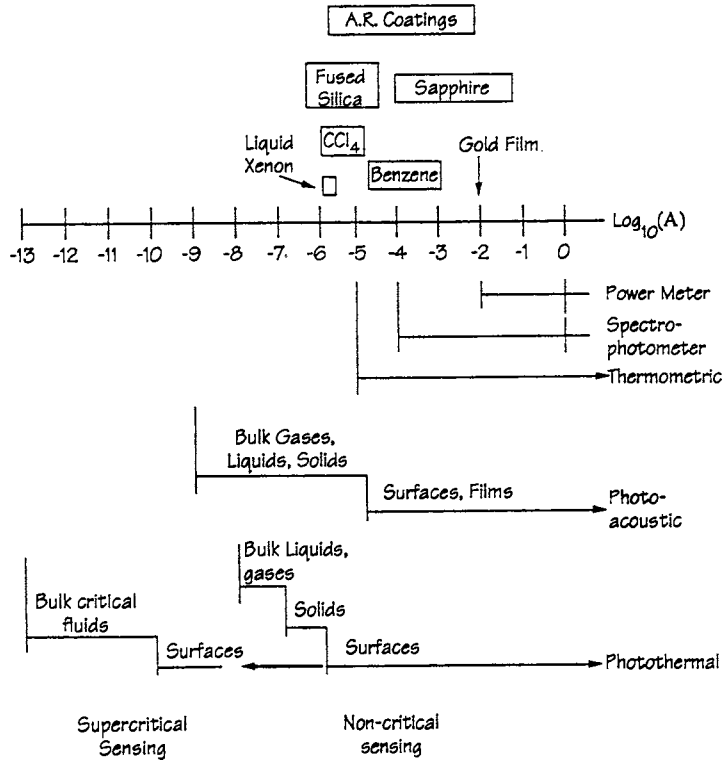

Fig. 3. A logarithmic guide to absorption measurements, giving the minimum detectable fractional absorption, $A \equiv P_{\text{absorbed}}/P_{\text{incident}}$, for various techniques, under a 1 W cw illumination. For bulk absorptions, the length l is taken to be 1 cm, where $A = \alpha l$. The arrows pointing to the right are intended to emphasize that these techniques can be used for opaque materials.

of samples for a variety of thermal, spectroscopic, and diagnostic studies. The review articles by Welsch [7], texts by Mandelis [15] and Sell [16], and others [17, 18] will quickly inform the interested reader.

PHOTOTHERMAL DEFLECTION II

Advantages and Disadvantages A

Figures 1 and 4–6 show several configurations for photothermal deflection measurements. The collinear arrangement (Figs. 1 and 6) senses the absorption at the location where the beams cross—either bulk or surface absorptions can be measured by choosing the location appropriately. In bulk measurements, the volume that contributes to the signal is set by the overlap of the heating and probe beams and the diameter of the heating beam, i.e., a cylinder $\sim$ 0.5 (mm long) $\times$ 0.05 (mm diameter). Surface measurements sense an area determined by the diameter of the heating beam, because the absorption at the surface is usually much stronger than the bulk absorption, so that the bulk can be neglected [19]. Treatments of the separation of bulk and surface contributions can be found elsewhere in [20–22], and examples in optical-constants measurements are discussed in Sections IID1 and IID13. The sensitivity for surface absorptions of solids can be increased strongly by immersing the sample in a fluid and placing the intersection of the probe and heating beams just above the surface, in the fluid. This is because the higher thermal-expansion coefficient of the fluid leads to a stronger optical effect (Section IIE.)

Though highly sensitive, the *accuracy* of this technique has been limited to the 10% level since the start of this research field. The difficulty in improving the accuracy arises because k is found from the amplitude of the deflection, which depends on quantities that are difficult to reproduce or know accurately at the site where the beams cross, principally the diameter of the heating and probe beams and the alignment between the two beams. The surface polish and sample handling must be specified for measurements of surface absorption, because the surface roughness and cleanliness strongly effect the absorption. Further, convection is an issue when working in liquids or at surfaces in air, and it is important in these types of measurements to reduce the heating power until good linearity of the signal with power is observed [6, 23]. Attempts to model these issues will be mentioned in Section II E. As a rule of thumb, only a careful calibration using known absorbers with thermophysical, geometrical, and optical properties chosen to match the unknowns will allow an accurate measurement of k. Photothermal deflection is, therefore, applied to the measurement of k in systems that de-

mand either a high sensitivity, a non-contact measurement, or a localized measurement. Photothermal deflection can also be applied to determine how much of the relaxation is thermal; transmission measurements reveal the total absorption, while photothermal techniques reveal only that portion of the absorption which relaxes thermally. For example, results from these two techniques are used by Montecchi and Masetti [24] to find the vibrational relaxation efficiency for films of gold, chromium, zinc selenide, and amorphous-carbon thin-films.

B Examples of Deflection Techniques

An example of the 10% accuracy available from deflection techniques is provided by the first exhaustive photothermal deflection study, which still serves as an instruction manual for getting started in this technique [1,3]. These authors demonstrate the accuracy of their collinear-deflection apparatus by achieving 10% agreement and repeatability between calculated and calibrated bulk-absorption measurements. They use a dye-laser heating beam to measure the spectrum of the sixth harmonic of theC—H stretching excitation of benzene at various concentrations of benzene in carbon tetrachloride from $\lambda = 580$ to 620 nm. The carbon tetrachloride serves as a non-absorbing medium in which the known amount of benzene present allows the authors to test the accuracy of the deflection measurements at various absorption levels against separate spectrophotometric measurements. In the same paper, the authors report a similar level of success for measurements of the surface-absorption spectra of In and CdS *films* on glass substrates, again calibrating the absorption in separate spectrophotometric measurements.

The "mirage" configuration shown in Fig. 4 allows the experimenter to work on opaque samples, and simplifies the process of scanning the sample [3]. Here the deflection arises from thermal expansion in the gas above the hot spot created by the absorption of the heating beam at the surface of the material. Changing the frequency and noting the phase shift in the response allows an analysis of the depth of the absorption. Alternatively, the probe beam can travel through the substrate, sensing the mirage effect from the (weaker) thermal expansion of the substrate material under the surface absorption [25]. This would be useful for detecting the absorption in processes for which the region above the surface is not optically good, such as laser ablation.

Although Murphy and Aamodt [23] find 10% accuracy and agreement with theory for mirage measurements on an electrically heated surface, in the more common case of heating from optical absorption, the agreement between the mirage measurements and theory is not as good [25, 26]. This presumably is because of the more complex geometry and alignment requirements. The convenience of the technique for imaging problems makes this an important

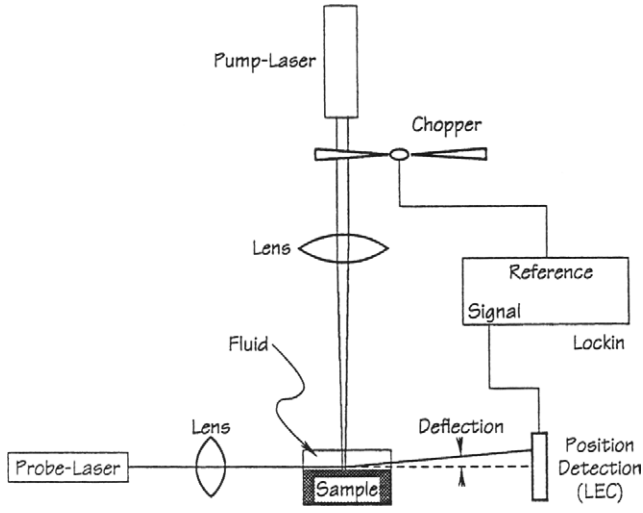

Fig. 4. A mirage photothermal-deflection apparatus using the refractive-index distortions created in the fluid or gas above the region of the absorption as a measure of the absorption.

technique, but until the mechanisms of the measurement are understood well enough to allow the measured amplitude to agree with theory, the transfer of absolute absorption levels from calibration samples to unknowns will have a larger margin of doubt than other photothermal techniques.

The remaining deflection techniques fall under the title *photothermal surface-deformation,* an example of which is shown in Fig. 5. These techniques offer advantages in imaging applications similar to the mirage technique, and in addition contain information about the thermal-expansion properties of the material itself (rather than the gas above the material.) Examples of these configurations of photothermal apparatus are available elsewhere [23, 27, 28]. A further advantage is that the surface-deformation approach gives agreement with theory closer to 10% [28, 29], presumably because the optical alignment is less demanding than for the mirage technique. Because the signal depends on the coefficient of thermal expansion of the material, surface-deflection techniques are typically used on metal films; it would be less appropriate on the low-thermal-expansion optical glasses, where one would turn to the collinear or mirage approach.

Summary of Strengths and Weaknesses C

Strengths of the deflection techniques thus generally include: 1) a combination of simplicity and very high sensitivity, 2) non-contact *in-situ* measurements, 3) adaptable to transparent, turbid or opaque samples, 4) either

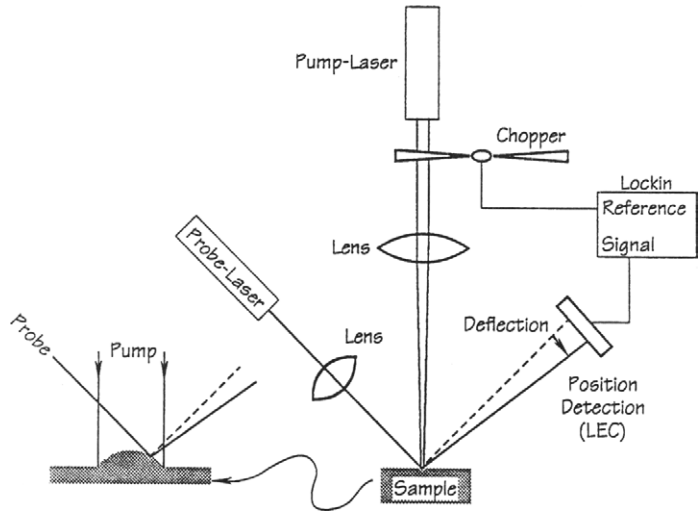

Fig. 5. A reflective photothermal deflection apparatus using the thermal expansion of the sample surface at the site of the absorption as a convex mirror, to change the angle of reflection in proportion to the absorption.

strongly absorbing or weakly absorbing and any phase (gas, liquid, solid), 5) either surface or bulk, spatial resolution to a few μm's, and 6) ability to measure dynamic processes. We should also mention that the technique has been used at cryogenic temperatures (see Section IID13). Weaknesses of the technique generally include: 1) necessity for careful optical alignment, 2) accuracy is not high, 3) modeling of 3-D heat flow is needed to understand full dynamic range, 4) provides only local measurements, and 5) requires laser with power $\gtrsim$ 100 mW. Because *deflection* measurements are localized, the measurement of k in bulk materials is probably better done using one of the *extended* techniques mentioned in the introduction—unless the surface absorption needs to be removed from the measurement. The dominant applications for *deflection* techniques today are the microscopy and characterization of surfaces, which will be evident from the following discussion. However, anyone using a single number for the absorption in a material must consider the possible effects of local variations if their application pushes the performance or depends critically on the performance of the material. The absorptance can vary locally by a factor of 100 around a surface, and 10 in bulk materials.

D Measurements of *k* Using Photothermal Deflection

The photothermal techniques yield the absorptance $A \equiv P_a/P$, where P_a is the power absorbed from a heating beam of power P in the material (see the

footnote in the introduction). In order to find the imaginary part of the refractive index, k, we first find from the absorptance A the absorption coefficient $\alpha(\text{cm}^{-1})$, which describes the spatial rate at which optical energy is converted into thermal energy, and then use $\alpha = 4\pi k/\lambda$. For example, in the simplest case of normal incidence on a semi-infinite material we have

$$A \equiv P_a/P_i = 1 - e^{-\alpha z}, \tag{1}$$

where z is the path length travelled in the absorbing material, and P_i is the power transmitted into the sample through the interface. Finding α from A can be a challenging problem: for the case of intereference coatings, Eq. (1) must take into account the multiple reflections of the heating beam within the coating, which requires careful calculation of the path length and interference effects [19, 30].

A detailed schematic of a collinear apparatus we used for precise measurement of optical absorptions is shown in Fig. 6. We include this to provide as detailed an example of an experimental set-up as we can. This is an implementation of the apparatus described by Jackson *et al.* [3], which still serves as an excellent cookbook for setting up such an apparatus, as well as for an introduction to the theory. Along with this, we recommend papers by Commandré et al. [19], Bennet *et al.* [26], Commandré and Pelletier [30] as examples of how to make a thorough study of the optical properties of a material using photothermal deflection (See Section IID14).

We now discuss materials for which k has been measured using photothermal deflection techniques. In all cases, the process involves an initial calibration using a known absorber with similar optical properties, such as the substrate thermophysical properties and film multilayer structure, in the case of thin films. We will attempt to present the strength and weakness of the individual measurements, bearing in mind that often the primary goal of the authors was to diagnose the presence of impurities or defects, rather than to produce absolute measurements of optical constants.

Aluminum Oxide and Fused Silica Glasses (Al_2O_3, SiO_2 Glasses) 1

Fused silica provides an excellent example of the role photothermal deflection can play in the measurement of optical properties: the absorption of this material is sufficiently low that it had not been measured yet [31]. The collinear-deflection technique has since been used to measure $\alpha \approx 10^{-6}$ cm^{-1} at 514.5 and 632.8 nm for synthetic fused silica, and $16\text{–}600 \times 10^{-6}$ cm^{-1} for natural fused silica [19, 32]. This gives an extinction coefficient for synthetic fused-silica of $k = 3 \times 10^{-12}$. The reason for using the deflection technique rather than an extended technique is that by crossing the beams in the bulk of the sample, the workers were able to avoid surface absorption effects which might dominate the bulk absorption. The loss in intensity due to reflections and scatter in these materials is small enough that workers take

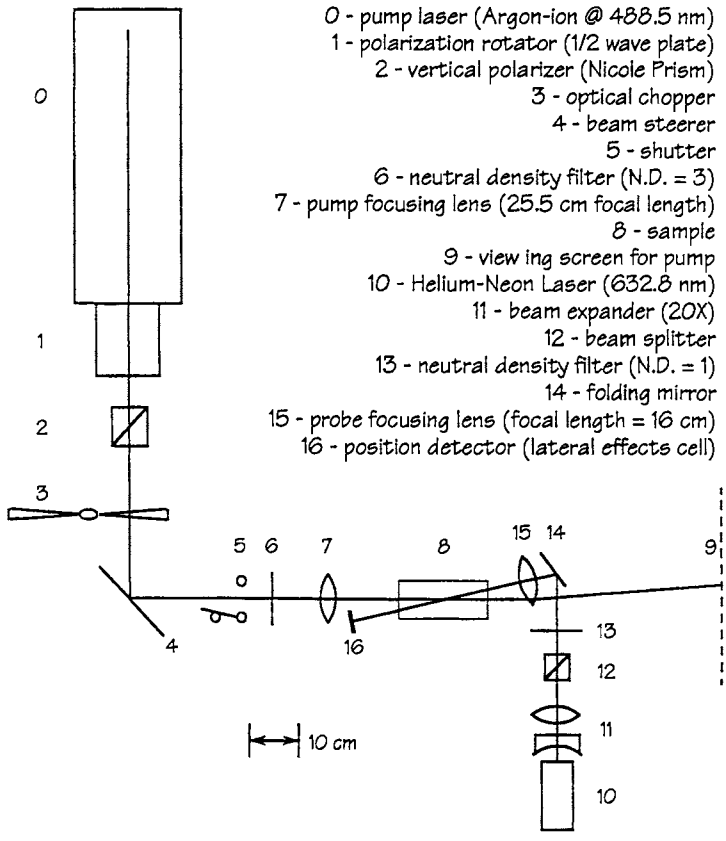

Fig. 6. A scale drawing of a typical photothermal deflection apparatus that allows a convenient variation of the power through rotation of the polarization of the Ar^+ output beam, and is characterized by a 20 μm radius probe beam and 50 μm radius heating beam at the sample location.

the intensity in the bulk to be equal to the intensity incident on the surface. Other techniques are generally forced to include the surface absorption with the bulk, and the surface absorption will usually be much stronger. We have not found bulk measurements using deflection techniques for sapphire. Our own work on surface absorptions in these materials reveals a wide range of absorptances, $10^{-5}-10^{-3}$ at 632.8 nm, depending on surface polish and cleaning [6] (recall that surface measurements can only report the fraction of light absorbed, not α). A good collection of different treatments of the problem of surface absorption in optical materials can be found elsewhere [18]. Several papers in the section on absorption losses in this reference show that surface absorptances in fused silica can be as low as $A = 10^{-6}$. Our own best fused-silica surfaces, which were superpolished by the same com-

pany that supplied some of the 10^{-6} surfaces reported in this collection, showed levels of 10^{-5}. This suggests the presence of a low-level contaminant on the surface, despite our use of modern UHV procedures to prepare the perfect sample. Workers in supercritical fluids should take note of this observation.

Amorphous Carbon Films (a-C:H) 2

Photothermal deflection was chosen for its sensitivity in recent work mapping the effects of hydrogenation on the optical absorption in amorphous-carbon films [33]. Results are given for α, which we convert to an approximate value of k using $k = \lambda\alpha/4\pi$. For example, at $\lambda = 0.6328$ μm, this gives $k = 2 \times 10^{-3}$ at an atomic fraction of hydrogen in the film of $X_H = 0.44$. This should be compared to the values $k = 0.217, 0.0348$ from transmission measurements, as tabulated by Piller [34], for which X_H was not quoted. A careful study of the absorption in a-C:H must include careful treatment of X_H, as in Compagnini *et al.* [33].

Copper (Cu) 3

The absorption spectrum of copper for $500\text{nm} < \lambda < 700\text{nm}$ is given by Spear and Russo [25] for a 0.2 μm-thick layer sputtered onto acrylic. This is a demonstration of the mirage technique performed in the substrate, and not an optical-properties paper, so the level is equivilant to the calibration from reflectance measurements, and no value for α is given. The experimental deflection is an order of magnitude lower than expected from theory, which seems to be a typical problem for the mirage approach, making it less desirable for the measurement of optical constants.

Gallium Arsenide and Amorphous Gallium Arsenide (GaAs, a-GaAs:H) 4

The absorption of 1 μm thick MBE layers of GaAs has been reported between 0.8 and 2 μm as a function of temperature of the substrate during growth [35]. The photothermal deflection technique was chosen for its sensitivity; these results fall into an area of low extinction coefficient in the subgap region not previously measured [31]. Subgap absorption-levels vary strongly with substrate growth temperature, $\alpha \approx 10^1$–10^3cm^{-1} as λ goes from 2 to 0.8μm. These results are used by the authors to determine defect-density behavior. Unhydrogenated amorphous GaAs layers show 100× higher absorption than the crystalline films and a shift to lower energies [36], similar to behavior observed for GaP (next section) and Se (Section IID7).

The hydrogenated amorphous film showed similar behavior to the crystalline film, however.

5 Gallium Phosphide (GaP)

The effect of substrate temperature during sputtering of amorphous GaP films appears to have only a slight effect on the optical absorption in the subgap region [37], in contrast to the behavior reported for GaAs (Section IID4). A smoothing of the exponential absorption edge is observed by these authors, similar to that found for amorphous Se (Section IID7), as well as a shift by a factor of 3 to lower energy compared to the absorption edge in crystalline GaP. The observed α ranges from 0.1 to 10^5 cm^{-1} as the wavelength decreases from 0.5 to 2.5 μm. Much of this region had not been explored before [38].

6 Amorphous Hydrogenated Germanium (a-Ge:H)

The amorphous thin-films of germanium and silicon (Section IID13) have been extensively studied with photothermal deflection, because the sensitivity allows the measurement of the absorption in the sub-gap region up into the more highly absorptive region where classical approaches work. For example, the region from 0.5 to 1.5 eV has been measured in a-Ge:H using photothermal deflection [39], showing the change from $\alpha = 10$ cm^{-1} at the flat absorption below the gap rising up to 10^5 cm^{-1} at the gap. Generally, these studies map the absorption as a function of the degree of hydrogenation and the defect density.

7 Amorphous GeSe and Selenium Films (a-GeSe, a-Se)

Annealing effects on 1–1.5 μm-thick GeSe films have been reported by Theye *et al.* [40], in which the authors use photothermal deflection in the subgap region. The resulting absorption ranges from $\alpha = 10^1$ to 10^3 cm^{-1} as λ goes from 1.2 to 0.5 μm. The authors find strongly reduced absorption with annealing over most of the range, but find an indication of *increased* absorption for the annealed sample at the lowest energy. Theye and co-workers later study absorption versus concentration of Se from 0 to 100% [41], over a broader range of wavelengths than their first study. The material shows a gradually increasing absorption with energy, $\alpha = 3$ to 10^5 cm^{-1} as the wavelength changes from $\lambda = 2.5$ to 0.5 μm. They note that the amorphous selenium films lack the sharp exponential absorption edge found in bulk Se.

Gold Films (Au) 8

Gold has been measured using photothermal deflection in demonstration measurements for a new surface-deformation technique [28]. The authors show the equivalence between the absorption measured on gold films using photothermal deflection with that measured using the reflectance, and demonstrate agreement between the expected and measured signal levels. The absorption coefficient they measure is $\alpha = 7.6 \times 10^5\ \text{cm}^{-1}$ at $\lambda = 0.488\ \mu\text{m}$, which gives $k = \lambda\alpha/4\pi = 2.4$, compared to $k \approx 1.8$ in Lynch and Hunter [42]. The difference is presumably due to differences in the deposition and surface finish of the film, and reinforces our point that reports of surface absorptions must include a careful specification of the surface condition at the time of measurement.

Indium Phosphide (InP) 9

Polished wafers of InP were tested by Horita *et al.* [43] for demonstrating a double-pass method to enhance the sensitivity of mirage detection. In addition, these workers used the high sensitivity to extend the measurements of k reported by Glembocki and Piller [44] to wavelengths between 1 and 1.2 μm, where the absorption had been too low to measure previously. The new results map smoothly onto the old ones, and dip down to $\alpha = 2 \times 10^{-2}\ \text{cm}^{-1}$ at 1.2 μm. As usual for the mirage technique, the calibration cannot be calculated correctly from theory. However, there is good overlap with the data of Glembocki and Piller [44], which is taken as the calibration. This is appropriate for their demonstration work, but leaves open the possibility of an offset (due, for example, to surface roughness) between the actual and reported absorption of the sample. We just want to emphasize the importance of an independent calibration and agreement with theoretical signal-levels in measurements of optical constants. The absorption of this material was also measured using photothermal deflection [45], as part of a study of the utility of photothermal deflection in the characterization of quantum wells. The authors report that they are successful in determining the absolute absorption of the quantum wells, and in addition report the absorption spectrum for the InP substrate from $\lambda = 1$ down to 2 μm, extending the work of Horita *et al.* [43] further into the relatively flat absorption region ($k \approx 10^{-2}$) below the gap at 1.3 eV.

Iron Disilicide ($FeSi_2$) 10

k and α are reported in Dimitriadis *et al.* [46] using photothermal deflection in conjunction with spectroscopic ellipsometry and X-ray diffraction in

a thorough study of this material between $\lambda = 0.5$ and 2.5 μm. Photothermal deflection was chosen for its sensitivity. The resulting k is found to grow from 1 to 3 with energy in this range, for both bulk and thin-film samples. The results establish a band gap at 0.8 μm.

11 *Lead Lanthanum Zirconate Titanate Ceramics (PLZT)*

The subgap absorption in this material has been measured in a study of the absorption centers and the effects of illumination [47]. The authors find a smooth increase in the absorption coefficient from 10^{-2} to 10^{2} cm^{-1}, for incident light between 1 and 3.5 eV. In the method of calibration, the authors show an appreciation for the need to duplicate the thermal properties of the unkown materials: they paint the surface of an identical sample with black paint to increase the absorption sufficiently to allow a cross-calibration with transmission. This still leaves serious doubt, however, in that the thermal impedance at the boundary between the paint and the sample will be very different from that of the surface absorption to the bulk in the unpainted material.

12 *Silicon (Si)*

The same work we discussed in the Section IID9 also reported measurements of α for a polished silicon wafer. Again, the results dip down smoothly from the literature values used for calibration [48], and end with $\alpha = 10^{-2}$, cm^{-1} at 1.2 μm, similar to InP. This small region is interesting because previous measurements had stopped at 1.1 μm [48], and Horita *et al.* [43] show that the absorption continues to plummet, dropping two more decades between 1.1 and 1.2 μm. Because work by Edwards [48] is used for calibration, the results of Horita *et al.* [43] are locked into consistency with the earlier work. A calibration offset may exist for this mirage work, as discussed in Section IID9.

13 *Amorphous Silicon and Hydrogenated Silicon (a-Si, a-Si:H)*

The absorptions of a-Si and a-Si:H thin films have now been measured using all of the techniques that we have mentioned. This work provides another example of the interplay between these techniques: The transmission work cited by Piller [34] lacks the sensitivity to measure the absorption in the sub-gap region of the thin film. Since then, photothermal (and other) techniques have measured the absorption in this region, revealing a wide variety of levels associated with different levels of hydrogenation (X_H) and

sample purity [49]. The surface absorption is distinguished from the film interior absorption by Umezu *et al.* [50] by studying the absorption versus the thickness of the film from 0.02 to 5 μm. The work is carried out at wavelengths starting in the supgap region and extending up over the band-edge, from 0.6 to 1.2 μm, for the purpose of exploring the nature of the surface states; α is not given. The difficulty in reaching conclusions about the absolute absorption α arises from the interpretation of interference effects, as we discussed in our general review of the technique. A treatment of this effect for amorphous silicon films can be found elsewhere [51]. These authors apply a thin-film optical analysis to extract α for 0.3 μm-thick films of a-Si:H between $\lambda = 0.6$ and 1.2 μm. They find α increasing from 10^1 to 10^4 cm^{-1} with energy in this region, with the gap edge at 0.8 μm. They attempt to resolve surface and bulk levels by fitting, to obtain the surface density of states and how these depend on light soaking and thermal annealing. A more thorough discussion of the application of thin-film optical analyis can be found in the work on TiO_2 discussed in the next section. A review of earlier work using photothermal deflection on a-Si can be found elsewhere [52]. Finally, we note that this material was studied at liquid-nitrogen temperatures, with α decreasing smoothly from 10^5 to 10^2 cm^{-1} between $\lambda = 0.5$ and 1.2 μm [53].

Titanium Dioxide Films (TiO_2) **14**

Photothermal techniques are critical for measuring k in TiO_2 (and other transparent films) where the extinction coefficient is so small in the entire visible region that it was previously inaccessible [31]. The optical properties of this material have been thoroughly measured in the literature using photothermal deflection [19, 26, 30]. This work gives $k = 1 \times 10^{-5}$–5×10^{-4}, depending principally on the sample roughness and preparation method, and independent of wavelength in the visible range where these studies were done. Note that the crossover from this flat region to the strong wavelength dependence evident in Ribarsky [54] for $\lambda < 0.4$ μm and $\lambda > 10$ μm has not been explored to our knowledge. The value of k reported at these wavelengths is $k \approx .05$, rising quickly to $k \approx 2$ [54]. This is one of the most studied materials, and one can go to the above references to find work on the effects of multilayer interference, and comparison with the more traditional techniques.

Zinc Sulfide (ZnS) **15**

A single layer of ZnS was used as a calibration signal by Commandré *et al.* [19]. In order to extract an extinction coefficient from their data, we cal-

culate k from the formula and parameters given by Commandré *et al.* [19] that take into account interference effects, with $n_1 = 2.4$ at $\lambda = 610$ nm [55]. This gives $k = 7 \times 10^{-4}$, somewhat higher than the value for cubic ZnS given by Palik and Addamiano [55], but not inconsistent with variations noted for surface absorptions in general. See references in Palik and Addamiano [55].

E Working Equations

Here we give the working equations for the simplest deflection measurement, a collinear deflection apparatus making bulk measurements. Our intention is to show, in general, how the different materials' properties affect the signal. The absolute calculation for a particular experiment must take into account any peculiarities of the new experiment and be verified against calibration standards. If such a comparison is unsuccessful, then the confidence in using the calibration standards to judge the absolute absorption of an unknown is diminished. Several workers have reported good success with models, treating the heat flow in the proper number of dimensions and taking into account the presence of surfaces [3, 6, 56–58].

When a material is heated, thermal expansion causes the density of the material to decrease, and this lowers the refractive index of the material—the speed of light increases as the density goes down. The optical effect of the change in density dominates the change in polarizability. This phenomenon is well described by a dipole approximation described by the Clausius-Mossotti equation [59], and if one takes the derivative of this equation with respect to density ρ, one finds a simple expression for the temperature derivative of the refractive index, dn/dT,

$$\frac{dn}{dT} = \frac{\partial n}{\partial \rho}\frac{\partial p}{\partial T} = -\frac{(n^2 - 1)(n^2 + 2)}{6n}\beta_p, \tag{2}$$

where we have substituted the thermal expansion coefficient at constant pressure β_p,

$$\beta_p \equiv -(1/\rho)(\partial \rho/\partial T)_p. \tag{3}$$

The signal turns out to be proportional to this term, so that the coefficient of thermal expansion plays a crucial role in the signal level: the sensitivity of the mirage approach is due to the thermal expansion in the gas above the heated surface, the use of sensing fluids in collinear measurements on solids is due to the 100× larger thermal expansion in liquids compared to solids, and the enhancement to the signal provided by supercritical fluids arises because the thermal-expansion coefficient diverges with proximity to the criti-

cal point [4, 6]. The coefficient of thermal expansion of liquids is β_p (liquid) $\approx 10^{-3}$ (K^{-1}), while for fused silica, β_p has the very low value 1.6×10^{-6} (K^{-1}). The strength of the thermal effect on n, therefore, varies from $dn/dT \approx 5 \times 10^{-4}$ or 0.03%, down to 7×10^{-7} or 5×10^{-5}% (K^{-1}). These are small effects, but they are entirely due to the process of interest, unlike the transmission approach, which deduces the absorption from the small amount of light lost from the incident beam.

The deflections are small enough that we can assume that a beam travelling in some direction z will always be deflected by gradients perpendicular to z, $\partial n/\partial r$, according to the simple expression

$$d\theta = \frac{1}{n}\frac{\partial n}{\partial r}dz, \tag{4}$$

where $d\theta$ is the angular deviation from the z-axis. This can be seen directly by considering the change in the velocity along the wavefront of a plane-wave travelling in a medium with a gradient in the refractive index along the wavefront [59]. We express this gradient in terms of the temperature gradient from which it arises, $\partial n/\partial r = (dn/dT)\partial T/\partial r$, and integrate this along the path of the probe-beam through the heated region of the sample. Assume this heated region arises from the absorption coefficient α (cm^{-1}) of a heating beam of power P, focused to a Gaussian waist-radius w_0 and chopped at a frequency ω. We take the heating and probe-beams to overlap at an angle ϕ, which gives an effective overlap length l of $l = 2w_0/\sin\phi$. If the frequency is low enough that a steady state is reached during each shutter opening, the effect will be limited by the thermal conductivity Λ of the sample, so that the final expression for the root-mean-square angular variation of the probe beam is:

$$\theta_{rms} = \frac{\beta_p}{\Lambda}\rho\frac{\partial n}{\partial \rho}\frac{\alpha l P}{\sqrt{2}\pi^2 w_0}\left[\frac{1 - e^{-2r^2/\omega_0^2}}{r/w_0}\right], \tag{5}$$

where we have assumed that the materials are transparent, i.e., that the power in the heating beam is not significantly diminished by the absorption before and while overlapping with the probe beam. If on the other hand, the frequency is high enough that the temperature is increasing at its maximum rate throughout the time the shutter is open, the signal is limited by the heat capacity of the sample c_p, and obeys

$$\theta_{rms} = \frac{\beta_p}{\omega\rho c_p}\rho\frac{\partial n}{\partial \rho}\frac{16\alpha l P}{\sqrt{2}\pi^2 w_0^3}\left[\frac{r}{w_0}e^{-2r^2/w_0^2}\right]. \tag{6}$$

The intermediate frequencies are described by integral equations that must be solved numerically [3, 6, 15, 16, 60].

The qualitative behavior common to both the low- and high-frequency forms is then a signal which is proportional to the illuminating power P and the absorption αl or A. The low-frequency signal level rolls-off to frequency-limited behavior at a frequency $f_r \equiv 4D/(\pi w_0^2)$, where D is the thermal diffusivity of the fluid, and w_0 is the waist radius of the heating beam. Low-frequency signals will be independent of frequency, and proportional to the ratio of the thermal-expansion coefficient β_p to the thermal conductivity Λ. The maximum signal will be found with the probe at $r = 0.8w_0$ from the axis of the heating beam. High-frequency signals fall off with frequency like $1/f$, and are proportional to the ratio of β_p to the constant-pressure heat capacity c_p. The probe position at maximum signal will move in, to a separation $r = w_0/2$ from the heating beam.

We repeat that the above calculations describe the signal in a collinear photothermal deflection experiment measuring the bulk absorption of a transparent material. We wanted to illustrate how the modulation frequency, heat capacity, thermal conductivity, and coefficient of thermal expansion affect the signal. These equations, and generalizations of these equations, have been applied successfully to predict signal levels in a variety of experimental situations, as mentioned in the first paragraph of this section.

III CONCLUSIONS

The photothermal deflection techniques are highly sensitive techniques of 10% accuracy which find their greatest applicability in characterizing the effects on materials of production processes and handling. These non-contact, *in-situ* inspection techniques are in demand in both research and industrial applications in semiconductors and optics [17, 18], and photothermal techniques have been applied to a broad range of sample geometries and materials [7]. The localized nature of these techniques has revealed the fact that impurities, defects, and surface conditions alter dramatically the local absorption level of a material [61]. This has shown us that we must think of a material as having a distribution of absorption levels in order to anticipate the behavior of the material in modern research and technology. The extended techniques we mentioned in the introduction are used more commonly than the deflection techniques for measuring "the" optical constants of materials, because they average over the local variations. However, if one wishes to separate bulk from surface absorption in a transparent material, the ability to choose the measurement location with the beam crossing in the collinear-deflection technique is very useful. One must also realize that the local variations are hidden by the extended techniques—and turn to a local technique to get a complete picture of k in demanding applications.

ACKNOWLEDGEMENTS

This work was supported by the Department of Physics at the University of Utah, 201 James Fletcher Building, University of Utah, Salt Lake City, UT 84112.

REFERENCES

1. A. C. Boccara, D. Fournier, W. B. Jackson, and N. M. Amer, Sensitive photothermal deflection technique for measuring absorption in optically thin media. *Opt. Lett.* **5**, 377 (1980).
2. J. D. Spear, R. E. Russo, and R. J. Silva, Collinear photothermal deflection spectroscopy with light-scattering samples. *Appl. Opt.* **29**, 4225 (1990).
3. W. B. Jackson, N. M. Amer, A. C. Boccara, and D. Fournier, Photothermal deflection spectroscopy and detection. *Appl. Opt.* **20**, 1333 (1981).
4. R. A. Leach and J. M. Harris, Supercritical fluids as spectroscopic solvents for thermooptical absorption measurements. *Anal. Chem.* **56**, 1481 (1984).
5. V. Loriette, L. Pinard, A. C. Boccara, and J. M. Mackowski, Multilayers coatings characterisation for interferometric gravitational waves detection, Optical Interference Coatings. (F. Abelès, ed.), *SPIE Proc.* **2253**, 1031 (1994).
6. M. E. Briggs and R. W. Gammon, Photothermal deflection in a supercritical fluid. *Int. J. Thermophys.* **16**, 1439 (1995).
7. E. Welsch, Photothermal measurements on optical thin films. *Appl. Opt.* **34**, 7239 (1995); E. Welsch, Absorption measurements, *in* "Handbook of Optical Properties, Volume 1, Thin Films for Optical Coatings." (R. E. Hummel and K. H. Guenther, eds.), CRC Press, Boca Raton, Florida, 1995.
8. J. Stone, Measurements of the absorption of light in low-loss liquids. *J. Opt. Soc. Am.* **62**, 327 (1972).
9. J. P. Gordon, R. C. C. Leite, R. S. Moore, S. P. S. Porto, and J. R. Whinnery, Long-transient effects in lasers with inserted liquid samples. *J. Appl. Phys.* **36**, 3 (1965).
10. D. Solimini, Loss measurement of organic materials at 6328 Å. *J. Appl. Phys.* **37**, 3314 (1966).
11. J. R. Whinnery, Laser measurement of optical absorption in liquids. *Acc. Chem. Res.* **7**, 225 (1974).
12. H. A. Schuessler, S. H. Chen, Z. Rong, Z. C. Tang, and E. C. Benck, Cavity-enhanced photothermal spectroscopy: Dynamics, sensitivity, and spatial resolution. *Appl. Opt.* **31**, 2669 (1992).
13. J. Stone, Thermooptical technique for the measurement of absorption loss spectrum in liquids. *Appl. Opt.* **12**, 1828 (1973).
14. D. L. Mazzoni and C. C. Davis, Trace detection of hydrazines by optical homodyne interferometry. *Appl. Opt.* **30**, 756 (1991).
15. A. Mandelis, ed., "Principles and Perspectives of Photothermal and Photoacoustic Phenomena." Elsevier, New York, 1992.
16. J. A. Sell, ed., "Photothermal Investigations of Solids and Fluids." (J. A. Sell, ed.), Academic Press, San Diego, 1989.
17. J. C. Murphy, J. W. M. Spicer, L. C. Aamodt, and B. S. H. Royce, eds., "Photoacoustic and Photothermal Phenomena II." Springer-Verlag, New York, 1990.
18. F. Abelès, ed., Optical Interference Coatings. *SPIE Proc.* **2253**, 1021 (1994).
19. M. Commandré, L. Bertrand, G. Albrand, and E. Pelletier, Measurement of absorption losses of optical thin film components by photothermal deflection spectroscopy. Optical Components and Systems. *SPIE* **805**, 128 (1987).
20. Y. X. Nie and L. Bertrand, Separation of surface and volume absorption by photothermal deflection. *J. Appl. Phys.* **65**, 438 (1994).
21. B. C. Li, Y. Deng, and J. Cheng, Separation of optical thin film and substrate absorption by obliquely-crossed photothermal deflection: Theory. *J. Mod. Opt.* **42**, 1093 (1995).

22. H. E. Bennett and D. K. Burge, Simple expressions for predicting the effect of volume and interface absorption and of scattering in high-reflectance or antireflectance multilayer coatings. *J. Opt. Soc. Am.* **70**, 268 (1980).
23. J. C. Murphy and L. C. Aamodt, Photothermal spectroscopy using optical beam probing: Mirage effect. *J. Appl. Phys.* **51**, 4580 (1980).
24. M. Montecchi and E. Masetti, Measurement of vibrational deexcitation efficiencies of gold, chormium, zinc selenide and amorphous carbon thin films. *Phys. Rev. B* **44**, 11649 (1991).
25. J. D. Spear and R. E. Russo, Transverse photothermal beam deflection within a solid. *J. Appl. Phys* **70**, 580 (1991).
26. J. M. Bennet, E. Pelletier, G. Albrand, J. P. Borgogno, B. Lazarides, C. K. Carniglia, R. A. Schmell, T. H. Allen, T. Tuttle-Hart, K. H. Guenther, and A. Saxer, Comparison of the properties of titanium dioxide films prepared by various techniques. *Appl. Opt.* **28**, 3303 (1989).
27. A. Rosencwaig, J. Opsal, and D. L. Willenborg, Thin-film thickness measurements with thermal waves. *J. Phys.* **6**, 483 (1983).
28. H. Saito, M. Haraguchi, and M. Fukui, New type of photothermal spectroscopic technique. *Appl. Opt.* **31**, 2047 (1992).
29. E. Welsch, H. G. Walther, K. Friedrich, and P. Eckardt, Separation of optical thin film and substrate absorption by means of photothermal surface deformation technique. *J. Appl. Phys.* **67**, 6575 (1990).
30. M. Commandré and E. Pelletier, Measurements of absorption losses in TiO_2 films by a collinear photothermal deflection technique. *Appl. Opt.* **29**, 4276 (1990).
31. E. D. Palik, ed., "Handbook of Optical Constants of Solids." Academic Press, Orlando, Florida, (1985).
32. K. A. Strain, J. Hough, N. A. Robertson, and K. Skeldon, Measurement of the absorptance of fused silica at $\lambda = 514.5$ nm. *Opt. Commun.* **117**, 385 (1995).
33. G. Compagnini, U. Zammit, K. N. Madhusoodanan, and G. Foti, Disorder and absorption edges in ion-irradiated hydrogenated amorphous carbon films. *Phys. Rev. B* **51**, 11168 (1995).
34. H. Piller, Silicon (amorphous), *in* "Handbook of Optical Constants of Solids" (E. D. Palik, ed.), Academic Press Orlando, Florida, p. 571, 1985.
35. M. H. Chan, S. K. So, K. T. Chan, and F. G. Kellert, Defect density measurements of low temperature grown molecular beam epitaxial GaAs by photothermal deflection spectroscopy. *Appl. Phys. Lett.* **67**, 834 (1995).
36. R. Murri and N. Pinto, Optical properties of amorphous gallium arsenide films. *J. Non-Cryst. Solids* **164–166**, 889 (1993).
37. N. Elgun and E. A. Davis, Transport and optical properties of a-GaP prepared at different substrate temperatures. *J. Phys.: Condens. Matter* **6**, 779 (1994).
38. A. Borghesi and G. Guizzetti, Gallium phosphide (GaP), *in* "Handbook of Optical Constants of Solids" (E. D. Palik, ed.), Academic Press, Orlando, Florida, p. 445, 1985.
39. L. Zanzig, W. Beyer, and H. Wagner, High quality hydrogenated amorphous germanium prepared by the hot wire technique. *Appl. Phys. Lett.* **67**, 1567 (1995).
40. M. L. Theye, M. F. Kotkata, K. M. Kandil, A. Gheorghiu, C. Senemaud, and J. Dixmier, Studies of evaporated amorphous $GeSe_2$ films as a function of annealing. *J. Non-Cryst. Solids* **137–138**, 963 (1991).
41. M. F. Kotkata, K. M. Kandil, and M. L. Theye, Optical studies of disorder and defects in amorphous Ge_xSe_{1-x} films as a function of composition. *J. Non-Cryst. Solids* **164–166, 1259 (1993).**
42. D. W. Lynch and W. R. Hunter, Optical constants of metals, *in* "Handbook of Optical Constants of Solids" (E. D. Palik, ed.), Academic Press, Orlando, Florida, p. 275, 1985.
43. S. Horita, E. Miyagoshi, M. Ishimaru, and T. Hata, Improvement of sensitivity of photothermal deflection spectroscopy by a double pass method. *Rev. Sci. Instrum.* **63**, 1909 (1992).

44. O. J. Glembocki and H. Piller, Indium phosphide, *in* "Handbook of Optical Constants of Solids" (E. D. Palik, ed.), Academic Press, Orlando, Florida, p. 503, 1985.
45. C. Wetzel, V. Petrova-Koch, F. Koch, and D. Grutzmacher, Photothermal deflection spectroscopy of InGaAs/InP quantum wells. *Semicond. Sci. Technol.* **5**, 702 (1990).
46. C. A. Dimitriadis, J. H. Werner, S. Logothetidis, M. Stutzmann, J. Weber, and R. Nesper, Electronic properties of semiconducting $FeSi_2$ films. *Appl. Phys.* **68**, 1726 (1990).
47. W. L. Warren, C. H. Seager, D. Dimos, and E. J. Friebele, Optically induced absorption and paramagnetism in lead lanthanum zirconate titanate ceramics. *Appl. Phys. Lett.* **61**, 2530 (1992).
48. D. F. Edwards, Silicon, *in* "Handbook of Optical Constants of Solids" (E. D. Palik, ed.), Academic Press, Orlando, Florida, p. 547, 1985.
49. See Chapter 3 by A. Mandelis, this volume.
50. I. Umezu, M. Daigo and K. Maeda, Investigation of surface passivation effect of a-SiN_x:H and a-Si:H by photothermal deflection spectroscopy. *Jpn. J. Appl. Phys.* **33**, L873 (1994).
51. F. Leblanc, Y. Maeda, K. Onisawa and T. Minemura, Bulk and surface densities of states of 0.3 μm thick hydrogenated amorphous-silicon films using photothermal deflection spectroscopy. *Phys. Rev. B* **50**, 14613 (1994).
52. G. Amato, G. Benedetto, L. Boarino, M. Maringelli, and R. Spagnolo, Photoacoustic and photothermal deflection spectroscopy of semiconductors. *IEE Proc. A 139*, 161 (1992).
53. S. Nonomura, H. Hayashi, and S. Nitta, Photothermal deflection spectroscopy at 77 K. *Rev. Sci. Instrum.* **60**, 657 (1989).
54. M. W. Ribarsky, Titanium dioxide (TiO_2) (rutile), *in* "Handbook of Optical Constants of Solids" (E. D. Palik, ed.), Academic Press, Orlando, Florida, p. 795, 1985.
55. E. D. Palik and A. Addamiano, Zinc Sulfide, *in* "Handbook of Optical Constants of Solids" (E. D. Palik, ed.), Academic Press, Orlando, Florida, p. 597, 1985.
56. A. Rose, R. Vyas, and R. Gupta, Pulsed photothermal deflection spectroscopy in a flowing medium: A quantitative investigation. *Appl. Opt.* **25**, 4626 (1986).
57. E. L. Lasalle, F. Lepoutre, and J. P. Roger, Probe beam size effects in photothermal deflection experiments. *J. Appl. Phys.* **64**, 1 (1988).
58. J. A. Sell, Optical ray tracing for crossed beam photothermal deflection spectroscopy. *Appl. Opt.* **26**, 336 (1987).
59. M. V. Klein, "Optics." Wiley, New York, 1970.
60. J. F. Power, Frequency modulation time delay thermal lens effect spectrometry: A new technique of transient photothermal calorimetry. *Appl. Opt.* **29**, 841 (1990).
61. N. Kaiser, H. Uhlig, U.B. Schallenberg, B. Anton, U. Kaiser, K. Mann, and E. Eva, High damage threshold Al_2O_3/SiO_2 dielectric coatings for excimer lasers. *Thin Solid Films* **260**, 86 (1995).

Chapter 5

Determination of the Optical Constants by Brillouin Scattering

HACÈNE BOUKARI
Institute for Physical Science and Technology
University of Maryland
College Park, Maryland

and

NICHOLAS LAGAKOS
Naval Research Laboratory
Washington, D.C.

I. Definition of Notation 121
II. Introduction 122
III. Background of Brillouin Scattering Technique 123
IV. Equations for Measurement of the Index of Refraction 125
A. Scattering in Transparent Materials 126
B. Scattering from Absorbing Materials 127
V. Fabry-Perot Interferometers 128
VI. Discussion 129
VII. Brillouin Scattering in Thin Slabs and Optical Fibers 134
VIII. Special Case of Transparent Thin Slabs 135
A. Side Illumination (90° External Scattering) 135
B. Edge Illumination (90° External Scattering) 138
C. Special Geometries 140
D. Examples 141
E. Side Illumination at Normal Incidence 144
IX. Brillouin Scattering in Optical Fibers 146
A. Examples 147
References 153

I DEFINITION OF NOTATION

k_i wavevector incident inside sample
k_s wavevector scattered inside

HANDBOOK OF OPTICAL CONSTANTS OF SOLIDS III

Copyright © 1998 by Academic Press.
All rights of reproduction in any form reserved
ISBN 0-12-544423-0/$25.00.

q	acoustic phonon wavevector
ω	angular frequency in rad/s
ν	frequency in Hertz
n	complex index of refraction
η	index of refraction
κ	extinction coefficient
α_0	absorption coefficient
β_0	phase coefficient
λ_0	wavelength in vacuum
$\lambda_i = \lambda_0/\eta$	wavelength in sample
θ	scattering angle
Ω	Brillouin line frequency
v_s	velocity of sound
F_R	reflective finesse
Δ	free spectral range
t	spacing between Fabry-Perot plates
R	reflectivity of Fabry-Perot plates
c	speed of light in vacuum
Γ_q	damping constant of acoustic phonon
γ_q	sound attenuation constant
η_f	index of refraction of medium between the Fabry-Perot plates
δ	optical skin depth
α, β, γ	angles describing side and edge illumination for thin films
d	film thickness
Y	Young's modulus
σ	Poisson's ratio
ρ	density
P	Pockels coefficient

II INTRODUCTION

Brillouin scattering is known to be a very valuable tool to investigate the elastic properties of various materials. Typically, one can derive considerable information about the acoustic phonons from the measured Brillouin peaks. The shift and the width of the peaks can be directly related to the phonon velocity and the phonon attenuation constant, respectively.

In a pioneering work, Sandercock [1] showed, however, that the Brillouin-scattering technique can be applied also to measure the optical constants of absorbing materials and determined accurately the refractive index and the absorption coefficient of germanium and silicon. For this purpose he used a high-resolution, multipass Fabry-Perot interferometer to examine the broadening effect due to absorption on the Brillouin peaks of these materials. In this chapter we describe this broadening effect and its usefulness in measuring the optical constants of absorbing materials.

BACKGROUND ON BRILLOUIN SCATTERING TECHNIQUE

In a typical Brillouin-scattering experiment, a laser beam is directed onto a scattering medium. The scattered light passes through a Fabry-Perot interferometer and is then collected by a detector positioned at a scattering angle, θ, with respect to the incident beam. One obtains, in principle, the spectrum of scattered light (see Fig. 1) from the scattering sample—a plot of the distribution of scattered intensities as a function of frequency. The shape of the measured spectrum depends on the underlying physical processes responsible for the scattering phenomenon. The theoretical task is to identify these processes and calculate the corresponding spectral lineshape.

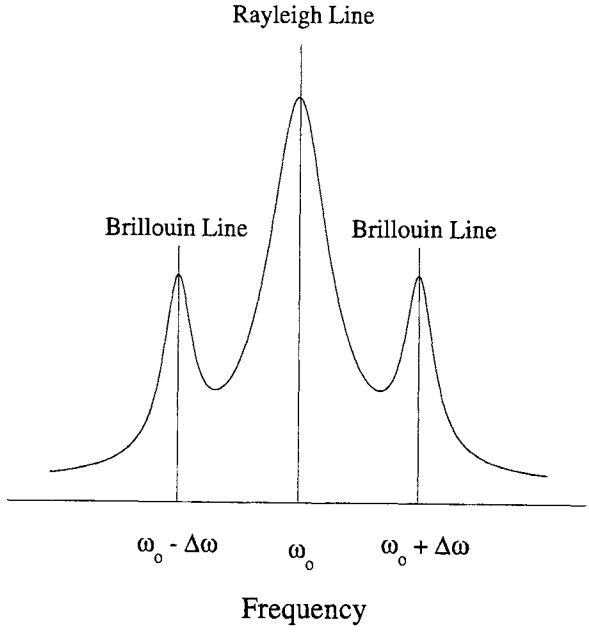

Fig. 1. Typical Brillouin spectrum of a fluid.

As an example, if we consider scattering from a single-component fluid sample, the spectrum of light scattered in a given direction contains three components for a fixed scattering geometry [2, 3]. First, a central Rayleigh line at a non-shifted frequency of the source. This elastic component is caused by density fluctuations in the fluid in thermodynamic equilibrium. These fluctuations cause, in turn, fluctuations in the dielectric constant responsible for the scattering of light. Second, two symmetric, shifted lines. These lines, commonly named Brillouin lines, are caused by inelastic scattering from longitudinal acoustic waves (phonons) propagating in the fluid at a frequency determined by the speed of sound.

In the case of crystals, the spectrum of most light-scattering experiments is composed of a central, non-shifted component and up to three pairs of the phonon components (Brillouin lines): one pair corresponds to longitudinal phonons, and two other pairs correspond to transverse phonons [4–6]. In contrast to the central component in fluids, the non-shifted line is caused by elastic scattering from imperfections either from the surface or bulk of the sample. The Brillouin lines are caused by a collective mode of vibrations of the molecules or atoms forming the sample crystal. We should mention that in crystals, additional components caused by other acoustic quasiparticles such as acoustic magnons, can appear in the spectrum [7].

In the following we will focus only on the Brillouin line as it pertains closely to the application of the Brillouin-scattering technique on the measurement of optical constants. First, there has been extensive progress in understanding and describing the details of the interaction of the incident beam with the scattering system, allowing the calculation of the complete spectral lineshape [4–6, 8]. Second, development of high-contrast, multipass Fabry-Perot interferometers has motivated several experimentalists into applying the Brillouin-scattering technique as a valuable tool in their investigation of elementary excitations in various materials. By increasing the contrast of the instrument, it is possible to detect the weak Brillouin lines and suppress the dominant Rayleigh line [1, 9–13].

The scattering processes can be examined within either a wave (classical) or a quasi-particle (quantum) picture. In the first picture the incident electromagnetic wave, $E \sim e^{i(\omega_i t - \mathbf{k}_i \mathbf{r})}$, is scattered, for example, by the sound waves acting as diffraction gratings. Here we define ω_i and $\mathbf{k}_i$ as the angular frequency and wavevector of the electric field. If the grating were fixed in space, the scattered light would have the frequency of the incident field, ω_i. However, since sound waves propagate with phase velocity, v_s, the gratings move with the same velocity as well. As a result, the back-reflected beam is reduced by a Doppler shift of $2v_s\omega_i/c_m$, c_m being the speed of light in the scattering medium [2]. One can further this analysis and apply the general Maxwell's equations coupled with the elastic properties of the materials to derive the scattering spectrum representing this Doppler-shift line, a challenging theoretical work for complicated structures of the system.

In the quasi-particle picture one can regard the same scattering process as inelastic collisions between photons and phonons [11]. The incident photon has an energy $\hbar\omega_i$ and momentum $\hbar\mathbf{k_i}$, whereas the scattered photon has an energy $\hbar\omega_s$ and momentum $\hbar\mathbf{k_s}$. Conservation of energy and momentum is then applied to extract the form of the normal-mode dispersion relations by requiring that

$$\hbar\mathbf{q} = \hbar\mathbf{k_i} \pm \hbar\mathbf{k_s} \quad (\textit{momentum conservation}), \tag{1}$$

$$\hbar\omega = \hbar\omega_i \pm \hbar\omega_s \quad (\textit{energy conservation}). \tag{2}$$

Two solutions are derived from the above relations: 1) $\mathbf{k_s} = \mathbf{q} - \mathbf{k_i}$ with $\omega_s = \omega - \omega_i$, and 2) $\mathbf{k_s} = \mathbf{k_i} - \mathbf{q}$ with $\omega_s = \omega_i - \omega$. The solutions $\mathbf{q}$ and ω correspond to the annihilation ("anti-Stokes") and creation ("Stokes") of a phonon, respectively. Note that in phonon creation, the scattered photon has a lower frequency than the incident photon, a consistent picture with red-shift tendency.

IV EQUATIONS FOR MEASUREMENT OF THE INDEX OF REFRACTION

We define the complex index of refraction as $n = \eta + i\kappa$, with κ as the extinction coefficient and η as the real-part of the index of refraction of the system (for simplicity we call η the index of refraction). Since our interest is in the measurement of η and κ of a material, our use of a measured Brillouin spectrum is directed to this purpose. So, unlike the common application of the Brillouin-scattering technique as a tool to investigate acoustic phonons in crystals or hydrodynamic modes in fluids, we intend to use the scattering property of the acoustic phonons to determine these optical constants. On the theoretical side, we need to determine the relation between η and κ of the scattering medium and the quantities that can be derived from the measured Brillouin spectrum. On the practical side, we need to design the appropriate spectrometer to measure accurately the Brillouin spectrum. More importantly, we need to discuss the limitations of the Brillouin-scattering technique.

We first note that the energy of acoustic phonons is, at most, of order $E = 10^{-2}$ eV, whereas energy of a visible photon is typically a few eV [11]. Second, for crystals the photon wavevectors are small (of order 10^5 cm^{-1}) compared with typical Brillouin-zone dimensions (of order 10^8 cm^{-1}) [11]. The length scale probed by visible light is long compared with distances between the atoms or molecules constituting the crystal, justifying the application of a continuum picture in the calculations. By applying the above observations, one can find that the magnitude of the wavevector of the incident photon in the medium is conserved in the scattering process. As a re-

sult the momentum-transfer vector q of the phonon probed by the experiment is given by:

$$q = |\mathbf{k_i} - \mathbf{k_s}| = 2k_i \sin(\theta/2), \tag{3}$$

with $|\mathbf{k_i}| = |\mathbf{k_s}|$ being the magnitude of the incident and scattering wavevectors inside the scattering medium. For a laser beam of wavelength λ_0 in vacuum, k_i is given by

$$k_i = \frac{2\pi\eta}{\lambda_0}, \tag{4}$$

where η is the index of refraction of the scattering medium.

The expression in Eq. (3) is commonly known as Bragg's condition. It is an exact relation for elastic scattering and an excellent approximation for most light-scattering situations. The q-value in Eq. (3) can be varied over a wide range by either varying θ or λ (see Eq. (4)) or both. For practical reasons, it is much easier to vary θ. In most experiments, however, θ is fixed and usually set at 90°, although backscattering configuration with $\theta = 180°$ has become a familiar configuration, especially for scattering from opaque materials and thin films.

A Scattering in Transparent Materials

In transparent materials ($\kappa = 0$) the wavevector of the probed phonon is determined uniquely by the wavelength of the incident laser beam and the scattering geometry, specifically the angle θ. The q-wavevector represents one specific Fourier-component of the phonon spectrum. For the observed Brillouin lines, the line shift, Ω, is directly related to the velocity of sound, v_s. This shift is

$$\Omega = v_s q = \frac{4\pi v_s \eta \sin(\theta/2)}{\lambda_0}, \tag{5}$$

where we use the expressions of Eqs. (3) and (4).

Immediately, one can see from Eq. (5) that the shift of the Brillouin line is directly proportional to the index of refraction. If v_s is known, η can be determined, since λ_0 and θ are known. If we neglect the width due to the inherent and natural lifetime of the scattering phonons as well as the width from the instrument (see Section B below), the lineshape of the Brillouin line is very sharp without a width, a theoretical $\delta(q)$-function centered at wavevector q, whose frequency is $\Omega = v_s q$. This can be explained by the uniqueness of the q-vector. The measured intensity is constructed from the

scattered electric fields that add up to form one single peak at the frequency, $\omega_i + \Omega$. Determination of η of transparent materials with such an approach is not commonly pursued, as η can be determined with higher precision using other optical techniques such as prism-minimum deviation and transmission-reflection techniques. The measured Brillouin spectrum is more appropriately used to determine v_s.

Scattering from Absorbing Materials B

Unlike transparent materials, absorbing materials are characterized by a complex refractive index, $n = \eta + i\kappa$, inducing a scale length over which the intensity of the optical field falls off exponentially in the medium. As the varying optical field traverses the material, a range of phonon wavevectors q is covered, adding up to the formed spectrum of the scattered beam [1, 12, 13]. This effect can be readily observed as a broadening of the Brillouin peaks. Here we note that this broadening is an additional effect to that due to the lifetime of the phonon.

For the backscattering configuration, two expressions have been applied to fit the observed Brillouin line, i.e., is, the distribution of the scattered intensity as a function of q wavevector. Initially, Sandercock [1] derived a Lorentzian distribution,

$$L(q) = \frac{1}{\pi} \frac{\alpha_0}{(\beta_0 - q)^2 + {\alpha_0}^2}, \tag{6}$$

where $\beta_0 = 2\omega_i\eta/c$ and $\alpha_0 = 2\omega_i\kappa/c$, ω_i being the angular frequency of the incident beam and c being the speed of light.

However, Dresselhaus and Pine [13] noted later that in the derivation of Eq. (6) the contribution from the reflected optical fields to the total spectrum was neglected. The lineshape of the Brillouin spectrum is not actually symmetric as the Lorentzian function of Eq. (6) suggests. For the same backscattering configuration, the lineshape is rather asymmetric around its maximum and is more accurately described by the following expression:

$$G(q) = \frac{Bq}{({\beta_0}^2 + {\alpha_0}^2 - q^2)^2 + (2q\alpha_0)^2}. \tag{7}$$

In contrast to Eq. (6), the expression in Eq. (7) vanishes at $q = 0$ and falls off as q^{-3} for large q. We further note that $G(q)$ in Eq. (7) and the Lorentzian in Eq. (6) are nearly identical in the limit of a weak absorbent ($\alpha_0 \ll \beta_0$). For a strong absorbent we have ($\alpha_0 \sim \beta_0$), and Eq. (7) appears to be appropriate to the real case.

The calculation for backscattering has been extended to an arbitrary direction of the incident beam [8, 12]. The situation becomes more complicated by the contribution of surface waves of the Rayleigh type to the scattered intensity. Further, the acoustic phonons (bulk) in solids are modified because longitudinal and transverse polarizations are coupled near the surface and cannot be considered independent.

V FABRY-PEROT INTERFEROMETERS

The frequency range of acoustic phonons falls in the Gigahertz, a range suitable to Fabry-Perot interferometers. Nowadays, high-resolution Fabry-Perot interferometers are commercially available and operated routinely to measure Brillouin spectra of various systems. A simple description of the interferometer and its principle of operation can be found in several textbooks [9, 10, 14]. In a simple design, a Fabry-Perot interferometer consists of two plane mirrors held parallel to each other. The inner surfaces are highly reflecting with a reflectivity exceeding 90%. If we examine the case of an ideal Fabry-Perot interferometer, where the plates are considered parallel and free of surface-defects, the instrumental function describing the interferometer is described by an Airy function:

$$I(\omega) = \frac{I_0}{[1 + F \sin^2(\pi\omega/\Delta)]}. \tag{8}$$

Equation (8) represents the lineshape that is obtained if an extremely narrow beam (described by a δ-like function) traverses the interferometer. In Eq. (8) we have $F = 4R/(1 - R)^2$ and $\Delta = c/2\eta_f t$ is the free spectral range, η_f being the index of the medium (usually air) between the mirror plates of reflectivity R, t the spacing between the plates, and c the speed of light in vacuum.

If one varies the spacing, t, or the index of refraction, η_f, one can change the condition of the transmission of light of a given frequency through the interferometer. If a scattered light contains two frequencies set at ω_0 and $\omega_0 + \delta\omega_0$ with ω_0 being at resonance frequency, the peak of the shifted line can be detected by varying t to cover at least one order of interference. Here the conditions for the observation of the shifted peak are determined by two important characteristics of the interferometer: finesse and contrast. First, the finesse, F_R, is the ratio of the free spectral range over the full width at half maximum of the Airy line and describes the capability of the instrument in separating various peaks. For an ideal interferometer it is defined as

$$F_R = \pi\sqrt{R}/(1 - R), \tag{9}$$

and depends only on the reflectivity.

Second, the contrast, C, is the ratio of the maximum over the minimum of the instrumental line, providing an idea on the power of the instrument to detect weak signals. For an ideal interferometer, it is given by

$$C = 1 + (4/\pi^2)F_R^2. \tag{10}$$

Both expressions of Eqs. (9) and (10) show that as R is increased, both finesse and contrast increase. In principle, one can then improve the performance of the interferometer by just changing R. However, imperfections such as surface defects and misalignment introduce a limit to the finesse and contrast [9, 10]. In the interferometers now available, F_R does not usually exceed ~ 50 and $C < 10^3$. This contrast number is particularly too small if one intends to measure very weak peaks, such as those of phonons in highly absorbing materials. For this purpose, a multipassing technique has been devised to increase the contrast [9, 10]. Here, the beam of light passes through the interferometer several times. It can be shown that the resultant contrast, C_n, is

$$C_n = C^n, \tag{11}$$

where n is the number of passes of the beam through the interferometer, and C is the contrast for one pass. In practice, two corner cubes are usually used to achieve multipassing by reflecting and appropriately directing the beam from the various facets of the two cubes. It is now possible to achieve a contrast as high as 10^{12}.

The schematic diagram of a typical set-up for the measurements of acoustic phonons by a multi-pass Fabry-Perot interferometer is shown in Fig. 2. The setup may operate either on 90°-geometry or in backscattering. The light of a laser beam (~200 mW) is focused and directed to a sample by the lens L_1 (90°) or L_2 (backscattering). The scattered light is collected by the lens L_2 and directed onto the input aperture of the Fabry-Perot interferometer. Here, the spacing between the plates t is scanned by piezoelectric rods to cover a number of orders of interference. The output beam passes through the collimator formed by the lenses L_2 and L_3, and is directed to a sensitive photomultiplier (PMT-1) usually with a low dark count (~1 ct/s). The output signal from the photomultiplier is amplified and further processed by a photon-counting circuit. The processed signal is fed to a multichannel analyzer. A second photomultiplier (PMT-2) in combination with a stabilization system is used in a feedback mode to control the plate separation by adjusting the piezoelectric spacers.

VI DISCUSSION

The main information obtained from a measured Brillouin spectrum are the line shift, the linewidth, and the distribution of intensity as a function of frequency, including the maximum peak.

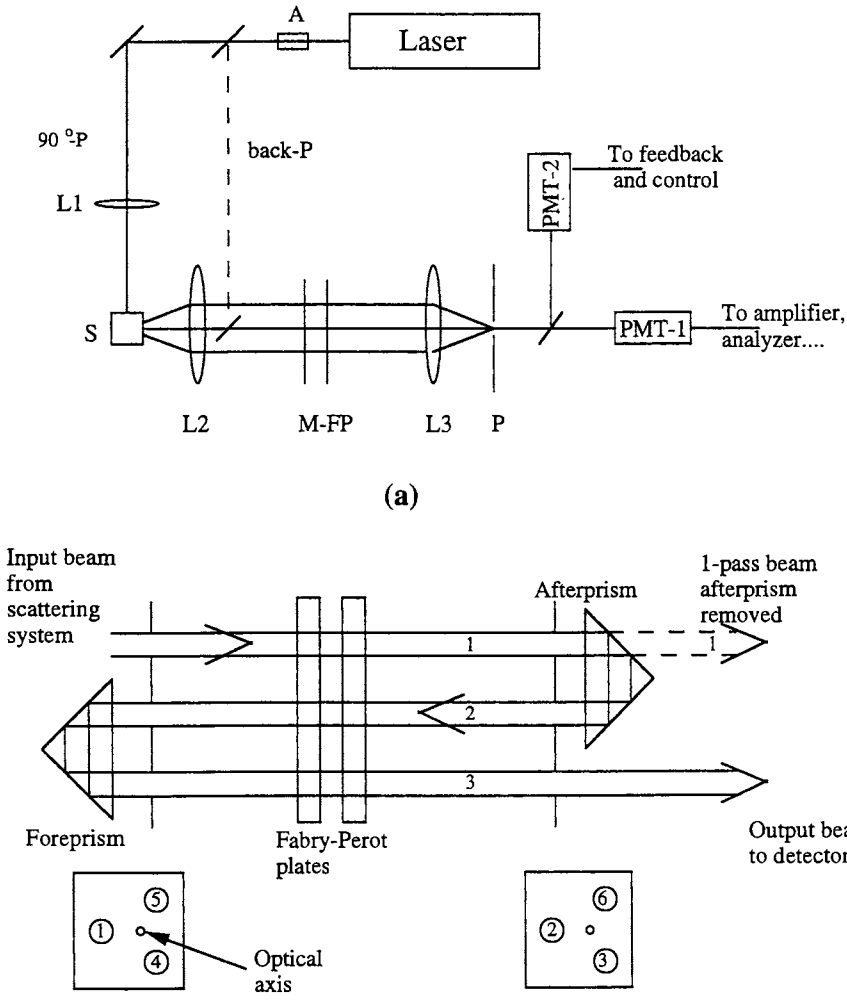

Fig. 2(a). Schematic diagram of an experimental setup to measure the Brillouin spectrum of a sample *S*. Two configurations are shown 90° (90°-*P*) and backscattering (back-*P*). L1, L2, and L3 are optical lenses, *M-FP* the Fabry-Perot interferometer, *P* the collecting pinhole, *PMT*-1 and *PMT*-2 the photomultiplier tubes. **(b)** Details of the 3-pass aperture and retroreflection prism of a 3-pass Fabry-Perot interferometer.

The line shift is directly related to the phonon velocity and is given by Eq. (5). Equation (5) shows that the shift depends on the velocity as well as the index of refraction. As discussed earlier for transparent materials, it is much more appropriate to use the Brillouin spectrum to determine the phonon velocity instead of η, since other optical techniques such as transmission-

reflection and prism-minimum deviation techniques are much more precise in measuring η. However, for practical reasons and experimental difficulties, the Brillouin-scattering technique is sometimes used to determine η. For example Zha *et al.* [15] applied the technique to investigate the effect of high pressure on transparent SiO_2 glass. For this purpose, they measured the Brillouin line shift at two different angles, 90° and 135°, (two q-vectors) and determined simultaneously both η and v_s from the ratio of the shifts. As the pressure was varied, they observed changes in η and v_s indicating changes in the structural properties of the glass. We should note, however, that this two-angle method is appropriate when the material is isotropic with one phonon velocity, therefore simplifying the problem. For anisotropic crystals, complications arise as the phonon velocity changes as a function of optical axis or q-vector. It is not possible then to separate η and v_s, since both vary as a function θ (q-vector).

Information on linewidth is much more useful in the case of absorbing materials as κ is related to the width. The experiments are performed in a backscattering configuration with a high-resolution, multi-pass Fabry-Perot interferometer, allowing the detection of weak Brillouin peaks [1, 16]. To get an accurate value of the width due to just broadening from absorption, corrections are needed to remove contributions from the phonon lifetime and the instrumental function that may include effects due to the finite size of the collection pinhole (see Refs. 9, 10, and 17–19 for more discussion).

Several methods have been developed to correct for contributions from the instrumental linewidth. One can fit the instrumental function with some familiar functions such as a Gaussian or Voigt function and deconvolute numerically the observed spectrum from the fitted instrumental function (see Refs. 17 and 18 and references therein). A more elaborate deconvolution scheme can be performed by first deriving an analytical form of the instrumental function (see Refs. 17–19 for more discussion). Here, the Airy function of the ideal Fabry-Perot interferometer is modified to include various defects in the instrument. Then, this analytical function is convoluted with the predicted scattering function (expression of Eq. (6) or Eq. (7) in our case). The resulting function is fit with the observed spectrum to determine the appropriate parameters (optical constants).

It is sometimes important to correct also for the broadening effect due to the finite size of the collecting pinhole on the spectrum. Indeed, the pinhole introduces a finite solid angle, collecting a range of q-wavevectors instead of the unique q defined in the above theoretical treatment. Experimentally, one has to compromise between reducing the pinhole size to avoid significant broadening and opening it to collect more signal [18].

In Table I we list η and κ for numerous materials which have been studied by Brillouin-scattering technique [20–36]. We should point out that only a few of these materials could yield linewidth information (Si, Ge, CdS, GaAs). Of particular interest is the ratio of the width of the lineshape to the

TABLE I

Index of Refraction and Extinction Coefficient of Numerous Materials

Material	η (5145 Å)	κ (5145 Å)	$\Delta\omega/\Omega = 2\kappa/\eta$	δ (cm)	Reference
CaF_2	1.43	$< 1 \times 10^{-7}$	$< 1.4 \times 10^{-7}$	> 41	[34, 35]
AlN	2.4	$< 1 \times 10^{-6}$	$< 1 \times 10^{-6}$	> 4.1	[36]
ZnO	2.05	$< 1 \times 10^{-6}$	$< 1 \times 10^{-6}$	> 4.1	[28]
GaP	3.55	1.2×10^{-3}	5.6×10^{-4}	3.41×10^{-3}	[23]
CdS†	2.7	4.1×10^{-3}	3.0×10^{-3}	1×10^{-3}	[20–22]
Si	4.21	0.06	0.028	6.82×10^{-5}	[1, 33]
GaAs	4.2	0.37	0.17	1.1×10^{-5}	[33]
TiN	1.2	1.6	2.66	2.56×10^{-6}	[32]
Ta	2.68	1.92	1.43	2.13×10^{-6}	[33]
Au	0.61	2.1	6.9	1.93×10^{-6}	[26, 29]
Ge	4.6	2.45	1.06	1.67×10^{-6}	[1, 33]
Cu	1.12	2.60	4.4	1.57×10^{-6}	[33]
Ni	1.7	3.1	3.77	1.33×10^{-6}	[25, 33]
Co	1.90	3.6	3.77	1.14×10^{-6}	[30]
Fe	2.8	3.7	2.64	1.11×10^{-6}	[33]
Mo	3.6	3.8	2.11	1.08×10^{-6}	[27]
Cr	2.75	4.46	3.24	9.2×10^{-7}	[33]
Al	0.84	6.2	14.7	6.6×10^{-7}	[24, 31, 33]

† Values for electric field polarization perpendicular to c-axis.

frequency shift. Assuming the lineshape to be Lorentzian, one can derive from Eq. (6)

$$\frac{\Delta\omega}{\Omega} = \frac{2\kappa}{\eta}, \tag{12}$$

where $\Delta\omega$ is the full width at half maximum of the line. Equation (12) can be expressed in terms of the absorption coefficient $\alpha_0 = 4\pi\kappa/\lambda_0$ or the skin depth $\delta = 1/\alpha_0$, yielding the following practical relation:

$$\frac{\Delta\omega}{\Omega} = \frac{2\kappa}{\eta} = \frac{\lambda_0}{2\pi\eta\delta}. \tag{13}$$

First, we emphasize that the relation in Eq. (12) is exact only when the lineshape is Lorentzian, a case applicable for low-absorbing materials such as Si. For highly absorbing systems such as Ge, the expression in Eq. (7) describes more accurately the measured lineshape, and Eq. (12) is just an approximation. We show in Fig. 3 the lineshape of the Brillouin lines of Si and Ge as measured by Sandercock [1]. Here we contrast the symmetric line observed for Si with the asymmetric line of Ge, a point already made by Dresselhaus and Pine [13].

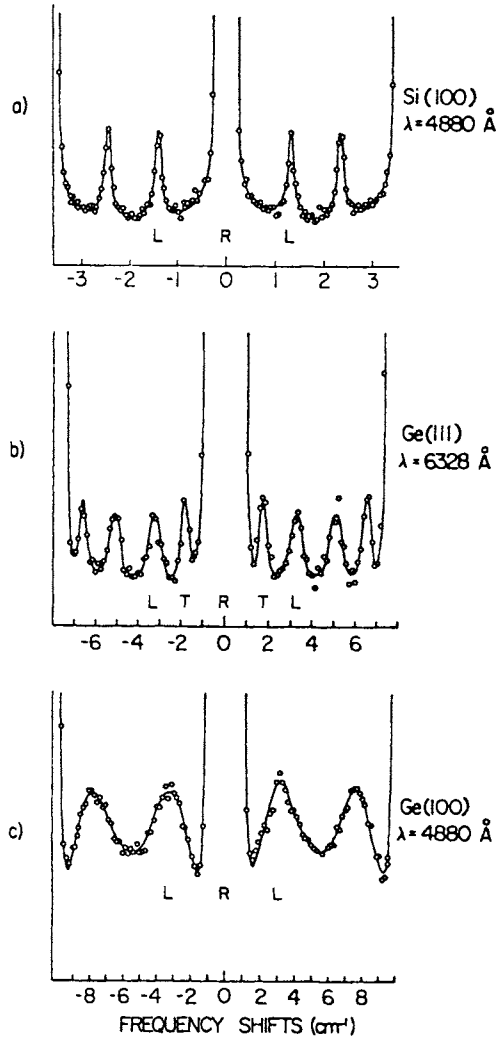

Fig. 3. Brillouin peaks of Si and Ge obtained by Sandercock [1].

Second, we note that the ratio, $\Delta\omega/\Omega$, can be obtained directly from the measured line. Sood and Cardona [16] measured the change in ratio $\Delta\omega/\Omega$ in Si as a function of concentration of a n-type dopant, which changes its absorption coefficient. We show in Fig. 4 their results. The determination of κ or η from the measured line requires previous knowledge of η or κ from another technique. If both η and κ are unknown, one needs the phonon velocity, v_s, which can be determined from ultrasonic measurements, for example. This approach was followed by Sandercock [1] in his analysis of his

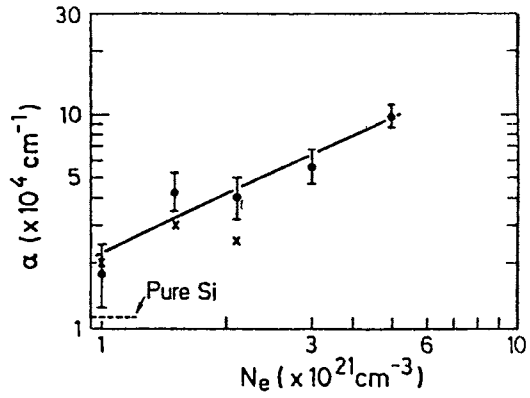

Fig. 4. Optical absorption coefficient of Si is shown as a function of concentration of dopant. The data were determined from the broadening of the measured Brillouin peaks. (From Sood and Cardona [16] with permission from the publisher.)

Si and Ge measurements. In this way, the Brillouin technique works as a complementary technique.

Third, Table I indicates further that the ratio in Eq. (12) becomes larger in highly absorbing materials such as metals. It may then be difficult to observe the peak, as its width can be larger than its frequency shift. Indeed, as κ is increased, the linewidth increases, extending the wings of the Brillouin peak to interfere with the next order of the Fabry-Perot lines. Another way, if the skin depth is of the order of the wavelength of the beam in the scattering medium ($\delta = \lambda_0/\eta$), Eq. 13 yields $\Delta\omega/\Omega \simeq 1/6$, showing a big broadening effect already. Since for metals, $\Delta\omega/\Omega \geq 2$, this is probably why bulk acoustic phonons have not been reported for metals. Practically speaking, materials with $0.01 < \Delta\omega/\Omega < 1$ show probably a measurable linewidth dependence on absorption.

VII BRILLOUIN SCATTERING IN THIN SLABS AND OPTICAL FIBERS

In the second part of this chapter, Brillouin scattering is considered in thin samples, such as thin slabs and single-mode optical fibers, where the dimension of the sample becomes of the same order as the light wavelength. Contrary to the bulk-sample case where both light and phonon energy and momentum are well defined, in thin samples, the light scattered over the thickness of the film develops an envelope of frequencies (and wavevectors), which, therefore, encompass more phonon energies and wavevectors. First, the formulas for calculating the refractive index in slabs are given for several convenient scattering geometries. Then, some examples of Brillouin spectra from the literature are considered, and the refractive index of the

samples is calculated using the given formulas. Finally, phonon propagation in thin slabs and single-mode fibers is discussed.

SPECIAL CASE OF TRANSPARENT THIN SLABS VIII

The refractive index η of a sample can be determined from the Brillouin shift Ω of an acoustic excitation or phonon from one of the two following relationships:

$$\Omega = \frac{4\pi v_s \eta}{\lambda_0} \sin\frac{\theta_s}{2}, \quad q = \frac{4\pi\eta}{\lambda_0} \sin\frac{\theta_s}{2}, \tag{14}$$

where v_s is the velocity of sound of the phonon generated by the light scattering, λ_0 is the wavelength of the incident light in vacuum, and θ_s is the scattering angle in the sample. The dispersion curve for acoustic phonons is given by $\Omega = \omega = qv_s$, where ω is often used, and q is the phonon wavevector. The Brillouin scattering in thin samples can be done by using side illumination [37–40] or edge illumination [40].

Side Illumination (90° External Scattering) A

Most Brillouin spectra in thin samples have been measured by using the side illumination, which is shown schematically in Fig. 5. In this figure, light is incident from the side of the sample (which has 1.458 refractive index, as that of silica), and the scattered light is observed at 90°. The internal scattered angle is not 90°. As can be seen from Fig. 5 (where the notation of Wang *et al.* [37] has been used), two different phonons are generated (created or destroyed depending on whether it is Stokes or anti-Stokes) with the refracted and reflected beams to produce the scattered light inside the sample. Note that for a typical material with $\eta = 1.5$, at a reflection most of the light is refracted out of the slab; only ~4% is reflected for modest angles of incidence. As shown in Fig. 5, in the first case, the phonon has q_1 wavevector, and the scattering angle is θ_1; while in the second case, the phonon has q_2 wavevector, and the scattering angle is θ_2. The two scattering angles can be determined from the following equations:

$$\theta_1 = \beta + \gamma, \quad \theta_2 = \pi - \beta + \gamma, \tag{15}$$

where β and γ are related to the refractive index η:

$$\eta\sin\beta = \sin\alpha, \quad \eta\sin\gamma = \cos\alpha, \tag{16}$$

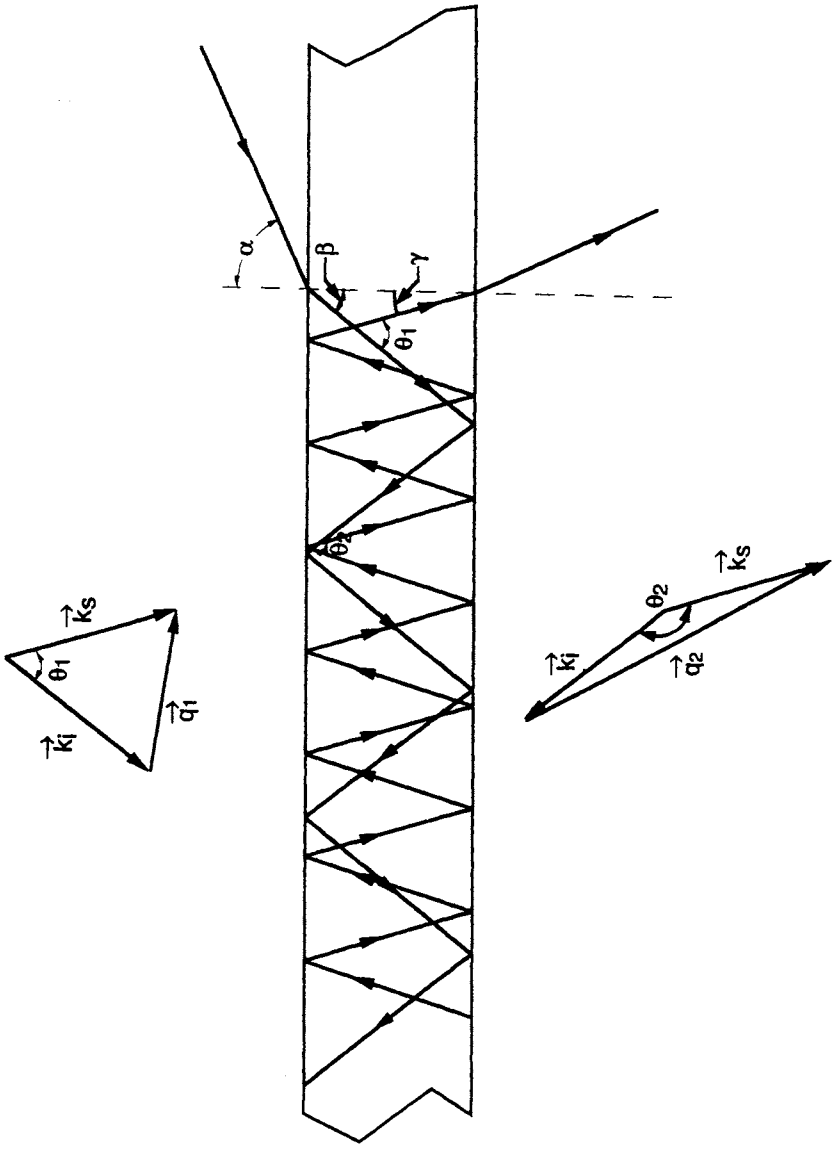

Fig. 5. Side illumination with 90° external scattering.

where α is the incident angle (not to be confused with the absorption coefficient, α_0) and β is the refraction angle (not to be confused with the phase coefficient, β_0). In the second Eq. (16), $\cos\alpha = \sin\alpha'$, since a 90° scattering is considered. Here, α' is the angle formed by the external scattered light and the normal to the sample surface. Note that in Fig. 5 the q_2 phonon is involved with near-backscattering internally.

Using the above equations, it can be shown that the phonon velocity v_s [Eq. (14)] can be expressed in terms of η and the incident angle α as follows [37]:

$$v_{s,1} = \frac{\Omega_1 \lambda_i}{[2\eta^2 + \sin 2\alpha - 2(\eta^4 - \eta^2 + \tfrac{1}{4}\sin^2 2\alpha)^{1/2}]^{1/2}}, \tag{17}$$

$$v_{s,2} = \frac{\Omega_2 \lambda_i}{[2\eta^2 + \sin 2\alpha + 2(\eta^4 - \eta^2 + \tfrac{1}{4}\sin^2 2\alpha)^{1/2}]^{1/2}}, \tag{18}$$

where Ω_1 and Ω_2 are the Brillouin shifts corresponding to the phonons with q_1 and q_2 wavevectors, respectively. For many transparent materials, one usually knows η in advance, so the phonon velocity is determined. For a cubic crystal oriented so that the principal axes are along the slab edges, these phonons will, in general, have different velocities. For an isotropic sample ($v_{s,1} = v_{s,2}$), from the above Eqs. (17) and (18), the following equation is obtained

$$\frac{{\Omega_1}^2}{{\Omega_2}^2} = \frac{2\eta^2 + \sin 2\alpha - 2(\eta^4 - \eta^2 + \tfrac{1}{4}\sin^2 2\alpha)^{1/2}}{2\eta^2 + \sin 2\alpha + 2(\eta^4 - \eta^2 + \tfrac{1}{4}\sin^2 2\alpha)^{1/2}}. \tag{19}$$

Fused silica can serve as an example of an isotropic sample. From this equation the refractive index η can be found from the Brillouin shifts Ω_1 and Ω_2 for any incident angle α.

45°–45° Scattering When the incident angle α is 45°, Eq. (19) has a very simple form. This geometry, in which the sample bisects the incident and the scattered light (45°–45°), has been used extensively in the literature to obtain the refractive index of thin samples and films [37–40]. In this case, $\beta = \gamma$ and $\alpha = 45°$ (see Fig. 5). The q_2 phonon is involved in internal backscattering. Then, from Eqs. (14), (15), and (16) one obtains:

$$v_{s,1} = \frac{\Omega_1 \lambda_i}{\sqrt{2}}, \tag{20}$$

$$v_{s,2} = \frac{\Omega_2 \lambda_i}{2\eta}. \tag{21}$$

Therefore, for an isotropic sample the refractive index η can be obtained from the following equation:

$$\eta = \frac{1}{\sqrt{2}} \frac{\Omega_2}{\Omega_1}. \tag{22}$$

B Edge Illumination (90° External Scattering)

This geometry, in which light is incident at the edge of the sample, has been discussed extensively by Takagi and Gammon [40], and it is shown schematically in Fig. 6. Our notation continues to be that found by Wang *et al.* [37]. One of the positive characteristics of this geometry is that the intensity of the phonon peaks is much stronger than that with the side illumination [40]. This is probably due to the larger volume per reflection implied by Fig. 6 compared to Fig. 5. Similarly to the side-illumination case, as can be seen from Fig. 6, two different phonons are involved in the scattering of the refracted and the reflected beams inside the sample. In the first case, the phonon has q_1 wavevector, and the scattering angle (inside the sample) is θ^*_1, while in the second case the phonon has q_2 wavevector, and the scattering angle is θ^*_2. The two scattering angles can be determined by the following equations:

$$\theta^*_1 = \pi - \beta - \gamma, \quad \theta^*_2 = \pi - \beta + \gamma, \tag{23}$$

where β and γ are related to the refractive index η through Eq. (16). Note that in Fig. 6, the q_2 phonon is involved with internal near-backscattering. Using Eqs. (14), (16), and (23) one obtains:

$$\nu^*_{s,1} = \frac{\Omega^*_1 \lambda_i}{[2\eta^2 - \sin 2\alpha + 2(\eta^4 - \eta^2 + \frac{1}{4}\sin^2 2\alpha)^{1/2}]^{1/2}}, \tag{24}$$

$$\nu^*_{s,2} = \frac{\Omega^*_2 \lambda_i}{[2\eta^2 + \sin 2\alpha + 2(\eta^4 - \eta^2 + \frac{1}{4}\sin^2 2\alpha)^{1/2}]^{1/2}}. \tag{25}$$

Note that Eqs. (18) and (25) are the same. From Eqs. (24) and (25) for an isotropic sample, we obtain the following equation:

$$\frac{\Omega^{*2}_1}{\Omega^{*2}_2} = \frac{2\eta^2 - \sin 2\alpha + 2(\eta^4 - \eta^2 + \frac{1}{4}\sin^2 2\alpha)^{1/2}}{2\eta^2 + \sin 2\alpha + 2(\eta^4 - \eta^2 + \frac{1}{4}\sin^2 2\alpha)^{1/2}}. \tag{26}$$

From this equation, the refractive index η can be found from the Brillouin shifts Ω^*_1 and Ω^*_2 for any incident angle α.

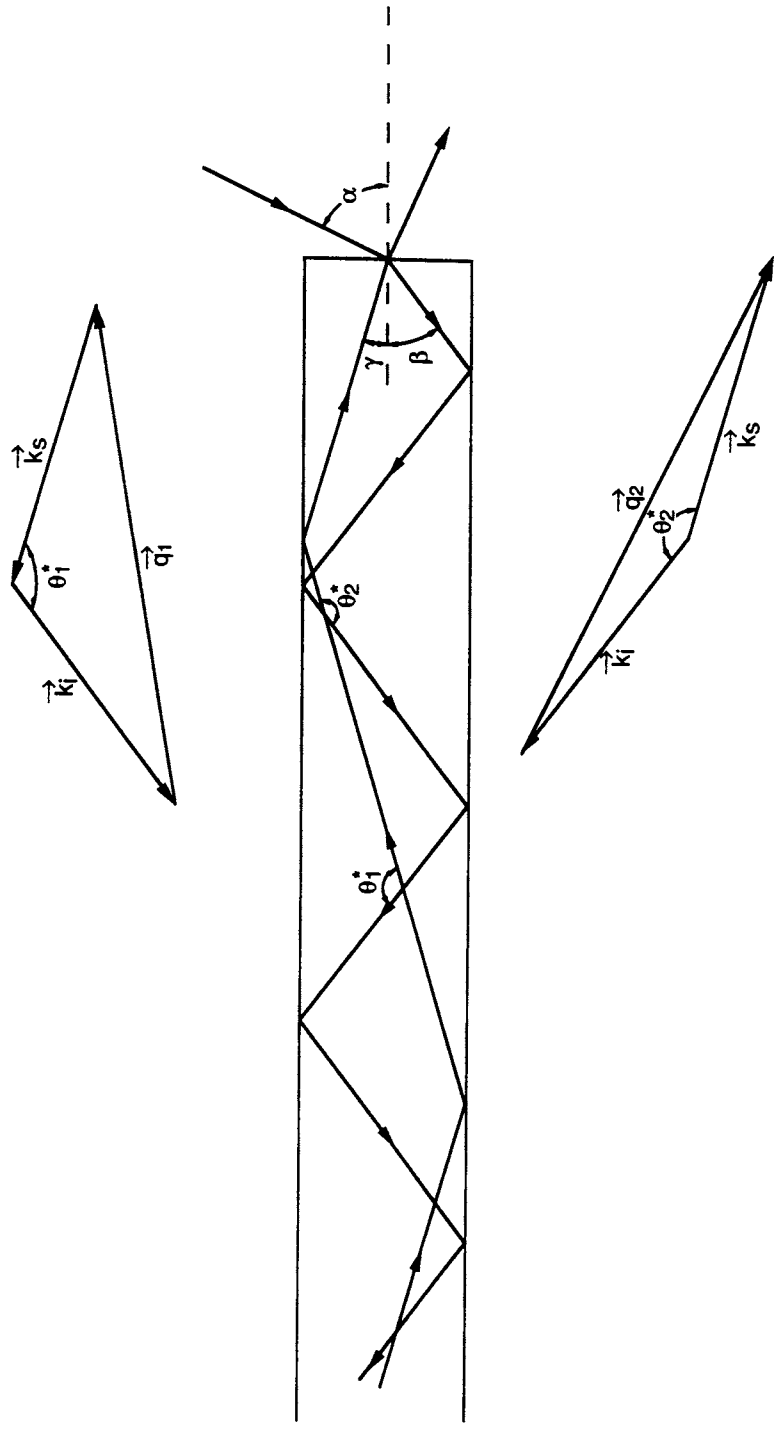

Fig. 6. Edge illumination with 90° external scattering.

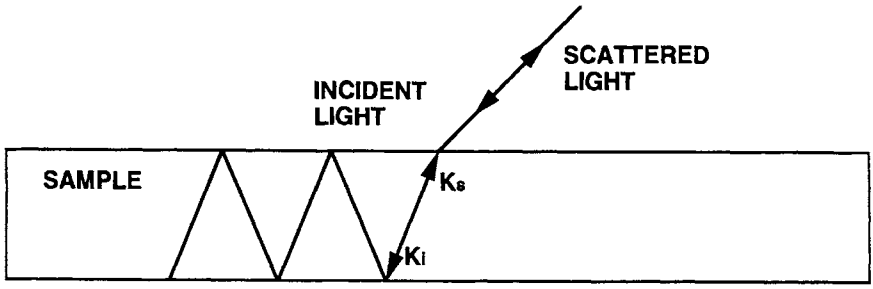

Fig. 7. Side illumination with 180° external backscattering.

45°–45° Scattering In this geometry we have $\beta = \gamma$ and $\alpha = 45°$. The q_2 phonon is involved exactly in backscattering internally. Then, from Eqs. (14), (16), and (23) one obtains:

$$v_{s,1} = \frac{\Omega^*{}_1 \lambda_i}{\sqrt{2}(2\eta^2 - 1)^{1/2}}, \tag{27}$$

$$v_{s,2} = \frac{\Omega^*{}_2 \lambda_i}{2\eta}. \tag{28}$$

Note that Eqs. (21) and (28) are the same. Therefore, the refractive index of an isotropic sample can be found from the following equation:

$$\eta = \frac{1}{\sqrt{2}[1 - \Omega^{*2}{}_1/\Omega^{*2}{}_2]^{1/2}}. \tag{29}$$

C Special Geometries

1 *External Backscattering*

Two examples of external backscattering (rather than 90° external scattering) are shown in Figs. 7 and 8, where backscattering is done from the side and the edge of the thin slab. For external backscattering for both side and edge illumination, the same phonon with wavevector q_2 is observed as described by Eqs. (18) and (25) or for the 45°–45° position, by Eqs. (21) and (28). Note that since only one q_2 phonon is observed (and q_2 is along k_s), Eqs. (17) and (24) are not pertinent. These results hold for an isotropic material or for a cubic material with the principal crystal axes along the edges of the thin slab. For an isotropic sample it can be shown from selection-rule analysis that for the backscattering geometry (180°), only the longitudinal phonon will be present, while no transverse phonon can be seen [41].

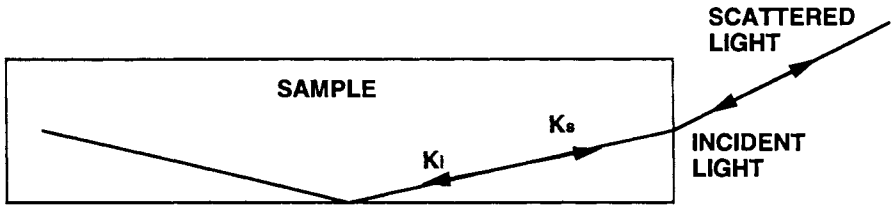

Fig. 8. Edge illumination with 180° external backscattering.

Classical 90° Scattering 2

For the traditional 90° scattering from a bulk sample shown in Fig. 9, $\theta_s = 90°$ in Eq. (14) and, thus:

$$v_s = \frac{\Omega\lambda_i}{\sqrt{2}\eta}. \tag{30}$$

Note that the phonon propagates at 45° to the plate edge. Contrary to the backscattering case, in the 90° scattering both the longitudinal phonon and the transverse phonons (only one transverse phonon for an isotropic sample) will be present.

Examples D

Here, some Brillouin spectra from thin plates and films are used from the literature to calculate their refractive index.

Isotropic Samples 1

Glass Plate The Brillouin spectra of a thin glass plate (150 μm thick) for the 45°–45° geometry for the side and edge illumination, is shown in

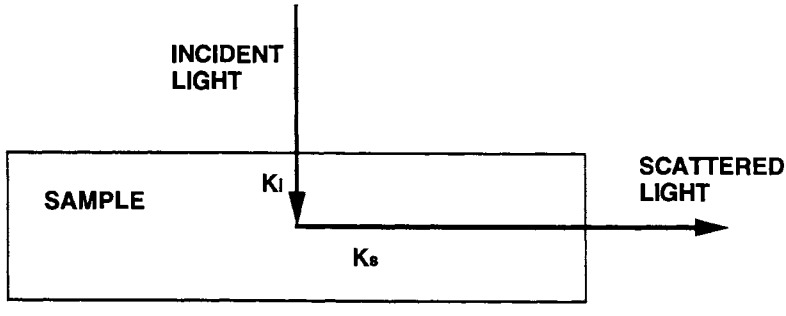

Fig. 9. Classical 90° scattering.

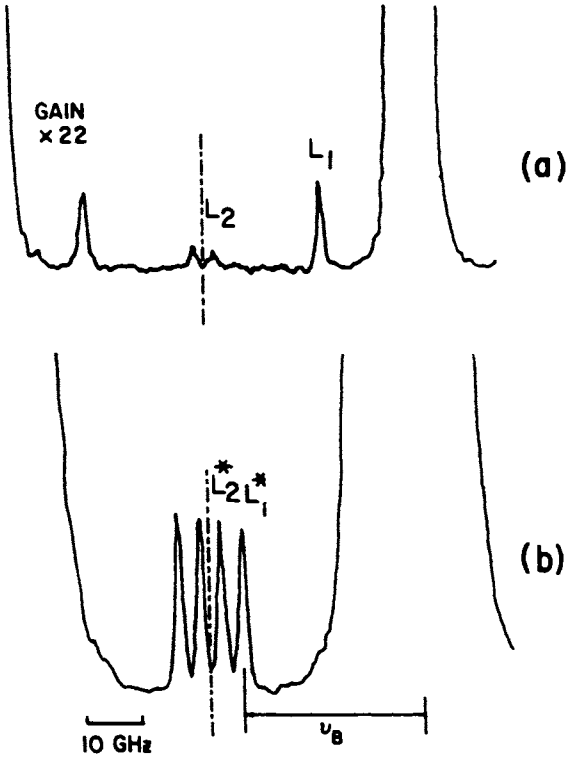

Fig. 10. Typical Brillouin spectra of thin glass plate (150 μm thick). $FSR = 77$; $\alpha = 45°$. (a) Side illumination; (b) Edge illumination. (After Takagi and Gammon [40].)

Fig. 10 [40]. The spectra were obtained using the VV scattering geometry, where only the longitudinal phonons can be seen for an isotropic sample.

In Fig. 10(a) the side illumination was used to obtain the ratio of the Brillouin shifts of the two longitudinal phonons L_1 and L_2 (with q_1 and q_2 wavevectors in Figs. 5 and 6). Then, using this ratio from Eq. (22), the refractive index of the isotropic thin glass plate is calculated to be 1.52.

In Fig. 10(b) the edge illumination was used to obtain the ratio of the Brillouin shifts of the two longitudinal phonons L^*_1 and L^*_2. Using this ratio, from Eq. (29) the refractive index of the thin glass plate is calculated to be 1.51, which is close to the 1.52 obtained from the side illumination. While this type of glass was not described, the fused-silica refractive index is 1.458, which is close to that obtained above.

Polymer Film: Mylar-PET The Brillouin spectra obtained from a polymer film, Mylar-PET, which is a commercial film used as a transparency sheet for overhead projectors can be seen elsewhere [40]. In this case, the side illumination and the 45°–45° scattering geometry were used to obtain

the Brillouin spectra shown in Fig. 11. From the ratio of the Brillouin shifts of the two longitudinal phonons L_1 and L_2, the refractive index of the isotropic Mylar-PET film is found from Eq. (22) to be 1.28. Most plastics have refractive indexes in the range 1.42–1.65, so this value appears too low [42, 43].

DNA Films The refractive index and the sound speed of DNA films has been studied using backscattering and 45°–45° geometry [39]. It was found that the refractive index decreases as the relative humidity of the DNA films increases (for dry DNA, $\eta = 1.50$).

Uniaxially Stretched Films 2

For nonisotropic films, the formulas given above for determining the refractive index are not expected to hold.

PET Film Brillouin scattering has been used in polyethylene terephalate (PET) films to study the sound velocity and the elastic constants as a function of the film stretching ratio [38]. The refractive index of the unoriented PET film is 1.588 at 4880 Å, which is within the range of plastics [42, 43]. It was found that, even though the refractive index of the film is not sensitive to stretching, the elastic constants strongly depend on the stretching ratio of the uniaxially stretched film [38]. The refractive index of the uniaxially stretched PET was found from the Brillouin spectra (side excitation; 45°–45° geometry) [38] using Eq. (22) to be 1.06, a value too low for plastics [42, 43]. This discrepancy is due probably to the fact that Eq. (22) holds only for isotropic samples.

Polyvinylidene Fluoride (PVF_2) Films Brillouin scattering was also used to study the sound velocity and the elastic constants of uniaxially stretched PVF_2 films [37]. Similar to the PET case, while the refractive index is not

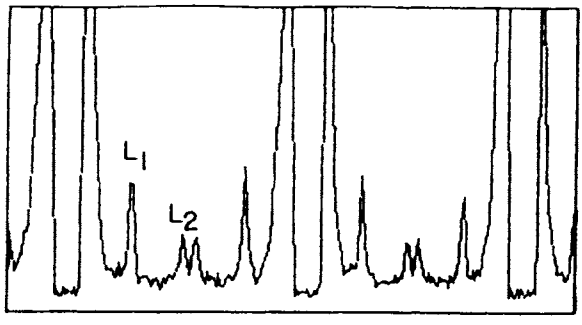

Fig. 11. Brillouin spectra of polymer film Mylar-PET with side illumination. *FSR* = 40 GHz. (After Takagi and Gammon [40].)

sensitive to stretching ($\eta = 1.43$), the sound velocity and the elastic constants are sensitive to the stretching ratio. From the Brillouin spectra (side illumination; 45°–45° geometry) seen elsewhere [37], it was found (using Eq. (22)) that the refractive index of the PVF_2 in the form I is 1.05, while in the form II it is 1.02, values too low for plastics. As in the previous case, this discrepancy is due probably to the fact that the film is not isotropic.

E Side Illumination at Normal Incidence

Brillouin scattering has been used to study phonon propagation in thin films. Following Sandercock [44], for the case of backscattering (180°) perpendicular to the film surface, we have the following distinct regimes.

a. With a real refractive index η, for a semi-infinite thick film, the Brillouin spectrum is typical with the normal Brillouin shift $\Omega = 2\eta k_0 v_s$, as illustrated in Fig. 12(a), where some instrumental and phonon-lifetime broadening of the peaks has been assumed.

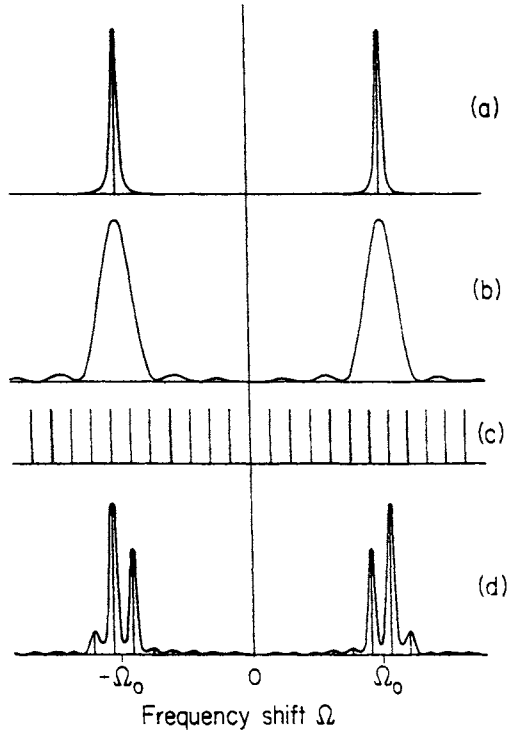

Fig. 12. (a) A normal Brillouin spectrum, (b) the expected spectrum from a thin supported film, (c) the possible frequency shifts in the spectrum from a thin unsupported film, and (d) the observable spectrum from a thin unsupported film. (After Sandercock [44].)

b. With a real η, there is a special case of a film supported on a substrate with the special properties that the substrate has the same acoustic impedance (so phonons can propagate across the boundary freely), but the substrate has very different elasto-optic properties, so that scattering occurring in the film is distinguishable from scattering in the substrate. Such a film/substrate sample probably does not exist, so the spectrum in Fig. 12(b) is not observable. Since film and substrate have the same acoustic properties, all values of q perpendicular to the surface are allowed. However, the Brillouin peaks are broadened due to the finite summation of the scattered electric fields as the incident beam traverses the film. The line shape is given by a $\sin^2 x/x^2$, as shown schematically in Fig. 12(b). Here, $x = (\Omega_0 - \Omega)d/2v_s$, where d is the film thickness, Ω_0 is the Brillouin shift corresponding to the phonon frequency, and Ω is the variable frequency.
c. If further, the film is unsupported, the boundary conditions require that the component of the phonon wavevector perpendicular to the surface be an integral multiple of π/d. In this case, the Brillouin spectrum would have peaks at the frequency shifts $\Omega = qv_s = p\pi v_s/d$ (p is an integer), as shown in Fig. 8(c).
d. Moreover, these phonon lines have a relative amplitude determined by the $\sin^2 x/x^2$ envelope (Fig. 8(b)). Thus, the resulting Brillouin spectrum will be similar to that shown in Fig. 12(d), where again, some instrumental and lifetime broadening has been assumed. The exact form of the peaks of Fig. 12(d) depends on the thickness d, but in general they show triplet or quadruplet structure within the main peak of the $\sin^2 x/x^2$ envelope. With reference to the dispersion curve shown schematically in Fig. 13, the quantized acoustic-phonon modes would be along the q-axis, while the measured phonon frequencies would occur along the ω-axis. Furthermore, the observed modes would be attenuated severely.
e. With a complex index of refraction n, a near-Lorentzian broadening of the Brillouin peaks occurs, as has been discussed in Section IVB. Therefore, the Brillouin components in Fig. 12(d) should be broadened.

From the above discussion the main conclusion is that while normal Brillouin scattering (from a large volume) determines precisely both the energy (from the spectrum) and the momentum (from the scattering geometry) of the phonon involved, the backscattering from a thin film normal to the surface measures phonons within a range of momenta and correspondingly, having a range of energies.

The predicted triplet in the Brillouin spectrum of a thin unsupported film (Fig. 12(d)) has been observed experimentally in Mn_2PS_4 films [44]. Figure 14 shows the observed Brillouin spectrum from two specimens of Mn_2PS_4 of thickness 1.1 and 2.0 μm. In both these spectra the triplets are clear; as the thickness of the film increases, however, the secondary peaks of the triplet get much weaker (Fig. 14(b)).

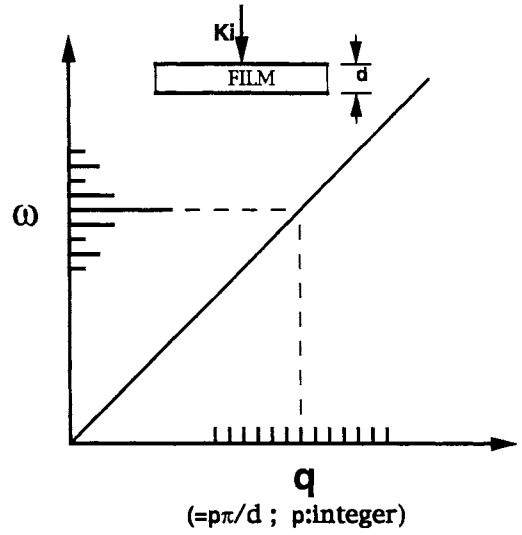

Fig. 13. Frequency vs. wavevector for acoustic phonons propagating perpendicular to the surface of a thin unsupported film. While the incident light energy and wavevector are well defined, the light backscattered over the thickness of the film contains an envelope of frequencies which contain several of the phonons, thus giving the multiple structure.

IX BRILLOUIN SCATTERING IN OPTICAL FIBERS

Brillouin scattering has also been used to study phonon propagation in optical fibers. Most of the work has been done with single-mode fibers in the core of which only one optical mode (photon) propagates. The core is surrounded by the cladding (clad) which has a slightly lower refractive index than that of the core, so that light can propagate in the core in a total-internal-reflection mode. In the simplest case of the backscattering geometry, which we consider here and in which only the longitudinal phonon is present, both the phonon and the photon are propagating almost along the fiber axis. Similar to the thin-film case, phonon propagation in single-mode fibers is expected to be strongly affected by the boundary conditions at the core-clad interface, since light is confined to propagate in the fiber core, which has a diameter (few microns) of the same order as the propagating light wavelength. Indeed, it has been found that [45]: the normal acoustic modes are linear combinations of transverse and longitudinal phonons in both the core and the clad, and the relative field amplitudes are dependent on the boundary conditions at both surfaces. Second, the density of phonon states is not uniform in q and ω space. Finally, the wavevector is not conserved in this acousto-optic interaction for a direction normal to the surface, i.e., the radial direction, and scattering is allowed over a continuum of phonons.

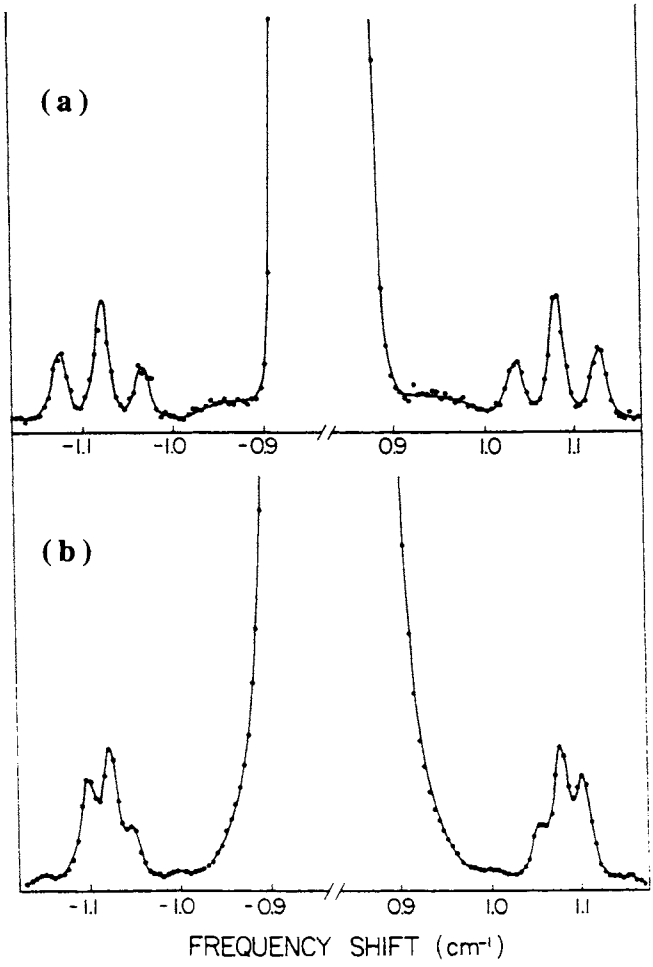

Fig. 14. Observed spectra from (a) and (b) two specimens of Mn_2PS_4 of thickness 1.1 and 2.0 μm, respectively. After Sandercock [44].

Even with the added complexities of a cylinder compared with a flat plate, some comparison can be made with the results for plates given in Eqs. (14–28).

Examples A

Brillouin scattering in optical fibers has been done using 180° and 90° geometry, which are shown schematically in Fig. 15.

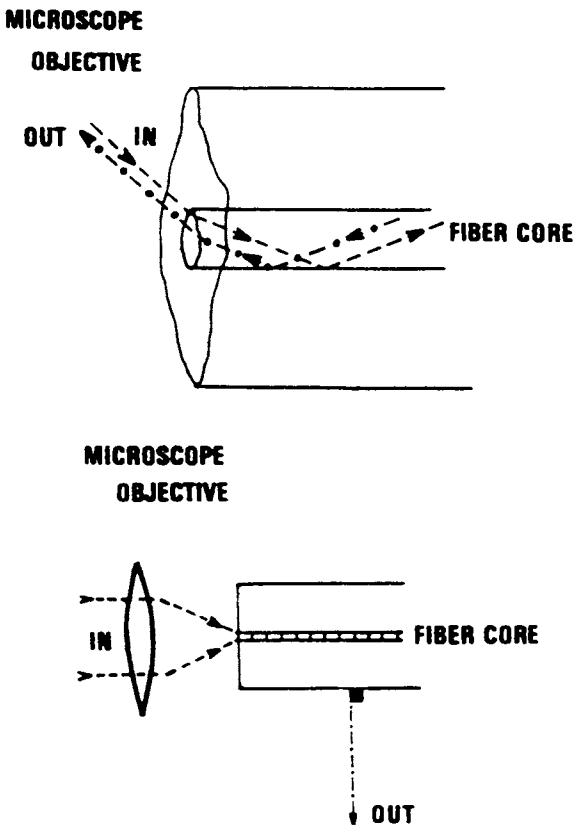

Fig. 15. Schematic of Brillouin scattering in an optical fiber (a) 180° scattering; (b) 90° scattering. After Thomas *et al.* [45].

1 *180° Scattering*

Using the Brillouin backscattering shown in Fig. 15, in which only the longitudinal phonon can be seen, phonon propagation has been studied in single-mode fibers (3 μm core diameter), which is shown in Fig. 16 [45]. In this figure we can see the longitudinal phonons propagating in the core only and in the core-clad space. In Thomas *et al.* [45] the refractive indexes of the core and the clad are given to be 1.462 and 1.457, respectively. From the spectrum of Fig. 16 and the refractive indexes, the sound velocities were calculated using Eq. (28) (backscattering phonon):

$$v_c = 6.026 \times 10^5 \quad \text{cm/sec}, \quad v_{cl} = 5.160 \times 10^5 \quad \text{cm/sec}. \tag{31}$$

Using Eq. (28), which has been derived for thin slabs, is an approximation for the cylindrical fibers, and it probably holds only for the optical rays passing through the fiber axis. These rays propagate in planes containing the

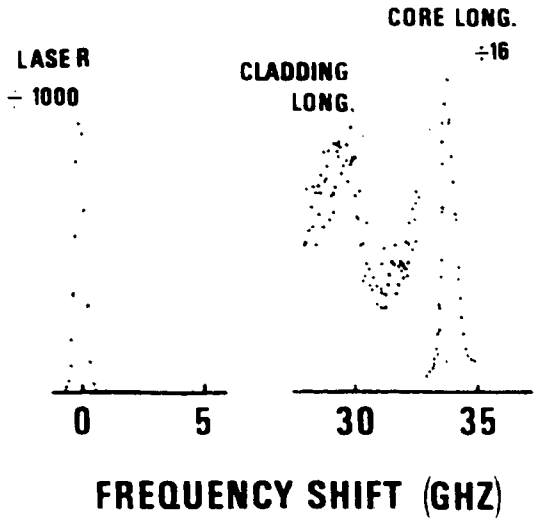

Fig. 16. Experimental Brillouin spectrum from a single optical fiber (180° scattering geometry). (After Thomas *et al.* [45].)

fiber axis. For the skew rays which do not pass through the fiber axis, the above equations would not hold; however, the skew modes attenuate fast in a fiber, and in the steady state of propagation only the rays passing through the center are present.

Even though the exact composition of the fiber was not given, as it can be seen below, the velocities listed in Eq. (31) correspond to standard fibers. In this example, the refractive indexes were given, and the sound velocities were found. However, the opposite is also true: Given the sound velocity, the refractive index can be found using the formula of Eq. (25) or (28).

90° Scattering 2

Single-Mode Fiber Using the 90° scattering shown in Fig. 15, the Brillouin spectrum was obtained in the fiber which was also used in Fig. 16, which is shown schematically in Fig. 17. This spectrum contains both the longitudinal phonons of the core and the clad and the transverse phonon of the core. For the Brillouin shift of the longitudinal core phonon (23.9 GHz), using Eq. (30), it is found that $\eta = 1.463$, a value very close to 1.462 found from the backscattering experiment of Fig. 16.

Single-Mode Fiber Preforms The elastic and elasto-optic (Pockels) coefficients of single-mode fibers have been studied doing Brillouin scattering

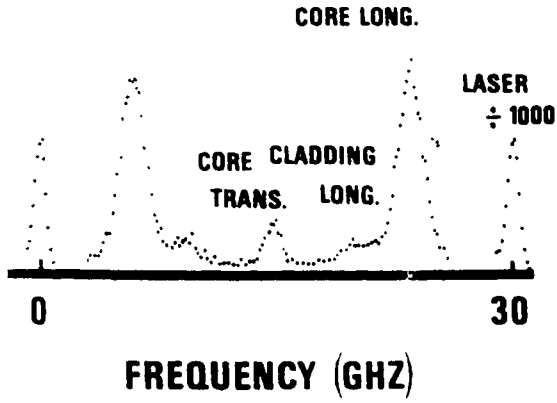

Fig. 17. Experimental Brillouin scattering from an optical fiber (classical 90° scattering geometry). (After Thomas *et al.* [45].)

(90°) on the glass preforms from which the fibers were drawn [46]. The preforms were cylinders 5 cm long and 7 mm in diameter with optically polished end faces. Two different fiber preforms were studied, one with numerical aperture $NA = 0.1$ composed of a fused-silica core with traces of GeO_2, and a clad of 5% B_2O_3 + 95% SiO_2 and another with $NA = 0.15$ composed of a 3% GeO_2 + 97% SiO_2 core, and a 15% B_2O_3 + 85% SiO_2 clad. The longitudinal (L) and the transverse (T) phonons were studied from the (V,V) and the (V,H) Brillouin spectra, respectively. The sound velocities of the phonons were calculated from Eq. (30), where the refractive index had been obtained using the prism method. From the two sound speeds, for an isotropic sample the elastic moduli, i.e., Young's modulus Y and Poisson's ratio σ, can be calculated using the following formulas:

$$Y = \rho v_T^2 \frac{(3v_L^2 - 4v_T^2)}{v_L^2 - v_T^2}, \quad \sigma = \frac{v_L^2 - 2v_T^2}{2(v_L^2 - v_T^2)}, \tag{32}$$

where ρ is the glass density.

The Pockels coefficients were also found by comparing the Brillouin spectra of the preforms to that of a fused-silica preform, whose Pockels coefficients are known, using the following formula for the L phonon [6]:

$$I = \frac{K\eta^8 P_{12}^2}{\rho v_s^2}, \tag{33}$$

where K is a geometrical and temperature factor, and P_{12} is the Pockels coefficient. Keeping the scattering geometry of the fused silica and the preforms identical, the K factor was eliminated by dividing the intensities of the spectra of the fused silica by those of the preforms [46]. This demonstrates the power of the Brillouin-scattering spectra from which, not only all the elastic moduli can be determined at once, but also the (very difficult to

measure) Pockels coefficients can by obtained. It should be also noticed from Eq. (33) that the intensity of the Brillouin spectra has the very strong dependence on the 8th power of the refractive index η.

The results of these experiments on the two fiber preforms for the coefficients of the longitudinal phonon for the core and the clad are listed below: Fiber $NA = 0.1$:

$$\eta_c = 1.4580, \quad \eta_{cl} = 1.4546, \quad v_{c,L} = 5.944 \times 10^5 \text{ cm/sec}, \quad v_{cl,L} = 5.605 \times 10^5 \text{ cm/sec}. \tag{34}$$

Fiber $NA = 0.15$:

$$\eta_c = 1.4624, \quad \eta_{cl} = 1.4547, \quad v_{c,L} = 5.806 \times 10^5 \text{ cm/sec}, \quad v_{cl,L} = 5.164 \times 10^5 \text{ cm/sec}. \tag{35}$$

A close comparison of the sound velocities in Eq. (31) to those in Eqs. (34) and (35) identifies the composition of the fiber used in the 180° scattering to be close to that of the 0.15 *NA*. Also the refractive indexes of these two glasses are very close ($\eta_c = 1.462$ vs. 1.4624, $\eta_{cl} = 1.457$ vs. 1.4547).

Edge Illumination (90° External Scattering) 3

Pyrex Glass The edge illumination (90° external scattering) has been used [40] to obtain the Brillouin spectrum of the longitudinal phonon of a 600 μm diameter glass rod (Pyrex), which is shown in Fig. 18(a). The incidence angle was ~45° for the 45°–45° geometry [47]. If the slab model holds for the cylinder, which seems to be the case in the examples above, two phonons should be observed in the cylinder. If $\Omega_1{}^{*2}/\Omega_2{}^{*2} = 0.844$ is obtained from Fig. 18(a), $\eta = 1.8$ is calculated from Eq. (29), while for Pyrex $\eta = 1.471$ [48]. The correct value for the refractive index of Pyrex can be found from Eq. (26) with $\alpha = 20°$ or 69° for the angle of incidence. Only with these incidence angles for a 90° external scattering, can the peaks shown in Fig. 18(a) correspond to $L_1{}^*$ and $L_2{}^*$ phonons discussed in Section VIII.B, as has been assumed by Takagi and Gammon [40].

Optical Fibers The Brillouin spectra of a multimode and a single-mode fiber are also given and are shown in Figs. 18(b) and 18(c), respectively [40]. For the multimode fiber, $\Omega_1{}^{*2}/\Omega_2{}^{*2} = 0.855$ (Fig. 18(b)), which gives $\eta = 1.8$ for the 45°–45° geometry; this is too large for an optical fiber, which is probably a high-silica glass. Conversely, Eq. (26) gives $\alpha = 17°$ or 72° (with $\eta = 1.458$ for silica), which is not in agreement with experiment.

For the single-mode fiber, $\Omega_1{}^{*2}/\Omega_2{}^{*2} = 0.849$ (Fig. 18(c)), which gives $\eta = 1.8$ for the 45°–45° geometry; again, this is too large for an optical fi-

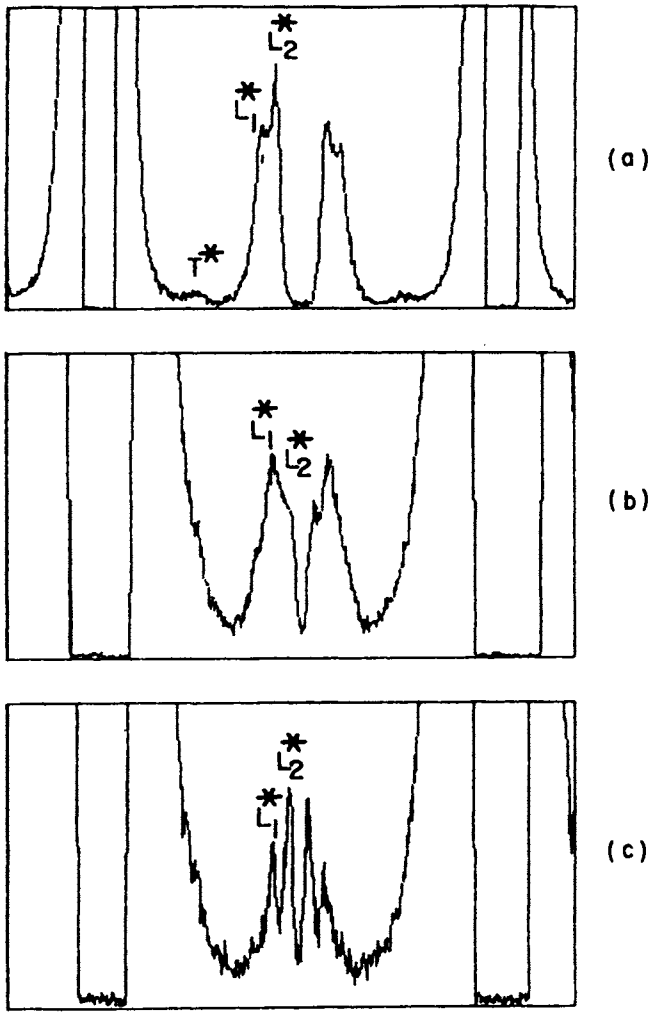

Fig. 18. Brillouin spectra with edge illumination at $FSR = 77$ GHz; (a) glass rod (600 μm), (b) multimode optical fiber, and (c) single-mode optical fiber. After Takagi and Gammon [40].

ber. Conversely, Eq. (26) gives $\alpha = 19°$ or $71°$, which is not in agreement with experiment.

However, for the case of the fibers another possibility is that the two longitudinal phonons correspond to the core and the clad phonons, similar to the ones observed in Figs. 16 and 17, and not to the L_1* and L_2* phonons, as were assigned by Tagaki and Gammon [40].

REFERENCES

1. J. R. Sandercock, *Phys. Rev. Lett.* **28**, 237 (1972).
2. B. Chu, "Laser Light Scattering." Academic Press, New York, 1974.
3. B. Berne and R. Pecora, "Dynamic Light Scattering." Wiley, New York, 1976.
4. G. B. Benedek and K. Fritsch, *Phys. Rev.* **149**, 647 (1966).
5. A. Griffin, *Rev. Mod. Phys.* **40**, 167 (1968).
6. M. Born and K. Huang, "Dynamic Theory of Crystal Lattices." Oxford Univ. Press (Clarendon) Oxford, 1954.
7. A. S. Borovik-Romanov and N. W. Kreines, *Phys. Rep.* **81**, 351 (1982).
8. N. L. Rowell and G. I. Stegeman, *Phys. Rev. B* **18**, 2598 (1978).
9. J. M. Vaughan, "The Fabry-Perot Interferometer." Hilger, London, 1989.
10. G. Hernandez, "Fabry-Perot Interferometers." Cambridge Univ. Press, Cambridge, 1986.
11. N. W. Ashcroft and N. D. Mermin, "Solid State Physics." Sanders College, Philadelphia, 1976.
12. R. Loudon, *J. Phys. C: Solid State Phys.* **11**, 403 1978.
13. G. Dresselhaus and A. S. Pine, *Solid State Commun.* **16**, 1001 (1975).
14. M. Born and E. Wolf, "Principles of Optics," Chap. 7, p. 328. Pergamon, London, 1959.
15. C. S. Zha, R. J. Hemsley, H. K. Mao, T. S. Duffy, and C. Meade, *Phys. Rev. B* **50**, 13105 (1994).
16. A. K. Sood and M. Cardona, *Solid State Commun.* **49**, 299 (1984).
17. E. D. Palik, H. Boukari, and R. W. Gammon, *Appl. Opt.* **34**, 58 (1995).
18. H. Boukari, E. D. Palik, and R. W. Gammon, *Appl. Opt.* **34**, 69 (1995).
19. E. D. Palik, H. Boukari, and R. W. Gammon, *Appl. Opt.* **35**, 48 (1996).
20. A. S. Pine, "Light Scattering in Solids: Topics in Applied Physics," (M. Cardona, ed.), Vol. 28, Chap. 6. Springer-Verlag, Berlin, 1975.
21. A. S. Pine, *Phys. Rev. B* **5**, 2997 (1972).
22. A. S. Pine, *Phys. Rev. B* **5**, 3003 (1972).
23. J. Zuk, H. Kiefte, and M. J. Clouter, *J. Appl. Phys.* **72**, 3504 (1992).
24. R. Bhadra, M. Grimsditch, I. K. Schuller, and F. Nizzoli, *Phys. Rev. B* **39**, 12456 (1989).
25. R. Jorna, D. Visser, V. Bortolani, and F. Nizzoli, *J. Appl. Phys.* **65**, 718 (1989).
26. B. Hillebrands, P. Baumgart, R. Mock, G. Güntherodt, and P. S. Bechthold, *J. Appl. Phys.* **58**, 3167 (1985).
27. J. A. Bell, W. R. Bennett, R. Zanoni, G. I. Stegeman, C. M. Falco, and F. Nizzoli, *Phys. Rev. B* **35**, 4127 (1987).
28. G. Carlotti, D. Fioretto, L. Palmieri, G. Socino, L. Verdini, and E. Verona, IEEE ultrasonic symposium, p. 1201, (1989).
29. M. Grimsditch, R. Bhadra, and I. K. Schuller, *Phys. Rev. Lett.* **58**, 1216 (1987).
30. S. Subramanian, R. Sooryankumar, G. A. Prinz, B. T. Jonker, and Y. U. Idzerda, *Phys. Rev. B* **49**, 17319 (1994).
31. F. Nizzoli, R. Bhadra, O. F. de Lima, M. B. Brodsky, and M. Grimsditch, *Phys. Rev. B* **37**, 1007 (1988).
32. M. Elena, M. Bonelli, C. E. Bottani, G. Ghislotti, A. Miotello, P. Mutti, and P. M. Ossi, *Thin Solid Films* **236**, 209 (1993).
33. J. R. Sandercock, *Solid State Commun.* **26**, 547 (1978).
34. J. M. Karanikas, R. Sooryakumar, and J. M. Phillips, *J. Appl. Phys.* **65**, 3407 (1989).
35. J. M. Karanikas, R. Sooryakumar, and J. M. Phillips, *Phys. Rev. B* **39**, 1388 (1989).
36. L. E. McNeil, M. Grimsditch, and R. H. French, *J. Am. Ceram. Soc.* **76**, 1132 (1993).
37. C. H. Wang, D. B. Cavanaugh, and Y. Hagashigaki, *J. Polym. Sci., (Polym. Phys. Ed.)* **19**, 941–950 (1981).
38. D. B. Cavanaugh and C. H. Wang, *J. Appl. Phys.* **52**, 5998 (1981).
39. M. B. Hakin, S. M. Lindsay, and J. Powell, *Biopolymers* **23**, 1185 (1984).
40. Y. Takagi and R. W. Gammon, *J. Appl. Phys.* **61**, 2030 (1987).

41. J. Pelous and R. Vacher, *Solid State Commun.* **16**, 279 (1975); R. Vacher and J. Pelous, Phys. Rev. *B* **14**, 823 (1976).
42. J. D. Lytle, Polymeric optics, *in* "Handbook of Optics, Devices, Measurements and Properties," (M. Bass, ed.), 2nd Ed., Vol. 2, Chap. 34. McGraw-Hill, New York, 1995.
43. B. H. Billings, Optics, *in* "American Institute of Physics Handbook," (D. E. Gray, ed.), 3rd Ed., Section 6, pp. 6–108. McGraw-Hill, New York, 1982.
44. J. R. Sandercock, *Phys. Rev. Lett.* **29**, 1735 (1972).
45. P. J. Thomas, N. l. Rowell, H. M. van Driel, and G. I. Stegeman, *Phys. Rev. B* **19**, 4986 (1979).
46. N. Lagakos, J. A. Bucaro, and R. Hughes, *Appl. Opt.* **19**, 3668 (1980).
47. Y. Takagi, private communication (1996).
48. J. Schroeder, *J. Non-Cryst. Solids* **40**, 549 (1980).

Chapter 6

Doped n-Type Silicon (n-Si)

MARK AUSLENDER and SHLOMO HAVA
Ben-Gurion University of the Negev
Department of Electrical and Computer Engineering
Beer-Sheva, Israel

I. Introduction 155
II. Contributions to Dielectric Function: Optical Properties versus Optical Constants 156
III. Semiclassical Theory of Free-Carrier Contribution to the Dielectric Function: The Drude Approximation 158
IV. Free-Carrier Contribution to the Dielectric Function in Quantum Absorption Regime: Generalized Drude Approach 159
V. Experimental Data Overview 162
VI. Generalized Drude Approximation for n-Si 166
A. Electron-Phonom Scattering 167
B. Electron-Impurity Scattering 168
VII. Tabulation of Optical Constants of Doped n-Si 171
References 185

INTRODUCTION I

The importance of knowing optical constants was excellently outlined in the introduction to *HOC I* [1]. In the case of silicon, one can also point out technologically important applications of this knowledge. A partial list includes the determination of epilayer thickness [2] and the losses in all-silicon integrated optical devices [3], silicon-wafer thermometry [4], IR emissivity, and absorbance enhancement in silicon gratings [5, 6]

To be self-contained, this critique includes an overview of dielectric-function partition and the relation of optical constants to measured optical properties (Section II), semiclassical, and quantum absorption theory (Sections III and IV). In order to avoid multiple repetition when citing textbook materials, we refer in advance to well-known books on optics [7], semiconductor optics [8], and physics [9], and quantum mechanics [10]; in Section IV we also introduce the generalized Drude approximation. Section V is an

HANDBOOK OF OPTICAL CONSTANTS OF SOLIDS III

Copyright © 1998 by Academic Press.
All rights of reproduction in any form reserved
ISBN 0-12-544423-0/$25.00.

overview of experimental data and the Drude formula with empirically adjusted parameters. In Section VI we present a first-principle theory of free-carrier contribution to optical constants in doped n-Si based on the generalized Drude approximation. We outline the calculations and emphasize the difficulties that the theory is faced with when being used to describe available experimental data.

II CONTRIBUTIONS TO DIELECTRIC FUNCTION: OPTICAL PROPERTIES VERSUS OPTICAL CONSTANTS

Electromagnetics of homogeneous material is completely defined by the dielectric function (DF): $\epsilon = \epsilon_1 + i\epsilon_2$, a function of radiation frequency ω or vacuum wavelength $\lambda = 2\pi c/\omega$. The basic quantity of optics, however, is *complex refractive index* $\sqrt{\epsilon} = n + ik$, where the *refractive index, n,* and *extinction coefficient, k,* are related to ϵ_1 and ϵ_2 via equations

$$n^2 - k^2 = \epsilon_1, \tag{1}$$

$$2nk = \epsilon_2. \tag{2}$$

The lattice and free-carriers, which arise from doping, give additive contributions to the DF:

$$\epsilon = \epsilon_l + \epsilon_c. \tag{3}$$

Here, $\epsilon_l = (n_l + ik_l)^2$ is the lattice contribution, and ϵ_c is that due to the carriers

$$\epsilon_c = i\frac{4\pi\sigma(\omega)}{\omega}, \tag{4}$$

where $\sigma(\omega)$ is conductivity at optical frequencies. Though doping also affects $\epsilon_l$via band-gap reduction [11], in the IR this effect is negligible as compared to ϵ_c. The tables of n_l and k_l for intrinsic silicon were presented by Edwards [12]; such tables for Si: O_2 were also reported [13]. In the near and mid IR, n_l decreases from 3.4490 at 5000 cm^{-1} to 3.4201 at 400 cm^{-1}, the largest values of $k_l \sim 10^{-3}$ are achieved in a narrow band near 606 cm^{-1}. It seems that this variation is negligible on the scale of ϵ_c for doping in excess of 10^{16} cm^{-3}; in most papers, n_l is taken to be constant, and k_l is neglected.

Experimentally, n and k are determined using measurements of various optical properties of quality samples with simple geometry. For smooth

opaque samples, the only quantity of interest is the complex amplitude reflectance

$$r = -\frac{\sqrt{\epsilon} - 1}{\sqrt{\epsilon} + 1} = \sqrt{R}\exp(i\Phi), \tag{5}$$

where R is the Fresnel reflectance of the sample's surface

$$R = |r|^2 = \frac{(n-1)^2 + k^2}{(n+1)^2 + k^2}, \tag{6}$$

and Φ is the argument of the complex reflectance

$$\tan(\Phi) = \frac{2k}{n^2 + k^2 - 1}. \tag{7}$$

The spectrum of R is measured using reflectometry techniques; with R measured, Φ is determined using Kramers-Kronig analysis (KKA) [14]. With both spectra available, Eqs. (6, 7) are solved simultaneously to yield n and k. For a transparent slab, the apparent reflectance R_a and transmittance T_a are measured. In many practical cases, interference oscillations (fringes) in the spectra of R_a and T_a are averaged out. This leads to simple equations:

$$R_a = R\left[1 + \left|1 - r^2\right|^2 \frac{\exp(-2\alpha d)}{1 - R^2\exp(-2\alpha d)}\right], \tag{8}$$

$$T_a = \left|1 - r^2\right|^2 \frac{\exp(-\alpha d)}{1 - R^2\exp(-2\alpha d)}, \tag{9}$$

in which d is the thickness of the slab, and

$$\alpha = \frac{4\pi k}{\lambda} \tag{10}$$

is the EM *power attenuation coefficient.* It is referred to as the *absorption coefficient* in the case $n > k$ ($\epsilon_1 > \epsilon_2$). At $n \gg k$, $r^2 = R$ in Eqs. (8, 9), and *spectral absorbance* $A = 1 - R_a - T_a$ takes the following form when used in silicon-wafer thermometry [4]:

$$A = \frac{(1-R)[1 - \exp(-\alpha d)]}{1 - R\exp(-\alpha d)}. \tag{11}$$

III SEMICLASSICAL THEORY OF FREE-CARRIER CONTRIBUTION TO THE DIELECTRIC FUNCTION: THE DRUDE APPROXIMATION

An approach to calculating ϵ_c, which combines an account of band structure and scattering with the merit of being simple, is based on quasi-classical Boltzmann transport equation. This is restricted by the requirement that the radiation quantum is much smaller than the mean electron energy: $\hbar\omega \ll \langle E \rangle$. In the relaxation-time approximation, the Boltzmann equation can be solved in a closed form for an arbitrary band spectrum $E(\mathbf{k})$. This gives in Eq. (4)

$$\epsilon_c = -\frac{4\pi e^2 N}{\omega}\langle(\omega + i\tau^{-1})^{-1}\mathbf{m}^{-1}\rangle. \tag{12}$$

Here, N is the carrier concentration, τ and $\mathbf{m}$ are the energy-dependent relaxation time and effective-mass tensors, respectively, $\langle ... \rangle$ denotes average over energies E with normalized-to-unity weight $-\frac{\partial f(E)}{\partial E}\cdot\frac{N(E)}{N}$, where $N(E)$ is the number of band states with energies less than E, and f is the Fermi-Dirac distribution. The conduction band in silicon has six equivalent minima (valleys) in the Γ-X directions. Constant-energy surfaces are those of revolution, so $\mathbf{m}$ has two principal values $m_\parallel$ and $m_\perp$. Near the minima ($E < 0.15$ eV), they are constant: $m_\parallel \approx 0.98m_0$, $m_\perp \approx 0.19m_0$, and the constant-energy surfaces are ellipsoids. At larger E's, the masses (mostly $m_\perp$) increase with increasing E, and the ellipsoids become warped [15]. The tensor τ has the same principal axes as $\mathbf{m}$, with principal values $\tau_\parallel$ and $\tau_\perp$. Deformation acoustic (DA)-phonon scattering is nearly isotropic ($\tau_\parallel \approx \tau_\perp$), and deformation optical (DO)-phonon and point-defect scattering are isotropic. For ionized-impurity scattering, tensor τ, introduced as an approximation, is essentially anisotropic.

At $\omega\tau \ll 1$, Eq. (12) gives

$$\epsilon_1 = n_1^2, \quad \epsilon_2 = 2n_1k_1 + n_1^2\frac{\omega_p^2\tau_{dc}}{\omega}, \tag{13}$$

and at $\omega\tau \gg 1$

$$\epsilon_1 = n_1^2(1 - \omega_p^2/\omega^2), \quad \epsilon_2 = 2n_1k_1 + n_1^2\frac{\omega_p^2}{\omega^3\tau_{ac}}. \tag{14}$$

In Eqs. (13, 14) ω_p is the electron plasma frequency defined by

$$\omega_p = \frac{1}{n_1}\sqrt{\frac{4\pi e^2 N}{m_c}}, \quad \frac{1}{m_c} = \langle\frac{1}{3m_\parallel} + \frac{2}{3m_\perp}\rangle, \tag{15}$$

τ_{dc} and $1/\tau_{ac}$ are the combined energy-valley averages of the tensor τ, and the tensor inverse to τ, respectively:

$$\tau_{dc} = m_c \left\langle \frac{\tau_\parallel}{3m_\parallel} + \frac{2\tau_\perp}{3m_\perp} \right\rangle, \tag{16}$$

$$\frac{1}{\tau_{ac}} = m_c \left\langle \frac{1}{3m_\parallel \tau_\parallel} + \frac{2}{3m_\perp \tau_\perp} \right\rangle. \tag{17}$$

The quantity m_c is called *optical* or *conductivity effective mass.* With the use of cyclotron-resonance data, the average in Eq. (15) is calculated trivially to give $m_c = 0.26m_0$.

If, for some reasons, τ_{dc} and τ_{ac} are close to each other, the two limits Eq. (13) and Eq. (14) may be interpolated by the simple formula

$$\epsilon = \epsilon_1 - \frac{n_1^2 \omega_p^2}{\omega(\omega + i\gamma)}, \quad \gamma = \frac{1}{\tau}, \tag{18}$$

which is the celebrated Drude (also Drude-Lorentz or Drude-Zener) equation, and τ is the relaxation time [8, 9, 16]. For isotropic τ, the closeness of τ_{dc} and τ_{ac} is certainly realized when carriers are degenerate. In n-Si with the valley density-of-state effective mass $m_d = m_\parallel^{1/3} m_\perp^{2/3} \approx 0.33m_0$, no degeneracy occurs unless $N \geq 10^{20}$ cm^{-3}.

In order to validate the Drude equation at all concentrations, the relation $\tau_{dc}/\tau_{ac} = 1.13$, valid for combined DA-phonon and point-defect scattering in non-degenerate statistics, is used. For ionized-impurity scattering another reason must be sought, because $\tau_{dc}/\tau_{ac} \gg 1$ even in the isotropic band. At heavy doping, the allowance of Eq. (18) implies the existence of a mechanism which 'binds' one-particle currents into collective variable, total current, which relaxes as a whole. This mechanism could be electron-electron (*e-e*) interaction, which smears an individual electron momentum but conserves the total one. Then the response of the electron plasma on an external EM field will be described in terms of total momentum, provided that the electron momentum exchange in *e-e* collisions becomes faster than the electron momentum relaxation due other mechanisms, as N increases over some value. However, this picture is only partially adequate because the *e-e* momentum-relaxation rate is of the same order of magnitude as that due to ionized impurities, though detailed estimates are not widely known especially for the anisotropic band.

IV FREE-CARRIER CONTRIBUTION TO THE DIELECTRIC FUNCTION IN QUANTUM ABSORPTION REGIME: GENERALIZED DRUDE APPROACH

The Boltzmann equation becomes invalid at $\hbar\omega > \langle E \rangle$, since in this case radiation influences the scattering process. In the quantum regime, the act of

scattering is a transition between initial state with momentum $\mathbf{k}$ and energy $E(\mathbf{k})$ and final state with momentum $\mathbf{k}'$ and energy $E(\mathbf{k}')$ with radiation quanta absorbed or emitted: $E(\mathbf{k}') = E(\mathbf{k}) \pm \hbar\omega$. In the quantum regime, ϵ_c was calculated in the terms of transition probabilities using time-dependent perturbation theory. The first calculations of this type were reported 40 years ago by Fan *et al.* in connection with the first IR-absorption measurements on Ge [17] and Si [18]. For DA-phonon scattering, the absorption coefficient (Eq.(10)) obeys a power law: $n\alpha \propto \omega^{-1.5} \propto \lambda^{1.5}$ at $\hbar\omega > \langle E \rangle$. At $\langle E \rangle/\hbar > \omega > 1/\tau$, quantum theory gives the same result as semiclassical theory or the Drude approximation at $\omega\tau > 1$ (Eqs. (14, 18) with Eqs. (2, 10))

$$n\alpha \approx \frac{n_1^2}{c\tau}\left(\frac{\omega_p}{\omega}\right)^2 \propto \lambda^2. \tag{19}$$

DO-phonon scattering in n-Ge was also considered by Fan *et al.* [17]; phonon-assisted absorption in a many-valley conduction band was studied by Meyer [19] and Rosenberg and Lax [20]. The method was recapitulated by Dumke [21] in 1960. Ionized impurity-assisted absorption in the Born approximation was studied by Meyer [19] and Rosenberg and Lax [20], and with Coulomb wave functions by Visvanathan [22] and Donovan [23]. It was found that in the quantum regime, $n\alpha \propto \omega^{-3.5} \propto \lambda^{3.5}$. The transition to Eq. (19) may not occur even after $\langle E \rangle$ exceeds $\hbar\omega$. The reason is, though the electron wave packet as a whole starts to move at thermal equilibrium, its breadth δr is still determined by the oscillations in radiation field: $\delta r = \sqrt{\hbar/2m^*\omega}$, m^* being an effective mass. So at $\delta r < r_s$ (screening length) the electrons 'feel' an unscreened impurity for which $n\alpha \propto \omega^{-3} \propto \lambda^3$ in the classical frequency region [22, 23], and the limit of Eq. (19) is reached only at $\delta r > r_s$. The calculations using transition probabilities require throwbacks to first principles, and are recast each time a new mechanism is considered. From the late 1960s to 1970s, studies devoted to the derivation of generalized Boltzmann equations, which could recover both quantum and classical regimes, were carried out. Having no room to review this subject here, we refer to the contribution of Jensen [24]. Note that at $\omega\tau \gg 1$, the quantum Boltzmann equation and the transition-probability methods give close results.

Kubo quantum-admittance formalism [25] with second quantization allowed researchers to automate the calculations at high frequencies in a reasonably correct, unified form. The Kubo formula for dynamical conductivity [25] reads

$$\sigma(\omega) = \int_0^\infty \exp(i\omega t) \int_0^{1/kT} \langle J_x(t - i\hbar s) J_x(0) \rangle_T \, dt ds. \tag{20}$$

Here, J_x is x −(or any) component of electric-current operator,

$$A(t) = \exp(it\mathcal{H}/\hbar) A \exp(-it\mathcal{H}/\hbar), \tag{21}$$

where $\mathscr{H}$ is a Hamiltonian, and $\langle ... \rangle_T$ stands for thermodynamic average with the temperature T. Using integration by parts with respect to time t, in Eq. (20) the free-carrier contribution (Eq. (4)) can be identically transformed to

$$\epsilon_c = -\frac{\Omega_p^2}{\omega^2}\left[1 + \frac{\Pi(\omega)}{i\omega}\right], \quad \Omega_p^2 = 4\pi \int_0^{1/kT} \langle J_x(i\hbar s) J_x(0)\rangle_T \, ds \tag{22}$$

with

$$\Pi(\omega) = 4\pi\Omega_p^{-2} \int_0^\infty \exp(i\omega t) \int_0^{1/kT} \langle \dot{J}_x(t + i\hbar s)\dot{J}_x(0)\rangle_T \, dtds, \tag{23}$$

where the upper dot denotes the time derivative:

$$\dot{A}(t) = \frac{i}{\hbar}[\mathscr{H}, A(t)].$$

Eq. (23) is convenient for the calculation at high frequencies. Indeed, $\Pi(\omega)$ is at least of *second order* with respect to the interactions, since the electric-current operator commutes with the kinetic energy part of $\mathscr{H}$. Thus, at $\omega\tau \gg 1$ the interactions can be neglected when considering the correlation function in Eq. (23). Then the lowest-order estimate of Eq. (23) $\Pi^{(2)}(\omega) = \Gamma(\omega)$ is obtained in a closed form as a sum of the contributions of different scattering mechanisms. It is expedient to note that in this approximation, the *e-e* interaction does not contribute to $\Gamma(\omega)$ for the isotropic band, where J_x is proportional to the total momentum.

With $\Pi(\omega)$ replaced by $\Gamma(\omega)$, Eq. (22) becomes a fragment of the high-frequency expansion of

$$\epsilon_c = -\frac{\Omega_p^2}{\omega[\omega + i\Gamma(\omega)]}. \tag{24}$$

The extention of Eq. (24) to all ω's is called the *generalized Drude approximation* (GDA). The structure of this type may formally be obtained from exact Eq.(22) using the Mori projection ansatz [26]. Of course, the prescription of the structure by no means validates GDA. The validity of GDA in the whole frequency range was extensively discussed by Sernelius [27]. It was applied to simple metals [28], and to an isotropic model of doped n-Si [29, 30]. GDA appears to be a good approximation if the *e-e* collisions dominate, as outlined in Section III.

Since $\Omega_p = n_1\omega_p$ in the leading approximation, the total DF (Eq. (10)) in GDA differs from the Drude formula (Eq. (19)) only in the presence of the relaxation-memory function $\Gamma(\omega)$ *instead of constant relaxation rate* γ. If the valleys are uncoupled, GDA must be applied separately to each valley. The calculations for the valleys of $\langle 100\rangle$, and $\langle 010\rangle$, $\langle 001\rangle$ types give, in

general, two different contributions $\Gamma_{\parallel}(\omega)$, and $\Gamma_{\perp}(\omega)$, respectively. The total DF in this case is

$$\epsilon = \epsilon_1 - \frac{4\pi Ne^2}{3m_{\parallel}\omega[\omega + i\Gamma_{\parallel}(\omega)]} - \frac{8\pi Ne^2}{3m_{\perp}\omega[\omega + i\Gamma_{\perp}(\omega)]}. \tag{25}$$

At the high-frequency limit only the average relaxation function

$$\Gamma(\omega) = \frac{m_c}{3}\left[\frac{\Gamma_{\parallel}(\omega)}{m_{\parallel}} + 2\frac{\Gamma_{\perp}(\omega)}{m_{\perp}}\right] \tag{26}$$

enters Eq. (25), thus comprising the first term of exact perturbation expansion as required. In the presence of a scattering, that couples the valleys, Eq. (25) must be changed (Eq. (3.8) [27]).

V EXPERIMENTAL DATA OVERVIEW

There exists a body of literature on the optical properties of variously doped n-Si crystals in the IR. The equilibrium solubility of atoms of As, P, and Sb in Si does not exceed $5 \times 10^{20}\text{cm}^{-3}$ [31]. The use of advanced ion-implantation technology increased the active dopant density far above this (up to 5×10^{21} cm^{-3}) and allowed plasma effects to be observed in the near IR [32–34].

Basically, these studies used reflection and/or transmission measurements. For bulk-doped samples at $N < 10^{19}\text{cm}^{-3}$, it is technologically possible to prepare slabs suitable for transmission measurements. With the use of Eqs. (6–10), optical constants are retrieved from measured values of R_a and T_a. As is seen from Eq. (14), extrapolating measured ϵ_1 to zero from the region $n \gg k$ gives the plasma frequency, and hence the optical effective mass m_c. Using this method, Spitzer and Fan [18] found $m_c = 0.27m_0$ for $N = 3.6 \times 10^{18}$ cm^{-3}, in excellent agreement with the value cited in Section II. It was pointed out by Fistul [31] that for heavier doping, the method has low reliability, as was seen from the result $m_c = 0.44m_0$ of Cardona *et al.* for $N = 6.5 \times 10^{19}$ and 1.1×10^{20} cm^{-3} [35]. At doping in excess of 10^{19} cm^{-3}, reflectometry was mostly used [33, 36–39]. A comprehensive study of reflection was made by Howarth and Gilbert [36], who measured 16 n-Si samples doped in the range $7.4 \times 10^{18}\text{cm}^{-3} - 1.67 \times 10^{20}\text{cm}^{-3}$. For ion-implanted n-Si layers, combined measurements of reflection and transmission were carried out by Streltsov and Titov [40], Miyao *et al.* [32], and Aspnes *et al.* [34].

Two approaches to processing reflectivity data of bulk-doped samples were used. The first one, which relied on the Drude model, was proposed by

Kukharski and Subashiev [38], and advocated by Lambert [41]. In this approach, ω_p and γ are found from the reflectivity minimum frequency, ω_{min} (wavelength λ_{min}), and the value of reflectivity minimum, R_{min}. With known ω_p, one can calculate m_c if N is measured and vice versa; this method is an improvement of widely used approximations: $(n-1)^2 \gg k^2$ or $n \sim 1$, $k \sim 0$ [17, 18, 35–37]. The method of Kukharski and Subashiev [38] was used also for doped n-Si layers in a homogeneous approximation [40] and modified by Slaoui and Siffert [33] for concentration profiles. The second approach is KKA giving n and k independently of the physical model (see Section II). However, as a rule, the retrieved n and k were not displayed, and again, the Drude model was used. Spitzer *et al.* [37] assumed $m_c = 0.28m_0$ and studied the influence of heat treatment on γ in a sample with $N = 7.5 \times 10^{19}$ cm^{-3}. Barta [39] expressed m_c and τ via ϵ_1 and ϵ_2, which were known after KKA (see Eqs. (1, 2)). The parameters were calculated at the zero of ϵ_1, which gave: $m_c = 0.31m_0$ and $m_c = 0.35m_0$ for two samples with $N = 9 \times 10^{19}$ cm^{-3} and 1.6×10^{20} cm^{-3}, respectively, and about the same value of the relaxation parameter $\gamma \sim 1.09 \times 10^{14}$ s^{-1} for both samples.

A variety of spectra of the absorption coefficient α was observed in n-Si. Dubrovsky in his thesis cited by Fistul [31] in the range of $N \sim (0.1 - 1) \times 10^{20} cm^{-3}$ and reported the dependence $\alpha \propto \lambda^{3.5}$, which is characteristic for ionized-impurity scattering (see Section IV). Balkanski *et al.* [42] measured $\alpha \propto \lambda^2$ at $4\mu m < \lambda < 6\mu m$ in bulk-doped samples with $N = 6 \times 10^{18}$, 10^{19} cm^{-3}. On the contrary, in ion-implanted layers with $N \sim (0.5 - 2) \times 10^{20} cm^{-3}$, the dependence $\alpha \propto \lambda^{1.5}$ was observed at $2\mu m < \lambda < 10\mu m$ [40]. Later this was also observed in laser-annealed poly-Si layers with a much larger concentration [34]. Based on the fact that this dependence is obtained for DA-phonon scattering (see Section VI), Streltsov and Titov [40] asserted that the phonon mechanism dominates the scattering processes in n-Si doped in excess of 10^{19} cm^{-3}.

On the one hand, the researchers were disposed to retrieve some physical information rather than tabulate optical constants. On the other hand, such restricted information can hardly be used in practice. For a fast and accurate approximation of optical constants in a wide range of N and ω, Humlíček and Wojtechovsky [43] proposed a KKA-adjusted Drude model for a best fit of reflectivity data. Using the data for the samples of Howarth and Gilbert [36] and three of their own [43], they found fitting values of ω_p and γ for each, and derived linear relations:

$$\begin{aligned} \gamma &= 113 + 0.208\ \omega_p \quad \text{(Si: Sb)}, \\ \gamma &= 153 + 0.265\ \omega_p \quad \text{(Si: As)}, \\ \gamma &= 194 + 0.174\ \omega_p \quad \text{(Si: P)}, \end{aligned} \tag{27}$$

where ω_p and γ are in units cm^{-1}, and $N \geq 5 \times 10^{18}$ cm^{-3}. The authors sought a dependence between m_c, as calculated using the definition of ω_p,

and N. Due to a large scatter, the result (Eq. (15) [43]) seemed so unphysical that they recommended substituting the value $m_c = 0.26m_0$ for interpolation of optical constants using Eq. (27). Thus, at $N \leq 10^{20}$ cm^{-3} it can be put in the Drude equation (Eq. (18)):

$$n_l^2\omega_p^2 = 3.452 \times 10^{-13} N\,\mathrm{cm}^{-2}, \tag{28}$$

where N is in units cm^{-3}.

Eq. (28) can be validated by fittting ω_p of Humlíček and Wojtechovsky [43] linearly to N. The result is shown in Fig. 1. We display only the fit for Si: As, which yields $m_c = 0.27m_0$. It fits the data reasonably well up to $\sim 8 \times 10^{19}$ cm^{-3}. The data for Si: Sb also have a small scatter and are fitted with $m_c = 0.28m_0$. The data for Si: P have larger scatter especially at the end concentrations. The linear fit using the data for $N \leq 10^{20}$ cm^{-3} gives $m_c = 0.29m_0$. The point $N = 1.67 \times 10^{20}$ cm^{-3} (not shown in Fig. 1) drops drastically below this fit. Including this point in the fit increases the value of m_c to $0.31m_0$; the calculation using only this point gives $m_c = 0.34m_0$, which are about the same as obtained by Barta [39]. Since m_c must be independent of impurity type, we conclude that its apparent increase at $N \leq 10^{20}$ cm^{-3} is a result of experimental uncertainty. This agrees with band-structure calculations of van Driel [15], which predicted different behavior of m_c: near-to-constant $m_c = (0.26 - 0.27)\ m_0$ at $N \leq 10^{20}$ cm^{-3}, and monotonic in-

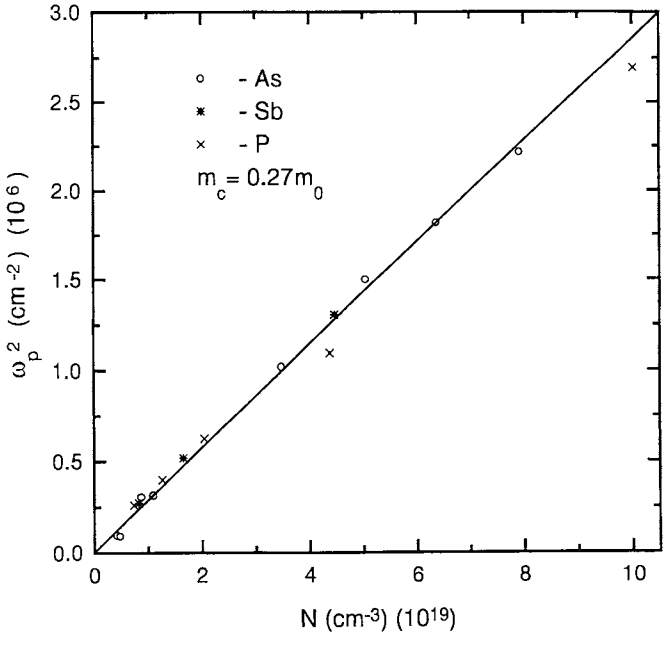

Fig. 1. Plasma frequency squared versus electron concentration for various doped n-Si. Si: As (o), Si: Sb (*), Si: P (×). Straight line is the best linear fit for Si: As giving $m_c = 0.27m_0$.

crease at $N > 10^{20}$ cm^{-3} to about $0.57m_0$ at 5×10^{21} cm^{-3}. This huge increase of m_c was observed in ion-implanted samples [32–34], whereas its onset is seen in the last two Si: P samples of Howarth and Gilbert [36]. As seen from Fig. 2, the agreement of theory [15] and experiment [32–34] is fair.

To derive a fit for γ at $N < 5 \times 10^{18}$ cm^{-3}, the transmission through four samples with $N = 1.4 \times 10^{16}$, 7.5×10^{16}, 10^{17}, and 1.15×10^{17} cm^{-3} was measured by Humlíček and Wojtechovsky [43]. It was found that there is a good agreement between the retrieved γ's and the inverse relaxation times extracted from the mobility data. Using a simplified empirical fit for the mobility, the authors obtained

$$\gamma = 35910 \frac{1 + (10^{-16} N/9.68)^{0.68}}{1427 + 52.2\,(10^{-16} N/9.68)^{0.68}} \text{ cm}^{-1}, \tag{29}$$

where, as usual, N is in units cm^{-3}. Even though optical data between 1.2×10^{17} cm^{-3} and 3.6×10^{18} cm^{-3} are missing, and the mobility data are uncertain, the γ values obtained from Eq. (29) and Eq. (27) match reasonably at $N = 5 \times 10^{18}$ cm^{-3}. To summarize, Eq. (18) (ω in units of cm^{-1}) with Eq. (28) and empirically adjusted relaxation parameter given by Eq. (29)

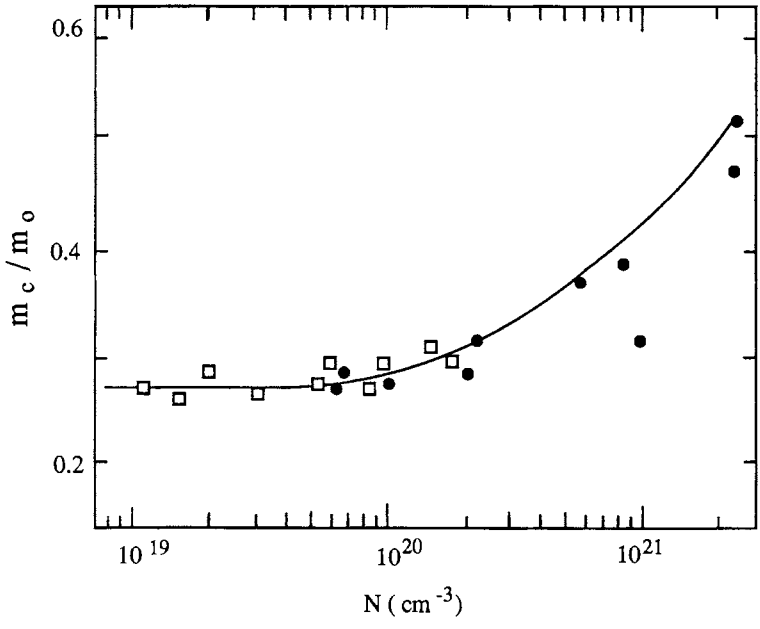

Fig. 2. Dependence of optical effective mass in n-Si on free-carrier concentration. The solid line represents theoretical curve after van Driel [15]. Open squares and solid circles are experimental data after Howarth and Gilbert [36] (□) and Miyao *et al.* [32] (●). Reprinted with permission.

or Eq. (27), can be used for modelling the optical constants in n-Si versus both wavenumber and electron concentration. At light doping, spectral variation of ϵ_l in Eq. (18) is to be taken into account. For this purpose, the real part of ϵ_l can be modeled using the known Sellmeier-type formula [12], and the imaginary part can be taken from the tables [12, 13]. At doping levels well above 10^{19} cm^{-3} the relaxation time τ retrieved from experimental data of Miyao *et al.* [32] and Slaoui and Siffert [33] is smoothly decreasing with the increase of N and then saturated to 3×10^{-15} s near $N = 5 \times 10^{21}$ cm^{-3} as shown in Fig. 3.

It is worthwhile to mention that the reflectivity data are affected by the state of the sample's surface. For example, Spitzer *et al.* [37] noted that for surfaces specially polished or etched, $R_{min} \sim 0.11$, whereas with standard polishing technique, values lower than 0.139 did not occur [36, 37]. Moreover, heat treatment, without affecting λ_{min}, lowered R_{min} to 0.067 [37]. An analysis of this reflectivity curve indicated that relaxation time must depend on λ [37].

VI GENERALIZED DRUDE APPROXIMATION FOR n-Si

In this section we consider all the necessary ingredients for the application of GDA to n-Si. This is done to point out that the results of this treat-

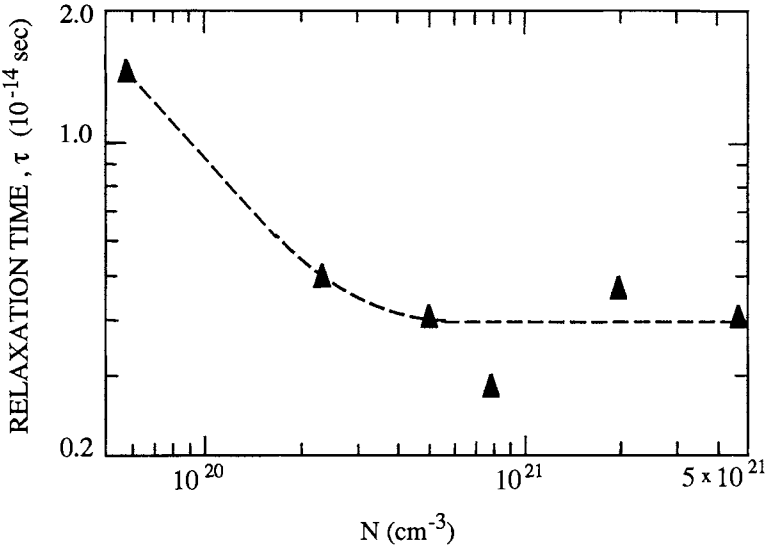

Fig. 3. Dependence of relaxation time τ, which enters the Drude Eq. (18), on free-carrier concentration in ion-implanted n-Si. Solid triangles are experimental data after Miyao *et al.* [32]; dashed line is a guide for the eye. Reprinted with permission.

ment conflict with the Drude approximation, since screened-impurity-potential models lead to a strong spectral dependence of the relaxation functions. In turn, the allowance of a constant τ contradicts some experimental data at short wavelengths [31, 34, 41], and, though less certainly, near λ_{min} [37]. Ideally, one might hope that for a much-studied material like n-Si, the theory and experiment would agree. In reality, poor knowledge of impurity potentials in heavily doped n-Si (see below), as well as the uncertainties of experimental data, make disagreement quite possible. Let us first consider the contributions to the relaxation functions existing in n-Si.

Electron-Phonon Scattering A

Electron-phonon scattering dominates in lightly doped n-Si. The actual mechanisms are DA-phonon and intervalley-phonon scattering. Unlike n-Ge, in n-Si, DO-phonon scattering is not allowed [44]. There are two types of intervalley scattering. In the first, *g*-type, an electron is transferred from a given valley to a valley with the same orientation, and in the second, *f*-type, to one of the four valleys with a different orientation. The *g*-transition uses an LO-phonon with wavevector at the point Δ and energy $\hbar\omega_{LO} \approx 735$K. Two *f*-transitions are assisted by the two phonons with wavevector at the point S: TO ($\hbar\omega_{TO} \approx 690$K) and LA ($\hbar\omega_{LA} \approx 510$K). Matrix elements of these transitions are unknown, but fortunately DA-phonon scattering more or less accounts for room-temperature mobility in lightly doped n-Si ($\mu_{300} \approx 1350$ cm^2 V^{-1}s^{-1}, the mobility relaxation time $\tau_0 \approx 2.00 \times 10^{-13}$ s). The intervalley processes contribute negligibly at room temperature because the corresponding phonon occupation numbers are rather small.

For DA-phonon scattering Eq. (23), neglecting weak anisotropy factors, gives:

$$\Gamma_{\upsilon}^{(ep)}(\omega) = \frac{\Gamma_{DA}}{F_{1/2}(\eta)} \int_0^{\infty} \frac{x}{\bar{\omega}} \ln\left[\frac{1 + \exp(\eta - x - \bar{\omega}^2/16x + \bar{\omega}/2)}{1 + \exp(\eta - x - \bar{\omega}^2/16x - \bar{\omega}/2)}\right] dx, \qquad \upsilon = \parallel, \perp, \quad (30)$$

where $\bar{\omega} = \hbar\omega/kT$, $\eta = \zeta/kT$ is the reduced chemical potential, $F_r(\eta)$ are the Fermi integrals,

$$\Gamma_{DA} = \frac{4\Xi_u^2}{3\hbar\rho u_l^2}\left(\frac{2m_d kT}{\pi\hbar^2}\right)^{3/2}, \quad (31)$$

where Ξ_u is shear-deformation potential, ρ is the crystal density, and u_l is the longitudinal sound velocity. With known values of $\Xi_u \approx 9.6$ eV, the band

and lattice parameters, one obtains $\Gamma_{DA} \approx 0.566 \times 10^{13}\ s^{-1}$ at $T = 300K$. In the non-degenerate case, one obtains

$$\Gamma^{(ep)}(\omega) = \Gamma_{DA}\left(\frac{\overline{\omega}}{4}\right)\sinh\left(\frac{\overline{\omega}}{2}\right)K_2\left(\frac{\overline{\omega}}{2}\right), \tag{32}$$

where $K_2(x)$ is the McDonald function. At $\overline{\omega}/\max(\eta,1) \gg 1$, Eq.(30) gives the asymptotic form of the absorption coefficient (see Section IV):

$$n\alpha^{(ep)} \approx \frac{16Ne^2}{9c\tau m_c\omega^2}\left(\frac{\pi\hbar\omega}{kT}\right)^{1/2}, \quad \tau = \tau_0 \exp(-\eta)F_{1/2}(\eta), \tag{33}$$

where τ_0 is DA-phonon mobility relaxation time for light doping. In Streltsov and Titov [40] the absorption spectra retrieved from the transmission data for ion-implanted Si: P layers with $N = (0.5 - 2) \times 10^{20}\ cm^{-3}$ were shown to fit Eq. (33). Using qualitative arguments, the authors stated that ionized-impurity scattering should 'switch-off' in the spectral interval under study, so observed absorption is due to acoustic phonons; the same conclusion was also drawn by Aspnes *et al.* [34]. At $N = 10^{20}\ cm^{-3}$ the fit by Streltsov and Titov [40] needed τ about 15 times smaller than τ_0, and the formula in Eq. (33) gives a factor ~ 3. The rest, however, is *not necessary* due to the increase of electron-phonon interaction as was claimed by Streltsov and Titov [40]. Actually, any short-range interaction leads to the same spectral dependence as given by Eq. (33), but with another τ_0. It might be the short-range part of electron-donor interaction (see next subsection). In this case, the asymptotic form in Eq. (33) is almost *independent* of T, whereas in the case of phonons, it is *linear* with respect to the temperature. Thus, the origin of $\lambda^{1.5}$-absorption spectrum can not be identified until its temperature dependence is studied experimentally. More seriously, the concept of Aspnes *et al.* [34] and Streltsov and Titov [40] implies impurity scattering *to play no role* also at DC. Indeed, the fit values of τ attributed by Streltsov and Titov [40] *solely* to electron-phonon interaction correspond to the mobilities in the range (61–88) $cm^2\ V^{-1}s^{-1}$, typical for the *measured* mobility at the studied concentrations.

B Electron-Impurity Scattering

A key problem in the theoretical description of electron-donor scattering is to determine the electron-donor interaction potential. Usually it is taken in the form of screened Coulomb potential

$$V_i(\mathbf{r}) = -\frac{e\exp(-|\mathbf{r} - \mathbf{R}_D|/r_s)}{\epsilon_l|\mathbf{r} - \mathbf{R}_D|}, \tag{34}$$

where e is the electron charge, $\mathbf{R}_D$ is a donor position, and r_s is a screening length. The lowest-order calculation of Eq. (23) with respect to this potential can be performed easily no matter what model for r_s is chosen. In the Debye-Thomas-Fermi model and isotropic valleys, the calculation was carried out in our paper [29]. In a theory that seems more consistent, the screening is not introduced but is *derived* in perturbative electron-gas calculations, electron-impurity, and *e-e* interactions being treated simultaneously. For many-valley bands such a calculation of Eq. (23) was performed by Sernelius [27] using a diagrammatic method. His result for the impurity contribution can be transformed to:

$$\Gamma_v^{(ei)}(\omega) = \frac{6e^2}{m_d\omega}\mathrm{Im}\int\frac{d^3q}{(2\pi)^3}q^2 a_\nu(\mathbf{q})V_i(\mathbf{q};\omega)V_i(\mathbf{q},0)[\chi_0(q,\omega) - \chi_0(q,0)], \quad (35)$$

where $a_\parallel(\mathbf{q}) = \cos^2\theta$, $a_\perp(\mathbf{q}) = 1/2\ \sin^2\theta$, $\chi_0(q,\omega)$ is the wavevector-frequency-dependent electron polarizability in one parabolic valley (Lindhard function) with effective mass m_d;

$$V_i(\mathbf{q},\omega) = \frac{-4\pi e}{\epsilon_l q^2\left(\dfrac{m_\parallel a_\parallel}{m_d} + \dfrac{m_\perp a_\perp}{m_d}\right) + 8\pi e^2\sum\limits_{k=1}^{3}\chi_0(q_k,\omega)} \quad (36)$$

is the space-time Fourier transform of the effective interaction potential, where: $q_1 = q$, $q_2 = qK^{1/2}\,[\cos^2\theta + K^{-1}(\cos^2\varphi + K^{-1}\sin^2\varphi)]^{1/2}$, $q_3 = qK^{1/2}\,[\cos^2\theta + K^{-1}(\sin^2\varphi + K^{-1}\cos^2\varphi)]^{1/2}$, $K = m_\parallel/m_\perp$, θ and φ being the polar and azimuthal angles, respectively. In the isotropic valleys Eq. (35) reduces to our result [29] by putting $\omega = 0$, $q = 0$ in the polarizability term of Eq. (36), that is also obtained using transition-probability method. Sernelius [27] obtained an expression for an *e-e* contribution that describes 'friction' damping of relative momentum of differently oriented valleys. It changes the structure of Eq. (25) at general ω, but at high frequencies contributes only an additive term to Eq. (26).

Both screening models take into consideration only the long-range part of electron-donor interaction potential. For uncompensated n-Si at $T = 300$K, because of full donor ionization, they predict independence of the scattering rate from impurity type. At the same time, there exists experimental evidence of such dependence for the mobility [31] and for IR reflectance [34] (see Section III). The dependence is probably due to a short-range potential, for which at least two sources can be pointed out. The first is the difference between the atomic potentials of Si and the donor atom, which is responsible for the deviation of dopant ionization energy from the Bohr energy, and for the difference in those for different dopants. These substitution potentials for the three dopants in Si were estimated by Viña and Cardona [11]. The second is a local deformation in the vicinity of the impurity that affects the valleys through the deformation potential the same way as the lattice

vibrations do. We have not found a reliable estimation of this effect in the literature. The near-IR absorption spectra [34, 40] offer an additional evidence that a short-range potential emerges with doping (see Subsection VIA).

The calculation of DC mobility is a crucial test for the model, because without agreeement between theory and experiment at DC, the disagreement will appear also in the IR. As is well known, the mobility calculated in the Born approximation with respect to the Debye-Thomas-Fermi potential, and isotropic-valley approximation (Brooks-Herring mobility) disagrees strongly with experimental data [45]. The calculations in GDA with (q, ω)-screening model (Eqs. (25, 35, 36)) include triple integration of complicated function with respect to q, θ, φ. This is a formidable task for desktop-computer simulations (a Cray-type supercomputer was used by Serrelius [27]). In our case $K^{1/2} \approx 2.27$, the mean values of $q_{2,3}$ appear to be close to q, so we could put $q_{2,3} = q$ in Eq. (35), but retain angular dependence through the functions $a_\nu(\mathbf{q})$. After this, the angle integration is carried out analytically. The relaxation functions are expressed via the integrals with respect to the reduced-energy variable x as in Eq. (30), but with much more complicated integrands. Despite this complexity, they still allow a fast desktop-computer calculation. The calculations become much faster in the Debye-Thomas-Fermi limit.

Neglecting e-e scattering, the DC relaxation time is found using GDA extrapolated to $\omega = 0$:

$$\tau = \frac{m_c}{3m_\parallel \Gamma_\parallel(0)} + \frac{2m_c}{3m_\perp \Gamma_\perp(0)}. \tag{37}$$

At maximum e-e scattering, τ changes from this value to $\Gamma^{-1}(0)$, where $\Gamma(\omega)$ is given by Eq. (26) [27]. We calculated τ for $N = 10^{17}$, 10^{18}, 10^{19}, and 10^{20} cm^{-3} and obtained: $\tau = 1.31 \times 10^{-13}$, $(7.22\text{–}7.07) \times 10^{-14}$, $(3.90\text{–}3.77) \times 10^{-14}$, and $(2.58\text{–}2.51) \times 10^{-14}$ s, respectively. The second value in the brackets shows the effect of e-e scattering, which thus proves to be small. Corresponding 'experimental' values of τ calculated using Eqs. (27–29) are: 1.08×10^{-13}, 4.22×10^{-14}, $(1.83\text{–}1.69) \times 10^{-14}$, and $(1.09\text{–}1.02) \times 10^{-14}$ s, respectively. In the last two data, the first value corresponds to Si: P and the second to Si: As; close values are extracted from the Irvin resistivity curves [46]. We see systematic discrepancy between the theoretical and experimental values of τ by a factor which increases with the increase of N from ~ 1.2 to $\sim 2.3 - 2.5$. The Debye-Thomas-Fermi model gives a larger factor (3.5–3.7 at $N = 10^{20}$ cm^{-3}). To the best of our knowledge this discrepancy has not yet been resolved, and is still discussed in the literature [47]. Thus, the disagreement between optical constants calculated by GDA using the screening models and those calculated using the empirically adjusted Drude approach [43], arises even if the static values of the relaxation functions are substituted into Eq. (25). Including full frequency de-

pendence does not make the situation better. Moreover, as seen from Fig. 4, the relaxation functions appear to strongly decrease with decreasing λ, so their values at short wavelengths are too small to account for observed absorption. In addition, at heavy doping ($N > 3 \times 10^{18}$ cm^{-3}) the relaxation functions acquire peaks near the plasma wavelength, which are more pronounced for $\Gamma_{\perp}$ (see Figs. 4, 5). Mathematically, these peaks arise from the poles of $V_i(\mathbf{q},\omega)$ in the complex (q,ω)-plane. Physically, they display the response of plasma waves excited by scattered electrons in the screening electron cloud, a feature that cannot appear in the Debye-Thomas-Fermi model. These peaks produce weak humps on the reflectivity curves near λ_{min}, which have never been observed experimentally. In our opinion, this is one more reason to recast the donor potential issue in n-Si.

TABULATION OF OPTICAL CONSTANTS OF DOPED n-Si VII

We tabulated n and k for practical use at nine concentrations in the range from 10^{16} cm^{-3} to 10^{20} cm^{-3}, with roughly a factor-of-three increase for each step, using the fit of Humlíček and Wojtechovsky [43] given by

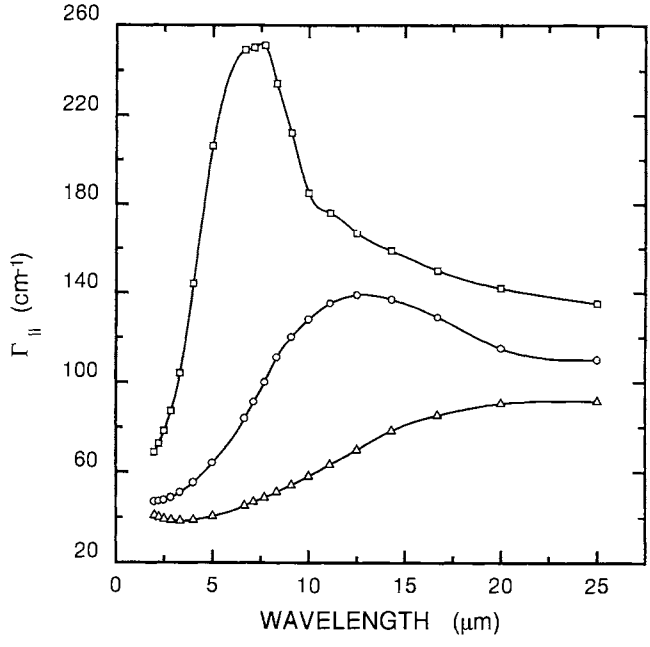

Fig. 4. Theoretical spectra of ⟨100⟩ relaxation function $\Gamma_{\parallel}$ calculated using Eqs. (35, 36) for three electron concentrations: (Δ) $N = 10^{19}$ cm^{-3}; (○) $N = 3 \times 10^{19}$ cm^{-3}; (□) $N = 10^{20}$ cm^{-3}.

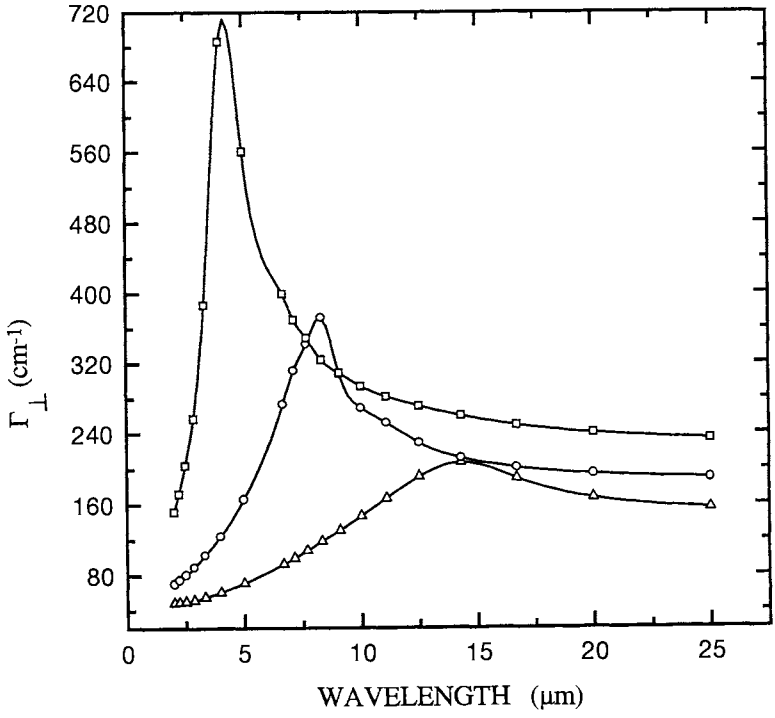

Fig. 5. Theoretical spectra of ⟨010⟩ relaxation function $\Gamma_\perp$ calculated using Eqs. (35, 36) for three electron concentrations: (Δ) $N = 10^{19}$ cm^{-3}; (○) $N = 3 \times 10^{19}$ cm^{-3}; (□) $N = 10^{20}$ cm^{-3}.

Eqs. (27, 28) and Drude Eq. (18). The results are placed in Tables I to IX in the columns headed by abbreviation 'HW'. For heavy doping we display different values for Si: P and Si: As. The fit for Si: Sb (first line of Eq. (27)) was not used because we found that three data points available for this dopant fit a linear function of N better than that of $\sqrt{N}$. Each table covers a spectral interval from 2μm either to 100μm at light and moderate dopings, or to 25μm at heavy doping. The tables can be easily extended to wider intervals using Eqs. (27, 28, 18).

For sake of comparison, in each table we added the columns with theoretical values calculated by us using Eqs. (35, 36) with Eq. (25) as outlined above; they are abbreviated by 'GDA'. It is seen that at light and moderate doping the disagreement between theory and the empirical fit is not so strong. It is more or less concordant with the disagreement at DC discussed above. In some cases, where the fit overestimates γ, theory may be in a better agreement with direct experimental data (see Fig. 6). At heavy doping (Tables VII–IX), the disagreement becomes more drastic especially near the peaks of the relaxation functions. Fig. 7 shows some plots of n and k.

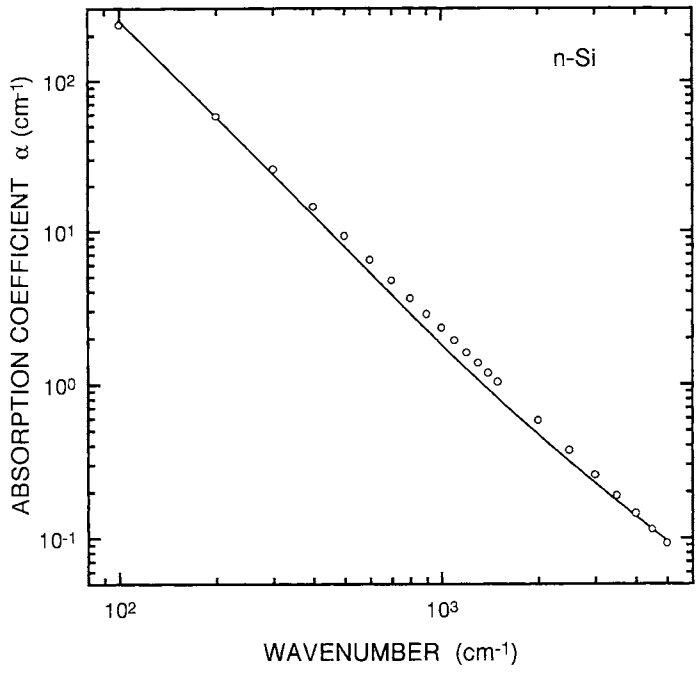

Fig. 6. Absorption spectrum for $N = 10^{17}$ cm^{-3} with lattice absorption extracted. The solid line represents theoretical curve. Open circles are the experimental data for Si: As [43].

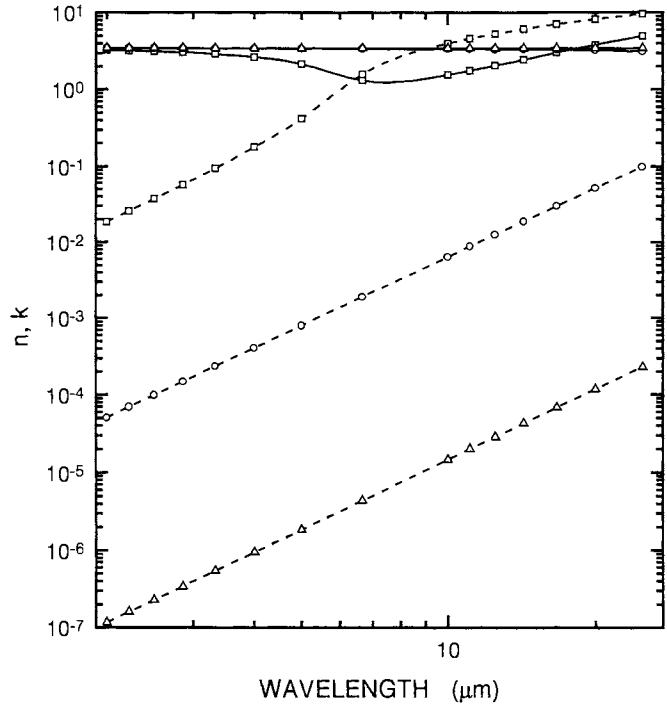

Fig. 7. Log-plot of n and k calculated using Eqs. (18, 27, 29) for three electron concentrations: (Δ) $N = 10^{16}$ cm^{-3}; (○) $N = 10^{18}$ cm^{-3}; (□) $N = 10^{20}$ cm^{-3}. Lines: solid-n, dashed-k. The difference in values of n as well as its spectral variation for (Δ) and (○) are small.

TABLE I

n-Si, $N = 10^{16}$ cm^{-3}

			n		k	
eV	cm^{-1}	μm	HW[a]	GDA[b]	HW[a]	GDA[b]
0.6199	5000	2.000	3.453	3.453	1.160 E–7	1.514 E–7
0.5579	4500	2.222	3.447	3.447	1.594 E–7	2.006 E–7
0.4959	4000	2.500	3.441	3.441	2.273 E–7	2.751 E–7
0.4339	3500	2.857	3.435	3.435	3.398 E–7	3.945 E–7
0.3720	3000	3.333	3.431	3.431	5.403 E–7	6.001 E–7
0.3100	2500	4.000	3.427	3.427	9.347 E–7	9.912 E–7
0.2480	2000	5.000	3.424	3.424	1.827 E–6	1.850 E–6
0.1860	1500	6.667	3.421	3.421	4.334 E–6	4.210 E–6
0.1240	1000	10.00	3.419	3.419	1.463 E–5	1.392 E–5
0.1116	900	11.11	3.419	3.419	2.006 E–5	1.910 E–5
0.09919	800	12.50	3.419	3.419	2.856 E–5	2.727 E–5
0.08679	700	14.29	3.418	3.418	4.262 E–5	4.092 E–5
0.07439	600	16.67	3.418	3.418	6.765 E–5	6.549 E–5
0.06199	500	20.00	3.417	3.417	1.168 E–4	1.143 E–4
0.04959	400	25.00	3.416	3.416	2.278 E–4	2.259 E–4
0.03720	300	33.33	3.413	3.413	5.382 E–4	5.413 E–4
0.03472	280	35.71	3.412	3.412	6.612 E–4	6.669 E–4
0.03224	260	38.46	3.411	3.411	8.247 E–4	8.341 E–4
0.02976	240	41.67	3.410	3.410	1.047 E–3	1.061 E–3
0.02728	220	45.45	3.408	3.408	1.356 E–3	1.379 E–3
0.02480	200	50.00	3.406	3.406	1.799 E–3	1.834 E–3
0.02232	180	55.56	3.399	3.399	3.481 E–3	3.563 E–3
0.01984	160	62.50	3.403	3.403	2.458 E–3	2.511 E–3
0.01736	140	71.43	3.394	3.394	5.154 E–3	5.284 E–3
0.01488	120	83.33	3.385	3.385	8.085 E–3	8.297 E–3
0.01240	100	100.0	3.372	3.372	1.370 E–2	1.405 E–2

[a] Values calculated using the fit of Ref. [43].
[b] Values calculated using GDA (unpublished)

TABLE II

n-Si, $N = 3 \times 10^{16}$ cm^{-3}

			n		*k*	
eV	cm^{-1}	μm	HW[a]	GDA[b]	HW[a]	GDA[b]
0.6199	5000	2.000	3.453	3.453	6.273 E–7	4.547 E–7
0.5579	4500	2.222	3.447	3.447	8.622 E–7	6.025 E–7
0.4959	4000	2.500	3.441	3.441	1.230 E–6	8.264 E–7
0.4339	3500	2.857	3.435	3.435	1.838 E–6	1.185 E–6
0.3720	3000	3.333	3.431	3.431	2.923 E–6	1.804 E–6
0.3100	2500	4.000	3.427	3.427	5.056 E–6	2.982 E–6
0.2480	2000	5.000	3.424	3.424	9.884 E–6	5.571 E–6
0.1860	1500	6.667	3.421	3.421	2.344 E–5	1.271 E–5
0.1240	1000	10.00	3.418	3.418	7.913 E–5	4.223 E–5
0.1116	900	11.11	3.417	3.418	1.085 E–4	5.808 E–5
0.09919	800	12.50	3.416	3.417	1.545 E–4	8.312 E–5
0.08679	700	14.29	3.415	3.416	2.306 E–4	1.251 E–4
0.07439	600	16.67	3.413	3.415	3.660 E–4	2.010 E–4
0.06199	500	20.00	3.410	3.413	6.320 E–4	3.528 E–4
0.04959	400	25.00	3.405	3.410	1.233 E–3	7.025 E–4
0.03720	300	33.33	3.394	3.402	2.913 E–3	1.704 E–3
0.03472	280	35.71	3.391		3.579 E–3	
0.03224	260	38.46	3.386		4.464 E–3	
0.02976	240	41.67	3.381		5.667 E–3	
0.02728	220	45.45	3.374		7.342 E–3	
0.02480	200	50.00	3.365	3.381	9.745 E–3	5.888 E–3
0.02232	180	55.56	3.352		1.887 E–3	
0.01984	160	62.50	3.336		1.332 E–2	
0.01736	140	71.43	3.311		2.796 E–2	
0.01488	120	83.33	3.275		4.391 E–2	
0.01240	100	100.0	3.218	3.279	7.453 E–2	4.695 E–2

TABLE III

n-Si, $N = 10^{17}$ cm^{-3}

			n		k	
eV	cm^{-1}	μm	HW[a]	GDA[b]	HW[a]	GDA[b]
0.6199	5000	2.000	3.453	3.453	2.856 E–6	1.519 E–6
0.5579	4500	2.222	3.446	3.446	3.925 E–6	2.013 E–6
0.4959	4000	2.500	3.440	3.440	5.598 E–6	2.763 E–6
0.4339	3500	2.857	3.435	3.435	8.369 E–6	3.965 E–6
0.3720	3000	3.333	3.430	3.430	1.331 E–5	6.042 E–6
0.3100	2500	4.000	3.426	3.426	2.302 E–5	1.000 E–5
0.2480	2000	5.000	3.422	3.423	4.500 E–5	1.875 E–5
0.2356	1900	5.263	3.421		5.250 E–5	
0.2232	1800	5.556	3.421		6.175 E–5	
0.2108	1700	5.882	3.420		7.331 E–5	
0.1984	1600	6.250	3.419		8.794 E–5	
0.1860	1500	6.667	3.418	3.419	1.067 E–4	4.300 E–5
0.1736	1400	7.143	3.417	3.419	1.313 E–4	5.268 E–5
0.1612	1300	7.692	3.4165	3.418	1.640 E–4	6.561 E–5
0.1488	1200	8.333	3.415	3.417	2.085 E–4	8.333 E–5
0.1364	1100	9.091	3.414	3.416	2.708 E–4	1.083 E–4
0.1240	1000	10.00	3.413	3.415	3.604 E–4	1.446 E–4
0.1116	900	11.11	3.410	3.413	4.944 E–4	1.997 E–4
0.09919	800	12.50	3.408	3.411	7.039 E–4	2.874 E–4
0.08679	700	14.29	3.404	3.409	1.051 E–3	4.355 E–4
0.07439	600	16.67	3.399	3.405	1.668 E–3	7.061 E–4
0.06199	500	20.00	3.390	3.400	2.882 E–3	1.255 E–3
0.05951	480	20.83	3.387		3.257 E–3	
0.05703	460	21.74	3.384		3.700 E–3	
0.05455	440	22.73	3.381		4.228 E–3	
0.05207	420	23.81	3.377		4.861 E–3	
0.04959	400	25.00	3.373	3.387	5.626 E–3	2.542 E–3
0.04771	380	26.32	3.368		6.561 E–3	
0.04463	360	27.78	3.365		7.715 E–3	
0.04215	340	29.41	3.356		9.156 E–3	
0.03968	320	31.25	3.348		1.098 E–2	
0.03720	300	33.33	3.338	3.362	1.332 E–2	6.326 E–3
0.03472	280	35.71	3.326		1.638 E–2	
0.03224	260	38.46	3.312		2.045 E–2	
0.02976	240	41.67	3.294		2.599 E–2	
0.02728	220	45.45	3.271		3.372 E–2	
0.02480	200	50.00	3.241	3.294	4.485 E–2	2.283 E–2
0.02232	180	55.56	3.201		6.147 E–2	
0.01984	160	62.50	3.146		8.744 E–2	
0.01736	140	71.43	3.069		1.304 E–1	
0.01488	120	83.33	2.956		2.068 E–1	
0.01240	100	100.0	2.786	2.957	3.567 E–1	1.995 E–1

TABLE IV

n-Si, $N = 3 \times 10^{17}$ cm^{-3}

			n		*k*	
eV	cm^{-1}	μm	HW[a]	GDA[b]	HW[a]	GDA[b]
0.6199	5000	2.000	3.452	3.453	1.286 E–5	4.580 E–6
0.5579	4500	2.222	3.446	3.446	1.768 E–5	6.078 E–6
0.4959	4000	2.500	3.439	3.440	2.522 E–5	8.355 E–6
0.4339	3500	2.857	3.434	3.434	3.770 E–5	1.202 E–5
0.3720	3000	3.333	3.429	3.429	5.995 E–5	1.837 E–5
0.3100	2500	4.000	3.424	3.425	1.037 E–4	3.056 E–5
0.2480	2000	5.000	3.419	3.420	2.028 E–4	5.774 E–5
0.2356	1900	5.263	3.417		2.365 E–4	
0.2232	1800	5.556	3.416		2.782 E–4	
0.2108	1700	5.882	3.415		3.304 E–4	
0.1984	1600	6.250	3.413		3.963 E–4	
0.1860	1500	6.667	3.412	3.415	4.811 E–4	1.344 E–4
0.1736	1400	7.143	3.410	3.413	5.918 E–4	1.654 E–4
0.1612	1300	7.692	3.408	3.412	7.393 E–4	2.071 E–4
0.1488	1200	8.333	3.405	3.410	9.401 E–4	2.647 E–4
0.1364	1100	9.091	3.402	3.408	1.221 E–3	3.466 E–4
0.1240	1000	10.00	3.398	3.405	1.625 E–3	4.671 E–4
0.1116	900	11.11	3.392	3.401	2.230 E–3	6.522 E–4
0.09919	800	12.50	3.385	3.396	3.177 E–3	9.513 E–4
0.08679	700	14.29	3.374	3.388	4.745 E–3	1.467 E–3
0.07439	600	16.67	3.358	3.377	7.542 E–3	2.431 E–3
0.06199	500	20.00	3.331	3.358	1.305 E–2	4.446 E–3
0.05951	480	20.83	3.324		1.476 E–2	
0.05703	460	21.74	3.316		1.678 E–2	
0.05455	440	22.73	3.306		1.918 E–2	
0.05207	420	23.81	3.295		2.207 E–2	
0.04959	400	25.00	3.283	3.324	2.556 E–2	9.367 E–3
0.04771	380	26.32	3.268		2.984 E–2	
0.04463	360	27.78	3.251		3.513 E–2	
0.04215	340	29.41	3.232		4.176 E–2	
0.03968	320	31.25	3.208		5.017 E–2	
0.03720	300	33.33	3.180	3.250	6.100 E–2	2.464 E–2
0.03472	280	35.71	3.145		7.522 E–2	
0.03224	260	38.46	3.103		9.424 E–2	
0.02976	240	41.67	3.051		1.203 E–1	
0.02728	220	45.45	2.985		1.571 E–1	
0.02480	200	50.00	2.900	3.041	2.107 E–1	9.695 E–2
0.02232	180	55.56	2.790		2.923 E–1	
0.01984	160	62.50	2.647		4.227 E–1	
0.01736	140	71.43	2.465		6.431 E–1	
0.01612	130	76.92	2.364		8.094 E–1	
0.01488	120	83.33	2.267		1.030 E 0	
0.01364	110	90.91	2.193		1.314 E 0	
0.01240	100	100.0	2.163	2.137	1.664 E 0	9.947 E–1

TABLE V

n-Si, $N = 10^{18}$ cm^{-3}

			n		k	
eV	cm^{-1}	μm	HW[a]	GDA[b]	HW[a]	GDA[b]
0.6199	5000	2.000	3.451	3.451	5.030 E–5	1.556 E–5
0.5579	4500	2.222	3.444	3.444	6.913 E–5	2.072 E–5
0.4959	4000	2.500	3.438	3.438	9.860 E–5	2.863 E–5
0.4339	3500	2.857	3.431	3.431	1.474 E–4	4.149 E–5
0.3720	3000	3.333	3.425	3.425	2.344 E–4	6.408 E–5
0.3100	2500	4.000	3.419	3.419	4.054 E–4	1.083 E–4
0.2480	2000	5.000	3.411	3.411	7.925 E–4	2.100 E–4
0.2356	1900	5.263	3.410		9.244 E–4	
0.2232	1800	5.556	3.407		1.087 E–3	
0.2108	1700	5.882	3.405		1.291 E–3	
0.1984	1600	6.250	3.402		1.548 E–3	
0.1860	1500	6.667	3.399	3.399	1.879 E–3	5.121 E–4
0.1736	1400	7.143	3.396	3.395	2.312 E–3	6.385 E–4
0.1612	1300	7.692	3.391	3.391	2.887 E–3	8.120 E–4
0.1488	1200	8.333	3.386	3.385	3.671 E–3	1.056 E–3
0.1364	1100	9.091	3.379	3.378	4.766 E–3	1.412 E–3
0.1240	1000	10.00	3.370	3.369	6.343 E–3	1.951 E–3
0.1116	900	11.11	3.358	3.357	8.700 E–3	2.804 E–3
0.09919	800	12.50	3.342	3.340	1.239 E–2	4.234 E–3
0.08679	700	14.29	3.318	3.315	1.848 E–2	6.806 E–3
0.07439	600	16.67	3.282	3.277	2.934 E–2	1.187 E–2
0.06199	500	20.00	3.224	3.213	5.068 E–2	2.309 E–2
0.05951	480	20.83	3.208		5.727 E–2	
0.05703	460	21.74	3.190		6.507 E–2	
0.05455	440	22.73	3.169		7.435 E–2	
0.05207	420	23.81	3.146		8.548 E–2	
0.04959	400	25.00	3.120	3.100	9.896 E–2	5.252 E–2
0.04771	380	26.32	3.090		1.154 E–1	
0.04463	360	27.78	3.055		1.358 E–1	
0.04215	340	29.42	3.014		1.612 E–1	
0.03968	320	31.25	2.967		1.934 E–1	
0.03720	300	33.33	2.912	2.844	2.349 E–1	1.525 E–1
0.03472	280	35.71	2.847		2.891 E–1	
0.03224	260	38.46	2.771		3.613 E–1	
0.02976	240	41.67	2.682		4.594 E–1	
0.02728	220	45.45	2.582		5.953 E–1	
0.02480	200	50.00	2.474	2.149	7.862 E–1	6.685 E–1
0.02232	180	55.56	2.374		1.054 E 0	
0.02108	170	58.82	2.337		1.222 E 0	
0.01984	160	62.50	2.314		1.416 E 0	
0.01860	150	66.67	2.312		1.634 E 0	
0.01736	140	71.43	2.336		1.875 E 0	
0.01612	130	76.92	2.388		2.137 E 0	
0.01488	120	83.33	2.474		2.420 E 0	
0.01364	110	90.91	2.596		2.723 E 0	
0.01240	100	100.0	2.758	2.122	3.048 E 0	3.868 E 0

TABLE VI

n-Si, $N = 3 \times 10^{18}$ cm^{-3}

			n		*k*	
eV	cm^{-1}	μm	HW[a]	GDA[b]	HW[a]	GDA[b]
0.6199	5000	2.000	3.447	3.447	2.482 E–4	4.914 E–5
0.5579	4500	2.222	3.439	3.439	3.412 E–4	6.614 E–5
0.4959	4000	2.500	3.431	3.431	4.866 E–4	9.264 E–5
0.4339	3500	2.857	3.423	3.423	7.275 E–4	1.367 E–4
0.3720	3000	3.333	3.414	3.414	1.157 E–3	2.168 E–4
0.3100	2500	4.000	3.403	3.403	2.001 E–3	3.807 E–4
0.2480	2000	5.000	3.386	3.386	3.913 E–3	7.826 E–4
0.2356	1900	5.263	3.382		4.565 E–3	
0.2232	1800	5.556	3.377		5.370 E–3	
0.2108	1700	5.882	3.371		6.376 E–3	
0.1984	1600	6.250	3.363		7.650 E–3	
0.1860	1500	6.667	3.355	3.354	9.286 E–3	2.097 E–3
0.1736	1400	7.143	3.345	3.343	1.142 E–2	2.683 E–3
0.1612	1300	7.692	3.332	3.330	1.427 E–2	3.510 E–3
0.1488	1200	8.333	3.317	3.314	1.815 E–2	4.714 E–3
0.1364	1100	9.091	3.297	3.293	2.358 E–2	6.531 E–3
0.1240	1000	10.00	3.272	3.266	3.141 E–2	9.391 E–3
0.1116	900	11.11	3.237	3.228	4.312 E–2	1.412 E–2
0.09919	800	12.50	3.190	3.176	6.148 E–2	2.244 E–2
0.08679	700	14.29	3.123	3.099	9.198 E–2	3.820 E–2
0.07439	600	16.67	3.023	2.980	1.466 E–1	7.099 E–2
0.06199	500	20.00	2.866	2.782	2.553 E–1	1.477 E–1
0.05951	480	20.83	2.825		2.892 E–1	
0.05703	460	21.74	2.780		3.294 E–1	
0.05455	440	22.73	2.729		3.774 E–1	
0.05207	420	23.81	2.674		4.352 E–1	
0.04959	400	25.00	2.615	2.435	5.052 E–1	3.728 E–1
0.04771	380	26.32	2.550		5.906 E–1	
0.04463	360	27.78	2.483		6.953 E–1	
0.04215	340	29.41	2.414		8.241 E–1	
0.03968	320	31.25	2.349		9.816 E–1	
0.03720	300	33.33	2.294	1.677	1.172 E 0	1.110 E 0
0.03472	280	35.71	2.258		1.398 E 0	
0.03224	260	38.46	2.249		1.659 E 0	
0.02976	240	41.67	2.277		1.953 E 0	
0.02728	220	45.45	2.347		2.275 E 0	
0.02480	200	50.00	2.464	1.600	2.625 E 0	3.324 E 0
0.02232	180	55.56	2.635		3.004 E 0	
0.01984	160	62.50	2.866		3.416 E 0	
0.01736	140	71.43	3.170		3.868 E 0	
0.01488	120	83.33	3.567		4.375 E 0	
0.01240	100	100.0	4.088	3.571	4.963 E 0	7.154 E 0

TABLE VII

n-Si, $N = 10^{19}$ cm^{-3}

			n		k	
eV	cm^{-1}	μm	HW[a]	GDA[b]	HW[a]	GDA[b]
0.6199	5000	2.000	3.432[P]		1.239 E–3	
			3.434[As]	3.433	1.233 E–3	1.929 E–4
0.5579	4500	2.222	3.420		1.703 E–3	
			3.422	3.422	1.695 E–3	2.672 E–4
0.4959	4000	2.500	3.408		2.432 E–3	
			3.410	3.409	2.419 E–3	3.883 E–4
0.4339	3500	2.857	3.392		3.641 E–3	
			3.395	3.394	3.620 E–3	6.013 E–4
0.3720	3000	3.333	3.372		5.802 E–3	
			3.376	3.375	5.765 E–3	1.015 E–3
0.3100	2500	4.000	3.342		1.007 E–2	
			3.349	3.346	1.000 E–2	1.940 E–3
0.2480	2000	5.000	3.290		1.984 E–2	
			3.301	3.296	1.963 E–2	4.478 E–3
0.2356	1900	5.263	3.275		2.319 E–2	
			3.288		2.293 E–2	
0.2232	1800	5.556	3.258		2.735 E–2	
			3.272		2.702 E–2	
0.2108	1700	5.882	3.237		3.257 E–2	
			3.253		3.214 E–2	
0.1984	1600	6.250	3.213		3.922 E–2	
			3.231		3.865 E–2	
0.1860	1500	6.667	3.184		4.782 E–2	
			3.205	3.190	4.706 E–2	1.413 E–2
0.1736	1400	7.143	3.148		5.916 E–2	
			3.173	3.155	5.810 E–2	1.883 E–2
0.1612	1300	7.692	3.105		7.444 E–2	
			3.133	3.110	7.292 E–2	2.577 E–2
0.1488	1200	8.333	3.050		9.557 E–2	
			3.084	3.054	9.330 E–2	3.636 E–2
0.1364	1100	9.091	2.979		1.257 E–1	
			3.021	2.981	1.222 E–1	5.321 E–2
0.1240	1000	10.00	2.888		1.703 E–1	
			2.940	2.884	1.645 E–1	8.135 E–2
0.1116	900	11.11	2.765[P]		2.395 E–1	
			2.833[As]	2.753	2.293 E–1	1.311 E–1
0.09919	800	12.50	2.598		3.541 E–1	
			2.688	2.572	3.345 E–1	2.240 E–1
0.08679	700	14.29	2.369		5.598 E–1	
			2.492	2.307	5.173 E–1	3.933 E–1
0.08431	680	14.71	2.315		6.194 E–1	
			2.447		5.692 E–1	
0.08183	660	15.15	2.259		6.878 E–1	
			2.399		6.281 E–1	

TABLE VII *(Continued)*

n-Si, $N = 10^{19}$ cm^{-3}

			n		*k*	
eV	cm^{-1}	μm	HW[a]	GDA[b]	HW[a]	GDA[b]
0.07935	640	15.63	2.201		7.662 E–1	
			2.349		6.952 E–1	
0.07690	620	16.13	2.142		8.562 E–1	
			2.299		7.717 E–1	
0.07439	600	16.67	2.085		9.591 E–1	
			2.248	1.847	8.588 E–1	7.106 E–1
0.07180	580	17.24	2.030		1.076 E–1	
			2.198		9.578 E–1	
0.06933	560	17.86	1.980		1.208 E 0	
			2.151		1.070 E 0	
0.06685	540	18.52	1.938		1.355 E 0	
			2.110		1.195 E 0	
0.06438	520	19.23	1.907		1.516 E 0	
			2.075		1.334 E 0	
0.06199	500	20.00	1.887		1.690 E 0	
			2.049	1.274	1.487 E 0	1.565 E 0
0.05951	480	20.83	1.882		1.876 E 0	
			2.035		1.653 E 0	
0.05703	460	21.74	1.890		2.072 E 0	
			2.034		1.830 E 0	
0.05455	440	22.73	1.914		2.277 E 0	
			2.047		2.018 E 0	
0.05207	420	23.81	1.954		2.492 E 0	
			2.075		2.217 E 0	
0.04959	400	25.00	2.009		2.716 E 0	
			2.118	1.197	2.424 E 0	2.943 E 0

[P, As] The superscripts denote Si: P, Si: As respectively.

TABLE VIII

n-Si, $N = 3 \times 10^{19}$ cm^{-3}

			n		k	
eV	cm^{-1}	μm	HW[a]	GDA[b]	HW[a]	GDA[b]
0.6199	5000	2.000	3.397[P]		4.082 E–3	
			3.395[As]	3.393	4.811 E–3	8.340 E–4
0.5579	4500	2.222	3.376		5.626 E–3	
			3.374	3.372	6.629 E–3	1.215 E–3
0.4959	4000	2.500	3.352		8.056 E–3	
			3.349	3.345	9.489 E–3	1.875 E–3
0.4339	3500	2.857	3.319		1.211 E–2	
			3.316	3.310	1.426 E–2	3.121 E–3
0.3720	3000	3.333	3.272		1.944 E–2	
			3.267	3.259	2.287 E–2	5.759 E–3
0.3100	2500	4.000	3.196		3.418 E–2	
			3.191	3.177	4.015 E–2	1.232 E–2
0.2480	2000	5.000	3.060		6.895 E–2	
			3.053	3.025	8.078 E–2	3.331 E–2
0.2356	1900	5.263	3.019		8.124 E–2	
			3.011		9.509 E–2	
0.2232	1800	5.556	2.971		9.671 E–2	
			2.963		1.131 E–1	
0.2108	1700	5.882	2.914		1.165 E–1	
			2.906		1.361 E–1	
0.1984	1600	6.250	2.846		1.423 E–1	
			2.838		1.660 E–1	
0.1860	1500	6.667	2.763		1.768 E–1	
			2.755	2.694	2.057 E–1	1.415 E–1
0.1736	1400	7.143	2.661		2.240 E–1	
			2.655	2.587	2.599 E–1	2.036 E–1
0.1612	1300	7.692	2.534		2.910 E–1	
			2.530	2.453	3.363 E–1	2.886 E–1
0.1488	1200	8.333	2.372		3.903 E–1	
			2.377	2.294	4.483 E–1	4.167 E–1
0.1364	1100	9.091	2.168		5.460 E–1	
			2.188	1.999	6.201 E–1	5.280 E–1
0.1240	1000	10.00	1.921		8.042 E–1	
			1.971	1.609	8.933 E–1	7.725 E–1
0.1116	900	11.11	1.675[P]		1.232 E 0	
			1.774[As]	1.221	1.317 E 0	1.308 E 0
0.09919	800	12.50	1.540		1.842 E 0	
			1.681	1.000	1.893 E 0	2.079 E 0
0.08679	700	14.29	1.571		2.565 E 0	
			1.737	0.966	2.572 E 0	2.948 E 0
0.08431	680	14.71	1.597		2.720 E 0	
			1.767		2.718 E 0	
0.08183	660	15.15	1.628		2.878 E 0	
			1.801		2.868 E 0	

TABLE VIII *(Continued)*

n-Si, $N = 3 \times 10^{19}$ cm^{-3}

			n		*k*	
eV	cm^{-1}	μm	HW[a]	GDA[b]	HW[a]	GDA[b]
0.07935	640	15.63	1.666		3.041 E 0	
			1.843		3.021 E 0	
0.07690	620	16.13	1.711		3.208 E 0	
			1.891		3.178 E 0	
0.07439	600	16.67	1.762		3.380 E 0	
			1.945	1.073	3.340 E 0	3.932 E 0
0.07180	580	17.24	1.820		3.557 E 0	
			2.007		3.506 E 0	
0.06933	560	17.86	1.886		3.739 E 0	
			2.076		3.677 E 0	
0.06685	540	18.52	1.959		3.928 E 0	
			2.153		3.853 E 0	
0.06438	520	19.23	2.042		4.123 E 0	
			2.238		4.035 E 0	
0.06199	500	20.00	2.134		4.325 E 0	
			2.332	1.318	4.223 E 0	5.134 E 0
0.05951	480	20.83	2.236		4.535 E 0	
			2.437		4.418 E 0	
0.05703	460	21.74	2.349		4.754 E 0	
			2.552		4.620 E 0	
0.05455	440	22.73	2.475		4.982 E–0	
			2.679		4.831 E–0	
0.05207	420	23.81	2.614		5.220 E 0	
			2.819		5.050 E 0	
0.04959	400	25.00	2.769		5.469 E 0	
			2.974	1.803	5.278 E 0	6.720 E 0

TABLE IX

n-Si, $N = 10^{20}$ cm^{-3}

			n		k	
eV	cm^{-1}	μm	HW[a]	GDA[b]	HW[a]	GDA[b]
0.6199	5000	2.000	3.270[P]		1.834 E–2	
			3.257[As]	3.247	2.403 E–2	6.131 E–3
0.5579	4500	2.222	3.219		2.549 E–2	
			3.203	3.190	3.341 E–2	9.701 E–3
0.4959	4000	2.500	3.151		3.698 E–2	
			3.130	3.112	4.845 E–2	1.664 E–2
0.4339	3500	2.857	3.053	3.000	5.671 E–2	
			3.027		7.432 E–2	3.232 E–2
0.3720	3000	3.333	2.902		9.410 E–2	
			2.867	2.828	1.233 E–1	8.053 E–2
0.3100	2500	4.000	2.644		1.765 E–1	
			2.597	2.577	2.314 E–1	2.549 E–1
0.2480	2000	5.000	2.138		4.176 E–1	
			2.087	1.990	5.461 E–1	5.336 E–1
0.2356	1900	5.263	1.981		5.226 E–1	
			1.939		6.796 E–1	
0.2232	1800	5.556	1.800		6.717 E–1	
			1.780		8.617 E–1	
0.2108	1700	5.882	1.604		8.873 E–1	
			1.626		1.107 E 0	
0.1984	1600	6.250	1.423		1.188 E 0	
			1.503		1.417 E 0	
0.1860	1500	6.667	1.295		1.566 E 0	
			1.429	0.971	1.777 E 0	1.902 E 0
0.1736	1400	7.143	1.237		1.989 E 0	
			1.411	0.893	2.172 E 0	2.369 E 0
0.1612	1300	7.692	1.239		2.437 E 0	
			1.442	0.873	2.591 E 0	2.859 E 0
0.1488	1200	8.333	1.291		2.911 E 0	
			1.518	0.872	3.037 E 0	3.387 E 0
0.1364	1100	9.091	1.390		3.418 E 0	
			1.642	0.913	3.514 E 0	3.960 E 0
0.1240	1000	10.00	1.540		3.971 E 0	
			1.817	0.985	4.034 E 0	4.603 E 0
0.1116	900	11.11	1.751[P]		4.584 E 0	
			2.057[As]	1.105	4.608 E 0	5.341 E 0
0.09919	800	12.50	2.042		5.278 E 0	
			2.378	1.278	5.251 E 0	6.216 E 0
0.08679	700	14.29	2.444		6.079 E 0	
			2.810	1.530	5.982 E 0	7.282 E 0
0.08431	680	14.71	2.542		6.255 E 0	
			2.913		6.141 E 0	
0.08183	660	15.15	2.646		6.437 E 0	
			3.022		6.305 E 0	

TABLE IX *(Continued)*

n-Si, $N = 10^{20}$ cm^{-3}

			n		*k*	
eV	cm^{-1}	μm	HW[a]	GDA[b]	HW[a]	GDA[b]
0.07935	640	15.63	2.758		6.625 E 0	
			3.139		6.474 E 0	
0.07690	620	16.13	2.877		6.820 E 0	
			3.262		6.649 E 0	
0.07439	600	16.67	3.006		7.022 E 0	
			3.395	1.911	6.829 E 0	8.630 E 0
0.07180	580	17.24	3.143		7.231 E 0	
			3.536		7.015 E 0	
0.06933	560	17.86	3.291		7.448 E 0	
			3.686		7.208 E 0	
0.06685	540	18.52	3.451		7.674 E 0	
			3.846		7.407 E 0	
0.06438	520	19.23	3.622		7.909 E 0	
			4.018		7.614 E 0	
0.06199	500	20.00	3.807		8.154 E 0	
			4.201	2.517	7.829 E 0	1.040 E+1
0.05951	480	20.83	4.006		8.409 E 0	
			4.398		8.052 E 0	
0.05703	460	21.74	4.222		8.675 E 0	
			4.608		8.285 E 0	
0.05455	440	22.73	4.455		8.954 E 0	
			4.835		8.528 E 0	
0.05207	420	23.81	4.707		9.245 E 0	
			5.078		8.782 E 0	
0.04959	400	25.00	4.982		9.551 E 0	
			5.340	3.551	9.048 E 0	1.285 E+1

To conclude, there exists a dicrepancy between theory and experiment for the DF of heavily doped n-Si. This inconsistency is due to an improper model of donor potential, to a much larger extent, than to theoretical shortcomings and experimental uncertainties.

REFERENCES

1. E. D. Palik, *in* "Handbook of Optical Constants of Solids" (E. D. Palik, ed.), p. 3. Academic Press, Orlando, Florida, 1985.
2. P. A. Shumann, Jr., R. P. Phillips, and P. J. Olshefski, *J. Electrochem. Soc.* **113**, 368 (1966).
3. B. R. Hemenway, O. Solgaard, and D. M. Bloom, *Appl. Phys. Lett.* **55**, 349 (1989).
4. J. C. Sturm and C. M. Reaves, *IEEE Trans. Electron Devices* **39**, 81 (1992); P. J. Timans, *J. Appl. Phys.* **74**, 6353 (1993).
5. P. J. Hesketh, J. N. Zemel, and B. Gebhart, *Phys. Rev. B* **37**, 10795 and 10813 (1988).
6. M. Auslender and S. Hava, *Infrared Phys. Technol.* **36**, 1077 (1995); M. Auslender, S. Hava, and J. N. Zemel, *Infrared Phys. Technol.* **37**, 367 (1996).

7. M. Born and E. Wolf, "Principles of Optics." Pergamon, Oxford, 1986.
8. T. S. Moss, "Optical Properties of Semiconductors." Academic Press, New York, 1959.
9. K. Seeger, "Semiconductor Physics" (Springer Series on Solid State Science, Vol. 40). Springer-Verlag, New York, 1982.
10. L. I. Shiff, "Quantum Mechanics." McGraw-Hill, Singapore, 1988.
11. L. Viña and M. Cardona, *Phys. Rev. B* **29**, 6739 (1984).
12. D. F. Edwards, *in* "Handbook of Optical Constants of Solids" (E. D. Palik, ed.), p. 547. Academic Press, Orlando, Florida, 1985.
13. D. E. Aspnes, *in* "Properties of Silicon," Vol. 2.6, p. 79 (Emis Data reviews Ser. No. 4). Inspec IEE, London, 1988.
14. D. Y. Smith, *in* "Handbook of Optical Constants of Solids" (E. D. Palik, ed.), p. 35. Academic Press, Orlando, Florida, 1985.
15. H. M. van Driel, *Appl. Phys. Lett.* **44**, 617 (1984).
16. P. Drude, "Theory of Optics." Dover, New York, 1902.
17. H. Y. Fan, W. G. Spitzer, and R. J. Collins, *Phys. Rev.* **101**, 569 (1956); H. Y. Fan, *Rep. Prog. Phys.* **14**, 119 (1956).
18. W. G. Spitzer and H. Y. Fan, *Phys. Rev.* **106**, 882 (1957).
19. H. J. G. Meyer, *Phys. Rev.* **112**, 298 (1958); H. J. G. Meyer, *J. Phys. Chem. Sol.* **8**, 264 (1959).
20. R. Rosenberg and M. Lax, *Phys. Rev.* **112**, 843 (1958).
21. W. Dumke, *Phys. Rev.* **124**, 1813 (1960).
22. S. Visvanathan, *Phys. Rev.* **120**, 379 (1960).
23. B. Donovan, *Proc. Phys. Soc. (London)* **A76**, 574 (1960).
24. B. Jensen, *in* "Handbook of Optical Constants of Solids" (E. D. Palik, ed.), p. 169. Academic Press, Orlando, Florida, 1985.
25. R. Kubo, *J. Phys. Soc. Jpn.* **12**, 570 (1957).
26. H. Mori, *Prog. Theor. Phys.* **34**, 399 (1965).
27. B. E. Sernelius, *Phys. Rev. B* **41**, 30 (1990).
28. W. Gotze and P. Wolfle, *Phys. Rev. B* **6**, 1226 (1972).
29. M. Auslender and S. Hava, *Phys. Status Solidi B* **174**, 565 (1992); M. Auslender and S. Hava, *Proc. SPIE* **1972**, 210 (1992).
30. S. Hava and M. Auslender, *Appl. Opt.* **32**, 1122 (1993).
31. V. I. Fistul, "Heavily Doped Semiconductors." Plenum, New York, 1969.
32. M. Miyao, T. Motooka, N. Natsuaki, and T. Tokuyama, *Solid State Commun.* **37**, 605 (1981).
33. A. Slaoui and P. Siffert, *Phys. Status Solidi A* **89**, 617 (1985).
34. D. E. Aspnes, A. A. Studna, and E. Kinsbron, *Phys. Rev. B* **29**, 768 (1984).
35. M. Cardona, W. Paul, and H. Brooks, *Z. Naturforsch.* **101**, 329 (1960).
36. L. E. Howarth and J. F. Gilbert, *J. Appl. Phys.* **34**, 236 (1963).
37. W. G. Spitzer, G. W. Gobeli, and F. A. Trumbore, *J. Appl. Phys.* **35**, 206 (1964).
38. A. A. Kukharski and V. K. Subashiev, *Sov. Phys. Solid State,* **8**, 603 (1966).
39. E. Barta, *Infrared Phys.* **17**, 111 (1976).
40. L. N. Streltsov and V. V. Titov, *Sov. Phys. Semicond. (Engl. Transl.)* **4**, 605 (1970).
41. L. M. Lambert, *Phys. Status Solidi A* **11**, 461 (1972).
42. M. Balkanski, E. Aziza, and E. Amzallag, *Phys. Status Solidi* **31**, 323 (1969).
43. J. Humlíček and K. Wojtechovsky, *Czech. J. Phys.* **B38**, 1033 (1988).
44. W. Harrison, *Phys. Rev.* **104**, 1281 (1956).
45. D. Chattopadhyay and H. J. Queisser, *Rev. Mod. Phys.* **53**, 745 (1981).
46. J. C. Irvin, *Bell Syst. Technol. J.* **41**, 387 (1962); S. M. Sze and J. C. Irvin, *Solid-State Electron.* **11**, 559 (1968).
47. H. K. Jung, H. Ohtsuka, K. Taniguchi, and C. Hamaguchi, *J. Appl. Phys.* **79**, 2559 (1996).

Chapter 7

Optical Parameters for the Materials in *HOC I, HOC II,* and *HOC III*

EDWARD D. PALIK
Institute for Physical Science and Technology
University of Maryland
College Park, Maryland

I. Introduction 187
II. The Parameters 187
References 225

INTRODUCTION I

In *HOC II,* we made an attempt to catalog certain optical parameters for all the materials in *HOC I* and *HOC II.* We have continued this work and present in Table I a listing of Material, Crystal Structure, Symmetry Class (Space Group), Unit-Cell Dimensions, Number of Molecular Units per Unit Cell and Primitive Cell, Number of Optic Modes, Optic Irreducible Representation, Acoustic Irreducible Representation, Transverse and Longitudinal Optic Frequencies (ω_T and ω_L), Plasma Frequency for a Metal ω_p (Drude), Fundamental Band Gap E_g (Direct or Indirect), and dc Dielectric Constant ϵ_o.

THE PARAMETERS II

Usually a cubic metal cannot support a transverse or longitudinal optic mode, and this is indicated with *None.* For a cubic diatomic metal, the LO mode may be degenerate with the TO mode, at least at the zone center. It is not obvious that the LO mode has any oscillator strength, since the free charges can move to cancel any longitudinal planes of charge the lattice tries to set up and maintain. We indicate our doubt with a (?). A dashed (- - -)

HANDBOOK OF OPTICAL CONSTANTS OF SOLIDS III

Copyright © 1998 by Academic Press.
All rights of reproduction in any form reserved
ISBN 0-12-544423-0/$25.00.

TABLE I

Collected Optical Parameters

Material	Crystal structure	Symmetry class space group	Unit cell dimensions (Å)	Molecular Units: Unit cell	Molecular Units: Primitive cell	No. of optic modes	Optic irreducible representation	Accoustic irr. rep.	ω_T (cm^{-1})	ω_L (cm^{-1})	ω_P Drude (eV)	E_g (eV)	ϵ_O
$Y_3Al_5O_{12}$	cubic	(230) Ia3d O_h^{10}	12.008	8	4	237	$5A_{1u}(0) + 3A_{1g}(R) + 5A_{2u}(0) + 5A_{2g}(0) + 10E_u(0) + 8E_g(R) + 14F_{1g}(0) + 17F_{1u}(IR) + 14F_{2g}(R) + 16F_{2u}(0)$	F_{1u}	Table a		----	6.5	10.6
Mo	bcc	(229) Im3m O_h^9	3.1473	2	1	0	None	F_{1u}	None	None	7.5	None	−21000
W			3.1646								6.4		−11000
Fe			2.8665								4.1		−50000
Cr			2.8839								xx		xx
Nb			3.3004								xx		xx
K			5.2								4.25		xx
Na			4.2906								5.91		xx
Li			3.5902								xx		xx
Ta			3.3058								6.2		xx
V			3.0240								5.2		−7200
Cs			6.091								xx		xx
Al_2MgO_4	cubic	(227) Fd3m O_h^7	8.0800	8	2	39	$A_{1g}(R) + 2A_{2u}(O) + E_g(R) + 2E_u(O) + F_{1g}(0) + 4F_{1u}(IR) + 3F_{2g}(R) + 2F_{2u}(0)$	F_{1u}	Table b		----	~8	8.29
$Al_{23}O_{27}N_5$	cubic	(227) Fd3m O_h^7	7.948	1	1	162	xxxx	F_{1u}	Table c		----	6–7	~9.36
Si	cubic diamond	(227) Fd3m O_h^7	5.4307	8	2	3	$F_{2g}(R)$	F_{1u}	521	521	----	1.1(i)	11.6
Ge			5.6573						301	301		0.66(i)	16.0
C			3.5667						1332	1332		5.2(i)	5.6
Sn-α gray			6.4912						xxx	?	~8.1	None	xx
Cu	fcc	(225) Fm3m O_h^5	3.6149	4	1	0	None	F_{1u}	None	None	7.4	None	−66000
Au			4.0782								9.0		−114000
Ir			3.8394								xx		xx

Ni			3.5238									4.9		−13000
Pt			3.9231									5.1		−5600
Rh			3.8031									3.8		−251000
Ag			4.0862									9.0		xx
Al			4.0495									14.8		−33000
Pd			3.8898									5.5		−126000
Yb			5.4862									10.0		xx
PbS	cubic NaCl	(225) Fm3m O_h^5	5.935	4	1	3	F_{1u}(IR)	F_{1u}	71	212	----		0.41(d)	169
PbSe			6.122						39	111			0.278(d)	210
PbTe			6.443						32	112			0.31(d)	414
SnTe			6.313						26	139			0.19(d)	1770
NaCl			5.64						164	266			8.6	5.90
KCl			6.2929						142	213			8.5	4.4
KI			7.0655						101	139			~6.2	4.94
LiF			4.0263						307	501			14.2(d)	9.06
KBr			6.6000						113	155			7.8	4.8
NaF			4.620						246	420			10.5	~5.7
MgO			4.215						396	729			7.8(d)	9.8
AgCl			5.547						106	196			3.2(i)	11.1
AgBr			5.7745						79	138			2.6(i)	12.4
CsF			6.008						131	248			10.0	~8.1
RbBr			6.854						88	117			7.7	4.9
RbI			7.342						75	103			~6.1	5.0
TiC			4.3186						537	?	xx		None	xx
TiN			4.235						488	?	xx			xx
HfN			4.512						xx	?	~3			xx
ZrN			4.61						450	?	~3			xx
VC			4.182						590	?	xx			xx
VN			4.128						507	?	xx			xx
CaF_2	cubic fluorite	(225) Fm3m O_h^5	5.4629	4	1	6	F_{1u}(IR) + F_{2g}(R)	F_{1u}	258 F_{1u} 322 F_{2g}	473	----		~11	6.7
BaF_2			6.2001						184 241	319			10.1	7.3
PbF_2-β			5.9273						102 256	337			5.7	27.4
SrF_2			5.7996						217 286	366			3.4	7.69

(continued)

TABLE I *(Continued)*

Collected Optical Parameters

Material	Crystal structure	Symmetry class space group	Unit cell dimensions (Å)	Molecular Units: Unit cell	Molecular Units: Primitive cell	No. of optic modes	Optic irreducible representation	Accoustic irr. rep.	ω_T (cm^{-1})	ω_L (cm^{-1})	ω_P Drude (eV)	E_g (eV)	ϵ_O
Cu_2O	cubic	(224) Pn3m O_h^4	4.2696	2	2	15	$A_{2u}(0) + E_u(0) + F_{2u}(0) + 2F_{1u}(IR) + F_{2g}(R)$	F_{1u}	613 F_{1u} 146 F_{1u} 220 F_{2g} 110 E_u 300 A_{2u}	638 149	----	2.17(d)	~7.5
$SrTiO_3$	cubic perovskite	(221) Pm3m O_h^1	3.9051	1	1	12	$3F_{1u}(IR) + F_{2u}(O)$	F_{1u}	88 F_{1u} 178 F_{1u} 594 F_{1u} xx F_{2u}	173 473 808	----	3.4	311
CsCl	cubic CsCl	(221) Pm3m O_h^1	4.121	1	1	3	$F_{1u}(IR)$	F_{1u}	99	160	----	8.1	6.34
CsBr			4.286						75	113		6.9	6.51
CsI			4.5667						62	93		6.4(d)	6.54
TlCl			3.8452						63	158		3.6	32.7
TlBr			3.9846						43	101		3.1	30.6
Mn-α	cubic	(217) I43m T_d^3	8.894	58	29	84	$5A_1(R) + 2A_2(0) + 7E(R) + 9F_1(0) + 12F_2(IR,R)$	F_2	xx	?	xx	None	xx
ZnS	cubic zincblende	(216) F43m T_d^2	5.4093	4	1	3	$F_2(IR,R)$	F_2	279	351	----	3.68(d)	8.35
ZnSe			5.6676						206	252		2.83(d)	9.0
ZnTe			6.089						179	206		2.3(d)	9.8
CdTe			6.480						141	169		1.5(d)	10.2
GaAs			5.6535						269	292		1.42(i)	13.0
GaP			5.4506						367	403		2.27(i)	11.1
InAs			6.0585						218	240		0.35(d)	14.1
InSb			6.4782						179	190		0.18(d)	17.7
InP			5.8688						304	345		1.34(d)	12.4
SiC-β			4.348						796	972		2.86	9.72
GaSb			6.118						227	237		0.75	15.7

AlSb			6.1347						318	340		1.61(i)	11.2
AlAs			5.62						362	404		2.15(i)	10.06
HgTe			6.460						116	139		0	xx
BN			3.6157						1055	1305		8	7.1
Y_2O_3	bcc	(206) Ia3 T_h^7	10.604	16	8	117	$4A_g(R) + 5A_u(0) + 4E_g(R) +$ $5E_u(0) + 14F_g(R) + 16F_u(IR)$	F_u	Table d		----	~6	11.4
FeS_2	cubic pyrite	(205) Pa3 T_h^6	5.4067	4	4	33	$A_g(R) + 2A_u(0) + E_g(R) +$ $2E_u(0) + 3F_g(R) + 5F_u(IR)$	F_u	Table e		----	~0.9(i)	26.1
$Bi_{12}SiO_{20}$	cubic	(197) I23 T^3	10.1043	2	1	96	8A(R) + 8E(R) + 24F(IR,R)	F	Table f		----	3.25	56
$Bi_{12}GeO_{20}$			10.143									3.25	40
Os	hcp	(194) $P6_3/mmc$ D_{6h}^4	a = 2.7352	2	2	3	$B_{1g}(O) + E_{2g}(R)$	$A_{2u} + E_{1u}$	xx E_{2g}		xx	None	xx
			c = 4.3190						xx B_{1g}				
Co-α			a = 2.5071						xx		4.0		−12000
			c = 4.0686						xx				
Be			a = 2.2866						463		xx		xx
			c = 3.5833						673				
Mg			a = 3.2093						120		xx		xx
			c = 5.2103						241				
Re			a = 2.7608						138		xx		xx
			c = 4.4582						271				
Ru			a = 2.7039						192		xx		xx
			c = 4.2817						267				
Ti			a = 2.950						137		2.5		−2800
			c = 4.686						188				
Dy			a = 3.5903						62		11.8		xx
			c = 5.6475						110				
Er			a = 3.5588						58		6.9		xx
			c = 5.5874						116				
Gd			a = 3.6360						59		9.1		xx
			c = 5.7826						102				
Tb			a = 3.6010						61		11.5		xx
			c = 5.6936						108				
Tm			a = 3.5375						68		6.5		xx
			c = 5.5546						118				
Ce-γ			a = 3.65						xx		8.9		xx
			c = 5.96						xx				
C	hexagonal graphite	(194) $P6_3/mmc$ D_{6h}^4	a = 2.456	4	4	9	$A_{2u}(IR\|) + 2B_{2g}(O) +$ $E_{1u}(IR\perp) + 2E_{2g}(R)$	$A_{2u} + E_{1u}$	Table g		----	xx	5.7(e)
			c = 6.696										

(continued)

TABLE I *(Continued)*

Collected Optical Parameters

Material	Crystal structure	Symmetry class space group	Unit cell dimensions (Å)	Molecular Units: Unit cell	Molecular Units: Primitive cell	No. of optic modes	Optic irreducible representation	Accoustic irr. rep.	ω_T (cm^{-1})	ω_L (cm^{-1})	ω_P Drude (eV)	E_g (eV)	ϵ_O
GaSe-β	hexagonal	(194) $P6_3/mmc$ D^4_{6h}	a = 3.755 c = 15.94	4	4	21	$2A_{1g}(R) + A_{2u}(IR\|) + 2B_{1u}(0) + 2B_{2g}(0) + 2E_{1g}(R) + E_{1u}(IR\perp) + 2E_{2g}(R) + 2E_{2u}(0)$	$A_{2u} + E_{1u}$	Table h		----	2.0(d)	10.6(o) 6.18(e)
GaSe-ϵ	hexagonal	(187) $P\bar{6}m2$ D^1_{3h}	a = 3.755 c = 15.954	4	4	21	$4A_1'(R) + 3A_2''(IR\|,R) + 3E'(IR\perp,R) + 4E''(R)$	$A_2'' + E'$	Table i		-----	~2.0	10.6(o) 6.18(e)
ZnS	hexagonal wurzite	(186) $P6_3mc$ C^4_{6v}	a = 3.811 c = 6.234	2	2	9	$A_1(IR\|,R) + 2B_1(0) + E_1(IR\perp,R) + 2E_2(R)$	$A_1 + E_1$	Table j		-----	3.91	~9.6(o)
CdS			a = 4.1348 c = 6.7490									2.55(d)	9.6(o) 10.7(e)
CdSe			a = 4.2999 c = 7.0109									1.75(d)	9.29(o) 10.16(e)
BeO			a = 2.698 c = 4.380									9.4	6.94(o) 7.65(e)
SiC 6H,$\alpha\Pi$			a = 3.076 c = 5.048									3.1	9.7(o) 10.0(e)
AgI-β			a = 4.5924 c = 7.5104									~5.6	6.8 xx
AlN			a = 3.1127 c = 4.9816									6.2(d)	xx xx
BN			a = 2.504 c = 10.01									3.9(i)	6.86(o) 5.06(e)
GaN			a = 3.1892 c = 5.1850									3.5	9.3(o) 10.4(e)
Si_3N_4-β	hexagonal	(176) $P6_3/m$ C^2_{6h}	a = 7.606 c = 2.909	2	2	39	$4A_g(R) + 2A_u(IR\|) + 3B_g(0) + 4B_u(0) + 2E_{1g}(R) + 4E_{1u}(IR\perp) + 5E_{2g}(R) + 2E_{2u}(0)$	$A_u + E_{1u}$	Table k		----	xx	xx
Al_2O_3	trigonal (hex)	(167) $R\bar{3}c$ D^6_{3d}	a = 5.128 α = 55°20′	6	2	27	$2A_{1g}(R) + 3A_{2g}(O) + 2A_{1u}(O) + 2A_{2u}(IR\|) + 5E_g(R) + 4E_u(IR\perp)$	$A_{2u} + E_u$	Table l		----	8.3	9.49(o) 11.4(e)
Ga_2O_3			a = 5.320 α = 55°48′									xx	24.1(o) 20.6(e)

$NaNO_3$	trigonal (hex)	(167) $R\bar{3}c$ D_{3d}^6	a = 6.3247 α = 47°16′	6	2	27	$A_{1g}(R) + 2A_{1u}(0) + 3A_{2g}(0) +$ $3A_{2u}(IR\parallel) + 4E_g(R) + 5E_u(IR\perp)$	$A_{2u} + E_u$	Table m		----	~5.1	6.85
$CaCO_3$			a = 4.9898 c = 17.060								---- ~8(o) ~9.5(o)		~8.6(o) ~8.3(e)
Sb	trigonal (hex)	(166) $R\bar{3}m$ D_{3d}^5	a = 4.5066 α = 57°6.5′	2	2	3	$A_{1g}(R) + E_g(R)$	$A_{2u} + E_u$	115 A_{1g} 150 Eg		xx	None	xx
Sm			a = 8.996 α = 73°13′						xx xx		~11.7		xx
$LiNbO_3$	trigonal (hex)	(161) R3c C_{3v}^6	a = 5.1483 c = 13.8631	2	2	27	$4A_1(IR\parallel,R) + 5A_2(O) + 9E(IR\perp,R)$	$A_1 + E$	Table n		----	~4.2	43.7(o) 25.6(e)
$LiTaO_3$			a = 5.1543 c = 13.7835								----	~4.5(o)	43.8(o) 46.8(e)
GaSe-γ	trigonal (hex)	(160) R3m C_{3v}^5	a = 3.755 c = 23.92	12	6	33	$11A_1(IR\parallel,R) + 11E(IR\perp,R)$	$A_1 + E$	Table o		----	~2.0	~6.18(o) ~10.6(e)
Si_3N_4-α	trigonal (hex)	(159) P31cC$_{3v}^4$	a = 7.753 c = 5.618	4	4	81	$13A_1(IR\parallel,R) + 14A_2(0) + 27E(IR\perp,R)$	$A_1 + E$	Table p		----	xx	~6.9
SiO_2	trigonal (hex)	(154) $P3_221$ D_3^4	a = 4.9130 c = 5.4046	3	3	24	$4A_1(R) + 4A_2(IR\parallel) + 8E(IR\perp,R)$	$A_2 + E$	Table q		----	~9	4.41(o) 4.62(e)
Se	trigonal (hex)	(152) $P3_121$ $_rD_3^4$	a = 4.3551 c = 4.9494	3	3	6	$A_1(R) + A_2(IR\parallel) + 2E(IR\perp,R)$	$A_2 + E$	Table r		----	~1.6(i)	7.40(o) 12.2(e)
Te			a = 4.4469 c = 5.9149									0.33(d)	30(o) 43(e)
Sn-β	tetragonal (white)	(141) $I4_1/amd$ D_{4h}^{19}	a = 5.8197 c = 3.1749	4	2	3	$B_{2g}(R) + E_g(R)$	$A_{2u} + E_u$	43 124		xx	None	xx
$ZrSiO_4$	tetragonal	(141) I4/amd D_{4h}^{19}	a = 6.6164 c = 6.0150	4	2	33	$2A_{1g}(R) + A_{1u}(0) + A_{2g}(0) +$ $3A_{2u}(IR\parallel) + 4B_{1g}(R) + B_{1u}(0) +$ $B_{2g}(R) + 2B_{2u}(0) + 5E_g(R) + 4E_u(IR\perp)$	$A_{2u} + E_u$	Table s		----	~2.5	xx(o) 10.7(e)
In	tetragonal	(139) I4/mmm D_{4h}^{17}	a = 3.253 c = 4.945	2	1	0	None	$A_{2u} + E_u$	None	None	xx	None	xx
Zn_3P_2	tetragonal	(137) $P4_2/nmc$ D_{4h}^{15}	a = 8.097 c = 11.45	8	8	117	$9A_{1g}(R) + 4A_{1u}(0) + 5A_{2g}(0) +$ $9A_{2u}(IR\parallel) + 10B_{1g}(R) + 5B_{1u}(0) +$ $4B_{2g}(R) + 9B_{2u}(0) + 16E_g(R) + 15E_u(IR\perp)$	$A_{2u} + E_u$	Table t		----	1.3	11
TiO_2	tetragonal SnO_2 rutile	(136) $P4_2/mnm$ D_{4h}^4	a = 4.5937 c = 2.9581	2	2	15	$A_{1g}(R) + A_{2g}(O) + A_{2u}(IR\parallel) +$ $B_{1g}(R) + 2B_{1u}(O) + B_{2g}(R) +$ $E_g(R) + 3E_u(IR\perp)$	$A_{2u} + E_u$	Table u		----	3.06(d,o) 4.3(d,e)	83.7(o) 165(e)

(continued)

TABLE I *(Continued)*

Collected Optical Parameters

Material	Crystal structure	Symmetry class space group	Unit cell dimensions (Å)	Molecular Units: Unit cell	Molecular Units: Primitive cell	No. of optic modes	Optic irreducible representation	Accoustic irr. rep.	ω_T (cm^{-1})	ω_L (cm^{-1})	ω_P Drude (eV)	E_g (eV)	ϵ_O
MgF_2			a = 4.623 c = 3.052									11	5.47(o) 4.62(e)
KH_2PO_4	tetragonal	(122) I42d $D_{2d}^{12} = V_d^{12}$	a = 7.448 c = 6.977	4	2	45	$4A_1(R) + 5A_2(0) + 6B_1(R) +$ $6B_2(IR\parallel,R) + 12E(IR\perp,R)$	$B_2 + E$	Table v		-----	4.96	~44(o) ~21(e)
$AgGaS_2$	tetragonal	(122) I42d $D_{2d}^{12} = V_d^{12}$	a = 5.757 c = 10.304	4	2	21	$A_1(R) + 2A_2(0) + 3B_1(R) +$ $3B_2(IR\parallel,R) + 6E(IR\perp,R)$	$B_2 + E$	Table w		-----	xx ~2.7(d,e)	~10.0(o) ~8.6(e)
$AgGaSe_2$			a = 5.973 c = 10.88									xx ~1.8(d,e)	8.9(o) 7.8(e)
$CdGeAs_2$			a = 5.9432 c = 11.216									xx 0.57(d,e)	18.2(o) 17.9(e)
$CuGaS_2$			a = 5.351 c = 10.480									2.55(d,o) 2.43(d,e)	8.9(o) 7.6(e)
$ZnGeP_2$			a = 5.466 c = 10.722									xx 2.4(d,e)	11.4(o) 11.6(e)
$NH_4H_2PO_4$	tetragonal	(122) I42d $D_{2d}^{12} = V_d^{12}$	a = 7.510 c = 7.564	4	2	69	$7A_1(R) + 7A_2(0) + 8B_1(R) +$ $9B_2(IR\parallel,R) + 19E(IR\perp,R)$	$B_2 + E$	Table x		----	9.92	~56(o) ~15(e)
Zn_3As_2	tetragonal	(110) $I4_1cd$ C_{4v}^{12}	a = 8.316 c = 11.76	32	16	237	$26A_1(IR\parallel,R) + 27A_2(0) +$ $27B_1(0) + 27B_2(R) + 65E(IR\perp,R)$	$A_1 + E$	Table y		----	0.93	10-11.8
$BaTiO_3$	tetragonal	(99) P4mm C_{4v}^1	a = 3.9920 c = 4.0361	1	1	12	$3A_1(IR\parallel,R) + B_1(R) + 4E(IR\perp,R)$	$A_1 + E$	Table z		----	3.27(o) 3.38(e)	xx 31.5(e)

S-α	orthorhombic	(70) Fddd $D_{2h}^{24} = V_h^{24}$	a = 10.467 b = 12.870 c = 24.493	128	32	93	$12A_g(R) + 12A_u(0) + 12B_{1g}(R) +$ $11B_{1u}(IR \parallel z) + 12B_{2g}(R) +$ $11B_{2u}(IR \parallel y) + 2B_{3g}(R) +$ $11B_{3u}(IR \parallel x)$	$B_{1u} +$ $B_{2u} +$ B_{3u}	Table aa	----	4.1(b) 4.2(a)	3.85(b) 3.65(a)
TlI	orthorhombic	(63) Cmcm $D_{2h}^{17} = V_h^{17}$	a = 4.582 b = 12.92 c = 5.251	4	2	9	$2A_u(0) + B_{1u}(IR \parallel z) +$ $3B_{2u}(IR \parallel y) + 3B_{3u}(IR \parallel x)$	$B_{1u} +$ $B_{2u} +$ B_{3u}	Table bb	----	2.8	37.3
$(CH_2)_n$	ortborbombic	(62) Pnma $D_{2h}^{16} = V_h^{16}$	a = 7.40 b = 4.93 c = 2.534	4	4	33	$6A_g(R) + 3A_u(0) + 6B_{1g}(R) +$ $2B_{1u}(IR \parallel z) + 3B_{2g}(R) +$ $5B_{2u}(IR \parallel y) + 3B_{3g}(R) + 5B_{3u}(IR \parallel x)$	$B_{1u} +$ $B_{2u} +$ B_{3u}	Table cc	----	xx	2.29(b) 2.32(c)
$KNbO_3$	orthorhombic	(38) Amm2 C_{2v}^{14}	a = 5.6896 b = 3.9692 c = 5.7256	2	1	12	$4A_1(IR \parallel z,R) + A_2(R) +$ $4B_1(IR \parallel x,R) + 3B_2(IR:y,R)$	$A_1 + B_1$ $+ B_2$	Table dd	----	3.46 3.43 3.46	150-x 985-y 44-z
CuO	monoclinic	(15) B2/b C_{2h}^6 C2/c	a = 4.6837 b = 3.4226 c = 5.1288 β = 99°29′	4	2	9	$A_g(R) + 3A_u(IR \parallel z) +$ $2B_g(R) + 3B_u(IR \parallel x,y)$	$A_u + 2B_u$	Table ee	----	~1.3i	18.1
ThF_4	monoclinic	(15) B2/b C_{2h}^6	a = 12.90 b = 10.93 c = 8.58 β = 126.4°	12	6	87	$20A_g(R) + 22A_u(IR \parallel z) +$ $22B_g(R) + 23B_u(IR \parallel x,y)$	$A_u + 2B_u$	Table ff	----	xx	xx
As_2S_3	monoclinic (unit cell)	(14) $P2_1/b,c$ C_{2h}^5	a = 11.475 b = 9.577 c = 4.256 β = 90°41′	4	4	57	$15A_g(R) + 14A_u(IR \parallel z) +$ $15B_g(R) + 13B_u(IR \parallel x,y)$	$A_u + 2B_u$	Table gg	----	2.43(a,d) 2.45(c,d)	15.2(a) 6.25(b) 13.0(c)
	orthorhombic (layer)	(31) $Pmm2_1$ C_{2v}^1		2	2	27	$7A_1(IR \parallel z,R) + 7A_2(R)$ $7B_1(IR \parallel x,R) + 6B_2(IR \parallel y,R)$					
As_2Se_3			a = 12.053 b = 9.890 c = 4.277 β = 90°28′								~2	14.4(a) 13.0(c)

TABLE I *(Continued)*

Collected Optical Parameters

Material	Crystal structure	Symmetry class space group	Unit cell dimensions (Å)	Molecular Units: Unit cell	Molecular Units: Primitive cell	No. of optic modes	Optic irreducible representation	Accoustic irr. rep.	ω_T (cm^{-1})	ω_L (cm^{-1})	ω_P Drude (eV)	E_g (eV)	ϵ_0
GaTe-α	monoclinic	(12) B2/m C_{2h}^3	a = 17.84 b = 4.07 c = 10.56	12	6	33	$12A_g(R) + 6B_g(R) + 5A_u(IR \parallel z) + 10B_u(IR \parallel x,y)$	$A_u + 2B_u$	Table hh		----	1.67(d) ~1.7	10.58(e) 9.66(o)
(TlBrI, KRS-5)									43	103	----	~2.47	32.5
(TlBrCl, KRS-6)									58	149		3.25	31.8
(AlGaAs) alloy													
(HgCdTe)													
(PbSnTe)													
(Ge-Si)													

(a-Si)			1.77	13.7
amorphous				
(a-SiO_2)		469	~9	3.8
		800		
		1094		
(a-SiO)		1020	~6	4.0
(a-Si_3N_4)		880		3.6
		490		
(a-As_2S_3)				7.45
(a-As_2Se_3)				9.0
(a-ThF_4)				
(a-C:H)				
Hg	liquid			
H_2O				78.3

TABLE a

$Y_3Al_5O_{12}$ [2]

17 F_{1u}(T)(IR)	F_{1u}(L)	14 F_{2g}(R)	8 E_g(R)	3 A_{1g}(R)	16 F_2(0)	14 F_{1g}(0)	10 E_u(0)	5 A_{2g}(0)	5 A_{2u}(0)	5 A_{1u}(0)
122	123	144	162	373	xx	xx	xx	xx	xx	xx
163	172	218	310	561	xx	xx	xx	xx	xx	xx
177	180	243	340	783	xx	xx	xx	xx	xx	xx
219	224	259	403		xx	xx	xx	xx	xx	xx
290	296	296	531		xx	xx	xx	xx	xx	xx
330	340	408	537		xx	xx	xx			
372	378	436	714		xx	xx	xx			
387	388	544	758		xx	xx	xx			
394	402	690			xx	xx	xx			
428	438	719			xx	xx	xx			
445	471	857			xx	xx				
472	511	xx			xx	xx				
516	549	xx			xx	xx				
569	585	xx			xx	xx				
692	712				xx					
723	765				xx					
782	840									

TABLE b

Al_2MgO_4 [2]

4 F_{1u}(T)(IR)	F_{1u}(L)(IR)	1 A_{1g}(R)	1 E_g(R)	3 F_{2g}(R)	2 A_{2u}(0)	2 E_u(0)	1 F_{1g}(0)	2 F_{2u}(0)
305	311	722	410	311	xx	xx	xx	xx
428	xx			492	xx	xx		xx
485	497			611				
670	800							

TABLE c

$Al_{23}O_{27}N_5$ [2]

(T)	(L)
346	xx
395	xx
495	551
634	718
768	869
920	969

TABLE d

Y_2O_3 [2]

16 $F_u(T)(IR)$	$F_u(L)(IR)$	4 $E_g(R)$	4 $A_g(R)$	14 $F_g(R)$	5 $A_u(0)$	5 $E_u(0)$
120	121	333	1184	131	xx	xx
172	173	830	xx	431	xx	xx
182	183	984	xx	469	xx	xx
241	242	xx	xx	596	xx	xx
303	315			xx	xx	xx
335	359			xx		
371	412			xx		
415	456			xx		
461	486			xx		
490	535			xx		
555	620			xx		
xx				xx		
xx				xx		
xx				xx		
xx						
xx						

TABLE e

FeS_2 [2, 19, 20]

5 $F_u(T)(IR)$	$F_u(L)(IR)$	1 $A_g(R)$	1 $E_g(R)$	3 $F_g(R)$	2 $A_u(0)$	2 $E_u(0)$
293	294	379	343	350	xx	xx
348	350			377	xx	xx
401	411			435		
412	421					
422	439					

TABLE f

$Bi_{12}SiO_{20}$ [21]

24 F(T)(IR,R)	F(L)(IR,R)	8 A(R)	8 E(R)
44	xx	92	68
51		149	88
59		171	132
89		282	252
99		331	xx
106		546	464
xx		785	626
115		xx	xx
136			
175			
195			
208			
237			
288			
314			
353			
367			
462			
496			
509			
531			
579			
609			
825			

$Bi_{12}GeO_{20}$ [21]

46	xx	89	68
52		148	97
57		170	130
99		273	236
106		326	306
124		543	458
xx		715	623
131		xx	xx
177			
xx			
xx			
207			
232			
271			
303			
338			
356			
459			
481			
xx			
526			
571			
600			
682			

This is the first example of a crystal with the same modes both IR and R active. Often, there is not a one-to-one correspondence, presumably because the IR or R intensity is too weak to be measured. Also, some of the high frequency bands may be combination bands.

TABLE g

C graphite [22]

1 $E_{1u}(T)(IR\perp)$	$E_{1u}(L)(IR\perp)$	1 $A_{2u}(T)(IR\parallel)$	$A_{2u}(L)(IR\parallel)$	2 $E_{2g}(R)$	2 $B_{2g}(O)$
1587.0	1587.5	867.8	868.1	42	127
				1575	xx

IR$\perp$ represents electric field E perpendicular to the c axis (ordinary) and IR$\parallel$ represents electric field E parallel to the c axis (extraordinary). This nomenclature will persist until the orthorhombic crystals are reached, whereupon we must revert to $E \parallel a$, $E \parallel b$, $E \parallel c$ notation. For the remaining monoclinic and triclinic unit cells, the situation becomes more complicated because we must choose a Cartesian coordinate system to describe atomic displacement and electric polarization whose x, y, z axes do not line up with all three a, b, c edges of the unit cell.

TABLE h

GaSe-β [23]

1 $E_{1u}(T)(IR\perp)$	$E_{1u}(L)$	1 $A_{2u}(T)(IR\parallel)$	$A_{2u}(L)$	2 $A_{1g}(R)$	2 $E_{1g}(R)$	2 $E_{2g}(R)$	2 $B_{1u}(0)$	2 $B_{2g}(0)$	2 $E_{2u}(0)$
213.9	254.7	xx	xx	134.6	60.1	19.1	xx	xx	xx
				307.8	249	213.1	xx	xx	xx

Sometimes we omit xx in the longitudinal-mode column because we do not know if such a mode exists until a zero in ϵ_R is found experimentally.

TABLE i

GaSe-ϵ [24]

3 $E'(T)(IR\parallel,R)$	$E'(L)$	3 $A_2''(T)(IR\perp,R)$	$A_2''(L)$	4 $A_1'(R)$	4 $E''(R)$
237	245.5	19.5	254.7	134.3	60.1
xx	xx	213.5	xx	308	211.9
xx	xx	xx	xx	xx	xx
				xx	xx

TABLE j

ZnS [2, 6]

1 $E_1(T)(IR\perp)$	$E_1(L)(IR\perp)$	1 $A_1(T)(IR\parallel)$	$A_1(L)(IR\parallel)$	2 $E_2(R)$	2 $B_1(0)$
224	352	274	352	55	xx
				280	xx
CdS [2, 6]					
243	307	234	305	44	xx
				252	xx
CdSe [2, 6]					
172	210	166	211	34	xx
				xx	xx
BeO [2, 6]					
722	1095	678	1085	340	xx
				684	xx
SiC-α-6H [2, 6]					
794	970	785	970	149	xx
				788	xx
AgI-β [2]					
106	124	106	124	17	xx
				112	xx
AlN [2, 6]					
672	895	659	888	655	xx
				xx	xx
BN [25]					
767	778	783	828	xx	xx
				xx	xx
GaN [2, 6]					
560	746	533	744	145	xx
				568	xx

TABLE k

Si_3N_4-β [26–30]

4 $E_{1u}(T)$ (IR⊥)		2 $A_u(T)$ (IR ∥)		4 $A_g(R)$	2 $E_{1g}(R)$	5 $E_{2g}(R)$	3 $B_g(0)$	4 $B_u(0)$	2 $E_{2u}(0)$
[30]	[27]	[28]	[29]	xx	[29]	[28]			
352						144	xx	xx	xx
371					184	186	xx	xx	xx
378	376	380			206	210	xx	xx	
406					227	229		xx	
443	445	447			449				
460					452	451			
495	496		495		456				
509					617	619			
	537				730	732			
578	580	580	582		742				
600					792				
675					802				
684	680				862	864			
854			854		927	928			
871					938	939			
893					1043	1047			
906	906	910	900						
941									
957									
	980	985	980						
1040	1040	1040	1051						

In most cases, too many lines are seen for each species. Splitting of degenerate modes and combination bands are sometimes invoked to ease this dilemma.

TABLE l

Al_2O_3 [6, 12]

4 $E_u(T)(IR\perp)$	$E_u(L)(IR\perp)$	2 $A_{2u}(T)(IR\parallel)$	$A_{2u}(L)(IR\parallel)$	2 $A_{1g}(R)$	5 $E_g(R)$	3 $A_{2g}(0)$	2 $A_{1u}(0)$
385	388	400	512	418	378	xx	xx
442	480	583	871	645	432	xx	xx
569	625				451	xx	
635	900				578		
					751		
Ga_2O_3 [31]*							
154	xx	xx	xx	xx	xx	xx	xx
230		xx		xx	xx	xx	xx
284					xx	xx	
320					xx		
370					xx		
430							
530							
680							
760							

*Polycrystalline sample measured in transmission. Modes not assigned.

TABLE m

$NaNO_3$ [32]

5 $E_u(T)(IR\perp)$	$E_u(L)(IR\perp)$	3 $A_{2u}(T)(IR\parallel)$	$A_{2u}(L)(IR\parallel)$	1 $A_{1g}(R)$	4 $E_g(R)$	2 $A_{1u}(0)$	3 $A_{2g}(0)$
87	98.5	51.5	90	xx	xx	xx	xx
175.5	184.5	214	262.5		xx	xx	xx
209	257.5	xx	xx		xx		xx
xx	xx				xx		
1356	1468						
$CaCO_3$ [2]							
102	123	92	136	1088	156	xx	xx
223	239	303	387		283	xx	xx
297	381	872	890		714		xx
712	715				1432		
1407	1549						

TABLE n

$LiNbO_3$ [33, 34]

9 E(T)(IR⊥,R)	E(L)(IR⊥,R)	4 A_1(T)(IR∥,R)	A_1(L)(IR∥,R)	5 A_2(0)
155	198	255	275	xx
238	243	276	333	xx
265	295	334	436	xx
325	371	633	876	xx
371	428			xx
431	454			
582	668			
668	739			
743	880			
$LiTaO_3$ [35]				
74	80	201	245	xx
140	163	253	347	xx
206	248	356	399	xx
251	278	600	864	xx
316	318			xx
383	452			
462	474			
596	648			
662	870			

TABLE o

GaSe-γ [36]

11 E(T)(IR⊥,R)	E(L)(IR⊥,R)	11 A_1(T)(IR∥,R)	A_1(L)(IR∥,R)
20.9	xx	133.5	xx
59.5	xx	235.7	246.5
208.7	xx	307.4	xx
213.9	253.2	xx	
xx		xx	
xx		xx	
xx		xx	
xx		xx	
xx		xx	
xx		xx	
xx		xx	

TABLE p

Si_3N_4-α [26-28, 30, 37]

27 E(T) (IR⊥,R)		13 A_1(T) (IR∥,R)		27 E(R)	13 A_1(R)	14 A_2(0)
[30]	[26]	[27]	[28]	[28]	[37]	
	305		300	153		xx
352	352		355	202	200	xx
371	375		375	231	232	xx
378				258	259	xx
406	403		412	282	280	xx
443				298		xx
460	461		463	306	302	xx
	488			321		xx
495	493	495	499	337		xx
	501			356	356	xx
509	510		518	361	365	xx
578		582	580	383		xx
600	605		600	391		xx
	660				404	xx
	668			460	460	
675	676			470		
684	684		688		484	
	750				505	
854	858	54	855	514	515	
	871		874	537		
893	895		895	569	572	
906		900	909	601	602	
941			935	667	668	
957				691	692	
	985	980	995	763		
1040	1045	1051	1040	848	845	
				868	868	
				914	915	
				951	948	
				975	976	
				1032	1034	
				1107		
					1122	
				1142		
					1205	

The analyses are incomplete. Note that the modes both IR and R active are shown separately. There is poor correlation between IR, R frequencies. Each IR frequency should have an equal R frequency. Raman experimental arrangement was not described adequately—polarization selection rules, etc. No IR polarization was used to distinguish ∥ and ⊥. Powders in mulls were often used.

TABLE q

SiO_2 [12]

8 E(T)(IR⊥,R)	E(L)(IR⊥,R)	4 A_2(T)(IR ∥)	A_2(L)IR ∥)	4 A_1(R)
127	129	364	387	207
265	270	489	547	356
394	403	777	789	464
450	510	1080	1240	1085
697	699			
796	809			
1076	1161			
1161	1236			

TABLE r

Se [38]

2 E(T)(IR⊥,R)	E(L)(IR⊥,R)	1 A_2(T)(IR ∥)	A_2(L)(IR ∥)	1 A_1(R)
144	150	102	106	237
225	225			
Te [38]				
92	106	90	96	120
144	145			

TABLE s

$ZrSiO_4$ [39]

4 $E_u(T)(IR\perp)$	$E_u(L)$	3 $A_{2u}(T)(IR\parallel)$	$A_{2u}(L)$	2 $A_{1g}(R)$	4 $B_{1g}(R)$	1 $B_{2g}(R)$	5 $E_g(R)$	1 $A_{1u}(0)$	1 $A_{2g}(0)$	1 $B_{1u}(0)$	2 $B_{2u}(0)$
287	351	338	478	439	214	266	201	xx	xx	xx	xx
389.5	417	608	646	974	393		225				xx
430.5	469	989	1106		1008		357				
885	1034						547				
							1008				

TABLE t

Zn_3P_2 [40, 41]

15 $E_u(T)(IR\perp)$	$E_u(L)$	9 $A_{2u}(T)(IR\parallel)$	$A_{2u}(L)$	9 $A_{1g}(R)$	10 $B_{1g}(R)$	4 $B_{2g}(R)$	16 $E_g(R)$	4 $A_{1u}(0)$	5 $A_{2g}(0)$	5 $B_{1u}(0)$	9 $B_{2u}(0)$
[40]	[40]			[40]	[41]	[40]					
T	L			VV		VH					
44	57			27.5		26					
64	66			37		34.5					
70.5	71			45		39					
78	78.5			50		45					
86	89			61.5		51					
103	104.5			70		61.5					
168.5	169			76		64.5					
182.5	184			86.5		70					
246	276			93		79					
285	307			125		84					
309.5	320			144		92					
338	345			159		94					
351	360			171		99.5					
				190.5		109					
				212		120					
				224.5		132					
				248.5		141					
				258		151.5					
				292		168.5					
				310.5		188					
				331		205					
				340		222					
				345		231.5					
				363		241.5					

(continued)

TABLE t (*Continued*)

Zn_3P_2 [40, 41]

15 $E_u(T)(IR\perp)$	$E_u(L)$	9 $A_{2u}(T)(IR\parallel)$	$A_{2u}(L)$	9 $A_{1g}(R)$	10 $B_{1g}(R)$	4 $B_{2g}(R)$	16 $E_g(R)$	4 $A_{1u}(0)$	5 $A_{2g}(0)$	5 $B_{1u}(0)$	9 $B_{2u}(0)$
				384		256					
				396.5		263					
				411		290					
				430		306.5					
				452		328.5					
				463.5		336					
				486		345					
				499		352.5					
				511		363					
						379.5					
						394					
						403.5					
						423					
						430					
						442					
						450					
						456					
						466.5					
						499					

TABLE u

TiO_2 [6, 42]

3 $E_u(T)(IR\perp)$	$E_u(L)$	2 $A_{2u}(T)(IR\parallel)$	$A_{2u}(L)$	1 $A_{1g}(R)$	1 $B_{1g}(R)$	1 $B_{2g}(R)$	1 $E_g(R)$	1 $A_{2g}(0)$	2 $B_{1u}(0)$
183	373	167	811	612	143	44	763	113	826
388	458	xx							xx
508	831								
MgF_2 [6, 42]									
247	303	399	625	410	92	515	295	326	xx
410	415	xx							xx
450	617								

TABLE v

KH_2PO_4 [2, 43]

12 E(T)(IR⊥,R)	E(L)(IR⊥)	6 $B_2(T)(IR\parallel,R)$	$B_2(L)(IR\parallel)$	4 $A_1(R)$	6 $B_1(R)$	5 $A_2(0)$
86 75	xx	80	xx	360	156	xx
102 95		174		514	479	xx
122 113		xx		918	570	xx
152 190		386		2700	1366	xx
206 320		510			1806	xx
526 490		1350			2390	
xx 530						
xx 568						
xx 960						
xx 1145						
xx 1325						
xx						

Infrared and Raman frequencies do not show a good one-to-one correlation for the *E* mode.

TABLE w

$AgGaS_2$ [2]

6 E(T)(IR⊥,R)	E(L)(IR⊥,R)	3 B_2(T)(IR∥,R)	B_2(L)(IR∥,R)	1 A_1(R)	3 B_1(R)	2 A_2(0)
63	64	195	199	295	118	xx
93	96	215	239		179	xx
158	160	366	400		334	
225	230					
323	347					
368	392					
$AgGaSe_2$ [2]						
78	78	195	199	179	125	xx
133	135	215	239		xx	xx
xx	112	366	400		xx	
160	163					
208	213					
247	274					
$CdGeAs_2$ [2]						
95	98	85	85	188	84	xx
159	161	203	210		167	xx
200	206	270	278		245	
255	258					
280	365					
$CuGaS_2$ [2]						
75	76	259	284	312	138	xx
95	98	339	369		203	xx
147	167	371	402		243	
260	278					
335	352					
365	387					
$ZnGeP_2$ [2]						
94	94	140	xx	328	120	xx
141	141	361	341		247	xx
201	206	411	401		389	
328	330					
369	375					
386	406					

TABLE x

$NH_4H_2PO_4$ [44]

19 E(T)(IR⊥,R)	E(L)(IR⊥,R)	9 B_2(T)(IR ∥,R)	B_2(L)(IR ∥,R)	7 A_1(R)	8 B_1(R)	7 A_2(0)
51	xx	76	xx	337	178	xx
70		198		520	474	xx
150		450		918	541	xx
164		xx		2700	1298	xx
350		xx		xx	1750	xx
540		xx		xx	2370	xx
xx		xx		xx	xx	xx
xx		xx			xx	
xx		xx				
xx						
xx						
xx						
xx						
xx						
xx						
xx						
xx						
xx						
xx						
xx						

TABLE y

Zn_3As_2 [45]

65 E(T)(IR⊥,R)	E(L)	26 A_1(T)(IR∥,R)	A_1(L)	27 B_2(R)	27 A_2(0)	27 B_1(0)
				[45, (HH)]		
xx	xx	xx	xx	34 xx	xx	xx
xx		xx		62 xx	xx	xx
xx		xx		68 xx	xx	xx
xx		xx		74 xx	xx	xx
xx		xx		92 xx	xx	xx
xx		xx		xx	xx	xx
xx		xx		xx	xx	xx
xx		xx	

TABLE y (*Continued*)

Zn_3As_2 [45]

65 E(T)(IR⊥,R)	E(L)	26 A_1(T)(IR ∥,R)	A_1(L)	27 B_2(R)	27 A_2(0)	27 B_1(0)
xx						
xx						
xx						
xx						
xx						
xx						
xx						
xx						
xx						
xx						
xx						
xx						
xx						
xx						
xx						
xx						
xx						
xx						
xx						
xx						

Neither the infrared nor Raman spectrum has been studied in detail or analyzed.

TABLE z

$BaTiO_3$ [2, 46]

4 E(T)(IR⊥,R)	E(L)(IR⊥,R)	3 A_1(T)(IR ∥,R)	A_1(L)(IR ∥,R)	1 B_1(R)
38	180	179	189	305
180	308	276	471	
308	466	515	725	
498	722			

TABLE aa

S [47]

11 B_{1u}(T)(IR ∥ z)	B_{1u}(L)	11 B_{2u}(T)(IR ∥ y)	B_{2u}(L)	11 B_{3u}(T)(IR ∥ x)	B_{3u}(L)	12 A_g	12 B_{1g}	12 B_{2g}	12 B_{3g}	12 A_u(0)
44	xx	35	xx	34	xx	45	40	30	30	xx
78		45		47		56	61	46	46	xx
151		74		57		92	79	56	61	xx
181		96		89		159	150	67	70	xx
213		158		155		199	188	79	86	xx
253		197		199		221	217	161	154	xx
408		238		239		249	244	188	183	xx
431		254		256		419	420	239	236	xx
464		437		435		441	434	253	253	xx
472		466		465		470	473	441	443	xx
476		476		471		474	473	472	468	xx
						477	478	472	472	xx

TABLE bb

TlI [48]*

1 B_{1u}(T)(IR ∥ z)	B_{1u}(L)	3 B_{2u}(T)(IR ∥ y)	B_{2u}(L)	3 B_{3u}(T)(IR ∥ x)	B_{3u}(L)	2 A_u(0)
52	xx	90	xx	xx	xx	xx
		xx		xx		xx
		xx		xx		

* polycrystalline sample

TABLE cc

$(CH_2)_n$ [49, 50]

2 B_{1u}(T)(IR ∥ z)	5 B_{2u}(T)(IR ∥ y)	5 B_{3u}(T)(IR ∥ x)	6 A_g(R)	6 B_{1g}(R)	3 B_{2g}(R)	3 B_{3g}(R)	3 A_u(O)
86	109	1043	141	1066	1070	101	55
736	721	1177	1138	1297	1293	1137	1041
1478	1472	xx	1175	1371	1373	1176	1181
2851	2853	xx	1445	xx		1458	
2921	2922	xx	2855	xx		2850	
			2885	xx		2889	

Most of the other observed modes in the IR are combination bands of these fundamentals.

TABLE dd

$KNbO_3$ [2]

4 A_1(T)(IR ∥ z,R)	A_1(L)	4 B_1(T)(IR ∥ x,R)	B_1(L)	3 B_2(T)(IR ∥ y,R)	B_2(L)	1 A_2(R)
190	193	187	190	56	189	283
290	296	243	294	195	425	
299	417	267	413	511	838	
607	827	534	842			

TABLE ee

CuO [51]

3 A_u(T)(IR ∥ z)	A_u(L)(IR ∥ z)	3 B_u(T)(IR ∥ x,y)	B_u(L)(IR ∥ x,y)	1 A_g(R)	2 B_g(R)
164	165	145	147	296	346
355	xx	480	593		636
421	xx	603	624		

For this crystal symmetry $a \approx b \approx c$ and $\beta = 99°29'$. The Cartesian coordinate system is taken as $y \parallel b$, $x \parallel a$, leaving z not quite $\parallel$ to c. Note that for species A_u, atomic displacement is along z, and for B_u, it is along x, y.

TABLE ff

ThF_4 [52]

22 $A_u(T)(IR \parallel z)$	$A_u(L)$	23 $B_u(T)(IR \parallel x,y)$	$B_u(L)$	20 $A_g(R)$	22 $B_g(R)$
xx	xx	135	xx	xx	xx
xx		185		xx	xx
xx		xx		xx	xx
xx		xx		xx	xx
xx		xx		xx	xx
xx		xx		xx	xx
xx		xx		xx	xx
xx		xx		xx	xx
xx		xx		xx	xx
xx		xx		xx	xx
xx		xx		xx	xx
xx		xx		xx	xx
xx		xx		xx	xx
xx		xx		xx	xx
xx		xx		xx	xx
xx		xx		xx	xx
xx		xx		xx	xx
xx		xx		xx	xx
xx		xx		xx	xx
xx		xx		xx	xx
xx		xx		xx	xx
xx		xx			xx
xx		xx			xx
		xx			

Obtained from reflection peaks of deposited thin films. Symmetry was not determined.

TABLE gg

As_2S_3 [53]

14 A_u(T)(IR ∥ b)	A_u(L)	15 B_u(T)(IR ∥ a)	B_u(L)	13 B_u(T)(IR ∥ c)	B_u(L)	15 A_g(R)	15 B_g(R)
186	xx	182	189	140	148	136	xx
386	392	246	xx	159	165	154	xx
xx		279	xx	185	189	204	xx
xx		293	328	201	203	311	xx
xx		348	354	260	xx	355	xx
xx		354	369	278	xx	382	xx
xx		369	370	307	326	xx	xx
xx		384	390	355	368	xx	xx
xx		xx		385	390	xx	xx
xx		xx		xx		xx	xx
xx		xx		xx		xx	xx
xx		xx		xx		xx	xx
xx		xx		xx		xx	xx
xx		xx				xx	xx
		xx				xx	xx
As_2Se_3 [53]							
xx	xx	106	108	94	97	xx	xx
xx		132	134	105	108	xx	xx
xx		201	209	132	136	xx	xx
xx		224	238	217	232	xx	xx
xx		249		248	250	xx	xx
xx		268		xx		xx	xx
xx		xx		xx		xx	xx
xx		xx		xx		xx	xx
xx		xx		xx		xx	xx
xx		xx		xx		xx	xx
xx		xx		xx		xx	xx
xx		xx		xx		xx	xx
xx		xx		xx		xx	xx
xx		xx				xx	xx
		xx				xx	xx

IR measurements were made with $E \| a$, $E \| b$, $E \| c$, which is probably $E \| x$, $E \| z$, but not quite $E \| y$.

TABLE hh

GaTe-α [54]

10 B_u(T)(IR ∥ x,y)	B_u(L)(IR ∥ x,y)	5 A_u(T)(IR ∥ z)	A_u(L)(IR ∥ z)	12 A_g(R)	6 B_g(R)
49	51	94	98	41	58
89	91	118	120	52	164
97	98	131	132	67	170
112	113	143	144	76	xx
124	125	174	199	110	xx
141	148			115	xx
157	160			155	
193	205			178	
212	214			208	
266	271			233	
				271	
				284	

It is important to establish the *xyz* Cartesian coordinate system with respect to the *a,b,c* edges of the unit cell and then make the appropriate polarization measurements, E ∥ *a*, E ∥ *b*, E ∥ *c* (not given by group theory), or E ∥ *x*, E ∥ *y*, E ∥ *z* (given by group theory).

line in the ω_p column signifies that a dielectric has no free-carrier plasma frequency, or in a semiconductor the free-carrier plasma is ignored. A dashed (- - -) line in the E_g column signifies there is no fundamental band gap (in a metal or semimetal). An xxx line in the ω_T, ω_L, ω_p, E_g or ϵ_o column signifies that we could not find a value for this parameter in the literature. Hopefully, this will be filled in later.

When the collection of ω_T, ω_L data is large for a given material, the reader is referred to a separate table often containing a reference.

Even though materials like ThF_4 (monoclinic) and Si_3N_4 (hexagonal and trigonal) have very little room-temperature optical data for crystalline forms, they were tabulated in *HOC I* and *HOC II* in polycrystalline or amorphous forms as deposited in thin films for technological applications. The crystalline parameters available are tabulated in Table I. Sometimes there is more than one crystal form of a material at room temperature, but only one form was critiqued. We often include parameters for the other forms in Table I. There are many optical glasses where the primary interest is the visible index of refraction which is controlled by "doping." Fused silica is an example in *HOC I*. We never tabulated *n* for the many optical glasses, but this is done elsewhere [1, 2].

The numbers in Table I have been obtained from several sources including the original reference to the experimental work. It is not practical to cite every reference. Many of the numbers are from several collections and reviews [3–7] and the references therein. In many cases values of ω_T and ω_L from different laboratories vary by ± a few wavenumbers. Values of E_g vary

by ± a very few tenths of an eV. Some modelling and analysis is necessary to determine whether the gap is direct or indirect.

The irreducible representations at the zone center (Γ point) are obtained from the original literature or were calculated for each symmetry using the reviews by Fateley *et al.* [8] and Rousseau *et al.* [9]. This requires that the site symmetry of each atom in the unit cell be known from other references [4, 5]. While there are 230 space groups in nature, the *HOC's* contain only about 39 (roughly 17%), but surely the *HOC's* contain at least 80% of the materials of optical interest in science and technology. Most of the naturally occuring minerals on Earth have orthorhombic, triclinic, or monoclinic symmetry (thus being biaxial) and have the most complicated optical properties.

On the basis of a Lorentz model for lattice vibrations, there are resonances in ϵ_I defining resonant frequencies for the lattice. The Lorentz model was developed to describe the reaction of a solid to the propagation properties of transverse EM waves in the material. We ultimately associate the resonances at ω_T with propagating transverse optical phonons in the material.

If the oscillator strength for each mode in the material is small, the real part of the dielectric constant ϵ_R is not driven negative (through zero); the medium then cannot support a propagating longitudinal electric field, and there is no ω_L. This is true for a material like polyethylene, but is not true for a material like crystalline SiO_2, where all ω_T's have accompanying ω_L's. If the material only has transverse oscillators, the irreducible representation completely describes the transverse modes giving their IR, R, and silent O activity. In fact, group theory only deals with *x, y, z* atomic displacements and seldom invokes the words transverse, longitudinal, or direction of propagation.

However, as a given oscillator strength increases, the real part of the dielectric constant will be driven to zero at a frequency defined as ω_L. This describes a propagating longitudinal mode with atomic displacements along the direction of propagation; it occurs at a frequency somewhat higher than ω_T. The ω_L mode is not necessarily counted by group theory. The ω_L mode is not directly observed as a resonant absorption line in an IR-reflection experiment, but is located at $\epsilon_R = 0$ and is found by locating the zeroes by Kramers-Kronig analysis of reflectivity R or by a Lorentz-model fit of R. Actually, the ω_L mode can be seen in a thin-film, non-normal-incidence transmission experiment [10] with *p*-polarization. It can also be inferred from reflection measurements at normal incidence as a function of crystal orientation and for a given crystal orientation as a function of angle of incidence [11].

As discussed by several authors [6, 12–14], the Raman-scattering experiment can be used to measure specific transverse and longitudinal phonons propagating in various directions in a uniaxial crystal like ZnS, for example. The principal modes are schematically represented in Fig. 1 for propagation along the *x, y,* and *z* axes, which are usually orthogonal and parallel to the

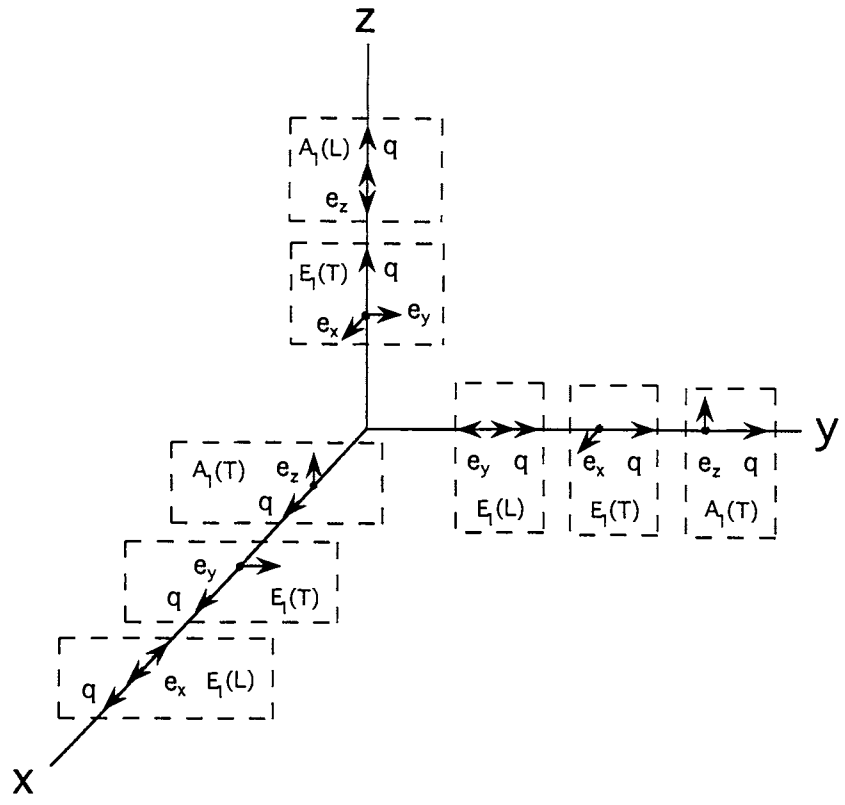

Fig. 1. Schematic representation of various A_1 and E_1 transverse and longitudinal optic modes propagating along principal directions in a CdS-type crystal. The z axis is the c optic axis. Wavevector is indicated by q and atomic displacement by e.

edges of the unit cell (except for monoclinic and triclinic symmetries). For arbitrary direction of propagation, modes are often mixed (transverse and longitudinal). For a C_{6h} crystal with hexagonal symmetry, the optic irreducible representaion is

$$\Gamma = A_1(\mathrm{IR}\|,\mathrm{R}) + 2B_1(\mathrm{O}) + E_1(\mathrm{IR}\perp,\mathrm{R}) + 2E_2(\mathrm{R}).$$

This gives 9 distinct (transverse) optic modes. The A_1 species is to be associated with e_z atomic displacements along the $z(c)$ axis, while the E_1 species is associated with e_x, e_y atomic displacements along the x and y axes. Since group theory is based on symmetry properties of atomic displacements, it tells little about direction of propagation of phonons with respect to atomic displacement of the lattice atoms. Thus, $A_1(\mathrm{IR}\|,\mathrm{R})$ can represent a transverse mode with dipole change (atomic displacement) $\|$ z. This could be a $A_1(T)$ mode propagating along x or y or an $A_1(L)$ mode propagating along z.

These three lattice vibrations have the same atomic displacement along z. Similar considerations for E_1(IR⊥,R) give an $E_1(T)$ species with atomic displacement along $x(y)$ and propagating along $y(x)$ or an $E_1(T)$ mode with atomic displacement along $x(y)$ and propagation along z; and an $E_1(L)$ with atomic displacement along $x(y)$ and propagating along $x(y)$. As mentioned before, the Raman experiment can measure each specific mode by proper orientation of the wave vectors q_i and q_s for the incident and scattered light. In the ω_T, ω_L tables, (for a non-cubic crystal), the total of optic modes will not match the number given by the irreducible representation, as the ω_L modes are "not included" in the irreducible representation.

The x, y, z axes are orthogonal. It is obvious how to define the x, y, z axes system with respect to the a, b, c edges of the unit cell for cubic, tetragonal, orthorhombic and hexagonal and trigonal symmetry (after a bit of thought). But for monoclinic and triclinic symmetries, the a, b, c axes cannot all be selected to coincide with the x, y, z system. The character tables are constructed with x, y, z axes with the resulting selection rules for IR- and Raman-active modes. However, IR experiments are often done with polarization $E \parallel a$, $E \parallel b$, $E \parallel c$. Apparently, the choice of the x, y, z coordinate system is somewhat different in Russian literature as slight systematic differences in irreducible representations seem to occur.

It is pertinent to ask which transverse and longitudinal phonons are observed in an IR reflection experiment. In Fig. 2(a) and (b) for the IR, we show typical reststrahlen reflection spectra of a CdS-type sample with the ω_T, ω_L frequencies marked for light polarizations $\parallel$ and $\perp z$. Note that ω_T (A_1) is somewhat less than ω_T (E_1); ω_L (A_1) is slightly less than ω_L (E_1). In the inset we show the experimental configuration of the sample. At the transverse frequencies light is resonantly absorbed (with a component of dipole moment $\parallel$ and $\perp z$. The longidudinal frequencies occur at the zeroes in ϵ_R. We are tempted to say that for $E \parallel z$ polarization, we measure all $A_1(T)$ modes propagating in the x-y plane; for $E \perp z$, we measure all $E_1(T)$ modes propagating in the x-z plane. Then, where are the corresponding $A_1(L)$ and $E_1(L)$ modes?

For $A_1(T)$ $(E \parallel z)$ with $q \parallel y$ and atomic dispacement $e \parallel z$, there is an $A_1(L)$ mode with $q \parallel z$ and atomic displacement $e \parallel z$. For $E_1(T)$ $(E \perp z)$ with q in the x-z plane and atomic displacement $e \parallel y$, there is an $E_1(L)$ with $q \parallel y$ and atomic displacement $e \parallel y$. A detailed examination of the several ω_T and ω_L frequencies of crystalline SiO_2 indeed suggests such a correlation.

Note that for cubic crystals the IR-active mode is always of F species in some form. Since this is a triply degenerate mode, one can always account for 2 T and 1 L modes. In non-cubic crystals the situation is more complicated. An $A_1(T)$ mode can often change species as the propagation direction is turned from z to x and, indeed, convert to an $E_1(T)$ mode.

Zone-center optic phonons which are silent or Raman active in a metal

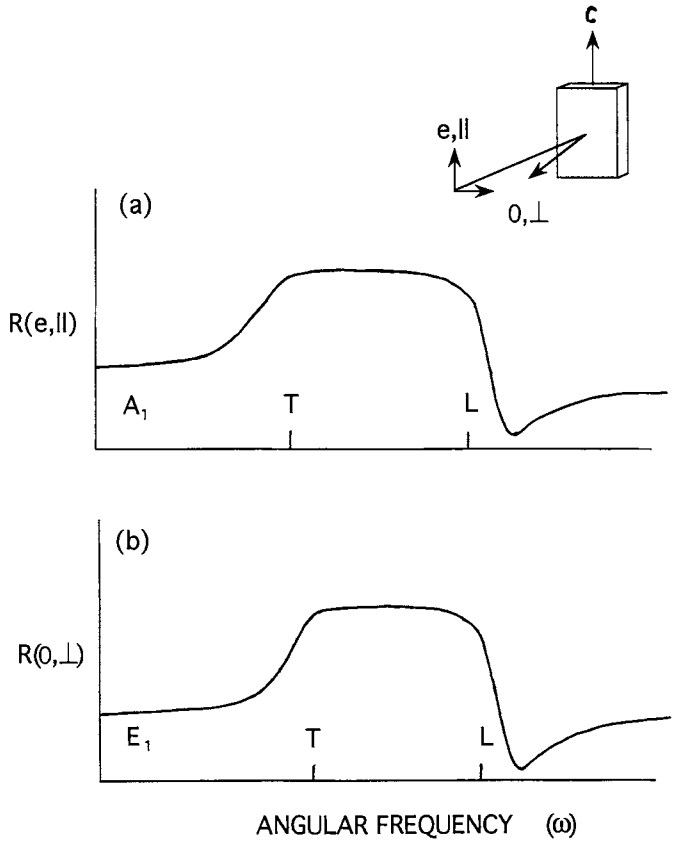

Fig. 2. (a) Reststrahlen spectrum of a CdS-type crystal for incident electric field $E \parallel c$ (extraordinary). Inset shows sample configuration with electric-field polarizations. (b) Reststrahlen spectrum of a CdS-type sample for incident electric field $E \perp c$ (ordinary).

(and therefore not possible or hard to see) can often be seen in neutron-scattering data [15, 16], at least the lower-energy modes. Note that the only metals in Table I which have IR-active modes are cubic Mn-α and the diatomic metals with cubic NaCl symmetry. Since the high free-electron concentration has driven the real dielectric function negative in the IR, these modes would be difficult to measure.

More detailed group theory can be used to calculate the dispersions curves for phonons propagating along various symmetry directions in the crystal, not just for long wavelength phonons at the zone center. This has been done in conjunction with neutron inelastic-scattering experiments. In this case, LA, TA, LO, and TO modes can be assigned to various branches of the dispersion curves in cubic diatomic metals and non-cublic metals such as Sn-β (tetragonal) [17, 18].

REFERENCES

1. A. M. Efimov, "Optical Constants of Inorganic Glasses." CRC Press, Boca Raton, Florida, 1995.
2. W. J. Tropf, M. E. Thomas, and T. J. Harris, Properties of crystals and glasses. *in* "Handbook of Optics, Volume II, Devices, Measurements and Properties" (M. Bass, E. W. Van Stryland, D. R. Wiliams, and W. L. Wolfe, eds.), 2nd Ed., Chap. 33. McGraw-Hill, New York, 1995.
3. K.-H. Hellwege, ed., "Landolt-Börnstein Numerical Data and Functional Relationships in Science and Technology." Springer-Verlag, Berlin, 1983; Several of the volumes treating semiconductors.
4. N. M. F. Henry and K. L. Lonsdak, eds., "International Tables for X-Ray Crystallography." Kynoch Press, Birmingham, U. K., 1952.
5. R. W. G. Wyckoff, "Crystal Structures," Vols. 1–4, Wiley (Interscience), New York, 1965.
6. G. R. Wilkinson, Raman spectra of ionic, covalent, and metallic crystals. *in* "Raman Effect" (A. Anderson, ed.), Vol. 2, Chap. 1. Dekker, New York, 1973.
7. D. E. Gray, ed., "American Institute of Physics Handbook." McGraw-Hill, New York, 1972.
8. W. G. Fateley, F. R. Dollish, M. T. McDevitt, and F. F. Bentley, "Infrared and Raman Selection Rules for Molecular and Lattice Vibrations: The Correlation Method." Wiley (Interscience), New York, 1972.
9. D. L. Rousseau, R. P. Bauman, and S. P. S. Porto, Normal mode determination in crystals. *J. Raman Spectrosc.* **10**, 253 (1981).
10. D. W. Berreman, Infrared absorption at longitudinal optic frequency in cubic crystal films. *Phys. Rev.* **130**, 2193 (1963).
11. C. Decius, R. Frech, and P. Brüesch, Infrared reflection from longitudinal modes in anisotropic crystals." *J. Chem. Phys.* **58**, 4056 (1973).
12. S. P. S. Porto and R. S. Krishnan, Raman effect of corundum. *J. Chem. Phys.* **47**, 1009 (1967).
13. S. M. Shapiro and J. D. Axe, Raman scattering from polar phonons. *Phys. Rev. B* **6**, 2420 (1972).
14. C. A. Arguello, D. L. Rousseau, and S. P. S. Porto, First-order Raman effect in wurtzite-type crystals. *Phys. Rev.* **181**, 1351 (1969).
15. K.-H. Helwege, ed., "Landolt-Börnstein Numerical Data and Functional Relationships in Science and Technology," Section III/Vol. 13a and Section III/Vol. 13b. Springer-Verlag, Berlin, 1983.
16. H. Bilz and W. Kress, "Phonon Dispersion Relations in Insulators." Springer-Verlag, Berlin, 1979.
17. S. H. Chen, Group-theoretical analysis of lattice vibrations in metallic β-Sn. *Phys. Rev.* **163**, 547 (1967).
18. J. M. Rowe, Crystal dynamics of metallic β-Sn at 110 K. *Phys. Rev.* **163**, 547 (1967).
    The preceeding and following references were used to obtain the vibration frequencies for many of the materials in *HOC I, II,* and *III.* The chemical formula for the material precedes the reference or can be inferred from the title of the reference.
    $Y_3Al_5O_{12}$: [2]
    Al_2MgO_4: [2]
    $Al_{23}O_{27}N_5$: [2]
    Y_2O_3: [2]
19. FeS_2: H. D. Lutz, G. Schneider, and G. Kliche, Far-infrared reflection spectra, TO- and LO-phonon frequencies, coupled and decoupled plasmon-phonon modes, dielectric constants, and effective dynamical charges of manganese, iron, and platinum group pyrite type compounds. *J. Phys. Chem. Solids* **46**, 437 (1985).
20. H. Vogt, T. Chattopadhyay, and H. J. Stolz, Complete first-order Raman spectra of the

pyrite structure compounds FeS_2, MnS_2 and SiP_2. *J. Phys. Chem. Solids* **44**, 869 (1983).
Y_2O_3: [2]
21. W. Wojdowski, Vibrational modes in $Bi_{12}GeO_{20}$ and $Bi_{12}SiO_{20}$. *Phys. Status Solidi B* **130**, 121 (1985).
22. C. F. Tuinstra and T. L. Koenig, Raman spectrum of graphite. *J. Chem. Phys.* **53**, 1126 (1970).
23. T. J. Wieting and J. L. Verble, Interlayer bonding and the lattice vibrations of β-GaSe. *Phys. Rev. B* **5**, 1473 (1972).
24. GaSe-ε: J. C. Irwin, R. M. Hoff, B. P. Clayman, and R. A. Bromley, Long wavelength lattice vibrations in GaS and GaSe. *Solid State Commun.* **13**, 1531 (1973).
ZnS: [2, 6]
CdS: [2, 6]
CdSe: [2, 6]
BeO: [2, 6]
SiC-α-6H: [2, 6]
AgI: [2, 6]
AlN: [2, 6]
BN: [25]
GaN: [2, 6]
25. R. Geick, C. H. Perry, and G. Rupprecht, Normal modes in hexagonal boron nitride. *Phys. Rev.* **146**, 543 (1966).
26. Si_3N_4-β: Y. N. Volgin and Y. I. Ukhanov, Vibrational spectra of silicon nitride. *Opt. Spectrosc.* **38**, 412 (1975); *Opt. Spektrosk.* **38**, 727 (1975).
27. Y. N. Volgin, G. P. Dubrovskii, and Y. I. Ukhanov, Lattice vibration spectrum of silicon nitride. *Sov. Phys. Solid State* **17**, 1089 (1975); *Fiz. Tverd. Tela (Leningrad)* **17**, 1671 (1975).
28. N. Wada, S. A. Solin, J. Wong, and S. Prochazka, Raman and IR absorption spectroscopic studies on α, β and amorphous Si_3N_4. *J. Non-Cryst. Solids* **43**, 7 (1981).
29. Y. N. Volgin, V. V. Baptizmanskii, Y. I. Ukhanov, and B. V. Chernovets, Vibrational spectra of β-Si_3N_4. *Sov. Phys. Solid State* **30**, 1105 (1988); *Fiz. Tverd. Tela (Leningrad)* **30**, 1910 (1988).
30. J. P. Luongo, Infrared characterization of α- and β-crystalline silicon nitride. *J. Electrochem. Soc.* **130**, 1560 (1983).
Al_2O_3: [6, 12]
31. Ga_2O_3: E. D. Palik, N. Ginsburg, R. T. Holm, and J. W. Gibson, Optical studies of the anodic oxide on GaAs. *J. Vac. Sci. Technol.* **15**, 1488 (1977).
32. F. Brehat and B. Wyncke, Analysis of the temperature-dependent infrared active modes in the ordered phase of sodium nitrate. *J. Phys. Chem.* **18**, 247 (1985).
$CaCO_3$: [2]
33. I. P. Kaminow and W. D. Johnston, Jr., Quantitative determination of source of the electro-optic effect in $LiNbO_3$ and $LiTaO_3$. *Phys. Rev.* **160**, 519 (1967).
34. R. Claus, Directional dispersion and assignment of optical phonons in $LiNbO_3$. *Z. Naturforsch.* **287A**, 1187 (1972).
35. $LiTaO_3$: J. L. Servoid and F. Gervais, Soft vibrational mode in $LiNbO_3$ and $LiTaO_3$. *Solid State Commun.* **31**, 387 (1979).
36. GaSe-γ: R. M. Hoff, J. C. Irwin and R. M. A. Lieth, Raman scattering in GaSe. *Can. J. Phys.* **53**, 1606 (1975).
37. Si_3N_4-α: T. Kuzuba, K. Kijima, and Y. Bando, Raman-active modes of alpha silicon nitride. *J. Chem. Phys.* **69**, 40 (1978).
SiO_2: [12]
38. Se: G. Lucovsky, A. Mooradian, W. Taylor, G. B. Wright, and R. C. Keezer, Identification of the fundamental vibrational modes of trigonal, α-monoclinic and amorphous films. *Solid State Commun.* **5**, 113 (1967).
Te: [6, 38]

39. P. Dawson, M. M. Hargreave, and G. R. Wilkinson, The vibrational spectrum of zircon ($ZrSiO_4$). *J. Phys. C: Solid State Phys.* **4**, 240 (1971).
40. J. Misiewicz, Optical vibrations in the Zn_3P_2 lattice. *J. Phys. Condens. Matter* **1**, 9283 (1991).
41. G. Pangilinan, R. Sooryakumar, and J. Misiewicz, Raman activity of Zn_3P_2. *Phys. Rev. B* **44**, 2582 (1991).
42. TiO_2: S. P. S. Porto, P. A. Fleury, and T. C. Damen, Raman spectra for TiO_2, MgF_2, ZnF_2, CrF_2, and MnF_2. *Phys. Rev.* **154**, 522 (1967).
43. KH_2PO_4: D. K. Agrawal and C. H. Perry, The temperature dependent Raman spectra of KDP, KD*P, KDA and ADP. *in* "Proceedings of the Second International Conference on Light Scattering Solids," (M. Balkanski, ed.), p. 429. Flammarion, Paris, 1971.
$AgGaS_2$: [2]
$AgGaSe_2$: [2]
$CdGeAs_2$: [2]
$CuGaS_2$: [2]
$ZnGeP_2$: [2]
44. $NH_4H_2PO_4$: T. Kawamura and A. Mitsuishi, *Technol. Rep. Osaka Univ.* **23**, 365 (1973).
45. J. Weszka, A. Zwick, and M. Renucci, Raman scattering in α-Zn_3As_2 crystals. *Acta Phys. Pol. A* **77**, 363 (1990).
46. A. Scalabrin, A. S. Chaves, D. S. Shin, and S. P. S. Porto, Temperature dependence of the A_1 and E optical phonons in $BaTiO_3$. *Phys. Status Solidi B* **79**, 731 (1977).
47. S. G. Gautier and M. Debeau, Spectres de vibration d'un monocristal de soufre orthorhombique. *Spectrochim. Acta* **30A**, 1193 (1974).
48. TlI: J. Claudel, A. Hadni, P. Strimer, and P. Vergnat, Absorption spectra of the thallous halides in the far infrared at low temperatures. *J. Phys. Chem. Solids* **29**, 1539 (1968).
49. $(CH_2)_x$: J. R. Nielsen and A. H. Wollett, Vibrational spectra of polyethylenes and related substances. *J. Chem. Phys.* **26**, 1391 (1957).
50. $(CH_2)_x$: R. Zbinden, "Infrared Spectroscopy of High Polymers." Academic Press, New York, 1964.
$KNbO_3$: [2]
51. S. Guda, D. Peebles, and T. J. Wieting, Zone-center (q = 0) optical phonons in CuO studied by Raman and infrared spectroscopy. *Phys. Rev. B* **43**, 13092 (1991).
52. ThF_4: H. Y. B. Mar, Infrared properties and morphology of ThF_4 films. *J. Vac. Sci. Technol.* **12**, 919 (1975).
53. R. Zallen, M. L. Slade, and A. T. Ward, Lattice vibrations and interlayer interactions in crystalline As_2S_3 and As_2Se_3. *Phys. Rev. B* **3**, 4257 (1971).
54. GaTe-α: M. N. Gasanly, B. M. Dzhavadov, V. I. Tagirov, and E. A. Vinogrdov, Vibrational spectra of a GaTe layer crystal. *Phys. Status. Solidi. (B)* **100**, K53 (1980).

Introduction to the Data for Several Metals

DAVID W. LYNCH
Department of Physics and Astronomy and
Ames Laboratory, USDOE
Iowa State University
Ames, Iowa
and
W. R. HUNTER
SFA Inc.
Largo, Maryland

INTRODUCTION I

Optical data are presented below for eight metals. Mg, In, and Sn are nearly-free-electron polyvalent metals, Ti, Mn, Re, and Ru are transition metals, and Sb is not really a metal, but rather a semimetal. The optical properties of all these metals in the visible and ultraviolet are determined by interband absorption. The threshold for such absorption is, in principle, zero for the transition metals. This means that a fit of the infrared optical properties with a free-electron or Drude model may not be possible. As a practical matter, for b.c.c. and h.c.p. metals there is a threshold for the onset of strong interband absorption, but at energies below this threshold, there is dispersion in the real part of the dielectric function due to the nearby rise in the imaginary part, so a region of "pure" Drude behavior may occur only at very low energies. The polyvalent metals have, in the absence of damping, a threshold for interband absorption, but damping is always present because of electron–electron scattering. For such metals, a Drude model may be fitted at long wavelengths, but the high-energy limit of such a fit is not known reliably at this time. For these reasons we do not report the parameters of Drude fits to the infrared optical properties of any of these metals.

There are four general methods for determining the optical properties (complex refractive index $[n + ik]$ or complex dielectric function $[\epsilon = \epsilon_1 +$

HANDBOOK OF OPTICAL CONSTANTS OF SOLIDS III

Copyright © 1998 by Academic Press.
All rights of reproduction in any form reserved
ISBN 0-12-544423-0/$25.00.

$i\epsilon_2$]) of a material, and in principle, one needs two measurements at each photon energy to determine the real and imaginary parts. Three of the general methods are photometric. When using the first, one measures the reflectance of an opaque sample or thin film, and a second quantity, such as the reflectance at another angle, the transmittance of the film, or the reflectance at nonnormal incidence with a different polarization. The second method is a variant of the first. One measures the reflectance over as wide a range of energies as possible and uses a dispersion integral, or Kramers–Kronig integral, to obtain the unmeasured phase shift upon reflection. These two quantities give the complex refractive index. This method requires, in principle, data over an infinite energy range: data that are usually supplied by the use of measurements of others, and the appeal to simple models for high and low energies. The third method is ellipsometry, which measures the ratio of reflectances for *s*- and *p*-polarized radiation and the relative phase shift between the two, both measured at large angles of incidence. The fourth method is a nonoptical method, electron-energy-loss spectroscopy, which gives a spectrum proportional to $\mathrm{Im}(-1/\epsilon)$. If measured over a wide energy range, this can yield $\mathrm{Re}(-1/\epsilon)$ in a dispersion integral, and ϵ can be obtained, although a scaling factor has to be introduced to obtain absolute units. These measurement methods, and references to them, are described in more detail elsewhere [1]. In the data, we have not made use of any measurements from electron-energy-loss spectroscopy.

By now these methods are able to achieve an accuracy of the order of 1%, but there are discrepancies between the results of different investigators of over 10%. Much of this can be assigned to differences in samples, and how sample deficiencies affect the measured quantities. The first three types of measurement make use of the Fresnel relations derived from Maxwell's equations for the interface between a sample and the ambient medium, air or vacuum in the cases at hand. The interface is assumed to be a mathematical plane and the medium just below it is assumed to be the same as in the bulk of that medium. Real surfaces are not like this. They may be rather rough; the material to be studied may have an oxide film, a cold-worked layer from polishing, or both. Thin films may be highly strained and they may not have the density of the bulk. The effects of these departures from ideality are different for different techniques, and they will depend on the photon energy. For example, an oxide layer may be transparent in the visible but absorbing in the ultraviolet. As a result of these effects, there is not as good agreement between the results of different investigators as may be desired. Moreover, the "correct" optical constants one wants to use may depend on the application. Data resulting from measurements made on strained films may be the best to use if one is calculating anticipated spectra for filters made of strained films.

Several of the materials whose optical constants are given later are anisotropic. These are uniaxial, and two independent spectra of complex optical

constants are required for a complete description of the optical properties of a single crystal. For a polycrystalline sample consisting of randomly oriented crystallites, the dielectric function is given by $\epsilon = (\epsilon_{\parallel} + 2\epsilon_{\perp})/3$, with the c-axis as the reference for polarization. However, films of these materials tend not to have randomly oriented crystallites; the c-axes tend to be oriented normal to the films. They may be closer to a single crystal for optical purposes than to a polycrystal. When available, we have reported a single set of data taken on polycrystalline bulk samples, but for such anisotropic materials, most of those reported here, the reader should consult the references, and should decide how to deal with the anisotropy.

REFERENCES

1. D. W. Lynch, *in* "Handbook on Synchrotron Radiation" (G. V. Marr, ed.), Vol. 2, Chap. 11. Elsevier, Amsterdam, 1987.

MAGNESIUM (Mg) II

Magnesium is a hexagonal close-packed metal. In single-crystal form it is optically anisotropic, uniaxial, with two independent components in the dielectric tensor, one for the electric field parallel to the c-axis and one for the perpendicular orientation. Polycrystalline films may have a texture, growing with the closest-packed plane, the basal plane, in the plane of the film, but with randomly oriented a-axes. If so, the film will be optically anisotropic. If there is truly random orientation of crystallites, the film is isotropic with a complex dielectric function $\epsilon = (\epsilon_{\parallel} + 2\,\epsilon_{\perp})/3$. Mg develops an oxide skin when exposed to air, typically MgO, which is unstable in that it does not protect the metal from further oxidation.

The data presented in Table I and Fig. 1 are those of Hagemann *et al* [1]. These are a result of a Kramers–Kronig analysis of the data of Gesell *et al.* [2], Daudé *et al.* [3], Hacman and Heitmann [4], Kröger and Tomboulian [5], and their own measurements. These represent results on polycrystalline films. Some measurements on single crystals have been published [6–8].

The location of the soft x-ray edges, shown by the short, vertical lines in Fig. 1, are taken from Siegbahn *et al.* [9].

REFERENCES

1. W. Hagemann, W. Gudat, and C. Kunz, *J. Opt. Soc. Am.* **65**, 742 (1975). The data appear in report DESY SR-74/7 from Deutsches Elektronen-Synchrotron, Notkestieg 1, D-2000 Hamburg 52, Germany.
2. T. F. Gesell, E. T. Arakawa, M. W. Williams, and N. R. Hamm, *Phys. Rev. B* **7**, 5141 (1973).
3. A. Daudé, M. Priol, and S. Robin, *Compt. Rend. Ser B* **264**, 1489 (1967).

4. D. Hacman and W. Heitmann, *Appl. Opt.* **12**, 895 (1967).
5. H. Kröger and D. H. Tomboulian, *Phys. Rev.* **130**, 152 (1957).
6. A. P. Lenham and D. M. Treherne, *J. Opt. Soc. Am.* **56**, 752 (1966).
7. D. Jones and A. H. Lettington, *Proc. Phys. Soc. (London)* **92**, 948 (1967).
8. R. H. W. Graves and A. P. Lenham, *J. Opt. Soc. Am.* **58**, 126 (1968).
9. K. Siegbahn, C. Nordling, A. Fahlman, R. Nordberg, K. Hamrin, J. Hedman, G. Johansson, T. Bergmark, S.-E. Karlsson, I. Lindgren, and B. Lindberg, *in* "ESCA Atomic, Molecular, and Solid State Structure Studied by Means of Electron Spectroscopy." Almquist & Wiksell, Uppsala, Sweden, 1967.

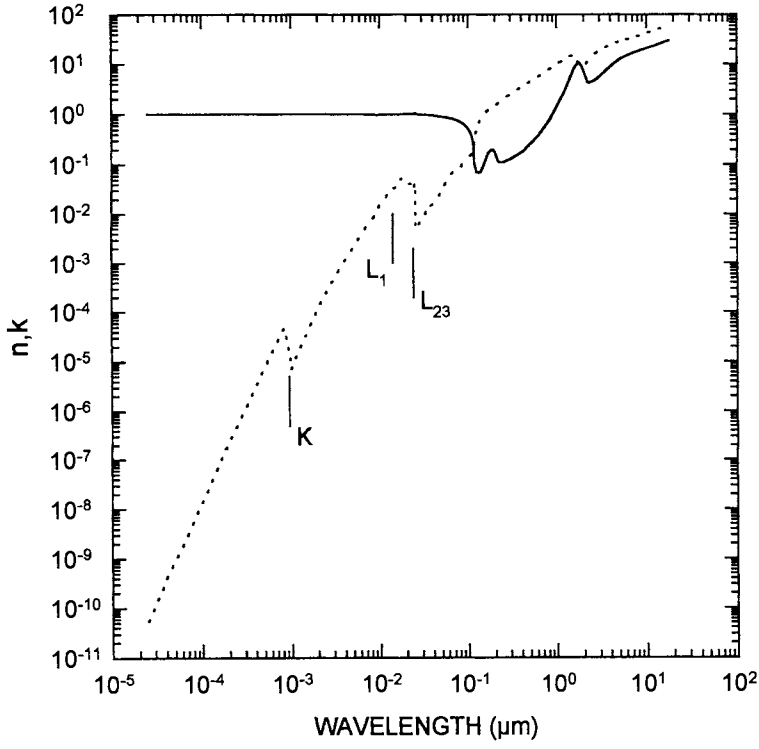

Fig. 1. Log–log plot of n (——) and k (- - - -) versus wavelength in micrometers for magnesium.

TABLE I

Values of n and k Obtained from Various References for Magnesium[a]

eV	cm^{-1}	μm	n	k
50000.	4.033E + 08	2.48E-05	9.999E-01 [1]	5.38E-11 [1]
40000.	3.226E + 08	3.10E-05	9.999E-01	1.35E-10
30000.	2.420E + 08	4.13E-05	9.999E-01	4.80E-10
20000.	1.613E + 08	6.20E-05	9.999E-01	2.04E-09
10000.	8.065E + 07	1.24E-04	9.999E-01	3.33E-08
8000.	6.452E + 07	1.55E-04	9.999E-01	8.27E-08
6000.	4.839E + 07	2.07E-04	9.999E-01	2.75E-07
4000.	3.226E + 07	3.10E-04	9.999E-01	1.19E-06
2000.	1.613E + 07	6.20E-04	9.999E-01	1.75E-05
1500.	1.210E + 07	8.27E-04	9.999E-01	4.76E-05
1300.	1.049E + 07	9.54E-04	9.999E-01	1.50E-05
1260.	1.016E + 07	9.84E-04	9.999E-01	8.15E-06
1250.	1.008E + 07	9.92E-04	9.999E-01	7.09E-06
1200.	9.679E + 06	1.03E-03	9.999E-01	8.94E-06
1000.	8.065E + 06	1.24E-03	9.990E-01	1.86E-05
800.	6.452E + 06	1.55E-03	9.996E-01	4.41E-05
600.	4.839E + 06	2.07E-03	9.990E-01	1.39E-04
500.	4.033E + 06	2.48E-03	9.987E-01	2.66E-04
450.	3.629E + 06	2.76E-03	9.984E-01	3.75E-04
400.	3.226E + 06	3.10E-03	9.977E-01	5.42E-04
350.	2.823E + 06	3.54E-03	9.974E-01	8.11E-04
300.	2.420E + 06	4.13E-03	9.963E-01	1.25E-03
250.	2.016E + 06	4.96E-03	9.948E-01	2.15E-03
200.	1.613E + 06	6.20E-03	9.923E-01	4.07E-03
180.	1.452E + 06	6.89E-03	9.911E-01	5.30E-03
160.	1.290E + 05	7.75E-03	9.891E-01	7.11E-03
150.	1.210E + 06	8.27E-03	9.881E-01	8.16E-03
145.	1.169E + 06	8.55E-03	9.871E-01	8.85E-03
140.	1.129E + 06	8.86E-03	9.860E-01	1.00E-02
135.	1.089E + 06	9.18E-03	9.489E-01	1.16E-02
130.	1.049E + 06	9.54E-03	9.846E-01	1.35E-02
125.	1.008E + 06	9.92E-03	9.847E-01	1.52E-02
120.	9.679E + 05	1.03E-02	9.846E-01	1.66E-02
115.	9.275E + 05	1.08E-02	9.844E-01	1.77E-02
110.	8.872E + 05	1.13E-02	9.829E-01	1.93E-02
105.	8.469E + 05	1.18E-02	9.815E-01	2.25E-02
100.	8.065E + 05	1.24E-02	9.815E-01	2.68E-02
95.	7.662E + 05	1.31E-02	9.838E-01	3.10E-02
90.	7.259E + 05	1.38E-02	9.860E-01	3.30E-02
89.	7.178E + 05	1.39E-02	9.870E-01	3.37E-02
88.	7.098E + 05	1.41E-02	9.870E-01	3.34E-02
87.	7.017E + 05	1.43E-02	9.870E-01	3.34E-02
86.	6.936E + 05	1.44E-02	9.870E-01	3.36E-02
84.	6.775E + 05	1.48E-02	9.880E-01	3.45E-02
82.	6.614E + 05	1.51E-02	9.880E-01	3.52E-02
80.	6.452E + 05	1.55E-02	9.870E-01	3.60E-02
78.	6.291E + 05	1.59E-02	9.860E-01	3.74E-02

(continued)

[a] The references from which the values were extracted are given in brackets.

TABLE I *(Continued)*

Magnesium

eV	cm^{-1}	μm	n	k
76.	6.130E + 05	1.63E-02	9.840E-01	4.14E-02
74.	5.968E + 05	1.68E-02	9.860E-01	4.75E-02
72.	5.807E + 05	1.72E-02	9.920E-01	5.26E-02
70.	5.646E + 05	1.77E-02	1.00	5.33E-02
68.	5.485E + 05	1.82E-02	1.005	5.03E-02
66.	5.323E + 05	1.88E-02	1.008	4.58E-02
64.	5.162E + 05	1.94E-02	1.008	4.32E-02
62.	5.001E + 05	2.00E-02	1.008	4.14E-02
60.	4.839E + 05	2.07E-02	1.008	4.09E-02
59.	4.759E + 05	2.10E-02	1.008	4.10E-02
58.	4.678E + 05	2.14E-02	1.009	4.08E-02
57.	4.597E + 05	2.18E-02	1.01	4.09E-02
56.	4.517E + 05	2.21E-02	1.01	4.18E-02
55.5	4.476E + 05	2.23E-02	1.012	4.12E-02
55.	4.436E + 05	2.25E-02	1.013	4.06E-02
54.5	4.396E + 05	2.27E-02	1.013	3.98E-02
54.	4.355E + 05	2.30E-02	1.014	4.01E-02
53.5	4.315E + 05	2.32E-02	1.015	4.07E-02
53.	4.275E + 05	2.34E-02	1.017	3.93E-02
52.5	4.234E + 05	2.36E-02	1.018	3.39E-02
52.	4.194E + 05	2.38E-02	1.019	3.76E-02
51.5	4.154E + 05	2.41E-02	1.02	3.72E-02
51.	4.113E + 05	2.43E-02	1.021	3.58E-02
50.5	4.073E + 05	2.46E-02	1.023	3.79E-02
50.	4.033E + 05	2.48E-02	1.03	4.17E-02
49.8	4.017E + 05	2.49E-02	1.04	4.18E-02
49.6	4.000E + 05	2.50E-02	1.05	3.38E-02
49.4	3.984E + 05	2.51E-02	1.053	1.06E-02
49.2	3.968E + 05	2.52E-02	1.04	4.92E-03
49.	3.952E + 05	2.53E-02	1.033	4.92E-03
48.5	3.912E + 05	2.56E-02	1.023	4.96E-03
48.	3.871E + 05	2.58E-02	1.018	5.02E-03
46.	3.710E + 05	2.70E-02	1.004	5.97E-03
44.	3.549E + 05	2.82E-02	0.997	6.86E-03
42.	3.388E + 05	2.95E-02	0.989	7.36E-03
40.	3.226E + 05	3.10E-02	0.982	8.84E-03
38.	3.065E + 05	3.26E-02	0.975	1.02E-02
36.	2.904E + 05	3.44E-02	0.967	1.41E-02
34.	2.742E + 05	3.65E-02	0.959	1.41E-02
32.	2.581E + 05	3.87E-02	0.95	1.54E-02
30.	2.420E + 05	4.13E-02	0.939	1.69E-02
28.	2.258E + 05	4.43E-02	0.924	1.96E-02
26.	2.097E + 05	4.77E-02	0.906	2.52E-02
24.	1.936E + 05	5.17E-02	0.885	3.30E-02
22.	1.774E + 05	5.64E-02	0.861	4.54E-02
20.	1.613E + 05	6.20E-02	0.833	5.92E-02
18.	1.452E + 05	6.89E-02	0.798	7.31E-02

TABLE I *(Continued)*

Magnesium

eV	cm^{-1}	μm	n	k
16.	1.290E + 05	7.75E-02	0.741	7.92E-02
15.	1.210E + 05	8.27E-02	0.692	9.16E-02
14.	1.129E + 05	8.86E-02	0.644	1.11E-01
13.	1.049E + 05	9.54E-02	0.577	1.27E-01
12.	9.679E + 04	1.03E-01	0.477	1.45E-01
11.5	9.275E + 04	1.08E-01	0.404	1.58E-01
11.	8.872E + 04	1.13E-01	0.293	1.76E-01
10.5	8.469E + 04	1.18E-01	0.11	2.96E-01
10.	8.065E + 04	1.24E-01	0.0723	4.99E-01
9.5	7.662E + 04	1.31E-01	0.0691	6.47E-01
9.	7.259E + 04	1.38E-01	0.0717	7.87E-01
8.5	6.856E + 04	1.46E-01	0.0858	9.26E-01
8.	6.452E + 04	1.55E-01	0.115	1.06
7.5	6.049E + 04	1.65E-01	0.155	1.19
7.3	5.888E + 04	1.70E-01	0.171	1.23
7.1	5.726E + 04	1.75E-01	0.184	1.27
6.9	5.565E + 04	1.80E-01	0.194	1.31
6.7	5.404E + 04	1.85E-01	0.199	1.35
6.5	5.243E + 04	1.91E-01	0.197	1.39
6.3	5.081E + 04	1.97E-01	0.187	1.44
6.1	4.920E + 04	2.03E-01	0.166	1.49
5.9	4.759E + 04	2.10E-01	0.14	1.56
5.7	4.597E + 04	2.18E-01	0.121	1.64
5.5	4.436E + 04	2.25E-01	0.112	1.74
5.	4.033E + 04	2.48E-01	0.111	2.00
4.	3.226E + 04	3.10E-01	0.132	2.63
3.	2.420E + 04	4.13E-01	0.184	3.66
2.	1.613E + 04	6.20E-01	0.382	5.74
1.5	1.210E + 04	8.27E-01	0.791	7.96
1.	8.065E + 03	1.24	2.977	12.8
0.9	7.259E + 03	1.38	4.776	14.5
0.8	6.452E + 03	1.55	8.269	15.5
0.7	5.646E + 03	1.77	11.2	10.2
0.65	5.243E + 03	1.91	8.809	8.98
0.6	4.839E + 03	2.07	6.056	9.33
0.55	4.436E + 03	2.25	4.194	12.2
0.5	4.033E + 03	2.48	4.509	14.7
0.45	3.629E + 03	2.76	5.056	16.8
0.4	3.226E + 03	3.10	6.069	19.5
0.35	2.823E + 03	3.54	7.519	22.2
0.3	2.420E + 03	4.13	9.516	25.1
0.25	2.016E + 03	4.96	12.3	28.8
0.2	1.613E + 03	6.20	15.2	32.6
0.15	1.210E + 03	8.27	18.9	37.6
0.1	8.065E + 02	12.4	23.8	48.8
0.07	5.646E + 02	17.7	30.3	60.2

III TITANIUM (Ti)

Ti is a hexagonal close-packed metal. In single-crystal form it is optically anisotropic, uniaxial, with two independent components in the dielectric tensor, one for the electric field parallel to the *c*-axis and one for the perpendicular orientation. Polycrystalline films may have a texture, growing with the closest-packed plane, the basal plane, in the plane of the film, but with randomly oriented *a*-axes. If so, the film will be optically anisotropic. If there is truly random orientation, the film is isotropic with a complex dielectric function $\epsilon = (\epsilon_{\parallel} + 2\epsilon_{\perp})/3$. Ti is quite reactive with air. (It is used as a getter pump in vacuum systems.) However, the oxide film is self-limiting, leading to a stable sample. Since there are so many oxides of Ti, it is difficult to model the optical properties of a Ti sample oxidized to equilibrium.

Ti is a transition metal. The incompletely filled 3*d* bands can give rise to interband optical absorption at arbitrarily small energies. This means that reliable fits of optical data to a Drude-model dielectric function cannot be made, except below some unknown low energy. Ordal *et al.* [1] were unable to fit the optical constants of Ti to a Drude model in the 1–12-μm wavelength region because of the presence of interband transitions. According to absorptivity measurements by Lynch *et al.* [2], these transitions give a strong absorption edge at 0.4 eV, although they are present, however weaker, at lower energies. Later, Ordal *et al.* [3] produced a Drude fit to the same data for energies below 0.37 eV.

Ordal *et al.* [4] measured absorptance spectra in the submillimeter-wave region and obtained optical constants by a Kramers–Kronig analysis, using their data and measurements from shorter wavelengths. The data we present in Table II and Fig. 2 are those of Ordal *et al.* [4] and Lynch *et al.* [2], measured on polycrystalline bulk samples and published by Weaver *et al.* [5], Wall *et al.* [6], and Sonntag *et al.* [7]. The last spectra were of the absorption coefficient. They were converted to spectra of the imaginary part of the complex refractive index with the assumption that the real part was unity. The data of Wall *et al.* are the only data on atomically clean surfaces. Comparison with the data of Lynch *et al.*, taken on electropolished surfaces, shows that in the vacuum ultraviolet the effect of the residual oxide is serious.

The data reported for the 1–10 μm region were taken at 4.2 K. At room temperature the peak will broaden considerably. The literature contains a number of additional reports on measurements of the optical constants of Ti [8–20] taken on bulk polycrystalline samples and on evaporated films by several techniques.

Smith [21] has measured the temperature dependence at two wavelengths, 5461 and 6328 Å.

Data in the soft x-ray region, from approximately 10^{-4} to 0.024 μm, are taken from Henke *et al.* [22], and the location of the soft x-ray edges, shown by the short, vertical lines in Fig. 1, are taken from Siegbahn *et al.* [23].

REFERENCES

1. M. A. Ordal, L. L. Long, R. J. Bell, S. E. Bell, R. R. Bell, R. W. Alexander, and C. A. Ward, *Appl. Opt.* **22**, 1099 (1983).
2. D. W. Lynch, C. G. Olson, and J. H. Weaver, *Phys. Rev. B* **11**, 3617 (1975).
3. M. A. Ordal, R. J. Bell, R. W. Alexander, L. L. Long, and M. R. Querry, *Appl. Opt.* **24**, 4493 (1985).
4. M. A. Ordal, R. J. Bell, R. W. Alexander, L. A. Newquist, and M. R. Querry, *Appl. Opt.* **27**, 1203 (1988).
5. J. H. Weaver, C. Krafka, D. W. Lynch, and E.-E. Koch, Physics Data, Optical Properties of Metals, Part I: The Transition Metals, Fachinformationszentrum Karlsruhe, 7514 Eggenstein-Leopoldshafen 2, Germany, 1981.
6. W. Wall, M. W. Ribarsky, and J. R. Stevenson, *J. Appl. Phys.* **51**, 661 (1980).
7. B. Sonntag, R. Haensel, and C. Kunz, *Solid State Commun.* **7**, 597 (1969).
8. G. Hass and A. P. Bradford, *J. Opt. Soc. Am.* **47**, 125 (1957).
9. G. A. Bolotin, A. N. Voloshinskii, M. M. Kirillova, M. M. Noskov, A. V. Sokolov, and B. A. Charikov, *Fiz. Met. Metalloved.* **13**, 823 (1962); *Phys. Met. Metall.* **13**, 24 (1962).
10. M. M. Kirillova and B. A. Charikov, *Opt. Spektrosk.* **17**, 254 (1963); *Opt. Spectrosc.* **17**, 134 (1963).
11. M. M. Kirillova and B. A. Charikov, *Fiz. Met. Metalloved.* **15**, 315 (1963); *Phys. Met. Metall.* **15**, 138 (1963).
12. A. P. Lukirskii, E. P. Savinov, O. A. Ershov, and Yu. F. Shepelev, *Opt. Spektrosk.* **16**, 310 (1964); *Opt. Spectrosc.* **16**, 168 (1964).
13. M. M. Kirillova and B. A. Charikov, *Fiz. Met. Metalloved.* **19**, 495 (1965); *Phys. Met. Metall.* **19**, 13 (1965).
14. A. P. Lenham and D. M. Treherne, *J. Opt. Soc. Am.* **56**, 1137 (1966).
15. M. M. Kirillova, L. V. Nomerovannaya, G. A. Bolotin, V. M. Mayevskiy, M. M. Noskov, and M. L. Bolotina, *Fiz. Met. Metalloved.* **25**, 459 (1968); *Phys. Met. Metall.* **25**, 81 (1968).
16. I. D. Mash and G. P. Motulevich, *Sov. Phys. JETP* **36**, 516 (1973).
17. P. B. Johnson and R. W. Christy, *Phys. Rev. B* **9**, 5056 (1974).
18. J. J. Carroll and A. J. Melmed, *J. Opt. Soc. Am.* **64**, 514 (1974).
19. G. Blondeau, M. Froelicher, M. Froment, and A. Hugot-LeGoff, *Thin Solid Films* **38**, 261 (1976).
20. R. Blickensderfer, D. K. Deardorff, and R. L. Lincoln, *J. Less Common Metals* **51**, 13 (1977).
21. T. Smith, *J. Opt. Soc. Am.* **62**, 774 (1972).
22. B. L. Henke, J. C. Davis, E. M. Gullikson, and R. C. C. Perera, "A Preliminary Report on X-Ray Photoabsorption Coefficients and Atomic Scattering Factors for 92 Elements in the 10–10,000 eV Region," Lawrence Berkeley Lab. Rep. LBL-26259, University of California, Berkeley, California, 1988.
23. K. Siegbahn, C. Nordling, A. Fahlman, R. Nordberg, K. Hamrin, J. Hedman, G. Johansson, T. Bergmark, S.-E. Karlsson, I. Lindgren, and B. Lindberg, "ESCA Atomic, Molecular, and Solid State Structure Studied by Means of Electron Spectroscopy." Almquist & Wiksell, Uppsala, Sweden, 1967.

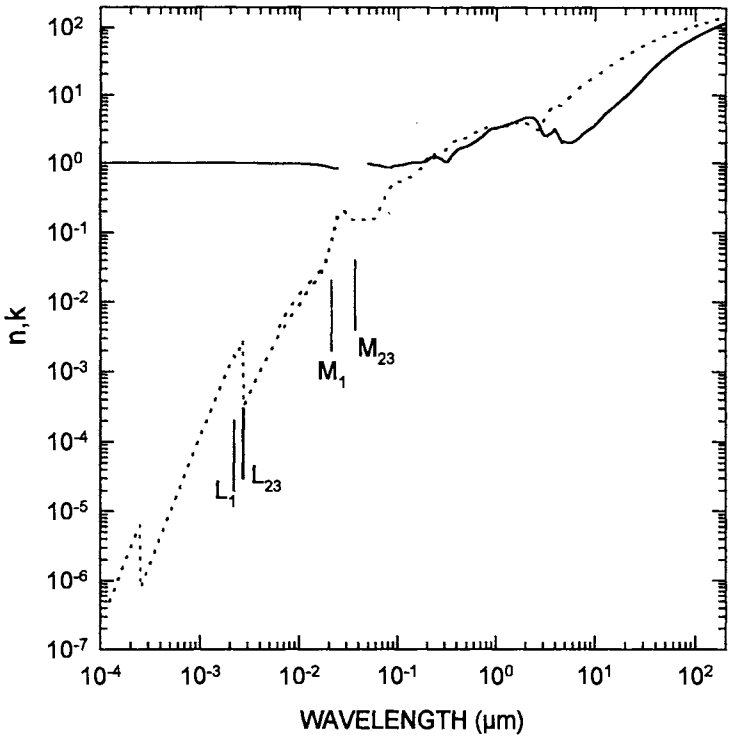

Fig. 2. Log–log plot of n (——) and k (- - - -) versus wavelength in micrometers for titanium.

TABLE II

Values of n and k Obtained from Various References for Titanium[a]

eV	cm^{-1}	μm	n	k
10000	8.101E + 07	1.23E-04	9.9999120E-01 [22]	4.89E-07 [22]
8558	6.902E + 07	1.45E-04	9.999880E-01	9.03E-07
7100	5.726E + 07	1.75E-04	9.999828E-01	1.80E-06
5294	4.269E + 07	2.34E-04	9.999720E-01	5.17E-06
5154	4.157E + 07	2.41E-04	9.999716E-01	5.67E-06
5018	4.048E + 07	2.47E-04	9.999729E-01	6.22E-06
4886	3.941E + 07	2.54E-04	9.999705E-01	7.97E-07
4758	3.837E + 07	2.61E-04	9.999670E-01	8.81E-07
3547	2.861E + 07	3.50E-04	9.999351E-01	2.63E-06
2575	2.077E + 07	4.81E-04	9.99874E-01	8.63E-06
1680	1.355E + 07	7.38E-04	9.99697E-01	4.13E-05
1470	1.186E + 07	8.43E-04	9.99603E-01	6.69E-05
1287	1.038E + 07	9.64E-04	9.99483E-01	1.08E-04
1126	9.081E + 06	1.10E-03	9.99330E-01	1.72E-04
1012	8.161E + 06	1.23E-03	9.99181E-01	2.49E-04
886	7.142E + 06	1.40E-03	9.9896E-01	3.94E-04
735	5.925E + 06	1.69E-03	9.9860E-01	7.40E-04
593	4.786E + 06	2.09E-03	9.9831E-01	1.48E-03
578	4.660E + 06	2.15E-03	9.9834E-01	1.61E-03
563	4.537E + 06	2.20E-03	9.9847E-01	1.52E-03
548	4.417E + 06	2.26E-03	9.9834E-01	1.65E-03
533	4.301E + 06	2.32E-03	9.9832E-01	1.80E-03
492	3.971E + 06	2.52E-03	9.9857E-01	2.31E-03
479	3.866E + 06	2.59E-03	9.9886E-01	2.52E-03
467	3.764E + 06	2.66E-03	9.9945E-01	2.74E-03
454	3.665E + 06	2.73E-03	1.000853	3.24E-04
442	3.568E + 06	2.80E-03	9.9946E-01	3.50E-04
431	3.475E + 06	2.88E-03	9.9887E-01	3.79E-04
321	2.591E + 06	3.86E-03	9.9588E-01	9.19E-04
215	1.736E + 06	5.76E-03	9.9028E-01	2.79E-03
200	1.613E + 06	6.20E-03		4.40E-03 [7]
190	1.532E + 06	6.53E-03		5.10E-03
180	1.452E + 06	6.89E-03		6.00E-03
170	1.371E + 06	7.29E-03		6.90E-03
160	1.290E + 06	7.75E-03		7.90E-03
152	1.227E + 06	8.15E-03	9.817E-01 [22]	6.23E-03 [22]
150	1.210E + 06	8.27E-03		9.10E-03 [7]
140	1.129E + 06	8.86E-03		1.05E-02
130	1.049E + 06	9.54E-03		1.20E-02
120	9.679E + 05	1.03E-02		1.39E-02
110	8.872E + 05	1.13E-02		1.60E-02
102	8.219E + 05	1.22E-02	9.611E-01 [22]	1.45E-02 [22]
100	8.065E + 05	1.24E-02		1.86E-02 [7]
95	7.662E + 05	1.31E-02		2.01E-02

(continued)

[a] The references from which the values were extracted are given in brackets.

TABLE II *(Continued)*

Titanium

eV	cm^{-1}	μm	n	k
90	7.259E + 05	1.38E-02		2.17E-02
85	6.856E + 05	1.46E-02		2.42E-02
80	6.452E + 05	1.55E-02		2.63E-02
75	6.049E + 05	1.65E-02		2.87E-02
74	5.968E + 05	1.68E-02		3.04E-02
72	5.807E + 05	1.72E-02		3.26E-02
70	5.646E + 05	1.77E-02		3.49E-02
68	5.485E + 05	1.82E-02		3.88E-02
66	5.323E + 05	1.88E-02		4.45E-02
64	5.162E + 05	1.94E-02		5.20E-02
62	5.001E + 05	2.00E-02		6.15E-02
60	4.839E + 05	2.07E-02		7.01E-02
55	4.436E + 05	2.25E-02		0.112
52	4.194E + 05	2.38E-02		0.151
50	4.033E + 05	2.48E-02		0.176
48	3.871E + 05	2.58E-02		0.194
46	3.710E + 05	2.70E-02		0.208
44	3.549E + 05	2.82E-02		0.209
42	3.388E + 05	2.95E-02		0.191
40	3.226E + 05	3.10E-02		0.164
38	3.065E + 05	3.26E-02		0.154
25	2.016E + 05	4.96E-02	0.991 [6]	0.151 [6]
24.50	1.976E + 05	5.06E-02	0.987	0.152
24.00	1.936E + 05	5.17E-02	0.982	0.153
23.50	1.895E + 05	5.28E-02	0.977	0.154
23.00	1.855E + 05	5.39E-02	0.972	0.154
22.50	1.815E + 05	5.51E-02	0.961	0.156
22.00	1.774E + 05	5.64E-02	0.951	0.158
21.50	1.734E + 05	5.77E-02	0.941	0.159
21.00	1.694E + 05	5.90E-02	0.936	0.160
20.50	1.653E + 05	6.05E-02	0.932	0.172
20.00	1.613E + 05	6.20E-02	0.930	0.188
19.50	1.573E + 05	6.36E-02	0.922	0.201
19.00	1.532E + 05	6.53E-02	0.920	0.217
18.50	1.492E + 05	6.70E-02	0.902	0.233
18.00	1.452E + 05	6.89E-02	0.891	0.253
17.50	1.411E + 05	7.08E-02	0.883	0.283
17.00	1.371E + 05	7.29E-02	0.882	0.312
16.50	1.331E + 05	7.51E-02	0.871	0.344
16.00	1.290E + 05	7.75E-02	0.852	0.382
15.50	1.250E + 05	8.00E-02	0.853	0.410
15.00	1.210E + 05	8.27E-02	0.860	0.436
14.50	1.169E + 05	8.55E-02	0.872	0.459
14.00	1.129E + 05	8.86E-02	0.892	0.505
13.50	1.089E + 05	9.18E-02	0.903	0.515
13.00	1.049E + 05	9.54E-02	0.912	0.521
12.50	1.008E + 05	9.92E-02	0.923	0.531

TABLE II *(Continued)*

Titanium

eV	cm^{-1}	μm	n	k
12.00	9.679E + 04	1.03E-01	0.932	0.537
11.50	9.275E + 04	1.08E-01	0.940	0.542
11.00	8.872E + 04	1.13E-01	0.951	0.552
10.50	8.469E + 04	1.18E-01	0.966	0.569
10.00	8.065E + 04	1.24E-01	0.993	0.604
9.50	7.662E + 04	1.31E-01	1.00 [2]	0.625 [2]
9.00	7.259E + 04	1.38E-01	1.01	0.645
8.50	6.856E + 04	1.46E-01	1.01	0.691
8.00	6.452E + 04	1.55E-01	1.02	0.763
7.50	6.049E + 04	1.65E-01	1.02	0.810
7.00	5.646E + 04	1.77E-01	1.03	0.873
6.50	5.243E + 04	1.91E-01	1.06	0.947
6.46	5.210E + 04	1.92E-01	1.07	1.11
6.36	5.130E + 04	1.95E-01	1.08	1.14
6.26	5.049E + 04	1.98E-01	1.09	1.16
6.20	5.001E + 04	2.00E-01	1.11	1.18
6.14	4.952E + 04	2.02E-01	1.12	1.19
6.08	4.904E + 04	2.04E-01	1.13	1.20
6.02	4.855E + 04	2.06E-01	1.15	1.21
5.90	4.759E + 04	2.10E-01	1.18	1.22
5.85	4.718E + 04	2.12E-01	1.19	1.22
5.79	4.670E + 04	2.14E-01	1.21	1.22
5.74	4.630E + 04	2.16E-01	1.22	1.22
5.69	4.589E + 04	2.18E-01	1.23	1.21
5.64	4.549E + 04	2.20E-01	1.23	1.21
5.59	4.509E + 04	2.22E-01	1.24	1.21
5.53	4.460E + 04	2.24E-01	1.24	1.20
5.49	4.428E + 04	2.26E-01	1.24	1.19
5.44	4.388E + 04	2.28E-01	1.23	1.19
5.39	4.347E + 04	2.30E-01	1.17	1.16
5.34	4.307E + 04	2.32E-01	1.18	1.41
5.30	4.275E + 04	2.34E-01	1.35	1.21
5.25	4.234E + 04	2.36E-01	1.28	1.20
5.21	4.202E + 04	2.38E-01	1.27	1.20
5.17	4.170E + 04	2.40E-01	1.25	1.20
5.12	4.130E + 04	2.42E-01	1.25	1.20
5.08	4.097E + 04	2.44E-01	1.24	1.21
5.00	4.033E + 04	2.48E-01	1.24	1.21
4.96	4.000E + 04	2.50E-01	1.23	1.21
4.92	3.968E + 04	2.52E-01	1.22	1.22
4.88	3.936E + 04	2.54E-01	1.22	1.22
4.84	3.904E + 04	2.56E-01	1.22	1.23
4.80	3.871E + 04	2.58E-01	1.21	1.23
4.77	3.847E + 04	2.60E-01	1.20	1.23
4.73	3.815E + 04	2.62E-01	1.19	1.24
4.66	3.759E + 04	2.66E-01	1.16	1.27

(continued)

TABLE II *(Continued)*

Titanium

eV	cm^{-1}	μm	n	k
4.66	3.759E + 04	2.66E-01	1.17	1.26
4.59	3.702E + 04	2.70E-01	1.17	1.29
4.56	3.678E + 04	2.72E-01	1.17	1.29
4.53	3.654E + 04	2.74E-01	1.16	1.30
4.49	3.621E + 04	2.76E-01	1.15	1.31
4.46	3.597E + 04	2.78E-01	1.14	1.32
4.43	3.573E + 04	2.80E-01	1.14	1.33
4.40	3.549E + 04	2.82E-01	1.13	1.33
4.36	3.517E + 04	2.84E-01	1.12	1.34
4.34	3.500E + 04	2.86E-01	1.11	1.36
4.30	3.468E + 04	2.88E-01	1.10	1.37
4.28	3.452E + 04	2.90E-01	1.09	1.38
4.25	3.428E + 04	2.92E-01	1.07	1.40
4.22	3.404E + 04	2.94E-01	1.06	1.42
4.19	3.379E + 04	2.96E-01	1.05	1.45
4.16	3.355E + 04	2.98E-01	1.05	1.47
4.13	3.331E + 04	3.00E-01	1.04	1.49
4.11	3.315E + 04	3.02E-01	1.04	1.52
4.08	3.291E + 04	3.04E-01	1.04	1.54
4.05	3.267E + 04	3.06E-01	1.03	1.57
4.03	3.250E + 04	3.08E-01	1.03	1.59
3.99	3.218E + 04	3.11E-01	1.04	1.62
3.97	3.202E + 04	3.12E-01	1.04	1.64
3.95	3.186E + 04	3.14E-01	1.04	1.67
3.92	3.162E + 04	3.16E-01	1.05	1.71
3.90	3.146E + 04	3.18E-01	1.06	1.73
3.87	3.121E + 04	3.20E-01	1.07	1.75
3.85	3.105E + 04	3.22E-01	1.08	1.78
3.80	3.065E + 04	3.26E-01	1.11	1.83
3.70	2.984E + 04	3.35E-01	1.17	1.90
3.60	2.904E + 04	3.44E-01	1.24	1.96
3.50	2.823E + 04	3.54E-01	1.30	2.01
3.40	2.742E + 04	3.65E-01	1.37	2.06
3.30	2.662E + 04	3.76E-01	1.44	2.09
3.20	2.581E + 04	3.87E-01	1.50	2.12
3.10	2.500E + 04	4.00E-01	1.55	2.15
3.00	2.420E + 04	4.13E-01	1.59	2.17
2.90	2.339E + 04	4.28E-01	1.63	2.21
2.80	2.258E + 04	4.43E-01	1.68	2.25
2.70	2.178E + 04	4.59E-01	1.71	2.29
2.60	2.097E + 04	4.77E-01	1.75	2.34
2.50	2.016E + 04	4.96E-01	1.78	2.39
2.40	1.936E + 04	5.17E-01	1.81	2.47
2.30	1.855E + 04	5.39E-01	1.86	2.56
2.20	1.774E + 04	5.64E-01	1.92	2.67
2.10	1.694E + 04	5.90E-01	2.01	2.77
2.00	1.613E + 04	6.20E-01	2.11	2.88

TABLE II *(Continued)*

Titanium

eV	cm^{-1}	μm	n	k
1.95	1.573E + 04	6.36E-01	2.16	2.93
1.90	1.532E + 04	6.53E-01	2.22	2.99
1.85	1.492E + 04	6.70E-01	2.29	3.05
1.80	1.452E + 04	6.89E-01	2.36	3.11
1.75	1.411E + 04	7.08E-01	2.44	3.17
1.70	1.371E + 04	7.29E-01	2.54	3.23
1.65	1.331E + 04	7.51E-01	2.65	3.24
1.60	1.290E + 04	7.75E-01	2.74	3.30
1.55	1.250E + 04	8.00E-01	2.87	3.33
1.50	1.210E + 04	8.27E-01	2.98	3.32
1.45	1.169E + 04	8.55E-01	3.08	3.31
1.40	1.129E + 04	8.86E-01	3.17	3.28
1.35	1.089E + 04	9.18E-01	3.23	3.26
1.30	1.049E + 04	9.54E-01	3.28	3.25
1.25	1.008E + 04	9.92E-01	3.31	3.26
1.20	9.679E + 03	1.03	3.35	3.30
1.15	9.275E + 03	1.08	3.40	3.35
1.10	8.872E + 03	1.13	3.47	3.40
1.05	8.469E + 03	1.18	3.54	3.46
1.00	8.065E + 03	1.24	3.62	3.52
0.98	7.904E + 03	1.27	3.65	3.55
0.96	7.743E + 03	1.29	3.69	3.57
0.94	7.582E + 03	1.32	3.73	3.60
0.92	7.420E + 03	1.35	3.77	3.62
0.90	7.259E + 03	1.38	3.80	3.65
0.88	7.098E + 03	1.41	3.85	3.69
0.86	6.936E + 03	1.44	3.93	3.73
0.84	6.775E + 03	1.48	3.94	3.65
0.82	6.614E + 03	1.51	3.94	3.80
0.80	6.452E + 03	1.55	4.04	3.82
0.78	6.291E + 03	1.59	4.11	3.85
0.76	6.130E + 03	1.63	4.18	3.87
0.74	5.968E + 03	1.68	4.25	3.88
0.72	5.807E + 03	1.72	4.32	3.89
0.70	5.646E + 03	1.77	4.38	3.89
0.68	5.485E + 03	1.82	4.44	3.90
0.66	5.323E + 03	1.88	4.52	3.90
0.64	5.162E + 03	1.94	4.60	3.88
0.62	5.001E + 03	2.00	4.66	3.83
0.60	4.839E + 03	2.07	4.71	3.77
0.58	4.678E + 03	2.14	4.74	3.71
0.56	4.517E + 03	2.21	4.75	3.62
0.54	4.355E + 03	2.30	4.73	3.50
0.52	4.194E + 03	2.38	4.62	3.35
0.50	4.033E + 03	2.48	4.43	3.22
0.49	3.952E + 03	2.53	4.29	3.15

(continued)

TABLE II *(Continued)*

Titanium

eV	cm^{-1}	μm	n	k
0.48	3.871E + 03	2.58	4.11	3.10
0.47	3.791E + 03	2.64	3.89	3.08
0.46	3.710E + 03	2.70	3.62	3.12
0.45	3.629E + 03	2.76	3.35	3.25
0.44	3.549E + 03	2.82	3.10	3.44
0.43	3.468E + 03	2.88	2.88	3.68
0.42	3.388E + 03	2.95	2.69	3.98
0.41	3.307E + 03	3.02	2.56	4.32
0.40	3.226E + 03	3.10	2.49	4.68
0.39	3.146E + 03	3.18	2.48	5.02
0.38	3.065E + 03	3.26	2.52	5.35
0.37	2.984E + 03	3.35	2.59	5.65
0.36	2.904E + 03	3.44	2.67	5.93
0.35	2.823E + 03	3.54	2.74	6.21
0.34	2.742E + 03	3.65	2.82	6.52
0.33	2.662E + 03	3.76	2.95	6.88
0.32	2.581E + 03	3.87	3.17	7.29
0.31	2.500E + 03	4.00	3.60	7.87
0.30	2.420E + 03	4.13	6.39	9.94
0.29	2.339E + 03	4.28	4.15	3.06
0.28	2.258E + 03	4.43	1.43	5.65
0.27	2.178E + 03	4.59	2.00	6.98
0.26	2.097E + 03	4.77	2.08	7.56
0.25	2.016E + 03	4.96	2.05	8.10
0.24	1.936E + 03	5.17	2.01	8.66
0.23	1.855E + 03	5.39	1.98	9.27
0.22	1.774E + 03	5.64	2.00	9.92
0.21	1.694E + 03	5.90	2.04	10.61
0.20	1.613E + 03	6.20	2.12	11.34
0.19	1.532E + 03	6.53	2.23	12.12
0.18	1.452E + 03	6.89	2.41	12.94
0.17	1.371E + 03	7.29	2.60	13.79
0.16	1.290E + 03	7.75	2.81	14.70
0.15	1.210E + 03	8.27	3.00	15.72
0.14	1.129E + 03	8.86	3.22	16.87
0.13	1.049E + 03	9.54	3.49	18.23
0.12	9.679E + 02	10.3	3.90	19.79
0.11	8.872E + 02	11.3	4.48	21.45
0.0992	8.000E + 02	12.5	5.2 [4]	24.40 [4]
0.0868	7.000E + 02	14.3	6.24	27.60
0.0744	6.000E + 02	16.7	7.58	31.80
0.0620	5.000E + 02	20.0	9.67	37.60
0.0558	4.500E + 02	22.2	11.20	41.30
0.0496	4.000E + 02	25.0	13.30	45.80
0.0434	3.500E + 02	28.6	16.30	51.50
0.0372	3.000E + 02	33.3	20.90	58.00
0.0310	2.500E + 02	40.0	27.20	65.90

TABLE II *(Continued)*

Titanium

eV	cm^{-1}	μm	n	k
0.0279	2.250E + 02	44.4	31.30	70.60
0.0248	2.000E + 02	50.0	36.20	75.80
0.0217	1.750E + 02	57.1	42.30	81.80
0.0186	1.500E + 02	66.7	49.90	88.90
0.0155	1.250E + 02	80.0	59.64	97.50
0.0124	1.000E + 02	100	72.50	108.40
0.0099	8.000E + 01	125	86.40	120.00
0.0081	6.500E + 01	154	100.50	131.90
0.0062	5.000E + 01	200	120.00	148.40

MANGANESE (Mn) IV

α-Mn has a complex unit cell, but the lattice is body-centered cubic. α-Mn, therefore, is optically isotropic. There is another cubic phase and a tetragonal phase at high temperature. Mn is quite reactive with oxygen, and this has an effect on all measurements at energies above a few electron volts. Not only does one expect a surface oxide on any film in air, but, as discussed by Atkinson [1], Mn films often contain MnO unless prepared in ultrahigh vacuum. Optical studies have not been carried out on such films.

Mn is a transition metal. The incompletely filled $3d$ bands can give rise to interband optical absorption at arbitrarily small energies. This means that reliable fits of optical data to a Drude-model dielectric function cannot be made, except below some unknown low energy.

With the exception of the work of Lenham and Treherne [2], all optical studies on Mn have been made on thin or thick films. All have possible effects from an oxide. The only infrared data are from Lenham and Treherne [2], obtained by ellipsometry on mechanically polished surfaces of bulk specimens that were not etched after polishing, and from Fouad and Amar [3], obtained on films. The latter match up well with the data of Johnson and Christy [4], taken in the 1–6-eV range on thin films. We present data in Table III and Fig. 3 from both these sources, and the soft x-ray absorption measurements of Sonntag *et al.* [5]. The latter were measurements of the absorption coefficient, converted to a spectrum of the imaginary part of the refractive index with the assumption that the real part was unity. There is a gap between these measurements and the data of Christy *et al.* [4]. In addition, there have been measurements by Steel [6] and Aagard [7].

Data in the soft x-ray region, from approximately 10^{-4} to 0.024 μm, are

taken from Henke *et al.* [8], and the location of the soft x-ray edges, shown by the short, vertical lines in Fig. 3, are taken from Siegbahn *et al.* [9].

REFERENCES

1. R. Atkinson, *Thin Solid Films* **37**, 195 (1976).
2. A. P. Lenham and D. M. Treherne, *J. Opt. Soc. Am.* **56**, 1137 (1966).
3. S. S. Fouad and A. H. Amar, *Physica B* **205**, 285 (1995).
4. P. B. Johnson and R. W. Christy, *Phys. Rev. B* **9**, 5056 (1974).
5. B. Sonntag, R. Haensel, and C. Kunz, *Solid State Commun.* **7**, 597 (1969).
6. M. R. Steel, *J. Phys. F: Metal Phys.* **4**, 873 (1974).
7. R. L. Aagard, *J. Opt. Soc. Am.* **64**, 1456 (1976).
8. B. L. Henke, J. C. Davis, E. M. Gullikson, and R. C. C. Perera, "A Preliminary Report on X-Ray Photoabsorption Coefficients and Atomic Scattering Factors for 92 Elements in the 10–10,000 eV Region," Lawrence Berkeley Lab. Rep. LBL-26259, University of California, Berkeley, California, 1988.
9. K. Siegbahn, C. Nordling, A. Fahlman, R. Nordberg, K. Hamrin, J. Hedman, G. Johansson, T. Bergmark, S.-E. Karlsson, I. Lindgren, and B. Lindberg, "ESCA Atomic, Molecular, and Solid State Structure Studied by Means of Electron Spectroscopy." Almquist & Wiksell, Uppsala, Sweden, 1967.

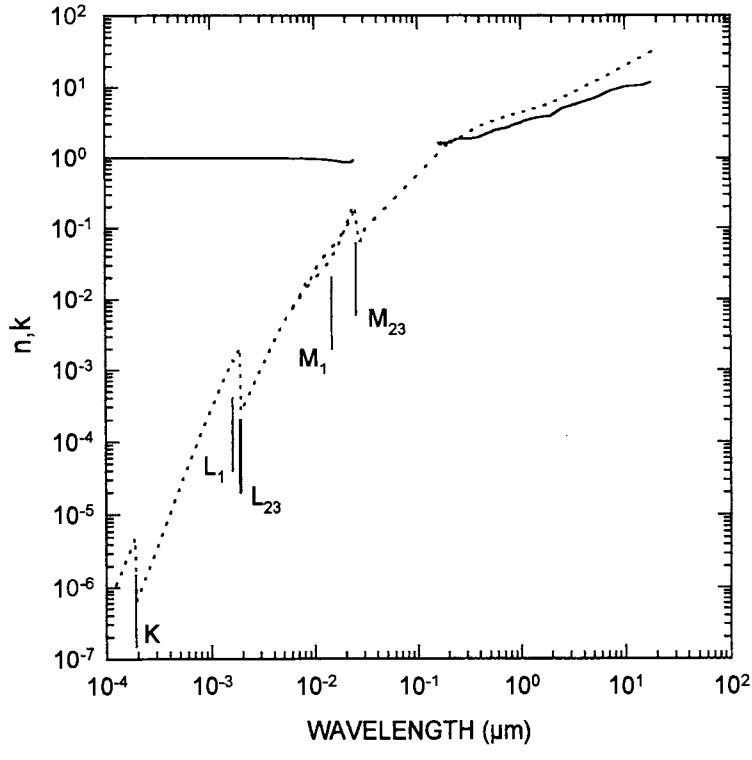

Fig. 3. Log–log plot of n (——) and k (- - - -) versus wavelength in micrometers for manganese.

TABLE III

Values of n and k Obtained from Various References for Manganese[a]

eV	cm^{-1}	μm	n	k
10000.	8.066E + 07	1.24E-04	9.999862E-01 [8]	1.09E-06 [8]
9117.	7.353E + 07	1.36E-04	9.999834E-01	1.54E-06
8123.	6.551E + 07	1.53E-04	9.999795E-01	2.33E-06
7237.	5.837E + 07	1.71E-04	9.999751E-01	3.52E-06
6752.	5.446E + 07	1.84E-04	9.999732E-01	4.48E-06
6598.	5.321E + 07	1.88E-04	9.999737E-01	4.85E-06
6447.	5.200E + 07	1.92E-04	9.999723E-01	6.54E-07
6300.	5.081E + 07	1.97E-04	9.999694E-01	7.11E-07
6156.	4.965E + 07	2.01E-04	9.999673E-01	7.74E-07
5117.	4.127E + 07	2.42E-04	9.999503E-01	1.53E-06
4061.	3.276E + 07	3.05E-04	9.999193E-01	3.63E-06
3299.	2.661E + 07	3.76E-04	9.99876E-01	7.90E-06
2227.	1.797E + 07	5.57E-04	9.99723E-01	3.41E-05
1768.	1.426E + 07	7.01E-04	9.99560E-01	7.92E-05
1539.	1.241E + 07	8.06E-04	9.99423E-01	1.30E-04
1309.	1.056E + 07	9.47E-04	9.99217E-01	2.28E-04
806.	6.501E + 06	1.54E-03	9.9845E-01	1.18E-03
686.	5.530E + 06	1.81E-03	9.9865E-01	1.79E-03
670.	5.404E + 06	1.85E-03	9.9886E-01	1.93E-03
655.	5.281E + 06	1.89E-03	9.9927E-01	2.08E-03
640.	5.160E + 06	1.94E-03	1.00384	2.59E-04
625.	5.042E + 06	1.98E-03	9.9931E-01	2.78E-04
611.	4.927E + 06	2.03E-03	9.9885E-01	2.98E-04
485.	3.911E + 06	2.56E-03	9.9677E-01	6.08E-04
403.	3.251E + 06	3.08E-03	9.9500E-01	1.10E-03
313.	2.521E + 06	3.97E-03	9.9158E-01	2.37E-03
237.	1.911E + 06	5.23E-03	9.863E-01	5.24E-03
232.	1.867E + 06	5.36E-03	9.857E-01	5.52E-03
200.	1.613E + 06	6.20E-03		7.80E-03 [5]
190.	1.532E + 06	6.53E-03		8.80E-03
180.	1.371E + 06	7.29E-03		1.15E-02
175.	1.415E + 06	7.07E-03	9.775E-01 [8]	1.01E-02 [8]
160.	1.290E + 06	7.75E-03		1.38E-02 [5]
150.	1.210E + 06	8.27E-03		1.70E-02
140.	1.129E + 06	8.86E-03		1.63E-02
136.	1.098E + 06	9.11E-03	9.668E-01 [8]	1.67E-02 [8]
130.	1.049E + 06	9.54E-03		2.18E-02 [5]
120.	9.679E + 05	1.03E-02		2.69E-02
111.	8.915E + 05	1.12E-02	9.531E-01 [8]	2.30E-02 [8]
110.	8.872E + 05	1.13E-02		3.20E-02 [5]
100.	8.065E + 05	1.24E-02		3.96E-02
98.5	7.942E + 05	1.26E-02	9.418E-01 [8]	2.75E-02 [8]
95.	7.662E + 05	1.31E-02		4.32E-02 [5]
90.	7.259E + 05	1.38E-02		4.67E-02
85.	6.856E + 05	1.46E-02		5.18E-02

(continued)

[a] The references from which the values were extracted are given in brackets.

TABLE III *(Continued)*

Manganese

eV	cm^{-1}	μm	n	k
83.8	6.756E + 05	1.48E-02	9.195E-01 [8]	3.95E-02 [8]
80.	6.452E + 05	1.55E-02		5.75E-02 [5]
75.	6.049E + 05	1.65E-02		6.39E-02
72.9	5.882E + 05	1.70E-02	0.894 [8]	5.72E-02 [8]
70.	5.646E + 05	1.77E-02		7.40E-02 [5]
65.	5.243E + 05	1.91E-02		9.03E-02
62.	5.004E + 05	2.00E-02	0.864 [8]	0.101 [8]
60.	4.839E + 05	2.07E-02		1.08E-01 [5]
58.	4.678E + 05	2.14E-02		1.16E-01
56.	4.517E + 05	2.21E-02		1.26E-01
55.3	4.458E + 05	2.24E-02	0.864 [8]	0.16 [8]
54.	4.355E + 05	2.30E-02		1.41E-01 [5]
52.	4.194E + 05	2.38E-02		1.67E-01
51.6	4.159E + 05	2.40E-02	0.927 [8]	0.188 [8]
50.	4.033E + 05	2.48E-02		1.96E-01 [5]
48.	3.871E + 05	2.58E-02		1.02E-01
46.	3.710E + 05	2.70E-02		6.38E-02
44.	3.549E + 05	2.82E-02		6.67E-02
42.	3.388E + 05	2.95E-02		8.38E-02
40.	3.226E + 05	3.10E-02		9.78E-02
6.6	5.323E + 04	1.88E-01	1.48 [4]	1.47 [4]
6.47	5.218E + 04	1.92E-01	1.55	1.5
6.35	5.122E + 04	1.95E-01	1.59	1.52
6.22	5.017E + 04	1.62E-01	1.62	1.55
6.1	4.920E + 04	2.03E-01	1.63	1.58
5.98	4.823E + 04	2.07E-01	1.67	1.61
5.85	4.718E + 04	2.12E-01	1.7	1.64
5.73	4.622E + 04	2.16E-01	1.72	1.67
5.6	4.517E + 04	2.21E-01	1.73	1.7
5.48	4.420E + 04	2.26E-01	1.74	1.73
5.36	4.323E + 04	2.31E-01	1.78	1.76
5.23	4.218E + 04	2.37E-01	1.81	1.79
5.11	4.121E + 04	2.43E-01	1.82	1.82
4.98	4.017E + 04	2.49E-01	1.82	1.86
4.86	3.920E + 04	2.55E-01	1.83	1.91
4.74	3.823E + 04	2.62E-01	1.84	1.94
4.61	3.718E + 04	2.69E-01	1.85	1.99
4.49	3.621E + 04	2.76E-01	1.86	2.03
4.36	3.517E + 04	2.84E-01	1.85	2.08
4.24	3.420E + 04	2.92E-01	1.85	2.14
4.12	3.323E + 04	3.01E-01	1.86	2.19
3.99	3.218E + 04	3.11E-01	1.86	2.25
3.87	3.121E + 04	3.20E-01	1.86	2.32
3.74	3.016E + 04	3.32E-01	1.86	2.38
3.62	2.920E + 04	3.43E-01	1.87	2.45
3.5	2.823E + 04	3.54E-01	1.89	2.51
3.37	2.718E + 04	3.68E-01	1.89	2.59

TABLE III *(Continued)*

Manganese

eV	cm^{-1}	μm	n	k
3.25	2.612E + 04	3.81E-01	1.92	2.67
3.12	2.516E + 04	3.97E-01	1.96	2.74
3.	2.420E + 04	4.13E-01	2.0	2.82
2.88	2.323E + 04	4.31E-01	2.06	2.9
2.75	2.218E + 04	4.51E-01	2.11	2.98
2.63	2.121E + 04	4.71E-01	2.19	3.06
2.5	2.016E + 04	4.96E-01	2.25	3.14
2.38	1.920E + 04	5.21E-01	2.32	3.23
2.26	1.823E + 04	5.49E-01	2.39	3.33
2.13	1.718E + 04	5.82E-01	2.47	3.43
2.01	1.621E + 04	6.17E-01	2.51	3.54
1.88	1.516E + 04	6.59E-01	2.56	3.65
1.76	1.420E + 04	7.04E-01	2.62	3.78
1.64	1.323E + 04	7.56E-01	2.7	3.91
1.51	1.218E + 04	8.21E-01	2.83	4.03
1.39	1.121E + 04	8.92E-01	2.97	4.18
1.26	1.016E + 04	9.84E-01	3.1	4.35
1.14	9.195E + 03	1.09	3.3	4.53
1.02	8.227E + 03	1.22	3.48	4.74
0.89	7.178E + 03	1.39	3.65	5.02
0.77	6.210E + 03	1.61	3.78	5.41
0.64	5.162E + 03	1.94	3.89	5.95
0.496	4.000E + 03	2.50	5.0 [3]	7.1 [3]
0.248	2.000E + 03	5.00	7.0	11.8
0.165	1.331E + 03	7.51	9.0	16.0
0.124	1.000E + 03	10.	10.3	20.7
0.099	7.985E + 02	12.5	10.5	24.0
0.083	6.694E + 02	14.9	10.8	28.0
0.071	5.726E + 02	17.5	11.7	31.5
0.062	5.001E + 02	20.		35.7

RUTHENIUM (Ru) V

Ruthenium is a hexagonal close-packed metal. In single-crystal form it is optically anisotropic, uniaxial, with two independent components in the dielectric tensor, one for the electric field parallel to the *c*-axis and one for the perpendicular orientation. Polycrystalline films may have a texture, growing with the closest-packed plane, the basal plane, in the plane of the film, but with randomly oriented *a*-axes. If so, the film will be optically anisotropic. If there is truly random orientation, the film is isotropic with a complex dielectric function $\epsilon = (\epsilon_{\parallel} + 2\epsilon_{\perp})/3$.

Ru is a transition metal. The incompletely filled 4*d* bands can give rise to interband optical absorption at arbitrarily small energies. This means that reliable fits of optical data to a Drude-model dielectric function cannot be made, except below some unknown low energy.

Reliable optical data over a wide spectral range do not exist for polycrystalline bulk samples or thin films of Ru. Therefore, we have chosen to use data taken from the basal plane of a single crystal ($\mathbf{E}\perp\mathbf{c}$) by Weaver *et al.* [1, 2]. These data are from a Kramers–Kronig inversion of absorptance and reflectance data. Where there is overlap of spectral regions, there is good agreement with the data of Kirillova *et al.* [3] obtained by ellipsometry, and with Cox *et al.* [4] from reflectance measurements on films taken at several angles of incidence. Additional measurements have been made by Kress and Lapeyre [5], and by Carroll and Melmed [6].

Data in the soft x-ray region, from approximately 10^{-4} to 0.024 μm, are taken from Henke *et al.* [7], and the location of the soft x-ray edges, shown by the short, vertical lines in Fig. 4, are taken from Siegbahn *et al.* [8]. In order to fill the small gap between the data of Henke *et al.* [7] and Weaver *et al.* [1, 2], we have incorporated some of the data of Cox *et al.* [4].

REFERENCES

1. J. H. Weaver, C. G. Olson, and D. W. Lynch, unpublished, 1981.
2. J. H. Weaver, C. Krafka, D. W. Lynch, and E.-E. Koch, Physics Data, Optical Properties of Metals, Part I: the Transition Metals, Fachinformationszentrum Karlsruhe, 7514 Eggenstein-Leopoldshafen 2, Germany, 1981.
3. M. M. Kirillova, L. V. Nomerovannaya, M. M. Noskov, N. B. Gorina, V. P. Polyakova, and E. M. Savitskii, *Fiz. Tverd. Tela (Leningrad)* **20**, 1718 (1978); *Sov. Phys. Solid State* **20**, 994 (1978).
4. J. T. Cox, G. Hass, J. B. Ramsey, and W. R. Hunter, *J. Opt. Soc. Am.* **64**, 423 (1974).
5. K. A. Kress and G. J. Lapeyre, *Phys. Rev. B* **2**, 2532 (1970).
6. J. J. Carroll and A. J. Melmed, *J. Opt. Soc. Am.* **66**, 1050 (1976).
7. B. L. Henke, J. C. Davis, E. M. Gullikson, and R. C. C. Perera, "A Preliminary Report on X-Ray Photoabsorption Coefficients and Atomic Scattering Factors for 92 Elements in the 10–10,000 eV Region," Lawrence Berkeley Lab. Rep. LBL-26259, University of California, Berkeley, California, 1988.
8. K. Siegbahn, C. Nordling, A. Fahlman, R. Nordberg, K. Hamrin, J. Hedman, G. Johansson, T. Bergmark, S.-E. Karlsson, I. Lindgren, and B. Lindberg, "ESCA Atomic, Molecular, and Solid State Structure Studied by Means of Electron Spectroscopy." Almquist & Wiksell, Uppsala, Sweden, 1967.

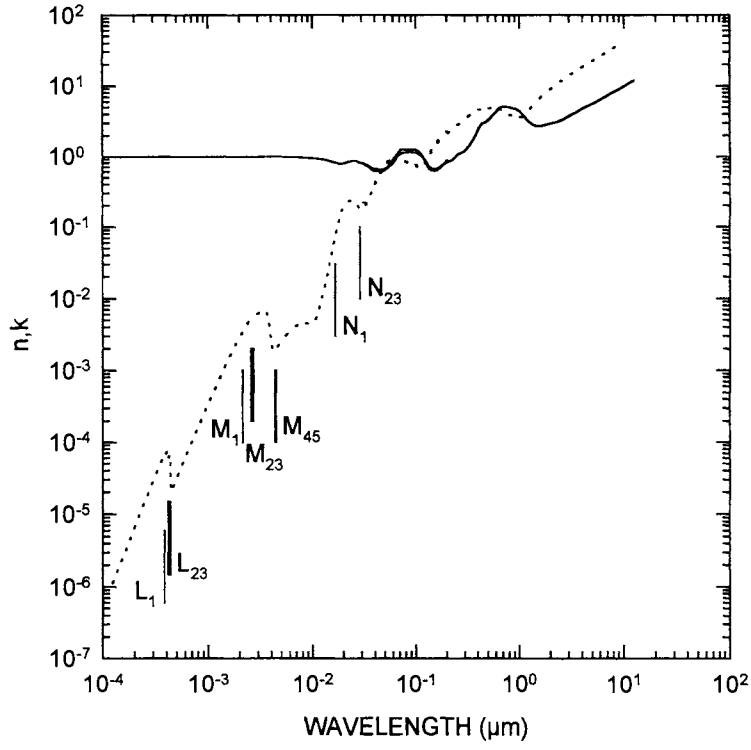

Fig. 4. Log–log plot of n (——) and k (- - - -) versus wavelength in micrometers for ruthenium.

TABLE IV

Values of n and k Obtained from Various References for Ruthenium[a]

eV	cm^{-1}	μm	n	k
10000.	8.066E + 07	1.24E-04	9.999778E-01 [7]	1.14E-06 [7]
9117.	7.353E + 07	1.36E-04	9.999731E-01	1.61E-06
8123.	6.551E + 07	1.53E-04	9.999660E-01	2.48E-06
7072.	5.704E + 07	1.73E-04	9.999550E-01	4.16E-06
6015.	4.852E + 07	2.06E-04	9.999379E-01	7.55E-06
5000.	4.033E + 07	2.48E-04	9.999111E-01	1.48E-05
4062.	3.276E + 07	3.05E-04	9.999870E-01	3.11E-05
3376.	2.723E + 07	3.67E-04	9.99830E-01	5.89E-05
3299.	2.661E + 07	3.76E-04	9.99827E-01	6.37E-05
3224.	2.600E + 07	3.85E-04	9.99828E-01	6.11E-05
3150.	2.541E + 07	3.94E-04	9.99820E-01	6.61E-05
3078.	2.483E + 07	4.03E-04	9.99817E-01	7.16E-05
3008.	2.426E + 07	4.12E-04	9.99821E-01	7.75E-05
2939.	2.371E + 07	4.21E-04	9.99825E-01	6.12E-05
2872.	2.317E + 07	4.32E-04	9.99822E-01	6.63E-05
2806.	2.264E + 07	4.42E-04	9.99825E-01	2.09E-05
2742.	2.212E + 07	4.52E-04	9.99786E-01	2.26E-05
2031.	1.638E + 07	6.10E-04	9.99538E-01	6.42E-05
1809.	1.459E + 07	6.85E-04	9.99410E-01	9.61E-05
1650.	1.330E + 07	7.52E-04	9.99286E-01	1.33E-04
1504.	1.213E + 07	8.24E-04	9.99139E-01	1.83E-04
1371.	1.106E + 07	9.04E-04	9.9897E-01	2.49E-04
1222.	9.854E + 06	1.01E-03	9.9871E-01	3.64E-04
1016.	8.191E + 06	1.22E-03	9.9817E-01	6.70E-04
825.	6.653E + 06	1.50E-03	9.9740E-01	1.29E-03
702.	5.660E + 06	1.77E-03	9.9672E-01	2.12E-03
611.	4.927E + 06	2.03E-03	9.9627E-01	3.11E-03
597.	4.814E + 06	2.08E-03	9.9620E-01	3.28E-03
583.	4.705E + 06	2.12E-03	9.9612E-01	3.46E-03
570.	4.597E + 06	2.18E-03	9.9604E-01	3.66E-03
557.	4.492E + 06	2.23E-03	9.9597E-01	3.90E-03
508.	4.096E + 06	2.44E-03	9.9611E-01	4.79E-03
496.	4.002E + 06	2.50E-03	9.9614E-01	4.94E-03
485.	3.911E + 06	2.56E-03	9.9617E-01	5.09E-03
474.	3.821E + 06	2.62E-03	9.9620E-01	5.23E-03
463.	3.734E + 06	2.68E-03	9.9620E-01	5.37E-03
452.	3.649E + 06	2.74E-03	9.9618E-01	5.53E-03
442.	3.565E + 06	2.80E-03	9.9619E-01	5.74E-03
327.	2.640E + 06	3.79E-03	9.9922E-01	4.60E-03
298.	2.407E + 06	4.15E-03	9.9584E-01	1.82E-03
292.	2.352E + 06	4.25E-03	9.9492E-01	1.90E-03
285.	2.299E + 06	4.35E-03	9.9416E-01	1.97E-03
278.	2.246E + 06	4.45E-03	9.9346E-01	2.04E-03
272.	2.195E + 06	4.56E-03	9.9277E-01	2.13E-03
266.	2.145E + 06	4.66E-03	9.9209E-01	2.24E-03
197.	1.588E + 06	6.30E-03	9.824E-01	3.79E-03

[a] The references from which the values were extracted are given in brackets.

TABLE IV *(Continued)*

Ruthenium

eV	cm^{-1}	μm	n	k
149.	1.204E + 06	8.31E-03	9.672E-01	4.57E-03
101.	8.127E + 05	1.23E-02	9.100E-01	1.02E-02
81.9	6.602E + 05	1.51E-02	0.844	4.02E-02
80.0	6.451E + 05	1.55E-02	0.835	4.78E-02
78.2	6.304E + 05	1.59E-02	0.827	5.68E-02
76.4	6.160E + 05	1.62E-02	0.820	6.59E-02
74.6	6.019E + 05	1.66E-02	0.812	7.53E-02
72.9	5.882E + 05	1.70E-02	0.805	8.60E-02
60.6	4.889E + 05	2.04E-02	0.808	2.05E-01
52.8	4.256E + 05	2.35E-02	0.853	2.35E-01
50.6	4.082E + 05	2.45E-02	0.865 [4]	0.233 [4]
49.6	4.000E + 05	2.50E-02	0.868	0.231
48.6	3.922E + 05	2.55E-02	0.868	0.228
47.7	3.846E + 05	2.60E-02	0.866	0.223
46.8	3.774E + 05	2.65E-02	0.860	0.215
45.9	3.704E + 05	2.70E-02	0.850	0.207
45.1	3.636E + 05	2.75E-02	0.835	0.197
44.3	3.571E + 05	2.80E-02	0.822	0.186
43.5	3.509E + 05	2.85E-02	0.815	0.177
42.8	3.448E + 05	2.90E-02	0.809	0.172
42.0	3.390E + 05	2.95E-02	0.804	0.168
41.3	3.333E + 05	3.00E-02	0.801	0.171
40.0	3.226E + 05	3.10E-02	0.787	0.183
40.0	3.226E + 05	3.10E-02	0.79 [1, 2]	0.22 [1, 2]
39.0	3.146E + 05	3.18E-02	0.77	0.22
38.7	3.125E + 05	3.20E-02	0.774 [4]	0.195 [4]
38.0	3.065E + 05	3.26E-02	0.75 [1, 2]	0.22 [1, 2]
37.6	3.030E + 05	3.30E-02	0.759 [4]	0.208 [4]
37.0	2.984E + 05	3.35E-02	0.73 [1, 2]	0.23 [1, 2]
36.0	2.904E + 05	3.44E-02	0.72	0.25
35.0	2.823E + 05	3.54E-02	0.70	0.26
34.5	2.783E + 05	3.59E-02	0.68	0.27
34.0	2.742E + 05	3.65E-02	0.67	0.28
33.5	2.702E + 05	3.70E-02	0.66	0.30
33.0	2.662E + 05	3.76E-02	0.65	0.31
32.5	2.621E + 05	3.81E-02	0.64	0.32
32.0	2.581E + 05	3.87E-02	0.63	0.34
31.5	2.541E + 05	3.94E-02	0.62	0.37
31.0	2.500E + 05	4.00E-02	0.61	0.40
30.5	2.460E + 05	4.07E-02	0.61	0.43
30.0	2.420E + 05	4.13E-02	0.62	0.45
29.5	2.379E + 05	4.20E-02	0.62	0.46
29.0	2.339E + 05	4.28E-02	0.61	0.48
28.5	2.299E + 05	4.35E-02	0.61	0.50
28.0	2.258E + 05	4.43E-02	0.60	0.53
27.5	2.218E + 05	4.51E-02	0.60	0.56

(continued)

TABLE IV *(Continued)*

Ruthenium

eV	cm^{-1}	μm	n	k
27.0	2.178E + 05	4.59E-02	0.60	0.59
26.5	2.137E + 05	4.68E-02	0.60	0.63
26.0	2.097E + 05	4.77E-02	0.61	0.66
25.5	2.057E + 05	4.86E-02	0.62	0.69
25.0	2.016E + 05	4.96E-02	0.64	0.73
24.5	1.976E + 05	5.06E-02	0.65	0.76
24.0	1.936E + 05	5.17E-02	0.67	0.79
23.5	1.895E + 05	5.28E-02	0.68	0.83
23.0	1.855E + 05	5.39E-02	0.71	0.87
22.5	1.815E + 05	5.51E-02	0.74	0.90
22.0	1.774E + 05	5.64E-02	0.77	0.94
21.8	1.754E + 05	5.70E-02	0.79	0.95
21.5	1.734E + 05	5.77E-02	0.80	0.97
21.3	1.714E + 05	5.83E-02	0.82	0.99
21.0	1.694E + 05	5.90E-02	0.85	1.01
20.8	1.674E + 05	5.98E-02	0.88	1.02
20.5	1.653E + 05	6.05E-02	0.91	1.03
20.3	1.633E + 05	6.12E-02	0.94	1.04
20.0	1.613E + 05	6.20E-02	0.97	1.04
19.8	1.593E + 05	6.28E-02	0.99	1.04
19.5	1.573E + 05	6.36E-02	1.02	1.04
19.3	1.553E + 05	6.44E-02	1.04	1.05
19.0	1.532E + 05	6.53E-02	1.07	1.05
18.8	1.512E + 05	6.61E-02	1.09	1.05
18.5	1.492E + 05	6.70E-02	1.12	1.05
18.3	1.472E + 05	6.79E-02	1.15	1.05
18.0	1.452E + 05	6.89E-02	1.19	1.04
17.8	1.432E + 05	6.99E-02	1.22	1.02
17.5	1.411E + 05	7.08E-02	1.25	1.00
17.3	1.391E + 05	7.19E-02	1.27	0.97
17.0	1.371E + 05	7.29E-02	1.28	0.94
16.8	1.351E + 05	7.40E-02	1.28	0.91
16.5	1.331E + 05	7.51E-02	1.28	0.89
16.3	1.311E + 05	7.63E-02	1.28	0.87
16.0	1.290E + 05	7.75E-02	1.27	0.85
15.8	1.274E + 05	7.85E-02	1.26	0.85
15.6	1.258E + 05	7.95E-02	1.25	0.85
15.4	1.242E + 05	8.05E-02	1.25	0.84
15.2	1.226E + 05	8.16E-02	1.25	0.84
15.0	1.210E + 05	8.27E-02	1.25	0.84
14.8	1.194E + 05	8.38E-02	1.25	0.84
14.6	1.178E + 05	8.49E-02	1.25	0.84
14.4	1.161E + 05	8.61E-02	1.25	0.84
14.2	1.145E + 05	8.73E-02	1.25	0.84
14.0	1.129E + 05	8.86E-02	1.26	0.84
13.8	1.113E + 05	8.98E-02	1.26	0.83
13.6	1.097E + 05	9.12E-02	1.27	0.83

TABLE IV *(Continued)*

Ruthenium

eV	cm^{-1}	μm	n	k
13.4	1.081E + 05	9.25E-02	1.27	0.82
13.2	1.065E + 05	9.39E-02	1.27	0.81
13.0	1.049E + 05	9.54E-02	1.27	0.79
12.8	1.032E + 05	9.69E-02	1.26	0.78
12.6	1.016E + 05	9.84E-02	1.25	0.77
12.4	1.000E + 05	1.00E-01	1.25	0.76
12.2	9.840E + 04	1.02E-01	1.24	0.75
12.0	9.679E + 04	1.03E-01	1.22	0.73
11.8	9.517E + 04	1.05E-01	1.20	0.72
11.6	9.356E + 04	1.07E-01	1.17	0.71
11.4	9.195E + 04	1.09E-01	1.14	0.70
11.2	9.033E + 04	1.11E-01	1.11	0.70
11.0	8.872E + 04	1.13E-01	1.08	0.70
10.8	8.711E + 04	1.15E-01	1.04	0.71
10.6	8.549E + 04	1.17E-01	0.99	0.72
10.4	8.388E + 04	1.19E-01	0.94	0.74
10.2	8.227E + 04	1.22E-01	0.90	0.77
10.0	8.065E + 04	1.24E-01	0.86	0.81
9.8	7.904E + 04	1.27E-01	0.82	0.84
9.6	7.743E + 04	1.29E-01	0.77	0.89
9.4	7.582E + 04	1.32E-01	0.73	0.95
9.2	7.420E + 04	1.35E-01	0.70	1.02
9.0	7.259E + 04	1.38E-01	0.69	1.09
8.8	7.098E + 04	1.41E-01	0.68	1.15
8.6	6.936E + 04	1.44E-01	0.66	1.22
8.4	6.775E + 04	1.48E-01	0.66	1.29
8.2	6.614E + 04	1.51E-01	0.65	1.36
8.0	6.452E + 04	1.55E-01	0.66	1.44
7.8	6.291E + 04	1.59E-01	0.66	1.51
7.6	6.130E + 04	1.63E-01	0.67	1.59
7.4	5.968E + 04	1.68E-01	0.68	1.67
7.2	5.807E + 04	1.72E-01	0.70	1.75
7.0	5.646E + 04	1.77E-01	0.73	1.82
6.8	5.485E + 04	1.82E-01	0.76	1.89
6.6	5.323E + 04	1.88E-01	0.78	1.97
6.4	5.162E + 04	1.94E-01	0.81	2.04
6.2	5.001E + 04	2.00E-01	0.82	2.11
6.0	4.839E + 04	2.07E-01	0.84	2.20
5.9	4.759E + 04	2.10E-01	0.85	2.24
5.8	4.678E + 04	2.14E-01	0.86	2.29
5.7	4.597E + 04	2.18E-01	0.87	2.34
5.6	4.517E + 04	2.21E-01	0.88	2.40
5.5	4.436E + 04	2.25E-01	0.90	2.45
5.4	4.355E + 04	2.30E-01	0.91	2.52
5.3	4.275E + 04	2.34E-01	0.94	2.58
5.2	4.194E + 04	2.38E-01	0.97	2.64

(continued)

TABLE IV *(Continued)*

Ruthenium

eV	cm^{-1}	μm	n	k
5.1	4.113E + 04	2.43E-01	1.00	2.70
5.0	4.033E + 04	2.48E-01	1.03	2.75
4.9	3.952E + 04	2.53E-01	1.06	2.81
4.8	3.871E + 04	2.58E-01	1.09	2.86
4.7	3.791E + 04	2.64E-01	1.11	2.91
4.6	3.710E + 04	2.70E-01	1.13	2.97
4.5	3.629E + 04	2.76E-01	1.14	3.04
4.4	3.549E + 04	2.82E-01	1.16	3.13
4.3	3.468E + 04	2.88E-01	1.18	3.21
4.2	3.388E + 04	2.95E-01	1.21	3.31
4.1	3.307E + 04	3.02E-01	1.25	3.42
4.0	3.226E + 04	3.10E-01	1.29	3.53
3.9	3.146E + 04	3.18E-01	1.35	3.64
3.8	3.065E + 04	3.26E-01	1.41	3.77
3.7	2.984E + 04	3.35E-01	1.50	3.90
3.6	2.904E + 04	3.44E-01	1.60	4.03
3.5	2.823E + 04	3.54E-01	1.71	4.16
3.4	2.742E + 04	3.65E-01	1.84	4.30
3.3	2.662E + 04	3.76E-01	2.00	4.43
3.2	2.581E + 04	3.87E-01	2.18	4.55
3.1	2.500E + 04	4.00E-01	2.40	4.64
3.0	2.420E + 04	4.13E-01	2.64	4.69
2.9	2.339E + 04	4.28E-01	2.87	4.64
2.8	2.258E + 04	4.43E-01	2.99	4.59
2.7	2.178E + 04	4.59E-01	3.06	4.59
2.6	2.097E + 04	4.77E-01	3.14	4.66
2.5	2.016E + 04	4.96E-01	3.27	4.77
2.4	1.936E + 04	5.17E-01	3.44	4.88
2.4	1.895E + 04	5.28E-01	3.56	4.94
2.3	1.855E + 04	5.39E-01	3.69	4.97
2.3	1.815E + 04	5.51E-01	3.82	4.99
2.2	1.774E + 04	5.64E-01	3.94	5.00
2.2	1.734E + 04	5.77E-01	4.05	5.03
2.1	1.694E + 04	5.90E-01	4.21	5.09
2.0	1.613E + 04	6.20E-01	4.61	5.06
1.9	1.532E + 04	6.53E-01	4.96	4.78
1.8	1.452E + 04	6.89E-01	5.10	4.45
1.7	1.371E + 04	7.29E-01	5.12	4.22
1.7	1.331E + 04	7.51E-01	5.11	4.11
1.6	1.290E + 04	7.75E-01	5.08	4.03
1.6	1.250E + 04	8.00E-01	5.04	3.94
1.5	1.210E + 04	8.27E-01	4.99	3.89
1.5	1.169E + 04	8.55E-01	4.93	3.83
1.4	1.129E + 04	8.86E-01	4.86	3.79
1.4	1.089E + 04	9.18E-01	4.77	3.75
1.3	1.049E + 04	9.54E-01	4.66	3.72
1.3	1.008E + 04	9.92E-01	4.51	3.68

TABLE IV *(Continued)*

Ruthenium

eV	cm^{-1}	μm	n	k
1.2	9.679E + 03	1.03E + 00	4.28	3.66
1.2	9.275E + 03	1.08E + 00	4.00	3.73
1.1	8.872E + 03	1.13E + 00	3.69	3.91
1.1	8.469E + 03	1.18E + 00	3.41	4.22
1.0	8.065E + 03	1.24E + 00	3.17	4.59
1.0	7.662E + 03	1.31E + 00	2.97	5.03
0.9	7.259E + 03	1.38E + 00	2.82	5.54
0.9	6.856E + 03	1.46E + 00	2.73	6.12
0.8	6.452E + 03	1.55E + 00	2.73	6.71
0.8	6.049E + 03	1.65E + 00	2.77	7.33
0.7	5.646E + 03	1.77E + 00	2.82	7.99
0.7	5.243E + 03	1.91E + 00	2.90	8.71
0.6	4.839E + 03	2.07E + 00	2.98	9.54
0.6	4.436E + 03	2.25E + 00	3.09	10.50
0.5	4.033E + 03	2.48E + 00	3.27	11.63
0.5	3.629E + 03	2.76E + 00	3.54	12.96
0.4	3.226E + 03	3.10E + 00	3.90	14.51
0.4	2.823E + 03	3.54E + 00	4.30	16.48
0.3	2.420E + 03	4.13E + 00	4.94	18.92
0.3	2.016E + 03	4.96E + 00	5.61	22.27
0.2	1.613E + 03	6.20E + 00	6.68	27.18
0.2	1.210E + 03	8.27E + 00	8.39	35.13
0.1	8.065E + 02	1.24E + 01	11.85	50.81

INDIUM (In) VI

Indium is a tetragonal metal. Its softness and low melting point are well known. In single-crystal form it is optically anisotropic and uniaxial, with two independent components in the dielectric tensor, one for the electric field parallel to the *c*-axis and one for the perpendicular orientation. Polycrystalline films may have a texture, growing with the closest-packed plane, the basal plane, in the plane of the film, but with randomly oriented *a*-axes. If so, the film will be optically anisotropic. If there is truly random orientation, the film is isotropic with a complex dielectric function $\epsilon = (\epsilon_{\parallel} + 2\epsilon_{\perp})/3$. Indium develops an oxide skin when exposed to air.

We present data in Table V and Fig. 5 for polycrystalline In, usually in the form of evaporated films. The film textures usually have not been determined. Studies of the anisotropy in single crystals have been carried out by Lenham and Treherne [1, 2], but on "hand-polished" single crystals. We list the infrared data of Golovashkin *et al.* [3], the visible and ultraviolet data of

Koyama *et al.* [4], and the vacuum ultraviolet and soft x-ray data of Hunter *et al.* [5, 6], Jezequel *et al.* [7], and Leveque *et al.* [8]. All these were taken on evaporated films. The last two references contain spectra of the absorption coefficient that have been converted to spectra of the imaginary part of the refractive index with the assumption that the real part is unity. Other measurements in the visible and near-ultraviolet region are found elsewhere [9–12], and additional measurements in the vacuum ultraviolet are reported by others [13–15]. Measurements at several temperatures were made by Golovashkin *et al.* [3] and Mathewson and Myers [12]. Hodgson [16] and Wilson and Rice [17] have made optical measurements on liquid In.

Data in the soft x-ray region, from approximately 10^{-4} to 0.024 μm, are taken from Henke *et al.* [18], and the location of the soft x-ray edges, shown by the short, vertical lines in Fig. 5, are taken from Siegbahn *et al.* [19].

REFERENCES

1. A. P. Lenham and D. M. Treherne, *Proc. Phys. Soc. (London)* **85**, 167 (1965).
2. A. P. Lenham and D. M. Treherne, *J. Opt. Soc. Am.* **56**, 752 (1966).
3. A. I. Golovashkin, I. S. Levchenko, G. P. Motulevich, and A. A. Shubin, *Sov. Phys. JETP* **24**, 1093 (1967).
4. R. Y. Koyama, N. V. Smith, and W. E. Spicer, *Phys. Rev. B* **8**, 2426, (1973).
5. W. R. Hunter, *J. Opt. Soc. Am.* **54**, 208 (1964).
6. W. R. Hunter, D. W. Angel, and R. Tousey, *Appl. Opt.* **4**, 891 (1965).
7. G. Jezequel, J. Thomas, and J. C. Lemonnier, *Solid State Commun.* **23**, 559 (1977).
8. G. Leveque, C. G. Olson, and D. W. Lynch, *Solid State Commun.* **51**, 377 (1984).
9. J. Bor and C. Bartholomew, *Proc. Phys. Soc. (London)* **90**, 1153 (1967).
10. A. Donnadieu and R. Garrigos, *Compt. Rend. Acad. Sci. Paris* **268**, B698 (1969).
11. M. L. Theye and G. Devant, *Thin Solid Films* **4**, 205 (1969).
12. A. G. Mathewson and H. P. Myers, *J. Phys. C* **5**, 2503 (1972).
13. W. C. Walker, O. P. Rustgi, and G. L. Wiessler, *J. Opt. Soc. Am.* **49**, 471 (1959).
14. J. C. Lemonnier, G. Stephan, Y. Le Calvez, and S. Robin, *J. Phys. Chem. Solids* **30**, 1147 (1969).
15. J. C. Lemonnier, G. Jezequel, and J. Thomas, *J. Phys. C* **8**, 2812 (1975).
16. J. Hodgson, *Philos. Mag.* **7**, 229 (1962).
17. E. G. Wilson and S. A. Rice, *Phys. Rev.* **145**, 55 (1966).
18. B. L. Henke, J. C. Davis, E. M. Gullikson, and R. C. C. Perera, "A Preliminary Report on X-Ray Photoabsorption Coefficients and Atomic Scattering Factors for 92 Elements in the 10–10,000 eV Region," Lawrence Berkeley Lab. Rep. LBL-26259, University of California, Berkeley, California, 1988.
19. K. Siegbahn, C. Nordling, A. Fahlman, R. Nordberg, K. Hamrin, J. Hedman, G. Johansson, T. Bergmark, S.-E. Karlsson, I. Lindgren, and B. Lindberg, "ESCA Atomic, Molecular, and Solid State Structure Studied by Means of Electron Spectroscopy." Almquist & Wiksell, Uppsala, Sweden, 1967.

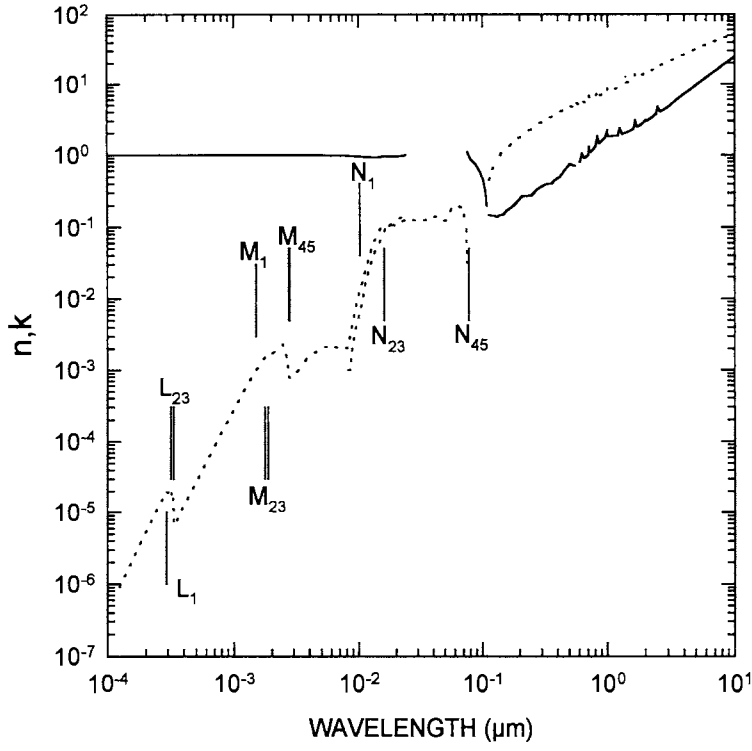

Fig. 5. Log–log plot of n (——) and k (- - - -) versus wavelength in micrometers for indium.

TABLE V

Values of n and k Obtained from Various References for Indium[a]

eV	cm^{-1}	μm	n	k
10000.	8.066E + 07	1.24E-04	9.999872E-01 [18]	9.04E-07 [18]
9117.	7.353E + 07	1.36E-04	9.999844E-01	1.27E-06
8122.	6.551E + 07	1.53E-04	9.999803E-01	1.95E-06
7236.	5.837E + 07	1.71E-04	9.999753E-01	2.99E-06
6156.	4.965E + 07	2.01E-04	9.999662E-01	5.40E-06
5117.	4.127E + 07	2.42E-04	9.999527E-01	1.05E-05
4558.	3.677E + 07	2.72E-04	9.999435E-01	1.58E-05
4454.	3.593E + 07	2.78E-04	9.999418E-01	1.71E-05
4353.	3.511E + 07	2.85E-04	9.999405E-01	1.86E-05
4253.	3.431E + 07	2.91E-04	9.999422E-01	2.01E-05
4156.	3.352E + 07	2.98E-04	9.999381E-01	1.90E-05
4061.	3.276E + 07	3.05E-04	9.999366E-01	2.06E-05
3968.	3.201E + 07	3.12E-04	9.999380E-01	2.24E-05
3878.	3.128E + 07	3.20E-04	9.999357E-01	1.77E-05
3789.	3.057E + 07	3.27E-04	9.999349E-01	1.92E-05
3703.	2.987E + 07	3.35E-04	9.999338E-01	6.59E-06
3618.	2.919E + 07	3.43E-04	9.999247E-01	7.17E-06
2872.	2.317E + 07	4.32E-04	9.99864E-01	1.64E-05
2176.	1.756E + 07	5.70E-04	9.99756E-01	4.29E-05
1727.	1.393E + 07	7.18E-04	9.99613E-01	9.36E-05
1504.	1.213E + 07	8.24E-04	9.99493E-01	1.48E-04
1340.	1.081E + 07	9.25E-04	9.99370E-01	2.17E-04
1166.	9.408E + 06	1.06E-03	9.99192E-01	3.43E-04
1015.	8.191E + 06	1.22E-03	9.9899E-01	5.42E-04
844.	6.809E + 06	1.47E-03	9.9876E-01	9.48E-04
734.	5.927E + 06	1.69E-03	9.9862E-01	1.35E-03
718.	5.792E + 06	1.73E-03	9.9863E-01	1.45E-03
701.	5.660E + 06	1.77E-03	9.9866E-01	1.54E-03
685.	5.530E + 06	1.81E-03	9.9875E-01	1.60E-03
670.	5.404E + 06	1.85E-03	9.9880E-01	1.56E-03
654.	5.281E + 06	1.89E-03	9.9878E-01	1.52E-03
639.	5.160E + 06	1.94E-03	9.9867E-01	1.53E-03
625.	5.042E + 06	1.98E-03	9.9861E-01	1.63E-03
507.	4.096E + 06	2.44E-03	9.9918E-01	2.36E-03
473.	3.821E + 06	2.62E-03	9.9975E-01	1.62E-03
463.	3.734E + 06	2.68E-03	9.9966E-01	1.20E-03
452.	3.649E + 06	2.74E-03	9.9926E-01	8.21E-04
442.	3.565E + 06	2.80E-03	9.9886E-01	7.66E-04
432.	3.484E + 06	2.87E-03	9.9855E-01	7.63E-04
422.	3.404E + 06	2.94E-03	9.9830E-01	7.83E-04
319.	2.580E + 06	3.88E-03	9.9581E-01	1.51E-03
236.	1.911E + 06	5.23E-03	9.9238E-01	2.13E-03
152.	1.232E + 06	8.12E-03	9.761E-01	2.06E-03
150.	1.210E + 06	8.27E-03		1.00E-03 [8]
145.	1.169E + 06	8.55E-03		1.00E-03
140.	1.129E + 06	8.86E-03		2.00E-03

[a] The references from which the values were extracted are given in brackets.

TABLE V *(Continued)*

Indium

eV	cm^{-1}	μm	n	k
135.	1.089E + 06	9.18E-03		3.00E-03
130.	1.049E + 06	9.54E-03		4.00E-03
127.	1.024E + 06	9.77E-03	9.581E-01 [18]	9.81E-03 [18]
125.	1.008E + 06	9.92E-03		5.00E-03 [8]
124.	1.001E + 06	9.99E-03	9.555E-01 [18]	1.14E-02 [18]
121.	9.778E + 05	1.02E-02	9.529E-01	1.32E-02
120.	9.679E + 05	1.03E-02		7.00E-03 [8]
118.	9.555E + 05	1.05E-02	9.500E-01 [18]	1.54E-02 [18]
115.	9.275E + 05	1.08E-02		1.00E-02 [8]
110.	8.872E + 05	1.13E-02		1.60E-02
105.	8.469E + 05	1.18E-02		2.20E-02
100.	8.065E + 05	1.24E-02		3.00E-02
96.2	7.761E + 05	1.29E-02	9.272E-01 [18]	5.68E-02 [18]
95.	7.662E + 05	1.31E-02		4.00E-02 [8]
90.	7.259E + 05	1.38E-02		5.00E-02
85.	6.856E + 05	1.46E-02		6.00E-02
83.8	6.756E + 05	1.48E-02	9.432E-01 [18]	9.34E-02 [18]
81.9	6.602E + 05	1.51E-02	9.479E-01	9.60E-02
80.	6.451E + 05	1.55E-02	9.527E-01	9.85E-02
80.	6.452E + 05	1.55E-02		7.70E-02 [8]
78.2	6.304E + 05	1.59E-02	9.569E-01 [18]	9.83E-02 [18]
76.4	6.160E + 05	1.62E-02	9.589E-01	9.77E-02
75.	6.049E + 05	1.65E-02		9.80E-02 [8]
74.6	6.019E + 05	1.66E-02	9.588E-01 [18]	9.76E-02 [18]
72.9	5.882E + 05	1.70E-02	9.584E-01	9.96E-02
71.3	5.747E + 05	1.74E-02	9.582E-01	1.02E-01
70.	5.646E + 05	1.77E-02		9.60E-02 [8]
69.6	5.616E + 05	1.78E-02	9.576E-01 [18]	1.06E-01 [18]
68.0	5.488E + 05	1.82E-02	9.591E-01	1.11E-01
65.	5.243E + 05	1.91E-02		1.08E-01 [8]
60.	4.839E + 05	2.07E-02		1.03E-01
59.2	4.778E + 05	2.09E-02	9.703E-01 [18]	1.32E-01 [18]
55.	4.436E + 05	2.25E-02		1.21E-01 [8]
54.0	4.356E + 05	2.30E-02	9.830E-01 [18]	1.43E-01 [18]
52.8	4.256E + 05	2.35E-02	9.860E-01	1.45E-01
51.6	4.159E + 05	2.40E-02	9.887E-01	1.48E-01
50.	4.033E + 05	2.48E-02		1.29E-01 [8]
45.	3.629E + 05	2.76E-02		1.26E-01
40.	3.226E + 05	3.10E-02		1.20E-01
28.5	2.299E + 05	4.35E-02		1.44E-01 [7]
28.0	2.258E + 05	4.43E-02		1.40E-01
27.5	2.218E + 05	4.51E-02		1.37E-01
27.0	2.178E + 05	4.59E-02		1.34E-01
26.5	2.137E + 05	4.68E-02		1.28E-01
26.0	2.097E + 05	4.77E-02		1.26E-01
25.5	2.057E + 05	4.86E-02		1.22E-01

(continued)

TABLE V *(Continued)*

Indium

eV	cm^{-1}	μm	n	k
25.0	2.016E + 05	4.96E-02		1.23E-01
24.5	1.976E + 05	5.06E-02		1.25E-01
24.0	1.936E + 05	5.17E-02		1.31E-01
23.5	1.895E + 05	5.28E-02		1.43E-01
23.0	1.855E + 05	5.39E-02		1.53E-01
22.5	1.815E + 05	5.51E-02		1.69E-01
22.0	1.774E + 05	5.64E-02		1.83E-01
21.5	1.734E + 05	5.77E-02		1.92E-01
21.0	1.694E + 05	5.90E-02		2.01E-01
20.5	1.653E + 05	6.05E-02		2.04E-01
20.0	1.613E + 05	6.20E-02		2.01E-01
19.5	1.573E + 05	6.36E-02		1.97E-01
19.0	1.532E + 05	6.53E-02		1.94E-01
18.5	1.492E + 05	6.70E-02		1.90E-01
18.0	1.452E + 05	6.89E-02		1.89E-01
17.9	1.444E + 05	6.93E-02		1.88E-01
17.8	1.436E + 05	6.97E-02		1.86E-01
17.7	1.428E + 05	7.00E-02		1.78E-01
17.6	1.420E + 05	7.04E-02		1.63E-01
17.5	1.411E + 05	7.08E-02		1.47E-01
17.4	1.403E + 05	7.13E-02		1.41E-01
17.3	1.395E + 05	7.17E-02		1.40E-01
17.2	1.387E + 05	7.21E-02		1.41E-01
17.1	1.379E + 05	7.25E-02		1.39E-01
17.0	1.371E + 05	7.29E-02		0.90 [4]
17.0	1.371E + 05	7.29E-02		1.37E-01 [7]
16.9	1.363E + 05	7.34E-02		1.31E-01
16.80	1.355E + 05	7.38E-02		1.22E-01
16.75	1.351E + 05	7.40E-02	1.10 [4]	.
16.70	1.347E + 05	7.42E-02		9.30E-02 [7]
16.60	1.339E + 05	7.47E-02		4.40E-02
16.50	1.331E + 05	7.51E-02		3.20E-02
16.50	1.331E + 05	7.51E-02	1.10 [4]	.
16.25	1.311E + 05	7.63E-02	1.02	
16.00	1.290E + 05	7.75E-02	0.97	
16.00	1.290E + 05	7.75E-02		2.60E-02 [7]
15.75	1.270E + 05	7.87E-02	0.92 [4]	.
15.50	1.250E + 05	8.00E-02	0.88	
15.25	1.230E + 05	8.13E-02	0.85	
15.00	1.210E + 05	8.27E-02	0.83	
14.75	1.190E + 05	8.41E-02	0.80 [4, 5, 6]	.
14.50	1.169E + 05	8.55E-02	0.77	
14.25	1.149E + 05	8.70E-02	0.75	
14.00	1.129E + 05	8.86E-02	0.72	5.00E-02
13.75	1.109E + 05	9.02E-02	0.68	
13.50	1.089E + 05	9.18E-02	0.65	7.00E-02
13.25	1.069E + 05	9.36E-02	0.61	

TABLE V *(Continued)*

Indium

eV	cm^{-1}	μm	n	k
13.00	1.049E + 05	9.54E-02	0.58	8.30E-02
12.75	1.028E + 05	9.72E-02	0.53	
12.50	1.008E + 05	9.92E-02	0.49	1.50E-01
12.25	9.880E + 04	1.01E-01	0.44	
12.00	9.679E + 04	1.03E-01	0.38	1.34E-01
11.75	9.477E + 04	1.06E-01	0.30	
11.50	9.275E + 04	1.08E-01	0.20 [4]	3.00E-01 [4]
11.00	8.872E + 04	1.13E-01	0.15	4.50E-01
10.50	8.469E + 04	1.18E-01	0.15	6.00E-01
10.00	8.065E + 04	1.24E-01	0.15	7.50E-01
9.50	7.662E + 04	1.31E-01	0.14	8.00E-01
9.00	7.259E + 04	1.38E-01	0.15	1.00
8.50	6.856E + 04	1.46E-01	0.15	1.15
8.00	6.452E + 04	1.55E-01	0.17	1.25
7.50	6.049E + 04	1.65E-01	0.18	1.35
7.00	5.646E + 04	1.77E-01	0.20	1.60
6.50	5.243E + 04	1.91E-01	0.23	1.70
6.00	4.839E + 04	2.07E-01	0.27	1.85
5.50	4.436E + 04	2.25E-01	0.27	2.10
5.00	4.033E + 04	2.48E-01	0.28	2.35
4.50	3.629E + 04	2.76E-01	0.34	2.70
4.00	3.226E + 04	3.10E-01	0.38	3.00
3.75	3.025E + 04	3.31E-01	0.40	3.20
3.50	2.823E + 04	3.54E-01	0.40	3.40
3.25	2.621E + 04	3.81E-01	0.45	3.70
3.00	2.420E + 04	4.13E-01	0.50	4.00
2.75	2.218E + 04	4.51E-01	0.60	4.30
2.50	2.016E + 04	4.96E-01	0.75	4.80
2.255	1.819E + 04	5.50E-01	0.70 [3]	4.70 [3]
2.250	1.815E + 04	5.51E-01	0.85	5.50
2.067	1.667E + 04	6.00E-01	0.80	5.02
2.000	1.613E + 04	6.20E-01	1.05	6.00
1.908	1.539E + 04	6.50E-01	0.90	5.42
1.771	1.428E + 04	7.00E-01	1.01	5.83
1.750	1.411E + 04	7.08E-01	1.30	6.90
1.722	1.389E + 04	7.20E-01	1.07	6.00
1.676	1.352E + 04	7.40E-01	1.13	6.18
1.653	1.333E + 04	7.50E-01	1.17	6.26
1.632	1.316E + 04	7.60E-01	1.19	6.31
1.550	1.250E + 04	8.00E-01	1.32	6.60
1.500	1.210E + 04	8.27E-01	1.85	8.00
1.459	1.177E + 04	8.50E-01	1.45	6.78
1.378	1.111E + 04	9.00E-01	1.59	7.18
1.305	1.053E + 04	9.50E-01	1.72	7.44
1.250	1.008E + 04	9.92E-01	2.25	8.80
1.240	1.000E + 04	1.00	1.81	7.77

(continued)

TABLE V *(Continued)*

Indium

eV	cm^{-1}	μm	n	k
1.127	9.090E + 03	1.10	1.84	8.38
1.033	8.332E + 03	1.20	1.87	9.00
1.000	8.065E + 03	1.24	2.40	10.60
0.954	7.694E + 03	1.30	1.95	9.70
0.886	7.146E + 03	1.40	2.06	10.35
0.827	6.670E + 03	1.50	2.19	11.00
0.775	6.251E + 03	1.60	2.33	11.80
0.750	6.049E + 03	1.65	3.10	14.00
0.729	5.880E + 03	1.70	2.49	12.50
0.689	5.557E + 03	1.80	2.64	13.10
0.653	5.267E + 03	1.90	2.80	13.60
0.620	5.001E + 03	2.00	3.13	15.00
0.620	5.001E + 03	2.00	2.97	14.50
0.564	4.549E + 03	2.20	3.30	15.60
0.539	4.347E + 03	2.30	3.48	16.30
0.517	4.170E + 03	2.40	3.81	17.60
0.517	4.170E + 03	2.40	3.65	16.90
0.500	4.033E + 03	2.48	4.80	18.00
0.477	3.847E + 03	2.60	4.00	18.30
0.413	3.331E + 03	3.00	4.70	20.90
0.354	2.855E + 03	3.50	6.00	23.90
0.310	2.500E + 03	4.00	7.27	26.70
0.248	2.000E + 03	5.00	9.77	32.20
0.207	1.670E + 03	5.99	12.40	37.20
0.155	1.250E + 03	8.00	18.40	45.30
0.124	1.000E + 03	10.00	24.80	51.90

VII TIN (Sn)

White tin, β-Sn, is a tetragonal metal. There is also a cubic phase, gray tin, α-Sn, with the diamond structure. Gray tin is the stable form below 18° C, but the transformation from white tin to gray tin is sluggish. We consider here only white tin. In single-crystal form it is optically anisotropic and uniaxial, with two independent components in the dielectric tensor, one for the electric field parallel to the *c*-axis and one for the perpendicular orientation. Polycrystalline films may have a texture, growing with the closest-packed plane, the basal plane, in the plane of the film, but with randomly oriented *a*-axes. If so, the film will be optically anisotropic. If there is truly random orientation, the film is isotropic with a complex dielectric function $\epsilon = (\epsilon_{\parallel} + 2\epsilon_{\perp})/3$. Sn develops an oxide skin when exposed to air, typically SnO_2 with a layer of SnO below.

The data reported in Table VI and Fig. 6 were taken on polycrystalline films. However, it is not at all clear that these films had randomly oriented grains. Schwartz [1] made ellipsometric measurements on an oriented single crystal and a polycrystalline film, and it is clear from his data that the spectrum of the film is neither that for **E** in the basal plane nor the polycrystalline average quoted above. Also, the structures in the spectra for the film are broader than those for the single crystal. The data are taken from Golovashkin and Motulevich [2, 3], MacRae *et al.* [4], Girouard and Truong [5], Jezequel *et al.* [6], and Haensel *et al.* [7]. The last have reported only absorption-coefficient spectra. These have been converted to spectra of the imaginary part of the refractive index with the assumption that the real part is unity. Other measurements have been reported by Lenham and Treherne [8] and Mahmoud [9].

Carotenuto *et al.* [10] measured the temperature derivative of the optical constants. Optical studies at different temperatures have been carried out by Schwartz [1] and Golovashkin and Motulevich [2, 3]. Hodgson [11], Comins [12], and Petrakian *et al.* [13] have measured the optical constants of liquid Sn.

Data in the soft x-ray region, from approximately 10^{-4} to 0.024 μm, are taken from Henke *et al.* [14], and the location of the soft x-ray edges, shown by the short, vertical lines in Fig. 6, are taken from Siegbahn *et al.* [15].

REFERENCES

1. H. Schwartz, *Phys. Status. Solidi. B* **44**, 603 (1971).
2. A. I. Golovashkin and G. P. Motulevich, *Sov. Phys. JETP* **19**, 310 (1964).
3. A. I. Golovashkin and G. P. Motulevich, *Sov. Phys. JETP* **20**, 44 (1965).
4. R. A. MacRae, E. T. Arakawa, and M. W. Williams, *Phys. Rev.* **162**, 615 (1967).
5. F. E. Girouard and V. V. Truong, *Appl. Opt.* **15**, 4144 (1981).
6. G. Jezequel, J. Thomas, and J. C. Lemonnier, *Solid State Commun.* **23**, 559 (1977).
7. R. Haensel, C. Kunz, T. Sasaki, and B. Sonntag, *Appl. Opt.* 7, 301 (1968).
8. A. P. Lenham and D. M. Treherne, J. *Opt. Soc. Am.* **56**, 752 (1966).
9. S. Mahmoud, *J. Mater. Sci.* **22**, 251 (1986).
10. C. Carotenuto, E. Colavita, S. Modesti, and M. Sommacal, *Phys. Rev. B* **14**, 5327 (1976).
11. J. N. Hodgson, *Philos. Mag.* **6**, 509 (1961).
12. N. R. Comins, *Philos. Mag.* **25**, 817 (1972).
13. J. P. Petrakian, A. R. Cathers, J. E. Parks, R. A. MacRae, T. A. Callcott, and E. T. Arakawa, *Phys. Rev. B* **21**, 3043 (1980).
14. B. L. Henke, J. C. Davis, E. M. Gullikson, and R. C. C. Perera, "A Preliminary Report on X-Ray Photoabsorption Coefficients and Atomic Scattering Factors for 92 Elements in the 10–10,000 eV Region," Lawrence Berkeley Lab. Rep. LBL-26259, University of California, Berkeley, California, 1988.
15. K. Siegbahn, C. Nordling, A. Fahlman, R. Nordberg, K. Hamrin, J. Hedman, G. Johansson, T. Bergmark, S.-E. Karlsson, I. Lindgren, and B. Lindberg, "ESCA Atomic, Molecular, and Solid State Structure Studied by Means of Electron Spectroscopy." Almquist & Wiksell, Uppsala, Sweden, 1967.

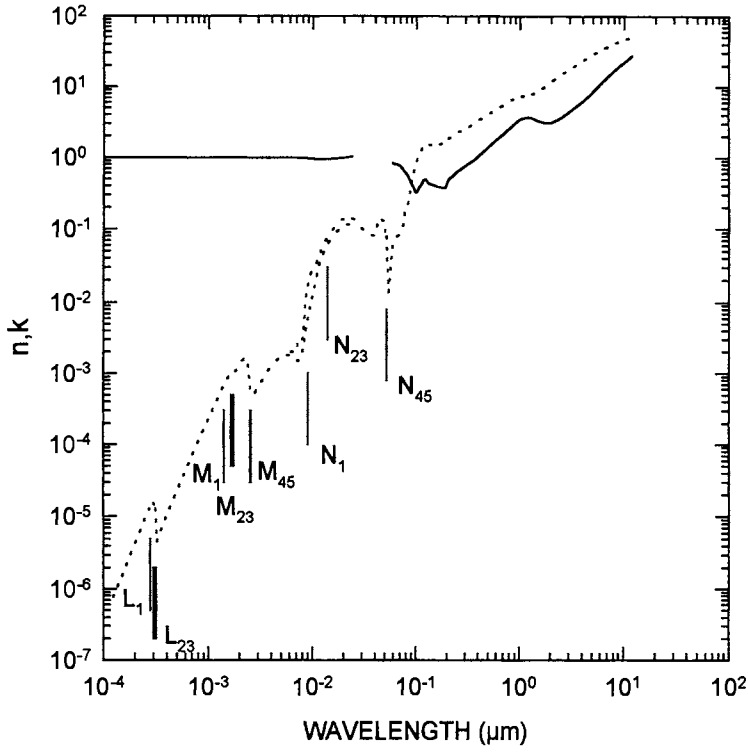

Fig. 6. Log–log plot of n (——) and k (- - - -) versus wavelength in micrometers for tin.

TABLE VI

Values of n and k Obtained from Various References for Tin[a]

eV	cm^{-1}	μm	n	k
10000.	8.066E + 07	1.24E-04	9.999900E-01 [14]	7.65E-07 [14]
9117.	7.353E + 07	1.36E-04	9.999878E-01	1.08E-06
8123.	6.551E + 07	1.53E-04	9.999847E-01	1.66E-06
7072.	5.704E + 07	1.75E-04	9.999800E-01	2.75E-06
6015.	4.852E + 07	2.06E-04	9.999728E-01	4.93E-06
5117.	4.127E + 07	2.42E-04	9.999641E-01	8.70E-06
4665.	3.763E + 07	2.66E-04	9.999591E-01	1.19E-05
4559.	3.677E + 07	2.72E-04	9.999582E-01	1.29E-05
4455.	3.593E + 07	2.78E-04	9.999575E-01	1.24E-05
4353.	3.511E + 07	2.85E-04	9.999561E-01	1.34E-05
4254.	3.431E + 07	2.91E-04	9.999555E-01	1.46E-05
4157.	3.352E + 07	2.98E-04	9.999568E-01	1.58E-05
4062.	3.276E + 07	3.05E-04	9.999540E-01	1.25E-05
3969.	3.201E + 07	3.12E-04	9.999551E-01	1.35E-05
3878.	3.128E + 07	3.20E-04	9.999519E-01	4.55E-06
3790.	3.057E + 07	3.27E-04	9.999456E-01	4.97E-06
2228.	1.797E + 07	5.57E-04	9.99818E-01	3.32E-05
1939.	1.564E + 07	6.39E-04	9.99760E-01	5.29E-05
1728	7.176E + 07	7.18E-04	9.99699E-01	7.77E-05
1688.	1.362E + 07	7.34E-04	9.99686E-01	8.38E-05
1504.	1.213E + 07	8.24E-04	9.99608E-01	1.22E-04
1403.	1.132E + 07	8.84E-04	9.99553E-01	1.54E-04
1309.	1.056E + 07	9.47E-04	9.99493E-01	1.93E-04
1194.	9.628E + 06	1.04E-03	9.99403E-01	2.62E-04
1088.	8.779E + 06	1.14E-03	9.99305E-01	3.55E-04
970.	7.821E + 06	1.28E-03	9.99184E-01	5.36E-04
825.	6.653E + 06	1.50E-03	9.99081E-01	8.24E-04
770.	6.208E + 06	1.61E-03	9.99090E-01	9.78E-04
752.	6.066E + 06	1.65E-03	9.99114E-01	1.02E-03
735.	5.927E + 06	1.69E-03	9.99154E-01	1.03E-03
718.	5.792E + 06	1.73E-03	9.99149E-01	1.00E-03
702.	5.660E + 06	1.77E-03	9.99082E-01	1.00E-03
611.	4.927E + 06	2.03E-03	9.99032E-01	1.42E-03
520.	4.191E + 06	2.39E-03	9.99873E-01	1.27E-03
508.	4.096E + 06	2.44E-03	9.99830E-01	9.19E-04
496.	4.002E + 06	2.50E-03	9.99638E-01	6.63E-04
485.	3.911E + 06	2.56E-03	9.99359E-01	5.34E-04
474.	3.821E + 06	2.62E-03	9.99132E-01	5.14E-04
463.	3.734E + 06	2.68E-03	9.9895E-01	5.12E-04
351.	2.830E + 06	3.53E-03	9.9717E-01	9.62E-04
299.	2.407E + 06	4.15E-03	9.9605E-01	1.36E-03
254.	2.048E + 06	4.88E-03	9.9457E-01	1.66E-03
200.	1.613E + 06	6.20E-03		2.00E-03 [7]
197.	1.588E + 06	6.30E-03	9.9049E-03 [14]	1.72E-03 [14]
190.	1.532E + 06	6.53E-03		2.00E-03 [7]

(continued)

[a] The references from which the values were extracted are given in brackets.

TABLE VI *(Continued)*

Tin

eV	cm^{-1}	μm	n	k
180.	1.452E + 06	6.89E-03		2.00E-03
170.	1.371E + 06	7.29E-03		3.00E-03
160.	1.290E + 06	7.75E-03		3.00E-03
156.	1.261E + 06	7.93E-03	9.808E-01 [14]	1.96E-03 [14]
155.	1.250E + 06	8.00E-03		3.00E-03 [7]
150.	1.210E + 06	8.27E-03		5.00E-03
145.	1.169E + 06	8.55E-03		1.10E-02
140.	1.129E + 06	8.86E-03		1.60E-02
135.	1.089E + 06	9.18E-03		2.00E-02
130.	1.049E + 06	9.54E-03		2.50E-02
125.	1.008E + 06	9.92E-03		2.70E-02
121.	9.778E + 05	1.02E-02	9.608E-01 [14]	1.53E-02 [14]
120.	9.679E + 05	1.03E-02		3.10E-02 [7]
115.	9.275E + 05	1.08E-02		3.40E-02
110.	8.872E + 05	1.13E-02		4.00E-02
105.	8.469E + 05	1.18E-02		4.80E-02
100.	8.065E + 05	1.24E-02		5.90E-02
98.5	7.942E + 05	1.26E-02	9.531E-01 [14]	4.66E-02 [14]
95.	7.662E + 05	1.31E-02		6.70E-02 [7]
90.	7.259E + 05	1.38E-02		7.80E-02
85.7	6.914E + 05	1.45E-02	9.571E-01 [14]	6.81E-02 [14]
85.	6.856E + 05	1.46E-02		8.90E-02 [7]
80.	6.452E + 05	1.55E-02		9.80E-02
75.	6.049E + 05	1.65E-02		0.111
72.9	5.882E + 05	1.70E-02	9.727E-01 [14]	9.21E-02 [14]
70.	5.646E + 05	1.77E-02		0.123 [7]
65.	5.243E + 05	1.91E-02		0.135
60.6	4.889E + 05	2.05E-02	9.984E-01 [14]	1.12E-01 [14]
60.	4.839E + 05	2.07E-02		0.143 [7]
55.	4.436E + 05	2.25E-02		0.146
51.7	4.159E + 05	2.40E-02	1.031 [14]	1.11E-01 [14]
50.	4.033E + 05	2.48E-02		0.137 [7]
45.	3.629E + 05	2.76E-02		0.113
40.	3.226E + 05	3.10E-02		0.098
33.	2.662E + 05	3.76E-02		0.082 [6]
32.5	2.621E + 05	3.81E-02		0.081
32.0	2.581E + 05	3.87E-02		0.081
31.5	2.541E + 05	3.94E-02		0.083
31.0	2.500E + 05	4.00E-02		0.089
30.5	2.460E + 05	4.07E-02		0.095
30.0	2.420E + 05	4.13E-02		0.105
29.5	2.379E + 05	4.20E-02		0.115
29.0	2.339E + 05	4.28E-02		0.124
28.5	2.299E + 05	4.35E-02		0.137
28.0	2.258E + 05	4.43E-02		0.140
27.5	2.218E + 05	4.51E-02		0.134
27.0	2.178E + 05	4.59E-02		0.134

TABLE VI *(Continued)*

Tin

eV	cm^{-1}	μm	n	k
26.5	2.137E + 05	4.68E-02		0.133
26.0	2.097E + 05	4.77E-02		0.131
25.5	2.057E + 05	4.86E-02		0.129
25.0	2.016E + 05	4.96E-02		0.121
24.9	2.008E + 05	4.98E-02		0.107
24.8	2.000E + 05	5.00E-02		0.086
24.7	1.992E + 05	5.02E-02		0.078
24.6	1.984E + 05	5.04E-02		0.077
24.5	1.976E + 05	5.06E-02		0.079
24.4	1.968E + 05	5.08E-02		0.081
24.3	1.960E + 05	5.10E-02		0.083
24.2	1.952E + 05	5.12E-02		0.082
24.1	1.944E + 05	5.14E-02		0.080
24.0	1.936E + 05	5.17E-02		0.079
23.8	1.916E + 05	5.22E-02		0.056
23.4	1.887E + 05	5.30E-02		0.022
23.0	1.855E + 05	5.39E-02		0.014
21.0	1.694E + 05	5.90E-02	0.84 [5]	0.060 [5]
20.0	1.613E + 05	6.20E-02	0.82	0.070
19.0	1.532E + 05	6.53E-02	0.8	0.080
18.0	1.452E + 05	6.89E-02	0.77	0.085
17.5	1.411E + 05	7.08E-02	0.74	0.090
17.0	1.371E + 05	7.29E-02	0.71	0.100
16.5	1.331E + 05	7.51E-02	0.68	0.120
16.0	1.290E + 05	7.75E-02	0.64	0.170
15.5	1.250E + 05	8.00E-02	0.60	0.190
15.0	1.210E + 05	8.27E-02	0.56	0.220
14.5	1.169E + 05	8.55E-02	0.51	0.270
14.0	1.129E + 05	8.86E-02	0.45	0.380
13.5	1.089E + 05	9.18E-02	0.41	0.520
13.0	1.049E + 05	9.54E-02	0.365	0.660
12.5	1.008E + 05	9.92E-02	0.32	0.830
12.0	9.679E + 04	1.03E-01	0.34	1.000
11.5	9.275E + 04	1.08E-01	0.38	1.150
11.0	8.872E + 04	1.13E-01	0.42	1.300
10.5	8.469E + 04	1.18E-01	0.475	1.480
10.0	8.065E + 04	1.24E-01	0.50	1.540
9.5	7.662E + 04	1.31E-01	0.44	1.520
9.0	7.259E + 04	1.38E-01	0.42	1.510
8.5	6.856E + 04	1.46E-01	0.41	1.500
8.0	6.452E + 04	1.55E-01	0.40	1.520
7.5	6.049E + 04	1.65E-01	0.39	1.540
7.0	5.646E + 04	1.77E-01	0.38	1.560
6.5	5.243E + 04	1.91E-01	0.37	1.580
6.0	4.839E + 04	2.07E-01	0.50 [4]	1.900 [4]
5.5	4.436E + 04	2.25E-01	0.55	2.050

(continued)

TABLE VI *(Continued)*

Tin

eV	cm^{-1}	μm	n	k
5.0	4.033E + 04	2.48E-01	0.63	2.300
4.5	3.629E + 04	2.76E-01	0.70	2.400
4.0	3.226E + 04	3.10E-01	0.80	2.600
3.5	2.823E + 04	3.54E-01	0.90	3.000
1.333	1.075E + 04	9.30E-01	3.15 [2]	7.280 [2]
1.253	1.011E + 04	9.90E-01	3.44	7.340
1.033	8.332E + 03	1.20E + 00	3.76	7.630
0.919	7.412E + 03	1.35E + 00	3.57	8.040
0.827	6.670E + 03	1.50E + 00	3.31	8.670
0.729	5.880E + 03	1.70E + 00	3.13	9.880
0.62	5.001E + 03	1.00E + 00	3.10	11.800
0.496	4.000E + 03	2.50E + 00	3.63	14.800
0.413	3.331E + 03	3.00E + 00	4.41	17.800
0.354	2.855E + 03	3.50E + 00	5.27	20.500
0.31	2.500E + 03	3.00E + 00	6.19	23.200
0.248	2.000E + 03	5.00E + 00	8.49	28.500
0.207	1.670E + 03	5.99E + 00	11.0	33.100
0.177	1.428E + 03	7.00E + 00	13.8	37.100
0.155	1.250E + 03	8.00E + 00	16.6	40.600
0.138	1.113E + 03	8.98E + 00	19.3	43.800
0.124	1.000E + 03	1.00E + 01	22.0	46.400
0.113	9.114E + 02	1.10E + 01	24.8	49.000
0.103	8.307E + 02	1.20E + 01	27.8	51.600

VIII ANTIMONY (Sb)

Antimony is a semimetal with a rhombohedral structure. In single-crystal form it is optically anisotropic and uniaxial, with two independent components in the dielectric tensor, one for the electric field parallel to the *c*-axis and one for the perpendicular orientation. Polycrystalline films may have a texture, growing with the closest-packed plane, the basal plane, in the plane of the film, but with randomly oriented *a*-axes. If so, the film will be optically anisotropic. If there is truly random orientation, the film is isotropic with a complex dielectric function $\epsilon = (\epsilon_{\parallel} + 2\epsilon_{\perp})/3$. Sb develops an oxide skin when exposed to air.

Cardona and Greenaway [1] have determined optical constants for a single crystal of Sb with **E** in the basal plane ($\mathbf{E} \perp \mathbf{c}$). We give their data in Table VII and Fig. 7. Data in a more limited, but overlapping, range have been taken by Aspnes [2], Strümpler and Lüth [3], and de Sande *et al.* [4]. Lenham and Treherne [5] and Lenham *et al.* [6] have made measurements in the infrared. Nanney [7] measured the infrared absorptance spectra of a single crystal with $\mathbf{E} \perp \mathbf{c}$ and $\mathbf{E} \parallel \mathbf{c}$ at 300 K and 4.2 K.

Data in the soft x-ray region, from approximately 10^{-4} to 0.024 μm, are taken from Henke *et al.* [8], and the location of the soft x-ray edges, shown by the short, vertical lines in Fig. 7, are taken from Siegbahn *et al.* [9].

REFERENCES

1. M. Cardona and D. L. Greenaway, *Phys. Rev.* **133**, A1685 (1964).
2. D. E. Aspnes, *Phys. Rev. B* **12**, 4008 (1975).
3. R. Strümpler and H. Lüth, *Thin Solid Films* **177**, 287 (1989).
4. J. C. G. de Sande, F. Vega, C. N. Afonso, C. Ortega, and J. Siejka, *Thin Solid Films* **249**, 195 (1994).
5. A. P. Lenham and D. M. Treherne, *J. Opt. Soc. Am.* **56**, 752 (1966).
6. A. P. Lenham, D. M. Treherne, and R. J. Metcalfe, *J. Opt. Soc. Am.* **55**, 1072 (1965).
7. C. Nanney, *Phys. Rev.* **129**, 109 (1963).
8. B. L. Henke, J. C. Davis, E. M. Gullikson, and R. C. C. Perera, "A Preliminary Report on X-Ray Photoabsorption Coefficients and Atomic Scattering Factors for 92 Elements in the 10–10,000 eV Region," Lawrence Berkeley Lab. Rep. LBL-26259, University of California, Berkeley, California, 1988.
9. K. Siegbahn, C. Nordling, A. Fahlman, R. Nordberg, K. Hamrin, J. Hedman, G. Johansson, T. Bergmark, S.-E. Karlsson, I. Lindgren, and B. Lindberg, "ESCA Atomic, Molecular, and Solid State Structure Studied by Means of Electron Spectroscopy." Almquist & Wiksell, Uppsala, Sweden, 1967.

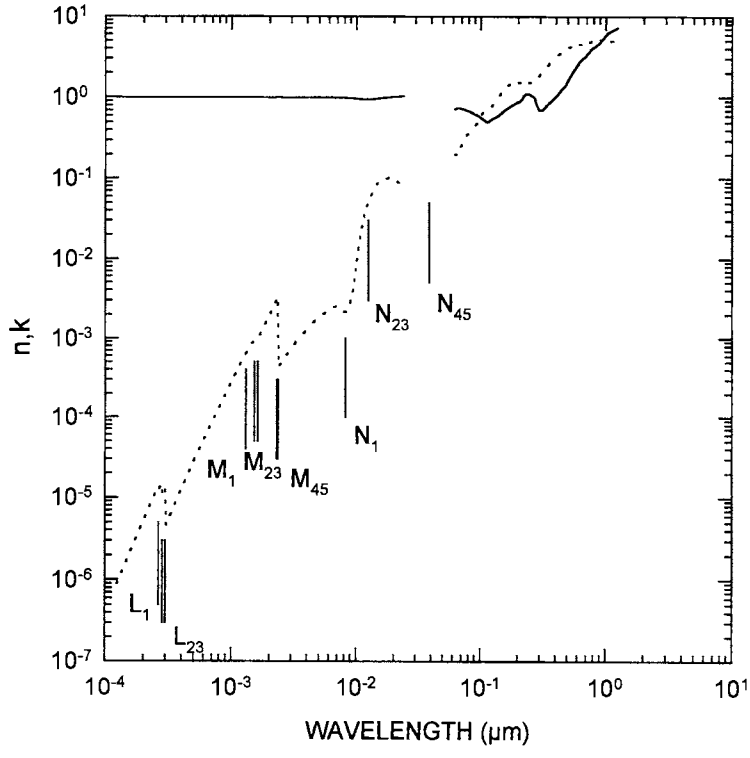

Fig. 7. Log–log plot of n (——) and k (- - - -) versus wavelength in micrometers for antimony.

TABLE VII

Values of n and k Obtained from Various References for Antimony[a]

eV	cm^{-1}	μm	n	k
10000.	8.066E + 07	1.24E-04	9.999885E-01 [8]	8.94E-07 [8]
9117.	7.353E + 07	1.36E-04	9.999860E-01	1.26E-06
8123.	6.551E + 07	1.53E-04	9.999824E-01	1.93E-06
7237.	5.837E + 07	1.71E-04	9.999779E-01	2.95E-06
6156.	4.965E + 07	2.01E-04	9.999701E-01	5.30E-06
5117.	4.127E + 07	2.42E-04	9.999591E-01	1.03E-05
4886.	3.941E + 07	2.54E-04	9.999566E-01	1.21E-05
4775.	3.851E + 07	2.60E-04	9.999558E-01	1.31E-05
4665.	3.763E + 07	2.66E-04	9.999551E-01	1.23E-05
4559.	3.667E + 07	2.72E-04	9.999533E-01	1.34E-05
4455.	3.593E + 07	2.78E-04	9.999529E-01	1.46E-05
4353.	3.511E + 07	2.85E-04	9.999532E-01	1.15E-05
4254.	3.431E + 07	2.91E-04	9.999506E-01	1.25E-05
4157.	3.352E + 07	2.98E-04	9.999512E-01	1.35E-05
4062.	3.276E + 07	3.05E-04	9.999467E-01	4.68E-06
3969.	3.201E + 07	3.12E-04	9.999412E-01	5.10E-06
2806.	2.264E + 07	4.42E-04	9.99868E-01	1.79E-05
2127.	1.716E + 07	5.83E-04	9.99766E-01	4.68E-05
1688.	1.362E + 07	7.34E-04	9.99632E-01	1.02E-04
1504.	1.213E + 07	8.24E-04	9.99542E-01	1.50E-04
1403.	1.132E + 07	8.84E-04	9.99480E-01	1.89E-04
1309.	1.056E + 07	9.47E-04	9.99411E-01	2.37E-04
1166.	9.408E + 06	1.06E-03	9.99284E-01	3.46E-04
1016.	8.191E + 06	1.22E-03	9.99135E-01	5.43E-04
970.	7.821E + 06	1.28E-03	9.99095E-01	6.10E-04
948.	7.642E + 06	1.31E-03	9.99070E-01	6.45E-04
926.	7.468E + 06	1.34E-03	9.99043E-01	6.84E-04
844.	6.809E + 06	1.47E-03	9.9899E-01	8.77E-04
825.	6.653E + 06	1.50E-03	9.9899E-01	8.97E-04
806.	6.501E + 06	1.54E-03	9.9897E-01	9.12E-04
788.	6.353E + 06	1.57E-03	9.9892E-01	9.28E-04
770.	6.208E + 06	1.61E-03	9.9886E-01	9.67E-04
752.	6.066E + 06	1.65E-03	9.9880E-01	1.03E-03
735.	5.927E + 07	1.69E-03	9.9876E-01	1.11E-03
611.	4.927E + 06	2.03E-03	9.9872E-01	2.03E-03
544.	4.389E + 06	2.28E-03	9.9997E-01	2.99E-03.
532.	4.289E + 06	2.33E-03	1.00143	3.23E-03
520.	4.191E + 06	2.39E-03	1.000883	4.40E-04
508.	4.096E + 06	2.44E-03	1.0000560	4.65E-04
496.	4.002E + 06	2.50E-03	9.9966E-01	4.91E-04
394.	3.177E + 06	3.15E-03	9.9788E-01	8.36E-04
298.	2.407E + 06	4.15E-03	9.9576E-01	1.38E-03
197.	1.588E + 06	6.30E-03	9.896E-01	2.37E-03
175.	1.415E + 06	7.07E-03	9.865E-01	2.51E-03
171.	1.383E + 06	7.23E-03	9.857E-01	2.51E-03
168.	1.351E + 06	7.40E-03	9.849E-01	2.44E-03

[a] The references from which the values were taken are given in brackets.

TABLE VII *(Continued)*

Antimony

eV	cm^{-1}	μm	n	k
164.	1.320E + 06	7.57E-03	9.839E-01	2.36E-03
160.	1.290E + 06	7.75E-03	9.828E-01	2.28E-03
156.	1.261E + 06	7.93E-03	9.815E-01	2.20E-03
153.	1.232E + 06	8.12E-03	9.801E-01	2.14E-03
149.	1.204E + 06	8.31E-03	9.785E-01	2.16E-03
121.	9.778E + 05	1.02E-02	9.545E-01	1.13E-02
101.	8.127E + 05	1.23E-02	9.431E-01	4.82E-02
98.5	7.942E + 05	1.26E-02	9.434E-01	5.27E-02
96.2	7.761E + 05	1.29E-02	9.439E-01	5.76E-02
94.	7.584E + 05	1.32E-02	9.452E-01	6.28E-02
80.	6.451E + 05	1.55E-02	9.688E-01	9.17E-02
71.3	5.747E + 05	1.74E-02	9.870E-01	9.89E-02
69.6	5.616E + 05	1.78E-02	9.907E-01	0.100
68.	5.488E + 05	1.82E-02	9.984E-01	0.101
66.5	5.363E + 05	1.86E-02	9.997E-01	0.101
56.6	4.562E + 05	2.19E-02	1.021	8.92E-02
51.5	4.159E + 05	2.40E-02	1.026	7.80E-02
20.	1.613E + 05	6.20E-02	0.72 [1]	0.2 [1]
19.	1.532E + 05	6.53E-02	0.75	0.2
18.	1.452E + 05	6.89E-02	0.74	0.25
17.	1.371E + 05	7.29E-02	0.72	0.3
16.	1.290E + 05	7.75E-02	0.7	0.35
15.	1.210E + 05	8.27E-02	0.67	0.4
14.	1.129E + 05	8.86E-02	0.63	0.45
13.	1.049E + 05	9.54E-02	0.6	0.5
12.	9.679E + 04	1.03E-01	0.55	0.65
11.	8.872E + 04	1.13E-01	0.5	0.7
10.	8.065E + 04	1.24E-01	0.55	0.8
9.	7.259E + 04	1.38E-01	0.6	1.
8.	6.452E + 04	1.55E-01	0.7	1.3
7.	5.646E + 04	1.77E-01	0.8	1.5
6.	4.839E + 04	2.07E-01	0.9	1.5
5.8	4.678E + 04	2.14E-01	0.95	1.6
5.6	4.517E + 04	2.21E-01	1.05	1.6
5.4	4.355E + 04	2.30E-01	1.1	1.6
5.2	4.194E + 04	2.38E-01	1.1	1.55
5.	4.033E + 04	2.48E-01	1.1	1.5
4.8	3.871E + 04	2.58E-01	1.05	1.55
4.6	3.710E + 04	2.70E-01	1.	1.6
4.4	3.549E + 04	2.82E-01	0.8	1.7
4.2	3.388E + 04	2.95E-01	0.7	1.85
4.	3.226E + 04	3.10E-01	0.7	2.1
3.	2.420E + 04	4.13E-01	1.1	3.3
2.8	2.258E + 04	4.43E-01	1.25	3.6
2.6	2.097E + 04	4.77E-01	1.4	3.9
2.4	1.936E + 04	5.17E-01	1.8	4.2

(continued)

TABLE VII *(Continued)*

Antimony

eV	cm^{-1}	μm	n	k
2.2	1.774E + 04	5.64E-01	2.2	4.45
2.	1.613E + 04	6.20E-01	2.8	4.5
1.8	1.452E + 04	6.89E-01	3.2	4.6
1.6	1.290E + 04	7.75E-01	4.	4.9
1.4	1.129E + 04	8.86E-01	4.6	5.1
1.2	9.679E + 03	1.03	6.2	5.1
1.	8.065E + 03	1.24	7.3	4.7

IX RHENIUM (Re)

Rhenium is a hexagonal close-packed metal. In single-crystal form it is optically anisotropic and uniaxial, with two independent components in the dielectric tensor, one for the electric field parallel to the *c*-axis and one for the perpendicular orientation. Polycrystalline films may have a texture, growing with the closest-packed plane, the basal plane, in the plane of the film, but with randomly oriented *a*-axes. If so, the film will be optically anisotropic. If there is truly random orientation, the film is isotropic with a complex dielectric function $\epsilon = (\epsilon_{\parallel} + 2\epsilon_{\perp})/3$.

Re is a transition metal. The incompletely filled 5*d* bands can give rise to interband optical absorption at arbitrarily small energies. This means that reliable fits of optical data to a Drude-model dielectric function cannot be made, except below some unknown low energy.

Reliable optical data over a wide spectral range do not exist for polycrystalline bulk samples or thin films of Re. Therefore, for Table VIII and Fig. 8, we have chosen to use data taken from the basal plane of a single crystal ($\mathbf{E}\perp\mathbf{c}$) by Weaver *et al.* [1, 2]. In the soft x-ray region the absorption-coefficient spectra of Haensel *et al.* [3] have been converted to spectra of the imaginary part of the complex refractive index with the assumption that the real party is unity. Additional optical measurements have been made by Nomerovannaya *et al.* [4] and others [5–8]. Nomerovannaya *et al.* made measurements at 295 and 77 K. Barnes [9] has made measurements of the temperature dependence at higher temperatures.

Data in the soft x-ray region, from approximately 10^{-4} to 0.024 μm, are taken from Henke *et al.* [10], and the location of the soft x-ray edges, shown by the short, vertical lines in Fig. 8 are taken from Siegbahn *et al.* [11].

REFERENCES

1. J. H. Weaver, C. G. Olson, and D. W. Lynch, unpublished.
2. J. H. Weaver, C. Krafka, D. W. Lynch, and E.-E. Koch, Physics Data, Optical Properties of Metals, Part I: the Transition Metals, Fachinformationszentrum Karlsruhe, 7514 Eggenstein-Leopoldshafen 2, Germany, 1981.
3. R. Haensel, K. Radler, B. Sonntag, and C. Kunz, *Solid State Commun.* **7**, 1495 (1969).
4. L. V. Nomerovannaya, M. M. Kirillova, M. M. Noskov, and G. A. Bolotin, *Fiz. Met. Metalloved.* **36**, 1197 (1973); *Phys. Met. Metall.* **36**, 66 (1973).
5. L. J. Leblanc, J. S. Farrell, and D. W. Juenker, *J. Opt. Soc. Am.* **54**, 956, (1964).
6. D. W. Juenker, L. J. Leblanc, and C. R. Martin, *J. Opt. Soc. Am.* **58**, 164 (1968).
7. J. T. Cox, G. Hass, J. B. Ramsey, and W. R. Hunter, *J. Opt. Soc. Am.* **62**, 781 (1972).
8. L. K. Thomas and S. Thurm, *J. Phys. F: Metal Phys.* **6**, 279 (1976).
9. B. T. Barnes, *J. Opt. Soc. Am.* **56**, 1546 (1966).
10. B. L. Henke, J. C. Davis, E. M. Gullikson, and R. C. C. Perera, "A Preliminary Report on X-Ray Photoabsorption Coefficients and Atomic Scattering Factors for 92 Elements in the 10–10,000 eV Region," Lawrence Berkeley Lab. Rep. LBL-26259, University of California, Berkeley, California, 1988.
11. K. Siegbahn, C. Nordling, A. Fahlman, R. Nordberg, K. Hamrin, J. Hedman, G. Johansson, T. Bergmark, S.-E. Karlsson, I. Lindgren, and B. Lindberg, "ESCA Atomic, Molecular, and Solid State Structure Studied by Means of Electron Spectroscopy." Almquist & Wiksell, Uppsala, Sweden, 1967.

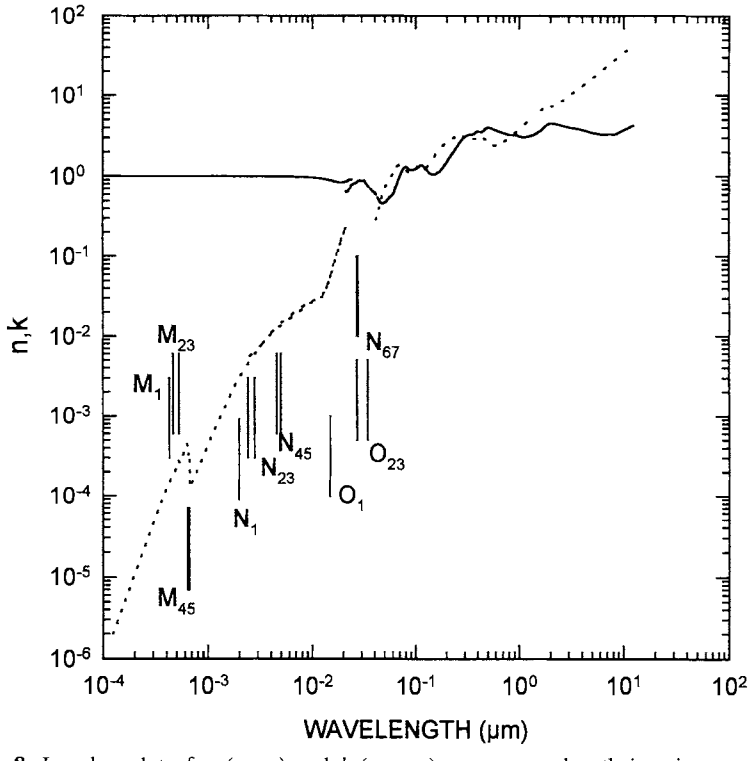

Fig. 8. Log–log plot of n (——) and k (- - - -) versus wavelength in micrometers for rhenium.

TABLE VIII

Values of n and k Obtained from Various References for Rhenium[a]

eV	cm^{-1}	μm	n	k
10000	8.065E + 07	1.24E-04	9.999689E-01 [10]	2.02E-06 [10]
8909.	7.186E + 07	1.39E-04	9.999592E-01	3.06E-06
7937.	6.402E + 07	1.56E-04	9.999479E-01	4.63E-06
7071.	5.703E + 07	1.75E-04	9.999337E-01	6.98E-06
6015.	4.852E + 07	2.06E-04	9.999078E-01	1.24E-05
5000.	4.033E + 07	2.48E-04	9.99866E-01	2.38E-05
4061.	3.276E + 07	3.05E-04	9.99800E-01	4.93E-05
3078.	2.483E + 07	4.03E-04	9.99675E-01	1.28E-04
3007.	2.426E + 07	4.12E-04	9.99664E-01	1.38E-04
2939.	2.371E + 07	4.22E-04	9.99655E-01	1.49E-04
2872.	2.316E + 07	4.32E-04	9.99641E-01	1.55E-04
2806.	2.264E + 07	4.42E-04	9.99628E-01	1.68E-04
2742.	2.212E + 07	4.52E-04	9.99617E-01	1.82E-04
2679.	2.161E + 07	4.63E-04	9.99610E-01	1.85E-04
2618.	2.112E + 07	4.73E-04	9.99593E-01	2.01E-04
2558.	2.064E + 07	4.85E-04	9.99579E-01	2.18E-04
2500.	2.017E + 07	4.96E-04	9.99567E-01	2.36E-04
2443.	1.971E + 07	5.07E-04	9.99561E-01	2.57E-04
2387.	1.926E + 07	5.19E-04	9.99575E-01	2.79E-04
2332.	1.882E + 07	5.31E-04	9.99552E-01	2.59E-04
2279.	1.839E + 07	5.44E-04	9.99530E-01	2.80E-04
2078.	1.676E + 07	5.97E-04	9.99512E-01	3.83E-04
2030.	1.638E + 07	6.10E-04	9.99530E-01	4.14E-04
1984.	1.601E + 07	6.25E-04	9.99580E-01	4.48E-04
1939.	1.564E + 07	6.39E-04	9.99635E-01	3.27E-04
1894.	1.528E + 07	6.54E-04	9.99686E-01	3.56E-04
1851.	1.493E + 07	6.70E-04	9.99600E-01	1.28E-04
1809.	1.459E + 07	6.85E-04	9.99493E-01	1.38E-04
1612.	1.300E + 07	7.69E-04	9.99205E-01	1.99E-04
1403.	1.132E + 07	8.84E-04	9.9888E-01	3.07E-04
1221.	9.854E + 06	1.01E-03	9.9850E-01	4.72E-04
1088.	8.778E + 06	1.14E-03	9.9811E-01	6.67E-04
1015.	8.190E + 06	1.22E-03	9.9785E-01	8.21E-04
904.	7.297E + 06	1.37E-03	9.9736E-01	1.14E-03
806.	6.501E + 06	1.54E-03	9.9679E-01	1.58E-03
685.	5.530E + 06	1.81E-03	9.9590E-01	2.44E-03
670.	5.404E + 06	1.85E-03	9.9576E-01	2.59E-03
654.	5.280E + 06	1.89E-03	9.9564E-01	2.76E-03
639.	5.160E + 06	1.94E-03	9.9553E-01	2.94E-03
625.	5.043E + 06	1.98E-03	9.9543E-01	3.09E-03
610.	4.927E + 06	2.03E-03	9.9531E-01	3.22E-03
596.	4.814E + 06	2.08E-03	9.9517E-01	3.36E-03
544.	4.389E + 06	2.28E-03	9.9450E-01	4.11E-03
531.	4.289E + 06	2.33E-03	9.9439E-01	4.34E-03
519.	4.192E + 06	2.39E-03	9.9427E-01	4.53E-03
507.	4.096E + 06	2.44E-03	9.9412E-01	4.72E-03

[a] The references from which the values were extracted are given in brackets.

TABLE VIII *(Continued)*

Rhenium

eV	cm^{-1}	μm	n	k
500.	4.033E + 06	2.48E-03		5.60E-03 [3]
496.	4.002E + 06	2.50E-03	9.9397E-01 [10]	4.92E-03 [10]
463.	3.734E + 06	2.68E-03	9.9346E-01	5.58E-03
452.	3.649E + 06	2.74E-03	9.9328E-01	5.82E-03
442.	3.566E + 06	2.80E-03	9.9310E-01	6.06E-03
432.	3.484E + 06	2.87E-03	9.9292E-01	6.30E-03
422.	3.404E + 06	2.94E-03	9.9272E-01	6.55E-03
400.	3.226E + 06	3.10E-03		7.30E-03 [3]
312.	2.521E + 06	3.97E-03	9.9002E-01 [10]	1.09E-02 [10]
300.	2.420E + 06	4.13E-03		1.14E-02 [3]
285.	2.299E + 06	4.35E-03	9.891E-01 [10]	1.25E-02 [10]
278.	2.246E + 06	4.45E-03	9.889E-01	1.29E-02
272.	2.195E + 06	4.56E-03	9.887E-01	1.33E-02
265.	2.145E + 06	4.66E-03	9.885E-01	1.37E-02
259.	2.096E + 06	4.77E-03	9.883E-01	1.40E-02
253.	2.048E + 06	4.88E-03	9.880E-01	1.44E-02
248.	2.001E + 06	5.00E-03	9.877E-01	1.48E-02
200.	1.613E + 06	6.20E-03		1.70E-02 [3]
196.	1.588E + 06	6.30E-03	9.836E-01 [10]	1.86E-02 [10]
170.	1.371E + 06	7.29E-03		2.00E-02 [3]
167.	1.351E + 06	7.40E-03	9.789E-01 [10]	2.16E-02 [10]
145.	1.176E + 06	8.50E-03	9.733E-01	2.48E-02
140.	1.129E + 06	8.86E-03		2.43E-02 [3]
124.	1.001E + 06	9.99E-03	9.633E-01 [10]	2.76E-02 [10]
120.	9.679E + 05	1.03E-02		2.76E-02 [3]
100.	8.065E + 05	1.24E-02		3.11E-02
100.	8.130E + 05	1.23E-02	9.364E-01 [10]	3.24E-02 [10]
90.	7.259E + 05	1.38E-02		4.22E-02 [3]
83.8	6.759E + 05	1.48E-02	8.919E-01 [10]	5.52E-02 [10]
80.	6.452E + 05	1.55E-02		6.93E-02 [3]
71.3	5.751E + 05	1.74E-02	8.479E-01 [10]	1.09E-01 [10]
70.	5.646E + 05	1.77E-02		1.25E-01 [3]
65.	5.243E + 05	1.91E-02		1.60E-01
60.6	4.888E + 05	2.05E-02	8.506E-01 [10]	2.11E-01 [10]
60.	4.839E + 05	2.07E-02		2.24E-01 [3]
59.	4.759E + 05	2.10E-02	0.65 [1]	.
58.	4.678E + 05	2.14E-02	0.64	
58.	4.678E + 05	2.14E-02		2.35E-01 [3]
57.	4.597E + 05	2.18E-02	0.65 [1]	.
56.	4.517E + 05	2.21E-02	0.66	
55.	4.436E + 05	2.25E-02	0.68	
55.	4.436E + 05	2.25E-02		2.44E-01 [3]
54.	4.355E + 05	2.30E-02	0.71 [1]	.
53.	4.275E + 05	2.34E-02	0.75	
52.	4.194E + 05	2.38E-02	0.77	
51.6	4.162E + 05	2.40E-02	9.120E-01 [10]	2.34E-01 [10]

(continued)

TABLE VIII *(Continued)*

Rhenium

eV	cm^{-1}	μm	n	k
51.	4.113E + 05	2.43E-02	0.79	
50.	4.033E + 05	2.48E-02	0.8	
50.	4.033E + 05	2.48E-02		2.30E-01 [3]
49.	3.952E + 05	2.53E-02	0.81 [1]	.
48.	3.871E + 05	2.58E-02	0.82	
47.	3.791E + 05	2.64E-02	0.83	
47.	3.791E + 05	2.64E-02		2.69E-01 [3]
46.	3.710E + 05	2.70E-02	0.84 [1]	.
45.	3.629E + 05	2.76E-02	0.87	
45.	3.629E + 05	2.76E-02		2.60E-01 [3]
44.	3.549E + 05	2.82E-02	0.88 [1]	.
43.	3.468E + 05	2.88E-02	0.88	
42.	3.388E + 05	2.95E-02	0.87	
41.	3.307E + 05	3.02E-02	0.87	
40.	3.226E + 05	3.10E-02	0.87	
40.	3.226E + 05	3.10E-02		1.70E-01 [3]
39.	3.146E + 05	3.18E-02	0.88 [1]	.
38.	3.065E + 05	3.26E-02	0.84	
37.	2.984E + 05	3.35E-02	0.8	
36.	2.904E + 05	3.44E-02	0.77	
35.	2.823E + 05	3.54E-02	0.74	
35.	2.823E + 05	3.54E-02		1.95E-01 [3]
34.	2.742E + 05	3.65E-02	0.7 [1]	.
33.	2.662E + 05	3.76E-02	0.67	
32.	2.581E + 05	3.87E-02	0.65	
31.	2.500E + 05	4.00E-02	0.64	
30.	2.420E + 05	4.13E-02	0.59	0.29 [1]
30.	2.420E + 05	4.13E-02		0.2919 [3]
29.	2.339E + 05	4.28E-02	0.55	0.34 [1]
28.	2.258E + 05	4.43E-02	0.51	0.41
27.6	2.226E + 05	4.49E-02	0.49	0.47
27.2	2.194E + 05	4.56E-02	0.48	0.50
26.8	2.162E + 05	4.63E-02	0.47	0.53
26.4	2.129E + 05	4.70E-02	0.46	0.57
26.0	2.097E + 05	4.77E-02	0.46	0.61
25.6	2.065E + 05	4.84E-02	0.46	0.64
25.2	2.033E + 05	4.92E-02	0.47	0.68
24.8	2.000E + 05	5.00E-02	0.47	0.72
24.4	1.968E + 05	5.08E-02	0.48	0.75
24.0	1.936E + 05	5.17E-02	0.49	0.79
23.6	1.903E + 05	5.25E-02	0.50	0.82
23.2	1.871E + 05	5.34E-02	0.52	0.85
22.8	1.839E + 05	5.44E-02	0.53	0.89
22.4	1.807E + 05	5.54E-02	0.55	0.92
22.0	1.774E + 05	5.64E-02	0.56	0.95
21.6	1.742E + 05	5.74E-02	0.57	0.98
21.2	1.710E + 05	5.85E-02	0.58	1.02

TABLE VIII *(Continued)*

Rhenium

eV	cm^{-1}	μm	n	k
20.8	1.678E + 05	5.96E-02	0.60	1.06
20.4	1.645E + 05	6.08E-02	0.61	1.10
20.2	1.629E + 05	6.14E-02	0.64	1.15
20.0	1.613E + 05	6.20E-02	0.65	1.17
19.8	1.597E + 05	6.26E-02	0.67	1.21
19.6	1.581E + 05	6.33E-02	0.72	1.25
19.6	1.581E + 05	6.33E-02	0.70	1.23
19.4	1.565E + 05	6.39E-02	0.74	1.27
19.2	1.549E + 05	6.46E-02	0.76	1.29
19.0	1.532E + 05	6.53E-02	0.79	1.31
18.8	1.516E + 05	6.59E-02	0.82	1.33
18.6	1.500E + 05	6.67E-02	0.85	1.35
18.4	1.484E + 05	6.74E-02	0.88	1.36
18.2	1.468E + 05	6.81E-02	0.92	1.37
18.0	1.452E + 05	6.89E-02	0.95	1.38
17.8	1.436E + 05	6.97E-02	0.99	1.39
17.6	1.420E + 05	7.04E-02	1.03	1.39
17.4	1.403E + 05	7.13E-02	1.06	1.39
17.2	1.387E + 05	7.21E-02	1.10	1.39
17.0	1.371E + 05	7.29E-02	1.14	1.38
16.8	1.355E + 05	7.38E-02	1.17	1.37
16.6	1.339E + 05	7.47E-02	1.21	1.35
16.4	1.323E + 05	7.56E-02	1.24	1.33
16.2	1.307E + 05	7.65E-02	1.26	1.30
16.0	1.290E + 05	7.75E-02	1.28	1.28
15.8	1.274E + 05	7.85E-02	1.29	1.26
15.6	1.258E + 05	7.95E-02	1.31	1.23
15.4	1.242E + 05	8.05E-02	1.31	1.20
15.2	1.226E + 05	8.16E-02	1.31	1.17
15.0	1.210E + 05	8.27E-02	1.29	1.14
14.8	1.194E + 05	8.38E-02	1.27	1.12
14.6	1.178E + 05	8.49E-02	1.24	1.12
14.4	1.161E + 05	8.61E-02	1.22	1.13
14.2	1.145E + 05	8.73E-02	1.21	1.14
14.0	1.129E + 05	8.86E-02	1.20	1.16
13.8	1.113E + 05	8.98E-02	1.19	1.18
13.6	1.097E + 05	9.12E-02	1.19	1.20
13.4	1.081E + 05	9.25E-02	1.20	1.21
13.2	1.065E + 05	9.39E-02	1.20	1.23
13.0	1.049E + 05	9.54E-02	1.21	1.25
12.8	1.032E + 05	9.69E-02	1.22	1.26
12.6	1.016E + 05	9.84E-02	1.23	1.27
12.4	1.000E + 05	1.00E-01	1.23	1.29
12.2	9.840E + 04	1.02E-01	1.25	1.30
12.0	9.679E + 04	1.03E-01	1.26	1.32
11.8	9.517E + 04	1.05E-01	1.28	1.33

(continued)

TABLE VIII *(Continued)*

Rhenium

eV	cm^{-1}	μm	n	k
11.6	9.356E + 04	1.07E-01	1.31	1.34
11.4	9.195E + 04	1.09E-01	1.33	1.34
11.2	9.033E + 04	1.11E-01	1.36	1.33
11.0	8.872E + 04	1.13E-01	1.37	1.31
10.8	8.711E + 04	1.15E-01	1.38	1.28
10.6	8.549E + 04	1.17E-01	1.36	1.25
10.4	8.388E + 04	1.19E-01	1.33	1.23
10.2	8.227E + 04	1.22E-01	1.29	1.22
10.0	8.065E + 04	1.24E-01	1.24	1.24
9.8	7.904E + 04	1.27E-01	1.20	1.27
9.6	7.743E + 04	1.29E-01	1.17	1.31
9.4	7.582E + 04	1.32E-01	1.14	1.36
9.2	7.420E + 04	1.35E-01	1.11	1.41
9.0	7.259E + 04	1.38E-01	1.09	1.46
8.8	7.098E + 04	1.41E-01	1.07	1.52
8.6	6.936E + 04	1.44E-01	1.06	1.58
8.4	6.775E + 04	1.48E-01	1.05	1.66
8.2	6.614E + 04	1.51E-01	1.05	1.74
8.0	6.452E + 04	1.55E-01	1.05	1.83
7.8	6.291E + 04	1.59E-01	1.08	1.93
7.6	6.130E + 04	1.63E-01	1.12	1.98
7.4	5.968E + 04	1.68E-01	1.12	2.08
7.2	5.807E + 04	1.72E-01	1.16	2.19
7.0	5.646E + 04	1.77E-01	1.22	2.28
6.8	5.485E + 04	1.82E-01	1.28	2.37
6.4	5.162E + 04	1.94E-01	1.42	2.56
6.2	5.001E + 04	2.00E-01	1.51	2.64
6.0	4.839E + 04	2.07E-01	1.61	2.74
5.9	4.759E + 04	2.10E-01	1.67	2.78
5.8	4.678E + 04	2.14E-01	1.73	2.81
5.7	4.597E + 04	2.18E-01	1.78	2.85
5.6	4.517E + 04	2.21E-01	1.84	2.88
5.5	4.436E + 04	2.25E-01	1.89	2.92
5.4	4.355E + 04	2.30E-01	1.96	2.96
5.3	4.275E + 04	2.34E-01	2.02	3.00
5.2	4.194E + 04	2.38E-01	2.10	3.04
5.1	4.113E + 04	2.43E-01	2.17	3.08
5.0	4.033E + 04	2.48E-01	2.25	3.12
4.9	3.952E + 04	2.53E-01	2.35	3.14
4.8	3.871E + 04	2.58E-01	2.44	3.17
4.7	3.791E + 04	2.64E-01	2.55	3.19
4.6	3.710E + 04	2.70E-01	2.67	3.18
4.5	3.629E + 04	2.76E-01	2.77	3.17
4.4	3.549E + 04	2.82E-01	2.88	3.15
4.3	3.468E + 04	2.88E-01	2.97	3.11
4.2	3.388E + 04	2.95E-01	3.05	3.06
4.1	3.307E + 04	3.02E-01	3.13	3.01

TABLE VIII *(Continued)*

Rhenium

eV	cm^{-1}	μm	n	k
4.0	3.226E + 04	3.10E-01	3.19	2.94
3.9	3.146E + 04	3.18E-01	3.22	2.88
3.8	3.065E + 04	3.26E-01	3.24	2.84
3.7	2.984E + 04	3.35E-01	3.24	2.81
3.6	2.904E + 04	3.44E-01	3.25	2.83
3.5	2.823E + 04	3.54E-01	3.28	2.84
3.4	2.742E + 04	3.65E-01	3.34	2.88
3.35	2.702E + 04	3.70E-01	3.39	2.90
3.30	2.662E + 04	3.76E-01	3.44	2.89
3.25	2.621E + 04	3.81E-01	3.50	2.88
3.20	2.581E + 04	3.87E-01	3.55	2.84
3.15	2.541E + 04	3.94E-01	3.57	2.79
3.10	2.500E + 04	4.00E-01	3.57	2.74
3.05	2.460E + 04	4.07E-01	3.56	2.71
3.00	2.420E + 04	4.13E-01	3.53	2.71
2.95	2.379E + 04	4.20E-01	3.51	2.72
2.90	2.339E + 04	4.28E-01	3.49	2.75
2.85	2.299E + 04	4.35E-01	3.51	2.83
2.80	2.258E + 04	4.43E-01	3.57	2.88
2.75	2.218E + 04	4.51E-01	3.65	2.91
2.70	2.178E + 04	4.59E-01	3.74	2.92
2.65	2.137E + 04	4.68E-01	3.83	2.88
2.60	2.097E + 04	4.77E-01	3.90	2.84
2.55	2.057E + 04	4.86E-01	3.96	2.78
2.50	2.016E + 04	4.96E-01	4.01	2.70
2.45	1.976E + 04	5.06E-01	4.01	2.60
2.40	1.936E + 04	5.17E-01	4.00	2.55
2.35	1.895E + 04	5.28E-01	3.97	2.47
2.30	1.855E + 04	5.39E-01	3.93	2.44
2.25	1.815E + 04	5.51E-01	3.89	2.40
2.20	1.774E + 04	5.64E-01	3.83	2.38
2.15	1.734E + 04	5.77E-01	3.78	2.39
2.10	1.694E + 04	5.90E-01	3.74	2.40
2.05	1.653E + 04	6.05E-01	3.69	2.41
2.00	1.613E + 04	6.20E-01	3.63	2.43
1.95	1.573E + 04	6.36E-01	3.59	2.46
1.90	1.532E + 04	6.53E-01	3.54	2.50
1.85	1.492E + 04	6.70E-01	3.51	2.57
1.80	1.452E + 04	6.89E-01	3.47	2.59
1.75	1.411E + 04	7.08E-01	3.42	2.65
1.70	1.371E + 04	7.29E-01	3.38	2.72
1.65	1.331E + 04	7.51E-01	3.34	2.80
1.60	1.290E + 04	7.75E-01	3.29	2.88
1.55	1.250E + 04	8.00E-01	3.25	3.01
1.50	1.210E + 04	8.27E-01	3.23	3.12
1.45	1.169E + 04	8.55E-01	3.22	3.25

(continued)

TABLE VIII *(Continued)*

Rhenium

eV	cm^{-1}	μm	n	k
1.40	1.129E + 04	8.86E-01	3.23	3.38
1.35	1.089E + 04	9.18E-01	3.24	3.46
1.30	1.049E + 04	9.54E-01	3.20	3.56
1.25	1.008E + 04	9.92E-01	3.14	3.70
1.20	9.679E + 03	1.03E + 00	3.08	3.89
1.15	9.275E + 03	1.08E + 00	3.04	4.14
1.10	8.872E + 03	1.13E + 00	3.05	4.39
1.05	8.469E + 03	1.18E + 00	3.07	4.65
1.00	8.065E + 03	1.24E + 00	3.09	4.96
0.95	7.662E + 03	1.31E + 00	3.17	5.27
0.90	7.259E + 03	1.38E + 00	3.26	5.61
0.85	6.856E + 03	1.46E + 00	3.39	5.95
0.80	6.452E + 03	1.55E + 00	3.55	6.32
0.77	6.210E + 03	1.61E + 00	3.65	6.53
0.75	6.049E + 03	1.65E + 00	3.77	6.75
0.73	5.888E + 03	1.70E + 00	3.94	6.94
0.70	5.646E + 03	1.77E + 00	4.13	7.09
0.68	5.485E + 03	1.82E + 00	4.30	7.19
0.65	5.243E + 03	1.91E + 00	4.44	7.26
0.63	5.081E + 03	1.97E + 00	4.52	7.31
0.60	4.839E + 03	2.07E + 00	4.53	7.40
0.57	4.597E + 03	2.18E + 00	4.51	7.53
0.55	4.436E + 03	2.25E + 00	4.45	7.73
0.50	4.033E + 03	2.48E + 00	4.34	8.26
0.45	3.629E + 03	2.76E + 00	4.17	9.03
0.40	3.226E + 03	3.10E + 00	3.99	10.15
0.35	2.823E + 03	3.54E + 00	3.93	11.54
0.30	2.420E + 03	4.13E + 00	3.73	13.44
0.25	2.016E + 03	4.96E + 00	3.47	16.27
0.20	1.613E + 03	6.20E + 00	3.28	20.66
0.15	1.210E + 03	8.27E + 00	3.28	28.08
0.10	8.065E + 02	1.24E + 01	4.25	42.83

Optical Constants of Eight Rare Earth Elements: (Ce), (Sm), (Gd), (Tb), (Dy), (Er), (Tm), and (Yb)

L. WARD
Coventry University
Coventry, U.K.

INTRODUCTION I

The 14 rare-earth elements or lanthanides lie in the periodic table between atomic numbers 58 and 71, cerium to lutecium, and are generally characterized by a basic electron configuration of $6s^2\ 5d^1$ and the progressive filling of the $4f$ electron shell. The exceptions to this rule are europium (atomic number 63), which has 7 $4f$ electrons and none in the $5d$ shell, and ytterbium (atomic number 70), which has 14 $4f$ and no $5d$; both of these elements have cubic structures. The rest are hexagonal and so are able to exhibit anisotropic optical properties; some researchers have reported values of optical constants with both $\mathbf{E} \| \mathbf{c}$ and $\mathbf{E} \perp \mathbf{c}$ (the c-axis is at right angles to the hexagonal plane), and these results have been included where suitable. The optical behavior of all the elements in this group between 10 and 10,000 eV is generally governed by the 3, 4, and $5d$ electrons ($M_{4,5}$, $N_{4,5}$, and O_{1-3}) as the $4f$ electrons lie in a narrow localized band and are shielded by the outer $5p$ and $6s$ electrons, which are in overlapping bands giving a high density of states close to the Fermi energy. This situation allows many quantum transitions between these bands and the Fermi energy at low photon energies (1 to 5 eV), giving rise to several absorption peaks in this spectral region. The general shapes of the Fermi surfaces and energy-band structures are complicated but similar in all the heavy rare-earth elements. However, the two elements Eu and Yb are much simpler in this respect, and they behave more like the transition metals.

It is proposed to deal firstly with these elements as a group and then to consider the individual elements later. Eight rare-earth elements will be con-

HANDBOOK OF OPTICAL CONSTANTS OF SOLIDS III

Copyright © 1998 by Academic Press.
All rights of reproduction in any form reserved
ISBN 0-12-544423-0/$25.00.

sidered in this survey: Ce, Sm, Gd, Tb, Dy, Er, Tm, and Yb. The first seven have hexagonal structures, whereas the last, Yb, is cubic. Ce is cubic below 100 K (α-phase) but becomes hexagonal (γ-phase) at higher temperatures.

All the rare-earth metals are highly reactive with oxygen and hydrogen (in water vapor); many of the older measurements that were made in air on solid materials are, therefore, suspect because of possible contamination from these sources, which will cause values of both n and k to be too small. Most modern experimenters have attempted to overcome this problem by carrying out measurements on polycrystalline thick films deposited in a very high vacuum, and so more faith should be given to these more recent results. Where any choice has been available, the later results have been quoted in this article, unless there were compelling reasons otherwise.

Some of the rare-earth metals exhibit paramagnetism at room temperature but become ferromagnetic or antiferromagnetic at lower temperatures. Thus, the light rare-earth metals (Ce to Eu) order antiferromagnetically at low temperatures, whereas the heavy rare-earths (Gd to Tm) may become either ferromagnetic or antiferromagnetic. These effects are connected with the coupling between the uncompensated magnetic moments of the $4f$ electrons and those of the outer electrons by a process known as s–f exchange coupling; depending on the sign of the coupling, either ferro- (positive coupling) or antiferromagnetism (negative coupling) will result. Thus, gadolinium becomes ferromagnetic with a Curie point of 293 K, whereas dysprosium firstly becomes antiferromagnetic with a Néel temperature of 179 K and then ferromagnetic below the Curie temperature of 85 K. Several authors have studied the optical properties of rare-earth metals in low-temperature regions and also at higher temperatures up to about 470 K in order to investigate the effects of these magnetic transformations. Where appropriate, sets of results in all these temperature regions have been included. The values of Curie and Néel temperatures quoted have been obtained from the *Handbook of Physics and Chemistry* [1].

At one time, the rare-earth metals were regarded merely as scientific curiosities that possessed a range of interesting theoretical properties, but now they are finding increasing practical use in a number of commercial applications: for example, as alloys for the storage of computer information, in superconductors, and in optical materials. In recent years, a significant trend in published work in this area has been devoted to the properties of alloys of rare-earth metals with erbium, gadolinium, and ytterbium. The optical properties of these alloys will not be discussed in this chapter, but useful references are Kuron *et al.* [2], Atkinson *et al.* [3], and Memon *et al.* [4]; a triennial conference held by the Rare Earths Research Group is devoted to the properties of such materials [5].

There are comparatively few direct results for n and k for the rare-earth elements. However, some authors have measured the absorption coefficient, α, which is related to k by the equation $\alpha = 4\pi k/\lambda$, so that k may be calcu-

lated, but no value is obtained for n. Similarly, the optical conductivity, σ, may be reported, and this is related to ϵ_2 by $\sigma = \epsilon_2\omega/4\pi$. If both α and ω are measured, n and k can then be determined. There are also scarcities of published values for very low energies (far infrared) and in the range 5–30 eV. Another problem in obtaining accurate data for n and k is that many authors publish their results in graphical form only. In general, it is possible to read off data from these graphs to at best about 1%.

There have been several reviews of the optical and electrical properties of the rare-earth metals. Gasgnier [6] divided his account into three energy ranges, viz.: 0–6 eV, 6–50 eV, and high energies (up to 300 eV). In the low-energy, long-wavelength region, he noted particularly the wide divergences in values by different authors, probably due to surface conditions, crystal structure, and contamination, mainly oxides and hydroxides, and this is borne out in the plots of n and k versus wavelength. The center energy range was dominated by the plasma resonances, whereas the high range featured the N_{4-5} absorption edge.

Knyazev and Noskov [7] have given an in-depth study of the optics of the lanthanides, also looking at different wavelength regions and considering free-electron and interband-absorption mechanisms and also the effect of magnetic transformations. In addition, these authors have published a large number of papers dealing with the optical properties of some of the individual elements, which will be referred to under the appropriate sections. Lynch [8] has given a broad review of the optical properties of these metals in an article in *The Rare Earths in Modern Science and Technology.*

Weaver *et al.* [9] followed their earlier survey of the optical properties of the transition elements by a similar collation of data from various authors that covered the lanthanides and the actinides; they present tables of values of ϵ_1, ϵ_2, n, and k between 0.1 and 5.0 eV.

Another source of the optical constants of the rare-earth metals is Volume 15b of "Landolt–Börnstein New Series" [10], which has tables of n and k versus wavelength for Dy, Sm, Tm, Tb, and Gd, as well as some graphs of σ versus λ for other elements in this group.

For all the rare-earth elements, Henke *et al.* [11, 12] have tables of values of the x-ray interaction coefficients, f_1 and f_2, from which n and k may be calculated, between photon energies of 30 and 10,000 eV, that is, 0.13 and 40 nm.

Thus, $n = 1 - r_0 N f_1 \lambda^2/2\pi$ and $k = r_0 N f_2 \lambda^2/2\pi$, where r_0 = classical electron radius = $2.8179\ 10^{-15}$ m, N = no. of atoms/unit volume = Avogadro's no. $\times$ density/atomic wt., and λ = wavelength in micrometers.

As with other metals, the optical properties of this group of elements are determined by the interactions of the bound and free electrons with the electric field of the incident wave. At wavelengths greater than about 1 μm the free-electron effects are dominant and Drude-like equations may be used to describe their optical properties. Knyazev and Noskov [13] used a two-term Drude equation to describe the properties of samarium, terbium, and dys-

prosium. This makes use of two values each for the electron-relaxation frequency, ω_t, and the plasma frequency, ω_p; the first term in this equation is much larger than the second and agrees well with the values of ω_t and ω_p quoted by other sources. At shorter wavelengths, that is, higher frequencies, interband transitions become significant, and each element shows a series of absorption edges due to the various electron shells; *L, M, N,* and *O* bands are the most significant, and values of the energies for these absorptions will be given for each element considered. Schuler [14] has given a general discussion of these properties, particularly the interband transitions near the symmetry points in the Brillouin zone, where the joint density of states is very high; he gives a table of possible electron transitions in this region.

All the lanthanides show three strong absorption edges in the high-energy region, the N_4 and N_5 transitions between 120 and 180 eV (7 to 10 nm); those between the M_4 and M_5 levels (3*d* electrons) in the range 900 to 1600 eV (0.78 to 1.4 nm); and the *L* band (2*p* electrons) between 6000 and 10,000 eV (0.13 to 0.20 nm). These lines move progressively to larger energies, i.e., shorter wavelengths, as the atomic number increases. The values of the energies of the *L, M, N* and *O* absorption bands quoted have been taken from either Kaye and Laby [15] or the *Physics Handbook* [16].

The energy region between 70 and 500 eV, which includes the N_4 and N_5 electron transitions, has been covered by several groups of workers. Tables by Henke *et al.* [12] cover this region but do not allow the accurate pinpointing of absorption peaks as the values of the photon energies quoted are too far apart. Gribovskii and Zimkina [17, 18] have reported values of the mass absorption coefficients, μ_m, for La, Ce, Pr, Nd, Sm, Gd, Tb, Dy, Ho, Er, Tm, and Yb between 70 and 500 eV, determined by transmission measurements. Their results can be used to calculate values of k ($k = \mu_m \rho \lambda/4\pi$ where ρ = density). In the later paper [18] they used x-ray emission to study the $N_{4,5}$ spectra of Gd, Tb, and Dy in this region.

Formichev *et al.* [19] have published graphs of the absorption coefficient against photon energy for all the rare-earth elements between 95 and 185 eV. Although these are useful in identifying absorption lines, the absorption scale is only arbitrary, and no quantitative information can be extracted. However, their figures give details of the fine-structure maxima for all the lanthanides. Another paper by the same group [20] extended the study to 500 eV for the elements Ce, Pr, Nd, Sm, Eu, Gd, Dy, and Ho. Similarly, Muto *et al.* [21] have studied Eu, Gd, Tb, Dy, and Ho in the 4*d*–4*f* excitation region between 140 and 180 eV using circularly polarized synchrotron radiation as a source to irradiate thin films (~10 nm thick) on polycarbonate cooled to liquid-nitrogen temperature; diagrams show the absorption coefficient (arbitrary units) versus photon energy. The absorption peaks are as follows: Eu 142 eV, Gd 148 eV, Tb 158 eV, Dy 165 eV, and Ho (a flat top) between 167 and 173 eV. These values were also confirmed in the work of Trebbia and Colliex [22].

Kunz [23] observed that all the foregoing results display the systematic absorption behavior due to the progressive lowering in energy of the empty *f* states until these states are finally filled at Lu. The large peak due to transitions into empty 4*f* states migrates towards the ionization limit, while the binding energy of the 4*d* levels increases, producing a shift in the whole absorption feature towards higher photon energies. Finally, when the 4*f* states are filled with 14 electrons, the peak disappears. The fine structures in the absorption coefficient are fairly simple in La but become increasingly complex as the number of filled *f* states increases; in Yb, however, when only one empty *f* state remains, the fine structures become simple again. Gerken *et al.* [24] have noted the energy differences between the emission spectra of the 4*f* electrons from the surface and from the bulk atoms for the lanthanides.

Weaver and Lynch [25] carried out measurements at 4.2 K on the elements Gd, Tb, Dy, Ho, Er, Tm, and Lu in solid form; they measured (a) the optical conductivity, σ, and (b) the optical absorptivity A, defined as $1 - R$ between 0.1 and 5.0 eV in both states of polarization. ϵ_2 may be calculated from σ as described earlier, and n may then be obtained from A using the normal-incidence formula for $1 - R$ [26] to compute ϵ_1. Their results are presented in great detail elsewhere [9]. However, there appear to be errors in all the values of k quoted for these elements. The values of k given in the present article have been recalculated from the values of n and ϵ_2, $(2\ n\ k)$, and now agree with Weaver and Lynch's values for ϵ_1, $(n^2 - k^2)$. In a private communication [27] these authors give optical constants up to 18 eV for dysprosium.

Dzionk *et al.* [28] were able to observe the 5p (*O*) excitations in Gd, Tb, Dy, Er, Tm, and Yb by using the photoionic yields from these elements.

Petrakian [29, 30] adopted a different technique by measuring the reflectance and transmittance of films of thickness d, calculating the absorptivity, A, now defined as $1 - R - T$, and then, using the Wolter formula [31], to obtain $\epsilon_2 = n\ A\ \lambda/2\ \pi\ d\ T$. Petrakian observed that all the lanthanides exhibited an absorption maximum between 5.5 and 6.5 eV, which he ascribed to indirect electron transitions between the 4*f* levels and the Fermi level. In addition, the heavy rare-earths gave an extra peak near 3.1 eV that was not thickness dependent and that he claimed was due to a direct interband transition.

Several authors have reported plasmons in the rare-earth metals. These include Bakulin *et al.* [32], Colliex *et al.* [33], Tsveiman *et al.* [34], and Zashkvara *et al.* [35]. Netzer *et al.* [36] used electron-energy-loss techniques to study plasmons in polycrystalline films of most of the rare-earth metals. Surface plasmons occurred between 4 and 5 eV, whereas bulk plasmons were found between 7 and 14 eV; in both cases, the plasmon energies increased with atomic number. The surface plasmon was found to be very sensitive to oxidation.

Data for each of the rare-earth elements are now presented.

II CERIUM

Crystal structure α = f.c.c., γ = h.c.p.; space group Fm3m O_h^5; atomic number 58; atomic weight 140.1; density α 8.16 $\times$ 10^3 kg/m^3, density γ 6.80 $\times$ 10^3 kg/m^3; electron configuration $4f^1$ $5d^1$ $6s^2$.

Cerium can exist in two phases; at low temperatures the α (f.c.c.) phase is present, and this changes to the γ (hex h.c.p.) phase above about 100 K.

The main absorption edges for cerium are 6516, 6131, and 5690 eV (L) and 1152, 902, and 883 (M_{3-5}) [15]. The $M_{1,2}$ edges occur at 1435 and 1273 eV, whereas N and O edges are at 289 (N_1), 207 ($N_{2,3}$), 112 (N_4), 108 (N_5), 38 (O_1), and 18 eV ($O_{2,3}$) [16]. Henke-model calculations of k [12] show peaks at 885 (M_5) and 131 eV. In the overlap region, the Haensel *et al.* [37] values of k determined from measurements of absorption using synchrotron radiation are in reasonable agreement with the Henke model and indicate a peak between 125 and 130 eV. Suzuki *et al.* [38] have also measured the absorption coefficient for cerium between 100 and 170 eV, recording a broad band peaking at 124 eV, when k = 0.0748, which is very close to the value of Haensel *et al.*

Results for polycrystalline cerium between 0.18 and 6.2 eV have been published by Kirillova *et al.* [39, 40] paying particular attention to the changes due to magnetic and phase transitions. The specimens were electropolished and finally cleaned by bombardment with argon ions; the optical technique used was ellipsometry. It was noted that both n and k increased with the duration of the argon cleaning process until saturation values were obtained after about 200 minutes. The values of both n and k were much larger at 293 K (γ-phase) than at 78 K (α-phase); peaks were observed in n and k in both the α- and γ-phases at about 5.8 eV, as also reported by Petrakian [41]. Two peaks were observed in the curves of conductance versus energy; in the γ-phase there was a narrow peak at 0.35 eV and a wider one at 1.6 eV, whereas in the α-phase the two peaks were of equal width and occurred at 0.75 and 1.8 eV. Kirillova *et al.* claimed that these features supported the theory that, on passing from γ to α, the $4f$ band delocated into a $4f'$ band.

The optical conductivity of thin films of α- and γ-cerium in the range 1.5 to 5.4 eV were studied by Rhee *et al.* [42] using ellipsometry. They found monotonic decreases in σ with energy for both phases and also that σ increased on passing from the γ- to the α-phase because of the increase in the number of electrons per unit volume associated with the change in density that occurs at the phase change.

Plasmons were observed by Zashkvara *et al.* [35]; the bulk plasmon occurred at 8.9 eV and the surface plasmon at 4.1 eV. They also observed the O_{2-3} transition at 20.3 eV and the O_1 transition at 38.6 eV.

Figure 1 shows a log-log plot of n (○) and k (△) versus λ for cerium and incorporating values from Henke [12], Haensel *et al.* [37], and Kirillova *et al.* [39, 40] at 295 K. The n and k curves cross at 0.14 μm, that is, 8.9 eV;

this value of the plasmon energy is in good agreement with that reported by Zashkvara *et al.* [35].

SAMARIUM III

Crystal structure trigonal; space group R3m D_{3d}^{5} atomic number 62; atomic weight 150.4; density 7.75×10^3 kg/m^3; electron configuration $4f^6\ 6s^2$.

Absorption edges for samarium occur at 7707 eV (L_1), 7278 (L_2), 6683 (L_3), 1388 (M_3), 1106 (M_4), and 1081 (M_5) [15]; 1728 (M_1), 1546 (M_2), 351 (N_1), 251 ($N_{2,3}$), 137 (N_4), 33 (O_1), and 26 eV ($O_{2,3}$) [16].

Data for the optical constants, n and k, of samarium at high energies have been obtained from Henke's model [12]; these show absorption peaks at about 1120 eV ($M_{4,5}$), and 138 eV (N_4); there is also a slight shoulder at 350 eV (N_1).

The results for k from Gribovskii and Zimkina [17, 18] overlap with Henke's for energies less than 150 eV, and there is reasonably good agreement in this region, the peak at 150 eV being well defined. Haensel *et al.* [37] used synchrotron radiation to determine the absorption coefficients of samarium between 70 and 180 eV, and their values of k agree with Henke's at 170 eV, but are less satisfactory at lower energies.

Knyazev and Noskov [43], working at 293 K, give tables of n and k between 1 and 3 eV. Other, later, sets of results have been published by the same authors [44] between 0.06 and 1.24 eV and at three different temperatures: 85, 293, and 460 K. Where these two groups of results touch at about 1.0 eV, the agreement is excellent. The Néel temperature of samarium is 109 K; results from Knazev and Noskov [44] span this temperature. No dramatic changes in n and k were observed over this magnetic transformation but, in general, k decreases while n increases with temperature up to 460 K over this energy range.

Values of the relaxation and plasma frequencies were calculated by Knyazev and Noskov [44] at all the three temperatures they used and are as follows:

T (K)	ω_t (eV)	ω_p (eV)
80	0.16	11.6
293	0.42	11.7
460	0.59	12.5

Figure 2 shows a log–log plot of n (○) and k (△) versus λ for samarium using values due to Henke [12] Haensel *et al.* [37], Gribovskii and Zimkina [17, 18], and Knyazev and Noskov [43]. It is not easy to get an accurate

value for the crossover point, so the plasma frequency has not been calculated.

IV GADOLINIUM

Crystal structure hex; Space group: $P6_3/mmc$ D_{6h}^4; atomic number 64; atomic weight 157.3; density 7.90×10^3 kg/m^3; electron structure $4f^7$ $5d^1$ $6s^2$.

The L_{1-3} edges are at 8343, 7898, and 7211eV, respectively, whereas the M_{3-5} occur at 1511, 1217, and 1185 eV [15]. The "Physics Handbook" [16] gives 1888 (M_1), 1695 (M_2), 383 (N_1), 311 (N_2), 272 (N_3), 147 (N_4), 142 (N_5), 43 (O_1), and 28 eV (O_2).

Henke *et al.* [12] found M-absorption peaks at 1672 eV (M_2) and 1181 eV (M_5) and also one at about 143 eV (N_5). Results from Gribovskii and Zimkina [17, 18] for k agree well with the Henke-model values at all the overlap energies and also show a clear peak at 146 eV. The O_1 peak near 31 eV is also visible.

Erskine and Flynn [45] have given data for α between 2 and 35 eV using the direct absorption technique. Absorption peaks were found at 7, 8, 24, and 33 eV. These authors claim good agreement with the more accurate ellipsometric measurements of Erskine *et al.* [46] in the overlap region between 4.5 and 5.5 eV (the latter only give ϵ_2, so they are not included in the table of results). Results from Erskine and Flynn fit well with Henke's at 30 eV. Another set of results covering the range 2 to 160 eV has been given by Cukier *et al.* [47]; they found a volume plasmon at 13 eV and the O_2 and O_3 peaks at 25 and 35 eV, respectively. Quemerais *et al.* [48] also covered gadolinium, presenting graphs of ϵ_1, ϵ_2, and σ versus energy up to 15 eV, which overlap with Erskine and Flynn. The agreement is not perfect, but is very good at 12 eV; there were peaks in conductance at 2 and 4–8 eV. Also covering this energy range were Weaver and Lynch [25] at 4.2 K and in both states of polarization; n was smaller for $\mathbf{E} \| \mathbf{c}$, whereas k was larger in this case. At this temperature n showed a peak at 2.0 μm; this was different from the results of Knyazev and Noskov [52], where n continued to increase with wavelength.

Miller *et al.* [49] obtained the optical constants and conductivity of gadolinium from reflectance ratios at oblique incidence on opaque films in the range 1.8 to 3.1 eV. They found optical transitions at 1.95, 2.15, 2.50, 2.75, and 3.1 eV, corresponding to a series of interband transitions. Miller *et al.* [50] used thermally modulated reflectance measurements to study Gd over the energy range 1.45 to 3.2 eV. Another worker with Gd was Myers [51], who employed ellipsometry on thin films; however, he failed to observe the detailed structures described by Miller *et al.* [49]. Instead, the conductivity

only showed some indistinct structure superimposed on a general monotonically decreasing background; a broad peak at 2 eV was identified as due to electron transitions from the Fermi level to the empty *d*-band.

Knyazev and Noskov [52] give values of n and k at 293 K between 1.2 and 3.4 eV. Their experimental technique was to measure the reflectance and phase change on reflection using the method of Bolotin *et al.* [53] on four polycrystalline flat mirrors, mechanically polished. Gadolinium became metallic, i.e., $k > n$ at 1.77 eV. A further series of results by these authors [54] covered the range 1 to 20 μm at temperatures of 80, 293, and 460 K; k was found to decrease with temperature, whereas n increased. There was good agreement where these two sets of values at 293 K touched at 1.0 eV. Knyazev *et al.* [55] have also reported on the infrared absorption of Gd, Tb, and Dy single crystals.

Hodgson and Clayet [56] measured the optical constants of gadolinium at temperatures of 105 and 293 K in the range 0.5 to 2.5 eV using the internal reflectance of evaporated films deposited on silica glass prisms. They found a decrease in n and an increase in k with temperature; they also discovered absorption bands at 0.7 and 1.1 eV. Their results were close to those of Weaver and Lynch [25] and also Krizek and Taylor [57], who employed ellipsometry on evaporated films over the range 0.5 to 2.5 eV and at temperatures of 56 and 300 K. It was only at low energies that ϵ_1 and σ changed rapidly because of the Drude free-electron contribution; there was also a peak at 2.0 eV caused by an interband transition. By assuming that the hexagonal gadolinium could be treated as isotropic, Krizek and Taylor were able to make a theoretical calculation of both the optical conductivity and ϵ_1; this gave the absorption band at 1.6 eV (293 K) and 1.8 eV (105 K).

Petrakian *et al.* [58, 59], who used the technique due to Querry [60] to measure the reflectances in both states of polarization, have reported values of the optical conductivity of gadolinium between 1 and 5 eV at temperatures between 10 K and 300 K. In the ferromagnetic state (below 293 K) an extra peak in conductivity was observed at 0.69 eV and was ascribed to the *s–p* exchange interaction; this peak increased in magnitude as the temperature decreased. Both n and k tended to decrease with temperature, particularly at the lower energies. They compared their results graphically with those of Hodgson and Clayet [56], Erskine *et al.* [46], and Knyazev and Noskov [52]. All the results from investigations over this energy range showed a peak in conductivity at about 1.5 eV and, in addition, two (Petrakian *et al.* [58, 59] and Knyazev and Noskov [52]) indicated a second peak at about 2.5 eV. The most striking feature of this graph, however, was the wide spread of the values of conductivity over this energy range among the various authors, those of Hodgson and Clayet being about three times greater than the values of Knyazev and Noskov, with the other two sets lying between. The results quoted here are taken from both papers by Petrakian *et al.* [58, 59].

Knyazev and Bolotin [61] used polarimetry to measure the optical con-

stants of single crystals of gadolinium both along the hexagonal axis (c) and in the basal plane (a). Transition to the magnetic ordered state was accompanied by the appearance of resonance absorption peaks in the near infrared that may be associated with quantum transitions of electrons between energy bands split by the exchange interaction between the $4f$ and the s and p electrons. This interaction depends on the orientation of the magnetic moment of the unfilled $4f$ shell and consequently may oscillate; if the period of the oscillations is different from that of the lattice, extra gaps form in the energy spectrum. This is the mechanism of exchange-split bands. At 80 K there was a clear extra peak due to this effect at 0.7 eV (1.77 μm) together with smaller peaks at 1.5 and 2.2 eV. The changes in n and k with temperature are comparatively small, but k tends to decrease with increase in temperature, whereas n increases.

Erskine *et al.* [46], using ellipsometry, have measured values of conductivity for gadolinium between 1.25 and 5.5 eV at temperatures of 80 and 295 K; however, σ on its own only allows the calculation of ϵ_2, so their results have not been quoted. But, they, too, present a graph of σ versus eV for gadolinium at room temperature comparing results from Schuler [14], Petrakian *et al.* [58, 59], Hodgson and Clayet [56], Knyazev and Noskov [52], and themselves. A strong peak was observed between 1.5 and 2.5 eV by all the authors, but a second peak at 5–6 eV was found only by Petrakian, Schuler, and themselves. There was again a wide spread in the values of conductivity from the various authors, the lowest being obtained by Knyazev and Noskov and the highest by Petrakian; this is probably due to the reactive nature of this element, which leads to surface contamination.

Daniels [62] claimed to observe plasmons (plasma resonance) at 16.2 eV for gadolinium, but Colliex *et al.* [33] gave a value of 14.2 eV, the difference being probably again due to surface contamination. Other values for plasmons are 9.9 eV (bulk) and 4.7 eV (surface) [35]. The theoretical value is 11.2 eV. Knyazev and Noskov [13] were able to deduce the relaxation and plasma frequencies from their double Drude-like equation and give the following values versus temperature.

T (K)	ω_t (eV)	ω_p (eV)
80	0.43	10.4
293	0.58	9.1
460	0.58	7.2

Ponosov and Bolotin [63], looking at Raman scattering spectra from single crystals of gadolinium, found evidence of a transverse optical phonon at 171.8 μm.

The values of n(○) and k(△) for gadolinium plotted in log–log form in Fig. 3 come from Henke [12], Haensel *et al.* [37], Gribovskii and Zimkina [17],

Knyazev and Noskov [52] (295 K), Krizek and Taylor [57], and Hodgson and Clayet [56]. The n–k plasmon crossover occurs at 10.0 eV, close to that given by Knyazev and Noskov. Figure 3 shows two sets of values for n at wavelengths greater than about 1 μm: those of Knyazev and Noskov [52], in which n increases steadily with wavelength, and those due to Weaver and Lynch at 4.2 K, where there is a peak at 2.0 μm.

TERBIUM V

Crystal structure h.c.p.; space group $P6_3/mmc$ D_{6h}^4; atomic number 65; atomic weight 158.9; density 8.23×10^3 kg/m^3; electron configuration $4f^2\ 6s^2$.

The L_{1-3} absorption edges occur at 8679, 8221, and 7484 eV, respectively, whereas M_{3-5} edges are found at 1583, 1275, and 1241 eV [15]. The "Physics Handbook" [16] gives the following edges in electron volts: 1970 (M_1), 1710 (M_2), 400, 322, 284, 152, 148 (N_{1-5}), 42, and 28 ($O_{1,2}$).

Henke-model results [12] show k peaking at 1240 eV (M_5) and 151 eV (N_4), then falling and rising again at 30 eV. In their overlap region (70 to 170 eV), the results for k from Gribovskii and Zimkina [17,18] show a general agreement with Henke-model values except at 150 eV, where their value is only half that of the Henke model at this peak in k. There is a sharp absorption peak at 151 eV, and the results from Gribovskii and Zimkana may be slightly off peak.

Knyazev and Noskov [64] have published results for terbium at 80, 293, and 450 K in the visible and infrared regions measured by polarimetry, the specimens being mechanically polished and chemically etched before being finally cleaned in an argon discharge. The polarization technique due to Beattie [65] was employed using one reflection in the visible and two for the infrared; an accuracy of between 3 and 5% was claimed.

Values of σ for terbium have also been published by Erskine *et al.* [46] between 1.25 and 5.5 eV and at two temperatures, 80 and 300 K, using an automatic ellipsometer. The Néel temperature of terbium is 230 K, whereas the Curie temperature is close by at 219.5 K. The results of these authors do not show any dramatic change in conductivity over the magnetic transformation points, but generally indicate a simple increase in σ with temperature. Miller *et al.* [49] report values between 1.8 and 3.1 eV using the technique of reflectance ratios; there were optical transitions at 1.90, 2.20, and 2.45 eV due to a number of interband transitions, but only these authors have reported such absorption detail. Krizek and Taylor [57] used ellipsometry to measure both ϵ_1 and σ for terbium films in a similar spectral region (0.35 and 2.5 eV) at temperatures of 20 and 300 K. Weaver and Lynch [25]

have reported values of n and k at 4.2 K for both states of polarization measured by ellipsometry. The agreement between their results and those of Krizek and Taylor is quite good; k increases with temperature over the whole energy range, whereas n decreases below 1.5 eV but increases above 1.5 eV. However, the values of n from Weaver and Lynch peak at 3 μm, whereas those of Knyazev and Noskov show a continuous increase with wavelength. The results of Knyazev *et al.* [55] on single crystals are also included.

Ponosov and Bolotin [63] have also studied terbium by Raman-scattering spectra and found an optical phonon at 166.9 μm.

Colliex *et al.* [33] give a value of the bulk plasmon as 13.3 eV. The following values of ω_t and ω_p were obtained by Knyazev and Noskov [54].

T (K)	ω_t (eV)	ω_p (eV)
80	0.31	11.2
293	0.53	11.5
460	0.86	12.6

$n(\circ)$ and $k(\triangle)$ versus λ for terbium are shown in log–log form in Fig. 4 using data from several references. The crossover of n and k (plasmon) occurs at 13.1 eV. Figure 4 gives two sets of points for n for wavelengths greater than 1.0 μm. The first, due to Knyazev and Noskov, shows n increasing with wavelength, but the second, from Weaver and Lynch [25] at 4.2 K, indicates n reaching a maximum at about 2 μm.

VI DYSPROSIUM

Crystal structure h.c.p.; space group $P6_3/mmc$ D_{6h}^4; atomic number 66; atomic weight 162.5; density 8.54×10^3 kg/m^3; electron configuration $4f^{10}\,6s^2$.

L-absorption edges occur at 9013 (L_1), 8553 (L_2), and 7762 eV (L_3); M_{3-5} peaks are located at 1642, 1333, and 1295 eV [15]. The following values are for other peaks: 2050 (M_1), 1845 (M_2), 419 (N_1), 339 (N_2), 297 (N_3), 158 (N_4), 155 (N_5), 66 (O_1), and 29 eV (O_2) [16].

Henke's model [12] shows absorption peaks at 1672 eV (M_3), 1295 eV (M_5) and 159 eV (N_4) and a shoulder at 443 eV (N_1). Results from Gribovskii and Zimkina [17, 18] for k below 170 eV are always lower than the Henke-model values by about 30% but show a peak at 160 eV.

A set of results has been published by Quemerais *et al.* [48] using multiangle reflectance measurements, which gives σ and ϵ_1 between 2 and 30 eV in graphical form; this is one of the few studies of the rare-earth elements to cover this spectral range. n and k have been calculated by the

method described earlier and show effects at the $5p^{3/2}$ and $5p^{1/2}$ thresholds. At 30 eV, their values of k are almost 30% lower than the ones from the Henke model, but are in line with those of Gribovskii and Zimkina.

Dysprosium has also been studied by Weaver and Lynch [25] in both the $\mathbf{E} \parallel \mathbf{c}$ and $\mathbf{E} \perp \mathbf{c}$ states of polarization over the energy range 0.1 to 5.0 eV and at 4.2 K as described earlier. As with some other rare-earth metals at this temperature, their values of n showed a peak in the infrared, whereas the results of other workers at higher temperatures show a steady increase in n with increasing wavelength. Krizek and Taylor [57], using ellipsometry, give values of n and k between 0.4 and 2.5 eV at 56 and 300 K; there is a small increase in both n and k as the temperature increases. There was evidence of slight structure in σ at 0.4 eV in the results at 56 and 97 K. Values of σ have also been reported by Erskine *et al.* [46] at 80 K between 1.25 and 5.5 eV, using their automatic-ellipsometer technique. These showed peaks at 22.1 eV ($O_{2,3}$) and 33.5 eV (O_1), but, as it is not possible to deduce n and k, their results have been omitted. Cukier *et al.* [47] found a plasmon at 14 eV and the O-peaks at 25 and 38 eV.

Knyazev *et al.* [40] have given values of n and k between 1 and 4 eV at 293 K and a further set of values occurs in their later paper [54]. Knyazev *et al.* [66] have reported work on single crystals of dysprosium at temperatures between 80 and 293 K both along the hexagonal axis (c) and in the basal plane (a). Dysprosium is paramagnetic at room temperature, becomes antiferromagnetic at 179 K, and finally ferromagnetic below 89 K. A peak developed in the calculated conductivity along the hexagon (c) axis as the temperature decreased for both the anti- and ferromagnetic states. Similar peaks occuring in the conductivity in the basal (a) plane were very much smaller. A further investigation into both states of polarization on single-crystal dysprosium has been carried out by Knyazev *et al.* [55].

Daniels [62] reported a bulk plasma resonance (plasmon) at 15.8 eV for Dy, whereas Colliex *et al.* [33] gave a figure of 14.0 eV, the presence of contamination probably accounting for the difference. Other values of these plasmons are 10.9 eV (bulk) and 5.2 eV (due to the metal–oxide interface) [35]. The following values of ω_t and ω_p were given by Knyazev and Noskov [13] from their double Drude model.

T (K)	ω_t (eV)	ω_p (eV)
80	0.20	10.8
293	0.39	11.8
460	0.64	13.6

Demers *et al.* [67] and also Ponosov and Bolotin [63] using Raman-scattering spectra have reported the presence of an optical phonon in dysprosium at 160.3 μm.

Figure 5 shows log–log plots of $n(\circ)$ and $k(\triangle)$ versus wavelength for dysprosium using data from Henke [12], Gribovskii and Zimkina [17, 18], Quemerais *et al.* [48], Weaver and Lynch [25], Knyazev and Noskov [40, 54], Knyazev *et al.* [55] and Krizek and Taylor [57]. The plasmon crossover between n and k is at 6.9 eV, considerably lower than that observed by Knyazev and Noskov [13].

VII ERBIUM

Crystal structure h.c.p.; space group $P6_3/mmc$ D_{6h}^4; atomic number 68; atomic weight 167.3; density 9.07×10^3 kg/m^3; electron configuration $4f^{12}\ 6s^2$.

L-type edges occur at 9725, 9243, and 8336 eV, corresponding to L_{1-3}, respectively, whereas M_{3-5} edges are at 1783, 1453, and 1409 eV [15]; $M_{1,2}$ are at 2211 and 2010 eV, and N_{1-5} are located at 453, 366, 320, 172, and 169 eV, respectively; $O_{1,2}$ occur at 64 and 33 eV [16].

The absorption peaks revealed by Henke's model [12] are at 1442 eV (M_4), 1401 eV (M_5) and 167 eV (N_5). The values of k derived from the Gribovskii and Zimkina data [17] between 170 and 70 eV are about 10% lower than those of the Henke model in the overlap region but show a sharp peak just above 170 eV.

The imaginary part of the dielectric constant, ϵ_2, can be calculated from values of the optical conductivity σ ($\sigma = \epsilon_2\ \omega/4\ \pi$). Weaver and Lynch [25] and also Krizek and Taylor [57], both using ellipsometry, report values of σ versus ω over the ranges 0.1–5.0 eV and 0.35–2.5 eV, respectively. Weaver and Lynch give values of n and k in two crystallographic directions at 4.2 K; for $\mathbf{E} \parallel \mathbf{c}$, n is larger than for $\mathbf{E} \perp \mathbf{c}$, whereas the opposite is the case for k. (The c-axis is at right angles to the hexagon.) In both orientations, n peaks at about 1.2 μm and then decreases with increasing wavelength. This is the only set of results for temperatures below the Curie point (20 K).

Values of n and k for bulk polycrystalline erbium have been reported by Knyazev and Noskov [68] over the range 0.06 to 4.4 eV and at temperatures between 56 and 293 K; these were determined by polarimetry. n increased with increasing temperature, while k decreased. Both n and k were monotonic between 0.06 and 0.27 eV at all temperatures, indicating that intraband transitions were dominant in this region. The electron relaxation frequency decreased with increasing temperature. Above 0.27 eV interband transitions took over, and there was a broad peak in conductivity centered about 2 eV. Below the Néel temperature (84 K), a new structure appeared in the conductivity at an energy of 0.28 eV, and this was ascribed to the transition to the antiferromagnetic state. In addition, Knyazev and Bolotin [69] measured n and k using ellipsometry on erbium single crystals; values for

both $\mathbf{E} \| \mathbf{c}$ and $\mathbf{E} \perp \mathbf{c}$ were obtained between 0.2 and 5.6 eV and at temperatures of 78 and 293 K, and the errors were estimated at between 2 and 5%. The conductivities in each state were calculated and, when plotted against energy, indicated quantum absorption mainly at about 0.7 eV in a band close to the Fermi surface. Erbium becomes antiferromagnetic at 85 K, and a new peak in the conductivity appeared at about 0.3 eV in both states of polarization for the values at 78 K; the value of this peak predicted from theory was 0.26 eV.

Demers *et al.* [67], using Raman-scattering techniques, discovered an optical phonon in erbium at about 160 μm.

Figure 6 shows log–log plots of $n(\circ)$ and $k(\triangle)$ versus λ for erbium using data from Henke [12], Gribovskii and Zimkina [17], Weaver and Lynch [25], Knyazev and Noskov [68], and Knyazev and Bolotin [69]. The crossover point gives the plasma frequency as 6.9 eV. At wavelengths greater than 1 μm two sets of points for n are plotted. That due to Knyazev and Noskov shows n steadily increasing, whereas that for Weaver and Lynch indicates a peak in n at about 1.5 μm, then a dip to 2.5 μm before n starts to rise again.

THULIUM VIII

Crystal structure h.c.p.; space group $P6_3/mmc$ D_{6h}^4; atomic number 69; atomic weight 168.9; density 9.325×10^3 kg/m^3; electron configuration $4f^{13}\ 6s^2$.

The main absorption edges are as follows: L_1 is at 10,097, L_2 at 9601, and L_3 at 8632 eV, whereas M_{3-5} are at 1861, 1515, and 1468 eV, respectively [15]. Other absorption edges from [16] are 2305 and 2088 ($M_{1,2}$), 470, 382, 333, 180, and 176 eV (N_{1-5}), and 51 and 30 eV ($O_{1,2}$).

The absorption peaks from Henke's model [12] are 1461 eV (M_5) and 183 eV. Gribovskii and Zimkina [17] give values of k between 70 and 170 eV showing a peak developing beyond 180 eV; the agreement with the Henke-model results is within 10%.

Weaver and Lynch [25] have given results for both $\mathbf{E} \| \mathbf{c}$ and $\mathbf{E} \perp \mathbf{c}$ between 0.1 and 5.0 eV at 4.2 K, which is below the Curie temperature of thulium (32 K). n and k are flat between 1 and 2 μm, but although k then resumes its steady increase with increasing wavelength, n decreases at greater wavelengths.

Knyazev and Noskov [70] have published results between 0.062 and 1.24 eV at 80, 293, and 450 K; as the temperature increased, k tended to increase, while n decreased. Knyazev and Bolotin [69] studied single crystals of thulium at 78 and 293 K also with $\mathbf{E} \| \mathbf{c}$ and $\mathbf{E} \perp \mathbf{c}$. Thulium remains paramagnetic down to 58 K, so no magnetic transformations were observed in this work.

Knyazev and Noskov [13] give the following values of ω_t:

T (K)	ω_t (eV)
80	2.93
293	1.00
450	0.69

Figure 7 shows log–log plots of $n(\circ)$ and $k(\triangle)$ versus λ for thulium using data from Henke [12], Gribovskii and Zimkina [17], Knyazev and Noskov [70], and Knyazev and Bolotin [69]; the crossover (plasma resonance) occurs at 6.5 eV, which is smaller than the value given by Knyazev and Noskov. Once again, there are two separate sets of points for n for wavelengths longer than 1 μm, those due to Knyazev and Bolotin and the others from Weaver and Lynch [25]. The latter show that n is flat between 1 and 2 μm and then continues to increase with increasing wavelength.

IX YTTERBIUM

Crystal structure f.c.c.; space group Fm3m O_h^5; atomic number 70; atomic weight 173.0; density 6.996×10^3 kg/m^3; electron configuration $4f^{14}6s^2$.

Ytterbium is the only rare-earth metal in this survey to have a cubic structure. Consequently, it does not exhibit anisotropic optical properties and, in fact, is considered to behave similarly to a transition metal.

The L-absorption edges are at 10479 eV (L_1), 9968 eV (L_2), and 8933 eV (L_3), whereas M_{3-5} occur at 1948, 1576, and 1528 eV [15]; M_1 is at 2397, M_2 at 2172 eV, and N_{1-5} at 487, 399, 346, 189, and 185 eV, whereas $O_{1,2}$ are 53 and 23 eV, respectively [16].

Henke's model [12] indicates absorption peaks at 1550 eV (M_5) and 1943 eV (M_3), as well as at 191 eV (N_4); there is also a shoulder at 393 eV (N_2). The studies of Gribovskii and Zimkina [17] overlap below 170 eV, and their values of k are in very good agreement (5%) with the those derived from Henke's model. No peak is indicated within their range of energies, but a shoulder occurs at 140 eV.

Studies of the optical constants of ytterbium (and europium) have been made by Endriz and Spicer [71] using reflectances over the range 0.5 to 11.5 eV and then employing Kramers–Kronig analysis to obtain ϵ_1, ϵ_2, σ, and α; an overall accuracy of only 20% was claimed for these results. These authors compared their results for these two rare-earth metals with those for the transition elements barium and strontium, which have similar crystal structures and electron configurations; the absorption graphs for these elements were very similar in shape, indicating that the absorption mechanisms were similar in all four elements.

Petrakian [72] measured the conductivity of Yb and also noted that this element behaves similarly to the alkali metal strontium in having broad absorption peaks near 3 and 6 eV. He also published a graph comparing the values of optical conductivity for ytterbium in the energy range 0–6 eV obtained by himself, Muller [73], and Hodgson and Cleyet [56]. These all show a strong peak between 1.5 and 2.0 eV whose height differs markedly between authors. For energies above 2.0 eV, the conductivity values of the three authors differ considerably; this spread is probably because of the differing surface conditions of the specimens.

Muller [73] also studied the same four elements and presented a graph of σ versus E between 0.5 and 5.5 eV. Although his results do not agree well with those of other workers, they have been included in the tables.

Idczak and Zukowska [74] used the ellipsometric technique devised by Idzak *et al.* [75] to measure n and k for thick ytterbium films (350 nm) in the infrared between 1 and 25 μm (0.05 to 0.62 eV); both n and k steadily increase with increasing wavelength in this region where the optical properties are dominated by the free electrons. In addition, Zukowska and Oleszkiewicz [76] have reported single values of n and k for ytterbium using a laser at 632.8 nm. ($n = 1.68$, $k = 3.22$.) They noted that both n and k decreased over a 24-hour period when the specimen was exposed to air, illustrating the effect of oxidation on the optical constants.

A plasmon was detected at 10.0 eV by Bakulin *et al.* [32] using electron energy loss.

Log–log plots of n (○) and k (△) versus λ are shown in Fig. 8, incorporating the results of Henke [12], Gribovskii and Zimkina [17], Endriz and Spicer [71], and Idzak and Zukowska [74]. The plasma frequency given by the crossover point is 11.5 eV, which agrees reasonably well with that just given.

REFERENCES

1. "Handbook of Chemistry and Physics," 1995/6, 76th Ed., pp. 4–115, CRC Press, Roca Raton, Florida, New York, London, and Tokyo.
2. Y.-S. Kuron, T. Suzuki, and T. Kasuya, Physical properties of actinides and rare earth compounds. *Jpn. J. App. Phys., Ser.* **8**, 104–116 (1993).
3. R. Atkinson, R. Gamble, P. F. Gu, and P. H. Lissberger, *Thin Solid Films* **162**, 89 (1988).
4. A. Memon, M. N. Khan, S. Al-Dallal, D. B. Tanner, and C. D. Porter, *Physica C* **185**, 1009 (1991).
5. 20th Rare Earths Research Conference, Monterey, California, Sept. 12–17, 1993.
6. M. Gasgnier, *Phys. Status Solidi A* **57**, 11 (1980).
7. Yu. V. Knyazev and M. M. Noskov, *Phys. Status Solidi B* **80**, 11 (1977).
8. D. W. Lynch, "The Rare Earths in Modern Science and Technology" (G. J. McCarthy and J. J. Rhyne, eds.), p. 461. Plenum, New York and London, 1978.
9. J. H. Weaver, C. Krafta, D. W. Lynch, and E. E. Koch, Physik Daten No. 18–2, Fachinformationszentrum, Karlsruhe, Germany, 1981.
10. "Landolt-Börnstein New Series, Volume III/15(b), Metals: Electronic Transport Phenomena" (K.-H. Kellwege and J. T. Olsen, eds.), Springer-Verlag, Heidelberg, 1985.
11. B. L. Henke, *Am. Inst. Phys., Conf. Proc.* **75**, 146 (1981).

12. B. L. Henke, P. Lee, T. J. Tanaka, R. Shimabukaro, and B. K. Fujikama, *At. Data Nucl. Data Tables* **27**, 1 (1982).
13. Yu. V. Knyazev and M. M. Noskov, *Phys. Met. Metall.* **32**, 1189 (1971).
14. C. C. Schuler, "Optical Properties and Electronic Structure of Metals and Alloys," p. 221. North-Holland, Publ., Amsterdam, 1966.
15. G. W. C. Kaye and T. H. Laby, "Tables of Physical and Chemical Constants," 16th Ed., pp. 384–385. Longmans, Harlow, U.K., 1995.
16. "Physics Handbook," pp. 72–76, Chartwell-Bratt, Bromley, U.K., 1980.
17. S. A. Gribovskii and T. M. Zimkina, *Opt. Spectrosc.* **35**, 104 (1973).
18. S. A. Gribovskii and T. M. Zimkina, *Sov. Phys. Solid State* **15**, 217 (1973).
19. V. A. Fomichev, T. M. Zimkina, S. A. Gribovskii, and I. I. Zhukova, *Sov. Phys. Solid State* **9**, 1163 (1967).
20. T. M. Zimkina, V. A. Fomichev, S. A. Gribovskii, and I. I. Zhukova, *Sov. Phys. Solid State* 9, 1128 (1967).
21. S. Muto, S.-Y. Pak, S. Imada, K. Yamaguchi, Y. Kagoshima, and T. Miyahara, *J. Phys. Soc. Jpn.* **63**, 1179 (1994).
22. P. Trebbia and C. Colliex, *Phys. Status Solidi B* **58**, 523 (1973).
23. C. Kunz, "Optical Properties of Solids—New Developments" (B. O. Seraphin, ed.), p. 473. North-Holland, Amsterdam, 1975.
24. F. Gerken, A. S. Flodstrom, J. Barth, L. I. Johannson, and C. Kunz, *Phys. Scr.* **32**, 43 (1985).
25. J. H. Weaver and D. W. Lynch, *Phys. Rev. Lett.* **34**, 1324 (1975).
26. L. Ward, "Optical Properties of Bulk Materials and Thin Films," 2nd Ed., p. 10. Institute of Physics Publ., Bristol, 1994.
27. J. H. Weaver, private communication, 1996.
28. C. Dzionk, W. Fiedler, M. V. Luche, and P. Zimmermann, *Phys. Rev. A* **41**, 3572 (1990).
29. J. P. Petrakian, *J. Opt. Soc. Am.* **62**, 401 (1972).
30. J. P. Petrakian, *Thin Solid Films* **38**, 83 (1976).
31. H. Wolter, *Z. Phys.* **105**, 269 (1937).
32. E. A. Bakulin, L. A. Balabanova, E. V. Sleppin, and V. V. Shcherbinina, *Sov. Phys. Solid State* **13**, 189 (1969).
33. C. Colliex, M. Gasgnier, and P. Trebbia, *J. Phys. (Paris)* **37**, 397 (1976).
34. E. V. Tsveiman, V. S. Red'kin, V. V. Zashkvara, and M. I. Kovsunskii, *Sov. Phys. Solid State* **58**, 156 (1975).
35. V. V. Zashkvara, E. V. Tsveiman, M. I. Kovsunskii, and V. S. Red'kin, *Sov. Phys. Solid State* **14**, 1564 (1972).
36. F. P. Netzer, G. Strasser, G. Rosina, and J. A. D. Matthew, *Surf. Sci.* **152/153**, 757 (1985).
37. R. Haensel, P. Rabe, and B. Sonntag, *Solid State Commun.* **8**, 1845 (1970).
38. S. Suzuki, T. Ishu, and T. Sagawa, *J. Phys. Soc. Jpn.* **38**, 156 (1975).
39. M. M. Kirillova, Yu. V. Knyazev, and Yu. I. Kuzmin, *Thin Solid Films* **234**, 527 (1993).
40. Yu. V. Knyazev, M. M. Kirillova, Yu. I. Kuzmin, and E. Z. Rivman, *Sov. J. Low Temp. Phys.* **17**, 1143 (1991).
41. J. P. Petrakian, *Thin Solid Films* **13**, 269 (1972).
42. J. T. Rhee, X. Wang, B. N. Harmon, and D. W. Lynch, *Phys. Rev. B* **51**, 17390 (1995).
43. Yu. V. Knyazev and M. M. Noskov, *Phys. Met. Metall.* **30**, 230 (1970).
44. Yu. V. Knyazev and M. M. Noskov, *Phys. Met. Metall.* **33**, 87 (1972).
45. J. L. Erskine and C. F. Flynn, *Phys. Rev. B* **14**, 2197 (1976).
46. J. L. Erskine, G. A. Blake, and C. W. Flaten, *J. Opt. Soc. Am.* **64**, 1322 (1974).
47. M. Cukier, B. Gauthe, and C. Wehenkehl, *J. Phys. (Paris)* **41**, 603 (1980).
48. A. Quemerais, B. Loisel, G. Jezequel, J. Thomas, and J. C. Lemonnier, *J. Phys. F* **11**, 293 (1981).
49. R. F. Miller, L. S. Julian, and A. J. Taylor, *J. Phys. F* **4**, 2338 (1974).
50. R. F. Miller, M. Syms, and L. S. Julien, *J. Phys. D* **12**, 1985 (1979).

51. H. P. Myers, *J. Phys. F* **6**, 141 (1976).
52. Yu. V. Knyazev and M. M. Noskov, *Phys. Met. Metall.* **32**, 71 (1971).
53. G. A. Bolotin, M. M. Noskov, and I. I. Sasovshaya, *Phys. Met. Metall.* **35**, 24 (1973).
54. Yu. V. Knyazev and M. M. Noskov, *Phys. Met. Metall.* **35**, 26 (1973).
55. Yu. V. Knyazev, M. M. Kirillova, and S. A. Nikitin, *Phys. Met. Metall.* **12**, 33 (1990).
56. J. N. Hodgson and B. Clayet, *J. Phys. C* **2**, 97 (1969).
57. J. Krizek and K. W. R. Taylor, *J. Phys. F* **5**, 774 (1975).
58. J. P. Petrakian, N. A. Mokhtar, and R. Fraisse, *Solid State Commun.* **24**, 377 (1977).
59. J. P. Petrakian, N. A. Mokhtar, and R. Fraisse, *J. Phys. F* **7**, 2431 (1977).
60. M. P. Querry, *J. Opt. Soc. Am.* **59**, 876 (1969).
61. Yu. V. Knyazev and G. A. Bolotin, *Phys. Met. Metall.* **58**, 70 (1984).
62. J. Daniels, *Opt. Commun.* **3**, 13 (1977).
63. Yu. S. Ponosov and G. A. Bolotin, *Sov. Phys. Solid State* **35**, 1437 (1993).
64. Yu. V. Knyazev and M. M. Noskov, *Opt. Spectrosc.* **38**, 672 (1975).
65. J. R. Beattie, *Philos. Mag.* **46**, 223 (1955).
66. Yu. V. Knyazev, T. A. Motveyena, and G. A. Bolotin, *Phys. Met. Metall.* **54**, 74 (1982).
67. R. I. Deners, S. Kong, M. V. Klein, R. Du, and C. P. Flynn, *Phys. Rev. B* **38**, 11523 (1988).
68. Yu. V. Knyazev and M. M. Noskov, *Sov. J. Low Temp. Phys.* **4**, 376 (1978).
69. Yu. V. Knyazev and G. A. Bolotin, *Phys. Met. Metall.* **61**, 57 (1986).
70. Yu. V. Knyazev and M. M. Noskov, *Opt. Spectrosc.* **43**, 424 (1977).
71. J. G. Endriz and W. E. Spicer, *Phys. Rev. B* **2**, 1466 (1970).
72. J. P. Petrakian, *Thin Solid Films* **20**, 297 (1974).
73. W. E. Muller, *Phys. Lett.* **17**, 82 (1965).
74. E. Idzak and K. Zukowska, *Thin Solid Films* **75**, 139 (1981).
75. E. Idzak, E. Oleszkiewicz, and K. Zukowska, *J. Phys. E* **22**, 410 (1989).
76. K. Zukowska and E. Oleszkiewicz, *Thin Solid Films* **224**, 217 (1993).

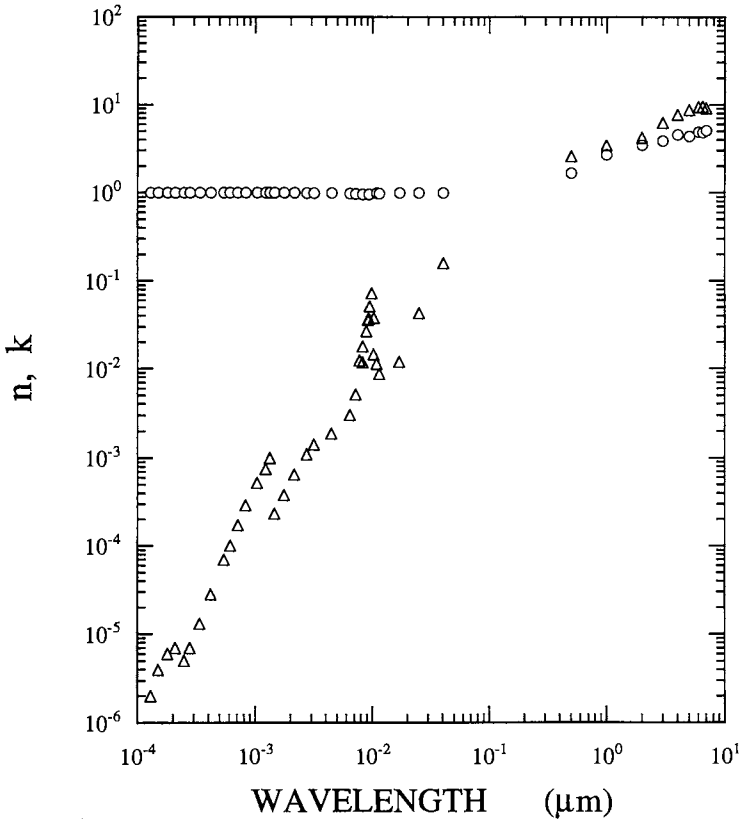

Fig. 1. Log–log plots of n (○) and k (△) versus wavelength in micrometers for cerium (unpolarized radiation).

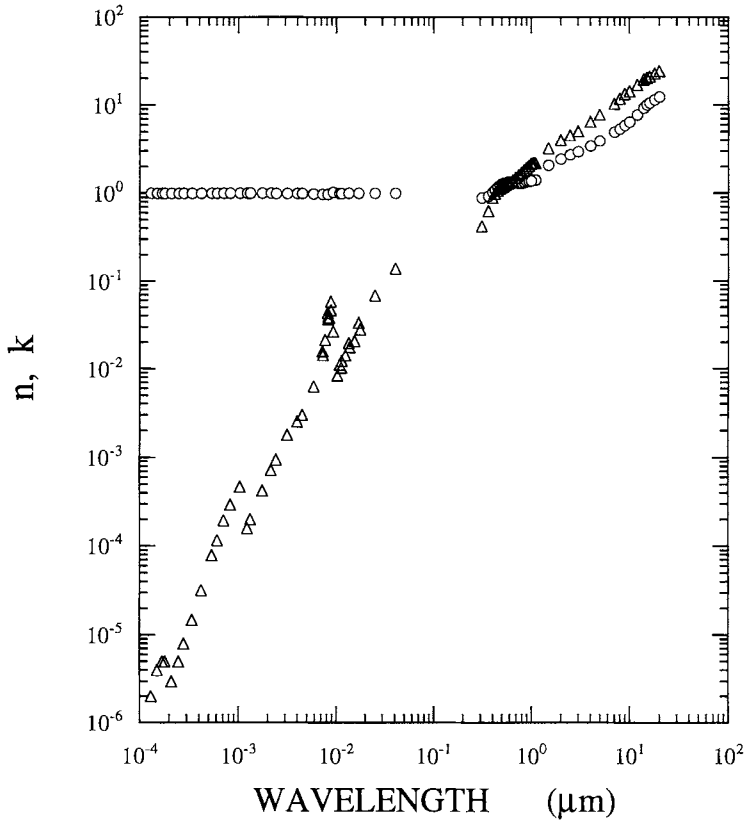

Fig. 2. Log–log plots of n (○) and k (△) versus wavelength in micrometers for samarium (unpolarized radiation).

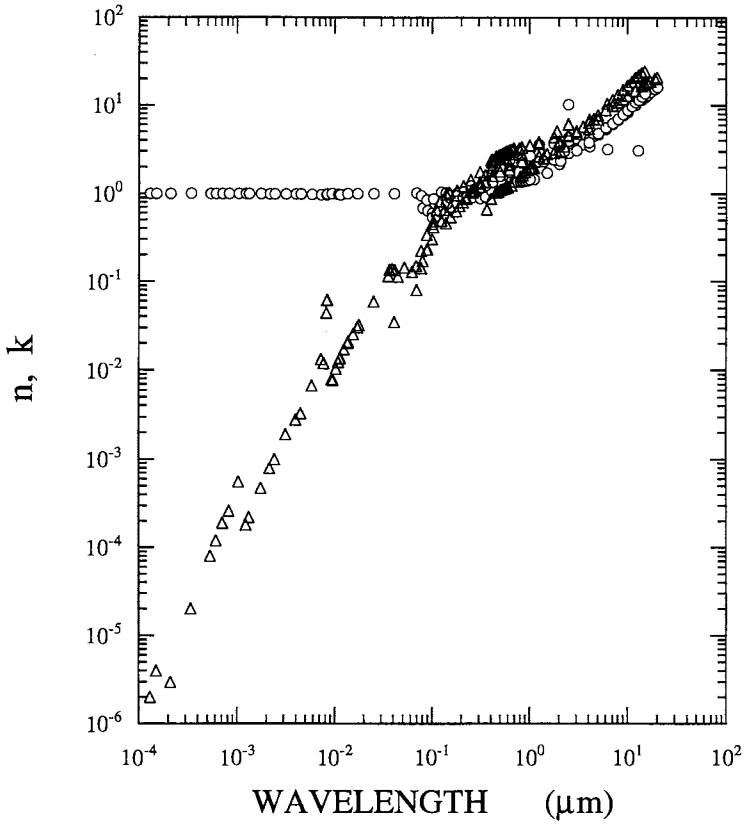

Fig. 3. Log–log plots of n (○) and k (△) versus wavelength in micrometers for gadolinium (unpolarized radiation or polarized $\mathbf{E} \parallel \mathbf{c}$).

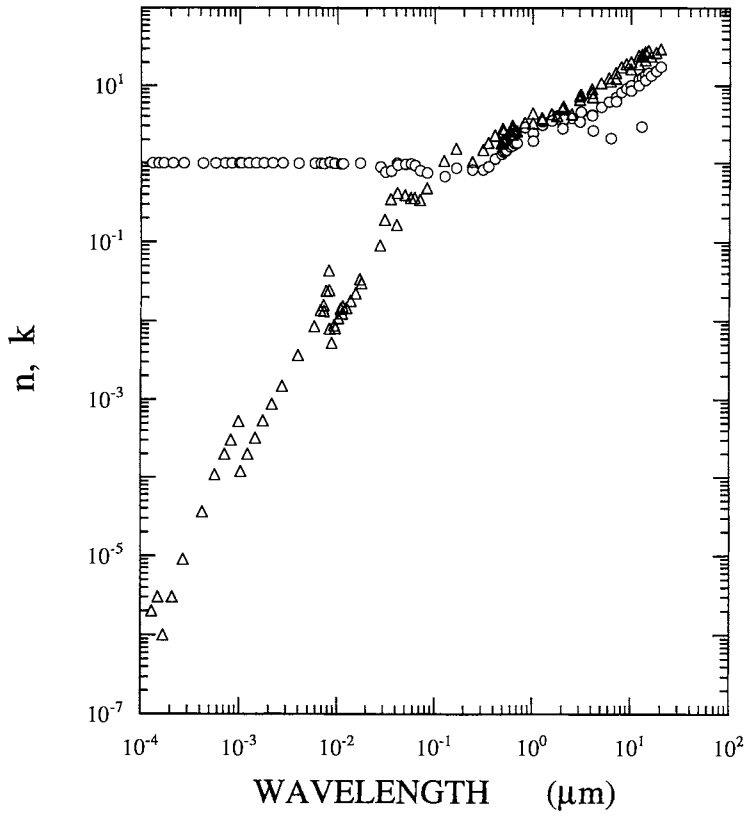

Fig. 4. Log–log plots of n (○) and k (△) versus wavelength in micrometers for terbium (unpolarized radiation or polarized $\mathbf{E} \parallel \mathbf{c}$).

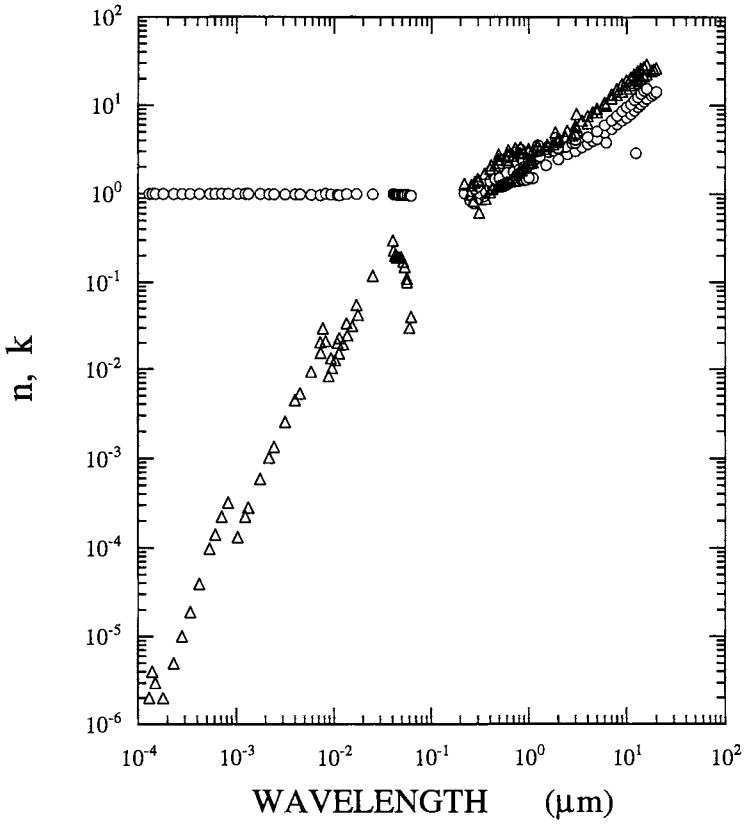

Fig. 5. Log–log plots of n (○) and k (△) versus wavelength in micrometers for dysprosium (unpolarized radiation or polarized $\mathbf{E} \parallel \mathbf{c}$).

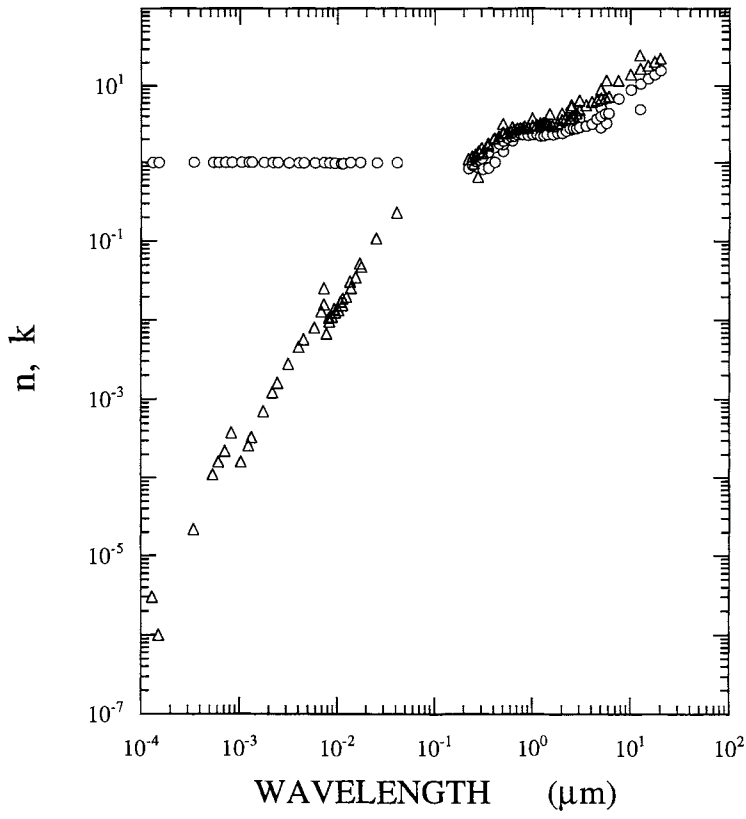

Fig. 6. Log–log plots of n (○) and k (△) versus wavelength in micrometers for erbium (unpolarized radiation or polarized $\mathbf{E} \parallel \mathbf{c}$).

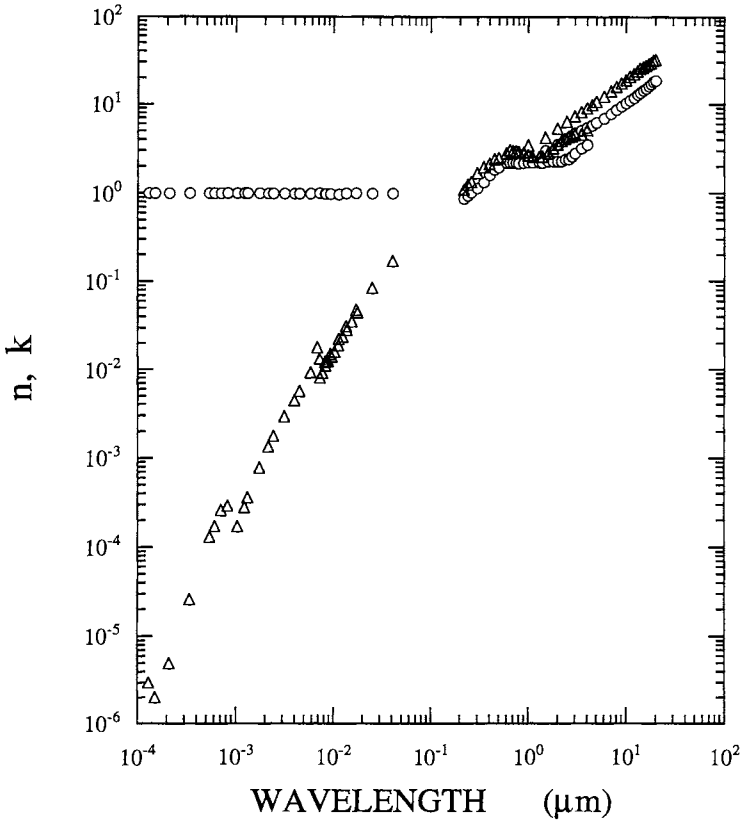

Fig. 7. Log–log plots of n (○) and k (△) versus wavelength in micrometers for thulium (unpolarized radiation or polarized $\mathbf{E} \parallel \mathbf{c}$).

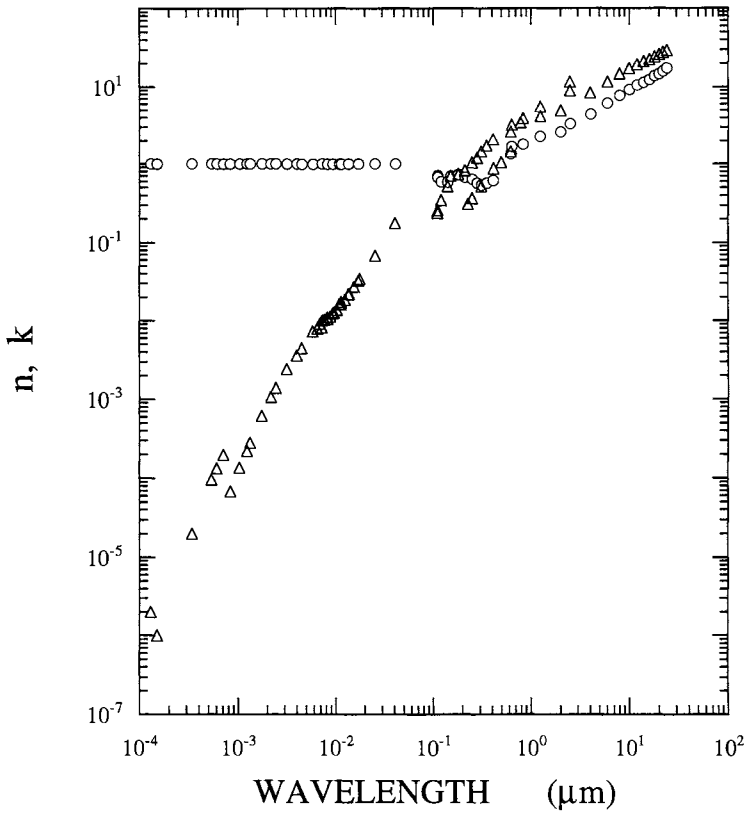

Fig. 8. Log–log plots of n (○) and k (△) versus wavelength in micrometers for ytterbium (unpolarized radiation).

TABLE I

Values of n and k for Cerium from Various References[a]

eV	cm^{-1}	μm	n	k	
9886.40	79738680	0.00013	1.000	0.000002	[12]
8047.80	64909460	0.00015	1.000	0.000004	
6930.30	55896272	0.00018	1.000	0.000006	
5898.80	47576720	0.00021	1.000	0.000007	
4952.20	39941932	0.00025	1.000	0.000005	
4466.30	36022900	0.00028	1.000	0.000007	
3691.70	29775376	0.00034	1.000	0.000013	
2984.30	24069848	0.00042	1.000	0.000028	
2293.20	18495786	0.00054	1.000	0.000069	
2042.40	16472960	0.00061	0.999	0.00010	
1740.00	14033955	0.00071	0.999	0.00017	
1486.70	11990966	0.00083	0.999	0.00029	
1188.00	9581804	0.00104	0.999	0.00052	
1011.70	8159858	0.00123	0.999	0.00075	
929.70	7498488	0.00133	0.999	0.00100	
851.50	6867766	0.00146	0.999	0.00023	
705.00	5686172	0.00176	0.999	0.00038	
572.80	4619914	0.00216	0.998	0.00065	
452.20	3647215	0.00274	0.997	0.00109	
392.40	3164899	0.00316	0.996	0.00141	
277.00	2234141	0.00448	0.993	0.00188	
192.60	1553414	0.00644	0.983	0.00302	
171.70	1384845	0.00722	0.977	0.00513	
151.10	1218696	0.00821	0.967	0.0118	
132.80	1071097	0.00934	0.961	0.0371	
114.00	919466	0.01088	0.991	0.0113	
108.50	875106	0.01143	0.983	0.00875	
72.40	583942	0.01713	1.000	0.0121	
49.30	397629	0.02515	1.000	0.0426	
30.50	245998	0.04065	1.000	0.1603	
160.0	1290478	0.00775		0.0123	[37]
150.0	1209824	0.00827		0.0179	
140.0	1129169	0.00886		0.0268	
135.0	1088847	0.00918		0.0358	
130.0	1048514	0.00954		0.0516	
125.0	1008186	0.00992		0.0734	
120.0	967859	0.01033		0.0378	
115.0	927531	0.01028		0.0146	
2.480	20000	0.50	1.54	2.66	[39]
1.240	10000	1.00	2.64	3.14	78 K
0.620	5000	2.00	3.90	4.50	
0.413	3333	3.00	4.13	5.52	
0.310	2500	4.00	4.09	6.73	
0.248	2000	5.00	3.12	7.99	

[a] The references from which the values were taken are given in brackets.

TABLE I (*Continued*)

Cerium

eV	cm^{-1}	μm	n	k	
0.207	1667	6.00	3.53	8.36	
0.191	1539	6.50	3.29	8.51	
0.177	1429	7.00	3.53	8.36	
2.400	20000	0.50	1.67	2.57	[39]
1.240	10000	1.00	2.68	3.44	295 K
0.620	5000	2.00	3.49	4.20	
0.413	3333	3.00	3.90	6.23	
0.310	2500	4.00	4.59	7.71	
0.248	2000	5.00	4.41	8.74	
0.207	1667	6.00	4.93	9.39	
0.191	1539	6.50	4.85	9.48	
0.177	1429	7.00	5.11	9.20	

TABLE II

Values of *n* and *k* for Samarium for Various References[a]

eV	cm^{-1}	μm	n	k	
9886.40	79738680	0.00013	1.000	0.000002	[12]
8047.80	64909460	0.00015	1.000	0.000004	
7478.20	60315356	0.00017	1.000	0.000005	
6930.30	55896272	0.00018	1.000	0.000005	
5898.80	47576720	0.00021	1.000	0.000003	
4952.20	39941932	0.00025	1.000	0.000005	
4466.30	36022900	0.00028	1.000	0.000008	
3691.70	29775376	0.00034	1.000	0.000015	
2984.30	24069848	0.00042	1.000	0.000032	
2293.20	18495786	0.00054	1.000	0.000078	
2042.40	16472960	0.00061	0.999	0.000115	
1740.00	14033955	0.00071	0.999	0.000196	
1486.70	11990966	0.00083	0.999	0.000295	
1188.00	9581804	0.00104	0.999	0.000465	
1011.70	8159858	0.00123	0.999	0.000158	
929.70	7498488	0.00133	0.999	0.000200	
705.00	5686172	0.00176	0.999	0.000426	
572.80	4619914	0.00216	0.998	0.000721	
511.30	4123886	0.00242	0.997	0.000950	
392.40	3164899	0.00316	0.996	0.00178	
311.70	2514014	0.00398	0.994	0.00251	
277.00	2234141	0.00448	0.993	0.00299	
212.20	1711497	0.00584	0.986	0.00633	
171.70	1384845	0.00722	0.975	0.0159	

(continued)

[a] The references from which the values were taken are given in brackets.

TABLE II *(Continued)*

Samarium

eV	cm^{-1}	μm	n	k	
151.10	1218696	0.00821	0.972	0.0433	
132.80	1071097	0.00934	1.030	0.0268	
114.00	919466	0.01088	0.997	0.0111	
108.50	875106	0.01143	0.992	0.0124	
91.50	737992	0.01355	1.000	0.0197	
72.40	583942	0.01713	1.000	0.0335	
49.30	397629	0.02515	1.000	0.0683	
30.50	245998	0.04065	1.000	0.1395	
170.0	1371133	0.00729		0.0144	[37]
160.0	1290478	0.00775		0.0215	
150.0	1209824	0.00827		0.0362	
148.0	1193693	0.00838		0.0380	
146.0	1177562	0.00849		0.0376	
140.0	1129169	0.00886		0.0465	
150.00	1209833	0.00826		0.0387	[17]
140.00	1129169	0.00886		0.0581	
120.00	967859	0.01033		0.0084	
110.00	887204	0.01127		0.0103	
100.00	806549	0.01240		0.0143	
90.00	725894	0.01377		0.0176	
80.00	645239	0.01550		0.0207	
70.00	564584	0.01771		0.0280	
3.966	31989.8	0.3126	0.89	0.42	[43]
3.397	27397.4	0.365	0.93	0.63	293 K
3.099	25000.0	0.400	1.02	0.89	
2.917	23529.4	0.425	1.09	0.98	
2.755	22222.2	0.450	1.17	1.07	
2.610	21052.6	0.475	1.22	1.12	
2.480	20000.0	0.500	1.27	1.16	
2.362	19047.6	0.525	1.29	1.19	
2.254	18181.8	0.550	1.31	1.24	
2.156	17391.3	0.575	1.33	1.28	
2.066	16666.7	0.600	1.33	1.32	
1.907	15384.7	0.650	1.31	1.39	
1.771	14285.7	0.700	1.31	1.49	
1.653	13333.3	0.750	1.30	1.58	
1.550	12500.0	0.800	1.30	1.70	
1.459	11764.7	0.850	1.32	1.81	
1.378	11111.1	0.900	1.35	1.91	
1.305	10526.3	0.950	1.37	2.02	
1.240	10000.0	1.000	1.38	2.12	
1.181	9523.8	1.050	1.40	2.16	
1.127	9090.9	1.100	1.41	2.16	
1.240	10000.0	1.00	1.39	2.16	[44]
0.827	6666.7	1.50	2.02	3.28	80 K
0.620	5000.0	2.00	2.37	4.13	

TABLE II *(Continued)*

Samarium

eV	cm^{-1}	μm	n	k	
0.496	4000.0	2.50	2.63	4.62	
0.413	3333.3	3.00	2.85	5.12	
0.354	2857.1	3.50	3.14	5.89	
0.310	2500.0	4.00	3.35	6.68	
0.248	2000.0	5.00	3.61	8.15	
0.207	1666.7	6.00	4.03	9.78	
0.177	1428.6	7.00	4.24	11.27	
0.155	1250.0	8.00	4.59	12.75	
0.138	1111.1	9.00	4.81	14.35	
0.124	1000.0	10.00	5.12	15.51	
0.103	833.3	12.00	5.88	18.52	
0.089	714.3	14.00	6.54	21.65	
0.083	666.7	15.00	7.03	22.86	
0.078	625.0	16.00	7.35	24.31	
0.073	588.2	17.00	7.82	25.38	
0.069	555.5	18.00	8.26	26.54	
0.065	526.3	19.00	8.53	27.40	
0.062	500.0	20.00	9.02	28.20	
1.240	10000.0	1.00	1.38	2.12	[44]
0.827	6666.7	1.50	2.07	3.24	293 K
0.620	5000.0	2.00	2.44	4.02	
0.496	4000.0	2.50	2.71	4.53	
0.413	3333.3	3.00	2.96	5.06	
0.310	2500.0	4.00	3.46	6.46	
0.248	2000.0	5.00	3.93	7.81	
0.177	1428.6	7.00	4.97	10.31	
0.155	1250.0	8.00	5.38	11.80	
0.138	1111.1	9.00	5.89	13.26	
0.124	1000.0	10.00	6.51	14.28	
0.103	833.3	12.00	7.76	16.79	
0.089	714.3	14.00	9.32	19.33	
0.083	666.7	15.00	10.08	20.18	
0.078	625.0	16.00	10.61	20.82	
0.069	555.5	18.00	11.55	22.62	
0.062	500.0	20.00	12.43	23.97	
1.240	10000.0	1.00	1.38	2.10	[44]
0.827	6666.7	1.50	2.12	3.18	460 K
0.354	2857.1	3.50	3.34	5.66	
0.248	2000.0	5.00	4.26	7.56	
0.177	1428.6	7.00	5.25	9.92	
0.138	1111.1	9.00	6.37	12.51	
0.103	833.3	12.00	8.38	15.72	
0.083	666.7	15.00	10.79	18.75	
0.073	588.2	17.00	12.26	19.91	
0.065	526.3	19.00	13.51	21.32	
0.062	500.0	20.00	13.98	21.94	

TABLE III

Values of n and k for Gadolinium for Various References[a]

eV	cm^{-1}	μm	n	k	
9886.40	79738680	0.00013	1.000	0.000002	[12]
8047.80	64909460	0.00015	1.000	0.000004	
5898.80	47576720	0.00021	1.000	0.000003	
3691.70	29775376	0.00034	1.000	0.00002	
2293.20	18495786	0.00054	1.000	0.00008	
2042.40	16472960	0.00061	0.999	0.00012	
1740.00	14033955	0.00071	0.999	0.00019	
1486.70	11990966	0.00083	0.999	0.00026	
1188.00	9581804	0.00104	1.000	0.00056	
1011.70	8159858	0.00123	0.999	0.00018	
929.70	7498488	0.00133	0.999	0.00022	
705.00	5686172	0.00176	0.998	0.00047	
572.80	4619914	0.00216	0.997	0.00079	
511.30	4123886	0.00242	0.997	0.0010	
392.40	3164899	0.00316	0.996	0.0019	
311.70	2514014	0.00398	0.994	0.0028	
277.00	2234141	0.00448	0.992	0.0033	
212.20	1711497	0.00584	0.986	0.0067	
171.70	1384845	0.00722	0.976	0.0132	
151.10	1218696	0.00821	0.974	0.0439	
148.70	1199339	0.00834	0.995	0.0622	
132.80	1071097	0.00934	0.999	0.0079	
114.00	919466	0.01088	0.980	0.0123	
108.50	875106	0.01143	0.977	0.0138	
91.50	737993	0.01355	1.000	0.0202	
72.40	583942	0.01713	1.000	0.0304	
49.30	397629	0.02515	1.000	0.0589	
30.50	245997	0.04065	1.000	0.0348	
160.00	1290635	0.00775		0.0120	[17]
150.00	1209970	0.00826		0.0613	
130.00	1048641	0.00954		0.0078	
120.00	967976	0.01033		0.0104	
110.00	887311	0.01127		0.0135	
100.00	806647	0.01240		0.0171	
90.00	725982	0.01377		0.0208	
80.00	645317	0.01550		0.0253	
70.00	564653	0.01771		0.0323	
35.00	282292	0.0354		0.115	[45]
34.00	274227	0.0365		0.135	
32.00	258096	0.0388		0.138	
30.00	241965	0.0413		0.133	
28.00	225834	0.0443		0.114	
24.00	193572	0.0517		0.144	
20.00	161310	0.0620		0.129	

[a] The references from which the values were taken are given in brackets.

TABLE III *(Continued)*

Gadolinium

eV	cm^{-1}	μm	n	k	
18.00	145179	0.0689		0.150	
16.00	129048	0.0775		0.223	
14.00	112917	0.0886		0.337	
12.00	96786	0.1033		0.417	
9.25	74606	0.1340		0.653	
8.00	64524	0.1550		0.719	
6.50	52426	0.1907		0.724	
4.00	32262	0.3100		1.308	
2.00	16131	0.6199		2.128	
15.00	120982	0.08	0.69	0.17	[48]
14.00	112917	0.09	0.64	0.23	
13.00	104851	0.10	0.60	0.30	
12.00	96786	0.10	0.54	0.45	
11.00	88720	0.11	0.56	0.66	
10.00	80655	0.12	0.63	0.81	
9.00	72589	0.14	0.76	0.98	
8.00	64524	0.15	0.92	1.04	
7.00	56458	0.18	1.01	1.09	
6.00	48393	0.21	1.06	1.21	
5.00	40328	0.25	1.12	1.43	
4.00	32262	0.31	1.20	1.75	
3.00	24197	0.41	1.64	2.27	
2.00	16131	0.62	2.35	2.81	
3.10	25003	0.400	1.41	2.39	[49]
3.00	24197	0.413	1.43	2.44	
2.90	23390	0.428	1.45	2.41	
2.80	22583	0.443	1.48	2.46	
2.75	22180	0.451	1.58	2.64	
2.70	21777	0.459	1.59	2.62	
2.60	20970	0.477	1.60	2.66	
2.50	20164	0.496	1.70	2.74	
2.40	19357	0.517	1.73	2.77	
2.30	18551	0.539	1.79	2.82	
2.25	18147	0.551	1.88	2.89	
2.20	17744	0.564	1.91	2.93	
2.15	17308	0.577	1.95	3.00	
2.10	16375	0.590	1.96	2.98	
2.00	16131	0.620	2.10	3.10	
1.90	15324	0.653	2.19	3.14	
1.85	14921	0.670	2.20	3.14	
1.80	14158	0.689	2.34	3.28	
3.397	27397	0.365	1.05	0.66	[52]

(continued)

TABLE III *(Continued)*

Gadolinium

eV	cm^{-1}	μm	n	k	
3.099	25000	0.400	1.12	0.88	293 K
2.755	22222	0.450	1.27	1.04	
2.610	21053	0.475	1.34	1.06	
2.480	20000	0.500	1.37	1.10	
2.362	19048	0.525	1.39	1.12	
2.254	18182	0.550	1.41	1.14	
2.156	17391	0.575	1.42	1.16	
2.066	16667	0.600	1.41	1.19	
1.907	15385	0.650	1.40	1.24	
1.771	14286	0.700	1.36	1.38	
1.550	12500	0.800	1.38	1.55	
1.459	11765	0.850	1.39	1.63	
1.378	11111	0.900	1.41	1.75	
1.305	10526	0.950	1.42	1.86	
1.240	10000	1.000	1.47	1.96	
1.181	9524	1.050	1.49	2.00	
1.127	9091	1.100	1.46	1.96	
1.240	10000	1.00	1.41	2.00	[54]
0.827	6667	1.50	1.70	3.20	80 K
0.620	5000	2.00	2.13	4.01	
0.413	3333	3.00	2.88	5.14	
0.354	2857	3.50	3.36	5.91	
0.310	2500	4.00	3.60	6.92	
0.276	2222	4.50	3.93	7.56	
0.248	2000	5.00	4.18	8.20	
0.207	1667	6.00	4.75	9.38	
0.177	1429	7.00	5.33	10.60	
0.155	1250	8.00	6.03	11.74	
0.124	1000	10.00	7.34	13.96	
0.103	833.3	12.00	8.72	16.25	
0.095	769.2	13.00	9.48	17.19	
0.089	714.3	14.00	10.28	18.07	
0.077	625.0	16.00	11.80	19.97	
0.073	588.2	17.00	12.40	20.71	
0.065	526.3	19.00	13.60	22.12	
0.062	500.0	20.00	14.18	23.24	
1.240	10000	1.00	1.47	1.96	[54]
0.827	6667	1.50	1.73	2.80	293 K
0.620	5000	2.00	2.18	3.89	
0.496	4000	2.50	2.91	4.48	
0.413	3333	3.00	3.26	5.05	
0.354	2857	3.50	3.61	5.71	
0.310	2500	4.00	4.07	6.34	
0.276	2222	4.50	4.52	7.03	
0.248	2000	5.00	4.69	7.72	

TABLE III *(Continued)*

Gadolinium

eV	cm^{-1}	μm	n	k	
0.207	1667	6.00	5.36	8.90	
0.177	1429	7.00	6.14	9.88	
0.155	1250	8.00	6.87	10.75	
0.138	1111	9.00	7.65	11.80	
0.124	1000	10.00	8.40	12.91	
0.103	833.3	12.00	10.12	14.82	
0.089	714.3	14.00	11.71	16.47	
0.083	666.7	15.00	12.45	17.27	
0.077	625.0	16.00	13.20	18.12	
0.073	588.2	17.00	14.09	18.85	
0.065	526.3	19.00	15.38	20.25	
0.062	500.0	20.00	16.20	20.89	
1.240	10000	1.00	1.51	1.95	[54]
0.827	6667	1.50	1.80	2.77	460 K
0.620	5000	2.00	2.30	3.82	
0.413	3333	3.00	3.56	5.02	
0.310	2500	4.00	4.28	6.25	
0.248	2000	5.00	5.06	7.48	
0.207	1667	6.00	5.72	8.46	
0.177	1429	7.00	6.59	9.58	
0.155	1250	8.00	7.47	10.32	
0.138	1111	9.00	8.35	11.40	
0.124	1000	10.00	9.21	12.32	
0.113	909.1	11.00	10.12	13.30	
0.095	769.2	13.00	11.75	15.10	
0.089	714.3	14.00	12.62	15.86	
0.083	666.7	15.00	13.41	16.65	
0.073	588.2	17.00	14.89	18.15	
0.069	555.6	18.00	15.60	18.84	
0.062	500.0	20.00	16.96	20.10	
2.50	20165	0.496	1.96	2.57	[57]
2.00	16132	0.620	2.41	2.93	56 K
1.50	12099	0.827	2.95	3.27	
1.00	8066	1.240	3.52	3.89	
0.50	4033	2.480	4.96	5.44	
2.50	20165	0.496	1.96	2.57	[57]
2.00	16132	0.620	2.44	2.91	300 K
1.50	12099	0.827	3.05	3.25	
1.00	8066	1.240	3.59	3.76	
0.50	4033	2.480	4.27	5.98	
2.50	20165	0.496	2.02	2.62	[56]
2.00	16132	0.620	2.48	2.94	105 K
1.80	14519	0.689	2.71	3.04	

(continued)

TABLE III *(Continued)*

Gadolinium

eV	cm^{-1}	μm	n	k	
1.50	12099	0.827	2.99	3.18	
1.20	9679	1.033	3.23	3.64	
1.00	8066	1.240	3.46	3.93	
0.70	5646	1.771	4.30	4.85	
0.50	4033	2.480	4.86	5.35	
2.50	20165	0.496	1.97	2.56	[56]
2.00	16132	0.620	2.42	2.96	293 K
1.60	12905	0.775	2.89	3.25	
1.50	12099	0.827	3.00	3.33	
1.00	8066	1.240	3.57	3.83	
0.65	5243	1.907	3.87	5.06	
0.50	4033	2.488	4.36	6.10	
5.0	40329	0.248	1.155	1.226	[58, 59]
4.5	36296	0.265	1.167	1.345	50 K
4.0	32263	0.310	1.171	1.543	
3.5	28230	0.354	1.238	1.833	
3.0	24198	0.413	1.381	2.119	
2.5	20165	0.496	1.631	2.357	
2.0	16132	0.620	2.119	2.917	
1.85	14922	0.670	2.310	2.845	
1.4	11292	0.886	2.417	2.719	
1.0	8066	1.240	2.786	3.071	
0.9	7259	1.378	2.81	3.11	
0.8	6452	1.550	3.07	3.39	
0.7	5646	1.771	3.84	3.98	
0.6	4839	2.066	3.22	3.55	
0.55	4439	2.253	4.17	4.28	
0.5	4033	2.480	7.03	5.07	
1.5	12099	0.827	2.21	2.49	[58, 59]
1.0	8066	1.240	2.61	2.80	100 K
0.9	7259	1.378	2.63	2.86	
0.8	6452	1.550	2.68	2.94	
0.7	5646	1.771	2.92	3.20	
0.65	5243	1.907	2.86	3.14	
0.6	4839	2.066	2.88	3.20	
0.55	4439	2.254	3.04	3.44	
0.5	4033	2.480	3.96	4.31	
5.0	40329	0.248	1.226	1.059	[58, 59]
4.5	36296	0.276	1.143	1.095	300 K
4.0	32263	0.310	1.171	1.190	
3.5	28230	0.354	1.250	1.371	
3.0	24198	0.413	1.357	1.583	
2.5	20165	0.496	1.583	1.786	
2.0	16132	0.620	1.774	1.881	

TABLE III *(Continued)*

Gadolinium

eV	cm^{-1}	μm	n	k	n	k	
1.5	12099	0.827	2.238	2.345			
1.0	8066	1.240	2.310	2.667			
0.9	7259	1.378	2.34	2.54			
0.7	5646	1.771	2.44	2.88			
0.6	4839	2.066	2.36	2.99			
0.55	4439	2.253	3.04	3.44			
0.5	4033	2.480	10.18	6.02			
			E ‖ c		**E ⊥ c**		
18.0	145284	0.069	1.02	0.08	[27]		
16.0	129142	0.077	0.95	0.14	4.2 K		
14.0	112999	0.088	0.85	0.23			
12.0	96856	0.103	0.88	0.48			
10.0	80714	0.124	1.05	0.49			
9.0	72642	0.138	1.03	0.46			
8.0	64571	0.155	0.97	0.54			
7.0	56500	0.177	0.95	0.63			
6.0	48428	0.206	0.92	0.79			
5.5	44392	0.225	0.91	0.88			
4.8	38725	0.26	0.91	1.04	0.82	1.03	[25]
4.0	32262	0.31	0.89	1.34	0.75	1.41	
3.5	28229	0.35	0.93	1.62	0.81	1.76	
3.0	24197	0.41	1.07	1.98	1.04	2.17	
2.5	20164	0.50	1.35	2.45	1.41	2.99	
2.0	16131	0.62	1.94	2.81	1.77	2.76	
1.5	12098	0.83	2.43	2.78	2.08	3.46	
1.0	8066	1.24	2.87	3.64	3.16	3.80	
0.7	5646	1.77	3.68	4.32	4.10	4.90	
0.5	4033	2.48	3.96	4.63	4.32	4.43	
0.3	2420	4.10	3.43	6.84	2.58	7.27	
0.2	1613	6.20	3.20	10.48	2.57	12.06	
0.1	806.6	12.80	3.12	21.35	3.32	21.61	
1.240	10000	1.00	2.7	3.5	2.4	3.5	[55]
0.620	5000	2.00	2.8	3.7	2.7	3.6	
0.413	3333	3.00	3.1	4.8	3.4	5.0	
0.310	2500	4.00	3.8	5.4	4.0	5.6	
0.248	2000	5.00	4.8	6.9	4.7	6.7	
0.207	1667	6.00	5.6	8.9	5.1	8.6	
0.177	1429	7.00	6.3	11.5	5.8	10.7	
0.155	1250	8.00	7.0	13.2	6.5	12.4	
0.138	1111	9.00	7.9	15.1	7.4	13.8	
0.124	1000	10.00	8.9	16.8	8.2	15.3	
0.113	909.1	11.00	9.8	18.7	9.2	16.7	
0.103	833.3	12.00	10.9	20.7	10.1	18.0	
0.095	769.2	13.00	11.6	22.1	10.8	19.3	
0.089	714.3	14.00	12.7	23.5	11.6	20.5	
0.083	666.7	15.00	13.8	24.5	12.5	21.8	

TABLE IV

Values of n and k for Terbium for Various References[a]

eV	cm^{-1}	μm	n	k	
9886.4	79748312.	0.00013	1.000	0.000002	[12]
8047.8	64917296	0.00015	1.000	0.000003	
7478.2	60322644	0.00017	1.000	0.000001	
5898.8	47582464	0.00021	1.000	0.000003	
4510.8	36386212	0.00027	1.000	0.000009	
2984.3	24072752	0.00042	1.000	0.000036	
2165.9	17471158	0.00057	1.000	0.00011	
1740.0	14035649	0.00071	1.000	0.00020	
1486.7	11992413	0.00083	1.000	0.00030	
1253.6	10112120	0.00099	1.000	0.00053	
1188.0	9582961	0.00104	1.000	0.00012	
1011.7	8160843	0.00123	1.000	0.00020	
851.5	6868595	0.00146	1.000	0.00032	
705.0	5686859	0.00176	0.998	0.00054	
572.8	4620471	0.00216	0.998	0.00087	
452.2	3647656	0.00274	0.996	0.00148	
311.7	2514317	0.00398	0.994	0.00364	
212.2	1711704	0.00584	0.988	0.00844	
183.3	1478583	0.00676	0.985	0.0137	
171.7	1385012	0.00722	0.983	0.0158	
151.1	1218843	0.00820	1.021	0.0436	
148.7	1199483	0.00834	1.018	0.0080	
132.8	1071227	0.00934	0.987	0.0088	
114.0	919577	0.01087	0.979	0.0142	
108.5	875212	0.01143	0.976	0.0154	
72.4	584012	0.01712	1.000	0.0339	
30.5	246027	0.04065	1.000	0.164	
170.0	1371299	0.00729		0.0134	[17]
160.0	1290635	0.00775		0.0239	
150.0	1209970	0.00826		0.0246	
140.0	1129305	0.00886		0.0052	
130.0	1048641	0.00954		0.0081	
120.0	967976	0.01033		0.0108	
110.0	887311	0.01127		0.0125	
100.0	806647	0.01240		0.0146	
90.0	725982	0.01377		0.0180	
80.0	645317	0.01550		0.0223	
70.0	564653	0.01771		0.0302	
45.0	362947	0.0276	0.89	0.09	[33]
40.0	322620	0.0310	0.77	0.19	
35.0	282292	0.0354	0.80	0.35	
30.0	241965	0.0413	0.94	0.42	
25.0	201637	0.0496	0.97	0.39	
22.0	177441	0.0564	0.98	0.36	
20.0	161310	0.0620	0.93	0.36	

[a] The references from which the values were taken are given in brackets.

TABLE IV *(Continued)*

Terbium

eV	cm^{-1}	μm	n	k	n	k	
17.5	141146	0.0708	0.81	0.34			
15.0	120982	0.0827	0.75	0.48			
10.0	80655	0.1240	0.68	1.07			
7.5	60491	0.1653	0.86	1.54			
				E ∥ c	**E ⊥ c**		
5.0	40328	0.24	0.82	1.04	0.81	1.06	[25]
4.0	32262	0.31	0.82	1.47	0.83	1.46	4.2 K
3.5	28229.	0.35	0.90	1.81	0.90	1.77	
3.0	24197	0.41	1.14	2.24	1.07	2.12	
2.5	20164	0.50	1.59	2.52	1.36	2.57	
2.0	16131	0.62	1.96	2.71	1.94	2.98	
1.0	8066	1.24	3.08	3.63	3.06	3.77	
0.7	5646	1.77	4.05	3.99	3.65	4.29	
0.5	4033	2.48	3.75	4.25	3.76	5.03	
0.3	2420	4.10	2.65	7.07	3.44	7.54	
0.2	1613	6.20	2.10	11.46	3.07	11.44	
0.1	807	12.80	2.94	24.07	3.09	23.76	
1.240	10000	1.00	2.4	4.3	2.2	4.0	[55]
0.620	5000	2.00	3.3	5.1	3.0	4.5	
0.413	3333	3.00	3.5	7.2	3.4	6.5	
0.310	2500	4.00	4.2	9.0	4.1	8.0	
0.248	2000	5.00	5.3	10.8	4.8	9.6	
0.207	1667	6.00	6.2	12.6	5.4	11.0	
0.177	1429	7.00	7.1	14.7	6.2	12.4	
0.155	1250	8.00	8.2	17.5	7.1	13.8	
0.138	1111	9.00	9.2	19.2	7.8	15.3	
0.124	1000	10.00	10.1	20.4	8.6	16.6	
0.103	833.3	12.00	12.2	24.3	10.2	19.6	
0.095	769.2	13.00	12.8	25.6	11.0	20.3	
0.089	714.3	14.00	13.7	27.2	11.8	21.5	
0.083	666.7	15.00	14.8	28.5	12.8	22.7	
2.60	20970	0.476	1.30	1.80	[49]		
2.50	20165	0.496	1.40	1.97			
2.40	19357	0.516	1.42	2.02			
2.30	18551	0.539	1.48	2.11			
2.10	16938	0.590	1.62	2.32			
2.00	16131	0.619	1.67	2.32			
1.90	15325	0.652	1.80	2.54			
1.80	14518	0.688	1.82	2.55			
2.50	20165	0.496	1.83	2.71	[57]		
2.00	16132	0.620	2.35	3.00	77 K		
1.50	12099	0.827	2.80	3.22			

(continued)

TABLE IV *(Continued)*

Terbium

eV	cm^{-1}	μm	n	k	
1.00	8066	1.240	3.40	3.75	
0.80	6453	1.550	3.72	4.22	
0.70	5646	1.771	3.82	4.64	
0.60	4840	2.066	3.98	5.23	
0.40	3226	3.099	4.68	7.07	
2.50	20165	0.496	1.87	2.74	[57]
2.00	16132	0.620	2.36	3.01	300 K
1.50	12099	0.827	2.86	3.27	
1.00	8066	1.240	3.40	3.75	
0.80	6453	1.550	3.47	4.25	
0.60	4840	2.066	3.67	5.34	
0.40	3226	3.099	4.57	7.67	
1.240	10000	1.00	1.79	3.26	[64]
0.620	5000	2.00	2.60	5.23	80 K
0.310	2500	4.00	3.65	8.45	
0.248	2000	5.00	4.26	10.04	
0.177	1429	7.00	5.56	13.46	
0.138	1111	9.00	6.90	16.37	
0.103	833.3	12.00	8.83	20.60	
0.089	714.3	14.00	10.14	23.30	
0.077	625.0	16.00	11.48	26.24	
0.069	555.6	18.00	13.10	29.01	
0.062	500.0	20.00	15.03	31.92	
1.240	10000	1.00	1.92	3.21	[64]
0.620	5000	2.00	2.78	4.94	293 K
0.413	3333	3.00	3.40	6.54	
0.310	2500	4.00	4.12	8.04	
0.177	1429	7.00	6.22	12.42	
0.124	1000	10.00	8.60	16.57	
0.103	833.3	12.00	10.18	19.06	
0.089	714.3	14.00	11.84	21.54	
0.077	625.0	16.00	13.66	24.10	
0.069	555.6	18.00	15.61	26.80	
0.062	500.0	20.00	17.63	29.51	
1.240	10000	1.00	2.20	3.05	[64]
0.620	5000	2.00	3.03	4.72	450 K
0.310	2500	4.00	4.51	7.76	
0.177	1429	7.00	7.10	11.74	
0.138	1111	9.00	8.80	14.15	
0.124	1000	10.00	9.74	15.47	
0.103	833.3	12.00	11.53	17.65	
0.089	714.3	14.00	13.64	20.16	
0.077	625.0	16.00	15.83	22.72	
0.069	555.6	18.00	17.72	24.95	
0.062	500.0	20.00	19.68	27.17	

TABLE V

Values of *n* and *k* for Dysprosium from Various References[a]

eV	cm^{-1}	μm	n	k	
9886.4	79738680	0.00013	1.000	0.000002	[12]
8638.9	69676976	0.00014	1.000	0.000004	
8047.8	64909460	0.00015	1.000	0.000003	
6930.3	55896272	0.00018	1.000	0.000002	
5414.7	43672220	0.00023	1.000	0.000005	
4466.3	36022900	0.00028	1.000	0.000010	
3691.7	29775376	0.00034	1.000	0.000019	
2984.3	24069848	0.00042	1.000	0.000039	
2293.2	18495786	0.00054	1.000	0.000097	
2042.4	16472960	0.00061	1.000	0.00014	
1740.0	14033955	0.00071	1.000	0.00022	
1486.7	11990966	0.00083	0.999	0.00032	
1188.0	9581804	0.00104	0.999	0.00013	
1011.7	8159858	0.00123	0.999	0.00022	
929.7	7498488	0.00133	0.999	0.00028	
705.0	5686172	0.00176	0.998	0.00059	
572.8	4619914	0.00216	0.997	0.00102	
511.3	4123886	0.00242	0.997	0.00135	
392.4	3164899	0.00316	0.995	0.00255	
311.7	2514014	0.00398	0.994	0.00445	
277.0	2234141	0.00448	0.993	0.00528	
212.2	1711497	0.00584	0.988	0.00936	
171.7	1384845	0.00722	0.979	0.0204	
151.1	1218696	0.00821	1.009	0.0210	
132.8	1071097	0.00934	0.989	0.0134	
114.0	919466	0.01088	0.980	0.0201	
108.5	875106	0.01143	0.978	0.0226	
91.5	737992	0.01355	1.000	0.0336	
72.4	583942	0.01713	1.000	0.0552	
49.3	397629	0.02515	1.000	0.1180	
30.5	245998	0.04065	1.000	0.2977	
170.0	1371134	0.00729		0.0154	[17]
160.0	1290479	0.00775		0.0295	
140.0	1129169	0.00886		0.0084	
130.0	1048514	0.00954		0.0104	
120.0	967859	0.01033		0.0127	
110.0	887204	0.01127		0.0153	
100.0	806549	0.01240		0.0194	
90.0	725894	0.01377		0.0244	
80.0	645239	0.01550		0.0316	
70.0	564458	0.01771		0.0422	
30.0	241965	0.0413	0.99	0.23	[48]
29.0	233899	0.0428	0.99	0.20	

(continued)

[a] The references from which the values were taken are given in brackets.

TABLE V *(Continued)*

Dysprosium

eV	cm^{-1}	μm	n	k			
28.0	225834	0.0443	0.98	0.19			
27.0	217768	0.0459	0.98	0.19			
26.0	209703	0.0477	0.98	0.19			
25.5	205670	0.0468	0.98	0.19			
25.0	201637	0.0496	0.98	0.19			
24.0	193572	0.0517	0.98	0.17			
23.0	185506	0.0539	0.98	0.15			
22.0	177441	0.0564	0.98	0.11			
21.7	175424	0.0570	0.98	0.10			
20.8	167359	0.0598	0.97	0.03			
20.0	161310	0.0620	0.97	0.04			
				E ∥ c		**E ⊥ c**	
5.00	40329	0.248	0.86	0.99	0.73	1.21	[25]
4.50	36295	0.276	0.79	0.84	0.73	1.32	4.2 K
4.00	32263	0.310	0.90	1.42	0.75	1.53	
3.50	28229	0.354	0.95	1.69	0.83	1.90	
3.00	24198	0.413	1.12	2.09	1.13	2.36	
2.50	20164	0.496	1.51	2.47	1.64	2.65	
2.00	16132	0.620	2.01	2.75	2.04	2.87	
1.50	12099	0.827	2.53	2.86	2.76	3.21	
1.00	10080	1.240	3.11	3.37	3.20	3.60	
0.80	6452	1.550	3.39	3.58	3.88	3.88	
0.60	4839	2.066	3.50	4.17	3.81	4.15	
0.40	3226	3.100	3.57	5.67	3.30	5.53	
0.20	1613	6.200	3.79	10.03	3.23	10.79	
0.10	806.5	12.400	2.91	20.02	2.23	22.79	
3.966	31990	0.313	1.04	0.62	[43]		
3.397	27397	0.365	1.06	0.89			
3.099	25000	0.400	1.18	1.05			
2.917	23529	0.425	1.24	1.15			
2.610	21053	0.475	1.37	1.20			
2.480	24000	0.500	1.40	1.23			
2.362	19048	0.525	1.41	1.24			
2.254	18182	0.550	1.44	1.28			
2.156	17391	0.575	1.44	1.31			
2.066	16667	0.600	1.40	1.34			
1.907	15385	0.650	1.41	1.40			
1.771	14286	0.700	1.38	1.54			
1.653	13333	0.750	1.40	1.64			
1.550	12500	0.800	1.41	1.76			
1.459	11765	0.850	1.43	1.85			
1.378	11111	0.900	1.43	1.96			
1.305	10526	0.950	1.45	2.09			
1.240	10000	1.000	1.52	2.19			

TABLE V *(Continued)*

Dysprosium

eV	cm^{-1}	μm	n	k	
1.181	9524	1.050	1.51	2.24	
1.127	9091	1.100	1.50	2.26	
1.240	10000	1.00	1.48	2.22	[54]
0.826	6667	1.50	2.06	3.30	80 K
0.620	5000	2.00	2.36	4.25	
0.496	4000	2.50	2.71	5.26	
0.413	3333	3.00	2.90	5.93	
0.354	2857	3.50	3.09	6.81	
0.310	2500	4.00	3.31	7.65	
0.275	2222	4.50	3.51	8.43	
0.248	2000	5.00	3.84	9.40	
0.207	1667	6.00	4.26	10.98	
0.177	1429	7.00	4.88	12.41	
0.155	1250	8.00	5.35	13.94	
0.138	1111	9.00	5.91	15.04	
0.124	1000	10.00	6.61	16.45	
0.103	833.3	12.00	7.75	19.10	
0.089	714.3	14.00	8.74	22.01	
0.077	625.0	16.00	9.92	24.40	
0.069	555.6	18.00	10.82	26.21	
0.065	526.3	19.00	11.22	27.12	
0.062	500.0	20.00	11.70	28.23	
1.240	10000	1.00	1.52	2.19	[54]
0.826	6667	1.50	2.10	3.25	293 K
0.620	5000	2.00	2.46	4.20	
0.496	4000	2.50	2.80	5.13	
0.413	3333	3.00	3.04	5.86	
0.354	2857	3.50	3.36	6.74	
0.310	2500	4.00	3.65	7.58	
0.275	2222	4.50	3.96	8.35	
0.248	2000	5.00	4.16	9.10	
0.207	1667	6.00	4.95	10.76	
0.177	1429	7.00	5.44	12.02	
0.155	1250	8.00	6.13	13.18	
0.138	1111	9.00	6.76	14.40	
0.124	1000	10.00	7.35	15.74	
0.113	909.1	11.00	8.02	16.92	
0.103	833.3	12.00	8.76	17.97	
0.095	769.2	13.00	9.57	19.24	
0.089	714.3	14.00	10.28	20.26	
0.083	666.7	15.00	11.07	21.51	
0.077	625.0	16.00	11.85	22.63	
0.069	555.6	18.00	12.95	24.46	
0.065	526.3	19.00	13.52	25.24	
0.062	500.0	20.00	14.27	26.42	

(continued)

TABLE V *(Continued)*

Dysprosium

eV	cm^{-1}	μm	n	k		
1.240	10000	1.00	1.62	2.16	[54]	
0.826	6667	1.50	2.33	3.17	460 K	
0.620	5000	2.00	2.63	4.09		
0.413	3333	3.00	3.34	5.65		
0.354	2857	3.50	3.63	6.61		
0.310	2500	4.00	3.97	7.39		
0.248	2000	5.00	4.48	8.87		
0.207	1667	6.00	5.38	10.60		
0.177	1429	7.00	5.85	11.71		
0.155	1250	8.00	6.79	12.96		
0.138	1111	9.00	7.42	14.10		
0.124	1000	10.00	8.15	15.40		
0.113	909.1	11.00	9.02	16.62		
0.103	833.3	12.00	9.70	17.65		
0.095	769.2	13.00	10.61	18.70		
0.089	714.3	14.00	11.41	19.61		
0.083	666.7	15.00	12.33	20.52		
0.077	625.0	16.00	13.31	21.60		
0.073	588.2	17.00	14.16	22.11		
0.069	555.6	18.00	14.95	22.91		
0.065	526.3	19.00	15.74	23.73		
0.062	500.0	20.00	16.43	25.09		

eV	cm^{-1}	μm	n	k	n	k	
			E ∥ c		**E ⊥ c**		
5.64	45455	0.22	0.92	1.19	0.96	1.24	[66]
4.77	38462	0.26	0.96	1.21	0.96	1.21	80 K
4.43	35714	0.28	1.06	1.25	1.07	1.29	
4.13	33333	0.30	1.10	1.42	1.14	1.43	
3.54	28571	0.35	1.25	1.64	1.25	1.74	
3.10	25000	0.40	1.35	1.96	1.38	2.05	
2.76	22222	0.45	1.53	2.09	1.57	2.17	
2.25	18182	0.55	1.72	2.31	1.77	2.37	
2.07	16667	0.60	1.80	2.44	1.85	2.49	
1.91	15385	0.65	1.90	2.54	1.93	2.68	
1.65	13333	0.75	2.08	2.66	2.15	2.87	
1.55	12500	0.80	2.13	2.74	2.22	2.95	
1.38	11111	0.90	2.21	2.95	2.30	3.15	
1.24	10000	1.00	2.33	3.08	2.40	3.18	
1.03	8333.3	1.20	2.61	3.25	2.62	3.21	
0.95	7692.3	1.30	2.79	3.26	2.76	3.34	
0.89	7142.9	1.40	2.91	3.37	2.87	3.46	
0.77	6250.0	1.60	3.10	3.56	3.05	3.60	
0.69	5555.6	1.80	3.23	3.79	3.09	3.75	
0.62	5000.0	2.00	3.36	4.05	3.31	3.96	
0.56	4545.5	2.20	3.53	4.19	3.52	4.06	

TABLE V *(Continued)*

Dysprosium

eV	cm^{-1}	μm	n	k	n	k	
0.52	4166.7	2.40	3.68	4.42	3.64	4.32	
0.48	3846.2	2.60	3.84	4.58	3.81	4.53	
0.44	3571.4	2.80	4.02	4.77	4.02	4.59	
0.41	3333.3	3.00	4.15	5.02	4.10	4.91	
5.64	45455	0.22	1.03	1.29	1.04	1.32	[66]
4.77	38462	0.26	1.09	1.26	1.07	1.28	293 K
4.43	35714	0.28	1.16	1.35	1.16	1.35	
4.13	33333	0.30	1.22	1.47	1.22	1.48	
3.10	25000	0.40	1.40	1.92	1.43	1.93	
2.76	22222	0.45	1.48	2.09	1.54	2.05	
2.48	20000	0.50	1.51	2.25	1.56	2.23	
2.07	16667	0.60	1.71	2.40	.75	2.43	
1.77	14286	0.70	1.78	2.67	1.88	2.70	
1.55	12500	0.80	1.88	2.89	2.02	2.92	
1.38	11111	0.90	2.02	2.96	2.14	2.98	
1.24	10000	1.00	2.20	3.04	2.24	3.08	
1.13	9090.9	1.10	2.38	3.05	2.40	3.16	
1.03	8333.3	1.20	2.50	3.12	2.46	3.21	
0.95	7692.3	1.30	2.64	3.18	2.59	3.21	
0.77	6250.0	1.60	2.97	3.42	2.77	3.62	
0.69	5555.6	1.80	3.09	3.66	2.95	3.78	
0.62	5000.0	2.00	3.23	3.85	3.06	3.99	
0.52	4166.7	2.40	3.39	4.36	3.28	4.42	
0.44	3571.4	2.80	3.73	4.59	3.64	4.63	
0.41	3333.3	3.00	3.76	4.86	3.67	4.83	
1.24	10000	1.00	2.4	3.2	2.3	3.1	[55]
0.62	5000	2.00	3.3	4.0	3.4	4.1	
0.413	3333	3.00	4.1	4.9	4.2	5.0	
0.310	2500	4.00	4.4	6.3	4.4	6.2	
0.248	2000	5.00	5.1	8.4	5.2	8.2	
0.207	1667	6.00	6.0	10.5	6.1	10.3	
0.177	1429	7.00	6.8	13.3	6.7	12.5	
0.155	1250	8.00	7.7	15.3	7.3	14.2	
0.138	1111	9.00	8.7	17.5	8.3	15.9	
0.124	1000	10.00	9.6	19.2	9.3	17.2	
0.113	909.1	11.00	10.3	20.7	10.2	19.0	
0.103	833.3	12.00	11.6	22.4	11.0	20.5	
0.095	769.2	13.00	12.4	24.3	11.8	22.4	
0.090	714.3	14.00	13.6	25.8	12.6	23.6	
0.083	666.7	15.00	14.8	26.8	13.4	25.0	
0.078	625.0	16.00	15.6	28.8	14.6	26.1	

(continued)

TABLE V *(Continued)*

Dysprosium

eV	cm^{-1}	μm	n	k	
2.50	20165	0.496	2.04	2.77	[57]
2.00	16132	0.620	2.15	2.76	80 K
1.70	13712	0.729	2.93	3.26	
1.50	12099	0.827	3.17	3.32	
1.00	8065.8	1.240	3.53	3.53	
0.66	5323.4	1.878	3.17	4.84	
0.40	3226.3	3.099	4.47	7.61	
2.50	20165	0.496	2.04	2.77	[57]
2.00	16132	0.620	2.58	3.11	300 K
1.70	13712	0.729	2.95	3.27	
1.50	12099	0.827	3.17	3.32	
1.00	8065.8	1.240	3.56	3.56	
0.66	5323.4	1.878	4.28	4.98	
0.40	3226.3	3.099	4.66	7.98	

TABLE VI

Values of *n* and *k* for Erbium from Various References[a]

eV	cm^{-1}	μm	n	k	
9886.4	79738680	0.00013	1.000	0.000003	[12]
8047.8	64909460	0.00015	1.000	0.000001	
3691.7	29775376	0.00034	1.000	0.000022	
2293.2	18495786	0.00054	1.000	0.00011	
2042.4	16472960	0.00061	1.000	0.00016	
1740.0	14033955	0.00071	1.000	0.00022	
1486.7	11990966	0.00083	1.000	0.00038	
1188.0	9581804	0.00104	0.999	0.00016	
1011.7	8159858	0.00123	0.999	0.00026	
929.7	7498488	0.00133	0.999	0.00033	
705.0	5686172	0.00176	0.998	0.00071	
572.8	4619914	0.00216	0.997	0.00122	
511.3	4123886	0.00242	0.997	0.00161	
392.4	3164899	0.00316	0.995	0.00278	
311.7	2514014	0.00398	0.994	0.00456	
277.0	2234141	0.00448	0.993	0.00564	
212.2	1711497	0.00584	0.990	0.00809	
171.7	1384845	0.00722	0.997	0.0258	
151.1	1218696	0.00821	0.986	0.0107	
132.8	1071097	0.00934	0.982	0.0138	
114.0	919466	0.01088	0.974	0.0171	
108.5	875106	0.01143	0.970	0.0188	
91.5	737992	0.01355	1.000	0.0306	
72.4	583942	0.01713	1.000	0.0518	

[a] The references from which the values were taken are given in brackets.

TABLE VI *(Continued)*

Erbium

eV	cm^{-1}	μm	n	k			
49.3	397629	0.02515	1.000	0.1090			
30.5	245998	0.04065	1.000	0.2315			
180.0	1451964	0.00689		0.0129	[17]		
170.0	1371299	0.00729		0.0158			
160.0	1290635	0.00775		0.0067			
150.0	1209970	0.00826		0.0095			
140.0	1129305	0.00886		0.0109			
130.0	1048641	0.00954		0.0124			
120.0	967976	0.01033		0.0134			
110.0	887311	0.01127		0.0155			
100.0	806647	0.01240		0.0197			
90.0	725982	0.01377		0.0258			
80.0	645317	0.01550		0.0347			
70.0	564653	0.01771		0.0473			
eV	cm^{-1}	μm	n	k	n	k	
				E ∥ c		**E ⊥ c**	
5.0	40328	0.25	0.90	0.97	0.81	0.98	[25]
4.5	36295	0.276	0.86	0.66	0.81	0.64	4.2 K
4.0	32262	0.31	0.82	1.32	0.80	1.43	
3.5	28229	0.35	0.85	1.65	0.89	1.81	
3.0	24197	0.41	1.01	2.07	1.19	2.23	
2.5	20164	0.50	1.40	2.48	1.73	2.54	
2.0	16131	0.62	1.93	2.89	2.25	2.65	
1.5	12098	0.83	2.57	2.96	2.66	2.37	
1.0	8065.5	1.24	2.99	3.14	2.72	2.77	
0.9	7258.9	1.378	3.06	3.22	2.64	2.83	
0.5	4032.8	2.48	2.70	5.24	2.03	5.48	
0.3	2016.4	4.96	2.88	8.75	2.45	9.55	
0.22	1774.4	5.63	3.24	11.75	3.17	12.80	
0.10	806.6	12.40	5.00	24.93	6.98	26.08	
2.48	20000	0.5	1.71	3.21		[68]	
1.24	10000	1.0	2.30	3.75		300 K	
0.83	6666.7	1.5	2.63	4.29			
0.62	5000.0	2.0	2.84	4.39			
0.50	4000.0	2.5	3.32	5.63			
0.41	3333.3	3.0	3.80	6.48			
0.25	2000.0	5.0	5.11	9.00			
0.17	1333.3	7.5	6.89	11.74			
0.12	1000.0	10.0	8.89	14.11			
0.10	800.0	12.5	10.63	16.63			
0.083	666.7	15.0	12.47	18.42			
0.071	571.4	17.5	14.16	20.53			
0.062	500.0	20.0	15.79	22.63			

(continued)

TABLE VI *(Continued)*

Erbium

eV	cm^{-1}	μm	n	k	n	k	
5.64	45455	0.22	0.84	1.10	0.82	1.14	[69]
5.17	41667	0.24	0.92	1.19	0.88	1.24	78 K
4.77	38462	0.26	1.03	1.26	1.01	1.28	
4.43	35714	0.28	1.08	1.40	1.06	1.38	
4.13	33333	0.30	1.14	1.52	1.13	1.44	
3.54	28571	0.35	1.34	1.75	1.32	1.58	
3.10	25000	0.40	1.56	2.03	1.54	1.84	
2.76	22222	0.45	1.75	2.20	1.75	2.02	
2.48	20000	0.50	1.90	2.39	1.94	2.26	
2.25	18182	0.55	2.08	2.45	2.09	2.43	
2.07	16667	0.60	2.17	2.53	2.19	2.66	
1.91	15385	0.65	2.21	2.69	2.24	2.77	
1.77	14286	0.70	2.31	2.78	2.36	2.74	
1.65	13333	0.75	2.36	2.82	2.42	2.76	
1.55	12500	0.80	2.32	2.80	2.41	2.94	
1.38	11111	0.90	2.27	2.84	2.41	3.21	
1.24	10000	1.00	2.30	2.99	2.48	3.39	
1.13	9090.9	1.10	2.30	3.09	2.45	3.52	
1.03	8333.3	1.20	2.21	3.22	2.42	3.45	
0.95	7692.3	1.30	2.23	3.26	2.40	3.34	
0.89	7142.9	1.40	2.30	3.10	2.40	3.20	
0.77	6250.0	1.60	2.30	3.00	2.40	3.40	
0.69	5555.6	1.80	2.40	3.20	2.50	3.50	
0.62	5000.0	2.00	2.40	3.60	2.60	3.80	
0.56	4545.5	2.20	2.60	3.80	2.70	4.00	
0.52	4166.7	2.40	2.80	3.80	2.90	4.20	
0.48	3846.2	2.60	2.80	4.10	2.90	4.60	
0.44	3571.4	2.80	2.80	4.40	3.00	4.90	
0.41	3333.3	3.00	2.90	4.80	3.10	5.10	
0.35	2857.1	3.50	3.00	5.60	3.20	5.90	
0.31	2500.0	4.00	3.20	6.20	3.50	6.20	
0.28	2222.2	4.50	3.70	6.50	3.80	6.50	
0.25	2000.0	5.00	4.00	6.90	4.20	6.70	
0.23	1818.2	5.50	4.30	7.00	4.50	6.60	
0.21	1666.7	6.00	4.40	7.30	4.70	6.70	

TABLE VII

Values of n and k for Thulium from Various References[a]

eV	cm^{-1}	μm	n	k	
9886.4	79738680	0.00013	1.000	0.000003	[12]
8047.8	64909460	0.00015	1.000	0.000002	
5898.8	47576720	0.00021	1.000	0.000005	
3691.7	29775376	0.00034	1.000	0.000026	
2293.2	18495786	0.00054	1.000	0.00013	
2042.4	16472960	0.00061	0.999	0.00017	
1740.0	14033955	0.00071	0.999	0.00026	
1486.7	11990966	0.00083	0.999	0.00029	
1188.0	9581804	0.00104	0.999	0.00017	
1011.7	8159858	0.00123	0.999	0.00028	
929.7	7498488	0.00133	0.999	0.00036	
705.0	5686172	0.00176	0.998	0.00078	
572.8	4619914	0.00216	0.997	0.00135	
511.3	4123886	0.00242	0.997	0.00177	
392.4	3164899	0.00316	0.996	0.00293	
331.7	2514014	0.00398	0.994	0.00444	
277.0	2234141	0.00448	0.993	0.00568	
212.2	1711497	0.00584	0.990	0.00927	
171.7	1384845	0.00722	1.005	0.0133	
151.1	1218696	0.00821	0.987	0.0122	
148.7	1199339	0.00834	0.986	0.0125	
132.8	1071097	0.00934	0.983	0.0152	
108.5	875106	0.01143	0.975	0.0224	
91.5	737992	0.01355	1.000	0.0316	
72.4	583942	0.01713	1.000	0.0475	
49.3	397629	0.02515	1.000	0.0843	
30.5	245998	0.04065	1.000	0.1707	
180.0	1451964	0.00689		0.0179	[17]
170.0	1371299	0.00729		0.0081	
160.0	1290635	0.00775		0.0092	
150.0	1209970	0.00826		0.0110	
140.0	1129305	0.00886		0.0125	
130.0	1048641	0.00954		0.0141	
120.0	967976	0.01033		0.0161	
110.0	887311	0.01127		0.0192	
100.0	806647	0.01240		0.0239	
90.0	725982	0.01377		0.0286	
80.0	645317	0.01550		0.0356	
70.0	564653	0.01771		0.0447	
1.240	10000.0	1.00	2.22	3.75	[70]
0.827	6666.7	1.50	2.67	4.40	80 K
0.620	5000.0	2.00	3.21	5.56	
0.496	4000.0	2.50	3.65	6.51	

(continued)

[a] The references from which the values were taken are given in brackets.

TABLE VII *(Continued)*

Thulium

eV	cm^{-1}	μm	n	k	n	k
0.413	3333.3	3.00	3.86	7.65		
0.354	2857.1	3.50	4.11	8.52		
0.310	2500.0	4.00	4.60	9.37		
0.276	2222.2	4.50	5.03	10.33		
0.248	2000.0	5.00	5.39	11.12		
0.207	1666.6	6.00	6.10	12.94		
0.177	1428.4	7.00	6.92	14.75		
0.155	1250.0	8.00	7.41	16.28		
0.138	1111.1	9.00	7.89	18.15		
0.124	1000.0	10.00	8.40	20.03		
0.113	909.1	11.00	8.68	21.46		
0.103	833.3	12.00	9.53	22.91		
0.095	769.2	13.00	10.02	24.30		
0.089	714.3	14.00	10.68	25.62		
0.083	666.7	15.00	11.35	26.97		
0.078	625.8	16.00	11.77	28.09		
0.073	588.2	17.00	12.21	29.40		
0.069	555.5	18.00	12.64	30.77		
0.065	526.3	19.00	13.10	31.94		
0.062	500.0	20.00	13.60	33.12		
1.240	10000.0	1.00	2.52	3.46	[70]	
0.827	6666.7	1.50	3.02	4.20	293 K	
0.620	5000.0	2.00	3.56	5.30		
0.496	4000.0	2.50	4.15	6.32		
0.413	3333.3	3.00	4.72	7.34		
0.354	2857.1	3.50	5.04	8.15		
0.310	2500.0	4.00	5.46	9.03		
0.276	2222.2	4.50	5.81	9.86		
0.248	2000.0	5.00	6.22	10.72		
0.207	1666.6	6.00	6.94	12.28		
0.177	1422.7	7.00	7.81	14.02		
0.155	1250.0	8.00	8.70	15.81		
0.138	1111.1	9.00	9.54	17.45		
0.124	1000.0	10.00	10.35	18.86		
0.113	909.1	11.00	11.13	20.65		
0.103	833.3	12.00	11.93	22.21		
0.095	769.2	13.00	12.85	23.68		
0.089	714.3	14.00	13.60	25.45		
0.083	666.7	15.00	14.46	26.31		
0.078	625.0	16.00	15.22	27.32		
0.073	588.2	17.00	16.15	28.50		
0.069	555.6	18.00	17.04	29.62		
0.065	526.3	19.00	18.04	31.24		
0.062	500.0	20.00	18.70	31.96		
1.240	10000.0	1.00	2.83	3.31	[70]	
0.827	6666.7	1.50	3.35	3.98	450 K	

TABLE VII *(Continued)*

Thulium

eV	cm^{-1}	μm	n	k			
0.620	5000.0	2.00	3.91	5.07			
0.496	4000.0	2.50	4.48	6.04			
0.413	3333.3	3.00	5.03	6.92			
0.354	2857.1	3.50	5.72	7.70			
0.310	2500.0	4.00	6.24	8.51			
0.276	2222.2	4.50	6.71	9.43			
0.248	2000.0	5.00	7.37	10.40			
0.207	1666.6	6.00	8.36	11.75			
0.177	1428.7	7.00	9.43	13.48			
0.155	1250.0	8.00	10.31	15.36			
0.138	1111.1	9.00	11.25	16.93			
0.124	1000.0	10.00	12.46	18.38			
0.113	909.1	11.00	13.40	20.02			
0.103	833.3	12.00	14.52	21.43			
0.095	769.2	13.00	15.31	22.90			
0.089	714.3	14.00	16.34	24.26			
0.083	666.7	15.00	17.65	25.55			
0.078	625.0	16.00	18.21	26.40			
0.073	588.2	17.00	19.20	27.83			
0.069	555.5	18.00	20.16	29.02			
0.062	500.0	20.00	22.03	31.02			
eV	cm^{-1}	μm	n	k	n	k	
				E ∥ c		**E ⊥ c**	
5.64	45455	0.22	0.87	1.10	0.86	1.09	[69]
5.17	41667	0.24	0.94	1.26	0.92	1.15	78 K
4.77	38462	0.26	1.03	1.34	1.01	1.20	
4.13	33333	0.30	1.15	1.68	1.18	1.40	
3.54	28571	0.35	1.33	1.96	1.29	1.80	
3.10	25000	0.40	1.60	2.13	1.55	1.98	
2.76	22222	0.45	1.85	2.40	1.81	2.16	
2.48	20000	0.50	1.97	2.49	1.92	2.39	
2.07	16667	0.60	2.19	2.80	2.13	2.64	
1.91	15385	0.65	2.23	3.03	2.19	2.81	
1.77	14286	0.70	2.21	2.98	2.23	3.03	
1.65	13333	0.75	2.19	2.98	2.20	3.36	
1.55	12500	0.80	2.18	2.92	2.23	3.48	
1.38	11111	0.90	2.20	2.86	2.24	3.50	
1.24	10000	1.00	2.21	2.66	2.26	3.44	
1.13	9090.9	1.10	2.22	2.56	2.29	3.33	
0.95	7692.3	1.30	2.21	2.55	2.33	3.37	
0.89	7142.9	1.40	2.20	2.60	2.30	3.20	
0.77	6250.0	1.60	2.30	2.80	2.40	3.20	
0.69	5555.6	1.80	2.30	3.20	2.50	2.90	
0.62	5000.0	2.00	2.30	3.50	2.50	2.90	

(continued)

TABLE VII *(Continued)*

Thulium

eV	cm^{-1}	μm	n	k	n	k	
0.56	4545.5	2.20	2.30	3.90	2.60	3.00	
0.52	4166.7	2.40	2.40	4.10	2.80	3.30	
0.48	3846.2	2.60	2.40	4.30	2.80	3.30	
0.44	3571.4	2.80	2.60	4.40	2.90	3.50	
0.41	3333.3	3.00	2.80	4.50	2.90	3.60	
0.35	2857.1	3.50	3.20	4.60	3.20	4.10	
0.31	2500.0	4.00	3.50	5.10	3.40	4.60	
5.0	40327	0.25	0.96	0.94	0.82	1.04	[25]
4.0	32262	0.31	0.90	1.28	0.81	1.51	4.2 K
3.5	28229	0.35	0.94	1.59	0.91	1.91	
3.0	24197	0.41	1.10	2.02	1.35	2.36	
2.5	20164	0.50	1.61	2.50	1.96	2.45	
2.0	16131	0.62	2.30	2.61	2.44	2.52	
1.5	12098	0.83	3.02	2.39	2.84	2.11	
1.0	8065.5	1.24	3.09	2.31	2.34	2.19	
0.5	4032.8	2.48	2.57	5.18	2.80	6.83	
0.3	2419.6	4.13	6.06	5.97	7.96	6.92	
0.2	1613.1	6.20	4.64	5.94	5.32	6.73	
0.1	806.6	12.40	2.21	14.91	2.75	16.60	

TABLE VIII

Values of n and k for Ytterbium from Various References[a]

eV	cm^{-1}	μm	n	k	
9886.4	79738700	0.00013	1.000	0.000002	[12]
8047.8	64909500	0.00015	1.000	0.000001	
3691.7	29775400	0.00034	1.000	0.000020	
2293.2	18495800	0.00054	1.000	0.000096	
2042.4	16473000	0.00061	0.999	0.000134	
1740.0	14034000	0.00071	0.999	0.000197	
1486.7	11991000	0.00083	0.999	0.000068	
1188.0	9581800	0.00104	0.999	0.000135	
1011.7	8159860	0.00123	0.999	0.000220	
929.7	7498490	0.00133	0.999	0.000282	
705.0	5686170	0.00176	0.998	0.000615	
572.8	4619910	0.00216	0.998	0.00106	
511.3	4123880	0.00242	0.998	0.00139	
392.4	3164900	0.00316	0.997	0.00242	
311.7	2514010	0.00398	0.996	0.00360	
277.0	2234140	0.00448	0.995	0.00441	
212.2	1711500	0.00584	0.994	0.00725	
171.7	1384850	0.00722	0.996	0.00812	
151.1	1218700	0.00821	0.991	0.01097	
132.8	1071100	0.00934	0.989	0.0123	
114.0	919466	0.01088	0.986	0.0160	
108.5	875106	0.01143	0.985	0.0171	
91.5	737992	0.01355	1.000	0.0217	
72.4	583942	0.01713	1.000	0.0321	
49.3	397629	0.02515	1.000	0.0680	
30.5	245998	0.04065	1.000	0.1799	
190.0	1532440	0.00652		0.0079	[17]
180.0	1451790	0.00689		0.0091	
170.0	1371130	0.00729		0.0100	
160.0	1290480	0.00775		0.0102	
140.0	1129170	0.00886		0.0112	
150.0	1209830	0.00826		0.0104	
130.0	1048520	0.00954		0.0126	
120.0	967859	0.01033		0.0136	
110.0	887204	0.01127		0.0161	
100.0	806549	0.01240		0.0184	
90.0	725894	0.01377		0.0219	
80.0	645239	0.01550		0.0272	
70.0	564584	0.01771		0.0340	
11.50	92756.9	0.11	0.71	0.24	[71]
11.00	88725.0	0.11	0.68	0.26	
10.00	80658.2	0.12	0.60	0.35	
9.00	72592.4	0.14	0.59	0.52	
8.00	64526.5	0.15	0.70	0.70	

[a] The references from which the values were taken are given in brackets.

TABLE VIII *(Continued)*

Ytterbium

eV	cm^{-1}	μm	n	k	
7.00	56460.7	0.18	0.73	0.73	
6.00	48394.9	0.21	0.68	0.82	
5.00	40329.1	0.25	0.64	1.03	
4.50	36296.2	0.28	0.57	1.19	
4.00	32263.3	0.31	0.54	1.45	
3.50	28230.4	0.35	0.57	1.71	
3.00	24197.5	0.41	0.62	2.09	
2.00	16131.6	0.62	1.34	2.61	
1.50	12098.7	0.83	1.79	3.90	
1.00	8065.8	1.24	2.28	5.49	
0.50	4032.9	2.48	3.37	8.91	
5.50	44361.9	0.225		0.31	[73]
5.00	40329.5	0.248		0.37	
4.00	32263.3	0.310		0.52	
3.00	24197.5	0.413		0.87	
2.50	20164.5	0.496		1.05	
2.00	16131.6	0.620		1.45	
1.60	12905.3	0.775		3.45	
1.00	8065.8	1.240		4.13	
0.50	4032.9	2.480		11.62	
1.959	15802.8	0.633	1.68	3.22	[76]
0.620	5000.0	2.0	2.63	4.92	[74]
0.310	2500.0	4.0	4.43	8.45	
0.207	1666.7	6.0	6.15	11.73	
0.155	1250.0	8.0	7.79	14.68	
0.124	1000.0	10.0	9.23	17.30	
0.104	833.3	12.0	10.58	19.43	
0.089	714.3	14.0	11.48	21.32	
0.078	625.0	16.0	12.38	22.47	
0.069	555.6	18.0	13.86	24.44	
0.062	500.0	20.0	14.84	26.16	
0.056	454.5	22.0	15.99	27.80	
0.052	416.7	24.0	17.47	29.27	

Cesium (Cs)

T. INAGAKI
Division of Natural Science
Osaka Kyoiku University
Osaka, Japan

and

E. T. ARAKAWA
Life Sciences Division
Oak Ridge National Laboratory
Oak Ridge, Tennessee

Cesium is a soft and ductile metal and chemically reactive. The crystalline structure is normally body-centered cubic. The melting point is the lowest (28°C) and the vapor pressure is the highest (ca. 7×10^{-7} torr at room temperature) among the alkali metals. Optical studies have been made usually under ultrahigh vacuum and at low temperatures. However, extensive studies have been made at room temperature [1–6], which is only several degrees below the melting point.

Mirror surfaces of cesium for optical measurements have been produced either by distillation and condensation onto a cooled substrate [1, 2, 6] or by gentle thermal evaporation [3–5, 7, 8, 10–12]. Some measurements have been made on quartz (or calcium fluoride)–Cs interfaces [3–5] to avoid contamination even under ultrahigh vacuum and to avoid the effects of roughening due to the high volatility of Cs. Most measurements have been made, however, on vacuum–cesium interfaces [1, 2, 6–12]. In addition, the optical properties of cesium in the form of semitransparent thin films and the thickness dependencies have been studied by several authors [7, 8, 11, 12] at low temperatures.

The optical properties of cesium in the near infrared to the ultraviolet have been relatively well established [5, 9]. The optical properties are essentially like those of nearly free electrons. The absorption properties given by the optical-conductivity curve show three prominent features: a tail of the Drude absorption below 0.6 eV, a weak absorption with the peak centered at 1.1 eV, and a strong absorption with the peak centered at 5.1 eV.

The weak absorption at 1.1 eV has been assigned conclusively as due to

HANDBOOK OF OPTICAL CONSTANTS OF SOLIDS III

Copyright © 1998 by Academic Press.
All rights of reproduction in any form reserved
ISBN 0-12-544423-0/$25.00.

an interband absorption, whose quantitative features are described by the single-pseudopotential model [5]. The observed onset of this absorption, 0.6 eV, is, however, significantly lower than the theoretical threshold energy, 0.97 eV, of the interband transition. To account for this discrepancy, the contribution from the intrinsic surface state to the total absorption in this region has been studied [13]. The strong absorption at 5.1 eV has been attributed either to an interband transition or to collective excitations [3, 4, 9]. These absorption features are common to the alkali metals except for lithium, but those observed for cesium are considerably stronger than for the other alkali metals [9].

The first modern measurement of the optical constants of cesium at room temperature was made by Mayer and Hietel [2, 6]. They measured a vacuum–cesium interface between 0.5 and 4.18 eV by ellipsometry. Their results show clearly the tail of a Drude absorption below 0.6 eV, the absorption band with peak at around 1.1 eV, and a gradual rise of the absorption above 3.5 eV after leveling off between 2 and 3.5 eV.

Smith [5] remeasured the optical constants of cesium at room temperature between 0.5 and 4.0 eV. He measured multiple (seven) reflections at quartz–cesium interfaces using a split-beam ellipsometer. His measurements reproduced the results of Mayer and Hietel [2, 6] in general. His n values below 1.0 eV are, however, considerably larger than those measured by Mayer and Hietel for vacuum–cesium interfaces. A Kramers–Kronig analysis made by the present authors using a reasonable extrapolation of the k values in the region below 0.5 eV yielded n values that were very close to Smith's values. Smith also found that his n and k values in the region above 2.0 eV agree well with the earlier data by Ives and Briggs [1], which were measured for vacuum–cesium interfaces in 1937.

The optical measurements of cesium have been extended into the vacuum ultraviolet above 6 eV by Whang *et al.* [3, 4] They measured the reflectance from quartz–cesium and calcium fluoride–cesium interfaces as a function of angle of incidence near the critical angle for total internal reflection. Since, in the region of their measurements between 3.6 and 9.6 eV, the k values are small (<0.2), the reflectance curve shows a steep rise at angles given by the n value of cesium relative to that of the substrate. The n values of cesium were obtained from the angle at which the reflectance curve exhibits the steepest rise, and the k values were obtained from the slope by taking account of the effects of the partial polarization of the incident light. Their result of the optical conductivity shows a strong absorption with the peak centered at 5.1 eV. Below 4.2 eV, their results show good agreement with those from Mayer and Hietel [2, 6] and Smith [5].

Whang *et al.* [3, 4] reported that reflectance values measured with calcium fluoride–cesium interfaces were significantly lower than those predicted by theoretical calculations and speculated that it was caused by contamination of the calcium fluoride–cesium interface. They later estimated [9] that

the uncertainty of their optical-conductivity values was less than 30%, and the normalization of the measured reflectance values to the theoretical values rendered the optical conductivity uncertain by an approximately constant factor over the full range of their measurement. A Kramers–Kronig analysis made by the present authors gave n values that are systematically smaller than those reported by Whang *et al.* by 0.080 in the entire range of their measurement. These discrepancies were found too large to attribute to any uncertainties involved in the present Kramers–Kronig analysis, indicating that the major part of the discrepancies came from the uncertainties in the experiments of Whang *et al.*

The optical constants of cesium at low temperatures were studied by Mayer and Hietel [2, 6] by ellipsometry. They measured vacuum–cesium interfaces at 90 and 195 K between 0.5 and 4.18 eV and compared the results with those obtained at room temperature. They found that the ϵ_1 values are rather insensitive to the temperature, but that the ϵ_2 values, and hence the optical conductivity, in the region of the interband transition above 0.6 eV increases, and the 1.1 eV peak shifts slightly to higher energies with decreasing temperature. As pointed out earlier for the room-temperature data, their data below 1.0 eV are possibly subject to a Kramers–Kronig inconsistency.

Monin and Boutry [10] also investigated the vacuum–cesium interface at low temperatures. They prepared the cesium layer at 77 K and measured n and k by ellipsometry between 2 and 5 eV. They found that, below 3 eV, the vacuum–cesium interface exhibited an irreversible change when it was heated to 195 K and cooled down again to 77 K.

The optical properties of cesium in the form of a thin, semitransparent film were studied by Steffen and Mayer [7] between 1.38 and 4.13 eV. They prepared cesium films on a quartz plate kept at 77 K with the thicknesses ranging from 7 to 240 nm. The thickness dependencies of the transmittance and the reflectance were measured by using p- and s-polarized photons incident at 30 and 60°. For the thinner films, they observed an absorption due to plasmon excitation when the photons were p-polarized. They reported the optical constants for the 160-nm-thick film, which did not differ much from those of bulk cesium measured at low temperature [6].

Steffen [11] later reported the optical constants of the rest of the films studied in the previous paper [7]. The ϵ_1 and ϵ_2 values reported for the 14.5-, 80.5-, and 107-nm-thick films show too large a scatter to define dependency of the optical constant values on film thickness.

Hanyu and Yamaguchi [8] also studied the optical properties of cesium films at low temperature between 2.1 and 6.2 eV. They prepared 150- to 170-nm-thick films on a quartz plate kept at 133 K and measured the transmittance and the reflectance of p- and s-polarized photons incident at 45°. The n and k values derived from these data above 3 eV do not differ much from those of bulk cesium measured at room temperature by Smith [5] and Whang *et al.* [4]. Below 3 eV, they found significant deviation of their ϵ_2

values from the bulk values and attributed it to a temperature effect. These authors also reported that the ϵ_2 values found for the 3-μm-thick opaque films were consistently smaller than those found for the 150- to 170-nm-thick films.

The optical constants of cesium in the region of the inner-shell excitation were studied by Sato *et al.* [12] using synchrotron radiation. They prepared semitransparent films of cesium on collodion films supported by metal-mesh screens kept at 77 K. Normal-incidence transmittances of the films were measured between 10 and 37 eV as a function of film thickness. The k values of the films were determined from the slope of the semilog plot of the inverse of the transmittance and the film thickness. Their data show a sharp rise of absorption at 11.8 eV followed by strong absorption extending to 30 eV with a peak at around 16 eV. This absorption was assigned to the transition of electrons in the outermost $5p$ shell to the Fermi and higher levels.

We have made a Kramers–Kronig analysis by combining the k-value data taken at room temperature in the various spectral regions. Below 0.5 eV, we used Drude values of k, which were evaluated from the dc conductivity of cesium to yield a smooth connection with the k values from Smith [5] at 0.5 eV. Between 0.5 and 3.4 eV and between 3.6 and 9.0 eV, we used the data from Smith [5] and Whang *et al.* [4], respectively. Between 10 and 30 eV, we used the data from Sato *et al.* [12] (measured at 77 K), and, above 30 eV, we used the semiempirical data from Henke *et al.* [14] derived from the atomic scattering factors. These data show good agreement with each other in the connecting regions, producing a smoothly connected single curve from $\sim$0 to 30 keV. The result of the sum-rule calculation on these k values was satisfactory.

The n values obtained from the Kramers–Kronig analysis are plotted in Fig. 1 and numerically tabulated in Table I together with the k values. Below 3.4 eV, the n values thus obtained agree well with the data from Smith [5], and between 3.6 and 9.0 eV, they are smaller than the values from Whang *et al.* [4] almost by a constant 0.080, as described earlier. We recommend these n and k values as the most reliable values of the optical constants of cesium at room temperature that are presently available.

ACKNOWLEDGMENT

Sponsored by the Office of Health and Environmental Research, U.S. Department of Energy, under Contract DE-AC05-96OR22464 with Lockheed Martin Energy Research Corporation.

REFERENCES

1. H. E. Ives and H. B. Briggs, *J. Opt. Soc. Am.* **27**, 395 (1937).
2. H. Mayer and B. Hietel, "Optical Properties and Electronic Structures of Metals and Alloys," (F. Abelés, ed.), pp. 47–59. North Holland, Publ., Amsterdam, 1966.
3. U. S. Whang, E. T. Arakawa, and T. A. Callcott, *Phys. Rev. Lett.* **25**, 646 (1970).

4. U. S. Whang, E. T. Arakawa, and T. A. Callcott, *J. Opt. Soc. Am.* **61**, 740 (1971).
5. N. V. Smith, *Phys. Rev. B* **2**, 2840 (1970).
6. H. Mayer and B. Hietel, *Z. Phys.* **254**, 232 (1972).
7. H. Steffen and H. Mayer, *Z. Phys.* **254**, 250 (1972).
8. T. Hanyu and S. Yamaguchi, *J. Phys. Soc. Jpn.* **37**, 994 (1974).
9. U. S. Whang, E. T. Arakawa, and T. A. Callcott, *Phys. Rev. B* **6**, 2109 (1972).
10. J. Monin and G. A. Boutry, *Phys. Rev. B* **9**, 1309 (1974).
11. H. Steffen, *Thin Solid Films* **21**, 59 (1974).
12. S. Sato, T. Miyahara, T. Hanyu, S. Yamaguchi, and T. Ishii, *J. Phys. Soc. Jpn.* **47**, 836 (1979).
13. R. Garron and H. Roubaud, *Surf. Sci.* **146**, 527 (1984).
14. L. Henke, E. M. Gullikson, and J. C. Davis, *At. Data Nucl. Data Tables* **54**, 181 (1993).

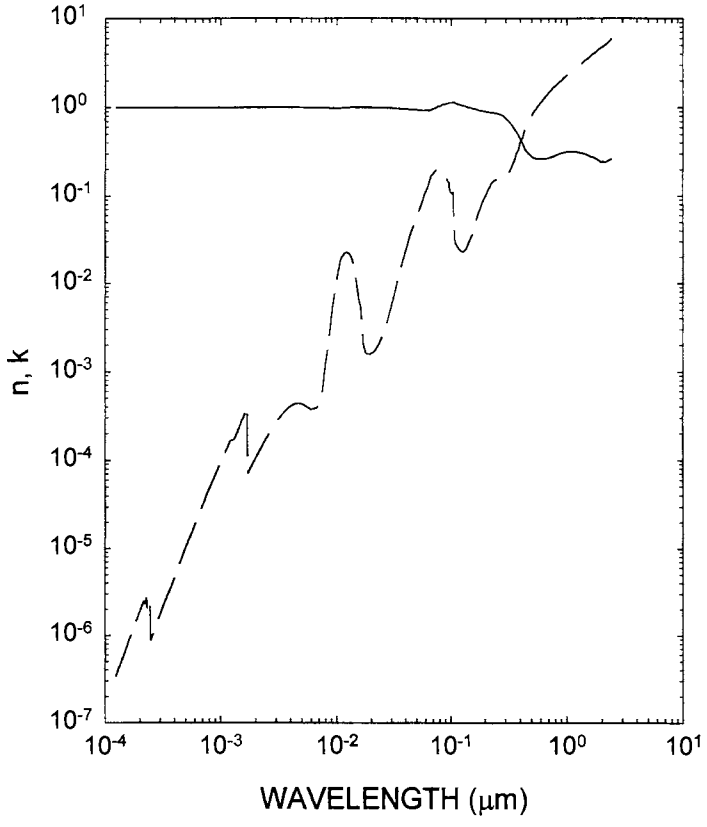

Fig. 1. Log–log plot of n (solid line) and k (dashed line) versus wavelength in micrometers for cesium.

TABLE I

Values of n and k for Cesium Obtained from Various References[a]

eV	cm^{-1}	μm	n	k
10000	8.065E + 07	1.240E-04	0.9999968	3.37E-07[14]
9542	7.696E + 07	1.299E-04	0.9999965	4.00E-07
9106	7.344E + 07	1.362E-04	0.9999961	4.75E-07
8689	7.008E + 07	1.427E-04	0.9999958	5.64E-07
8291	6.687E + 07	1.495E-04	0.9999954	6.68E-07
7912	6.381E + 07	1.567E-04	0.9999949	7.92E-07
7549	6.089E + 07	1.642E-04	0.9999945	9.37E-07
7204	5.810E + 07	1.721E-04	0.999994	1.11E-06
6874	5.544E + 07	1.804E-04	0.9999935	1.31E-06
6560	5.291E + 07	1.890E-04	0.9999929	1.54E-06
6260	5.049E + 07	1.981E-04	0.9999923	1.82E-06
5973	4.818E + 07	2.076E-04	0.9999919	2.14E-06
5700	4.597E + 07	2.175E-04	0.9999919	2.22E-06
5439	4.387E + 07	2.280E-04	0.9999912	2.62E-06
5190	4.186E + 07	2.389E-04	0.9999906	2.27E-06
4952	3.994E + 07	2.504E-04	0.9999902	8.83E-07
4726	3.812E + 07	2.624E-04	0.9999882	1.04E-06
4509	3.637E + 07	2.750E-04	0.9999866	1.23E-06
4303	3.471E + 07	2.881E-04	0.999985	1.46E-06
4106	3.312E + 07	3.020E-04	0.9999833	1.72E-06
3918	3.160E + 07	3.165E-04	0.9999815	2.03E-06
3739	3.016E + 07	3.316E-04	0.9999795	2.40E-06
3568	2.878E + 07	3.475E-04	0.9999774	2.82E-06
3404	2.745E + 07	3.642E-04	0.999975	3.33E-06
3249	2.620E + 07	3.816E-04	0.9999724	3.92E-06
3100	2.500E + 07	4.000E-04	0.9999696	4.61E-06
2958	2.386E + 07	4.192E-04	0.9999666	5.43E-06
2823	2.277E + 07	4.392E-04	0.9999632	6.38E-06
2693	2.172E + 07	4.604E-04	0.9999596	7.50E-06
2570	2.073E + 07	4.824E-04	0.9999556	8.82E-06
2452	1.978E + 07	5.057E-04	0.9999513	1.04E-05
2340	1.887E + 07	5.299E-04	0.9999466	1.22E-05
2233	1.801E + 07	5.552E-04	0.9999414	1.43E-05
2131	1.719E + 07	5.818E-04	0.9999359	1.67E-05
2033	1.640E + 07	6.099E-04	0.9999299	1.96E-05
1940	1.565E + 07	6.391E-04	0.9999235	2.29E-05
1852	1.494E + 07	6.695E-04	0.9999166	2.69E-05
1767	1.425E + 07	7.017E-04	0.9999092	3.14E-05
1686	1.360E + 07	7.354E-04	0.9999015	3.67E-05
1609	1.298E + 07	7.706E-04	0.999893	4.29E-05
1535	1.238E + 07	8.077E-04	0.999885	4.95E-05
1465	1.182E + 07	8.463E-04	0.999877	5.67E-05
1398	1.128E + 07	8.869E-04	0.999867	6.50E-05
1334	1.076E + 07	9.294E-04	0.999857	7.44E-05
1273	1.027E + 07	9.740E-04	0.999847	8.53E-05
1215	9.800E + 06	1.020E-03	0.999837	9.84E-05

[a] The references from which the values were taken are given in brackets.

TABLE I *(Continued)*

Cesium

eV	cm^{-1}	μm	n	k
1159	9.348E + 06	1.070E-03	0.999828	1.13E-04
1106	8.920E + 06	1.121E-03	0.99982	1.29E-04
1055	8.509E + 06	1.175E-03	0.999811	1.48E-04
1007	8.122E + 06	1.231E-03	0.999815	1.68E-04
961.0	7.751E + 06	1.290E-03	0.999812	1.71E-04
917.0	7.396E + 06	1.352E-03	0.999793	1.85E-04
875.0	7.057E + 06	1.417E-03	0.999781	2.15E-04
835.0	6.735E + 06	1.485E-03	0.999782	2.51E-04
796.8	6.427E + 06	1.556E-03	0.999799	2.95E-04
760.3	6.132E + 06	1.631E-03	0.999858	3.47E-04
725.5	5.852E + 06	1.709E-03	1.000264	6.94E-05
692.3	5.584E + 06	1.791E-03	0.999877	7.82E-05
660.6	5.328E + 06	1.877E-03	0.999797	8.82E-05
630.4	5.084E + 06	1.967E-03	0.999739	9.98E-05
601.5	4.851E + 06	2.061E-03	0.999688	1.12E-04
574.0	4.630E + 06	2.160E-03	0.999639	1.26E-04
547.7	4.417E + 06	2.264E-03	0.99959	1.41E-04
522.7	4.216E + 06	2.372E-03	0.99954	1.58E-04
498.7	4.022E + 06	2.486E-03	0.999487	1.75E-04
475.9	3.838E + 06	2.605E-03	0.999432	1.95E-04
454.1	3.663E + 06	2.730E-03	0.999372	2.17E-04
433.3	3.495E + 06	2.861E-03	0.999313	2.40E-04
413.5	3.335E + 06	2.998E-03	0.999248	2.63E-04
394.6	3.183E + 06	3.142E-03	0.999179	2.87E-04
376.5	3.037E + 06	3.293E-03	0.999105	3.11E-04
359.3	2.898E + 06	3.451E-03	0.999025	3.36E-04
342.8	2.765E + 06	3.617E-03	0.99894	3.59E-04
327.2	2.639E + 06	3.789E-03	0.99884	3.81E-04
312.2	2.518E + 06	3.971E-03	0.99874	4.01E-04
297.9	2.403E + 06	4.162E-03	0.99862	4.18E-04
284.3	2.293E + 06	4.361E-03	0.99849	4.30E-04
271.3	2.188E + 06	4.570E-03	0.99835	4.36E-04
258.8	2.087E + 06	4.791E-03	0.99817	4.36E-04
247.0	1.992E + 06	5.020E-03	0.99798	4.30E-04
235.7	1.901E + 06	5.260E-03	0.99774	4.18E-04
224.9	1.814E + 06	5.513E-03	0.99746	4.01E-04
214.6	1.731E + 06	5.778E-03	0.99712	3.85E-04
204.8	1.652E + 06	6.054E-03	0.99672	3.78E-04
195.4	1.576E + 06	6.345E-03	0.99625	3.84E-04
186.5	1.504E + 06	6.648E-03	0.9957	3.88E-04
177.9	1.435E + 06	6.969E-03	0.995	4.30E-04
169.8	1.370E + 06	7.302E-03	0.99414	5.34E-04
162.0	1.307E + 06	7.654E-03	0.9931	7.64E-04
154.6	1.247E + 06	8.020E-03	0.99185	1.15E-03
147.5	1.190E + 06	8.406E-03	0.99028	1.86E-03
140.8	1.136E + 06	8.806E-03	0.9885	3.17E-03

(continued)

TABLE I *(Continued)*

Cesium

eV	cm^{-1}	μm	n	k
134.3	1.083E + 06	9.232E-03	0.9868	5.30E-03
128.2	1.034E + 06	9.671E-03	0.9854	8.35E-03
122.3	9.864E + 05	1.014E-02	0.9852	1.22E-02
116.7	9.412E + 05	1.062E-02	0.9862	1.66E-02
111.4	8.985E + 05	1.113E-02	0.9898	2.02E-02
106.3	8.574E + 05	1.166E-02	0.99366	2.21E-02
101.4	8.178E + 05	1.223E-02	0.99814	2.25E-02
96.77	7.805E + 05	1.281E-02	1.00282	2.20E-02
92.35	7.448E + 05	1.343E-02	1.0074	1.99E-02
88.12	7.107E + 05	1.407E-02	1.0108	1.53E-02
84.09	6.782E + 05	1.474E-02	1.0118	1.06E-02
80.24	6.472E + 05	1.545E-02	1.0104	6.83E-03
76.57	6.176E + 05	1.619E-02	1.00904	5.35E-03
73.06	5.893E + 05	1.697E-02	1.00804	2.06E-03
69.72	5.623E + 05	1.778E-02	1.00458	1.62E-03
66.53	5.366E + 05	1.864E-02	1.00248	1.59E-03
63.48	5.120E + 05	1.953E-02	1.00072	1.58E-03
60.58	4.886E + 05	2.047E-02	0.999	1.64E-03
57.80	4.662E + 05	2.145E-02	0.99738	1.72E-03
55.16	4.449E + 05	2.248E-02	0.996	1.88E-03
52.63	4.245E + 05	2.356E-02	0.99358	2.10E-03
50.23	4.051E + 05	2.468E-02	0.99154	2.38E-03
47.93	3.866E + 05	2.587E-02	0.9896	2.77E-03
45.73	3.688E + 05	2.711E-02	0.9865	3.32E-03
43.64	3.520E + 05	2.841E-02	0.9837	4.12E-03
41.64	3.358E + 05	2.978E-02	0.9808	5.17E-03
39.74	3.205E + 05	3.120E-02	0.9778	6.64E-03
37.92	3.058E + 05	3.270E-02	0.9738	8.62E-03
36.00	2.904E + 05	3.444E-02	0.9700	1.13E-02
34.00	2.742E + 05	3.647E-02	0.9655	1.53E-02
32.00	2.581E + 05	3.875E-02	0.9600	2.02E-02
30.00	2.420E + 05	4.133E-02	0.9540	2.71E-02[12]
29.00	2.339E + 05	4.275E-02	0.9504	3.18E-02
28.00	2.258E + 05	4.428E-02	0.9483	3.69E-02
27.00	2.178E + 05	4.592E-02	0.9459	4.20E-02
26.00	2.097E + 05	4.769E-02	0.9423	4.77E-02
25.00	2.016E + 05	4.959E-02	0.9378	5.46E-02
24.00	1.936E + 05	5.166E-02	0.9340	6.47E-02
23.00	1.855E + 05	5.391E-02	0.9318	7.49E-02
22.00	1.774E + 05	5.636E-02	0.9290	8.90E-02
21.00	1.694E + 05	5.904E-02	0.9296	1.06E-01
20.00	1.613E + 05	6.199E-02	0.9328	1.22E-01
19.50	1.573E + 05	6.358E-02	0.9312	1.33E-01
19.00	1.532E + 05	6.526E-02	0.9352	1.52E-01
18.75	1.512E + 05	6.613E-02	0.9405	1.60E-01
18.50	1.492E + 05	6.702E-02	0.9490	1.69E-01
18.25	1.472E + 05	6.794E-02	0.9574	1.72E-01

TABLE I *(Continued)*

Cesium

eV	cm^{-1}	μm	n	k
18.00	1.452E + 05	6.888E-02	0.9640	1.76E-01
17.75	1.432E + 05	6.985E-02	0.9700	1.79E-01
17.50	1.411E + 05	7.085E-02	0.9761	1.84E-01
17.25	1.391E + 05	7.188E-02	0.9832	1.88E-01
17.00	1.371E + 05	7.293E-02	0.99192	1.93E-01
16.75	1.351E + 05	7.402E-02	1.00000	1.96E-01
16.50	1.331E + 05	7.514E-02	1.00841	1.98E-01
16.25	1.311E + 05	7.630E-02	1.0250	1.97E-01
16.00	1.290E + 05	7.749E-02	1.0326	1.93E-01
15.75	1.270E + 05	7.872E-02	1.0380	1.90E-01
15.50	1.250E + 05	7.999E-02	1.0444	1.91E-01
15.25	1.230E + 05	8.130E-02	1.0536	1.92E-01
15.00	1.210E + 05	8.266E-02	1.0658	1.91E-01
14.75	1.190E + 05	8.406E-02	1.079	1.85E-01
14.50	1.169E + 05	8.551E-02	1.0857	1.72E-01
14.25	1.149E + 05	8.701E-02	1.0878	1.65E-01
14.00	1.129E + 05	8.856E-02	1.0909	1.62E-01
13.75	1.109E + 05	9.017E-02	1.0964	1.61E-01
13.50	1.089E + 05	9.184E-02	1.108	1.57E-01
13.25	1.069E + 05	9.358E-02	1.114	1.47E-01
13.00	1.049E + 05	9.537E-02	1.124	1.44E-01
12.75	1.028E + 05	9.724E-02	1.136	1.22E-01
12.50	1.008E + 05	9.919E-02	1.127	1.10E-01
12.25	9.880E + 04	1.012E-01	1.125	1.06E-01
12.10	9.759E + 04	1.025E-01	1.127	1.05E-01
12.00	9.679E + 04	1.033E-01	1.132	1.07E-01
11.80	9.517E + 04	1.051E-01	1.153	1.10E-01
11.75	9.477E + 04	1.055E-01	1.160	5.79E-02
11.50	9.275E + 04	1.078E-01	1.130	3.17E-02
11.25	9.074E + 04	1.102E-01	1.112	2.86E-02
11.00	8.872E + 04	1.127E-01	1.0963	2.71E-02
10.60	8.549E + 04	1.170E-01	1.0778	2.50E-02
10.20	8.227E + 04	1.216E-01	1.0618	2.33E-02
9.80	7.904E + 04	1.265E-01	1.0467	2.29E-02
9.40	7.582E + 04	1.319E-01	1.0318	2.35E-02
9.04	7.291E + 04	1.372E-01	1.019	2.50E-02[4]
8.74	7.049E + 04	1.419E-01	1.003	2.80E-02
8.39	6.767E + 04	1.478E-01	0.992	3.20E-02
8.07	6.509E + 04	1.536E-01	0.980	3.60E-02
7.76	6.259E + 04	1.598E-01	0.968	4.10E-02
7.63	6.154E + 04	1.625E-01	0.961	4.60E-02
7.35	5.928E + 04	1.687E-01	0.950	5.50E-02
7.08	5.710E + 04	1.751E-01	0.935	6.40E-02
6.82	5.501E + 04	1.818E-01	0.925	7.20E-02
6.66	5.372E + 04	1.862E-01	0.920	7.90E-02
6.53	5.267E + 04	1.899E-01	0.915	8.40E-02

(continued)

TABLE I *(Continued)*

Cesium

eV	cm^{-1}	μm	n	k
6.32	5.097E + 04	1.962E-01	0.905	9.30E-02
6.09	4.912E + 04	2.036E-01	0.896	1.01E-01
5.86	4.726E + 04	2.116E-01	0.888	1.15E-01
5.72	4.613E + 04	2.168E-01	0.883	1.22E-01
5.43	4.380E + 04	2.283E-01	0.873	1.38E-01
5.22	4.210E + 04	2.375E-01	0.865	1.47E-01
5.00	4.033E + 04	2.480E-01	0.858	1.53E-01
4.80	3.871E + 04	2.583E-01	0.845	1.57E-01
4.60	3.710E + 04	2.695E-01	0.830	1.59E-01
4.40	3.549E + 04	2.818E-01	0.808	1.62E-01
4.20	3.388E + 04	2.952E-01	0.775	1.64E-01
4.00	3.226E + 04	3.100E-01	0.730	1.69E-01
3.80	3.065E + 04	3.263E-01	0.678	1.91E-01
3.60	2.904E + 04	3.444E-01	0.618	2.24E-01
3.397	2.740E + 04	3.650E-01	0.548	2.70E-01[5]
3.351	2.703E + 04	3.700E-01	0.535	3.00E-01
3.204	2.584E + 04	3.870E-01	0.480	3.33E-01
3.100	2.500E + 04	4.000E-01	0.441	4.00E-01
2.952	2.381E + 04	4.200E-01	0.388	4.58E-01
2.818	2.273E + 04	4.400E-01	0.340	5.70E-01
2.638	2.128E + 04	4.700E-01	0.303	6.83E-01
2.417	1.949E + 04	5.130E-01	0.273	8.53E-01
2.226	1.795E + 04	5.570E-01	0.263	9.84E-01
2.033	1.640E + 04	6.099E-01	0.261	1.16E + 00
1.842	1.486E + 04	6.731E-01	0.266	1.36E + 00
1.625	1.311E + 04	7.630E-01	0.280	1.65E + 00
1.400	1.129E + 04	8.856E-01	0.303	1.98E + 00
1.219	9.832E + 03	1.017E + 00	0.318	2.36E + 00
1.046	8.436E + 03	1.185E + 00	0.317	2.75E + 00
0.923	7.444E + 03	1.343E + 00	0.306	3.14E + 00
0.864	6.969E + 03	1.435E + 00	0.298	3.41E + 00
0.818	6.598E + 03	1.516E + 00	0.288	3.56E + 00
0.777	6.267E + 03	1.596E + 00	0.280	3.77E + 00
0.734	5.920E + 03	1.689E + 00	0.273	4.02E + 00
0.702	5.662E + 03	1.766E + 00	0.265	4.19E + 00
0.675	5.444E + 03	1.837E + 00	0.257	4.34E + 00
0.651	5.251E + 03	1.905E + 00	0.251	4.54E + 00
0.626	5.049E + 03	1.981E + 00	0.239	4.70E + 00
0.608	4.904E + 03	2.039E + 00	0.246	4.86E + 00
0.587	4.734E + 03	2.112E + 00	0.241	5.04E + 00
0.572	4.613E + 03	2.168E + 00	0.243	5.15E + 00
0.512	4.130E + 03	2.422E + 00	0.263	5.90E + 00

Zirconium Nitride (ZrN)
Hafnium Nitride (HfN)

CARL G. RIBBING and ARNE ROOS
Institute of Technology
Uppsala University
Uppsala, Sweden

The three transition-metal nitrides TiN, ZrN, and HfN belong to a larger group of compounds having NaCl or A15 structure with extreme stability in a generalized sense, i.e., hardness, chemical inertness, and high melting point and Young's modulus. This stability is the basis for their widespread technical use as hard materials on cutting tools, abrasive applications, etc. The larger family of materials includes carbides, nitrides, and oxides of group IVB to VIB transition metals such as vanadium, niobium, tantalum, molybdenum, and tungsten. There are numerous possible stoichiometry variations, since many of these compounds can form stable solid solutions with each other over wide ranges of composition. The basic reason for the high stability is their bonding, which is an intricate mixture of covalent bonds and ionic contributions. Of the three nitrides mentioned, only the two heavier ones constitute the subject of this critique. TiN, which is by far the most investigated of the three, was covered in Vol. II of this handbook [1]. The electronic configurations for the two metals are $[Kr]4d^2 5s^2$ and $[Xe]4f^{14}5d^2 6s^2$, respectively, which form highly directional bonds with N: $1s^2 2s^2 2p^3$ by hybridization. A characteristic and unusual result of this intricate bonding is that these two compounds (as well as TiN) are "ceramic" in terms of hardness, inertness, and directed bonds, but "metallic" with characteristically high electrical and thermal conductivity [2], in fact higher than that of the metal Ti. ZrN becomes superconducting for $T < 10$ K, significantly higher than the critical temperature for the metal T_c (Zr) ≈ 0.55 K. The room-temperature cubic unit-cell sizes of ZrN and HfN are 0.4577 and 0.4526 nm, respectively [2].

The *optical* applications of materials from this group are much less important than their tribological ones, but in particular TiN is used as a cos-

HANDBOOK OF OPTICAL CONSTANTS OF SOLIDS III

Copyright © 1998 by Academic Press.
All rights of reproduction in any form reserved
ISBN 0-12-544423-0/$25.00.

metic coating to replace gold in situations when a noble metal would not be sufficiently wear-resistant. ZrN and HfN have a less yellow but still bright appearance. Their possible use of a color standard has been discussed [3]. This adds to the metallic features just mentioned, and it signals a *free-electron-like* optical behavior that is striking for at least two reasons. Empirical chemical considerations, as well as advanced theoretical calculations, predict that the electrons close to the Fermi-level have a pure *d*-character in spite of the hybridization mentioned earlier. Based on this, one would expect a transition-metal-like behavior and a dull, greyish appearance. This is what is observed for the three carbides of Ti, Zr, and Hf, but the nitrides are radically different. This qualitative shift for only one *p*-electron more or less on the metaloid atom was pointed out by Karlsson [4]. It was suggested to exploit this free-electron-like character of the nitrides in stable optical coatings that are selectively transmitting [5]. Early attempts to prepare a bulk, selective solar absorber from compounds within this group of materials were not sucessful [6–8]. Lately, the use of an inhomogeneously oxidized surface has shown more promise [9].

Free-electron-like optical properties are conventionally described with the Drude-oscillator formalism [10], which models the intraband excitations of an electron gas. In this case of the transition metal nitrides, the *d*-electrons just below the Fermi surface constitute the electron gas. The low dispersion of typical *d*-bands makes it unusual to associate *d*-band compounds with free-electron behavior. Even more striking is that the optical behavior of these nitrides also indicates that interband excitations do not occur at low photon energies, or are at least strongly suppressed. It was suggested that in analogy with atomic spectroscopy, transitions between *d*-bands are forbidden to first order by the selection rule $\Delta l = \pm 1$ [4]. This explanation leaves open the question why the common transition metals, e.g., Fe and Ni, exhibit interband transitions [11] and are not free-electron-like.

In this connection it was of primary interest to compare the experimental optical data with results of band-structure calculations, in particular if integrated to partial densities of state. Already in the period between 1960 and 1970, band-structure calculations correctly predicted general trends within a group such as TiC, TiN, and TiO with regard to the energy band gap [12]. Eibler *et al.* [13] performed LCAO-APW calculations that were well adapted to distinguish between the bands of different character and that gave a more detailed picture than the general chemical arguments above. From the partial density of states a joint density of state function (JDOS) was calculated that, as expected, did not show any suppression at low excitation energies. The matrix elements were approximated in such a way as to show some **k**-dependence, and the product, as an approximation to the imaginary part of the interband dielectric function, $\epsilon_{2,\mathrm{ib}}$, was compared to the corresponding experimental quantity. It was interesting to note that while the JDOS did not show strong supression of *d–d* interband excitations, some of this quench-

ing appeared as a consequence of the matrix-element variation. This point was emphasized further by LMTO calculations [14]. A leap forward in the theoretical understanding has been taken with more recent LMTO calculations of Delin *et al.* [15]. Using the energy-band structure and fully variable matrix elements, an *ab initio* interband dielectric function was calculated. The supression of low-energy interband excitations is confirmed as a consequence of the vanishing dipole excitation probability. A semiempirical Drude-type intraband contribution was added, which resulted in very good agreement between theoretical and experimental reflectance spectra.

Relatively few experimental determinations of the complex index of refraction or dielectric function for bulk samples of *zirconium nitride* have been published. In particular, single crystalline studies are scarce. Schlegel *et al.* [16] prepared ZrN single-crystal samples by CVD growth on a heated graphite substrate from a chloride vapor. The resulting single crystals were polished and the normal-incidence bulk reflectance was measured for photon energies from 0.03 to 12 eV. The spectrum had an interval with high and almost wavelength-independent reflectance in the infrared region and a sharp drop to a minimum in the blue/ultraviolet region, as characteristic for a free-electron-like metal. At shorter wavelengths the reflectance again increases as a consequence of interband excitations. This reflectance spectrum was used as an input to Kramers–Kronig calculations giving primarily the complex dielectric function from which the complex refractive index $N(\lambda) = n(\lambda) + ik(\lambda)$ is easily obtained. The early work of Knosp *et al.* [17] with high-temperature sintered nitrides and carbonitrides had already pointed out that only the nitrides, in contrast to the carbides and even the pure metal, are optically free-electron-like in the visible range. They report reflectance spectra and the dielectric function for the limited wavelength interval 275–750 nm.

For their measurements Karlsson *et al.* [7] also used opaque samples deposited upon molybdenum in a CVD process very similar to that of Schlegel, but at a lower temperature, resulting in a polycrystalline dense film that was subsequently polished to ensure specular reflectance. The room-temperature reflectance spectrum was recorded and Kramers–Kronig inverted as in the two previous cases. The NIR reflectance was about the same, 85–90% in all three cases, but the reflectance minima differed both in magnitude and position [7, 16, 17]. We recall that application of the Drude model requires the introduction of a screening constant in the standard expression:

$$\tilde{\epsilon} = \epsilon_1(\infty) - \frac{\omega_p^2 \tau}{\omega^2 \tau + i\omega}, \tag{1}$$

where $\epsilon_1(\infty) > 1$ is the simplest possible representation, a screening constant, of the dispersion caused by higher-energy excitations not included in the

Drude model. The Drude-model reflectance edge for valence electrons with effective optical mass m^* and volume density n in SI units:

$$\hbar\omega_p = \sqrt{\frac{ne^2}{\epsilon_0 m^*}}. \tag{2}$$

The screening constant corresponds to a rigid shift upward of the real part of the dielectric function $\epsilon_1(\omega)$, which displaces the zero of the corresponding Drude function to a lower photon energy. The plasma edge is therefore shifted by the interband excitations of lower-lying electrons, and if the plasma resonance is sharp, that is, $\omega_p\tau \gg 1$, the screened reflectance-edge position is approximately given by.

$$\hbar\omega_p^* = \sqrt{\frac{ne^2}{\epsilon_1(\infty)\epsilon_0 m^*}}. \tag{3}$$

Equations (1)–(3) apply to the transition-metal nitrides almost as well as to the noble metals, and we find that high IR reflectance, steep plasma edge, and a deep reflectance minimum before the onset of interband transitions all indicate a long relaxation time and therefore a more perfect structure. The reflectance minimum was clearly lower in Refs. [17] and [7], which gives them some preference. The free-electron-like part of the dielectric function was used to calculate the Drude parameters, the plasma and relaxation energies: $\hbar\omega_p$ and $\hbar/\tau$. A comparison revealed some scatter in ω_p-values and lower relaxation energies, that is, longer relaxations times, reported by Knosp and Goretzki [17] and Karlsson *et al.* [7] than by Schlegel *et al.* [16], which somewhat surprisingly indicates fewer defects in the polycrystalline films than in the epitaxial layer.

Using the Drude parameters, the intraband contribution can be subtracted from the experimental dielectric function over the entire experimental region. The remaining, interband-excitation part of the dielectric function is relevant for comparison with band-structure calculations and density-of-state functions, in particular the conspicuous threshold for interband transitions, the position of which explains the color of these nitrides, as well as for the three noble metals. This threshold is close to the reflectance minimum just mentioned, and for ZrN Karlsson *et al.* located it to be at ≈3.5 eV [7]. François *et al.* [18] sputtered 480-nm-thick films on 400° C glass and stainless-steel substrates and measured the bulk-reflectance spectra at elevated temperatures, up to 700° C. The dielectric function was calculated by Kramers–Kronig integration for various temperatures. Already for moderately high temperatures the Drude relaxation time decreased, and at the more elevated temperatures a reduction of the screened plasma energy was also observed. These authors report a lower threshold, 1.5 eV, for interband excitations than previous studies, and also a local maximum in the interband contribution to

ϵ_2 at 2.5 eV, which is not present in papers by Karlsson *et al.* [7] and Schlegel [16]. The resulting optical constants, calculated from their dielectric function, are included in the enlarged-wavelength-scale diagrams in Figs. 2a and b.

Edlou *et al.* [19] deposited the three nitrides on room-temperature optical glass, fused silica, or silicon substrates. Two samples were opaque and two semitransparent with thicknesses 30–40 nm. Reflectance measurements as well as spectroscopic ellipsometry were performed to determine the optical constants. They note that the real part of their refractive index is ≤ 1 in most of the visible range. They also observed that, in particular for the longer wavelengths, the n-values increase, while the k-values are approximately constant when the films are made thinner.

Some reported optical measurements were made on opaque, otherwise unspecified samples and gave results that are difficult to reconcile with present knowledge. Presumably because of oxidation, the material appears dielectric or at least with a dielectric surface layer [20, 21]. The appearance of slowly varying n-values > 1 over the visible range is a typical indicator of such problems [1].

A number of studies on the deposition, mainly by reactive sputtering, of ZrN films and in most cases for tribological applications have been published [22]. The number of detailed reports on the optical constants of opaque or semitransmitting films is limited. In particular, very little has been done outside the visible and near-infrared regions. The report of EELS measurements by Pflüger *et al.* [23] is one of few exceptions, showing plasmon losses at 3.6 and 22.3 eV. We have used data from their diagram in Table II for the photon-energy range 10–50 eV. However, they report a refractive index value $n > 1.1$ at 600 nm and a reduction of the critical temperature for superconductivity T_c to < 5 K, which indicates sample oxidation. We have therefore placed less faith in their results for the visible and infrared regions.

Compared to the much-more-investigated TiN films, ZrN films pose a problem in their poor adhesion to common substrate materials. Bonnot *et al.* [8] sputtered their opaque films reactively upon 500° C silicon or glass substrates. They do not report optical constants, but confirm the transition from ZrN as a strongly colored, free-electron-like metal to the grey, transition-metal-like ZrC by also reporting reflectance spectra for zirconium carbonitrides. Veszelei *et al.* [24] studied optically opaque and semitransmitting ZrN films, reactively sputtered onto heated glass substrates. The optical constants for opaque films were determined by two independent methods: Kramers–Kronig integration of reflectance data was used over the range 0.3–25 μm, beyond which the extrapolation parameter was determined with reflectance measurements using polarized light at 60° incidence [25] at a few short wavelengths. The second method used was spectroscopic ellipsometry for λ from 0.28 to 1 μm. The two methods agreed to within 5% at all wavelengths. The values obtained for opaque films are quoted in Table II. One notices

that the n-values for opaque films are clearly <1, that is, noble-metal-like, over the entire visible region. The variation of the optical constants with film thickness was systematically studied [26], and the same trend as had previously been noted for TiN [27] was established. With decreasing film thickness, the n-values for the visible region increase, and the k-values decrease. For a film thickness < 30 nm, no n-values < 1 are obtained. The usual determination of the intraband part was made without the standard asumption of total dominance for Drude behavior by using the screened version (1) and noting that it corresponds to an exact relation between the real and imaginary parts,

$$\epsilon_1 = \epsilon_1(\infty) - \epsilon_2 \omega\tau, \tag{4}$$

so that the linearity of the plot ϵ_1 versus $\omega\epsilon_2$ will verify that the Drude model is valid, and the slope of the straight line will give an experimental value for the relaxation time τ. In the subsequent step, the second Drude parameter ω_p is determined from the slope of ϵ_1 versus $[(\hbar/\tau)^2 + (\hbar\omega)^2]^{-1}$. It was demonstrated that the screened Drude model very closely predicted the optical constants over the wavelength range 0.3–2 μm, with the constant parameter values $\epsilon_1(\infty) = 6.1$, $\hbar\omega_p = 7.1$ eV, and variations only in τ from 2.3 to 0.49 fs to cover film thicknesses from 300 down to 11 nm.

The number of optical studies of *hafnium nitride* is even more limited than for ZrN. We have not been able to find any report of optical measurements on hafnium-nitride single crystals. The thesis of Fluck on the optical properties of hafnium carbonitrides is a standard reference [28]. Fluck's samples were prepared by sintering at 30 MPa at a temperature of 2800° C in a protective atmosphere of nitrogen. The result was bulk, polycrystalline samples with 10–20 μm grain size. Fluck measured the reflectance spectra over the range 0.1–6.2 eV for the carbonitride series HfC_xN_{1-x} and noted the transition from the noble-metal-like behavior of the nitride, to the transition-metal character of the carbide. He also modeled his spectra with Drude theory, compared with band-structure calculations, and extracted the number of free electrons as a function of composition. However, he only reported values for $\epsilon_2(\omega)$ for samples with $x \geq 0.07$.

Early optical measurements at one wavelength (632.8 nm) on rf-sputtered HfN_x films resulted in optical constants characteristic of a partly oxidized film [29]. Karlsson *et al.* prepared opaque HfN films by CVD deposition in a process similar to that for ZrN [7]. They measured normal-incidence reflectance, made Kramers–Kronig calculations, reported optical constants for λ (0.3–2.1 μm) and separated the intra- and interband contributions to the dielectric function. The n-values were <1 for the visible region and the relaxation energy, $\hbar/\tau$, only 0.45 eV, which indicates a less-defected structure than the sintered samples with $\hbar/\tau = 1.4$ eV.

Thin-film deposition of HfN with reactive dc sputtering and accurate structure determinations was studied in detail by Johansson [30]. It appears as if

the dc sputtering results in less-oxidized films. Two studies of reactively sputtered films give optical constants for the wavelength interval in which measurements can be carried out in air [19, 31]. Edlou *et al.* [19] used spectroscopic ellipsometry to determine $n(\lambda)$ and $k(\lambda)$ for λ from 240 to 1640 nm. Strømme *et al.* [31] combined Kramers–Kronig inversion and ellipsometry to obtain data for the λ-range 230–2000 nm as in Veszelei [24]. Both sets of data are included in Figs. 4a and b. In Table III we quote the data of Karlsson *et al.* [7] considering the lower n-values and higher k-values in the visible region. In one part of the spectrum we have used the data of Strømme *et al.* [31] because of their two independent measurements and wider wavelength range. An increase of the n-values with decreasing film thickness is pointed out elsewhere [19, 31]. A systematic study of the variation of the Drude parameters with film thickness was carried out by Strømme. As for the case with ZrN [26], it is shown that the variation, both in n and in k, can be modeled with a variation of the relaxation time τ alone. An opaque 380-nm-thick film had $\tau = 1.86$ fs, which monotonically decreases to $\tau = 0.60$ fs for a 15-nm-thick film, a variation that is comparable with, but smaller than, that reported for ZrN.

In Fig. 1 we have the standard log–log plot of the optical constants for ZrN from Table II, selected as described below. In Figs. 2a and 2b we have given the more detailed behavior of $n(\lambda)$ and $k(\lambda)$, respectively, in the wavelength range of most optical interest and therein included data from several reports mentioned above. It is striking that there are considerable differences between the various refractive-index curves, $n(\lambda)$ in Fig. 2a, while the extinction coefficients, $k(\lambda)$, in 2b closely agree. In Figs. 3, 4a, and 4b the corresponding representation of HfN-data is given.

In Table I we have collected the Drude parameters for the two materials converted to one set of units, otherwise as reported by the various authors. In Tables II and III, i.e., the major collection of optical constants versus photon energy, we have made the following selection among the available sets of data according to the criteria indicated earlier. For ZrN the high-photon-energy data (10 keV–30 eV) were calculated from atomic data and the density according to Henke [32]. In the range 28–8 eV, the values were extracted from Pflüger *et al.* [23] and at lower energies than 8 eV from Veszelei *et al.* [24]. For HfN in Table III the same source of high-energy data was used [32], which left a gap to the next source for 11–4 eV, an interval where Ref. [31] was used. For 4 eV and below we have chosen the values from Karlsson *et al.* [7]. It should be noted that the Henke values have merely been interpolated across the various atomic absorption edges.

ACKNOWLEDGMENT

We acknowledge many useful and stimulating discussions with Ass. Prof. Björn Karlsson, The Älvkarleby Laboratory, State Power Board, on the subject of this critique.

REFERENCES

1. J. Pflüger and J. Fink, *in* "Handbook of Optical Constants of Solids II" (E. D . Palik, ed.), Chap. 13, Section VIII, p. 307. Academic Press, Orlando, Florida, 1991.
2. L. E. Toth, "Refractory Materials: A Series of Monographs, Volume 7: Transition Metal Carbides and Nitrides." Academic Press, New York, 1971.
3. A. Mumtaz and W. H. Class, Color of titanium nitride prepared by reactive dc magnetron sputtering. *J. Vac. Sci. Technol.* **20**, 345 (1982).
4. B. Karlsson, Optical properties of solids for solar energy conversion. Thesis, Acta Universitatis Upsaliensis No. 620, Uppsala University, Uppsala, Sweden (1981).
5. B. Karlsson and C.-G. Ribbing, Optical properties of transparent heat-mirrors based on thin films of TiN, ZrN and HfN. *Proc SPIE* **324**, 52 (1982); see also B. Zega, M. Kornmann, and J. Amiguet, *Thin Solid Films* **45**, 577 (1977)—Abstract only.
6. L. Roux, J. Hanus, J. C. François, and M. Sigrist, The optical properties of titanium nitrides and carbides: Spectral selectivity and photothermal conversion of solar energy. *Sol. Energy Mater.* **7**, 299 (1982).
7. B. Karlsson, R. P. Shimshock, B. O. Seraphin, and J. C. Haygarth, Optical properties of CVD-coated TiN, ZrN and HfN. *Sol. Energy Mater.* **7**, 401 (1983).
8. A. M. Bonnot, H. Belkhir, D. Pailharey, and P. Mathiez, Reactively sputtered zirconium carbides, carbonitrides and nitride thin films-optical properties. *Sol. Energy Mater.* **14**, 375 (1986).
9. M. Lazarov, A. Brunotte, T. Eisenhammer, R. Sizmann, W. Graf, and W. Wittwer, Effects of roughness in TiN_xO_y-Cu selective absorbers. *Proc. SPIE* **1727**, 34 (1992).
10. F. Wooten, "Optical Properties of Solids," 1st Ed. Academic Press, New York, 1972.
11. P. B. Johnson and R. W. Christy, Optical constants of transition metals: Ti, V, Cr, Mn, Fe, Co, Ni and Pd. *Phys. Rev. B* **9**, 5056 (1974).
12. J.-L. Calais, Band structure of transition metal compounds. *Adv. Phys.* **26**, 847 (1977).
13. R. Eibler, M. Dorrer, and A. Neckel, Calculation of the imaginary part $\epsilon_2(\omega)$ of the dielectric function for TiN and ZrN. *J. Phys. C: Solid State Phys.* **16**, 3137 (1983).
14. A. G. Nargizyan and S. N. Rashkeev, Microscopic analysis of the characteristic energy loss spectra of 3d- and 4d-transition metal carbides and nitrides. *Z. Phys. B Condens. Matter* **82**, 217 (1991).
15. A. Delin, O. Eriksson, R. Ahuja, B. Johansson, M. S. S. Brooks, T. Gasche, S. Auluck, and J. M. Wills, Optical properties of the group IVB refractory metal compounds. *Phys. Rev. B* **54**, 1673 (1996).
16. A. Schlegel, P. Wachter, J. J. Nickl, and H. Lingg, Optical properties of TiN and ZrN. *J. Phys. C: Solid State Phys.* **10**, 4889 (1977).
17. H. Knosp and H. Goretzki, Mikroreflexionsmessungen an druckgesinterten Proben der System Titan-TiN-TiC und Zirkonium-ZrN-ZrC. *Z. Metallkd.* **60**, 587 (1969) and also in H. Knosp and V. Gerold, Die Optische Konstanten in den Systemen Titan-TiN-TiC und Zirconium-ZrN-ZrC. *Z. Metallkd.* **60**, 627 (1969).
18. J. C. François, J. Casset, G. Chassaing, P. Gravier, and M. Sigrist, Optical properties of ZrN as a function of temperature. *J. Appl. Phys.* **58**, 3841 (1985).
19. S. M. Edlou, J. C. Simons, G. A. Al-Jumaily, and N. A. Raouf, Optical and electrical properties of reactively sputtered TiN, ZrN and HfN thin films. *Proc. SPIE* **2262**, 96 (1994).
20. S. A. Kutolin, L. F. Belova, R. N. Samoilova, and O. M. Kotenko, Optical properties and physicochemical spectra of nitrides with the NaCl structure. *Izv. Akad. Nauk SSSR, Met.* **12**, 1299 (1976).
21. B. A. Atamanenko, M. U. Belyi, P. I. Drozd, G. G. Tsebulya, and I. A. Shaikevich, Optical properties of zirconium nitride. *Izv. Akad. Nauk SSSR, Met.* **23**, 1037 (1987).
22. J. E. Sundgren and H. T. G. Hentzell, Critical review: A review of the present state of art in hard coatings grown from the vapor phase. *J. Vac. Sci. Technol. A* **4**, 2259 (1986).

23. J. Pflüger, J. Fink, W. Weber, K. P. Bohnen, and G. Crecelius, Dielectric properties of ZrN, NbC and NbN as determined by electron-energy-loss spectroscopy. *Phys. Rev. B* **31**, 1244 (1985).
24. M. Veszelei, K. Andersson, K. Järrendahl, C.-G. Ribbing, and H. Arwin, Optical constants and Drude analysis of sputtered zirconium nitride films. *Appl. Opt.* **33**, 1993 (1994).
25. J. E. Nestell and R. W. Christy, Derivation of optical constants of metals from thin-film measurements at oblique incidence. *Appl. Opt.* **11**, 643 (1972).
26. M. Veszelei, K. E. Andersson, and A. Roos, Optical characterization of sputtered semi-transparent zirconium nitride films. *Opt. Mater.* **2**, 257 (1993).
27. E. Valkonen, C.-G. Ribbing, and J.-E. Sundgren, Optical constants of thin TiN films: Thickness and preparation effects. *Appl. Opt.* **25**, 3624 (1986).
28. F. W. Fluck, Optische Untersuchungen an Hafniumcarbonitriden HfC_xN_{1-x}. Thesis, Juni 1978, Fakultät für Physik, University of Karlsruhe, Karlsruhe, Germany (1978).
29. P. R Aron and A. Grill, Some properties of RF-sputtered hafnium nitride coatings. *Thin Solid Films* **96**, 87 (1982).
30. B. O. Johansson, Structure and properties of titanium- and hafnium- nitride films prepared by reactive magnetron sputtering. Thesis No. 122, Linköping University, Linköping, Sweden (1984).
31. M. Strømme, R. Karmhag, and C. G. Ribbing, Optical constants of sputtered hafnium nitride films. Intra- and interband contributions. *Opt. Mater.* **4**, 629 (1995).
32. We acknowledge M Sc. Bjoern Gaalnander for demonstrating the E. M. Gullikson website: http://grace.lbl.gov/optical_constants/getdb2.html, which was used for calculating our data.

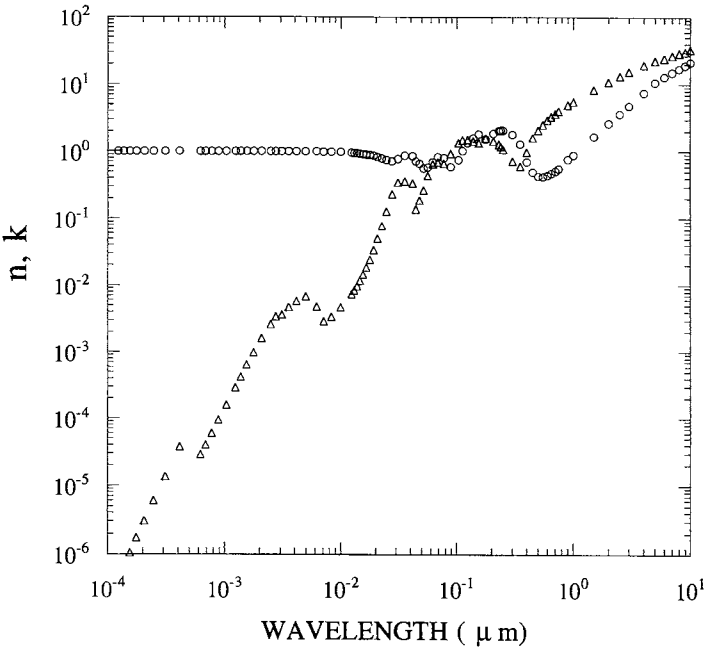

Fig. 1. Complex refractive index, n (○) and k (△), versus photon energy from the x-ray region to the infrared for ZrN according to Table II.

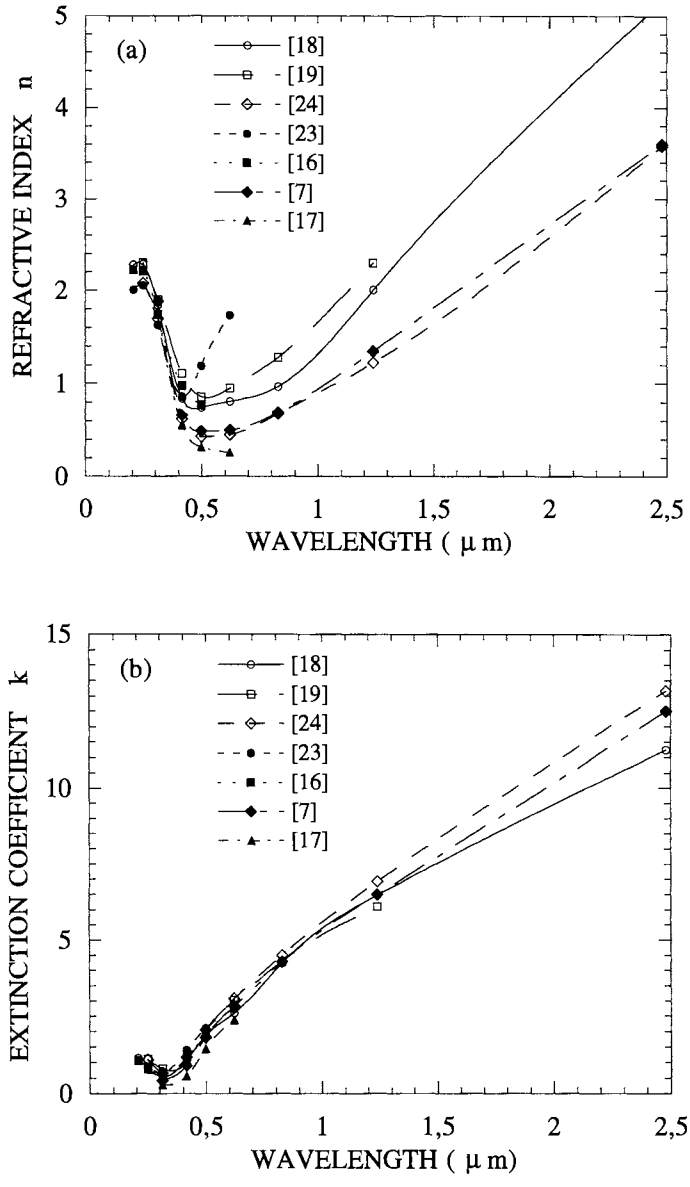

Fig. 2. (a) ZrN n-values versus wavelength in the UV–VIS–NIR range, with values from the different references as indicated in the figure. (b) k-values versus wavelength in the UV–VIS–NIR range, with values from the different references as indicated in the figure.

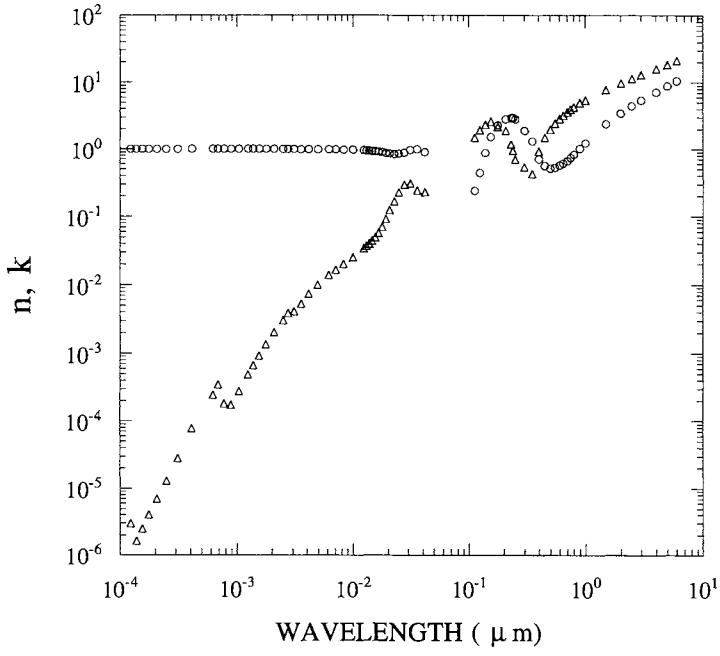

Fig. 3. Complex refractive index, n (○) and k (△), versus photon energy from the x-ray region to the infrared for HfN according to Table III.

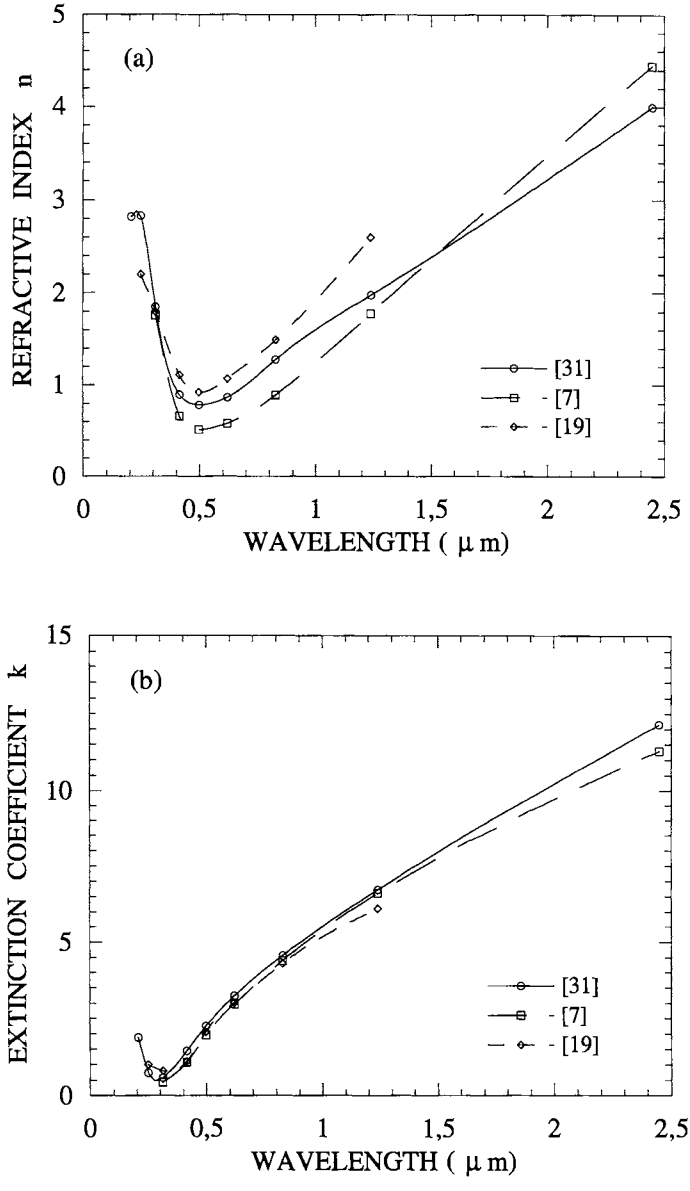

Fig. 4. (a) HfN n-values versus wavelength in the UV–VIS–NIR range with values from the different references as indicated in the figure. (b) k-values versus wavelength in the UV–VIS–NIR range with values from the different references as indicated in the figure.

TABLE I

Drude Parameters: Screened Plasma Energy According to Eq. (3), Drude Plasma Energy According to Eq. (2), Relaxation Energy and Screening Constant as Obtained from the the Indicated Sources

Reference	$\hbar\omega_p^*$ (eV)	$\hbar\omega_p$ (eV)	$\hbar/\tau$ (eV)	$\epsilon_1(\infty)$
ZrN Ref. [7]	3.2	7.17	0.35	
[16]	3.1	7.32	0.62	
[17]	3.20	6.77	0.24	≈7
[18]	3.08	7.35	0.59	
[19]	3.07	6.1	0.73	(2.31)[a]
[24, 26]	3.19	7.35	0.29	6.1
HfN [7]	3.0	7.32	0.45	
[28]	3.11	8.63	1.40	7.7
[19]	3.17	6.1	0.9	(2.74)[a]
[31]	3.88	7.78	0.35	6.4

[a] The two $\epsilon_1(\infty)$-values from Ref. [19] are not comparable with the others because a two-oscillator model was used in the fitting procedure.

TABLE II

Values of *n* and *k* for ZrN Obtained from Various References[a]

e V	cm^{-1}	μm	n	k
1.000E + 4	8.065E + 7	1.240E-1	1.00E + 0 [32]	4.53E-7 [32]
9.000E + 3	7.259E + 7	1.378E-1	1.00E + 0	6.75E-7
8.000E + 3	6.452E + 7	1.550E-1	1.00E + 0	1.05E-6
7.000E + 3	5.646E + 7	1.771E-1	1.00E + 0	1.72E-6
6.000E + 3	4.839E + 7	2.067E-1	1.00E + 0	3.07E-6
5.000E + 3	4.033E + 7	2.480E-1	1.00E + 0	6.01E-6
4.000E + 3	3.226E + 7	3.100E-1	1.00E + 0	1.36E-5
3.000E + 3	2.420E + 7	4.133E-1	1.00E + 0	3.80E-5
2.000E + 3	1.613E + 7	6.200E-1	1.00E + 0	2.86E-5
1.800E + 3	1.452E + 7	6.889E-1	1.00E + 0	4.03E-5
1.600E + 3	1.290E + 7	7.750E-1	1.00E + 0	6.04E-5
1.400E + 3	1.129E + 7	8.857E-1	9.99E-1	9.55E-5
1.200E + 3	9.679E + 6	1.033E + 0	9.99E-1	1.61E-4
1.000E + 3	8.065E + 6	1.240E + 0	9.99E-1	2.91E-4
9.000E + 2	7.259E + 6	1.378E + 0	9.99E-1	4.22E-4
8.000E + 2	6.452E + 6	1.550E + 0	9.98E-1	6.44E-4
7.000E + 2	5.646E + 6	1.771E + 0	9.98E-1	9.90E-4
6.000E + 2	4.839E + 6	2.067E + 0	9.97E-1	1.58E-3
5.000E + 2	4.033E + 6	2.480E + 0	9.97E-1	2.58E-3
4.500E + 2	3.629E + 6	2.756E + 0	9.96E-1	3.37E-3
4.000E + 2	3.226E + 6	3.100E + 0	9.97E-1	3.63E-3
3.500E + 2	2.823E + 6	3.543E + 0	9.96E-1	4.64E-3

(continued)

[a] The references from which the values were taken are given in brackets.

TABLE II *(Continued)*

ZrN

e V	cm^{-1}	μm	n	k
3.000E + 2	2.420E + 6	4.133E + 0	9.95E-1	5.76E-3
2.500E + 2	2.016E + 6	4.960E + 0	9.95E-1	6.73E-3
2.000E + 2	1.613E + 6	6.200E + 0	9.94E-1	4.77E-3
1.750E + 2	1.411E + 6	7.086E + 0	9.89E-1	2.90E-3
1.500E + 2	1.210E + 6	8.267E + 0	9.82E-1	3.36E-3
1.250E + 2	1.008E + 6	9.920E + 0	9.71E-1	4.68E-3
1.000E + 2	8.065E + 5	1.240E + 1	9.51E-1	7.31E-3
9.500E + 1	7.662E + 5	1.305E + 1	9.45E-1	8.30E-3
9.000E + 1	7.259E + 5	1.378E + 1	9.37E-1	9.66E-3
8.500E + 1	6.856E + 5	1.459E + 1	9.28E-1	1.16E-2
8.000E + 1	6.452E + 5	1.550E + 1	9.17E-1	1.43E-2
7.500E + 1	6.049E + 5	1.653E + 1	9.03E-1	1.83E-2
7.000E + 1	5.646E + 5	1.771E + 1	8.85E-1	2.42E-2
6.500E + 1	5.243E + 5	1.908E + 1	8.62E-1	3.40E-2
6.000E + 1	4.839E + 5	2.067E + 1	8.33E-1	5.03E-2
5.500E + 1	4.436E + 5	2.255E + 1	7.96E-1	7.82E-2
5.000E + 1	4.033E + 5	2.480E + 1	7.51E-1	1.29E-1
4.500E + 1	3.629E + 5	2.756E + 1	7.14E-1	2.28E-1
4.000E + 1	3.226E + 5	3.100E + 1	7.81E-1	3.49E-1
3.500E + 1	2.823E + 5	3.543E + 1	8.64E-1	3.58E-1
3.000E + 1	2.420E + 5	4.133E + 1	8.47E-1	3.35E-1
2.800E + 1	2.258E + 5	4.429E + 1	7.21E-1 [23]	1.39E-1 [23]
2.600E + 1	2.097E + 5	4.769E + 1	6.60E-1	1.89E-1
2.400E + 1	1.936E + 5	5.167E + 1	5.66E-1	2.65E-1
2.200E + 1	1.774E + 5	5.636E + 1	5.80E-1	4.31E-1
2.000E + 1	1.613E + 5	6.200E + 1	6.90E-1	6.52E-1
1.800E + 1	1.452E + 5	6.889E + 1	8.27E-1	6.95E-1
1.600E + 1	1.290E + 5	7.750E + 1	7.97E-1	6.59E-1
1.400E + 1	1.129E + 5	8.857E + 1	5.95E-1	9.24E-1
1.200E + 1	9.679E + 4	1.033E + 2	7.52E-1	1.33E + 0
1.100E + 1	8.874E + 4	1.127E + 2	1.02E + 0	1.47E + 0
1.000E + 1	8.065E + 4	1.240E + 2	1.35E + 0	1.49E + 0
8.999E + 0	7.258E + 4	1.378E + 2	1.57E + 0	1.43E + 0
8.000E + 0	6.452E + 4	1.550E + 2	1.82E + 0	1.35E + 0
7.002E + 0	5.647E + 4	1.771E + 2	1.54E + 0 [24]	1.58E + 0 [24]
5.999E + 0	4.838E + 4	2.067E + 2	1.85E + 0	1.43E + 0
5.391E + 0	4.348E + 4	2.300E + 2	2.04E + 0	1.28E + 0
5.167E + 0	4.167E + 4	2.400E + 2	2.08E + 0	1.19E + 0
4.960E + 0	4.000E + 4	2.500E + 2	2.07E + 0	1.07E + 0
4.769E + 0	3.847E + 4	2.600E + 2	2.04E + 0	9.66E-1
4.593E + 0	3.704E + 4	2.700E + 2	1.99E + 0	8.90E-1
4.429E + 0	3.572E + 4	2.800E + 2	1.93E + 0	8.22E-1
4.276E + 0	3.449E + 4	2.900E + 2	1.86E + 0	7.60E-1
4.133E + 0	3.334E + 4	3.000E + 2	1.79E + 0	7.13E-1
4.000E + 0	3.226E + 4	3.100E + 2	1.70E + 0	6.69E-1
3.875E + 0	3.125E + 4	3.200E + 2	1.60E + 0	6.48E-1
3.758E + 0	3.031E + 4	3.300E + 2	1.52E + 0	6.32E-1

TABLE II *(Continued)*

ZrN

e V	cm^{-1}	μm	n	k
3.647E + 0	2.942E + 4	3.400E + 2	1.41E + 0	5.99E-1
3.543E + 0	2.857E + 4	3.500E + 2	1.29E + 0	5.99E-1
3.444E + 0	2.778E + 4	3.600E + 2	1.17E + 0	6.19E-1
3.351E + 0	2.703E + 4	3.700E + 2	1.04E + 0	6.68E-1
3.263E + 0	2.632E + 4	3.800E + 2	9.20E-1	7.60E-1
3.179E + 0	2.564E + 4	3.900E + 2	8.23E-1	8.55E-1
3.100E + 0	2.500E + 4	4.000E + 2	7.06E-1	9.76E-1
3.024E + 0	2.439E + 4	4.100E + 2	6.35E-1	1.12E + 0
2.952E + 0	2.381E + 4	4.200E + 2	5.85E-1	1.24E + 0
2.884E + 0	2.326E + 4	4.300E + 2	5.45E-1	1.36E + 0
2.818E + 0	2.273E + 4	4.400E + 2	5.17E-1	1.48E + 0
2.756E + 0	2.222E + 4	4.500E + 2	4.97E-1	1.59E + 0
2.696E + 0	2.174E + 4	4.600E + 2	4.84E-1	1.69E + 0
2.638E + 0	2.128E + 4	4.700E + 2	4.55E-1	1.80E + 0
2.583E + 0	2.084E + 4	4.800E + 2	4.44E-1	1.90E + 0
2.531E + 0	2.041E + 4	4.900E + 2	4.35E-1	1.99E + 0
2.480E + 0	2.000E + 4	5.000E + 2	4.28E-1	2.09E + 0
2.431E + 0	1.961E + 4	5.100E + 2	4.23E-1	2.18E + 0
2.385E + 0	1.923E + 4	5.200E + 2	4.20E-1	2.27E + 0
2.340E + 0	1.887E + 4	5.300E + 2	4.21E-1	2.35E + 0
2.296E + 0	1.852E + 4	5.400E + 2	4.19E-1	2.44E + 0
2.255E + 0	1.818E + 4	5.500E + 2	4.23E-1	2.52E + 0
2.214E + 0	1.786E + 4	5.600E + 2	4.28E-1	2.60E + 0
2.175E + 0	1.755E + 4	5.700E + 2	4.23E-1	2.68E + 0
2.138E + 0	1.724E + 4	5.800E + 2	4.26E-1	2.76E + 0
2.102E + 0	1.695E + 4	5.900E + 2	4.32E-1	2.84E + 0
2.067E + 0	1.667E + 4	6.000E + 2	4.39E-1	2.92E + 0
2.033E + 0	1.640E + 4	6.100E + 2	4.46E-1	2.99E + 0
2.000E + 0	1.613E + 4	6.200E + 2	4.51E-1	3.07E + 0
1.968E + 0	1.587E + 4	6.300E + 2	4.56E-1	3.14E + 0
1.937E + 0	1.563E + 4	6.400E + 2	4.63E-1	3.22E + 0
1.908E + 0	1.539E + 4	6.500E + 2	4.69E-1	3.29E + 0
1.879E + 0	1.515E + 4	6.600E + 2	4.77E-1	3.36E + 0
1.851E + 0	1.493E + 4	6.700E + 2	4.86E-1	3.44E + 0
1.824E + 0	1.471E + 4	6.800E + 2	4.93E-1	3.51E + 0
1.797E + 0	1.449E + 4	6.900E + 2	5.09E-1	3.58E + 0
1.771E + 0	1.429E + 4	7.000E + 2	5.13E-1	3.64E + 0
1.746E + 0	1.409E + 4	7.100E + 2	5.17E-1	3.71E + 0
1.722E + 0	1.389E + 4	7.200E + 2	5.28E-1	3.78E + 0
1.699E + 0	1.370E + 4	7.300E + 2	5.38E-1	3.85E + 0
1.676E + 0	1.352E + 4	7.400E + 2	5.47E-1	3.92E + 0
1.653E + 0	1.333E + 4	7.500E + 2	5.57E-1	3.99E + 0
1.632E + 0	1.316E + 4	7.600E + 2	5.68E-1	4.06E + 0
1.610E + 0	1.299E + 4	7.700E + 2	5.80E-1	4.13E + 0
1.590E + 0	1.282E + 4	7.800E + 2	5.93E-1	4.20E + 0
1.570E + 0	1.266E + 4	7.900E + 2	6.15E-1	4.27E + 0

(continued)

TABLE II *(Continued)*

ZrN

e V	cm^{-1}	μm	n	k
1.459E + 0	1.177E + 4	8.500E + 2	6.99E-1	4.64E + 0
1.378E + 0	1.111E + 4	9.000E + 2	7.57E-1	4.95E + 0
1.305E + 0	1.053E + 4	9.500E + 2	8.17E-1	5.25E + 0
1.240E + 0	1.000E + 4	1.000E + 3	8.86E-1	5.55E + 0
1.127E + 0	9.092E + 3	1.100E + 3	1.02E + 0	6.13E + 0
1.033E + 0	8.334E + 3	1.200E + 3	1.17E + 0	6.71E + 0
9.538E-1	7.693E + 3	1.300E + 3	1.33E + 0	7.27E + 0
8.857E-1	7.144E + 3	1.400E + 3	1.49E + 0	7.82E + 0
8.267E-1	6.667E + 3	1.500E + 3	1.68E + 0	8.36E + 0
7.750E-1	6.251E + 3	1.600E + 3	1.85E + 0	8.87E + 0
7.294E-1	5.883E + 3	1.700E + 3	2.04E + 0	9.39E + 0
6.889E-1	5.556E + 3	1.800E + 3	2.19E + 0	9.87E + 0
6.526E-1	5.264E + 3	1.900E + 3	2.43E + 0	1.04E + 1
6.200E-1	5.001E + 3	2.000E + 3	2.62E + 0	1.09E + 1
5.905E-1	4.762E + 3	2.100E + 3	2.83E + 0	1.14E + 1
5.636E-1	4.546E + 3	2.200E + 3	3.03E + 0	1.18E + 1
5.391E-1	4.348E + 3	2.300E + 3	3.20E + 0	1.23E + 1
5.167E-1	4.167E + 3	2.400E + 3	3.39E + 0	1.28E + 1
4.960E-1	4.000E + 3	2.500E + 3	3.65E + 0	1.33E + 1
4.769E-1	3.847E + 3	2.600E + 3	4.05E + 0	1.37E + 1
4.593E-1	3.704E + 3	2.700E + 3	4.08E + 0	1.41E + 1
4.429E-1	3.572E + 3	2.800E + 3	4.32E + 0	1.45E + 1
4.276E-1	3.449E + 3	2.900E + 3	4.56E + 0	1.49E + 1
4.133E-1	3.333E + 3	3.000E + 3	4.75E + 0	1.54E + 1
3.100E-1	2.500E + 3	4.000E + 3	7.43E + 0	1.94E + 1
2.480E-1	2.000E + 3	5.000E + 3	1.07E + 1	2.22E + 1
2.066E-1	1.666E + 3	6.002E + 3	1.28E + 1	2.43E + 1
1.771E-1	1.428E + 3	7.003E + 3	1.49E + 1	2.68E + 1
1.550E-1	1.250E + 3	8.000E + 3	1.71E + 1	2.87E + 1
1.378E-1	1.111E + 3	9.001E + 3	1.91E + 1	3.04E + 1
1.240E-1	1.000E + 3	1.000E + 4	2.11E + 1	3.27E + 1
1.127E-1	9.091E + 2	1.100E + 4	2.35E + 1	3.35E + 1
1.033E-1	8.331E + 2	1.200E + 4	2.50E + 1	3.51E + 1
9.536E-2	7.691E + 2	1.300E + 4	2.70E + 1	3.63E + 1
8.853E-2	7.141E + 2	1.401E + 4	2.85E + 1	3.72E + 1
8.258E-2	6.661E + 2	1.501E + 4	3.03E + 1	3.85E + 1
7.750E-2	6.251E + 2	1.600E + 4	3.25E + 1	3.87E + 1
7.291E-2	5.881E + 2	1.701E + 4	3.41E + 1	3.84E + 1
6.882E-2	5.551E + 2	1.802E + 4	3.47E + 1	4.04E + 1
6.523E-2	5.261E + 2	1.901E + 4	3.63E + 1	4.08E + 1
6.200E-2	5.001E + 2	2.000E + 4	3.71E + 1	4.03E + 1
5.903E-2	4.761E + 2	2.101E + 4	3.82E + 1	4.32E + 1
5.630E-2	4.541E + 2	2.203E + 4	3.99E + 1	4.15E + 1
5.382E-2	4.341E + 2	2.304E + 4	4.01E + 1	4.17E + 1
5.159E-2	4.161E + 2	2.404E + 4	4.01E + 1	4.21E + 1

TABLE III

Values of n and k for HfN Obtained from Various References[a]

eV	cm^{-1}	μm	n	k
1.000E + 4	8.065E + 7	1.240E-4	1.00E + 0 [32]	2.97E-6 [32]
9.000E + 3	7.259E + 7	1.378E-4	1.00E + 0	1.63E-6
8.000E + 3	6.452E + 7	1.550E-4	1.00E + 0	2.50E-6
7.000E + 3	5.646E + 7	1.771E-4	1.00E + 0	4.02E-6
6.000E + 3	4.839E + 7	2.067E-4	1.00E + 0	6.94E-6
5.000E + 3	4.033E + 7	2.480E-4	1.00E + 0	1.31E-5
4.000E + 3	3.226E + 7	3.100E-4	1.00E + 0	2.84E-5
3.000E + 3	2.420E + 7	4.133E-4	1.00E + 0	7.70E-5
2.000E + 3	1.613E + 7	6.200E-4	1.00E + 0	2.41E-4
1.800E + 3	1.452E + 7	6.889E-4	1.00E + 0	3.48E-4
1.600E + 3	1.290E + 7	7.750E-4	1.00E + 0	1.80E-4
1.400E + 3	1.129E + 7	8.857E-4	9.99E-1	1.74E-4
1.200E + 3	9.679E + 6	1.033E-3	9.99E-1	2.78E-4
1.000E + 3	8.065E + 6	1.240E-3	9.98E-1	4.88E-4
9.000E + 2	7.259E + 6	1.378E-3	9.98E-1	6.64E-4
8.000E + 2	6.452E + 6	1.550E-3	9.98E-1	9.31E-4
7.000E + 2	5.646E + 6	1.771E-3	9.97E-1	1.36E-3
6.000E + 2	4.839E + 6	2.067E-3	9.96E-1	2.04E-3
5.000E + 2	4.033E + 6	2.480E-3	9.95E-1	3.02E-3
4.500E + 2	3.629E + 6	2.756E-3	9.95E-1	3.88E-3
4.000E + 2	3.226E + 6	3.100E-3	9.95E-1	4.12E-3
3.500E + 2	2.823E + 6	3.543E-3	9.93E-1	5.35E-3
3.000E + 2	2.420E + 6	4.133E-3	9.91E-1	7.31E-3
2.500E + 2	2.016E + 6	4.960E-3	9.89E-1	9.97E-3
2.000E + 2	1.613E + 6	6.200E-3	9.85E-1	1.39E-2
1.750E + 2	1.411E + 6	7.086E-3	9.82E-1	1.65E-2
1.500E + 2	1.210E + 6	8.267E-3	9.77E-1	2.01E-2
1.250E + 2	1.008E + 6	9.920E-3	9.69E-1	2.54E-2
1.000E + 2	8.065E + 5	1.240E-2	9.53E-1	3.43E-2
9.500E + 1	7.662E + 5	1.305E-2	9.47E-1	3.70E-2
9.000E + 1	7.259E + 5	1.378E-2	9.41E-1	4.02E-2
8.500E + 1	6.856E + 5	1.459E-2	9.33E-1	4.42E-2
8.000E + 1	6.452E + 5	1.550E-2	9.23E-1	4.96E-2
7.500E + 1	6.049E + 5	1.653E-2	9.09E-1	5.76E-2
7.000E + 1	5.646E + 5	1.771E-2	8.92E-1	7.09E-2
6.500E + 1	5.243E + 5	1.908E-2	8.73E-1	9.15E-2
6.000E + 1	4.839E + 5	2.067E-2	8.55E-1	1.25E-1
5.500E + 1	4.436E + 5	2.255E-2	8.45E-1	1.69E-1
5.000E + 1	4.033E + 5	2.480E-2	8.48E-1	2.30E-1
4.500E + 1	3.629E + 5	2.756E-2	8.88E-1	2.95E-1
4.000E + 1	3.226E + 5	3.100E-2	9.67E-1	3.13E-1
3.500E + 1	2.823E + 5	3.543E-2	9.98E-1	2.43E-1
3.000E + 1	2.420E + 5	4.133E-2	8.94E-1	2.29E-1
1.100E + 1	8.872E + 4	1.127E-1	2.40E-1 [31]	1.49E + 0 [31]
1.000E + 1	8.065E + 4	1.240E-1	4.43E-1	1.92E + 0

(continued)

[a] References from which the values were taken are given in brackets.

TABLE III *(Continued)*

HfN

eV	cm^{-1}	μm	n	k
8.999E + 0	7.258E + 4	1.378E-1	8.70E-1	2.31E + 0
8.000E + 0	6.452E + 4	1.550E-1	1.52E + 0	2.57E + 0
7.002E + 0	5.647E + 4	1.771E-1	2.26E + 0	2.18E + 0
5.999E + 0	4.838E + 4	2.067E-1	2.82E + 0	1.87E + 0
5.391E + 0	4.348E + 4	2.300E-1	2.95E + 0	1.19E + 0
5.167E + 0	4.167E + 4	2.400E-1	2.96E + 0	9.42E-1
4.960E + 0	4.000E + 4	2.500E-1	2.80E + 0	6.94E-1
4.769E + 0	3.846E + 4	2.600E-1	2.63E + 0	5.38E-1
4.593E + 0	3.704E + 4	2.700E-1	2.30E + 0	4.32E-1
4.429E + 0	3.572E + 4	2.800E-1	2.17E + 0	4.75E-1
4.276E + 0	3.449E + 4	2.900E-1	2.01E + 0	4.87E-1
4.133E + 0	3.333E + 4	3.000E-1	1.91E + 0	5.38E-1
4.000E + 0	3.226E + 4	3.100E-1	1.76E + 0 [7]	4.30E-1 [7]
3.875E + 0	3.125E + 4	3.200E-1	1.66E + 0	4.10E-1
3.758E + 0	3.031E + 4	3.300E-1	1.56E + 0	4.05E-1
3.647E + 0	2.941E + 4	3.400E-1	1.44E + 0	4.05E-1
3.543E + 0	2.858E + 4	3.500E-1	1.31E + 0	4.30E-1
3.444E + 0	2.778E + 4	3.600E-1	1.17E + 0	4.70E-1
3.351E + 0	2.703E + 4	3.700E-1	1.05E + 0	5.40E-1
3.263E + 0	2.632E + 4	3.800E-1	9.00E-1	6.40E-1
3.180E + 0	2.565E + 4	3.900E-1	7.80E-1	7.70E-1
3.100E + 0	2.500E + 4	4.000E-1	7.10E-1	9.20E-1
3.024E + 0	2.439E + 4	4.100E-1	6.60E-1	1.04E + 0
2.952E + 0	2.381E + 4	4.200E-1	6.30E-1	1.16E + 0
2.884E + 0	2.326E + 4	4.300E-1	6.00E-1	1.28E + 0
2.818E + 0	2.273E + 4	4.400E-1	5.70E-1	1.40E + 0
2.756E + 0	2.223E + 4	4.500E-1	5.60E-1	1.50E + 0
2.696E + 0	2.174E + 4	4.600E-1	5.40E-1	1.60E + 0
2.638E + 0	2.128E + 4	4.700E-1	5.30E-1	1.70E + 0
2.583E + 0	2.083E + 4	4.800E-1	5.20E-1	1.80E + 0
2.531E + 0	2.041E + 4	4.900E-1	5.15E-1	1.89E + 0
2.480E + 0	2.000E + 4	5.000E-1	5.10E-1	1.98E + 0
2.431E + 0	1.961E + 4	5.100E-1	5.10E-1	2.07E + 0
2.385E + 0	1.924E + 4	5.200E-1	5.10E-1	2.16E + 0
2.340E + 0	1.887E + 4	5.300E-1	5.15E-1	2.25E + 0
2.296E + 0	1.852E + 4	5.400E-1	5.25E-1	2.34E + 0
2.255E + 0	1.819E + 4	5.500E-1	5.30E-1	2.42E + 0
2.214E + 0	1.786E + 4	5.600E-1	5.35E-1	2.51E + 0
2.175E + 0	1.754E + 4	5.700E-1	5.40E-1	2.59E + 0
2.138E + 0	1.724E + 4	5.800E-1	5.50E-1	2.67E + 0
2.102E + 0	1.695E + 4	5.900E-1	5.60E-1	2.75E + 0
2.067E + 0	1.667E + 4	6.000E-1	5.70E-1	2.83E + 0
2.033E + 0	1.640E + 4	6.100E-1	5.80E-1	2.90E + 0
2.000E + 0	1.613E + 4	6.200E-1	5.85E-1	2.97E + 0
1.968E + 0	1.587E + 4	6.300E-1	5.90E-1	3.05E + 0
1.937E + 0	1.562E + 4	6.400E-1	6.00E-1	3.12E + 0
1.908E + 0	1.539E + 4	6.500E-1	6.10E-1	3.20E + 0

TABLE III *(Continued)*

HfN

eV	cm^{-1}	μm	n	k
1.879E + 0	1.516E + 4	6.600E-1	6.20E-1	3.26E + 0
1.851E + 0	1.493E + 4	6.700E-1	6.30E-1	3.33E + 0
1.823E + 0	1.470E + 4	6.800E-1	6.40E-1	3.40E + 0
1.797E + 0	1.449E + 4	6.900E-1	6.50E-1	3.47E + 0
1.771E + 0	1.428E + 4	7.000E-1	6.60E-1	3.55E + 0
1.746E + 0	1.408E + 4	7.100E-1	6.75E-1	3.62E + 0
1.722E + 0	1.389E + 4	7.200E-1	6.90E-1	3.70E + 0
1.699E + 0	1.370E + 4	7.300E-1	7.10E-1	3.77E + 0
1.676E + 0	1.352E + 4	7.400E-1	7.25E-1	3.85E + 0
1.653E + 0	1.333E + 4	7.500E-1	7.40E-1	3.92E + 0
1.632E + 0	1.316E + 4	7.600E-1	7.60E-1	4.00E + 0
1.610E + 0	1.299E + 4	7.700E-1	7.80E-1	4.05E + 0
1.590E + 0	1.282E + 4	7.800E-1	7.95E-1	4.11E + 0
1.570E + 0	1.266E + 4	7.900E-1	8.15E-1	4.17E + 0
1.550E + 0	1.250E + 4	8.000E-1	8.30E-1	4.24E + 0
1.459E + 0	1.177E + 4	8.500E-1	9.30E-1	4.56E + 0
1.378E + 0	1.111E + 4	9.000E-1	1.03E + 0	4.93E + 0
1.305E + 0	1.053E + 4	9.500E-1	1.15E + 0	5.20E + 0
1.240E + 0	1.000E + 4	1.000E + 0	1.24E + 0	5.45E + 0
1.181E + 0	9.525E + 3	1.050E + 0	1.38E + 0	5.65E + 0
1.127E + 0	9.090E + 3	1.100E + 0	1.45E + 0	5.90E + 0
1.078E + 0	8.695E + 3	1.150E + 0	1.60E + 0	6.15E + 0
1.033E + 0	8.332E + 3	1.200E + 0	1.70E + 0	6.40E + 0
9.920E-1	8.001E + 3	1.250E + 0	1.82E + 0	6.65E + 0
9.539E-1	7.694E + 3	1.300E + 0	1.95E + 0	6.85E + 0
9.185E-1	7.408E + 3	1.350E + 0	2.05E + 0	7.05E + 0
8.857E-1	7.144E + 3	1.400E + 0	2.18E + 0	7.30E + 0
8.552E-1	6.898E + 3	1.450E + 0	2.25E + 0	7.50E + 0
8.267E-1	6.668E + 3	1.500E + 0	2.40E + 0	7.75E + 0
7.750E-1	6.251E + 3	1.600E + 0	2.60E + 0	8.20E + 0
7.294E-1	5.883E + 3	1.700E + 0	2.81E + 0	8.60E + 0
6.889E-1	5.556E + 3	1.800E + 0	3.02E + 0	9.00E + 0
6.526E-1	5.264E + 3	1.900E + 0	3.22E + 0	9.30E + 0
6.200E-1	5.001E + 3	2.000E + 0	3.45E + 0	9.70E + 0
5.905E-1	4.763E + 3	2.100E + 0	3.68E + 0	1.01E + 1
5.636E-1	4.546E + 3	2.200E + 0	3.90E + 0	1.04E + 1
5.391E-1	4.348E + 3	2.300E + 0	4.10E + 0	1.07E + 1
5.167E-1	4.167E + 3	2.400E + 0	4.30E + 0	1.11E + 1
4.960E-1	4.000E + 3	2.500E + 0	4.50E + 0	1.14E + 1
4.769E-1	3.846E + 3	2.600E + 0	4.68E + 0	1.17E + 1
4.593E-1	3.704E + 3	2.700E + 0	4.86E + 0	1.20E + 1
4.429E-1	3.572E + 3	2.800E + 0	5.04E + 0	1.23E + 1
4.276E-1	3.449E + 3	2.900E + 0	5.22E + 0	1.26E + 1
4.133E-1	3.333E + 3	3.000E + 0	5.40E + 0	1.29E + 1
3.100E-1	2.500E + 3	4.000E + 0	7.10E + 0	1.56E + 1
2.480E-1	2.000E + 3	5.000E + 0	8.80E + 0	1.80E + 1
2.067E-1	1.667E + 3	6.000E + 0	1.05E + 1	2.10E + 1

Aluminum Nitride (AlN)

S. LOUGHIN
Lockheed Martin Corporation
Philadelphia, Pennsylvania

and

R. H. FRENCH
DuPont Central Research & Development,
Wilmington, Delaware

INTRODUCTION I

Aluminum nitride (AlN) is a wurtzite structure (space group $P6_3mc$) ceramic material, with lattice parameters [1] of $\vec{a} = \vec{b} = 3.11$ Å and $\vec{c} = 4.98$ Å. The volume of the unit cell is 41.71 Å^3 with two formula units per cell. Interest in this material increased after the pioneering work of Slack [2], who along with McNelly [3, 4], synthesized high-purity single crystals with thermal conductivities of up to 275 W m^{-1} K^{-1}. Since then, this material has found increasing technological application [5] motivating considerable study in theoretical [6–14] and experimental [15] investigations. Here, we critique the literature on the optical properties of AlN, rendering [16] selected data in a table of the real and imaginary components of the index of refraction.

AlN has an affinity for oxygen [17, 18] and all commercially available material contains some oxygen. Previous investigators have correlated oxygen content to changes in thermal conductivity, shifts in luminescence features [19], and changes in the energy dependence of the reflectance spectrum [20] of AlN. A number of authors [21–24] have discussed the thermal stability and oxidation of AlN, noting that AlN is easily oxidized by reaction with water or by heating in the presence of oxygen. Much work [25, 26] has focused on how oxygen is accommodated in AlN and its effect on the electronic structure. Because the electronic structure is altered by the presence of oxygen [27], the optical results most characteristic of the pure phase are obtained on nonaqueously polished samples that have been prepared with

Copyright © 1998 by Academic Press.
All rights of reproduction in any form reserved
ISBN 0-12-544423-0/$25.00.

careful attention to minimize oxygen impurities. The difficulty of obtaining and maintaining an oxygen-free AlN surface has complicated many of the experimental investigations of the optical properties of this material. Data from investigations on single crystals or on thin films where oxygen was controlled or mitigated are included in Table I, although a substantially larger body of work is reviewed.

II BAND GAP, BAND-EDGE ABSORPTION, AND BIREFRINGENCE

Estimates of the band gap of AlN from optical measurements have been reported by a number of investigators [28–30] and range from about 5.8 to 6.2 eV. Chu and Kelm [31] report optical absorbance in the region below the fundamental edge and a band gap of 5.9 ± 0.2 eV. Aita *et al.* [32] report a band-gap energy of 6.18 eV.

Zarwasch *et al.* [33] measured the optical absorption of AlN thin films prepared by sputter deposition over the range of 3 to 6.5 eV and discussed their results in comparison to those of Aita *et al.* [32]. Both of these investigations focused on absorption just below the band edge in thin films, which Zarwasch *et al.* attributed to localized states arising from crystalline disorder in the film. The single crystals grown by Slack and McNelly [3, 4] also exhibit absorption below the band edge; however, this has been attributed to nitrogen vacancies [34]. Kaplan and Gerhardt [35] have studied the role of carbon impurities in UV-induced absorption at 0.650 μm. Perry and Rutz [36] measured optical density over the range 5.2–6.4 eV, noting the presence of two absorption features below the fundamental edge attributed to vacancies or oxygen impurities, and report band-gap values of 6.28 eV at 5 K and 6.20 eV at 300 K. Bauer *et al.* [37] prepared films by pyrolytic and plasmachemical vapor deposition and provided the spectral dependence of the real index between 0.1 and 0.4 μm, as well as the absorption coefficient from 4 to 7 eV. They measured band gaps of 5.93 and 6.0 eV with temperature dependancies of -2.8×10^{-4} and -2.5×10^{-4} eV/K, respectively. Barovskii *et al.* [38] reported absorption spectra for oriented, epitaxial AlN films over the range of 2–6 eV and reported the band gap as 5.92 ± 0.05 eV at 300 K.

The temperature dependence of the band gap has been studied in further detail by Guo and Yoshida [39], who provide parameters for the Varshni equation,

$$\Delta E_g(T) = \frac{\alpha T^2}{\beta + T}, \tag{1}$$

and the Bose–Einstein expression,

$$\Delta E_g(T) = \frac{2a_B}{\exp\left(\frac{\Theta}{T}\right) - 1}, \tag{2}$$

over the temperature range 0–300 K as follows: $\alpha = 1.799$ (meV/K) and $\beta = 1462$ K in Eq. (1), and $a_B = 471$ (meV) and $\Theta = 725$ K in Eq. (2).

Yamashita *et al.* [30] prepared epitaxial thin films and obtained spectra for both (**E⊥a**) and (**E∥a**). Ideally, the (**E⊥c**) and (**E∥c**) response would have been compared, however by comparing the ordinary response from (**E⊥a**) with a mixed ordinary–extraordinary response from (**E∥a**), they were able to determine the birefringence of AlN reporting a Δn of order 10^{-2} at about 5 eV, which they attribute to dichroism in the 7- to 8-eV region. They found a direct gap of 6.2 eV but suggested that the Γ_{1v}–Γ_{1c} transition for (**E⊥c**) occurs at lower energy than the Γ_{6v}–Γ_{1c} transition for (**E∥c**) due to crystal-field splitting. Lin *et al.* [40] have studied second-order optical nonlinearity of AlN thin films as a function of incidence angle at a single wavelength (1.06 μm) and have found the effect to be several times larger than that observed in KTP or quartz. Slack [41] reports an index value of 2.2 at 0.589 μm averaged over all directions, and an anisotropy of the index of about 2.3%.

VACUUM ULTRAVIOLET RANGE III

The onset of interband transitions occurs in the UV at approximately 6.1 eV or 0.2 μm. Optical properties in the vacuum UV have been reported by several investigators. Michailin *et al.* [42] employed synchrotron radiation and provide reflectance results between 6 and 40 eV, as well as luminescence. They report features in the reflectance at 7.8 and 8.6 eV.

Jones *et al.* [43] have measured the complex index of refraction below the fundamental absorption edge by ellipsometry, and then used these data in combination with VUV reflectance data of Loughin *et al.* [44] to determine n and k. The ellipsometric data were obtained from a thin-film sample prepared by reactive sputtering, whereas the VUV reflectance data were obtained from a single-crystal specimen prepared by Slack and McNelly [3, 4] and polished non aqueously to avoid oxidation.

The VUV energy range has also been studied by electron-energy-loss spectroscopy [45, 46], although in most cases these results are consistent with those for oxidized material [47].

IV UV/VISIBLE RANGE

Demiryont *et al.* [48] measured thin-film samples of AlN and obtained values for both n and k in this region. Geidur and Yaskov [49] have reported a model for the dispersion of the refractive index of AlN based on experimental data of Roskovcová *et al.* [50]. Optical properties have also been reported by Legrand *et al.* [51], who present the following expression for the index of AlN thin films prepared by sputter deposition over the range of 250 to 800 nm in λ:

$$n = \left[\alpha \exp(-\frac{\lambda}{\beta})\right] + \gamma. \tag{3}$$

α is 2.09, β is 0.1319 μm, and γ varies from 1.8 to 2.5 depending on the nitrogen partial flow rate used in preparing the film. Slack [41] provides the absorption spectrum of single-crystal AlN with less than 340 ppm oxygen over the range 0.25 μm to 10^4 μm.

V INFRARED RANGE

Carlone *et al.* [52] have reported on infrared optical absorption due to phonons, which they used for comparison with Raman-spectroscopy results. Although their IR absorption spectra were not presented quantitatively, they indicate that for **(E⊥c)**, strong absorption occurs between 800 and 610 cm^{-1}, and they identify these wave numbers as associated with the E_1(LO) and E_1(TO) modes, respectively. McNeil *et al.* [53] present more recent work on the vibration spectrum of this material obtained with specimens from the single crystals grown by Slack and McNelly [3, 4]. Lewis [54] presents transmission data for AlN thin films between 3 and 15 μm, but these are difficult to interpret because of absorption bands due to ammonium chloride in the films. IR spectra are also given by Li *et al.* [55], but no scale is given for their absorption results. Once again, the work of Slack [41] is considered to be most representative of oxygen-free material.

VI TABLE AND FIGURES

Table I summarizes the available data on the complex index of refraction, $n + ik$, over the wavelength range of $\lambda = 0.0289$ μm (42 eV) to 9440 μm (0.00013 eV). These data are presented graphically in Fig. 1, which shows

the real part of the index, n, and Fig. 2, which shows the imaginary part, k, also referred to as the extinction coefficient. The bulk of the data presented in the table are taken from five references: Demiryont *et al.* [48], Geidur and Yaskov [49], Jones *et al.* [43], Slack [41], and Zhilyakov and Kostanovskii [56].

Aside from the general information described earlier, extraordinary ray response data are not available, and the tabular data given here are for the ordinary ray response, with the exception of the polycrystalline films of either Zhilyakov and Kostanovskii [56] or Jones *et al.* [43], averaging both ordinary and extraordinary ray response. The latter data are annotated in the reference column with an "(e)," to distinguish ellipsometric measurements on thin-film samples from their analysis combining both ellipsometric and VUV measurements.

REFERENCES

1. H. Schulz and K. H. Thiemann, Crystal structure refinement of AlN and GaN. *Solid State Commun.* **23**, 815–819 (1977).
2. G. A. Slack, Nonmetallic crystals with high thermal conductivity. *J. Phys. Chem. Solids* **34**, 321–335 (1973).
3. G. A. Slack and T. F. McNelly, Growth of high purity AlN crystals. *J. Cryst. Growth.* **34**, 263–279 (1976).
4. G. A. Slack and T. F. McNelly, AlN single crystals. *J. Cryst. Growth* **42**, 560–563 (1977).
5. L. M. Sheppard, Aluminum nitride: A versatile but challenging material. *Ceram. Bull.* **69**, 1801–1812 (1990).
6. B. Hejda and K. Hauptmanová, Energy band structure of AlN. *Phys. Status Solidi* **36**, K95–K99 (1969).
7. D. Jones and A. H. Lettington, The electronic band structures of the wide band gap semiconductors GaN and AlN. *Solid State Commun.* **11**, 701–705 (1972).
8. A. Kobayashi, O. F. Sankey, S. M. Volz and J. D. Dow, Semiempirical tight-binding band structures of wurtzite semiconductors: AlN, CdS, CdSe, ZnS, and ZnO. *Phys. Rev. B* **28**, 935–945 (1983).
9. M.-Z. Huang and W.-Y. Ching, A minimal basis semi-ab initio approach to the band structures of semiconductors. *J. Phys. Chem. Solids* **46**, 977–995 (1985).
10. W.-Y. Ching and B. N. Harmon, Electronic structure of AlN. *Phys. Rev. B* **34**, 5305–5308 (1986).
11. R. V. Kasowski and F. S. Ohuchi, Electronic structure of Cu overlayers on AlN. *Phys. Rev. B* **35**, 9311–9313 (1987).
12. Y.-N. Xu and W.-Y. Ching, Electronic, optical, and structural properties of some wurtzite crystals. *Phys. Rev. B* **48**, 4335–4351 (1993).
13. E. Ruiz, S. Alvarez, and P. Alemany, Electronic structure and properties of AlN. *Phys. Rev. B* **49**, 7115–7123 (1994).
14. A. K. Solanki, A. Kashyap, T. Nautiyal, and S. Auluck, Optical properties of AlN. *Solid State Commun.* **94** 1009–1012 (1995).
15. F. S. Ohuchi, Cu-AlN interface: electronic structure and adhesion. *J. Phys. (Paris)* **49**, C5-783–789 (1988); *J. Appl. Phys.* **62**, 2286–2289 (1987).
16. F. Wooten, *"Optical Properties of Solids,"* pp. 28 and 49. Academic Press, San Diego, 1972.
17. K. H. Jack, Review: Sialons and related nitrogen ceramics. *J. Mater. Sci.* **11**, 1135–1158 (1976).

18. J. W. McCauley and N. D. Corbin, *Report Submitted to NATO Advanced Study Inst. on Nitrogen Ceramics,* (Aug 1981). see also N. D. Corbin, *The Influences of Carbon, Nitrogen, and Argon on Aluminum Oxynitride Spinel Formation.* Master's Thesis, Massachusetts Institute of Technology, Cambridge (June 1982).
19. J. H. Harris, R. A. Youngman, and R. G. Teller, On the nature of the oxygen related defect in aluminum nitride. *J. Mater. Res.* **5**, 1763–1773 (1990).
20. J. H. Harris and R. A. Youngman, Light induced defects in aluminum nitride ceramics. *J. Mater. Res.* **8**, 154–162 (1993).
21. T. J. Mroz, Jr., Aluminum nitride. *Ceram. Bull.* **70**, 849–850 (1991).
22. M. Sternitzke, Growth of oxide layers on thin aluminum nitride samples measured by electron energy loss spectroscopy. *J. Am. Ceram. Soc.* **76**, 2289–2294 (1993).
23. M. Sternitzke and G. Müller, EELS study of oxygen diffusion in aluminum nitride. *J. Am. Ceram. Soc.* 77, 737–742 (1994).
24. A. Abid, R. Bensalem, and B. J. Sealy, The thermal stability of AlN." *J. Mater. Sci.* **21**, 1301–1304 (1986).
25. A. D. Westwood, R. A. Youngman, M. R. McCartney, A. N. Cormack, and M. R. Notis, Oxygen incorporation in aluminum nitride via extended defects: Part I. Refinement of the structural model for the planar inversion domain boundary. *J. Mater. Res.* **10**, 1270–1286 (1995); A. D. Westwood, R. A. Youngman, M. R. McCartney, A. N. Cormack, and M. R. Notis, Oxygen incorporation in aluminum nitride via extended defects: Part II. Structure of curved inversion domain boundaries and defect formation. *J. Mater. Res.* **10**, 1287–1300 (1995).
26. F. Ansart, H. Ganda, R. Saporte and J. P. Traverse, Study of the oxidation of aluminum nitride coatings at high temperature. *Thin Solid Films* **260**, 38–46 (1995).
27. S. Pacesová and L. Jastrabík, Radiative recombination at deep impurity centers in AlN : O. *Czech. J. Phys.* **B29**, 913–923 (1979).
28. M. Morita, K. Tsubouchi, and N. Mikoshiba, Optical absorption and cathodoluminescence of epitaxial aluminum nitride films. *Jpn. J. Appl. Phys.* **21**, 1102–1103 (1982).
29. G. Radhakrishnan, Properties of AlN films grown at 350 K by gas-phase excimer laser photolysis. *J. Appl. Phys.* **78**, 6000–6005 (1995).
30. H. Yamashita, K. Fukui, S. Misawa, and S. Yoshida, Optical properties of AlN epitaxial thin films in the vacuum ultraviolet region. *J. Appl. Phys.* **50**, 896–898 (1979).
31. T. L. Chu and R. W. Kelm, Jr., The preparation and properties of aluminum nitride films. *J. Electrochem. Soc.* **122**, 995–1000 (1975).
32. C.R. Aita, C. J. G. Kubiak, and F. Y. H. Shih, Optical behavior near the fundamental absorption edge of sputter-deposited microcrystalline aluminum nitride. *J. Appl. Phys.* **66**, 4360–4364 (1989).
33. R. Zarwasch, E. Rille, and H. K. Pulker, Fundamental optical absorption edge of reactively direct current magnetron sputter-deposited AlN thin films. *J. Appl. Phys.* **71**, 5275–5277 (1992).
34. G. A. Slack, private communication (1996).
35. J. C. Kaplan and R. A. Gerhardt, Effect of trace carbon on the UV-induced behavior of aluminum nitride ceramics. *J. Mater. Res.* **9**, 2209–2212 (1994).
36. P. B. Perry and R. F. Rutz, The optical absorption edge of single crystal AlN prepared by a close spaced vapor process. *Appl. Phys. Lett.* **33**, 319–321 (1978).
37. J. Bauer, L. Biste, and D. Bolze, Optical properties of aluminum nitride prepared by chemical and plasmachemical vapour deposition. *Phys. Status Solidi A* **39**, 173–181 (1977).
38. N. V. Barovskii, U. D. Kudakov, E. B. Sokolov, and V. G. Sredin, Growth and optical properties of AlN epitaxial layers. *Izv. Akad. Nauk SSSR, Neorg. Mat.* **19**, 1589–1591 (1983); *Bull. Acad. Sci USSR. Inorg. Mater.* **19,** 1406 (1983).
39. Q. Guo and A. Yoshida, Temperature dependence of band gap change in InN and AlN. *Jpn. J. Appl. Phys.* **33**, 2453–2456 (1994).

40. W. P. Lin, P. M. Lundquist, G. K. Wong, E. D. Rippert, and J. B. Ketterson, Second order optical nonlinearities of radio frequency sputter-deposited AlN thin films. *Appl. Phys. Lett.* **63**, 2875–2877 (1993).
41. G. A. Slack, "Advanced Materials for Optical Windows," General Electric Technical Information Series No. 79CRD071, under ONR contract N00014-77-C-0649, Schenectady, June 1979.
42. V. V. Michailin, V. E. Oranovskii, S. Pacesová, J. Pastrnák, and A. S. Salamatov, Optical properties of AlN single crystals in the energy region 3 to 40 eV. *Phys. Status Solidi B* **55**, K51–K53 (1973).
43. D. J. Jones, R. H. French, H. Müllejans, S. Loughin, and P. F. Garcia, Optical properties of aluminum nitride determined from vacuum ultraviolet spectroscopy and spectroscopic ellipsometry. To be published.
44. S. Loughin, R. H. French, W.-Y. Ching, Y.-N. Xu, and G. A. Slack, Electronic structure of aluminum nitride: theory and experiment. *Appl. Phys. Lett.* **63**, 1182–1184 (1993).
45. C. G. Olson, J. H. Sexton, D. W. Lynch, A. J. Bevolo, H. R. Shanks, B. N. Harmon, W.-Y. Ching, and D. M. Wieliczka, Photoelectron and electron energy loss spectra of epitaxial aluminum nitride. *Solid State Commun.* **56**, 35–37 (1985).
46. M. Gautier, J. P. Duraud, and C. LeGressus, Electronic structure of an AlN film produced by ion implantation studied by electron spectroscopy. *J. Appl. Phys.* **61**, 574–580 (1987).
47. A. D. Dorneich, R. H. French, H. Müllejans, S. Loughin, and M. Rühle, Quantitative analysis of valence electron energy-loss spectra of aluminum nitride. J. Microsc. to be published.
48. H. Demiryont, L.R. Thompson, and G.J. Collins, Optical properties of aluminum oxinitrides deposited by laser-assisted CVD. *Appl. Opt.* **25**, 1311–1318 (1986).
49. S. A. Geidur and A. D. Yaskov, Dispersion of refractive index and photoelastic effect in semiconductors with a wurtzite structure. *Opt. Spectrosc.* **48**, 618–622 (1980).
50. L. Roskovcová, J. Pastrnák and R. Babusková, The dispersion of the refractive index and the birefringence of AlN. *Phys. Status Solidi* **20**, K29 (1967); J. Pastrnák and L. Roskovcová, Refraction index measurements on AlN single crystal. *Phys. Status Solidi* **14**, K5 (1966).
51. P. B. Legrand, M. Wautelet, B. Dugnoille, J. P. Dauchot and M. Hecq, Optical properties of sputter-deposited aluminum nitride films on silicon. *Thin Solid Films* **248**, 220–223 (1994).
52. C. Carlone, K. M. Lakin, and H. R. Shanks, Optical phonons of aluminum nitride. *J. Appl. Phys.*, **55**, 4010–4014 (1984).
53. L. E. McNeil, M. Grimsditch, and R. H. French, Vibrational spectroscopy of aluminum nitride. *J. Am. Ceram. Soc.* **76**, 1132–1136, (1993).
54. D. W. Lewis, Properties of aluminum nitride derived from $AlCl_3 \cdot NH_3$. *J. Electrochem. Soc.* **117**, 978–982 (1970).
55. Li Xinjiao, Xu Zechuan, He Ziyou, Cao Huazhe, Su Wuda, Chen Zhongcai, Zhou Feng, and Wang Enguang, On the properties of AlN thin films grown by low temperature reactive R. F. sputtering. *Thin Solid Films* **139**, 261–274 (1986).
56. P. A. Zhilyakov and A. V. Kostanovskii, Optical properties of thin films of aluminum nitride. *Teplofiz. Vys. Temp.* **30**, 290–293 (1992).

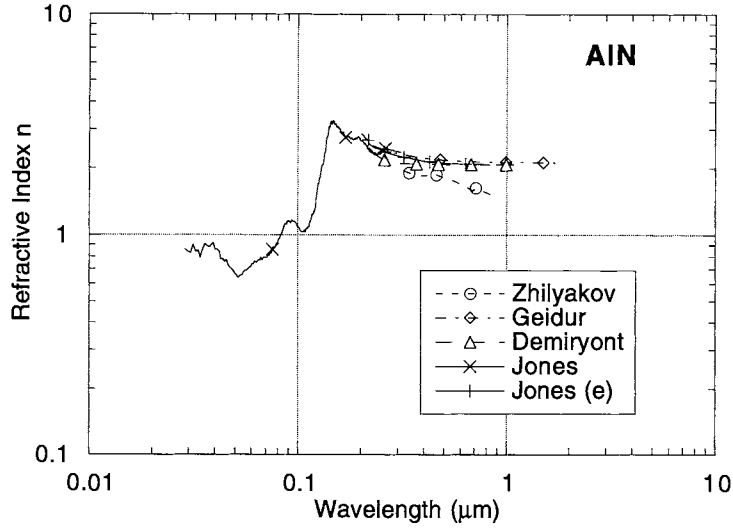

Fig. 1. Log–log plot of n (from Table I) versus wavelength in micrometers for aluminum nitride.

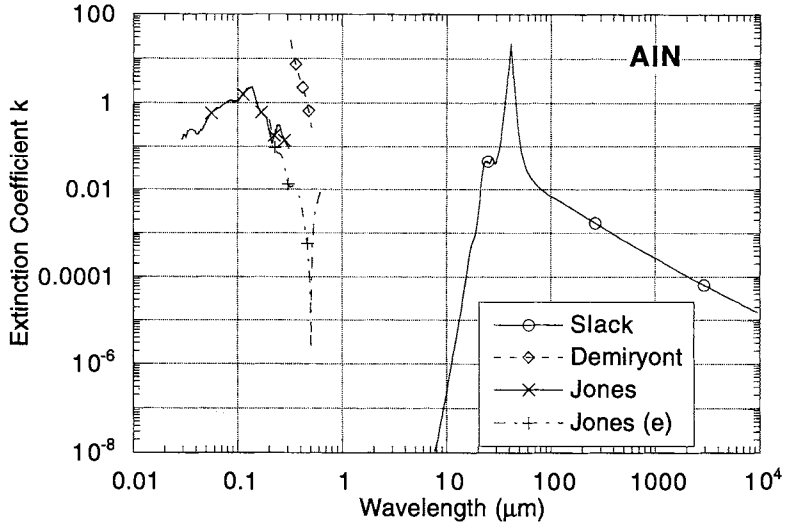

Fig. 2. Log–log plot of k (from Table I) versus wavelength in micrometers for aluminum nitride.

TABLE I

Values of n and k for Aluminum Nitride Obtained from Various References[a]

eV	cm^{-1}	μm	n	k
42.97	346581.	0.0289	0.856 [43]	0.148 [43]
41.70	336312.	0.0297	0.836	0.155
40.50	326634.	0.0306	0.830	0.189
39.36	317498.	0.0315	0.896	0.176
38.29	308858.	0.0324	0.837	0.160
37.28	300677.	0.0333	0.851	0.228
36.32	292917.	0.0341	0.790	0.235
35.40	285548.	0.0350	0.861	0.254
34.53	278541.	0.0359	0.910	0.255
33.71	271870.	0.0368	0.885	0.249
32.92	265510.	0.0377	0.879	0.242
32.17	259441.	0.0385	0.905	0.229
31.45	253644.	0.0394	0.918	0.231
30.76	248100.	0.0403	0.864	0.195
30.10	242793.	0.0412	0.864	0.195
29.47	237708.	0.0421	0.842	0.195
28.87	232832.	0.0429	0.784	0.224
28.29	228152.	0.0438	0.780	0.233
27.73	223656.	0.0447	0.764	0.252
27.19	219335.	0.0456	0.767	0.233
26.68	215177.	0.0465	0.730	0.256
26.18	211169.	0.0474	0.715	0.280
25.70	207312.	0.0482	0.700	0.310
25.24	203594.	0.0491	0.690	0.322
24.80	200006.	0.0500	0.667	0.365
24.37	196543.	0.0509	0.661	0.397
23.95	193198.	0.0518	0.639	0.444
23.55	189964.	0.0526	0.651	0.447
23.17	186837.	0.0535	0.657	0.491
22.79	183812.	0.0544	0.656	0.521
22.43	180882.	0.0553	0.683	0.559
22.07	178045.	0.0562	0.688	0.580
21.73	175295.	0.0570	0.687	0.588
21.40	172629.	0.0579	0.698	0.623
21.08	170043.	0.0588	0.713	0.654
20.77	167533.	0.0597	0.721	0.652
20.47	165097.	0.0606	0.738	0.670
20.18	162730.	0.0615	0.741	0.672
19.89	160430.	0.0623	0.756	0.694
19.61	158194.	0.0632	0.749	0.709
19.34	156019.	0.0641	0.757	0.741
19.08	153904.	0.0650	0.767	0.743
18.83	151845.	0.0659	0.769	0.766
18.58	149840.	0.0667	0.787	0.754
18.34	147888.	0.0676	0.770	0.782

(continued)

[a] The references from which the values were taken are given in brackets.

TABLE I *(Continued)*

Aluminum Nitride

eV	cm^{-1}	μm	n	k
18.10	145986.	0.0685	0.790	0.815
17.87	144132.	0.0694	0.788	0.799
17.65	142325.	0.0703	0.793	0.837
17.43	140563.	0.0711	0.793	0.859
17.21	138843.	0.0720	0.808	0.895
17.01	137165.	0.0729	0.811	0.911
16.80	135528.	0.0738	0.831	0.936
16.61	133928.	0.0747	0.833	0.956
16.41	132367.	0.0755	0.859	0.979
16.22	130841.	0.0764	0.878	0.980
16.04	129350.	0.0773	0.873	0.978
15.86	127892.	0.0782	0.892	1.022
15.68	126467.	0.0791	0.919	1.028
15.51	125074.	0.0800	0.920	1.070
15.34	123711.	0.0808	0.947	1.059
15.17	122377.	0.0817	0.961	1.109
15.01	121072.	0.0826	0.992	1.086
14.85	119792.	0.0835	1.005	1.121
14.70	118541.	0.0844	1.033	1.112
14.55	117316.	0.0852	1.057	1.123
14.40	116116.	0.0861	1.104	1.184
14.25	114940.	0.0870	1.122	1.102
14.11	113788.	0.0879	1.114	1.087
13.97	112658.	0.0888	1.144	1.149
13.83	111551.	0.0896	1.160	1.099
13.70	110466.	0.0905	1.150	1.082
13.56	109401.	0.0914	1.149	1.091
13.43	108357.	0.0923	1.133	1.063
13.31	107332.	0.0932	1.151	1.084
13.18	106327.	0.0940	1.162	1.100
13.06	105340.	0.0949	1.147	1.078
12.94	104371.	0.0958	1.146	1.084
12.82	103420.	0.0967	1.153	1.096
12.71	102486.	0.0976	1.129	1.064
12.59	101569.	0.0985	1.123	1.095
12.48	100668.	0.0993	1.104	1.073
12.37	99789.5	0.1002	1.082	1.103
12.26	98920.8	0.1011	1.081	1.141
12.16	98067.1	0.1020	1.061	1.130
12.05	97228.0	0.1029	1.043	1.177
11.95	96393.9	0.1037	1.039	1.211
11.85	95583.1	0.1046	1.032	1.229
11.75	94785.8	0.1055	1.025	1.276
11.65	94001.7	0.1064	1.031	1.321
11.56	93230.5	0.1073	1.046	1.346
11.47	92471.8	0.1081	1.030	1.365
11.37	91725.4	0.1090	1.060	1.435

TABLE I *(Continued)*

Aluminum Nitride

eV	cm^{-1}	μm	n	k
11.28	90990.9	0.1099	1.071	1.449
11.19	90268.1	0.1108	1.070	1.485
11.10	89556.7	0.1117	1.082	1.511
11.02	88848.6	0.1126	1.090	1.557
10.93	88159.3	0.1134	1.102	1.616
10.85	87480.6	0.1143	1.139	1.660
10.76	86812.3	0.1152	1.155	1.700
10.68	86154.1	0.1161	1.184	1.738
10.60	85505.8	0.1170	1.230	1.774
10.52	84867.2	0.1178	1.232	1.760
10.44	84238.1	0.1187	1.248	1.852
10.37	83618.2	0.1196	1.280	1.883
10.29	83007.4	0.1205	1.294	1.932
10.22	82398.7	0.1214	1.332	2.033
10.14	81805.5	0.1222	1.436	2.137
10.07	81220.8	0.1231	1.532	2.142
10.00	80644.4	0.1240	1.614	2.151
9.928	80076.1	0.1249	1.698	2.159
9.859	79515.8	0.1258	1.704	2.086
9.790	78963.2	0.1266	1.783	2.181
9.723	78418.3	0.1275	1.823	2.148
9.656	77880.9	0.1284	1.881	2.171
9.590	77344.8	0.1293	1.955	2.196
9.525	76821.9	0.1302	2.025	2.191
9.461	76306.0	0.1311	2.061	2.159
9.398	75797.0	0.1319	2.071	2.151
9.335	75294.8	0.1328	2.125	2.209
9.274	74799.2	0.1337	2.240	2.279
9.213	74310.1	0.1346	2.329	2.273
9.153	73827.3	0.1355	2.392	2.264
9.094	73350.7	0.1363	2.551	2.317
9.036	72880.3	0.1372	2.724	2.295
8.978	72410.6	0.1381	2.784	2.174
8.921	71952.1	0.1390	2.800	2.104
8.865	71499.4	0.1399	2.973	2.106
8.809	71052.3	0.1407	3.082	1.999
8.755	70610.8	0.1416	3.059	1.870
8.701	70174.8	0.1425	3.102	1.809
8.647	69744.1	0.1434	3.220	1.739
8.594	69318.6	0.1443	3.247	1.614
8.542	68898.3	0.1451	3.175	1.511
8.491	68483.1	0.1460	3.183	1.473
8.439	68068.2	0.1469	3.282	1.412
8.389	67662.9	0.1478	3.288	1.301
8.340	67262.4	0.1487	3.240	1.213
8.290	66866.6	0.1496	3.171	1.153

(continued)

TABLE I *(Continued)*

Aluminum Nitride

eV	cm^{-1}	μm	n	k
8.242	66475.5	0.1504	3.140	1.118
8.194	66088.9	0.1513	3.179	1.064
8.147	65706.7	0.1522	3.175	0.998
8.100	65329.0	0.1531	3.073	0.967
8.054	64955.5	0.1540	3.069	0.952
8.008	64586.4	0.1548	3.067	0.919
7.962	64217.2	0.1557	3.080	0.884
7.917	63856.4	0.1566	3.057	0.837
7.873	63499.5	0.1575	3.021	0.811
7.829	63146.7	0.1584	3.021	0.772
7.786	62797.7	0.1592	2.997	0.741
7.743	62452.6	0.1601	2.961	0.721
7.701	62111.2	0.1610	2.923	0.708
7.659	61773.6	0.1619	2.922	0.695
7.618	61439.6	0.1628	2.890	0.685
7.576	61105.4	0.1637	2.891	0.667
7.536	60778.6	0.1645	2.920	0.637
7.496	60455.3	0.1654	2.880	0.606
7.456	60135.3	0.1663	2.831	0.600
7.417	59818.8	0.1672	2.796	0.598
7.378	59505.5	0.1681	2.786	0.597
7.339	59195.6	0.1689	2.754	0.610
7.301	58888.8	0.1698	2.755	0.617
7.264	58585.2	0.1707	2.761	0.603
7.226	58284.7	0.1716	2.808	0.592
7.189	57983.9	0.1725	2.756	0.589
7.153	57689.5	0.1733	2.773	0.574
7.117	57398.1	0.1742	2.767	0.563
7.081	57109.7	0.1751	2.770	0.551
7.045	56824.1	0.1760	2.767	0.527
7.010	56541.4	0.1769	2.743	0.531
6.976	56261.4	0.1777	2.717	0.531
6.941	55984.2	0.1786	2.724	0.527
6.907	55709.8	0.1795	2.743	0.511
6.873	55438.0	0.1804	2.736	0.499
6.840	55165.8	0.1813	2.721	0.492
6.807	54899.3	0.1822	2.703	0.492
6.774	54635.3	0.1830	2.697	0.490
6.742	54373.9	0.1839	2.688	0.499
6.709	54115.0	0.1848	2.687	0.497
6.678	53858.5	0.1857	2.725	0.477
6.646	53604.4	0.1866	2.715	0.482
6.615	53352.7	0.1874	2.705	0.471
6.584	53103.4	0.1883	2.723	0.465
6.553	52856.4	0.1892	2.735	0.444
6.523	52608.9	0.1901	2.739	0.439
6.493	52366.5	0.1910	2.724	0.428

TABLE I *(Continued)*

Aluminum Nitride

eV	cm^{-1}	μm	n	k
6.463	52126.3	0.1918	2.745	0.413
6.433	51888.3	0.1927	2.745	0.401
6.404	51652.4	0.1936	2.767	0.367
6.375	51418.7	0.1945	2.775	0.340
6.346	51187.1	0.1954	2.767	0.312
6.318	50957.5	0.1962	2.739	0.307
6.290	50730.0	0.1971	2.728	0.280
6.262	50502.0	0.1980	2.730	0.258
6.234	50278.6	0.1989	2.702	0.258
6.206	50057.1	0.1998	2.670	0.258
6.179	49837.6	0.2007	2.663	0.250
6.152	49619.9	0.2015	2.665	0.244
6.150	49602.7	0.2016	2.858 (e)	0.413 (e)
6.125	49404.2	0.2024	2.653	0.235
6.100	49199.4	0.2033	2.836 (e)	0.383 (e)
6.099	49190.3	0.2033	2.667	0.204
6.073	48978.3	0.2042	2.647	0.213
6.050	48796.2	0.2049	2.823 (e)	0.351 (e)
6.047	48768.1	0.2051	2.634	0.185
6.021	48559.7	0.2059	2.634	0.170
6.000	48392.9	0.2066	2.807 (e)	0.322 (e)
5.995	48350.8	0.2068	2.608	0.177
5.969	48145.9	0.2077	2.570	0.188
5.950	47989.6	0.2084	2.765 (e)	0.298 (e)
5.944	47942.8	0.2086	2.569	0.177
5.919	47741.4	0.2095	2.586	0.151
5.900	47586.3	0.2101	2.736 (e)	0.243 (e)
5.894	47541.6	0.2103	2.580	0.144
5.870	47343.6	0.2112	2.557	0.139
5.850	47183.1	0.2119	2.709 (e)	0.216 (e)
5.846	47147.1	0.2121	2.538	0.130
5.821	46952.3	0.2130	2.532	0.117
5.800	46779.8	0.2138	2.712 (e)	0.195 (e)
5.797	46759.1	0.2139	2.512	0.116
5.774	46567.5	0.2147	2.479	0.134
5.750	46376.5	0.2156	2.688 (e)	0.135 (e)
5.750	46375.3	0.2156	2.460	0.133
5.726	46186.8	0.2165	2.455	0.122
5.703	45999.8	0.2174	2.463	0.117
5.700	45973.2	0.2175	2.680 (e)	0.121 (e)
5.680	45814.4	0.2183	2.420	0.139
5.657	45630.4	0.2192	2.396	0.154
5.650	45570.0	0.2194	2.586 (e)	0.123 (e)
5.636	45454.1	0.22	2.463 [48]	
5.635	45447.9	0.2200	2.386 [43]	0.163 [43]
5.612	45266.9	0.2209	2.381	0.166

(continued)

TABLE I *(Continued)*

Aluminum Nitride

eV	cm^{-1}	μm	n	k
5.600	45166.7	0.2214	2.567 (e)	0.115 (e)
5.590	45087.3	0.2218	2.391	0.161
5.568	44909.1	0.2227	2.379	0.174
5.550	44763.4	0.2234	2.533 (e)	0.108 (e)
5.546	44732.3	0.2236	2.359	0.191
5.524	44554.9	0.2244	2.360	0.177
5.503	44380.9	0.2253	2.368	0.181
5.500	44360.1	0.2254	2.521 (e)	0.101 (e)
5.481	44208.2	0.2262	2.364	0.189
5.460	44036.9	0.2271	2.338	0.198
5.450	43956.9	0.2275	2.498 (e)	0.095 (e)
5.439	43866.9	0.2280	2.342	0.196
5.418	43698.2	0.2288	2.340	0.200
5.400	43553.6	0.2296	2.491 (e)	0.090 (e)
5.397	43530.8	0.2297	2.331	0.210
5.391	43477.8	0.23	2.348 [48]	
5.391	43429.3	0.230	2.523 [49]	
5.377	43364.7	0.2306	2.315 [43]	0.225 [43]
5.356	43199.9	0.2315	2.305	0.240
5.350	43150.3	0.2317	2.481 (e)	0.084 (e)
5.336	43036.3	0.2324	2.299	0.254
5.315	42872.0	0.2333	2.312	0.250
5.300	42747.0	0.2339	2.471 (e)	0.080 (e)
5.296	42710.9	0.2341	2.331	0.243
5.276	42551.0	0.2350	2.352	0.234
5.256	42392.2	0.2359	2.337	0.243
5.250	42343.8	0.2362	2.463 (e)	0.077 (e)
5.236	42234.7	0.2368	2.320	0.253
5.217	42078.3	0.2377	2.304	0.263
5.200	41940.5	0.2384	2.455 (e)	0.073 (e)
5.198	41923.0	0.2385	2.291	0.285
5.179	41769.0	0.2394	2.284	0.303
5.166	41666.3	0.24	2.272 [48]	
5.166	41619.8	0.240	2.485 [49]	
5.160	41616.0	0.2403	2.289 [43]	0.310 [43]
5.150	41537.2	0.2407	2.448 (e)	0.072 (e)
5.141	41462.4	0.2412	2.313	0.308
5.122	41311.7	0.2421	2.344	0.305
5.103	41162.0	0.2429	2.352	0.308
5.100	41133.9	0.2431	2.441 (e)	0.069 (e)
5.085	41013.5	0.2438	2.357	0.308
5.067	40866.0	0.2447	2.358	0.305
5.050	40730.7	0.2455	2.436 (e)	0.070 (e)
5.049	40719.5	0.2456	2.362	0.309
5.031	40574.1	0.2465	2.367	0.313
5.013	40429.8	0.2473	2.367	0.313
5.000	40327.4	0.2480	2.425 (e)	0.070 (e)

TABLE I *(Continued)*

Aluminum Nitride

eV	cm^{-1}	μm	n	k
4.995	40286.5	0.2482	2.374	0.310
4.977	40144.1	0.2491	2.394	0.301
4.960	40001.2	0.2500	2.402	0.299
4.959	39999.6	0.25	2.221 [48]	
4.959	39955.0	0.250	2.447 [49]	
4.950	39924.1	0.2505	2.413 [43]	0.070 [43]
4.942	39860.9	0.2509	2.403	0.300
4.925	39721.6	0.2518	2.400	0.302
4.908	39583.2	0.2526	2.398	0.304
4.900	39520.9	0.2530	2.402 (e)	0.068 (e)
4.891	39445.8	0.2535	2.400	0.306
4.874	39309.3	0.2544	2.410	0.301
4.857	39173.8	0.2553	2.433	0.285
4.850	39117.6	0.2556	2.391 (e)	0.065 (e)
4.840	39039.3	0.2562	2.447	0.278
4.824	38905.6	0.2570	2.451	0.279
4.807	38772.8	0.2579	2.451	0.271
4.800	38714.3	0.2583	2.381 (e)	0.065 (e)
4.791	38639.5	0.2588	2.449	0.258
4.774	38508.6	0.2597	2.458	0.252
4.769	38461.2	0.26	2.180 [48]	
4.769	38418.3	0.260	2.416 [49]	
4.758	38378.5	0.2606	2.468 [43]	0.247 [43]
4.750	38311.0	0.2610	2.372 (e)	0.063 (e)
4.742	38249.3	0.2614	2.465	0.237
4.726	38121.0	0.2623	2.462	0.227
4.711	37993.6	0.2632	2.468	0.219
4.700	37907.8	0.2638	2.362 (e)	0.060 (e)
4.695	37867.0	0.2641	2.472	0.211
4.679	37741.2	0.2650	2.465	0.205
4.664	37616.3	0.2658	2.459	0.199
4.650	37504.5	0.2666	2.352 (e)	0.056 (e)
4.648	37490.7	0.2667	2.460	0.192
4.633	37367.5	0.2676	2.459	0.186
4.618	37245.0	0.2685	2.452	0.185
4.603	37123.3	0.2694	2.445	0.183
4.600	37101.2	0.2695	2.343 (e)	0.052 (e)
4.592	37036.7	0.27	2.146 [48]	
4.592	36995.4	0.270	2.389 [49]	
4.588	37002.4	0.2703	2.443 [43]	0.178 [43]
4.573	36882.3	0.2711	2.441	0.173
4.558	36763.0	0.2720	2.439	0.171
4.550	36697.9	0.2725	2.335 (e)	0.047 (e)
4.543	36644.5	0.2729	2.436	0.169
4.529	36526.7	0.2738	2.434	0.165
4.514	36409.6	0.2747	2.432	0.162

(continued)

TABLE I *(Continued)*

Aluminum Nitride

eV	cm^{-1}	μm	n	k
4.500	36294.7	0.2755	2.327 (e)	0.042 (e)
4.500	36292.0	0.2755	2.430	0.159
4.485	36176.5	0.2764	2.428	0.157
4.471	36061.7	0.2773	2.425	0.154
4.457	35947.6	0.2782	2.423	0.151
4.450	35891.4	0.2786	2.320 (e)	0.037 (e)
4.443	35834.2	0.2791	2.421	0.148
4.429	35721.6	0.2799	2.419	0.146
4.428	35713.9	0.28	2.127 [48]	
4.428	35674.1	0.280	2.366 [49]	
4.415	35609.7	0.2808	2.417 [43]	0.143 [43]
4.401	35498.4	0.2817	2.415	0.141
4.400	35488.1	0.2818	2.312 (e)	0.033 (e)
4.388	35387.9	0.2826	2.413	0.138
4.374	35278.0	0.2835	2.411	0.136
4.360	35167.6	0.2844	2.409	0.134
4.350	35084.8	0.2850	2.305 (e)	0.030 (e)
4.347	35059.1	0.2852	2.407	0.132
4.333	34951.3	0.2861	2.405	0.129
4.320	34844.1	0.2870	2.403	0.127
4.307	34737.6	0.2879	2.401	0.125
4.300	34681.6	0.2883	2.297 (e)	0.025 (e)
4.294	34631.7	0.2888	2.398	0.124
4.281	34526.5	0.2896	2.396	0.122
4.275	34482.4	0.29	2.116 [48]	
4.275	34444.0	0.290	2.346 [49]	
4.268	34421.9	0.2905	2.394 [43]	0.120 [43]
4.255	34317.9	0.2914	2.392	0.119
4.250	34278.3	0.2917	2.288 (e)	0.022 (e)
4.242	34214.6	0.2923	2.389	0.117
4.229	34110.7	0.2932	2.387	0.116
4.217	34008.7	0.2940	2.385	0.115
4.204	33907.2	0.2949	2.383	0.113
4.200	33875.0	0.2952	2.281 (e)	0.019 (e)
4.191	33806.3	0.2958	2.382	0.112
4.179	33706.0	0.2967	2.380	0.111
4.167	33606.3	0.2976	2.378	0.109
4.154	33507.3	0.2984	2.376	0.108
4.150	33471.7	0.2988	2.274 (e)	0.017 (e)
4.142	33408.7	0.2993	2.375	0.107
4.133	33333.0	0.3	2.104 [48]	
4.133	33295.8	0.300	2.329 [49]	
4.130	33310.8	0.3002	2.373 [43]	0.106 [43]
4.118	33213.4	0.3011	2.371	0.105
4.106	33115.6	0.3020	2.370	0.103
4.100	33068.5	0.3024	2.268 (e)	0.015 (e)
4.094	33019.3	0.3029	2.368	0.102

TABLE I *(Continued)*

Aluminum Nitride

eV	cm^{-1}	μm	n	k
4.082	32923.7	0.3037	2.367	0.101
4.070	32828.6	0.3046	2.365	0.100
4.059	32734.0	0.3055	2.364	0.099
4.050	32665.2	0.3061	2.262 (e)	0.013 (e)
4.047	32640.0	0.3064	2.362	0.098
4.035	32546.5	0.3073	2.361	0.097
4.024	32453.5	0.3081	2.359	0.096
4.012	32361.1	0.3090	2.358	0.094
4.000	32261.9	0.3100	2.257 (e)	0.012 (e)
3.999	32257.8	0.31	2.103 [48]	
3.999	32221.8	0.310	2.314 [49]	
3.950	31858.6	0.3139	2.251 [43]	0.012
3.900	31455.4	0.3179	2.245	0.011
3.875	31249.7	0.32	2.100 [48]	26.007 [48]
3.875	31214.8	0.320	2.300 [49]	
3.875	31249.7	0.32	1.950 [56]	[56]
3.850	31052.1	0.3220	2.240 [43]	0.011 [43]
3.800	30648.8	0.3263	2.235 (e)	0.011 (e)
3.757	30302.7	0.33	2.097 [48]	16.997 [48]
3.757	30268.9	0.330	2.287 [49]	
3.750	30245.6	0.3306	2.230 [43]	0.011 [43]
3.700	29842.3	0.3351	2.224 (e)	0.012 (e)
3.650	29439.0	0.3397	2.219 (e)	0.012 (e)
3.647	29411.5	0.34	2.094 [48]	12.270 [48]
3.647	29378.7	0.340	2.275 [49]	
3.647	29411.5	0.34	1.910 [56]	[56]
3.600	29035.7	0.3444	2.214 [43]	0.012 [43]
3.550	28632.5	0.3493	2.208 (e)	0.012 (e)
3.542	28539.3	0.350	2.265 [49]	
3.542	28571.2	0.35	1.880 [56]	[56]
3.500	28229.2	0.3542	2.202 [43]	0.012 [43]
3.450	27825.9	0.3594	2.196 (e)	0.011 (e)
3.444	27777.5	0.36	2.093 [48]	7.405 [48]
3.444	27746.5	0.360	2.255 [49]	
3.400	27422.6	0.3647	2.190 [43]	0.011 [43]
3.351	27026.8	0.37	2.092 [48]	5.620 [48]
3.351	26996.6	0.370	2.246 [49]	
3.350	27019.4	0.3701	2.184 [43]	0.010 [43]
3.300	26616.1	0.3757	2.177 (e)	0.009 (e)
3.263	26315.5	0.38	2.092 [48]	4.616
3.263	26286.2	0.380	2.238 [49]	
3.250	26212.8	0.3815	2.171 [43]	0.008 [43]
3.200	25809.5	0.3875	2.166 (e)	0.007 (e)
3.179	25640.8	0.39	2.091 [48]	3.796
3.179	25612.2	0.390	2.231 [49]	
3.179	25640.8	0.39	1.850 [56]	

(continued)

TABLE I *(Continued)*

Aluminum Nitride

eV	cm^{-1}	μm	n	k
3.150	25406.3	0.3936	2.161	0.006
3.100	25003.0	0.3999	2.156 (e)	0.005 (e)
3.100	24999.8	0.4	2.090 [48]	3.024 [48]
3.100	24971.9	0.400	2.224 [49]	
3.050	24599.7	0.4065	2.151 [43]	0.005 [43]
3.024	24390.0	0.41	2.089 [48]	2.620 [48]
3.024	24362.8	0.410	2.218 [49]	
3.000	24196.4	0.4133	2.146 [43]	0.004 [43]
2.952	23809.3	0.42	2.088 [48]	2.234 [48]
2.952	23782.7	0.420	2.212 [49]	
2.952	23809.3	0.42	1.860 [56]	
2.950	23793.2	0.4203	2.142 [43]	0.003 [43]
2.900	23389.9	0.4275	2.138 (e)	0.002 (e)
2.883	23255.6	0.43	2.087 [48]	1.868 [48]
2.883	23229.6	0.430	2.206 [49]	
2.850	22986.6	0.4350	2.135 [43]	0.002 [43]
2.818	22727.1	0.44	2.086 [48]	1.587 [48]
2.818	22701.7	0.440	2.201 [49]	
2.800	22583.3	0.4428	2.131 [43]	0.001 [43]
2.755	22222.0	0.45	2.085 [48]	1.289 [48]
2.755	22197.2	0.450	2.196 [49]	
2.750	22180.1	0.4509	2.128 [43]	0.001 [43]
2.700	21776.8	0.4592	2.124 (e)	0.001 (e)
2.695	21738.9	0.46	2.085 [48]	1.047 [48]
2.695	21714.7	0.460	2.191 [49]	
2.695	21738.9	0.46	1.870 [56]	
2.650	21373.5	0.4679	2.121 [43]	0.001 [43]
2.638	21276.4	0.47	2.084 [48]	0.842 [48]
2.638	21252.7	0.470	2.187 [49]	
2.600	20970.2	0.4769	2.118 [43]	0.000 [43]
2.583	20833.1	0.48	2.084 [48]	0.664 [48]
2.583	20809.9	0.480	2.184 [49]	
2.550	20567.0	0.4862	2.115 [43]	0.000 [43]
2.530	20408.0	0.49	2.084 [48]	0.542 [48]
2.530	20385.2	0.490	2.180 [49]	
2.500	20163.7	0.4959	2.112 [43]	0.000 [43]
2.480	19999.8	0.5	2.083 [48]	0.426 [48]
2.480	19977.5	0.500	2.177 [49]	
2.450	19760.4	0.5061	2.109 [43]	0.000 [43]
2.431	19607.7	0.51	2.083 [48]	0.277 [48]
2.431	19585.8	0.510	2.174 [49]	
2.400	19357.2	0.5166	2.106 [43]	0.000 [43]
2.384	19230.6	0.52	2.082 [48]	
2.384	19209.1	0.520	2.171 [49]	
2.350	18953.9	0.5276	2.102 [43]	0.000 [43]
2.339	18846.7	0.530	2.168 [49]	
2.300	18550.6	0.5391	2.100 [43]	0.000 [43]

TABLE I *(Continued)*

Aluminum Nitride

eV	cm^{-1}	μm	n	k
2.296	18497.7	0.540	2.166 [49]	
2.267	18281.4	0.547	2.080 [48]	
2.254	18161.4	0.550	2.163 [49]	
2.254	18181.6	0.55	1.760 [56]	
2.250	18147.3	0.5510	2.098 [43]	0.000 [43]
2.214	17837.0	0.560	2.161 [49]	
2.200	17744.1	0.5636	2.096 [43]	0.000 [43]
2.175	17524.1	0.570	2.159 [49]	
2.150	17340.8	0.5767	2.095 [43]	0.000 [43]
2.141	17271.0	0.579	2.079 [48]	
2.138	17222.0	0.580	2.157 [49]	
2.101	16930.1	0.590	2.156	
2.100	16937.5	0.5904	2.094 [43]	0.000 [43]
2.066	16647.9	0.600	2.154 [49]	
2.066	16666.5	0.60	1.700 [56]	
2.050	16534.2	0.6048	2.093 [43]	0.000 [43]
2.033	16375.0	0.610	2.153 [49]	
2.029	16366.5	0.611	2.078 [48]	
2.000	16131.0	0.6199	2.092 [43]	0.000 [43]
2.000	16110.9	0.620	2.152 [49]	
1.968	15855.2	0.630	2.150	
1.950	15727.7	0.6358	2.092 [43]	0.000 [43]
1.937	15607.4	0.640	2.149 [49]	
1.928	15552.0	0.643	2.078 [48]	
1.907	15367.3	0.650	2.147 [49]	
1.900	15324.4	0.6525	2.091 [43]	0.001 [43]
1.879	15134.5	0.660	2.146 [49]	
1.851	14908.6	0.670	2.145	
1.850	14921.1	0.6702	2.090 [43]	0.002 [43]
1.837	14814.7	0.675	2.078 [48]	
1.823	14689.3	0.680	2.144 [49]	
1.800	14517.9	0.6888	2.089 [43]	0.003 [43]
1.797	14476.4	0.690	2.144 [49]	
1.797	14492.6	0.69	1.580 [56]	
1.771	14269.6	0.700	2.143 [49]	
1.751	14124.2	0.708	2.078 [48]	
1.750	14114.6	0.7085	2.087 [43]	0.004 [43]
1.746	14068.7	0.710	2.142 [49]	
1.746	14084.4	0.71	1.630 [56]	
1.722	13873.3	0.720	2.141 [49]	
1.700	13711.3	0.7293	2.085 [43]	0.005 [43]
1.698	13683.2	0.730	2.140 [49]	
1.675	13513.4	0.74	2.077 [48]	
1.675	13498.3	0.740	2.139 [49]	
1.653	13318.3	0.750	2.138	
1.650	13308.0	0.7514	2.083 [43]	0.006 [43]

(continued)

TABLE I *(Continued)*

Aluminum Nitride

eV	cm^{-1}	μm	n	k
1.631	13143.1	0.760	2.138 [49]	
1.610	12972.4	0.770	2.137	
1.606	12953.2	0.772	2.077 [48]	
1.600	12904.8	0.7749	2.081 [43]	0.007 [43]
1.590	12806.1	0.780	2.136 [49]	
1.569	12644.0	0.790	2.136	
1.550	12501.5	0.7999	2.079 [43]	0.008 [43]
1.550	12485.9	0.800	2.135 [49]	
1.542	12437.7	0.804	2.076 [48]	
1.531	12331.8	0.810	2.135 [49]	
1.512	12181.4	0.820	2.134	
1.500	12098.2	0.8266	2.076 [43]	0.010 [43]
1.494	12034.6	0.830	2.134 [49]	
1.483	11961.6	0.836	2.075 [48]	
1.476	11891.4	0.840	2.134 [49]	
1.459	11751.5	0.850	2.133	
1.442	11614.8	0.860	2.133	
1.430	11533.9	0.867	2.075 [48]	
1.425	11481.3	0.870	2.132 [49]	
1.409	11350.8	0.880	2.132	
1.393	11223.3	0.890	2.132	
1.379	11123.4	0.899	2.074 [48]	
1.378	11098.6	0.900	2.131 [49]	
1.362	10976.6	0.910	2.131	
1.348	10857.3	0.920	2.131	
1.348	10869.5	0.92	1.460 [56]	
1.333	10740.6	0.930	2.131 [49]	
1.332	10741.0	0.931	2.073 [48]	
1.319	10626.3	0.940	2.131 [49]	
1.305	10514.5	0.950	2.130	
1.292	10404.9	0.960	2.130	
1.287	10384.1	0.963	2.073 [48]	
1.278	10297.7	0.970	2.130 [49]	
1.265	10192.6	0.980	2.130	
1.252	10089.6	0.990	2.129	
1.246	10050.2	0.995	2.072 [48]	
1.240	9988.7	1.000	2.129 [49]	
1.228	9889.8	1.010	2.129	
1.216	9792.9	1.020	2.129	
1.207	9737.0	1.027	2.072 [48]	
1.204	9697.8	1.030	2.129 [49]	
1.192	9604.6	1.040	2.129	
1.181	9513.1	1.050	2.128	
1.170	9433.9	1.06	2.072 [48]	
1.170	9423.3	1.060	2.128 [49]	
1.159	9335.3	1.070	2.128	
1.148	9248.8	1.080	2.128	

TABLE I *(Continued)*

Aluminum Nitride

eV	cm^{-1}	μm	n	k
1.137	9164.0	1.090	2.128	
1.135	9157.4	1.092	2.072 [48]	
1.127	9080.7	1.100	2.127 [49]	
1.117	8998.9	1.110	2.127	
1.107	8918.5	1.120	2.127	
1.103	8896.7	1.124	2.072 [48]	
1.097	8839.6	1.130	2.127 [49]	
1.088	8762.1	1.140	2.127	
1.078	8685.9	1.150	2.127	
1.072	8643.0	1.157	2.072 [48]	
1.069	8611.0	1.160	2.126 [49]	
1.060	8537.4	1.170	2.126	
1.051	8465.0	1.180	2.126	
1.042	8393.9	1.190	2.126	
1.033	8324.0	1.200	2.126	
1.025	8255.2	1.210	2.126	
1.016	8187.5	1.220	2.125	
1.008	8120.9	1.230	2.125	
0.9999	8055.4	1.240	2.125	
0.9919	7991.0	1.250	2.125	
0.9840	7927.6	1.260	2.125	
0.9763	7865.2	1.270	2.125	
0.9686	7803.7	1.280	2.125	
0.9611	7743.2	1.290	2.125	
0.9537	7683.7	1.300	2.125	
0.9464	7625.0	1.310	2.124	
0.9393	7567.2	1.320	2.124	
0.9322	7510.3	1.330	2.124	
0.9253	7454.3	1.340	2.124	
0.9184	7399.1	1.350	2.124	
0.9116	7344.7	1.360	2.123	
0.9050	7291.1	1.370	2.123	
0.8984	7238.2	1.380	2.123	
0.8920	7186.1	1.390	2.123	
0.8856	7134.8	1.400	2.123	
0.8793	7084.2	1.410	2.123	
0.8731	7034.3	1.420	2.122	
0.8670	6985.1	1.430	2.122	
0.8610	6936.6	1.440	2.122	
0.8551	6888.8	1.450	2.122	
0.8492	6841.6	1.460	2.122	
0.8434	6795.1	1.470	2.121	
0.8377	6749.2	1.480	2.121	
0.8321	6703.9	1.490	2.121	
0.8266	6659.2	1.500	2.120	
0.8211	6615.1	1.510	2.120	

(continued)

TABLE I *(Continued)*

Aluminum Nitride

eV	cm^{-1}	μm	n	k
0.8157	6571.5	1.520	2.119	
0.8104	6528.6	1.530	2.119	
0.8051	6486.2	1.540	2.120	
0.7999	6444.4	1.550	2.119	
0.7948	6403.0	1.560	2.119	
0.7897	6362.3	1.570	2.118	
0.7847	6322.0	1.580	2.118	
0.7798	6282.2	1.590	2.117	
0.7749	6243.0	1.600	2.117	
0.7701	6204.2	1.610	2.117	
0.7653	6165.9	1.620	2.116	
0.7606	6128.1	1.630	2.116	
0.7560	6090.7	1.640	2.116	
0.7514	6053.8	1.650	2.114	
0.7469	6017.3	1.660	2.114	
0.7424	5981.3	1.670	2.114	
0.7380	5945.7	1.680	2.114	
0.7336	5910.5	1.690	2.114	
0.7293	5875.7	1.700	2.114	
0.7251	5841.4	1.710	2.114	
0.7208	5807.4	1.720	2.114	
0.7167	5773.8	1.730	2.114	
0.7126	5740.7	1.740	2.114	
0.7085	5707.9	1.750	2.114	
0.1616	1303.2	7.67		1.086E-08 [41]
0.1579	1273.5	7.85		1.271E-08
0.1543	1244.5	8.04		1.596E-08
0.1508	1216.2	8.22		2.053E-08
0.1474	1188.5	8.41		2.681E-08
0.1440	1161.4	8.61		3.638E-08
0.1407	1135.0	8.81		4.863E-08
0.1375	1109.2	9.02		6.453E-08
0.1344	1083.9	9.23		8.562E-08
0.1313	1059.3	9.44		1.120E-07
0.1283	1035.1	9.66		1.460E-07
0.1254	1011.6	9.89		1.897E-07
0.1226	988.55	10.12		2.609E-07
0.1198	966.05	10.35		3.720E-07
0.1170	944.06	10.59		5.140E-07
0.1144	922.57	10.84		6.893E-07
0.1118	901.57	11.09		9.291E-07
0.1092	881.05	11.35		1.254E-06
0.1068	860.99	11.61		1.665E-06
0.1043	841.39	11.89		2.214E-06
0.1019	822.24	12.16		2.928E-06
0.0996	803.53	12.45		3.961E-06
0.0974	785.23	12.74		5.542E-06

TABLE I *(Continued)*

Aluminum Nitride

eV	cm^{-1}	μm	n	k
0.0951	767.36	13.03		8.169E-06
0.0930	749.89	13.34		1.102E-05
0.0909	732.82	13.65		1.406E-05
0.0888	716.14	13.96		2.033E-05
0.0868	699.84	14.29		2.917E-05
0.0848	683.91	14.62		4.115E-05
0.0829	668.34	14.96		5.822E-05
0.0810	653.13	15.31		8.514E-05
0.0791	638.26	15.67		1.293E-04
0.0773	623.73	16.03		1.945E-04
0.0756	609.54	16.41		2.796E-04
0.0739	595.66	16.79		3.754E-04
0.0722	582.10	17.18		4.652E-04
0.0705	568.85	17.58		5.686E-04
0.0689	555.90	17.99		6.595E-04
0.0674	543.25	18.41		7.701E-04
0.0658	530.88	18.84		9.159E-04
0.0643	518.80	19.28		1.293E-03
0.0629	506.99	19.72		1.909E-03
0.0614	495.45	20.18		2.987E-03
0.0600	484.17	20.65		4.857E-03
0.0587	473.15	21.13		9.321E-03
0.0573	462.38	21.63		1.646E-02
0.0560	451.86	22.13		2.474E-02
0.0547	441.57	22.65		3.459E-02
0.0535	431.52	23.17		0.043
0.0523	421.70	23.71		0.045
0.0511	412.10	24.27		0.042
0.0499	402.72	24.83		0.045
0.0488	393.55	25.41		0.041
0.0477	384.59	26.00		0.040
0.0466	375.84	26.61		0.046
0.0455	367.28	27.23		0.052
0.0445	358.92	27.86		0.049
0.0435	350.75	28.51		0.044
0.0425	342.77	29.17		0.038
0.0415	334.97	29.85		0.042
0.0406	327.34	30.55		0.054
0.0397	319.89	31.26		0.064
0.0388	312.61	31.99		0.083
0.0379	305.49	32.73		0.113
0.0370	298.54	33.50		0.171
0.0362	291.74	34.28		0.277
0.0353	285.10	35.08		0.457
0.0345	278.61	35.89		0.755
0.0338	272.27	36.73		1.276

(continued)

TABLE I *(Continued)*

Aluminum Nitride

eV	cm^{-1}	μm	n	k
0.0330	266.07	37.58		2.208
0.0322	260.02	38.46		3.481
0.0315	254.10	39.36		5.366
0.0308	248.31	40.27		10.156
0.0301	242.66	41.21		21.656
0.0294	237.14	42.17		10.903
0.0287	231.74	43.15		5.243
0.0281	226.46	44.16		2.957
0.0274	221.31	45.19		1.619
0.0268	216.27	46.24		0.875
0.0262	211.35	47.32		0.484
0.0256	206.54	48.42		0.282
0.0250	201.84	49.55		0.167
0.0245	197.24	50.70		0.108
0.0239	192.75	51.88		0.078
0.0234	188.36	53.09		0.061
0.0228	184.08	54.33		0.049
0.0223	179.89	55.59		0.041
0.0218	175.79	56.89		0.034
0.0213	171.79	58.21		0.029
0.0208	167.88	59.57		0.026
0.0203	164.06	60.95		0.023
0.0199	160.32	62.37		0.021
0.0194	156.67	63.83		0.019
0.0190	153.11	65.31		1.795E-02
0.0186	149.62	66.83		1.651E-02
0.0181	146.22	68.39		1.535E-02
0.0177	142.89	69.98		1.427E-02
0.0173	139.64	71.61		1.334E-02
0.0169	136.46	73.28		1.255E-02
0.0165	133.35	74.99		1.190E-02
0.0162	130.32	76.74		1.126E-02
0.0158	127.35	78.52		1.073E-02
0.0154	124.45	80.35		1.023E-02
0.0151	121.62	82.22		9.806E-03
0.0147	118.85	84.14		9.432E-03
0.0144	116.14	86.10		8.994E-03
0.0141	113.50	88.11		8.623E-03
0.0138	110.92	90.16		8.244E-03
0.0134	108.39	92.26		7.923E-03
0.0131	105.93	94.41		7.601E-03
0.0128	103.51	96.61		7.317E-03
0.0125	101.16	98.86		7.125E-03
0.0123	98.86	101.16		6.921E-03
0.0120	96.60	103.51		6.725E-03
0.0117	94.41	105.93		6.527E-03
0.0114	92.26	108.39		6.314E-03

TABLE I *(Continued)*

Aluminum Nitride

eV	cm^{-1}	μm	n	k
0.0112	90.16	110.92		6.145E-03
0.0109	88.10	113.50		5.956E-03
0.0107	86.10	116.15		5.729E-03
0.0104	84.14	118.85		5.554E-03
0.0102	82.22	121.62		5.377E-03
0.0100	80.35	124.45		5.203E-03
0.0097	78.52	127.35		5.028E-03
0.0095	76.74	130.32		4.838E-03
0.0093	74.99	133.35		4.679E-03
0.0091	73.28	136.46		4.515E-03
0.0089	71.61	139.64		4.343E-03
0.0087	69.98	142.89		4.193E-03
0.0085	68.39	146.22		4.078E-03
0.0083	66.83	149.62		3.963E-03
0.0081	65.31	153.11		3.836E-03
0.0079	63.83	156.68		3.719E-03
0.0077	62.37	160.32		3.604E-03
0.0076	60.95	164.06		3.491E-03
0.0074	59.57	167.88		3.375E-03
0.0072	58.21	171.79		3.244E-03
0.0071	56.89	175.79		3.134E-03
0.0069	55.59	179.89		3.032E-03
6.735E-03	54.32	184.08		2.928E-03
6.582E-03	53.09	188.37		2.835E-03
6.432E-03	51.88	192.75		2.744E-03
6.286E-03	50.70	197.24		2.657E-03
6.143E-03	49.54	201.84		2.572E-03
6.003E-03	48.42	206.54		2.469E-03
5.866E-03	47.32	211.35		2.388E-03
5.733E-03	46.24	216.27		2.310E-03
5.602E-03	45.19	221.31		2.230E-03
5.475E-03	44.16	226.46		2.160E-03
5.350E-03	43.15	231.74		2.086E-03
5.228E-03	42.17	237.14		2.024E-03
5.109E-03	41.21	242.66		1.969E-03
4.993E-03	40.27	248.31		1.891E-03
4.879E-03	39.35	254.10		1.824E-03
4.768E-03	38.46	260.02		1.755E-03
4.660E-03	37.58	266.07		1.690E-03
4.554E-03	36.73	272.27		1.640E-03
4.450E-03	35.89	278.61		1.577E-03
4.349E-03	35.08	285.10		1.527E-03
4.250E-03	34.28	291.74		1.486E-03
4.153E-03	33.50	298.54		1.439E-03
4.059E-03	32.73	305.49		1.394E-03
3.966E-03	31.99	312.61		1.343E-03

(continued)

TABLE I *(Continued)*

Aluminum Nitride

eV	cm^{-1}	μm	n	k
3.876E-03	31.26	319.89		1.296E-03
3.788E-03	30.55	327.34		1.262E-03
3.701E-03	29.85	334.97		1.217E-03
3.617E-03	29.17	342.77		1.178E-03
3.535E-03	28.51	350.75		1.146E-03
3.454E-03	27.86	358.92		1.110E-03
3.376E-03	27.23	367.28		1.079E-03
3.299E-03	26.61	375.84		1.044E-03
3.224E-03	26.00	384.59		1.004E-03
3.150E-03	25.41	393.55		9.721E-04
3.079E-03	24.83	402.72		9.353E-04
3.009E-03	24.27	412.10		9.020E-04
2.940E-03	23.71	421.70		8.724E-04
2.873E-03	23.17	431.52		8.406E-04
2.808E-03	22.65	441.57		8.131E-04
2.744E-03	22.13	451.86		7.870E-04
2.681E-03	21.63	462.38		7.622E-04
2.620E-03	21.13	473.15		7.391E-04
2.561E-03	20.65	484.17		7.133E-04
2.502E-03	20.18	495.45		6.915E-04
2.446E-03	19.72	506.99		6.732E-04
2.390E-03	19.28	518.80		6.517E-04
2.335E-03	18.84	530.89		6.337E-04
2.282E-03	18.41	543.25		6.155E-04
2.230E-03	17.99	555.91		5.946E-04
2.180E-03	17.58	568.85		5.786E-04
2.130E-03	17.18	582.10		5.591E-04
2.081E-03	16.79	595.66		5.385E-04
2.034E-03	16.41	609.54		5.232E-04
1.988E-03	16.03	623.74		5.037E-04
1.943E-03	15.67	638.26		4.878E-04
1.898E-03	15.31	653.13		4.755E-04
1.855E-03	14.96	668.35		4.622E-04
1.813E-03	14.62	683.91		4.499E-04
1.772E-03	14.29	699.84		4.372E-04
1.731E-03	13.96	716.14		4.229E-04
1.692E-03	13.65	732.83		4.116E-04
1.653E-03	13.34	749.90		3.987E-04
1.616E-03	13.03	767.36		3.841E-04
1.579E-03	12.74	785.24		3.718E-04
1.543E-03	12.45	803.53		3.597E-04
1.508E-03	12.16	822.24		3.498E-04
1.474E-03	11.88	841.40		3.416E-04
1.440E-03	11.61	861.00		3.308E-04
1.407E-03	11.35	881.05		3.213E-04
1.375E-03	11.09	901.57		3.126E-04
1.344E-03	10.84	922.57		3.025E-04

TABLE I *(Continued)*

Aluminum Nitride

eV	cm^{-1}	μm	n	k
1.313E-03	10.59	944.06		2.934E-04
1.283E-03	10.35	966.05		2.843E-04
1.254E-03	10.12	988.56		2.752E-04
1.226E-03	9.89	1011.58		2.677E-04
1.198E-03	9.66	1035.14		2.604E-04
1.170E-03	9.44	1059.26		2.532E-04
1.144E-03	9.23	1083.93		2.464E-04
1.118E-03	9.02	1109.18		2.384E-04
1.092E-03	8.81	1135.01		2.303E-04
1.068E-03	8.61	1161.45		2.228E-04
1.043E-03	8.41	1188.50		2.140E-04
1.019E-03	8.22	1216.19		2.069E-04
9.963E-04	8.04	1244.52		1.996E-04
9.736E-04	7.85	1273.51		1.926E-04
9.514E-04	7.67	1303.17		1.876E-04
9.298E-04	7.50	1333.52		1.819E-04
9.086E-04	7.33	1364.59		1.766E-04
8.879E-04	7.16	1396.37		1.719E-04
8.677E-04	7.00	1428.90		1.658E-04
8.479E-04	6.84	1462.18		1.608E-04
8.286E-04	6.68	1496.24		1.564E-04
8.098E-04	6.53	1531.09		1.513E-04
7.914E-04	6.38	1566.75		1.465E-04
7.733E-04	6.24	1604.25		1.417E-04
7.557E-04	6.10	1640.59		1.369E-04
7.385E-04	5.96	1678.81		1.331E-04
7.217E-04	5.82	1717.91		1.290E-04
7.053E-04	5.69	1757.93		1.252E-04
6.892E-04	5.56	1798.88		1.217E-04
6.735E-04	5.43	1840.78		1.179E-04
6.582E-04	5.31	1883.65		1.146E-04
6.432E-04	5.19	1927.53		1.118E-04
6.286E-04	5.07	1972.43		1.082E-04
6.143E-04	4.95	2018.37		1.050E-04
6.003E-04	4.84	2065.39		1.016E-04
5.866E-04	4.73	2113.49		9.772E-05
5.733E-04	4.62	2162.72		9.459E-05
5.602E-04	4.52	2213.10		9.139E-05
5.475E-04	4.42	2264.65		8.852E-05
5.350E-04	4.32	2317.40		8.616E-05
5.228E-04	4.22	2371.38		8.368E-05
5.109E-04	4.12	2426.62		8.131E-05
4.993E-04	4.03	2483.14		7.912E-05
4.879E-04	3.94	2540.98		7.704E-05
4.768E-04	3.85	2600.17		7.483E-05
4.660E-04	3.76	2660.73		7.250E-05

(continued)

TABLE I *(Continued)*

Aluminum Nitride

eV	cm^{-1}	μm	n	k
4.554E-04	3.67	2722.71		7.020E-05
4.450E-04	3.59	2786.13		6.829E-05
4.349E-04	3.51	2851.03		6.631E-05
4.250E-04	3.43	2917.43		6.424E-05
4.153E-04	3.35	2985.39		6.280E-05
4.059E-04	3.27	3054.93		6.135E-05
3.966E-04	3.20	3126.09		5.972E-05
3.876E-04	3.13	3198.90		5.826E-05
3.788E-04	3.05	3273.42		5.658E-05
3.701E-04	2.99	3349.66		5.485E-05
3.617E-04	2.92	3427.69		5.353E-05
3.535E-04	2.85	3507.53		5.166E-05
3.454E-04	2.79	3589.23		4.983E-05
3.376E-04	2.72	3672.83		4.856E-05
3.299E-04	2.66	3758.38		4.718E-05
3.224E-04	2.60	3845.93		4.590E-05
3.150E-04	2.54	3935.51		4.467E-05
3.079E-04	2.48	4027.18		4.329E-05
3.009E-04	2.43	4120.99		4.210E-05
2.940E-04	2.37	4216.98		4.095E-05
2.873E-04	2.32	4315.20		3.967E-05
2.808E-04	2.26	4415.72		3.860E-05
2.744E-04	2.21	4518.57		3.748E-05
2.681E-04	2.16	4623.82		3.628E-05
2.620E-04	2.11	4731.53		3.537E-05
2.561E-04	2.07	4841.74		3.446E-05
2.502E-04	2.02	4954.52		3.350E-05
2.446E-04	1.97	5069.92		3.259E-05
2.390E-04	1.93	5188.01		3.157E-05
2.335E-04	1.88	5308.86		3.063E-05
2.282E-04	1.84	5432.52		2.994E-05
2.230E-04	1.80	5559.06		2.906E-05
2.180E-04	1.76	5688.55		2.821E-05
2.130E-04	1.72	5821.05		2.751E-05
2.081E-04	1.68	5956.64		2.679E-05
2.034E-04	1.64	6095.39		2.612E-05
1.988E-04	1.60	6237.37		2.540E-05
1.943E-04	1.57	6382.65		2.444E-05
1.898E-04	1.53	6531.32		2.372E-05
1.855E-04	1.50	6683.46		2.306E-05
1.813E-04	1.46	6839.14		2.233E-05
1.772E-04	1.43	6998.44		2.172E-05
1.731E-04	1.40	7161.45		2.115E-05
1.692E-04	1.36	7328.27		2.061E-05
1.653E-04	1.33	7498.96		2.016E-05
1.616E-04	1.30	7673.64		1.962E-05
1.579E-04	1.27	7852.38		1.901E-05

TABLE I *(Continued)*

Aluminum Nitride

eV	cm^{-1}	μm	n	k
1.543E-04	1.24	8035.28		1.849E-05
1.508E-04	1.22	8222.45		1.793E-05
1.474E-04	1.19	8413.98		1.738E-05
1.440E-04	1.16	8609.96		1.693E-05
1.407E-04	1.14	8810.51		1.649E-05
1.375E-04	1.11	9015.74		1.610E-05
1.344E-04	1.08	9225.74		1.573E-05
1.313E-04	1.06	9440.64		1.529E-05

Bismuth Silicon Oxide ($Bi_{12}SiO_{20}$) Bismuth Germanium Oxide ($Bi_{12}GeO_{20}$)

E. D. PALIK
Institute for Physical Science and Technology
University of Maryland
College Park, Maryland

$Bi_{12}SiO_{20}$ (BSO) and $Bi_{12}GeO_{20}$ (BGO) are cubic crystals with space group symmetry I23 T^3, containing two molecular units per unit cell. Some of the properties making these materials of technological interest include low ultrasonic velocity, small acoustic damping up to 1 GHz, and large piezoelectric, photorefractive [1], photoelastic [2], and electrooptic (nonlinear index) [3] effects.

Although being cubic results in isotropic intensity transmission and reflection properties for linearly polarized light, both crystals are gyrotropic, showing optical activity [4], the rotation of the plane of polarization of linearly polarized light being proportional to the thickness of the crystal. Thus, the angle of rotation is given by

$$\phi = \frac{\pi d}{\lambda}(n_l - n_r), \tag{1}$$

where n_l and n_r are the indices of refraction for left and right circularly polarized light, respectively. This is similar to the optical activity of "isotropic" sugar solutions, where the activity depends on the left- and right-handedness of the microscopic molecular structure, which is left- or right-handed for any direction through the solution.

Since several of the papers examined deal with both BSO and BGO, while others deal with one or the other, we will review them from high to low photon energy with no preference. We give the n and k data in Tables I and II and Figs. 1 and 2.

Futro [5] has measured the reflectivity of BGO from 1.5 to 8.5 eV in two

HANDBOOK OF OPTICAL CONSTANTS OF SOLIDS III

Copyright © 1998 by Academic Press.
All rights of reproduction in any form reserved
ISBN 0-12-544423-0/$25.00.

steps. From 1.5 to 5.5 eV, near-normal-incidence reflectivity was measured with a Zeiss SPM-2 prism monochromator and a high-pressure xenon arc. From 5.5 to 8.5 eV a vacuum UV Hilger and Watts E766 grating monochromator was used along with a low-pressure ac discharge hydrogen lamp. An Al reference mirror was used. Although the reflectivity of BSO was also measured, no analysis of it was given. The reflectivity data were Kramers–Kronig analyzed using a suitable extrapolation for reflectivity to high frequency. The data read from a small graph of n and k (which was enlarged) are collected in Table II and Fig. 2. Near the band gap, k is much too large compared to the other direct measurements of k to be discussed. This has to do with the poor accuracy of the K-K method when $k \ll 1$. Where $k > 1$, the values of n and k are probably not good to more than two significant figures, if that.

Aldrich *et al.* [6] give several properties of BSO and BGO. Their samples were grown by the Czochralski method. Different samples showed positive and negative optical activity. For BGO the loss tangent at low frequency was determined to be 0.0035, which gives a low-frequency dielectric constant $\epsilon_0 = 40$. The band gap was found to be 3.15–3.25 eV. The index of refraction was measured by the prism minimum-deviation method from 400 to 700 nm. These data have been quoted by subsequent workers [7, 8], who have fitted a Sellmeier-type equation to the data. For BSO, the loss tangent at low frequency was 0.0015, which gives a low-frequency dielectric constant $\epsilon_0 = 56$. The band gap was 3.15–3.25 eV.

The absorption in the vicinity of the band edge of BGO and BSO has been measured in detail. There are comments to the effect that the band gaps are similar [6], the indices are similar [6], the reflectivities are similar [4], etc. Grabmaier and Oberschmid [9] studied the optical absorption near the band gap with many doped single crystals of BSO and BGO. They state that undoped BGO is yellow in color and has a band gap $E_g = 3.2$ eV. They measured the transmittance and calculated the absorption coefficient, assuming the reflectivity was given by the index of refraction analyzed by Vedam and Hennessey [7]. There was an order-of-magnitude change in the absorption coefficient as the dopants were changed. Therefore, we expect values of k to vary significantly from lab to lab, especially if the samples are not well characterized. We determined k for just the undoped samples of BSO and BGO from graphs and list its values in Tables I and II and Figs. 1 and 2. The values of k for BGO are much smaller than those of Futro in the band gap, indicating poor accuracy for the K-K method used in by Futro. [5].

Toyoda *et al.* [10, 11] studied the optical properties of the band edge of BSO as a function of temperature, attempting to fit their data with an Urbach-rule equation. Two types of faceting can be obtained from the solid–liquid interface of a growing crystal. These produce facet-core-free and facet-core samples. Although the optical differences are small, the type of sample does

affect the technical properties of interest. We read expanded graphs to get k for 293 K and list values in Table I and Fig. 1. These k data compare well with data of Grabmaier and Oberschmid.

Zengfa *et al.* [12] measured the transmittance and reflectance of a BSO sample with a thickness of 1.09 mm in the spectral region 300–550 nm, using a UN-365 UV-VIS spectrometer, and determined both n and k. The analysis of Zengfa *et al.* is not clear. They give the transmittance of a slab as

$$T = \frac{(1 - R)^2 \exp(-\alpha d)}{(1 - R^2 \exp(-2\alpha d)}, \tag{2}$$

where R must be the bulk reflectivity, which is

$$R = \frac{(n - 1)^2 + k^2}{(n + 1)^2 + k^2}. \tag{3}$$

This applies to a semi-infinite sample or to one that is wedged, so there are no multiple-reflection effects. For $k/n \ll 1$, they use

$$n = \frac{(1 + \sqrt{R})}{(1 - \sqrt{R})} \tag{4}$$

to determine n; it appears they used the measured reflectance for R. However, their sample surely had multiple-reflection effects, since it was presumably plane parallel. However, bulk reflectivity should not equal sample reflectance in transparent regions. We compare the results of Zengfa *et al.* and Toyota *et al.* in Table I. Note that in the band-gap region 3.5–3.1 eV, the k values of Zenga *et al.* [10, 11] are considerably smaller than those of Toyota *et al.* and Grabmaier and Oberschmid [9].

Tropf *et al.* [13] cite work of Gospodinov *et al.* [14], who fitted n data for BSO in the spectral region 0.48–0.7 μm with a Sellmeier-type equation of the form

$$n^2 = 2.72777 + \frac{3.01705\,\lambda^2}{\lambda^2 - (0.2661)^2}. \tag{5}$$

They also give an equation for BGO of the form

$$n^2 - 1 = \frac{4.601\,\lambda^2}{\lambda^2 - (0.242)^2} \tag{6}$$

for the spectral region 0.4–0.7 μm (citing Burattini *et al.* [8] and Vedam and Hennessey [7]). Although both of these groups try to fit the data of Al-

drich *et al.* [6] for BGO, the exact form of Eq. (6) is not given in these references. However, Burattini *et al.* do fit the data of Aldrich *et al.* and their own data with a more complicated equation discussed later. We used Eq. (5) to calculate n for BSO and give the results in Table I and Fig. 1. We defer using Eq. (6) until we discuss the BGO data of Burattini *et al.* Burattini *et al.* [8] measured n and k for BGO in the spectral region 1.2–5.0 μm. The {100} plane was the plane of the slab samples. They were ground with carborundum and polished with diamond paste. Thickness was ~200 μm, so although multiple-refection effects were present, no interference fringes were resolved. The transmittance T and the reflectance R were measured with a double-beam spectrophotometer. The reflection standard was a gold mirror. The transmittance standard was a polished Si wafer. To analyze the data, they used complicated expressions relating αd to R and T and R_1 to R and T. They defined α as the absorption coefficient, d as the sample thickness, transmittance as T, reflectance as R of the slab sample (measured quantities), and single-surface reflectivity as R_1 (reflection from a semi-infinite sample or from the front surface of a wedged sample). R_1 is of the form of Eq. (3) with the change in notation noted.

A Hertzberger-type equation of the form

$$n - n_0 = \frac{a_1}{\lambda^2 - \lambda_o^2} + \frac{a_2}{(\lambda^2 - \lambda_o^2)^2} + a_3 \lambda^2 + a_4 \lambda^4 \tag{7}$$

was used to fit the data and also data of Aldrich *et al.* [6]. The fitting parameters were $\lambda_0 = 0.1675$ μm, $n_0 = 2.4098$, $a_1 = 3.26 \times 10^{-2}$ μm^2, $a_2 = 4.69 \times 10^{-3}$ μm^4, $a_3 = -6.07 \times 10^{-3}$ μm^{-2}, $a_4 = 1.15 \times 10^{-4}$ μm^{-4}. Uncertainty (or deviation of the experimental data from the calculated) was $\Delta n = 4.23 \times 10^{-4}$. No Δk was given, but surely k is not known to four significant figures. The data are given in Table II and Fig. 2. The absorption shown is multiphonon absorption, which continues to increase to lower energy until the reststrahlen region is reached.

Wojdowski *et al.* [15, 16] measured the far-infrared reflectivity of both BSO and BGO materials. The angle of incidence was 8°. The crystals were grown by the Czochralski method. Samples were unoriented, but since the crystals are cubic, this should pose no problem. The samples were mechanically polished with corundum powder and diamond paste. They used a single-pass grating spectrometer to measure R from 50 to 900 cm^{-1} both at 300 K and near-liquid-nitrogen temperature (90 K). Although they were primarily interested in the lattice-vibration frequencies and group-theory analysis of the vibration modes, they did determine ϵ_1 and ϵ_2. A K-K analysis, not described in detail (especially the end limits), was performed to obtain ϵ_1 and ϵ_2. Although graphs of ϵ_1 and ϵ_2 were not given in the papers, Nazarewicz [17] did provide us a plot of room-temperature ϵ_1 and ϵ_2, which we enlarged. After extracting ϵ_1 and ϵ_2, we calculated n and k. These are dis-

played in Tables I and II and Figs. 1 and 2. Near the absorption lines where ϵ_1 and ϵ_2 were less than unity (and hard to read from a plot), the calculated values of k often showed sharp downward dips before rising to the peaks. A classical-oscillator model does not show such structure. It is not known whether this is an artifact or a physical phenomenon. For BGO between 700 and 800 cm^{-1}, there appears to be some residual absorption probably due to the two-phonon absorption.

Wojdowski [18] also measured the transmittance of thin evaporated films of BSO and BGO, primarily to determine vibration frequencies.

Zengfa *et al.* [12] used a Fourier-transform spectrometer to measure the reflectivity of BSO in the 50–1500 cm^{-1} region. Details of sample preparation and experimental procedure are lacking; room temperature was not defined. A K-K analysis was performed to obtain ϵ_1 and ϵ_2 and n and k. The limits of integration were not clearly discussed, especially accounting for absorption (reflection) below 50 cm^{-1} and above the band gap. Zengfa *et al.* did not cite earlier work of Wojdowski *et al.* [15] and Brody *et al.* [19]. These works might have been useful in their K-K analysis.

Examination of k indicates that the apparent resolution of Zengfa *et al.* [12] was significantly less than that of Wojdowski *et al.*, [15] and more lines were observed in the spectra of Wojdowski *et al.* For example, a triplet of lines between 535 and 610 cm^{-1} are clearly resolved by Wojdowski *et al.* but only partly resolved by Zengfa *et al.*

Although we favor the data of Wojdowski *et al.* [15] because of the higher resolution, we decided to show the n and k data of Zengfa *et al.* and Wojdowski *et al.* in Table I to compare the results for BSO. There is serious mismatch in frequencies, implying that the wave number was not carefully measured by one or the other of the groups. For most of the peaks in k the Zengfa *et al.* [12] data were on the average about 5 cm^{-1} higher than the Wojdowski *et al.* [15] data. This discrepancy points out a general problem in the calibration of spectrometers and comparing spectra of significantly different resolution. Once the spectra are shifted, so the peaks in k "agree," the magnitudes of n and k are usually within $\pm 30\%$ of each other. Such differences are to be expected, because of accuracy considerations in measuring R with a Fourier-transform spectrometer and a grating specrometer; we assume the reference mirror was an aluminum mirror in both cases.

Brody *et al.* [19] used a Fourier-transform spectrometer to measure the transmittance of thin slabs in the millimeter-wave region (15–4 cm^{-1}) for both BSO and BGO samples. Room temperature was not defined. Presumably, they used at least two thicknesses of slabs and fitted the transmittance to obtain both n and k, since channel spectra were observed. We extracted values of n and k from a graph and display them in Tables I and II and Figs. 1 and 2. Note that there are no vibration bands in this region, all of them presumably being above 15 cm^{-1}. Note that the value of n at 70 cm^{-1} is smaller than the n measured at 15 cm^{-1}. There may be another vibration

band between 70 and 15 cm^{-1}, which could account for this mismatch, or the 70 cm^{-1} data are in error due to problems with the K-K analysis.

For BGO, extrapolation to low frequency gives a dc dielectric constant $\epsilon_0 = 38.6$, in close agreeement with a loss-tangent measurement of $\epsilon_o = 40$ of Aldrich *et al.* For BSO, extrapolation to low frequency gives $\epsilon_0 = 40.7$, in poor agreement with a loss-tangent measurement of $\epsilon_0 = 56$.

REFERENCES

1. A. Grunnet-Jepsen, I. Aubrecht, and L. Solynar, Investigation of the internal field in photorefractive materials and measurement of the effective electro-optic coefficient, *J. Opt. Soc. Am. B* **12**, 921 (1995).
2. P. I. Ropot, Determination of the photoelastic constant of optically active cubic crystals by a polarization method. *Opt. Spectrosc.* **70**, 217 (1991); *Opt. Spektrosk.* **70**, 371 (1991).
3. Y. V. Shaldin and D. A. Belogurov, Dispersion of the nonlinear refractive index of gyrotropic sillenite-type crystals. *Sov. Phys. Solid State* **15**, 1846 (1974).
4. P. Hennessey and K. Vedam, Piezo- and thermo-optical properties of $Bi_{12}GeO_{20}$, I. Optical rotatory dispersion. *J. Opt. Soc. Am.* **65**, 436 (1975).
5. A. T. Futro, Analysis of reflectivity spectrum and band structure of $Bi_{12}GeO_{20}$. *J. Phys. Chem. Solids* **40**, 201 (1979).
6. R. E. Aldrich, S. L. Hou, and M. L. Harvill, Electrical and optical properties of $Bi_{12}SiO_{20}$. *J. Appl. Phys.* **42**, 493 (1971).
7. K. Vedam and P. Hennessey, Piezo- and thermo-optical properties of $Bi_{12}GeO_{20}$, II. Refractive index. *J. Opt. Soc. Am.* **65**, 442 (1975).
8. E. Burattini, G. Cappuccio, M. Grandolfo, P. Vecchia, and S.M. Efendiev, Near-infrared refractive index of bismuth germanium oxide [$Bi_{12}GeO_{20}$]. *J. Opt. Soc. Am.* **73**, 495 (1983).
9. B. C. Grabmaier and R. Oberschmid, Properties of pure and doped $Bi_{12}GeO_{20}$ and $Bi_{12}SiO_{20}$ crystals. *Phys. Status Solidi A* **96**, 199 (1986).
10. T. Toyoda, H. Nakanishi, S. Endo and T. Irie, The fitting parameters of exponential optical absorption in $Bi_{12}SiO_{20}$. *J. Phys. C: Solid State Phys.* **19**, L259 (1986).
11. T. Toyoda, S. Maruyama, H. Nakanishi, S. Endo, and T. Irie, The fundamental absorption edge in $Bi_{12}SiO_{20}$, *J. Phys. D: Appl. Phys.* **19**, 909 (1986).
12. L. Zengfa, S. Dazhao, Y. Xiaoyan, S. Sufa, and Z. Wanlin, Study of the optical properties of $Bi_{12}SiO_{20}$. *Infrared Phys.* **31**, 59 (1991).
13. W. J. Tropf, M. E. Thomas, and T. J. Harris, Properties of crystals and glasses. *In* "Handbook of Optics, Devices, Measurements & Properties" (M. Bass, ed.), Vol. 2, Chap. 33, McGraw-Hill, New York, 1995.
14. M. Gospodinov, S. Haussuhl, P. Sreshtarov, V. Tassev, and N. Petkov, Physical properties of cubic $Bi_{12}SiO_{20}$. *Bulg. J. Phys.* **15**, 140 (1988).
15. W. Wojdowski, T. Lukasiewicz, W. Nazarewicz, and J. Zmija, Infrared studies of lattice vibrations in $Bi_{12}GeO_{20}$ and $Bi_{12}SiO_{20}$ crystals. *Phys. Status Solidi B* **94**, 649 (1979).
16. W. Wojdowski, Vibrational modes in $Bi_{12}GeO_{20}$ and $Bi_{12}SiO_{20}$ crystals. *Phys. Status Solidi B* **130**, 121 (1985).
17. W. Nazarewicz, private communication, 1996.
18. W. Wojdowski, Infrared spectra of thin films of $Bi_{12}GeO_{20}$ and $Bi_{12}SiO_{20}$. *Phys. Status Solidi B* **123**, K101 (1984).
19. P. S. Brody, J. P. Sattler, and G. J. Simonis, Near-millimeter refractive indices, absorption coefficients, and electrooptic coefficients in ferroelectric and other crystals. *Ferroelectrics* **59**, 319 (1983).

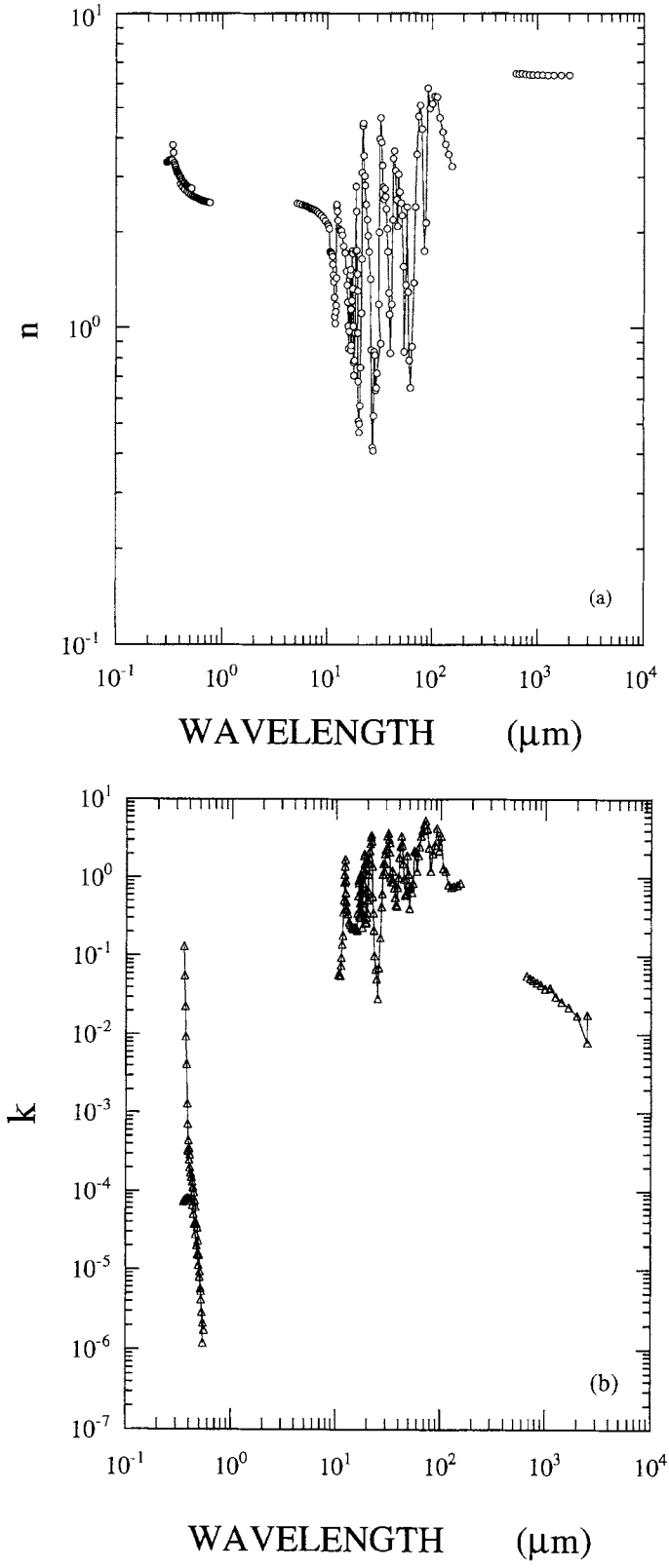

Fig. 1. (a) Log–log plot of n (○) versus wavelength in micrometers for $Bi_{12}SiO_{20}$. Some data from Toyoda *et al.* [11] and Zengfa *et al.* [12] are omitted. (b) Log–log plot of k (△) versus wavelength in micrometers for $Bi_{12}SiO_{20}$.

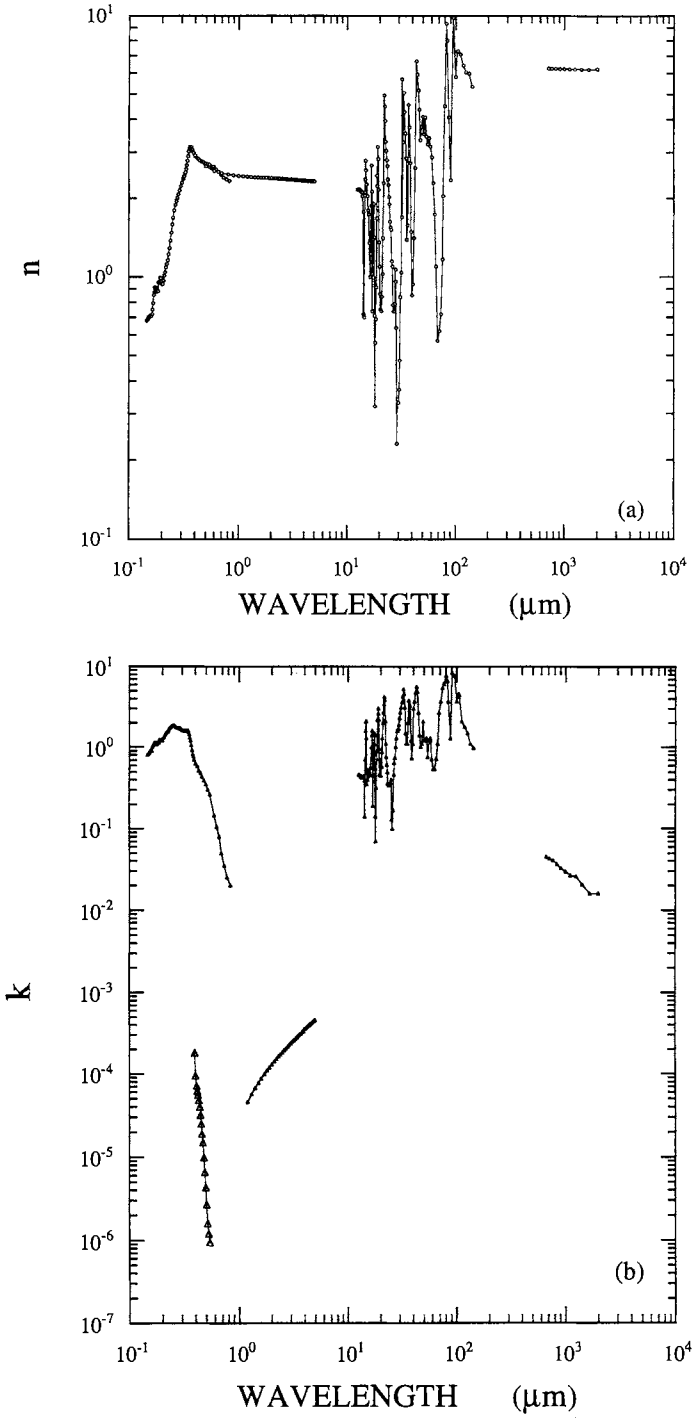

Fig. 2. (a) Log–log plot of n (○) versus wavelength in micrometers for $Bi_{12}GeO_{20}$. (b) Log–log plot of k (▲) versus wavelength in micrometers for $Bi_{12}GeO_{20}$.

TABLE I

Values of n and k for $Bi_{12}SiO_{20}$ from Various References[a]

eV	cm^{-1}	μm	n	k	n	k	k
4.133	33333	0.30	3.341[12]				
4.065	32787	0.305	3.360				
4.000	32258	0.31	3.379				
3.936	31746	0.315	3.394				
3.875	31250	0.32	3.404				
3.815	30769	0.325	3.410				
3.757	30303	0.33	3.410				
3.701	29851	0.335	3.400				
3.647	29412	0.34	3.800				
3.594	28986	0.345	3.590				
3.542	28571	0.35	3.329	7.27E-5[12]			
3.493	28169	0.355	3.280				
3.440	27778	0.36	3.224	7.59E-5			
3.397	27397	0.365	3.170				
3.351	27027	0.37	3.130	7.80E-5			
3.306	26667	0.375	3.100				
3.263	26316	0.38	3.075	7.98E-5			
3.220	25974	0.385	3.050				
3.179	25641	0.39	3.024	8.04E-5			
3.139	25316	0.395	3.005				
3.100	25000	0.40	2.983	7.97E-5	2.853[14]		
3.024	24390	0.41	2.944	7.80E-5			
2.952	23810	0.42	2.909	7.35E-5	2.787		
2.883	23256	0.43	2.880	6.50E-5			
2.818	22727	0.44	2.850	5.00E-5	2.736		
2.755	22222	0.45	2.823	3.76E-5			
2.695	21739	0.46	2.805	2.75E-5	2.695		
2.638	21277	0.47	2.789	1.98E-5			
2.583	20833	0.48	2.777	1.53E-5	2.661		
2.530	20408	0.49	2.768	1.13E-5			
2.480	20000	0.50	2.760	7.96E-6	2.634		
2.431	19608	0.51	2.759	5.68E-6			
2.384	19231	0.52		4.14E-6	2.611		
2.296	18519	0.54		2.15E-6	2.591		
2.254	18182	0.55		1.75E-6			
2.214	17857	0.56			2.574		
2.138	17241	0.58			2.559		
2.066	16667	0.60			2.546		
2.000	16129	0.62			2.535		
1.937	15625	0.64			2.525		
1.879	15152	0.66			2.516		
1.823	14706	0.68			2.508		
1.771	14286	0.70			2.501		
1.722	13889	0.72			2.494		
1.675	13514	0.74			2.489		
1.631	13158	0.76			2.483		

(continued)

[a] The references from which the values were taken are given in brackets.

TABLE I *(Continued)*

$Bi_{12}SiO_{20}$

eV	cm^{-1}	μm	n	k	n	k	k
						fcf	fc
3.5	28229	0.3542				1.3E-1[11]	1.2E-1[11]
3.45	27826	0.3594				5.6E-2	5.4E-2
3.4	27423	0.3647				2.3E-2	2.4E-2
3.35	27019	0.3701				9.4E-3	1.0E-2
3.3	26616	0.3757				4.2E-3	4.6E-3
3.25	26213	0.3815				1.3E-3	1.8E-3
3.2	25810	0.3875		3.3E-4[9]		7.1E-4	9.6E-4
3.15	25406	0.3936		3.2E-4		4.4E-4	6.3E-4
3.10	25003	0.4000		2.5E-4		3.5E-4	5.1E-4
3.05	24600	0.4065		2.0E-4		2.9E-4	4.5E-4
3.0	24196	0.4133		1.7E-4			
2.95	23793	0.4203		1.5E-4			
2.9	23390	0.4275		1.3E-4			
2.85	22987	0.4350		1.1E-4			
2.8	22583	0.4428		9.5E-5			
2.75	22180	0.4509		7.5E-5			
2.7	21777	0.4592		6.2E-5			
2.65	21374	0.4679		3.8E-5			
2.6	20970	0.4769		3.4E-5			
2.55	20567	0.4862		2.3E-5			
2.5	20164	0.4959		1.5E-5			
2.45	19760	0.5061		9.3E-6			
2.4	19357	0.5166		5.3E-6			
2.35	18954	0.5276		2.9E-6			
2.3	18551	0.5391		1.2E-6			
0.2418	1950	5.128	2.47[12]				
0.2294	1850	5.405	2.46				
0.2170	1750	5.714	2.44				
0.2046	1650	6.061	2.43				
0.1984	1600	6.250	2.42				
0.1922	1550	6.452	2.41				
0.1860	1500	6.667	2.40				
0.1798	1450	6.896	2.38				
0.1736	1400	7.143	2.37				
0.1674	1350	7.407	2.36				
0.1612	1300	7.692	2.34				
0.1550	1250	8.000	2.32				
0.1488	1200	8.333	2.29				
0.1426	1150	8.696	2.26				
0.1364	1100	9.091	2.22				
0.1302	1050	9.524	2.17				
0.1240	1000	10.00	2.12				
0.1215	980	10.20	2.09				
0.1190	960	10.42	2.05				
0.1178	950	10.53			1.73[17]	5.8E-2[17]	
0.1165	940	10.64	2.01		1.72	5.8E-2	

TABLE I *(Continued)*

$Bi_{12}SiO_{20}$

eV	cm^{-1}	μm	n	k	n	k	k
0.1153	930	10.75			1.72	5.8E-2	
0.1141	920	10.87	1.96		1.72	5.8E-2	
0.1183	910	10.99			1.70	5.6E-2	
0.1116	900	11.11	1.85		1.67	7.5E-2	
0.1103	890	11.23	1.83	4.0E-2[12]	1.58	9.5E-2	
0.1091	880	11.36	1.75	9.0E-2	1.46	1.4E-1	
0.1079	870	11.49	1.64	1.2E-1	1.39	1.8E-1	
0.1066	860	11.63	1.50	1.5E-1	1.24	3.6E-1	
0.1054	850	11.76	1.15	2.2E-1	1.08	5.1E-1	
0.1041	840	11.90	2.00	1.5E + 0	1.03	8.7E-1	
0.1038	837	11.95		2.1E + 0			
0.1035	835	11.98			1.12	1.1E + 0	
0.1029	830	12.05	3.00	1.3E + 0	1.17	1.4E + 0	
0.1023	825	12.12			1.43	1.7E + 0	
0.1017	820	12.19	2.63	3.3E-1	2.41	9.1E-1	
0.1010	815	12.27			2.45	6.3E-1	
0.1004	810	12.34	2.44	3.0E-2	2.33	4.9E-1	
0.09919	800	12.50			2.18	3.9E-1	
0.09795	790	12.66	2.24				
0.09671	780	12.82			2.05	3.4E-1	
0.09547	770	12.99	2.14				
0.09423	760	13.16			2.03	2.7E-1	
0.09299	750	13.33	2.00				
0.09175	740	13.51			2.02	2.5E-1	
0.09051	730	13.70	1.90				
0.08927	720	13.89			1.96	2.3E-1	
0.08803	710	14.08	1.79				
0.08679	700	14.29			1.80	2.2E-1	
0.08555	690	14.49	1.67				
0.08431	680	14.71			1.72	2.3E-1	
0.08307	670	14.92	1.54				
0.08183	660	15.15			1.50	2.3E-1	
0.08059	650	15.38	1.39	9.0E-2	1.36	2.2E-1	
0.07935	640	15.62	1.25	1.1E-1	1.20	2.1E-1	
0.07811	630	15.87	1.08	2.0E-1	1.01	3.5E-1	
0.07687	620	16.13	0.98	4.9E-1	0.86	5.8E-1	
0.07625	615	16.26			0.97	9.2E-1	
0.07563	610	16.39	1.11	7.8E-1	1.46	8.6E-1	
0.07501	605	16.53			1.52	3.3E-1	
0.07439	600	16.67	1.12	7.6E-1	1.14	3.1E-1	
0.07377	595	16.81			0.85	4.7E-1	
0.07315	590	16.95	1.10	1.1E + 0	0.88	6.8E-1	
0.07265	586	17.06		1.1E + 0			
0.07253	585	17.09			1.21	1.1E + 0	
0.07191	580	17.24	1.37	1.1E-1	1.74	1.0E + 0	
0.07129	575	17.39			1.71	3.5E-1	
0.07067	570	17.54	1.20	8.1E-1	1.32	2.3E-1	

(continued)

TABLE I *(Continued)*

$Bi_{12}SiO_{20}$

eV	cm^{-1}	μm	n	k	n	k	k
0.07005	565	17.70			1.01	3.5E-1	
0.06943	560	17.86	0.85	1.2E + 0	0.78	6.4E-1	
0.06881	555	18.02			0.71	8.4E-1	
0.06819	550	18.18	0.64	1.6E + 0	0.79	1.3E + 0	
0.06757	545	18.35			0.96	1.9E + 0	
0.06732	543	18.42		2.3E + 0			
0.06695	540	18.52	0.90	2.3E + 0	1.74	2.0E + 0	
0.06633	535	18.69			2.80	1.5E + 0	
0.06571	530	18.87	1.40	1.9E + 0	2.33	6.4E-1	
0.06509	525	19.05			1.75	2.6E-1	
0.06447	520	19.23	1.77	1.5E + 0	1.47	2.7E-1	
0.06410	517	19.34		1.4E + 0			
0.06385	515	19.42			1.30	3.1E-1	
0.06323	510	19.61	1.40	1.7E + 0	0.96	3.6E-1	
0.06261	505	19.80			0.68	5.1E-1	
0.06199	500	20.00	1.00	2.5E + 0	0.51	6.8E-1	
0.06137	495	20.20			0.47	1.1E + 0	
0.06075	490	20.41	0.96	3.3E + 0	0.50	1.5E + 0	
0.06013	485	20.62			0.57	1.8E + 0	
0.05951	480	20.83	1.30	4.2E + 0	0.75	2.2E + 0	
0.05914	477	20.96		5.1E + 0			
0.05889	475	21.05			1.11	2.7E + 0	
0.05827	470	21.28	2.00	3.1E + 0	1.64	3.3E + 0	
0.05763	465	21.51			3.10	3.5E + 0	
0.05703	460	21.74	5.20	1.5E + 0	4.38	2.9E + 0	
0.05641	455	21.98			4.48	1.4E + 0	
0.05579	450	22.22	5.00	4.4E-1	3.51	5.7E-1	
0.05517	445	22.47			3.02	3.5E-1	
0.05455	440	22.73	4.00	2.3E-1	2.82	2.1E-1	
0.05331	430	23.25	3.20	1.4E-1	2.45	1.0E-1	
0.05207	420	23.81	2.70	2.0E-1	2.19	6.8E-2	
0.05083	410	24.39	2.40	3.0E-1	1.95	5.1E-2	
0.04959	400	25.00	2.05	4.5E-1	1.73	2.9E-2	
0.04835	390	25.64	1.90	6.1E-1	1.42	7.1E-2	
0.04711	380	26.31	1.53	8.8E-1	0.85	1.7E-1	
0.04587	370	27.03	1.22	1.5E + 0	0.42	4.2E-1	
0.04525	365	27.40			0.41	6.1E-1	
0.04463	360	27.78	1.21	2.1E + 0	0.53	1.1E + 0	
0.04401	355	28.17			0.84	1.5E + 0	
0.04339	350	28.57	1.29	2.6E + 0	0.82	1.2E + 0	
0.04277	345	28.99			0.64	1.5E + 0	
0.04215	340	29.41	1.55	3.2E + 0	0.65	2.0E + 0	
0.04154	335	29.85			0.72	2.3E + 0	
0.04129	333	30.03		3.6E + 0			
0.04091	330	32.30	2.20	3.3E + 0	0.89	2.8E + 0	
0.04030	325	30.77			1.18	3.4E + 0	
0.03967	320	31.25	3.80	2.5E + 0	2.00	3.7E + 0	

TABLE I *(Continued)*

$Bi_{12}SiO_{20}$

eV	cm^{-1}	μm	n	k	n	k	k
0.03906	315	31.75			3.98	3.1E + 0	
0.03843	310	32.26	4.38	1.8E + 0	4.65	2.1E + 0	
0.03782	305	32.79			3.88	1.0E + 0	
0.03719	300	33.33	4.10	1.2E + 0	3.27	8.9E-1	
0.03658	295	33.90			2.79	8.9E-1	
0.03595	290	34.48	3.75	9.4E-1	2.55	1.2E + 0	
0.03534	285	35.09			2.75	8.7E-1	
0.03471	280	35.71	3.50	7.8E-1	2.60	7.3E-1	
0.03410	275	36.36			2.37	5.5E-1	
0.03347	270	37.04	2.80	7.4E-1	2.05	4.4E-1	
0.03286	265	37.74			1.73	4.3E-1	
0.03224	260	38.46	2.30	1.3E + 0	1.28	7.4E-1	
0.03162	255	39.22			1.10	1.0E + 0	
0.03100	250	40.00	1.88	2.9E + 0	0.83	1.8E + 0	
0.03062	247	40.48		3.2E + 0			
0.03038	245	40.82			1.18	2.5E + 0	
0.02976	240	41.67	2.70	2.6E + 0	2.19	3.4E + 0	
0.02914	235	42.55			3.44	2.6E + 0	
0.02852	230	43.48	3.95	1.3E + 0	3.64	1.5E + 0	
0.02790	225	44.44			3.15	9.5E-1	
0.02752	222	45.04		1.1E + 0			
0.02728	220	45.45	3.80	1.2E + 0	2.54	5.9E-1	
0.02666	215	46.51			2.09	6.2E-1	
0.02604	210	47.62	3.10	1.4E + 0	3.06	1.9E + 0	
0.02542	205	48.78			2.69	1.1E + 0	
0.02480	200	50.00	3.10	9.6E-1	2.48	4.0E-1	
0.02418	195	51.28			2.26	7.7E-1	
0.02356	190	52.63	2.20	1.3E + 0	1.55	6.4E-1	
0.02294	185	54.05			0.84	8.4E-1	
0.02232	180	55.55	1.82	2.5E + 0	1.36	2.2E + 0	
0.02170	175	57.14			2.41	2.1E + 0	
0.02108	170	58.82	1.80	2.9E + 0	1.29	1.2E + 0	
0.02046	165	60.61			0.79	1.9E + 0	
0.01984	160	62.50	1.93	4.8E + 0	0.65	2.5E + 0	
0.01922	155	64.52			0.87	3.4E + 0	
0.01860	150	66.67	1.80	6.4E + 0	1.38	4.0E + 0	
0.01798	145	68.97			2.41	4.8E + 0	
0.01736	140	71.43	3.20	4.3E + 0	3.55	5.3E + 0	
0.01674	135	74.07			4.70	4.2E + 0	
0.01612	130	76.92	6.15	3.1E + 0	5.10	2.4E + 0	
0.01562	126	79.35		2.0E + 0			
0.01550	125	80.00			4.29	1.2E + 0	
0.01488	120	83.33	5.00	3.1E + 0	1.74	2.0E + 0	
0.01426	115	86.96			2.14	2.6E + 0	
0.01364	110	90.91	4.00	4.4E + 0	5.80	4.3E + 0	
0.01302	105	95.24			4.99	2.2E + 0	
0.01240	100	100.0	5.80	3.8E + 0	5.15	3.4E + 0	

(continued)

TABLE I *(Continued)*

$Bi_{12}SiO_{20}$

eV	cm^{-1}	μm	n	k	n	k	k
0.01178	95	105.3			5.45	1.3E + 0	
0.01116	90	111.1	6.80	2.6E + 0	5.43	1.2E + 0	
0.01054	85	117.6			4.65	8.1E-1	
0.009919	80	125.0	6.70	2.1E + 0	4.19	7.4E-1	
0.009299	75	133.3			3.82	7.7E-1	
0.008679	70	142.8	6.48	2.0E + 0	3.55	7.9E-1	
0.008059	65	153.8			3.24	8.5E-1	
0.007439	60	166.7	6.28	2.0E + 0			
0.006199	50	200.0	6.00	2.4E + 0			
0.001984	16	625.0	6.450[19]				
0.001860	15	666.7	6.438	5.62E-2[19]			
0.001736	14	714.3	6.451	5.28E-2			
0.001612	13	769.2	6.415	5.01E-2			
0.001488	12	833.3	6.405	4.64E-2			
0.001364	11	909.1	6.397	4.34E-2			
0.001240	10	1000	6.390	3.89E-2			
0.001116	9	1111	6.382	3.97E-2			
0.0009919	8	1250	6.379	3.08E-2			
0.0008679	7	1428	6.378	2.61E-2			
0.0007439	6	1667	6.378	2.25E-2			
0.0006199	5	2000	6.380	1.75E-2			
0.0004959	4	2500		7.95E-3			
0.0004959	4	2500		1.79E-2			

TABLE II

Values of n and k for $Bi_{12}GeO_{20}$ from Various References[a]

eV	cm^{-1}	μm	n	k	k
8.5	68557	0.1459	0.680[5]	0.805[5]	
8.4	67750	0.1476	0.685	0.825	
8.3	66943	0.1494	0.690	0.840	
8.2	66137	0.1512	0.700	0.860	
8.1	65330	0.1531	0.703	0.880	
8.0	64524	0.1550	0.705	0.900	
7.9	63717	0.1569	0.710	0.904	
7.8	62911	0.1590	0.710	0.906	
7.7	62104	0.1610	0.710	1.00	
7.6	61298	0.1631	0.720	1.04	
7.5	60491	0.1653	0.75	1.09	
7.4	59685	0.1675	0.795	1.12	
7.3	58878	0.1698	0.85	1.13	
7.25	58475	0.1710	0.87	1.13	

[a] The references from which the values were taken are given in brackets.

TABLE II *(Continued)*

$Bi_{12}GeO_{20}$

eV	cm^{-1}	μm	n	k	k
7.2	58071	0.1722	0.91	1.12	
7.15	57668	0.1734	0.90	1.10	
7.1	57265	0.1746	0.905	1.10	
7.05	56862	0.1759	0.89	1.08	
7.0	56458	0.1771	0.875	1.10	
6.95	56055	0.1784	0.895	1.13	
6.9	55652	0.1797	0.905	1.12	
6.85	55249	0.1810	0.90	1.12	
6.8	54845	0.1823	0.89	1.13	
6.75	54442	0.1837	0.88	1.15	
6.7	54039	0.1851	0.88	1.20	
6.65	53635	0.1864	0.95	1.23	
6.6	53232	0.1879	0.96	1.21	
6.55	52829	0.1893	0.955	1.20	
6.5	52426	0.1907	0.95	1.21	
6.45	52022	0.1922	0.96	1.23	
6.4	51619	0.1937	0.995	1.23	
6.35	51216	0.1953	0.99	1.21	
6.3	50813	0.1968	0.96	1.20	
6.25	50409	0.1984	0.945	1.23	
6.2	50006	0.2000	0.935	1.26	
6.1	49199	0.2033	0.94	1.32	
6.0	48393	0.2066	0.97	1.39	
5.9	47586	0.2101	1.01	1.43	
5.8	46780	0.2138	1.04	1.49	
5.7	45973	0.2175	1.09	1.53	
5.6	45167	0.2214	1.12	1.57	
5.5	44360	0.2254	1.16	1.61	
5.4	43554	0.2296	1.22	1.69	
5.3	42747	0.2339	1.29	1.76	
5.2	41940	0.2384	1.38	1.80	
5.1	41134	0.2431	1.48	1.835	
5.0	40327	0.2480	1.59	1.85	
4.9	39521	0.2530	1.69	1.86	
4.8	38714	0.2583	1.80	1.83	
4.7	37908	0.2638	1.89	1.785	
4.6	37101	0.2695	1.955	1.75	
4.5	36295	0.2755	2.01	1.715	
4.4	35488	0.2818	2.08	1.715	
4.3	34682	0.2883	2.15	1.70	
4.2	33875	0.2952	2.23	1.665	
4.1	33068	0.3024	2.30	1.63	
4.0	32262	0.3100	2.365	1.60	
3.95	31859	0.3139	2.40	1.585	
3.9	31455	0.3179	2.435	1.58	
3.85	31052	0.3220	2.48	1.585	

(continued)

TABLE II *(Continued)*

$Bi_{12}GeO_{20}$

eV	cm^{-1}	μm	n	k	k
3.8	30649	0.3263	2.52	1.60	
3.75	30246	0.3306	2.59	1.61	
3.7	29842	0.3351	2.68	1.605	
3.65	29439	0.3397	2.78	1.605	
3.6	29036	0.3444	2.90	1.55	
3.55	28632	0.3493	3.02	1.45	
3.5	28229	0.3542	3.105	1.31	
3.45	27826	0.3594	3.135	1.20	
3.4	27423	0.3647	3.14	1.06	
3.35	27019	0.3701	3.13	0.92	
3.3	26616	0.3757	3.08	0.815	
3.25	26213	0.3815	3.02	0.77	
3.2	25810	0.3875	2.98	0.705	
3.15	25406	0.3936			1.8E-4[9]
3.1	25003	0.4000	2.91	0.63	9.5E-5
3.05	24600	0.4065			7.1E-5
3.0	24196	0.4133	2.865	0.58	6.2E-5
2.95	23793	0.4203			5.5E-5
2.9	23390	0.4275	2.83	0.52	4.8E-5
2.85	22987	0.4350			4.0E-5
2.8	22583	0.4428	2.795	0.48	3.2E-5
2.75	22180	0.4509			2.5E-5
2.7	21777	0.4592	2.765	0.435	1.9E-5
2.65	21374	0.4679			1.5E-5
2.6	20970	0.4769	2.75	0.39	9.9E-6
2.55	20567	0.4862			6.6E-6
2.5	20164	0.4959	2.73	0.35	4.3E-6
2.45	19760	0.5061			2.7E-6
2.4	19357	0.5166	2.705	0.30	1.6E-6
2.35	18954	0.5276			1.2E-6
2.3	18551	0.5391	2.695	0.265	9.4E-7
2.1	16938	0.5904	2.65	0.145	
2.0	16131	0.6199	2.585	0.105	
1.9	15324	0.6526	2.53	0.08	
1.8	14518	0.6888	2.47	0.05	
1.7	13711	0.7293	2.41	0.035	
1.6	12905	0.7749	2.37	0.025	
1.5	12098	0.8266	2.335	0.02	
3.100	25000	0.4	2.926[8]		
2.480	20000	0.5	2.651		
2.066	16667	0.6	2.549		
1.771	14286	0.7	2.499		
1.550	12500	0.8	2.472		
1.378	11111	0.9	2.454		
1.240	10000	1.0	2.442		
1.127	9091	1.1	2.434		

TABLE II *(Continued)*

$Bi_{12}GeO_{20}$

eV	cm^{-1}	μm	n	k	k
1.033	8333	1.2	2.427	4.57E-5[8]	
0.9537	7692	1.3	2.421	5.62E-5	
0.8856	7143	1.4	2.416	6.67E-5	
0.8266	6667	1.5	2.412	7.73E-5	
0.7749	6250	1.6	2.409	8.78E-5	
0.7293	5882	1.7	2.405	9.84E-5	
0.6888	5556	1.8	2.402	1.09E-4	
0.6526	5263	1.9	2.399	1.19E-4	
0.6199	5000	2.0	2.396	1.30E-4	
0.5904	4762	2.1	2.393	1.41E-4	
0.5636	4545	2.2	2.390	1.51E-4	
0.5391	4348	2.3	2.387	1.62E-4	
0.5166	4167	2.4	2.384	1.72E-4	
0.4959	4000	2.5	2.382	1.83E-4	
0.4769	3846	2.6	2.379	1.93E-4	
0.4592	3704	2.7	2.376	2.04E-4	
0.4428	3571	2.8	2.373	2.14E-4	
0.4275	3448	2.9	2.371	2.25E-4	
0.4133	3333	3.0	2.368	2.35E-4	
0.4000	3226	3.1	2.366	2.46E-4	
0.3875	3125	3.2	2.363	2.56E-4	
0.3757	3030	3.3	2.360	2.67E-4	
0.3647	2941	3.4	2.358	2.78E-4	
0.3542	2857	3.5	2.355	2.88E-4	
0.3444	2778	3.6	2.353	2.99E-4	
0.3351	2703	3.7	2.351	3.09E-4	
0.3263	2632	3.8	2.348	3.20E-4	
0.3179	2564	3.9	2.346	3.30E-4	
0.3100	2500	4.0	2.344	3.51E-4	
0.3024	2439	4.1	2.342	3.62E-4	
0.2952	2381	4.2	2.340	3.72E-4	
0.2883	2326	4.3	2.339	3.83E-4	
0.2818	2273	4.4	2.337	3.93E-4	
0.2755	2222	4.5	2.336	4.04E-4	
0.2695	2174	4.6	2.334	4.14E-4	
0.2638	2128	4.7	2.333	4.25E-4	
0.2583	2083	4.8	2.332	4.36E-4	
0.2530	2041	4.9	2.332	4.46E-4	
0.2480	2000	5.0	2.331	4.57E-4	
0.09919	800	12.50	2.17[17]	4.6E-1[17]	
0.09795	790	12.66	2.17	4.6E-1	
0.09671	780	12.82	2.17	4.6E-1	
0.09547	770	12.99	2.17	4.4E-1	
0.09423	760	13.16	2.17	4.4E-1	
0.09299	750	13.33	2.14	4.2E-1	

(continued)

TABLE II *(Continued)*

$Bi_{12}GeO_{20}$

eV	cm^{-1}	μm	n	k	k
0.09175	740	13.51	2.14	4.2E-1	
0.09051	730	13.70	2.12	4.3E-1	
0.08927	720	13.89	2.05	4.4E-1	
0.08803	710	14.08	1.78	3.9E-1	
0.08679	700	14.29	0.72	1.4E-1	
0.08617	695	14.39	0.71	7.1E-1	
0.08555	690	14.49	0.70	1.6E + 0	
0.08493	685	14.60	2.06	2.1E + 0	
0.08468	683	14.64	2.12	2.1E + 0	
0.08431	680	14.71	2.37	1.3E + 0	
0.08369	675	14.81	2.79	5.4E-1	
0.08307	670	14.92	2.57	3.5E-1	
0.08183	660	15.15	2.27	4.0E-1	
0.08059	650	15.38	2.05	4.4E-1	
0.07935	640	15.62	1.80	5.0E-1	
0.07811	630	15.87	1.74	4.6E-1	
0.07687	620	16.13	1.35	5.6E-1	
0.07563	610	16.39	1.00	1.0E + 0	
0.07501	605	16.53	1.23	1.4E + 0	
0.07439	600	16.67	1.88	1.6E + 0	
0.07377	595	16.81	2.68	4.5E-1	
0.07315	590	16.95	2.13	1.9E-1	
0.07253	585	17.09	1.03	9.8E-1	
0.07191	580	17.24	0.74	6.7E-1	
0.07129	575	17.39	1.40	1.1E + 0	
0.07104	573	17.45	1.88	1.5E + 0	
0.07067	570	17.54	1.92	8.3E-1	
0.07005	565	17.70	1.91	3.9E-1	
0.06943	560	17.86	1.42	1.4E-1	
0.06881	555	18.02	0.71	7.0E-2	
0.06819	550	18.18	0.32	3.2E-1	
0.06757	545	18.35	0.56	9.0E-1	
0.06695	540	18.52	0.69	1.4E + 0	
0.06633	535	18.69	0.91	2.2E + 0	
0.06571	530	18.87	1.68	3.0E + 0	
0.06534	527	18.98	2.45	2.6E + 0	
0.06509	525	19.05	2.24	2.2E + 0	
0.06447	520	19.23	3.15	9.5E-1	
0.06385	515	19.42	2.83	7.1E-1	
0.06323	510	19.61	2.17	4.6E-1	
0.06261	505	19.80	1.36	5.9E-1	
0.06199	500	20.00	1.10	4.5E-1	
0.06137	495	20.20	0.86	5.8E-1	
0.06075	490	20.41	0.75	8.7E-1	
0.06013	485	20.62	0.84	1.3E + 0	
0.05951	480	20.83	0.74	2.0E + 0	
0.05889	475	21.05	0.84	2.7E + 0	

TABLE II *(Continued)*

$Bi_{12}GeO_{20}$

eV	cm^{-1}	μm	n	k	k
0.05827	470	21.28	1.03	3.4E + 0	
0.05763	465	21.51	1.41	4.2E + 0	
0.05703	460	21.74	2.30	3.9E + 0	
0.05641	455	21.98	4.95	2.1E + 0	
0.05579	450	22.22	4.50	1.1E + 0	
0.05517	445	22.47	3.95	7.6E-1	
0.05455	440	22.73	3.30	6.1E-1	
0.05393	435	22.99	3.04	4.9E-1	
0.05331	430	23.25	2.81	3.6E-1	
0.05269	425	23.53	2.67	3.4E-1	
0.05207	420	23.81	2.37	3.6E-1	
0.05145	415	24.10	2.26	3.5E-1	
0.05083	410	24.39	2.03	3.7E-1	
0.05021	405	24.69	1.91	3.7E-1	
0.04959	400	25.00	1.63	4.0E-1	
0.04897	395	25.32	1.55	1.3E-1	
0.04835	390	25.64	1.52	9.9E-2	
0.04773	385	25.97	1.15	1.7E-1	
0.04711	380	26.31	1.10	4.6E-1	
0.04649	375	26.67	0.78	6.4E-1	
0.04587	370	27.03	0.74	7.4E-1	
0.04525	365	27.40	0.74	1.0E + 0	
0.04463	360	27.78	0.79	1.3E + 0	
0.04401	355	28.17	1.07	1.6E + 0	
0.04389	354	28.25	0.96	1.6E + 0	
0.04339	350	28.57	0.64	1.6E + 0	
0.04277	345	28.99	0.23	1.7E + 0	
0.04215	340	29.41	0.34	1.9E + 0	
0.04154	335	29.85	0.33	2.3E + 0	
0.04091	330	30.30	0.37	2.7E + 0	
0.04030	325	30.77	0.48	3.1E + 0	
0.03967	320	31.25	0.84	3.6E + 0	
0.03906	315	31.75	1.04	4.3E + 0	
0.03868	312	32.05	5.70	4.3E + 0	
0.03843	310	32.26	1.70	5.3E + 0	
0.03782	305	32.79	3.29	4.6E + 0	
0.03719	300	33.33	5.08	3.1E + 0	
0.03658	295	33.90	4.28	1.5E + 0	
0.03595	290	34.48	3.55	1.1E + 0	
0.03534	285	35.09	2.85	1.1E + 0	
0.03471	280	35.71	1.39	2.0E + 0	
0.03410	275	36.36	1.58	3.8E + 0	
0.03347	270	37.04	4.56	3.3E + 0	
0.03286	265	37.74	3.74	1.2E + 0	
0.03224	260	38.46	2.74	7.3E-1	
0.03162	255	39.22	1.49	1.1E + 0	

(continued)

TABLE II *(Continued)*

$Bi_{12}GeO_{20}$

eV	cm^{-1}	μm	n	k	k
0.03100	250	40.00	0.85	3.0E + 0	
0.03038	245	40.82	0.94	3.7E + 0	
0.02976	240	41.67	1.41	4.8E + 0	
0.02914	235	42.55	2.62	5.7E + 0	
0.02852	230	43.48	6.67	4.9E + 0	
0.02790	225	44.44	5.94	2.7E + 0	
0.02728	220	45.45	5.18	1.4E + 0	
0.02666	215	46.51	4.37	1.0E + 0	
0.02604	210	47.62	3.35	1.1E + 0	
0.02542	205	48.78	3.75	2.1E + 0	
0.02480	200	50.00	4.10	1.2E + 0	
0.02418	195	51.28	3.52	1.2E + 0	
0.02356	190	52.63	4.08	1.3E + 0	
0.02294	185	54.05	3.45	7.5E-1	
0.02232	180	55.55	3.22	1.2E + 0	
0.02182	176	56.82	3.41	1.3E + 0	
0.02170	175	57.14	3.40	1.2E + 0	
0.02108	170	58.82	3.16	7.1E-1	
0.02046	165	60.61	2.88	5.4E-1	
0.01984	160	62.50	2.30	5.4E-1	
0.01922	155	64.52	1.74	7.2E-1	
0.01860	150	66.67	1.10	1.1E + 0	
0.01798	145	68.97	0.57	2.7E + 0	
0.01736	140	71.43	0.62	3.7E + 0	
0.01674	135	74.07	0.72	5.5E + 0	
0.01624	131	76.34	1.17	6.2E + 0	
0.01512	130	76.92	2.05	6.1E + 0	
0.01550	125	80.00	4.51	7.8E + 0	
0.01513	122	81.97	9.35	6.7E + 0	
0.01488	120	83.33	8.00	3.7E + 0	
0.01426	115	86.96	4.08	1.3E + 0	
0.01364	110	90.91	2.36	8.5E + 0	
0.01302	105	95.24	9.83	7.7E + 0	
0.01240	100	100.0	5.81	3.7E + 0	
0.01190	96	104.2	7.27	4.6E + 0	
0.01178	95	105.3	7.31	4.5E + 0	
0.01116	90	111.1	7.10	2.1E + 0	
0.01054	85	117.6	6.43	1.8E + 0	
0.009919	80	125.0	6.06	1.5E + 0	
0.009299	75	133.3	5.98	1.1E + 0	
0.008679	70	142.8	5.33	9.8E-1	
0.001860	15	666.7		4.50E-2[19]	
0.001736	14	714.3	6.270[19]	4.26E-2	
0.001612	13	769.2	6.259	4.04E-2	
0.001488	12	833.3	6.250	3.64E-2	
0.001364	11	909.1	6.240	3.25E-2	
0.001240	10	1000	6.232	2.94E-2	

TABLE II *(Continued)*

$Bi_{12}GeO_{20}$

eV	cm^{-1}	μm	n	k	k
0.001116	9	1111	6.226	2.65E-2	
0.0009919	8	1250	6.220	2.58E-2	
0.0008679	7	1428	6.217	2.04E-2	
0.0007439	6	1667	6.210	1.59E-2	
0.0006199	5	2000	6.212	1.59E-2	

Boron Nitride (BN)

GARY L. DOLL
Materials Science Department
Timken Research
Canton, Ohio

INTRODUCTION I

The optical functions of the hexagonal and cubic phases of BN (hBN and cBN, respectively) are not nearly as well defined as those of other group III nitrides. This is due in large part to the fact that single-crystal samples either do not exist (which is the case for hexagonal boron nitride) or are extremely rare (as in the case of cubic boron nitride) [1]. Optical studies on the optically anisotropic hBN have been performed on preferentially oriented, polycrystalline samples with $\vec{E} \perp \hat{c}$ and $\vec{E} \parallel \hat{c}$ polarization. In these samples, it is difficult to obtain a complete separation of the two polarizations because the typical mosaic spread of the c-axes is greater than 20°, and because pure a-faces are not easily obtained. In this critique, we have not included experiments performed on BN films. The reasons for this are that the optical constants of these films can vary greatly with film properties such as stoichiometry, homogeneity, crystallinity, and purity, to name a few. For the most part, these types of film properties have not been correlated with optical properties that have been reported. As we shall see, the optical properties of bulk BN materials are not that well defined.

The hexagonal phase of BN is isostructural to graphite in that it is composed of planes of BN hexagons stacked along the c-axis in an ABA configuration. hBN has the space group $D_{4h}^6(\mathrm{P6_3/mmc})$, which has the irreducible representation

$$\Gamma = 2E_{2g} + A_{2u} + E_{1u} + 2B_{1g},$$

where the E_{2g} modes are Raman-active, the B_{1g} modes are silent (optically inactive), and the A_{2u} and E_{1u} modes are infrared-active. Whereas the A_{2u} modes are out-of-plane vibrations excited by light polarized parallel to the hBN c-axis ($\vec{E} \parallel \hat{c}$), the E_{1u} modes are in-plane vibrations excited by light

HANDBOOK OF OPTICAL CONSTANTS OF SOLIDS III

Copyright © 1998 by Academic Press.
All rights of reproduction in any form reserved
ISBN 0-12-544423-0/$25.00.

polarized perpendicular to the c-axis ($\vec{E} \perp \hat{c}$). The A_{2u} and E_{1u} modes are polar, which means that the longitudinal-optical or LO mode has a higher energy than the transverse-optical or TO mode.

cBN has the zincblende structure with the space group T_d^2, ($F\bar{4}3m$). Its phonon modes are of T_2 symmetry, and are polar, so that the energy of the cBN LO vibration is also higher than the TO polarization energy.

II cBN

Selected optical constants n and k for cBN taken from three sources are collected in Table I and plotted in Fig. 1. Tabulated values of the optical constants were not included in any of the sources.

Gielisse *et al.* [2] provided the first reported examination of the cBN optical constants. Although this study covered the energy range 400 to 4000 cm^{-1}, the optical constants could only be deduced from their data over the energy range 400 to 1800 cm^{-1}. In this study, Gielisse *et al.* measured the reflectivity of a collection of small single crystals compressed into compacts that were ground and polished. Their normal-incidence reflectivity was modeled using a four-parameter fit to the equations

$$\epsilon_1(\omega) = \epsilon_\infty + 4\pi\rho\omega_0^2 \frac{{\omega_0}^2 - \omega^2}{(\omega_0^2 - \omega^2)^2 + \Gamma^2\omega^2} \tag{1}$$

$$\epsilon_2(\omega) = 4\pi\rho\omega_0^2 \frac{\Gamma\omega}{(\omega_0^2 - \omega^2)^2 + \Gamma^2\omega^2}, \tag{2}$$

where ϵ_0 is the high-frequency limiting value of the dielectric constant, ω_0 is the Brillouin-zone-center, TO phonon-mode energy, $4\pi\rho$ is the strength of the resonance, Γ and is the phonon width or the damping constant. Good agreement between the calculated and measured reflectivity was found for the following parameters: $\epsilon_\infty = 4.5$, $4\pi\rho = 2.6$, $\omega_0 = 1065$ cm^{-1}, and $\Gamma = 40.5$ cm^{-1}. The static dielectric constant ϵ_0 was calculated to be 7.1 from the equation

$$\epsilon_0 = \epsilon_\infty + 4\pi\rho. \tag{3}$$

We calculated the values of $\epsilon_1(\omega)$ and $\epsilon_2(\omega)$ using the above parameters, then derived n and k by the equations

$$\begin{aligned} 2n^2 &= \sqrt{\epsilon_1^2 + \epsilon_2^2} + \epsilon_1 \\ 2k^2 &= \sqrt{\epsilon_1^2 + \epsilon_2^2} - \epsilon_1 \end{aligned} \tag{4}$$

The results are shown in Fig. 1 and listed in Table I. The energy of the LO mode was deduced to be 1340 cm^{-1} from the Lyddane–Sachs–Teller relationship $\omega_{LO} = \omega_{TO}(\epsilon_0/\epsilon_\infty)^{1/2}$.

Eremets *et al.* [3] have reported the optical properties of cBN over the energy range 500 to 28,000 cm^{-1}. Single crystals of cBN 0.45 μm thick by 150 μm square were studied in reflection and transmission, and n and k were deduced by fitting the interference fringes with equations proposed by Heavens [4]. Although n and k were neither tabulated nor shown in a form suitable for our purposes, the dielectric functions were described by a Sellmeier model that considers the contribution to $\epsilon(\omega)$ from phonons and electronic transitions. The Sellmeier model used by the authors is expressed as

$$\epsilon = \epsilon_{ph} + \epsilon_{elec} - \epsilon_\infty, \tag{5}$$

where

$$\epsilon_{elec} - 1 = \frac{\epsilon_\infty - 1}{1 - [\hbar\omega/E_0]^2}, \tag{6}$$

and ϵ_{ph} is described by Eqs. (1), (2), and (3). Using this approach, they were able to approximate the reflectance and transmittance over the measured energy range. We first calculated the dielectric functions using Eq. (5) with the parameters $\epsilon_0 = 6.8$, $\epsilon_\infty = 4.46$, $E_0 = 104{,}850$ cm^{-1}, $\omega_0 = 1055.7$ cm^{-1}, and $\Gamma = 0.005$ cm^{-1}, which were given by the authors. Eremets *et al.* also report the LO mode energy to be 1304.8 cm^{-1}. We suspect that the value of Γ given by Eremets *et al.* in [3] is incorrect, since it appears to be too small to describe phonon linewidths in these types of samples. Nevertheless, using the preceding parameters, we calculated n and k from Eq. (4). The results of this calculation are gathered in Table I and plotted in Fig. 1.

Miyata *et al.* [5] have reported the optical properties of a cBN single crystal having an area of 5 mm^2 and a thickness (d) of 0.16 mm. The sample was measured over the energy range 2 to 23 eV by reflectance and 2 to 6 eV by transmittance. In the energy range 2 to 6 eV where both R and T were measured, n and k were derived from the expressions

$$\begin{aligned} k &= \frac{\lambda}{4\pi d} \ln \frac{(1-R)^2}{T} \\ n &= \frac{R + 1 + [(R+1)^2 - (R-1)^2(1+k^2)]^{1/2}}{1-R}. \end{aligned} \tag{7}$$

To determine the optical constants from the reflectance at higher photon energy, a Kramers–Kronig relation was employed where the values of the phase-change integral were set equal to those calculated from the optical

constants in the energy region 2.5 to 5.5 eV. Their results for n and k, which we extracted from their figure, are listed in Table I and plotted in Fig. 1.

As can be seen in Fig. 1, some discrepancy exists between the data published by Gielisse *et al.* [2] and Eremets *et al.* [3] in the vicinity of the cBN IR-active phonon. Whereas Gielisse *et al.* [2] quote the energy of the TO phonon of their sample to be 1065 cm^{-1}, Eremets *et al.* [3] have determined the energy to be 1055.7 cm^{-1} for their material. One might expect this sort of discrepancy to be sample dependent. As we would expect from Eqs. (1) and (2), Fig. 1 shows us that the suspiciously low value of $\Gamma = 0.005$ cm^{-1} reported by Eremets *et al.* has a much more pronounced effect on k than on n in the region of the IR-active cBN phonon. Gielisse *et al.* [2] and Eremets *et al.* [3] derive similar values for ϵ_0 and ϵ_∞. The method used to deduce n and k from Eremets *et al.* [3] does not account for multiphonon absorption that is present at energies between 2000 cm^{-1} and 4000 cm^{-1}, so the optical constants in that energy range are not accurate. There is good agreement in the values of n derived from Eremets *et al.* [3] and Miyata *et al.* [5] where the data overlap in the energy region 2 to 3.5 eV. The onset for optical absorption was determined to be 6.1 $\pm$ 0.2 eV from Miyata *et al.* [5], and several absorption edges are also present at higher photon energies.

III hBN

The first examination of the optical properties of hBN was performed by Geick *et al.* [6] on pyrolytic hBN with a mosaic spread in the c-axis of 30°, where the c-axis is the direction normal to the BN hexagonal planes. The reflectivity was measured at near-normal incidence in $\vec{E} \perp \hat{c}$ and $\vec{E} \parallel \hat{c}$ polarizations over the energy range 300 to 2000 cm^{-1}. With this mosaic spread, a complete separation of the polarizations is not possible, but the experiment did provide first evidence for the identification of the in-plane (E_{1u}) and out-of-plane (A_{2u}) IR-active phonons in hBN. The dielectric functions were obtained from a Kramers–Kronig transformation of the reflectance data. No details of how the phase integral was extended to lower and higher energies in order to perform the transformation were given. We have calculated n and k using Eq. (4) from a digitization of their figures for ϵ_1 and ϵ_2 obtained with $\vec{E} \perp \hat{c}$ polarization. We show the results in Table II and Fig. 2. The presence of the low-frequency A_{2u} phonon near 13 μm illustrates the contribution that the crystallographic mosaic spread of the c-axis makes to the optical spectra of these types of samples. To our knowledge, there has been no optical spectrum taken on hBN samples that does not contain a mixture of these polarizations. The authors fit their dielectric functions to an oscillator model similar to Eqs. (1) and (2) but that contains contributions from both polarizations to account for the mosaic spread of the hBN crystallites. For the $\vec{E} \parallel \hat{c}$ polarization, the parameters that provided the best fit to

the data are $\epsilon_\infty = 4.10$, $\epsilon_0 = 5.09$, $\omega_{TO}^{A2u} = 783\ cm^{-1}$, $\omega_{LO}^{A2u} = 828\ cm^{-1}$, $4\pi\rho^{A2u} = 3.26 \times 10^5\ cm^{-2}$, $\Gamma^{A2u} = 8.0\ cm^{-1}$, $\omega_{TO}^{E1u} = 1510\ cm^{-1}$, $\omega_{LO}^{E1u} = 1595\ cm^{-1}$, $4\pi\rho^{E1u} = 1.04 \times 10^6\ cm^{-1}$, and $\Gamma^{E1u} = 80\ cm^{-1}$. For the $\vec{E}\perp\hat{c}$ polarization, the parameters that provided the best fit to the data are $\epsilon_\infty = 4.95$, $\epsilon_0 = 7.04$, $\omega_{TO}^{A2u} = 767\ cm^{-1}$, $\omega_{LO}^{A2u} = 778\ cm^{-1}$, $4\pi\rho^{A2u} = 1.23 \times 10^5\ cm^{-2}$, $\Gamma^{A2u} = 35.0\ cm^{-1}$, $\omega_{TO}^{E1u} = 1367\ cm^{-1}$, $\omega_{LO}^{E1u} = 1610\ cm^{-1}$, $4\pi\rho^{E1u} = 3.49 \times 10^6\ cm^{-1}$, and $\Gamma^{E1u} = 29\ cm^{-1}$. We do not display the $\vec{E}\parallel\hat{c}$ optical constants in either Fig. 2 or Table II.

Hoffman *et al.* [7] examined the $\vec{E}\perp\hat{c}$ optical reflectivity spectrum on a similar sample of pyrolytic hBN, with a mosaic spread slightly larger than that of Geick *et al.* [6] over the energy range 0.05 to 10 eV. The dielectric functions were obtained from a Kramers–Kronig transformation of the reflectance data. For purposes of integrating the phase-shift integral of the transformation, the data were extended below 0.045 eV by treating R as a constant, from 10 to 30 eV by using data from Mamy *et al.* [8], from 30 to 100 eV as $R \approx \omega^{-1}$, and thereafter as $R \approx \omega^{-4}$. We have calculated n and k using Eq. (4) from a digitization of their figures for ϵ_1 and ϵ_2, and we show the results in Table II and Fig. 2. As is evident in the figure, there is agreement in the energies of the E_{1u} and A_{2u} phonons between the two studies, but disagreement in the oscillator strengths of the vibrations. This is probably related to orientational and structural differences between the samples examined in the two studies. Another item of note is that the values of k are relatively high in the region between the ir-active phonons and the electronic band gap near 5 eV. The authors believe that this is not intrinsic to hBN, but rather is related to the rather large amounts of impurities and defects in the sample. The authors also examined the phonon region of ϵ_2 by fitting the data with an oscillator model similar to the one used by Geick *et al.* [6] for the $\vec{E}\perp\hat{c}$ polarization. The best fit to the data was achieved with the following parameters: $\omega_{TO}^{A2u} = 770\ cm^{-1}$, $4\pi\rho^{A2u} = 3.8 \times 10^4\ cm^{-2}$, $\Gamma^{A2u} = 18\ cm^{-1}$, $\omega_{TO}^{E1u} = 1383\ cm^{-1}$, $4\pi\rho^{E1u} = 7.5 \times 10^5\ cm^{-1}$, and $\Gamma^{E1u} = 30\ cm^{-1}$. Values for ϵ_∞ and ϵ_0 were not given in the paper, so a determination of the LO-mode energies from the data is not possible.

REFERENCES

1. J. H. Edgar, *in* "Properties of Group III Nitrides" (J. H. Edgar, ed.), p. 7. INSPEC, The Institute of Electrical Engineers, London, 1994.
2. P. J. Gielisse, S. S. Mitra, J. N. Plendl, R. D. Griffis, L. C. Mansur, R. Marshall, and E. A. Pascoe, *Phys. Rev.* **155**, 1039 (1967).
3. M. I. Eremets, M. Gauthier, A. Polian, J. C. Chervin, J. M. Besson, G. A. Dubitskii, and Y. Y. Semenova, *Phys. Rev. B* **52**, 8854 (1995).
4. O. S. Heavens, *Rep. Prog. Phys.* **23**, 1 (1960).
5. N. Miyata, K. Moriki, O. Mishima, M. Fujisawa, and T. Hattori, *Phys. Rev. B* **40**, 12028 (1989).
6. R. Geick, C. H. Perry, and G. Rupprecht, *Phys. Rev.* **146**, 543 (1966).
7. D. M. Hoffman, G. L. Doll, and P. C. Eklund, *Phys. Rev. B* **30**, 6052 (1984).
8. R. Mamy, J. Thomas, G. Jezequel, and J. C. Lemonnier, *J. Phys. (Paris) Lett.* **42**, 473 (1981).

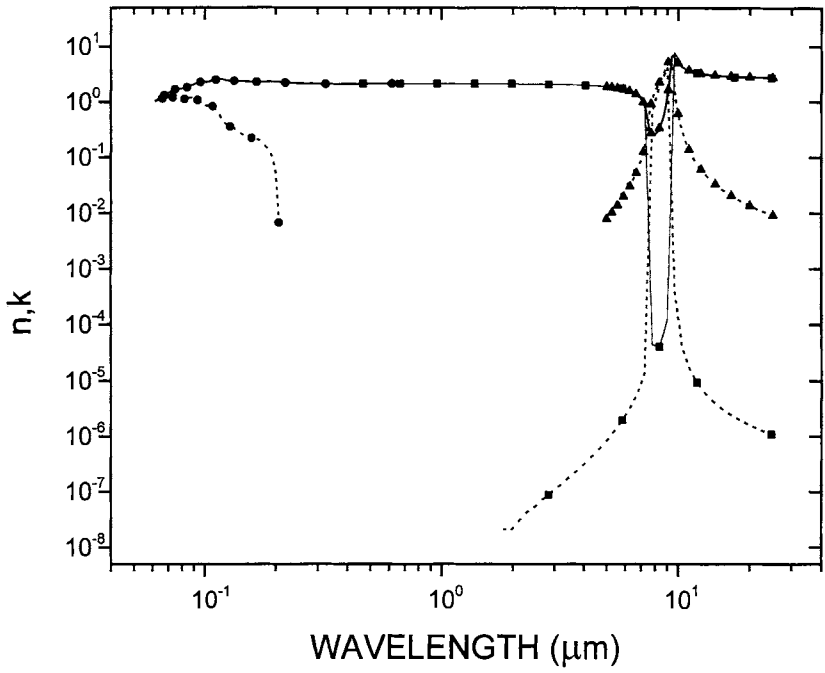

Fig. 1. Log–log plot of n (solid line) and k (dashed line) versus wavelength in micrometers for cBN. The data for n and k were derived from Gielisse *et al.* [2] (triangles), Eremets *et al.* [3] (squares), and Miyata *et al.* [5] (circles).

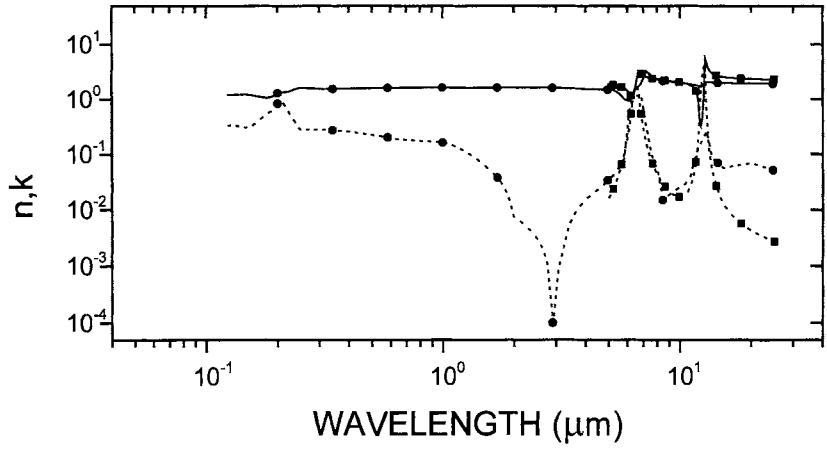

Fig. 2. Log–log plot of n (solid line) and k (dashed line) versus wavelength in micrometers for hBN obtained from $\vec{E} \perp \hat{c}$ polarization. The data for n and k were derived from Geick *et al.* [6] (squares) and Hoffman *et al.* [7] (circles).

TABLE I

Values of n and k for Cubic BN from Various References[a]

eV	cm^{-1}	μm	n	k
2.00E1	1.613E5	6.200E-2	1.0389 [5]	1.03E0 [5]
1.98E1	1.599E5	6.257E-2	1.0552	1.05E0
1.96E1	1.584E5	6.315E-2	1.0872	1.07E0
1.95E1	1.569E5	6.374E-2	1.1212	1.09E0
1.93E1	1.555E5	6.434E-2	1.1534	1.10E0
1.91E1	1.540E5	6.495E-2	1.1830	1.12E0
1.89E1	1.525E5	6.558E-2	1.2125	1.13E0
1.87E1	1.511E5	6.621E-2	1.2421	1.15E0
1.85E1	1.496E5	6.686E-2	1.2735	1.16E0
1.84E1	1.481E5	6.752E-2	1.3081	1.17E0
1.82E1	1.467E5	6.820E-2	1.3427	1.17E0
1.80E1	1.452E5	6.889E-2	1.3773	1.18E0
1.78E1	1.437E5	6.959E-2	1.4112	1.19E0
1.76E1	1.423E5	7.031E-2	1.4433	1.20E0
1.75E1	1.408E5	7.104E-2	1.4776	1.20E0
1.73E1	1.393E5	7.179E-2	1.5162	1.20E0
1.71E1	1.379E5	7.255E-2	1.5547	1.20E0
1.69E1	1.364E5	7.333E-2	1.5935	1.20E0
1.67E1	1.349E5	7.413E-2	1.6344	1.20E0
1.65E1	1.335E5	7.495E-2	1.6713	1.17E0
1.64E1	1.320E5	7.578E-2	1.6835	1.14E0
1.62E1	1.305E5	7.663E-2	1.6957	1.11E0
1.60E1	1.291E5	7.750E-2	1.7079	1.10E0
1.58E1	1.276E5	7.839E-2	1.7154	1.08E0
1.56E1	1.261E5	7.930E-2	1.7178	1.07E0
1.55E1	1.247E5	8.024E-2	1.7249	1.09E0
1.53E1	1.232E5	8.119E-2	1.7388	1.10E0
1.51E1	1.217E5	8.217E-2	1.7560	1.11E0
1.49E1	1.203E5	8.317E-2	1.7780	1.13E0
1.47E1	1.188E5	8.420E-2	1.8105	1.14E0
1.45E1	1.173E5	8.525E-2	1.8516	1.15E0
1.44E1	1.159E5	8.633E-2	1.8959	1.16E0
1.42E1	1.144E5	8.744E-2	1.9390	1.18E0
1.40E1	1.129E5	8.857E-2	1.9822	1.16E0
1.38E1	1.115E5	8.974E-2	2.0369	1.15E0
1.36E1	1.100E5	9.093E-2	2.0906	1.13E0
1.35E1	1.085E5	9.216E-2	2.1344	1.11E0
1.33E1	1.071E5	9.342E-2	2.1804	1.07E0
1.31E1	1.056E5	9.472E-2	2.2249	1.03E0
1.29E1	1.041E5	9.606E-2	2.2513	9.82E-1
1.27E1	1.027E5	9.743E-2	2.2628	9.35E-1
1.25E1	1.012E5	9.884E-2	2.2689	8.93E-1
1.24E1	9.973E4	1.003E-1	2.2648	8.60E-1
1.22E1	9.826E4	1.018E-1	2.2604	8.36E-1
1.20E1	9.679E4	1.033E-1	2.2583	8.45E-1
1.18E1	9.533E4	1.049E-1	2.2822	8.55E-1

(continued)

[a] The references from which the values were taken are given in brackets.

TABLE I *(Continued)*

Cubic BN

eV	cm^{-1}	μm	n	k
1.16E1	9.386E4	1.066E-1	2.3384	8.65E-1
1.15E1	9.239E4	1.083E-1	2.4265	8.28E-1
1.13E1	9.093E4	1.100E-1	2.4467	7.62E-1
1.11E1	8.946E4	1.118E-1	2.4702	7.19E-1
1.09E1	8.799E4	1.137E-1	2.5046	6.76E-1
1.07E1	8.653E4	1.156E-1	2.5368	5.94E-1
1.05E1	8.506E4	1.176E-1	2.5357	5.13E-1
1.04E1	8.359E4	1.197E-1	2.5046	4.38E-1
1.02E1	8.213E4	1.218E-1	2.4598	4.15E-1
1.00E1	8.066E4	1.240E-1	2.4147	3.92E-1
9.82E0	7.919E4	1.263E-1	2.3900	3.69E-1
9.64E0	7.773E4	1.287E-1	2.3733	3.57E-1
9.45E0	7.626E4	1.312E-1	2.3647	3.45E-1
9.27E0	7.479E4	1.337E-1	2.3561	3.30E-1
9.09E0	7.333E4	1.364E-1	2.3470	3.11E-1
8.91E0	7.186E4	1.392E-1	2.3362	2.91E-1
8.73E0	7.039E4	1.421E-1	2.3268	2.70E-1
8.55E0	6.893E4	1.451E-1	2.3204	2.56E-1
8.36E0	6.746E4	1.483E-1	2.3086	2.44E-1
8.18E0	6.599E4	1.516E-1	2.2960	2.32E-1
8.00E0	6.453E4	1.550E-1	2.2835	2.26E-1
7.82E0	6.306E4	1.586E-1	2.2749	2.20E-1
7.64E0	6.159E4	1.624E-1	2.2690	2.14E-1
7.45E0	6.013E4	1.663E-1	2.2687	2.08E-1
7.27E0	5.866E4	1.705E-1	2.2733	2.03E-1
7.09E0	5.720E4	1.749E-1	2.2766	1.86E-1
6.91E0	5.573E4	1.795E-1	2.2762	1.65E-1
6.73E0	5.426E4	1.843E-1	2.2782	1.45E-1
6.55E0	5.280E4	1.894E-1	2.2919	1.24E-1
6.36E0	5.133E4	1.949E-1	2.3032	9.62E-2
6.18E0	4.986E4	2.006E-1	2.2913	5.15E-2
6.00E0	4.840E4	2.067E-1	2.2692	6.72E-3
5.82E0	4.693E4	2.131E-1	2.2160	
5.64E0	4.546E4	2.200E-1	2.1981	
5.45E0	4.400E4	2.273E-1	2.1912	
5.27E0	4.253E4	2.352E-1	2.1752	
5.09E0	4.106E4	2.436E-1	2.1471	
4.91E0	3.960E4	2.526E-1	2.1286	
4.73E0	3.813E4	2.623E-1	2.1258	
4.55E0	3.666E4	2.728E-1	2.1186	
4.36E0	3.520E4	2.842E-1	2.1148	
4.18E0	3.373E4	2.965E-1	2.1073	
4.00E0	3.226E4	3.100E-1	2.0969	
3.82E0	3.080E4	3.248E-1	2.0909	
3.64E0	2.933E4	3.410E-1	2.0852	
3.55E0	2.862E4	3.490E-1	2.1111 [3]	
3.45E0	2.786E4	3.590E-1	2.0791 [5]	

TABLE I *(Continued)*

Cubic BN

eV	cm^{-1}	μm	n	k
3.30E0	2.663E4	3.760E-1	2.1110 [3]	
3.27E0	2.640E4	3.789E-1	2.0744 [5]	
3.09E0	2.493E4	4.012E-1	2.0794	
3.07E0	2.477E4	4.040E-1	2.1109 [3]	
2.91E0	2.346E4	4.263E-1	2.0815 [5]	
2.86E0	2.305E4	4.340E-1	2.1107 [3]	
2.73E0	2.200E4	4.547E-1	2.0837 [5]	
2.66E0	2.144E4	4.660E-1	2.1105 [3]	
2.55E0	2.053E4	4.871E-1	2.0935 [5]	
2.47E0	1.995E4	5.010E-1	2.1103 [3]	
2.36E0	1.907E4	5.246E-1	2.1021 [5]	
2.30E0	1.856E4	5.390E-1	2.1101 [3]	
2.18E0	1.760E4	5.683E-1	2.1109 [5]	
2.14E0	1.727E4	5.790E-1	2.1098 [3]	
2.00E0	1.613E4	6.200E-1	2.1231 [5]	
1.99E0	1.606E4	6.230E-1	2.1095 [3]	
1.85E0	1.494E4	6.690E-1	2.1091	
1.72E0	1.390E4	7.190E-1	2.1087	
1.60E0	1.293E4	7.730E-1	2.1082	
1.49E0	1.203E4	8.310E-1	2.1076	
1.39E0	1.120E4	8.930E-1	2.1069	
1.29E0	1.042E4	9.600E-1	2.1061	
1.20E0	9.690E3	1.032E0	2.1052	
1.12E0	9.015E3	1.109E0	2.1042	
1.04E0	8.387E3	1.193E0	2.1029	
9.67E-1	7.803E3	1.282E0	2.1015	
9.00E-1	7.259E3	1.378E0	2.0999	
8.37E-1	6.754E3	1.481E0	2.0979	
7.79E-1	6.283E3	1.592E0	2.0957	
7.25E-1	5.846E3	1.711E0	2.0931	
6.74E-1	5.438E3	1.839E0	2.0901 [3]	2.11E-8 [3]
6.27E-1	5.060E3	1.977E0	2.0865	2.11E-8
5.84E-1	4.707E3	2.125E0	2.0823	2.98E-8
5.43E-1	4.379E3	2.284E0	2.0774	4.21E-8
5.05E-1	4.074E3	2.455E0	2.0716	5.16E-8
4.70E-1	3.790E3	2.639E0	2.0647	6.99E-8
4.37E-1	3.526E3	2.836E0	2.0566	8.69E-8
4.07E-1	3.281E3	3.049E0	2.0468	1.13E-7
3.78E-1	3.052E3	3.277E0	2.0351	1.46E-7
3.52E-1	2.840E3	3.522E0	2.0210	1.90E-7
3.28E-1	2.642E3	3.786E0	2.0037	2.50E-7
3.05E-1	2.458E3	4.069E0	1.9825	3.33E-7
2.83E-1	2.287E3	4.374E0	1.9559	4.51E-7
2.64E-1	2.127E3	4.701E0	1.9222	6.21E-7
2.48E-1	2.000E3	5.001E0	2.8450 [2]	1.75E-2 [2]
2.47E-1	1.990E3	5.026E0	2.8440	1.74E-2
2.45E-1	1.980E3	5.051E0	2.8430	1.73E-2

(continued)

TABLE I *(Continued)*

Cubic BN

eV	cm^{-1}	μm	n	k
2.45E-1	1.979E3	5.053E0	1.8785 [3]	8.75E-7 [3]
2.44E-1	1.970E3	5.077E0	2.8420 [2]	1.72E-2 [2]
2.43E-1	1.960E3	5.103E0	2.8410	1.72E-2
2.42E-1	1.950E3	5.129E0	2.8400	1.71E-2
2.41E-1	1.940E3	5.156E0	2.8400	1.70E-2
2.39E-1	1.930E3	5.182E0	2.8390	1.69E-2
2.38E-1	1.920E3	5.209E0	2.8380	1.69E-2
2.37E-1	1.910E3	5.237E0	2.8370	1.68E-2
2.36E-1	1.900E3	5.264E0	2.8360	1.67E-2
2.34E-1	1.890E3	5.292E0	2.8350	1.67E-2
2.33E-1	1.880E3	5.320E0	2.8350	1.66E-2
2.32E-1	1.870E3	5.349E0	2.8340	1.65E-2
2.31E-1	1.860E3	5.377E0	2.8330	1.65E-2
2.29E-1	1.850E3	5.406E0	2.8320	1.64E-2
2.28E-1	1.841E3	5.432E0	1.8202 [3]	1.27E-6 [3]
2.28E-1	1.840E3	5.436E0	2.8310 [2]	1.63E-2 [2]
2.27E-1	1.830E3	5.465E0	2.8310	1.63E-2
2.26E-1	1.820E3	5.496E0	2.8300	1.62E-2
2.24E-1	1.810E3	5.526E0	2.8290	1.61E-2
2.23E-1	1.800E3	5.557E0	2.8280	1.61E-2
2.22E-1	1.790E3	5.588E0	2.8270	1.60E-2
2.21E-1	1.780E3	5.619E0	2.8270	1.59E-2
2.19E-1	1.770E3	5.651E0	2.8260	1.59E-2
2.18E-1	1.760E3	5.683E0	2.8250	1.58E-2
2.17E-1	1.750E3	5.715E0	2.8240	1.57E-2
2.16E-1	1.740E3	5.748E0	2.8240	1.57E-2
2.14E-1	1.730E3	5.781E0	2.8230	1.56E-2
2.13E-1	1.720E3	5.815E0	2.8220	1.55E-2
2.12E-1	1.713E3	5.839E0	1.7395 [3]	1.94E-6 [3]
2.12E-1	1.710E3	5.849E0	2.8210 [2]	1.55E-2 [2]
2.11E-1	1.700E3	5.883E0	2.8200	1.54E-2
2.10E-1	1.690E3	5.918E0	2.8200	1.53E-2
2.08E-1	1.680E3	5.953E0	2.8190	1.53E-2
2.07E-1	1.670E3	5.989E0	2.8180	1.52E-2
2.06E-1	1.660E3	6.025E0	2.8170	1.52E-2
2.05E-1	1.650E3	6.062E0	2.8170	1.51E-2
2.03E-1	1.640E3	6.099E0	2.8160	1.50E-2
2.02E-1	1.630E3	6.136E0	2.8150	1.50E-2
2.01E-1	1.620E3	6.174E0	2.8150	1.49E-2
2.00E-1	1.610E3	6.212E0	2.8140	1.49E-2
1.98E-1	1.600E3	6.251E0	2.8130	1.48E-2
1.98E-1	1.594E3	6.276E0	1.6215 [3]	3.16E-6 [3]
1.97E-1	1.590E3	6.290E0	2.8120 [2]	1.47E-2 [2]
1.96E-1	1.580E3	6.330E0	2.8120	1.47E-2
1.95E-1	1.570E3	6.371E0	2.8110	1.46E-2
1.93E-1	1.560E3	6.411E0	2.8100	1.46E-2
1.92E-1	1.550E3	6.453E0	2.8090	1.45E-2

TABLE I *(Continued)*

Cubic BN

eV	cm^{-1}	μm	n	k
1.91E-1	1.540E3	6.495E0	2.8090	1.44E-2
1.90E-1	1.530E3	6.537E0	2.8080	1.44E-2
1.88E-1	1.520E3	6.580E0	2.8070	1.43E-2
1.87E-1	1.510E3	6.624E0	2.8070	1.43E-2
1.86E-1	1.500E3	6.668E0	2.8060	1.42E-2
1.85E-1	1.490E3	6.713E0	2.8050	1.41E-2
1.84E-1	1.483E3	6.745E0	1.4327 [3]	5.75E-6 [3]
1.83E-1	1.480E3	6.758E0	2.8050 [2]	1.41E-2 [2]
1.82E-1	1.470E3	6.804E0	2.8040	1.40E-2
1.81E-1	1.460E3	6.851E0	2.8030	1.40E-2
1.80E-1	1.450E3	6.898E0	2.8020	1.39E-2
1.79E-1	1.440E3	6.946E0	2.8020	1.39E-2
1.77E-1	1.430E3	6.994E0	2.8010	1.38E-2
1.76E-1	1.420E3	7.044E0	2.8000	1.38E-2
1.75E-1	1.410E3	7.094E0	2.8000	1.37E-2
1.74E-1	1.400E3	7.144E0	2.7990	1.36E-2
1.72E-1	1.390E3	7.196E0	2.7980	1.36E-2
1.71E-1	1.380E3	7.248E0	2.7980	1.35E-2
1.71E-1	1.379E3	7.251E0	1.0721 [3]	1.35E-5 [3]
1.70E-1	1.370E3	7.301E0	2.7970 [2]	1.35E-2 [2]
1.69E-1	1.360E3	7.354E0	2.7960	1.34E-2
1.67E-1	1.350E3	7.409E0	2.7960	1.34E-2
1.66E-1	1.340E3	7.464E0	2.7950	1.33E-2
1.65E-1	1.330E3	7.520E0	2.7940	1.33E-2
1.64E-1	1.320E3	7.577E0	2.7940	1.32E-2
1.62E-1	1.310E3	7.635E0	2.7930	1.32E-2
1.61E-1	1.300E3	7.694E0	2.7920	1.31E-2
1.60E-1	1.290E3	7.753E0	2.7920	1.31E-2
1.59E-1	1.283E3	7.793E0		6.64E-1 [3]
1.59E-1	1.280E3	7.814E0	2.7910 [2]	1.30E-2 [2]
1.57E-1	1.270E3	7.875E0	2.7910	1.30E-2
1.56E-1	1.260E3	7.938E0	2.7900	1.29E-2
1.55E-1	1.250E3	8.001E0	2.7890	1.29E-2
1.54E-1	1.240E3	8.066E0	2.7890	1.28E-2
1.52E-1	1.230E3	8.132E0	2.7880	1.27E-2
1.51E-1	1.220E3	8.198E0	2.7870	1.27E-2
1.50E-1	1.210E3	8.266E0	2.7870	1.26E-2
1.49E-1	1.200E3	8.335E0	2.7860	1.26E-2
1.48E-1	1.194E3	8.377E0		1.98E0 [3]
1.48E-1	1.190E3	8.405E0	2.7860 [2]	1.25E-2 [2]
1.46E-1	1.180E3	8.476E0	2.7850	1.25E-2
1.45E-1	1.170E3	8.549E0	2.7840	1.24E-2
1.44E-1	1.160E3	8.622E0	2.7840	1.24E-2
1.43E-1	1.150E3	8.697E0	2.7830	1.23E-2
1.41E-1	1.140E3	8.774E0	2.7820	1.23E-2
1.40E-1	1.130E3	8.851E0	2.7820	1.23E-2
1.39E-1	1.120E3	8.930E0	2.7810	1.22E-2

(continued)

TABLE I *(Continued)*

Cubic BN

eV	cm^{-1}	μm	n	k
1.38E-1	1.111E3	9.004E0	0.0001 [3]	4.17E0 [3]
1.38E-1	1.110E3	9.011E0	2.7810 [2]	1.22E-2 [2]
1.36E-1	1.100E3	9.093E0	2.7800	1.21E-2
1.35E-1	1.090E3	9.176E0	2.7790	1.21E-2
1.34E-1	1.080E3	9.261E0	2.7790	1.20E-2
1.33E-1	1.070E3	9.348E0	2.7780	1.20E-2
1.31E-1	1.060E3	9.436E0	2.7780	1.19E-2
1.30E-1	1.050E3	9.526E0	2.7770	1.19E-2
1.29E-1	1.040E3	9.617E0	2.7770	1.18E-2
1.28E-1	1.033E3	9.678E0	7.7797 [3]	4.00E-4 [3]
1.28E-1	1.030E3	9.711E0	2.7760 [2]	1.18E-2 [2]
1.26E-1	1.020E3	9.806E0	2.7750	1.17E-2
1.25E-1	1.010E3	9.903E0	2.7750	1.17E-2
1.24E-1	1.000E3	1.000E1	2.7740	1.16E-2
1.23E-1	9.900E2	1.010E1	2.7740	1.16E-2
1.21E-1	9.800E2	1.021E1	2.7730	1.15E-2
1.20E-1	9.700E2	1.031E1	2.7720	1.15E-2
1.19E-1	9.615E2	1.040E1	4.2651 [3]	4.07E-5 [3]
1.19E-1	9.600E2	1.042E1	2.7720 [2]	1.15E-2 [2]
1.18E-1	9.500E2	1.053E1	2.7710	1.14E-2
1.17E-1	9.400E2	1.064E1	2.7710	1.14E-2
1.15E-1	9.300E2	1.076E1	2.7700	1.13E-2
1.14E-1	9.200E2	1.087E1	2.7700	1.13E-2
1.13E-1	9.100E2	1.099E1	2.7690	1.12E-2
1.12E-1	9.000E2	1.111E1	2.7690	1.12E-2
1.11E-1	8.945E2	1.118E1	3.5726 [3]	1.65E-5 [3]
1.10E-1	8.900E2	1.124E1	2.7680 [2]	1.11E-2 [2]
1.09E-1	8.800E2	1.137E1	2.7670	1.11E-2
1.08E-1	8.700E2	1.150E1	2.7670	1.11E-2
1.07E-1	8.600E2	1.163E1	2.7660	1.10E-2
1.05E-1	8.500E2	1.177E1	2.7660	1.10E-2
1.04E-1	8.400E2	1.191E1	2.7650	1.09E-2
1.03E-1	8.322E2	1.202E1	3.2627 [3]	9.35E-6 [3]
1.03E-1	8.300E2	1.205E1	2.7650 [2]	1.09E-2 [2]
1.02E-1	8.200E2	1.220E1	2.7640	1.08E-2
1.00E-1	8.100E2	1.235E1	2.7640	1.08E-2
9.92E-2	8.000E2	1.250E1	2.7630	1.08E-2
9.79E-2	7.900E2	1.266E1	2.7630	1.07E-2
9.67E-2	7.800E2	1.282E1	2.7620	1.07E-2
9.60E-2	7.742E2	1.292E1	3.0865 [3]	6.17E-6 [3]
9.55E-2	7.700E2	1.299E1	2.7620 [2]	1.06E-2 [2]
9.42E-2	7.600E2	1.316E1	2.7610	1.06E-2
9.30E-2	7.500E2	1.334E1	2.7610	1.05E-2
9.17E-2	7.400E2	1.352E1	2.7600	1.05E-2
9.05E-2	7.300E2	1.370E1	2.7600	1.05E-2
8.93E-2	7.203E2	1.389E1	2.9735 [3]	4.45E-6 [3]
8.93E-2	7.200E2	1.389E1	2.7590 [2]	1.04E-2 [2]

TABLE I *(Continued)*

Cubic BN

eV	cm^{-1}	μm	n	k
8.80E-2	7.100E2	1.409E1	2.7590	1.04E-2
8.68E-2	7.000E2	1.429E1	2.7580	1.03E-2
8.55E-2	6.900E2	1.450E1	2.7570	1.03E-2
8.43E-2	6.800E2	1.471E1	2.7570	1.03E-2
8.31E-2	6.701E2	1.493E1	2.8952 [3]	3.41E-6 [3]
8.31E-2	6.700E2	1.493E1	2.7560 [2]	1.02E-2 [2]
8.18E-2	6.600E2	1.515E1	2.7560	1.02E-2
8.06E-2	6.500E2	1.539E1	2.7550	1.01E-2
7.93E-2	6.400E2	1.563E1	2.7550	1.01E-2
7.81E-2	6.300E2	1.588E1	2.7540	1.01E-2
7.73E-2	6.234E2	1.604E1	2.8383 [3]	2.72E-6 [3]
7.69E-2	6.200E2	1.613E1	2.7540 [2]	1.00E-2 [2]
7.56E-2	6.100E2	1.640E1	2.7530	9.97E-3
7.44E-2	6.000E2	1.667E1	2.7530	9.93E-3
7.31E-2	5.900E2	1.695E1	2.7530	9.89E-3
7.19E-2	5.800E2	1.724E1	2.7954 [3]	2.24E-6 [3]
7.19E-2	5.800E2	1.725E1	2.7520 [2]	9.85E-3 [2]
7.07E-2	5.700E2	1.755E1	2.7520	9.81E-3
6.94E-2	5.600E2	1.786E1	2.7510	9.78E-3
6.82E-2	5.500E2	1.819E1	2.7510	9.74E-3
6.69E-2	5.400E2	1.852E1	2.7500	9.70E-3
6.69E-2	5.396E2	1.854E1	2.7623 [3]	1.88E-6 [3]
6.57E-2	5.300E2	1.887E1	2.7500 [2]	9.66E-3 [2]
6.45E-2	5.200E2	1.923E1	2.7490	9.62E-3
6.32E-2	5.100E2	1.961E1	2.7490	9.58E-3
6.22E-2	5.020E2	1.992E1	2.7361 [3]	1.61E-6 [3]
6.20E-2	5.000E2	2.000E1	2.7480 [2]	9.55E-3 [2]
6.07E-2	4.900E2	2.041E1	2.7480	9.51E-3
5.95E-2	4.800E2	2.084E1	2.7470	9.47E-3
5.83E-2	4.700E2	2.128E1	2.7470	9.43E-3
5.79E-2	4.670E2	2.142E1	2.7151 [3]	1.40E-6 [3]
5.70E-2	4.600E2	2.174E1	2.7460 [2]	9.40E-3 [2]
5.58E-2	4.500E2	2.223E1	2.7460	9.36E-3
5.45E-2	4.400E2	2.273E1	2.7450	9.32E-3
5.39E-2	4.345E2	2.302E1	2.6981 [3]	1.23E-6 [3]
5.33E-2	4.300E2	2.326E1	2.7450 [2]	9.28E-3 [2]
5.21E-2	4.200E2	2.381E1	2.7440	9.25E-3
5.08E-2	4.100E2	2.440E1	2.7440	9.21E-3
5.01E-2	4.043E2	2.474E1	2.6841 [3]	1.09E-6 [3]
4.96E-2	4.000E2	2.501E1	2.7440 [2]	9.17E-3 [2]

TABLE II

Values of n and k for Hexagonal BN from Various References[a]

eV	cm^{-1}	μm	n	k
1.000E1	8.066E4	1.240E-1	1.1905 [7]	3.3E-1 [7]
9.479E0	7.646E4	1.308E-1	1.1903	3.3E-1
8.985E0	7.248E4	1.380E-1	1.1949	3.2E-1
8.517E0	6.870E4	1.456E-1	1.2040	3.1E-1
8.074E0	6.512E4	1.536E-1	1.1799	3.0E-1
7.653E0	6.173E4	1.620E-1	1.1281	3.7E-1
7.255E0	5.852E4	1.709E-1	1.0819	4.4E-1
6.877E0	5.547E4	1.803E-1	1.0470	5.3E-1
6.518E0	5.258E4	1.902E-1	1.1054	6.2E-1
6.179E0	4.984E4	2.007E-1	1.2790	8.3E-1
5.857E0	4.724E4	2.117E-1	1.3301	8.4E-1
5.552E0	4.478E4	2.234E-1	1.3589	5.6E-1
5.263E0	4.245E4	2.356E-1	1.5082	4.0E-1
4.989E0	4.024E4	2.486E-1	1.5987	2.8E-1
4.729E0	3.814E4	2.622E-1	1.5810	2.8E-1
4.483E0	3.616E4	2.766E-1	1.5631	2.8E-1
4.249E0	3.427E4	2.918E-1	1.5450	2.8E-1
4.028E0	3.249E4	3.079E-1	1.5266	2.8E-1
3.818E0	3.079E4	3.248E-1	1.5193	2.7E-1
3.619E0	2.919E4	3.426E-1	1.5270	2.7E-1
3.430E0	2.767E4	3.615E-1	1.5346	2.6E-1
3.252E0	2.623E4	3.813E-1	1.5422	2.6E-1
3.082E0	2.486E4	4.023E-1	1.5496	2.5E-1
2.922E0	2.357E4	4.244E-1	1.5566	2.5E-1
2.770E0	2.234E4	4.477E-1	1.5637	2.4E-1
2.625E0	2.118E4	4.723E-1	1.5707	2.3E-1
2.489E0	2.007E4	4.983E-1	1.5778	2.2E-1
2.359E0	1.903E4	5.256E-1	1.5849	2.2E-1
2.236E0	1.804E4	5.545E-1	1.5920	2.1E-1
2.120E0	1.710E4	5.850E-1	1.5992	2.0E-1
2.009E0	1.621E4	6.172E-1	1.6049	1.9E-1
1.905E0	1.536E4	6.511E-1	1.6050	1.9E-1
1.805E0	1.456E4	6.868E-1	1.6056	1.8E-1
1.711E0	1.380E4	7.246E-1	1.6061	1.8E-1
1.622E0	1.308E4	7.644E-1	1.6067	1.8E-1
1.538E0	1.240E4	8.064E-1	1.6072	1.7E-1
1.458E0	1.176E4	8.507E-1	1.6078	1.7E-1
1.382E0	1.114E4	8.975E-1	1.6084	1.7E-1
1.310E0	1.056E4	9.468E-1	1.6090	1.7E-1
1.241E0	1.001E4	9.988E-1	1.6096	1.6E-1
1.177E0	9.492E3	1.054E0	1.6099	1.6E-1
1.116E0	8.998E3	1.112E0	1.6094	1.4E-1
1.057E0	8.529E3	1.173E0	1.6090	1.3E-1
1.002E0	8.085E3	1.237E0	1.6088	1.1E-1
9.501E-1	7.664E3	1.305E0	1.6087	9.9E-2
9.006E-1	7.265E3	1.377E0	1.6088	8.4E-2

[a] The references from which the values were taken are given in brackets.

TABLE II *(Continued)*

Hexagonal BN

eV	cm^{-1}	μm	n	k
8.537E-1	6.886E3	1.452E0	1.6093	6.9E-2
8.092E-1	6.527E3	1.532E0	1.6100	5.7E-2
7.671E-1	6.187E3	1.616E0	1.6109	4.7E-2
7.271E-1	5.865E3	1.705E0	1.6118	3.7E-2
6.893E-1	5.560E3	1.799E0	1.6128	2.7E-2
6.534E-1	5.270E3	1.898E0	1.6138	1.7E-2
6.193E-1	4.995E3	2.002E0	1.6149	7.4E-3
5.871E-1	4.735E3	2.112E0	1.6161	6.3E-3
5.565E-1	4.489E3	2.228E0	1.6173	5.3E-3
5.275E-1	4.255E3	2.351E0	1.6184	4.2E-3
5.000E-1	4.033E3	2.480E0	1.6196	3.2E-3
4.740E-1	3.823E3	2.616E0	1.6208	2.2E-3
4.493E-1	3.624E3	2.760E0	1.6142	1.1E-3
4.259E-1	3.435E3	2.912E0	1.6023	1.0E-4
4.037E-1	3.256E3	3.072E0	1.5904	8.6E-4
3.827E-1	3.087E3	3.240E0	1.5783	2.2E-3
3.627E-1	2.926E3	3.418E0	1.5661	5.4E-3
3.438E-1	2.773E3	3.606E0	1.5539	8.6E-3
3.259E-1	2.629E3	3.804E0	1.5415	1.2E-2
3.090E-1	2.492E3	4.013E0	1.5291	1.5E-2
2.929E-1	2.362E3	4.234E0	1.5166	1.8E-2
2.776E-1	2.239E3	4.467E0	1.5040	2.2E-2
2.632E-1	2.123E3	4.712E0	1.4913	2.6E-2
2.494E-1	2.012E3	4.971E0	1.4785	3.4E-2
2.480E-1	2.000E3	5.001E0	0.0337 [6]	8.3E-1 [6]
2.467E-1	1.990E3	5.026E0	0.0347	8.4E-1
2.455E-1	1.980E3	5.051E0	0.0358	8.5E-1
2.442E-1	1.970E3	5.077E0	0.0370	8.6E-1
2.430E-1	1.960E3	5.103E0	0.0382	8.7E-1
2.418E-1	1.950E3	5.129E0	0.0395	8.8E-1
2.405E-1	1.940E3	5.156E0	0.0409	8.9E-1
2.393E-1	1.930E3	5.182E0	0.0423	9.0E-1
2.380E-1	1.920E3	5.209E0	0.0439	9.2E-1
2.368E-1	1.910E3	5.237E0	0.0455	9.3E-1
2.365E-1	1.907E3	5.244E0	1.4657 [7]	4.1E-2 [7]
2.356E-1	1.900E3	5.264E0	0.0472 [6]	9.4E-1 [6]
2.343E-1	1.890E3	5.292E0	0.0491	9.5E-1
2.331E-1	1.880E3	5.320E0	0.0511	9.7E-1
2.318E-1	1.870E3	5.349E0	0.0532	9.8E-1
2.306E-1	1.860E3	5.377E0	0.0555	9.9E-1
2.294E-1	1.850E3	5.406E0	0.0579	1.0E0
2.281E-1	1.840E3	5.436E0	0.0605	1.0E0
2.269E-1	1.830E3	5.465E0	0.0633	1.0E0
2.256E-1	1.820E3	5.496E0	0.0663	1.1E0
2.244E-1	1.810E3	5.526E0	0.0696	1.1E0
2.241E-1	1.808E3	5.532E0	1.2721 [7]	5.6E-2 [7]
2.232E-1	1.800E3	5.557E0	0.0732 [6]	1.1E0 [6]

(continued)

TABLE II *(Continued)*

Hexagonal BN

eV	cm^{-1}	μm	n	k
2.219E-1	1.790E3	5.588E0	0.0771	1.1E0
2.207E-1	1.780E3	5.619E0	0.0813	1.1E0
2.194E-1	1.770E3	5.651E0	0.0860	1.2E0
2.182E-1	1.760E3	5.683E0	0.0911	1.2E0
2.170E-1	1.750E3	5.715E0	0.0967	1.2E0
2.157E-1	1.740E3	5.748E0	0.1029	1.2E0
2.145E-1	1.730E3	5.781E0	0.1098	1.2E0
2.132E-1	1.720E3	5.815E0	0.1175	1.3E0
2.125E-1	1.714E3	5.836E0	0.9780 [7]	8.3E-2 [7]
2.120E-1	1.710E3	5.849E0	0.1261 [6]	1.3E0 [6]
2.108E-1	1.700E3	5.883E0	0.1358	1.3E0
2.095E-1	1.690E3	5.918E0	0.1469	1.4E0
2.083E-1	1.680E3	5.953E0	0.1594	1.4E0
2.070E-1	1.670E3	5.989E0	0.1739	1.4E0
2.058E-1	1.660E3	6.025E0	0.1906	1.5E0
2.046E-1	1.650E3	6.062E0	0.2101	1.5E0
2.033E-1	1.640E3	6.099E0	0.2330	1.6E0
2.021E-1	1.630E3	6.136E0	0.2603	1.6E0
2.014E-1	1.624E3	6.157E0	0.9087 [7]	7.4E-1 [7]
2.008E-1	1.620E3	6.174E0	0.2930 [6]	1.7E0 [6]
1.996E-1	1.610E3	6.212E0	0.3329	1.8E0
1.984E-1	1.600E3	6.251E0	0.3821	1.8E0
1.971E-1	1.590E3	6.290E0	0.4437	1.9E0
1.959E-1	1.580E3	6.330E0	0.5220	2.0E0
1.946E-1	1.570E3	6.371E0	0.6230	2.1E0
1.934E-1	1.560E3	6.411E0	0.7549	2.2E0
1.922E-1	1.550E3	6.453E0	0.9284	2.3E0
1.909E-1	1.540E3	6.495E0	1.1541	2.4E0
1.909E-1	1.540E3	6.495E0	1.4838 [7]	1.1E0 [7]
1.897E-1	1.530E3	6.537E0	1.4357 [6]	2.4E0 [6]
1.884E-1	1.520E3	6.580E0	1.7536	2.3E0
1.872E-1	1.510E3	6.624E0	2.0515	2.1E0
1.860E-1	1.500E3	6.668E0	2.2592	1.8E0
1.847E-1	1.490E3	6.713E0	2.3459	1.5E0
1.835E-1	1.480E3	6.758E0	2.3346	1.2E0
1.822E-1	1.470E3	6.804E0	2.2666	9.6E-1
1.810E-1	1.460E3	6.851E0	2.1738	7.8E-1
1.810E-1	1.460E3	6.852E0	1.8762 [7]	1.2E0 [7]
1.798E-1	1.450E3	6.898E0	2.0746 [6]	6.5E-1 [6]
1.785E-1	1.440E3	6.946E0	1.9778	5.4E-1
1.773E-1	1.430E3	6.994E0	1.8871	4.6E-1
1.760E-1	1.420E3	7.044E0	1.8035	4.0E-1
1.748E-1	1.410E3	7.094E0	1.7270	3.5E-1
1.736E-1	1.400E3	7.144E0	1.6572	3.1E-1
1.723E-1	1.390E3	7.196E0	1.5934	2.7E-1
1.715E-1	1.384E3	7.229E0	3.2662 [7]	3.0E-1 [7]
1.711E-1	1.380E3	7.248E0	1.5348 [6]	2.4E-1 [6]

TABLE II *(Continued)*

Hexagonal BN

eV	cm^{-1}	μm	n	k
1.698E-1	1.370E3	7.301E0	1.4808	2.2E-1
1.686E-1	1.360E3	7.354E0	1.4310	2.0E-1
1.674E-1	1.350E3	7.409E0	1.3847	1.8E-1
1.661E-1	1.340E3	7.464E0	1.3415	1.7E-1
1.649E-1	1.330E3	7.520E0	1.3010	1.6E-1
1.636E-1	1.320E3	7.577E0	1.2629	1.5E-1
1.626E-1	1.311E3	7.626E0	2.5572 [7]	9.5E-2 [7]
1.624E-1	1.310E3	7.635E0	1.2270 [6]	1.4E-1 [6]
1.612E-1	1.300E3	7.694E0	1.1929	1.3E-1
1.599E-1	1.290E3	7.753E0	1.1604	1.2E-1
1.587E-1	1.280E3	7.814E0	1.1293	1.1E-1
1.575E-1	1.270E3	7.875E0	1.0995	1.1E-1
1.562E-1	1.260E3	7.938E0	1.0707	1.0E-1
1.550E-1	1.250E3	8.001E0	1.0429	9.7E-2
1.541E-1	1.243E3	8.045E0	2.3066 [7]	5.2E-2 [7]
1.537E-1	1.240E3	8.066E0	1.0159 [6]	9.2E-2 [6]
1.525E-1	1.230E3	8.132E0	0.9896	8.8E-2
1.513E-1	1.220E3	8.198E0	0.9637	8.5E-2
1.500E-1	1.210E3	8.266E0	0.9383	8.2E-2
1.488E-1	1.200E3	8.335E0	0.9133	7.9E-2
1.475E-1	1.190E3	8.405E0	0.8884	7.6E-2
1.463E-1	1.180E3	8.476E0	0.8636	7.4E-2
1.461E-1	1.178E3	8.487E0	2.1397 [7]	1.5E-2 [7]
1.451E-1	1.170E3	8.549E0	0.8387 [6]	7.2E-2 [6]
1.438E-1	1.160E3	8.622E0	0.8137	7.1E-2
1.426E-1	1.150E3	8.697E0	0.7883	6.9E-2
1.413E-1	1.140E3	8.774E0	0.7625	6.8E-2
1.401E-1	1.130E3	8.851E0	0.7361	6.7E-2
1.389E-1	1.120E3	8.930E0	0.7089	6.7E-2
1.385E-1	1.117E3	8.954E0	2.0910 [7]	1.8E-2 [7]
1.376E-1	1.110E3	9.011E0	0.6806 [6]	6.7E-2 [6]
1.364E-1	1.100E3	9.093E0	0.6510	6.7E-2
1.351E-1	1.090E3	9.176E0	0.6198	6.8E-2
1.339E-1	1.080E3	9.261E0	0.5865	6.9E-2
1.327E-1	1.070E3	9.348E0	0.5506	7.1E-2
1.314E-1	1.060E3	9.436E0	0.5115	7.4E-2
1.313E-1	1.059E3	9.446E0	2.0411 [7]	2.1E-2 [7]
1.302E-1	1.050E3	9.526E0	0.4680 [6]	7.9E-2 [6]
1.289E-1	1.040E3	9.617E0	0.4189	8.6E-2
1.277E-1	1.030E3	9.711E0	0.3619	9.8E-2
1.265E-1	1.020E3	9.806E0	0.2943	1.2E-1
1.252E-1	1.010E3	9.903E0	0.2159	1.6E-1
1.244E-1	1.004E3	9.965E0	1.9899 [7]	2.5E-2 [7]
1.240E-1	1.000E3	1.000E1	0.1460 [6]	2.3E-1 [6]
1.227E-1	9.900E2	1.010E1	0.1060	3.2E-1
1.215E-1	9.800E2	1.021E1	0.0848	4.0E-1
1.203E-1	9.700E2	1.031E1	0.0721	4.7E-1

(continued)

TABLE II *(Continued)*

Hexagonal BN

eV	cm^{-1}	μm	n	k
1.190E-1	9.600E2	1.042E1	0.0637	5.4E-1
1.180E-1	9.514E2	1.051E1	1.9374 [7]	2.9E-2 [7]
1.178E-1	9.500E2	1.053E1	0.0579 [6]	6.1E-1 [6]
1.165E-1	9.400E2	1.064E1	0.0539	6.8E-1
1.153E-1	9.300E2	1.075E1	0.0511	7.5E-1
1.141E-1	9.200E2	1.087E1	0.0494	8.2E-1
1.128E-1	9.100E2	1.099E1	0.0486	9.0E-1
1.118E-1	9.019E2	1.109E1	1.8669 [7]	3.8E-2 [7]
1.116E-1	9.000E2	1.111E1	0.0487 [6]	9.7E-1 [6]
1.103E-1	8.900E2	1.124E1	0.0499	1.1E0
1.091E-1	8.800E2	1.137E1	0.0521	1.2E0
1.079E-1	8.700E2	1.150E1	0.0559	1.3E0
1.066E-1	8.600E2	1.163E1	0.0616	1.4E0
1.060E-1	8.549E2	1.170E1	1.7817 [7]	9.8E-2 [7]
1.054E-1	8.500E2	1.177E1	0.0703 [6]	1.5E0 [6]
1.041E-1	8.400E2	1.191E1	0.0837	1.7E0
1.029E-1	8.300E2	1.205E1	0.1053	1.9E0
1.017E-1	8.200E2	1.220E1	0.1430	2.2E0
1.005E-1	8.104E2	1.234E1	1.6951 [7]	1.7E-1 [7]
1.004E-1	8.100E2	1.235E1	0.2187 [6]	2.6E0 [6]
9.918E-2	8.000E2	1.250E1	0.4147	3.3E0
9.794E-2	7.900E2	1.266E1	1.3238	4.8E0
9.670E-2	7.800E2	1.282E1	5.8255	2.9E0
9.546E-2	7.700E2	1.299E1	3.9641	5.7E-1
9.523E-2	7.682E2	1.302E1	2.0660 [7]	2.6E-1 [7]
9.422E-2	7.600E2	1.316E1	3.0979 [6]	2.5E-1 [6]
9.298E-2	7.500E2	1.334E1	2.6422	1.5E-1
9.174E-2	7.400E2	1.352E1	2.3552	9.9E-2
9.050E-2	7.300E2	1.370E1	2.1550	7.3E-2
9.027E-2	7.281E2	1.374E1	2.0118 [7]	8.3E-2 [7]
8.926E-2	7.200E2	1.389E1	2.0058 [6]	5.7E-2 [6]
8.802E-2	7.100E2	1.409E1	1.8895	4.6E-2
8.678E-2	7.000E2	1.429E1	1.7958	3.9E-2
8.557E-2	6.902E2	1.449E1	1.9709 [7]	6.9E-2 [7]
8.554E-2	6.900E2	1.450E1	1.7184 [6]	3.3E-2 [6]
8.430E-2	6.800E2	1.471E1	1.6532	2.9E-2
8.306E-2	6.700E2	1.493E1	1.5973	2.5E-2
8.182E-2	6.600E2	1.515E1	1.5489	2.3E-2
8.111E-2	6.543E2	1.529E1	1.9582 [7]	5.6E-2 [7]
8.059E-2	6.500E2	1.539E1	1.5063 [6]	2.1E-2 [6]
7.935E-2	6.400E2	1.563E1	1.4687	1.9E-2
7.811E-2	6.300E2	1.588E1	1.4350	1.7E-2
7.689E-2	6.202E2	1.613E1	1.9517 [7]	5.8E-2 [7]
7.687E-2	6.200E2	1.613E1	1.4048 [6]	1.6E-2 [6]
7.563E-2	6.100E2	1.640E1	1.3774	1.5E-2
7.439E-2	6.000E2	1.667E1	1.3525	1.4E-2
7.315E-2	5.900E2	1.695E1	1.3297	1.3E-2

TABLE II *(Continued)*

Hexagonal BN

eV	cm^{-1}	μm	n	k
7.288E-2	5.879E2	1.701E1	1.9451 [7]	6.1E-2 [7]
7.191E-2	5.800E2	1.724E1	1.3087 [6]	1.2E-2 [6]
7.067E-2	5.700E2	1.755E1	1.2895	1.2E-2
6.943E-2	5.600E2	1.786E1	1.2716	1.1E-2
6.909E-2	5.572E2	1.795E1	1.9385 [7]	6.3E-2 [7]
6.819E-2	5.500E2	1.819E1	1.2551 [6]	1.1E-2 [6]
6.695E-2	5.400E2	1.852E1	1.2396	1.0E-2
6.571E-2	5.300E2	1.887E1	1.2253	9.6E-3
6.549E-2	5.282E2	1.893E1	1.9319 [7]	6.6E-2 [7]
6.447E-2	5.200E2	1.923E1	1.2118 [6]	9.2E-3 [6]
6.323E-2	5.100E2	1.961E1	1.1992	8.8E-3
6.208E-2	5.007E2	1.998E1	1.9260 [7]	6.8E-2 [7]
6.199E-2	5.000E2	2.000E1	1.1874 [6]	8.4E-3 [6]
6.075E-2	4.900E2	2.041E1	1.1763	8.1E-3
5.951E-2	4.800E2	2.084E1	1.1658	7.7E-3
5.884E-2	4.746E2	2.107E1	1.9216 [7]	6.4E-2 [7]
5.827E-2	4.700E2	2.128E1	1.1559 [6]	7.4E-3 [6]
5.703E-2	4.600E2	2.174E1	1.1466	7.1E-3
5.579E-2	4.500E2	2.223E1	1.1377	6.9E-3
5.578E-2	4.499E2	2.223E1	1.9172 [7]	6.0E-2 [7]
5.455E-2	4.400E2	2.273E1	1.1294 [6]	6.6E-3 [6]
5.331E-2	4.300E2	2.326E1	1.1214	6.4E-3
5.287E-2	4.265E2	2.345E1	1.9128 [7]	5.6E-2 [7]
5.207E-2	4.200E2	2.381E1	1.1139 [6]	6.1E-3 [6]
5.083E-2	4.100E2	2.439E1	1.1068	5.9E-3
5.012E-2	4.043E2	2.474E1	1.9084 [7]	5.2E-2 [7]
4.959E-2	4.000E2	2.500E1	1.1000 [6]	5.7E-3 [6]
4.835E-2	3.900E2	2.565E1	1.0935	5.5E-3
4.711E-2	3.800E2	2.632E1	1.0874	5.3E-3
4.587E-2	3.700E2	2.703E1	1.0816	5.1E-3
4.463E-2	3.600E2	2.778E1	1.0760	4.9E-3
4.339E-2	3.500E2	2.858E1	1.0707	4.7E-3
4.215E-2	3.400E2	2.942E1	1.0657	4.5E-3
4.091E-2	3.300E2	3.031E1	1.0609	4.3E-3
3.967E-2	3.200E2	3.126E1	1.0563	4.2E-3
3.843E-2	3.100E2	3.226E1	1.0520	4.0E-3
3.719E-2	3.000E2	3.334E1	1.0479	3.9E-3

Cadmium Germanium Arsenide ($CdGeAs_2$)

J. C. RIFE*
Naval Research Laboratory
Washington, D.C.

$CdGeAs_2$ is a tetragonally bonded semiconductor with the chalcopyrite structure and a direct band gap of 0.57 eV at room temperature. The structure, growth, and optical and electronic properties of the chalcopyrite semiconductors have been reviewed in the book by Shay and Wernick [1]. Properties have also been summarized in the Landolt–Börnstein series [2]. The II–IV–V_2 chalcopyrite lattice is equivalent to the III–V semiconductor crystal structure, but with ordering of the II and IV components and so a doubling of the unit cell along the *c*-axis. The chalcopyrite lattice is typically compressed along the *c*-axis, leading to a crystalline electric field and birefringence with n_e ($\mathbf{E} \| \mathbf{c}$) > n_o ($\mathbf{E} \perp \mathbf{c}$) (positive uniaxial crystal). Chalcopyrite semiconductors are also optically active because of varying degrees of tetragonal distortion [3]. The $CdGeAs_2$ crystal structure, in particular, is compressed 5.6% along the *c*-axis. Studies of the crystalline and amorphous phases of $CdGeAs_2$ show that the amorphous phase has a density 2.5% higher [4]. The band structure of $CdGeAs_2$ has been discussed by several authors [5–7].

Since $CdGeAs_2$ has a large nonlinear coefficient due to its covalent bonding and can be phase-matched because of its birefringence, it is of great interest for second-harmonic generation. A 27% energy-conversion efficiency has been obtained in doubling the 10.6-μm CO_2 laser [8]. Fourth-harmonic generation has also been reported [9].

The optical constants, *n* and *k*, listed in Table I and plotted in Fig. 1 are derived from sources discussed in more detail later. The optical constants were taken from tables, calculated from formulae, or extracted from graphs where necessary. The table has more significant figures than justified by the

* The views presented are those of the author and do not represent the views of the Department of Defense or its components.

HANDBOOK OF OPTICAL CONSTANTS OF SOLIDS III ISBN 0-12-544423-0/$25.00.

extraction in some cases; consult the original work for the actual experimental resolution. Measurements made using polarized radiation were favored for inclusion here; in such cases, the optical constants have been given for both $\mathbf{E} \| \mathbf{c}$ and $\mathbf{E} \perp \mathbf{c}$. All measurements used were made on single crystals at room temperature, except where noted in the text. The discussion of measurements below gives references to additional work on polycrystalline or amorphous specimens.

I X-RAY TO BAND-GAP ABSORPTION EDGE

The optical constants, n and k, for the range from 10,000 to 11 eV have been calculated from the scattering factors of the elements of Henke *et al.* [10] using the compound formula and a density of 5.58 gm/cm^3 [4]. In Fig. 1, the K-edge ($1s$) transitions of As and Ge appear at 1.0 and 1.1×10^{-4} μm; the $L_{2,3}$ ($2p$) transitions of Cd at 3.3×10^{-4} μm and those of As and Ge near 1×10^{-3} μm; and the $M_{4,5}$ ($3d$) transitions of Cd at 3.0×10^{-3} μm. The calculated edges are a good approximation on the scale of Fig. 1, but the scatttering factors of the elements cannot predict the compound edge locations or structure to high degree (edge within 5 or 10 eV) because of core-level chemical shifts and bonding-dependent redistribution of the absorption at and just above the edges.

Optical constants for the 11- to 1-eV range have been taken from Goryunova *et al.* [11]. They extracted optical constants for single-crystal and amorphous samples from a Kramers-Kronig analysis of unpolarized, room-temperature reflectance data. Zlatkin *et al.* subsequently made polarized reflectance measurements from 5.5 to 1.5 eV at 195 and 100 K that showed relatively small but significant polarization-dependent structure, but they reported no optical constants [12]. Artus *et al.* made unpolarized reflectance measurements from 25 to 1.2 eV, but derived no optical constants [13]. Their data are similar to previous room-temperature results, but with more structure at lower energy, and show a smooth fall-off above 8 eV in contrast to the results of Goryunova *et al.*

II BAND-GAP ABSORPTION EDGE

Measurements of the absorption coefficient at the absorption edge have been reported by a number of authors. Isomura *et al.* give the absorption coefficient ($\alpha = 4\pi k/\lambda$) for $\mathbf{E} \| \mathbf{c}$ and $\mathbf{E} \perp \mathbf{c}$ from 0.73 to 0.5 eV and derive values of the energy gap in good agreement with those obtained using elec-

troreflectance [14]. Hong *et al.* give the absorption coefficient from 0.8 to 0.123 eV for polycrystalline and amorphous specimens [15]. Madelon *et al.* present the near-edge absorption coefficient for four temperatures from 4.2 to 260 K [16]. Bendorius *et al.* give the pressure dependence of the edge [17]. Several other absorption edge measurements of the amorphous state have also been reported [18, 19].

BAND GAP III

In the transparent gap region from the energy gap at 2.2 to 18 μm where the two-phonon lattice absorption sets in, the index of refraction for $\mathbf{E} \| \mathbf{c}$ and $\mathbf{E} \perp \mathbf{c}$ has been reported by Boyd *et al.* [20]. They determined the index by the minimum-deviation method; however, results for other individual crystals could vary slightly from their results, depending on doping. Their data have been reduced to an analog formula by Wemple *et al.* [21] and by Bhar [22]. The latter finds a good fit to a special Sellmeier form,

$$n^2 = A + \frac{B}{1 - \dfrac{C}{\lambda^2}} + \frac{D}{1 - \dfrac{E}{\lambda^2}},$$

where for n_o $(A,B,C,D,E) = (10.1064, 2.2988, 1.0872, 1.6247, 1370)$ and for n_e $(A,B,C,D,E) = (11.8018, 1.2152, 2.6971, 1.6922, 1370)$; λ is the wavelength in microns.

Absorption in the gap region is sensitive to impurities and doping. Iseler *et al.* [8] observe, for *p*-type doped crystals, a residual shoulder on the intrinsic absorption edge for wavelengths up to 5.5 μm, an absorption band near 5.5 μm due to valence-band hole transitions in the *p*-type material that disappears in going from temperatures of 300 to 77 K, and three-phonon absorption at 13.5 μm. Absorption in *n*-type crystals is a minimum at the band edge and rises from there because of free-electron intraband transitions [7]. The shoulder at 5.5 μm could present a difficulty for second-harmonic generation. In that regard, Barnes *et al.* [23] measured the temperature dependence of the absorption coefficient at 10.6 μm and the index of refraction at 5.6 μm; however, their absorption coefficient was an order of magnitude larger than that determined by Iseler *et al.* Mamedov and Osmanov [24] also observed the temperature dependence in *p*-type samples and an impurity absorption at 9.5 μm. Boyd *et al.* [20] measured the gap absorption as well, but their measurements were limited on the low-absorption side by sample size.

IV LATTICE ABSORPTION IN THE INFRARED

Transmission in the two-phonon lattice absorption region from 13 to 25 μm was measured by Boltovets *et al.* [25], but the absorption coefficient is not given. The optical constants for $\mathbf{E} \| \mathbf{c}$ and $\mathbf{E} \perp \mathbf{c}$ in the one-phonon region from 20 to 200 μm were derived by dispersion analysis from polarized reflectivity measurements by Holah *et al.* [26]. With j harmonic oscillators, the formula for the dielectric constant $\epsilon(\nu)$ is

$$\epsilon(\nu) = \epsilon_\infty + \sum_j \frac{S_j \nu^2{}_j}{(\nu^2{}_j - \nu^2 - i\nu\gamma_j},$$

where S_j is the oscillator strength, ν_j the frequency in cm^{-1}, and γ_j the damping of the jth oscillator in cm^{-1}. For $\mathbf{E} \| \mathbf{c}$, Holah *et al.* derive the two oscillators $(S_j, \nu_j, \gamma_j) = (1.06, 270, 5.6)$ and $(1.40, 203, 7.6)$ with $\epsilon_\infty = 15.4$; and for $\mathbf{E} \perp \mathbf{c}$, they give the five oscillators $(S_j, \nu_j, \gamma_j) = (1.07, 272, 4.0)$, $(0.10, 255, 4.5)$, $(1.12, 200, 12.7)$, $(0.39, 159, 4.5)$, and $(0.28, 95, 5.0)$ with $\epsilon_\infty = 15.2$. The analysis yields an ϵ_0 of 17.9 for $\mathbf{E} \| \mathbf{c}$ and 18.2 for $\mathbf{E} \perp \mathbf{c}$. Their data are given in the graph and table. Zlatkin *et al.* [27] and Goryunova *et al.* [11] previously had measured the lattice reflectivity with unpolarized light and derived the optical constants from 20 to 80 μm for single-crystal and amorphous specimens. They obtained a ϵ_∞ of 14.3 and a ϵ_0 of 18.7. More recently, Hong *et al.* reported the optical constants from unpolarized reflectance and transmission measurements from 18 to 200 μm for polycrystalline and amorphous samples [15]. The phonon frequencies have been calculated for $CdGeAs_2$ by Antropova *et al.* [28].

REFERENCES

1. J. L. Shay and J. H. Wernick, "Ternary Chalcopyrite Semiconductors: Growth, Electronic Properties, and Applications." Pergamon, New York, 1975.
2. Landolt-Börnstein, "Semiconductors—Physics of Ternary Compounds" (K.-H. Hellwege and O. Madelung, eds.), Vol. 17h. Springer-Verlag, New York, 1985.
3. G. A. Babonas, A. S. Martsinkyavichyus, and A. Yu. Shileika, *Sov. Phys. J.* **29**, 617 (1986).
4. L. Červinka, R. Hosemann, and W. Vogel, *J. Non-Cryst. Solids* **3**, 294 (1970).
5. N. A. Goryunova, A. S. Poplavnoi, Yu. I. Polygalov, and V. A. Chaldyshev, *Phys. Status Solidi* **39 B**, 9 (1970).
6. J. L. Shay and E. Buehler, *Phys. Rev. B* **3**, 2598 (1971).
7. H. Kidal, *Phys. Rev. B* **10**, 5082 (1974).
8. G. W. Iseler, H. Kildal, and N. Menyuk, *J. Electron Mater.* **7**, 737 (1978).
9. H. Kildal and G. W. Iseler, *Phys. Rev. B* **19**, 5218 (1979).
10. B. L. Henke, P. Lee, T. J. Tanaka, R. L. Shimabukuro, and B. J. Fujikawa, *At. Data Nucl. Data Tables* **27** (1982); B. L. Henke, J. C. Davis, E. M. Gullikson, and R. C. C. Perera, *Lawrence Berkeley Laboratory Report* **LBL-26259** (1988).
11. N. A. Goryunova, E. F. Gross, L. B. Zlatkin, and E. K. Ivanov, *J. Non-Cryst. Solids* **4**, 57 (1970).

12. L. B. Zlatkin, E. K. Ivanov, G. F. Karavaev, and V. A. Chaldyshev, *Sov. Phys. Semicond. (Engl. Transl.)* **5**, 1794 (1972).
13. L. Artus, Y. Bertand, C. Ance, and A. Lopez-Soler, *Solid State Commun.* **57**, 649 (1986).
14. S. Isomura, S. Takahashi, and K. Masumoto, *Jpn. J. Appl. Phys.* **16,** 1723 (1977).
15. K. S. Hong, R. F. Speyer, and R. A. Condrate, Sr., *J. Phys. Chem. Solids* **51**, 969 (1990).
16. R. Madelon, M. Shaimi, A. Hairie, E. Paumier, and B. Mercey, *Solid State Commun.* **50**, 545 (1984).
17. R. Bendorius, V. D. Prochukhan, and A. Šileika, *Phys. Status Solidi B* **53,** 745 (1972).
18. V. Vorlíček, *Phys. Status Solidi B* **67**, 731 (1975).
19. V. D. Okunev and A.G. Yurov, *Sov. Tech. Phys. Lett.* **5**(2), 64 (1979).
20. G. D. Boyd, E. Buehler, F. G. Storz, and J. H. Wernick, *IEEE J. Quantum Electron.* **QE-8**, 419 (1972).
21. S. H. Wemple, J. D. Gabbe, and G. D. Boyd, *J. Appl. Phys.* **46,** 3597 (1975).
22. G. C. Bhar, *Appl. Opt.* **15**, 305 (1976).
23. N. P. Barnes, R. C. Eckhardt, D. J. Gettemy, and L. B. Edgett, *IEEE J. Quantum Electron.* **QE-15**, 1074 (1979).
24. B. Kh. Mamedov and É. O. Osmanov, *Sov. Phys. Semicond. (Engl. Transl.)* **5**, 1120 (1972).
25. N. S. Boltovets, B. Kh. Mamedov, and É. O. Osmanov, *Sov. Phys. Semicond. (Engl. Transl.)* **4**, 499 (1970).
26. G. D. Holah, A. Miller, W. D. Dunnett, and G. W. Iseler, *Solid State Commun.* **23**, 75 (1977).
27. L. B. Zlatkin, Yu. F. Markov, A. I. Stekhanov, and M. S. Shur, *J. Phys. Chem. Solids* **31**, 567 (1970).
28. E. V. Antropova, A. A. Kopytov, and A. S. Poplavnoi, *Opt. Spectrosc.* **64**, 766 (1988).

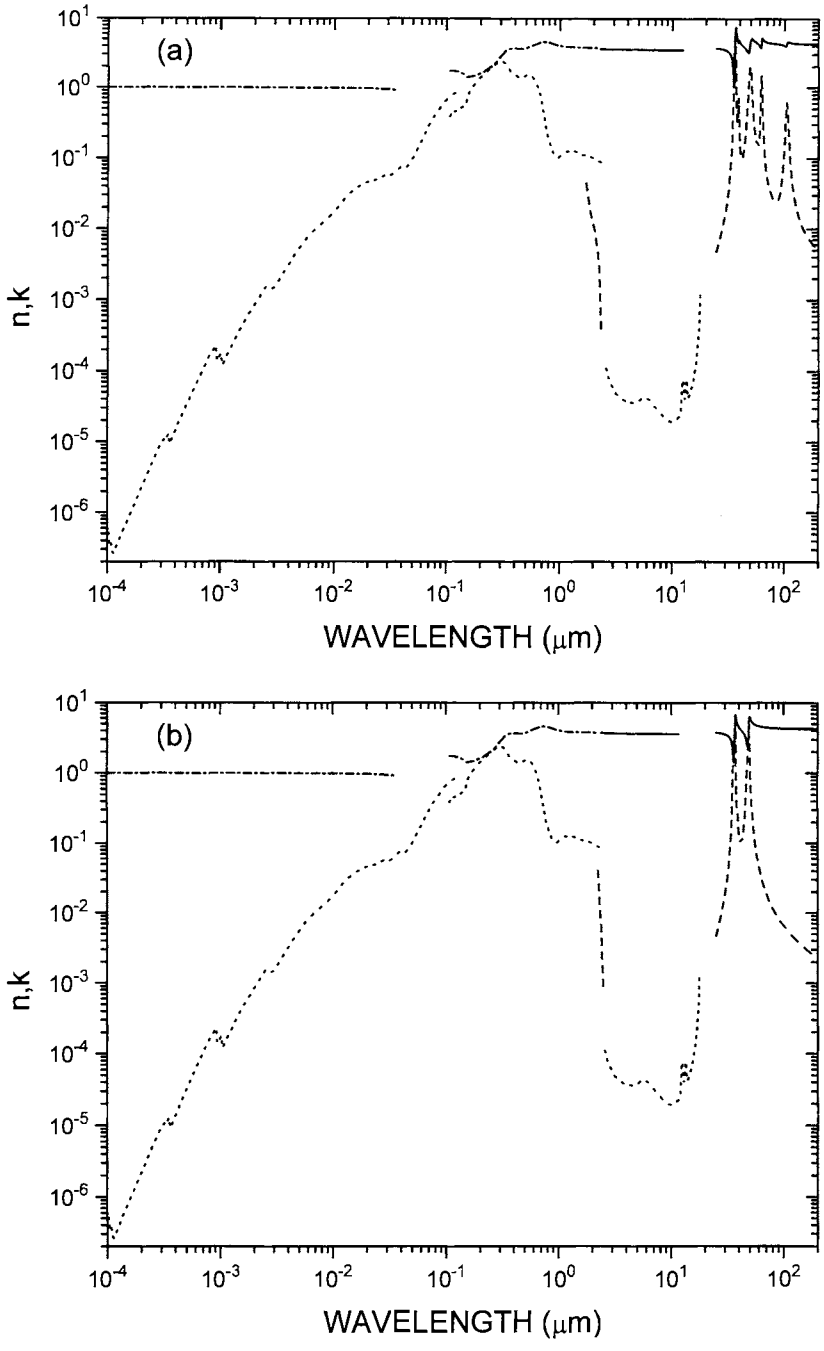

Fig. 1. (a) Log–log plot of n_o (solid line) and k_o (dashed line), $\mathbf{E}\perp\mathbf{c}$, versus wavelength for $CdGeAs_2$. (b) Log–log plot of n_e (solid line) and k_e (dashed line), $\mathbf{E}\parallel\mathbf{c}$, versus wavelength for $CdGeAs_2$. Unpolarized n (dash-dot line) and k (dotted line) are plotted on both graphs, where polarized data was not available.

TABLE I

Values of n and k for $CdGeAs_2$ Obtained from Various References[a]

eV	cm^{-1}	μm	1-n	k
			[10]	[10]
3.000E4	2.420E8	4.133E-5	1.13E-6	4.01E-8
2.010E4	1.622E8	6.167E-5	2.50E-6	9.51E-8
1.277E4	1.030E8	9.708E-5	6.02E-6	5.06E-7
1.243E4	1.003E8	9.971E-5	6.26E-6	5.57E-7
1.211E4	9.766E7	1.024E-4	6.50E-6	6.13E-7
1.179E4	9.506E7	1.052E-4	6.68E-6	3.44E-7
1.148E4	9.259E7	1.080E-4	7.21E-6	3.79E-7
1.118E4	9.017E7	1.109E-4	7.57E-6	2.81E-7
1.088E4	8.772E7	1.140E-4	8.11E-6	2.61E-7
1.060E4	8.547E7	1.170E-4	8.64E-6	2.89E-7
1.005E4	8.104E7	1.234E-4	9.66E-6	3.56E-7
8.114E3	6.545E7	1.528E-4	1.51E-5	8.02E-7
6.048E3	4.878E7	2.050E-4	2.73E-5	2.38E-6
4.053E3	3.269E7	3.059E-4	5.79E-5	1.02E-5
3.843E3	3.100E7	3.226E-4	6.38E-5	1.13E-5
3.741E3	3.018E7	3.314E-4	6.62E-5	1.25E-5
3.643E3	2.939E7	3.403E-4	6.93E-5	1.17E-5
3.548E3	2.861E7	3.495E-4	7.06E-5	1.29E-5
3.454E3	2.786E7	3.590E-4	7.74E-5	9.24E-6
3.363E3	2.712E7	3.687E-4	8.30E-5	1.02E-5
3.274E3	2.641E7	3.787E-4	8.83E-5	1.13E-5
3.023E3	2.438E7	4.102E-4	1.05E-4	1.53E-5
2.025E3	1.633E7	6.122E-4	2.29E-4	6.49E-5
1.510E3	1.218E7	8.210E-4	3.43E-4	1.64E-4
1.432E3	1.155E7	8.661E-4	3.66E-4	1.94E-4
1.394E3	1.124E7	8.895E-4	3.68E-4	2.10E-4
1.357E3	1.095E7	9.135E-4	3.56E-4	2.28E-4
1.321E3	1.066E7	9.383E-4	2.90E-4	1.38E-4
1.287E3	1.038E7	9.637E-4	3.76E-4	1.50E-4
1.253E3	1.010E7	9.897E-4	4.05E-4	1.62E-4
1.220E3	9.843E6	1.016E-3	4.07E-4	1.76E-4
1.188E3	9.579E6	1.044E-3	4.64E-4	1.20E-4
1.157E3	9.328E6	1.072E-3	5.13E-4	1.31E-4
1.012E3	8.163E6	1.225E-3	7.16E-4	2.04E-4
9.096E2	7.337E6	1.363E-3	8.92E-4	2.88E-4
7.958E2	6.418E6	1.558E-3	1.14E-3	4.36E-4
6.096E2	4.916E6	2.034E-3	1.75E-3	8.70E-4
4.922E2	3.970E6	2.519E-3	2.24E-3	1.52E-3
4.666E2	3.764E6	2.657E-3	2.24E-3	1.48E-3
4.543E2	3.664E6	2.729E-3	2.36E-3	1.44E-3
4.425E2	3.569E6	2.802E-3	2.51E-3	1.43E-3
4.308E2	3.475E6	2.878E-3	2.69E-3	1.44E-3
4.194E2	3.383E6	2.956E-3	2.88E-3	1.47E-3
4.084E2	3.294E6	3.036E-3	3.11E-3	1.52E-3
3.480E2	2.807E6	3.563E-3	4.35E-3	2.31E-3

(continued)

[a] References given in brackets.

TABLE I *(Continued)*

$CdGeAs_2$

eV	cm^{-1}	μm	1-n	k
			[10]	[10]
1.987E2	1.602E6	6.241E-3	9.12E-3	8.53E-3
1.521E2	1.227E6	8.150E-3	1.23E-2	1.27E-2
1.020E2	8.224E5	1.216E-2	2.16E-2	2.59E-2
4.959E1	4.000E5	2.500E-2	4.04E-2	5.14E-2
3.067E1	2.474E5	4.042E-2	1.11E-1	7.45E-2
2.001E1	1.614E5	6.195E-2		1.93E-1
1.492E1	1.204E5	8.308E-2		4.48E-1
9.999E0	8.065E4	1.240E-1		8.76E-1
eV	cm^{-1}	μm	n	k
			[11]	[11]
1.140E1	9.191E4	1.088E-1	1.75E0	4.03E-1
1.120E1	9.033E4	1.107E-1	1.74E0	4.30E-1
1.100E1	8.873E4	1.127E-1	1.74E0	4.16E-1
1.080E1	8.711E4	1.148E-1	1.72E0	4.28E-1
1.060E1	8.547E4	1.170E-1	1.71E0	4.41E-1
1.040E1	8.389E4	1.192E-1	1.71E0	4.54E-1
1.020E1	8.224E4	1.216E-1	1.70E0	4.67E-1
9.999E0	8.065E4	1.240E-1	1.69E0	4.66E-1
9.801E0	7.905E4	1.265E-1	1.69E0	4.79E-1
9.596E0	7.740E4	1.292E-1	1.66E0	4.92E-1
9.400E0	7.582E4	1.319E-1	1.65E0	5.05E-1
9.198E0	7.418E4	1.348E-1	1.62E0	5.18E-1
8.997E0	7.257E4	1.378E-1	1.59E0	5.17E-1
8.800E0	7.097E4	1.409E-1	1.56E0	5.57E-1
8.598E0	6.935E4	1.442E-1	1.53E0	5.83E-1
8.400E0	6.775E4	1.476E-1	1.49E0	5.83E-1
8.200E0	6.614E4	1.512E-1	1.44E0	6.49E-1
7.999E0	6.452E4	1.550E-1	1.37E0	7.57E-1
7.798E0	6.289E4	1.590E-1	1.38E0	8.51E-1
7.602E0	6.131E4	1.631E-1	1.43E0	9.58E-1
7.402E0	5.970E4	1.675E-1	1.45E0	9.85E-1
7.200E0	5.807E4	1.722E-1	1.44E0	1.05E0
7.001E0	5.647E4	1.771E-1	1.47E0	1.12E0
6.801E0	5.485E4	1.823E-1	1.50E0	1.20E0
6.598E0	5.322E4	1.879E-1	1.54E0	1.27E0
6.401E0	5.163E4	1.937E-1	1.56E0	1.33E0
6.199E0	5.000E4	2.000E-1	1.62E0	1.40E0
6.001E0	4.840E4	2.066E-1	1.66E0	1.48E0
5.799E0	4.677E4	2.138E-1	1.70E0	1.56E0
5.600E0	4.517E4	2.214E-1	1.77E0	1.65E0
5.400E0	4.355E4	2.296E-1	1.83E0	1.74E0
5.201E0	4.195E4	2.384E-1	1.90E0	1.82E0
4.999E0	4.032E4	2.480E-1	2.01E0	1.94E0
4.800E0	3.871E4	2.583E-1	2.10E0	2.04E0

TABLE I *(Continued)*

$CdGeAs_2$

eV	cm^{-1}	μm	n	k		
			[11]	[11]		
4.601E0	3.711E4	2.695E-1	2.24E0	2.15E0		
4.400E0	3.549E4	2.818E-1	2.45E0	2.27E0		
4.200E0	3.388E4	2.952E-1	2.72E0	2.34E0		
4.000E0	3.226E4	3.100E-1	3.06E0	2.37E0		
3.800E0	3.065E4	3.263E-1	3.32E0	2.28E0		
3.600E0	2.904E4	3.444E-1	3.55E0	2.01E0		
3.400E0	2.742E4	3.647E-1	3.65E0	1.73E0		
3.200E0	2.581E4	3.875E-1	3.65E0	1.61E0		
3.000E0	2.420E4	4.133E-1	3.70E0	1.47E0		
2.800E0	2.258E4	4.428E-1	3.68E0	1.37E0		
2.600E0	2.097E4	4.769E-1	3.62E0	1.41E0		
2.400E0	1.936E4	5.166E-1	3.78E0	1.51E0		
2.200E0	1.774E4	5.636E-1	4.01E0	1.45E0		
2.000E0	1.613E4	6.199E-1	4.30E0	1.14E0		
1.800E0	1.452E4	6.888E-1	4.56E0	6.55E-1		
1.600E0	1.290E4	7.749E-1	4.57E0	2.08E-1		
1.400E0	1.129E4	8.856E-1	4.28E0	1.13E-1		
1.200E0	9.681E3	1.033E0	4.01E0	1.12E-1		
9.999E-1	8.065E3	1.240E0	3.87E0	1.25E-1		
7.999E-1	6.452E3	1.550E0	3.80E0	1.11E-1		
6.001E-1	4.840E3	2.066E0	3.77E0	9.67E-2		
eV	cm^{-1}	μm	n_o	k_o	n_e	k_e
				[14]		[14]
7.309E-1	5.895E3	1.696E0		6.42E-2		
7.235E-1	5.836E3	1.714E0		4.94E-2		
7.147E-1	5.764E3	1.735E0		4.14E-2		
7.060E-1	5.694E3	1.756E0		3.55E-2		
7.000E-1	5.646E3	1.771E0		3.08E-2		
6.913E-1	5.576E3	1.794E0		2.66E-2		
6.823E-1	5.503E3	1.817E0		2.39E-2		
6.768E-1	5.458E3	1.832E0		2.19E-2		
6.689E-1	5.395E3	1.854E0		1.93E-2		
6.618E-1	5.338E3	1.873E0		1.81E-2		
6.558E-1	5.289E3	1.891E0		1.70E-2		
6.468E-1	5.217E3	1.917E0		1.55E-2		
6.401E-1	5.163E3	1.937E0		1.43E-2		
6.343E-1	5.116E3	1.955E0		1.35E-2		
6.280E-1	5.065E3	1.974E0		1.28E-2		
6.225E-1	5.021E3	1.992E0		1.19E-2		
6.157E-1	4.966E3	2.014E0		1.13E-2		
6.096E-1	4.917E3	2.034E0		1.03E-2		
6.031E-1	4.864E3	2.056E0		9.64E-3		
5.983E-1	4.825E3	2.072E0		8.93E-3		
5.926E-1	4.779E3	2.092E0		8.12E-3		

(continued)

TABLE I *(Continued)*

$CdGeAs_2$

eV	cm^{-1}	μm	n_o	k_o	n_e	k_e
				[14]		[14]
5.867E-1	4.732E3	2.113E0		7.35E-3		
5.809E-1	4.685E3	2.134E0		6.70E-3		
5.759E-1	4.645E3	2.153E0		5.71E-3		
5.705E-1	4.601E3	2.173E0		4.92E-3		
5.651E-1	4.558E3	2.194E0				5.29E-2
5.644E-1	4.552E3	2.197E0		4.80E-3		
5.602E-1	4.518E3	2.213E0				4.79E-2
5.594E-1	4.512E3	2.216E0		4.18E-3		
5.558E-1	4.483E3	2.231E0				4.45E-2
5.558E-1	4.483E3	2.231E0		3.48E-3		
5.510E-1	4.444E3	2.250E0				4.06E-2
5.490E-1	4.428E3	2.258E0		2.61E-3		
5.456E-1	4.401E3	2.272E0				3.37E-2
5.451E-1	4.397E3	2.274E0		1.91E-3		
5.410E-1	4.363E3	2.292E0				2.71E-2
5.397E-1	4.353E3	2.297E0		1.28E-3		
5.358E-1	4.322E3	2.314E0				2.12E-2
5.344E-1	4.310E3	2.320E0		6.60E-4		
5.326E-1	4.296E3	2.328E0				1.60E-2
5.314E-1	4.286E3	2.333E0		4.00E-4		
5.272E-1	4.252E3	2.352E0				1.22E-2
5.227E-1	4.216E3	2.372E0				9.35E-3
5.180E-1	4.178E3	2.394E0				7.19E-3
5.141E-1	4.147E3	2.412E0				5.25E-3
5.103E-1	4.116E3	2.430E0				3.76E-3
5.059E-1	4.080E3	2.451E0				2.80E-3
5.007E-1	4.039E3	2.476E0				2.06E-3
4.961E-1	4.001E3	2.499E0				1.47E-3
4.926E-1	3.973E3	2.517E0				9.10E-4

eV	cm^{-1}	μm	n_o	k	n_e
			[20]	[8]	[20]
5.391E-1	4.348E3	2.300E0	3.608E0		
5.166E-1	4.167E3	2.400E0	3.597E0		3.755E0
4.959E-1	4.000E3	2.500E0	3.590E0		3.732E0
4.769E-1	3.846E3	2.600E0	3.582E0	1.10E-4	3.716E0
4.592E-1	3.704E3	2.700E0	3.577E0	8.62E-5	3.703E0
4.428E-1	3.571E3	2.800E0	3.572E0	7.49E-5	3.693E0
4.275E-1	3.448E3	2.900E0	3.568E0	6.47E-5	3.685E0
4.133E-1	3.333E3	3.000E0	3.565E0	5.85E-5	3.678E0
4.000E-1	3.226E3	3.100E0	3.562E0	5.20E-5	3.671E0
3.875E-1	3.125E3	3.200E0	3.558E0	4.85E-5	3.666E0
3.647E-1	2.941E3	3.400E0	3.554E0	4.35E-5	3.657E0
3.444E-1	2.778E3	3.600E0	3.550E0	4.09E-5	3.651E0
3.263E-1	2.632E3	3.800E0	3.547E0	3.87E-5	3.645E0

TABLE I *(Continued)*

$CdGeAs_2$

eV	cm^{-1}	μm	n_o	k	n_e
			[20]	[8]	[20]
3.100E-1	2.500E3	4.000E0	3.544E0	3.73E-5	3.640E0
2.952E-1	2.381E3	4.200E0	3.542E0	3.67E-5	3.637E0
2.818E-1	2.273E3	4.400E0	3.539E0	3.63E-5	3.633E0
2.695E-1	2.174E3	4.600E0	3.537E0	3.59E-5	3.630E0
2.583E-1	2.083E3	4.800E0	3.535E0	3.63E-5	3.627E0
2.480E-1	2.000E3	5.000E0	3.534E0	3.71E-5	3.625E0
2.254E-1	1.818E3	5.500E0	3.529E0	4.17E-5	3.618E0
2.066E-1	1.667E3	6.000E0	3.525E0	4.12E-5	3.613E0
1.907E-1	1.538E3	6.500E0	3.522E0	3.76E-5	3.610E0
1.771E-1	1.429E3	7.000E0	3.520E0	3.24E-5	3.607E0
1.653E-1	1.333E3	7.500E0	3.518E0	2.84E-5	3.605E0
1.550E-1	1.250E3	8.000E0	3.516E0	2.53E-5	3.603E0
1.459E-1	1.176E3	8.500E0	3.514E0	2.28E-5	3.601E0
1.378E-1	1.111E3	9.000E0	3.512E0	2.08E-5	3.599E0
1.305E-1	1.053E3	9.500E0	3.510E0	1.97E-5	3.597E0
1.240E-1	1.000E3	1.000E1	3.508E0	1.93E-5	3.594E0
1.181E-1	9.524E2	1.050E1	3.505E0	1.98E-5	3.592E0
1.127E-1	9.091E2	1.100E1	3.503E0	2.07E-5	3.590E0
1.078E-1	8.696E2	1.150E1	3.500E0	2.23E-5	3.587E0
1.033E-1	8.333E2	1.200E1	3.498E0	2.56E-5	
1.026E-1	8.278E2	1.208E1		2.86E-5	
4.686E-1	3.779E3	1.213E1		3.33E-5	
4.647E-1	3.748E3	1.222E1		4.62E-5	
4.602E-1	3.712E3	1.226E1		5.13E-5	
4.518E-1	3.644E3	1.232E1		6.13E-5	
4.375E-1	3.529E3	1.235E1		6.91E-5	
4.287E-1	3.458E3	1.244E1		7.59E-5	
9.919E-2	8.000E2	1.250E1	3.495E0		
4.176E-1	3.368E3	1.258E1		7.54E-5	
4.089E-1	3.298E3	1.267E1		6.51E-5	
3.966E-1	3.199E3	1.275E1		5.55E-5	
3.759E-1	3.032E3	1.281E1		4.67E-5	
3.605E-1	2.908E3	1.292E1		4.18E-5	
3.403E-1	2.745E3	1.303E1		4.01E-5	
3.189E-1	2.572E3	1.314E1		4.37E-5	
2.939E-1	2.370E3	1.322E1		5.02E-5	
2.788E-1	2.249E3	1.330E1		5.97E-5	
2.658E-1	2.144E3	1.335E1		6.70E-5	
2.527E-1	2.038E3	1.341E1		7.43E-5	
2.454E-1	1.979E3	1.348E1		7.79E-5	
2.398E-1	1.934E3	1.360E1		7.52E-5	
2.322E-1	1.873E3	1.364E1		6.87E-5	
2.276E-1	1.836E3	1.366E1		6.31E-5	
2.229E-1	1.798E3	1.372E1		5.73E-5	
2.163E-1	1.745E3	1.376E1		4.99E-5	
2.080E-1	1.677E3	1.379E1		4.54E-5	

(continued)

TABLE I *(Continued)*

$CdGeAs_2$

eV	cm^{-1}	μm	n_o	k	n_e
			[20]	[8]	[20]
2.024E-1	1.632E3	1.383E1		4.22E-5	
1.968E-1	1.588E3	1.405E1		4.27E-5	
1.931E-1	1.557E3	1.443E1		4.80E-5	
1.885E-1	1.521E3	1.470E1		5.32E-5	
1.838E-1	1.483E3	1.519E1		6.43E-5	
1.818E-1	1.466E3	1.552E1		7.74E-5	
1.773E-1	1.430E3	1.596E1		1.00E-4	
1.720E-1	1.388E3	1.658E1		1.52E-4	
1.645E-1	1.327E3	1.697E1		2.26E-4	
1.606E-1	1.295E3	1.739E1		3.60E-4	
1.564E-1	1.262E3	1.764E1		5.24E-4	
1.514E-1	1.221E3	1.774E1		7.04E-4	
1.472E-1	1.187E3	1.783E1		9.41E-4	
1.434E-1	1.156E3	1.788E1		1.23E-3	

eV	cm^{-1}	μm	n_o	k_o	n_e	k_e
			[26]	[26]	[26]	[26]
4.959E-2	4.000E2	2.500E1	3.71E0	4.77E-3	3.75E0	4.70E-3
4.649E-2	3.750E2	2.667E1	3.66E0	7.00E-3	3.70E0	7.03E-3
4.339E-2	3.500E2	2.857E1	3.58E0	1.14E-2	3.62E0	1.17E-2
4.030E-2	3.250E2	3.077E1	3.42E0	2.25E-2	3.49E0	2.37E-2
3.720E-2	3.000E2	3.333E1	2.99E0	7.58E-2	3.12E0	7.92E-2
3.670E-2	2.960E2	3.378E1	2.84E0	1.05E-1	3.00E0	1.07E-1
3.620E-2	2.920E2	3.425E1	2.60E0	1.58E-1	2.82E0	1.56E-1
3.571E-2	2.880E2	3.472E1	2.23E0	2.77E-1	2.57E0	2.49E-1
3.521E-2	2.840E2	3.521E1	1.55E0	6.76E-1	2.15E0	4.75E-1
3.472E-2	2.800E2	3.571E1	1.04E0	2.14E0	1.54E0	1.23E0
3.447E-2	2.780E2	3.597E1	1.19E0	3.12E0	1.43E0	1.97E0
3.422E-2	2.760E2	3.623E1	1.71E0	4.31E0	1.61E0	2.85E0
3.397E-2	2.740E2	3.650E1	3.17E0	5.75E0	2.19E0	3.85E0
3.372E-2	2.720E2	3.676E1	6.60E0	5.53E0	3.54E0	4.78E0
3.348E-2	2.700E2	3.704E1	7.45E0	2.47E0	5.77E0	4.44E0
3.323E-2	2.680E2	3.731E1	6.58E0	1.13E0	6.67E0	2.56E0
3.298E-2	2.660E2	3.759E1	5.91E0	6.50E-1	6.29E0	1.35E0
3.273E-2	2.640E2	3.788E1	5.45E0	4.40E-1	5.82E0	8.00E-1
3.248E-2	2.620E2	3.817E1	5.11E0	3.44E-1	5.46E0	5.26E-1
3.224E-2	2.600E2	3.846E1	4.84E0	3.22E-1	5.19E0	3.75E-1
3.199E-2	2.580E2	3.876E1	4.60E0	4.02E-1	4.98E0	2.83E-1
3.174E-2	2.560E2	3.906E1	4.56E0	6.65E-1	4.82E0	2.24E-1
3.162E-2	2.550E2	3.922E1	4.73E0	7.29E-1	4.75E0	2.02E-1
3.149E-2	2.540E2	3.937E1	4.88E0	6.02E-1	4.68E0	1.84E-1
3.124E-2	2.520E2	3.968E1	4.83E0	3.14E-1	4.57E0	1.56E-1
3.100E-2	2.500E2	4.000E1	4.69E0	1.96E-1	4.48E0	1.37E-1
3.050E-2	2.460E2	4.065E1	4.47E0	1.23E-1	4.32E0	1.13E-1
3.000E-2	2.420E2	4.132E1	4.31E0	1.03E-1	4.18E0	1.02E-1

TABLE I *(Continued)*

$CdGeAs_2$

eV	cm^{-1}	μm	n_o	k_o	n_e	k_e
			[26]	[26]	[26]	[26]
2.951E-2	2.380E2	4.202E1	4.19E0	9.94E-2	4.06E0	1.01E-1
2.901E-2	2.340E2	4.274E1	4.08E0	1.06E-1	3.93E0	1.09E-1
2.852E-2	2.300E2	4.348E1	3.97E0	1.22E-1	3.80E0	1.28E-1
2.802E-2	2.260E2	4.425E1	3.86E0	1.51E-1	3.64E0	1.64E-1
2.752E-2	2.220E2	4.505E1	3.74E0	2.01E-1	3.45E0	2.33E-1
2.703E-2	2.180E2	4.587E1	3.59E0	2.88E-1	3.17E0	3.77E-1
2.653E-2	2.140E2	4.673E1	3.42E0	4.54E-1	2.76E0	7.40E-1
2.604E-2	2.100E2	4.762E1	3.24E0	7.89E-1	2.43E0	1.76E0
2.579E-2	2.080E2	4.808E1	3.21E0	1.06E0	2.65E0	2.58E0
2.554E-2	2.060E2	4.854E1	3.29E0	1.41E0	3.39E0	3.38E0
2.529E-2	2.040E2	4.902E1	3.55E0	1.77E0	4.73E0	3.69E0
2.517E-2	2.030E2	4.926E1	3.76E0	1.91E0	5.45E0	3.44E0
2.504E-2	2.020E2	4.951E1	4.02E0	1.99E0	5.98E0	2.95E0
2.480E-2	2.000E2	5.000E1	4.56E0	1.95E0	6.30E0	1.85E0
2.455E-2	1.980E2	5.051E1	4.98E0	1.64E0	6.12E0	1.14E0
2.430E-2	1.960E2	5.102E1	5.15E0	1.25E0	5.85E0	7.39E-1
2.405E-2	1.940E2	5.155E1	5.17E0	9.28E-1	5.63E0	5.12E-1
2.381E-2	1.920E2	5.208E1	5.10E0	6.90E-1	5.44E0	3.74E-1
2.356E-2	1.900E2	5.263E1	5.01E0	5.25E-1	5.30E0	2.85E-1
2.306E-2	1.860E2	5.376E1	4.83E0	3.30E-1	5.08E0	1.81E-1
2.257E-2	1.820E2	5.495E1	4.68E0	2.29E-1	4.93E0	1.25E-1
2.244E-2	1.810E2	5.525E1	4.65E0	2.12E-1	4.90E0	1.16E-1
2.232E-2	1.800E2	5.556E1	4.61E0	1.98E-1	4.87E0	1.07E-1
2.182E-2	1.760E2	5.682E1	4.49E0	1.60E-1	4.77E0	8.04E-2
2.133E-2	1.720E2	5.814E1	4.36E0	1.49E-1	4.70E0	6.29E-2
2.108E-2	1.700E2	5.882E1	4.28E0	1.57E-1	4.67E0	5.62E-2
2.083E-2	1.680E2	5.952E1	4.19E0	1.80E-1	4.64E0	5.06E-2
2.058E-2	1.660E2	6.024E1	4.07E0	2.35E-1	4.62E0	4.57E-2
2.033E-2	1.640E2	6.098E1	3.92E0	3.67E-1	4.59E0	4.16E-2
2.009E-2	1.620E2	6.173E1	3.75E0	7.24E-1	4.57E0	3.80E-2
1.984E-2	1.600E2	6.250E1	4.11E0	1.45E0	4.55E0	3.49E-2
1.959E-2	1.580E2	6.329E1	5.13E0	1.17E0	4.53E0	3.21E-2
1.934E-2	1.560E2	6.410E1	5.16E0	5.22E-1	4.52E0	2.96E-2
1.909E-2	1.540E2	6.494E1	4.98E0	2.70E-1	4.50E0	2.75E-2
1.885E-2	1.520E2	6.579E1	4.85E0	1.68E-1	4.49E0	2.55E-2
1.860E-2	1.500E2	6.667E1	4.75E0	1.18E-1	4.47E0	2.38E-2
1.835E-2	1.480E2	6.757E1	4.68E0	8.96E-2	4.46E0	2.22E-2
1.810E-2	1.460E2	6.849E1	4.63E0	7.21E-2	4.45E0	2.08E-2
1.785E-2	1.440E2	6.944E1	4.59E0	6.03E-2	4.44E0	1.95E-2
1.761E-2	1.420E2	7.042E1	4.55E0	5.19E-2	4.43E0	1.83E-2
1.736E-2	1.400E2	7.143E1	4.52E0	4.56E-2	4.42E0	1.73E-2
1.686E-2	1.360E2	7.353E1	4.47E0	3.70E-2	4.40E0	1.54E-2
1.637E-2	1.320E2	7.576E1	4.43E0	3.15E-2	4.38E0	1.38E-2
1.587E-2	1.280E2	7.813E1	4.40E0	2.78E-2	4.37E0	1.24E-2
1.537E-2	1.240E2	8.065E1	4.37E0	2.55E-2	4.36E0	1.12E-2
1.488E-2	1.200E2	8.333E1	4.34E0	2.45E-2	4.34E0	1.02E-2

(continued)

TABLE I *(Continued)*

$CdGeAs_2$

eV	cm^{-1}	μm	n_o	k_o	n_e	k_e
			[26]	[26]	[26]	[26]
1.438E-2	1.160E2	8.621E1	4.31E0	2.49E-2	4.33E0	9.25E-3
1.389E-2	1.120E2	8.929E1	4.28E0	2.77E-2	4.32E0	8.44E-3
1.364E-2	1.100E2	9.091E1	4.26E0	3.06E-2	4.32E0	8.08E-3
1.339E-2	1.080E2	9.259E1	4.24E0	3.54E-2	4.31E0	7.73E-3
1.314E-2	1.060E2	9.434E1	4.21E0	4.33E-2	4.31E0	7.40E-3
1.289E-2	1.040E2	9.615E1	4.18E0	5.72E-2	4.31E0	7.08E-3
1.265E-2	1.020E2	9.804E1	4.14E0	8.36E-2	4.30E0	6.79E-3
1.240E-2	1.000E2	1.000E2	4.08E0	1.40E-1	4.30E0	6.51E-3
1.215E-2	9.800E1	1.020E2	4.02E0	2.78E-1	4.30E0	6.24E-3
1.190E-2	9.600E1	1.042E2	4.14E0	5.59E-1	4.29E0	5.98E-3
1.178E-2	9.500E1	1.053E2	4.36E0	6.20E-1	4.29E0	5.86E-3
1.165E-2	9.400E1	1.064E2	4.55E0	5.17E-1	4.29E0	5.74E-3
1.141E-2	9.200E1	1.087E2	4.61E0	2.48E-1	4.29E0	5.51E-3
1.116E-2	9.000E1	1.111E2	4.55E0	1.26E-1	4.28E0	5.29E-3
1.091E-2	8.800E1	1.136E2	4.50E0	7.49E-2	4.28E0	5.07E-3
1.066E-2	8.600E1	1.163E2	4.46E0	5.02E-2	4.28E0	4.87E-3
1.041E-2	8.400E1	1.190E2	4.43E0	3.65E-2	4.27E0	4.67E-3
1.017E-2	8.200E1	1.220E2	4.41E0	2.82E-2	4.27E0	4.49E-3
9.919E-3	8.000E1	1.250E2	4.39E0	2.28E-2	4.27E0	4.31E-3
9.671E-3	7.800E1	1.282E2	4.38E0	1.90E-2	4.27E0	4.13E-3
9.423E-3	7.600E1	1.316E2	4.37E0	1.62E-2	4.26E0	3.97E-3
6.199E-3	5.000E1	2.000E2	4.29E0	4.98E-3	4.24E0	2.24E-3

Copper Gallium Sulfide ($CuGaS_2$)

J. C. RIFE*
Naval Research Laboratory
Washington, D.C.

$CuGaS_2$ is a tetragonally bonded semiconductor with the chalcopyrite structure and a direct band gap of 2.49 eV at room temperature. The structure, growth, and optical and electronic properties of the chalcopyrite semiconductors have been reviewed in the book by Shay and Wernick [1]. Properties have also been summarized in the Landolt–Börnstein series [2]. The I–III–VI_2 chalcopyrite lattice is equivalent to the II–VI zincblende semiconductor crystal structure but with ordering of the I and III components and so a doubling of the unit cell along the *c*-axis. The chalcopyrite lattice is typically compressed along the *c*-axis leading to a crystalline electric field and birefringence with n_e ($\mathbf{E} \| \mathbf{c}$) $> n_o$ ($\mathbf{E} \perp \mathbf{c}$), (positive uniaxial crystal). Chalcopyrite semiconductors are also optically active because of varying degrees of tetragonal distortion [3]. The $CuGaS_2$ crystal structure, in particular, is compressed 2.0% along the *c*-axis. The band structure of $CuGaS_2$ has been calculated by several authors [4–7]. $CuGaS_2$ has a band gap about 1.1 eV less than that of its analog, ZnS, which has a direct band gap of 3.6 eV in cubic form. This property is displayed by other I–III–VI_2 chalcopyrites and their analogs as well. This has been attributed to *p–d* hybridization as a result of Cu *d*-orbitals in the valence band [5, 6] and to difference in the lengths of the Cu–S and Ga–S bonds [7].

$CuGaS_2$ is promising for green-blue light emitting devices since it can be doped *p*-type and form a heterojunctions with II–VI materials, which can only be doped *n*-type [1, 8]. Stimulation at 592 nm has also been obtained from a $CuGa(S_{0.65}Se_{0.35})_2/CuAl_{0.3}Ga_{0.7}(S_{0.65}Se_{0.35})_2$ double heterostructure device pumped by the third harmonic of a Nd:YAG laser [9].

The optical constants, *n* and *k*, listed in Table I and plotted in Fig. 1 are derived from sources discussed in more detail later. The optical constants were taken from tables, calculated from formulae, or extracted from graphs

* The views presented are those of the author and do not represent the views of the Department of Defense or its components.

ISBN 0-12-544423-0/$25.00.

where necessary. The table here has more significant figures than justified in some cases; consult the original work for the actual experimental resolution. Measurements made using polarized radiation were favored for inclusion here; in such cases, the optical constants have been given for both $\mathbf{E} \| \mathbf{c}$ and $\mathbf{E} \perp \mathbf{c}$. All measurements used were made on single crystals at room temperature, except where noted in the text.

I X-RAY TO BAND-GAP ABSORPTION EDGE

The optical constants, n and k, for the range from 10,000 to 26 eV have been calculated from the scattering factors of the elements of Henke *et al.* [10] using the compound formula and a density of 4.35 gm/cm^3. In Fig. 1, the K-edge ($1s$) transitions of Ga and Cu appear at 1.2 and 1.4×10^{-4} μm and of S at 5.0×10^{-4} μm, and the $L_{2,3}$ ($2p$) transitions of Ga and Cu at 1.1 and 1.3×10^{-3} μm and of S at 7.6×10^{-3} μm. The calculated edges are a good approximation on the scale of Fig. 1, but the scattering factors of the elements cannot predict the compound edge locations or structure to high degree (edge within 5 or 10 eV) because of core-level chemical shifts and bonding-dependent redistribution of the absorption at and just above the edges. Detailed $CuGaS_2$ absorption structure at the Cu K edge has been measured by Ballal and Mande [11].

For the fundamental electronic transitions in the 26 to 2.45 eV range, here, optical constants are taken from Rife *et al.* [12]. They extracted optical constants for a single stoichiometric "yellow"/"orange" crystal sample from a Kramers–Kronig analysis of polarized, 80-K reflectance data. Other measurements in this range are the unpolarized reflectance of Ringeissen *et al.* [13] from 6 to 3.5 eV of "orange" crystals at 4.2 K and that of Hengehold and Pedrotti [14] from 11 to 2.5 eV of "green" crystals at room temperature.

II BAND-GAP ABSORPTION EDGE

Measurements of the absorption coefficient at the absorption edge have been reported by a several authors. Tell and Kasper [5] measured the absorption coefficient from 2.58 to 2.48 eV for $\mathbf{E} \perp \mathbf{c}$ at 2 K. Kobayashi *et al.* [15] measured the absorption coefficient from 2.53 to 2.40 eV for $\mathbf{E} \perp \mathbf{c}$ at 77, 213, and 293 K, removing a background likely due to a Fe impurity. Gonzalez *et al.* [16] obtained the pressure dependance of the $CuGaS_2$ edge at room temperature and zero hydrostatic pressure from 2.48 to 2.52 eV, but their absorption coefficient is lower for a given energy than that of Kobayashi *et al.*

BAND GAP III

In the transparent gap region from 0.5 to 13 μm, where the two-phonon lattice absorption sets in, the index of refraction at room temperature, the temperature derivative for $\mathbf{E} \| \mathbf{c}$ and $\mathbf{E} \perp \mathbf{c}$, and the absorption coefficient for unpolarized light have been reported by Boyd *et al.* [17]. They determined the index by the minimum-deviation method; however, results for other individual crystals could vary slightly from their results, depending on impurities or doping. Their refractive-index data have been reduced to an analog formula by Wemple *et al.* [18] and by Bhar and Ghosh [19] for 20 and 120° C and more extreme temperatures. The latter find a good fit for 20° C to a special Sellmeier form,

$$n^2 = A + \frac{B}{1 - \dfrac{C}{\lambda^2}} + \frac{D}{1 - \dfrac{E}{\lambda^2}},$$

where for n_o $(A,B,C,D,E) = (3.9064, 2.3065, 0.1149, 1.5479, 738.43)$ and for n_e $(A,B,C,D,E) = (4.3165, 1.8692, 0.1364, 1.7575, 738.43)$; λ is the wavelength in microns. At 120° C, these parameters are n_o $(A,B,C,D,E) = (4.0984, 2.1419, 0.1225, 1.5755, 738.43)$ and n_e $(A,B,C,D,E) = (4.4834, 1.7316, 0.1453, 1.7785, 738.43)$.

LATTICE ABSORPTION IN THE INFRARED IV

Several authors have studied the phonon modes of $CuGaS_2$ by transmission [20, 21] and Raman spectroscopies [20, 22]. Baars and Koschel [23] measured the polarized reflectance from 50 to 500 cm^{-1} and derived optical constants by Kramers–Kronig analysis and fitting to dispersion of a set of harmonic oscillators. Their dispersion formula for the dielectric constant $\epsilon(\nu)$ is

$$\epsilon(\nu) = \epsilon_\infty + \sum_j \frac{S_j \nu^2{}_j}{(\nu^2{}_j - \nu^2 - i\nu\gamma_j)},$$

where S_j is the oscillator strength, ν_j is the frequency in cm^{-1}, and γ_j is the damping of the jth oscillator in cm^{-1}. For $\mathbf{E} \| \mathbf{c}$, they give two oscillators out of a possible three $(S_j, \nu_j, \gamma_j) = (0.27, 364, 2.7)$ and $(1.20, 330, 2.49)$ with $\epsilon_\infty = 6.1$; and for $\mathbf{E} \perp \mathbf{c}$, they give the four oscillators out of a possible six $(S_j, \nu_j, \gamma_j) = (0.04, 387, 3.60)$, $(0.56, 364, 3.44)$, $(0.55, 345, 6.85)$, and $(1.54, 259, 15.02)$ with $\epsilon_\infty = 6.2$. Baars and Koschel obtained values for ϵ_0

of 7.6 for $\mathbf{E} \| \mathbf{c}$ and 8.9 for $\mathbf{E} \perp \mathbf{c}$. They observed two additional peaks in the $\mathbf{E} \perp \mathbf{c}$ reflectance at 148 and 93 cm^{-1}, but reported no oscillator parameters for them.

REFERENCES

1. J. L. Shay and J. H. Wernick, "Ternary Chalcopyrite Semiconductors: Growth, Electronic Properties, and Applications." Pergamon, New York, 1975.
2. Landolt-Börnstein, "Semiconductors—Physics of Ternary Compounds" (K.-H. Hellwege and O. Madelung, eds.), Vol. 17h. Springer-Verlag, New York, 1985.
3. G. A. Babonas, A. S. Martsinkyavichyus, and A. Yu. Shileika, *Sov. Phys. J.* **29**, 617 (1986).
4. A. S. Poplavnoi and Yu. I. Polygalov, *Inorg. Mater.* **7**, 1527 and 1531 (1971).
5. B. Tell and H. M. Kasper, *Phys. Rev.* **B 7**, 740 (1973).
6. B. Tell and P. M. Bridenbaugh, *Phys. Rev.* **B 12**, 3330 (1975).
7. J. E. Jaffe and A. Zunger, *Phys. Rev.* **B 28**, 5822 (1983).
8. H. Kukimoto, Proceedings of the Ninth International Conference on Ternary and Multinary Compounds. *Jpn. J. Appl. Phys. Suppl.* **32-3**, 10 (1993).
9. M. Yamamoto, T. Ogawa, K. Hara, J. Yoshino, and H. Kukimoto, *Jpn. J. Appl. Phys.* **33**, L624 (1994).
10. B. L. Henke, P. Lee, T. J. Tanaka, R. L. Shimabukuro, and B. J. Fujikawa, *At. Data Nucl. Data Tables* **27**, 1 (1982); B. L. Henke, J. C. Davis, E. M. Gullikson, and R. C. C. Perera, *Lawrence Berkeley Laboratory Report* **LBL-26259** (1988).
11. M. M. Ballal and C. Mande, *J. Phys. C: Solid State Phys.* **11**, 837 (1978).
12. J. C. Rife, R. N. Dexter, P. M. Bridenbaugh, and B. W. Veal, *Phys. Rev. B* **10**, 4491 (1977); J. C. Rife, Unpublished Ph.D. Thesis University of Wisconsin, Madison (1976).
13. J. Ringeissen, J. L. Regoline, and S. Lewonczuk, *Surf. Sci.* **37**, 777 (1973).
14. R. L. Hengehold and F. L. Pedrotti, *J. Appl. Phys.* **46**, 5202 (1975).
15. S. Kobayashi, N. Tsuboi, and F. Kaneko, *Jpn. J. of Appl. Phys.* **26**, 220 (1987).
16. J. Gonzalez, E. Calderon, T. Tinoco, J. P. Itie, A. Polian, and E. Moya, *J. Phys. Chem. Solids* **56**, 507 (1995).
17. G. D. Boyd, H. Kasper, and J. H. McFee, *IEEE J. Quanum Electron.* **QE-7**, 563 (1971).
18. S. H. Wemple, J. D. Gabbe, and G. D. Boyd, *J. Appl. Phys.* **46**, 3597 (1975).
19. G. C. Bhar and G.C. Ghosh, *IEEE J. Quantum Electron.* **QE-16**, 838 (1980); G. C. Bhar and G. C. Ghosh, *J. Opt. Soc. Am.* **69**, 730 (1979).
20. W. H. Koschel and M. Bettini, *Phys. Status Solidi B* **72**, 729 (1975).
21. N. V. Joshi, *J. Chem. Phys. Solids* **40**, 93 (1979).
22. J. P. van der Ziel, A. E. Meixner, H. M. Kasper, and J. A. Ditzenberger, *Phys. Rev.* **B 9**, 4286 (1974).
23. J. Baars and W. H. Koschel, *Solid State Commun.* **11** 1513 (1972).

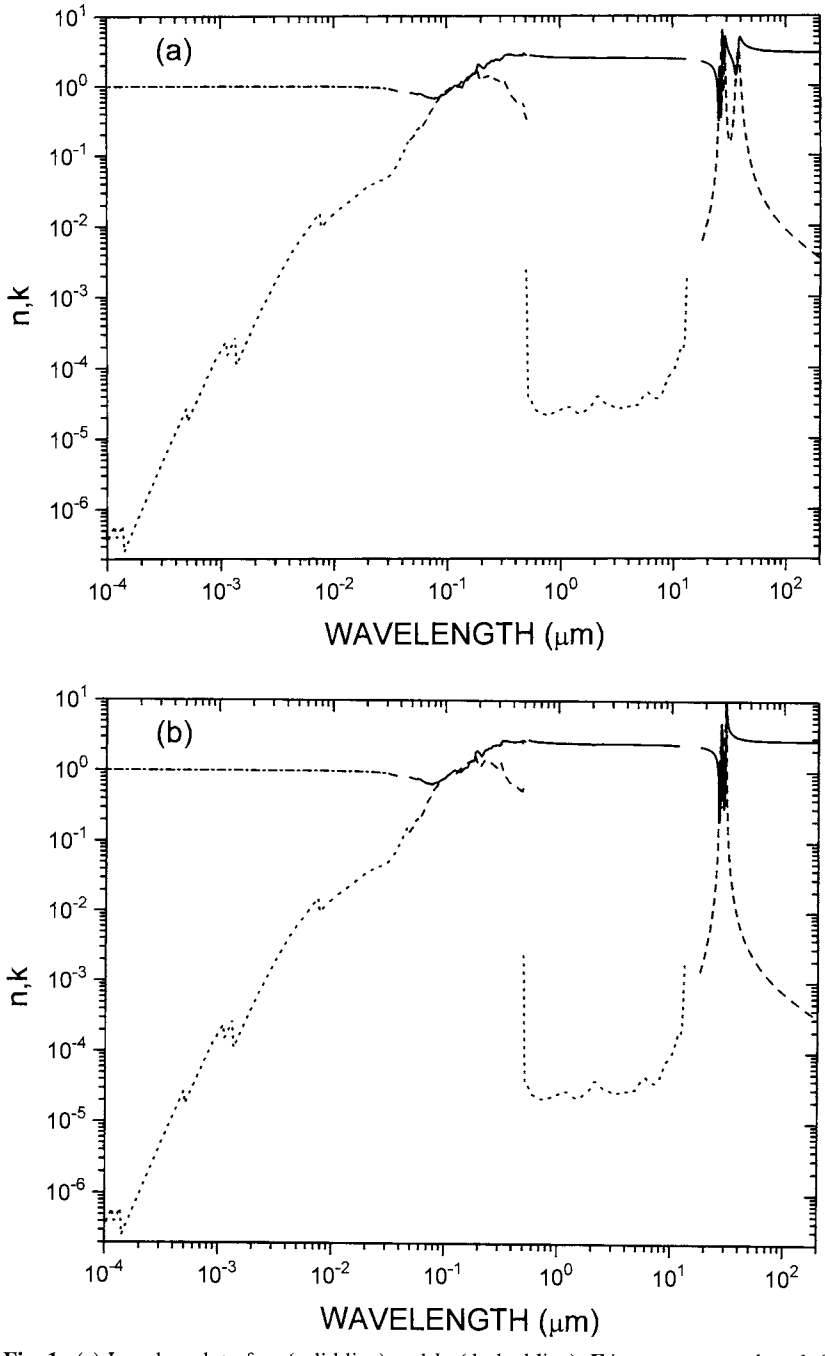

Fig. 1. (a) Log–log plot of n_o (solid line) and k_o (dashed line), $\mathbf{E} \perp \mathbf{c}$, versus wavelength for $CuGaS_2$. (b) Log–log plot of n_e (solid line) and k_e (dashed line), $\mathbf{E} \parallel \mathbf{c}$, versus wavelength for $CuGaS_2$. Unpolarized n (dash-dot line) and k (dotted line) are plotted on both graphs, where polarized data were not available.

TABLE I

Values of n and k for $CuGaS_2$ Obtained from Various References[a]

eV	cm^{-1}	μm	1-n	k
			[10]	[10]
3.000E4	2.420E8	4.133E-5	9.50E-7	1.18E-8
2.010E4	1.622E8	6.167E-5	2.09E-6	5.54E-8
1.499E4	1.209E8	8.272E-5	3.76E-6	1.68E-7
1.118E4	9.017E7	1.109E-4	6.62E-6	4.93E-7
1.088E4	8.772E7	1.140E-4	6.91E-6	5.42E-7
1.060E4	8.547E7	1.170E-4	7.21E-6	5.96E-7
1.031E4	8.319E7	1.202E-4	7.45E-6	4.01E-7
1.005E4	8.104E7	1.234E-4	7.99E-6	4.08E-7
9.778E3	7.886E7	1.268E-4	8.46E-6	4.51E-7
9.523E3	7.680E7	1.302E-4	8.94E-6	4.97E-7
9.273E3	7.479E7	1.337E-4	9.36E-6	5.47E-7
9.024E3	7.278E7	1.374E-4	9.72E-6	6.02E-7
8.787E3	7.087E7	1.411E-4	1.04E-5	2.53E-7
8.557E3	6.901E7	1.449E-4	1.10E-5	2.80E-7
8.332E3	6.720E7	1.488E-4	1.17E-5	3.10E-7
6.048E3	4.878E7	2.050E-4	2.28E-5	1.05E-6
4.053E3	3.269E7	3.059E-4	5.13E-5	4.70E-6
2.645E3	2.133E7	4.688E-4	1.15E-4	2.22E-5
2.575E3	2.077E7	4.815E-4	1.19E-4	2.44E-5
2.507E3	2.022E7	4.945E-4	1.22E-4	2.68E-5
2.441E3	1.969E7	5.079E-4	1.26E-4	1.79E-5
2.377E3	1.917E7	5.216E-4	1.38E-4	1.97E-5
2.314E3	1.867E7	5.357E-4	1.48E-4	2.17E-5
1.820E3	1.468E7	6.812E-4	2.41E-4	5.14E-5
1.394E3	1.124E7	8.895E-4	3.84E-4	1.31E-4
1.188E3	9.579E6	1.044E-3	4.60E-4	2.05E-4
1.157E3	9.328E6	1.072E-3	4.63E-4	2.21E-4
1.126E3	9.083E6	1.101E-3	4.36E-4	2.38E-4
1.096E3	8.842E6	1.131E-3	4.72E-4	1.54E-4
1.067E3	8.606E6	1.162E-3	5.24E-4	1.67E-4
1.039E3	8.382E6	1.193E-3	5.61E-4	1.81E-4
9.856E2	7.949E6	1.258E-3	6.11E-4	2.21E-4
9.596E2	7.740E6	1.292E-3	6.15E-4	2.45E-4
9.343E2	7.536E6	1.327E-3	5.14E-4	2.71E-4
9.096E2	7.337E6	1.363E-3	6.63E-4	1.12E-4
8.856E2	7.143E6	1.400E-3	7.46E-4	1.23E-4
8.622E2	6.954E6	1.438E-3	8.13E-4	1.36E-4
6.965E2	5.618E6	1.780E-3	1.36E-3	2.89E-4
5.056E2	4.078E6	2.452E-3	2.57E-3	8.41E-4
3.976E2	3.207E6	3.118E-3	3.95E-3	1.79E-3
3.045E2	2.456E6	4.072E-3	5.91E-3	3.85E-3
1.987E2	1.602E6	6.241E-3	8.80E-3	1.04E-2
1.738E2	1.402E6	7.132E-3	7.88E-3	1.40E-2
1.693E2	1.365E6	7.325E-3	6.97E-3	1.48E-2
1.648E2	1.329E6	7.523E-3	4.63E-3	1.56E-2

[a]References given in brackets.

TABLE I *(Continued)*

$CuGaS_2$

eV	cm^{-1}	μm	1-n	k		
			[10]	[10]		
1.605E2	1.294E6	7.726E-3	3.93E-3	9.64E-3		
1.563E2	1.260E6	7.935E-3	6.87E-3	1.02E-2		
1.521E2	1.227E6	8.150E-3	8.12E-3	1.07E-2		
1.262E2	1.018E6	9.824E-3	1.24E-2	1.46E-2		
1.020E2	8.224E5	1.216E-2	1.68E-2	1.94E-2		
7.602E1	6.131E5	1.631E-2	2.70E-2	2.81E-2		
4.959E1	4.000E5	2.500E-2	5.45E-2	4.28E-2		
4.006E1	3.231E5	3.095E-2	9.34E-2	5.11E-2		
3.413E1	2.753E5	3.633E-2	1.45E-1	7.28E-2		
2.987E1	2.409E5	4.151E-2		1.10E-1		
2.757E1	2.224E5	4.497E-2		1.50E-1		
2.614E1	2.108E5	4.744E-2		1.83E-1		
eV	cm^{-1}	μm	n_o	k_o	n_e	k_e
			[12]	[12]	[12]	[12]
2.590E1	2.089E5	4.787E-2	7.94E-1	1.70E-1	8.12E-1	1.37E-1
2.550E1	2.057E5	4.862E-2	7.95E-1	1.78E-1	8.08E-1	1.43E-1
2.500E1	2.016E5	4.959E-2	7.95E-1	1.85E-1	8.03E-1	1.49E-1
2.450E1	1.976E5	5.060E-2	7.92E-1	1.88E-1	7.96E-1	1.50E-1
2.400E1	1.936E5	5.166E-2	7.82E-1	1.95E-1	7.82E-1	1.64E-1
2.350E1	1.895E5	5.276E-2	7.75E-1	2.08E-1	7.77E-1	1.78E-1
2.300E1	1.855E5	5.390E-2	7.68E-1	2.19E-1	7.69E-1	1.87E-1
2.290E1	1.847E5	5.414E-2	7.64E-1	2.21E-1	7.66E-1	1.89E-1
2.280E1	1.839E5	5.438E-2	7.60E-1	2.26E-1	7.61E-1	1.94E-1
2.270E1	1.831E5	5.462E-2	7.58E-1	2.32E-1	7.60E-1	2.03E-1
2.260E1	1.823E5	5.486E-2	7.58E-1	2.38E-1	7.61E-1	2.08E-1
2.250E1	1.815E5	5.510E-2	7.60E-1	2.47E-1	7.64E-1	2.15E-1
2.240E1	1.807E5	5.535E-2	7.67E-1	2.53E-1	7.71E-1	2.18E-1
2.230E1	1.799E5	5.560E-2	7.71E-1	2.50E-1	7.72E-1	2.16E-1
2.220E1	1.791E5	5.585E-2	7.69E-1	2.51E-1	7.71E-1	2.17E-1
2.210E1	1.783E5	5.610E-2	7.67E-1	2.57E-1	7.72E-1	2.20E-1
2.200E1	1.774E5	5.635E-2	7.76E-1	2.63E-1	7.79E-1	2.21E-1
2.180E1	1.758E5	5.687E-2	7.82E-1	2.52E-1	7.75E-1	2.13E-1
2.160E1	1.742E5	5.740E-2	7.72E-1	2.53E-1	7.63E-1	2.20E-1
2.140E1	1.726E5	5.793E-2	7.74E-1	2.60E-1	7.70E-1	2.28E-1
2.120E1	1.710E5	5.848E-2	7.72E-1	2.56E-1	7.65E-1	2.23E-1
2.100E1	1.694E5	5.904E-2	7.69E-1	2.62E-1	7.64E-1	2.28E-1
2.080E1	1.678E5	5.961E-2	7.68E-1	2.61E-1	7.61E-1	2.25E-1
2.060E1	1.662E5	6.018E-2	7.60E-1	2.59E-1	7.50E-1	2.25E-1
2.040E1	1.645E5	6.077E-2	7.52E-1	2.65E-1	7.41E-1	2.32E-1
2.020E1	1.629E5	6.138E-2	7.47E-1	2.70E-1	7.35E-1	2.36E-1
2.000E1	1.613E5	6.199E-2	7.40E-1	2.73E-1	7.27E-1	2.42E-1
1.900E1	1.533E5	6.525E-2	7.07E-1	3.17E-1	6.89E-1	2.88E-1
1.800E1	1.452E5	6.888E-2	6.85E-1	3.81E-1	6.68E-1	3.55E-1
1.700E1	1.371E5	7.293E-2	6.74E-1	4.38E-1	6.59E-1	4.22E-1

(continued)

TABLE I *(Continued)*

$CuGaS_2$

eV	cm^{-1}	μm	n_o	k_o	n_e	k_e
			[12]	[12]	[12]	[12]
1.600E1	1.291E5	7.749E-2	6.62E-1	5.24E-1	6.56E-1	5.21E-1
1.500E1	1.210E5	8.265E-2	6.79E-1	6.12E-1	6.92E-1	5.96E-1
1.480E1	1.194E5	8.377E-2	6.80E-1	6.35E-1	6.92E-1	6.10E-1
1.460E1	1.178E5	8.492E-2	6.86E-1	6.59E-1	6.92E-1	6.29E-1
1.440E1	1.161E5	8.610E-2	6.95E-1	6.84E-1	6.97E-1	6.55E-1
1.420E1	1.145E5	8.731E-2	7.12E-1	7.06E-1	7.10E-1	6.77E-1
1.400E1	1.129E5	8.856E-2	7.30E-1	7.21E-1	7.23E-1	6.95E-1
1.380E1	1.113E5	8.984E-2	7.42E-1	7.28E-1	7.36E-1	7.09E-1
1.360E1	1.097E5	9.116E-2	7.46E-1	7.36E-1	7.46E-1	7.22E-1
1.340E1	1.081E5	9.252E-2	7.47E-1	7.53E-1	7.51E-1	7.37E-1
1.320E1	1.065E5	9.392E-2	7.50E-1	7.75E-1	7.58E-1	7.57E-1
1.300E1	1.049E5	9.537E-2	7.55E-1	7.98E-1	7.69E-1	7.79E-1
1.280E1	1.032E5	9.686E-2	7.66E-1	8.27E-1	7.82E-1	7.99E-1
1.260E1	1.016E5	9.840E-2	7.83E-1	8.53E-1	7.97E-1	8.19E-1
1.240E1	1.000E5	9.998E-2	8.03E-1	8.77E-1	8.13E-1	8.40E-1
1.220E1	9.840E4	1.016E-1	8.27E-1	8.97E-1	8.33E-1	8.59E-1
1.200E1	9.679E4	1.033E-1	8.50E-1	9.11E-1	8.54E-1	8.74E-1
1.180E1	9.518E4	1.051E-1	8.70E-1	9.21E-1	8.74E-1	8.87E-1
1.160E1	9.356E4	1.069E-1	8.85E-1	9.32E-1	8.93E-1	9.00E-1
1.140E1	9.195E4	1.088E-1	8.98E-1	9.51E-1	9.10E-1	9.11E-1
1.120E1	9.034E4	1.107E-1	9.21E-1	9.70E-1	9.28E-1	9.28E-1
1.100E1	8.872E4	1.127E-1	9.47E-1	9.84E-1	9.53E-1	9.44E-1
1.080E1	8.711E4	1.148E-1	9.76E-1	9.89E-1	9.89E-1	9.50E-1
1.060E1	8.550E4	1.170E-1	9.98E-1	9.84E-1	1.01E0	9.40E-1
1.040E1	8.388E4	1.192E-1	1.01E0	9.75E-1	1.02E0	9.34E-1
1.020E1	8.227E4	1.215E-1	9.99E-1	9.70E-1	1.02E0	9.28E-1
1.000E1	8.066E4	1.240E-1	9.82E-1	9.91E-1	1.01E0	9.27E-1
9.800E0	7.905E4	1.265E-1	9.73E-1	1.03E0	1.00E0	9.42E-1
9.600E0	7.743E4	1.291E-1	9.89E-1	1.06E0	9.97E-1	9.62E-1
9.400E0	7.582E4	1.319E-1	9.87E-1	1.07E0	9.77E-1	9.90E-1
9.200E0	7.421E4	1.348E-1	9.47E-1	1.13E0	9.65E-1	1.05E0
9.000E0	7.259E4	1.378E-1	9.78E-1	1.25E0	9.94E-1	1.11E0
8.800E0	7.098E4	1.409E-1	1.07E0	1.32E0	1.04E0	1.16E0
8.600E0	6.937E4	1.442E-1	1.17E0	1.33E0	1.08E0	1.19E0
8.400E0	6.775E4	1.476E-1	1.22E0	1.30E0	1.11E0	1.21E0
8.200E0	6.614E4	1.512E-1	1.21E0	1.32E0	1.12E0	1.25E0
8.000E0	6.453E4	1.550E-1	1.25E0	1.38E0	1.14E0	1.31E0
7.800E0	6.291E4	1.589E-1	1.31E0	1.42E0	1.21E0	1.42E0
7.600E0	6.130E4	1.631E-1	1.39E0	1.45E0	1.36E0	1.41E0
7.400E0	5.969E4	1.675E-1	1.47E0	1.45E0	1.40E0	1.39E0
7.200E0	5.807E4	1.722E-1	1.51E0	1.44E0	1.42E0	1.39E0
7.000E0	5.646E4	1.771E-1	1.50E0	1.50E0	1.41E0	1.50E0
6.800E0	5.485E4	1.823E-1	1.65E0	1.64E0	1.67E0	1.70E0
6.700E0	5.404E4	1.850E-1	1.80E0	1.67E0	1.88E0	1.55E0
6.600E0	5.323E4	1.878E-1	1.97E0	1.60E0	1.94E0	1.43E0
6.400E0	5.162E4	1.937E-1	2.04E0	1.29E0	1.92E0	1.22E0

TABLE I *(Continued)*

$CuGaS_2$

eV	cm^{-1}	μm	n_o	k_o	n_e	k_e
			[12]	[12]	[12]	[12]
6.200E0	5.001E4	2.000E-1	1.91E0	1.20E0	1.80E0	1.16E0
6.000E0	4.839E4	2.066E-1	1.83E0	1.20E0	1.68E0	1.22E0
5.800E0	4.678E4	2.138E-1	1.79E0	1.33E0	1.74E0	1.43E0
5.600E0	4.517E4	2.214E-1	1.92E0	1.45E0	1.94E0	1.42E0
5.500E0	4.436E4	2.254E-1	2.02E0	1.45E0	2.00E0	1.37E0
5.400E0	4.356E4	2.296E-1	2.09E0	1.40E0	2.02E0	1.35E0
5.300E0	4.275E4	2.339E-1	2.11E0	1.38E0	2.05E0	1.35E0
5.200E0	4.194E4	2.384E-1	2.15E0	1.38E0	2.10E0	1.33E0
5.100E0	4.114E4	2.431E-1	2.24E0	1.38E0	2.13E0	1.30E0
5.000E0	4.033E4	2.480E-1	2.29E0	1.29E0	2.13E0	1.28E0
4.900E0	3.952E4	2.530E-1	2.27E0	1.25E0	2.16E0	1.31E0
4.800E0	3.872E4	2.583E-1	2.28E0	1.24E0	2.25E0	1.30E0
4.700E0	3.791E4	2.638E-1	2.32E0	1.26E0	2.29E0	1.24E0
4.600E0	3.710E4	2.695E-1	2.38E0	1.21E0	2.31E0	1.21E0
4.500E0	3.630E4	2.755E-1	2.39E0	1.16E0	2.35E0	1.20E0
4.400E0	3.549E4	2.818E-1	2.38E0	1.13E0	2.37E0	1.14E0
4.300E0	3.468E4	2.883E-1	2.37E0	1.12E0	2.37E0	1.12E0
4.200E0	3.388E4	2.952E-1	2.37E0	1.19E0	2.37E0	1.11E0
4.100E0	3.307E4	3.024E-1	2.43E0	1.19E0	2.34E0	1.16E0
4.000E0	3.226E4	3.100E-1	2.49E0	1.24E0	2.48E0	1.31E0
3.900E0	3.146E4	3.179E-1	2.63E0	1.23E0	2.73E0	1.17E0
3.800E0	3.065E4	3.263E-1	2.74E0	1.14E0	2.73E0	1.00E0
3.700E0	2.984E4	3.351E-1	2.80E0	1.03E0	2.73E0	9.05E-1
3.600E0	2.904E4	3.444E-1	2.82E0	9.34E-1	2.72E0	8.25E-1
3.500E0	2.823E4	3.542E-1	2.83E0	8.50E-1	2.69E0	7.60E-1
3.400E0	2.742E4	3.646E-1	2.82E0	7.76E-1	2.68E0	7.10E-1
3.300E0	2.662E4	3.757E-1	2.81E0	6.94E-1	2.65E0	6.78E-1
3.200E0	2.581E4	3.874E-1	2.78E0	6.49E-1	2.64E0	6.56E-1
3.100E0	2.500E4	3.999E-1	2.76E0	6.19E-1	2.62E0	6.33E-1
3.000E0	2.420E4	4.133E-1	2.75E0	5.95E-1	2.63E0	6.26E-1
2.900E0	2.339E4	4.275E-1	2.74E0	5.79E-1	2.64E0	6.09E-1
2.800E0	2.258E4	4.428E-1	2.75E0	5.59E-1	2.65E0	5.85E-1
2.750E0	2.218E4	4.508E-1	2.76E0	5.48E-1	2.65E0	5.74E-1
2.700E0	2.178E4	4.592E-1	2.76E0	5.37E-1	2.69E0	5.94E-1
2.650E0	2.137E4	4.678E-1	2.76E0	5.41E-1	2.71E0	5.38E-1
2.600E0	2.097E4	4.768E-1	2.86E0	5.91E-1	2.71E0	4.69E-1
2.550E0	2.057E4	4.862E-1	2.92E0	3.94E-1	2.78E0	6.09E-1
2.500E0	2.016E4	4.959E-1	2.82E0	3.37E-1	2.73E0	4.41E-1

eV	cm^{-1}	μm	n	k
				[15]
2.400E0	1.935E4	5.167E-1		3.98E-5
2.410E0	1.944E4	5.144E-1		5.80E-5
2.420E0	1.952E4	5.123E-1		8.20E-5
2.429E0	1.959E4	5.104E-1		1.12E-4

(continued)

TABLE I *(Continued)*

$CuGaS_2$

eV	cm^{-1}	μm	n	k	
				[15]	
2.434EO	1.964E4	5.093E-1		1.46E-4	
2.438E0	1.967E4	5.085E-1		1.98E-4	
2.443E0	1.971E4	5.075E-1		2.74E-4	
2.449E0	1.975E4	5.063E-1		4.09E-4	
2.453E0	1.979E4	5.054E-1		6.03E-4	
2.458E0	1.983E4	5.044E-1		9.22E-4	
2.460E0	1.984E4	5.039E-1		1.06E-3	
2.463E0	1.987E4	5.034E-1		1.16E-3	
2.465E0	1.988E4	5.029E-1		1.20E-3	
2.468E0	1.991E4	5.023E-1		1.23E-3	
2.470E0	1.992E4	5.020E-1		1.24E-3	
2.474E0	1.995E4	5.012E-1		1.29E-3	
2.476E0	1.997E4	5.008E-1		1.35E-3	
2.478E0	1.999E4	5.004E-1		1.41E-3	
2.482E0	2.002E4	4.995E-1		1.68E-3	
2.487E0	2.006E4	4.985E-1		2.03E-3	
2.493E0	2.011E4	4.973E-1		2.60E-3	
eV	cm^{-1}	μm	n_o	k	n_e
			[17]	[17]	[17]
2.254E0	1.818E4	5.500E-1	2.763E0		2.781E0
2.101E0	1.695E4	5.529E-1		3.33E-5	
2.066E0	1.667E4	5.900E-1	2.709E0	2.64E-5	2.714E0
2.033E0	1.639E4	6.000E-1	2.698E0	2.55E-5	2.702E0
2.000E0	1.613E4	6.100E-1	2.689E0	2.50E-5	2.691E0
1.968E0	1.587E4	6.200E-1	2.680E0	2.46E-5	2.682E0
1.937E0	1.563E4	6.300E-1	2.672E0	2.42E-5	2.673E0
1.907E0	1.538E4	6.400E-1	2.664E0	2.39E-5	2.665E0
1.771E0	1.429E4	6.500E-1	2.658E0	2.35E-5	2.637E0
1.653E0	1.333E4	7.000E-1	2.629E0	2.21E-5	2.627E0
1.550E0	1.250E4	7.500E-1	2.610E0	2.18E-5	2.606E0
1.459E0	1.176E4	8.000E-1	2.593E0	2.22E-5	2.589E0
1.378E0	1.111E4	8.500E-1	2.579E0	2.30E-5	2.574E0
1.305E0	1.053E4	9.000E-1	2.568E0	2.38E-5	2.563E0
1.240E0	1.000E4	9.500E-1	2.559E0	2.48E-5	2.554E0
1.127E0	9.091E3	1.000E0	2.552E0	2.56E-5	2.546E0
1.033E0	8.333E3	1.100E0	2.541E0	2.71E-5	2.535E0
9.537E-1	7.692E3	1.200E0	2.532E0	2.78E-5	2.527E0
8.856E-1	7.143E3	1.300E0	2.526E0	2.61E-5	2.520E0
7.749E-1	6.250E3	1.400E0	2.521E0	2.33E-5	2.515E0
6.888E-1	5.556E3	1.422E0		2.26E-5	
6.199E-1	5.000E3	1.600E0	2.514E0	2.40E-5	2.507E0
5.636E-1	4.545E3	1.800E0	2.509E0	2.70E-5	2.503E0
5.166E-1	4.167E3	2.000E0	2.505E0	3.55E-5	2.449E0
4.769E-1	3.846E3	2.200E0	2.502E0	3.93E-5	2.496E0

TABLE I *(Continued)*

$CuGaS_2$

eV	cm^{-1}	μm	n_o	k	n_e
			[17]	[17]	[17]
4.428E-1	3.571E3	2.400E0	2.499E0	3.33E-5	2.493E0
4.133E-1	3.333E3	2.600E0	2.498E0	3.03E-5	2.491E0
3.875E-1	3.125E3	2.800E0	2.496E0	2.91E-5	2.489E0
3.647E-1	2.941E3	3.000E0	2.495E0	2.77E-5	2.489E0
3.444E-1	2.778E3	3.200E0	2.493E0	2.69E-5	2.487E0
3.263E-1	2.632E3	3.400E0	2.492E0	2.69E-5	2.485E0
3.100E-1	2.500E3	3.600E0	2.491E0	2.71E-5	2.484E0
2.755E-1	2.222E3	3.800E0	2.490E0	2.76E-5	2.483E0
2.480E-1	2.000E3	4.000E0	2.488E0	2.81E-5	2.482E0
2.254E-1	1.818E3	4.500E0	2.487E0	2.93E-5	2.480E0
2.066E-1	1.667E3	4.915E0		3.01E-5	
1.907E-1	1.538E3	5.000E0	2.484E0	3.17E-5	2.477E0
1.771E-1	1.429E3	5.500E0	2.480E0	4.14E-5	2.473E0
1.653E-1	1.333E3	6.000E0	2.477E0	4.51E-5	2.469E0
1.550E-1	1.250E3	6.500E0	2.474E0	3.99E-5	2.466E0
1.459E-1	1.176E3	7.000E0	2.472E0	3.72E-5	2.462E0
1.378E-1	1.111E3	7.348E0		3.67E-5	
1.305E-1	1.053E3	7.500E0	2.467E0	3.79E-5	2.458E0
1.240E-1	1.000E3	8.000E0	2.464E0	4.40E-5	2.454E0
1.181E-1	9.524E2	8.500E0	2.459E0	5.77E-5	2.449E0
1.127E-1	9.091E2	9.000E0	2.454E0	7.23E-5	2.444E0
1.078E-1	8.696E2	9.126E0		7.65E-5	
1.033E-1	8.333E2	9.500E0	2.449E0	8.12E-5	2.438E0
9.919E-2	8.000E2	1.000E1	2.443E0	9.11E-5	2.431E0
9.537E-2	7.692E2	1.050E1	2.437E0	1.09E-4	2.423E0
2.242E0	1.809E4	1.100E1	2.431E0	1.38E-4	2.418E0
2.214E0	1.786E4	1.150E1	2.428E0	1.76E-4	2.412E0
2.178E0	1.757E4	1.184E1		1.99E-4	
2.135E0	1.722E4	1.200E1	2.417E0	1.95E-4	
2.060E0	1.661E4	1.229E1		1.88E-4	
1.963E0	1.583E4	1.250E1	2.409E0	2.23E-4	
1.806E0	1.457E4	1.300E1	2.400E0	9.23E-4	
1.682E0	1.357E4	1.306E1		1.06E-3	
1.556E0	1.255E4	1.314E1		1.44E-3	
1.402E0	1.131E4	1.325E1		2.04E-3	

eV	cm^{-1}	μm	n_o	k_o	n_e	k_e
			[23]	[23]	[23]	[23]
6.199E-2	5.000E2	2.000E1	2.11E0	1.10E-2	2.21E0	2.64E-3
5.579E-2	4.500E2	2.222E1	1.87E0	2.51E-2	2.05E0	6.25E-3
5.207E-2	4.200E2	2.381E1	1.49E0	6.04E-2	1.83E0	1.39E-2
5.158E-2	4.160E2	2.404E1	1.39E0	7.24E-2	1.78E0	1.61E-2
5.108E-2	4.120E2	2.427E1	1.28E0	9.00E-2	1.73E0	1.87E-2
5.059E-2	4.080E2	2.451E1	1.13E0	1.18E-1	1.67E0	2.22E-2
5.009E-2	4.040E2	2.475E1	9.13E-1	1.73E-1	1.59E0	2.70E-2

(continued)

TABLE I *(Continued)*

$CuGaS_2$

eV	cm^{-1}	μm	n_o	k_o	n_e	k_e
			[23]	[23]	[23]	[23]
4.959E-2	4.000E2	2.500E1	5.90E-1	3.33E-1	1.50E0	3.36E-2
4.910E-2	3.960E2	2.525E1	3.35E-1	8.00E-1	1.38E0	4.37E-2
4.860E-2	3.920E2	2.551E1	3.47E-1	1.36E0	1.22E0	6.04E-2
4.798E-2	3.870E2	2.584E1	1.36E0	1.81E0	9.23E-1	1.08E-1
4.761E-2	3.840E2	2.604E1	8.78E-1	1.07E0	6.12E-1	2.03E-1
4.711E-2	3.800E2	2.632E1	3.80E-1	1.71E0	2.27E-1	7.83E-1
4.662E-2	3.760E2	2.660E1	3.65E-1	2.39E0	2.05E-1	1.39E0
4.612E-2	3.720E2	2.688E1	5.02E-1	3.21E0	2.76E-1	2.08E0
4.563E-2	3.680E2	2.717E1	1.08E0	4.62E0	6.10E-1	3.19E0
4.538E-2	3.660E2	2.732E1	2.25E0	5.78E0	1.37E0	4.22E0
4.513E-2	3.640E2	2.747E1	5.50E0	5.48E0	4.31E0	4.25E0
4.488E-2	3.620E2	2.762E1	5.85E0	2.26E0	4.35E0	1.34E0
4.439E-2	3.580E2	2.793E1	3.83E0	8.43E-1	2.71E0	3.82E-1
4.389E-2	3.540E2	2.825E1	2.60E0	1.03E0	1.77E0	3.04E-1
4.339E-2	3.500E2	2.857E1	2.13E0	2.32E0	7.17E-1	6.61E-1
4.302E-2	3.470E2	2.882E1	3.16E0	3.38E0	3.49E-1	1.54E0
4.277E-2	3.450E2	2.899E1	4.47E0	3.18E0	3.11E-1	2.04E0
4.240E-2	3.420E2	2.924E1	5.05E0	1.62E0	3.29E-1	2.78E0
4.191E-2	3.380E2	2.959E1	4.45E0	6.60E-1	4.81E-1	4.00E0
4.141E-2	3.340E2	2.994E1	3.97E0	3.67E-1	1.14E0	6.19E0
4.092E-2	3.300E2	3.030E1	3.64E0	2.50E-1	9.13E0	8.71E0
4.042E-2	3.260E2	3.067E1	3.40E0	1.94E-1	7.34E0	9.61E-1
3.992E-2	3.220E2	3.106E1	3.21E0	1.66E-1	5.65E0	3.36E-1
3.943E-2	3.180E2	3.145E1	3.06E0	1.54E-1	4.89E0	1.76E-1
3.893E-2	3.140E2	3.185E1	2.91E0	1.52E-1	4.45E0	1.11E-1
3.844E-2	3.100E2	3.226E1	2.78E0	1.58E-1	4.15E0	7.65E-2
3.794E-2	3.060E2	3.268E1	2.65E0	1.73E-1	3.95E0	5.65E-2
3.744E-2	3.020E2	3.311E1	2.52E0	1.98E-1	3.79E0	4.36E-2
3.695E-2	2.980E2	3.356E1	2.38E0	2.37E-1	3.66E0	3.48E-2
3.645E-2	2.940E2	3.401E1	2.22E0	2.97E-1	3.56E0	2.85E-2
3.596E-2	2.900E2	3.448E1	2.04E0	3.92E-1	3.48E0	2.37E-2
3.546E-2	2.860E2	3.497E1	1.83E0	5.50E-1	3.41E0	2.01E-2
3.496E-2	2.820E2	3.546E1	1.60E0	8.23E-1	3.35E0	1.73E-2
3.447E-2	2.780E2	3.597E1	1.45E0	1.26E0	3.30E0	1.50E-2
3.397E-2	2.740E2	3.650E1	1.47E0	1.82E0	3.25E0	1.32E-2
3.348E-2	2.700E2	3.704E1	1.72E0	2.44E0	3.21E0	1.17E-2
3.298E-2	2.660E2	3.759E1	2.30E0	3.06E0	3.18E0	1.04E-2
3.248E-2	2.620E2	3.817E1	3.35E0	3.39E0	3.15E0	9.34E-3
3.211E-2	2.590E2	3.861E1	4.28E0	3.11E0	3.13E0	8.64E-3
3.174E-2	2.560E2	3.906E1	4.86E0	2.39E0	3.11E0	8.02E-3
3.124E-2	2.520E2	3.968E1	4.93E0	1.47E0	3.08E0	7.28E-3
3.075E-2	2.480E2	4.032E1	4.70E0	9.15E-1	3.06E0	6.65E-3
3.025E-2	2.440E2	4.098E1	4.45E0	6.09E-1	3.04E0	6.09E-3
2.976E-2	2.400E2	4.167E1	4.25E0	4.31E-1	3.02E0	5.60E-3
2.926E-2	2.360E2	4.237E1	4.08E0	3.20E-1	3.00E0	5.16E-3
2.876E-2	2.320E2	4.310E1	3.94E0	2.47E-1	2.99E0	4.77E-3

TABLE I *(Continued)*

$CuGaS_2$

eV	cm^{-1}	μm	n_o	k_o	n_e	k_e
			[23]	[23]	[23]	[23]
2.827E-2	2.280E2	4.386E1	3.83E0	1.97E-1	2.97E0	4.42E-3
2.777E-2	2.240E2	4.464E1	3.74E0	1.60E-1	2.96E0	4.11E-3
2.728E-2	2.200E2	4.545E1	3.67E0	1.33E-1	2.95E0	3.83E-3
2.678E-2	2.160E2	4.630E1	3.60E0	1.12E-1	2.94E0	3.57E-3
2.628E-2	2.120E2	4.717E1	3.55E0	9.62E-2	2.92E0	3.34E-3
2.579E-2	2.080E2	4.808E1	3.50E0	8.33E-2	2.91E0	3.13E-3
2.529E-2	2.040E2	4.902E1	3.45E0	7.29E-2	2.90E0	2.93E-3
2.480E-2	2.000E2	5.000E1	3.41E0	6.42E-2	2.90E0	2.76E-3
1.860E-2	1.500E2	6.667E1	3.15E0	2.02E-2	2.82E0	1.37E-3
1.240E-2	1.000E2	1.000E2	3.04E0	8.74E-3	2.78E0	7.15E-4
6.199E-3	5.000E1	2.000E2	3.00E0	3.51E-3	2.76E0	3.12E-4

Gallium Selenide (GaSe)

DAVID F. EDWARDS
Tracy, California

Gallium selenide (GaSe) is a semiconductor that has recently received much attention because of its potential applications. GaSe has been proposed as the active compound for use in photovoltaic devices [1, 2], as intercalation electrodes in electrochemical lithium cells [3, 4], and as a nonlinear optical medium [5]. GaSe is also of interest because of its physical properties. The compound belongs to the family of metal chalcogens that crystallize in a layered structure. Each layer consists of four atomic sheets, Se–Ga–Ga–Se, that are bound together by strong forces, mostly covalent. The forces between layers are of the weak van der Waals type. The layer structure of GaSe is D_{3h} hexagonal symmetry with two formula units per layer unit cell [6–8]. Because of the different ways of stacking adjacent layers, GaSe crystallizes under several modifications. So far, four modifications have been proposed [9]. These are β (space group D_{6h}^4),γ (C_{3v}^5),ϵ (D_{3h}^1), and δ (C_{6v}^4). Several researchers [10, 11] question the existence of the β-structure and propose that γ-GaSe is a very rare modification [12] . The data reported in this chapter are for the ϵ-type modification. The interested reader is referred to the review paper by Fernelius [13] for an extensive compilation of the growth, structural and mechanical, thermal, electrical, and optical properties of single-crystal GaSe.

COMPLEX INDEX OF REFRACTION I

Brebner and Deverin [14] were among the first to report index-of-refraction measurements for GaSe. Their data were for a limited wavelength region in the vicinity of the band gap and for an undefined crystalline modification. Since this first report, a number of groups have reported index values using different techniques and different experimental conditions and crystalline modifications. A few developed analytical expressions that accurately represent their experimental data. Adachi and Shindo [15] used spec-

HANDBOOK OF OPTICAL CONSTANTS OF SOLIDS III

Copyright © 1998 by Academic Press.
All rights of reproduction in any form reserved
ISBN 0-12-544423-0/$25.00.

troscopic ellipsometery to measure the complex dielectric function, $\epsilon(\omega) = \epsilon_1(\omega) + i\epsilon_2(\omega)$, in the 2.0–5.0 eV photon-energy range for ϵ-GaSe. The layered structure of GaSe allows for easy cleavage with the crystallographic c-axis in the cleavage plane. From their measured data they have developed a mathematical model of the spectral dependence of $\epsilon(\omega)$ at energies below and above the fundamental absorption edge. Their model is based on the Kramers–Kronig transformation and is strongly connected with the electronic energy-band structure of the material. From their model the index of refraction, n, and extinction coefficient, k, have been calculated for selected wavelengths and are listed in Table I for light polarized perpendicular (n_o, k_o) and parallel (n_e, k_e) to the crystallographic c-axis. These data are plotted in Figs. 1 and 2, respectively. Other authors report optical measurements for this band-gap region, but only Adachi and Shindo [15] have developed a theoretical model that accurately represents their data over an extended wavelength region.

According to Adachi and Shindo [15], for light polarized perpendicular to the c-axis the complex dielectric function is the sum of the following three dispersive and one nondispersive terms. The contribution to $\epsilon(\omega)$ corresponding to the one-electron approximation for a transition from one of the three valence bands to the conduction band is

$$\epsilon(\omega) = -BX_1^{-2} ln(1 - X_1^2). \tag{1}$$

There is an additional contribution of the saddle-point exciton at this critical point given by

$$\epsilon(\omega) = B_\chi/(1 - X_1) \tag{2}$$

with

$$X_1 = (\hbar\omega + i\Gamma)/E_1. \tag{3}$$

The B's and Γ are, respectively, the strength and broadening parameters of these transitions.

The contribution to $\epsilon(\omega)$ corresponding to transitions from a second valence band to the conduction band is characterized as that of a damped harmonic oscillator,

$$\epsilon(\omega) = C/[(1 - X_3^2) - iX_3\gamma], \tag{4}$$

with

$$X_3 = \hbar\omega/E_3,$$

where C is the strength parameter and γ is the dimensionless broadening parameter. In these equations $\hbar\omega$ is the photon energy (eV), and E_1 and E_3 are the energies corresponding to critical points as resolved by the dielectric-function spectra. The B, B_χ, and C are adjustable parameters. The critical-point energies, E_1 and E_3, are adjusted to obtain better fits to the dielectric-function data. The values of these parameters are listed in Table II. To the

sum of Eqs. (1), (2), and (4) is added $\epsilon_{1\infty}$, the nondispersive term, to improve the fit. This term is assumed to arise from other higher-lying gap contributions.

The refractive index, n_o, and extinction coefficient, k_o, are obtained from the real and imaginary parts of the sum of Eqs. (1), (2), and (4) plus $\epsilon_{1\infty}$. It follows that

$$\epsilon(\omega)^{1/2} = n(\omega) + ik(\omega),$$

and

$$n(\omega) = \left(\frac{[\epsilon_1(\omega)^2 + \epsilon_2(\omega)^2]^{1/2} + \epsilon_1(\omega)}{2} \right)^{1/2}, \tag{5}$$

$$k(\omega) = \left(\frac{[\epsilon_1(\omega)^2 + \epsilon_2(\omega)^2]^{1/2} - \epsilon_1(\omega)}{2} \right)^{1/2}. \tag{6}$$

For photon energies greater than 0.1 eV the theoretical curve for n_o (n) is in good agreement with the experimental data of Adachi and Shindo [15] and those of Toullec *et al.* [16], Wasscher and Dieleman [17], and Piccioli *et al.* [18]. For photon energies below 0.1 eV the theoretical curve shows poor fit with the data of Piccioli *et al.* [18]. The reason given is that Adachi and Shindo did not take into account the reststrahlen dispersion. For this reststrahlen region the radiation field strongly interacts with the fundamental lattice vibrations [19].

An expression was also developed by Adachi and Shindo for the complex dielectric function for light polarized parallel to the c-axis. They fitted the experimental data of Toullec *et al.* [16] to a steplike absorption edge. The contribution to $\epsilon(\omega)$ for this type of transition is given by

$$\epsilon(\omega) = -AX_0^{-2}\ln(1 - X_0^2), \tag{7}$$

with

$$X_0 = (\hbar\omega + i\Gamma)/E_0,$$

where A and Γ are, respectively, the strength and broadening parameters and E_0 is the energy of the steplike edge. The extraordinary refractive indices n_e ($n\|$) and extinction coefficient k_e ($k\|$), are calculated from Eq. (7) plus the nondispersive term, $\epsilon_{1\infty}$, using Eqs. (5) and (6). The results are listed in Table I and plotted in Fig. 2.

Piccioli and co-workers [16, 18] have measured the ordinary and extraordinary optical constants for ϵ-GaSe between 0.45 and 330 μm. Three measuring techniques were used to cover this range. For the GaSe transparent region (12 to 33 μm and 70 to 330 μm) the index was determined from interference fringes produced by multiple internal reflections from the parallel faces of the sample. For the 0.45- to 0.62-μm region the index was determined from the reflectance of the sample of known thickness and which

had one face coated with aluminum. In the reststrahlen region (30–70 μm) the indices were determined from the infrared reflectance on thick samples. A Kramers–Kronig analysis of these reflectance data gives values of the transverse and longitudinal optical modes, ω_{TO} and ω_{LO}.

Piccioli and co-workers [16, 18] developed a theoretical fit of their data assuming the complex dielectric function to be a combination of electronic transitions (a polynomial development) and of lattice vibrations (a damped harmonic oscillator). Their expression as a function of wavenumber, ω, is

$$\epsilon(\omega) = A\omega^6 + B\omega^4 + C\omega^2 + \epsilon_\infty + \frac{(\omega_{LO}^2 - \omega_{TO}^2)\epsilon_\infty}{\omega_{TO}^2 - \omega^2 - i\Gamma\omega}, \tag{8}$$

where Γ is the damping of the harmonic oscillator, ω_{TO} and ω_{LO} are, respectively, the transverse and longitudinal optical-phonon wavenumbers, and A, B, C are parameters determined by a mean-square fit to the data. The index of refraction, n, and the extinction coefficient, k, are found from the real and imaginary parts of Eq. (8). Values for the parameters in Eq. (8) are given in Table III. The Piccioli *et al.* indices are listed in Table I for ϵ-GaSe as calculated using Eq. (8) and the parameters of Table III. According to Piccioli *et al.*, the calculated ordinary index of refraction reproduces the experimental results with a standard deviation of 0.002. The exception is for the band-gap region (0.619μm), where the measured n_o and k_o values deviate from those calculated by about 0.0075. Shown in Figs. 1 and 2 are the ordinary and extraordinary index of refraction and extinction coefficient, respectively, as calculated by the preceding equations. With reference to the extinction coefficient curves, it is not clear why the k values of Adachi and Shindo [15] are so much larger than those of Piccioli *et al.* One would expect the k values to decrease abruptly for photon energies below the band gap. As pointed out by Piccioli *et al.*, in the energy-gap region the transmission of the sample decreases so rapidily that important errors on the energy extreme could not be avoided. For this region their method was to measure the reflectance of a sample of known thickness and which was coated with aluminum on one face. It is not clear, but this could have a significant effect on the reflectance values and thus the smaller k values in this region.

II THERMAL COEFFICIENTS

The temperature variation of the ordinary index of refraction was measured by Antonioli *et al.* [20] for temperatures from 300 to 75 K in the 0.5- to 2.5-eV energy range. Their results are given by the expression

$$n(h\nu) = A + B(h\nu) + C(h\nu)^3, \tag{9}$$

where the phenomenological coefficients are given in Table IV for four selected temperatures. The reader is referred to the original report [20] for the complete coefficient list of 10 temperatures between 300 and 75 K. Antonioli *et al.* report the relative error for the refractive index $\Delta n/n \approx 10^{-3}$ for all the temperatures over the entire energy range investigated, with the exception of the spectral region around the exciton energy (619 nm). The 300-K values of Antionoli *et al.* are in good agreement with those of Piccioli *et al.* [18] for the 0.5- to 2.5-eV energy region.

The temperature dependence of the energy gap of ϵ-GaSe as reported by Reddy *et al.* [21] is

$$E_g = 2.137 \exp(-T \times 10^{-4}/0.61), \tag{10}$$

where T is the temperature for the range 0 to 300 K, and the energy gap, E_g, is in eV.

PRESSURE COEFFICIENT III

Gauthier *et al.* [22] have measured the refractive index of room-temperature ϵ-GaSe in the region of the direct-gap energy (1.5 to 1.9 eV) for hydrostatic pressures up to 8 GPa. They report no evidence of a phase transition, indicating that the layered structure of ϵ-GaSe is stable for this pressure range. They also found the relative variation of the index with pressure to be the same for their measured spectral region, indicating that the index dispersion does not vary significantly with pressure. From their data for the relative variation of index, the following polynomial was fit by a least-squares technique.

$$\frac{n}{n(0)} = 0.99977 + 1.8130 \times 10^{-2}p - 3.9367 \times 10^{-3}p^2 + 4.4431 \times 10^{-4}p^3 - 1.8098 \times 10^{-5}p^4, \tag{11}$$

where $n(0)$ is the atmospheric-pressure index and p is the hydrostatic pressure in GPa. They report a precision of better than 1% for $n(\lambda,p)$.

REFERENCES

1. A. Segura, J. P. Guesdon, J. M. Besson, and A. Chevy, *Rev. Phys. Appl.* **14**, 253 (1979).
2. C. Clemen, X. I. Saldana, P. Munz, and E. Butcher, *Phys. Status Solidi A* **49**, 437 (1978).
3. C. Julien and E. Hatzikkraniotis, *Mater. Lett.* **5**, 134 (1988).
4. Z. D. Kovalyuk, M. N. Pyrla, A. I. Seredyuk, and K. D. Tovstyuk, *Inorg. Mater.* **21**, 1444 (1985).
5. C. Hirliman, J. F. Morhange, M. A. Kanehisa, A. Chevy, and C. H. Brito-Cruz, *Appl. Phys. Lett.* **55**, 2307 (1989).

6. H. Hahn and G. Z. Frank, *Anorg. Allg. Chem.* **278**, 340 (1955).
7. K. Schubert, E. Dorre, and M. Kluge, *Z. Metallkd.* **46**, 216 (1955).
8. F. Jellinek and H. Hahn, *Z. Naturforsch.* **B16,** 713 (1961).
9. A. Kuhn, A. Chevy, and R. Chevalier, *Phys. Status Solidi A* **31, 469, (1975).**
10. A. Polian, K. Kunc, and A. Kuhn, *Solid State Commun.* **19,** 1079 (1976).
11. A. Gouskov, J. Camassel, and L. Gouskov, *Prog. Cryst. Growth Charact.* **5,** 323 (1982).
12. E. Finkman and A. Rizzo, *Solid State Commun.* **15,** 1841 (1974).
13. N. C. Fernelius, *Prog. Cryst. Growth Charat.* **28**, 275 (1994).
14. J. L. Brebner and J. A. Deverin, *Helv. Phys. Acta* **38,** 650 (1965).
15. S. Adachi and Y. Shindo, *J. Appl. Phys.* **71**, 428 (1992).
16. R. Le Toullec, N. Piccioli, M. Mejatty, and M. Balkanski, *Ital. Nuovo Cimento.* **38B**, 159 (1977).
17. J. O. Wasscher and J. Dieleman, *Phys. Lett.* **A39**, 279 (1972).
18. N. Piccioli, R. Le Toullec, M. Mejatty, and M. Balkanski, *Appl. Opt.* **16,** 1236 (1977).
19. See, for instance, M. Balkanski, *in* "Optical Properties of Soilds" (F. Abeles, ed.), p. 529. North-Holland Publ., Amsterdam, 1972.
20. G. Antonioli, D. Bianchi, and P. Franzosi, *Appl. Opt.* **18**, 3847 (1979).
21. R. R. Reddy, M. Ravi Kumar, and T. V. R. Rao, *Infrared Phys.* **34,** 103 (1993).
22. M. Gauthier, A. Polian, J. M. Besson, and A. Chevy, *Phys. Rev. B* **40**, 3837 (1989).

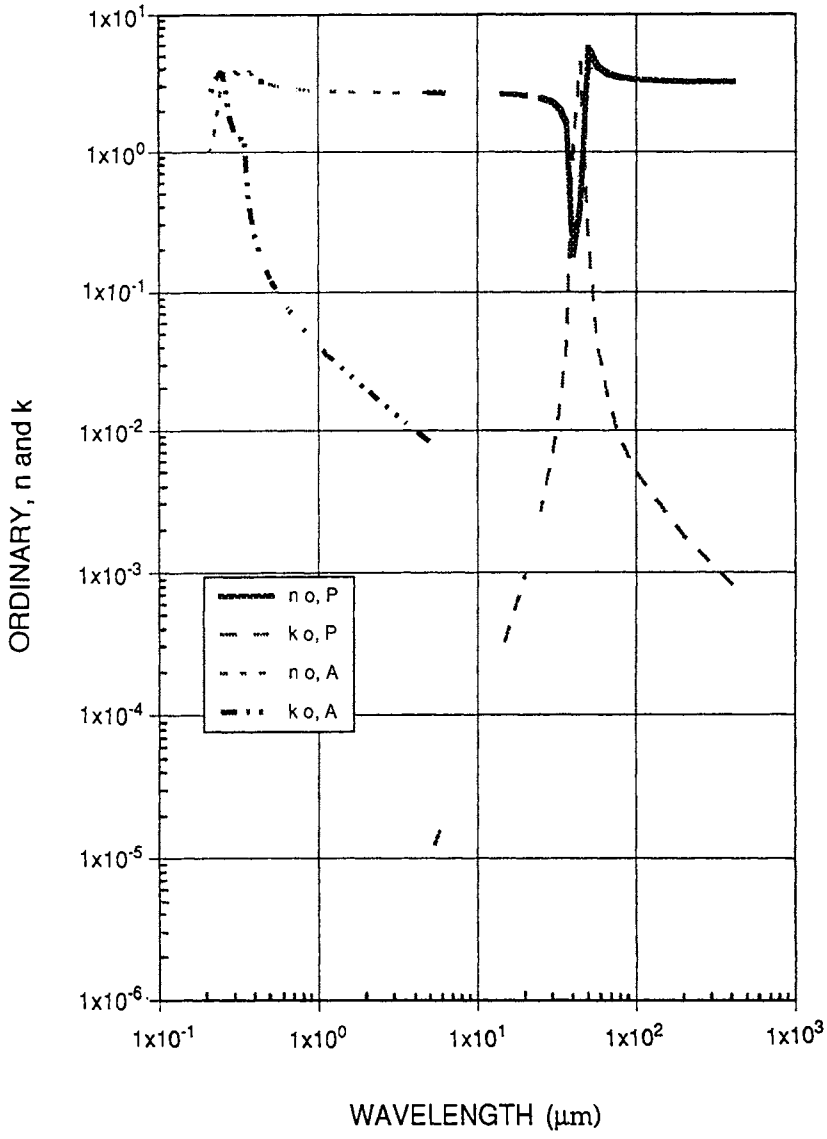

Fig. 1. Log–log plot of ordinary n_o and k_o versus wavelength in micrometers for ϵ-GaSe. The curves n_o,A and k_o,A are calculated from the sum of Eqs. (1), (2), (4), and $\epsilon_{1\infty} = 1.25$. The curves n_o,P and k_o,P are calculated from Eq. (8).

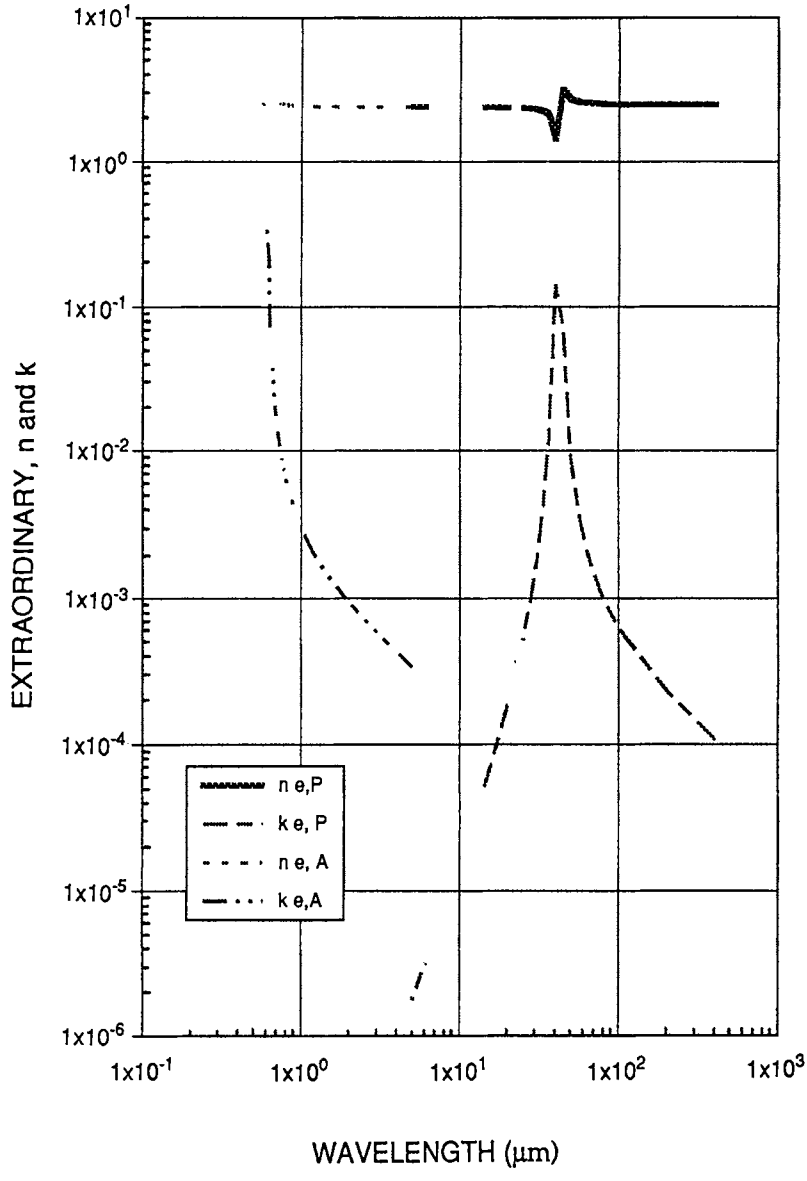

Fig. 2. Log–log plot of extraordinary n_e and k_e versus wavelength in micrometers for ϵ-GaSe. The curves n_e,A and k_e,A are calculated from the sum of Eq. (7) and $\epsilon_{1\infty} = 4.9$. The curves n_e,P and k_e,P are calculated from Eq. (8).

TABLE I

Values of n and k for ε-GaSe as Calculated from the Expressions of Adachi and Shindo [15] and Piccioli *et al.* [16, 18]

eV	cm^{-1}	μm	$n_o(P)$	$k_o(P)$	$n_e(P)$	$k_e(P)$	$n_o(A)$	$k_o(A)$	$n_e(A)$	$k_e(A)$
6.00	48309	0.207					1.00451 [15]	2.60550 [15]		
5.95	47907	0.209					1.03292	2.66138		
5.90	47504	0.211					1.06430	2.71991		
5.85	47101	0.212					1.09908	2.78124		
5.80	46699	0.214					1.13777	2.84549		
5.75	46296	0.216					1.18099	2.91279		
5.70	45894	0.218					1.22946	2.98323		
5.65	45491	0.220					1.28404	3.05683		
5.60	45089	0.222					1.34730	3.13354		
5.50	44686	0.224					1.41574	3.21320		
5.00	44283	0.226					1.49544	3.29542		
5.45	43881	0.228					1.58647	3.37957		
5.40	43478	0.230					1.69067	3.46464		
5.35	43076	0.232					1.81006	3.54905		
5.30	42673	0.234					1.94680	3.63049		
5.25	42271	0.237					2.10295	3.70570		
5.20	41868	0.239					2.28015	3.77020		
5.15	41465	0.241					2.47909	3.81818		
5.10	41063	0.244					2.69870	3.84256		
5.05	40660	0.246					2.93529	3.83555		
5.00	40258	0.248					3.18170	3.78976		
4.95	39855	0.251					3.42720	3.70010		
4.90	39453	0.253					3.65850	3.56579		
4.85	39050	0.256					3.86214	3.39166		
4.80	38647	0.259					4.02747	3.18787		
4.75	38245	0.261					4.14898	2.96771		
4.70	37842	0.264					4.22682	2.74465		

(continued)

TABLE I *(Continued)*

ϵ-GaSe

eV	cm^{-1}	μm	n_o(P)	k_o(P)	n_e(P)	k_e(P)	n_o(A)	k_o(A)	n_e(A)	k_e(A)
4.65	37440	0.267					4.26569	2.52983		
4.55	36634	0.273					4.25599	2.15190		
4.50	36232	0.276					4.22252	1.99429		
4.45	35829	0.279					4.17839	1.85759		
4.40	35427	0.282					4.12830	1.74029		
4.35	35024	0.286					4.07574	1.64041		
4.30	34622	0.289					4.02321	1.55586		
4.25	34219	0.292					3.97245	1.48466		
4.20	33816	0.296					3.92466	1.42501		
4.15	33414	0.299					3.88061	1.37539		
4.10	33011	0.303					3.84085	1.33457		
4.05	32609	0.307					3.80573	1.30168		
4.00	32206	0.311					3.77557	1.27623		
3.95	31804	0.314					3.75804	1.25832		
3.90	31401	0.318					3.73254	1.24886		
3.85	30998	0.323					3.72316	1.24886		
3.80	30596	0.327					3.72909	1.23648		
3.75	30193	0.331					3.76591	1.29431		
3.70	29791	0.336					3.86252	1.32114		
3.65	29388	0.340					4.02957	1.27878		
3.60	28986	0.345					4.17863	1.10447		
3.55	28583	0.350					4.20760	8.7237E-1		
3.50	28180	0.355					4.14411	6.8188E-1		
3.45	27778	0.360					4.04945	5.5000E-1		
3.40	27375	0.365					3.95357	4.6035E-1		

3.35	26973	0.371		3.86555	3.9730E-1
3.30	26570	0.376		3.78686	3.5091E-1
3.25	26167	0.382		3.71674	3.1529E-1
3.20	25765	0.388		3.65396	2.8692E-1
3.15	25362	0.394		3.59736	2.6364E-1
3.10	24960	0.401		3.54597	2.4405E-1
3.05	24557	0.407		3.49899	2.2724E-1
3.00	24155	0.414		3.45579	2.1258E-1
2.95	23752	0.421		3.41586	1.9962E-1
2.90	23349	0.428		3.37878	1.8804E-1
2.86	23000	0.435	3.3179		
2.85	22947	0.436		3.34421	1.7760E-1
2.84	22850	0.438	3.3064		
2.82	22725	0.440	3.2970		
2.80	22544	0.444		3.31187	1.6810E-1
2.76	22225	0.450	3.2607		
2.75	22142	0.452		3.28152	1.5942E-1
2.70	21739	0.460		3.25297	1.5143E-1
2.65	21337	0.469		3.22604	1.4404E-1
2.60	20934	0.478		3.23006	1.3718E-1
2.55	20531	0.487		3.17651	1.3079E-1
2.50	20129	0.497		3.15367	1.2481E-1
2.48	20000	0.500	3.1226		
2.45	19726	0.507		3.13198	1.1920E-1
2.40	19324	0.518		3.11136	1.1393E-1
2.35	18921	0.529		3.09173	1.0896E-1
2.30	18519	0.540		3.07303	1.0426E-1
2.26	18175	0.550	3.0336 [18]		
2.25	18116	0.552		3.05520	9.9813E-2

(continued)

TABLE I *(Continued)*

ϵ-GaSe

eV	cm^{-1}	μm	n_o(P)	k_o(P)	n_e(P)	k_e(P)	n_o(A)	k_o(A)	n_e(A)	k_e(A)
2.20	17713	0.565					3.03819		2.49335 [15]	4.1439E-1 [15]
2.15	17311	0.578					3.02194	9.1579E-2	2.54691	4.1643E-1
2.10	16908	0.591					3.00642	8.7758E-2	2.61759	4.0900E-1
2.07	16650	0.601	2.9729							
2.05	16506	0.606					2.99158	8.4114E-2	2.7182	3.7344E-1
2.00	16103	0.621					2.97738	8.0632E-2	2.8225	2.1940E-1
1.95	15700	0.637					2.96381	7.7301E-2	2.73322	7.2733E-2
1.91	15375	0.650	2.9299							
1.90	15298	0.654					2.95082	7.4110E-2	2.65709	3.7473E-2
1.85	14895	0.671					2.93838	7.1048E-2	2.60927	2.4244E-2
1.80	14493	0.690					2.92648	6.8107E-2	2.57582	1.7502E-2
1.77	14275	0.701	2.8976							
1.75	14090	0.710					2.91509	6.5278E-2	2.55064	1.3464E-2
1.70	13688	0.731					2.90418	6.2553E-2	2.53077	1.0793E-2
1.65	13325	0.750	2.8730							
1.65	13285	0.753					2.89379	5.9926E-2	2.51456	8.9065E-3
1.60	12882	0.776					2.88375	5.7389E-2	2.50101	7.5083E-3
1.55	12500	0.800	2.8537							
1.55	12480	0.801					2.87420	5.4937E-2	2.48948	6.4340E-3
1.50	12077	0.828					2.86505	5.2565E-2	2.47953	5.5848E-3
1.46	11750	0.851	2.8377	4.2147E-8						
1.45	11675	0.857					2.85631	5.0267E-2	2.47084	4.8941E-3
1.40	11272	0.887					2.84795	4.8039E-2	2.46319	4.3320E-3
1.38	11100	0.901	2.8250	5.5777E-8						
1.35	10870	0.920					2.83997	4.5875E-2	2.456396	3.8579E-3

1.31	10525	0.950	2.8145	6.0664E-8						
1.30	10467	0.955					2.83235	4.3772E-2	2.45032	3.4554E-3
1.25	10064	0.994					2.82508	4.1727E-2	2.44486	3.1095E-3
1.24	10000	1.000	2.8056	7.8850E-8		2.1073E-8				
1.20	9662	1.035					2.81815	3.9734E-2	2.43994	2.8091E-3
1.15	9259	1.080					2.81156	3.7792E-2	2.43549	2.5458E-3
1.10	8857	1.129					2.80528	3.4044E-2	2.43145	2.3131E-3
1.05	8454	1.183					2.79932	3.4044E-2	2.42778	2.1056E-3
1.0000	8052	1.242					2.79366	3.2232E-2	2.41443	1.9195E-3
0.9500	7649	1.307					2.78830	3.0459E-2	2.42138	1.7514E-3
0.9000	7246	1.380					2.78323	2.8721E-2	2.41859	1.5985E-3
0.8500	6844	1.461					2.77845	2.7015E-2	2.41605	1.4587E-3
0.8000	6441	1.553					2.77395	2.5341E-2	2.41373	1.3301E-3
0.7500	6039	1.656					2.76971	2.3695E-2	2.41161	1.2112E-3
0.7000	5636	1.774					2.76575	2.2075E-2	2.40969	1.1007E-3
0.6500	5233	1.911					2.76205	2.0479E-2	2.40794	9.9744E-4
0.6210	5000	2.000	2.7459 [18]	6.2974E-7 [18]		1.1151E-7 [18]				
0.6000	4831	2.070					2.75862	1.8906E-2	2.40636	9.0048E-4
0.5500	4428	2.258					2.75542	1.7353E-2	2.40494	8.0898E-4
0.5000	4026	2.484					2.75250	1.5818E-2	2.40366	7.2221E-4
0.4500	3623	2.760					2.74982	1.4300E-2	2.40253	6.3954E-4
0.4000	3221	3.105					2.74738	1.2796E-2	2.40153	5.6037E-4
0.3500	2818	3.549					2.74519	1.1306E-2	2.40066	4.8421E-4
0.3105	2500	4.000	2.7286	5.1258E-6	2.4045	8.9630E-7				
0.3000	2415	4.140					2.74324	9.8277E-3	2.39992	4.1059E-4
0.2500	2013	4.968					2.74153	8.3592E-3	2.39929	3.3907E-4
0.2484	2000	5.000	2.7245	1.0110E-5	2.4021	1.7703E-6				
0.2049	1650	6.061	2.7204	1.8229E-5	2.4005	3.1976E-6				
0.2000	1610	6.210					2.74005	6.8990E-3	2.39879	2.6926E-4

(continued)

TABLE I *(Continued)*

ε-GaSe

eV	cm^{-1}	μm	n_o(P)	k_o(P)	n_e(P)	k_e(P)	n_o(A)	k_o(A)	n_e(A)	k_e(A)
0.1553	1250	8.000	2.7120	4.3139E-5	2.3981	7.5976E-6				
0.1500	1208	8.280					2.73881	5.4456E-3	2.3984	2.0080E-4
0.1242	1000	10.000	2.7012	8.7524E-5	2.3956	1.5497E-5				
0.1000	805	12.420					2.73780	3.9975E-3		1.3332E-4
0.0869	700	14.286	2.6687	2.8601E-4	2.3890	5.1486E-5				
0.0776	625	16.000	2.6511	4.2644E-4	2.3856	7.7458E-5				
0.0683	550	18.182	2.6240	6.8385E-4	2.3802	1.2594E-4				
0.0652	525	19.048	2.6115	8.1808E-4	2.3777	1.5162E-4				
0.0621	500	20.000	2.5965	9.9241E-4	2.3747	1.8534E-4				
0.0500	403	24.840						2.5531E-3		6.6498E-5
0.0497	400	25.000	2.4878	2.6447E-3	2.3523	5.2160E-4				
0.0435	350	28.571	2.3616	5.3937E-3	2.3247	1.1314E-3				
0.0404	325	30.769	2.2479	8.6346E-3	2.2985	1.9113E-3				
0.0373	300	33.333	2.0525	1.5949E-2	2.2500	3.8504E-3				
0.0342	275	36.364	1.6339	4.0131E-2	2.1326	1.1290E-2				
0.0311	250	40.000	0.1824	1.0295E + 0	1.4470	1.4084E-1				
0.0279	225	44.444	0.4115	4.5493E + 0	3.1580	7.5688E-2				
0.0248	200	50.000	5.7381	2.3813E-1	2.6869	9.4049E-3				
0.0217	175	57.143	4.1270	4.0770E-2	2.5855	3.4295E-3				
0.0186	150	66.667	3.6961	1.6398E-2	2.5420	1.7213E-3				
0.0155	125	80.000	3.4979	8.5744E-3	2.5185	9.9852E-4				
0.0124	100	100.000	3.3879	5.0204E-3	2.5043	6.1952E-4				
0.0062	50	200.000	3.2826	1.7673E-3	2.4900	2.3056E-4				
0.0031	25	400.000	3.2614	8.1678E-4	2.4870	1.0776E-4				

TABLE II

Parameters Used in the Calculation of the Optical Constants for ε-GaSe [15] from Eqs. (1)–(4) and (7)

Parameter	Ordinary	Extraordinary
E_0(eV)		2.00
A		0.85
Γ(meV)		30
E_1(eV)	3.63	
B	2.27	
B_χ	0.17	
Γ(eV)	0.13	
E_3(eV)	4.89	
C	3.8	
γ	0.17	
$\epsilon_{1\infty}$	1.25	4.9

TABLE III

Parameters Used in the Calculation of the Optical Constants for ε-GaSe [16, 18] from Eq. (8)

Parameter	Ordinary		Extraordinary
ω_{LO} (cm^{-1})	254.7		245.5
ω_{TO} (cm^{-1})	213.5		237
Γ (cm^{-1})	3		2.8
ϵ_∞	7.443		5.76
A (cm^6)		$6.105\ 10^{-27}$	
B (cm^4)		$1.8564\ 10^{-18}$	
C (cm^2)		$4.0499\ 10^{-9}$	

TABLE IV

Coefficients of the Thermal Dependence of the Refractive Index Dispersion Relation [20] to be Used in Eq. (9)

T(K)	A	B (eV^{-1})	C (eV^{-3})
300	2.716	0.04053	0.01986
225	2.709	0.04059	0.01916
150	2.702	0.04116	0.01831
75	2.697	0.04186	0.01774

Gallium Telluride (GaTe)

DAVID F. EDWARDS
Tracy, California

Gallium telluride, GaTe, is a layered semiconductor belonging to the III–VI metal-chalcogen family of GaS, GaSe, and GaTe. The crystal structure of GaTe, however, is considerably more complex than the structures of GaS and GaSe. These layered crystals are made up of weakly interacting two-dimensional sheets, each four atoms thick, which, when stacked in a variety of ways, give the full three-dimensional structure. Two modifications, one stable and the other metastable, have been reported for GaTe [1]. The stable modification, α-GaTe, has a monoclinic structure with space group C_{2h}^3 – C2/m. The metastable modification, β-GaTe, is hexagonal with space group D_{6h}^4 – C6/mmc. The hexagonal phase converts to the monoclinic phase at high temperatures. Only the stable modification, α-GaTe, is of interest here.

The crystal structure of monoclinic α-GaTe is shown in Fig. 1 [2]. The crystallographic *abc*-axes are indicated. The coordinate axes *(xyz)* are not shown, but the *a* and *b* axes are in the *x* and *y* directions, respectively. The easy cleavage plane for these layered crystals is the *x*–*y* plane with *z* normal to this plane.

Girlanda *et al.* [3] have measured the reflectance of a freshly cleaved α-GaTe sample at the fundamental absorption edge using light polarized in different directions inside the *x*–*y* plane. They report reflection spectra for $\mathbf{E}\perp\mathbf{b}$ and $\mathbf{E}\parallel\mathbf{b}$ for the 2–6 eV photon-energy range. They also measured the reflectance for unpolarized radiation in the same energy region. Unfortunately, insufficient data are given to allow the determination of *n* and *k*. However, their reflectance spectra do show appreciable variation for the two polarizations, both in intensity and in the energies of the main peaks at the absorption edge. These variations are strong evidence of the expected polarization dependence of *n* and *k* for a monoclinic crystal.

Levêque *et al.* [4] have made similar measurements of the reflectance of α-GaTe in the 2.5- to 26-eV energy range using polarized synchrotron radiation. Their measurements were for normal and oblique incidence on a freshly cleaved surface. Two reflectance curves permit the determination of

HANDBOOK OF OPTICAL CONSTANTS OF SOLIDS III

Copyright © 1998 by Academic Press.
All rights of reproduction in any form reserved
ISBN 0-12-544423-0/$25.00.

the complex refractive-index tensor from which they extract the three complex refractive indices relative to the *xyz* crystallographic directions. Given in Table I are the n and k values for three polarizations ($\mathbf{E}\|\mathbf{x}$, $\mathbf{E}\|\mathbf{y}$, $\mathbf{E}\|\mathbf{z}$) resulting from their measurements and analysis. The n and k values are plotted in Figs. 2 and 3, respectively, as functions of the wavelength.

This work is particularly interesting because they have deduced three different dielectric constants of a biaxial crystal only from reflectance measurements. A total of eight reflectance curves were needed ($\mathbf{E}\|\mathbf{a}$, $\mathbf{E}\perp\mathbf{a}$, $\mathbf{E}\|\mathbf{b}$, $\mathbf{E}\perp\mathbf{b}$, for two angles of incidence). They also show that their results are consistent with the Kramers–Kronig relations. They do note, however, that their method has inherent systematic errors because of neglecting the nondiagonal terms of the dielectric tensor.

Grasso *et al.* [5] have measured the optical constants of room-temperature α-GaTe in the spectral region of the energy gap (1.0 to 6.0 eV). The real and imaginary parts of the complex refractive index (n,k) were obtained from the normal incidence reflectivity spectrum using a rapidly converging Kramers–Kronig transform. For these measurements it is assumed unpolarized light and cleaved *xy*-surfaces were used. The room temperature n and k values are listed in Table II and are shown in Figs. 4 and 5, respectively.

Tatsuyama *et al.* [6] have also measured the room-temperature optical constants of α-GaTe using reflectance and transmittance measurements on single crystals. The samples were cleaved along the easy planes, and the radiation was unpolarized and near normal incidence. Their measurements were in a narrow spectral region about the energy gap (1.7 eV). The absorption coefficient was calculated from the relation

$$\alpha = \frac{1}{d} \ln \frac{(1-R)^2 + \sqrt{(1-R)^4 + T^2R^2}}{2T},$$

where d is the sample thickness, R the reflectance, and T the transmittance. The extinction coefficient, k, has been calculated using

$$k = \frac{\lambda\alpha}{4\pi},$$

where λ is the wavelength. Tatsuyama *et al.* obtained their index of refraction values from the reflectance assuming k is small:

$$n = \frac{1+\sqrt{R}}{1-\sqrt{R}}.$$

The Tatsuyama *et al.* n and k values are listed in Table II. The spectral dependence of n and k is given in Figs. 4 and 5, respectively. Tatsuyama *et al.*

also report absorption values (and thus k values) for sample temperature of 77 K for the 1.5- to 2.0-eV spectral region.

Brebner *et al.* [7] and Grandolfo *et al.* [8] also report absorption-coefficient data for the 1.7-eV spectral region. Both groups used unpolarized light on samples cleaved along the x–y plane.

Mead and Genzel [9] report room-temperature, far-infrared optical constants (n,k) of α-GaTe for $\mathbf{E}\perp\mathbf{b}$ for the 50- to 350-cm^{-1} frequency region. Their measuring technique was that of asymmetric Fourier transform spectroscopy. They point out that the great advantage of this technique is that both the real and imaginary parts of the index of refraction can be measured directly in a single experiment. Their measurements were on the $(\bar{2}01)$ cleavage plane. The crystal structure of α-GaTe allows 33 degrees of freedom to be assigned to the phonon modes. It is therefore expected that the n and k spectra would be highly structured as shown in Figs. 4 and 5. The spectra show three strong reststrahlen bands with peaks at 146, 160, and 200 cm^{-1}. Weaker bands are noted at 89, 103, 115, 126, and 216 cm^{-1}. Mead and Genzel suggest that the missing infrared-active lattice modes may be too weak to detect. n and k values as read from Figs. 4 and 5 are listed in Table II.

REFERENCES

1. S. A. Semiletov and V. A. Vlasov, *Kristallografia* **8**, 877 (1963); *Sov. Phys. Crystallogr.* **8**, 704 (1964).
2. W. B. Pearson, *Acta Crystallogr.* **17**, 1 (1964).
3. R. Girlanda, V. Grasso, G. Mondio, and E. Doni, *Solid State Commun.* **57**, 253 (1986).
4. G. Levêque, C. G. Olson, and D. W. Lynch, *J. Phys. (Paris)* **45**, 1699 (1984).
5. V. Grasso, G. Mondio, and G. Saitta, *Phys. Lett.* **64A**, 95 (1973).
6. C. Tatsuyama, Y. Watanabe, C. Hamaguchi, and J. Nakai, *J. Phys. Soc. Jpn.* **29**, 150 (1970).
7. J. L. Brebner, G. Fischer, and E. Mooser, *J. Phys. Chem. Solids* **23**, 1417 (1962).
8. M. Grandolfo, E. Gratton, F. Anfosso Somma, and P. Vecchia, *Phys. Status Solidi B* **48**, 729 (1971).
9. D. G. Mead and L. Genzel, *Infrared Phys.* **18**, 555 (1978).

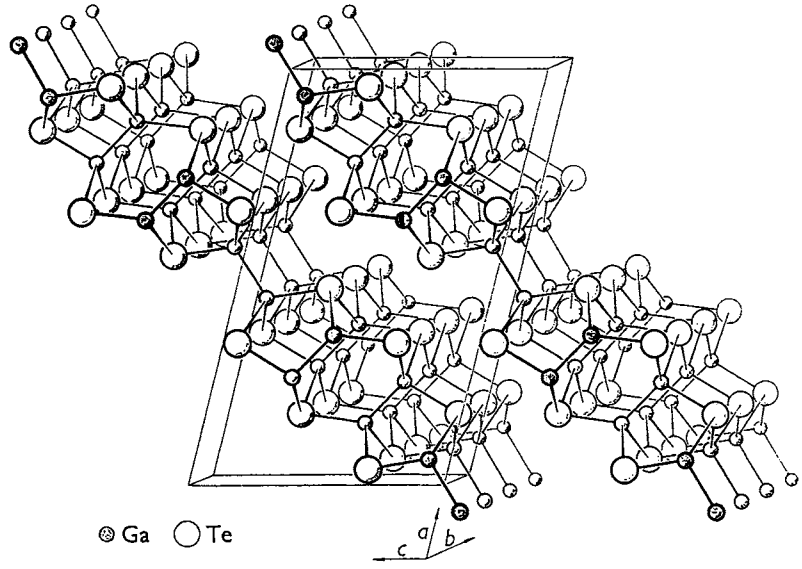

Fig. 1. The GaTe structure (monoclinic), after Pearson [2].

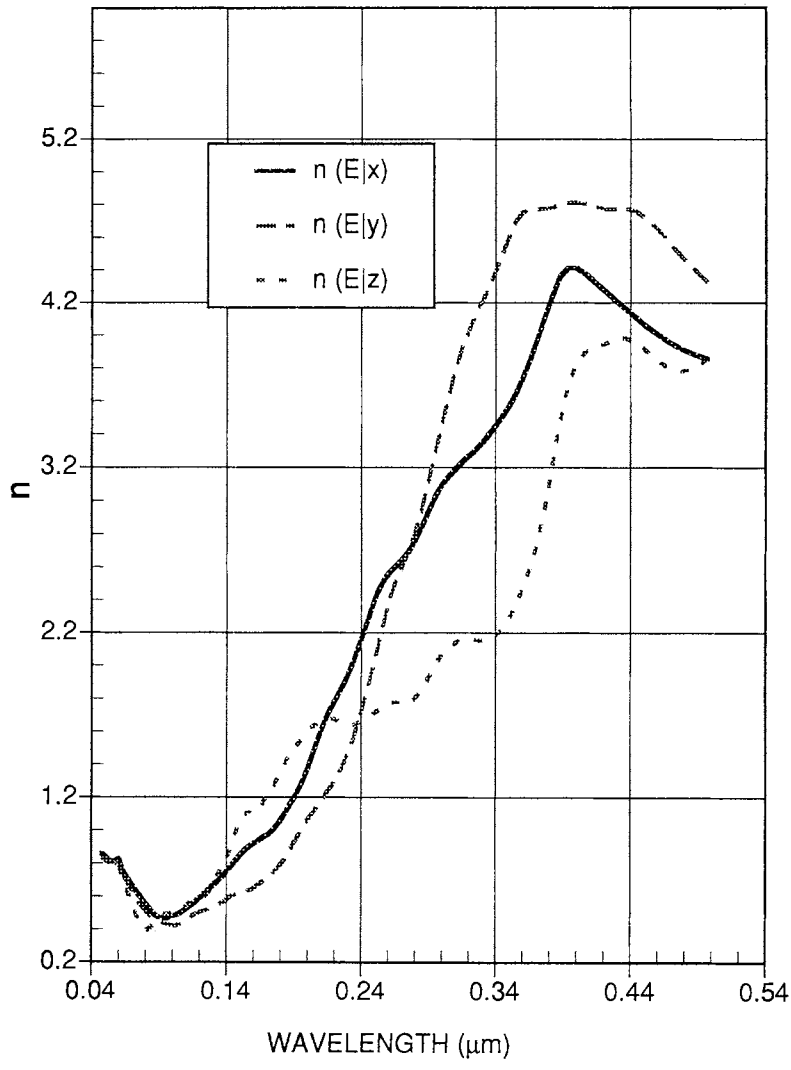

Fig. 2. Plot of n versus wavelength in microns as calculated by Levêque *et al.* [4].

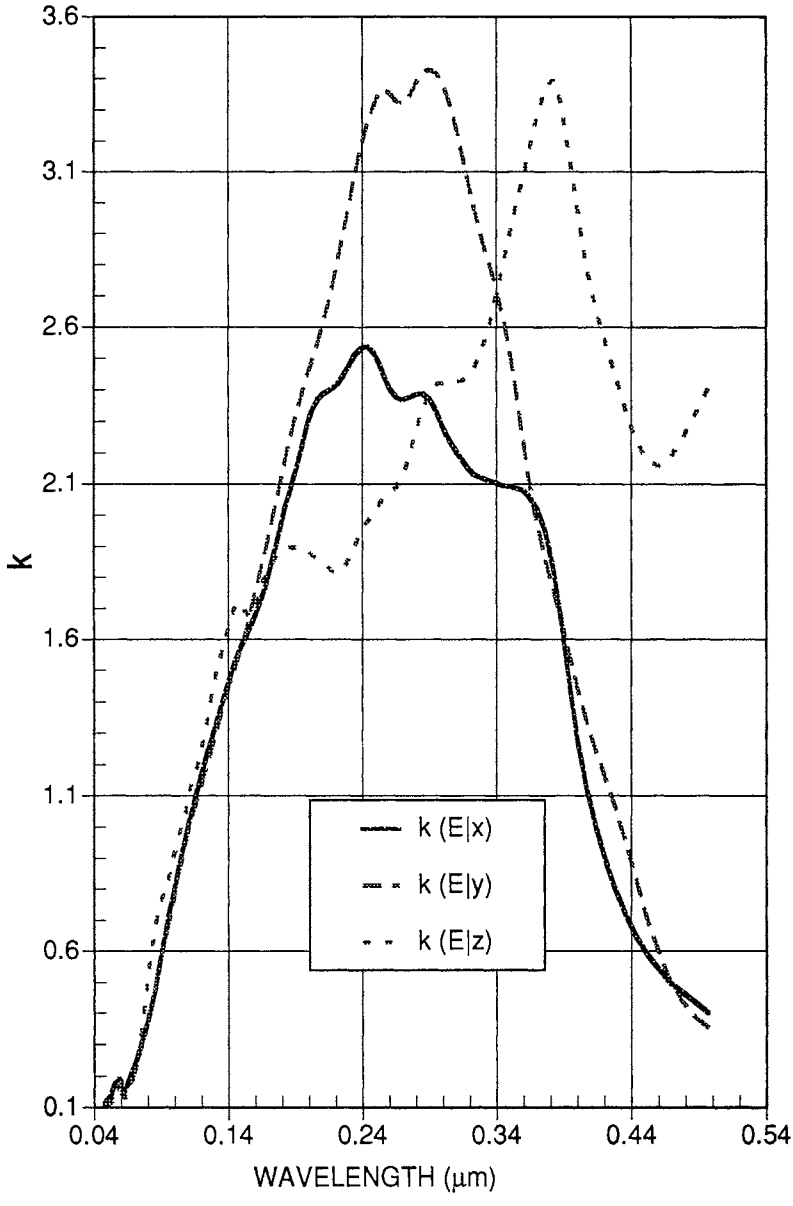

Fig. 3. Plot of k versus wavelength in microns as calculated by Levêque *et al.* [4].

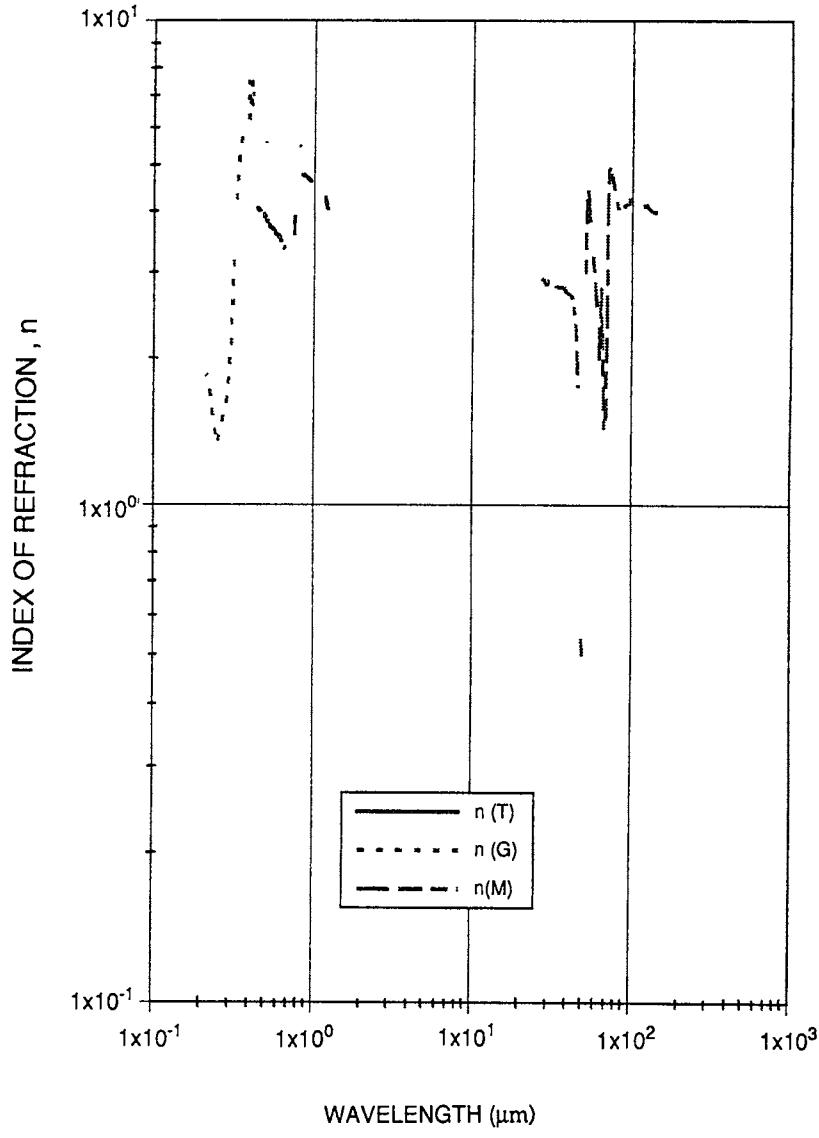

Fig. 4. Log–log plot of n versus wavelength (micrometers). The curve $n(T)$ is from Tatsuyama *et al.* [6], curve n (G) from Grasso *et al.* [5], and curve $n(M)$ from Mead and Genzel [9].

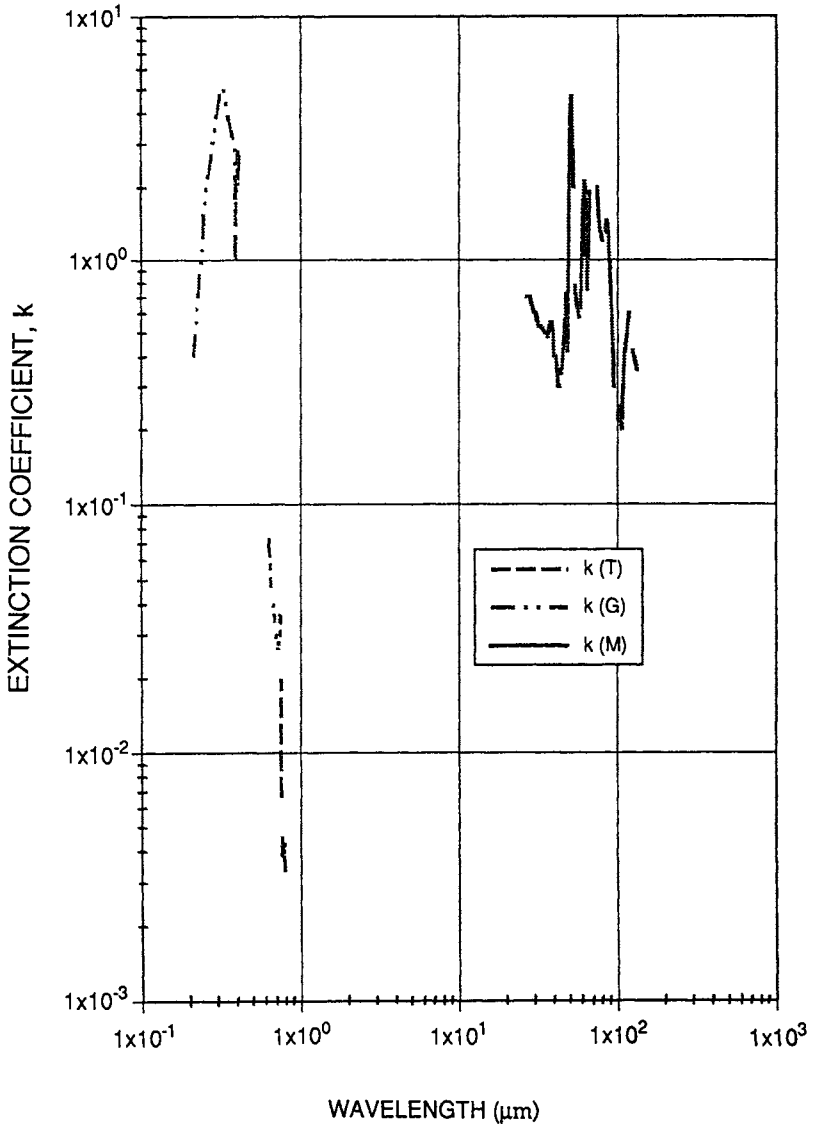

Fig. 5. Log–log plot of k versus wavelength (micrometers). The curve $k(T)$ is from Tatsuyama *et al.* [6], curve $k(G)$ from Grasso *et al.* [5], and curve $k(M)$ from Mead and Genzel [9].

TABLE I

Values of n and k for GaTe as Calculated by Levêque *et al.* [4]

eV	cm^{-1}	μm	n(E∥x)	n(E∥y)	n(E∥z)	k(E∥x)	k(E∥y)	k(E∥z)
26.10	210145	0.0476	0.8587	0.8579	0.8336	0.1100	0.1081	0.0933
25.80	207729	0.0481	0.8552	0.8547	0.8294	0.1128	0.1103	0.0939
25.50	205314	0.0487	0.8513	0.8507	0.8255	0.1161	0.1128	0.0986
25.20	202899	0.0493	0.8475	0.8466	0.8211	0.1196	0.1164	0.1004
24.90	200483	0.0499	0.8438	0.8436	0.8173	0.1231	0.1202	0.1051
24.60	198068	0.0505	0.8399	0.8412	0.8133	0.1266	0.1232	0.1064
24.30	195652	0.0511	0.8358	0.8386	0.8096	0.1301	0.1249	0.1098
24.00	193237	0.0518	0.8308	0.8344	0.8036	0.1330	0.1255	0.1069
23.80	191626	0.0522	0.8265	0.8300	0.7981	0.1354	0.1260	0.1096
23.60	190016	0.0526	0.8211	0.8245	0.7920	0.1394	0.1280	0.1131
23.40	188406	0.0531	0.8166	0.8192	0.7850	0.1449	0.1314	0.1145
23.20	186795	0.0535	0.8133	0.8144	0.7786	0.1515	0.1363	0.1207
23.00	185185	0.0540	0.8114	0.8116	0.7725	0.1584	0.1420	0.1226
22.80	183575	0.0545	0.8117	0.8104	0.7672	0.1653	0.1469	0.1320
22.60	181965	0.0550	0.8133	0.8095	0.7652	0.1702	0.1505	0.1399
22.40	180354	0.0554	0.8146	0.8084	0.7648	0.1735	0.1532	0.1448
22.20	178744	0.0559	0.8154	0.8065	0.7633	0.1758	0.1554	0.1458
22.00	177134	0.0565	0.8157	0.8037	0.7585	0.1773	0.1582	0.1481
21.90	176329	0.0567	0.8150	0.8021	0.7562	0.1779	0.1603	0.1516
21.80	175523	0.0570	0.8140	0.8011	0.7528	0.1786	0.1627	0.1502
21.70	174718	0.0572	0.8130	0.8006	0.7501	0.1806	0.1655	0.1579
21.60	173913	0.0575	0.8124	0.8007	0.7481	0.1824	0.1680	0.1579
21.50	173108	0.0578	0.8123	0.8014	0.7469	0.1852	0.1709	0.1666
21.40	172303	0.0580	0.8132	0.8033	0.7469	0.1878	0.1735	0.1677
21.30	171498	0.0583	0.8162	0.8070	0.7485	0.1901	0.1752	0.1751
21.20	170692	0.0586	0.8199	0.8118	0.7530	0.1902	0.1741	0.1777
21.10	169887	0.0589	0.8235	0.8153	0.7563	0.1870	0.1691	0.1756
21.00	169082	0.0591	0.8231	0.8143	0.7555	0.1821	0.1629	0.1737
20.90	168277	0.0594	0.8194	0.8101	0.7535	0.1804	0.1600	0.1777
20.80	167472	0.0597	0.8179	0.8084	0.7551	0.1831	0.1609	0.1822
20.70	166667	0.0600	0.8228	0.8120	0.7652	0.1814	0.1589	0.1855
20.60	165862	0.0603	0.8288	0.8134	0.7763	0.1776	0.1502	0.1732
20.50	165056	0.0606	0.8287	0.8080	0.7743	0.1653	0.1399	0.1588
20.40	164251	0.0609	0.8194	0.7973	0.7650	0.1551	0.1337	0.1506
20.30	163446	0.0612	0.8076	0.7867	0.7560	0.1523	0.1330	0.1479
20.20	162641	0.0615	0.7994	0.7794	0.7516	0.1541	0.1341	0.1492
20.10	161836	0.0618	0.7948	0.7732	0.7475	0.1542	0.1337	0.1421
20.00	161031	0.0621	0.7887	0.7656	0.7386	0.1518	0.1333	0.1376
19.90	160225	0.0624	0.7794	0.7574	0.7304	0.1514	0.1341	0.1381
19.80	159420	0.0627	0.7711	0.7495	0.7223	0.1538	0.1362	0.1354
19.60	157810	0.0634	0.7576	0.7356	0.7046	0.1601	0.1420	0.1355
19.40	156200	0.0640	0.7469	0.7236	0.6874	0.1667	0.1484	0.1354
19.20	154589	0.0647	0.7366	0.7120	0.6694	0.1732	0.1550	0.1411
19.00	152979	0.0654	0.7268	0.7010	0.6528	0.1799	0.1623	0.1481
18.70	150564	0.0664	0.7120	0.6854	0.6286	0.1909	0.1729	0.1600
18.40	148148	0.0675	0.6982	0.6685	0.6038	0.2028	0.1847	0.1756
18.10	145733	0.0686	0.6843	0.6525	0.5791	0.2149	0.1972	0.1890

(continued)

TABLE I *(Continued)*

Gallium Telluride

eV	cm^{-1}	μm	n(E‖x)	n(E‖y)	n(E‖z)	k(E‖x)	k(E‖y)	k(E‖z)
17.80	143317	0.0698	0.6705	0.6350	0.5526	0.2276	0.2112	0.2083
17.50	140902	0.0710	0.6553	0.6181	0.5254	0.2416	0.2267	0.2305
17.20	138486	0.0722	0.6406	0.5998	0.4978	0.2569	0.2442	0.2562
16.90	136071	0.0735	0.6251	0.5828	0.4698	0.2738	0.2641	0.2866
16.60	133655	0.0748	0.6102	0.5659	0.4443	0.2924	0.2851	0.3284
16.30	131240	0.0762	0.5944	0.5488	0.4224	0.3118	0.3086	0.3667
16.00	128824	0.0776	0.5791	0.5335	0.4019	0.3336	0.3338	0.4191
15.70	126409	0.0791	0.5633	0.5176	0.3927	0.3570	0.3604	0.4777
15.40	123994	0.0806	0.5470	0.5024	0.3916	0.3812	0.3896	0.5319
15.10	121578	0.0823	0.5281	0.4882	0.3977	0.4083	0.4215	0.5828
14.80	119163	0.0839	0.5093	0.4771	0.4099	0.4415	0.4551	0.6342
14.50	116747	0.0857	0.4929	0.4664	0.4270	0.4795	0.4891	0.6752
14.20	114332	0.0875	0.4789	0.4567	0.4421	0.5215	0.5246	0.7173
13.90	111916	0.0894	0.4705	0.4474	0.4655	0.5666	0.5621	0.7549
13.60	109501	0.0913	0.4670	0.4393	0.4810	0.6136	0.6022	0.7778
13.30	107085	0.0934	0.4651	0.4339	0.4891	0.6578	0.6437	0.8086
13.00	104670	0.0955	0.4635	0.4287	0.4932	0.7074	0.6855	0.8339
12.70	102254	0.0978	0.4737	0.4228	0.4936	0.7572	0.7313	0.8770
12.40	99839	0.1002	0.4765	0.4201	0.5066	0.7997	0.7821	0.9220
12.10	97424	0.1026	0.4808	0.4221	0.5183	0.8520	0.8355	0.9576
11.80	95008	0.1053	0.4919	0.4287	0.5233	0.9065	0.8906	0.9989
11.50	92593	0.1080	0.5077	0.4408	0.5284	0.9600	0.9461	1.0495
11.20	90177	0.1109	0.5263	0.4581	0.5463	1.0123	0.9989	1.1081
10.90	87762	0.1139	0.5459	0.4764	0.5738	1.0645	1.0472	1.1569
10.60	85346	0.1172	0.5672	0.4920	0.5891	1.1177	1.0931	1.1948
10.30	82931	0.1206	0.5915	0.5036	0.5913	1.1737	1.1409	1.2524
10.00	80515	0.1242	0.6195	0.5126	0.6038	0.2286	1.1945	1.3335
9.80	78905	0.1267	0.6386	0.5196	0.6269	1.2660	1.2347	1.3946
9.60	77295	0.1294	0.6585	0.5288	0.6600	1.3041	1.2776	1.4541
9.40	75684	0.1321	0.6789	0.5408	0.7032	1.3437	1.3223	1.5103
9.20	74074	0.1350	0.7016	0.5552	0.7510	1.3863	1.3673	1.5572
9.00	72464	0.1380	0.7279	0.5710	0.7981	1.4293	1.4127	1.6014
8.80	70853	0.1411	0.7568	0.5885	0.8499	1.4731	1.4579	1.6527
8.60	69243	0.1444	0.7903	0.6052	0.9236	1.5168	1.5018	1.7018
8.40	67633	0.1479	0.8274	0.6179	1.0160	1.5564	1.5466	1.7204
8.20	66023	0.1515	0.8623	0.6256	1.0842	1.5908	1.5976	1.6982
8.00	64412	0.1553	0.8919	0.6328	1.1117	1.6254	1.6599	1.6772
7.85	63205	0.1582	0.9105	0.6425	1.1087	1.6536	1.7147	1.6775
7.70	61997	0.1613	0.9267	0.6591	1.1033	1.6862	1.7714	1.7127
7.55	60789	0.1645	0.9424	0.6773	1.1280	1.7249	1.8284	1.7690
7.40	59581	0.1678	0.9585	0.6973	1.1803	1.7693	1.8886	1.8100
7.25	58374	0.1713	0.9765	0.7195	1.2296	1.8235	1.9533	1.8329
7.10	57166	0.1749	1.0025	0.7459	1.2752	1.8869	2.0235	1.8612
6.95	55958	0.1787	1.0412	0.7788	1.3345	1.9558	2.0996	1.8870
6.80	54750	0.1826	1.0919	0.8224	1.3993	2.0224	2.1799	1.8977
6.65	53543	0.1868	1.1476	0.8780	1.4547	2.0863	2.2580	1.8974
6.50	52335	0.1911	1.2083	0.9400	1.5054	2.1536	2.3296	1.8960

TABLE I *(Continued)*

Gallium Telluride

eV	cm^{-1}	μm	n(E ∥ x)	n(E ∥ y)	n(E ∥ z)	k(E ∥ x)	k(E ∥ y)	k(E ∥ z)
6.40	51530	0.1941	1.2546	0.9823	1.5376	2.2017	2.3748	1.8923
6.30	50725	0.1971	1.3085	1.0246	1.5697	2.2522	2.4189	1.8901
6.20	49919	0.2003	1.3742	1.0661	1.6023	2.3019	2.4626	1.8830
6.10	49114	0.2036	1.4509	1.1059	1.6285	2.3422	2.5077	1.8690
6.00	48309	0.2070	1.5323	1.1449	1.6474	2.3703	2.5569	1.8563
5.90	47504	0.2105	1.6112	1.1854	1.6642	2.3857	2.6105	1.8477
5.80	46699	0.2141	1.6823	1.2266	1.6784	2.3948	2.6692	1.8346
5.70	45894	0.2179	1.7455	1.2707	1.6799	2.4038	2.7370	1.8200
5.60	45089	0.2218	1.8032	1.3227	1.6685	2.4186	2.8132	1.8151
5.50	44283	0.2258	1.8631	1.3856	1.6504	2.4442	2.8982	1.8267
5.40	43478	0.2300	1.9349	1.4638	1.6387	2.4768	2.9892	1.8599
5.30	42673	0.2343	2.0220	1.5616	1.6425	2.5085	3.0830	1.9008
5.20	41868	0.2388	2.1247	1.6812	1.6594	2.5317	3.1719	1.9419
5.10	41063	0.2435	2.2398	1.8200	1.6821	2.5379	3.2497	1.9758
5.00	40258	0.2484	2.3581	1.9742	1.7061	2.5198	3.3129	2.0088
4.92	39614	0.2524	2.4443	2.1126	1.7278	2.4857	3.3529	2.0340
4.84	38969	0.2566	2.5136	2.2606	1.7500	2.4435	3.3658	2.0569
4.76	38325	0.2609	2.5639	2.3973	1.7702	2.4017	3.3523	2.0755
4.68	37681	0.2654	2.5995	2.5056	1.7790	2.3747	3.3265	2.0913
4.60	37037	0.2700	2.6352	2.5910	1.7727	2.3679	3.3206	2.1246
4.52	36393	0.2748	2.6843	2.6800	1.7733	2.3749	3.3419	2.1845
4.44	35749	0.2797	2.7515	2.7953	1.7979	2.3847	3.3828	2.2609
4.36	35105	0.2849	2.8380	2.9463	1.8521	2.3881	3.4187	2.3368
4.28	34461	0.2902	2.9374	3.1242	1.9301	2.3703	3.4315	2.3922
4.20	33816	0.2957	3.0323	3.3155	2.0134	2.3284	3.4150	2.4208
4.15	33414	0.2993	3.0824	3.4392	2.0606	2.2924	3.3888	2.4225
4.10	33011	0.3029	3.1224	3.5616	2.0942	2.2577	3.3508	2.4207
4.05	32609	0.3067	3.1574	3.6829	2.1188	2.2273	3.0009	2.4230
4.00	32206	0.3105	3.1912	3.7991	2.1420	2.2013	3.2371	2.4281
3.95	31804	0.3144	3.2254	3.9067	2.1585	2.1767	3.1624	2.4309
3.90	31401	0.3185	3.2573	3.9992	2.1607	2.1526	3.0787	2.4392
3.85	30998	0.3226	3.2863	4.0799	2.1577	2.1338	3.0007	2.4639
3.80	30596	0.3268	3.3174	4.1561	2.1556	2.1227	2.9245	2.5019
3.75	30193	0.3312	3.3560	4.2296	2.1557	2.1161	2.8540	2.5542
3.70	29791	0.3357	3.4007	4.3082	2.1628	2.1090	2.7874	2.6229
3.65	29388	0.3403	3.4509	4.3980	2.1843	2.1027	2.7187	2.7069
3.60	28986	0.3450	3.5059	4.4972	2.2255	2.0953	2.6353	2.8005
3.55	28583	0.3499	3.5676	4.6022	2.2885	2.0911	2.5298	2.8973
3.50	28180	0.3549	3.6418	4.6942	2.3701	2.0872	2.3926	2.9918
3.45	27778	0.3600	3.7334	4.7519	2.4684	2.0792	2.2350	3.0855
3.40	27375	0.3653	3.8408	4.7693	2.5853	2.0563	2.0863	3.1819
3.35	26973	0.3707	3.9631	4.7716	2.7357	2.0170	1.9631	3.2854
3.30	26570	0.3764	4.1017	4.7731	2.9479	1.9482	1.8574	3.3743
3.25	26167	0.3822	4.2437	4.7813	3.2152	1.8326	1.7621	3.3955
3.20	25765	0.3881	4.3586	4.7988	3.4862	1.6639	1.6638	3.3207
3.15	25362	0.3943	4.4142	4.8135	3.7052	1.4651	1.5535	3.1632
3.10	24960	0.4006	4.4098	4.8105	3.8428	1.2777	1.4404	2.9714

(continued)

TABLE I *(Continued)*

Gallium Telluride

eV	cm^{-1}	μm	n(E ∥ x)	n(E ∥ y)	n(E ∥ z)	k(E ∥ x)	k(E ∥ y)	k(E ∥ z)
3.05	24557	0.4072	4.3723	4.8002	3.9061	1.1235	1.3372	2.7917
3.00	24155	0.4140	4.3245	4.7845	3.9287	0.9986	1.2407	2.6541
2.95	23752	0.4210	4.2730	4.7744	3.9483	0.8902	1.1550	2.5489
2.90	23349	0.4283	4.2180	4.7734	3.9733	0.8002	1.0641	2.4507
2.85	22947	0.4358	4.1662	4.7747	3.9833	0.7208	0.9584	2.3406
2.80	22544	0.4436	4.1110	4.7605	3.9565	0.6490	0.8339	2.2410
2.75	22142	0.4516	4.0550	4.7146	3.9028	0.5921	0.7078	2.1765
2.70	21739	0.4600	4.0072	4.6486	3.8418	0.5432	0.5983	2.1576
2.65	21337	0.4687	3.9565	4.5694	3.7956	0.4988	0.5065	2.1843
2.60	20934	0.4777	3.9146	4.4836	3.7807	0.4671	0.4374	2.2424
2.55	20531	0.4871	3.8821	4.4033	3.8013	0.4357	0.3881	2.3181
2.50	20129	0.4968	3.8546	4.3293	3.8583	0.4009	0.3520	2.4024

TABLE II

Values of n and k for α-GaTe as Given by Grasso *et al.* [5], Tatsuyama *et al.* [6], and Mead and Genzel [9]

eV	cm^{-1}	μm	n [6]	k [6]	n [5]	k [5]	n [9]	k [9]
5.900	47504	0.211			1.93			
5.850	47101	0.212				0.40		
5.800	46699	0.214			1.86	0.42		
5.700	45894	0.218			1.80	0.50		
5.600	45089	0.222			1.75	0.56		
5.500	44283	0.226			1.70	0.65		
5.400	43478	0.230			1.62	0.77		
5.300	42673	0.234			1.54	0.90		
5.200	41868	0.239			1.47	1.03		
5.100	41063	0.244			1.40	1.25		
5.000	40258	0.248			1.33	1.57		
4.900	39452	0.253			1.34	1.75		
4.800	38647	0.259			1.40	2.00		
4.700	37842	0.264			1.46	2.25		
4.600	37037	0.270			1.50	2.42		
4.500	36232	0.276			1.56	2.73		
4.400	35427	0.282			1.58	3.05		
4.300	34622	0.289			1.68	3.40		
4.200	33816	0.296			1.83	3.80		
4.100	33011	0.303			2.14	4.20		
4.000	32206	0.311			2.70	4.65		
3.900	31401	0.318			3.28	5.05		
3.850	30998	0.323				5.15		
3.800	30596	0.327			4.10	5.14		
3.700	29791	0.336			5.00	4.70		
3.600	28986	0.345			5.43	4.20		
3.500	28180	0.355			5.80	3.78		
3.400	27375	0.365			5.94	3.45		
3.300	26570	0.376			6.03	3.16		
3.250	26167	0.382				3.00		
3.200	25765	0.388			6.16	2.95		
3.100	24960	0.401			6.50	2.83		
3.000	24155	0.414			7.00	2.70		
3.100	24960	0.401			7.55	2.00		
3.200	25765	0.388			7.55	1.00		
2.850	22947	0.436	4.12					
2.850	22947	0.436			7.70			
2.800	22544	0.444	4.07					
2.760	22222	0.450	4.05					
2.710	21820	0.458	4.01					
2.700	21739	0.460			6.75	0.15		
2.670	21498	0.465	3.97					
2.650	21337	0.469				0.08		
2.600	20934	0.478	3.98					
2.600	20934	0.478			6.10	0.08		

(continued)

TABLE II *(Continued)*

Gallium Telluride

eV	cm^{-1}	μm	n [6]	k [6]	n [5]	k [5]	n [9]	k [9]
2.560	20612	0.485	3.96					
2.540	20451	0.489	3.92					
2.500	20129	0.497	3.89					
2.500	20129	0.497			5.62	0.10		
2.500	20129	0.497			5.60			
2.470	19887	0.503	3.85					
2.440	19646	0.509	3.82					
2.400	19324	0.518	3.80					
2.400	19324	0.518			5.30	0.10		
2.370	19082	0.524	3.76					
2.350	18921	0.529	3.73					
2.310	18599	0.538	3.71					
2.300	18519	0.540			5.10	0.14		
2.280	18357	0.545	3.70					
2.230	17955	0.557	3.67					
2.200	17713	0.565			4.96	0.20		
2.190	17633	0.567	3.64					
2.160	17391	0.575	3.60					
2.130	17150	0.583	3.59					
2.100	16908	0.591			4.87	0.30		
2.090	16828	0.594	3.58					
2.060	16586	0.603	3.56					
2.020	16264	0.615	3.53					
2.010	16184	0.618	3.50					
2.000	16103	0.621	3.48					
2.000	16103	0.621			4.80	0.45		
1.985	15982	0.626		7.87E-02				
1.980	15942	0.627	3.44					
1.970	15862	0.630		7.32E-02				
1.953	15725	0.636		6.73E-02				
1.940	15620	0.640		6.22E-02				
1.925	15499	0.645		5.49E-02				
1.920	15459	0.647	3.38					
1.910	15378	0.650	3.36					
1.910	15378	0.650		5.10E-02				
1.900	15298	0.654		4.68E-02				
1.900	15298	0.654			4.72	0.55		
1.865	15016	0.666		4.08E-02				
1.850	14895	0.671	3.30					
1.850	14895	0.671		4.01E-02				
1.832	14750	0.678		3.78E-02				
1.825	14694	0.681		3.57E-02				
1.811	14581	0.686		3.38E-02				
1.800	14493	0.690			4.60	0.80		
1.797	14469	0.691		3.19E-02				
1.790	14412	0.694	3.33					
1.785	14372	0.696		3.05E-02				

TABLE II *(Continued)*

Gallium Telluride

eV	cm^{-1}	μm	n [6]	k [6]	n [5]	k [5]	n [9]	k [9]
1.770	14251	0.702		2.90E-02				
1.760	14171	0.706	3.31					
1.760	14171	0.706		2.78E-02				
1.750	14090	0.710			4.52			
1.745	14050	0.712		2.66E-02				
1.734	13961	0.716		2.62E-02				
1.725	13889	0.720		2.64E-02				
1.720	13849	0.722	3.31					
1.717	13824	0.723		2.73E-02				
1.710	13768	0.726		2.89E-02				
1.705	13728	0.728		3.01E-02				
1.700	13688	0.731	3.25					
1.700	13688	0.731		3.08E-02				
1.700	13688	0.731				1.25		
1.700	13688	0.731			4.75			
1.695	13647	0.733		3.32E-02				
1.687	13583	0.736		3.57E-02				
1.680	13527	0.739		3.65E-02				
1.675	13486	0.741		2.95E-02				
1.670	13446	0.744	3.28					
1.670	13446	0.744		2.01E-02				
1.664	13398	0.746		1.16E-02				
1.660	13366	0.748		7.14E-03				
1.653	13309	0.751		6.58E-03				
1.650	13285	0.753	3.33					
1.644	13237	0.755		6.01E-03				
1.642	13221	0.756	3.60					
1.638	13188	0.758	3.90					
1.638	13188	0.758		4.83E-03				
1.630	13124	0.762		3.64E-03				
1.622	13060	0.766	4.34					
1.622	13060	0.766		3.05E-03				
1.618	13027	0.768	4.60					
1.615	13003	0.769		1.84E-03				
1.606	12931	0.773		1.85E-03				
1.600	12882	0.776	4.72					
1.600	12882	0.776		2.47E-03				
1.600	12882	0.776			5.43	0.95		
1.595	12842	0.779		3.72E-03				
1.588	12786	0.782		4.36E-03				
1.580	12721	0.786		4.38E-03				
1.570	12641	0.791		3.34E-03				
1.560	12560	0.796	4.71					
1.550	12480	0.801			5.49			
1.500	12077	0.828			5.48	0.65		
1.470	11836	0.845	4.78					

(continued)

TABLE II *(Continued)*

Gallium Telluride

eV	cm^{-1}	μm	n [6]	k [6]	n [5]	k [5]	n [9]	k [9]
1.420	11433	0.875	4.75					
1.400	11272	0.887			5.44	0.50		
1.370	11031	0.907	4.72					
1.300	10467	0.955	4.63					
1.300	10467	0.955			5.38	0.37		
1.240	9984	1.002	4.57					
1.200	9662	1.035			5.32	0.30		
1.120	9018	1.109	4.42					
1.100	8857	1.129			5.25	0.26		
1.060	8535	1.172	4.28					
1.020	8213	1.218	4.06					
1.000	8052	1.242			5.20	0.25		
4.66E-02	375	26.667						0.70
4.60E-02	370	27.027					2.90	0.70
4.53E-02	365	27.397					2.92	0.70
4.47E-02	360	27.778					2.92	0.70
4.41E-02	355	28.169					2.90	0.70
4.35E-02	350	28.571					2.85	0.66
4.28E-02	345	28.986					2.83	0.64
4.22E-02	340	29.412					2.85	0.62
4.16E-02	335	29.851					2.88	0.60
4.10E-02	330	30.303					2.90	0.60
4.04E-02	325	30.769					2.90	0.58
3.97E-02	320	31.250					2.90	0.56
3.91E-02	315	31.746					2.88	0.53
3.85E-02	310	32.258					2.85	0.53
3.79E-02	305	32.787					2.84	0.53
3.73E-02	300	33.333					2.82	0.52
3.66E-02	295	33.898					2.80	0.52
3.60E-02	290	34.483					2.80	0.50
3.54E-02	285	35.088					2.80	0.50
3.48E-02	280	35.714					2.80	0.50
3.42E-02	275	36.364					2.80	0.48
3.35E-02	270	37.037					2.80	0.52
3.29E-02	265	37.736						0.55
3.29E-02	265	37.736					2.80	
3.23E-02	260	38.462					2.75	0.55
3.17E-02	255	39.216					2.71	0.50
3.11E-02	250	40.000					2.73	0.40
3.04E-02	245	40.816					2.72	0.40
2.98E-02	240	41.667					2.70	0.35
2.92E-02	235	42.553					2.65	0.30
2.86E-02	230	43.478						0.30
2.86E-02	230	43.478					2.55	
2.79E-02	225	44.444					2.40	0.34
2.73E-02	220	45.455					2.13	0.40
2.67E-02	215	46.512					1.75	0.52

TABLE II *(Continued)*

Gallium Telluride

eV	cm^{-1}	μm	n [6]	k [6]	n [5]	k [5]	n [9]	k [9]
2.61E-02	210	47.619						0.72
2.61E-02	210	47.619					1.20	
2.56E-02	206	48.544						0.42
2.55E-02	205	48.780					0.54	0.63
2.48E-02	200	50.000					0.50	3.40
2.43E-02	196	51.020						4.66
2.42E-02	195	51.282					3.00	4.68
2.36E-02	190	52.632					4.45	2.00
2.35E-02	189	52.910					4.45	
2.30E-02	185	54.054					4.15	0.78
2.24E-02	180	55.556					3.65	0.65
2.17E-02	175	57.143						0.58
2.17E-02	175	57.143					3.25	
2.11E-02	170	58.824					3.00	0.63
2.05E-02	165	60.606					2.50	1.60
2.01E-02	162	61.728						2.10
1.99E-02	160	62.500					1.94	2.00
1.93E-02	155	64.516					2.80	0.75
1.86E-02	150	66.667					1.75	1.90
1.83E-02	147	68.027					1.43	
1.80E-02	145	68.966						3.95
1.80E-02	145	68.966					1.50	
1.74E-02	140	71.429					4.90	3.10
1.70E-02	137	72.993					5.00	
1.68E-02	135	74.074					4.80	2.00
1.61E-02	130	76.923					4.45	1.35
1.55E-02	125	80.000						1.20
1.55E-02	125	80.000					4.20	
1.49E-02	120	83.333					4.00	1.30
1.45E-02	117	85.470						1.45
1.44E-02	116	86.207					3.96	
1.43E-02	115	86.957					4.00	1.40
1.37E-02	110	90.909					4.15	0.80
1.30E-02	105	95.238					4.14	0.30
1.28E-02	103	97.087					4.27	
1.24E-02	100	100.000					4.25	0.22
1.22E-02	98	102.041						0.25
1.18E-02	95	105.263					4.00	0.21
1.17E-02	94	106.383						0.20
1.12E-02	90	111.111					3.95	0.40
1.06E-02	85	117.647						0.60
1.06E-02	85	117.647					4.10	
1.02E-02	82	121.951					4.15	
9.94E-03	80	125.000					4.10	0.42
9.32E-03	75	133.333					4.00	0.35
8.69E-03	70	142.857					4.00	

Iron Pyrite (FeS_2)

E. D. PALIK
Institute for Physical Science and Technology
University of Maryland
College Park, Maryland

Iron pyrite is called "fool's gold" because to the untrained prospector, it looks very much like gold. However, comparison of the optical constants in the visible spectral region easily distinguishes between the two materials. While the reflectivity $R = \sim 0.40$ at 3 eV for both Au and FeS_2, it rises rapidly to $R = 0.97$ at 1.6 eV for Au and continues to rise into the near IR, while for FeS_2 it rises to a peak $R = 0.65$ at 1.6 eV, then drops to $R = 0.44$ at 0.5 eV. This gives the characteristic yellow color, but this color should be brighter for Au and duller for FeS_2.

Iron pyrite is a cubic semiconductor of space group symmetry class Pa3 (T_h^6). The optic irreducible representation is

$$A_g(\mathrm{R}) + 2A_u(0) + E_g(\mathrm{R}) + 2E_u(0) + 5F_u(\mathrm{IR}), \tag{1}$$

where we define R, Raman; IR, infrared; 0, silent. This predicts 33 optic modes. There is an additional F_u triply degenerate acoustic mode to complete the total irreducible representation.

The far-IR lattice-vibration region has been studied by Verble and Wallis [1] and Lutz *et al.* [2, 3]. Verble and Wallis measured the reflectivity (at an undesignated room temperature) of a natural single-crystal sample in the region 190–660 cm^{-1} with a Perkin-Elmer Model 301 spectrophotometer. An aluminum mirror served as a reference standard. Both Kramers–Kronig (K-K) and Lorentz-oscillator-model analyses were performed. The K-K analysis gave a small, nearly constant $k = \sim 0.2$ above 460 to 650 cm^{-1}, which the Lorentz-oscillator model ignored. Although five F_u IR modes were expected, only four were observed. The Lorentz-oscillator model gives

$$\begin{aligned} n^2 - k^2 = \epsilon_{\mathrm{R}} &= \epsilon_\infty + \sum_j \frac{4\pi \rho_j \omega_j^2 (\omega_j^2 - \omega^2)}{(\omega_j^2 - \omega^2)^2 + (\gamma_j \omega_j \omega)^2} \\ 2nk = \epsilon_{\mathrm{I}} &= \sum_j \frac{4\pi \rho_j \omega_j^2 \omega}{(\omega_j^2 - \omega^2)^2 + (\gamma_j \omega_j \omega)^2}. \end{aligned} \tag{2}$$

HANDBOOK OF OPTICAL CONSTANTS OF SOLIDS III

Copyright © 1998 by Academic Press.
All rights of reproduction in any form reserved
ISBN 0-12-544423-0/$25.00.

We can just as well define the damping parameter as $\Gamma_j = \gamma_j\ \omega_j$, so Γ_j has units of cm^{-1} and signifies the FWHM of the jth absorption line. The angular frequency is ω; the oscillator strength is ρ; ω_j is the jth resonant frequency. The fitting parameters are given in Table I for Verble and Wallis [1]. The calculated values of n and k are listed in Table II.

Lutz *et al.* [3] performed similar reflectivity measurements (at an undesignated room temperature) with a Fourier-transform spectrometer in the spectral range 30–700 cm^{-1}. Polycrystalline FeS_2 samples were prepared by heating stoichiometric mixtures of the elements in evacuated fused-quartz tubes at high temperature. Such samples were hot pressed and polished; some natural crystalline samples were also used. There were considerable differences in the two sets of reflectivity data. For the natural crystals they determined oscillator parameters, some of which were similar to and some drastically different from those found by Verble and Wallis. Because we are suspicious of how well a Fourier-transform spectrometer can measure R, we will not use these data; we do list the fitting parameters for the natural crystal in Table I for Lutz *et al.* [3]. Note the difference in notation by Verble and Wallis [1] and Lutz *et al.* [3] regarding Γ and γ. However, Lutz *et al.* [3] did measure all five IR modes in transmittance using powdered material in a CsI matrix, while Verble and Wallis could not find one mode in reflectivity in the vicinity of 422 cm^{-1}.

Toward the near IR we could find no measurements of index of refraction n up to the the vicinity of the fundamental indirect band gap at $E_g = \sim 0.7$ eV. Therefore, we have to extrapolate the Lorentz-oscillator-model results [1] up to 0.5 eV.

The various natural crystals and deposited thin films used by the many researchers must have had significantly different properties, since there were significant differences in n and k.

We summarize some of the papers [4–10], and list others [11–14] for the reader's further interest.

Ferrer *et al.* [4]: Natural samples and flash-evaporated films on a glass substrate; Cary Model 2415 spectrophotometer at normal incidence; both R and T measured in spectral region 0.5–5.5 eV; K-K analysis; room temperature not specified; peak $R = 0.53$ at 1.7 eV. K-K analysis is notorious for giving inaccurate values of k when k is small (less than a few tenths).

There have been numerous measurements of the extinction coefficient k in the band-gap region. Ferrer *et al.* [4] noticed significant variations among these works when they attempted to fit the absorption coefficient α (cm^{-1}) with a formula of the form

$$(\alpha\ h\ \nu)^n = B\ (h\ \nu - E_o), \tag{3}$$

where ν is the frequency in Hz; for direct transitions $E_o = E_g$; for indirect transitions $E_o = E_g + E_p$, with E_p being the associated phonon energy; and $n = \frac{1}{2}, \frac{1}{3}, 2, \frac{2}{3}$ for allowed and forbidden indirect transitions and allowed and

forbidden direct transitions, respectively. This n is not to be confused with the index of refraction. Equation (3) was derived for parabolic conduction and valence bands. They analyzed their own data and could not definitely decide between allowed and forbidden indirect. When they noted that the several sets of data of other workers gave drastically different values of E_g and n (direct and indirect, allowed and forbidden), they concluded that Eq. (3) is not applicable for FeS_2 because the bands are rather flat. We include in Table II some data of Ferrer *et al.* that hint that the band gap $E_g = 1.1$ eV and is allowed indirect.

Bither *et al.* [5]: Samples grown by high-pressure reaction of high-purity reactants (Fe,S) pelleted first at room temperature and then inserted into an anvil press that could be heated; near-normal-incidence reflectivity measured in spectral region 0.5–5.0 eV; Perkin-Elmer 112 monochromator; as-grown crystal faces; room temperature was 300 K; K-K analysis using an extrapolation formula to high frequency; peak $R = 0.62$ at 1.7 eV. Also, the reflectance was measured as a function of angle of incidence (θ), and n and k were directly computed. However, it is not clear which set of data are given in the figures, and no comparisons are made of the two sets of data.

Schlegel and Wachter [6]: Natural crystals; reflectivity measured in the IR spectral region 0.03–0.5 eV; thin-film transmittance measured from 0.03 to 1.1 eV and showed peculiar constant level of absorption with $\alpha = \sim 1.4 \times 10^3$ cm^{-1} from 0.06 to 0.8 eV; also, lowest lattice mode showed a splitting (277, 290 cm^{-1}); this was not seen by Verble and Wallis and Lutz *et al.;* reflectivity also measured from 0.5 to 12 eV; K-K analysis used, but extrapolation method not mentioned; peak $R = 0.53$ at 1.7 eV.

Kou and Seehra [7]: Two thin-film natural samples of low and high resistivity; low-resistivity sample showed free-carrier absorption; high-resistivity sample showed a constant background absorption below the band gap; spectral region was 0.7–1.0 eV; residual absorption was presumably subtracted out on α (cm^{-1}) versus (eV) plot. The formula used was

$$I_t/I_o = \frac{(1 - R^2)\exp(-\alpha d).}{1 - R^2\exp(-2\,\alpha\, d)} \tag{4}$$

This formula contains multiple-reflection effects but does not show interference fringes. Since R was nearly constant at $R = 0.43$ in the narrow spectral region covered, and if $R^2\exp(-2\,\alpha\, d) \ll 1$, one can measure the optical density $D_o = \log_{10}(I_t/I_o)$ and from this obtain

$$\alpha\, d = 2.303\, D_o - 4.606\, \log_{10}(1 - R). \tag{5}$$

Since D_o varies rapidly with wavelength in the band-gap region, its absorption in the first term is superimposed on a nearly constant second term. This second term is computed to be ~ 125 cm^{-1} for $d = 90$ μm and $R = 0.43$. The observed absorption is 720 cm^{-1}. For a second film with $d = 150$ μm,

the calculated value is 75 cm^{-1}, but a background absorption of 400 cm^{-1} was measured. Kuo and Seehra do not directly say that the observed constant absorption is this constant term. Also, thin films with $d = 90$ μm and $d = 150$ μm give somewhat different values of α after the background absorption is subtracted. For example, at 0.8 eV, $(\alpha h\nu) = 5.5$ for $d = 90$ μm and 4.0 for 150 μm. This is unusual.

We have occasionally noticed that workers will subtract off a background absorption at the k or α level. This is not quite proper. Linear optics suggests that the dielectric constants are additive; for example, a Drude model described by $\epsilon(D)$ can be added to a Lorentz model described by $\epsilon(L)$, and can be added to a constant-background lattice model described by ϵ_∞. When tempted to make such a subtraction at the k level, the worker should actually calculate the error introduced by adding or subtracting k's instead of ϵ_I's.

However, we have elected to include the k data in Table II for the $d = 150$ μm sample for comparison with other data to be discussed next. It will be obvious that the materials must vary to produce such variations in n and k [4, 7–9].

Yang *et al.* [8]: Synthetic single crystals grown by chemical-vapor-transport method; thin plates made by diamond-saw cutting and polishing down to 30 μm; transmission near normal incidence measured with a Bruker model IFS 120HR in the spectral region 0.8–1.3 eV; room temperature was 300 K. Data analysis was similar to that of Kou and Seehra [7]. Since the absorption was about a factor of 5 smaller than measured by Kuo and Seehra, and the spectral region was somewhat wider, we choose to present these band-edge data in Table II. Analysis was done with the indirect-allowed-transition model similar to the method of Kuo and Seehra. However, Yang *et al.* had variations in absorption for samples of different thickness (like Kuo and Seehra). They did estimate that $E_g = 0.93$ eV at 300 K.

Suga *et al.* [9]: Natural crystals polished and etched; p-polarized reflectivity spectrum using a 1-m Seya-Namioka monochromator attached to the beam line of a 0.4-GeV electron storage ring; 3000–400 Å; with additional, presumably new, unpublished data of Sato in the region 0.3–4 eV; room temperature not specified; peak $R = 0.64$ at 1.7 eV.

Sato [10]: Thin films made by a chemical vapor-transport reaction; surfaces etched; double-beam refectivity spectrometer in the spectral region 0.5–4.4 eV; K-K analysis using the VUV data of Suga *et al.;* room temperature not specified; peak $R = 0.54$ at 1.7 eV.

We finally choose the data of Suga *et al.* because they used natural crystals; there was no free-carier absorption below E_g as was the case with the data of Sato; also below E_g, $n = 5.0$ at 0.5 eV, above (but approaching) the value $n = 4.617$ of Verble and Wallis. The reflection peak near 1.7 eV is the highest at $R = \sim 0.64$ compared to $R = \sim 0.54$ for Sato and ~ 0.53 for

Ferrer *et al.* There is a proverb saying that bigger (reflectivity) is better, especially in the interband region where strong transitions give peaks in R; these peaks can be supressed by native oxides and poorly prepared surfaces.

Because of the possible use of FeS_2 as a solar-energy material, several methods of growing it economically have been tried. These include polycrystal films made from powdered FeS_2 heated in a fused-quartz ampule with a detailed heating cycle for days [11]; spray pyrolysis deposition on a hot fused-quartz plate utilizing solutions of ferric salts and sulfo-organic compounds [12, 13]; iron films made by flash evaporation on a glass substrate were placed into vacuum sealed glass ampules with sulfur with temperatures as high as 500 K applied for many hours [14]. There were signficant differences in the band-gap data of such thin films, and we cannot use the optical constants obtained from such samples. Unfortunately, even the natural crystals seem to vary in their optical constants, suggesting other impurity and structure problems.

In all these papers the n and k data were presented in small graphs which were enlarged by photocopying and then read. We estimate that n and k are uncertain to $\pm 10\%$ when read this way; this is above and beyond the experimental uncertainties seldom discussed in the various papers.

There are data for the temperature dependence of the band gap [8, 15], but they are not of direct interest here. No data could be found above 25 eV. However, Suguiro [16] measured the K x-ray absorption edge of S in FeS_2 near 2472 eV with some structure observed. No absolute values of absorption coefficient were determined.

Lastly, the data in Table II are plotted in Fig. 1.

REFERENCES

1. J. L. Verble and R. F. Wallis, Infrared studies of lattice vibrations in iron pyrite. *Phys. Rev.* **182**, 783 (1969).
2. H. D. Lutz, G. Schneider, and G. Kliche, Far-infrared reflection spectra, TO- and LO-phonon frequencies, coupled and decoupled plasmon-phonon modes, dielectric constants, and effective dynamical charges of manganese, iron, and platinum group pyrite type compounds. *J. Phys. Chem. Solids* **46**, 437 (1985).
3. H. D. Lutz, G. Kliche, and H. Haeuseler, Far-infrared reflection spectra, optical and dielectric constants, and effective charges of the pyrite type compounds FeS_2, MnS_2, $MnSe_2$ and $MnTe_2$. *Z. Naturforsch.* **36a**, 184 (1981).
4. I. J. Ferrer, D. M. Nevskaia, C. de las Heras, and C. Sanchez, About the band gap nature of FeS_2 as determined from optical and photo-electrochemical measurements. *Solid State Commun.* **74**, 913 (1990).
5. T. A. Bither, R. J. Bouchard, W. H. Cloud, P. C. Donohue, and W. J. Siemons, Transition metal pyrite dichalcogenides. High-pressure synthesis and correlation of properties. *Inorg. Chem.* **7**, 2208 (1968).
6. A. Schlegel and P. Wachter, Optical properties, phonons and electronic structure of iron pyrite (FeS_2). *J. Phys. C: Solid State Phys.* **9**, 3363 (1976).

7. W. W. Kou and M. S. Seehra, Optical absorption in iron pyrite (FeS_2). *Phys. Rev. B* **18**, 7062 (1978).
8. T.-R. Yang, J.-T. Yu, J.-K. Huang, S.-H. Chen, M.-Y. Tsay, and Y.-S. Huang, Optical-absorption study of synthetic pyrite FeS_2 single crystals. *J. Appl. Phys.* **77**, 1710 (1995).
9. S. Suga, K. Inoue, M. Taniguchi, S. Shin, M. Seki, K. Sato, and T. Teranishi, Vacuum ultraviolet reflectance spectra and band structures of pyrites (FeS_2, CoS_2 and NiS_2) and NiO measured with synchrotron radiation. *J. Phys. Soc. Jpn.* **52**, 1848 (1983).
10. K. Sato, Reflectivity spectra and optical constants of pyrites (FeS_2, CoS_2 and NiS_2) between 0.2 and 4.4 eV. *J. Phys. Soc. Jpn.* **53**, 1617 (1984).
11. A. Ennaoui, S. Fiechter, H. Goslowsky, and H. Tributsch, Photoactive synthetic polycrystalline pyrite (FeS_2). *J. Electrochem. Soc.* **132**, 1579 (1985).
12. A. K. Abass, Z. A. Ahmed, and R. E. Tahir, Interband transitions of chemically deposited pyrite FeS_2 films in the fundamental absorption region between 1 and 3.8 eV. *Phys. Status Solidi A* **97**, 243 (1986).
13. A. K. Abass, Z. A. Ahmed, and R. E. Tahir, Absorption edge measurements in chemically deposited pyrite FeS_2 thin layers. *J. Appl. Phys.* **61**, 2339 (1987).
14. I. J. Ferrer and C. Sanchez, Characterization of FeS_2 thin films prepared by thermal sulfidation of flash evaporated iron. *J. Appl. Phys.* **70**, 641 (1991).
15. M. S. Seehra and S. S. Seehra, Temperature dependence of the band gap of FeS_2. *Phys. Rev. B* **19**, 6620 (1979).
16. C. Sugiura, Sulfur K x-ray absorption spectra of FeS, FeS_2, and Fe_2S_3. *J. Chem. Phys.* **74**, 215 (1981).

TABLE I

Lorentz-Oscillator-Model Parameters Obtained from Fitting Measured Reflectivities from Verble and Wallis [1] and Lutz *et al.* [3][a]

	ω_j (cm^{-1})		ρ_j		Γ_j (cm^{-1})	
j	[1]	[3]	[1]	[3]	[1]	[3]
1	293	293	0.0258	0.027	1.46	2.78
2	348	348	0.065	0.033	1.95	0.83
3	402	401	0.27	0.255	5.23	3.97
4	415	412	0.022	0.026	9.13	13.93
5		422		0.00079		10.04

[a] $\epsilon_\infty = 21.32$ [1]; 19.80 [3].

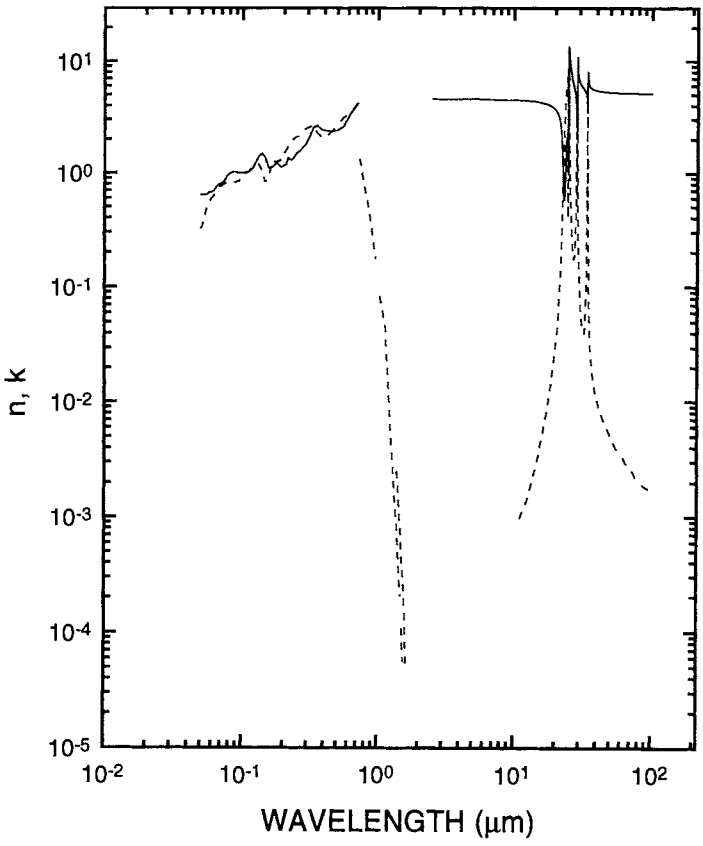

Fig. 1. Log–log plot of n (—) and k (----) versus wavelength in micrometers for iron pyrite.

TABLE II

Values of n and k for Iron Pyrite Obtained from Various References[a]

eV	cm−1	μm	n	k	k	k
25.0	201600.	0.04959	0.64[9]	3.2E-1[9]		
24.5	197600.	0.05061	0.64	3.4E-1		
24.0	193600.	0.05166	0.64	3.8E-1		
23.5	189500.	0.05276	0.64	4.1E-1		
23.0	185500.	0.05391	0.64	4.6E-1		
22.5	181500.	0.05510	0.65	4.9E-1		
22.0	177400.	0.05636	0.66	5.2E-1		
21.5	173400.	0.05767	0.68	5.6E-1		
21.0	169400.	0.05904	0.68	5.9E-1		
20.5	165300.	0.06048	0.68	6.1E-1		
20.0	161300.	0.06199	0.70	6.3E-1		
19.5	157300.	0.06358	0.73	6.7E-1		
19.0	153200.	0.06525	0.77	7.0E-1		
18.5	149200.	0.06702	0.79	7.3E-1		
18.0	145200.	0.06888	0.80	7.6E-1		
17.5	141100.	0.07085	0.82	7.8E-1		
17.0	137100.	0.07293	0.84	8.0E-1		
16.5	133100.	0.07514	0.89	8.1E-1		
16.0	129000.	0.07749	0.95	8.2E-1		
15.5	125000.	0.0800	0.99	8.3E-1		
15.0	121000.	0.08265	1.00	8.3E-1		
14.5	116900.	0.08551	1.02	8.3E-1		
14.0	112900.	0.08856	1.02	8.3E-1		
13.5	108900.	0.09184	1.01	8.4E-1		
13.0	104800.	0.09537	1.00	8.6E-1		
12.5	100800.	0.09919	1.00	9.2E-1		
12.0	96780.	0.1003	1.00	9.8E-1		
11.5	92750.	0.1078	1.02	1.01E0		
11.0	88720.	0.1127	1.04	1.06E0		
10.5	84690.	0.1181	1.10	1.12E0		
10.0	80650.	0.1240	1.23	1.19E0		
9.5	76620.	0.1305	1.41	1.21E0		
9.0	72570.	0.1378	1.48	1.02E0		
8.5	68560.	0.1459	1.38	8.3E-1		
8.0	64520.	0.1550	1.10	9.6E-1		
7.5	60490.	0.1653	1.13	1.27E0		
7.0	56460.	0.1771	1.23	1.25E0		
6.5	52420.	0.1907	1.12	1.30E0		
6.0	48390.	0.2066	1.18	1.60E0		
5.75	46380.	0.2156	1.37	1.73E0		
5.5	44360.	0.2254	1.30	1.81E0		
5.25	42340.	0.2362	1.36	2.02E0		
5.0	40330.	0.2480	1.49	2.10E0		
4.75	38310.	0.2610	1.56	2.15E0		
4.5	36290.	0.2755	1.68	2.32E0		
4.25	34280.	0.2917	1.80	2.50E0		

[a] References given in brackets.

TABLE II *(Continued)*

Iron Pyrite

eV	cm−1	μm	n	k	k	k
4.0	32260.	0.3100	2.12	2.60E0		
3.75	30240.	0.3306	2.59	2.65E0		
3.5	28230.	0.3542	2.65	2.24E0		
3.25	26210.	0.3815	2.44	2.08E0		
3.0	24200.	0.4133	2.38	2.10E0		
2.75	22180.	0.4508	2.35	2.34E0		
2.5	20160.	0.4959	2.40	2.67E0		
2.25	18150.	0.5510	2.60	3.12E0		
2.0	16130.	0.6199	3.38	3.46E0		
1.75	14110.	0.7085	4.20	4.30E0		
1.7	13710.	0.7293			1.33E0[4]	
1.6	12900.	0.7749			8.63E-1	
1.5	12100.	0.8265	6.65	4.09E0	5.92E-1	
1.4	11290.	0.8856			3.52E-1	
1.3	10480.	0.9537			1.74E-1	
1.25	10080.	0.9919	5.90	1.0E0		
1.2	9678.	1.033			8.22E-2	
1.1	8872.	1.127			4.48E-2	
1.02	8227.	1.215			8.25E-3[8]	
1.00	8065.	1.240	5.45	5.1E-1	5.82E-3	
0.98	7904.	1.265			3.82E-3	
0.96	7743.	1.291			2.60E-3	
0.94	7581.	1.319			1.71E-3	
0.92	7420.	1.348			1.21E-3	
0.90	7257.	1.378			8.79E-4	2.5E-3[7]
0.88	7098.	1.409			6.02E-4	1.9E-3
0.86	6936.	1.442			3.20E-4	1.2E-3
0.84	6775.	1.476			2.02E-4	7.0E-4
0.83	6694.	1.494				5.2E-4
0.82	6614.	1.512			1.07E-4	4.1E-4
0.80	6452.	1.550			5.56E-5	2.6E-4
0.78	6291.	1.589				1.4E-4
0.76	6130.	1.631				4.9E-5
0.75	6049.	1.653	5.12			
0.74	5968.	1.675				2.7E-6
0.4959	4000.	2.500	4.60[1]			
0.4339	3500.	2.857	4.60			
0.3719	3000.	3.333	4.60			
0.3097	2500.	4.000	4.59			
0.2480	2000.	5.000	4.59			
0.1860	1500.	6.667	4.57			
0.1240	1000.	10.00	4.51			
0.1116	900.	11.11	4.49	9.76E-4[1]		
0.0991	800.	12.50	4.44	1.38E-3		
0.0867	700.	14.28	4.37	2.58E-3		
0.08183	660.	15.15	4.32	3.52E-3		
0.08059	650.	15.38	4.30	3.78E-3		

(continued)

TABLE II *(Continued)*

Iron Pyrite

eV	cm−1	μm	n	k	k	k
0.07935	640.	15.62	4.29	4.26E-3		
0.07811	630.	15.87	4.27	4.68E-3		
0.07687	620.	16.13	4.25	5.07E-3		
0.07563	610.	19.39	4.23	5.61E-3		
0.07439	600.	16.67	4.21	6.25E-3		
0.07315	590.	16.95	4.18	7.04E-3		
0.07191	580.	17.24	4.15	7.87E-3		
0.07067	570.	17.54	4.12	9.00E-3		
0.06943	560.	17.86	4.08	1.03E-2		
0.06819	550.	18.18	4.04	1.19E-2		
0.06695	540.	18.52	3.99	1.39E-2		
0.06571	530.	18.87	3.93	1.64E-2		
0.06447	520.	19.23	3.86	1.97E-2		
0.06323	510.	19.61	3.77	2.41E-2		
0.06199	500.	25.00	3.67	3.03E-2		
0.06075	490.	20.41	3.54	3.91E-2		
0.05951	480.	20.83	3.37	5.26E-2		
0.05827	470.	21.28	3.14	7.50E-2		
0.05703	460.	21.74	2.79	1.17E-1		
0.05579	450.	22.22	2.22	2.20E-1		
0.05455	440.	22.73	1.01	7.96E-1		
0.05393	435.	22.99	0.612	1.81E0		
0.05331	430.	23.25	0.584	2.78E0		
0.05269	425.	23.53	0.706	3.80E0		
0.05207	420.	23.81	1.10	5.00E0		
0.05182	418.	23.92	1.44	5.49E0		
0.05158	416.	24.04	1.88	5.82E0		
0.05145	415.	24.10	2.03	5.89E0		
0.05133	414.	24.15	2.08	5.97E0		
0.05108	412.	24.27	2.00	6.44E0		
0.05083	410.	24.39	2.08	7.40E0		
0.05058	408.	24.51	2.58	8.74E0		
0.05034	406.	24.63	3.84	10.4E0		
0.05021	405.	24.69	5.01	11.4E0		
0.05009	404.	24.75	6.81	12.2E0		
0.04997	403.	24.81	9.31	12.3E0		
0.04984	402.	24.87	11.9	11.0E0		
0.04972	401.	24.94	13.5	8.50E0		
0.04959	400.	25.00	13.6	6.09E0		
0.04947	399.	25.06	13.1	4.36E0		
0.04935	398.	25.12	12.3	3.21E0		
0.04910	396	25.25	11.0	1.93E0		
0.04835	390.	25.64	8.69	7.06E-1		
0.04711	380.	26.31	7.05	2.81E-1		
0.04587	370.	27.02	6.15	1.73E-1		
0.04463	360.	27.78	5.22	1.96E-1		
0.04389	354.	28.25	3.76	6.11E-1		

TABLE II *(Continued)*

Iron Pyrite

eV	cm−1	μm	n	k	k	k
0.04364	352.	28.41	2.45	1.83E0		
0.04352	351.	28.49	2.15	3.40E0		
0.04339	350.	28.57	2.67	5.37E-1		
0.04327	349.	28.65	4.65	7.69E0		
0.04315	348.	28.73	9.63	7.60E0		
0.04302	347.	28.82	10.9	3.30E0		
0.04290	346.	28.90	9.70	1.47E0		
0.04401	345.	28.98	8.82	8.24E-1		
0.04265	344.	29.07	8.24	5.32E-1		
0.04240	342.	29.24	7.54	2.85E-1		
0.04215	340.	29.41	7.13	1.86E-1		
0.04091	330.	30.30	6.26	6.58E-2		
0.03967	320.	31.25	5.90	4.33E-2		
0.03843	310.	32.26	5.61	3.95E-2		
0.03720	300.	33.33	5.10	9.26E-2		
0.03695	298.	33.56	4.82	1.65E-1		
0.03670	296.	33.78	4.18	4.61E-1		
0.03657	295.	33.90	3.52	1.11E0		
0.03645	294.	34.01	3.45	3.30E0		
0.03633	293.	34.13	7.23	4.52E-1		
0.03620	292.	34.25	8.05	1.42E0		
0.03608	291.	34.36	7.28	5.40E-1		
0.03596	290.	34.48	6.83	2.81E-1		
0.03571	288.	34.72	6.38	1.21E-1		
0.03546	286.	34.96	6.16	7.13E-2		
0.03472	280.	35.71	5.86	3.09E-2		
0.03348	270.	37.04	5.66	1.74E-2		
0.03224	260.	38.46	5.56	1.29E-2		
0.03100	250.	40.00	5.48	1.04E-2		
0.02976	240.	41.67	5.43	8.68E-3		
0.02852	230.	43.48	5.38	7.43E-3		
0.02728	220.	45.45	5.34	6.47E-3		
0.02604	210.	47.62	5.31	5.69E-3		
0.02490	200.	50.00	5.28	5.07E-3		
0.02356	190.	52.63	5.26	4.47E-3		
0.02232	180.	55.56	5.24	3.91E-3		
0.02108	170.	58.82	5.22	3.52E-3		
0.01984	160.	62.50	5.20	3.24E-3		
0.01860	150.	66.67	5.19	2.76E-3		
0.01736	140.	71.43	5.18	2.58E-3		
0.01612	130.	76.92	5.16	2.18E-3		
0.01488	120.	83.33	5.15	1.95E-3		
0.01364	110.	90.91	5.14	1.80E-3		
0.01240	100.	100.0	5.14	1.69E-3		

Silicon (Si) Revisited (1.1–3.1 eV)

JON GEIST
Olney, Maryland

I THE INDEX OF REFRACTION OF SILICON IN THE VISIBLE AND VERY NEAR IR

A Introduction

At room temperature, the extinction coefficient, k, of nominally pure, single-crystal silicon increases from less than 10^{-6} at the onset of the indirect transition to almost 1 at 370 nm. On the other hand, the real part of the index of refraction, n, of silicon at room temperature varies by less than a factor of 2 over the same spectral range.

Transmission measurements are the most accurate way to determine $k \ll 1$, but they require impractically thin samples for wavelengths less than about 550 nm. More accurate values of k can be deduced from reflectance or ellipsometric measurements below this wavelength. Only reflectance and ellipsometric measurements can be used to measure n except at the longest wavelengths of this spectral region because of the large values of the absorption coefficient $\alpha = 4\ \pi\ k/\lambda$ over most of the region.

The extinction-coefficient data will be considered first, then the index data. But first, a few generalizations about the data to be discussed can be made. All of the measurements discussed here were carried out at nominal room temperature, but very few authors reported the exact temperature, so corrections among the different data sets for small differences in measurement temperature are not possible. All of the authors used single-crystal material that was pure enough to preclude extrinsic effects in the spectral region of their measurements. All authors were concerned with the effect of surface films, surface roughness, and surface damage, and most attempted to minimize or correct for the effects of these imperfections in the measured data. On the other hand, there was no consensus at all about how to do this.

HANDBOOK OF OPTICAL CONSTANTS OF SOLIDS III

Copyright © 1998 by Academic Press.
All rights of reproduction in any form reserved
ISBN 0-12-544423-0/$25.00.

B Extinction Coefficient

A large number of references report k spectra for nominally pure, single-crystal silicon at room temperature, but the agreement among most of these spectra is very poor. In fact, just two of these, the room-temperature data of Jellison [1] and Weakliem and Redfield [2], have been selected as having a satisfactory combination of range and accuracy over the spectral region of interest here. Furthermore, an analytic model was used to summarize the data of Jellison [1] and Weakliem and Redfield [2]. This model is given by

$$k(h\nu) = f(h\nu)\ [1.23985 \times 10^{-4}\ \text{cm eV}/h\nu][g(h\nu)/h\nu]/4\pi \tag{1}$$

$$g(h\nu) = \sum_{i=1}^{2} \sum_{j=-1}^{1} \{C_{i,j}[L(h\nu - \epsilon_1 + jd\epsilon_i)]^2\} + C_3[2L(h\nu - \epsilon_3)]^{N+dN\,h\nu} \tag{2}$$

$$f(h\nu) = \exp\{K_4 L(h\nu - \epsilon_4) + K_5 L(h\nu - \epsilon_5)\} \tag{3}$$

$$L(\epsilon) = (\epsilon + |\epsilon|)/2eV, \tag{4}$$

where $j = 0$ is not used in the sum over j, $|\epsilon|$ indicates the absolute value of ϵ, $h\nu$ is the photon energy = 1.23985 μm eV/λ, λ is the vacuum wavelength, and the values of the parameters in Eqs. (1)–(4) are given in Table I.

This model is an extension of the fit of $g(h\nu)$ that was reported by Geist *et al.* [3] to the absorption-coefficient data of Weakliem and Redfield [2]. The terms under the double sum in Eq. (2) describe the onset of the indirect (phonon-assisted) transition in silicon according to quantum band theory as described in by Macfarlane *et al.* [4]. The C_3 term in Eq. (2) is an empirical term to describe the effect of the nonparabolic nature of the bands away from the silicon band edge. The function $f(h\nu)$ is an empirical correction factor that was fitted to the ratio of the data of Jellison [1] to the values calculated from $g(h\nu)$ for photon energies greater than those used to adjust the parameters in $g(h\nu)$.

The k values calculated from the model given in Eqs. (1)–(4) are shown in Fig. 1 over the range from 370 to 1170 nm. (The kink between 1000 and 1100 nm is real, as discussed by Macfarlane *et al.* [4].) The model fits the data of Jellison [1] and Weakliem and Redfield [2] very well from 390 to 1130 nm, considering that k(390 nm)/k(1130 nm) > 35,000. The quality of the fit over this range is shown in Fig. 2, which plots the ratio of the reported data points to those calculated from the model.

A few other data sets are also plotted in Fig. 2 as consistency checks. Note that the temperature coefficient of k is of the order of 0.5%/K at room temperature between 400 and 800 nm [9]. Thus, the major differences in Fig. 2, are not due to the use of different temperatures for nominal room temperature by the authors of the different references, although some of the smaller differences might be.

The data of Weakliem and Redfield [2] were chosen for fitting for a number of reasons. First, three different sample thicknesses (5.50, 249, and 797 μm) were used in the transmission measurements reported therein. This has the virtue of covering a large range of extinction coefficient and also of providing a good consistency check on the k values in spectral regions where the transmission measurements overlap. Second, it was already shown by Geist *et al.* [3] that the data of Weakliem and Redfield [2] agree well with the data of Macfarlane *et al.* [4] (not shown in Fig. 2) at the longer wavelengths, and with a single high-accuracy datum point at 633 nm [5] that is shown in Fig. 2. Another virtue of this data set is that tabulated numerical values were available to the author [10]. Finally, note that the two thinner samples were measured at 297 K, and the thickest sample was measured at 299 K.

A portion of a second data set [6] of k data that was derived from transmission measurements is also shown in Fig. 2 as a consistency check on the model fit to the data of Weakliem and Redfield [2]. The points shown in Fig. 2 for these data were read from an enlarged copy of a different version of Fig. 11 by Gentile *et al.* [11]. Notice that the k data of Vol'fson and Subashiev [6] differ from the model by a uniform $3.4 \pm 0.5\%$ over the spectral region for which the data of Vol'fson and Subashiev [6] are plotted. This is consistent with a 3.4% error between the sample-thickness measurements upon which the two data sets were based.

The consistency of Eqs. (1)–(4) with the data of Vol'fson and Subashiev [6] is important because the agreement between the k values derived from the 5.50-μm-thick sample and the 249-μm-thick sample used by Weakliem and Redfield [2] is not as good as might be desired. The consistency also shows that fitting a function that is based on physical principles to the data tends to ignore the less-accurate data points.

The data of Jellison [1] were chosen for fitting for a number of reasons. First, the two-channel, polarization-modulation ellipsometric technique on which these data were based is more accurate for $k < 1$ than more conventional ellipsometric techniques such as rotating-analyzer ellipsometry. Second, these data were corrected for the presence of a thin native-oxide layer on the silicon surface. Third, Jellison [1] includes a careful uncertainty analysis that estimates about 1, 4, and 10% uncertainties at 400, 500, and 600 nm, respectively. Finally, these data agree with the high-accuracy datum point at 633 nm [5] mentioned earlier and with another high-accuracy datum point that was also based on transmission measurements using samples of different thicknesses (4.80, 5.93, 8.80, and 10.82 μm) at 546 nm [7] within the uncertainties estimated in [1, 5, 7]. This level of agreement tends to confirm the choice of the data from Jellison [1] based on the first three reasons. A final virtue of this data set is that tabulated numerical values were published in Jellison [1].

A portion of another set [8] of k data is also shown in Fig. 2 as a consistency check of the model around 400 nm. These k values were obtained in a

very different way: from a Kramers–Kronig analysis of reflectance data. These k values also include a correction for the effect of the native oxide. The rapid increase of the difference between that data points of Philipp [8] and the data points of Jellison [1] with increasing wavelength is not considered a problem with the latter, since a Kramers–Kronig analysis is not well suited to determining the smaller k values at the longer wavelengths.

Notice that the data of Jellison [1] and Weakliem and Redfield [2] agree very well in the center of their overlap region. Such agreement is usually considered a good sign of consistency. However, the agreement between the data sets of Jellison [1] and Weakliem and Redfield [2] in the overlap region may be fortuitous. Actually, the data of Jellison [1] were normalized to agree with another data set [12] that does not agree well with that of Weakliem and Redfield [2], but the normalization was carried out in a spectral region where the data of Dash and Newman [12] do not agree with those of Weakliem and Redfield [2], either. Therefore, the agreement at 633 nm might be a coincidence that has no bearing on the actual uncertainty of either data set in the overlap region. The independent agreement of both data sets with the high-accuracy datum point from Geist *et al.* [5] at 633 nm suggests that the data from Jellison [1] and Weakliem and Redfield [2] are indeed reliable in the overlap region.

The author knows of no other data set covering this spectral region that is comparable to that of Jellison [1] and Weakliem and Redfield [2] with respect to the virtues just mentioned. In fact, most of the k values in other data sets differ so much from the data shown in Fig. 2 that they would not even show up in Fig. 2.

Plus or minus 10% should be a very conservative uncertainty on k from this model over the 400 to 1130 nm spectral region, whereas $\pm$ 5% would appear to be a reasonable estimated one-standard-deviation equivalent uncertainty where such is required.

Before turning attention to n, note that the k values given in Table III at the end of this section are quite different from those given in by Edwards [13]. Also, note that the k values in Table III are not the data points reported by Jellison [1] and Weakliem and Redfield [2], but the values calculated from the model of Eqs. (1)–(4). Finally, note that k decreases so rapidly with increasing wavelength in this spectral region that great care is needed during interpolation of the data in Table III to avoid incurring significant errors. This is particularly so at the ends of the table. For this reason, it is probably safer to calculate k values from Eqs. (1)–(4) directly rather than to try to interpolate them from Table III.

C Real Part of the Index of Refraction

The choice among the various sets of n data is not as straightforward as was the case with the k data. Nevertheless, a model was fitted to the room-

temperature data in Jellison [1] and to three room-temperature data points from Edwards [13]. The model is given by

$$n(h\nu) = y(h\nu)z(h\nu) \tag{5}$$

$$z(h\nu) = N_0 + h\nu(N_1 + h\nu(N_2 + h\nu(N_3 + h\nu N_4))) \tag{6}$$

$$y(h\nu) = \exp\{y_6(h\nu)[K_{61} + y_6(h\nu)K_{62}] + y_7(h\nu)[K_{71} + y_7(h\nu)K_{72}]\} \tag{7}$$

$$y_m(h\nu) = 2L(h\nu - \epsilon_m), \tag{8}$$

where $m = 6, 7$, the function $L(\epsilon)$ is defined in Eq. (4), and the values of the parameters needed in Eqs. (5)–(8) are given in Table II. The model fits the n data of Jellison [1] and Edwards [13] reasonably well from 390 to 1200 nm, as shown in Fig. 3 [14]. This figure plots the ratio of the reported data points to those calculated from the model.

A few other data sets are also plotted in Fig. 3 as consistency checks. Note that the temperature coefficient of n is of the order of 0.025%/K at room temperature [9]. Thus the major differences in Fig. 3 are not due to the use of different temperatures as nominal room temperature by the authors of the different references, although the smaller differences might be.

The data of Jellison [1] were chosen partially because the quality of these data had already been established in connection with the selection of the k data, but also because they are recent, and they agree well at 546.1 nm with the value reported in by Taft [7]. The latter value has been characterized by Aspnes and Studna [14] as "most probably, the best data" among the more than 15 data points (ranging from 4.004 to 4.151) that have been reported at this wavelength.

Three data points between 1100 and 1200 nm were selected from Edwards [13] because these are derived from measurements of the angle of minimum deviation, which should be considerably more accurate than ellipsometric or reflectance measurements. Data points from two other widely referenced [8, 14] index spectra are also shown in Fig. 3 for comparison. Ellipsometric measurements were used by Aspnes and Studna [14], whereas a Kramers–Kronig analysis of reflectance measurements was used by Philipp [8].

The model of Eqs. (5)–(8) was fitted only to the plus signs in Fig. 3. The plus signs below 900 nm are from Jellison [1] and those above 1100 nm are from Edwards [13]. Jellison [1] estimated the uncertainty of the data used in Fig. 3 at less than 0.6% between 400 and 800 nm. Therefore, the model of Eqs. (5)–(8) fits the data from Jellison [1] to well within the estimated uncertainty of the data except near 400 nm and at wavelengths longer than 800 nm, where the error in the fit approaches the estimated error.

Since the two other spectra [8, 14] included in Fig. 3 have very similar shapes, it is somewhat disconcerting that the spectrum from Jellison [1] has a different shape below about 550 nm. On the other hand, Jellison [1] agrees better with Taft [7] at 546.1 nm, and Jellison [1] devoted a significant amount of time to estimating and reporting the uncertainties in his measurements. In

light of (i) the small but not negligible inconsistencies among the data shown in Fig. 3, (ii) the uncertainty estimate provided by Jellison [1], and (iii) the lack of good coverage over an extended region from about 800 to 1100 nm, a conservative uncertainty estimate might be $\pm 1\%$ for wavelengths greater than 550 nm, and $+1$–2% for shorter wavelengths. It is not possible to assign a convincing "one-standard-deviation equivalent" uncertainty for the model of Eqs. (5)–(8) in light of the inconsistencies shown in the data in Fig. 3.

Table III contains n and k data calculated from Eqs. (1)–(8) at 0.05-eV intervals from 1.10 to 3.10 eV. Data about the variation of n and k with temperature at different wavelengths can be found elsewhere [2, 9, 15]. Finally, note that Gentile *et al.* [11] review a wider variety of k data, but reaches similar conclusions to those given here.

ACKNOWLEDGEMENT

The author thanks T. R. Gentile for providing a preprint of the appendix reviewing k data in Gentile *et al.* [11], a different version of Fig. 11 in Gentile *et al.* [11], a computer disk containing data keyed from Jellison [1], and other useful information about the data reviewed by Gentile *et al.* [11].

REFERENCES

1. G. E. Jellison Jr., Optical functions of silicon determined by two-channel polarization modulation ellipsometry. *Opt. Mater.* **1**, 41–47 (1992).
2. H. A. Weakliem and D. Redfield, Temperature dependence of the optical properties of silicon. *J. Appl. Phys.* **50**, 1491–1493 (1979).
3. J. Geist, A. Migdall, and H. P. Baltes, Analytic representation of the silicon absorption coefficient in the indirect transition region. *Appl. Opt.* **27**, 3777–3779 (1988).
4. G. G. Macfarlane, T. P. McLean, J. E. Quarington, and V. Roberts, Fine structure in the absorption-edge spectrum of silicon. *Phys. Rev.* **111**, 1245–1254 (1958); G. G. Macfarlane, P. T. McLean, J. E. Quarington, and V. Roberts, Exiton and phonon effects in the absorption spectra of germanium and silicon. *J. Phys. Chem. Solids* **8**, 388–392 (1959).
5. J. Geist, A. R. Schaefer, J.-F. Song, Y. H. Wang, and E. F. Zalewski, An accurate value for the absorption coefficient of silicon at 633 nm. *J. Res. Natl. Inst. Stand. Technol.* **95**, 549–558 (1990).
6. A. A. Vol'fson and V. K. Subashiev, Fundamental absorption edge of silicon heavily doped with donor or acceptor impurities. *Sov. Phys. Semicond. (Engl. Transl.)* **1**, 327–332 (1967), which includes a pure-silicon reference.
7. E. A. Taft, The optical constants of silicon and dry oxygen oxides of silicon at 5461 Å. *J. Electrochem. Soc.* **125**, 968–971 (1978).
8. H. R. Philipp, Influence of oxide layers on the determination of the optical properties of silicon. *J. Appl. Phys.* **43**, 2835–2839 (1972); H. R. Philipp personal communication, 1979.
9. G. E. Jellison, Jr. and F. A. Modine, Optical functions of silicon at elevated temperatures. *J. Appl. Phys.* **76**, 3758–3761 (1994).
10. H. A. Weakliem personal communication, 1979.
11. T. R. Gentile, J. M. Houston, and C. L. Cromer, Realization of a scale of absolute spectral

response using the National Institute of Standards and Technology high-accuracy cyrogenic radiometer. *Appl. Opt.* **35**, 4392–4403 (1996).
12. W. C. Dash and R. Newman, Intrinsic optical absorption spectra in single-crystal germanium and silicon at 77° K and 300° K. *Phys. Rev.* **99**, 1151–1155 (1955).
13. D. F. Edwards, Silicon (Si). *in* "Handbook of Optical Constants of Solids" (E. D. Palik, ed.), pp. 547–569. Academic Press, Orlando, Florida, 1985.
14. D. E. Aspnes and A. A. Studna, Dielectric functions and optical parameters of Si, Ge, GaP, GaAs, GaSb, InP, InAs, and InSb from 1.5 to 6.0 eV. *Phys. Rev. B* **27**, 985–1009 (1983).
15. G. E. Jellison, Jr., and D. H. Lowndes, Optical absorption coefficients of silicon at 1.152 μ at elevated temperatures. *Appl. Phys. Lett.* **41**, 594–596 (1982).

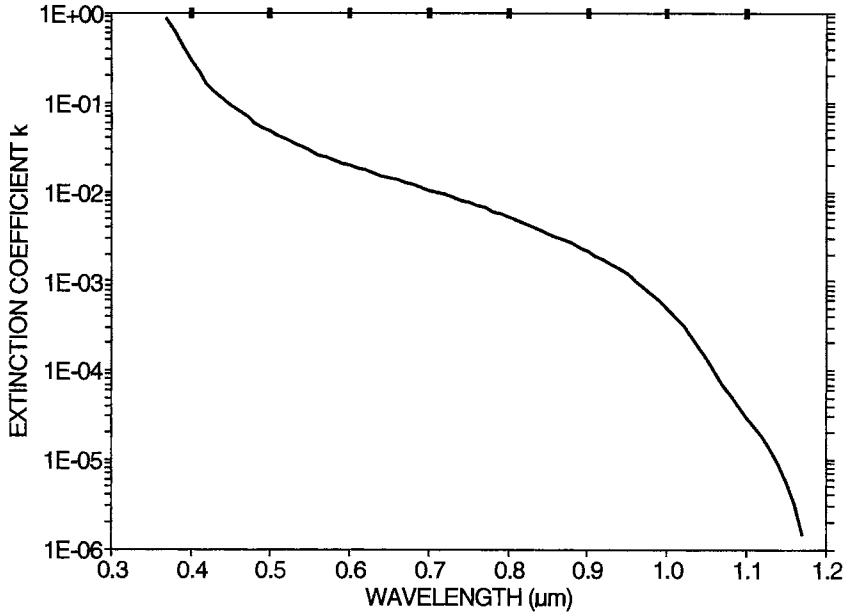

Fig. 1. The extinction coefficient of a pure silicon crystal at room temperature from 370 to 1170 nm as calculated from Eqs. (1)–(4) to represent the data of Jellison [1] and Weakliem and Redfield [2].

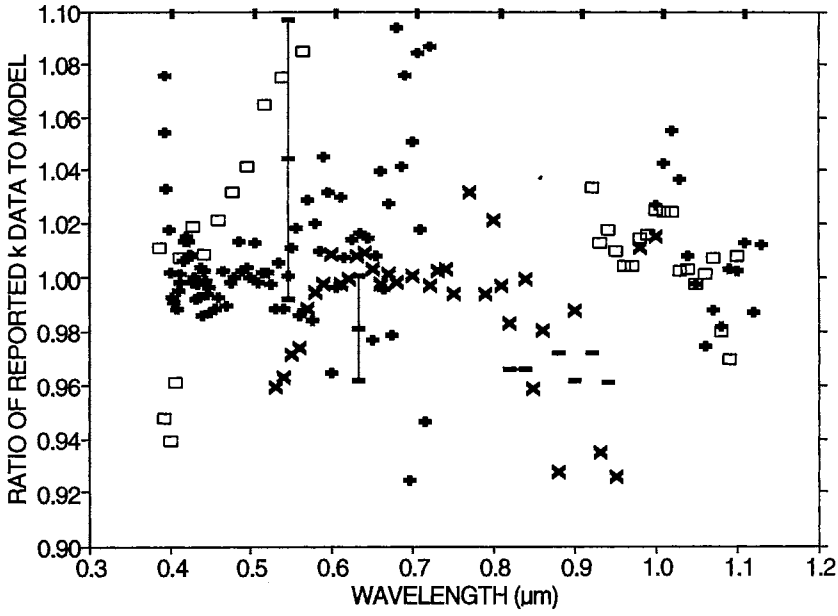

Fig. 2. The ratio of the k values reported by some different authors to the k values calculated from Eqs. (1)–(4) at the same wavelengths: plus signs below 800 nm from Jellison [1], x's from Weakliem and Redfield [2]; plus signs and open boxes above 800 nm also from Weakliem and Redfield [2]; 633-nm data point with error bars from Giest *et al.* [5]; minus signs from Vol'fson and Subashiev [6]; 546-nm data point with error bars from Taft [7]; open boxes below 600 nm from Philipp [8].

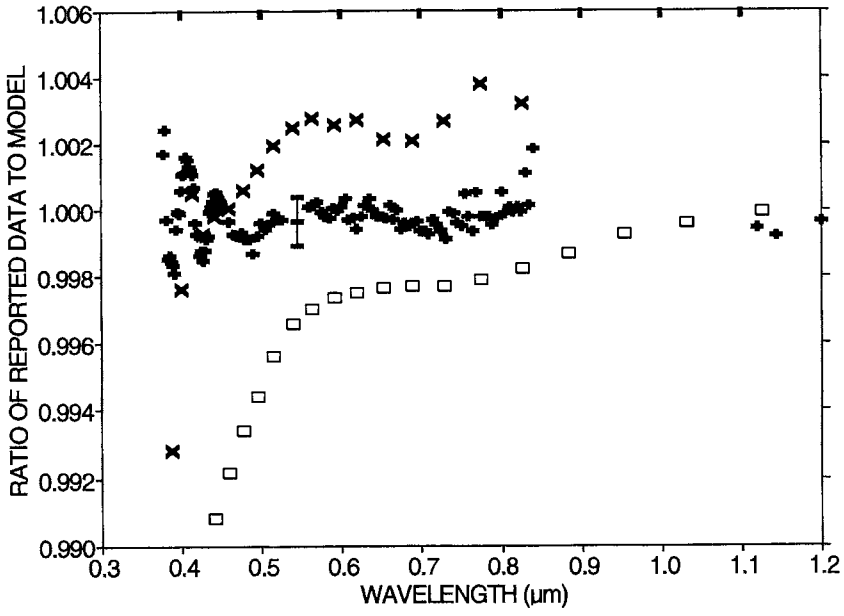

Fig. 3. The ratio of the n values reported by some different authors to the n values calculated from Eqs. (5)–(8) at the same wavelengths: plus signs below 900 nm from Jellison [1]; plus signs above 1100 nm from Edwards [13]; 546-nm data point with error bars from Taft [7]; open boxes from Philipp [8]; and x's from Aspnes and Studna [14].

TABLE I

Parameters for Use in Eqs. (1)–(4) to Describe the Extinction Coefficient of Pure Silicon at Room Temperature from 400 to 1180 nm

Parameter	Value
ϵ_1	1.09969 eV
$d\epsilon_1$	0.0583148 eV
$C_{1,-1}$	5030.02 cm^{-1} eV
$C_{1,+1}$	483.916 cm^{-1} eV
ϵ_2	(not used)
$d\epsilon_2$	0.0220161 eV
$C_{2,-2}$	1634.30 cm^{-1} eV
$C_{2,+2}$	79.4079 cm^{-1} eV
ϵ_3	1.40985 eV
C_3	1046.08 cm^{-1} eV
N	0.394122
dN	1.23084 eV^{-1}
ϵ_4	2.15362 eV
K_4	0.210102
ϵ_5	2.95893 eV
K_5	1.03681

TABLE II

Parameters for Use in Eqs. (5)–(8) to Describe the Index of Refraction of Pure Silicon at Room Temperature from 390 to 1200 nm

Parameter	Value
N_0	3.76289
N_1	−1.02862
N_2	1.19270
N_3	−0.504529
N_4	0.0909420
ϵ_6	2.74717 eV
K_{61}	0.00891406
K_{62}	0.0292730
ϵ_7	2.97648 eV
K_{71}	−0.0012589
K_{72}	0.197000

TABLE III

Values of n and k for Silicon Obtained from Various References

eV	cm^{-1}	μm	n	k
3.10	25000	0.4000	5.5832	2.96E-01
3.05	24600	0.4065	5.3834	2.40E-01
3.00	24200	0.4133	5.2195	1.96E-01
2.95	23790	0.4203	5.0855	1.62E-01
2.90	23390	0.4275	4.9647	1.40E-01
2.85	22990	0.4350	4.8544	1.21E-01
2.80	22580	0.4428	4.7539	1.05E-01
2.75	22180	0.4509	4.6627	9.19E-02
2.70	21780	0.4592	4.5828	8.05E-02
2.65	21370	0.4679	4.5085	7.08E-02
2.60	20970	0.4769	4.4394	6.25E-02
2.55	20570	0.4862	4.3749	5.54E-02
2.50	20160	0.4959	4.3149	4.92E-02
2.45	19760	0.5061	4.2589	4.39E-02
2.40	19360	0.5166	4.2068	3.93E-02
2.35	18950	0.5276	4.1582	3.52E-02
2.30	18550	0.5391	4.1128	3.16E-02
2.25	18150	0.5510	4.0704	2.84E-02
2.20	17740	0.5636	4.0307	2.56E-02
2.15	17340	0.5767	3.9936	2.31E-02
2.10	16940	0.5904	3.9588	2.10E-02
2.05	16530	0.6048	3.9261	1.91E-02
2.00	16130	0.6199	3.8953	1.73E-02
1.95	15730	0.6358	3.8662	1.57E-02
1.90	15320	0.6526	3.8388	1.41E-02
1.85	14920	0.6702	3.8127	1.26E-02
1.80	14520	0.6888	3.7880	1.12E-02
1.75	14110	0.7085	3.7644	9.92E-03
1.70	13710	0.7293	3.7419	8.65E-03
1.65	13310	0.7514	3.7204	7.45E-03
1.60	12900	0.7749	3.6999	6.30E-03
1.55	12500	0.7999	3.6801	5.22E-03
1.50	12100	0.8266	3.6611	4.21E-03
1.45	11690	0.8551	3.6429	3.29E-03
1.40	11290	0.8856	3.6254	2.47E-03
1.35	10890	0.9184	3.6087	1.75E-03
1.30	10490	0.9537	3.5926	1.11E-03
1.25	10080	0.9919	3.5773	5.87E-04
1.20	9679	1.033	3.5628	2.21E-04
1.15	9275	1.078	3.5491	5.55E-05
1.10	8872	1.127	3.5362	1.39E-05

Silicon (Si) Revisited (1.4–6.0 eV)

DAVID F. EDWARDS
Tracy, California

Adachi [1, 2] has developed a method for the calculation of the complex dielectric function, $\epsilon(\omega) = \epsilon_1(\omega) + i\,\epsilon_2(\omega)$, of Si based on a simplified model of the energy-band structure of the material. This model covers the optical response of Si over the entire range of photon energies (0–6.0 eV) and is based on the Kramers–Kronig transformation. The calculation takes into account the effects of interband transitions at the major energy–band critical points and indirect band gap. The model relies on the measured critical point energies of Lautenschlager *et al.* [3]. This group measured the dielectric function of Si by ellipsometry in the 1.7- to 5.7-eV photon-energy range. For the Adachi model the strength and damping parameters were adjusted to optimize the fit to experimental data. The experimental data of Aspens and Studna [4] were used for the fit of the $\epsilon_2(\omega)$ calculation. These experimental data were obtained from spectroscopic ellipsometry. For the $\epsilon_1(\omega)$ calculation the experimental data of Philipp and Ehrenreich [5] were used for energies below 1.5 eV and those in the 1.5- to 6.0-eV range from Aspens and Studna [4]. In order to improve the $\epsilon_1(\omega)$ fit, the nondispersive term, $\epsilon_{1\infty}$, was added to the sum of the dispersive terms. The spectral dependence of the refractive index, n, and the extinction coefficient, k, were calculated from the real and imaginary parts of $\epsilon(\omega)$. The details of these calculations are given later.

Overall, the continuous analytical functions for n and k are in satisfactory agreement with experiment concerning the simplicity of the model and complexity of the problem. The calculated k values appear to be about 9–10% too small in the energy region greater than about 4.27 eV. The fit of the calculated n values is much better for energies less than 3.38 eV than for energies greater than this value. For purpose of this review article, only n and k values in the 3.0- to 6.0 eV-range are tabulated. The 1.10- to 3.1-eV data of Geist (included in this volume) appear to give a more accurate fit to experimental data.

For the interband transitions, E_1, along the $\langle 111 \rangle$ direction of the Brillouin zone (near 3.4 eV), the contributions to ϵ_2 are

HANDBOOK OF OPTICAL CONSTANTS OF SOLIDS III

Copyright © 1998 by Academic Press.
All rights of reproduction in any form reserved
ISBN 0-12-544423-0/$25.00.

$$\begin{aligned} \epsilon_2(\omega) &= \pi\chi_1^{-2}[B_1 - B_{11}(E_1 - \hbar\omega)^{0.5} \quad (\hbar\omega < E_1) \\ &= \pi B_1 \chi_1^{-2} \qquad\qquad\qquad\qquad (\hbar\omega \geq E_1), \end{aligned} \tag{1}$$

where $\chi_1 = \hbar\omega/E_1$.

The contribution of the E_1 transition to $\epsilon_1(\omega)$ is

$$\epsilon_1(\omega) = -B_1\chi_1^{-2}\ln|1 - \chi_1^2|. \tag{2}$$

The B's are the strength parameters. The numerical parameters used in the calculations are listed in Table I.

At the $\langle 100 \rangle$ edge of the Brillouin zone (near 4.3 eV), the E_2 transition has two contributions to the dielectric function . The first is characterized by a damped harmonic oscillator,

$$\epsilon_2(\omega) = C\chi_2\gamma/[(1 - \chi_2^2)^2 + \chi_2^2\gamma^2] \tag{3}$$

and

$$\epsilon_1(\omega) = C(1 - \chi_2^2)/[(1 - \chi_2^2)^2 + \chi_2^2\gamma^2] \tag{4}$$

with

$$\chi_2 = \hbar\omega/E_2,$$

where C and γ are, respectively, the strength and damping parameters of the oscillator.

The second contribution for the E_2 transition is

$$\epsilon_2(\omega) = \pi F\chi_2^{-2}H(\chi_{cl} - 1) \tag{5}$$

with

$$\chi_1 = \hbar\omega/E_1$$

and

$$\epsilon_1(\omega) = -F\chi_2^{-2}/\ln\left|\frac{1 - \chi_{cl}^2}{1 - \chi_2^2}\right|. \tag{6}$$

Here F is the strength parameter and

$$\begin{aligned} H(y) &= 1 \text{ for } y \geq 0 \\ &= 0 \text{ for } y < 0. \end{aligned}$$

The E_1' transitions near 5.3 eV are to a higher valence band. They are assumed by Adachi to be of the form of damped harmonic oscillators:

$$\epsilon_2(\omega) = C_a\gamma_a\chi_a/[1 - \chi_a^2)^2 + \chi_a^2\gamma_a^2] \tag{7}$$

$$\epsilon_1(\omega) = C_a(1 - \chi_a^2)/[(1 - \chi_a^2)^2 + \chi_a^2\gamma_a^2], \tag{8}$$

with

$$\chi_a = \hbar\omega/E_a,$$

where E_a is the energy of the oscillator.

The contribution of the indirect transition to $\epsilon_2(\omega)$ is

$$\epsilon_2(\omega) = \frac{D}{\hbar\omega^2}(\hbar\omega - E_g^{id} \pm \hbar\omega_q)^2 H(1 - \chi_g), \tag{9}$$

with

$$\chi_g = (E_g^{id} \pm \hbar\omega_q)/\hbar\omega,$$

where D is the direct-transition strength parameter and $\hbar\omega_q$ is the phonon energy associated with the indirect transition. Adachi states that there is no contribution of the indirect transition to $\epsilon_1(\omega)$.

The nondispersive term, $\epsilon_{1\infty}(= 1.8$ eV), is added to the sum of Eqs. (2), (4), (6), and (8) for the final summation of the $\epsilon_1(\omega)$.

The complex refractive index, $n^*(\omega)$, is

$$n^*(\omega) = n(\omega) + ik(\omega) = \epsilon(\omega)^{1/2}, \tag{10}$$

where n and k are, respectively, the real refractive index and the extinction coefficient. From Eq. (10), the optical constants are

$$n(\omega) = \left(\frac{(\epsilon_1(\omega)^2 + \epsilon_2(\omega)^2)^{1/2} + \epsilon_1(\omega)}{2}\right)^{1/2} \tag{11}$$

$$k(\omega) = \left(\frac{(\epsilon_1(\omega)^2 + \epsilon_2(\omega)^2)^{1/2} - \epsilon_1(\omega)}{2}\right)^{1/2}. \tag{12}$$

Listed in Table II are n and k values for the energy range 3.0 to 6.0 eV (0.207 to 0.414 μm) as calculated from Eqs. (11) and (12) and the parameters of Table I.

REFERENCES

1. S. Adachi, *Phys. Rev. B* **38**, 12966 (1988).
2. S. Adachi, *J. Appl. Phys.* **66**, 3224 (1989).
3. P. Lautenschlager, N. Garriga, L. Viña, and M. Cardona, *Phys. Rev. B* **36**, 4821 (1987).
4. D. E. Aspens and A. A. Studna, *Phys. Rev. B* **27** 985 (1983).
5. H. R. Philipp and H. J. Ehrenreich, *Phys. Rev.* **129**, 1550 (1963).

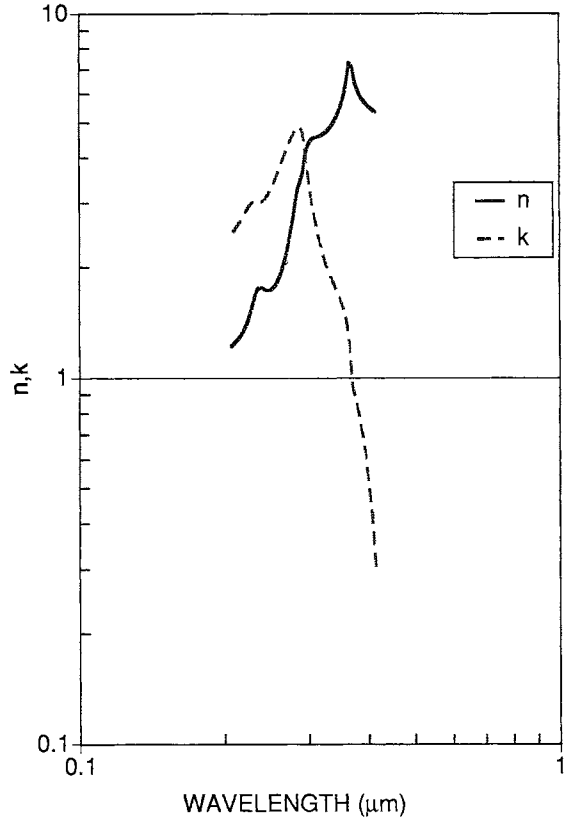

Fig. 1. Log–log plot of n and k versus wavelength in microns for silicon as calculated from Eqs. (1)–(12).

TABLE 1

Parameters Used in the Calculation of $n(\omega)$ and $k(\omega)$ (at room temperature)

E_1(eV)	3.38
B_1	5.22
B_{11} ($eV^{-0.5}$)	7.47
E_2(eV)	4.27
C	3.01
γ	0.127
F	3.51
$\Gamma[E_2]$ (eV)	0.04
E_a (eV)	5.32
C_a	0.21
γ_a	0.089
E_g^{ID}(eV)	1.12
D	0.89
$\epsilon_{1\infty}$	1.8

TABLE II

Values of n and k for Silicon Calculated from Eqs. (1)–(12)

eV	cm^{-1}	μm	n	k
6.00	48309	0.2070	1.2215	2.4570
5.95	47907	0.2087	1.2338	2.4961
5.90	47504	0.2105	1.2472	2.5373
5.85	47101	0.2123	1.2622	2.5808
5.80	46699	0.2141	1.2791	2.6269
5.75	46296	0.2160	1.2987	2.6758
5.70	45894	0.2179	1.3217	2.7275
5.65	45491	0.2198	1.3494	2.7819
5.60	45089	0.2218	1.3835	2.8386
5.55	44686	0.2238	1.4259	2.8958
5.50	44283	0.2258	1.4785	2.9506
5.45	43881	0.2279	1.5418	2.9974
5.40	43478	0.2300	1.6127	3.0292
5.35	43076	0.2321	1.6813	3.0403
5.30	42673	0.2343	1.7337	3.0333
5.25	42271	0.2366	1.7600	3.0216
5.20	41868	0.2388	1.7624	3.0214
5.15	41465	0.2412	1.7516	3.0421
5.10	41063	0.2435	1.7385	3.0847
5.05	40660	0.2459	1.7300	3.1459
5.00	40258	0.2484	1.7297	3.2220
4.95	39855	0.2509	1.7388	3.3103
4.90	39452	0.2535	1.7583	3.4092
4.85	39050	0.2561	1.7888	3.5180
4.80	38647	0.2588	1.8318	3.6365
4.75	38245	0.2615	1.8893	3.7647
4.70	37842	0.2643	1.9641	3.9025
4.65	37440	0.2671	2.0601	4.0490
4.60	37037	0.2700	2.1823	4.2024
4.55	36634	0.2730	2.3365	4.3582
4.50	36232	0.2760	2.5280	4.5085
4.45	35829	0.2791	2.7588	4.6407
4.40	35427	0.2823	3.0209	4.7384
4.35	35024	0.2855	3.2832	4.7922
4.30	34622	0.2888	3.4479	4.8588
4.25	34219	0.2922	3.6423	4.6901
4.20	33816	0.2957	4.0828	4.0766
4.15	33414	0.2993	4.3189	3.6196
4.10	33011	0.3029	4.4468	3.2317
4.05	32609	0.3067	4.5097	2.9100
4.00	32206	0.3105	4.5401	2.6504
3.95	31804	0.3144	4.5611	2.4436
3.90	31401	0.3185	4.5874	2.2789
3.85	30998	0.3226	4.6281	2.1460
3.80	30596	0.3268	4.6890	2.0366
3.75	30193	0.3312	4.7742	1.9436

(continued)

TABLE 2 *(Continued)*

Silicon

eV	cm^{-1}	μm	n	k
3.70	29791	0.3357	4.8877	1.8616
3.65	29388	0.3403	5.0349	1.7859
3.60	28986	0.3450	5.2236	1.7122
3.55	28583	0.3499	5.4679	1.6359
3.50	28180	0.3549	5.7966	1.5505
3.45	27778	0.3600	6.2842	1.4427
3.40	27375	0.3653	7.2958	1.2577
3.35	26973	0.3707	7.0864	0.9453
3.30	26570	0.3764	6.3887	0.8896
3.25	26167	0.3822	6.0408	0.8075
3.20	25765	0.3881	5.8121	0.7171
3.15	25362	0.3943	5.6458	0.6215
3.10	24960	0.4006	5.5186	0.5210
3.05	24557	0.4072	5.4189	0.4156
3.00	24155	0.4140	5.3399	0.3050

Silicon–Germanium Alloys (Si_xGe_{1-x}) Revisited

J. HUMLÍČEK
Masaryk University, Faculty of Science
Department of Solid State Physics
Brno, Czech Republic

Silicon and germanium form a continuous series of crystalline alloys, Si_xGe_{1-x}. Their optical constants have been compiled for three compositions x ($\approx$ 0.80, 0.50, and 0.25) in *HOC II* [1]. Optical constants of both constituents are available in the critiques of Potter (Ge, [2]) and Edwards (Si, [3]). Recently, the silicon-rich alloys from the range $1 < x < 0.75$ have become important in silicon-based thin-film structures. Very thin epitaxial alloy layers of a few tens of nanometers can accomodate the silicon—substrate lattice constant, resulting in appreciable strain that influences the optical response [4]. Thicker films are (at least partly) relaxed. Most of the recent work not covered by Humlíček *et al.* [1] has been done on the epitaxial films.

In the present critique we (i) compile a comprehensive database for $x \approx 0.80$ from the x-ray to the far-infrared region, including data taken on the relaxed films, and (ii) provide narrowly spaced, interpolated data over the compositions, within the spectral range from UV to NIR. In Table I we list n and k data obtained for the compositions equal or close to $x = 0.80$. The spectra from several sources are plotted in Fig. 1. In the x-ray region, the data were calculated using the Henke model [5, 6]. The calculation is based on the data for pure Si and Ge, and on the assumption of independent contributions of the atomic cross-sections of both constituents. The only input for the particular alloy composition x consisted in the density of 2.93 g/cm^3, obtained by linear interpolation between $x = 1$ and $x = 0$. Let us note that the model does not take into account the valence-band structure of the alloy, resulting in the loss of accuracy with decreasing photon energy. In the UV range, we use the results of reflectance measurements [7], discussed in detail by Humlíček *et al.* [1]. The range of fundamental interband transitions has been covered by several spectroellipsometric studies [4, 8, 9]. The main problem influencing the accuracy of the optical data consists in the

HANDBOOK OF OPTICAL CONSTANTS OF SOLIDS III

Copyright © 1998 by Academic Press.
All rights of reproduction in any form reserved
ISBN 0-12-544423-0/$25.00.

quality of sample surfaces. A significant improvement might be obtained with the high-quality (relaxed) epitaxial layers, with an appropriate procedure for the removal of the influence of substrate and overlayer [4]. We have selected data of Pickering and Carline [4] and Humlíček *et al.* [8] for the two entries of Table I; they are in a fairly good agreement. We expect the thin-film data of Pickering and Carline [4] to be more reliable, especially for the low extinction at the lowest photon energies; consequently, we display also values of k below 0.3 reported by Pickering and Carline [4]. The low extinction values obtained on bulk samples are considered to be unreliable [1] in the results of Humlíček *et al.* [8] and are therefore skipped in Table I. At the band edge, we include the k data resulting from an interpolation scheme using the gap and phonon energy as functions of the concentration [1]. The parametrization used the absorption measurements of Braunstein *et al.* [10]. We complement the extinction data with the values of refractive index obtained using the Kramers–Kronig transformation of the ellipsometric data above the edge [11]. It should be noted that the latter work corrects the erroneous results obtained for the refractive index found elsewhere [12, 13], where n has been related to the position of the indirect band gap. The rich spectral structure due to lattice vibrations in the infrared changes very strongly with the alloy composition and displays both first- and higher-order phonon processes [1]. We therefore complement the data of Table I by the plot of the absorption coefficient of silicon-rich alloys [14] shown in Fig. 2. Besides a number of multiphonon bands and an extrinsic, oxygen-related band at $\sim$1100 cm^{-1}, two distinct absorption peaks at $\sim$400 and $\sim$500 cm^{-1} reveal the "Ge–Si" and "Si–Si" vibrations [15], respectively. They represent a convenient fingerprint of alloying in the optical constants of the Si-rich materials.

In Fig. 3 we plot n and k data obtained from the databases of others [7, 8, 10, 11] by linear interpolation over compositions with steps of 0.1. The concentration dependence is fairly smooth in the whole spectral interval, except for k in the range of the indirect band gap (because of the crossover of the conduction-band minima for $x \approx 0.15$ [10]). Consequently, the corresponding data in Table II are expected to provide a reasonable basis for intermediate compositions.

REFERENCES

1. J. Humlíček, F. Lukeš, and E. Schmidt, *in* "Handbook of Optical Constants of Solids II" (E. D. Palik, ed.), p. 607. Academic Press, San Diego, 1991.
2. R. F. Potter, *in* "Handbook of Optical Constants of Solids" (E. D. Palik, ed.), p. 465. Academic Press, Orlando, Florida, 1985.
3. D. F. Edwards, *in* "Handbook of Optical Constants of Solids" (E. D. Palik, ed.), p. 465. Academic Press, Orlando, Florida, 1985.
4. C. Pickering and R. T. Carline, *J. Appl. Phys.* **75**, 4642 (1994); C. Pickering, private information, 1994.
5. B. L. Henke, P. Lee, T. J. Tanaka, R. L. Shimobukuro, and B. K. Fujikama, *At. Data Nucl. Data Tables* **27**, 1 (1982).

6. B. L. Henke, J. C. Davis, E. M. Gullikson, and R. C. C. Perera, *Lawrence Berkeley Laboratory Report No.* **LBL–26259** (1988).
7. E. Schmidt, *Phys. Status. Solidi* **27**, 57 (1968).
8. J. Humlíček, M. Garriga, M. I. Alonso, and M. Cardona, *J. Appl. Phys.* **65**, 2827 (1989).
9. G. E. Jellison Jr., T. E. Haynes, and H. H. Burke, *Opt. Mater.* **2**, 105 (1993).
10. R. Braunstein, A. R. Moore, and F. Herman, *Phys. Rev.* **109**, 695 (1958).
11. J. Humlíček, A. Roeseler, T. Zettler, M. G. Kekoua, and E. Khoutsishvili, *Appl. Opt.* **31**, 90 (1992).
12. J. J. Miceli and D. P. Naughton, *Appl. Opt.* **27**, 500 (1988).
13. D. P. Naughton, J. J. Miceli, and D. T. Moore, *Appl. Opt.* **27**, 505 (1988).
14. M. Lorenc and J. Humlíček, unpublished data, 1996.
15. G. M. Zinger, I. P. Ipatova, and A. V. Subashiev, *Sov. Phys. Semicond. (Engl. Transl.)* **11**, 383 (1977).

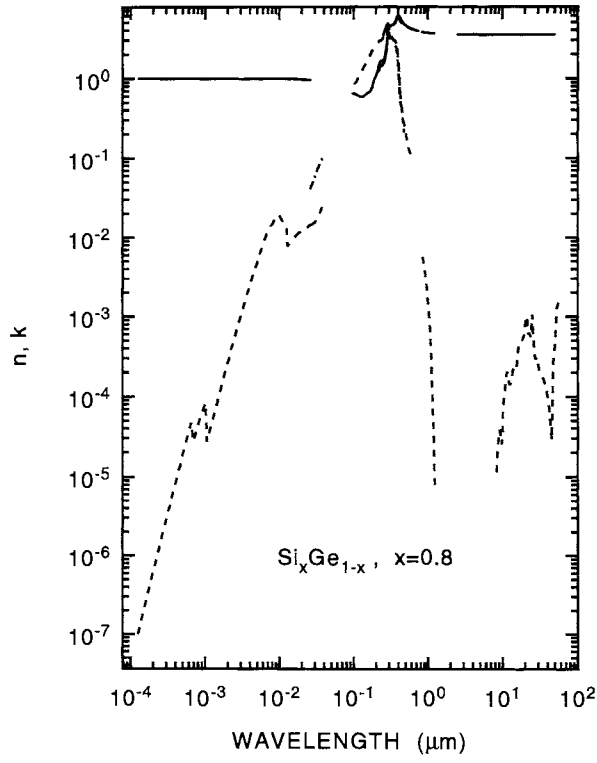

Fig. 1. Log–log plot of n (solid lines) and k (dashed lines) versus wavelength in microns for Si_xGe_{1-x}, $x = 0.8$.

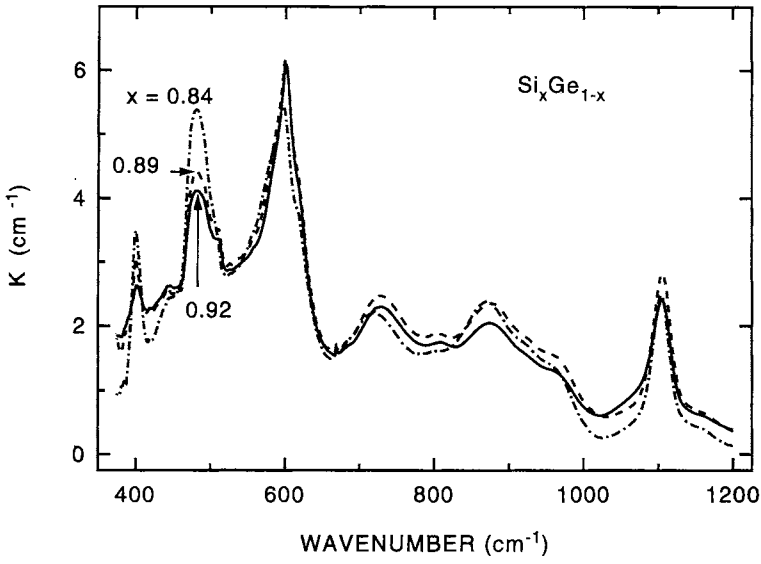

Fig. 2. Linear/linear plot of absorption coefficient for three compositions x of Si_xGe_{1-x} versus wavenumber.

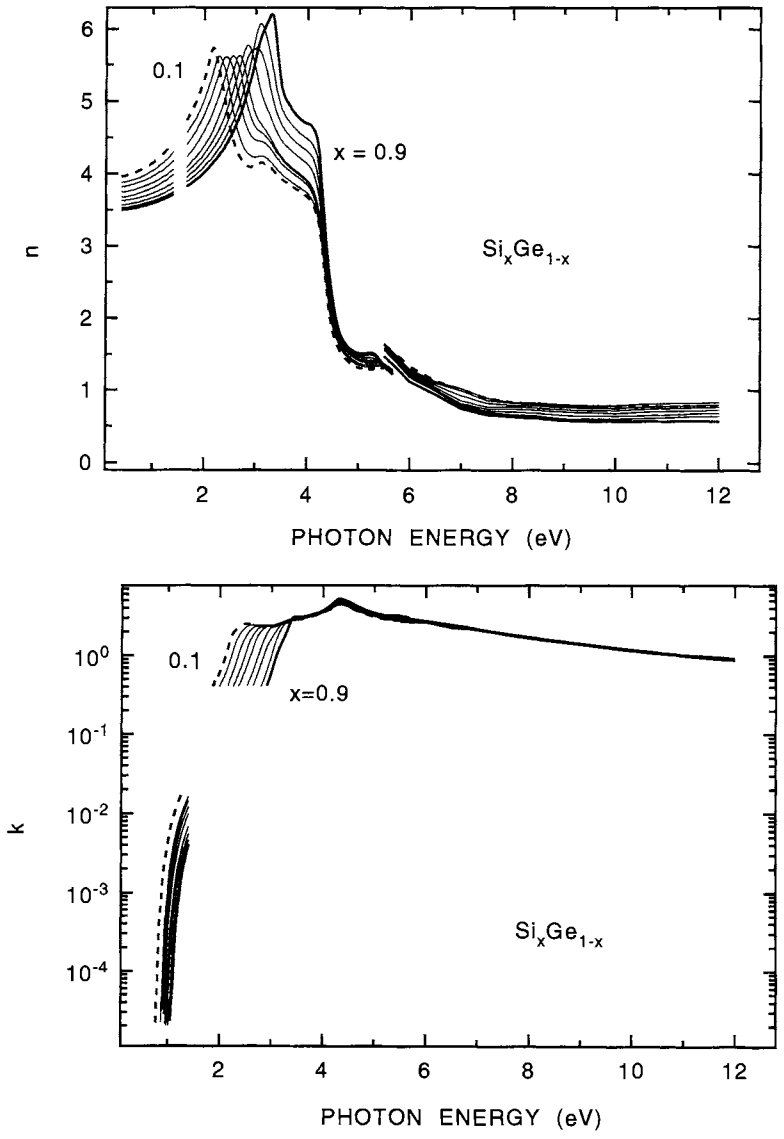

Fig. 3. Optical constants for Si_xGe_{1-x} with the composition $x = 0.1$ (dashed lines), 0.2, . . ., 0.8 in steps of 0.1 (thin solid lines) and 0.9 (solid lines). Linear–linear plot of n versus photon energy. Log–linear plot of k versus photon energy.

TABLE 1

Values of n and k for Si_xGe_{1-x}, $x \approx 0.80$, from Various References[a]

eV	cm^{-1}	Å	n	n	k	k
9918.	79,990,000	1.25	0.99999418 [5, 6]		1.001E-07 [5, 6]	
3306.	26,660,000	3.75	0.9999461		6.569E-06	
1983.	15,990,000	6.25	0.999869		4.122E-05	
1416.	11,420,000	8.75	0.999762		5.731E-05	
1102.	8,888,000	11.2	0.999622		3.470E-05	
901.7	7,272,000	13.7	0.999398		6.973E-05	
762.9	6,153,000	16.2	0.999140		1.268E-04	
661.2	5,333,000	18.7	0.99884		2.109E-04	
583.4	4,705,000	21.2	0.99851		3.259E-04	
522.0	4,210,000	23.7	0.99814		4.761E-04	
472.3	3,809,000	26.2	0.99775		6.615E-04	
431.2	3,478,000	28.7	0.99733		8.898E-04	
396.7	3,199,000	31.2	0.99689		1.156E-03	
367.3	2,962,000	33.7	0.99642		1.474E-03	
342.0	2,758,000	36.2	0.99594		1.844E-03	
319.9	2,580,000	38.7	0.99546		2.274E-03	
300.5	2,424,000	41.2	0.99497		2.767E-03	
283.3	2,285,000	43.7	0.99451		3.312E-03	
268.0	2,162,000	46.2	0.99407		3.901E-03	
254.3	2,051,000	48.7	0.99364		4.522E-03	
241.8	1,950,000	51.2	0.99321		5.207E-03	
206.8	1,668,000	59.9	0.99199		8.090E-03	
180.7	1,457,000	68.6	0.99191		1.170E-02	
160.4	1,294,000	77.2	0.99327		1.414E-02	
144.2	1,163,000	85.9	0.99374		1.680E-02	
131.0	1,057,000	94.6	0.99707		1.915E-02	
120.0	968,300	103.	0.999334		1.813E-02	
110.7	893,400	111.	0.99877		1.596E-02	
102.8	829,100	120.	0.99771		1.503E-02	
95.9	773,500	129.	0.999833		7.868E-03	
89.8	725,000	137.	0.99570		8.488E-03	
84.5	682,100	146.	0.99285		9.095E-03	
79.8	644,000	155.	0.99045		9.698E-03	
75.6	610,000	163.	0.9882		1.029E-02	
71.8	579,300	172.	0.9860		1.088E-02	
68.3	551,600	181.	0.9839		1.142E-02	
65.2	526,500	189.	0.9817		1.167E-02	
62.4	503,500	198.	0.9793		1.193E-02	
59.8	482,400	207.	0.9768		1.221E-02	
57.4	463,100	215.	0.9741		1.251E-02	
55.2	445,200	224.	0.9713		1.284E-02	
53.1	428,600	233.	0.9683		1.322E-02	
51.2	413,300	241.	0.9653		1.362E-02	

[a] The reference from which the values were extracted is given in brackets next to the first value. The nominal alloy compositions are: $x = 0.80$ [5, 6], $x = 0.803$ [7], $x = 0.782$ [8], $x = 0.805$ [4], $x = 0.782$ [10,11], $x = 0.80$ [14].

TABLE I *(Continued)*

Si_xGe_{1-x}, $x \approx 0.80$

eV	cm^{-1}	Å	n	n	k	k
49.4	399,000	250.	0.9623		1.402E-02	
47.8	385,600	259.	0.9592		1.428E-02	
12.8	103,200	0.09686	0.64 [7]		0.78 [7]	
12.2	98,420	0.1016	0.65		0.84	
11.3	91,910	0.1088	0.63		0.92	
10.5	85,470	0.1170	0.61		1.04	
9.80	79,050	0.1265	0.60		1.20	
8.99	72,560	0.1378	0.60		1.40	
8.20	66,130	0.1512	0.65		1.63	
7.79	62,890	0.1590	0.67		1.76	
7.00	56,460	0.1771	0.77		2.18	
6.80	54,850	0.1823	0.87		2.30	
6.59	53,220	0.1879	0.95		2.38	
6.40	51,620	0.1937	1.02		2.45	
6.19	50,000	0.2000	1.08		2.57	
6.00	48,400	0.2066	1.18		2.71	
5.70	45,970	0.2175	1.40		2.89	
5.62	45,320	0.2206	1.27 [8]		3.06 [8]	
5.56	44,840	0.2230	1.30		3.08	
5.49	44,360	0.2254	1.35		3.11	
5.44	43,870	0.2279	1.40		3.13	
5.37	43,390	0.2305	1.44		3.13	
5.32	42,900	0.2331	1.47		3.14	
5.26	42,420	0.2357	1.48		3.15	
5.20	41,940	0.2384	1.48		3.18	
5.13	41,450	0.2412	1.48		3.23	
5.08	40,970	0.2441	1.48		3.29	
5.02	40,480	0.2470	1.49		3.37	
4.99	40,320	0.2480		1.520 [4]		3.412 [4]
4.95	40,000	0.2500	1.51		3.45	
4.94	39,920	0.2505		1.540		3.491
4.89	39,510	0.2531	1.53	1.568	3.55	3.581
4.83	39,030	0.2562	1.57	1.599	3.66	3.673
4.79	38,710	0.2583		1.641		3.770
4.78	38,550	0.2594	1.61		3.78	
4.74	38,300	0.2611		1.687		3.878
4.72	38,060	0.2627	1.68		3.93	
4.69	37,900	0.2638		1.741		4.003
4.66	37,580	0.2661	1.76		4.08	
4.64	37,500	0.2667		1.824		4.140
4.59	37,090	0.2696	1.87	1.929	4.26	4.287
4.54	36,610	0.2731	2.03	2.085	4.46	4.447
4.49	36,290	0.2756		2.269		4.610
4.48	36,130	0.2768	2.26		4.66	
4.44	35,880	0.2787		2.522		4.769
4.41	35,640	0.2805	2.56		4.84	
4.39	35,480	0.2818		2.826		4.885

(continued)

TABLE I *(Continued)*

Si_xGe_{1-x}, $x \approx 0.80$

eV	cm^{-1}	Å	n	n	k	k
4.35	35,160	0.2844	2.96		4.98	
4.34	35,080	0.2851		3.172		4.967
4.29	34,670	0.2884	3.48	3.586	4.97	4.864
4.23	34,190	0.2924	3.93	3.927	4.73	4.683
4.19	33,870	0.2952		4.188		4.427
4.18	33,710	0.2966	4.20		4.40	
4.14	33,460	0.2988		4.314		4.175
4.12	33,230	0.3009	4.33		4.11	
4.09	33,060	0.3024		4.394		3.957
4.06	32,740	0.3054	4.40		3.88	
4.04	32,660	0.3062		4.441		3.771
3.99	32,250	0.3100	4.44	4.470	3.69	3.616
3.94	31,770	0.3147	4.47	4.488	3.55	3.496
3.89	31,450	0.3180		4.509		3.393
3.87	31,290	0.3196	4.51		3.42	
3.84	31,040	0.3221		4.538		3.305
3.81	30,810	0.3246	4.54		3.32	
3.79	30,640	0.3263		4.569		3.228
3.75	30,320	0.3298	4.59		3.24	
3.74	30,240	0.3307		4.594		3.161
3.69	29,830	0.3351	4.64	4.629	3.16	3.100
3.63	29,350	0.3406	4.69	4.668	3.10	3.050
3.59	29,030	0.3444		4.717		3.014
3.57	28,870	0.3463	4.75		3.05	
3.54	28,620	0.3493		4.774		2.983
3.52	28,390	0.3522	4.82		3.01	
3.49	28,220	0.3543		4.859		2.956
3.45	27,900	0.3583	4.94		2.98	
3.44	27,820	0.3594		4.959		2.923
3.39	27,410	0.3647	5.09	5.090	2.95	2.895
3.34	26,930	0.3712	5.29	5.264	2.89	2.840
3.29	26,610	0.3758		5.458		2.749
3.28	26,450	0.3780	5.55		2.76	
3.24	26,210	0.3815		5.660		2.587
3.21	25,970	0.3851	5.82		2.52	
3.19	25,800	0.3875		5.846		2.342
3.15	25,480	0.3924	6.01		2.17	
3.14	25,400	0.3937		5.997		2.048
3.09	25,000	0.4000	6.11	6.089	1.73	1.686
3.03	24,510	0.4079	6.04	6.044	1.30	1.311
2.99	24,190	0.4133		5.897		1.000
2.97	24,030	0.4161	5.86		0.95	
2.94	23,790	0.4203		5.708		0.776
2.91	23,550	0.4246	5.64		0.73	
2.89	23,380	0.4276		5.518		0.638
2.86	23,060	0.4335	5.44		0.56	
2.84	22,980	0.4351		5.352		0.535

TABLE I *(Continued)*

Si_xGe_{1-x}, $x \approx 0.80$

eV	cm^{-1}	Å	n	n	k	k
2.79	22,580	0.4429	5.26	5.209	0.44	0.461
2.74	22,090	0.4525	5.11	5.078	0.37	0.394
2.69	21,770	0.4593		4.967		0.346
2.68	21,610	0.4626	4.97		0.30	
2.64	21,370	0.4679		4.857		0.299
2.61	21,130	0.4732	4.85			
2.59	20,960	0.4769		4.766		0.271
2.55	20,640	0.4843	4.75			
2.54	20,560	0.4863		4.705		0.254
2.49	20,160	0.4960	4.65	4.645		0.237
2.43	19,680	0.5081	4.57	4.568		0.210
2.39	19,350	0.5167		4.492		0.187
2.37	19,190	0.5210	4.49			
2.34	18,950	0.5277		4.418		0.166
2.31	18,710	0.5344	4.41			
2.29	18,540	0.5391		4.348		0.149
2.25	18,220	0.5486	4.35			
2.24	18,140	0.5511		4.288		0.135
2.19	17,740	0.5636	4.29	4.236		0.124
2.13	17,260	0.5794	4.23	4.191		0.116
2.09	16,930	0.5905		4.148		0.108
2.08	16,770	0.5961	4.18			
2.04	16,530	0.6049		4.107		0.100
2.01	16,290	0.6138	4.13			
1.99	16,120	0.6200		4.066		0.091
1.95	15,800	0.6326	4.08			
1.90	15,320	0.6526	4.04			
1.84	14,840	0.6738	4.00			
1.78	14,350	0.6965	3.97			
1.72	13,870	0.7208	3.93			
1.65	13,380	0.7469	3.90			
1.40	11,290	0.8856	3.75 [10, 11]		4.63E-03 [10, 11]	
1.38	11,130	0.8984	3.74		4.19E-03	
1.35	10,960	0.9117	3.73		3.77E-03	
1.33	10,800	0.9253	3.72		3.37E-03	
1.31	10,640	0.9393	3.72		2.99E-03	
1.30	10,480	0.9537	3.71		2.62E-03	
1.28	10,320	0.9686	3.70		2.27E-03	
1.26	10,160	0.9840	3.70		1.95E-03	
1.23	10,000	0.9999	3.69		1.64E-03	
1.21	9,840	1.016	3.68		1.36E-03	
1.20	9,679	1.033	3.68		1.10E-03	
1.18	9,517	1.050	3.67		8.68E-04	
1.16	9,356	1.068	3.67		6.60E-04	
1.13	9,195	1.087	3.66		4.80E-04	
1.12	9,033	1.107	3.65		3.29E-04	
1.10	8,872	1.127	3.65		2.08E-04	

(continued)

TABLE I *(Continued)*

Si_xGe_{1-x}, $x \approx 0.80$

eV	cm^{-1}	Å	n	n	k	k
1.08	8,711	1.148	3.64		1.20E-04	
1.05	8,549	1.169	3.64		6.56E-05	
1.03	8,388	1.192	3.63		4.01E-05	
1.02	8,227	1.215	3.63		2.15E-05	
0.1000	8,065	1.239	3.62		8.44E-06	
0.9800	7,904	1.265	3.62		1.30E-06	
0.1488	1,200	8.330			1.05E-05 [14]	
0.1438	1,160	8.620			1.92E-05	
0.1388	1,120	8.930			3.18E-05	
0.1339	1,080	9.260			3.77E-05	
0.1289	1,040	9.620			2.78E-05	
0.1240	1,000	10.00			3.22E-05	
0.1190	960	10.42			9.31E-05	
0.1141	920	10.87			1.27E-04	
0.1091	880	11.36			1.91E-04	
0.1042	840	11.90			1.84E-04	
0.09919	800	12.50			1.41E-04	
0.09421	760	13.16			1.59E-04	
0.08926	720	13.89			2.15E-04	
0.08557	690	14.49			2.37E-04	
0.08184	660	15.15			2.21E-04	
0.07687	620	16.13			3.63E-04	
0.07192	580	17.24			5.00E-04	
0.06942	560	17.86			5.17E-04	
0.06447	520	19.23			5.30E-04	
0.06075	490	20.41			9.45E-04	
0.05826	470	21.28			9.21E-04	
0.05580	450	22.22			6.06E-04	
0.05330	430	23.26			5.97E-04	
0.05145	415	24.10			5.55E-04	
0.05022	405	24.69			9.63E-04	
0.04897	395	25.32			8.23E-04	
0.04711	380	26.32			4.42E-04	
0.04463	360	27.78			2.91E-04	
0.04214	340	29.42			2.85E-04	
0.03720	300	33.33			1.88E-04	
0.03224	260	38.46			1.24E-04	
0.02728	220	45.45			2.84E-05	
0.02480	200	50.00			4.28E-04	
0.02232	180	55.55			1.49E-03	

TABLE II

Values of n and k for Si_xGe_{1-x}, Interpolated for Various x[a]

eV	cm^{-1}	μm	n	k	n	k
			$x = 0.90$		$x = 0.70$	
12.00	96,780	0.1033	0.57 [7]	0.88 [7]	0.68 [7]	0.87 [7]
11.00	88,720	0.1127	0.57	1.01	0.66	0.98
10.00	80,650	0.1240	0.57	1.19	0.64	1.16
9.00	72,580	0.1378	0.58	1.42	0.65	1.39
8.00	64,520	0.1550	0.63	1.72	0.70	1.67
7.00	56,450	0.1771	0.74	2.19	0.79	2.16
6.00	48,390	0.2066	1.12	2.74	1.20	2.71
5.00	40,320	0.2480	1.52 [8]	3.45 [8]	1.47 [8]	3.35 [8]
4.90	39,520	0.2530	1.54	3.62	1.51	3.50
4.80	38,710	0.2583	1.60	3.83	1.58	3.69
4.70	37,900	0.2638	1.69	4.09	1.68	3.91
4.60	37,100	0.2695	1.88	4.43	1.84	4.18
4.50	36,290	0.2755	2.24	4.80	2.12	4.49
4.40	35,480	0.2818	2.81	5.11	2.60	4.79
4.30	34,680	0.2883	3.66	5.21	3.36	4.86
4.20	33,870	0.2952	4.43	4.66	3.98	4.45
4.10	33,060	0.3024	4.64	4.09	4.22	3.99
4.00	32,260	0.3100	4.69	3.72	4.31	3.67
3.90	31,450	0.3179	4.74	3.48	4.36	3.44
3.80	30,640	0.3263	4.80	3.32	4.42	3.28
3.70	29,840	0.3351	4.89	3.18	4.49	3.14
3.60	29,030	0.3444	5.01	3.10	4.57	3.04
3.50	28,220	0.3542	5.24	3.09	4.68	2.97
3.40	27,420	0.3647	5.87	2.94	4.86	2.91
3.30	26,610	0.3757	6.21	2.07	5.14	2.80
3.20	25,810	0.3875	6.05	1.46	5.45	2.52
3.10	25,000	0.4000	5.87	0.99	5.67	2.10
3.00	24,190	0.4133	5.59	0.62	5.72	1.65
2.90	23,390	0.4275	5.28		5.68	1.21
2.80	22,580	0.4428	5.02		5.50	0.79
2.70	21,770	0.4592	4.82		5.24	0.52
2.60	20,970	0.4769	4.65		5.00	
2.50	20,160	0.4959	4.50		4.82	
2.40	19,350	0.5166	4.37		4.64	
2.30	18,550	0.5391	4.27		4.50	
2.20	17,740	0.5636	4.18		4.38	
2.10	16,930	0.5904	4.09		4.28	
2.00	16,130	0.6199	4.02		4.19	
1.90	15,320	0.6526	3.95		4.11	
1.80	14,510	0.6888	3.90		4.04	
1.70	13,710	0.7293	3.84		3.98	
1.40	11,290	0.8856	3.72 [11]	4.03E-03 [10]	3.81 [11]	5.50E-03 [10]

(continued)

[a] The references from which the dataset for interpolation was taken are given in brackets next to the first value.

TABLE II *(Continued)*

Si_xGe_{1-x}

eV	cm^{-1}	μm	n	k	n	k
			$x = 0.90$		$x = 0.70$	
1.38	11,130	0.8984	3.71	3.59E-03	3.80	5.02E-03
1.36	10,960	0.9117	3.70	3.18E-03	3.79	4.56E-03
1.32	10,640	0.9393	3.69	2.42E-03	3.77	3.68E-03
1.30	10,480	0.9537	3.68	2.07E-03	3.77	3.28E-03
1.28	10,320	0.9686	3.67	1.74E-03	3.76	2.89E-03
1.26	10,160	0.9840	3.67	1.44E-03	3.75	2.52E-03
1.24	10,000	0.9999	3.66	1.17E-03	3.74	2.17E-03
1.22	9,840	1.016	3.65	9.17E-04	3.73	1.84E-03
1.20	9,679	1.033	3.65	6.97E-04	3.73	1.54E-03
1.18	9,517	1.050	3.64	5.07E-04	3.72	1.26E-03
1.16	9,356	1.068	3.64	3.49E-04	3.72	1.01E-03
1.14	9,195	1.087	3.63	2.23E-04	3.71	7.80E-04
1.12	9,033	1.107	3.62	1.31E-04	3.70	5.83E-04
1.10	8,872	1.127	3.62	7.14E-05	3.70	4.16E-04
1.08	8,711	1.148	3.61	4.24E-05	3.69	2.80E-04
1.06	8,549	1.169	3.61	2.32E-05	3.69	1.78E-04
			$x = 0.60$		$x = 0.50$	
12.00	96,780	0.1033	0.73 [7]	0.88 [7]	0.77 [7]	0.88 [7]
11.00	88,720	0.1127	0.71	0.99	0.75	0.99
10.00	80,650	0.1240	0.68	1.15	0.72	1.15
9.00	72,580	0.1378	0.70	1.38	0.73	1.37
8.00	64,520	0.1550	0.74	1.64	0.77	1.63
7.00	56,450	0.1771	0.81	2.14	0.85	2.12
6.00	48,390	0.2066	1.21	2.70	1.23	2.68
5.00	40,320	0.2480	1.44 [8]	3.29 [8]	1.43 [8]	3.17 [8]
4.90	39,520	0.2530	1.48	3.44	1.47	3.32
4.80	38,710	0.2583	1.55	3.61	1.54	3.48
4.70	37,900	0.2638	1.65	3.81	1.63	3.66
4.60	37,100	0.2695	1.80	4.07	1.77	3.89
4.50	36,290	0.2755	2.05	4.36	2.01	4.16
4.40	35,480	0.2818	2.50	4.65	2.41	4.42
4.30	34,680	0.2883	3.21	4.72	3.04	4.47
4.20	33,870	0.2952	3.79	4.36	3.56	4.17
4.10	33,060	0.3024	4.03	3.94	3.80	3.81
4.00	32,260	0.3100	4.13	3.63	3.90	3.53
3.90	31,450	0.3179	4.19	3.41	3.97	3.32
3.80	30,640	0.3263	4.25	3.24	4.03	3.17
3.70	29,840	0.3351	4.31	3.11	4.09	3.05
3.60	29,030	0.3444	4.38	3.01	4.15	2.95
3.50	28,220	0.3542	4.46	2.93	4.23	2.88
3.40	27,420	0.3647	4.59	2.86	4.34	2.80
3.30	26,610	0.3757	4.76	2.77	4.47	2.70
3.20	25,810	0.3875	4.94	2.63	4.60	2.58
3.10	25,000	0.4000	5.14	2.51	4.69	2.47

TABLE II *(Continued)*

			Si_xGe_{1-x}			
eV	cm^{-1}	μm	n	k	n	k
			$x = 0.60$		$x = 0.50$	
3.00	24,190	0.4133	5.43	2.30	4.82	2.41
2.90	23,390	0.4275	5.72	1.86	5.06	2.32
2.80	22,580	0.4428	5.72	1.26	5.38	2.06
2.60	20,970	0.4769	5.23	0.54	5.51	1.01
2.50	20,160	0.4959	5.03		5.26	0.68
2.40	19,350	0.5166	4.80		5.03	0.46
2.30	18,550	0.5391	4.64		4.83	
2.20	17,740	0.5636	4.50		4.65	
2.10	16,930	0.5904	4.38		4.50	
2.00	16,130	0.6199	4.28		4.39	
1.90	15,320	0.6526	4.19		4.29	
1.80	14,510	0.6888	4.12		4.20	
1.70	13,710	0.7293	4.05		4.12	
1.40	11,290	0.8856	3.88 [11]	6.78E-03 [10]	3.99 [11]	9.86E-03 [10]
1.38	11,130	0.8984	3.87	6.24E-03	3.98	9.14E-03
1.36	10,960	0.9117	3.86	5.71E-03	3.97	8.43E-03
1.34	10,800	0.9253	3.85	5.20E-03	3.96	7.75E-03
1.32	10,640	0.9393	3.84	4.70E-03	3.95	7.09E-03
1.30	10,480	0.9537	3.84	4.23E-03	3.94	6.44E-03
1.28	10,320	0.9686	3.83	3.78E-03	3.92	5.82E-03
1.26	10,160	0.9840	3.82	3.34E-03	3.91	5.22E-03
1.24	10,000	0.9999	3.81	2.93E-03	3.90	4.65E-03
1.22	9,840	1.016	3.80	2.53E-03	3.90	4.11E-03
1.20	9,679	1.033	3.80	2.17E-03	3.89	3.59E-03
1.18	9,517	1.050	3.79	1.82E-03	3.88	3.09E-03
1.16	9,356	1.068	3.78	1.50E-03	3.87	2.63E-03
1.14	9,195	1.087	3.78	1.21E-03	3.86	2.20E-03
1.12	9,033	1.107	3.77	9.52E-04	3.85	1.80E-03
1.10	8,872	1.127	3.76	7.20E-04	3.84	1.44E-03
1.08	8,711	1.148	3.76	5.20E-04	3.84	1.12E-03
1.06	8,549	1.169	3.75	3.54E-04	3.83	8.31E-04
1.04	8,388	1.192	3.75	2.23E-04	3.82	5.86E-04
1.02	8,227	1.215	3.74	1.29E-04	3.81	3.85E-04
1.00	8,065	1.239	3.73	7.58E-05	3.81	2.29E-04
0.9800	7,904	1.265	3.73	4.34E-05	3.80	1.21E-04
0.9600	7,743	1.291	3.72	2.12E-05	3.80	6.01E-05
			$x = 0.40$		$x = 0.30$	
12.00	96,780	0.1033	0.80 [7]	0.89 [7]	0.83 [7]	0.90 [7]
11.00	88,720	0.1127	0.78	0.99	0.82	0.99
10.00	80,650	0.1240	0.75	1.14	0.78	1.13
9.00	72,580	0.1378	0.76	1.37	0.78	1.36
8.00	64,520	0.1550	0.79	1.63	0.82	1.64
7.00	56,450	0.1771	0.92	2.11	0.99	2.09
6.00	48,390	0.2066	1.24	2.64	1.26	2.60

(continued)

TABLE II *(Continued)*

Si_xGe_{1-x}

eV	cm^{-1}	μm	n	k	n	k
			$x = 0.40$		$x = 0.30$	
5.00	40,320	0.2480	1.41 [8]	3.20 [8]	1.37 [8]	3.19 [8]
4.90	39,520	0.2530	1.46	3.34	1.42	3.33
4.80	38,710	0.2583	1.52	3.50	1.48	3.49
4.70	37,900	0.2638	1.61	3.68	1.57	3.68
4.50	36,290	0.2755	1.98	4.18	1.92	4.18
4.40	35,480	0.2818	2.39	4.45	2.33	4.47
4.30	34,680	0.2883	3.02	4.51	2.98	4.52
4.20	33,870	0.2952	3.53	4.21	3.49	4.22
4.10	33,060	0.3024	3.78	3.86	3.73	3.87
4.00	32,260	0.3100	3.88	3.58	3.84	3.59
3.90	31,450	0.3179	3.95	3.37	3.91	3.38
3.80	30,640	0.3263	4.01	3.22	3.96	3.23
3.70	29,840	0.3351	4.07	3.09	4.02	3.10
3.60	29,030	0.3444	4.13	2.98	4.08	2.99
3.50	28,220	0.3542	4.21	2.90	4.14	2.90
3.40	27,420	0.3647	4.30	2.82	4.23	2.81
3.30	26,610	0.3757	4.42	2.71	4.33	2.71
3.20	25,810	0.3875	4.52	2.58	4.41	2.58
3.10	25,000	0.4000	4.57	2.47	4.44	2.46
3.00	24,190	0.4133	4.64	2.42	4.46	2.40
2.90	23,390	0.4275	4.79	2.40	4.53	2.40
2.80	22,580	0.4428	5.05	2.32	4.69	2.41
2.70	21,770	0.4592	5.40	2.06	4.97	2.35
2.60	20,970	0.4769	5.60	1.60	5.31	2.14
2.50	20,160	0.4959	5.56	1.06	5.55	1.71
2.40	19,350	0.5166	5.34	0.68	5.60	1.22
2.30	18,550	0.5391	5.10	0.46	5.43	0.78
2.20	17,740	0.5636	4.91		5.19	0.52
2.10	16,930	0.5904	4.73		4.98	
2.00	16,130	0.6199	4.60		4.82	
1.90	15,320	0.6526	4.46		4.67	
1.80	14,510	0.6888	4.36		4.55	
1.70	13,710	0.7293	4.27		4.44	
1.40	11,290	0.8856	4.06 [11]	1.21E-02 [10]	4.18 [11]	1.43E-02 [10]
1.38	11,130	0.8984	4.05	1.13E-02	4.16	1.34E-02
1.36	10,960	0.9117	4.04	1.04E-02	4.15	1.25E-02
1.34	10,800	0.9253	4.03	9.64E-03	4.14	1.16E-02
1.32	10,640	0.9393	4.02	8.87E-03	4.12	1.07E-02
1.30	10,480	0.9537	4.01	8.12E-03	4.11	9.83E-03
1.28	10,320	0.9686	3.99	7.39E-03	4.10	9.00E-03
1.26	10,160	0.9840	3.98	6.69E-03	4.09	8.19E-03
1.24	10,000	0.9999	3.97	6.01E-03	4.08	7.41E-03
1.22	9,840	1.016	3.97	5.36E-03	4.06	6.66E-03
1.20	9,679	1.033	3.96	4.74E-03	4.05	5.94E-03
1.18	9,517	1.050	3.95	4.15E-03	4.04	5.25E-03

TABLE II *(Continued)*

Si_xGe_{1-x}

eV	cm^{-1}	μm	n	k	n	k
			$x = 0.40$		$x = 0.30$	
1.16	9,356	1.068	3.94	3.59E-03	4.03	4.60E-03
1.14	9,195	1.087	3.93	3.06E-03	4.03	3.97E-03
1.12	9,033	1.107	3.92	2.57E-03	4.02	3.39E-03
1.10	8,872	1.127	3.91	2.11E-03	4.01	2.84E-03
1.08	8,711	1.148	3.91	1.70E-03	4.00	2.34E-03
1.04	8,388	1.192	3.89	9.90E-04	3.98	1.46E-03
1.02	8,227	1.215	3.88	7.04E-04	3.98	1.09E-03
1.00	8,065	1.239	3.88	4.67E-04	3.97	7.71E-04
0.9800	7,904	1.265	3.87	2.82E-04	3.96	5.07E-04
0.9600	7,743	1.291	3.87	1.51E-04	3.95	3.02E-04
0.9400	7,582	1.318	3.86	7.21E-05	3.94	1.58E-04
0.9200	7,420	1.347	3.85	3.31E-05	3.94	7.37E-05
			$x = 0.20$		$x = 0.10$	
12.00	96,780	0.1033	0.83 [7]	0.91 [7]	0.79 [7]	0.94 [7]
11.00	88,720	0.1127	0.82	1.00	0.78	1.04
10.00	80,650	0.1240	0.79	1.15	0.77	1.20
9.00	72,580	0.1378	0.80	1.38	0.79	1.41
8.00	64,520	0.1550	0.83	1.65	0.83	1.69
7.00	56,450	0.1771	1.02	2.09	1.01	2.12
6.00	48,390	0.2066	1.29	2.59	1.33	2.61
5.00	40,320	0.2480	1.35 [8]	3.10 [8]	1.31 [8]	3.09 [8]
4.90	39,520	0.2530	1.39	3.24	1.34	3.22
4.80	38,710	0.2583	1.45	3.40	1.40	3.38
4.70	37,900	0.2638	1.53	3.58	1.48	3.57
4.60	37,100	0.2695	1.66	3.80	1.59	3.80
4.50	36,290	0.2755	1.87	4.07	1.79	4.09
4.40	35,480	0.2818	2.28	4.37	2.22	4.42
4.30	34,680	0.2883	2.92	4.40	2.90	4.43
4.20	33,870	0.2952	3.40	4.10	3.38	4.10
4.10	33,060	0.3024	3.63	3.75	3.59	3.75
4.00	32,260	0.3100	3.72	3.49	3.68	3.48
3.90	31,450	0.3179	3.78	3.29	3.74	3.29
3.80	30,640	0.3263	3.83	3.14	3.78	3.14
3.70	29,840	0.3351	3.89	3.02	3.83	3.02
3.60	29,030	0.3444	3.94	2.91	3.88	2.91
3.50	28,220	0.3542	4.00	2.82	3.93	2.82
3.40	27,420	0.3647	4.08	2.74	4.00	2.73
3.30	26,610	0.3757	4.16	2.64	4.08	2.63
3.20	25,810	0.3875	4.22	2.51	4.13	2.50
3.10	25,000	0.4000	4.24	2.39	4.15	2.38
3.00	24,190	0.4133	4.23	2.32	4.12	2.30
2.90	23,390	0.4275	4.25	2.33	4.09	2.29
2.80	22,580	0.4428	4.32	2.36	4.13	2.33
2.70	21,770	0.4592	4.47	2.40	4.22	2.39

(continued)

TABLE II *(Continued)*

Si_xGe_{1-x}

eV	cm^{-1}	μm	n	k	n	k
			$x = 0.20$		$x = 0.10$	
2.60	20,970	0.4769	4.74	2.41	4.37	2.45
2.50	20,160	0.4959	5.12	2.27	4.64	2.50
2.40	19,350	0.5166	5.44	1.92	5.06	2.39
2.30	18,550	0.5391	5.61	1.42	5.38	2.09
2.20	17,740	0.5636	5.47	0.88	5.72	1.60
2.10	16,930	0.5904	5.22	0.58	5.58	0.95
1.90	15,320	0.6526	4.85		5.08	0.49
1.80	14,510	0.6888	4.72		4.93	
1.70	13,710	0.7293	4.61		4.78	
1.40	11,290	0.8856	4.30 [11]	1.62E-02 [10]	4.45 [11]	2.65E-02 [10]
1.38	11,130	0.8984	4.29	1.52E-02	4.44	2.51E-02
1.36	10,960	0.9117	4.27	1.42E-02	4.42	2.38E-02
1.34	10,800	0.9253	4.25	1.32E-02	4.40	2.24E-02
1.32	10,640	0.9393	4.23	1.22E-02	4.38	2.11E-02
1.30	10,480	0.9537	4.22	1.13E-02	4.36	1.98E-02
1.28	10,320	0.9686	4.20	1.04E-02	4.34	1.86E-02
1.26	10,160	0.9840	4.19	9.47E-03	4.32	1.73E-02
1.24	10,000	0.9999	4.18	8.61E-03	4.31	1.61E-02
1.22	9,840	1.016	4.16	7.78E-03	4.29	1.49E-02
1.20	9,679	1.033	4.15	6.98E-03	4.28	1.38E-02
1.18	9,517	1.050	4.14	6.21E-03	4.26	1.27E-02
1.16	9,356	1.068	4.13	5.48E-03	4.25	1.16E-02
1.14	9,195	1.087	4.12	4.78E-03	4.24	1.05E-02
1.12	9,033	1.107	4.11	4.12E-03	4.22	9.49E-03
1.10	8,872	1.127	4.09	3.50E-03	4.21	8.51E-03
1.08	8,711	1.148	4.08	2.92E-03	4.20	7.56E-03
1.06	8,549	1.169	4.07	2.39E-03	4.19	6.66E-03
1.04	8,388	1.192	4.06	1.90E-03	4.17	5.80E-03
1.02	8,227	1.215	4.05	1.46E-03	4.16	4.99E-03
1.00	8,065	1.239	4.04	1.08E-03	4.15	4.23E-03
0.9800	7,904	1.265	4.04	7.48E-04	4.14	3.53E-03
0.9600	7,743	1.291	4.03	4.78E-04	4.13	2.88E-03
0.9400	7,582	1.318	4.02	2.72E-04	4.12	2.29E-03
0.9200	7,420	1.347	4.01	1.33E-04	4.12	1.76E-03
0.9000	7,259	1.377	4.00	6.07E-05	4.11	1.31E-03
0.8800	7,098	1.408	3.99	2.22E-05	4.10	9.15E-04

Silver Chloride (AgCl), Silver Bromide (AgBr), Silver Iodide (AgI)

MASATO TAZAWA
National Industrial Research Institute of Nagoya
Nagoya, Japan
and
ARMAND HADNI
Université Henri Poincaré, Nancy
Vandœuvre-les-Nancy, France

AgCl (CUBIC) I

The optical constants from the visible to the UV region were determined in the energy range 2–21 eV by means of reflectivity measurements at room temperature and a Kramers–Kronig (K-K) analysis by White and Straley in 1968 [1]. They were revised in 1974 [2]. The purpose of the revision was to eliminate an unphysical negative dip in the absorption edge occurring at 3.2 eV and caused by an inadequate fitting. Their apparatus consisted of a McPherson model 225 1-m VUV scanning monochromator and a slightly modified Tropel S-2 reflectometer. The K-K analysis was based on reflectivity values over four energy regions: (1) From 0.0 to 3.0 eV, the reflectivity was computed from literature values of the index of refraction [3, 4]. (2) From 3.1 to 14.0 eV, the experimentally determined values of the reflectivity were least-square fitted in four subregions. (3) From 14.1 to 21.1 eV, the experimentally determined values of the reflectivity were fitted to an exponential curve. (4) Beyond 21.1 eV, the reflectivity was inferred by using the extrapolation formula

$$\ln R(E) = -A \ln(E/E_f) + \ln R_f,$$

where E and R are the photon energy and the reflectivity, respectively, f denotes the last-measured data point, and A is an energy-independent, adjustable parameter. They used $A = 2.027$ and $E_f = 21.1$ eV.

Carrera and Brown [5] have also given the optical constants from 3.5 to

Copyright © 1998 by Academic Press.
All rights of reproduction in any form reserved
ISBN 0-12-544423-0/$25.00.

6.7 eV and from 30 to 240 eV at room, liquid-nitrogen, and liquid-helium temperatures. They observed the transmission of two thin films with a different thickness, deposited by vacuum evaporation onto a thin, transparent substrate of Formvar (polyvinyl formal resin) or Lucite (methyl methacrylate resin). In order to obtain the extinction coefficient k, they used the following expressions:

$$D_2 - D_1 = \alpha(t_2 - t_1)/2.303$$
$$k = \lambda\alpha/4\pi = (hc/4\pi E)\alpha,$$

where D and t are the optical density and the thickness, α is the absorption coefficient in cm^{-1}, E is the photon energy, and λ is the wavelength. They obtained the refractive index n by means of a K-K analysis using their own k values and those of White and Straley [1]. In the UV range, a Cary model 14R spectrophotometer was used, and in the extreme UV range, a modified Hilger-Watts E580 was used with the synchrotron radiation from the 240-MeV electron storage ring of the University of Wisconsin.

The optical constants in the mid-IR region were obtained by Tilton et al. [4] with a 31° prism of silver chloride used at the minimum deviation, and a Perkin-Elmer infrared spectrometer equipped with a calibrated screw for operation of the Littrow mirror. These optical constants were used by White and co-workers [1, 2]. Tilton *et al.* [4] determined the refractive index from 578 nm to 20.56 μm. The extinction coefficients were not obtained.

Hadni *et al.* [6] measured the far-IR reflectivity of a single crystal at room temperature, 80 K, and 25 K by means of a grating spectrometer. The optical constants shown in Table IV were obtained by a K-K analysis. They also gave the parameter values of the Lorentz oscillators by fitting the reflectivity with two Lorentz oscillators. Table I gives these parameters, and

$$(n + ik)^2 = \epsilon_{RV} + \sum_{j=1}^{2} \frac{4\pi\rho_j\nu_j^2}{\nu_j^2 - \nu^2 - i\nu\nu_0\delta_j}.$$

Two Lorentz oscillators were needed, and the stronger one corresponds to the one-phonon transition to the transverse optic mode with a wave vector $q = 0$ and the other one, about 10 times weaker, corresponds to a two-phonon addition process, probably TA + TO.

Values of n and k from these various references are listed in Table IV, and the data are plotted in Fig. 1.

II AgBr (CUBIC)

The optical constants in the UV range were first obtained by Carrera and Brown [5] at room temperature and at liquid-nitrogen and liquid-helium tem-

peratures. Their experimental method was the same one used for AgCl. The optical constants are, however, limited between 4 and 6.8 eV, probably because of the lack of a wide enough range for the K-K analysis.

White [7] also reported the optical constants between 3 and 16 eV at room temperature. The method was the same as in the case of AgCl.

In the mid-IR region, McCarthy [8] measured a refractive index of 2.167 and 2.162 at 9.93 and 12.67 μm, respectively, at 313 K.

In the far-IR region, Hadni *et al.* [6] reported the optical constants determined by a K-K analysis at room temperature (shown in Table V), 80 K, and 25 K. The experimental procedure was the same as in the case of AgCl, but the samples were not single crystals; they were pellets. Two Lorentz oscillators were also needed for AgBr; the stronger one corresponds to the TO mode and the weaker one to the TA + TO mode (see Table II).

Values of n and k from these various references are listed in Table V, and the data are plotted in Fig. 2.

β-AgI (HEXAGONAL), STABLE FOR $T < T_c = 147°$ C III

Ageev *et al.* [9] have obtained the optical constants of polycrystalline samples prepared by treating, in iodine vapor at room temperature, thin films of silver deposited by vacuum evaporation on glass substrates. To find the optical constants averaged over the random arrangement of crystallites in the film, they measured both transmission and reflection between 1000 and 370 nm using an SF-4 spectrophotometer. They gave the optical constants between 370 and 460 nm.

Bedikyan *et al.* [10] reported the dielectric constant in the region extending from 2.7 to 4.0 eV at 90, 293, and 393 K. Their β-AgI films (2H polytype) were prepared by treating in iodine vapor thin Ag films evaporated in vacuum onto a quartz substrate, and they were textured with a preferred orientation of the c-axis perpendicular to the substrate. The optical constants were determined by measuring the transmission (perhaps in normal incidence) of the films over a wide spectral range (0.22–1.2 μm), then treating the measured data by means of a K-K analysis. The error in the determination of n and k should amount to 0.1 for n and 0.02 for k. However, the optical constants that are said to have been "determined" are shown neither in tables nor in figures.

Cochrane [11] has also measured the absorption coefficient and the refractive index of single crystals at 293 K. He used single crystals of β-AgI grown by the slow evaporation of either an HI solution saturated with AgI, or a KI solution saturated with AgI. Although there were impurities of potassium and sodium, detected by spectrochemical analysis and flame photometry, no differences were observed in the optical behavior of crystals obtained by the two methods. Platelike specimens were prepared by cleaving

prism-shaped single crystals perpendicular to the *c*-axis with a razor blade. The absorption coefficients were determined from transmission measurements at normal incidence in the wavelength range 200–750 nm carried out in a Perkin-Elmer PE 350 spectrophotometer.

In the far-IR, Hadni *et al.* [6] reported the effective optical constants shown in Table VI obtained by K-K analysis. The experiment was the same one as in the case of AgCl, except that the samples were not single crystals, but pellets. Two Lorentz oscillators were also needed for AgI at room temperature (Table III); the stronger one corresponds to the TO mode and the weaker one to the TA + LA mode, an addition process that is IR-active.

Funke and Jost [12] also reported the optical constants in the frequency range from 8.5×10^{11} to 6×10^{12} Hz using Fourier spectrophotometry. The samples, which were prepared by reaction of silver with iodine in the dark at about 170°C, were probably polycrystalline. The reflectivity and transmission measurements were carried out with the spectrophotometers LR 100 (using a lamellar grating interferometer) and FS 720 (using a Michelson interferometer). The resultant optical constants are said to be accurate within 2%.

Values of n and k from these various references are listed in Table VI, and the data are plotted in Fig. 3.

IV α-AgI (CUBIC), STABLE FOR $T > T_c = 147°$ C

It is well known since the pioneering work of Strock[13] that the dc conductivity of AgI, which is very small at room temperature (β-AgI), increases dramatically at the phase transition when the cubic phase occurs for $T > T_c$, with values comparable to those found in aqueous solutions of electrolytes. The AgI is the archetype of superionic conductors with applications to solid-state batteries. The far-IR and mid-IR spectra are known [12, 14–16], but the optical constants have only been published in terms of dynamic conductivity between 10 and 250 cm^{-1}.

REFERENCES

1. J. J. White III and J. W. Straley, *J. Opt. Soc. Am.* **58**, 759 (1968).
2. R. S. Bauer, W. E. Spicer, and J. J. White III, *J. Opt. Soc. Am.* **64**, 830 (1974).
3. H. Schröter, *Z. Phys.* **67**, 24 (1931).
4. L. W. Tilton, E. K. Plyler, and R. E. Stephens, *J. Opt. Soc. Am.* **40**, 540 (1950).
5. N. J. Carrera and F. C. Brown, *Phys. Rev. B* **4**, 3651 (1971).
6. A. Hadni, J. Claudel, and P. Strimer, *Appl. Opt.* **7**, 1159 (1968).
7. J. J. White III, *J. Opt. Soc. Am.* **62**, 212 (1972).
8. D. E. McCarthy, *Appl. Opt.* **12**, 409 (1973).
9. L. A. Ageev, V. K. Miloslavskii, and I. N. Shklyarevskii, *Opt. Spectrosc.* **31**, 561 (1971).
10. L. D. Bedikyan, V. K. Miloslavskii, and L. A. Ageev, *Opt. Spectrosc.* **47**, 225 (1979).
11. G. Cochrane, *J. Phys. D* **7**, 748 (1974).

12. K. Funke and A. Jost, *Ber. Bunsen-Ges. Phys. Chem.* **75**, 436 (1971).
13. L. W. Strock, *Z. Phys. Chem. B* **25**, 411 (1934).
14. W. Jost, K. Funke, and A. Jost, *Z. Naturforsch. A* **25**, 983 (1970).
15. P. Brüesch, S. Strässler, and H. R. Zeller, *Phys. Status Solidi A* **31**, 217 (1975).
16. G. Burns, F. H. Dacol, and M. W. Shafer, *Phys. Rev. B* **16**, 1416 (1977).

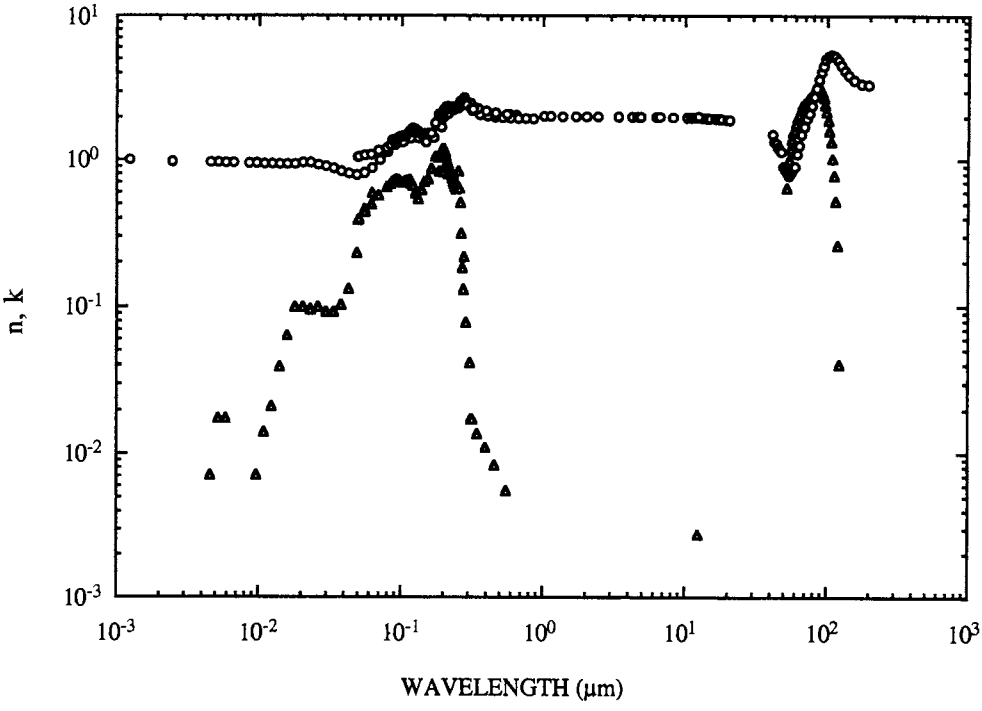

Fig. 1. Log–log plot of n (open circles) and k (open triangles) versus wavelength in micrometers for silver chloride.

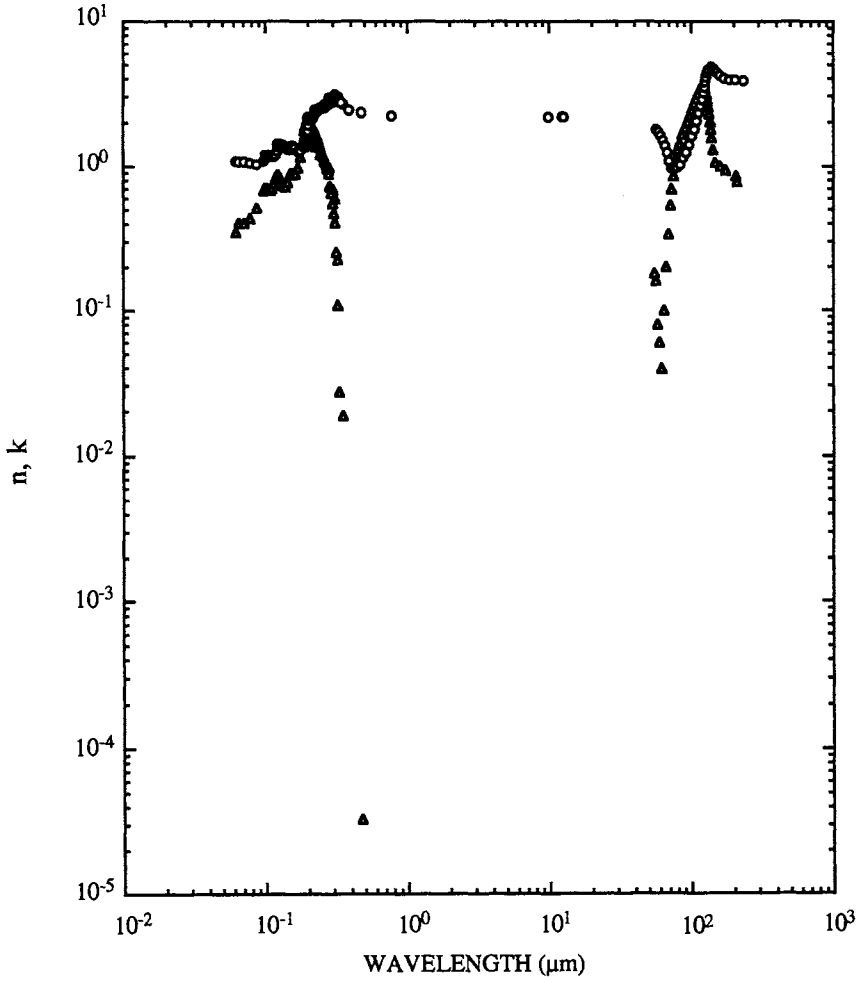

Fig. 2. Log–log plot of n (open circles) and k (open triangles) versus wavelength in micrometers for silver bromide.

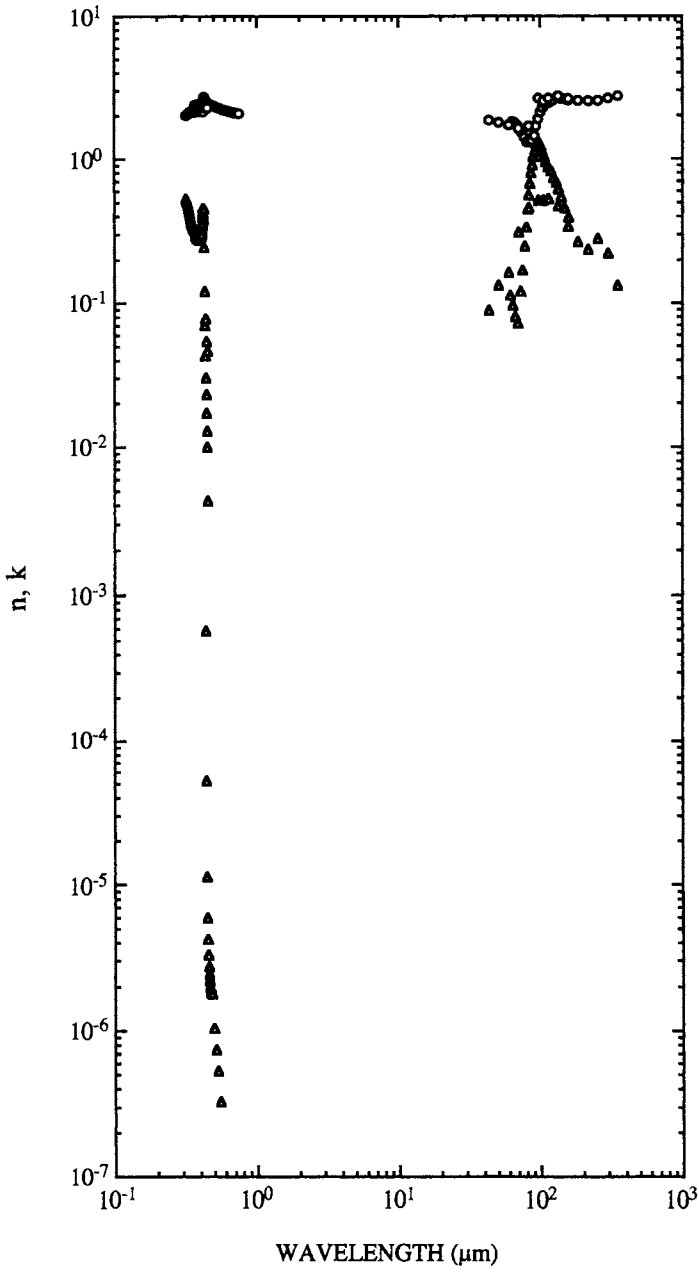

Fig. 3. Log–log plot of n (open circles) and k (open triangles) versus wavelength in micrometers for silver iodide.

TABLE I

Lorentz Oscillators Analysis of AgCl

T(K)	$\nu_1(cm^{-1})$	ρ_1	δ_1	$\nu_2(cm^{-1})$	ρ_2	δ_2	ϵ_{RV}
290	105	0.56	0.33	138	0.05	0.20	3.9
80	114	0.45	0.05	141	0.04	0.15	3.9
25	119	0.43	0.03	142	0.03	0.15	3.9

TABLE II

Lorentz Oscillators Analysis of AgBr

T(K)	$\nu_1(cm^{-1})$	ρ_1	δ_1	$\nu_2(cm^{-1})$	ρ_2	δ_2	ϵ_{RV}
290	79	0.61	0.32	105	0.020	0.25	4.5
80	84	0.52	0.10	120	0.015	0.20	4.5
25	85	0.48	0.028	122	0.010	0.20	4.5

TABLE III

Lorentz Oscillators Analysis of AgI

T(K)	$\nu_1(cm^{-1})$	ρ_1	δ_1	$\nu_2(cm^{-1})$	ρ_2	δ_2	ϵ_{RV}
290	103	0.14	0.36	80	0.01	0.10	4.91
80	106	0.14	0.10				4.91
25	106	0.14	0.04				4.91

TABLE IV

Values of n and k Obtained from Various References for AgCl[a]

eV	cm^{-1}	μm	n	k
1000.	8065000.	0.001240	1.000 [5]	0.000 [5]
504.3	4068000.	0.002458	0.967	0.000
270.7	2183000.	0.004581	0.961	0.007
239.0	1928000.	0.005188	0.961	0.018
211.0	1702000.	0.005876	0.954	0.018
186.3	1503000.	0.006654	0.954	0.000
145.3	1172000.	0.008535	0.947	0.000
128.3	1035000.	0.009666	0.947	0.007
113.3	913400.	0.01095	0.941	0.014
100.0	806500.	0.01240	0.941	0.021
88.30	712200.	0.01404	0.934	0.039
77.96	628800.	0.01590	0.934	0.064
68.84	555200.	0.01801	0.934	0.099
60.78	490200.	0.02040	0.954	0.099
53.67	432900.	0.02310	0.954	0.096
47.39	382200.	0.02616	0.921	0.099
41.84	337500.	0.02963	0.901	0.092
36.95	298000.	0.03356	0.868	0.092
32.62	263100.	0.03801	0.829	0.103
28.80	232300.	0.04304	0.803	0.131
25.43	205100.	0.04875	0.783	0.230
25.00	201600.	0.04959	1.044 [2]	0.386 [2]
24.60	198400.	0.05041	1.051	0.395
22.46	181100.	0.05521	0.809 [5]	0.461 [5]
22.36	180400.	0.05545	1.072 [2]	0.441 [2]
20.13	162300.	0.06161	1.086	0.497
19.83	159900.	0.06253	0.875 [5]	0.592 [5]
17.89	144300.	0.06931	1.156 [2]	0.568 [2]
17.51	141200.	0.07082	0.993 [5]	
15.65	126200.	0.07921	1.204 [2]	0.648 [2]
15.46	124700.	0.08020	1.132 [5]	
14.76	119000.	0.08401	1.267 [2]	0.684 [2]
14.31	115400.	0.08664	1.371	0.703
13.86	111800.	0.08943	1.336	0.720
13.65	110100.	0.09083	1.270 [5]	
13.42	108200.	0.09241	1.392 [2]	0.734 [2]
12.97	104600.	0.09560	1.427	0.731
12.52	101000.	0.09901	1.455	0.703
12.08	97390.	0.1027	1.462	0.698
12.05	97210.	0.1029	1.329 [5]	
11.63	93780.	0.1066	1.469 [2]	0.712 [2]
11.18	90180.	0.1109	1.524	0.726
10.73	86570.	0.1155	1.594	0.728
10.64	85830.	0.1165	1.415 [5]	
10.29	82960.	0.1205	1.664 [2]	0.662 [2]

(continued)

[a] References are indicated in brackets.

TABLE IV *(Continued)*

AgCl

eV	cm^{-1}	μm	n	k
9.840	79360.	0.1260	1.636	0.588
9.397	75790.	0.1319	1.421 [5]	
9.390	75750.	0.1320	1.573 [2]	0.538 [2]
8.940	72140.	0.1386	1.510	0.621
8.500	68530.	0.1459	1.517	0.703
8.297	66920.	0.1494	1.329 [5]	
8.050	64930.	0.1540	1.524 [2]	0.734 [2]
7.600	61320.	0.1631	1.531	0.869
7.326	59090.	0.1692	1.428 [5]	
7.160	57710.	0.1733	1.810 [2]	1.062 [2]
6.772	54620.	0.1831	2.075 [5]	1.044 [5]
6.710	54110.	0.1850	2.019	0.836
6.684	53910.	0.1855	2.053	1.044
6.596	53200.	0.1880	2.039	1.070
6.509	52500.	0.1905	2.053	1.122
6.469	52170.	0.1917	1.691	
6.421	51790.	0.1931	2.082	1.174
6.333	51080.	0.1958	2.131	1.200
6.260	50500.	0.1980	1.984 [2]	0.828 [2]
6.246	50370.	0.1985	2.202 [5]	1.200 [5]
6.158	49670.	0.2013	2.273	1.165
6.070	48960.	0.2043	2.309	1.122
5.982	48250.	0.2072	2.351	1.044
5.895	47540.	0.2103	2.351	0.974
5.810	46890.	0.2133	2.095 [2]	0.800 [2]
5.807	46840.	0.2135	2.344 [5]	0.922 [5]
5.719	46130.	0.2168	2.344	0.870
5.712	46070.	0.2171	2.205	
5.632	45420.	0.2202	2.337	0.835
5.544	44710.	0.2236	2.337	0.791
5.456	44010.	0.2272	2.330	0.748
5.370	43290.	0.2310	2.227 [2]	0.789 [2]
5.368	43300.	0.2310	2.323 [5]	0.713 [5]
5.281	42590.	0.2348	2.316	0.687
5.193	41880.	0.2388	2.309	0.652
5.105	41180.	0.2429	2.287	0.626
5.043	40680.	0.2458	2.284	
5.018	40470.	0.2471	2.280	0.635
4.930	39760.	0.2515	2.301	0.652
4.920	39680.	0.2520	2.332 [2]	0.836 [2]
4.842	39050.	0.2561	2.422	0.635
4.754	38350.	0.2608	2.564	0.504
4.739	38220.	0.2616	2.547	
4.667	37640.	0.2657	2.599	0.313
4.579	36930.	0.2708	2.571	0.183
4.491	36220.	0.2761	2.507	0.130
4.470	36070.	0.2772	2.715 [2]	0.218 [2]

TABLE IV *(Continued)*

AgCl

eV	cm^{-1}	μm	n	k
4.453	35920.	0.2784	2.448 [5]	
4.316	34810.	0.2873	2.422 [5]	0.078 [5]
4.030	32460.	0.3080	2.471 [2]	0.041 [2]
3.965	31980.	0.3127	2.287 [5]	0.017 [5]
3.932	31710.	0.3153	2.211	
3.877	31270.	0.3198	2.259	0.017
3.580	28860.	0.3465	2.276 [2]	0.014 [2]
3.472	28000.	0.3571	2.073 [5]	
3.130	25280.	0.3960	2.186 [2]	0.011 [2]
3.065	24720.	0.4045	2.020 [5]	
2.707	21830.	0.4581	1.987	
2.680	21640.	0.4621	2.123 [2]	0.008 [2]
2.390	19280.	0.5188	1.974 [5]	
2.240	18040.	0.5545	2.081 [2]	0.006 [2]
2.145	17300.	0.5780	2.069 [4]	
2.110	17020.	0.5876	1.961 [5]	
1.926	15530.	0.6438	2.055 [4]	
1.863	15030.	0.6654	1.948 [5]	
1.645	13270.	0.7536	1.948	
1.453	11720.	0.8535	1.941	
1.222	9860.	1.014	2.022 [4]	
1.098	8857.	1.129	2.018	
0.9050	7299.	1.370	2.012	
0.7293	5882.	1.700	2.008	
0.6138	4950.	2.020	2.006	
0.5102	4115.	2.430	2.004	
0.3657	2950.	3.390	2.001	
0.2924	2358.	4.240	1.999	
0.2684	2165.	4.620	1.998	
0.2546	2053.	4.870	1.998	
0.1981	1597.	6.260	1.994	
0.1925	1553.	6.440	1.994	
0.1873	1511.	6.620	1.993	
0.1508	1217.	8.220	1.988	
0.1199	967.1	10.34	1.979	
0.1124	906.6	11.03	1.975	
0.1081	871.8	11.47	1.973	
0.1045	843.2	11.86	1.971	
0.09379	756.4	13.22	1.963	
0.08658	698.3	14.32	1.956	
0.08277	667.6	14.98	1.951	
0.07560	609.8	16.40	1.940	
0.07336	591.7	16.90	1.936	
0.07134	575.4	17.38	1.932	
0.06966	561.8	17.80	1.928	
0.06827	550.7	18.16	1.925	
0.06262	505.1	19.80	1.909	

(continued)

TABLE IV *(Continued)*

AgCl

eV	cm^{-1}	μm	n	k
0.06030	486.4	20.56	1.901	
0.03000	241.7	41.38	1.506 [6]	
0.02920	235.7	42.42	1.343	
0.02830	228.2	43.83	1.302	
0.02750	221.8	45.08	1.221	
0.02680	215.9	46.32	1.180	
0.02600	209.9	47.64	1.140	
0.02510	202.8	49.32	0.895	
0.02450	197.6	50.60	0.855	
0.02390	192.7	51.88		0.640 [6]
0.02370	191.3	52.28	0.814	
0.02330	188.3	53.10		0.840
0.02300	185.7	53.85	0.773	
0.02280	184.3	54.27		1.000
0.02230	180.2	55.48		1.200
0.02220	179.4	55.75	0.814	
0.02190	177.0	56.49		1.400
0.02160	174.6	57.27	0.855	
0.02150	173.8	57.54		1.560
0.02100	169.8	58.91		1.620
0.02080	167.9	59.57	0.895	
0.02060	166.1	60.19		1.800
0.02010	162.1	61.69		1.960
0.02010	161.9	61.76	1.099	
0.01950	157.7	63.43		2.080
0.01940	156.7	63.80	1.262	
0.01900	153.2	65.26		2.240
0.01870	151.2	66.14	1.506	
0.01850	149.2	67.03		2.400
0.01790	144.0	69.42	1.709	
0.01770	143.1	69.86		2.500
0.01720	138.5	72.21	1.954	
0.01710	137.9	72.51		2.600
0.01650	133.5	74.92		2.740
0.01640	132.5	75.45	2.116	
0.01590	128.6	77.74		2.840
0.01580	127.4	78.50	2.401	
0.01540	124.2	80.52		3.000
0.01520	122.6	81.55	2.767	
0.01490	120.6	82.94		3.160
0.01470	118.3	84.56	3.174	
0.01440	116.1	86.11		3.300
0.01410	113.5	88.11	3.622	
0.01380	111.3	89.86		3.180
0.01350	109.1	91.64	4.070	
0.01340	108.1	92.54		2.980
0.01310	105.6	94.74	4.477	

TABLE IV *(Continued)*

AgCl

eV	cm^{-1}	μm	n	k
0.01300	104.8	95.38		2.740
0.01280	103.2	96.88		2.440
0.01270	102.4	97.67	4.965	
0.01250	100.8	99.20		2.180
0.01210	97.58	102.5		1.900
0.01210	97.22	102.9	5.209	
0.01190	96.37	103.8		1.600
0.01150	93.15	107.4		1.340
0.01150	92.46	108.2	5.291	
0.01130	91.53	109.3		1.020
0.01100	89.11	112.2		0.780
0.01080	87.30	114.5	5.169	
0.01070	86.69	115.3		0.520
0.01040	83.87	119.2		0.260
0.01030	82.94	120.6	4.884	
0.01000	81.05	123.4		0.040
0.009800	78.97	126.6	4.517	
0.009200	74.60	134.0	4.151	
0.008700	70.24	142.4	3.866	
0.008000	64.29	155.6	3.581	
0.007000	56.75	176.2	3.378	
0.006300	50.80	196.9	3.337	

TABLE V

Values of n and k Obtained from Various References for AgBr[a]

eV	cm^{-1}	μm	n	k
20.00	161300.	0.06199	1.083 [7]	0.350 [7]
19.05	153600.	0.06509	1.075	0.406
17.46	140800.	0.07101	1.075	0.406
15.87	128000.	0.07811	1.052	0.438
14.29	115200.	0.08679	1.036	0.519
12.70	102400.	0.09764	1.091	0.681
12.40	100000.	0.1000	1.200	0.710
12.38	99860.	0.1001	1.130	0.713
12.06	97300.	0.1028	1.177	0.706
11.75	94740.	0.1055	1.200	0.694
11.43	92180.	0.1085	1.192	0.688
11.11	89620.	0.1116	1.169	0.713
10.79	87060.	0.1149	1.169	0.763
10.48	84500.	0.1184	1.200	0.831
10.16	81940.	0.1220	1.278	0.869
10.10	81460.	0.1228	1.430	0.880
9.841	79370.	0.1260	1.364	0.844
9.524	76810.	0.1302	1.418	0.788
9.206	74250.	0.1347	1.403	0.744
8.889	71690.	0.1395	1.348	0.725
8.571	69130.	0.1446	1.309	0.775
8.254	66570.	0.1502	1.317	0.881
8.100	65330.	0.1531	1.380	0.900
7.937	64010.	0.1562	1.387	0.881
7.619	61450.	0.1627	1.348	0.888
7.302	58890.	0.1698	1.270	0.975
6.984	56330.	0.1775	1.286	1.163
6.667	53770.	0.1860	1.379	1.369
6.596	53200.	0.1880	1.423 [5]	1.773 [5]
6.506	52470.	0.1906	1.508	1.864
6.416	51750.	0.1933	1.569	1.918
6.349	51210.	0.1953	1.590 [7]	1.569 [7]
6.326	51020.	0.1960	1.654 [5]	2.018 [5]
6.236	50300.	0.1988	1.754	2.082
6.200	50010.	0.2000	2.170 [7]	1.650 [7]
6.146	49570.	0.2017	1.915 [5]	2.091 [5]
6.056	48850.	0.2047	2.078	2.055
6.032	48650.	0.2060	2.018 [7]	1.588 [7]
5.966	48120.	0.2078	2.162 [5]	1.927 [5]
5.876	47400.	0.2110	2.169	1.864
5.787	46670.	0.2143	2.185	1.827
5.714	46090.	0.2170	2.135 [7]	1.406 [7]
5.697	45950.	0.2176	2.215 [5]	1.809 [5]
5.607	45220.	0.2211	2.239	1.791
5.517	44500.	0.2247	2.315	1.718
5.500	44360.	0.2254	2.440 [7]	1.400 [7]

[a] References are indicated in brackets.

TABLE V *(Continued)*

AgBr

eV	cm^{-1}	μm	n	k
5.427	43770.	0.2285	2.354 [5]	1.655 [5]
5.397	43530.	0.2297	2.346 [7]	1.369 [7]
5.337	43050.	0.2323	2.400 [5]	1.600 [5]
5.247	42320.	0.2363	2.446	1.527
5.157	41600.	0.2404	2.462	1.436
5.079	40970.	0.2441	2.509 [7]	1.213 [7]
5.067	40870.	0.2447	2.477 [5]	1.355 [5]
4.978	40150.	0.2491	2.500	1.273
4.888	39420.	0.2537	2.500	1.200
4.798	38700.	0.2584	2.515	1.164
4.762	38410.	0.2604	2.618 [7]	1.094 [7]
4.708	37970.	0.2634	2.531 [5]	1.091 [5]
4.618	37250.	0.2685	2.546	1.036
4.528	36520.	0.2738	2.600	0.964
4.444	35850.	0.2790	2.805 [7]	0.944 [7]
4.438	35800.	0.2794	2.685 [5]	0.891 [5]
4.400	35490.	0.2818	2.930 [7]	0.980 [7]
4.348	35070.	0.2851	2.731 [5]	0.727 [5]
4.258	34350.	0.2912	2.731	0.655
4.169	33620.	0.2974	2.739	0.555
4.127	33290.	0.3004	2.961 [7]	0.694 [7]
4.079	32900.	0.3040	2.754 [5]	0.473 [5]
4.000	32260.	0.3100	3.090 [7]	0.600 [7]
3.989	32170.	0.3108	2.808 [5]	0.409 [5]
3.899	31450.	0.3180	2.900	0.255
3.810	30730.	0.3255	2.984 [7]	0.225 [7]
3.809	30720.	0.3255	2.892 [5]	0.109 [5]
3.719	30000.	0.3334	2.839	0.027
3.629	29270.	0.3416	2.723	0.000
3.492	28170.	0.3550	2.649 [7]	0.019 [7]
3.175	25610.	0.3906	2.416	0.000
2.600	20970.	0.4769	2.330	0.000
1.587	12800.	0.7811	2.205	
0.1249	1008.	9.926	2.167 [8]	
0.1000	806.5	12.40	2.174 [7]	
0.09795	790.0	12.66	2.162 [8]	
0.02254	181.8	55.01		0.180 [6]
0.02184	176.1	56.77		0.160
0.02180	176.1	56.79	1.787 [6]	
0.02119	170.9	58.51		0.080
0.02100	169.7	58.93	1.727	
0.02054	165.7	60.36		0.060
0.02020	162.9	61.39	1.627	
0.01994	160.9	62.17		0.040
0.01950	157.2	63.61	1.506	
0.01925	155.2	64.42		0.100

(continued)

TABLE V *(Continued)*

AgBr

eV	cm^{-1}	μm	n	k
0.01880	152.0	65.79	1.386	
0.01855	149.6	66.84		0.200
0.01820	147.2	67.93	1.245	
0.01790	144.4	69.27		0.340
0.01770	142.8	70.03	1.084	
0.01735	140.0	71.45		0.540
0.01700	136.7	73.15	0.964	
0.01695	136.7	73.14		0.700
0.01645	132.7	75.35		0.860
0.01620	130.3	76.75	0.964	
0.01596	128.7	77.71		1.100
0.01550	125.1	79.94	0.984	
0.01546	124.7	80.22		1.300
0.01491	120.2	83.17		1.440
0.01480	119.0	84.03	1.024	
0.01436	115.8	86.34		1.660
0.01410	113.4	88.18	1.145	
0.01371	110.6	90.42		1.840
0.01340	108.2	92.42	1.245	
0.01316	106.2	94.19		2.020
0.01280	102.9	97.18	1.406	
0.01262	101.7	98.29		2.240
0.01222	98.53	101.5		2.440
0.01220	98.50	101.5	1.606	
0.01177	94.91	105.4		2.700
0.01170	94.50	105.8	1.787	
0.01147	92.49	108.1		2.900
0.01130	91.30	109.5	2.028	
0.01107	89.28	112.0		3.140
0.01100	88.50	113.0	2.309	
0.01072	86.46	115.7		3.380
0.01060	85.30	117.2	2.590	
0.01030	83.20	120.2	2.851	
0.01022	82.44	121.3		3.500
0.01010	81.20	123.2	3.173	
0.009919	80.00	125.0	3.454	
0.009872	79.62	125.6		3.360
0.009869	79.60	125.6	3.775	
0.009720	78.40	127.6	4.076	
0.009623	77.61	128.8		3.060
0.009500	76.80	130.2	4.378	
0.009473	76.41	130.9		2.800
0.009400	75.60	132.3	4.619	
0.009374	75.60	132.3		2.560
0.009274	74.80	133.7		2.300
0.009075	73.19	136.6		2.020
0.008975	72.39	138.1		1.800

TABLE V *(Continued)*

AgBr

eV	cm^{-1}	μm	n	k
0.008900	71.60	139.7	4.819	
0.008875	71.58	139.7		1.580
0.008676	69.97	142.9		1.300
0.008500	68.40	146.2	4.639	
0.008376	67.56	148.0		1.060
0.008100	65.50	152.7	4.418	
0.007800	62.70	159.5	4.197	
0.007728	62.33	160.4		1.000
0.007200	58.30	171.5	3.996	
0.007080	57.10	175.1		0.940
0.006600	53.50	186.9	3.916	
0.006000	48.70	205.3	3.916	
0.005983	48.26	207.2		0.860
0.005883	47.45	210.7		0.780
0.005300	42.60	234.7	3.855	

TABLE VI

Values of n and k Obtained from Various References for AgI[a]

eV	cm^{-1}	μm	n	k
3.900	31460.	0.3179	2.001 [10]	0.535 [10]
3.860	31130.	0.3212	2.015	0.519
3.820	30810.	0.3246	2.029	0.505
3.780	30490.	0.3280	2.048	0.486
3.740	30170.	0.3315	2.074	0.460
3.700	29840.	0.3351	2.100	0.438
3.660	29520.	0.3387	2.112	0.414
3.620	29200.	0.3425	2.117	0.390
3.580	28880.	0.3463	2.125	0.367
3.540	28550.	0.3502	2.123	0.356
3.500	28230.	0.3542	2.123	0.344
3.460	27910.	0.3583	2.122	0.335
3.420	27590.	0.3625	2.125	0.327
3.380	27260.	0.3668	2.129	0.322
3.356	27070.	0.3694	2.377 [9]	0.296 [9]
3.340	26940.	0.3712	2.133 [10]	0.319 [10]
3.310	26700.	0.3746	2.138	0.316
3.270	26380.	0.3791	2.144	0.313
3.260	26300.	0.3803	2.391 [9]	0.284 [9]
3.230	26050.	0.3838	2.149 [10]	0.312 [10]
3.190	25730.	0.3887	2.148	0.310
3.182	25660.	0.3897	2.394 [9]	0.279 [9]
3.150	25410.	0.3936	2.153 [10]	0.309 [10]

(continued)

[a] References are indicated in brackets.

TABLE VI *(Continued)*

AgI

eV	cm^{-1}	μm	n	k
3.110	25080.	0.3987	2.169	0.307
3.102	25020.	0.3997	2.385 [9]	0.275 [9]
3.070	24760.	0.4038	2.194 [10]	0.303 [10]
3.030	24440.	0.4092	2.227	0.301
3.028	24430.	0.4094	2.391 [9]	0.292 [9]
3.013	24300.	0.4115	2.382	0.307
3.000	24200.	0.4132	2.388	0.328
2.990	24120.	0.4146	2.160 [10]	0.356 [10]
2.983	24060.	0.4156	2.400 [9]	0.353 [9]
2.969	23940.	0.4176	2.427	0.399
2.958	23860.	0.4191	2.474	0.425
2.950	23790.	0.4203	2.121 [10]	0.457 [10]
2.942	23730.	0.4215	2.547 [9]	0.417 [9]
2.927	23610.	0.4235	2.621	0.381
2.910	23470.	0.4260	2.284 [10]	0.453 [10]
2.907	23450.	0.4265	2.706 [9]	0.245 [9]
2.887	23290.	0.4294	2.703	0.122
2.875	23190.	0.4312	2.496 [11]	
2.870	23150.	0.4320	2.430 [10]	0.121 [10]
2.868	23130.	0.4324	2.653 [9]	0.071 [9]
2.848	22970.	0.4353	2.588	0.043
2.839	22900.	0.4370		5.8E-04 [11]
2.830	22830.	0.4381	2.366 [10]	0.078 [10]
2.829	22820.	0.4382	2.538 [9]	0.030 [9]
2.818	22730.	0.4400		5.3E-05 [11]
2.810	22670.	0.4412	2.500 [9]	0.023 [9]
2.797	22560.	0.4430		1.1E-05 [11]
2.792	22520.	0.4441	2.474 [9]	0.017 [9]
2.790	22500.	0.4444	2.290 [10]	0.055 [10]
2.776	22390.	0.4470		6.0E-06 [11]
2.773	22370.	0.4471	2.459 [9]	0.013 [9]
2.755	22220.	0.4500		4.3E-06 [11]
2.755	22220.	0.4500	2.444 [9]	0.010 [9]
2.750	22180.	0.4508	2.261 [10]	0.046 [10]
2.746	22150.	0.4515	2.441 [11]	
2.735	22060.	0.4530		3.3E-06 [11]
2.720	21940.	0.4559	2.424 [9]	0.004 [9]
2.715	21900.	0.4570		2.8E-06 [11]
2.695	21740.	0.4600		2.4E-06
2.685	21660.	0.4618	2.394 [9]	
2.676	21580.	0.4630		2.2E-06 [11]
2.657	21430.	0.4670		2.0E-06
2.638	21280.	0.4700		1.8E-06
2.600	20970.	0.4769	2.378 [11]	
2.583	20830.	0.4800		1.8E-06
2.496	20130.	0.4970		1.0E-06
2.468	19910.	0.5023	2.327	

TABLE VI *(Continued)*

AgI

eV	cm^{-1}	μm	n	k
2.415	19480.	0.5130		7.5E-07
2.350	18950.	0.5277	2.280	
2.339	18870.	0.5300		5.3E-07
2.254	18180.	0.5500		3.3E-07
2.242	18080.	0.5530	2.241	
2.143	17290.	0.5784	2.202	
2.053	16560.	0.6038	2.171	
1.971	15890.	0.6292	2.145	
1.894	15280.	0.6546	2.122	
1.823	14710.	0.6799	2.102	
1.758	14180.	0.7053	2.086	
1.697	13690.	0.7307	2.076	
1.653	13330.	0.7500	2.067	
0.02857	230.4	43.41	1.842 [12]	0.090 [12]
0.02432	196.1	50.99	1.782	0.134
0.02070	167.0	59.89	1.708	0.163
0.02015	162.5	61.53		0.113 [6]
0.01959	158.0	63.29	1.806 [6]	
0.01935	156.1	64.08		0.097
0.01885	152.0	65.79	1.766	
0.01855	149.6	66.85		0.081
0.01810	146.0	68.49	1.706	
0.01780	143.5	69.67		0.073
0.01762	142.1	70.36	1.619 [12]	0.312 [12]
0.01736	140.0	71.43	1.605 [6]	
0.01704	137.5	72.75		0.121 [6]
0.01671	134.8	74.18	1.505	
0.01654	133.4	74.95		0.169
0.01607	129.6	77.16	1.405	
0.01594	128.6	77.78		0.250
0.01549	124.9	80.04		0.339
0.01542	124.4	80.39	1.304	
0.01514	122.1	81.90		0.452
0.01500	121.0	82.65	1.678 [12]	0.460 [12]
0.01499	120.9	82.72		0.565 [6]
0.01478	119.2	83.89	1.304 [6]	
0.01474	118.9	84.13		0.677
0.01444	116.4	85.88		0.798
0.01418	114.4	87.41	1.345	
0.01414	114.0	87.71		0.903
0.01394	112.4	88.97		1.032
0.01364	110.0	90.91	1.445	
0.01354	109.2	91.61		1.129
0.01329	107.2	93.28	1.686	
0.01328	107.1	93.33		1.242

(continued)

TABLE VI *(Continued)*

AgI

eV	cm^{-1}	μm	n	k
0.01293	104.3	95.87		1.339
0.01285	103.6	96.53	1.886	
0.01277	103.0	97.08	2.644 [12]	0.520 [12]
0.01253	101.1	98.93		1.282 [6]
0.01240	100.0	100.0	2.107 [6]	
0.01228	99.06	101.0		1.210
0.01198	96.63	103.5		1.121
0.01195	96.40	103.7	2.268	
0.01178	95.04	105.2	2.525 [12]	0.520 [12]
0.01163	93.80	106.6		1.032 [6]
0.01146	92.40	108.2	2.388 [6]	
0.01138	91.78	109.0		0.952
0.01093	88.14	113.5		0.879
0.01087	87.69	114.0	2.644 [12]	0.535 [12]
0.01081	87.20	114.7	2.448 [6]	
0.01043	84.10	118.9		0.823 [6]
0.01022	82.40	121.4	2.528	
0.009976	80.46	124.3		0.742
0.009524	76.82	130.2		0.686
0.009423	76.00	131.6	2.689	
0.009255	74.65	134.0	2.733 [12]	0.475 [12]
0.009224	74.39	134.4		0.621 [6]
0.008927	72.00	138.9	2.629 [6]	
0.008823	71.16	140.5		0.548
0.008431	68.00	147.1	2.609	
0.008321	67.12	149.0		0.460
0.007935	64.00	156.3	2.549	
0.007879	63.55	157.4	2.614 [12]	0.342 [12]
0.007820	63.07	158.5		0.395 [6]
0.006707	54.10	184.8	2.540 [12]	0.267 [12]
0.005710	46.05	217.1	2.525	0.238
0.004861	39.21	255.1	2.540	0.282
0.004138	33.38	299.6	2.644	0.223
0.003523	28.41	352.0	2.733	0.134

Silver Gallium Selenide ($AgGaSe_2$)
Silver Gallium Sulfide ($AgGaS_2$)

LUIS ARTÚS
Instituto Jaime Almera
Consejo Superior de Investigaciones Cientificas (C.S.I.C.)
Barcelona, SPAIN

$AgGaS_2$ and $AgGaSe_2$ are I–III–VI_2 compounds that belong to the chalcopyrite family. All these compounds have space-group symmetry $I\bar{4}2d$, and they are considered as derived from II–VI binary zincblende semiconductors. In ideal chalcopyrite crystals, the c parameter of the unit cell should be twice the a parameter, and the anions should be at equal distance from both cations, ocupying positions $(\frac{1}{4}, \frac{1}{4}, \frac{1}{8})$ and their equivalent positions in the unit cell. However, two important structural anomalies take place in real ternary chalcopyrite compounds. One is the so-called tetrahedral distortion, which takes into account the displacement of the anions toward the smaller cations; it is characterized by the parameter u, defined as

$$u = \tfrac{1}{4} + (d_{AC}{}^2 - d_{BC}{}^2)/a,$$

where d_{AC} and d_{BC} stand for the distances existing between the anions and cations I and III, respectively. The second structural change corresponds to the tetragonal compression that makes the c parameter different from twice the a parameter. This tetragonal compression is measured by the parameter $\mu = c/2a$. For $AgGaS_2$ these structural parameters take the values $u = 0.304$ and $\mu = 0.894$, whereas for $AgGaSe_2$ the values are $u = 0.276$ and $\mu = 0.896$ [1].

In the II–VI zincblende compounds, the fundamental gap corresponds to transitions occurring at the center of the Brillouin zone between the threefold-degenerate Γ_{15} level, which constitutes the top of the valence band, and the nondegenerate Γ_1 level, which constitutes the bottom of the conduction band. In the $AgGaS_2$ and $AgGaSe_2$ chalcopyrite compounds, because of the existence of the tetragonal crystal field, the threefold degeneracy of the Γ_{15} level is lifted in such a way that a nondegenerate Γ_4 level lies above a doubly degenerate Γ_5 level. If the spin–orbit interaction is taken into account, Γ_5

HANDBOOK OF OPTICAL CONSTANTS OF SOLIDS III

Copyright © 1998 by Academic Press.
All rights of reproduction in any form reserved
ISBN 0-12-544423-0/$25.00.

splits into Γ_6 and Γ_7, whereas Γ_4 and Γ_1 convert into Γ_7 and Γ_6, respectively. So, three structures can be observed in the fundamental-gap region in the optical spectra of the $AgGaS_2$ and $AgGaSe_2$ chalcopyrite compounds. The first one corresponds to transitions that occur at the fundamental gap between Γ_7 and Γ_6 levels, and it is labeled the A transition. The two other structures are due to transitions ocurring between Γ_6 and Γ_6 levels (B transition) and between Γ_7 and Γ_6 levels (C transition).

I OPTICAL PROPERTIES OF $AgGaSe_2$

For $AgGaSe_2$, these three structures A, B, and C have been measured at 5 K by means of reflectivity at near-normal incidence to take place at 1.804, 2.00, and 2.27 eV, respectively [2]. Taking into account the excitonic character of the A transition, the measurement of the fundamental excitonic state, as well as of its first excited state, allowed the determination of the gap value of $AgGaSe_2$ at liquid-helium temperatures to be $E_g = 1.824$ eV [2]. A similar value of $E_g = 1.830$ eV has been reported by other authors [3]. The pressure dependence of the band gap was found to be 5.3 meV/kbar with an atmospheric-pressure band-gap value of 1.80 eV at 300 K by means of absorption measurements under hydrostatic pressure [4]. An anomalous dependence of the band gap on temperature was found between 5 and 300 K [5]. So, a positive temperature coefficient $+1.0 \times 10^{-4}$ eV K^{-1} was found between 5 and 70 K, whereas a negative temperature coefficient of -1.4×10^{-4} eV K^{-1} was found between 110 and 300 K. This anomalous behavior of the band gap with temperature is related to the hybridization between the *d* orbitals of Ag and the Se *p* orbitals that takes place in the $AgGaSe_2$ compound.

At energies higher than the fundamental band gap, only unpolarized reflectivity measurements performed at room temperature from 1.2 to 25 eV [6] and polarized wavelength-modulated reflectivity performed at room temperature and 10 K up to 5.5 eV [7] have been reported. To estimate the *n* and *k* values in this energy region, a Kramers–Kronig analysis from the unpolarized reflectivity data reported up to 25 eV [6] has been carried out. At higher energies, we used the extrapolation suggested by Cardona and Greenaway [8], who consider a minus fourth-power reflectivity dependence of the energy. For the low-energy end, we have fitted an analytical curve to the monotonically decreasing reflectivity data measured below the band gap, which has been extrapolated to zero energy. The values of the refractive indices obtained by using this extrapolation are consistent with the values of the refractive indices obtained experimentally in the transparent region [9]. The values obtained for *n* and *k* from the fundamental-band-gap energy up to 25 eV are listed in Table I.

Optical absorption on thin films of thickness between 250 and 750 nm in the range 3.0–1.5 eV were reported [10], and the corresponding values of the extinction coefficient k in this energy range are listed in Table I. To read the values of the absorption coefficient from the graph displayed by Murthy *et al.* [10], we have digitized the curve. Hereafter, the same procedure has been carried out to obtain the data from the different reported graphs. Soliman [11] measured the transmittance and reflectance of thin films with different thickness in the range 0.5–2.0 μm and, from these experimental data, he calculated n and k by means of Murmann's formulae. The reported data have been listed in Table I.

Experimental measurements of n or k have been reported in the transparent region of this compound. Boyd *et al.* [9] determined accurately the refractive indices by measuring the minimum-deviation angle on a prism of angle close to 20° cut from the crystal boule. They measured n_o and n_e values in the range 0.725–13.5 μm with four decimal figures as shown in Table I. According to these authors, the presence of imperfections in their samples precludes obtaining reliable absolute values of the absorption-coefficient dispersion, and they could only determine relative variations of the absorption coefficient with wavelength. Consequently, the corresponding k values are not listed in Table I.

We have fitted the measured values of Boyd *et al.* [9] to the modified Sellmeier-type dispersion formula [12] of the form

$$n^2 = A + \frac{B}{\lambda^2 - C} + \frac{D\lambda^2}{E\lambda^2 - 1}.$$

The fit has been performed using the 43 reported experimental points. When the wavelengths are expressed in micrometers, the following parameters for the n_o and n_e dispersions in the range 0.725–13.5 μm are obtained:

A_o =	1.002933	A_e =	1.000687
B_o =	8.596864E03	B_e =	1.308038E04
C_o =	−2.523862E03	C_e =	−3.035824E03
D_o =	1.399621E01	D_e =	4.860614
E_o =	5.725267	E_e =	3.512771

Here, the subindices o or e denote ordinary or extraordinary rays, respectively. The RMS deviation of the measured refractive indices and the values calculated from the preceeding dispersion formula are 0.48% and 0.70% for n_o and n_e, respectively.

Catella *et al.* [13] performed polarized mid-IR transmission in the region below the band gap on several different samples. The values of the extinction coefficient k listed in Table I are obtained from their transmission curves for ordinary and extraordinary rays in the range 0.73–2.6 μm.

Reflectivity measurements in the reststrahlen region have been reported

by several authors [14–16]. Kanellis and Kampas [14] calculated from the polarized reflectivity data, using the classical dispersion theory, the n and k dispersion curves from 400 to 10 cm^{-1} for both polarizations. The values they obtained are listed in Table I.

The data of Table I are plotted in Figs. 1a and b for $AgGaSe_2$.

II OPTICAL PROPERTIES OF $AgGaS_2$

The three electronic transitions near the fundamental gap have been found to be at 2.679, 2.91, and 2.94 eV for A, B, and C transitions, respectively, from reflectivity measurements at 5 K [17]. The differences found in the gap values reported for this compound are greater than usual, which can be explained taking into account that $AgGaS_2$ crystals are frequently found to be nonstoichiometric. Some authors [18] have observed variation of the color of the crystals depending on their proximity to the stoichiometric composition. At liquid-helium temperature, excitonic behavior has been found by several authors, who reported values of about 2.72 eV for the fundamental gap [17, 19, 20]. A fundamental-band-gap value of 2.70 eV at room temperature and a pressure dependence of this gap of 2.2 meV/kbar were found by absorption measurements under hydrostatic pressure [4]. As happens for the $AgGaSe_2$ compound, the $AgGaS_2$ crystals also present an anomalous behavior of the fundamental band gap with temperature: The temperature coefficient was positive up to 80 K with a value of 1.0×10^{-4} eV K^{-1}, whereas from 110 K to room temperature the coefficient was found to be -2.2×10^{-4} eV K^{-1} [5].

At energies higher than the fundamental gap, unpolarized reflectivity measurements at room temperature from 1.2 up to 25 eV [6] and to 10 eV [21] have been reported, as well as polarized reflectivity at 80 K up to 7 eV [22]. By applying a Kramers–Kronig analysis to the reflectivity data [6] using the extrapolations discussed earlier, the n and k dispersions from 25 eV to the band-gap energy have been calculated, and their values are listed in Table II. Absorption measurements on polycrystalline $AgGaS_2$ at room temperature have been performed up to about 7 eV [23]. The values of the extinction coefficient k obtained from these measurements are listed in Table II.

In the transparent region, the indices n_o and n_e were measured in the range 0.49–13.0 μm by the minimum-deviation-angle method on a prism of angle close to 30° cut from the crystal boule [24]. The values are given in Table II. Absorption-coefficient measurements were also performed up to 12.5 μm, but according to the authors, the presence of cracks and voids in the crystal made absolute values unreliable, and consequently, only relative variations are meaningful.

We have fitted the measured values of Boyd *et al.* [24] to the modified

Sellmeier-type dispersion formula mentioned earlier. The fit has been performed using the 50 reported experimental points. The following parameters have been obtained for the n_o and n_e dispersions in the range 0.49–13.0 μm when the wavelength is in micrometers:

A_o =	0.966201	A_e =	1.000010
B_o =	2.689302E03	B_e =	3.372195E03
C_o =	−9.541617E02	C_e =	−1.061937E03
D_o =	1.903090E01	D_e =	1.007695E01
E_o =	9.426157	E_e =	7.290825

The RMS deviation between the measured refractive indices and the values calculated from the dispersion formula are 3.7% and 0.97% for n_o and n_e, respectively.

The existence of optical activity in a non-enantiomorphous crystal was first demonstrated by Hobden [25] by taking advantage of the unusual property that, for the $AgGaS_2$ crystal, the birefringence changes sign at 4974 Å. So, the accidental isotropy of the crystal at this wavelength allowed its optical activity to be seen without the difficulties arising from the presence of birefringence. Measurement of n_o and n_e by the prism method for six different wavelengths in the transparent region up to 0.67 μm was also reported in this paper, the measured values being close to those obtained by Boyd *et al.* [24].

Chemla *et al.* [26] measured the transmission of the crystal in the range 0.5–13.0 μm for ordinary and extraordinary rays. The extinction coefficients k listed in Table II have been obtained from these transmission curves. The temperature dependence of the refractive indices of $AgGaS_2$ crystals was determined by Bhar *et al.* [27] by means of the classical minimum-deviation technique controlling the prism temperature from room temperature up to 90° C. The nondispersive value of the thermooptic coefficient dn/dT was found to be 15.5×10^{-5}/°C in the temperature range studied.

In the reststrahlen region, polarized reflectivity measurements were performed from 400 to 40 cm^{-1} by Holah *et al.* [28]. By using the classical dispersion theory, they calculated the n and k dispersion curves throughout this range. The corresponding values are listed in Table II.

The data in Table II are plotted in Figs. 2a and b for $AgGaS_2$.

REFERENCES

1. H. W. Spiess, V. Haeberln, G. Brandt, A. Rauber, and J. Schneider, *Phys. Status Solidi B* **62**, 183 (1974).
2. L. Artús, Y. Bertrand, and C. Ance, *J. Phys. C: Solid State Phys.* **19**, 5937 (1986).
3. B. Tell and H. M. Kasper, *Phys. Rev. B* **4**, 4455 (1971).
4. A. Jayaraman, V. Narayanamurti, H. M. Kasper, M. A. Chin, and R. G. Maines, *Phys. Rev. B* **14**, 3516 (1976).
5. L. Artús and Y. Bertrand, *Solid State Commun.* **61**, 733 (1987).

6. L. Artús, Y. Bertrand, and A. López-Soler, *J. Phys. C: Solid State Phys.* **20**, 111 (1987).
7. B. Sermage and G. Fishman, *Inst. Phys. Confer. Ser.* **35**, 139 (1977).
8. M. Cardona and D. L. Greenaway, *Phys. Rev.* **133**, 1685 (1964).
9. G. D. Boyd, H. M. Kasper, J. H. McFee, and F. G. Storz, *IEEE J. Quantum Electron.* **8**, 900 (1972).
10. Y. S. Murthy, B. S. Naidu, and P. J. Reddy, *Vacuum* **41**, 1448 (1990).
11. H. S. Soliman, *J. Phys. D: Appl. Phys.* **28**, 764 (1995).
12. F. Zernike, *J. Opt. Soc. Am.* **54**, 1215 (1964).
13. G. C. Catella, L. R. Shiozawa, J. R. Hietanen, R. C. Eckardt, R. K. Route, R. S. Feigelson, D. G. Cooper, and C. L. Marquardt, *Appl. Opt.* **32**, 3948 (1993).
14. G. Kanellis and K. Kampas, *J. Phys.(Paris)* **38**, 833 (1977).
15. A. Miller, G. D. Holah, W. D. Dunnett, and G. Iseler, *Phys. Status Solidi B* **78**, 569 (1976).
16. J. Camassel, L. Artús and J. Pascual, *Phys. Rev. B* **41**, 5717 (1990).
17. L. Artús and Y. Bertrand, *J. Phys. C: Solid State Phys.* **20**, 1365 (1987).
18. P. Korczak and C. Staff, *J. Cryst. Growth* **41**, 146 (1974).
19. B. Tell and H. M. Kasper, *Phys. Rev. B* **6**, 3008 (1972).
20. P. Yu, W. J. Anderson, and Y. S. Park, *Solid State Commun.* **13**, 1883 (1973).
21. R. L. Hengehold and F. L. Pedrotti, *J. Appl. Phys.* **46**, 5202 (1975).
22. J. Austinat, H. Nelkowski, and W. Scrittenlacher, *Solid State Commun.* **37**, 285 (1981).
23. H. V. Campe, *J. Phys. Chem. Solids* **44**, 1019 (1983).
24. G. D. Boyd, H. Kasper, and J. H. McFee, *IEEE J. Quantum Electron* **7**, 563 (1971).
25. M. V. Hobden, *Nature (London)* **216**,678 (1967); M. V. Hobden, *Acta Crystallogr. A* **24**, 676 (1968).
26. D. S. Chemla, P. J. Kupecek, D. S. Robertson, and R. C. Smith, *Opt. Commun.* **3**, 29 (1971).
27. G. C. Bhar, D. K. Ghosh, P. S. Ghosh, and D. Schmitt, *Appl. Opt.* **22**, 2492 (1983).
28. G. D. Holah, J. S. Webb, and H. Montgomery, *J. Phys. C: Solid State Phys.* **7**, 3875 (1974).

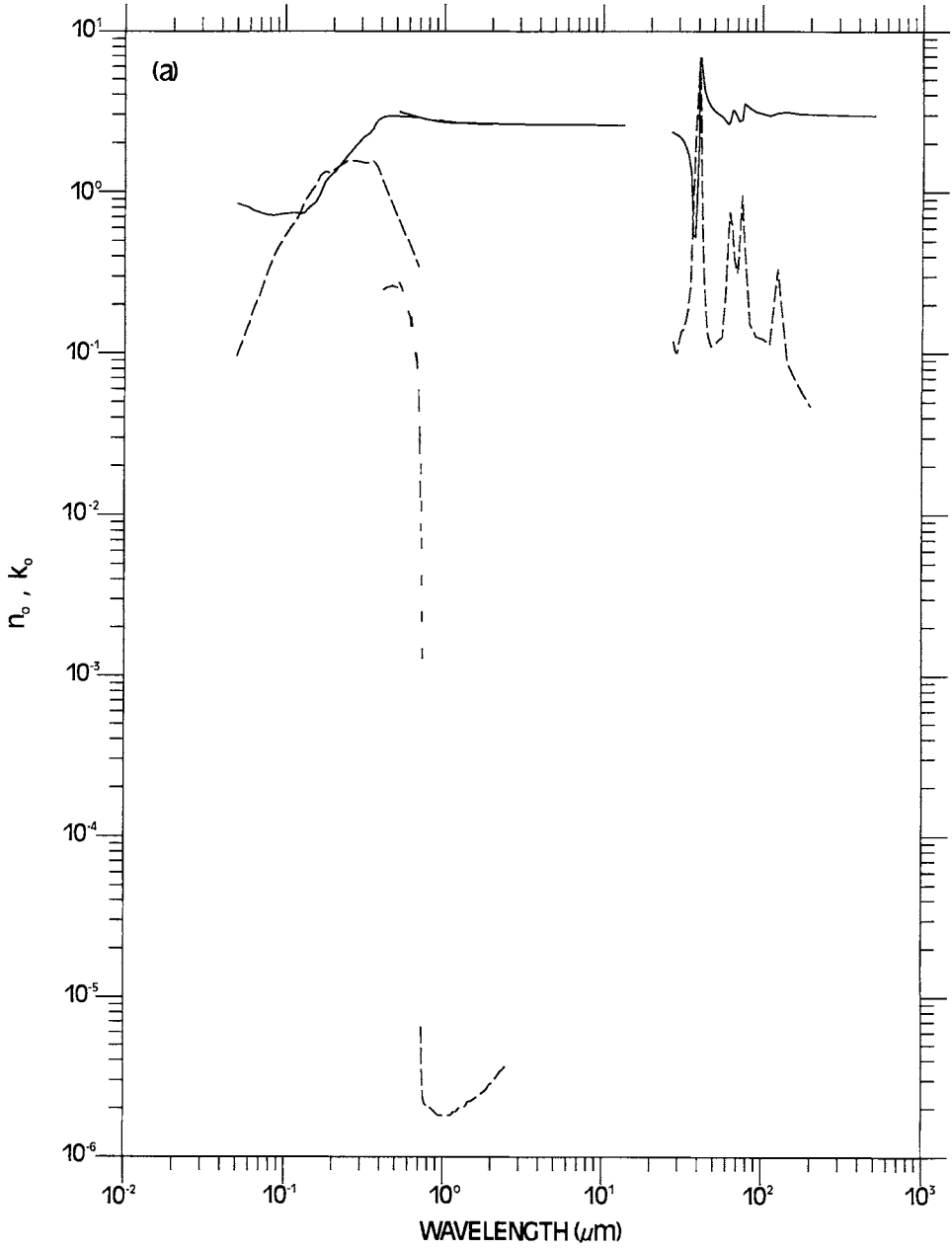

Fig. 1. (a) Log–log plot of n_o (solid line) and k_o (dashed line) versus wavelength in micrometers for silver gallium selenide ($AgGaSe_2$).

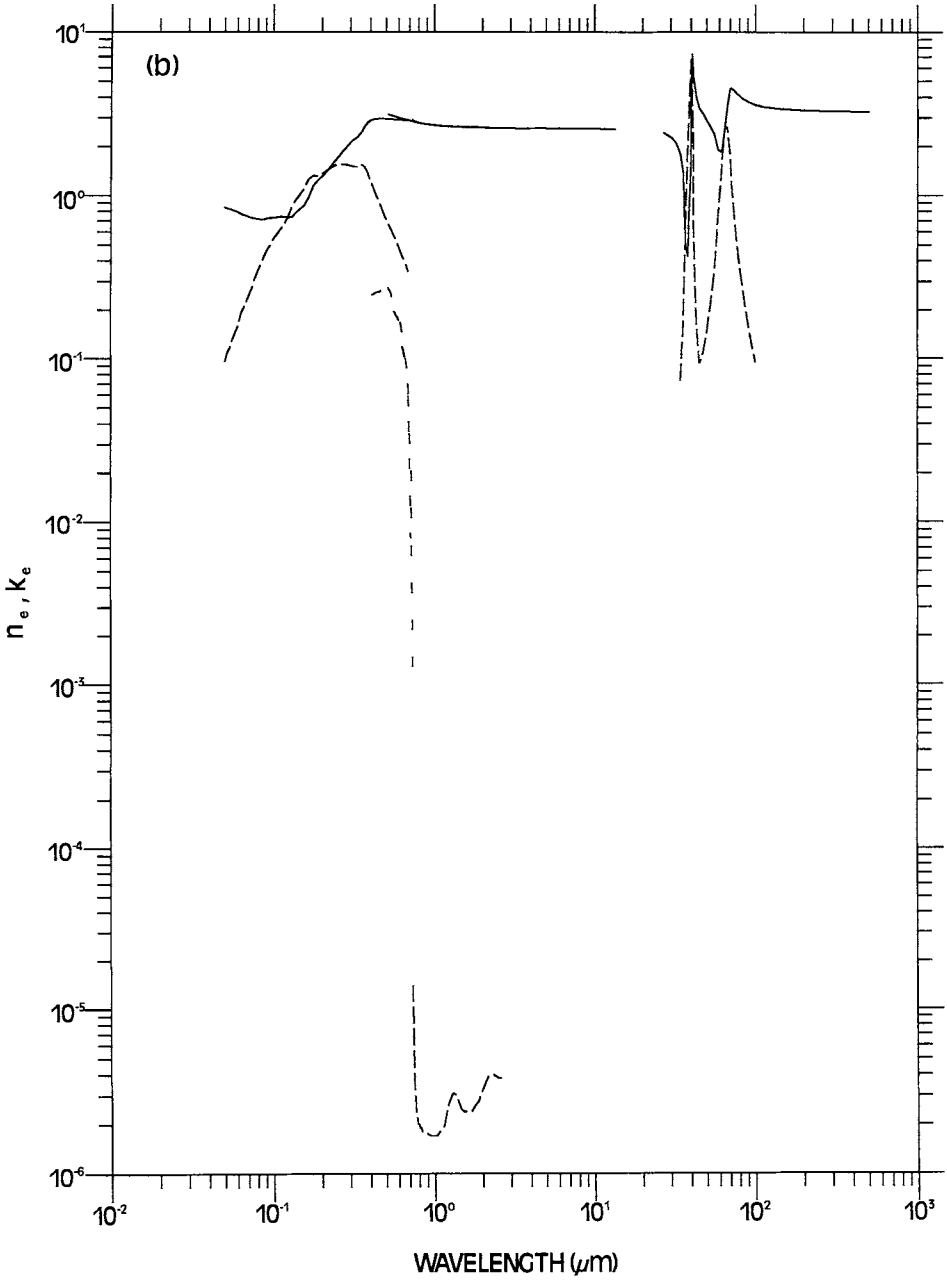

Fig. 1. (b) Log–log plot of n_e (solid line) and k_e (dashed line) versus wavelength in micrometers for silver gallium selenide ($AgGaSe_2$).

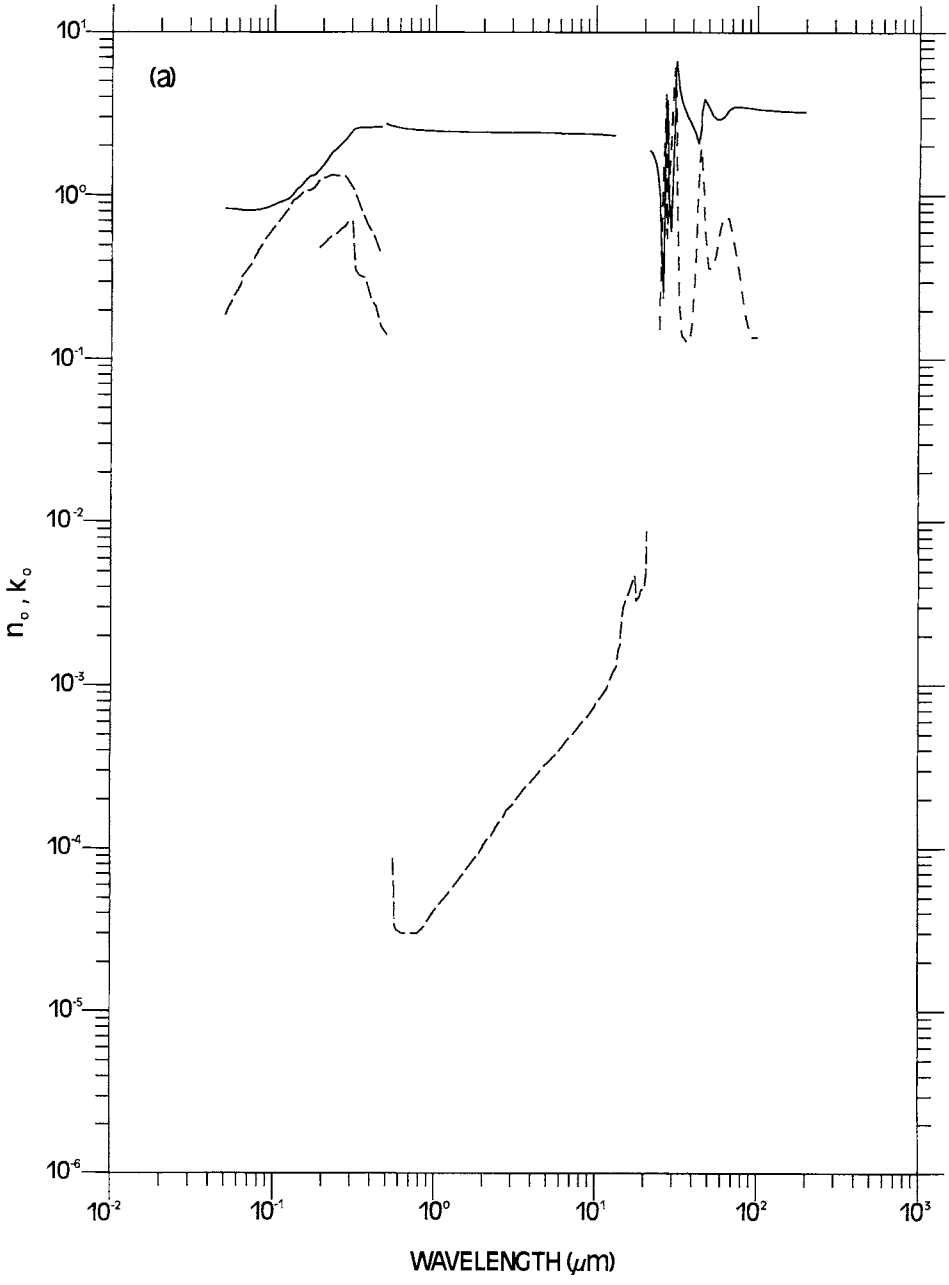

Fig. 2. (a) Log–log plot of n_o (solid line) and k_o (dashed line) versus wavelength in micrometers for silver gallium sulfide ($AgGaS_2$).

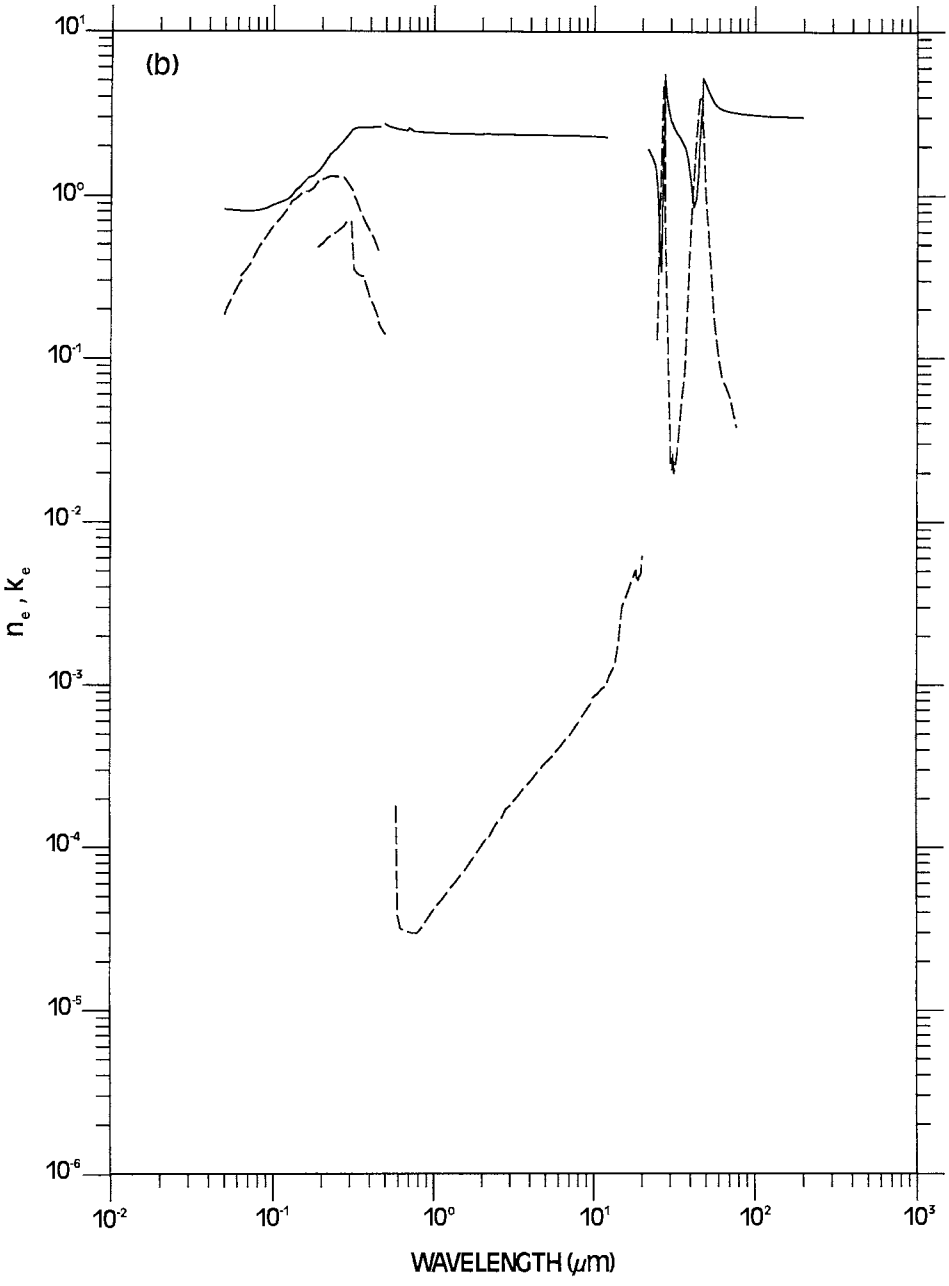

Fig. 2. (b) Log–log plot of n_e (solid line) and k_e (dashed line) versus wavelength in micrometers for silver gallium sulfide ($AgGaS_2$).

TABLE I

Values of n and k for $AgGaSe_2$ Obtained from Various References[a]

eV	cm^{-1}	μm	n	k
25.0	2.016E5	0.04959	0.845 [6]	0.095 [6]
24.0	1.936E5	0.05166	0.835	0.106
23.0	1.855E5	0.05390	0.824	0.119
22.0	1.774E5	0.05636	0.812	0.133
21.0	1.694E5	0.05904	0.799	0.151
20.5	1.653E5	0.06048	0.791	0.160
19.0	1.532E5	0.06358	0.768	0.195
18.0	1.452E5	0.06889	0.748	0.227
17.5	1.411E5	0.07085	0.739	0.248
17.0	1.371E5	0.07293	0.732	0.270
16.0	1.290E5	0.07749	0.721	0.321
15.5	1.250E5	0.07997	0.721	0.345
15.0	1.210E5	0.08266	0.716	0.372
14.5	1.169E5	0.08555	0.715	0.405
14.0	1.129E5	0.08856	0.719	0.437
13.5	1.089E5	0.09184	0.725	0.467
13.0	1.049E5	0.09537	0.730	0.495
12.5	1.008E5	0.09919	0.731	0.527
12.0	9.679E4	0.1033	0.734	0.564
11.5	9.275E4	0.1078	0.739	0.605
11.0	8.872E4	0.1127	0.743	0.643
10.5	8.469E4	0.1181	0.738	0.681
10.0	8.066E4	0.1240	0.731	0.749
9.50	7.662E4	0.1305	0.738	0.852
9.00	7.259E4	0.1378	0.784	0.933
8.50	6.856E4	0.1459	0.825	1.010
8.00	6.452E4	0.1550	0.864	1.097
7.50	6.049E4	0.1653	0.965	1.252
7.00	5.646E4	0.1771	1.146	1.324
6.50	5.243E4	0.1907	1.247	1.311
6.00	4.839E4	0.2066	1.341	1.378
5.50	4.436E4	0.2254	1.493	1.470
5.00	4.032E4	0.2478	1.683	1.553
4.50	3.630E4	0.2755	1.911	1.552
4.00	3.226E4	0.3100	2.175	1.512
3.90	3.146E4	0.3179	2.211	1.501
3.80	3.065E4	0.3263	2.253	1.502
3.70	2.984E4	0.3351	2.298	1.514
3.60	2.904E4	0.3444	2.372	1.543
3.50	2.823E4	0.3542	2.438	1.546
3.40	2.742E4	0.3647	2.602	1.508
3.30	2.662E4	0.3757	2.712	1.442
3.20	2.581E4	0.3874	2.804	1.353
3.10	2.500E4	0.3999	2.868	1.243
3.00	2.420E4	0.4133	2.905	1.141
2.90	2.339E4	0.4275	2.925	1.047

(continued)

[a] References shown in brackets.

TABLE I *(Continued)*

$AgGaSe_2$

eV	cm^{-1}	μm	n	k
2.80	2.258E4	0.4428	2.938	0.964
2.70	2.178E4	0.4592	2.951	0.885
2.60	2.097E4	0.4769	2.952	0.804
2.50	2.016E4	0.4960	2.943	0.732
2.40	1.936E4	0.5166	2.933	0.672
2.30	1.855E4	0.5391	2.927	0.616
2.20	1.774E4	0.5636	2.918	0.563
2.10	1.694E4	0.5904	2.917	0.507
2.00	1.613E4	0.6199	2.905	0.451
1.90	1.532E4	0.6526	2.889	0.400
1.80	1.452E4	0.6888	2.894	0.345
3.02	2.436E4	0.4105		0.247 [10]
2.93	2.363E4	0.4232		0.252
2.84	2.291E4	0.4366		0.257
2.75	2.218E4	0.4509		0.259
2.65	2.137E4	0.4679		0.262
2.55	2.057E4	0.4862		0.259
2.48	2.000E4	0.4999		0.257
2.40	1.936E4	0.5166		0.254
2.33	1.879E4	0.5321		0.245
2.26	1.823E4	0.5486		0.226
2.19	1.766E4	0.5661		0.196
2.14	1.726E4	0.5794		0.186
2.09	1.686E4	0.5932		0.179
2.04	1.645E4	0.6078		0.167
2.00	1.613E4	0.6199		0.142
1.95	1.573E4	0.6358		0.119
1.90	1.532E4	0.6526		0.103
1.85	1.492E4	0.6702		0.088
1.80	1.452E4	0.6888		0.066
1.79	1.444E4	0.6927		0.056
1.78	1.436E4	0.6965		0.041
1.76	1.420E4	0.7045		0.028
1.75	1.412E4	0.7085		0.016
1.74	1.403E4	0.7126		0.011
1.73	1.395E4	0.7167		0.008
2.398	1.934E4	0.517	3.124 [11]	0.276 [11]
2.300	1.855E4	0.539	3.089	0.255
2.218	1.789E4	0.559	3.058	0.219
2.138	1.724E4	0.580	3.028	0.204
2.070	1.669E4	0.599	2.999	0.190
2.009	1.621E4	0.617	2.974	0.168
1.937	1.563E4	0.640	2.943	0.133
1.884	1.520E4	0.658	2.922	0.108
1.829	1.475E4	0.678	2.898	0.084
1.771	1.429E4	0.700	2.872	0.040

TABLE I *(Continued)*

$AgGaSe_2$

eV	cm^{-1}	μm	n	k
1.720	1.387E4	0.721	2.850	0.019
1.676	1.351E4	0.740	2.831	0.001
1.636	1.319E4	0.758	2.812	
1.554	1.253E4	0.798	2.781	
1.481	1.195E4	0.837	2.754	
1.382	1.115E4	0.897	2.727	
1.309	1.056E4	0.947	2.710	
1.216	9.804E3	1.020	2.690	
1.128	9.099E3	1.099	2.674	
1.033	8.333E3	1.200	2.661	
0.9530	7.686E3	1.301	2.651	
0.8856	7.143E3	1.400	2.644	
0.8260	6.662E3	1.501	2.639	
0.7739	6.242E3	1.602	2.634	
0.7280	5.872E3	1.703	2.631	
0.6872	5.543E3	1.804	2.629	
0.6512	5.252E3	1.904	2.625	
0.6199	5.000E3	2.000	2.624	

eV	cm^{-1}	μm	n_o	k_o	n_e	k_e
1.710	1.379E4	0.725	2.8452 [9]		2.8932 [9]	
1.653	1.333E4	0.750	2.8191		2.8415	
1.550	1.250E4	0.800	2.7849		2.7866	
1.459	1.177E4	0.850	2.7598		2.7522	
1.378	1.111E4	0.900	2.7406		2.7275	
1.306	1.053E4	0.950	2.7552		2.7085	
1.240	1.000E4	1.00	2.7132		2.6934	
1.127	9.091E3	1.10	2.6942		2.6712	
1.033	8.333E3	1.20	2.6806		2.6554	
0.9537	7.692E3	1.30	2.6705		2.6438	
0.8856	7.143E3	1.40	2.6624		2.6347	
0.7749	6.250E3	1.60	2.6516		2.6224	
0.6889	5.556E3	1.80	2.6432		2.6131	
0.6119	5.000E3	2.00	2.6376		2.6071	
0.5635	4.545E3	2.20	2.6336		2.6027	
0.5166	4.167E3	2.40	2.6304		2.5992	
0.4768	3.846E3	2.60	2.6286		2.5968	
0.4428	3.571E3	2.80	2.6261		2.5943	
0.4132	3.333E3	3.00	2.6245		2.5925	
0.3875	3.125E3	3.20	2.6231		2.5912	
0.3646	2.941E3	3.40	2.6221		2.5899	
0.3444	2.778E3	3.60	2.6213		2.5889	
0.3263	2.632E3	3.80	2.6200		2.5876	
0.3100	2.500E3	4.00	2.6189		2.5863	
0.2755	2.222E3	4.50	2.6166		2.5840	
0.2480	2.000E3	5.00	2.6144		2.5819	

(continued)

TABLE I *(Continued)*

$AgGaSe_2$

eV	cm^{-1}	μm	n_o	k_o	n_e	k_e
0.2254	1.818E3	5.50	2.6128		2.5800	
0.2067	1.667E3	6.00	2.6113		2.5784	
0.1907	1.538E3	6.50	2.6094		2.5765	
0.1772	1.429E3	7.00	2.6070		2.5743	
0.1653	1.333E3	7.50	2.6049		2.5723	
0.1550	1.250E3	8.00	2.6032		2.5704	
0.1458	1.176E3	8.50	2.6009		2.5681	
0.1377	1.111E3	9.00	2.5988		2.5659	
0.1306	1.053E3	9.50	2.5964		2.5635	
0.1240	1.000E3	10.0	2.5939		2.5608	
0.1181	9.524E2	10.5	2.5917		2.5585	
0.1127	9.091E2	11.0	2.5890		2.5555	
0.1078	8.696E2	11.5	2.5868		2.5536	
0.1033	8.333E2	12.0	2.5837		2.5505	
0.09919	8.000E2	12.5	2.5805		2.5473	
0.09537	7.692E2	13.0	2.5771		2.5439	
0.09184	7.407E2	13.5	2.5731		2.5404	
1.692	1.364E4	0.733		6.5E-06 [13]		1.4E-05 [13]
1.680	1.355E4	0.738		4.0E-06		1.0E-05
1.666	1.344E4	0.744		2.9E-06		5.5E-06
1.655	1.335E4	0.749		2.5E-06		3.7E-06
1.644	1.326E4	0.754		2.3E-06		2.9E-06
1.631	1.316E4	0.760		2.2E-06		2.5E-06
1.606	1.295E4	0.772		2.1E-06		2.2E-06
1.581	1.276E4	0.784		2.1E-06		2.0E-06
1.560	1.258E4	0.795		2.0E-06		2.0E-06
1.538	1.241E4	0.806		2.0E-06		1.9E-06
1.518	1.224E4	0.817		2.0E-06		1.9E-06
1.496	1.206E4	0.829		2.0E-06		1.8E-06
1.474	1.189E4	0.841		2.0E-06		1.8E-06
1.325	1.068E4	0.936		1.8E-06		1.7E-06
1.204	9.709E3	1.03		1.8E-06		1.7E-06
1.159	9.346E3	1.07		1.8E-06		1.8E-06
1.097	8.850E3	1.13		1.8E-06		1.9E-06
1.060	8.547E3	1.17		1.9E-06		2.3E-06
1.016	8.197E3	1.22		1.9E-06		2.7E-06
0.9763	7.874E3	1.27		2.0E-06		3.0E-06
0.9465	7.634E3	1.31		2.0E-06		3.1E-06
0.9117	7.353E3	1.36		2.0E-06		3.0E-06
0.8793	7.092E3	1.41		2.1E-06		2.7E-06
0.8551	6.897E3	1.45		2.2E-06		2.5E-06
0.8266	6.667E3	1.50		2.2E-06		2.4E-06
0.7749	6.250E3	1.60		2.3E-06		2.4E-06
0.7336	5.917E3	1.69		2.4E-06		2.4E-06
0.6966	5.618E3	1.78		2.5E-06		2.6E-06
0.6595	5.319E3	1.88		2.6E-06		2.8E-06

TABLE I *(Continued)*

$AgGaSe_2$

eV	cm^{-1}	μm	n_o	k_o	n_e	k_e
0.6274	5.076E3	1.97		2.8E-06		3.2E-06
0.5990	4.831E3	2.07		2.9E-06		3.6E-06
0.5713	4.608E3	2.17		3.1E-06		3.9E-06
0.5367	4.329E3	2.31		3.4E-06		4.0E-06
0.5166	4.167E3	2.40		3.5E-06		3.9E-06
0.4959	4.000E3	2.50		3.7E-06		3.8E-06
0.4787	3.861E3	2.59		3.8E-06		3.8E-06
46.00E-3	371	26.95	2.348 [14]		2.420 [14]	
44.76E-3	361	27.70	2.317	0.118 [14]	2.389	
43.52E-3	351	28.49	2.280	0.102	2.354	
42.28E-3	341	29.33	2.247	0.100	2.307	
41.04E-3	331	30.21	2.191	0.122	2.277	
39.80E-3	321	31.15	2.114	0.137	2.201	
38.56E-3	311	32.15	2.024	0.141	2.107	
37.32E-3	301	33.22	1.870	0.159	1.961	
36.08E-3	291	34.36	1.697	0.188	1.784	0.073 [14]
34.72E-3	280	35.71	1.351	0.269	1.389	0.145
33.48E-3	270	37.04	0.544	0.913	0.488	0.658
32.36E-3	261	38.31	0.528	2.410	0.422	2.150
31.12E-3	251	39.84	1.826	4.744	1.519	5.197
30.87E-3	249	40.16	3.655	5.637	4.264	6.776
30.50E-3	246	40.65	6.862	5.770	7.291	4.945
30.00E-3	242	41.32	6.850	2.657	5.912	1.982
29.88E-3	241	41.49	6.124	1.403	5.324	0.572
28.64E-3	231	43.29	4.226	0.282	3.960	0.171
27.40E-3	221	45.25	3.690	0.132	3.425	0.093
26.04E-3	210	47.62	3.361	0.110	3.135	0.109
24.80E-3	200	50.00	3.169	0.112	2.879	0.138
23.56E-3	190	52.63	3.054	0.120	2.639	0.205
22.19E-3	179	55.87	2.935	0.126	2.376	0.342
21.08E-3	170	58.82	2.748	0.229	1.911	0.741
20.33E-3	164	60.98	2.642	0.456	1.854	1.115
19.84E-3	160	62.50	2.747	0.752	1.928	1.746
19.09E-3	154	64.94	3.225	0.613	2.644	2.591
18.47E-3	149	67.11	3.133	0.381	3.341	2.621
17.73E-3	143	69.93	2.872	0.317	4.493	1.784
17.36E-3	140	71.43	2.744	0.408	4.523	1.160
16.61E-3	134	74.63	2.799	0.959	4.348	0.723
16.12E-3	130	76.92	3.541	0.550	4.192	0.501
14.88E-3	120	83.33	3.304	0.152	3.926	0.280
13.64E-3	110	90.91	3.135	0.127	3.730	0.158
12.40E-3	100	100.0	3.053	0.123	3.581	0.095
11.16E-3	90.0	111.1	2.969	0.113	3.497	
9.919E-3	80.0	125.0	3.095	0.335	3.444	
8.679E-3	70.0	142.9	3.119	0.088	3.387	
7.439E-3	60.0	166.7	3.051	0.064	3.349	

(continued)

TABLE I *(Continued)*

$AgGaSe_2$

eV	cm^{-1}	μm	n_o	k_o	n_e	k_e
6.199E-3	50.0	200.0	3.028	0.047	3.317	
4.959E-3	40.0	250.0	3.005		3.298	
3.720E-3	30.0	333.3	2.988		3.285	
2.480E-3	20.0	500.0	2.971		3.260	

TABLE II

Values of n and k for $AgGaS_2$ Obtained from Various References[a]

eV	cm^{-1}	μm	n	k
25.0	2.016E5	0.04959	0.827 [6]	0.185 [6]
24.0	1.936E5	0.05166	0.822	0.206
23.0	1.855E5	0.05390	0.822	0.222
22.0	1.774E5	0.05636	0.816	0.245
21.0	1.694E5	0.05904	0.815	0.264
20.0	1.613E5	0.06199	0.810	0.291
19.5	1.573E5	0.06358	0.807	0.306
19.0	1.532E5	0.06226	0.805	0.321
18.5	1.492E5	0.06702	0.803	0.341
18.0	1.452E5	0.06889	0.805	0.360
17.5	1.411E5	0.07085	0.807	0.374
17.0	1.371E5	0.07293	0.805	0.396
16.5	1.331E5	0.07514	0.808	0.416
16.0	1.290E5	0.07749	0.810	0.439
15.5	1.250E5	0.08000	0.813	0.464
15.0	1.210E5	0.08266	0.819	0.491
14.5	1.169E5	0.08555	0.826	0.515
14.0	1.129E5	0.08856	0.832	0.545
13.5	1.089E5	0.09184	0.842	0.577
13.0	1.049E5	0.09537	0.858	0.610
12.5	1.009E5	0.09919	0.874	0.637
12.0	9.679E4	0.1033	0.886	0.669
11.6	9.356E4	0.1069	0.900	0.698
11.0	8.872E4	0.1127	0.917	0.742
10.5	8.469E4	0.1181	0.934	0.790
10.0	8.066E4	0.1240	0.958	0.846
9.50	7.662E4	0.1305	1.008	0.925
9.00	7.259E4	0.1378	1.083	0.955
8.50	6.856E4	0.1459	1.126	1.007
8.00	6.452E4	0.1550	1.213	1.063
7.50	6.049E4	0.1653	1.292	1.058
7.00	5.646E4	0.1771	1.317	1.110
6.50	5.243E4	0.1907	1.415	1.240
6.00	4.839E4	0.2066	1.564	1.266

[a] References given in brackets.

TABLE II *(Continued)*

$AgGaS_2$

eV	cm^{-1}	μm	n	k
5.50	4.436E4	0.2254	1.784	1.314
5.00	4.033E4	0.2478	1.939	1.305
4.50	3.630E4	0.2755	2.173	1.283
4.00	3.226E4	0.3100	2.515	1.080
3.90	3.146E4	0.3179	2.542	1.006
3.80	3.065E4	0.3263	2.569	0.944
3.70	2.984E4	0.3351	2.578	0.875
3.60	2.904E4	0.3444	2.590	0.820
3.50	2.823E4	0.3542	2.589	0.766
3.40	2.742E4	0.3647	2.590	0.717
3.30	2.662E4	0.3757	2.587	0.672
3.20	2.581E4	0.3874	2.586	0.634
3.10	2.500E4	0.3999	2.586	0.600
3.00	2.420E4	0.4133	2.597	0.566
2.90	2.339E4	0.4275	2.609	0.518
2.80	2.258E4	0.4428	2.601	0.468
2.75	2.218E4	0.4509	2.601	0.450
2.70	2.178E4	0.4592	2.606	0.429
6.54	5.275E4	0.1896		0.479 [23]
6.29	5.073E4	0.1971		0.496
6.06	4.888E4	0.2046		0.510
5.80	4.678E4	0.2138		0.539
5.55	4.476E4	0.2234		0.559
5.31	4.283E4	0.2335		0.569
5.05	4.073E4	0.2455		0.590
4.80	3.871E4	0.2583		0.620
4.56	3.678E4	0.2719		0.643
4.32	3.484E4	0.2870		0.693
4.06	3.275E4	0.3054		0.687
3.91	3.154E4	0.3171		0.350
3.71	2.992E4	0.3342		0.329
3.51	2.831E4	0.3532		0.320
3.41	2.750E4	0.3636		0.320
3.32	2.678E4	0.3735		0.291
3.20	2.581E4	0.3875		0.258
3.11	2.508E4	0.3987		0.235
2.90	2.339E4	0.4275		0.208
2.70	2.178E4	0.4592		0.158
2.50	2.016E4	0.4959		0.141

eV	cm^{-1}	μm	n_o	k_o	n_e	k_e
2.531	2.041E4	0.490	2.7148 [24]		2.7287 [24]	
2.480	2.000E4	0.500	2.6916		2.6867	
2.362	1.905E4	0.525	2.6503		2.6239	
2.254	1.818E4	0.550	2.6190		2.5834	
2.156	1.739E4	0.575	2.5944		2.5537	

(continued)

TABLE II *(Continued)*

$AgGaS_2$

eV	cm^{-1}	μm	n_o	k_o	n_e	k_e
2.067	1.667E4	0.600	2.5748		2.5303	
1.984	1.600E4	0.625	2.5577		2.5116	
1.908	1.539E4	0.650	2.5437		2.4961	
1.837	1.482E4	0.675	2.5310		2.4824	
1.772	1.429E4	0.700	2.5205		2.5706	
1.653	1.333E4	0.750	2.5049		2.4540	
1.550	1.250E4	0.800	2.4909		2.4395	
1.459	1.177E4	0.850	2.4802		2.4279	
1.377	1.111E4	0.900	2.4716		2.4192	
1.306	1.053E4	0.950	2.4644		2.4118	
1.240	1.000E4	1.00	2.4582		2.4053	
1.127	9.091E3	1.10	2.4486		2.3954	
1.033	8.333E3	1.20	2.4414		2.3881	
0.9537	7.692E3	1.30	2.4359		2.3819	
0.8856	7.143E3	1.40	2.4315		2.3781	
0.8266	6.667E3	1.50	2.4280		2.3745	
0.7749	6.250E3	1.60	2.4252		2.3716	
0.6889	5.556E3	1.80	2.4206		2.3670	
0.6199	5.000E3	2.00	2.4164		2.3637	
0.5635	4.545E3	2.20	2.4161		2.3684	
0.5166	4.167E3	2.40	2.4119		2.3583	
0.4768	3.846E3	2.60	2.4102		2.3567	
0.4428	3.571E3	2.80	2.4094		2.3559	
0.4132	3.333E3	3.00	2.4080		2.3545	
0.3875	3.125E3	3.20	2.4068		2.3534	
0.3646	2.941E3	3.40	2.4062		2.3522	
0.3444	2.778E3	3.60	2.4046		2.3511	
0.3263	2.632E3	3.80	2.4024		2.3491	
0.3100	2.500E3	4.00	2.4024		2.3488	
0.2755	2.222E3	4.50	2.4003		2.3461	
0.2480	2.000E3	5.00	2.3955		2.3419	
0.2254	1.818E3	5.50	2.3938		2.3401	
0.2067	1.667E3	6.00	2.3908		2.3369	
0.1907	1.538E3	6.50	2.3874		2.3334	
0.1772	1.429E3	7.00	2.3827		2.3291	
0.1653	1.333E3	7.50	2.3787		2.3252	
0.1550	1.250E3	8.00	2.3757		2.3219	
0.1458	1.176E3	8.50	2.3699		2.3163	
0.1377	1.111E3	9.00	2.3663		2.3121	
0.1306	1.053E3	9.50	2.3606		2.3064	
0.1240	1.000E3	10.0	2.3548		2.3012	
0.1181	9.524E2	10.5	2.3486		2.2948	
0.1127	9.091E2	11.0	2.3417		2.2880	
0.1078	8.696E2	11.5	2.3329		2.2789	
0.1033	8.333E2	12.0	2.3266		2.2716	
0.09919	8.000E2	12.5	2.3177			
0.09537	7.692E2	13.0	2.3076			

TABLE II *(Continued)*

$AgGaS_2$

eV	cm^{-1}	μm	n_o	k_o	n_e	k_e
2.522	2.034E4	0.4916	2.700 [25]		2.710 [25]	
2.472	1.994E4	0.5016	2.683		2.676	
2.270	1.831E4	0.5461	2.619		2.585	
2.145	1.730E4	0.5780	2.587		2.546	
2.110	1.702E4	0.5876	2.579		2.537	
1.857	1.498E4	0.6678	2.529		2.481	
2.234	1.802E4	0.555		8.6E-05 [26]		
2.175	1.754E4	0.570		3.3E-05		
2.112	1.704E4	0.587		3.1E-05		1.8E-04 [26]
2.070	1.669E4	0.599		3.1E-05		3.9E-05
1.990	1.605E4	0.623		3.0E-05		3.2E-05
1.887	1.522E4	0.657		3.0E-05		3.1E-05
1.705	1.376E4	0.727		3.0E-05		3.0E-05
1.556	1.255E4	0.797		3.0E-05		3.0E-05
1.425	1.149E4	0.870		3.3E-05		3.3E-05
1.328	1.071E4	0.934		3.7E-05		3.7E-05
1.241	1.001E4	0.999		4.1E-05		4.1E-05
1.042	8.403E3	1.19		5.1E-05		5.1E-05
0.8920	7.194E3	1.39		6.2E-05		6.2E-05
0.7897	6.369E3	1.57		7.2E-05		7.2E-05
0.7045	5.682E3	1.76		8.5E-05		8.5E-05
0.6424	5.181E3	1.93		9.6E-05		9.6E-05
0.5904	4.762E3	2.10		1.1E-04		1.1E-04
0.5414	4.367E3	2.29		1.2E-04		1.2E-04
0.5020	4.049E3	2.47		1.4E-04		1.4E-04
0.4643	3.745E3	2.67		1.5E-04		1.5E-04
0.4382	3.534E3	2.83		1.7E-04		1.7E-04
0.4119	3.322E3	3.01		1.8E-04		1.8E-04
0.4092	3.300E3	3.03		1.8E-04		1.8E-04
0.3397	2.740E3	3.65		2.3E-04		2.3E-04
0.2931	2.364E3	4.23		2.7E-04		2.7E-04
0.2545	2.053E3	4.87		3.2E-04		3.2E-04
0.2266	1.828E3	5.47		3.6E-04		3.6E-04
0.2030	1.637E3	6.11		4.1E-04		4.1E-04
0.1851	1.493E3	6.70		4.6E-04		4.6E-04
0.1694	1.366E3	7.32		5.0E-04		5.1E-04
0.1566	1.263E3	7.92		5.5E-04		5.7E-04
0.1461	1.178E3	8.49		6.0E-04		6.3E-04
0.1364	1.100E3	9.09		6.5E-04		7.0E-04
0.1292	1.042E3	9.60		7.0E-04		7.7E-04
0.1252	1.010E3	9.90		7.4E-04		8.3E-04
0.1042	8.403E2	11.9		9.6E-04		1.0E-03
0.09184	7.407E2	13.5		1.3E-03		1.3E-03
0.08670	6.993E2	14.3		1.8E-03		1.8E-03

(continued)

TABLE II *(Continued)*

$AgGaS_2$

eV	cm^{-1}	μm	n_o	k_o	n_e	k_e
0.08266	6.667E2	15.0		3.0E-03		3.0E-03
0.07005	5.650E2	17.7		4.7E-03		
0.06927	5.587E2	17.9		3.3E-03		
0.06739	5.435E2	18.4		3.4E-03		5.1E-03
0.06595	5.319E2	18.8		3.5E-03		4.3E-03
0.06457	5.208E2	19.2		3.8E-03		4.6E-03
0.06293	5.076E2	19.7		3.9E-03		4.8E-03
0.06168	4.975E2	20.1		3.9E-03		6.2E-03
0.05990	4.831E2	20.7		4.9E-03		
0.05932	4.785E2	20.9		8.7E-03		
57.41E-3	463	21.60	1.875 [28]		1.931 [28]	
56.28E-3	454	22.03	1.826		1.870	
55.05E-3	444	22.52	1.759		1.792	
53.81E-3	434	23.04	1.665		1.721	
52.45E-3	423	23.64	1.522		1.591	
51.21E-3	413	24.21	1.319		1.439	
49.84E-3	402	24.88	1.010	0.152 [28]	1.112	0.131 [28]
48.73E-3	393	25.45	0.471	0.475	0.568	0.554
47.36E-3	382	26.18	0.237	1.507	0.340	1.838
46.12E-3	372	26.88	1.721	3.329	1.819	4.605
45.75E-3	369	27.10	3.029	4.177	2.063	4.645
45.13E-3	364	27.47	3.810	1.513	5.526	3.417
45.01E-3	363	27.55	3.674	0.546	5.185	0.870
43.77E-3	353	28.33	0.988	1.082	3.868	0.257
42.40E-3	342	29.24	0.605	2.250	3.200	0.079
41.16E-3	332	30.12	1.398	4.421	2.856	0.023
40.17E-3	324	30.86	3.580	6.061	2.696	0.021
39.92E-3	322	31.06	5.690	5.554	2.625	0.026
39.30E-3	317	31.55	6.652	2.394	2.550	0.020
38.81E-3	313	31.95	5.846	0.866	2.498	0.021
37.69E-3	304	32.89	4.408	0.246	2.377	0.026
36.33E-3	293	34.13	3.721	0.139	2.268	0.038
34.96E-3	282	35.46	3.362	0.134	2.100	0.058
33.72E-3	272	36.76	3.059	0.125	1.969	0.083
32.48E-3	262	38.17	2.842	0.126	1.694	0.198
31.24E-3	252	39.68	2.617	0.172	1.305	0.504
29.88E-3	241	41.49	2.345	0.374	0.855	1.227
28.76E-3	232	43.10	2.060	1.090	0.964	2.216
27.77E-3	224	44.64	2.550	1.947	1.416	3.374
27.52E-3	222	45.05	3.195	1.850	2.013	3.831
26.53E-3	214	46.73	3.897	1.020	3.419	4.050
26.16E-3	211	47.39	3.801	0.637	5.216	2.657
24.92E-3	201	49.75	3.502	0.364	4.695	0.912
23.56E-3	190	52.63	3.091	0.358	4.110	0.435
22.32E-3	180	55.56	2.938	0.437	3.679	0.187
21.08E-3	170	58.82	2.915	0.619	3.458	0.111

TABLE II *(Continued)*

$AgGaS_2$

eV	cm^{-1}	μm	n_o	k_o	n_e	k_e
19.84E-3	160	62.50	3.048	0.754	3.353	0.077
18.60E-3	150	66.67	3.332	0.723	3.292	0.065
17.48E-3	141	70.92	3.473	0.546	3.241	0.056
16.12E-3	130	76.92	3.482	0.345	3.193	0.038
14.88E-3	120	83.33	3.454	0.203	3.153	
13.64E-3	110	90.91	3.420	0.135	3.129	
12.40E-3	100	100.0	3.373	0.136	3.104	
11.16E-3	90	111.1	3.333		3.069	
9.919E-3	80	125.0	3.300		3.051	
8.679E-3	70	142.9	3.276		3.048	
7.439E-3	60	166.7	3.248		3.031	
6.323E-3	51	196.1	3.230		3.017	

Zinc Arsenide (Zn_3As_2)

J. MISIEWICZ and K. JEZIERSKI
Institute of Physics
Technical University of Wroclaw
Wroclaw, Poland

Zinc arsenide, Zn_3As_2, is a member of the II–V group of semiconducting compounds [1]. It posseses a tetragonal unit cell described by $I4_1cd \equiv C_{4v}^{12}$ symmetry. Optical properties of this material are not intensively studied, mainly because of the relatively high and temperature-independent concentration of holes in the range of $10^{17}cm^{-3}$, which results in a very limited range of possible applications of Zn_3As_2 in semiconductor devices.

Infrared optical processes are dominated by strong absorption when the photon energy decreases below 0.8 eV [2]. Within this energy region there are very intense intraband and defect-related transitions observed even at 5 K by Sujak-Cyrul *et al.* [3]. Within the 0.9–1 eV energy range, a strong increase of absorption connected with the fundamental absorption edge is observed by Misiewicz and Pawlikowski [2]. Above an energy of 1 eV, absorption was investigated only on polycrystalline thin films [4]. Żdanowicz and Pawlikowski [5] determined a refractive index equal to 3.85 from interference fringes observed in transmission spectra for polycrystalline Zn_3As_2 thin films within the wavelength range 3–20 μm. The values of extinction coefficient given in Table I for energies smaller than 1.5 eV are derived directly from the absorption coefficient determined by means of transmission measurements [2–4].

The reflectivity spectrum for Zn_3As_2 measured within the energy range 1–5 eV is presented elsewhere [6]. The high-energy spectrum up to 12 eV was published by Sobolev *et al.* [7]. Zivitz and Stevenson [8] presented reflectivity obtained by using a glow-discharge lamp source (up to 20 eV) and a synchrotron radiation source (up to 30 eV) utilizing polycrystal samples. These spectra covered the whole energy range from 1 eV up to 30 eV, and from them one spectrum was constructed in order to perform the Kramers–Kronig analysis. It was necessary to reject the reflectivity data for the synchrotron-radiation source, because for these data negative values of the extinction coefficient for high energies were obtained. Therefore, the values

HANDBOOK OF OPTICAL CONSTANTS OF SOLIDS III

Copyright © 1998 by Academic Press.
All rights of reproduction in any form reserved
ISBN 0-12-544423-0/$25.00.

of n and k given in Table I covered the energy range up to 20 eV. In the Kramers–Kronig calculations [9] the values of extinction coefficient below 1.5 eV were assumed to be equal to those known from the experiment [2–4]. The spectra of n and k for unpolarized light over a wide spectral range are presented in Fig. 1.

The measured optical spectra of Zn_3As_2 showed anisotropy, which was observed by Misiewicz *et al.* for the fundamental absorption edge [10] and in the reflectivity spectra within the visible and ultraviolet energy range [11]. The measurements were performed at room temperature by using x-ray oriented Zn_3As_2 single crystals obtained from a gas-transport growth method. The double grating Carl-Zeiss GDM-1000 monochromator equipped with linear polarizers from Carl-Zeiss and a Hamamatsu photomultiplier were utilized. Within the 0.9–1.0 eV energy range, a HgCdTe-based detector was used. The determined values of n_e, n_o and k_e, k_o are also included in Table I and presented in Figs. 2 and 3.

REFERENCES

1. E. K. Arushanov, *Prog. Cryst. Growth Charact.* **25**, 131 (1992).
2. J. Misiewicz and J. M. Pawlikowski, *Solid State Commun.* **32**, 687 (1979).
3. B. Sujak-Cyrul, B. Kolodka, J. Misiewicz, and J. M. Pawlikowski, *J. Phys. Chem. Solids* **43**, 1045 (1982).
4. B. Kołodka, J. Misiewicz, and J. M. Pawlikowski, *Acta Phys. Pol.* **A62**, 63 (1982).
5. W. Żdanowicz and J. M. Pawlikowski, *Acta Phys. Pol.* **A38**, 11 (1970).
6. J. Misiewicz, J. Wróbel, B. Sujak-Cyrul, and F. Królicki, *Opt. Appl.* **10**, 75 (1980).
7. V. V. Sobolev, N. N. Syrbu, T.A. Zjubina, and I. A. Ugai, *Fiz. Tekh. Poluprovadn. (Leningrad.)* **5**, 327 (1971).
8. M. Zivitz and J. R. Stevenson, *Phys. Rev. B* **10**, 2457 (1974).
9. K. Jezierski, *J. Phys. C: Solid State Phys.* **17**, 475 (1984).
10. J. Misiewicz, J. M. Wróbel, and K. Jezierski, *Solid State Commun.* **86**, 509 (1993).
11. J. Misiewicz, J. Wróbel, and K. Jezierski, *J. Phys. C: Solid State Phys.* **17**, 3091 (1984).

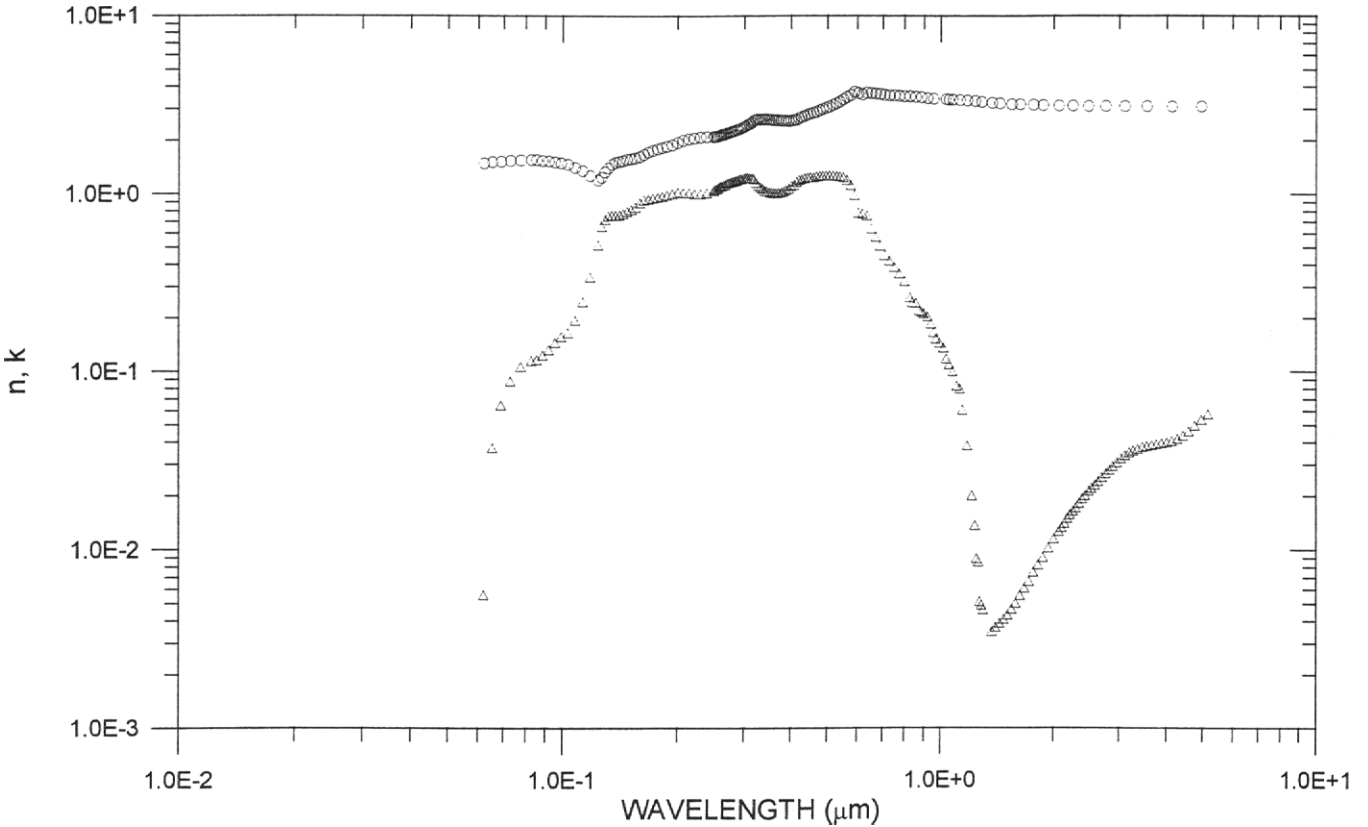

Fig. 1. Log–log plot of n (circles) and k (triangles) versus wavelength in micrometers for zinc arsenide (Zn_3As_2). Data are for unpolarized light for monocrystal samples [2, 6–8] and for polycrystal samples [4].

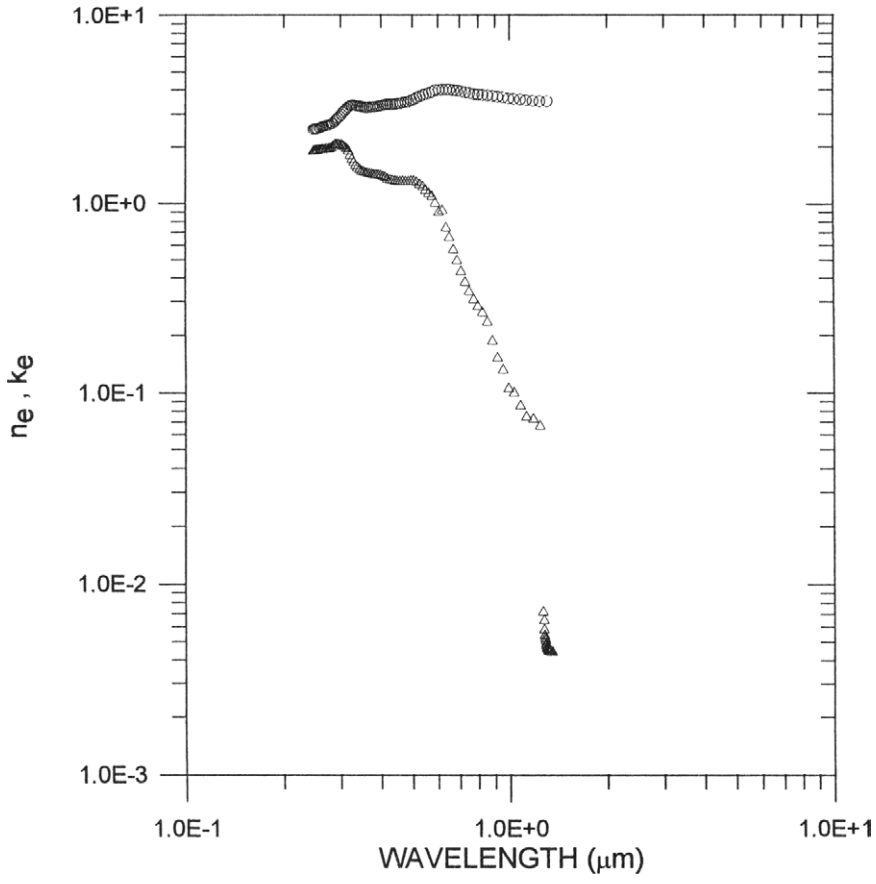

Fig. 2. Log–log plot of n_e (circles) and k_e (triangles) versus wavelength in micrometers for zinc arsenide (Zn_3As_2).

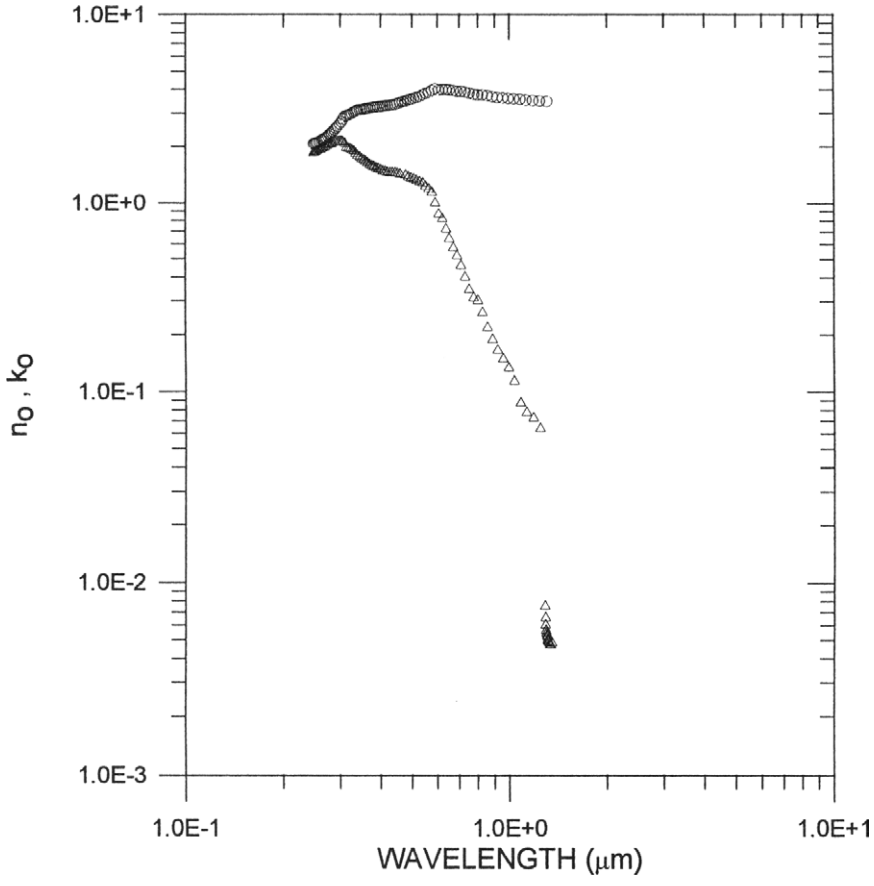

Fig. 3. Log–log plot of n_o (circles) and k_o (triangles) versus wavelength in micrometers for zinc arsenide (Zn_3As_2).

TABLE I

Values of n and k Obtained from Various References for Zinc Arsenide[a]

eV	cm^{-1}	μm	n	k
20	161,300	0.06199	1.4921 [8]	0.0056 [8]
19	153,200	0.06526	1.51	0.0372
18	145,200	0.06888	1.522	0.0646
17	137,100	0.07293	1.537	0.0885
16	129,000	0.07749	1.552	0.107
15	121,000	0.08266	1.562	0.115
14.5	116,900	0.08551	1.554	0.117
14	112,900	0.08856	1.544	0.124
13.5	108,900	0.09184	1.53	0.133
13	104,900	0.09537	1.514	0.146
12.5	100,800	0.09919	1.497	0.157
12	96,780	0.1033	1.466	0.165
11.5	92,750	0.1078	1.408	0.195
11	88,720	0.1127	1.351	0.248
10.5	84,690	0.1181	1.271	0.341
10	80,650	0.1240	1.199 [7]	0.516 [7]
9.8	79,040	0.1265	1.238	0.658
9.6	77,430	0.1292	1.331	0.718
9.4	75,810	0.1319	1.401	0.753
9.2	74,200	0.1348	1.467	0.763
9	72,590	0.1378	1.505	0.758
8.8	70,980	0.1409	1.526	0.761
8.6	69,360	0.1442	1.544	0.776
8.4	67,750	0.1476	1.564	0.796
8.2	66,140	0.1512	1.582	0.816

8	64,520	0.1550	1.594	0.843				
7.8	62,910	0.1590	1.626	0.89				
7.6	61,300	0.1631	1.674	0.922				
7.4	59,680	0.1675	1.723	0.938				
7.2	58,070	0.1722	1.764	0.945				
7	56,460	0.1771	1.796	0.955				
6.8	54,850	0.1823	1.829	0.97				
6.6	53,230	0.1879	1.862	0.985				
6.4	51,620	0.1937	1.898	1.005				
6.2	50,010	0.2000	1.952	1.023				
6	48,390	0.2066	2.002	1.018				
5.8	46,780	0.2138	2.039	1.012				
5.6	45,170	0.2214	2.066	1.004				
5.4	43,550	0.2296	2.087	1.006				
5.2	41,940	0.2384	2.099	1.012				
eV	cm^{-1}	μm	n_e	k_e	n_o	k_o	n	k
5	40,330	0.2480	2.49 [11]	1.931 [11]	2.072 [11]	1.885 [11]	2.105 [6]	1.048 [6]
4.95	39,920	0.2505	2.495	1.937	2.077	1.896	2.116	1.062
4.9	39,520	0.2530	2.503	1.943	2.087	1.918	2.117	1.068
4.85	39,120	0.2556	2.511	1.948	2.102	1.935	2.123	1.091
4.8	38,710	0.2583	2.526	1.959	2.12	1.958	2.144	1.106
4.75	38,310	0.2610	2.544	1.963	2.144	1.976	2.161	1.111
4.7	37,910	0.2638	2.56	1.967	2.167	1.993	2.171	1.119
4.65	37,500	0.2666	2.577	1.971	2.191	2.011	2.177	1.129
4.6	37,100	0.2695	2.595	1.975	2.218	2.029	2.197	1.152
4.55	36,700	0.2725	2.614	1.978	2.243	2.047	2.219	1.161

(continued)

[a] References given in brackets.

TABLE I *(Continued)*

Zinc Arsenide

eV	cm^{-1}	μm	n_e	k_e	n_o	k_o	n	k
4.5	36,290	0.2755	2.627	1.983	2.279	2.077	2.241	1.17
4.45	35,890	0.2786	2.639	1.994	2.323	2.09	2.259	1.174
4.4	35,490	0.2818	2.66	2.019	2.359	2.108	2.279	1.184
4.35	35,080	0.2850	2.687	2.042	2.4	2.126	2.297	1.189
4.3	34,680	0.2883	2.736	2.077	2.453	2.15	2.314	1.201
4.25	34,280	0.2917	2.802	2.093	2.515	2.16	2.339	1.215
4.2	33,880	0.2952	2.863	2.087	2.571	2.163	2.367	1.222
4.15	33,470	0.2988	2.916	2.082	2.631	2.171	2.394	1.229
4.1	33,070	0.3024	2.99	2.086	2.712	2.176	2.429	1.239
4.05	32,660	0.3061	3.064	2.055	2.789	2.149	2.467	1.239
4	32,260	0.3100	3.126	2.024	2.881	2.114	2.503	1.233
3.95	31,860	0.3139	3.193	1.989	2.921	2.016	2.535	1.229
3.9	31,460	0.3179	3.274	1.935	2.93	1.998	2.6	1.219
3.85	31,050	0.3220	3.329	1.839	2.965	1.978	2.636	1.159
3.8	30,650	0.3263	3.339	1.751	3.002	1.949	2.639	1.122
3.75	30,250	0.3306	3.335	1.682	3.047	1.924	2.636	1.097
3.7	29,840	0.3351	3.327	1.625	3.084	1.874	2.648	1.078
3.65	29,440	0.3397	3.306	1.576	3.106	1.828	2.64	1.048
3.6	29,040	0.3444	3.3	1.548	3.124	1.792	2.638	1.041
3.55	28,630	0.3493	3.28	1.509	3.138	1.758	2.632	1.027
3.5	28,230	0.3542	3.268	1.497	3.154	1.73	2.627	1.022
3.45	27,830	0.3594	3.26	1.482	3.172	1.702	2.623	1.017
3.4	27,420	0.3647	3.255	1.475	3.188	1.673	2.614	1.015
3.35	27,020	0.3701	3.261	1.47	3.203	1.644	2.609	1.02
3.3	26,620	0.3757	3.263	1.458	3.212	1.619	2.601	1.027
3.25	26,210	0.3815	3.267	1.454	3.228	1.598	2.595	1.041

3.2	25,810	0.3875	3.285	1.452	3.237	1.572	2.597	1.058
3.15	25,410	0.3936	3.298	1.44	3.247	1.554	2.587	1.075
3.1	25,000	0.4000	3.32	1.434	3.26	1.535	2.606	1.112
3.05	24,600	0.4065	3.34	1.417	3.269	1.518	2.609	1.128
3	24,200	0.4133	3.36	1.4	3.285	1.505	2.634	1.177
2.95	23,790	0.4203	3.373	1.375	3.296	1.486	2.677	1.207
2.9	23,390	0.4275	3.379	1.359	3.302	1.481	2.718	1.22
2.85	22,990	0.4350	3.388	1.349	3.325	1.485	2.751	1.231
2.8	22,580	0.4428	3.4	1.338	3.35	1.477	2.801	1.249
2.75	22,180	0.4509	3.409	1.329	3.382	1.473	2.843	1.244
2.7	21,780	0.4592	3.421	1.33	3.411	1.46	2.874	1.248
2.65	21,370	0.4679	3.443	1.333	3.446	3.453	2.909	1.258
2.6	20,970	0.4769	3.47	1.332	3.49	1.439	2.955	1.271
2.55	20,570	0.4862	3.496	1.332	3.529	1.414	3.007	1.277
2.5	20,160	0.4959	3.541	1.338	3.566	1.392	3.058	1.275
2.45	19,760	0.5061	3.585	1.333	3.601	1.37	3.106	1.276
2.4	19,360	0.5166	3.656	1.326	3.644	1.353	3.174	1.281
2.35	18,950	0.5276	3.716	1.287	3.69	1.331	3.237	1.268
2.3	18,550	0.5391	3.773	1.25	3.752	1.305	3.312	1.265
2.25	18,150	0.5510	3.823	1.201	3.814	1.262	3.402	1.249
2.2	17,740	0.5636	3.869	1.156	3.871	1.221	3.514	1.205
2.15	17,340	0.5767	3.924	1.111	3.973	1.168	3.598	1.129
2.1	16,940	0.5904	4.001	1.027	4.043	1.019	3.738	0.993
2.05	16,530	0.6048	4.015	0.915	3.993	0.888	3.676	0.786
2	16,130	0.6199	4.029	0.939	4.018	0.837	3.616	0.779
1.95	15,730	0.6358	4.03	0.757	4.016	0.736	3.688	0.761
1.9	15,320	0.6526	4.041	0.672	3.992	0.653	3.677	0.641
1.85	14,920	0.6702	4.018	0.576	3.961	0.584	3.65	0.576

(continued)

TABLE I *(Continued)*

Zinc Arsenide

eV	cm^{-1}	μm	n_e	k_e	n_o	k_o	n	k
1.8	14,520	0.6888	3.984	0.504	3.934	0.529	3.641	0.513
1.75	14,110	0.7085	3.947	0.441	3.919	0.47	3.6	0.454
1.7	13,710	0.7293	3.907	0.388	3.882	0.409	3.579	0.423
1.65	13,310	0.7514	3.864	0.346	3.853	0.352	3.559	0.389
1.6	12,900	0.7749	3.829	0.314	3.788	0.319	3.547	0.359
1.55	12,500	0.7999	3.793	0.289	3.77	0.309	3.535	0.325
1.5	12,100	0.8266	3.777	0.268	3.757	0.266	3.523	0.263 [4]
1.48	11,940	0.8377						0.247
1.45	11,690	0.8551	3.761	0.239	3.724	0.223	3.51	0.245
1.42	11,450	0.8731						0.222
1.4	11,290	0.8856	3.748	0.19	3.689	0.193	3.499	0.218
1.38	11,130	0.8984						0.214
1.35	10,890	0.9184	3.693	0.155	3.653	0.17	3.458	0.205
1.32	10,650	0.9393						0.187
1.3	10,480	0.9537	3.676	0.134	3.626	0.152	3.432	0.167
1.28	10,320	0.9686						0.154
1.25	10,080	0.9919	3.63	0.1071	3.599	0.136		0.146
1.22	9,840	1.016						0.137
1.2	9,678	1.033	3.602	0.102	3.582	0.116	3.399	0.119
1.18	9,517	1.051					3.392	0.11
1.15	9,275	1.078	3.584	0.087	3.556	0.089	3.38	0.101
1.12	9,033	1.107						8.37E-2
1.1	8,870	1.127	3.547	0.076	3.52	0.079	3.368	8.07E-2
1.08	8,711	1.148						6.12E-2
1.05	8,469	1.181	3.529	0.074	3.502	0.074	3.352	3.85E-2
1.02	8,227	1.216						2.03E-2

1	8,005	1.240	3.511	0.068	3.484	0.065	3.317	1.38E-2 [2]
0.99	7,985	1.252						8.97E-3
0.98	7,904	1.265		7.3E-3 [10]				8.63E-3
0.975	7,864	1.272		6.58E-3				
0.9725	7,844	1.275		5.88E-3				
0.97	7,824	1.278		5.49E-3				5.19E-3
0.9675	7,803	1.282		5.30E-3				
0.965	7,783	1.285		5.16E-3		7.7E-3 [10]		
0.9625	7,763	1.288		4.97E-3		6.66E-3		
0.96	7,743	1.291		4.88E-3		6.11E-3	3.283	4.93E-3
0.9575	7,723	1.295		4.74E-3		5.72E-3		
0.955	7,702	1.298		4.70E-3		5.53E-3		
0.9525	7,682	1.302		4.66E-3		5.39E-3		
0.95	7,662	1.305	3.502	4.62E-3	3.475	5.30E-3		4.67E-3
0.9475	7,642	1.309		4.58E-3		5.15E-3		
0.945	7,622	1.312		4.56E-3		5.06E-3		
0.9425	7,602	1.316		4.55E-3		5.02E-3		
0.94	7,582	1.319		4.51E-3		4.98E-3		
0.935	7,541	1.326		4.50E-3		4.91E-3		
0.93	7,501	1.333		4.51E-3		4.83E-3		
0.925	7,461	1.340		4.48E-3		4.80E-3		
0.92	7,420	1.348		4.50E-3		4.93E-3		

eV	cm^{-1}	μm	n	k
0.9	7,259	1.378	3.246 [2]	3.51E-3 [2]
0.88	7,098	1.409		3.70E-3
0.86	6,936	1.442	3.227	3.90E-3

(continued)

TABLE I *(Continued)*

Zinc Arsenide

eV	cm^{-1}	μm	n	k
0.84	6,775	1.476		4.11E-3
0.82	6,614	1.512		4.33E-3
0.8	6,452	1.550	3.202	4.69E-3
0.78	6,291	1.589		5.06E-3
0.76	6,130	1.631	3.188	5.58E-3
0.74	5,968	1.675		6.13E-3
0.72	5,807	1.722		6.71E-3
0.7	5,646	1.771	3.17	7.54E-3
0.68	5,485	1.823		8.27E-3
0.66	5,323	1.879	3.159	9.11E-3
0.64	5,162	1.937		1.03E-2
0.62	5,001	2.000		1.16E-2
0.6	4,839	2.066	3.144	1.27E-2
0.59	4,759	2.101		1.34E-2
0.58	4,678	2.138		1.41E-2
0.57	4,597	2.175		1.51E-2
0.56	4,517	2.214		1.58E-2
0.55	4,436	2.254	3.133	1.66E-2
0.54	4,355	2.296		1.73E-2
0.53	4,275	2.339		1.83E-2
0.52	4,194	2.384		1.94E-2
0.51	4,113	2.431		2.03E-2
0.5	4,033	2.480	3.124	2.14E-2
0.49	3,952	2.530		2.23E-2
0.48	3,871	2.583		2.32E-2
0.47	3,791	2.638		2.43E-2

TABLE I *(Continued)*

Zinc Arsenide

eV	cm^{-1}	μm	n	k
0.46	3,710	2.695		2.56E-2
0.45	3,629	2.755	3.117	2.68E-2
0.44	3,549	2.818		2.81E-2
0.43	3,468	2.883		2.95E-2
0.42	3,387	2.952		3.10E-2
0.41	3,307	3.024		3.26E-2
0.4	3,226	3.100	3.113	3.40E-2
0.39	3,145	3.179		3.52E-2
0.38	3,065	3.263		3.61E-2
0.37	2,984	3.351		3.69E-2
0.36	2,904	3.444		3.77E-2
0.35	2,823	3.542	3.113	3.83E-2
0.34	2,742	3.647		3.86E-2
0.33	2,662	3.757		3.92E-2
0.32	2,581	3.875		3.95E-2
0.31	2,501	3.999		4.01E-2
0.3	2,419	4.133	3.109	4.08E-2
0.29	2,339	4.275		4.18E-2
0.28	2,258	4.428		4.37E-2
0.27	2,178	4.592		4.60E-2
0.26	2,097	4.769		4.97E-2
0.25	2,016	4.959	3.103	5.37E-2
0.24	1,936	5.166		5.75E-2

Zinc Phosphide (Zn_3P_2)

J. MISIEWICZ and K. JEZIERSKI
Institute of Physics
Technical University of Wroclaw
Wroclaw, Poland

Zn_3P_2 belongs to the group of II–V semiconducting compounds [1]. It possesses the tetragonal crystal structure described by $P4_2/nmc \equiv D_{4h}^{15}$ space symmetry group. The unit cell of Zn_3P_2 is characterized by the dimensions ratio $c/a \approx \sqrt{2}$ and consists of 40 atoms. The crystal structure of Zn_3P_2 may be regarded as a Na_2O lattice (or anti-fluoride lattice) in which one-quarter of the metal sites are vacant. The main interest of this material arises from its very high photoconductivity within the solar spectrum [2]. Compared to the well-known semiconductors, the number of papers for Zn_3P_2 is limited. The optical properties of this compound were measured over a wide range of photon energies from 3 meV up to 11 eV. The measurements were performed for unpolarized light and for Zn_3P_2 samples with c-axis parallel to the surface, so the results are mixed with both components, $E \| c$ and $E \perp c$. Therefore, the optical constants tabulated later as n and k should be regarded as the average ones. Only within the energy range of 1.35–5 eV were measurements done for the polarizations $E \| c$ and $E \perp c$, so n_e, k_e as well as n_o, k_o could be tabulated.

In the far-infrared region of 30–400 cm^{-1} the reflectivity measurements were performed by Misiewicz *et al.* [3] by using a Bruker model 113 V Fourier interferometer at room and low temperatures. High-quality Zn_3P_2 single crystals with high resistivity and hole concentrations of $\sim 10^{13} cm^{-3}$ were used. To determine the refractive index n and extinction coefficient k the measured spectra were analyzed with the help of a classical oscillator model [4]. The use of the oscillator model gives us the set of parameters that characterize zone center transverse lattice modes in Zn_3P_2 by the formulas

$$\epsilon_1(\omega) = \epsilon_\infty + \sum_{i=1}^{18} \frac{f_i \, \omega_{Ti}^2 (\omega_{Ti}^2 - \omega^2)}{(\omega_{Ti}^2 - \omega^2)^2 + \Gamma_i^2 \omega^2} \tag{1}$$

HANDBOOK OF OPTICAL CONSTANTS OF SOLIDS III

Copyright © 1998 by Academic Press.
All rights of reproduction in any form reserved
ISBN 0-12-544423-0/$25.00.

$$\epsilon_2(\omega) = \sum_{i=1}^{18} \frac{f_i\, \omega_{Ti}^2\, \Gamma_i\, \omega}{(\omega_{Ti}^2 - \omega^2)^2 + \Gamma_i^2 \omega^2}, \tag{2}$$

where ϵ_1 and ϵ_2 are average values of the dielectric constants, ω_{Ti} is the transverse-mode frequency, f_i is the oscillator strength, and Γ_i is the damping parameter. Parameters obtained by Misiewicz *et al.* [4] for room temperature and 10 K are given in Table I. Phonon frequencies determined from the classical oscillator model correspond well with those observed in Raman-scattering experiments [5, 6]. Frequencies of 16 longitudinal optical phonons are determined and shown elsewhere [5]. The n and k values obtained with Eqs. (1) and (2) within the range 30–400 cm^{-1} are presented in Table II. These data are very close to the ones obtained by Kramers–Kronig analysis of reflectivity spectra [3].

The knowledge of the osillator strengths enables us to determine the static dielectric constant, which is given by

$$\epsilon_S = \epsilon_\infty + \sum_{i=1}^{N} f_i. \tag{3}$$

The value of ϵ_∞ was assumed to be equal to 11 $\pm$ 1.5 in accordance with the data obtained for monocrystals and thin films [7–12]. The value of ϵ_S determined from Eq. 3 was equal to 33 (at 300 K) and was within the range of values determined from electrical measurements for Zn_3P_2 grown by different methods [13].

Within the 380–1200 cm^{-1} wave-number range, where there are multiphonon transitions, the optical-constant measurements were carried out with both the Fourier interferometer and Beckman spectrometer [3, 5]. The transmission spectrum within the 400–750 cm^{-1} wave-number range was presented by Radautsan *et al.* [14]. For energies smaller than 0.2 eV (1600 cm^{-1}) a strong absorption increase is observed in high-concentration Zn_3P_2 samples ($p \geq 10^{17}$ cm^{-3}) [15]. Within the 0.2–1.3 eV energy range, optical constants do not vary much. The refractive index for this range was found equal to 3.3 $\pm$ 0.1 [7–9]. The fundamental absorption edge for bulk Zn_3P_2 was investigated from 1.3 to 1.6 eV elsewhere [8, 9, 16–19]. Data presented in these papers are in good agreement, except for results published by Sobolev and Syrbu [19]. For energy higher than 1.6 eV, only transmission data for thin films are available [8–12]. The high-quality thin films of Zn_3P_2 with thicknesses below 0.5 μm were obtained by thermal vacuum evaporation onto the glass substrate. A standard optical system was used in the optical measurements.

The values of extinction coefficient given in Table II for energies smaller than 1.6 eV are derived directly from the absorption coefficient determined by means of transmission measurements [5, 15]. High-quality Zn_3P_2 single

crystals of two types, with hole concentrations higher than 10^{17} cm^{-3} and lower than 10^{16} cm^{-3}, were used in the measurements. The transmission was measured with high-resolution spectrometers, according to the wavenumber range: with a GDM 1000 from 0.77 to 1.3 μm, with a Carry II from 1.2 to 2.5 μm, and with a Beckman spectrophotometer from 2.5 to 10 μm.

In the visible and ultraviolet regions the values of n and k are provided by Kramers–Kronig analysis of the reflectivity spectra for single crystals of Zn_3P_2. The published reflectivity spectra were measured within different energy ranges, namely by Sobolev and Syrbu [19] within the energy range of 1–12 eV, by Misiewicz and Jezierski [20] within the 4–11 eV energy range, by Fagen [8] from 1.4 to 5 eV, by Jezierski *et al.* [21] from 2.2 to 5.8 eV, and by Misiewicz *et al.* [7] from 1.2 to 5.2 eV. The values of reflectivity presented by Sobolev and Syrbu [19] are much smaller than those reported by Misiewicz and Jezierski [20], especially for energies higher than 3.5 eV. This difference is related to the quality of the samples. Therefore, the Kramers–Kronig analysis was performed only for the spectrum with higher reflectivity values [20]. The n and k values are given in Table II for energies greater than 5 eV.

For the lower energies K-K analysis was based on the reflectivity spectrum chosen from the spectra published by Jezierski *et al.* [21]. The chosen spectrum was characterized by the highest reflectivity value ($R = 0.524$) at the second maximum. This value indicates a good-quality sample with a well-prepared surface. The surface preparation involved polishing with aluminum-oxide powder of decreasing grain size (1.0, 0.3, and 0.05 μm) and etching in 1% bromine–methanol solution [21]. It is worthwhile to notice that the highest value obtained by Fagen ($R = 0.5$ at the second peak) [8] is very close to that just mentioned. The values from K-K analysis for the spectrum chosen from those measured by Jezierski *et al.* [21] are tabulated for the energy range 1.93–5.7 eV.

For energies lower than 2.2 eV, the reflectivity was calculated by K-K analysis [22] from a knowledge of the absorption coefficient in this range. For energies lower than 1.93 eV, the n values given in Table II were characteristic of the K-K analysis of the reflectivity spectra measured down to 1.2 eV, for example, the spectrum given by Misiewicz *et al.* [7]. These values of n are decreasing to the value 3.32 with decreasing energy. The spectra for n and k for unpolarized light over a wide spectral range are presented in Fig. 1.

The measured optical spectra of Zn_3P_2 showed anisotropy, which was observed for the fundamental absorption edge [16, 18] and in the reflectivity spectra within the visible and ultraviolet energy range [23]. The measurements were performed at room temperature by using x-ray oriented Zn_3P_2 single crystals obtained from a gas-transport growth method. A double-grating Carl-Zeiss GDM-1000 monochromator equipped with linear polarizers from Carl-Zeiss and a Hamamatsu photomultiplier were utilized. Within the 0.9–1.0 eV energy range, a HgCdTe-based detector was used. The de-

termined values of n_e, n_o and k_e, k_o are also included in Table II and presented in Figs. 2 and 3.

The small birefringence in Zn_3P_2 was measured within the 0.5–1.44 eV energy range [24, 25]. The birefringence value increased from 0.0156 at 0.5 eV, through 0.0165 at 1.1 eV and 0.0176 at 1.30 eV, up to 0.0200 at 1.44 eV.

REFERENCES

1. E. K. Arushanov, *Prog. Cryst. Growth Charact.* **25**, 131 (1992).
2. J. M. Pawlikowski, *Rev. Solid State Sci.* **2**, 581 (1988); J. Misiewicz, L. Bryja, K. Jezierski, J. Szatkowski, N. Mirowska, Z. Gumienny, and E. Placzek-Popko, *Microelectron. J.* **25**, 23 (1994).
3. J. Misiewicz, J. M. Wróbel, and B. P. Clayman, *Solid State Commun.* **66**, 747 (1988).
4. J. Misiewicz, A. Lemiec, K. Jezierski, J. M. Wróbel, and B. P. Clayman, *Infrared Phys. Technol.* **35**, 775 (1994).
5. J. Misiewicz, *J. Phys. Condens. Matter* **1**, 9283 (1989).
6. G. Pangilinan, R. Sooryakumar, and J. Misiewicz, *Phys. Rev. B* **44**, 2582 (1991).
7. J. Misiewicz, J. Wróbel, and B. Sujak-Cyrul, *Opt. Appl.* **10**, 75 (1980).
8. E. A. Fagen, *J. Appl. Phys.* **50**, 6505 (1979).
9. L. Żdanowicz, W. Żdanowicz, D. Petelenz, and K. Kloc, *Acta Phys. Pol.* **A57**, 159 (1980).
10. K. R. Murali, B. S. V. Gopalam, and J. Sabhanadri, *Thin Solid Films* **136**, 275 (1986).
11. J. L. Deiss, B. Elidrissi, M. Robino, and R. Weil, *Appl. Phys. Lett.* **49**, 969 (1986).
12. A. Weber, P. Sutter, and H. von Kanel, *J. Appl. Phys.* **75**, 7448 (1994).
13. A. Subrahmanyam, K. R. Murali, B. S. V. Gopalam, and J. Sobhanadri, *Phys. Status Solidi A* **88**, 681 (1985).
14. R. S. Radautsan, N. N. Syrbu, J. J. Nebola, and K. J. Volodina, *Sov. Phys. Solid State* **19**, 1290 (1977).
15. J. Misiewicz, *J. Phys. Chem. Solids* **50**, 1013 (1988).
16. V. Munoz, D. Decroix, A. Chery, and J. M. Besson, *J. Appl. Phys.* **60**, 3282 (1986).
17. J. M. Pawlikowski, J. Misiewicz, and N. Mirowska, *J. Phys. Chem. Solids* **40**, 1027 (1979).
18. J. Misiewicz, *J. Phys. Condens. Matter* **2**, 2053 (1990).
19. V. V. Sobolev and N. N. Syrbu, *Phys. Status Solidi B* **64**, 423 (1974).
20. J. Misiewicz and K. Jezierski, *Solid State Commun.* **70**, 465 (1989).
21. K. Jezierski, J. Misiewicz, and F. Królicki, *Phys. Status Solidi A* **112**, K135 (1989).
22. K. Jezierski, *J. Phys. C: Solid State Phys.* **17**, 475 (1984).
23. J. Misiewicz, J. Wróbel, and K. Jezierski, *J. Phys. C: Solid State Phys.* **17**, 3091 (1984).
24. J. Misiewicz and J. A. Gaj, *Phys Status Solidi B* **105**, K23 (1981).
25. J. Misiewicz, N. Mirowska, and Z. Gumienny, *Phys. Status Solidi A* **83**, K51 (1984).

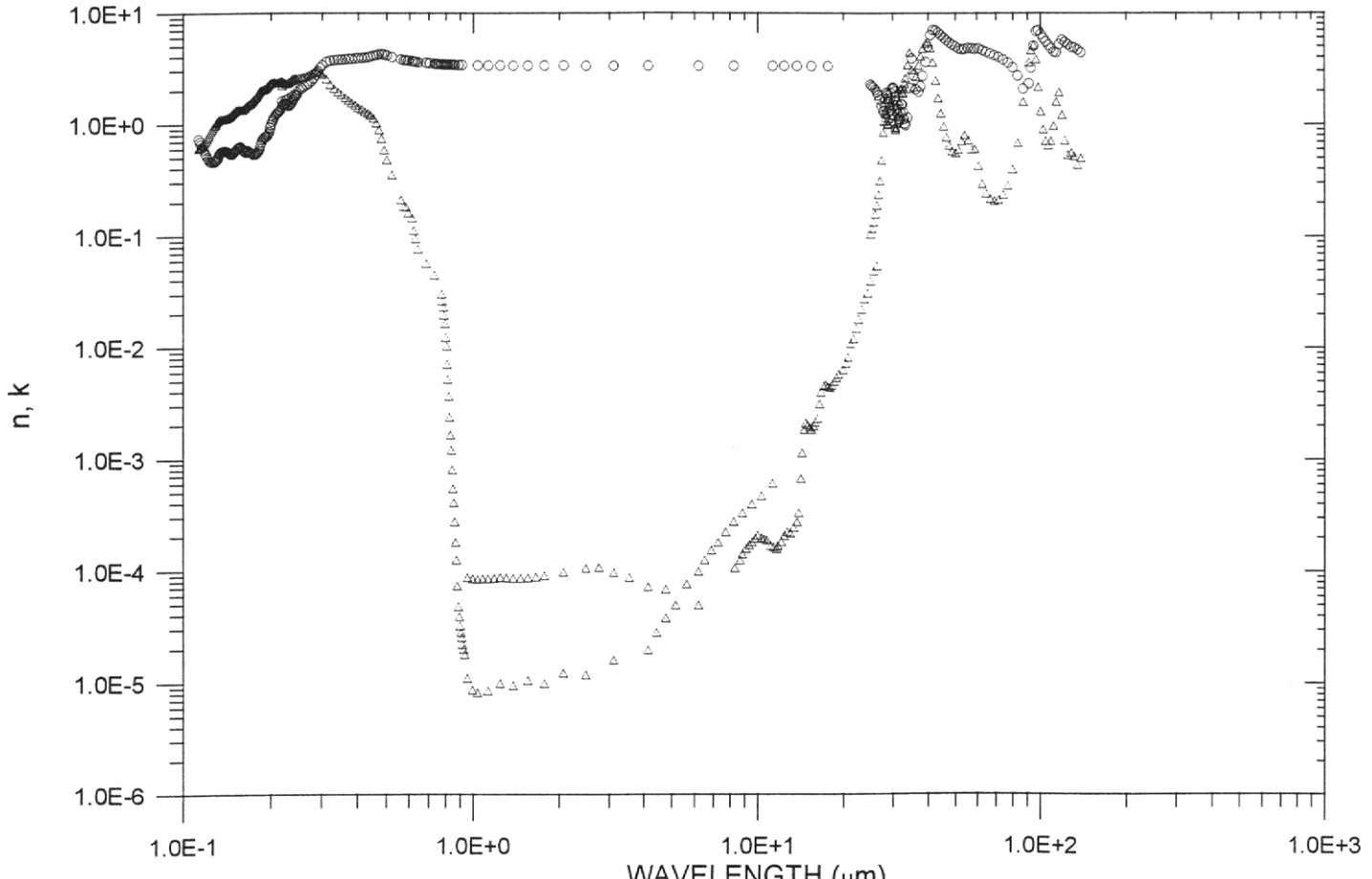

Fig. 1. Log–log plot of n (circles) and k (triangles) versus wavelength in micrometers for zinc phosphide.

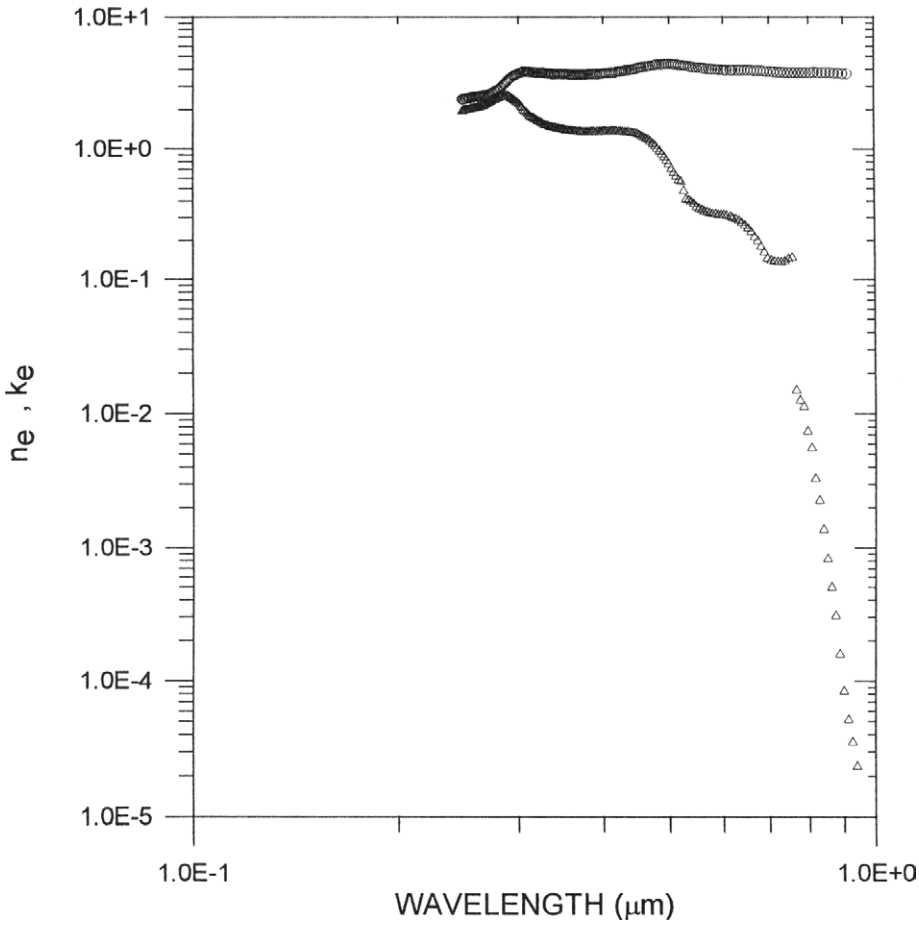

Fig. 2. Log–log plot of n_e (circles) and k_e (triangles) versus wavelength in micrometers for zinc phosphide.

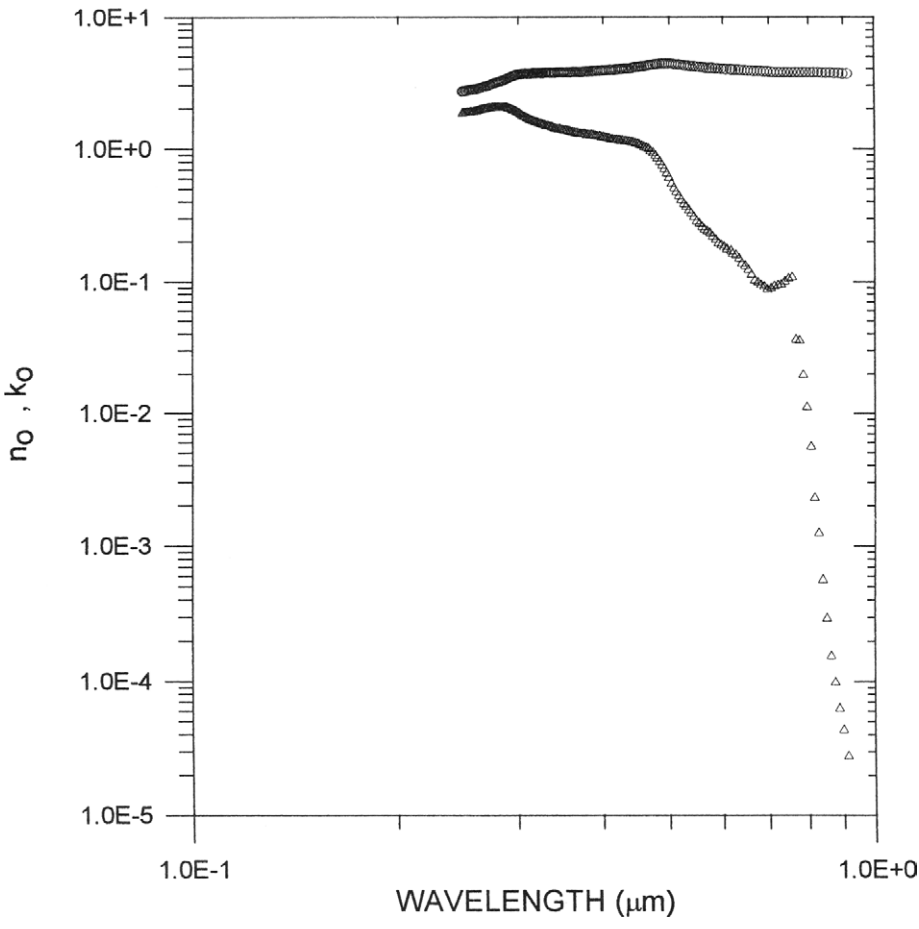

Fig. 3. Log–log plot of n_o (circles) and k_o (triangles) versus wavelength in micrometers for zinc phosphide.

TABLE I

Values of the Oscillator Parameters Obtained from a Fit to the Zn_3P_2 Reflectivity Spectrum in the Reststrahlen Region from Misiewicz *et al.* [4]

	10 K			300 K		
i	ω_{Ti} (cm^{-1})	f_i	Γ_i (cm^{-1})	ω_{Ti} (cm^{-1})	f_i	Γ_i (cm^{-1})
1	46	10.32	5.5	40	3.2	5.39
2	48	0.01	0.36	44	4.16	4.09
3	52	2.2	3.54	48	5.79	6.99
4	62	0.27	1.21	64	0.35	2.88
5	70	0.27	1.06	70	0.18	5.51
6	77	0.11	1.02	77	0.09	3.11
7	89	1.54	3.56	86	1.12	5.35
8	105	0.19	2.59	105	0.15	5.96
9	112	0.23	2.76	112	0.23	18.9
10	171	0.39	4.2	169	0.13	9.37
11	184	0.68	4.96	184	0.57	20.4
12	252	4.86	9.15	246	6.03	24.1
13	287	1.06	6.01	287	0.61	7.11
14	302	0.02	1.7	—	—	—
15	314	0.11	2.61	310	0.08	7.37
16	331	0.03	4.33	331	0.03	7.91
17	341	0.2	8.06	337	0.14	11.1
18	357	0.1	7.75	353	0.1	10.5

TABLE II

Values of n and k Obtained from Various References for Zinc Phosphide[a]

eV	cm^{-1}	μm	n	k
11	88,720	0.1127	0.739 [20]	0.615 [20]
10.9	87,910	0.1137	0.702	0.626
10.8	87,110	0.1148	0.665	0.637
10.7	86,300	0.1159	0.629	0.657
10.6	85,490	0.1170	0.601	0.671
10.5	84,690	0.1181	0.564	0.696
10.4	83,880	0.1192	0.538	0.721
10.3	83,070	0.1204	0.511	0.756
10.2	82,270	0.1216	0.493	0.788
10.1	81,460	0.1228	0.472	0.831
10	80,650	0.1240	0.469	0.872
9.9	79,850	0.1252	0.464	0.912
9.8	79,040	0.1265	0.467	0.949
9.7	78,230	0.1278	0.47	0.987
9.65	77,830	0.1285	0.473	1.005
9.6	77,430	0.1292	0.476	1.025
9.55	77,030	0.1298	0.48	1.045
9.5	76,620	0.1305	0.489	1.07
9.45	76,220	0.1312	0.505	1.087
9.4	75,810	0.1319	0.523	1.108
9.35	75,410	0.1326	0.55	1.11
9.3	75,010	0.1333	0.56	1.11
9.25	74,610	0.1340	0.569	1.111
9.2	74,200	0.1348	0.575	1.112
9.15	73,800	0.1355	0.578	1.113

(continued)

[a] References given in brackets.

TABLE II *(Continued)*

Zinc Phosphide

eV	cm^{-1}	μm	n	k
9.1	73,400	0.1362	0.581	1.115
9.05	72,990	0.1370	0.582	1.119
9	72,590	0.1378	0.582	1.122
8.95	72,190	0.1385	0.58	1.127
8.9	71,780	0.1393	0.579	1.133
8.85	71,380	0.1401	0.578	1.14
8.8	70,980	0.1409	0.575	1.146
8.75	70,570	0.1417	0.571	1.154
8.7	70,170	0.1425	0.566	1.163
8.65	69,770	0.1433	0.56	1.173
8.6	69,360	0.1442	0.551	1.19
8.55	68,960	0.1450	0.548	1.206
8.5	68,560	0.1459	0.546	1.227
8.45	68,150	0.1467	0.548	1.246
8.4	67,750	0.1476	0.551	1.268
8.35	67,350	0.1485	0.561	1.287
8.3	66,940	0.1494	0.568	1.305
8.25	66,540	0.1503	0.58	1.321
8.2	66,140	0.1512	0.591	1.335
8.15	65,730	0.1521	0.608	1.346
8.1	65,330	0.1531	0.619	1.348
8.05	64,930	0.1540	0.624	1.35
8	64,520	0.1550	0.631	1.353
7.95	64,120	0.1560	0.635	1.353
7.9	63,720	0.1569	0.634	1.351
7.85	63,310	0.1579	0.624	1.344
7.8	62,910	0.1590	0.603	1.36

7.75	62,510	0.1600	0.597	1.377		
7.7	62,100	0.1610	0.587	1.389		
7.65	61,700	0.1621	0.572	1.41		
7.6	61,300	0.1631	0.564	1.446		
7.55	60,890	0.1642	0.578	1.473		
7.5	60,490	0.1653	0.583	1.488		
7.45	60,090	0.1664	0.587	1.501		
7.4	59,680	0.1675	0.581	1.511		
7.35	59,280	0.1687	0.569	1.53		
7.3	58,880	0.1698	0.561	1.555		
7.25	58,470	0.1710	0.553	1.582		
7.2	58,070	0.1722	0.546	1.614		
7.15	57,670	0.1734	0.542	1.65		
7.1	57,260	0.1746	0.543	1.686		
7.05	56,860	0.1759	0.545	1.723		
7	56,460	0.1771	0.546	1.764		
6.95	56,050	0.1784	0.554	1.807		
6.9	55,650	0.1797	0.563	1.855		
6.85	55,250	0.1810	0.582	1.903		
6.8	54,850	0.1823	0.605	1.96		
6.75	54,440	0.1837	0.654	2.007		
6.7	54,040	0.1851	0.701	2.024		
6.65	53,640	0.1864	0.732	2.035		
6.6	53,230	0.1879	0.751	2.051		
eV	cm^{-1}	μm	n	k	n	k
6.55	52,830	0.1893	0.769	2.069		
6.5	52,420	0.1907	0.778	2.091		
6.45	52,020	0.1922	0.783	2.126		
6.4	51,620	0.1937	0.798	2.175		
6.35	51,210	0.1953	0.825	2.223		

(continued)

TABLE II *(Continued)*

Zinc Phosphide

eV	cm^{-1}	μm	n	k	n	k
6.3	50,810	0.1968	0.862	2.294		
6.25	50,410	0.1984	0.942	2.337		
6.2	50,010	0.2000	1.004	2.355		
6.15	49,600	0.2016	1.062	2.363		
6.1	49,200	0.2033	1.113	2.372		
6.05	48,800	0.2049	1.168	2.384		
6	48,390	0.2066	1.221	2.375		
5.95	47,990	0.2084	1.259	2.355		
5.9	47,590	0.2101	1.271	2.355		
5.85	47,180	0.2119	1.29	2.371		
5.8	46,780	0.2138	1.321	2.391		
5.75	46,380	0.2156	1.363	2.423		
5.7	45,970	0.2175	1.435	2.425		
5.687	45,870	0.218			1.616 [21]	2.225 [21]
5.65	45,570	0.2194	1.496	2.405		
5.6	45,170	0.2214	1.528	2.365		
5.55	44,760	0.2234	1.539	2.342		
5.535	44,640	0.224			1.651	2.307
5.5	44,360	0.2254	1.531	2.308		
5.45	43,960	0.2275	1.493	2.315		
5.438	43,860	0.228			1.691	2.35
5.4	43,550	0.2296	1.476	2.363		
5.344	43,100	0.232			1.726	2.403
5.35	43,150	0.2317	1.486	2.429		
5.3	42,750	0.2339	1.524	2.484		
5.254	42,380	0.236			1.78	2.458
5.25	42,340	0.2362	1.579	2.551		
5.2	41,940	0.2384	1.666	2.57		

5.166	41,670	0.24			1.843	2.506		
5.15	41,540	0.2407	1.731	2.572				
5.1	41,130	0.2431	1.789	2.579				
5.061	40,820	0.245			1.93	2.568		
5.05	40,730	0.2455	1.85	2.573				
eV	cm^{-1}	μm	n_e	k_e	n_o	k_o	n	k
5	40,330	0.2480	2.388 [23]	1.988 [23]	2.692 [23]	1.879 [23]		
4.98	40,170	0.2490	2.399	2	2.705	1.891		
4.96	40,000	0.2500	2.408	2.009	2.72	1.896	2.024 [21]	2.608 [21]
4.94	39,840	0.2510	2.417	2.017	2.732	1.899		
4.92	39,680	0.2520	2.426	2.026	2.743	1.904		
4.9	39,520	0.2530	2.429	2.036	2.758	1.906		
4.88	39,360	0.2541	2.443	2.051	2.765	1.91		
4.86	39,200	0.2551	2.457	2.059	2.772	1.917	2.102	2.637
4.84	39,040	0.2562	2.467	2.068	2.782	1.92		
4.82	38,880	0.2572	2.478	2.077	2.789	1.927		
4.8	38,710	0.2583	2.487	2.086	2.8	1.938		
4.78	38,550	0.2594	2.497	2.095	2.81	1.944		
4.769	38,460	0.26					2.185	2.669
4.76	38,390	0.2605	2.505	2.104	2.82	1.956		
4.74	38,230	0.2616	2.513	2.117	2.832	1.967		
4.72	38,070	0.2627	2.523	2.13	2.846	1.979		
4.7	37,910	0.2638	2.534	2.142	2.859	1.991		
4.68	37,750	0.2649	2.538	2.149	2.881	2.007	2.252	2.714
4.66	37,580	0.2661	2.545	2.168	2.903	2.011		
4.64	37,420	0.2672	2.548	2.192	2.918	2.02		
4.62	37,260	0.2684	2.552	2.219	2.936	2.033		
4.6	37,100	0.2695	2.573	2.245	2.958	2.042		
4.592	37,040	0.27					2.325	2.78
4.58	36,940	0.2707	2.573	2.272	2.985	2.053		

(continued)

TABLE II *(Continued)*

Zinc Phosphide

eV	cm^{-1}	μm	n_e	k_e	n_o	k_o	n	k
4.56	36,780	0.2719	2.604	2.299	3.009	2.056		
4.54	36,620	0.2731	2.609	2.33	3.029	2.062		
4.52	36,460	0.2743	2.648	2.361	3.057	2.07		
4.509	36,370	0.275					2.447	2.858
4.5	36,290	0.2755	2.682	2.395	3.085	2.073		
4.48	36,130	0.2768	2.723	2.419	3.111	2.075		
4.46	35,970	0.2780	2.746	2.444	3.147	2.074		
4.44	35,810	0.2792	2.794	2.472	3.168	2.07		
4.428	35,710	0.28					2.58	2.928
4.42	35,650	0.2805	2.828	2.505	3.192	2.068		
4.4	35,490	0.2818	2.888	2.525	3.215	2.072		
4.38	35,330	0.2831	2.939	2.553	3.243	2.072		
4.36	35,170	0.2844	3.014	2.573	3.271	2.073		
4.35	35,080	0.285					2.784	3.009
4.34	35,000	0.2857	3.085	2.575	3.298	2.073		
4.32	34,840	0.2870	3.15	2.581	3.334	2.076		
4.3	34,680	0.2883	3.222	2.584	3.374	2.07		
4.28	34,520	0.2897	3.307	2.573	3.41	2.055		
4.275	34,480	0.29					3.017	3.004
4.26	34,360	0.2910	3.381	2.539	3.442	2.043		
4.24	34,200	0.2924	3.44	2.502	3.475	2.026		
4.22	34,040	0.2938	3.536	2.457	3.529	1.997		
4.203	33,900	0.295					3.217	2.915
4.2	33,880	0.2952	3.572	2.425	3.544	1.98		
4.18	33,710	0.2966	3.619	2.376	3.569	1.963		
4.16	33,550	0.2980	3.656	2.329	3.599	1.935		
4.14	33,390	0.2995	3.698	2.29	3.625	1.905		
4.133	33,330	0.3					3.378	2.81

4.12	33,230	0.3009	3.748	2.239	3.645	1.872		
4.1	33,070	0.3024	3.769	2.177	3.658	1.844		
4.08	32,910	0.3039	3.799	2.121	3.659	1.805		
4.06	32,750	0.3054	3.871	2.031	3.688	1.776		
4.04	32,580	0.3069	3.847	1.984	3.692	1.761		
4.02	32,420	0.3084	3.827	1.941	3.688	1.736		
4	32,260	0.31	3.828	1.885	3.696	1.713	3.645	2.548
3.98	32,100	0.3115	3.832	1.831	3.704	1.684		
3.96	31,940	0.3131	3.814	1.801	3.703	1.672		
3.94	31,780	0.3147	3.802	1.773	3.708	1.655		
3.92	31,620	0.3163	3.797	1.746	3.708	1.636		
3.9	31,450	0.3179	3.788	1.725	3.709	1.629		
3.88	31,290	0.3195	3.791	1.69	3.723	1.611		
3.875	31,250	0.32					3.751	2.271
3.86	31,130	0.3212	3.784	1.657	3.732	1.584		
3.84	30,970	0.3229	3.774	1.637	3.722	1.567		
3.82	30,810	0.3246	3.771	1.619	3.724	1.565		
3.8	30,650	0.3263	3.765	1.588	3.731	1.548		
3.78	30,490	0.3280	3.755	1.564	3.737	1.533		
3.76	30,330	0.3297	3.744	1.547	3.737	1.52		
3.757	30,300	0.33					3.775	2.078
3.74	30,160	0.3315	3.73	1.533	3.738	1.512		
3.72	30,000	0.3333	3.722	1.516	3.742	1.498		
3.7	29,840	0.3351	3.711	1.507	3.745	1.492		
3.68	29,680	0.3369	3.702	1.494	3.753	1.477		
3.66	29,520	0.3388	3.704	1.484	3.758	1.458		
3.647	29,410	0.34					3.793	1.943
3.64	29,360	0.3406	3.698	1.476	3.757	1.451		
3.62	29,200	0.3425	3.7	1.458	3.767	1.435		
3.6	29,040	0.3444	3.692	1.455	3.765	1.43		
3.58	28,870	0.3463	3.687	1.449	3.769	1.423		

(continued)

TABLE II *(Continued)*

Zinc Phosphide

eV	cm^{-1}	μm	n_e	k_e	n_o	k_o	n	k
3.56	28,710	0.3483	3.689	1.44	3.771	1.412		
3.542	28,570	0.35					3.821	1.837
3.54	28,550	0.3502	3.682	1.43	3.772	1.408		
3.52	28,390	0.3522	3.68	1.419	3.779	1.397		
3.5	28,230	0.3542	3.675	1.412	3.784	1.388		
3.48	28,070	0.3563	3.672	1.406	3.789	1.379		
3.46	27,910	0.3583	3.667	1.405	3.792	1.373		
3.444	27,780	0.36					3.85	1.733
3.44	27,750	0.3604	3.667	1.398	3.8	1.36		
3.42	27,580	0.3625	3.665	1.395	3.8	1.351		
3.4	27,420	0.3647	3.665	1.39	3.805	1.342		
3.38	27,260	0.3668	3.67	1.381	3.813	1.327		
3.36	27,100	0.3690	3.667	1.381	3.811	1.324		
3.351	27,030	0.37					3.87	1.641
3.34	26,940	0.3712	3.666	1.38	3.814	1.32		
3.32	26,780	0.3734	3.667	1.377	3.813	1.32		
3.3	26,620	0.3757	3.671	1.373	3.83	1.318		
3.28	26,450	0.378	3.671	1.373	3.837	1.297		
3.263	26,320	0.38					3.886	1.558
3.26	26,290	0.3803	3.674	1.37	3.841	1.295		
3.24	26,130	0.3827	3.674	1.372	3.844	1.293		
3.22	25,970	0.385	3.676	1.378	3.853	1.296		
3.2	25,810	0.3875	3.682	1.378	3.865	1.286		
3.18	25,650	0.3899	3.692	1.377	3.878	1.275	3.914	1.483
3.16	25,490	0.3924	3.697	1.38	3.887	1.27		
3.14	25,330	0.3949	3.706	1.386	3.895	1.265		
3.12	25,160	0.3974	3.715	1.383	3.907	1.253		
3.1	25,000	0.4	3.722	1.387	3.913	1.246	3.935	1.411

3.08	24,840	0.4025	3.736	1.389	3.921	1.236		
3.06	24,680	0.4052	3.749	1.388	3.93	1.231		
3.04	24,520	0.4078	3.756	1.386	3.941	1.22		
3.024	24,390	0.41					3.954	1.356
3.02	24,360	0.4105	3.764	1.391	3.951	1.207		
3	24,200	0.4133	3.78	1.403	3.958	1.204		
2.98	24,030	0.4161	3.782	1.409	3.969	1.192		
2.96	23,870	0.4189	3.873	1.389	3.977	1.19		
2.952	23,810	0.42					3.981	1.304
2.94	23,710	0.4217	3.876	1.382	3.988	1.187		
2.92	23,550	0.4246	3.881	1.378	4	1.18		
2.9	23,390	0.4275	3.898	1.378	4.011	1.177		
2.883	23,250	0.43					4.013	1.254
2.88	23,230	0.4305	3.92	1.376	4.028	1.171		
2.86	23,070	0.4335	3.941	1.375	4.044	1.169		
2.84	22,910	0.4366	3.97	1.37	4.063	1.157		
2.82	22,740	0.4397	3.997	1.362	4.081	1.15		
2.818	22,730	0.44					4.069	1.207
2.8	22,580	0.4428	4.027	1.354	4.105	1.139		
2.78	22,420	0.4460	4.058	1.342	4.123	1.125		
2.76	22,260	0.4492	4.091	1.33	4.147	1.117		
2.755	22,220	0.45					4.145	1.139
2.74	22,100	0.4525	4.137	1.31	4.177	1.1		
2.72	21,940	0.4558	4.169	1.276	4.203	1.078		
2.7	21,780	0.4592	4.188	1.245	4.216	1.055		
2.695	21,740	0.46					4.215	1.031
2.68	21,610	0.4626	4.211	1.225	4.241	1.044		
2.66	21,540	0.4661	4.244	1.206	4.28	1.023		
2.64	21,290	0.4696	4.282	1.169	4.301	0.988		
2.638	21,280	0.47					4.265	0.889
2.62	21,130	0.4732	4.311	1.126	4.331	0.959		
2.6	20,970	0.4769	4.338	1.081	4.358	0.915		

(continued)

TABLE II *(Continued)*

Zinc Phosphide

eV	cm^{-1}	μm	n_e	k_e	n_o	k_o	n	k
2.583	20,830	0.48					4.275	0.748
2.58	20,810	0.4806	4.357	1.034	4.378	0.872		
2.56	20,650	0.4843	4.369	0.983	4.393	0.821		
2.54	20,490	0.4881	4.379	0.933	4.401	0.768		
2.53	20,410	0.49					4.226	0.59
2.52	20,320	0.4920	4.388	0.891	4.405	0.723		
2.5	20,160	0.4959	4.397	0.841	4.408	0.673		
2.48	20,000	0.4999	4.4	0.788	4.402	0.62	4.166	0.482
2.46	19,840	0.5040	4.398	0.727	4.389	0.563		
2.44	19,680	0.5081	4.384	0.678	4.369	0.523		
2.42	19,520	0.5123	4.364	0.635	4.343	0.487		
2.4	19,360	0.5166	4.344	0.594	4.322	0.454		
2.384	19,230	0.52					4.032	0.356
2.38	19,200	0.5209	4.313	0.579	4.299	0.425		
2.36	19,030	0.5254	4.3	0.495	4.276	0.397		
2.34	18,870	0.5299	4.276	0.424	4.251	0.378		
2.32	18,710	0.5344	4.237	0.418	4.232	0.354		
2.3	18,550	0.5391	4.2	0.408	4.211	0.337		
2.28	18,390	0.5438	4.175	0.392	4.189	0.316		
2.26	18,230	0.5486	4.152	0.368	4.17	0.294		
2.24	18,070	0.5535	4.121	0.358	4.15	0.282		
2.22	17,900	0.5585	4.096	0.349	4.131	0.265		
2.214	17,860	0.56					3.846	0.214 [15]
2.2	17,740	0.5636	4.075	0.342	4.11	0.253		
2.18	17,580	0.5687	4.051	0.337	4.089	0.246		
2.16	17,420	0.5740	4.032	0.332	4.075	0.238	3.786	0.185
2.14	17,260	0.5794	4.013	0.327	4.065	0.224		
2.13	17,180	0.5821					3.76	0.183

2.12	17,100	0.5848	4	0.327	4.046	0.213		
2.1	16,940	0.5904	3.988	0.321	4.031	0.2		
2.09	16,860	0.5932					3.731	0.161
2.08	16,780	0.5961	3.978	0.322	4.016	0.194		
2.06	16,610	0.6019	3.97	0.321	4.001	0.188		
2.04	16,450	0.6078	3.965	0.316	3.986	0.18		
2.03	16,370	0.6108					3.701	0.146
2.02	16,290	0.6158	3.958	0.311	3.975	0.175		
2	16,130	0.6199	3.954	0.305	3.961	0.167	3.681	0.113
1.98	15,970	0.6262	3.949	0.299	3.949	0.163		
1.97	15,890	0.6294					3.649	0.095
1.96	15,810	0.6326	3.948	0.291	3.942	0.154		
1.94	15,650	0.6391	3.948	0.279	3.929	0.141		
1.93	15,570	0.6424					3.611	0.077
1.92	15,490	0.6458	3.944	0.267	3.918	0.136		
1.9	15,320	0.6526	3.941	0.254	3.907	0.127		
1.88	15,160	0.6595	3.938	0.238	3.895	0.117		
1.86	15,000	0.6666	3.93	0.218	3.879	0.105		
1.84	14,840	0.6738	3.921	0.203	3.862	0.102		
1.82	14,680	0.6812	3.911	0.184	3.849	0.097		
1.81	14,600	0.6850					3.576 [7]	0.057
1.8	14,520	0.6888	3.895	0.166	3.834	0.094		
1.78	14,360	0.6965	3.875	0.149	3.82	0.089		
1.76	14,200	0.7045	3.851	0.143	3.803	0.091	3.534	
1.74	14,030	0.7126	3.831	0.141	3.793	0.095		
1.72	13,870	0.7208	3.817	0.14	3.782	0.096		
1.7	13,710	0.7293	3.802	0.139	3.773	0.098	3.503	0.045
1.68	13,550	0.7380	3.784	0.141	3.764	0.103	3.489	
1.66	13,390	0.7469	3.776	0.148	3.761	0.109	3.477	
1.64	13,230	0.7560	3.771	0.152	3.759	0.111	3.47	
1.62	13,070	0.7653	3.768	1.53E-2 [18]	3.761	3.72E-2 [18]	3.466	

(continued)

TABLE II *(Continued)*

Zinc Phosphide

eV	cm^{-1}	μm	n_e	k_e	n_o	k_o	n	k
1.6	12,900	0.7749	3.767	1.29E-2	3.759	3.64E-2	3.462	3.02E-2
1.59	12,820	0.7798						2.61E-2
1.58	12,740	0.7847	3.77	1.16E-2	3.762	2.0E-2	3.459	2.31E-2
1.57	12,660	0.7897						1.95E-2
1.56	12,580	0.7948	3.78	7.59E-3	3.763	1.14E-2	3.458	1.64E-2
1.55	12,500	0.7999						1.24E-2
1.54	12,420	0.8051	3.793	5.7E-3	3.765	5.7E-3	3.457	1.03E-2
1.53	12,340	0.8104						7.09E-3
1.52	12,260	0.8157	3.798	3.37E-3	3.768	2.34E-3	3.455	5.19E-3
1.51	12,180	0.8211						3.66E-3
1.5	12,100	0.8266	3.793	2.3E-3	3.762	1.28E-3	3.452	2.37E-3
1.49	12,020	0.8321						1.65E-3
1.48	11,940	0.8377	3.787	1.4E-3	3.751	5.73E-4	3.448	1.20E-3
1.47	11,860	0.8434						8.05E-4
1.46	11,780	0.8492	3.779	8.45E-4	3.743	3.01E-4	3.441	5.41E-4
1.45	11,690	0.8551						4.08E-4
1.44	11,610	0.8610	3.767	5.14E-4	3.733	1.58E-4	3.429	2.74E-4
1.43	11,530	0.8670	0.867					1.79E-4
1.42	11,450	0.8731	3.755	3.13E-4	3.723	1.01E-4		1.25E-4
1.41	11,370	0.8793	0.8793					7.35E-5
1.4	11,290	0.8856	3.743	1.62E-4	3.712	6.41E-5	3.42	4.79E-5
1.39	11,210	0.8920	0.892					3.90E-5
1.38	11,130	0.8984	3.729	8.58E-5	3.702	4.43E-5		3.22E-5
1.37	11,050	0.9050	0.905					2.81E-5
1.36	10,970	0.9117	3.709	5.29E-5	3.69	2.83E-5	3.408	2.54E-5
1.35	10,890	0.9184	0.9184					2.19E-5
1.34	10,810	0.9253		3.61E-5				1.99E-5
1.33	10,730	0.9322	0.9322					1.78E-5

eV	cm^{-1}	μm	n	k	k
1.3	10,480	0.9537		1.1E-5 [15]	8.7E-5 [15]
1.25	10,080	0.9919		8.68E-6	8.44E-5
1.2	9,678	1.033	3.397 [7]	8.22E-6	8.39E-5
1.15	9,275	1.078			8.49E-5
1.1	8,872	1.127	3.387	8.52E-6	8.52E-5
1.05	8,469	1.181			8.55E-5
1	8,065	1.240	3.376	9.87E-6	8.68E-5
0.95	7,662	1.305			8.62E-5
0.9	7,260	1.378	3.367	9.43E-6	8.55E-5
0.85	6,856	1.459			8.59E-5
0.8	6,452	1.550	3.358	1.05E-5	8.63E-5
0.75	6,049	1.653			8.81E-5
0.7	5,646	1.771	3.35	9.87E-6	9.02E-5
0.6	4,839	2.066	3.344	1.23E-5	9.65E-5
0.5	4,033	2.480	3.338	1.18E-5	1.05E-4
0.45	3,629	2.755			1.07E-4
0.4	3,226	3.100	3.334	1.60E-5	9.62E-5
0.35	2,823	3.542			8.74E-5
0.3	2,420	4.133	3.33	1.97E-5	7.23E-5
0.28	2,258	4.428		2.82E-5	
0.26	2,097	4.769		3.79E-5	6.83E-5
0.24	1,936	5.166		4.93E-5	
0.22	1,774	5.636		7.62E-5	
0.2	1,613	6.199	3.327	9.87E-5	4.93E-5
0.19	1,532	6.525		1.25E-4	
0.18	1,452	6.888		1.53E-4	
0.17	1,371	7.293		1.80E-4	
0.16	1,290	7.749		2.22E-4	
0.15	1,209	8.266	3.325	2.76E-4	

(continued)

TABLE II *(Continued)*

Zinc Phosphide

eV	cm^{-1}	μm	n	k	k
0.1488	1,200	8.332			1.06E-4 [5]
0.1426	1,150	8.695			1.25E-4
0.1401	1,130	8.850			1.41E-4
0.14	1,129	8.856		3.31E-4	
0.1364	1,100	9.090			1.59E-4
0.1327	1,070	9.343			1.71E-4
0.1302	1,050	9.523			1.82E-4
0.13	1,048	9.537		3.95E-4	
0.1265	1,020	9.801			1.95E-4
0.1240	1,000	9.999			2.07E-4
0.1203	970	10.31			1.97E-4
0.12	968	10.33		4.69E-4	
0.1178	950	10.52			1.93E-4
0.1153	930	10.75			1.88E-4
0.1116	900	11.11			1.68E-4
0.11	887.2	11.27	3.324	6.10E-4	
0.1091	880	11.36			1.63E-4
0.1066	860	11.63			1.57E-4
0.1054	850	11.76			1.68E-4
0.1029	830	12.05		1.82E-4 [5]	
0.1004	810	12.35	3.324	2.06E-4	
0.0979	790	12.66		2.22E-4	
0.0955	770	12.98		2.17E-4	
0.0930	750	13.33		2.44E-4	
0.0905	730	13.70	3.324	2.73E-4	
0.0893	720	13.88		3.31E-4	
0.0880	710	14.09		6.73E-4	

0.0868	700	14.28		1.14E-3	
0.0855	690	14.50		1.85E-3	
0.0843	680	14.71		2.11E-3	
0.0831	670	14.92		2.02E-3	
0.0818	660	15.16		1.93E-3	
0.0806	650	15.38	3.324	1.84E-3	
0.0794	640	15.61		1.99E-3	
0.0781	630	15.87		2.15E-3	
0.0769	620	16.12		2.31E-3	
0.0756	610	16.40		3.13E-3	
0.0744	600	16.66		3.98E-3	
0.0732	590	16.94		4.58E-3	
0.0719	580	17.24		4.66E-3	
0.0707	570	17.54	3.323	4.46E-3	
0.0694	560	17.86		4.41E-3	
0.0682	550	18.18		4.63E-3	
0.0670	540	18.51		5.01E-3	
0.0657	530	18.87		5.41E-3	
0.0645	520	19.22		5.81E-3	
0.0620	500	20.00		6.36E-3	
0.0608	490	20.39		7.30E-3	
0.0595	480	20.84		8.29E-3	
0.0583	470	21.27		1.10E-2	
0.0570	460	21.75		1.21E-2	
0.0558	450	22.22		1.50E-2	
0.0546	440	22.71		1.81E-2	
0.0533	430	23.26		2.22E-2	
0.0521	420	23.80		2.75E-2	
0.0508	410	24.41		3.11E-2	
0.04959	400	25.00	2.276 [4]	0.105 [4]	3.98E-2 [5]
0.04897	395	25.32	2.212	0.118	

(continued)

TABLE II *(Continued)*

Zinc Phosphide

eV	cm^{-1}	μm	n	k	k
0.04835	390	25.64	2.139	0.135	4.90E-2
0.04773	385	25.98	2.053	0.158	
0.04711	380	26.32	1.951	0.189	5.45E-2
0.04649	375	26.67	1.825	0.236	
0.04587	370	27.03	1.665	0.316	
0.04525	365	27.40	1.463	0.48	
0.04463	360	27.78	1.302	0.85	
0.04439	358	27.93	1.334	1.063	
0.04414	356	28.09	1.473	1.255	
0.04389	354	28.25	1.699	1.333	
0.04364	352	28.41	1.887	1.243	
0.04339	350	28.57	1.918	1.089	
0.04315	348	28.73	1.826	1.002	
0.04290	346	28.90	1.697	1.022	
0.04265	344	29.07	1.598	1.141	
0.04240	342	29.24	1.586	1.325	
0.04215	340	29.41	1.699	1.501	
0.04191	338	29.58	1.911	1.568	
0.04166	336	29.76	2.097	1.475	
0.04141	334	29.94	2.156	1.322	
0.04116	332	30.12	2.147	1.205	
0.04092	330	30.30	2.112	1.072	
0.04067	328	30.49	1.982	0.946	
0.04042	326	30.67	1.792	0.899	
0.04017	324	30.86	1.592	0.928	
0.03992	322	31.06	1.402	1.023	
0.03968	320	31.25	1.239	1.178	
0.03943	318	31.44	1.121	1.384	

0.03918	316	31.64	1.07	1.629
0.03893	314	31.84	1.111	1.888
0.03868	312	32.05	1.282	2.095
0.03844	310	32.25	1.514	2.087
0.03819	308	32.46	1.506	1.918
0.03794	306	32.68	1.3	1.916
0.03769	304	32.89	1.123	2.087
0.03744	302	33.11	1.027	2.332
0.03720	300	33.33	0.994	2.606
0.03658	295	33.89	1.151	3.413

eV	cm^{-1}	μm	n	k
0.03596	290	34.48	2.123	4.425
0.03534	285	35.08	3.91	3.107
0.03472	280	35.71	2.766	2.172
0.03410	275	36.36	2.067	2.676
0.03348	270	37.03	1.965	3.396
0.03286	265	37.73	2.199	4.108
0.03234	260	38.34	2.728	4.796
0.03162	255	39.21	3.638	5.372
0.03100	250	39.99	4.978	5.531
0.03038	245	40.81	6.358	4.858
0.02976	240	41.66	7.045	3.598
0.02914	235	42.55	7.017	2.48
0.02852	230	43.47	6.702	1.732
0.02790	225	44.44	6.339	1.264
0.02728	220	45.45	6.004	0.967
0.02666	215	46.51	5.709	0.775
0.02604	210	47.61	5.449	0.652
0.02542	205	48.77	5.217	0.581

(continued)

TABLE II *(Continued)*

Zinc Phosphide

eV	cm^{-1}	μm	n	k
0.02480	200	49.99	5.005	0.56
0.02418	195	51.28	4.823	0.6
0.02356	190	52.62	4.716	0.711
0.02294	185	54.05	4.767	0.809
0.02232	180	55.55	4.858	0.725
0.02170	175	57.14	4.799	0.599
0.02108	170	58.82	4.759	0.605
0.02046	165	60.60	4.787	0.429
0.01984	160	62.49	4.63	0.297
0.01922	155	64.51	4.472	0.243
0.01860	150	66.66	4.322	0.219
0.01798	145	68.96	4.169	0.21
0.01736	140	71.42	4.003	0.215
0.01674	135	74.06	3.81	0.236
0.01612	130	76.91	3.567	0.287
0.01550	125	79.99	3.235	0.4
0.01488	120	83.32	2.738	0.69
0.01426	115	86.95	2.096	1.588
0.01364	110	90.90	2.329	3.618
0.01339	108	92.60	3.203	4.646
0.01314	106	94.36	5.063	5.162
0.01289	104	96.19	6.885	3.851
0.01265	102	98.01	6.965	2.173
0.01240	100	99.99	6.445	1.307
0.01215	98	102.0	5.944	0.904
0.01190	96	104.2	5.523	0.716
0.01165	94	106.4	5.151	0.654
0.01141	92	108.7	4.794	0.711

0.01116	90	111.1	4.457	0.973
0.01091	88	113.6	4.409	1.602
0.01066	86	116.3	5.253	1.949
0.01041	84	119.1	5.724	1.226
0.01017	82	121.9	5.493	0.722
0.00992	80	125.0	5.181	0.536
0.00967	78	128.2	4.924	0.559
0.00942	76	131.6	4.9	0.52
0.00917	74	135.2	4.665	0.434
0.00893	72	138.8	4.436	0.504
0.00868	70	142.8	4.331	0.62
0.00843	68	147.1	4.182	0.614
0.00818	66	151.6	3.852	0.819
0.00794	64	156.1	4.19	1.371
0.00769	62	161.2	4.22	0.807
0.00744	60	166.6	3.731	0.783
0.00719	58	172.4	3.244	1.041
0.00694	56	178.6	2.778	1.606
0.00670	54	185.0	2.56	2.549
0.00645	52	192.2	2.853	3.685
0.00620	50	200.0	3.804	4.696
0.00595	48	208.4	5.223	4.949
0.00570	46	217.5	6.082	4.734
0.00546	44	227.1	7.621	4.604
0.00521	42	238.0	8.142	3.008
0.00496	40	250.0	8.186	2.444
0.00471	38	263.2	8.279	1.522
0.00446	36	278.0	7.881	0.874
0.00422	34	293.8	7.493	0.562
0.00397	32	312.3	7.196	0.395
0.00372	30	333.3	6.97	0.295

Zinc Germanium Phosphide ($ZnGeP_2$)

J. C. RIFE*
Naval Research Laboratory
Washington, D.C.

$ZnGeP_2$ is a tetragonally bonded semiconductor with the chalcopyrite structure and an effective direct band gap of 2.34 eV at room temperature. The structure, growth, and optical and electronic properties of the chalcopyrite semiconductors have been reviewed in the book by Shay and Wernick [1]. Properties have also been summarized in the Landolt-Börnstein series [2]. The II–IV–V_2 chalcopyrite lattice is equivalent to the III–V semiconductor crystal structure, but with ordering of the II and IV components and so a doubling of the unit cell along the c-axis. The chalcopyrite lattice is typically compressed along the c-axis, leading to a crystalline electric field and birefringence with n_e $(\mathbf{E} \| \mathbf{c}) > n_o$ $(\mathbf{E} \perp \mathbf{c})$, (positive uniaxial crystal). Chalcopyrite semiconductors are also optically active because of varying degrees of tetragonal distortion [3]. The $ZnGeP_2$ crystal structure, in particular, is compressed 2.0% along the c-axis. The $ZnGeP_2$ band gap was given earlier as only an effective direct one at 2.34 eV because, in fact, the lowest-energy electronic transition to the conduction-band minimum is at 1.99 eV at 300 K [4]. That is the weak "pseudodirect" band gap due to the fact that the III–V analog, GaP, has an indirect gap, and the indirect gap is folded to the zone center in the band structure of $ZnGeP_2$. The band structure of $ZnGeP_2$ has been calculated by several authors [5–7].

$ZnGeP_2$ is the most promising material for optical parametric oscillation, where tunable, mid-infrared light is generated from a shorter-wavelength pump laser. This is because $ZnGeP_2$ has a large nonlinear coefficient due to its covalent bonding, can be phase-matched because of its birefringence, has a wide transparency range (0.6 to 13 μm), and can sustain higher pumping powers because of its high thermal conductivity. Attempts to maximize performance by minimizing absorption in the band gap due to defects and im-

* The views presented are those of the author and do not represent the views of the Department of Defense or its components.

HANDBOOK OF OPTICAL CONSTANTS OF SOLIDS III
ISBN 0-12-544423-0/$25.00.

purities are referenced later. Useful second-harmonic generation in $ZnGeP_2$ is limited by its insufficient birefringence.

The optical constants, n and k, listed in Table I and plotted in Fig. 1 are derived from sources discussed in more detail later. The optical constants were taken from tables, calculated from formulae, or extracted from graphs where necessary. The table here has more significant figures than justified in some cases; consult the original work for the actual experimental resolution. Measurements made using polarized radiation were favored for inclusion here; in such cases, the optical constants have been given for both $\mathbf{E} \| \mathbf{c}$ and $\mathbf{E} \perp \mathbf{c}$. All measurements used were made on single crystals at room temperature, except where noted in the text. The following discussion of measurements gives references to additional work on polycrystalline or amorphous specimens.

I X-RAY TO BAND-GAP ABSORPTION EDGE

The optical constants, n and k, for the range from 10,000 to 20 eV have been calculated from the scattering factors of the elements of Henke *et al.* [8] using the compound formula and a density of 4.17 gm/cm^3. In Fig. 1, the K-edge ($1s$) transitions of Ge and Zn appear at 1.1 and 1.3×10^{-4} μm and of P at 5.8×10^{-4} μm; the $L_{2,3}$ ($2p$) transitions of Ge and Zn at 1.0 and 1.2×10^{-3} μm and of P at 9.1×10^{-3} μm; and the $M_{4,5}$ ($3d$) transitions of Ge at 4.1×10^{-2} μm. The calculated edges are a good approximation on the scale of Fig. 1, but the scatttering factors of the elements cannot predict the compound edge locations or structure to high degree (edge within 5 or 10 eV) because of core-level chemical shifts and bonding-dependent redistribution of the absorption at and just above the edges.

Optical constants for the fundamental electronic transitions in the 20 to 2.2 eV range are from Rife *et al.* [9]. They extracted optical constants for single-crystal samples from a Kramers–Kronig analysis of polarized, 80-K temperature reflectance data. De Alvarez and co-workers measured the reflectance from 2 to 5.5 eV at 5 and 300 K and compared with theory, but reported no optical constants [6].

II BAND-GAP ABSORPTION EDGE

Measurements of the absorption coefficient at the absorption edge have been reported by a number of authors with considerable scatter in the data, probably because of the variation of crystal quality and the psuedodirect gap. Isomura and Masumoto [10] give the absorption coefficient ($\alpha = 4\pi k/\lambda$) at

300, 207, and 99 K for unpolarized light from 2.1 to 0.9 eV. Gorban *et al.* show the absorption edge from 2.2 to 1.7 eV at 293 and 80 K, the lower temperature revealing pseudodirect transitions at 2.168 and 2.086 eV [11]. Bendorius *et al.* give the pressure dependence [12].

BAND GAP III

In the transparent gap region from 0.6 to 13 μm, where the two-phonon lattice absorption sets in, the index of refraction for $\mathbf{E} \| \mathbf{c}$ and $\mathbf{E} \perp \mathbf{c}$ has been reported by Boyd *et al.* [13]. They determined the index by the minimum deviation method; however, results for other individual crystals could vary slightly from their results, depending on doping. Their data have been reduced to an analog formula by Wemple *et al.* [14] and by Bhar and Ghosh [15]. At 20° C, the latter find a good fit to a special Sellmeier form,

$$n^2 = A + \frac{B}{1 - \dfrac{C}{\lambda^2}} + \frac{D}{1 - \dfrac{E}{\lambda^2}},$$

where for n_o (A, B, C, D, E) = (4.4733, 5.2658, 0.1338, 1.4909, 662.55) and for n_e (A, B, C, D, E) = (4.6332, 5.3422, 0.1426, 1.4580, 662.55); λ is the wavelength in microns. At 70° C, they find that n_o (A, B, C, D, E) = (4.4492, 5.3338, 0.1353, 1.4736, 662.55) and n_e (A, B, C, D, E) = (4.5717, 5.4513, 0.1435, 1.4262, 662.55). Bhar and Ghosh have also published the temperature dependence of the Sellmeier coefficients for temperatures as high as 400° C and low as −180° C [16].

Absorption in the gap region is sensitive to impurities and doping. Boyd *et al.* [17] measured absorption of high-quality samples in the gap. They observed a large shoulder between 0.6 and 3 μm that has since been attributed to defects. Considerable effort has been expended in the study of this absorption and methods for its reduction, since it is the primary limitation in optical parametric oscillator applications [18–21].

LATTICE ABSORPTION IN THE INFRARED IV

Poplavnoi [22] has reviewed infrared absorption and Raman scattering in $ZnGeP_2$ and a number of other II–IV–V_2 semiconductors. The optical constants in the infrared have been determined by a number of authors from polarized reflectance and transmittance measurements. Most recently, Voitsekhovskii *et al.* [23] have derived a set of harmonic oscillators that match

their data for both polarizations over the 10 to 600 cm^{-1} range and consider the overall picture of the dielectric characteristics in that range complete. Their results compare well with the previous work above 200 cm^{-1} of Miller *et al.* [24] and Markov *et al.* [25], but they find additional modes at 120 and 142 cm^{-1} and measure absorption in the 10 to 120 cm^{-1} range due to free-carrier absorption arising from impurities. Their formula for the dielectric constant $\epsilon(\nu)$ is

$$\epsilon(\nu) = \epsilon_\infty + \sum \frac{S_j \nu^2_j}{(\nu^2_j - \nu^2 - i\nu\gamma_j)},$$

where S_j is the oscillator strength, ν_j is the frequency in cm^{-1}, and γ_j is the damping of the jth oscillator in cm^{-1}. For $\mathbf{E} \| \mathbf{c}$, Voitsekhovskii *et al.* give the three oscillators (S_j, ν_j, γ_j) = (0.48, 397, 7.4), (1.15, 345, 5.5), and (0.02, 120, 0.55) with $\epsilon_\infty = 9.96$; for $\mathbf{E} \perp \mathbf{c}$ they give the five oscillators (S_j, ν_j, γ_j) = (0.50, 386, 3.0), (0.64, 368, 2.3), (0.34, 327, 6.0), (0.18, 202, 4.3), and (0.025, 141.5, 0.72), with $\epsilon_\infty = 9.73$. They determine ϵ_0 (at 13 cm^{-1}) to be 11.6 for $\mathbf{E} \| \mathbf{c}$ and 11.4 for $\mathbf{E} \perp \mathbf{c}$.

REFERENCES

1. J. L. Shay and J. H. Wernick, "Ternary Chalcopyrite Semiconductors: Growth, Electronic Properties, and Applications." Pergamon, New York, 1975.
2. Landolt-Börnstein, "Semiconductors—Physics of Ternary Compounds" (K.-H. Hellwege and O. Madelung, eds.), Vol. 17h, Springer-Verlag, New York, 1985.
3. G. A. Babonas, A. S. Martsinkyavichyus, and A. Yu. Shileika, *Sov. Phys. J.* **29**, 617 (1986).
4. A. Shileika, *Surf. Sci.* **37**, 730 (1973).
5. A. S. Poplavnoi and Y. I. Polygalov, *Sov. Phys. J.* **13**, 766 and 849 (1970).
6. C. V. de Alvarez and M. L. Cohen, *Phys. Rev. Lett.* **20**, 979 (1973); C. V. de Alvarez, M. L. Cohen, S. E. Kohn, Y. Petroff, and Y. R. Shen, *Phys. Rev. B* **10**, 5175 (1974).
7. J. E. Jaffe and A. Zunger, *Phys. Rev. B* **30**, 741 (1984).
8. B. L. Henke, P. Lee, T. J. Tanaka, R. L. Shimabukuro, and B. J. Fujikawa, *At. Data Nucl. Data Tables* **27**, 1 (1982); B. L. Henke, J. C. Davis, E. M. Gullikson, and R. C. C. Perera, *Lawrence Berkeley Laboratory Report* **LBL-26259** (1988).
9. J. C. Rife, R. N. Dexter, P. M. Bridenbaugh, and B. W. Veal, *Phys. Rev. B* **10**, 4491 (1977); J. C. Rife, Unpublished Ph.D. Thesis, University of Wisconsin, Madison (1976).
10. S. Isomura and K. Masumoto, *Phys. Status Solidi A* **13**, 223 (1972).
11. I. S. Gorban, V. A. Goryna, V. V. Lugovskii, and I. I. Tychina, *Sov. Phys. Solid State* **16**, 1029 (1974).
12. R. Bendorius, V. D. Prochukhan, and A. Šileika, *Phys. Status Solidi B* **53**, 745 (1972).
13. G. D. Boyd, E. Buehler, and F. G. Storz, *Appl. Phys. Lett.* **18**, 301 (1970).
14. S. H. Wemple, J. D. Gabbe, and G. D. Boyd, *J. Appl. Phys.* **46**, 3597 (1975).
15. G. C. Bhar and G. Ghosh, *J. Opt. Soc. Am.* **69**, 730 (1979).
16. G. C. Bhar and G. C. Ghosh, *IEEE J. Quantum Electron.* **QE-16**, 838 (1980).
17. G. D. Boyd, E. Buehler, F. G. Storz, and J. H. Wernick, *IEEE J. Quantum Electron.* **QE-8**, 419 (1972).
18. P. G. Schunemann, P. J. Drevinsky, M. C. Ohmer, W. C. Mitchel, and N. C. Fernelius, *Mater. Res. Soc. Symp.* **354**, 729 (1995).

19. M. H. Rakowsky, W. J. Lauderdale, R. A. Mantz, R. Pandey, and P. J. Drevinsky, *Mater. Res. Soc. Symp.* **354**, 735 (1995).
20. V. N. Brudnyi, V. A. Novikov, and E. A. Popova, *Sov. Phys. J.* **29**, 679 (1986).
21. Yu.V. Rud, *Sov. Phys. Semicond. (Engl. Transl.)* **28**, 633 (1994); *Fiz. Tekh. Poluprovodn. (St. Petersburg)* **28**, 1105 (1994).
22. A. S. Poplavnoi, *Sov. Phys. J.* **29**, 587 (1986).
23. V. V. Voitsekhovskii, A. A. Volkov, G. A. Komandin, and Yu. A. Shakir, *Sov. Phys. Solid State* **37**, 1198 (1995); *Fiz. Tverd. Tela (St. Petersburg)* **37**, 2199 (1995).
24. A. Miller, G. D. Holah, and W. C. Clark, *J. Phys. Chem. Solids,* **35**, 685 (1974).
25. Yu. F. Markov, V. S. Grigoreva, B. S. Zadokhin, and T. V. Rybakova, *Opt. Spectrosc.* **36**, 93 (1974).

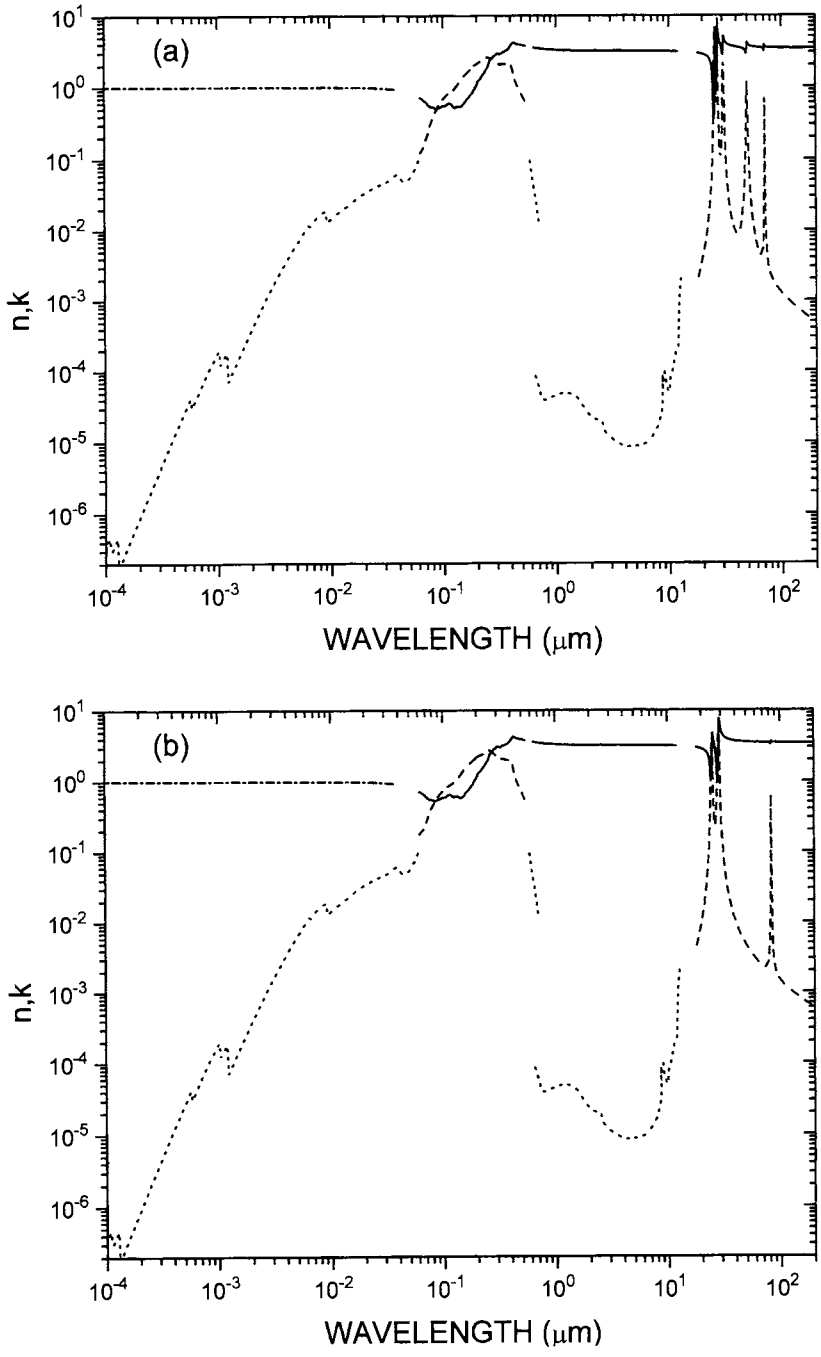

Fig. 1. (a) Log–log plot of n_o (solid line) and k_o (dashed line), $\mathbf{E} \perp \mathbf{c}$, versus wavelength for $ZnGeP_2$. (b) Log–log plot of n_e (solid line) and k_e (dashed line), $\mathbf{E} \parallel \mathbf{c}$, versus wavelength for $ZnGeP_2$. Unpolarized n (dash-dot line) and k (dotted line) are plotted on both graphs, where polarized data was not available.

TABLE I

Values of n and k for $ZnGeP_2$ Obtained from Various References[a]

eV	cm^{-1}	μm	1−n	k
			[8]	[8]
3.000E4	2.420E8	4.133E-5	8.90E-7	1.24E-8
2.010E4	1.622E8	6.167E-5	1.97E-6	5.76E-8
1.211E4	9.766E7	1.024E-4	5.36E-6	3.79E-7
1.179E4	9.506E7	1.052E-4	5.60E-6	4.18E-7
1.148E4	9.259E7	1.080E-4	5.84E-6	4.60E-7
1.118E4	9.017E7	1.109E-4	6.02E-6	3.35E-7
1.088E4	8.772E7	1.140E-4	6.44E-6	3.07E-7
1.060E4	8.547E7	1.170E-4	6.85E-6	3.38E-7
1.031E4	8.319E7	1.202E-4	7.21E-6	3.73E-7
1.005E4	8.104E7	1.234E-4	7.57E-6	4.13E-7
9.778E3	7.886E7	1.268E-4	7.81E-6	4.59E-7
9.523E3	7.680E7	1.302E-4	7.93E-6	1.75E-7
9.273E3	7.479E7	1.337E-4	8.88E-6	1.94E-7
9.024E3	7.278E7	1.374E-4	9.42E-6	2.15E-7
8.114E3	6.545E7	1.528E-4	1.19E-5	3.24E-7
6.048E3	4.878E7	2.050E-4	2.16E-5	9.88E-7
4.053E3	3.269E7	3.059E-4	4.88E-5	4.44E-6
2.314E3	1.867E7	5.357E-4	1.41E-4	3.42E-5
2.253E3	1.818E7	5.502E-4	1.47E-4	3.76E-5
2.194E3	1.770E7	5.651E-4	1.50E-4	4.13E-5
2.136E3	1.723E7	5.804E-4	1.51E-4	3.07E-5
2.080E3	1.678E7	5.961E-4	1.67E-4	3.38E-5
2.025E3	1.633E7	6.122E-4	1.79E-4	3.71E-5
1.593E3	1.285E7	7.784E-4	2.82E-4	8.58E-5
1.394E3	1.124E7	8.895E-4	3.41E-4	1.32E-4
1.287E3	1.038E7	9.637E-4	3.66E-4	1.69E-4
1.253E3	1.010E7	9.897E-4	3.63E-4	1.83E-4
1.220E3	9.843E6	1.016E-3	3.37E-4	1.98E-4
1.188E3	9.579E6	1.044E-3	3.81E-4	1.24E-4
1.157E3	9.328E6	1.072E-3	4.16E-4	1.34E-4
1.126E3	9.083E6	1.101E-3	4.41E-4	1.45E-4
1.096E3	8.842E6	1.131E-3	4.60E-4	1.56E-4
1.067E3	8.606E6	1.162E-3	4.73E-4	1.69E-4
1.039E3	8.382E6	1.193E-3	4.69E-4	1.83E-4
1.012E3	8.163E6	1.225E-3	4.28E-4	7.13E-5
9.856E2	7.949E6	1.258E-3	5.47E-4	7.81E-5
9.596E2	7.740E6	1.292E-3	6.04E-4	8.55E-5
7.958E2	6.418E6	1.558E-3	9.71E-4	1.66E-4
5.932E2	4.785E6	2.090E-3	1.81E-3	4.53E-4
3.976E2	3.207E6	3.118E-3	3.81E-3	1.68E-3
2.965E2	2.391E6	4.182E-3	6.04E-3	3.93E-3
2.040E2	1.646E6	6.077E-3	8.50E-3	1.04E-2
1.442E2	1.163E6	8.597E-3	5.77E-3	1.79E-2
1.404E2	1.133E6	8.829E-3	4.75E-3	1.83E-2
1.367E2	1.103E6	9.068E-3	2.64E-3	1.86E-2

(continued)

[a] References given in brackets.

TABLE I *(Continued)*

$ZnGeP_2$

eV	cm^{-1}	μm	1−n	k		
1.331E2	1.074E6	9.313E-3	2.68E-3	1.28E-2		
1.296E2	1.045E6	9.565E-3	5.50E-3	1.34E-2		
1.262E2	1.018E6	9.824E-3	6.72E-3	1.40E-2		
9.927E1	8.006E5	1.249E-2	1.22E-2	1.92E-2		
7.402E1	5.970E5	1.675E-2	1.95E-2	2.77E-2		
4.959E1	4.000E5	2.500E-2	3.57E-2	4.09E-2		
3.413E1	2.753E5	3.633E-2	7.63E-2	5.71E-2		
3.323E1	2.680E5	3.731E-2	7.94E-2	5.94E-2		
3.236E1	2.610E5	3.832E-2	8.13E-2	6.11E-2		
3.151E1	2.541E5	3.935E-2	8.31E-2	6.08E-2		
3.067E1	2.474E5	4.042E-2	8.52E-2	5.85E-2		
2.987E1	2.409E5	4.151E-2		5.33E-2		
2.908E1	2.346E5	4.263E-2		4.99E-2		
2.831E1	2.284E5	4.379E-2		4.79E-2		
2.757E1	2.224E5	4.497E-2		4.78E-2		
2.684E1	2.165E5	4.619E-2		4.86E-2		
2.614E1	2.108E5	4.744E-2		4.97E-2		
2.413E1	1.946E5	5.139E-2		5.75E-2		
2.227E1	1.796E5	5.567E-2		7.19E-2		
2.001E1	1.614E5	6.195E-2		1.10E-1		
eV	cm^{-1}	μm	n_o	k_o	n_e	k_e
			[9]	[9]	[9]	[9]
1.995E1	1.609E5	6.215E-2	7.06E-1	1.22E-1	7.03E-1	1.76E-1
1.975E1	1.593E5	6.277E-2	7.01E-1	1.25E-1	7.05E-1	1.77E-1
1.950E1	1.573E5	6.358E-2	6.94E-1	1.28E-1	6.97E-1	1.81E-1
1.925E1	1.553E5	6.441E-2	6.82E-1	1.31E-1	6.89E-1	1.86E-1
1.900E1	1.533E5	6.525E-2	6.71E-1	1.39E-1	6.81E-1	1.93E-1
1.875E1	1.512E5	6.612E-2	6.61E-1	1.44E-1	6.73E-1	1.97E-1
1.850E1	1.492E5	6.702E-2	6.45E-1	1.52E-1	6.60E-1	2.03E-1
1.825E1	1.472E5	6.793E-2	6.34E-1	1.65E-1	6.48E-1	2.13E-1
1.800E1	1.452E5	6.888E-2	6.25E-1	1.76E-1	6.40E-1	2.22E-1
1.775E1	1.432E5	6.985E-2	6.13E-1	1.85E-1	6.26E-1	2.29E-1
1.750E1	1.411E5	7.085E-2	6.01E-1	1.97E-1	6.11E-1	2.43E-1
1.725E1	1.391E5	7.187E-2	5.88E-1	2.07E-1	5.99E-1	2.59E-1
1.700E1	1.371E5	7.293E-2	5.66E-1	2.23E-1	5.80E-1	2.72E-1
1.675E1	1.351E5	7.402E-2	5.53E-1	2.47E-1	5.66E-1	2.99E-1
1.650E1	1.331E5	7.514E-2	5.42E-1	2.70E-1	5.61E-1	3.22E-1
1.625E1	1.311E5	7.630E-2	5.34E-1	2.95E-1	5.48E-1	3.41E-1
1.600E1	1.290E5	7.749E-2	5.30E-1	3.20E-1	5.44E-1	3.72E-1
1.575E1	1.270E5	7.872E-2	5.27E-1	3.42E-1	5.45E-1	3.96E-1
1.550E1	1.250E5	7.999E-2	5.24E-1	3.64E-1	5.44E-1	4.16E-1
1.525E1	1.230E5	8.130E-2	5.22E-1	3.85E-1	5.39E-1	4.38E-1
1.500E1	1.210E5	8.265E-2	5.20E-1	4.04E-1	5.38E-1	4.60E-1
1.450E1	1.170E5	8.550E-2	5.00E-1	4.54E-1	5.29E-1	5.11E-1
1.425E1	1.149E5	8.700E-2	5.01E-1	4.86E-1	5.26E-1	5.42E-1

TABLE I *(Continued)*

$ZnGeP_2$

eV	cm^{-1}	μm	n_o	k_o	n_e	k_e
1.400E1	1.129E5	8.856E-2	5.04E-1	5.14E-1	5.35E-1	5.74E-1
1.375E1	1.109E5	9.017E-2	5.10E-1	5.43E-1	5.46E-1	5.99E-1
1.350E1	1.089E5	9.184E-2	5.17E-1	5.66E-1	5.55E-1	6.18E-1
1.325E1	1.069E5	9.357E-2	5.15E-1	5.90E-1	5.53E-1	6.40E-1
1.300E1	1.049E5	9.537E-2	5.22E-1	6.20E-1	5.60E-1	6.69E-1
1.275E1	1.028E5	9.724E-2	5.33E-1	6.47E-1	5.70E-1	6.95E-1
1.250E1	1.008E5	9.918E-2	5.43E-1	6.66E-1	5.80E-1	7.15E-1
1.225E1	9.881E4	1.012E-1	5.44E-1	6.84E-1	5.83E-1	7.34E-1
1.200E1	9.681E4	1.033E-1	5.43E-1	7.12E-1	5.84E-1	7.58E-1
1.175E1	9.479E4	1.055E-1	5.51E-1	7.43E-1	5.88E-1	7.92E-1
1.150E1	9.276E4	1.078E-1	5.63E-1	7.70E-1	6.03E-1	8.22E-1
1.125E1	9.074E4	1.102E-1	5.78E-1	7.92E-1	6.21E-1	8.47E-1
1.100E1	8.873E4	1.127E-1	5.89E-1	8.04E-1	6.37E-1	8.61E-1
1.075E1	8.673E4	1.153E-1	5.88E-1	8.14E-1	6.43E-1	8.71E-1
1.050E1	8.467E4	1.181E-1	5.77E-1	8.31E-1	6.36E-1	8.81E-1
1.025E1	8.264E4	1.210E-1	5.54E-1	8.47E-1	6.19E-1	9.04E-1
9.999E0	8.065E4	1.240E-1	5.28E-1	9.00E-1	6.05E-1	9.45E-1
9.747E0	7.862E4	1.272E-1	5.13E-1	9.58E-1	6.00E-1	9.96E-1
9.501E0	7.663E4	1.305E-1	5.25E-1	1.02E0	6.08E-1	1.04E0
9.253E0	7.463E4	1.340E-1	5.35E-1	1.07E0	6.13E-1	1.08E0
8.997E0	7.257E4	1.378E-1	5.34E-1	1.12E0	5.99E-1	1.12E0
8.750E0	7.057E4	1.417E-1	5.31E-1	1.19E0	5.83E-1	1.18E0
8.498E0	6.854E4	1.459E-1	5.41E-1	1.27E0	5.79E-1	1.27E0
8.249E0	6.653E4	1.503E-1	5.65E-1	1.35E0	5.96E-1	1.36E0
7.999E0	6.452E4	1.550E-1	6.02E-1	1.43E0	6.26E-1	1.46E0
7.749E0	6.250E4	1.600E-1	6.40E-1	1.51E0	6.75E-1	1.54E0
7.501E0	6.050E4	1.653E-1	6.85E-1	1.59E0	7.24E-1	1.62E0
7.251E0	5.848E4	1.710E-1	7.23E-1	1.67E0	7.67E-1	1.70E0
7.001E0	5.647E4	1.771E-1	7.79E-1	1.77E0	8.28E-1	1.80E0
6.950E0	5.605E4	1.784E-1	7.93E-1	1.78E0	8.41E-1	1.82E0
6.900E0	5.565E4	1.797E-1	8.03E-1	1.80E0	8.54E-1	1.84E0
6.850E0	5.525E4	1.810E-1	8.11E-1	1.82E0	8.69E-1	1.86E0
6.801E0	5.485E4	1.823E-1	8.17E-1	1.84E0	8.83E-1	1.88E0
6.749E0	5.444E4	1.837E-1	8.28E-1	1.87E0	8.95E-1	1.90E0
6.702E0	5.405E4	1.850E-1	8.45E-1	1.89E0	9.06E-1	1.92E0
6.652E0	5.365E4	1.864E-1	8.65E-1	1.92E0	9.21E-1	1.95E0
6.602E0	5.325E4	1.878E-1	8.85E-1	1.94E0	9.44E-1	1.98E0
6.550E0	5.283E4	1.893E-1	9.05E-1	1.96E0	9.68E-1	2.00E0
6.502E0	5.244E4	1.907E-1	9.26E-1	1.99E0	9.90E-1	2.02E0
6.451E0	5.203E4	1.922E-1	9.46E-1	2.01E0	1.01E0	2.03E0
6.401E0	5.163E4	1.937E-1	9.67E-1	2.03E0	1.03E0	2.05E0
6.352E0	5.123E4	1.952E-1	9.89E-1	2.05E0	1.05E0	2.07E0
6.300E0	5.081E4	1.968E-1	1.01E0	2.07E0	1.08E0	2.09E0
6.249E0	5.040E4	1.984E-1	1.04E0	2.10E0	1.10E0	2.12E0
6.199E0	5.000E4	2.000E-1	1.06E0	2.12E0	1.13E0	2.14E0
6.150E0	4.960E4	2.016E-1	1.10E0	2.15E0	1.15E0	2.16E0
6.102E0	4.921E4	2.032E-1	1.14E0	2.17E0	1.19E0	2.19E0

(continued)

TABLE I *(Continued)*

$ZnGeP_2$

eV	cm^{-1}	μm	n_o	k_o	n_e	k_e
6.051E0	4.880E4	2.049E-1	1.19E0	2.17E0	1.24E0	2.20E0
6.001E0	4.840E4	2.066E-1	1.21E0	2.16E0	1.27E0	2.19E0
5.949E0	4.798E4	2.084E-1	1.23E0	2.17E0	1.29E0	2.20E0
5.901E0	4.760E4	2.101E-1	1.24E0	2.18E0	1.30E0	2.20E0
5.851E0	4.719E4	2.119E-1	1.25E0	2.19E0	1.32E0	2.22E0
5.799E0	4.677E4	2.138E-1	1.26E0	2.22E0	1.34E0	2.24E0
5.751E0	4.638E4	2.156E-1	1.29E0	2.24E0	1.36E0	2.25E0
5.700E0	4.598E4	2.175E-1	1.32E0	2.27E0	1.38E0	2.27E0
5.651E0	4.558E4	2.194E-1	1.35E0	2.29E0	1.40E0	2.30E0
5.600E0	4.517E4	2.214E-1	1.38E0	2.31E0	1.43E0	2.32E0
5.550E0	4.476E4	2.234E-1	1.42E0	2.32E0	1.47E0	2.34E0
5.501E0	4.437E4	2.254E-1	1.44E0	2.34E0	1.50E0	2.35E0
5.450E0	4.396E4	2.275E-1	1.47E0	2.35E0	1.53E0	2.37E0
5.400E0	4.355E4	2.296E-1	1.50E0	2.37E0	1.55E0	2.39E0
5.351E0	4.316E4	2.317E-1	1.53E0	2.40E0	1.58E0	2.41E0
5.301E0	4.275E4	2.339E-1	1.55E0	2.43E0	1.61E0	2.44E0
5.249E0	4.234E4	2.362E-1	1.60E0	2.46E0	1.65E0	2.47E0
5.201E0	4.195E4	2.384E-1	1.65E0	2.48E0	1.69E0	2.49E0
5.151E0	4.155E4	2.407E-1	1.70E0	2.49E0	1.74E0	2.51E0
5.100E0	4.114E4	2.431E-1	1.75E0	2.50E0	1.78E0	2.53E0
5.050E0	4.073E4	2.455E-1	1.78E0	2.52E0	1.82E0	2.55E0
4.999E0	4.032E4	2.480E-1	1.82E0	2.54E0	1.87E0	2.57E0
4.950E0	3.992E4	2.505E-1	1.87E0	2.58E0	1.90E0	2.60E0
4.901E0	3.953E4	2.530E-1	1.93E0	2.62E0	1.96E0	2.65E0
4.851E0	3.912E4	2.556E-1	2.01E0	2.65E0	2.04E0	2.68E0
4.800E0	3.871E4	2.583E-1	2.11E0	2.66E0	2.12E0	2.71E0
4.750E0	3.831E4	2.610E-1	2.22E0	2.67E0	2.22E0	2.73E0
4.700E0	3.791E4	2.638E-1	2.32E0	2.62E0	2.35E0	2.72E0
4.651E0	3.751E4	2.666E-1	2.38E0	2.54E0	2.43E0	2.66E0
4.601E0	3.711E4	2.695E-1	2.40E0	2.51E0	2.50E0	2.62E0
4.550E0	3.670E4	2.725E-1	2.44E0	2.49E0	2.56E0	2.58E0
4.500E0	3.630E4	2.755E-1	2.49E0	2.48E0	2.61E0	2.54E0
4.450E0	3.589E4	2.786E-1	2.56E0	2.46E0	2.65E0	2.51E0
4.400E0	3.549E4	2.818E-1	2.62E0	2.40E0	2.71E0	2.48E0
4.350E0	3.509E4	2.850E-1	2.64E0	2.36E0	2.77E0	2.46E0
4.301E0	3.469E4	2.883E-1	2.68E0	2.33E0	2.82E0	2.39E0
4.250E0	3.428E4	2.917E-1	2.71E0	2.31E0	2.85E0	2.35E0
4.200E0	3.388E4	2.952E-1	2.76E0	2.29E0	2.89E0	2.33E0
4.151E0	3.348E4	2.987E-1	2.82E0	2.26E0	2.95E0	2.30E0
4.100E0	3.307E4	3.024E-1	2.85E0	2.18E0	2.99E0	2.23E0
4.050E0	3.267E4	3.061E-1	2.87E0	2.12E0	3.03E0	2.17E0
4.000E0	3.226E4	3.100E-1	2.86E0	2.08E0	3.03E0	2.10E0
3.950E0	3.186E4	3.139E-1	2.85E0	2.06E0	3.02E0	2.05E0
3.900E0	3.146E4	3.179E-1	2.84E0	2.05E0	3.01E0	2.03E0
3.850E0	3.106E4	3.220E-1	2.84E0	2.05E0	2.99E0	2.01E0
3.800E0	3.065E4	3.263E-1	2.85E0	2.06E0	2.99E0	2.02E0
3.750E0	3.025E4	3.306E-1	2.88E0	2.09E0	3.01E0	2.06E0

TABLE I *(Continued)*

$ZnGeP_2$

eV	cm^{-1}	μm	n_o	k_o	n_e	k_e
3.700E0	2.984E4	3.351E-1	2.93E0	2.10E0	3.08E0	2.07E0
3.650E0	2.944E4	3.397E-1	3.00E0	2.08E0	3.13E0	2.03E0
3.600E0	2.904E4	3.444E-1	3.01E0	2.04E0	3.17E0	1.99E0
3.551E0	2.864E4	3.492E-1	3.02E0	2.05E0	3.16E0	1.96E0
3.500E0	2.823E4	3.542E-1	3.07E0	2.08E0	3.18E0	1.98E0
3.450E0	2.782E4	3.594E-1	3.13E0	2.06E0	3.23E0	1.98E0
3.401E0	2.743E4	3.646E-1	3.18E0	2.04E0	3.27E0	1.96E0
3.350E0	2.702E4	3.701E-1	3.21E0	2.04E0	3.31E0	1.96E0
3.300E0	2.662E4	3.757E-1	3.24E0	2.05E0	3.34E0	1.96E0
3.250E0	2.621E4	3.815E-1	3.32E0	2.11E0	3.40E0	1.99E0
3.200E0	2.581E4	3.874E-1	3.43E0	2.09E0	3.48E0	1.99E0
3.150E0	2.541E4	3.936E-1	3.55E0	2.09E0	3.58E0	1.98E0
3.100E0	2.501E4	3.999E-1	3.69E0	2.05E0	3.69E0	1.96E0
3.050E0	2.460E4	4.065E-1	3.84E0	1.97E0	3.82E0	1.94E0
3.000E0	2.420E4	4.133E-1	3.99E0	1.86E0	3.97E0	1.84E0
2.950E0	2.379E4	4.203E-1	4.11E0	1.65E0	4.12E0	1.68E0
2.900E0	2.339E4	4.275E-1	4.11E0	1.45E0	4.19E0	1.49E0
2.850E0	2.299E4	4.350E-1	4.09E0	1.29E0	4.16E0	1.29E0
2.800E0	2.258E4	4.428E-1	4.00E0	1.16E0	4.11E0	1.18E0
2.750E0	2.218E4	4.508E-1	3.97E0	1.09E0	4.07E0	1.05E0
2.700E0	2.178E4	4.592E-1	3.90E0	1.01E0	4.02E0	9.74E-1
2.650E0	2.138E4	4.678E-1	3.88E0	9.73E-1	3.97E0	9.08E-1
2.600E0	2.097E4	4.768E-1	3.86E0	9.18E-1	3.95E0	8.54E-1
2.550E0	2.057E4	4.862E-1	3.84E0	8.64E-1	3.91E0	7.87E-1
2.500E0	2.017E4	4.959E-1	3.83E0	8.06E-1	3.88E0	7.49E-1
2.450E0	1.976E4	5.060E-1	3.81E0	7.36E-1	3.87E0	7.01E-1
2.400E0	1.936E4	5.166E-1	3.75E0	6.92E-1	3.85E0	6.33E-1
2.350E0	1.895E4	5.276E-1	3.73E0	6.58E-1	3.79E0	5.71E-1
2.300E0	1.855E4	5.390E-1	3.70E0	6.27E-1	3.76E0	5.42E-1

eV	cn^{-1}	μm	n	k
				[10]
2.109E0	1.701E4	5.880E-1		9.36E-2
1.997E0	1.610E4	6.210E-1		4.94E-2
1.867E0	1.506E4	6.640E-1		2.64E-2
1.749E0	1.410E4	7.090E-1		1.13E-2

eV	cm^{-1}	μm	n_o	k	n_e
			[13]	[17]	[13]
1.937E0	1.563E4	6.400E-1	3.505E0		3.580E0
1.879E0	1.515E4	6.600E-1	3.476E0	7.78E-5	3.547E0
1.823E0	1.471E4	6.800E-1	3.448E0	6.73E-5	3.516E0
1.771E0	1.429E4	7.000E-1	3.423E0	5.72E-5	3.489E0
1.653E0	1.333E4	7.500E-1	3.373E0	3.94E-5	3.432E0
1.550E0	1.250E4	8.000E-1	3.336E0	3.92E-5	3.392E0

(continued)

TABLE I *(Continued)*

$ZnGeP_2$

eV	cm^{-1}	μm	n_o	k	n_e
1.459E0	1.176E4	8.500E-1	3.306E0	4.10E-5	3.359E0
1.378E0	1.111E4	9.000E-1	3.283E0	4.29E-5	3.334E0
1.305E0	1.053E4	9.500E-1	3.264E0	4.46E-5	3.312E0
1.240E0	1.000E4	1.000E0	3.248E0	4.62E-5	3.295E0
1.127E0	9.091E3	1.100E0	3.223E0	4.84E-5	3.269E0
1.033E0	8.333E3	1.200E0	3.205E0	4.89E-5	3.249E0
9.537E-1	7.692E3	1.300E0	3.192E0	4.79E-5	3.235E0
8.856E-1	7.143E3	1.400E0	3.182E0	4.54E-5	3.224E0
7.749E-1	6.250E3	1.600E0	3.167E0	3.71E-5	3.208E0
6.888E-1	5.556E3	1.800E0	3.156E0	2.76E-5	3.197E0
6.199E-1	5.000E3	2.000E0	3.149E0	2.18E-5	3.189E0
5.636E-1	4.545E3	2.200E0	3.143E0	2.05E-5	3.183E0
5.166E-1	4.167E3	2.400E0	3.139E0	1.98E-5	3.178E0
4.769E-1	3.846E3	2.600E0	3.136E0	1.42E-5	3.175E0
4.428E-1	3.571E3	2.800E0	3.133E0	1.22E-5	3.172E0
4.133E-1	3.333E3	3.000E0	3.130E0	1.12E-5	3.169E0
3.875E-1	3.125E3	3.200E0	3.128E0	1.04E-5	3.167E0
3.647E-1	2.941E3	3.400E0	3.126E0	9.85E-6	3.165E0
3.444E-1	2.778E3	3.600E0	3.126E0	9.36E-6	3.163E0
3.263E-1	2.632E3	3.800E0	3.124E0	8.87E-6	3.162E0
3.100E-1	2.500E3	4.000E0	3.122E0	8.45E-6	3.161E0
2.952E-1	2.381E3	4.200E0	3.121E0	8.50E-6	3.160E0
2.755E-1	2.222E3	4.500E0	3.119E0	8.57E-6	3.156E0
2.638E-1	2.128E3	4.700E0	3.117E0	8.61E-6	3.154E0
2.480E-1	2.000E3	5.000E0	3.115E0	8.68E-6	3.153E0
2.254E-1	1.818E3	5.500E0	3.113E0	9.00E-6	3.152E0
2.066E-1	1.667E3	6.000E0	3.110E0	9.33E-6	3.148E0
1.907E-1	1.538E3	6.500E0	3.106E0	1.07E-5	3.145E0
1.771E-1	1.429E3	7.000E0	3.104E0	1.20E-5	3.142E0
1.653E-1	1.333E3	7.500E0	3.099E0	1.48E-5	3.138E0
1.550E-1	1.250E3	8.000E0	3.096E0	1.82E-5	3.135E0
1.459E-1	1.176E3	8.500E0	3.092E0	2.91E-5	3.131E0
1.441E-1	1.162E3	8.603E0		5.57E-5	
1.419E-1	1.144E3	8.739E0		9.10E-5	
1.378E-1	1.111E3	9.000E0	3.088E0	8.94E-5	3.127E0
1.354E-1	1.092E3	9.157E0		7.21E-5	
1.305E-1	1.053E3	9.500E0	3.084E0	5.55E-5	3.123E0
1.255E-1	1.012E3	9.879E0		4.94E-5	
1.245E-1	1.004E3	9.962E0		6.50E-5	
1.240E-1	1.000E3	1.000E1	3.079E0	7.18E-5	3.118E0
1.181E-1	9.524E2	1.050E1	3.074E0	9.75E-5	3.114E0
1.150E-1	9.276E2	1.078E1			1.20E-4
1.127E-1	9.091E2	1.100E1	3.069E0	1.47E-4	3.109E0
1.099E-1	8.865E2	1.128E1		1.81E-4	
1.078E-1	8.696E2	1.150E1	3.062E0	1.94E-4	3.101E0
1.043E-1	8.410E2	1.189E1		2.10E-4	
1.038E-1	8.368E2	1.195E1		2.43E-4	

TABLE I *(Continued)*

$ZnGeP_2$

eV	cm^{-1}	μm	n_o	k	n_e	
1.033E-1	8.333E2	1.200E1	3.055E0	3.89E-4	3.095E0	
1.021E-1	8.237E2	1.214E1		8.97E-4		
1.006E-1	8.110E2	1.233E1		1.34E-3		
9.871E-2	7.962E2	1.256E1		1.83E-3		
9.747E-2	7.862E2	1.272E1		1.23E-3		
eV	cm^{-1}	μm	n_o	k_o	n_e	k_e
			[23]	[23]	[23]	[23]
6.819E-2	5.500E2	1.818E1	2.92E0	2.15E-3	2.95E0	4.57E-3
6.199E-2	5.000E2	2.000E1	2.82E0	4.30E-3	2.85E0	9.61E-3
5.579E-2	4.500E2	2.222E1	2.57E0	1.29E-2	2.58E0	3.35E-2
4.959E-2	4.000E2	2.500E1	3.81E-1	1.17E0	2.33E0	3.36E0
4.922E-2	3.970E2	2.519E1	3.62E-1	1.89E0	4.07E0	3.19E0
4.885E-2	3.940E2	2.538E1	4.52E-1	2.68E0	4.67E0	1.70E0
4.835E-2	3.900E2	2.564E1	9.64E-1	4.27E0	4.14E0	7.14E-1
4.786E-2	3.860E2	2.591E1	5.80E0	5.59E0	3.67E0	4.01E-1
4.736E-2	3.820E2	2.618E1	4.76E0	9.12E-1	3.33E0	2.81E-1
4.687E-2	3.780E2	2.646E1	3.05E0	5.88E-1	3.05E0	2.36E-1
4.637E-2	3.740E2	2.674E1	1.23E0	1.92E0	2.77E0	2.33E-1
4.587E-2	3.700E2	2.703E1	2.22E0	5.87E0	2.46E0	2.71E-1
4.563E-2	3.680E2	2.717E1	7.67E0	6.71E0	2.28E0	3.13E-1
4.513E-2	3.640E2	2.747E1	6.37E0	6.48E-1	1.80E0	4.99E-1
4.463E-2	3.600E2	2.778E1	5.15E0	2.37E-1	1.17E0	1.11E0
4.414E-2	3.560E2	2.809E1	4.59E0	1.40E-1	9.71E-1	2.29E0
4.364E-2	3.520E2	2.841E1	4.24E0	1.08E-1	1.32E0	3.71E0
4.315E-2	3.480E2	2.874E1	3.98E0	1.02E-1	2.91E0	5.66E0
4.240E-2	3.420E2	2.924E1	3.63E0	1.36E-1	7.30E0	2.27E0
4.191E-2	3.380E2	2.959E1	3.36E0	2.22E-1	6.10E0	8.01E-1
4.141E-2	3.340E2	2.994E1	2.98E0	5.10E-1	5.39E0	4.03E-1
4.092E-2	3.300E2	3.030E1	2.87E0	1.63E0	4.97E0	2.44E-1
4.054E-2	3.270E2	3.058E1	4.36E0	2.14E0	4.75E0	1.81E-1
4.017E-2	3.240E2	3.086E1	4.94E0	9.53E-1	4.58E0	1.40E-1
3.968E-2	3.200E2	3.125E1	4.55E0	3.27E-1	4.41E0	1.04E-1
3.918E-2	3.160E2	3.165E1	4.29E0	1.60E-1	4.28E0	8.11E-2
3.868E-2	3.120E2	3.205E1	4.12E0	9.54E-2	4.18E0	6.51E-2
3.819E-2	3.080E2	3.247E1	4.01E0	6.43E-2	4.10E0	5.36E-2
3.769E-2	3.040E2	3.289E1	3.92E0	4.69E-2	4.03E0	4.49E-2
3.720E-2	3.000E2	3.333E1	3.86E0	3.60E-2	3.97E0	3.83E-2
3.100E-2	2.500E2	4.000E1	3.50E0	8.75E-3	3.63E0	1.02E-2
2.790E-2	2.250E2	4.444E1	3.38E0	1.48E-2	3.56E0	6.64E-3
2.752E-2	2.220E2	4.505E1	3.35E0	1.82E-2	3.55E0	6.33E-3
2.703E-2	2.180E2	4.587E1	3.31E0	2.62E-2	3.54E0	5.96E-3
2.604E-2	2.100E2	4.762E1	3.14E0	9.37E-2	3.53E0	5.29E-3
2.554E-2	2.060E2	4.854E1	2.92E0	3.26E-1	3.52E0	5.00E-3
2.504E-2	2.020E2	4.951E1	3.64E0	1.17E0	3.51E0	4.72E-3
2.455E-2	1.980E2	5.051E1	3.93E0	2.44E-1	3.51E0	4.47E-3

(continued)

TABLE I *(Continued)*

$ZnGeP_2$

eV	cm^{-1}	μm	n_o	k_o	n_e	k_e
2.405E-2	1.940E2	5.155E1	3.74E0	7.86E-2	3.50E0	4.23E-3
2.356E-2	1.900E2	5.263E1	3.64E0	3.83E-2	3.50E0	4.01E-3
2.306E-2	1.860E2	5.376E1	3.59E0	2.30E-2	3.49E0	3.81E-3
2.257E-2	1.820E2	5.495E1	3.55E0	1.56E-2	3.49E0	3.62E-3
2.207E-2	1.780E2	5.618E1	3.53E0	1.14E-2	3.48E0	3.44E-3
2.157E-2	1.740E2	5.747E1	3.51E0	8.88E-3	3.48E0	3.27E-3
2.108E-2	1.700E2	5.882E1	3.49E0	7.19E-3	3.47E0	3.12E-3
2.058E-2	1.660E2	6.024E1	3.48E0	6.03E-3	3.47E0	2.97E-3
2.009E-2	1.620E2	6.173E1	3.47E0	5.21E-3	3.46E0	2.83E-3
1.959E-2	1.580E2	6.329E1	3.45E0	4.66E-3	3.46E0	2.70E-3
1.909E-2	1.540E2	6.494E1	3.44E0	4.39E-3	3.45E0	2.58E-3
1.860E-2	1.500E2	6.667E1	3.42E0	4.67E-3	3.45E0	2.48E-3
1.810E-2	1.460E2	6.849E1	3.39E0	7.66E-3	3.45E0	2.38E-3
1.754E-2	1.415E2	7.067E1	3.51E0	7.02E-1	3.44E0	2.29E-3
1.736E-2	1.400E2	7.143E1	3.60E0	3.97E-2	3.44E0	2.27E-3
1.686E-2	1.360E2	7.353E1	3.48E0	5.34E-3	3.43E0	2.23E-3
1.637E-2	1.320E2	7.576E1	3.46E0	3.16E-3	3.43E0	2.29E-3
1.587E-2	1.280E2	7.813E1	3.44E0	2.48E-3	3.42E0	2.62E-3
1.562E-2	1.260E2	7.937E1	3.44E0	2.28E-3	3.41E0	3.16E-3
1.513E-2	1.220E2	8.197E1	3.43E0	2.00E-3	3.35E0	1.39E-2
1.463E-2	1.180E2	8.475E1	3.43E0	1.80E-3	3.52E0	1.31E-2
1.413E-2	1.140E2	8.772E1	3.42E0	1.64E-3	3.46E0	2.86E-3
1.364E-2	1.100E2	9.091E1	3.42E0	1.50E-3	3.45E0	1.95E-3
1.314E-2	1.060E2	9.434E1	3.41E0	1.39E-3	3.44E0	1.64E-3
1.240E-2	1.000E2	1.000E2	3.41E0	1.24E-3	3.43E0	1.42E-3
6.199E-3	5.000E1	2.000E2	3.39E0	4.76E-4	3.41E0	5.85E-4

Aluminum Oxide (Al_2O_3) Revisited

WILLIAM J. TROPF and MICHAEL E. THOMAS
Applied Physics Laboratory
The Johns Hopkins University
Laurel, Maryland

In a previous volume of this series, Gervais [1] reviewed the optical properties of aluminum oxide. We extend his chapter by providing additional information, much of it recent. Table I gives the anisotropic optical constants of aluminum oxide from 0 to 116 eV.

The hexagonal (rhombohedral) form of aluminum oxide is variously called α-Al_2O_3, alumina (usually applied to the non-fully-dense polycrystalline ceramic), corundum (mineral name), ruby (red [chromium containing] corundum), or sapphire (blue corundum; also frequently used to denote the pure, synthetic crystal). It is a hard, stable material melting at 2319 K. The space group is $R\bar{3}c$ (or D_{3d}^6) with six formula units per unit cell. Room-temperature cell dimensions are 4.759 Å (a-axis) and 12.989 Å (c-axis), giving an x-ray density of 3.987 g/cm^2. Atomic coordinates are as follows: aluminum atoms occupy the 12(c) sites at 0, 0, 0.347 (with point symmetry 3 or C_3) and the oxygen atoms occupy 18(e) sites at 0.306, 0, $\frac{1}{4}$ (with point symmetry 2 or C_2).

Aluminum oxide is a negative, uniaxial crystal transparent from 0.145 to 5.0 μm (ordinary ray) and 0.147 to 5.2 μm (extraordinary ray). Optical anisotropy is small from the extreme ultraviolet through the infrared, becoming larger in the microwave region. Optical-quality crystalline aluminum oxide (or "sapphire") is made by several techniques including Czochralski growth, flame fusion (Verneuil method), the heat-exchanger method (HEM), and the edge-defined, film-fed growth (EFG) techniques. The high mechanical and dielectric strength of aluminum oxide make it a desirable laser host material. Chromium- and titanium-doped aluminum oxide are common solid-state laser-gain media.

Gervais [1] used a compilation of optical constants for amorphous aluminum oxide [2] that do not contain information on the anisotropy of the crystalline state. We supplement this information with single-crystal and polarization measurements as discussed in the following.

Tomiki *et al.* [3] provided the complex dielectric constant, determined

Copyright © 1998 by Academic Press.
All rights of reproduction in any form reserved
ISBN 0-12-544423-0/$25.00.

from a Kramers–Kronig analysis, in digital form with three decimal places. About 600 points were provided for both principal values, covering the range from 6.2 to 119 eV for the real component and above 9 to 119 eV for the imaginary component. Reflectance-measurement accuracy is better than 2.2% ($E > 7.3$ eV) and less accurate at higher energy [4]; therefore, the second decimal place of n and k is uncertain. The complex refractive index (n and k) values determined from selected points of these data are listed in Table I.

Harman *et al.* [5] used Tomiki's data to represent the optical constants of aluminum oxide from 1 to 30 eV using the classical oscillator model with 13 modes. The model reproduces the imaginary refractive index well, but agreement with the real refractive index is poor.

French *et al.* [6] provided the complex refractive index of the ordinary ray of crystalline aluminum oxide determined from an average of several measurements. Optical constants were determined from a Kramers–Kronig analysis of reflectance (to 42 eV, resolution 0.01 to 0.1 eV) and electron-energy-loss (to 140 eV, resolution approximately 0.7 eV) spectra. Optical constants above 119 eV are taken from the electron-energy-loss data, and selected reflectance-measurement values (below 42 eV) are provided in Table I.

Aluminum oxide has a direct band gap of 8.8 eV. Excitonic absorption leads up to the absorption peaks at 9 and 13 eV, which are maxima in the interband transitions between the upper valence band of oxygen ($2p^6$) to the conduction band of triply ionized aluminum ($3s + 3p$ states). Other features at higher frequencies include a plasma oscillation peaking near 25 eV and transitions from oxygen ($2s^2$) to aluminum ($3p$ states) in the 33 to 45 eV region. At higher energies, photoabsorption by the inner core electrons, beginning at the $L_{2,3}$ edge, dominate the spectrum.

Tomiki *et al.* [4] also give the temperature dependence of exciton absorption at the UV edge of the transparent region (8.5–9.0 eV) between 10 and 297 K and fit their measurements to an Urbach rule formulation:

$$\beta(E, T) = \beta_0 \exp(-\sigma_s(T)(E_0 - E)/k_B T), \tag{1a}$$

where $\beta(E, T)$ is the absorption coefficient as a function of energy (E) and temperature (T), and k_B is Boltzmann's constant. The slope parameter $\sigma_s(T)$ is given by

$$\sigma_s(T) = \sigma_{s0}(2k_B T/E_{s0}) \tanh(E_{s0}/2k_B T). \tag{1b}$$

Constants of Eq. (1) are $\beta_0 = 3.87 \times 10^7$ cm^{-1}, $E_0 = 9.314$ eV, $\sigma_{s0} = 0.672$, and $E_{s0} = 33.79$ meV for the ordinary ray (or $\mathbf{E} \perp c$-axis) and $\beta_0 = 1.117 \times 10^7$ cm^{-1}, $E_0 = 9.249$ eV, $\sigma_{s0} = 0.505$, and $E_{s0} = 31.87$ meV for the extraordinary ray (or $\mathbf{E} \parallel c$-axis). The ordinary-ray results agree well with the measurement of Thomas *et al.* [7] near the edge of transparency. Values of the imaginary part of the refractive index between 8.5 and 9.0 eV given in Table I are calculated from this equation using Tomiki's constants.

At energy lower than 8.5 eV, aluminum oxide continues to exhibit considerable absorption due to trace impurities and defects. Innocenzi *et al.* [8] review prior measurements and present chemical analyses and laser-calorimetry absorption data on several aluminum-oxide crystals grown by the Czochralski method. They found that the absorption coefficient between 0.9 and 8.5 eV could be represented by a "weak-absorption-tail" model of the form

$$\beta(E) = \beta_0 \cdot 10^{E/E_0}, \tag{2}$$

where $\beta_0 = 3.13 \times 10^{-5}$ cm^{-1} and $E_0 = 1.7$ eV. Evans [9] performed a similar absorption study using transmission measurements. This work studied aluminum-oxide crystals grown by different techniques and included optical anisotropy. Evans identified the major spectral features as trace impurities and oxygen vacancies (F and F^+ centers). Single-crystal aluminum oxide has very low ultraviolet and visible scatter loss.

Chandrasekharan and Damany [10] measured the ultraviolet birefringence of aluminum oxide between 3.9 and 8.7 eV. The birefringence ($n_e - n_o$) is zero at 0.1426 μm, rises rapidly to -0.0010 at 0.147 μm, has a minimum value of -0.0013 at 0.1595 μm, then slowly falls to -0.0010 near 0.223 μm. Their results generally agree with whose of Tomiki given in Table I and closely match the refractive index and direct birefringence measurements of Jeppesen [11].

Refractive-index data for aluminum oxide in the transparent region are given by several sources [11–15]; measurements [11, 12] are given in Table I. Unfortunately, the preponderance of measurements is for the ordinary ray. Jeppesen [11] measured near-ultraviolet and visible refractive indices at 24° C between 0.25 and 0.7 μm, and Malitson [12] determined the ordinary-ray refractive index between 0.26 and 5.6 μm at 24° C. Malitson [12] and Malitson and Dodge [13] give the refractive index in the form of a Sellmeier-type dispersion formula,

$$n^2(\lambda) - 1 = \sum_i \frac{A_i \lambda^2}{\lambda^2 - \lambda_i^2}, \tag{3}$$

based on minimum-dispersion prism measurements, where the constants A_i and λ_i are given in Table II. Malitson (private communication, 7/11/96) gives the accuracy of the dispersion equation as $\pm 2 \times 10^{-5}$ over the 0.2 to 5.5 μm range.

Harman *et al.* [5] made ellipsometric measurements of both principal values of the dielectric constant of single-crystal aluminum oxide between 1.2 and 5.4 eV. They provide their data as a dispersion equation that agrees reasonably well with the values in Table I (differences in third decimal place).

DeFranzo and Pazol [14] measured the ordinary- and extraordinary-ray refractive index in the visible from 20 to 295 K for aluminum-oxide crystals

grown with the HEM and EFG techniques. The HEM crystal exhibited consistently higher refractive index, between 0.0015 and 0.0020 throughout the measurement range. The indices of both materials appear lower than the measurements of Malitson [12].

Several references give the temperature dependence of the refractive index of aluminum oxide [11, 12, 14–19]. These values are tabulated in Table III. Note that Jeppesen [11] and Feldman *et al.* [17] determined $dn_e/dT > dn_o/dT$, while DeFranzo and Pazol [14] obtained $dn_e/dT < dn_o/dT$. The many dn_o/dT values generally agree, although differences may be 20% or more.

Dodge *et al.* [20] measured the birefringent refractive index of ruby (Al_2O_3 with 0.062% Cr_2O_3 by weight) in the visible. Results are very close to those of Jeppesen [11] for pure aluminum oxide. As the concentration of Cr_2O_3 increases, both refractive indices rise, as shown by the measurements of Mandarino [21]. Wilson [22] measured the temperature coefficient of the refractive index of ruby at 0.633 μm and found $dn_e/dT > dn_o/dT$, in agreement with the measurement of Jeppesen [11].

At the infrared edge of transparency, loss rises because of multiphonon absorption. Several measurements of this loss have been made [23–26]. In aluminum oxide, the absorption falls exponentially with increasing frequency. Deutsch [23] models the absorption coefficient, $\beta(\nu)$, as

$$\beta(\nu) = \beta_0 \exp(-\gamma\nu/\nu_{LO}), \tag{4}$$

where ν is frequency (usually in wave numbers), β_0 is a normalizing constant, ν_{LO} is the maximum longitudinal optical frequency of the material, and γ is another constant (typically between 4 and 5). For aluminum oxide, Deutsch [23], and Thomas and co-workers [24, 25] determined these constants as given in Table IV. Multiphonon-absorption data given in Table I come from measurements by Thomas and co-workers [24, 25] and Gervais *et al.* [26]. Thomas *et al.* [24] gives a multiphonon-absorption model covering all temperatures to the melt.

Harrington *et al.* [27] measured infrared absorption coefficients of aluminum-oxide crystals at HF and DF multiline wavelengths using laser calorimetry. Measured absorption coefficients at DF laser wavelengths (nominally at 3.8μm or 2630 cm^{-1}) were 2.4×10^{-2} and 2.5×10^{-2} cm^{-1} for crystals from Crystal Systems (HEM growth method) and Union Carbide (Czochralski growth), respectively. These values are essentially the intrinsic multiphonon absorption. At HF laser wavelengths (nominally at 2.7 μm or 3700 cm^{-1}), absorption coefficients were 3.4×10^{-3} and 2.6×10^{-3} cm^{-1} for the same samples, far above the intrinsic levels. Aluminum oxide can exhibit significant absorption due to hydrogen, resulting in an OH^- vibrational band peaking at 3278 cm^{-1} [28].

The fundamental lattice vibrations have been studied by Barker [29], Gervais and co-workers [26, 30], and Hoffmann [31]. All model the complex

refractive index in the reststrahlen region. Barker gives the optical modes of aluminum oxide as

$$\Gamma = 2A_{1g}(\mathrm{R}) + 2A_{1u}(-) + 3A_{2g}(-) + 2A_{2u}(\mathrm{IR},\mathbf{E} \parallel \mathbf{c}) + 5E_g(\mathrm{R}) + 4E_u(\mathrm{IR},\mathbf{E} \perp \mathbf{c}), \quad (5)$$

and Table V summarizes measured locations of the infrared-active modes. Porto and Krishnan [32] make the following assignments to the Raman-active modes: A_{1g} vibrations at 418 and 645 cm^{-1} and E_g vibrations at 378, 432, 451, 578, and 751 cm^{-1}.

Refractive indices for the region of fundamental lattice vibrations given in Table I are calculated by the method of Gervais and co-workers [26, 30], essentially duplicating the results reported in 1991 [1]. Real refractive index is calculated over the 200 to 1400 cm^{-1} interval and at 100 cm^{-1} for comparison to low-frequency measurements. The imaginary index is calculated between 200 and 1000 cm^{-1} to avoid regions of multiphonon absorption, which are not represented by this model.

Barker [29] gives a classical oscillator model for the far-infrared optical constants of aluminum oxide, and Harman *et al.* [5] give a refined model based on reanalysis of Barker's reflectance data.

Below 300 cm^{-1}, absorption arises from the red wing of the one-phonon resonances and from multiphonon difference bands. Several measurements of the real refractive index and absorption coefficient [33–38] cover the 5–200 cm^{-1} region. Values from these references are given in Table I.

Low-frequency measurements (1 MHz) of Fontella *et al.* [39], made by the method of substitution, give the static dielectric constant as $\epsilon_o = 9.395 \pm 0.005$ (or $n_o = 3.065 \pm 0.001$) for the ordinary ray ($\mathbf{E} \perp \mathbf{c}$) and $\epsilon_e = 11.589 \pm 0.005$ (or $n_e = 3.404 \pm 0.001$) for the extraordinary ray ($\mathbf{E} \parallel \mathbf{c}$). These values agree well with extrapolated values from Russell and Bell [33], Loewenstein *et al.* [34], Roberts and Coon [37], and Grischkowsky *et al.* [38].

Figures 1 and 2 shows a composite of the principal values of the complex refractive index of aluminum oxide taken from all of the data sources.

ACKNOWLEDGMENTS

We thank Professor T. Tomiki, University of Ryukyus (retired), for graciously providing digital data from his measurements. We acknowledge and greatly appreciate the information provided by Mr. I. H. Malitson, (NBS, retired) on refractive-index measurements and dispersion equations. We also thank Dr. R. H. French and Mr. D. J. Jones of DuPont Company for reanalyzing their measurements and providing their data in digital form.

REFERENCES

1. F. Gervais, Aluminum oxide (Al_2O). *in* "Handbook of Optical Constants of Solids II," (E. D. Palik, ed.), pp. 761–775. Academic Press, San Diego, 1991.
2. H.-J. Hagemann, W. Gudat, and C. Kunz, Optical constants from the far infrared to the

x-ray region: Mg, Al, Cu, Ag, Au, Bi, C, and Al_2O_3. *J. Opt. Soc. Am.* **65**, 742–744 (1975); H.-J. Hagemann, W. Gudat, and C. Kunz, Optical constants from the far infrared to the x-ray region: Mg, Al, Cu, Ag, Au, Bi, C, and Al_2O_3, *DESY* **SR-74/7** (Hamburg, 1974).

3. T. Tomiki, Y. Ganaha, T. Futemma, T. Shikenbaru, Y. Aiura, M. Yuri, S. Sato, H. Fututani, H. Kato, T. Miyahara, J. Tamashiro, and A. Yonesu, Anisotropic optical spectra of α-Al_2O_3 single crystals in the vacuum ultraviolet region. II. Spectra of optical constants. *J. Phys. Soc. Jpn.* **62**, 1372–1387 (1993).
4. T. Tomiki, Y. Ganaha, T. Shikenbaru, T. Futemma, M. Yuri, Y. Aiura, S. Sato, H. Fukutani, H. Kato, T. Miyahara, A. Yonesu, and J. Tamashiro, Anisotropic optical spectra of α-Al_2O single crystals in the vacuum ultraviolet region. I. Spectra of absorption tail and reflectivity. *J. Phys. Soc. Jpn.* **62**, 573–584 (1993).
5. A. K. Harman, S. Ninomiya, and S. Adachi, Optical constants of sapphire (α-Al_2O_3) single crystals. *J. Appl. Phys.* **76**, 8032–8036 (1994).
6. R. H. French, H. Müllejans, and D. J. Jones, Optical properties of aluminum oxide determined from vacuum ultraviolet and electron energy loss spectroscopies. *J. Am. Ceram. Soc.* submitted.
7. M. E. Thomas, W. J. Tropf, and S. L. Gilbert, Vacuum-ultraviolet characterization of sapphire, ALON, and spinel near the band gap. *Opt. Eng.* **32**, 1340–1343 (1993).
8. M. E. Innocenzi, R. T. Swimm, M. Bass, R. H. French, A. B. Villaverde, and M. R. Kokta, Room-temperature optical absorption in undoped α-Al_2O_3. *J. Appl. Phys.* **67**, 7542–7546 (1990).
9. B. D. Evans, Optical transmission in undoped crystalline α-Al_2O_3 grown by several techniques. *J.Appl. Phys.* **70**, 3995–3997 (1991).
10. V. Chandrasekharan and H. Damany, Birefringence of sapphire, magnesium fluoride, and quartz in the vacuum ultraviolet, and retardation plates. *Appl. Opt.* **7**, 939–941 (1968); V. Chandrasekharan and H. Damany, Anomalous dispersion of birefringence of sapphire and magnesium fluoride in the vacuum ultraviolet. *Appl. Opt.* **8**, 671–675 (1969).
11. M. A. Jeppesen, Some optical, thermo-optical, and piezo-optical properties of synthetic sapphire. *J. Opt. Soc. Am.* **48**, 629–632 (1958).
12. I. H. Malitson, Refraction and dispersion of synthetic sapphire. *J. Opt. Soc. Am.* **52**, 1377–1379 (1962); I. H. Malitson, F. V. Murphy, and W. S. Rodney, Refractive index of synthetic sapphire. *J. Opt. Soc. Am.* **48**, 72–73 (1958).
13. I. H. Malitson and M. J. Dodge, Refractive index and birefringence of synthetic sapphire. *J. Opt. Soc. Am.* **62**, 1405 (1972); the cited dispersion equation is given in M. J. Dodge, Refractive index. *in* "Handbook of Laser Science and Technology, Volume IV, Optical Material: Part 2" (M. J. Weber, ed.), CRC Press, Boca Raton, Florida, 1986.
14. A. C. DeFranzo and B. G. Pazol, Index of refraction measurements on sapphire at low temperatures and visible wavelengths. *Appl. Opt.* **32**, 2224–2234 (1993).
15. J. Tapping and M. L. Reilly, Index of refraction of sapphire between 24 and 1060°C for wavelengths of 633 and 799 nm. *J. Opt. Soc. Am. A* **3**, 610–616 (1986).
16. E. S. Zouboulis and M. Grimsditch, Refractive index and elastic properties of single-crystal corundum (α-Al_2O_3) up to 2100 K. *J. Appl. Phys.* **70**, 772–776 (1991).
17. A. Feldman, D. Horowitz, R. M. Walker, and M. J. Dodge, "Optical Materials Characterization Final Technical Report, February 1, 1978–September 30, 1978," NBS Technical Note 993, February 1979.
18. V. I. Bukatyi, Yu. V. Goncharov, V. N. Krasnopevtsev, A. M. Shaiduk, V. P. Lushev, A. A. Pavlenko, and M. G. Potapov, Study of the temperature dependence of the refractive index of sapphire. *Opt. Spectrosc.* **56**, 283–285 (1984).
19. C. H. Lange and D. D. Duncan, Temperature coefficient of refractive index for candidate optical windows. *SPIE Proc.* **1326**, 71–78 (1990).
20. M. J. Dodge, I. H. Malitson, and A. I. Mahan, A special method for precise refractive index measurement of uniaxial optical media. *Appl. Opt.* **8**, 1703–1705 (1969).

21. J. A. Mandarino, Refraction, absorption, and biabsorption in synthetic ruby. *Am. Mineral.* **44**, 961–973 (1959).
22. K. E. Wilson, Thermo-optics of nonlinear crystals and laser materials. Ph.D. Dissertation, University of Southern California, Los Angeles (January 1980).
23. T. F. Deutsch, Absorption coefficient of infrared laser window materials. *J. Phys. Chem. Solids* **34**, 2091–2104 (1973); also see T. F. Deutsch, Laser window materials—An overview. *J. Electron. Mater.* **4**, 663–719 (1975).
24. M. E. Thomas, R. I. Joseph, and W. J. Tropf, Infrared transmission properties of sapphire, spinel, yttria, and ALON as a function of temperature and frequency. *Appl. Opt.* **27**, 239–245 (1988).
25. M. E. Thomas, Infrared properties of the extraordinary ray multiphonon processes in sapphire. *Appl. Opt.* **28**, 3277–3278 (1989).
26. F. Gervais, D. Billard, and B. Piriou, High temperature phonon self-energy: An application to infrared spectra of corundum Al_2O_3. *Rev. Int. Haut. Temp. Refract.* **12**, 58–62 (1975).
27. J. A. Harrington, D. A. Gregory, and W. F. Ott, Infrared absorption in chemical laser window materials. *Appl. Opt.* **15**, 1953–1959 (1976).
28. T. J. Turner and J. H. Crawford, V Centers in single crystal Al_2O_3. *Solid State Commun.* **17**, 167–169 (1975).
29. A. S. Barker, Infrared lattice vibrations and dielectric dispersion in corundum. *Phys. Rev.* **132**, 1474–1481 (1963).
30. F. Gervais and B. Piriou, Anharmonicity in several-polar-mode crystals: Adjusting phonon self-energy of LO and TO modes in Al_2O_3 and TiO_2 to fit infrared reflectivity. *J. Phys. C* **7**, 2374–2386 (1974).
31. C. Hoffmann, Optical constants of infrared active phonons as a function of temperature. Masters Essay, The Johns Hopkins University, Baltimore, Maryland (1988).
32. S. P. S. Porto and R. S. Krishnan, Raman effect of corundum. *J. Chem Phys.* **47**, 1009–1012 (1967).
33. E. E. Russell and E. E. Bell, Optical constants of sapphire in the far infrared. *J. Opt. Soc. Am.* **57**, 543–544 (1967).
34. E. V. Loewenstein, D. R. Smith, and R. L. Morgan, Optical constants of far infrared materials 2: Crystalline solids. *Appl. Opt.* **12**, 398–406 (1973).
35. W. B. Cook and S. Perkowitz, Temperature dependence of the far-infrared ordinary-ray optical constants of sapphire. *Appl. Opt.* **24**, 1773–1775 (1985).
36. V. P. Bystrov, Yu. G. Goncharov, G. V. Kozlov, and A. F. Kupriyanenko, Dielectric properties of optical crystals at submillimeter wavelengths. *Sov. Phys. Tech. Phys. (Engl. Transl.)* **31** 1206–1207 (1986).
37. S. Roberts and D. D. Coon, Far-infrared properties of quartz and sapphire. *J. Opt. Soc. Am.* **52**, 1023–1029 (1962).
38. D. Grischkowsky, S. Keiding, M. van Exter, and C. Fattinger, Far-infrared time-domain spectroscopy with terahertz beams of dielectrics and semiconductors. *J. Opt. Soc. Am. B* **7**, 2006–2015 (1990).
39. J. Fontella, C. Andeen, and D. Schuele, Low-frequency dielectric constants of α-quartz, sapphire, MgF_2, and MgO. *J. Appl. Phys.* **45**, 2852–2854 (1974).

NOTE ADDED IN PROOF

Temperature-dependence of the ultraviolet absorption edge, based on exciton and band locations, is given by French, *et al.*, [40] from 0 K to the melt.

40. R. H. French, D. J. Jones, and S. Loughin, Interband electronic structure of α-alumina up to 2167 K. *J. Am. Ceram. Soc.* **77**, 412-422 (1994).

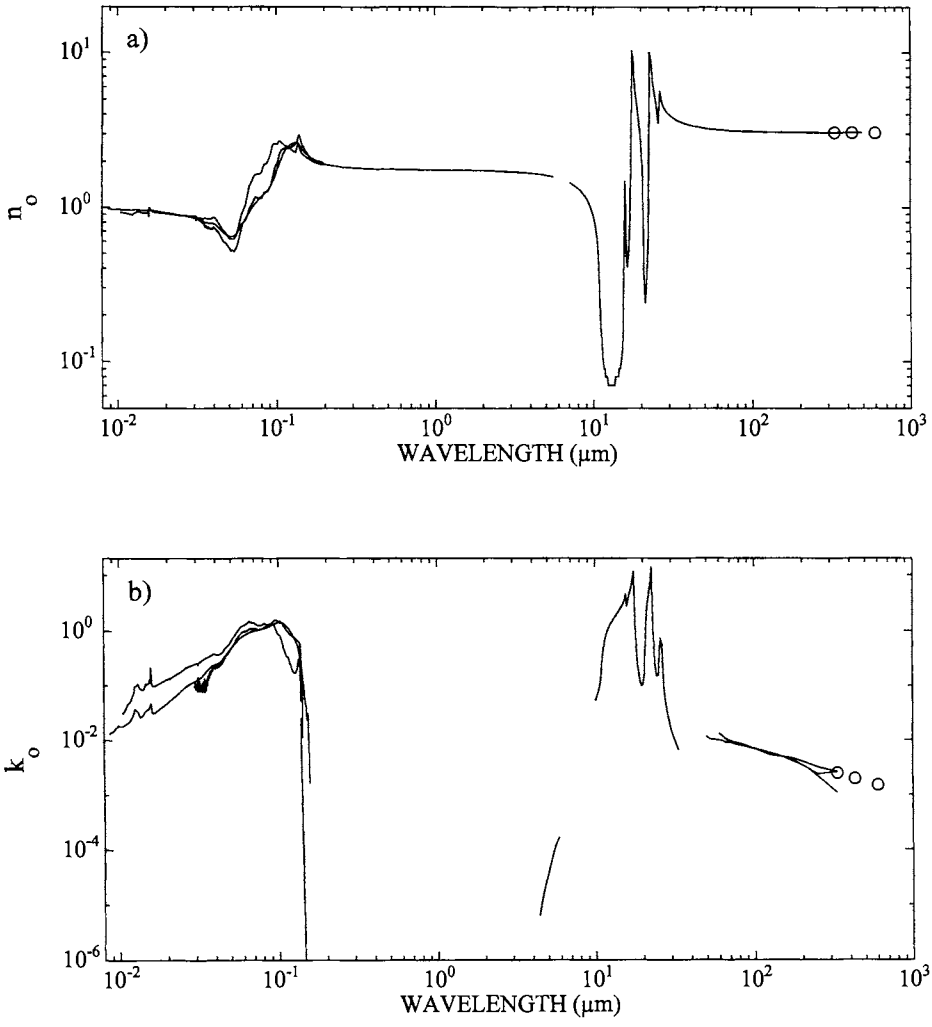

Fig. 1. (a) Log–log plot of the ordinary-ray index of refraction n_o versus wavelength in micrometers for aluminum oxide. (b) Log–log plot of the ordinary-ray extinction coefficient k_o versus wavelength in micrometers for aluminum oxide. Lines are data sets of many points; scattered data are indicated by circles.

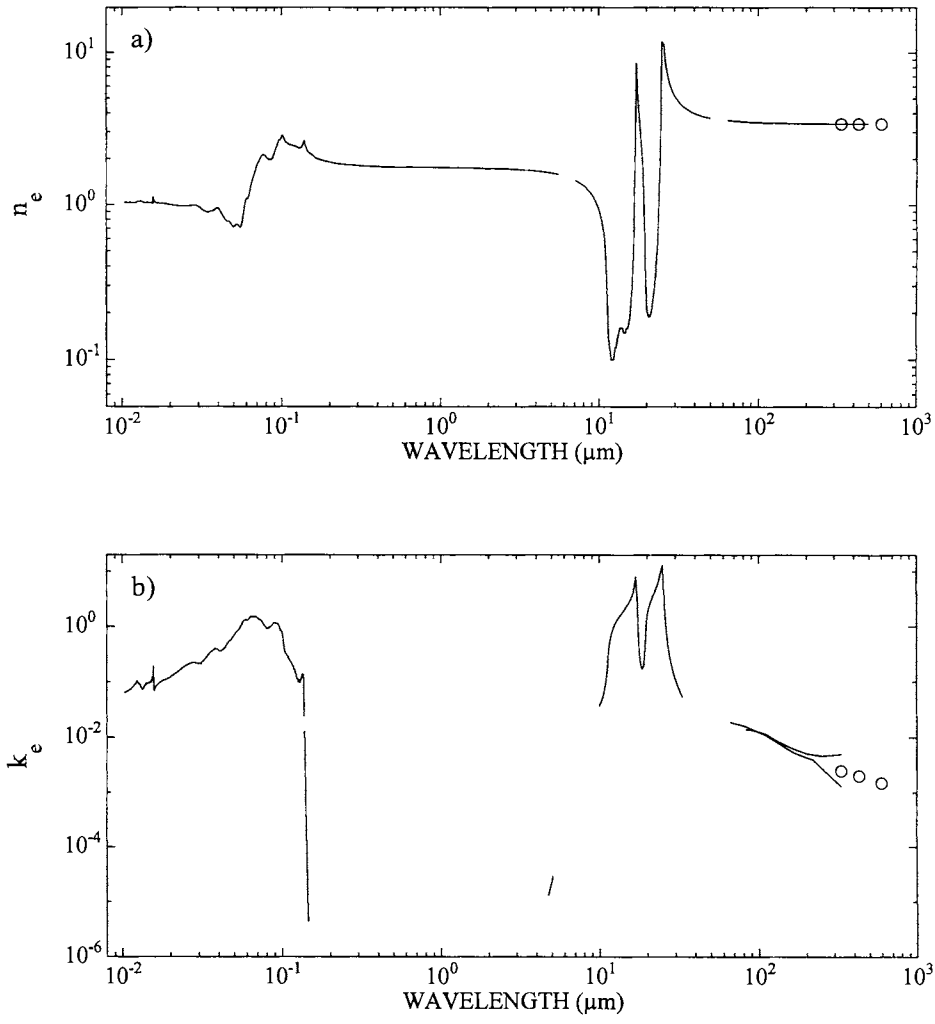

Fig. 2. (a) Log–log plot of the extraordinary-ray index of refraction n_e versus wavelength in micrometers for aluminum oxide. (b) Log–log plot of the extraordinary-ray extinction coefficient k_e versus wavelength in micrometers for aluminum oxide. Lines are data sets of many points; scattered data are indicated by circles.

TABLE I

Values of n and k for Aluminum Oxide (Al_2O_3) from Various References[a]

eV	cm^{-1}	μm	n_o	k_o	n_e	k_e
142.000	1145298	0.008731	0.975 [6]	0.0130 [6]		
141.020	1137394	0.008792	0.975	0.0135		
140.040	1129490	0.008854	0.975	0.0138		
139.000	1121102	0.008920	0.975	0.0139		
138.030	1113278	0.008982	0.975	0.0140		
137.050	1105374	0.009047	0.975	0.0141		
136.010	1096986	0.009116	0.975	0.0143		
135.040	1089162	0.009181	0.974	0.0145		
134.000	1080774	0.009253	0.974	0.0147		
133.020	1072870	0.009321	0.974	0.0150		
132.040	1064966	0.009390	0.973	0.0156		
131.010	1056659	0.009464	0.973	0.0161		
130.030	1048754	0.009535	0.973	0.0165		
129.050	1040850	0.009608	0.973	0.0168		
128.010	1032462	0.009686	0.973	0.0170		
127.040	1024639	0.009760	0.973	0.0174		
126.000	1016250	0.009840	0.973	0.0182		
125.020	1008346	0.009917	0.974	0.0182		
124.050	1000523	0.009995	0.974	0.0178		
123.010	992135	0.010079	0.973	0.0177		
122.030	984231	0.010160	0.973	0.0177		
121.060	976407	0.010242	0.973	0.0177		
120.020	968019	0.010330	0.972	0.0177		
119.897	967027	0.01034			1.035 [3]	0.063 [3]
118.800	958179	0.01044	0.972 [6]	0.0178 [6]		
118.691	957300	0.01045			1.037	0.064
118.182	953195	0.01049	0.929 [3]	0.031 [3]		
118.081	952380	0.01050			1.035	0.064
117.577	948315	0.01055	0.928	0.032		
117.477	947508	0.01055			1.035	0.065
116.967	943395	0.01060	0.927	0.032		
116.868	942597	0.01061			1.035	0.066
116.363	938523	0.01066	0.927	0.033		
116.265	937733	0.01066			1.034	0.066
115.453	931184	0.01074	0.925	0.034		
115.356	930402	0.01075			1.034	0.068
114.546	923868	0.01082	0.924	0.036		
114.441	923022	0.01083			1.034	0.069
113.936	918949	0.01088	0.923	0.036		
113.842	918190	0.01089			1.033	0.069
113.032	911657	0.01097	0.921	0.038		
112.929	910827	0.01098			1.033	0.070
112.122	904318	0.01106	0.919	0.040		
112.021	903503	0.01107			1.033	0.071
111.217	897018	0.01115	0.918	0.042		

[a] References given in brackets.

TABLE I *(Continued)*

Aluminum Oxide (Al_2O_3)

eV	cm^{-1}	μm	n_o	k_o	n_e	k_e
111.108	896139	0.01116			1.032	0.072
110.307	889679	0.01124	0.918	0.045		
110.199	888808	0.01125	0.918	0.045	1.031	0.073
108.692	876653	0.01141	0.916	0.046	1.030	0.076
107.776	869265	0.01150	0.914	0.048	1.030	0.077
106.874	861990	0.01160	0.912	0.049	1.028	0.079
105.961	854626	0.01170	0.909	0.051	1.028	0.082
105.054	847311	0.01180	0.907	0.054	1.029	0.085
104.145	839979	0.01191	0.904	0.058	1.029	0.087
103.235	832640	0.01201	0.902	0.062	1.030	0.089
102.020	822840	0.01215	0.900	0.068	1.031	0.093
101.113	815525	0.01226	0.895	0.072	1.032	0.098
100.206	808209	0.01237	0.892	0.088	1.040	0.104
99.299	800894	0.01249	0.906	0.098	1.050	0.100
98.082	791078	0.01264	0.913	0.099	1.052	0.094
97.175	783763	0.01276	0.918	0.102	1.053	0.090
96.269	776456	0.01288	0.922	0.102	1.053	0.088
95.051	766632	0.01304	0.931	0.107	1.054	0.084
94.142	759300	0.01317	0.940	0.101	1.052	0.078
93.236	751993	0.01330	0.942	0.094	1.048	0.074
92.025	742226	0.01347	0.939	0.087	1.039	0.074
91.119	734918	0.01361	0.935	0.087	1.034	0.078
90.204	727539	0.01374	0.936	0.086	1.031	0.082
89.294	720199	0.01389	0.932	0.083	1.030	0.086
88.083	710432	0.01408	0.925	0.085	1.031	0.093
87.178	703132	0.01422	0.922	0.087	1.033	0.092
86.268	695793	0.01437	0.915	0.094	1.032	0.095
85.055	686009	0.01458	0.920	0.105	1.033	0.095
84.149	678702	0.01473	0.925	0.104	1.032	0.096
83.239	671362	0.01490	0.922	0.108	1.031	0.100
82.028	661595	0.01511	0.923	0.107	1.032	0.099
81.116	654239	0.01528	0.917	0.115	1.025	0.109
79.996	645206	0.01550	0.929	0.130	1.043	0.118
79.934	644706	0.01551	0.929	0.129	1.042	0.117
79.903	644456	0.01552	0.930	0.129	1.043	0.117
79.846	643996	0.01553	0.931	0.127	1.043	0.115
79.784	643496	0.01554	0.930	0.126	1.042	0.114
79.723	643004	0.01555	0.931	0.124	1.041	0.113
79.661	642504	0.01556	0.930	0.122	1.038	0.112
79.600	642012	0.01558	0.927	0.119	1.035	0.112
79.539	641520	0.01559	0.923	0.115	1.030	0.113
79.483	641069	0.01560	0.916	0.113	1.025	0.117
79.422	640577	0.01561	0.907	0.114	1.018	0.124
79.361	640085	0.01562	0.893	0.120	1.017	0.137
79.300	639593	0.01563	0.881	0.133	1.017	0.155
79.239	639101	0.01565	0.874	0.157	1.030	0.176
79.178	638609	0.01566	0.883	0.183	1.056	0.186

(continued)

TABLE I *(Continued)*

Aluminum Oxide (Al_2O_3)

eV	cm^{-1}	μm	n_o	k_o	n_e	k_e
79.118	638125	0.01567	0.906	0.206	1.088	0.183
79.057	637633	0.01568	0.939	0.214	1.116	0.161
78.997	637149	0.01569	0.968	0.200	1.116	0.124
78.936	636657	0.01571	0.978	0.175	1.108	0.108
78.876	636173	0.01572	0.976	0.157	1.089	0.102
78.816	635689	0.01573	0.965	0.151	1.081	0.107
78.756	635205	0.01574	0.959	0.157	1.083	0.115
78.691	634681	0.01576	0.964	0.165	1.092	0.114
78.631	634197	0.01577	0.976	0.166	1.100	0.107
78.571	633713	0.01578	0.989	0.162	1.104	0.094
78.511	633229	0.01579	0.997	0.150	1.099	0.082
78.452	632753	0.01580	0.998	0.134	1.091	0.074
78.387	632229	0.01582	0.993	0.125	1.083	0.071
78.328	631753	0.01583	0.990	0.120	1.076	0.070
78.268	631269	0.01584	0.986	0.117	1.070	0.070
78.209	630793	0.01585	0.982	0.114	1.066	0.071
78.145	630277	0.01587	0.979	0.111	1.063	0.071
78.086	629801	0.01588	0.977	0.110	1.060	0.072
78.027	629325	0.01589	0.975	0.109	1.058	0.073
77.963	628809	0.01590	0.973	0.107	1.056	0.073
77.905	628341	0.01591	0.972	0.107	1.054	0.074
77.846	627865	0.01593	0.970	0.106	1.053	0.075
77.782	627349	0.01594	0.968	0.105	1.051	0.075
77.724	626881	0.01595	0.967	0.104	1.050	0.076
77.661	626373	0.01596	0.966	0.103	1.049	0.076
77.602	625897	0.01598	0.965	0.103	1.048	0.076
77.539	625389	0.01599	0.964	0.103	1.047	0.077
77.481	624921	0.01600	0.963	0.102	1.046	0.077
77.100	621849	0.01608	0.958	0.100		
77.000	621042	0.01610			1.040	0.080
76.501	617017	0.01621	0.952	0.098	1.036	0.083
75.901	612178	0.01634	0.947	0.098		
75.499	608936	0.01642			1.031	0.087
75.002	604927	0.01653	0.942	0.099	1.029	0.088
74.398	600056	0.01667	0.939	0.100	1.026	0.091
74.101	597660	0.01673	0.938	0.100	1.025	0.092
73.499	592805	0.01687	0.935	0.100	1.024	0.094
72.001	580723	0.01722	0.930	0.104	1.022	0.099
71.101	573464	0.01744	0.928	0.106	1.020	0.100
70.199	566189	0.01766	0.926	0.108	1.019	0.103
68.999	556510	0.01797	0.923	0.111	1.017	0.105
68.101	549267	0.01821	0.921	0.114	1.015	0.107
66.900	539581	0.01853	0.920	0.117	1.013	0.110
65.999	532314	0.01879	0.918	0.120	1.012	0.111
65.101	525071	0.01905	0.917	0.123	1.009	0.113
64.201	517812	0.01931	0.915	0.126	1.007	0.115
63.001	508133	0.01968	0.915	0.130	1.003	0.119

TABLE I *(Continued)*

Aluminum Oxide (Al_2O_3)

eV	cm^{-1}	μm	n_o	k_o	n_e	k_e
62.101	500874	0.01997	0.913	0.131	0.999	0.122
61.200	493607	0.02026	0.911	0.134	0.997	0.126
60.001	483937	0.02066	0.911	0.136	0.995	0.130
59.100	476670	0.02098	0.905	0.139	0.992	0.135
58.201	469419	0.02130	0.903	0.143	0.990	0.139
56.999	459724	0.02175	0.900	0.148	0.986	0.144
56.099	452465	0.02210	0.897	0.152	0.983	0.149
55.200	445214	0.02246	0.895	0.157	0.980	0.155
54.000	435536	0.02296	0.892	0.164	0.977	0.164
53.101	428285	0.02335	0.890	0.169	0.976	0.171
52.200	421018	0.02375	0.888	0.174	0.977	0.178
51.000	411339	0.02431	0.884	0.182	0.976	0.185
50.099	404072	0.02475	0.881	0.188	0.976	0.193
49.200	396822	0.02520	0.879	0.196	0.977	0.199
48.000	387143	0.02583	0.878	0.207	0.979	0.207
47.100	379884	0.02632	0.879	0.216	0.980	0.212
46.199	372617	0.02684	0.880	0.223	0.982	0.217
45.000	362947	0.02755	0.881	0.230	0.985	0.222
44.099	355680	0.02812	0.881	0.236	0.988	0.224
43.200	348429	0.02870	0.880	0.241	0.989	0.221
42.000	338750	0.02952	0.882 [3]	0.249 [3]	0.983	0.215
			0.859 [6]	0.098 [6]		
41.100	331491	0.03017	0.875 [3]	0.252 [3]	0.967	0.214
40.200	324232	0.03084	0.882	0.256	0.960	0.216
39.000	314554	0.03179	0.859	0.269	0.931	0.235
38.100	307295	0.03254	0.854	0.282	0.916	0.252
37.200	300036	0.03333	0.851	0.297	0.906	0.274
36.000	290357	0.03444	0.849	0.316	0.894	0.309
35.100	283098	0.03532	0.851	0.329	0.900	0.338
34.200	275839	0.03625	0.846	0.339	0.907	0.356
33.000	266161	0.03757	0.842	0.361	0.916	0.390
32.100	258902	0.03862	0.843	0.379	0.941	0.396
31.200	251643	0.03974	0.859	0.387	0.950	0.380
30.000	241964	0.04133	0.841	0.367	0.901	0.360
29.100	234705	0.04261	0.800	0.379	0.858	0.384
28.302	228269	0.04381	0.764	0.400	0.814	0.416
27.984	225704	0.04431	0.749	0.411	0.798	0.439
27.673	223196	0.04480	0.731	0.427	0.787	0.465
27.369	220744	0.04530	0.716	0.448	0.780	0.490
27.072	218349	0.04580	0.706	0.472	0.778	0.512
27.013	217873	0.04590	0.605 [6]	0.317 [6]		
26.891	216889	0.04611	0.596	0.328		
26.799	216147	0.04626	0.592	0.335		
26.780	215994	0.04630	0.703 [3]	0.492 [3]	0.776	0.534
26.738	215655	0.04637	0.590 [6]	0.344 [6]		
26.616	214671	0.04658	0.593	0.353		
26.496	213703	0.04679	0.698 [3]	0.508 [3]	0.776	0.550

(continued)

TABLE I *(Continued)*

Aluminum Oxide (Al_2O_3)

eV	cm^{-1}	μm	n_o	k_o	n_e	k_e
26.494	213687	0.04680	0.593 [6]	0.359 [6]		
26.311	212211	0.04712	0.594	0.369		
26.219	211469	0.04729	0.590	0.371		
26.217	211453	0.04729	0.691 [3]	0.519 [3]	0.772	0.562
26.127	210727	0.04745	0.590 [6]	0.376 [6]		
26.005	209743	0.04768	0.584	0.380		
25.944	209251	0.04779	0.676 [3]	0.538 [3]	0.760	0.575
25.914	209009	0.04784	0.582 [6]	0.386 [6]		
25.700	207283	0.04824	0.575	0.396		
25.676	207089	0.04829	0.666 [3]	0.556 [3]	0.744	0.595
25.609	206549	0.04841	0.572 [6]	0.399 [6]		
25.425	205065	0.04877	0.560	0.419		
25.414	204976	0.04879	0.652 [3]	0.578 [3]	0.730	0.625
25.303	204081	0.04900	0.559 [6]	0.426 [6]		
25.212	203347	0.04918	0.557	0.431		
25.158	202911	0.04928	0.640 [3]	0.604 [3]	0.723	0.655
25.120	202605	0.04936	0.552 [6]	0.438 [6]		
24.907	200887	0.04978	0.545	0.461		
24.906	200879	0.04978	0.629 [3]	0.633 [3]	0.717	0.688
24.815	200145	0.04996	0.544 [6]	0.465 [6]		
24.723	199403	0.05015	0.540	0.474		
24.659	198887	0.05028	0.622 [3]	0.667 [3]	0.717	0.725
24.601	198419	0.05040	0.536 [6]	0.481 [6]		
24.510	197685	0.05059	0.531	0.495		
24.418	196943	0.05078	0.621 [3]	0.698 [3]	0.725	0.756
24.418	196943	0.05078	0.529 [6]	0.500 [6]		
24.204	195217	0.05123	0.522	0.537		
24.180	195023	0.05128	0.620 [3]	0.728 [3]	0.733	0.782
24.113	194483	0.05142	0.524 [6]	0.542 [6]		
24.021	193741	0.05162	0.523	0.558		
23.948	193152	0.05177	0.620 [3]	0.758 [3]	0.739	0.804
23.930	193007	0.05181	0.527 [6]	0.564 [6]		
23.808	192023	0.05208	0.527	0.577		
23.720	191313	0.05227	0.622 [3]	0.785 [3]	0.742	0.825
23.716	191281	0.05228	0.526 [6]	0.581 [6]		
23.502	189555	0.05276	0.524	0.608		
23.496	189507	0.05277	0.618 [3]	0.817 [3]	0.741	0.845
23.411	188821	0.05296	0.523 [6]	0.616 [6]		
23.319	188079	0.05317	0.520	0.627		
23.277	187740	0.05327	0.619 [3]	0.851 [3]	0.734	0.868
23.228	187345	0.05338	0.517 [6]	0.638 [6]		
23.106	186361	0.05366	0.515	0.663		
23.061	185998	0.05376	0.622 [3]	0.890 [3]	0.724	0.898
23.014	185619	0.05387	0.517 [6]	0.678 [6]		
22.922	184877	0.05409	0.522	0.695		
22.849	184288	0.05426	0.631 [3]	0.927 [3]	0.714	0.938
22.800	183893	0.05438	0.527 [6]	0.707 [6]		

TABLE I *(Continued)*

Aluminum Oxide (Al_2O_3)

eV	cm^{-1}	μm	n_o	k_o	n_e	k_e
22.709	183159	0.05460	0.529	0.720		
22.642	182619	0.05476	0.642 [3]	0.962 [3]	0.709	0.985
22.617	182417	0.05482	0.531 [6]	0.734 [6]		
22.526	181683	0.05504	0.535	0.752		
22.438	180973	0.05526	0.653 [3]	1.000 [3]	0.712	1.039
22.404	180699	0.05534	0.543 [6]	0.766 [6]		
22.312	179957	0.05557	0.546	0.786		
22.238	179360	0.05575	0.668 [3]	1.039 [3]	0.723	1.098
22.220	179215	0.05580	0.554 [6]	0.797 [6]		
22.129	178481	0.05603	0.560	0.815		
22.041	177771	0.05625	0.690 [3]	1.077 [3]	0.747	1.158
22.007	177497	0.05634	0.574 [6]	0.828 [6]		
21.915	176755	0.05658	0.581	0.848		
21.847	176207	0.05675	0.716 [3]	1.110 [3]	0.784	1.217
21.824	176021	0.05681	0.593 [6]	0.854 [6]		
21.702	175037	0.05713	0.602	0.874		
21.658	174682	0.05725	0.742 [3]	1.142 [3]	0.834	1.266
21.610	174295	0.05737	0.614 [6]	0.885 [6]		
21.518	173553	0.05762	0.625	0.896		
21.471	173174	0.05775	0.772 [3]	1.170 [3]	0.892	1.300
21.427	172819	0.05786	0.636 [6]	0.907 [6]		
21.305	171835	0.05820	0.655	0.918		
21.287	171690	0.05824	0.803 [3]	1.196 [3]	0.948	1.321
21.213	171093	0.05845	0.665 [6]	0.923 [6]		
21.122	170359	0.05870	0.675	0.934		
21.107	170238	0.05874	0.839 [3]	1.216 [3]	1.003	1.331
21.000	169375	0.05904	0.691 [6]	0.946 [6]		
20.929	168802	0.05924	0.871 [3]	1.226 [3]	1.051	1.326
20.908	168633	0.05930	0.703 [6]	0.950 [6]		
20.816	167891	0.05956	0.714	0.961		
20.755	167399	0.05974	0.895 [3]	1.237 [3]	1.083	1.313
20.725	167157	0.05982	0.729 [6]	0.965 [6]		
20.603	166173	0.06018	0.743	0.973		
20.584	166020	0.06023	0.917 [3]	1.245 [3]	1.095	1.304
20.511	165431	0.06045	0.756 [6]	0.974 [6]		
20.420	164697	0.06072	0.770	0.987		
20.415	164657	0.06073	0.932 [3]	1.258 [3]	1.098	1.310
20.328	163955	0.06099	0.787 [6]	0.978 [6]		
20.249	163318	0.06123	0.948 [3]	1.276 [3]	1.099	1.333
20.085	161995	0.06173	0.966	1.298	1.111	1.368
20.084	161987	0.06173	0.793 [6]	0.978 [6]		
19.992	161245	0.06202	0.800	0.983		
19.925	160705	0.06223	0.986 [3]	1.318 [3]	1.134	1.406
19.840	160019	0.06249	0.815 [6]	0.997 [6]		
19.767	159430	0.06272	1.007 [3]	1.343 [3]	1.169	1.448
19.748	159277	0.06278	0.820 [6]	0.992 [6]		
19.657	158543	0.06307	0.821	0.998		

(continued)

TABLE I *(Continued)*

Aluminum Oxide (Al_2O_3)

eV	cm^{-1}	μm	n_o	k_o	n_e	k_e
19.611	158172	0.06322	1.034 [3]	1.372 [3]	1.218	1.481
19.565	157801	0.06337	0.824 [6]	1.010 [6]		
19.473	157059	0.06367	0.833	1.025		
19.458	156938	0.06372	1.068 [3]	1.397 [3]	1.273	1.505
19.382	156325	0.06397	0.843 [6]	1.033 [6]		
19.307	155720	0.06422	1.106 [3]	1.422 [3]	1.331	1.515
19.290	155583	0.06427	0.850 [6]	1.039 [6]		
19.199	154849	0.06458	0.861	1.058		
19.158	154518	0.06472	1.152 [3]	1.443 [3]	1.384	1.515
19.138	154357	0.06478	0.873 [6]	1.066 [6]		
19.016	153373	0.06520	0.891	1.071		
19.012	153341	0.06521	1.201 [3]	1.452 [3]	1.429	1.510
18.954	152873	0.06541	0.901 [6]	1.079 [6]		
18.893	152381	0.06562	0.912	1.083		
18.868	152179	0.06571	1.247 [3]	1.456 [3]	1.468	1.507
18.832	151889	0.06584	0.923 [6]	1.084 [6]		
18.771	151397	0.06605	0.932	1.087		
18.726	151034	0.06621	1.292 [3]	1.449 [3]	1.504	1.504
18.680	150663	0.06637	0.951 [6]	1.093 [6]		
18.588	149921	0.06670	0.967	1.087		
18.587	149913	0.06671	1.330 [3]	1.441 [3]	1.540	1.508
18.497	149187	0.06703	0.974 [6]	1.082 [6]		
18.449	148800	0.06720	1.364 [3]	1.430 [3]	1.582	1.507
18.375	148203	0.06747	0.993 [6]	1.087 [6]		
18.313	147703	0.06770	1.392 [3]	1.420 [3]	1.623	1.504
18.283	147461	0.06781	0.998 [6]	1.080 [6]		
18.191	146719	0.06816	1.014	1.092		
18.180	146630	0.06820	1.417 [3]	1.412 [3]	1.666	1.502
18.100	145985	0.06850	1.017 [6]	1.077 [6]		
18.048	145566	0.06870	1.442 [3]	1.407 [3]	1.710	1.492
18.008	145243	0.06885	1.028 [6]	1.093 [6]		
17.947	144751	0.06908	1.036	1.091		
17.918	144517	0.06920	1.469 [3]	1.401 [3]	1.757	1.483
17.886	144259	0.06932	1.044 [6]	1.094 [6]		
17.825	143767	0.06956	1.056	1.097		
17.790	143485	0.06969	1.496 [3]	1.395 [3]	1.804	1.459
17.764	143275	0.06980	1.064 [6]	1.091 [6]		
17.703	142783	0.07004	1.069	1.088		
17.664	142469	0.07019	1.525 [3]	1.388 [3]	1.839	1.428
17.642	142291	0.07028	1.073 [6]	1.085 [6]		
17.581	141799	0.07052	1.077	1.084		
17.540	141469	0.07069	1.554 [3]	1.373 [3]	1.865	1.401
17.520	141307	0.07077	1.080 [6]	1.086 [6]		
17.459	140815	0.07102	1.087	1.093		
17.417	140476	0.07119	1.579 [3]	1.358 [3]	1.884	1.376
17.398	140323	0.07126	1.102 [6]	1.102 [6]		
17.337	139831	0.07151	1.112	1.094		

TABLE I *(Continued)*

Aluminum Oxide (Al_2O_3)

eV	cm^{-1}	μm	n_o	k_o	n_e	k_e
17.296	139501	0.07168	1.601 [3]	1.338 [3]	1.904	1.364
17.276	139339	0.07177	1.112 [6]	1.082 [6]		
17.184	138597	0.07215	1.130	1.098		
17.177	138541	0.07218	1.616 [3]	1.316 [3]	1.927	1.348
17.123	138105	0.07241	1.139 [6]	1.087 [6]		
17.093	137863	0.07254	1.140	1.080		
17.059	137589	0.07268	1.626 [3]	1.299 [3]	1.952	1.337
17.032	137371	0.07280	1.145 [6]	1.079 [6]		
16.970	136871	0.07306	1.154	1.077		
16.943	136653	0.07318	1.636 [3]	1.284 [3]	1.985	1.324
16.909	136379	0.07332	1.153 [6]	1.062 [6]		
16.848	135887	0.07359	1.156	1.063		
16.828	135726	0.07368	1.640 [3]	1.265 [3]	2.019	1.299
16.787	135395	0.07386	1.165 [6]	1.063[6]		
16.726	134903	0.07413	1.159	1.045		
16.715	134814	0.07418	1.639 [3]	1.256 [3]	2.046	1.268
16.665	134411	0.07440	1.154 [6]	1.042 [6]		
16.604	133919	0.07467	1.641 [3]	1.251 [3]	2.071	1.239
16.604	133919	0.07467	1.158 [6]	1.050 [6]		
16.543	133427	0.07495	1.155	1.042		
16.494	133032	0.07517	1.643 [3]	1.247 [3]	2.090	1.203
16.482	132935	0.07522	1.150 [6]	1.041 [6]		
16.391	132201	0.07564	1.155 [3]	1.050 [3]		
16.385	132153	0.07567	1.646	1.245	2.104	1.170
16.299	131459	0.07607	1.148 [6]	1.042 [6]		
16.279	131298	0.07616	1.647 [3]	1.242 [3]	2.116	1.137
16.207	130717	0.07650	1.144 [6]	1.052 [6]		
16.173	130443	0.07666	1.648 [3]	1.246 [3]	2.122	1.100
16.116	129983	0.07693	1.149 [6]	1.062 [6]		
16.085	129733	0.07708	1.148	1.060		
16.068	129596	0.07716	1.651 [3]	1.249 [3]	2.125	1.068
15.994	128999	0.07752	1.144 [6]	1.064 [6]		
15.965	128765	0.07766	1.652 [3]	1.255 [3]	2.120	1.033
15.902	128257	0.07797	1.145 [6]	1.075 [6]		
15.864	12795	10.07816	1.656 [3]	1.267 [3]	2.112	1.005
15.841	127765	0.07827	1.148 [6]	1.085 [6]		
15.763	127136	0.07866	1.661 [3]	1.277 [3]	2.100	0.979
15.750	127031	0.07872	1.157 [6]	1.091 [6]		
15.664	126338	0.07915	1.668 [3]	1.293 [3]	2.085	0.957
15.658	126289	0.07918	1.146 [6]	1.083 [6]		
15.566	125547	0.07965	1.680 [3]	1.314 [3]	2.065	0.941
15.566	125547	0.07965	1.140 [6]	1.102 [6]		
15.475	124813	0.08012	1.142	1.125		
15.470	124773	0.08015	1.699 [3]	1.335 [3]	2.047	0.933
15.383	124071	0.08060	1.147 [6]	1.145 [6]		
15.374	123999	0.08065	1.728 [3]	1.356 [3]	2.030	0.928
15.292	123337	0.08108	1.166 [6]	1.174 [6]		

(continued)

TABLE I *(Continued)*

Aluminum Oxide (Al_2O_3)

eV	cm^{-1}	μm	n_o	k_o	n_e	k_e
15.280	123241	0.08114	1.763 [3]	1.367 [3]	2.014	0.929
15.200	122595	0.08157	1.176 [6]	1.181 [6]		
15.187	122490	0.08164	1.802 [3]	1.372 [3]	2.003	0.935
15.139	122103	0.08190	1.192 [6]	1.199 [6]		
15.095	121748	0.08214	1.838 [3]	1.364 [3]	1.995	0.940
15.047	121361	0.08240	1.205 [6]	1.196 [6]		
15.004	121014	0.08263	1.866 [3]	1.353 [3]	1.987	0.946
14.956	120627	0.08290	1.222 [6]	1.218 [6]		
14.914	120289	0.08313	1.892 [3]	1.340 [3]	1.982	0.954
14.864	119885	0.08341	1.243 [6]	1.214 [6]		
14.825	119571	0.08363	1.909 [3]	1.321 [3]	1.978	0.963
14.773	119151	0.08393	1.246 [6]	1.214 [6]		
14.737	118861	0.08413	1.919 [3]	1.310 [3]	1.974	0.974
14.681	118409	0.08445	1.263 [6]	1.224 [6]		
14.651	118167	0.08463	1.924 [3]	1.301 [3]	1.970	0.987
14.565	117474	0.08513	1.933	1.303	1.971	1.004
14.529	117183	0.08534	1.265 [6]	1.220 [6]		
14.480	116788	0.08563	1.942 [3]	1.302 [3]	1.975	1.022
14.437	116441	0.08588	1.271 [6]	1.233 [6]		
14.396	116111	0.08612	1.950 [3]	1.306 [3]	1.981	1.041
14.376	115949	0.08624	1.270 [6]	1.234 [6]		
14.315	115457	0.08661	1.271	1.246		
14.314	115449	0.08662	1.961 [3]	1.315 [3]	1.989	1.061
14.254	114965	0.08698	1.276 [6]	1.258 [6]		
14.232	114788	0.08712	1.977 [3]	1.327 [3]	2.003	1.086
14.193	114473	0.08736	1.274 [6]	1.262 [6]		
14.151	114135	0.08762	2.001 [3]	1.338 [3]	2.023	1.109
14.132	113981	0.08773	1.274 [6]	1.279 [6]		
14.071	113489	0.08811	2.024 [3]	1.343 [3]	2.047	1.131
14.071	113489	0.08811	1.285 [6]	1.304 [6]		
14.010	112997	0.08850	1.295	1.319		
13.992	112852	0.08861	2.049 [3]	1.351 [3]	2.081	1.152
13.949	112505	0.08888	1.307 [6]	1.335 [6]		
13.914	112223	0.08911	2.076 [3]	1.357 [3]	2.117	1.164
13.888	112013	0.08928	1.320 [6]	1.349 [6]		
13.837	111602	0.08960	2.105 [3]	1.361 [3]	2.155	1.171
13.827	111521	0.08967	1.330 [6]	1.359 [6]		
13.766	111029	0.09007	1.338	1.369		
13.760	110981	0.09011	2.132 [3]	1.363 [3]	2.193	1.172
13.704	110529	0.09047	1.343 [6]	1.383 [6]		
13.685	110376	0.09060	2.164 [3]	1.372 [3]	2.228	1.169
13.643	110037	0.09088	1.355 [6]	1.408 [6]		
13.610	109771	0.09110	2.199 [3]	1.376 [3]	2.265	1.165
13.582	109545	0.09129	1.375 [6]	1.434 [6]		
13.536	109174	0.09160	2.246 [3]	1.384 [3]	2.294	1.153
13.521	109053	0.09170	1.394 [6]	1.452 [6]		
13.463	108586	0.09209	2.292 [3]	1.376 [3]	2.325	1.150

TABLE I *(Continued)*

Aluminum Oxide (Al_2O_3)

eV	cm^{-1}	μm	n_o	k_o	n_e	k_e
13.460	108561	0.09211	1.413 [6]	1.469 [6]		
13.399	108069	0.09253	1.435	1.491		
13.390	107997	0.09260	2.346 [3]	1.373 [3]	2.351	1.143
13.338	107577	0.09296	1.461 [6]	1.513 [6]		
13.319	107424	0.09309	2.402 [3]	1.350 [3]	2.389	1.147
13.277	107085	0.09338	1.494 [6]	1.538 [6]		
13.248	106851	0.09359	2.454 [3]	1.319 [3]	2.432	1.137
13.216	106593	0.09381	1.538 [6]	1.560 [6]		
13.178	106287	0.09408	2.499 [3]	1.278 [3]	2.473	1.122
13.155	106101	0.09425	1.578 [6]	1.563 [6]		
13.109	105730	0.09458	2.534 [3]	1.232 [3]	2.517	1.104
13.094	105609	0.09469	1.604 [6]	1.556 [6]		
13.040	105174	0.09508	2.560 [3]	1.186 [3]	2.560	1.078
13.033	105117	0.09513	1.632 [6]	1.561 [6]		
12.972	104625	0.09558	2.581 [3]	1.142 [3]	2.603	1.044
12.972	104625	0.09558	1.670 [6]	1.573 [6]		
12.911	104133	0.09603	1.708	1.574		
12.905	104085	0.09608	2.596 [3]	1.096 [3]	2.639	0.999
12.850	103641	0.09649	1.745 [6]	1.572 [6]		
12.838	103545	0.09658	2.605 [3]	1.052 [3]	2.661	0.948
12.789	103149	0.09695	1.789 [6]	1.569 [6]		
12.772	103012	0.09708	2.609 [3]	1.010 [3]	2.664	0.901
12.728	102657	0.09741	1.816 [6]	1.548 [6]		
12.707	102488	0.09757	2.607 [3]	0.972 [3]	2.661	0.871
12.667	102165	0.09788	1.840 [6]	1.536 [6]		
12.643	101972	0.09807	2.600 [3]	0.939 [3]	2.663	0.855
12.606	101673	0.09835	1.886 [6]	1.533 [6]		
12.579	101456	0.09857	2.592 [3]	0.912 [3]	2.679	0.848
12.545	101181	0.09883	1.903 [6]	1.499 [6]		
12.516	100948	0.09906	2.584 [3]	0.892 [3]	2.710	0.835
12.484	100689	0.09932	1.895 [6]	1.470 [6]		
12.453	100439	0.09956	2.577 [3]	0.876 [3]	2.757	0.808
12.422	100189	0.09981	1.905 [6]	1.472 [6]		
12.391	99939.4	0.1001	2.571 [3]	0.867 [3]	2.790	0.758
12.361	99697.4	0.1003	1.918 [6]	1.476 [6]		
12.330	99447.4	0.1006	2.578 [3]	0.864 [3]	2.822	0.702
12.300	99205.4	0.1008	1.943 [6]	1.486 [6]		
12.269	98955.4	0.1011	2.589 [3]	0.854 [3]	2.838	0.629
12.239	98713.4	0.1013	1.975 [6]	1.493 [6]		
12.209	98471.4	0.1016	2.601 [3]	0.844 [3]	2.826	0.557
12.178	98221.4	0.1018	1.999 [6]	1.493 [6]		
12.149	97987.5	0.1021	2.622 [3]	0.834 [3]	2.808	0.498
12.117	97729.4	0.1023	2.048 [6]	1.504 [6]		
12.090	97511.7	0.1026	2.651 [3]	0.812 [3]	2.775	0.447
12.056	97237.4	0.1028	2.100 [6]	1.499 [6]		
12.032	97043.9	0.1030	2.667 [3]	0.776 [3]	2.745	0.409
11.995	96745.4	0.1034	2.129 [6]	1.478 [6]		

(continued)

TABLE I *(Continued)*

Aluminum Oxide (Al_2O_3)

eV	cm^{-1}	μm	n_o	k_o	n_e	k_e
11.974	96576.1	0.1035	2.678 [3]	0.743 [3]	2.706	0.380
11.934	96253.4	0.1039	2.177 [6]	1.469 [6]		
11.917	96116.3	0.1040	2.687 [3]	0.708 [3]	2.680	0.362
11.873	95761.4	0.1044	2.227 [6]	1.446 [6]		
11.860	95656.6	0.1045	2.687 [3]	0.673 [3]	2.651	0.345
11.812	95269.4	0.1050	2.254 [6]	1.410 [6]		
11.804	95204.9	0.1050	2.691 [3]	0.639 [3]	2.624	0.336
11.751	94777.5	0.1055	2.288 [6]	1.380 [6]		
11.748	94753.3	0.1055	2.678 [3]	0.604 [3]	2.610	0.328
11.693	94309.7	0.1060	2.677	0.580	2.587	0.317
11.690	94285.5	0.1061	2.307 [6]	1.344 [6]		
11.638	93866.1	0.1065	2.668 [3]	0.548 [3]	2.570	0.315
11.629	93793.5	0.1066	2.324 [6]	1.314 [6]		
11.584	93430.5	0.1070	2.655 [3]	0.523 [3]	2.565	0.311
11.568	93301.5	0.1072	2.362 [6]	1.285 [6]		
11.531	93003.0	0.1075	2.645 [3]	0.502 [3]	2.552	0.300
11.507	92809.5	0.1077	2.366 [6]	1.241 [6]		
11.477	92567.5	0.1080	2.638 [3]	0.479 [3]	2.541	0.295
11.446	92317.5	0.1083	2.357 [6]	1.210 [6]		
11.425	92148.1	0.1085	2.620 [3]	0.457 [3]	2.535	0.286
11.385	91825.5	0.1089	2.380 [6]	1.191 [6]		
11.373	91728.7	0.1090	2.613 [3]	0.441 [3]	2.517	0.280
11.324	91333.5	0.1095	2.397 [6]	1.162 [6]		
11.321	91309.3	0.1095	2.593 [3]	0.423 [3]	2.515	0.280
11.270	90898.0	0.1100	2.586	0.413	2.510	0.271
11.263	90841.5	0.1101	2.400 [6]	1.131 [6]		
11.219	90486.6	0.1105	2.575 [3]	0.397 [3]	2.503	0.263
11.202	90349.5	0.1107	2.405 [6]	1.105 [6]		
11.169	90083.3	0.1110	2.564 [3]	0.383 [3]	2.495	0.255
11.141	89857.5	0.1113	2.412 [6]	1.080 [6]		
11.119	89680.1	0.1115	2.549 [3]	0.370 [3]	2.487	0.250
11.079	89357.5	0.1119	2.427 [6]	1.051 [6]		
11.069	89276.8	0.1120	2.538 [3]	0.362 [3]	2.481	0.244
11.020	88881.6	0.1125	2.526	0.354	2.471	0.241
11.018	88865.5	0.1125	2.415 [6]	1.020 [6]		
10.972	88494.4	0.1130	2.515 [3]	0.350 [3]	2.475	0.236
10.957	88373.5	0.1132	2.392 [6]	1.005 [6]		
10.924	88107.3	0.1135	2.510 [3]	0.345 [3]	2.461	0.228
10.896	87881.5	0.1138	2.408 [6]	0.998 [6]		
10.876	87720.2	0.1140	2.502 [3]	0.338 [3]	2.463	0.226
10.835	87389.5	0.1144	2.423 [6]	0.982 [6]		
10.829	87341.1	0.1145	2.494 [3]	0.337 [3]	2.454	0.219
10.782	86962.0	0.1150	2.500	0.336	2.457	0.214
10.774	86897.5	0.1151	2.431 [6]	0.962 [6]		
10.735	86582.9	0.1155	2.499 [3]	0.325 [3]	2.448	0.205
10.713	86405.5	0.1157	2.453 [6]	0.936 [6]		
10.689	86211.9	0.1160	2.503 [3]	0.314 [3]	2.444	0.200

TABLE I *(Continued)*

Aluminum Oxide (Al_2O_3)

eV	cm^{-1}	μm	n_o	k_o	n_e	k_e
10.652	85913.5	0.1164	2.438 [6]	0.908 [6]		
10.644	85849.0	0.1165	2.505 [3]	0.294 [3]	2.439	0.195
10.598	85478.0	0.1170	2.485	0.279	2.435	0.192
10.591	85421.5	0.1171	2.420 [6]	0.895 [6]		
10.553	85115.0	0.1175	2.487 [3]	0.273 [3]	2.437	0.184
10.509	84760.1	0.1180	2.476	0.256	2.427	0.175
10.500	84687.5	0.1181	2.449 [6]	0.871 [6]		
10.465	84405.2	0.1185	2.458 [3]	0.251 [3]	2.422	0.171
10.438	84187.5	0.1188	2.430 [6]	0.851 [6]		
10.421	84050.4	0.1190	2.458 [3]	0.252 [3]	2.415	0.169
10.378	83703.6	0.1195	2.458	0.242	2.415	0.168
10.377	83695.5	0.1195	2.422 [6]	0.845 [6]		
10.292	83009.9	0.1205	2.441 [3]	0.218 [3]	2.417	0.157
10.286	82961.5	0.1205	2.439 [6]	0.831 [6]		
10.249	82663.1	0.1210	2.437 [3]	0.210 [3]	2.409	0.147
10.207	82324.4	0.1215	2.427	0.198	2.405	0.143
10.194	82219.5	0.1216	2.444 [6]	0.815 [6]		
10.166	81993.7	0.1220	2.411 [3]	0.192 [3]	2.402	0.138
10.133	81727.5	0.1224	2.454 [6]	0.802 [6]		
10.124	81654.9	0.1225	2.406 [3]	0.190 [3]	2.401	0.130
10.083	81324.2	0.1230	2.395	0.184	2.393	0.122
10.072	81235.5	0.1231	2.452 [6]	0.792 [6]		
10.043	81001.6	0.1235	2.386 [3]	0.182 [3]	2.385	0.119
10.011	80743.5	0.1238	2.464 [6]	0.783 [6]		
10.002	80670.9	0.1240	2.378 [3]	0.179 [3]	2.380	0.117
9.962	80348.3	0.1245	2.370	0.177	2.376	0.113
9.951	80255.6	0.1246	2.476 [6]	0.770 [6]		
9.923	80033.8	0.1249	2.362 [3]	0.175 [3]	2.369	0.112
9.890	79763.6	0.1254	2.475 [6]	0.762 [6]		
9.883	79711.1	0.1255	2.356 [3]	0.174 [3]	2.369	0.112
9.844	79396.6	0.1260	2.348	0.173	2.370	0.107
9.829	79271.6	0.1261	2.491 [6]	0.754 [6]		
9.806	79090.1	0.1264	2.343 [3]	0.172 [3]	2.363	0.100
9.767	78778.8	0.1269	2.510 [6]	0.739 [6]		
9.767	78775.5	0.1269	2.335 [3]	0.171 [3]	2.353	0.100
9.729	78469.1	0.1274	2.328	0.172	2.350	0.103
9.706	78286.8	0.1277	2.514 [6]	0.726 [6]		
9.691	78162.6	0.1279	2.319 [3]	0.175 [3]	2.348	0.108
9.653	77856.1	0.1284	2.314	0.180	2.357	0.106
9.645	77794.0	0.1285	2.528 [6]	0.716 [6]		
9.616	77557.7	0.1289	2.310 [3]	0.185 [3]	2.351	0.098
9.584	77302.0	0.1294	2.548 [6]	0.701 [6]		
9.579	77259.2	0.1294	2.306 [3]	0.192 [3]	2.347	0.097
9.543	76968.9	0.1299	2.310	0.196	2.338	0.101
9.523	76809.2	0.1302	2.559 [6]	0.686 [6]		
9.506	76670.5	0.1304	2.303 [3]	0.199 [3]	2.342	0.109
9.470	76380.1	0.1309	2.302	0.209	2.347	0.111

(continued)

TABLE I *(Continued)*

Aluminum Oxide (Al_2O_3)

eV	cm^{-1}	μm	n_o	k_o	n_e	k_e
9.462	76317.2	0.1310	2.569 [6]	0.675 [6]		
9.434	76089.7	0.1314	2.301 [3]	0.218 [3]	2.350	0.112
9.401	75824.4	0.1319	2.588 [6]	0.665 [6]		
9.399	75807.4	0.1319	2.298 [3]	0.233 [3]	2.351	0.116
9.371	75578.4	0.1323	2.600 [6]	0.658 [6]		
9.363	75517.1	0.1324	2.307 [3]	0.257 [3]	2.362	0.116
9.340	75332.4	0.1327	2.613 [6]	0.652 [6]		
9.328	75234.8	0.1329	2.335 [3]	0.272 [3]	2.355	0.121
9.310	75086.4	0.1332	2.624 [6]	0.645 [6]		
9.293	74952.5	0.1334	2.346 [3]	0.282 [3]	2.375	0.133
9.279	74839.6	0.1336	2.636 [6]	0.640 [6]		
9.259	74678.3	0.1339	2.377 [3]	0.303 [3]	2.390	0.133
9.249	74593.6	0.1341	2.648 [6]	0.636 [6]		
9.224	74396.0	0.1344	2.429 [3]	0.310 [3]	2.403	0.136
9.218	74347.6	0.1345	2.665 [6]	0.632 [6]		
9.190	74121.8	0.1349	2.477 [3]	0.294 [3]	2.430	0.137
9.188	74101.6	0.1349	2.690 [6]	0.625 [6]		
9.157	73855.6	0.1354	2.518 [3]	0.270 [3]	2.448	0.134
9.157	73854.8	0.1354	2.725 [6]	0.613 [6]		
9.126	73608.8	0.1359	2.765	0.592		
9.123	73581.4	0.1359	2.563 [3]	0.237 [3]	2.488	0.130
0.096	73362.8	0.1363	2.807 [6]	0.563 [6]		
9.090	73315.2	0.1364	2.604 [3]	0.184 [3]	2.526	0.107
9.065	73116.8	0.1368	2.845 [6]	0.526 [6]		
9.057	73049.1	0.1369	2.621 [3]	0.117 [3]	2.562	0.076
9.035	72870.0	0.1372	2.878 [6]	0.482 [6]		
9.024	72782.9	0.1374	2.619 [3]	0.052 [3]	2.603	0.024
9.004	72624.0	0.1377	2.907 [6]	0.430 [6]		
8.991	72516.7	0.1379	2.605 [3]	0.025 [4]	2.616	0.013 [4]
8.974	72378.0	0.1382	2.929 [6]	0.372 [6]		
8.959	72258.6	0.1384	2.572 [3]	0.012 [4]	2.618	7.64E-03
8.943	72132.0	0.1386	2.942 [6]	0.310 [6]		
8.927	72000.5	0.1389	2.526 [3]	5.81E-03 [4]	2.590	4.37E-03
8.913	71886.0	0.1391	2.943 [6]	0.246 [6]		
8.895	71742.4	0.1394	2.489 [3]	2.79E-03 [4]	2.549	2.51E-03
8.882	71639.2	0.1396	2.933 [6]	0.183 [6]		
8.863	71484.3	0.1399	2.449 [3]	1.34E-03 [4]	2.511	1.44E-03
8.852	71393.2	0.1401	2.912 [6]	0.125 [6]		
8.832	71234.3	0.1404	2.417 [3]	6.60E-04 [4]	2.474	8.37E-04
8.821	71147.2	0.1406	2.881 [6]	0.075 [6]		
8.801	70984.3	0.1409	2.392 [3]	3.25E-04 [4]	2.447	4.88E-04
8.791	70901.2	0.1410	2.841 [6]	0.037 [6]		
8.770	70734.3	0.1414	2.357 [3]	1.60E-04 [4]	2.419	2.84E-04
8.760	70654.4	0.1415	2.797 [6]	0.011 [6]		
8.739	70484.2	0.1419		7.85E-05 [4]	2.398	1.66E-04
8.730	70408.4	0.1420	2.753 [6]	0.0 [6]		
8.708	70234.2	0.1424	2.326 [3]	3.86E-05 [4]	2.375	9.66E-05

TABLE I *(Continued)*

Aluminum Oxide (Al_2O_3)

eV	cm^{-1}	μm	n_o	k_o	n_e	k_e
8.648	69750.3	0.1434	2.279	9.78E-06	2.336	3.40E-05
8.588	69266.3	0.1444	2.246	2.48E-06	2.273	1.20E-05
8.529	68790.5	0.1454	2.242	6.41E-07	2.247	4.28E-06
8.471	68322.7	0.1464	2.231		2.225	
8.414	67862.9	0.1474	2.210		2.207	
8.358	67411.3	0.1483	2.188		2.195	
8.302	66959.6	0.1493	2.174		2.183	
8.193	66080.5	0.1513	2.150		2.161	
8.034	64798.1	0.1543	2.127		2.125	
7.932	63975.4	0.1563	2.105		2.102	
7.832	63168.8	0.1583	2.081		2.083	
7.735	62386.5	0.1603	2.070		2.053	
7.687	61999.3	0.1613	2.059		2.040	
7.663	61805.8	0.1618			2.033	
7.593	61241.2	0.1633	2.044			
7.547	60870.2	0.1643	2.037		2.013	
7.457	60144.3	0.1663	2.020			
7.435	59966.8	0.1668			2.000	
7.412	59781.3	0.1673	2.014			
7.325	59079.6	0.1693	1.995		1.988	
7.250	58474.7	0.1710	1.986			
7.219	58224.7	0.1717			1.977	
7.198	58055.3	0.1722	1.975			
7.116	57394.0	0.1742	1.969		1.970	
7.076	57071.3	0.1752	1.967			
7.016	56587.4	0.1767			1.962	
6.996	56426.1	0.1772	1.962			
6.918	55797.0	0.1792	1.953		1.953	
6.880	55490.5	0.1802	1.947			
6.824	55038.8	0.1817			1.948	
6.805	54885.6	0.1822	1.940			
6.731	54288.7	0.1842	1.933		1.938	
6.695	53998.4	0.1852	1.930			
6.624	53425.7	0.1872	1.930		1.929	
6.554	52861.2	0.1892	1.929		1.922	
6.469	52175.6	0.1917	1.936		1.919	
6.386	51506.2	0.1942	1.930		1.918	
6.305	50852.9	0.1966	1.924		1.915	
6.226	50215.7	0.1991	1.920		1.908	
6.1993	50000.0	0.2000	1.91271 [13]		1.90163 [13]	
5.6357	45454.5	0.2200	1.87817		1.86774	
5.1661	41666.7	0.2400	1.85446		1.84453	
4.8890	39432.2	0.2536	1.844 [11]		1.834 [11]	
4.7687	38461.5	0.2600	1.8376		1.8280	
4.6752	37707.4	0.26520	1.83360 [12]		1.82411 [13]	
4.4280	35714.3	0.2800	1.8242 [11]		1.8149 [11]	
4.4225	35669.7	0.28035	1.82427 [12]		1.81490 [13]	

(continued)

TABLE I *(Continued)*

Aluminum Oxide (Al_2O_3)

eV	cm^{-1}	μm	n_o	k_o	n_e	k_e
4.2848	34559.0	0.28936	1.81949		1.81021	
4.1784	33700.7	0.29673	1.81595		1.80674	
4.1328	33333.3	0.3000	1.8147 [11]		1.8056 [11]	
4.1034	33096.1	0.30215	1.81351 [12]		1.80437 [13]	
3.9612	31948.9	0.3130	1.80906		1.80005	
3.7571	30303.0	0.3300	1.8035 [11]		1.7947 [11]	
3.7105	29926.7	0.33415	1.80184 [12]		1.79293 [13]	
3.5770	28850.0	0.34662	1.79815		1.78940	
3.4340	27696.9	0.36105	1.79450		1.78579	
3.3967	27396.1	0.36502	1.7935 [11]		1.7849 [11]	
			1.79358 [12]		1.78488 [13]	
3.1739	25599.0	0.39064	1.78826		1.77970	
3.0640	24712.3	0.40466	1.78582		1.77730	
			1.78571 [11]		1.77724 [11]	
2.8448	22944.7	0.43583	1.78110		1.77275	
			1.78120 [12]		1.77279 [13]	
2.5505	20570.6	0.48613	1.77547 [11]		1.76724 [11]	
2.2705	18312.7	0.54607	1.77067		1.76254	
			1.77078 [12]		1.76258 [13]	
2.1489	17332.2	0.576960	1.76884		1.76069	
2.1411	17269.2	0.57907	1.76871		1.76057	
2.1039	16969.3	0.5893	1.76808 [11]		1.75999 [11]	
1.9257	15531.6	0.64385	1.76547 [12]		1.75739 [13]	
			1.76538 [11]		1.75734 [11]	
1.8892	15237.4	0.65628	1.76485		1.75682	
1.7950	14477.6	0.69072	1.76351		1.75549	
1.7549	14153.9	0.70652	1.76303 [12]		1.75500 [13]	
1.4550	11735.4	0.85212	1.75885		1.75090	
1.3862	11180.7	0.89440	1.75796		1.74994	
1.2228	9862.1	1.01398	1.75547		1.74794 [12]	
1.0985	8860.1	1.12866	1.75339		1.74549 [13]	
0.9068	7313.8	1.36728	1.74936		1.74148	
0.8887	7168.2	1.39506	1.74888		1.74101	
0.8106	6538.0	1.52952	1.74660		1.73874	
0.7323	5906.0	1.6932	1.74368		1.73584	
0.7254	5850.9	1.70913	1.74340		1.73555	
0.6838	5515.5	1.81307	1.74144		1.73362	
0.6325	5101.8	1.9601	1.73833		1.73074	
0.5760	4645.5	2.1526	1.73444		1.72670	
0.5512	4445.8	2.24929	1.73231		1.72455	
0.5332	4300.3	2.32542	1.73057		1.72279	
0.5087	4102.7	2.4374	1.72783		1.72011	
0.3822	3082.7	3.2439	1.70437		1.69688	
0.3795	3061.1	3.2668	1.70356		1.69612	
0.3754	3027.9	3.3026	1.70231		1.69491	
0.3723	3002.7	3.3303	1.70140		1.69397	
0.3623	2922.3	3.422	1.69818		1.69077	

TABLE I *(Continued)*

Aluminum Oxide (Al_2O_3)

eV	cm^{-1}	μm	n_o	k_o	n_e	k_e
0.3535	2851.4	3.5070	1.69504		1.68772	
0.3345	2697.8	3.7067	1.68746		1.68021	
0.3100	2500.0	4.000	1.67523 [13]	1.30E-06 [26]	1.66825	
0.2976	2400.0	4.167	1.66777	2.60E-06	1.66094	
0.2914	2350.0	4.2553	1.66371 [12]		1.65690	
0.2852	2300.0	4.348	1.65920 [13]	5.78E-06	1.65257	
0.2824	2278.0	4.3898	1.65714	6.29E-06 [24]	1.65056	
0.2728	2200.0	4.545	1.64928	1.12E-05 [26]	1.64289	
0.2705	2181.0	4.5830	1.64732	1.24E-05 [24]	1.64099	
0.2616	2110.0	4.7393	1.63894	2.03E-05 [25]	1.63284	1.32E-05 [25]
0.2604	2100.0	4.762	1.63769	2.99E-05 [26]	1.63163	
0.2585	2085.0	4.7962	1.63579	2.29E-05 [24]	1.62978	
0.2503	2018.6	4.954	1.62665 [12]		1.62102	
0.2480	2000.0	5.000	1.62403 [13]	3.76E-05 [26]	1.61839	
0.2465	1988.0	5.0302	1.62223	3.96E-05 [24]	1.61664	
0.2460	1984.0	5.0403	1.62162	3.85E-05 [25]	1.61605	2.73E-05
0.2452	1978.0	5.0556	1.62070	4.17E-05	1.61516	2.93E-05
0.2410	1943.4	5.1456	1.61514 [12]		1.60983	
0.2356	1900.0	5.263	1.60775 [13]	6.53E-05 [26]	1.60266	
0.2346	1892.0	5.2854	1.60631	6.98E-05 [24]	1.60127	
0.2318	1869.5	5.349	1.60202 [12]		1.59727	
0.2288	1845.4	5.419	1.59735		1.59277	
0.2232	1800.0	5.556	1.58808	1.20E-04 [26]	1.58375	
0.2227	1796.0	5.5679	1.58721	1.22E-04 [24]	1.58291	
0.2223	1793.1	5.577	1.58638		1.58230	
0.2108	1700.0	5.882		2.14E-04 [26]		
0.2107	1699.0	5.8858		1.69E-04 [24]		
0.1984	1600.0	6.250		5.82E-04 [26]		
0.1860	1500.0	6.667		1.50E-03		
0.1736	1400.0	7.143	1.459 [30]	3.60E-03	1.44 [26]	
0.1674	1350.0	7.407	1.42		1.41	
0.1612	1300.0	7.692	1.38		1.38	
0.1550	1250.0	8.000	1.34		1.34	
0.1488	1200.0	8.333	1.29		1.29	
0.1426	1150.0	8.696	1.22		1.23	
0.1364	1100.0	9.091	1.14		1.16	
0.1302	1050.0	9.524	1.03		1.06	
0.1240	1000.0	10.00	0.88	0.053 [30]	0.94	0.037 [26]
0.1227	990.0	10.10	0.84	0.057	0.90	0.039
0.1215	980.0	10.20	0.80	0.062	0.87	0.042
0.1203	970.0	10.31	0.75	0.068	0.83	0.045
0.1190	960.0	10.42	0.70	0.075	0.79	0.049
0.1178	950.0	10.53	0.64	0.084	0.74	0.054
0.1165	940.0	10.64	0.57	0.097	0.69	0.061
0.1153	930.0	10.75	0.48	0.117	0.64	0.069
0.1141	920.0	10.87	0.38	0.153	0.57	0.081
0.1128	910.0	10.99	0.27	0.224	0.49	0.098

(continued)

TABLE I *(Continued)*

Aluminum Oxide (Al_2O_3)

eV	cm^{-1}	μm	n_o	k_o	n_e	k_e
0.1116	900.0	11.11	0.18	0.344	0.39	0.128
0.1103	890.0	11.24	0.14	0.468	0.28	0.192
0.1091	880.0	11.36	0.12	0.579	0.18	0.312
0.1079	870.0	11.49	0.10	0.680	0.14	0.440
0.1066	860.0	11.63	0.09	0.774	0.12	0.553
0.1054	850.0	11.76	0.09	0.864	0.11	0.655
0.1041	840.0	11.90	0.08	0.951	0.10	0.750
0.1029	830.0	12.05	0.08	1.04	0.10	0.840
0.1017	820.0	12.20	0.08	1.12	0.10	0.927
0.1004	810.0	12.35	0.07	1.21	0.10	1.01
0.09919	800.0	12.50	0.07	1.29	0.11	1.09
0.09795	790.0	12.66	0.07	1.38	0.12	1.18
0.09671	780.0	12.82	0.07	1.47	0.12	1.26
0.09547	770.0	12.99	0.07	1.57	0.13	1.34
0.09423	760.0	13.16	0.07	1.66	0.14	1.42
0.09299	750.0	13.33	0.07	1.77	0.15	1.50
0.09175	740.0	13.51	0.07	1.87	0.16	1.58
0.09051	730.0	13.70	0.08	1.99	0.16	1.66
0.08927	720.0	13.89	0.08	2.11	0.16	1.75
0.08803	710.0	14.08	0.08	2.24	0.16	1.85
0.08679	700.0	14.29	0.08	2.39	0.15	1.96
0.08555	690.0	14.49	0.09	2.55	0.15	2.08
0.08431	680.0	14.71	0.09	2.74	0.15	2.22
0.08307	670.0	14.93	0.10	2.96	0.16	2.37
0.08183	660.0	15.15	0.12	3.24	0.16	2.55
0.08059	650.0	15.38	0.16	3.66	0.17	2.75
0.07935	640.0	15.63	0.58	4.56	0.19	3.00
0.07811	630.0	15.87	1.48	2.77	0.23	3.32
0.07687	620.0	16.13	0.47	3.56	0.29	3.74
0.07563	610.0	16.39	0.41	4.28	0.41	4.36
0.07439	600.0	16.67	0.49	5.10	0.73	5.43
0.07315	590.0	16.95	0.75	6.30	2.37	7.85
0.07191	580.0	17.24	1.69	8.61	8.50	3.27
0.07067	570.0	17.54	10.26	11.28	5.36	0.678
0.06943	560.0	17.86	9.10	1.53	3.96	0.313
0.06819	550.0	18.18	6.55	0.507	3.11	0.206
0.06695	540.0	18.52	5.28	0.255	2.45	0.174
0.06571	530.0	18.87	4.46	0.158	1.84	0.186
0.06447	520.0	19.23	3.82	0.115	1.13	0.278
0.06323	510.0	19.61	3.24	0.099	0.34	0.932
0.06199	500.0	20.00	2.64	0.106	0.21	1.64
0.06075	490.0	20.41	1.83	0.163	0.19	2.17
0.05951	480.0	20.83	0.38	1.03	0.19	2.64
0.05827	470.0	21.28	0.24	2.62	0.20	3.10
0.05703	460.0	21.74	0.32	4.16	0.23	3.61
0.05579	450.0	22.22	0.73	6.68	0.28	4.19
0.05455	440.0	22.73	10.08	14.01	0.36	4.91

TABLE I *(Continued)*

Aluminum Oxide (Al_2O_3)

eV	cm^{-1}	μm	n_o	k_o	n_e	k_e
0.05331	430.0	23.26	8.57	0.764	0.52	5.88
0.05207	420.0	23.81	6.36	0.257	0.89	7.38
0.05083	410.0	24.39	5.36	0.152	2.16	10.22
0.04959	400.0	25.00	4.64	0.156	11.82	12.96
0.04835	390.0	25.64	3.53	0.732	11.36	2.26
0.04711	380.0	26.32	5.64	0.552	8.54	0.804
0.04587	370.0	27.03	4.77	0.097	7.18	0.422
0.04463	360.0	27.78	4.44	4.55E-02	6.36	0.264
0.04339	350.0	28.57	4.23	2.83E-02	5.82	0.182
0.04215	340.0	29.41	4.08	1.97E-02	5.42	0.133
0.04092	330.0	30.30	3.95	1.45E-02	5.11	0.101
0.03968	320.0	31.25	3.85	1.10E-02	4.87	7.99E-02
0.03844	310.0	32.26	3.77	8.55E-03	4.67	6.44E-02
0.03720	300.0	33.33	3.69	6.68E-03	4.51	5.30E-02
0.03596	290.0	34.48	3.63		4.37	
0.03472	280.0	35.71	3.57		4.25	
0.03348	270.0	37.04	3.52		4.15	
0.03224	260.0	38.46	3.48		4.06	
0.03100	250.0	40.00	3.43		3.98	
0.02976	240.0	41.67	3.40		3.91	
0.02852	230.0	43.48	3.36		3.85	
0.02728	220.0	45.45	3.33		3.79	
0.02604	210.0	47.62	3.30		3.74	
0.02480	200.0	50.00	3.260 [34]	0.0117 [35]		
0.02480	200.0	50.00	3.28 [26]		3.70	
0.02356	190.0	52.63	3.241 [34]	0.0103		
0.02232	180.0	55.56	3.218	0.0103		
0.02187	176.4	56.69	3.2113 [33]			
0.02124	171.3	58.38	3.2018			
0.02108	170.0	58.82	3.198 [34]	0.0100		
0.02062	166.3	60.13	3.1921 [33]	0.0130 [33]		
0.02000	161.3	62.00	3.1854			
0.01984	160.0	62.50	3.180 [34]	0.00975 [35]		
0.01937	156.2	64.02	3.1795 [33]		3.6042 [33]	
0.01875	151.2	66.14	3.1696	0.0104 [33]	3.5856	0.0189 [33]
0.01860	150.0	66.67	3.164 [34]	0.0101 [34]		
0.01811	146.1	68.45	3.1623 [33]		3.5746	
0.01749	141.1	70.87	3.1549		3.5612	
0.01736	140.0	71.43	3.149 [34]	0.0091		
0.01687	136.1	73.48	3.1485 [33]	0.0092 [33]	3.5508	0.0173
0.01624	131.0	76.34	3.1422		3.5375	
0.01612	130.0	76.92	3.136 [34]	0.00898 [35]		
0.01562	126.0	79.37	3.1357 [33]		3.5279	
0.01499	120.9	82.71	3.1304	0.0085 [33]	3.5185	0.0158
0.01488	120.0	83.33	3.125 [34]	0.0080 [34]	3.524 [34]	0.0139 [34]
0.01437	115.9	86.28	3.1249 [33]		3.5081 [33]	
0.01375	110.9	90.17	3.1198		3.4998	

(continued)

TABLE I *(Continued)*

Aluminum Oxide (Al_2O_3)

eV	cm^{-1}	μm	n_o	k_o	n_e	k_e
0.01364	110.0	90.91	3.114 [34]	0.0074	3.502 [34]	0.0137
0.01312	105.8	94.52	3.1249 [33]	0.0074 [33]	3.5081 [33]	0.0134 [33]
0.01250	100.8	99.21	3.1198		3.4993	
0.01240	100.0	100.0	3.105 [34]	0.0069 [34]	3.485 [34]	0.0127 [34]
			3.12 [30]	0.0070 [35]	3.42 [26]	
0.01188	95.8	104.4	3.1147 [33]		3.4908 [33]	
0.01125	90.7	110.3	3.1019	0.0063 [33]	3.4689	0.0111 [33]
0.01116	90.0	111.1	3.097 [34]	0.0065 [34]	3.470 [34]	0.0115 [34]
0.01063	85.7	116.7	3.0982 [33]		3.4625 [33]	
0.00999	80.6	124.1	3.0941		3.4569	
0.00992	80.0	125.0	3.090 [34]	0.0058	3.455 [34]	0.0093
0.00937	75.6	132.3	3.0906 [33]	0.0052 [33]	3.4510 [33]	0.0080 [33]
0.00875	70.6	141.6	3.0870		3.4440	
0.00868	70.0	142.9	3.085 [34]	0.0052 [34]	3.445 [34]	0.0076 [34]
0.00812	65.5	152.7	3.0843 [33]		3.4391 [33]	
0.00750	60.5	165.3	3.0822	0.0047 [33]	3.4334	0.0053 [33]
0.00744	60.0	166.7	3.080 [34]	0.0044 [34]	3.436 [34]	0.0062 [34]
0.00687	55.4	180.5	3.0795 [33]		3.4294 [33]	
0.00625	50.4	198.4	3.0770		3.4260	
0.00620	50.0	200.0	3.076 [34]	0.0035	3.428 [34]	0.0051
0.00563	45.4	220.3	3.0752 [33]	0.0030 [33]	3.4232 [33]	0.0039 [33]
0.00500	40.3	248.1	3.0740		3.4187	
0.00496	40.0	250.0	3.072 [34]	0.0024 [34]	3.420 [34]	0.0046 [34]
0.00438	35.3	283.3	3.0720 [33]		3.4163 [33]	
0.00374	30.2	331.1	3.0704	0.0011 [33]	3.4234	0.0013 [33]
0.00372	30.0	333.3	3.069 [34]	0.0027 [34]	3.415 [34]	0.0050 [34]
0.00372	30.0	333.3	3.06 [36]	0.0025 [36]	3.40 [36]	0.0025 [36]
0.00312	25.2	396.8	3.0698 [33]		3.4129 [33]	
0.00289	23.3	428.6	3.06 [36]	0.0020	3.40 [36]	0.0020
0.00250	20.2	495.0	3.0688 [33]		3.4111 [33]	
0.00207	16.7	600.0	3.05 [36]	0.0015	3.39 [36]	0.0015
0	0	∞	3.068 [34]		3.406 [34]	
			3.067 [33]		3.408 [33]	
			3.066 [39]		3.404 [39]	

TABLE II

Sellmeier Dispersion Equation Constants for Aluminum Oxide

Term (Eq. [4])	Malitson [12] o-ray	Malitson and Dodge [13] o-ray	Malitson and Dodge [13] e-ray
λ_1	0.06144821	0.0726631	0.0740298
λ_2	0.1106997	0.1193242	0.1216529
λ_3	17.92656	18.028251	20.072248
A_1	1.023798	1.4313493	1.5039759
A_2	1.058264	0.65054713	0.55069141
A_3	5.280792	5.3414021	6.5927379
Temperature:	24° C	20° C	20° C
Wavelength:	0.26–5.5 μm	0.2–5.5 μm	0.2–5.5 μm

[a] Corrects error of Ref. [13].

TABLE III

Thermo-optical Coefficients of Aluminum Oxide

Wavelength (μm)	dn/dT (10^{-6}/K) o-ray	dn/dT (10^{-6}/K) e-ray	Temperature (°C)	Reference
~0.26	20		24	[12]
0.4047	14.1		24	[12]
0.4579	11.7	12.8	20	[17]
0.475	16	12	22	[14]
0.4358	13.9		24	[12]
0.502	16	12	22	[14]
0.5145	16.5		27	[16]
0.5461	13.1		24	[12]
	13.7		20–700	[18]
0.552	14	12	22	[14]
0.5770	13.1		24	[12]
0.5791	13.1		24	[12]
	14.0		20–700	[18]
0.5893	13.6	14.7	50	[11]
0.603	14	11	22	[12]
0.633	12.8		24	[15]
	11.7		24	[19]
	13.0[a]	14.2[a]	30–45	[22]
0.6438	12.8		24	[12]
0.651	13	12	22	[14]
0.701	13	9.7	22	[14]
0.7065	12.6		24	[12]
0.799	12.4		24	[15]
~4	10		24	[12]

[a] Ruby measurement.

TABLE IV

Constants for Infrared Absorption Coefficient of Aluminum Oxide

	Model parameters			
Orientation	β_0 (cm^{-1})	γ	ν_{LO} (cm^{-1})	Reference
o-ray	55222	5.03	900	[23]
o-ray	94778	5.28	914	[24]
e-ray	33523	4.73	871	[25]

TABLE V

Transverse (and Longitudinal) Optical Phonon Frequencies in Aluminum Oxide

Mode	Barker [29]	Gervais [26,30]	Hoffmann [31]
E_u (**E** $\perp$ **c**)	385 (388)	384.6 (387.7)	384
E_u (**E** $\perp$ **c**)	442 (480)	439.3 (482)	439
E_u (**E** $\perp$ **c**)	569 (625)	569.5 (630.5)	568
E_u (**E** $\perp$ **c**)	635 (900)	635 (908)	633
A_{1g} (**E** $\parallel$ **c**)	400 (512)	399.5 (514)	—
A_{1g} (**E** $\parallel$ **c**)	583 (871)	584 (886.5)	—

Barium Fluoride (BaF_2)

MICHAEL E. THOMAS and WILLIAM J. TROPF
Applied Physics Laboratory
The Johns Hopkins University
Laurel, Maryland

Barium fluoride is a general-purpose optical window material that offers a wide range of transparency, from the ultraviolet to the long-wave infrared (0.15 to 12 μm), with low reflectance loss and low dispersion. This combination of broad transparency and low dispersion is rare in optical window materials used in infrared systems. It allows experimenters to conveniently perform initial system alignment in the visible and then switch to the IR with only minor correction of the optical components. Furthermore, barium fluoride has good surface hardness (Knoop scale 78 kg/mm^2), and it is not attacked by water vapor, though immersion in water causes surface damage. It has moderate flexure strength (27 MPa) and is very brittle, requiring careful handling. Thus, barium fluoride is better suited for laboratory than to field work. It is also a relatively inexpensive single-crystal material that is readily available from a number of vendors.

Barium fluoride is a cubic crystal with the fluorite structure, space group Fm3m (O_h^5), with four formula units per unit cell. The lattice constant is 6.2001 Å, giving a theoretical density of 4.886 g/cm^3. The atomic arrangement is barium atoms occupy the 4(a) sites (m3m or O_h symmetry), and the fluorine atoms occupy the 8(c) sites ($\bar{4}$3m or T_d symmetry). Melting point is 1641 K.

Ultraviolet reflectance of bulk BaF_2 was measured by Ganin *et al.* [1] up to 20 eV at room temperature and liquid-helium temperature. Rubloff [2] has measured the room-temperature reflectance up to 36 eV. Unfortunately, these measurements are not reduced to optical constants. However, similar measurements from 10 to 33 eV by Nisar and Robin [3] have been reduced to optical constants utilizing the Kramers–Kronig relation. Thin-film optical constant data is available from transmittance and reflectance measurements by Zukic *et al.* [4], but only between 0.12 and 0.2 μm. These results extend the Nisar and Robin data set down to 6.2 eV. These data are listed in Table I and plotted in Fig. 1.

The Urbach tail represents absorption below the band gap, defining the

HANDBOOK OF OPTICAL CONSTANTS OF SOLIDS III

Copyright © 1998 by Academic Press.
All rights of reproduction in any form reserved
ISBN 0-12-544423-0/$25.00.

end of transparency. The room-temperature absorption coefficient was determined from transmission measurements by Tomiki and Miyata [5] in the spectral range from 9.1 to 9.35 eV and fitted to the functional form

$$\beta_{abs}(E,T) = \beta_{U0}\exp[\sigma_s(T)(E - E_g)/k_BT], \tag{1}$$

where β_{abs} is the absorption coefficient (typically in units of cm^{-1}); β_{U0} is a scaling coefficient (in units of cm^{-1}), E_g is the band-gap energy at absolute zero temperature, typically given in electron volts; k_B is Boltzmann's constant; and T is temperature in Kelvins. The exponential factor $\sigma_s(T)$ is given by the equation

$$\sigma_s(T) = \sigma_0 \frac{2k_BT}{E_p} \tanh \frac{E_p}{2k_BT}, \tag{2}$$

where E_p is an effective acoustic-phonon energy of the material. The Urbach tail parameters for BaF_2 are $\beta_{U0} = 4.17 \times 10^8$ cm^{-1}, $E_g = 10.162$ eV, $\sigma_0 = 0.58$, and $E_p = 0.04$ eV. The room-temperature values for k in Table I and Fig. 1 for this spectral region are generated using Eqs. (1) and (2).

The room-temperature (25° C) index of refraction from the ultraviolet to the infrared (0.27 to 10.3 μm) has been measured by Malitson [6] using a prism and the minimum-deviation technique. A Sellmeier model of the form

$$n^2(\lambda,T) = 1 + \sum_i \frac{\lambda^2 \Delta\epsilon_i(T)}{\lambda^2 - \lambda_i^2(T)} \tag{3}$$

is used to accurately represent the data (± 0.00002). Model parameters are listed in Table II. A comprehensive analysis on a variety of data sets was perfomed by Li [7]. A Sellmeier formula was also generated covering the range from 0.15 to 15 μm at $T = 20°$ C. The Li model parameters are also listed in Table II. Because the Sellmeier model has a physical basis, the extrapolation to higher frequencies beyond the experimental limit is justified. The values for n in Table I and Fig. 1 for the spectral region from 650 to 67,000 cm^{-1} are generated by the preceding formula. A temperature-dependent Sellmeier model covering the range from 100 to 450 K has been developed by Tropf [8]. Room-temperature thermo-optic coefficients, measured at different wavelengths, are listed in Table III [6, 9–13]. Notice that the thermo-optic coefficients are negative. This gives BaF_2 some athermal performance as an optical element. An athermal material has the property that

$$\frac{d(n(T)L(T))}{dT} = 0.$$

The value of the optical-path derivative as given above for BaF_2 is 7.5×10^{-6} nL per Kelvin at visible and near-infrared wavelengths. Thus, BaF_2 is useful for optical designs that require insensitivity to temperature.

Laser-calorimetry data [14] at DF (3.8 μm) and HF (2.7 μm) laser wavelengths indicate low-level absorption in roughly the middle of the transparency range of BaF_2. Material obtained from Adolf Meller had absorption-coefficient values of 2.0×10^{-4} cm^{-1} at the DF laser wavelength and 1.4×10^{-4} cm^{-1} at the HF laser wavelength. Material obtained from Optovac had absorption-coefficient values of 2.0×10^{-3} cm^{-1} at the DF laser wavelength and 1.8×10^{-3} cm^{-1} at the HF laser wavelength. The lowest values are listed in Table I and plotted in Fig. 1. The low-level absorption and the near-athermal performance of BaF_2 make it a candidate window material for high-power laser applications.

The multiphonon absorption (multiple-quanta lattice vibrations) edge marks the end of infrared transparency. Absorption-coefficient measurements by Deutsch [15] are represented by the simple formula

$$\beta_{abs}(\nu) = \beta_0 \exp\left(-\gamma \frac{\nu}{\nu_0}\right), \tag{4}$$

where for BaF_2, $\beta_0 = 49.641$ cm^{-1} and $\nu_0/\gamma = 75.9$ cm^{-1} at room temperature. The values of k in the spectral range from 800 to 1250 cm^{-1} in Table I and Fig. 1 are obtained from this formula. The data cover the three-phonon to four-phonon regions. Temperature-dependent experimental data on the absorption coefficient are described in Lipson *et al.* [16]. A temperature-dependent multiphonon model has been developed by Thomas *et al.* [17] and applied to BaF_2. Measurements in the two-phonon region are reported by Kaiser *et al.* [18]. The experimental results are listed in Table I and plotted in Fig. 1.

The one-phonon (one-quantum fundamental lattice vibrations) region is opaque and therefore characterized by reflectance measurements. A room-temperature reflectance measurement is reported by Kaiser *et al.* [18]. Temperature-dependent data are available from Hoffmann [19]. The classical-oscillator model is often used to fit the reflectance data and then to derive the optical constants. The classical-oscillator model is expressed in terms of the relative permittivity, $\epsilon_r(\nu,T)$, as given by[1]

$$\epsilon_r(\nu,T) = \epsilon_\infty(T) + \sum_i \frac{\Delta\epsilon_i(T)\nu_i^2(T)}{\nu_i^2(T) - \nu^2 + j\Gamma_i(\nu,T)\nu}, \tag{5}$$

where $\Delta\epsilon_i$, Γ_i, and ν_i are the ith-mode strength, line width, and long-wavelength transverse optical frequency, ν_{TO}, respectively. The sum on i is over all transverse optical modes. For BaF_2, there is only one allowed

[1] The expression uses the engineering convention for a time harmonic field of $\exp(-j\omega t)$. To convert to the convention commonly used in the *HOC* series, use $i = -j$.

infrared-active vibrational mode based on group theory of a perfect lattice. This is formally stated as

$$\Gamma = F_{1u}(\mathrm{IR}) + F_{2g}(\mathrm{R}).$$

The first mode is infrared active (mode 1 in Table IV), and the second mode is Raman active (241 cm^{-1} [20]). Table IV lists the classical-oscillator-model parameters used to fit the experimental data. More than one mode is needed to account for impurities and defects in real materials. Also, the high-frequency edge of the reflectance spectrum must include two-phonon contributions (see mode 4, Hoffmann [19], in Table IV). The n and k values in Table I and Fig. 1 are generated by Eq. (5) and the parameters from Hoffmann [19].

Below ν_{TO}, the index of refraction, n, is determined by extrapolation of the classical-oscillator model with reasonable accuracy. The absorption coefficient has been measured by Bosomworth [21]. Table I and Fig. 1 list and display the resulting values.

The static-dielectric constant data is the sum of all the strengths of higher frequency oscillators, including vibrational and electronic. Using Eq. (5), the static dielectric constant, $\epsilon_s(T) = \epsilon_r'(0,T)$, becomes

$$\epsilon_s(T) = \epsilon_\infty(T) + \sum_i \Delta\epsilon_i(T). \tag{6}$$

Based on the parameters listed in Table IV, we expect the value of ϵ_s to be between 6.73 and 7.63. Experimental results, obtained from capacitance bridges operating from 1 kHz to 1 MHz, produce values from 7.28 to 7.36, with most results closer to the higher value [13, 22–24]. The corresponding refractive index value is $n_s = 2.71$. Because the static dielectric constant predicted by the Hoffmann [19] parameters is close to the experimental result, his model parameters are used in the calculations of n in Table I and Fig. 1 below ν_{TO}. The static-index values are located incorrectly at 1×10^4 μm; however, there is little difference in the value of n_s at the measured wavelength and the plotted wavelength.

Whenever possible, physically based models are used to represent experimental measurements in Table I and Fig. 1. The models tend to reduce noise and allow interpolation and extrapolation to obtain meaningful results where no experimental data exist. In some case, the models discussed in this section also allow temperature-dependent data to be obtained.

REFERENCES

1. V. A. Ganin, M. G. Karin, V. K. Sidorin, K. K. Sidorin, N. V. Starostin, G. P. Startsev, and M. P. Shepilov, Optical constants and energy-band structure of fluorite-type crystals. *Sov. Phys. Solid State* **16**, 2313–2318 (1975).
2. G. W. Rubloff, Far-infrared reflectance spectra and the electronic structure of ionic crystals. *Phys. Rev. B* **5**, 662–684 (1972).

3. M. Nisar and S. Robin, Far ultraviolet electronic spectra of SrF_2 and BaF_2. *Pak. J. Sci. Ind. Res.* **17**, 49–54 (1974).
4. M. Zukic, D. G. Torr, J. F. Spann, and M. R. Torr, Vacuum ultraviolet thin films. 1: Optical constants of BaF_2, CaF_2, LaF_3, MgF_2, Al_2O_3, HfO_2 and SiO_2 thin films. *Appl. Opt.* **29**, 4284–4292 (1990).
5. T. Tomiki and T. Miyata, Optical studies of alkali fluorides and alkaline earth fluorides in VUV region. *J. Phys. Soc. Jpn.* **27**, 658–678 (1969).
6. I. H. Malitson, Refractive properties of barium fluoride. *J. Opt. Soc. Am.* **54**, 628–632 (1964).
7. H. H. Li, Refractive index of alkaline earth halides and its wavelength and temperature derivatives. *J. Phys. Chem. Ref. Data* **9**, 161–289 (1980).
8. W. J. Tropf, Temperature-dependent refractive index models for BaF_2, CaF_2, MgF_2, SrF_2, LiF, NaF, KCl, ZnS and ZnSe. *Opt. Eng.* **34**, 1369–1373 (1995).
9. A. Feldman, D. Horowitz, R. M. Walker, and M. J. Dodge, "Optical Materials Characterization Final Technical Report, February 1, 1978–September 30, 1978," NBS Technical Note 993, February 1979.
10. H. G. Lipson, Y. F. Tsay, B. Bendow, and P. A. Ligor, Temperature dependence of the refractive index of alkaline earth fluorides. *Appl. Opt.* **15**, 2352–2354 (1976).
11. Y. F. Tsay, H. G. Lipson, and P. A. Ligor, The temperature variation of the thermo-optic coefficient of CaF_2. *J. Appl. Phys.* **48**, 1953–1955 (1977).
12. R. J. Harris, G. T. Johnson, G. A. Kepple, P. C. Krok, and H. Mukai, Infrared thermooptic coefficient measurement of polycrystalline ZnSe, ZnS, CdTe, CaF_2 and BaF_2, single crystal KCl, and TI-20 glass. *Appl. Opt.* **16**, 436–438 (1977).
13. M. Wintersgill, J. Fontanella, C. Andeen, and D. Schuele, The temperature variation of the dielectric constant of "pure" CaF_2, SrF_2, BaF_2, and MgO. *J. Appl. Phys.* **50**, 8259–8261 (1979).
14. J. A. Harrington, D. A. Gregory, and W. F. Otto, Jr., Infrared absorption in chemical laser window materials. *Appl. Opt.* **15**, 1953–1959 (1976).
15. T. F. Deutsch, Absorption coefficient of infrared laser window materials. *J. Phys. Chem. Solids* **34**, 2091–2104 (1973).
16. H. G. Lipson, B. Bendow, N. E. Massa, and S. S. Mitra, Multiphonon infrared absorption in the transparent regime of alkaline-earth fluorides. *Phys. Rev. B* **13**, 2614–2619 (1976).
17. M. E. Thomas, R. I. Joseph, and W. J. Tropf, Infrared transmission properties of sapphire, spinel, yttria and ALON as a function of temperature and frequency. *Appl. Opt.* **27**, 239 (1988); M. E. Thomas, Temperature dependence of the complex index of refraction. *In* "Handbook of Optical Constants of Solids II" (E. D. Palik, ed.), pp. 177–201. Academic Press, Orlando, Florida, 1991; M. E. Thomas, A computer code for modeling optical properties of window materials, in Window and Dome Technologies and Materials. *Proc. of SPIE* **1112**, 260–267 (1989).
18. W. Kaiser, W. G. Spitzer, R. H. Kaiser, and L. E. Howarth, Infrared properties of CaF_2, SrF_2, and BaF_2. *Phys. Rev.* **127**, 1950–1954 (1962).
19. C. E. Hoffmann, Optical constants of infrared active phonons as a function of frequency and temperature. M.S. Thesis, Johns Hopkins University, Baltimore, Maryland (1988).
20. I. Richman, Longitudinal optical phonons in CaF_2, SrF_2 and BaF_2. *J. Chem. Phys.* **41**, 2836–2837 (1966).
21. D. R. Bosomworth, Far-infrared optical properties of CaF_2, SrF_2, BaF_2, and CdF_2. *Phys. Rev.* **157**, 709–715 (1967).
22. K. V. Rao and A. Smakula, Dielectric properties of alkaline earth fluoride single crystals. *J. Appl. Phys.* **37**, 319–323 (1965).
23. C. Andeen, J. Fontanella, and D. Schuele, Low-frequency dielectric constants of the alkaline earth fluorides by the method of substitution. *J. Appl. Phys.* **42**, 2216–2219 (1971).
24. G. A. Samara, Temperature and pressure dependence of the dielectric properties of PbF_2 and the alkaline-earth fluorides. *Phys. Rev. B* **13**, 4529–4544 (1976).

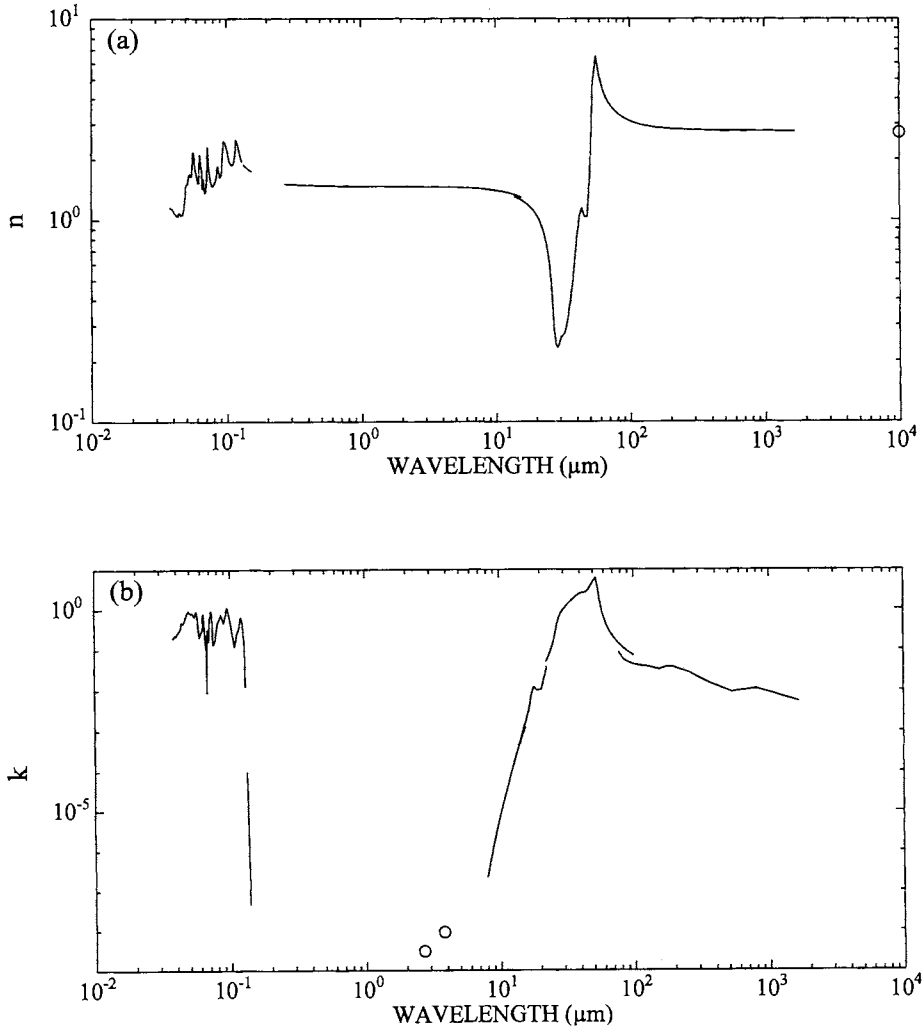

Fig. 1. (a) Log–log plot of the room-temperature index of refraction, n, for BaF_2 versus wavelength in microns. (b) Log–log plot of the room-temperature extinction coefficient, k, for BaF_2 versus wavelength in microns. Isolated data points are indicated with a symbol.

TABLE I

Values of n and k for BaF_2 from Various References[a]

eV	cm^{-1}	μm	n	k
32.91	265400	0.03767	1.149 [3]	0.1900 [3]
31.71	255800	0.03910	1.134	0.2208
31.42	253500	0.03946	1.130	0.2263
31.20	251600	0.03974	1.118	0.2138
30.35	244800	0.04086	1.084	0.2436
29.97	241700	0.04137	1.077	0.2614
28.91	233100	0.04289	1.040	0.3217
28.71	231600	0.04318	1.043	0.3344
28.60	230700	0.04335	1.044	0.3767
28.52	230000	0.04348	1.046	0.4149
28.40	229100	0.04365	1.052	0.4468
28.22	227600	0.04393	1.081	0.4727
27.47	221600	0.04514	1.074	0.4452
27.27	219900	0.04547	1.056	0.4568
27.07	218300	0.04580	1.054	0.4885
26.81	216200	0.04625	1.063	0.5393
26.46	213400	0.04686	1.058	0.6116
25.75	207700	0.04816	1.153	0.7983
25.55	206100	0.04853	1.196	0.8265
25.35	204500	0.04891	1.251	0.8610
25.22	203400	0.04916	1.323	0.9051
25.03	201900	0.04954	1.440	0.9275
24.72	199400	0.05016	1.479	0.8579
24.51	197700	0.05059	1.507	0.8247
24.18	195000	0.05128	1.517	0.8062
24.02	193700	0.05162	1.561	0.7774
23.89	192700	0.05189	1.604	0.8146
23.73	191400	0.05225	1.649	0.8438
23.52	189700	0.05271	1.680	0.8169
23.34	188200	0.05313	1.686	0.7727
22.91	184700	0.05413	1.638	0.7006
22.66	182800	0.05471	1.659	0.6882
22.48	181300	0.05515	1.702	0.7341
22.14	178600	0.05600	2.116	0.8357
22.03	177700	0.05627	2.163	0.8987
21.86	176300	0.05671	2.155	0.8533
21.76	175500	0.05698	2.123	0.7893
21.66	174700	0.05724	2.072	0.7178
21.58	174100	0.05744	2.031	0.6405
21.49	173400	0.05768	1.972	0.5627
21.43	172800	0.05786	1.926	0.4945
21.34	172100	0.05811	1.870	0.4196
21.26	171400	0.05833	1.825	0.3641
21.15	170600	0.05861	1.781	0.2973
20.86	168300	0.05943	1.685	0.2063
20.23	163100	0.06130	1.527	0.2784

(continued)

[a] References given in brackets.

TABLE I *(Continued)*

Barium Fluoride

eV	cm^{-1}	μm	n	k
19.97	161100	0.06208	1.529	0.3039
19.79	159700	0.06264	2.096	0.3464
19.73	159200	0.06283	2.102	0.3943
19.71	159000	0.06290	2.094	0.4627
19.65	158500	0.06309	2.073	0.5899
19.65	158500	0.06310	2.073	0.6628
19.64	158400	0.06314	2.068	0.7318
19.56	157700	0.06340	2.014	0.7757
19.44	156800	0.06377	1.953	0.7318
19.37	156300	0.06399	1.917	0.6568
19.25	155300	0.06439	1.805	0.4843
19.14	154300	0.06479	1.813	0.3468
19.05	153600	0.06509	1.812	0.2730
18.96	153000	0.06538	1.726	0.2107
18.86	152100	0.06573	1.504	0.1616
18.76	151300	0.06608	1.433	0.1349
18.52	149400	0.06693	1.597	0.0961
18.48	149100	0.06708	1.582	0.0543
18.40	148400	0.06739	1.523	0.0086
18.33	147900	0.06763	1.473	0.0611
18.32	147732	0.06769	1.462	0.1209
18.31	147764	0.06773	1.457	0.1668
18.30	147600	0.06775	1.456	0.2168
18.29	147500	0.06779	1.446	0.2674
18.24	147100	0.06797	1.417	0.3101
18.09	145900	0.06855	1.363	0.2612
18.05	145600	0.06869	1.365	0.2027
17.94	144700	0.06910	1.372	0.1651
17.80	143600	0.06965	1.381	0.2058
17.72	142900	0.06998	1.427	0.2497
17.67	142500	0.07018	1.457	0.3108
17.63	142200	0.07034	1.474	0.3856
17.61	142000	0.07041	1.480	0.4522
17.59	141800	0.07050	1.489	0.5121
17.54	141400	0.07070	1.508	0.5679
17.43	140600	0.07114	1.622	0.6246
17.29	139500	0.07171	2.288	0.6744
17.22	138900	0.07199	2.246	0.7235
17.21	138800	0.07203	2.241	0.7717
17.21	138800	0.07203	2.241	0.8344
17.20	138800	0.07204	2.239	0.8843
17.14	138300	0.07233	2.105	0.9368
16.98	137000	0.07301	1.885	0.9063
16.94	136600	0.07318	1.855	0.8525
16.86	136000	0.07354	1.820	0.7332
16.72	134800	0.07416	1.737	0.4620
16.63	134100	0.07456	1.686	0.2532

TABLE I *(Continued)*

Barium Fluoride

eV	cm^{-1}	μm	*n*	*k*
16.61	134000	0.07464	1.676	0.1981
16.48	132900	0.07522	1.619	0.1388
16.32	131600	0.07596	1.550	0.1405
16.04	129400	0.07729	1.481	0.1644
15.86	127900	0.07820	1.467	0.2023
15.73	126800	0.07884	1.477	0.2521
15.61	125900	0.07940	1.485	0.3047
15.43	124400	0.08037	1.507	0.4231
15.26	123000	0.08127	1.526	0.4748
15.07	121600	0.08225	1.551	0.5121
14.96	120700	0.08287	1.586	0.5555
14.81	119400	0.08374	1.639	0.5974
14.59	117700	0.08498	1.814	0.6492
14.50	116900	0.08553	1.845	0.7024
14.42	116300	0.08600	1.845	0.7457
14.22	114700	0.08721	1.755	0.6855
14.00	112900	0.08856	1.645	0.5621
13.89	112000	0.08925	1.633	0.5027
13.76	111000	0.09013	1.655	0.4675
13.63	109900	0.09096	1.675	0.5213
13.57	109500	0.09134	1.684	0.5859
13.29	107200	0.09326	2.210	0.7223
13.25	106900	0.09356	2.366	0.7724
13.21	106500	0.09388	2.415	0.8294
13.18	106300	0.09410	2.428	0.8841
13.11	105700	0.09460	2.457	1.001
12.98	104700	0.09552	2.443	1.113
12.86	103800	0.09638	2.427	1.052
12.81	103300	0.09678	2.416	0.9956
12.77	103000	0.09708	2.399	0.9291
12.71	102500	0.09755	2.367	0.8661
12.65	102100	0.09799	2.337	0.7979
12.57	101300	0.09867	2.291	0.7258
12.51	100900	0.09909	2.269	0.6605
12.41	100100	0.09987	2.230	0.5781
12.34	99540	0.1005	2.203	0.506
12.25	98760	0.1013	2.161	0.4437
12.15	97960	0.1021	2.094	0.3779
12.05	97210	0.1029	2.033	0.3087
11.96	96420	0.1037	1.982	0.2574
11.78	95010	0.1053	1.928	0.2154
11.48	92600	0.1080	1.882	0.121
11.31	91200	0.1097	1.873	0.1532
11.04	89010	0.1123	1.908	0.2276
10.94	88230	0.1133	1.932	0.2623
10.80	87140	0.1148	2.133	0.2967
10.66	86000	0.1163	2.491	0.3385

(continued)

TABLE I *(Continued)*

Barium Fluoride

eV	cm^{-1}	μm	n	k
10.54	85040	0.1176	2.465	0.3917
10.46	84400	0.1185	2.447	0.4592
10.41	83960	0.1191	2.417	0.5208
10.38	83720	0.1195	2.398	0.5806
10.27	82800	0.1208	2.328	0.6321
10.12	81650	0.1225	2.236	0.5717
10.07	81190	0.1232	2.199	0.5121
10.01	80700	0.1239	2.163	0.4417
9.953	80260	0.1246	2.132	0.3712
9.891	79750	0.1254	2.094	0.3053
9.850	79440	0.1259	2.075	0.2423
9.771	78810	0.1269	2.038	0.1713
9.716	78370	0.1276	2.013	0.1095
9.646	77800	0.1285	1.980	0.06145
9.590	77350	0.1293	1.954	0.01223
9.321	75180	0.1330	1.882 [4]	
9.357	75470	0.1325		9.759E-5 [5]
9.287	74910	0.1335		2.589E-5
9.218	74350	0.1345		7.004E-6
9.214	74320	0.1346	1.873	
9.150	73800	0.1355		1.932E-6
9.137	73690	0.1357	1.857	
9.083	73260	0.1365		5.431E-7
9.017	72730	0.1375		1.555E-7
8.975	72390	0.1381	1.834	
8.952	72200	0.1385		4.535E-8
8.808	71040	0.1408	1.815	
8.697	70150	0.1426	1.800	
8.538	68860	0.1452	1.782	
8.396	67710	0.1477	1.767	
8.099	65320	0.1531	1.741	
8.266	66670	0.15	1.678 [7]	
6.199	50000	0.20	1.557	
4.959	40000	0.25	1.519	
4.133	33330	0.30	1.501	
4.592	37037	0.27	1.51031 [6]	
3.874	31250	0.32	1.49636	
3.350	27027	0.37	1.48821	
2.952	23809	0.42	1.48301	
2.637	21276	0.47	1.47946	
2.384	19230	0.52	1.47691	
2.175	17543	0.57	1.47503	
1.999	16129	0.62	1.47358	
1.850	14925	0.67	1.47245	
1.722	13888	0.72	1.47153	
1.610	12987	0.77	1.47078	
1.512	12195	0.82	1.47016	

TABLE I *(Continued)*

Barium Fluoride

eV	cm^{-1}	μm	n	k
1.425	11494	0.87	1.46963	
1.347	10869	0.92	1.46917	
1.278	10309	0.97	1.46877	
1.215	9803	1.02	1.46842	
1.158	9345	1.07	1.46811	
1.107	8928	1.12	1.46783	
1.059	8547	1.17	1.46757	
1.016	8196	1.22	1.46733	
0.976	7874	1.27	1.46710	
0.939	7575	1.32	1.46689	
0.904	7299	1.37	1.46669	
0.873	7042	1.42	1.46651	
0.843	6802	1.47	1.46632	
0.815	6578	1.52	1.46615	
0.789	6369	1.57	1.46598	
0.765	6172	1.62	1.46581	
0.742	5988	1.67	1.46565	
0.720	5813	1.72	1.46549	
0.700	5649	1.77	1.46533	
0.681	5494	1.82	1.46517	
0.663	5347	1.87	1.46501	
0.645	5208	1.92	1.46485	
0.629	5076	1.97	1.46470	
0.613	4950	2.02	1.46454	
0.598	4830	2.07	1.46438	
0.584	4716	2.12	1.46422	
0.571	4608	2.17	1.46406	
0.558	4504	2.22	1.46390	
0.546	4405	2.27	1.46374	
0.534	4310	2.32	1.46358	
0.523	4219	2.37	1.46341	
0.512	4132	2.42	1.46325	
0.501	4048	2.47	1.46308	
0.492	3968	2.52	1.46291	
0.482	3891	2.57	1.46273	
0.473	3816	2.62	1.46256	
0.464	3745	2.67	1.46238	
0.459	3704	2.70		3.03E-9 [14]
0.455	3676	2.72	1.46220	
0.447	3610	2.77	1.46202	
0.439	3541	2.82	1.46184	
0.432	3484	2.87	1.46165	
0.424	3424	2.92	1.46146	
0.417	3367	2.97	1.46127	
0.410	3311	3.02	1.46107	
0.403	3257	3.07	1.46088	
0.397	3205	3.12	1.46068	

(continued)

TABLE I *(Continued)*

Barium Fluoride

eV	cm^{-1}	μm	n	k
0.391	3154	3.17	1.46047	
0.385	3105	3.22	1.46027	
0.379	3058	3.27	1.46006	
0.373	3012	3.32	1.45985	
0.367	2967	3.37	1.45964	
0.362	2923	3.42	1.45942	
0.357	2881	3.47	1.45920	
0.352	2840	3.52	1.45898	
0.347	2801	3.57	1.45876	
0.342	2762	3.62	1.45853	
0.337	2724	3.67	1.45830	
0.333	2688	3.72	1.45806	
0.328	2652	3.77	1.45783	
0.326	2632	3.80		9.07E-9 [14]
0.324	2617	3.82	1.45759	
0.320	2583	3.87	1.45734	
0.316	2551	3.92	1.45710	
0.312	2518	3.97	1.45685	
0.308	2487	4.02	1.45660	
0.304	2457	4.07	1.45634	
0.300	2427	4.12	1.45608	
0.297	2398	4.17	1.45582	
0.293	2369	4.22	1.45556	
0.290	2341	4.27	1.45529	
0.287	2314	4.32	1.45502	
0.283	2288	4.37	1.45475	
0.280	2262	4.42	1.45447	
0.277	2237	4.47	1.45419	
0.274	2212	4.52	1.45391	
0.271	2188	4.57	1.45362	
0.268	2164	4.62	1.45333	
0.265	2141	4.67	1.45304	
0.262	2118	4.72	1.45274	
0.259	2096	4.77	1.45244	
0.257	2074	4.82	1.45214	
0.254	2053	4.87	1.45183	
0.252	2032	4.92	1.45153	
0.249	2012	4.97	1.45121	
0.246	1992	5.02	1.45090	
0.244	1972	5.07	1.45058	
0.242	1953	5.12	1.45026	
0.239	1934	5.17	1.44993	
0.237	1915	5.22	1.44960	
0.235	1897	5.27	1.44927	
0.233	1879	5.32	1.44893	
0.230	1862	5.37	1.44860	
0.228	1845	5.42	1.44825	

TABLE I *(Continued)*

Barium Fluoride

eV	cm^{-1}	μm	n	k
0.226	1828	5.47	1.44791	
0.224	1811	5.52	1.44756	
0.222	1795	5.57	1.44721	
0.220	1779	5.62	1.44685	
0.218	1763	5.67	1.44649	
0.216	1748	5.72	1.44613	
0.214	1733	5.77	1.44576	
0.213	1718	5.82	1.44540	
0.211	1703	5.87	1.44502	
0.209	1689	5.92	1.44465	
0.207	1675	5.97	1.44427	
0.205	1661	6.02	1.44388	
0.204	1647	6.07	1.44350	
0.202	1633	6.12	1.44311	
0.200	1620	6.17	1.44271	
0.199	1607	6.22	1.44232	
0.197	1594	6.27	1.44192	
0.196	1582	6.32	1.44151	
0.194	1569	6.37	1.44110	
0.193	1557	6.42	1.44069	
0.191	1545	6.47	1.44028	
0.190	1533	6.52	1.43986	
0.188	1522	6.57	1.43944	
0.187	1510	6.62	1.43901	
0.185	1499	6.67	1.43858	
0.184	1488	6.72	1.43815	
0.183	1477	6.77	1.43772	
0.181	1466	6.82	1.43728	
0.180	1455	6.87	1.43683	
0.179	1445	6.92	1.43638	
0.177	1434	6.97	1.43593	
0.176	1424	7.02	1.43548	
0.175	1414	7.07	1.43502	
0.174	1404	7.12	1.43456	
0.172	1394	7.17	1.43409	
0.171	1385	7.22	1.43363	
0.170	1375	7.27	1.43315	
0.169	1366	7.32	1.43268	
0.168	1356	7.37	1.43220	
0.167	1347	7.42	1.43171	
0.165	1338	7.47	1.43122	
0.164	1329	7.52	1.43073	
0.163	1321	7.57	1.43024	
0.162	1312	7.62	1.42974	
0.161	1303	7.67	1.42923	
0.160	1295	7.72	1.42873	
0.159	1287	7.77	1.42822	

(continued)

TABLE I *(Continued)*

Barium Fluoride

eV	cm^{-1}	μm	n	k
0.158	1278	7.82	1.42770	
0.157	1270	7.87	1.42718	
0.156	1262	7.92	1.42666	
0.155	1254	7.97	1.42613	
0.155	1250.0	8.0	1.4259 [7]	2.225E-7 [15]
0.146	1176.5	8.5	1.4204	6.228E-7
0.138	1111.1	9.0	1.4145	1.560E-6
0.131	1052.6	9.5	1.4082	3.558E-6
0.124	1000.0	10.0	1.4014	7.494E-6
0.118	952.4	10.5	1.3942	1.474E-5
0.113	909.1	11.0	1.3865	2.731E-5
0.108	869.6	11.5	1.3783	4.805E-5
0.103	833.3	12.0	1.3697	8.082E-5
0.100	800.0	12.5	1.3604	0.000131
0.095	769.2	13.0	1.3506	0.000204
0.0919	740.7	13.5	1.3402	0.000308
0.0886	714.3	14.0	1.3292	0.000453
0.09016	727.2	13.75	1.3040 [19]	0.000400 [18]
0.08740	704.9	14.19	1.2921	0.00057
0.08530	688.0	14.53	1.2821	0.00077
0.08363	674.5	14.83	1.2735	0.00098
0.08209	662.1	15.10	1.2650	0.00123
0.07894	636.7	15.71	1.2455	0.00177
0.07780	627.5	15.94	1.2377	0.00223
0.07660	617.8	16.92	1.2289	0.00270
0.07577	611.1	16.36	1.2226	0.00301
0.07396	596.5	16.76	1.2077	0.00441
0.07318	590.2	16.94	1.2008	0.00546
0.07242	584.1	17.12	1.1939	0.00666
0.07168	578.1	17.29	1.1867	0.00805
0.07068	570.1	17.54	1.1767	0.00936
0.06991	563.9	17.73	1.1685	0.01038
0.06908	557.2	17.94	1.1593	0.01159
0.06828	550.7	18.16	1.1498	0.01196
0.06745	544.0	18.38	1.1395	0.01145
0.06591	531.6	18.81	1.1190	0.01019
0.06528	526.5	18.99	1.1099	0.01003
0.06391	515.5	19.40	1.0888	0.01026
0.06270	505.7	19.77	1.0682	0.01027
0.06094	491.5	20.34	1.0348	0.01023
0.05998	483.8	20.67	1.0145	0.01131
0.05943	479.3	20.86	1.0019	0.01275
0.05855	472.2	21.18	0.9806	0.01703
0.05739	462.9	21.60	0.9501	0.02099
0.05673	457.6	21.85	0.9311	0.02337
0.05599	451.6	22.14	0.9010	0.02939
0.05564	448.8	22.28	0.8967	0.03298

TABLE I *(Continued)*

Barium Fluoride

eV	cm^{-1}	μm	n	k
0.05543	447.1	22.36	0.8895	0.03795
0.05455	440	22.37	0.8579	0.05890 [19]
0.05331	430	23.26	0.8074	0.0694
0.05207	420	23.81	0.7483	0.0834
0.05083	410	24.39	0.6778	0.1032
0.04959	400	25.00	0.5922	0.1334
0.04835	390	25.64	0.4873	0.1845
0.04711	380	26.32	0.3691	0.2801
0.04587	370	27.03	0.2800	0.4304
0.04463	360	27.78	0.2411	0.5931
0.04339	350	28.57	0.2325	0.7473
0.04215	340	29.41	0.2426	0.8911
0.04091	330	30.30	0.2603	1.020
0.03967	320	31.25	0.2672	1.147
0.03843	310	32.26	0.2725	1.296
0.03719	300	33.33	0.2940	1.463
0.03595	290	34.48	0.3367	1.644
0.03471	280	35.71	0.4014	1.835
0.03347	270	37.04	0.4902	2.040
0.03223	260	38.46	0.6235	2.260
0.03099	250	40.00	0.8233	2.4592
0.02975	240	41.67	1.0499	2.568
0.02851	230	43.48	1.139	2.609
0.02727	220	45.45	1.036	2.869
0.02603	210	47.62	1.038	3.590
0.02479	200	50.00	1.636	4.911
0.02355	190	52.63	4.894	6.135
0.02231	180	55.56	6.461	2.095
0.02107	170	58.82	5.168	0.787
0.01983	160	62.50	4.431	0.4251
0.01859	150	66.67	3.987	0.2735
0.01735	140	71.43	3.690	0.1935
0.01611	130	76.92	3.477	0.1449
0.01599	128.94	77.55	3.458 [19]	0.0875 [20]
0.01590	128.23	77.99	3.446	0.0846
0.01576	127.13	78.66	3.427	0.0801
0.01556	125.50	79.68	3.400	0.0751
0.01538	124.01	80.64	3.377	0.0708
0.01523	122.81	81.42	3.359	0.0667
0.01505	121.40	82.37	3.338	0.0644
0.01489	120.12	83.25	3.320	0.0600
0.01446	116.66	85.72	3.273	0.0549
0.01398	112.78	88.67	3.226	0.0512
0.01337	107.86	92.71	3.172	0.0480
0.01275	102.86	97.22	3.123	0.0448
0.01211	97.65	102.4	3.078	0.0428
0.01137	91.67	109.1	3.031	0.0409

(continued)

TABLE I *(Continued)*

Barium Fluoride

eV	cm^{-1}	μm	n	k
0.01063	85.77	116.6	2.991	0.0395
0.01003	80.87	123.6	2.961	0.0385
0.00949	76.53	130.7	2.937	0.0390
0.00877	70.71	141.4	2.909	0.0347
0.00799	64.46	155.1	2.881	0.0326
0.00712	57.45	174.1	2.855	0.0373
0.00643	51.89	192.7	2.837	0.0374
0.00484	39.00	256.4	2.803	0.0272
0.00414	33.40	299.4	2.792	0.0203
0.00330	26.59	376.2	2.781	0.0141
0.00234	18.90	529	2.772	0.0090
0.00155	12.50	800	2.766	0.0108
0.00074	6.00	1666.7	2.763	0.0053
0.0	0	∞	2.713 [13]	0.0

TABLE II

Room-temperature Sellmeier Model Parameters

ith mode		$\Delta\epsilon_i$	λ_i
Malitson model [6]			
	1	0.643356	0.057789
	2	0.506762	0.10968
	3	3.8261	46.3864
Li model [7]			
	1	0.33973	0.0
	2	0.81070	0.10065
	3	0.19652	29.87
	4	4.52469	63.82

TABLE III

Thermo-optical Coefficients of Barium Fluoride

Wavelength (μm)	dn/dT (10^{-6}/K)	Measurement temperature (°C)	Reference
0.3250	−15.6	37	[11]
0.4047	−15.0	15–55	[6]
0.4416	−16.3	37	[11]
0.4579	−15.6	20	[9]
0.5461	−15.2	15–55	[6]
0.6328	−16.0	20	[9]
	−16.7	37	[10, 11]
	−16.4	25–65	[12]
0.6563	−15.2	15–55	[6]
0.7679	−15.5	15–55	[6]
1.15	−16.2	20	[9]
	−17.1	37	[10, 11]
	−16.8	25–65	[12]
3.39	−15.9	20	[9]
	−16.8	37	[10, 11]
	−16.3	25–65	[12]
10.6	−14.5	20	[9]
∞	290	7–47	[13]

TABLE IV

Room-Temperature Classical Oscillator Model Parameters

Mode number i	ν_i (cm^{-1})	$\Delta\epsilon_i$	Γ_i/ν_i	Reference
1	184	4.5	0.020	[18]
2	278	0.07	0.30	
$\epsilon_\infty = 2.16$				
1	188	4.5	0.069	[19]
2	236	0.96	0.21	
3	278	0.015	0.15	
4	328	0.014	0.125	
$\epsilon_\infty = 2.141$				

Calcium Carbonate, Calcite ($CaCO_3$)

WILLIAM J. TROPF
Applied Physics Laboratory
The Johns Hopkins University
Laurel, Maryland

Calcite (or calcspar) is the mineral name of the low-pressure, hexagonal form of calcium carbonate, $CaCO_3$. (Orthorhombic aragonite [high-pressure form] and the rare hexagonal mineral vaterite are isomorphs found in nature.) Calcite is the principal constituent of limestone, marble, and chalk. The mineral Iceland spar is a pure, colorless, optical-quality form of calcite. The outstanding optical feature of calcite is its very high (negative) birefringence, making it a useful material for polarizers. Calcite is soft (3 on the Mohs scale) and dissociates into calcium oxide and carbon dioxide above 1170 K.

Crystalline calcite has a hexagonal (rhombohedral) structure, the space group is $R\bar{3}c$ (or D_{3d}^6), and the lattice dimensions are $a = 4.9900$ and $c = 17.060$. The unit cell contains six formula units (30 atoms), giving a theoretical density of 2.711 g/cm^3. Calcium atoms occupy 6(b) sites (with $\bar{3}$ or $C_{3i}[S_6]$ point symmetry), carbon atoms are in the 6(a) sites (32 or D_3 point symmetry), and the oxygen atoms are in the 18(e) sites (C_2 point symmetry).

Ultraviolet optical constants of calcite were determined from a Kramers–Kronig analysis of reflectance measurements by Kondo *et al.* [1] from 5 to 12 eV and from polarized reflection measurements by Uzan *et al.* [2] from 6 to 9.5 eV. There are considerable differences in the two results, but they agree on the basic features. The ordinary ray is dominated by a strong absorption peak near 8 eV, while the extraordinary-ray absorption becomes strong near 9.5 eV. The ordinary-ray absorption is explained by Kondo as arising from a transition from the A_1' state to an excited E' state of the carbonate radical. Values in Table I from 6.7 to 11.7 eV are from the measurements of Kondo *et al.* [1] with an additional value at 10.2 eV from variable-angle reflection measurements of Stéphan *et al.* [3].

Uzan *et al.* [4] also determined the absorption coefficients in the 6.5–7.3 eV region from transmission measurements of thin samples. These data are also included in Table I.

Copyright © 1998 by Academic Press.
All rights of reproduction in any form reserved
ISBN 0-12-544423-0/$25.00.

Smakula [5] summarizes the available refractive-index values. The accurate data listed in Table I are nearly a century old and come primarily from minimum-deviation prism measurements by Martens (0.2–0.77 μm, measured at 18° C [6]), by Gifford (measured at 15° C [7]), and by Carvallo (0.62–2.32 μm, measured at 20° C [8, 9]), supplemented by a single-wavelength measurement of Barbaron (0.55 μm, 18° C [10]). A standard Sellmeier dispersion equation of the form

$$n^2(\lambda) - 1 = \sum_i \frac{A_i \lambda^2}{\lambda^2 - \lambda_i^2} \tag{1}$$

can be used to represent the refractive index in the transparent region. Values of the constants A_i and λ_i are given by Ramachandran [11] and Tropf *et al.* [12] and are listed in Table II. These dispersion formulae are based on the data cited earlier, but are accurate only to the third decimal place. A few sources [10, 13, 14] give the temperature dependence of the refractive index. All measurements are in the ultraviolet or visible spectral regions. Table III lists the values of dn/dT with references. Ramachandran [11] also gives a temperature-dependent dispersion relationship based on these data.

The fundamental infrared and Raman spectra of calcite have been extensively studied. Optical modes of calcite are

$$\begin{aligned} \Gamma = {} & A_{1g}(\mathrm{R}) + 3A_{2g}(-) + 2A_{1u}(-) + 3A_{2u}(\mathrm{IR},\mathbf{E} \parallel \mathbf{c}) \\ & + 4E_g(\mathrm{R}) + 5E_u(\mathrm{IR},\mathbf{E} \perp \mathbf{c}), \end{aligned} \tag{2}$$

where the Raman frequencies are given by Porto *et al.* [15] as a A_{1g} vibration at 1088 cm^{-1} and E_g vibrations at 156, 283, 714, and 1432 cm^{-1}. Infrared-active modes have been extensively studied using reflection and emission measurements [16–23], including determination of temperature dependence [16], and measurements made at oblique angles with respect to the principal axes [20]. Table IV summarizes the location of the infrared-active optical modes measured by several authors. Of special interest are the classical-oscillator dispersion models of Hellwege *et al.* [19] and Long *et al.* [22], which can be used to calculate optical constants. Model calculations from Long *et al.* [22] are used to provide the optical constants given in Table I from 0 to 2500 cm^{-1}. Selected results of a Kramers–Kronig analysis of reflectivity [24] near several of the optical modes are also included in Table I.

Measurements made in the submillimeter region [25] given in Table I agree well with low-frequency model results [22]. The microwave (10 GHz) impedance measurement of Demau [26] gives the low-frequency dielectric constant as $\epsilon_o = 8.680$ ($n_o = 2.946$) and $\epsilon_e = 8.307$ ($n_e = 2.882$).

Figures 1 and 2 show a composite of the principal values of the complex refractive index of calcite taken from all of the data sources.

REFERENCES

1. S. Kondo, H. Yamashita, and K. Nakamura, Optical properties of calcite in the vacuum ultraviolet. *J. Phys. Soc. Jpn.* **34**, 711–714 (1973).
2. E. Uzan, H. Damany, and V. Chandrasekharan, Optical properties of calcite in the Schumann region. *Opt. Commun.* **1**, 221–222 (1969).
3. G. Stéphan, Y. Le Calvez, and S. Robin, A method to determine the complex refractive indices of an absorbing uniaxial crystal. *C. R. Acad. Sci. (Paris)* **265**, 281–284 (1967).
4. E. Uzan, H. Damany, and V. Chandrasekharan, Determination of the absorption indices of calcite in the dichroic region. *Opt. Commun.* **2**, 273–275 (1969); also see J. Schellman, V. Chandrasekharan, H. Damany, and J. Romand, Dichroic absorption of calcite in the Schumann region. *C. R. Acad. Sci. (Paris)* **260**, 117–120 (1965).
5. A. Smakula, "Single Crystals: Growth, Production, and Application," p. 400, Springer-Verlag, Berlin, 1962; also see B. H. Billings, Optics. *In* "American Institute of Physics Handbook," (D. E. Gray, ed.), 3rd Ed. McGraw-Hill, New York, 1972. Note: several typographic errors occur in these references.
6. F. F. Martens, On the dispersion of ultraviolet light. *Ann. Phys. (Leipzig)* **7**, 603–640 (1901).
7. J. W. Gifford, The refractive indices of fluorite, quartz, and calcite. *Proc. R. Soc. London* **70**, 329–340 (1902).
8. E. Carvallo, Precise measurement of the infrared dispersion of Iceland spar. *C. R. Acad. Sci (Paris)* **126**, 950–953 (1898).
9. E. Carvallo, On the unusual dispersion of Iceland spar. *J. Phys. Radium* **9**, 465–479 (1900).
10. M. Barbaron, Optical constants of calcite at low temperatures. *C. R. Acad. Sci (Paris)* **229**, 875–876 (1949).
11. G. N. Ramachandran, Birefringence of crystals and its temperature variation, Part I: Calcite and aragonite. *Proc. Indian Acad. Sci. B* **A26**, 77–92 (1947).
12. W. J. Tropf, M. E. Thomas, and T. Harris, Properties of crystals and glasses. *in* "Optical Society of America Handbook of Optics" (M. Bass, ed.), 2nd Ed. McGraw-Hill, New York, 1994.
13. F. J. Micheli, On the influence of temperature on ultraviolet dispersion of fluorite, rock salt, quartz, and calcite. *Ann. Phys. (Leipzig)* **7**, 772–790 (1902).
14. J. O. Reed, On the influence of temperature on the refraction and dispersion of single crystals and glasses. *Ann. Phys. Chem. (Leipzig)* **65**, 707–744 (1898).
15. S. P. S. Porto, J. A. Giordmaine, and T. C. Damen, Depolarization of raman scattering in calcite. *Phys. Rev.* **147**, 608–611 (1966).
16. T. Sakuria and T. Sato, Temperature dependence of vibrational spectra in calcite by means of emissivity measurement. *Phys. Rev. B* **4**, 583–591 (1971).
17. P. J. Ring, Dispersion analysis of the isomorphs sodaniter and calcite. *Infrared Phys.* **12**, 237–249 (1972).
18. R. K. Vincent, Emission polarization study on quartz and calcite. *Appl. Opt.* **11**, 1942–1945 (1972).
19. K. H. Hellwege, W. Lesch, M. Plihal, and G. Schaack, Two phonon absorption spectra and dispersion of phonon branches in crystals of the calcite structure. *Z. Phys.* **232**, 61–86 (1970).
20. R. Frech and H. Nichols, Infrared reflectivity of calcite: Oblique phonons. *Phys. Rev. B* **17**, 2275–2779 (1978).
21. C. Pastorek and J. C. Declus, Infrared vibrational intensities, dipole derivatives, and charge flux parameters for BF_3, CO_3^{2-}, and NO_3^-. *J. Phys. Chem.* **83**, 1379–1385 (1979).
22. L. L. Long, M. R. Querry, R. J. Bell, and R. W. Alexander, Optical properties of calcite and gypsum in crystalline and powdered form in the infrared and far-infrared. *Infrared Phys.* **34**, 191–201 (1993).
23. E. V. Antropova and A. S. Poplavnoi, Optical properties of calcite-structure crystals in the infrared region. *Opt. Spectrosc.* **79**, 445–449 (1995).

24. F. Matossi and V. Hohler, Optical constants of calcite in the region of fundamental frequencies. *Z. Naturforsch.* **22A**, 1516–1524 (1967).
25. V. P. Bystrov, Yu. G. Goncharov, G. V. Kozlov, and A. F. Kupriyanenko, Dielectric properties of optical crystals at submillimeter wavelengths. *Sov. Phys. Tech. Phys. (Engl. Transl.)* **31**, 1206–1207 (1986).
26. C. Demau, Measurement of the dielectric constants and dielectric anisotropies of various crystals at X-band. *J. Phys. (Paris)* **24,** 284–285 (1963).

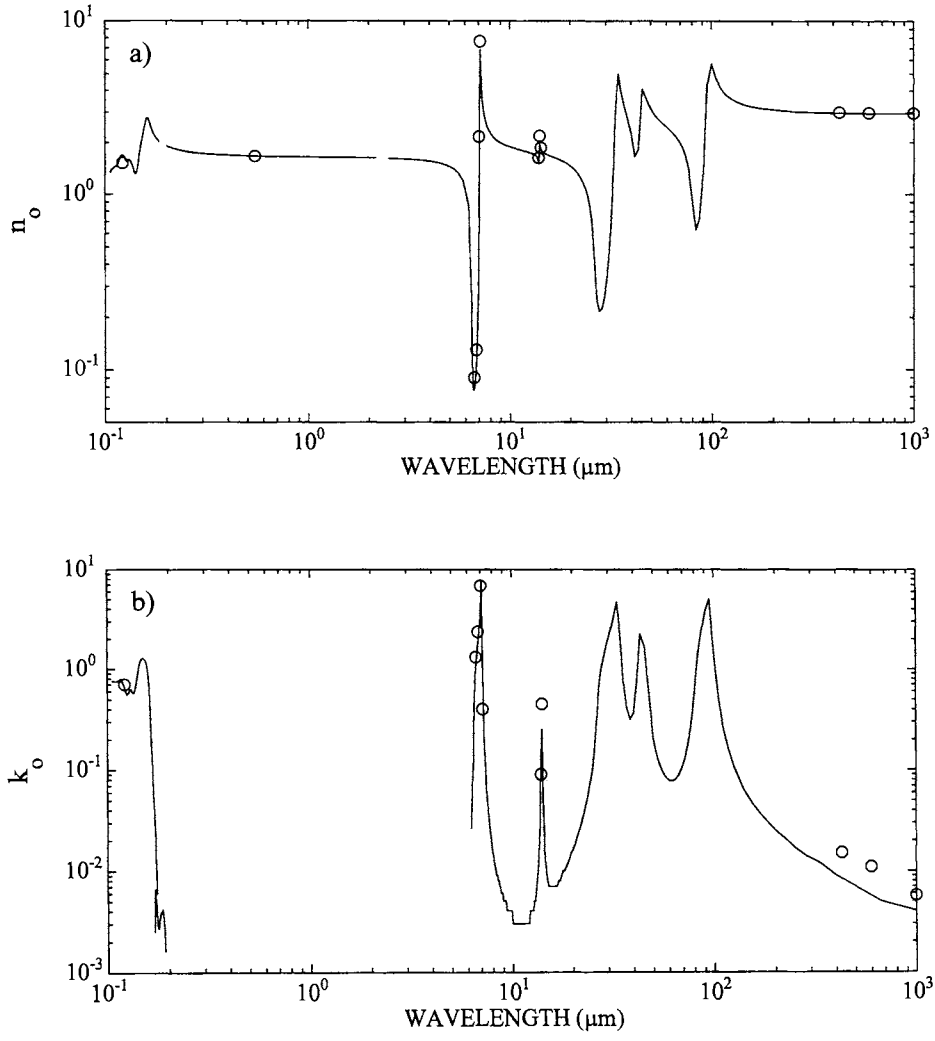

Fig. 1. (a) Log–log plot of the ordinary-ray index of refraction n_o versus wavelength in micrometers for calcium carbonate (calcite). (b) Log–log plot of the ordinary-ray extinction coefficient, k_o versus wavelength in micrometers for calcium carbonate (calcite). Lines are data sets of many points; scattered data are indicated by circles.

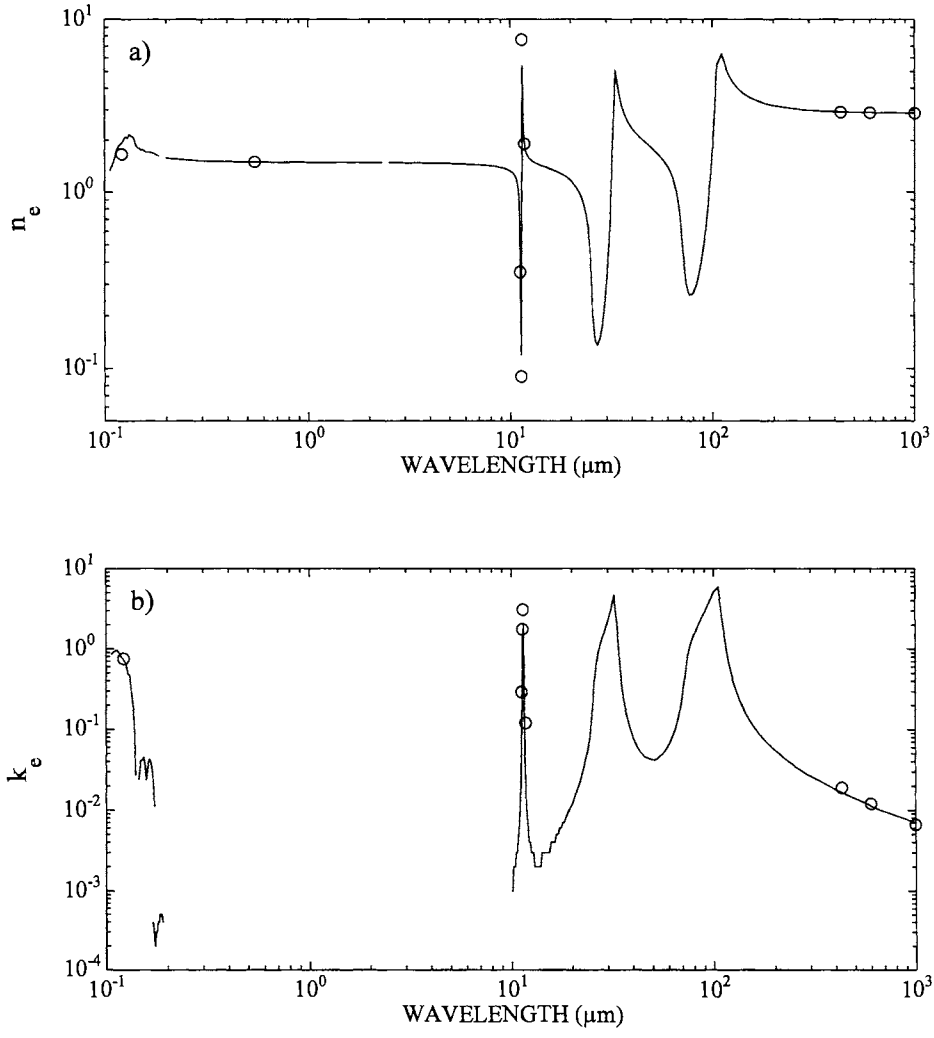

Fig. 2. (a) Log–log plot of the extraordinary-ray index of refraction n_e versus wavelength in micrometers for calcium carbonate (calcite). (b) Log–log plot of the extraordinary-ray extinction coefficient k_e versus wavelength in micrometers for calcium carbonate (calcite). Lines are data sets of many points; scattered data are indicated by circles.

TABLE I

Values of n and k for Calcium Carbonate (Calcite) from Various References[a]

eV	cm^{-1}	μm	n_o	k_o	n_e	k_e
11.7000	94366.1	0.1060	1.34 [1]	0.751 [1]	1.33 [1]	0.846 [1]
11.6000	93559.6	0.1069	1.36	0.757	1.35	0.867
11.5000	92753.0	0.1078	1.39	0.757	1.38	0.887
11.4000	91946.5	0.1088	1.40	0.754	1.41	0.906
11.3000	91139.9	0.1097	1.42	0.752	1.45	0.922
11.2000	90333.4	0.1107	1.43	0.752	1.49	0.939
11.1000	89526.8	0.1117	1.44	0.754	1.55	0.949
11.0000	88720.3	0.1127	1.45	0.759	1.60	0.959
10.9000	87913.7	0.1137	1.46	0.767	1.67	0.957
10.8000	87107.2	0.1148	1.49	0.777	1.75	0.927
10.7000	86300.6	0.1159	1.51	0.789	1.80	0.889
10.6000	85494.1	0.1170	1.56	0.787	1.84	0.854
10.5000	84687.5	0.1181	1.62	0.765	1.86	0.817
10.4000	83881.0	0.1192	1.66	0.729	1.89	0.780
10.3000	83074.4	0.1204	1.68	0.689	1.91	0.751
10.2000	82267.9	0.1216	1.69	0.644	1.94	0.732
10.1962	82236.8	0.1216	1.51 [3]	0.70 [3]	1.65 [3]	0.75 [3]
10.1000	81461.3	0.1228	1.67 [1]	0.606 [1]	1.97 [1]	0.707 [1]
10.0000	80654.8	0.1240	1.65	0.573	2.01	0.678
9.9000	79848.3	0.1252	1.60	0.555	2.06	0.632
9.8000	79041.7	0.1265	1.56	0.566	2.09	0.553
9.7000	78235.2	0.1278	1.54	0.599	2.07	0.484
9.6000	77428.6	0.1292	1.54	0.628	2.06	0.478
9.5000	76622.1	0.1305	1.57	0.632	2.10	0.464
9.4000	75815.5	0.1319	1.58	0.600	2.15	0.370
9.3000	75009.0	0.1333	1.55	0.581	2.14	0.283
9.2000	74202.4	0.1348	1.51	0.578	2.12	0.223
9.1000	73395.9	0.1362	1.45	0.605	2.10	0.175
9.0000	72589.3	0.1378	1.39	0.662	2.09	0.109
8.9000	71782.8	0.1393	1.33	0.742	2.04	0.027
8.8000	70976.2	0.1409	1.31	0.847	1.95	
8.7000	70169.7	0.1425	1.34	1.002	1.85	
8.6000	69363.1	0.1442	1.44	1.126	1.81	0.024
8.5000	68556.6	0.1459	1.58	1.204	1.80	0.030
8.4000	67750.0	0.1476	1.74	1.252	1.79	0.041
8.3000	66943.5	0.1494	1.90	1.273	1.77	0.041
8.2000	66136.9	0.1512	2.05	1.265	1.76	0.043
8.1000	65330.4	0.1531	2.21	1.236	1.75	0.045
8.0000	64523.8	0.1550	2.37	1.182	1.75	0.037
7.9000	63717.3	0.1569	2.54	1.045	1.73	0.024
7.8000	62910.7	0.1590	2.73	0.843	1.71	0.031
7.7000	62104.2	0.1610	2.78	0.588	1.70	0.039
7.6000	61297.6	0.1631	2.74	0.307	1.70	0.042
7.5000	60491.1	0.1653	2.61	0.132	1.70	0.040
7.4000	59684.6	0.1675	2.46	0.067	1.70	0.032

(continued)

[a] References given in brackets.

TABLE I *(Continued)*

Calcium Carbonate (Calcite)

eV	cm^{-1}	μm	n_o	k_o	n_e	k_e
7.3364	59171.6	0.1690		0.0025 [4]		0.0004 [4]
7.3000	58878.0	0.1698	2.34	0.035 [1]	1.69	0.022 [1]
7.2506	58479.5	0.1710		0.0066 [4]		0.0003 [4]
7.2000	58071.5	0.1722	2.26	0.018 [1]	1.68	0.011 [1]
7.1668	57803.5	0.1730		0.0041 [4]		0.0002 [4]
7.1000	57264.9	0.1746	2.20	0.006 [1]	1.67	
7.0849	57142.9	0.1750		0.0029 [4]		0.0003
7.0048	56497.2	0.1770		0.0027		0.0003
7.0000	56458.4	0.1771	2.14		1.66	
6.9265	55865.9	0.1790		0.0033		0.0004
6.9000	55651.8	0.1797	2.09		1.64	
6.8500	55248.6	0.1810		0.0037		0.0004
6.8000	54845.3	0.1823	2.05		1.63	
6.7751	54644.8	0.1830		0.0039		0.0005
6.7019	54054.1	0.1850		0.0041		0.0005
6.7000	54038.7	0.1851	2.02		1.62	
6.6302	53475.9	0.1870		0.0036		0.0005
6.5601	52910.1	0.1890		0.0027		0.0004
6.4914	52356.0	0.1910		0.0016		0.0004
6.2307	50253.8	0.19899			1.57796 [6]	
6.1965	49977.5	0.20009	1.90284 [6]		1.57649	
6.0637	48906.9	0.20447	1.88242		1.57081	
5.9546	48027.0	0.20821	1.86733		1.56640	
5.9074	47646.3	0.20988	1.8608110 [7]			
5.8739	47375.9	0.21108	1.85692 [6]		1.56327	
5.7815	46630.9	0.21445	1.84558		1.55976	
			1.8458240 [7]		1.5599225 [7]	
5.6501	45570.5	0.21944	1.8307980		1.5551219	
5.6496	45566.4	0.21946	1.83075 [6]		1.55496 [6]	
5.5351	44642.9	0.22400	1.81890		1.55105	
5.4736	44147.6	0.22651	1.8130351 [7]		1.5491444 [7]	
5.3651	43272.2	0.23110	1.8023942		1.5455001	
5.3606	43235.8	0.23129	1.80233 [6]		1.54541 [6]	
5.1063	41184.5	0.24281	1.78111		1.53782	
5.0692	40885.4	0.24459	1.7796645 [7]		1.5373101 [7]	
4.9528	39946.8	0.25033	1.76968 [6]		1.53358 [6]	
4.8185	38863.3	0.25731	1.7605000 [7]		1.5301212 [7]	
4.8184	38862.6	0.25732	1.76038 [6]		1.53005 [6]	
4.7107	37993.9	0.26320	1.75343		1.52736	
4.6331	37367.8	0.26761	1.74864		1.52547	
4.5107	36381.1	0.27487	1.7415041 [7]		1.5226617	
			1.74139 [6]		1.52261 [6]	
4.4023	35506.3	0.28164	1.73538		1.52018	
4.2553	34320.9	0.29137	1.72774		1.51705	
4.0862	32957.5	0.30342	1.7195881 [7]		1.5136464 [7]	
4.0225	32443.6	0.30823	1.71657 [6]		1.51240 [6]	
3.9703	32022.5	0.31228	1.71425		1.51140	

TABLE I *(Continued)*

Calcium Carbonate (Calcite)

eV	cm^{-1}	μm	n_o	k_o	n_e	k_e
3.7539	30276.9	0.33029	1.7051544 [7]		1.5074581 [7]	
3.6428	29380.8	0.34036	1.70078 [6]		1.50562 [6]	
3.4565	27878.3	0.35870	1.69297		1.50267	
3.4339	27695.8	0.36107	1.6931606 [7]		1.5022352 [7]	
3.1435	25354.0	0.39442	1.68397 [6]		1.49810 [6]	
3.1296	25241.8	0.39617	1.6832956 [7]		1.4977742 [7]	
3.0227	24379.2	0.41019	1.68014 [6]		1.49640 [6]	
2.8564	23038.0	0.43407	1.67552		1.49430	
			1.6755174 [7]		1.4942419 [7]	
2.8077	22645.6	0.44159	1.67423 [6]		1.49373 [6]	
2.6502	21375.2	0.46783	1.67024		1.49190	
2.5504	20569.8	0.48615	1.66785		1.49074	
2.5504	20569.8	0.48615	1.6678308 [7]		1.4907407 [7]	
2.4377	19661.6	0.50861	1.66527 [6]		1.48956 [6]	
2.3526	18974.9	0.52701	1.6634145 [7]		1.4887055 [7]	
2.3226	18732.6	0.53383	1.66277 [6]		1.48841 [6]	
2.3175	18691.6	0.5350	1.662671 [8]		1.488421 [8]	
2.2708	18315.0	0.5460	1.66193 [10]		1.48840 [10]	
2.2704	18311.7	0.54610	1.66168 [6]		1.48793 [6]	
2.2113	17834.8	0.56070	1.66046		1.48736	
2.2112	17834.5	0.56071	1.6604550 [7]		1.4873449 [7]	
2.1039	16969.0	0.58931	1.658369 [8]		1.486449 [8]	
			1.65835 [6]		1.48640 [6]	
			1.6583551 [7]		1.4863915 [7]	
2.0138	16242.5	0.6157			1.485677 [8]	
1.9748	15927.6	0.62784	1.65592 [6]		1.48529 [6]	
1.9566	15780.8	0.6337			1.485200 [8]	
1.9256	15530.8	0.64388	1.65504		1.48490 [6]	
1.8991	15317.2	0.6529			1.484722 [8]	
1.8891	15236.8	0.65630	1.65437		1.48459 [6]	
			1.6543988 [7]		1.4845685 [7]	
1.8483	14907.6	0.6708	1.653688 [8]		1.484331 [8]	
			1.65367 [6]		1.48426 [6]	
1.8420	14856.6	0.6731			1.484283 [8]	
1.7840	14388.5	0.6950	1.652581 [8]		1.483834 [8]	
1.7548	14153.1	0.70656	1.6520702 [7]		1.4835315 [7]	
1.7256	13917.9	0.7185	1.651581 [8]		1.483396 [8]	
1.6676	13449.9	0.7435	1.650611		1.482976	
1.6144	13020.8	0.7680	1.649741		1.482607	
1.6139	13016.8	0.76824	1.64974 [6]		1.48259 [6]	
			1.6497403 [7]		1.4825523 [7]	
1.6079	12968.5	0.7711	1.649650 [8]		1.482566 [8]	
1.5596	12578.6	0.7950	1.6488640 [7]		1.4821645 [7]	
1.5485	12489.1	0.8007	1.648687 [8]		1.482156 [8]	
1.4893	12012.0	0.8325	1.647724		1.481756	
1.4299	11532.7	0.8671	1.646759		1.481365	
1.3705	11053.4	0.9047	1.645784		1.480984	

(continued)

TABLE I *(Continued)*

Calcium Carbonate (Calcite)

eV	cm^{-1}	μm	n_o	k_o	n_e	k_e
1.3106	10570.8	0.9460	1.644800		1.480602	
1.2506	10086.7	0.9914	1.643798		1.480221	
1.1902	9599.7	1.0417	1.642762		1.479849	
1.1299	9113.3	1.0973	1.641675		1.479477	
1.0696	8626.6	1.1592	1.640511		1.479096	
1.0090	8138.0	1.2288	1.639262		1.478704	
0.9738	7854.2	1.2732	1.638487			
0.9486	7651.1	1.3070	1.637894		1.478312	
0.9396	7578.6	1.3195	1.637670			
0.9060	7307.3	1.3685	1.636809			
0.8883	7164.4	1.3958	1.636366		1.477891	
0.8720	7032.8	1.4219	1.635898			
0.8382	6760.4	1.4792	1.634901			
0.8281	6679.1	1.4972	1.634571		1.477441	
0.8044	6487.6	1.5414	1.633811			
0.7707	6216.2	1.6087	1.632611			
0.7679	6193.5	1.6146			1.476950	
0.7373	5947.1	1.6815	1.631266			
0.7090	5718.5	1.7487			1.476381	
0.7039	5677.3	1.7614	1.629741			
0.6707	5409.2	1.8487	1.628002			
0.6496	5239.7	1.9085			1.475733	
0.6372	5139.5	1.9457	1.626023			
0.6039	4870.7	2.0531	1.623717			
0.5905	4762.4	2.0998			1.474919	
0.5709	4604.3	2.1719	1.620995			
0.5334	4302.4	2.3243			1.473918	
0.4959	4000.0	2.500	1.614 [22]		1.473 [22]	
0.4649	3750.0	2.667	1.609		1.472	
0.4339	3500.0	2.857	1.603		1.472	
0.4030	3250.0	3.077	1.596		1.470	
0.3720	3000.0	3.333	1.586		1.469	
0.3410	2750.0	3.636	1.572		1.467	
0.3100	2500.0	4.000	1.550		1.465	
0.2790	2250.0	4.444	1.515		1.462	
0.2480	2000.0	5.000	1.448		1.457	
0.2356	1900.0	5.263	1.401		1.455	
0.2232	1800.0	5.556	1.326		1.452	
0.2108	1700.0	5.882	1.190		1.448	
0.1984	1600.0	6.250	0.853	0.026 [22]	1.443	
0.1922	1550.0	6.452	0.233	0.174	1.441	
0.1909	1540.0	6.494	0.107	0.437	1.440	
0.1897	1530.0	6.536	0.084	0.650	1.440	
0.1885	1520.0	6.579	0.077	0.836	1.439	
0.1872	1510.0	6.623	0.077	1.015	1.438	
			0.09 [24]	1.31 [24]		
0.1860	1500.0	6.667	0.079 [22]	1.197 [22]	1.438	

TABLE I *(Continued)*

Calcium Carbonate (Calcite)

eV	cm^{-1}	μm	n_o	k_o	n_e	k_e
0.1847	1490.0	6.711	0.086	1.389	1.437	
0.1835	1480.0	6.757	0.096	1.601	1.436	
0.1823	1470.0	6.803	0.112	1.842	1.436	
			0.13 [24]	2.35 [24]		
0.1810	1460.0	6.849	0.136 [22]	2.130 [22]	1.435	
0.1798	1450.0	6.897	0.176	2.489	1.434	
0.1785	1440.0	6.944	0.248	2.970	1.433	
0.1773	1430.0	6.993	0.402	3.687	1.433	
0.1761	1420.0	7.042	0.864	4.960	1.432	
			2.16 [24]	6.85 [24]		
0.1748	1410.0	7.092	3.878 [22]	7.485 [22]	1.431	
0.1736	1400.0	7.143	6.865	1.869	1.430	
			7.67 [24]	0.40 [24]		
0.1723	1390.0	7.194	4.969 [22]	0.553 [22]	1.429	
0.1711	1380.0	7.246	4.109	0.273	1.428	
0.1699	1370.0	7.299	3.622	0.166	1.427	
0.1686	1360.0	7.353	3.306	0.113	1.426	
0.1674	1350.0	7.407	3.081	0.083	1.425	
0.1661	1340.0	7.463	2.912	0.063	1.424	
0.1649	1330.0	7.519	2.780	0.050	1.423	
0.1637	1320.0	7.576	2.674	0.041	1.422	
0.1624	1310.0	7.634	2.587	0.034	1.421	
0.1612	1300.0	7.692	2.513	0.029	1.420	
0.1599	1290.0	7.752	2.451	0.025	1.418	
0.1587	1280.0	7.813	2.396	0.022	1.417	
0.1575	1270.0	7.874	2.349	0.019	1.416	
0.1562	1260.0	7.937	2.307	0.017	1.414	
0.1550	1250.0	8.000	2.270	0.015	1.413	
0.1537	1240.0	8.065	2.237	0.014	1.411	
0.1525	1230.0	8.130	2.207	0.012	1.410	
0.1513	1220.0	8.197	2.180	0.011	1.408	
0.1500	1210.0	8.264	2.155	0.010	1.406	
0.1488	1200.0	8.333	2.132	0.009	1.404	
0.1475	1190.0	8.403	2.111	0.009	1.402	
0.1463	1180.0	8.475	2.092	0.008	1.400	
0.1451	1170.0	8.547	2.074	0.008	1.398	
0.1438	1160.0	8.621	2.057	0.007	1.396	
0.1426	1150.0	8.696	2.041	0.007	1.394	
0.1413	1140.0	8.772	2.027	0.006	1.391	
0.1401	1130.0	8.850	2.013	0.006	1.388	
0.1389	1120.0	8.929	2.000	0.006	1.385	
0.1376	1110.0	9.009	1.988	0.005	1.382	
0.1364	1100.0	9.091	1.976	0.005	1.379	
0.1351	1090.0	9.174	1.965	0.005	1.375	
0.1339	1080.0	9.259	1.955	0.005	1.372	
0.1327	1070.0	9.346	1.945	0.004	1.367	
0.1314	1060.0	9.434	1.935	0.004	1.363	

(continued)

TABLE I *(Continued)*

Calcium Carbonate (Calcite)

eV	cm^{-1}	μm	n_o	k_o	n_e	k_e
0.1302	1050.0	9.524	1.926	0.004	1.358	
0.1289	1040.0	9.615	1.917	0.004	1.352	
0.1277	1030.0	9.709	1.908	0.004	1.346	
0.1265	1020.0	9.804	1.900	0.004	1.339	
0.1252	1010.0	9.901	1.892	0.004	1.331	
0.1240	1000.0	10.000	1.885	0.003	1.323	0.001 [22]
0.1227	990.0	10.101	1.877	0.003	1.312	0.001
0.1215	980.0	10.204	1.870	0.003	1.300	0.002
0.1203	970.0	10.309	1.863	0.003	1.286	0.002
0.1190	960.0	10.417	1.856	0.003	1.269	0.002
0.1178	950.0	10.526	1.849	0.003	1.247	0.003
0.1165	940.0	10.638	1.842	0.003	1.219	0.003
0.1153	930.0	10.753	1.836	0.003	1.181	0.004
0.1141	920.0	10.870	1.829	0.003	1.126	0.006
0.1128	910.0	10.989	1.822	0.003	1.038	0.010
0.1116	900.0	11.111	1.816	0.003	0.873	0.020
0.1103	890.0	11.236	1.810	0.003	0.368	0.106
0.1103	890.0	11.236			0.35 [24]	0.29 [24]
0.1091	880.0	11.364	1.803	0.003	0.120 [22]	1.373 [22]
					0.09 [24]	1.75 [24]
0.1079	870.0	11.494	1.797	0.003	5.387 [22]	2.064 [22]
					7.62 [24]	3.06 [24]
0.1066	860.0	11.628	1.790	0.003	2.288 [22]	0.052 [22]
0.1054	850.0	11.765	1.783	0.003	1.913	0.018
					1.90 [24]	0.12 [24]
0.1041	840.0	11.905	1.777	0.003	1.760 [22]	0.009 [22]
0.1029	830.0	12.048	1.770	0.003	1.676	0.006
0.1017	820.0	12.195	1.762	0.004	1.621	0.004
0.1004	810.0	12.346	1.755	0.004	1.583	0.004
0.0992	800.0	12.500	1.747	0.004	1.554	0.003
0.0979	790.0	12.658	1.738	0.004	1.531	0.003
0.0967	780.0	12.821	1.729	0.005	1.513	0.003
0.0955	770.0	12.987	1.718	0.005	1.497	0.002
0.0942	760.0	13.158	1.705	0.007	1.483	0.002
0.0930	750.0	13.333	1.688	0.009	1.470	0.002
0.0917	740.0	13.514	1.663	0.013	1.459	0.002
0.0905	730.0	13.699	1.619	0.028	1.448	0.002
0.0893	720.0	13.889	1.505	0.133	1.439	0.002
			1.62 [24]	0.09 [24]		
0.0880	710.0	14.085	1.951 [22]	0.251 [22]	1.429	0.003
			2.18 [24]	0.45 [24]		
0.0868	700.0	14.286	1.828 [22]	0.038 [22]	1.420	0.003
			1.86 [24]			
0.0855	690.0	14.493	1.772 [22]	0.016	1.411	0.003
0.0843	680.0	14.706	1.743	0.010	1.402	0.003
0.0831	670.0	14.925	1.723	0.008	1.393	0.003
0.0818	660.0	15.152	1.707	0.007	1.385	0.003

TABLE I *(Continued)*

Calcium Carbonate (Calcite)

eV	cm^{-1}	μm	n_o	k_o	n_e	k_e
0.0806	650.0	15.385	1.693	0.007	1.376	0.003
0.0794	640.0	15.625	1.680	0.007	1.366	0.004
0.0781	630.0	15.873	1.668	0.007	1.357	0.004
0.0769	620.0	16.129	1.656	0.007	1.347	0.004
0.0756	610.0	16.393	1.643	0.007	1.336	0.004
0.0744	600.0	16.667	1.630	0.007	1.326	0.005
0.0732	590.0	16.949	1.617	0.008	1.314	0.005
0.0719	580.0	17.241	1.604	0.008	1.302	0.006
0.0707	570.0	17.544	1.589	0.009	1.289	0.006
0.0694	560.0	17.857	1.574	0.010	1.275	0.007
0.0682	550.0	18.182	1.557	0.010	1.260	0.007
0.0670	540.0	18.519	1.540	0.011	1.243	0.008
0.0657	530.0	18.868	1.520	0.012	1.225	0.009
0.0645	520.0	19.231	1.500	0.013	1.206	0.010
0.0632	510.0	19.608	1.477	0.015	1.184	0.011
0.0620	500.0	20.000	1.452	0.016	1.160	0.012
0.0608	490.0	20.408	1.424	0.018	1.132	0.014
0.0595	480.0	20.833	1.393	0.021	1.101	0.016
0.0583	470.0	21.277	1.357	0.024	1.066	0.019
0.0570	460.0	21.739	1.317	0.027	1.024	0.022
0.0558	450.0	22.222	1.271	0.032	0.975	0.027
0.0546	440.0	22.727	1.217	0.038	0.916	0.033
0.0533	430.0	23.256	1.152	0.046	0.843	0.041
0.0521	420.0	23.810	1.073	0.057	0.750	0.055
0.0508	410.0	24.390	0.974	0.074	0.623	0.079
0.0496	400.0	25.000	0.843	0.102	0.434	0.138
0.0484	390.0	25.641	0.662	0.157	0.204	0.366
0.0471	380.0	26.316	0.404	0.318	0.144	0.664
0.0459	370.0	27.027	0.248	0.659	0.136	0.928
0.0446	360.0	27.778	0.217	0.990	0.147	1.198
0.0434	350.0	28.571	0.225	1.314	0.173	1.501
0.0422	340.0	29.412	0.260	1.669	0.226	1.874
0.0409	330.0	30.303	0.335	2.096	0.339	2.385
0.0397	320.0	31.250	0.496	2.667	0.648	3.205
0.0384	310.0	32.258	0.934	3.535	2.118	4.672
0.0372	300.0	33.333	2.713	4.689	5.076	2.060
0.0360	290.0	34.483	4.971	2.212	3.818	0.563
0.0347	280.0	35.714	3.946	0.761	3.152	0.264
0.0335	270.0	37.037	3.230	0.414	2.778	0.157
0.0322	260.0	38.462	2.726	0.318	2.533	0.107
0.0310	250.0	40.000	2.252	0.363	2.356	0.079
0.0298	240.0	41.667	1.656	0.765	2.217	0.062
0.0285	230.0	43.478	1.815	2.227	2.102	0.052
0.0273	220.0	45.455	4.071	1.703	2.000	0.046
0.0248	200.0	50.000	3.137	0.209	1.810	0.042
0.0242	195.0	51.282	2.991	0.161	1.761	0.042
0.0236	190.0	52.632	2.872	0.130	1.710	0.043

(continued)

TABLE I *(Continued)*

Calcium Carbonate (Calcite)

eV	cm^{-1}	μm	n_o	k_o	n_e	k_e
0.0229	185.0	54.054	2.770	0.110	1.656	0.046
0.0223	180.0	55.556	2.679	0.096	1.598	0.049
0.0217	175.0	57.143	2.595	0.087	1.533	0.053
0.0211	170.0	58.824	2.514	0.081	1.461	0.060
0.0205	165.0	60.606	2.433	0.078	1.377	0.068
0.0198	160.0	62.500	2.350	0.078	1.278	0.081
0.0192	155.0	64.516	2.260	0.081	1.156	0.101
0.0186	150.0	66.667	2.159	0.088	1.000	0.134
0.0180	145.0	68.966	2.040	0.102	0.785	0.201
0.0174	140.0	71.429	1.891	0.125	0.490	0.387
0.0167	135.0	74.074	1.691	0.170	0.304	0.774
0.0161	130.0	76.923	1.395	0.269	0.261	1.153
0.0155	125.0	80.000	0.931	0.577	0.265	1.523
0.0149	120.0	83.333	0.630	1.386	0.297	1.922
0.0143	115.0	86.957	0.730	2.374	0.364	2.389
0.0136	110.0	90.909	1.323	3.737	0.499	2.988
0.0130	105.0	95.238	4.336	5.036	0.803	3.842
0.0124	100.0	100.00	5.677	1.508	1.733	5.206
0.0118	95.0	105.26	4.651	0.520	5.471	5.800
0.0112	90.0	111.11	4.107	0.263	6.273	1.850
0.0105	85.0	117.65	3.790	0.160	5.088	0.715
0.00992	80.0	125.00	3.585	0.108	4.408	0.379
0.00930	75.0	133.33	3.441	0.079	3.994	0.236
0.00868	70.0	142.86	3.334	0.060	3.718	0.161
0.00806	65.0	153.85	3.252	0.047	3.521	0.117
0.00744	60.0	166.67	3.188	0.038	3.374	0.089
0.00682	55.0	181.82	3.136	0.031	3.261	0.069
0.00620	50.0	200.00	3.094	0.025	3.172	0.055
0.00558	45.0	222.22	3.059	0.021	3.102	0.044
0.00496	40.0	250.00	3.031	0.017	3.045	0.035
0.00434	35.0	285.71	3.007	0.014	2.999	0.028
0.00372	30.0	333.33	2.988	0.012	2.962	0.023
0.00310	25.0	400.00	2.973	0.009	2.932	0.018
0.00289	23.3	428.57	2.987 [25]	0.015 [25]	2.915 [25]	0.019 [25]
0.00248	20.0	500.00	2.961 [22]	0.007 [22]	2.909 [22]	0.014 [22]
0.00207	16.7	600.00	2.968 [25]	0.011 [25]	2.888 [25]	0.012 [25]
0.00186	15.0	666.67	2.952 [22]	0.005 [22]	2.892 [22]	0.010 [22]
0.00124	10.0	1000.0	2.945	0.004	2.880	0.007
			2.950 [25]	0.0057 [25]	2.862 [25]	0.0066 [25]
0.000620	5.0	2000.0	2.941 [22]	0.002 [22]	2.873 [22]	0.003 [22]
0.000372	3.0	3333.3	2.946 [26]	0.0 [26]	2.883 [26]	0.0 [26]
0	0.0	∞	2.940 [22]	0.0 [22]	2.871 [22]	0.0 [22]

TABLE II

Sellmeier Dispersion Equation Constants for Calcite

	Ramachandran [11]		Tropf [12]	
Term [Eq. (1)]	n_o	n_e	n_o	n_e
λ_1	0.0500	0.0500	0.0588	0.07897
λ_2	0.1000	0.1000	0.141	0.142
λ_3	0.1535	0.1535	0.197	11.468
λ_4	6.7	11.3	7.005	—
A_1	0.43257	0.45899	0.8559	1.0856
A_2	0.82932	0.69835	0.8391	0.0988
A_3	0.43376	0.02680	0.0009	0.317
A_4	0.61855	0.30018	0.6845	—
Range (μm)	0.2–2.1		0.2–2.2	

TABLE III

Thermo-optical Coefficients of Calcite (in Vacuum)

Wavelength (μm)	dn_o/dT (10^{-6}/K)	dn_e/dT (10^{-6}/K)	Temperature[a] (°C)	Reference
0.211	20.0		$\overline{T} = 61.5$	[13]
0.214	18.8	24.3	$\overline{T} = 61.5$	[13]
0.219	16.7	23.5	$\overline{T} = 61.5$	[13]
0.224	15.0		$\overline{T} = 61.5$	[13]
0.226		20.8	$\overline{T} = 61.5$	[13]
0.231	12.5	22.0	$\overline{T} = 61.5$	[13]
0.257	8.1	17.6	$\overline{T} = 61.5$	[13]
0.274	6.4	16.3	$\overline{T} = 61.5$	[13]
0.288	5.4	15.7	$\overline{T} = 61.5$	[13]
0.298	4.7	15.3	$\overline{T} = 61.5$	[13]
0.313	3.8		$\overline{T} = 61.5$	[13]
0.325	3.4	14.4	$\overline{T} = 61.5$	[13]
0.340	2.7	13.7	$\overline{T} = 61.5$	[13]
0.361	2.4	13.4	$\overline{T} = 61.5$	[13]
0.436	1.44	11.92	$\overline{T} = 57.1$	[14]
0.441	2.1	12.1	$\overline{T} = 61.5$	[13]
0.467	2.0		$\overline{T} = 61.5$	[13]
	1.34	11.79	$\overline{T} = 57.1$	[14]
0.480	1.8	11.8	$\overline{T} = 61.5$	[13]
0.508	1.7	11.3	$\overline{T} = 61.5$	[13]
0.546	0.5	12.0	−100 to 18	[10]
0.589	1.2	11.1	$\overline{T} = 61.5$	[13]
	0.78	10.94	$\overline{T} = 57.1$	[14]
0.643	0.9	10.8	$\overline{T} = 61.5$	[13]
0.656	0.71	10.62	$\overline{T} = 57.1$	[14]

[a] $\overline{T}$ is the mean measurement temperature.

TABLE IV

Transverse (and Longitudinal) Optical Phonon Frequencies in Calcite ($CaCO_3$)

Mode	Hellwege [19]	Long [22]	Pastorek [21]
E_u (**E**⊥**c**)	102(123)	104.1	
E_u (**E**⊥**c**)	223(239)	223.3	
E_u (**E**⊥**c**)	297(381)	295.6	
E_u (**E**⊥**c**)	712(715)	713.2	711.9(713.2)
E_u (**E**⊥**c**)	1407(1599)	1406.8	1408(1551.5)
A_{2u} (**E**∥**c**)	92(136)	94.6	
A_{2u} (**E**∥**c**)	303(387)	304.9	
A_{2u} (**E**∥**c**)	872(890)	870.8	869.8(887.4)

Cesium Bromide (CsBr)

W. J. MOORE
Naval Research Laboratory
Washington, D.C.

Values for the room-temperature refractive index, n, and the extinction coefficient, k, for CsBr presented in Fig. 1 and Table I are based on measurements by Dianov and Irisova [1] at 2.31 mm, Geick [2] from 275 to 31 μm, Rodney and Spindler [3] from 39 to 0.36 μm, Matthews [4] near 0.2 μm, Eby *et al.* [5] from 0.19 to 0.11 μm, Cardona *et al.* [6] from 1.77×10^{-2} to 7.3×10^{-3} μm, and Henke and co-workers [7, 8] from 0.124 to 4.13×10^{-5} μm.

Data are quoted, in most cases, as presented in these references with suitable unit conversion and standardization. Exceptions include the region 0.2 to 55 μm, where the values from Rodney and Spindler [3] and those of Geick [2] are presented as combined and critiqued by Li [9]. Refractive indices and extinction coefficients in the region 0.124 to 4.13×10^{-5} μm were calculated from atomic scattering coefficients of the component materials. The optical-density data of Eby *et al.* [5] in the region 0.11 to 0.19 μm have been scaled to compensate for uncertainty in sample thickness. Where data were originally published as an x–y plot only, we have scanned and digitized these plots in order to provide tabulated results.

The plotted results of Fig. 1 contain all points tabulated in the original references and a high data point density for the scanned x–y plots. Data points tabulated in Table I include only the minimum point density that adequately reproduces the structure apparent in the original.

Additional data at room temperature can be found in Vergnat *et al.* [10], Jones *et al.* [11], and Plyler and Phelps [12]. Low-temperature data and the temperature coefficient of n near room temperature can be found in Dianov and Irisova [1], Vergnat *et al.* [10], Havinga and Bosman [13], Selvarajan *et al.* [14], and Li [9].

At very long wavelengths the "2 mm" result of Dianov and Irisova [1] is an early example of a technique later generalized for simultaneous acquisition of a range of frequencies and known as dispersive Fourier-transform-

Copyright © 1998 by Academic Press.
All rights of reproduction in any form reserved
ISBN 0-12-544423-0/$25.00.

spectroscopy. In the Dianov and Irisova application the source was a monochromatic microwave oscillator at 2.31 mm [15] feeding a Michelson interferometer in a hybrid waveguide/optical configuration. The sinusoidal interference pattern due to moving one mirror was measured with no sample, then again with the sample in the moving mirror arm. The refractive index was determined from the shift in phase between the two measurements. The samples used were described only as crystals with no comment on purity.

Vergnat *et al.* [10] found refractive indices and extinction coefficients for the Cs halides at 290, 80, and 25 K from analysis of reflection measurements in the 200 to 1000 μm spectral region. Their static value for n at 290 K was 2.56, which equals Dianov and Irisova's 2-mm interferometric value at 300 K. The CsBr sample used was a single crystal.

In the reststrahlen region Geick [2] determined n and k by analyzing measurement of transmission and reflection of CsBr samples ranging from 0.2 μm to 1 cm thick. Samples from 0.2 to 2.5 μm thick were vacuum deposited onto cellulose-acetate films. Those with thicknesses from 25 μm to 1 cm were cut from thicker commercial samples or used as received.

Rodney and Spindler [3] measured the refractive index of CsBr prisms by the minimum-deviation method from 0.365 to 39.22 μm. The results were quoted to six significant figures. Two samples, grown by different organizations, were studied. Differences between the two sets of refractive-index data were described as "several units in the fifth decimal," that is, less than $\pm 0.007\%$. These data overlap those of Geick [2] in the 31 to 39.22 micron range. At 31 μm Geick gets $n = 1.606$, while Rodney and Spindler's result interpolates to 1.60546. Agreement is better than 0.04%. However, at 39 μm Geick gets $n = 1.565$, while Rodney and Spindler's data interpolates to 1.56144; agreement here has dropped to 0.23%. Li [9] critiqued these results and recommended an analytic expression of the Sellmeier form as accurate to five places in the region 0.21 to 55 μm at 293 K:

$$n^2 = 1.14600 + \frac{1.26628\,\lambda^2}{\lambda^2 - (0.120)^2} + \frac{0.01137\,\lambda^2}{\lambda^2 - (0.146)^2} + \frac{0.00975\,\lambda^2}{\lambda^2 - (0.16)^2} + \frac{0.00672\,\lambda^2}{\lambda^2 - (0.173)^2} + \frac{0.34557\,\lambda^2}{\lambda^2 - (0.187)^2} + \frac{3.76339\,\lambda^2}{\lambda^2 - (136.05)^2}. \quad (1)$$

This equation yields 1.60613 and 1.56486 at 31 and 39 μm, respectively; these values are slightly increased over the Rodney and Spindler results in the long-wavelength region but blend smoothly with those of Geick. Data points in Fig. 1 and Table I were calculated with Eq. (1).

Plyler and Phelps [12] have measured transmission in the region 0.32 to 38 μm. The samples were grown from the melt using highly purified charge material. We have extracted extinction coefficients from these data and find values not exceeding 1×10^{-5} at all wavelengths between 0.32 and 24 μm. This value is believed to be at the limit of the absorption measuring capability of their experiment and so should be taken as an upper limit to k only.

Matthews [4] has measured transmission of good-quality crystalline CsBr throughout its transparent spectral range. We have scanned and digitized his plots in the near ultraviolet, converted to approximate extinction coefficient, and tabulated and plotted the result to indicate the onset of opacity as energy increases in that region.

Eby *et al.* [5] have measured optical density in the 0.11 to 0.19 μm region of thin films of alkali halides evaporated in vacuum onto LiF substrates. Reflection and substrate effects were minimized by tabulating the difference in optical density of films with estimated thicknesses of 100 and 1000 Å. Data were presented as a plot of optical density versus energy. The CsBr plot has been scanned and digitized. Because there was no accurate thickness determination, the conversion from optical density to extinction coefficient has an undetermined scaling factor. The raw results calculated with their estimates of sample thickness fall below the extinction coefficients calculated from the atomic scattering coefficients of the constituent Cs and Br with cooperative effects neglected. Considerable structure attributed to exciton absorption was found in these spectra. Consequently, they contain useful data but are complicated by the scaling uncertainty. The Eby *et al.* extinction-coefficient data in Fig. 1 and in Table I have been scaled by a factor of 5 in order to bring the absorption by the crystal above that expected for the constituent atoms.

Cardona *et al.* [6] have studied absorption by Cs and Rb halides evaporated in vacuum onto carbon foils supported by a copper grid in the spectral region from 1.77×10^{-2} to 7.3×10^{-3} μm. Sample thickness was measured to an accuracy of about 20% by a quartz oscillator. These data were presented as absorption coefficient versus energy. The CsBr plot was scanned and digitized as described earlier.

At wavelengths shorter than 7.3×10^{-3} μm we have only the calculation of n and k based on atomic scattering factors for the constituent atoms published by Henke and co-workers [7, 8]. The calculation is described in the CsI critique by Eldridge [16] and on the Lawrence Berkeley Laboratory Internet Web site www-cxro.lbl.gov/optical_constants. Agreement between calculated values for extinction coefficient and those measured by Cardona *et al.* [6] is quite good, typically within the 20% error in sample-thickness determination.

ACKNOWLEDGMENTS

The contributions of K. Matthews of Crystran, Ltd. who provided unpublished near-ultraviolet transmission spectra, and W. R. Hunter, who calculated n and k from atomic scattering factors, are gratefully acknowledged.

REFERENCES

1. E. M. Dianov and N. A. Irisova, *Sov. Phys. Solid State* **8**, 1807 (1967).
2. R. Geick, *Z. Phys.* **163**, 499 (1961).
3. W. S. Rodney and R. J. Spindler, *J. Res. NBS* **51**, 123 (1953).

4. "Crystran Ltd. Handbook." Crystran, Poole, U.K.; K. Matthews, private communication, 1996.
5. J. E. Eby, K. J. Teegarden, and D. B. Dutton, *Phys. Rev.* **116**, 1099 (1959).
6. M. Cardona, R. Haensel, D. W. Lynch, and B. Sonntag, *Phys. Rev. B* **2**, 1117 (1970).
7. B. L. Henke, E. M. Gullikson, and J. C. Davis, *At. Data Nucl. Data Tables* **54**, 181 (1993).
8. E. M. Gullikson, private communication, 1996.
9. H. H. Li, *J. Phys. Chem. Ref. Data* **5**, 329 (1976).
10. P. Vergnat, J. Claudel, A. Hadni, P. Strimer, and F. Vermillard, *J. Phys. (Paris)* **30**, 723 (1969).
11. G. O. Jones, D. H. Martin, P. A. Mawer, and C. H. Perry, *Proc. R. Soc. London A* **261**, 10 (1961).
12. E. K. Plyler and F. P. Phelps, *J. Opt. Soc. Am.* **41**, 209 (1951).
13. E. E. Havinga and A. J. Bosman, *Phys. Rev.* **140**, A292 (1965).
14. A. Selvarajan, J. L. Swedberg, A. G. DeBell, and W. L. Wolfe, *Appl. Opt.* **18**, 3116 (1979).
15. E. A. Vinogradov, E. M. Dianov, and N. A. Irisova, *Radio Eng. Electron. Phys.* **10**, 1547 (1965).
16. J. E. Eldridge, *in* "Handbook of Optical Constants of Solids II" (E. D. Palik, ed.), p. 851. Academic Press, Orlando, Florida, 1991.

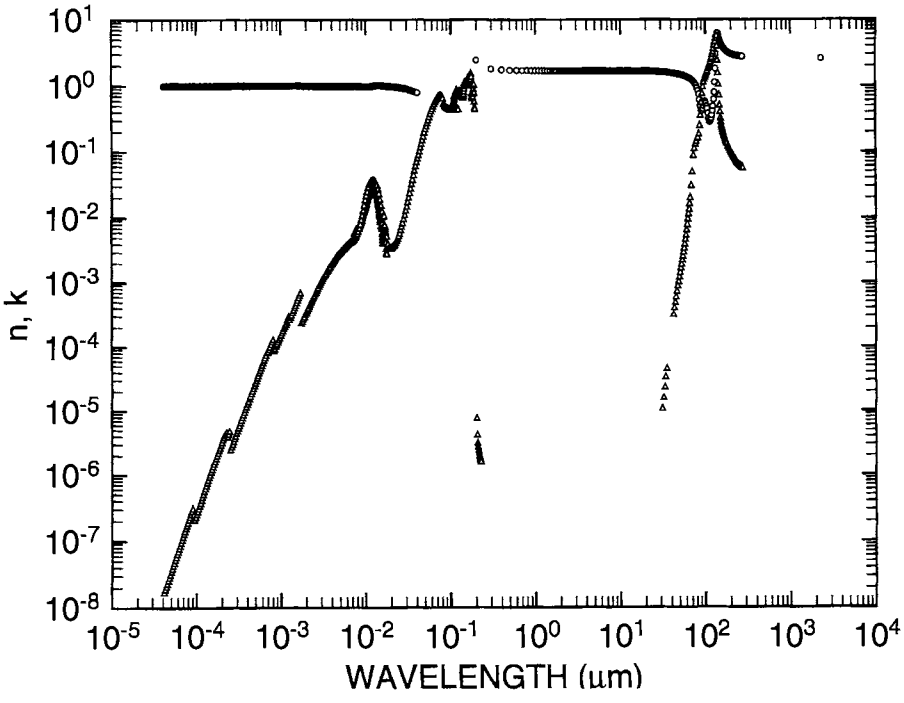

Fig. 1. Log–log plot of n (circles) and k (triangles) versus wavelength in micrometers for cesium bromide.

TABLE I

Values of *n* and *k* for Cesium Bromide from Various References[a]

eV	cm^{-1}	μm	n	k
3.000E4	2.420E8	4.13E-5	1.00 [7, 8]	1.74E-8 [7, 8]
2.556E4	2.061E8	4.85E-5	1.00	3.19E-8
2.178E4	1.757E8	5.69E-5	1.00	5.82E-8
1.856E4	1.497E8	6.68E-5	1.00	1.06E-7
1.624E4	1.310E8	7.64E-5	1.00	1.74E-7
1.421E4	1.146E8	8.73E-5	1.00	2.84E-7
1.384E4	1.116E8	8.96E-5	1.00	3.13E-7
1.312E4	1.058E8	9.45E-5	1.00	2.09E-7
1.211E4	9.766E7	1.02E-4	1.00	2.83E-7
1.031E4	8.319E7	1.20E-4	1.00	5.13E-7
8.787E3	7.087E7	1.41E-4	1.00	9.29E-7
7.487E3	6.039E7	1.66E-4	1.00	1.66E-6
6.381E3	5.147E7	1.94E-4	1.00	2.95E-6
5.735E3	4.625E7	2.16E-4	1.00	4.28E-6
5.018E3	4.047E7	2.47E-4	1.00	4.86E-6
4.885E3	3.940E7	2.54E-4	1.00	2.52E-6
4.510E3	3.638E7	2.75E-4	1.00	3.37E-6
3.843E3	3.100E7	3.23E-4	1.00	6.02E-6
3.274E3	2.641E7	3.79E-4	1.00	1.07E-5
2.790E3	2.250E7	4.44E-4	1.00	1.88E-5
2.377E3	1.917E7	5.22E-4	1.00	3.3E-5
2.025E3	1.633E7	6.12E-4	1.00	5.73E-5
1.820E3	1.468E7	6.81E-4	1.00	8.22E-5
1.636E3	1.319E7	7.58E-4	1.00	1.1E-4
1.551E3	1.251E7	7.99E-4	1.00	1.3E-4
1.510E3	1.218E7	8.21E-4	1.00	8.77E-5
1.394E3	1.124E7	8.90E-4	1.00	1.11E-4
1.287E3	1.038E7	9.64E-4	1.00	1.41E-4
1.096E3	8.842E6	1.13E-3	1.00	2.27E-4
9.096E2	7.337E6	1.36E-3	1.00	3.4E-4
7.958E2	6.418E6	1.56E-3	1.00	5.3E-4
7.345E2	5.924E6	1.69E-3	1.00	6.98E-4
7.154E2	5.770E6	1.73E-3	1.00	2.36E-4
6.602E2	5.325E6	1.88E-3	1.00	2.96E-4
5.625E2	4.537E6	2.20E-3	1.00	4.69E-4
4.793E2	3.865E6	2.59E-3	1.00	7.24E-4
4.084E2	3.294E6	3.04E-3	1.00	1.1E-3
3.480E2	2.807E6	3.56E-3	1.00	1.6E-3
2.965E2	2.391E6	4.18E-3	1.00	2.25E-3
2.526E2	2.037E6	4.91E-3	1.00	2.96E-3
2.152E2	1.736E6	5.76E-3	0.99	3.69E-3
1.834E2	1.479E6	6.76E-3	0.99	4.38E-3
1.648E2	1.329E6	7.52E-3	0.99	5.06E-3

(continued)

[a] Tabulation of *n* and *k* as a function of photon energy (electron volts), wave number (inverse centimeters), and wavelength (microns). References for the data are given in brackets and apply to all data below the brackets until a new reference appears.

TABLE I *(Continued)*

Cesium Bromide

eV	cm^{-1}	μm	n	k
1.521E2	1.227E6	8.15E-3	0.99	6.3E-3
1.367E2	1.103E6	9.07E-3	0.98	1.1E-2
1.262E2	1.018E6	9.82E-3	0.98	1.88E-2
1.165E2	9.398E5	1.06E-2	0.98	2.93E-2
1.047E2	8.446E5	1.18E-2	0.99	3.71E-2
9.407E1	7.587E5	1.32E-2	1.00	3.41E-2
8.920E1	7.194E5	1.39E-2	1.01	2.76E-2
8.457E1	6.821E5	1.47E-2	1.03	1.92E-2
8.020E1	6.468E5	1.55E-2	1.00	1.26E-2
7.402E1	5.970E5	1.68E-2	1.00	7.87E-3
7.017E1	5.659E5	1.77E-2	0.99	5.33E-3
6.652E1	5.365E5	1.86E-2	0.98	3.47E-3
6.306E1	5.086E5	1.97E-2	0.98	3.5E-3
5.518E1	4.450E5	2.25E-2	0.96	4.27E-3
4.702E1	3.792E5	2.64E-2	0.93	7.53E-3
4.340E1	3.500E5	2.86E-2	0.91	1.12E-2
4.006E1	3.231E5	3.10E-2	0.89	1.76E-2
3.698E1	2.982E5	3.35E-2	0.86	2.8E-2
3.413E1	2.753E5	3.63E-2	0.83	4.48E-2
3.151E1	2.541E5	3.94E-2	0.80	7.13E-2
2.908E1	2.346E5	4.26E-2		1.04E-1
2.684E1	2.165E5	4.62E-2		1.53E-1
2.478E1	1.998E5	5.00E-2		2.26E-1
2.287E1	1.845E5	5.42E-2		3.09E-1
1.949E1	1.572E5	6.36E-2		5.39E-1
1.660E1	1.339E5	7.47E-2		7.23E-1
1.574E1	1.270E5	7.88E-2		7.14E-1
1.492E1	1.204E5	8.31E-2		5.54E-1
1.341E1	1.082E5	9.24E-2		4.66E-1
1.080E1	8.710E4	1.15E-1		4.42E-1
1.174E1	9.470E4	1.06E-1		4.42E-1
1.695E2	1.367E6	7.316E-3		5.850E-3 [6]
1.684E2	1.358E6	7.362E-3		5.930E-3
1.673E2	1.350E6	7.409E-3		5.940E-3
1.663E2	1.341E6	7.457E-3		6.020E-3
1.656E2	1.335E6	7.489E-3		6.080E-3
1.634E2	1.318E6	7.587E-3		6.240E-3
1.624E2	1.310E6	7.636E-3		6.500E-3
1.645E2	1.327E6	7.538E-3		6.120E-3
1.616E2	1.304E6	7.670E-3		6.750E-3
1.613E2	1.301E6	7.687E-3		6.760E-3
1.606E2	1.295E6	7.722E-3		6.510E-3
1.599E2	1.289E6	7.756E-3		6.360E-3
1.588E2	1.281E6	7.808E-3		6.520E-3
1.577E2	1.272E6	7.861E-3		6.640E-3

(continued)

TABLE I *(Continued)*

Cesium Bromide

eV	cm^{-1}	μm	n	k
1.567E2	1.264E6	7.914E-3		6.760E-3
1.556E2	1.255E6	7.969E-3		6.890E-3
1.545E2	1.246E6	8.024E-3		6.940E-3
1.534E2	1.238E6	8.080E-3		7.030E-3
1.524E2	1.229E6	8.136E-3		7.120E-3
1.513E2	1.220E6	8.194E-3		7.180E-3
1.502E2	1.212E6	8.252E-3		7.240E-3
1.492E2	1.203E6	8.311E-3		7.330E-3
1.481E2	1.195E6	8.371E-3		7.430E-3
1.474E2	1.189E6	8.412E-3		7.510E-3
1.467E2	1.183E6	8.452E-3		7.590E-3
1.460E2	1.177E6	8.493E-3		7.710E-3
1.453E2	1.172E6	8.535E-3		7.790E-3
1.442E2	1.163E6	8.598E-3		7.930E-3
1.431E2	1.154E6	8.662E-3		8.120E-3
1.421E2	1.146E6	8.727E-3		8.350E-3
1.410E2	1.137E6	8.793E-3		8.580E-3
1.403E2	1.131E6	8.838E-3		8.800E-3
1.392E2	1.123E6	8.905E-3		9.120E-3
1.382E2	1.114E6	8.974E-3		9.450E-3
1.371E2	1.106E6	9.043E-3		9.950E-3
1.360E2	1.097E6	9.114E-3		1.040E-2
1.350E2	1.089E6	9.185E-3		1.090E-2
1.339E2	1.080E6	9.258E-3		1.130E-2
1.328E2	1.071E6	9.333E-3		1.180E-2
1.318E2	1.063E6	9.408E-3		1.230E-2
1.307E2	1.054E6	9.484E-3		1.280E-2
1.297E2	1.046E6	9.562E-3		1.320E-2
1.286E2	1.037E6	9.641E-3		1.360E-2
1.275E2	1.029E6	9.721E-3		1.410E-2
1.265E2	1.020E6	9.803E-3		1.460E-2
1.254E2	1.012E6	9.886E-3		1.520E-2
1.251E2	1.009E6	9.914E-3		1.530E-2
1.240E2	1.000E6	9.999E-3		1.600E-2
1.229E2	9.911E5	1.009E-2		1.670E-2
1.219E2	9.833E5	1.017E-2		1.740E-2
1.208E2	9.747E5	1.026E-2		1.820E-2
1.198E2	9.662E5	1.035E-2		1.920E-2
1.186E2	9.569E5	1.045E-2		2.000E-2
1.176E2	9.488E5	1.054E-2		2.110E-2
1.166E2	9.407E5	1.063E-2		2.200E-2
1.156E2	9.320E5	1.073E-2		2.270E-2
1.145E2	9.234E5	1.083E-2		2.340E-2
1.134E2	9.149E5	1.093E-2		2.430E-2
1.123E2	9.058E5	1.104E-2		2.500E-2
1.113E2	8.977E5	1.114E-2		2.590E-2

(continued)

TABLE I *(Continued)*

Cesium Bromide

eV	cm^{-1}	μm	n	k
1.103E2	8.896E5	1.124E-2		2.678E-2
1.091E2	8.803E5	1.136E-2		2.750E-2
1.085E2	8.749E5	1.143E-2		2.780E-2
1.073E2	8.658E5	1.155E-2		2.780E-2
1.063E2	8.576E5	1.166E-2		2.770E-2
1.060E2	8.547E5	1.170E-2		2.770E-2
1.053E2	8.489E5	1.178E-2		2.820E-2
1.042E2	8.403E5	1.190E-2		2.880E-2
1.031E2	8.313E5	1.203E-2		2.960E-2
1.020E2	8.230E5	1.215E-2		3.010E-2
1.010E2	8.143E5	1.228E-2		2.980E-2
9.991E1	8.058E5	1.241E-2		2.920E-2
9.879E1	7.968E5	1.255E-2		2.810E-2
9.770E1	7.880E5	1.269E-2		2.670E-2
9.664E1	7.794E5	1.283E-2		2.490E-2
9.589E1	7.734E5	1.293E-2		2.460E-2
9.515E1	7.675E5	1.303E-2		2.400E-2
9.443E1	7.616E5	1.313E-2		2.290E-2
9.372E1	7.559E5	1.323E-2		2.250E-2
9.301E1	7.502E5	1.333E-2		2.390E-2
9.232E1	7.446E5	1.343E-2		2.420E-2
9.090E1	7.331E5	1.364E-2		2.210E-2
8.939E1	7.210E5	1.387E-2		1.860E-2
9.776E1	7.885E5	1.268E-2		1.282E-2
8.831E1	7.123E5	1.404E-2		1.630E-2
8.756E1	7.062E5	1.416E-2		1.520E-2
8.682E1	7.003E5	1.428E-2		1.340E-2
8.574E1	6.916E5	1.446E-2		1.120E-2
8.469E1	6.831E5	1.464E-2		1.340E-2
8.394E1	6.770E5	1.477E-2		1.050E-2
8.327E1	6.716E5	1.489E-2		8.950E-3
8.184E1	6.601E5	1.515E-2		1.000E-2
8.146E1	6.570E5	1.522E-2		8.950E-3
8.035E1	6.481E5	1.543E-2		7.270E-3
7.968E1	6.427E5	1.556E-2		8.290E-3
7.892E1	6.365E5	1.571E-2		6.020E-3
7.822E1	6.309E5	1.585E-2		4.740E-3
7.749E1	6.250E5	1.600E-2		4.190E-3
7.677E1	6.192E5	1.615E-2		4.390E-3
7.606E1	6.135E5	1.630E-2		5.050E-3
7.537E1	6.079E5	1.645E-2		5.870E-3
7.464E1	6.020E5	1.661E-2		6.950E-3
7.407E1	5.974E5	1.674E-2		7.240E-3
7.336E1	5.917E5	1.690E-2		7.400E-3
7.302E1	5.889E5	1.698E-2		6.880E-3
7.263E1	5.858E5	1.707E-2		6.040E-3

(continued)

TABLE I *(Continued)*

Cesium Bromide

eV	cm^{-1}	μm	n	k
7.229E1	5.831E5	1.715E-2		6.320E-3
7.154E1	5.770E5	1.733E-2		4.440E-3
7.117E1	5.741E5	1.742E-2		3.480E-3
7.081E1	5.711E5	1.751E-2		3.010E-3
7.013E1	5.656E5	1.768E-2		2.880E-3
1.134E1	9.149E4	1.093E-1		5.69E-1 [5]
1.124E1	9.066E4	1.103E-1		6.25E-1
1.115E1	8.993E4	1.112E-1		6.79E-1
1.105E1	8.913E4	1.122E-1		7.28E-1
1.095E1	8.834E4	1.132E-1		7.75E-1
1.086E1	8.757E4	1.142E-1		8.12E-1
1.076E1	8.681E4	1.152E-1		8.40E-1
1.066E1	8.598E4	1.163E-1		8.64E-1
1.056E1	8.518E4	1.174E-1		8.79E-1
1.047E1	8.446E4	1.184E-1		8.70E-1
1.038E1	8.368E4	1.195E-1		8.44E-1
1.027E1	8.285E4	1.207E-1		8.23E-1
1.008E1	8.130E4	1.230E-1		8.17E-1
9.887E0	7.974E4	1.254E-1		8.35E-1
9.793E0	7.899E4	1.266E-1		8.42E-1
9.694E0	7.819E4	1.279E-1		8.48E-1
9.596E0	7.740E4	1.292E-1		8.45E-1
9.501E0	7.663E4	1.305E-1		8.13E-1
9.400E0	7.582E4	1.319E-1		7.80E-1
9.357E0	7.547E4	1.325E-1		7.71E-1
9.260E0	7.468E4	1.339E-1		7.81E-1
9.211E0	7.429E4	1.346E-1		7.79E-1
9.110E0	7.348E4	1.361E-1		7.54E-1
9.017E0	7.273E4	1.375E-1		7.23E-1
8.920E0	7.194E4	1.390E-1		6.97E-1
8.825E0	7.117E4	1.405E-1		6.78E-1
8.725E0	7.037E4	1.421E-1		7.16E-1
8.676E0	6.998E4	1.429E-1		7.63E-1
8.628E0	6.959E4	1.437E-1		8.33E-1
8.580E0	6.920E4	1.445E-1		9.25E-1
8.533E0	6.882E4	1.453E-1		1.02E0
8.486E0	6.845E4	1.461E-1		1.10E0
8.389E0	6.766E4	1.478E-1		1.17E0
8.338E0	6.725E4	1.487E-1		1.16E0
8.244E0	6.649E4	1.504E-1		1.10E0
8.146E0	6.570E4	1.522E-1		1.04E0
7.953E0	6.414E4	1.559E-1		1.02E0
7.852E0	6.333E4	1.579E-1		1.12E0
7.759E0	6.258E4	1.598E-1		1.28E0
7.711E0	6.219E4	1.608E-1		1.34E0

(continued)

TABLE I *(Continued)*

Cesium Bromide

eV	cm^{-1}	μm	n	k
7.663E0	6.180E4	1.618E-1		1.35E0
7.565E0	6.101E4	1.639E-1		1.24E0
7.469E0	6.024E4	1.660E-1		1.12E0
7.420E0	5.984E4	1.671E-1		1.10E0
7.323E0	5.907E4	1.693E-1		1.17E0
7.225E0	5.828E4	1.716E-1		1.38E0
7.175E0	5.787E4	1.728E-1		1.52E0
7.130E0	5.750E4	1.739E-1		1.56E0
7.081E0	5.711E4	1.751E-1		1.39E0
7.033E0	5.672E4	1.763E-1		1.05E0
6.981E0	5.631E4	1.776E-1		7.90E-1
6.884E0	5.552E4	1.801E-1		6.64E-1
6.835E0	5.513E4	1.814E-1		6.56E-1
6.738E0	5.435E4	1.840E-1		7.78E-1
6.691E0	5.397E4	1.853E-1		9.14E-1
6.644E0	5.359E4	1.866E-1		1.04E0
6.595E0	5.319E4	1.880E-1		1.07E0
6.546E0	5.280E4	1.894E-1		8.00E-1
6.512E0	5.252E4	1.904E-1		5.86E-1
6.464E0	5.214E4	1.918E-1		4.81E-1
6.414E0	5.173E4	1.933E-1		4.52E-1
6.138E0	4.950E4	2.020E-1		7.86E-6 [4]
6.075E0	4.900E4	2.041E-1		4.29E-6
6.013E0	4.850E4	2.062E-1		3.21E-6
5.949E0	4.798E4	2.084E-1		2.78E-6
5.887E0	4.748E4	2.106E-1		2.49E-6
5.826E0	4.699E4	2.128E-1		2.27E-6
5.764E0	4.649E4	2.151E-1		2.08E-6
5.700E0	4.598E4	2.175E-1		1.96E-6
5.638E0	4.548E4	2.199E-1		1.83E-6
5.575E0	4.496E4	2.224E-1		1.72E-6
5.513E0	4.446E4	2.249E-1		1.62E-6
6.199E0	5.000E4	0.2	2.4393 [9]	
4.133E0	3.333E4	0.3	1.8048	
3.100E0	2.500E4	0.4	1.7357	
2.480E0	2.000E4	0.5	1.7095	
2.066E0	1.667E4	0.6	1.6964	
1.771E0	1.429E4	0.7	1.6888	
1.550E0	1.250E4	0.8	1.6840	
1.378E0	1.111E4	0.9	1.6808	
1.240E0	1.000E4	1.0	1.6785	
6.199E-1	5.000E3	2.0	1.6711	
4.133E-1	3.333E3	3.0	1.6695	
3.100E-1	2.500E3	4.0	1.6687	

(continued)

TABLE I *(Continued)*

Cesium Bromide

eV	cm^{-1}	μm	n	k
2.480E-1	2.000E3	5.0	1.6679	
2.066E-1	1.667E3	6.0	1.6671	
1.771E-1	1.429E3	7.0	1.6662	
1.550E-1	1.250E3	8.0	1.6653	
1.378E-1	1.111E3	9.0	1.6642	
1.240E-1	1.000E3	10	1.6630	
1.127E-1	9.091E2	11	1.6617	
1.033E-1	8.333E2	12	1.6602	
9.537E-2	7.692E2	13	1.6587	
8.856E-2	7.143E2	14	1.6570	
8.266E-2	6.667E2	15	1.6552	
7.749E-2	6.250E2	16	1.6532	
7.293E-2	5.882E2	17	1.6511	
6.888E-2	5.556E2	18	1.6489	
6.526E-2	5.263E2	19	1.6465	
6.199E-2	5.000E2	20	1.6440	
5.904E-2	4.762E2	21	1.6413	
5.636E-2	4.545E2	22	1.6385	
5.391E-2	4.348E2	23	1.6356	
5.166E-2	4.167E2	24	1.6324	
4.959E-2	4.000E2	25	1.6292	
4.769E-2	3.846E2	26	1.6258	
4.592E-2	3.704E2	27	1.6222	
4.428E-2	3.571E2	28	1.6184	
4.275E-2	3.448E2	29	1.6145	
4.133E-2	3.333E2	30	1.6104	
4.000E-2	3.226E2	31	1.6061	
3.875E-2	3.125E2	32	1.6017	
3.757E-2	3.030E2	33	1.5970	
3.647E-2	2.941E2	34	1.5922	
3.542E-2	2.857E2	35	1.5871	
3.444E-2	2.778E2	36	1.5819	
3.351E-2	2.703E2	37	1.5764	
3.263E-2	2.632E2	38	1.5708	
3.179E-2	2.564E2	39	1.5649	
3.100E-2	2.500E2	40	1.5587	
3.024E-2	2.439E2	41	1.5524	
2.952E-2	2.381E2	42	1.5457	
2.883E-2	2.326E2	43	1.5389	
2.818E-2	2.273E2	44	1.5317	
2.755E-2	2.222E2	45	1.5243	
2.695E-2	2.174E2	46	1.5166	
2.638E-2	2.128E2	47	1.5085	
2.583E-2	2.083E2	48	1.5002	
2.530E-2	2.041E2	49	1.4916	
2.480E-2	2.000E2	50	1.4826	

(continued)

TABLE I *(Continued)*

Cesium Bromide

eV	cm^{-1}	μm	n	k
2.431E-2	1.961E2	51	1.4732	
2.384E-2	1.923E2	52	1.4635	
2.339E-2	1.887E2	53	1.4534	
2.296E-2	1.852E2	54	1.4429	
2.254E-2	1.818E2	55	1.4320	
4.000E-2	3.226E2	31	1.606 [2]	1.10E-5 [2]
3.875E-2	3.125E2	32	1.601	1.62E-5
3.757E-2	3.030E2	33	1.597	2.37E-5
3.647E-2	2.941E2	34	1.592	3.38E-5
3.542E-2	2.857E2	35	1.587	4.65E-5
3.444E-2	2.778E2	36	1.582	
3.351E-2	2.703E2	37	1.577	
3.263E-2	2.632E2	38	1.571	
3.179E-2	2.564E2	39	1.565	
3.100E-2	2.500E2	40	1.558	
3.024E-2	2.439E2	41	1.552	
2.952E-2	2.381E2	42	1.546	3.23E-4
2.883E-2	2.326E2	43	1.539	4.07E-4
2.818E-2	2.273E2	44	1.532	5.00E-4
2.755E-2	2.222E2	45	1.524	6.10E-4
2.695E-2	2.174E2	46	1.516	7.40E-4
2.638E-2	2.128E2	47	1.508	9.00E-4
2.583E-2	2.083E2	48	1.500	1.05E-3
2.530E-2	2.041E2	49	1.491	1.23E-3
2.480E-2	2.000E2	50	1.482	1.45E-3
2.431E-2	1.961E2	51	1.472	1.70E-3
2.384E-2	1.923E2	52	1.462	1.97E-3
2.339E-2	1.887E2	53	1.451	2.29E-3
2.296E-2	1.852E2	54	1.440	2.65E-3
2.254E-2	1.818E2	55	1.429	3.10E-3
2.214E-2	1.786E2	56	1.417	3.55E-3
2.175E-2	1.754E2	57	1.405	4.10E-3
2.138E-2	1.724E2	58	1.390	4.85E-3
2.101E-2	1.695E2	59	1.380	5.60E-3
2.066E-2	1.667E2	60	1.365	6.70E-3
2.033E-2	1.639E2	61	1.350	8.13E-3
2.000E-2	1.613E2	62	1.330	9.73E-3
1.968E-2	1.587E2	63	1.315	1.16E-2
1.937E-2	1.563E2	64	1.300	1.37E-2
1.907E-2	1.538E2	65	1.285	1.66E-2
1.879E-2	1.515E2	66	1.270	2.04E-2
1.823E-2	1.471E2	68	1.240	3.13E-2
1.771E-2	1.429E2	70	1.200	5.07E-2
1.722E-2	1.389E2	72	1.160	8.93E-2
1.675E-2	1.351E2	74	1.110	1.15E-1

(continued)

TABLE I *(Continued)*

Cesium Bromide

eV	cm^{-1}	μm	n	k
1.631E-2	1.316E2	76	1.060	1.34E-1
1.590E-2	1.282E2	78	1.000	1.46E-1
1.550E-2	1.250E2	80	0.924	1.61E-1
1.512E-2	1.220E2	82	0.842	1.68E-1
1.476E-2	1.190E2	84	0.744	1.90E-1
1.442E-2	1.163E2	86	0.618	2.57E-1
1.409E-2	1.136E2	88	0.497	3.64E-1
1.378E-2	1.111E2	90	0.426	5.69E-1
1.348E-2	1.087E2	92	0.416	7.80E-1
1.319E-2	1.064E2	94	0.449	9.80E-1
1.292E-2	1.042E2	96	0.495	1.15E0
1.265E-2	1.020E2	98	0.551	1.29E0
1.240E-2	1.000E2	100	0.579	1.39E0
1.216E-2	9.804E1	102	0.541	1.49E0
1.192E-2	9.615E1	104	0.491	1.59E0
1.170E-2	9.434E1	106	0.449	1.68E0
1.148E-2	9.259E1	108	0.382	1.82E0
1.127E-2	9.091E1	110	0.321	1.93E0
1.107E-2	8.929E1	112	0.287	2.06E0
1.088E-2	8.772E1	114	0.284	2.16E0
1.069E-2	8.621E1	116	0.299	2.31E0
1.051E-2	8.475E1	118	0.323	2.51E0
1.033E-2	8.333E1	120	0.359	2.72E0
1.016E-2	8.197E1	122	0.417	3.00E0
9.999E-3	8.065E1	124	0.490	3.27E0
9.840E-3	7.937E1	126	0.622	3.70E0
9.686E-3	7.813E1	128	0.801	4.18E0
9.537E-3	7.692E1	130	1.13	4.70E0
9.393E-3	7.576E1	132	1.80	5.27E0
9.253E-3	7.463E1	134	3.00	6.00E0
9.117E-3	7.353E1	136	4.89	5.74E0
8.984E-3	7.246E1	138	6.24	4.01E0
8.856E-3	7.143E1	140	6.10	2.47E0
8.731E-3	7.042E1	142	5.72	1.59E0
8.610E-3	6.944E1	144	5.29	1.07E0
8.492E-3	6.849E1	146	5.07	7.39E-1
8.377E-3	6.757E1	148	4.81	5.20E-1
8.266E-3	6.667E1	150	4.59	4.14E-1
8.157E-3	6.579E1	152	4.38	3.31E-1
8.051E-3	6.494E1	154	4.23	2.90E-1
7.948E-3	6.410E1	156	4.11	2.58E-1
7.847E-3	6.329E1	158	3.99	2.38E-1
7.749E-3	6.250E1	160	3.88	2.21E-1
7.653E-3	6.173E1	162	3.78	2.06E-1
7.560E-3	6.098E1	164	3.69	1.95E-1
7.469E-3	6.024E1	166	3.61	1.83E-1

(continued)

TABLE I *(Continued)*

Cesium Bromide

eV	cm^{-1}	μm	n	k
7.380E-3	5.952E1	168	3.54	1.74E-1
7.293E-3	5.882E1	170	3.47	1.66E-1
7.208E-3	5.814E1	172	3.42	1.59E-1
7.126E-3	5.747E1	174	3.36	1.53E-1
7.045E-3	5.682E1	176	3.32	1.47E-1
6.965E-3	5.618E1	178	3.28	1.42E-1
6.888E-3	5.556E1	180	3.24	1.37E-1
6.702E-3	5.405E1	185	3.16	1.24E-1
6.526E-3	5.263E1	190	3.10	1.14E-1
6.358E-3	5.128E1	195	3.05	1.07E-1
6.199E-3	5.000E1	200	3.00	9.98E-2
6.048E-3	4.878E1	205	2.97	9.45E-2
5.904E-3	4.762E1	210	2.94	8.94E-2
5.767E-3	4.651E1	215	2.92	8.49E-2
5.636E-3	4.545E1	220	2.90	8.11E-2
5.510E-3	4.444E1	225	2.88	7.72E-2
5.391E-3	4.348E1	230	2.86	7.42E-2
5.276E-3	4.255E1	235	2.85	7.05E-2
5.166E-3	4.167E1	240	2.83	6.83E-2
5.061E-3	4.082E1	245	2.82	6.61E-2
4.959E-3	4.000E1	250	2.80	6.44E-2
4.862E-3	3.922E1	255	2.79	6.27E-2
4.769E-3	3.846E1	260	2.78	6.15E-2
4.679E-3	3.774E1	265	2.77	6.04E-2
4.592E-3	3.704E1	270	2.77	5.89E-2
4.509E-3	3.636E1	275	2.76	5.77E-2
5.367E-4	4.329E0	2.31E3	2.56 [1]	

Cesium Chloride (CsCl)

JOHN E. ELDRIDGE
Department of Physics
University of British Columbia
Vancouver, British Columbia, Canada

The room-temperature values of n and k tabulated here (Table I, Fig. 1) were obtained from the following works and references therein: In the far-infrared region, the reststrahlen values of n from 10 to 245 cm^{-1} and values of k from 100 to 245 cm^{-1} are from Shimizu *et al.* [1]; these are supplemented with values of k from 75 to 98 cm^{-1}, just below the peak, from Vergnat *et al.* [2]. In the transparent region from 250 cm^{-1} (40 μm) to 55,556 cm^{-1} (0.18 μm), values of n have been calculated by Li [3], who used the results of Wulff and co-workers [4–6] as the basis for the data generation; finally, in the low-energy x-ray region from 100 eV (12.4 nm) to 2000 eV (0.62 nm), *calculated* values of n and k are from Henke *et al.* [7].

Cesium chloride, which has cubic symmetry Pm3m (O_h^1), is very hygroscopic and highly soluble in water (1.62 g/cm^3). It is, therefore, an unsatisfactory material for making optical parts, despite its broad transparent range. Because of this, very few measurements of the refractive index or extinction coefficient have been made.

The far-infrared reststrahlen data were obtained by Shimizu *et al.* [1] by measuring the near-normal-incidence reflectivity of single crystals. These were polished with 0.3 μm particle size alumina dissolved in ethyl alcohol. After polishing, the samples were cleaned with methyl alcohol. The n and k data presented here were obtained after a Kramers–Kronig analysis. The measured reflectivity was higher than that obtained by Vergnat *et al.* [2], who used a pressed-powder sample, and for this reason was considered the more accurate. However, the high- and low-frequency extrapolations required for the Kramers–Kronig analysis were obviously in error, since the values of k just below the reststrahlen peak are negative. For this reason we have substituted the k values from Vergnat *et al.* [2], which were obtained from a Lorentz-oscillator fit to the reflectivity, in this small region. For the same reason one can see a discontinuity in Table I in going from the low-accuracy n data in the high-frequency wing of the restrahlen peak at 245 cm^{-1}, from

HANDBOOK OF OPTICAL CONSTANTS OF SOLIDS III

Copyright © 1998 by Academic Press.
All rights of reproduction in any form reserved
ISBN 0-12-544423-0/$25.00.

Shimuzu *et al.* [1], to the more accurate data of Li [3] at 250 cm^{-1}. The lowest-frequency n value, of 2.67 at 10 cm^{-1}, however, compares well with $\sqrt{\epsilon_s}$, equal to 2.64, where ϵ_s is the static dielectric constant with a value of 6.95 measured by Lowndes and Martin [8]. These same authors measured ω_T, the frequency of the zero-wave-vector transverse-optic (TO) phonon, to be 99.5 $\pm$ 0.5 cm^{-1}, in good agreement with the ~99.5 cm^{-1} frequency of the maximum value of the product nk (since $\epsilon_2 = 2nk$) using the values presented here.

The absorption in the wings of the reststrahlen band, away from the TO mode at ω_T, is due to two- and higher-phonon sum and difference processes by which the TO mode can relax when energy and momentum are conserved, producing broad structure in these regions. This absorption has been calculated by Shimizu *et al.* [9], but the agreement is not very satisfactory.

In the wide transparent region from 40 μm (250 cm^{-1}) to 0.18 μm (55,556 cm^{-1}), Li [3] has tabulated accurate values of n. He found only four sets of refractive-index data in the literature but considered the three works by Wulff and co-workers [4–6] to be sufficiently reliable to be used as the basis for the reference-data generation. These were corrected to 293 K, the chosen reference temperature. Using the infrared absorption peak at 100.5 μm (99.5 cm^{-1}, as mentioned earlier) plus the four measured absorption peaks in the vacuum ultraviolet [10–12] at 0.119 μm (10.42 eV), 0.137 μm (9.05 eV), 0.145 μm (8.55 eV), and 0.162 μm (7.65 eV), Li fitted the Wulff data to a dispersion equation of the Sellmeier type,

$$n^2 = 1.33013 + \frac{0.98369\lambda^2}{\lambda^2 - (0.119)^2} + \frac{0.00009\lambda^2}{\lambda^2 - (0.137)^2} + \frac{0.00018\lambda^2}{\lambda^2 - (0.145)^2} + \frac{0.30914\lambda^2}{\lambda^2 - (0.162)^2} + \frac{4.320\lambda^2}{\lambda^2 - (100.5)^2}, \quad (1)$$

where λ is in units of micrometers. In practical use the contributions of the third and fourth terms are small and can be neglected. Values from Eq. (1) are listed in Table I, although to greater accuracy than warranted by the experiment for the purpose of smoothness and internal comparison. Wulff's measurements of minimum deviation were performed on prismatic crystal specimens suspended in organic solutions. Uncertainties of 0.0001 were quoted.

No values of k above the far-infrared reststrahlen region have been found, nor values of n beyond Wulff's measurements [4–6]. Many studies of total absorption at energies above the transparent region have been performed, usually through thin films, which yield spectra of the absorption coefficient μ either in arbitrary or in absolute units. Those performed before 1977 have been summarized by Haelbich *et al.* [13]. In particular, Teegarden and Baldini [14] give μ in arbitrary units at 10 K between 7.4 and 12 eV, whereas

Saito *et al.* [15] continue this region up to 24 eV at room temperature. Cardona *et al.* [16] give μ in absolute units from 70 to 190 eV. They made the thin films, from 10 to 1000 nm thick, by *in situ* evaporation and measured the thickness to an accuracy of $\pm 20\%$ by an oscillating quartz. These spectra contain the same features as would the k spectra and can be used to obtain an approximate value of k, since the true absorption coefficient α is related to k through $\alpha = 4\pi k\nu$, where ν is in wave numbers (cm^{-1}), whereas μ was obtained without correcting for the surface reflectivity. Values of k obtained using this relationship are within 50% of those calculated from Henke *et al.* [7]. μ in arbitrary units is given by Iguchi *et al.* [17] from 200 to 280 eV. The absorption at the Cl K edge at 2.8 kV is given by Kiyono and Sugiura [18] and the Cl L edges at 5 kV by the same authors [19].

For several materials, good agreement has been found previously in the soft x-ray region between experimental values and those calculated using the atomic scattering factors of Henke *et al.* [7]. We have therefore tabulated the calculated values of n and k for CsCl between 100 eV and 2000 eV. In scattering theory, the complex refractive index is given as

$$n = 1 - \delta - ik, \tag{2}$$

where

$$\delta = \frac{r_0\lambda^2}{2\pi} Nf_1 \tag{3}$$

$$k = \frac{r_0\lambda^2}{2\pi} Nf_2. \tag{4}$$

Here $r_0 = e^2/mc^2$, the classical electron radius, equal to 2.814×10^{-13} cm; λ is the wavelength; N is the density of molecules per unit volume, equal in this case to 14.26×10^{21} CsCl molecules per cm^3; and f_1 and f_2 are the sum of the individual Cs and Cl atomic scattering factors, which are listed elsewhere [7].

REFERENCES

1. H. Shimizu, Y. Ohbayashi, K. Yamamoto, K. Abe, M. Midorikawa, and Y. Ishibashi, *J. Phys. Soc. Jpn.* **39**, 448 (1975).
2. P. P. Vergnat, J. Claudel, A. Hadni, P. Strimer, and F. Vermillard, *J. Phys. (Paris)* **30**, 723 (1969).
3. H. H. Li, *J. Phys. Chem. Ref. Data* **5**, 329 (1976).
4. P. Wulff and D. Schaller, *Z. Kristallogr.* **87**, 43 (1934).
5. P. Wulff and T. F. Anderson, *Z. Phys.* **94**, 28 (1935).
6. P. Wulff and A. Heigl, *Z. Kristallogr.* **77**, 84 (1931).
7. B. L. Henke, P. Lee, T. J. Tanaka, R. L. Shimabukuro, and B. K. Fujukawa, *in* "Low Energy X-Ray Diagnostics-1981," (D. T. Attwood and B. L. Henke, eds.), AIP Conf. Proc. No. 75, p. 340. American Institute of Physics, New York, 1981.
8. R. P. Lowndes and D. H. Martin, *Proc. R. Soc. London A.* **308**, 473 (1969).

9. H. Shimizu, Y. Ohbayashi, K. Yamamoto, K. Abe, and Y. Ishibashi, *J. Phys. Soc. Jpn.* **40**, 1684 (1976).
10. R. Hilsch and R. W. Pohl, *Z. Phys.* **59**, 812 (1930).
11. E. G. Schneider and H. M. O'Brian, *Phys. Rev.* **51**, 293 (1937).
12. G. N. Ramachandran, *Proc. Indian Acad. Sci. Sect. A* **25A**, 481 (1947).
13. R. P. Haelbich, M. Iwan, and E. E. Koch, "Physik Daten-Physics Data," p. 152. Fachinformation Zentrum, Karlsruhe, Germany, 1977.
14. K. Teegarden and G. Baldini, *Phys. Rev.* **155**, 896 (1967).
15. H. Saito, S. Saito, R. Onaka, and B. Ikeo, *J. Phys. Soc. Jpn.* **24**, 1095 (1968).
16. M. Cardona, R. Haensel, D. W. Lynch, and B. Sonntag, *Phys. Rev. B* **2**, 1117 (1970).
17. Y. Iguchi, T. Sagawa, S. Sato, M. Watanabe, H. Yamashita, A. Ejiri, M. Sasonuma, S. Nakai, M. Nakamura, A. Yamaguchi, Y. Nakai, and T. Oshio, *Solid State Commun.* **6**, 575 (1968).
18. S. Kiyono and C. Sugiura, *Sci. Rep. Tohoku Univ.* **30**, 9 (1965).
19. C. Sugiura and S. Kiyono, *Technol. Rep. Tohoku Univ.* **35**, 119 (1970).

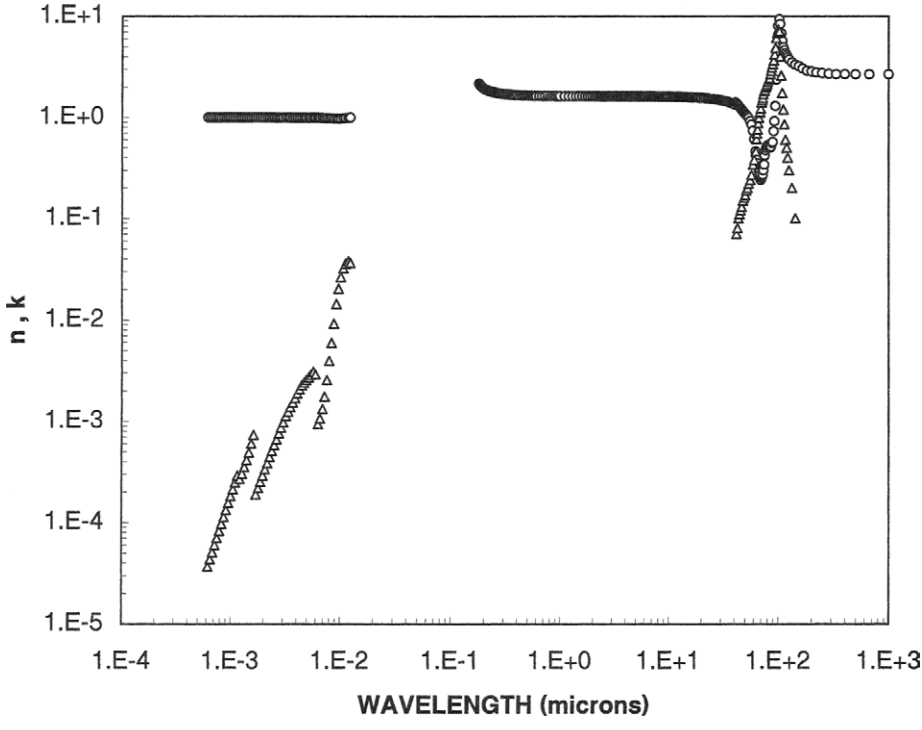

Fig. 1. Log–log plot of n (○) and k (△) versus wavelength in micrometers for cesium chloride.

TABLE I

Values of n and k for Cesium Chloride from Various References[a]

eV	cm^{-1}	nm	n	k
2000	16131000	0.620	0.99984 [7]	3.67 E-5 [7]
1905	15365000	0.651	0.99982	4.33 E-5
1815	14639000	0.683	0.99980	5.09 E-5
1730	13953000	0.717	0.99979	5.99 E-5
1648	13292000	0.752	0.99977	7.02 E-5
1570	12663000	0.790	0.99974	8.26 E-5
1496	12066000	0.829	0.99972	9.69 E-5
1426	11501000	0.869	0.99970	1.13 E-4
1358	10953000	0.913	0.99967	1.33 E-4
1294	10437000	0.958	0.99964	1.56 E-4
1233	9944700	1.006	0.99962	1.83 E-4
1175	9476900	1.055	0.99959	2.13 E-4
1119	9025300	1.108	0.99957	2.49 E-4
1067	8605900	1.162	0.99956	2.90 E-4
1016	8194500	1.220	0.99956	2.70 E-4
968	7807400	1.281	0.99949	3.03 E-4
923	7444400	1.343	0.99944	3.53 E-4
879	7089600	1.411	0.99941	4.14 E-4
838	6758900	1.480	0.99938	4.91 E-4
798	6436300	1.554	0.99939	6.01 E-4
760	6129800	1.631	0.99950	7.33 E-4
725	5847500	1.710	1.00036	1.90 E-4
690	5565200	1.797	0.99951	2.19 E-4
658	5307100	1.884	0.99932	2.52 E-4
627	5057100	1.977	0.99918	2.91 E-4
597	4815100	2.077	0.99905	3.35 E-4
569	4589300	2.179	0.99892	3.85 E-4
542	4371500	2.288	0.99879	4.43 E-4
516	4161800	2.403	0.99865	5.09 E-4
492	3968200	2.520	0.99850	5.80 E-4
469	3782700	2.644	0.99836	6.61 E-4
447	3605300	2.774	0.99820	7.59 E-4
426	3435900	2.910	0.99803	8.64 E-4
406	3274600	3.054	0.99787	9.76 E-4
386	3113300	3.212	0.99769	1.13 E-3
368	2968100	3.369	0.99750	1.24 E-3
351	2831000	3.532	0.99732	1.38 E-3
334	2693900	3.712	0.99710	1.53 E-3
318	2564800	3.899	0.99688	1.70 E-3
303	2443800	4.092	0.99666	1.88 E-3
289	2330900	4.290	0.99644	2.07 E-3
275	2218000	4.509	0.99622	2.27 E-3
262	2113200	4.732	0.99600	2.41 E-3

(continued)

[a] Tabulation of n and k as a function of photon energy (electron volts), wave number (inverse centimeters), and wavelength (nm or μm). References for the data are given in brackets and apply to all data below the brackets until a new reference appears.

TABLE I *(Continued)*

Cesium Chloride

eV	cm^{-1}	nm	n	k
250	2016400	4.959	0.99574	2.56 E-3
238	1919600	5.209	0.99545	2.72 E-3
227	1830900	5.462	0.99518	2.88 E-3
216	1742100	5.740	0.99501	3.07 E-3
206	1661500	6.019	0.99553	2.90 E-3
196	1580800	6.326	0.99391	9.37 E-4
187	1508200	6.630	0.99208	1.06 E-3
178	1435700	6.965	0.99023	1.32 E-3
170	1371100	7.293	0.98836	1.76 E-3
162	1306600	7.653	0.98609	2.55 E-3
154	1242100	8.051	0.98337	3.93 E-3
147	1185600	8.434	0.98065	5.96 E-3
140	1129200	8.856	0.97762	9.20 E-3
133	1072700	9.322	0.97520	1.44 E-2
127	1024300	9.763	0.97485	2.03 E-2
121	975920	10.25	0.97647	2.65 E-2
115	927530	10.78	0.98048	3.22 E-2
110	887200	11.27	0.98551	3.58 E-2
104	838810	11.92	0.99318	3.76 E-2
100	806550	12.40	0.99848	3.65 E-2

eV	cm^{-1}	μm	n	k
6.888	55556	0.180	2.16918 [3]	
6.738	54348	0.184	2.09684	
6.595	53191	0.188	2.04273	
6.458	52083	0.192	2.00270	
6.326	51020	0.196	1.96580	
6.199	50000	0.200	1.93711	
6.078	49020	0.204	1.91275	
5.961	48077	0.208	1.89176	
5.848	47170	0.212	1.87345	
5.740	46296	0.216	1.85730	
5.636	45455	0.220	1.84294	
5.535	44643	0.224	1.83008	
5.438	43860	0.228	1.81848	
5.344	43103	0.232	1.80797	
5.254	42373	0.236	1.79839	
5.166	41667	0.240	1.78963	
5.081	40984	0.244	1.78158	
4.999	40323	0.248	1.77416	
4.920	39683	0.252	1.76731	
4.843	39063	0.256	1.76095	
4.769	38462	0.260	1.75504	
4.696	37879	0.264	1.74953	
4.626	37313	0.268	1.74438	
4.558	36765	0.272	1.73957	
4.492	36232	0.276	1.73505	
4.428	35714	0.280	1.73080	
4.366	35211	0.284	1.72681	

TABLE I *(Continued)*

Cesium Chloride

eV	cm^{-1}	μm	n	k
4.305	34722	0.288	1.72305	
4.246	34247	0.292	1.71949	
4.189	33784	0.296	1.71613	
4.133	33333	0.300	1.71295	
4.000	32258	0.310	1.70570	
3.875	31250	0.320	1.69931	
3.757	30303	0.330	1.69364	
3.647	29412	0.340	1.68859	
3.542	28571	0.350	1.68407	
3.444	27778	0.360	1.68000	
3.351	27027	0.370	1.67631	
3.263	26316	0.38	1.67297	
3.179	25641	0.39	1.66993	
3.100	25000	0.40	1.66714	
2.952	23810	0.42	1.66225	
2.818	22727	0.44	1.65810	
2.695	21739	0.46	1.65453	
2.583	20833	0.48	1.65146	
2.480	20000	0.50	1.64878	
2.384	19231	0.52	1.64643	
2.296	18519	0.54	1.64435	
2.214	17857	0.56	1.64252	
2.138	17241	0.58	1.64088	
2.066	16667	0.60	1.63941	
1.937	15625	0.64	1.63690	
1.823	14706	0.68	1.63484	
1.722	13889	0.72	1.63313	
1.631	13158	0.76	1.63169	
1.550	12500	0.80	1.63047	
1.476	11905	0.84	1.62942	
1.409	11364	0.88	1.62852	
1.348	10870	0.92	1.62773	
1.292	10417	0.96	1.62704	
1.240	10000	1.00	1.62643	
1.127	9091	1.10	1.62518	
1.033	8333	1.20	1.62423	
0.954	7692	1.30	1.62348	
0.886	7143	1.40	1.62288	
0.827	6667	1.50	1.62239	
0.775	6250	1.60	1.62198	
0.729	5882	1.70	1.62162	
0.689	5556	1.80	1.62132	
0.653	5263	1.90	1.62105	
0.620	5000	2.00	1.62082	
0.590	4762	2.10	1.62060	
0.564	4545	2.20	1.62041	
0.539	4348	2.30	1.62023	

(continued)

TABLE I *(Continued)*

Cesium Chloride

eV	cm^{-1}	μm	n	k
0.517	4167	2.40	1.62006	
0.496	4000	2.50	1.61990	
0.4769	3846	2.6	1.61975	
0.4592	3704	2.7	1.61961	
0.4428	3571	2.8	1.61947	
0.4275	3448	2.9	1.61934	
0.4133	3333	3.0	1.61921	
0.4000	3226	3.1	1.61908	
0.3875	3125	3.2	1.61895	
0.3757	3030	3.3	1.61882	
0.3647	2941	3.4	1.61870	
0.3542	2857	3.5	1.61857	
0.3444	2778	3.6	1.61845	
0.3351	2703	3.7	1.61832	
0.3263	2632	3.8	1.61820	
0.3179	2564	3.9	1.61807	
0.3100	2500	4.0	1.61795	
0.3024	2439	4.1	1.61782	
0.2952	2381	4.2	1.61769	
0.2883	2326	4.3	1.61756	
0.2818	2273	4.4	1.61743	
0.2755	2222	4.5	1.61729	
0.2695	2174	4.6	1.61716	
0.2638	2128	4.7	1.61702	
0.2583	2083	4.8	1.61688	
0.2530	2041	4.9	1.61674	
0.2480	2000	5.0	1.61660	
0.2384	1923	5.2	1.61631	
0.2296	1852	5.4	1.61601	
0.2214	1786	5.6	1.61570	
0.2138	1724	5.8	1.61538	
0.2066	1667	6.0	1.61505	
0.2000	1613	6.2	1.61471	
0.1937	1563	6.4	1.61436	
0.1879	1515	6.6	1.61401	
0.1823	1471	6.8	1.61364	
0.1771	1429	7.0	1.61326	
0.1722	1389	7.2	1.61287	
0.1675	1351	7.4	1.61248	
0.1631	1316	7.6	1.61207	
0.1590	1282.0	7.8	1.61165	
0.1550	1250.0	8.0	1.61122	
0.1512	1219.5	8.2	1.61078	
0.1476	1190.5	8.4	1.61032	
0.1442	1162.8	8.6	1.60986	
0.1409	1136.4	8.8	1.60939	
0.1378	1111.1	9.0	1.60890	

TABLE I *(Continued)*

Cesium Chloride

eV	cm^{-1}	μm	n	k
0.1348	1087.0	9.2	1.60841	
0.1319	1063.8	9.4	1.60790	
0.1292	1041.7	9.6	1.60738	
0.1265	1020.4	9.8	1.60685	
0.1240	1000.0	10.0	1.60631	
0.1192	961.5	10.4	1.60520	
0.1148	925.9	10.8	1.60404	
0.1107	892.9	11.2	1.60283	
0.1069	862.1	11.6	1.60158	
0.1033	833.3	12.0	1.60028	
0.1000	806.5	12.4	1.59893	
0.0969	781.3	12.8	1.59754	
0.0939	757.6	13.2	1.59609	
0.0912	735.3	13.6	1.59460	
0.0886	714.3	14.0	1.59306	
0.0861	694.4	14.4	1.59147	
0.0838	675.7	14.8	1.58983	
0.0816	657.9	15.2	1.58814	
0.0795	641.0	15.6	1.58640	
0.0775	625.0	16.0	1.58460	
0.0756	609.8	16.4	1.58276	
0.0738	595.2	16.8	1.58086	
0.0721	581.4	17.2	1.57891	
0.0704	568.2	17.6	1.57690	
0.0689	555.6	18.0	1.57484	
0.0674	543.5	18.4	1.57272	
0.0659	531.9	18.8	1.57055	
0.0646	520.8	19.2	1.56832	
0.0633	510.2	19.6	1.56604	
0.0620	500.0	20.0	1.56369	
0.0590	476.2	21.0	1.55758	
0.05636	454.5	22.0	1.55108	
0.05391	434.8	23.0	1.54418	
0.05166	416.7	24.0	1.53688	
0.04959	400.0	25.0	1.52915	
0.04769	384.6	26.0	1.52098	
0.04592	370.4	27.0	1.51235	
0.04428	357.1	28.0	1.50323	
0.04275	344.8	29.0	1.49361	
0.04133	333.3	30.0	1.48346	
0.04000	322.6	31.0	1.47275	
0.03875	312.5	32.0	1.46146	
0.03757	303.0	33.0	1.44954	
0.03647	294.1	34.0	1.43698	
0.03542	285.7	35.0	1.42372	
0.03444	277.8	36.0	1.40973	
0.03351	270.3	37.0	1.39495	

(continued)

TABLE I *(Continued)*

Cesium Chloride

eV	cm^{-1}	μm	n	k
0.03263	263.2	38.0	1.37935	
0.03179	256.4	39.0	1.36285	
0.03100	250.0	40.0	1.34539	
0.03038	245.0	40.82	1.41 [1]	0.07 [1]
0.02976	240.0	41.67	1.38	0.80
0.02914	235.0	42.55	1.35	0.10
0.02852	230.0	43.48	1.31	0.11
0.02790	225.0	44.44	1.27	0.12
0.02728	220.0	45.45	1.24	0.13
0.02666	215.0	46.51	1.20	0.15
0.02604	210.0	47.62	1.16	0.16
0.02542	205.0	48.78	1.12	0.17
0.02480	200.0	50.00	1.09	0.19
0.02418	195.0	51.28	1.06	0.20
0.02356	190.0	52.63	1.03	0.22
0.02294	185.0	54.05	0.99	0.24
0.02232	180.0	55.56	0.92	0.27
0.02170	175.0	57.14	0.85	0.34
0.02108	170.0	58.82	0.74	0.38
0.02046	165.0	60.61	0.61	0.46
0.01984	160.0	62.50	0.46	0.61
0.01959	158.0	63.29	0.42	0.69
0.01934	156	64.10	0.38	0.76
0.01909	154	64.94	0.35	0.88
0.01885	152	65.79	0.33	0.99
0.01860	150	66.67	0.30	1.11
0.01835	148	67.57	0.29	1.14
0.01810	146	68.49	0.27	1.22
0.01785	144	69.44	0.24	1.41
0.01761	142	70.42	0.25	1.49
0.01736	140	71.43	0.26	1.56
0.01711	138	72.46	0.27	1.70
0.01686	136	73.53	0.30	1.83
0.01661	134	74.63	0.34	1.87
0.01637	132	75.76	0.42	1.98
0.01612	130	76.92	0.472	2.06
0.01587	128	78.13	0.499	2.14
0.01562	126	79.37	0.519	2.25
0.01537	124	80.65	0.529	2.37
0.01513	122	81.97	0.520	2.44
0.01488	120	83.33	0.505	2.67
0.01463	118	84.75	0.502	2.90
0.01438	116	86.21	0.512	3.13
0.01413	114	87.72	0.559	3.36
0.01389	112	89.29	0.57	3.66
0.01364	110	90.91	0.73	4.20
0.01339	108	92.59	0.92	4.89

TABLE I *(Continued)*

Cesium Chloride

eV	cm^{-1}	μm	n	k
0.01314	106	94.34	1.30	6.11
0.01289	104	96.15	2.37	6.87
0.01277	103	97.09	3.04	7.03
0.01265	102	98.04	4.20	7.40
0.01252	101	99.01	5.32	7.38
0.01240	100	100.0	8.02	7.10
0.01227	99	101.0	8.75	5.10
0.01215	98	102.0	9.35	4.00 [2]
0.01203	97	103.1	8.90	3.19
0.01190	96	104.2	8.40	2.60
0.01165	94	106.4	6.79	1.75
0.01141	92	108.7	5.72	1.20
0.01116	90	111.1	4.96	0.85
0.01091	88	113.6	4.62	0.60
0.01066	86	116.3	4.31	0.50
0.01041	84	119.0	4.12	0.40
0.01017	82	122.0	3.93	0.30
0.00992	80	125.0	3.74	0.20
0.00930	75	133.3	3.51	0.10
0.00868	70	142.9	3.32	
0.00806	65	153.8	3.21	
0.00744	60	166.7	3.05	
0.00682	55	181.8	2.90	
0.00620	50	200.0	2.86	
0.00558	45	222.2	2.79	
0.00496	40	250.0	2.75	
0.00434	35	285.7	2.71	
0.00372	30	333.3	2.69	
0.00310	25	400.0	2.68	
0.00248	20	500.0	2.67	
0.00186	15	666.7	2.67	
0.00124	10	1000.0	2.67	

Cesium Fluoride (CsF)

JOHN E. ELDRIDGE
Department of Physics
University of British Columbia
Vancouver, British Columbia, Canada

Cesium fluoride has cubic symmetry Fm3m (O_h^5), with the NaCl structure, which consists of two interpenetrating face-centered cubic lattices, one of Na and one of Cl. It is extremely hygroscopic and soluble in water (3.67 g/cm^3) and is, therefore, a very unsatisfactory material for making optical parts and consequently has been little studied. Only one measurement of refractive index has been found, and no measurements of extinction coefficient.

The room-temperature values of n and k tabulated here (Table I, Fig. 1) were *calculated* and are taken from two references [1, 2]. Li [1] used the one refractive-index datum point together with several other input data as the basis for the generation of his dispersion equation of the Sellmeier type, for n throughout the wide transparent region,

$$n^2 = 1.60 + \frac{0.56\lambda^2}{\lambda^2 - (0.121)^2} + \frac{5.92\lambda^2}{\lambda^2 - (78.74)^2}, \tag{1}$$

where λ is in units of micrometers. The one refractive-index measurement was made by Spangenberg [3] for a single spectral line, the sodium D line at a wavelength of 0.5893 μm, using the immersion method. He gave two values for n, one for α-CsF (equal to 1.478, and this is the one used by Li [1]), and one for β-CsF. [The α phase is the NaCl structure mentioned earlier, which is stable at elevated temperatures. The β phase is the CsCl structure, which consists of two interpenetrating cubic lattices of Cs and Cl, one displaced from the other by the vector 0.5, 0.5, 0.5. This phase of CsF is stable only at normal temperatures.] The other input data include the 78.74-μm wavelength (127 cm^{-1}) of the zero-wave-vector transverse optic (TO) phonon, which resonates in the far-infrared region and was measured by Lowndes and Martin [4], and the value of 8.08 for the static dielectric constant ϵ_s, and 2.16 for the high-frequency dielectric constant ϵ_∞, measured

HANDBOOK OF OPTICAL CONSTANTS OF SOLIDS III

Copyright © 1998 by Academic Press.
All rights of reproduction in any form reserved
ISBN 0-12-544423-0/$25.00.

by the same authors [4]. This value of ϵ_s predicts a low-frequency value of n, given by $\sqrt{\epsilon_s}$, of 2.84. In the second term of Eq. 1 the 0.121 μm is the average wavelength of the three peaks observed in the ultraviolet by Schneider and O'Brian [5]. Values from Eq. 1 are listed in Table I, although to far greater accuracy than warranted by the experiments, for the purpose of smoothness and internal comparison. Because of the paucity of input data, only the values of n between 0.3 μm and 2 μm are recommended; those outside this range are classified by Li as provisional.

Several studies of total absorption at energies above the transparent region have been performed, usually through thin films, which yield spectra of the absorption coefficient μ either in arbitrary or in absolute units. Those performed before 1977 have been summarized by Haelbich *et al.* [6]. In particular, Watanabe *et al.* [7] give μ in arbitrary units at room temperature between 8 and 32 eV. Cardona *et al.* [8] give μ in absolute units from 70 to 190 eV. They made the thin films, from 10 to 1000 nm thick, by *in situ* evaporation and measured the thickness to an accuracy of $\pm 20\%$ by an oscillating quartz. These spectra contain the same features as would the k spectra and can be used to obtain an approximate value of k, since the true absorption coefficient α is related to k through $\alpha = 4\pi k\nu$, where ν is in wave numbers (cm^{-1}), whereas μ was obtained without correcting for the surface reflectivity. Values of k obtained using this relationship are within 50% of those calculated from Henke *et al.* [2] (see below and Table I). μ in arbitrary units is given by Vinogradov *et al.* [9] from 680 to 720 eV. The absorption at the Cl L edges near 5 keV is given by Sugiura and Kiyono [10].

For several materials, good agreement has been found previously in the soft x-ray region between experimental values and those calculated using the atomic scattering factors of Henke *et al.* [2]. We have therefore tabulated the *calculated* values of n and k for CsF between 100 and 2000 eV. In scattering theory, the complex refractive index is given as

$$n = 1 - \delta - ik, \tag{2}$$

where

$$\delta = \frac{r_0\lambda^2}{2\pi} N f_1 \tag{3}$$

$$k = \frac{r_0\lambda^2}{2\pi} N f_2. \tag{4}$$

Here $r_0 = e^2/mc^2$, the classical electron radius, equal to 2.814×10^{-13} cm; λ is the wavelength; N is the density of molecules per unit volume, equal in this case to 16.31×10^{21} CsF molecules per cm^3; and f_1 and f_2 are the sum of the individual Cs and F atomic scattering factors, which are listed by Henke *et al.* [2].

REFERENCES

1. H. H. Li, *J. Phys. Chem. Ref. Data* **5**, 329 (1976).
2. B. L. Henke, P. Lee, T. J. Tanaka, R. L. Shimabukuro, and B. K. Fujukawa, *in* "Low Energy X-Ray Diagnostics-1981" (D. T. Attwood and B. L. Henke, eds.), AIP Conf. Proc. No. 75, p. 340. American Institute of Physics, New York, 1981.
3. K. Spangenberg, *Z. Kristallogr.* **57**, 494 (1923).
4. R. P. Lowndes and D. H. Martin, *Proc. R. Soc. London A.* **308**, 473 (1969).
5. E. G. Schneider and H. M. O'Brian, *Phys. Rev.* **51**, 293 (1937).
6. R. P. Haelbich, M. Iwan, and E. E. Koch, "Physik Daten-Physics Data," p. 152. Fachinformation Zentrum, Karlsruhe, Germany, 1977.
7. M. Watanabe, H. Nishida, and A. Ejiri, "Vacuum Ultraviolet Radiation Physics" (E. E. Koch, R. Haensel, and C. Kunz, eds.), p. 370. Pergamon-Vieweg, Braunschweig, Germany, 1974.
8. M. Cardona, R. Haensel, D. W. Lynch, and B. Sonntag, *Phys. Rev. B* **2**, 1117 (1970).
9. A. S. Vinogradov, T. M. Zimkina, and Yu. F. Mal'tsev, *Sov. Phys. Solid State* **11**, 2721 (1970).
10. C. Sugiura and S. Kiyono, *Technol. Rep. Tohoku Univ.* **35**, 119 (1970).

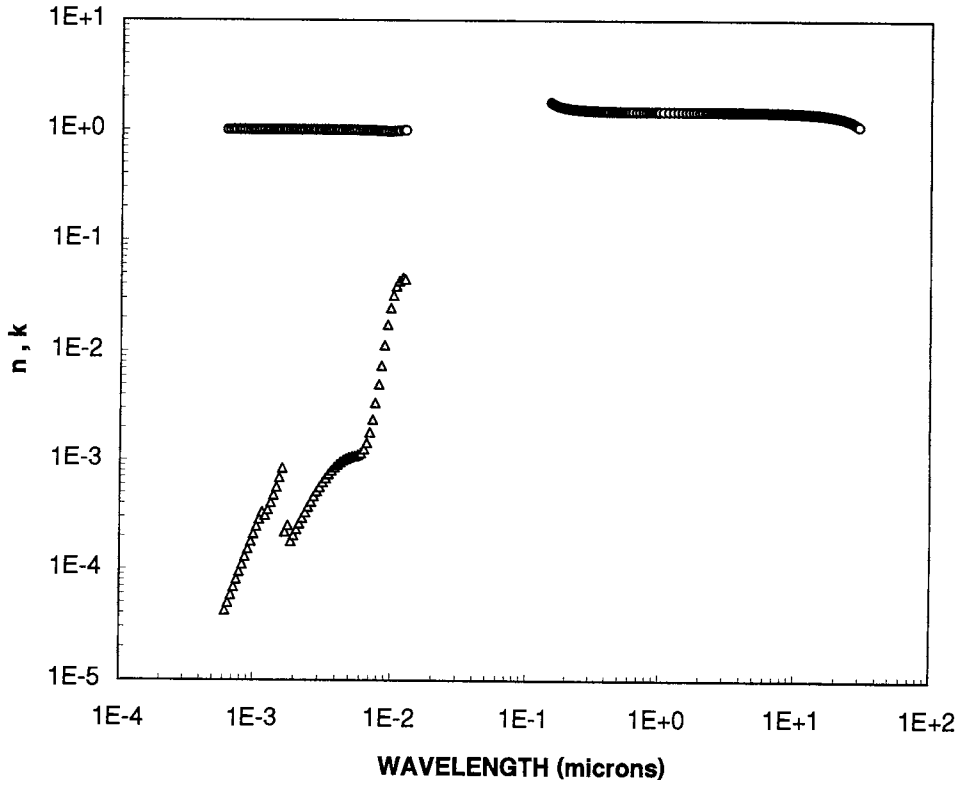

Fig. 1. Log–log plot of n (○) and k (△) versus wavelength in micrometers for cesium fluoride.

TABLE I

Values of n and k for Cesium Fluoride from Various References[a]

eV	cm^{-1}	nm	n	k
2000	16131000	0.620	0.99983 [2]	4.21 E-5 [2]
1905	15365000	0.651	0.99982	4.96 E-5
1815	14639000	0.683	0.99980	5.84 E-5
1730	13953000	0.717	0.99978	6.88 E-5
1648	13292000	0.752	0.99976	8.07 E-5
1570	12663000	0.790	0.99974	9.49 E-5
1496	12066000	0.829	0.99971	1.11 E-5
1426	11501000	0.869	0.99969	1.30 E-4
1358	10953000	0.913	0.99966	1.53 E-4
1294	10437000	0.958	0.99964	1.79 E-4
1233	9944700	1.006	0.99961	2.10 E-4
1175	9476900	1.055	0.99959	2.45 E-4
1119	9025300	1.108	0.99957	2.86 E-4
1067	8605900	1.162	0.99957	3.33 E-4
1016	8194500	1.220	0.99958	3.10 E-4
968	7807400	1.281	0.99951	3.49 E-4
923	7444400	1.343	0.99947	4.06 E-4
879	7089600	1.411	0.99944	4.76 E-4
838	6758900	1.480	0.99943	5.64 E-4
798	6436300	1.554	0.99946	6.90 E-4
760	6129800	1.631	0.99962	8.43 E-4
725	5847500	1.710	1.00064	2.19 E-4
690	5565200	1.797	0.99977	2.51 E-4
658	5307100	1.884	0.99952	1.79 E-4
627	5057100	1.977	0.99936	2.03 E-4
597	4815100	2.077	0.99923	2.30 E-4
569	4589300	2.179	0.99910	2.60 E-4
542	4371500	2.288	0.99897	2.93 E-4
516	4161800	2.403	0.99883	3.30 E-4
492	3968200	2.520	0.99869	3.69 E-4
469	3782700	2.644	0.99855	4.11 E-4
447	3605300	2.774	0.99839	4.63 E-4
426	3435900	2.910	0.99822	5.13 E-4
406	3274600	3.054	0.99805	5.63 E-4
386	3113300	3.212	0.99784	6.23 E-4
368	2968100	3.369	0.99763	6.80 E-4
351	2831000	3.532	0.99740	7.38 E-4
334	2693900	3.712	0.99714	7.98 E-4
318	2564800	3.899	0.99685	8.57 E-4
303	2443800	4.092	0.99655	9.09 E-4
289	2330900	4.290	0.99621	9.57 E-4
275	2218000	4.509	0.99580	1.00 E-3
262	2113200	4.732	0.99536	1.03 E-3

[a] Tabulation of n and k as a function of photon energy (electron volts), wave number (inverse centimeters), and wavelength (nm or μm). References for the data are given in brackets and apply to all data below the brackets until a new reference appears.

TABLE I *(Continued)*

Cesium Fluoride

eV	cm^{-1}	nm	*n*	*k*
250	2016400	4.959	0.99485	1.06 E-3
238	1919600	5.209	0.99423	1.08 E-3
227	1830900	5.462	0.99353	1.09 E-3
216	1742100	5.740	0.99265	1.12 E-3
206	1661500	6.019	0.99164	1.16 E-3
196	1580800	6.326	0.99037	1.26 E-3
187	1508200	6.630	0.98894	1.44 E-3
178	1435700	6.965	0.98710	1.80 E-3
170	1371100	7.293	0.98510	2.36 E-3
162	1306600	7.653	0.98261	3.34 E-3
154	1242100	8.051	0.97956	5.02 E-3
147	1185600	8.434	0.97648	7.45 E-3
140	1129200	8.856	0.97303	1.13 E-2
133	1072700	9.322	0.97028	1.74 E-2
127	1024300	9.763	0.96988	2.44 E-2
121	975920	10.25	0.97174	3.17 E-2
115	927530	10.78	0.97633	3.85 E-2
110	887200	11.27	0.98210	4.28 E-2
104	838810	11.92	0.99089	4.54 E-2
100	806550	12.40	0.99700	4.45 E-2
eV	cm^{-1}	μm	*n*	*k*
8.265	66667	0.150	1.78976 [1]	
8.051	64935	0.154	1.75027	
7.847	63291	0.158	1.71878	
7.653	61728	0.162	1.69310	
7.469	60241	0.166	1.67177	
7.293	58824	0.170	1.65378	
7.125	57471	0.174	1.63840	
6.965	56180	0.178	1.62513	
6.812	54945	0.182	1.61356	
6.666	53763	0.186	1.60338	
6.525	52632	0.190	1.59438	
6.391	51546	0.194	1.58635	
6.262	50505	0.198	1.57916	
6.138	49505	0.202	1.57269	
6.018	48544	0.206	1.56682	
5.904	47619	0.210	1.56150	
5.793	46729	0.214	1.55664	
5.687	45872	0.218	1.55219	
5.585	45045	0.222	1.54810	
5.486	44248	0.226	1.54434	
5.390	43478	0.230	1.54086	
5.298	42735	0.234	1.53764	
5.209	42017	0.238	1.53465	

(continued)

TABLE I *(Continued)*

Cesium Fluoride

eV	cm^{-1}	μm	n	k
5.123	41322	0.242	1.53187	
5.040	40650	0.246	1.52927	
4.959	40000	0.250	1.52684	
4.881	39370	0.254	1.52457	
4.805	38760	0.258	1.52245	
4.732	38168	0.262	1.52045	
4.661	37594	0.266	1.51857	
4.592	37037	0.270	1.51679	
4.525	36496	0.274	1.51512	
4.460	35971	0.278	1.51354	
4.396	35461	0.282	1.51205	
4.335	34965	0.286	1.51063	
4.275	34483	0.290	1.50929	
4.217	34014	0.294	1.50802	
4.160	33557	0.298	1.50681	
4.065	32787	0.305	1.50483	
3.936	31746	0.315	1.50228	
3.815	30769	0.325	1.50000	
3.701	29851	0.335	1.49797	
3.594	28986	0.345	1.49614	
3.492	28169	0.355	1.49449	
3.397	27397	0.365	1.49299	
3.306	26667	0.375	1.49162	
3.220	25974	0.385	1.49038	
3.139	25316	0.395	1.48924	
3.024	24390	0.41	1.48771	
2.883	23256	0.43	1.48593	
2.755	22222	0.45	1.48440	
2.638	21277	0.47	1.48308	
2.530	20408	0.49	1.48194	
2.431	19608	0.51	1.48093	
2.339	18868	0.53	1.48004	
2.254	18182	0.55	1.47925	
2.175	17544	0.57	1.47855	
2.101	16949	0.59	1.47792	
2.000	16129	0.62	1.47709	
1.878	15152	0.66	1.47616	
1.771	14286	0.70	1.47539	
1.675	13514	0.74	1.47474	
1.589	12821	0.78	1.47419	
1.512	12195	0.82	1.47371	
1.442	11628	0.86	1.47330	
1.378	11111	0.90	1.47293	
1.319	10638	0.94	1.47261	
1.265	10204	0.98	1.47233	
1.181	9524	1.05	1.47190	

TABLE I *(Continued)*

Cesium Fluoride

eV	cm^{-1}	μm	n	k
1.078	8696	1.15	1.47140	
0.9918	8000	1.25	1.47099	
0.9184	7407	1.35	1.47064	
0.8550	6897	1.45	1.47035	
0.7999	6452	1.55	1.47008	
0.7514	6061	1.65	1.46984	
0.7085	5714	1.75	1.46961	
0.6702	5405	1.85	1.46940	
0.6358	5128	1.95	1.46919	
0.6048	4878	2.05	1.46899	
0.5767	4651	2.15	1.46880	
0.5510	4444	2.25	1.46860	
0.5276	4255	2.35	1.46840	
0.5060	4082	2.45	1.46821	
0.4862	3922	2.55	1.46801	
0.4678	3774	2.65	1.46781	
0.4508	3636	2.75	1.46760	
0.4350	3509	2.85	1.46739	
0.4203	3390	2.95	1.46718	
0.4065	3279	3.05	1.46697	
0.3936	3175	3.15	1.46674	
0.3815	3077	3.25	1.46652	
0.3701	2985	3.35	1.46629	
0.3594	2899	3.45	1.46605	
0.3492	2817	3.55	1.46581	
0.3397	2740	3.65	1.46556	
0.3306	2667	3.75	1.46531	
0.3220	2597	3.85	1.46505	
0.3139	2532	3.95	1.46478	
0.3061	2469	4.05	1.46451	
0.2987	2410	4.15	1.46424	
0.2917	2353	4.25	1.46395	
0.2850	2299	4.35	1.46366	
0.2786	2247	4.45	1.46337	
0.2725	2198	4.55	1.46307	
0.2666	2151	4.65	1.46276	
0.2610	2105	4.75	1.46244	
0.2556	2062	4.85	1.46212	
0.2505	2020	4.95	1.46180	
0.2431	1961	5.10	1.46129	
0.2339	1887	5.30	1.46060	
0.2254	1818	5.50	1.45988	
0.2175	1754	5.70	1.45913	
0.2101	1695	5.90	1.45836	
0.2032	1639	6.10	1.45756	
0.1968	1587	6.3	1.45673	

(continued)

TABLE I *(Continued)*

Cesium Fluoride

eV	cm^{-1}	μm	n	k
0.1907	1538	6.5	1.45588	
0.1850	1493	6.7	1.45499	
0.1797	1449	6.9	1.45408	
0.1746	1408	7.1	1.45315	
0.1698	1370	7.3	1.45218	
0.1653	1333	7.5	1.45119	
0.1610	1299	7.7	1.45017	
0.1569	1266	7.9	1.44911	
0.1531	1235	8.1	1.44804	
0.1494	1205	8.3	1.44693	
0.1459	1176	8.5	1.44579	
0.1425	1149	8.7	1.44463	
0.1393	1124	8.9	1.44343	
0.1362	1099	9.1	1.44221	
0.1333	1075	9.3	1.44095	
0.1305	1053	9.5	1.43967	
0.1278	1031	9.7	1.43835	
0.1252	1010	9.9	1.43701	
0.1215	980.4	10.2	1.43494	
0.1170	943.4	10.6	1.43206	
0.1127	909.1	11.0	1.42907	
0.1088	877.2	11.4	1.42594	
0.1051	847.5	11.8	1.42269	
0.1016	819.7	12.2	1.41931	
0.09840	793.7	12.6	1.41580	
0.09537	769.2	13.0	1.41215	
0.09252	746.3	13.4	1.40836	
0.08984	724.6	13.8	1.40444	
0.08731	704.2	14.2	1.40037	
0.08492	684.9	14.6	1.39616	
0.08265	666.7	15.0	1.39180	
0.08051	649.4	15.4	1.38729	
0.07847	632.9	15.8	1.38263	
0.07653	617.3	16.2	1.37781	
0.07469	602.4	16.6	1.37283	
0.07293	588.2	17.0	1.36769	
0.07125	574.7	17.4	1.36239	
0.06965	561.8	17.8	1.35691	
0.06812	549.5	18.2	1.35126	
0.06666	537.6	18.6	1.34542	
0.06525	526.3	19.0	1.33941	
0.06391	515.5	19.4	1.33220	
0.06262	505.1	19.8	1.32681	
0.06048	487.8	20.5	1.31513	
0.05767	465.1	21.5	1.29734	
0.05510	444.4	22.5	1.27814	

TABLE I *(Continued)*

Cesium Fluoride

eV	cm^{-1}	μm	n	k
0.05276	425.5	23.5	1.25743	
0.05060	408.2	24.5	1.23508	
0.04862	392.2	25.5	1.21094	
0.04678	377.4	26.5	1.18483	
0.04508	363.6	27.5	1.15655	
0.04350	350.9	28.5	1.12584	
0.04203	339.0	29.5	1.09242	

Beta-Gallium Oxide (β-Ga_2O_3)

DAVID F. EDWARDS
Tracy, California

Gallium oxide, Ga_2O_3, has been shown [1] to exist in five phases; only one phase, called β-Ga_2O_3, is stable. At one time crystals of β-Ga_2O_3 doped with small amounts of Cr^{3+} ions were believed to have important applications as a MASER material [2, 3]. More recently the semiconductor industry has focused attention on the anodic oxide on GaAs made up of amorphous Ga_2O_3 and As_2O_3 [4]. β-Ga_2O_3 crystals also have interesting scientific properties. They can be either insulators or conductors, depending on the growth conditions. For either condition the crystals are layered material similar to GaSe and GaTe, also in this volume.

The crystal structure of the stable phase, β-Ga_2O_3, is monoclinic with lattice parameters of $a = 12.23$ Å, $b = 3.04$ Å, $c = 5.80$ Å, and $\alpha = 103.7°$ [5]. Geller [6] has determined that the most probable space group of β-Ga_2O_3 is C_{2h}^3 – C 2/m with four Ga_2O_3 molecules per unit cell.

The four metastable phases of Ga_2O_3 have been designated by Roy *et al.* [1] as α-, γ-, δ-, and ϵ-. The α-Ga_2O_3 has been identified to be hexagonal, analogous to α-Al_2O_3. The γ-Ga_2O_3 was originally reported by Böhm [7] to be analogous to γ-Al_2O_3 with the spinel structure (O_h^7 – Fd3m). Roy *et al.* were not able to confirm this relationship. The structure of δ-Ga_2O_3 is body centered cubic with space group T_h^7—Ia3. Large particles of this crystalline phase were found to be birefringent with an apparent index of refraction of about 1.8. The structure of ϵ-Ga_2O_3 could not be determined by Roy *et al.*, but they report its symmetry to be lower than hexagonal or tetragonal.

Single crystals of β-Ga_2O_3 have been grown by the Verneuil technique [8], the chemical transport method [9], and the vapor-phase reaction method [10]. The most extensive optical measurements on relatively large single crystals of β-Ga_2O_3 have been reported by Matsumoto *et al.* [10]. Their single-crystal platelets of β-Ga_2O_3 were grown by vapor-phase Ga/HCl/O_2/Ar reaction and were insulators [11]. The crystalline platelets consisted of layers parallel to the (100) direction. The major cleavage plane is (100), and the secondary one is (001). β-Ga_2O_3, being monoclinic and thus biaxial, has a triaxial ellipsoidal refractive-index surface. Based on their index mea-

HANDBOOK OF OPTICAL CONSTANTS OF SOLIDS III

Copyright © 1998 by Academic Press.
All rights of reproduction in any form reserved
ISBN 0-12-544423-0/$25.00.

surements Matsumoto *et al.* speculate as to the orientation of the principal dielectric axes (X , Y , Z) with respect to the crystallographic axes (*a*, *b*, *c*). They conclude that the *b*-axis is parallel to the Z-axis, and the *a*- and *c*-axes are approximately parallel to X and Y, respectively. They assume the electric polarization to be the easiest when the electric vector of the incident light is parallel to the (100) plane. They identify this condition as that for measuring the largest index. Their conclusions for the three indices are as follows: n_z for $\mathbf{E} \| \mathbf{b}$, n_y for $\mathbf{E} \| \mathbf{c}$, and n_x for $\mathbf{E} \perp \mathbf{b}$ and $\mathbf{c}$. The platelet orientations allowed only n_y and n_z measurements; no measurements of n_x were possible. The expected anisotropy between n_y and n_z appears to be small and could not be distinguished because of experimental error.

Matsumoto *et al.* [10] determined the refractive indices from the interference fringes produced by the multiple internal reflections in the thin platelets. These are called channel spectra. As noted by this writer [12], special care must be exercised in using channel spectra for the visible and near infrared because of the very large fringe order and the difficulty in its determination. For the channel-spectra technique the flatness, wedge, and platelet thickness can be the determining factors in the accuracy of the index values. For the Matsumoto *et al.* data the accuracy of the index values is limited by the approximately 5% accuracy of their platelet-thickness measurement.

The indices of refraction, n_y and n_z, as reported by Matsumoto *et al.*, are shown in Fig. 1. These data are listed in Table I as read from the figure. The solid curve in the figure is the least-squares fit of these combined data. The formulas given next, were used for the calculated average values listed in the table. For convenience, separate formulas are given for the ultraviolet and visible regions.

Ultraviolet (2775 Å $\leq \lambda \leq$ 3025 Å):

$$n_{uv} = -2.6396 + 9.7307/\lambda^4 + 4.0975 \times 10^7/\lambda^2,$$

where λ is in angstrom units.

Visible (3050 Å $\leq \lambda \leq$ 6900 Å):

$$n_{vis} = 1.3168 + 0.5179/\lambda^4 + 4.2114 \times 10^6/\lambda^2.$$

No vaccum UV determination of n and k could be found in the literature. The far-infrared reflection spectrum of sintered polycrystalline β-Ga_2O_3 showed weak reststrahlen bands, but no analysis could be done to obtain n and k [4]. A rough estimate of the dielectric constant, ϵ_0, can be made using the Clausius–Mossotti equation,

$$\frac{M}{\rho}\left(\frac{\epsilon - 1}{\epsilon + 2}\right) = \frac{4\pi}{3} N_0 \alpha,$$

where M is the molecular weight, ρ the density, N_0 Avogadro's constant, and α the total polarizability per molecule. For β-Ga_2O_3, $\alpha = 8.80$ Å^3 [13], yielding the approximate value for the dielectric constant $\epsilon_0 = 7.9$.

REFERENCES

1. R. Roy, V. G. Hill, and E. F. Osborn, *J. Am. Chem. Soc.* **74**, 719 (1952).
2. C. Kikuchi, University of Michigan, Willow Run Laboratory, private communication (1960).
3. M. Peter and A. L. Schawlow, *Bull. Am. Phys. Soc. Ser. II,* **5**, 158 (1960).
4. E. D. Palik, N. Ginsburg, R. T. Holm, and J. W. Gibson, *J. Vac. Sci. Technol.* **15**, 1488 (1978); and references therein.
5. J. A. Kohn, G. Katz, and J. D. Broder, *Am. Miner.* **42**, 398 (1975).
6. S. Geller, *J. Chem. Phys.* **33**, 676 (1960).
7. J. Böhm, *Angew. Chem.* **53**, 131 (1940).
8. A. B. Chase, *J. Am. Ceram. Soc.* **47**, 470 (1964).
9. H. Juskowiak and A. Pajaczkowska, *J. Mater. Sci.* **21**, 3430 (1986).
10. T. Matsumoto, M. Aoki, A. Kinoshita, and T. Aono, *Jpn. J. Appl. Phys.* **13**, 737 and 1578 (1974).
11. M. R. Lorenz, J. F. Woods, and R. J. Gambino, *J. Phys. Chem. Solids* **28**, 403 (1967).
12. D. F. Edwards, *in* "Handbook of Optical Constants of Solids," (E. D. Palik, ed.), p. 547. Academic Press, Orlando, Florida, 1985.
13. R. D. Shannon, M. A. Subraminian, T. H. Allik, H. Kimura, M. R. Kokta, M. H. Randels, and G. R. Rossman, *J. Appl. Phys.* **67**, 3798 (1990).

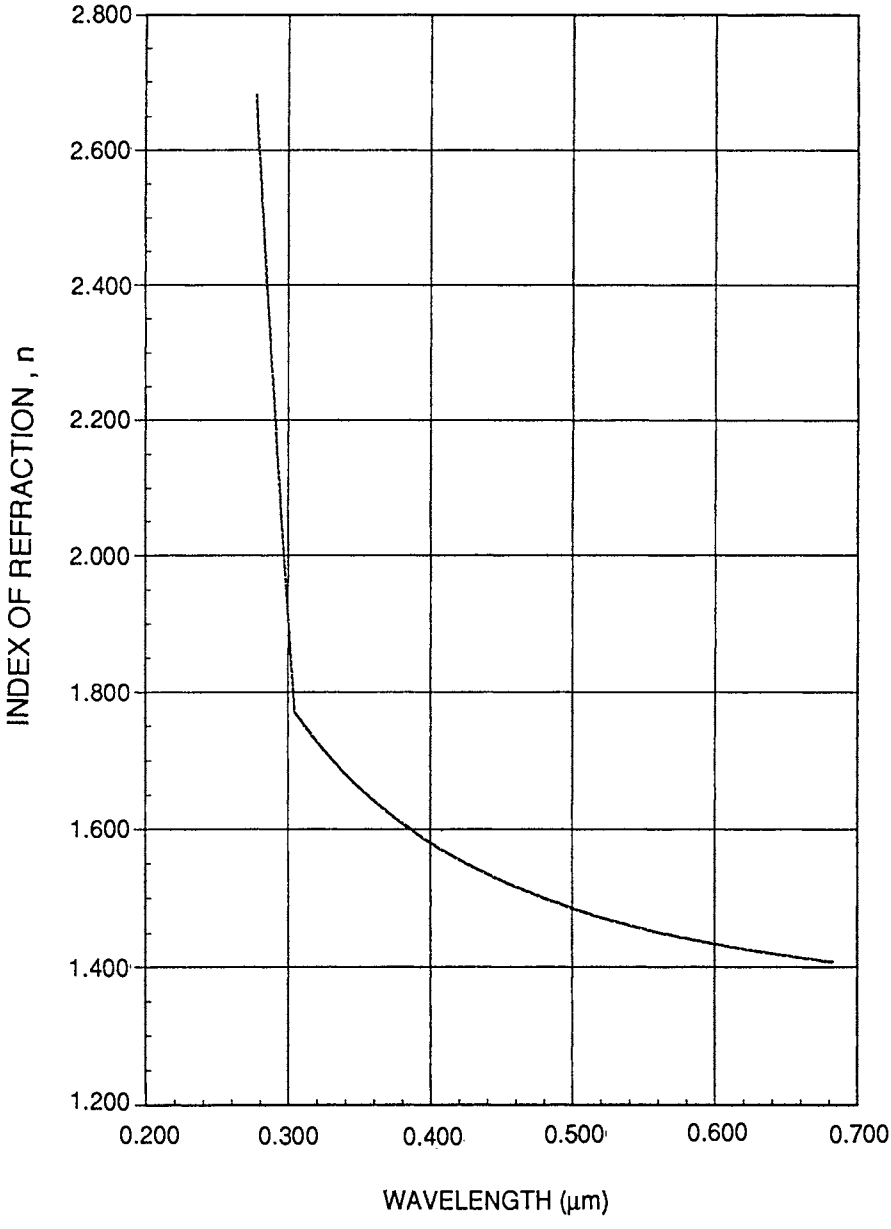

Fig. 1. Average values of index of refraction n versus wavelength in micrometers for β-Ga_2O_3.

TABLE I

Values of Index of Refraction n for β-Ga_2O_3 from Ref. [10]

eV	cm^{-1}	Å	n_{calc}	n_y	n_z
4.4757	36036	2775	2.6814		2.7750 [10]
4.4357	35714	2800	2.5868		
4.3965	35398	2825	2.4947		
4.3579	35088	2850	2.4050	2.5250 [10]	2.4000
4.3200	34783	2875	2.3177	2.0250	
4.2828	34483	2900	2.2326		
4.2462	34188	2925	2.1496		
4.2102	33898	2950	2.0688		
4.1748	33613	2975	1.9900		
4.1400	33333	3000	1.9132	1.8600	
4.1058	33058	3025	1.8382		1.9750
4.0721	32787	3050	1.7695		
4.0390	32520	3075	1.7622		
4.0065	32258	3100	1.7550		
3.9744	32000	3125	1.7480	1.6650	1.7100
3.9429	31746	3150	1.7412		
3.9118	31496	3175	1.7346		
3.8813	31250	3200	1.7281		
3.8512	31008	3225	1.7217		
3.8215	30769	3250	1.7155	1.7300	
3.7924	30534	3275	1.7094		
3.7636	30303	3300	1.7035		
3.7353	30075	3325	1.6977		
3.7075	29851	3350	1.6921		1.6250
3.6800	29630	3375	1.6865		
3.6529	29412	3400	1.6811	1.7700	
3.6263	29197	3425	1.6758		
3.6000	28986	3450	1.6706		
3.5741	28777	3475	1.6656		
3.5486	28571	3500	1.6606		
3.5234	28369	3525	1.6557		
3.4986	28169	3550	1.6510		
3.4741	27972	3575	1.6463	1.7250	
3.4500	27778	3600	1.6418		
3.4262	27586	3625	1.6373		
3.4027	27397	3650	1.6329		
3.3796	27211	3675	1.6286		
3.3568	27027	3700	1.6244		
3.3342	26846	3725	1.6203		
3.3120	26667	3750	1.6163		
3.2901	26490	3775	1.6123		
3.2684	26316	3800	1.6084		
3.2471	26144	3825	1.6046		
3.2260	25974	3850	1.6009		
3.2052	25806	3875	1.5973		
3.1846	25641	3900	1.5937		
3.1643	25478	3925	1.5902		

(continued)

TABLE I *(Continued)*

β-Ga_2O_3

eV	cm^{-1}	Å	n_{calc}	n_y	n_z
3.1443	25316	3950	1.5867		
3.1245	25157	3975	1.5833		
3.1050	25000	4000	1.5800		
3.0857	24845	4025	1.5768		
3.0667	24691	4050	1.5736		
3.0479	24540	4075	1.5704		
3.0293	24390	4100	1.5673		1.6000
3.0109	24242	4125	1.5643		
2.9928	24096	4150	1.5613		
2.9749	23952	4175	1.5584		
2.9571	23810	4200	1.5555	1.5300	
2.9396	23669	4225	1.5527		
2.9224	23529	4250	1.5500		
2.9053	23392	4275	1.5472		
2.8884	23256	4300	1.5446		
2.8717	23121	4325	1.5419		
2.8552	22989	4350	1.5394		
2.8389	22857	4375	1.5368		
2.8227	22727	4400	1.5343		
2.8068	22599	4425	1.5319		
2.7910	22472	4450	1.5295		
2.7754	22346	4475	1.5271		
2.7600	22222	4500	1.5248		
2.7448	22099	4525	1.5225		
2.7297	21978	4550	1.5202		
2.7148	21858	4575	1.5180		
2.7000	21739	4600	1.5158		
2.6854	21622	4625	1.5137		
2.6710	21505	4650	1.5116	1.4750	
2.6567	21390	4675	1.5095		
2.6426	21277	4700	1.5074		
2.6286	21164	4725	1.5054		
2.6147	21053	4750	1.5035		
2.6010	20942	4775	1.5015		1.5250
2.5875	20833	4800	1.4996		
2.5741	20725	4825	1.4977	1.5700	
2.5608	20619	4850	1.4958		
2.5477	20513	4875	1.4940		
2.5347	20408	4900	1.4922		
2.5218	20305	4925	1.4904		
2.5091	20202	4950	1.4887		
2.4965	20101	4975	1.4870		
2.4840	20000	5000	1.4853		
2.4716	19900	5025	1.4836		
2.4594	19802	5050	1.4819		
2.4473	19704	5075	1.4803		
2.4353	19608	5100	1.4787		

TABLE I *(Continued)*

β-Ga_2O_3

eV	cm^{-1}	Å	n_{calc}	n_y	n_z
2.4234	19512	5125	1.4771		
2.4117	19417	5150	1.4756		
2.4000	19324	5175	1.4741		
2.3885	19231	5200	1.4725		
2.3770	19139	5225	1.4711		
2.3657	19048	5250	1.4696		
2.3545	18957	5275	1.4681		1.5700
2.3434	18868	5300	1.4667		
2.3324	18779	5325	1.4653		
2.3215	18692	5350	1.4639		
2.3107	18605	5375	1.4626		
2.3000	18519	5400	1.4612		
2.2894	18433	5425	1.4599	1.4900	
2.2789	18349	5450	1.4586		
2.2685	18265	5475	1.4573		
2.2582	18182	5500	1.4560		
2.2480	18100	5525	1.4548		
2.2378	18018	5550	1.4535		1.4500
2.2278	17937	5575	1.4523		
2.2179	17857	5600	1.4511		
2.2080	17778	5625	1.4499	1.4750	
2.1982	17699	5650	1.4487		
2.1885	17621	5675	1.4476		
2.1789	17544	5700	1.4464		
2.1694	17467	5725	1.4453		
2.1600	17391	5750	1.4442		
2.1506	17316	5775	1.4431		
2.1414	17241	5800	1.4420		
2.1322	17167	5825	1.4409		
2.1231	17094	5850	1.4399		
2.1140	17021	5875	1.4388		
2.1051	16949	5900	1.4378		
2.0962	16878	5925	1.4368		
2.0874	16807	5950	1.4358		
2.0787	16736	5975	1.4348		
2.0700	16667	6000	1.4338		
2.0614	16598	6025	1.4328		
2.0529	16529	6050	1.4319	1.4250	
2.0444	16461	6075	1.4309		
2.0361	16393	6100	1.4300		
2.0278	16327	6125	1.4291		
2.0195	16260	6150	1.4281		
2.0113	16194	6175	1.4272		
2.0032	16129	6200	1.4264		
1.9952	16064	6225	1.4255		
1.9872	16000	6250	1.4246		
1.9793	15936	6275	1.4238		

(continued)

TABLE I *(Continued)*

β-Ga_2O_3

eV	cm^{-1}	Å	n_{calc}	n_y	n_z
1.9714	15873	6300	1.4229		
1.9636	15810	6325	1.4221	1.3050	
1.9559	15748	6350	1.4212		
1.9482	15686	6375	1.4204		1.4300
1.9406	15625	6400	1.4196		
1.9331	15564	6425	1.4188		
1.9256	15504	6450	1.4180		
1.9181	15444	6475	1.4172		
1.9108	15385	6500	1.4165		
1.9034	15326	6525	1.4157		
1.8962	15267	6550	1.4150		
1.8890	15209	6575	1.4142		
1.8818	15152	6600	1.4135		
1.8747	15094	6625	1.4128		1.3650
1.8677	15038	6650	1.4120		
1.8607	14981	6675	1.4113		
1.8537	14925	6700	1.4106	1.3600	
1.8468	14870	6725	1.4099		
1.8400	14815	6750	1.4092		
1.8332	14760	6775	1.4086		
1.8265	14706	6800	1.4079		
1.8198	14652	6825	1.4072		

Lead Fluoride (PbF_2)

MÁRCIA A. F. DESTRO and ALVARO J. DAMIÃO
Instituto de Estudos Avançados—CTA
São José dos Campos, SP, Brasil

Lead fluoride is a transparent insulator over a wide range of the optical spectrum from the ultraviolet to the middle infrared. It has a medium refractive index in the visible (1.77) and a low index in the infrared (1.63), when compared to other transparent materials. It is an electronic insulator with a large energy band gap, $E_g = 5.84$ eV at 298 K [1]. The melting point is 1095 K [2].

Lead fluoride can be found in two different crystalline structures, the cubic fluorite structure (space group Fm3m—O_h^5, β-phase) or in an orthorhombic structure (space group Pmnb—V_{2h}^{16}, α-phase). Sample preparation is very important when studying PbF_2, as even the grinding process can affect the crystalline structure and its transition temperature. For a strain-free material the initial temperature of α- to β-PbF_2 transformation is 328° C, and the heat necessary to this transformation is 1630 J/mol [3]. The transition temperature around 600 K, is controversial, probably because of kinetic effects [4]. Both phases exhibit relatively high ionic conductivity, and the cubic phase becomes a "superionic" conductor at high temperature, where its conductivity attains at $\geq$800 K what seems to be one of the highest values for any known solid ionic conductor [5, 6].

Three main approaches appear in the literature for studying optical properties of PbF_2:

Crystal [7–9]
Superionic conductor at high temperatures [1, 10, 11]
Thin films [12, 13]

With these approaches, part of the data was obtained using crystals and part using thin films, depending mainly on the technique used and on the specific application.

Eijkelenkamp [14] used the diffuse-reflection technique to ascertain the positions of optical transitions of finely grained powders for α- and β-PbF_2,

HANDBOOK OF OPTICAL CONSTANTS OF SOLIDS III

Copyright © 1998 by Academic Press.
All rights of reproduction in any form reserved
ISBN 0-12-544423-0/$25.00.

between 3 and 7 eV, and he showed some results of heat treatment on α-PbF_2 powder.

The index of refraction of β-PbF_2 at $\lambda = 589.3$ nm increases linearly with pressure, as well as the strain, with a slope of 7.76×10^{-4}/kbar up to 4.8 kbar, when a irreversible phase transformation to α-PbF_2 occurs [15].

When the crystal is heated at $T_c \cong 700$ K, well below the melting temperature 1095 K, an ionic disorder occurs. About 40% of the fluorine ions leave their normal sites in the anion sublattice, and the crystal becomes a superionic conductor. This disorder manifests itself in the Raman scattering and in the temperature dependence of the lattice constant [10]. Hayes *et al.* [11] carried out a Raman study of disorder in PbF_2 at high temperatures, and Kosacki and Zalibowski [10] made measurements of temperature and frequency dependence of the dielectric constant and dielectric loss function. In their article a figure shows the temperature dependence of dielectric constant ϵ' for PbF_2 crystals at the frequencies of 1 kHz, 10 kHz, 100 kHz, and 0.5 MHz.

Moss and Peacock [16] measured the transmission of cut and polished 6.7-mm-thick specimens using a Leiss double monochromator fitted with NaCl, KBr, or CsI prisms. A diagram in their article shows the results, corrected for surface losses.

Findley *et al.* [1] obtained, at near-normal incidence, the absolute reflectance spectra of polished β-PbF_2 crystal 3 mm thick from 4 to 10 eV, in the vicinity of the fundamental absorption edge, at temperatures between 298 and 800 K. There are three figures in their paper showing the reflectance and the imaginary part ϵ_2 of the dielectric response at three temperatures, 298, 613, and 773 K.

The optical data are presented in Table I, for crystals and thin films. They were obtained by a variety of optical techniques. Special attention must be paid to the fact that the sample preparation process can change the crystalline structure and its transition temperature; then the data presented on Table I are not exclusive for α- or β-phase, but most probably a mixture of the two phases.

Malitson and Dodge [8] and Jones [2] measured the refractive index of lead-fluoride prisms by means of the minimum-deviation method. Malitson and Dodge [8] used a synthetic prism at 20° C from 0.28 to 11.9 μm. Jones [2] used a prism with an angle of approximately 62.5° and faces approximately 3×3 cm^2, the room temperature varying between 17.5 and 19.5° C, and showed the transmission for a 1-cm-thick crystal, from UV to near IR regions (200 to 1000 nm) for a clear specimen, after 6-hour exposure to light from a Hg arc and to neutron bombardment.

Dodge [17], using the Malitson and Dodge data [8], obtained the parameters of a Sellmeier dispersion equation. The fitting range of λ is 0.3 to 11.9 μm:

$$n^2 = 1 + \sum_i \frac{A_i \lambda^2}{\lambda^2 - \lambda_i^2}. \quad (1)$$

$\lambda_1 = 0.00034911$ $\lambda_2 = 0.17144455$ $\lambda_3 = 0.28125513$ $\lambda_4 = 796.67469$
$A_1 = 0.66959342$ $A_2 = 1.3086319$ $A_3 = 0.01670641$ $A_4 = 2007.8865$

These calculated data are listed in Table I.

Aurora *et al.* [5] measured the temperature variation of the coefficients of linear thermal expansion and optical length for PbF_2 crystals, using an interferometer with a He–Ne laser over the temperature range of 300–1300 K. They calculated the temperature variation of the molecular polarizability, energy band gap, refractive-index variation with density, and the strain-polarizability parameter. This information was obtained to verify the applicability of this material for laser windows and other optical components.

Beaumont *et al.* [7] presented the optical constants of PbF_2 between its fundamental absorption edge at 5.7 eV and 130 eV, obtained from reflectivity and transmission measurements. For the reflectivity experiments (8–60 eV), they used polished single crystals with cubic structure and evaporated films that were thick enough to make negligible the interference effects due to reflections from the rear surface. The reflectivity was Kramers–Kronig analyzed. Transmission measurements (16–130 eV) were obtained from evaporated thin films on a zapon substrate. The reflectivity (above 8 eV) and transmission data presented were obtained with synchrotron radiation from NINA, the electron synchrotron at Daresbury laboratory. Beaumont *et al.* showed figures for the reflection spectrum at 77 K (2–30 eV), the real and imaginary parts of the dielectric constant (2–30 eV), the absorption coefficient at 77 K (2–30 eV) and at 290 K (30–130 eV) measured on evaporated thin films, and a single-crystal XPS spectrum (0–32 eV). It was found that absorption coefficients obtained from the K-K analysis of the reflectivity data agreed with those obtained from transmission measurements in the photon energy region where the spectra overlapped. Selected data of Beaumont *et al.* [7] are listed in Table I.

Axe *et al.* [9] made infrared reflectivity measurements between 10 and 150 μm at room temperature on samples of cubic (probably single) crystal 2 inches in length cut and polished using standard metallographic procedures. The reflectivity was measured by a point-by-point comparison with an aluminized surface in a Perkin-Elmer model 301 spectrometer. The measurements were corrected for the reflectivity of the aluminum but not for the off-axis configuration (the angle of incidence was 9°). The reflectivity was fitted with an oscillator model and by Kramers–Kronig analysis.The n and k values listed in Table I were obtained from our reading of a graph of Axe *et al.* [9]. The low-frequency dielectric constants were determined by measuring the capacitance of sample disks of material several millimeters thick in a conventional Schering bridge circuit.

Harrington *et al.* [18] used calorimetry to measure the absorption of low-loss thin dielectric films to be used as antireflection and enhanced-reflection coatings at the common IR laser wavelengths. The absorption coefficients were measured in film–bar combination (film with $\lambda/2$ at 5.3 μm thick, at one end of the KCl bar) using a conventional vacuum calorimeter and a CO_2 laser delivering approximately 5 W of cw power. The fractional power αL absorbed by the films was obtained directly from the temperature–time curves using a three-slope calculation. Using this fractional power, the extinction coefficient k, defined by $N = n - ik$, where N is the complex index of refraction, is computed for the film. Finally, the absorption coefficient α is obtained from $k = \alpha\lambda/4\pi$.

Pulker [12] reviewed the basic optical properties of the main dielectric materials in the form of single thin films to help the design of optical thin-film multilayers. Besides optical data, information is also presented on their preparation, structure, and mechanical properties. When the starting material was PbF_2, using a resistive evaporation (boat) at a temperature of 850° C, the information obtained was as follows: a β-PbF_2 film structure, with a packing density of 0.91, when substrate temperature (T_s) was 30° C, having a good transmittance ($\alpha < 10^{-3}$ cm^{-1}) from 0.25 to 17 μm and refractive index (T_s = 30° C) of 1.98 for 0.3 μm and 1.75 for 0.55 μm. The film was soft, and it had a compressive stress for thicknesses smaller than 0.1 μm, and a tensile stress for thicknesses larger than 0.1 μm.

Bennett *et al.* [19] critically investigated the technique for determining the optical constants of a metal by overcoating it with a dielectric film of known optical constants. They measured the thickness, transmittances, reflectances, and wavelengths of the interference maxima and minima for samples of lead fluoride on quartz and lead fluoride on aluminum. There were appreciable changes with time in the optical constants of lead fluoride films deposited on a substrate at room temperature. However, when the substrate was heated to 80° C, the change in k with time was from 0.008 to 0.007. Evaporation rates of about 100 Å/min were used with a pressure of about 10^{-5} torr and a coating distance of 46 cm. By mounting the substrates on a turntable rotating at 65 rpm, films 9000 Å in thickness could be formed. The thickness of the lead-fluoride film was determined by a multiple-beam interferometric technique using fringes of equal chromatic order. All absolute reflectance and transmittance measurements were made using the NOTS absolute reflectometer. The refractive index n was determined from the measured wavelengths of the interference maxima and minima in transmission produced by the lead fluoride film on fused quartz. Data from Bennett *et al.* [19] are listed in Table I.

Destro *et al.* [13, 20, 21] studied the optical and crystalline properties of PbF_2 thin films as a function of the substrate temperature during deposition, keeping other evaporation conditions as constant as possible. The films were evaporated on a BK7 Schott glass substrate. The residual

pressure of the chamber was 10^{-5} torr, and the crucible was made of tungsten and coated with aluminum oxide (Al_2O_3). A typical current of 100 A and a voltage of 5 V were employed. A Varian bell-jar evaporation system was used, and the substrate was heated by IR light. The thickness, $\approx$800 nm, was measured using a quartz monitor. The deposition rate varied from 0.5 to 0.75 nm/s. After the film deposition, the vacuum chamber was opened in the presence of N_2, when the sample reached room temperature. Some of the samples were obtained while the substrate holder was rotating, but the majority were obtained with the substrate holder standing still. The optical-characterization techniques used were channel spectra, guided modes, ellipsometry [13, 20], and envelope [21]. A Perkin-Elmer Lambda 9 spectrophotometer coupled to a computer was used for the spectral measurements. Using the same points of the maxima and minima, it was possible to obtain n, k, and the thickness of these thin films with the envelope technique. A Gaertner L117 ellipsometer was used to obtain the ellipsometric results; the data were reduced by the program described by McCrakin [22]. The coupling of the light to the film through a prism was used to obtain the guided-modes results. The He–Ne and argon laser beams were combined to obtain the measurements at five different wavelengths. A Rigaku's Bragg–Brentano x-ray diffractometer was used to verify the occurrence of changes in the crystalline phase and the existence of a preferential crystalline direction as a function of substrate temperature. A figure in Destro *et al.* [13] shows the change in the preferential orientation from β-PbF_2 $\langle 111 \rangle$ to β-PbF_2 $\langle 200 \rangle$, when the temperature increased. The parameters of Cauchy dispersion equations for thin films around 760 nm thick, measured with guided-modes technique [20], using λ in the range 400 to 650 nm, are

$$\begin{gathered} n = A + B\lambda^{-2} + C\lambda^{-4} \\ A = 1.726 \qquad B = 1.157 \times 10^4 \qquad C = 3.774 \times 10^8, \end{gathered} \tag{2}$$

and measured with the envelope technique [21], using λ in the range 400 to 800 nm, are

$$A = 1.7 \qquad B = 1.9 \times 10^4 \qquad C = -4.0 \times 10^8.$$

Data of Destro and co-workers [13, 21] are listed in Table I.

Baumeister *et al.* [23] measured the index of refraction of a single-layer PbF_2 film, $\lambda/4$ optically thick, at 16 μm. They obtained identical transmittance for thin films of the ZnSe and the PbF_2 on germanium substrates and from knowledge of the substrate index n_s, of the air n_0, and of the coating (ZnSe) n_2. They found the index of the second coating (PbF_2) using the relation $n_1 n_2 = n_0 n_s$. The thin films were made in a Balzer BA-500 chamber using a thermal heated platinum boat. The evaporation run started at pressures in the range of $1\text{–}3 \times 10^{-6}$ torr, the optimum evaporation rate was

found to be about 0.1 μm/min, and the chamber temperature was 100–150° C. Data of Baumeister *et al.* [23] are listed in Table I.

Bezuidenhout *et al.* [24] report on the optical, structural, and chemical properties of vacuum evaporated thin films of PbF_2 on Schott K-50 glass, quartz glass, silicon, germanium and sapphire discs as substrates, with the growth rate between 1 and 2 nm/s. The pressure during evaporation was below 2×10^{-6} torr, and the substrate temperature was 150° C. The layer thickness was obtained by measurements of fringe dislocation over a step (interferometric method), and the optical properties were calculated on the turning points of reflectance and transmittance spectra, which were measured with a Beckman UV 5270 from 0.7 to 2.0 μm and a Perkin-Elmer 983 from 2.0 to 12 μm. Data of Bezuidenhout *et al.* [24] are listed in Table I.

Sankur [25] compared thin-film optical data, refractive index, and extinction coefficient, obtained from reflectance and transmittance spectral analysis. The films were prepared by e-beam, pulsed, and cw laser deposition. For cw evaporation Sankur found that the refractive index, for 632.8 nm, is independent of the evaporation rate between 0.1 and 100 Å/s. The source material was a mixture of α- and β-PbF_2 in pellet form. The films were grown on glass and low-conductivity Si substrate at room temperature at pressures of 2×10^{-7} torr. Data of Sankur [25] are listed in Table I.

Many of the n and k data in Table I are plotted in Fig. 1.

REFERENCES

1. P. R. Findley, Z. Wu, and W. C. Walker, *Phys. Rev. B* **28**, 4761 (1983).
2. D. A. Jones, *Proc. Phys. Soc. (London) B* **68**, 165 (1955).
3. J. P. Auffredic, R. Couple and D. Louër, *J. Mater. Sci.* **20**, 2119 (1985).
4. O. K. Nikol'skaya and L. N. Dem'yantes, *Inorg. Mater.* **30**, 1097 (1994).
5. T. S. Aurora, S. M. Day, and D. O. Pederson, *J. Appl. Phys.* **76**, 2122 (1994).
6. S. Palchoudhuri and G. K. Bichile, *Solid State Commun.* **69**, 271 (1989).
7. J. H. Beaumont, A. J. Bourdillon, and J. Bordas, *J. Phys. C* **10**, 761 (1977).
8. I. H. Malitson and M. J. Dodge, *J. Opt. Soc. Am.* **59**, 500A (1969).
9. J. D. Axe, J. W. Gaglianello, and J. E. Scardefield, *Phys. Rev.* **139**, A1211 (1965).
10. I. Kosacki and K. Zalibowski, *Phys. Status Solidi A* **108**, 765 (1988).
11. W. Hayes, A. J. Rushworth, J. F. Ryan, R. J. Elliot, and W. G. Kleppmann, *J. Phys. C* **10**, L111 (1977).
12. H. K. Pulker, *Appl. Opt.* **18**, 1969 (1979).
13. M. A. F. Destro, R. A. Stempniak, and A. J. Damião, *Appl. Opt.* **32**, 7106 (1993).
14. A. J. H. Eijkelenkamp, *Phys. Status Solidi B* **76**, 153 (1976).
15. E. D. D. Schmidt and K. Vedam, *J. Phys. Chem. Solids* **27**, 1563 (1966).
16. T. S. Moss and A. G. Peacock, *Infrared Phys.* **1**, 104 (1961).
17. M. J. Dodge, *in* "CRC Handbook of Laser Science and Technology" (M. J. Weber, ed.), Vol 4, Optical Materials, Part 2: Properties, CRC Press, Boca Raton, Florida, 1986.
18. J. A. Harrington, M. Braunstein, and E Rudisill, *Appl. Opt.* **16**, 2843 (1977).
19. J. M. Bennett, E. J. Ashley, and H. E. Bennett, *Appl. Opt.* **4**, 961 (1965).
20. M. A. F. Destro, Propriedades Ópticas e Cristalinas de Filmes Finos de Fluoreto de Chumbo. M. S. Thesis, Instituto Tecnológico de Aeronáutica—CTA, São José dos Campos—SP, Brazil, 1991 (in Portuguese).

21. M. A. F. Destro and A. J. Damião, Techical Report, Instituto de Estudos Avaçados—CTA, IEAv/RP-002/95, February 1995 (in Portuguese).
22. F. L. McCrakin, "A FORTRAN program for analysis of ellipsometer measurements," U.S. Natl. Bur. Stand. Tech. Note 479, Washington, D.C., 1969.
23. P. Baumeister, J. Pritts, D. Lees, and D. F. Edwards, *Appl. Opt.* **18**, 3127 (1979).
24. D. F. Bezuidenhout, B. Theron, and R. Pretorius, *S. Afr. J. Phys.* **10**, 23 (1987).
25. H. Sankur, *Appl. Opt.* **25**, 1962 (1986).

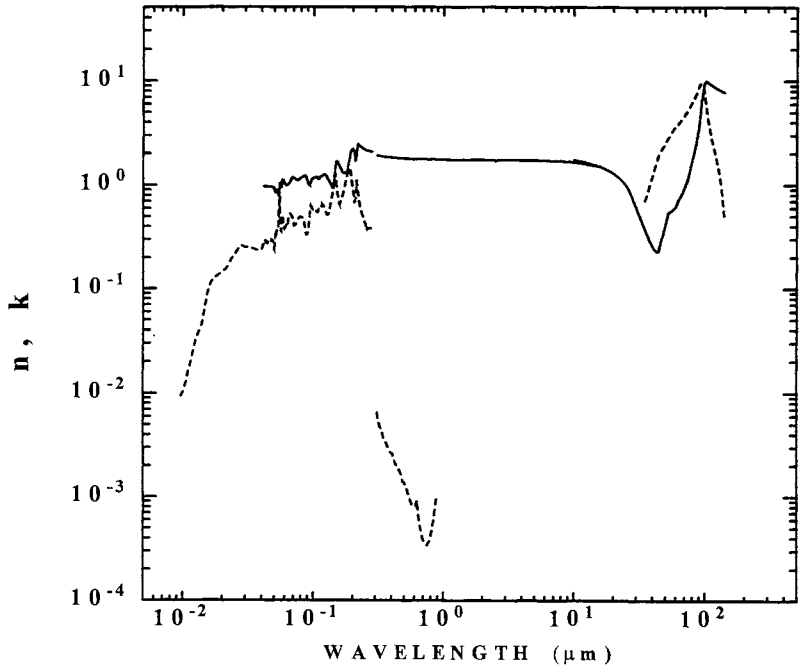

Fig. 1. Log–log plot of n (———) and k (-------) versus wavelength in micrometers for lead fluoride.

TABLE I

Values of *n* and *k* for Lead Fluoride Obtained from Various References[a, b, c]

eV	cm^{-1}	μm	n	k
130	1048512	0.0095373		9.11E-3 [7]
128	1032381	0.0096863		9.40E-3
126	1016250	0.0098401		9.79E-3
124	1000119	0.0099988		1.01E-2
122	983988	0.010163		1.06E-2
120	967857	0.010332		1.15E-2
118	951726	0.010507		1.24E-2
116	935595	0.010688		1.32E-2
114	919464	0.010876		1.47E-2
112	903333	0.011070		1.63E-2
110	887202	0.011271		1.79E-2
108	871071	0.011480		1.96E-2
106	854940	0.011697		2.19E-2
104	838809	0.011922		2.42E-2
102	822679	0.012155		2.71E-2
100	806548	0.012398		3.01E-2
98	790417	0.012652		3.32E-2
96	774286	0.012915		3.54E-2
94	758155	0.013190		3.78E-2
92	742024	0.013477		4.04E-2
90	725893	0.013776		4.27E-2
88	709762	0.014089		4.76E-2
86	693631	0.014417		5.74E-2
84	677500	0.014760		6.58E-2
82	661369	0.015120		7.82E-2
80	645238	0.015498		9.00E-2
78	629107	0.015895		1.06E-1
76	612976	0.016314		1.14E-1
74	596845	0.016755		1.19E-1
72	580714	0.017220		1.25E-1
70	564583	0.017712		1.30E-1
68	548452	0.018233		1.32E-1
66	532321	0.018786		1.37E-1
64	516190	0.019373		1.40E-1
62	500059	0.019998		1.46E-1
60	483929	0.020664		1.52E-1
58	467798	0.021377		1.54E-1
56	451767	0.022140		1.67E-1 [7]
54	435536	0.022960		1.84E-1
52	419405	0.023843		2.01E-1
50	403274	0.024797		2.15E-1
48	387143	0.025830		2.25E-1
46	371012	0.026953		2.57E-1

[a] Measured on thin films.
[b] Not at room temperature.
[c] References are indicated in brackets.

TABLE I *(Continued)*

PbF_2

eV	cm^{-1}	μm	n	k
44	354881	0.028178		2.61E-1
42	338750	0.029520		2.47E-1
40	322619	0.030996		2.54E-1
38	306488	0.032628		2.47E-1
36	290357	0.034440		2.45E-1
34	274226	0.036466		2.32E-1
32	258095	0.038745		2.37E-1
30	241964	0.041328		2.30E-1
30.0	241964	0.041328	0.963 [7][b]	2.95E-1 [7][b]
29.0	233899	0.042753	0.963	2.95E-1
28	225833	0.044280		2.47E-1 [7]
28.0	225833	0.044280	0.963	2.95E-1 [7][b]
27.0	217768	0.045920	0.958	2.97E-1
26.5	213735	0.046787	0.958	2.97E-1
26	209702	0.047687		2.71E-1 [7]
26.0	209702	0.047687	0.958	2.97E-1 [7][b]
25.5	205670	0.048622	0.953	2.98E-1
25.0	201637	0.049594	0.942	2.81E-1
24.8	200024	0.049994	0.926	2.42E-1
24.6	198411	0.050400	0.873	2.51E-1
24.4	196798	0.050814	0.823	2.97E-1
24.2	195184	0.051234	0.848	3.59E-1
24	193571	0.051660		2.94E-1 [7]
24.0	193571	0.051660	0.872	3.61E-1 [7][b]
23.8	191958	0.052095	0.845	3.66E-1
23.6	190345	0.052536	0.871	4.24E-1
23.4	188732	0.052985	0.888	3.99E-1
23.2	187119	0.053442	0.851	3.93E-1
23.0	185506	0.053907	0.746	4.55E-1
22.8	183893	0.054379	0.780	6.40E-1
22.6	182280	0.054861	0.956	7.84E-1
22.4	180667	0.055351	1.17	4.25E-1
22.2	179054	0.055849	1.05 [7][b]	3.45E-1 [7][b]
22.0	177440	0.056357	0.963	3.58E-1
21.8	175827	0.056874	0.880	4.54E-1
21.6	174214	0.057401	1.03	5.97E-1
21.4	172601	0.057937	1.16	5.10E-1
21.2	170988	0.058484	1.12	4.23E-1
21.0	169375	0.059041	1.07	3.87E-1
20.8	167762	0.059608	1.05	3.79E-1
20.6	166149	0.060187	1.02	3.81E-1
20.4	164536	0.060777	0.993	3.97E-1
20.2	162923	0.061379	0.990	4.13E-1
20.0	161309	0.061993	1.00	4.39E-1
19.8	159696	0.062619	1.00	4.14E-1
19.6	158083	0.063258	0.988	4.09E-1

(continued)

TABLE I *(Continued)*

PbF_2

eV	cm^{-1}	μm	n	k
19.4	156470	0.063910	1.01	4.84E-1
19.2	154857	0.064576	1.02	5.04E-1
19.0	153244	0.065255	1.03	5.29E-1
18.5	149211	0.067019	1.12	5.33E-1
18.0	145179	0.068881	1.18	4.95E-1
17.5	141146	0.070849	1.16	4.07E-1
17.0	137113	0.072932	1.11	4.11E-1
16.5	133080	0.075143	1.10	4.53E-1
16.0	129048	0.077491	1.12	4.89E-1
15.5	125015	0.079990	1.16	4.99E-1
15.0	120982	0.082657	1.19	4.84E-1
14.8	119369	0.083774	1.20	4.65E-1
14.6	117756	0.084921	1.23	4.18E-1
14.4	116143	0.086101	1.22	3.67E-1
14.2	114530	0.087313	1.20	3.33E-1
14.0	112917	0.088561	1.14	3.23E-1
13.8	111304	0.089844	1.09	3.30E-1
13.6	109690	0.091166	1.02	3.81E-1
13.4	108077	0.092526	0.969	4.58E-1
13.2	106464	0.093928	0.982	5.34E-1
13.0	104851	0.095373	1.05	6.28E-1
12.8	103238	0.096863	1.14	6.12E-1
12.6	101625	0.098401	1.15	5.69E-1
12.4	100012	0.099988	1.17	5.52E-1
12.2	98399	0.10163	1.17 [7][b]	5.55E-1 [7][b]
12.0	96786	0.10332	1.18	5.62E-1
11.8	95173	0.10507	1.21	5.63E-1
11.6	93559	0.10688	1.19	5.35E-1
11.4	91946	0.10876	1.13	5.37E-1
11.2	90333	0.11070	1.12	6.21E-1
11.0	88720	0.11271	1.23	6.48E-1
10.8	87107	0.11480	1.20	5.90E-1
10.6	85494	0.11697	1.22	6.53E-1
10.4	83881	0.11922	1.26	6.26E-1
10.2	82268	0.12155	1.27	5.94E-1
10.0	80655	0.12398	1.26	5.52E-1
9.8	79042	0.12651	1.20	5.09E-1
9.6	77429	0.12915	1.13	5.05E-1
9.4	75815	0.13190	1.10	5.44E-1
9.2	74202	0.13477	1.04	6.34E-1
9.0	72589	0.13776	0.983	7.52E-1
8.8	70976	0.14089	0.894	8.94E-1
8.7	70170	0.14251	0.939	1.06E0
8.6	69363	0.14417	1.06	1.21E0
8.5	68556	0.14586	1.26	1.26E0
8.4	67750	0.14760	1.46	1.32E0

TABLE I *(Continued)*

PbF_2

eV	cm^{-1}	μm	n	k
8.3	66943	0.14938	1.62	1.10E0
8.2	66137	0.15120	1.72	8.71E-1
8.1	65330	0.15307	1.66	8.12E-1
8.0	64524	0.15498	1.60	7.47E-1
7.8	62911	0.15895	1.52	6.52E-1
7.6	61298	0.16314	1.39	7.05E-1
7.4	59684	0.16755	1.31	7.97E-1
7.2	58071	0.17220	1.29	9.30E-1
7.0	56458	0.17712	1.27	1.10E0
6.8	54845	0.18233	1.34	1.26E0
6.7	54039	0.18505	1.51	1.38E0
6.6	53232	0.18786	1.66	1.44E0
6.5	52426	0.19075	1.86	1.50E0
6.4	51619	0.19373	2.08	1.24E0
6.3	50812	0.19680	2.2	1.02E0
6.2	50006	0.19998	2.19	9.01E-1
6.1	49199	0.20325	2.15 [7][b]	7.90E-1 [7][b]
6.0	48393	0.20664	2.15	6.51E-1
5.9	47586	0.21014	1.71	5.83E-1
5.8	46779	0.21377	1.66	1.08E0
5.7	45973	0.21752	2.50	8.78E-1
5.6	45167	0.22140	2.44	7.75E-1
5.4	43554	0.22960	2.33	5.99E-1
5.2	41940	0.23843	2.24	4.89E-1
5.0	40327	0.24797	2.17	4.41E-1
4.8	38714	0.25830	2.13	3.73E-1
4.6	37101	0.26953	2.10	3.96E-1
4.4	35488	0.28178	2.08	3.79E-1
4.2	33875	0.29520	2.06	3.58E-1
4.0	32262	0.30996	2.05	3.40E-1
4.133	33333	0.30	1.9366 [17]	
4.015	32383	0.3088	1.915 [19][a]	6.5E-3 [19][a]
3.889	31368	0.3188	1.887	4.6E-3
3.714	29958	0.3338	1.882	4.8E-3
3.581	28885	0.3462	1.854	3.7E-3
3.542	28571	0.35	1.8542 [17]	
3.401	27435	0.3645	1.849 [19][a]	3.5E-3
3.254	26247	0.3810	1.826 [19][a]	2.6E-3
3.100	25000	0.40	1.8180 [17]	
3.065	24722	0.4045	1.824 [19][a]	2.6E-3
3.064	24712	0.40466	1.8155 [2][b]	
		0.412	1.7922 [21][a]	4.6E-4 [21][a]
2.959	23866	0.419	1.793 [13][a]	
2.906	23441	0.4266	1.804 [19][a]	1.8E-3 [19][a]
2.856	23039	0.43404	1.8023 [2][b]	
		0.444	1.7800 [21][a]	2.7E-4 [21][a]

(continued)

TABLE I *(Continued)*

PbF_2

eV	cm^{-1}	μm	n	k
2.773	22364	0.44715	1.7974	
2.755	22222	0.45	1.7964 [17]	
2.749	22173	0.451	1.781 [13][a]	
2.716	21906	0.4565	1.801 [19][a]	2.1E-3 [19][a]
2.650	21376	0.46781	1.7907 [2][b]	
2.602	20986	0.4765	1.7841 [13][a]	
		0.479	1.7689 [21][a]	2.2E-4 [21][a]
2.583	20834	0.47999	1.7872 [2][b]	
2.550	20571	0.48613	1.7856	
2.543	20509	0.4876	1.787 [19][a]	1.4E-3 [19][a]
2.541	20492	0.488	1.7809 [13][a]	
2.535	20450	0.489	1.771 [13][a]	
2.519	20317	0.49219	1.7841 [2][b]	
2.497	20141	0.4965	1.7789 [13][a]	
2.480	20000	0.50	1.7822 [17]	
2.438	19663	0.50858	1.7803 [2][b]	
2.410	19436	0.5145	1.7749 [13][a]	
		0.525	1.7571 [21][a]	5.7E-5 [21][a]
2.349	18950	0.5277	1.785 [19][a]	1.4E-3 [19][a]
2.317	18692	0.535	1.761 [13][a]	
2.270	18313	0.54607	1.7729 [2][b]	
2.254	18182	0.55	1.7722 [17]	
2.171	17510	0.5711	1.771 [19][a]	6.0E-4
		0.580	1.7462 [21][a]	4.1E-5 [21][a]
2.110	17019	0.58756	1.7665 [2][b]	
2.105	16978	0.58900	1.7663	
2.103	16961	0.58959	1.7663	
2.098	16920	0.591	1.751 [13][a]	
2.066	16667	0.60	1.7649 [17]	
1.981	15977	0.6259	1.764 [19][a]	9.0E-4 [19][a]
1.959	15803	0.6328	1.7570 [13][a]	~0 [13][a]
1.959	15803	0.6328	1.76 [25][a]	
1.926	15532	0.64385	1.7599 [2][b]	
1.907	15385	0.65	1.7593 [17]	
		0.651	1.7357 [21][a]	~0 [21][a]
1.889	15237	0.65628	1.7587 [2][b]	
1.873	15106	0.662	1.743 [13][a]	
1.857	14974	0.66781	1.7577 [2][b]	
1.795	14477	0.69075	1.7558	
1.789	14430	0.6930	1.758 [19][a]	3.0E-4 [19][a]
1.771	14286	0.70	1.7550 [17]	
1.755	14154	0.70652	1.7545 [2][b]	
		0.735	1.7267 [21][a]	2.3E-4 [21][a]
1.653	13333	0.75	1.77 [24][a]	
1.653	13333	0.75	1.7516 [17]	
1.642	13245	0.755	1.740 [13][a]	

TABLE I *(Continued)*

PbF_2

eV	cm^{-1}	μm	n	k
1.595	12862	0.7775	1.753 [19][a]	2.0E-4 [19][a]
1.550	12500	0.80	1.7488 [17]	
1.550	12500	0.8	1.75 [24][a]	
1.459	11765	0.85	1.79	
1.459	11765	0.85	1.7465 [17]	
1.399	11285	0.8861	1.748 [19][a]	~0 [19][a]
1.378	11111	0.9	1.77 [24][a]	
1.378	11111	0.90	1.7445 [17]	
1.305	10526	0.95	1.7429	
1.240	10000	1.0	1.77 [24][a]	
1.240	10000	1.00	1.7415 [17]	
1.203	9699	1.031	1.744 [19][a]	~0
1.181	9524	1.05	1.7403 [17]	
1.127	9091	1.1	1.72 [24][a]	
1.127	9091	1.10	1.73921 [17]	
1.078	8696	1.15	1.7383	
1.033	8333	1.2	1.72 [24][a]	
1.033	8333	1.20	1.7374 [17]	
1.002	8084	1.237	1.743 [19][a]	~0
0.992	8000	1.25	1.7366 [17]	
0.954	7692	1.3	1.73 [24][a]	
0.954	7692	1.30	1.7360 [17]	
0.918	7407	1.35	1.7353	
0.886	7143	1.4	1.74 [24][a]	
0.886	7143	1.40	1.7347 [17]	
0.855	6897	1.45	1.7342	
0.827	6667	1.5	1.73 [24][a]	
0.827	6667	1.50	1.7337 [17]	
0.802	6472	1.545	1.742 [19][a]	~0
0.800	6452	1.55	1.7332 [17]	
0.775	6250	1.6	1.72 [24][a]	
0.775	6250	1.60	1.7328 [17]	
0.751	6061	1.65	1.7324	
0.729	5882	1.70	1.7320	
0.708	5714	1.75	1.7316	
0.689	5556	1.8	1.75 [24][a]	
0.689	5556	1.80	1.7312 [17]	
0.670	5405	1.85	1.7308	
0.653	5263	1.90	1.7305	
0.636	5128	1.95	1.7302 [17]	
0.620	5000	2.0	1.77 [24][a]	
0.620	5000	2.00	1.7298 [17]	
0.605	4878	2.05	1.7295	
0.602	4859	2.058	1.740 [19][a]	~0 [19][a]
0.590	4762	2.10	1.7292 [17]	
0.577	4651	2.15	1.7289	

(continued)

TABLE I *(Continued)*

PbF_2

eV	cm^{-1}	μm	n	k
0.564	4545	2.20	1.7285	
0.551	4444	2.25	1.7282	
0.539	4348	2.30	1.7279	
0.528	4255	2.35	1.7276	
0.517	4167	2.40	1.7273	
0.506	4082	2.45	1.7270	
0.4959	4000	2.50	1.7267	
0.4959	4000	2.5	1.7 [24][a]	
0.4862	3922	2.55	1.7264 [17]	
0.4769	3846	2.60	1.7261	
0.4679	3774	2.65	1.7258	
0.4592	3704	2.70	1.7255	
0.4509	3636	2.75	1.7252	
0.4428	3571	2.80	1.7249	
0.4350	3509	2.85	1.7246	
0.4275	3448	2.90	1.7243	
0.4203	3390	2.95	1.7239	
0.4133	3333	3.00	1.7236	
0.4133	3333	3.0	1.7 [24][a]	
0.4016	3239	3.087	1.740 [19][a]	~0
0.3875	3125	3.20	1.7223 [17]	
0.3647	2941	3.40	1.7210	
0.3444	2778	3.60	1.7196	
0.3263	2632	3.80	1.7181	
0.3100	2500	4.0	1.7 [24][a]	
0.3100	2500	4.00	1.7166 [17]	
0.2952	2381	4.20	1.7150	
0.2818	2273	4.40	1.7134	
0.2695	2174	4.60	1.7117	
0.2583	2083	4.80	1.7099	
0.2480	2000	5.0	1.7 [24][a]	
0.2480	2000	5.00	1.7080 [17]	
0.2339	1887	5.3		2.5E-4 [18][a]
0.2254	1818	5.50	1.7031	
0.2066	1667	6.00	1.6977	
0.2008	1620	6.174	1.740 [19][a]	
0.1907	1538	6.50	1.6918 [17]	
0.1771	1429	7.00	1.6854	
0.1653	1333	7.50	1.6786	
0.1550	1250	8.0	1.7 [24][a]	
0.1550	1250	8.00	1.6712 [17]	
0.1459	1176	8.50	1.6634	
0.1378	1111	9.00	1.6550	
0.1305	1053	9.5	1.69 [24][a]	
0.1305	1053	9.50	1.6461 [17]	
0.1240	1000	10.0	1.6367	

TABLE I *(Continued)*

PbF_2

eV	cm^{-1}	μm	n	k
0.1240	1000	10.0	1.73 [9]	
0.1181	952.4	10.5	1.6268 [17]	
0.1170	943.4	10.6	1.63 [23][a]	
0.1127	909.1	11.0	1.6163 [17]	
0.1078	869.6	11.5	1.6052	
0.1042	840.3	11.9	1.5960	
0.08266	666.7	15.0	1.58 [9]	
0.07749	625.0	16.0	1.5 [23][a]	
0.06199	500.0	20.0	1.41 [9]	
0.04959	400.0	25.0	1.00	
0.04133	333.3	30.0	0.707	
0.03542	285.7	35.0		0.707 [9]
0.03100	250.0	40.0		1.22
0.02917	235.3	42.5	0.157	1.59
0.02755	222.2	45.0	0.248	2.02
0.02610	210.5	47.5	0.331	2.26
0.02480	200.0	50.0	0.402	2.48
0.02362	190.5	52.5	0.537	2.79
0.02254	181.8	55.0	0.558	3.13
0.02156	173.9	57.5	0.581	3.44
0.02066	166.7	60.0	0.615	3.66
0.01984	160.0	62.5	0.710	3.87
0.01907	153.8	65.0	0.797 [9]	4.10 [9]
0.01837	148.1	67.5	0.845	4.44
0.01771	142.9	70.0	0.961	4.68
0.01710	137.9	72.5	1.05	5.01
0.01653	133.3	75.0	1.20	5.43
0.01600	129.0	77.5	1.51	5.81
0.01550	125.0	80.0	1.66	6.31
0.01503	121.2	82.5	2.00	6.75
0.01459	117.6	85.0	2.30	7.40
0.01417	114.3	87.5	2.96	8.11
0.01378	111.1	90.0	3.74	8.95
0.01340	108.1	92.5	5.08	9.64
0.01305	105.3	95.0	7.06	9.99
0.01272	102.6	97.5	8.69	8.69
0.01240	100.0	100.0	10.3	6.87
0.01210	97.56	102.5	10.1	5.36
0.01181	95.24	105.0	9.69	4.23
0.01153	93.02	107.5	9.46	3.54
0.01127	90.91	110.0	9.29	3.04
0.01102	88.89	112.5	9.13	2.71
0.01078	86.96	115.0	8.97	2.43
0.01055	85.11	117.5	8.82	2.18
0.01033	83.33	120.0	8.64	1.91
0.01012	81.63	122.5	8.48	1.71

(continued)

TABLE I *(Continued)*

PbF_2

eV	cm^{-1}	μm	n	k
0.009919	80.00	125.0	8.36	1.53
0.009724	78.43	127.5	8.23	1.34
0.009537	76.92	130.0	8.12	1.17
0.009184	74.07	135.0	7.95	0.849
0.008856	71.43	140.0	7.83	0.511
0.008551	68.97	145.0	7.75	0.226

Lithium Tantalate ($LiTaO_3$)

FRANÇOIS GERVAIS
Laboratoire d'Electrodynamique des Matériaux Avancés
Faculté des Sciences & Techniques, Université François Rabelais
Tours, France

and

VICENTE FONSECA
Centre de Recherches sur la Physique des Hautes Températures
Centre National de la Recherche Scientifique
Orléans, France

$LiTaO_3$ crystallizes in the pseudo-ilmenite 3m structure. It was found to be ferroelectric by Matthias and Remeika in 1949 [1]. The Curie temperature is ~890 K. Although the spontaneous polarization is not as large as in the parent compound $LiNbO_3$, there are many possible technical applications of $LiTaO_3$ related to the large electro-optic coefficient [2]. High-quality single crystals may be grown by the Czochralski pulling method. The system is uniaxial, and optical properties measured on a single crystal are, therefore, anisotropic. The anisotropy of the refractive index in the visible region, mainly related to the anisotropy of the oxygen polarizability, is surprisingly small, ~0.2% in the visible region. In the millimeter-wave range, the anisotropy remains small (~2%) also. These small anisotropies are related to the fact that the structure of $LiTaO_3$ derives from the cubic perovskite structure. However, at intermediate frequencies, the anisotropy of the structure induces very different lattice dynamical properties and band structure, so that the spectra of the index of refraction n and extinction coefficient k are very different for the polarizations parallel and perpendicular to the ferroelectric c axis.

The availability of synchrotron-radiation sources allowed the first measurements of optical response of this material at high energies, as well as for many other materials in the past 20 years. Reflection spectra in the op-

HANDBOOK OF OPTICAL CONSTANTS OF SOLIDS III

Copyright © 1998 by Academic Press.
All rights of reproduction in any form reserved
ISBN 0-12-544423-0/$25.00.

tical range 2–35 eV were obtained with the aid of the storage ring at the Stoughton Synchrotron Radiation Center of the University of Wisconsin. Data were published by Mamedov and co-workers [3, 4], but they are, unfortunately, restricted to a single surface orientation, for the crystal cut perpendicular to the ferroelectric (FE) c-axis. Measurements parallel to the ferroelectric axis would be highly desirable to complement the data. The purpose of the measurements was to study the electronic excitations in relation to partial hybridization of atomic orbitals, but not properly to determine the optical constants n and k which are not displayed in the papers. Only the maxima of the imaginary part of the dielectric response $\epsilon = n - ik$ are discussed. In the absence of other studies devoted to the specific measurement of these spectra, we have attempted to extract information useful for the present purpose from reflectivity. This was done by Kramers–Kronig (K-K) analysis. But, by doing so, and even after proper extrapolation of low-frequency data, we realized that the absorption coefficient (or the imaginary part of the dielectric function, or the imaginary part of the inverse dielectric function equally well) found by K-K inversion is negative below 34,000 cm^{-1} (see also Fig. 3 of Mamedov [4]), which is obviously meaningless physically. We made, therefore, the slightest correction of all the data (-2.5%) to recover physically reasonable values, viz., the real part of the dielectric response which tends towards unity at infinite frequency and positive values of the imaginary part everywhere. The minimum correction according to these criteria gives the results of n and k listed in Table I. Whereas the accuracy of the highest k values is little affected by this correction, the accuracy of lowest values is poor. New measurements are, therefore, highly desirable. Indices n are less affected by the uncertainty.

Absorption in the range 3.2–4.7 eV was measured by Kase and Ohi [5]. The deduced k values ($k = \alpha/4\pi\sigma$, where α is the absorption coefficient and σ the wave number) are much more accurate than the estimation in this region by K-K analysis for the reasons given earlier. Note that a slight shift of the band edge is found by comparing the values of Mamedov [3] and these data.

The indices of refraction of $LiTaO_3$ prisms measured over its entire range of transmission (0.4 to 4 μm) and for both principal directions are reported by Bond [6]. Results are listed in Tables I and II. Note that one value, 2.0299, in Table IV of Bond [6] does not extrapolate to neighboring values and is most likely a misprint.

The earliest set of measurements in the infrared complemented by data processing was performed by Barker *et al.* [7] in 1970. Several single crystals cut parallel or perpendicular to the FE axis from boules grown by the Czochralski pulling technique were used. Infrared reflection measurements were performed with a prism spectrometer. Complementary transmission measurements performed on 30- and 147-μm-thick thin slabs made use of a Michelson interferometer. Gervais and Servoin [7, 8] also remeasured the

spectra with a prism spectrometer. The same authors [9–11] later performed a complete study of the temperature dependence of infrared reflectivity, including both sides of the ferroelectric–paraelectric (FE-PE) phase transition, with a modern Fourier-transform infrared spectrometer. These spectra were obtained on single crystals also cut from Czochralski-grown boules. Unfortunately, in none of these studies were the spectra of n and k given explicitly.

In single crystals, the dielectric function $\epsilon = n - ik$ can be modeled. As soon as a dielectric-function model fits the infrared reflectivity, one may deduce the optical constants more accurately than with a K-K analysis. The absorption coefficient is extremely high in the atomic-vibration region, because of the large polar character of the vibrations in such a ferroelectric crystal. The penetration depth of the infrared radiation is found to be less than 1 μm at a peak, corresponding to a normal vibration mode. As a result, the infrared beam in these narrow spectral regions probes the surface of the sample rather than the bulk. The result is then very sensitive to the alterations of the crystal surface. Conversely, far from normal modes, the penetration depth of the infrared beam is much larger. Disorder or alteration of the sample surface increases mode damping and, therefore, lowers the reflectivity. Fitting the spectra can minimize the spurious effects of the surface by comparison with a K-K analysis because the damping coefficient is then averaged over a wide spectral range (with larger penetration depth on an average) in the former case instead of being determined near the mode frequency, where disorder may alter the result.

Barker *et al.* [7] fitted their spectra with the usual dielectric-function model

$$\epsilon = \epsilon_\infty + \sum_j \Delta\epsilon_j \frac{\Omega_{j\mathrm{TO}}^2}{\Omega_{j\mathrm{TO}}^2 - \omega^2 + i\gamma_{j\mathrm{TO}}\omega}. \tag{1}$$

ϵ_∞ is the high-frequency dielectric constant; $\Delta\epsilon_j$, $\Omega_{j\mathrm{TO}}$, and $\gamma_{j\mathrm{TO}}$ are the oscillator strength, the frequency, and the damping of the jth TO (transverse optic) mode, respectively.

A factorization over poles and zeroes of the dielectric response in the form

$$\epsilon = \epsilon_\infty \prod_j \frac{\Omega_{j\mathrm{LO}}^2 - \omega^2 + i\gamma_{j\mathrm{LO}}\omega}{\Omega_{j\mathrm{LO}}^2 - \omega^2 + i\gamma_{j\mathrm{TO}}\omega} \tag{2}$$

was preferred by others [7–11]. Here the index LO refers to longitudinal optic modes. The reason invoked by the authors is that in systems that are highly polar and where the Coulombic field splits the polar modes into transverse and longitudinal components (the later being possibly twice more energetic than the former), phonons can have very different decays, and then dampings can be very different. Conversely, identical dampings are implicitly assumed for the TO and LO components by the model Eq. (1). Results

deduced from the fit to the reflectivity data with the dielectric-function model Eq. (2) are compared to K-K transformed data of Barker *et al.* [7] and from Servoin [11] in Table I. Data are given for the electric field of infrared radiation polarized perpendicular to the crystal c-axis (ordinary ray). The overall agreement is good.

The situation for the polarization parallel to the FE c-axis is more complicated. Indeed, neither model, Eq. (1) or (2), is able to fit the data correctly. This is why some authors [7–11] introduced a phonon self-energy function that yields in practice a frequency dependence of the damping function of certain modes (including the soft FE mode) to get a good fit to reflectivity data. But this procedure introduces many more fitting parameters and is, therefore, questionable. At least, it is nonstandard. Here we preferred to adopt a compromise and fitted with the general model Eq. (2), by just adding an overdamped mode at low frequency to take account of the bump that develops at low frequency on heating [10–12]. Results are satisfactory. They are compared with K-K analyses in Table II.

Lowest-frequency values of k in Tables I and II are those of Barker [7], deduced from absorption-coefficient measurements in thin slabs.

Much of the n and k data in Table I and II is plotted in Figs. 1 and 2.

As mentioned earlier, the temperature dependence of infrared reflection spectra has been studied in detail elsewhere [10–12]. In particular, it was shown that, whereas a soft vibrational mode is observed on approaching the temperature of the FE-PE phase transition, the soft mode alone does not explain the behavior of the dielectric constant. A soft mode assumes a displacive-type phase transition, whereas a discrepancy of ϵ_0 measured in the very far infrared and in the radio-frequency range is rather indicative of an order–disorder-type phase transition. These experimental observations were, therefore, understood in terms of a crossover from displacive to order–disorder behavior in a model for ferroelectrics proposed by Müller and co-workers [13].

REFERENCES

1. B. T. Matthias and J. P. Remeika, *Phys. Rev.* **76**, 1886 (1949).
2. P. V. Lenzo, E. H. Turner, E. G. Spencer, and A. A. Balman, *Appl. Phys. Lett.* **8**, 81 (1966).
3. A. M. Mamedov, *Ferroelectrics* **45**, 55 (1982).
4. A. M. Mamedov, M. A. Osman, and L. C. Hajieva, *Appl. Phys. A* **34**, 189 (1984).
5. S. Kase and K. Ohi, *Ferroelectrics* **8**, 419 (1974).
6. W. L. Bond, *J. Appl. Phys.* **36**, 1674 (1965).
7. A. S. Barker, A. A. Ballman, and J. A. Ditzenberger, *Phys. Rev. B* **2**, 4233 (1970).
8. F. Gervais and J. L. Servoin, *Phys. Rev. B* **15**, 4532 (1977).
9. J. L. Servoin and F. Gervais, *Appl. Opt.* **16**, 2952 (1977).
10. J. L. Servoin and F. Gervais, *Solid State Commun.* **31**, 387 (1979).
11. J. L. Servoin, Ph.D. Thesis, University of Orléans, France (1980).
12. F. Gervais, *in* "Infrared and Millimeter Waves," (K. J. Button, ed.), Vol. 8, p. 279. Academic Press, New York, 1983.
13. K. A. Müller, Y. Luspin, J. L. Servoin, and F. Gervais, *J. Phys. Lett.* **43**, 537 (1982).

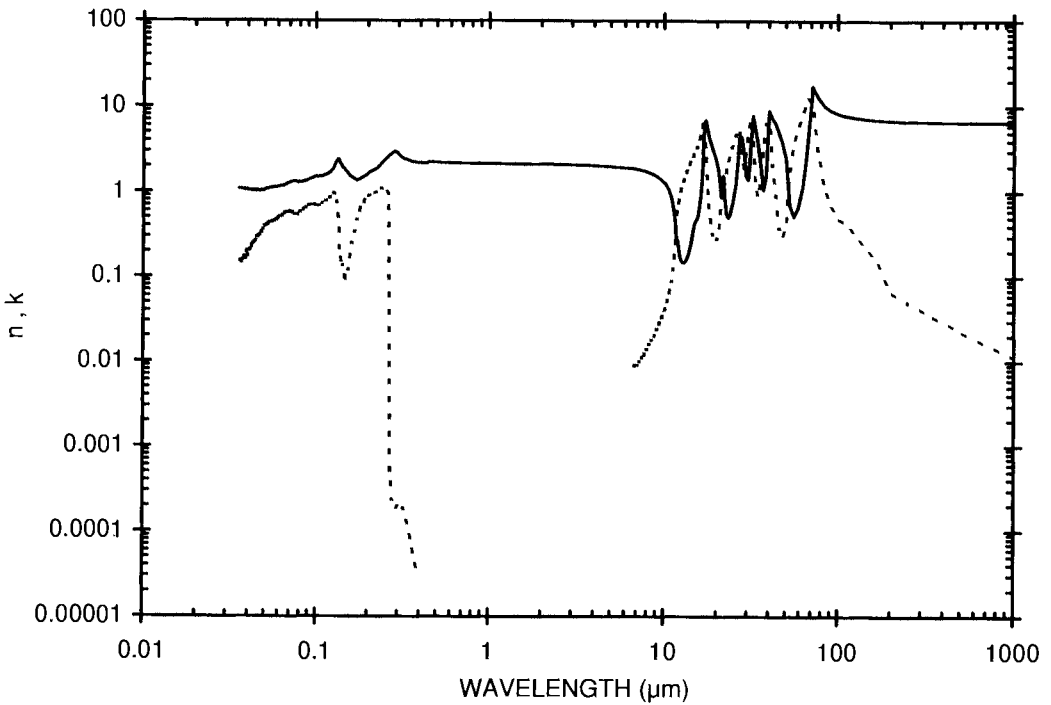

Fig. 1. Log–log plot of $n_\perp$ (—) and $k_\perp$ (---) versus wavelength in micrometers for lithium tantalate.

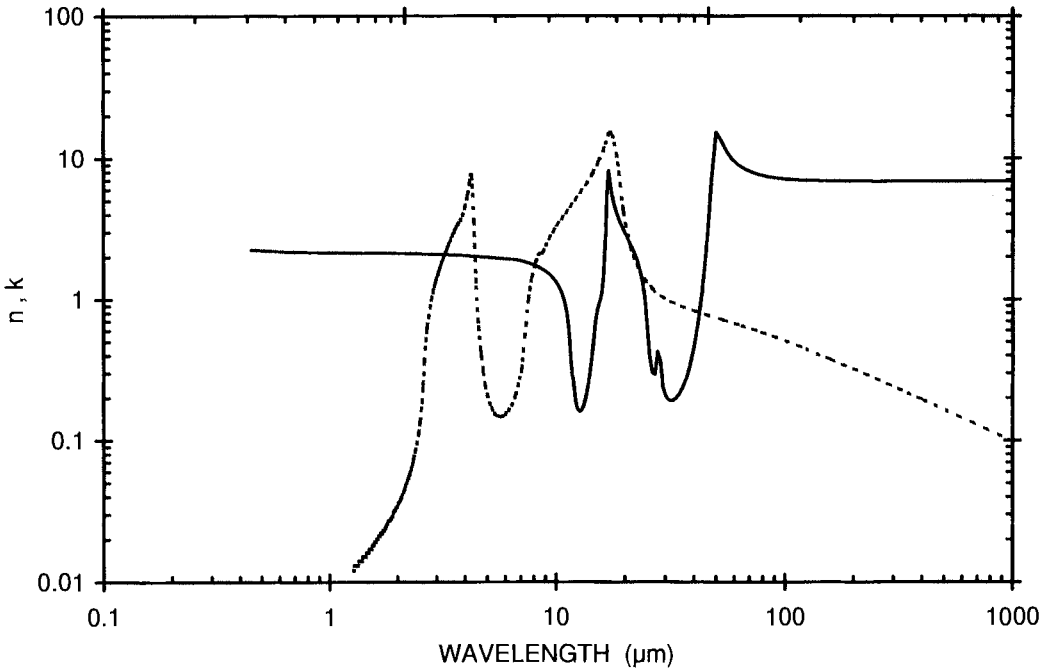

Fig. 2. Log–log plot of $n_{\|}$ (—) and $k_{\|}$ (---) versus wavelength in micrometers for lithium tantalate.

TABLE I

Values of $n_\perp$ and $k_\perp$ for Lithium Tantalate from Various References

eV	cm ^{1}	μm	$n_\perp$	$k_\perp$	$n_\perp$	$k_\perp$	$n_\perp$	$k_\perp$
35.0	282000	0.03546	1.082 [3]	0.145 [3]				
34.8	281000	0.03559	1.080	0.147				
34.7	280000	0.03571	1.080	0.149				
34.6	279000	0.03584	1.080	0.152				
34.5	278000	0.03597	1.080	0.154				
34.3	277000	0.03610	1.082	0.155				
34.2	276000	0.03623	1.083	0.155				
34.1	275000	0.03636	1.084	0.155				
34.0	274000	0.03650	1.085	0.152				
33.8	273000	0.03663	1.082	0.149				
33.7	272000	0.03676	1.075	0.148				
33.6	271000	0.03690	1.070	0.154				
33.5	270000	0.03704	1.070	0.158				
33.4	269000	0.03717	1.072	0.159				
33.2	268000	0.03731	1.070	0.159				
33.1	267000	0.03745	1.068	0.160				
33.0	266000	0.03759	1.065	0.161				
32.9	265000	0.03774	1.062	0.164				
32.7	264000	0.03788	1.061	0.169				
32.6	263000	0.03802	1.061	0.173				
32.5	262000	0.03817	1.063	0.176				
32.4	261000	0.03831	1.070	0.177				
32.2	260000	0.03846	1.068	0.168				
32.1	259000	0.03861	1.057	0.162				

(continued)

TABLE I *(Continued)*

Lithium Tantalate

eV	cm^{-1}	μm	$n_\perp$	$k_\perp$	$n_\perp$	$k_\perp$	$n_\perp$	$k_\perp$
32.0	258000	0.03876	1.047	0.173				
31.9	257000	0.03891	1.044	0.182				
31.7	256000	0.03906	1.045	0.193				
31.6	255000	0.03922	1.054	0.203				
31.5	254000	0.03937	1.067	0.197				
31.4	253000	0.03953	1.068	0.189				
31.2	252000	0.03968	1.063	0.180				
31.1	251000	0.03984	1.048	0.174				
31.0	250000	0.04000	1.037	0.197				
30.9	249000	0.04016	1.045	0.201				
30.7	248000	0.04032	1.047	0.204				
30.6	247000	0.04049	1.051	0.204				
30.5	246000	0.04065	1.051	0.201				
30.4	245000	0.04082	1.046	0.199				
30.3	244000	0.04098	1.038	0.202				
30.1	243000	0.04115	1.034	0.209				
30.0	242000	0.04132	1.032	0.216				
29.9	241000	0.04149	1.033	0.222				
29.8	240000	0.04167	1.035	0.229				
29.6	239000	0.04184	1.046	0.233				
29.5	238000	0.04202	1.043	0.218				
29.4	237000	0.04219	1.023	0.231				
29.3	236000	0.04237	1.036	0.247				
29.1	235000	0.04255	1.043	0.243				
29.0	234000	0.04274	1.045	0.237				
28.9	233000	0.04292	1.039	0.231				
28.8	232000	0.04310	1.021	0.236				

28.6	231000	0.04329	1.021	0.254
28.5	230000	0.04348	1.028	0.263
28.4	229000	0.04367	1.039	0.261
28.3	228000	0.04386	1.036	0.254
28.1	227000	0.04405	1.028	0.265
28.0	226000	0.04425	1.040	0.263
27.9	225000	0.04444	1.024	0.259
27.8	224000	0.04464	1.015	0.272
27.6	223000	0.04484	1.023	0.293
27.5	222000	0.04505	1.035	0.291
27.4	221000	0.04525	1.040	0.287
27.3	220000	0.04545	1.038	0.282
27.2	219000	0.04566	1.024	0.280
27.0	218000	0.04587	1.025	0.298
26.9	217000	0.04608	1.029	0.295
26.8	216000	0.04630	1.018	0.300
26.7	215000	0.04651	1.022	0.318
26.5	214000	0.04673	1.031	0.309
26.4	213000	0.04695	1.013	0.317
26.3	212000	0.04717	1.020	0.333
26.2	211000	0.04739	1.029	0.342
26.0	210000	0.04762	1.040	0.338
25.9	209000	0.04785	1.039	0.332
25.8	208000	0.04808	1.027	0.342
25.7	207000	0.04831	1.038	0.344
25.5	206000	0.04854	1.026	0.343
25.4	205000	0.04878	1.033	0.361
25.3	204000	0.04902	1.034	0.354
25.2	203000	0.04926	1.021	0.367
25.0	202000	0.04950	1.024	0.389
24.9	201000	0.04975	1.045	0.394

(continued)

TABLE I *(Continued)*

Lithium Tantalate

eV	cm^{-1}	μm	$n_\perp$	$k_\perp$	$n_\perp$	$k_\perp$	$n_\perp$	$k_\perp$
24.8	200000	0.05000	1.051	0.388				
24.7	199000	0.05025	1.041	0.399				
24.5	198000	0.05051	1.061	0.406				
24.4	197000	0.05076	1.060	0.400				
24.3	196000	0.05102	1.059	0.408				
24.2	195000	0.05128	1.072	0.419				
24.1	194000	0.05155	1.080	0.412				
23.9	193000	0.05181	1.076	0.408				
23.8	192000	0.05208	1.074	0.413				
23.7	191000	0.05236	1.073	0.424				
23.6	190000	0.05263	1.089	0.434				
23.4	189000	0.05291	1.098	0.426				
23.3	188000	0.05319	1.092	0.420				
23.2	187000	0.05348	1.091	0.432				
23.1	186000	0.05376	1.101	0.434				
22.9	185000	0.05405	1.104	0.432				
22.8	184000	0.05435	1.101	0.434				
22.7	183000	0.05464	1.105	0.443				
22.6	182000	0.05495	1.112	0.441				
22.4	181000	0.05525	1.109	0.440				
22.3	180000	0.05556	1.112	0.447				
22.2	179000	0.05587	1.116	0.449				
22.1	178000	0.05618	1.118	0.451				
21.9	177000	0.05650	1.120	0.452				
21.8	176000	0.05682	1.120	0.454				
21.7	175000	0.05714	1.123	0.465				
21.6	174000	0.05747	1.133	0.460				

21.4	173000	0.05780	1.128	0.455
21.3	172000	0.05814	1.124	0.462
21.2	171000	0.05848	1.122	0.470
21.1	170000	0.05882	1.127	0.481
21.0	169000	0.05917	1.136	0.485
20.8	168000	0.05952	1.137	0.478
20.7	167000	0.05988	1.131	0.494
20.6	166000	0.06024	1.144	0.502
20.5	165000	0.06061	1.152	0.495
20.3	164000	0.06098	1.145	0.506
20.2	163000	0.06135	1.158	0.510
20.1	162000	0.06173	1.163	0.510
20.0	161000	0.06211	1.165	0.510
19.8	160000	0.06250	1.164	0.518
19.7	159000	0.06289	1.178	0.518
19.6	158000	0.06329	1.172	0.518
19.5	157000	0.06369	1.181	0.527
19.3	156000	0.06410	1.181	0.516
19.2	155000	0.06452	1.164	0.531
19.1	154000	0.06494	1.175	0.549
19.0	153000	0.06536	1.187	0.559
18.8	152000	0.06579	1.199	0.560
18.7	151000	0.06623	1.206	0.561
18.6	150000	0.06667	1.208	0.567
18.5	149000	0.06711	1.224	0.573
18.3	148000	0.06757	1.232	0.570
18.2	147000	0.06803	1.235	0.576
18.1	146000	0.06849	1.252	0.580
18.0	145000	0.06897	1.261	0.573
17.9	144000	0.06944	1.260	0.570
17.7	143000	0.06993	1.269	0.579

(continued)

TABLE I *(Continued)*

Lithium Tantalate

eV	cm^{-1}	μm	$n_\perp$	$k_\perp$	$n_\perp$	$k_\perp$	$n_\perp$	$k_\perp$
17.6	142000	0.07042	1.284	0.572				
17.5	141000	0.07092	1.285	0.563				
17.4	140000	0.07143	1.287	0.570				
17.2	139000	0.07194	1.300	0.570				
17.1	138000	0.07246	1.306	0.562				
17.0	137000	0.07299	1.308	0.557				
16.9	136000	0.07353	1.311	0.554				
16.7	135000	0.07407	1.316	0.550				
16.6	134000	0.07463	1.316	0.541				
16.5	133000	0.07519	1.312	0.538				
16.4	132000	0.07576	1.312	0.536				
16.2	131000	0.07634	1.310	0.526				
16.1	130000	0.07692	1.296	0.525				
16.0	129000	0.07752	1.280	0.535				
15.9	128000	0.07813	1.276	0.552				
15.7	127000	0.07874	1.285	0.565				
15.6	126000	0.07937	1.290	0.569				
15.5	125000	0.08000	1.293	0.573				
15.4	124000	0.08065	1.294	0.578				
15.3	123000	0.08130	1.295	0.583				
15.1	122000	0.08197	1.296	0.589				
15.0	121000	0.08264	1.297	0.597				
14.9	120000	0.08333	1.297	0.608				
14.8	119000	0.08403	1.304	0.618				
14.6	118000	0.08475	1.306	0.628				
14.5	117000	0.08547	1.321	0.648				
14.4	116000	0.08621	1.335	0.636				

14.3	115000	0.08696	1.326	0.644
14.1	114000	0.08772	1.332	0.667
14.0	113000	0.08850	1.353	0.668
13.9	112000	0.08929	1.356	0.674
13.8	111000	0.09009	1.369	0.688
13.6	110000	0.09091	1.391	0.691
13.5	109000	0.09174	1.395	0.684
13.4	108000	0.09259	1.410	0.699
13.3	107000	0.09346	1.423	0.696
13.1	106000	0.09434	1.426	0.698
13.0	105000	0.09524	1.447	0.701
12.9	104000	0.09615	1.448	0.705
12.8	103000	0.09709	1.468	0.710
12.6	102000	0.09804	1.489	0.709
12.5	101000	0.09901	1.501	0.694
12.4	100000	0.1000	1.504	0.688
12.3	99000	0.1010	1.515	0.680
12.2	98000	0.1020	1.501	0.671
12.0	97000	0.1031	1.500	0.682
11.9	96000	0.1042	1.507	0.690
11.8	95000	0.1053	1.516	0.691
11.7	94000	0.1064	1.512	0.689
11.5	93000	0.1075	1.508	0.702
11.4	92000	0.1087	1.510	0.729
11.3	91000	0.1099	1.529	0.740
11.2	90000	0.1111	1.542	0.750
11.0	89000	0.1124	1.554	0.765
10.9	88000	0.1136	1.573	0.776
10.8	87000	0.1149	1.590	0.785
10.7	86000	0.1163	1.598	0.803
10.5	85000	0.1176	1.625	0.819

(continued)

TABLE I *(Continued)*

Lithium Tantalate

eV	cm^{-1}	μm	$n_\perp$	$k_\perp$	$n_\perp$	$k_\perp$	$n_\perp$	$k_\perp$
10.4	84000	0.1190	1.659	0.837				
10.3	83000	0.1205	1.672	0.855				
10.2	82000	0.1220	1.722	0.870				
10.0	81000	0.1235	1.759	0.903				
9.92	80000	0.1250	1.812	0.927				
9.79	79000	0.1266	1.915	0.958				
9.67	78000	0.1282	2.031	0.936				
9.55	77000	0.1299	2.157	0.889				
9.42	76000	0.1316	2.270	0.763				
9.30	75000	0.1333	2.344	0.628				
9.17	74000	0.1351	2.411	0.418				
9.05	73000	0.1370	2.222	0.214				
8.93	72000	0.1389	2.117	0.171				
8.80	71000	0.1408	2.027	0.123				
8.68	70000	0.1429	1.917	0.136				
8.55	69000	0.1449	1.906	0.138				
8.43	68000	0.1471	1.826	0.081				
8.31	67000	0.1493	1.746	0.105				
8.18	66000	0.1515	1.704	0.103				
8.06	65000	0.1538	1.621	0.121				
7.94	64000	0.1563	1.576	0.149				
7.81	63000	0.1587	1.503	0.200				
7.69	62000	0.1613	1.487	0.250				
7.56	61000	0.1639	1.447	0.277				
7.44	60000	0.1667	1.427	0.335				
7.32	59000	0.1695	1.393	0.372				
7.19	58000	0.1724	1.355	0.470				

7.07	57000	0.1754	1.379	0.537	
6.94	56000	0.1786	1.385	0.590	
6.82	55000	0.1818	1.430	0.669	
6.70	54000	0.1852	1.453	0.700	
6.57	53000	0.1887	1.484	0.752	
6.45	52000	0.1923	1.526	0.795	
6.32	51000	0.1961	1.558	0.824	
6.20	50000	0.2000	1.616	0.877	
6.08	49000	0.2041	1.675	0.899	
5.95	48000	0.2083	1.719	0.909	
5.83	47000	0.2128	1.754	0.927	
5.70	46000	0.2174	1.795	0.952	
5.58	45000	0.2222	1.830	0.984	
5.46	44000	0.2273	1.897	1.053	
5.33	43000	0.2326	2.007	1.096	
5.21	42000	0.2381	2.118	1.089	
5.08	41000	0.2439	2.236	1.082	
4.96	40000	0.2500	2.349	1.053	
4.84	39000	0.2564	2.470	1.007	
4.71	38000	0.2632	2.590	0.940	
4.59	37000	0.2703	2.720	0.837	5.1E-04 [5]
4.46	36000	0.2778	2.836	0.697	2.3E-04
4.34	35000	0.2857	2.957	0.496	1.9E-04
4.22	34000	0.2941	2.896	0.173	1.9E-04
4.09	33000	0.3030	2.686	0.002	2.0E-04
3.97	32000	0.3125	2.558		2.0E-04
3.84	31000	0.3226	2.428		1.8E-04
3.72	30000	0.3333	2.398		1.5E-04
3.60	29000	0.3448	2.330		1.1E-04
3.47	28000	0.3571	2.256		7.9E-05
3.35	27000	0.3704	2.232		5.4E-05

(continued)

TABLE I *(Continued)*

Lithium Tantalate

eV	cm^{-1}	μm	$n_\perp$	$k_\perp$	$n_\perp$	$k_\perp$	$n_\perp$	$k_\perp$
3.22	26000	0.3846	2.197			3.8E-05		
3.10	25000	0.4000	2.183					
2.98	24000	0.4167	2.161					
2.85	23000	0.4348	2.155					
2.73	22000	0.4545	2.155					
2.60	21000	0.4762	2.134					
2.48	20000	0.5000	2.130					
2.755	22222	0.45			2.2420 [6]			
2.480	20000	0.50			2.2160			
2.066	16667	0.60			2.1834			
1.771	14286	0.70			2.1652			
1.550	12500	0.80			2.1538			
1.378	11111	0.90			2.1454			
1.240	10000	1.00			2.1391			
1.033	8333	1.20			2.1305			
0.8856	7143	1.40			2.1236			
0.7749	6250	1.60			2.1174			
0.6888	5556	1.80			2.1120			
0.6199	5000	2.00			2.1066			
0.5636	4545	2.20			2.1009			
0.5166	4167	2.40			2.0951			
0.4769	3846	2.60			2.0891			
0.4428	3571	2.80			2.0825			
0.4133	3333	3.00			2.0755			
0.3875	3125	3.20			2.0680			
0.3647	2941	3.40			2.0601			
0.3444	2778	3.60			2.0513			

0.3263	2632	3.80			2.0424	
0.3100	2500	4.00			2.0335	
0.2108	1700	5.882	1.879 [7]			
0.2095	1690	5.917	1.875			
0.2083	1680	5.952	1.872			
0.2071	1670	5.988	1.868			
0.2058	1660	6.024	1.864			
0.2046	1650	6.061	1.861			
0.2033	1640	6.098	1.857			
0.2021	1630	6.135	1.854			
0.2009	1620	6.173	1.850			
0.1996	1610	6.211	1.847			
0.1984	1600	6.250	1.843	0.001 [7]		
0.1971	1590	6.289	1.839	0.002		
0.1959	1580	6.329	1.836	0.003		
0.1947	1570	6.369	1.832	0.004		
0.1934	1560	6.410	1.828	0.005		
0.1922	1550	6.452	1.825	0.006		
0.1909	1540	6.494	1.821	0.007		
0.1897	1530	6.536	1.818	0.007		
0.1885	1520	6.579	1.814	0.008		
0.1872	1510	6.623	1.810	0.009		
0.1860	1500	6.667	1.807	0.009		
0.1847	1490	6.711	1.803	0.009	1.887 [11]	0.008 [11]
0.1835	1480	6.757	1.799	0.009	1.882	0.008
0.1823	1470	6.803	1.796	0.008	1.877	0.009
0.1810	1460	6.849	1.792	0.006	1.872	0.009
0.1798	1450	6.897	1.786	0.003	1.867	0.009
0.1785	1440	6.944	1.779	0.003	1.862	0.009
0.1773	1430	6.993	1.773	0.003	1.856	0.009
0.1761	1420	7.042	1.766	0.004	1.850	0.009

(continued)

TABLE I *(Continued)*

Lithium Tantalate

eV	cm^{-1}	μm	$n_\perp$	$k_\perp$	$n_\perp$	$k_\perp$	$n_\perp$	$k_\perp$
0.1748	1410	7.092	1.760	0.005	1.845	0.010		
0.1736	1400	7.143	1.753	0.006	1.839	0.010		
0.1723	1390	7.194	1.747	0.007	1.833	0.010		
0.1711	1380	7.246	1.740	0.009	1.826	0.010		
0.1699	1370	7.299	1.733	0.010	1.820	0.011		
0.1686	1360	7.353	1.727	0.012	1.813	0.011		
0.1674	1350	7.407	1.720	0.014	1.806	0.011		
0.1661	1340	7.463	1.714	0.015	1.799	0.011		
0.1649	1330	7.519	1.707	0.017	1.792	0.012		
0.1637	1320	7.576	1.700	0.018	1.785	0.012		
0.1624	1310	7.634	1.694	0.019	1.777	0.012		
0.1612	1300	7.692	1.687	0.019	1.769	0.012		
0.1599	1290	7.752	1.680	0.019	1.760	0.013		
0.1587	1280	7.813	1.673	0.016	1.752	0.013		
0.1575	1270	7.874	1.663	0.014	1.743	0.014		
0.1562	1260	7.937	1.654	0.015	1.734	0.014		
0.1550	1250	8.000	1.644	0.017	1.724	0.014		
0.1537	1240	8.065	1.634	0.019	1.715	0.015		
0.1525	1230	8.130	1.624	0.021	1.704	0.015		
0.1513	1220	8.197	1.614	0.024	1.694	0.016		
0.1500	1210	8.264	1.604	0.026	1.683	0.016		
0.1488	1200	8.333	1.594	0.029	1.672	0.017		
0.1475	1190	8.403	1.584	0.031	1.660	0.017		
0.1463	1180	8.475	1.574	0.033	1.648	0.018		
0.1451	1170	8.547	1.564	0.034	1.635	0.018		
0.1438	1160	8.621	1.554	0.034	1.621	0.019		
0.1426	1150	8.696	1.543	0.033	1.608	0.020		

0.1413	1140	8.772	1.533	0.027	1.593	0.020		
0.1401	1130	8.850	1.521	0.010	1.578	0.021		
0.1389	1120	8.929	1.502	0.005	1.562	0.022		
0.1376	1110	9.009	1.482	0.008	1.546	0.023		
0.1364	1100	9.091	1.461	0.014	1.528	0.024		
0.1351	1090	9.174	1.440	0.024	1.510	0.025		
0.1339	1080	9.259	1.418	0.034	1.491	0.026		
0.1327	1070	9.346	1.395	0.046	1.471	0.027		
0.1314	1060	9.434	1.371	0.058	1.450	0.029		
0.1302	1050	9.524	1.345	0.070	1.427	0.030		
0.1289	1040	9.615	1.318	0.082	1.403	0.032		
0.1277	1030	9.709	1.289	0.091	1.378	0.033		
0.1265	1020	9.804	1.258	0.099	1.352	0.035		
0.1252	1010	9.901	1.234	0.109	1.323	0.037		
0.1240	1000	10.00	1.215	0.121	1.293	0.040		
0.1227	990	10.10	1.195	0.133	1.260	0.042	1.200 [a]	0.007 [a]
0.1215	980	10.20	1.173	0.144	1.225	0.045	1.173	0.048
0.1203	970	10.31	1.148	0.154	1.188	0.049	1.144	0.035
0.1190	960	10.42	1.121	0.161	1.147	0.053	1.095	0.052
0.1178	950	10.53	1.092	0.165	1.102	0.058	1.058	0.078
0.1165	940	10.64	1.059	0.166	1.053	0.063	1.036	0.089
0.1153	930	10.75	1.022	0.161	0.999	0.070	0.956	0.101
0.1141	920	10.87	0.979	0.146	0.939	0.078	0.919	0.094
0.1128	910	10.99	0.862	0.184	0.870	0.089	0.840	0.113
0.1116	900	11.11	0.740	0.200	0.792	0.104	0.779	0.129
0.1103	890	11.24	0.658	0.192	0.700	0.125	0.706	0.141
0.1091	880	11.36	0.600	0.187	0.589	0.161	0.587	0.153
0.1079	870	11.49	0.466	0.216	0.457	0.229	0.442	0.225
0.1066	860	11.63	0.315	0.315	0.335	0.362	0.321	0.371
0.1054	850	11.76	0.272	0.505	0.285	0.520	0.281	0.533
0.1041	840	11.90	0.239	0.628	0.269	0.632	0.282	0.636

(continued)

[a] Best fit of model Eq. (2) to reflectivity data of Ref. [11].

TABLE I *(Continued)*

Lithium Tantalate

eV	cm^{-1}	μm	$n_\perp$	$k_\perp$	$n_\perp$	$k_\perp$	$n_\perp$	$k_\perp$
0.1029	830	12.05	0.207	0.748	0.227	0.733	0.243	0.719
0.1017	820	12.20	0.194	0.879	0.189	0.853	0.196	0.829
0.1004	810	12.35	0.180	1.001	0.167	0.978	0.166	0.953
0.09919	800	12.50	0.180	1.120	0.155	1.100	0.151	1.074
0.09795	790	12.66	0.180	1.238	0.150	1.220	0.140	1.189
0.09671	780	12.82	0.183	1.354	0.148	1.339	0.132	1.306
0.09547	770	12.99	0.194	1.473	0.149	1.458	0.126	1.430
0.09423	760	13.16	0.207	1.589	0.152	1.580	0.128	1.557
0.09299	750	13.33	0.221	1.708	0.159	1.706	0.135	1.685
0.09175	740	13.51	0.235	1.829	0.168	1.837	0.145	1.819
0.09051	730	13.70	0.246	1.960	0.183	1.974	0.162	1.958
0.08927	720	13.89	0.260	2.113	0.203	2.119	0.189	2.105
0.08803	710	14.08	0.304	2.274	0.232	2.274	0.225	2.251
0.08679	700	14.29	0.357	2.442	0.274	2.436	0.269	2.405
0.08555	690	14.49	0.433	2.605	0.331	2.601	0.324	2.562
0.08431	680	14.71	0.501	2.761	0.396	2.758	0.386	2.715
0.08307	670	14.93	0.572	2.944	0.445	2.914	0.441	2.864
0.08183	660	15.15	0.652	3.131	0.468	3.104	0.472	3.034
0.08059	650	15.38	0.684	3.420	0.490	3.366	0.485	3.256
0.07935	640	15.63	0.815	3.800	0.543	3.715	0.503	3.586
0.07811	630	15.87	1.040	4.362	0.660	4.174	0.598	4.030
0.07687	620	16.13	1.695	5.012	0.899	4.796	0.826	4.605
0.07563	610	16.39	3.027	5.438	1.433	5.684	1.286	5.381
0.07439	600	16.67	4.495	4.884	2.897	6.878	2.424	6.397
0.07315	590	16.95	5.479	3.548	6.462	6.308	5.256	6.423
0.07191	580	17.24	5.383	2.098	6.992	2.713	6.593	3.712
0.07067	570	17.54	4.778	1.234	5.750	1.257	5.869	1.889

0.06943	560	17.86	4.287	0.822	4.831	0.736	5.080	1.130
0.06819	550	18.18	3.801	0.571	4.179	0.503	4.459	0.726
0.06695	540	18.52	3.363	0.376	3.680	0.382	3.954	0.451
0.06571	530	18.87	2.978	0.322	3.268	0.316	3.440	0.281
0.06447	520	19.23	2.609	0.340	2.903	0.281	2.977	0.243
0.06323	510	19.61	2.298	0.372	2.557	0.270	2.592	0.273
0.06199	500	20.00	2.008	0.443	2.204	0.283	2.256	0.323
0.06075	490	20.41	1.698	0.498	1.806	0.334	1.894	0.378
0.05951	480	20.83	1.309	0.713	1.296	0.505	1.455	0.508
0.05827	470	21.28	1.030	1.215	0.867	1.230	0.949	0.998
0.05703	460	21.74	1.307	1.299	1.542	1.289	1.458	1.365
0.05579	450	22.22	0.819	1.376	0.810	1.260	0.894	1.230
0.05455	440	22.73	0.624	1.847	0.541	1.831	0.560	1.784
0.05331	430	23.26	0.604	2.383	0.498	2.348	0.469	2.334
0.05207	420	23.81	0.748	2.873	0.545	2.844	0.527	2.857
0.05083	410	24.39	0.994	3.339	0.678	3.341	0.673	3.384
0.04959	400	25.00	1.354	3.714	0.865	3.861	0.913	3.943
0.04835	390	25.64	1.791	4.129	1.212	4.567	1.350	4.598
0.04711	380	26.32	2.650	4.537	2.213	5.416	2.289	5.277
0.04587	370	27.03	4.144	3.916	4.398	4.970	4.339	5.135
0.04463	360	27.78	3.991	2.009	4.442	2.650	4.755	2.608
0.04339	350	28.57	2.658	1.725	2.908	1.945	3.118	1.732
0.04215	340	29.41	1.448	2.630	1.546	2.857	1.725	2.576
0.04092	330	30.30	1.714	4.258	1.398	4.644	1.405	4.223
0.03968	320	31.25	3.979	5.776	3.141	7.097	3.054	6.689
0.03844	310	32.26	5.468	3.144	7.877	3.970	7.339	3.971
0.03720	300	33.33	4.736	1.561	5.614	1.255	5.553	1.303
0.03596	290	34.48	3.415	1.081	3.859	0.875	3.832	0.730
0.03472	280	35.71	2.037	1.411	2.060	1.338	1.942	1.142
0.03348	270	37.04	1.048	3.226	1.058	3.487	1.079	3.228
0.03224	260	38.46	2.081	5.458	1.569	6.282	1.436	5.666

(continued)

TABLE I *(Continued)*

Lithium Tantalate

eV	cm^{-1}	μm	$n_\perp$	$k_\perp$	$n_\perp$	$k_\perp$	$n_\perp$	$k_\perp$
0.03100	250	40.00	5.409	5.824	8.997	8.705	5.581	7.540
0.02976	240	41.67	5.967	3.231	7.365	2.041	7.966	3.011
0.02852	230	43.48	5.538	2.043	6.450	0.921	6.248	1.143
0.02728	220	45.45	4.732	1.537	5.017	0.376	4.861	0.642
0.02604	210	47.62	4.285	1.164	3.855	0.293	3.762	0.501
0.02480	200	50.00	2.595	0.829	2.531	0.406	2.364	0.557
0.02356	190	52.63	0.883	2.352	0.705	1.797	0.896	1.976
0.02232	180	55.56	1.159	4.311	0.515	3.796	0.409	3.787
0.02108	170	58.82	1.596	5.845	0.653	5.655	0.443	5.665
0.01984	160	62.50	2.461	7.855	1.137	8.124	0.881	8.340
0.01860	150	66.67	6.245	10.345	3.288	12.701	4.150	12.382
0.01736	140	71.43	11.762	7.685	17.429	10.457	12.580	10.900
0.01612	130	76.92	11.076	2.801	12.825	1.876	13.134	3.878
0.01488	120	83.33	9.729	1.158	10.319	0.780	10.668	1.620
0.01364	110	90.91	8.426	0.670	9.077	0.443	9.331	1.123
0.01240	100	100.0	7.904	0.483	8.331	0.289	8.662	0.925
0.01116	90	111.1		0.433 [b]	7.834	0.204	8.198	0.746
0.009919	80	125.0		0.321	7.482	0.151	7.902	0.618
0.008679	70	142.9		0.226	7.222	0.115	7.657	0.486
0.007439	60	166.7		0.156	7.026	0.088	7.454	0.416
0.006199	50	200.0			6.878	0.067	7.308	0.366
0.004959	40	250.0			6.767	0.050	7.239	0.337
0.003720	30	333.3			6.686	0.036	7.211	0.290
0.002480	20	500.0			6.631	0.023	7.210	0.207
0.001240	10	1000.0			6.599	0.011		

[b] Calculated from absorption coefficient of Ref. [7].

TABLE II

Values of $n_\parallel$ and $k_\parallel$ for Lithium Tantalate from Various References

eV	cm^{-1}	μm	$n_\parallel$	$k_\parallel$	$n_\parallel$	$k_\parallel$	$n_\parallel$	$k_\parallel$
2.755	22222	0.45	2.2468 [6]					
2.480	20000	0.50	2.2205					
2.066	16667	0.60	2.1878					
1.771	14286	0.70	2.1696					
1.550	12500	0.80	2.1578					
1.378	11111	0.90	2.1493					
1.240	10000	1.00	2.1432					
1.033	8333	1.20	2.1341					
0.8856	7143	1.40	2.1273					
0.7749	6250	1.60	2.1213					
0.6888	5556	1.80	2.1170					
0.6199	5000	2.00	2.1115					
0.5636	4545	2.20	2.1053					
0.5166	4167	2.40	2.0993					
0.4769	3846	2.60	2.0936					
0.4428	3571	2.80	2.0871					
0.4133	3333	3.00	2.0799					
0.3875	3125	3.20	2.0727					
0.3647	2941	3.40	2.0649					
0.3444	2778	3.60	2.0561					
0.3263	2632	3.80	2.0473					
0.3100	2500	4.00	2.0377					
0.2108	1700	5.882			1.932 [7]			
0.2095	1690	5.917			1.929			
0.2083	1680	5.952			1.925			

(continued)

TABLE II *(Continued)*

Lithium Tantalate

eV	cm^{-1}	μm	$n_{\parallel}$	$k_{\parallel}$	$n_{\parallel}$	$k_{\parallel}$	$n_{\parallel}$	$k_{\parallel}$
0.2071	1670	5.988			1.921			
0.2058	1660	6.024			1.918			
0.2046	1650	6.061			1.914			
0.2033	1640	6.098			1.910			
0.2021	1630	6.135			1.905			
0.2009	1620	6.173			1.900			
0.1996	1610	6.211			1.895			
0.1984	1600	6.250			1.890			
0.1971	1590	6.289			1.885			
0.1959	1580	6.329			1.880			
0.1947	1570	6.369			1.875			
0.1934	1560	6.410			1.870			
0.1922	1550	6.452			1.866			
0.1909	1540	6.494			1.861			
0.1897	1530	6.536			1.856			
0.1885	1520	6.579			1.851			
0.1872	1510	6.623			1.846			
0.1860	1500	6.667			1.841			
0.1847	1490	6.711			1.837		1.905 [a]	0.012 [a]
0.1835	1480	6.757			1.832		1.900	0.012
0.1823	1470	6.803			1.827		1.895	0.013
0.1810	1460	6.849			1.822		1.890	0.013
0.1798	1450	6.897			1.817		1.885	0.013
0.1785	1440	6.944			1.812		1.880	0.013
0.1773	1430	6.993			1.808		1.875	0.013
0.1761	1420	7.042			1.803		1.870	0.014
0.1748	1410	7.092			1.798		1.864	0.014

[a] Best fit of model Eq. (2) to reflectivity data of Ref. [11].

0.1736	1400	7.143	1.793	1.858	0.014
0.1723	1390	7.194	1.788	1.853	0.014
0.1711	1380	7.246	1.783	1.846	0.015
0.1699	1370	7.299	1.778	1.840	0.015
0.1686	1360	7.353	1.773	1.834	0.015
0.1674	1350	7.407	1.768	1.827	0.015
0.1661	1340	7.463	1.763	1.820	0.016
0.1649	1330	7.519	1.758	1.813	0.016
0.1637	1320	7.576	1.752	1.806	0.016
0.1624	1310	7.634	1.747	1.799	0.017
0.1612	1300	7.692	1.741	1.791	0.017
0.1599	1290	7.752	1.735	1.783	0.017
0.1587	1280	7.813	1.729	1.775	0.018
0.1575	1270	7.874	1.716	1.766	0.018
0.1562	1260	7.937	1.704	1.757	0.019
0.1550	1250	8.000	1.691	1.748	0.019
0.1537	1240	8.065	1.680	1.738	0.020
0.1525	1230	8.130	1.668	1.729	0.020
0.1513	1220	8.197	1.656	1.718	0.021
0.1500	1210	8.264	1.645	1.708	0.021
0.1488	1200	8.333	1.634	1.697	0.022
0.1475	1190	8.403	1.622	1.685	0.022
0.1463	1180	8.475	1.611	1.673	0.023
0.1451	1170	8.547	1.599	1.661	0.023
0.1438	1160	8.621	1.587	1.648	0.024
0.1426	1150	8.696	1.576	1.634	0.025
0.1413	1140	8.772	1.564	1.620	0.026
0.1401	1130	8.850	1.551	1.606	0.027
0.1389	1120	8.929	1.539	1.590	0.027
0.1376	1110	9.009	1.526	1.574	0.028
0.1364	1100	9.091	1.513	1.557	0.029

(continued)

TABLE II *(Continued)*

Lithium Tantalate

eV	cm^{-1}	μm	$n_{\parallel}$	$k_{\parallel}$	$n_{\parallel}$	$k_{\parallel}$	$n_{\parallel}$	$k_{\parallel}$
0.1351	1090	9.174			1.499		1.539	0.031
0.1339	1080	9.259			1.484		1.520	0.032
0.1327	1070	9.346			1.465		1.501	0.033
0.1314	1060	9.434			1.436		1.480	0.034
0.1302	1050	9.524			1.412		1.458	0.036
0.1289	1040	9.615			1.389		1.435	0.037
0.1277	1030	9.709			1.366		1.410	0.039
0.1265	1020	9.804			1.343		1.383	0.041
0.1252	1010	9.901			1.319		1.355	0.043
0.1240	1000	10.00	1.275 [11]		1.293		1.325	0.046
0.1227	990	10.10	1.208		1.264		1.293	0.049
0.1215	980	10.20	1.176		1.230		1.258	0.052
0.1203	970	10.31	1.143		1.177		1.221	0.055
0.1190	960	10.42	1.112		1.153		1.180	0.059
0.1178	950	10.53	1.068		1.144		1.135	0.064
0.1165	940	10.64	1.030	0.011 [11]	1.122	0.002 [7]	1.087	0.070
0.1153	930	10.75	0.978	0.003	1.066	0.042	1.032	0.077
0.1141	920	10.87	0.920	0.023	0.992	0.055	0.972	0.086
0.1128	910	10.99	0.853	0.031	0.920	0.068	0.903	0.097
0.1116	900	11.11	0.799	0.042	0.871	0.038	0.824	0.112
0.1103	890	11.24	0.713	0.048	0.841	0.006	0.732	0.134
0.1091	880	11.36	0.605	0.063	0.788	0.001	0.621	0.169
0.1079	870	11.49	0.462	0.120	0.672	0.001	0.488	0.234
0.1066	860	11.63	0.336	0.246	0.522	0.023	0.358	0.362
0.1054	850	11.76	0.265	0.394	0.403	0.117	0.293	0.525
0.1041	840	11.90	0.237	0.521	0.293	0.225	0.267	0.652
0.1029	830	12.05	0.201	0.631	0.233	0.377	0.227	0.768

0.1017	820	12.20	0.168	0.755	0.191	0.500	0.192	0.900
0.1004	810	12.35	0.150	0.879	0.152	0.621	0.173	1.033
0.09919	800	12.50	0.141	1.000	0.137	0.762	0.164	1.164
0.09795	790	12.66	0.137	1.116	0.127	0.886	0.160	1.294
0.09671	780	12.82	0.135	1.234	0.122	1.007	0.161	1.424
0.09547	770	12.99	0.136	1.354	0.121	1.137	0.165	1.556
0.09423	760	13.16	0.142	1.478	0.138	1.258	0.172	1.692
0.09299	750	13.33	0.153	1.605	0.152	1.369	0.184	1.834
0.09175	740	13.51	0.169	1.735	0.162	1.486	0.200	1.984
0.09051	730	13.70	0.189	1.869	0.172	1.609	0.224	2.142
0.08927	720	13.89	0.211	2.011	0.188	1.745	0.257	2.313
0.08803	710	14.08	0.241	2.168	0.215	1.883	0.303	2.496
0.08679	700	14.29	0.290	2.336	0.247	2.028	0.368	2.691
0.08555	690	14.49	0.359	2.502	0.289	2.182	0.459	2.896
0.08431	680	14.71	0.438	2.677	0.341	2.343	0.577	3.098
0.08307	670	14.93	0.537	2.852	0.407	2.516	0.713	3.287
0.08183	660	15.15	0.656	3.008	0.487	2.691	0.836	3.465
0.08059	650	15.38	0.698	3.152	0.567	2.852	0.919	3.682
0.07935	640	15.63	0.717	3.419	0.597	3.088	0.986	4.014
0.07811	630	15.87	0.781	3.822	0.663	3.443	1.112	4.537
0.07687	620	16.13	0.964	4.458	0.858	3.911	1.440	5.350
0.07563	610	16.39	1.577	5.375	1.263	4.640	2.401	6.618
0.07439	600	16.67	3.338	6.328	2.407	5.274	5.687	7.585
0.07315	590	16.95	5.713	4.842	4.436	5.134	8.143	3.503
0.07191	580	17.24	5.925	2.732	5.212	3.122	6.638	1.320
0.07067	570	17.54	5.248	1.514	4.722	2.070	5.529	0.685
0.06943	560	17.86	4.592	1.044	4.335	1.484	4.814	0.434
0.06819	550	18.18	4.133	0.779	3.888	1.116	4.311	0.312
0.06695	540	18.52	3.738	0.608	3.609	0.943	3.932	0.244
0.06571	530	18.87	3.408	0.537	3.337	0.809	3.627	0.203
0.06447	520	19.23	3.156	0.524	3.070	0.735	3.372	0.178

(continued)

TABLE II *(Continued)*

Lithium Tantalate

eV	cm^{-1}	μm	$n_{\parallel}$	$k_{\parallel}$	$n_{\parallel}$	$k_{\parallel}$	$n_{\parallel}$	$k_{\parallel}$
0.06323	510	19.61	2.981	0.513	2.914	0.711	3.150	0.162
0.06199	500	20.00	2.816	0.487	2.773	0.672	2.949	0.152
0.06075	490	20.41	2.649	0.457	2.643	0.621	2.763	0.148
0.05951	480	20.83	2.493	0.439	2.507	0.583	2.584	0.146
0.05827	470	21.28	2.331	0.424	2.383	0.525	2.408	0.149
0.05703	460	21.74	2.173	0.417	2.207	0.486	2.230	0.155
0.05579	450	22.22	2.006	0.419	2.019	0.473	2.044	0.165
0.05455	440	22.73	1.831	0.426	1.836	0.478	1.845	0.181
0.05331	430	23.26	1.635	0.441	1.633	0.496	1.623	0.206
0.05207	420	23.81	1.407	0.458	1.429	0.528	1.363	0.249
0.05083	410	24.39	1.118	0.511	1.134	0.521	1.041	0.334
0.04959	400	25.00	0.710	0.660	0.725	0.733	0.646	0.560
0.04835	390	25.64	0.457	1.072	0.465	1.119	0.387	0.991
0.04711	380	26.32	0.347	1.446	0.394	1.531	0.302	1.400
0.04587	370	27.03	0.324	1.798	0.415	1.864	0.294	1.773
0.04463	360	27.78	0.410	2.124	0.529	2.118	0.424	2.083
0.04339	350	28.57	0.399	2.215	0.513	2.211	0.368	2.126
0.04215	340	29.41	0.256	2.482	0.358	2.476	0.237	2.446
0.04092	330	30.30	0.217	2.817	0.323	2.818	0.203	2.779
0.03968	320	31.25	0.211	3.137	0.329	3.164	0.192	3.112
0.03844	310	32.26	0.203	3.487	0.381	3.529	0.191	3.458
0.03720	300	33.33	0.220	3.865	0.460	3.892	0.198	3.829
0.03596	290	34.48	0.247	4.280	0.553	4.279	0.211	4.240
0.03472	280	35.71	0.293	4.750	0.669	4.713	0.235	4.706
0.03348	270	37.04	0.356	5.302	0.844	5.232	0.273	5.248
0.03224	260	38.46	0.476	5.980	1.119	5.794	0.338	5.902
0.03100	250	40.00	0.720	6.835	1.546	6.449	0.450	6.723

0.02976	240	41.67	1.179	7.901	2.176	7.017	0.659	7.809
0.02852	230	43.48	2.088	9.176	2.818	7.678	1.107	9.354
0.02728	220	45.45	3.886	10.580	4.044	8.653	2.294	11.765
0.02604	210	47.62	7.019	10.982	6.104	8.727	6.685	15.217
0.02480	200	50.00	10.181	9.309	7.970	7.654	15.148	10.271
0.02356	190	52.63	11.441	6.088	8.955	6.460	13.288	4.126
0.02232	180	55.56	10.919	3.643	9.902	4.964	11.150	2.352
0.02108	170	58.82	9.839	2.296	9.387	2.934	9.830	1.667
0.01984	160	62.50	8.906	1.685	8.906	2.242	8.969	1.330
0.01860	150	66.67	8.256	1.431	8.425	1.629	8.374	1.138
0.01736	140	71.43	7.850	1.301	7.915	1.261	7.945	1.017
0.01612	130	76.92	7.548	1.168	7.607	1.020	7.630	0.932
0.01488	120	83.33	7.345	1.102	7.311	0.812	7.396	0.868
0.01364	110	90.91	7.181	1.014	7.052	0.660	7.222	0.814
0.01240	100	100.0	7.089	0.964	6.793	0.575	7.093	0.764
0.01116	90	111.1	7.018	0.882		0.566 [b]	7.001	0.713
0.009919	80	125.0	6.952	0.793		0.419	6.937	0.658
0.008679	70	142.9	6.933	0.695		0.284	6.894	0.598
0.007439	60	166.7	6.895	0.611		0.161	6.867	0.531
0.006199	50	200.0	6.879	0.512			6.852	0.457
0.004959	40	250.0	6.858	0.415			6.845	0.375
0.003720	30	333.3	6.849	0.309			6.843	0.288
0.002480	20	500.0	6.862	0.223			6.843	0.195
0.001240	10	1000.0					6.844	0.098

[b] Calculated from absorption coefficient of Ref. [7].

Potassium Iodide (KI)

MICHAEL E. THOMAS
Applied Physics Laboratory
The Johns Hopkins University
Laurel, Maryland

Potassium iodide offers a wide range of transparency, from the ultraviolet to the far infrared (0.25 to 38 μm). It is a soft material (Knoop scale 5 kg/mm^2) that is easily scratched, and it is highly hygroscopic. It has a flexure strength less than that of KBr (11 MPa). These mechanical properties limit the general utility of this optical material.

Potassium iodide is a cubic crystal with the sodium-chloride structure, space group Fm3m (O_h^5), with four formula units per unit cell. The lattice constant is 7.06555 Å, giving a theoretical density of 3.126 g/cm^3. The atomic arrangement is potassium atoms occupy the 4(a) sites and the iodine atoms occupy the 4(b) sites (both sites with m3m or O_h symmetry). Melting point is 954 K.

Ultraviolet reflectance of bulk KI was measured by Blechschmidt *et al.* [1] from 12 to 27 eV at room temperature. A Kramers–Kronig analysis yielded the optical constants in this spectral range. Tomiki *et al.* [2] measured the room-temperature (295 K) reflectance from 5 to 9 eV. Unfortunately, only the imaginary part of the permittivity was published. To complete the data set for this review, a Hilbert transform of the imaginary part of the permittivity was numerically computed to obtain the real part. The result was checked against the measured reflectance for validation. Knowing the permittivity, the optical constants were obtained. These data are listed in Table I and plotted in Fig. 1.

The Urbach tail represents absorption below the band gap, defining the end of bulk transparency. The room-temperature absorption coefficient was determined from transmission measurements by Tomiki *et al.* [3] in the spectral range from 5.0 to 5.4 eV and fitted to the functional form

$$\beta_{\text{abs}}(E,T) = \beta_{\text{U0}}\exp[\sigma_s(T)(E - E_g)/k_B T], \tag{1}$$

where β_{abs} is the absorption coefficient (typically in units of cm^{-1}); β_{U0} is a scaling coefficient in units of cm^{-1}; E_g is the band-gap energy at absolute-

HANDBOOK OF OPTICAL CONSTANTS OF SOLIDS III

Copyright © 1998 by Academic Press.
All rights of reproduction in any form reserved
ISBN 0-12-544423-0/$25.00.

zero temperature, typically given in units of eV; k_B is Boltzmann's constant; and T is temperature in Kelvins. The exponential factor $\sigma_s(T)$ is given by the equation

$$\sigma_s(T) = \sigma_0 \frac{2k_B T}{E_P} \tanh \frac{E_P}{2k_B T}, \tag{2}$$

where E_p is an effective acoustic-phonon energy of the material. The Urbach tail parameters for KI are $\beta_{U0} = 6.0 \times 10^9$ cm^{-1}, $E_g = 5.890$ eV, $\sigma_0 = 0.83$, and $E_p = 0.0045$ eV. Additional measurements of the Urbach edge covering the temperature range from 300 to 900 K are reported by Matienssen [4]. The room-temperature (295 K) values for k in Table I and Fig. 1 for this spectral region are generated using Eqs. (1) and (2).

The room-temperature (20° C) index of refraction from the ultraviolet to the far infrared (0.25 to 50 μm) has been determined by Li [5] using data from a variety of different sources. A Sellmeier model of the form

$$n^2(\lambda,T) = 1 + \sum_i \frac{\lambda^2 \Delta\epsilon_i(T)}{\lambda^2 - \lambda_i^2(T)} \tag{3}$$

is used to represent the data accurately. A Sellmeier model determined from a single consistent data sets at 311 K and 339 K is reported by Ramachandran [6]. Model parameters are listed in Table II. Because the Sellmeier model has a physical basis, the extrapolation to higher frequencies beyond the experimental limit is justified. The values for n in Table I and Fig. 1 for the spectral regions indicated are generated by the Sellmeier formula. Experimental results are reported by Korth [7] from 0.55 to 29 μm at a temperature of 311 K. Experimental results in the visible region are reported by Lowndes and Martin [8] at temperatures of 2 and 290 K. Near-room-temperature thermo-optic coefficients measured at different wavelengths are listed in Table III [7, 9, 10]. Notice that the thermo-optic coefficients at wavelengths longer than 0.3 μm are negative. This gives KI some athermal performance as an optical element. An athermal material has the property that

$$\frac{d(n(T)L(T))}{dT} = 0.$$

The value of the optical-path derivative as given above for KI is $15.7 \times 10^{-6} nL$ per Kelvin at visible and near-infrared wavelengths. Thus, KI is useful for optical designs in the far infrared that require some insensitivity to temperature.

The multiphonon absorption (multiple-quanta lattice vibrations) edge marks the end of infrared transparency. Absorption-coefficient measurements are represented by the simple formula [11]

$$\beta_{abs}(\nu) = \beta_0 \exp\left(-\gamma \frac{\nu}{\nu_0}\right), \tag{4}$$

where for KI, $\beta_0 = 4294\ cm^{-1}$ and $\nu_0/\gamma = 35.1\ cm^{-1}$ at room temperature. The values of k in the spectral range from 225 to 500 cm^{-1} in Table I and Fig. 1 are obtained from this formula. The data cover the three-phonon to four-phonon regions. Temperature-dependent data on the absorption coefficient are described in Li [11]. A temperature-dependent multiphonon model has been developed by Thomas *et al.* [12] and applied to KI. Measurements in the two-phonon region are reported by Berg and Bell [13] and Pai *et al.* [14]. These results are listed in Table I and plotted in Fig. 1.

The one-phonon (one-quanta fundamental lattice vibrations) region is opaque and therefore characterized by reflectance measurements. Room-temperature reflectance measurement is reported by Berg and Bell [13]. Room-temperature measurement using a dispersive Fourier transform spectrometer is reported by Pai *et al.* [14]. The classical-oscillator model is often used to fit the reflectance data and then to derive the optical constants. The classical-oscillator model is expressed in terms of the relative permittivity, $\epsilon_r(\nu,T)$, as[1]

$$\epsilon_r(\nu,T) = \epsilon_\infty(T) + \sum_i \frac{\Delta\epsilon_i(T)\nu_i^2(T)}{\nu_i^2(T) - \nu^2 + j\Gamma_i(\nu,T)\nu}, \tag{5}$$

where $\Delta\epsilon_i(T)$, $\Gamma_i(\nu,T)$, and $\nu_i(T)$ are the ith-mode strength, line width, and long-wavelength transverse optical frequency, ν_{TO}, respectively. The sum on i is over all transverse optical modes. For KI, there is only one allowed infrared active vibrational mode based on group theory of a perfect lattice. This is formally stated as

$$\Gamma = F_{1u}(\text{IR}).$$

The mode is infrared active (mode 1 in Table IV). Table IV lists the classical-oscillator-model parameters used to fit the experimental data [15]. More than one mode is needed to account for impurities and defects in real materials. Also, the high-frequency edge of the reflectance spectrum must include two-phonon contributions (see mode 2 in Table IV). A complete theoretical description of the infrared properties of KI is given by Hardy and Karo [16]. Unfortunately, the value of ϵ_∞ used by Hadni *et al.* [15] is not consistent with the value from the Sellmeier model mentioned previously. For this reason the joining of the Sellmeier model and the one-phonon model is not smooth. Good agreement with the static dielectric constant is obtained. The n and k values in Table I and Fig. 1 come from Berg and Bell [13] and Pai *et al.* [14].

[1] The expression uses the engineering convention for a time harmonic field of $\exp(-j\omega t)$. To convert to the convention commonly used in the *HOC* series use $i = -j$.

Below ν_{TO}, the index of refraction, n, and the extinction coefficient, k, have been measured by Berg and Bell [13], and Pai *et al* [13]. Table I and Fig. 1 list and display the resulting values.

The static-dielectric-constant data is the sum of all the strengths of higher-frequency oscillators including vibrational and electronic. Using Eq. (5), the static dielectric constant, $\epsilon_s(T) = \epsilon_r'(0,T)$, becomes

$$\epsilon_s(T) = \epsilon_\infty(T) + \sum_i \Delta\, \epsilon_i(T). \tag{6}$$

Based on the parameters listed in Table IV, we expect the value of ϵ_s to be 5.11. Experimental results, obtained from capacitance bridges operating from 1 kHz to 1 MHz, microwave techniques, or reflection measurements using a Fourier transform spectrometer produce values from 5.00 to 5.12, with the best results closer to the higher value [5, 10, 13, 16, 17]. The representative refractive index value is $n_s = 2.256$. The static-index values incorrectly are located at 1×10^4 μm in Fig. 1; however, there is little difference in the value of n_s at the measured wavelength and the plotted wavelength.

Whenever possible, physically based models are used to represent experimental measurements in Table I and Fig. 1. The models tend to reduce noise and allow interpolation and extrapolation to obtain meaningful results where no experimental data exists. In some case, the models discussed in this section also allow temperature-dependent data to be obtained.

REFERENCES

1. D. Blechschmidt, R. Klucker and M. Skibowski, Dielectric properties of KCl, KBr, and KI single crystals in the extreme ultraviolet up to 35 eV. *Phys. Status Solidi* **36**, 625–634 (1959).
2. T. Tomiki, T. Miyata, and H. Tsukamoto, Temperature dependence of the fundamental spectra of potassium-halides in the Schumann ultraviolet (4.4–13.5 eV), *J. Phys. Soc. Jpn.* **35**, 495–507 (1973).
3. T. Tomiki, T. Mayata, and H. Tsukamoto, The Urbach rule for the sodium- and potassium-halides. *Z. Naturforsch.* **29A**, 145–157 (1974).
4. W. Martienssen, The optical absorption edge in ionic crystals. *J. Phys. Chem. Solids* **8**, 294–296 (1959).
5. H. H. Li, Refractive index of alkali halides and its wavelength and temperature derivatives. *J. Phys. Chem. Ref. Data* **5**, 329–528 (1976).
6. G. N. Ramachandran, Thermo-optic behavior of solids V. Alkali halides. *Proc. Indian Acad. Sci. Sect. A* **25**, 481–497 (1947).
7. K. Korth, Dispersion measurements on potassium bromide and potassium iodide in the infrared region. *Z. Phys.* **84**, 677–685 (1933).
8. R. P. Lowndes and D. H. Martin, Dielectric dispersion and the structures of ionic lattices. *Proc. R. Soc. London A* **308**, 473–496 (1969).
9. H. Harting, The optical aspect of some crystals and their representation by the Hartmann equation. *Z. Instrum.* **63**, 125–131 (1943).
10. R. P. Lowndes and D. H. Martin, Dielectric constants of ionic crystals and their variations with temperature and pressure. *Proc. R. Soc. London A* **316**, 351–375 (1970).

11. H. H. Li, The infrared absorption coefficient of alkali halides. *Int. J. Thermophys.* **1**, 97–134 (1980).
12. M. E. Thomas, R. I. Joseph, and W. J. Tropf, Infrared transmission properties of sapphire, spinel, yttria and ALON as a function of temperature and frequency. *Appl. Opt.* **27**, 239–245 (1988); M. E. Thomas, Temperature dependence of the complex didex of refraction. *in* "Handbook of Optical Constants of Solids II" (E. D. Palik, ed.), Chap 8, pp. 177–201. Orlando, Florida, Academic Press, 1991; M. E. Thomas, A computer code for modeling optical properties of window materials, in window and dome technologies and materials. *Proc. of SPIE* **1112**, 260–267 (1989).
13. J. I. Berg and E. E. Bell, Far-infrared optical constants of KI. *Phys. Rev.* **B 4**, 3572–3580 (1971).
14. K. F. Pai, T. J. Parker, N. E. Tornberg, R. P. Lowndes and W. G. Chambers, Determination of the complex refractive indices of solids in the far-infrared by dispersive fourier transform spectroscopy-I. Alkali halides. *Infrared Phys.* **18**, 199–214 (1978).
15. A. Hadni, J. Claudel, G. Morlet, and P. Strimer, Transmission and reflection spectra of pure and doped potassium iodide at low temperatures. *Appl. Opt.* **7**, 161–165 (1968).
16. J. R. Hardy and A. M. Karo, Theoretical study of the long-wavelength optical properties of NaCl, KCl, KBr and KI. *Phys. Rev.* **B 26**, 3327–3337 (1982).
17. C. Demau, Measurement of the diclectric constants and dielectric anisotropies of various crystals at X-band. *J. Phys. (Paris)* **24**, 284–285 (1963).

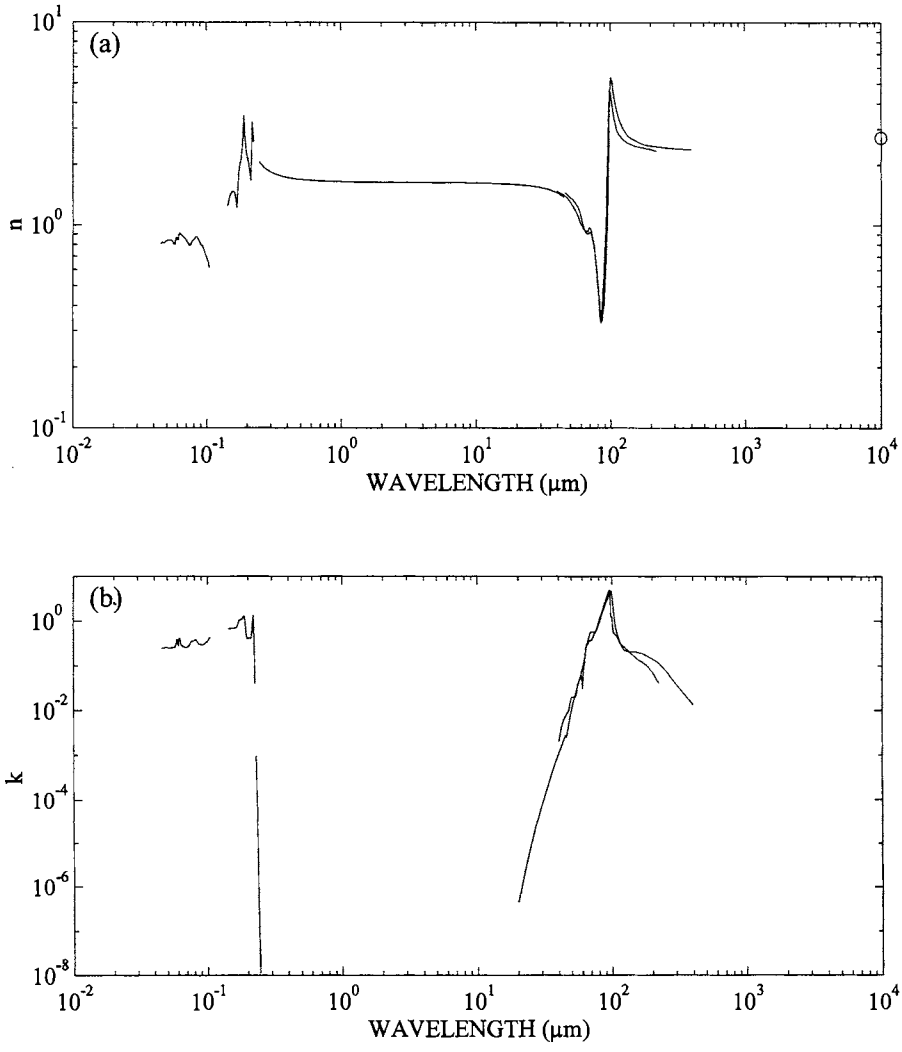

Fig. 1. (a) Log–log plot of the room-temperature index of refraction, n, for KI versus wavelength in micrometers. (b) Log–log plot of the room-temperature extinction coefficient, k, for KI versus wavelength in micrometers. Isolated data points are indicated with a symbol.

TABLE I

Values of n and k for Potassium Iodide from Various References[a]

eV	cm^{-1}	μm	n	k
27.34	220500	0.04536	0.8020 [1]	0.2474 [1]
26.65	214900	0.04653	0.8210	0.2464
26.07	210200	0.04757	0.8122	0.2507
25.76	207800	0.04813	0.8097	0.2548
25.27	203800	0.04907	0.8198	0.2614
24.84	200400	0.04991	0.8314	0.2547
24.52	197700	0.05057	0.8339	0.2500
24.10	194400	0.05145	0.8370	0.2467
23.51	189600	0.05275	0.8403	0.2487
22.88	184600	0.05419	0.8412	0.2519
22.28	179700	0.05565	0.8296	0.2546
21.81	175900	0.05684	0.8029	0.2591
21.61	174300	0.05738	0.8002	0.2693
21.49	173300	0.05769	0.7988	0.2904
21.39	172500	0.05796	0.7976	0.3102
21.32	172000	0.05815	0.8043	0.3314
21.26	171500	0.05831	0.8147	0.3475
21.27	171500	0.05830	0.8140	0.3651
21.12	170400	0.05869	0.8379	0.3959
20.89	168500	0.05934	0.8655	0.3807
20.81	167800	0.05958	0.8618	0.3653
20.78	167600	0.05965	0.8605	0.3451
20.64	166500	0.06008	0.8532	0.3067
20.53	165600	0.06040	0.8476	0.2746
20.48	165200	0.06054	0.8456	0.3082
20.50	165400	0.06048	0.8465	0.3306
20.42	164700	0.06071	0.8432	0.3545
20.20	163000	0.06137	0.8427	0.3973
20.10	162100	0.06169	0.8585	0.4219
19.99	161300	0.06201	0.8858	0.4050
19.96	161000	0.06212	0.8947	0.3873
19.81	159800	0.06259	0.9048	0.3420
19.79	159600	0.06265	0.9056	0.3275
19.75	159300	0.06277	0.9071	0.3139
19.64	158400	0.06314	0.9091	0.3020
19.52	157400	0.06352	0.9044	0.2898
19.31	155700	0.06421	0.8963	0.2772
19.07	153800	0.06503	0.8871	0.2677
17.97	145000	0.06899	0.8556	0.2527
16.94	136600	0.07319	0.8016	0.2775
16.86	136000	0.07355	0.7965	0.2906
16.80	135500	0.07382	0.7933	0.3061
16.64	134200	0.07452	0.7871	0.3193
16.60	133900	0.07470	0.7856	0.3411
16.26	131100	0.07627	0.8013	0.3458

(continued)

[a] References given in brackets.

TABLE I *(Continued)*

Potassium Iodide

eV	cm^{-1}	μm	n	k
15.95	128600	0.07775	0.8240	0.3532
15.72	126800	0.07889	0.8339	0.3590
15.59	125700	0.07954	0.8395	0.3648
15.53	125300	0.07983	0.8419	0.3745
15.15	122200	0.08186	0.8612	0.3898
15.08	121600	0.08222	0.8653	0.3798
15.02	121200	0.08252	0.8682	0.3708
14.77	119100	0.08393	0.8750	0.3394
14.65	118200	0.08463	0.8683	0.3280
14.36	115800	0.08635	0.8523	0.3039
13.65	110100	0.09081	0.7963	0.2951
13.27	107000	0.09343	0.7838	0.2996
12.66	102100	0.09790	0.7115	0.3367
12.60	101600	0.09838	0.7066	0.3403
12.42	100200	0.09984	0.6936	0.3507
12.00	96780	0.1033	0.6457	0.4120
11.92	96180	0.1040	0.6369	0.4264
11.84	95480	0.1047	0.6137	0.4411
8.610	69440	0.1440	1.242 [2]	0.675 [2]
8.486	68440	0.1461	1.281	0.684
8.362	67440	0.1483	1.369	0.6879
8.238	66440	0.1505	1.410	0.6841
8.114	65440	0.1528	1.437	0.683
7.990	64440	0.1552	1.456	0.6875
7.866	63440	0.1576	1.464	0.6895
7.742	62440	0.1601	1.459	0.6985
7.618	61440	0.1628	1.436	0.7025
7.494	60440	0.1654	1.343	0.7254
7.370	59440	0.1682	1.215	0.8313
7.246	58440	0.1711	1.431	1.003
7.122	57440	0.1741	1.777	1.061
6.998	56440	0.1772	1.961	1.069
6.874	55440	0.1804	2.069	1.101
6.750	54440	0.1837	2.318	1.206
6.626	53440	0.1871	2.742	1.298
6.502	52440	0.1907	3.449	0.9769
6.378	51440	0.1944	2.659	0.4732
6.254	50440	0.1982	2.284	0.3918
6.130	49440	0.2023	2.159	0.4171
6.006	48440	0.2064	2.055	0.4087
5.882	47440	0.2108	1.848	0.4104
5.758	46440	0.2153	1.655	0.76
5.634	45440	0.2201	3.219	1.3
5.510	44440	0.2250	2.583	0.040
5.391	43480	0.230	2.391 [5]	0.00095 [3]
5.344	43100	0.232	2.325	0.00021

TABLE I *(Continued)*

Potassium Iodide

eV	cm^{-1}	μm	*n*	*k*
5.298	42740	0.234	2.272	4.8E-5
5.254	42370	0.236	2.229	1.1E-5
5.209	42020	0.238	2.192	2.7E-6
5.166	41670	0.240	2.161	6.6E-7
5.123	41320	0.242	2.133	1.7E-7
5.081	40980	0.244	2.109	4.3E-8
5.040	40650	0.246	2.087	1.3E-8
4.959	40000	0.25	2.0493	
3.542	28571	0.35	1.7595	
2.755	22222	0.45	1.6979	
2.254	18182	0.55	1.6723	
1.907	15385	0.65	1.6589	
1.653	13333	0.75	1.6509	
1.458	11765	0.85	1.6457	
1.305	10526	0.95	1.6422	
1.181	9523.8	1.05	1.6396	
1.078	8695.7	1.15	1.6377	
0.9990	8000	1.25	1.6363	
0.9184	7407.4	1.35	1.6351	
0.8551	6896.6	1.45	1.6342	
0.7999	6451.6	1.55	1.6335	
0.7514	6060.6	1.65	1.6328	
0.7085	5714.3	1.75	1.6323	
0.6702	5405.4	1.85	1.6319	
0.6358	5128.2	1.95	1.6315	
0.6048	4878	2.05	1.6312	
0.5510	4444.4	2.25	1.6306	
0.5061	4081.6	2.45	1.6302	
0.4679	3773.6	2.65	1.6298	
0.4350	3508.8	2.85	1.6295	
0.4065	3278.7	3.05	1.6292	
0.3815	3076.9	3.25	1.6289	
0.3594	2898.6	3.45	1.6287	
0.3397	2739.7	3.65	1.6285	
0.3220	2597.4	3.85	1.6282	
0.3061	2469.1	4.05	1.628	
0.2917	2352.9	4.25	1.6278	
0.2786	2247.2	4.45	1.6276	
0.2666	2150.5	4.65	1.6274	
0.2556	2061.9	4.85	1.6272	
0.2455	1980.2	5.05	1.6270	
0.2362	1904.8	5.25	1.6268	
0.2275	1834.9	5.45	1.6266	
0.2194	1769.9	5.65	1.6264	
0.2119	1709.4	5.85	1.6262	
0.2049	1652.9	6.05	1.6259	

(continued)

TABLE I *(Continued)*

Potassium Iodide

eV	cm^{-1}	μm	n	k
0.1984	1600.0	6.25	1.6257	
0.1922	1550.4	6.45	1.6255	
0.1864	1503.8	6.65	1.6253	
0.1810	1459.9	6.85	1.6250	
0.1759	1418.4	7.05	1.6248	
0.1710	1379.3	7.25	1.6245	
0.1664	1342.3	7.45	1.6242	
0.1621	1307.2	7.65	1.6240	
0.1579	1273.9	7.85	1.6237	
0.1540	1242.2	8.05	1.6234	
0.1503	1212.1	8.25	1.6231	
0.1467	1183.4	8.45	1.6229	
0.1433	1156.1	8.65	1.6226	
0.1401	1129.9	8.85	1.6223	
0.1370	1105.0	9.05	1.6219	
0.1340	1081.1	9.25	1.6216	
0.1312	1058.2	9.45	1.6213	
0.1285	1036.3	9.65	1.6210	
0.1259	1015.2	9.85	1.6206	
0.1234	995.02	10.05	1.6203	
0.1210	975.61	10.25	1.6199	
0.1186	956.94	10.45	1.6196	
0.1164	938.97	10.65	1.6192	
0.1143	921.66	10.85	1.6188	
0.1122	904.98	11.05	1.6185	
0.1102	888.89	11.25	1.6181	
0.1083	873.36	11.45	1.6177	
0.1064	858.37	11.65	1.6173	
0.1046	843.88	11.85	1.6169	
0.1029	829.88	12.05	1.6164	
0.1012	816.33	12.25	1.6160	
0.09959	803.21	12.45	1.6156	
0.09801	790.51	12.65	1.6152	
0.09649	778.21	12.85	1.6147	
0.09501	766.28	13.05	1.6142	
0.09357	754.72	13.25	1.6138	
0.09218	743.49	13.45	1.6133	
0.09083	732.6	13.65	1.6128	
0.08952	722.02	13.85	1.6124	
0.08824	711.74	14.05	1.6119	
0.08701	701.75	14.25	1.6114	
0.08580	692.04	14.45	1.6108	
0.08463	682.59	14.65	1.6103	
0.08349	673.4	14.85	1.6098	
0.08238	664.45	15.05	1.6093	
0.08025	647.25	15.45	1.6082	

TABLE I *(Continued)*

Potassium Iodide

eV	cm^{-1}	μm	*n*	*k*		
0.07822	630.91	15.85	1.6071			
0.07630	615.38	16.25	1.6059			
0.07446	600.6	16.65	1.6047			
0.07272	586.51	17.05	1.6035			
0.07105	573.07	17.45	1.6022			
0.06946	560.22	17.85	1.6009			
0.06794	547.95	18.25	1.5996			
0.06648	536.19	18.65	1.5982			
0.06508	524.93	19.05	1.5968			
0.06374	514.14	19.45	1.5954			
0.06246	503.78	19.85	1.5939			
0.06199	500.0	20.0	1.5933	4.448E-7 [11]		
0.05904	476.1	21.0	1.5894	9.203E-7		
0.05636	454.5	22.0	1.5853	1.786E-6		
0.05391	434.8	23.0	1.5809	3.279E-6		
0.05166	416.7	24.0	1.5762	5.734E-6		
0.04959	400.0	25.0	1.5712	9.602E-6		
0.04769	384.6	26.0	1.5660	1.548E-5		
0.04592	370.4	27.0	1.5604	2.412E-5		
0.04428	357.1	28.0	1.5545	3.646E-5		
0.04275	344.8	29.0	1.5483	5.364E-5		
0.04133	333.3	30.0	1.5417	7.699E-5		
0.03999	322.6	31.0	1.5347	0.000109		
0.03874	312.5	32.0	1.5273	0.000149		
0.03757	303.0	33.0	1.5195	0.000201		
0.03647	294.1	34.0	1.5112	0.000267		
0.03542	285.7	35.0	1.5024	0.000349		
0.03444	277.8	36.0	1.4931	0.000450		
0.03351	270.3	37.0	1.4832	0.000573		
0.03263	263.2	38.0	1.4727	0.000720		
0.03179	256.4	39.0	1.4615	0.000896		
0.03100	250.0	40.0	1.4497	0.00110		
eV	cm^{-1}	μm	*n*	*k*	*n*	*k*
0.03024	243.9	41.0	1.4370	0.00134		
0.02952	238.1	42.0	1.4235	0.00163		
0.02883	232.6	43.0	1.4090	0.00195		
0.02818	227.3	44.0	1.3935	0.00232		
0.02755	222.2	45.0	1.3769	0.00274		
0.03100	250	40.0			1.47 [14]	0.002 [14]
0.02976	240	41.7			1.45	0.004
0.02852	230	43.5			1.43	0.006
0.02728	220	45.5	1.454 [13]	0.002 [13]	1.40	0.008
0.02666	215	46.5	1.437	0.004		
0.02604	210	47.6	1.424	0.005	1.37	0.01

(continued)

TABLE I *(Continued)*

Potassium Iodide

eV	cm^{-1}	μm	n	k	n	k
0.02542	205	48.8	1.400	0.007	1.34	0.015
0.02480	200	50.0	1.380	0.010	1.31	0.02
0.02418	195	51.3		0.014	1.28	0.02
0.02356	190	52.6	1.338	0.019	1.24	0.02
0.02331	188	53.2			1.23	0.02
0.02306	186	53.8			1.21	0.02
0.02294	185	54.1	1.305	0.027		
0.02281	184	54.4			1.19	0.025
0.02257	182	55.0			1.18	0.03
0.02232	180	55.6	1.272	0.035	1.16	0.04
0.02207	178	56.2			1.14	0.04
0.02182	176	56.8			1.13	0.045
0.02170	175	57.1	1.234	0.048		
0.02157	174	57.5			1.10	0.05
0.02133	172	58.1			1.08	0.05
0.02108	170	58.8	1.174	0.066	1.05	0.06
0.02083	168	59.5			1.02	0.05
0.02058	166	60.2			1.01	0.03
0.02046	165	60.6	1.083	0.092		
0.02033	164	61.0			1.00	0.07
0.02009	162	61.7			0.98	0.1
0.01984	160	62.5	0.984	0.149	0.96	0.15
0.01959	158	63.3	0.960	0.235	0.95	0.2
0.01934	156	64.1	0.938	0.275	0.94	0.26
0.01909	154	64.9	0.922	0.308	0.94	0.28
0.01885	152	65.8	0.912	0.342	0.93	0.31
0.01860	150	66.7	0.905	0.393	0.93	0.33
0.01835	148	67.6	0.904	0.453	0.93	0.35
0.01810	146	68.5	0.908	0.530	0.95	0.37
0.01785	144	69.4	0.915	0.558	0.97	0.36
0.01761	142	70.4	0.919	0.568	0.97	0.37
0.01736	140	71.4	0.913	0.564	0.95	0.4
0.01711	138	72.5	0.894	0.560	0.91	0.45
0.01686	136	73.5	0.862	0.564	0.86	0.5
0.01661	134	74.6	0.825	0.573	0.81	0.54
0.01637	132	75.8	0.778	0.593	0.75	0.59
0.01612	130	76.9	0.709	0.634	0.71	0.67
0.01587	128	78.1	0.615	0.710	0.64	0.77
0.01562	126	79.4	0.535	0.813	0.57	0.92
0.01537	124	80.6	0.464	0.942	0.49	1.11
0.01513	122	82.0	0.399	1.100	0.43	1.26
0.01488	120	83.3	0.351	1.277	0.38	1.42
0.01463	118	84.7	0.330	1.485	0.34	1.6
0.01438	116	86.2	0.340	1.714	0.38	1.87
0.01413	114	87.7	0.369	2.001	0.48	2.27
0.01389	112	89.3	0.425	2.342	0.59	2.75

TABLE I *(Continued)*

Potassium Iodide

eV	cm^{-1}	μm	n	k	n	k
0.01364	110	90.9	0.528	2.718	0.75	3.28
0.01339	108	92.6	0.682	3.169	1.03	3.96
0.01314	106	94.3	0.961	3.787	1.66	4.51
0.01289	104	96.2	1.597	4.387	2.92	4.88
0.01265	102	98.0	3.692	4.788	4.62	1.24
0.01240	100	100.0	5.371	3.770	4.54	1.24
0.01215	98	102.0	5.177	2.302	4.09	0.58
0.01190	96	104.2	4.742	1.168	3.72	0.51
0.01166	94	106.4	4.313	0.732	3.39	0.48
0.01141	92	108.7	3.976	0.543	3.16	0.45
0.01116	90	111.1	3.706	0.439	2.97	0.39
0.01091	88	113.6	3.503	0.359	2.88	0.33
0.01066	86	116.3	3.342	0.300	2.80	0.3
0.01042	84	119.1	3.197	0.254	2.75	0.28
0.01017	82	122.0	3.064	0.228	2.69	0.27
0.00992	80	125.0	2.974	0.213	2.65	0.25
0.00930	75	133.3	2.788	0.202	2.57	0.21
0.00868	70	142.9	2.694	0.203	2.51	0.17
0.00806	65	153.9	2.625	0.200	2.46	0.14
0.00744	60	166.7	2.555	0.187	2.44	0.12
0.00682	55	181.8	2.504	0.164	2.41	0.1
0.00620	50	200.0	2.475	0.139	2.38	0.07
0.00558	45	222.2	2.453	0.113	2.33	0.04
0.00496	40	250.0	2.433	0.077		
0.00434	35	285.7	2.409	0.046		
0.00372	30	333.3	2.390	0.026		
0.00310	25	400.0	2.372	0.013		
0.0	0	∞	2.256 [15]			

TABLE II

Room-Temperature Sellmeier Model Parameters

ith Mode	$\Delta\epsilon_i$	λ_i
Li model, $T = 293$ K, 0.25–50 μm [5]		
1	0.47285	0.0
2	0.41222	0.129
3	0.44163	0.175
4	0.16076	0.187
5	0.33571	69.44
6	1.92474	98.04
Ramachandran model, $T = 339$ K, 0.253–0.615 μm [6]		
1	0.4532	0.0
2	0.2150	0.1290
3	0.8027	0.1805
4	0.1780	0.2190
Ramachandran model, $T = 311$ K, 4.0–29.0 μm [6]		
1	1.6499	0.0
2	2.530	102.0

TABLE III

Thermo-optical Coefficients of Potassium Iodide

Wavelength (μm)	dn/dT (10^{-6}/K)	Measurement Temperature (°C)	Reference
0.24828	131	20	[9]
0.25365	102	20	[9]
0.26537	42	20	[9]
0.28936	0	20	[9]
0.54	−50	38	[7]
0.33415	−22	20	[9]
1.08303	−43	20	[9]
5.0	−45	20	[5]
10.0	−44	20	[5]
∞	373	27	[10]

TABLE IV

Room-Temperature Classical Oscillator-Model Parameters

Mode number i	ν_i [cm^{-1}]	$\Delta\epsilon_i$	Γ_i/ν_i	Reference
1	102	2.136	0.084	[15]
2	316	0.276	0.3	
		$\epsilon_\infty = 2.7$		

Potassium Niobate ($KNbO_3$)

IVAN BIAGGIO
Nonlinear Optics Laboratory
Institute of Quantum Electronics
Swiss Federal Institute of Technology
Zürich, Switzerland

Potassium niobate is a perovskite ferroelectric crystal with orthorhombic structure and space group Bmm2 at room temperature. Upon cooling from the high-temperature cubic phase, it undergoes a series of phase transitions to a tetragonal, orthorhombic, and rhombohedral phase at temperatures of 418, 203, and $-50°$ C, respectively. On heating, the orthorhombic-to-tetragonal phase transition takes place at 223° C. The orthorhombic nonprimitive unit cell contains twice as many atoms as the cubic phase primitive cell. The orthorhombic crystallographic a-axis is oriented along the (101) direction derived from the cube of the ideal perovskite structure, the b-axis is along (010), and the c-axis is along $(\bar{1}01)$. The $+c$-axis is, by definition, parallel to the spontaneous polarization. The corresponding lattice parameters are $a_o = 0.56896$ nm, $b_o = 0.39692$ nm, and $c_o = 0.57256$ nm [1, 2]. With this choice of crystallographic axes, the space group is labeled Bmm2, because the b-face of the orthorhombic unit cell is centered. It is important to note that the refractive indices in the visible spectral range obey $n_b > n_a > n_c$, and that, although this is the convention most often used in the optics literature relating to $KNbO_3$, another convention has been proposed [3, 4] and is sometimes used. In this alternative convention the a and b axes are interchanged with respect to the definition used here and the space group is labeled Amm2.

Index matching for second-harmonic generation is possible through angle and temperature tuning for fundamental wavelengths longer than 850 nm and up to a few micrometers [5].

The UV and band-edge data has been measured by Wiesendanger [6] up to a photon energy of 10 eV. Wiesendanger used single-domain crystals grown from a top-seeded, flux-growth technique, and poled a few degrees below the orthorhombic–tetragonal phase transition (poling of the crystal is performed by application of an electric field and makes sure that the ferro-

Copyright © 1998 by Academic Press.
All rights of reproduction in any form reserved
ISBN 0-12-544423-0/$25.00.

electric polarization is oriented in the same direction throughout the crystal sample). Vacuum-ultraviolet reflectivity was measured with polarized light at near-normal incidence in the range between 3 and 10 eV. Reproducibility of the reflectance values for each polarization was better than 0.01. Anisotropy effects are observed especially in the low-energy part below 7 eV, with differences in reflectivity up to 0.12. Above 7 eV these differences are less marked. The optical constants were derived from the measured reflectivity spectra by Kramers–Kronig analysis for every polarization. For the Kramers–Kronig analysis the data had to be extrapolated. Details of the extrapolation affected the absolute values of the optical constants but had little influence on the positions of the different peaks or on the relative magnitudes of the optical constants for different light polarizations. We take the (n, k) data directly from the plots published by Wiesendanger. Note that the k values are slightly too high in the low-energy region around 3.5 eV, especially for k_b. This is apparent when comparing to the band-edge absorption measurements presented later.

Mamedov and Gadzhieva [7] measured UV reflectivity up to a photon energy of 35 eV. We do not use their data here because it is not clear what the polarization of their light source was. Qualitatively, the structure they observe below 10 eV is similar to the measurements of Wiesendanger. Above 10 eV, the reflectivity slowly decreases, with a not-well-pronounced, strongly broadened maximum around 17 eV, which has a reflectivity more than 5 times smaller than the peaks observed below 10 eV.

Wiesendanger [6] also studied the band-edge absorption with polarized light in the energy range from 3.1 to 3.3 eV and found an Urbach-rule behavior, with the absorption coefficient α increasing exponentially with the photon energy. The slopes of the $\ln(\alpha)$ versus photon energy lines were the same for all polarization of the light, but the absorption for light polarized along b was approximately twice the absorption observed for light polarized along a or c. The latter was found to be 100 cm^{-1} at a photon energy of 3.31 eV. The data presented in the table is Wiesendanger's Urbach-rule fit to his absorption measurements.

Montemezzani *et al.* [8] measured the transmittivity of thin $KNbO_3$ crystals in a UV spectrophotometer between 3.2 and 3.5 eV for light polarized along the c- and the b-axis. The samples were prepared by gluing $KNbO_3$ platelets with polished a face onto fused-silica substrates using polymethyl methacrylate (PMMA) and subsequently polishing the crystals to final thicknesses of 25 and 70 μm. They obtained absorption-coefficient values with a precision of about 10% and observed the deviation from the Urbach-rule behavior for light energies higher than 3.3 eV. The results for the two samples were within the 10% error margin. The data we present in Tables IV–VI are the average of the data of both samples. Wiesendanger has shown that at the band edge the absorption for a- and c-polarized light is equal within experimental uncertainty. Therefore, we use the data measured by Montemezzani *et al.* with c-polarized light also in the table for k_a.

The refractive-index data in the wavelength range 400–3400 nm were measured by Zysset *et al.* [9] at six different temperatures between 22 and 180° C. The refractive indices were measured for the three light polarizations using the minimum-deviation technique and three different prisms. The prisms were obtained from high-optical-quality boules of nominally pure $KNbO_3$ grown by the top-seeded-solution technique [10]. All prisms had the *c*-axis oriented parallel to the apex of the prism. Two of them had the *b*-axis in the prism-bisecting plane, and a third one the *a*-axis. This allowed the measurement of n_a in one prism, measurements of n_b in two prisms, and measurements of n_c in all three samples. The orientation of the prisms was controlled by x-ray scattering to better than 30 arcmin, and the process of fabricating the prisms introduced an error of less than 30 arcmin. The refractive indices were measured at 22 different wavelengths between 404.66 and 3400 nm. The maximum error for a single data point was estimated to be ± 0.0003. The scattering of the experimental data of the various samples was within the error margin. The data were fitted with a two-term Sellmeier oscillator model with an IR correction term:

$$n^2 - 1 = S_1 \frac{\lambda^2 \lambda_1^2}{\lambda^2 - \lambda_1^2} + S_2 \frac{\lambda^2 \lambda_2^2}{\lambda_2 - \lambda_2^2} - D\lambda^2, \tag{1}$$

where n is the refractive index at vacuum wavelength λ, S_i, λ_i are the strengths and wavelengths of the two UV oscillators, and D is the coefficient of an IR correction term. The term $-D\lambda^2$ is the limiting form of the complete oscillator term $S_{IR}/(\lambda_{IR}^{-2} - \lambda^{-2})$ when $\lambda << \lambda_{IR}$. The simplified form is enough to fit the refractive indices over the 400–3400 nm range with the required accuracy. The IR term gives a small correction of less than 0.1 in the visible, but dominates the dispersion for wavelengths longer than 2μm. The refractive indices calculated with Eq. (1) and the parameters in Table I have a maximum error of ± 0.00025, or approximately 0.01% of the index values. In Table I we list the Sellmeier coefficients to be used to calculate the three principal refractive indices at 22° C using Eq. (1). We refer to Zysset *et al.* [9] for the high-temperature data.

Jundt *et al.* [11] refitted the complete data set of Zysset *et al.* using an ad hoc dispersion formula that gives the refractive index at all wavelengths between 400 and 3400 nm and at all temperatures in the orthorhombic phase:

$$\begin{aligned} n^2 - 1 = {} & (S_1 + b_1 F + b_2 G) \frac{\lambda^2 \lambda_1^2}{\lambda^2 - (\lambda_1 + b_3 F + b_4 G)^2} \\ & + (S_2 + b_5 F) \frac{\lambda^2 \lambda_2^2}{\lambda^2 - (\lambda_2 + b_6 F)^2} - (D + b_7 F)\lambda^2 + b_8 F \lambda^4, \end{aligned} \tag{2}$$

with $F = (\vartheta + 273.15)^2 - (22 + 273.15)^2$ and $G = \vartheta - 22$, where ϑ is the crystal temperature in °C. This expression gives the $KNbO_3$ refractive indi-

ces over the whole temperature range as accurately as the Sellmeier fits using Eq. (1). The parameters are given in Table II.

Note that in Zysset *et al.* [9] and Jundt *et al.* [11] the oscillator energies in electron volts are given, rather than their wavelength in nanometers, and that in these two publications different conversion factors were used to transform from the fitted wavelengths to the energy in electron volts given in Tables I and V. These conversion factors are given in the table footnotes.

Absorption losses in the visible and near infrared have been measured in high-quality $KNbO_3$ samples by Busse *et al.* [12] and are generally around 3% per centimeter at a wavelength of 500 nm for light polarized parallel to the *c*-axis, and less than 0.5% per centimeter between 800 and 1064 nm for light polarization along the *b*-axis. We did not find precise absorption data in the spectral range from 1 to 10 μm, but from a transmission measurement performed in 1-mm-thick plates in our laboratory, we know that the absorption remains low up to a wavelength of $\sim$5 μm. At wavelengths longer than 5 μm the transmission of the sample decreases, and it becomes less than 1% (corresponding to an absorption coefficient of approximately 45 cm^{-1}, or $k = 3 \times 10^{-3}$) at wavelengths longer than 8 μm.

The optical phonon reflection branches have been measured at optical frequencies between 100 and 1000 cm^{-1} by Bozinis and Hurrell [13] and by Fontana *et al.* [14]. Fontana *et al.* fitted the reflectivity $R = |(n + ik) - 1|^2/|(n + ik) + 1|^2$ with the factorized form of the dielectric function $\epsilon = (n + ik)^2$:

$$\epsilon(\omega) = \epsilon_\infty \prod_{i=1}^{4} \frac{\Omega^2(\mathrm{LO}_i) - \omega^2 + i\,\omega\,\gamma(\mathrm{LO}_i)}{\Omega^2(\mathrm{TO}_i) - \omega^2 + i\,\omega\,\gamma(\mathrm{TO}_i)}, \tag{3}$$

where ϵ_∞ is the dielectric constant at optical frequencies, and Ω,γ are the frequencies and dampings of the transversal optical (TO) and longitudinal optical (LO) vibrational modes.

Fontana *et al.* [14] do not state explicitly the value of ϵ_∞ they used in their fit and only measured the reflectivity spectrum for light polarized along the *b*-axis at room temperature. Bozinis and Hurrell give spectra for all light polarizations, but their data are less precise, and they do not explicitly derive the dielectric constant from it.

We used Eq. (3) to fit the *b*-polarization data of Fontana *et al.* [14] and the *a*- and *c*-polarization data of Bozinis and Hurrell [13]. For all fits we imposed the constraint that the limiting values of the dielectric constant at low and high frequencies correspond to the independently determined values. That is, we fixed $\epsilon(\lambda = 1.5\mu\mathrm{m})$ to the values given by Zysset *et al.* [9] (at 1.5 μm $n_a = 2.1992$, $n_b = 2.2341$, $n_c = 2.1029$) and $\epsilon(\omega = 0)$ to the clamped values of the dielectric constants determined by Zgonik *et al.* [15] ($\epsilon_a = 34 \pm 2$, $\epsilon_b = 780 \pm 22$, $\epsilon_c = 24 \pm 2$). These are the values of the dielectric constant at electric-field frequencies where the optical vibrational modes contribute to the polarization but the acoustic modes do not.

The parameters obtained from the fit and from the published data of Fontana *et al.* [14] and Bozinis and Hurrell [13] are given in Table III. From the dielectric function calculated from Eq. (3) we then obtain the values of n and k for wavelengths longer than 10 μm. In the tables for (n_a,k_a) and (n_c,k_c) we give a reference to the work of Bozinis and Hurrell for the data in this spectral range. This refers to the original reflectivity data from which the optical constants were extracted.

The fit for the *b*-polarized, room-temperature reflectivity data of Fontana *et al.* was good and could reproduce their experimental data within the scatter of the data points. The experimental data points in the measurements of Bozinis and Hurrell have a larger uncertainty. Moreover, their data below $\sim 300\ cm^{-1}$ suffer from poor precision and calibration uncertainty. Their measured reflectivity values at low frequency are too low when compared to the clamped dielectric permittivity values [15]. Because of this, a fit to the Bozinis and Hurrell [13] data below $300\ cm^{-1}$ was not possible. The parameters characterizing the two oscillators found in this range were taken from the published frequency values of Bozinis and Hurrell, and only their linewidth was fitted whenever this led to a better fit of the data above $300\ cm^{-1}$. The parameters given in Table III for *a*- and *c*-polarizations should not be used to calculate the dielectric constant at frequencies between 100 and $300\ cm^{-1}$. Although the limiting value for low frequency is correct, the resonance structure between 100 and $300 cm^{-1}$ is not well determined. For these reasons we do not give any (n_a,k_a) and (n_c,k_c) data for frequencies in this spectral range. We estimate the accuracy of n and k determined by the foregoing method to be approximately $\pm 10\%$ for *b*-polarization. The accuracy for *a*- and *c*-polarization is lower, approximately $\pm 20\%$. The accuracy is expected to be worse whenever k or n peaks at a narrow resonance.

REFERENCES

1. L. Katz and H. D. Megaw, The structure of potassium niobate at room temperature: The solution of a pseudosymmetric structure by Fourier methods. *Acta Crystallogr.* **22**, 639–648 (1967).
2. U. J. Flückiger, Darstellung und Eigenschaften von reinen und dotierten, eindomänigen $KNbO_3$ Kristallen. Ph. D. Dissertation, University of Zurich, Zurich (1976).
3. D. A. Roberts, Simplified characterization of uniaxial and biaxial nonlinear optical crystals: A plea for standardization of nomenclature and conventions. *IEEE J. Quantum Electron.* **28**, 2057–2074 (1992).
4. D. A. Roberts and T. R. Meeker, Proposed revisions for the polar orthorhombic class, *in* IEEE/ANSI Std 176. *IEEE Transactions on Ultrasonics and Frequency Control* **39**, 165–166 (1992).
5. I. Biaggio, P. Kerkoc, L.-S. Wu, and P. Günter, Refractive indices of orthorhombic $KNbO_3$. II. Phase matching configurations for nonlinear-optical interactions. *J. Opt. Soc. Am. B* **9**, 507–517 (1992).
6. E. Wiesendanger, Dielectric, mechanical, and optical properties of orthorhombic $KNbO_3$. *Ferroelectrics* **6**, 263–281 (1974).
7. A. M. Mamedov and L. S. Gadzhieva, Optical properties of potassium niobate in the fundamental absorption region. *Sov. Phys. Solid State* **26**, 1732–1733 (1984).

8. G. Montemezzani, P. Rogin, M. Zgonik, and P. Günter, Interband photorefractive effects: Theory and experiments in $KNbO_3$. *Phys. Rev. B* **49**, 2484–2502 (1994).
9. B. Zysset, I. Biaggio, and P. Günter, Refractive indices of orthorhombic $KNbO_3$. I. Dispersion and temperature dependence. *J. Opt. Soc. Am. B* **9**, 380–386 (1992).
10. J. Hulliger, R. Gutmann, and H. Wüest, Growth of large size $KNbO_3$ crystals and epitaxial layers of $KTa_{1-x}Nb_xO_3$. *J. Cryst. Growth* **128**, 897–902 (1993).
11. D. H. Jundt, P. Günter, and B. Zysset, A temperature-dependent dispersion equation for $KNbO_3$. *Nonlinear Opt.* **4**, 341–345 (1993).
12. L. E. Busse, L. Goldberg, and M. R. Surette, Absorption losses in MgO-doped and undoped potassium niobate. *J. Appl. Phys.* **75**, 1102–1110 (1994).
13. D. G. Bozinis and J. P. Hurrell, Optical modes and dielectric properties of ferroelectric orthorhombic $KNbO_3$. *Phys. Rev. B* **13**, 3109–3120 (1976).
14. M. D. Fontana, G. Métrat, J. L. Servoin, and F. Gervais, Infrared spectroscopy in $KNbO_3$ through the successive ferroelectric phase transitions. *J. Phys. C: Solid State Phys.* **16**, 483–514 (1984).
15. M. Zgonik, R. Schlesser, I. Biaggio, E. Voit, J. Tcherry, and P. Günter, Material constants of $KNbO_3$ relevant for electro- and acousto-optics, *J. Appl. Phys.* **74**, 1287–1297 (1993).

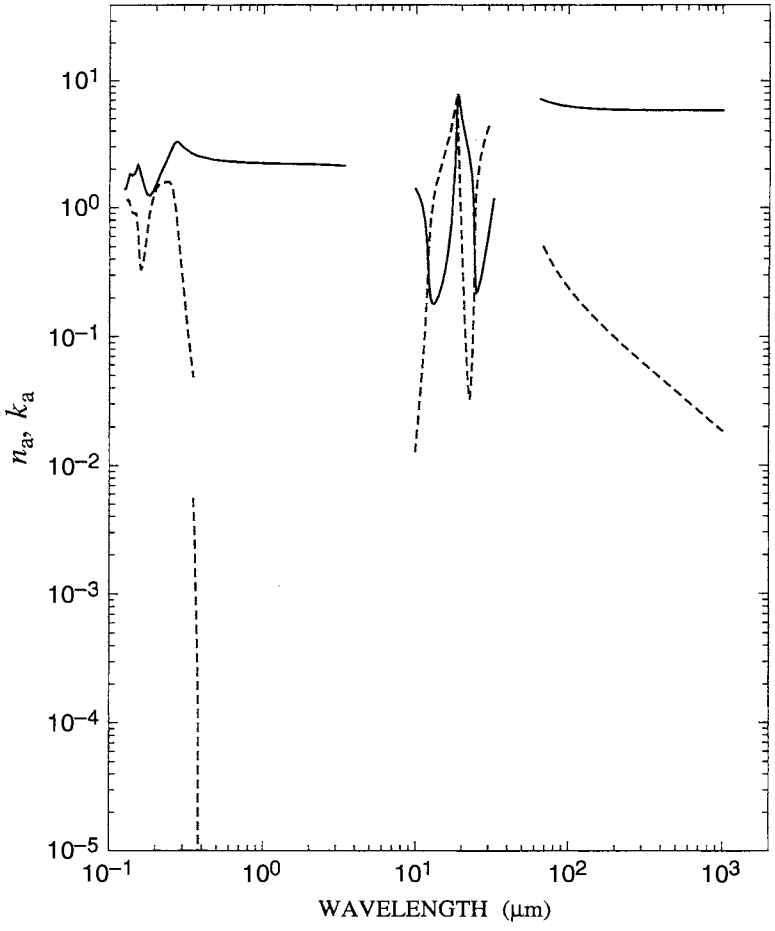

Fig. 1. Log–log plot of n_a (———) and k_a (- - - -) versus wavelength in micrometers for potassium niobate.

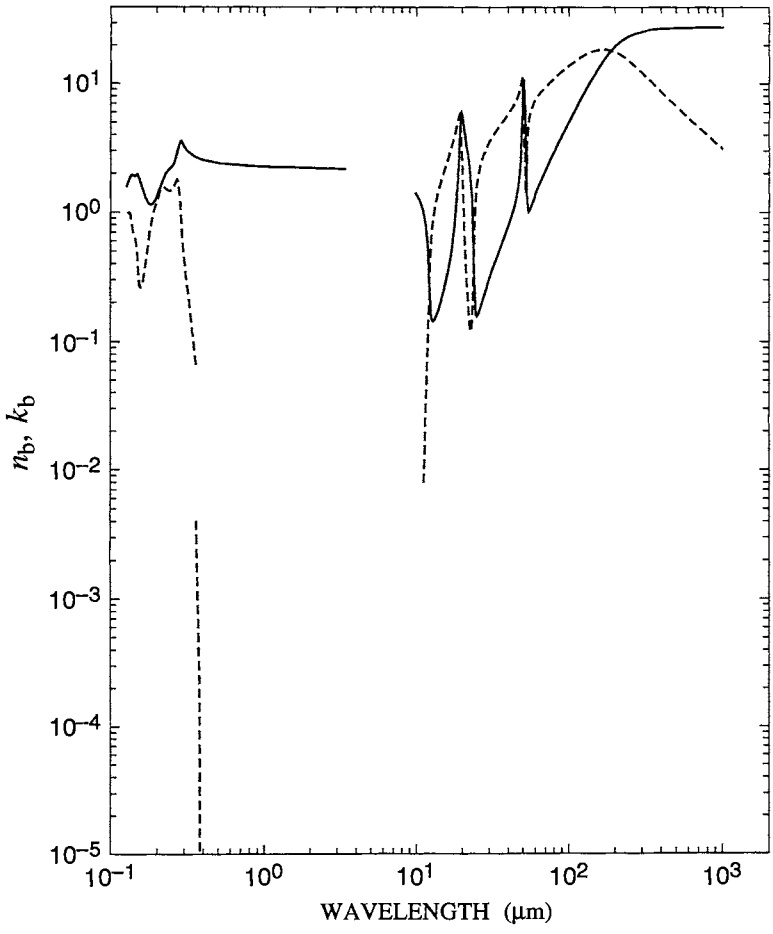

Fig. 2. Log–log plot of n_b (———) and k_b (- - - -) versus wavelength in micrometers for potassium niobate.

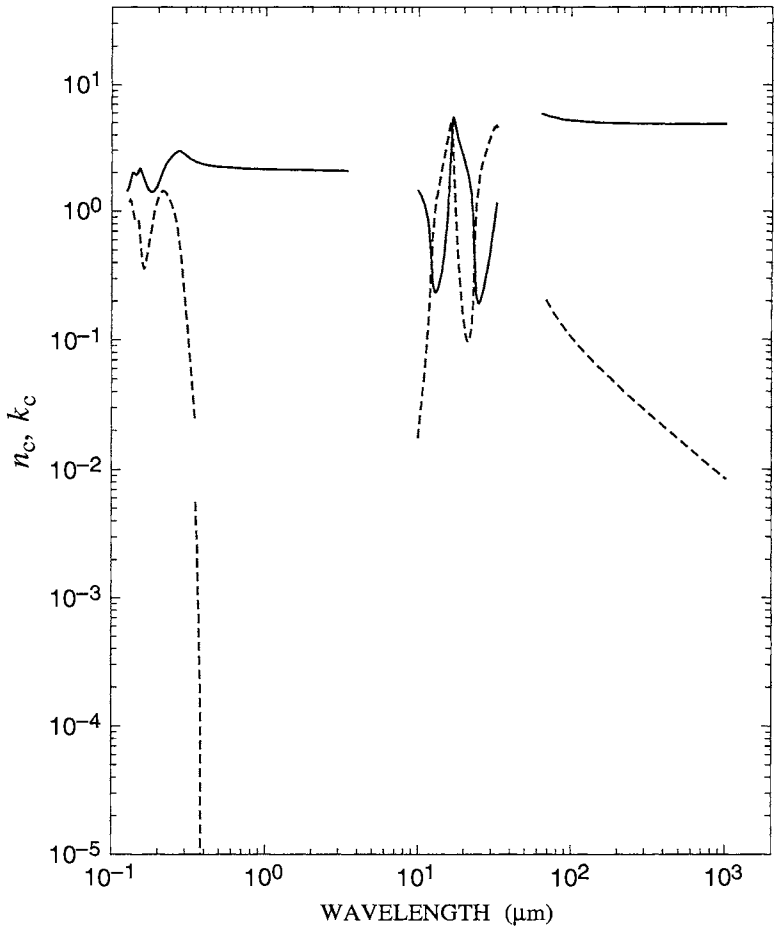

Fig. 3. Log–log plot of n_c (———) and k_c (- - - -) versus wavelength in micrometers for potassium niobate.

TABLE I

Parameters to Calculate the 22°C Refractive Indices in the Spectral range from 0.4 μm to 3.4 μm from Eq. (1).[a]

Parameter	n_a	n_b	n_c
S_1 [μm^{-2}]	20.05519	19.37347	16.0917
S_2 [μm^{-2}]	149.8408	135.4992	165.4431
E_1 [eV]	4.802660	4.545782	4.857787
E_2 [eV]	9.604319	9.049686	10.356684
D [μm^{-2}]	0.02517432	0.02845018	0.01943289

[a] $\lambda_i = (1.23986\ \mu m\ eV) / E_i$.

TABLE II

Parameters to Calculate the Refractive Indices in the Spectral Range from 0.4 μm to 3.4 μm from Eq. (2).[a]

Parameter	n_a	n_b	n_c
S_1 [μm^{-2}]	17.381	19.456	16.086
S_2 [μm^{-2}]	142.40	134.95	166.258
E_1 [eV]	4.7288	4.5492	4.8553
E_2 [eV]	9.1082	9.0392	10.3834
D [μm^{-2}]	0.02513	0.02837	0.01939
b_1 [μm^{-2}]	-2.018×10^{-5}	-5.263×10^{-5}	-3.267×10^{-5}
b_2 [μm^{-2}]	-1.32×10^{-3}	-1.65×10^{-3}	-2.8×10^{-3}
b_3 [μm]	1.231×10^{-7}	2.38×10^{-7}	1.89×10^{-7}
b_4 [μm]	-1.82×10^{-5}	-6.78×10^{-5}	-2.48×10^{-5}
b_5 [μm^{-2}]	0.9017×10^{-4}	2.0536×10^{-4}	1.990×10^{-4}
b_6 [μm]	0.796×10^{-7}	1.767×10^{-7}	1.75×10^{-7}
b_7 [μm^{-2}]	-5.58×10^{-9}	-12.2×10^{-9}	-2.7×10^{-9}
b_8 [μm^{-4}]	-4.4×10^{-10}	-3.3×10^{-10}	-5.7×10^{-10}

[a] $\lambda = (1.239852\ \mu m\ eV) / E$.

TABLE III

Parameters to Calculate the Dielectric Function from Eq. (3)[a]

Parameter	ϵ_a [b]	ϵ_b [c]	ϵ_c [b]
ϵ_∞	5.0753	5.2717	4.6065
$\Omega(TO_1)$	187.0	198.5	190.0
$\Omega(TO_2)$	243.0	53.0	267.8
$\Omega(TO_3)$	262.9	—	290.0
$\Omega(TO_4)$	537.1	512.1	601.5
$\Omega(LO_1)$	190.0	189.7	193.0
$\Omega(LO_2)$	254.0	420.1	429.9
$\Omega(LO_3)$	412.7	—	296.0
$\Omega(LO_4)$	833.9	822.3	824.8
$\gamma(TO_1)$	3.0	5.1	3.0
$\gamma(TO_2)$	25.0	61.5	15.1
$\gamma(TO_3)$	26.6	—	14.0
$\gamma(TO_4)$	22.3	27.1	33.1
$\gamma(LO_1)$	3.0	2.8	3.0
$\gamma(LO_2)$	12.0	4.8	8.4
$\gamma(LO_3)$	4.6	—	3.0
$\gamma(LO_4)$	27.1	17.6	31.0

[a] The frequencies Ω and γ have units [cm^{-1}].

[b] Eq. (3) is valid between 300 and 1000 cm^{-1} with an accuracy of ~20%.

[c] Eq. (3) is valid between 0 and 1000 cm^{-1} with an accuracy of ~10%.

TABLE IV

Values for n_a and k_a for Potassium Niobate Obtained from Various References

eV	cm^{-1}	μm	n_a	k_a
10.0	80655	0.1240	1.43 [6]	0.89 [6]
9.9	79849	0.1252	1.40	0.93
9.8	79042	0.1265	1.39	0.99
9.7	78236	0.1278	1.42	1.06
9.6	77429	0.1292	1.47	1.11
9.5	76623	0.1305	1.55	1.14
9.4	75816	0.1319	1.64	1.16
9.3	75010	0.1333	1.72	1.14
9.2	74203	0.1348	1.80	1.10
9.1	73396	0.1362	1.83	1.03
9.0	72590	0.1378	1.81	0.97
8.9	71783	0.1393	1.79	0.93
8.8	70977	0.1409	1.79	0.91
8.7	70170	0.1425	1.80	0.90
8.6	69364	0.1442	1.83	0.90
8.5	68557	0.1459	1.87	0.91
8.4	67751	0.1476	1.93	0.91
8.3	66944	0.1494	2.01	0.89
8.2	66137	0.1512	2.12	0.81
8.1	65331	0.1531	2.15	0.64
8.0	64524	0.1550	2.07	0.46
7.9	63718	0.1569	1.94	0.37
7.8	62911	0.1590	1.82	0.34
7.7	62105	0.1610	1.72	0.34
7.6	61298	0.1631	1.62	0.35
7.5	60492	0.1653	1.54	0.37
7.4	59685	0.1675	1.47	0.41
7.3	58878	0.1698	1.40	0.46
7.2	58072	0.1722	1.34	0.53
7.1	57265	0.1746	1.29	0.61
7.0	56459	0.1771	1.26	0.71
6.9	55652	0.1797	1.24	0.81
6.8	54846	0.1823	1.24	0.91
6.7	54039	0.1851	1.26	1.00
6.6	53233	0.1879	1.28	1.08
6.5	52426	0.1907	1.32	1.16
6.4	51619	0.1937	1.37	1.23
6.3	50813	0.1968	1.43	1.31
6.2	50006	0.2000	1.50	1.38
6.1	49200	0.2033	1.58	1.45
6.0	48393	0.2066	1.67	1.50
5.9	47587	0.2101	1.76	1.54
5.8	46780	0.2138	1.85	1.57
5.7	45974	0.2175	1.95	1.57
5.6	45167	0.2214	2.05	1.58

TABLE IV *(Continued)*

$KNbO_3$

eV	cm^{-1}	μm	n_a	k_a
5.5	44360	0.2254	2.14	1.58
5.4	43554	0.2296	2.23	1.59
5.3	42747	0.2339	2.33	1.59
5.2	41941	0.2384	2.45	1.60
5.1	41134	0.2431	2.58	1.60
5.0	40328	0.2480	2.75	1.56
4.9	39521	0.2530	2.92	1.48
4.8	38715	0.2583	3.07	1.35
4.7	37908	0.2638	3.19	1.17
4.6	37101	0.2695	3.27	0.96
4.5	36295	0.2755	3.27	0.75
4.4	35488	0.2818	3.21	0.55
4.3	34682	0.2883	3.12	0.41
4.2	33875	0.2952	3.03	0.31
4.1	33069	0.3024	2.94	0.23
4.0	32262	0.3100	2.86	0.17
3.9	31456	0.3179	2.79	0.13
3.8	30649	0.3263	2.73	0.10
3.7	29843	0.3351	2.67	0.07
3.6	29036	0.3444	2.63	0.06
3.5	28229	0.3542	2.59	0.05
3.4	27423	0.3647	2.55	0.03
3.54	28552	0.3502		5.46E-3 [8]
3.50	28229	0.3542		4.18E-3
3.45	27826	0.3594		2.54E-3
3.40	27423	0.3647		1.33E-3
3.35	27020	0.3701		6.11E-4
3.30	26616	0.3757		2.49E-4
3.30	26616	0.3757		2.19E-4 [6]
3.25	26213	0.3815		6.96E-5
3.20	25810	0.3875		2.22E-5
3.15	25406	0.3936		7.05E-6
3.10	25003	0.3999		2.25E-6
3.05	24600	0.4065		7.15E-7
3.00	24197	0.4133		2.28E-7
3.351	27027	0.370	2.5386 [9]	
3.263	26316	0.380	2.5103	
3.179	25641	0.390	2.4859	
3.100	25000	0.400	2.4646	
3.024	24390	0.410	2.4459	
2.952	23810	0.420	2.4293	
2.883	23256	0.430	2.4145	
2.818	22727	0.440	2.4012	

(continued)

TABLE IV *(Continued)*

$KNbO_3$

eV	cm^{-1}	μm	n_a	k_a
2.755	22222	0.450	2.3892	
2.695	21739	0.460	2.3783	
2.638	21277	0.470	2.3684	
2.583	20833	0.480	2.3594	
2.530	20408	0.490	2.3511	
2.480	20000	0.500	2.3434	
2.431	19608	0.510	2.3364	
2.384	19231	0.520	2.3298	
2.339	18868	0.530	2.3238	
2.296	18519	0.540	2.3181	
2.254	18182	0.550	2.3129	
2.214	17857	0.560	2.3080	
2.175	17544	0.570	2.3034	
2.138	17241	0.580	2.2991	
2.101	16949	0.590	2.2950	
2.066	16667	0.600	2.2912	
2.000	16129	0.620	2.2842	
1.937	15625	0.640	2.2780	
1.879	15152	0.660	2.2723	
1.823	14706	0.680	2.2673	
1.771	14286	0.700	2.2627	
1.722	13889	0.720	2.2585	
1.675	13514	0.740	2.2547	
1.631	13158	0.760	2.2512	
1.590	12821	0.780	2.2479	
1.550	12500	0.800	2.2449	
1.512	12195	0.820	2.2422	
1.476	11905	0.840	2.2396	
1.442	11628	0.860	2.2372	
1.409	11364	0.880	2.2350	
1.378	11111	0.900	2.2329	
1.348	10870	0.920	2.2309	
1.319	10638	0.940	2.2290	
1.292	10417	0.960	2.2273	
1.265	10204	0.980	2.2256	
1.240	10000	1.0	2.2240	
1.127	9091	1.1	2.2172	
1.033	8333	1.2	2.2117	
0.9537	7692	1.3	2.2070	
0.8856	7143	1.4	2.2029	
0.8266	6667	1.5	2.1992	
0.7749	6250	1.6	2.1958	
0.7293	5882	1.7	2.1925	
0.6888	5556	1.8	2.1893	
0.6525	5263	1.9	2.1862	
0.6199	5000	2.0	2.1832	

TABLE IV *(Continued)*

$KNbO_3$

eV	cm^{-1}	μm	n_a	k_a
0.5636	4545	2.2	2.1770	
0.5166	4167	2.4	2.1706	
0.4769	3846	2.6	2.1640	
0.4428	3571	2.8	2.1571	
0.4133	3333	3.0	2.1498	
0.3875	3125	3.2	2.1421	
0.3647	2941	3.4	2.1340	
0.1364	1100	9.091	1.60 [13]*	
0.1240	1000	10.00	1.39	
0.1178	950	10.53	1.23	0.03 [13]*
0.1116	900	11.11	0.99	0.06
0.1054	850	11.76	0.56	0.18
0.1017	820	12.20	0.25	0.54
0.09919	800	12.50	0.19	0.81
0.09299	750	13.33	0.18	1.38
0.08679	700	14.29	0.22	1.95
0.08059	650	15.38	0.31	2.67
0.07439	600	16.67	0.58	3.82
0.07191	580	17.24	0.88	4.63
0.06943	560	17.86	1.77	6.02
0.06819	550	18.18	3.09	7.02
0.06757	545	18.35	4.36	7.38
0.06695	540	18.52	6.11	7.06
0.06571	530	18.87	7.85	3.75
0.06447	520	19.23	6.76	1.59
0.06199	500	20.00	4.87	0.43
0.05951	480	20.83	3.78	0.15
0.05703	460	21.74	2.96	0.05
0.05455	440	22.73	2.18	0.03
0.05207	420	23.81	1.14	0.13
0.04959	400	25.00	0.22	1.49
0.04711	380	26.32	0.26	2.46
0.04463	360	27.78	0.37	3.28
0.04215	340	29.41	0.54	4.13
0.03967	320	31.25	0.85	5.14
0.03720	300	33.33	1.51	6.46
0.01240	100	100.00	6.26	0.24
0.006199	50	200.00	5.93	0.10
0	0		5.83 [15]	

* The reflectivity data from which n and k were derived are from Ref. [13].

TABLE V

Values for n_b and k_b for Potassium Niobate Obtained from Various References

eV	cm^{-1}	μm	n_b	k_b
10.0	80655	0.1240	1.55 [6]	0.88 [6]
9.9	79849	0.1252	1.56	0.91
9.8	79042	0.1265	1.58	0.93
9.7	78236	0.1278	1.61	0.95
9.6	77429	0.1292	1.65	0.97
9.5	76623	0.1305	1.70	0.99
9.4	75816	0.1319	1.77	1.00
9.3	75010	0.1333	1.84	0.98
9.2	74203	0.1348	1.90	0.94
9.1	73396	0.1362	1.94	0.85
9.0	72590	0.1378	1.95	0.78
8.9	71783	0.1393	1.93	0.72
8.8	70977	0.1409	1.92	0.68
8.7	70170	0.1425	1.91	0.65
8.6	69364	0.1442	1.91	0.63
8.5	68557	0.1459	1.92	0.62
8.4	67751	0.1476	1.96	0.55
8.3	66944	0.1494	1.96	0.46
8.2	66137	0.1512	1.92	0.37
8.1	65331	0.1531	1.84	0.30
8.0	64524	0.1550	1.75	0.27
7.9	63718	0.1569	1.67	0.26
7.8	62911	0.1590	1.60	0.26
7.7	62105	0.1610	1.52	0.27
7.6	61298	0.1631	1.46	0.29
7.5	60492	0.1653	1.39	0.32
7.4	59685	0.1675	1.33	0.36
7.3	58878	0.1698	1.28	0.41
7.2	58072	0.1722	1.23	0.47
7.1	57265	0.1746	1.19	0.54
7.0	56459	0.1771	1.17	0.61
6.9	55652	0.1797	1.15	0.70
6.8	54846	0.1823	1.15	0.79
6.7	54039	0.1851	1.15	0.87
6.6	53233	0.1879	1.17	0.95
6.5	52426	0.1907	1.19	1.03
6.4	51619	0.1937	1.22	1.10
6.3	50813	0.1968	1.27	1.16
6.2	50006	0.2000	1.32	1.23
6.1	49200	0.2033	1.38	1.31
6.0	48393	0.2066	1.46	1.39
5.9	47587	0.2101	1.54	1.48
5.8	46780	0.2138	1.64	1.53
5.7	45974	0.2175	1.74	1.56
5.6	45167	0.2214	1.85	1.57
5.5	44360	0.2254	1.94	1.55

TABLE V *(Continued)*

$KNbO_3$

eV	cm^{-1}	μm	n_b	k_b
5.4	43554	0.2296	2.03	1.52
5.3	42747	0.2339	2.10	1.49
5.2	41941	0.2384	2.15	1.47
5.1	41134	0.2431	2.18	1.47
5.0	40328	0.2480	2.23	1.48
4.9	39521	0.2530	2.29	1.52
4.8	38715	0.2583	2.39	1.59
4.7	37908	0.2638	2.55	1.69
4.6	37101	0.2695	2.81	1.78
4.5	36295	0.2755	3.16	1.70
4.4	35488	0.2818	3.46	1.34
4.3	34682	0.2883	3.57	0.84
4.2	33875	0.2952	3.39	0.55
4.1	33069	0.3024	3.20	0.41
4.0	32262	0.3100	3.06	0.31
3.9	31456	0.3179	2.95	0.24
3.8	30649	0.3263	2.87	0.19
3.7	29843	0.3351	2.80	0.14
3.6	29036	0.3444	2.74	0.11
3.5	28229	0.3542	2.69	0.08
3.4	27423	0.3647	2.64	0.06
3.43	27665	0.3615		3.99E-3 [8]
3.40	27423	0.3647		2.81E-3
3.35	27020	0.3701		1.24E-3
3.30	26616	0.3757		4.63E-4
3.30	26616	0.3757		4.39E-4 [6]
3.25	26213	0.3815		1.40E-4
3.20	25810	0.3875		4.44E-5
3.15	25406	0.3936		1.41E-5
3.10	25003	0.3999		4.50E-6
3.05	24600	0.4065		1.43E-6
3.00	24197	0.4133		4.57E-7
3.3509	27027	0.370	2.6646 [9]	
3.2627	26316	0.380	2.6253	
3.1791	25641	0.390	2.5919	
3.0996	25000	0.400	2.5633	
3.0240	24390	0.410	2.5384	
2.9520	23810	0.420	2.5167	
2.8834	23256	0.430	2.4974	
2.8178	22727	0.440	2.4802	
2.7552	22222	0.450	2.4649	
2.6953	21739	0.460	2.4510	
2.6380	21277	0.470	2.4385	

(continued)

TABLE V *(Continued)*

$KNbO_3$

eV	cm^{-1}	μm	n_b	k_b
2.5830	20833	0.480	2.4271	
2.5303	20408	0.490	2.4167	
2.4797	20000	0.500	2.4072	
2.4311	19608	0.510	2.3984	
2.3843	19231	0.520	2.3903	
2.3393	18868	0.530	2.3828	
2.2960	18519	0.540	2.3759	
2.2543	18182	0.550	2.3695	
2.2140	17857	0.560	2.3634	
2.1752	17544	0.570	2.3578	
2.1377	17241	0.580	2.3526	
2.1014	16949	0.590	2.3476	
2.0664	16667	0.600	2.3430	
1.9997	16129	0.620	2.3346	
1.9373	15625	0.640	2.3270	
1.8785	15152	0.660	2.3203	
1.8233	14706	0.680	2.3142	
1.7712	14286	0.700	2.3087	
1.7220	13889	0.720	2.3037	
1.6755	13514	0.740	2.2991	
1.6314	13158	0.760	2.2949	
1.5895	12821	0.780	2.2911	
1.5498	12500	0.800	2.2875	
1.5120	12195	0.820	2.2843	
1.4760	11905	0.840	2.2812	
1.4417	11628	0.860	2.2784	
1.4089	11364	0.880	2.2757	
1.3776	11111	0.900	2.2733	
1.3477	10870	0.920	2.2709	
1.3190	10638	0.940	2.2687	
1.2915	10417	0.960	2.2667	
1.2651	10204	0.980	2.2647	
1.2398	10000	1.0	2.2629	
1.1271	9091	1.1	2.2549	
1.0332	8333	1.2	2.2485	
0.9537	7692	1.3	2.2431	
0.8856	7143	1.4	2.2384	
0.8266	6667	1.5	2.2341	
0.7749	6250	1.6	2.2302	
0.7293	5882	1.7	2.2265	
0.6888	5556	1.8	2.2229	
0.6525	5263	1.9	2.2194	
0.6199	5000	2.0	2.2159	
0.5636	4545	2.2	2.2089	
0.5166	4167	2.4	2.2018	
0.4769	3846	2.6	2.1944	
0.4428	3571	2.8	2.1867	

TABLE V *(Continued)*

$KNbO_3$

eV	cm^{-1}	μm	n_b	k_b
0.4133	3333	3.0	2.1785	
0.3875	3125	3.2	2.1699	
0.3647	2941	3.4	2.1608	
0.1364	1100	9.091	1.60 [14]	
0.1240	1000	10.00	1.38	
0.1178	950	10.53	1.23	
0.1116	900	11.11	1.01	
0.1054	850	11.76	0.65	0.06 [14]
0.09919	800	12.50	0.16	0.61
0.09299	750	13.33	0.15	1.17
0.08679	700	14.29	0.19	1.66
0.08059	650	15.38	0.27	2.20
0.07439	600	16.67	0.43	2.92
0.07191	580	17.24	0.56	3.33
0.06943	560	17.86	0.81	3.90
0.06695	540	18.52	1.43	4.77
0.06447	520	19.23	3.76	5.69
0.06323	510	19.61	5.71	4.33
0.06199	500	20.00	5.69	2.14
0.05951	480	20.83	4.01	0.56
0.05703	460	21.74	2.82	0.21
0.05455	440	22.73	1.82	0.12
0.05207	420	23.81	0.42	0.42
0.04959	400	25.00	0.16	1.68
0.04711	380	26.32	0.18	2.33
0.04463	360	27.78	0.23	2.85
0.04215	340	29.41	0.28	3.33
0.03967	320	31.25	0.35	3.80
0.03720	300	33.33	0.43	4.29
0.03472	280	35.71	0.54	4.82
0.03224	260	38.46	0.68	5.44
0.02976	240	41.67	0.89	6.23
0.02728	220	45.45	1.31	7.44
0.02604	210	47.62	1.95	8.67
0.02480	200	50.00	7.63	11.0
0.02455	198	50.51	10.7	7.57
0.02418	195	51.28	7.99	2.34
0.02356	190	52.63	2.42	1.88
0.02232	180	55.56	1.04	5.78
0.01984	160	62.50	1.55	7.99
0.01736	140	71.43	2.23	9.65
0.01488	120	83.33	3.26	11.5
0.01240	100	100.00	5.02	13.8
0.009919	80	125.00	8.35	16.6
0.006199	50	200.00	19.6	17.8
0	0		27.9 [15]	

(continued)

TABLE VI

Values for n_c and k_c for Potassium Niobate Obtained from Various References

eV	cm^{-1}	μm	n_c	k_c
10.0	80655	0.1240	1.44 [6]	0.92 [6]
9.9	79849	0.1252	1.44	0.98
9.8	79042	0.1265	1.45	1.02
9.7	78236	0.1278	1.48	1.07
9.6	77429	0.1292	1.53	1.13
9.5	76623	0.1305	1.62	1.19
9.4	75816	0.1319	1.71	1.22
9.3	75010	0.1333	1.81	1.20
9.2	74203	0.1348	1.89	1.15
9.1	73396	0.1362	1.96	1.06
9.0	72590	0.1378	1.99	0.97
8.9	71783	0.1393	1.97	0.90
8.8	70977	0.1409	1.94	0.85
8.7	70170	0.1425	1.92	0.83
8.6	69364	0.1442	1.91	0.84
8.5	68557	0.1459	1.93	0.85
8.4	67751	0.1476	1.98	0.86
8.3	66944	0.1494	2.06	0.83
8.2	66137	0.1512	2.14	0.74
8.1	65331	0.1531	2.15	0.60
8.0	64524	0.1550	2.08	0.48
7.9	63718	0.1569	1.98	0.41
7.8	62911	0.1590	1.88	0.37
7.7	62105	0.1610	1.79	0.36
7.6	61298	0.1631	1.71	0.36
7.5	60492	0.1653	1.65	0.38
7.4	59685	0.1675	1.58	0.42
7.3	58878	0.1698	1.53	0.46
7.2	58072	0.1722	1.47	0.51
7.1	57265	0.1746	1.44	0.57
7.0	56459	0.1771	1.42	0.64
6.9	55652	0.1797	1.40	0.72
6.8	54846	0.1823	1.40	0.80
6.7	54039	0.1851	1.41	0.88
6.6	53233	0.1879	1.43	0.97
6.5	52426	0.1907	1.46	1.05
6.4	51619	0.1937	1.50	1.12
6.3	50813	0.1968	1.55	1.18
6.2	50006	0.2000	1.61	1.25
6.1	49200	0.2033	1.69	1.31
6.0	48393	0.2066	1.79	1.37
5.9	47587	0.2101	1.89	1.41
5.8	46780	0.2138	2.01	1.43
5.7	45974	0.2175	2.12	1.42
5.6	45167	0.2214	2.23	1.40
5.5	44360	0.2254	2.33	1.37

TABLE VI *(Continued)*

$KNbO_3$

eV	cm^{-1}	μm	n_c	k_c
5.4	43554	0.2296	2.42	1.32
5.3	42747	0.2339	2.51	1.27
5.2	41941	0.2384	2.59	1.21
5.1	41134	0.2431	2.67	1.14
5.0	40328	0.2480	2.74	1.07
4.9	39521	0.2530	2.81	1.00
4.8	38715	0.2583	2.87	0.91
4.7	37908	0.2638	2.92	0.80
4.6	37101	0.2695	2.95	0.67
4.5	36295	0.2755	2.97	0.55
4.4	35488	0.2818	2.93	0.43
4.3	34682	0.2883	2.87	0.33
4.2	33875	0.2952	2.80	0.24
4.1	33069	0.3024	2.72	0.17
4.0	32262	0.3100	2.66	0.12
3.9	31456	0.3179	2.60	0.09
3.8	30649	0.3263	2.54	0.06
3.7	29843	0.3351	2.49	0.04
3.6	29036	0.3444	2.45	0.03
3.5	28229	0.3542	2.41	0.02
3.4	27423	0.3647	2.38	0.002
3.54	28552	0.3502		5.46E-3 [8]
3.50	28229	0.3542		4.18E-3
3.45	27826	0.3594		2.54E-3
3.40	27423	0.3647		1.33E-3
3.35	27020	0.3701		6.11E-4
3.30	26616	0.3757		2.49E-4
3.30	26616	0.3757		2.19E-4 [6]
3.25	26213	0.3815		6.96E-5
3.20	25810	0.3875		2.22E-5
3.15	25406	0.3936		7.05E-6
3.10	25003	0.3999		2.25E-6
3.05	24600	0.4065		7.15E-7
3.00	24197	0.4133		2.28E-7
3.351	27027	0.370	2.3761 [9]	
3.263	26316	0.380	2.3536	
3.179	25641	0.390	2.3342	
3.100	25000	0.400	2.3172	
3.024	24390	0.410	2.3023	
2.952	23810	0.420	2.2890	
2.883	23256	0.430	2.2771	
2.818	22727	0.440	2.2664	

(continued)

TABLE VI *(Continued)*

$KNbO_3$

eV	cm^{-1}	μm	n_c	k_c
2.755	22222	0.450	2.2568	
2.695	21739	0.460	2.2481	
2.638	21277	0.470	2.2401	
2.583	20833	0.480	2.2328	
2.530	20408	0.490	2.2261	
2.480	20000	0.500	2.2199	
2.431	19608	0.510	2.2142	
2.384	19231	0.520	2.2090	
2.339	18868	0.530	2.2041	
2.296	18519	0.540	2.1995	
2.254	18182	0.550	2.1953	
2.214	17857	0.560	2.1913	
2.175	17544	0.570	2.1875	
2.138	17241	0.580	2.1841	
2.101	16949	0.590	2.1808	
2.066	16667	0.600	2.1777	
2.000	16129	0.620	2.1720	
1.937	15625	0.640	2.1669	
1.879	15152	0.660	2.1624	
1.823	14706	0.680	2.1583	
1.771	14286	0.700	2.1545	
1.722	13889	0.720	2.1511	
1.675	13514	0.740	2.1480	
1.631	13158	0.760	2.1452	
1.590	12821	0.780	2.1425	
1.550	12500	0.800	2.1401	
1.512	12195	0.820	2.1378	
1.476	11905	0.840	2.1358	
1.442	11628	0.860	2.1338	
1.409	11364	0.880	2.1320	
1.378	11111	0.900	2.1303	
1.348	10870	0.920	2.1287	
1.319	10638	0.940	2.1271	
1.292	10417	0.960	2.1257	
1.265	10204	0.980	2.1244	
1.240	10000	1.0	2.1231	
1.127	9091	1.1	2.1175	
1.033	8333	1.2	2.1130	
0.9537	7692	1.3	2.1092	
0.8856	7143	1.4	2.1059	
0.8266	6667	1.5	2.1029	
0.7749	6250	1.6	2.1001	
0.7293	5882	1.7	2.0974	
0.6888	5556	1.8	2.0949	
0.6525	5263	1.9	2.0924	
0.6199	5000	2.0	2.0899	

TABLE VI *(Continued)*

$KNbO_3$

eV	cm^{-1}	μm	n_c	k_c
0.5636	4545	2.2	2.0849	
0.5166	4167	2.4	2.0797	
0.4769	3846	2.6	2.0744	
0.4428	3571	2.8	2.0689	
0.4133	3333	3.0	2.0630	
0.3875	3125	3.2	2.0568	
0.3647	2941	3.4	2.0503	
0.1364	1100	9.091	1.61 [13]*	
0.1240	1000	10.00	1.42	0.02 [13]*
0.1178	950	10.53	1.28	0.04
0.1116	900	11.11	1.07	0.07
0.1054	850	11.76	0.70	0.16
0.09919	800	12.50	0.26	0.74
0.09299	750	13.33	0.25	1.42
0.08679	700	14.29	0.35	2.18
0.08059	650	15.38	0.78	3.43
0.07563	610	16.39	3.47	5.14
0.07687	620	16.13	2.13	4.85
0.07439	600	16.67	5.10	4.28
0.07315	590	16.95	5.53	2.59
0.07191	580	17.24	5.08	1.49
0.06943	560	17.86	4.09	0.61
0.06695	540	18.52	3.41	0.31
0.06447	520	19.23	2.92	0.19
0.06199	500	20.00	2.50	0.13
0.05951	480	20.83	2.09	0.10
0.05703	460	21.74	1.63	0.10
0.05455	440	22.73	0.98	0.18
0.05207	420	23.81	0.23	0.99
0.04959	400	25.00	0.19	1.77
0.04711	380	26.32	0.23	2.41
0.04463	360	27.78	0.31	3.05
0.04215	340	29.41	0.46	3.76
0.01240	100	100.00	5.21	0.10
0.006199	50	200.00	4.97	0.04
0	0		4.90 [15]	

* The reflectivity data from which n and k were derived are from Ref. [13].

Rubidium Bromide (RbBr)

IVAN OHLÍDAL
Department of Solid State Physics
Faculty of Sciences
Masaryk University Brno
Brno, Czech Republic

and

MILOSLAV OHLÍDAL
Institute of Physical Engineering
Technical University
Brno, Czech Republic

Single crystals of rubidium bromide exhibit the cubic structure of NaCl (O_h^5-Fm3m space group).

Rubidium bromide is a hygroscopic material similar to the other rubidium halides. Surfaces of optical components fabricated from RbBr crystals must be prepared with great care. Roughness of the surfaces of the RbBr components achieved by the usual polishing procedures causes a considerable decrease in transmittance of these components, at shorter wavelengths in particular [1]. This is probably caused by the fact that these procedures cause surface roughness that is characterized by relatively large values of the heights of the surface irregularities [1]. In practice the spectral region 0.25–40 μm can be considered as the region of transparency of RbBr.

So far, only four sets of optical-constant data have been published for RbBr in the literature. Three of these sets are summarized in this work. The room-temperature values of the refractive index n and the extinction coefficient k tabulated here (see Table I and Fig. 1) were obtained from the following papers: the 54.05 μm (0.02294 eV) to 0.21 μm (5.904 eV) values of n are calculated using the dispersion formula published in the Li paper [2]; the 0.656 μm (1.890 eV) to 0.486 μm (2.551 eV) values of n are from Sprockhoff [3]; and 222.2 μm (45 cm^{-1}) to 50.00 μm (200 cm^{-1}) values of n and k were presented by Pai *et al.*[4].

Copyright © 1998 by Academic Press.
All rights of reproduction in any form reserved
ISBN 0-12-544423-0/$25.00.

The Li formula employed for calculating the refractive-index data of RbBr in the region 54.00 μm $\geq \lambda \geq$ 0.21 μm was constructed in the form

$$n^2 = 1.45931 + \frac{0.16301\,\lambda^2}{\lambda^2 - (0.123)^2} + \frac{0.29841\,\lambda^2}{\lambda^2 - (0.146)^2} + \frac{0.17198\,\lambda^2}{\lambda^2 - (0.155)^2} + \frac{0.12186\,\lambda^2}{\lambda^2 - (0.178)^2} + \frac{0.13039\,\lambda^2}{\lambda^2 - (0.191)^2} + \frac{2.520\,\lambda^2}{\lambda^2 - (114.29)^2}, \tag{1}$$

where λ is in micrometers.

The values of n calculated by means of the Li formula (see Table I) correspond to the RbBr single crystal because this formula was obtained on the basis of the important Kublitzky refractive-index data [5]. The primary Kublitzky data were measured for prisms formed with the RbBr single crystal by means of the method of minimum deviation at selected wavelengths in the spectral region 0.578 μm $\geq \lambda \geq$ 0.219 μm [5]. Li constructed his formula of the Sellmeier type in such a way that the wavelengths of the ultraviolet absorption peaks and the wavelength of the fundamental infrared absorption peak λ_I found by direct measurements are included in this formula. The values of the adjustable parameters of the formula mentioned (e.g., 0.16301) were sought by fitting the Kublitzky data by means of the least-squares method [2]. This means that the values of the refractive index n can be calculated using the Li dispersion formula at wavelengths beyond the Kublitzky's data in both directions, that is, at wavelengths belonging to the near-UV and the IR regions.

On the basis of the Kublitzky data, Radhakrishnan [6] also derived the following empirical dispersion formula expressing the spectral dependence of the refractive index n of the RbBr single crystal in the region 0.546 μm $\geq \lambda \geq$ 0.219 μm:

$$n^2 = 1.4500 + \frac{0.2000\,\lambda^2}{\lambda^2 - 0.015129} + \frac{0.3651\,\lambda^2}{\lambda^2 - 0.022650} + \frac{0.3224\,\lambda^2}{\lambda^2 - 0.033124}, \tag{2}$$

λ is also in micrometers.

This formula gives wavelengths of ultraviolet absorption peaks that agree closely with those obtained by direct measurements [7, 8] but gives no information concerning the infrared absorption peak. Extrapolated values of n for the long wavelengths, that is, for the IR wavelengths, as given by the Radhakrishnan formula have large uncertainties in contrast to those given by the Li formula expressed with Eq. (1). This means that the Radhakrish-

nan dispersion formula is not an adequate one for use in a wide wavelength range, that is, in both the mid-IR and the far-IR regions in particular. Thus, the Radhakrishnan formula only correlates the dispersion in both the visible and the near UV with absorption bands in the UV region.

Sprockhoff [3] measured the values of n of RbBr using the method of minimum deviation as well. He determined the refractive-index value of the RbBr single crystal at the following wavelengths: 0.486, 0.589 and 0.656 μm (see Table I).

The errors of the refractive-index data calculated using Eq. (1) are dependent on wavelength. (The greatest and/or smallest errors in n are equal to $\pm$ 0.02 in the regions 0.21–0.22 μm and 40.00–60.00 μm and/or $\pm$ 0.002 in the region 0.40–1.50 μm.) In the Sprockhoff and Kublitzky data the errors of the values of n can be estimated as $\pm$ 0.001.

Pai *et al.* [4] determined the spectral dependences of n and k characterizing RbBr bulk samples (i.e., single crystals) by means of amplitude and phase reflection measurements made by dispersive Fourier transform spectroscopy in the region 222.2 μm $\geq \lambda \geq$ 50 μm. The errors in the optical constants n and k evaluated in this way are also dependent on wavelength. (The greatest and/or smallest errors in both n and k are equal to $\pm$ 0.10 and/or $\pm$ 0.01 at the wavelength of about 116 μm and/or in the interval 93 μm $\geq \lambda \geq$ 50 μm [4].) Spectral dependences of n and k in the vicinity of the maximum value of k at the wavelength of the fundamental infrared absorption peak λ_I are related to the TO phonon mode. The fine structures in the curves of n and k in the far-IR region may be caused by multiple-phonon absorption processes. In the visible there is very good agreement between the refractive-index data calculated using the Li formula [2] and measured by Kublitzky [5] on one side and those presented by Sprockhoff [3] on the other side (see Table I). Similarly, one can see a relatively good agreement between the values of n calculated by means of the Li formula and those determined by Pai *et al.* [4] in the region 54.00 μm $\geq \lambda \geq$ 50.00 μm (see Table I). Both the facts mentioned give support for the correctness and reliability of the optical-constant data presented for the RbBr single crystal in this paper.

From Eq. (1) and the spectral dependence of k determined by Pai *et al.* [4], one can see that there is a good agreement between the value of λ_I used in the Li formula [2] and that implied by the data of Pai *et al.*

It should be noted that in the parts of the IR region in which RbBr is a weakly absorbing material ($k \leq 0.1$), more precise values of k can be determined by transmittance measurements of sufficiently thin RbBr slabs than by means of the experimental techniques used by Pai *et al.* [4]. Thus far, these measurements of the transmittance of the RbBr slabs have not been performed in the IR region. Unfortunately, measurements enabling us to evaluate the values of the extinction coefficient k of the RbBr single crystals or RbBr thin films in the UV region have not been carried out, either.

The optical-constant data presented here are the room-temperature

data, as pointed out earlier. However, strictly speaking, there are small differences at temperatures corresponding to the data summarized. Namely, the refractive-index data obtained by means of the Li dispersion formula [2], the values of n determined by Sprockhoff [3] and the values of n and k published by Pai *et al.* [4] correspond to 293 K, 298 K, and 300 K, respectively. Both the Radhakrishnan formula [6] and the Kublitzky data correspond to 308 K. This means that at first Li reduced the Kublitzky refractive-index data from 308 to 293 K to obtain his formula in the form presented. He performed these corrections by using empirical parameters to construct a formula for dn/dT, enabling him to carry out the mentioned corrections of the Kublitzky values of n [2] (dn/dT denotes the derivative of the refractive index with respect to temperature T).

In conclusion, it is possible to state that the optical-constant data summarized here represent the best values of the refractive index n characterizing the RbBr single crystal in the region 222.2 μm $\geq \lambda \geq$ 0.21 μm and the best values of the extinction coefficient k of the same material in the region 222.2 μm $\geq \lambda \geq$ 50 μm.

REFERENCES

1. D. E. McCarthy, *Appl. Opt.* **7**, 1243 (1968).
2. H. H. Li, J. Phys. *Chem. Ref. Data* **5**, 329 (1976).
3. M. Sprockhoff, *Neues Jahrb. Mineral. Geol. Palaeontol., Beilageband* **18**, 117 (1904).
4. K. F. Pai, T. J. Parker, N. E. Tornberg, R. P. Lowndes, and W. G. Chambers, *Infrared Phys.* **18**, 199 (1978).
5. A. Kublitzky, *Ann. Phys.* **20**, 793 (1934).
6. T. Radhakrishnan, *Proc. Indian Acad. Sci. Sect. A* **27**, 165 (1948).
7. R. Hilsch and R. W. Pohl, *Z. Phys.* **59**, 812 (1930).
8. E. G. Schneider and H. M. O'Bryan, *Phys. Rev.* **51**, 293 (1937).

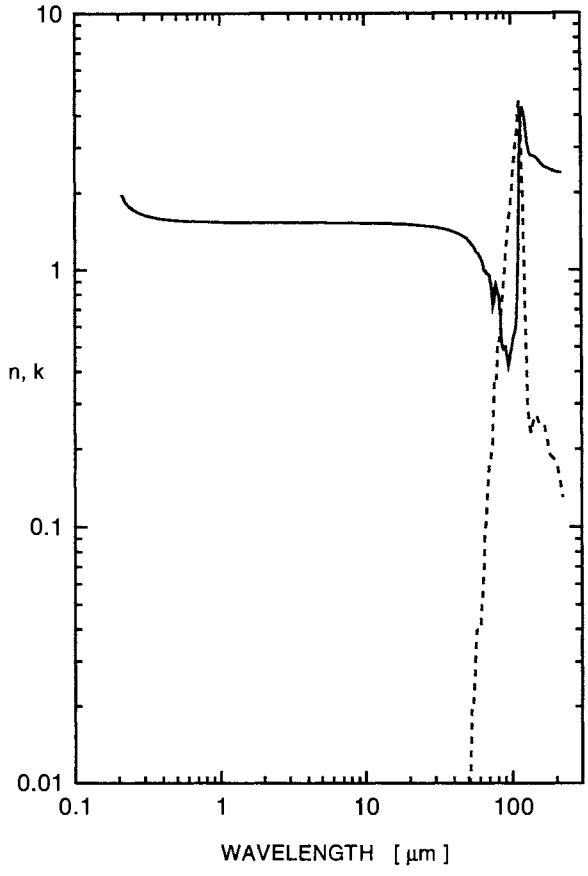

Fig. 1. Log–log plot of n (solid line) and k (dashed line) versus wavelength in micrometers for RbBr.

TABLE I

Values of n and k for Rubidium Bromide as Obtained from Various References[a]

eV	cm^{-1}	μm	n	k
5.904	47,620	0.210	1.962 [2]	
5.848	47,170	0.212	1.936	
5.794	46,730	0.214	1.913	
5.740	46,300	0.216	1.893	
5.687	45,870	0.218	1.875	
5.636	45,450	0.220	1.858	
5.585	45,050	0.222	1.844	
5.535	44,640	0.224	1.830	
5.486	44,250	0.226	1.818	
5.438	43,860	0.228	1.807	
5.391	43,480	0.230	1.796	
5.344	43,100	0.232	1.787	
5.299	42,740	0.234	1.777	
5.254	42,370	0.236	1.769	
5.209	42,020	0.238	1.761	
5.166	41,670	0.240	1.754	
5.123	41,320	0.242	1.747	
5.081	40,980	0.244	1.740	
5.040	40,650	0.246	1.734	
4.999	40,320	0.248	1.728	
4.959	40,000	0.250	1.722	
4.920	39,680	0.252	1.717	
4.881	39,370	0.254	1.712	
4.843	39,060	0.256	1.707	
4.806	38,760	0.258	1.703	
4.769	38,460	0.260	1.698	
4.732	38,170	0.262	1.694	
4.696	37,880	0.264	1.690	
4.661	37,590	0.266	1.686	
4.626	37,310	0.268	1.683	
4.592	37,040	0.270	1.679	
4.558	36,760	0.272	1.676	
4.525	36,500	0.274	1.673	
4.492	36,230	0.276	1.669	
4.460	35,970	0.278	1.666	
4.428	35,710	0.280	1.664	
4.397	35,460	0.282	1.661	
4.366	35,210	0.284	1.658	
4.335	34,970	0.286	1.655	
4.305	34,720	0.288	1.653	
4.275	34,480	0.290	1.651	
4.246	34,250	0.292	1.648	
4.217	34,010	0.294	1.646	
4.189	33,780	0.296	1.644	
4.161	33,560	0.298	1.642	

(continued)

[a] References given in brackets.

TABLE I *(Continued)*

Rubidium Bromide

eV	cm^{-1}	μm	n	k
4.133	33,330	0.300	1.640	
4.065	32,790	0.305	1.635	
4.000	32,260	0.310	1.630	
3.936	31,750	0.315	1.626	
3.875	31,250	0.320	1.622	
3.815	30,770	0.325	1.618	
3.757	30,300	0.330	1.615	
3.701	29,850	0.335	1.612	
3.647	29,410	0.340	1.609	
3.594	28,990	0.345	1.606	
3.542	28,570	0.350	1.603	
3.493	28,170	0.355	1.601	
3.444	27,780	0.360	1.598	
3.397	27,400	0.365	1.596	
3.351	27,030	0.370	1.594	
3.306	26,670	0.375	1.592	
3.263	26,320	0.380	1.590	
3.220	25,970	0.385	1.588	
3.179	25,640	0.390	1.587	
3.139	25,320	0.395	1.585	
3.100	25,000	0.400	1.583	
3.024	24,390	0.410	1.580	
2.952	23,810	0.420	1.578	
2.883	23,260	0.430	1.575	
2.818	22,730	0.440	1.573	
2.755	22,220	0.450	1.571	
2.695	21,740	0.460	1.569	
2.638	21,280	0.470	1.567	
2.583	20,830	0.480	1.566	
2.551	20,580	0.486	1.565 [3]	
2.530	20,410	0.490	1.564 [2]	
2.480	20,000	0.500	1.563	
2.431	19,610	0.510	1.561	
2.384	19,230	0.520	1.560	
2.339	18,870	0.530	1.559	
2.296	18,520	0.540	1.558	
2.254	18,180	0.550	1.557	
2.214	17,860	0.560	1.556	
2.175	17,540	0.570	1.555	
2.138	17,240	0.580	1.554	
2.105	16,980	0.589	1.553 [3]	
2.101	16,950	0.590	1.553 [2]	
2.066	16,670	0.600	1.552	
2.000	16,130	0.620	1.551 [2]	
1.937	15,630	0.640	1.550	
1.890	15,240	0.656	1.548 [3]	

(continued)

TABLE I *(Continued)*

Rubidium Bromide

eV	cm^{-1}	μm	n	k
1.879	15,150	0.660	1.548 [2]	
1.823	14,710	0.680	1.547	
1.771	14,290	0.700	1.546	
1.722	13,890	0.720	1.546	
1.675	13,510	0.740	1.545	
1.631	13,160	0.760	1.544	
1.590	12,820	0.780	1.543	
1.550	12,500	0.800	1.543	
1.512	12,200	0.820	1.542	
1.476	11,900	0.840	1.542	
1.442	11,630	0.860	1.541	
1.409	11,360	0.880	1.541	
1.378	11,110	0.900	1.540	
1.348	10,870	0.920	1.540	
1.319	10,640	0.940	1.539	
1.292	10,420	0.960	1.539	
1.265	10,200	0.980	1.539	
1.240	10,000	1.00	1.538	
1.181	9,524	1.05	1.538	
1.127	9,091	1.10	1.537	
1.078	8,696	1.15	1.537	
1.033	8,333	1.20	1.536	
0.9919	8,000	1.25	1.536	
0.9537	7,692	1.30	1.535	
0.9184	7,407	1.35	1.535	
0.8856	7,143	1.40	1.535	
0.8551	6,897	1.45	1.535	
0.8266	6,667	1.50	1.534	
0.7749	6,250	1.60	1.534	
0.7293	5,882	1.70	1.534	
0.6888	5,556	1.80	1.533	
0.6526	5,263	1.90	1.533	
0.6199	5,000	2.00	1.533	
0.5636	4,545	2.20	1.532	
0.5166	4,167	2.40	1.532	
0.4769	3,846	2.60	1.532	
0.4428	3,571	2.80	1.532	
0.4133	3,333	3.00	1.532	
0.3542	2,857	3.50	1.531	
0.3100	2,500	4.00	1.531	
0.2755	2,222	4.50	1.530	
0.2480	2,000	5.00	1.530	
0.2066	1,667	6.00	1.529	
0.1771	1,429	7.00	1.528	
0.1550	1,250	8.00	1.527	
0.1378	1,111	9.00	1.526	

TABLE I *(Continued)*

Rubidium Bromide

eV	cm^{-1}	μm	n	k
0.1240	1,000	10.0	1.525	
0.1127	909.1	11.0	1.524	
0.1033	833.3	12.0	1.522	
0.09537	769.2	13.0	1.521	
0.08856	714.3	14.0	1.519	
0.08266	666.7	15.0	1.517	
0.07999	645.2	15.5	1.516	
0.07749	625.0	16.0	1.515	
0.07514	606.1	16.5	1.514	
0.07293	588.2	17.0	1.513	
0.07085	571.4	17.5	1.511	
0.06888	555.6	18.0	1.510	
0.06702	540.5	18.5	1.509	
0.06526	526.3	19.0	1.508	
0.06358	512.8	19.5	1.506	
0.06199	500.0	20.0	1.505	
0.06048	487.8	20.5	1.504	
0.05904	476.2	21.0	1.502	
0.05767	465.1	21.5	1.501	
0.05636	454.5	22.0	1.499	
0.05510	444.4	22.5	1.498	
0.05391	434.8	23.0	1.496	
0.05276	425.5	23.5	1.495	
0.05166	416.7	24.0	1.493	
0.05061	408.2	24.5	1.491	
0.04959	400.0	25.0	1.489	
0.04862	392.2	25.5	1.488	
0.04769	384.6	26.0	1.486	
0.04679	377.4	26.5	1.484	
0.04592	370.4	27.0	1.482	
0.04509	363.6	27.5	1.480	
0.04428	357.1	28.0	1.478	
0.04350	350.9	28.5	1.476	
0.04275	344.8	29.0	1.474	
0.04203	339.0	29.5	1.471	
0.04133	333.3	30.0	1.469	
0.04065	327.9	30.5	1.467	
0.04000	322.6	31.0	1.465	
0.03936	317.5	31.5	1.462	
0.03875	312.5	32.0	1.460	
0.03815	307.7	32.5	1.457	
0.03757	303.0	33.0	1.455	
0.03701	298.5	33.5	1.452	
0.03647	294.1	34.0	1.449	
0.03594	289.9	34.5	1.446	
0.03542	285.7	35.0	1.444	

(continued)

TABLE I *(Continued)*

Rubidium Bromide

eV	cm^{-1}	μm	n	k
0.03493	281.7	35.5	1.441	
0.03444	277.8	36.0	1.438	
0.03397	274.0	36.5	1.435	
0.03351	270.3	37.0	1.432	
0.03306	266.7	37.5	1.429	
0.03263	263.2	38.0	1.425	
0.03220	259.7	38.5	1.422	
0.03179	256.4	39.0	1.419	
0.03139	253.2	39.5	1.415	
0.03100	250.0	40.0	1.412	
0.03061	246.9	40.5	1.408	
0.03024	243.9	41.0	1.405	
0.02988	241.0	41.5	1.401	
0.02952	238.1	42.0	1.397	
0.02917	235.3	42.5	1.393	
0.02883	232.6	43.0	1.389	
0.02850	229.9	43.5	1.385	
0.02818	227.3	44.0	1.381	
0.02786	224.7	44.5	1.376	
0.02755	222.2	45.0	1.372	
0.02725	219.8	45.5	1.368	
0.02695	217.4	46.0	1.363	
0.02666	215.1	46.5	1.358	
0.02638	212.8	47.0	1.354	
0.02610	210.5	47.5	1.349	
0.02583	208.3	48.0	1.344	
0.02556	206.2	48.5	1.338	
0.02530	204.1	49.0	1.333	
0.02505	202.0	49.5	1.328	
0.02480	200	50.00	1.322	
			1.31 [4]	0.01 [4]
0.02418	195	51.28	1.308 [2]	
			1.29 [4]	0.01 [4]
0.02356	190	52.63	1.291 [2]	
			1.27 [4]	0.02 [4]
0.02294	185	54.05	1.272 [2]	
			1.25 [4]	0.02 [4]
0.02232	180	55.56	1.22	0.03
0.02170	175	57.14	1.18	0.04
0.02108	170	58.82	1.16	0.04
0.02046	165	60.61	1.13	0.04
0.02009	162	61.73	1.11	0.05
0.01984	160	62.50	1.09	0.05
0.01959	158	63.29	1.07	0.06
0.01934	156	64.10	1.04	0.07
0.01909	154	64.94	1.00	0.09

TABLE I *(Continued)*

Rubidium Bromide

eV	cm^{-1}	μm	n	k
0.01885	152	65.79	0.99	0.10
0.01860	150	66.67	0.99	0.11
0.01835	148	67.57	0.97	0.13
0.01810	146	68.49	0.96	0.14
0.01785	144	69.44	0.96	0.17
0.01761	142	70.42	0.95	0.18
0.01736	140	71.43	0.91	0.18
0.01711	138	72.46	0.88	0.20
0.01686	136	73.53	0.80	0.21
0.01661	134	74.63	0.72	0.27
0.01637	132	75.76	0.75	0.36
0.01612	130	76.92	0.84	0.38
0.01587	128	78.13	0.87	0.37
0.01562	126	79.37	0.84	0.44
0.01537	124	80.65	0.81	0.53
0.01513	122	81.97	0.78	0.52
0.01488	120	83.33	0.69	0.56
0.01463	118	84.75	0.55	0.67
0.01438	116	86.21	0.50	0.76
0.01413	114	87.72	0.49	0.86
0.01389	112	89.29	0.50	0.99
0.01364	110	90.91	0.50	1.14
0.01339	108	92.59	0.45	1.30
0.01314	106	94.34	0.42	1.46
0.01289	104	96.15	0.44	1.61
0.01265	102	98.04	0.47	1.76
0.01240	100	100.0	0.49	1.99
0.01215	98.0	102.0	0.54	2.33
0.01190	96.0	104.2	0.56	2.68
0.01165	94.0	106.4	0.59	3.05
0.01141	92.0	108.7	0.73	3.46
0.01116	90.0	111.1	1.25	4.12
0.01091	88.0	113.6	2.66	4.56
0.01066	86.0	116.3	4.26	3.31
0.01041	84.0	119.0	4.27	1.95
0.01017	82.0	122.0	4.08	1.17
0.00992	80.0	125.0	3.62	0.52
0.00967	78.0	128.2	3.12	0.29
0.00942	76.0	131.6	2.87	0.25
0.00917	74.0	135.1	2.78	0.23
0.00893	72.0	138.9	2.78	0.25
0.00868	70.0	142.9	2.76	0.27
0.00843	68.0	147.1	2.73	0.27
0.00806	65.0	153.8	2.65	0.25
0.00744	60.0	166.7	2.53	0.25
0.00682	55.0	181.8	2.47	0.19
0.00620	50.0	200.0	2.41	0.18
0.00558	45.0	222.2	2.39	0.13

Rubidium Iodide (RbI)

IVAN OHLÍDAL and DANIEL FRANTA
Department of Solid State Physics
Faculty of Sciences
Masaryk University Brno
Brno, Czech Republic

Single crystals of rubidium iodide exhibit the cubic structure of NaCl (O_h^5-Fm3m space group).

Rubidium iodide crystals are widely used for manufacturing various optical components employed especially in the infrared region. This is due to the fact that RbI crystals exhibit a broad range of transparency from the near UV (0.24 μm) to the far IR (64 μm).

RbI is the most hygroscopic material of the rubidium halides. Considerable care has to be devoted to preparing surfaces of the optical components fabricated from RbI crystals, since these surfaces play an important role in their transparency properties. The gradual decrease in transmittance at shorter wavelengths is due to surface scattering that is caused by roughness of the surfaces of the components prepared by usual procedures of polishing, and not by absorption or scattering within the material itself [1]. This is probably caused by the fact that usual polishing procedures yield roughness of surfaces of the RbI components, exhibiting relatively large values of the heights of the surface irregularities.

There are few data of the optical constants available for RbI, similar to the other rubidium halides. The room-temperature values of the refractive index n and the extinction coefficient k tabulated here (see Table I and Fig. 1) were obtained from the following papers: the 0.25 μm (4.959 eV) to 0.18 μm (6.888 eV) results are from the paper of Baldini and Rigaldi [2]; the 0.26 μm (4.769 eV) to 0.23 μm (5.391 eV) values of n and k are obtained on the basis of measurements presented in the article of Fröhlich *et al.* [3]; the 64 μm (0.01937 eV) to 0.24 μm (5.166 eV) refractive-index data were calculated by means of the dispersion formula presented in the paper of Li [4]; the 0.656 μm (1.890 eV) to 0.486 μm (2.551 eV) values of n are from the paper of Sprockhoff [5]; and the 222.2 μm (45 cm^{-1}) to 52.63 μm (190 cm^{-1}) values of n and k were published by Pai *et al.* [6].

HANDBOOK OF OPTICAL CONSTANTS OF SOLIDS III

Copyright © 1998 by Academic Press.
All rights of reproduction in any form reserved
ISBN 0-12-544423-0/$25.00.

The values of n and k presented by Baldini and Rigaldi [2] were obtained by interpreting spectral dependences of the reflectances and transmittance of a RbI thin film with the thickness of 0.042 μm (the error of the thickness was ± 0.003 μm). The RbI film was prepared by sublimation onto a fused-silica plate in the vacuum chamber employed simultaneously for the optical measurements (temperature of the fused-silica substrate during the deposition of the RbI film is not specified in the paper of Baldini and Rigaldi [2], but one can assume that it was about room temperature). Thus, the spectral dependences of both the reflectances R and R' of the film for incidence of light from the ambient side and the substrate side, respectively, could be measured together with the transmittance T of the film corresponding to incidence of light from the ambient side in the spectral region of interest ($R \neq R'$ and $T = T'$, if the film under investigation is absorbing, where T' denotes the transmittance of the film corresponding to incidence of light from the substrate side). The authors measured the values of these three different optical quantities, that is, the values of R, R' and T, at selected wavelengths at near-normal incidence of light. They then determined the value of the thickness and the values of n and k by solving the three equations expressing R, R', and T by means of a numerical procedure at the wavelengths of interest without any auxiliary measurements [2]. The spectral dependences of the optical constants of the RbI film determined in this way correspond to absorption caused by excitons in this region. Uncertainty of the optical-constant data was reported to be about 1%. It should be noted that the wavelengths of the ultraviolet absorption peaks derived from the work by Baldini and Rigaldi [2] are inconsistent with those observed for bulk material of RbI [7, 8].

In the region $0.260\ \mu\text{m} \geq \lambda \geq 0.230\ \mu\text{m}$, we calculated the values of the refractive index n and extinction coefficient k by means of the values of parameters characterizing resonances on the lower exciton–polariton branch in RbI single crystals evaluated with three-photon difference-frequency generation (TP-DFG) by Fröhlich *et al.* [3]. Namely, as a modern method of nonlinear optical spectroscopy, the TP-DFG method opens up new possibilities to study elementary excitations in solids and, moreover, in the corresponding spectral region this method allows the determination of the spectral dependences of the optical constants of thick bulk samples of the single crystals in a reliable way. Therefore, the values of positions and widths of the resonance peaks (i.e., the values of the parameters characterizing resonances) determined for the RbI single crystal by the TP-DFG method at room temperature in the paper of Fröhlich *et al.* [3] were used to calculate the spectral dependences of n and k of RbI for the region of the exponential tail of the excitonic absorption edge, that is, for the region mentioned earlier. Equations enabling us to carry out these calculations are introduced in the paper mentioned [3]. Unfortunately, uncertainties in the values of the parameters determined with the TP-DFG method (and needed for calculating n and k)

are not introduced in the paper of Fröhlich *et al.*, and so it is not possible to estimate an accuracy of the optical constants calculated. Thus, it is impossible to compare the values of n and k determined by Baldini and Rigaldi [2] with those calculated on the basis of the TP-DFG method in an exact way. In spite of this fact, it is evident that there are nonnegligible differences between the Baldini and Rigaldi data and the data calculated. This statement is especially true for the region $0.238\ \mu m \geq \lambda \geq 0.230\ \mu m$ (see Table I). One can expect that the values of n and k calculated on the basis of the TP-DFG measurements are more reliable than those determined by Baldini and Rigaldi. The values of the optical constants obtained by Baldini and Rigaldi are probably influenced by defects frequently occurring in thin solid films. The RbI thin film studied by Baldini and Rigaldi probably exhibited polycrystalline structure (structure of this film was not examined), and thus the defects such as columnar structure, impurities, and roughness of the boundaries could considerably affect the correctness of the data presented. This conclusion is also supported by the fact that the wavelengths of the ultraviolet absorption peaks corresponding to the Baldini and Rigaldi data are inconsistent with those observed for the RbI single crystals in direct measurements [7, 8].

In the region $64.00\ \mu m \geq \lambda \geq 0.24\ \mu m$, that is, in the region of transparency of RbI, the refractive-index data obtained on the basis of the Li results [4] are introduced. This author employed the important refractive-index data published by Kublitzky [9] to obtain the following empirical dispersion formula for the refractive index of RbI:

$$n^2 = 1.60563 + \frac{0.00947\lambda^2}{\lambda^2 - (0.120)^2} + \frac{0.01073\lambda^2}{\lambda^2 - (0.134)^2} + \frac{0.00136\lambda^2}{\lambda^2 - (0.156)^2} + \frac{0.41864\lambda^2}{\lambda^2 - (0.179)^2} + \frac{0.41771\lambda^2}{\lambda^2 - (0.187)^2} + \frac{0.13707\lambda^2}{\lambda^2 - (0.223)^2} + \frac{2.36091\lambda^2}{\lambda^2 - (132.45)^2}, \quad (1)$$

λ denotes the wavelengths in micrometers.

Thus, this formula of the Sellmeier type was utilized for calculating the values of n within the spectral region of transparency of RbI [4]. These refractive-index values correspond to the RbI single crystal, since Kublitzky [9] measured the values of n characterizing RbI prisms by the method of minimum deviation at selected wavelengths in the spectral region $0.578\ \mu m \geq \lambda \geq 0.254\ \mu m$.

Sprockhoff [5] also measured the values of n of RbI by means of the method of minimum deviation. He determined the refractive-index values of the single crystal for the following three wavelengths: 0.486, 0.589, and 0.656 μm (see Table I).

The uncertainties of the refractive-index values determined by means of Eq. (1) are dependent on wavelength. (The smallest and/or greatest uncertainties in n are equal to ± 0.002 in the region $1.5\ \mu\text{m} \geq \lambda \geq 0.4\ \mu\text{m}$ and/or ± 0.02 in regions $0.25\ \mu\text{m} \geq \lambda \geq 0.24\ \mu\text{m}$ and $64\ \mu\text{m} \geq \lambda \geq 50\ \mu\text{m}$). The errors of n in Sprockhoff's measurements can be estimated as ± 0.001.

One can see that the values of n determined using Eq. (1) agree very well with those calculated on the basis of the TP-DFG measurements. Similarly, there is a very good agreement between values of n determined by means of Eq. (1) and those measured by Sprockhoff. These facts gives significant support for the correctness and reliability of the n values of bulk RbI presented here for both the visible and the region 0.23–0.38 μm. It should be noted that in the region $0.546\ \mu\text{m} \geq \lambda \geq 0.25\ \mu\text{m}$ by treating the Kublitzky data, Radhakrishnan [10] obtained the empirical dispersion formula of the Sellmeier type expressing the spectral dependence of n of the RbI single crystal in the following form:

$$n^2 = 1.6017 + \frac{0.01749\lambda^2}{\lambda^2 - 0.015625} + \frac{0.83466\lambda^2}{\lambda^2 - 0.033489} + \frac{0.13917\lambda^2}{\lambda^2 - 0.049729}, \tag{2}$$

λ is also in micrometers.

This formula yields the wavelengths of three ultraviolet absorption peaks, which agree with those studied for bulk material by direct measurements [7, 8] but gives no information concerning the infrared absorption peak. Thus, the Radhakrishnan formula [10] can not be used to calculate the values of n in a wide spectral region. Namely, the extrapolated refractive-index values for the IR wavelengths using this formula have large uncertainties compared to those obtained using the Li formula [4]. This is caused by the fact that Radhakrishnan only correlated his formula with the wavelengths of the absorption peaks in the UV region found in the independent way, while Li performed the correlation of his formula not only with these ultraviolet wavelengths, but also with the wavelength of the fundamental infrared absorption peak λ_I found by direct measurements. This fact enables us to use the Li formula in the IR region in which RbI is a nonabsorbing material. It should be noted that the values of the adjustable parameters of both the empirical dispersion formulas mentioned (e.g., the value of 0.00947 in the Li formula) were found by fitting the Kublitzky data [9] by means of the least-squares method.

Pai *et al.* [6] determined the spectral dependences of n and k characterizing RbI bulk samples (i.e., the single crystals) using amplitude and phase reflection measurements made by dispersive Fourier transform spectroscopy in the region $222.2\ \mu\text{m} \geq \lambda \geq 52.63\ \mu\text{m}$. The errors of n and k determined in this way are also dependent on wavelength. (The greatest and/or smallest

errors in both n and k are equal to ± 0.13 and/or ± 0.01 at the wavelength of about 132 μm and/or in the interval 106 $\mu m \geq \lambda \geq 54$ μm [6].) Spectral dependences of n and k in the vicinity of the maximum value of k at the wavelength of the fundamental infrared absorption peak λ_I are related to one-photon absorption, corresponding to the TO phonon mode. The fine structures of the curves expressing the spectral dependences of n and k in the region 60–90 μm may be caused by multiple-phonon processes of absorption. In the region 64.52 $\mu m \geq \lambda \geq 52.63$ μm, very good agreement exists between the refractive-index data presented by Pai *et al.* [6] and those calculated using the Li formula [4] (see Table I). This agreement again gives support for the correctness and reliability of the n and k values of bulk RbI introduced for the infrared region here. However, it is necessary to point out that more precise values of k will be able to be determined using transmittance measurements of sufficiently thin RbI slabs in the intervals of the infrared region in which RbI is weakly absorbing ($k \leq 0.1$), if these measurements are ever performed.

From Eq. (1) and the spectral dependence of k determined by Pai *et al.* [6], one can see that there is relatively good agreement between the value of λ_I used in the Li formula and that implied by the data of Pai *et al.*

The optical-constant data presented in this paper are the room-temperature data, as emphasized earlier. However, strictly speaking there are small differences at temperatures corresponding to the data summarized. Namely, Baldini and Rigaldi's data [2] and the data derived from the TP-DFG measurements [3] correspond to 298 K. Li's values of n [4], Sprockhoff's values of n [5], and the data of Pai *et al.* [6] correspond to 293, 298, and 300 K, respectively. Both the Radhakrishnan formula [10] and the Kublitzky measurements were for 309 K. Thus, to obtain his formula in the form presented at first, Li [4] reduced the Kublitzky data of n from 309 to 293 K by using empirical parameters enabling him to construct a dn/dT formula that was employed for the corrections mentioned (dn/dT denotes the derivative of the refractive index n with respect to temperature T).

In conclusion, one can state that the data of n and k summarized in this work represent the best values of these optical constants characterizing bulk RbI in the spectral region 222.2 $\mu m \geq \lambda \geq 0.23$ μm (i.e., these data consist of the data based on the TP-DFG method, the Li data [4], the Sprockhoff [5] values of n, and the data of Pai *et al.* [6]). The data of n and k presented by Baldini and Rigaldi [2] can serve as the values of the optical constants of RbI usable for applications in the first approximation.

REFERENCES

1. D. E. McCarthy, *Appl. Opt.* **7**, 1243 (1968).
2. G. Baldini and L. Rigaldi, *J. Opt. Soc. Am.* **69**, 495 (1970).
3. D. Fröhlich, P. Köhler, W. Nieswand, and T. Rappen, *Phys. Rev. B* **43**, 12590 (1991).
4. H. H. Li, *J. Phys. Chem. Ref. Data* **5**, 329 (1976).

5. M. Sprockhoff, *Neues Jahrb. Mineral. Geol. Palaeontol., Beilageband* **18**, 117 (1904).
6. K. F. Pai, T. J. Parker, N. E. Tornberg, R. P. Lowndes, and W. G. Chambers, *Infrared Phys.* **18**, 199 (1978).
7. R. Hilsch and R. W. Pohl, *Z. Phys.* **59**, 812 (1930).
8. E. G. Schneider and H. M. O'Bryan, *Phys. Rev.* **51**, 293 (1937).
9. A. Kublitzky, *Ann. Phys.* **20**, 793 (1934).
10. T. Radhakrishnan, *Proc. Indian Acad. Sci. Sect. A* **27**, 165 (1948).

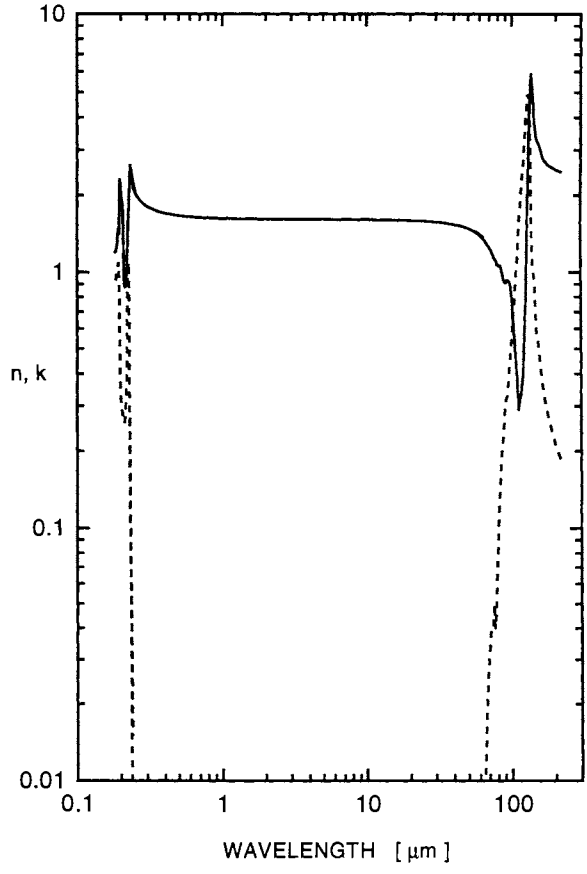

Fig. 1. Log–log plot of n (solid line) and k (dashed line) versus wavelength in micrometers for RbI.

TABLE I

Values of n and k for Rubidium Iodide as Obtained from Various References[a]

eV	cm^{-1}	μm	n	k
6.888	55,560	0.180	1.193 [2]	0.857 [2]
6.812	54,950	0.182	1.199	0.884
6.738	54,350	0.184	1.215	0.928
6.666	53,760	0.186	1.254	0.986
6.595	53,190	0.188	1.318	1.040
6.526	52,630	0.190	1.412	1.054
6.458	52,090	0.192	1.494	1.096
6.391	51,550	0.194	1.415	0.953
6.326	51,020	0.196	2.299	0.509
6.262	50,510	0.198	2.153	0.339
6.199	50,000	0.200	1.998	0.314
6.138	49,500	0.202	1.903	0.298
6.078	49,020	0.204	1.830	0.286
6.019	48,540	0.206	1.706	0.277
5.961	48,080	0.208	1.032	0.267
5.904	47,620	0.210	0.896	0.257
5.848	47,170	0.212	0.873	0.262
5.794	46,730	0.214	0.883	0.281
5.740	46,300	0.216	0.925	0.326
5.687	45,870	0.218	1.000	0.423
5.636	45,460	0.220	1.172	0.627
5.585	45,050	0.222	1.432	0.978
5.535	44,640	0.224	1.706	1.096
5.486	44,250	0.226	1.984	0.951
5.438	43,860	0.228	2.262	0.469
5.391	43,480	0.230	2.488	0.112
			2.636 [3]	0.270 [3]
5.344	43,100	0.232	2.540 [2]	0.069 [2]
			2.461 [3]	0.0751 [3]
5.299	42,740	0.234	2.497 [2]	0.046 [2]
			2.355 [3]	0.0213 [3]
5.254	42,370	0.236	2.419 [2]	0.028 [2]
			2.280 [3]	0.0062 [3]
5.209	42,020	0.238	2.343 [2]	0.015 [2]
			2.223 [3]	0.0018 [3]
5.166	41,670	0.240	2.272 [2]	
			2.177 [3]	
			2.155 [4]	
5.123	41,320	0.242	2.220 [2]	
			2.140 [3]	
			2.123 [4]	
5.081	40,980	0.244	2.171 [2]	
			2.108 [3]	
			2.094 [4]	

(continued)

[a] References given in brackets.

TABLE I *(Continued)*

Rubidium Iodide

eV	cm^{-1}	μm	n	k
5.040	40,650	0.246	2.131 [2]	
			2.081 [3]	
			2.070 [4]	
4.999	40,320	0.248	2.092 [2]	
			2.057 [3]	
			2.048 [4]	
4.959	40,000	0.250	2.059 [2]	
			2.036 [3]	
			2.028 [4]	
4.920	39,680	0.252	2.017 [3]	
			2.010 [4]	
4.881	39,370	0.254	2.000 [3]	
			1.994 [4]	
4.843	39,060	0.256	1.984 [3]	
			1.979 [4]	
4.806	38,760	0.258	1.970 [3]	
			1.966 [4]	
4.769	38,460	0.260	1.957 [3]	
			1.953 [4]	
4.732	38,170	0.262	1.941	
4.696	37,880	0.264	1.930	
4.661	37,590	0.266	1.920	
4.626	37,310	0.268	1.910	
4.592	37,040	0.270	1.901	
4.558	36,760	0.272	1.893	
4.525	36,500	0.274	1.885	
4.492	36,230	0.276	1.877	
4.460	35,970	0.278	1.870	
4.428	35,710	0.280	1.863	
4.397	35,460	0.282	1.856	
4.366	35,210	0.284	1.850	
4.335	34,970	0.286	1.844	
4.305	34,720	0.288	1.838	
4.275	34,480	0.290	1.833	
4.246	34,250	0.292	1.828	
4.217	34,010	0.294	1.823	
4.189	33,780	0.296	1.818	
4.161	33,560	0.298	1.813	
4.133	33,330	0.300	1.809	
4.065	32,790	0.305	1.798	
4.000	32,260	0.310	1.789	
3.936	31,750	0.315	1.780	
3.875	31,250	0.320	1.772	
3.815	30,770	0.325	1.765	
3.757	30,300	0.330	1.758	
3.701	29,850	0.335	1.752	

TABLE I *(Continued)*

Rubidium Iodide

eV	cm^{-1}	μm	n	k
3.647	29,410	0.340	1.746	
3.594	28,990	0.345	1.741	
3.542	28,570	0.350	1.736	
3.493	28,170	0.355	1.731	
3.444	27,780	0.360	1.727	
3.397	27,400	0.365	1.722	
3.351	27,030	0.370	1.718	
3.306	26,670	0.375	1.715	
3.263	26,320	0.380	1.711	
3.220	25,970	0.385	1.708	
3.179	25,640	0.390	1.705	
3.139	25,320	0.395	1.702	
3.100	25,000	0.400	1.699	
3.024	24,390	0.410	1.694	
2.952	23,810	0.420	1.689	
2.883	23,260	0.430	1.685	
2.818	22,730	0.440	1.681	
2.755	22,220	0.450	1.677	
2.695	21,740	0.460	1.674	
2.638	21,280	0.470	1.671	
2.583	20,830	0.480	1.668	
2.551	20,580	0.486	1.667 [5]	
2.530	20,410	0.490	1.665 [4]	
2.480	20,000	0.500	1.663	
2.431	19,610	0.510	1.661	
2.384	19,230	0.520	1.659	
2.339	18,870	0.530	1.657	
2.296	18,520	0.540	1.655	
2.254	18,180	0.550	1.653	
2.214	17,860	0.560	1.652	
2.175	17,540	0.570	1.650	
2.138	17,240	0.580	1.649	
2.105	16,980	0.589	1.647 [5]	
2.101	16,950	0.590	1.647 [4]	
2.066	16,670	0.600	1.646	
2.000	16,130	0.620	1.644	
1.937	15,625	0.640	1.642	
1.890	15,240	0.656	1.640 [5]	
1.879	15,150	0.660	1.640 [4]	
1.823	14,710	0.680	1.638	
1.771	14,290	0.700	1.637	
1.722	13,890	0.720	1.635	
1.675	13,510	0.740	1.634	
1.631	13,160	0.760	1.633	
1.590	12,820	0.780	1.632	
1.550	12,500	0.800	1.631	

(continued)

TABLE I *(Continued)*

Rubidium Iodide

eV	cm^{-1}	μm	n	k
1.512	12,200	0.820	1.630	
1.476	11,900	0.840	1.629	
1.442	11,630	0.860	1.628	
1.409	11,360	0.880	1.627	
1.378	11,110	0.900	1.627	
1.348	10,870	0.920	1.626	
1.319	10,640	0.940	1.625	
1.292	10,420	0.960	1.625	
1.265	10,200	0.980	1.624	
1.240	10,000	1.00	1.624	
1.181	9,524	1.05	1.623	
1.127	9,091	1.10	1.622	
1.078	8,696	1.15	1.621	
1.033	8,333	1.20	1.620	
0.9919	8,000	1.25	1.620	
0.9537	7,692	1.30	1.619	
0.9184	7,407	1.35	1.619	
0.8856	7,143	1.40	1.618	
0.8551	6,897	1.45	1.618	
0.8266	6,667	1.50	1.617	
0.7749	6,250	1.60	1.617	
0.7293	5,882	1.70	1.616	
0.6888	5,556	1.80	1.616	
0.6526	5,263	1.90	1.616	
0.6199	5,000	2.00	1.615	
0.5637	4,545	2.20	1.615	
0.5166	4,167	2.40	1.614	
0.4769	3,846	2.60	1.614	
0.4428	3,571	2.80	1.614	
0.4133	3,333	3.00	1.613	
0.3542	2,857	3.50	1.613	
0.3100	2,500	4.00	1.613	
0.2755	2,222	4.50	1.612	
0.2480	2,000	5.00	1.612	
0.2066	1,667	6.00	1.611	
0.1771	1,429	7.00	1.611	
0.1550	1,250	8.00	1.610	
0.1378	1,111	9.00	1.609	
0.1240	1,000	10.0	1.609	
0.1127	909.1	11.0	1.608	
0.1033	833.3	12.0	1.607	
0.09537	769.2	13.0	1.606	
0.08856	714.3	14.0	1.604	
0.08266	666.7	15.0	1.603	
0.07999	645.2	15.5	1.602	
0.07749	625.0	16.0	1.602	

TABLE I *(Continued)*

Rubidium Iodide

eV	cm^{-1}	μm	n	k
0.07514	606.1	16.5	1.601	
0.07293	588.2	17.0	1.600	
0.07085	571.4	17.5	1.600	
0.06888	555.6	18.0	1.599	
0.06702	540.5	18.5	1.598	
0.06526	526.3	19.0	1.597	
0.06358	512.8	19.5	1.596	
0.06199	500.0	20.0	1.596	
0.06048	487.8	20.5	1.595	
0.05904	476.2	21.0	1.594	
0.05767	465.1	21.5	1.593	
0.05636	454.5	22.0	1.592	
0.05510	444.4	22.5	1.591	
0.05391	434.8	23.0	1.590	
0.05276	425.5	23.5	1.589	
0.05166	416.7	24.0	1.588	
0.05061	408.2	24.5	1.587	
0.04959	400.0	25.0	1.585	
0.04862	392.2	25.5	1.584	
0.04769	384.6	26.0	1.583	
0.04679	377.4	26.5	1.582	
0.04592	370.4	27.0	1.581	
0.04509	363.6	27.5	1.579	
0.04428	357.1	28.0	1.578	
0.04350	350.9	28.5	1.577	
0.04275	344.8	29.0	1.575	
0.04203	339.0	29.5	1.574	
0.04133	333.3	30.0	1.573	
0.04065	327.9	30.5	1.571	
0.04000	322.6	31.0	1.570	
0.03936	317.5	31.5	1.568	
0.03875	312.5	32.0	1.567	
0.03815	307.7	32.5	1.565	
0.03757	303.0	33.0	1.563	
0.03701	298.5	33.5	1.562	
0.03647	294.1	34.0	1.560	
0.03594	289.9	34.5	1.558	
0.03542	285.7	35.0	1.557	
0.03493	281.7	35.5	1.555	
0.03444	277.8	36.0	1.553	
0.03397	274.0	36.5	1.551	
0.03351	270.3	37.0	1.549	
0.03306	266.7	37.5	1.548	
0.03263	263.2	38.0	1.546	
0.03220	259.7	38.5	1.544	
0.03179	256.4	39.0	1.542	

(continued)

TABLE I *(Continued)*

Rubidium Iodide

eV	cm^{-1}	μm	n	k
0.03139	253.2	39.5	1.540	
0.03100	250.0	40.0	1.537	
0.03061	246.9	40.5	1.535	
0.03024	243.9	41.0	1.533	
0.02988	241.0	41.5	1.531	
0.02952	238.1	42.0	1.529	
0.02917	235.3	42.5	1.526	
0.02883	232.6	43.0	1.524	
0.02850	229.9	43.5	1.522	
0.02818	227.3	44.0	1.519	
0.02786	224.7	44.5	1.517	
0.02755	222.2	45.0	1.514	
0.02725	219.8	45.5	1.512	
0.02695	217.4	46.0	1.509	
0.02666	215.1	46.5	1.506	
0.02638	212.8	47.0	1.504	
0.02610	210.5	47.5	1.501	
0.02583	208.3	48.0	1.498	
0.02556	206.2	48.5	1.495	
0.02530	204.1	49.0	1.492	
0.02505	202.0	49.5	1.489	
0.02480	200.0	50.0	1.486	
0.02455	198.0	50.5	1.483	
0.02431	196.1	51.0	1.480	
0.02407	194.2	51.5	1.477	
0.02384	192.3	52.0	1.473	
0.02362	190.5	52.5	1.470	
0.02356	190.0	52.63	1.46 [6]	
0.02339	188.7	53.0	1.466 [4]	
0.02317	186.9	53.5	1.463	
0.02296	185.2	54.0	1.459	
0.02294	185.0	54.05	1.46 [6]	
0.02275	183.5	54.5	1.456 [4]	
0.02254	181.8	55.0	1.452	
0.02234	180.2	55.5	1.448	
0.02232	180.0	55.56	1.44 [6]	
0.02214	178.6	56.0	1.445 [4]	
0.02194	177.0	56.5	1.441	
0.02175	175.4	57.0	1.437	
0.02170	175.0	57.14	1.43 [6]	0.01 [6]
0.02156	173.9	57.5	1.433 [4]	
0.02138	172.4	58.0	1.428	
0.02119	170.9	58.5	1.424	
0.02108	170.0	58.82	1.41 [6]	0.01 [6]
0.02101	169.5	59.0	1.420 [4]	
0.02084	168.1	59.5	1.416	

TABLE I *(Continued)*

Rubidium Iodide

eV	cm^{-1}	μm	n	k
0.02066	166.7	60.0	1.411	
0.02049	165.3	60.5	1.406	
0.02046	165.0	60.61	1.39 [6]	0.01 [6]
0.02033	163.9	61.0	1.402 [4]	
0.02016	162.6	61.5	1.397	
0.02000	161.3	62.0	1.392	
0.01984	160.0	62.50	1.387	
			1.37 [6]	0.01 [6]
0.01968	158.7	63.0	1.382 [4]	
0.01953	157.5	63.5	1.377	
0.01937	156.3	64.0	1.372	
0.01922	155	64.52	1.34 [6]	0.01 [6]
0.01860	150	66.67	1.30	0.02
0.01798	145	68.97	1.27	0.03
0.01736	140	71.43	1.23	0.04
0.01711	138	72.46	1.21	0.04
0.01686	136	73.53	1.18	0.04
0.01661	134	74.63	1.16	0.05
0.01637	132	75.76	1.13	0.04
0.01612	130	76.92	1.12	0.04
0.01587	128	78.13	1.10	0.06
0.01562	126	79.37	1.07	0.08
0.01537	124	80.65	1.06	0.10
0.01513	122	81.97	1.06	0.14
0.01488	120	83.34	1.06	0.16
0.01463	118	84.75	1.02	0.20
0.01438	116	86.21	0.98	0.22
0.01413	114	87.72	0.94	0.24
0.01389	112	89.29	0.91	0.29
0.01364	110	90.91	0.91	0.32
0.01339	108	92.59	0.93	0.33
0.01314	106	94.34	0.93	0.37
0.01289	104	96.15	0.92	0.43
0.01265	102	98.04	0.88	0.49
0.01240	100	100.0	0.79	0.57
0.01215	98.0	102.0	0.64	0.67
0.01190	96.0	104.2	0.55	0.78
0.01165	94.0	106.4	0.46	0.93
0.01141	92.0	108.7	0.37	1.12
0.01116	90.0	111.1	0.29	1.38
0.01091	88.0	113.6	0.32	1.67
0.01066	86.0	116.3	0.34	2.05
0.01041	84.0	119.0	0.40	2.48
0.01017	82.0	122.0	0.56	3.08
0.00992	80.0	125.0	0.83	3.93
0.00967	78.0	128.2	1.52	4.93

(continued)

TABLE I *(Continued)*

Rubidium Iodide

eV	cm^{-1}	μm	n	k
0.00942	76.0	131.6	4.26	4.80
0.00917	74.0	135.1	5.89	2.41
0.00893	72.0	138.9	4.97	1.07
0.00868	70.0	142.9	3.80	0.94
0.00843	68.0	147.1	3.33	0.59
0.00818	66.0	151.5	3.19	0.52
0.00794	64.0	156.3	3.04	0.44
0.00769	62.0	161.3	2.87	0.38
0.00744	60.0	166.7	2.73	0.33
0.00682	55.0	181.8	2.60	0.26
0.00620	50.0	200.0	2.51	0.21
0.00558	45.0	222.2	2.46	0.18

Sodium Nitrate ($NaNO_3$)

EDWARD D. PALIK
Institute for Physical Science and Technology

and

R. KHANNA
Department of Chemistry and Biochemistry
University of Maryland
College Park, Maryland

Sodium nitrate ($NaNO_3$) is isomorphic with $CaCO_3$ (calcite). Unlike calcite, $NaNO_3$ is water soluble and, hence, not particularly suitable as an industrial birefringent material. The interest in $NaNO_3$ is principally due to an order–disorder phase transition it undergoes in the temperature range 150 to 276° C. In the room-temperature phase sodium nitrate is a trigonal crystal with space group symmmetry R3c (D_{3d}). The unit cell contains two $NaNO_3$ formula units; the two NO_3^- ions are oriented in planes perpendicular to the optic axis. Above the phase transition, the NO_3^- ions are randomly oriented in the same plane.

The optical characteristics of $NaNO_3$ have been determined from the vacuum UV (95,000 cm^{-1}) to the far IR (10 cm^{-1}). The values of n(o), k(o), n(e) and k(e) specifying the ordinary and extraordinary optical constants obtained in this critique are listed in Table I and plotted in Fig. 1.

The ultraviolet region has been studied by Uzan *et al.* [1] and Yamashita [2]. Measurements of reflectivity were made as a function of angle of incidence with *s*- and *p*-polarized light [1]. The sample was mechanically polished with the *c*-axis presumably in the plane. The polarized reflectivity was measured on a cleaved (1011) surface at normal incidence and treated by Kramers–Kronig (K-K) analysis by Yamashita [2]. Although we prefer the angle-of-incidence technique with polarized light, the sample, being mechanically polished, presents several problems depending on the depth of damage, the crystal orientation within the optical skin depth $\delta = 1/\alpha = \lambda/4\pi k$, and the effect of water on the surface while the sample is being prepared and inserted into the vacuum spectrometer. In fact, Yamashita demon-

Copyright © 1998 by Academic Press.
All rights of reproduction in any form reserved
ISBN 0-12-544423-0/$25.00.

strated for reflectivity results with mechanical polishing that there was a significant variation in R, with R(polished) always smaller than R(cleaved). However, his analysis for the cleaved surface was more complicated. The sample had the c-axis at 43°49′ to the surface, so with normal incidence one can measure $\mathbf{E}\perp\mathbf{c}$ directly but not $\mathbf{E}\parallel\mathbf{c}$, only $\mathbf{E}\parallel\mathbf{c}'$, where $\mathbf{c}'$ is a direction in the surface containing the plane of incidence, the c-axis and the c'-axis. It was then necessary to use K-K analysis and the equation for the dielectric ellipsoid (with both real and imaginary parts) to obtain ϵ(e); ϵ(o) was directly measured.

Because there is folklore saying that bigger (reflectivity) is better, we choose to exhibit the data of Yamashita [2] in Table I. Plots of the real and imaginary plots of ϵ(o) and ϵ(e) were expanded and read. This can be done at best to two significant figures, but we give n(o), k(o) and n(e), k(e) to three or four figures to show trends and structures in the spectrum. The absolute values are surely uncertain to $\pm 10\%$ and even more for small values of k.

There do not seem to be any measurements of the refractive indices throughout the visible. The refractive indices reported in the "CRC Handbook of Chemistry and Physics" [3], presumably for the Na D line, are n(o) = 1.587 and n(e) = 1.336. There is little or no absorption and, consequently, no significant dispersion in the visible region. We include these two values in Table I.

We could find no measurements of n(o) or n(e) in the vis–near IR spectral region that might be fitted with a Sellmeier-type dispersion equation.

Greenberg and Hallgren [4] measured the near-IR (2–15 μm) transmittance of films grown in the interstices of a fine-mesh platinum screen; we assume the sample was polycrystalline. They observed several weak bands in the 3–6 μm region, which they assigned as overtone or combination bands. They also assigned fundamental bands at $\nu_3 = 1400\ \text{cm}^{-1}$, $\nu_2 = 833\ \text{cm}^{-1}$, and $\nu_4 = 719\ \text{cm}^{-1}$. Just above the melting point an additional weak absorption line at $1047\ \text{cm}^{-1}$ was assigned to ν_1, which is inactive in the room-temperature crystal phase. The ν notation refers to the internal vibration modes of the NO_3^- molecule. Because of the lack of information on sample thickness, these data could not be used to obtained the optical constants.

Frech and Nichols [5] measured the (ordinary) reflectance of the strong vibration band at 7.1 μm. This oscillator makes a significant contribution to the reflectance, whereas the weak band at $833\ \text{cm}^{-1}$ is probably too weak to show up in reflection. Interestingly, Frech and Nichols assume a classical oscillator with a frequency-dependent damping constant to explain a sharp dip in the reststrahlen peak at $1448\ \text{cm}^{-1}$. They found $\omega_T = 1356\ \text{cm}^{-1}$ and $\omega_L = 1468\ \text{cm}^{-1}$ and used $\epsilon_\infty = 2.518$, which corresponds to $n(\text{o})^2$ at 0.5890 μm as given in Table I. We calculated n(o) and k(o) using a classical oscillator model with the frequency-dependent damping constant given by Frech and Nicols [5]. Our calculation did not quite reproduce the measured reflectivity, giving a peak reflectivity of 0.86 compared to the measured value of 0.80. Therefore, we only give n and k to 2–3 figures. The values of n(o)

were extrapolated from 1700 up to 10,000 cm^{-1}. We also extrapolated n(o) to somewhat lower frequency to note how it blended into the lower-frequency data of Brehat and Wyncke [6], to be discussed later.

The far-infrared region 10–600 cm^{-1} has been studied by Brehat and Wyncke [6]. $NaNO_3$ crystals were grown by the Bridgman method. Several plates of (1010) orientation were mechanically polished. Both $\mathbf{E} \| \mathbf{c}$ (A_{2u} modes) and $\mathbf{E} \| \mathbf{a}$ (E_u modes) were measured; here $\mathbf{E} \| \mathbf{a}$ is equivalent to $\mathbf{E} \perp \mathbf{c}$. Measurements were made at temperatures from 10 to 549 K. Room-temperature spectra were shown at 299 K for A_{2u} modes and 303 K for E_u modes. Infrared reflectivity was measured at a 10° angle of incidence with a grating spectrometer. In addition, transmission measurements were made at 7–18 cm^{-1} using a monochromatic spectrometer with a tunable electron-beam, backward-wave oscillator [7]. A factorized form of the dielectric function was used to fit the reflectivity:

$$\epsilon(\omega) = \epsilon_\infty \frac{(\omega - i\gamma_{LR})}{(\omega - i\gamma_{TR})} \prod_j \frac{(\omega_{Lj}^2 - \omega^2 + i\omega\gamma_{Lj})}{(\omega_{Tj}^2 - \omega^2 + i\omega\gamma_{Tj})}, \tag{1}$$

Here, ω_j and γ_j are the frequencies and damping constants of the transverse and longitudinal polar lattice mode j, ϵ_∞ is the high-frequency dielectric constant, and γ_{TR} and γ_{LR} are damping factors for a relaxation mode assumed to be at $\omega = 0$. Although the Lorentz model is often used for several independent oscillators, a dielectric function of the form of Eq. (1) is sometimes used when the Lorentz model does not fit the reflectivity data well. One appears to be adding more adjustable parameters to obtain a better fit. Much more-detailed models are discussed by Gervais and Piriou [8] and Berreman and Unterwald [9]. The fitting parameters are listed in Table II; here we have obtained the relaxation parameters at 300 K from a graph showing their temperature dependence by Brehat and Wyncke [6]. Equation (1) at $\omega = 0$ gives the dc dielectric constants as $\epsilon(0)\perp = 5.96$ and $\epsilon(0)\| = 8.51$. We have calculated n(o,⊥), k(o,⊥), n(e,∥), k(e,∥) and list the data in Table I. The n and k for the three transmittance measurements are listed at 9.3, 13.3, and 17.3 cm^{-1} for comparison with the oscillator model; here $T = 26°$ C for (o) and $T = 30°$ C for (e).

The drastic mismatch in n(o) near 1000 cm^{-1} from Frech and Nichols [5] and Brehat and Wyncke [6] is due to the fact that Brehat and Wynke omitted the strong oscillator near 1400 cm^{-1} [5] from their model given in Eq. (1). In principle, the reader can do this to obtain somewhat better n(o) data in this spectral region.

REFERENCES

1. E. Uzan, H. Damany, and V. Chandrasekharan, Proprietes optique du nitrate de sodium dans la region de Schumann. *Opt. Commun.* **2**, 84 (1970).
2. H. Yamashita, Optical properties of sodium nitrate in the vacuum ultraviolet region. *J. Phys. Soc. Jpn.* **33**, 1407 (1972).

3. R. C. Weast, ed., "CRC Handbook of Chemistry and Physics," 53rd Ed., The Chemical Rubber Co., Cleveland, Ohio, 1972.
4. G. Greenberg and L. J. Hallgren, Infrared absorption spectra of alkali metal nitrates and nitrites above and below the melting point. *J. Chem. Phys.* **33**, 900 (1960).
5. R. Frech and H. Nichols, Anomalous infrared reflectivity minimum in $NaNO_3$. *Phys. Rev. B* **19**, 1243 (1979).
6. F. Brehat and B. Wyncke, Analysis of the temperature-dependent infrared active lattice modes in the ordered phase of sodium nitrate. *J. Phys. C: Solid State Phys.* **18**, 4247 (1985).
7. B. Wyncke, F. Brehat, and G. V. Kozlov, Low-frequency dielectric response function of sodium nitrate. *Phys. Status Solidi B* **129**, 531 (1985).
8. F. Gervais and B. Piriou, Temperature dependence of transverse- and longitudinal-optic modes in TiO_2 (rutile). *Phys. Rev. B* **10**, 1646 (1974).
9. D. W. Berreman and F. C. Unterwald, Adjusting poles and zeroes of dielectric dispersion to fit reststrahlen of $PrCl_3$ and $LaCl_3$. *Phys. Rev.* **174**, 791 (1968).

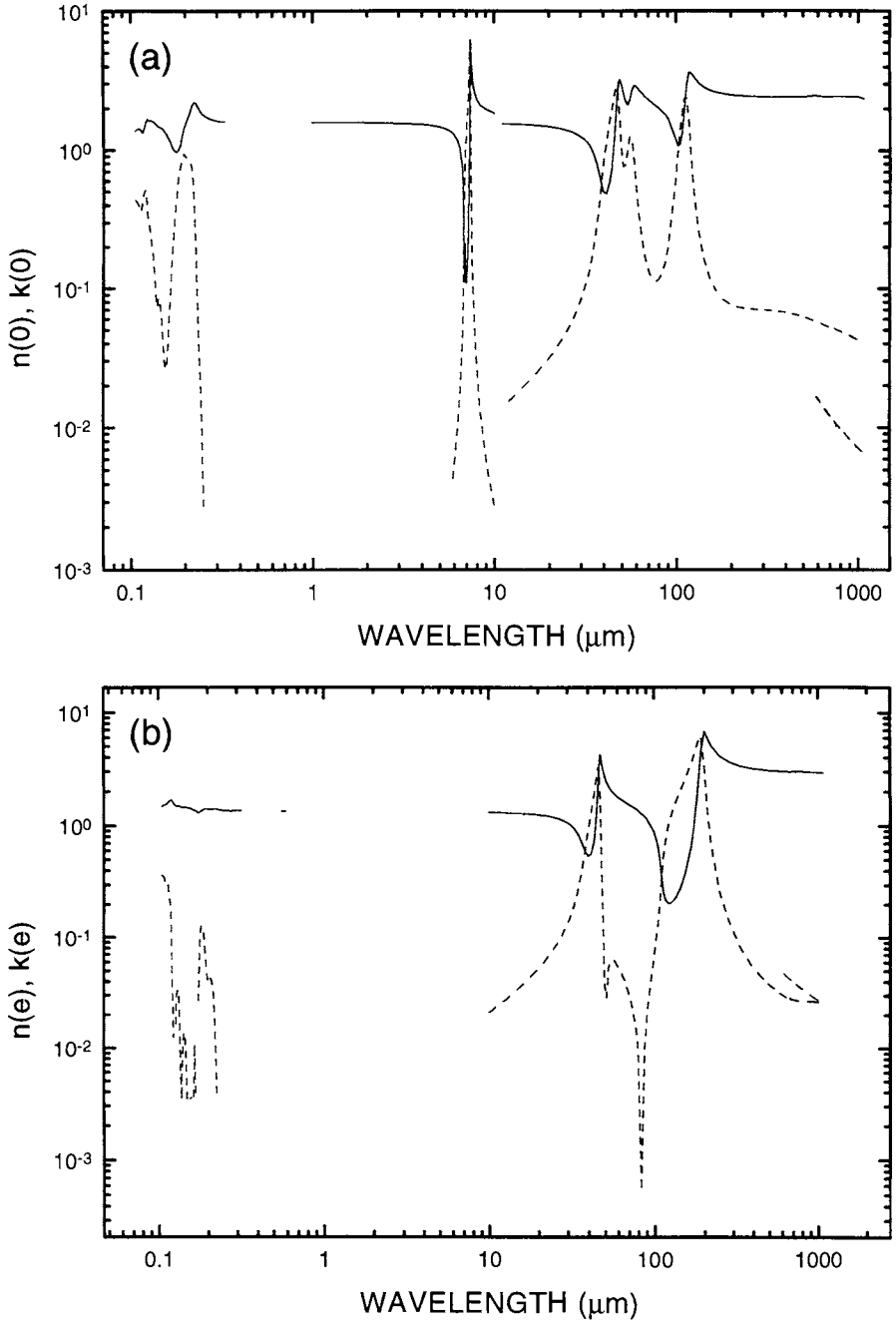

Fig. 1. (a) Log–log plot of n(o) (solid line) and k(o) (dashed line) versus wavelength in micrometers for sodium nitrate. (b) Log–log plot of n(e) (solid line) and k(e) (dashed line) versus wavelength in micrometers for sodium nitrate.

TABLE I

Values of n and k for Sodium Nitrate as Obtained from Various References[a]

eV	cm^{-1}	μm	n(o)	k(o)	n(e)	k(e)
11.8	95170	0.1051	1.374 [2]	4.36E-1 [2]	1.480 [2]	3.61E-1 [2]
11.7	94370	0.1060	1.388	4.33E-1	1.490	3.62E-1
11.6	93560	0.1069	1.404	4.28E-1	1.503	3.59E-1
11.5	92750	0.1078	1.413	4.22E-1	1.514	3.53E-1
11.4	91950	0.1088	1.421	4.11E-1	1.522	3.41E-1
11.3	91140	0.1097	1.424	4.00E-1	1.531	3.26E-1
11.2	90330	0.1107	1.424	3.86E-1	1.541	3.08E-1
11.1	89530	0.1117	1.420	3.69E-1	1.546	3.00E-1
11.0	88720	0.1127	1.403	3.59E-1	1.556	3.02E-1
10.9	87910	0.1137	1.380	3.69E-1	1.579	3.10E-1
10.8	87110	0.1148	1.344	4.09E-1	1.609	3.01E-1
10.7	86300	0.1159	1.341	4.47E-1	1.627	2.45E-1
10.6	85490	0.1170	1.393	4.80E-1	1.642	2.19E-1
10.5	84690	0.1181	1.454	5.05E-1	1.659	2.08E-1
10.4	83880	0.1192	1.516	5.19E-1	1.688	1.71E-1
10.3	83070	0.1204	1.578	5.10E-1	1.681	9.51E-2
10.2	82270	0.1216	1.638	4.30E-1	1.646	3.64E-2
10.1	81460	0.1228	1.660	3.55E-1	1.621	2.46E-2
10.0	80650	0.1240	1.646	3.15E-1	1.587	1.25E-2
9.9	79850	0.1252	1.639	2.95E-1	1.552	
9.8	79040	0.1265	1.635	2.75E-1	1.519	
9.7	78240	0.1278	1.631	2.51E-1	1.506	1.65E-2
9.6	77430	0.1292	1.627	2.24E-1	1.490	3.02E-2
9.5	76620	0.1305	1.619	1.94E-1	1.490	3.35E-2
9.4	75820	0.1319	1.609	1.77E-1	1.490	3.02E-2
9.3	75010	0.1333	1.594	1.50E-1	1.486	3.02E-2
9.2	74200	0.1348	1.576	1.26E-1	1.483	1.68E-2
9.1	73400	0.1362	1.553	1.11E-1	1.473	6.79E-3
9.0	72590	0.1378	1.525	8.84E-2	1.459	3.43E-3
8.9	71780	0.1393	1.495	7.35E-2	1.449	6.89E-3
8.8	70980	0.1409	1.475	8.13E-2	1.445	1.03E-2
8.7	70170	0.1425	1.458	8.57E-2	1.445	1.38E-2
8.6	69360	0.1442	1.454	7.90E-2	1.445	1.38E-2
8.5	68560	0.1459	1.447	6.90E-2	1.445	1.03E-2
8.4	67750	0.1476	1.436	6.09E-2	1.445	6.91E-3
8.3	66940	0.1494	1.411	4.60E-2	1.442	3.46E-3
8.2	66140	0.1512	1.386	3.60E-2	1.438	
8.1	65330	0.1531	1.356	2.94E-2	1.435	
8.0	64520	0.1550	1.330	2.63E-2	1.428	3.50E-3
7.9	63720	0.1569	1.292	2.70E-2	1.417	3.53E-3
7.8	62910	0.1590	1.257	3.18E-2	1.403	3.56E-3
7.7	62100	0.1610	1.217	4.10E-2	1.382	
7.6	61300	0.1631	1.176	6.37E-2	1.371	3.64E-3
7.5	60490	0.1653	1.130	8.84E-2	1.363	1.09E-2
7.4	59680	0.1675	1.076	1.39E-1	1.360	3.86E-3

[a] References given in brackets.

TABLE I *(Continued)*

Sodium Nitrate

eV	cm^{-1}	μm	n(o)	k(o)	n(e)	k(e)
7.3	58880	0.1698	1.031	1.84E-1	1.349	3.70E-3
7.2	58070	0.1722	1.001	2.49E-1	1.311	
7.1	57260	0.1746	0.991	3.22E-1	1.300	2.69E-2
7.0	56460	0.1771	0.973	3.95E-1	1.301	6.14E-2
6.9	55650	0.1797	0.969	4.89E-1	1.319	1.09E-1
6.8	54850	0.1823	0.987	5.87E-1	1.347	1.26E-1
6.7	54040	0.1851	1.029	6.85E-1	1.369	1.24E-1
6.6	53230	0.1879	1.092	7.64E-1	1.386	1.11E-1
6.5	52430	0.1907	1.204	8.42E-1	1.399	8.57E-2
6.4	51620	0.1937	1.319	8.78E-1	1.405	6.40E-2
6.3	50810	0.1968	1.446	9.43E-1	1.404	4.62E-2
6.2	50010	0.2000	1.519	8.98E-1	1.396	3.93E-2
6.1	49200	0.2033	1.618	8.89E-1	1.393	4.30E-2
6.0	48390	0.2066	1.705	8.70E-1	1.393	4.30E-2
5.9	47590	0.2101	1.804	8.58E-1	1.393	3.94E-2
5.8	46780	0.2138	1.941	8.24E-1	1.396	3.22E-2
5.7	45970	0.2175	2.075	7.46E-1	1.400	2.14E-2
5.6	45170	0.2214	2.174	5.74E-1	1.400	1.07E-2
5.5	44360	0.2254	2.212	3.38E-1	1.396	3.57E-3
5.4	43550	0.2296	2.147	1.74E-1	1.385	
5.3	42750	0.2339	2.046	8.06E-2	1.378	
5.2	41940	0.2384	1.952	3.58E-2	1.371	
5.1	41130	0.2431	1.881	2.12E-2	1.367	
5.0	40330	0.2480	1.822	1.09E-2	1.363	
4.9	39520	0.2530	1.783	2.80E-3	1.361	
4.8	38710	0.2583	1.740		1.360	
4.7	37910	0.2638	1.717		1.356	
4.6	37100	0.2695	1.688		1.352	
4.5	36290	0.2755	1.667		1.352	
4.4	35490	0.2818	1.652		1.352	
4.3	34680	0.2883	1.640		1.356	
4.2	33880	0.2952	1.624		1.360	
4.1	33070	0.3024	1.615		1.363	
4.0	32260	0.3100	1.612		1.363	
2.105	16980	0.5890	1.587 [3]		1.336 [3]	
1.240	10000	1.000	1.584 [5]			
1.116	9000	1.111	1.583			
0.9919	8000	1.250	1.582			
0.8679	7000	1.429	1.581			
0.7439	6000	1.667	1.579			
0.6199	5000	2.000	1.576			
0.4959	4000	2.500	1.569			
0.4339	3500	2.857	1.562			
0.3720	3000	3.333	1.552			

(continued)

TABLE I *(Continued)*

Sodium Nitrate

eV	cm^{-1}	μm	n(o)	k(o)	n(e)	k(e)
0.3472	2800	3.571	1.544			
0.3224	2600	3.846	1.535			
0.2976	2400	4.167	1.521			
0.2728	2200	4.545	1.501			
0.2480	2000	5.000	1.466			
0.2356	1900	5.263	1.438			
0.2232	1800	5.556	1.396			
0.2108	1700	5.882	1.33	4.4E-3 [5]		
0.2046	1650	6.061	1.27	6.3E-3		
0.1984	1600	6.250	1.19	9.8E-3		
0.1922	1550	6.452	1.05	1.8E-2		
0.1860	1500	6.667	0.77	4.3E-2		
0.1847	1490	6.711	0.66	5.8E-2		
0.1835	1480	6.757	0.51	8.6E-2		
0.1823	1470	6.803	0.29	1.8E-1		
0.1820	1468	6.812	0.24	2.4E-1		
0.1818	1466	6.821	0.20	2.8E-1		
0.1815	1464	6.831	0.17	3.4E-1		
0.1813	1462	6.840	0.15	4.0E-1		
0.1810	1460	6.849	0.14	4.6E-1		
0.1808	1458	6.859	0.13	5.1E-1		
0.1805	1456	6.868	0.12	5.6E-1		
0.1804	1455	6.873	0.12	5.9E-1		
0.1803	1454	6.878	0.12	6.1E-1		
0.1802	1453	6.882	0.12	6.4E-1		
0.1800	1452	6.887	0.13	6.6E-1		
0.1799	1451	6.892	0.14	6.8E-1		
0.1798	1450	6.897	0.15	7.1E-1		
0.1797	1449	6.901	0.18	7.3E-1		
0.1795	1448	6.906	0.21	7.6E-1		
0.1794	1447	6.911	0.21	7.8E-1		
0.1793	1446	6.916	0.18	8.0E-1		
0.1792	1445	6.920	0.15	8.2E-1		
0.1790	1444	6.925	0.13	8.4E-1		
0.1789	1443	6.930	0.12	8.6E-1		
0.1788	1442	6.935	0.12	8.9E-1		
0.1785	1440	6.944	0.11	9.3E-1		
0.1779	1435	6.969	0.11	1.1E0		
0.1773	1430	6.993	0.11	1.2E0		
0.1767	1425	7.018	0.11	1.3E0		
0.1761	1420	7.042	0.12	1.4E0		
0.1754	1415	7.067	0.13	1.5E0		
0.1748	1410	7.092	0.14	1.7E0		
0.1742	1405	7.117	0.16	1.8E0		
0.1736	1400	7.143	0.18	2.0E0		
0.1723	1390	7.194	0.24	2.4E0		

TABLE I *(Continued)*

Sodium Nitrate

eV	cm^{-1}	μm	n(o)	k(o)	n(e)	k(e)
0.1711	1380	7.246	0.38	3.0E0		
0.1699	1370	7.299	0.77	4.1E0		
0.1692	1365	7.326	1.34	5.0E0		
0.1686	1360	7.353	2.97	6.1E0		
0.1680	1355	7.380	6.20	4.8E0		
0.1674	1350	7.407	6.07	2.0E0		
0.1668	1345	7.435	5.10	9.5E-1		
0.1661	1340	7.463	4.45	5.6E-1		
0.1649	1330	7.519	3.69	2.7E-1		
0.1637	1320	7.576	3.27	1.6E-1		
0.1624	1310	7.634	2.99	1.1E-1		
0.1612	1300	7.692	2.80	7.8E-2		
0.1587	1280	7.813	2.54	4.7E-2		
0.1562	1260	7.937	2.38	3.1E-2		
0.1537	1240	8.065	2.27	2.3E-2		
0.1513	1220	8.197	2.18	1.7E-2		
0.1488	1200	8.333	2.12	1.3E-2		
0.1364	1100	9.091	1.95	5.3E-3		
0.1240	1000	10.00	1.86	2.8E-3		
0.1240	1000	10.00	1.558 [6]	1.26E-2 [6]	1.322 [6]	2.11E-2 [6]
0.1116	900	11.11	1.552	1.42E-2	1.317	2.38E-2
0.09919	800	12.59	1.544	1.63E-2	1.310	2.74E-2
0.08679	700	14.29	1.532	1.93E-2	1.300	3.23E-2
0.07439	600	16.67	1.512	2.38E-2	1.283	3.98E-2
0.06199	500	20.00	1.475	3.15E-2	1.251	5.24E-2
0.05951	480	20.83	1.464	3.38E-2	1.242	5.61E-2
0.05703	460	21.74	1.451	3.65E-2	1.231	6.05E-2
0.05455	440	22.73	1.435	3.98E-2	1.218	6.57E-2
0.05207	420	23.81	1.417	4.37E-2	1.202	7.20E-2
0.04959	400	25.00	1.394	4.87E-2	1.182	7.99E-2
0.04835	390	25.64	1.380	5.18E-2	1.170	8.47E-2
0.04711	380	26.32	1.364	5.52E-2	1.157	9.01E-2
0.04587	370	27.03	1.347	5.93E-2	1.142	9.64E-2
0.04463	360	27.78	1.327	6.40E-2	1.125	1.04E-1
0.04339	350	28.57	1.304	6.97E-2	1.105	1.13E-1
0.04215	340	29.41	1.277	7.66E-2	1.082	1.23E-1
0.04091	330	30.30	1.245	8.52E-2	1.055	1.36E-1
0.03968	320	31.25	1.207	9.62E-2	1.022	1.53E-1
0.03843	310	32.26	1.160	1.11E-1	0.981	1.75E-1
0.03720	300	33.33	1.102	1.31E-1	0.931	2.05E-1
0.03595	290	34.48	1.027	1.60E-1	0.867	2.48E-1
0.03472	280	35.71	0.929	2.06E-1	0.786	3.16E-1
0.03347	270	37.04	0.796	2.88E-1	0.688	4.29E-1
0.03224	260	38.46	0.630	4.56E-1	0.591	6.18E-1
0.03100	250	40.00	0.504	7.58E-1	0.538	8.97E-1

(continued)

TABLE I *(Continued)*

Sodium Nitrate

eV	cm^{-1}	μm	n(o)	k(o)	n(e)	k(e)
0.02976	240	41.67	0.486	1.15E0	0.558	1.28E0
0.02852	230	43.48	0.591	1.65E0	0.717	1.86E0
0.02790	225	44.44	0.729	1.97E0	0.946	2.31E0
0.02728	220	45.45	1.000	2.35E0	1.549	2.95E0
0.02697	217.5	45.98	1.236	2.56E0	2.256	3.27E0
0.02666	215	46.51	1.581	2.75E0	3.406	3.12E0
0.02635	212.5	47.06	2.067	2.83E0	4.188	2.02E0
0.02604	210	47.62	2.633	2.68E0	4.006	9.89E-1
0.02573	207.5	48.19	3.065	2.24E0	3.590	4.75E-1
0.02542	205	48.78	3.199	1.71E0	3.237	2.31E-1
0.02480	200	50.00	2.933	1.01E0	2.762	3.66E-2
0.02418	195	51.28	2.560	7.63E-1	2.468	2.85E-2
0.02356	190	52.63	2.262	7.78E-1	2.269	5.30E-2
0.02294	185	54.05	2.120	9.87E-1	2.123	6.17E-2
0.02232	180	55.56	2.290	1.25E0	2.011	6.34E-2
0.02170	175	57.14	2.711	1.21E0	1.921	6.18E-2
0.02108	170	58.82	2.916	8.34E-1	1.845	5.85E-2
0.02046	165	60.61	2.843	5.14E-1	1.780	5.43E-2
0.01984	160	62.50	2.700	3.33E-1	1.721	4.96E-2
0.01860	150	66.67	2.449	1.79E-1	1.617	3.95E-2
0.01736	140	71.43	2.260	1.26E-1	1.520	2.86E-2
0.01612	130	76.92	2.097	1.12E-1	1.418	1.62E-2
0.01550	125	80.00	2.015	1.15E-1	1.362	8.93E-3
0.01488	120	83.33	1.924	1.27E-1	1.298	5.46E-4
0.01426	115	86.96	1.815	1.51E-1	1.226	9.60E-3
0.01364	110	90.91	1.674	2.01E-1	1.139	2.27E-2
0.01240	100	100.0	1.187	6.25E-1	0.887	6.97E-2
0.01209	97.5	102.6	1.081	9.52E-1	0.794	9.24E-2
0.01178	95	105.3	1.111	1.39E0	0.680	1.27E-1
0.01147	92.5	108.1	1.352	1.90E0	0.533	1.90E-1
0.01116	90	111.1	1.943	2.38E0	0.364	3.27E-1
0.01085	87.5	114.3	2.962	2.40E0	0.258	5.41E-1
0.01054	85	117.6	3.634	1.62E0	0.219	7.50E-1
0.01023	82.5	121.2	3.588	9.13E-1	0.206	9.45E-1
0.009919	80	125.0	3.371	5.48E-1	0.204	1.13E0
0.009299	75	133.3	3.030	2.62E-1	0.223	1.52E0
0.008679	70	142.9	2.827	1.62E-1	0.273	1.98E0
0.008059	65	153.8	2.699	1.18E-1	0.378	2.58E0
0.007439	60	166.7	2.611	9.58E-2	0.648	3.51E0
0.007129	57.5	173.9	2.578	8.88E-2	0.986	4.24E0
0.006819	55	181.8	2.550	8.36E-2	1.816	5.31E0
0.006509	52.5	190.5	2.526	7.98E-2	4.348	6.20E0
0.006199	50	200.0	2.504	7.69E-2	6.773	3.33E0
0.005889	47.5	210.5	2.487	7.48E-2	5.842	1.30E0
0.005573	45	222.2	2.471	7.33E-2	4.995	6.55E-1
0.004959	40	250.0	2.447	7.14E-2	4.079	2.58E-1

TABLE I *(Continued)*

Sodium Nitrate

eV	cm^{-1}	μm	n(o)	k(o)	n(e)	k(e)
0.004339	35	285.7	2.431	7.04E-2	3.616	1.35E-1
0.003720	30	333.3	2.421	6.94E-2	3.342	8.09E-2
0.003100	25	400.0	2.417	6.74E-2	3.165	5.31E-2
0.002480	20	500.0	2.418	6.31E-2	3.047	3.74E-2
0.002145	17.3	578.0	2.47 [7]	1.62E-2 [7]	3.00 [7]	5.33E-2 [7]
0.001860	15	666.7	2.424 [6]	5.51E-2 [6]	2.968 [6]	2.84E-2 [6]
0.001649	13.3	751.9	2.45 [7]	1.02E-2 [7]	2.98 [7]	3.69E-2 [7]
0.001240	10	1000	2.432 [6]	4.18E-2 [6]	2.919 [6]	2.43E-2 [6]
0.001153	9.3	1075	2.35 [7]	6.18E-3 [7]	2.90 [7]	2.60E-2 [7]

TABLE II

Coupled Oscillator Parameters from Brehat and Wyncke [6]

	ϵ_∞	ω_T (cm^{-1})	γ_T (cm^{-1})	ω_L (cm^{-1})	γ_L (cm^{-1})	γ_{TR} (cm^{-1})	γ_{LR} (cm^{-1})
A_{2u}	1.8	51.5	4.5	90	5	3.5	3.6
		214	8	262.5	37		
E_u	2.5	87	8	98.5	9	26.5	29.4
		175.5	19	184.5	19		
		209	14	257.5	25		

Strontium Fluoride (SrF_2)

MICHAEL E. THOMAS
Applied Physics Laboratory
The Johns Hopkins University
Laurel, Maryland

Strontium fluoride offers a wide range of transparency, from the ultraviolet to the long-wave infrared (0.13 to 11 μm), with low reflectance loss and low dispersion. This combination of broad transparency and low dispersion is rare in optical-window materials used in infrared systems. Like BaF_2, it allows experimenters to conveniently perform initial system alignment in the visible and then switch to the IR with only minor correction of the optical components. Furthermore, strontium fluoride has good surface hardness (Knoop scale 150 kg/mm^2) and is not hygroscopic. It has a flexure strength between those of CaF_2 (90 MPa) and BaF_2 (27 MPa).

Strontium fluoride is a cubic crystal with the fluorite structure, space group Fm3m (O_h^5), with four formula units per unit cell. The lattice constant is 5.7996 Å, giving a theoretical density of 4.277 g/cm^3. The atomic arrangement is strontium atoms occupy the 4(a) sites (m3m or O_h symmetry), and the fluorine atoms occupy the 8(c) sites ($\bar{4}$3m or T_d symmetry). Melting point is 1750 K.

Ultraviolet reflectance of bulk SrF_2 was measured by Ganin *et al.* [1] up to 20 eV at room temperature and liquid-helium temperature. Rubloff [2] measured the room-temperature reflectance up to 36 eV. Unfortunately, these measurements are not reduced to optical constants. However, similar measurements from 10 to 36 eV by Nisar and Robin [3] have been reduced to optical constants using the Kramers–Kronig relation. These data are listed in Table I and plotted in Fig. 1.

The Urbach tail represents absorption below the band gap, defining the end of transparency. The room-temperature absorption coefficient was determined from transmission measurements by Tomiki and Miyata [4] in the spectral range from 9.5 to 9.8 eV and fitted to the functional form

$$\beta_{abs}(E, T) = \beta_{U0}\exp[\sigma_s(T)(E - E_g)/k_BT], \quad (1)$$

where β_{abs} is the absorption coefficient (typically in units of cm^{-1}), β_{U0} is

HANDBOOK OF OPTICAL CONSTANTS OF SOLIDS III

Copyright © 1998 by Academic Press.
All rights of reproduction in any form reserved
ISBN 0-12-544423-0/$25.00.

a scaling coefficient (in units of cm^{-1}), E_g is the band-gap energy at absolute zero temperature (typically given in units of eV), k_B is Boltzmann's constant, and T is temperature in Kelvins. The exponential factor $\sigma_s(T)$ is given by the equation

$$\sigma_s(T) = \sigma_0 \frac{2k_B T}{E_p} \tanh \frac{E_p}{2k_B T}, \tag{2}$$

where E_p is an effective acoustic-phonon energy of the material. The Urbach tail parameters for SrF_2 are $\beta_{U0} = 1.35 \times 10^9$ cm^{-1}, $E_g = 10.670$ eV, $\sigma_0 = 0.60$, and $E_p = 0.044$ eV. The room-temperature (295 K) values for k in Table I and Fig. 1 for this spectral region are generated using Eqs. (1) and (2).

The room-temperature (25° C) index of refraction from the ultraviolet to the infrared (0.22 to 11.5 μm) has been measured by Feldman *et al.* [5] using a prism and the minimum-deviation technique. A Sellmeier model of the form

$$n^2(\lambda, T) = 1 + \sum_i \frac{\lambda^2 \Delta\epsilon_i(T)}{\lambda^2 - \lambda_i^2(T)} \tag{3}$$

is used to represent the data accurately. Model parameters are listed in Table II. A comprehensive analysis on a variety of data sets was performed by Li [6]. A Sellmeier formula was also generated covering the range from 0.15 to 14 μm at $T = 20°$ C. The Li model parameters are also listed in Table II. Because the Sellmeier model has a physical basis, the extrapolation to higher frequencies beyond the experimental limit is justified. The values for n in Table I and Fig. 1 for the spectral regions indicated are generated by the appropriate formula. A temperature-dependent Sellmeier model covering the range from 100 to 450 K has been developed by Tropf [7]. Near-room-temperature thermo-optic coefficients measured at different wavelengths are listed in Table III [5, 8–10]. Notice that the thermo-optic coefficients are negative. This gives SrF_2 some athermal performance as an optical element. An athermal material has the property that

$$\frac{d(n(T)L(T))}{dT} = 0.$$

The value of the optical-path derivative as given earlier for SrF_2 is 6.9×10^{-6} nL per Kelvin at visible and near infrared wavelengths. Thus, SrF_2 is useful for optical designs that require insensitivity to temperature.

Laser-calorimetry data [11] at DF (3.8 μm) and HF (2.7 μm) laser wavelengths indicate low-level absorption in roughly the middle of the transparency range of SrF_2. Material obtained from Optovac had absorption-

coefficient values of 2.0×10^{-4} cm^{-1} at the DF laser wavelength and 1.4×10^{-4} cm^{-1} at the HF laser wavelength. The corresponding k values are listed in Table I and plotted in Fig. 1. The low-level absorption and the near athermal performance of SrF_2 make it a candidate window material for high-power laser applications.

The multiphonon absorption (multiple-quanta lattice vibrations) edge marks the end of infrared transparency. Absorption-coefficient measurements by Deutsch [12] are represented by the simple formula

$$\beta_{abs}(\nu) = \beta_0 \exp\left(-\gamma \frac{\nu}{\nu_0}\right), \tag{4}$$

where for SrF_2, $\beta_0 = 22{,}548$ cm^{-1} and $\nu_0/\gamma = 90.4$ cm^{-1} at room temperature. The values of k in the spectral range from 820 to 1300 cm^{-1} in Table I and Fig. 1 are obtained from this formula. The data cover the three-phonon to four-phonon regions. Temperature-dependent experimental data on the absorption coefficient is described in Lipson *et al.* [13]. A temperature-dependent multiphonon model has been developed by Thomas *et al.* [14] and applied to SrF_2. Measurements in the two-phonon region are reported by Kaiser *et al.* [15]. The experimental results are listed in Table I and plotted in Fig. 1.

The one-phonon (one-quanta fundamental lattice vibrations) region is opaque and therefore characterized by reflectance measurements. A room-temperature reflectance measurement is reported by Kaiser *et al.* [15]. The classical-oscillator model is often used to fit the reflectance data and then to derive the optical constants. The classical-oscillator model is expressed in terms of the relative permittivity, $\epsilon_r(\nu,T)$, as given by[1]

$$\epsilon_r(\nu,T) = \epsilon_\infty(T) + \sum_i \frac{\Delta\epsilon_i(T)\nu_i^2(T)}{\nu_i^2(T) - \nu^2 + j\Gamma_i(\nu,T)\nu}, \tag{5}$$

where $\Delta\epsilon_i(T)$, $\Gamma_i(\nu,T)$ and $\nu_i(T)$ are the ith-mode strength, linewidth, and long-wavelength transverse optical frequency, ν_{TO}, respectively. The sum on i is over all transverse optical modes. For SrF_2, there is only one allowed infrared-active vibrational mode based on group theory of a perfect lattice. This is formally stated as

$$\Gamma = F_{1u}(\mathrm{IR}) + F_{2g}(\mathrm{R}).$$

The first mode is infrared active (mode 1 in Table IV), and the second mode is Raman active (286 cm^{-1} [16]). Table IV lists the classical-oscillator model parameters used to fit the experimental data. More than one mode is needed

[1] The expression uses the engineering convention for a time harmonic field of $\exp(-j\omega t)$. To convert to the convention commonly used in the *HOC* series, use $i = -j$.

to account for impurities and defects in real materials. Also, the high-frequency edge of the reflectance spectrum must include two-phonon contributions (see mode 2 in Table IV). Unfortunately, the value of ϵ_∞ used by Kaiser *et al.* is not consistent with the value from the Sellmeier models mentioned previously, and the same is true for the static dielectric constant. For this reason the model parameters have been modified to agree with these limiting values and still match the reflectance spectrum. These modified values are listed in Table IV. The n and k values in Table I and Fig. 1 are generated by Eq. (5) and the modified parameters in Table IV.

Below ν_{TO}, the index of refraction, n, is determined by extrapolation of the classical-oscillator model with reasonable accuracy. The absorption coefficient has been measured by Bosomworth [17]. Table I and Fig. 1 list and display the resulting values. The values are above the one-phonon red wing because multiphonon difference bands are also included in this spectral region.

The static-dielectric-constant data is the sum of all the strengths of higher-frequency oscillators including vibrational and electronic. Using Eq. (5), the static dielectric constant, $\epsilon_s(T) = \epsilon_r'(0,T)$, becomes

$$\epsilon_s(T) = \epsilon_\infty(T) + \sum_i \Delta\epsilon_i(T). \tag{6}$$

Based on the parameters listed in Table IV, we expect the value of ϵ_s to be between 6.14 and 6.5. Experimental results, obtained from capacitance bridges operating from 1 kHz to 1 MHz, produce values from 6.45 to 6.48, with most results closer to the higher value [18–21]. The corresponding refractive index value is $n_s = 2.543$. The static-index values incorrectly are located at 1×10^4 μm; however, there is little difference in the value of n_s at the measured wavelength and the plotted wavelength.

Whenever possible, physically based models are used to represent experimental measurements in Table I and Fig. 1. The models tend to reduce noise and allow interpolation and extrapolation to obtain meaningful results where no experimental data exists. In some case, the models discussed in this section also allow temperature-dependent data to be obtained.

REFERENCES

1. V. A. Ganin, M. G. Karin, V. K. Sidorin, K. K. Sidorin, N. V. Starostin, G. P. Startsev, and M. P. Shepilov, Optical constants and energy-band structure of fluorite-type crystals. *Sov. Phys. Solid State* **16**, 2313–2318 (1975).
2. G. W. Rubloff, Far-infrared reflectance spectra and the electronic structure of ionic crystals. *Phys. Rev. B* **5**, 662–684 (1972).
3. M. Nisar and S. Robin, Far ultraviolet electronic spectra of SrF_2 and BaF_2. *Pak. J. Sci. Ind. Res.* **17**, 49–54 (1974).
4. T. Tomiki and T. Miyata, Optical studies of alkali fluorides and alkaline earth fluorides in VUV region. *J. Phys. Soc. Jpn.* **27**, 658–678 (1969).

5. A. Feldman, D. Horowitz, R. M. Walker, and M. J. Dodge, Optical Materials Characterization Final Technical Report, February 1, 1978–September 30, 1978. *NBS Technical Note* **993** (February 1979).
6. H. H. Li, Refractive index of alkaline earth halides and its wavelength and temperature derivatives. *J. Phys. Chem. Ref. Data* **9**, 161–289 (1980).
7. W. J. Tropf, Temperature-dependent refractive index models for BaF_2, CaF_2, MgF_2, SrF_2, LiF, NaF, KCl, ZnS and ZnSe. *Opt. Eng.* **34**, 1369–1373 (1995).
8. Y. F. Tsay, H. G. Lipson, and P. A. Ligor, The temperature variation of the thermo-optic coefficient of CaF_2. *J. Appl. Phys.* **48**, 1953–1955 (1977).
9. H. G. Lipson, Y. F. Tsay, B. Bendow, and P. A. Ligor, Temperature dependence of the refractive index of alkaline earth fluorides. *Appl. Opt.* **15**, 2352–2354 (1976).
10. M. Wintersgill, J. Fontanella, C. Andeen, and D. Schuele, The temperature variation of the dielectric constant of "pure" CaF_2, SrF_2, BaF_2, and MgO. *J. Appl. Phys.* **50**, 8259–8261 (1979).
11. J. A. Harrington, D. A. Gregory, and W. F. Otto, Jr., Infrared absorption in chemical laser window materials. *Appl. Opt.* **15**, 1953–1959 (1976).
12. T. F. Deutsch, Absorption coefficient of infrared laser window materials. *J. Phys. Chem. Solids* **34**, 2091–2104 (1973).
13. H. G. Lipson, B. Bendow, N. E. Massa, and S. S. Mitra, Multiphonon infrared absorption in the transparent regime of alkaline-earth fluorides. *Phys. Rev. B* **13**, 2614–2619 (1976).
14. M. E. Thomas, R. I. Joseph, and W. J. Tropf, Infrared transmission properties of sapphire, spinel, yttria and ALON as a function of temperature and frequency. *Appl. Opt.* **27**, 239–245 (1988); M. E. Thomas, Temperature dependence of the complex index of refraction, *in* "Handbook of Optical Constants of Solids II" (E. D. Palik ed.), Chap. 8, pp. 177–201. Academic Press, Orlando, Florida, 1991; M. E. Thomas, A computer code for modeling optical properties of window materials, in window and dome technologies and materials. *Proc. of SPIE* **1112**, 260–267 (1989).
15. W. Kaiser, W. G. Spitzer, R. H. Kaiser, and L. E. Howarth, Infrared properties of CaF_2, SrF_2, and BaF_2. *Phys. Rev.* **127**, 1950–1954 (1962).
16. I. Richman, Longitudinal optical phonons in CaF_2, SrF_2 and BaF_2. *J. Chem. Phys.* **41**, 2836–2837 (1966).
17. D. R. Bosomworth, Far-infrared optical properties of CaF_2, SrF_2, BaF_2, and CdF_2. *Phys. Rev.* **157**, 709–715 (1967).
18. K. V. Rao and A. Smakula, Dielectric properties of alkaline earth fluoride single crystals. *J. Appl. Phys.* **37**, 319–323 (1965).
19. C. Andeen, J. Fontanella, and D. Schuele, Low-frequency dielectric constants of the alkaline earth fluorides by the method of substitution. *J. Appl. Phys.* **42**, 2216–2219 (1971).
20. G. A. Samara, Temperature and pressure dependence of the dielectric properties of PbF_2 and the alkaline-earth fluorides. *Phys. Rev. B* **13**, 4529–4544 (1976).
21. M. Wintersgill, J. Fontanella, C. Andeen, and D. Schuele, The temperature variation of the dielectric constant of "pure" CaF_2, SrF_2, BaF_2, and MgO. *J. Appl. Phys.* **50**, 8259–8261 (1979).

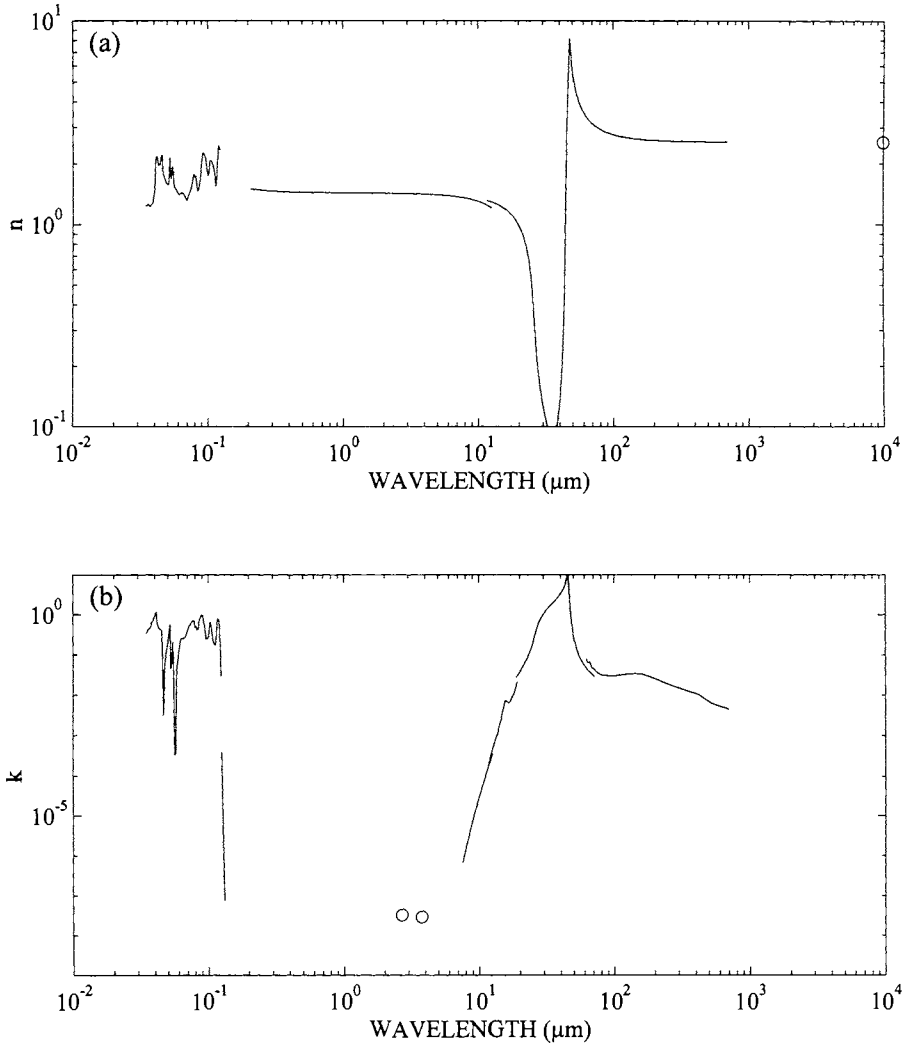

Fig. 1. (a) Log–log plot of the room-temperature index of refraction, n, for SrF_2 versus wavelength in microns. (b) Log–log plot of the room-temperature extinction coefficient, k, for SrF_2 versus wavelength in microns. Isolated data points are indicated with a symbol.

TABLE I

Values of n and k for Strontium Fluoride from Various References[a]

eV	cm^{-1}	μm	n	k
35.90	289500	0.03454	1.242	0.3412 [3]
35.24	284300	0.03518	1.236	0.3963
34.94	281800	0.03549	1.261	0.4173
34.58	278900	0.03586	1.266	0.4291
33.63	271200	0.03687	1.236	0.4696
33.15	267300	0.03740	1.225	0.5356
32.97	265900	0.03761	1.237	0.5875
32.72	263900	0.03789	1.261	0.6360
32.12	259000	0.03861	1.272	0.6871
31.98	257900	0.03878	1.274	0.7286
31.84	256800	0.03894	1.293	0.7873
31.21	251700	0.03973	1.407	0.9057
31.03	250300	0.03996	1.448	0.9605
30.90	249200	0.04013	1.480	1.011
30.74	248000	0.04033	1.536	1.064
30.68	247400	0.04042	1.584	1.115
30.39	245100	0.04080	1.991	1.150
30.33	244700	0.04087	2.051	1.112
30.30	244400	0.04092	2.075	1.063
30.26	244100	0.04097	2.102	1.007
30.21	243600	0.04104	2.137	0.9336
30.13	243000	0.04115	2.154	0.8745
30.06	242500	0.04124	2.146	0.8165
29.97	241700	0.04137	2.143	0.7493
29.86	240800	0.04152	2.150	0.6764
29.76	240000	0.04167	2.158	0.6196
29.64	239000	0.04184	2.149	0.5502
28.85	232700	0.04298	1.951	0.4337
28.58	230500	0.04338	1.971	0.4471
28.35	228700	0.04373	1.976	0.4198
28.15	227000	0.04405	1.969	0.4257
27.68	223300	0.04479	2.180	0.4002
27.43	221200	0.04520	2.193	0.1579
27.33	220400	0.04537	2.197	0.07584
27.05	218200	0.04584	2.007	0.00311
26.77	215900	0.04632	1.773	0.00451
26.47	213500	0.04684	1.748	0.03753
26.15	210900	0.04742	1.702	0.07288
25.26	203700	0.04909	1.604	0.1530
25.01	201700	0.04957	1.589	0.1877
24.56	198100	0.05048	1.568	0.2835
24.42	196900	0.05078	1.565	0.3399
24.20	195200	0.05124	1.613	0.5235
24.10	194400	0.05145	1.789	0.5621

(continued)

[a] References given in brackets.

TABLE I *(Continued)*

Strontium Fluoride

eV	cm^{-1}	μm	n	k
23.99	193500	0.05169	2.013	0.5311
23.93	193000	0.05180	2.110	0.4473
23.77	191700	0.05217	2.123	0.0440
23.50	189500	0.05276	1.746	0.0500
23.20	187100	0.05344	1.680	0.1000
22.92	184900	0.05409	1.820	0.2068
22.75	183500	0.05449	1.910	0.1012
22.64	182600	0.05476	1.925	0.0427
22.44	181000	0.05525	1.813	0.00551
22.13	178500	0.05603	1.592	0.00033
21.77	175600	0.05695	1.523	0.00037
21.54	173700	0.05756	1.499	0.02126
21.28	171700	0.05825	1.477	0.05195
20.96	169000	0.05916	1.447	0.0827
20.20	162900	0.06139	1.403	0.2047
19.71	159000	0.06291	1.434	0.2516
19.46	157000	0.06370	1.431	0.2553
19.17	154600	0.06468	1.431	0.2538
18.86	152100	0.06575	1.419	0.2518
18.45	148800	0.06718	1.387	0.2706
18.21	146900	0.06808	1.364	0.3070
17.76	143300	0.06980	1.319	0.3907
17.59	141900	0.07049	1.319	0.4455
17.43	140600	0.07114	1.348	0.4962
17.26	139200	0.07185	1.383	0.5240
17.03	137400	0.07280	1.411	0.5437
16.83	135800	0.07365	1.437	0.5801
16.34	131800	0.07590	1.536	0.6662
16.13	130100	0.07687	1.607	0.6928
15.92	128400	0.07790	1.709	0.6637
15.76	127200	0.07865	1.766	0.6845
15.71	126700	0.07892	1.764	0.6449
15.69	126500	0.07903	1.764	0.5219
15.64	126200	0.07925	1.762	0.4731
15.42	124400	0.08042	1.704	0.5124
15.20	122600	0.08155	1.737	0.4517
15.15	122200	0.08186	1.706	0.4011
14.80	119400	0.08378	1.501	0.4348
14.63	118000	0.08472	1.452	0.5763
14.57	117500	0.08508	1.466	0.6442
14.38	116000	0.08623	1.520	0.7740
14.27	115100	0.08688	1.564	0.8387
14.19	114500	0.08736	1.601	0.8853
14.07	113500	0.08814	1.677	0.9228
14.00	112900	0.08855	1.736	0.9694
13.74	110800	0.09022	2.055	0.9530

TABLE I *(Continued)*

Strontium Fluoride

eV	cm^{-1}	μm	n	k
13.60	109700	0.09116	2.185	0.8583
13.53	109200	0.09160	2.225	0.8077
13.43	108300	0.09231	2.245	0.6814
13.38	107900	0.09269	2.254	0.6182
13.31	107300	0.09317	2.241	0.5482
13.11	105800	0.09454	2.206	0.3949
12.84	103500	0.09658	2.105	0.2394
12.34	99540	0.1005	1.738	0.2703
12.28	99020	0.1010	1.759	0.3342
12.24	98760	0.1013	1.770	0.3888
12.19	98360	0.1017	1.786	0.4590
12.14	97930	0.1021	1.803	0.5389
12.09	97540	0.1025	1.818	0.6044
12.02	96930	0.1032	1.991	0.6413
11.92	96120	0.1040	2.059	0.5856
11.87	95700	0.1045	2.060	0.5012
11.81	95240	0.1050	2.060	0.4392
11.71	94440	0.1059	2.062	0.3726
11.58	93390	0.1071	2.029	0.3015
11.45	92320	0.1083	2.006	0.2424
11.32	91270	0.1096	1.973	0.1942
11.09	89460	0.1118	1.857	0.1697
10.91	88010	0.1136	1.691	0.2072
10.84	87460	0.1143	1.620	0.2625
10.79	87060	0.1149	1.582	0.3263
10.76	86770	0.1152	1.554	0.3936
10.72	86430	0.1157	1.545	0.4574
10.67	86050	0.1162	1.572	0.6011
10.64	85830	0.1165	1.623	0.6730
10.58	85330	0.1172	1.766	0.7409
10.52	84860	0.1178	1.925	0.8018
10.30	83060	0.1204	2.415	0.6704
10.29	83000	0.1205	2.423	0.6066
10.27	82840	0.1207	2.443	0.5469
10.25	82630	0.1210	2.446	0.4814
10.24	82570	0.1211	2.441	0.4262
10.21	82360	0.1214	2.426	0.3630
10.17	82040	0.1219	2.402	0.2947
10.15	81900	0.1221	2.394	0.2326
10.10	81460	0.1228	2.370	0.1654
10.05	81070	0.1234	2.335	0.1017
10.01	80750	0.1238	2.315	0.0293
9.879	79680	0.1255	1.746 [6]	0.0003826 [4]
9.801	79050	0.1265	1.735	8.702E-5
9.724	78430	0.1275	1.725	2.026E-5
9.649	77820	0.1285	1.716	4.823E-6

(continued)

TABLE I *(Continued)*

Strontium Fluoride

eV	cm^{-1}	μm	n	k
9.574	77220	0.1295	1.707	1.174E-6
9.501	76630	0.1305	1.699	2.922E-7
9.429	76050	0.1315	1.691	7.428E-8
8.266	66670	0.150	1.594	
7.085	57140	0.175	1.534	
6.199	50000	0.200	1.504	
5.510	44440	0.225	1.486	
5.904	47619	0.21	1.49513 [5]	
4.959	40000	0.25	1.47336	
3.999	32258	0.31	1.45725	
3.542	28571	0.35	1.45131	
3.024	24390	0.41	1.44556	
2.755	22222	0.45	1.44309	
2.431	19608	0.51	1.44029	
2.254	18182	0.55	1.43906	
2.032	16393	0.61	1.43740	
1.907	15384	0.65	1.43675	
1.746	14084	0.71	1.43560	
1.653	13333	0.75	1.43527	
1.531	12346	0.81	1.43435	
1.362	10989	0.91	1.43343	
1.228	9901.0	1.01	1.43269	
1.117	9009.0	1.11	1.43206	
1.025	8264.5	1.21	1.43151	
0.9464	7633.6	1.31	1.43100	
0.8793	7092.2	1.41	1.43051	
0.8211	6622.5	1.51	1.43003	
0.7701	6211.2	1.61	1.42956	
0.7251	5847.9	1.71	1.42909	
0.6850	5524.9	1.81	1.42861	
0.6491	5235.6	1.91	1.42812	
0.6168	4975.1	2.01	1.42761	
0.5876	4739.3	2.11	1.42709	
0.5610	4524.9	2.21	1.42656	
0.5367	4329.0	2.31	1.42601	
0.5145	4149.4	2.41	1.42544	
0.4940	3984.1	2.51	1.42485	
0.4750	3831.4	2.61	1.42424	
0.4590	3703.7	2.70		3.20E-8 [11]
0.4575	3690.0	2.71	1.42361	
0.4412	3558.7	2.81	1.42296	
0.4261	3436.4	2.91	1.42228	
0.4119	3322.3	3.01	1.42159	
0.3987	3215.4	3.11	1.42087	
0.3862	3115.3	3.21	1.42013	
0.3746	3021.1	3.31	1.41937	

TABLE I *(Continued)*

Strontium Fluoride

eV	cm^{-1}	μm	*n*	*k*
0.3636	2932.5	3.41	1.41858	
0.3532	2849.0	3.51	1.41778	
0.3434	2770.1	3.61	1.41694	
0.3342	2695.4	3.71	1.41609	
0.3260	2631.6	3.80		2.90E-8 [11]
0.3254	2624.7	3.81	1.41521	
0.3171	2557.5	3.91	1.41430	
0.3092	2493.8	4.01	1.41337	
0.3017	2433.1	4.11	1.41242	
0.2945	2375.3	4.21	1.41144	
0.2877	2320.2	4.31	1.41044	
0.2811	2267.6	4.41	1.40941	
0.2749	2217.3	4.51	1.40835	
0.2689	2169.2	4.61	1.40727	
0.2633	2123.1	4.71	1.40617	
0.2578	2079.0	4.81	1.40503	
0.2525	2036.7	4.91	1.40388	
0.2475	1996.0	5.01	1.40269	
0.2426	1956.9	5.11	1.40148	
0.2380	1919.4	5.21	1.40024	
0.2335	1883.2	5.31	1.39898	
0.2292	1848.4	5.41	1.39768	
0.2250	1814.9	5.51	1.39636	
0.2210	1782.5	5.61	1.39502	
0.2171	1751.3	5.71	1.39364	
0.2134	1721.2	5.81	1.39223	
0.2098	1692.1	5.91	1.39080	
0.2063	1663.9	6.01	1.38934	
0.2029	1636.7	6.11	1.38785	
0.1997	1610.3	6.21	1.38633	
0.1965	1584.8	6.31	1.38478	
0.1934	1560.1	6.41	1.38320	
0.1905	1536.1	6.51	1.38159	
0.1876	1512.9	6.61	1.37995	
0.1848	1490.3	6.71	1.37828	
0.1821	1468.4	6.81	1.37658	
0.1794	1447.2	6.91	1.37485	
0.1769	1426.5	7.01	1.37308	
0.1744	1406.5	7.11	1.37128	
0.1720	1387.0	7.21	1.36946	
0.1696	1368.0	7.31	1.36759	
0.1673	1349.5	7.41	1.36570	
0.1651	1331.6	7.51	1.36377	
0.1629	1314.1	7.61	1.36181	
0.1608	1297.0	7.71	1.35981	
0.1588	1280.4	7.81	1.35778	

(continued)

TABLE I *(Continued)*

Strontium Fluoride

eV	cm^{-1}	μm	n	k
0.1567	1264.2	7.91	1.35572	
0.1548	1248.4	8.01	1.35362	
0.1531	1234.6	8.1	1.3517 [6]	1.7035E-6 [12]
0.1442	1162.8	8.6	1.3405	4.11E-6
0.1363	1098.9	9.1	1.3283	8.58E-6
0.1292	1041.7	9.6	1.3151	1.71E-5
0.1228	990.1	10.1	1.3800	3.17E-5
0.1170	943.4	10.6	1.2854	5.58E-5
0.1117	900.9	11.1	1.2686	9.36E-5
0.1069	862.1	11.6	1.2505	0.0150
0.10609	855.7	11.69	1.3156	0.000173 [15]
0.10037	809.5	12.35	1.3002	0.000361
0.09776	788.5	12.68	1.2921	0.000502
0.09526	768.3	13.02	1.2835	0.000631
0.09346	753.8	13.27	1.2768	0.000780
0.09161	738.9	13.53	1.2695	0.000955
0.08967	723.2	13.83	1.2611	0.00120
0.08838	712.8	14.03	1.2552	0.00159
0.08485	684.4	14.61	1.2373	0.00252
0.08200	661.4	15.12	1.2206	0.00432
0.07944	640.7	15.61	1.2035	0.00719
0.07867	634.5	15.76	1.1979	0.00702
0.07795	628.7	15.91	1.1926	0.00708
0.07686	619.9	16.13	1.1840	0.00682
0.07584	611.7	16.35	1.1756	0.00644
0.07463	601.9	16.61	1.1649	0.00619
0.07280	587.2	17.03	1.1474	0.00693
0.06859	553.2	18.08	1.0991	0.0107
0.06486	523.1	19.12	1.0442	0.0206
0.06447	520	19.23	1.038[2]	0.0297[2]
0.06323	510	19.61	1.015	0.0331
0.06199	500	20.00	0.991	0.0370
0.06075	490	20.41	0.964	0.0416
0.05951	480	20.83	0.934	0.0470
0.05827	470	21.28	0.901	0.0535
0.05703	460	21.74	0.864	0.0612
0.05579	450	22.22	0.822	0.0708
0.05455	440	22.73	0.774	0.0826
0.05331	430	23.26	0.719	0.0977
0.05207	420	23.81	0.655	0.118
0.05083	410	24.39	0.578	0.146
0.04959	400	25.00	0.486	0.189
0.04835	390	25.64	0.380	0.261
0.04711	380	26.32	0.282	0.378
0.04587	370	27.03	0.219	0.519
0.04463	360	27.78	0.181	0.660

[2] Results obtained from modified classical-oscillator parameters in Table IV.

TABLE I *(Continued)*

Strontium Fluoride

eV	cm^{-1}	μm	n	k
0.04339	350	28.57	0.156	0.800
0.04215	340	29.41	0.137	0.940
0.04092	330	30.30	0.122	1.087
0.03968	320	31.25	0.110	1.243
0.03844	310	32.26	0.0998	1.413
0.03720	300	33.33	0.0925	1.602
0.03596	290	34.48	0.0881	1.818
0.03472	280	35.71	0.0876	2.071
0.03348	270	37.04	0.0923	2.379
0.03224	260	38.46	0.106	2.770
0.03100	250	40.00	0.136	3.304
0.02976	240	41.67	0.208	4.121
0.02852	230	43.48	0.448	5.668
0.02728	220	45.45	3.166	10.930
0.02604	210	47.62	8.167	1.012
0.02480	200	50.00	5.525	0.272
0.02356	190	52.63	4.534	0.136
0.02232	180	55.56	3.994	0.0855
0.02108	170	58.82	3.648	0.0594
0.01984	160	62.50	3.406	0.0445
0.01860	150	66.67	3.227	0.0349
0.01736	140	71.43	3.090	0.0282
0.01995	160.9	62.14	3.426	0.0792 [17]
0.01993	160.7	62.21	3.422	0.0766
0.01989	160.4	62.34	3.415	0.0746
0.01980	159.7	62.63	3.399	0.0725
0.01969	158.8	62.96	3.383	0.0687
0.01948	157.1	63.66	3.349	0.0643
0.01921	154.9	64.55	3.309	0.0620
0.01876	151.3	66.10	3.248	0.0650
0.01860	150.0	66.67	3.227	0.0593
0.01849	149.2	67.04	3.214	0.0550
0.01837	148.2	67.50	3.199	0.0509
0.01815	146.4	68.32	3.173	0.0472
0.01781	143.7	69.60	3.136	0.0454
0.01748	141.0	70.94	3.102	0.0436
0.01721	138.8	72.03	3.076	0.0416
0.01701	137.2	72.89	3.057	0.0385
0.01670	134.7	74.26	3.029	0.0362
0.01589	128.2	78.02	2.964	0.0329
0.01531	123.5	80.99	2.922	0.0315
0.01482	119.5	83.66	2.890	0.0306
0.01370	110.5	90.51	2.825	0.0295
0.01299	104.8	95.42	2.790	0.0294
0.01235	99.6	100.4	2.761	0.0298
0.01172	94.5	105.8	2.735	0.0304

(continued)

TABLE I *(Continued)*

Strontium Fluoride

eV	cm^{-1}	μm	n	k
0.01102	88.9	112.5	2.710	0.0312
0.01044	84.2	118.8	2.690	0.0318
0.00978	78.9	126.8	2.670	0.0331
0.00924	74.5	134.2	2.655	0.0333
0.00872	70.3	142.2	2.642	0.0335
0.00824	66.5	150.4	2.630	0.0330
0.00769	62.0	161.3	2.618	0.0327
0.00720	58.1	172.2	2.608	0.0304
0.00664	53.6	186.6	2.598	0.0275
0.00595	48.0	208.4	2.587	0.0239
0.00534	43.1	232.1	2.578	0.0204
0.00481	38.8	258.0	2.571	0.0176
0.00359	29.0	344.8	2.559	0.0127
0.00293	23.7	422.7	2.554	0.0101
0.00239	19.3	519.0	2.550	0.0062
0.00178	14.4	697.0	2.547	0.0045
0.0	0.0	∞	2.543 [21]	0.0

TABLE II

Room-Temperature Sellmeier Model Parameters

ith mode	$\Delta\epsilon_i$	λ_i
Feldman *et al.* model		
1	0.67805894	0.05628989
2	0.37140533	0.10801027
3	3.8484723	34.649040
Li model		
1	0.33973	0.0
2	0.70970	0.09597
3	0.1788	26.03
4	3.8796	45.60

TABLE III

Thermo-optical Coefficients of Strontium Fluoride

Wavelength (μm)	dn/dT (10^{-6}/K)	Measurement temperature (°C)	Reference
0.3250	−10.8	37	[8]
0.4416	−11.6	37	[8]
0.4579	−12.0	20	[5]
0.6328	−12.4	20	[5]
	−12.0	37	[8, 9]
1.15	−12.6	20	[5]
	−12.7	37	[8, 9]
3.39	−12.4	20	[5]
	−13.0	37	[8, 9]
10.6	−9.8	20	[5]
∞	265	7–47	[10]

TABLE IV

Room-Temperature Classical Oscillator Model Parameters

Mode number i	ν_i (cm^{-1})	$\Delta\epsilon_i$	Γ_i/ν_i	Reference
1	217	4.0	0.0170	[16]
2	316	0.07	0.25	
$\epsilon_\infty = 2.07$				
Modified				
1	217	4.3	0.017	[see text]
2	360	0.6	0.25	
$\epsilon = 2.05$				

Orthorhombic Sulfur (α-S)

KIRK A. FULLER
Department of Atmospheric Science
Colorado State University
Fort Collins, Colorado

HARRY D. DOWNING
Department of Physics and Astronomy
Stephen F. Austin State University
Nacogdoches, Texas

MARVIN R. QUERRY
Department of Physics
University of Missouri
Kansas City, Missouri

OVERVIEW I

Although elemental sulfur has a high propensity for catenation and, therefore, occurs in a wide variety of molecular allotropes [1], the only completely stable molecule in the solid phase is cyclo-octasulfur. The cyclo-S_8 molecules also constitute a large fraction of the melt throughout the liquid phase, although helical molecules are more prevalent at temperatures above about 498 K [2].

Cyclo-octasulfur is frequently referred to as λ sulfur (λ-S). From λ-S, strongly birefringent orthorhombic crystals or weakly birefringent monoclinic crystals may be assimilated. These two crystallographic allotropes are known as α- and β-S, respectively. At room temperature, α-S is the only thermodynamically stable modification of the element. Pure β-S may be very long-lived below about 198 K, and it tends to convert only slowly to the orthorhombic modification between 200 K and about 366 K, [3, 4]. The longest-lived transient polymorph of sulfur is a polymeric form known as μ-S, which can be preserved for several years, but is unstable against x-rays and sunlight [5]. μ-S is composed of long helical molecules that dominate

HANDBOOK OF OPTICAL CONSTANTS OF SOLIDS III

Copyright © 1998 by Academic Press.
All rights of reproduction in any form reserved
ISBN 0-12-544423-0/$25.00.

the more viscous, high-temperature melt and is insoluble in carbon disulfide. All other modifications convert to α-S with half-lives ranging from a few seconds to more than a year.

Terrestrially, native sulfur is found in sedimentary formations in association with gypsum and limestone, and it is produced by volcanic and fumarolic activity (such as at Yellowstone National Park). Pure sulfur is almost nonexisting in Earth's atmosphere. Extraterrestrially, an abundance of elemental sulfur is expected to occur in the clouds of Venus [6]. Elemental sulfur also is generally believed to exist, at least in small regions, on the surface of the Jovian moon Io [7], and possibly in the polar regions of Mercury [8].

The morphology of both natural and synthetic specimens of α-S ranges from cryptocrystalline masses or fine-grained aggregates to large crystals of well-formed basal pinachoidal or dipyramidal habits. The λ-S molecules are weakly held in the crystals almost exclusively by van der Waals forces [9]. Crystalline sulfur is a soft, brittle material, and is difficult to polish. The crystals display poor cleavage and tend to fracture conchoidally. Sulfur also is a poor conductor of heat, and thermal expansion from handling may result in fracturing or spallation of a specimen.

In part because of the instability of allotropes other than α-sulfur, related optical data are sparse and a comprehensive review of their optical constants is not possible now. Therefore, data for α-S, along with some discussion of the optical properties of liquid sulfur, are presented in this review. Furthermore, α-S's poor cleavage, difficulties in polishing, and the sensitivity of its bulk morphology and optical properties to thermodynamic history and trace impurities have resulted in limited consistency of measurements from one study to another.

In particular, the primary crystal data tabulated here are restricted to refractive-index measurements with polarization components along the *a*- and *b*-axes, and thus exclude polarization with components along the *c*-axis of the α-S crystal. As such, they are the only polarimetric measurements on sulfur that are available throughout the UV–mid-IR. It must be remembered, however, that near-normal-incidence reflectance R and corresponding refractive index n are significantly higher when the incident radiant flux has its electric field aligned with the *c*-axis. The absorption index can display a strong polarization dependence, as well. In order to give some understanding of how the optical constants of more general orientations may differ from the *a*- and *b*-axis data displayed in the graph, values of n and k for cryptocrystalline or amorphous samples are included as supplemental data in our tabulations, where possible.

Reviews of the optical and thermodynamic properties are given by Fuller and co-workers [10, 11], Moses and Nash [7], Young [12], Stuedel [2], and Meyer [1, 5, 13]. Although the literature on the spectral features of α-S is somewhat extensive, it certainly is not comprehensive. A considerable amount of work has been published on the transmission spectra of this allo-

trope in the infrared [14–23]. Sasson *et al.* [24] measured the visible and near-IR reflectance of unpolarized light from polycrystalline melt–freeze samples in which the *c*-axis of the crystallites tended to align normal to the substrates onto which they were frozen. Kurrelmeyer [25] and Spear and Adams [26] measured the absorption coefficient in the visible region, while investigating the photoconductivity of α-S. Its reflectance spectrum was studied with unpolarized UV light by Cook and Spear [27] and polarimetrically by Emerald *et al.* [28]. Sulfur absorbs too strongly in the UV region to permit detailed measurements of transmittance spectra. Although most references just cited pertain to single orthorhombic crystals, there also have been measurements of the optical properties of powdered (orthorhombic) and molten sulfur [24, 29–33]. Because of its weak absorption of radiant flux throughout much of the visible and infrared, powdered sulfur has found use as a diffuse reflectance standard in those spectral regions.

The IR absorption spectrum of α-S displays bands of attenuation centered around the following wave-number positions: 191, 243, 435, 470, 509, 549, 584, 618, 659, 679, 711, 845, 903, and 936 cm^{-1} [21], as well as 986, 1050, and 1298 cm^{-1} [16–18]. The bands at 191, 243, and 470 cm^{-1} are relatively strong and correspond, respectively, to the E_1, B_2, and E_1 irreducible representations of the S_8 molecule. The remaining bands listed are combinations and overtones that are rather weak, with the exception of the feature at 845 cm^{-1}, which is of moderate strength. (Care should be taken with regard to spectra of crystals grown in CS_2 solutions. Such specimens will possess solvent inclusions, and the strong ν_3 fundamental of CS_2, which occurs at about 1510 cm^{-1}, has been mistaken for a combination band of λ-S.)

For information on the absorption spectrum of sulfur in the far IR, the low-temperature studies of Gautier and Debeau [22] and Anderson and Boczar [23] are recommended, although one cannot glean information on the optical constants in this region, because insufficient detail was provided regarding their samples. In the intermediate infrared Barrow [27] investigated some effects of birefringence on the transmittance of α-S over the 1500–700 cm^{-1} range. Bernstein and Powling [16] and Srb and Vaško [19] also provided absorption spectra for α-S over the 1600–400 cm^{-1} and 1800–400 cm^{-1} regions, respectively.

Fuller *et al.* [10] measured the near-normal specular reflectance $R_\perp$ and $R_\parallel$ of the (111) plane of an orthorhombic sulfur crystal at room temperature with respective polarizations having projections perpendicular and parallel to the *c*-axis of the crystal. The reflectance R_C, in unpolarized radiation, of a cryptocrystalline melt freeze was also obtained. Note that the subscript is a capital "C" and does not refer to a crystallographic axis, but rather to the cryptocrystalline nature of the sample. Optical constants were determined from Kramers–Kronig phase-shift analysis of the reflectance data, although *k* was too small to be determined accurately throughout much of the range. The scatter in the reflectance data was on the order of 0.5% or less. It was

concluded that over the range 5000–180 cm^{-1}, the near-normal-incidence reflectance of the (111) face of an α-S crystal in unpolarized radiation is about 0.11 ± 0.005, that the corresponding values of n are around 1.99 ± 0.05, and that the reflectance and refractive index, respectively, do not fall below 0.097 ± 0.003 and 1.90 ± 0.03 or rise above 0.148 ± 0.004 and 2.25 ± 0.03 as the polarization of the incident beam is varied. These limits correspond to the extrema encountered at the endpoints of regions of anomalous dispersion. Over most of the spectrum, it was observed that $R_\perp \approx 0.100 \pm 0.002$, $R_C \approx 0.112 \pm 0.002$, $R_\parallel \approx 0.125 \pm 0.002$, $n_\perp \approx 1.92 \pm 0.01$, $n_C \approx 2.00 \pm 0.01$, and $n_\parallel \approx 2.09 \pm 0.01$.

Fuller *et al.* [10] found that scattering from the microcrystallites that were formed in the frozen-melt sample as it cooled to room temperature (a large fraction of this material probably underwent a transition from β-S to α-S) led to a noticeable contribution to an *apparent* reflectance by backscattered radiation. As the sequence of λ-S bands beginning with those centered near 936 and 903 cm^{-1} is approached, there is a corresponding increase in $k(\nu)$ that attenuates the internally scattered radiation before a detectable amount emerges from the sample, and the average reflectance below 1000 cm^{-1} drops by about 2% from its value at higher energies. The scatter in n_C was not observed to be more than about 1.5%, even in the raw data, where problems associated with volume scattering occurred.

The general decrease in the transmittance of α-S below 1000 cm^{-1} along with a window in the region of 760 cm^{-1} can be easily seen in the published spectra of the element. The role of multiple scattering in the foregoing context is exemplified in the diffuse reflectance spectra of Nash [32], where the influence of the increased k values beginning near 1000 cm^{-1} and the 760 cm^{-1} window is particularly strong. Similar structure appears in diffuse spectra at about 1300 cm^{-1}. Such features are important in helping to determine the abundance of sulfur on the surfaces of solar-system bodies.

II EXTRAPOLATION TO DIFFERENT TEMPERATURES

Wong [34] measured the IR reflectance of molten sulfur from 2 to 22μm at 423 and 473 K. By paralleling R_C to Wong's data, estimates of this reflectance were obtained over domains that extended out to 5000 cm^{-1}. Based on these extrapolations, n_C was found to range between 2.00 and 2.01. The density of α-S at room temperature is about 2.07 g/cm^3. One can use this and the density of the melt at around 423 K, which is about 1.78 g/cm^3 [13, 35], to obtain, via the Lorentz–Lorenz equation, approximations of refractive indices at this temperature based on one's knowledge of these indices at room temperature. This leads to values for n_C of between 1.84 and 1.85

at 423 K. (Because the optical properties of cryptocrystalline and amorphous sulfur are not expected to differ significantly, the subscript C is used in describing amorphous sulfur, as well.) Upon correcting R_C for the contribution of backscatter attributed to the granularities in the microcrystalline sample, estimated to be about 2%, the refractive index of what would constitute *solid* amorphous λ-sulfur at 300 K and 5000 cm^{-1} is found to be 1.99, giving a refractive index $n_C \approx 1.83$ for liquid (amorphous) λ-S at 423 K. Wong [34] has found the melt at 423 K to have a refractive index of 1.81 ± 0.02 throughout most of the 5000–450 cm^{-1} region. Sasson and Arakawa [33] conducted studies similar to ours over the 25,000 to 5000 cm^{-1} interval and determined n_C (5000) for the melt to be 1.84 ± 0.01 at a temperature of 428 K.

The Lorentz–Lorenz formula is only an approximation when applied to solids or liquids [36, 37]; furthermore, it is being applied here to a temperature regime in which a crystalline material of strong birefringence transforms to a liquid and, therefore, amorphous structure. The formula has been used successfully, however, in the study of water [38] and has produced excellent results when applied to sulfuric-acid solutions of varying concentration [39]. Furthermore, in view of the weak intermolecular coupling between λ-S molecules in both the solid and liquid phases, it is quite likely that the polarizabilities of the molecule, which are ultimately responsible for the refractive index of the bulk material, are very nearly the same in either phase. Support for this latter argument is found in the results of a study conducted by Robertson *et al.* [40] on the optical constants of solid NH_3.

If the thermal expansion coefficient of α-S is assumed to be no larger than about 20×10^{-5}/K from room temperature [3, 13], down to about 100 K, then the change in refractive index is expected to be only on the order of a few hundredths of a percent.

THE TABULATED DATA III

For this critique, values for n and k in the far-UV–x-ray region were calculated with the Henke model [41]. A density of 2.07 g/cm^3 was assumed, and crystallographic orientation was neglected even though ⊥ is specified in Table I.

The data of Emerald *et al.* [28] was chosen for the UV. They measured the reflectance for polarization parallel to the *a*- and *b*-axes for up to 12 eV, from which the optical constants were obtained with Kramers–Kronig analysis. Professor Zallen kindly provided original figures [28], from which the numerical values were extracted by scanning. To maintain consistency with data at lower energies, values presented here for n and k in the UV are simple averages of those obtained for the two polarizations. The variation of optical properties with polarization is illustrated by a peak reflectance at 9.5 eV,

which dominated the spectra of Cook and Spear [27], but was not nearly as strong and occurred at a somewhat lower energy in the work reported by Emerald *et al.*

The orientation of the polycrystalline samples in the measurements made by Sasson *et al.* [24] are compatible with the UV work of Emerald *et al.* [28], and their values for n have been selected for tabulation in the visible to near-IR. The high transparency of sulfur in the vis–near-IR coupled with scattering losses from their samples prevented Sasson *et al.* from obtaining k values for α-S. The slight mismatch in the values of n reported by Emerald *et al.* and by Sasson *et al.* is believed to be due to some variation in crystal orientation in the polycrystalline samples of Sasson *et al.* In view of the previous discussion on extrapolation to other temperatures, one may reasonably expect to estimate n_C in the visible via the Lorentz–Lorenz approximation.

Spear and Adams [26] measured the absorption coefficient ($\alpha = 4\pi k\nu$) of the near-UV absorption edge using unpolarized light incident on thin sections taken from single crystals. Further into the visible, values for k are taken from the early work of Kurrelmeyer, who measured the absorption coefficient for unpolarized light incident along the c-axis. A baseline absorbance of zero was forced at 0.700 μm, rendering data for $\lambda > 0.600$ μm questionable. The measurements of Sasson and Arakawa [33] are used for the near IR, although this latter work dealt with the low-temperature melt, and it is unclear how similar the k-values are to those for the room-temperature solid; they likely provide an upper bound. It is worth noting that the absorption edge seen in these works is responsible for the characteristic yellow color of sulfur. Because of preferential absorption of shorter wavelengths, the light emerging from sulfur at room temperature appears yellow. As the temperature rises, thermal broadening of the band centered at about 4 eV carries the absorption edge further into the visible, and the hue darkens. Conversely, the absorption edge recedes into the UV with decreasing temperature, rendering sulfur crystals colorless below about $-50°$ C.

Further into the IR, the n-values obtained by Fuller *et al.* [10] for incident irradiance normal to the (111) crystal plane and with polarization perpendicular to the c-axis are used. The refractive indices were obtained from Kramers–Kronig analysis, and data were also collected for the orthogonal polarization and for a cryptocrystalline melt freeze. By far the most prominent features in the reflectance spectra of Fuller *et al.* are the bands centered near 190 and 240 cm^{-1}, respectively. Because of extrapolations beyond experimental range that are required by K-K analysis, it is difficult to be sure of the uncertainty in k below 250 cm^{-1}, but based on several different extrapolations, $k(190)$ was not found to change by more than about ± 0.01 and $k(240)$ varied by no more than about ± 0.003. A strong dependence on polarization of the band at 240 cm^{-1} was observed, and the E_1 band at

190 cm^{-1} appears only as a shoulder on what is a very strong B_2 absorption in the case of $\perp$ or *ab* polarization.

The band arising from the ν_5 fundamental at 470 cm^{-1} was easily distinguished in all spectra. Values of $k(470)$ were found to range between 0.016 ($k_{\parallel}$) and 0.019 ($k_{\perp}$). Rather than lying somewhere between $k_{\parallel}$ and $k_{\perp}$, the value of k_C was found to be 0.023. This anomalously high value is attributed to both particle-size effects and experimental uncertainty.

The most important combination band appearing in the transmittance and diffuse reflectance spectra of α-S is the $\nu_{10} + \nu_3$ combination, which is centered at about 845 cm^{-1}. As calculated from transmission spectra of various authors, peak values of $k(845)$ 0.001 to 0.004.

All other absorption bands are quite weak. Their influence on R and n is on the order of at most 0.3%, and any k values obtained via the Kramers–Kronig relations from such faint structures are quite unreliable. Above 675 cm^{-1} numerical values for k were obtained by electronically scanning graphs presented in Barrow's paper. Unpolarized light incident on the (110) plane was used because the transmission of the band at 845 cm^{-1} was too low at the desired polarization to allow the absorption index to be extracted. After correcting for reflection losses with the use of measurements made by Fuller *et al.*, values for k were taken from the spectra of Srb and Vaško between 675 and 500 cm^{-1}. Below 500 cm^{-1}, the k values provided by Fuller *et al.* [10] are used, but supplemental values are also provided from the Srb and Vaško's work between 450 and 410 cm^{-1}.

Data for optical constants in the far IR are not available, though work is planned for this region. In view of mm–far-IR instrumentation planned by NASA, there are additional features, especially absorption at around 74 cm^{-1}, that warrant investigation.

To provide some idea of the optical constants associated with more arbitrary polarizations or crystallographic orientations, those of the melt freeze are included in the tabulated values. Attention is called to the differences between the two sets of data at energies below about 250 cm^{-1}.

Crystal structure [42] and electric-vector polarization are discussed in the caption of Fig. 1.

ACKNOWLEDGMENTS

We are grateful to Dr. W. R. Hunter (SFA, Inc., 1401 McCormick Dr., Largo, MD 20774) for calculation of n and k in the far-UV–x-ray region, and we also wish to thank Philip Gabriel for his assistance in electronically scanning many of the graphs from which the tabulated data were obtained.

REFERENCES

1. B. Meyer, Elemental sulfur. *Chem. Rev.* **76**, 367–388 (1976).
2. R. Stuedel, Homocyclic sulfur molecules. *Top. Curr. Chem.* **102**, 147–176 (1981).

3. E. D. Eastman and W. C. McGavock, Heat capacity and entropy of rhombic and monoclinic sulfur. *J. Am. Chem. Soc.* **59**, 145–151 (1937).
4. E. D. West, Heat capacity of sulfur from 25 to 450K, the heats and temperatures of transition and fusion. *J. Am. Chem. Soc.* **81**, 29–37 (1959).
5. B. Meyer, Solid allotropes of sulfur. *Chem. Rev.* **64**, 429–451 (1964).
6. A. T. Young, Venus cloud microphysics. *Icarus* **56**, 568–577 (1983).
7. J. I. Moses and D. B. Nash, Phase transformations and the spectral reflectance of solid sulfur: Can metastable sulfur allotropes exist on Io? *Icarus* **89**, 277–304 (1991).
8. A. L. Sprague, D. M. Hunten, and K. Lodders, Sulfur at Mercury, elemental at the poles and sulfides in the regolith. *Icarus* **118**, 211–215 (1995).
9. A. R. Adams and W. E. Spear, Charge transport in orthorhombic sulphur crystals. *J. Phys. Chem. Solids* **25**, 1113–1118 (1964).
10. K. A. Fuller, H. D. Downing, and M. R. Querry, Infrared optical properties of orthorhombic sulfur. *Appl. Opt.* **30**, 4081–4093 (1991).
11. K. A. Fuller, Elemental sulfur and its optical properties in the infrared. M. S. Thesis, Stephen F. Austin State University, Nacogdoches, Texas (1984).
12. A. T. Young, No sulfur flows on Io. *Icarus* **58**, 197–226 (1984).
13. B. Meyer, "Sulfur, Energy and Environment." Elsevier, New York, 1979.
14. W. W. Coblentz, Optical notes. *Phys. Rev.* **19**, 89–97 (1904).
15. R. B. Barnes, Measurements in the long wavelength infrared from 20 μm to 135 μm. *Phys. Rev.* **39**, 562–575 (1932).
16. H. J. Bernstein and J. Powling, The vibrational spectra and structure of inorganic molecules. II. Sulfur S_8, sulfur chloride S_2Cl_2, phosphorous P_4. *J. Chem. Phys.* **18**, 1018–1023 (1950).
17. G. M. Barrow, The infrared spectra of oriented rhombic sulfur crystals with polarized radiation. *J. Chem. Phys.* **21**, 219–222 (1953).
18. V. D. Neff and T. H. Walnut, Effect of temperature on the intensity and structure of bands in the infrared spectrum of rhombic sulfur. *J. Chem. Phys.* **35**, 1723–1729 (1961).
19. I. Srb and A. Vaško, Remark on the infrared spectrum of rhombic sulfur. *J. Chem. Phys.* **37**, 1892–1893 (1962).
20. C. E. MacNeill, Infrared transmittance of rhombic sulfur. *J. Opt. Soc. Am.* **53**, 398–399 (1963).
21. D. W. Scott, J. P. McCullough, and F. H. Kruse, Vibrational assignment and force constants of S_8 from a normal coordinate treatment. *J. Mol. Spectrosc.* **13**, 313–320 (1964).
22. G. Gautier and M. Debeau, Spectres vibration d'un monocristal de soufre orthorhombique. *Spectrochim. Acta Part A* **30**, 1193–1198 (1974).
23. A. Anderson and P. G. Boczar, Far infrared spectrum of orthorhombic sulfur. *Chem. Phys. Lett.* **43**, 506–511 (1976).
24. R. Sasson, R. Wright, E. T. Arakawa, B. N. Khare, and C. Sagan, Optical properties of solid and liquid sulfur at visible and infrared wavelengths. *Icarus* **64**, 368–374 (1985).
25. B. Kurrelmeyer, The photoelectric conductivity of sulphur. *Phys. Rev.* **30**, 893–910 (1927).
26. W. E. Spear and A. R. Adams, Photogeneration of charge carriers and related optical properties in orthorhombic sulphur. *J. Chem. Phys. Solids* **27**, 281–289 (1966).
27. B. E. Cook and W. E. Spear, The optical properties of orthorhombic sulphur in the vacuum ultraviolet. *J. Phys. Chem. Solids* **30**, 1125–1134 (1969).
28. R. L. Emerald, R. E. Drews, and R. Zallen, Polarization-dependent optical properties of orthorhombic sulfur in the ultraviolet. *Phys. Rev. B* **14**, 808–813 (1976).
29. B. Meyer, M. Gouterman, D. Jensen, T. Oommen, and T. Stroyer-Hansen, The spectrum of sulfur and its allotropes. *Adv. Chem. Ser.* **110**, 53–72 (1972).
30. N. M. Nelson, D. C. Pieri, S. M. Bologa, D. B. Nash, and C. Sagan, The reflection spectrum of liquid sulfur: Implications for Io. *Icarus* **56**, 409–413 (1983).
31. J. Gradie and J. Veverka, Photometric properties of sulfur. *Icarus* **58**, 227–245 (1984).

32. D. B. Nash, Mid-infrared reflectance spectra (2.3–22μm) of sulfur, gold, KBr, MgO, and Halon. *Appl. Opt.* **25**, 2427–2433 (1986).
33. R. Sasson and E. T. Arakawa, Temperature dependence of index of refraction, reflection, and extinction coefficient of liquid sulfur in the 0.4–2.0 μm wavelength range. *Appl. Opt.* **25**, 2675–2680 (1986).
34. M. Wong, The infrared optical constants of molten sulfur at 150° and 200°C. M. S. Thesis Stephen F. Austin State University, Nacogdoches, Texas, (1984).
35. A. M. Kellas, The determination of the molecular complexity of liquid sulphur. *J. Chem. Soc.* **113**, 903–922 (1918).
36. L. Brillouin, "Wave Propagation and Group Velocity," Academic Press, New York, 1960.
37. J. D. Jackson, "Classical Electrodynamics," 2nd Ed. Wiley, New York, 1975.
38. L. W. Pinkley, P. P. Sethna, and D. Williams, Optical constants of water in the infrared: Influence of temperature. *J. Opt. Soc. Am.* **67**, 494–499 (1977).
39. L. W. Pinkley and D. Williams, The infrared optical constants of sulfuric acid at 250K. *J. Opt. Soc. Am.* **66**, 122–124 (1976).
40. C. W. Robertson, H. D. Downing, B. Curnutte, and D. Williams, Optical constants of solid ammonia in the infrared. *J. Opt. Soc. Am.* **65**, 432–435 (1975).
41. B. L. Henke, E. M. Gullikson, and J. C. Davis, X-ray interactions: Photoabsorption, scattering, transmission, and reflection at E = 50-30000 eV, Z = 1-92. *At. Data Nucl. Data Tables* **54**, 181 (1993).
42. A. S. Cooper, W. L. Bond, and S. C. Abrahams, The lattice and molecular constants in orthorhombic sulfur. *Acta Crystallogr.* **14**, 1008 (1961).

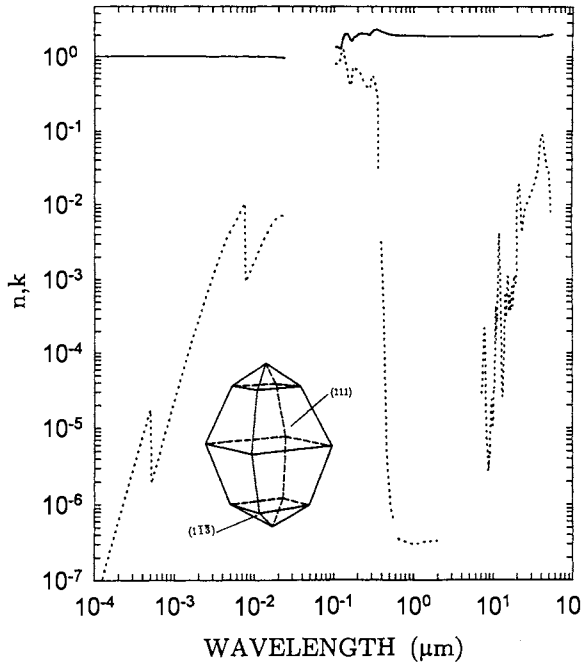

Fig. 1. Log–log plot of n (———) and k (- - - -) versus wavelength in micrometers for α-S. The symmetry of the orthorhombic crystals is F*ddd* with lattice constants of Cooper *et al.* [42]

$$a : b : c = 10.46 : 12.87 : 24.49.$$

The c-axis of the orthorhombic crystal lies along the length of the crystal. The *ab*-plane contains the middle horizontal parallelogram shown in the figure, with the a-axis lying along the diagonal that extends out of the plane of the figure. The primary tabulated data (columns 4 and 5) involve incident radiation with electric vector contained in the *ab*-plane. The direction of incidence for the primary data is along the c-axis for the UV-VIS region and perpendicular to it in the IR.

TABLE I

Values for *n* and *k* for Orthorhombic Sulfur Obtained from Various References[a]

eV	cm^{-1}	μm	$n_{\perp}$	$k_{\perp}$	n_{supp}	k_{supp}
.300E + 05	.242E + 09	.413E-04	1.000 [41]	.123E-08 [41]		
.292E + 05	.236E + 09	.425E-04	1.000	.137E-08		
.284E + 05	.229E + 09	.436E-04	1.000	.153E-08		
.277E + 05	.223E + 09	.448E-04	1.000	.171E-08		
.270E + 05	.217E + 09	.460E-04	1.000	.190E-08		
.263E + 05	.212E + 09	.472E-04	1.000	.212E-08		
.256E + 05	.206E + 09	.485E-04	1.000	.236E-08		
.249E + 05	.201E + 09	.498E-04	1.000	.263E-08		
.242E + 05	.195E + 09	.512E-04	1.000	.293E-08		
.236E + 05	.190E + 09	.526E-04	1.000	.327E-08		
.230E + 05	.185E + 09	.540E-04	1.000	.364E-08		
.224E + 05	.180E + 09	.554E-04	1.000	.406E-08		
.218E + 05	.176E + 09	.569E-04	1.000	.452E-08		
.212E + 05	.171E + 09	.585E-04	1.000	.503E-08		
.206E + 05	.167E + 09	.601E-04	1.000	.560E-08		
.201E + 05	.162E + 09	.617E-04	1.000	.624E-08		
.196E + 05	.158E + 09	.633E-04	1.000	.695E-08		
.191E + 05	.154E + 09	.651E-04	1.000	.773E-08		
.186E + 05	.150E + 09	.668E-04	1.000	.860E-08		
.181E + 05	.146E + 09	.686E-04	1.000	.957E-08		
.176E + 05	.142E + 09	.705E-04	1.000	.107E-07		
.171E + 05	.138E + 09	.774E-04	1.000	.118E-07		
.167E + 05	.135E + 09	.743E-04	1.000	.132E-07		
.162E + 05	.131E + 09	.764E-04	1.000	.147E-07		
.158E + 05	.128E + 09	.784E-04	1.000	.163E-07		
.154E + 05	.124E + 09	.805E-04	1.000	.181E-07		
.150E + 05	.121E + 09	.827E-04	1.000	.201E-07		
.146E + 05	.118E + 09	.850E-04	1.000	.224E-07		
.142E + 05	.115E + 09	.878E-04	1.000	.248E-07		
.138E + 05	.112E + 09	.896E-04	1.000	.276E-07		
.135E + 05	.109E + 09	.920E-04	1.000	.307E-07		
.131E + 05	.106E + 09	.945E-04	1.000	.341E-07		
.128E + 05	.103E + 09	.971E-04	1.000	.378E-07		
.124E + 05	.100E + 09	.997E-04	1.000	.420E-07		
.121E + 05	.976E + 08	.102E-03	1.000	.467E-07		
.118E + 05	.951E + 08	.105E-03	1.000	.518E-07		
.115E + 05	.926E + 08	.108E-03	1.000	.575E-07		
.112E + 05	.901E + 08	.111E-03	1.000	.639E-07		
.109E + 05	.878E + 08	.114E-03	1.000	.709E-07		
.106E + 05	.855E + 08	.117E-03	1.000	.787E-07		
.103E + 05	.832E + 08	.120E-03	1.000	.873E-07		
.100E + 05	.810E + 08	.123E-03	1.000	.967E-07		
.978E + 04	.789E + 08	.127E-03	1.000	.107E-06		
.952E + 04	.768E + 08	.130E-03	1.000	.119E-06		
.927E + 04	.748E + 08	.134E-03	1.000	.132E-06		

(continued)

[a] References given in brackets.

TABLE I *(Continued)*

Orthorhombic Sulfur

eV	cm^{-1}	μm	$n_\perp$	$k_\perp$	n_{supp}	k_{supp}
.903E + 04	.728E + 08	.137E-03	1.000	.146E-06		
.879E + 04	.709E + 08	.141E-03	1.000	.162E-06		
.856E + 04	.690E + 08	.145E-03	1.000	.180E-06		
.833E + 04	.672E + 08	.149E-03	1.000	.199E-06		
.811E + 04	.654E + 08	.153E-03	1.000	.221E-06		
.790E + 04	.637E + 08	.157E-03	1.000	.245E-06		
.769E + 04	.620E + 08	.161E-03	1.000	.271E-06		
.749E + 04	.604E + 08	.166E-03	1.000	.301E-06		
.729E + 04	.588E + 08	.170E-03	1.000	.333E-06		
.710E + 04	.573E + 08	.175E-03	1.000	.369E-06		
.691E + 04	.558E + 08	.179E-03	1.000	.409E-06		
.673E + 04	.543E + 08	.184E-03	1.000	.453E-06		
.655E + 04	.529E + 08	.189E-03	1.000	.502E-06		
.638E + 04	.515E + 08	.194E-03	1.000	.556E-06		
.621E + 04	.501E + 08	.200E-03	1.000	.616E-06		
.605E + 04	.488E + 08	.205E-03	1.000	.682E-06		
.589E + 04	.475E + 08	.211E-03	1.000	.755E-06		
.573E + 04	.463E + 08	.216E-03	1.000	.835E-06		
.558E + 04	.450E + 08	.222E-03	1.000	.924E-06		
.544E + 04	.438E + 08	.228E-03	1.000	.102E-05		
.529E + 04	.427E + 08	.234E-03	1.000	.113E-05		
.515E + 04	.416E + 08	.241E-03	1.000	.125E-05		
.502E + 04	.405E + 08	.247E-03	1.000	.138E-05		
.489E + 04	.394E + 08	.254E-03	1.000	.153E-05		
.476E + 04	.384E + 08	.261E-03	1.000	.169E-05		
.463E + 04	.374E + 08	.268E-03	1.000	.187E-05		
.451E + 04	.364E + 08	.275E-03	1.000	.207E-05		
.439E + 04	.354E + 08	.282E-03	1.000	.228E-05		
.428E + 04	.345E + 08	.290E-03	1.000	.252E-05		
.416E + 04	.336E + 08	.298E-03	1.000	.278E-05		
.405E + 04	.327E + 08	.306E-03	1.000	.307E-05		
.395E + 04	.318E + 08	.314E-03	1.000	.339E-05		
.384E + 04	.310E + 08	.323E-03	1.000	.374E-05		
.374E + 04	.302E + 08	.331E-03	1.000	.413E-05		
.364E + 04	.294E + 08	.340E-03	1.000	.455E-05		
.355E + 04	.286E + 08	.350E-03	1.000	.502E-05		
.345E + 04	.279E + 08	.359E-03	1.000	.553E-05		
.336E + 04	.271E + 08	.369E-03	1.000	.609E-05		
.327E + 04	.264E + 08	.379E-03	1.000	.671E-05		
.319E + 04	.257E + 08	.389E-03	1.000	.738E-05		
.310E + 04	.250E + 08	.399E-03	1.000	.812E-05		
.302E + 04	.244E + 08	.410E-03	1.000	.893E-05		
.294E + 04	.237E + 08	.421E-03	1.000	.982E-05		
.287E + 04	.231E + 08	.433E-03	1.000	.108E-04		
.279E + 04	.225E + 08	.444E-03	1.000	.119E-04		
.272E + 04	.219E + 08	.456E-03	1.000	.130E-04		

TABLE I *(Continued)*

Orthorhombic Sulfur

eV	cm^{-1}	μm	$n_\perp$	$k_\perp$	n_{supp}	k_{supp}
.264E + 04	.213E + 08	.469E-03	1.000	.143E-04		
.258E + 04	.208E + 08	.481E-03	1.000	.157E-04		
.251E + 04	.202E + 08	.495E-03	1.000	.172E-04		
.244E + 04	.197E + 08	.508E-03	1.000	.186E-05		
.238E + 04	.192E + 08	.522E-03	1.000	.207E-05		
.231E + 04	.187E + 08	.536E-03	1.000	.230E-05		
.225E + 04	.182E + 08	.550E-03	1.000	.255E-05		
.219E + 04	.177E + 08	.565E-03	1.000	.282E-05		
.214E + 04	.172E + 08	.580E-03	1.000	.313E-05		
.208E + 04	.168E + 08	.596E-03	1.000	.346E-05		
.203E + 04	.163E + 08	.612E-03	1.000	.383E-05		
.197E + 04	.159E + 08	.629E-03	1.000	.423E-05		
.192E + 04	.155E + 08	.646E-03	1.000	.467E-05		
.187E + 04	.151E + 08	.663E-03	1.000	.516E-05		
.182E + 04	.147E + 08	.681E-03	1.000	.570E-05		
.177E + 04	.143E + 08	.700E-03	1.000	.630E-05		
.173E + 04	.139E + 08	.719E-03	1.000	.695E-05		
.168E + 04	.136E + 08	.738E-03	1.000	.766E-05		
.164E + 04	.132E + 08	.758E-03	1.000	.844E-05		
.159E + 04	.128E + 08	.778E-03	1.000	.930E-05		
.155E + 04	.125E + 08	.799E-03	1.000	.102E-04		
.151E + 04	.122E + 08	.821E-03	1.000	.113E-04		
.147E + 04	.119E + 08	.843E-03	1.000	.125E-04		
.143E + 04	.115E + 08	.866E-03	1.000	.137E-04		
.139E + 04	.112E + 08	.890E-03	1.000	.152E-04		
.136E + 04	.109E + 08	.914E-03	1.000	.167E-04		
.132E + 04	.107E + 08	.938E-03	1.000	.185E-04		
.129E + 04	.104E + 08	.964E-03	1.000	.204E-04		
.125E + 04	.101E + 08	.990E-03	1.000	.225E-04		
.122E + 04	.984E + 07	.102E-02	1.000	.248E-04		
.119E + 04	.958E + 07	.104E-02	1.000	.274E-04		
.116E + 04	.933E + 07	.107E-02	1.000	.303E-04		
.113E + 04	.908E + 07	.110E-02	1.000	.334E-04		
.110E + 04	.884E + 07	.113E-02	1.000	.369E-04		
.107E + 04	.861E + 07	.116E-02	1.000	.407E-04		
.104E + 04	.838E + 07	.119E-02	1.000	.449E-04		
.101E + 04	.816E + 07	.123E-02	1.000	.496E-04		
.985E + 03	.795E + 07	.126E-02	1.000	.547E-04		
.959E + 03	.774E + 07	.129E-02	1.000	.603E-04		
.934E + 03	.753E + 07	.133E-02	1.000	.665E-04		
.910E + 03	.734E + 07	.136E-02	0.999	.733E-04		
.886E + 03	.714E + 07	.140E-02	0.999	.808E-04		
.862E + 03	.695E + 07	.144E-02	0.999	.891E-04		
.840E + 03	.677E + 07	.148E-02	0.999	.981E-04		
.817E + 03	.659E + 07	.152E-02	0.999	.108E-03		
.796E + 03	.642E + 07	.156E-02	0.999	.119E-03		

(continued)

TABLE I *(Continued)*

Orthorhombic Sulfur

eV	cm^{-1}	μm	$n_\perp$	$k_\perp$	n_{supp}	k_{supp}
.775E + 03	.625E + 07	.160E-02	0.999	.131E-03		
.755E + 03	.609E + 07	.164E-02	0.999	.144E-03		
.735E + 03	.592E + 07	.169E-02	0.999	.159E-03		
.715E + 03	.577E + 07	.173E-02	0.999	.175E-03		
.696E + 03	.562E + 07	.178E-02	0.999	.192E-03		
.678E + 03	.547E + 07	.183E-02	0.999	.210E-03		
.660E + 03	.532E + 07	.188E-02	0.999	.231E-03		
.643E + 03	.518E + 07	.193E-02	0.999	.255E-03		
.626E + 03	.505E + 07	.198E-02	0.999	.279E-03		
.609E + 03	.492E + 07	.203E-02	0.999	.306E-03		
.593E + 03	.479E + 07	.209E-02	0.999	.335E-03		
.578E + 03	.466E + 07	.215E-02	0.999	.367E-03		
.563E + 03	.454E + 07	.220E-02	0.999	.402E-03		
.548E + 03	.442E + 07	.226E-02	0.999	.440E-03		
.533E + 03	.430E + 07	.232E-02	0.999	.480E-03		
.519E + 03	.419E + 07	.239E-02	0.999	.525E-03		
.506E + 03	.408E + 07	.245E-02	0.998	.573E-03		
.492E + 03	.397E + 07	.252E-02	0.998	.625E-03		
.479E + 03	.387E + 07	.259E-02	0.998	.683E-03		
.467E + 03	.376E + 07	.266E-02	0.998	.746E-03		
.454E + 03	.366E + 07	.273E-02	0.998	.814E-03		
.442E + 03	.357E + 07	.280E-02	0.998	.887E-03		
.431E + 03	.347E + 07	.288E-02	0.998	.965E-03		
.419E + 03	.338E + 07	.296E-02	0.998	.105E-02		
.408E + 03	.329E + 07	.304E-02	0.998	.114E-02		
.398E + 03	.321E + 07	.312E-02	0.998	.124E-02		
.387E + 03	.312E + 07	.320E-02	0.998	.135E-02		
.377E + 03	.304E + 07	.329E-02	0.997	.146E-02		
.367E + 03	.296E + 07	.338E-02	0.997	.157E-02		
.357E + 03	.288E + 07	.347E-02	0.997	.170E-02		
.348E + 03	.281E + 07	.356E-02	0.997	.183E-02		
.339E + 03	.273E + 07	.366E-02	0.997	.198E-02		
.330E + 03	.266E + 07	.376E-02	0.997	.214E-02		
.321E + 03	.259E + 07	.386E-02	0.997	.231E-02		
.313E + 03	.252E + 07	.397E-02	0.997	.249E-02		
.305E + 03	.246E + 07	.407E-02	0.997	.269E-02		
.297E + 03	.239E + 07	.418E-02	0.997	.291E-02		
.289E + 03	.233E + 07	.430E-02	0.997	.314E-02		
.281E + 03	.227E + 07	.441E-02	0.997	.339E-02		
.274E + 03	.221E + 07	.453E-02	0.997	.361E-02		
.267E + 03	.215E + 07	.465E-02	0.996	.381E-02		
.259E + 03	.209E + 07	.478E-02	0.996	.401E-02		
.253E + 03	.204E + 07	.491E-02	0.996	.422E-02		
.246E + 03	.198E + 07	.504E-02	0.996	.444E-02		
.240E + 03	.193E + 07	.518E-02	0.996	.467E-02		
.233E + 03	.188E + 07	.532E-02	0.996	.491E-02		

TABLE I *(Continued)*

Orthorhombic Sulfur

eV	cm^{-1}	μm	$n_{\perp}$	$k_{\perp}$	n_{supp}	k_{supp}
.227E + 03	.183E + 07	.546E-02	0.996	.517E-02		
.221E + 03	.178E + 07	.561E-02	0.996	.544E-02		
.215E + 03	.174E + 07	.576E-02	0.996	.573E-02		
.210E + 03	.169E + 07	.592E-02	0.996	.606E-02		
.204E + 03	.165E + 07	.608E-02	0.996	.646E-02		
.199E + 03	.160E + 07	.624E-02	0.997	.688E-02		
.193E + 03	.156E + 07	.641E-02	0.997	.732E-02		
.188E + 03	.152E + 07	.658E-02	0.997	.778E-02		
.183E + 03	.148E + 07	.676E-02	0.998	.825E-02		
.179E + 03	.144E + 07	.694E-02	0.998	.873E-02		
.174E + 03	.140E + 07	.713E-02	0.999	.924E-02		
.169E + 03	.137E + 07	.733E-02	1.001	.978E-02		
.165E + 03	.133E + 07	.752E-02	1.004	.103E-01		
.161E + 03	.129E + 07	.773E-02	1.006	.928E-03		
.156E + 03	.126E + 07	.793E-02	1.001	.988E-03		
.152E + 03	.123E + 07	.815E-02	1.000	.105E-02		
.148E + 03	.119E + 07	.837E-02	0.999	.112E-02		
.144E + 03	.116E + 07	.860E-02	0.998	.120E-02		
.140E + 03	.113E + 07	.883E-02	0.997	.128E-02		
.137E + 03	.110E + 07	.907E-02	0.996	.138E-02		
.133E + 03	.108E + 07	.931E-02	0.996	.147E-02		
.130E + 03	.105E + 07	.957E-02	0.995	.157E-02		
.126E + 03	.102E + 07	.982E-02	0.994	.168E-02		
.123E + 03	.991E + 06	.101E-01	0.994	.179E-02		
.120E + 03	.965E + 06	.104E-01	0.993	.191E-02		
.117E + 03	.940E + 06	.106E-01	0.992	.204E-02		
.113E + 03	.915E + 06	.109E-01	0.991	.218E-02		
.110E + 03	.890E + 06	.112E-01	0.991	.231E-02		
.108E + 03	.867E + 06	.115E-01	0.990	.246E-02		
.105E + 03	.844E + 06	.118E-01	0.989	.264E-02		
.102E + 03	.822E + 06	.122E-01	0.988	.283E-02		
.993E + 02	.801E + 06	.125E-01	0.988	.303E-02		
.966E + 02	.779E + 06	.128E-01	0.987	.321E-02		
.941E + 02	.759E + 06	.132E-01	0.986	.340E-02		
.916E + 02	.739E + 06	.135E-01	0.985	.361E-02		
.892E + 02	.719E + 06	.139E-01	0.984	.382E-02		
.869E + 02	.701E + 06	.143E-01	0.983	.403E-02		
.846E + 02	.682E + 06	.147E-01	0.982	.426E-02		
.823E + 02	.664E + 06	.151E-01	0.981	.449E-02		
.802E + 02	.647E + 06	.155E-01	0.980	.474E-02		
.781E + 02	.630E + 06	.159E-01	0.979	.497E-02		
.760E + 02	.613E + 06	.163E-01	0.977	.519E-02		
.740E + 02	.597E + 06	.168E-01	0.976	.546E-02		
.721E + 02	.582E + 06	.172E-01	0.975	.575E-02		
.702E + 02	.566E + 06	.177E-01	0.973	.597E-02		
.683E + 02	.551E + 06	.182E-01	0.972	.618E-02		

(continued)

TABLE I *(Continued)*

Orthorhombic Sulfur

eV	cm^{-1}	μm	$n_{\perp}$	$k_{\perp}$	n_{supp}	k_{supp}
.665E + 02	.536E + 06	.186E-01	0.970	.637E-02		
.648E + 02	.523E + 06	.191E-01	0.968	.653E-02		
.631E + 02	.509E + 06	.197E-01	0.967	.665E-02		
.614E + 02	.495E + 06	.202E-01	0.965	.673E-02		
.598E + 02	.482E + 06	.207E-01	0.963	.688E-02		
.582E + 02	.469E + 06	.213E-01	0.960	.699E-02		
.567E + 02	.457E + 06	.219E-01	0.958	.693E-02		
.557E + 02	.449E + 06	.225E-01	0.955	.693E-02		
.537E + 02	.433E + 06	.231E-01	0.953	.693E-02		
.523E + 02	.422E + 06	.237E-01	0.950	.686E-02		
.118E + 02	.952E + 05	.105E + 00	1.340 [28]	.795E + 00 [28]		
.117E + 02	.944E + 05	.106E + 00	1.344	.793E + 00		
.116E + 02	.936E + 05	.107E + 00	1.352	.789E + 00		
.115E + 02	.928E + 05	.108E + 00	1.358	.783E + 00		
.114E + 02	.920E + 05	.109E + 00	1.359	.778E + 00		
.113E + 02	.911E + 05	.110E + 00	1.358	.775E + 00		
.112E + 02	.903E + 05	.111E + 00	1.352	.771E + 00		
.111E + 02	.895E + 05	.112E + 00	1.348	.770E + 00		
.110E + 02	.887E + 05	.113E + 00	1.338	.775E + 00		
.109E + 02	.879E + 05	.114E + 00	1.332	.782E + 00		
.108E + 02	.871E + 05	.115E + 00	1.326	.798E + 00		
.107E + 02	.863E + 05	.116E + 00	1.318	.815E + 00		
.106E + 02	.855E + 05	.117E + 00	1.308	.834E + 00		
.105E + 02	.847E + 05	.118E + 00	1.296	.853E + 00		
.104E + 02	.839E + 05	.119E + 00	1.281	.880E + 00		
.103E + 02	.831E + 05	.120E + 00	1.272	.930E + 00		
.102E + 02	.823E + 05	.122E + 00	1.272	.101E + 01		
.101E + 02	.815E + 05	.123E + 00	1.301	.109E + 01		
.100E + 02	.806E + 05	.124E + 00	1.358	.116E + 01		
.990E + 01	.798E + 05	.125E + 00	1.432	.121E + 01		
.980E + 01	.790E + 05	.126E + 00	1.503	.124E + 01		
.970E + 01	.782E + 05	.128E + 00	1.599	.125E + 01		
.960E + 01	.774E + 05	.129E + 00	1.705	.125E + 01		
.950E + 01	.766E + 05	.131E + 00	1.802	.122E + 01		
.940E + 01	.758E + 05	.132E + 00	1.877	.117E + 01		
.930E + 01	.750E + 05	.133E + 00	1.947	.112E + 01		
.920E + 01	.742E + 05	.135E + 00	2.009	.106E + 01		
.910E + 01	.734E + 05	.136E + 00	2.040	.986E + 00		
.900E + 01	.726E + 05	.138E + 00	2.047	.914E + 00		
.890E + 01	.718E + 05	.139E + 00	2.045	.851E + 00		
.880E + 01	.710E + 05	.141E + 00	2.049	.807E + 00		
.870E + 01	.702E + 05	.142E + 00	2.061	.778E + 00		
.860E + 01	.694E + 05	.144E + 00	2.079	.742E + 00		
.850E + 01	.686E + 05	.146E + 00	2.089	.692E + 00		
.840E + 01	.678E + 05	.148E + 00	2.078	.635E + 00		
.830E + 01	.669E + 05	.149E + 00	2.044	.577E + 00		

TABLE I *(Continued)*

Orthorhombic Sulfur

eV	cm^{-1}	μm	$n_\perp$	$k_\perp$	n_{supp}	k_{supp}
.820E + 01	.661E + 05	.151E + 00	2.005	.526E + 00		
.810E + 01	.653E + 05	.153E + 00	1.962	.484E + 00		
.800E + 01	.645E + 05	.155E + 00	1.907	.450E + 00		
.790E + 01	.637E + 05	.157E + 00	1.848	.423E + 00		
.780E + 01	.629E + 05	.159E + 00	1.790	.405E + 00		
.770E + 01	.621E + 05	.161E + 00	1.737	.399E + 00		
.760E + 01	.613E + 05	.163E + 00	1.692	.423E + 00		
.750E + 01	.605E + 05	.165E + 00	1.659	.473E + 00		
.740E + 01	.597E + 05	.168E + 00	1.648	.534E + 00		
.730E + 01	.589E + 05	.170E + 00	1.672	.593E + 00		
.720E + 01	.581E + 05	.172E + 00	1.723	.653E + 00		
.710E + 01	.573E + 05	.175E + 00	1.782	.702E + 00		
.700E + 01	.565E + 05	.177E + 00	1.833	.727E + 00		
.690E + 01	.556E + 05	.180E + 00	1.868	.725E + 00		
.680E + 01	.548E + 05	.182E + 00	1.883	.709E + 00		
.670E + 01	.540E + 05	.185E + 00	1.891	.684E + 00		
.660E + 01	.532E + 05	.188E + 00	1.903	.670E + 00		
.650E + 01	.524E + 05	.191E + 00	1.923	.672E + 00		
.640E + 01	.516E + 05	.194E + 00	1.951	.678E + 00		
.630E + 01	.508E + 05	.197E + 00	1.984	.680E + 00		
.620E + 01	.500E + 05	.200E + 00	2.018	.667E + 00		
.610E + 01	.492E + 05	.203E + 00	2.043	.655E + 00		
.600E + 01	.484E + 05	.207E + 00	2.063	.643E + 00		
.590E + 01	.476E + 05	.210E + 00	2.085	.623E + 00		
.580E + 01	.468E + 05	.214E + 00	2.097	.592E + 00		
.570E + 01	.460E + 05	.218E + 00	2.103	.566E + 00		
.560E + 01	.452E + 05	.221E + 00	2.102	.541E + 00		
.550E + 01	.444E + 05	.225E + 00	2.101	.515E + 00		
.540E + 01	.436E + 05	.230E + 00	2.096	.487E + 00		
.530E + 01	.428E + 05	.234E + 00	2.087	.461E + 00		
.520E + 01	.419E + 05	.238E + 00	2.082	.438E + 00		
.510E + 01	.411E + 05	.243E + 00	2.077	.421E + 00		
.500E + 01	.403E + 05	.248E + 00	2.076	.410E + 00		
.490E + 01	.395E + 05	.253E + 00	2.074	.403E + 00		
.480E + 01	.387E + 05	.258E + 00	2.062	.393E + 00		
.470E + 01	.379E + 05	.264E + 00	2.042	.378E + 00		
.460E + 01	.371E + 05	.269E + 00	2.015	.363E + 00		
.450E + 01	.363E + 05	.275E + 00	1.985	.356E + 00		
.440E + 01	.355E + 05	.282E + 00	1.990	.370E + 00		
.430E + 01	.347E + 05	.288E + 00	2.065	.435E + 00		
.420E + 01	.339E + 05	.295E + 00	2.150	.516E + 00		
.410E + 01	.331E + 05	.302E + 00	2.217	.552E + 00		
.400E + 01	.323E + 05	.310E + 00	2.275	.539E + 00		
.390E + 01	.315E + 05	.318E + 00	2.322	.498E + 00		
.380E + 01	.306E + 05	.326E + 00	2.353	.435E + 00		
.370E + 01	.298E + 05	.335E + 00	2.380	.370E + 00		

(continued)

TABLE I *(Continued)*

Orthorhombic Sulfur

eV	cm^{-1}	μm	$n_{\perp}$	$k_{\perp}$	n_{supp}	k_{supp}
.360E + 01	.290E + 05	.344E + 00	2.395	.313E + 00		
.350E + 01	.282E + 05	.354E + 00	2.376	.249E + 00		
.344E + 01	.277E + 05	.360E + 00	2.360	.287E-01		
.340E + 01	.274E + 05	.365E + 00	2.339			
.330E + 01	.266E + 05	.376E + 00	2.293			
.320E + 01	.258E + 05	.387E + 00	2.247			
.315E + 01	.254E + 05	.394E + 00	2.230	.313E-02 [26]		
.292E + 01	.236E + 05	.425E + 00	2.160	.338E-03		
.277E + 01	.223E + 05	.448E + 00	2.130	.356E-04		
.263E + 01	.212E + 05	.471E + 00	2.090	.375E-05		
.248E + 01	.200E + 05	.500E + 00	2.030 [24]	.174E-05 [25]		
.243E + 01	.197E + 05	.510E + 00	2.020	.122E-05		
.238E + 01	.192E + 05	.520E + 00	2.020	.931E-06		
.234E + 01	.189E + 05	.530E + 00	2.010	.844E-06		
.230E + 01	.185E + 05	.540E + 00	2.010	.752E-06		
.225E + 01	.182E + 05	.550E + 00	2.000	.711E-06		
.221E + 01	.179E + 05	.560E + 00	2.000	.668E-06		
.218E + 01	.175E + 05	.570E + 00	1.990	.624E-06		
.214E + 01	.172E + 05	.580E + 00	1.990	.600E-06		
.210E + 01	.169E + 05	.590E + 00	1.980	.587E-06		
.207E + 01	.167E + 05	.600E + 00	1.990			
.191E + 01	.154E + 05	.650E + 00	1.980	.350E-06 [33]		
.177E + 01	.143E + 05	.700E + 00	1.970	.330E-06		
.165E + 01	.133E + 05	.750E + 00	1.970	.330E-06		
.155E + 01	.125E + 05	.800E + 00	1.960	.320E-06		
.146E + 01	.118E + 05	.850E + 00	1.955	.312E-06		
.138E + 01	.111E + 05	.900E + 00	1.950	.305E-06		
.130E + 01	.105E + 05	.950E + 00	1.950	.298E-06		
.124E + 01	.100E + 05	.100E + 01	1.950	.290E-06		
.118E + 01	.952E + 04	.105E + 01	1.947	.294E-06		
.113E + 01	.909E + 04	.110E + 01	1.945	.298E-06		
.108E + 01	.870E + 04	.115E + 01	1.942	.301E-06		
.103E + 01	.833E + 04	.120E + 01	1.940	.305E-06		
.992E + 00	.800E + 04	.125E + 01	1.940	.309E-06		
.954E + 00	.769E + 04	.130E + 01	1.940	.312E-06		
.918E + 00	.741E + 04	.135E + 01	1.940	.316E-06		
.886E + 00	.714E + 04	.140E + 01	1.940	.320E-06		
.855E + 00	.690E + 04	.145E + 01	1.940	.321E-06		
.827E + 00	.667E + 04	.150E + 01	1.940	.322E-06		
.800E + 00	.645E + 04	.155E + 01	1.940	.323E-06		
.775E + 00	.625E + 04	.160E + 01	1.940	.323E-06		
.751E + 00	.606E + 04	.165E + 01	1.940	.324E-06		
.729E + 00	.588E + 04	.170E + 01	1.940	.325E-06		
.709E + 00	.571E + 04	.175E + 01	1.940	.326E-06		
.689E + 00	.556E + 04	.180E + 01	1.940	.327E-06		
.670E + 00	.540E + 04	.185E + 01	1.940	.328E-06		

TABLE I *(Continued)*

Orthorhombic Sulfur

eV	cm^{-1}	μm	$n_\perp$	$k_\perp$	n_{supp}	k_{supp}
.653E + 00	.526E + 04	.190E + 01	1.940	.328E-06		
.636E + 00	.513E + 04	.195E + 01	1.940	.329E-06		
.620E + 00	.500E + 04	.200E + 01	1.926 [10]		2.003 [10]	
.558E + 00	.450E + 04	.222E + 01	1.926		2.003	
.496E + 00	.400E + 04	.250E + 01	1.926		2.003	
.434E + 00	.350E + 04	.286E + 01	1.926		2.003	
.372E + 00	.300E + 04	.333E + 01	1.926		2.003	
.310E + 00	.250E + 04	.400E + 01	1.926		2.003	
.248E + 00	.200E + 04	.500E + 01	1.926		2.003	
.186E + 00	.150E + 04	.667E + 01	1.926		2.003	
.185E + 00	.149E + 04	.671E + 01	1.925		2.003	
.184E + 00	.148E + 04	.676E + 01	1.925		2.003	
.182E + 00	.147E + 04	.680E + 01	1.925		2.003	
.181E + 00	.146E + 04	.685E + 01	1.925		2.003	
.180E + 00	.145E + 04	.690E + 01	1.925		2.003	
.178E + 00	.144E + 04	.694E + 01	1.925		2.003	
.177E + 00	.143E + 04	.699E + 01	1.925		2.003	
.176E + 00	.142E + 04	.704E + 01	1.925		2.003	
.175E + 00	.141E + 04	.709E + 01	1.924		2.003	
.174E + 00	.140E + 04	.714E + 01	1.924	.288E-04 [17]	2.003	
.173E + 00	.140E + 04	.717E + 01	1.924	.303E-04	2.003	
.172E + 00	.139E + 04	.719E + 01	1.924	.315E-04	2.003	
.172E + 00	.138E + 04	.722E + 01	1.924	.329E-04	2.003	
.171E + 00	.138E + 04	.725E + 01	1.924	.356E-04	2.003	
.170E + 00	.138E + 04	.727E + 01	1.924	.374E-04	2.003	
.170E + 00	.137E + 04	.730E + 01	1.924	.396E-04	2.002	
.169E + 00	.136E + 04	.733E + 01	1.924	.429E-04	2.002	
.169E + 00	.136E + 04	.735E + 01	1.924	.465E-04	2.002	
.168E + 00	.136E + 04	.738E + 01	1.924	.554E-04	2.002	
.167E + 00	.135E + 04	.741E + 01	1.924	.660E-04	2.002	
.167E + 00	.134E + 04	.743E + 01	1.923	.790E-04	2.002	
.166E + 00	.134E + 04	.746E + 01	1.923	.926E-04	2.002	
.166E + 00	.134E + 04	.749E + 01	1.923	.108E-03	2.002	
.165E + 00	.133E + 04	.752E + 01	1.923	.127E-03	2.002	
.164E + 00	.132E + 04	.755E + 01	1.922	.148E-03	2.002	
.164E + 00	.132E + 04	.758E + 01	1.921	.166E-03	2.002	
.163E + 00	.132E + 04	.761E + 01	1.921	.192E-03	2.002	
.162E + 00	.131E + 04	.763E + 01	1.920	.211E-03	2.002	
.162E + 00	.130E + 04	.766E + 01	1.921	.217E-03	2.002	
.161E + 00	.130E + 04	.769E + 01	1.921	.218E-03	2.002	
.161E + 00	.130E + 04	.772E + 01	1.921	.216E-03	2.002	
.160E + 00	.129E + 04	.775E + 01	1.922	.213E-03	2.002	
.159E + 00	.128E + 04	.778E + 01	1.923	.206E-03	2.002	
.159E + 00	.128E + 04	.781E + 01	1.923	.184E-03	2.002	
.158E + 00	.128E + 04	.784E + 01	1.924	.158E-03	2.002	
.157E + 00	.127E + 04	.787E + 01	1.926	.132E-03	2.002	

(continued)

TABLE I *(Continued)*

Orthorhombic Sulfur

eV	cm^{-1}	μm	$n_\perp$	$k_\perp$	n_{supp}	k_{supp}
.157E + 00	.126E + 04	.791E + 01	1.926	.101E-03	2.002	
.156E + 00	.126E + 04	.794E + 01	1.927	.771E-04	2.002	
.156E + 00	.126E + 04	.797E + 01	1.927	.624E-04	2.002	
.155E + 00	.125E + 04	.800E + 01	1.927	.457E-04	2.002	
.154E + 00	.124E + 04	.803E + 01	1.927	.329E-04	2.002	
.154E + 00	.124E + 04	.806E + 01	1.927	.258E-04	2.002	
.153E + 00	.124E + 04	.810E + 01	1.927	.187E-04	2.002	
.153E + 00	.123E + 04	.813E + 01	1.927	.154E-04	2.002	
.152E + 00	.122E + 04	.816E + 01	1.927	.132E-04	2.002	
.151E + 00	.122E + 04	.820E + 01	1.927	.110E-04	2.002	
.151E + 00	.122E + 04	.823E + 01	1.927	.979E-05	2.002	
.150E + 00	.121E + 04	.826E + 01	1.927	.815E-05	2.002	
.149E + 00	.120E + 04	.830E + 01	1.927	.734E-05	2.002	
.149E + 00	.120E + 04	.833E + 01	1.927	.610E-05	2.002	
.148E + 00	.120E + 04	.837E + 01	1.927	.584E-05	2.002	
.147E + 00	.119E + 04	.840E + 01	1.927	.506E-05	2.002	
.147E + 00	.118E + 04	.844E + 01	1.927	.508E-05	2.002	
.146E + 00	.118E + 04	.848E + 01	1.927	.429E-05	2.002	
.146E + 00	.118E + 04	.851E + 01	1.927	.433E-05	2.002	
.145E + 00	.117E + 04	.855E + 01	1.927	.435E-05	2.002	
.144E + 00	.116E + 04	.858E + 01	1.927	.357E-05	2.002	
.144E + 00	.116E + 04	.862E + 01	1.927	.277E-05	2.002	
.143E + 00	.116E + 04	.866E + 01	1.927	.343E-05	2.002	
.143E + 00	.115E + 04	.870E + 01	1.927	.279E-05	2.002	
.142E + 00	.114E + 04	.873E + 01	1.927	.317E-05	2.002	
.141E + 00	.114E + 04	.877E + 01	1.927	.302E-05	2.002	
.141E + 00	.114E + 04	.881E + 01	1.927	.367E-05	2.002	
.140E + 00	.113E + 04	.885E + 01	1.927	.319E-05	2.002	
.140E + 00	.112E + 04	.889E + 01	1.927	.431E-05	2.002	
.139E + 00	.112E + 04	.893E + 01	1.927	.449E-05	2.002	
.138E + 00	.112E + 04	.897E + 01	1.927	.456E-05	2.002	
.138E + 00	.111E + 04	.901E + 01	1.927	.482E-05	2.002	
.137E + 00	.110E + 04	.905E + 01	1.927	.464E-05	2.002	
.136E + 00	.110E + 04	.909E + 01	1.927	.547E-05	2.002	
.136E + 00	.110E + 04	.913E + 01	1.927	.690E-05	2.002	
.135E + 00	.109E + 04	.917E + 01	1.927	.812E-05	2.002	
.134E + 00	.108E + 04	.922E + 01	1.927	.872E-05	2.002	
.134E + 00	.108E + 04	.926E + 01	1.927	.102E-04	2.002	
.133E + 00	.108E + 04	.930E + 01	1.927	.109E-04	2.002	
.133E + 00	.107E + 04	.935E + 01	1.927	.133E-04	2.002	
.132E + 00	.106E + 04	.939E + 01	1.927	.152E-04	2.002	
.131E + 00	.106E + 04	.943E + 01	1.927	.175E-04	2.002	
.131E + 00	.106E + 04	.948E + 01	1.927	.207E-04	2.002	
.130E + 00	.105E + 04	.952E + 01	1.927	.214E-04	2.002	
.130E + 00	.104E + 04	.957E + 01	1.927	.233E-04	2.002	
.129E + 00	.104E + 04	.961E + 01	1.927	.234E-04	2.002	

TABLE I *(Continued)*

Orthorhombic Sulfur

eV	cm^{-1}	μm	$n_{\perp}$	$k_{\perp}$	n_{supp}	k_{supp}
.128E + 00	.104E + 04	.966E + 01	1.927	.223E-04	2.002	
.128E + 00	.103E + 04	.971E + 01	1.927	.187E-04	2.002	
.127E + 00	.102E + 04	.976E + 01	1.927	.156E-04	2.002	
.126E + 00	.102E + 04	.980E + 01	1.927	.135E-04	2.002	
.126E + 00	.102E + 04	.985E + 01	1.927	.107E-04	2.001	
.125E + 00	.101E + 04	.990E + 01	1.927	.118E-04	2.001	
.125E + 00	.100E + 04	.995E + 01	1.927	.124E-04	2.001	
.124E + 00	.100E + 04	.100E + 02	1.927	.130E-04	2.001	
.123E + 00	.995E + 03	.101E + 02	1.927	.260E-04	2.001	
.123E + 00	.990E + 03	.101E + 02	1.927	.304E-04	2.001	
.122E + 00	.985E + 03	.101E + 02	1.926	.331E-04	2.001	
.122E + 00	.980E + 03	.102E + 02	1.926	.289E-04	2.001	
.121E + 00	.975E + 03	.103E + 02	1.926	.349E-04	2.001	
.120E + 00	.970E + 03	.103E + 02	1.926	.395E-04	2.001	
.120E + 00	.965E + 03	.104E + 02	1.926	.433E-04	2.000	
.119E + 00	.960E + 03	.104E + 02	1.926	.579E-04	2.000	
.118E + 00	.955E + 03	.105E + 02	1.926	.912E-04	2.000	
.118E + 00	.950E + 03	.105E + 02	1.926	.161E-03	1.999	
.117E + 00	.945E + 03	.106E + 02	1.926	.296E-03	1.998	
.116E + 00	.940E + 03	.106E + 02	1.926	.430E-03	1.998	
.116E + 00	.935E + 03	.107E + 02	1.926	.434E-03	2.000	
.115E + 00	.930E + 03	.108E + 02	1.925	.315E-03	2.001	
.115E + 00	.925E + 03	.108E + 02	1.926	.198E-03	2.002	
.114E + 00	.920E + 03	.109E + 02	1.926	.150E-03	2.003	
.113E + 00	.915E + 03	.109E + 02	1.926	.157E-03	2.003	
.113E + 00	.910E + 03	.110E + 02	1.926	.262E-03	2.002	
.112E + 00	.905E + 03	.111E + 02	1.926	.312E-03	2.001	
.112E + 00	.900E + 03	.111E + 02	1.926	.280E-03	2.001	
.111E + 00	.895E + 03	.112E + 02	1.926	.301E-03	2.002	
.110E + 00	.890E + 03	.112E + 02	1.926	.420E-03	2.003	
.110E + 00	.885E + 03	.113E + 02	1.926	.607E-03	2.001	
.109E + 00	.880E + 03	.114E + 02	1.926	.848E-03	1.999	
.108E + 00	.875E + 03	.114E + 02	1.926	.102E-02	1.997	
.108E + 00	.870E + 03	.115E + 02	1.926	.119E-02	1.996	
.107E + 00	.865E + 03	.116E + 02	1.925	.131E-02	1.995	
.107E + 00	.860E + 03	.116E + 02	1.924	.167E-02	1.994	
.106E + 00	.855E + 03	.117E + 02	1.924	.237E-02	1.995	
.105E + 00	.850E + 03	.118E + 02	1.924	.334E-02	1.995	
.105E + 00	.845E + 03	.118E + 02	1.924	.419E-02	1.997	
.104E + 00	.840E + 03	.119E + 02	1.925	.307E-02	1.998	
.104E + 00	.835E + 03	.120E + 02	1.926	.220E-02	2.000	
.103E + 00	.830E + 03	.121E + 02	1.926	.149E-02	2.003	
.102E + 00	.825E + 03	.121E + 02	1.926	.109E-02	2.004	
.102E + 00	.820E + 03	.122E + 02	1.926	.810E-03	2.005	
.101E + 00	.815E + 03	.123E + 02	1.926	.647E-03	2.005	
.100E + 00	.810E + 03	.124E + 02	1.926	.486E-03	2.005	

(continued)

TABLE I *(Continued)*

Orthorhombic Sulfur

eV	cm^{-1}	μm	$n_\perp$	$k_\perp$	n_{supp}	k_{supp}
.998E-01	.805E + 03	.124E + 02	1.926	.297E-03	2.005	
.992E-01	.800E + 03	.125E + 02	1.926	.200E-03	2.005	
.986E-01	.795E + 03	.126E + 02	1.926	.141E-03	2.005	
.979E-01	.790E + 03	.127E + 02	1.926	.103E-03	2.005	
.973E-01	.785E + 03	.127E + 02	1.926	.716E-04	2.004	
.967E-01	.780E + 03	.128E + 02	1.925	.442E-04	2.004	
.961E-01	.775E + 03	.129E + 02	1.925	.296E-04	2.004	
.955E-01	.770E + 03	.130E + 02	1.925	.257E-04	2.004	
.949E-01	.765E + 03	.131E + 02	1.925	.262E-04	2.004	
.942E-01	.760E + 03	.132E + 02	1.925	.269E-04	2.004	
.936E-01	.755E + 03	.132E + 02	1.924	.344E-04	2.004	
.930E-01	.750E + 03	.133E + 02	1.924	.422E-04	2.004	
.924E-01	.745E + 03	.134E + 02	1.924	.525E-04	2.004	
.918E-01	.740E + 03	.135E + 02	1.924	.695E-04	2.004	
.911E-01	.735E + 03	.136E + 02	1.923	.964E-04	2.004	
.905E-01	.730E + 03	.137E + 02	1.923	.134E-03	2.004	
.899E-01	.725E + 03	.138E + 02	1.923	.201E-03	2.004	
.893E-01	.720E + 03	.139E + 02	1.923	.425E-03	2.004	
.887E-01	.715E + 03	.140E + 02	1.923	.593E-03	2.004	
.880E-01	.710E + 03	.141E + 02	1.922	.612E-03	2.004	
.874E-01	.705E + 03	.142E + 02	1.921	.502E-03	2.004	
.868E-01	.700E + 03	.143E + 02	1.920	.447E-03	2.004	
.862E-01	.695E + 03	.144E + 02	1.919	.306E-03 [19]	2.003	
.856E-01	.690E + 03	.145E + 02	1.919	.364E-03	2.003	
.849E-01	.685E + 03	.146E + 02	1.919	.478E-03	2.003	
.843E-01	.680E + 03	.147E + 02	1.919	.569E-03	2.003	
.837E-01	.675E + 03	.148E + 02	1.918	.671E-03	2.002	
.831E-01	.670E + 03	.149E + 02	1.918	.872E-03	2.001	
.825E-01	.665E + 03	.150E + 02	1.919	.103E-02	2.000	
.818E-01	.660E + 03	.151E + 02	1.920	.111E-02	1.999	
.812E-01	.655E + 03	.153E + 02	1.922	.994E-03	1.998	
.806E-01	.650E + 03	.154E + 02	1.924	.666E-03	1.998	
.800E-01	.645E + 03	.155E + 02	1.927	.440E-03	2.001	
.794E-01	.640E + 03	.156E + 02	1.930	.368E-03	2.004	
.787E-01	.635E + 03	.158E + 02	1.931	.373E-03	2.009	
.781E-01	.630E + 03	.159E + 02	1.933	.443E-03	2.013	
.775E-01	.625E + 03	.160E + 02	1.933	.560E-03	2.013	
.769E-01	.620E + 03	.161E + 02	1.932	.609E-03	2.013	
.763E-01	.615E + 03	.163E + 02	1.931	.524E-03	2.016	
.756E-01	.610E + 03	.164E + 02	1.930	.409E-03	2.019	
.750E-01	.605E + 03	.165E + 02	1.930	.378E-03	2.019	
.744E-01	.600E + 03	.167E + 02	1.930	.401E-03	2.019	
.738E-01	.595E + 03	.168E + 02	1.930	.494E-03	2.016	
.732E-01	.590E + 03	.170E + 02	1.930	.705E-03	2.014	
.725E-01	.585E + 03	.171E + 02	1.929	.801E-03	2.012	
.719E-01	.580E + 03	.172E + 02	1.929	.628E-03	2.010	

TABLE I *(Continued)*

Orthorhombic Sulfur

eV	cm^{-1}	μm	$n_\perp$	$k_\perp$	n_{supp}	k_{supp}
.713E-01	.575E + 03	.174E + 02	1.928	.485E-03	2.009	
.707E-01	.570E + 03	.175E + 02	1.927	.443E-03	2.007	
.701E-01	.565E + 03	.177E + 02	1.926	.476E-03	2.009	
.694E-01	.560E + 03	.179E + 02	1.925	.650E-03	2.010	
.688E-01	.555E + 03	.180E + 02	1.924	.936E-03	2.008	
.682E-01	.550E + 03	.182E + 02	1.924	.113E-02	2.006	
.676E-01	.545E + 03	.184E + 02	1.923	.108E-02	2.007	
.670E-01	.540E + 03	.185E + 02	1.923	.986E-03	2.009	
.663E-01	.535E + 03	.187E + 02	1.923	.907E-03	2.007	
.657E-01	.530E + 03	.189E + 02	1.923	.880E-03	2.004	
.651E-01	.525E + 03	.190E + 02	1.923	.966E-03	2.003	
.645E-01	.520E + 03	.192E + 02	1.923	.107E-02	2.003	
.639E-01	.515E + 03	.194E + 02	1.923	.113E-02	2.003	
.632E-01	.510E + 03	.196E + 02	1.923	.120E-02	2.002	
.626E-01	.505E + 03	.198E + 02	1.923	.125E-02	2.002	
.620E-01	.500E + 03	.200E + 02	1.922	.900E-02 [10]	2.002	.130E-02 [19]
.614E-01	.495E + 03	.202E + 02	1.921	.102E-01	2.001	.133E-02
.608E-01	.490E + 03	.204E + 02	1.920	.114E-01	2.001	.134E-02
.601E-01	.485E + 03	.206E + 02	1.921	.137E-01	1.995	.460E-02 [10]
.595E-01	.480E + 03	.208E + 02	1.921	.159E-01	1.990	.920E-02
.589E-01	.475E + 03	.210E + 02	1.924	.172E-01	1.995	.160E-01
.583E-01	.470E + 03	.213E + 02	1.927	.186E-01	2.000	.229E-01
.576E-01	.465E + 03	.215E + 02	1.931	.176E-01	2.016	.194E-01
.570E-01	.460E + 03	.217E + 02	1.934	.166E-01	2.033	.160E-01
.564E-01	.455E + 03	.220E + 02	1.935	.137E-01	2.027	.800E-02
.558E-01	.450E + 03	.222E + 02	1.936	.108E-01	2.021	.181E-02 [19]
.552E-01	.445E + 03	.225E + 02	1.935	.835E-02	2.016	.205E-02
.545E-01	.440E + 03	.227E + 02	1.934	.590E-02	2.011	.253E-02
.539E-01	.435E + 03	.230E + 02	1.931	.505E-02	2.011	.278E-02
.533E-01	.430E + 03	.233E + 02	1.929	.420E-02	2.011	.263E-02
.527E-01	.425E + 03	.235E + 02	1.928	.470E-02	2.010	.242E-02
.521E-01	.420E + 03	.238E + 02	1.927	.520E-02	2.009	.207E-02
.514E-01	.415E + 03	.241E + 02	1.926	.585E-02	2.009	.173E-02
.508E-01	.410E + 03	.244E + 02	1.925	.650E-02	2.008	.169E-02
.502E-01	.405E + 03	.247E + 02	1.925	.725E-02	2.008	
.496E-01	.400E + 03	.250E + 02	1.925	.800E-02	2.008	
.490E-01	.395E + 03	.253E + 02	1.925	.835E-02	2.008	
.483E-01	.390E + 03	.256E + 02	1.925	.870E-02	2.008	
.477E-01	.385E + 03	.260E + 02	1.924	.915E-02	2.007	
.471E-01	.380E + 03	.263E + 02	1.924	.960E-02	2.007	
.465E-01	.375E + 03	.267E + 02	1.924	.995E-02	2.007	
.459E-01	.370E + 03	.270E + 02	1.924	.103E-01	2.007	
.452E-01	.365E + 03	.274E + 02	1.924	.108E-01	2.007	
.446E-01	.360E + 03	.278E + 02	1.924	.113E-01	2.006	
.440E-01	.355E + 03	.282E + 02	1.923	.117E-01	2.005	
.434E-01	.350E + 03	.286E + 02	1.923	.121E-01	2.004	

(continued)

TABLE I *(Continued)*

Orthorhombic Sulfur

eV	cm^{-1}	μm	$n_\perp$	$k_\perp$	n_{supp}	k_{supp}
.428E-01	.345E + 03	.290E + 02	1.923	.126E-01	2.003	
.421E-01	.340E + 03	.294E + 02	1.923	.132E-01	2.002	
.415E-01	.335E + 03	.299E + 02	1.923	.136E-01	2.000	
.409E-01	.330E + 03	.303E + 02	1.922	.139E-01	1.999	
.403E-01	.325E + 03	.308E + 02	1.921	.146E-01	1.998	
.397E-01	.320E + 03	.312E + 02	1.921	.152E-01	1.998	
.391E-01	.315E + 03	.318E + 02	1.921	.159E-01	1.996	
.384E-01	.310E + 03	.323E + 02	1.920	.167E-01	1.994	
.378E-01	.305E + 03	.328E + 02	1.919	.178E-01	1.993	
.372E-01	.300E + 03	.333E + 02	1.919	.188E-01	1.992	
.366E-01	.295E + 03	.339E + 02	1.918	.201E-01	1.990	
.360E-01	.290E + 03	.345E + 02	1.917	.214E-01	1.988	
.353E-01	.285E + 03	.351E + 02	1.916	.232E-01	1.986	
.347E-01	.280E + 03	.357E + 02	1.915	.250E-01	1.984	
.341E-01	.275E + 03	.364E + 02	1.912	.286E-01	1.980	
.335E-01	.270E + 03	.370E + 02	1.909	.321E-01	1.976	
.329E-01	.265E + 03	.377E + 02	1.906	.422E-01	1.971	.600E-03 [10]
.322E-01	.260E + 03	.385E + 02	1.902	.524E-01	1.966	.120E-02
.316E-01	.255E + 03	.392E + 02	1.911	.657E-01	1.955	.162E-01
.310E-01	.250E + 03	.400E + 02	1.919	.789E-01	1.944	.313E-01
.304E-01	.245E + 03	.408E + 02	1.939	.844E-01	1.969	.458E-01
.298E-01	.240E + 03	.417E + 02	1.958	.900E-01	1.993	.603E-01
.291E-01	.235E + 03	.425E + 02	1.975	.810E-01	2.013	.451E-01
.285E-01	.230E + 03	.435E + 02	1.993	.720E-01	2.033	.299E-01
.279E-01	.225E + 03	.444E + 02	1.997	.587E-01	2.020	.158E-01
.273E-01	.220E + 03	.455E + 02	2.001	.455E-01	2.006	.160E-02
.267E-01	.215E + 03	.465E + 02	1.998	.388E-01	1.991	.145E-02
.260E-01	.210E + 03	.476E + 02	1.995	.322E-01	1.976	.130E-02
.254E-01	.205E + 03	.488E + 02	1.999	.318E-01	1.964	.281E-01
.248E-01	.200E + 03	.500E + 02	2.003	.315E-01	1.951	.550E-01
.242E-01	.195E + 03	.513E + 02	2.016	.233E-01	1.968	.843E-01
.236E-01	.190E + 03	.526E + 02	2.028	.150E-01	1.985	.114E + 00
.229E-01	.185E + 03	.540E + 02	2.037	.750E-02	2.080	0.912E-01
.223E-01	.180E + 03	.556E + 02	2.046		2.176	.686E-01

Cubic Thallium(I) Halides

WILLIAM J. TROPF
Applied Physics Laboratory
The Johns Hopkins University
Laurel, Maryland

Most of the univalent thallium [thallium(I) or thallous] halides have the cubic cesium-chloride structure (space group Pm3m or O_h^5). Exceptions are thallium fluoride and the low-temperature (below 170° C) form of thallium iodide, which are both orthorhombic. Cubic forms of the thallium(I) halides are important optical materials because of their high refractive index, far-infrared transparency, relative insolubility in water, and moderate strength. Thallium halides are miscible in all concentrations; eutectic mixtures are typically used to improve composition homogeneity [1]. The cubic eutectic mixtures of thallium-halide crystals with the designations KRS-5 and KRS-6[1] are especially important. The usual composition of KRS-5 is 54.3 mole-percent TlI and of KRS-6 is 70.2 mole percent TlCl, with the balance being thallium bromide for both. Single crystals of pure and mixed thallous halides are grown by the Stockbarger technique. Table I summarizes the physical properties of thallous-halide crystals.

THALLIUM CHLORIDE I

Thallium chloride has a direct band gap of 3.4 eV [1]. Unlike most materials, the band gap increases with temperature, by about 0.02 eV from 0 to 200 K. Optical constants in the region of fundamental electronic absorption from the band gap to about 20 eV were determined by Hinson and Stevenson [2] and Frandon and LaHaye [3] from Kramers–Krönig analyses of reflection and energy-loss spectra, respectively. Absorption immediately above the band gap has been determined from transmission measurements by Martienssen [4] and Tutihasi [5]. These results are given in Table II.

[1] KRS is an abbreviation for the German term Kristalle aus dem *S*chmeltzfluß, or crystal from the fused melt.

Copyright © 1998 by Academic Press.
All rights of reproduction in any form reserved
ISBN 0-12-544423-0/$25.00.

Strong absorption begins with exciton formation at the band gap followed by interband transitions between the valence band of chlorine and the conduction band of thallium. A thallium-valence-electron plasma oscillation occurs around 7.2 eV and a chlorine $4p$ electron plasma resonance occurs near 12.4 eV.

Smakula [6] reports low-level absorption at the ultraviolet and infrared edges of transparency.

Refractive index in the visible transparent region has been measured by Barth [7] (method unknown, probably index matching), Schröter [8] (minimum-deviation method), and Takahei and Kobayashi [9] (prism refraction method). Barth's data are lower that those from other sources by 0.015 to 0.020. The later two references give dispersion equations only. McCarthy [10] gives interferometrically measured refractive indices in the infrared at 45° C, which have been corrected to room temperature (20° C) by adding 0.006. The dispersion equation of Schröter [8] is

$$\frac{n^2(\lambda)-1}{n^2(\lambda)+2} = 0.47856 + \frac{0.07858}{\lambda^2 - 0.08277} - 0.00881\lambda^2 \tag{1}$$

for the 0.435 to 0.660 μm range, and the dispersion equation of Takahei and Kobayashi [9] is

$$n^2(\lambda) = (2.146)^2 + \frac{1.780}{(\lambda/0.2651)^2 - 1} + \frac{0.0778}{(\lambda/0.3532)^2 - 1} \tag{2}$$

for the 0.390 to 0.635 μm range. Wavelengths are in micrometers in both cases. Table II has the data of Barth and McCarthy and selected calculated values from the dispersion equations.

The temperature change of the refractive index due to electronic absorption, dn_∞/dT, of thallium chloride is determined by Takahei and Kobayashi [9] to be -154×10^{-6}/K over the interval 40 to 300 K and as -194×10^{-6}/K by Shanker and Sundaraj [11] (using $n_\infty = 2.146$). This latter dn/dT value was used to correct the McCarthy data (see earlier discussion) to room temperature.

Low-level infrared absorption of thallium chloride, up to the region of fundamental lattice vibration absorption, was measured by Hidaka *et al.* [12]. They model the absorption coefficient in the 500 to 1100 cm^{-1} region with the equation

$$\beta(\nu) = \beta_0 \exp(-\nu/\nu_0) \tag{3}$$

with $\beta_0 = 6$ cm^{-1}, $\nu_0 = 100$ cm^{-1}, and ν is in wave numbers.

Infrared reflection measurements have been made by Mitsuishi *et al.* [13], Lowndes [14], and Claudel *et al.* [15]. Thallium chloride, like the other cubic thallous halides, has only a single (degenerate) Raman-inactive, infrared-

active optical mode (F_{1u}). Lowndes uses a model of the complex refractive index (n) of the form

$$n^2(\nu) = \epsilon(\nu) = \epsilon_\infty \frac{\nu_{LO}^2 - \nu^2 - i\gamma_{LO}\nu}{\nu_{TO}^2 - \nu^2 - i\gamma_{TO}\nu}, \tag{4}$$

where the transverse and longitudinal frequencies of thallium chloride are $\nu_{TO} = 62\ cm^{-1}$ and $\nu_{LO} = 173\ cm^{-1}$, with widths of $\gamma_{TO} = 7.7\ cm^{-1}$ and $\gamma_{LO} = 20\ cm^{-1}$, and $\epsilon_\infty = 4.60$.

Claudel *et al.* [15] used a classical oscillator model of the form

$$n^2(\nu) = \epsilon(\nu) = \epsilon_\infty + \sum_j \frac{4\pi\rho_j\nu_{TOj}^2}{\nu_{TOj}^2 - \nu^2 - i\gamma_j\nu} \tag{5}$$

with two far-infrared modes to represent their data. Their model parameters are $\rho_1 = 2.20$, $\rho_2 = 0.05$, $\nu_{TO1} = 63\ cm^{-1}$, $\nu_{TO2} = 120\ cm^{-1}$, $\gamma_1 = 0.08$, $\gamma_2 = 0.6$, and $\epsilon_\infty = 4.4$. Both models, which generally agree within 10%, are used to calculate the optical constants given in Table II.

The room-temperature, low-frequency (1–100 kHz) dielectric constant was measured as $\epsilon_0 = 32.7 \pm 0.2$ (or $n = 5.72 \pm 0.02$) by Lowndes [16], $\epsilon_0 = 32.4 \pm 0.1$ (or $n = 5.70 \pm 0.01$) by Lowndes and Martin [17], and $\epsilon_0 = 32.3 \pm 0.2$ (or $n = 5.68 \pm 0.02$) by Samara [18] using capacitance techniques. The low-frequency dielectric constant has a large, negative temperature dependence: $d\epsilon_0/dT = -0.012\ K^{-1}$ [16–18] and $d\epsilon_0/dT = -0.01216\ K^{-1}$ [11] (or $dn/dT = -0.0011\ K^{-1}$).

Table II gives all the optical-constant data for thallium chloride and Fig. 1 shows the data graphically.

THALLIUM BROMIDE II

Thallium bromide has a direct band gap of 3.0 eV [1]. Like thallium chloride, the band gap increases with temperature, by about 0.02 eV from 0 to 200 K. Optical constants in the region of fundamental electronic absorption from the band gap to about 20 eV were determined by Hinson and Stevenson [2] and Frandon and LaHaye [3] from a Kramers–Kronig analysis of reflection and energy-loss spectra, respectively. These results are given in Table III.

Strong absorption begins with exciton formation at the band gap followed by interband transitions between the valence band of bromine and the conduction band of thallium. A thallium-valence-electron plasma oscillation occurs around 6.7 eV and bromine $4p$ electron plasma resonance occurs near 11.8 eV.

Smakula [6] reports low-level absorption at the ultraviolet and infrared edges of transparency.

Refractive index in the visible transparent region has been measured by Barth [7], Schröter [8], and Takahei and Kobayashi [9]. Barth's data is lower that the other sources by 0.020. The latter two references give dispersion equations only. McCarthy [10] gives refractive indices in the infrared at 45° C which have been corrected to room temperature (20° C) by adding 0.006. The dispersion equation of Schröter [8] is

$$\frac{n^2(\lambda) - 1}{n^2(\lambda) + 2} = 0.48484 + \frac{0.10279}{\lambda^2 - 0.090000} - 0.0047896\lambda^2 \qquad (6)$$

for the 0.435 to 0.660 μm range, and the dispersion equation of Takahei and Kobayashi [9] is

$$n^2(\lambda) = (2.273)^2 + \frac{2.582}{(\lambda/0.2736)^2 - 1} + \frac{0.0789}{(\lambda/0.3986)^2 - 1} \qquad (7)$$

for the 0.390 to 0.635 μm range. Wavelengths are in micrometers in both cases. Table III has the data of Barth and McCarthy and selected calculated values from the dispersion equations.

The temperature change of the refractive index due to electronic absorption, dn_∞/dT, of thallium bromide is determined by Takahei and Kobayashi [9] to be -180×10^{-6}/K over the interval 40 to 300 K and as -229×10^{-6}/K by Shanker and Sundaraj [11] (using $n_\infty = 2.27$). This latter dn/dT value was used to correct the McCarthy data (see above) to room temperature.

Infrared reflection measurements have been made by Mitsuishi *et al.* [13], Lowndes [14], and Claudel *et al.* [15]. Lowndes uses the model of the complex refractive index (n) given by Eq. (4) with the transverse and longitudinal frequencies of thallium bromine are $\nu_{TO} = 47$ cm^{-1} and $\nu_{LO} = 116$ cm^{-1}, with widths are $\gamma_{TO} = 4.0$ cm^{-1} and $\gamma_{LO} = 17.5$ cm^{-1}, and $\epsilon_\infty = 5.15$. Claudel *et al.* [15] uses the classical oscillator model of Eq. (5) with two far-infrared modes to represent their data. Their model parameters are $\rho_1 = 1.98$, $\rho_2 = 0.02$, $\nu_{TO1} = 47.5$ cm^{-1}, $\nu_{TO2} = 137.5$ cm^{-1}, $\gamma_1 = 0.10$, $\gamma_2 = 0.5$, and $\epsilon_\infty = 5.4$. Both models give similar results, with agreement typically 20%. The Lowndes model is used to calculate the optical constants given in Table III.

Pai *et al.* [19] measured the room-temperature complex dielectric constant of thallium bromide between 22 and 190 cm^{-1} using dispersive Fourier transform spectroscopy. These data are also given in Table III.

The room-temperature, low-frequency (1–100 kHz) dielectric constant of thallium bromide was measured as $\epsilon_0 = 30.6 \pm 0.2$ (or $n = 5.53 \pm 0.01$) by Lowndes [16] and Lowndes and Martin [17], and $\epsilon_0 = 30.0 \pm 0.2$ (or

$n = 5.48 \pm 0.02$) by Samara [18] using capacitance techniques. The low-frequency dielectric constant has a large, negative temperature dependence: $d\epsilon_0/dT = -0.013\ K^{-1}$ [16, 17], $d\epsilon_0/dT = -0.011\ K^{-1}$ [18], and $d\epsilon_0/dT = -0.01295\ K^{-1}$ [11] (or $dn/dT \approx -0.0012\ K^{-1}$).

Table III gives all the optical constant data for thallium bromide and Fig. 2 shows the data graphically.

THALLIUM IODIDE III

Little is known about the optical properties of thallium iodide. Thallium iodide is orthorhombic at room temperature and 1 atmosphere (see Table I) and does not revert to the cubic (CsCl) structure until temperature is raised to 170° C or pressure to 5000 atm. The orthorhombic form (space group Cmcm or D_{2h}^{17}) has four molecules per unit cell. The thallium and iodide atoms both occupy 4(c) sites (C_{2v} symmetry). The band gap of thallium iodide is 2.7 eV (orthorhombic structure) or about 2.1–2.2 eV for the cubic structure (extrapolated from pressure-dependent absorption measurements [20]).

Optical constants in the region of fundamental electronic absorption from the band gap to about 22 eV were determined by Frandon and LaHaye [3] from a Kramers–Kronig analysis of an energy-loss spectrum of a thin film of thallium iodide measured in transmission. The authors state that the measured crystals (TlCl, TlBr, and TlI) all have cubic symmetry. Most likely the thallium iodide film is orthorhombic (optical constants are consistent with the band gap) and polycrystalline. These results are given in Table IV.

Barth [7] measured the refractive index (method unknown) of metastable cubic thallium iodide at room temperature by quickly cooling and carefully handling the crystals. (Note that comparison of Barth's measurements of the refractive index of TlCl and TlBr, made at the same time, are lower than those of other researchers; see above). His values are given in Table IV.

Unpolarized infrared reflection measurements of orthorhombic TlI were made by Claudel *et al.* [15], probably with a polycrystalline sample. They used the classical-oscillator model of Eq. (5) with two far-infrared modes to represent their data. The model parameters are $\rho_1 = 1.12$, $\rho_2 = 0.05$, $\nu_{TO1} = 51\ cm^{-1}$, $\nu_{TO2} = 90\ cm^{-1}$, $\gamma_1 = 0.02$, $\gamma_2 = 0.5$, and $\epsilon_\infty = 6.1$. These results indicate that the optical modes of different crystallographic directions are very similar. This model was used to provide the far-infrared optical constants in Table IV.

Samara [18] measured the room-temperature, low-frequency (10 kHz) dielectric constant of polycrystalline orthorhombic thallium iodide as $\epsilon_0 = 21.2 \pm 0.2$ (or $n = 4.60 \pm 0.02$) and extrapolated the dielectric constant of cubic thallium iodide as $\epsilon_0 = 29.6 \pm 0.5$ (or $n = 5.44 \pm 0.05$) from its

pressure variation using a capacitance technique. Von Hippel [21] gives $\epsilon_0 = 21.8$ (1 kHz–10 MHz) for (orthorhombic) TlI at 25° C and $\epsilon_0 = 37.3$ (10 MHz) for (cubic) TlI at 193° C. Note that the orthorhombic values agree well with the value of 20.9 obtained from the model of Claudel *et al.* [15].

Table IV gives all the optical-constant data for thallium iodide, and Fig. 3 shows the data graphically.

IV MIXED THALLOUS HALIDES KRS-5 AND KRS-6

The mixed crystals KRS-5 and KRS-6 are less studied than TlCl and TlBr, but more optically important. Optical properties of these materials were originally studied by Barth [7], and later they were developed in Germany during World War II (see Hettner and Leisegang [22]). Further study of these mixtures improved optical uniformity by accurately finding the eutectic compositions [23]. The actual composition of some measured materials given later may differ from the eutectic mixture and have different optical constants.

Takahei and Kobayashi [9] measured low-temperature reflectance of pure and mixed crystals of TlCl–TlBr and derived dispersion equations for several mixtures at different temperatures. Their results give the band gap of KRS-6 as 3.25 eV. Absorption-edge measurements of Smakula [6] and room-temperature reflectance measurements of Tropf [24] indicate a band gap of ≈2.45–2.50 eV for KRS-5.

Tropf [24] measured the absorption coefficient of KRS-5 at the visible edge of transparency between 20 and 209° C and fit his data to an Urbach-rule model of the form

$$\beta(\nu, T) = \beta_0 \exp\left(-\sigma_s hc(\nu_g - \nu)/k_B T\right), \tag{8}$$

where $\beta(\nu,T)$ is the absorption coefficient as a function of wave number (ν) and temperature (T). Fixed quantities are Planck's constant (h), Boltzmann's constant (k_B), and the speed of light (c). Material-dependent parameters are the slope parameter, $\sigma_s = 0.9418$, a constant over the measured temperature range; $\beta_0 = 1.8063\ \text{cm}^{-1}$; and $\nu_g = 17{,}474\ \text{cm}^{-1}$.

The only measurement of room-temperature visible absorption of KRS-6 are the absorption-edge transmission and laser-calorimetry measurements of Mori and Izawa [25]. Their measurements are included in Table VI and were fitted to the sum of two exponential absorption edges with absorption coefficient, $\beta(\nu)$, each having the form

$$\beta(\nu) = \beta_0 \exp(\nu/\nu_0), \tag{9}$$

where $\beta_0 = 1 \times 10^{-34}\ \text{cm}^{-1}$ and $\nu_0 = 301.3\ \text{cm}^{-1}$ for the fundamental absorption-edge component and $\beta_0 = 5.62 \times 10^{-6}\ \text{cm}^{-1}$ and $\nu_0 = 2258.3$

cm^{-1} for the weak-absorption-tail component. These two components combine to model the absorption edge from 15,000 to 25,000 cm^{-1}, with fundamental absorption dominating above 23,000 cm^{-1}. (Extrapolated values to 26,600 cm^{-1} are given in Table VI.)

The KRS-5 Urbach-edge model of Tropf [24], Eq. (8), gives room-temperature (295 K) constants $\beta_0 = 2.5 \times 10^{-35}$ cm^{-1} and $\nu_0 = 217.7$ cm^{-1}, when recast into the form of Eq. (9). These values were used to calculate the imaginary part of the refractive index of KRS-5 at the electronic absorption edge between 17,000 and 19,000 cm^{-1} (2.10 to 2.35 eV).

The refractive index of KRS-5 was measured using the minimium-deviation method by Hettner and Leisegang [22] for a composition 56 mol % TlI, by Tilton *et al.* [26] for compositions of 58 and 58.3 mol % TlI, and at three near-ambient temperatures by Rodney and Malitson [27] for a composition of 54.3 mol % thallium iodide. Barth [7] also provided data for several TlBr-TlI mixtures including 50 and 60 mol % thallium iodide. Rodney and Malitson's measurements at 25° C are given in Table V. Tilton *et al.* provide a dispersion equation and Rodney and Malitson give a five-term Sellmeier equation for their data. Tropf [24] developed this equally accurate three-term Sellmeier dispersion equation based on the Rodney and Malitson 25° C measurements (0.57 to 39.4 μm):

$$n^2(\lambda) - 1 = \frac{3.7442390\lambda^2}{\lambda^2 - (0.2079603)^2} + \frac{0.9189162\lambda^2}{\lambda^2 - (0.3765643)^2} + \frac{12.5444602\lambda^2}{\lambda^2 - (165.6525518)^2}. \tag{10}$$

Wavelength (λ) is in micrometers. He also gives three-term Sellmeier models for their data at 19 and 31° C, as well as a less-accurate, temperature-dependent Sellmeier model.

The refractive index of KRS-6 was measured using the minimum-deviation method by Hettner and Leisegang [22] for a highly noneutectic composition, 60 mol % TlCl (which will have a higher index) and by Takahei and Kobayashi [9] for a composition with 68 mol % TlCl. The dispersion equation of Takahei and Kobayashi is

$$n^2(\lambda) = (2.186)^2 + \frac{1.877}{(\lambda/0.2828)^2 - 1} + \frac{0.0296}{(\lambda/0.3748)^2 - 1} \tag{11}$$

for the 0.390 to 0.635 μm range; wavelengths are in micrometers. The data of Hettner and Leisegang and calculations from the visible-wavelength dispersion equation of Takahei and Kobayashi are given in Table IV.

Barth [7] used a Lorentz–Lorenz molar-refractivity formulation to estimate the visible refractive index of mixed TlBr–TlI crystals of various com-

positions. Craig [28] later refined Barth's calculation and obtained a good fit to his data.

Rodney and Malitson [27] give dn/dT for KRS-5 as -254×10^{-6}/K at 0.577 μm, decreasing to -233×10^{-6}/K at 11.025 μm, and to -154×10^{-6}/K at 39.38 μm. Tropf [24] measured an average dn/dT for KRS-5 as -232×10^{-6}/K over the 700–1000 cm^{-1} (10–14.3 μm) spectral range and the temperature interval of 22 to 209° C, consistent with the Rodney and Malitson results. The temperature change of the refractive index due to electronic absorption, dn_∞/dT, of KRS-6 (68 mol % TlCl) was determined by Takahei and Kobayashi [9] to be -160×10^{-6}/K over the interval 40 to 300 K. Afanas'ev and Nosov [29] give $dn/dT = -254 \times 10^{-6}$/K for KRS-5 and $dn/dT = -234 \times 10^{-6}$/K for KRS-6 at 0.633 μm.

Absorption of KRS-5 and KRS-6 in the transparent region has been extensively studied, primarily for infrared fibers. Available data includes the laser-calorimetry measurements of Harrington *et al.* [30] on crystalline KRS-5 at HF and DF laser wavelengths; transmission measurements on long polycrystalline KRS-5 fibers at 10.6 μm by Harrington and Standlee [31]; laser calorimetry at 1, 5, and 10 μm by Belousov *et al.* [32] on crystalline KRS-5 and KRS-6; carbon-monoxide laser calorimetry measurements of Nosov *et al.* [33] on crystalline KRS-5 and KRS-6; and differential-spectrophotometry measurements of Hidaka *et al.* [12] on crystalline KRS-5. This last set of measurements covers a broad spectral range (500–1150 cm^{-1}) and is included in Table V. Typical measured infrared absorption coefficients in the transparent range of these materials are on the order of 10^{-3} to 10^{-5}/cm.

Absorption at the infrared edge of transparency was measured by Smakula [6] and by Dianov *et al.* [34] for both KRS-5 and KRS-6, and for KRS-5 alone by Hidaka *et al.* [12] and by Tropf [24]. The infrared absorption coefficient, $\beta(\nu)$, can also be modeled as a exponential edge using Eq. (3). For KRS-5 at room temperature, Hidaka *et al.* give $\beta_0 = 5400$ and $\nu_0 = 25$ cm^{-1}; Dianov *et al.* give $\beta_0 = 20700$ and $\nu_0 = 25$ cm^{-1}; and Tropf gives $\beta_0 = 7700$ and $\nu_0 = 27.1$ cm^{-1}. For KRS-6, Dianov *et al.* give $\beta_0 = 10810$ and $\nu_0 = 43$ cm^{-1}. Values of the imaginary refractive index at the infrared absorption edge in Tables IId and IIe come from Tropf [24] and Dianov *et al.* [34] for KRS-5 and KRS-6, respectively. (Note: Dianov *et al.* also gives model parameters for the visible absorption edges of KRS-5 and KRS-6. These values appear to be in error.)

There is little data on optical constants of KRS-5 and KRS-6 in the region of fundamental optical absorption. The reflectance measurements of Mitsuishi *et al.* [13] were fit to a the dispersion model of Eq. (4), and the following parameters provided a good fit: for KRS-5, $\nu_{TO} = 43$ cm^{-1}, $\nu_{LO} = 103$ cm^{-1}, $\gamma_{TO} = 7$ cm^{-1}, $\gamma_{LO} = 25$ cm^{-1}, and $\epsilon_\infty = 5.66$; for KRS-6, $\nu_{TO} = 58$ cm^{-1}, $\nu_{LO} = 149$ cm^{-1}, $\gamma_{TO} = 8$ cm^{-1}, $\gamma_{LO} = 35$ cm^{-1}, and $\epsilon_\infty = 4.85$. These values were used to calculate far-infrared optical constants given in Tables V and VI.

The room-temperature, low-frequency (measurement method unknown, accuracy of 2% or better) dielectric constants of KRS-5 (58 mol % TlI) and KRS-6 (60 mol % TlCl[2]) are given by von Hippel [21] as $\epsilon_0 = 32.5$ (or $n = 5.70$) for frequencies from 10 kHz to 10 MHz and $\epsilon_0 = 31.8$ (or $n = 5.64$) at 100 kHz, respectively. Von Hippel also gives $d\epsilon_0/dT = -0.0091\ K^{-1}$ for KRS-5 at 1 MHz and $d\epsilon_0/dT = -0.0075\ K^{-1}$ for KRS-6 at 10 MHz.

Tables V and VI give all the optical constant data for KRS-5 and KRS-6, respectively. Figures 4 and 5 shows the same data graphically.

REFERENCES

1. C. W. Jurgensen and H. G. Drickamer, High-pressure studies of the absorption edges of three thallous halides. *Phys. Rev. B* **30**, 7202–7205 (1984).
2. D. C. Hinson and J. R. Stevenson, Optical constants of TlCl and TlBr with a comparison of the Kramers-Krönig and "two-angle" methods of data analysis. *Phys. Rev.* **159,** 711–716 (1967).
3. J. Frandon and B. LaHaye, Electron loss characteristics of TlCl, TlBr, TlI and calculated optical constants from 3 to 25 eV. *J. Phys (Paris)* **33**, 229–235 (1972).
4. W. Martienssen, The optical absorption edge in ionic crystals. *J. Phys. Chem. Solids* **8**, 294–296 (1959).
5. S. Tutihasi, Ultraviolet absorption in thallous halides. *J. Phys. Chem. Solids* **12**, 344–348 (1960).
6. A. Smakula, Synthetic crystals and polarizing materials. *Opt. Acta* **9**, 205–222 (1962).
7. T. F. W. Barth, Optical properties of mixed crystals. *Am. J. Sci.* **219**, 135–146 (1930); also see T. Barth, Some new immersion melts of high refraction. *Am. Mineral.* **14**, 358–361 (1929).
8. H. Schröter, On the refractive indices of some heavy-metal halides in the visible and calculation of interpolation formulas for dispersion. *Z. Phys.* **67**, 24–36 (1931).
9. K. Takahei and K. Kobayashi, Reflectivity spectra of TlCl-TlBr mixed crystals, *J. Phys. Soc. Jpn.* **43**, 891–898 (1977).
10. D. E. McCarthy, Refractive index measurements of TlBr and TlCl in the IR. *Appl. Opt.* **4**, 878–879 (1965).
11. J. Shanker and R. Sundaraj, Dielectric and anharmonic behavior of silver halides, thallous halides, alkaline earth fluorides, and lead fluoride crystals. *Phys. Status Solidi B* **115**, 67–74 (1968).
12. T. Hidaka, T. Morikawa, and J. Shimada, Spectroscopic small loss measurements on infrared transparent materials. *Appl. Opt.* **19**, 3763–3766 (1980).
13. A. Mitsuishi, Y. Yamada, and H. Yoshinaga, Reflection measurements on reststrahlen crystals in the far-infrared region. *J. Opt. Soc. Am.* **52**, 14–16 (1962).
14. R. P. Lowndes, Anharmonicity in the silver and thallium halides: Far-infrared dielectric response. *Phys. Rev. B* **6**, 1490–1498 (1972).
15. J. Claudel, A. Handi, P. Strimer, and P. Vergnat, Absorption spectra and reflection of the thallium halides in the far infrared at low temperatures. *J. Phys. Chem. Solids* **29**, 1539–1544 (1968).
16. R. P. Lowndes, Anharmonicity in the silver and thallium halides: Low-frequency dielectric response. *Phys. Rev. B* **6**, 4667–4674 (1972).
17. R. P. Lowndes and D. H. Martin, Dielectric constants of ionic crystals and their variations with temperature and pressure. *Proc. R. Soc. (London) A* **316**, 351–375 (1970).

[2] Composition of 60% TlBr, 40% TlCl stated; this is undoubtedly an error. Molar percentage assumed corresponding to the composition of this era.

18. G. A. Samara, Temperature and pressure dependence of the dielectric constants of the thallous halides. *Phys. Rev.* **165**, 959–969 (1968).
19. K. F. Pai, T. J. Parker, N. E. Tornberg, and R. P. Lowndes, Determination of the complex refractive indices of solids in the far-infrared by dispersive fourier transform spectroscopy—II. Pseudo-displacement ferroelectrics. *Infrared Phys.* **18**, 327–336 (1978).
20. J. C. Zahner and H. G. Drickamer, The effect of pressure on the absorption edge in heavy-metal halides. *J. Phys. Chem. Solids* **11**, 92–96 (1959).
21. A. R. von Hippel, ed., "Dielectric Materials and Applications." Wiley, New York, 1954.
22. G. Hettner and G. Leisegang, Dispersion of mixed crystals TlBr-TlI (KRS 5) and TlCl-TlBr (KRS 6) in the infrared. *Optik* **3**, 305–314 (1948).
23. A. Smakula, J. Kalnajs, and V. Sils, Inhomogeneity of thallium halide mixed crystals and its elimination. *J. Opt. Soc. Am.* **43**, 698–701 (1953).
24. A. Z. Tropf, M. E. Thomas, and W. J. Tropf, Optical properties of KRS-5. To be published in *Proc. SPIE* **3060** (1997).
25. H. Mori and T. Izawa, A new loss mechanism in ultralow loss optical fiber materials. *J. Appl. Phys.* **51**, 2270–2271 (1980).
26. L. W. Tilton, K. Plyler, and R. E. Stephens, Refractive indices of thallium bromide-iodide crystals for visible and infrared radiant energy. *J. Res. Natl. Bur. Stand. (U.S.)* **43**, 81–86 (1949).
27. W. S. Rodney, and I. H. Malitson, Refraction and dispersion of thallium bromide iodide. *J. Opt. Soc. Am.* **46**, 956–961 (1956).
28. H. Craig, A simple model for refractive indices in mixed crystals and glasses. *Geochim. Comochim. Acta* **56**, 3001–3006 (1992).
29. I. I. Afanas'ev and V. B. Nosov, Temperature increments of the refractive indices of certain single crystals. *Sov. J. Opt. Technol.* **46**, 281–283 (1979).
30. J. A. Harrington, D. A. Gregory, and W. F. Otto, Jr., Infrared absorption in chemical laser window materials. *Appl. Opt.* **15**, 1953–1959 (1976).
31. J. A. Harrington and A. G. Standlee, Attenuation at 10.6 mm in loaded and unloaded polycrystalline KRS-5 fibers. *Appl. Opt.* **22**, 3073–3078 (1983).
32. A. P. Belousov, E. M. Dianov, I. S. Lisitskii, T. M. Nesterova, V. G. Plotnichenko, and V. K. Sysoev, Single crystals of thallium halides with optical losses below 10 dB/km. *Sov. J. Quantum Electron.* **12**, 496–497 (1982).
33. V. B. Nosov, G. T. Petrovskii, M. V. Serzhantova, and A. V. Shatilov, Calorimetric measurements of the volume and surface absorption of IR materials in the 5-6 mm spectral region. *Sov. J. Opt. Technol.* **56**, 238–240 (1989).
34. E. M. Dianov, N. S. Lisitskii, V. G. Plotnichenko, V. B. Sulimov, and V. K. Sysoev, Evaluation of minimum possible optical losses in thallium halides. *Opt. Spectrosc.* **56**, 281–283 (1984); also see E. M. Dianov, N. S. Lisitsky, V. G. Plotnichenko, V. K. Sysoev, V. B. Sulimov, and L. N. Butvina, Evaluation of optical loss minima in thallium halide crystals. *Fiber Integr. Opt.* **5**, 125–133 (1985). (Note error in Table 1 of the latter reference.)

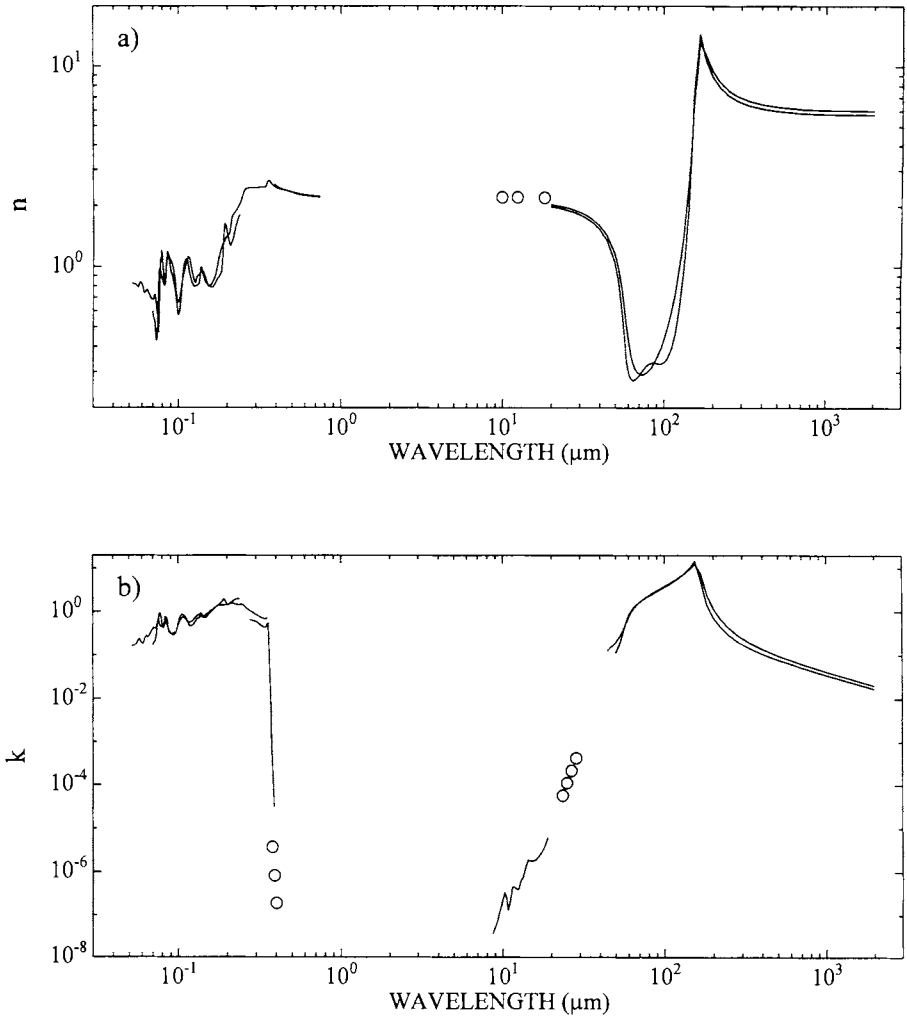

Fig. 1. (a) Log–log plot of the index of refraction n versus wavelength in micrometers for thallium(I) chloride. (b) Log–log plot of the extinction coefficient k versus wavelength in micrometers for thallium(I) chloride. Lines are data sets of many points; scattered data are indicated by circles.

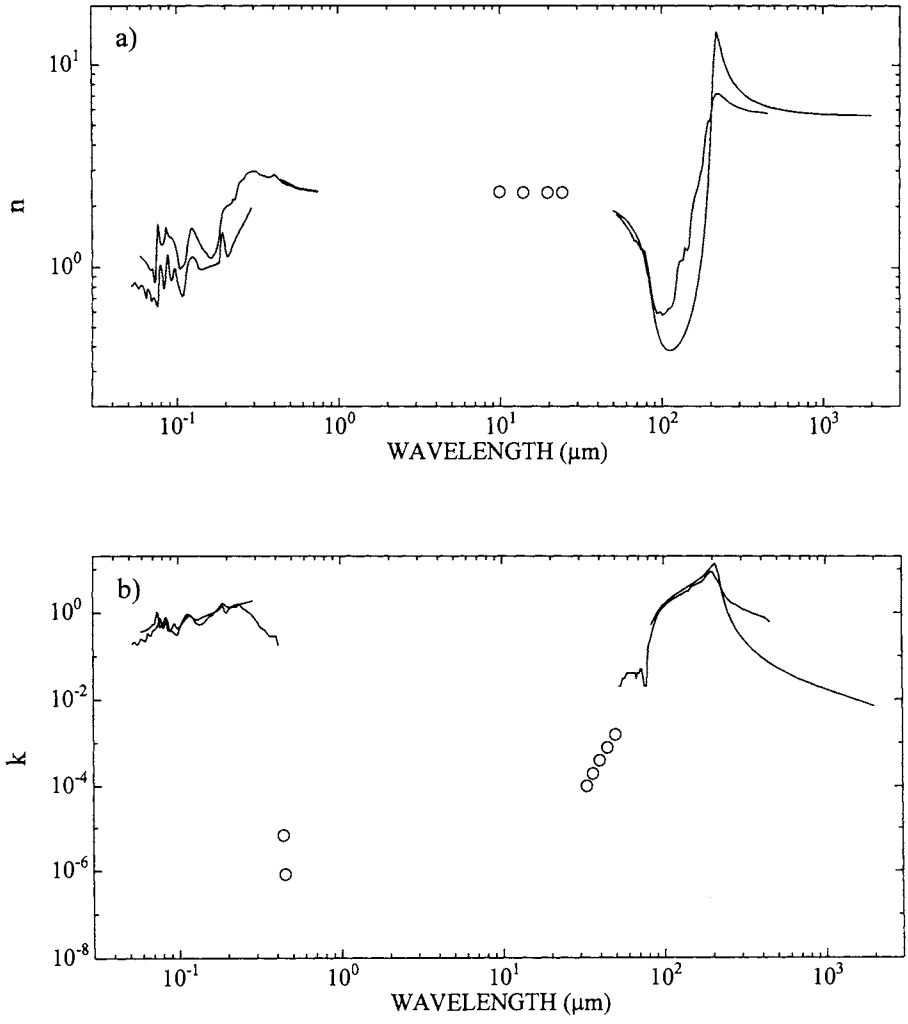

Fig. 2. (a) Log–log plot of the index of refraction n versus wavelength in micrometers for thallium(I) bromide. (b) Log–log plot of the extinction coefficient k versus wavelength in micrometers for thallium(I) bromide. Lines are data sets of many points; scattered data are indicated by circles.

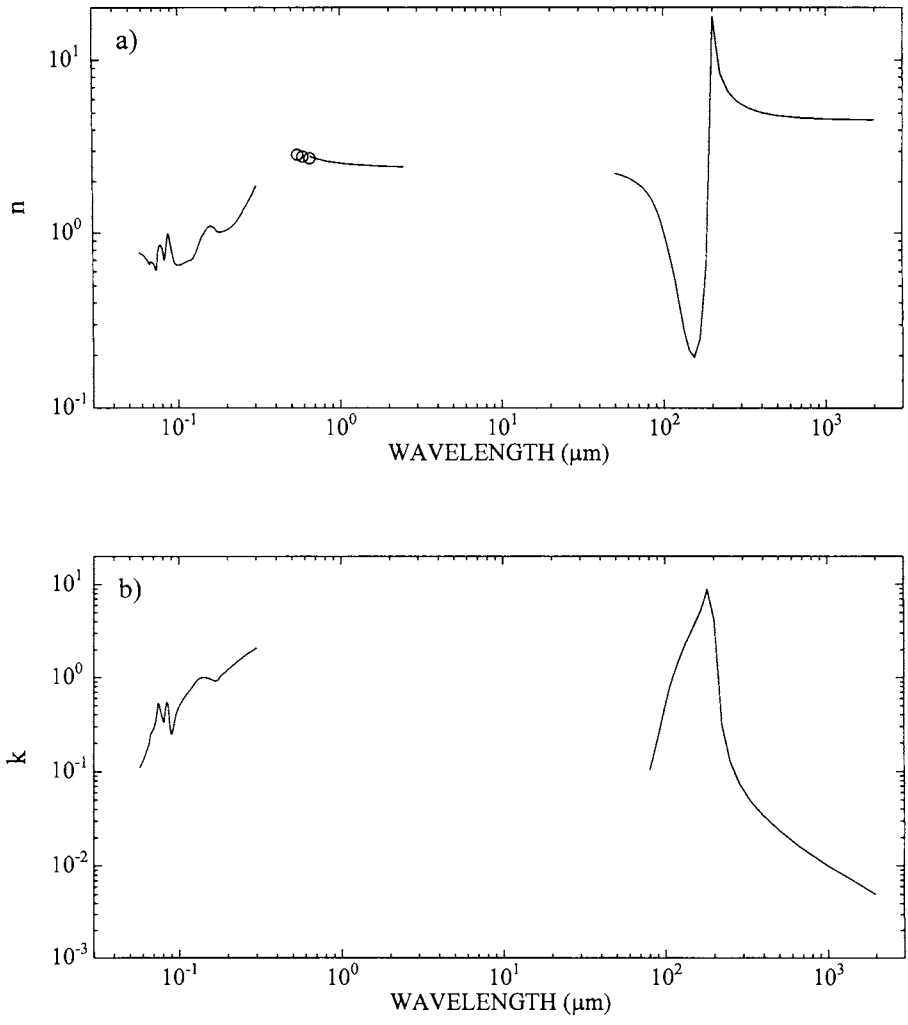

Fig. 3. (a) Log–log plot of the index of refraction n versus wavelength in micrometers for thallium(I) iodide. (b) Log–log plot of the extinction coefficient k versus wavelength in micrometers for thallium(I) iodide. Lines are data sets of many points; scattered data are indicated by circles.

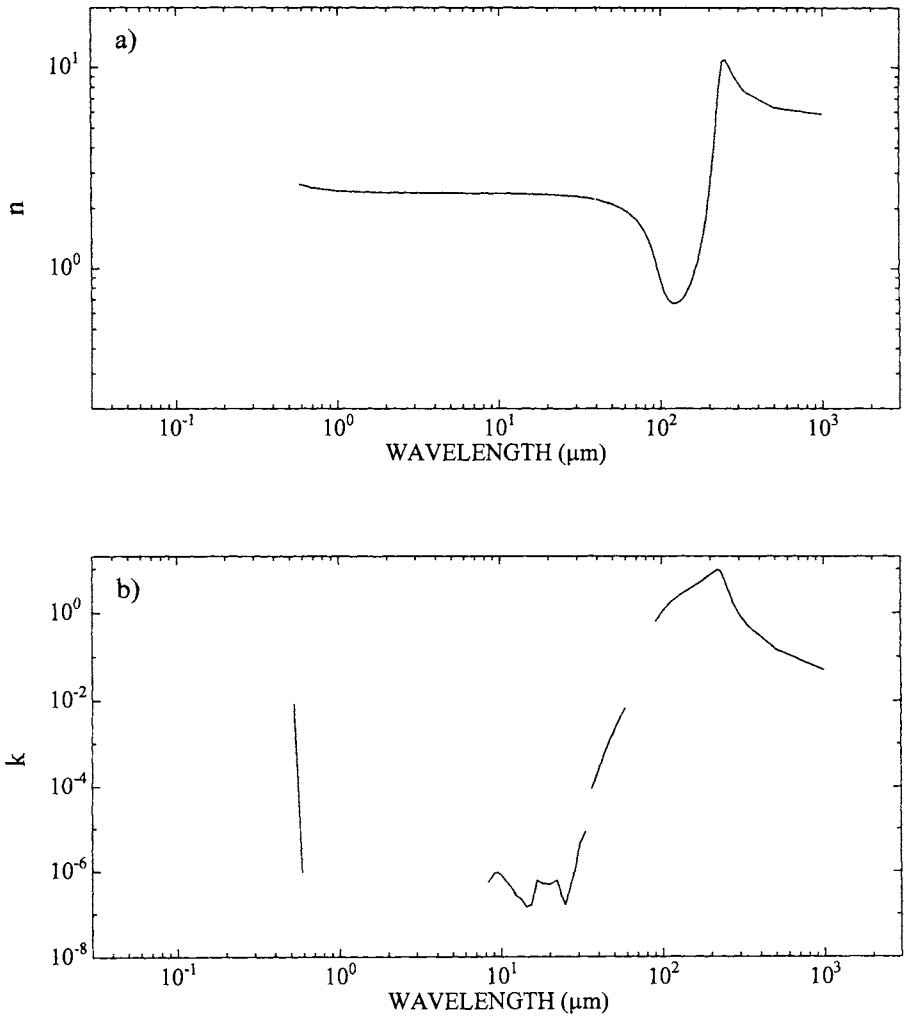

Fig. 4. (a) Log–log plot of the index of refraction n versus wavelength in micrometers for KRS-5. (b) Log–log plot of the extinction coefficient k versus wavelength in micrometers for KRS-5.

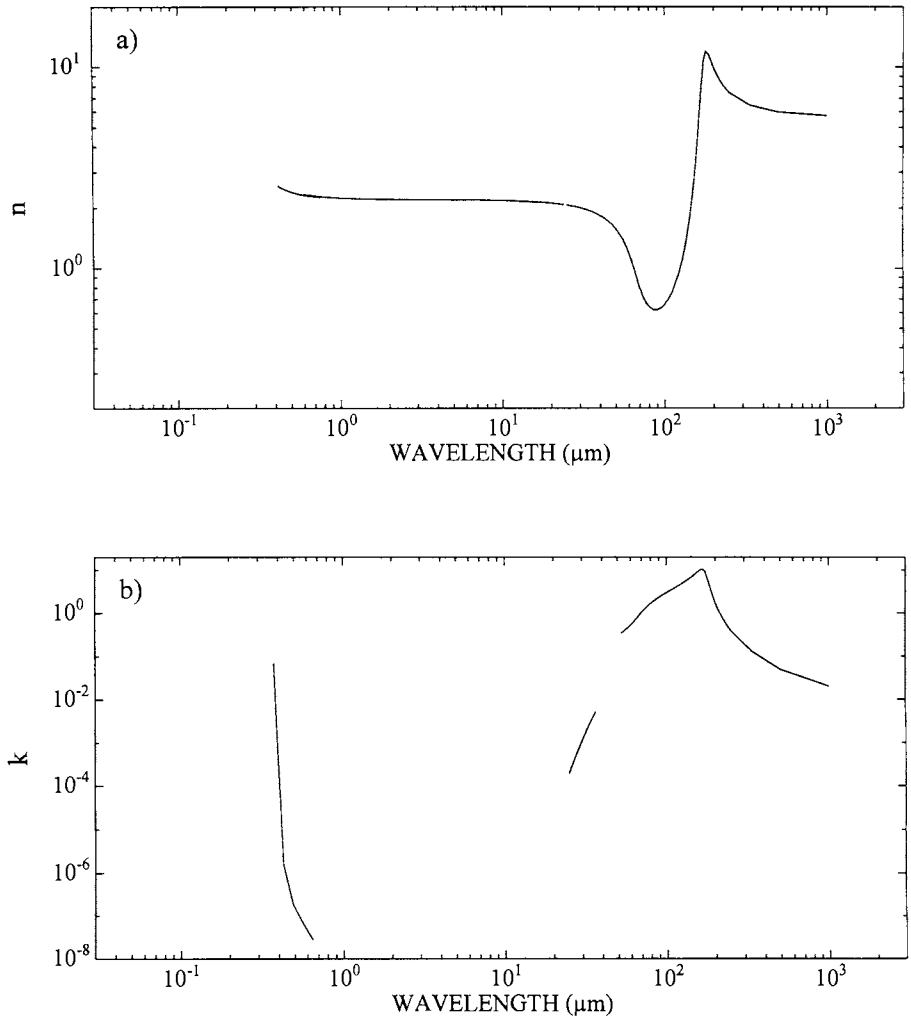

Fig. 5. (a) Log–log plot of the index of refraction n versus wavelength in micrometers for KRS-6. (b) Log–log plot of the extinction coefficient k versus wavelength in micrometers for KRS-6.

TABLE 1

Properties of Pure and Mixed Thallium(I) Halides

Material	Crystal Structure and Space Group	Lattice Constants (Å)	Density (g/cm^3)	Melting Point (°C)
TlF	Orthorhombic: Fmmm	$a = 5.495$; $b = 6.080$; $c = 5.180$	8.573	326
TlCl	Cubic: Pm3m	$a = 3.84247$	7.020	430.2
TlCl–TlBr	Cubic: Pm3m	$a = 3.88946$	7.142	422.9
TlBr	Cubic: Pm3m	$a = 3.98588$	7.455	460.5
TlBr–TlI	Cubic: Pm3m	$a = 4.11826$	7.365	413.9
TlI	Cubic: Pm3m	$a = 4.2099$[a]	7.373	441.8
TlI	Orthorhombic: Cmcm	$a = 4.582$; $b = 12.92$; $c = 5.251$	7.079	~170[b]

[a] extrapolated to room temperature and pressure.
[b] Phase change from orthorhombic to cubic.

TABLE II

Values of *n* and *k* for Thallium Chloride from Various References

eV	cm^{-1}	μm	*n*	*k*	*n*	*k*
23.800	191958.4	0.05209	0.821 [3]	0.162 [3]		
23.600	190345.3	0.05254	0.821	0.162		
23.400	188732.2	0.05299	0.822	0.164		
23.200	187119.1	0.05344	0.820	0.165		
23.000	185506.0	0.05391	0.817	0.167		
22.800	183892.9	0.05438	0.814	0.169		
22.600	182279.9	0.05486	0.810	0.173		
22.400	180666.8	0.05535	0.804	0.180		
22.200	179053.7	0.05585	0.798	0.189		
22.000	177440.6	0.05636	0.791	0.203		
21.800	175827.5	0.05687	0.787	0.221		
21.600	174214.4	0.05740	0.805	0.234		
21.400	172601.3	0.05794	0.825	0.234		
21.200	170988.2	0.05848	0.831	0.222		
21.000	169375.1	0.05904	0.830	0.206		
20.800	167762.0	0.05961	0.820	0.194		
20.600	166148.9	0.06019	0.805	0.183		
20.400	164535.8	0.06078	0.779	0.180		
20.200	162922.7	0.06138	0.752	0.193		
20.000	161309.6	0.06199	0.736	0.219		
19.800	159696.5	0.06262	0.739	0.244		
19.600	158083.4	0.06326	0.750	0.262		
19.400	156470.3	0.06391	0.762	0.274		
19.200	154857.2	0.06458	0.767	0.264		
19.000	153244.1	0.06526	0.747	0.257		
18.800	151631.0	0.06595	0.729	0.266		
18.600	150017.9	0.06666	0.716	0.286		

TABLE II *(Continued)*

Thallium Chloride

eV	cm^{-1}	μm	n	k	n	k
18.400	148404.8	0.06738	0.702	0.309		
18.200	146791.7	0.06812	0.693	0.332		
18.000	145178.6	0.06888	0.685	0.356		
17.900	144372.1	0.06927	0.683	0.370		
17.800	143565.5	0.06965	0.681	0.383	0.596 [2]	0.173 [2]
17.700	142759.0	0.07005	0.681	0.399	0.579	0.171
17.600	141952.5	0.07045	0.688	0.411	0.561	0.176
17.500	141145.9	0.07085	0.703	0.422	0.550	0.189
17.400	140339.4	0.07126	0.714	0.426	0.547	0.197
17.300	139532.8	0.07167	0.722	0.420	0.538	0.203
17.200	138726.3	0.07208	0.718	0.411	0.516	0.208
17.100	137919.7	0.07251	0.700	0.408	0.484	0.212
17.000	137113.2	0.07293	0.676	0.417	0.449	0.229
16.900	136306.6	0.07336	0.644	0.437	0.429	0.272
16.800	135500.1	0.07380	0.617	0.465	0.434	0.329
16.700	134693.5	0.07424	0.592	0.485	0.458	0.422
16.600	133887.0	0.07469	0.559	0.517	0.505	0.518
16.500	133080.4	0.07514	0.490	0.596	0.633	0.643
16.400	132273.9	0.07560	0.471	0.665	0.778	0.710
16.300	131467.3	0.07606	0.486	0.742	0.898	0.622
16.200	130660.8	0.07653	0.627	0.846	0.953	0.544
16.100	129854.2	0.07701	0.803	0.910	0.974	0.501
16.000	129047.7	0.07749	0.908	0.900	0.967	0.474
15.900	128241.1	0.07798	1.079	0.795	0.946	0.457
15.800	127434.6	0.07847	1.152	0.755	0.924	0.445
15.700	126628.0	0.07897	1.199	0.695	0.904	0.445
15.600	125821.5	0.07948	1.172	0.555	0.884	0.449
15.500	125014.9	0.07999	1.109	0.456	0.864	0.457
15.400	124208.4	0.08051	1.021	0.431	0.846	0.468
15.300	123401.8	0.08104	0.963	0.422	0.830	0.480
15.200	122595.3	0.08157	0.894	0.443	0.816	0.505
15.100	121788.8	0.08211	0.853	0.465	0.803	0.545
15.000	120982.2	0.08266	0.829	0.507	0.804	0.637
14.900	120175.7	0.08321	0.824	0.560	0.818	0.749
14.800	119369.1	0.08377	0.844	0.630	0.906	0.657
14.700	118562.6	0.08434	0.980	0.743	0.984	0.580
14.600	117756.0	0.08492	1.105	0.706	1.045	0.528
14.500	116949.5	0.08551	1.181	0.660	1.086	0.489
14.400	116142.9	0.08610	1.180	0.557	1.104	0.454
14.300	115336.4	0.08670	1.151	0.431	1.111	0.421
14.200	114529.8	0.08731	1.134	0.370	1.111	0.394
14.100	113723.3	0.08793	1.108	0.332	1.108	0.371
14.000	112916.7	0.08856	1.058	0.320	1.102	0.353
13.900	112110.2	0.08920	1.012	0.318	1.095	0.335
13.800	111303.6	0.08984	0.982	0.315	1.082	0.321
13.700	110497.1	0.09050	0.951	0.312	1.066	0.312
13.600	109690.5	0.09117	0.925	0.308	1.048	0.303

(continued)

TABLE II *(Continued)*

Thallium Chloride

eV	cm^{-1}	μm	n	k	n	k
13.500	108884.0	0.09184	0.903	0.307	1.029	0.296
13.400	108077.4	0.09253	0.881	0.310	1.006	0.290
13.300	107270.9	0.09322	0.857	0.314	0.981	0.287
13.200	106464.3	0.09393	0.834	0.319	0.950	0.285
13.100	105657.8	0.09465	0.810	0.326	0.915	0.290
13.000	104851.2	0.09537	0.782	0.320	0.874	0.299
12.900	104044.7	0.09611	0.753	0.311	0.820	0.310
12.800	103238.1	0.09686	0.710	0.318	0.762	0.323
12.700	102431.6	0.09763	0.671	0.346	0.719	0.348
12.600	101625.1	0.09840	0.628	0.380	0.690	0.379
12.500	100818.5	0.09919	0.593	0.426	0.671	0.429
12.400	100012.0	0.09999	0.573	0.489	0.665	0.479
12.300	99205.4	0.1008	0.576	0.576	0.667	0.525
12.200	98398.9	0.1016	0.592	0.657	0.681	0.564
12.100	97592.3	0.1025	0.621	0.721	0.697	0.600
12.000	96785.8	0.1033	0.666	0.767	0.734	0.634
11.900	95979.2	0.1042	0.712	0.807	0.771	0.667
11.800	95172.7	0.1051	0.771	0.843	0.807	0.697
11.700	94366.1	0.1060	0.837	0.852	0.844	0.719
11.600	93559.6	0.1069	0.912	0.839	0.878	0.732
11.500	92753.0	0.1078	0.980	0.815	0.908	0.737
11.400	91946.5	0.1088	1.025	0.798	0.937	0.732
11.300	91139.9	0.1097	1.049	0.769	0.964	0.716
11.200	90333.4	0.1107	1.075	0.738	0.991	0.692
11.100	89526.8	0.1117	1.085	0.699	1.024	0.652
11.000	88720.3	0.1127	1.087	0.654	1.056	0.615
10.900	87913.7	0.1137	1.086	0.604	1.086	0.578
10.800	87107.2	0.1148	1.033	0.584	1.114	0.544
10.700	86300.6	0.1159	0.987	0.566	1.115	0.511
10.600	85494.1	0.1170	0.949	0.552	1.107	0.483
10.500	84687.5	0.1181	0.912	0.551	1.082	0.462
10.400	83881.0	0.1192	0.878	0.559	1.041	0.458
10.300	83074.4	0.1204	0.852	0.572	0.993	0.462
10.200	82267.9	0.1216	0.829	0.589	0.952	0.469
10.100	81461.3	0.1228	0.817	0.610	0.917	0.481
10.000	80654.8	0.1240	0.803	0.641	0.885	0.497
9.900	79848.3	0.1252	0.793	0.675	0.858	0.516
9.800	79041.7	0.1265	0.795	0.701	0.838	0.547
9.700	78235.2	0.1278	0.798	0.728	0.828	0.599
9.600	77428.6	0.1292	0.800	0.757	0.859	0.652
9.500	76622.1	0.1305	0.802	0.785	0.885	0.675
9.400	75815.5	0.1319	0.807	0.813	0.899	0.682
9.300	75009.0	0.1333	0.813	0.838	0.905	0.691
9.200	74202.4	0.1348	0.825	0.867	0.911	0.714
9.100	73395.9	0.1362	0.882	0.863	0.920	0.780
9.000	72589.3	0.1378	0.985	0.910	0.938	0.785
8.900	71782.8	0.1393	0.987	0.862	0.948	0.774

TABLE II *(Continued)*

Thallium Chloride

eV	cm^{-1}	μm	n	k	n	k
8.800	70976.2	0.1409	0.942	0.780	0.953	0.742
8.700	70169.7	0.1425	0.910	0.759	0.941	0.719
8.600	69363.1	0.1442	0.876	0.783	0.919	0.708
8.500	68556.6	0.1459	0.850	0.815	0.896	0.711
8.400	67750.0	0.1476	0.832	0.843	0.868	0.724
8.300	66943.5	0.1494	0.819	0.871	0.842	0.755
8.200	66136.9	0.1512	0.810	0.899	0.818	0.792
8.100	65330.4	0.1531	0.808	0.926	0.798	0.833
8.000	64523.8	0.1550	0.799	0.964	0.793	0.876
7.900	63717.3	0.1569	0.792	1.004	0.800	0.923
7.800	62910.7	0.1590	0.790	1.049	0.808	0.977
7.700	62104.2	0.1610	0.785	1.085	0.820	1.034
7.600	61297.6	0.1631	0.785	1.124	0.837	1.081
7.500	60491.1	0.1653	0.799	1.172	0.857	1.124
7.400	59684.6	0.1675	0.813	1.217	0.878	1.184
7.300	58878.0	0.1698	0.831	1.268	0.908	1.248
7.200	58071.5	0.1722	0.850	1.317	0.955	1.303
7.100	57264.9	0.1746	0.866	1.365	1.014	1.347
7.000	56458.4	0.1771	0.877	1.422	1.085	1.382
6.900	55651.8	0.1797	0.897	1.492	1.148	1.402
6.800	54845.3	0.1823	0.917	1.572	1.205	1.400
6.700	54038.7	0.1851	0.944	1.654	1.254	1.395
6.600	53232.2	0.1879	1.142	1.779	1.293	1.392
6.500	52425.6	0.1907	1.482	1.941	1.324	1.396
6.400	51619.1	0.1937	1.623	1.802	1.339	1.407
6.300	50812.5	0.1968	1.587	1.618	1.395	1.411
6.200	50006.0	0.2000	1.475	1.403	1.410	1.415
6.100	49199.4	0.2033	1.377	1.418	1.431	1.441
6.000	48392.9	0.2066	1.296	1.497	1.454	1.499
5.900	47586.3	0.2101	1.270	1.594	1.580	1.560
5.800	46779.8	0.2138	1.320	1.684	1.735	1.594
5.700	45973.2	0.2175	1.369	1.734	1.798	1.548
5.600	45166.7	0.2214	1.460	1.810	1.834	1.499
5.500	44360.1	0.2254	1.557	1.875	1.868	1.472
5.400	43553.6	0.2296	1.648	1.927	1.906	1.449
5.300	42747.0	0.2339	1.727	1.952	1.957	1.439
5.200	41940.5	0.2384	1.801	1.966	2.020	1.441
5.100	41133.9	0.2431			2.100	1.447
5.000	40327.4	0.2480			2.207	1.444
4.900	39520.9	0.2530			2.325	1.402
4.800	38714.3	0.2583			2.408	1.262
4.700	37907.8	0.2638			2.428	1.178
4.600	37101.2	0.2695			2.438	1.112
4.500	36294.7	0.2755		0.634 [5]	2.449	1.053
4.400	35488.1	0.2818		0.630	2.458	0.997
4.300	34681.6	0.2883		0.621	2.453	0.941
4.200	33875.0	0.2952		0.602	2.450	0.884

(continued)

TABLE II *(Continued)*

Thallium Chloride

eV	cm^{-1}	μm	n	k	n	k
4.100	33068.5	0.3024		0.572	2.451	0.835
4.000	32261.9	0.3100		0.534	2.454	0.789
3.900	31455.4	0.3179		0.497	2.461	0.747
3.800	30648.8	0.3263		0.462	2.468	0.711
3.700	29842.3	0.3351		0.434	2.467	0.683
3.600	29035.7	0.3444		0.436	2.474	0.683
3.500	28229.2	0.3542		0.531	2.633	0.703
						0.495 [4]
3.480	28067.9	0.3563		0.533		0.433
3.460	27906.6	0.3583		0.424		0.324
3.440	27745.3	0.3604		0.212		0.210
3.420	27583.9	0.3625		0.0890		0.111
3.400	27422.6	0.3647		0.0412	2.656	0.0590
3.380	27261.3	0.3668		0.0187		0.0248
3.360	27100.0	0.3690		0.0083		0.00961
3.340	26938.7	0.3712		0.0039		0.00401
3.320	26777.4	0.3734		0.0019		0.00153
3.300	26616.1	0.3757		0.0009	2.550	5.73E-4
3.280	26454.8	0.3780		0.0004		2.91E-4
3.263	26315.8	0.3800				3.74E-6 [6]

eV	cm^{-1}	μm	n	n	n	k
3.200	25809.5	0.3875			2.49	3.03E-5 [4]
3.179	25641.0	0.3900		2.5474 [9]		8.25E-7 [6]
3.100	25003.0	0.4000		2.5050	2.46	1.91E-7
3.024	24390.2	0.4100		2.4714		
3.000	24196.4	0.4133		2.4618	2.42	
2.844	22935.8	0.436	2.4112 [8]	2.4079	2.400 [7]	
2.271	18315.0	0.546	2.2856	2.2826	2.270	
2.145	17301.0	0.578	2.2681	2.2640	2.253	
2.105	16977.9	0.589	2.2629	2.2586	2.247	
1.907	15384.6	0.650	2.2402	2.2345	2.223	
1.653	13333.3	0.750	2.2155	2.2094	2.198	

eV	cm^{-1}	μm	n	k	n	k
0.1426	1150.0	8.696		3.51E-8 [12]		
0.1333	1075.0	9.302		7.41E-8		
0.1302	1050.0	9.524		1.13E-7		
0.1271	1025.0	9.756		1.58E-7		
0.1240	1000.0	10.00	2.199 [10]	2.41E-7		
0.1209	975.0	10.26		3.45E-7		
0.1178	950.0	10.53		2.62E-7		
0.1147	925.0	10.81		1.32E-7		
0.1116	900.0	11.11		2.25E-7		
0.1085	875.0	11.43		4.56E-7		
0.1054	850.0	11.76		4.68E-7		

TABLE II *(Continued)*

Thallium Chloride

eV	cm^{-1}	μm	n	k	n	k
0.1023	825.0	12.12		4.23E-7		
0.0994	802.0	12.47	2.197			
0.0992	800.0	12.50		4.05E-7		
0.0961	775.0	12.90		6.34E-7		
0.0930	750.0	13.33		7.57E-7		
0.0899	725.0	13.79		1.22E-6		
0.0868	700.0	14.29		1.86E-6		
0.0837	675.0	14.81		1.84E-6		
0.0806	650.0	15.38		1.81E-6		
0.0775	625.0	16.00		1.91E-6		
0.0744	600.0	16.67		2.31E-6		
0.0713	575.0	17.39		2.86E-6		
0.0682	550.0	18.18		3.93E-6		
0.0676	545.0	18.35	2.188			
0.06509	525.0	19.05		6.23E-6		
0.06199	500.0	20.00	2.029 [14]		1.979 [15]	
0.05889	475.0	21.05	2.015		1.966	
0.05579	450.0	22.22	2.000		1.950	
0.05269	425.0	23.53	1.981		1.930	5.71E-5 [6]
0.04959	400.0	25.00	1.959		1.907	1.11E-4
0.04649	375.0	26.67	1.931		1.878	2.16E-4
0.04339	350.0	28.57	1.896		1.843	4.24E-4
0.04030	325.0	30.77	1.852		1.797	
0.03720	300.0	33.33	1.794		1.736	
0.03410	275.0	36.36	1.715		1.654	
0.03100	250.0	40.00	1.604		1.537	
0.02790	225.0	44.44	1.437	0.128 [14]	1.358	
0.02480	200.0	50.00	1.157	0.196	1.049	0.113 [15]
0.02356	190.0	52.63	0.984	0.255	0.848	0.171
0.02232	180.0	55.56	0.751	0.372	0.563	0.321
0.02108	170.0	58.82	0.498	0.635	0.334	0.687
0.02046	165.0	60.61	0.414	0.817	0.295	0.882
0.01984	160.0	62.50	0.362	1.003	0.278	1.066
0.01922	155.0	64.52	0.330	1.187	0.273	1.240
0.01860	150.0	66.67	0.310	1.369	0.276	1.410
0.01798	145.0	68.97	0.299	1.553	0.283	1.579
0.01736	140.0	71.43	0.293	1.741	0.293	1.748
0.01674	135.0	74.07	0.291	1.936	0.305	1.921
0.01612	130.0	76.92	0.295	2.140	0.317	2.099
0.01550	125.0	80.00	0.302	2.358	0.327	2.286
0.01488	120.0	83.33	0.313	2.593	0.332	2.489
0.01426	115.0	86.96	0.331	2.850	0.334	2.714
0.01364	110.0	90.91	0.354	3.136	0.331	2.973
0.01302	105.0	95.24	0.387	3.458	0.329	3.275
0.01240	100.0	100.0	0.432	3.829	0.333	3.636
0.01178	95.0	105.3	0.495	4.267	0.350	4.073
0.01116	90.0	111.1	0.588	4.798	0.390	4.615

(continued)

TABLE II *(Continued)*

Thallium Chloride

eV	cm^{-1}	μm	n	k	n	k
0.01054	85.0	117.6	0.731	5.466	0.469	5.312
0.00992	80.0	125.0	0.974	6.349	0.625	6.259
0.00930	75.0	133.3	1.443	7.599	0.968	7.666
0.00868	70.0	142.9	2.573	9.521	1.955	10.087
0.00806	65.0	153.8	6.400	12.135	7.200	14.464
0.00744	60.0	166.7	13.222	7.565	14.443	5.057
0.00682	55.0	181.8	11.316	2.509	10.692	1.481
0.00620	50.0	200.0	9.433	1.150	8.841	0.716
0.00558	45.0	222.2	8.303	0.649	7.807	0.428
0.00496	40.0	250.0	7.575	0.410	7.151	0.284
0.00434	35.0	285.7	7.077	0.277	6.703	0.200
0.00372	30.0	333.3	6.722	0.194	6.383	0.146
0.00310	25.0	400.0	6.464	0.138	6.150	0.107
0.00248	20.0	500.0	6.277	0.098	5.980	0.078
0.00186	15.0	666.7	6.143	0.067	5.859	0.055
0.00124	10.0	1000.0	6.053	0.042	5.778	0.035
0.00062	5.0	2000.0	6.001	0.020	5.731	0.017
0.0	0.0		5.985	0.000	5.716	0.000
			5.72 [16]		5.68 [18]	

TABLE III

Values of *n* and k for Thallium Bromide from Various References

eV	cm^{-1}	μm	n	k	n	k
23.800	191958.4	0.05209	0.804 [3]	0.188 [3]		
23.600	190345.3	0.05254	0.807	0.197		
23.400	188732.2	0.05299	0.811	0.205		
23.200	187119.1	0.05344	0.821	0.212		
23.000	185506.0	0.05391	0.830	0.214		
22.800	183892.9	0.05438	0.836	0.209		
22.600	182279.9	0.05486	0.837	0.198		
22.400	180666.8	0.05535	0.828	0.191		
22.200	179053.7	0.05585	0.821	0.188		
22.000	177440.6	0.05636	0.813	0.188		
21.800	175827.5	0.05687	0.803	0.191		
21.600	174214.4	0.05740	0.791	0.201		
21.400	172601.3	0.05794	0.782	0.217		
21.200	170988.2	0.05848	0.787	0.238		
21.000	169375.1	0.05904	0.800	0.248	1.135 [2]	0.369 [2]
20.900	168568.5	0.05932	0.805	0.247	1.131	0.368
20.800	167762.0	0.05961	0.809	0.245	1.127	0.369
20.700	166955.4	0.05990	0.812	0.243	1.123	0.369
20.600	166148.9	0.06019	0.813	0.241	1.120	0.371
20.500	165342.3	0.06048	0.813	0.238	1.115	0.373
20.400	164535.8	0.06078	0.810	0.235	1.111	0.375
20.300	163729.2	0.06108	0.807	0.232	1.106	0.377

TABLE III *(Continued)*

Thallium Bromide

eV	cm^{-1}	μm	n	k	n	k
20.200	162922.7	0.06138	0.803	0.230	1.102	0.378
20.100	162116.2	0.06168	0.798	0.228	1.097	0.380
20.000	161309.6	0.06199	0.792	0.227	1.093	0.382
19.900	160503.1	0.06230	0.784	0.225	1.088	0.385
19.800	159696.5	0.06262	0.775	0.225	1.082	0.388
19.700	158890.0	0.06294	0.765	0.225	1.077	0.390
19.600	158083.4	0.06326	0.752	0.231	1.072	0.394
19.500	157276.9	0.06358	0.736	0.242	1.067	0.397
19.400	156470.3	0.06391	0.718	0.256	1.063	0.400
19.300	155663.8	0.06424	0.706	0.274	1.058	0.404
19.200	154857.2	0.06458	0.702	0.300	1.052	0.410
19.100	154050.7	0.06491	0.725	0.323	1.046	0.415
19.000	153244.1	0.06526	0.758	0.333	1.040	0.421
18.900	152437.6	0.06560	0.773	0.329	1.032	0.426
18.800	151631.0	0.06595	0.782	0.325	1.025	0.433
18.700	150824.5	0.06630	0.781	0.316	1.016	0.440
18.600	150017.9	0.06666	0.775	0.306	1.008	0.446
18.500	149211.4	0.06702	0.768	0.297	0.999	0.453
18.400	148404.8	0.06738	0.761	0.294	0.991	0.463
18.300	147598.3	0.06775	0.751	0.293	0.983	0.473
18.200	146791.7	0.06812	0.738	0.295	0.976	0.482
18.100	145985.2	0.06850	0.723	0.301	0.973	0.496
18.000	145178.6	0.06888	0.706	0.317	0.970	0.511
17.900	144372.1	0.06927	0.680	0.343	0.970	0.525
17.800	143565.5	0.06965	0.678	0.364	0.973	0.538
17.700	142759.0	0.07005	0.686	0.382	0.982	0.551
17.600	141952.5	0.07045	0.696	0.397	0.983	0.545
17.500	141145.9	0.07085	0.701	0.398	0.972	0.543
17.400	140339.4	0.07126	0.704	0.400	0.939	0.549
17.300	139532.8	0.07167	0.704	0.403	0.903	0.566
17.200	138726.3	0.07208	0.701	0.410	0.866	0.597
17.100	137919.7	0.07251	0.694	0.420	0.843	0.674
17.000	137113.2	0.07293	0.688	0.433	0.841	0.772
16.900	136306.6	0.07336	0.680	0.446	0.850	0.860
16.800	135500.1	0.07380	0.671	0.462	0.916	0.958
16.700	134693.5	0.07424	0.661	0.482	1.054	1.033
16.600	133887.0	0.07469	0.647	0.509	1.211	0.996
16.500	133080.4	0.07514	0.650	0.524	1.392	0.914
16.400	132273.9	0.07560	0.635	0.586	1.543	0.787
16.300	131467.3	0.07606	0.651	0.629	1.622	0.694
16.200	130660.8	0.07653	0.693	0.671	1.591	0.554
16.100	129854.2	0.07701	0.795	0.723	1.510	0.478
16.000	129047.7	0.07749	0.925	0.748	1.431	0.462
15.900	128241.1	0.07798	0.997	0.713	1.378	0.469
15.800	127434.6	0.07847	1.016	0.653	1.342	0.481
15.700	126628.0	0.07897	1.024	0.593	1.313	0.494
15.600	125821.5	0.07948	1.018	0.537	1.303	0.510

(continued)

TABLE III *(Continued)*

Thallium Bromide

eV	cm^{-1}	μm	n	k	n	k
15.500	125014.9	0.07999	0.992	0.497	1.293	0.531
15.400	124208.4	0.08051	0.968	0.465	1.291	0.555
15.300	123401.8	0.08104	0.938	0.446	1.290	0.581
15.200	122595.3	0.08157	0.878	0.458	1.296	0.611
15.100	121788.8	0.08211	0.813	0.486	1.308	0.651
15.000	120982.2	0.08266	0.784	0.533	1.329	0.705
14.900	120175.7	0.08321	0.795	0.579	1.368	0.756
14.800	119369.1	0.08377	0.815	0.628	1.420	0.790
14.700	118562.6	0.08434	0.863	0.667	1.477	0.755
14.600	117756.0	0.08492	0.935	0.699	1.549	0.649
14.500	116949.5	0.08551	0.992	0.683	1.566	0.491
14.400	116142.9	0.08610	1.064	0.645	1.529	0.418
14.300	115336.4	0.08670	1.148	0.576	1.488	0.395
14.200	114529.8	0.08731	1.152	0.524	1.464	0.388
14.100	113723.3	0.08793	1.129	0.460	1.444	0.390
14.000	112916.7	0.08856	1.075	0.412	1.428	0.391
13.900	112110.2	0.08920	1.017	0.395	1.420	0.390
13.800	111303.6	0.08984	0.960	0.384	1.412	0.389
13.700	110497.1	0.09050	0.912	0.398	1.407	0.388
13.600	109690.5	0.09117	0.876	0.425	1.403	0.387
13.500	108884.0	0.09184	0.861	0.451	1.395	0.383
13.400	108077.4	0.09253	0.864	0.484	1.387	0.377
13.300	107270.9	0.09322	0.872	0.519	1.378	0.367
13.200	106464.3	0.09393	0.887	0.549	1.368	0.355
13.100	105657.8	0.09465	0.920	0.564	1.356	0.343
13.000	104851.2	0.09537	0.966	0.566	1.337	0.334
12.900	104044.7	0.09611	0.984	0.527	1.316	0.324
12.800	103238.1	0.09686	0.981	0.496	1.293	0.318
12.700	102431.6	0.09763	0.976	0.463	1.265	0.315
12.600	101625.1	0.09840	0.940	0.443	1.233	0.313
12.500	100818.5	0.09919	0.902	0.433	1.198	0.310
12.400	100012.0	0.09999	0.861	0.432	1.161	0.323
12.300	99205.4	0.1008	0.838	0.443	1.120	0.360
12.200	98398.9	0.1016	0.815	0.456	1.072	0.401
12.100	97592.3	0.1025	0.797	0.481	1.026	0.450
12.000	96785.8	0.1033	0.780	0.511	0.992	0.494
11.900	95979.2	0.1042	0.761	0.544	0.985	0.525
11.800	95172.7	0.1051	0.744	0.580	0.987	0.550
11.700	94366.1	0.1060	0.729	0.616	0.997	0.573
11.600	93559.6	0.1069	0.719	0.655	1.003	0.595
11.500	92753.0	0.1078	0.719	0.697	1.009	0.618
11.400	91946.5	0.1088	0.724	0.742	1.015	0.642
11.300	91139.9	0.1097	0.732	0.799	1.024	0.669
11.200	90333.4	0.1107	0.762	0.844	1.035	0.697
11.100	89526.8	0.1117	0.811	0.897	1.051	0.726
11.000	88720.3	0.1127	0.862	0.928	1.082	0.757
10.900	87913.7	0.1137	0.912	0.938	1.146	0.800

TABLE III *(Continued)*

Thallium Bromide

eV	cm^{-1}	μm	n	k	n	k
10.800	87107.2	0.1148	0.960	0.935	1.217	0.837
10.700	86300.6	0.1159	1.015	0.909	1.285	0.861
10.600	85494.1	0.1170	1.044	0.892	1.342	0.881
10.500	84687.5	0.1181	1.070	0.870	1.395	0.892
10.400	83881.0	0.1192	1.089	0.848	1.455	0.892
10.300	83074.4	0.1204	1.101	0.827	1.499	0.867
10.200	82267.9	0.1216	1.115	0.805	1.538	0.827
10.100	81461.3	0.1228	1.124	0.784	1.553	0.784
10.000	80654.8	0.1240	1.127	0.766	1.559	0.737
9.900	79848.3	0.1252	1.125	0.747	1.547	0.687
9.800	79041.7	0.1265	1.121	0.728	1.522	0.642
9.700	78235.2	0.1278	1.112	0.713	1.489	0.606
9.600	77428.6	0.1292	1.096	0.702	1.459	0.579
9.500	76622.1	0.1305	1.078	0.693	1.432	0.563
9.400	75815.5	0.1319	1.061	0.688	1.407	0.550
9.300	75009.0	0.1333	1.037	0.691	1.381	0.540
9.200	74202.4	0.1348	1.008	0.709	1.360	0.537
9.100	73395.9	0.1362	0.985	0.726	1.339	0.536
9.000	72589.3	0.1378	0.983	0.747	1.319	0.541
8.900	71782.8	0.1393	0.981	0.768	1.297	0.546
8.800	70976.2	0.1409	0.978	0.789	1.273	0.553
8.700	70169.7	0.1425	0.976	0.808	1.249	0.573
8.600	69363.1	0.1442	0.978	0.823	1.231	0.593
8.500	68556.6	0.1459	0.982	0.840	1.214	0.616
8.400	67750.0	0.1476	0.986	0.857	1.198	0.653
8.300	66943.5	0.1494	0.990	0.875	1.188	0.692
8.200	66136.9	0.1512	0.995	0.891	1.177	0.730
8.100	65330.4	0.1531	0.999	0.904	1.161	0.768
8.000	64523.8	0.1550	1.004	0.917	1.141	0.801
7.900	63717.3	0.1569	1.006	0.931	1.124	0.837
7.800	62910.7	0.1590	1.008	0.947	1.116	0.861
7.700	62104.2	0.1610	1.012	0.964	1.108	0.876
7.600	61297.6	0.1631	1.014	0.983	1.111	0.913
7.500	60491.1	0.1653	1.017	1.005	1.127	0.966
7.400	59684.6	0.1675	1.022	1.026	1.145	1.023
7.300	58878.0	0.1698	1.028	1.045	1.162	1.083
7.200	58071.5	0.1722	1.027	1.074	1.186	1.141
7.100	57264.9	0.1746	1.032	1.108	1.219	1.203
7.000	56458.4	0.1771	1.049	1.152	1.257	1.268
6.900	55651.8	0.1797	1.042	1.223	1.321	1.337
6.800	54845.3	0.1823	1.056	1.262	1.429	1.419
6.700	54038.7	0.1851	1.279	1.404	1.607	1.592
6.600	53232.2	0.1879	1.443	1.446	1.736	1.643
6.500	52425.6	0.1907	1.476	1.294	1.844	1.611
6.400	51619.1	0.1937	1.396	1.078	1.905	1.531
6.300	50812.5	0.1968	1.313	1.001	1.946	1.452
6.200	50006.0	0.2000	1.188	1.033	1.972	1.387

(continued)

TABLE III *(Continued)*

Thallium Bromide

eV	cm^{-1}	μm	n	k	n	k
6.100	49199.4	0.2033	1.129	1.136	1.989	1.370
6.000	48392.9	0.2066	1.133	1.246	2.003	1.354
5.900	47586.3	0.2101	1.159	1.332	2.019	1.339
5.800	46779.8	0.2138	1.190	1.399	2.039	1.369
5.700	45973.2	0.2175	1.240	1.443	2.061	1.401
5.600	45166.7	0.2214	1.288	1.479	2.139	1.383
5.500	44360.1	0.2254	1.329	1.502	2.155	1.343
5.400	43553.6	0.2296	1.374	1.530	2.152	1.364
5.300	42747.0	0.2339	1.421	1.554	2.281	1.495
5.200	41940.5	0.2384	1.464	1.576	2.478	1.550
5.100	41133.9	0.2431	1.506	1.597	2.601	1.428
5.000	40327.4	0.2480	1.548	1.620	2.651	1.313
4.900	39520.9	0.2530	1.590	1.643	2.689	1.238
4.800	38714.3	0.2583	1.645	1.680	2.726	1.191
4.700	37907.8	0.2638	1.698	1.718	2.776	1.141
4.600	37101.2	0.2695	1.747	1.755	2.860	1.056
4.500	36294.7	0.2755	1.805	1.801	2.904	0.991
4.400	35488.1	0.2818	1.874	1.850	2.936	0.918
4.300	34681.6	0.2883	1.957	1.900	2.952	0.836
4.200	33875.0	0.2952			2.955	0.742
4.100	33068.5	0.3024			2.960	0.649
4.000	32261.9	0.3100			2.970	0.576
3.900	31455.4	0.3179			2.913	0.482
3.800	30648.8	0.3263			2.858	0.441
3.700	29842.3	0.3351			2.843	0.417
3.600	29035.7	0.3444			2.825	0.387
3.500	28229.2	0.3542			2.795	0.339
3.400	27422.6	0.3647			2.760	0.291
3.300	26616.1	0.3757			2.767	0.284
3.200	25809.5	0.3875			2.790	0.285
3.100	25003.0	0.4000			2.857	0.289
3.000	24196.4	0.4133			2.819	0.180
2.900	23389.9	0.4275			2.709	
2.818	22727.3	0.4400			6.8E-6 [6]	
2.800	22583.3	0.4428			2.637	
2.755	22222.2	0.4500			8.2E-7	
2.700	21776.8	0.4592			2.580	
2.600	20970.2	0.4769			2.539	

eV	cm^{-1}	μm	n	n	n	n
2.844	22935.8	0.436	2.7111 [8]	2.6917 [9]	2.652 [7]	
2.271	18315.0	0.546	2.4744	2.4743	2.452	
2.145	17301.0	0.578	2.4448	2.4462	2.424	
2.105	16977.9	0.589	2.4364	2.4380	2.418	
1.907	15384.6	0.650	2.4001	2.4021	2.384	
1.653	13333.3	0.750	2.3634	2.3652	2.350	

TABLE III *(Continued)*

Thallium Bromide

eV	cm^{-1}	μm	n	k	n	k
0.1242	1002.0	9.98	2.343 [10]			
0.0889	717.0	13.95	2.326			
0.0627	506.0	19.76	2.326			
0.0508	410.0	24.39	2.326			
0.0372	300.0	33.33				0.0001 [6]
0.0341	275.0	36.36				0.0002
0.0310	250.0	40.00				0.00039
0.0279	225.0	44.44				0.00077
0.0248	200.0	50.00			1.907 [15]	0.00155
0.0236	190.0	52.63	1.82 [19]	0.02 [19]	1.861	
0.0229	185.0	54.05	1.78	0.02	1.835	
0.0223	180.0	55.56	1.74	0.03	1.805	
0.0217	175.0	57.14	1.70	0.03	1.772	
0.0211	170.0	58.82	1.64	0.04	1.736	
0.0205	165.0	60.61	1.58	0.04	1.695	
0.0198	160.0	62.50	1.53	0.04	1.648	
0.0192	155.0	64.52	1.46	0.04	1.595	
0.0186	150.0	66.67	1.38	0.04	1.533	
0.0183	148.0	67.57	1.35	0.03	1.506	
0.0181	146.0	68.49	1.36	0.04	1.477	
0.0179	144.0	69.44	1.35	0.04	1.446	
0.0176	142.0	70.42	1.33	0.04	1.413	
0.0174	140.0	71.43	1.30	0.05	1.378	
0.0171	138.0	72.46	1.28	0.05	1.340	
0.0169	136.0	73.53	1.25	0.04	1.300	
0.0166	134.0	74.63	1.23	0.03	1.256	
0.0164	132.0	75.76	1.23	0.02	1.209	
0.0161	130.0	76.92	1.21	0.02	1.158	
0.0159	128.0	78.13	1.20	0.02	1.102	
0.0156	126.0	79.37	1.14	0.10	1.043	
0.0154	124.0	80.65	1.05	0.18	0.978	
0.0151	122.0	81.97	0.99	0.22	0.910	
0.0149	120.0	83.33	0.91	0.28	0.838	0.519 [15]
0.0146	118.0	84.75	0.82	0.35	0.765	0.587
0.0144	116.0	86.21	0.75	0.44	0.695	0.667
0.0141	114.0	87.72	0.69	0.55	0.631	0.760
0.0139	112.0	89.29	0.65	0.68	0.577	0.862
0.0136	110.0	90.91	0.62	0.82	0.531	0.971
0.0134	108.0	92.59	0.59	0.93	0.495	1.083
0.0131	106.0	94.34	0.59	1.03	0.466	1.196
0.0129	104.0	96.15	0.60	1.13	0.443	1.311
0.0126	102.0	98.04	0.60	1.24	0.425	1.428
0.0124	100.0	100.00	0.58	1.36	0.411	1.545
0.0122	98.0	102.04	0.58	1.46	0.400	1.665
0.0119	96.0	104.17	0.59	1.55	0.392	1.787
0.0117	94.0	106.38	0.60	1.67	0.386	1.912
0.0114	92.0	108.70	0.62	1.80	0.383	2.041

(continued)

TABLE III *(Continued)*

Thallium Bromide

eV	cm^{-1}	μm	n	k	n	k
0.0112	90.0	111.11	0.62	1.92	0.381	2.174
0.0109	88.0	113.64	0.63	2.02	0.381	2.313
0.0107	86.0	116.28	0.65	2.11	0.384	2.457
0.0104	84.0	119.05	0.69	2.19	0.388	2.610
0.0102	82.0	121.95	0.79	2.33	0.394	2.770
0.0099	80.0	125.00	0.97	2.46	0.403	2.941
0.0097	78.0	128.21	1.07	2.59	0.414	3.124
0.0094	76.0	131.58	1.08	2.72	0.428	3.321
0.0092	74.0	135.14	1.08	2.96	0.446	3.535
0.0089	72.0	138.89	1.25	3.10	0.469	3.768
0.0087	70.0	142.86	1.21	3.14	0.497	4.026
0.0084	68.0	147.06	1.26	3.73	0.533	4.313
0.0082	66.0	151.52	1.73	4.11	0.579	4.637
0.0079	64.0	156.25	2.05	4.34	0.639	5.009
0.0077	62.0	161.29	2.26	4.63	0.719	5.441
0.0074	60.0	166.67	2.47	4.85	0.830	5.956
0.0072	58.0	172.41	2.81	5.18	0.990	6.585
0.0069	56.0	178.57	3.16	6.13	1.235	7.379
0.0067	54.0	185.19	4.21	7.13	1.647	8.427
0.0064	52.0	192.31	5.17	8.44	2.429	9.879
0.0062	50.0	200.00	5.37	8.68	4.233	11.932
0.0060	48.0	208.33	6.73	6.55	9.167	13.595
0.0057	46.0	217.39	7.19	5.10	14.658	8.314
0.0055	44.0	227.27	7.19	3.64	13.099	3.386
0.0052	42.0	238.10	6.96	2.51	11.137	1.673
0.0050	40.0	250.00	6.77	1.99	9.808	0.974
0.0047	38.0	263.16	6.50	1.66	8.891	0.627
0.0045	36.0	277.78	6.34	1.53	8.226	0.431
0.0042	34.0	294.12	6.19	1.34	7.722	0.309
0.0040	32.0	312.50	6.08	1.16	7.329	0.229
0.0037	30.0	333.33	5.98	1.08	7.015	0.174
0.0035	28.0	357.14	5.90	0.95	6.758	0.134
0.0032	26.0	384.62	5.85	0.87	6.546	0.105
0.0030	24.0	416.67	5.82	0.77	6.369	0.083
0.0027	22.0	454.55	5.76	0.60	6.220	0.066
0.00248	20.0	500.00			6.095	0.053
0.00186	15.0	666.67			5.860	0.030
0.00124	10.0	1000.0			5.711	0.017
0.00062	5.0	2000.0			5.628	0.007
0.0	0.0		5.53 [16]		5.601	0.0
			5.53 [15]		5.48 [18]	

TABLE IV

Values of n and k Obtained for Polycrystalline Orthorhombic (and Cubic as Noted) Thallium Iodide

eV	cm^{-1}	μm	n	k
21.500	173407.8	0.05767	0.775 [3]	0.110 [3]
21.200	170988.2	0.05848	0.768	0.115
21.000	169375.1	0.05904	0.763	0.120
20.800	167762.0	0.05961	0.759	0.125
20.600	166148.9	0.06019	0.755	0.130
20.400	164535.8	0.06078	0.751	0.135
20.200	162922.7	0.06138	0.745	0.141
20.000	161309.6	0.06199	0.738	0.147
19.800	159696.5	0.06262	0.730	0.153
19.600	158083.4	0.06326	0.722	0.161
19.400	156470.3	0.06391	0.713	0.169
19.200	154857.2	0.06458	0.704	0.180
19.000	153244.1	0.06526	0.691	0.192
18.800	151631.0	0.06595	0.676	0.213
18.600	150017.9	0.06666	0.662	0.235
18.400	148404.8	0.06738	0.678	0.253
18.200	146791.7	0.06812	0.683	0.261
18.000	145178.6	0.06888	0.681	0.268
17.800	143565.5	0.06965	0.675	0.278
17.600	141952.5	0.07045	0.669	0.291
17.400	140339.4	0.07126	0.662	0.310
17.200	138726.3	0.07208	0.645	0.335
17.000	137113.2	0.07293	0.613	0.381
16.800	135500.1	0.07380	0.616	0.456
16.600	133887.0	0.07469	0.742	0.530
16.500	133080.4	0.07514	0.788	0.529
16.400	132273.9	0.07560	0.809	0.517
16.300	131467.3	0.07606	0.823	0.496
16.200	130660.8	0.07653	0.836	0.474
16.100	129854.2	0.07701	0.845	0.453
16.000	129047.7	0.07749	0.852	0.431
15.900	128241.1	0.07798	0.855	0.411
15.800	127434.6	0.07847	0.852	0.395
15.700	126628.0	0.07897	0.842	0.382
15.600	125821.5	0.07948	0.830	0.368
15.500	125014.9	0.07999	0.818	0.352
15.400	124208.4	0.08051	0.806	0.335
15.300	123401.8	0.08104	0.774	0.333
15.200	122595.3	0.08157	0.730	0.364
15.100	121788.8	0.08211	0.704	0.408
15.000	120982.2	0.08266	0.710	0.453
14.900	120175.7	0.08321	0.730	0.490
14.800	119369.1	0.08377	0.769	0.524
14.700	118562.6	0.08434	0.823	0.539
14.600	117756.0	0.08492	0.880	0.539

(continued)

TABLE IV *(Continued)*

Orthorhombic (and Cubic as Noted) Thallium Iodide

eV	cm^{-1}	μm	n	k
14.500	116949.5	0.08551	0.927	0.524
14.400	116142.9	0.08610	0.964	0.493
14.300	115336.4	0.08670	0.988	0.437
14.200	114529.8	0.08731	0.988	0.365
14.100	113723.3	0.08793	0.963	0.314
14.000	112916.7	0.08856	0.928	0.287
13.900	112110.2	0.08920	0.895	0.267
13.800	111303.6	0.08984	0.862	0.252
13.700	110497.1	0.09050	0.831	0.249
13.600	109690.5	0.09117	0.802	0.258
13.500	108884.0	0.09184	0.769	0.270
13.400	108077.4	0.09253	0.741	0.290
13.300	107270.9	0.09322	0.724	0.308
13.200	106464.3	0.09393	0.706	0.329
13.100	105657.8	0.09465	0.686	0.353
13.000	104851.2	0.09537	0.673	0.376
12.900	104044.7	0.09611	0.666	0.395
12.800	103238.1	0.09686	0.661	0.414
12.700	102431.6	0.09763	0.657	0.432
12.600	101625.1	0.09840	0.656	0.449
12.500	100818.5	0.09919	0.657	0.465
12.400	100012.0	0.09999	0.658	0.479
12.300	99205.4	0.1008	0.658	0.493
12.200	98398.9	0.1016	0.658	0.508
12.100	97592.3	0.1025	0.658	0.522
12.000	96785.8	0.1033	0.659	0.536
11.900	95979.2	0.1042	0.660	0.549
11.800	95172.7	0.1051	0.662	0.563
11.700	94366.1	0.1060	0.665	0.576
11.600	93559.6	0.1069	0.668	0.589
11.500	92753.0	0.1078	0.671	0.603
11.400	91946.5	0.1088	0.673	0.617
11.300	91139.9	0.1097	0.676	0.632
11.200	90333.4	0.1107	0.679	0.647
11.100	89526.8	0.1117	0.681	0.663
11.000	88720.3	0.1127	0.684	0.678
10.900	87913.7	0.1137	0.688	0.690
10.800	87107.2	0.1148	0.692	0.702
10.700	86300.6	0.1159	0.696	0.714
10.600	85494.1	0.1170	0.698	0.728
10.500	84687.5	0.1181	0.698	0.746
10.400	83881.0	0.1192	0.698	0.764
10.300	83074.4	0.1204	0.700	0.780
10.200	82267.9	0.1216	0.706	0.799
10.100	81461.3	0.1228	0.712	0.818
10.000	80654.8	0.1240	0.718	0.837
9.900	79848.3	0.1252	0.732	0.861

TABLE IV *(Continued)*

Orthorhombic (and Cubic as Noted) Thallium Iodide

eV	cm^{-1}	μm	n	k
9.800	79041.7	0.1265	0.746	0.884
9.700	78235.2	0.1278	0.760	0.908
9.600	77428.6	0.1292	0.780	0.924
9.500	76622.1	0.1305	0.799	0.940
9.400	75815.5	0.1319	0.823	0.955
9.300	75009.0	0.1333	0.847	0.965
9.200	74202.4	0.1348	0.870	0.975
9.100	73395.9	0.1362	0.892	0.983
9.000	72589.3	0.1378	0.913	0.992
8.900	71782.8	0.1393	0.938	0.996
8.800	70976.2	0.1409	0.957	0.996
8.700	70169.7	0.1425	0.976	0.996
8.600	69363.1	0.1442	0.994	0.995
8.500	68556.6	0.1459	1.012	0.994
8.400	67750.0	0.1476	1.031	0.992
8.300	66943.5	0.1494	1.048	0.987
8.200	66136.9	0.1512	1.064	0.982
8.100	65330.4	0.1531	1.077	0.976
8.000	64523.8	0.1550	1.088	0.970
7.900	63717.3	0.1569	1.093	0.961
7.800	62910.7	0.1590	1.096	0.952
7.700	62104.2	0.1610	1.095	0.942
7.600	61297.6	0.1631	1.090	0.931
7.500	60491.1	0.1653	1.081	0.922
7.400	59684.6	0.1675	1.066	0.919
7.300	58878.0	0.1698	1.050	0.918
7.200	58071.5	0.1722	1.027	0.926
7.100	57264.9	0.1746	1.016	0.949
7.000	56458.4	0.1771	1.011	0.977
6.900	55651.8	0.1797	1.010	1.010
6.800	54845.3	0.1823	1.012	1.041
6.700	54038.7	0.1851	1.014	1.071
6.600	53232.2	0.1879	1.016	1.100
6.500	52425.6	0.1907	1.020	1.129
6.400	51619.1	0.1937	1.026	1.158
6.300	50812.5	0.1968	1.034	1.189
6.200	50006.0	0.2000	1.042	1.219
6.100	49199.4	0.2033	1.051	1.246
6.000	48392.9	0.2066	1.060	1.273
5.900	47586.3	0.2101	1.074	1.307
5.800	46779.8	0.2138	1.088	1.341
5.700	45973.2	0.2175	1.102	1.375
5.600	45166.7	0.2214	1.116	1.409
5.500	44360.1	0.2254	1.141	1.450
5.400	43553.6	0.2296	1.167	1.488
5.300	42747.0	0.2339	1.199	1.527
5.200	41940.5	0.2384	1.233	1.567

(continued)

TABLE IV *(Continued)*

Orthorhombic (and Cubic as Noted) Thallium Iodide

eV	cm^{-1}	μm	n	k
5.100	41133.9	0.2431	1.269	1.609
5.000	40327.4	0.2480	1.311	1.654
4.900	39520.9	0.2530	1.363	1.704
4.800	38714.3	0.2583	1.412	1.751
4.700	37907.8	0.2638	1.457	1.795
4.600	37101.2	0.2695	1.512	1.847
4.500	36294.7	0.2755	1.572	1.891
4.400	35488.1	0.2818	1.633	1.927
4.300	34681.6	0.2883	1.713	1.982
4.200	33875.0	0.2952	1.796	2.040
4.100	33068.5	0.3024	1.882	2.078
2.271	18315.0	0.546	2.85† [7]	
2.105	16977.9	0.589	2.78†	
1.907	15384.6	0.650	2.72†	
1.90	15324.4	0.653	2.790 [3]	
1.80	14517.9	0.689	2.740	
1.70	13711.3	0.729	2.700	
1.60	12904.8	0.775	2.660	
1.50	12098.2	0.827	2.620	
1.40	11291.7	0.886	2.590	
1.30	10485.1	0.954	2.570	
1.20	9678.6	1.033	2.540	
1.10	8872.0	1.127	2.520	
1.00	8065.5	1.240	2.500	
0.90	7258.9	1.378	2.490	
0.80	6452.4	1.550	2.470	
0.70	5645.8	1.771	2.450	
0.60	4839.3	2.066	2.440	
0.50	4032.7	2.480	2.430	
0.0248	200.0	50.00	2.230 [15]	
0.0242	195.0	51.28	2.216	
0.0236	190.0	52.63	2.200	
0.0229	185.0	54.05	2.183	
0.0223	180.0	55.56	2.164	
0.0217	175.0	57.14	2.143	
0.0211	170.0	58.82	2.120	
0.0205	165.0	60.61	2.093	
0.0198	160.0	62.50	2.064	
0.0192	155.0	64.52	2.031	
0.0186	150.0	66.67	1.993	
0.0180	145.0	68.97	1.950	
0.0174	140.0	71.43	1.900	
0.0167	135.0	74.07	1.842	
0.0161	130.0	76.92	1.774	
0.0155	125.0	80.00	1.693	0.104 [15]
0.0149	120.0	83.33	1.597	0.135
0.0143	115.0	86.96	1.482	0.180

† Cubic thallium iodide

TABLE IV *(Continued)*

Orthorhombic (and Cubic as Noted) Thallium Iodide

eV	cm^{-1}	μm	*n*	*k*
0.0136	110.0	90.91	1.344	0.248
0.0130	105.0	95.24	1.182	0.353
0.0124	100.0	100.0	1.005	0.512
0.0118	95.0	105.3	0.834	0.734
0.0112	90.0	111.1	0.679	1.008
0.0105	85.0	117.6	0.526	1.342
0.0099	80.0	125.0	0.385	1.770
0.0093	75.0	133.3	0.278	2.314
0.0087	70.0	142.9	0.214	3.008
0.0081	65.0	153.8	0.196	3.950
0.0074	60.0	166.7	0.251	5.444
0.0068	55.0	181.8	0.656	8.853
0.0062	50.0	200.0	17.685	4.132
0.0056	45.0	222.2	8.373	0.316
0.0050	40.0	250.0	6.584	0.128
0.0043	35.0	285.7	5.779	0.074
0.0037	30.0	333.3	5.320	0.048
0.0031	25.0	400.0	5.029	0.034
0.0024	20.0	500.0	4.836	0.024
0.0018	15.0	666.7	4.706	0.016
0.0012	10.0	1000.0	4.623	0.010
0.00062	5.0	2000.0	4.576	0.005
0.0	0.0		4.561	0.0
			4.60 [18]	
			5.44† [18]	

TABLE V

Values of *n* and *k* for KRS-5 from Various References

eV	cm^{-1}	μm	*n*	*k*
2.3557	19000.0	0.5263		8.38E-3 [24]
2.2937	18500.0	0.5405		8.66E-4
2.2317	18000.0	0.5556		8.95E-5
2.1697	17500.0	0.5714		9.26E-6
2.1489	17332.2	0.57696	2.62758 [27]	4.33E-6
2.1413	17270.7	0.57902	2.62505	3.27E-6
2.1077	17000.0	0.5882		9.59E-7
1.9257	15531.6	0.64385	2.56454	
1.7949	14477.0	0.69075	2.53470	
1.4550	11735.4	0.85212	2.47448	
1.3862	11180.7	0.8944	2.46470	
1.2228	9862.1	1.01398	2.44416	
1.1697	9434.0	1.0600		8.44E-11 [31]
1.0985	8860.1	1.12866	2.43090	

(continued)

TABLE V *(Continued)*

KRS-5

eV	cm^{-1}	μm	n	k
0.90679	7313.7	1.3673	2.41385	
0.88878	7168.5	1.395	2.41242	
0.81061	6538.0	1.52952	2.40658	
0.73225	5906.0	1.6932	2.40143	
0.72540	5850.7	1.7092	2.40105	
0.68384	5515.5	1.81308	2.39851	
0.62933	5075.9	1.9701	2.39553	
0.53322	4300.7	2.3252	2.39076	
0.36266	2925.0	3.4188	2.38386	
0.29118	2348.5	4.258	2.38142	
0.22380	1805.1	5.54		3.53E-10
0.18527	1494.3	6.692	2.37680	
0.14878	1200.0	8.333		5.64E-7 [12]
0.14258	1150.0	8.696		7.00E-7
0.13638	1100.0	9.091		8.97E-7
0.13018	1050.0	9.524		9.25E-7
0.12750	1028.4	9.724	2.37132	
0.12399	1000.0	10.000		8.24E-7
0.11779	950.0	10.526		6.35E-7
0.11697	943.4	10.60		4.22E-9 [31]
0.11236	906.2	11.035	2.36857	
0.11159	900.0	11.111		5.03E-7 [12]
0.10539	850.0	11.765		3.67E-7
0.09919	800.0	12.500		2.58E-7
0.09299	750.0	13.333		2.18E-7
0.08679	700.0	14.286		1.48E-7
0.08676	699.8	14.29	2.36023	
0.08277	667.6	14.98	2.35824	
0.08059	650.0	15.385		1.58E-7
0.08009	646.0	15.48	2.35667	
0.07439	600.0	16.667		6.13E-7
0.07126	574.7	17.40	2.35022	
0.06827	550.7	18.16	2.34755	
0.06819	550.0	18.182		5.05E-7
0.06199	500.0	20.000		4.95E-7
0.06027	486.1	20.57	2.33816	
0.05690	458.9	21.79	2.33290	
0.05579	450.0	22.222		6.13E-7
0.05448	439.4	22.76	2.32851	
0.05269	425.0	23.529		2.88E-7
0.05205	419.8	23.82	2.32338	
0.04959	400.0	25.00		1.64E-7
0.04928	397.5	25.16	2.31696	
0.04774	385.1	25.97	2.31260	
0.04656	375.5	26.63	2.30902	
0.04339	350.0	28.571		1.01E-6
0.04159	335.5	29.81	2.28988	

TABLE V *(Continued)*

KRS-5

eV	cm^{-1}	μm	n	k
0.04030	325.0	30.769		4.39E-6
0.03911	315.5	31.70	2.27730	
0.03757	303.0	33.00	2.26821	
0.03720	300.0	33.333		8.49E-6
0.03596	290.0	34.48	2.25740	
0.03410	275.0	36.364		8.75E-5 [24]
0.03301	266.2	37.56	2.23243	1.25E-4
0.03148	253.9	39.38	2.21621	2.06E-4
0.03100	250.0	40.00	2.21 [13]	2.42E-4
0.02976	240.0	41.67	2.19	3.64E-4
0.02852	230.0	43.48	2.17	5.49E-4
0.02728	220.0	45.45	2.15	8.30E-4
0.02604	210.0	47.62	2.13	1.26E-3
0.02480	200.0	50.00	2.10	1.91E-3
0.02356	190.0	52.63	2.06	2.91E-3
0.02232	180.0	55.56	2.02	4.44E-3
0.02108	170.0	58.82	1.97	6.80E-3
0.01984	160.0	62.50	1.91	
0.01860	150.0	66.67	1.83	
0.01736	140.0	71.43	1.73	
0.01612	130.0	76.92	1.60	
0.01587	128.0	78.13	1.56	
0.01562	126.0	79.37	1.53	
0.01537	124.0	80.65	1.49	
0.01513	122.0	81.97	1.45	
0.01488	120.0	83.33	1.41	
0.01463	118.0	84.75	1.36	
0.01438	116.0	86.21	1.31	
0.01413	114.0	87.72	1.26	
0.01389	112.0	89.29	1.21	
0.01364	110.0	90.91	1.15	0.63 [13]
0.01339	108.0	92.59	1.09	0.69
0.01314	106.0	94.34	1.03	0.75
0.01289	104.0	96.15	0.98	0.83
0.01265	102.0	98.04	0.92	0.92
0.01240	100.0	100.0	0.87	1.01
0.01215	98.0	102.0	0.82	1.12
0.01190	96.0	104.2	0.78	1.23
0.01165	94.0	106.4	0.75	1.35
0.01141	92.0	108.7	0.72	1.47
0.01116	90.0	111.1	0.70	1.59
0.01091	88.0	113.6	0.69	1.73
0.01066	86.0	116.3	0.68	1.86
0.01041	84.0	119.0	0.67	2.00
0.01017	82.0	122.0	0.67	2.15
0.00992	80.0	125.0	0.67	2.30
0.00967	78.0	128.2	0.68	2.46

(continued)

TABLE V *(Continued)*

KRS-5

eV	cm^{-1}	μm	*n*	*k*
0.00942	76.0	131.6	0.69	2.64
0.00917	74.0	135.1	0.70	2.82
0.00893	72.0	138.9	0.72	3.01
0.00868	70.0	142.9	0.75	3.22
0.00843	68.0	147.1	0.78	3.45
0.00818	66.0	151.5	0.83	3.70
0.00794	64.0	156.3	0.88	3.97
0.00769	62.0	161.3	0.96	4.28
0.00744	60.0	166.7	1.05	4.63
0.00719	58.0	172.4	1.18	5.03
0.00694	56.0	178.6	1.35	5.49
0.00670	54.0	185.2	1.59	6.04
0.00645	52.0	192.3	1.95	6.71
0.00620	50.0	200.0	2.52	7.52
0.00595	48.0	208.3	3.48	8.48
0.00570	46.0	217.4	5.22	9.42
0.00546	44.0	227.3	8.11	9.42
0.00521	42.0	238.1	10.70	7.09
0.00496	40.0	250.0	10.92	4.20
0.00471	38.0	263.2	10.08	2.46
0.00446	36.0	277.8	9.21	1.54
0.00422	34.0	294.1	8.50	1.03
0.00397	32.0	312.5	7.95	0.72
0.00372	30.0	333.3	7.51	0.53
0.00248	20.0	500.0	6.30	0.15
0.00124	10.0	1000.0	5.83	0.05
0.0	0.0		5.70	0.0
			5.70 [21]	

TABLE VI

Values of *n* and *k* for KRS-6 from Various References

eV	cm^{-1}	μm	*n*	*k*
3.3000	26616.1	0.3757		0.0697 [25]
3.2000	25809.5	0.3875		0.00493
3.1000	25003.0	0.4000		0.000349
3.0508	24606.0	0.4064		9.46E-5
3.0240	24390.2	0.4100	2.5754 [9]	4.66E-5
2.9771	24012.0	0.4165	2.5516	1.35E-5
2.9559	23840.9	0.4194	2.5417	7.71E-6
2.8955	23353.3	0.4282	2.5155	1.56E-6
2.8437	22935.8	0.4360	2.4951	
2.5407	20491.8	0.4880	2.4021	1.90E-7
2.4098	19436.3	0.5145	2.3716	1.26E-7

TABLE VI *(Continued)*

KRS-6

eV	cm^{-1}	μm	*n*	*k*
2.2708	18315.0	0.5460	2.3437	
2.1821	17599.4	0.5682	2.3280	6.16E-8
2.1451	17301.0	0.5780	2.3218	
2.1039	16969.3	0.5893	2.3154	
			2.3367 [22]	
2.0664	16666.7	0.6000	2.3294	
1.9160	15453.6	0.6471	2.2884 [9]	2.71E-08
1.9075	15384.6	0.650	2.2873	
1.7712	14285.7	0.700	2.2982 [22]	
			2.2708 [9]	
1.6531	13333.3	0.750	2.2582	
1.5498	12500.0	0.80	2.2660 [22]	
1.3776	11111.1	0.90	2.2510	
1.2399	10000.0	1.00	2.2404	
1.1697	9434.0	1.06		6.77E-10 [32]
1.1271	9090.9	1.10	2.2321	
1.0332	8333.3	1.20	2.2255	
0.9537	7692.3	1.30	2.2212	
0.8856	7142.9	1.40	2.2176	
0.8266	6666.7	1.50	2.2148	
0.7749	6250.0	1.60	2.2124	
0.7293	5882.4	1.70	2.2103	
0.6888	5555.6	1.80	2.2086	
0.6526	5263.2	1.90	2.2071	
0.6199	5000.0	2.00	2.2059	
0.5636	4545.5	2.20	2.2039	
0.5166	4166.7	2.40	2.2024	
0.4769	3846.2	2.60	2.2011	
0.4428	3571.4	2.80	2.2001	
0.4133	3333.3	3.00	2.1990	
0.3542	2857.1	3.50	2.1972	
0.3100	2500.0	4.00	2.1956	
0.2755	2222.2	4.50	2.1942	
0.2480	2000.0	5.00	2.1928	
0.2238	1805.1	5.54		6.17E-10
0.2066	1666.7	6.00	2.1900	
0.1771	1428.6	7.00	2.1870	
0.1550	1250.0	8.00	2.1839	
0.1378	1111.1	9.00	2.1805	
0.1240	1000.0	10.00	2.1767	
0.1170	943.4	10.60		1.18E-09
0.1127	909.1	11.00	2.1723	
0.10332	833.3	12.00	2.1674	
0.09537	769.2	13.00	2.1620	
0.08856	714.3	14.00	2.1563	
0.08266	666.7	15.00	2.1504	
0.07749	625.0	16.00	2.1442	

(continued)

TABLE VI *(Continued)*

KRS-6

eV	cm^{-1}	μm	n	k
0.07293	588.2	17.00	2.1377	
0.06888	555.6	18.00	2.1309	
0.06526	526.3	19.00	2.1236	
0.06199	500.0	20.00	2.1154	
0.05904	476.2	21.00	2.1067	
0.05636	454.5	22.00	2.0976	
0.05391	434.8	23.00	2.0869	
0.05166	416.7	24.00	2.0752	
0.04959	400.0	25.00	2.07 [13]	1.96E-4 [34]
0.04649	375.0	26.67	2.05	3.74E-4
0.04339	350.0	28.57	2.03	7.17E-4
0.04030	325.0	30.77	2.00	1.38E-3
0.03720	300.0	33.33	1.96	2.68E-3
0.03410	275.0	36.36	1.91	5.22E-3
0.03100	250.0	40.00	1.83	
0.02976	240.0	41.67	1.80	
0.02852	230.0	43.48	1.76	
0.02728	220.0	45.45	1.71	
0.02604	210.0	47.62	1.65	
0.02480	200.0	50.00	1.58	
0.02356	190.0	52.63	1.49	0.34 [13]
0.02232	180.0	55.56	1.39	0.40
0.02108	170.0	58.82	1.25	0.49
0.01984	160.0	62.50	1.09	0.62
0.01959	158.0	63.29	1.06	0.65
0.01934	156.0	64.10	1.02	0.69
0.01909	154.0	64.94	0.99	0.73
0.01885	152.0	65.79	0.95	0.77
0.01860	150.0	66.67	0.92	0.82
0.01835	148.0	67.57	0.89	0.87
0.01810	146.0	68.49	0.85	0.93
0.01785	144.0	69.44	0.82	0.99
0.01761	142.0	70.42	0.79	1.05
0.01736	140.0	71.43	0.77	1.12
0.01711	138.0	72.46	0.74	1.19
0.01686	136.0	73.53	0.72	1.26
0.01661	134.0	74.63	0.70	1.33
0.01637	132.0	75.76	0.69	1.41
0.01612	130.0	76.92	0.67	1.48
0.01587	128.0	78.13	0.66	1.56
0.01562	126.0	79.37	0.65	1.64
0.01537	124.0	80.65	0.64	1.73
0.01513	122.0	81.97	0.63	1.81
0.01488	120.0	83.33	0.63	1.90
0.01463	118.0	84.75	0.62	1.99
0.01438	116.0	86.21	0.62	2.09
0.01413	114.0	87.72	0.62	2.18

TABLE VI *(Continued)*

KRS-6

eV	cm^{-1}	μm	n	k
0.01389	112.0	89.29	0.62	2.28
0.01364	110.0	90.91	0.62	2.39
0.01339	108.0	92.59	0.63	2.49
0.01314	106.0	94.34	0.63	2.61
0.01289	104.0	96.15	0.64	2.73
0.01265	102.0	98.04	0.65	2.85
0.01240	100.0	100.0	0.66	2.98
0.01215	98.0	102.0	0.68	3.12
0.01190	96.0	104.2	0.69	3.26
0.01165	94.0	106.4	0.71	3.42
0.01141	92.0	108.7	0.74	3.58
0.01116	90.0	111.1	0.76	3.76
0.01091	88.0	113.6	0.80	3.95
0.01066	86.0	116.3	0.84	4.16
0.01041	84.0	119.0	0.89	4.39
0.01017	82.0	122.0	0.94	4.64
0.00992	80.0	125.0	1.02	4.92
0.00967	78.0	128.2	1.10	5.23
0.00942	76.0	131.6	1.22	5.58
0.00917	74.0	135.1	1.36	5.97
0.00893	72.0	138.9	1.56	6.44
0.00868	70.0	142.9	1.82	6.98
0.00843	68.0	147.1	2.20	7.62
0.00818	66.0	151.5	2.76	8.38
0.00794	64.0	156.3	3.65	9.27
0.00769	62.0	161.3	5.15	10.18
0.00744	60.0	166.7	7.59	10.61
0.00719	58.0	172.4	10.55	9.33
0.00694	56.0	178.6	12.00	6.42
0.00670	54.0	185.2	11.64	3.96
0.00645	52.0	192.3	10.75	2.50
0.00620	50.0	200.0	9.91	1.66
0.00595	48.0	208.3	9.20	1.16
0.00570	46.0	217.4	8.63	0.85
0.00546	44.0	227.3	8.17	0.63
0.00521	42.0	238.1	7.78	0.49
0.00496	40.0	250.0	7.47	0.38
0.00372	30.0	333.3	6.46	0.13
0.00248	20.0	500.0	5.97	0.05
0.00124	10.0	1000.0	5.73	0.02
0.0	0.0		5.66	0.0
			5.63 [21]	

Yttrium Aluminum Garnet ($Y_3Al_5O_{12}$)

WILLIAM J. TROPF
Applied Physics Laboratory
The Johns Hopkins University
Laurel, Maryland

Yttrium aluminum garnet (YAG or yttrogarnet), is a synthetic, nonmagnetic material with the chemical formula $Y_3Al_5O_{12}$ or $Y_3Al_2(AlO_4)_3$. It is a host medium for rare-earth-doped, solid-state lasers, a low-loss material for acoustic devices, and a gemstone. YAG crystals have body-centered cubic crystalline structure with space group Ia3d (or O_h^{10}). The unit cell has an edge dimension of 12.008 Å [1] and contains eight formula units, giving a theoretical density of 4.554 g/cm^3. The yttrium atoms occupy the 24(c) sites (222 or D_2 point symmetry), aluminum(1) atoms occupy the 16(a) sites ($\bar{3}$ or $C_{3i}[S_6]$ point symmetry), aluminum(2) atoms occupy the 24(d) sites ($\bar{4}$ or S_4 point symmetry), and the oxygen atoms occupy the 96(h) sites (1 or C_1 point symmetry). YAG undergoes a phase change at 2193 K.

Optical constants above the electronic band gap have been extensively studied by Tomiki *et al.* [2–5] using Kramers–Kronig analyses of reflectance spectra. Professor Tomiki provided approximately 750 values of the complex dielectric constant at 297 K [4], from the band edge at 6.4 eV to 116 eV, in digital form with three decimal places. Selected values of the complex refractive index (n and k) determined from these data are given in Table I.

Yttrium aluminum garnet has a direct band gap at 6.5 eV. The lowest-energy feature in the electronic absorption is excitonic absorption (see later discussion). Interband transitions from the upper valence band of oxygen ($2p^6$) to the conduction bands of yttria ($4d + 5s$ states) dominate the structure from 7 to 15 eV. Optical constants between 15 and 26 eV are mainly due to interband transitions from the oxygen valence bands to conduction bands of yttrium ($5d + 6s$ levels) and aluminum ($3s + 3p$ levels). The valence electrons form a plasma oscillation centered at 23.4 eV.

Inner-core yttria electron transitions occur in the 26 to 35 eV region. At energies above 29.3 eV, absorption is mainly due to transitions from oxygen ($2s^2$) bands to the aluminum ($3p$) conduction band. Plasma oscillations from

HANDBOOK OF OPTICAL CONSTANTS OF SOLIDS III

Copyright © 1998 by Academic Press.
All rights of reproduction in any form reserved
ISBN 0-12-544423-0/$25.00.

the full bands of yttria ($4p^6$) and oxygen ($2s^2$) peak near 36.2 eV. At higher energies, yttria and aluminum electron transitions dominate, especially the prominent aluminum $L_{2,3}$ transitions near 77 eV.

Tomiki *et al.* [3, 5] determined the temperature dependence of exciton absorption between 10 and 297 K from transmission measurements (6.5–7.0 eV) and fitted their data to an Urbach-rule formulation,

$$\beta(E, T) = \beta_0 \exp(-\sigma_s(T)(E_0 - E)/k_B T), \tag{1a}$$

where $\beta(E,T)$ is the absorption coefficient as a function of energy (E) and temperature (T), and k_B is Boltzmann's constant. The slope parameter $\sigma_s(T)$ is given by

$$\sigma_s(T) = \sigma_{s0}\ (2kT/E_{s0}) \tanh(E_{s0}/2kT). \tag{1b}$$

Constants of Eq. (1) are $\beta_0 = 4.093 \times 10^5$ cm^{-1}, $E_0 = 7.047$ eV, $\sigma_{s0} = 0.558$, and $E_{s0} = 36.5$ meV [5]. Values of the imaginary part of the refractive index between 6.4 and 6.6 eV given in Table I are calculated from this equation.

Slack *et al.* [6] measured YAG absorption at 300 K in the vicinity of the Urbach absorption edge. Imaginary index values between 4.5 and 6.6 eV in Table I are taken from his measurements. Values below 6.4 eV are dominated by extrinsic absorption but are similar to those reported by Tomiki *et al.* [2, 3, 5].

Refractive-index measurements in the transparent region are surprisingly sparse. The most comprehensive data set, covering 0.4 to 4.0 μm, is the minimum-deviation prism measurement of Bond [7]. Other measurements (primarily from interferometric techniques) are those of Shchavelev *et al.* [8], McCollum *et al.* [9], and Wilson [10], which are restricted to the visible. Data given in Table I are from Bond [7], Shchavelev *et al.* [8], and McCollum *et al.* [9],

Several sources give Sellmeier dispersion relationships for YAG in the form

$$n^2(\lambda) - 1 = \sum_i \frac{A_i \lambda^2}{\lambda^2 - \lambda_i^2}, \tag{2}$$

where the constants A_i and λ_i are given in Table II. These dispersion formulas are either based on the data of Bond (see [2, 11]) or on visible measurements [12, 13]. Several sources give the temperature dependence of the refractive index [14–16]. All are restricted to the visible or near infrared. Table III lists values of dn/dT with references.

Absorption from the infrared edge of transparency through the region of fundamental lattice vibrations was measured by Slack *et al.* [6] and DeShazer *et al.* [17]. Imaginary-refractive-index values from 840 to 2350 cm^{-1} derived from these measurements are included in Table I.

The fundamental infrared lattice vibrations are studied by Hurrell *et al.* [18], Thirumavalavan *et al.* [19], Gledhill *et al.* [20], and Hofmeister and Campbell [21]. Hurrell *et al.* give the optical irreducible representation as

$$\Gamma = 5A_{1u}(-) + 3A_{1g}(R) + 5A_{2u}(-) + 5A_{2g}(-) + 10E_u(-) + 8E_g(R) + 14F_{1g}(-) + 17F_{1u}(IR) + 14F_{2g}(R) + 16F_{2u}(-) \quad (3)$$

and make the following assignments to the Raman-active modes: A_{1g} vibrations at 373, 561, and 783 cm^{-1}; E_g vibrations at 162, 310, 340, 403, 531, 537, 714, and 758 cm^{-1}; and 11 of 14 F_{2g} modes located at 144, 218, 243, 259, 296, 408, 436, 544, 690, 719, and 857 cm^{-1}. Table IV summarizes measured locations of the infrared-active modes from several sources.

Optical constants in Table I for the region of fundamental lattice vibrations are derived from the models of Gledhill *et al.* [20] and Hofmeister and Campbell [21]. Gledhill *et al.* measured room-temperature reflectivity and fitted the data to a dispersion model of the form

$$n^2(\nu) = \epsilon(\nu) = \epsilon_\infty \sum_j \frac{\nu_{\mathrm{LO}_j}^2 - \nu^2 - i\gamma_{\mathrm{LO}_j}\nu}{\nu_{\mathrm{TO}_j}^2 - \nu^2 - i\gamma_{\mathrm{TO}_j}\nu}, \quad (4)$$

where ν_{TO} and ν_{LO} are the transverse and longitudinal infrared-active optical mode frequencies, γ_{TO} and γ_{LO} are the respective mode widths, and ϵ_∞ the high-frequency (electronic) contribution to the dielectric constant. Hofmeister and Campbell also made reflectivity measurements, preformed a Kramers–Krönig analysis on their data, and fit the resulting optical constants to a Lorentzian (classical) oscillator model of the form

$$n^2(\nu) = \epsilon(\nu) = \epsilon_\infty + \sum_j \frac{f_j \nu_{\mathrm{TO}_j}^2}{\nu_{\mathrm{TO}_j}^2 - \nu^2 - i\gamma_j\nu}, \quad (5)$$

where ν_{TO} is transverse infrared-active optical mode frequency, γ is the mode width, f is the oscillator strength, and ϵ_∞ the high-frequency (electronic) contribution to the dielectric constant. These models were used to calculate the real index between 200 and 2350 cm^{-1} and the imaginary index between 200 and 835 cm^{-1} (or to 1000 cm^{-1} for [21]).

Real refractive index and absorption coefficient below 100 cm^{-1} for Nd-doped YAG were measured by Zhan and Coleman [22] using channeled-spectrum (interference) technique, who also provide a Sellmeier-type dispersion relationship for this regime,

$$n^2 = 9.42 + \frac{0.983\ \nu_0^2}{\nu_0^2 - \nu^2}, \quad (6)$$

where ν is in wave numbers, and ν_0 is the lowest-frequency infrared-active vibration (set to 123 cm^{-1}). In Table I, real-refractive-index values are cal-

culated from this equation, and the imaginary values are derived from the measured absorption coefficient.

The low-frequency (1 MHz) dielectric constant was determined by Shannon *et al.* [23] as $\epsilon = 10.60 \pm 0.05$ (giving $n = 3.26 \pm 0.01$) using a parallel-plate capacitance technique. This value is included in Table I, as well as limiting values from the infrared models of Gledhill *et al.* [20] and Hofmeister and Campbell [21], and the refractive-index model of Zhan and Coleman [22] based on Eq. (6).

Figure 1 shows a composite of the complex refractive index of yttrium aluminum garnet.

ACKNOWLEDGMENT

The author thanks Professor T. Tomiki, University of Ryukyus (retired), for graciously providing digital data from his measurements.

REFERENCES

1. H. S. Yoder and M. L. Keith, Complete substitution of aluminum for silicon: The systems $3MnO \times Al_2O_3 \cdot 3SiO_2 - 3Y_2O_3 \cdot 5Al_2O_3$. *Am. Mineral.* **36**, 519–533 (1951).
2. T. Tomiki, J. Tamashiro, M. Hiraoka, N. Hirata, and T. Futemma, A determination of the spectra of $Y_3Al_5O_{12}$ (YAG)—Reflectivity and intrinsic tail absorptivity in VUV region. *J. Phys. Soc. Jpn.* **57**, 4429–4433 (1988).
3. T. Tomiki, F. Fukudome, M. Kaminao, M. Fujisawa, Y. Tanahara, and T. Futemma, Optical spectra of $Y_3Al_5O_{12}$ (YAG) single crystals in the vacuum ultraviolet region. *J. Phys. Soc. Jpn.* **58**, 1801–1810 (1989).
4. T. Tomiki, Y. Ganaha, T. Shikenbaru, T. Futemma, M. Yuri, Y. Aiura, H. Fukutani, H. Kato, J. Tamashiro, T. Miyahara, and A. Yonesu, Optical spectra of $Y_3Al_5O_{12}$(YAG) single crystals in the vacuum ultraviolet region. II. *J. Phys. Soc. Jpn.* **62**, 1388–1400 (1993).
5. T. Tomiki, Y. Isa, Y. Kadekawa, Y. Ganaha, N. Toyokawa, T. Miyazato, M. Miyazato, T. Kohatsu, H. Shimabukuro, and J. Tamashiro, Optical absorption of single crystals of $Y_3Al_5O_{12}$ and $Y_3Al_5O_{12}$:Nd^{3+} in the UV fundamental absorption edge region. *J. Phys. Soc. Jpn.* **65**, 1106–1113 (1996).
6. G. A. Slack, D. W. Oliver, R. M Chrenko, and S. Roberts, Optical absorption of $Y_3Al_5O_{12}$ from 10− to 55,000 cm^{-1} wave numbers. *Phys. Rev.* **177**, 1308–1314 (1969).
7. W. L. Bond, Measurement of the refractive index of several crystals. *J. Appl. Phys.* **36**, 1674–1677 (1965).
8. O. S. Shchavelev, V. A. Babkina, and Z. S. Mal'tseva, Thermo-optic properties, expansion coefficient and refractive index of yttrium aluminum garnet. *Sov. J. Opt. Technol.* **40**, 623–624 (1973).
9. B. C. McCollum, W. R. Bekebrede, M. Kestigian, and A. B. Smith, Refractive index measurements on magnetic garnet films. *Appl. Phys. Lett.* **23**, 702–703 (1973).
10. K. E. Wilson, Thermo-optics of nonlinear crystals and laser materials. Ph.D. Dissertation, University of Southern California, Los Angeles (January 1980).
11. W. J. Tropf, M. E. Thomas, and T. J. Harris, Properties of crystals and glasses, *in* "Optical Society of America Handbook of Optics" (M. Bass, ed.), 2nd Ed., Chap. 33, McGraw-Hill, New York, 1994.
12. S. H. Wemple and W. J. Tabor, Refractive index behavior of garnets. *J. Appl. Phys.* **44**, 1395–1396 (1973).

13. E. V. Zharikov, Yu. S. Privis, P. A. Studenikin, V. A. Chikov, V. D. Shigorin, and I. A. Shcherbakov, Temperature-wise measurements of refractive indices of rare-earth garnets. *Sov. Phys. Crystallogr.* **34**, 712–714 (1989).
14. J. D. Foster and L. M. Osterink, Index of refraction and expansion thermal coefficients of Nd:YAG. *Appl. Opt.* **7**, 2428–2429 (1968).
15. D. D. Young, K. C. Jungling, T. L. Williamson, and E. R. Nichols, Holographic interferometry measurement of the thermal refractive index coefficient and thermal expansion coefficient of Nd:YAG and Nd:YALO. *IEEE J. Quantum Electon.* **QE-8**, 720–721 (1972).
16. P. R. Stoddart, P. E. Ngoepe, P. M. Mjwara, J. D. Comins, and G. A. Saunders, High-temperature elastic constants of yttrium aluminum garnet. *J. Appl. Phys.* **73**, 7298–7301 (1993).
17. L. G. DeShazer, S. C. Rand, and B. A. Wechsler, Laser crystals, *in* "CRC Handbook of Laser Science and Technology," (M. J. Weber, ed.), Vol. 5. pp. 281–338, CRC Press, Boca Raton, Florida, 1988.
18. J. P. Hurrell, S. P. S. Porto, I. F. Chang, S. S. Mitra, and R. P. Bauman, Optical phonons of yttrium aluminum garnet. *Phys. Rev.* **173**, 851–856 (1968).
19. M. Thirumavalavan, J. Kumar, F. D. Gnanam, and P. Ramasamy, Vibrational spectra of $Y_3Al_5O_{12}$ crystals grown from Ba- and Pb-based Flux systems. *Infrared Phys.* **26**, 101–103 (1986).
20. G. A. Gledhill, P. M. Nikolić, A. Hamilton, S. Stojilković, V. Blagojević, P. Mihajlović, and S. Djurić, FIR optical properties of single crystal $Y_3Al_5O_{12}$ (YAG). *Phys. Status Solidi B* **163**, K123–K128 (1991).
21. A. M. Hofmeister and K. R. Campbell, Infrared Spectroscopy of yttrium aluminum, yttrium gallium, and yttrium iron garnets. *J. Appl. Phys.* **72**, 638–646 (1992).
22. Y. Zhan and P. D. Coleman, Far-IR properties of $Y_3Al_5O_{12}$, $LiYF_4$, $Cs_2NaDyCl_6$, and Rb_2NaYF_6. *Appl. Opt.* **23**, 548–551 (1984).
23. R. D. Shannon, M. A. Subramanian, T. H. Allik, H. Kimura, M. R. Kokta, M. H. Randles, and G. R. Rossman, Dielectric constants of yttrium and rare-earth garnets, the polarizability of gallium oxide, and the oxide additive rule. *J. Appl. Phys.* **67**, 3798–3802 (1990).

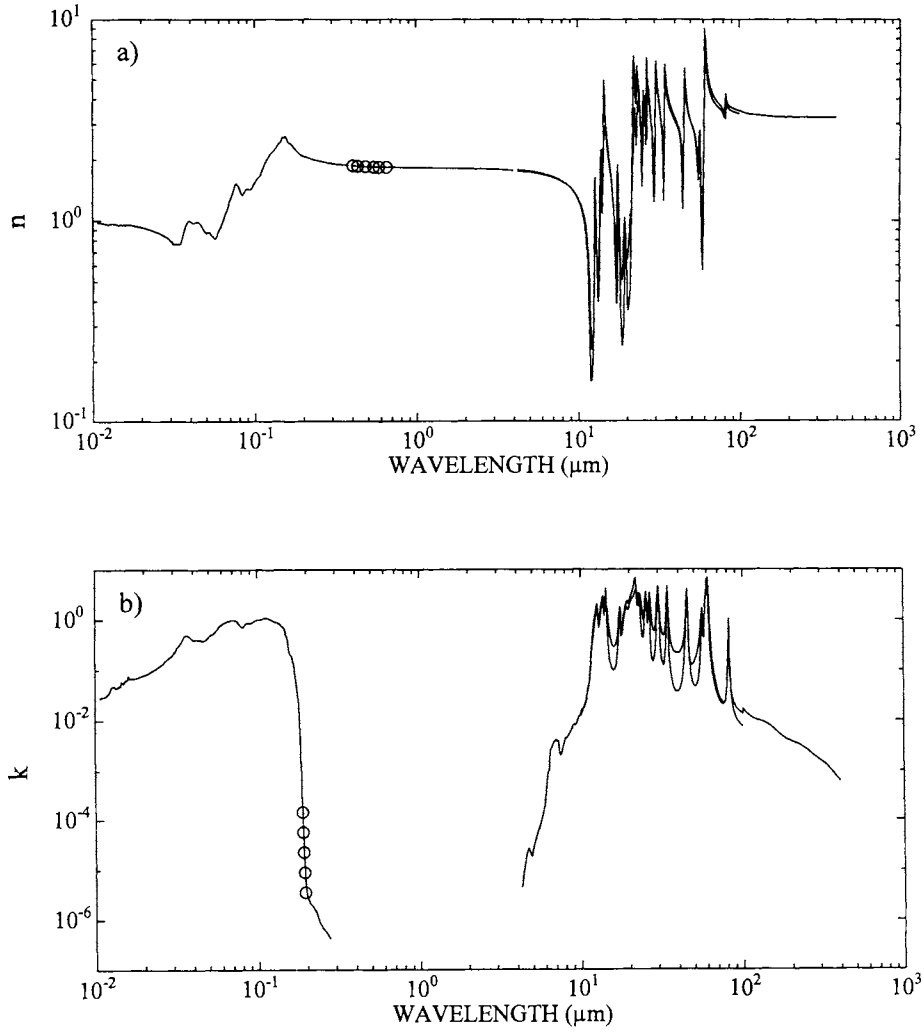

Fig. 1. (a) Log–log plot of the index of refraction n versus wavelength in micrometers for yttrium aluminum garnet. (b) Log–log plot of the extinction coefficient k versus wavelength in micrometers for yttrium aluminum garnet. Lines are data sets of many points; scattered data are indicated by circles.

TABLE I

Values of *n* and *k* for Yttrium Aluminum Garnet (YAG) from Various References

eV	cm^{-1}	μm	*n*	*k*	*n*	*k*
115.982	935451	0.01069	0.978 [4]	0.028 [4]		
114.758	925578	0.01080	0.977	0.028		
113.539	915747	0.01092	0.976	0.028		
112.315	905874	0.01104	0.975	0.029		
111.098	896059	0.01116	0.974	0.029		
109.877	886211	0.01128	0.973	0.029		
108.654	876347	0.01141	0.972	0.029		
107.439	866547	0.01154	0.971	0.030		
106.416	858296	0.01165	0.969	0.030		
105.403	850126	0.01176	0.967	0.030		
104.593	843593	0.01185	0.966	0.032		
103.571	835350	0.01197	0.965	0.033		
102.552	827131	0.01209	0.963	0.033		
101.535	818929	0.01221	0.961	0.035		
100.523	810766	0.01233	0.959	0.038		
99.506	802564	0.01246	0.958	0.041		
98.998	798466	0.01252	0.959	0.043		
98.487	794345	0.01259	0.959	0.044		
97.981	790264	0.01265	0.960	0.046		
97.473	786167	0.01272	0.961	0.046		
96.962	782045	0.01279	0.962	0.047		
96.456	777964	0.01285	0.962	0.047		
95.941	773810	0.01292	0.962	0.047		
95.439	769761	0.01299	0.963	0.048		
94.928	765640	0.01306	0.964	0.049		
94.422	761559	0.01313	0.965	0.049		
93.914	757461	0.01320	0.966	0.048		
93.404	753348	0.01327	0.966	0.047		
92.894	749235	0.01335	0.965	0.046		
92.388	745154	0.01342	0.965	0.045		
91.875	741016	0.01349	0.964	0.044		
91.367	736919	0.01357	0.962	0.044		
90.858	732813	0.01365	0.961	0.044		
90.348	728700	0.01372	0.959	0.045		
89.844	724635	0.01380	0.959	0.046		
89.333	720514	0.01388	0.958	0.046		
88.827	716432	0.01396	0.958	0.047		
88.315	712303	0.01404	0.957	0.048		
87.808	708214	0.01412	0.956	0.049		
87.301	704124	0.01420	0.956	0.048		
86.794	700035	0.01428	0.954	0.048		
86.286	695938	0.01437	0.950	0.048		
85.773	691800	0.01446	0.948	0.054		
85.266	687711	0.01454	0.951	0.059		
84.759	683622	0.01463	0.954	0.058		
84.252	679533	0.01472	0.955	0.058		
83.740	675403	0.01481	0.956	0.056		

(continued)

TABLE I *(Continued)*

Yttrium Aluminum Garnet (YAG)

eV	cm^{-1}	μm	n	k	n	k
83.234	671322	0.01490	0.954	0.055		
82.723	667201	0.01499	0.952	0.055		
82.218	663128	0.01508	0.950	0.056		
81.709	659022	0.01517	0.948	0.058		
81.201	654925	0.01527	0.947	0.061		
80.688	650787	0.01537	0.949	0.064		
80.182	646706	0.01546	0.951	0.065		
79.672	642593	0.01556	0.951	0.064		
79.163	638488	0.01566	0.951	0.064		
78.646	634318	0.01576	0.949	0.063		
78.160	630398	0.01586	0.945	0.068		
77.641	626212	0.01597	0.947	0.074		
77.153	622276	0.01607	0.953	0.076		
76.633	618082	0.01618	0.957	0.072		
76.116	613912	0.01629	0.957	0.069		
75.605	609791	0.01640	0.955	0.068		
75.097	605693	0.01651	0.955	0.068		
74.586	601572	0.01662	0.954	0.068		
74.078	597475	0.01674	0.953	0.068		
73.573	593402	0.01685	0.953	0.067		
73.061	589272	0.01697	0.952	0.068		
72.553	585175	0.01709	0.951	0.068		
71.946	580279	0.01723	0.950	0.068		
71.334	575343	0.01738	0.949	0.068		
70.723	570415	0.01753	0.948	0.069		
70.115	565511	0.01768	0.948	0.069		
69.502	560567	0.01784	0.946	0.069		
68.892	555647	0.01800	0.944	0.070		
68.281	550719	0.01816	0.943	0.071		
67.751	546444	0.01830	0.942	0.072		
67.150	541597	0.01846	0.941	0.072		
66.849	539169	0.01855	0.940	0.073		
66.249	534330	0.01872	0.939	0.073		
65.649	529491	0.01889	0.938	0.075		
65.050	524659	0.01906	0.936	0.076		
64.451	519828	0.01924	0.935	0.076		
63.851	514989	0.01942	0.934	0.078		
63.251	510150	0.01960	0.933	0.078		
62.650	505302	0.01979	0.932	0.078		
62.048	500447	0.01998	0.929	0.080		
61.449	495616	0.02018	0.928	0.081		
60.849	490776	0.02038	0.926	0.083		
60.251	485953	0.02058	0.926	0.082		
59.648	481090	0.02079	0.921	0.083		
59.049	476259	0.02100	0.919	0.086		
58.450	471427	0.02121	0.917	0.088		
57.850	466588	0.02143	0.916	0.088		

TABLE I *(Continued)*

Yttrium Aluminum Garnet (YAG)

eV	cm^{-1}	μm	n	k	n	k
57.249	461741	0.02166	0.913	0.090		
56.650	456909	0.02189	0.911	0.092		
56.049	452062	0.02212	0.909	0.094		
55.450	447231	0.02236	0.906	0.096		
54.851	442400	0.02260	0.904	0.098		
54.251	437560	0.02285	0.901	0.100		
53.650	432713	0.02311	0.898	0.101		
53.051	427882	0.02337	0.895	0.104		
52.449	423026	0.02364	0.893	0.106		
51.851	418203	0.02391	0.889	0.109		
51.250	413356	0.02419	0.886	0.112		
50.650	408517	0.02448	0.882	0.116		
50.051	403685	0.02477	0.879	0.118		
49.450	398838	0.02507	0.875	0.122		
48.850	393999	0.02538	0.871	0.126		
48.251	389167	0.02570	0.867	0.129		
47.650	384320	0.02602	0.863	0.133		
47.050	379481	0.02635	0.859	0.138		
46.450	374642	0.02669	0.854	0.143		
45.849	369794	0.02704	0.849	0.148		
45.250	364963	0.02740	0.844	0.153		
44.650	360124	0.02777	0.838	0.160		
44.051	355292	0.02815	0.834	0.167		
43.450	350445	0.02854	0.829	0.173		
42.850	345606	0.02893	0.823	0.181		
42.249	340758	0.02935	0.818	0.188		
41.650	335927	0.02977	0.808	0.190		
41.051	331096	0.03020	0.793	0.207		
40.449	326241	0.03065	0.790	0.228		
39.850	321409	0.03111	0.773	0.230		
39.249	316562	0.03159	0.768	0.264		
38.650	311731	0.03208	0.772	0.285		
38.050	306892	0.03258	0.772	0.303		
37.450	302052	0.03311	0.770	0.323		
36.850	297213	0.03365	0.765	0.349		
36.250	292374	0.03420	0.765	0.383		
35.650	287534	0.03478	0.775	0.424		
35.050	282695	0.03537	0.808	0.468		
34.450	277856	0.03599	0.854	0.491		
33.850	273016	0.03663	0.900	0.498		
33.250	268177	0.03729	0.942	0.487		
32.650	263338	0.03797	0.970	0.471		
32.050	258499	0.03868	0.992	0.451		
31.450	253659	0.03942	1.000	0.421		
30.850	248820	0.04019	0.991	0.401		
30.250	243981	0.04099	0.978	0.401		
29.650	239141	0.04182	0.973	0.405		

(continued)

TABLE I *(Continued)*

Yttrium Aluminum Garnet (YAG)

eV	cm^{-1}	μm	n	k	n	k
28.960	233576	0.04281	0.977	0.407		
28.302	228269	0.04381	0.982	0.408		
27.673	223196	0.04480	0.981	0.393		
27.072	218349	0.04580	0.964	0.381		
26.496	213703	0.04679	0.938	0.383		
25.944	209251	0.04779	0.913	0.394		
25.414	204976	0.04879	0.889	0.414		
24.906	200879	0.04978	0.872	0.447		
24.418	196943	0.05078	0.870	0.483		
23.948	193152	0.05177	0.877	0.501		
23.496	189507	0.05277	0.869	0.511		
23.061	185998	0.05376	0.852	0.534		
22.642	182619	0.05476	0.838	0.566		
22.238	179360	0.05575	0.826	0.604		
21.847	176207	0.05675	0.820	0.651		
21.471	173174	0.05775	0.825	0.712		
21.107	170238	0.05874	0.857	0.765		
20.755	167399	0.05974	0.894	0.795		
20.415	164657	0.06073	0.915	0.819		
20.085	161995	0.06173	0.940	0.854		
19.767	159430	0.06272	0.972	0.882		
19.611	158172	0.06322	0.988	0.895		
19.458	156938	0.06372	1.005	0.909		
19.307	155720	0.06422	1.025	0.922		
19.158	154518	0.06472	1.045	0.930		
19.012	153341	0.06521	1.064	0.937		
18.868	152179	0.06571	1.082	0.943		
18.726	151034	0.06621	1.099	0.948		
18.587	149913	0.06671	1.114	0.952		
18.449	148800	0.06720	1.126	0.960		
18.313	147703	0.06770	1.142	0.971		
18.180	146630	0.06820	1.161	0.980		
18.048	145566	0.06870	1.181	0.990		
17.918	144517	0.06920	1.205	0.997		
17.790	143485	0.06969	1.230	0.999		
17.664	142469	0.07019	1.254	1.000		
17.540	141469	0.07069	1.277	0.995		
17.417	140476	0.07119	1.295	0.992		
17.296	139501	0.07168	1.313	0.989		
17.177	138541	0.07218	1.331	0.987		
17.059	137589	0.07268	1.350	0.986		
16.943	136653	0.07318	1.372	0.986		
16.828	135726	0.07368	1.399	0.984		
16.715	134814	0.07418	1.427	0.974		
16.604	133919	0.07467	1.455	0.959		
16.494	133032	0.07517	1.481	0.938		
16.385	132153	0.07567	1.499	0.907		

TABLE I *(Continued)*

Yttrium Aluminum Garnet (YAG)

eV	cm^{-1}	μm	n	k	n	k
16.279	131298	0.07616	1.511	0.882		
16.173	130443	0.07666	1.518	0.851		
16.068	129596	0.07716	1.518	0.821		
15.965	128765	0.07766	1.510	0.793		
15.864	127951	0.07816	1.498	0.775		
15.763	127136	0.07866	1.487	0.759		
15.664	126338	0.07915	1.474	0.744		
15.566	125547	0.07965	1.461	0.734		
15.470	124773	0.08015	1.446	0.723		
15.374	123999	0.08065	1.429	0.716		
15.280	123241	0.08114	1.408	0.713		
15.187	122490	0.08164	1.384	0.715		
15.095	121748	0.08214	1.364	0.729		
15.004	121014	0.08263	1.351	0.745		
14.914	120289	0.08313	1.342	0.763		
14.825	119571	0.08363	1.337	0.783		
14.737	118861	0.08413	1.338	0.803		
14.651	118167	0.08463	1.344	0.821		
14.565	117474	0.08513	1.353	0.837		
14.480	116788	0.08563	1.364	0.847		
14.396	116111	0.08612	1.375	0.855		
14.314	115449	0.08662	1.386	0.861		
14.232	114788	0.08712	1.397	0.866		
14.151	114135	0.08762	1.407	0.867		
14.071	113489	0.08811	1.416	0.868		
13.992	112852	0.08861	1.426	0.867		
13.914	112223	0.08911	1.431	0.863		
13.837	111602	0.08960	1.435	0.861		
13.760	110981	0.09011	1.435	0.857		
13.685	110376	0.09060	1.433	0.857		
13.610	109771	0.09110	1.431	0.858		
13.536	109174	0.09160	1.428	0.862		
13.463	108586	0.09209	1.426	0.868		
13.390	107997	0.09260	1.424	0.876		
13.319	107424	0.09309	1.423	0.885		
13.248	106851	0.09359	1.423	0.894		
13.178	106287	0.09408	1.424	0.906		
13.109	105730	0.09458	1.428	0.918		
13.040	105174	0.09508	1.433	0.929		
12.972	104625	0.09558	1.438	0.941		
12.905	104085	0.09608	1.447	0.955		
12.838	103545	0.09658	1.459	0.965		
12.772	103012	0.09708	1.469	0.973		
12.707	102488	0.09757	1.480	0.982		
12.643	101972	0.09807	1.492	0.990		
12.579	101456	0.09857	1.505	0.997		
12.516	100948	0.09906	1.518	1.001		

(continued)

TABLE I *(Continued)*

Yttrium Aluminum Garnet (YAG)

eV	cm^{-1}	μm	n	k	n	k
12.453	100439	0.0996	1.531	1.005		
12.391	99939.4	0.1001	1.543	1.007		
12.330	99447.4	0.1006	1.554	1.010		
12.269	98955.4	0.1011	1.565	1.011		
12.209	98471.4	0.1016	1.576	1.013		
12.149	97987.5	0.1021	1.585	1.012		
12.090	97511.7	0.1026	1.592	1.013		
12.032	97043.9	0.1030	1.600	1.016		
11.974	96576.1	0.1035	1.611	1.019		
11.917	96116.3	0.1040	1.616	1.014		
11.860	95656.6	0.1045	1.621	1.021		
11.804	95204.9	0.1050	1.627	1.022		
11.748	94753.3	0.1055	1.632	1.028		
11.719	94519.4	0.1058	1.636	1.031		
11.609	93632.2	0.1068	1.648	1.038		
11.502	92769.2	0.1078	1.658	1.058		
11.462	92446.5	0.1082	1.668	1.070		
11.356	91591.6	0.1092	1.702	1.085		
11.252	90752.8	0.1102	1.733	1.093		
11.150	89930.1	0.1112	1.763	1.102		
11.050	89123.6	0.1122	1.800	1.109		
10.952	88333.1	0.1132	1.835	1.105		
10.856	87558.9	0.1142	1.871	1.103		
10.761	86792.6	0.1152	1.903	1.090		
10.668	86042.5	0.1162	1.929	1.080		
10.576	85300.5	0.1172	1.954	1.071		
10.486	84574.6	0.1182	1.983	1.061		
10.398	83864.9	0.1192	2.004	1.044		
10.311	83163.2	0.1202	2.023	1.035		
10.225	82469.5	0.1213	2.044	1.027		
10.141	81792.0	0.1223	2.073	1.019		
10.058	81122.6	0.1233	2.094	0.998		
9.977	80469.3	0.1243	2.113	0.984		
9.897	79824.1	0.1253	2.126	0.967		
9.818	79186.9	0.1263	2.145	0.959		
9.740	78557.8	0.1273	2.160	0.941		
9.664	77944.8	0.1283	2.169	0.929		
9.589	77339.9	0.1293	2.189	0.926		
9.515	76743.0	0.1303	2.204	0.910		
9.442	76154.3	0.1313	2.213	0.901		
9.370	75573.5	0.1323	2.240	0.901		
9.299	75000.9	0.1333	2.257	0.882		
9.229	74436.3	0.1343	2.277	0.873		
9.161	73887.9	0.1353	2.294	0.856		
9.093	73339.4	0.1364	2.307	0.845		
9.027	72807.1	0.1373	2.336	0.838		
8.961	72274.8	0.1384	2.352	0.815		

TABLE I *(Continued)*

Yttrium Aluminum Garnet (YAG)

eV	cm^{-1}	μm	*n*	*k*	*n*	*k*
8.896	71750.5	0.1394	2.371	0.803		
8.833	71242.4	0.1404	2.399	0.785		
8.770	70734.3	0.1414	2.411	0.754		
8.708	70234.2	0.1424	2.412	0.739		
8.647	69742.2	0.1434	2.440	0.734		
8.586	69250.2	0.1444	2.446	0.715		
8.527	68774.3	0.1454	2.486	0.717		
8.468	68298.5	0.1464	2.522	0.687		
8.410	67830.7	0.1474	2.578	0.640		
8.391	67677.4	0.1478	2.578	0.613		
8.334	67217.7	0.1488	2.583	0.567		
8.279	66774.1	0.1498	2.581	0.522		
8.224	66330.5	0.1508	2.574	0.487		
8.169	65886.9	0.1518	2.577	0.460		
8.116	65459.4	0.1528	2.585	0.428		
8.063	65032.0	0.1538	2.593	0.387		
8.010	64604.5	0.1548	2.598	0.331		
7.959	64193.2	0.1558	2.565	0.275		
7.908	63781.8	0.1568	2.533	0.242		
7.858	63378.5	0.1578	2.497	0.219		
7.808	62975.3	0.1588	2.467	0.209		
7.759	62580.1	0.1598	2.444	0.206		
7.710	62184.9	0.1608	2.433	0.202		
7.663	61805.8	0.1618	2.421	0.195		
7.615	61418.6	0.1628	2.415	0.190		
7.569	61047.6	0.1638	2.412	0.180		
7.523	60676.6	0.1648	2.409	0.165		
7.477	60305.6	0.1658	2.402	0.149		
7.432	59942.6	0.1668	2.396	0.133		
7.388	59587.8	0.1678	2.386	0.115		
7.344	59232.9	0.1688	2.373	0.0974		
7.301	58886.1	0.1698	2.356	0.0838		
7.258	58539.3	0.1708	2.342	0.0726		
7.215	58192.4	0.1718	2.326	0.0630		
7.173	57853.7	0.1728	2.313	0.0549		
7.132	57523.0	0.1738	2.298	0.0479		
7.091	57192.3	0.1748	2.285	0.0431		
7.051	56869.7	0.1758	2.275	0.0369		
7.011	56547.1	0.1768	2.261	0.0318		
6.971	56224.5	0.1779	2.252	0.0271		
6.932	55909.9	0.1789	2.241	0.0205		
6.893	55595.4	0.1799	2.228	0.0159		
6.855	55288.9	0.1809	2.217	0.0129		
6.817	54982.4	0.1819	2.208	0.00806		
6.780	54684.0	0.1829	2.195	0.00406		
6.743	54385.5	0.1839	2.183	0.00204		0.0020 [6]
6.600	53232.2	0.1879		1.44E-4 [5]		1.51E-4

(continued)

TABLE I *(Continued)*

Yttrium Aluminum Garnet (YAG)

eV	cm^{-1}	μm	*n*	*k*	*n*	*k*
6.550	52828.9	0.1893		5.71E-5		6.25E-5
6.500	52425.6	0.1907	2.120	2.26E-5		2.78E-5
6.450	52022.3	0.1922		8.96E-6		1.37E-5
6.400	51619.1	0.1937		3.55E-6		6.01E-6
6.250	50409.3	0.1984	2.088			3.03E-6
6.000	48392.9	0.2066	2.059			2.18E-6
5.750	46376.5	0.2156	2.033			1.84E-6
5.500	44360.1	0.2254	2.009			1.44E-6
5.250	42343.8	0.2362	1.987			9.06E-7
5.000	40327.4	0.2480	1.968			6.85E-7
4.750	38311.0	0.2610	1.950			5.67E-7
4.500	36294.7	0.2755	1.933			4.23E-7
4.250	34278.3	0.2917	1.918			
4.000	32261.9	0.3100	1.905			
3.750	30245.6	0.3306	1.892			
3.500	28229.2	0.3542	1.881			
3.250	26212.8	0.3815	1.871			
3.0996	25000	0.4000	1.8650 [7]			
3.0614	24691.4	0.4050			1.85977 [8]	
2.8568	23041.5	0.4340			1.85282	
2.8437	22935.8	0.4360			1.85246	
2.7552	22222.2	0.4500	1.8532			
2.5511	20576.1	0.4860			1.84367	
2.4797	20000	0.5000	1.8450			
2.11	17018.4	0.5876			1.83260	
2.105	16977.9	0.5890			1.83247	
2.0664	16666.7	0.6000	1.8347			
1.89	15243.9	0.6560			1.82785	
1.7712	14285.7	0.70	1.8285			
1.5498	12500	0.80	1.8245			
1.3776	11111.1	0.90	1.8222			
1.2399	10000	1.00	1.8197			
1.1271	9090.9	1.10	1.8170			
1.0332	8333.3	1.20	1.8152			
0.8856	7142.9	1.40	1.8121			
0.7749	6250.0	1.60	1.8093			
0.6888	5555.6	1.80	1.8065			
0.6199	5000.0	2.00	1.8035			
0.5636	4545.5	2.20	1.8004			
0.5166	4166.7	2.40	1.7970			
0.4769	3846.2	2.60	1.7935			
0.4428	3571.4	2.80	1.7896			
0.4133	3333.3	3.00	1.7855			
0.3875	3125.0	3.20	1.7810			
0.3647	2941.2	3.40	1.7764			
0.3444	2777.8	3.60	1.7713			
0.3263	2631.6	3.80	1.7659			

TABLE I *(Continued)*

Yttrium Aluminum Garnet (YAG)

eV	cm^{-1}	μm	n	k	n	k
0.3100	2500.0	4.00	1.7602			
0.2914	2350.0	4.2553	1.76 [20]	4.51E-6 [6]	1.77 [21]	
0.2901	2340.0	4.2735	1.75	4.97E-6	1.77	
0.2889	2330.0	4.2918	1.75	5.63E-6	1.77	
0.2876	2320.0	4.3103	1.75	6.30E-6	1.77	
0.2864	2310.0	4.3290	1.75	6.99E-6	1.77	
0.2852	2300.0	4.3478	1.75	7.76E-6	1.77	
0.2839	2290.0	4.3668	1.75	8.63E-6	1.77	
0.2827	2280.0	4.3860	1.75	9.55E-6	1.77	
0.2814	2270.0	4.4053	1.75	1.05E-5	1.77	
0.2802	2260.0	4.4248	1.75	1.13E-5	1.77	
0.2790	2250.0	4.4444	1.75	1.23E-5	1.77	
0.2777	2240.0	4.4643	1.75	1.33E-5	1.77	
0.2765	2230.0	4.4843	1.75	1.45E-5	1.76	
0.2752	2220.0	4.5045	1.75	1.58E-5	1.76	
0.2740	2210.0	4.5249	1.75	1.70E-5	1.76	
0.2728	2200.0	4.5455	1.75	1.83E-5	1.76	
0.2715	2190.0	4.5662	1.75	1.95E-5	1.76	
0.2703	2180.0	4.5872	1.75	2.09E-5	1.76	
0.2690	2170.0	4.6083	1.74	2.23E-5	1.76	
0.2678	2160.0	4.6296	1.74	2.35E-5	1.76	
0.2666	2150.0	4.6512	1.74	2.46E-5	1.76	
0.2653	2140.0	4.6729	1.74	2.56E-5	1.76	
0.2641	2130.0	4.6948	1.74	2.65E-5	1.76	
0.2628	2120.0	4.7170	1.74	2.64E-5	1.76	
0.2616	2110.0	4.7393	1.74	2.59E-5	1.76	
0.2604	2100.0	4.7619	1.74	2.50E-5	1.76	
0.2591	2090.0	4.7847	1.74	2.38E-5	1.75	
0.2579	2080.0	4.8077	1.74	2.28E-5	1.75	
0.2566	2070.0	4.8309	1.74	2.19E-5	1.75	
0.2554	2060.0	4.8544	1.74	2.10E-5	1.75	
0.2542	2050.0	4.8780	1.74	2.01E-5	1.75	
0.2529	2040.0	4.9020	1.73	1.89E-5	1.75	
0.2517	2030.0	4.9261	1.73	1.89E-5	1.75	
0.2505	2020.0	4.9505	1.73	2.02E-5	1.75	
0.2492	2010.0	4.9751	1.73	2.24E-5	1.75	
0.2480	2000.0	5.0000	1.73	2.45E-5	1.75	
0.2467	1990.0	5.0251	1.73	2.64E-5	1.75	
0.2455	1980.0	5.0505	1.73	2.84E-5	1.74	
0.2443	1970.0	5.0761	1.73	3.08E-5	1.74	
0.2430	1960.0	5.1020	1.73	3.30E-5	1.74	
0.2418	1950.0	5.1282	1.73	3.51E-5	1.74	
0.2405	1940.0	5.1546	1.72	3.71E-5	1.74	
0.2393	1930.0	5.1813	1.72	3.91E-5	1.74	
0.2381	1920.0	5.2083	1.72	4.11E-5	1.74	
0.2368	1910.0	5.2356	1.72	4.30E-5	1.74	
0.2356	1900.0	5.2632	1.72	4.49E-5	1.74	

(continued)

TABLE I *(Continued)*

Yttrium Aluminum Garnet (YAG)

eV	cm^{-1}	μm	n	k	n	k
0.2343	1890.0	5.2910	1.72	4.74E-5	1.74	
0.2331	1880.0	5.3191	1.72	5.02E-5	1.73	
0.2319	1870.0	5.3476	1.72	5.29E-5	1.73	
0.2306	1860.0	5.3763	1.72	5.62E-5	1.73	
0.2294	1850.0	5.4054	1.71	5.97E-5	1.73	
0.2281	1840.0	5.4348	1.71	6.30E-5	1.73	
0.2269	1830.0	5.4645	1.71	6.63E-5	1.73	
0.2257	1820.0	5.4945	1.71	6.99E-5	1.73	
0.2244	1810.0	5.5249	1.71	7.38E-5	1.72	
0.2232	1800.0	5.5556	1.71	7.77E-5	1.72	
0.2219	1790.0	5.5866	1.71	8.31E-5	1.72	
0.2207	1780.0	5.6180	1.71	8.85E-5	1.72	
0.2195	1770.0	5.6497	1.70	9.53E-5	1.72	
0.2182	1760.0	5.6818	1.70	1.02E-4	1.72	
0.2170	1750.0	5.7143	1.70	1.10E-4	1.72	
0.2157	1740.0	5.7471	1.70	1.19E-4	1.71	
0.2145	1730.0	5.7803	1.70	1.29E-4	1.71	
0.2133	1720.0	5.8140	1.70	1.40E-4	1.71	
0.2120	1710.0	5.8480	1.70	1.53E-4	1.71	
0.2108	1700.0	5.8824	1.69	1.70E-4	1.71	
0.2095	1690.0	5.9172	1.69	1.79E-4	1.71	
0.2083	1680.0	5.9524	1.69	1.88E-4	1.70	
0.2071	1670.0	5.9880	1.69	2.16E-4	1.70	
0.2058	1660.0	6.0241	1.69	2.55E-4	1.70	
0.2046	1650.0	6.0606	1.68	3.34E-4	1.70	
0.2033	1640.0	6.0976	1.68	4.65E-4	1.70	
0.2021	1630.0	6.1350	1.68	6.05E-4	1.70	
0.2009	1620.0	6.1728	1.68	7.27E-4	1.69	
0.1996	1610.0	6.2112	1.68	8.56E-4	1.69	
0.1984	1600.0	6.2500	1.68	9.51E-4	1.69	
0.1971	1590.0	6.2893	1.67	9.84E-4	1.69	
0.1959	1580.0	6.3291	1.67	1.01E-3	1.68	
0.1947	1570.0	6.3694	1.67	1.18E-3	1.68	
0.1934	1560.0	6.4103	1.67	1.64E-3	1.68	
0.1922	1550.0	6.4516	1.66	2.09E-3	1.68	
0.1909	1540.0	6.4935	1.66	2.54E-3	1.68	
0.1897	1530.0	6.5359	1.66	2.75E-3	1.67	
0.1885	1520.0	6.5789	1.66	2.82E-3	1.67	
0.1872	1510.0	6.6225	1.65	2.87E-3	1.67	
0.1860	1500.0	6.6667	1.65	3.15E-3	1.66	
0.1847	1490.0	6.7114	1.65	3.33E-3	1.66	
0.1835	1480.0	6.7568	1.65	3.49E-3	1.66	
0.1823	1470.0	6.8027	1.64	3.66E-3	1.66	
0.1810	1460.0	6.8493	1.64	3.88E-3	1.65	
0.1798	1450.0	6.8966	1.64	3.97E-3	1.65	
0.1785	1440.0	6.9444	1.64	3.94E-3	1.65	
0.1773	1430.0	6.9930	1.63	4.02E-3	1.64	

TABLE I *(Continued)*

Yttrium Aluminum Garnet (YAG)

eV	cm^{-1}	μm	n	k	n	k
0.1761	1420.0	7.0423	1.63	3.84E-3	1.64	
0.1748	1410.0	7.0922	1.63	3.83E-3	1.64	
0.1736	1400.0	7.1429	1.62	3.89E-3	1.63	
0.1723	1390.0	7.1942	1.62	3.94E-3	1.63	
0.1711	1380.0	7.2464	1.61	3.88E-3	1.63	
0.1699	1370.0	7.2993	1.61	3.50E-3	1.62	
0.1686	1360.0	7.3529	1.61	2.47E-3	1.62	
0.1674	1350.0	7.4074	1.60	2.18E-3	1.61	
0.1661	1340.0	7.4627	1.60	2.07E-3	1.61	
0.1649	1330.0	7.5188	1.60	2.10E-3	1.60	
0.1637	1320.0	7.5758	1.59	2.18E-3	1.60	
0.1624	1310.0	7.6336	1.59	2.28E-3	1.60	
0.1612	1300.0	7.6923	1.58	2.72E-3	1.59	
0.1599	1290.0	7.7519	1.58	2.96E-3	1.59	
0.1587	1280.0	7.8125	1.57	3.21E-3	1.58	
0.1575	1270.0	7.8740	1.57	3.58E-3	1.57	
0.1562	1260.0	7.9365	1.56	4.07E-3	1.57	
0.1550	1250.0	8.0000	1.56	4.43E-3	1.56	
0.1537	1240.0	8.0645	1.55	4.49E-3	1.56	
0.1525	1230.0	8.1301	1.54	4.41E-3	1.55	
0.1513	1220.0	8.1967	1.54	4.48E-3	1.54	
0.1500	1210.0	8.2645	1.53	4.74E-3	1.54	
0.1488	1200.0	8.3333	1.53	4.99E-3	1.53	
0.1475	1190.0	8.4034	1.52	5.25E-3	1.52	
0.1463	1180.0	8.4746	1.51	5.51E-3	1.52	
0.1451	1170.0	8.5470	1.50	5.80E-3	1.51	
0.1438	1160.0	8.6207	1.50	6.17E-3	1.50	
0.1426	1150.0	8.6957	1.49	6.51E-3	1.49	
0.1413	1140.0	8.7719	1.48	6.90E-3	1.48	
0.1401	1130.0	8.8496	1.47	7.31E-3	1.47	
0.1389	1120.0	8.9286	1.46	7.69E-3	1.46	
0.1376	1110.0	9.0090	1.45	8.04E-3	1.45	
0.1364	1100.0	9.0909	1.44	8.22E-3	1.44	
0.1351	1090.0	9.1743	1.43	8.02E-3	1.43	
0.1339	1080.0	9.2593	1.42	7.98E-3	1.41	
0.1327	1070.0	9.3458	1.41	8.18E-3	1.40	
0.1314	1060.0	9.4340	1.39	8.88E-3	1.39	
0.1302	1050.0	9.5238	1.38	9.72E-3	1.37	
0.1289	1040.0	9.6154	1.36	0.0105	1.36	
0.1277	1030.0	9.7087	1.35	0.0116	1.34	
0.1265	1020.0	9.8039	1.33	0.0120	1.32	
0.1252	1010.0	9.9010	1.31	0.0125	1.30	
0.1240	1000.0	10.000	1.30	0.0142	1.28	0.0122 [20]
0.1234	995.0	10.050	1.29	0.0148	1.27	0.0127
0.1227	990.0	10.101	1.28	0.0157	1.26	0.0133
0.1221	985.0	10.152	1.26	0.0161	1.24	0.0139
0.1215	980.0	10.204	1.25	0.0166	1.23	0.0146

(continued)

TABLE I *(Continued)*

Yttrium Aluminum Garnet (YAG)

eV	cm^{-1}	μm	n	k	n	k
0.1209	975.0	10.256	1.24	0.0171	1.22	0.0153
0.1203	970.0	10.309	1.23	0.0171	1.20	0.0160
0.1196	965.0	10.363	1.22	0.0172	1.19	0.0169
0.1190	960.0	10.417	1.20	0.0174	1.18	0.0178
0.1184	955.0	10.471	1.19	0.0182	1.16	0.0188
0.1178	950.0	10.526	1.17	0.0187	1.14	0.0198
0.1172	945.0	10.582	1.16	0.0196	1.12	0.0210
0.1165	940.0	10.638	1.14	0.0206	1.11	0.0223
0.1159	935.0	10.695	1.13	0.0216	1.09	0.0238
0.1153	930.0	10.753	1.11	0.0225	1.07	0.0254
0.1147	925.0	10.811	1.09	0.0242	1.04	0.0272
0.1141	920.0	10.870	1.07	0.0259	1.02	0.0293
0.1134	915.0	10.929	1.05	0.0285	0.99	0.0316
0.1128	910.0	10.989	1.03	0.0384	0.97	0.0343
0.1122	905.0	11.050	1.00	0.0427	0.94	0.0374
0.1116	900.0	11.111	0.97	0.0462	0.90	0.0410
0.1110	895.0	11.173	0.95	0.0492	0.87	0.0453
0.1103	890.0	11.236	0.92	0.0528	0.83	0.0505
0.1097	885.0	11.299	0.88	0.0571	0.79	0.0568
0.1091	880.0	11.364	0.85	0.0637	0.74	0.0648
0.1085	875.0	11.429	0.80	0.0938	0.68	0.0752
0.1079	870.0	11.494	0.76	0.116	0.62	0.0894
0.1072	865.0	11.561	0.71	0.158	0.55	0.110
0.1066	860.0	11.628	0.65	0.216	0.46	0.143
0.1060	855.0	11.696	0.58	0.250	0.35	0.204
0.1054	850.0	11.765	0.50	0.298	0.25	0.313
0.1048	845.0	11.834	0.41	0.353	0.20	0.446
0.1041	840.0	11.905	0.32	0.413	0.17	0.574
0.1035	835.0	11.976	0.27	0.419 [19]	0.16	0.694
0.1029	830.0	12.048	0.24	0.546	0.16	0.810
0.1023	825.0	12.121	0.23	0.668	0.16	0.926
0.1017	820.0	12.195	0.23	0.788	0.18	1.05
0.1010	815.0	12.270	0.25	0.909	0.20	1.17
0.1004	810.0	12.346	0.27	1.04	0.23	1.31
0.0998	805.0	12.422	0.32	1.17	0.28	1.47
0.0992	800.0	12.500	0.39	1.32	0.37	1.66
0.0986	795.0	12.579	0.51	1.49	0.56	1.87
0.0979	790.0	12.658	0.74	1.65	0.93	2.05
0.0973	785.0	12.739	1.14	1.67	1.50	1.85
0.0967	780.0	12.821	1.47	1.30	1.62	1.24
0.0961	775.0	12.903	1.34	0.864	1.31	0.879
0.0955	770.0	12.987	1.02	0.704	0.94	0.808
0.0948	765.0	13.072	0.72	0.775	0.64	0.945
0.0942	760.0	13.158	0.54	0.984	0.47	1.18
0.0936	755.0	13.245	0.48	1.22	0.41	1.43
0.0930	750.0	13.333	0.49	1.44	0.40	1.67
0.0924	745.0	13.423	0.55	1.66	0.44	1.92

TABLE I *(Continued)*

Yttrium Aluminum Garnet (YAG)

eV	cm^{-1}	μm	n	k	n	k
0.0917	740.0	13.514	0.67	1.88	0.53	2.19
0.0911	735.0	13.605	0.88	2.09	0.71	2.48
0.0905	730.0	13.699	1.24	2.24	1.03	2.78
0.0899	725.0	13.793	1.73	2.11	1.60	2.94
0.0893	720.0	13.889	1.91	1.57	2.22	2.58
0.0886	715.0	13.986	1.52	1.24	2.25	1.94
0.0880	710.0	14.085	1.10	1.49	1.77	1.71
0.0874	705.0	14.184	1.09	1.98	1.31	2.11
0.0868	700.0	14.286	1.44	2.39	1.35	3.03
0.0862	695.0	14.388	2.04	2.53	2.60	4.17
0.0855	690.0	14.493	2.63	2.26	4.93	2.70
0.0849	685.0	14.599	2.92	1.75	4.31	1.00
0.0843	680.0	14.706	2.92	1.29	3.65	0.520
0.0837	675.0	14.815	2.80	0.973	3.22	0.337
0.0831	670.0	14.925	2.65	0.762	2.92	0.247
0.0825	665.0	15.038	2.50	0.619	2.70	0.195
0.0818	660.0	15.152	2.37	0.519	2.52	0.162
0.0812	655.0	15.267	2.25	0.448	2.36	0.140
0.0806	650.0	15.385	2.13	0.396	2.23	0.125
0.0800	645.0	15.504	2.03	0.358	2.11	0.114
0.0794	640.0	15.625	1.93	0.329	2.01	0.106
0.0787	635.0	15.748	1.84	0.309	1.90	0.101
0.0781	630.0	15.873	1.75	0.295	1.80	0.0983
0.0775	625.0	16.000	1.66	0.286	1.71	0.0974
0.0769	620.0	16.129	1.57	0.284	1.61	0.0986
0.0763	615.0	16.260	1.48	0.287	1.51	0.102
0.0756	610.0	16.393	1.38	0.297	1.40	0.108
0.0750	605.0	16.529	1.27	0.316	1.28	0.119
0.0744	600.0	16.667	1.15	0.350	1.15	0.136
0.0738	595.0	16.807	1.02	0.409	1.00	0.165
0.0732	590.0	16.949	0.87	0.515	0.81	0.224
0.0725	585.0	17.094	0.72	0.712	0.56	0.374
0.0719	580.0	17.241	0.65	1.030	0.39	0.701
0.0713	575.0	17.391	0.79	1.485	0.39	1.09
0.0707	570.0	17.544	1.66	1.744	0.62	1.55
0.0701	565.0	17.699	1.87	0.739	1.53	1.59
0.0694	560.0	17.857	1.40	0.471	1.46	0.678
0.0688	555.0	18.018	1.06	0.486	0.93	0.501
0.0682	550.0	18.182	0.80	0.613	0.51	0.672
0.0676	545.0	18.349	0.62	0.816	0.32	0.984
0.0670	540.0	18.519	0.54	1.04	0.26	1.25
0.0663	535.0	18.692	0.51	1.26	0.24	1.49
0.0657	530.0	18.868	0.54	1.47	0.26	1.71
0.0651	525.0	19.048	0.63	1.68	0.30	1.94
0.0645	520.0	19.231	0.84	1.81	0.40	2.17
0.0639	515.0	19.417	1.03	1.69	0.62	2.38
0.0632	510.0	19.608	0.91	1.56	0.92	2.31

(continued)

TABLE I *(Continued)*

Yttrium Aluminum Garnet (YAG)

eV	cm^{-1}	μm	n	k	n	k
0.0626	505.0	19.802	0.74	1.66	0.81	2.07
0.0620	500.0	20.000	0.66	1.85	0.53	2.19
0.0614	495.0	20.202	0.65	2.05	0.39	2.49
0.0608	490.0	20.408	0.68	2.26	0.36	2.81
0.0601	485.0	20.619	0.75	2.47	0.38	3.16
0.0595	480.0	20.833	0.87	2.67	0.43	3.55
0.0589	475.0	21.053	1.07	2.81	0.55	4.02
0.0583	470.0	21.277	1.08	2.88	0.76	4.63
0.0577	465.0	21.505	1.15	3.23	1.20	5.45
0.0570	460.0	21.739	1.46	3.60	2.32	6.55
0.0564	455.0	21.978	2.01	3.89	5.27	6.72
0.0558	450.0	22.222	2.90	3.87	6.56	3.52
0.0552	445.0	22.472	3.59	2.93	5.22	1.93
0.0546	440.0	22.727	2.87	2.11	3.89	1.91
0.0539	435.0	22.989	2.36	2.77	3.81	3.36
0.0533	430.0	23.256	3.02	3.24	5.84	2.51
0.0527	425.0	23.529	3.79	2.83	5.19	1.00
0.0521	420.0	23.810	3.97	2.05	4.42	0.588
0.0515	415.0	24.096	3.68	1.40	3.81	0.454
0.0508	410.0	24.390	3.11	1.01	3.21	0.450
0.0502	405.0	24.691	2.22	0.988	2.43	0.670
0.0496	400.0	25.000	1.47	2.24	1.60	2.12
0.0490	395.0	25.316	2.84	3.34	4.41	3.55
0.0484	390.0	25.641	3.47	2.27	3.82	1.85
0.0477	385.0	25.974	3.90	1.61	4.12	0.841
0.0471	380.0	26.316	2.64	1.44	2.37	1.32
0.0465	375.0	26.667	2.51	3.34	6.40	3.40
0.0459	370.0	27.027	4.98	2.45	4.90	0.393
0.0453	365.0	27.397	4.43	1.14	4.14	0.198
0.0446	360.0	27.778	3.87	0.770	3.71	0.153
0.0440	355.0	28.169	3.42	0.626	3.36	0.147
0.0434	350.0	28.571	2.97	0.588	3.01	0.172
0.0428	345.0	28.986	2.39	0.698	2.55	0.260
0.0422	340.0	29.412	1.59	1.39	1.75	0.661
0.0419	338.0	29.586	1.43	2.04	1.33	1.24
0.0417	336.0	29.762	1.55	2.81	1.23	2.17
0.0414	334.0	29.940	2.05	3.64	1.56	3.26
0.0412	332.0	30.120	3.16	4.27	2.72	4.52
0.0409	330.0	30.303	4.69	3.96	5.44	4.39
0.0407	328.0	30.488	5.40	2.74	6.16	2.01
0.0404	326.0	30.675	5.27	1.80	5.49	0.932
0.0402	324.0	30.864	4.96	1.27	4.95	0.535
0.0399	322.0	31.056	4.66	0.974	4.57	0.355
0.0397	320.0	31.250	4.41	0.796	4.30	0.260
0.0394	318.0	31.447	4.19	0.681	4.09	0.204
0.0392	316.0	31.646	4.01	0.604	3.91	0.170
0.0389	314.0	31.847	3.84	0.551	3.76	0.148

TABLE I *(Continued)*

Yttrium Aluminum Garnet (YAG)

eV	cm^{-1}	μm	n	k	n	k
0.0387	312.0	32.051	3.68	0.516	3.62	0.134
0.0384	310.0	32.258	3.53	0.494	3.49	0.126
0.0382	308.0	32.468	3.38	0.485	3.36	0.125
0.0379	306.0	32.680	3.21	0.491	3.22	0.129
0.0377	304.0	32.895	3.03	0.516	3.06	0.141
0.0374	302.0	33.113	2.81	0.574	2.88	0.167
0.0372	300.0	33.333	2.54	0.692	2.64	0.219
0.0369	298.0	33.557	2.20	0.948	2.29	0.338
0.0367	296.0	33.784	1.85	1.52	1.72	0.697
0.0365	294.0	34.014	1.84	2.49	1.25	1.894
0.0362	292.0	34.247	2.59	3.68	1.90	3.754
0.0360	290.0	34.483	4.67	4.04	5.61	4.466
0.0357	288.0	34.722	5.80	2.28	5.95	1.202
0.0355	286.0	34.965	5.40	1.17	5.07	0.463
0.0352	284.0	35.211	4.96	0.738	4.59	0.252
0.0350	282.0	35.461	4.64	0.539	4.30	0.164
0.0347	280.0	35.714	4.41	0.433	4.10	0.120
0.0345	278.0	35.971	4.23	0.369	3.96	0.0941
0.0342	276.0	36.232	4.09	0.327	3.84	0.0776
0.0340	274.0	36.496	3.98	0.298	3.75	0.0665
0.0337	272.0	36.765	3.88	0.277	3.67	0.0587
0.0335	270.0	37.037	3.79	0.262	3.60	0.0529
0.0332	268.0	37.313	3.72	0.250	3.53	0.0485
0.0330	266.0	37.594	3.65	0.240	3.48	0.0452
0.0327	264.0	37.879	3.59	0.233	3.42	0.0426
0.0325	262.0	38.168	3.53	0.227	3.38	0.0407
0.0322	260.0	38.462	3.47	0.222	3.33	0.0392
0.0320	258.0	38.760	3.42	0.219	3.28	0.0382
0.0317	256.0	39.063	3.37	0.217	3.24	0.0375
0.0315	254.0	39.370	3.32	0.215	3.20	0.0372
0.0312	252.0	39.683	3.27	0.215	3.15	0.0372
0.0310	250.0	40.000	3.22	0.216	3.11	0.0377
0.0307	248.0	40.323	3.17	0.218	3.06	0.0386
0.0305	246.0	40.650	3.12	0.221	3.02	0.0401
0.0303	244.0	40.984	3.07	0.226	2.97	0.0423
0.0300	242.0	41.322	3.01	0.233	2.91	0.0454
0.0298	240.0	41.667	2.94	0.242	2.85	0.0499
0.0295	238.0	42.017	2.87	0.256	2.78	0.0563
0.0293	236.0	42.373	2.79	0.275	2.70	0.0657
0.0290	234.0	42.735	2.70	0.302	2.60	0.0801
0.0288	232.0	43.103	2.58	0.342	2.48	0.103
0.0285	230.0	43.478	2.44	0.409	2.31	0.145
0.0283	228.0	43.860	2.23	0.527	2.06	0.231
0.0280	226.0	44.248	1.95	0.774	1.64	0.464
0.0278	224.0	44.643	1.65	1.36	1.14	1.30
0.0275	222.0	45.045	1.74	2.48	1.46	2.80
0.0273	220.0	45.455	3.29	3.91	3.96	4.10

(continued)

TABLE I *(Continued)*

Yttrium Aluminum Garnet (YAG)

eV	cm^{-1}	μm	n	k	n	k
0.0270	218.0	45.872	5.65	1.92	5.29	1.35
0.0268	216.0	46.296	4.81	0.559	4.50	0.469
0.0265	214.0	46.729	4.24	0.267	4.05	0.239
0.0263	212.0	47.170	3.91	0.176	3.78	0.149
0.0260	210.0	47.619	3.69	0.142	3.60	0.106
0.0258	208.0	48.077	3.53	0.129	3.46	0.0817
0.0255	206.0	48.544	3.40	0.125	3.35	0.0672
0.0253	204.0	49.020	3.29	0.126	3.26	0.0581
0.0250	202.0	49.505	3.19	0.131	3.18	0.0523
0.0248	200.0	50.000	3.10	0.138	3.10	0.0489
0.0245	198.0	50.505	3.02	0.148	3.02	0.0472
0.0243	196.0	51.020	2.93	0.160	2.95	0.0470
0.0241	194.0	51.546	2.84	0.177	2.87	0.0483
0.0238	192.0	52.083	2.74	0.199	2.79	0.0513
0.0236	190.0	52.632	2.63	0.230	2.69	0.0568
0.0233	188.0	53.191	2.51	0.274	2.59	0.0660
0.0231	186.0	53.763	2.35	0.344	2.45	0.0822
0.0228	184.0	54.348	2.17	0.466	2.27	0.114
0.0226	182.0	54.945	1.95	0.713	2.01	0.198
0.0223	180.0	55.556	1.88	1.24	1.58	0.576
0.0221	178.0	56.180	2.61	1.68	2.33	1.49
0.0218	176.0	56.818	2.78	0.743	2.36	0.491
0.0216	174.0	57.471	1.95	0.588	1.62	0.444
0.0213	172.0	58.140	1.14	1.20	0.74	1.14
0.0211	170.0	58.824	0.92	2.33	0.57	2.38
0.0208	168.0	59.524	1.13	3.56	0.78	3.82
0.0206	166.0	60.241	1.97	5.20	1.87	6.22
0.0203	164.0	60.976	5.40	6.80	8.97	5.77
0.0201	162.0	61.728	7.93	2.64	7.04	0.998
0.0198	160.0	62.500	6.56	0.887	5.74	0.387
0.0196	158.0	63.291	5.71	0.423	5.11	0.211
0.0193	156.0	64.103	5.21	0.245	4.73	0.135
0.0191	154.0	64.935	4.87	0.159	4.47	0.0953
0.0188	152.0	65.789	4.64	0.111	4.29	0.0718
0.0186	150.0	66.667	4.46	0.0822	4.15	0.0567
0.0183	148.0	67.568	4.31	0.0636	4.04	0.0463
0.0181	146.0	68.493	4.20	0.0509	3.95	0.0389
0.0179	144.0	69.444	4.10	0.0421	3.87	0.0335
0.0176	142.0	70.423	4.02	0.0357	3.80	0.0294
0.0174	140.0	71.429	3.95	0.0310	3.75	0.0262
0.0171	138.0	72.464	3.89	0.0275	3.69	0.0239
0.0169	136.0	73.529	3.83	0.0249	3.65	0.0221
0.0166	134.0	74.627	3.78	0.0230	3.60	0.0210
0.0164	132.0	75.758	3.72	0.0220	3.56	0.0206
0.0161	130.0	76.923	3.67	0.0222	3.51	0.0214
0.0159	128.0	78.125	3.60	0.0250	3.46	0.0247
0.0156	126.0	79.365	3.50	0.0376	3.39	0.0358

TABLE I *(Continued)*

Yttrium Aluminum Garnet (YAG)

eV	cm^{-1}	μm	n	k	n	k
0.0154	124.0	80.645	3.27	0.129	3.24	0.0901
0.0151	122.0	81.967	4.23	1.01	3.18	0.994
0.0149	120.0	83.333	3.92	0.0933	3.82	0.123
0.0146	118.0	84.746	3.77	0.0412	3.64	0.0373
0.0144	116.0	86.207	3.70	0.0282	3.56	0.0214
0.0141	114.0	87.719	3.65	0.0227	3.52	0.0157
0.0139	112.0	89.286	3.62	0.0197	3.49	0.0129
0.0136	110.0	90.909	3.59	0.0178	3.46	0.0112
0.0134	108.0	92.593	3.57	0.0165	3.44	0.0100
0.0131	106.0	94.340	3.55	0.0155	3.42	0.00916
0.0129	104.0	96.154	3.53	0.0147	3.41	0.00849
0.0126	102.0	98.039	3.51	0.0141	3.39	0.00794
0.0124	100.0	100.00	3.50	0.0135	3.38	0.00748
			3.510 [22]	0.0167 [22]		
0.0118	95.0	105.26	3.443	0.0140		
0.0112	90.0	111.11	3.396	0.0121		
0.0105	85.0	117.65	3.362	0.0108		
0.0099	80.0	125.00	3.335	0.0099		
0.0093	75.0	133.33	3.314	0.00922		
0.0087	70.0	142.86	3.298	0.00838		
0.0081	65.0	153.85	3.284	0.00688		
0.0074	60.0	166.67	3.273	0.00542		
0.0068	55.0	181.82	3.263	0.00437		
0.0062	50.0	200.00	3.255	0.00375		
0.0056	45.0	222.22	3.249	0.00323		
0.0050	40.0	250.00	3.243	0.00252		
0.0043	35.0	285.71	3.239	0.00179		
0.0037	30.0	333.33	3.235	0.00125		
0.0031	25.0	400.0	3.232	0.00060		
0.0	0.0		3.26 [20]	0.0	3.18 [21]	0.0
			3.225 [22]		3.26 [23]	

TABLE II

Sellmeier Dispersion Equation Constants for Yttrium Aluminum Garnet

Term [(Eq. (2)]	Tomiki [2]	Tropf [11]	Wemple [12]	Zharikov [13]
λ_1	0.11227	0.1095	0.1117	0.1110
λ_2		17.825		
A_1	2.2831	2.293	2.2883	2.2736
A_2		3.705		
Range (μm)	0.4–1	0.4–4	0.4–0.9	0.4-0.6

TABLE III

Thermo-optical Coefficients of Yttrium Aluminum Garnet

Wavelength (μm)	dn/dT (10^{-6}/K)	Temperature (°C)	Reference
0.4579	11.9	30–45	[10]
0.4765	12.0	30–45	[10]
0.4880	11.6	30–45	[10]
0.4965	11.4	30–45	[10]
0.5017	11.4	30–45	[10]
0.508	10.2	20–120	[8]
0.5146	10.6	30–45	[10]
	12.2	27	[16]
0.546	11.5	23–372	[13]
0.6328	10.4	30–45	[10]
	9.86	75–110	[15]
	7.3[a]	27–58	[14]
0.644	9.4	20–120	[8]
1.06	10.0	23–372	[13]
1.0642	9.1	30–45	[10]

[a] Neodynium-doped YAG.

TABLE IV

Transverse (and Longitudinal) Optical Phonon Frequencies in Yttrium Aluminum Garnet

Mode	Gledhill [20]	Hoffmeister [21]	Hurrell [18]
F_{1u}	122.25(122.65)	121.7(122.2)	119(125)
F_{1u}	163.4(172.3)	164.2(173.0)	165(181)
F_{1u}	177.5(180.2)	177.9(179.8)	
F_{1u}	219.0(224)	219.6(224.7)	217.8(227)
F_{1u}	289.7(296.0)	288.8(295.8)	289(298)
F_{1u}	330.2(340)	328.5(338.0)	329(341)
F_{1u}	372.5(378)	374.3(380.4)	370(379)
F_{1u}	387.3(388)	388.3(391.2)	—
F_{1u}	394.5(402.5)	395.1(402.4)	392(403)
F_{1u}	427.8(438.3)	430.6(438.6)	429(437)
F_{1u}	445.5(471.5)	451(547.8?)	466(471)
F_{1u}	472.3(510.8)	—	482(505)
F_{1u}	516.5(549.0)	509.7(506.3?)	521(551)
F_{1u}	569.2(585.0)	565(582.6)	569.5(591.8)
F_{1u}	692.0(712.0)	690/3(708.4)	690(707)
F_{1u}	723(765)	720.8(766.5)	737(769)
F_{1u}	782(840.5)	784.9(857.7)	811(921)?

Zircon ($ZrSiO_4$)

EDWARD D. PALIK
Institute for Physical Science and Technology
and
R. KHANNA
Department of Chemistry and Biochemistry
University of Maryland
College Park, Maryland

The interest in zircon is primarily as a gemstone. Many varieties and colors are found all over the world. The colors are due to the impurities, which give line absorption in the visible. We will not discuss these extrinsic effects in any detail. Many of the properties of zircon are summarized by Deer *et al.* [1].

$ZrSiO_4$ is a tetragonal crystal with space group symmetry I4/amd (D_{4h}). The clear crystal is termed high zircon, but containing impurities, it may have various colors. A somewhat amorphous phase made up of some SiO_2 and ZrO_2 is called low zircon and bears a green color [2].

The crystal form should have four E_u ($\mathbf{E}\perp\mathbf{c}$) and three A_{2u} ($\mathbf{E}\parallel\mathbf{c}$) vibration modes in the infrared spectral region. The IR from 200 to 1100 cm^{-1} has been studied by Dawson *et al.* [3]. Gem-quality crystals from Ceylon were oriented, cut, and mechanically polished. An RIIC Michelson interferometer FS-720 was used at low frequencies, while single-beam and double-beam grating spectrometers (both built in the King's College physics department) were used at higher frequencies. The samples were either at 300 K or 100 K. Wire-grid polarizers were made of gold lines on AgCl or polyethylene sheets. The reflectivity spectrum was Kramers–Kronig (K-K) analyzed, but no mention was made of including the high-frequency reflectivity above the band gap. No Lorentz-oscillator analysis of reflectivity was made (which is often useful for comparison). The absorption spectrum was also measured for samples of thickness 0.3 to 3 mm with the *c*-axis in the plane of the samples. The data were presented in small graphs of ϵ' (real dielectric function) and ϵ'' (imaginary dielectric function) for polarization $\parallel$(e) and $\perp$(o) to the *c*-axis. These graphs were expanded by photocopying and read, and the 300 K data are listed in Table I. There is a significant

HANDBOOK OF OPTICAL CONSTANTS OF SOLIDS III

Copyright © 1998 by Academic Press.
All rights of reproduction in any form reserved
ISBN 0-12-544423-0/$25.00.

uncertainty in n and k, especially where these parameters are changing rapidly. Although we include n to three figures and k to two figures, the reading uncertainty is surely $\pm 20\%$. There is also an uncertainty in the wave number of probably ± 3 cm^{-1}. Four E_u modes are observed. Three A_{2u} modes are seen with a hint of a fourth one.

The A_{2u} modes ($\mathbf{E} \| \mathbf{c}$) have been measured by Gervais *et al.* [4]. The sample was a natural crystal, mechanically polished and then annealed at 1300 K. Both a K-K analysis and an oscillator model have been used to fit the reflectivity. The oscillator model gave the complex dielectric function as

$$\epsilon = \epsilon' - i\epsilon'' = \epsilon_\infty + \sum_j \frac{\Delta\epsilon_j \, \omega_j^2}{(\omega_j^2 - \omega^2 + i\Gamma_j\omega)}.$$

The parameters at 295 K for four oscillators are given in Table II. Note that group theory predicts only three A_{2u} modes, and a fourth mode has been added at high frequency for the model fit. The dc dielectric constant is calculated to be $\epsilon'_o(\mathrm{e}) = 10.71$.

We have calculated n(e) and k(e) to extend and fill in the gaps of the data of Dawson *et al.* [3] and also give them in Table I. The magnitudes of n and k are similar for the two sets of data, but do differ by $\pm 20\%$ in places if account is taken of the mode frequencies being slightly different. This gives slightly shifted spectra.

Dawson *et al.* [3] measured the transmittance of thin plates at 100 and 300 K with polarized radiation. They displayed absorption spectra with arbitrary but linear ordinate. They also gave the peak absorption coefficient $\alpha = 4\pi k/\lambda$ at three points in the spectrum. (We assume these are low-temperature data; if this is the wrong choice, there are up to 20% differences.) These are ($\perp$: 887 cm^{-1}, 85000 cm^{-1}; 1900 cm^{-1}, 70 cm^{-1}; 2750 cm^{-1}, ~0 cm^{-1}); ($\|$: 994 cm^{-1}, 93000 cm^{-1}; 1900 cm^{-1}, 100 cm^{-1}; 2750 cm^{-1}, 1.4 cm^{-1}). Assuming we can make the comparison of absorption coefficient with arbitrary absorption, we have calculated k in the two- and three-phonon absorption region near 1900 and 2800 cm^{-1}, respectively. We did not use a grid fine enough to show all the details of the observed spectral lines. The results are listed in Table I.

We could find no near-IR, visible data for n(o) and n(e) obtained by prism minimum-deviation methods.

Many books on gems give the indices of refraction at the Na D line (0.5890 μm) but usually do not quote the source. Clear high zircon has n(o) = 1.925 and n(e) = 1.984 in one gem book [5] and is given a range of values n(o) = 1.924–1.934 and n(e) = 1.970–1.977 in another book [1]. However, because of the ubiquitous presence of impurities, which change the color of the gem, these constants can vary drastically; therefore, we should focus on clear high zircon.

Vance [6] has measured the visible and near-IR transmittance of various

gem stones of low zircon at 15 and 290 K. The spectra contain many weak, sharp lines attributed to impurity atoms of U and Th. It is believed that high zircon containing U and Th degenerates into low zircon over the years because of the radioactive decay of the impurity atoms. Only the low-temperature spectra are given in graphs, and they are labeled as σ polarized. The atomic impurities often appear only in σ or π polarization. We assume this refers to and perpendicular and parallel to the c-axis of the crystal. The c-axis was presumably located in the plane of these gem samples. One σ spectrum shows the onset of band-edge absorption. Even though the spectrum was obtained at 15 K, we have smoothed out the impurity structure and show k(o) in Table II, since we can find no detailed study of the absorption edge at room temperature. This is not quite the correct thing to do, since low zircon is an "amorphous" mixture of SiO_2 and ZrO_2 (but showing a c-axis). But the band gap of crystalline SiO_2 is $\sim$ 9 eV, while that of crystalline ZrO_2 (zirconia) is $\sim$ 3 eV. We would expect a mixture to have a band gap somewhere in between these limits. Deer *et al.* [1] gives several references to optical absorption studies, but none of these were quantitative regarding k.

We could find no data above the band gap into the UV that could yield the optical constants and, therefore, cannot obtain an accurate value of the band gap.

The data listed in Table I are plotted in Fig. 1. The ordinary n(o) and k(o), primarily from Dawson *et al.* [3], are shown in Fig. 1a; the extraordinary n(e) and k(e), primarily from Dawson *et al.* [3] are shown in Fig. 1b; the extraordinary n(e) and k(e) from Gervais *et al.* [4] are shown in Fig. 1c for comparison.

ACKNOWLEDGMENT

We thank James E. Shigley, Director of Research, Gemological Institute of America, 1630 Stewart St., Santa Monica, CA 90404-4088 for kindly providing us with a copy of the zircon section of Deer *et al.* [1].

REFERENCES

1. W. A. Deer, R. A. Howie, and J. Zussman, "Rock-Forming Minerals," Vol. 1A, 2nd Ed., Orthosilicates, p. 431. Longmans, London, 1982.
2. R. Webster, "Gems," p. 131. Newnes-Butterworth, London, 1975.
3. P. Dawson, M. M. Hargreave, and G. R. Wilkinson, The vibrational spectrum of zircon ($ZrSiO_4$). *J. Phys. C: Solid State Phys.* **4**, 240 (1971).
4. F. Gervais, B. Piriou, and F. Cabannes, Anharmonicity in silicate crystals: temperature dependence of Au type vibrational modes in $ZrSiO_4$ and $LiAlSi_2O_6$. *J. Phys. Chem. Solids* **34**, 1785 (1973).
5. R. T. Liddicoat, Jr., "Handbook of Gem Identification," p. 272. Gemological Institute of America, Santa Monica, CA, 1969.
6. E. R. Vance, The anomolous optical absorption spectrum of low zircon. *Minerol. Mag.* **39**, 709 (1974).

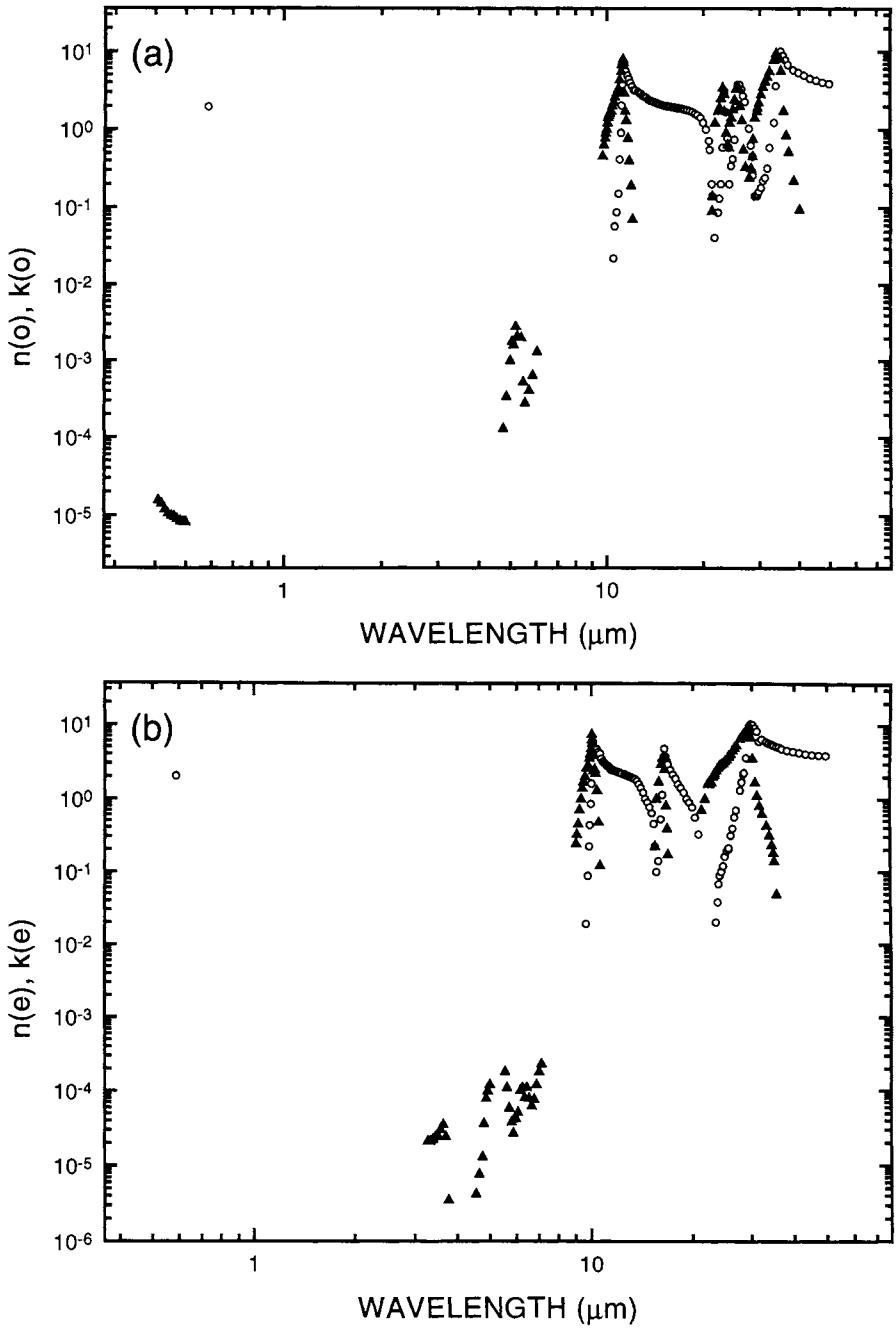

Fig. 1. (a) Log–log plot of n(o) (○○○) and k(o) (▲▲▲) versus wavelength in micrometers for zircon, primarily from Dawson et al. [3]. (b) Log–log plot of n(e) (○○○) and k(e) (▲▲▲) versus wavelength in micrometers for zircon, primarily from Dawson *et al.* [3].

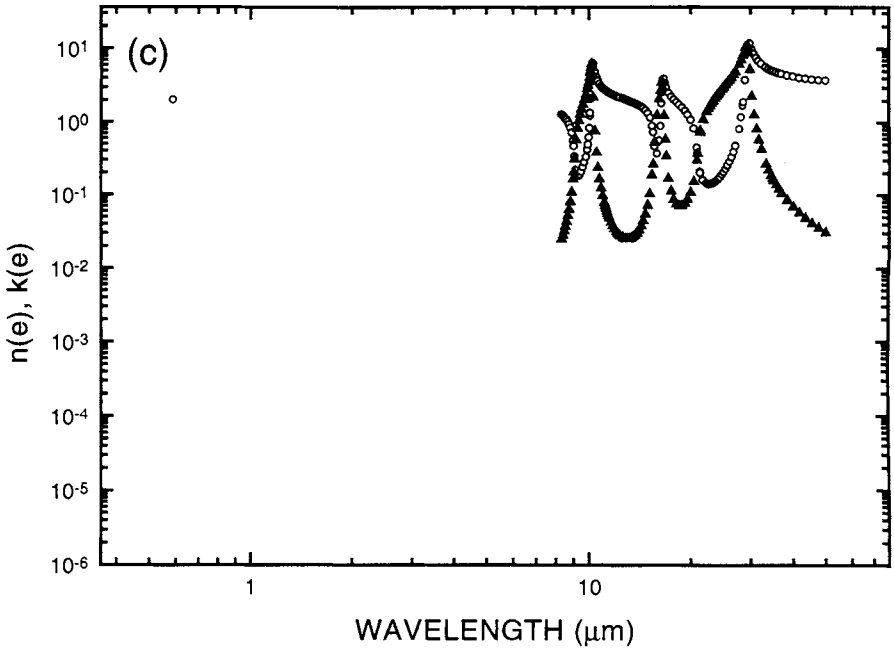

Fig. 1, cont'd. (c) Log–log plot of n(e) (○○○) and k(e) (▲▲▲) versus wavelength in micrometers for zircon, primarily from Gervais *et al.* [4].

TABLE I

Values of n and k for Zircon ($ZrSiO_4$) Obtained from Various References

eV	cm^{-1}	μm	n(o)	k(o)	n(e)	n(e)	k(e)	k(e)
3.024	24390	0.41		1.55E-5 [6]				
2.952	23810	0.42		1.40E-5				
2.883	23256	0.43		1.19E-5				
2.818	22727	0.44		1.05E-5				
2.755	22222	0.45		9.77E-6				
2.695	21739	0.46		9.51E-6				
2.638	21277	0.47		8.86E-6				
2.583	20833	0.48		8.40E-6				
2.530	20408	0.49		8.18E-6				
2.480	20000	0.50		8.15E-6				
2.105	16980	0.5890	1.925 [5]		1.984 [5]			
0.3782	3050	3.279					2.1E-5 [3]	
0.3720	3000	3.333					2.1E-5	
0.3658	2950	3.390					2.2E-5	
0.3596	2900	3.448					2.4E-5	
0.3534	2850	3.509					2.5E-5	
0.3472	2800	3.571					3.0E-5	
0.3410	2750	3.636					3.5E-5	
0.3348	2700	3.704					2.4E-5	
0.3286	2650	3.774					3.5E-6	
0.2728	2200	4.545					4.2E-6	
0.2666	2150	4.651					7.7E-6	
0.2604	2100	4.762		1.3E-4 [3]			1.3E-5	
0.2573	2075	4.819					3.6E-5	
0.2542	2050	4.878		3.4E-4			7.9E-5	
0.2511	2025	4.938					9.8E-5	
0.2480	2000	5.000		1.0E-3			1.2E-4	

0.2449	1975	5.063	1.8E-3				
0.2418	1950	5.128	1.6E-3				
0.2387	1925	5.195	2.8E-3				
0.2356	1900	5.263	2.1E-3				
0.2294	1850	5.405	2.0E-3				
0.2263	1825	5.479	5.3E-4				
0.2232	1800	5.556	2.8E-4			1.8E-4	
0.2201	1775	5.634				1.1E-4	
0.2170	1750	5.714	4.1E-4			5.8E-5	
0.2139	1725	5.797				3.8E-5	
0.2108	1700	5.882	6.4E-4			2.7E-5	
0.2077	1675	5.970				4.2E-5	
0.2046	1650	6.061	1.3E-3			5.1E-5	
0.2015	1625	6.154				1.0E-4	
0.1984	1600	6.250				1.1E-4	
0.1953	1575	6.349				8.0E-5	
0.1922	1550	6.452				1.1E-4	
0.1891	1525	6.557				7.9E-5	
0.1860	1500	6.667				6.2E-5	
0.1829	1475	6.780				7.6E-5	
0.1798	1450	6.897				1.2E-4	
0.1767	1425	7.018				1.8E-4	
0.1736	1400	7.143				2.3E-4	
0.1488	1200	8.333		1.26 [4]			2.48E-2 [4]
0.1475	1190	8.403		1.22			2.80E-2
0.1463	1180	8.475		1.18			3.19E-2
0.1451	1170	8.547		1.13			3.68E-2
0.1438	1160	8.621		1.08			4.30E-2
0.1426	1150	8.696		1.01			5.13E-2
0.1413	1140	8.772		0.932			6.27E-2
0.1401	1130	8.850		0.836			7.95E-2

(continued)

TABLE I *(Continued)*

$ZrSiO_4$

eV	cm^{-1}	μm	*n*(o)	*k*(o)	*n*(e)	*n*(e)	*k*(e)	*k*(e)
0.1389	1120	8.929				0.714		1.07E-1
0.1376	1110	9.009				0.549		1.62E-1
0.1371	1106	9.041				0.467	2.4E-1 [3]	2.02E-1
0.1364	1100	9.091				0.338	3.2E-1	3.09E-1
0.1351	1090	9.174				0.218	4.5E-1	5.72E-1
0.1339	1080	9.259				0.186	7.1E-1	8.17E-1
0.1327	1070	9.346				0.180	1.0E0	1.04E0
0.1314	1060	9.434				0.189	1.4E0	1.27E0
0.1302	1050	9.524				0.208	1.7E0	1.50E0
0.1289	1040	9.615				0.238	2.0E0	1.75E0
0.1277	1030	9.709		4.5E-1 [3]	0.019 [3]	0.279	2.6E0	2.04E0
0.1265	1020	9.804		6.3E-1	0.088	0.332	2.8E0	2.39E0
0.1252	1010	9.901		7.7E-1	0.22	0.418	3.5E0	2.86E0
0.1246	1005	9.950		8.9E-1	0.43	0.493	4.0E0	3.17E0
0.1240	1000	10.00		1.0E0	0.86	0.613	4.7E0	3.56E0
0.1234	995	10.05		1.2E0	1.61	0.820	6.2E0	4.06E0
0.1227	990	10.10		1.4E0	5.20	1.21	5.6E0	4.72E0
0.1226	989	10.11		1.4E0	5.48	1.33	5.5E0	4.88E0
0.1221	985	10.15		1.5E0	5.88	2.07	3.8E0	5.58E0
0.1215	980	10.20		1.6E0	4.69	4.07	2.4E0	6.18E0
0.1209	975	10.26		1.7E0	4.48	6.41	2.5E0	4.42E0
0.1203	970	10.31		1.7E0	4.58	6.23	2.2E0	2.18E0
0.1190	960	10.42		2.0E0	4.65	4.85	1.3E0	7.46E-1
0.1178	950	10.53	0.022 [3]	2.2E0	4.27	4.08	4.7E-1	3.82E-1
0.1165	940	10.64	0.057	2.6E0	4.00	3.62	1.2E-1	2.37E-1
0.1153	930	10.75	0.086	2.9E0	3.46	3.31		1.64E-1
0.1141	920	10.87	0.15	3.3E0	3.16	3.09		1.22E-1

0.1128	910	10.99	0.41	4.3E0	3.00	2.92		9.54E-2
0.1116	900	11.11	0.90	5.5E0	2.83	2.79		7.72E-2
0.1110	895	11.17	2.01	6.7E0	2.79	2.73		7.02E-2
0.1103	890	11.23	3.74	7.3E0	2.74	2.68		6.42E-2
0.1097	885	11.30	6.35	7.1E0	2.69	2.63		5.91E-2
0.1091	880	11.36	6.95	2.9E0	2.64	2.58		5.47E-2
0.1085	875	11.43	5.76	1.7E0	2.55	2.54		5.08E-2
0.1079	870	11.49	5.53	1.3E0	2.45	2.50		4.75E-2
0.1066	860	11.63	4.86	7.7E-1	2.41	2.43		4.19E-2
0.1054	850	11.76	4.38	4.0E-1	2.37	2.37		3.76E-2
0.1041	840	11.90	3.94	1.9E-1	2.32	2.31		3.42E-2
0.1029	830	12.05	3.54	7.1E-2	2.28	2.26		3.15E-2
0.1017	820	12.19	3.17		2.24	2.21		2.94E-2
0.1004	810	12.34	3.16		2.19	2.16		2.78E-2
0.09919	800	12.59	3.00		2.14	2.12		2.65E-2
0.09795	790	12.66	2.91		2.10	2.07		2.57E-2
0.09671	780	12.82	2.83		2.05	2.03		2.52E-2
0.09547	770	12.99	2.68		2.00	1.99		2.50E-2
0.09423	760	13.16	2.61		1.95	1.94		2.51E-2
0.09299	750	13.33	2.55		1.90	1.90		2.56E-2
0.09175	740	13.51	2.39		1.83	1.85		2.66E-2
0.09051	730	13.70	2.32		1.73	1.80		2.80E-2
0.08927	720	13.89	2.28		1.58	1.74		3.02E-2
0.08803	710	14.08	2.24		1.41	1.68		3.32E-2
0.08679	700	14.29	2.19		1.22	1.62		3.77E-2
0.08555	690	14.49	2.14		1.00	1.54		4.42E-2
0.08431	680	14.70	2.10		0.89	1.44		5.44E-2
0.08307	670	14.92	2.05		0.77	1.32		7.15E-2
0.08183	660	15.15	2.02		0.63	1.15		1.04E-1
0.08059	650	15.38	2.00		0.45	0.882		1.85E-1
0.08009	646	15.48	1.98		0.22	0.726	2.2E-1	2.62E-1
0.07935	640	15.62	1.97		0.099	0.466	1.0E0	5.35E-1

(continued)

TABLE I *(Continued)*

$ZrSiO_4$

eV	cm^{-1}	μm	n(o)	k(o)	n(e)	n(e)	k(e)	k(e)
0.07811	630	15.87	1.95		0.14	0.368	1.7E0	1.24E0
0.07687	620	16.13	1.92		0.52	0.560	2.9E0	2.10E0
0.07625	615	16.26	1.91		1.14	0.886	3.5E0	2.71E0
0.07563	610	16.39	1.90		3.32	1.82	3.6E0	3.48E0
0.07538	608	16.45	1.89		3.71	2.57	3.7E0	3.62E0
0.07501	605	16.53	1.88		4.73	3.81	2.5E0	2.96E0
0.07439	600	16.67	1.87		3.69	3.91	8.1E-1	1.22E0
0.07377	595	16.81	1.86		3.19	3.36	3.9E-1	5.77E-1
0.07315	590	16.95	1.84		2.92	2.97	1.7E-1	3.39E-1
0.07191	580	17.24	1.82		2.45	2.51		1.69E-1
0.07067	570	17.54	1.79		2.12	2.23		1.11E-1
0.06943	560	17.86	1.76		1.87	2.03		8.56E-2
0.06819	550	18.18	1.73		1.58	1.87		7.40E-2
0.06695	540	18.52	1.67		1.41	1.72		6.97E-2
0.06571	530	18.87	1.58		1.22	1.58		7.04E-2
0.06447	520	19.23	1.52		1.00	1.43		7.56E-2
0.06323	510	19.61	1.41		0.89	1.26		8.65E-2
0.06199	500	20.00	1.22		0.77	1.07		1.07E-1
0.06075	490	20.41	1.00		0.55	0.814		1.50E-1
0.05951	480	20.83	0.71		0.32	0.446		2.99E-1
0.05926	478	20.92	0.55			0.368		3.71E-1
0.05827	470	21.28	0.20	9.0E-2		0.207	7.0E-1	7.21E-1
0.05815	469	21.32	0.14	1.4E-1		0.198		7.61E-1
0.05703	460	21.74	0.041	1.2E0		0.158	1.0E0	1.08E0
0.05573	450	22.22	0.086	1.7E0		0.143	1.6E0	1.39E0
0.05517	445	22.47	0.13	1.9E0		0.140	1.6E0	1.54E0
0.05455	440	22.73	0.20	2.5E0		0.140	1.7E0	1.68E0

0.05393	435	22.99	0.59	3.4E0		0.142	2.0E0	1.83E0
0.05337	430	23.23	3.13	2.8E0		0.144	2.1E0	1.96E0
0.05331	430	23.25	2.97	1.7E0		0.145	2.2E0	1.98E0
0.05269	425	23.53	1.67	9.0E-1	0.020	0.150	2.4E0	2.13E0
0.05207	420	23.81	0.78	6.4E-1	0.038	0.156	2.6E0	2.29E0
0.05170	417	23.98	0.59	5.9E-1	0.068	0.161	2.7E0	2.39E0
0.05145	415	24.10	0.20	1.2E0	0.088	0.165	2.8E0	2.46E0
0.05083	410	24.39	0.34	1.4E0	0.10	0.175	2.9E0	2.64E0
0.05021	405	24.69	0.42	1.8E0	0.12	0.189	3.0E0	2.83E0
0.04959	400	25.00	0.74	2.4E0	0.16	0.205	3.2E0	3.03E0
0.04897	395	25.32	1.94	3.3E0	0.19	0.226	3.4E0	3.26E0
0.04835	390	25.64	3.54	3.4E0	0.20	0.252	3.7E0	3.51E0
0.04829	389	25.67	3.75	3.5E0	0.21	0.256	3.8E0	3.53E0
0.04773	385	25.97	3.74	2.0E0	0.31	0.286	4.0E0	3.79E0
0.04711	380	26.32	3.27	1.30E0	0.39	0.331	4.5E0	4.11E0
0.04649	375	26.67	2.70	5.5E-1	0.55	0.392	4.9E0	4.48E0
0.04587	370	27.03	2.26	3.3E-1	0.70	0.478	5.3E0	4.92E0
0.04463	360	27.78	1.03	2.4E-1	1.31	0.807	6.5E0	6.17E0
0.04401	355	28.17	0.63	3.2E-1	1.70	1.16	7.1E0	7.11E0
0.04352	351	28.49	0.45	4.5E-1	2.17	1.70	7.6E0	8.14E0
0.04339	350	28.57	0.26	7.5E-1	2.26	1.90	7.7E0	8.45E0
0.04277	345	28.98	0.14	1.4E0	3.58	3.79	7.0E0	10.4E0
0.04215	340	29.41	0.14	1.7E0	7.43	9.03	8.1E0	10.8E0
0.04191	338	29.58	0.15	1.9E0	9.67	11.2	9.7E0	8.82E0
0.04153	335	29.85	0.16	2.2E0	10.3	11.6	6.8E0	5.21E0
0.04091	330	30.30	0.18	2.8E0	10.1	9.84	3.5E0	2.28E0
0.04029	325	30.77	0.22	3.5E0	9.11	8.41	1.7E0	1.26E0
0.03968	320	31.25	0.24	4.1E0	8.26	7.46	1.1E0	8.11E-1
0.03905	315	31.75	0.32	4.7E0	5.97	6.79	8.0E-1	5.71E-1
0.03843	310	32.26	0.59	5.5E0	6.43	6.30	6.2E-1	4.26E-1
0.03720	300	33.33	1.23	7.7E0	5.93	5.60	4.2E-1	2.67E-1
0.03657	295	33.90	3.60	9.4E0	5.66	5.35	3.1E-1	2.21E-1

(continued)

TABLE I *(Continued)*

$ZrSiO_4$

eV	cm^{-1}	μm	n(o)	k(o)	n(e)	n(e)	k(e)	k(e)
0.03595	290	34.48	7.91	8.2E0	5.48	5.14	2.3E-1	1.85E-1
0.03558	287	34.84	9.70	8.1E0	5.36	5.03	1.8E-1	1.68E-1
0.03533	285	35.09	10.0	5.6E0	5.29	4.96	1.4E-1	1.58E-1
0.03472	280	35.71	8.82	1.7E0	5.10	4.81	4.9E-2	1.37E-1
0.03409	275	36.36	7.73	8.4E-1	5.00	4.68		1.20E-1
0.03347	270	37.04	6.73	5.2E-1	4.79	4.56		1.05E-1
0.03224	260	38.46	5.75	2.2E-1	4.53	4.36		8.41E-2
0.03100	250	40.00	5.29	9.4E-2	4.41	4.20		6.85E-2
0.02976	240	41.67	4.90		4.24	4.07		5.70E-2
0.02852	230	43.48	4.47		4.04	3.96		4.80E-2
0.02728	220	45.45	4.24		3.94	3.87		4.10E-2
0.02604	210	47.62	4.00		3.91	3.79		3.53E-2
0.02480	200	50.00	3.87		3.87	3.72		3.07E-2

TABLE II

Oscillator Parameters for A_{2u} Vibrational Modes at 295 K; $\epsilon_\infty = 3.8$

$\Delta\epsilon_j$	ω_j (cm^{-1})	Γ_j (cm^{-1})
5.75	339	9.5
0.36	605.7	9.5
0.78	977	12.2
0.022	1020	65

This page is intentionally left blank